ELECTROCHEMICAL SCIENCE

Stress Corrosion in the Grids of the Lead-Acid Storage Battery

A. C. Simon

U. S. Naval Research Laboratory, Washington, D. C.

ABSTRACT

In the lead-acid storage battery, the antimonial-lead grids which support the lead-dioxide active material usually fail by corrosion which occurs in two stages. In the first stage the attack on the lead-antimony alloy was uniform and nonselective. The lead was converted to an adherent layer of PbO_2, and the antimony of the alloy disappeared from the corrosion product. After a certain thickness of this deposit was built up, the attack underwent a change. Corrosion proceeded at a faster rate in the areas of eutectic between individual primary lead dendrites and in particular at grain boundaries. In this second stage the antimony did not disappear from the corrosion product, and the dark material formed did not appear identical to the PbO_2 of the first stage. The examination gave evidence that the greater specific volume of the corrosion product in the second stage introduced sufficient stress to accelerate the attack at grain boundaries and eventually led to cracking. The change from first to second stage appeared to be the result of reduced acidity in the corrosion layer after a sufficient depth of corrosion product had formed.

The active material of the plates used in lead-acid storage batteries is pasted on a metallic grid which is usually a lead-antimony alloy. This grid supports the active material and conducts electricity, and in both functions it is vital to the proper performance of the battery. Corrosion of this grid through the action of the dilute sulfuric acid electrolyte and the electrolytic current during charge and discharge of the battery normally takes place uniformly over the entire metal surface and forms a protective layer of PbO_2. In such circumstances the grid material corrodes at such a slow rate that it might be expected to last for many years under normal conditions of operation. Unfortunately certain areas in the metal surface corrode at a much accelerated rate, so that the actual life of the grid is less than anticipated. When examined, the grid bars are usually found to be separated at numerous points, and as a consequence the pellets of active material are found to be loosened. Conductivity is lost between the active material and the grid as well as between various portions of the grid and the posts for external connection to the battery.

This accelerated corrosion at certain points has been variously attributed to impurity inclusions, casting defects, and design imperfections. In the absence of obvious impurity or casting defects the corrosion is most often attributed to stress. This stress is sometimes considered as developing from the rather heavy load of active material on the grid, which is after all of fairly low creep resistance, or from stresses set up in the corrosion layer itself. Less frequently the stress on the grid has been attributed to actual expansion in the active material. Stress from either the corrosion layer or the active material is a definite possibility as the products of corrosion can be expected to have a greater volume than the original alloy, and it can also be expected that the active material will undergo a considerable change in volume in the conversion from PbO_2 to $PbSO_4$ and the reverse.

The author was fortunate in obtaining from a battery manufacturer several samples of grids that illustrate stress-corrosion cracking and offer an opportunity to study it as it progresses.

The purpose here is to report only some rather unusual features of the microscopic examination of this cracking phenomenon in the lead-antimony alloy when used as a grid in the dilute sulfuric electrolyte. It thus appears unnecessary to refer to the extensive literature either of stress-corrosion cracking or of corrosion in the lead alloys.

Observations

The battery plates examined were all of the same type and had been used on an intermittent cycle type of operation for up to ten years. The samples were mounted for metallographic preparation in such a way that the prepared section would extend across the grid and active material and would be parallel to the plate surface. This gave maximum probability of sectioning the cracks that were known to be present from previously obtained radiographs.

Upon microscopic examination the grids of the ten-year-old batteries were found to contain numerous cracks that extended entirely through the grid member. Although these cracks could be found at practically any location along the grid member, the majority were near the points where vertical and horizontal members intersected. Examination of a number of these cracks established that the cracks were following grain boundaries in almost every case.

A few exceptions were found near the center of a section where a single grain not favorably located for extension of an existing intergranular crack had been fractured. In these rare cases, however, this transverse crack was plainly the result of existing and extensive grain boundary corrosion which extended up to each side of the grain in question.

Examples of the type of intergranular corrosion and cracking which was found are shown in Fig. 1. There was no set pattern to this corrosion mechanism. In one case a corroded grain boundary might extend entirely across the section without a visible crack appearing, as in Fig. 1A. In other cases the outer portions of the interconnecting grain boundaries might show a crack at one or both sides of the section while the remaining side or center of the grid had either not yet corroded or had corroded without visible separation. An example of this is shown in Fig. 1B, where the outer portions of the continuous grain boundary have opened into a visible crack while the center portion, around the misaligned grain, has not yet separated although it has suffered intergranular

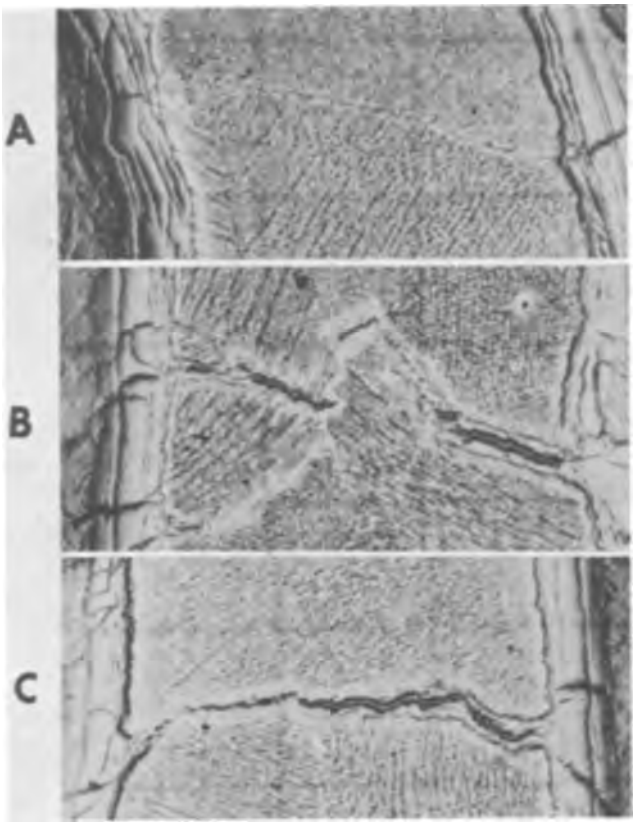

Fig. 1. Examples of the destructive intergranular corrosion that caused failure of the grids: (A) corroded but not yet showing cracking, (B) corroded and cracked but not yet completely separated, and (C) total failure. The side of one square in the dimensional grid measures 528μ. Original magnification 45X.

corrosion. It is believed that the ultimate fate of all examples of intergranular corrosion would be that of complete separation as shown in Fig. 1C.

It should also be remarked at this point that observation of a single cross section at the site of a cracked or corroded boundary leaves much to be inferred. The visible imperfection which so clearly proceeds along the grain boundary in the plane of the photograph or section must also extend above and below this plane. In other planes the grain boundary corrosion or actual cracking may be more or less extensive than in the plane which is visible. Yet the conditions that exist in these other planes or sections will influence the appearance of the visible section and may produce anomalies in the visible section for which there is no apparent reason. Despite this fact it is believed that a sufficient number of sections have been examined to arrive at an approximation of the mechanics of the process.

If this corrosion is stress induced, it is necessary to determine whether this stress is attributable to the active material. The approximately 51% increase in specific volume as PbO_2 is converted to $PbSO_4$ is certainly capable of creating stress in the grid, provided the active material is not free to relieve this stress in other directions. Such stress could be produced either continuously by a slow accumulation of unreactive $PbSO_4$ over an extended period of charge-discharge cycling or intermittently by a repeated conversion of the reactive PbO_2 to reactive $PbSO_4$ on each discharge cycle.

Several factors seemed to indicate that the stress was being exerted by the active material. The active material itself was unusually hard, cohesive, and well retained in the grid even after periods of use of up to 10 years. Examination of this active material from plates supposedly in the fully charged condition showed the presence of a large amount of sulfate.

Since the corrosion product on the grid bars builds up slowly over the period of use and because this product is hard and brittle, one would suppose that any stress that was sufficient to cause intergranular corrosion and actual cracking at the grain boundary would first cause the brittle corrosion product to crack. Moreover, since the corrosion product appears to undergo no visible change between charge and discharge, such a crack would remain visible with no means of repairing itself. For this reason a very careful examination was made of the corrosion product in the vicinity of any visible intergranular corrosion or where there were cases of actual cracking.

It was found that in the majority of cases where intergranular corrosion was just beginning or had not proceeded to a depth exceeding the diameter of the average grain there were no cracks through the corrosion product in a direction perpendicular to the metal surface. In the few cases where cracks did occur under these conditions they did not extend entirely through the corrosion product.

The corrosion product was found to be cracked only in directions either essentially parallel to or perpendicular to the metal surface. Cracks paralleling the metal surface divided the corrosion product into distinct layers. Any cracks that were directed perpendicular to the metal surface at the point where intergranular corrosion had begun had usually only penetrated the inner layer of corrosion product that was next to the metal-corrosion product interface. No perpendicularly directed cracks in other layers were found to lie close enough to be caused by or to influence the spot where intergranular corrosion was beginning. Although all of the outer layers showed cracks perpendicular to the metal-corrosion product interface, these cracks were not aligned with one another in adjacent layers and appeared to have no relation to metal structure defects. They were judged to be the result of internal stresses within the corrosion product itself. Thus there was nothing seen in the case of the slight or moderate intergranular corrosion that would indicate that such corrosion was being initiated by stresses set up in the active material.

In the case of severe intergranular corrosion extending through or nearly through the entire grid member or where actual cracking had occurred at grain boundaries there were still cases where no cracks occurred perpendicular to the surface, but this was the exception. Such cracks in the grid metal were more often accompanied by cracks in the adjacent corrosion product. These cracks in the corrosion product were studied carefully, and it was determined that in the majority of cases cracking did not extend to the outer surface of the corrosion product and also that the end of the crack farthest from the metal surface narrowed out of existence. It is evident that a crack would be wider at its outermost portion if the stress was being applied by the pellets of active material. In those few cases where the cracks did extend through the corrosion product they also extended for a considerable distance into the active material itself, and again the crack narrowed at the end in the active material.

An examination of the contact surface between corrosion product and active material also revealed that there was an actual space between the two in many areas. This would not be expected if the active material was actually applying stress to the grid.

It was therefore decided that the active material had not exerted stress on the grid despite its unusual hardness and undoubted large volume changes.

The next most likely source of stress was in the corrosion product itself. As will be brought out in the subsequent discussion the volume increase that occurs in the conversion of Pb to PbO_2 will vary depending on the amount of antimony in the alloy, but a theoretical maximum of about 20% increase in specific volume is a possibility. A cohesive corrosion product,

firmly attached to the metal surface, might produce a considerable sustained stress.

Continued microscopic examination of the corrosion product revealed first of all that only a small portion of the total thickness of corrosion product would be effective in the promotion of stress. As was previously mentioned cracks parallel to the metal surface divided the total thickness of corrosion product into a number of layers. There were both major and minor cracks. The major cracks were fairly equally spaced and one may imagine that they represent major stress relief as a definite thickness of corrosion product is exceeded. The minor cracks had less definite spacing between them and extended for shorter distances so that they did not divide the material into definite layers. The minor cracks appeared to become more numerous near the metal surface and as the depth of corrosion product increased. These minor cracks extend to within 10μ or less of the metal surface so that the corrosion product was not truly adherent at a greater distance. It thus became obvious that any stress produced by the surface corrosion product would not be increased as the thicknes of corrosion product increased. Only that portion of the corrosion product within about 10μ of the metal surface would be effective in creating stress. As new corrosion took place at the interior of this thin layer, that portion exceeding the 10μ thickness would shed off and thus would no longer be a contributor to the stress of the metal.

There was another factor involved, however, which undoubtedly did contribute to stress. In addition, and unlike the surface corrosion described above which applied a fairly constant stress, this condition became steadily worse as the service life of the battery was extended.

The lead-antimony alloy under consideration and indeed most alloy compositions used in battery grid construction are of a very nonuniform nature. In such material the primary dendrites form first during the freezing process and constitute the skeletons of the individual grains. These primary lead dendrites, which contain only small amounts of antimony in solid solution, usually form an intricate branched structure within which the nearly eutectic proportions of lead and antimony subsequently freeze. This nearly eutectic mixture is itself made up of actual particles of precipitated antimony in a matrix of lead.

Despite this decided lack of homogeneity it was noted that corrosion begins as a remarkably uniform process with no tendency to attack preferentially either grain boundaries or other points of nonuniformity. After a time which may perhaps either depend on length of service or thickness of corrosion product there is a definite shift to a very preferential type of attack. At this time the attack becomes most pronounced at grain boundaries, slightly less pronounced in the interdendritic spaces containing the eutectic type of material and least in those areas occupied by the primary dendritic branches. In addition, where previously the antimony particles were attacked and dissolved from the corrosion product right down to its boundary with the metal, now it is found that the preferentially attacked areas contain all the original segregated and precipitated antimony in unchanged form. In other words attack and dissolution of antimony has apparently ceased, although those areas containing the most antimony are being preferentially attacked.

The black PbO_2 that forms in these areas of most pronounced attack does not appear as dark as that formed at the earlier stage of corrosion when both were viewed by polarized light. When viewed by vertical illumination the hardness and reflectivity of this area of preferential attack was different when compared with the earlier corrosion. (Hardness was judged by the relative elevations of various regions, as the samples had been intentionally relief polished.)

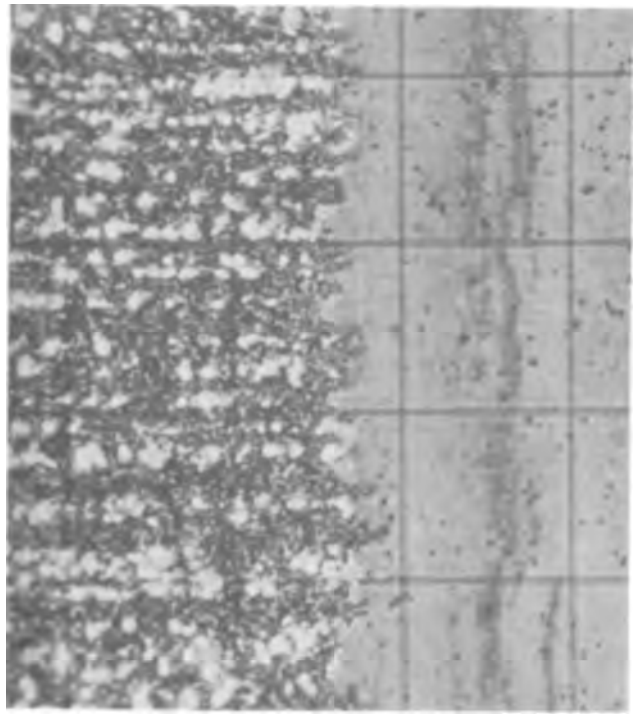

Fig. 2. Pattern of corrosion after 1½ years service. Note that the corrosion-metal interface is fairly smooth and that no antimony appears in the corrosion product; 2μ squares. Original magnification 800X.

As said previously the preferential attack occurred both at grain boundaries and in the spaces between individual arms of the primary dendrite that made up individual grains. This attack on the interdendritic spaces of individual crystals appeared to be at its worst when these spaces between dendritic arms were aligned perpendicular to the surface, but in any case the attack at the grain boundary was always more severe than elsewhere. Once this preferential type of attack began on the grain boundary it became progressively more severe until it had penetrated far beyond the interdendritic penetration. The deeper this attack penetrated into the grain boundary and the further that it proceeded from the surface the greater became the tendency for an interdendritic attack originating from the grain boundary to branch out into the two adjacent grains. This meant that the further the corrosion penetrated into the metal along a grain boundary the greater became the volume of PbO_2 liberated in and adjacent to the boundary and consequently the greater the internal stress that acted as a wedge to force the grain boundary open.

The appearance of the corrosion product after 1½ years of service is shown in Fig. 2. The right-hand part of the photograph shows the corrosion product. To the left is pictured the alloy. The darkly motled bands represent primary lead dendrites and the strings of brightly reflective particles represent antimony in the eutectic areas between primary dendrites. It will be seen that while the interface between metal and corrosion product is not a straight line the variation in rate for the various portions of this grain are slight, so that for all practical purposes the attack may still be considered to be uniform. While not visible in the photograph the same was true at grain boundaries and from one grain to another. It will also be noted that nowhere in the corrosion product are any of the small bright particles of antimony to be found, these having dissolved as the PbO_2 was formed.

Figure 3 shows the condition of the corrosion-metal interface after 7 years of service. This grain is similarly oriented to that shown previously so that the dendritic arms of the primary crystal are perpendicular to the interface. Under these conditions the most

Fig. 3. Same grain structure and orientation as shown in Fig. 2, but here is shown the type of interdendritic attack that was found after 7 years of service. It will be noted that the corrosion-metal interface is no longer smooth and that the particles of antimony originally in the metal now appear in that portion of the corrosion that extends into the metal. Note that no similar material appears in the surface layer of corrosion that does not extend into the metal and appears in right hand portion of the photograph; 28μ squares. Original magnification 800X.

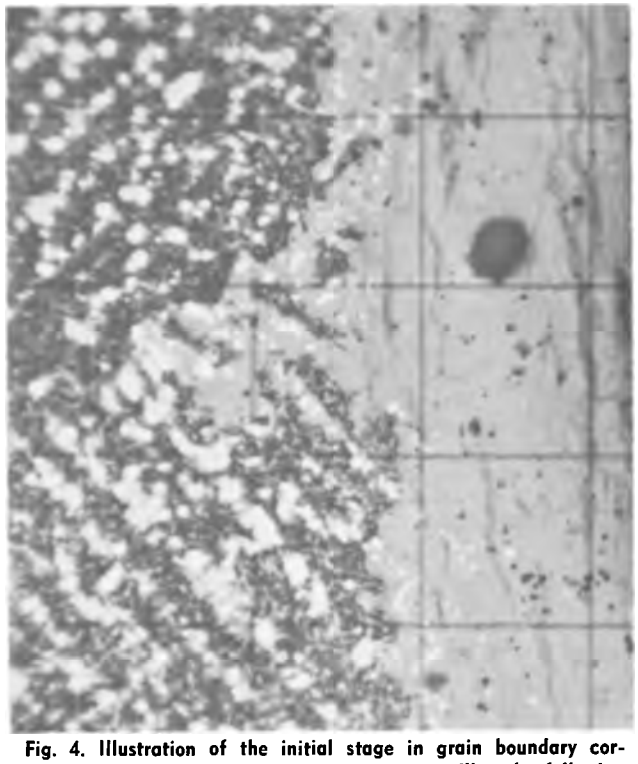

Fig. 4. Illustration of the initial stage in grain boundary corrosion. Note that the actual corrosion appears still to be following interdendritic as well as grain boundaries and that process occurs too extensively to suggest that a microcrack may be responsible; 28μ squares. Original magnification 800X.

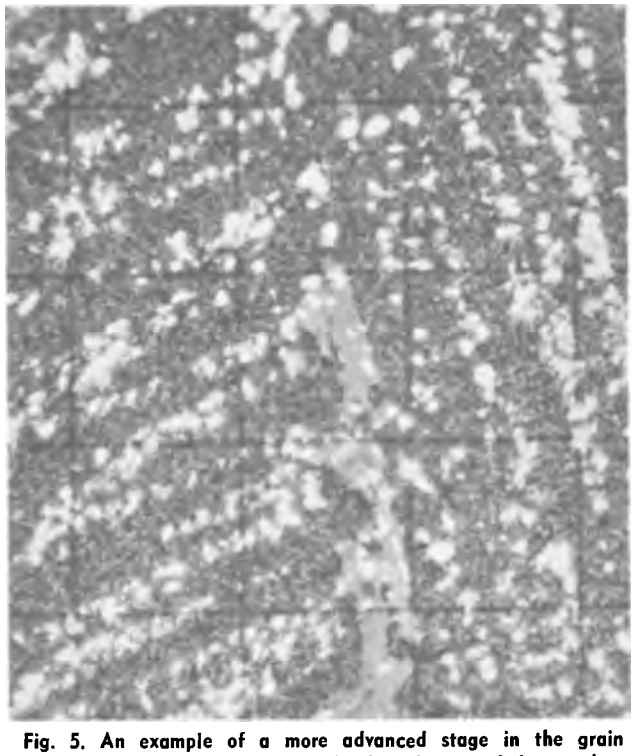

Fig. 5. An example of a more advanced stage in the grain boundary corrosion. Note particularly that the corroded area does not appear to widen with increasing depth and that no actual crack in the metal appears ahead of the corroded portion. Again note the presence of antimony particles in the corroded area; 28μ squares. Original magnification 800X.

severe attack on individual grains occurs. It can be seen that in this case the attack has become very preferential. This can be noted in the center vertical row of squares across which the corrosion product extends. It will be noted that this attack appears to be confined only to the antimony-rich areas (areas containing the bright antimony particles). The lead-rich areas (areas containing dark, mottled material with no bright particles) are much less severely attacked. It will also be noted that in the areas of preferential attack the antimony particles have not been dissolved out. In the actual viewing it was also evident that the reflectivity of the corrosion product in the areas of preferential attack was different from that of the continuous layer of corrosion product that covers the surface and is seen in the right vertical line of squares. Finally the numerous small cracks should be noted that appear in the corrosion product almost up to its interface with the metal.

Figure 4 shows the intersection of a grain boundary with the corrosion interface. The boundary between these two grains in the metal extends to the left through the center horizontal row of squares, and along this boundary corrosion has occurred. It will be noted that in this area and at the interface between metal and corrosion product metallic particles of antimony appear. It will also be seen that the corrosion is not so selective at the grain boundary as to appear to be following a crack nor does any crack appear in the corrosion product.

This can still be considered to be true when the penetration along the grain boundary has proceeded to a considerably greater depth as shown in Fig. 5. This figure also clearly shows the terminus of the corrosion and it will be noted that there is nothing to indicate a crack or defect in the metal ahead of the corrosion. Even the presence of a grain boundary cannot be readily seen, but its presence can be deduced from the different orientations of the primary dendrites to either side of the corroded layer. This becomes a great deal more evident at somewhat lower magnification. It will also be noted in this and other photographs of the series that the random positions of

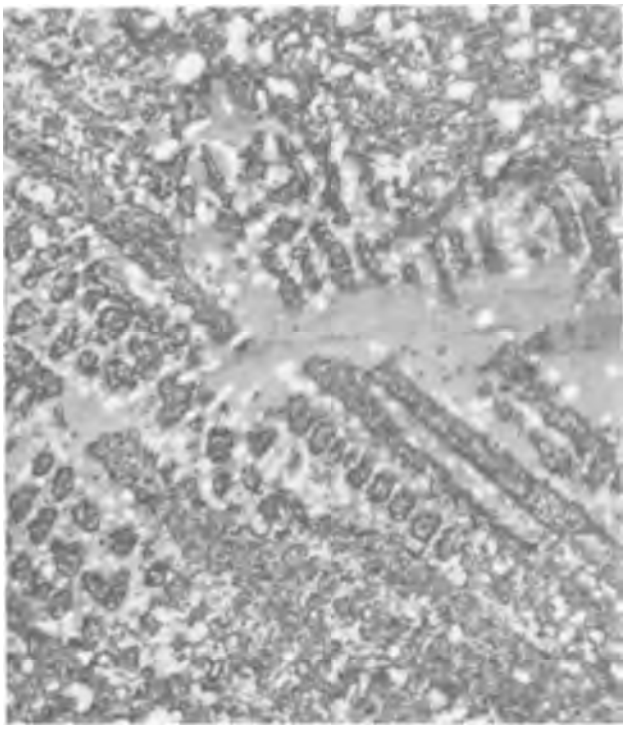

Fig. 6. Illustration of the very intensive interdendritic attack that proceeds outward from each side of the intergranular corrosion when a considerable depth within the metal has been reached. This might be considered as a third stage in the process illustrated by Fig. 4 and 5 and that stage during which actual cracking may occur. Original magnification 800X.

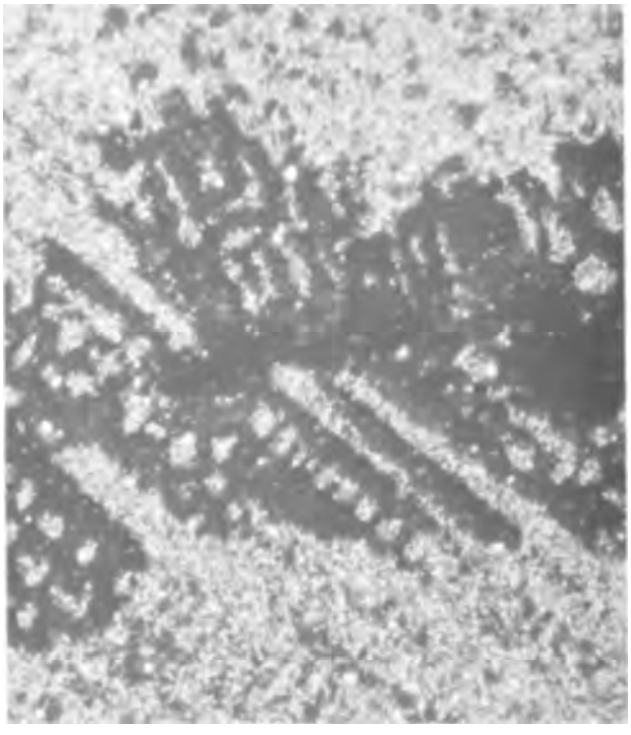

Fig. 7. Some area and magnification as used in Fig. 6 but here illuminated by polarized light to emphasize the extent of the corrosion. The corrosion product is the black area.

the antimony particles throughout the corroded area would also indicate that there was no actual break present during or before corrosion.

As the corrosion proceeds deeper into the grain boundary there is begun a decided preferential corrosion into each adjacent grain provided the orientation of these is suitable. This is shown in Fig. 6 where it can be seen that a very preferential and deep attack has been made into the antimony rich areas at each side of the grain boundary. Again is to be noticed the absence of anything resembling a crack and the antimony particles scattered throughout the corroded area. One does not appreciate the true extent of this corrosion until the same area is seen in polarized light (Fig. 7). While this photograph does not show as much detail as Fig. 6 it serves to illustrate clearly the extent to which corrosion has spread into adjacent grains from the corroded grain boundary and the interdendritic nature of this attack. When compared with Fig. 6 it also serves to identify those areas which represent corrosion. Corroded areas appear black in Fig. 7, a uniform gray in Fig. 6.

Discussion

In a previous report (1) the microstructure and intergranular corrosion of these plates was discussed in greater detail, and additional illustrations representing this phenomenon were presented. Some of the material was reexamined, and the considerably modified present paper is the result.

The mechanism of corrosion for pure lead and for the lead-antimony alloy is different in some physical aspects. Under the conditions existing in the lead-acid storage battery the lead grid becomes covered with a coating of lead dioxide which is formed from the metal. This is usually considered to be a dense and protective covering for the underlying metal, and in the absence of more than trace impurities this is probably true. In the lead-antimony alloy the as-cast surface does not form a continuous homogeneous layer but contains numerous impurities which consist of small particles of antimony and also contains antimony atoms in a solid solution.

It can be demonstrated that the antimony particles are removed from this surface by anodic corrosion even before the lead begins its conversion to lead dioxide. This will naturally result in voids in the protective layer. Since corrosion-product cross sections of considerable thickness reveal no antimony as a solid material and since antimony continues to deposit at the negative plate, it can be assumed that this removal of antimony continues for a considerable time as the lead dioxide builds up from the lead of the alloy.

The most immediate effect of this antimony removal is a reduced volume in the conversion from lead to PbO_2. When antimony is alloyed with lead the resultant alloy will have a specific volume greater than that of lead. As the amount of antimony in the alloy is increased, the specific volume will also increase.

While the corrosion product from pure lead will have a specific volume approximately 20% greater than the lead from which it was formed, that from the lead-antimony alloy will be less than this amount.

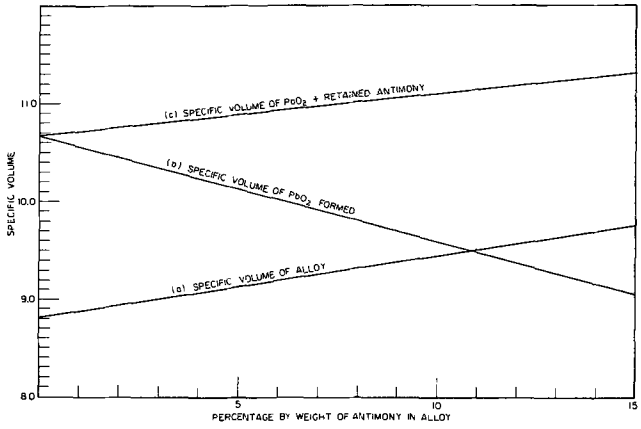

Fig. 8. Illustration of the manner in which specific volume of the alloy and of its corrosion product vary with change in the antimony content of the alloy.

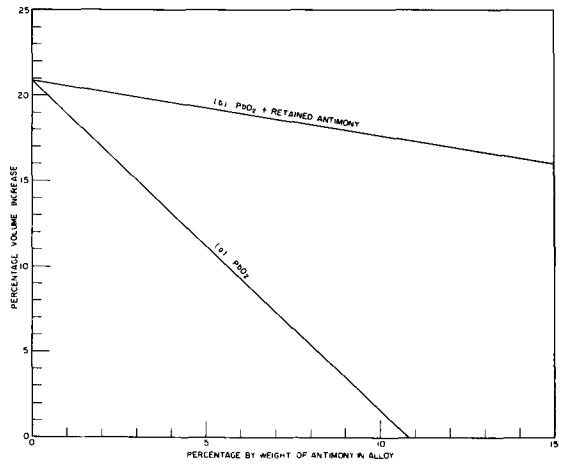

Fig. 9. Relationship between the antimony content of the alloy and the percentage volume increase as the alloy corrodes and is converted to lead dioxide. It will be noted that the volume decreases with increase of antimony in the alloy.

For, if the specific volume of the antimony is not added to that of the corrosion product, the latter will depend entirely on the lead portion of the alloy. As the amount of antimony in the alloy is increased and continues to be removed in the corrosion process, the specific volume of the corrosion product should decrease. A point is then reached where the specific volume of the alloy is greater than that of the corrosion product. This is graphically shown in curves (a) and (b) of Fig. 8. Curve (a) shows the increase in specific volume of the alloy with increase in amount of antimony and curve (b) shows the decrease in specific volume for the corrosion product formed from such alloys when the antimony is removed from consideration.

As has already been seen, a point is reached in the corrosion process when the antimony is no longer removed from the corrosion but remains behind to add to its bulk. In this case the specific volume of the antimony must be added to that of the lead dioxide; the specific volume of the corrosion product does not decrease with increasing antimony content in the alloy, but instead increases at almost the same rate as does the specific volume of the alloy (Fig. 8). This is shown by curve (c). The actual conditions can be expressed perhaps a little more clearly by plotting per cent of antimony in the alloy against the actual percentage volume increase in each case (Fig. 9).

In Fig. 9 curve (a) illustrates the percentage specific volume decrease as the antimony content is increased toward 11%, at which point there is no volume change. This is true provided the type of corrosion process that is taking place removes antimony from the corrosion product. Curve (b) shows the much slower decrease in specific volume that occurs with increasing amounts of antimony in the alloy provided the corrosion process does not remove the antimony from the corrosion product.

It is a well-known fact that lead grids shed corrosion product at an alarming rate whereas lead-antimony alloys retain their products of corrosion much better. It is probable that the entire difference may lie in the above discussed volume changes and not in alloy structure characteristics as some have supposed.

Lead-calcium alloys, unlike pure lead, do not shed corrosion product at such high rates when used as battery grids, and this fact might dispute the above conclusion. Microscopic examination has shown, however, that the entire corrosion process in lead-calcium alloys differs from that discussed here and in particular that the corrosion product appears to be softer and less cohesive than that obtained from lead or its alloys with antimony. Unlike the latter, lead-calcium alloys form a corrosion product that disintegrates and blends with the surrounding active material only a short distance from the metal surface. So definite is this tendency that the true extent of the corrosion layer is impossible to determine. A material so lacking in internal cohesion is able to adjust to large volume changes without visible spalling more easily than is the more brittle and cohesive pure lead corrosion product.

The stress that acts to remove the corrosion product is developed within it and is relieved in two ways. A study of this shedding process revealed that as the volume of corrosion product is increased around the periphery of a grid member, the stress increases in a circumferential direction and is relieved by a breaking away and increase in diameter of a stressed portion. This repeated process results in a series of corrosion layers that appear to be parallel to the metal surface when viewed in a plane section and as concentric layers when viewed in cross section.

At the same time that stress is developing around the periphery of the grid member a similar stress is developing along its length. This cannot be relieved as simply as the circumferential stress, even after breakaway has occurred, because portions of this corrosion product are prevented from longitudinal expansion by the configuration of the grid which is such that a blockage is provided by every grid bar crossing. The result of this restriction is that longitudinal cracks occur and the resultant long strips take a pronounced bow away from the surface to relieve their internal stress. It is unlikely that any great portion of this type of stress is transferred to the grid metal.

The net result of these processes on micrography is that the grid cross section is seen surrounded with a series of concentric layers of corrosion product with each layer containing a number of transverse cracks. When viewing a section cut parallel to the surface a series of nearly parallel layers of corrosion product are seen, but the spacing between two adjacent layers is at a maximum midway between crossing grid bars and is at a minimum near such intersections. As the amount of antimony in the alloy is increased the number of layers decreases and the spacing between adjacent layers also decreases.

Definite series of alloys with up to 11% antimony and various types of operation should be prepared to support this observation, which is based on random sampling of plates with various amounts of antimony and similar but uncontrolled periods of service.

It can be seen from Fig. 9 that even 5% of antimony in an alloy will reduce the specific volume increase by half with a corresponding improvement in the retention of corrosion product and reduced cracking. However the presence of 5% antimony offers hardly any reduction in specific volume when the second stage of corrosion begins and antimony remains in the corrosion product. In this case the volume increase is almost as great as that for pure lead, and the stress developed will be similar. Since a major portion of this stress is developed in the grain boundary, failure is inevitable.

The above may serve to explain the destructive stress developed in the second stage, but it does not explain why this transition in the mechanism of corrosion should take place. It would appear that the corrosion product is initially and for a time sufficiently porous to allow adequate acid penetration for maintaining the original type of corrosion. In this original type of corrosion attack either was not preferential or occurred at such a rate that preferential characteristics were masked. Despite the development of cracks both circumferentially and longitudinally a sufficient thickness of deposit must eventually form to prevent adequate acid being present to maintain the original process. If this is indeed the reason, then once the second stage is initiated it should be self-perpetuating because of its preferential nature and the confined conditions under which it occurs.

The initial penetration at the grain boundary is not believed to be caused by stress on the grid. The weakness at the grain boundary is believed to be caused by microporosity developed during solidification of the alloy.

When primary crystallization of an alloy is completed, a portion of the available metal has already solidified. In the case of the lead-antimony series the amount will depend on the quantity of antimony in the alloy. In the case under discussion it is evident from the well-developed primary branching in each grain and the relatively large amount of primary as compared with eutectic that a major portion of this alloy had solidified during primary crystallization and that a relatively small amount of eutectic melt remained in the channels between the primary dendrites.

Microscopic study of the freezing process in this alloy system during solidification reveals that solidification is arrested when formation of the primary crystals of lead is completed and does not proceed until eutectic crystallization is started by the appearance of antimony crystals. In addition the eutectic freezing does not take place in these alloys as a simultaneous shower of crystals. Instead one or more nuclei are formed within the grain, and the crystallization of the eutectic proceeds from these points by a tortuous route along the various channels left between dendritic branches of the grain. This process also proceeds with relative slowness and can be visually followed.

Eutectic nucleation occurs at more than one place in the grain, and from these points it spreads throughout the remaining channels of the grain. This final freezing causes a reduction in volume, and it is unlikely that sufficient liquid either remains or could reach these areas to fill all voids. As a consequence microporosity in these eutectic areas undoubtedly occurs. Since the nucleation of the eutectic appears to occur within the grain, an even greater porosity must result at the grain boundary from which liquid metal is withdrawn to feed the areas where freezing is occurring.

There is evidence other than the present corrosion to indicate that the grain boundary in these alloys may be microporous. When castings of these alloys were made very thin, on the order of 5 mils (0.127 mm) in thickness, the individual grains could be seen distinctly, as could the primary dendritic structure and the grain boundaries. This sharp demarcation was caused by the pronounced shrinkage of the eutectic portion of the material.

It was discovered that with very careful teasing the film could be separated into individual grains with easy and distinct separation taking place along the grain boundaries. These individual grains were then mounted so that the formerly mating surfaces could be examined; it was found that these showed no evidence of tearing or fracturing. Although there was no evidence of any actual welding at the grain boundary, the foil gave every evidence of being completely normal before separation and could be handled and bent in a normal manner. Microscopic examination of the boundary before separation showed the usual grain boundary structure. The appearance of the grain boundary after separation appeared similar to that seen in the casting defect known as a cold shut.

Burbank (2) has described a process for converting a thin metal film into a chemical replica for the purpose of microscopic examination by transmitted light. The thin cast films described above were converted to a translucent chemical replica by the use of an acetic acid-hydrogen peroxide solution. When examined under the microscope by transmitted light these replicas were found to reproduce the structure of the metal faithfully as seen by metallographic preparation of metal sections but in considerable more detail. These films were reasonably coherent and stable throughout the grain and showed no tendency to be weaker at the junction between primary and secondary structure. However at the grain boundaries there was definite weakness, and as before the film could be easily separated into areas corresponding to the original metal grains (Fig. 10). In addition examination of these grain boundaries at high magnification and with transmitted light produced no evidence that a crack existed before separation.

Fig. 10. Chemical replica of a portion of very thin Pb-Sb alloy cast foil containing 1% Sb illuminated by transmitted light. The dark dots in parallel rows represent segregated antimony concentrated at intersections of primary lead dendritic branches of the crystals. The boundary between the large lower grain and the small grain at center is intact, but separation has occurred cleanly along most of the boundary between lower and upper grain and between upper and center grain. Original magnification 50X.

It is therefore concluded that these boundaries were not in any way welded or soldered together in the freezing process but were merely in very intimate contact and were being held together by atomic forces similar to those which hold a plated coating to the base metal.

Although the conditions encountered at the boundary of a very thin cast grain may not duplicate the conditions at the boundary of a metal in bulk, and

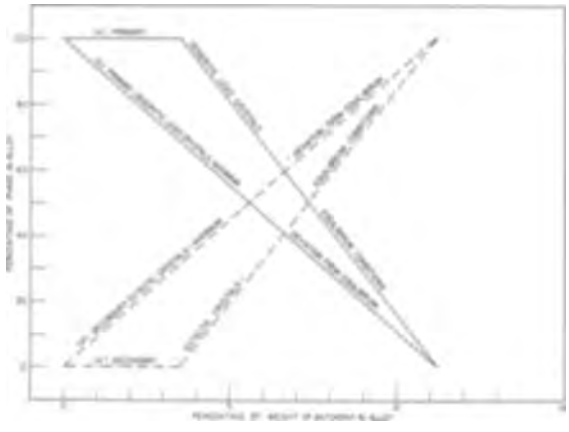

Fig. 11. Illustration of the relative amounts of primary crystallization (in the form of lead-rich dendritic crystals) and of eutectic crystallization present at the final solidification for alloys with various antimony contents.

although eventual diffusion, recrystallization, and resultant grain boundary migration eventually alter this condition, it still seems reasonable to expect considerable microporosity at the grain boundary.

It must be emphasized, however, that the extent of this microporosity and its distribution will change with change in antimony content in the alloy. The effect of changing the alloy composition of the lead-antimony alloys and the manner such changes influence the relative amounts of primary dendritic and secondary eutectic crystallization have been discussed elsewhere (3). It will suffice here to refer to Fig. 11 which shows the relative percentage of the two types of crystallization as the amount of antimony in the alloy is increased. Curves (a) and (a') represent the relative portions when freezing takes place under equilibrium conditions, while curves (b) and (b') show the greatest possible variation that could occur. All actual castings are represented somewhere between these two extremes. It will be realized that when the greater portion of the material freezes as primary dendrites, the remainder and still liquid portion may be confined in narrow passages between primary dendritic arms and as a thin film at the grain boundaries. Under these conditions the freezing of the final eutectic portion will take place with decided porosity at intergranular portions. When the major portion of the material remains liquid after the freezing out of the primary dendrites, the individual and much less complexly grown crystals of primary are separated from one another by large masses of still liquid material and indeed may be floating freely in the latter when final solidification takes place. In such a case final eutectic crystallization probably produces much less microporosity.

Since both volume change in the corrosion product and amount of microporosity in the alloy are reduced as the amount of antimony in the alloy is increased, there may be here the explanation for the lack of success in the numerous attempts to reduce the amount of antimony below that currently used in the industry.

In the process of corrosion that has been described grain boundary corrosion took place without visible cracks being present either in the metal or the original surface corrosion layer. This indicates a fundamental grain boundary weakness rather than corrosion initiated by external strain.

If microporosity is accepted, then its presence may also help to explain another puzzling feature, namely, the change from a uniform to selective mode of attack. With the freezing conditions present at the mold face it is unlikely that microporosity would extend entirely to the surface; the surface would almost certainly be sound. While there are unquestionably other differences in the mode of attack after a definite thickness of corrosion product has been formed, the selective characteristic of this attack might be attributable to penetration beyond the sound surface layer and its encounter with a porous remainder.

The type of corrosion described here is probably much more common than is generally realized. The vast majority of batteries used in such applications as starting, lighting, and ignition, simply do not survive other difficulties long enough for this type of corrosion to become the major problem. It is inherently a problem of the heavier grids used for industrial purposes, and it is suspected that examination of those in long use would reveal many cases of this type of attack.

Manuscript received Aug. 15, 1966. This paper was presented at the Philadelphia Meeting, Oct. 9-14, 1966.

Any discussion of this paper will appear in a Discussion Section to be published in the December 1967 JOURNAL.

REFERENCES

1. A. C. Simon, NRL Rpt 6387, April 1966.
2. J. Burbank, *J. Metals*, **5**, 55 (1953).
3. A. C. Simon and E. L. Jones, *This Journal*, **100**, 1 (1953).

High Rate Battery Electrodes

Clarence M. Shepherd and Harry C. Langelan

U. S. Naval Research Laboratory, Washington, D. C.

ABSTRACT

It has been shown previously that metal plates of controlled porosities and high surface areas can be produced by the electrolytic reduction of metal compounds subjected to controlled physical pressure during electrolysis. When these plates are discharged as anodes in test batteries their capacities and ampere hour efficiencies are found to increase rapidly as the porosity increases. At porosities of 85-90%, high efficiencies were obtained for extremely high discharge rates over a range of temperatures extending down as low as —60°C. Similar results were obtained with high porosity cathodic active materials. The active materials thus tested included zinc, cadmium lead Ag_2O, and AgO, all of which were highly successful, thus indicating that the technique can be applied to a wide range of batteries and active materials.

Theoretically, there are a very large number of substances that can be used as the active material in battery anodes or cathodes. From a practical viewpoint, this use is not feasible with a majority of these materials since they polarize heavily and can operate only at very low current densities. Since polarization is a monotonic increasing function of the current density, all materials have some limit to the current density at which they may be discharged practically and beyond which limit the drop in the value of the potential is too large to be acceptable for practical purposes. Any physical factor that increases the surface area of the active material decreases the polarization by decreasing the current density expressed in terms of discharge current per unit of surface area and thus makes it feasible for the material to be discharged at much higher rates.

Shepherd and Langelan (1) have shown that metal plates of controlled porosities can be produced by the electrolytic reduction of metal compounds which are subjected to controlled physical pressure during the electrolysis. The porosity of the metal plate is a function of the pressure applied during formation and is also dependent on the particular compound or mixture of compounds being reduced. A wide range of porosities was obtained in this manner from metals of the normal electronegative group such as silver, bismuth, tin, lead, antimony, zinc, cadmium, copper, and mixtures of these including mercury (1). The porosity, P, which is often expressed as a per cent, is defined as that fraction of the total volume of the material that is occupied by pores or void spaces.

Since the surface area of a metal plate increases with increase in porosity, a number of zinc electrodes of various porosities were prepared from ZnO and discharged in a AgO-Zn-KOH cell, in an effort to determine the effect of porosity on cell capacity (1). The results are shown in Fig. 1 where the ampere hour efficiency and the capacity in minutes are plotted as a function of the porosity. The efficiency increases

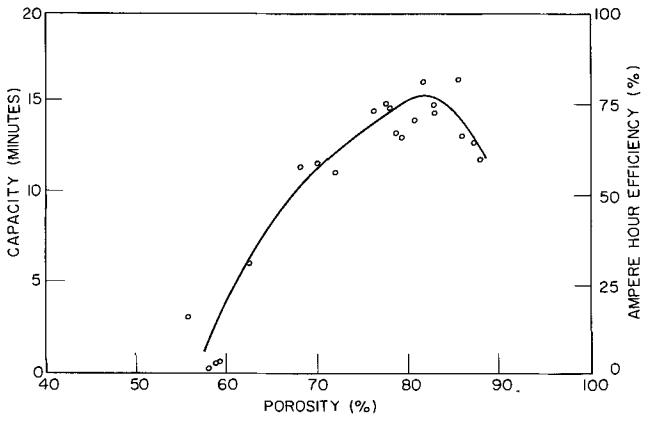

Fig. 1. Effect of zinc electrode porosity on capacity and efficiency, 20°C, 40% KOH, 730 ma/cm².

from close to 0% at 58% porosity up to a maximum of slightly over 75% at 82% porosity. As the porosity is increased beyond this peak value, the metal structure becomes flimsier and anodic dissolution causes high resistance paths and crumbling of the metal. As a result, the capacity and efficiency then decrease as the porosity increases.

On the basis of this information it was felt that an electrode of high porosity could be constructed which could be discharged at much higher rates and still have high ampere hour efficiencies for discharge times considerably less than the 15 min shown in Fig. 1. The information presented here is the result of an exploratory investigation designed to determine if such high rate electrodes could be prepared from zinc and also from other active materials; to determine if porosity was a major factor affecting the capacity of such electrodes; and to determine some of the major factors affecting the design, formation, and operation of high rate electrodes, thus opening the door to future investigations of a more highly detailed and quantitative nature.

High Rate Anodes

A cell or battery consists of components such as an anode, cathode, electrolyte, separators, grids, connectors, etc., all of which must be designed, assembled, and tested under appropriate conditions before the cell can be feasible for consideration in commercial competition with other power sources. The test results shown here are not meant to imply that a commercial cell is now available. However, as soon as a high rate anode and cathode have been tested in a common electrolyte as shown here and found to have suitable characteristics, the major obstacle standing in the path of constructing a high rate cell or battery has been eliminated.

The porous metal anode was suspended in a test cell between cathodes containing an excess of moderately high rate AgO as the active material. Under these conditions the metal anodes were always found to fail first. The effective spacing was 0.075 cm which was large enough to prevent any physical contact between the electrodes and thus eliminated the need for a separator. The presence of a separator tends to decrease the cell potential and also the capacity to a widely varying degree that depends on the physical properties of the separator and the discharge conditions for the cell. Thus, the data taken in the above manner represent an optimum as far as separators are concerned and present a standard against which the use of various separators can be tested in a specific, commercial cell.

A number of porous zinc electrodes of various porosities were formed by the electrolytic reduction of pasted ZnO, $ZnCO_3$, or mixtures of ZnO and $ZnCO_3$ under controlled physical pressures in 15% KOH electrolyte (1). Porosities as high as 92% were obtained

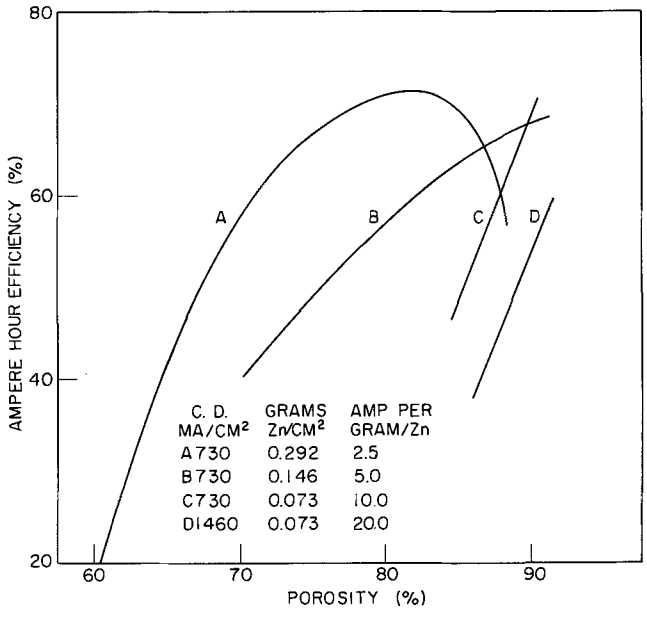

Fig. 2. Effect of porosities on efficiencies of zinc electrodes at 20°C.

by reducing $ZnCO_3$ under the comparatively light pressure of 0.054 kg/cm². A number of discharges were made at constant current covering a range of porosities, current densities, and electrode thicknesses. The results are shown in Fig. 2 where the ampere hour efficiency is plotted as a function of the porosity for various current densities and amounts of zinc. In each case, the efficiency and consequently the cell capacity increases rapidly with increasing porosity. In curve D, discharges are being obtained in slightly over one minute at efficiencies up to 60%. Figure 2 shows, as would be expected, that an increase in current density at a given porosity decreases efficiency. It also shows that a given efficiency can be maintained, within limits, by increasing the porosity as the current density increases. The current density is defined here in amperes per square centimeter, 1 cm² being defined as the area of an electrode 1 cm square. It would seem more logical to define current density as an active material current density measured in amperes per gram of zinc, since this value would be inversely proportional to the theoretical discharge time at 100% efficiency. Consequently the capacity of an electrode, at a given porosity and active material current density should be fairly constant but would tend to decrease as the thickness of the electrode increased.

The fact that ampere hour efficiencies of as much as 60% were obtained on cells discharging in as little as 1 min indicated that a further study should be made in this extremely high rate area. A number of cells were evaluated by means of constant resistance discharges. The average potential and the cutoff poten-

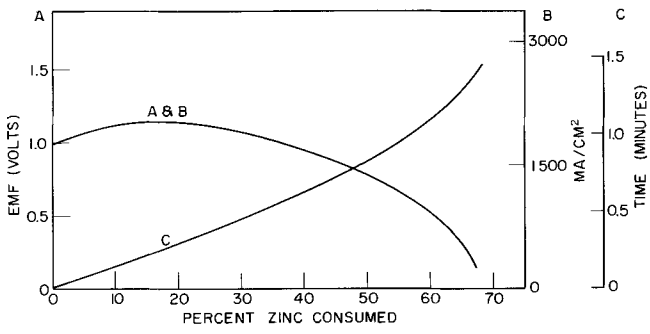

Fig. 3. High rate zinc electrode, constant resistance discharge at 23°C, AgO-Zn-32% KOH, 0.0577 g/cm² of 91.6% porous zinc. A, Potential; B, current density; C, time.

tial as well as the capacity are difficult to evaluate in a constant resistance discharge, since the potential tends to drop slowly with time in the manner shown in Fig. 3, which is in sharp contrast with the constant current discharges of Fig. 7 where the potential is fairly constant throughout most of the discharge and drops off rapidly near the end. However, many uses of a cell approximate constant current discharge conditions.

Occasionally in the past a cell has been observed, particularly at low temperatures, which was incapable of discharging through any type of load. Once started by extraneous means, a cell of this type would sometimes be capable of discharging on its own with satisfactory characteristics. If such a cell were discharged by the usual method of forcing a constant current through the cell and recording the potential, an initial period would be observed where the potential would be less than zero. If this period were too short to be detected by the recording equipment, it would never be known that the cell was incapable of practical operation without being started by an externally applied potential. The constant resistance discharges showed that this problem did not occur with these high porosity electrodes at high rates.

A large number of highly porous zinc electrodes of varying porosity were discharged at various high rates at temperatures varying from 23° to —60°C. A typical discharge is shown in Fig. 3 where the potential, the time, and the current density at 23°C have been plotted as a per cent of the total zinc that has been consumed at any given time. A discharge current equivalent to almost 2000 ma/cm² was maintained for nearly a minute at better than 50% efficiency. To check their durability, one of the cells tested at —60°C was short circuited for 6 sec followed by an immediate discharge through a constant resistance. The results are shown in Fig. 4 and indicate that the short circuit had no apparent effect on the Zn electrode characteristics.

The extremely high rates and efficiencies involved here can best be appreciated by comparison with existing types of electrodes. In Fig. 5, curve A, estimated values of the limiting current densities at various temperatures for the high porosity, high rate electrode are compared with those of a conventional electrode, curve B, recently developed for commercial high rate usage. The high porosity electrode has limiting current densities that are more than ten to thirty times higher than the conventional electrode.

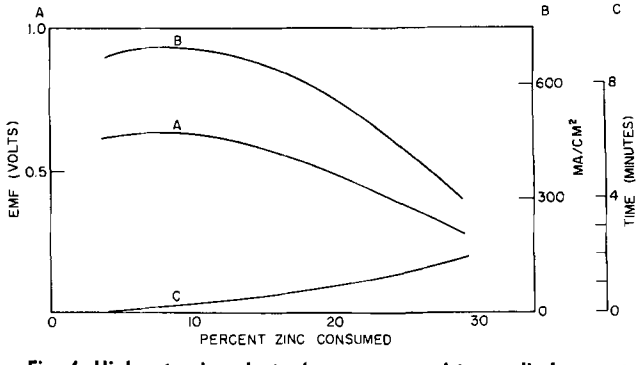

Fig. 4. High rate zinc electrode, constant resistance discharge at —60°C, AgO-Zn-32% KOH, 0.070 g/cm² of 91.4% porous zinc. A, Potential; B, current density; C, time.

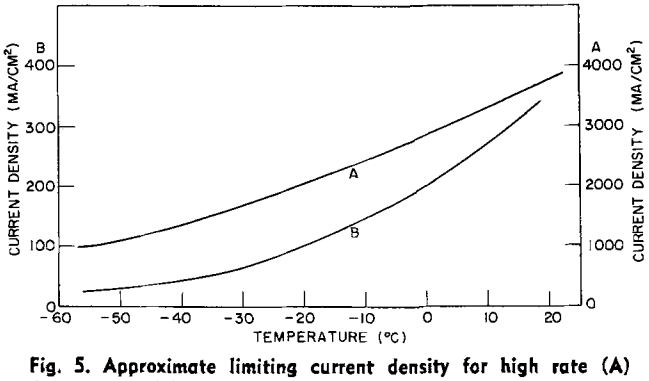

Fig. 5. Approximate limiting current density for high rate (A) and conventional (B) electrodes.

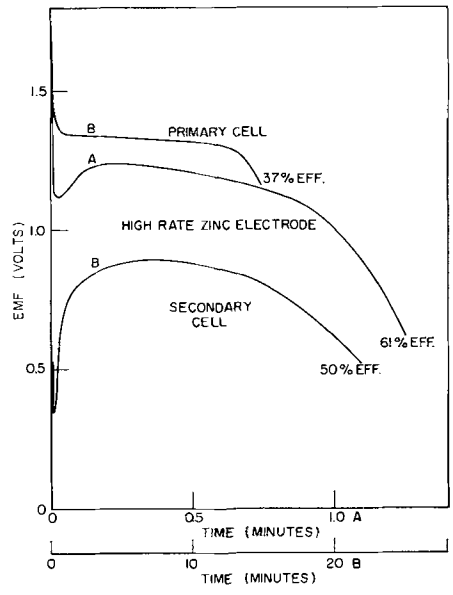

Fig. 6. Comparison of high rate zinc electrode battery with conventional silver zinc batteries.

In Fig. 6, where the potential is a function of the constant current discharge time, a higher efficiency and better characteristics are obtained for the high rate zinc electrode which is discharged in about 1 min, than are obtained for two commercial cells which were discharged in about 20 min. Commercial cells with higher efficiencies than these may be available, but these were the only two in which the weights of the active materials were known.

If the high surface area of the high porosity zinc electrode is the chief reason for its ability to discharge with high efficiencies at high rates and low temperatures then it should be possible to form high rate electrodes from other metals. High porosity cadmium electrodes were prepared by the electrolytic reduction of cadmium oxalate under 0.054 kg/cm² pressure in 15% KOH electrolyte. They were discharged against AgO cathodes in 32% KOH at constant current densities up to 1460 ma/cm². The results are shown in Fig. 7 where the emf is plotted against time throughout the discharge. High efficiencies were obtained, even in discharges that lasted as little as 1 min. Excellent results were also obtained at low temperatures. High porosity lead electrodes were

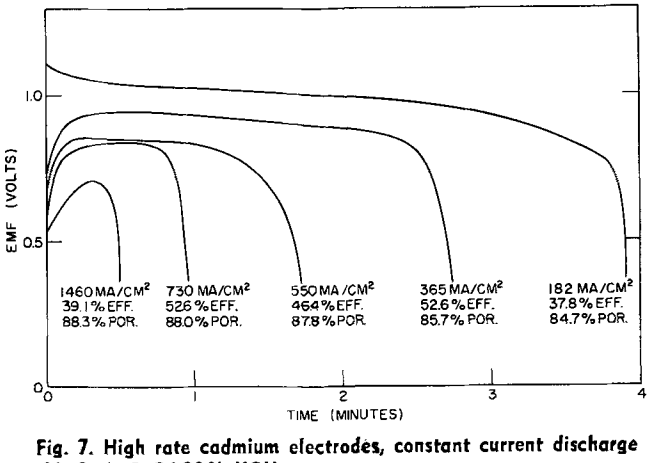

Fig. 7. High rate cadmium electrodes, constant current discharge at 20°C, AgO-Cd-32% KOH.

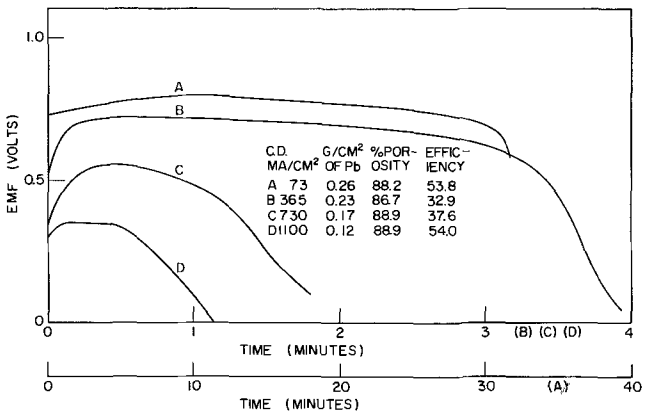

Fig. 8. High rate lead electrodes, constant current discharge at 20°C, AgO-Pb-32% KOH.

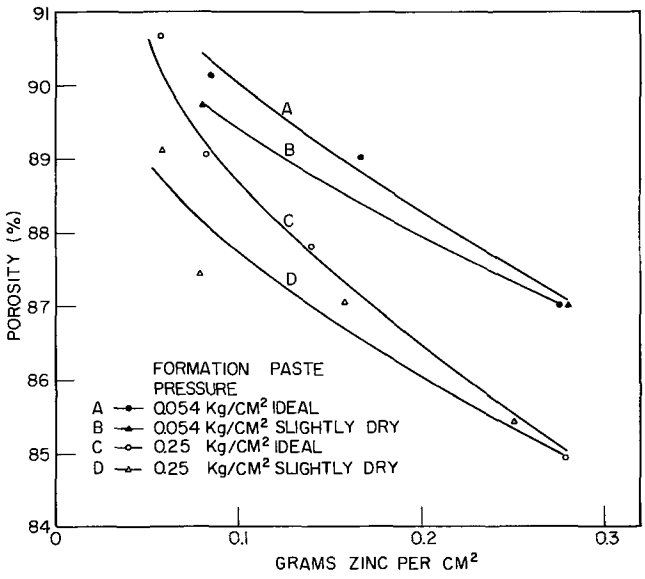

Fig. 9. Variation of porosity with the amount of zinc per unit area.

prepared by the electrolytic reduction of lead cyanamid and lead thiocyanate in 15% KOH electrolyte under 0.054 kg/cm² pressure. These were discharged against AgO cathodes in a 32% KOH electrolyte at constant current densities up to 1100 ma/cm² and discharge times of as little as 1 min. The results are shown in Fig. 8. The high capacities and efficiencies obtained at extremely high rates from the zinc, cadmium, and lead high porosity electrodes indicate that other high porosity, active materials should also make excellent high rate electrodes.

In every case, there was a large increase in temperature during a high rate discharge which would be capable under many conditions of seriously affecting cell capacity and other characteristics, particularly at low, ambient temperatures where the change in capacity with change in temperature is relatively large. This increase in temperature, which measured as much as 30°C, varies widely with changes in cell construction and operating conditions and consequently can have a serious effect on cell design. In the case of a large, closely packed, well insulated cell, containing a minimum of electrolyte, the temperature increase during discharge would be higher. Consequently, the discharge characteristics would be much better at low ambient temperatures than those obtained by the test procedures described here and illustrated in Fig. 4 and 12.

Electrode Pasting

There are a large number of problems involved in the pasting of the grids for the formation of the high porosity electrodes (2). Since the paste is subjected to physical pressure during reduction it cannot be put in the pockets of a commercial grid but must be set on top of a wire screen. Under these conditions the pasted material must be quite stiff in order to avoid flowing. This type of pasting is not particularly easy and is to a certain extent an art (2). An ideal paste gives on reduction a porous metal plate having optimum properties in regard to such characteristics as strength and cohesiveness. This ideal paste is a stiff paste and is almost dry, is slightly flexible and doughy, is not crumbly or sticky, and is cohesive and will flow to a certain extent when placed under pressure. The percentage of liquid present in a particular power-liquid combination is either constant or fixed within narrow limits. There is an extremely wide variation in the pasting properties of various compounds as defined in terms of ease of pasting and quality of paste. It was possible to divide all the compounds tested into five arbitrary groups ranging from "very good" to "very poor." This grouping was found to be a function of particle size and the water content of the ideal paste. The average water content of each group is approximately a linear function of the average geometric mean diameter. In going from the "very poor" to the "very good" paste group, the average water content increases from 32 to 60%, while the average particle size decreases from 1.2 to 0.3μ. Consequently, the finest size of particles make the best pastes and should be used wherever possible (2).

Since the water content of the paste is critical, slight variations in the paste composition might be expected to have an effect on the electrode porosity. The porosity of the metal obtained by electrolytic reduction of a pasted electrode is shown in Fig. 9 to be a function of the amount of zinc per unit area. The porosity decreases as the amount of zinc increases which is equivalent to saying that the porosity decreases as the thickness of the electrode increases. Similar results were obtained with lead. Results are shown in Fig. 9 for two different physical pressures applied throughout the reduction and show, as has been done previously, that the porosity decreases as the formation pressure is increased. A comparison shown here of ideally pasted electrodes with electrodes that were pasted slightly on the dry side indicate that the latter give a slightly lower porosity.

The control of metal porosity by the use of controlled physical pressure during reduction presents a number of problems which are now fairly well understood. This method has been successful in preparing porous metals from the normal electronegative group previously mentioned but has not been successful with the transition metals. It has been shown that the porosity of the metal plate is seriously affected by the choice of metal compound being reduced (1). If it is assumed that the volume of the porous metal plate at the end of the reduction at zero pressure equals the volume of the paste at the start, then the weight of the metal per cubic centimeter is

$$(1-P)\rho = (1-p)\,dP_m \qquad [1]$$

where P is the porosity expressed as a fraction, ρ is the metal density, p is the ratio of the volume of liquid in the paste to the volume of paste, d is the density of the compound being reduced, and P_m is the percentage of metal in this compound. Equation [1] can be rewritten in the form

$$1-P = (1-p)M_c \qquad [2]$$

where $M_c = dP_m/\rho$ = cubic centimeter of metal contained in a cubic centimeter of the compound.

A plot of $1 - P$ *vs.* M_c should give a straight line with the slope $(1 - p)$. Values of the porosity, P, at zero formation pressures were obtained by extrapolation from porosity-pressure curves and were plotted in Fig. 10 against cubic centimeter of metal per cubic

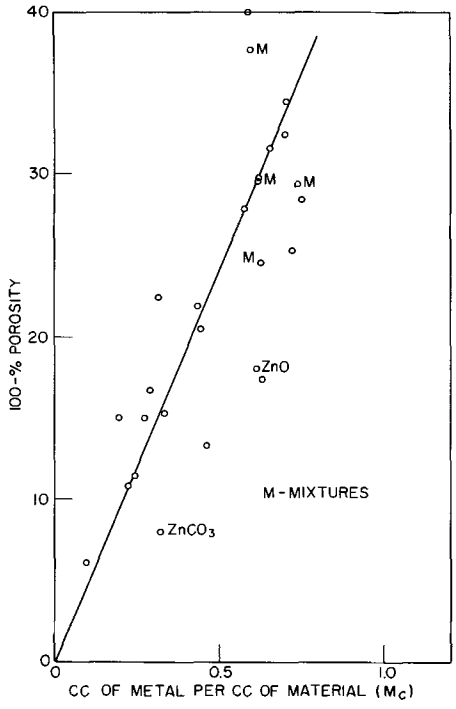

Fig. 10. Effect of cubic centimeter of metal per cubic centimeter of material on porosity.

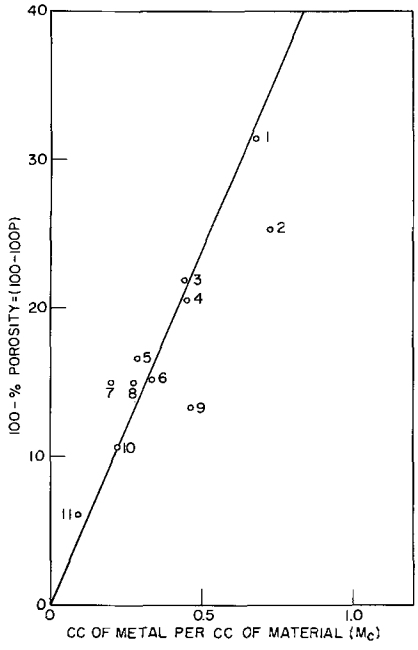

Fig. 11. Effect of cubic centimeter of lead per cubic centimeter of compound on porosity. Lead compounds; 1, oxide (PbO); 2, oxide (Pb_3O_4); 3, maleate (tribasic); 4, carbonate; 5, formate; 6, oxalate; 7, chlorphthalosilicate; 8, cyanate; 9, cyanamid; 10, thiocyanate; 11, stearate.

centimeter of compound for various compounds of zinc, lead, cadmium, silver, tin, copper, antimony, bismuth, and several mixtures of some of these compounds including mercury. The straight line fitted to this data has a slope of 0.48 which corresponds to a liquid content of 52% in the paste, which is about what would be expected (2). There is an appreciable scatter in the data of Fig. 10 due to the fact that each ideally pasted compound has its own particular value of p. In addition, the relationship is probably affected by such factors as the solubility of the compound in the electrolyte and its particle size distribution and shape factor. The two zinc compounds fall well below the line and indicate that the slope may also be dependent on the particular metal being formed. The data for the lead compounds alone have been plotted in Fig. 11 and the scatter, though definite, is much less than in Fig. 10. Porosities of lead from less than 70% up to 94% are shown here and any desired porosity in this range could be obtained by using a single compound or a suitable mixture of two or more of these compounds. All of these compounds were reduced to the porous metal in a 15% KOH electrolyte. The same metal porosity was obtained for Pb formed from PbO in 25% H_2SO_4 as in 15% KOH. It seems likely that the choice of electrolyte will have little effect on the metal porosity as long as the compound will reduce satisfactorily in that electrolyte. The very high porosities are obtained from compounds having a low value of M_c. Organic compounds containing a low percentage of metal tend to have low densities and consequently a low value of M_c. Not all compounds will reduce to the metal by electrolytic reduction under pressure. As a rough rule those compounds that are soluble in the electrolyte or are moderately good conductors of electricity tend to reduce. The best chance of obtaining very high porosities appears to be by the use of a metal salt of a high molecular weight organic acid.

If the use of pressure during the electrolytic reduction could be eliminated, the paste could be applied into the pockets of a conventional grid and thus eliminate most of the problems involved in pasting on top of a wire screen grid to form high porosity electrodes. A careful selection of metal compounds or mixtures thereof obviates the use of pressure to control metal porosity. However, a light pressure during reduction may be necessary in many cases in order to obtain optimum physical properties of the reduced metal electrode. It seems probable that a light pressure could be applied successfully to a pasted conventional grid particularly if a slight excess of paste were used.

If a high rate battery is to be constructed, a high rate cathode is needed in addition to the available high rate metal anodes. The problems involved in preparing high porosity cathodes from such materials as AgO and PbO_2 are similar to those involved in producing high rate metal anodes, but appear to be much more difficult, possibly because they have received less study. The major problem involved is the difficulty of getting good adherence between the active material and the grid. Although an Ag_2O electrode can be easily produced that operates at very high efficiencies at extremely high rates, a study was started on the AgO electrode since it is theoretically capable of producing almost double the capacity of the Ag_2O in terms of ampere hours per unit weight.

AgO electrodes were prepared by oxidation of various silver compounds pasted on a silver screen grid. Cathodes containing up to 87% porous AgO were formed in this manner. A number of cells were discharged under various conditions. A typical result is shown in Fig. 12 where the potential in volts, the current density, and the time are plotted as a func-

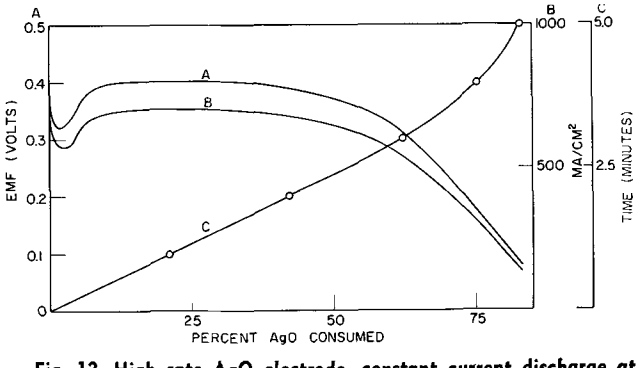

Fig. 12. High rate AgO electrode, constant current discharge at —40°C, AgO-Zn-32% KOH, 0.117 g/cm² of 86.9% porous AgO.

tion of the per cent of AgO consumed throughout a discharge made at —40°C.

A 71% porous PbO_2 electrode was prepared which was capable of discharging at moderately high rates. Both the AgO, the Ag_2O and the PbO_2 electrodes could be recycled.

The data indicated that the maximum efficiency on an efficiency porosity curve may be obtained at about 92% porosity at very high discharge rates as compared to 82% at the much lower rate illustrated in Fig. 1. At 92% porosity there are 11½ cc of electrolyte contained in the electrode for each cubic centimeter of Zn giving a total weight of active material plus electrolyte of about 27.6g. At 84% porosity there are 5¼ cc of electrolyte per cubic centimeter of Zn giving a total of about 14.1g. Thus, a drop in porosity that might be expected to decrease the capacity about 25% gives a decrease in the electrode weight of about 35%. Obviously the porosity that gives a peak capacity does not give a minimum weight. A 92 or 94% porous electrode is fairly flimsy. Rough calculations indicate that the maximum optimum porosity ever needed will be about 85 to 86%. Such an electrode, prepared on top of a wire screen, has fairly good physical strength which would be even better if a conventional grid were used. High porosity metal plates can be produced by other methods such as felt fiber or metallurgical techniques. Whether such electrodes will give the capacities obtained here probably depends on their pore size distribution and surface area. The successful reduction of a metal compound by the methods described here probably depends on the establishment of a network of relatively low resistance electrolytic paths filled with electrolyte and leading to virtually all the available active material. Since they must be there for formation to be possible, they will also be there for the purposes of discharge.

Conclusions

The results of this exploratory investigation show that high rate anodes and cathodes can be prepared that are capable of operating at high ampere hour efficiencies at temperatures down to as low as —60°C, thus pointing the way to the possibility of producing commercial cells capable of discharging with high efficiencies at extremely high rates. What may be of greater importance is the fact that this work shows that the porosity of the active material is a major factor of utmost importance in determining the capacity and other characteristics of many if not all cells which have porous electrodes.

Manuscript received May 5, 1966; revised manuscript received August 9, 1966. This paper was presented at the Buffalo Meeting, Oct. 10-14, 1965.

Any discussion of this paper will appear in a Discussion Section to be published in the December 1967 JOURNAL.

REFERENCES

1. C. M. Shepherd and H. C. Langelan, *This Journal*, **109**, 657 (1962).
2. C. M. Shepherd and H. C. Langelan, *ibid.*, **109**, 661 (1962).

The Formation and Discharge of Copper Chloride in an Organic Electrolyte

M. L. Bhaskara Rao

Laboratory for Physical Science, P. R. Mallory & Co. Inc., Burlington, Massachusetts

ABSTRACT

The electrochemical charge and discharge characteristics of copper electrodes in 1M $LiAlCl_4$ in propylene carbonate have been investigated. Oxidation of copper occurs with 100% efficiency yielding a sparingly soluble CuCl. The discharge efficiency of the precipitated salt is low (~50-75%). Analyses of the electrolyte during discharge have indicated the unusual phenomenon of an increase in the solubility of the salt which accounts for the low utilization efficiencies. An explanation is proposed based on the formation of a copper chloride complex. The significance of the observed results is discussed in relation to the development of organic electrolyte batteries.

It was recognized early that high energy density cell systems operating under room temperature and atmospheric pressure conditions would most probably comprise light transition metal salt cathodes and light alkali metal anodes in nonprotonic electrolytes such as can be obtained with certain organic solvents and inorganic salts. Several investigations have been conducted in recent years aimed at this possibility. It is the purpose of the present investigation to examine the suitability of one of the light transition metal chlorides, copper chloride, for a cathode in such cells.

It has been reported (1-3) that in propylene carbonate solutions of lithium tetrachloroaluminate only silver and nickel form insoluble salts on anodization of the bulk metal. Hence, the investigations conducted hitherto have concentrated on these two metals. It is not clear from the previous work whether the observed high solubility of copper, iron and cobalt chloride salts is due to the inherent solubility of the salt in the solvent, to the presence of impurities like water (4), or to ionic equilibria involving electrolyte salt. Experiments in our laboratory had shown that such processes were not only possible but that they were, indeed, operative in the copper chloride system. Thus it is of interest to consider copper chloride and other cathode salts which have been reported hitherto to be unsatisfactory for solubility reasons.

Previous work on the rechargeability of copper chloride electrodes in chloride ion containing organic electrolytes (1, 2) was limited to lithium chloride solutions in butyrolactone and dimethylformamide, and to lithium tetrachloroaluminate solutions in propylene carbonate. It was possible to charge and discharge copper electrodes reversibly only in the latter electrolyte. Porous copper electrodes operated at an efficiency of 65-75% (2). The causes of the failure to achieve 100% efficiency were not apparent from this work. It is the purpose of this paper to present the results of further work on this system, to interpret the observed behavior, and to indicate areas in which further study is required. Although attention is focused on the copper chloride system, it is apparent that the phenomena are of general relevance to cathode operation in organic electrolyte cells.

Experimental

Solvent.— Propylene carbonate, obtained from Matheson, Coleman, and Bell, was first passed through

a column of Linde 4A molecular sieves to remove part of the water initially present in the solvent. The propylene carbonate was then vacuum distilled at 3-5 mm Hg and the useful fractions collected at 89°-91°C. The water content of the various fractions was analyzed by gas chromatography and found to be between 0.002 and 0.5% by weight, depending on the fraction considered. Solvent fraction containing 0.002 to 0.005% (wt) water was used in the present experiments.

Electrolyte solution.—Various procedures for the preparation of solutions of lithium tetrachloroaluminate have been described (1-3). The most common method involves the controlled addition of stoichiometric quantities of $AlCl_3$ and LiCl to propylene carbonate. Such solutions become discolored and give evidence of extensive side reactions, probably the decomposition of solvent catalyzed by $AlCl_3$. We have adopted another procedure, previously reported (2), involving the direct formation of $LiAlCl_4$ through fusion of solid $AlCl_3$ and LiCl at 200°C. All the operations of premixing the salt, melting, and cooling were carried out in a dry atmosphere to exclude hydrolytic processes. The electrolyte was prepared by dissolving known amounts of this salt in given volumes of distilled solvent. Normally, such electrolytes were more stable than those obtained by other procedures, as evidenced by the very slight discoloration. The specific conductivity of 1M electrolyte solution was 5×10^{-3} ohm^{-1} cm^{-1}.

The cell.—All experiments were carried out in a Pyrex glass H-cell with a sintered glass frit separating the two compartments. Known volumes (25-50 ml) of electrolyte were used in the working electrode compartment. The cell had a cover suitable for holding the electrodes and also had provision for admitting dry, inert gas for deaeration and for maintaining a dry atmosphere over the electrolyte.

Electrodes.—Solid copper foils of 99.99% purity and thickness between 2 and 30 mils were employed to make working electrodes with superficial areas of 2 to 20 sq cm. Porous copper electrodes were also used in the present experiments. They were 2 sq cm in projected area, 0.076 cm thick, and were designated by the manufacturer (Clevite Corporation) to have a porosity of 62%. After the electrodes were cut to the required size, copper leads were attached by spot welding. Solid copper electrodes were cleaned in dilute nitric acid followed by rinsing in distilled water and acetone. Porous copper electrodes were used without any pretreatment. In order to prevent the shedding of products formed during anodization, a layer of Whatman No. 40 filter paper was wrapped around the working electrode.

Measuring set-up.—All measurements were made at a constant current provided by an Electronic Measurements Inc. electronically controlled constant current supply Model 620. The counter electrode was a strip of lithium metal in the counter electrode compartment of the H-cell.

The potentials of the working electrode reported were measured relative to a silver wire situated in the same solution 2-3 mm away from the former. Thus, the reported valves of potential include potential differences due to IR in the electrolyte. The reproducibility of the reference electrode was ±0.05v as evidenced by a series of open-circuit measurements with reference to a lithium electrode in the same solution. The potentials were measured with an electrometer, E-H Research Laboratories Model 230 and were recorded by feeding the output of the electrometer to a potentiometric recorder, Mosley Autograph 680.

Anodic and cathodic measurements were made at currents between 0.5 and 10 ma cm^{-2}, based on the projected electrode area. Most of the measurements were performed in agitated solution, using a magnetic stirrer.

Analytical techniques.—Dropping mercury electrode polarography was used to identify and to estimate the dissolved copper ion species formed in solution during electrolysis. For this purpose, 1-ml aliquots of the electrolyte from the working electrode compartment were added to a thoroughly deaerated, known volume of aqueous 1M HCl contained in the polarographic cell. Such a medium preserves the ratio of copper (I) and copper (II), since copper (I) will not disproportionate (5), and no copper metal is present to reduce copper (II) to copper (I). This procedure for analysis allowed the unequivocal identification and estimation of the copper ion species initially present in the working electrode compartment. In other respects the polarographic measurements were conventional and the results were compared against known solutions of copper (I) and copper (II) in aqueous 1M HCl. A Metrohm Polarecord Model E-261 was used in this work.

Specific experiments.—The following experiments were done: (*A*) Charge-discharge behavior of solid copper electrodes. Solid copper electrodes of known dimensions were submerged in a solution of 1M $LiAlCl_4$ in propylene carbonate in the working electrode compartment of the cell. The electrodes were anodically charged to capacities of 2.5 to 10 ma-hr cm^{-2} at 0.5 to 10 ma cm^{-2}. The charged electrodes were subsequently discharged at various current densities. Both the variation of electrode potential with time and the utilization efficiency were investigated. The utilization efficiency is calculated by dividing the coulombs recovered on cathodization by the coulombs passed during the preceding anodization.

(*B*) Composition of electroformed salt. A 20 cm^2 area electrode was anodized at 10 ma for 15 hr. A large amount of insoluble salt formed on the electrode. The electrode and the adhering salt were repeatedly rinsed in propylene carbonate and then dried. The composition of the salt was determined by x-ray diffraction, using a Phillips Type 422730 x-ray diffraction unit. For the cell constants, copper radiation (no filter) was employed.

(*C*) Maximum possible loading. The maximum anodization that an electrode could sustain was determined by charging anodically a 2-mil thick copper foil of approximately 20 ma-hr theoretical capacity (based on a one-electron oxidation). This electrode could be smoothly charged to capacity of greater than 18 ma-hr. Further charging was limited by the physical discontinuity of the metal due to the exhaustion of the metal rather than to passivation problems.

(*D*) Solubility measurements.—At various intervals of time during the charging and discharging of the electrode, 1 ml aliquots were taken from the working electrode compartment and analyzed to determine the nature and concentration of the dissolved copper species.

(*E*) Open-circuit stability of the charged electrodes. Solid copper electrodes were anodized at 5 ma cm^{-2} in 30 ml of solution to a capacity of 3.25 ma-hr cm^{-2} and were allowed to stand on open circuit in stirred solution for 5½ hr. The solutions were analyzed for dissolved copper species before and after the open-circuit stand.

(*F*) Effect of electrolyte composition on charge-discharge efficiency. The charge-discharge behavior of solid and porous copper electrodes was studied as described above in electrolytes of altered composition. The electrolyte was a propylene carbonate solution, 1M in $LiAlCl_4$ and 0.5M in $AlCl_3$.

Results and Discussion

The Charging Process

The anodic charging of copper metal electrodes in a propylene carbonate solution, 1M in $LiAlCl_4$, produced a partially soluble greenish white salt on the electrode. No change in the color of the solution was ob-

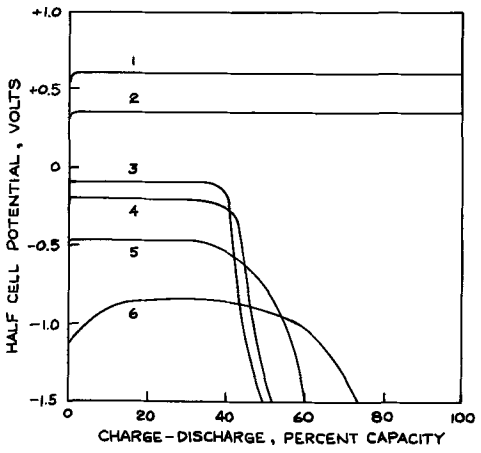

Fig. 1. Charge-discharge behavior of copper electrodes in 1M $LiAlCl_4$. Capacity of charging: 2.5 ma-hr cm^{-2}. Curves 1 and 2 refer to anodic charging at 2.5 and 0.5 ma cm^{-2}; curves 3 to 6 are for discharge at 0.5, 2.5, 5, and 10 ma cm^{-2}, respectively.

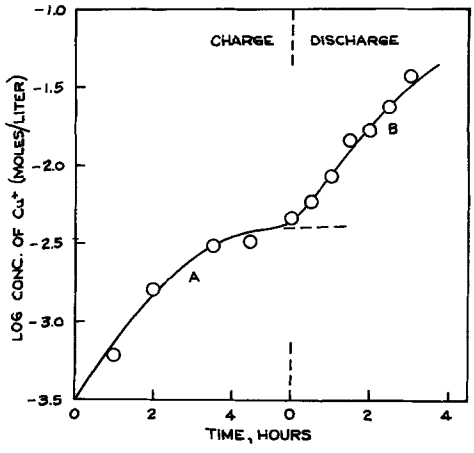

Fig. 2. Build up of copper (I) concentration in the working solution during charge and discharge of 10 cm^2 copper electrodes in 50 cc, 1M $LiAlCl_4$ at 20 ma.

served due to the dissolution of the salt. The charging curves, shown as curves 1 and 2 in Fig. 1, exhibited a single plateau. The salt remaining on the electrode was analyzed by x-ray diffraction as described above. The results are shown in Table I. Only three lines were observed, and these are compared with the ASTM data for CuCl. The data in Table I provide conclusive proof that the bulk of the salt produced on anodic charging was CuCl.

The electrolyte composition was analyzed during anodic charging. The results are shown as curve A of Fig. 2. Only copper (I) was found in solution. The concentration of copper (I) increased initially and then leveled off at a value which is assumed to be the point of saturation. This conclusion is supported by the observation that when an anodically charged copper electrode was allowed to stand on open circuit for as long as 5½ hr, there was no further significant change in the concentration of copper (I) in solution. From these data we may calculate the solubility of copper (I) in this electrolyte to be 4.64×10^{-3} M 1^{-1} at 25°C.

It is concluded that the only product of the anodic charging of copper metal in propylene carbonate, 1M in $LiAlCl_4$, is slighlty soluble CuCl. Since there was no evidence of copper (II) in solution, it must be concluded that, at the saturation concentration of copper (I), disproportionation is negligible.

The Discharge Process

Cathodic discharge curves for the product formed during anodic charging are shown as curves 3 to 6, Fig. 1. These discharge curves were obtained on electrodes which had been anodically charged to a capacity of 2.5 ma-hr cm^{-2}. A single discharge plateau was observed. The utilization efficiencies, calculated as described above, varied with the discharge current density from approximately 50% at 0.5 to 2.5 ma cm^{-2} to 70% at 10 ma cm^{-2}. It was also observed that the color of the solution in contact with the working electrode changed from a light to deeper yellow upon discharge.

Since the utilization efficiencies observed were rather less than 100% it was necessary to analyze the probable causes of the observed inefficiencies. The following phenomena and properties may cause a low efficiency: (*a*) parasitic oxidation and reduction reactions; (*b*) trapping of electroactive material in electrode regions not accessible to electron transfer due to shedding or irregular current density distribution; and (*c*) solubilization of active material in the electrolyte and the diffusion of solubilized species away from the electrode. In the present case, it was possible to ascertain the causes of the low utilization efficiency. During the investigations, the variation of the copper (I) concentration in the solution was also measured as a function of the depth of discharge. Surprisingly, the copper (I) concentration increased during the discharge cycle. The observed buildup is presented in Fig. 2, curve B. It may be seen that the Cu^+ ion concentration increased sharply from 4.64×10^{-3} moles/l at the end of the charge cycle to 2.72×10^{-2} moles/l at the end of the discharge cycle. The observed result was unexpected and seems to have no parallel in electrode processes occurring in aqueous systems.

Table I. Results

dA (Literature, CuK_α radiation)	I/I^o (Literature)	dA (Observed)	I/I^o (Observed)
3.127	100	3.1552	100
1.9148	55	1.9225	54
1.6332	32	1.6407	29

It was possible to account fully for the loss of efficiency from the magnitude of estimated concentrations of the dissolved copper (I) species. In a typical experiment, a coulombic equivalent of 4.1×10^{-3} moles of electricity were used for the charging of the electrode, and an equivalent of 2.46×10^{-3} moles were recovered from discharge. The analysis of the solution for the Cu^+ ion concentration after the discharge cycle indicated the presence of 1.68×10^{-3} mole of Cu^+ ions in the solution which accounted for the low efficiency on discharge. It was interesting to note that the data indicated a current efficiency of 100% for the chloride salt formation process. Obviously some ionic process occurred during the discharge that resulted in the production of a copper species more soluble than CuCl. The following explanation may be offered at this time to explain the observed behavior.

Earlier investigations (2) of copper salt systems in organic electrolyte media had led to the suggestion that there is a strong tendency for copper chloride to form more soluble $CuCl_2^-$ ions in the presence of free chloride ions. The exact experiments in this regard concerned measurement of the conductivity of propylene carbonate suspensions of insoluble CuCl and insoluble LiCl. The conductivity of the equilibrium solution in contact with different proportions of CuCl and LiCl increased linearly till equimolar amounts of CuCl and LiCl were present. Thereafter the conductivity did not increase appreciably with further addition of LiCl. The observed increase in conductivity up to 1:1 mole ratio has been explained on the basis of formation of a more soluble $CuCl_2^-$ complex. This led to the formulation of a reaction mechanism involving the cathodic generation of this complex to account for

the increased solubility observed in the present experiments.

To examine why more copper (I) goes into solution on cathodic discharge than on anodic charge, it is convenient to consider the following equilibria.

$$AlCl_4^- = AlCl_3 + Cl^- \quad [1]$$

and

$$CuCl_2^- = CuCl + Cl^- \quad [2]$$

and the reversible electrode reaction

$$Cu + Cl^- = CuCl + e^- \quad [3]$$

The equilibrium for reaction [1] lies predominately to the left, as is known from the fact that LiCl, which is relatively insoluble in propylene carbonate, does not precipitate in 1M $LiAlCl_4$ solution in propylene carbonate. The equilibrium for reaction [2] lies predominately to the left also, in the presence of a sufficiently large chloride concentration. This is not the case for the $LiAlCl_4$ solution, and there is little tendency for the CuCl to go into solution, as attested by the solubility for copper (I) in this solution of 4.64×10^{-3} M l^{-1}.

At the electrode/solution interface the net reaction during anodization involves the consumption of chloride ions (reaction [3] from left to right), and, hence, there is even less tendency for the dissolution of copper (I) through formation of $CuCl_2^-$. It is reasonable to assume that the aluminum chloride generated in the above reaction may diffuse away from the electrode. Consequently, at the beginning of discharge the concentration of $AlCl_3$ at the electrode/solution interface would be less than needed for reversing the quasi-equilibrium steps involved during charging. As such, part of the Cl^- ions released during discharge (reaction [3] from right to left) become available for combination with undischarged CuCl to form the soluble $CuCl_2^-$ species as in

$$2CuCl + e^- = Cu + CuCl_2^- \quad [4]$$

Thus, the formation and diffusion of $CuCl_2^-$ away from the electrode would account for the observed increase in the Cu^+ ion concentration in solution and the low efficiency on discharge. Whether or not the CuCl is reprecipitated from $CuCl_2^-$ and $AlCl_3$ in the bulk of the solution needs to be investigated.

The following experiments were designed to take advantage of this postulated mechanism to improve the utilization efficiency of the copper electrode.

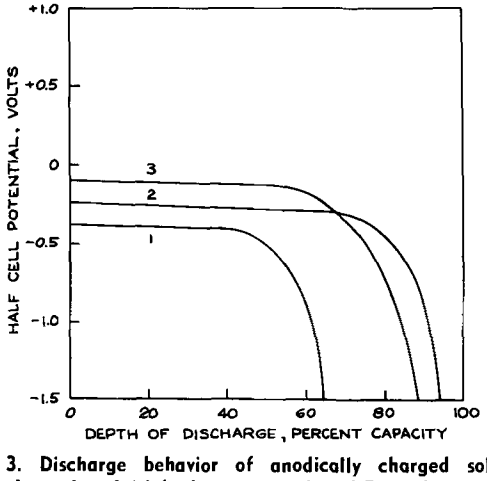

Fig. 3. Discharge behavior of anodically charged solid and porous electrodes. Initial charge capacity: 2.5 ma-hr cm^{-2}; discharge current density: 2.5 ma cm^{-2}. Curve 1 and 2 discharge of electroformed CuCl on solid and porous copper electrode in 1M $LiAlCl_4$ containing 0.5M $AlCl_3$ in propylene carbonate; curve 3 discharge of electroformed CuCl on porous copper electrode in 1M $LiAlCl_4$ in propylene carbonate.

1. Increasing the current density of discharge should increase the utilization efficiency since a larger fraction of the soluble $CuCl_2^-$ species would be reduced before they can leave the domain of reduction, the electrode. The results shown by curves 5 and 6, Fig. 1, demonstrate that this did, indeed, occur.

2. Increasing the porosity of the electrode should increase the utilization efficiency since the tortuous channels of the porous electrode would impede the diffusion of the $CuCl_2^-$ species into the solution, and a larger fraction of the salt should be reduced. This did occur, as is demonstrated by curve 3, Fig. 3, where a cathodic utilization of 85% was realized with the porous electrode under conditions where the solid electrode would have only yielded a utilization efficiency of 50%.

3. Increasing the concentration of $AlCl_3$ should increase the utilization efficiency. This may be seen from an examination of reactions [1] and [2]. The larger the concentration of $AlCl_3$, the more effective will be the competition of $AlCl_3$ for chloride ions, and the smaller will be the degree of complexation of CuCl with chloride ions. This was demonstrated to occur as shown by curves 1 and 2, Fig. 3, and curve 4, Fig. 1. In the 1M $LiAlCl_4$ solution containing 0.5M $AlCl_3$ the utilization efficiency was greater than 90%, whereas, under similar conditions, the utilization efficiency was only 50% when additional $AlCl_3$ was not present.

Conclusions

(*A*) In propylene carbonate, 1M in $LiAlCl_4$, the primary product of the anodic oxidation of copper metal is CuCl. CuCl may be cathodically reduced; the primary problem is the strong tendency of CuCl to form chlorocuprate (I) complexes, which are soluble in this solvent. The tendency toward complexation may be repressed by the appropriate control of the complexation equilibria through the addition of species which preferentially combine with chloride ions.

(*B*) The fraction of copper (I) which, through complexation, escapes into the solution before cathodic reduction may be retarded through the use of high current densities and porous electrodes.

(*C*) Under optimum conditions of current density, electrode porosity, and equilibrium control (through the addition of $AlCl_3$) it has been possible to cycle copper electrodes in propylene carbonate solutions of $LiAlCl_4$ with better than 95% utilization efficiency.

Acknowledgment

The author wishes to express his thanks to Dr. Per Bro, Dr. R. G. Selim, and Dr. K. R. Hill for their helpful discussion, to Mr. L. B. Griffiths and Mr. Salvatore Fantasia for x-ray diffraction measurements and acknowledge and thank the technical assistance of Mr. Paul M. Nichol.

This work was carried out under UAERDL Contract DA-44-009-AMC-1537(T).

Manuscript received June 30, 1966; revised manuscript received August 23, 1966. This paper was presented at the Philadelphia Meeting, Oct. 9-14, 1966.

Any discussion of this paper will appear in a Discussion Section to be published in the December 1967 JOURNAL.

REFERENCES

1. J. E. Chilton and G. M. Cook, Lockheed Missiles & Space Co. Air Force Contract No. AF 33(616)-7957; Project No. 8173, Task No. 817304, Technical Documentary Report, No. ASD-TDR-62-837, Dec. 1962.
2. K. R. Hill and R. G. Selim, P. R. Mallory & Co., NASA Contract No. NAS 3-2780, Final Report, Aug. 15, 1965. Also, R. G. Selim, K. R. Hill and M. L. B. Rao, P. R. Mallory & Co. Inc., NASA Contract No. NAS 3-6017, Final Report, Feb. 14, 1965.

3. Lithium Nickel Halide Secondary Battery Investigation. Gulton Industries Inc. Air Force Contract No. AF 33(615)-1266 Project No. 8173, Task No. 817304. Technical Progress Reports.
4. William-Sidney Harris, "Electrochemical Studies in Cyclic Esters," Thesis. University of California, 1958.
5. Kolthoff and Lingane, "Polarography," Vol. 2, 2nd ed., Chap. 28, Interscience Publishers, Inc., New York (1952).

Studies of Hydrocarbon Fuel Cell Anodes by the Multipulse Potentiodynamic Method

III. Behavior of Saturated Hydrocarbons on Conducting Porous Teflon Electrodes with a Phosphoric Acid Electrolyte

L. W. Niedrach and M. Tochner[1]

General Electric Research & Development Center, Schenectady, New York

ABSTRACT

The behavior of methane through butane fuels parallels that previously observed with methane, ethane, and propane with a perchloric acid electrolyte although quantitative differences are observed. A temperature range from 60° to 120° was covered. With both electrolytes all of the hydrocarbons form one class of surface species which is oxidized at relatively low potentials. Hydrocarbons above methane form a second more refractory class of surface species in both cases. As the molecular weight of the fuel increases, greater quantities of the refractory species accumulate on the electrode. These species play a role in determining the maximum current that can be carried by the electrode. They seem connected with the current and voltage oscillations frequently encountered with hydrocarbon fuel cells.

The behavior of ethane and related hydrocarbons on smooth platinum electrodes in the presence of a perchloric acid electrolyte has been previously investigated with the multipulse potentiodynamic (MPP) method in this laboratory (1, 2). More recently the method has been extended to porous fuel cell anodes of more complex structure with which the behavior of methane and ethane was examined in detail, and a few preliminary experiments were performed with propane (3, 4). For this purpose a miniature version of a previously described (5) conducting-porous-Teflon fuel cell electrode (containing platinum black as catalyst) was employed. The electrolyte was again perchloric acid.

The work with porous-Teflon electrodes has now been extended to phosphoric acid systems in the temperature range from 60° to 120°C. Saturated linear hydrocarbons from methane through butane have been included in the new studies which are the subject of the present paper.

As in the previous work, particular attention was given to the behavior of the species that form on the surface of the electrode. In addition data were again obtained to relate this behavior to the over-all polarization curves for the fuel electrodes.

Experimental

The equipment and general procedures utilized in these investigations have been described previously (3). In brief, the 0.2 cm diameter Teflon-bonded, platinum black electrode was mounted in a three compartment, Teflon cell. Platinized platinum flags served as the hydrogen reference and counter electrodes. The former communicated with the working anode through a Luggin capillary. The cell was operated in an air thermostat enabling control of the temperature to within 0.1°C.

The 75% phosphoric acid electrolyte solution used for this work was prepared from reagent grade phosphoric acid and quartz distilled water. Electrolytic grade hydrogen was used in the reference electrode chamber, and Phillips research grade hydrocarbons were used as the fuels. Tank argon, deoxygenated by passage over heated copper turnings, was used as the "fuel" for obtaining solvent blanks. Tank argon was also used for degassing the solution.

The electronic instrumentation and circuit have been described previously (6).

The potential-time sequence applied to the anode for adsorption studies at constant potential is shown in Fig. 1. The significance of the steps is covered below.

(*A*) Pretreatment step (15 sec) to remove oxidizable impurities and to produce a layer of "adsorbed oxygen" which serves to block fuel adsorption. The solution is vigorously stirred and purged with argon to remove molecular oxygen and oxidation products formed.

(*B*) Potential step, during which the oxygen layer formed in (*A*) is maintained, and the solution is purged for an additional minute. The solution is then allowed to become quiescent for 1 min.

(*C*) Reduction step (15 sec) during which the adsorbed oxygen layer is reduced. At this low potential (0.06v) the adsorption of hydrocarbons is blocked. This step was included so that the reduction of the surface and the adsorption of the hydrocarbon would not occur simultaneously. However, omission of this step

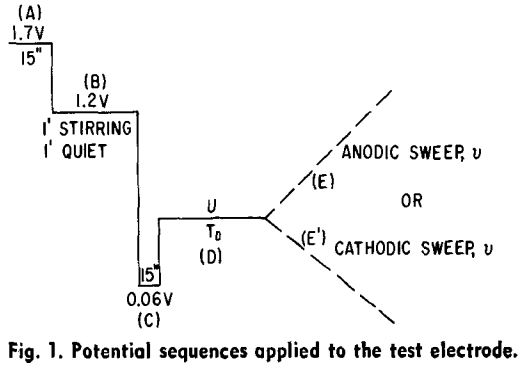

Fig. 1. Potential sequences applied to the test electrode.

[1] Present address: Silicone Products Department, General Electric Company, Waterford, New York.

was found to have no detectable effect on the equilibrations.

(*D*) Adsorption step, during which the hydrogen from (*C*) is rapidly oxidized, exposing a reproducibly clean surface for adsorption. The duration of this step is the adsorption time, T_D.

(*E*) Anodic sweep at 0.1 v/sec. The adsorbed fuel is oxidized and the surface covered with a layer of adsorbed oxygen. Subtraction of the charge due to surface oxidation from the total charge yields the charge required to oxidize the surface species derived from the adsorbed fuel.

(*E'*) Alternative to (*E*), a cathodic sweep at 0.025 v/sec which is used for determination of the "real" surface area of the electrode from the charge $_sQ_H$ corresponding to hydrogen deposition. In this case, argon is substituted for the hydrocarbon fuel.

The rationale behind the various steps has been discussed in detail elsewhere (1-3, 6).

Polarization curves were obtained by application of steps (A)-(D) of Fig. 1 before each measurement of current at a particular potential *U*. At each potential a 10-min equilibration was performed to allow the system to approach steady state before the final current measurement was made.

The work was completed over an interval of three months. During this period the area under the oxygen adsorption wave showed a variation of only ±3%. This is in agreement with a similar small variation in the real surface area of the electrode. It was also found that the blank traces were reproducible over the full range of equilibration periods used, thereby indicating that contamination of the electrode did not occur during the equilibrations.

Results

Each of the four hydrocarbons under study was examined over a range of equilibration times, potentials, and temperatures. As in the earlier work current-potential traces were obtained with a linear anodic sweep to determine the behavior of the adlayer on the electrode towards oxidation. In addition polarization curves were also obtained.

In Fig. 2, a set of current-potential traces is shown for the four fuels after various equilibration times at 0.3v with the 75% phosphoric acid electrolyte at 100°C. The general form of the traces is similar to that previously observed with the perchloric acid electrolyte at 60°C. In particular it is to be noted that only the single wave 1 is again observed with methane. This wave, which occurs at potentials below those at which the surface itself is normally oxidized, is also evident in the case of the higher hydrocarbons, but the latter also show a broad second wave which extends from about 0.8v to oxygen evolution potentials. With the ethane a clear indication is seen of a new, third wave which overlaps wave 2 and has a peak at about 0.9v. It is also to be noted that the charge required to oxidize the adlayer from the higher hydrocarbons is much larger than that required for methane. In addition, the rising portion of wave 1 shifts noticeably to higher potentials as the coverage increases.

The effects of the equilibration potential on the oxidation traces are shown for the four fuels in Fig. 3-6. Here again the temperature was 100°C and standard equilibration times of 10 min were employed. Over the range of temperatures investigated this time was found adequate to establish essentially a steady-state coverage except in the case of methane at low potentials. Again, as in the case of the perchloric acid a marked effect of potential is seen. The maximum charge required for oxidation of the adlayer occurs in the vicinity of 0.2v. This probably also corresponds to maximum surface coverage with adsorbate, but because of the unknown oxidation states of the specific surface species involved, this cannot be stated with certainty. The hypothesis is however supported by the related work of Brummer *et al.* with propane on wire electrodes (7).

It is to be noted that following equilibrations at 0.6v the amount of residual wave 2 increases with the molecular weight of the fuel. The new wave 3 for ethane is conspicuous after equilibrations at 0.2, 0.3, and 0.4v. It cannot be detected in the traces for propane and butane, possibly because of overlapping from a pronounced tail from wave 2.

The observed effects of potential at 100°C are also representative of the trends seen at 60°, 80°, and 120°C. However, there is a general tendency for the

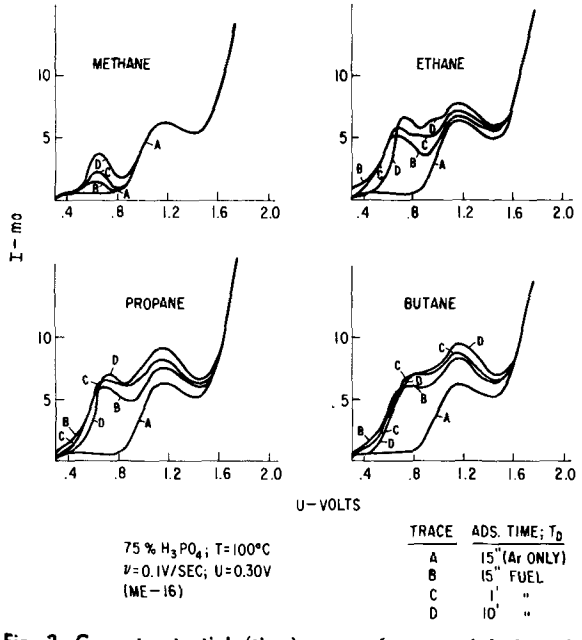

Fig. 2. Current-potential (time) traces for several hydrocarbons after different adsorption times.

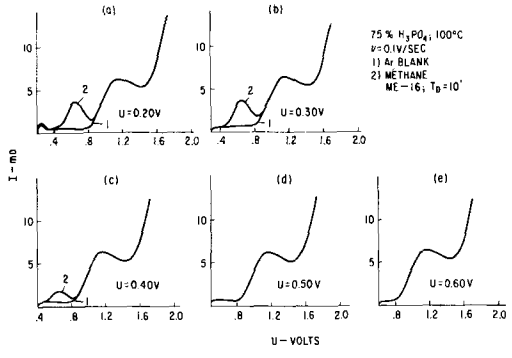

Fig. 3. Current-potential (time) traces for methane adsorbed at several potentials.

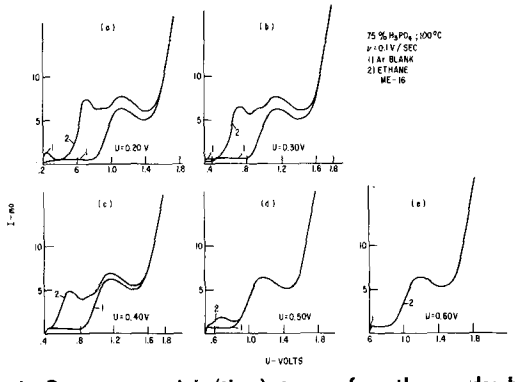

Fig. 4. Current-potential (time) traces for ethane adsorbed at several potentials.

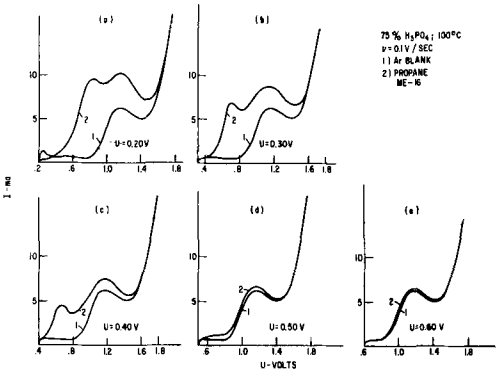

Fig. 5. Current-potential (time) traces for propane adsorbed at several potentials.

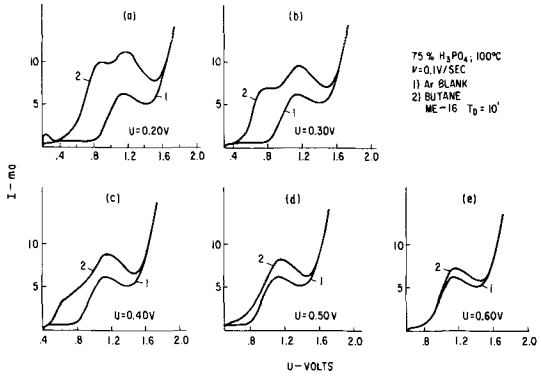

Fig. 6. Current-potential (time) traces for butane adsorbed at several potentials.

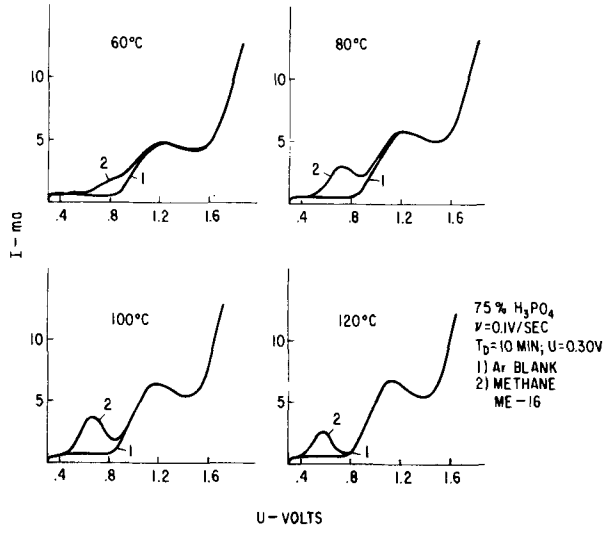

Fig. 7. Current-potential (time) traces for methane adsorbed at several temperatures.

oxidation waves to become more distinct and for wave 1 to grow in at the expense of wave 2 as the temperature is increased. This is illustrated in Fig. 7-10 with data obtained at 0.3v. Similar trends had been observed with the perchloric acid electrolyte over the temperature range from 25° to 80°C (3). The traces obtained with the phosphoric acid electrolyte at 60° and 80°C are, however, somewhat more diffuse than those with perchloric acid at the corresponding temperatures. As in the case of the perchloric acid electrolyte, methane shows only a single wave throughout.

The charge, $Q_{E_{tot}}$, associated with the oxidation of all carbonaceous species in the adlayer was determined at 100°C and 0.3v after different adsorption times, T_D. This was done conventionally by integrating the area enclosed by the solvent blank trace and the fuel trace (1-3, 6). It is to be noted that hydrogen formed by dissociation during the initial adsorption step is not included in these measurements. These data for the four fuels are shown in Fig. 11. The data have been normalized to charge per unit of "real" surface area as determined by cathodic deposition of hydrogen on the electrode. A conversion factor of 0.21 mcoul/cm^2 was employed in calculating the real area (8).

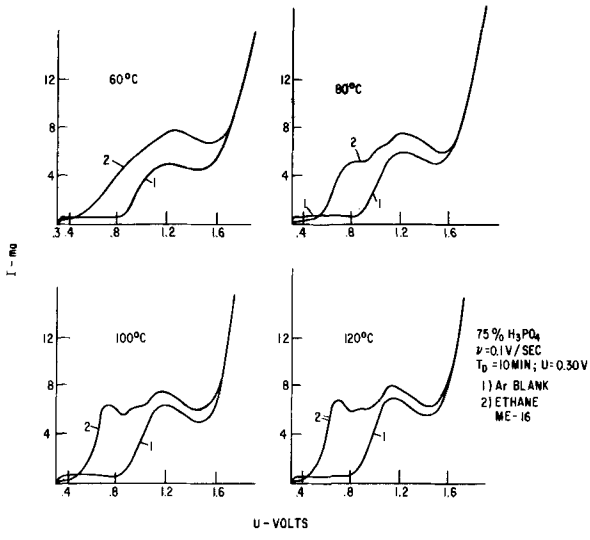

Fig. 8. Current-potential (time) traces for ethane adsorbed at several temperatures.

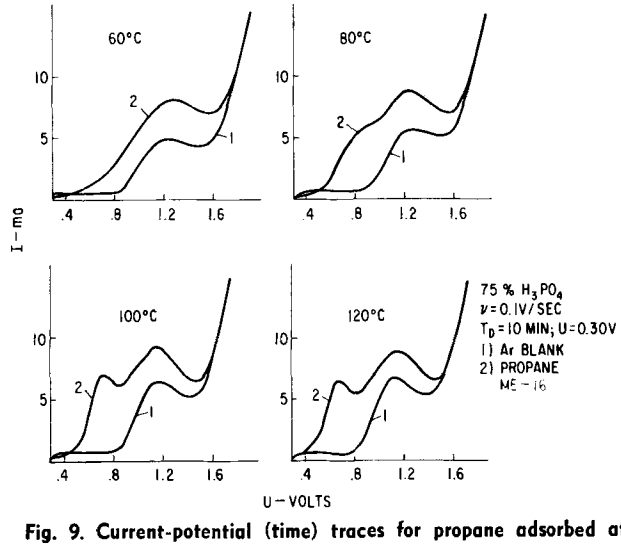

Fig. 9. Current-potential (time) traces for propane adsorbed at several temperatures.

At the temperature of these experiments the rates of accumulation of oxidizable species on the electrode surface are considerably higher than had been encountered in the work at 60°C with perchloric acid. This made it impossible to estimate initial adsorption rates as was reported earlier for the lower temperature work with perchloric acid. For ethane, propane, and butane, even for the shortest equilibrations, $Q_{E_{tot}}$ varies with the logarithm of time as had been observed at intermediate times with the perchloric acid at the lower temperature. In the case of methane a parabolic relationship between $Q_{E_{tot}}$ and time is followed at the shorter equilibration times. This contrasts with the linear relationship previously observed with the perchloric acid. As was noted in the

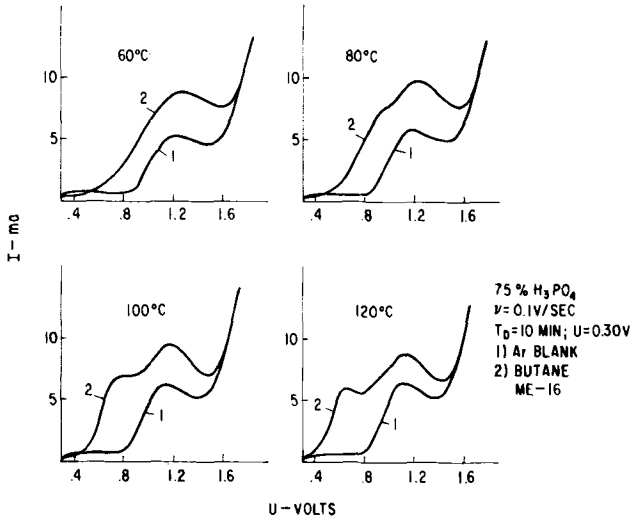

Fig. 10. Current-potential (time) traces for butane adsorbed at several temperatures.

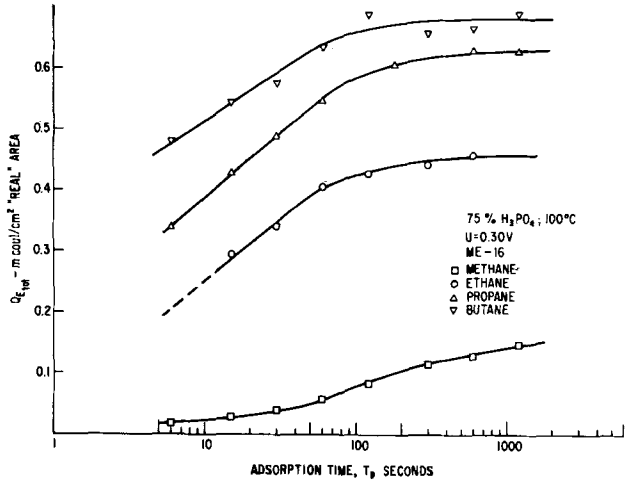

Fig. 11. Variation in surface charge with time for several hydrocarbons.

earlier work, $Q_{E_{tot}}$ eventually levels off to a steady-state value when the rate of adsorption equilibrates with the rate of oxidation. The total surface charge at steady state decreases with decreasing molecular weight of the fuel with the largest increment occurring between ethane and methane.

In addition to the examination of the adlayer, steady-state polarization curves were obtained for the four fuels at 60°, 80°, 100°, and 120°C. The family of polarization curves shown in Fig. 12 for ethane is representative of the effect of temperature on all of the fuels. In this figure the abscissa is expressed in terms of current density per unit geometrical area as well as per unit real area for the electrode. The presence of both scales enables one to relate the polarization curves to the present studies as well as the performance curves of fuel cells. The form of these curves is similar to those previously reported for methane (4) and ethane (3) with the perchloric acid electrolyte.

The polarization curves for the four fuels have been related to the steady-state values of Q_{E_1} and $Q_{E_{tot}}$ at the representative temperature of 100°C in Fig. 13-16. Here Q_{E_1} refers to the charge associated with the oxidation of species of wave 1; the values of Q_{E_1} were obtained by dropping a perpendicular from the minimum on the fuel oxidation trace and integrating

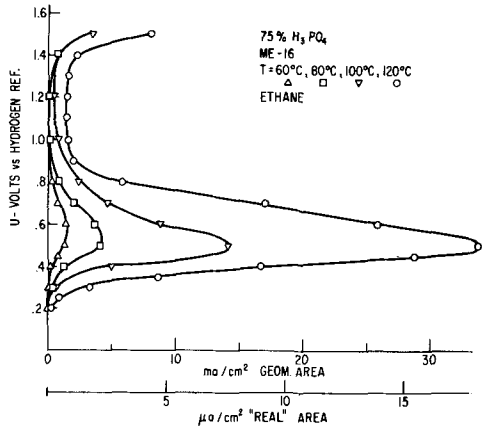

Fig. 12. Polarization curves for ethane at several temperatures

the area between curves 1 and 2 to the left of it in Fig. 3-6. In the case of butane the overlap of the individual waves prevented the determination of Q_{E_1}.

In general the form of the polarization curves is similar to those reported earlier for the perchloric acid system at lower temperatures. A comparison of the curves for ethane at 60°C with the two electrolytes reveals, however, that the maximum current with the phosphoric acid electrolyte is about 33% of that obtained with the perchloric acid. As with the perchloric acid electrolyte, the maximum currents occur at potentials at which there is still adsorbed fuel on the electrode surface.

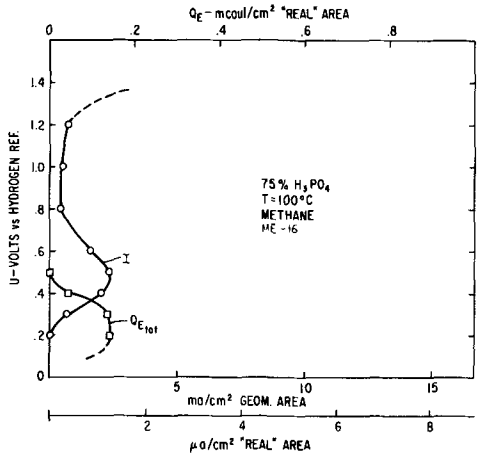

Fig. 13. Polarization and surface charge curves for methane

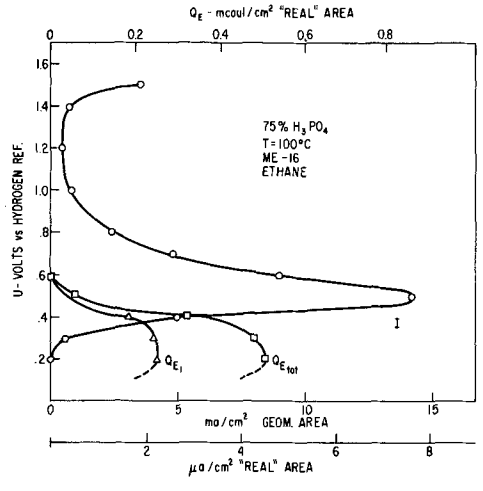

Fig. 14. Polarization and surface charge curves for ethane

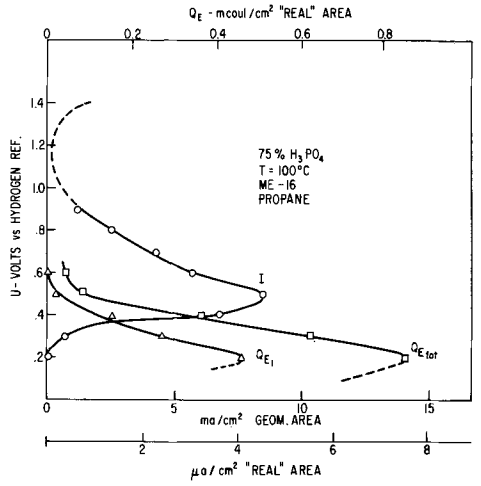

Fig. 15. Polarization and surface charge curves for propane

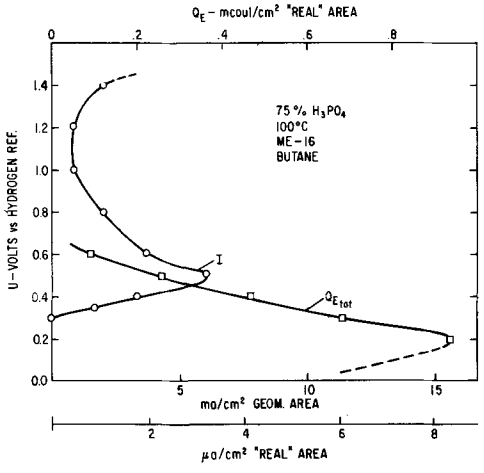

Fig. 16. Polarization and surface charge curves for butane

The maximum current occurred at about 0.5v with all of the fuels. A slight trend of the maximum toward lower voltages was evident as the temperature was increased. Arrhenius plots for the maximum currents for the four fuels indicated similar activation energies in all cases. This is shown by the normalized data plotted in Fig. 17. An average activation energy derived from these data is 14 kcal/mole.

Discussion

All of the results with the phosphoric acid electrolyte show marked similarities to those obtained with the perchloric acid. This includes the single oxidation wave for adsorbed methane, the multiple waves for ethane and propane, the similar effects of increasing the temperature, and the similar relationships between the polarization curves and the charges required for oxidation of the adlayers, *i.e.*, Q_{E1} and $Q_{E\text{tot}}$. These parallels indicate the absence of gross qualitative effects of the ionic double layer on the adsorption and surface behaviors of hydrocarbons on platinum electrodes. However, more subtle effects result in detectable quantitative differences between the two electrolytes. For example, the maximum current observed with ethane at 60°C with a perchloric acid electrolyte was 2.5 μa/cm² of real area and with the phosphoric acid 0.8 μa/cm². This undoubtedly reflects, in part, a stronger anion adsorption from the phosphoric acid electrolyte.

The new and more extensive data that have been obtained with propane and butane also support the earlier suggestion that similar surface reactions and surface intermediates are involved with all of the

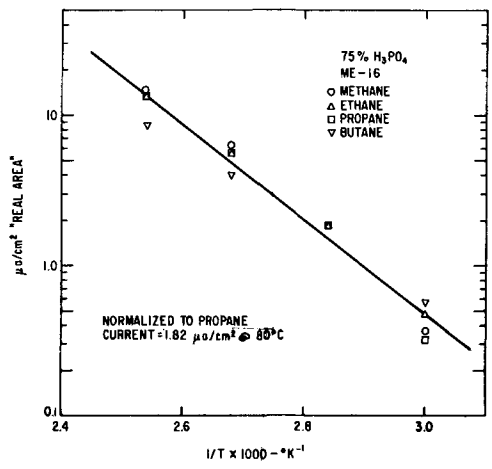

Fig. 17. Arrhenius plots for normalized maximum currents from several hydrocarbons.

saturated hydrocarbons above methane. Thus it appears that following the initial adsorption step two important reaction paths are available (1-4). The desirable path involves cracking to form a partially oxygenated intermediate which is oxidized further to CO_2 at relatively low overvoltages. The second path results in the accumulation of relatively refractory multiple carbon species on the surface. With the higher hydrocarbons it is likely that a variety of such species of different chain length form on the surface since it has been observed that propane produces C_2 species even at 25°C (9).

Increases in the values of Q_{E1} and $Q_{E\text{tot}}$ are also in strong evidence as the molecular weight of the fuel increases; *e.g.*, compare the areas between the blanks and the hydrocarbon traces in Fig. 3-6 as well as the surface charge curves in Fig. 13-16. The increase at 0.5-0.6v in going from methane to butane is of particular interest since it undoubtedly plays an important role in determining the magnitude of the maximum adsorption rate and hence the maximum current that can be drawn from an electrode, although other factors such as anion adsorption, surface oxidation, and bonding of water to the surface can also exert an influence. The accumulation of these refractory species, which can be removed at still higher potentials, is also suspect as an important cause of the current and voltage oscillations frequently encountered with hydrocarbon fuel cells (10, 11). One would expect in view of the trends in surface coverage so far observed that still higher molecular weight hydrocarbons would be more prone toward such oscillations. This has indeed been observed with operating fuel cells (12).

Because of the partial oxidation and cracking reactions, it is not possible to relate Q_{E1} and $Q_{E\text{tot}}$ directly to surface coverage. It is evident, however, from the data in Fig. 11 that the oxidizable species accumulate more rapidly as the molecular weight is increased, with the greatest increment occurring between methane and ethane. A similar trend is evident for the plateau representing steady-state coverage. In part this appears to relate to an increasing proportion of the species of wave 2 as the molecular weight increases. These relatively refractory species are believed to be partially dehydrogenated, but nonoxygenated.

The rate laws in all cases appear to be similar to the extent that a region in which $Q_{E\text{tot}}$ varies with the logarithm of the time precedes the eventual region of equilibrium coverage. The parabolic relationship for methane at low surface coverages (short equilibration times) suggests that mass transport effects may be important under these conditions. Lower solubility of methane in phosphoric acid than perchloric acid may account for the deviation from the initial linear

rate law that had previously been observed with the latter electrolyte. It is possible that similar deviations occur for the higher hydrocarbons at short equilibration times.

In the absence of adsorption rates on the "clean" surface it is not possible to compare these rates directly with the maximum current obtainable on the polarization curve as was done previously. From the data at longer equilibration times, however, it would appear that the initial adsorption rates of the four gases on the clean surfaces are in the order butane > propane > ethane >> methane. With the exception of methane this is the reverse order of the maximum currents as seen by the data of Fig. 13-16. Clearly then the adsorption of butane and propane is more hindered at the maximum than is methane or ethane.

Summary and Conclusions

The behavior of the model saturated hydrocarbons, methane through butane, on platinum-catalyzed electrodes is similar with perchloric acid and phosphoric acid electrolytes. With both electrolytes the adlayer on the electrode contains C_1 species some of which are undoubtedly oxygenated. The adlayers from the higher hydrocarbons also contain relatively refractory multiple carbon species, the coverage with such species increasing with the molecular weight of the fuel. These similarities and trends imply that a corresponding behavior will be followed by all saturated hydrocarbons.

In all cases the anodic performance is strongly influenced by the rate of adsorption and the ability of the catalyst to promote "cracking" of C-C bonds as well as the reaction of C_1 radicals with water. Accumulation of the refractory multiple-carbon species on the surface in turn influences the adsorption rate and results in maximum currents that can be markedly lower than those anticipated on the basis of adsorption rates on clean surfaces. It is also likely that these accumulated species play an important role in connection with the current and voltage oscillations that are frequently encountered with hydrocarbon fuel cells.

Acknowledgments

The authors are indebted to S. Gilman for many helpful discussions. This work is a part of the program under contracts DA-44-009-AMC-479(T) and DA-44-009-ENG-4909, ARPA Order No. 247 with the U.S. Army Engineer Research and Development Laboratories, Ft. Belvoir, Virginia, to develop a technology which will facilitate the design and fabrication of practical military fuel cell power plants for operation on ambient air and hydrocarbon fuels.

Manuscript received March 1, 1966; revised manuscript received Sept. 10, 1966.

Any discussion of this paper will appear in a Discussion Section to be published in the December 1967 JOURNAL.

REFERENCES

1. S. Gilman, *Trans. Faraday Soc.*, **61**, 2546, 2561 (1965).
2. S. Gilman, in "Hydrocarbon Fuel Cell Technology," B. S. Baker, Editor, p. 349, Academic Press, New York (1965).
3. L. W. Niedrach, S. Gilman, and I. Weinstock, *This Journal*, **112**, 1161 (1965).
4. L. W. Niedrach, *ibid.*, **113**, 645 (1966).
5. L. W. Niedrach and H. R. Alford, *ibid.*, **112**, 117 (1965).
6. S. Gilman, *J. Phys. Chem.*, **67**, 78 (1963).
7. S. B. Brummer, J. I. Ford, and M. J. Turner, *ibid.*, **69**, 3424 (1965).
8. F. G. Will and C. A. Knorr, *Z. Elektrochem.*, **64**, 258 (1960).
9. L. W. Niedrach, *This Journal*, **111**, 1309 (1964).
10. M. J. Schlatter, in "Fuel Cell Systems," R. F. Gould, Editor, p. 292, Advances in Chemistry Series 47, American Chemical Society, Washington, 1965.
11. H. Binder *et al.*, *This Journal*, **112**, 355 (1965).
12. P. J. Chludzinski *et al.*, Unpublished results.

The Kinetics of Oxidation of Plutonium Metal and a Plutonium-3.4 a/o Aluminum Alloy at Temperatures from 140° to 550°C

J. G. Schnizlein and D. F. Fischer

Argonne National Laboratory, Argonne, Illinois

ABSTRACT

The kinetics of oxidation of reactor grade plutonium and ultrapure plutonium were studied in oxygen and air at temperatures from 140° through 550°C. Paralinear rate laws apply over the entire range with a change of mechanism between 300° and 400°C. In the low-temperature range (140°-300°C) the process is postulated to be controlled by a compact layer of Pu_2O_3. Simultaneous growth of this layer and linear oxidation to PuO_2 results in paralinear kinetics whose rate constants are

$$k_{\text{parabolic}} = 1.6 \times 10^{15} \left[\exp\left(-27{,}400/RT\right)\right] (\mu g/cm^2)^2/\text{min}$$
$$k_{\text{linear}} = 1.6 \times 10^{8} \left[\exp\left(-16{,}800/RT\right)\right] (\mu g/cm^2)/\text{min}$$

Above 400°C the oxide produced is more protective and is postulated to include a layer of $PuO_{1.6}$ consistent with phase diagram studies. Paralinear kinetics are followed with simultaneous rate constants

$$k_{\text{parabolic}} = 1.8 \times 10^{12} \left[\exp\left(-22{,}500/RT\right)\right] (\mu g/cm^2)^2/\text{min}$$
$$k_{\text{linear}} = 8.8 \times 10^{9} \left[\exp\left(-26{,}400/RT\right)\right] (\mu g/cm^2)/\text{min}$$

The presence of moisture has no effect above 215°C, but causes a marked increase in the oxidation at lower temperatures. As little as 180 ppm moisture caused the linear rate at 190°C to accelerate an order of magnitude.

The presence of 3.4 a/o aluminum in plutonium markedly reduced the oxidation rates at temperatures below 400°C but only slightly reduced oxidation rates at higher temperatures.

The literature on the oxidation of plutonium is understandably limited because of the extreme toxicity and comparatively recent production of plutonium metal (1). Early studies at Los Alamos (2) and in Great Britain (3), conducted in air at temperatures below 100°C, demonstrated a marked increase of oxidation in the presence of moisture. Waber (4, 5) and Sackman (6) have reported that in humid air oxidation rates of plutonium follow logarithmic, parabolic, linear, and accelerating rate laws for extended periods of time. Sackman (7) showed that the oxidation rate at 25°C in moist argon (95% relative humidity, RH) is between 4 and 25 times that in moist air. He concluded, in agreement with Waber, that air oxidation produces a protective film and inhibits the faster reaction with moisture. The observation by Thompson (8) that oxidation is faster at 175°C in 360 mm oxygen with 35-40 ppm moisture than in 760 mm oxygen with 35 ppm moisture is consistent with the competitive reaction. In air at 255°C, with 38 ppm moisture, however, oxidation did not appear to accelerate and the higher pressure (760 mm) resulted in a slightly higher rate than was the case at 360 mm as might be expected for a slight pressure dependence. At the higher temperature no effect of small amounts of moisture was observed.

In dry air at low temperatures, parabolic behavior was usually observed. Sackman (6) observed that oxidation in dry air at 100°C would be represented by a succession of parabolic-shaped curves. The first parabolic rate continued nine days during which period the weight gain was 2.4 mg/cm². This would correspond to a film of plutonium oxide less than 20μ thick. It was thought that the rate of oxidation is limited by diffusion of oxygen ions through a thin film of PuO or Pu_2O_3. The oxide observed after completion of the experiment was PuO_2.

In studies of the oxidation of plutonium at higher temperatures, Waber (5) observed accelerating oxidation in oxygen at 345° and 400°C; Dempsey and Kay (9), using air as the oxidant, observed two-stage linear oxidation at 303°C, parabolic at 416°C, and initially parabolic at 487°C (accelerating to ignition after 300 min). The protective nature of the oxide film at 416°C, when the metal has a delta phase structure, resulted in a lower oxidation rate than at lower temperatures. Notley *et al.* (10) later demonstrated that the oxidation rate passes through a minimum in the vicinity of 416°C. Since the relative amount of adherent oxide to porous oxide increased when the temperature was increased from 400° to 450°C, they proposed that the minimum oxidation rate could be a net result of the increased thickness of adherent oxide and the simultaneous increase of the rate of oxygen diffusion with increased temperature. X-ray diffraction studies showed the readily removable oxide to be PuO_2 and the adherent interfacial oxide to include both cubic and hexagonal Pu_2O_3. Properties and phase relationships of the oxides in the plutonium-oxygen system were reported by Holley *et al.* (11), Chikalla *et al.* (12), and recently by Gardner, Markin, and Street (13). Markin and Rand (14) very recently revised the temperature scale.

The addition of aluminum to plutonium is known to extend the range of stability of the delta phase. The phase diagrams determined by investigators from the Soviet Union (15) and from Los Alamos (16) indicate 3.4 a/o (atom per cent) aluminum stabilized the delta phase from about 290° to 520°C. Without aluminum present the delta phase is stable from 320° to 450°C. Ignition temperatures of the 3.4 a/o aluminum alloy are also higher than for pure plutonium (17). Waber (18) and Sackman (6) have shown that addition of aluminum confers considerable oxidation resistance to plutonium in moist air at temperatures below 100°C.

The present investigation of the oxidation of plutonium at temperatures from 140° to 550°C covers a wider temperature range than any previous study. The objectives have been to provide data on the kinetics of oxidation and information about the rate-controlling mechanisms to aid in understanding the

Table I. Impurities in plutonium materials

	Plutonium from alloy program, Hanford,[a] ppm	Electrolytic high-purity plutonium from Metallurgy Div., ANL,[b] ppm
Mg	180	—
Fe	198	30
Ca	100	—
Cu	50	—
Pb	50	—
Ni	23	18
Mn	20	1
Ag	10	—
Al	—	5
Cr	5	18
Sn	3	—
Si	2	16
Am	—	38
U	—	22
C	260	19
O_2	110	5
N_2	105	13
H_2	3	1.3
Total	1119	186

[a] Metallic element concentrations were obtained by three separate spectrographic analyses (average value tabulated), carbon by combustion, and hydrogen, oxygen, and nitrogen by gas analysis. The analyses were performed by Hanford Atomic Products Operation.
[b] Metallic element concentrations (except Si, Am, and U) obtained by spectrographic analyses. Those less than the limit of detection are indicated by dashes. Si, Am, U, C, O_2, N_2, and H_2 were determined by chemical methods.

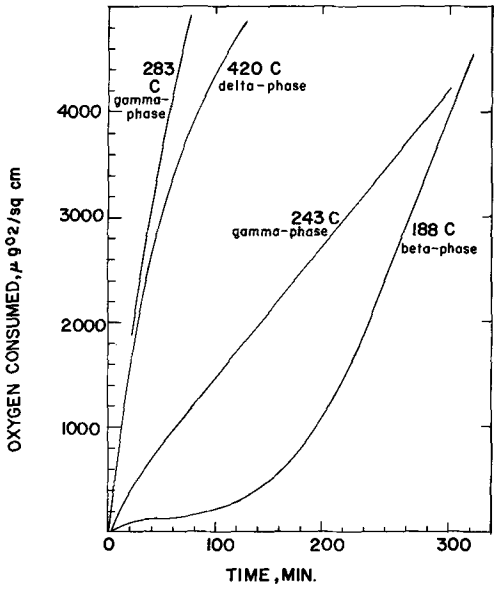

Fig. 1. Selected plutonium oxidation experiments

ignition behavior. The study of preoxidation at high temperature was made to provide insight on the importance of the oxide produced and the understanding of the mechanism of oxidation. The relative effects of the presence of moisture on the oxidation at various temperatures have been evaluated. Isothermal oxidation of a plutonium-3.4 a/o aluminum alloy was studied to aid in understanding the effect of aluminum on the ignition behavior and to evaluate the possible effect of a stabilized delta phase.

Material and Procedure

Plutonium samples of high-purity, reactor grade were obtained from Hanford[1] in the form of 5 and 10 mm cubes. Concentrations of metallic impurities totaled less than 700 ppm. A few samples of ultrapure plutonium were obtained from Metallurgy Division, ANL.[2] The plutonium for these samples was produced by electrolysis of a fused salt mixture and was purer by an order of magnitude than the Hanford material. The electrolytic plutonium was 99.84 a/o pure. Analytical data on impurities in the two supplies of plutonium are presented in Table I. Prior to oxidation the cubes were polished through 600 grit silicon carbide metallographic paper.

Oxygen and air from cylinders were used for most of these studies without further purification. To avoid the use of contaminated gas, each gas cylinder was sampled and analyzed by mass spectrography prior to use. Typical analysis expressed in volume per cent was as follows: oxygen 99.7 O_2, 0.3 N_2, 0.01 Ar, 0.03 H_2O; air 20.7 O_2, 78.5 N_2, 0.92 Ar, 0.1 H_2O.

Because of the extreme toxicity of plutonium, all operations were performed in a glove box. The box atmosphere was dry nitrogen to avoid accidental oxidation during sample preparation and handling. The course of oxidation was followed by the increase in weight of a sample. A recording balance which automatically adds weights (Ainsworth model 1 AU) was equipped with a temperature transducer (19) to permit continuous measurement of the sample temperature without interfering with the operation of the balance.

At about 480°C problems were encountered with self-heating due to the high oxidation rates and minimal heat loss from the sample. Dempsey (7) observed ignition after 300 min in a furnace at 478°C. This self-heating was markedly minimized by clamping two stainless steel plates onto the plutonium sample. These stainless plates served as heat sinks so that during oxidation a sample initially at 541°C was maintained at 557°C after 0.6 min. Control experiments at 350° and 460°C showed no detectible effect of the plates on the oxidation data.

Experimental Results

Reactor grade plutonium.—Oxidation experiments were performed at temperatures from 140° through 550°C in oxygen or air. In general, the observation of somewhat different behavior in the temperature ranges of each of the different phases (see Fig. 1) is consistent with that reported by Dempsey and Kay (7). In the range of the beta phase (120°-220°C), a three-stage oxidation was observed. The third stage showed a linear rate of 20 (μg O_2/cm^2)/min which did not appear to be temperature dependent. This third stage was shown to be caused by very small moisture content in the oxidizing gas (see below). In the range of the gamma phase (220°-320°C), after an initial deviation, an apparently linear rate was observed, ranging from 80 to 200 (μg/cm^2)/min. In the range of the delta phase (320°-450°C) a minimum in the oxidation rate was observed, indicating a change in the mechanism. Above 400°C the oxide becomes more protective so that the extent of oxidation after 15 min is less at 420° than at 283°C. Through the range of the delta prime phase (450°-480°C) and into the epsilon phase (480°-640°C) to the maximum temperature studied at 558°C, the oxidation is initially parabolic followed by a linear rate. The linear rate was 1200 (μg/cm^2)/min at 558°C.

By careful examination of the initial portion of each oxidation run, it was possible to show an initial fit to the parabolic rate law. Figure 2 illustrates the initial parabolic rate law agreement for the same selected experimental data presented in Fig. 1. The value of the parabolic rate constant in (μg O_2/cm^2)^2/min is included with each temperature.

An Arrhenius plot of the parabolic rate constants is presented in Fig. 3. It is apparent that the same initial rate control process is in effect over the temperature range from 140° to 300°C. Application of the method of least squares to all the data in this temperature range provided an apparent activation energy of 29.2 ± 1.4 kcal/mole, and the pre-exponential of 5.5 x 10^{16} (μg O_2/cm^2)^2/min. Above 400°C a somewhat dif-

[1] Prepared under the supervision of O. J. Wick, R. W. Steward, T. Nelson, P. G. Pallmer, and R. R. King of Hanford Atomic Products Operation, General Electric Company, Richland, Washington.

[2] Through the courtesy of G. B. O'Keefe, Metallurgy Division, Argonne National Laboratory.

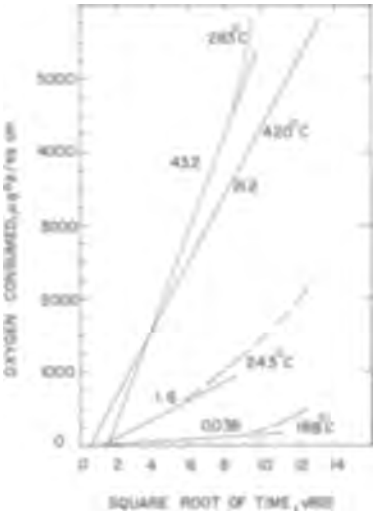

Fig. 2. Parabolic plots for selected plutonium oxidation experiments. Temperature and rate constant $\times 10^{-4}$ indicated on each line $(\mu g/cm^2)^2/min$.

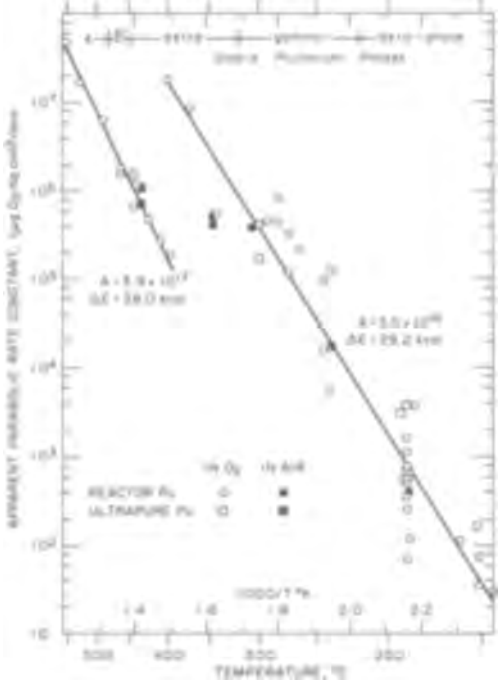

Fig. 3. Initial parabolic oxidation rate data

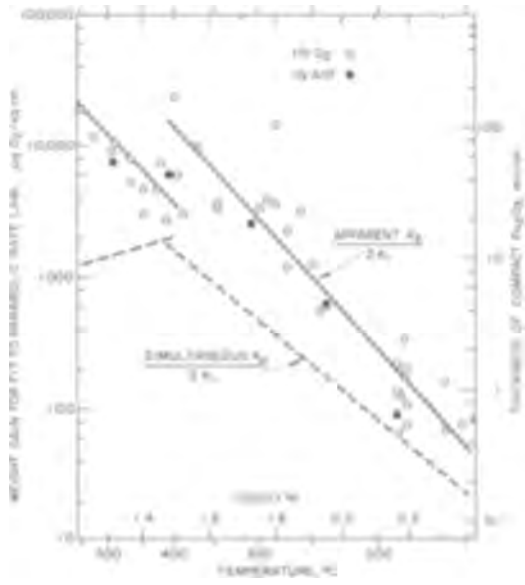

Fig. 4. Compact film thickness based on weight gain at deviation from parabolic rate law and ratio of parabolic-to-linear rate constants.

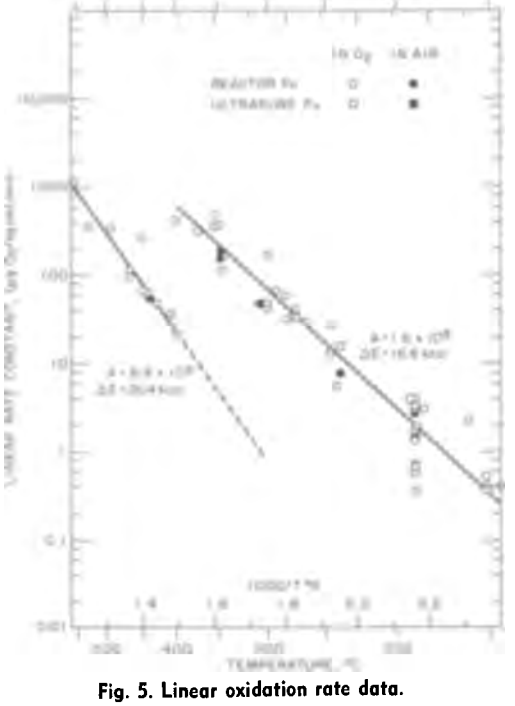

Fig. 5. Linear oxidation rate data.

ferent rate limiting process is indicated by an apparent activation energy of 38.0 ± 2.5 kcal/mole and a preexponential of 3.9 x 10^{17} $(\mu g\ O_2/cm^2)^2/min$. These activation energies are reasonable values for solid-state diffusion of oxygen ions through a thickening oxide film.

Subsequent to the parabolic portion, the adherent layer of compact oxide should remain essentially constant in thickness. Figure 4 illustrates the extent of oxidation at which the oxidation deviates from the fit to a parabolic rate law at various temperatures. Calculated on the basis of densities of plutonium oxides and the extent of oxygen consumed, the thickness varies from approximately 0.5μ at 150°C to 50μ at 350°C. Above 400°C the compact film is more protective, and the apparent thickness increases from about 20μ at 400°C to about 100μ at 550°C.

The linear rate constants for the oxidation subsequent to the parabolic portion are presented in an Arrhenius plot in Fig. 5. The activation energy for the linear process from 140° to 400°C was calculated by least squares method to be 16.8 ± 0.7 kcal/mole. The pre-exponential was 1.6 x 10^8 $(\mu g\ O_2/cm^2)/min$. Above 400°C the more protective underlying film causes the linear process to have an apparent activation energy of 26.4 ± 1.8 kcal/mole and a pre-exponential of 8.8 x 10^9 $(\mu g\ O_2/cm^2)min$.

Electrolytic ultrapure plutonium.—Isothermal oxidations were performed at 151°, 190°, 192°, 240°, 300°, and 438°C with the limited number of samples of ultrapure plutonium which had been prepared by electrolysis from fused salts. The results showed the same characteristic behavior as was observed with reactor grade plutonium obtained from Hanford. All rate constants obtained with the ultrapure plutonium were within the limits of deviations of the other data.

Effect of preoxidation at high temperature.—Two experiments were performed to test whether or not the oxide formed during the high-temperature process (above 400°C) would remain more protective when oxidation was continued at a lower temperature

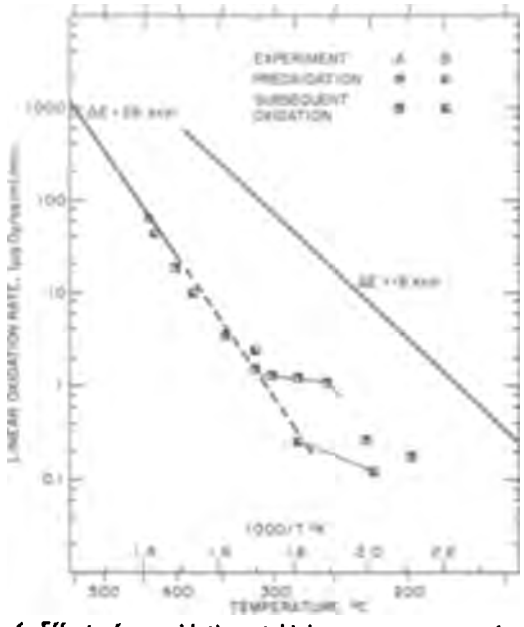

Fig. 6. Effect of preoxidation at high temperature on subsequent oxidation at lower temperature.

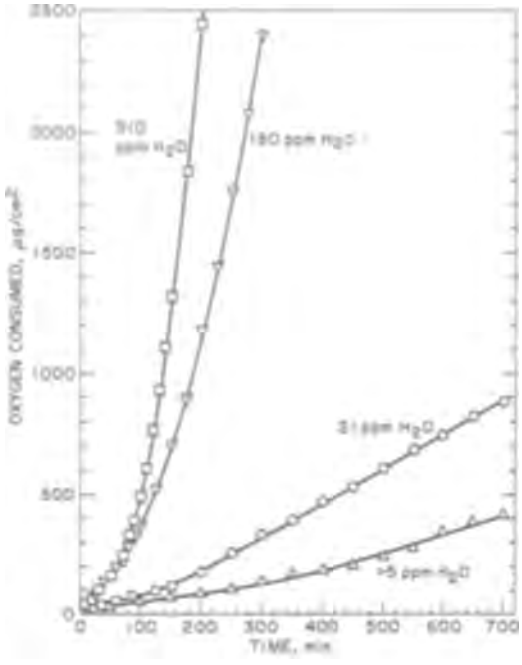

Fig. 7. Effect of moisture on oxidation of plutonium at 190°C in oxygen.

than that normally produced at lower temperatures. Ultrapure plutonium samples were oxidized at 430° and 440°C until 6500 and 11,000 μg O_2/cm^2, respectively, were consumed. The oxidations were proceeding at linear rates of 43 and 63 ($\mu g/cm^2$)/min, respectively. Then, without removal of the oxygen, the temperature was decreased and controlled at a new lower temperature. After a new linear rate was determined, the temperature was reduced again. The linear rate observed at each temperature was markedly lower than the rate expected from the data for low-temperature oxidation. However, when the sample was cooled to room temperature overnight and then reheated, a higher rate was again observed indicating that the reduced oxidation rate below 250°C caused by preoxidation is only temporary.

These data are compared with the previously determined data on the Arrhenius plot in Fig. 6. It is evident from the agreement to an extrapolation (dotted line) of the high-temperature data that the oxide produced at the higher temperature was stable to 318°C in the first experiment and 280°C in the second experiment.

Effect of moisture.—Most of the oxidation experiments were performed in oxygen or air containing a few hundred parts per million moisture. At temperatures below 210°C the oxidation rate would accelerate after a period of time under these conditions. The final rate ranged from 12 to 25 (μg O_2/cm^2)/min at temperatures near 140°C and from 16 to 30 (μg O_2/cm^2)/min near 190°C. This third stage was essentially independent of temperature while the initial parabolic rates and intermediate linear rates varied with temperature consistent with the activation energies deduced from experiments between 215° and 320°C.

The moisture content of the oxidizing gas could be maintained at low values only by exercising extreme care. It was also necessary to eliminate cellulose-type filters used to avoid escape of plutonium from the glove box. Experiments performed with less than five parts per million moisture in the oxygen at 300° and 440°C were, within normal limits, the same as those performed with moisture contents of a few hundred parts per million. Two experiments with 20,000 ppm moisture in air were also performed at 430°C with no evident effect on the oxidation.

In contrast, at 190° and 150°C the third stage was eliminated by the use of extremely dry oxygen (< 5 ppm moisture). The high oxidation rate, 20 ($\mu g/cm^2$)/min, previously called a third stage in the oxidation between 100° and 200°C, is thus attributable to moisture. It is noteworthy that this high rate can be produced by a moisture content as low as 180 ppm and is a similar value to that observed by Dempsey (9) with 10,000 ppm (55% relative humidity) in air at 205°C. In our work, as little as 20 ppm moisture in the oxygen caused some acceleration in the oxidation curve. Figure 7 illustrates the oxidation behavior of plutonium in oxygen at 190°C with four levels of moisture content, 510, 180, 21, and < 5 ppm.

Another experiment illustrated the behavior when the moisture content was changed during the course of an oxidation at 190°C. When the moisture content was increased from 21 to 180 ppm the oxidation rate increased quickly from 1.2 to 1.5 ($\mu g/cm^2$)/min, then further increased to 3.4 with 510 ppm moisture content, and then decreased to 0.71 with 21 ppm moisture content.

Interestingly, extrapolation of the linear rate data obtained above 215°C with or without moisture and the linear data between 200° and 140° under dry conditions agrees within a factor of 2 with the data obtained under dry conditions below 100°C by Kolodney (2), Waber (4), and Sackman (6). They found increases due to moisture to be factors of 100 to 1000.

Effect of aluminum addition to plutonium.—Isothermal oxidation of 5-mm cubes of plutonium-3.4 a/o aluminum alloy have been performed at temperatures from 150° through 588°C on the thermobalance. The results obtained in a few runs in air were not different from those obtained in oxygen. In general, a paralinear behavior was observed which was similar to that of unalloyed plutonium, but at all temperatures the rates for the alloy were lower. Oxidation data for plutonium-3.4 a/o aluminum are compared with data for unalloyed plutonium at a few selected temperatures in Fig. 8. The data for the initial portion of the reaction can be treated as an apparent parabolic or as simultaneous parabolic and linear process as will be explained in the discussion below. The apparent parabolic, simultaneous parabolic, and subsequent linear rate constants obtained are presented in Table II. The parabolic rate constants for the plutonium-3.4 a/o aluminum alloy are compared with those for unalloyed plutonium in Fig. 9, while the linear constants for the alloyed and unalloyed metal are compared in Figure 10.

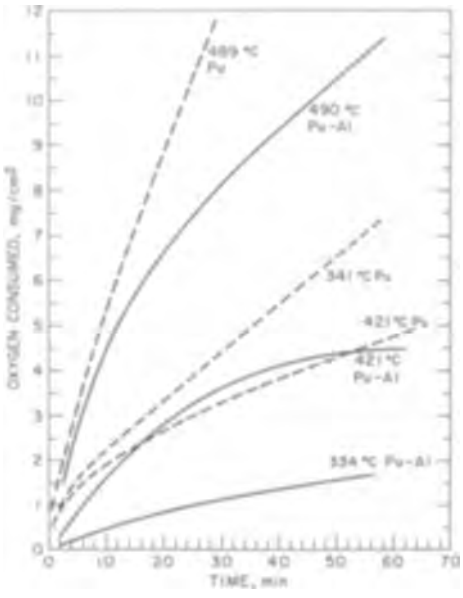

Fig. 8. Oxidation data for plutonium and plutonium-3.4 a/o aluminum alloy in oxygen.

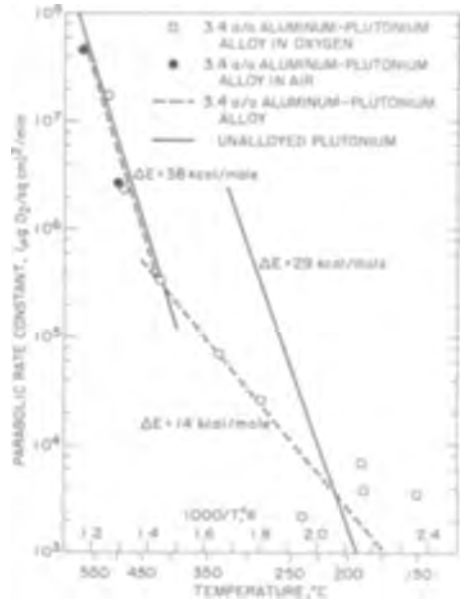

Fig. 9. Parabolic oxidation data for plutonium and plutonium-3.4 a/o aluminum alloy.

In the high-temperature region (above 420°C), the parabolic rate constants for the alloy are very similar to those for unalloyed plutonium. The linear rate constants are about a factor of two lower, but indicate the same activation energy. This is consistent with the observed ignition temperatures which are approximately 70° higher than those for unalloyed plutonium in the high-temperature regime (17).

At lower temperatures (below 420°C), both parabolic and linear rates are very much lower and indicate different activation energies than for unalloyed plutonium. The activation energy for the parabolic process is about 14 kcal/mole and for the linear process about 13 kcal/mole.

Discussion

Previous literature on the oxidation of plutonium has tended to attach considerable importance to the stable phases of the metal. This study indicates consistent activation energies over the temperature ranges of several metal phases. The same process appears to occur through the temperature ranges of the beta and gamma phase and may be extrapolated to include the range of the alpha phase. Another applies over the range of delta, delta prime, and epsilon phases. Thus, it is more appropriate to consider the control process to be attributed to the oxide. The principal features in the kinetics of oxidation reached are the observed

Table II. Oxidation data for plutonium-3.4 a/o aluminum alloy ($\mu g\ O_2/cm^2)^n$/min

Temp, °C	Parabolic rate constant ($\times 10^{-4}$) ($n = 2$)	Simultaneous parabolic rate constant ($\times 10^{-4}$) ($n = 2$)	Subsequent linear rate constant ($n = 1$)
150	0.35[a]	0.38[a]	0.01[a]
188	0.38[a]	0.19[a]	0.01[a]
190	0.69	0.064	1.45
238	0.22	—	0.68
283	2.65	1.62	2.25
334	7.08	3.86	8.2
421	33.5	55.8	22.8
490[b]	237.0	127.0	98.5
500[b, c]	265.0	114.0	146.0
539[b]	1,764.0	475.0	333.0
588[b, c]	4,726.0	—	1,555.0

[a] The limit of sensitivity of the balance introduces large uncertainty because total weight gain was less than 1 mg.
[b] Runs performed with a heat sink.
[c] Runs performed in air. All other runs were performed in oxygen.

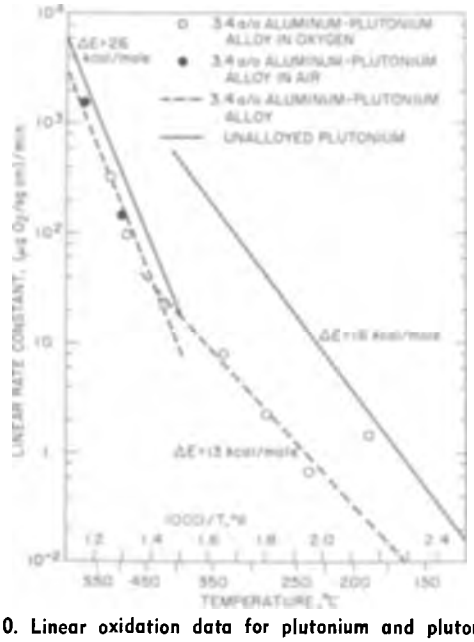

Fig. 10. Linear oxidation data for plutonium and plutonium-3.4 a/o aluminum alloy.

paralinear process and the change of mechanism between 300° and 400°C. Only speculations about the observed effects of moisture and aluminum are possible at this time.

Paralinear kinetics.—Paralinear kinetics have been observed for the oxidation of numerous metals (20). The mechanism to explain this behavior is usually initial growth of a compact adherent oxide film to a limited thickness. The growth process results in a parabolic rate law. When the outer portion becomes porous or is further oxidized to a higher oxide which affords less protection, in a manner that leaves a constant thickness of compact oxide, a linear rate law results. The parabolic rate constants presented in the previous section (Fig. 3) were determined from the original data and would apply to the case of a compact oxide undergoing a change, at some time after a finite thickness was formed, as a consecutive process.

Alternatively, if both compact and porous oxide are formed initially the two processes can be considered to be simultaneous. Simultaneous processes

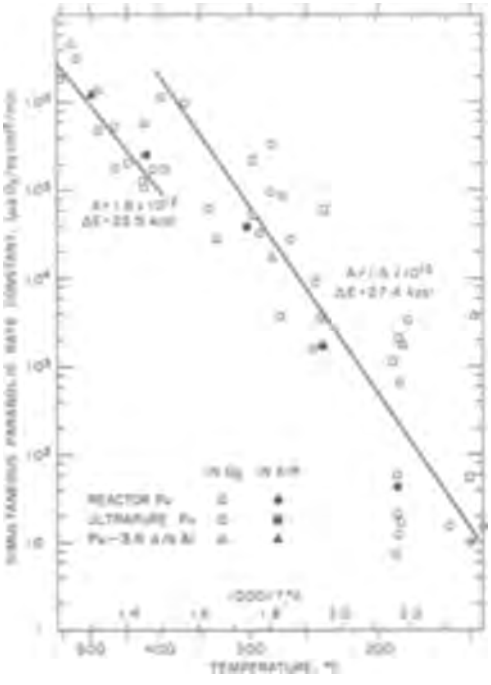

Fig. 11. Simultaneous parabolic rate data

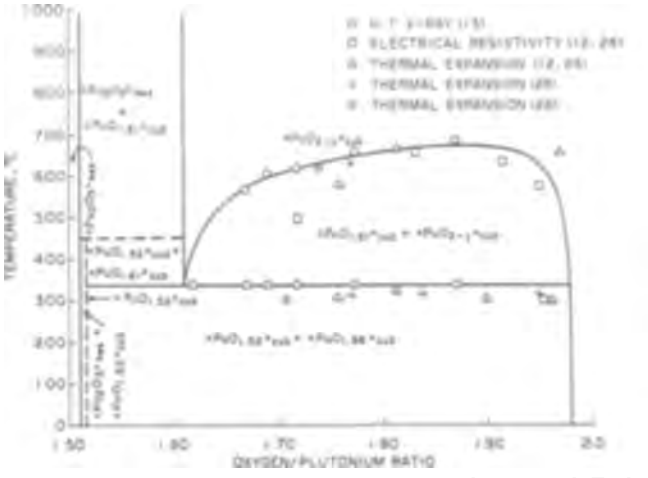

Fig. 12. Plutonium-oxygen phase diagram. Courtesy of T. L. Markin (14).

have been discussed by Haycock (21), Jepson and Aylmore (22), and Wajszel (23). The linear process is assumed constant from the beginning of the oxidation and is predominant after a long time of reaction.

The ease of oxidation of lower oxides to PuO_2 makes it more probable that the reactions occur simultaneously rather than consecutively. Parabolic rate constants for simultaneous reaction were redetermined for each experiment by subtracting the portion of oxygen consumption attributable to the linear process near the end of the experiment. An Arrhenius plot of these parabolic rate constants for a simultaneous process in Fig. 11 indicate an activation energy of 27.4 ± 3.3 kcal/mole and pre-exponential of 1.6 x 10^{15} (μg $O_2/cm^2)^2$/min for the low-temperature region and an activation energy of 22.5 ± 3.9 kcal/mole and pre-exponential of 1.8 x 10^{12} (μg $O_2/cm^2)^2$/min for the high temperatures. The activation energies for initial parabolic oxidation process, whether consecutive or simultaneous with the linear process, are reasonable values for solid-state diffusion of oxygen ions through a compact oxide. No data on oxygen diffusion in plutonium oxides have been found in published literature.

Mechanism change between 300° and 400°C.—The change in kinetics between 300° and 400°C results in a minimum in the over-all oxidation rates at about 400°C. It has been tempting to attribute this behavior to a property of the delta phase metal since early studies (5) had shown ". . . alloying elements that stabilize the delta phase confer substantial corrosion resistance . . .". However, it is more appropriate to attribute the kinetic change to the oxide film. Notley (10) postulated the minimum rate to be the net result of increased film thickness and increase of oxygen diffusion at higher temperature. If the compact film is to become thicker, the extent of oxidation attributable to the parabolic rate law should become greater at 400°C. Consideration of the extent of oxidation for parabolic rate law fit presented in Fig. 4 does not indicate an increase of film thickness between 300° and 400°C.

Haycock (21) deduced the following relationship between compact film thickness and rate constants.

$$\frac{d\mu}{dt} = \frac{k_p}{2\mu} - \frac{bk_l}{a}$$

where μ is the compact film thickness, t is time, k_p is the parabolic rate constant, k_l is the linear rate constant, and b and a are the conversion factors for thickness of porous and compact films, respectively.

As μ approaches a thickness given by $k_p/2\mu = bk_l/a$ then $d\mu/dt$ approaches zero. The inner layer, therefore, approaches a constant thickness $\mu = (a/b)\ k_p/2k_l$. Considered as a consecutive process, the thickness of stable compact film (data points) agree well with this relationship between rate constants and film thickness $\mu = k_p/2k_l$,[3] which is represented by the solid line in Fig. 4. If the linear and parabolic processes are considered to occur simultaneously and the ratio of the new reduced parabolic rate law constant to $2k_l$ is calculated, the dashed line in Fig. 4 is obtained. This relationship indicates thinner compact films at all temperatures and nearly constant film thickness above 400°C. This leads to the conclusions that a change of the compact oxide film occurs between 300° and 400°C and that the diffusion of oxygen through that oxide is reduced.

Chikalla (12) and McNeilly (24) have pointed out discontinuities in thermal expansion and electrical resistivity measurements of plutonium oxides with an oxygen-to-plutonium ratio between 1.64 and 1.98 at approximately 300°C. The plutonium-oxygen phase diagram given by Chikalla and associates (12), Gardner (13), and most recently by Markin and Rand (14) indicates a phase change in the oxide above 300°C. The plutonium-oxygen phase diagram according to Markin and Rand (14) has been reproduced for convenience in Fig. 12. The modification by Gardner (13) in the region of oxygen-to-plutonium ratios between 1.5 and 1.61 makes it reasonable to attribute the decreased oxidation rate above 400°C to the formation of the cubic phase $PuO_{1.61}$ in addition to the partially protective layer of Pu_2O_3. The pre-oxidation experiments demonstrate that when formed at higher temperature the new oxide is stable down to about 300°C. The rapid transformations and inability by Gardner (13) to quench the single phase material to room temperature explains the observation by Notley (10) of hexagonal and cubic Pu_2O_3 in the compact oxide from most experiments.

Effect of moisture.—The presence of moisture during the oxidation of plutonium does not influence the rate at temperatures above 215°C, but even very small amounts cause marked acceleration at temperatures below 200°C. The observation of an even higher

[3] The correction a/b is considered negligibly close to unity since the relationships of weight gain to film thickness for various oxides are very similar. 1 mg O_2/cm^2 is equivalent to 7.2μ hexagonal Pu_2O_3, 8.0μ cubic Pu_2O_3, and 7.4μ PuO_2 thickness.

rate in moist helium than in moist air leads to the conclusion that the presence of moisture causes partial breakdown of the protective layer of oxide formed in oxygen. The near absence of temperature dependence of the high oxidation rate of ~20 (μg O_2/cm^2)/min observed in oxygen or air containing a few hundred parts per million moisture may be the result of a balance between the formation of a protective layer by oxygen reaction and its destruction by reaction with moisture. This may occur by formation of a hydrated oxide or plutonium hydroxide. Sackman (6) reported that weight gains of plutonium on complete oxidation in moist air were greater than calculated for PuO_2 and correspond to $PuO_2 \cdot 0.1\ H_2O$. No information on the stabilities of hydrated oxide or hydroxide under these conditions appear available at this time.

Effect of addition of 3.4 a/o aluminum.—Addition of 3.4 a/o aluminum to plutonium improves the oxidation resistance at all temperatures. The high-temperature process is very similar to that of pure plutonium. Further speculations about the decreased oxidation are heuristic without knowledge of the effects of aluminum oxide on the phase diagram of plutonium oxides. The increase in the simultaneous parabolic rate constants without apparent change of activation energy in the high-temperature region might indicate an increase of oxygen ion diffusion through $PuO_{1.61}$. The linear rate may be lower because of a slightly thicker compact film. In the low-temperature region the presence of aluminum seems to cause a completely different oxidation process than for pure plutonium. In addition, the change of activation energy of the process at about 420°C does not indicate that the decreased oxidation should be attributed to delta phase stabilization. Further study of the effect of varied aluminum content should be informative.

Conclusion

The oxidation of plutonium between 140° and 550°C in air or oxygen follows paralinear kinetics with a change of mechanism between 300° and 400°C. Below 300°C the initial protective oxide is probably hexagonal Pu_2O_3. If this film has a limited thickness of stability and the linear process is a result of subsequent formation of porous oxide on the outside, the apparent parabolic rate constant is defined.

$$k_p = 5.5 \times 10^{16} [\exp(-29{,}200/RT)]\ (\mu g\ O_2/cm^2)^2/min$$

If the linear process occurs simultaneously from the beginning the parabolic rate constant is

$$k_p' = 1.6 \times 10^{15} [\exp(-27{,}400/RT)]\ (\mu g\ O_2/cm^2)^2/min$$

The linear rate constant between 140° and 300°C is

$$k = 1.6 \times 10^{8} [\exp(-16{,}800/RT)]\ (\mu g\ O_2/cm^2)/min$$

Above 400°C additional protectiveness of the oxide is observed which is attributed to the formation of cubic $PuO_{1.61}$ in addition to the hexagonal Pu_2O_3. This is consistent with the most recent phase diagram of the plutonium-oxygen system (14). If the paralinear kinetics is considered to be a consecutive process, the apparent parabolic rate constant is defined

$$k_p = 3.9 \times 10^{17} [\exp(-38{,}000/RT)]\ (\mu g\ O_2/cm^2)^2/min$$

If the linear process occurs simultaneously from the beginning, the parabolic rate constant is

$$k_p' = 1.8 \times 10^{12} [\exp(-22{,}500/RT)]\ (\mu g\ O_2/cm^2)^2/min$$

The linear rate constant above 400°C to the maximum temperature studied of 558°C is

$$k = 8.8 \times 10^{9} [\exp(-26{,}400/RT)]\ (\mu g\ O_2/cm^2)/min$$

If plutonium is preoxidized above 400°C, the linear rate continues to fit the high-temperature equation down to approximately 300°C.

The presence of moisture does not affect the oxidation above 215°C. Below this temperature very small quantities of moisture causes marked acceleration to a linear rate of about 20 (μg O_2/cm^2)/min in the temperature range of 100°-190°C.

The content of 3.4 a/o aluminum in the plutonium alloy causes only small changes in the high-temperature regime but marked differences at lower temperatures.

Manuscript received Dec. 6, 1965.

Any discussion of this paper will appear in a Discussion Section to be published in the December 1967 JOURNAL.

REFERENCES

1. S. Fried *et al.*, "The Microscale and Micrometallurgy of Plutonium Metal," "The Metal Plutonium," A. S. Coffinberry and W. N. Miner, Editors, p. 18, University of Chicago Press, Chicago (1961).
2. K. S. Covert and M. Kolodney, "Protection of Plutonium Against Atmospheric Oxidation," LA-314, June 1945.
3. D. Dean, A. E. Kay, B. W. Lowthian, R. F. Powell, and E. Dempsey, Unpublished data communicated by E. Dempsey to Physical Society Conference on "Materials for Nuclear Engineering," July 11, 1957 [K. Q. Bagley, *Nuclear Eng.*, **2**, 461 (Nov. 1957)].
4. J. T. Waber, Proc. Second UN International Conference on Peaceful Uses of Atomic Energy, Geneva, **6**, 204 (1958).
5. J. T. Waber and E. S. Wright, "The Corrosion of Plutonium," Presented AEC-ASM Conf., Chicago (1957). Also Chapter XVIII, "The Metal Plutonium," A. S. Coffinberry and W. N. Miner, Editors, p. 194, University of Chicago Press, Chicago (1961).
6. J. F. Sackman, International Conference on the Metallurgy of Plutonium, Grenoble, p. 222, Cleaver Hume, Ltd., London (1961).
7. J. F. Sackman, *Nature*, **197**, 587 (1963).
8. M. A. Thompson, Private communication.
9. E. Dempsey and A. E. Kay, *J. Inst. Metals*, **86**, 379 (1958).
10. M. J. F. Notley, E. N. Hodkin, and J. A. C. Davidson, UKAEA-AERE-R 4070 (1962).
11. C. E. Holley, Jr., R. N. R. Mulford, E. J. Huber, Jr., E. L. Head, F. H. Ellinger, and C. W. Bjorklund, Proc. Second UN International Conference on Peaceful Uses of Atomic Energy, Geneva, **6**, 215 (1958).
12. T. D. Chikalla, C. E. McNeilly, and R. E. Skavdahl, The Plutonium-Oxygen System, HW-74802 (1962).
13. E. R. Gardner, T. L. Markin, and R. S. Street, *J. Inorg. Nuc. Chem.*, **27**, 541 (1965).
14. T. L. Markin and M. H. Rand, Thermodynamic Data for Plutonium Oxides, Symposium on Thermodynamics, Vienna, July 1965.
15. A. A. Bochvar *et al.*, Proceedings Second UN International Conference on Peaceful Uses of Atomic Energy, Geneva, **6**, 184 (1958).
16. F. W. Schonfeld, "Plutonium Phase Diagrams," "The Metal Plutonium," A. S. Coffinberry and W. N. Miner, Editors, p. 255, University of Chicago Press, Chicago (1961).
17. J. G. Schnizlein and D. F. Fischer, "Ignition Behavior of Plutonium Metal and Certain Binary Alloys," To be published.
18. J. T. Waber, W. M. Olson, and R. B. Roof, *J. Nucl. Mat.*, **3**, 201 ((1961).
19. J. G. Schnizlein, John Brewer, and D. F. Fischer, *Rev. Sci. Inst.*, **36**, 591 (1965).
20. O. Kubaschewski and B. E. Hopkins, "Oxidation of Metals and Alloys," p. 35, Butterworths, London (1962).
21. E. W. Haycock, *This Journal*, **106**, 771 (1959).
22. W. B. Jepson and D. W. Aylmore, *ibid.*, **108**, 942 (1961).
23. D. Wajszel, *ibid.*, **110**, 942 (1961).
24. C. E. McNeilly, *J. Nucl. Mat.*, **11**, 53 (1964).
25. N. H. Brett and L. E. Russell, "Plutonium 1960," p. 397, Cleaver-Hume Press, Ltd., London (1961).
26. J. M. Leblanc and H. Andriesson, EURAEC-434 (1962).

Free Energy of Formation of Cupric Oxide

L. R. Bidwell

Metallurgy and Ceramics Research Laboratory,

Aerospace Research Laboratories, Wright-Patterson Air Force Base, Ohio

ABSTRACT

The standard molar free energy change for the oxidation of cuprous oxide to cupric oxide was determined over the temperature range 973°-1273°K using galvanic cells employing calcia stabilized zirconia as the electrolyte. The measurements predict a temperature of 1298°K for the decomposition of cupric oxide in air, in good agreement with the generally accepted value of 1299°K. The standard molar free energies of formation of cupric oxide were calculated from the experimental data using previously determined values for $\Delta G^\circ_{Cu_2O}$. The results can be represented by the equation

$$\Delta G^\circ_{CuO} = -35{,}750 + 19.97T \pm 100 \text{ cal mole}^{-1}$$

which is somewhat less negative than values estimated from calorimetric and dissociation pressure measurements.

The best available data for the standard molar free energy of formation of cupric oxide at elevated temperatures have been estimated from calorimetric and dissociation pressure measurements (1-3). The uncertainty in these data is of the order of 4 kcal mole^{-1}. This work was undertaken to obtain more accurate data for use in an investigation of the thermodynamic properties of solid copper-platinum alloys (4) by solid galvanic cell techniques (5).

Experimental

Since excellent data for $\Delta G^\circ_{Cu_2O}$ were available from previous work in this Laboratory (6), ΔG°_{CuO} could be obtained by determining the free energy change for the reaction

$$Cu_2O + \tfrac{1}{2}\, O_2 \rightleftharpoons 2\, CuO \qquad [1]$$

from the open-circuit potential of the following cell

$$Cu_2O, CuO \mid Zr_{0.85}\, Ca_{0.15}\, O_{1.85} \mid O_2\ (air) \qquad [I]$$

Solid galvanic cells employing calcia stabilized zirconia as the electrolyte have been used with considerable success by Kiukkola and Wagner (7, 8) and by many others to determine the standard free energies of formation of oxides at elevated temperatures. The essentially pure ionic conductivity of this electrolyte at high temperatures and at oxygen pressures of 10^{-15} atm and greater has been well established (7-10). Thus, the difference in the chemical potential of oxygen at the anode and at the cathode of the above cell, and hence the change in free energy for [1], is related to the electrical potential of the cell by the relationships

$$\mu_{O_2}{}^a - \mu_{O_2}{}^c = -\Delta G_{[1]} = 2\mathbf{F}E \qquad [2]$$

where **F** is Faraday's constant.

The experimental apparatus used in this work was similar to that employed in a previous investigation (5), with the exception of several important modifications. The cell was enclosed within a gas-tight quartz reaction tube that could be evacuated. The cell holder was modified to permit the use of an air electrode. This was achieved by substituting a closed-end calcia-stabilized zirconia tube containing an internal spring-loaded platinum electrical contact for the mullite push-rod. A gas-tight seal between the zirconia tube and the tapered brass holder was accomplished with a compression O-ring. The mixed copper oxide anode tablet was separated from the zirconia tube by a disk of electrolyte material. This prevented the cathode tube from being contaminated so that it need not be replaced when using different types of anodes. The zirconia tube and the mullite thrust reversal tube were independently spring-loaded to the tapered brass joint in order to keep the cell components in firm electrical contact at all temperatures. A combustion boat containing a 3:1 mixture of CuO and Cu_2O was placed in the hot zone of the furnace to keep the anode environment at the proper oxygen pressure.

The preparation of the electrolyte tablets has been described in an earlier publication (5). The closed-end cathode tube was obtained from the Zirconium Corporation. The mixed oxide anode tablets were prepared from Baker reagent grade Cu_2O and CuO obtained by oxidizing some of the Cu_2O in air. A 1:1 mixture of the two oxides was blended and cold-pressed in a hardened steel die at 50 tsi into tablets 6 mm in diameter by 3 mm thick.

At the beginning of an experiment, the cell apparatus was evacuated to approximately 10^{-3} Torr with a mechanical vacuum pump. The quartz reaction tube was then sealed from the pump and the furnace heated to temperature. The gas pressure within the anode compartment was thus largely dictated by reaction [1]. Cell potentials were measured to 0.1 mv with increasing and decreasing temperature over the temperature range 973°-1273°K with a L&N K-3 potentiometer and a high sensitivity galvanometer. Temperatures were measured with a Pt-13% Rh thermocouple placed within 1 mm of the electrolyte tablet. The thermocouple used for this purpose was calibrated against a second thermocouple that had been calibrated by the National Bureau of Standards. The resulting temperature measurements are therefore believed to be accurate to within ± 1°K.

The observed cell voltages were very stable with time and the cells appeared to be thermodynamically reversible. No tendency for polarization could be detected. After a small current had been passed through a cell by momentarily unbalancing the potentiometer, the potential returned to its initial value almost immediately. Data that were recorded with increasing or decreasing temperatures did not exhibit any systematic differences.

Results

The average values of the cell potentials for four separate experimental runs are listed in Table I. The reproducibility, as indicated, was better than ± 1 mv at all temperatures except 1273°K, where the scatter was somewhat greater (± 1.9 mv). The latter is undoubtedly an indication that the combustion boat of mixed copper oxides had difficulty in establishing the relatively high oxygen pressure required for equilibrium between CuO and Cu_2O at that temperature. The experimental data are well represented by the linear equation

$$E\,(\text{mv}) = 678.7 \pm 1.0 - 0.5228T \qquad [3]$$

Table I. Electromotive force of cell

Cu_2O, CuO | electrolyte | O_2 (air)

Temperature, °K	Number of determinations	E, mv	cal mole^{-1} $\Delta G°_{[1]}$	cal mole^{-1} $\Delta G°_{CuO}$
973	5	170.0 ± 0.7	−9,350	−16,320
1023	5	143.9 ± 0.4	−8,220	−15,320
1073	6	117.7 ± 0.7	−7,090	−14,320
1123	6	91.6 ± 0.9	−5,970	−13,320
1173	6	65.5 ± 0.5	−4,840	−12,330
1223	6	39.3 ± 0.5	−3,710	−11,330
1273	5	13.2 ± 1.9	−2,580	−10,330

calculated by a least squares analysis. This equation predicts a temperature of 1298°K for the decomposition of CuO in air (*i.e.*, E = O and Cu_2O, CuO, and air are in equilibrium), which is in excellent agreement with the generally accepted value of 1299°K (11).

The standard free energy changes, $\Delta G°_{[1]}$, for reaction [1] calculated from the relationship

$$\Delta G°_{[1]} = -2FE + 1/2\ RT \ln p_{O_2}\ (\text{air}) \qquad [4]$$

are listed in Table I. Since at 1 mv uncertainty in the cell potential corresponds to approximately 50 cal mole^{-1} uncertainty in ΔG, the accuracy of $\Delta G°_{[1]}$ should be ±50 cal mole^{-1} or better. The standard states tacitly assumed by this calculation are Cu_2O saturated with oxygen, CuO saturated with copper, and pure oxygen at 1 atm pressure.

Previous solid galvanic cell measurements involving Cu, Cu_2O; Ni, NiO; Fe, Fe_xO; and air electrodes that have been carried out in this Laboratory have yielded reliable, self-consistent free energy data from which the standard molar free energy of formation of Cu_2O over the temperature range 973°-1273°K was determined to be (6)

$$\Delta G°_{Cu_2O} = -40{,}200 + 17.37T \pm 100 \text{ cal mole}^{-1} \qquad [5]$$

Using these values for $\Delta G°_{Cu_2O}$, the standard molar free energies of formation of CuO were calculated from the relationship

$$\Delta G°_{CuO} = 1/2\ (\Delta G°_{Cu_2O} + \Delta G°_{[1]}) \qquad [6]$$

These results are listed in Table I and are well represented by the linear equation

$$\Delta G°_{CuO} = -35{,}750 + 19.97T \pm 100 \text{ cal mole}^{-1} \qquad [7]$$

Discussion

It should be pointed out that the standard state for Cu_2O used in Eq. [5] is Cu_2O saturated with copper, whereas, the standard state employed in this investigation in [4] is Cu_2O saturated with oxygen. The above calculation of $\Delta G°_{CuO}$ therefore assumes that

$$\mu_{Cu_2O(Cu)} = \mu_{Cu_2O(CuO)} \qquad [8]$$

i.e., that the chemical potential of Cu_2O in equilibrium with Cu is equal to the chemical potential of Cu_2O in equilibrium with CuO. This assumption should be valid since Cu_2O is a compound of essentially fixed composition (11). Wagner (12) has shown that the chemical potential of phases whose composition does not deviate greatly from stoichiometry is essentially constant.

Table II. Standard molar free energies of formation of CuO

Temperature, °K	cal mole^{-1} Calculated Eq. [13]	cal mole^{-1} Wicks and Block (2)
1000	−15,780	−16,050
1100	−13,780	−14,100
1200	−11,790	−12,150
1300	−9,790	−10,250

Taking into account both the uncertainties in $\Delta G°_{Cu_2O}$ and in the experimental measurements, the values of $\Delta G°_{CuO}$ calculated from Eq. [7] should be accurate within approximately ± 100 cal mole^{-1} over the 973°-1273°K temperature range of this investigation. Values of $\Delta G°_{CuO}$ calculated at several temperatures are compared, in Table II, with data recently tabulated by Wicks and Block (2). As can be seen, the agreement is reasonably good, however, the differences that exist are much larger than the uncertainties in the present experimental data. Since the methods used to determine $\Delta G°_{CuO}$ in this investigation represent a more direct measurement than the values calculated from dissociation pressure and heat content data, they are to be preferred.

Acknowledgments

The author would like to thank Mr. D. F. Frank for his assistance in the experimental portion of this investigation. He would also like to thank Dr. F. E. Rizzo and Dr. H. A. Lipsitt for their helpful discussion of the work.

Manuscript received June 13, 1966; revised manuscript received Aug. 19, 1966.

Any discussion of this paper will appear in a Discussion Section to be published in the December 1967 JOURNAL.

REFERENCES

1. J. P. Coughlin, Bur. of Mines Bull. No. 542, p. 20 (1954).
2. C. E. Wicks and F. E. Block, Bur. of Mines Bull. No. 605, p. 42 (1963).
3. M. Olette and M. F. Ancey-Moret, *Rev. Met.*, **60**, 569 (1963).
4. L. R. Bidwell, W. J. Schulz, and R. K. Saxer, To be published.
5. L. R. Bidwell and R. Speiser, *Acta Met.*, **13**, 61 (1965).
6. F. E. Rizzo, L. R. Bidwell, and D. F. Frank, To be published.
7. K. Kiukkola and C. Wagner, *This Journal*, **104**, 308 (1957).
8. K. Kiukkola and C. Wagner, *ibid.*, **104**, 379 (1957).
9. W. D. Kingery, J. Pappis, M. E. Doty, and D. C. Hill, *J. Am. Ceram. Soc.*, **42**, 393 (1959).
10. H. Schmalzried, *Z. Elektrochem.*, **66**, 572 (1962).
11. M. Hansen and K. Anderko, "Constitution of Binary Alloys," McGraw-Hill Book Co., New York (1958).
12. C. Wagner and W. Schottky, *Z. phys. Chem.*, **B11**, 163 (1930).

The Effects of Crystallographic Orientation and Oxygen Pressure on the Oxidation of Iron

W. E. Boggs, R. H. Kachik, and G. E. Pellissier

Applied Research Laboratory, United States Steel Corporation, Monroeville, Pennsylvania

ABSTRACT

When clean iron is exposed to oxygen at temperatures of 200°-400°C, a film of Fe_3O_4 forms rapidly on the surface. Soon after this a second phase, α-Fe_2O_3, begins to form in the outer surface of the Fe_3O_4 layer. The rates of nucleation and lateral growth of the second phase depend on the oxygen pressure and on the crystallographic orientation of the Fe_3O_4 matrix which is determined by the crystallographic orientation of the iron substrate. When the oxygen pressure is high and/or when the close-packed oxygen-ion planes in the Fe_3O_4 are parallel to the surface, the rate of formation of the second oxide phase is high, and rapid coverage of the Fe_3O_4 phase occurs. Conversely, when the oxygen pressure is low and/or when the close-packed oxygen-ion planes in the Fe_3O_4 are not parallel to the surface, the rate of formation of the α-Fe_2O_3 phase is lower and the coverage of the Fe_3O_4 by a layer of α-Fe_2O_3 proceeds more slowly. Coverage of the Fe_3O_4 by α-Fe_2O_3 reduces the iron-oxidation rate by reducing the flux of iron ions outward through the Fe_3O_4 layer. Thus, the more rapidly the α-Fe_2O_3 layer forms, the more quickly the rate of oxidation is reduced. The order of oxidation rate with oxygen pressure, 0.01 > 0.1 > 10 Torr, and with iron crystallographic orientation, (001) > (112) > (111) > (011), can be explained by this mechanism.

The effect of oxygen pressure on the oxidation of polycrystalline zone-refined iron has been reported in a recently published paper (1). The rate of oxidation of 99.94% polycrystalline iron increases as the oxygen pressure is decreased from 100 to 0.01 Torr in the temperature range 200°-400°C. The oxidation kinetics are characterized by an initial period of high oxidation rate followed by a period of low oxidation rate. X-ray analyses of the films stripped from the specimens after oxidation for increasing lengths of time indicated that the period of high oxidation rate was associated with the growth of a layer of Fe_3O_4, while the period of low oxidation rate was associated with the growth of α-Fe_2O_3.

Electron microscopic examination of the stripped oxide films revealed that the initial films were extremely fine-grained as though composed of very fine crystallites. The oxide associated with each iron grain formed an individual single-crystal electron diffraction pattern of the cubic oxide, Fe_3O_4, an indication that the orientation of the oxide depended on the orientation of the iron substrate. As the oxidation was allowed to proceed for successively longer times, the oxide films assumed a coarse-grained, herringbone texture suggestive of a Widmanstätten structure. Selected-area electron diffraction analysis revealed that the herringbone texture of the latter films was imparted by crystals of α-Fe_2O_3 grown into the initially formed Fe_3O_4 layer.

At the high oxygen pressures, 10 and 100 Torr, large numbers of acicular α-Fe_2O_3 platelets formed and grew together rapidly into a closely interlocked Widmanstätten structure. At the lower oxygen pressures, 0.1 and 0.01 Torr, the α-Fe_2O_3 platelets were fewer in number and grew together more slowly. Replicas of oxidized and partially stripped specimens revealed that the surfaces of the α-Fe_2O_3 platelets were indented in the oxygen-oxide interface and that the metal surface beneath these crystals was raised above the remainder of the oxide-metal interface (1) so that the Fe_3O_4 layer was thinner under the α-Fe_2O_3 crystals. Replicas of the α-Fe_2O_3-Fe_3O_4 interface obtained after electrometric reduction (2, 3) of the α-Fe_2O_3 crystals revealed that this oxide-oxide interface was rougher than were either the O_2-oxide or the oxide-metal interfaces. Thus, it appeared that the α-Fe_2O_3 platelets grew into the Fe_3O_4 phase from sites of α-Fe_2O_3 nucleation at the Fe_3O_4-gas interface.

These experimental observations suggested the following mechanism to explain the fact that thicker oxide films were formed at the lower oxygen pressures than were formed at the higher oxygen pressures: the p-type semiconductor oxide, Fe_3O_4, forms first on the surface of the metal at these temperatures (200°-400°C) and oxygen pressures (0.01-100 Torr); the film grows thicker as iron ions move outward through lattice defects (cation vacancies) in the oxide; the vacancies are formed at the O_2-Fe_3O_4 interface when oxygen is incorporated into the Fe_3O_4 lattice.

The concentration of vacancies, and consequently the amount of iron moving through the Fe_3O_4 lattice, is dependent on the amount of oxygen available at the outer surface of the Fe_3O_4 layer. Thus, if a film of α-Fe_2O_3 is interposed between the Fe_3O_4 layer and the oxygen atmosphere, the amount of oxygen available to react with the Fe_3O_4 and form the iron-carrying vacancies will be drastically reduced. In consequence, the over-all oxidation rate will be reduced. Because the rates of nucleation and growth of the α-Fe_2O_3 platelets are higher at the higher oxygen pressures than at the lower oxygen pressures, Fe_3O_4 is exposed to gaseous oxygen for a longer time at the low oxygen pressures. This allows the high rate of Fe_3O_4 growth to persist longer at the low oxygen pressures and results in thicker oxide films than are formed at the higher oxygen pressures.

The proposed mechanism appears to explain, qualitatively at least, the observed kinetic and structural aspects of the oxidation of polycrystalline zone-refined iron foils in the temperature range 200°-400°C and over the oxygen-pressure range 0.01-100 Torr. However, the expected typical Widmanstätten pattern of the α-Fe_2O_3 platelets did not develop on all the iron grains in each foil. This suggested that the orientation of the iron substrate has an effect on the nucleation of α-Fe_2O_3 even through the intervening layer of Fe_3O_4. Accordingly, an investigation of the effect of iron substrate orientation on the morphology of the α-Fe_2O_3 platelets and on the rates of oxidation was undertaken.

Materials and Experimental Work

Single crystals of iron, grown by the strain-anneal method, were obtained in the (001), (011), (111), and (112) orientations. The approximately 1 cm square crystals were mechanically ground, spark-machined,

and electropolished into thin wafers of weights suitable for vacuum microbalance experiments. A 30-gauge platinum-20%-iridium wire was spot-welded to one corner of each crystal for support in the microbalance. A disturbed area, only 1 mm in radius, was produced on one surface of each crystal by the spot welding. Laue back-reflection patterns, obtained at this stage in the preparation, demonstrated that the crystals were not otherwise damaged. The surface treatment prior to oxidation was the same as that used on the polycrystalline foils (1). Because the greatest pressure effect was observed at 350°C, all the single-crystal oxidation experiments were carried out at this temperature. Oxygen pressures were 10, 0.1, and 0.01 Torr. Only one crystal suitable for kinetic studies was available in each orientation; consequently, the specimens were cleaned after each experiment and used again.

The oxide films were examined *in situ* by optical microscopy. Stripped oxide films and replicas of the interfaces were examined by electron microscopy. The crystal structure and orientations of the oxides were determined by electron diffraction analysis. Asymmetric specimen-support grids were used in this work so that the orientation relationships between the metal and the oxide could be preserved within a few degrees throughout the examination of the various types of replicas.

Results and Discussion

Kinetic data.—The results of the kinetic experiments at 350°C and at oxygen pressures of 10 and 0.1 Torr are shown in Fig. 1. Each curve, as plotted, is the average of two experiments on each crystal face. The agreement within the sets of data obtained at 10 Torr was quite good. Although the agreement among the data obtained at 0.1 Torr was not as good, there was no overlap among the sets of data for the different conditions, an indication that the effects of iron orientation and oxygen pressure were real.

As was observed in the experiments on polycrystalline iron foils (1), these rate curves consist of a short period of high oxidation rate followed by a period of very low oxidation rate. In each instance, more oxide was formed at 0.1 Torr than was formed at 10 Torr. The order of reaction rates with respect to the crystallographic orientation of the iron was (001) > (112) > (111) > (011), the same as that observed by Wagner, Lawless, and Gwathmey (4).

The curve for polycrystalline iron oxidized at 10 Torr and 350°C lies above the curve for the (112) Fe face and below the curve for the (001) Fe face. This suggests that the polycrystalline iron foils had a preferred orientation approaching (001). This supposition is strengthened by the observation that the oxide microstructures observed on the polycrystalline iron foils were, for the most part, similar to those found on the (001) face of the iron single crystal.

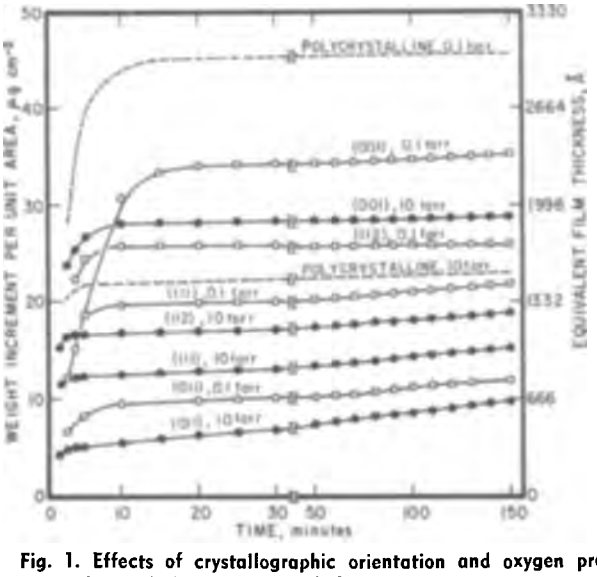

Fig. 1. Effects of crystallographic orientation and oxygen pressure on the oxidation of iron at 350°C.

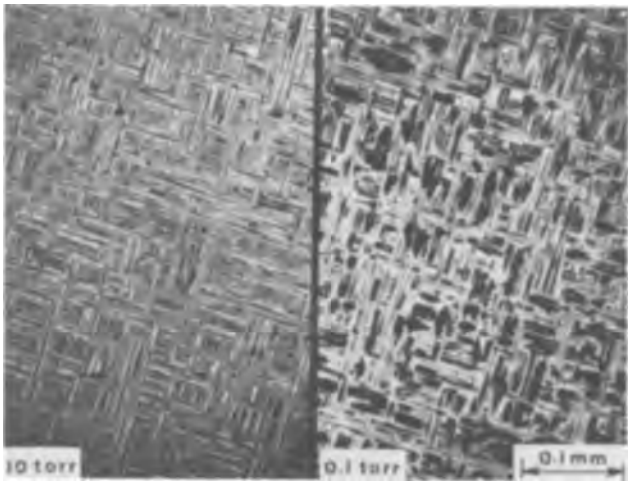

Fig. 2. Optical micrograph of oxide formed on the (001) Fe face in 150 min at 350°C.

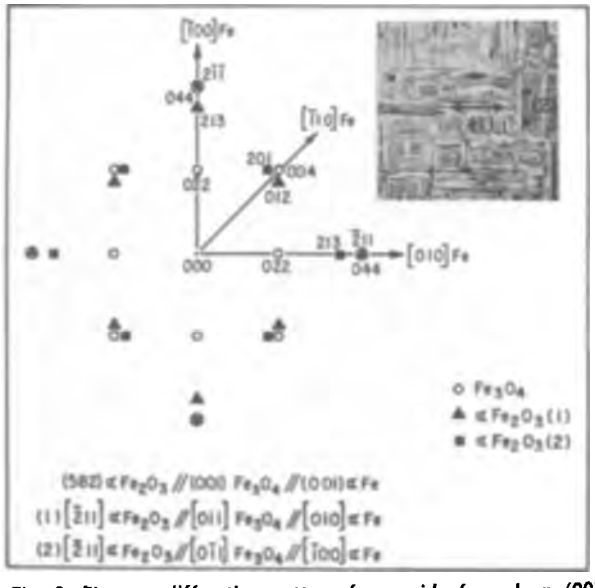

Fig. 3. Electron diffraction pattern from oxide formed on (001) α-Fe face at 350°C.

Morphology and orientation of the oxides.—(001) α-Fe.—The orientation of the cubic oxide Fe_3O_4 films that formed initially on the (001) iron face was the same as that reported in the literature (4, 5): (001) Fe_3O_4 // (001) α-Fe. A layer of acicular α-Fe_2O_3 crystals formed over the initial oxide film in a Widmanstätten pattern such as that shown in the optical micrographs of Fig. 2. The α-Fe_2O_3 layer was composed of two families of parallel crystals. The crystals of one family intersected the crystals of the other at 90°. The electron diffraction pattern obtained from such an α-Fe_2O_3-Fe_3O_4 film is interpreted in Fig. 3. The long axes of one family of α-Fe_2O_3 crystals, labeled 1 in the inset, were parallel to the [010] direction of the iron substrate and the long axes of the other family, labeled 2, were parallel to the [100] iron direction. The crystallographic orientations of α-Fe_2O_3 are given in rhombohedral coordinates that were derived from the electron-diffraction data using matrix algebra (6).

The ridged structure of the α-Fe_2O_3 crystals is evident in electron micrographs of replicas of the oxide-gas interface, Fig. 4. This same type of morphology is

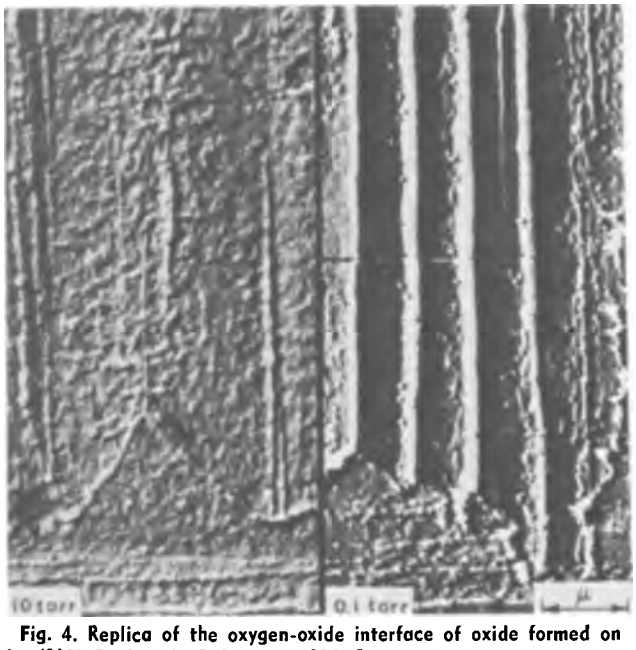

Fig. 4. Replica of the oxygen-oxide interface of oxide formed on the (001) Fe face in 150 min at 350°C.

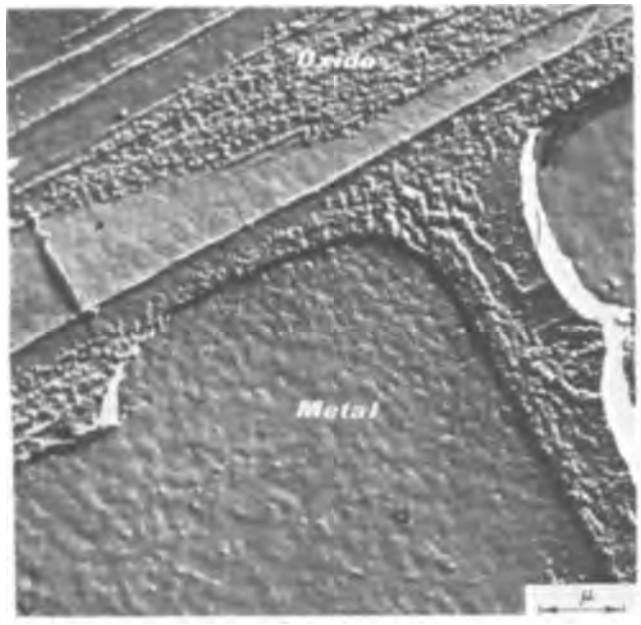

Fig. 6. Replica of partially stripped surface of (001) α-Fe crystal showing oxide at O_2-oxide interface and metal at oxide-metal interface; oxide formed in 150 min at 350°C and 10 Torr.

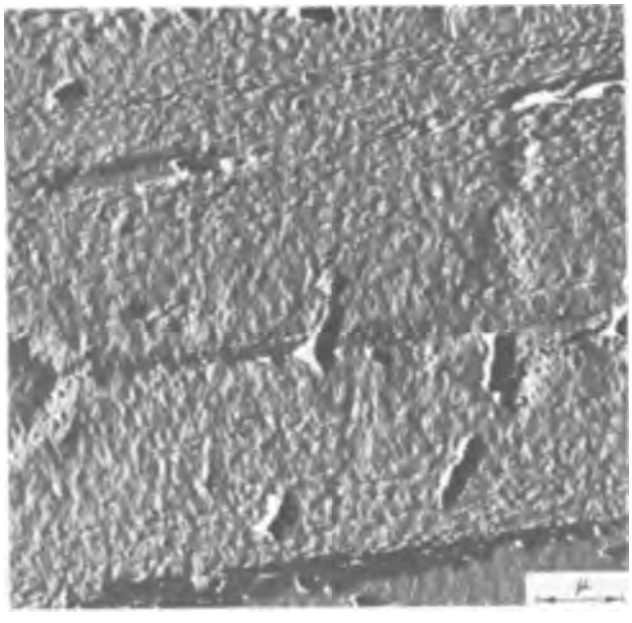

Fig. 5. Replica of the α-Fe_2O_3-Fe_3O_4 interface of oxide formed on the (001) Fe face in 150 min at 350°C and 10 Torr.

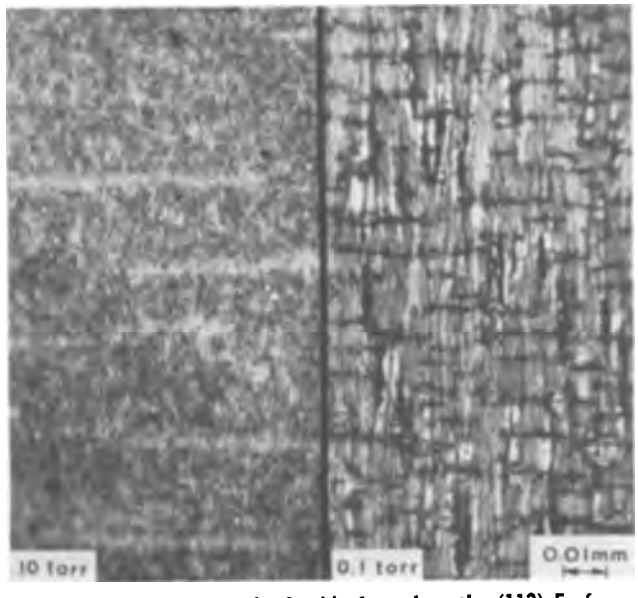

Fig. 7. Optical micrograph of oxide formed on the (112) Fe face in 150 min at 350°C.

also evident in replicas of the α-Fe_2O_3-Fe_3O_4 interface, obtained after electrometric reduction (2, 3) of the α-Fe_2O_3, Fig. 5. The ridging exhibited by these replicas suggests that the oxide interfaces are composed of microscopic facets.

The effect of oxygen pressure on the size of the α-Fe_2O_3 platelets is illustrated by the optical micrographs of Fig. 2. At the lower oxygen pressure, 0.1 Torr, somewhat fewer platelets were formed, and they became larger than those formed at 10 Torr. The crystals formed at 0.1 Torr were also in higher topographical relief than those formed at 10 Torr as is shown in Fig. 4. The oxide-metal interface was much smoother than the α-Fe_2O_3-Fe_3O_4 interface or the oxygen-α-Fe_2O_3 interface, as is shown in Fig. 6

(112) α-Fe.—Optical micrographs of the oxide formed on the (112) α-Fe face in 150 min at 350°C are shown in Fig. 7. This oxide is characterized by a profusion of small acicular crystals oriented with their long axes parallel to the [111] α-Fe direction. The crystals formed at 0.1 Torr were much larger than those formed at 10 Torr.

The electron diffraction patterns obtained from the oxide formed on the (112) iron face are interpreted in Fig. 8. The (011) Fe_3O_4 plane was parallel to the (112) α-Fe face as has been reported in the literature (5). However, the directional relationship found in this study between the Fe_3O_4 and the iron, $[3\bar{1}\bar{1}]$ Fe_3O_4 // [111] α-Fe, was different from that found by Sewell and Cohen (5). The α-Fe_2O_3 crystals formed over the Fe_3O_4 with the (573) α-Fe_2O_3 plane parallel to the (011) Fe_3O_4 and the (112) α-Fe. Diffraction patterns from two sets of α-Fe_2O_3 crystals are evident in Fig. 8. The two sets of α-Fe_2O_3 crystals are clearly evident in the replica of the oxide-oxygen interface shown in Fig. 9.

Certain reflections from a cubic crystalline phase that are forbidden by diffraction theory for Fe_3O_4 are indicated by diamonds in the electron diffraction pattern of Fig. 8. These reflections are characteristic of the cubic oxide phase γ-Fe_2O_3, and were in the same crystallographic orientation as the cubic Fe_3O_4 crystals

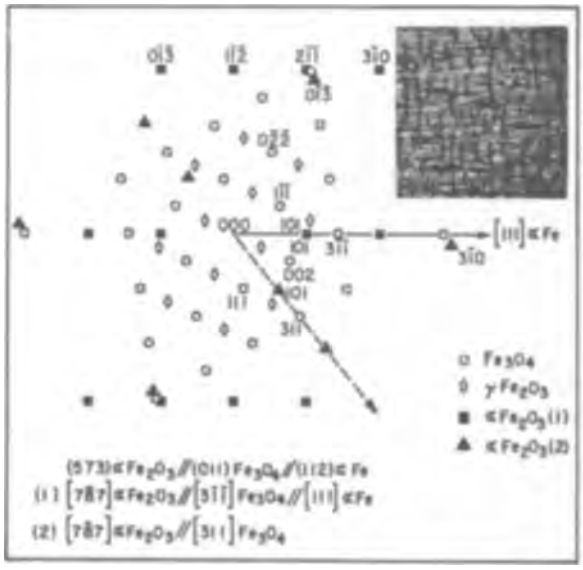

Fig. 8. Electron diffraction pattern from oxide formed on (112) α-Fe face at 350°C.

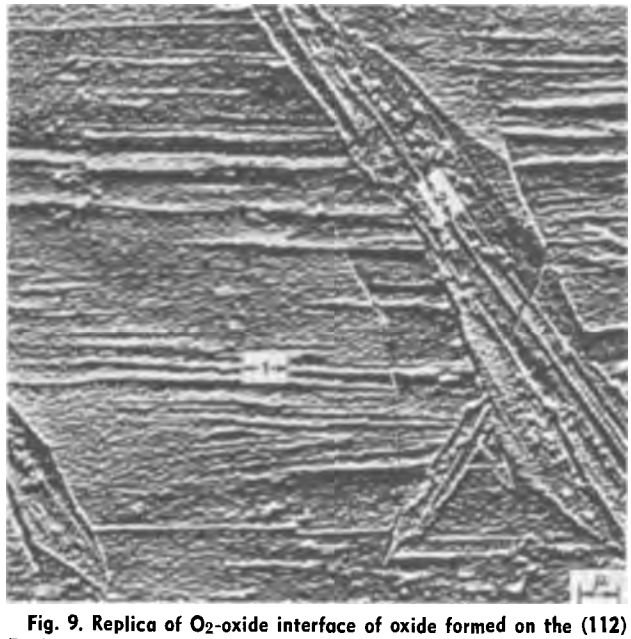

Fig. 9. Replica of O_2-oxide interface of oxide formed on the (112) Fe face in 150 min at 350°C and 0.1 Torr showing major (1) and minor (2) α-Fe_2O_3 orientations

indicated by the open circles. The Fe_3O_4 reflections could also be indexed as γ-Fe_2O_3. However, since no γ-Fe_2O_3 reflections appeared in the third order (that is, there were 011, 022, and 044 reflections but no 033 reflections), it is believed that Fe_3O_4 was the major cubic oxide phase present in these films.

Replicas of the O_2-α-Fe_2O_3, the α-Fe_2O_3-Fe_3O_4, and the Fe_3O_4-α-Fe interfaces are shown in the electron micrographs of Fig. 10. Traces of the α-Fe_2O_3 platelets are evident at all the interfaces. However, the α-Fe_2O_3-Fe_3O_4 interface was in higher topographic relief than was the outer surface of the oxide. This is believed to be evidence of the inward growth of the α-Fe_2O_3 phase from the oxide-gas interface. It is also evident that the planes of contact between the oxide phases were different from those shown to be parallel to the (112) α-Fe face, Fig. 8.

(111) α-Fe.—The effect of oxygen pressure on the size, numbers, and orientation of the α-Fe_2O_3 platelets was most clearly demonstrated in the oxidation of the (111) α-Fe face. The oxide formed at 10 Torr and

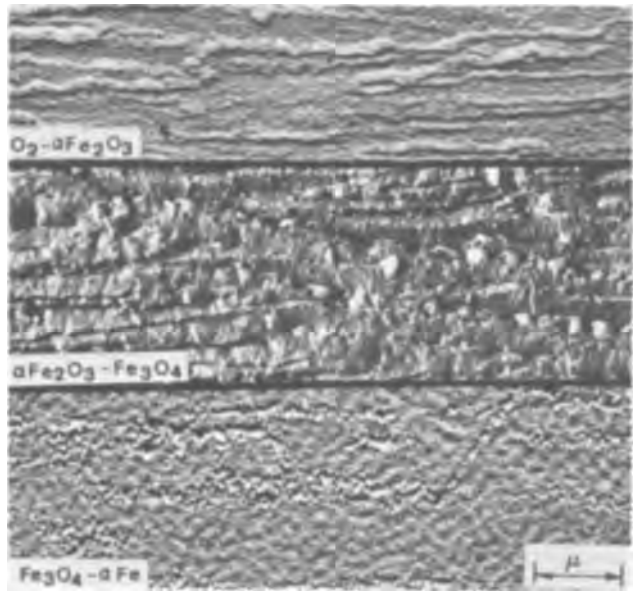

Fig. 10. Replicas of the O_2-α-Fe_2O_3, α-Fe_2O_3-Fe_3O_4, and Fe_3O_4-α-Fe interfaces of oxide formed on (112) α-Fe in 150 min at 350°C and 10 Torr.

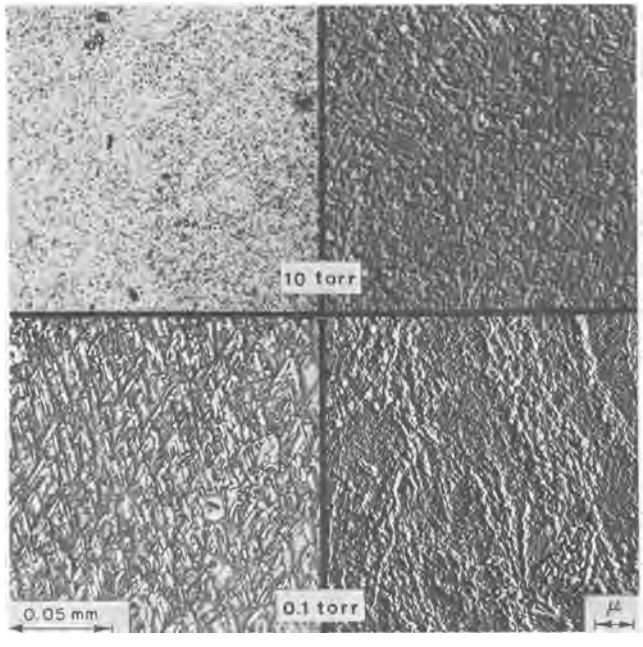

Fig. 11. Optical and electron micrographs of oxide formed on (111) Fe face in 150 min at 350°C.

350°C in 150 min was composed of very fine crystals that exhibited little evidence of morphological or crystallographic orientation in optical and in electron micrographs, Fig. 11, or in electron diffraction patterns. In contrast, Widmanstätten patterns of relatively large acicular crystals were found in the oxide formed at 0.1 Torr and 350°C for 150 min. These crystals were oriented with their long axes nearly parallel to the $[\bar{1}01]$ and $[\bar{1}10]$ directions in the iron crystal, and they intersected each other at an angle of about 50°. The surface of the metal at the oxide-metal interface was smoother than the surface of the oxide at the oxygen-oxide interface (Fig. 12), but was considerably rougher than the original metal surface; traces of the acicular α-Fe_2O_3 crystals were evident in the underlying metal surface.

Two (111) oriented α-Fe crystals were studied. The first crystal (α) was tilted about 2° in the $[2\bar{1}\bar{1}]$ di-

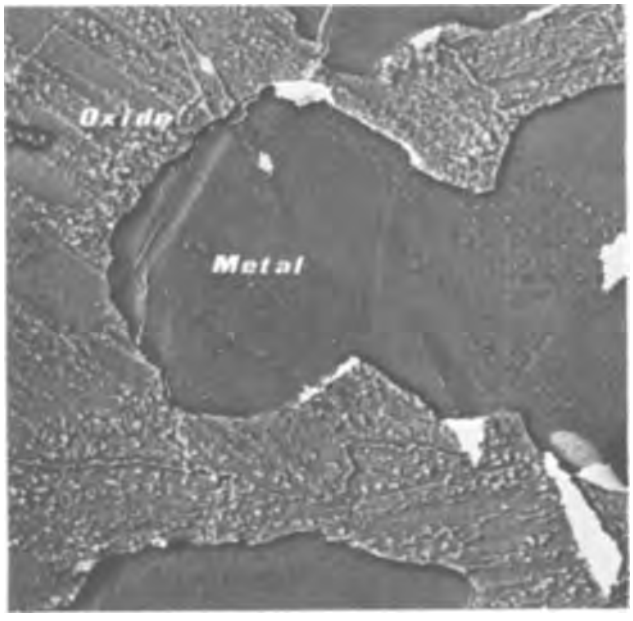

Fig. 12. Replica of partially stripped surface of (111) α-Fe crystal showing oxide at O_2-oxide interface, and metal at oxide-metal interface. Oxide formed in 150 min at 350°C and 0.1 Torr. Note traces of α-Fe_2O_3 crystals at both interfaces (arrow).

rection and 1° in the $[01\bar{1}]$ direction, whereas the second crystal (β) was tilted <2° in the $[2\bar{1}\bar{1}]$ direction only. Two orientations of Fe_3O_4 were observed; the $(\bar{2}10)$ Fe_3O_4 plane formed parallel to the (111) α-Fe plane on iron crystal (α), as shown in Fig. 13, but the $(1\bar{1}0)$ Fe_3O_4 plane formed parallel to the (111) α-Fe face on iron crystal (β), Fig. 14. However, the same orientations of α-Fe_2O_3 with respect to the orientation of the iron substrate were observed on both crystals.

(011) α-Fe.—No evidence of morphological orientation effects was found in the oxide formed at oxygen pressures of 10 or 0.1 Torr and 350°C for 150 min on the (011) α-Fe face, Fig. 15. As is shown in Fig. 16, the oxide was stripped from this face in irregular patches, and there was little difference between the appearance of the oxygen-oxide interface and that of the metal at the oxide-metal interface. The α-Fe_2O_3-Fe_3O_4 interface was also quite smooth, as is shown in Fig. 17.

Electron diffraction patterns from Fe_3O_4 alone could

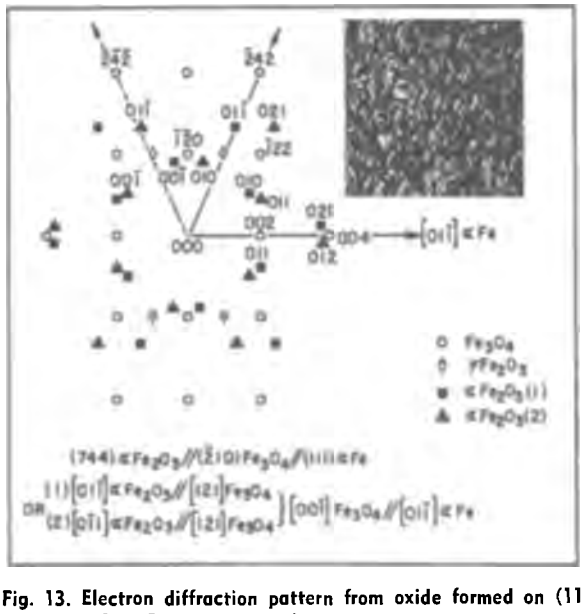

Fig. 13. Electron diffraction pattern from oxide formed on (111) α-Fe face at 350°C (iron crystal α).

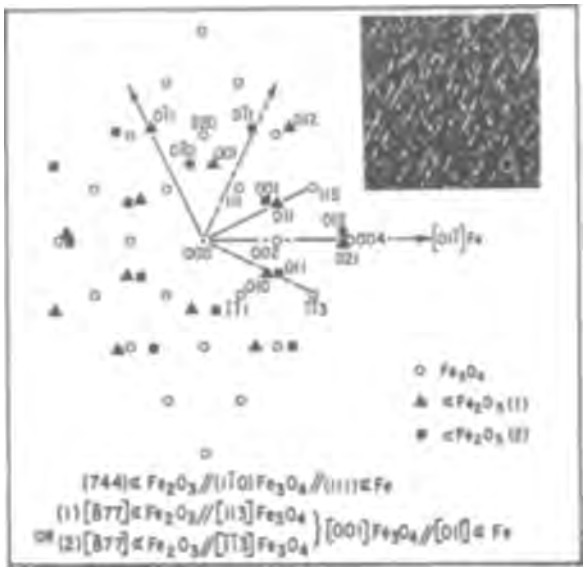

Fig. 14. Electron diffraction pattern from oxide formed on (111) α-Fe face at 350°C (iron crystal β).

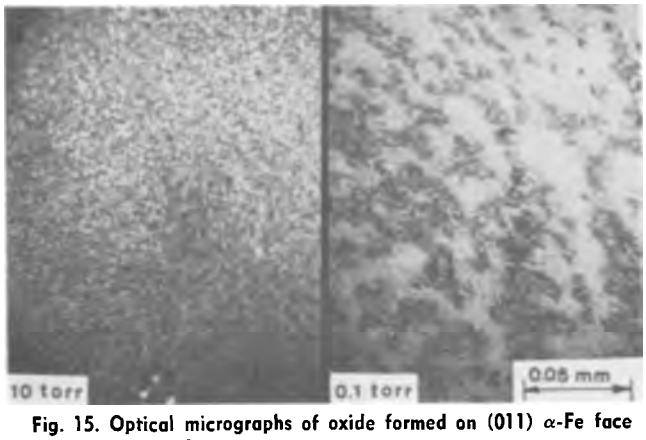

Fig. 15. Optical micrographs of oxide formed on (011) α-Fe face in 150 min at 350°C.

be obtained from oxide formed in short times (2-5 min) at low pressures (0.01 and 0.1 Torr) on the (001), (112), and (111) iron faces. In contrast, the diffraction patterns obtained from the oxide formed on the (011) α-Fe face always demonstrated the presence of both α-Fe_2O_3 and Fe_3O_4 in the single orientation relationship shown in Fig. 18. Apparently, the nucleation and lateral growth of the α-Fe_2O_3 phase over the Fe_3O_4 phase was much more rapid on the (011) α-Fe face than on any of the other iron faces studied.

Moire fringes (7), seldom observed in the transmission electron micrographs of oxide stripped from the other iron faces, were always observed in micrographs of the oxide formed on the (011) α-Fe face, Fig. 19. These fringes, which appear in electron micrographs as parallel black stripes running through a crystal, are a diffraction effect obtained when the electron beam passes through one crystal and then through a second crystal, the lattice spacing or orientation of which is slightly different from that of the first crystal.

The combined evidence of the smooth interfaces, the single diffraction pattern, and the moire fringes suggests that the preferred orientation for α-Fe_2O_3 on Fe_3O_4 is that illustrated by the diffraction pattern, Fig. 18, with the (111) plane of α-Fe_2O_3 parallel to the (111) plane of Fe_3O_4.

Nucleation of α-Fe_2O_3.—The evidence presented in the foregoing sections demonstrates that the nucleation and lateral growth of α-Fe_2O_3 on Fe_3O_4 is influenced not only by the oxygen pressure, but also by the crystallographic orientation of the Fe_3O_4 layer. The early stages in the growth of α-Fe_2O_3 platelets were

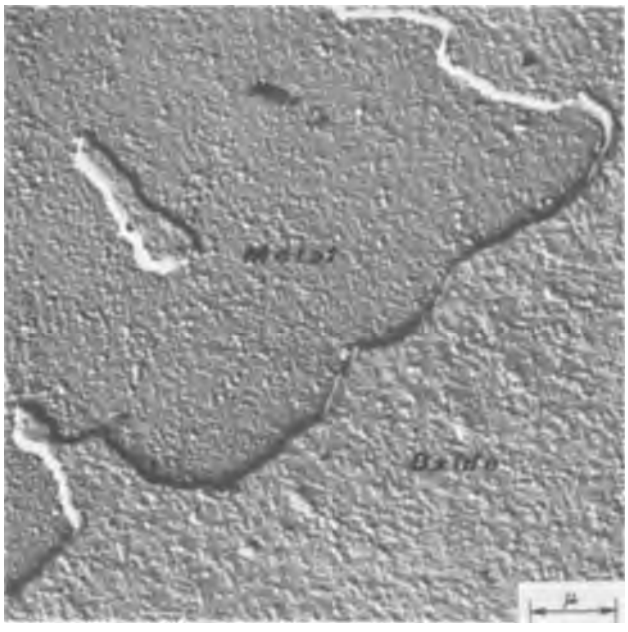

Fig. 16. Replica of partially stripped surface of (011) Fe crystal showing metal at the oxide-metal interface and oxide at the O_2-oxide interface; oxide formed at 350°C and 0.1 Torr.

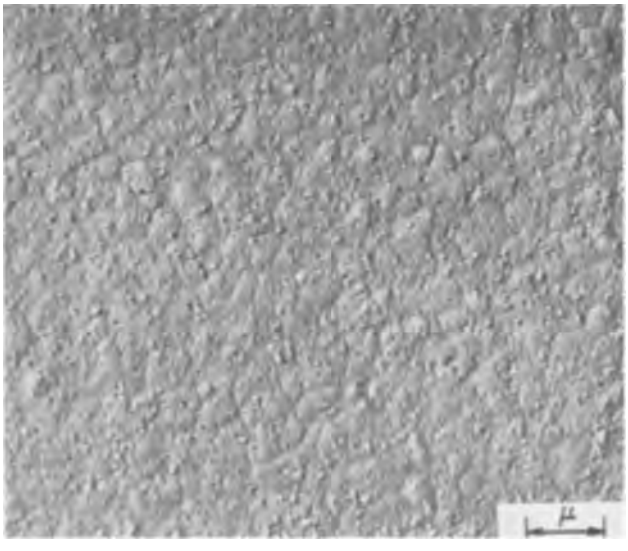

Fig. 17. Replica of the α-Fe_2O_3-Fe_3O_4 interface of oxide formed on the (011) α-Fe face in 150 min at 350°C and 10 Torr.

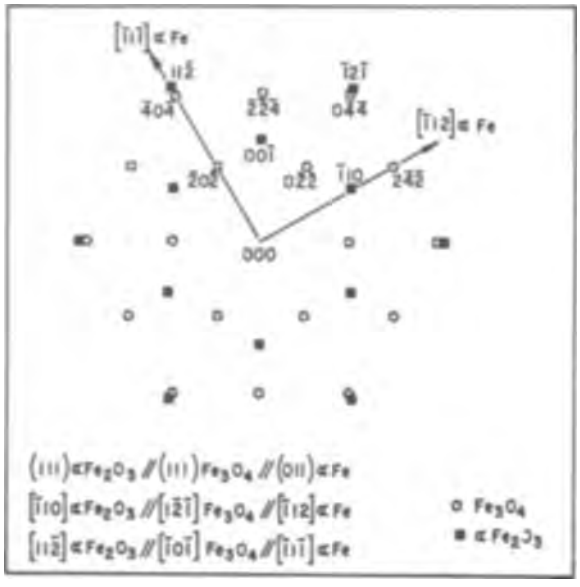

Fig. 18. Electron diffraction pattern from oxide formed on (011) α-Fe face at 350°C.

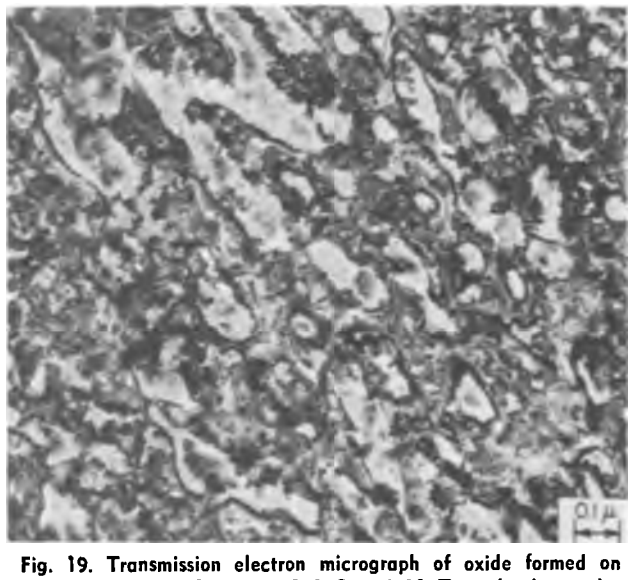

Fig. 19. Transmission electron micrograph of oxide formed on (011) iron face in 60 min at 350°C and 10 Torr showing moire fringes caused by difference in lattice spacing of two parallel layers of oxide crystal phases, α-Fe_2O_3 and Fe_3O_4.

examined in oxide films prepared by oxidizing the four iron single crystals for 2 min at 350°C and oxygen pressures of 0.01, 0.1, and 10 Torr, respectively. The resulting 12 oxide specimens were stripped from the iron substrates, and the α-Fe_2O_3 crystallites were counted in a small area of each film to obtain an estimate of α-Fe_2O_3 nucleation rates. Typical areas of some of these oxide films are shown in the micrographs of Fig. 20. The results of these counts projected to a number of α-Fe_2O_3 crystallites per square centimeter are presented in Table I. The correlation between the number of α-Fe_2O_3 crystallites and the over-all oxidation rate is clearly evident, that is, the smaller the number of α-Fe_2O_3 crystallites, the greater is the over-all oxidation rate. This evidence supports the argument presented in the previous paper (1) that the formation of a continuous layer of α-Fe_2O_3 lowers the rate of oxidation of iron by diminishing the flux of iron ions outward through the Fe_3O_4 layer.

Evidence cited above, in connection with the oxidation of the (011) iron face, suggests that the preferred orientation for the two iron oxide phases is such that the (111) α-Fe_2O_3 plane is formed parallel to the (111) Fe_3O_4 plane. This orientation relationship has been observed by Sewell and Cohen (5) in the oxidation of the (001) and (112) faces of iron, and also by other investigators in mineral specimens of hematite on magnetite (8). The closest-packed oxygen planes in both iron oxide phases are parallel to the respective (111) planes. The arrangement of the oxygen ions parallel to the (111) planes in the two oxide phases is similar, that is, close-packed hexagonal, with an ion spacing (oxygen-to-oxygen) of 2.90Å in α-Fe_2O_3 and 2.97Å in Fe_3O_4 (9). Thus, the transition from Fe_3O_4 to α-Fe_2O_3 is least discontinuous (10) when the (111) planes in each phase are parallel. Furthermore, the boundary between the two phases will be most coherent when these planes are parallel (11). From these considerations, it is inferred that the nucleation and lateral growth rates of α-Fe_2O_3 will be highest when the (111) plane of Fe_3O_4 is parallel to the gross surface, as is the case for the oxidation of the (011) iron face. This hypothesis is supported by the data presented in Table I.

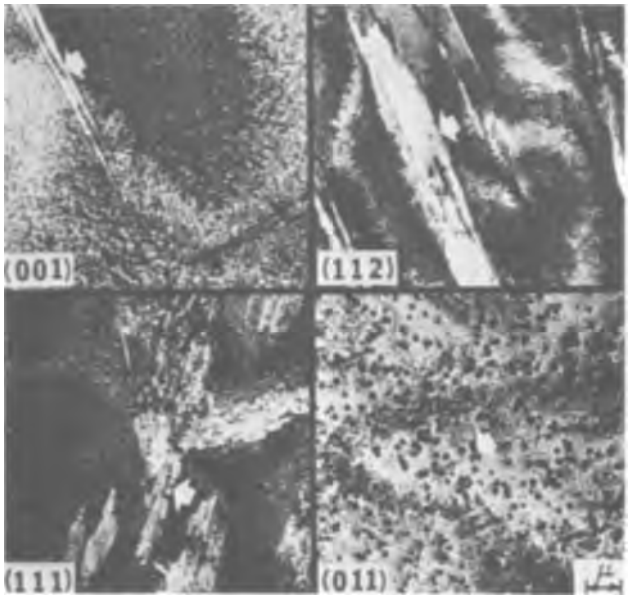

Fig. 20. Transmission electron micrographs of oxides formed on the four iron crystal faces in 2 min at 350°C and 0.1 Torr showing effect of Fe_3O_4 orientation on the number of α-Fe_2O_3 platelets.

The angles between the (111) plane of Fe_3O_4 and the gross surface planes of each of the four iron crystals are shown in Table II. There appears to be a correlation between these angles and the number of α-Fe_2O_3 crystallites, Table I. When the (111) Fe_3O_4 plane is parallel to the gross surface plane, as it is in the case of Fe_3O_4 formed on the (011) iron face, the number of α-Fe_2O_3 crystallites observed is high. Conversely, when the angle between the gross surface plane and the (111) plane of Fe_3O_4 is high, as it is in the case of Fe_3O_4 formed on the (001) face of iron, the number of α-Fe_2O_3 crystallites observed is low.

The roughness shown in electron micrographs of replicas of the α-Fe_2O_3-Fe_3O_4 interfaces of all of the oxide films, except those formed on the (011) face of iron, suggest faceting that is believed to occur parallel to the (111) Fe_3O_4 plane. Thus, the geometry of the interface between the two oxides that form on the four different iron faces is currently believed to be represented approximately by the sketches shown

Table I. Influence of oxygen pressure and iron orientation on the nucleation of α-Fe_2O_3 at 350°C

Orientation of iron crystal	Number of α-Fe_2O_3 platelets formed in 2 min at 10 Torr	0.1 Torr	0.01 Torr
(001)	3.2×10^6 cm^{-2}	1.7×10^4 cm^{-2}	None observed
(112)	9.6×10^7 cm^{-2}	1.0×10^6 cm^{-2}	2.1×10^4 cm^{-2}
(111)	1.2×10^9 cm^{-2}	5.9×10^6 cm^{-2}	3.4×10^5 cm^{-2}
(011)	$>2 \times 10^{10}$ cm^{-2}	8.5×10^5 cm^{-2}	5.8×10^7 cm^{-2}

increasing oxidation rate (↑ and →)

Table II. Angles of intersection of the (111) plane in Fe_3O_4 with the oxide-gas interface

Iron crystal face	Parallel Fe_3O_4 plane	Angles between the surface plane and the (111) plane in Fe_3O_4
(001) Fe	(001) Fe_3O_4	55°
(112) Fe	(011) Fe_3O_4	35°, 90°
(111) Fe	(210) Fe_3O_4	39°, 75°
(011) Fe	(111) Fe_3O_4	0°, 71°

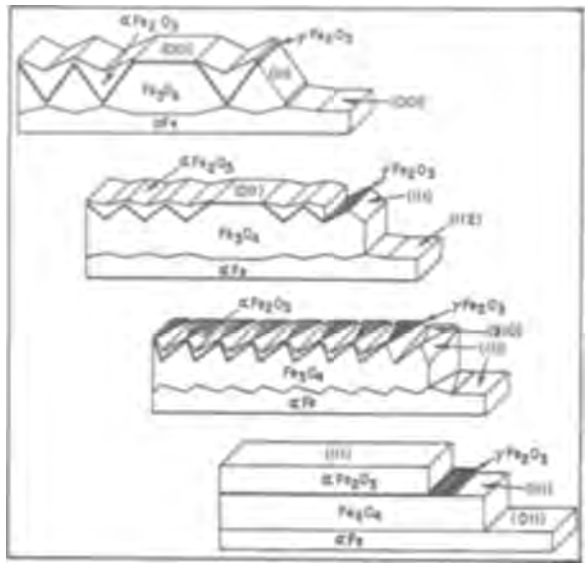

Fig. 21. Current concept of the arrangement of the oxides formed on the four iron crystal faces.

in Fig. 21. Independent electrochemical evidence obtained by Cohen (2, 3, 5) strongly suggests that a thin layer of γ-Fe_2O_3 exists between the α-Fe_2O_3 and the Fe_3O_4. Accordingly, such a layer is indicated in these sketches, although the only experimental evidence of γ-Fe_2O_3 obtained in the present study is that of the extra reflections from cubic crystals shown in Fig. 8 and 13.

Summary and Conclusions

The oxidation of four differently oriented iron single crystals at 350°C and oxygen pressures of 10, 0.1, and 0.01 Torr has been investigated. Kinetic data have been related to morphological data so that a reasonable model for the oxidation process can be deduced. It appears that the mechanism producing the difference in oxidation rates for different iron orientations is similar to that suggested in the previous paper to explain the increase in oxidation rate with decreasing oxygen pressure.

When clean iron is exposed to oxygen at temperatures of 200°-400°C, a film of Fe_3O_4 rapidly covers the surface. It appears that this film is composed of very small crystallites, all in essentially the same orientation, so that single-crystal electron diffraction patterns are obtained from the stripped films. The orientation of this oxide is determined by the orientation of the iron substrate. The formation of the Fe_3O_4 layer is so rapid under the experimental conditions that morphological evidence of the nucleation of the individual Fe_3O_4 crystallites was not obtained.

Soon after the formation of the Fe_3O_4 layer, crystallites of α-Fe_2O_3 begin to form in its outer surface. The number of these α-Fe_2O_3 platelets and the rate with which they spread laterally are dependent not only on the oxygen pressure but also on the crystallographic orientation of the Fe_3O_4 matrix. At high oxygen pressures (10 Torr in these experiments), a large number of α-Fe_2O_3 platelets are formed, and they grow rapidly. At low oxygen pressures (0.1 Torr), fewer platelets are formed, and they grow laterally much more slowly. It also appears that large numbers of α-Fe_2O_3 crystallites are formed, and they grow together rapidly when the close-packed oxygen plane of Fe_3O_4, the (111), is parallel to the gross iron surface [in this instance, the (011) α-Fe face]. These crystallites are fewer in number and grow together more slowly when the (111) Fe_3O_4 plane intersects the gross iron surface. These observations are demonstrated when the crystal counts in Table I are compared with the angles between the (111) Fe_3O_4 planes and the gross surface planes listed in Table II. It is evident that the number of α-Fe_2O_3 platelets

observed decreases, not only as the oxygen pressure decreases, but also as the angles between the (111) Fe_3O_4 planes and the gross surface planes increase from 0° over the (011) α-Fe face to 55° over the (001) α-Fe face. Replicas of the α-Fe_2O_3-Fe_3O_4 interface indicate that the actual interfaces between the two oxide phases are not parallel to the original iron surface except for the oxides formed over the (011) α-Fe face. Thus, it is suspected that the α-Fe_2O_3 phase forms on facets parallel to the (111) planes in the Fe_3O_4 layer, and that the rate of formation of these facets is related to the angle with which they intersect the gross surface plane.

This study tends to confirm the mechanism proposed in the previous paper to explain the effect of oxygen pressure on the rate of oxidation of iron: The formation of an outer layer of α-Fe_2O_3 over the surface of the Fe_3O_4 reduces the area of direct contact between the latter and gaseous oxygen. This reduces the number of cation-carrying vacancies formed at this interface, thereby reducing the flux of iron ions outward through the film. This reduction in iron-ion diffusion through the Fe_3O_4 layer reduces the oxidation rate. Thus, a correlation is observed between the number of α-Fe_2O_3 crystallites and the over-all oxidation rate. When the number is high, the α-Fe_2O_3 forms rapidly and the over-all oxidation rate is low. Conversely, when the number is low, the α-Fe_2O_3 film forms more slowly, and the over-all oxidation rate is high.

Manuscript received June 20, 1966; revised manuscript received Aug. 15, 1966. This paper was presented at the Philadelphia Meeting, Oct. 9-14, 1966.

Any discussion of this paper will appear in a Discussion Section to be published in the December 1967 JOURNAL.

REFERENCES

1. W. E. Boggs, R. H. Kachik, and G. E. Pellissier, *This Journal*, **112**, 539 (1965).
2. C. D. Stockbridge, P. B. Sewell, and M. Cohen, *ibid.*, **108**, 928 (1961).
3. P. B. Sewell and M. Cohen, *ibid.*, **111**, 501 (1964).
4. J. B. Wagner, Jr., K. R. Lawless, and A. T. Gwathmey, *Trans. AIME*, **221**, 257 (1961).
5. P. B. Sewell and M. Cohen, *This Journal*, **111**, 508 (1964).
6. T. G. Nilan, "An Application of Matrix Algebra to Geometric Crystallography," To be published.
7. G. A. Basset, J. W. Menter, and D. W. Pashley, "Structure and Properties of Thin Films," pp. 18-23, John Wiley & Sons, Inc., New York (1959).
8. C. Palanche, H. Berman, and C. Frondell, Editors, "'Dana' System of Mineralogy," 7th ed., p. 527, John Wiley & Sons, New York (1952).
9. C. D. Nicholls, *Adv. in Phys.*, **4**, 124 and 126 (1955).
10. A. Guinier, *Solid State Phys.*, **9**, 328 (1959).
11. A. Kelly and R. B. Nicholson, *Progress in Materials Science*, **10**, 153, 284 (1963).

Noncathodic Effects of the Permanganate Ion in the Anodic Passivation of Iron[1]

G. H. Cartledge

Chemistry Division, Oak Ridge National Laboratory, Oak Ridge, Tennessee

ABSTRACT

Iron actively reduces the permanganate ion at concentrations and pH values at which both chromate and pertechnetate ions inhibit corrosion effectively. The electrostatic polarization hypothesis of inhibition by such ions suggests, however, that the permanganate ion should probably manifest the same noncathodic effects as the inhibiting ions, if its reduction at the interface could be avoided. Anodic passivation of iron in permanganate solutions has therefore been conducted at potentials too noble for the cathodic process to occur. The polarization data showed that passivation was facilitated exactly as was previously found for the chromate and pertechnetate ions. The contrasting behavior of MnO_4^-, TcO_4^-, and ReO_4^- is discussed in relation to different theories of the action of the XO_4^{n-} inhibitors.

The permanganate ion is not generally considered to be an inhibitor of the corrosion of iron and steel, and very little study has been made of its interaction with the metals. In a comparison of the action of several oxyanions with iron, Mirolyubov, Tomaschov, and Zhuk (1) reported the ion to accelerate attack by cathodic stimulation. Hoar and Evans (2) showed that the permanganate ion, having no buffering capacity, differs from the chromate ion in being unable to precipitate ferrous ions completely as a hydrous ferric oxide without addition of alkali. In connection with the hypothesis of inhibition previously proposed (3-5), this failure to inhibit corrosion was ascribed to the strong oxidizing power of the ion, which resulted in its rapid consumption at the interface. Since it is plausible to regard the Mn-O bonds as having a considerable degree of polarity, however, it might be expected that the ion would exhibit the same noncathodic effects as were demonstrated recently for both chromate and pertechnetate ions, provided its reduction were prevented (6). The polarization data of the present study show clearly that MnO_4^- has a noncathodic activity in diminishing the charge and current density required for passivation.

[1] Research sponsored by the United States Atomic Energy Commission under contract with Union Carbide Corporation.

Experimental

Tests for inhibition.—The results of one set of several experiments carried out with 0.1% carbon steel in potassium permanganate of different concentrations and pH values are shown in Table I.

Corrosion was not instantaneously stifled under any of these conditions. Even in the $10^{-1}f$ solution, a

Table I. Tests for inhibition in aerated solutions

$[MnO_4^-]$	pH	Observations
$10^{-3}f$	4.1	Rusting and fading; in 7 hr, almost colorless and much rust
$10^{-3}f$	5.0	Spotting at once; in 14 da, colorless and some loose rust
$10^{-1}f$	3.05	In 1 hr, brassy film 56 da, no visible change, wt = 0.4031g 80 da, no visible change, wt = 0.4029g 103 da, no visible change, wt = 0.4032g 192 da, no visible change, wt = 0.4030g 248 da, no visible change, wt = 0.4031g

heavy, brass-colored film formed quickly, after which no more than a very slow reduction of the anions continued, in agreement with the observed constancy in weight over a period of several months. Subsequent measurements of electrode potentials of iron specimens confirmed the absence of appreciable polarization of the Mn(IV-VII) couple potential when the permanganate concentration was 10^{-1} or $10^{-2}f$ (pH $\geq$ 2.80). In the $10^{-3}f$ solution at pH 4, the couple potential was polarized by 100 mv or more by the corrosion process.

Another experiment was made to determine whether the permanganate ion, with its noble reduction potential, might inhibit attack if admixed with the pertechnetate ion under conditions in which the pertechnetate alone does not inhibit (low pH in the presence of sufficient sulfate ions). The metal was again 0.1% carbon steel (*ca.* 2 cm^2) and the solutions had the following compositions:

(*a*) $KTcO_4$, $10^{-3}f$, $KMnO_4$, $10^{-3}f$, H_2SO_4, $5\times10^{-3}f$; pH 2.16

(*b*) $KTcO_4$, $10^{-3}f$, - - - - - - H_2SO_4, $5\times10^{-3}f$; pH 2.12

The solutions were open to the air. Bubbles formed on the metal in (*b*) within 3 min while the specimen darkened; no bubbles formed in (*a*), but the metal darkened and turbidity developed within 5 min. In 1 hr, the permanganate color in (*a*) was completely bleached, and the metal had a nearly black film which resembled that produced in certain commercial coating processes. After the permanganate color disappeared, evolution of hydrogen was seen on both specimens. At 2.4 hr, the loose corrosion products were brushed away under running water and the specimens were weighed. The loss in weight was 2.6 mg for (*a*) and 1.7 mg for (*b*). It is clear that, under the chosen conditions, the permanganate ion held the potential above that for evolution of hydrogen so long as it lasted, and, at the same time, stimulated the attack on the metal.

Anodic polarization of iron in permanganate solutions.—In order to detect a noncathodic effect of the permanganate ion, if one exists, it is first necessary to ascertain empirically the potential of the permanganate ion and its reduction product under the conditions of concentration and acidity to be used. Then, following the procedure applied in the thorough study of the pertechnetate ion (6), it is necessary only to polarize the iron electrode anodically at a constant potential which is considerably noble to these couple potentials. A noncathodic action will then be seen as a resulting fall of the initial anodic current density to a low value (passivation), without the intervention of the very high current densities requisite for passivation in noninhibiting environments (sulfate, for example).

The Armco iron electrodes were electrocleaned and alternately passivated in HNO_3 and activated in HCl just before being connected to the polarizing circuit and inserted into the electrolyte. A rapid stream of helium swept out oxygen and provided agitation. A 0.1f $KMnO_4$ stock solution was prepared, aged for four days, then siphoned off from the sediment and adjusted to pH 3.60 by Dowex-50 resin that had been freed of substances that reduce permanganate and left in the acid form. Other solutions were prepared by dilution and similarly adjusted to the desired pH values.

The anodic current at a fixed potential was recorded until it fell to an essentially constant value. The cell was then switched quickly to a vibrating reed electrometer and recorder (for following the change of potential on open circuit) by a relay device activated by a multipole switch.[2] The charge passed during passivation was determined by graphical integration of the recorder chart. In order to insure that the potentiostat was set at a potential more noble than that of the Mn(IV-VII) couple under the experimental conditions, this value was determined using a platinum wire coated with the reduction product by cathodic polarization. The details of these measurements are indicated in the following section.

[2] The author is indebted to Mr. M. B. Noggle, of the Instrumentation and Controls Division, for the design and construction of this device.

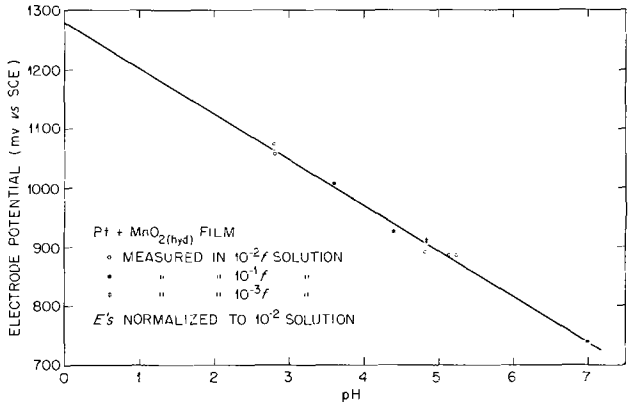

Fig. 1. Variation of the potential of the Mn(IV-VII) couple with pH.

Results

The Couple potential.—The composition of the reduction product from permanganate ion in the pH range 2.8-7.0 and in the presence of an excess of the anion is expected, on chemical grounds, to approximate a hydrous oxide of Mn(IV). Latimer (7) gives an electrode potential for the following couple:

$$MnO_2 \text{ (pyrolusite)} + 2H_2O \rightleftharpoons MnO_4^- + 4H^+ + 3e^-; \quad V_h^\circ = 1.69v$$

It is not known how much this value changes with the probable hydration of the dioxide or whether, indeed, the stoichiometry of the actual cathodic process conforms definitely to the above equation. Measurements were made, therefore, in 10^{-1}, 10^{-2}, and $10^{-3}f$ $KMnO_4$ at pH values ranging from 2.80 to 7.00. Oxygen was excluded by a rapid stream of helium. Although there was evidence of a slight aging effect on the potential of the filmed platinum electrode, the potential responded rather rapidly to changes in pH or concentration.[3] Figure 1 shows that measurements over a considerable range of concentration and pH are in good agreement with the indicated equation, dV/dpH being —78, rather than the theoretical —79 mv/pH. The data for 10^{-1} and $10^{-3}f$ solutions have been normalized to $10^{-2}f$ in accordance with the Nernst equation for the indicated couple. Figure 1 is a least-squares fit of the data and gives V_h° = 1.562 $\pm$ 0.007v.

The manganese couple potential is more noble than the reversible potential for evolution of oxygen in all the solutions used. Hence, the charges computed from the potentiostatic polarization curves are necessarily maximum values for the passivating charge. The data indicate, however, that the overvoltage for discharge of oxygen is large and the contribution of this reaction to the total charge is quite small when the potentiostat is held only 0.1-0.2v above the calculated manganese couple potential, since in such instances the total anodic current density fell to values in the μa/cm^2 region.

Passivation and behavior on open circuit.—Measurements were made at permanganate concentrations of 10^{-1}, 10^{-2}, and $10^{-3}f$, and over the pH range of 2.80-4.82. Results were similar in all cases: a very brief

[3] An example of the rapid equilibration after polarization may be seen in Fig. 3, which shows the ennobling of the oxide-coated platinum cathode from the low potential at which it was held during a passivation experiment.

surge of anodic current was followed by a rapid decrease to an essentially constant value in the microampere per square centimeter range, leaving the metal bright and visually free of any manganese oxide. The potential fell rapidly when the electrode was put on open circuit, but it did not go into the active region below the Flade potential and, at the two higher concentrations, ultimately approximated the stable value shown by a platinum wire coated with the manganese reduction product. The charge passed during passivation increased with the applied potential, owing to evolution of oxygen. Figures 2 and 3 show the temporal sequence of measurements for both the polarizing current density and subsequent change of potential on open circuit for two typical experiments with $10^{-2}f$ $KMnO_4$ at *p*H 2.80. In Fig. 2, the polarizing potential was 180 mv noble to the Mn(IV-VII) couple potential; in this case, the total charge was 16 mc/cm². In Fig. 3, the polarizing potential was 330 mv above the couple potential and the charge was 580 mc/cm². If it is assumed that the constant current density of 310 μa/cm² finally reached represented evolution of oxygen throughout the experiment, the net charge applicable to the passivation process is reduced to 80 mc/cm². Charges observed in the various concentrations were consistently in the range of a few mc/cm² and final current densities were as low as < 1 μa/cm² for the lower polarizing potentials. The very brief initial surge of current varied in the range of a few milliamperes per square centimeter.

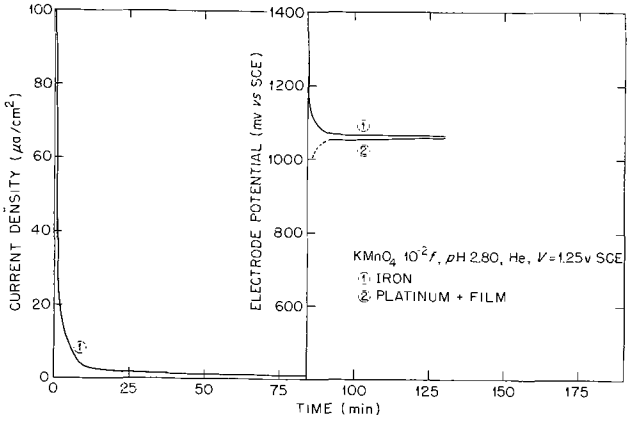

Fig. 2. Passivating current density and open-circuit potential of iron in $10^{-2}f$ $KMnO_4$ at *p*H 2.80; polarization at 1.25v (SCE).

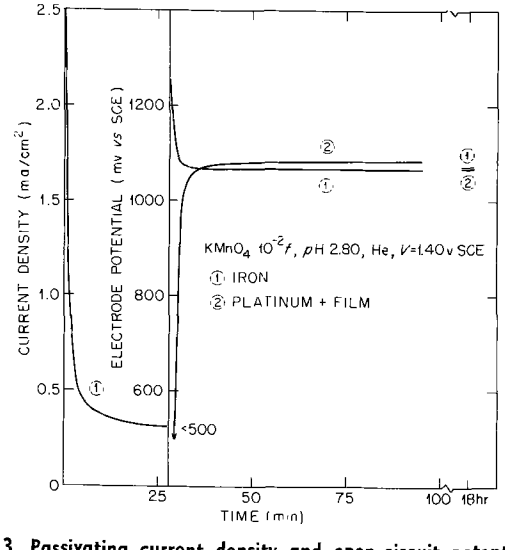

Fig. 3. Passivating current density and open-circuit potential of iron in $10^{-2}f$ $KMnO_4$ at *p*H 2.80; polarization at 1.40v (SCE).

For permanganate concentrations of both 10^{-1} and $10^{-2}f$, the potential of the iron electrode on open circuit exhibited the behavior shown in Fig. 2 and 3. The potential usually went through a very shallow minimum before coming back to a value within a few millivolts of the potential of the Mn(IV-VII) couple. At $10^{-3}f$, the permanganate ion was unable to maintain the passive state produced under anodic polarization after current was discontinued. The potential on open circuit fell 100 mv or more below the potential of the Mn(IV-VII) couple and the electrode corroded visibly. The system came to a mixed potential with the couple potential cathodically polarized by the continuing dissolution of the imperfectly passivated iron electrode. These observations are in agreement with the contrast shown in Table I between $10^{-1}f$ and $10^{-3}f$ solutions, the $10^{-1}f$ solution being able both to produce and to maintain the passive state.[4]

The influence of sulfate ions.—Anodic polarization of the iron electrode was conducted also in mixtures of permanganate and sulfate ions. In $10^{-3}f$ $(K,H)_2SO_4$ at *p*H 4.18, the full voltage of the potentiostat was applied to the cell without passivation.[5] Similarly, in $5 \times 10^{-2}f$ sulfate at *p*H 2.30, with lower cell resistance, the full anodic output of 16.5 ma/cm² failed to passivate the electrode. A mixed solution containing $5 \times 10^{-2}f$ $SO_4^=$ and $5 \times 10^{-2}f$ MnO_4^- at *p*H 3.86 was then used. In two experiments, the potentiostat was set at 1.10 and 1.20v (SCE), respectively. The initial surges of current fell only to 21 and 32 $\mu a/cm^2$. Although the potential of the iron did not fall into the active region on open circuit, considerable attack was evident both in the prompt formation of visible film and in the depression of the potential below the calculated couple potential. In a mixture that was $10^{-2}f$ in MnO_4^- and $10^{-1}f$ in $SO_4^=$ at *p*H 4, a polarizing potential of 1.10v (SCE) gave approximately constant current densities of 390 and 524 μa/cm², in two successive experiments. After the second polarization, the potential fell quickly to —510 mv (SCE) on open circuit. It may be concluded, therefore, that sulfate ions act antagonistically in this case also, although the permanganate ion is more tolerant of their presence than are the pertechnetate and chromate ions.

Cathodic polarization of the Mn(IV-VII) *couple.*—The film-coated platinum electrode used as cathode in the polarization experiments was subjected to cathodic polarization in $10^{-1}f$ $KMnO_4$ at *p*H 3.82. The re-

[4] Corrosion of the iron electrode in the $10^{-3}f$ solution even when the mixed potential is relatively noble is in no way inconsistent with the well-known observation that the metal has a very low corrosion rate at such potentials, if passivated anodically in sulfuric acid. The difference in behavior emphasizes the contrast between the simple surface film produced by passivation in the strongly acidic solution and the composite, nonprotective film resulting from action between the metal and the reducible anion at higher *p*H values.

[5] This means that the resistance of the $10^{-3}f$ sulfate solution held the current at too low a value for passivation, whereas in the permanganate solution of the same concentration and comparable resistance, passivation was readily achieved.

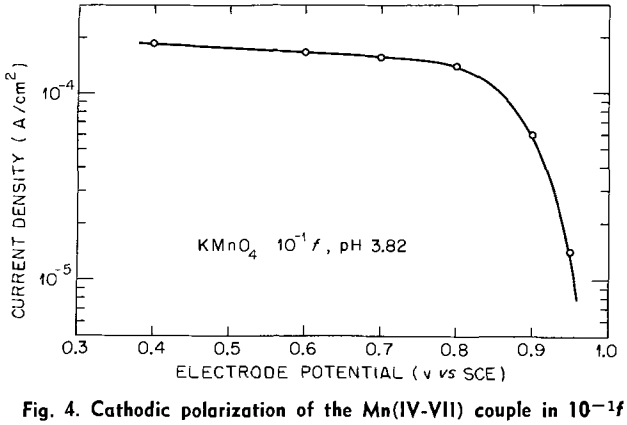

Fig. 4. Cathodic polarization of the Mn(IV-VII) couple in $10^{-1}f$ $KMnO_4$ at *p*H 3.82.

sults (Fig. 4) show that a limiting current density of about 0.2 ma/cm^2 is reached even at the relatively high concentration of permanganate ions. This current density is of the proper magnitude to represent the diffusion current for protons. Reduction of the permanganate ion is thus considerably faster than that of chromate ions at a similar *p*H, as may be seen by comparison of Fig. 4 with Fig. 6 of ref. (6), in which the limiting current density (before evolution of hydrogen) is an order of magnitude smaller.

Discussion

The experiments demonstrate that the permanganate ion is able to passivate iron or low-carbon steel only at concentrations substantially greater than those effective with the pertechnetate and chromate ions. At $10^{-1}f$ and *p*H 3, however, no loss in weight occurred over a long period and the exchange current of the Mn(IV-VII) couple was sufficient to maintain the passive electrode at essentially the reversible potential of the couple. In a $10^{-3}f$ solution at *p*H 5, on the contrary, active corrosion proceeded with reduction of the anions and extensive polarization of the couple potential.

At all three concentrations and over a *p*H range between 2.80 and 4.82, a noncathodic effect was manifest since passivation was observed at current densities which failed to produce passivation in sulfate solutions of comparable concentration and acidity. As in the previous experiments (6), the total charges accumulated during passivation at potentials noble to the anion couple potential were in the range of a few mc/cm^2, in spite of the fact that this charge included whatever amount of oxygen may have been simultaneously evolved. It was shown also that sulfate ions act antagonistically toward the inhibiting action of the permanganate ions, again emphasizing the importance of competing adsorption in the inhibitory process.

A comparison of the XO_4^-'s of the three transition metals of the seventh group of the periodic system shows the subtle character of the property associated with inhibitory action. The permanganate ion has vigorous oxidizing action, yet fails to inhibit corrosion except at relatively high concentrations. The perrhenate ion fails to inhibit at any concentration, even if its solution is artificially made to simulate a pertechnetate solution with respect to radiolytic products and oxidizing power (4). The pertechnetate ion, of intermediate electrode potential, is effective even at very low concentrations at least up to 250°C, although it contributes little to the requisite cathodic current if oxygen, or, still better, hydrogen peroxide is simultaneously present (8). Also, its inhibition is destroyed by noninhibitive anions at moderate concentration. None of the three anions is capable of buffering the interface.

The evidence supports the conclusion that although inhibition by all the XO_4^{n-} ions involves oxidation of iron to a composite film of low dissolution rate, the primary function of the $CrO_4^=$, MnO_4^-, and TcO_4^- ion is their noncathodic action at the interface. In practice, atmospheric oxygen is the chief oxidant (9). The property from which the specific, noncathodic action of these anions derives is therefore not buffering capacity, reducibility, nor formation of an insoluble salt with the cations. The effectiveness of the pertechnetate ion at higher temperatures indicates that the property is not very sensitive to rise of temperature.

As suggested previously (3-5), the difference between inhibiting and noninhibiting XO_4^{n-} ions may be associated with the contrasting polarity of their X-O bonds and the resulting field existing in close proximity to the ions. This field would act precisely in the double layer, across which the reactants in corrosion or passivation, respectively, must pass. Such an electrostatic polarization hypothesis led to the discovery of the remarkable effectiveness of the pertechnetate ion in 1952. Evans (10) used a related concept in 1961, but did not recognize the essential difference between the sulfate and chromate ions with respect to internal polarity and the consequent difference between the short-range fields adjacent to the ions.

The electrocapillary effects of ions in the double layer have been more or less successfully treated for completely polarized electrodes, but the situation becomes more complicated when Faradaic processes are in operation, as in corroding systems. In such cases, a simple treatment in terms of a ψ potential is incomplete, even if possible, since the identity of the rate-determining process can change with the ionic population in the interface, as well as with the potential. That is, the electrochemical rate equation can be altered both in the exponential function containing the net change of potential across the Helmholtz layer and also in the pre-exponential terms which depend on the "chemical" parts of the process. The noncathodic action of the XO_4^{n-} inhibitors is discussed from these points of view in another paper (11).

Manuscript received Jan. 17, 1966; revised manuscript received July 21, 1966.

Any discussion of this paper will appear in a Discussion Section to be published in the December 1967 JOURNAL.

REFERENCES

1. E. N. Mirolyubov, N. D. Tomashov, and N. P. Zhuk, *Trudy Chetvertogo Soveshchaniya po Elektrokhimii*, **1956**, 609.
2. T. P. Hoar and U. R. Evans, *J. Chem. Soc., London*, 1831 (1932).
3. G. H. Cartledge, *J. Phys. Chem.*, **59**, 979 (1955).
4. G. H. Cartledge, *ibid.*, **60**, 32 (1956).
5. G. H. Cartledge, *Z. Elektrochem.*, **62**, 684 (1958).
6. G. H. Cartledge, *This Journal*, **113**, 328 (1966).
7. W. M. Latimer, "Oxidation Potentials," 2 ed., p. 238; Prentice-Hall, Inc., New York (1952).
8. G. H. Cartledge, *J. Phys. Chem.*, **64**, 1882 (1960).
9. G. H. Cartledge, *ibid.*, **65**, 1361 (1961).
10. U. R. Evans, "First International Congress on Metallic Corrosion," p. 3; Butterworths, London, 1961.
11. G. H. Cartledge, *Brit. Corrosion J.*, **1**, 293 (1966).

Ellipsometric-Potentiostatic Studies of Iron Passivity

I. Anodic Film Growth in Slightly Basic Solutions

Jerome Kruger and Joan P. Calvert

National Bureau of Standards, Washington, D. C.

ABSTRACT

Cathodically reduced iron was anodically oxidized at potentials in the passive region of the anodic polarization curve in slightly basic sodium borate-boric acid solutions by means of a potentiostat. The kinetics of film growth were studied using an ellipsometer coupled with a fast recording technique, which enabled a determination of the rate of film formation for times less than 1 sec. This study of the kinetics of film growth using a nonelectrochemical technique agreed with kinetic results based on total charge measurements. Three stages of growth were detected: (*i*) First stage—growth limited by a diffusion process in the solution; (*ii*) Second stage—start of limitation of growth by the film involving the combination of several processes difficult to characterize by any rate law; (*iii*) Third stage—growth obeying either a logarithmic or inverse logarithmic rate law. The latter was found to imply that the passive film consisted of an outer layer poorly conductive for electrons.

Earlier ellipsometric studies (1) from our laboratory dealt with the kinetics of growth of passive films on iron in inorganic passivating solutions. As had been found by other techniques (2), that work showed a direct logarithmic growth law of a three-dimensional oxide film was observed. The work to be reported here extends these *in situ* ellipsometric studies on immersed surfaces to the growth of the passive films on iron by means of potentiostatic anodic polarization in slightly basic sodium borate-boric acid solution. This method of passivation has an advantage over both open-circuit passivation in oxidizing solutions and galvanostatic anodic polarization. Potentiostatic anodic polarization enables us to control more carefully the driving force for growth and maintain these conditions throughout the entire growth process, the rate being controlled by the process taking place. Thus, perhaps, we have a better chance to sort out these processes than for the case where the rate is fixed and the driving force changes (galvanostatic oxidation).

There already exists in the recent literature a set of excellent papers by Nagayama and Cohen (3, 4) and Sato and Cohen (5, 6) that deal with the anodic oxidation of iron under the same conditions as those used in this study. Our work complements and extends these studies in two ways: (*A*) By studying film growth using the optical technique of ellipsometry we have a direct nonelectrochemical way of measuring film thickness that does not depend on any possible current producing reactions not involved in film formation. (*B*) We are able to study the early stages ($<$ 10 sec) of the film formation process that are generally neglected in studies of the kinetics of passive film growth.

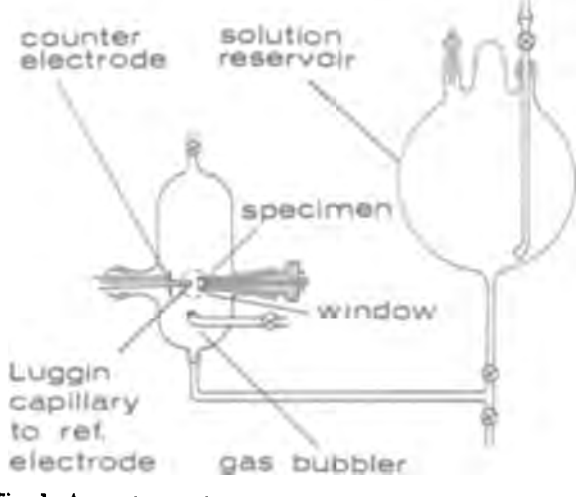

Fig. 1. Apparatus used to study the growth of films by anodic polarization with the ellipsometer. The drawing is not to scale.

This work differs from other *in situ* ellipsometric studies (7-11) on metals exhibiting passivity in one or both of two ways: (*a*) emphasis is placed on the kinetics of film growth and (*b*) the electrolyte is chosen so that little oxide film dissolution occurs. This is important because it leads to metal dissolution and surface roughening. Such an effect would present a complication in the interpretation of the ellipsometric measurements. This is so because the change in the optical parameters measured could be attributed to both film growth and to surface roughening. In this study roughening has been minimized by working in a neutral electrolyte and by growing the passive film rapidly, *i.e.*, by using a fast rise potentiostat to sweep the potential directly from the cathodic region to a potential in the passive region of the potentiostatic anodic polarization curve. The latter minimizes the roughening that would occur in going slowly through the active region before attaining passivity as was recently done in an ellipsometric study of passivity (10). A less ambiguous way of studying the active-passive transition is by going from the passive region to the active one. This will be the concern of the second paper in this series on the decay of passive films.

Cell, Material, and Procedure

Cell.—Figure 1 shows the cell used to observe the iron surface with the ellipsometer, measure its potential, and polarize the surface. The cell consisted of a gas bubbler, two glass windows, a platinum gauze counter electrode 2.25 cm^2 in area, and a Luggin capillary leading through a wetted closed stopcock to the saturated calomel electrode which served as the reference electrode.

The salt bridge was the solution used in the experiments and was drawn directly from the reaction cell through the Luggin capillary. Figure 1 shows also the iron specimen with an exposed area of 1.2 cm^2, mounted in a Teflon holder, and inserted into the cell. Solution was stored in the 2-liter reservoir and introduced into the bottom of the cell as shown in Fig. 1. Around 75 ml of solution were used in a run. This filled about half the cell.

Materials.—Solutions were made up using water of a conductivity of 7×10^{-7} mho or better and analyzed reagent grade H_3BO_3 and $Na_2B_4O_7 \cdot 10H_2O$. The acid

solution used was 0.3*N* and the salt 0.1*N*. Various *p*H's were obtained by mixing these solutions together in the following volume ratios of acid to salt to obtain the *p*H's used in this study: *p*H 7.4, 10/1, *p*H 8.4, 2/1, and *p*H 9.1, 1/4. The solutions were then checked with a *p*H meter. Once the solution was mixed it was placed in the 2-liter solution reservoir and deaerated by prolonged (24 hr) bubbling with purified 99.99% He prior to the introduction of the solution into the cell.

The iron was obtained from the Battelle Memorial Institute and was refined by a floating zone technique. It has less than 10 ppm gaseous impurities and less than 130 ppm metallic impurities.[1]

The specimens were large-grained (average grain size, 3 mm^2). Two specimens were used which had single crystal surfaces exposed to the solution. These were prepared by the strain-anneal technique.

Procedure.—The iron specimen surfaces were first mechanically polished (final polish 1/4 diamond abrasive), then electropolished using the perchloric acid polishing procedures described by Nagayama and Cohen (3), and finally washed in spectrographic grade methanol, dried in a jet of pure oxygen and placed in the cell. Once the iron specimen was placed in the cell and deaerated solution was admitted in the cell, it was possible to reduce any existing oxide film on the iron surface prior to growing a film by polarizing the surface galvanostatically to a cathodic potential. After cathodically reducing the iron surface, the solution was completely replaced by fresh solution with the metal surface maintained at the reduction potential. This step used by Nagayama and Cohen (3) was found to be essential in order to minimize the effect of ferrous ions. Also, oxygen had to be excluded as rigorously as possible in order to obtain reproducible results. When the film was so reduced, optical readings could be made[2] and the surface then brought rapidly by the potentiostat to an anodic potential where films start to form. Film formation was carried out in the potential region −0.4 to +0.8v. All potentials are referred to a saturated calomel electrode. All experiments were carried out at room temperature, 25°±1°C.

Ellipsometric-potentiostatic technique.—Detailed descriptions of ellipsometry in general and the experimental aspects of using ellipsometry in making *in situ* studies of the oxidation and corrosion of metal surfaces are discussed elsewhere (12). Therefore, the discussion here will be confined to the ellipsometric-potentiostatic technique used in this study which allows the kinetics of anodic film growth to be studied during the early stages of film formation at times as short as tenths of a second. The procedure used was an adaption of one recently reported by Reddy and Bockris (13) and consisted of the following: (*i*) After the surface was cathodically cleaned and readings taken, the ellipsometer was set at its extinction point (a minimum of light impinging on the photomultiplier tube). (*ii*) The photomultiplier tube was connected through an amplifier, which was a high impedance electrometer, to a fast two channel recorder of the direct recording galvanometer type with a frequency response as high as 100 Hz. This recorded the photocurrent along with the electrochemical current or potential. (*iii*) The surface was polarized anodically using the potentiostat[3] to potentials where film growth occurs. As soon as the film formed on the metal, the ellipsometer was no longer at the extinction point and the intensity of the light reaching the photomultiplier tube increased. For films <50Å, this was approximately a linear measure of the amount of film formed. This method depends also on the fact that for oxide films on iron Δ, the relative phase retardation, is the optical parameter that is sensitively changing with film growth (< 50Å) while the other optical parameter measured tan ψ, the relative amplitude reduction, is only slightly altered (14). Once the rate of film growth had slowed down (after a minute) more precise readings could be made by hand and the slower parts of the growth process studied. The circuit used to carry out such a technique is given elsewhere (12).

A complex refractive index used for the film formed was 2.5-0.3i (λ = 5461Å). This value was that found for the oxide formed on iron in a gaseous oxidation study (15). For reasons given elsewhere (14) it was reasonable to use in measuring the thickness of the very thin films observed in this study.

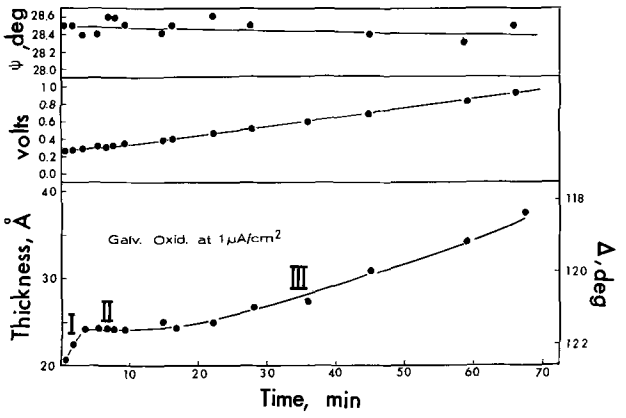

Fig. 2. Optical and electrochemical changes occurring during the galvanostatic oxidation of polycrystalline iron in a solution of pH 8.3. The specimen was pre-oxidized at 0.08v for 1 hr and then oxidized at a constant current density of 1 μa/cm^2.

Results and Discussion

Comparison between ellipsometric and coulometric film thickness measurements.—As a preliminary to the study of film growth kinetics a comparison between optical and coulometric anodic film thickness measurements was made. For this purpose galvanostatic rather than potentiostatic growth was employed. The conditions of growth were essentially the same as those used by Sato and Cohen (5); namely, the iron surface was pre-oxidized at 0.08v for 1 hr and then oxidized at a constant current of 1 μa/cm^2. The optical and coulometric results obtained in a solution of *p*H 8.3 are shown in Fig. 2. All the ellipsometric points shown were measured by the more accurate technique of placing the ellipsometer at extinction rather than the more rapid technique described in the experimental section. The thickness values given in this figure are based on the refractive index value n_2 given for the oxide earlier, 2.5-0.3i. The time is, of course directly proportional to the total charge used in the growth process.

With respect to the ellipsometric measurements, there are three separate regions in the relative phase retardation, Δ *vs.* time plot; before the arrest in Δ-values (called region I), during the arrest (region II), and after the arrest where steady growth occurs (region III). A potential arrest similar to that obtained by Sato and Cohen (5) appears to correspond to the arrest in Δ-values, but this would not be evident from our curve were it not for much more pronounced Δ-value arrest. The relation between the coulometric and the ellipsometric measurements differs in each of these regions and will be considered separately. We will consider only the variations of Δ because, as Fig. 2 shows, the variation of ψ with film growth is slight

[1] Gaseous impurities (ppm): O_2 (vacuum fusion), 2.1; S (colorimetric); 4 ± 3; C (combustion-conductometric), 3 ± 3; N_2 (vacuum fusion), 0.5; H_2 (vacuum fusion), 0.3.
Major metallic impurities (ppm): Al, 15; Cr, 5; Co, 5; Cu, 7; Ni, 20; P, 9; Si, 10.

[2] This cathodic reduction was also used as a check to determine whether roughening had occurred during film growth. Only when the same optical parameters were obtained after reducing a film formed during a given run, was the kinetic data obtained during that run considered valid.

[3] The potentiostat used was a commercial instrument whose rise time as determined under the conditions of these experiments was around 20 msec.

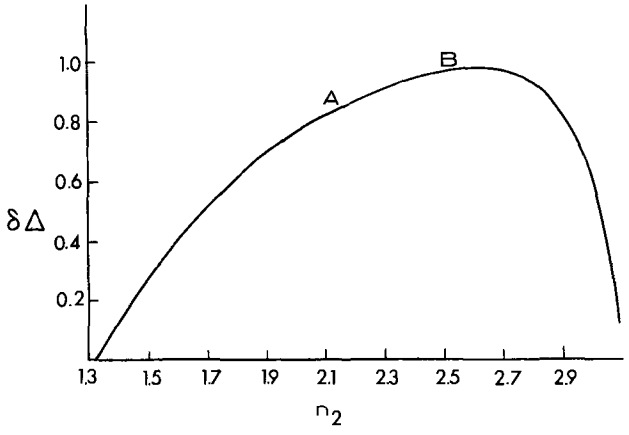

Fig. 3. Theoretically calculated curve showing the effect of varying n_2, the refractive index of the oxide film, on $\delta\Delta$, the change in the phase retardation that occurs on the growth of a 5Å film.

for films whose thickness lies in the range of interest of this study (40Å or less).

Region I.—Before the Δ-value arrest, a film is formed where 0.2 mC/cm^2 are required to cause a change of 1° in Δ as measured ellipsometrically. This compares with a value of 0.9 mC/cm^2 that one would calculate for a film assumed to be Fe_2O_3, density of 5 g/cm^3 and roughness factor of unity having the n_2 given above. This would thus suggest that during the stage before the potential arrest we have a film that has a density lower than 5 and thus probably an n_2 lower than 2.5-0.3i. It is likely that this would mean a film with many empty spaces or perhaps a film made up of discrete separated crystallites of oxide. Such a film probably behaves optically as a continuous film of low refractive index.

Region II.—At the arrest, the empty spaces in the film have filled up sufficiently to shift its n_2 value into a range where a change in n_2 does not appreciably change Δ, as long as the effective thickness is constant. This can be seen from Fig. 3 which shows the result of a calculation of the effect of varying the oxide's refractive index, n_2 on Δ, the change in Δ brought about by the growth of a 5Å film. Between points A and B in Fig. 3 there is only a small change in Δ with n_2. Thus, it would be possible to use up charge without appreciably changing Δ by forming oxide to fill the empty spaces in the film. As long as empty spaces are present and the solution has access to the substrate on which the film is growing, a constant potential would be expected. When the substrate becomes completely covered, the potential then changes and more nearly continuous film grows during the steady growth stage.

Two other explanations may be suggested to explain the Δ-value arrest. It may be related to Sato and Cohen's (6) observation that the outer layer of the passive film has a lower iron content and the process involved is the formation of iron-ion vacancies or excess oxygen ions. Such a process should not produce any observable change in Δ or ψ. Another possibility is that the arrest is associated with the introduction of protons into the Fe_2O_3 lattice, this being necessary for passivation according to some recent ideas of Bloom and Goldenberg (16). Because of the size and mass of the proton, its introduction into the film would probably be even less detectable ellipsometrically than the production of iron-ion vacancies.

Region III.—When the potential and film thickening arrest stage is over, the steady growth stage of a passive film commences. In the steady growth region the attainment of a steady value for the refractive index of the film is a more reasonable assumption than for regions I and II. It is this region that offers the best opportunity to compare the ellipsometrically determined thickness with the coulometrically determined values. A value of 0.242 mC/cm^2 per optically measured angstrom is obtained from Fig. 3. Using the density and composition assumptions described earlier, a thickness ratio of 1.3 can be calculated. Since ellipsometric thickness measurements do not depend on a knowledge of the roughness factor, while electrochemical ones do, the thickness ratio represents the surface roughness factor. A reasonable value for an electropolished surface is 1.3.

Variation of film thickness with potential and pH.—A determination of the variation of film thickness measured at a given time with overpotential[4] is important because it gives us an idea of the fields [or more correctly overfields (17)] involved. Figure 4 shows this variation for three solutions of different pH's used in this study, for a 1 hr polarization at a given potential. At an overpotential of around 0.5v the slope changes for the 7.4 pH solution. This overpotential corresponds to a potential of around —0.2v (SCE) and is near the potential that Nagayama and Cohen (4) call E_a^2, a potential below which Fe^{++} is observed in solution (called by them "region A"), and above which the concentration of Fe^{++} is too low for analysis ("region B"). Very little or no change in slope was observed for the 9.1 and 8.4 pH solutions in the passive region of the polarization curve, roughly between —0.6 to +0.85v (SCE). Our optically determined value for the differential field (dV/dX) [see (17)], for a solution of the same pH, 8.4, as that studied by Nagayama and Cohen (3) agrees with their value to better than 5% for potentials above E_a^2.

The fact that (dV/dX) is greater[5] at the lowest pH (above E_a^2) means phenomenologically that the barrier that the ions must surmount for the film to grow is higher than that existing in the film formed in the pH 9.1 solution.

Below E_a^2 for the 7.4 pH solution, the change in (dV/dX) to a lower value points to a lower barrier. The work of Nagayama and Cohen (4) indicated for the film formed in "region A" has a higher percentage of iron in its outer layer and is less protective because ferrous ions are found in solution. Thus a higher iron content in the film may be related to a lower barrier to the movement of ions.

[4] Our overvoltage values are assumed to be the difference in potential between the potential during film growth, V, as provided by the potentiostat and the open-circuit potential measured after the iron surface has been cathodically reduced. At equilibrium under these circumstances in the pH range used for this study, an oxide film does exist on the metal surface (18). The equilibrium values, E_o, for the solutions shown in Fig. 4 are for pH 7.4, —0.71, for 8.4, —0.75, and for 9.1, —0.78.

[5] It should be noted that since Fig. 4 is a plot of X *vs.* V, the value of (dV/dX) is the reciprocal of the slopes shown in the figure. Also it should be pointed out the current was almost constant when X was measured, $(dV/dX) \approx (\partial V/\partial X)_i$.

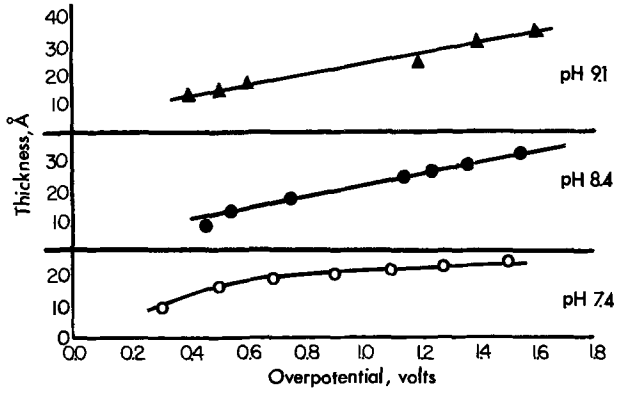

Fig. 4. Comparison of the change in film thickness with overpotential in solutions pH 7.4 (open circles), 8.4 (closed circles), and 9.1 (triangles) used in this study. Specimens were polarized potentiostatically 1 hr at potentials shown.

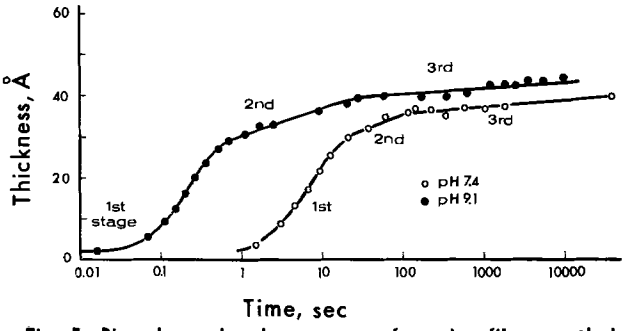

Fig. 5. Plot shows the three stages of passive film growth in solutions of pH 7.4 (open circles) and 9.1 (closed circles) for potentiostatic growth at 0.8v. This also shows that the onset of the three stages is affected by pH. Plot is logarithmic in time.

Stages of film growth.—A rapid recording technique described earlier was used to follow the kinetics of potentiostatic film growth. The growth of the passive film can be followed for times from less than 1 sec to any chosen longer time. Three stages in the growth process can be identified. These three stages are shown in Fig. 5 which also shows the variation in the onset of the stages as affected by *p*H. The division of the growth curve into these three stages is somewhat arbitrary but, except for those times during the growth process when there is a transition between stages, we do not have any difficulty in separating the stages. Strictly speaking, the second stage may not be a true stage in a kinetics sense, because it may be only a transition between the first and third stages. It will be so labeled, however, because there is a possibility, for reasons given in the section where it is discussed, that it may be a true stage.

First stage growth.—Figure 6 shows that the film growth during the first stage in the formation of the passive film follows a square root of time dependence. This was found to give a better fit than either a linear or logarithmic dependence by using a computer programmed for this purpose. Figure 6 also shows that the slope of the straight line plot of thickness *vs.* $\sqrt{t}$, is higher for the solution with the highest *p*H. This linear relationship between the thickness and $\sqrt{t}$ which is obtained by the integration of the diffusion equation (19) suggests that a diffusion process is controlling the rate of film growth during the first stage. Initially, it was thought that OH^- ions were the diffusing species controlling the growth process because the rate increased with an increase in *p*H. However, if the buffering action of a solution is good, the process could not be limited by OH^- diffusion because a well buffered solution would instantaneously supply a given concentration of OH^- ions. Calculations[6] indicate that for the solutions used the buffering action is poor, particularly for the 7.4 *p*H solution. Hence, the situation is complex with diffusion of not only OH^- ions, but also that of borate and boric acid being involved. For this reason the usual diffusion equation (19), which allows one to determine the diffusion coefficient, cannot be used. We can only give an empirical equation

$$x = k_1\sqrt{t} + C \qquad [1]$$

where k_1, the slope of the lines in Fig. 6 is *p*H dependent. This strong *p*H dependence suggests that the most important feature of the first stage is that it is controlled by diffusion through the solution rather than through the film.

To determine if the diffusion of a reacting species, such as oxygen, could be controlling in the first stage, an experiment was carried out using a solution saturated with oxygen. As Fig. 7 shows the concentration of oxidizing species was so high that the first stage $\sqrt{t}$ dependence was over so rapidly that our measuring technique could not detect it. The results obtained could also be due to a change in mechanism that occurs in the oxygen saturated solution.

Second stage growth.—The first stage ends at that point in the growth process at which there is a departure from the linear relationship between thickness and $\sqrt{t}$. When this occurs diffusion through the solution is no longer the rate-controlling step, and we begin to observe a change in the type of rate law governing the process. We call this second stage growth. It appears to be the transition between the solution limited growth of the first stage and the steady-state film limited growth of the third stage. Since the second stage is a transitory one, it is difficult to characterize the type of rate law governing the growth process. Because of this uncertainty, we will not attempt to fit a specific rate law, but will instead just point out the following three qualitative observations:

1. The rate of growth is greater than that in the third stage. This may indicate that the composition of the film formed during the second stage differs from that of the third. It is assumed that a more protective layer, one where ion movement is more difficult, is formed during the latter stage.

2. The possibility of diffusion of Fe^{++} ions in solution being rate controlling is ruled out because current measurements made simultaneously with the optical measurements show that for the coulombs passed all of the Fe^{++} produced have gone into producing the film measured optically at the point of transition between the first and second stages. Film growth during the second stage can therefore not use the Fe^{++} ions present in solution.

[6] The authors are indebted to Dr. William M. Schwarz, Jr., of the Electrochemistry Section of NBS, for making these calculations and pointing out their implications.

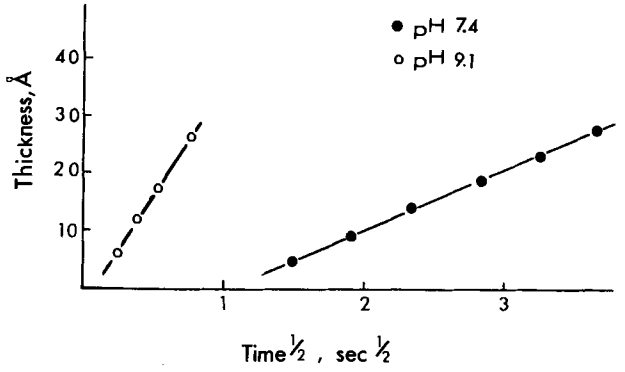

Fig. 6. Plot of film thickness vs. square root of time at pH = 7.4 (closed circles) and pH = 9.1 (open circles) for potentiostatic growth at 0.8v.

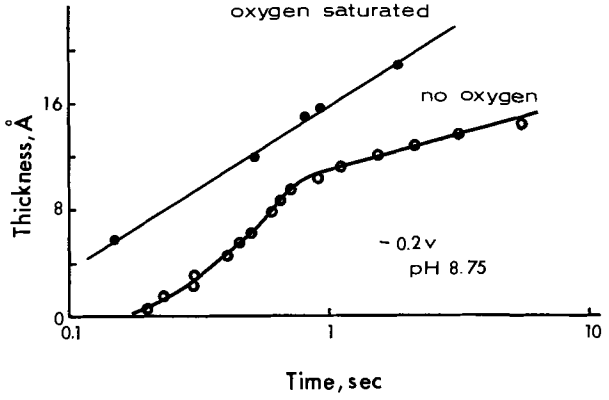

Fig. 7. Plot of film thickness vs. log of time in an oxygen saturated (closed circles) and He saturated solution (open circles). The oxidations were carried out at —0.2v in a solution of pH = 8.75.

Table I. Field, E, existing during the transition from first to second stage kinetics

pH	Potential, v	Overpotential, v	$X^*_{1\to 2}$, Å	(10^6 E v/cm)
9.1	0.8	1.58	27.5	5.8
	0.6	1.38	21.0	6.5
	0.4	1.18	17.9	6.5
7.4	0.8	1.51	22.5	6.8
	0.6	1.31	18.3	7.2
	0.4	1.11	15.4	7.2

* X_{1-2} is the thickness at which there occurs a transition from first to second stage kinetics.

3. When the thickness at which a change from first stage to second stage occurs is divided into the overpotential at which growth is occurring, it is found that this ratio, E, is roughly the same regardless of potential (see Table I). E is the field across the film, assuming that the film is a sufficiently good insulator to support such a field. Thus the first stage may end at that point in time when the field across the film has dropped to a value low enough so that passage of ions through the film becomes rate determining. This assumes that the growth process is field dependent. The results of Table I indicate this may be so.

Third growth stage.—This is the steady-state growth stage and occurs after about the first minute of the growth process. The growth that occurs during this stage is one that has been studied almost exclusively in most other kinetic studies of anodic oxidation. As Fig. 8a and b show this stage fits equally well either the logarithmic (x *vs.* ln t) or inverse logarithmic ($1/x$ *vs.* ln t) rate laws. Figure 9 is for single crystal specimens. A few experiments were carried out using two single crystal surfaces of (110) and (311) orientations. Figure 9 shows that the orientation of the metal surface also affects the rate. This aspect which is of great importance was not gone into in much detail in this study, but will be explored further in later studies. It is interesting to point out, however, that the (110) surface (the closest packed surface in the bcc system) exhibited the higher rate. This fits well with another study (1) that showed that the (110) forms the least protective film.

The logarithmic law implies a number of different mechanisms that are listed by Sato and Cohen (5). None of these require the existence of a large field dependent on film thickness to promote the growth process. Figure 8a shows the direct logarithmic rate is independent of potential (approximately parallel lines for different potentials), but the intercept varies with potential. These results agree with the empirical equation obtained by Sato and Cohen (5) for the same system. They give the expression for current as follows

$$i = k \exp\ (V - Q/B) \qquad [2]$$

where i is the current, V the potential, and Q the total charge accumulated in forming the film; k and B are constants. To compare their coulometric results with our optical ones Equation [2] is integrated and the film thickness, X, introduced in place of charge using the factor determined experimentally (0.242 mC/cm²/Å)

$$x = \frac{B}{0.242} \ln (t + t_o) + \frac{B\beta}{0.242} V + C \qquad [3]$$

The t_o in Eq. [3] is a constant with the unit of time, resulting from the integration, whose value depends on the time scale selected. On the basis of the empirical expression they obtained and because their rate constant B is temperature dependent,[7] they concluded that the various mechanisms leading to direct logarithmic growth do not fit. Instead, they proposed a "place exchange" mechanism for the oxidation of iron. This mechanism involves film grown by the simultaneous exchange of positions between oxygen and iron ions for all layers of these two species forming the film. In this way, oxygen at the solution interface is incorporated into the film while, likewise, iron at the metal-oxide interface is also incorporated.

The average values for a large number of runs obtained for the constants B and β by this ellipsometric study compared with those obtained by Sato and Cohen by electrochemical measurements and are shown in Table II. This agreement is reasonble for the pH 8.4 considering the fact that different iron was used and various assumptions were made with regard to the density and optical constants of the oxide, and the roughness factor of the surfaces. It can be seen from Table II and Fig. 4, however, that this study does indicate that β was found to vary with pH, whereas Sato and Cohen did not find any variation. Whether these variations are real or due to the differences in the two techniques of measurements, *e.g.*, the optical constants of the films formed at different pH's may vary, we cannot say. Possible reasons for the

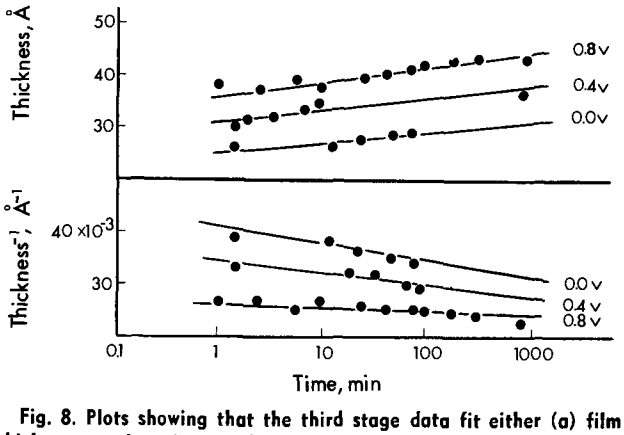

Fig. 8. Plots showing that the third stage data fit either (a) film thickness vs. log time or (b) reciprocal of film thickness vs. log time at potentials shown.

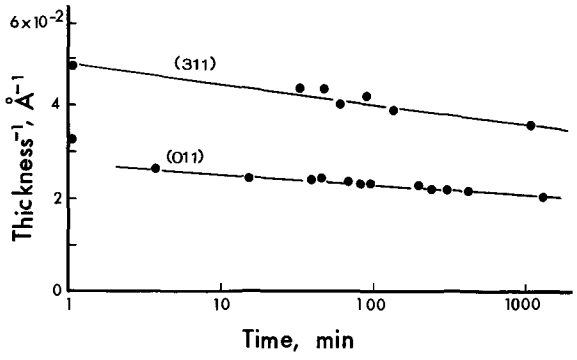

Fig. 9. Plot of reciprocal of film thickness vs. log time for (311) and (110) surfaces.

[7] If B were not as temperature dependent as Sato and Cohen (5) found, electron transport through the film could be rate limiting. Such a process would lead to a logarithmic law.

Table II. Average values of B and β

	pH	B/0.242, Å	β, v^{-1}
Sato and Cohen	8.4	0.77	19.2
Nagayama and Cohen	8.4		20*
This study	9.1	0.76 ± 0.1	28 ± 1*
	8.3	1.08 ± 0.3	18 ± 1*
	7.4	1.04 ± 0.3	12 ± 1*

* These values are based on A *vs.* η or A *vs.* V curves similar to that of Fig. 4, since, as can be seen from Eq. [3], the slope of this curve for a fixed time is $B\beta/0.242$.

variation of β with pH were given in the earlier section on the variation of film thickness with potential and pH.

Empirically, our results can be reasonably related to those obtained by Sato and Cohen and treated in the same way but using optical rather than electrochemical measurements. We will now consider in detail the other way of looking at the data which, as Fig. 8 shows, fit an inverse logarithmic growth equally well. When this type of growth is observed, we can consider the rate to be controlled by the current of Fe^{++} over an activation barrier, W. For such a process a plot of the reciprocal of the film thickness *vs.* the log of time should yield a straight line. Figure 8b shows such a plot for 3 different potentials, all above E_a^2. The rationale behind such a plot is based on the approximate integration of the equation for the ion current (20) neglecting the backward field, whose effect is small at potentials above E_a^2 where virtually no Fe^{++} ions are found in solution. This equation is

$$i = 2a^* n \nu ze \exp - \left[\frac{W - zea^*\eta/X}{kT} \right] \qquad [4]$$

where n is the number of mobile ions per unit volume, ν, the frequency, ze the charge on the mobile ion, η the overvoltage, a^* the activation jump distance, and X is the film thickness. An approximate integration of the equation gives

$$\frac{1}{X} = \text{Const.} - \frac{1}{X_1} \ln t \qquad [5]$$

where

$$\frac{1}{X_1} = \frac{kT}{zea^*\eta}$$

This is the inverse logarithmic rate law derived by Cabrera and Mott (21). From the expression for $1/X_1$ as derived from this theory, we can see that we would expect a plot of X_1 *vs.* η to yield a straight line. Figure 10 is such a plot for the two extreme pH solutions studied. Each point represents the averages of at least three runs. It can be seen that the values for both solutions fit reasonably well a straight line, the 7.4 pH solution showing more scatter.

Since the dependence of X_1 on η, as shown in Fig. 10, is reasonably linear and because an indirect logarithmic rate law is observed, we can consider the mechanism of passive film growth on iron in nearly neutral solutions as being similar to that for aluminum or tantalum, namely, field assisted migration of cations through the film to react with oxygen or OH^- at the solution-oxide interface. This mechanism has indeed been proposed for iron by Vetter (22), Ord (23) more recently, and others. A difficulty, however, arises when comparing the mechanism of passive film growth on iron to that of aluminum or tantalum. The oxides on the latter two metals are very poorly conductive for electrons and can thus support large fields. However, the oxide film on iron is assumed to be a good electronic conductor (22) and would thus not be able to support the 10^6-10^7 v/cm field necessary to pull cations through the film. The assumption that the passive film on iron is a good electronic conductor is probably based mostly on the fact that one gets oxygen evolution when a thin film is still present and at fairly low potentials as compared to aluminum (24). However, as the Pourbaix diagram for iron shows (18) at the oxygen evolution (transpassive) potentials the possibility of a change in the nature of the film exists. Electron diffraction studies from our laboratory (25) have indicated that the γFe_2O_3 found for films formed in the passive region is not found for films formed at potentials in the transpassive region. While still at passive potentials, however, the existence of γFe_2O_3 at the outer part of the film is most probable (3, 25). This oxide is probably a very poor electronic conductor (26) and could support the field required by the theory. As Nagayama and Cohen (3), Vetter (27), and others have pointed out, there exists a strong possibility that the γFe_2O_3 exists as an outer layer of the passive film next to the solution with Fe_3O_4 being next to the metal. Since Fe_3O_4 is a good electronic conductor, the field just postulated would exist only across the poorly conductive γFe_2O_3. In line with this, Vetter (27) has postulated that all of the potential drop in a passive film is across the outer layer. The reasonableness of this concept can be seen if we first calculate a value for the jump distance, a^*, using the slope from Fig. 10 and the expression for X_1 in Eq. [5]. The values in this plot are based on the assumption that the field is across the entire film. Such an assumption leads to a value of around 10Å for a^*, assuming that the mobile ion has a charge of 2. Estimates of a^* for the (110) and (311) surfaces were 8.3 and 4.6Å, respectively. Vetter (22), assuming that the ferric ions are mobile, obtained a value of 5.5Å for films formed in H_2SO_4 solution. Our value as well as Vetter's appears to be abnormally high. However, if the field is only across a poorly conducting outer layer of the passive film, the value of X_1 becomes roughly equal to the product of the fraction of the film that is poorly conducting and the value of X_1 obtained by assuming the field is across the entire film, *i.e.*, the values plotted in Fig. 10. An estimate of this fraction can be obtained from the work of Nagayama and Cohen (3), from the ratio of the charge required to reduce the outer layer to the total charge accumulated in forming the film. The fraction obtained using this assumption and their data is around 1/3. With this assumption the value of a^* becomes 3Å, a most reasonable value. Using this value for a^* or the larger value and either 1/3 the limiting thicknesses shown in Fig. 4 or the whole thickness, the same values for an estimate of W, the activation barrier can be made from the approximate expression for the limiting thickness (22)

$$X_L = \frac{Zea^*\eta}{W - 39kT} \qquad [6]$$

A value of 1.8 ev (41 kcal/mole) was obtained for the pH 9.1 solution and 2.0 ev (46 kcal/mole) for pH 7.4. Values estimated for the single crystal surfaces are about 1.5 ev for both orientations studied. All the values of W are rather high compared to the valve metals (18). This is reasonable in light of the fact that the passive film on iron is much thinner than that on the valve metals such as Al or Ta.

It must be emphasized that the reasonable value of 3Å for a^* is based on the assumption that the field is only across that part of the film that has a low concentration of iron, the part that Nagayama and Cohen concluded contains iron vacancies and Fe^{+6} ions. If the field is across all of the γFe_2O_3 they found to be present, a^* becomes much larger, around 7Å. Therefore, if the field assisted cation migration theory is valid, it

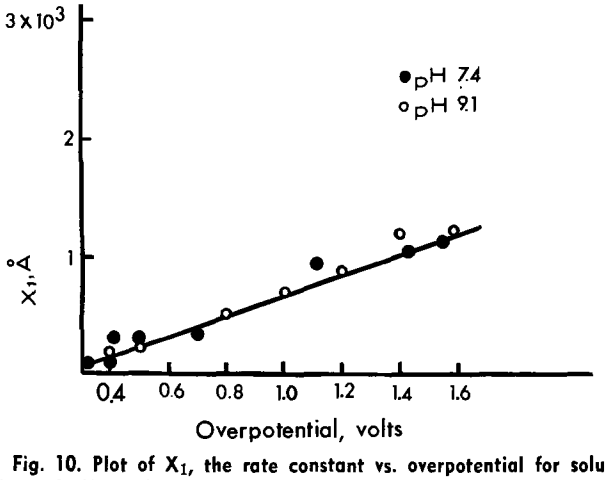

Fig. 10. Plot of X_1, the rate constant vs. overpotential for solutions of pH 7.4 (closed circles) and 9.1 (open circles).

is more reasonable to expect that the field is only across a vacancy rich or, using Bloom and Goldenberg's model (16), a proton rich outer third of the total film. This portion would be expected to be more poorly conducting than a more stoichiometric γFe_2O_3 and would thus be able to support a large field.

Recent work by Ord and DeSmet (28) combining ellipsometric and capacitance measurements on the same system described here indicate that the field is only across the outer part of the film as proposed here. Electrode capacity studies by Wisdom and Hackerman (29) also indicate that the passive film over a wide range of pH has two sorts of material, the last formed being responsible for passivity, and being different from bulk oxides.

Another indication of the importance of the composition of the outer part of the passive film and its bearing on the fields in the film can be obtained by considering film growth at potentials below E_a^2. Here a measurable concentration of Fe^{++} is present in solutions, and thus a more complicated set of conditions exist. Because of this it has been difficult to obtain completely reproducible results. The reason for this lies in the fact that two factors affecting the rate in opposite ways are probably present. The first factor, the increase in importance of a backward field[8] with decrease in overvoltage, tends to decrease the rate and is probably responsible for the appearance of Fe^{++} ions in solution. The second factor, a less protective film which would tend to increase the rate, is probably present on films formed at potentials below E_a^2 as indicated by results of Nagayama and Cohen (3). They found a higher concentration of iron which they ascribed to a lower concentration of defects in the films formed below E_a^2. Loosely expressed, they found the higher the concentration of defects, the more protective the film was.

This model concerned with field assisted movement of cations through a poorly conducting outer layer neglects the movement of cations through the inner layer. Electron diffraction studies (30) give a clue to the manner in which this may occur. These studies indicate that this inner layer is highly oriented, but made up of a very high concentration of grain boundaries or pipes of Fe_3O_4 so that easy diffusion of Fe^{++} is a good possibility. In this manner passage of Fe^{++} through the inner layer would be relatively easy. The second stage growth may thus be a combination of an easy diffusion growth through the inner "porous" Fe_3O_4 and the formation of an outer γFe_2O_3 that becomes more and more nonconductive and less porous with time until it can support a field that assists cation movement until the field becomes too small. Since the second stage is thus a mixture it is difficult to characterize by a simple rate law.

Summary

These studies have shown that by the use of the optical technique of ellipsometry we were able to get reasonable agreement with other studies on the same system using an entirely different way of measuring the amount of film, coulometry. Three growth stages were observed which were interpreted as follows: (*i*) First Stage, growth limited by the rate of diffusion of some species through the solution giving a process where the thickness is proportional to $\sqrt{t}$; (*ii*) second stage, the onset of the limitation of growth by the film but because it is a combination of two or more processes difficult to characterize by any rate law; (*iii*) third stage, described equally well by either a logarithmic or inverse logarithmic rate law. The consequences of the former have been interpreted elsewhere (5). The latter was shown to imply that the passive film involves a film whose outer layer is poorly conductive for electrons allowing a high field to be built up which assists the movement of cations through the film to the solution interface where they are oxidized.

This study has shown that rate studies are not able to decide definitely between the above two mechanisms in a slightly basic solution.

[8] This backward field should be part of Eq. [4], but was left out for simplicity and because it is unimportant until η becomes small (17).

Acknowledgment

The authors are grateful to M. C. Bloom, R. E. Howard, M. Cohen, and A. T. Fromhold, Jr., for many helpful discussions.

Manuscript received June 17, 1966; revised manuscript received Sept. 8, 1966. This paper was presented at the Buffalo Meeting, Oct. 10-14, 1966.

Any discussion of this paper will appear in a Discussion Section to be published in the December 1967 JOURNAL.

REFERENCES

1. J. Kruger, *This Journal*, **110**, 654 (1963).
2. D. M. Brasher and A. H. Kingsbury, *Trans. Faraday Soc.*, **54**, 1214 (1958).
3. M. Nagayama and M. Cohen, *This Journal*, **109**, 781 (1962).
4. M. Nagayama and M. Cohen, *ibid.*, **110**, 670 (1963).
5. N. Sato and M. Cohen, *ibid.*, **111**, 512 (1964).
6. N. Sato and M. Cohen, *ibid.*, **111**, 519 (1964).
7. L. Tronstad, *Trans. Faraday Soc.*, **29**, 502 (1933).
8. M. A. Barrett, "Ellipsometry in the Measurement of Surfaces and Thin Films," E. Passaglia, R. R. Stromberg, and J. Kruger, Editors, p. 213, N.B.S. Misc. Pub. 256, U.S. Government Printing Office, Washington (1964).
9. P. C. S. Hayfield and G. W. T. White, *ibid.*, p. 157.
10. A. K. N. Reddy, M. G. B. Rao, and J. O'M. Bockris, *J. Chem Phys.*, **42**, 2246 (1965).
11. V. V. Andreeva, *Corrosion*, **20**, 35t (1964).
12. J. Kruger, *ibid.*, **22**, 88 (1966).
13. A. K. N. Reddy and J. O'M. Bockris, "Ellipsometry in the Measurement of Surfaces and Thin Films," see (8) p. 229.
14. J. Kruger, *ibid.*, p. 131.
15. A. B. Winterbottom, *J. Iron and Steel Inst.*, **165**, 9 (1950).
16. M. C. Bloom and L. Goldenberg, *Corrosion Sci.*, **5**, 623 (1965).
17. L. Young, "Anodic Oxide Films," p. 10, Academic Press, New York (1961).
18. M. Pourbaix, "Atlas D'Equilibres Electrochemiques," p. 312, Gauthier-Villars and Cie, Paris (1963).
19. P. Delahay, "New Instrumental Methods in Electrochemistry," p. 51, Interscience Publishers, New York (1954).
20. L. Young, *op. cit.*, p. 15.
21. N. Cabrera and N. F. Mott, *Rep. Prog. Phys.*, **12**, 163 (1949).
22. K. J. Vetter, *Z. F. Elektrochem.*, **58**, 230 (1954).
23. J. L. Ord, *This Journal*, **113**, 213 (1966).
24. T. P. Hoar, Proc. 3rd Meeting, CITCE, Berne 1951, p. 146, Manfredi, Milan (1952).
25. J. Kruger, C. L. Foley, and C. J. Bechtoldt, To be published
26. R. Matejec, *Mitt. Forschungs der Agfa*, Leverkusen-Muenchen, **3**, 273 (1961).
27. K. J. Vetter, *This Journal*, **110**, 597 (1963).
28. J. L. Ord and D. J. DeSmet, *ibid.*, **113**, 1258 (1966).
29. N. E. Wisdom, Jr., and N. Hackerman, *ibid.*, **110**, 318 (1963).
30. P. B. Sewell, C. D. Stockbridge, and M. Cohen, *ibid.*, **108**, 933 (1961).

A Study of the Inclusion of a Radioactive Addition Agent in Bright Nickel

Warren R. Doty

Electrochemistry Department, Research Laboratories, General Motors Corporation

and Bernard J. Riley[1]

Physics Department, Research Laboratories, General Motors Corporation, Warren, Michigan

ABSTRACT

C-14 allyl and C-14 quinaldine labeled N-allyl quinaldinium bromide (NAQ) were prepared and their inclusion in bright nickel deposits studied. The amount of NAQ inclusion was found to depend on the mass transfer processes, the diffusion layer thickness, and the catalytic state of the nickel deposit.

Previous publications from this laboratory on the mechanism of leveling in bright nickel plating have shown that radioactively labeled addition agents can be used to study the problem (1-3). Work with C-14 and S-35 labeled sodium allyl sulfonate (SAS) demonstrated that slightly more radioactivity was incorporated in the nickel deposit adjacent to peaks rather than valleys of a microprofile surface. These results are in agreement with the general theory of leveling which postulates that a thinner diffusion layer above peaks facilitates transfer of addition agents to these areas, while the relatively thicker diffusion layer above valleys impedes transfer (4, 5). Adsorption of the addition agent or its reduction product leads to localized polarization and partly inhibits deposition of nickel ions. The net effect is the deposition of slightly more metal in the valleys than on the peaks.

In addition to the leveling phenomena the effect of other plating variables, such as *p*H, current density, and concentration of other addition agents on the amount of inclusion of the labeled compound, can also be determined. As is well known, in bright nickel plating, two or more addition agents are necessary to achieve the desired results. Addition agents are categorized as class I and class II brighteners, and a member of each class must be used (6). SAS is a typical class I brightener. The class II brightener used with SAS in the earlier work was N-allyl quinaldinium bromide (NAQ).

The results obtained with C-14 and S-35 labeled SAS in combination with nonradioactive NAQ have been reported (3) and are in agreement with the known behavior of class I brighteners. Recently Edwards also reported similar results with two other S-35 labeled class I brighteners (7, 8).

Relatively little work has been done, however, on the inclusion of class II brighteners.[2] Because of the commercial importance of class II brighteners and the very low concentrations that are normally employed, this problem seemed worthy of study by the radioisotope method.

The class II brightener chosen for study was NAQ, primarily because some experimental technique had been developed in its use from the earlier work. Which carbon atom should be labeled was the next decision. In any study involving radioactive compounds, it is necessary to be certain that the labeled portion of the molecule represents the behavior of the whole molecule in all reactions. Purity, availability, and cost of the radioactive intermediates are other factors.

C-14 allyl bromide (3 position) meets all of the latter considerations. Reacting this compound with quinaldine as shown in reaction 1 forms C-14A NAQ. Previous work had shown, however, that some of the NAQ was cleaved during electrolysis at the allyl-to-nitrogen bond and that propene was identified in the gases (mainly hydrogen) which had escaped the cathode (3). The use of C-14A NAQ, therefore, is suspect as correctly representing the behavior of NAQ if only the deposit is to be counted. Nevertheless, C-14A NAQ was prepared because at the time no source for C-14 quinaldine was available.

Later, after the inclusion studies were under way, a supplier of C-14 quinaldine (8a position) was located. A sample of C-14Q NAQ was prepared and the inclusion experiments repeated. With both functional parts of the NAQ molecule labeled, comparison of the relative inclusion of each part could now be made.

Experimental

Synthesis of NAQ.—Quinaldine and allyl bromide react to form the quaternary compound, NAQ.

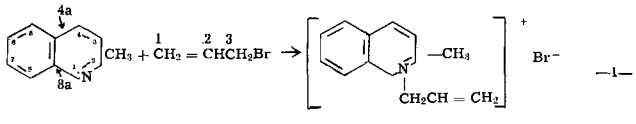

—1—

As reaction 1 proceeds the liquid reactants are consumed and a solid product formed. In order to moderate the reaction and minimize the occlusion of starting materials in the NAQ, the use of an inert solvent is necessary. Vanderkooi (9) had used isopropanol for this purpose. This same solvent was used in this work before it was discovered that allyl bromide reacts with most of the lower alcohols. One of the products of the solvolysis reaction is HBr which combines with quinaldine and precipitates as quinaldine hydrobromide.

Both radioactive NAQ preparations were contaminated with quinaldine hydrobromide to different degrees and had to be purified. Details of the purification procedure (neutralization and solvent extraction) are omitted in the interest of brevity, but will be supplied on request. Pertinent data of the purified products are summarized in Table I.

Pure nonradioactive NAQ was prepared by refluxing a 1:2 mole ratio of quinaldine and allyl bromide at 70°C for 48 hr with an equal volume of nitrobenzene. Excess allyl bromide was removed by distillation. After cooling to room temperature, the product was filtered and washed with isopropanol. The crude product (mp 225°-228°C) was found by infrared and ultra-

[1] Now with the Military Vehicles Organization, General Motors Corporation, Warren, Michigan.

[2] After this work was completed, a study of class II brighteners was published by J. Edwards and M. J. Levett, *Trans. Inst. Metal Finishing*, 44, 27 1966).

Table I. Radioactive NAQ data

Sample	Volume, ml	Concentration, mg/ml	Activity, cpm/ml	Specific activity, millicuries/millimole
C-14A NAQ	5	13.2	3.5×10^7	0.48
C-14Q NAQ	10	6.15	3.9×10^7	1.15

Table II. Plating solutions and conditions

Bath composition:	300 g/liter $NiSO_4 \cdot 6H_2O$	
	30 g/liter $NiCl_2 \cdot 6H_2O$	
	30 g/liter H_3BO_3	
Plating conditions:	pH	3.0*
	Current density	43 ma/cm²*
	Temperature	60°C
	Agitation	200 rpm
	Addition agents	
	SAS	2000 mg/liter*
	NAQ	4 mg/liter

* Items were studied as individual variables in which case all the other conditions were maintained at the above values.

violet analyses to be free of major contamination. Both spectra were unchanged by recrystallization of the NAQ from isopropanol-water. Melting point of the recrystallized NAQ was 227°-228°C.

Sodium Allyl Sulfonate.—Sodium allyl sulfonate is available as 2-propene-1-sulfonic acid sodium salt.[3] It can be prepared by scaling up a previously described synthesis (1). In this case the procedure is modified to include the dropwise addition of allyl bromide to a well-stirred sodium sulfite solution. The concentration of SAS in the stock solution can be determined by the bromate-bromide method.

Equipment and other conditions.—The plating cell, related equipment, and the method of preparing foil samples for proportional counting are described in earlier reports (1, 2). A circular stainless steel shield was substituted for the previously used lead shield. The area (1 cm²) of the hole remained the same. The change of materials was made because the natural radioisotopes in lead constituted a large background compared to some of the samples. Other conditions are summarized in Table II.

Results

Autoradiography.—The autoradiogram shown in Fig. 1 is representative of a deposit plated in a C-14Q NAQ solution. Deposits from a bath containing C-14A NAQ gave identical autoradiograms.

The cathode from which the foils were removed had a peak-to-valley height of 0.072 cm and a peak-to-peak separation of 0.161 cm. The autoradiogram in Fig. 1 shows a greater darkening occurred on the part of the film next to the peaks as compared to the valleys, indicating more radioactivity was included in the nickel deposited on the peaks. Since the same results were found for C-14A and C-14Q NAQ, it can be concluded that the whole NAQ ion is preferentially incorporated in the deposit on the peaks.

Inclusion of NAQ.—For every data point, at least two and as many as 10 samples were prepared for counting. As is the case with the measurement of low levels of radioactivity, the agreement between replicate samples can sometimes be poor. Therefore, no measurements were discarded unless it was certain that an error had been made in the sample preparation.

From the general shape of the inclusion curve, an equation was selected and the method of least squares used to obtain the best fit to the data. The mathematical procedure was carried out by a computer. The equations used to represent the inclusion curves will be given in subsequent sections.

[3] Eastman Kodak Company.

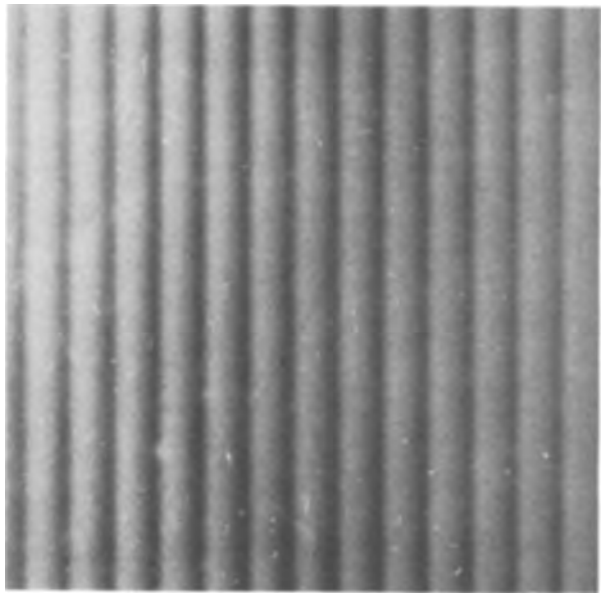

Fig. 1. Autoradiogram of the top of a foil containing C-14Q NAQ

It was convenient to treat and to plot the data in terms of "apparent" inclusion. Apparent inclusion is defined as the observed count rate of the sample without correction for self-absorption. It is known in radioisotope work that the count rate for beta radiation increases as a function of sample thickness until an "infinite" thickness is attained. Above infinite thickness the count rate becomes constant. Since the infinite thickness for C-14 beta radiation in a nickel matrix is 12μ, the sample thickness of 13μ used in this work was infinitely thick. Small variations in sample thickness thus have little effect on the observed or apparent count rate.

The true count rate, N_o, can be calculated from the apparent count rate, N, by correcting for the self-absorption of C-14 beta radiation. The correction is expressed by

$$\frac{N}{N_o} = e^{-\alpha t} \qquad [1]$$

where α is the linear absorption coefficient of nickel and t is the nickel thickness. The major problem in applying Eq. [1] is the difficulty of accurately measuring t. Small errors in t will lead to large errors in N_o.

One of the benefits of fitting a curve to the data is that differences in sample thickness are eliminated, and an average thickness for all samples may be assumed. Eighteen samples were measured, and an average of 1.32×10^{-4} cm was found. Using this value for t, and 2.14×10^3 cm^{-1} for α, Eq. [1] reduces to

$$N_o = 16.9\,N \qquad [2]$$

Any value of "apparent NAQ" inclusion in the following figures can be converted to total NAQ inclusion by Eq. [2].

Effect of NAQ concentration.—Inclusion of C-14A and C-14Q NAQ in nickel deposits as a function of NAQ concentration in the plating bath is shown in Fig. 2. These curves were fitted to the equation

$$y = Ax^1 + Bx^2 + Cx^3 \qquad [3]$$

where y is the apparent NAQ inclusion in the deposit and x the NAQ concentration in the bath in milligrams per liter. A, B, and C are empirically determined constants having the following values:

	A	B	C
C-14Q NAQ	11.05	1.070	—0.0169
C-14A NAQ	10.91	0.067	0.0207

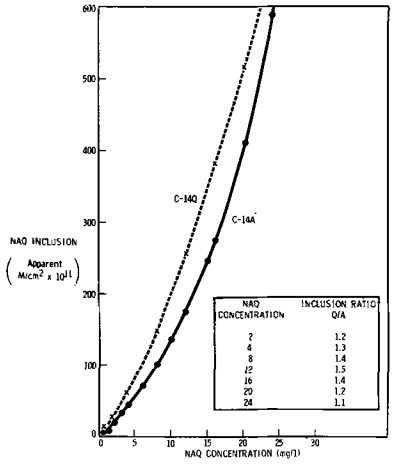

Fig. 2. Inclusion of NAQ vs. NAQ concentration

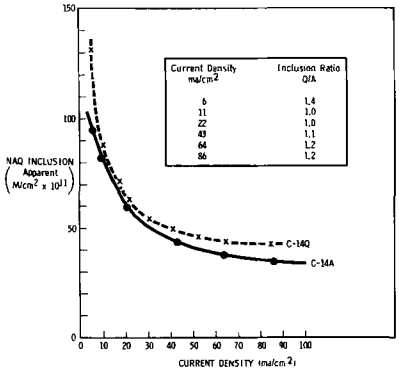

Fig. 3. Inclusion of NAQ vs. current density

According to Eq. [3], inclusion is proportional to NAQ concentration in the bath only at low concentrations of NAQ where the effect of the Bx^2 and Cx^3 terms is small. At higher concentrations of NAQ, the effect of the Bx^2 and Cx^3 terms increases; and, as Fig. 2 shows, both the C-14A and C-14Q inclusion curves bend toward the y axis. Over the concentration range investigated (0-25 mg/liter NAQ), Eq. [3] states that NAQ inclusion increases as a power function of its concentration in the bath, *i.e.*, NAQ increases its own inclusion.

Effect of current density.—Quantities of included C-14A and C-14Q NAQ are shown in Fig. 3 as functions of current density. These curves were fitted to the equation

$$y_i = Aw^{\circ} + Bw^{-1} + Cw^{-2} \qquad [4]$$

where y_i is the apparent NAQ inclusion and w is the current density in milliamperes per square centimeter. A, B, and C are empirically determined constants having the following values:

	A	B	C
C-14Q NAQ	35.83	534.6	— 290.4
C-14A NAQ	25.64	795.4	—2255.0

From Eq. [4] it can be seen that the amount of inclusion will be determined by the Bw^{-1} term at high current densities while it will be dependent on both Bw^{-1} and Cw^{-2} at low current densities.

It has been suggested that inclusion of class II brighteners is diffusion limited at higher plating current densities (5, 7). If this were true, the rate of inclusion, μ_i should level off and become constant after a critical current density is exceeded. The rate of inclusion can be calculated from the apparent inclusion values of Fig. 3 by converting these values to total

Table III. Rate of inclusion of NAQ

Current density, ma/cm²	Plating time, sec	μ_i C-14Q, M/cm²-sec × 10^{12}	μ_i C-14A, M/cm²-sec × 10^{12}
6	12,000	1.84	1.34
11	6,000	2.41	2.34
22	3,000	3.50	3.40
43	1,500	5.53	4.95
64	1,000	7.65	6.42
86	750	9.35	7.92

inclusion using Eq. [2] and dividing by the appropriate plating times. The data are shown in Table III where it can be seen that μ_i increases steadily with current density. No limiting μ_i is reached.

Effect of SAS concentration.—Inclusion of C-14A and C-14Q NAQ as a function of SAS concentration in the plating bath is shown in Fig. 4. From 0 to 400 mg/liter, there is a rapid rise in NAQ inclusion; this portion of the curve is approximated by two straight lines. Above 400 mg/liter, the curve was fitted to the equation

$$y_i = Az^{\circ} + Bz^{-1} + Cz^{-2} \qquad [5]$$

where y_i is the apparent NAQ inclusion and z is the SAS concentration in grams per liter. A, B, and C are empirically determined constants having the following values:

	A	B	C
C-14Q	36.72	27.35	5.44
C-14A	18.27	46.65	—9.12

This equation is the same as the one used to express inclusion as a function of current density and can be interpreted similarly.

The cathode potential as a function of SAS concentration is also shown in Fig. 4. Cathode potentials were measured with a L&N potentiometer using a fiber tip saturated calomel electrode in a Luggin capillary. The salt bridge was filled with saturated NaCl to prevent crystallization of potassium-nickel sulfate in the capillary tip.

An interpretation of Fig. 4 can be given by considering the inclusion curves to be the resultant of two competing phenomena, both of which depend upon SAS concentration.

In the region 0 to 400 mg/liter of SAS, many things occur simultaneously: SAS inclusion in the deposit is rapidly increasing (3); NAQ inclusion is also increasing; cathode potentials shows a smooth increase; the appearance of the deposit changes from dull to bright. It is believed that inclusion of SAS serves to create surface adsorption sites at a rapid rate (8). In support of

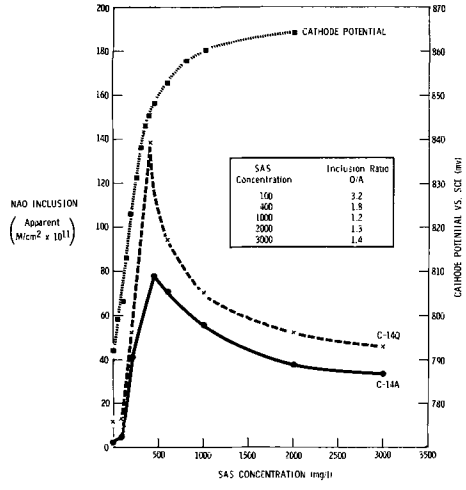

Fig. 4. Inclusion of NAQ vs. SAS concentration

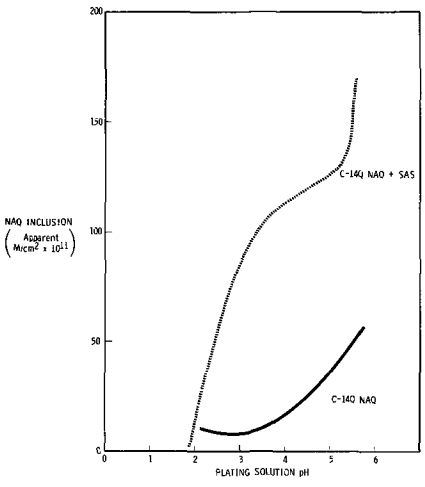

Fig. 5. Inclusion of NAQ vs. pH

this point is the evidence of greatly reduced grain size, even when low concentrations of class I brighteners are employed (10). More sites are created than can be filled by the SAS, and consequently NAQ inclusion rises to a maximum.

In the region above 400 mg/liter of SAS, the regular decrease in NAQ inclusion is due to increasing competition of SAS ions for adsorption sites. From other work (3) it is known that SAS inclusion continues to increase up to approximately 1 g/liter, then levels off and becomes fairly constant. Creation of adsorption sites would probably follow the SAS inclusion curve, but NAQ ions would have to compete with increasingly larger amounts of SAS in order to occupy these sites.

The Effect of pH.—The inclusion of C-14Q NAQ as a function of *p*H in the plating bath is shown in Fig. 5. Only C-14Q NAQ was used for these experiments because it represents better the behavior of the NAQ molecule. As *p*H increases over the range 3.0-5.0, the amount of NAQ included in the deposit increases. With 2 g-liter of SAS in the bath, the same general trend of NAQ inclusion with *p*H is found, but over a much wider range. These results again suggest an effect of plating conditions on the surface density of adsorption sites. Increasing *p*H increases the amount of codeposited colloidal nickel hydroxide which affects the crystallographic structure of the deposit and, hence, the density of adsorption sites. Similar inclusion results were observed by Edwards and Levett (8) for low concentrations of saccharin.

It should be pointed out that these *p*H data were determined in a smaller plating cell and with a slightly different method of sample preparation to obtain more efficient use of the radioactive NAQ. Results are comparable among themselves, but absolute values may differ from data shown in Fig. 2, 3, and 4.

Discussion

All of the inclusion results can be explained by consideration of the principles involved in mass transfer, diffusion layer thickness, and catalytic activity of a surface.

The three modes of mass transfer participate to varying degrees in the movement of addition agent ion, depending on whether the addition agents are in the bulk solution or near the cathode-solution interface. Hydrodynamic flow, caused by agitation and convection currents, is the main mode of transport for all ions in the bulk solution. Diffusion and electrical migration becomes significant at the cathode-solution interface (11). However, the effect of electrical migration usually can be neglected for addition agents because of the large concentrations of nickel and other inorganic ions that are normally present. Thus diffusion is generally concluded to be in the main process by which addition agents move through the cathode-solution interface (5, 7, 8).

The rate of diffusion, μ_d, is given by the well-known equation

$$\mu_d = \frac{D(C_b - C_o)}{\delta} \qquad [6]$$

where c_b and C_o = the bulk and interfacial concentrations, D = diffusion coefficient, δ = diffusion layer thickness.

Since D is a constant at a given temperature and C_b is fixed experimentally, the first approximation of the amount of NAQ inclusion will depend on C_o. However, C_o will depend on the rate of supply, μ_d, and the rate of inclusion, μ_i. Factors affecting the rate of supply are straightforward and are given by the terms of Eq. [6]. Rates of inclusion vary with the concentrations of SAS or hydrogen ions and will be explained later by postulating different numbers of adsorption sites created by addition agent inclusion.

Factors affecting rate of supply of NAQ are C_b and δ, but δ is a function of both the hydrodynamic conditions and the current density. Figure 2 shows that when C_b is increased NAQ inclusion also increases. There appears to be no limit to the amount NAQ that can be included in nickel. Only brittleness of the deposit limited the highest NAQ concentration to 25 mg/liter in this study.

Excluding convection effects the thickness of δ is constant when adjacent to smooth surfaces, but is affected by a microprofile surface (5). The autoradiogram (Fig. 1) shows inclusion of NAQ in the deposit is slightly larger above peaks than in valleys. A δ that is relatively thinner next to peaks and thicker next to valleys can account for the differences in diffusion of NAQ to these areas (12).

Because of the importance of agitation on δ and μ_d, it was attempted to maintain reasonably constant hydrodynamic conditions by using constant stirring speed, temperature, solution composition, cell geometry, and electrode shape. It is believed that δ was reproducible to within 15% for each variable investigated except *p*H. This can be shown by calculating μ_i from the inclusion data in Fig. 2, 3, 4, and 5 at the common point (4 mg/liter NAQ, 43 ma/cm²; 2000 mg/liter SAS; and *p*H 3.0).

Data from	Variable	μ_i C-14Q NAQ	μ_i C-14A NAQ
Fig. 2	NAQ	6.8×10^{-12} M/cm²-sec	5.2×10^{-12} M/cm²-sec
Fig. 3	CD	5.5×10^{-12} M/cm²-sec	5.0×10^{-12} M/cm²-sec
Fig. 4	SAS	5.9×10^{-12} M/cm²-sec	4.4×10^{-12} M/cm²-sec
Fig. 5	*p*H	9.7×10^{-12} M/cm²-sec	—

The average μ_i excluding that of Fig. 5, is $6.1 \pm 0.6 \times 10^{-12}$ M/cm²-sec for C-14Q NAQ and $4.9 \pm 0.5 \times 10^{-12}$ M/cm²-sec for C-14A NAQ. The experiments with *p*H as the variable were done in a smaller sized cell and indicate a smaller δ was probably obtained because of different hydrodynamic conditions.

The amount of NAQ inclusion shown in Fig. 4 and 5 is directly proportional to μ_i. Although the plating conditions should have given a reasonably constant μ_d, it can be seen from the figures that μ_i varies widely. From Fig. 4 the maximum μ_i for C-14Q NAQ is 15.7×10^{-12} M/cm²-sec and occurs at 400 mg/liter of SAS. This is approximately 2.5 times the average μ_i found previously when the SAS concentration was 2000 mg/liter. Similarly, the highest μ_i calculated from the data of Fig. 5 is 18.8×10^{-12} M/cm²-sec or nearly double the rate at *p*H 3.0. Neither the change in SAS concentration nor *p*H would be expected to have affected μ_d or δ. Therefore, changes in μ_i cannot be explained by changes in rate of supply of the NAQ but rather by differences in the catalytic properties of the nickel surface. Adsorption sites, according to Edwards and Levett (8), are created by inclusion of either class I or class II brighteners. The density of sites depends on the relative concentrations of the two brighteners as well as their effectiveness. This hy-

pothesis is applied in more detail in the Results section.

The mechanism of NAQ inclusion is believed to require an initial adsorption step followed by a partial reduction or cleavage of the ion. Possible reduction products were, at first, thought to be propene (3) (collected in the cathode gases) and quinaldine which can be isolated from used baths in large amounts (~25%) by solvent extraction. However, when nickel samples containing C-14A and C-14Q NAQ were dissolved anodically, the Q/A ratio of the anolytes was 1:1 or the same as that contained in the sample. If the C-14A part of NAQ were included as propene, it should have volatilized during dissolution. It was found that the C-14A material was water soluble, not extractable from basic solution, and not distillable up to 110°C. Therefore, it appears that only a small portion of the cleaved NAQ is lost as propene, and the remainder of the allyl part is included in some other chemical form.

The tentative distribution of inclusion products found for C-14Q NAQ is 40% NAQ, 40% quinaldine, 20% reduced NAQ and quinaldine, probably as the corresponding 1, 2, 3, 4-tetrahydro-compounds. The same distribution occurring for C-14A NAQ products can account for 50% of the C-14A activity (NAQ plus reduced NAQ). The rest of the C-14A activity has not been identified.

The above results were obtained from samples plated at 43 ma/cm^2 with 2 g/liter SAS and 10 mg/liter NAQ in the bath. However, the plating cell and current density distribution were different than that used in the earlier work. The ratio of included products will probably change when any of these variables are changed. Some idea of the differences in the included products can be found by comparing the Q/A ratios shown in the inserts of Fig. 2, 3, and 4. Note how large the Q/A ratio is at intermediate NAQ concentrations, low current density or low SAS concentrations. It is believed that the Q/A ratio indicates changes in the catalytic activity of the adsorption sites that are created when different amounts of SAS or NAQ are included.

Manuscript received April 18, 1966; revised manuscript received July 27, 1966. This paper was presented at the Washington Meeting, Oct. 11-15, 1964.

Any discussion of this paper will appear in a Discussion Section to be published in the December 1967 JOURNAL.

REFERENCES

1. S. E. Beacom and B. J. Riley, *This Journal*, **106**, 309 (1959).
2. S. E. Beacom and B. J. Riley, *ibid.*, **107**, 785 (1960).
3. S. E. Beacom and B. J. Riley, *ibid.*, **108**, 758 (1961).
4. J. D. Thomas, *Proc. Am. Electroplaters' Soc.*, **43**, 60 (1956).
5. O. Kardos and D. G. Foulke, "Advances in Electrochemistry and Electrochemical Engineering," Vol. 2, C. W. Tobias, Editor, Interscience Publishers, New York (1962).
6. W. L. Pinner, B. B. Knapp, and M. B. Diggin, "Modern Electroplating," 2nd ed., F. A. Lowenheim, Editor, p. 271-277, John Wiley & Sons, Inc., New York, (1963).
7. J. Edwards, *Trans. Inst. of Metal Finishing*, **39**, 52 (1962); **41**, 140 (1964).
8. J. Edwards and M. J. Levett, *ibid.*, **41**, 147 (1964).
9. N. Vanderkooi, Jr., Doctoral Dissertation, Wayne State Univ., 1958.
10. R. Weil and H. C. Cook, *This Journal*, **109**, 295 (1962).
11. E. Lyons, "Modern Electroplating," 2nd ed., F. A. Lowenheim, Editor, p. 19, John Wiley & Sons, Inc., New York (1963).
12. S. E. Beacom, *Plating*, **46**, 814 (1959).

Surface Roughness Effects in the Electrodeposition of Copper in the Limiting Current Range

N. Ibl and K. Schadegg[1]

Department of Industrial and Engineering Chemistry, Swiss Federal Institute of Technology, Zurich, Switzerland

ABSTRACT

Copper was deposited at high mass transfer rates (rotating disk cathode) in the range of the limiting current of mass transfer. The roughness of the deposit was characterized by impedance measurements. Galvanostatic and potentiostatic experiments, in which the potential, or the current, was measured as a function of time, were also carried out. The various methods used show that a very rough deposit is formed when the limiting current is reached. The results are discussed from the viewpoint of the methodology of electrochemical determination of mass transfer coefficients and from that of the mechanism of metal powder formation at high current densities.

In a previous investigation of the electrodeposition of copper (1) a study was made of the transition from a compact to a powdery deposit[2] which takes place when the current density is increased to a certain value. It was found that this transition occurs when the limiting current of mass transport is reached. The experiments were carried out with nonacidified $CuSO_4$ solutions, under conditions of natural convection, *i.e.*, at rather low mass transfer rates. In the present work copper was deposited from acidified $CuSO_4$ solutions at a rotating disk electrode, which ensured high mass transfer rates under well-defined hydrodynamic conditions. The concentration, speed of rotation, and current density were varied within a wide range. The roughness of the deposit was characterized by impedance measurements. Under otherwise comparable conditions the imaginary component of the vector impedance (reactance) gives a relative measure for the surface area of the deposit. The change in surface area in the limiting current region was also followed by measuring the variation of cathode potential with time at constant current, or the variation of current with time at constant potential.

[1] Present address: Département de Chimie, Université Laval, Quebec, Canada.

[2] A comprehensive review of the literature on electrolytic metal powders has been given in two previous papers (2, 3).

Experimental

The cathode was a rotating stainless steel disk, 1 cm in diameter, embedded in araldite to minimize edge effects. The outer inert annulus of araldite was 2.5 mm wide. The coupling between driving motor and rotating disk assembly was a magnetic one to avoid transmission of vibrations. The anode was a stationary

disk of electrolytic copper, 6 cm in diameter, located 4.5 cm from the rotating disk.

Before each run the deposit from the previous experiment was stripped off the stainless steel cathode, the latter degreased by a treatment with trichloroethylene vapor followed by a cathodic cleaning in an alkaline bath. A copper plate 10μ thick was then deposited on the stainless steel with a current density equal to 5% of the limiting current corresponding to the conditions of the given experiment. Finally, copper was deposited on this plate under the chosen conditions. In Fig. 2, 3, and 6 each point corresponds to a new run, with a freshly prepared surface as indicated above. The same applies to the various curves of Fig. 1, 4, and 5. All reagents used were "pro analysi." The cell was thermostated at 25° ± 0.05°C. The experiments were carried out in deaerated solutions under a N_2 atmosphere.

After switching off the d-c, the cathode was connected with a platinized platinum electrode (ϕ 1 cm), and the impedance of this system was measured with a Wheatstone bridge similar to that employed previously (1). An oscilloscope was used as null detector. The a.c. (250 cycles) applied to the cell had an amplitude of 10 mv. The impedance of the cell was balanced by a resistor and a capacitor in parallel. The reactance R_b was calculated from their resistance R and capacitance C by the relation

$$R_b = \frac{R^2\omega C}{1 + (R\omega C)^2} \qquad [1]$$

where ω is the angular frequency. Both the imaginary and the real part of the impedance decrease with increasing surface area of the metal deposited on the cathode, but the reactance (in contrast to the real component of the impedance) does not include the electrolyte resistance and, therefore, undergoes a much larger relative change when the roughness increases.

A number of impedance measurements were also carried out during the metal deposition by superimposing a.c. on the electrolysis current (Fig. 3). Suitable capacitors prevented the d.c. from flowing through any of the branches of the Wheatstone bridge except through the electrolysis cell.

In general, the metal was deposited under galvanostatic conditions. The current was kept constant by using a large voltage source and a high resistance in series with the electrolysis cell. In a series of typical runs the cathode potential was recorded as function of the electrolysis time. The potential was measured with a Knick high-impedance voltmeter against a copper reference electrode dipping into a solution of the same composition as that being electrolyzed. The reference electrode was connected to the cathode by a fine vertical Luggin capillary reaching to 0.5 mm of the center of the rotating disk.

In addition to the galvanostatic experiments, potentiostatic measurements were also made. The cathode potential was kept constant with an electronic potentiostat (Tacussel PR-2000). The current was measured as voltage drop over a resistor and recorded as function of time by feeding this voltage to a compensating pen and ink recorder.

Results

Figures 1 to 5 present a selection of the results obtained. A more complete account of the results and of the experimental procedure is given in (4). The $CuSO_4$ concentration ranged from 0.05 to 0.7M, the rotation speed of the disk from 300 to 6000 rpm. In general, the curves were of the same shape for all concentrations and speeds employed, so that only one typical curve or family of curves is shown in each case. The theoretical limiting current i_L, as indicated in some of the figures, was calculated from the relation (5)

$$i_L = 0.602\, AzFc_0 D^{2/3} \nu^{-1/6} \omega^{1/2} \qquad [2]$$

where z = charge of cation (for copper, z = 2),

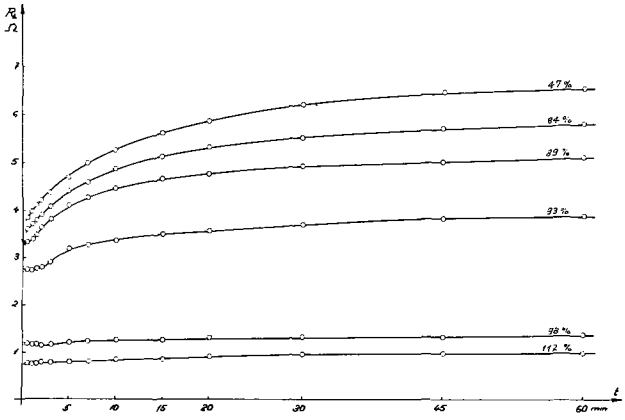

Fig. 1. Variation of reactance with time after switching off the d.c. The copper was deposited from 0.05M $CuSO_4$ + 1.5M H_2SO_4 at 300 rpm with a current indicated on each curve in per cent of the limiting current calculated from Eq. [2]. The metal remained in contact with the solution after switching off the d.c.

F = Faraday's constant (96500 Cb), c_0 = concentration of $CuSO_4$, D = diffusion coefficient, ν = kinematic viscosity, ω = angular velocity of rotation of disk, A = area of disk (0.785 cm^2). The numerical coefficient (0.602) applies for a Schmidt number of 1000, which is approximately the value usually prevailing in aqueous electrolysis. The following average values for ν and D were used (6) for 0.05M $CuSO_4$ + 1.5M H_2SO_4, and 0.7M $CuSO_4$ + 1.5M H_2SO_4, respectively: ν = 1.101 and 1.308 x 10^{-2} cm^2 sec^{-1}, D = 6.50 and 5.14 x 10^{-6} cm^2 sec^{-1}. The values of i_L shown in the figures were calculated for the projected electrode area (0.785 cm^2), *i.e.*, the area of the flat disk, before roughness formation sets in. Migration effects were not taken into account. The reasons are similar to those given by Wilke *et al.* (6), who used acidified $CuSO_4$ solutions of the same concentration range as in the present work. An additional reason why in the present case a more refined treatment would not be justified is that the limiting current was not very accurately defined (see later). In any case, because of the smallness of the effects involved, taking migration into account would not change anything in the conclusions reached.

In Fig. 1 the reactance is plotted against the time which has elapsed after the d.c. has been switched off. On each curve the current at which the metal has been deposited is given in per cent of the limiting current. In all experiments the reactance increased with time during a relatively long period, except when the metal had been deposited at a current close to or larger than the limiting value. This indicates that the surface of freshly deposited metal is unstable. It seems that a smoothing of the surface takes place for several minutes after the electrolysis current has been switched off.[3]

Figure 2 shows the variation of the reactance with the current at which the copper has been deposited. Because of its variation with time the reactance was always measured after the same time interval (30 sec) following switching off the d.c. in order to get comparable results. It is seen that the reactance drops off sharply when the deposition current reaches the limiting value i_L. This indicates a strong increase in surface area at the limiting current. The reactance measured during metal deposition (with a.c. superimposed on the d.c.) goes through a marked maximum at the limiting current (Fig. 3). This can be interpreted as being due to two effects acting in

[3] Alternative interpretations would be (a) the formation of an oxide layer (b) adsorption or desorption effects. However, these explanations appear less likely than a smoothing due to recrystallization processes, because of the fact that no increase of reactance with time occurs when the metal has been deposited at or above the limiting current, *i.e.*, when the deposit is very rough or powdery.

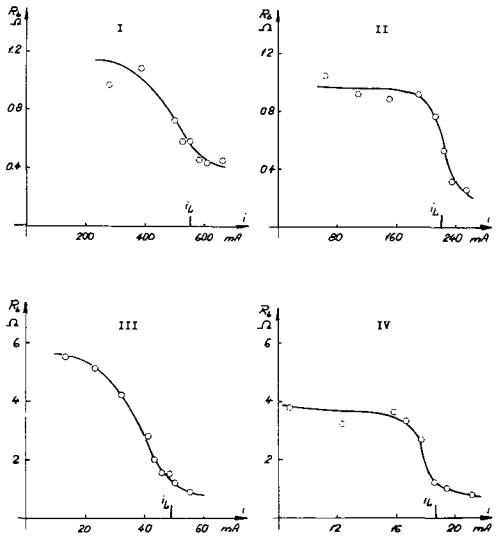

Fig. 2. Variation of the reactance R_b with the current of metal deposition (R_b measured after switching off this current). Deposition conditions: I, 0.7M $CuSO_4$, 1.5M H_2SO_4, 2000 rpm; II, 0.7M $CuSO_4$, 1.5M H_2SO_4, 300 rpm; III, 0.05M $CuSO_4$, 1.5M H_2SO_4, 2000 rpm; IV, 0.05M $CuSO_4$, 1.5M H_2SO_4, 300 rpm.

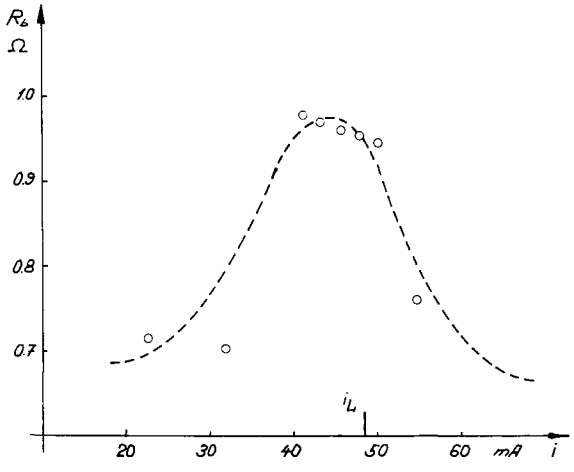

Fig. 3. Variation of reactance R_b with current (R_b measured during metal deposition); 0.05M $CuSO_4$ + 1.5M H_2SO_4, 2000 rpm.

opposite direction. The reactance due to concentration overvoltage, ${}_cR_b{}^*$, increases strongly when the electrolysis current i approaches the limiting current, i_L, according to the equation

$$ {}_cR_b{}^* = \frac{{}_cR_b}{1 - i/i_L} \qquad [3]^4 $$

which has been derived by Gerischer (7). On the other hand, the formation of a rough or powdery deposit in the limiting current range tends to decrease the reactance. When this effect prevails, the over-all reactance decreases again, as is seen on the right branch of the curve of Fig. 3.

In the case of the impedance measurements during metal deposition this decrease of reactance with increasing d.c. is probably not only due to the dependence of the reactance on the surface area as such, but also to an indirect influence of the increase in surface area. For a rough surface (with peaks of a height comparable to the thickness of the diffusion layer), the limiting current is larger than the value calculated for the projected electrode area; therefore, if we calculate i_L from Eq. [2] for the projected electrode area (*i.e.*, without taking the roughness formation into account) and if we electrolyze with a current i which is not much larger than i_L, then, this current i is no longer larger than the limiting current once a rough deposit has started to form and the departure from the limiting current condition causes a decrease of the reactance according to Eq. [3].

A similar influence of an increase of the surface area was observed on the galvanostatic curves, a sample of which is shown in Fig. 4. When the copper is deposited below the limiting current, the overvoltage is virtually independent of electrolysis time. In the limiting current range, however, the overvoltage strongly decreases with time: for instance, for $i = 1.12 i_L$ (i_L being calculated for the projected electrode area) the overvoltage decreases by about 400 mv within 2 min after the beginning of electrolysis.[5] This is due to the onset of the formation of a rough or powdery deposit at the limiting current and to the resulting increase of the limiting current. Figures 5a and 5b show the variation of current with electrolysis time at constant cathode potential. Instead of the decrease of overvoltage observed in the galvanostatic case, we have in the potentiostatic experiments an increase of current with time when a rough deposit is formed. The increase of current occurs only if the potential is more negative than a certain value. As can be seen from a comparison of Fig. 5a and 5b, this potential is less negative with concentrated than with dilute solutions. A similar shift of the potential for the start of the increase of current with time was observed when the speed of rotation was increased. It is not impossible that at very high speeds of rotation and high concentrations the formation of a powdery or very rough deposit would start at potentials less than that corresponding to zero interfacial concentration, *i.e.*, below the limiting current. However, within the range of concentrations and speeds of rotation studied in this work, the strong increase of current with time always occurred within the limiting current range.

It is to be noted, however, that the limiting current was not very well defined in spite of the well-defined hydrodynamics, because the current distri-

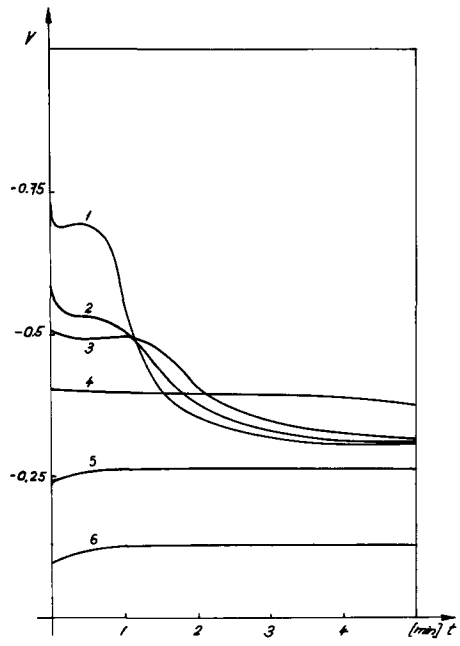

Fig. 4. Variation of overvoltage with time at constant current i (for 0.05M $CuSO_4$, 1.5M H_2SO_4); 1000 rpm: 1, i = 1.12 i_L; 2, i = 0.95 i_L; 3, i = 0.90 i_L; 4, i = 0.84 i_L; 5, i = 0.47 i_L; 6, i = 0.15 i_L.

[4] ${}_cR_b = RT/z^2F^2c_o(2D\omega)^{1/2}$, with ω = angular frequency, R = gas constant, T = abs. temperature. ${}_cR_b$ represents the reactance due to concentration overvoltage in an a-c circuit without superimposed d.c.

[5] A similar decrease of the overvoltage with electrolysis time in the electrodeposition of metal powders has also been reported in other papers (8-10).

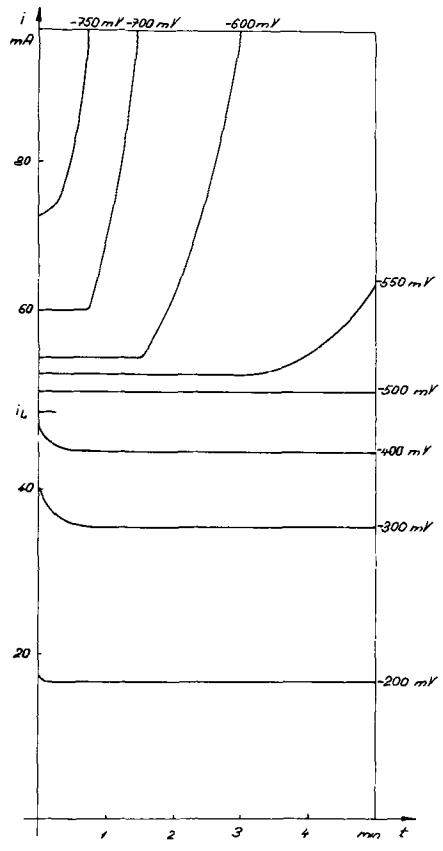

Fig. 5. Variation of current with time under potentiostatic conditions. For each curve the cathode potential was kept constant at the value indicated (which is referred to a copper reference electrode immersed in a solution of the same concentration as that being electrolyzed).

Fig. 5a. 0.05M $CuSO_4$, 1.5M H_2SO_4; 2000 rpm

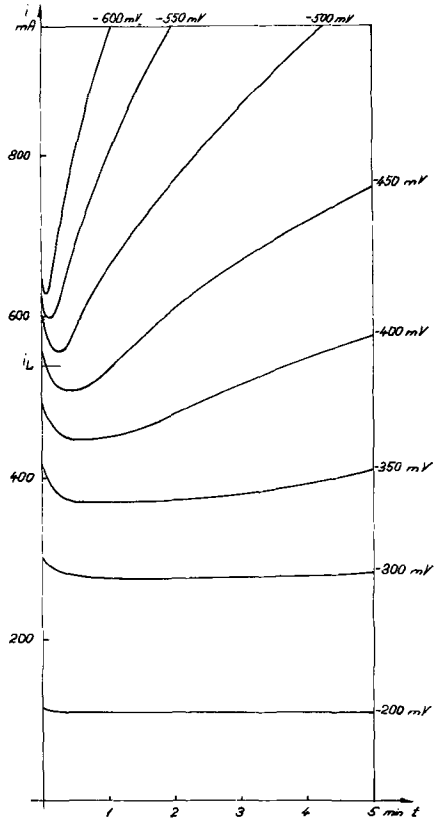

Fig. 5b. 0.7M $CuSO_4$, 1.5M H_2SO_4; 2000 rpm

bution at a disk is not uniform below the limiting current. When the current is increased, the limiting current is thus reached first toward the edge of the disk, so that the formation of a rough deposit starts at the edge and successively spreads over the whole electrode area. Owing to the roughness at the edge, the average limiting current for the whole disk can thus be increased before the limiting current condition is reached for the whole electrode area. There is thus a limiting current range rather than a well-defined limiting current. From current voltage measurements the uncertainty in the limiting current was estimated at 5-10% in most cases. The potentiostatic measurements yielded consistently higher limiting currents than the galvanostatic experiments (the current voltage curve being in both cases obtained by plotting the current, or the potential, measured after the same time on the potentiostatic or galvanostatic curves, respectively). Similar observations have been made by Emelyanenko and Baibarova (11).

The appearance of the deposits obtained at the limiting current was more reddish in color, and their adherence to the electrode was better than in the case of our previous study (1).[6] This appears to be due to the fact that strongly acidified solutions were used in the present case, compared to the neutral solutions employed earlier (rather than to the change in the rate of the mass transport owing to the increased stirring). However, the rule, that a deposit with a strongly increased surface is formed at the limiting current, holds true regardless of whether the solution is acid or not.

Discussion

The four methods used (galvanostatic and potentiostatic procedures, impedance measurements with and without d.c.) gave concordant results showing that a very rough deposit is formed when the limiting current is reached. This rule, which has been found previously for unstirred systems (1, 8, 9), is therefore also valid for strongly agitated solutions.

These results are of importance for the methodology of the electrochemical determination of mass transfer coefficients (12), which can be obtained very conveniently from the limiting current as given by the current voltage curve. The deposition of copper from acidified solutions has been repeatedly used as indicator reaction for this purpose in recent years [see for instance (13-16)].

Correct values of the mass transfer coefficient will be obtained only if the effective electrode area does

[6] It could thus well be that it is only the formation of a very rough deposit (rather than the formation of powder itself) which is linked to the limiting current. However, even at rotating disks with acidified solutions a powdery, loose deposit is eventually obtained when one waits long enough, or when the current is sufficiently above the limiting value calculated for the projected area.

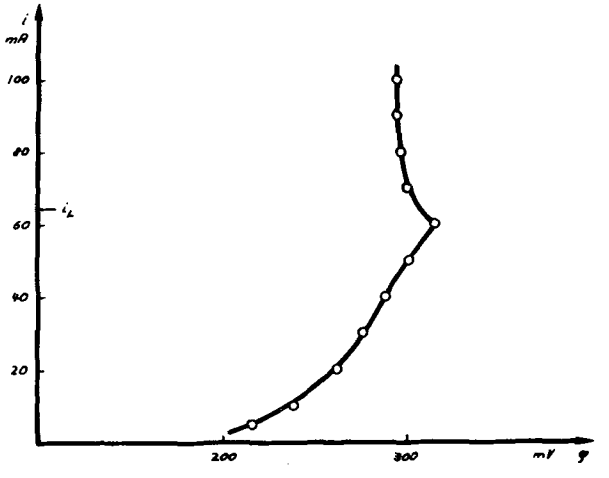

Fig. 6. Current voltage curve (derived from galvanostatic measurements) 0.1M $CuSO_4$, 1.5M H_2SO_4; 1000 rpm.

not change during the measurements for the current voltage curve. The roughness of the deposit, which develops at the limiting current, is thus a great potential source of error.[7] This is illustrated drastically by the current voltage curve of Fig. 6, which exhibits even a negative slope for currents larger than the limiting value. For each current setting the cathode potential was read after 5 min and under these conditions the influence of the increase of surface area becomes predominant. In order to avoid distortions of the current voltage curve the measurements should be made as rapidly as possible. However, one is usually interested in the steady-state mass transfer coefficients, and one must thus wait long enough for the steady state to be established. A compromise with respect to time must therefore be found. Fortunately, the onset of roughness occurs only after some time, as can be seen from Fig. 4 and 5. As long as the current is not much higher than the limiting current, this induction period is substantially longer than the galvanostatic "transition time" (17, 18) elapsing until zero concentration at the cathode surface is reached.[8] This leaves one some "freedom of action" when taking the current voltage curve and makes it more hopeful to find a satisfactory compromise with respect to measurement time. It might well be, however, that the possibility of finding such a compromise, allowing one to obtain reliable mass transfer coefficients, depends on the experimental conditions. From the experiments of this study it would appear, for instance, that dilute solutions are more favorable than concentrated ones. A closer examination of this question would be valuable for the methodology of the electrochemical measurements of mass transfer rates. Of course, the above difficulty does not arise when a redox reaction (such as the reduction of ferricyanide to ferrocyanide) is used as indicator instead of metal deposition. However, the ferricyanide system is not suitable for the study of natural convection and has also some other minor disadvantages.

Let us now briefly discuss the results from the viewpoint of the mechanism of electrolytic powder formation. A number of theories have been proposed. They have been reviewed in an earlier paper (2). An interesting interpretation based on quantum mechanics has been developed by Calusaru and Atanasiu (20). According to this theory, the electrons from the metal are transferred to the cations by the tunnel effect over a distance which substantially increases at the limiting current because the electrode potential becomes very negative and, at the same time, the supply of cations to be discharged is limited. The cations are thus discharged at some distance in front of the interface. When this neutralization distance becomes larger than the lattice parameter, powder is formed. An alternative explanation has been based on mass transfer considerations (2), (21). Below the limiting current the current distribution tends to be uniform because of the activation overvoltage, but at the limiting current the influence of mass transfer becomes predominant, and small peaks present by chance grow faster than the flat parts around them because of the differences in the mass transfer rates of the cations being discharged. There is thus, at the limiting current, a sort of instability with respect to small scale heterogeneities of the surface (21). A rough deposit results and, when the roughness has become very strong, this leads eventually for mechanical reasons to the formation of a loose metal which can easily be stripped off the electrode. The characteristics of such more or less powdery deposits can then much depend on circumstances and be strongly affected by factors such as the adsorption of inhibitors. The present work does not allow clear conclusions regarding these processes, but at least the following can be said with respect to the primary roughness formation. The induction period observed before the onset of roughness (see above and Fig. 4 and 5) as well as the direction in which the potential of the onset of roughness formation shifts when the concentration or the speed of rotation is changed (see above and Fig. 5) are difficult to interpret in terms of the tunnel effect theory and speak for a mass transfer mechanism, at least of the roughness formation.

[7] Although the major roughness increase takes place in the limiting current range, some roughness develops progressively already when one approaches the limiting current and it appears that under certain conditions an appreciable roughness has already formed at 50% of the limiting current, for instance [see Fig. 8 of ref. (1)]. This makes the question of the roughness formation even more important from the viewpoint of the methodology of the electrochemical determination of mass transfer coefficients.

[8] The relationships given in (17) and (18) for the calculation of the transition time apply to the case that there is no convection. This gives a first approximation sufficient for a comparison of the order of magnitude with that of the induction period. A more refined calculation is given in (4). For the potentiostatic case, an accurate calculation taking convection into account can be made on the basis of the Olander theoretical treatment (19): at 300 rpm the mass transfer rate drops in half a second to a value which differs from the figure for the steady state by only 5%. The authors thank Dr. J. R. Selman (University of California, Berkeley) for having drawn their attention to this paper.

Acknowledgment

Thanks are due to the Swiss Aluminium Funds for its support of this research work. We are indebted to Mr. A. M. Frei for his help in the development of the experimental technique.

Manuscript received Jan. 31, 1966; revised manuscript received Sept. 6, 1966. This paper was presented at the Buffalo Meeting Oct. 10-14, 1965.

Any discussion of this paper will appear in a Discussion Section to be published in the December 1967 JOURNAL.

REFERENCES

1. N. Ibl, *Helv. Chim. Acta*, **37**, 1149 (1954).
2. N. Ibl, "Advances in Electrochemistry and Electrochemical Engineering," vol. 2, p. 49, P. Delahay and C. W. Tobias, Editors, Interscience Publishers, New York (1962).
3. N. Ibl, *Chem. Ing. Tech.*, **36**, 601 (1964).
4. K. Schadegg, Thesis, Eidg. Technische Hochschule, Zurich, No. 3744 (1966).
5. D. P. Gregory and A. C. Riddiford, *J. Chem. Soc.*, **1956**, 3756.
6. C. R. Wilke, M. Eisenberg, and C. W. Tobias, *This Journal*, **100**, 513 (1953).
7. H. Gerischer, *Z. physik. Chem.*, **1**, 278 (1954).
8. M. Loshkarev, A. Ozerov, and N. Kudryavtsev, *Zhur. Priklad. Khim.*, **22**, 294 (1949).
9. D. N. Gritsan, *Uchenye Zapiski Kharkov. Gosuderstv. Univ.*, **95**; Trudy Khim. Fak. No. **18**, 93 (1957); *C. A.*, **54**, 5290b (1960).
10. N. Ibl, R. Keller, and K. Killer, Comptes rendus de la 9ème réunion du Comité International de Thermodynamique et de Cinétique Electrochimiques (CITCE) à Paris, p. 283, Butterworth, (1959).
11. G. A. Emelyanenko and E. Ya. Baibarova, *Ukrain. Khim. Zhur.*, **25**, 727 (1959).
12. P. Grassmann, N. Ibl, and J. Trüb, *Chem. Ing. Tech.*, **33**, 529 (1961).
13. T. K. Ross and A. A. Wragg, *Electrochim. Acta*, **10**, 1093 (1965).
14. J. C. Bazán and A. J. Arvía, *ibid.*, **9**, 17 (1964).
15. G. Wranglén and O. Nilsson, *ibid.*, **7**, 121 (1962).
16. G. Schütz, *Int. J. Heat Mass Transfer*, **6**, 873 (1963).
17. P. Delahay, "New Instrumental Methods in Electrochemistry," p. 184, Interscience Publishers, New York (1954).
18. N. Ibl and G. Trümpler, *Helv. Chem. Acta*, **34**, 1217 (1951).
19. D. R. Orlander, *Int. J. Heat and Mass Transfer*, **5**, 825 (1962).
20. A. Calusaru and I. Atanasiu, *Rev. Roum. Métallurgie*, **5**, 291 (1960).
21. N. Ibl, *Galvanotech. u. Oberflächenschutz*, **7**, 256 (1966).

Kinetics of Nitrogen Transfer through an Iron Surface

E. T. Turkdogan and P. Grieveson[1]

Edgar C. Bain Laboratory for Fundamental Research,
United States Steel Corporation, Monroeville, Pennsylvania

ABSTRACT

A study has been made of the kinetics of nitrogenization and denitrogenization of γ-iron at 1000°C in the presence of nitrogen, water vapor, and hydrogen in the gas phase. For a given ratio, p_{H_2}/p_{H_2O}, the rate is shown to be directly proportional to the square root of the nitrogen partial pressure. It is shown that under these conditions nitrogen transfer is dominantly controlled by the surface reaction rather than by diffusion. A rate equation is derived for the condition of almost complete coverage of surface sites by adsorbed oxygen atoms. The rate equation derived for this limiting case states that the rate of nitrogen reaction on the surface of iron, for a given nitrogen activity, is inversely proportional to the activity of oxygen in the system. This is in agreement with the experimental observations.

In previous work by the authors (1, 2) on kinetics of solution of nitrogen in purified iron (in α, γ, or δ state), the reaction rate was found to be controlled essentially by the process of diffusion in samples thicker than 0.05 cm. It was shown explicitly that in purified nitrogen the phase boundary reaction with purified iron approached the state of equilibrium in a short reaction time. In unpurified nitrogen, on the other hand, the approach to metal-gas phase boundary equilibrium was found to be much slower. Other investigators (3-7) have also demonstrated that the rate of nitrogen solution in liquid iron is retarded markedly with increasing oxygen content of the iron. Although many rate data have been published, understanding of the nature of this phase boundary reaction with liquid or solid iron containing oxygen remains to be developed.

In an attempt to advance the present knowledge of the kinetics of phase boundary reactions in gas-metal systems at elevated temperature, a study was made of the effect of oxygen on the rate of the reaction of nitrogen with purified γ-iron at 1000°C; the results obtained are presented in this paper.

Experimental

The experimental technique, apparatus, and materials used were the same as those discussed in the previous two papers (1, 2). The material used was vacuum-carbon deoxidized Plastiron rolled to 0.051 cm thick sheet. The impurity contents were: C, Mn < 0.01%; S, P < 0.002%; each of the other usual impurities < 0.004%. The oxygen content of the nitrogen atmosphere was controlled by introducing appropriate mixtures of hydrogen and water vapor into the reacting atmosphere. Depending on the gas composition required, a mixture of hydrogen, argon, and nitrogen was allowed to pass through a long column containing a mixture of oxalic acid dihydrate and 10% anhydrous oxalic acid. The temperature of the oxalic acid dihydrate column was controlled by a thermostatically regulated water bath. Using a total gas flow rate of 200 cc/min at about 0.96 atm, the gas compositions employed in the nitrogenization and denitrogenization experiments were within the following range: 0.0 to 0.92 atm N_2, 0.0 to 0.90 atm Ar and p_{H_2O}/p_{H_2} from 0.03 to 0.3. The ratio p_{H_2O}/p_{H_2} was less than the critical value of 0.67 which is required for the oxidation of iron to wustite at 1000°C.

The temperature dependence of the water vapor pressure of oxalic acid dihydrate, as determined by Baxter and Lansing (8), is given by the following expression

$$\log p_{H_2O} = 18.053 - \frac{9661}{250 + T} \qquad [1]$$

where p_{H_2O} is in mm Hg and T is in °K. This was later confirmed by Bookey and Tombs (9). A series of tests carried out in the present work also gave water vapor pressures in agreement with Eq. [1] within 2% over the temperature range of 20°-50°C.

The iron strips, 3 x 1.5 x 0.051 cm, were cleaned and treated in an atmosphere of purified hydrogen for 17 hr at 1000°C before the reacting gas was introduced. At the end of a specified reaction time, the sample was withdrawn rapidly to the water-cooled end of the reaction tube and analyzed for nitrogen. The reproducibility of chemical analysis was within about 4 ppm.

Results

The results given in Fig. 1 show the retarding effect of oxygen in the atmosphere (as given by p_{H_2O}/p_{H_2}) on the rate of nitrogenization of iron. The dashed curve in Fig. 1 is that calculated for a solid state diffusion-controlled process, using $D = 1.12 \times 10^{-7}$ cm²/sec for the diffusivity (1) of nitrogen in γ-iron at 1000°C. Comparison of the experimental results with the calculated broken curve shows the strong influence of oxygen, or oxygen-bearing gaseous species, on the rate of the nitrogen-iron interfacial reaction.

In one series of experiments, the samples were initially annealed for 17 hr at 1000°C in a hydrogen-water vapor mixture having the ratio $p_{H_2O}/p_{H_2} = 0.064$ (solid triangles in Fig. 1). The rate of nitrogenization of these samples was found to be the same as those in another series (open triangles in Fig. 1) in which the samples were annealed in dry hydrogen prior to the nitrogenization experiment in an atmosphere with $p_{H_2O}/p_{H_2} = 0.064$. This finding indicates that the rate of saturation of the surface of iron with chemisorbed oxygen, in the particular atmosphere employed, is a relatively fast reaction.

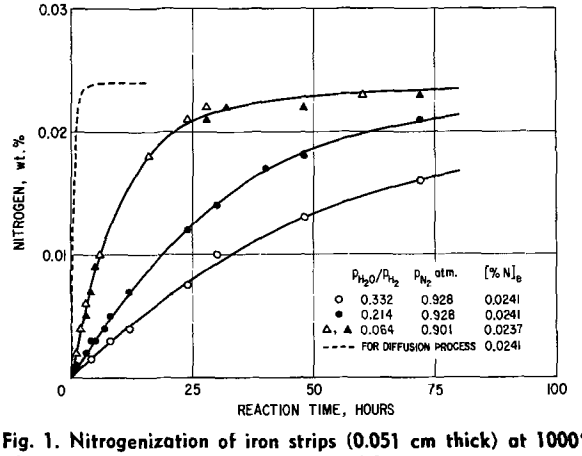

Fig. 1. Nitrogenization of iron strips (0.051 cm thick) at 1000°C in $N_2 + H_2O + H_2$ at total pressure of 0.96 atm.

[1] Present address: University of Newcastle, Newcastle-upon-Tyne, England.

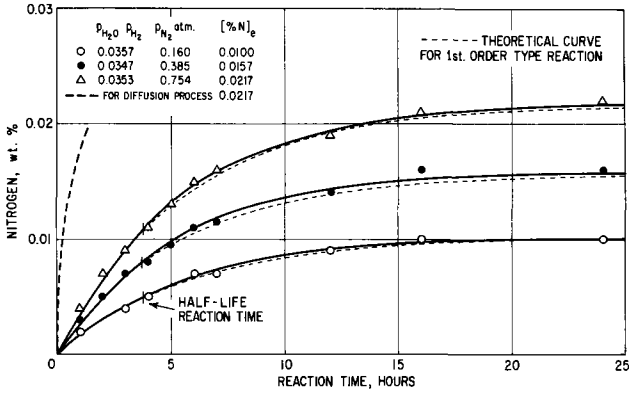

Fig. 2. Nitrogenization of iron strips (0.051 cm thick) at 1000°C in $N_2 + H_2O + H_2$ at total pressure of 0.96 atm.

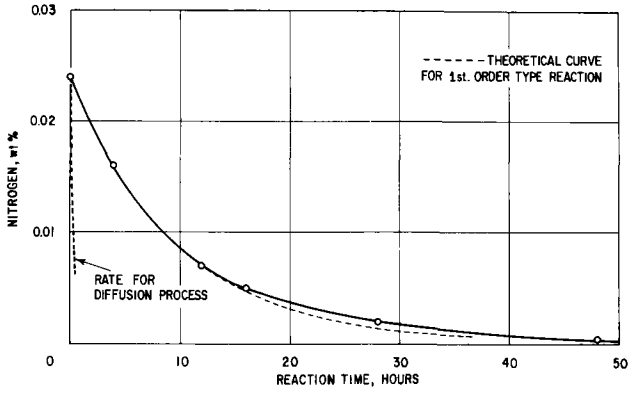

Fig. 3. Denitrogenization of iron strips (0.051 cm thick, containing 0.024% N) at 1000°C in $Ar + H_2O + H_2$ with $p_{H_2O}/p_{H_2} = 0.064$ at total pressure of 0.96 atm.

In another series of experiments, iron was nitrogenized in atmospheres of various nitrogen partial pressures with $p_{H_2O}/p_{H_2} = 0.035$. The results obtained are given in Fig. 2; as would be expected, the rate of nitrogenization decreases with decreasing partial pressure of nitrogen. It should be noted that the half-time of the reaction is independent of nitrogen partial pressure. The dotted curves given in Fig. 2 are calculated from the half-time for a first-order type of reaction. These theoretical rate curves are very close to those drawn through the experimental data.

The values of $[\%N]_e$ given in Fig. 1 and 2 are the calculated equilibrium (1) nitrogen concentrations.

The results in Fig. 3 are for denitrogenization of iron (initial uniform nitrogen content being 0.024% N) at 1000°C in argon with $p_{H_2O}/p_{H_2} = 0.064$. Comparison of the results with the dashed curve for the solid state diffusion-controlled reaction indicates that the presence of oxygen-bearing species in the atmosphere also markedly lowers the rate of denitrogenization. Again, the results compare favorably with the theoretical dotted curve for a first-order type of reaction.

It is apparent from these experimental results that the interstitial diffusion of nitrogen in iron does not play a prominent role in the control of the rate of nitrogenization or denitrogenization of iron strips (0.051 cm thick) when oxygen is present in the reacting gas. In order to verify this indication, a thicker iron strip (0.51 cm thick) was reacted with nitrogen at 1000°C with $p_{N_2} = 0.91$ atm and $p_{H_2O}/p_{H_2} = 0.052$. After a given reaction time, the metal was sectioned parallel to its surface and each layer analyzed for nitrogen. As seen from the results given in Fig. 4, the nitrogen distribution across the sample is essentially uniform. Since in the rate studies much thinner strip was used (0.051 cm thick), the surface nitrogen concentration in solution can in all cases be taken to

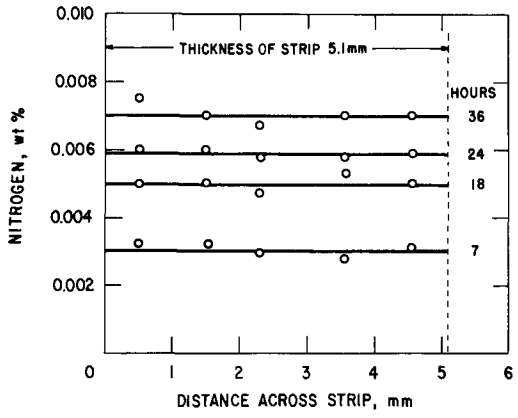

Fig. 4. Nitrogen profiles in iron strip after reaction in 0.914 atm N_2 ($+p_{H_2O}/p_{H_2} = 0.052$) at 1000°C.

be almost the same as those determined by analyzing the entire sample.

Reference should be made here to a recent experimental work of Podgurski (10) of this Laboratory on denitrogenization of iron at 442°C in H_2O-H_2 atmospheres. In this case the reaction product was found to be ammonia, and the rate was observed to be controlled by nitrogen diffusion in the bulk iron phase ($\sim$0.05 cm thick). Since at 1000°C the equilibrium ammonia concentration is very low, the presence of hydrogen in the atmosphere is not expected to enhance the rate of nitrogen reaction at the surface of iron.

For a first-order type of reaction the rate equation has the following form for nitrogenization and denitrogenization

$$\frac{d(\%N)}{dt} = -\frac{2q}{l}[(\%N)_e - (\%N)] \qquad [2]$$

where q = rate parameter for given temperature and p_{H_2}/p_{H_2O} ratio, l = thickness of iron strip, $[\%N]_e$ = nitrogen content of iron in equilibrium with the atmosphere, and $[\%N]$ = uniform nitrogen content of iron at a particular reaction time t.

Upon integration of Eq. [2], the following logarithmic expression is obtained

$$\log \frac{(\%N)_e - (\%N)}{(\%N)_e - (\%N)_o} = -\frac{2q}{2.303\,l}t \qquad [3]$$

where $(\%N)_o$ is the initial nitrogen content of the sample at $t = 0$. In all cases $(\%N)_o$ was about 3 ppm, or less, after hydrogen annealing at 1000°C.

The experimental results on nitrogenization and denitrogenization of iron are plotted in Fig. 5 and 6 in

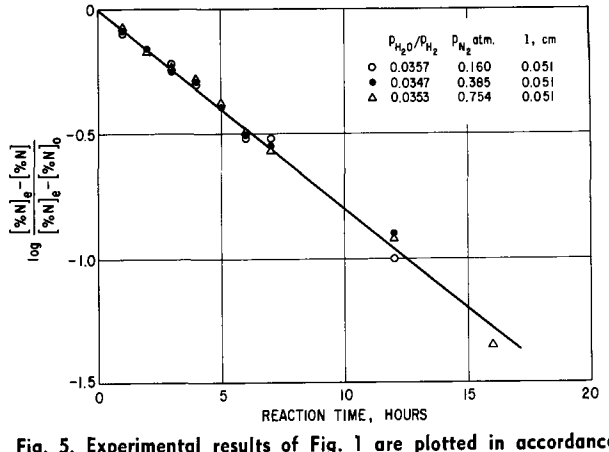

Fig. 5. Experimental results of Fig. 1 are plotted in accordance with the rate Eq. [3] for nitrogenization of iron at 1000°C.

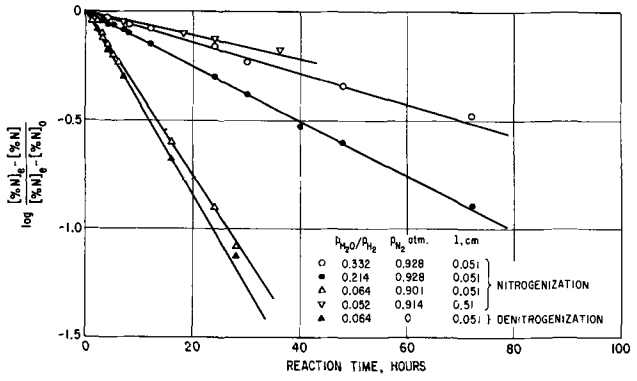

Fig. 6. Experimental results of Fig. 2 and 3 are plotted in accordance with the rate Eq. [3] for nitrogenization and denitrogenization of iron at 1000°C.

accordance with the rate Eq. [3], which appears to be supported reasonably well by the experimental data. The rate parameter q is computed from the slopes of the lines in Fig. 5 and 6 and the thickness of the iron strip, and is plotted against the ratio p_{H_2}/p_{H_2O} in Fig. 7. The line drawn through the points and the origin of the coordinates should of course be terminated at $p_{H_2}/p_{H_2O} = 1.49$ below which iron is oxidized to wustite.

Theoretical

One often refers to retardation of surface reactions on poisoned surfaces without identifying the implications involved in the so-called poisoning effect. There are two effects to be considered. One of them is an increase in the free energy of activation of the surface reaction involving adsorption and desorption of nitrogen. The other is that of retardation of transport of nitrogen through the few available vacant surface sites; that is, if the extent of surface coverage by a contaminant is very high, the fewness of the sites available for nitrogen atoms may create a bottleneck for the passage of nitrogen across the surface layer. The second effect would not appear to be the rate-controlling step for the system considered; however, the rate equation derived for such a transport process in the subsurface region is given in the Appendix.

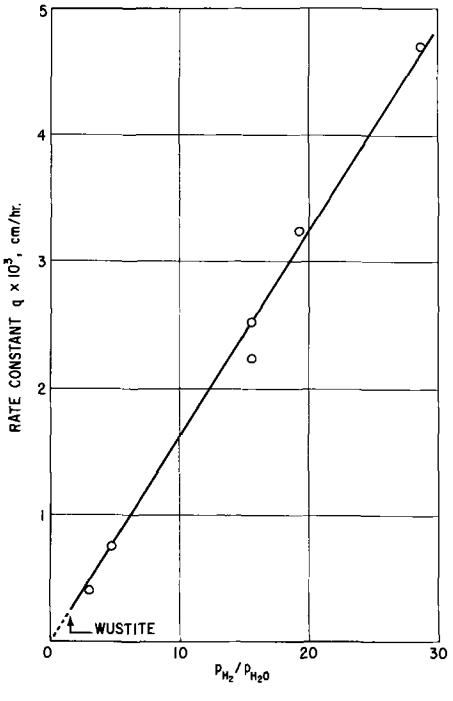

Fig. 7. Rate parameter q for nitrogenization of iron at 1000°C as a function of p_{H_2}/p_{H_2O} in the gas phase.

Thermodynamics of contaminated surface.—In the simple model to be considered, all the sites on the iron surface available for the adsorption of oxygen and nitrogen atoms are taken to be initially of the same kind, the total number being Γ sites/cm²

$$\Gamma = n_O + n_N + n_\ddagger + n_\square \qquad [4]$$

where the subscripts indicate the adsorbed atomic species, ‡ being the activated state of the nitrogen atom and the subscript □ is that for vacant sites.

In the thermodynamic treatment of the surface coverage in a monolayer by the classical statistics, the adsorbed atoms of different species are assumed to be completely interchangeable without affecting the internal energy. Then, the number of ways of distributing Γ elements[2] is given by

$$\frac{\Gamma!}{n_O! n_N! n_\ddagger! n_\square!}$$

The partition function, Q, for such as assemblage becomes

$$Q = \text{const.} \cdot \Gamma! \left[\frac{(g_O)^{n_O}}{n_O!} \cdot \frac{(g_N)^{n_N}}{n_N!} \cdot \frac{(g_\ddagger)^{n_\ddagger}}{n_\ddagger!} \cdot \frac{(g_\square)^{n_\square}}{n_\square!} \right] \qquad [5]$$

where g is the partition function of the element indicated by the subscript. By applying Stirling's approximation

$$\ln Q = \Gamma \ln \Gamma + \sum_i (n_i \ln g_i - n_i \ln n_i) + \text{const.} \qquad [6]$$

where the subscript i indicates terms for a particular element; it is to be remembered also that the summation $\sum_i n_i$ is equal to Γ. Differentiating ln Q with respect to a particular element n_j gives the chemical potential μ_j of that adsorbed species, thus

$$\left(\frac{\partial F}{\partial n_j}\right)_{P,T,\Gamma} = -kT\left(\frac{\partial \ln Q}{\partial n_j}\right)_{T,V,\Gamma} = \mu_j \qquad [7]$$

or

$$-\left(\frac{\partial \ln Q}{\partial n_j}\right)_{T,V,\Gamma} = \frac{\mu_j^o}{kT} + \ln a_j \qquad [8]$$

where μ_j^o is the chemical potential of j in the standard state and a_j its activity. In differentiating Eq. [6], it is to be remembered that $n_\square = \Gamma - \sum_i n_i$; the final form of the equation now becomes

$$a_j = k_j \frac{n_j}{n_\square} \qquad [9]$$

where k_j is a temperature dependent proportionality factor containing all the constant terms.

An important point to be noted is that the proportionality factor k_j for a particular adsorbed species and a given temperature is a constant only when the state of the monolayer satisfies one of the following idealized conditions for which the preceding treatment applies: (*i*) For small coverage in the surface no adjacent sites are occupied, therefore no change in the internal energy of the surface. (*ii*) One of the species occupies most of the surface sites, and that further increase in adsorption in the monolayer hardly affects the energy of the surface. Furthermore, the other species adsorbed on this nearly saturated surface cannot occupy adjacent sites; therefore interaction between them can be neglected. (*iii*) The adsorbed atoms of different species are completely interchangeable without affecting the internal energy of the surface, *i.e.*, an ideal monolayer.

[2] The word, element, is used here in a general sense, including vacant surface sites.

When most of the surface sites on iron are occupied by adsorbed oxygen atoms, condition (*ii*) stated above will apply. For this limiting case, the activities of the adsorbed species may now be given in terms of the fractions of sites occupied, θ, using the general Eq. [9]

$$\theta_O + \theta_N + \theta_\ddagger + \theta_\square = 1.0 \quad [10]$$

$$a_O = k_O \frac{\theta_O}{\theta_\square} \quad [11]$$

$$a_N = k_N \frac{\theta_N}{\theta_\square} \quad [12]$$

$$a_\ddagger = k_\ddagger \frac{\theta_\ddagger}{\theta_\square} \quad [13]$$

where a is the activity of the species indicated by the subscript and k's are temperature-dependent constants. For the limiting case of $\theta_O \rightarrow 1.0$, the fraction of vacant sites may be represented in terms of oxygen activity from Eq. [11]

$$\theta_\square = k_O \frac{1}{a_O} \quad [14]$$

Kinetics of nitrogen reaction.—As shown experimentally, the rate of nitrogenization and denitrogenization of solid iron is directly proportional to nitrogen activity, *i.e.*, to the square root of the corresponding nitrogen partial pressure. The same observation was made by previous workers on the rate of nitrogen reaction with liquid iron containing some oxygen. When most of the surface sites are covered with oxygen atoms, there is little probability for nitrogen atoms to occupy adjacent surface sites, at least for nitrogen activities corresponding to $p_{N_2} \leq 1.0$ atm. Therefore, it would appear reasonable to assume that, whatever may be the nature of the slow surface nitrogen reaction, the activated state for the reaction involves an atom of nitrogen.

There are two possible types of slow reaction steps when most of the surface sites are occupied with chemisorbed oxygen atoms.

(*i*) In the case of nitrogenization, for example, the nitrogen molecules in the gas phase first encounter the upper surface of the adsorbed oxygen monolayer, where equilibrium is assumed to exist between gaseous nitrogen and that adsorbed on the chemisorbed oxygen. The rate-controlling reaction step is considered to be the jump of a nitrogen atom from the outer surface of the oxygen layer to the activated state over a vacant nitrogen site on the surface of iron.

(*ii*) The other possibility is that the nitrogen chemisorption on a few available sites on the surface of iron is in equilibrium with the gaseous nitrogen. The slow reaction step is that due to the jump of the nitrogen atom from the chemisorbed site to the bulk metal phase.

The rate equation derived is identical in form for these two possible reaction steps, and, furthermore, no differentiation can be made between them from the available rate data. The sum of the reactions involved in either case leads to the following over-all reaction equilibrium

$$\tfrac{1}{2}\,N_2\ (\text{gas}) = N_\ddagger\ (\text{activated state}) \quad [15]$$

$$N_\ddagger\ (\text{activated state}) \rightarrow \underline{N}\ \text{dissolved in iron}$$

For the reaction [15] the equilibrium constant $K_\ddagger$ is given by

$$K_\ddagger = \frac{a_\ddagger}{\sqrt{p_{N_2}}} \quad [16]$$

The fraction of sites occupied by the activated nitrogen is obtained from the sum of Eq. [13], [14], and [16] for the limiting case of $\theta_O \rightarrow 1.0$:

$$\theta_\ddagger = \frac{K_\ddagger k_O}{k_\ddagger} \frac{1}{a_O} \sqrt{p_{N_2}} \quad [17]$$

Now, by invoking the theory of absolute reaction rates, a rate equation may be derived from [17]

$$\frac{dn}{dt} = -\frac{kT}{h} \Gamma \theta_\ddagger$$

where dn/dt is the rate in gram-atom N/cm^2 sec, kT/h is the universal rate. Substituting $\theta_\ddagger$ from Eq. [17] gives

$$\frac{dn}{dt} = -k' \frac{1}{a_o} \sqrt{p_{N_2}} \quad [18]$$

where k' is the specific rate constant which is equal to the product of all the other constants for a given temperature, *i.e.*

$$k' = \frac{kT}{h} \frac{K_\ddagger k_O}{k_\ddagger} \Gamma$$

According to the proposed reaction model yielding Eq. [18], when the surface of solid or liquid iron is nearly saturated with chemisorbed oxygen, the rate of nitrogenization is inversely proportional to the activity of oxygen in the system.

In view of the microscopic reversibility of the reaction process, the rate equation for denitrogenization must be based on a similar model. That is, either (*i*) a nitrogen atom adsorbed on the surface of iron, in equilibrium with the bulk phase, goes through an activated state in the process of jumping onto the chemisorbed oxygen layer, or (*ii*) a nitrogen atom in solution in the bulk phase goes through an activated state in the process of jumping into a vacant site on the surface of iron. These are the two possible slow reactions corresponding to the reverse of nitrogenization, and the rate equation is again identical in form.

The net rate equation involving a forward and reverse nitrogen reaction on the surface of iron contaminated with an oxygen monolayer is derived in a manner similar to those given above

$$\frac{dn}{dt} = -k'' \frac{1}{a_O} [(\%N)_e - (\%N)] \quad [19]$$

where k'' is the specific rate constant, $(\%N)_e$ is the nitrogen content of iron when in equilibrium with a given nitrogen partial pressure of the gas phase and (%N) is the nitrogen content of iron at time, t.

Equation [3] for a first-order type of reaction is the integrated form of Eq. [19]. It is seen that the rate parameter q (in Eq. [3]) derived from the slopes of the lines in Fig. 5 and 6 is directly proportional to k''/a_O of Eq. [19]. If the oxygen activity is sufficiently high that the limiting case of $\theta_O \rightarrow 1.0$ is satisfied, then the rate parameter q should be inversely proportional to the oxygen activity.

As seen from the results in Fig. 7, the experimentally determined rate parameter, q, is directly proportional to the ratio p_{H_2}/p_{H_2O} (which is inversely proportional to oxygen activity), at least within the range studied ($p_{H_2}/p_{H_2O} < 30$).

Discussion and Conclusions

In a recent study by Swisher and Turkdogan (11) of the rate of decarburization of liquid iron, the oxygen chemisorption isotherm for liquid iron-oxygen system was derived from the available surface tension data. At oxygen activities corresponding to % O in iron > 0.024%, the oxygen coverage in the monolayer corresponds to $\theta_O > 0.9$ at 1550°C. For the present purpose, the oxygen activity may be defined as $a_O = 1.0$ at oxygen saturation for iron-iron oxide equilibrium. The oxygen solubility limit in liquid iron at 1550°C is 0.17% O, giving $a_O = 0.14$ for 0.024% O content. That is, for liquid iron containing oxygen, chemisorption corresponds to $0.9 < \theta_O < 1.0$ when a_O

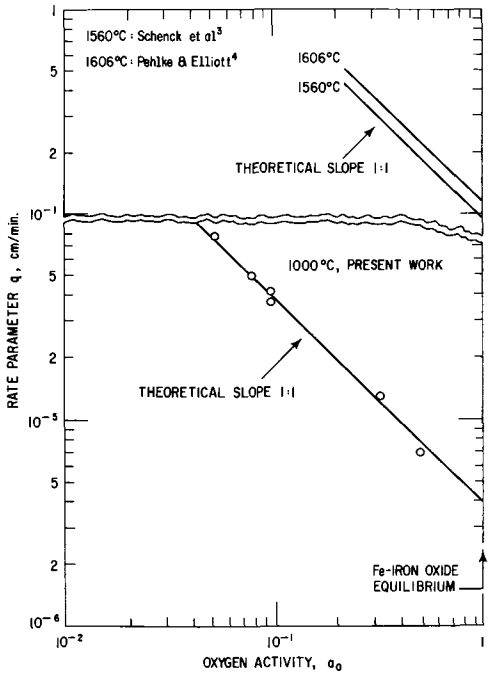

Fig. 8. Logarithmic plot of rate of nitrogen reaction on the surface of solid or liquid iron as a function of oxygen activity for which $\theta_O \rightarrow 1.0$.

> 0.14; for this range, the extent of coverage may be approximated to the limiting case of $\theta_O \rightarrow 1.0$.

At 1000°C, H_2-H_2O mixture corresponding to the iron-wustite equilibrium is given by the ratio $p_{H_2}/p_{H_2O} = 1.49$. The oxygen activity may be defined with respect to this critical ratio, *e.g.*, $a_O = 0.05$ for $p_{H_2}/p_{H_2O} = 30$ at 1000°C. Since the rate of nitrogen reaction with iron at 1000°C is a linear function of p_{H_2}/p_{H_2O} for the range studied, from the foregoing discussion it would follow that $\theta_O \rightarrow 1.0$ when $a_O > 0.05$.

From these observations it may be deduced that monolayer saturation with oxygen on solid iron is approached at oxygen activities (with respect to iron-iron oxide equilibrium) lower than those required for liquid iron surface.

As illustrated elsewhere (1), the rate of nitrogen reaction on liquid iron surface, determined by Schenck *et al.* (5) and Pehlke and Elliott (6), is inversely proportional to the oxygen content of iron for the range % O > 0.04 for which $\theta_O \rightarrow 1.0$. This evidence provides further support to the proposed reaction model.

The rate data on nitrogen reaction on solid and liquid iron surfaces are compared in Fig. 8 where the rate parameter q is plotted against the activity of oxygen in iron on a log-log scale. The results for 1000°C are those reproduced from Fig. 7; the line drawn through the points in Fig. 8 has the theoretical slope of unity. The lines, of course, terminate at $a_O = 1$ at which iron oxide forms.

Neglecting for the present the difference between the surfaces of solid and liquid iron, an estimate may be made of the temperature coefficient of the rate of nitrogen reaction. From the slope of the line of ln (q/T) *vs.* $1/T$ plot, the temperature coefficient of the reaction rate is found to correspond to about 78 kcal/g-atom N. It is to be realized that this is not the true heat of activation of the reaction considered, but it is the sum of all the heat terms associated with the constants contained in the rate equation.

The main conclusion to be drawn from this study is that at 1000°C and oxygen activities $a_O > 0.05$ (relative to iron-wustite equilibrium) the oxygen chemisorption in a monolayer on the surface of iron approaches saturation, *i.e.*, $\theta_O \rightarrow 1.0$. The rate equation derived for this limiting case of oxygen chemisorption states that the rate of nitrogen reaction on the surface of iron, for a given nitrogen activity, is inversely proportional to the activity of oxygen in the system. The experimental results for 1000°C and for liquid iron are found to be consistent with this theoretical analysis. On the basis of the experimental evidence, the activated state of nitrogen in the surface reaction is taken to be that containing an atom of nitrogen. The rate-controlling reaction step on highly contaminated surface may be due either to the jump of a nitrogen atom from the outer surface of the oxygen layer to the activated state over a vacant nitrogen site on the surface of iron, or to the jump of the nitrogen atom from the chemisorbed site to the bulk metal phase. The rate equation for either process is identical in form. Additional rate studies on this system at different temperatures may assist in the clarification of this uncertainty.

Acknowledgment

The authors wish to express their indebtedness to L. S. Darken for his counsel in the progress of this work, and particularly for his valuable contribution in the development of the theory. The authors would also like to express their thanks to R. S. Walsh and G. W. Momeyer of this Laboratory for carrying out the experimental and analytical work respectively.

Manuscript received Aug. 15, 1966.

Any discussion of this paper will appear in a Discussion Section to be published in the December 1967 JOURNAL.

REFERENCES

1. P. Grieveson and E. T. Turkdogan, *Trans. Met. Soc. AIME*, **230**, 407 (1964).
2. P. Grieveson and E. T. Turkdogan, *ibid.*, **230**, 1604 (1964).
3. G. Naeser, *Stahl u. Eisen*, **68**, 375 (1948).
4. W. A. Fischer and A. Hoffmann, *Arch. Eisenhuttenw.*, **31**, 215 (1960).
5. H. Schenck, M. G. Frohberg, and H. Heinemann, *ibid.*, **33**, 593 (1962).
6. R. D. Pehlke and J. F. Elliott, *Trans. Met. Soc. AIME*, **227**, 844 (1963).
7. P. Kozakevitch and G. Urbain, *Rev. Met.*, **60**, 143 (1963).
8. G. P. Baxter and J. E. Lansing, *J. Am. Chem. Soc.*, **42**, 419 (1920).
9. J. B. Bookey and N. C. Tombs, *J. Iron Steel Inst.*, **172**, 86 (1952).
10. H. H. Podgurski, Private communication.
11. J. H. Swisher and E. T. Turkdogan, To be published.

APPENDIX

Nitrogen Transport in Subsurface Region

When the extent of surface coverage with chemisorbed oxygen is very high, the paucity of sites available for nitrogen atoms may create a bottleneck for the passage of nitrogen across the surface layer. Although this is not the slow reaction step in the system already considered, it may play an important role in the kinetics of other similar reactions on poisoned surfaces. With this point in view, a particular rate equation applicable for such a transport process in the subsurface region will be given here; for convenience, the nitrogen reaction may again be taken as an example.

If there are a very few sites on the surface of iron available for occupation by nitrogen atoms, there will be radial diffusion of nitrogen atoms to or from these sites in the subsurface region. As an approximation and for mathematical convenience, this subsurface region may be considered to consist of hemispheres of equal size having centers at nitrogen surface sites or at vacant sites. Outside the hemispherical diffusion zone in the bulk phase the nitrogen concentration is taken to be uniform.

The solution of Fick's second law yields the following expression for diffusion in a hemispherical shell at a particular time t

$$F = 2\pi D \frac{c_e - c}{1/r_s - 1/r_o} \quad [20]$$

where F = nitrogen flow per nitrogen site, g-atom N/sec, D = nitrogen diffusivity in the metal, c_e = nitrogen concentration in solution near the surface nitrogen site, g-atom N/cm³, in equilibrium with the gas phase, c = uniform nitrogen concentration in solution in the bulk phase outside the diffusion zone, g-atom N/cm³, r_s = radius of inner hemispherical shell surrounding the surface nitrogen site, and r_o = radius of hemispherical shell which is equivalent to the thickness of the subsurface region.

If there is a total number Γ of sites/cm² at the surface of which θ_N and $\theta_\square$ are fractions of nitrogen covered and of vacant sites, the total number of hemispherical diffusion zones is

$$\chi = (\theta_N + \theta_\square)\Gamma = (1 - \theta_0)\Gamma \text{ per unit area} \quad [21]$$

For a close-packed arrangement of these hemispherical diffusion zones assumed to be uniform in size, the radius r_o is given by

$$r_o = \frac{1}{\sqrt{\pi(1 - \theta_0)\Gamma}} \quad [22]$$

The radius r_s of the inner hemispherical shell around the surface nitrogen atom may be taken to be half of the iron-iron interatomic distance d

$$r_s = \frac{d}{2} \quad [23]$$

By substituting Eq. [21]-[23] in [20], the rate of nitrogen transfer across the unit area of the surface is given by

$$\frac{dn}{dt} = \chi F = 2\pi D(1 - \theta_0)\Gamma \frac{c_e - c}{2/d - \sqrt{\pi(1 - \theta_0)\Gamma}} \quad [24]$$

where dn/dt is the rate of nitrogen transfer in g-atom N/cm² sec.

Since the maximum possible value of Γ is about 10^{15} sites/cm², Eq. [24] may be simplified for small values of $(1 - \theta_0) < 10^{-2}$.

$$\frac{dn}{dt} = q_t(c_e - c) \quad [25]$$

where

$$q_t = \pi d D \Gamma (1 - \theta_0) \quad [26]$$

For the condition that $\theta_0 >> (\theta_N + \theta_\square)$, it is permissible to take $1 - \theta_0 \simeq \theta_\square$ and substituting its equivalence from Eq. [14] in [26] gives

$$q_t = \pi d D \Gamma k_0 \frac{1}{a_0} \quad [27]$$

It is to be noted that the rate Eq. [25]-[27] are similar in form to those given in Eq. [19] for the surface reaction involving monatomic nitrogen in the activated state.

For the ratios p_{H_2}/p_{H_2O} from 3 to 30, the rate parameter q at 1000°C is within the range 1.4 x 10^{-7} to 1.4 x 10^{-6} cm/sec. If the observed rate were that limited by the transport process in the subsurface region, q may be set equal to q_t of Eq. [26]. Taking $\Gamma = 10^{15}$ sites/cm², $d = 3.64 \times 10^{-8}$ cm and $D = 1.1 \times 10^{-7}$ cm²/sec, the value of $(1 - \theta_O)$ would then fall within the range 10^{-8}-10^{-7}. That is, if $(1 - \theta_O)$ were less than 10^{-7} in the experiments considered for $\theta_O \rightarrow 1.0$, diffusion in the subsurface region would become the rate-controlling step. This limiting case is not considered to be reached in the system studied.

Cathode Processes in Molten Nitrates and Nitrites

H. E. Bartlett[1] and K. E. Johnson[2]

Department of Chemistry, Sir John Cass College, London, England

ABSTRACT

Fused $NaNO_3$ is reduced electrolytically first to nitrite and oxide. This process, however, is mixed as exact correspondence is not obtained between the nitrite produced and the coulombs passed. On further reduction of $NaNO_3$ there is an increasing contribution from various other cathodic processes including the production of colored species containing oxidized cathode metal. Reduction of KNO_3 and $NaNO_2$ also gives rise to mixed electrode processes and the formation of colored species in the cathode compartment. Ag^+/Ag is shown to be a suitable reference couple for fused $NaNO_2$.

About 120 years ago, Hittorf (1) attempted the preparation of alkali metals by electrolysis of their fused nitrates and, although his object was not achieved, he observed the formation of brightly colored liquids in the vicinity of gold and platinum cathodes. More recently (2, 3) it has been shown that the $NaNO_3$-KNO_3 eutectic melt is reduced in two discernible stages. In the first stage nitrite and sparingly soluble sodium oxide are produced, and at a more negative potential, with a platinum cathode, an unstable green solution, postulated as being a metastable solution of alkali metal, is said to be formed (3). In conflict with this postulate of the instability of the alkali metals in molten nitrate are the claims of Arvia and co-workers (4, 5) to have measured the standard reversible potential for a Na^+/Na couple in molten sodium nitrate and molten sodium nitrite. In order to resolve this conflict we have studied the current-voltage curves of fused sodium nitrate, fused potassium nitrate, and fused sodium nitrite and have examined the electrolytic reduction products of each of these melts using various metals as cathodes.

Experimental

The starting materials were AnalaR grade chemicals. The sodium nitrite was dried by heating at about 150°C *in vacuo* for 12 hr whereas the sodium and potassium nitrates were dried by bubbling dried nitrogen through their melts. Once molten, the salts were kept under an atmosphere of dried nitrogen.

The cell assembly consisted of a well-lagged 3-necked flask stoppered with silicone bungs, through which passed 1 cm diameter filter tubes cut off below the sintered glass disks (porosity No. 3 or 4) to form the electrode compartments. The flask was heated by a mantle, the power to which was controlled by a simmerstat. With this arrangement the temperature of the melt, as determined by a chromel-alumel thermocouple, could be maintained to ± 1°C.

Ag^+/Ag reference electrodes (6, 7) were made by simple addition or by coulometric generation of Ag^+ ions in compartments containing silver wires.

[1] Present address: Atomic Energy Board, Pretoria, South Africa.

[2] Present address: Chemistry Department, University of Saskatchewan, Regina, Saskatchewan, Canada.

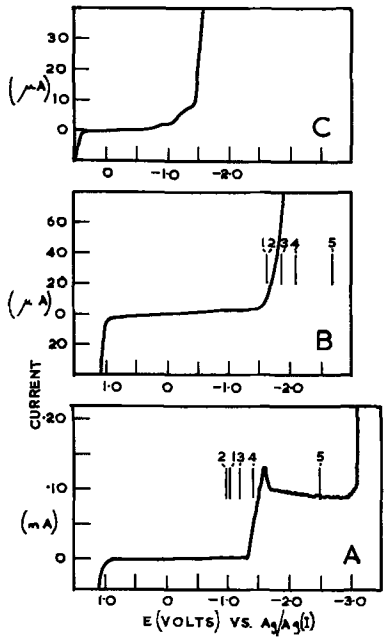

Fig. 1. Current voltage curves with platinum micro-electrodes. A, Sodium nitrate at 340°C; B, Potassium nitrate at 350°C; C, Sodium nitrite at 302°C. The lines numbered 1 to 5 in A and B mark the standard reversible decomposition voltage $E°$ of reactions 1 to 5 in Table measured from the anodic decomposition wave.

The constant current for coulometric generation was supplied by a Metrohm coulometer (ME211) whereas the somewhat larger currents needed for the massive electrolyses were derived either from a Wadsworth potentiostat when experiments were conducted at controlled cathode potentials, or from an Eliminac power supply when it was necessary to apply a large potential difference across the systems.

Platinum microelectrodes, made by sealing platinum wire (0.020 cm in diameter) into Pyrex glass and grinding the ends off flush, and an Ag^+/Ag counter electrode were used to obtain the current voltage curves.

These current voltage curves were recorded either on a Tinsley 13/1 or a Cambridge photographic polarograph.

The reducing power of the catholytes was determined by adding the cold, ground-up compartments and their contents to standard solutions of Ce^{4+} or chloramine T, stirring until all but the glass had dissolved and then back titrating with sodium thiosulfate. (The equivalent of the reducing agent is defined as the number of moles of reducing agent multiplied by the number of electrons involved in its oxidation back to nitrate and is equal to the number of moles of Ce^{4+} or chloramine T used to oxidize the catholyte. Such a definition is required as the reducing agent produced in electrolysis is unknown.)

The rhodium or platinum which went into solution at the cathode was determined as follows:

The catholytes were dissolved in water, any salt still adhering to the electrode being washed off into the solution. Concentrated HCl was then added and the solution evaporated down to dryness. The residue was strongly heated to decompose any nitrate.

When it was cold, more HCl was added and the evaporation and heating repeated to decompose most of the nitrate. The residue v as then dissolved in HCl and stannous chloride solution added. The Pt or Rh were determined colorimetrically (8).

Ag was determined gravimetrically and Co colorimetrically.

Results

Sodium nitrate.—Figure 1A depicts the current-voltage curve obtained for $NaNO_3$ at 340°C, using a platinum microelectrode and an Ag^+/Ag counter-electrode.

This current-voltage curve, which has the same profile as that for a $NaNO_3$-KNO_3 melt (2, 3) may be subdivided conveniently into three distinct regions: the peak, the afterpeak, and the ultimate decomposition wave.

Preparative electrolyses, at controlled potentials, were conducted in separate compartments within the melt, using platinum foil cathodes. Table I gives the results of these experiments.

In addition to the preparative electrolyses at controlled potentials, a number of electrolyses were conducted at high current densities (500 ma cm^{-2}) using various metals as cathodes and, in every case, colored solutions or precipitates were formed in the catholytes (see Table II).

Potassium nitrate.—Figure 1B shows the current-voltage curve obtained for KNO_3 at 350°C using a platinum microelectrode and an Ag^+/Ag counter electrode.

Unlike the corresponding curve for $NaNO_3$, the current-voltage curve for KNO_3 shows only a single cathodic decomposition wave and hence most of the preparative electrolyses were conducted at only the one potential.

During these preparative electrolyses at platinum foil cathodes, it was observed that dark green solutions were formed in the cathode compartments and that only a very small volume of gas was evolved. Neither red catholytes nor sparks could be observed in these experiments.

Further preparative electrolyses were conducted, using other metals as cathodes and in all cases, either colored solutions or precipitates were formed (Table II).

The analyses of the cathode compartments showed that the amount of reducing agent obtained depended on the metal used as cathode. With a platinum cathode there were 1.11 equivalents of reducing agent per Faraday and with a silver cathode 1.52 equivalents per Faraday. It is important to realize that it is impossible to produce more than one equivalent of reducing agent per Faraday unless, in the course of the electrochemical reaction, the metal is oxidized. With these electrolyses in the KNO_3, the metal was in fact oxidized; in the case of the platinum 0.144 mole of platinum per Faraday was found in the catholyte and in the case of silver, silver oxide was isolated from the aqueous extract of the catholyte.

Table I. Results of preparative electrolyses in sodium nitrate

Controlled potential	Observations	Analyses of catholyte (i) Reducing agent	Analyses of catholyte (ii) platinum
Peak potential −1.35v *vs.* Ag/Ag+ reference	Cathode became covered with a white deposit. Catholyte went yellow. Qualitative tests on solidified melt showed that nitrite was present.	0.94 equivalent per Faraday. Expressed as nitrite: −0.47 moles per Faraday (average of 3 determinations)	None
After-peak −2.5v *vs.* Ag/Ag+ reference	Cathode became covered with a dark deposit. Catholyte—red solution. On agitation of electrode green solution formed.	Irreproducible but results ranged from 0.70 to 0.90 equiv. per Faraday	Detected qualitatively
Ultimate decomposition −3.1v *vs.* Ag/Ag+ reference	As for the after-peak potential.	As for the after-peak potential	In green solution approx. 0.03 moles per Faraday. In red solution—detected qualitatively.

Table II. Cathodic corrosion products in fused $NaNO_2$ and KNO_3

Solvent	Cathode	Description of catholyte	Cold catholyte	Action of H_2O
$NaNO_3$	Pt	Orange, turned green on shaking cathode. Sparks observed when orange product formed in quantity without agitation.	Orange unchanged. Green to blue near m.pt. then brown	Decomposed, Pt^{2+} in solution
	Stainless steel	Dark brown precipitate and yellow solution	Dark brown	Fe_2O_3 aq.
$NaNO_2$	Pt	Red, turning green as gas evolved		
	Ag	Yellow precipitate	Yellow	Ag^+ in solution, some $Ag_2N_2O_2$
	Co	Burgundy red	Blue-green	Co^{3+} in solution
KNO_3	Pt	Dark green	Dark green	NO evolved Pt^{2+} in solution
	Rh	Yellow-brown turned green on agitation		Rh^{3+} in solution
	Ag	Dirty-brown	Dirty-brown	Ag_2O

Table III. Cathode processes, over-all cell reactions, and reversible decomposition potentials for $NaNO_3$ and KNO_3

	Cathode process	Over-all cell reaction	$E°_{600°K}$ M = Na	$E°_{625°K}$ M = K
1.	$NO_3^- + 2e^- = NO_2^- + O^{2-}$	$3MNO_3 = MNO_2 + M_2O + 2NO_2 + O_2$	−2.03	−2.64
2.	$NO_3^- + 5e^- = \frac{1}{2}N_2 + 3\,O^{2-}$	$6MNO_3 = \frac{1}{2}N_2 + 3M_2O + 5NO_2 + \frac{5}{2}O_2$	−1.97	−2.63
3.	$2NO_3^- + 8e^- = N_2O + 5\,O^{2-}$	$10MNO_3 = N_2O + 5M_2O + 8NO_2 + 4\,O_2$	−2.18	−2.87
4.	$NO_3^- + 3e^- = NO + 2\,O^{2-}$	$4MNO_3 = NO + 2M_2O + 3NO_2 + \frac{3}{2}O_2$	−2.39	−3.13
5.	$M^+ + e^- = M$	$MNO_3 = M + NO_2 + \frac{1}{2}O_2$	−3.49	−3.73

Sodium nitrite.—In some work on molten $NaNO_2$, Calandra and Arvia (5) have used an Ag^+/Ag electrode in $NaNO_3$-KNO_3 as a reference electrode. This was connected to the nitrite through a Luggin-Haber tip. However, since a reference electrode without the complication of two different solvent systems is preferable, a Ag^+/Ag reference electrode in molten $NaNO_2$ was established.

Figure 2 is a Nernst plot for a concentration cell experiment in molten $NaNO_2$ at 302°C, a line of the slope predicted by the Nernst equation being drawn through the experimental points. The Ag^+ was produced by anodic generation with a current efficiency of 100% (coulombs passed 8.88, weight of silver expected 9.937 mg, weight of silver found 9.94 mg).

Figure 1C is the current-voltage curve obtained for $NaNO_2$ at 302°C, and as with the potassium nitrate there is only a single reduction wave.

Preparative electrolyses were conducted at the potential of this reduction wave, using various metals as cathodes, and in every case the metal was corroded (Table II).

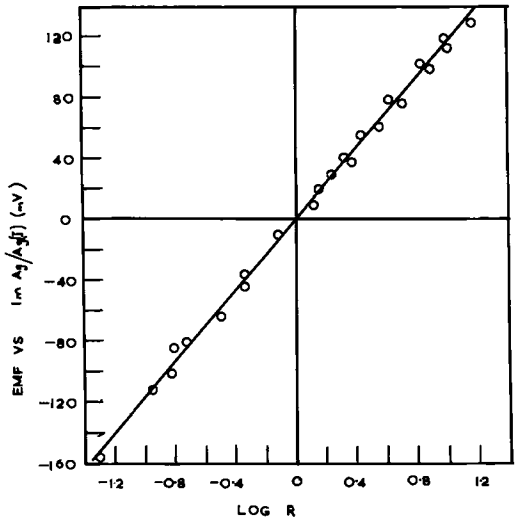

Fig. 2. Nernst plot for Ag/Ag (I) concentration cells in $NaNO_2$ at 302°C. R is the ratio of Ag (I) concentrations in the two compartments.

In contrast to either of the nitrates, the platinum foil anodes used in the sodium nitrite were corroded and, over a period of time, a green coloration developed in the anolyte.

Discussion

Unless otherwise specified this discussion is restricted to the results obtained with platinum electrodes.

At the peak potential in the molten sodium nitrate, the favored electrolytic process appears to be the reduction of the nitrate ion to nitrite and oxide, in accord with the work of Swofford and Laitinen (3). However, the fact that only 0.47 mole of nitrite per Faraday was found analytically indicates that other processes may also occur at, or before the peak potential. Among these processes could be (*a*) nitrogen evolution, (*b*) nitrous oxide evolution, or (c) nitric oxide evolution [cf. the production of nitrite, nitrous oxide, and nitrogen by reduction of nitrate with calcium metal or sodium amalgam (9) and the thermal evolution of nitrogen and nitric oxide from sodium nitrate (10)]. The standard reversible decomposition potentials (11) for each of these evolution reactions, for the production of the alkali metal, and for the formation of the alkali metal nitrite are given in Table III. For the purposes of calculating these standard reversible decompositions, it is assumed that reversible cells of the type

$$Pt, NO_2, O_2 / NaNO_3 // Na_2O, NaNO_3 / N_2, Pt$$

are formed when the melt is electrolytically decomposed. Working on these assumptions, the potentials at which reactions 1 to 5 occur in the sodium nitrate are marked on Fig. 1A: processes 1 to 3 should all occur before a potential of —1.35v *vs.* the Ag^+/Ag reference electrode.

At potentials beyond —1.35v *vs.* the reference electrode there is an increasing contribution from the gaseous evolution reactions and from other reactions, as evidenced by the smaller quantities of reducing agent found, by the appearance of the red and green colorations, and the identification of platinum in the catholytes. These mixed processes occur over a fairly wide potential span, and it is suggested that the sharp rise in current at —3.1v is not due to any one of these processes involving the reduction of the nitrate anion, as the products formed during the after-peak process are substantially the same as formed at —3.1v. The

sharp rise in current at −3.1v is more likely to be due to the breakdown of the sodium oxide film on the cathode. Metallic sodium should be thus produced and would then reduce the nitrate ion. At high current densities, this sodium, produced in fairly large quantities, would be partially shielded from the nitrate by a protective layer of sodium oxide, but when the nitrate does reach the sodium, a violent reaction in the form of sparks is not unexpected as the value for ΔG°_{600} for the reaction

$$5Na + NaNO_3 = 3Na_2O + \tfrac{1}{2}N_2$$

is −173.7 kcal mole^{-1}. Incidentally, this high negative value of ΔG°_{600} and the fact that sparks are observed at the cathode during electrolyses at high current densities would suggest that Arvia, Calandra, and Triaca's (4) claims to have measured the potential of a reversible Na^+/Na electrode are suspect.

The electrolytic reduction processes in potassium nitrate differ in some respects from the corresponding reductions in sodium nitrate, although in both cases it is the nitrate anion that is being reduced. Some of these differences could be explained in terms of the relative insolubility of sodium oxide in nitrate melts and the solubility of potassium oxide in potassium nitrate (3). Thus, there is no peak formed on the current-voltage curve of potassium nitrate as the electrode processes are not inhibited by an insoluble oxide layer. Also, as there is no alkali metal oxide film on the cathode in the KNO_3, there is little chance of forming alkali metal in large concentrations, with the result that no sparks are observed at the cathode on electrolysis of KNO_3 at high current densities.

The preparative electrolyses in molten sodium nitrite showed that the reduction processes in this medium are at least as complicated as those occurring in nitrate. Unfortunately, it is not feasible to analyze a nitrite for reducing agent and the oxide analyses were very unreliable due to the attack of the glass by the oxide. The fact that some silver hyponitrite was found in the catholyte when a silver cathode was used indicates that hyponitrite may be formed as an intermediate.

A reasonable explanation of the appearance of cathode metals in solution may be the attack of the cathode metal by one of the other cathode reduction products. The catholytes formed with platinum cathodes resemble those of aqueous platinum nitrosyl complexes (12, 13), and the brown compound formed in the nitrates when stainless steel cathodes were used is similar in appearance to $Fe(NO)_4$ and the $FeNO^{2+}$ ion which occurs as the "brown ring" compound in tests for the presence of nitrate in aqueous solutions.[3]

Further evidence suggesting that the green complex formed at the platinum cathodes in the nitrates may be a nitrosyl-type complex is that NO is evolved from the catholytes when water is added to them. Also with the sodium nitrite, in contrast of the nitrates, a green color develops in the anode compartment as well as in the cathode compartment. This may indicate that NO is formed as an intermediate in the oxidation of the nitrite and that this NO then chemically reacts with the platinum to form the green platinum nitrosyl type complex.

Acknowledgment

It is a pleasure to acknowledge the support of this work by Texas Instruments, Inc., including a maintenance grant (to H.E.B.).

Manuscript received April 28, 1966; revised manuscript received Aug. 27, 1966.

Any discussion of this paper will appear in a Discussion Section to be published in the December 1967 JOURNAL.

REFERENCES

1. W. Hittorf, *Poggendorfe Ann. Phys.*, **72**, 481 (1847).
2. G. J. Hills and K. E. Johnson, "Advances in Polarography," p. 974, Pergamon Press, London (1961).
3. H. S. Swofford and H. A. Laitinen, *This Journal*, **110**, 814 (1963).
4. A. J. Arvia, A. J. Calandra, and W. E. Triaca, *Electrochim. Acta*, **9**, 1417 (1964).
5. A. J. Calandra and A. J. Arvia, *ibid.*, **10**, 474 (1965).
6. D. G. Hill, J. Braunstein, and M. Blander, *J. Phys. Chem.*, **64**, 1038 (1960).
7. M. Blander, F. F. Blankenship, and R. F. Newton, *ibid.*, **63**, 1259 (1959).
8. G. H. Ayres, B. L. Tuffly, and J. S. Forrester, *Anal. Chem.*, **27**, 1742 (1965).
9. B. J. Brough and D. H. Kerridge, *Inorg. Chem.*, **4**, 1353 (1965).
10. B. D. Bond and P. W. M. Jacobs, *J. Chem. Soc.*, To be published.
11. H. E. Bartlett and K. E. Johnson, *Can. J. Chem.*, **44**, 2119 (1966).
12. R. Levitus and J. Ruskovan, *J. Inorg. and Nuclear Chem.*, 1534 (1963).
13. W. P. Griffiths, J. Lewis, and G. Wilkinson, *J. Chem. Soc.*, 775 (1961).

[3] In this context, it is interesting that the presence of nitrate in aqueous systems can be confirmed by adding a Pt (II) salt to the solution under test (instead of ferrous sulfate as is usually the case) and then adding concentrated sulfuric acid, when a green ring is formed at the sulfuric acid/solution interface.

The Free Energy of Formation of Palladium Oxide

J. Stuart Warner

Henry Krumb School of Mines, Columbia University, New York, New York

ABSTRACT

The equilibrium oxygen pressure for the reaction $2PdO(c) \rightleftarrows 2Pd(c) + O_2(g)$ was accurately measured over the temperature range 910°-1145°K. The following working equation for the oxygen pressure is valid over the experimental range.

$$\log P_{O_2} = 31.905 - 6.29 \log T - \frac{14{,}510}{T} \pm 0.006$$

The following expressions, valid from 298°-1200°K, apply to the formation of one mole of PdO(c)

$$\Delta F^\circ_f = -27{,}013 + 14.0\,T \log T - 6.16 \times 10^{-3} T^2 - 0.1 \times 10^5 T^{-1} - 12.190\,T \pm 100 \text{ cal/mole}$$

$$\Delta H^\circ_f = -27{,}013 - 6.08\,T + 6.16 \times 10^{-3} T^2 - 0.2 \times 10^5 T^{-1} \pm 400 \text{ cal/mole}$$

The heat of formation and entropy of PdO(c) at 298.15°K were found to be −28,345 ± 400 cal/mole and 8.60 ± 0.3 eu, respectively.

In an earlier paper (1), the author pointed out certain advantages that could be realized if the decomposition of a metal sulfate were carried out in the presence of an oxygen-controlling couple. The reaction

$$4CuO(c) \rightleftarrows 2Cu_2O(c) + O_2(g) \qquad (A)$$

was employed to maintain a known partial pressure of oxygen over a sample of $CoSO_4$ and its decomposition products. While the CuO/Cu_2O couple was satisfactory for that particular study, its relatively low equilibrium oxygen pressure and its ability to remove SO_3 from the gas phase, forming the stable compound $CuO \cdot CuSO_4$, restricted its use to the study of the more stable sulfates.

A search of the literature revealed that the PdO/Pd couple produced an oxygen pressure suitable for the study of less stable sulfates and did not itself form sulfates stable at high temperatures. Unfortunately as reported by Coughlin (2), the free energy of formation of PdO was uncertain to ± 2000 cal/mole. This large uncertainty would have seriously affected any thermodynamic properties derived for a sulfate decomposed in the presence of the PdO/Pd couple. It was therefore decided to make an accurate redetermination of the equilibrium oxygen pressure of the following reaction

$$2PdO(c) \rightleftarrows 2Pd(c) + O_2(g) \qquad (B)$$

Experimental Apparatus

An apparatus, suitable for the static determination of a variety of equilibria between gases and condensed phases of fixed composition, was designed and constructed. Since the gas phase was usually produced by some reaction of the condensed phases, it was essential that the apparatus accommodate a substantial quantity of reactants in its isothermal zone while keeping the gas volume to a minimum. This goal was achieved through the use of special furnace control circuitry, a crucible of unusual design, and an electromechanical transducer for pressure measurement.

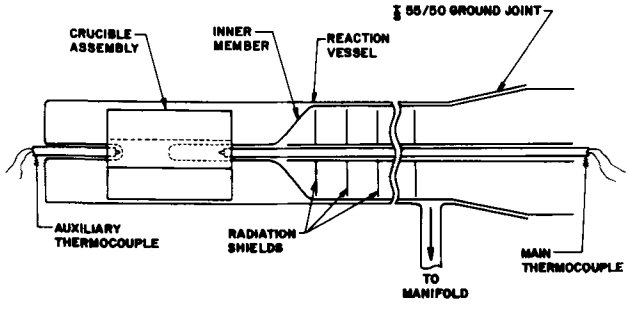

Fig. 1. Reaction vessel and crucible assembly

The reaction vessel, shown schematically in Fig. 1, was a 45 mm ID fused silica tube, 24⅝ in. in length including the Vycor female joint. The inner member, a 41 mm OD fused silica tube, carried the main thermocouple well and permitted the large crucible assembly to be sealed into the reaction vessel without creating much dead volume. The vessel was inserted about 16 in. into a tube furnace so that the crucible assembly rested at the center of the furnace.

The Nichrome heating element was wound evenly on a grooved Alundum core, 2 in. ID and 24 in. long with two taps dividing the winding into three 8-in. sections. The furnace control circuit, patterned after one described by Smith (3), could make as much as an 8 in. length of the 2 in. ID tube isothermal within ±1°C. Such control was particularly important because of the asymmetrical arrangement of the reaction vessel within the furnace. The average difference in temperature at the two thermocouples for the measurements to be reported was only 0.4°C. The furnace element was supplied with heating and cooling currents by a potentiometric controller in parallel with a rheostat. The furnace winding and the controller were supplied electrical power from separate constant voltage transformers. Since the controller had a wide dead band, a small Guoy modulator (4) was placed in series with the control thermocouple whose hot junction was in contact with the furnace winding. This crude form of proportioning control maintained the temperature of the isothermal zone constant within a few tenths of a degree for several hours and within one degree over a day.

The pick-a-back crucible assembly detailed in Fig. 2 was constructed from 0.010 in. platinum sheet. This design reduced the necessary length of the isothermal zone to 3½ in. It could accommodate relatively large volumes of reagents in separate containers, which arrangement was usually necessary in sulfate studies to prevent undesirable side reactions between the sulfate, its decomposition products, and an oxygen-controlling couple. A very important feature of the assembly was that it allowed the main and auxiliary thermocouples (see Fig. 1) to "see" only the interior of the assembly and the surface of the material in the lower crucible. This configuration permitted an accurate measurement of the temperature of the condensed phases.

Temperatures were measured with Pt-Pt/10% Rh thermocouples and an L&N Type K-3 Universal Potentiometer with guarded circuitry. The thermocouples were calibrated in accordance with NBS Circular 950 at the freezing points of zinc, aluminum, silver, and

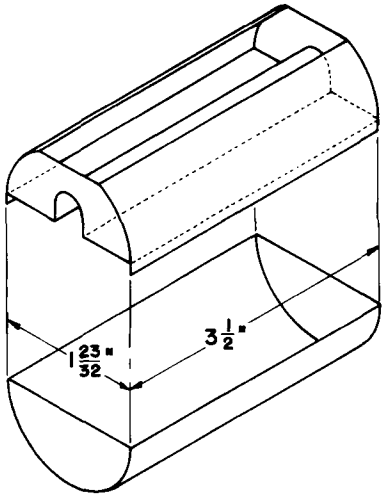

Fig. 2. Crucible assembly

copper. The silver, of 99.999% purity, was obtained commercially, the other metals from NBS. The reported temperatures are probably accurate to at least ±1°C.

The pressure of the system was measured by a miniature electromanometer system (Consolidated Electrodynamics). This device was preferred to a simple manometer because it had a much smaller dead volume and could be treated to resist attack by gaseous SO_3 arising from the decomposition of sulfates. (The author could find no manometric fluid which did not react with SO_3 or absorb significant quantities of gas.) The reaction gases were admitted to a small bellows in the thermostatted pressure balance. The interior of the bellows was gold-flashed for corrosion resistance. An associated servo-amplifier gave a ± 10 vdc output for a ± 15 psi pressure differential between the bellows and the reference cavity of the balance, which was normally evacuated to a pressure of a few microns. The output voltage was divided by a Kelvin-Varley type divider and then measured by the Type K-3 potentiometer or displayed on a potentiometric recorder.

A large-bore (22 mm ID) mercury manometer was constructed and installed in a special housing to insure an accurate determination of the mercury's temperature. Pressures could be measured on this manometer to ± 0.1 mm Hg with a cathetometer. The electromanometer was calibrated at 100 different points by comparing its electrical output with the pressure read on the mercury manometer when both devices were connected in parallel across the same pressure difference. The voltage-pressure data were correlated by a quadratic least squares equation. There was a slight hysteresis effect so different equations were used for increasing and decreasing pressures. By using the quadratic equations, pumping continuously on the reference cavity, maintaining the temperature of the pressure balance constant to within ± ½°C, and correcting for zero drift, one could measure pressures accurately to better than ± 0.1 mm Hg for a few months at a time. The arrangement of the manifold permitted the calibration to be checked at any time during the experiment.

Sample Preparation

Since Hansen (5) reported a continuous series of solid solutions between Pd and Pt, the PdO/Pd couple was contained in a half-cylindrical liner of fused silica which fitted snugly into the lower half of the crucible assembly. The empty upper half of the crucible was set in place to act as a radiation shield. An investigation of the system Pd-Si (6) revealed that, if there were any terminal solubility of Si in Pd, it was less than 0.1 a/o. This fact, together with the great difference in stability of PdO and SiO_2, indicated that no reaction should be expected between the couple and the silica liner. Preliminary experiments lasting several weeks left the liner absolutely clear and unetched.

These early experiments were not very satisfactory because of a slow approach to equilibrium. This was found to be caused by sintering of the Pd, creating a serious reduction in surface area. To prevent this sintering, Pd was mixed with an equal volume of silica which had been crushed to −200 mesh and leached repeatedly until free of iron. The metal was completely oxidized with dry tank oxygen in the reaction vessel at 700°C. The system was cooled, opened, and more Pd added to the mixture of PdO and SiO_2. Two thorough studies were made of this mixture with excellent results. The approach to equilibrium was reasonably fast in both directions, and the equilibrium oxygen pressure did not appear to depend on the amount of oxide present. Finally, x-ray diffraction patterns of the mixture made after the experiment were in excellent agreement with the patterns for PdO, Pd, and SiO_2 given in the ASTM Index.

Experimental Method and Results

The crucible assembly was inserted into the reaction vessel and the inner member sealed in place with Apiezon T grease. The thermocouples were positioned as shown in Fig. 1. The entire system was evacuated to $<5\mu$ then isolated from the mechanical pump and allowed to stand overnight to test for leaks. The system was heated and continuously evacuated for about 1½ hr until its temperature reached 500°C.

The procedure followed in all measurements was to bring the furnace close to the desired temperature, allow it to come to thermal equilibrium, then adjust its controls to minimize the temperature difference across the crucible assembly. Experience proved that subsequent constancy of pressure and both temperatures for ½ hr was sufficient to insure attainment of equilibrium. A small amount of gas was then removed in order to check the zero of the electromanometer and the pressure allowed to re-establish itself. Sometimes the furnace temperature was lowered slightly to approach equilibrium from above. The first experimental point was obtained at a pressure of several Torr, the entire gas phase being removed repeatedly to insure the absence of adsorbed gases. The data in the first two columns of Table I were obtained in this manner.

Correlation of the Data

Implicit in the equation for reaction (B) is the assumption that palladium oxide is a stoichiometric compound. Although the literature offers no evidence to the contrary, it appears that this hypothesis has not been tested. The equilibrium constant for this reaction may be expressed as follows

$$K = \frac{a^2_{Pd} P_{O_2}}{a^2_{PdO}}$$

Schmahl and Minzl (7) reported that the solubility of Pd in the oxide, if any, is very small. Raub and Plate (8) claimed to have found a small solubility of oxygen in Pd that decreased rapidly with decreasing temperature and amounted to only 0.038 a/o at 1173°K. In view of these facts Pd and PdO were assumed to have been pure substances throughout the experiment. The equilibrium constant was simplified accordingly.

$$K = P_{O_2} \qquad [1]$$

Heat capacity equations given by Kelley (9) were employed to derive the following expressions for ΔC°_p and Σ for reaction (B)

$$\Delta C^\circ_p = 12.16 - 24.64 \times 10^{-3} T - 0.4 \times 10^5 T^{-2} \qquad [2]$$

Table I. Experimental data and sigma function for the reaction $2PdO(c) = 2Pd(c) + O_2(g)$

T, °K	log P_{O_2}	Σ, cal/mole-°K	$10^4/T$, °K^{-1}
909.2	−2.667	83.820	10.999
909.2	−2.667	83.820	10.999
928.4	−2.391	82.576	10.772
929.1	−2.384	82.544	10.764
945.3	−2.154	81.503	10.579
945.4	−2.152	81.495	10.578
950.0	−2.094	81.231	10.526
950.2	−2.097	81.245	10.525
950.3	−2.097	81.245	10.524
969.5*	−1.843	80.091	10.315
971.8	−1.816	79.967	10.290
972.1	−1.814	79.958	10.288
991.3	−1.579	78.886	10.088
991.6*	−1.575	78.868	10.085
993.6	−1.553	78.767	10.065
1012.9*	−1.325	77.720	9.873
1013.0	−1.325	77.720	9.872
1015.8	−1.293	77.573	9.845
1034.4*	−1.0854	76.615	9.667
1037.3	−1.0550	76.475	9.640
1057.3	−0.8435	75.493	9.458
1058.9	−0.8252	75.408	9.444
1079.9*	−0.6118	74.413	9.260
1081.5	−0.5975	74.345	9.246
1081.7	−0.5944	74.331	9.245
1081.8	−0.5940	74.329	9.244
1101.6	−0.4030	73.433	9.078
1103.1	−0.3873	73.359	9.065
1122.1	−0.21582	72.548	8.912
1124.0	−0.19576	72.454	8.897
1124.8	−0.18471	72.402	8.891
1144.7	−0.00473	71.547	8.736
1144.9	−0.00258	71.537	8.734

* Equilibrium approached from high oxygen side.

$$\Sigma = -4.5756 \log P_{O_2} + 28.0 \log T - 12.32 \times 10^{-3}T - 0.2 \times 10^{5}T^{-2} \quad [3]$$

The values of Σ calculated from the experimental data are reported in Table I. These were correlated with reciprocal temperature by a linear least squares method, resulting in the following equation.

$$\Sigma = I + \frac{\Delta H^\circ_0}{T} = 24.381 + \frac{54{,}025}{T} \pm 0.029 \text{ cal/mole-°K} \quad [4]$$

The uncertainty quoted for Sigma represents two standard deviations of the data points about the correlating line. This scatter agrees quite well with that predicted from Eq. [3] assuming the errors in measuring temperature and pressure were 1°K and 0.1 Torr, respectively.

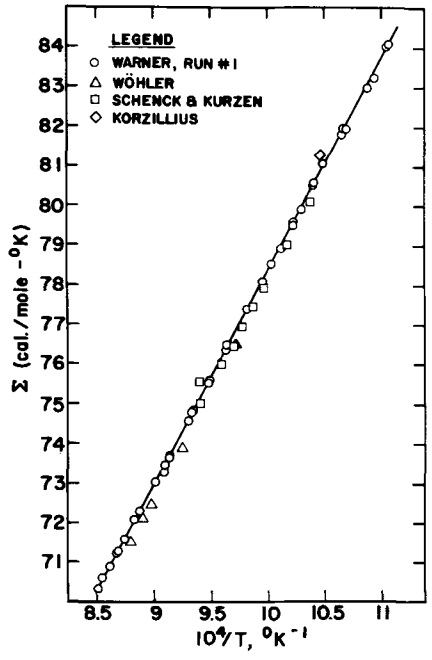

Fig. 3. Σ vs. $10^4/T$ for the reaction $2PdO(c) \rightleftarrows 2Pd(c) + O_2(g)$

Equation [4] has been graphed on Fig. 3 along with values of Sigma calculated from other experimental investigations of reaction (B). The data given in Table I were not plotted because their deviation from the correlating line could scarcely be detected even on a very large graph. When comparing data from various sources in Fig. 3, it is convenient to remember that the difference in Sigma values multiplied by the temperature at which the comparison is made equals the difference in the values of ΔF°_T for reaction (B); *i.e.*, $T(\delta\Sigma)_T = \delta(\Delta F^\circ_T)$ cal/mole. For example, the small scatter in the data of Table I may be expressed as $\delta(\Delta F^\circ_T) = \pm 0.029\ T$. This uncertainty is less than 35 cal/mole over the experimental range of temperature.

The data points labeled "Warner, Run No. 1" resulted from an earlier experiment performed with the dispersed couple in an uncovered silica crucible placed beneath the main thermocouple well. The thermocouple had not been calibrated, but the manufacturer supplied a calibration based on the wire from which it was made. This run covered a temperature range from 903° to 1177°K and developed oxygen pressures up to 1.84 atm. The sixty experimental points were correlated as described above and the resulting equation for Σ was compared with Eq. [4]. In terms of ΔF°_T the data for run No. 1 were 100 cal/mole less positive at the lowest experimental temperature and 10 cal/mole less negative at the highest experimental temperature. When both sets of data were extrapolated to room temperature, run No. 1 was only about 330 cal/mole less positive. Although the earlier experiment generally yielded slightly higher pressures, it was felt that these small differences could be readily explained in terms of the improved temperature measurement in the final experiment.

Since the completion of the author's experiments, another recent study of reaction (*B*) appeared in the literature. Schmahl and Minzl (7) used a thermobalance to determine when a small sample of the couple had come to equilibrium with a controlled oxygen pressure. They reported the following equation, said to describe their 14 data points lying between about 1020° and 1120°K

$$\log P_{O_2} = -\frac{11152}{T} + 9.726 \quad [5]$$

The data appeared to have very little scatter, but no quantitative measure could be obtained as the individual equilibrium points were not reported. In terms of ΔF°_T for reaction (B), their data were found to coincide with the author's at 1120°K and to be about 170 cal/mole less positive at 1020°K. These investigators mentioned that their experiments took a very long time, (experiments No. 1 and No. 2 took over two months), which fact may have been due to sintering of the Pd content of their couple. If this were true, it is not surprising that they found somewhat larger oxygen pressures than the author.

With the exception of one point of Schenck and Kurzen (10) and the sole point of Korzillius (11), all of the older data also lay on the high oxygen pressure side of Eq. [4]. The maximum deviation from the line was 500 cal/mole for Wohler (12), 350 cal/mole for Schenck and Kurzen, and 380 cal/mole for Korzillius.

The data of all five investigators agree extremely well within the experimental temperature range. However, the results of this investigation are preferred for the care taken in measuring temperature and pressure, the precision of the results over a wide range of temperatures, and because, in measurements of this type, the lowest pressures are probably the most accurate, all other things being equal. Equation [4] will be used for all subsequent calculations.

By combining Eq. [3] and [4] the following five-term equation for log P_{O_2} was derived

$$\log P_{O_2} = -\frac{11{,}805}{T} + 6.119 \log T - 2.693 \times 10^{-3}T - 0.044 \times 10^{5}T^{-2} - 5.328 \pm 0.0063 \quad [6]$$

A simple three-term equation was derived for log P_{O_2} which was valid over the actual experimental range of temperatures.

$$\log P_{O_2} = 31.905 - 6.29 \log T - \frac{14{,}510}{T} \quad [7]$$

Equation [7] gives excellent agreement with [6] at 900°, 1000°, and 1100°K, but differs from the preferred values by 0.01 log units at 800°K and by 0.004 log units at 1200°K. However, these deviations are comparable to the uncertainty in Eq. [6].

Thermodynamic Properties of PdO

The following expressions for the change in various thermodynamic properties accompanying reaction (B) were calculated by combining Eq. [2], [3], and [4] with the appropriate thermodynamic relations

$$\Delta F^\circ_T = 54{,}025 - 28.0\,T \log T + 12.32 \times 10^{-3}T^2 + 0.2 \times 10^{5}T^{-1} + 24.381\,T \pm 200 \text{ cal/mole} \quad [8]$$

$$\Delta H^\circ_T = 54{,}025 + 12.16\,T - 12.32 \times 10^{-3}T^2 + 0.4 \times 10^{5}T^{-1} \pm 800 \text{ cal/mole} \quad [9]$$

$$\Delta S^\circ_T = -12.221 + 28.0 \log T - 24.64 \times 10^{-3}T + 0.2 \times 10^{5}T^{-2} \pm 0.5 \text{ eu} \quad [10]$$

Equations [11] and [12] give the standard free energy of formation and the heat of formation of one mole of PdO.

$$\Delta F^\circ_f = -27{,}013 + 14.0\,T \log T - 6.16 \times 10^{-3}T^2 - 0.1 \times 10^{5}T^{-1} - 12.190\,T \pm 100 \text{ cal/mole} \quad [11]$$

$$\Delta H^\circ_f = -27{,}013 - 6.08\,T + 6.16 \times 10^{-3}T^2 - 0.2 \times 10^{5}T^{-1} \pm 400 \text{ cal/mole} \quad [12]$$

The heat of formation of PdO at 298.15°K was calculated to be −28,345 ± 400 cal/mole.

From Eq. [10], $\Delta S^\circ_{298.15}$ was calculated to be 49.94 ± 0.5 eu. This value was combined with the entropies of Pd(c) and O_2(g) given by Kelley (13) to determine $S^\circ_{298.15}$ for PdO(c).

$$49.94 \pm 0.5 = 2[9.06 \pm 0.05] + 49.01 \pm 0.01 - 2S^\circ_{298.15}(\text{PdO}) \quad [13]$$

$$S^\circ_{298.15}(\text{PdO}) = 8.60 \pm 0.3 \text{ eu} \quad [14]$$

Discussion of Results

The second-law correlation of the experimental data indicates that PdO has a smaller entropy at 298.15°K than does Pd. This is unusual, but not rare as CaO, MgO, and SrO also have reported entropies smaller than those of the corresponding metal, within the precision of the measurements.

Kellogg (14) has indicated the value of C_p for PdO at 298.15°K seems low compared with the heat capacity of comparable compounds. The data in Table I were correlated using a modified expression for the heat capacity of PdO, but the calculated value of $S^\circ_{298.15}$ was even smaller than that given in Eq. [14].

From the data given by Coughlin (2) for ΔF°_f and ΔH°_f at 298.15°K, it was apparent that he estimated a value of $S^\circ_{298.15}$ for PdO by Latimer's (15) method. This estimate, 13.2 eu, could not be used in a third-law correlation that honored the experimental points. It was probably for this reason that he assigned such a large uncertainty to ΔF°_f.

It appears that a third-law determination of the entropy of PdO is needed for clarification of these results.

Summary

The equilibrium oxygen pressure of the PdO/Pd couple in the range 800°-1200°K is given by the expression

$$\log P_{O_2} = 31.905 - 6.29 \log T - \frac{14{,}510}{T} \pm 0.006$$

The heat of formation and entropy of PdO at 298.15°K were found to be −28,345 ± 400 cal/mole and 8.60 ± 0.3 eu, respectively.

Acknowledgments

The author wishes to thank Mr. R. J. Slusar for his careful assistance in making many of the measurements and Professor H. H. Kellogg for his helpful suggestions in correlating the data and preparing the manuscript. The National Science Foundation supported this work through its grant G24464.

Manuscript received September 2, 1966.

Any discussion of this paper will appear in a Discussion Section to be published in the December 1967 JOURNAL.

REFERENCES

1. J. S. Warner, *Trans. Met. Soc. AIME*, **221**, 591 (1961).
2. J. P. Coughlin, *U. S. Bur. Mines Bull. 542* (1954).
3. R. P. Smith, *Acta Met.*, **1**, 578 (1953).
4. L. S. Darken, *Rev. Sci. Instr.*, **20**, 323 (1949).
5. M. Hansen, "Constitution of Binary Alloys," 2d ed., McGraw-Hill Book Co., Inc., New York (1958).
6. N. K. Rao and H. Winterhager, *Trans. Indian Inst. Metals*, **10**, 139 (1956-57).
7. N. G. Schmahl and E. Minzl, *Z. Phys. Chem. N. F.*, **47**, 142 (1965).
8. E. Raub and W. Plate, *Z. Metallkunde*, **48**, 529 (1957).
9. K. K. Kelley, *U. S. Bur. Mines Bull. 584* (1960).
10. R. Schenck and F. Kurzen, *Z. anorg u. allgem. Chem.*, **220**, 97 (1934).
11. H. Korzillius, Ph.D. Dissertation, Marburg, 1937.
12. L. Wohler, *Z. Elektrochem.*, **12**, 781 (1906).
13. K. K. Kelley and E. G. King, *U. S. Bur. Mines Bull. 592* (1961).
14. H. H. Kellogg, Private communication.
15. W. M. Latimer, "Oxidation Potentials," 2d ed., p. 359, Prentice-Hall, Inc., New York (1952).

Cation Effects on the Potentials of Zero Charge of Gold, Silver, and Mercury Electrodes

D. D. Bodé, Jr., T. N. Andersen, and H. Eyring

Rate Processes Institute, University of Utah, Salt Lake City, Utah

ABSTRACT

The potentials of zero charge of the mercury, silver, and gold electrodes were measured in aqueous salt solutions containing tetra-alkylammonium and some other cations. The open-circuit scrape method was used in the case of the solid electrodes, and the streaming electrode method was used for mercury. For mercury the potential of zero charge (pzc) shifts either positive or negative with increasing electrolyte concentration, depending on the relative adsorbabilities of the cation and anion. In the case of gold and silver the pzc is more cathodic in tetra-alkylammonium or cesium salt solutions than in solutions containing sodium ions. This difference in trend for mercury from the gold or silver electrode, with cation variation, reflects the variance in metal-anion *vs.* metal-cation interactions on the different metals.

Adsorbable cations markedly affect the kinetics of electrode processes in a manner which is not explicable without a fairly detailed knowledge of the inner double layer (1, 2). Although a knowledge of the potential of zero charge is needed for such studies, this reference point has seldom been directly measured in solutions containing adsorbable cations for electrodes other than mercury.

The present study presents measurements of the pzc on gold and silver electrodes by the "open-circuit scrape" method (3) in solutions containing cesium and tetra-alkylammonium ions. The above method has been tested on gold and silver electrodes in simple aqueous salt solutions (4) and has also recently proven successful in producing pzc values for solid gallium (5), which are in good agreement with the values obtained from the electrocapillary maximum of the liquid metal (6). Since the mobilities of the tetra-alkylammonium ions in water are lower than those of the common inorganic ions (7) it was feared that mass transfer may not be fast enough to insure equilibrium adsorption conditions for the above pzc measurements. Therefore, potentials of a streaming mercury electrode (sme) were measured in tetra-alkylammonium iodide solutions and compared with the electrocapillary maxima available in the literature (8), in order to test the effectiveness of mass transfer at the sme. From these results the applicability of the open-circuit scrape method to these systems could be ascertained, based on the similarity of this method to the sme method for obtaining the pzc. Results of the above tests lead us to believe that kinetic complications do not seriously interfere with the open-circuit scrape experiments, nor with the streaming electrode potentials over a majority of the concentration ranges studied.

Experimental Methods

Streaming mercury electrode.—An air-tight Pyrex glass cell housed the electrolyte. Into the lid was sealed a capillary of approximately 0.04 mm diameter which was joined to an adjustable mercury reservoir. Triply distilled mercury could then be passed from the reservoir into the solution at controlled rates. The saturated calomel reference electrode made ionic contact, through an agar-saturated KCl salt bridge, to a side compartment of the main cell. This compartment contained the solution under investigation and was separated from the main cell compartment by means of a closed stopcock. Solutions were prepared from salts of reagent grade and water which was redistilled from a basic permanganate solution.

After cleaning and assembling the cell, the solution was admitted, and nitrogen of 99.996% purity was bubbled for 30 min. The solution was at room temperature (23.5° + 1.5°C). The potential of the sme *vs.* the reference electrode was measured with a L&N K-3 potentiometer and recorded as V_o *vs.* the normal hydrogen electrode using the I.U.P.A.C.-Stockholm sign convention. The results of Grahame and co-workers (9) with KCl solutions were reproduced within 5 mv, which was satisfactory agreement for the present work considering the degree of care taken in purifying chemicals, maintaining constant temperature and standardization of reference electrodes [besides the fact that direct measurements of the potential of the sme were made, rather than the more accurate methods used by Grahame *et al.* (9)].

The apparatus, materials, and procedure for the open-circuit scrape method were described in a previous paper (4).

Experimental Results

The abbreviation Me, Et, Pr, Bu will be used for the alkyl part of the cation, R_4N^+, where R is the methyl, ethyl, n-propyl, and n-butyl group, respectively.

The pzc obtained with the sme in tetra-alkylammonium iodide solutions are compared with the electrocapillary maxima of mercury in the same solutions (8) in Fig. 1. Considering differences of more than 15 mv as being significant we see that the zero charge potentials measured by the two methods are in agreement for Me_4NI, Et_4NI, and Pr_4NI from the most dilute concentrations studied [0.005, 0.003, and 0.01M, respectively, by ref. (8)] to concentrations of 0.05-0.1M, depending on the solution. In more concentrated solutions it is seen that the electrocapillary results level out and become more positive while the sme values continue to become more negative. Although the pres-

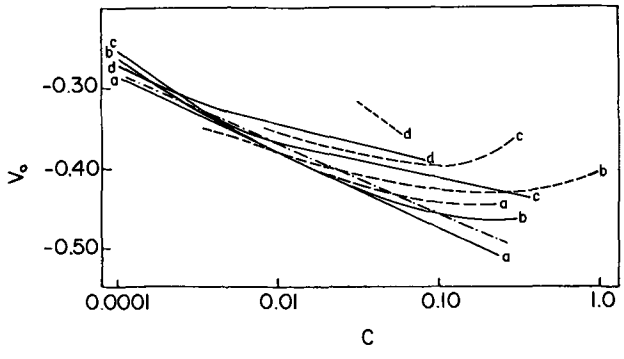

Fig. 1. Potential of zero charge, V_o (vs. NHE) vs. concentration (moles/liter). Dashed lines (----) electrocapillary maxima (8); solid lines this work; chain line (—.—.—) KI solutions [Grahame (13)]: (a) Me_4NI, (b) Et_4NI, (c) Pr_4NI, and (d) Bu_4NI.

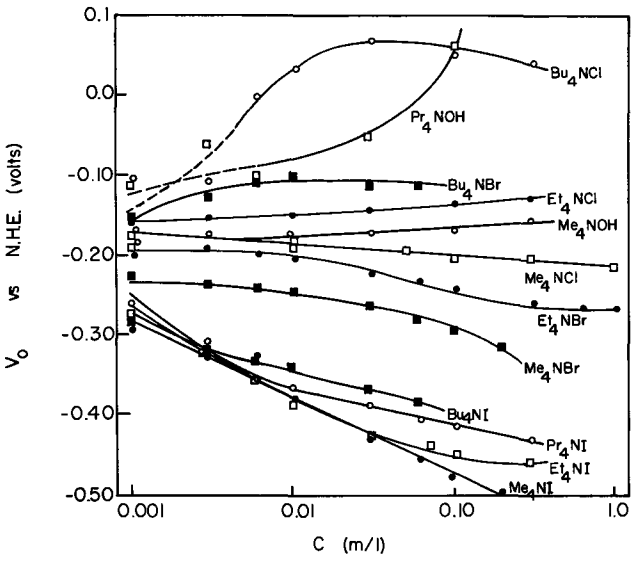

Fig. 2. Potential of zero charge, V_o, vs. concentration, c (moles/liter), for streaming mercury electrode in various aqueous solutions.

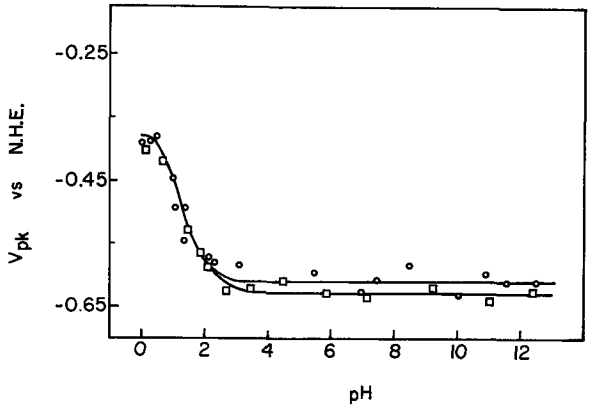

Fig. 3. Peak potential, V_{pk}, (in volts) vs. pH for the silver electrode in 0.1M solutions: ○ NaCl+(HCl or NaOH); □ CsCl + (HCl or NaOH).

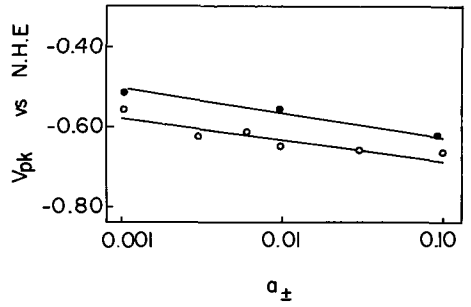

Fig. 4. Peak potential, V_{pk} (in volts), vs. activity (in moles/liter) for the silver electrode: • NaCl, ○ Et_4NCl.

ent results do little to explain the observed differences, it can be seen that slow mass transfer, in the case of the sme, is not the cause of the differences. If this were so, the discrepancies would be consistently present in dilute rather than concentrated solutions. Other investigators have also found that mass transfer need not be considered for tetra-alkylammonium ions at moderate concentrations (2). In the concentrated solutions one might presume that the sme measurements out-run some process involved in double layer formation, such as chemibonding of cations to specifically adsorbed anions (assuming the electrocapillary maximum values to be correct). The convergence of the pzc from the two methods for Bu_4NI, with increasing concentration, does not agree with the trends found for the other solutions and may indicate that experimental errors account for more than 15 mv difference between the two methods.

The potentials of zero charge for the sme in various tetra-alkylammonium solutions are shown in Fig. 2 as a function of concentration. Results shown in Fig. 1 for the iodides indicate that the sme in Fig. 2 should agree closely with the electrocapillary maximum results at least up to 0.1M, and even when there is some divergence it is by no means certain which procedure is most accurate. No results are available in the literature to compare with values given in Fig. 2 for the bromides, chlorides, and hydroxides.

From comparing the sme and electrocapillary results, one may safely assume that mass transfer considerations can be neglected in the open-circuit scrape experiments (in which the solution is in a state of rapid movement), and thus the transient peak potential, V_{pk}, is expected to yield the potential of zero charge. Figures 3 and 4 show peak potentials for silver in chloride solutions containing Na^+, Cs^+, and Et_4N^+ cations. From previous pH and anion work (4) we may interpret, as the pzc, all the V_{pk} values in Fig. 4 and those in the linear V_{pk} *vs.* pH region in Fig.

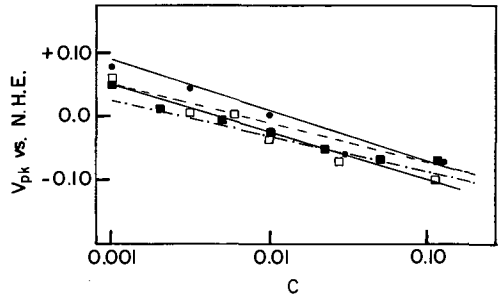

Fig. 5. Peak potential (in volts) vs. concentration (in moles/liter) for the gold electrode: ■ Me_4NOH, □ Et_4NCl, • Me_4NCl (---, NaCl; —.—.—, NaOH).

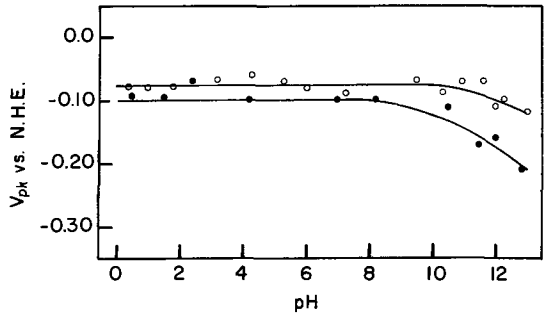

Fig. 6. Peak potential (in volts) vs. pH for the gold electrode: • 0.1N Et_4NCl + (HCl or NaOH), ○ 0.1N Me_4NCl + (HCl or Me_4NOH).

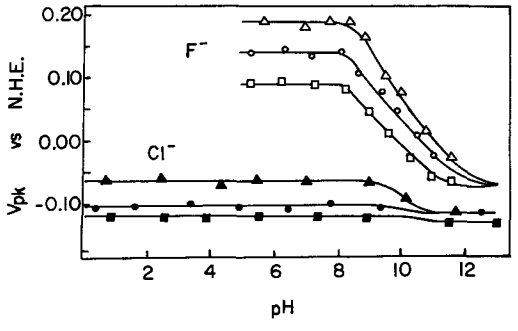

Fig. 7. Peak potential (in volts) vs. pH for the gold electrode in 0.1N fluoride (F^-) and chloride (Cl^-) solutions of Na^+ (triangles), Rb^+ (circles), and Cs^+ (squares).

3. For pH < 3, the hydrogen evolution reaction occurs so rapidly that charge is transferred to the electrode before the potential is measured. Figures 5, 6, and 7 show the V_{pk} for gold electrodes in solutions containing various large cations. In these figures all V_{pk} values are considered to be the pzc (4), and the deviations of the V_{pk} potentials from the horizontal at high pH arise from preferential adsorption of hydroxyl over the chloride or fluoride ions (4) in the alkaline region.

Discussion

When there is no electronic charge on the metal (*i.e.*, at the pzc) the change in potential brought about by the electrolyte is due to several causes. We write for this, ΔV, change in potential

$$\Delta V = \Delta V_{ad} + \Delta V_{dif} + \Delta V_{dip} + \Delta W \quad [1]$$

Here ΔW is the change in the work function of the electron which is added in charging the electrode with the change of the electrolyte. We consider ΔW to be negligible in our experiments. ΔV_{dip} arises from the orientation of dipoles at the interface. ΔV_{dif} is the potential arising from the diffuse double layer, and ΔV_{ads} is due to the closer approach to the surface of ions of one charge over that of the counter ions. We now write

$$\Delta V_{ad} = \sum_i \frac{4\pi q_i \gamma_i}{\epsilon_i} \quad [2]$$

Here q_i is the surface density of the adsorbed ions, i; γ_i is the difference in distance from the electrode to an adsorbed ion and its counter ion (10), *i.e.*, the distance between the inner and outer Helmholtz layer for this pair of ions; ϵ_i is the effective dielectric constant for the ith kind of ions.

If one plots data for various sources (11-13) for ΔV_{ad} against q_i either changing concentration or the kind of ion at a fixed concentration, nearly straight lines are obtained. This is understandable if ΔV_{ad} is the large term in ΔV and if γ_i is roughly constant for different ions. We accordingly neglect all terms in ΔV except ΔV_{ad} in our subsequent discussion.

When only one ion is adsorbed we therefore write

$$\Delta V = \frac{4\pi q_i \gamma_i}{\epsilon_i} \quad [3]$$

In this case ΔV measures the amount of adsorbed ions q_i providing γ_i/ϵ_i is known. The anodic shift, ΔV, has been observed for mercury in sodium sulfate or sulfuric acid to which tetra-alkylammonium ions have been added (14, 15). It is assumed that the OH^- ion is only slightly adsorbed on Hg, since the potential of zero charge for a 0.1*N* KOH solution is near to that for KF (9), and the KF is known to show negligible specific adsorption (11). Thus the pzc for Me_4NOH and Pr_4NOH in Fig. 2 should indicate the extent of cation adsorption.

Assuming that a simple competitive adsorption exists between anions and cations, the relative positions of the pzc in Fig. 2 may be explained assuming that the adsorbability decreases in the order $I^- > Bu_4N^+ > Br^- > Et_4N^+ > Cl^- > Me_4N^+ > OH^-$. Pr_4N^+ lies immediately to the left or right of Br^-. A minimum or maximum in the pzc *vs.* log c plot appears for the electrocapillary curves in the case of Et_4NI and Pr_4NI (cf. Fig 1) and for the streaming electrode in the case of Bu_4NCl and Bu_4NBr (cf. Fig. 2). This indicates that the sign of the preferentially adsorbed ion changes with progressive adsorption.

When both the cations and anions adsorb as in the case of most of the salts in Fig. 2, the interpretation of the pzc becomes more complicated, since the potential shift due to either ion may be compensated by that due to the opposite ion. When two ions are competitively adsorbed we write

$$\Delta V = \frac{4\pi q_1 \gamma_1}{\epsilon_1} + \frac{4\pi q_2 \gamma_2}{\epsilon_2} \quad [4]$$

Devanathan and Fernando (8) used their measurements to estimate the amount of adsorbed cation and anion. Actually they could only measure the sums of the concentrations in the adsorbed and diffuse layer for each ion. They then estimated the amount of adsorbed iodide ion. Using this value they calculated q_{ad} for the cation. In this way they arrived at stronger adsorption of the tetra-alkylammonium than of the iodide ions. This seems inconsistent with the fact that the zero charge potential of tetra-alkylammonium iodides are markedly negative with respect to KF for which neither ion is adsorbed. This explains the discrepancy between their order and ours for ion adsorption.

The potentials of zero charge for gold and silver (Fig. 3-7) show a surprising anomaly with respect to mercury. Thus the pzc for gold and silver shifts negatively for tetra-alkylammonium ions over the values for the comparatively small H^+, Li^+, or Na^+ ions. Such results require that the negative charge be nearer to the metal than the positive charge. This requires that there be some metal-anion interaction which is stronger than the metal-cesium or tetra-alkylammonium interaction. To understand these results we must suppose that the preferential adsorption of anions is enhanced by large cations. This would be explained if ion pairs are adsorbed with the negative ion next to the metal. Analogous "bridges" have been discussed by Frumkin (1). If the adsorbed ion pairs decrease the dielectric constants in Eq. [4], we see that ΔV will be enhanced in such cases. With mercury there is no evidence of preferential orientation of the negative end of such ion pairs as may exist toward the metal. Selective orientation of ion pairs depending on the metal is consistent with the known differences in tendencies to form coordination compounds as exemplified by the difference of gold and mercury in complexing with the cyanide ion.

The enhancement of anion adsorption by tetra-alkylammonium ions is an already familiar phenomenon in certain kinetic processes (1, 17). The formation of metal-anion-cation bridges has also been invoked in explaining corrosion inhibition by organic cations (17) and in a variety of other reaction rates (1).

Acknowledgments

The authors wish to acknowledge the National Aeronautics and Space Administration under Grant No. NaG (T-79) and the Atomic Energy Commission under Contract No. AT (11-1) 1144 for financial support of this project.

Manuscript received June 6, 1966; revised manuscript received Sept. 7, 1966.

Any discussion of this paper will appear in a Discussion Section to be published in the December 1967 JOURNAL.

REFERENCES

1. A. N. Frumkin, *Trans. Faraday Soc.*, **55**, 156 (1959).
2. P. Delahay, "Double Layer and Electrode Kinetics," Chap. 9, Interscience Publishers, New York (1965).
3. T. N. Andersen, R. S. Perkins, and H. Eyring, *J. Am. Chem. Soc.*, **86**, 4496 (1964); R. S. Perkins, R. C. Livingston, T. N. Andersen, and H. Eyring, *J. Phys. Chem.*, **69**, 3329 (1965).
4. D. D. Bodé, Jr., Thesis, University of Utah, 1966; D. D. Bodé, Jr., T. N. Andersen, and H. Eyring, *J. Phys. Chem.*, To be published.
5. R. S. Perkins, Thesis, University of Utah, 1967.
6. A. Frumkin, N. Polianovskaya, N. Grigorgev, and I. Bagstskaya, *Electrochim. Acta*, **10**, 793 (1965).
7. E. R. Nightingale, *J. Phys. Chem.*, **63**, 1381 (1959).
8. M. A. V. Devanathan and M. J. Fernando, *Trans. Faraday Soc.*, **58**, 368 (1962).
9. D. C. Grahame, E. M. Coffin, J. I. Cummings, and M. A. Pöth, *J. Am. Chem. Soc.*, **74**, 1207 (1952).
10. D. C. Grahame, *Z. Elecktrochem.*, **62**, 264 (1958).

11. D. C. Grahame and B. A. Soderberg, *J. Chem. Phys.*, **22**, 449 (1954).
12. H. Wroblowa, Z. Kovac, and J. O'M. Bockris, *Trans. Faraday Soc.*, **61**, 1523 (1965).
13. D. C. Grahame, *J. Am. Chem. Soc.*, **80**, 4201 (1958).
14. G. Gouy, *Ann. Chim. Phys.*, **9**, 75 (1906).
15. A. N. Frumkin, *Ergeb. exakt. Naturw*, **7**, 235 (1928).
16. A. Frumkin, "Proceedings of the Second International Congress of Surface Activity (London)," Vol. 3, p. 58 (1957).
17. N. Hackerman, Private communication.

Technical Note

The Anodic Oxidation of Yttrium Thin Films

J. R. Rairden

General Electric Company, Research and Development Center, Schenectady, New York

As part of a study of the properties of vacuum deposited thin films of yttrium, it has been observed that these films can be anodized to form thin, apparently dense, oxide films on the surface.

The yttrium was deposited onto 1 x 3 in. microscope slides from a water-cooled, electron-beam heated source using equipment that has been described previously (1). The evaporation source was a 100g ingot of 99.9% yttrium metal heated with a beam power of 250 ma at 14 kv. Prior to deposition, the slides located 10 in. from the source, were heated to about 300°C; then the yttrium was deposited in a vacuum of 1 x 10^{-5} mm Hg at a rate of approximately 30-40 Å/sec. X-ray diffraction analyses indicated that only very fine grained elemental yttrium is deposited with a slight amount of preferred orientation of (001)-type reflections.

During evaporation, the yttrium was deposited through a stencil mask so that the film coated an area 1.8 x 7.0 cm on the glass.

Electroplaters masking tape was used to define a film area on the slide approximately 1.8 x 4.5 cm, and this area of the film was completely immersed in the solution during anodization.

Several anodizing solutions were tried; the best one found, based on low-leakage current and high scintillation voltage, was a solution consisting of: 156g ammonium pentaborate, 1124g ethylene glycol, and 720 ml water.

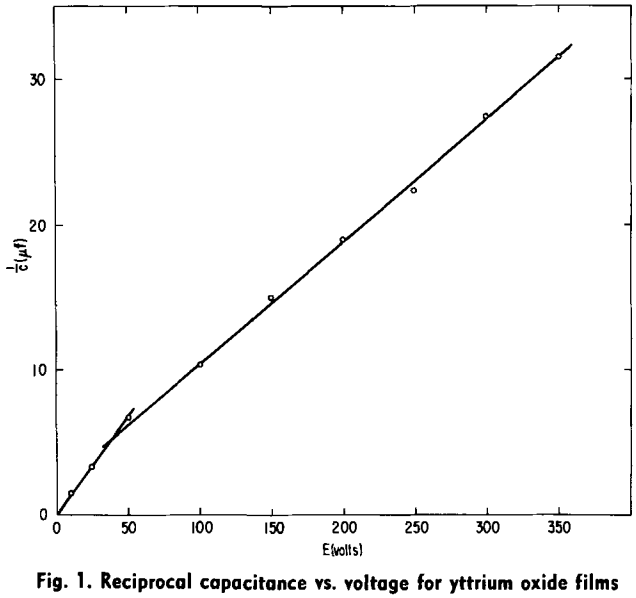

Fig. 1. Reciprocal capacitance vs. voltage for yttrium oxide films

A platinum foil cathode was used for all experiments. Using a constant voltage power supply, the anodic voltage was increased manually at a rate so that the current density was about 5-8 ma/cm². When the terminal voltage was reached, the current was allowed to decrease to, typically, 10-20 μa. For instance, using these conditions, it took about 1 min to anodize to 300v and about 3 min at voltage for the current to decrease to the minimum value.

The oxide films formed showed strong interference colors similar to those observed when tantalum or niobium is anodized. X-ray diffractometer traces taken of anodized films yielded patterns characteristic of yttrium; the oxide being too thin and/or of too small particle size to yield a pattern. Electron diffraction patterns showed three broad, diffuse halos at "d" values of 3.07, 1.98, and 1.16Å. These diffraction data indicate that the surface oxide is "amorphous" or of very small particle size which is similar to the structure of the anodic oxide formed on tantalum.

Capacitance values for the oxide films were measured at 1 kc in the anodizing electrolyte using a General Radio Company Type 650-A bridge. The reciprocal capacitance *vs.* voltage is shown in Fig. 1. It is interesting to note that this curve appears to have two linear regions; one from 0 to about 50v, and another above 50v. Scintillation occurs in the region of 375-400v. No quantitative measurements of capacitance reproducibility were made; however, it was observed that films anodized to a given voltage show identical interference colors.

Samples of several different thicknesses of yttrium were deposited; then the metal film was completely converted to oxide by anodization. These experiments indicate that for anodization above 50v, the "oxide build" is (14.8 Å/v + 300Å) ± 0.5 Å/v. By calculation, the dielectric constant of the anodic yttrium oxide is 16.5 ± 0.5. By comparing the thickness of the oxide to the thickness of the original yttrium film, it was determined that the volume ratio of oxide to metal is 1.36 ± 0.03 for the films examined. All film thickness measurements were made using a Sloan Instrument Corporation Model M-100 Angstrometer.

Acknowledgments

Helpful discussions with Dr. D. A. Vermilyea are gratefully acknowledged. R. L. Cormia kindly performed the film thickness measurements.

Manuscript received Aug. 23, 1966.

Any discussion of this paper will appear in a Discussion Section to be published in the December 1967 JOURNAL.

REFERENCE

1. J. R. Rairden and C. A. Neugebauer, *Proc. IEEE*, **52**, 1234 (1964).

SOLID STATE SCIENCE

The Growth and Crystallographic Properties of Calcium Fluor- and Chlorapatite Crystals

J. S. Prener

General Electric Company, Research and Development Center, Schenectady, New York

ABSTRACT

Stoichiometric crystals of $Ca_5(PO_4)_3F$ and $Ca_5(PO_4)_3Cl$ were grown by slowly cooling solutions of the polycrystalline apatites in fused $CaCl_2$ or CaF_2. While fluorapatite is hexagonal, optical and x-ray observations indicate that $Ca_5(PO_4)_3Cl$ has a monoclinic $P2_1/b$ space group. All crystals of this compound are highly twinned. At about 200°C a transition to a hexagonal phase ($P6_3/m$) occurs. Loss of $CaCl_2$ from the crystals leads to a stabilization of the hexagonal phase whereas at low concentrations F ion impurities have the opposite effect. Some previous observations on the luminescence of $Ca_5(PO_4)_{3-x}(MnO_4)_xCl$ can now be understood in terms of the lower symmetry structure.

The calcium apatites [$Ca_5(PO_4)_3X$; X = F, Cl, OH] form an important class of natural and synthetic compounds. Fluorapatite is the major ore of phosphorous, hydroxyapatite makes up the mineral portion of bones and teeth in all animals, and the mixed fluorchlorapatites constitute the base for the major phosphor component in fluorescent lamps. Structural, optical, and other significant properties of these compounds can best be determined and studied using single crystals of good quality. The first part of this paper describes the solution growth methods used for obtaining fairly large, stoichiometric crystals of both fluor- and chlorapatite. Recently Young and Elliott (1) in some preliminary experiments have found it possible, by heating in steam, to convert the crystals of chlorapatite grown by us from solution (but not natural mineral chlorapatite) into single crystals of hydroxyapatite. These contained only 6% of the original Cl. Thus for the first time, large crystals of this biologically important material may become available for study. The fluorapatite crystals grown from solution have been used in optical and EPR studies of color center formation on x-ray irradiation (2).

In the latter part of this paper some optical and crystallographic properties of the solution grown crystals are described. In particular the availability of chlorapatite of sufficiently high purity and good stoichiometry has revealed that at room temperature the structure is monoclinic, not hexagonal as previously reported (3). Preliminary x-ray diffraction studies on these crystals have already been reported by Young and Elliott (1). We describe here some optical studies on the twinning and birefringence of chlorapatite which reveal its lower symmetry. The observation of a transition at about 200°C from a monoclinic to hexagonal form is described, and the effects of stoichiometry and fluoride content on the transition temperature are discussed. Even though the present evidence therefore clearly indicates that stoichiometric, pure, $Ca_5(PO_4)_3Cl$ does not have a true apatite structure at room temperature, we shall for convenience refer to this compound as calcium chlorapatite in this paper.

Solution Growth of Apatite Crystals

Single crystals of fluorapatite have been grown previously by the Kyropoulus method, but stoichiometric chlorapatite could not be grown by this method due to the rapid loss of $CaCl_2$ by vaporization at the high temperatures required for fusion (*ca.* 1650°C) (4, 5). No chemical analysis was reported for the fluorapatite crystals, but these too may be off stoichiometry for the same reason. Furthermore, crystals grown from the melt at such high temperatures tend to be severely strained due to the large temperature gradients present during growth. In contrast, crystal growth from solution takes place at much lower temperatures under almost isothermal conditions.

In the methods to be described below, the formation of apatites that are halide deficient is averted through the use of CaF_2 or $CaCl_2$ as the solvents. These solvents provide a halide-rich surround for the growing crystals.

The phase diagrams of the pseudobinary systems CaF_2-$Ca_5(PO_4)_3F$ (calcium fluorapatite) and $CaCl_2$-$Ca_5(PO_4)_3Cl$ (calcium chlorapatite) were determined by Nacken (6), and his results are reproduced in Fig. 1. In the fluoride system there is a simple eutectic at 1205°C. In the chloride system there is one intermediate solid phase. Besides chlorapatite, $Ca_5(PO_4)_3Cl$, there exists the incongruently melting compound Ca_2PO_4Cl corresponding to the mineral spodiosite. The eutectic temperature is 770°C and the incongruent melting point occurs at 1040°C. In growing chlorapatite crystals from a $CaCl_2$ solution, therefore, growth must take place above 1040°C. It is not of course possible to grow Ca_2PO_4Cl from a melt of the same composition, but rather large (0.4 cm) well-formed crystals of this material have been obtained from solutions of $Ca_5(PO_4)_3Cl$ in $CaCl_2$ at temperatures below 1040°C (7).

The solutions, from which crystals of the apatites were grown, were made up by fusing mixtures of microcrystalline $Ca_5(PO_4)_3F$ [1] or $Ca_5(PO_4)_3Cl$ [1] and either CaF_2 of $CaCl_2$. The CaF_2 used consisted of small

[1] The apatites were made by solid phase reactions and kindly supplied by the Chemical Products Plant of the General Electric Company, Cleveland, Ohio.

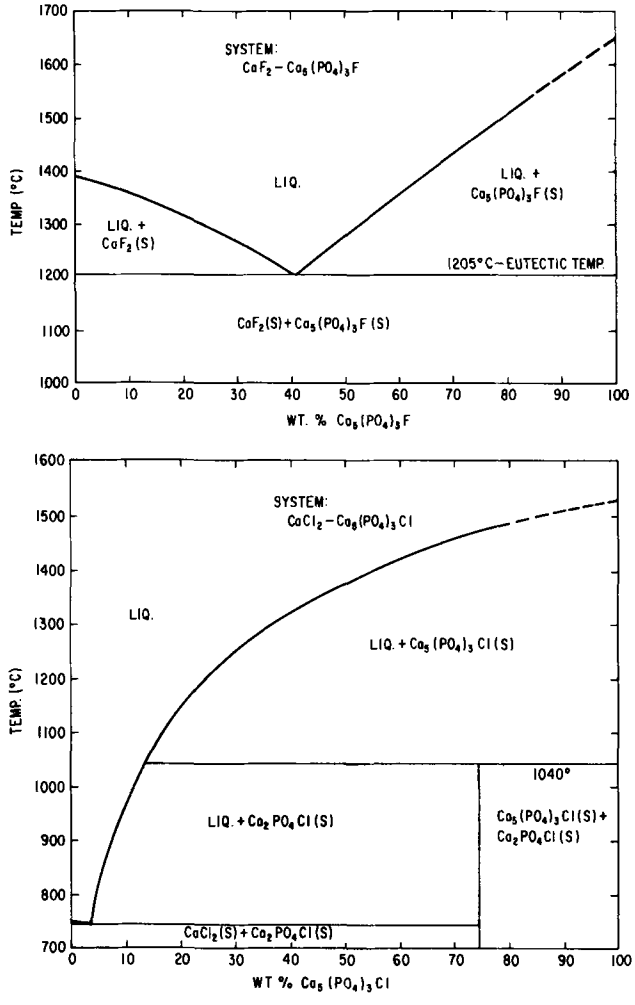

Fig. 1. Phase diagrams of the pseudobinary systems CaF_2-$Ca_3(PO_4)_2$ (top) and $CaCl_2$-$Ca_3(PO_4)_2$ (bottom) (6).

crystalline chips obtained from the Harshaw Chemical Company. The $CaCl_2$ was prepared by dehydrating AR $CaCl_2 \cdot 2H_2O$ in a stream of anhydrous HCl at 500°C. Typical compositions of the mixtures suitable for crystal growth are given in Table I.

The mixtures were contained in 100 ml platinum crucibles having a ⅛ in. lip around the top. For the chlorapatite, the crucibles were tightly covered by crimping 20 mil Pt foil around the lip and placed in the central, isothermal region of a wire wound furnace. For the fluorapatite, it was necessary to use the arrangement shown in Fig. 2. Whereas chlorapatite crystals could be separated very easily from the $CaCl_2$ matrix by leaching with hot water, fluorapatite crystals could not be separated from the solidified CaF_2. It was therefore necessary to effect a separation of the liquid and solid crystalline phases at a temperature above the 1205°C eutectic. The high-temperature separation was accomplished by inverting the furnace for several hours at the end of the crystal growing run (temperature about 1220°C). The liquid phase passed through the Pt gauze which retained the fluorapatite crystals. After cooling to room temperature,

Table I. Typical compositions used for growth of apatites from solution in fused salts

Compound	Wt. halide, g	Wt. apatite, g	Liquidus temp, °C	Temp of growth, °C
$Ca_5(PO_4)_3F$	45.0	55.0	1325	1375-1220
$Ca_5(PO_4)_3Cl$	60.0	23.5	1230	1280-1060

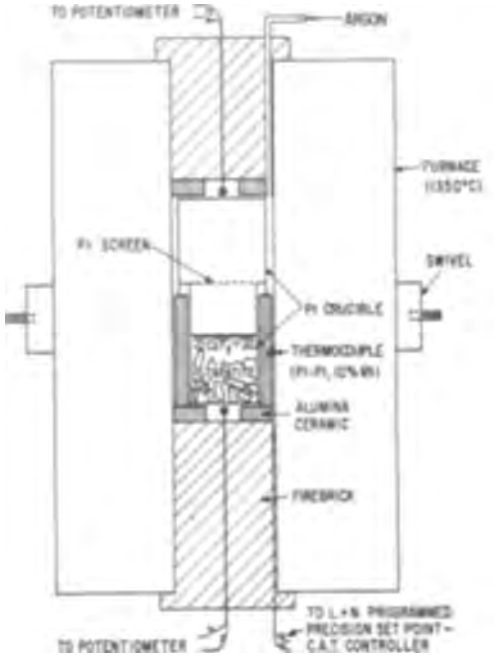

Fig. 2. Furnace and crucible used to grow crystals of $Ca_5(PO_4)_3F$ from fused CaF_2 solutions.

the crystals could be washed free of any adhering CaF_2 by boiling in an aqueous 20% solution of $Al(NO_3)_3 \cdot 9H_2O$.

Crystal growth runs were carried out as follows. The mixture of apatite powder and halide was soaked at temperatures some 50°C above the liquidus temperature for 10 to 20 hr in order to insure complete solution and then cooled at linear rates of 2-4°C/hr. Uniform cooling rates and precise temperature control (better than ±0.2°C) could be attained by driving the set-point potentiometer of a L&N Precision Set Point C.A.T. controller with a synchronous motor and suitable gear train. During cooling, when the temperature of the melt dropped below the liquidus temperature, crystallites of the apatites spontaneously nucleated in the melt or on the walls of the Pt crucible. Many crystals grew under these conditions, usually resulting in a large number of small crystals in addition to some larger ones. In the growth of fluorapatite, we cycled the temperature several times up and down some 20°C below the liquidus temperature. In this way the smallest of crystallites were redissolved leaving a fewer number of the larger crystallites which then acted as a sink for further growth. We were able to obtain many large crystals of fluorapatite (Fig. 3). The largest chlorapatite crystals obtained were 3-4 mm. The apatite crystals generally grew in the form of hexagonal prisms bounded by the faces of the $\{10\bar{1}0\}$ form. In many cases inclusions of the flux in thin rods parallel to the hexagonal axis were seen by microscopic examination, but it was always possible to find a large number of flux free crystals. The chlorapatites cleaved extremely easily perpendicular to the hexagonal axis, but no easy cleavage was observed in the fluorapatite crystals.

A number of mixed fluor- and chlorapatite crystals were grown by the use of mixtures of CaF_2 and $CaCl_2$ as the solvent and $Ca_5(PO_4)_3Cl$ powder as the source of apatite. In Table II we list the composition of the charges and the atomic ratio, $F/(Cl + F)$, in the charge as well as in the crystals. No attempt was made to determine the uniformity of the composition among the many crystals grown or within a single crystal.

It can be seen that the crystals are richer in F than the melt from which they grow. The ratio of the atomic fraction of F in the crystals to that in the charge is 2.0 ± 0.5 from the data shown in Table II.

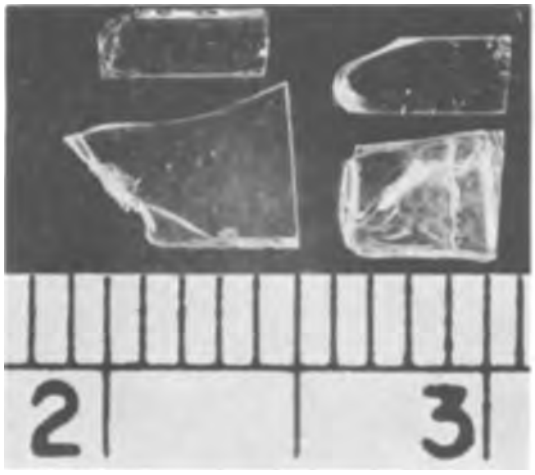

Fig. 3. Some fluorapatite crystals grown from fused CaF_2 solutions by slow cooling. The three transparent crystals have been cut and polished on the $10\bar{1}0$ faces. The scale is in centimeters.

Properties of the Apatite Crystals

Samples of both fluor- and chlorapatite crystals were analyzed for Ca, PO_4, and halide and the results are given in Table III.[2]

Since the accuracy of the chemical analyses was probably of the order of 0.1 w/o, the results given in Table II indicate that the apatite crystals were very near the stoichiometric composition.

The optical absorption of thin polished slabs of apatite crystals was measured at room temperature. A Cary Model 14 spectrophotometer was used down to 2000Å and a 1M normal incidence grating vacuum monochromator (8) was used for measurements at shorter wavelengths. The absorption coefficients of fluor- and chlorapatite are given in Fig. 4 and 5. Fluorapatite has essentially no strong absorption down to 1600Å (7.75 ev). The onset of strong absorption at this wavelength is probably intrinsic in origin [see also ref. (4)]. By way of comparison, fluorapatite crystals grown from the melt have a strong absorption band (200 cm^{-1}) peaking at 1900Å (4). This band is not intrinsic, but is due either to impurities or to a departure from stoichiometry for the melt-grown crystals since the absorption coefficient in this region

[2] The analyses were performed by the Quality Control and Testing Laboratory of the Chemical Products Plant, General Electric Company, Cleveland, Ohio.

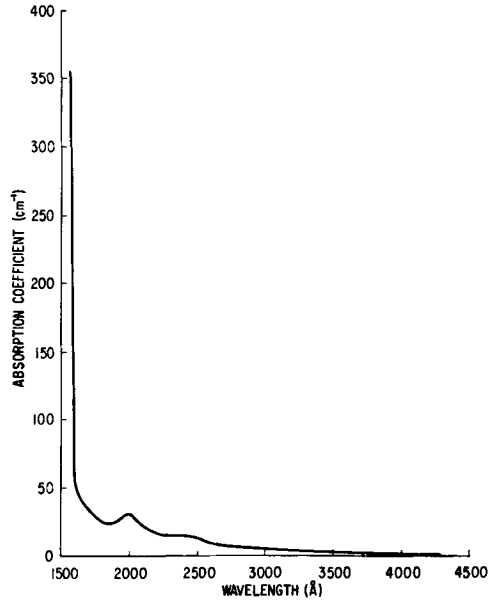

Fig. 4. Optical absorption of a $Ca_5(PO_4)_3F$ single crystal grown from solution.

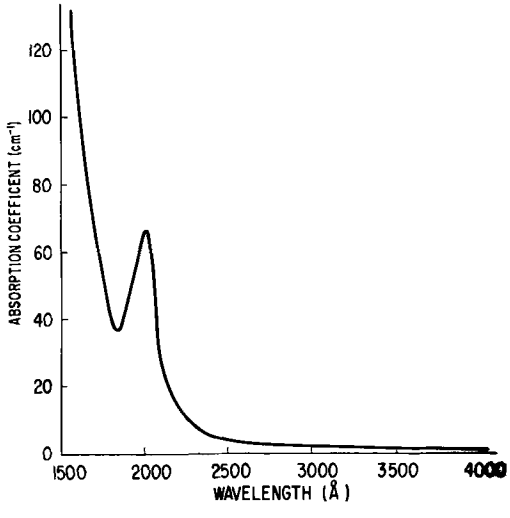

Fig. 5. Optical absorption of a $Ca_5(PO_4)_3Cl$ single crystal grown from solution.

Table II. Composition of charges and the F/(Cl + F) atomic ratios in crystals of mixed fluor- and chlorapatite

Wt. $Ca_5(PO_4)_3Cl$, g	Wt. $CaCl_2$, g	Wt. CaF_2, g	F/(Cl + F) in charge	F/(Cl + F) in crystals
11.7	29.7	0.3	0.014	0.03
11.7	28.5	1.5	0.067	0.09
11.7	27.9	2.1	0.093	0.16
11.7	27.0	3.0	0.13	0.36

Table III. Analysis of fluor- and chlorapatite

	Wt % halogen		Wt % Ca		Wt % PO_4	
	Found	Calc.	Found	Calc.	Found	Calc.
$Ca_5(PO_4)_3F$[a]	3.73	3.77	39.7	39.7	56.5	56.5
$Ca_5(PO_4)_3Cl$[b]	6.72	6.81	38.5	38.5	54.2	54.7

[a] It was necessary to correct analytical results for 0.17 wt % occluded CaF_2 solvent which could not be removed by washing the powdered charge with a hot concentrated $Al(NO_3)_3$ solution.
[b] Analytical sample analyzed for 1.5% $Ca_2P_2O_7$ as a separate phase. This again may have been an occluded phase.

for the solution grown crystals is only about 30 cm^{-1}. Strong optical absorption in chlorapatite also starts at about 1600Å, and again this probably represents an intrinsic edge. Solution-grown chlorapatite crystals have an absorption band (65 cm^{-1}) at 2000Å. It is again probably not intrinsic and has also been seen as a very strong optical absorption in diffuse reflectance spectra of chlorapatite powders (4). The origin of these impurity or defect absorption bands is being investigated.

Lattice constants of both fluor- and chlorapatite were obtained from single crystal c-axis rotation photographs. Based on a hexagonal unit cell (see, however, the next section) the measured lattice constants are given in Table IV and compared with previous determinations. The agreement of our results on single crystals with previous values determined using polycrystalline material is seen to be very good.

Microscopic examination under crossed polaroids using a quartz wedge showed fluorapatite to be uniaxial negative. For white light, the difference between the two principal refractive indices ($n_\omega - n_\epsilon$) was found to be 0.0019. The space group of fluorapatite as determined from x-ray precession photographs was

Table IV. Lattice constants of fluor- and chlorapatite

	a_0, A	c_0, A	Ref.
$Ca_5(PO_4)_3F$	9.364 ± 0.001	6.89 ± 0.05	Our value
	9.364 ± 0.005	6.879 ± 0.005	(9)
$Ca_5(PO_4)_3Cl$	9.640 ± 0.001	6.73 ± 0.05	Our value
	9.634 ± 0.005	6.783 ± 0.005	(1)

hexagonal $P6_3/m$, and the intensities of the various observed reflections were in agreement with those of previous studies of natural and synthetic fluorapatite. In contrast to fluorapatite, sections of solution grown chlorapatite crystals cut perpendicular to the apparent hexagonal c-axis appeared very weakly birefringent under crossed polaroids. The difference between the two principal refractive indices in this plane, $n_\gamma - n_\beta$, was found to be about 0.0002. Calcium chlorapatite is biaxial, and the true symmetry must therefore be lower than hexagonal. Young and Elliott (1) have already found from x-ray diffraction studies on some of these crystals that the true symmetry of chlorapatite was monoclinic $P2_1/b$, the monoclinic unit cell arising from a doubling of one of the a axes of a hexagonal cell. We were able to confirm their observations using x-ray precision camera techniques. The strong reflections indicated a hexagonal lattice. However, along one direction of the reciprocal lattice (which we take as b*) weak reflections were found half-way between the main reflections, thus indicating a doubled b-axis. The absence of odd k-indices in hko reflections and of odd l-indices in 001 reflections limit the space group to monoclinic $P2_1/b$. For monoclinic $Ca_5(PO_4)_3Cl$, Fig. 6 shows the relationship between the unit cell directions a, b, and c and the directions of the principal refractive indices (*i.e.*, the orientation of the indicatrix).

All crystals of chlorapatite when examined under crossed polaroids were found to be multiply twinned. In Fig. 7a, b, and c are shown microphotographs of a thin crystal slab cut perpendicular to the c-axis (taken as the unique axis of the monoclinic cell to coincide with the pseudo-hexagonal c-axis) as seen by transmitted light between crossed polaroids. The crystal was rotated 120° between each photograph. This crystal (as well as all other crystals examined) consists of three interpenetrating twins each having a common c-axis but oriented 120° to each other in the a-b plane. The 120° angle between the a and b axes and the fact that $b_0 = 2a_0$ results in the growth of mimetic twins having apparent hexagonal symmetry. The twinning planes are 120 and $1\bar{2}0$ and Fig. 8 shows the relationship between adjacent twins and the observed twinning planes.

Phase Transition in Chlorapatite

A large number of crystals of $Ca_5(PO_4)_3Cl$, cut perpendicular to the c-axis, were observed between

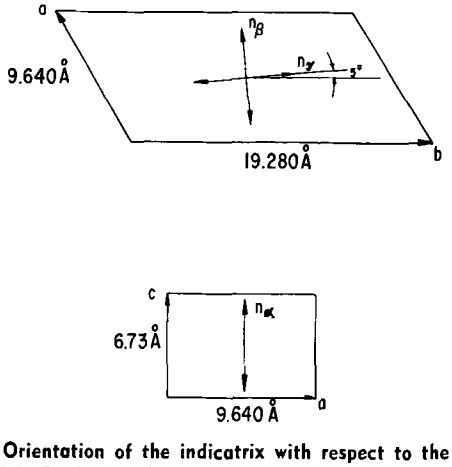

Fig. 6. Orientation of the indicatrix with respect to the unit cell in monoclinic $Ca_5(PO_4)_3Cl$.

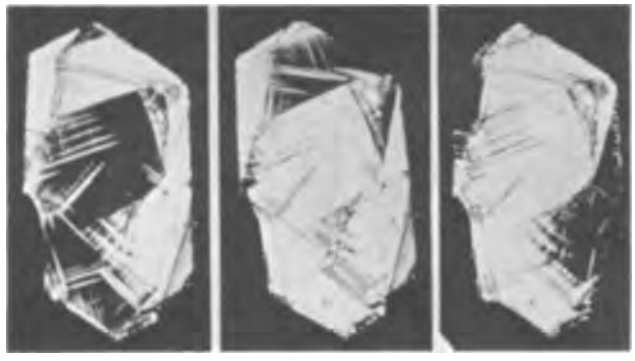

Fig. 7a, b, c (left, center, right). Microphotographs of a $Ca_5(PO_4)_3Cl$ crystal slab cut perpendicular to the c-axis (pseudohexagonal axis) and viewed through crossed polaroids. In each successive picture, the crystal is rotated 120°. The long dimension of the crystal was 4 mm.

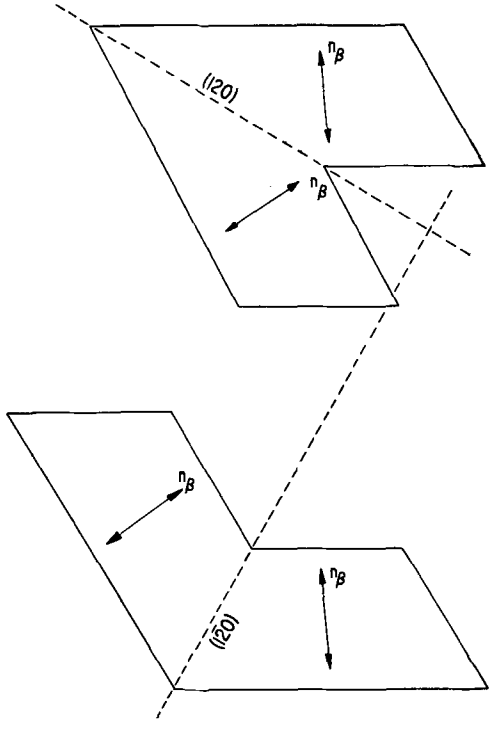

Fig. 8. Orientation of adjacent twins in $Ca_5(PO_4)_3Cl$ and the observed twinning planes. The two other adjacent sets of twins are obtained by two 120° rotations.

crossed polaroids while being heated on a microscope hot stage. At temperatures varying between 185° to 210°, for different crystals, the birefringence disappeared, the crystals becoming optically isotropic in this plane but not in a perpendicular plane. Because of the low birefringence of monoclinic apatite, observations were greatly aided by the use of a gypsum unit retardation plate. Below the transition temperature, at a suitable orientation of the crystal, the three twins show up as second order bright blue, first order bright orange and red-violet, whereas above the transition temperature, the entire crystal appears red-violet. The transition was found to be a perfectly reversible one. With each temperature cycle, however, the twinning patterns in many areas of the crystals changed drastically. For example, Fig. 9 shows the same crystal and orientation as in Fig. 7a, after one temperature cycle through the transition point. The change in the twinning pattern is obvious from the photograph. This transition was also studied by x-ray diffraction. Below the transition temperature, as already described, the space group is monoclinic $P2_1/b$, but above the transition temperature the observed re-

Fig. 9. Same crystal and orientation as one in Fig. 7a after one temperature cycle through the phase transition point.

flections are consistent with the hexagonal space group $P6_3/m$. The only obvious changes in the x-ray diffraction pattern as one goes through the transition is the disappearance of the odd k reflections in hkl ($l \neq 0$) resulting from the doubling of the hexagonal cell.

The real differences in the transition temperature observed in different crystals suggested that either deviations from stoichiometry, impurities, or both could effect this transition. To study the effect of stoichiometric deviations we heated chlorapatite crystals in vacuum at various temperatures and for various lengths of time. The results on two typical crystals are summarized in Table V. X-ray diffraction patterns taken of these heated crystals after they had become optically isotropic in the a-b plane again showed that their symmetry was hexagonal $P6_3/m$ with an apatite structure. We attributed the continuous lowering of the transition temperature and the final stabilization of the hexagonal form to a loss of $CaCl_2$ from the structure since it has been shown that there is a loss of $CaCl_2$ when chlorapatite powders are heated at temperatures of 900°-1000°C (10). Furthermore, we were able to restore the monoclinic form by reheating the hexagonal crystals in $CaCl_2$ vapor at 900°C for about 15 hr. Microscopic examination revealed that these crystals were now extremely highly twinned on a microscopic scale. These results on the effect of stoichiometry explain why $Ca_5(PO_4)_3Cl$ grown from the melt at about 1650°C are optically uniaxial (5).

Table V. Effect of heating chlorapatite in vacuum on the transition temperature

Heating temperature, °C	Time, hr	Transition temperature, °C
	Crystal I	
As grown	—	202
703	15	202
792	15	193
814	15	174
834	15	Optically isotropic down to 6°K
	Crystal II	
As grown	—	198
800	40	170
800	50	161
800	60	155
800	70	143
800	85	Optically isotropic down to 6°K

Table VI. Monoclinic-to-hexagonal transition temperatures of $Ca_5(PO_4)_3$ (F,Cl) crystals

Atomic ratio, F/(Cl + F)	Transition temperature, °C
0.0	200
0.03	223
0.09	315
0.16	310
0.36	Optically isotropic down to 6°K

Natural mineral chlorapatite is also apparently always optically uniaxial. Since mineral chlorapatite always appears to contain considerable amounts of F(11), we also studied the effect of the F content in chlorapatite on the transition temperature. The composition of the crystals of $Ca_5(PO_4)_3(F, Cl)$ used are given in Table II. In Table VI are listed the observed monoclinic-to-hexagonal transition temperatures as measured optically. It is quite apparent from the results on Table VI that small amounts of F in the chlorapatite lattice tend to stabilize the monoclinic form, but that somewhere between an atomic ratio of F/(Cl + F) of 0.16-0.36, the hexagonal form becomes the stable one. Presumably other impurities can act in a similar manner in stabilizing the hexagonal form of chlorapatite when present in sufficient concentrations. Young and Elliott (1) for example state that OH groups replacing Cl stabilize the hexagonal form.

Discussion

The structure of $Ca_5(PO_4)_3F$ (hexagonal space group $P6_3/m$) has been investigated many times (1, 3, 12). In the fluorapatite structure the two F^- ions per unit cell lie in the twofold positions (a) at 00¼ and 00¾. They are thus located in columns parallel to the hexagonal c-axis; each F^- ion lying on the mirror planes at $z = ¼$ and ¾ and in the center of a Ca^{2+} triangle. All six PO_4 tetrahedra per unit cell are crystallographically equivalent.

The location of the F^- ions and the surrounding Ca^{2+} ions are shown in Fig. 10a. Previous x-ray diffraction studies of chlorapatite have indicated that its space group symmetry was the same as that of fluorapatite (3). Because of the larger size of the Cl^- ions, however, it seemed most probable that they were in the twofold positions (a) at 000 and 00½, halfway between the mirror planes. However, as we have pointed out, x-ray diffraction and optical studies on single crystals of stoichiometric $Ca_5(PO_4)_3Cl$ have shown that the true symmetry at temperatures below 200°C is monoclinic $P2_1/b$. The monoclinic unit cell can be derived from a hexagonal cell by doubling one of the hexagonal a axes. In this lower symmetry struc-

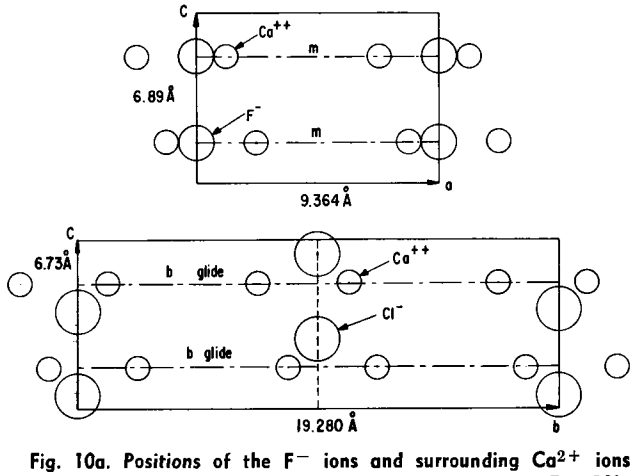

Fig. 10a. Positions of the F^- ions and surrounding Ca^{2+} ions projected on an a-c plane in the fluorapatite structure; Fig. 10b, possible positions of the Cl^- ions projected on the b-c plane in the monoclinic form of the $Ca_5(PO_4)_3Cl$ structure. The ionic sizes are drawn ½ scale for clarity.

ture all the atoms most probably lie on the fourfold general positions (e). As a consequence of this, the twelve P atoms per unit monoclinic cell will lie on three crystallographically inequivalent sets of positions (e). By a suitable choice of parameters, the general equivalent position of the $P2_1/b$ space group can be made close to or even the same as those of $P6_3/m$. The similarity in the strong reflections of $Ca_5(PO_4)_3Cl$ above and below the monoclinic-hexagonal transition indicates that the atomic positions in the monoclinic and hexagonal forms of chlorapatite are indeed not very different. Hence the term pseudo-hexagonal symmetry used to describe the low-temperature form. That there are, however, slight but measurable differences in the surroundings of the three sets of P atoms is shown by the fluorescence studies in fluor- and chlorapatites and spodiosite (Ca_2PO_4Cl) doped with small amounts of MnO_4^{-3} (7). The MnO_4^{-3} ion substitutes for the PO_4^{-3} ion in these materials. At 78°K in fluorapatite and spodiosite a strong, sharp fluorescent emission line is observed at 8640 and 8410 cm^{-1}, respectively. In chlorapatite three lines, of about equal intensity and separated by 5 cm^{-1}, are observed near 8600 cm^{-1}. These lines are due to electronic transitions between the excited ^1E and ground $^3A_2$ states of the e^2 configuration of the tetrahedral MnO_4^{-3} ion. Crystal field splittings of the ^1E state due to deviations from perfect T_d symmetry are also observed and vary from about 110 cm^{-1} in fluorapatite and 166 cm^{-1} in chlorapatite to 293 cm^{-1} in spodiosite. The origin of the 5 cm^{-1} splitting of the fluorescent line observed only in chlorapatite was attributed to a splitting of the threefold spin degenerate $^3A_2$ state. It was not understood why a similar splitting was not observed in fluorapatite or spodiosite. In view of the structural considerations discussed above, it seems most probable now that the three closely spaced equally intense lines observed in chlorapatite are in fact due to the presence of equal numbers of Mn^{5+} on the three different sets of P positions. The small value of the splitting indicates again that the three sets of P positions are structurally not very different from each other. Incidentally, the much larger crystal field splitting (arising from deviations from T_d symmetry mentioned above) in spodiosite as compared to the apatites is also reflected in the large distortion of the PO_4 tetrahedra found from x-ray diffraction studies of Ca_2PO_4Cl (13).

At temperatures near 200°C, we have found that monoclinic $Ca_5(PO_4)_3Cl$ undergoes a reversible transition to a hexagonal form and that the x-ray diffraction patterns of the high-temperature form are consistent with the hexagonal space group $P6_3/m$ and an apatite structure. Young and Elliott (1) have suggested that the lower symmetry of chlorapatite compared to fluorapatite arises primarily from the positions of the halide ions. They indicated that the four Cl^- ions per unit monoclinic cell could lie on the fourfold (e) positions (with $x = 0$ and $y = \frac{1}{4}$ and the origin on the twofold screw axis) $00z$; $0, \frac{1}{2}z$; $0, 0, \frac{1}{2}+z$; $0, \frac{1}{2}-z$ of the $P2_1/b$ space group. From considerations of ionic size and typical Ca-Cl bond distances they further suggest a possible value of 0.413 for the z parameter. The effect of moving the Cl^- ions away from positions halfway between the mirror planes of the apatite structure ($z = 0, \frac{1}{2}$) is to lower the symmetry to $P2_1/b$ and to replace the mirror planes by b glide planes. These proposed geometrical features of the monoclinic structure are illustrated in Fig. 10b. Considering only the Cl^- ions, the observed monoclinic-to-hexagonal transition can occur in two ways. Above the transition temperature the Cl^- ions may be shifted to mean positions at $z = 0$ and $\frac{1}{2}$, thus raising the symmetry to hexagonal. These shifts would be accompanied of course by corresponding small displacements of the other atoms to positions consistent with the hexagonal space group. On the other hand, the higher symmetry above the transition temperature can be achieved by a statistical disordering, within each column of Cl^- ions, of the sign of the z parameter. We have no experimental evidence as to which mechanism operates in the reversible transition at about 200°C. We do, however, have evidence that the hexagonal off-stoichiometric chlorapatite which results from the loss of $CaCl_2$ when $Ca_5(PO_4)_3Cl$ is heated in vacuum is a disordered phase. We have measured the fluorescence spectrum of MnO_4^{-3} ions in this hexagonal phase, and find that at 6°K the three closely spaced lines are still observed but much broadened when compared to those in the monoclinic form. At 77°K only one broad line was observed. We may conclude therefore that there exist small coherent regions (containing a small number of unit cells) with the monoclinic structure having the three inequivalent P sites. Between neighboring regions, however, there is no structural coherence. If the structurally coherent regions are small enough, the symmetry would appear to be hexagonal as far as the birefringence or x-ray diffraction effects are concerned. The line broadening may be due to lattice strains introduced by the disordering. This type of disordering as well as the stabilization of the hexagonal structure by Cl vacancies can be made plausible when we consider again the suggested Cl^- ion positions. In the monoclinic form the Cl-Cl distance along a column is given by $c_0/2 = 3.39$Å. Keeping any one Cl^- ion fixed and changing the sign of the z parameter of a neighboring Cl in the chain would put the two Cl ions a distance $c_0(2z-\frac{1}{2})$Å apart. Taking $z = 0.413$, we get a value of 2.20Å, a distance considerably smaller than twice the ionic radius of Cl^-, 3.62Å. Complete statistical disordering in the Cl^- ion positions does not therefore seem reasonable from size considerations. Such a shift in a Cl^- ion position could, however, take place adjacent to a Cl^- vacancy. In fact, a Cl^- vacancy would constitute locally an effective positive charge and would tend to attract a neighboring Cl^- ion. We might imagine therefore, that the presence of Cl^- vacancies destroys the structural coherence between neighboring coherent regions. A schematic diagram of such a possible effect of vacancies on the Cl^- ion positions in a Cl column is shown in Fig. 11 (a) and (b). The coherent regions

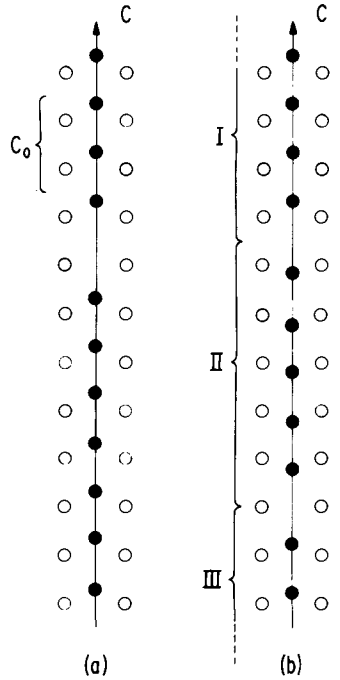

Fig. 11. Schematic representation of the possible disorder in the Cl^- positions produced by a vacancy. The open circles represent Ca^{2+} ions and the closed circles are Cl^- ions. In (a) the monoclinic arrangement of Cl^- ions is shown together with one vacancy. In (b) the movement of the Cl^- ions in region II has produced small structurally coherent regions marked by the brackets.

along the c-axis are bracketed. The structure shown in (b) is obtained by a change in the sign of the z parameter of the Cl^- ions in region II. This role of vacancies in $Ca_5(PO_4)_3Cl$ bears a certain resemblance to the role of F^- ion impurities in promoting one-dimensional disorder in the orientation of OH groups in hydroxyapatite (14).

The role of small concentrations of F^- ion impurity in stabilizing the monoclinic form of chlorapatite is uncertain. It may only be that the mixed fluor- chlorapatite crystals are more stoichiometric. On the other hand the F^- ions, presumably residing in the center of the Ca^{2+} triangles at $z = \frac{1}{4}$ and $\frac{3}{4}$, would provide a fixed negative charge in the halide column. If effectively positively charged vacancies lower the transition temperature and finally stabilize the hexagonal form by providing space for the nearby Cl^- ions to move, then any fixed negative charge in the halide column might have the opposite effect. At this time it seems fruitless to try to speculate further on this point. At a sufficiently high F content, the fixed F^- ions at positions consistent with the hexagonal space group would lead to the hexagonal apatite structure. This we have observed to occur at an atomic ratio of $F/(F + Cl)$ somewhere between 0.16 and 0.36.

The marked twinning observed in crystals of $Ca_5(PO_4)_3Cl$ is also understandable. In the high-temperature hexagonal phase there are three equivalent directions, 120° apart in the plane perpendicular to the c-axis. As the crystal cools through the transition temperature any one of these directions can give rise to the doubled axis of the monoclinic structure. A nucleus of the monoclinic cell once formed with a particular orientation will tend to grow with this orientation until it meets a twin with another orientation. Hence, the formation of the highly twinned crystals and the change in the twinning pattern with each temperature cycle through the transition point can be understood.

Acknowledgments

The author would like to thank A. M. LaTorre for his technical assistance, Dr. W. Roth for his help with the x-ray work, and Dr. P. D. Johnson for taking the absorption data in the vacuum ultraviolet.

Manuscript received June 14, 1966; revised manuscript received Aug. 26, 1966. This paper was presented at the Cleveland Meeting, May 1-6, 1966.

Any discussion of this paper will appear in a Discussion Section to be published in the December 1967 JOURNAL.

REFERENCES

1. R. A. Young and J. C. Elliott, *Archives of Oral Biology*, **11**, 699 1966.
2. W. W. Piper, L. C. Kravitz, R. K. Swank, and J. S. Prener, Abstract No. 149, 1965, Int. Symp. on Color Centers in Alkali Halides, University of Illinois, Urbana, Ill., p. 115.
3. S. B. Hendricks, M. E. Jefferson, and V. M. Mosely, *Z. Krist.*, **81**, 352 (1932).
4. P. D. Johnson, *This Journal*, **108**, 160 (1961).
5. P. D. Johnson, H. P. Kallman, and G. M. Spruch, Editors, "Luminescence of Organic and Inorganic Materials," pp. 563-575, John Wiley & Sons, Inc., New York (1962).
6. R. Nacken, *Centr. Mineral. Geol.*, **1912**, 545 (1912).
7. J. D. Kingsley, J. S. Prener, and B. Segall, *Phys. Rev.*, **137**, A189 (1965).
8. P. D. Johnson, *J. Opt. Soc. Am.*, **42**, 278 (1952); *Rev. Sci. Inst.*, **28**, 833 (1957).
9. H. Brasseur, "Proc. Int. Symp. on React. Solids, Gothenburg, 1952, Pt. 1, p. 363-367 (1954).
10. R. Hickok, Private communication.
11. C. Palache, H. Berman, and C. Frondel, "The System of Mineralogy," Vol. II, pp. 877-889, John Wiley & Sons, Inc., New York (1951).
12. S. Naráy-Szabó, *Z. Krist.*, **75**, 387 (1957).
13. M. Greenblatt, E. Banks, and B. Post, To be published.
14. M. I. Kay, R. A. Young, and A. S. Posner, *Nature*, **204**, 1050 (1964).

Emission Spectra of Impurity Activated (Zn,Cd) (S,Se,Te) Phosphors

III. Self-Activated Phosphors

W. Lehmann

Westinghouse Electric Corporation, Research and Development Center, Pittsburgh, Pennsylvania

ABSTRACT

The blue SA-emission of self-activated ZnS phosphors, due to the sole incorporation of a donor impurity, shifts monotonically toward red if Zn is gradually replaced by Cd. In contrast, gradual replacement of S in ZnS by Se causes little or no shift but replacement of the blue band of ZnS by an orange band in ZnSe. Again, the latter shifts monotonically into the infrared if Zn is replaced by Cd but is replaced by another band, also in the infrared, if Se is replaced by Te. The dependences are demonstrated in recombination term schemes assuming predominantly ionic crystal bonding and validity of the Schön-Klasens model of luminescence.

Emission spectra due to copper and silver, respectively, in (Zn,Cd) (S,Se,Te) phosphors as functions of the composition of the binary or ternary host material were reported in two earlier papers (1, 2). This present paper deals with a similar investigation on self-activated phosphors whose emission is due to the incorporation of a donor impurity (*e.g.*, Cl or Al). The ordinarily observed emission of self-activated ZnS consists of a single, although rather broad, band (SA-emission band) in the blue region of the visible spectrum and is frequently described in the literature (3-12). Relatively little is published on the SA-emission of (Zn,Cd)S (3, 13) and of Zn(S,Se) (3, 14), and practically nothing of the other II-VI compounds.

Our investigations were limited to powder phosphors prepared, excited (by ultraviolet radiation at 77°K), and measured as described in ref. (1). The evaluation of the measured emission spectra was the most problematic part of the investigation since the blue SA-emission band in ZnS, and the corresponding band in the other II-VI compounds, is only one of several which can be observed, especially at low tem-

peratures. The additional emission bands are not necessarily due to contaminations of the materials with undesired impurities, *e.g.*, copper, but some are probably due to native lattice defects with or without participation of the added donor impurity. Particularly troublesome were the following additional emission bands:

(*a*) A very broad and featureless emission extending from the blue over the whole visible range into the infrared, and with a peak position in the neighborhood of 2.0 ev appears in ZnS prepared with Ga or In. This emission sometimes dominates so much (especially in case of indium) that no other emission can be observed. Examples are shown in Fig. 1. It is probably related to an essentially similar emission reported by Apple and Williams (15) in ZnS:Cu and ZnS:Ag containing Ga or In. Its intensity decreases fairly rapidly with gradual replacement of ZnS by CdS and somewhat slower if ZnS is replaced by ZnSe.

(*b*) A band of moderate width appears in phosphors containing Al, Ga, or In (but ordinarily not in phosphors made with Cl, Br, or I) at about 0.3 ev higher quantum energy than the SA-emission. Its peak position in ZnS is about 2.95 ev (λ = 420 nm, violet). Details on this emission will be described in a separate publication. Examples are shown in Fig. 1.

(*c*) The SAL-emission (16) which is observed at about 0.6 ev higher quantum energy than the SA-emission. Its peak position is about 3.2 ev (λ = 397 nm, near-ultraviolet).

(*d*) Near-edge emission (at about 3.6 ev in ZnS) of a more or less complex spectral distribution appears in many self-activated phosphors. It is usually readily distinguished from the other emission bands.

This rather complex situation observed already in binary II-VI compounds (*e.g.*, ZnS or ZnSe) becomes still more complicated within some ternary mixtures [*e.g.*, Zn(S,Se)] where new emission bands may appear as a function of the host crystal composition. Close overlap of the generally rather broad and structureless bands is then unavoidable so that a clear identification frequently cannot be made.

All concentrations in this paper are given in terms of mole per cent based on 100% of the combined host material. The indicated impurity concentrations are those added before firing and not necessarily identical (especially in cases of the volatile halides) with the concentrations retained in the phosphors after firing.

Zinc Sulfide

The peak position and the width of the blue emission band (SA-emission) of self-activated ZnS phosphors are slightly uncertain and vary from sample to sample within small limits [similar to what is observed in cases of activation by copper (1) and by silver (2)]. Typical widths (measured at 50% of peak) are about 0.50 ev at room temperature and 0.30-0.35 ev at 77°K. A dependence of the peak position on the crystal structure (cubic or hexagonal) and on the donor impurity used seems to exist but is small and almost lost in the general uncertainty. In particular, we are not able to confirm a significant difference between ZnS phosphors prepared either with halides (Cl, Br, or I) or with group III-B elements (Al or Ga) as reported by Prener and Weil (8). The following peak positions were measured within these investigations as averages over many samples, all excited by ultraviolet of 3.40 ev (λ = 365 nm) at 77°K:

cubic	ZnS: (Cl, Br, or I)	2.61 ev
cubic	ZnS: (Al or Ga)	2.65 ev
hexagonal	ZnS: (Cl, Br, or I)	2.64 ev
hexagonal	ZnS:Al	2.62 ev

The peak position of the blue SA-emission depends to a small but measurable extent on the quantum energy (*i.e.*, on the wavelength) of the exciting ultraviolet radiation, quite in contrast to the luminescence of Cu- or Ag-activated ZnS phosphors where no such dependence was detected. Generally, excitation "across the band gap" (~3.8 ev in ZnS at 77°K) gives a peak position at slightly higher quantum energy than excitation with lower quantum energy. Some actual emission spectra, all measured on the same phosphor sample under different excitation conditions, are shown in Fig. 2.

Hexagonal Zinc-Cadmium Sulfide

The blue emission band of hexagonal ZnS prepared with the aid of a halide (Cl, Br, or I) shifts gradually toward red as Zn is replaced by Cd (3, 13) without significant change in band width and shape. Examples are shown in Fig. 3. In our work, the SA-emission dominated over all others only in the spectra of (Zn,Cd)S:halide phosphors containing low Cd concentrations but it could be followed up to 100% CdS

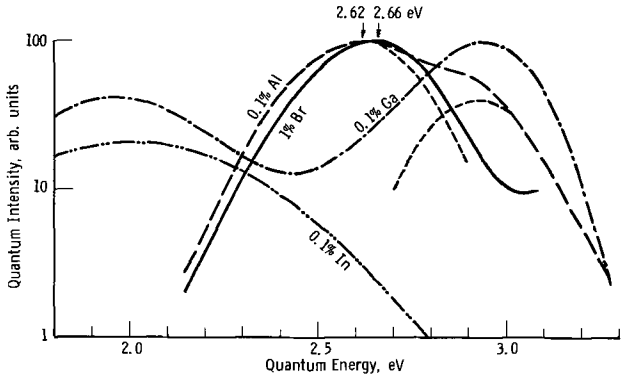

Fig. 1. Emission spectra of four different samples of hexagonal, self-activated ZnS excited by ultraviolet of 3.95 ev (λ = 313 nm) at 77°K.

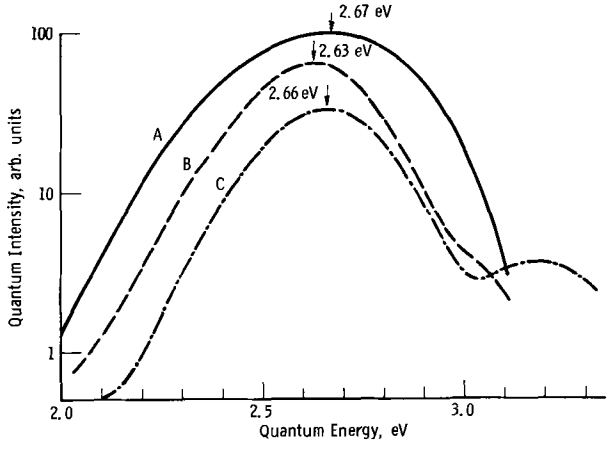

Fig. 2. Emission spectra measured on a single sample of hexagonal, self-activated ZnS:Br(1%). A, excited by 3.40 ev (λ = 365 nm) at room temperature; B, excited by 3.40 ev (λ = 365 nm) at 77°K; C, excited by 3.95 ev (λ = 313 nm) at 77°K.

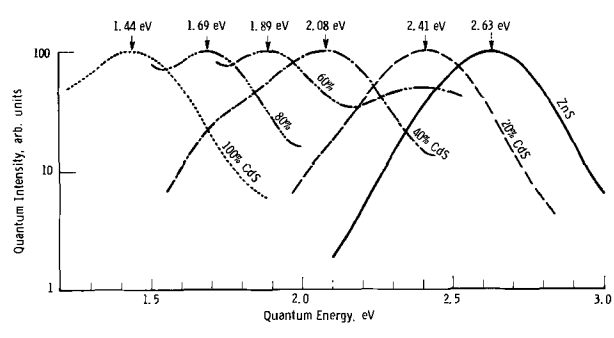

Fig. 3. Emission spectra of hexagonal (Zn,Cd)S:Br(1%) excited by ultraviolet of 3.40 ev (λ = 365 nm) at 77°K.

where the peak position is near 1.45 ev (λ = 855 nm).

Emission spectra of self-activated (Zn,Cd)S prepared with Ga or In differ somewhat from those made with the help of a halide. The peak position of the SA-band is at roughly 0.05-0.08 ev lower quantum energy (in contrast to ZnS phosphors where this difference is smaller).

The II-VI compounds can approximately be considered to be ionic compounds where the conduction band belongs to the cation (Zn or Cd) and the valence band to the anion (S, Se, or Te). Hence, a variation of the Zn/Cd ratio in (Zn,Cd)S phosphors means mainly a variation of the conduction band while, in a first approximation, the valence band remains unchanged. This approach is shown in Fig. 4 where the edge of the valence band is represented as a horizontal straight line while the edge of the conduction band is curved according to the dependence of the band gap on the Zn/Cd ratio.

The electron transition responsible for the emissions of copper or silver activated ZnS phosphors is generally ascribed to be from the edge (or from a level very near to the edge) of the conduction band into empty acceptor levels somewhat above the top of the valence band (Schön-Klasens model). The nature of the electron transition responsible for the SA-emission of self-activated phosphors is not as well known but the Schön-Klasens model may, somewhat empirically, be applied here also. The result is shown in Fig. 4 where the quantum energies corresponding to the peak positions of the measured emission bands are plotted downward from the curved edge of the conduction band. The so-determined term positions are connected by two separate curves. Curve A corresponds to the SA-emission of two separate phosphor series, (Zn,Cd)S:Cl and (Zn,Cd)S:Br, both of which gave practically identical results. Curve B corresponds to the SA-emission of a series of (Zn, Cd)S:Ga phosphors; it is obtained so far only with gallium. Attempts to replace Ga by Al failed (probably because of the too high reactivity of Al with traces of oxygen), and indium did not produce well-developed SA-emission bands. Curve B is very closely a horizontal straight line, but Curve A deviates somewhat from the horizontal in the direction of the variation of the conduction band edge although to a far lesser degree than the latter.

Cubic Zinc Sulfo-Selenide

The blue emission band of self-activated ZnS is reported to be gradually replaced by a green band if the sulfur is gradually replaced by selenium (3, 14). This is essentially confirmed in our measurements on cubic Zn(S,Se):halide phosphors. All three halides Cl, Br, and I give similar results. Some emission spectra of self-activated Zn(S,Se):Br phosphors are shown in Fig. 5 and 6. It is seen that replacement of only 1% of sulfur by selenium causes the green band (peak ~2.3 ev) to appear, and both bands, the green and the blue, are of comparable intensity at about 5% of ZnSe (Fig. 5). The bands are rather broad so that their peak positions can only be estimated because of strong overlap. Both bands shift slowly toward lower quantum energies as more ZnS is replaced by ZnSe (Fig. 6). Simultaneously, the "blue" band decreases in intensity until the SA-emission of ZnSe consists only of the "green" band which by then is shifted to orange (peak ~2.0 ev). Hence, the SA-emission of ZnSe:halide consists only of one band just as that of ZnS although there is no direct connection between the bands.

A variation of the host crystal composition from ZnS to ZnSe means a variation of the valence band, while the conduction band remains constant, if the II-VI compounds are considered to be ionic compounds.The Schön-Klasens model of electron recombination can be assumed here also. Hence, the quantum energies corresponding to the peaks of the measured emission bands are plotted downward from the horizontal edge of the conduction band. The points so obtained in Fig. 7 are connected by two separate curves corresponding to the two SA-bands of Zn(S, Se):Br. The curves deviate only slightly from the horizontal, much less than the edge of the valence band varies over the same range. A discontinuity near 100% of ZnS [as observed in cases of activation by copper (1) and by silver (2)] cannot be detected.

Cubic Zinc Seleno-Telluride

Emission spectra of self-activated Zn(Se,Te) phosphors do not seem to be reported elsewhere. Our work on this system was confined to phosphors prepared

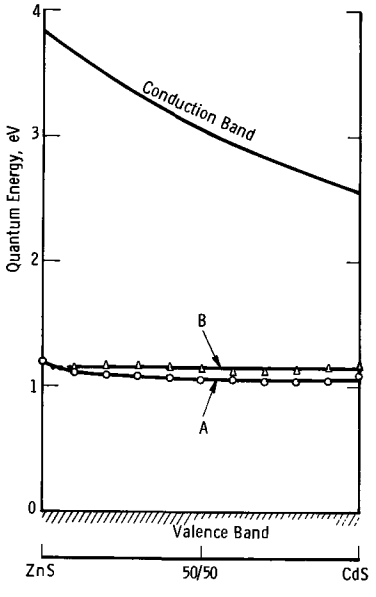

Fig. 4. Recombination term scheme of hexagonal, self-activated (Zn,Cd)S at 77°K. Curve A, 1% Cl or Br added. Curve B, 0.1% Ga added before friing.

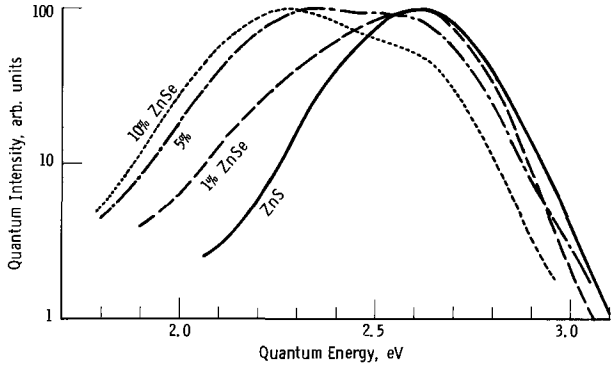

Fig. 5. Emission spectra of cubic, self-activated Zn(S,Se):Br excited by ultraviolet of 3.40 ev (λ = 365 nm) at 77°K.

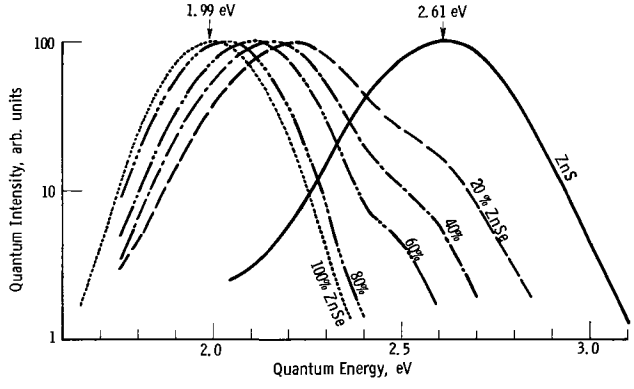

Fig. 6. Emission spectra of cubic, self-activated Zn(S,Se):Br excited by ultraviolet of 3.40 ev (λ = 365 nm) at 77°K.

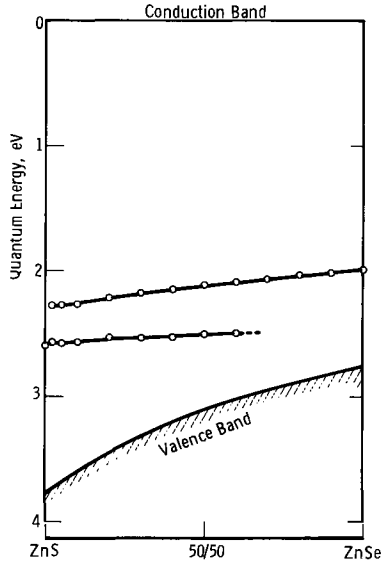

Fig. 7. Recombination term scheme of cubic, self-activated Zn(S,Se):Br at 77°K.

with the addition of 1% of Br (added as $ZnBr_2$) and fired at 800°C.

The orange emission band of self-activated ZnSe:Br (peak ~2.0 ev) can be followed up to roughly 10% of ZnTe after which it disappears. Instead of it, another emission band builds up at about 1.58 ev (Fig. 8). It is strong for a ZnTe concentration as low as 1%, can be followed up to roughly 20 to 30% of ZnTe and, apparently, shows up again in 100% of ZnTe at 1.51 ev (Fig. 9). The writer considers this latter emission band to be the analog of similar bands observed in cases of activation by Cu (1.7-1.75 ev) (1) and by Ag (~1.8 ev) (2).

A third emission band appears at about 1.29 ev in Zn(Se,Te):Br containing 10% of ZnTe (Fig. 8). In striking contrast to all others, its position is not nearly constant but shifts steadily with increasing ZnTe concentration toward higher quantum energy until it reaches 1.89 ev in ZnTe:Br (Fig. 9). The band may be identical with an emission in ZnTe reported by Dietz, Thomas, and Hopfield (17). It does not seem to be in any way related to the SA-emission bands of these phosphors but details are still unknown, and it is included in Fig. 8-10 only out of curiosity.

A fourth emission band is observed in Zn(Se,Te) phosphors containing high ZnTe concentrations. It appears in appreciable intensity in the neighborhood of 1 ev[1] (Fig. 9). It seems to be independent of any particular impurity and not related to the SA-emission, but details are still unknown.

[1] The spectral limit of the phototube used in these investigations.

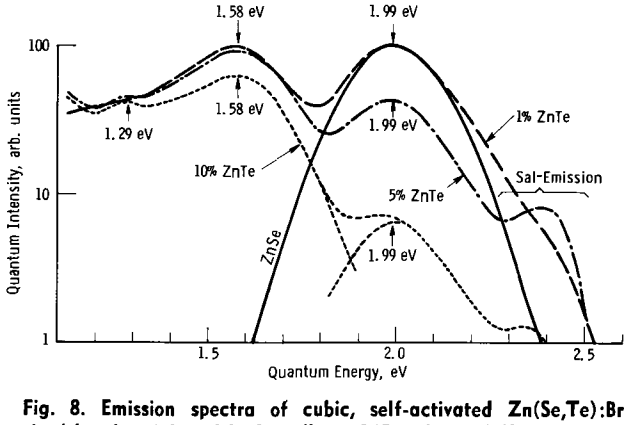

Fig. 8. Emission spectra of cubic, self-activated Zn(Se,Te):Br excited by ultraviolet of 3.40 ev (λ = 365 nm) at 77°K.

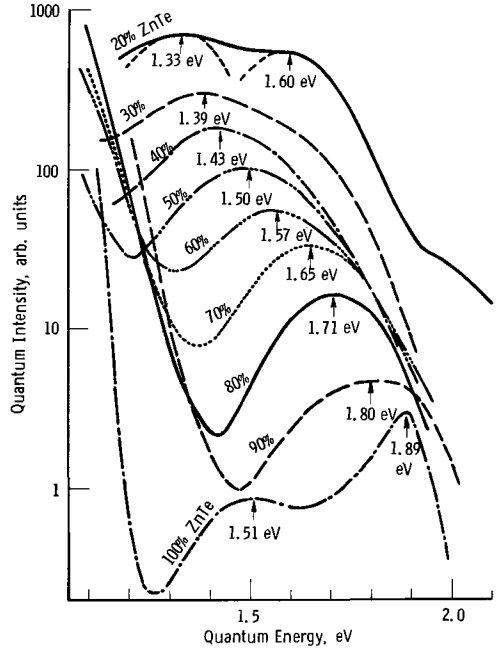

Fig. 9. Emission spectra of cubic, self-activated Zn(Se,Te):Br excited by ultraviolet of 3.40 ev (λ = 365 nm) at 77°K.

Assumption of ionic crystal binding and of the Schön-Klasens model of luminescence permits one to plot the quantum energies corresponding to the peaks of the emission bands downward from the horizontal edge of the conduction band to determine the energy position of the center responsible for the emission as a function of the Se/Te ratio. This gives the term scheme of Fig. 10 where the obtained points are connected by three curves. Curves A and B correspond to the SA-emission of Zn(Se,Te) phosphors and resemble very similar curves obtained in the case of Zn(S,Se) (Fig. 7). Both curves are very nearly horizontal straight lines. Curve C, corresponding to the unknown emission band of variable position, is also very nearly straight but not horizontal. This emission band may possibly be a close superposition of several narrower sub-bands.[2]

Zinc-Cadmium Selenides

The SA-emission of cubic ZnSe consists essentially, or only, of a single band with the peak at about 2.0

[2] Suggested by the referent.

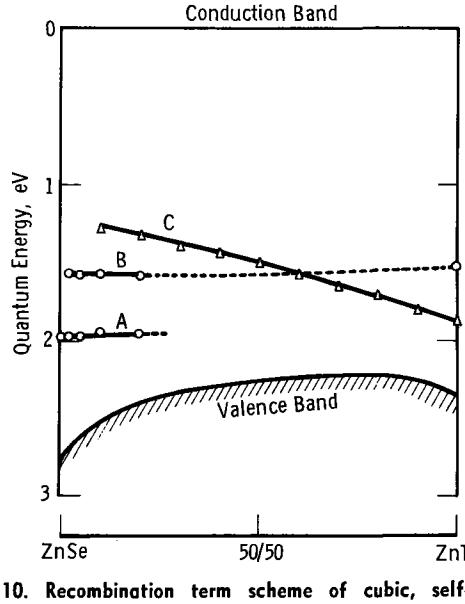

Fig. 10. Recombination term scheme of cubic, self-activated Zn(Se,Te):Br at 77°K.

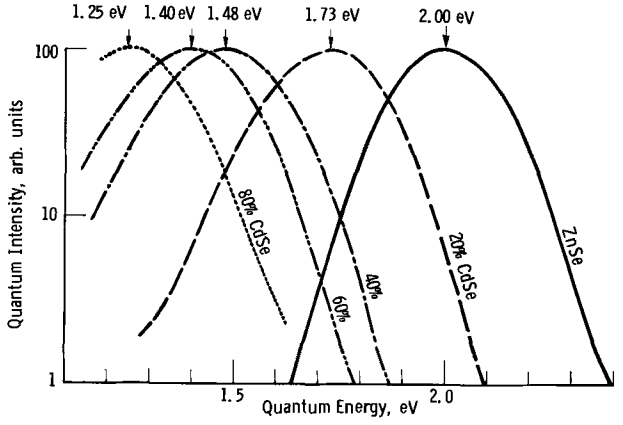

Fig. 11. Emission spectra of self-activated (Zn,Cd)Se:Br excited by ultraviolet of 3.40 ev (λ = 365 nm) at 77°K.

ev. Gradual replacement of ZnSe by CdSe causes a gradual shift of the emission band toward lower quantum energies (*i.e.*, into the infrared) without any significant change of band width and shape, all analogous to what is observed in corresponding sulfide phosphors. Some measured spectra are shown in Fig. 11.[3] If the Schön-Klasens model of luminescence is used and the quantum energies corresponding to the peaks of the emission bands are plotted downward from the curved edge of the conduction band, one obtains the recombination term scheme of Fig. 12 where all points scatter closely about a curve approaching a horizontal straight line. A slight curvature near 100% ZnSe seems to be present (analogous to curve A, Fig. 4, for corresponding sulfide phosphors) but is rather weak. The slight discontinuity near 40% of CdSe is reproducible and seems to be correlated to the phase transition from cubic to hexagonal. Extrapolation of the curve toward 100% CdSe indicates a probable peak position of the SA-emission of self-activated CdSe:Br, at 77°K, near 1.07 ev (λ = 1160 nm).

Discussion

No emission spectra of Zn(S,Se) containing Al, Ga, or In nor any spectrum of Cd(S,Se) phosphors are presented here. These phosphors were made but their emission spectra were very confusing and did not permit clear distinction between the various bands and their dependences on the S/Se ratio. Obviously, there is too much overlap of too many and too broad bands. Nevertheless, the dependence of the SA-emission on the host crystal composition can fairly unambiguously be deduced even from those spectra which are given in the figures of this paper. The main observations can be summarized as follows:

The SA-emission of self-activated binary compounds ZnS, ZnSe, CdS, and (probably) CdSe containing halide ions as donors consists essentially of one rather broad band. Gradual replacement of the zinc by cadmium either in the sulfides or in the selenides causes a steady shift of the emission band toward lower quantum energy. By contrast, gradual replacement of sulfur in ZnS by Se causes little shift of the emission but gradual replacement of the one emission band by another. The same behavior is expected also within Cd(S,Se):halide phosphors. The situation within the Zn(Se,Te) system is somewhat confused by an emission band with the peculiar shift toward higher quantum energy with increasing ZnTe-concentration. Although this band is, so far, observed only in self-activated Zn(Se,Te), chances are that it is not related to the SA-emission. If its presence is neglected, the emission spectrum of self-activated Zn(Se,Te):halide follows the general pattern, *i.e.*, the single SA-band in ZnSe is gradually replaced by another one in ZnTe.

This behavior of the SA-emission in the entire (Zn,Cd)(S,Se,Te) system resembles very much what is observed in the case of silver activation, *i.e.*, the SA-emission in the whole system consists of three bands. One band requires the presence of sulfur, another the presence of selenium, and the third that of tellurium. It is admittedly tempting to assume that each one of the three bands belongs to a particular recombination center which, besides others, contains either one sulfur or one selenium or one tellurium ion, but arguments presented in the case of silver activation (2) speak against this simple assumption.

[3] The emission spectrum of self-activated, 100% CdSe could not be measured because of instrumental limitations.

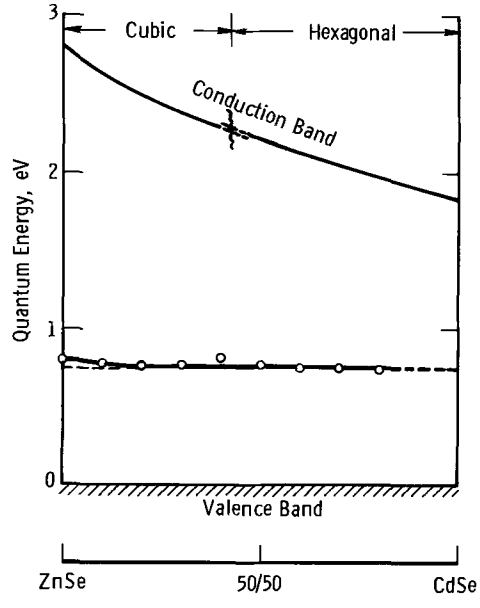

Fig. 12. Recombination term scheme of self-activated (Zn,Cd)Se:Br at 77°K.

Acknowledgment

The author wishes to express his thanks to H. F. Ivey and to W. A. Thornton for proof-reading and helpful suggestions, and to H. H. Dorman for much careful work in preparation and measurements.

Manuscript received May 24, 1966; revised manuscript received Aug. 5, 1966.

Any discussion of this paper will appear in a Discussion Section to be published in the December 1967 JOURNAL.

REFERENCES

1. W. Lehmann, *This Journal*, **113**, 449 (1966).
2. W. Lehmann, *ibid.*, **113**, 788 (1966).
3. H. W. Leverenz, "An Introduction to Luminescence of Solids," John Wiley & Sons, Inc., New York (1950).
4. R. H. Bube, *J. Chem. Phys.*, **20**, 708 (1952).
5. W. van Gool and A. P. Cleiren, *Philips Research Repts*, **15**, 238 (1960)
6. F. A. Kröger and J. E. Hellingman, *This Journal*, **93**, 156 (1948).
7. F. A. Kröger and J. Dickhoff, *Physica*, **16**, 297 (1950).
8. J. S. Prener and D. J. Weil, *This Journal*, **106**, 409 (1959).
9. H. Treptow, *Czech. J. Phys.*, **13**, 115 (1963).
10. J. S. Prener and F. E. Williams, *J. Chem. Phys.*, **25**, 361 (1956).
11. R. E. Shrader and S. Larach, *Phys. Rev.*, **103**, 1899 (1956).
12. T. Koda and S. Shionoya, *ibid.*, **136**, A541 (1964).
13. Y. M. Khozhainov and A. A. Bundel, *Optics and Spectroscopy*, **18**, 574 (1965).
14. A. A. Bundel, Z. I. Guretskaya, and M. N. Noskova, *ibid.*, **11**, 352 (1961).
15. E. F. Apple and F. A. Williams, *This Journal*, **106**, 224 (1959).
16. S. Rotschild, *ibid.*, **110**, 28 (1963).
17. R. E. Dietz, D. G. Thomas, and J. J. Hopfield, *Phys. Rev. Letters*, **8**, 391 (1962).

Peroxide Etching of Germanium

W. Primak and R. Kampwirth

Argonne National Laboratory, Argonne, Illinois

and Y. Dayal[1]

Argonne National Laboratory, Argonne, Illinois, and Illinois Institute of Technology, Chicago, Illinois

ABSTRACT

Etching with 3% hydrogen peroxide is useful for removing fractional micron layers of germanium. The etching rate is insensitive to concentration, but it is sensitive to pH, showing a minimum of about 0.021 μ/min at pH 4, a region recommended for controlled etching experiments; to temperature, showing a change of a factor 2 from 20° to 30°C; and to some foreign ions, *e.g.*, about twice as great for sulfate ions present in solutions as when phosphate ions are present. The etching rate is different for different orientations; among those tested, slowest for the [111], fastest for [201] in acid solution and [100] in alkaline solution. Mechanically polished surfaces possess an enhanced etching rate. The enhancement is removed by heavy ion bombardment, but not by light ion bombardment. The etching rate of normal germanium surfaces is not affected appreciably by heavy ion bombardment, but the etch pit density is greatly increased. Photomicrographs of the etched surfaces are given.

Etching by 3% aqueous hydrogen peroxide was used by Bredov and co-workers (1) to remove thin (fractional micron) layers of germanium for the purpose of determining the depth of penetration of alkali metal ions. The method was adopted by Davies, McIntyre, and Sims (2) who repeated these experiments and reported a variability in the peroxide etching rate. They reported a large increase in etching rate with increase in peroxide concentration and a decrease in etching rate on bombardment with cesium ions. We adopted the peroxide etching technique to determine the depth of the electrical conductivity change produced by ion bombardment. Since we could not determine weight losses because of attached metal leads, it was necessary to know the etching rate of normal and ion-bombarded germanium. The present investigation was begun when an irregularity in our results indicated a considerable alteration in etching rate during a set of successive etchings.

There are detailed reports of investigations of the etching rates of peroxide solutions containing hydrofluoric acid (3), but these solutions etch far too rapidly to be used for removing fractional micron layers. Camp (3) reports one experiment in which ". . . it was found that a [111] surface is etched by 1 part 30% H_2O_2 in 5 parts water at 26°C at a rate of 0.0275 μ/min."

Procedure

Most of the germanium used in these studies was purchased under the specification n-type, single crystal, lineage free, highest resistivity, nearly intrinsic, high purity, <111>, from the Eagle-Pitcher Company. One piece used for [100] orientation studies was a Kyropoulos grown crystal of very high purity. Plates of desired orientation were cut with a diamond saw. They were then lapped successively with 19 and 9.5μ alumina abrasive. Final surface treatments used for various studies were (*a*) CP4 etched, (*b*) mechanically polished with Linde A on silk cloth followed by Linde A on Microcloth followed by a 1-min etching in hydrogen peroxide, (c) etch polished with a sodium hypochlorite solution on Pellan Pan-W cloth (4) followed by a brief (1-10 sec) etching with CP4.

Irradiations were performed in a Cockcroft-Walton machine operated at energies from 20 to 140 kev. The ions used for the various studies were H^+, D^+, He^+, Ne^+, and A^+. For all the studies described here, one of two masks were used. The first shielded half the specimen and provided a sharp boundary. The second had six small rectangular openings which could be covered or uncovered individually or successively to prepare as many differently irradiated areas on the specimen. The specimens were irradiated in a clean mercury pumped (liquid nitrogen trapped) chamber maintained below 10^{-6} Torr.

The original etching studies were performed with reagent grade 3% aqueous hydrogen peroxide from several different manufacturers. Later studies were performed with 30% aqueous hydrogen peroxide diluted with distilled water to the desired concentration.

Hydrogen peroxide concentrations were determined by permanganate titration after addition of sulfuric acid as described in the U. S. Pharmacopoeia XII (5).

Germanium content of the etching solutions both before and after etching was determined as described by Hillebrant and Hoste (6) by forming the colored complex ion with phenylfluorone (2, 6, 7-trihydroxy-9-phenyl-isoxanthene-3-one D in 0.5*N* hydrochloric acid). The complex compound was extracted with benzyl alcohol, diluted to volume and measured spectrophotometrically at 505 mμ. The determination was made on an aliquot in which the peroxide was destroyed by hydroxylamine.

The pH was determined with a glass electrode and the PHM4C instrument made by Radiometer (Copenhagen).

Peroxide etching was performed in vessels 3-6 in. in diameter with 100-200 ml of solution. Specimens were grasped by the edges with a stainless steel forceps and held in a horizontal plane while the solution was stirred by means of a magnetic stirrer. After the desired etching time elapsed, the specimen was rinsed with distilled water, washed in distilled water for 2 min in a vessel like the one used for etching, and then blown dry with clean air or nitrogen. Drying in a desiccator before weighing was found to be unnecessary. The specimens were weighed on a Mettler microbalance to within 10 μg. The etching rates were computed from the weight changes and the area (calculated from the dimensions determined with a comparator), known density, measured weight, and etching times measured with a stop watch.

The differential etching rate for irradiated and unirradiated areas was determined by measuring the

[1] Ph.D. thesis student at Argonne National Laboratory from Illinois Institute of Technology; present address, General Electric Company, Atomic Products Division, San Jose, California. Part of the material presented here is taken from a dissertation submitted by Y. Dayal in partial fulfillment of Ph.D. requirements.

height of the step formed at the boundary of the irradiated area with a Zeiss interference microscope.

Results

Effect of concentration, pH, temperature, orientation.—When evidence of a variation in etching rate appeared during the course of a series of etchings of a set of specimens, the variation was at first attributed to peroxide concentration because hydrogen peroxide is considered a labile chemical, and the age of our reagents was unknown. Accordingly, the etching rates were determined for 2% and 4% peroxide. The two etching rates were found to be about the same.

The *p*H of the hydrogen peroxide from our stockrooms was then determined and was found to vary widely. According to the analyses given on the labels, sulfuric acid is an additive, presumably to control decomposition and its concentration employed by different manufacturers differs considerably. Accordingly, the effect of *p*H on the etching rate was determined, first by using 3% peroxide from different sources, then diluted 30% peroxide made up variously with sulfuric acid, saturated with carbon dioxide, and buffered with KH_2PO_4, NaOH, and H_3PO_4. Results for plates whose faces were perpendicular to the direction stated are given in Fig. 1.

It is seen that the etching rate is greatly dependent on *p*H and possesses a minimum in the neighborhood of *p*H 4.5. For the results given in Fig. 1, no effort was made to control H_2O_2 concentrations closely. Further experiments at controlled *p*H confirmed the etching rate to be independent of peroxide concentration at these concentrations. The etching rate for CO_2 saturated solutions was found to be the same at 1.8% and 6% H_2O_2 used to etch the [111] face. For KH_2PO_4-NaOH solutions buffered at *p*H 6, the etching rates remained within ±7% over the range of peroxide concentrations 1-4.8% for the four orientations given in Fig. 1. The variations found here were typical of those found for the conditioning of a clean (CP4 etched) surface; an abnormally high (by 7-15%) etching rate gradually falls during half an hour of etching to the stable value reported in Fig. 1.

To confirm that the weight losses are a correct measure of the etching rate, germanium assays were made of several peroxide baths after etching. The assays agreed with the weight losses to within 5% when the not insignificant germanium content of the reagents (apparently arising largely by leaching germanium from the glass reagent bottles and chemical glassware) was corrected for. This proves that in the

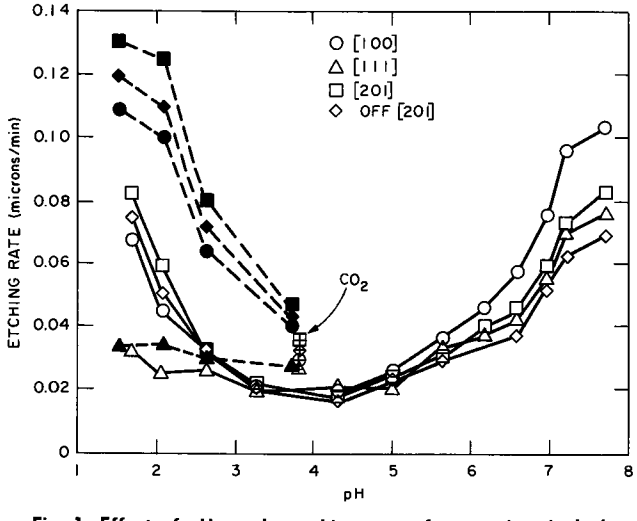

Fig. 1. Effect of *p*H on the etching rate of germanium in hydrogen peroxide, concentrations between 1.5 and 3%. Unshaded points are for H_3PO_4-KH_2PO_4-NaOH buffers, shaded points are for sulfuric acid addition to peroxide, and the crossed points are for CO_2 saturated solutions. Etching temperature is 24°C.

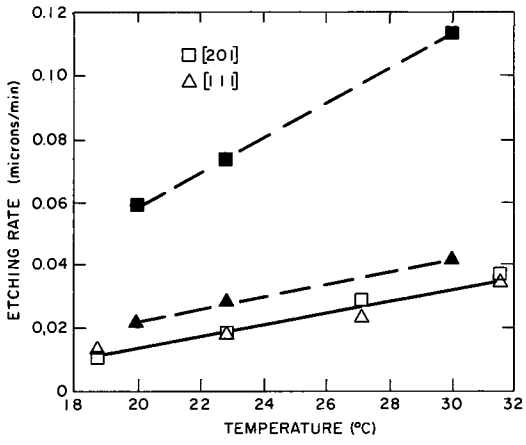

Fig. 2. Effect of temperature on the etching rate of germanium with peroxide (~3%) at *p*H 3.8; open points for phosphate buffered, shaded points for sulfuric acid addition.

etching the germanium goes into solution in the etching bath.

The temperature dependence was determined over a range of temperatures near room temperature; the results are shown in Fig. 2. It is seen that there is an increase of about a factor of 2 in etching rate for a 10°C temperature rise.

Effects of ion bombardment and mechanical polishing.—The original experiments for determining the effect of ion bombardment on the etching rate were performed with mechanically polished plates because it was thought necessary to have optically flat surfaces for the interferometric observations. These experiments were performed with H^+, Ne^+, and A^+ in the 100 kev region, as described above, with half the specimen masked. No effect was seen with H^+. From the fact that a step of 1/20 fringe height is easily visible, the etching rates must have been the same within a few per cent. With Ne^+ 140 kev, and A^+ 100 kev, definite steps were seen. Some examples of these steps taken from our collection of photographs are shown in Fig. 3. In all cases the bombarded area etched more slowly. The etching seems to progress in a manner described fully by a number of writers (7) for the etching of polished glass surfaces; namely, that as the etching progresses, the character of the lapping is revealed and scratches become more prominent. In these specimens the etching rate of the irradiated areas was the slower. The behavior of a typical case is shown in Fig. 4. The maximum differences in etching rates calculated from such curves was 20-30%. A direct comparison of the etching rates of the mechanically polished and CP4 etched surfaces prior to bombardment was made before the factors affecting the etching rate were known. The average values for several determinations were 0.024 μ/min for CP4 etched surfaces and 0.030 μ/min for mechanically polished surfaces. While these values are not reliable, they do afford some direct evidence that on unbombarded surfaces the etching rate is faster for the mechanically polished than for CP4 etched specimens.

When these experiments were repeated with chemically polished surfaces which had been lightly etched with CP4, again no effect was seen for H^+ or He^+ bombarded surfaces. For the Ne^+ bombarded surface an increase in etch pit density was found. Two examples are shown in Fig. 5. Although the etching rate for the bombarded area appears to be about the same as for the unbombarded area, there is a marked variation in etching rate at the boundary of the bombarded area. Passing from the unbombarded area, there is a sharp ridge of about the depth of the major radiation effect, and beyond it a broader shallow depression.

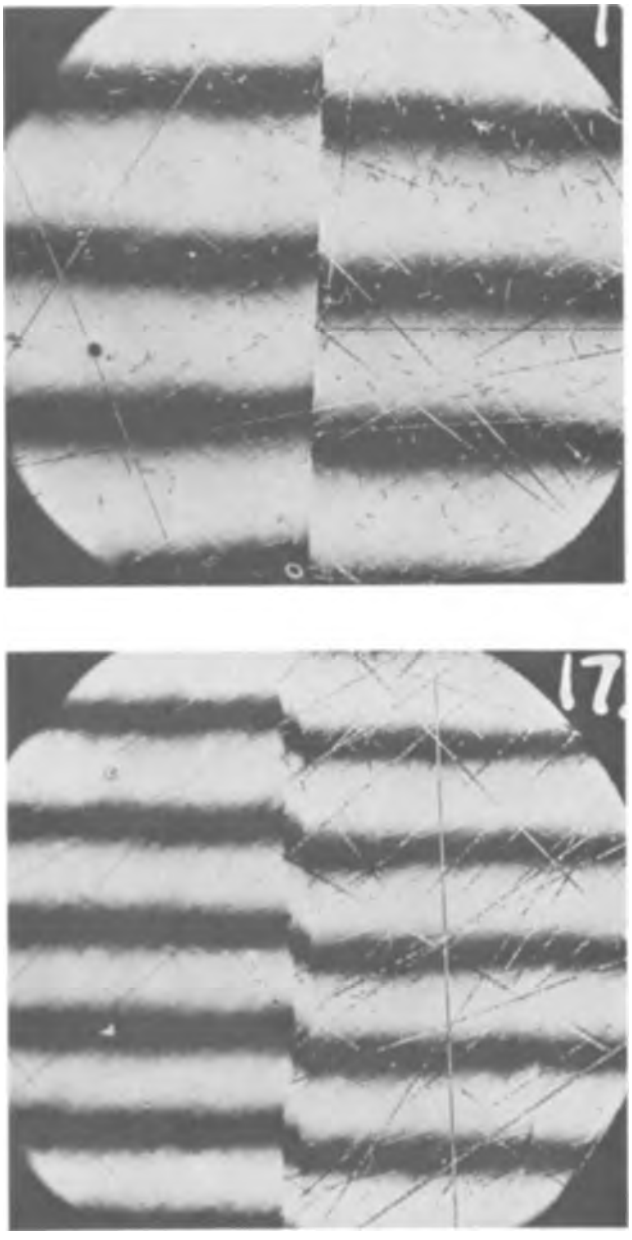

Fig. 3. Appearance of a [111] mechanically polished surface, left side bombarded and the whole plate etched. The contour interval indicated by the fringes is 0.27μ. A, 100 kev A^+ bombardment 300 $\mu C/cm^2$ after 12 min etching. The fringes are spaced at 157μ across the specimen; B, 140 kev Ne^+ bombardment 300 $\mu C/cm^2$ after 10 min of etching. The fringes are spaced 106μ across the specimen. It is not known whether the complex boundary was caused by the ion beam shifting or was the depletion layer effect described in the Discussion. (A, top; B, bottom)

Discussion

The large pH effect found for the peroxide etching rate of germanium indicates the etching is largely controlled by the solubility of the amphoteric oxide surface layer.

The ridge which is formed at the boundary of the bombarded layer, we suppose, is evidence of the effect of the depletion layer on the electrochemical reaction involved in the oxidation of the germanium. It provides evidence for one of the possible mechanisms for the oxidation; namely: that the oxidation occurs by electrons passing through the germanium dioxide film from the solution to the germanium. The unbombarded germanium is n-type. The bombarded area is strongly p-type. Thus in the field of the p-n junction, the electrons move toward the bombarded material preventing oxidation at the p-n junction where a

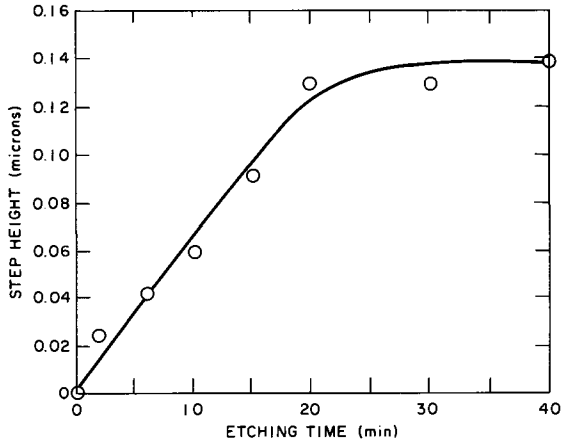

Fig. 4. Development of the step in etching a mechanically polished specimen bombarded with 140 kev Ne^+, 300 $\mu C/cm^2$. The etching rate was about 0.024 μ/min.

ridge develops, and causes an enhanced solution rate just beyond where a valley develops. We suppose these effects do not appear when etching in depth (*i.e.*, at the boundary parallel to the surface) because the p-region here merges very gradually into the n-region below and as the etching proceeds the strongly p-type material is removed before the boundary is approached.

Since the etching rates for bombarded and unbombarded chemically polished surfaces are the same, the slower etching rate found for the bombarded half of the mechanically polished surfaces is attributed to a release of the strain of mechanical polishing in bombardment. This is suggested also by the appearance of the surfaces on etching as described above. This confirms the earlier result that the etching rate of a mechanically polished surface is greater than the

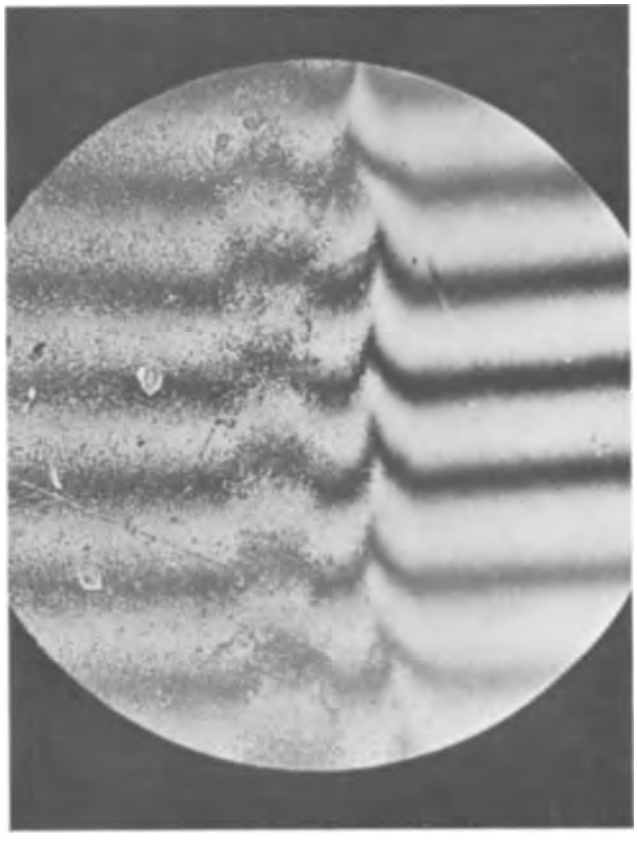

Fig. 5A. Appearance of a [111] surface bombarded with 140 kev ions after 17 min etching. Fringes mark a contour interval of 0.28μ. The fringes are spaced about 40μ along the surface.

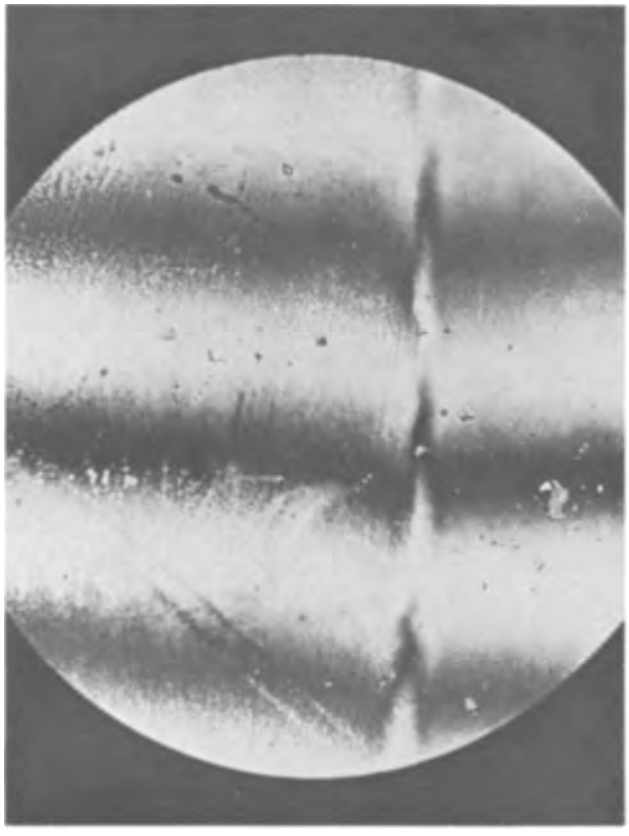

Fig. 5B. Appearance of a [111] surface bombarded with 80 kev Ne^+ ions. The fringes mark a contour interval of 0.28μ and are spaced about 84μ along the surface.

etching rate of a chemically polished surface. The strain of mechanical polishing is released by Ne^+ and A^+ bombardment, but not by the light ions, a point which is of significance in the theory of the radiation damage.

Davies *et al.* (2) report a decrease of a factor of 3 in the etching rate caused by 5 kev Cs^+ ion bombardment. We have not had the opportunity to confirm this result. Since ion bombardment alone did not affect our etching rates and since the Cs would be expected to raise the *p*H, hence increasing the peroxide etching rate, we speculate some other chemical or physical effect may be involved; *e.g.*, scavenging of the peroxide ion by the Cs in the lattice, a gas barrier produced from Cs reacting with water, or the formation of a protective film of greater integrity or with lower diffusion constants than in the absence of Cs.

Recommendations for Etching

For some time CO_2 saturated solutions made from diluted 30% peroxide (Superoxol) were employed in this laboratory. However, in our vessels loss of CO_2 was found to be substantial in 10-min etching periods causing a change from *p*H 3.8 to *p*H 4.2-5.2. The etching solution currently in use is made by taking 175 ml of 3-4% hydrogen peroxide (made by diluting 30% hydrogen peroxide) and 25 ml of 0.2M KH_2PO_4 containing 12 ml/l of 1*N* phosphoric acid. This gives a 2.7-3% H_2O_2 solution of *p*H 3.8. Temperature is controlled to $\pm\frac{1}{2}$°C which insures etching rates constant to a few per cent. Such batches have been used for etching as much as 8 cm^2 for as long as 10 min. Specimens are suspended in the etching solution at mid-depth and the solution is stirred with Teflon-coated magnetic stirring bars at a speed well below that causing splashing or air entrainment.

Acknowledgments

The authors are indebted to R. W. Bane and K. J. Jensen for advice and for the analytical results reported, to D. F. Powers and E. C. Yoder for specimen preparation, to J. O. Kartunen for specimen orientation, and to W. Ramler and his staff for performing the ion bombardments. This paper is based on work performed under the auspices of the United States Atomic Energy Commission.

Manuscript received July 23, 1966; revised manuscript received Sept. 9, 1966.

Any discussion of this paper will appear in a Discussion Section to be published in the December 1967 JOURNAL.

REFERENCES

1. We have not examined these papers. The reference may be found in the ref. (2) below.
2. J. A. Davies, J. D. McIntyre, and G. Sims, *Can. J. Chem.*, **40**, 1605 (1962).
3. P. R. Camp, *This Journal*, **102**, 586 (1955); J. Bloem and J. C. Van Versen, *ibid.*, **109**, 33 (1962); T. E. Burgers, *ibid.*, **109**, 341 (1962).
4. A. Reisman and R. Rohr, *ibid.*, **111**, 1425 (1964).
5. "The Pharmacopoeia of the United States of America," Twelfth Revision, Mack Printing Co., Easton, Pa. (1942).
6. A. Hillebrant and J. Hoste, *An. Chim. Acta*, **18**, 569 (1958).
7. L. Motz, "Surface Preparation News," Vol. 1, No. 2, Geoscience Instruments Corp., New York, April, 1964.

The Ternary Condensed Phase Diagram of the Ga-As-Te System

M. B. Panish

Bell Telephone Laboratories, Incorporated, Murray Hill, New Jersey

ABSTRACT

The condensed phase diagram for the Ga-As-Te system has been partially constructed on the basis of data obtained from DTA, electron beam microprobe, and x-ray studies. No regions of extensive solid solubility of Te in GaAs were observed. DTA data indicate that a region of ternary solid solution based on the Ga_2Te_3 structure exists in the Ga_2Te_3 region of the diagram. There is some evidence for a ternary compound in the arsenic rich region.

Interest in the Ga-As-Te system stems mainly from the growing usefulness of Te doped GaAs as a semiconductor for solid-state laser and electroluminescent diode applications. In this paper are presented the results of the first part of a study of the Ga-As-Te system which will include determination of both the liquidus isotherms in the GaAs primary phase field and the solidus isotherms representing the equilibrium

concentrations of Te in crystals which are in equilibrium with liquidus compositions along the liquidus isotherms.

The primary object of this present work is to present the ternary liquidus isotherms in the GaAs primary phase field and to establish whether there are regions in this phase field where there is extensive solid solubility of Te in GaAs.

Most work with III-V-VI systems has been done for the $A^{III}B^{V}$-$A_2^{III}C_3^{VI}$ binary systems (1) where there is particular interest in the $A_2^{III}C_3^{VI}$ compounds, which crystallize in a tetrahedral lattice with built-in vacancies. These compounds might therefore be expected to have extensive solid solubility with the $A^{III}B^{V}$ compounds. In addition to solid solution formation, III-V-VI systems are likely to be complicated by ternary compound formation such as has been suggested by Hahn and Thiele (2) for In_2AsSe and demonstrated for $InAs_3Se_3$ by Luzhnaya *et al.* (3). Liquid immiscibility has been observed in the InSb-InSe system by O'Kane and Stemple (4).

Experimental

Semiconductor grade arsenic and tellurium with purities better than 99.999% were used in this work. Reclaimed gallium with purity better than 99.99% was used, and for many of the runs semiconductor grade GaAs was used instead of the elements. The use of GaAs was necessary when the relative amounts of Ga and As were high in order to prevent explosions resulting from the exothermic reaction of the elements. For several samples in the high arsenic part of the phase diagram, GaAs, As_2Te_3, and As were used as starting materials. As_2Te_3 was prepared from the elements.

Fused silica capsules with a volume of about 13 cc which were about 2/3 filled with melt were used for the differential thermal analysis experiments. Experimental details are very similar to those which have already been described for the study of the Ga-As-Zn ternary (5, 6) and several other systems (7, 8). The precision to which thermal effect temperatures are reported is ±3°C except where otherwise indicated.

X-ray analysis of the DTA (differential thermal analysis) samples was done by standard powder techniques and electron beam microprobe analyses were obtained for several of the samples.

Binary Phase Systems

Ga-As.—Gallium and arsenic form a single congruently melting compound, GaAs, with a reported melting point of 1238°C (9). Thurmond (10) has utilized the solubility measurements of Köster and Thoma (9) and Hall (11), along with an adaptation of the regular solution treatment of Vieland (12) to construct the binary GaAs liquidus curves. The melting point of GaAs was recently measured by this author (6) and a value of 1237° ± 2°C was obtained.

Ga-Te.—Gallium and tellurium form two congruently melting compounds, GaTe and Ga_2Te_3. The melting point of Ga_2Te_3 has been reported as 792° (13) and 790°C (14), and that of GaTe as 835° (13) and 824°C (14). In this work the melting points of Ga_2Te_3 and GaTe were found to be 789° ± 3° and 827° ± 3°C, respectively. Two other tellurides, Ga_3Te_2 and $GaTe_3$, have been suggested on the basis of thermal analysis studies (13). These compounds were reported to decompose below their melting points. A phase corresponding to $GaTe_3$ has been identified in a metallographic study (15), but in the same study Ga_3Te_2 was not identified. A region of liquid immiscibility on the gallium rich side of the binary phase diagram has been reported but not confirmed (13).

A thermal effect which could be attributed to a peritectic formation of Ga_3Te_2 was noted in the work reported here; however, this thermal effect could equally well be attributed to the formation of a two liquid region. X-ray analysis did not reveal Ga_3Te_2 in any of the cooled DTA samples. No compositions which would yield information about $GaTe_3$ were studied.

As-Te.— There is very little information available about the arsenic-tellurium system. Only one compound, As_2Te_3, has been reported (16). The melting point of 362°C is in agreement with that of 362° ± 3°C obtained in this work. Hansen (16) gives a tentative phase diagram based on the work of Pelahon (17) in which As_2Te_3 is assumed to melt congruently and in which a region of liquid immiscibility is shown in the arsenic rich region.

Table I. Thermal effects in the Ga-As-Te system

Atom per cent Ga	As	Te	T_1, °C	T_2, °C	T_3, °C	T_4, °C	T_4', °C	T_5, °C	Fig. 1 cut
67.5	15.0	17.5	1061	—	—	—	—	736	—
50.0	50.0	—	1237**	—	—	—	—	—	—
50.0	—	50.0	827	—	—	—	—	—	A
50.0	10.0	40.0	1053	—	828	—	—	743	A
50.0	20.0	30.0	1127	—	819	—	—	744	A
50.0	30.0	20.0	1161	—	824	—	—	≈750	A
50.0	40.0	10.0	1198	—	821	—	—	*	A
40.0	—	60.0	797	—	—	—	—	—	B
40.8	4.2	55.0	870	856	—	817	—	—	B
42.1	9.9	48.1	993	≈880	—	≈825	—	—	B
44.1	19.9	36.0	1097	≈850	772	≈825	—	—	B
45.9	29.1	25.0	1146	≈850	771	≈815	—	—	B
47.6	37.4	15.0	1181	≈860	768	≈815	—	—	B
7.5	7.5	85.0	365	—	—	345	335	—	C
12.5	12.5	75.0	*	—	—	340	338	—	C
20.0	20.0	60.0	592	(≈520)	—	345	340	—	C
27.5	27.5	45.0	887	(≈530)	—	342	*	—	C
35.0	35.0	30.0	1069	—	—	343	*	—	C
42.5	42.5	15.0	1171	—	—	≈340	*	—	C
—	40.0	60.0	362	—	—	—	—	—	D
4.2	40.8	55.0	366	—	*	*	—	—	D
7.3	41.5	51.2	340	—	—	—	—	—	D
10.5	42.0	47.5	485	—	342	—	—	—	D
12.5	42.5	45.0	≈548	≈520	—	347	—	—	D
17.2	43.5	39.3	≈778	≈522	—	340	—	—	D
18.7	43.8	37.5	855	≈537	—	340	—	—	D
23.2	44.8	32.0	967	≈520	—	342	—	—	D
25.0	45.0	30.0	1004	≈537	—	350	—	—	D
27.0	45.5	27.5	1039	≈534	—	348	—	—	D
37.0	47.5	15.0	1157	≈545	—	343	—	—	D
23.0	50.0	27.0	996	573	—	338	—	—	—
19.6	60.0	20.4	1000	657	—	340	—	—	—

Note: where ≈ values are given, thermal effects were very slight and the precision may be no better than ±10°C. Where brackets are used, the existence of the thermal effect is doubtful.
* Not observed.
** Ref. (6).

Results

The temperatures at which thermal effects were observed when melts of various compositions were cooled are given in Table I. Most of the experimental data were obtained from samples with over-all compositions on the GaAs-GaTe, GaAs-Ga_2Te_3, GaAs-Te, and GaAs-As_2Te_3 binary cuts of the ternary phase diagram.

In each case T_1 represents the temperature at which the surface of primary crystallization was reached. For those cuts in which a thermal effect has been interpreted below as the temperature at which the cooling mixture reaches a peritectic boundary between two primary phase fields the thermal effect has been referred to as T_2. For those cuts in which a thermal effect has been interpreted below as the temperature at which the cooling mixture reaches a eutectic boundary between two primary phases, the thermal effect has been referred to as T_3. Thermal effects which appear to result from ternary eutectic or peritectic points are referred to as T_4, and those which are presumed to result from the formation of a second liquid phase are referred to as T_5.

Construction of the Ternary Phase Diagram

The ternary phase diagram (Fig. 1) is drawn in such a manner as to be consistent with the DTA and x-ray data for the various binary cuts discussed below and with the experimental data obtained for other points in the ternary system. Most of the experimental data were obtained for compositions in the GaAs primary phase field.

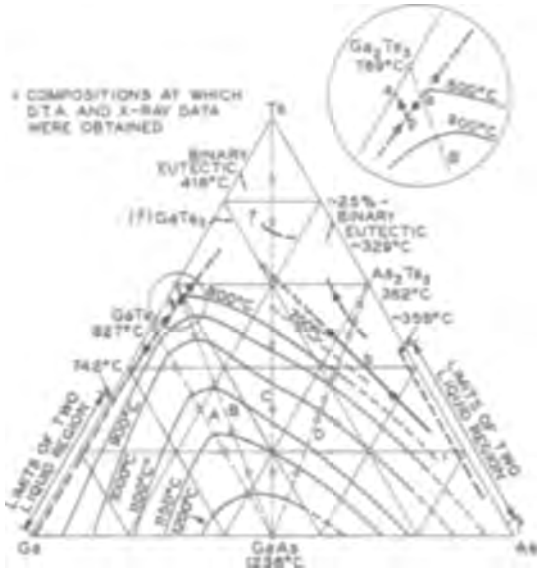

Fig. 1. The Ga-As-Te ternary phase diagram; Units are atom per cent.

Other regions of the phase diagram have not been studied in detail. As will be discussed below, there seem to be several ternary peritectic or eutectic points near 340°C. The location of these points on the phase diagram has not been determined in this work.

There is some evidence for a ternary compound which forms peritectically over a wide range of ternary liquidus compositions in the gallium poor regions of the phase diagram. This compound, if it does exist, is apparently consumed in a ternary peritectic reaction and is not observed in powder x-ray photographs.

The GaAs-GaTe *cut.*—The thermal effect data for the GaAs-GaTe binary cut, which are tabulated in Table I are plotted in Fig. 2. The primary phase separating at T_1 is GaAs. The concentration of Te in solid solution with the GaAs is apparently below the limit of detection of the x-ray powder photographs, and no line smearing or shifting was observed.

The secondary phase GaTe precipitates at T_3 along with GaAs. Although the GaAs-GaTe cut appears on the basis of Fig. 2 to be simple eutectic, the thermal effect noted as T_5 corresponds to approximately the temperature at which two liquids are found in the Ga-Te binary. In order for some of the liquid to reach the two liquid region near the binary, the GaTe phase precipitating must be somewhat richer in Te than the stoichiometric compound. The possibility that the peritectic formation of Ga_3Te_2 gives rise to T_5 and that

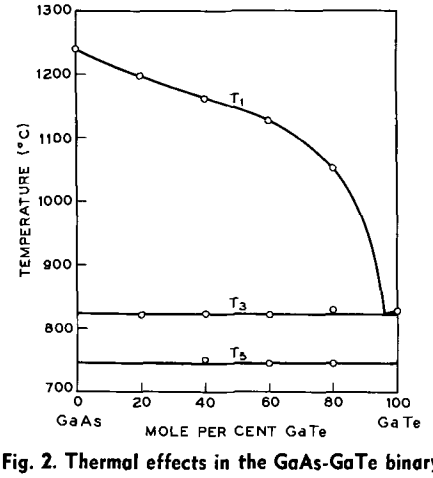

Fig. 2. Thermal effects in the GaAs-GaTe binary.

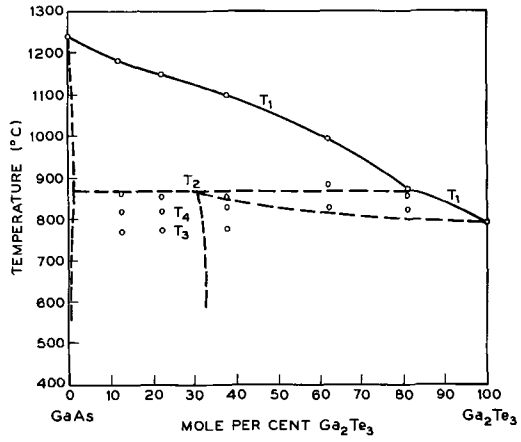

Fig. 3. Thermal effects and illustrative phase boundaries for the GaAs-Ga_2Te_3 binary. The dashed curves are intended to indicate only the shape of the phase boundaries in this cut.

the thermal effect due to the formation of the two liquids either does not occur at all or is hidden in the T_5 effect cannot be discounted.

No evidence for ternary compound formation such as that reported for the InAs-InSe system (3) was obtained.

The GaAs-Ga_2Te_3 *cut.*—The most complicated differential thermal analysis cooling curves obtained in the Ga-As-Te system were found with melts with over-all composition in the GaAs-Ga_2Te_3 cut. The T_1 liquidus is plotted as a solid curve in Fig. 3. Other thermal effects were noted which are interpreted here to indicate that the GaAs-Ga_2Te_3 system is not a true binary since the crystallization paths must be out of the plane of that system.

To illustrate the nonbinary behavior of this system, the DTA cooling curves are shown schematically in Fig. 4. For each cooling curve in Fig. 4, T_1 is the temperature at which the first solid appears, and each of the T_1 points is representative of a liquid with a composition on the GaAs-Ga_2Te_3 binary cut. If the GaAs precipitates with a small amount of Te in solid solution, the crystallization path will deviate only slightly from the GaAs-Ga_2Te_3 cut. The second thermal effect, T_2, will be observed when the liquidus composition reaches the boundary of the Ga_2Te_3 primary phase field between points a and p on Fig. 1. If the system remains in equilibrium as the mixture is cooled still further, the liquid composition will move along the two phase boundary a-p to a ternary pertectic (p), if the second solid is relatively rich in Te, at which time

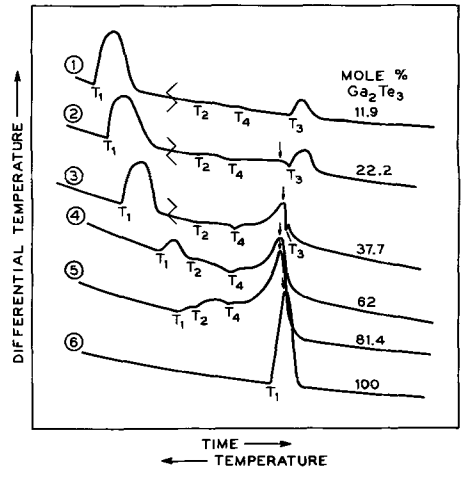

Fig. 4. Schematic DTA curves for samples with compositions on the GaAs-Ga_2Te_3 binary.

the thermal effect T_4 will be noted. At the ternary peritectic the reaction

$$\text{liquid} + \text{GaAs} \rightarrow \text{GaTe}$$

occurs, and with further cooling the liquidus composition will move along p-e (Fig. 1) until the binary eutectic is reached at e (thermal effect T_3).

The curve a-p is assumed here to represent the intersection of primary phase boundaries of a solid solution based on the Ga_2Te_3 structure but with variable ternary composition, and Te doped GaAs. Woolley and Smith (18) have shown that extensive solid solutions of Ga_2Te_3 and GaAs exist and that equilibrium in the solid solution region occurs very slowly. It is not expected, therefore, that the cooling curves of Fig. 4 represent equilibrium systems. Although the thermal effects T_2, T_3, and T_4 are observed for most of the curves obtained by cooling liquid mixtures with over-all compositions in the GaAs primary phase field of the GaAs-Ga_2Te_3 cut a different type of thermal effect (indicated in Fig. 4 by an arrow) rapidly gains in importance as the starting composition becomes closer to pure Ga_2Te_3. This thermal effect may be interpreted as being due to the nonequilibrium precipitation of the above mentioned solid solution with coring as the temperature overshoots T_4 and the peritectic reaction cannot be completed.

The analysis presented above is consistent with a binary section such as is illustrated approximately by the dashed and full curves of Fig. 3. A miscibility gap exists in the solid between GaAs-Te solid solutions and solid solutions based on Ga_2Te_3. The above analysis is also consistent with the studies of Woolley and Smith (18) who used long annealing procedures in an attempt to produce equilibrium phases in the GaAs-Ga_2Te_3 binary. They were not able to produce single phase behavior on the GaAs side of the system; however, on the Ga_2Te_3 rich side, extensive solid solubility of GaAs in Ga_2Te_3 was demonstrated.

Woolley and Smith noted that it was possible that they did not attain equilibrium and that the two-phase condition observed was due only to the fact that the diffusion rates were too low. If this were the case, and at equilibrium there were a complete series of solid solutions, the T_2, T_3, and T_4 thermal effects noted in this work would not have been observed. In such a situation T_1 would have been observed, and the GaAs-Ga_2Te_3 solid solution would precipitate with severe coring. As a result of the coring Ga_2Te_3 would precipitate as a separate phase when the temperature had approximately reached the melting point of the pure compound, and a large thermal effect would have been noted at that temperature.

X-ray powder photographs of the cooled DTA samples in this section do not show coring in the case of GaAs. Since the solid solubility of Te in GaAs is apparently quite small and probably below the limits of detection in the powder photographs this is not surprising. The Ga_2Te_3 powder diffraction lines showed evidence of severe coring for all of the samples on this cut. A lattice constant variation of from 5.88 to 5.77Å was noted.

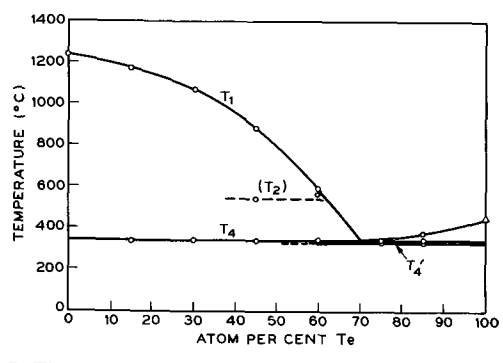

Fig. 5. Thermal effects in the GaAs-Te binary; Units are atom per cent for all components.

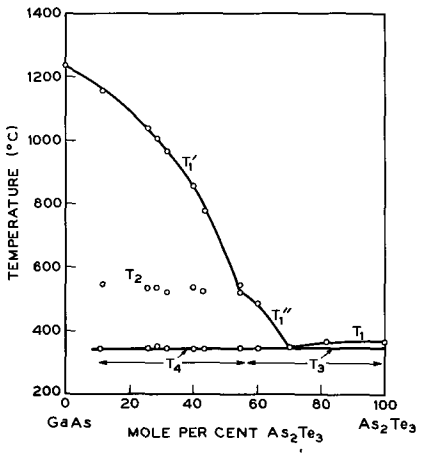

Fig. 6. Thermal effects in the GaAs-As_2Te_3 binary

The GaAs-Te *cut.*—The thermal effect data for this cut are plotted in Fig. 5. The shape of the T_1 liquidus curve is that of a simple eutectic system with the GaAs primary phase field occupying the major portion of the diagram. A very slight thermal effect was noted on two of the cooling curves, and this has been designated T_2 because it appears to be the same effect designated T_2 on the GaAs-As_2Te_3 cut and on several other cooling curves in the high arsenic region of the phase diagram. If, as discussed below, this represents the peritectic formation of a ternary compound, the system is obviously not a simple eutectic type and is not binary in nature. Two other thermal effects, designated T_4 and T_4', were noted in the DTA curves. These may result from a ternary peritectic and eutectic near 340°C. No attempt has been made to study the high Te region of this phase diagram and the composition at which these points occur has not been determined. The x-ray data for all samples on this cut are discussed below with the data for the GaAs-As_2Te_3 cut.

The GaAs-As_2Te_3 *cut.*—The thermal effect data obtained when solutions with over-all compositions along this cut were cooled are shown in Fig. 6. The T_1 liquidus curve resembles that for a binary system with a peritectic point. A small thermal effect (T_2) was noted for all cooling curves where T_1 was greater than T_2. A large thermal effect was observed in almost all the cooling curves at about 340°C.

If T_2 represents the peritectic formation of the compound GaAs-As_2Te_3 [by analogy to the In-As-Se system discussed by Luzhnaya *et al.* (3)], it would be expected that DTA curves obtained for compositions on the GaAs-As_2Te_3 cut would show a greater thermal effect at T_2 than nearby compositions in the ternary system. Actually greater T_2 thermal effects were noted for several compositions at higher As concentrations on the 1000° isotherm. The ternary compound is therefore not GaAs-As_2Te_3, and its actual composition has not been determined in this work.

The thermal effect at 340°C (T_4) may be ascribed to the intersection of curve b (Fig. 1) with a ternary peritectic point involving the peritectic formation of the Ga_2Te_3 based solid solution when the starting composition of the mixture is less than 55 mole % As_2Te_3. For mixtures with starting compositions greater than 55 mole % As_2Te_3, the thermal effect (T_3) at about the same temperature appears to result from the intersection of the liquidus crystallization path with the As_2Te_3 primary phase field. The x-ray powder photographs of cooled DTA samples with over-all compositions along the GaAs-Te and GaAs-As_2Te_3 cuts are quite interesting. The compounds identified by their x-ray patterns in each

Table II. Room temperature phases observed in cooled DTA samples with over-all compositions on the GaAs-Te and GaAs-As_2Te_3 cuts

Starting composition, Atom % Ga	As	Te	Phases observed GaAs	Ga_2Te_3*	As_2Te_3	Te	As
42.5	42.5	15.0	√	√	√		
35.0	35.0	30.0	√	√	√		
27.5	27.5	45.0	√	√	√		
20.0	20.0	60.0	**	√	√		
12.5	12.5	75.0		√	√	√	
7.5	7.5	85.0		√	√	√	
37.0	47.5	15.0	√	√	√		√
27.0	45.5	27.5	√	√	√		√
23.2	44.8	32.0	√	√	√		√
12.5	42.5	45.0	√	√	√		√
10.5	42.0	47.5		√	√		√
4.2	40.8	55.0		**	√		**
	40.0	60.0			√		
23.0	50.0	27.0	√	√	√		√
19.6	60.0	20.4	√	√	√		√

* Generally several lines for this compound indicated the presence of a solid solution of variable composition but with structure and lattice parameter similar to that of Ga_2Te_3.
** Very small amount.

sample are given in Table II. These x-ray patterns are consistent with the interpretation that the T_2 thermal effect in Fig. 5 and 6 is due to the peritectic formation of a ternary compound if we assume that the compound formed decomposes at a ternary peritectic point on further cooling to yield the Ga_2Te_3 based solid solution. The presence of As in all samples with starting compositions on the GaAs-As_2Te_3 cut and several samples with higher As starting compositions may indicate that there is a second unidentified ternary peritectic which permits the liquidus to reach the reported two liquid region on the Te-As binary. Details in this region of the phase diagram cannot be drawn on the basis of the data presented here.

Electron beam microprobe studies of several DTA samples along the GaAs-As_2Te_3 cut are consistent with the room temperature powder x-ray studies. GaAs, As_2Te_3, and As were observed where expected from the powder photographs. The Ga_2Te_3 phase had a variable composition and was difficult to study because it appeared to react under the impact of the electron beam.

Conclusion

A major part of the condensed ternary phase diagram for the gallium-arsenic-tellurium system has been constructed on the basis of data obtained from differential thermal analysis and x-ray studies. Unlike several other III-V-VI systems (18-22), no regions of extensive solid solubility of tellurium in GaAs were observed. The GaAs-GaTe cut shows essentially pseudobinary eutectic characteristics although it appears that the GaTe phase may be Te rich. The GaAs-Ga_2Te_3 cut is not a true pseudobinary and has a considerable region in which the liquid is in equilibrium with a ternary solid solution with a structure based on Ga_2Te_3. The GaAs-Te cut resembles, on the basis of the DTA studies, a binary eutectic, but a consideration of the x-ray data and the DTA data of the GaAs-As_2Te_3 cut reveals the possibility that a peritectic boundary may intersect the cut at about 62.5 atom % Te. DTA and x-ray studies of the GaAs-Te cut and the GaAs-As_2Te_3 cut have provided information which suggests the existence of a ternary compound which reacts at one or more ternary peritectics to yield a solid solution of GaAs and Ga_2Te_3. The composition of this compound is not known.

It is interesting to note that the shapes of the isotherms in the GaAs primary phase field are very similar to those in the In-As-Se system (3).

Acknowledgments

The author would like to thank P. Schmidt for some of the x-ray analyses and for a number of useful discussions of their interpretation. Other x-ray analyses were done by Mrs. V. Compton and Mrs. A. M. Hunt. H. Schreiber performed the electron beam microprobe analysis and aided in their interpretation. S. Sumski prepared the DTA samples. Discussions with C. D. Thurmond were very helpful.

Manuscript received May 27, 1966; revised manuscript received Aug. 19, 1966. This paper was presented at the Philadelphia Meeting, Oct. 9-14, 1966.

Any discussion of this paper will appear in a Discussion Section to be published in the December 1967 JOURNAL.

REFERENCES

1. J. C. Woolley, "Compound Semiconductors," Chap. 3, Reinhold Publishing Co., New York (1962).
2. H. Hahn and D. Thiele, *Z. Anorg. Chem.*, **303**, 147 (1960).
3. N. P. Luzhnaya, G. K. Slovnova, Z. S. Medvedeva, and A. A. Eliseev, *Russian J. Inorg. Chem.*, **9**, 642 (1964).
4. D. F. O'Kane and N. R. Stemple, *This Journal*, **113**, 289 (1966).
5. M. B. Panish, *J. Phys. Chem. Solids*, **27**, 291 (1966).
6. M. B. Panish, *This Journal*, In press.
7. M. B. Panish, *ibid.*, **113**, 224 (1966).
8. M. B. Panish, *J. Less Common Metals*, **10**, 416 (1966).
9. W. Köster and B. Thoma, *Z. Metallkunde*, **40**, 291 (1955).
10. C. D. Thurmond, *J. Phys. Chem. Solids*, **26**, 785 (1965).
11. R. N. Hall, *This Journal*, **110**, 385 (1963).
12. L. Vieland, *Acta Met.*, **11**, 137 (1963).
13. P. C. Newman, J. C. Brice, and H. C. Wright, Philips Research Rept., **16**, 41 (1961).
14. W. Klemm and H. U. Vogel, *Z. Anorg. Chem.*, **219**, 45 (1964).
15. J. R. Dale, *Nature*, **197**, 242 (1963).
16. M. Hansen, "The Constitution of Binary Alloys," McGraw-Hill Book Co., New York (1958).
17. H. Phelabon as reported in ref (15).
18. J. C. Woolley and B. A. Smith, *Proc. Phys. Soc. (London)*, **72**, 867 (1958).
19. N. A. Goryunova and V. S. Grigoreva, *Zhur. Tekh. Fiz.*, **26**, 2157 (1956).
20. J. C. Woolley and P. M. Keating, *J. Less Common Metals*, **3**, 194 (1961).
21. N. A. Goryunova and S. I. Radautsan, *Dokl. Akad. Nauk. SSSR*, **121**, 848 (1958).
22. N. A. Goryunova and S. I. Radautsan, *Zhur. Tekh. Fiz.*, **28**, 1917 (1958).
23. J. C. Woolley, C. M. Gillett, and J. A. Evans, *J. Phys. Chem. Solids*, **16**, 138 (1960).

Printable Insulated-Gate Field-Effect Transistors

Y. T. Sihvonen, S. G. Parker, and D. R. Boyd

Corporate Research and Engineering, Texas Instruments Incorporated, Dallas, Texas

ABSTRACT

Graphic means for fabricating active circuit elements have been examined in an exploratory program. Compatible and complementary semiconductor-, dielectric-, and metal-inks have been developed and tested. Their use in various juxtaposed and overlayed configurations has produced operational insulated-gate field-effect transistors. The ultimate goal is to establish processes compatible with existing processes for silk-screened resistors and capacitors and produce high-volume, low-cost active circuits. Four types of graphically produced transistors typically exhibit two characteristic modes of behavior; high transconductance ($\leq$2000 μmhos) coupled with poor frequency response ($<$100 cps); and low transconductance ($\leq$20 μmhos) coupled with better frequency response ($>$100 cps). These behaviors correlate with gate-dielectric parameters. Various organic and inorganic gate-dielectric materials have been tested; best results to date have been obtained with nitrocellulose, silicate cement, glyceryl monostearate, or barium titanate in association with CdS:CdSe. Sintering of the semiconductor layer and post-processing of the inks after each printing deposition have been found necessary to enhance device performance. The times involved with these operations are comparable to conventional screened conductor, resistor and capacitor processing periods.

Printing processes as applied to the manufacture of film-type electronic circuitry hitherto have been limited to combinations of passive elements, *i.e.*, resistors and capacitors connected by conductive paths to which active elements, i.e., diodes and transistors, are annexed in "chip" or package form. Partially negating the economic advantages of such printing operations are processing costs associated with fabricating and inserting the active elements.

The possibility of printing active elements as well as passive ones has received impetus from recent achievements with evaporated polycrystalline semiconductor films. Inasmuch as diodes and transistors can be readily fabricated from such films, it is not unreasonable to expect that active devices should be realizable by the deposition and processing of special "inks" either wet or dry in appropriate configurations on suitable substrates. The envisioned payoff for such a successful coalescence of printing disciplines with semiconductor concepts would be high volume production of components and networks attractively competitive costwise with components and networks manufactured by other means. The accuracy and speed with which modern printing presses produce meaningful patterns and designs are well exemplified by the high-quality color designs seen in the better magazines and books. Intricate overlayed and juxtaposed dot or dash configurations produced by multiprint operations are common practice, and to rapidly generate a million complex designs or pictures indistinguishable from each other to the n^{th} dot is generally taken for granted by artisans of the trade.

The purpose of this paper is to summarize results of an investigation into problems associated with printing active devices by means compatible with existing silk-screen processes for depositing resistors and capacitors. Effort has been expended in developing and testing various semiconductor-, dielectric-, and metal-inks, using these to print operational insulated-gate field-effect transistors, and evaluating their performance. Transistor components have received most study to date because they are considered vital for complete success of the over-all concept. Our studies involving printed diodes and wholly printed circuits are incomplete and will not be included in this paper.

Fabrication Considerations and Materials

Device types.—The Graphic Active Devices (GAD's) successfully printed are fundamentally similar to the evaporated insulated-gate field effect transistor developed by Wiemer (1). In such a device, the majority carrier concentration in the semiconductor film is controlled by an electric field applied to a dielectric overlay. Four variations of the structure are shown in Fig. 1: (a) and (b) are coplanar types having all layers on the same side of the semiconductor layer, and (c) and (d) are staggered types having the gate layer and source-drain layers on opposing sides of the semiconductor layer.

Substrates.—The choice of an appropriate substrate to receive the ink layers for GAD types (a) and (d) has been dictated by mechanical considerations and by the necessity to minimize undesirable reactions between the semiconductor and the substrate during post deposition heat treatments. For a variety of experimental inks, high-purity alumina has been especially useful as a passive substrate for it has good film adherence qualities and is nonreactive under a wide variety of fabrication processes. These alumina substrates, for convenience in measuring device parameters, were shaped to fit a standard four-lead TO-5 header. Protection against open-environment influences was afforded by polystyrene plastic coatings or by canning units in dry nitrogen.

Type (c) GAD's, wherein the gate insulator serves both as the substrate and the printing surface, require strong rigid materials that have both good in-

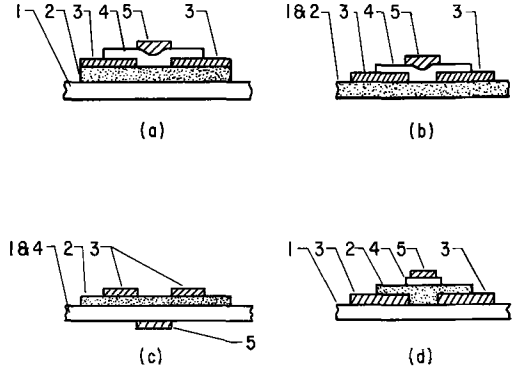

Fig. 1. Four types of GAD's in cross section: (a) planar structure on passive substrate; (b) planar structure on semiconductor substrate; (c) staggered structure on dielectric substrate; (d) staggered structure on passive substrate. 1, Substrate; 2, semiconductor; 3, source and drain electrodes; 4, insulator-dielectric; 5, gate.

sulating properties and relatively high dielectric coefficients. The advantages in printing this kind of device are that one material (an auxiliary substrate) is eliminated and that printing operations proceed on both broad areas simultaneously, thereby reducing the number of serial processing steps.

Type (b) GAD's utilize a pressed and sintered wafer of the semiconductor material that serves as both the substrate and active material. This approach is attractive because a separate substrate is not required, and it achieves the ultimate simplicity envisioned for printing and processing complete circuits of R's, C's, and active devices on the same wafer. To form these substrates, powder (typically CdS:CdSe powder of 99.999% purity) is compressed to 1 mm thick in a die at 20,000 psi and then fired at 550°C in air for 1 hr to recrystallize and bond the particles. Surface resistance approximates 10^3 ohms/sq and the pellet withstands relatively rough handling. Source and drain contacts, the gate insulator, and the gate are applied directly to the surface by one of several procedures to be described. Insulation of elements is achieved by diffusing appropriate dopants to create high-resistance boundaries.

Semiconducting layer.—Deposition and treatment. Various satisfactory inks which could be screen-deposited and processed into semiconducting layers were empirically developed by first concocting a screenable mix, and then adjusting the semiconducting and doping constituents for best device performance. A very useful ink and one employed for most GAD development work has been prepared by the following procedure: (*A*) A mixed compound of CdS:CdSe is made by mixing equal portions (by weight) of 99.999% purity CdS and CdSe and sintering at 950°C for 4 hr in a H_2S ambient of 1 atm. After cooling, the conglomeration is ground to 80 mesh with a porcelain mortar and pestle. (*B*) A slurry is made by the addition of distilled H_2O and $CdCl_2$ solution so that the $CdCl_2 \cdot 2\frac{1}{2} H_2O$ to CdS:CdSe weight ratio is 1:10. This slurry is dried on a hot plate at 100°C. (*C*) The final ink is prepared by mixing 10g of the dried CdS:CdSe material with 40 cc of a carrier solution of 5% (by weight) ethylcellulose in butyl cellusolve, and then ball milling for 16 hr. Inks stored for more than 24 hr required only simple stirring to properly resuspend the semiconducting particles.

In use, the CdS:CdSe ink is transferred to substrates in controlled thicknesses ranging from 2 to 25μ by screening through a 100 mesh silk-screen and is then predried to remove the carrier solvent. The resulting raw film exhibits high electrical resistance (> 1 Mohm), adheres well to most types of substrates and withstands considerable abuse before showing physical damage.

Sintering is required to activate the raw film. The $CdCl_2$ present serves as a flux that promotes particle fusion and granule regrowth at temperatures well below the normal CdS:CdSe sublimation point, and it also dopes the CdS:CdSe particles with Cl donors, bringing the resistance of the film into the desired range of 10^3 to 10^5 ohm/sq. The sintering operation is typically carried out at 570°C under conditions of limited air. Poor bonding strength and film homogeneity would result with insufficient $CdCl_2$ while excess $CdCl_2$ unfavorably affected device stability and frequency response. In the latter case, unreacted $CdCl_2$ could be satisfactorily removed by leaching.

Post treatment.—The application of surface activating agents (surfactants) to the sintered semiconductor layer prior to printing the gate insulator dielectric has been found to have beneficial effects on device performance. The surfactants used most extensively have been Lewis-type bases such as triethanol amine lauryl sulfate (TALS), glyceryl monostearate (GMS), sodium lauryl sulfate (SLS), dimethyl glyceryl stearate (DGS), ethanol amine (EA), and NH_3 gas. Best results were consistently achieved with NH_3 gas which was able to penetrate better into the inked film and envelop the CdS:CdSe granules. The liquid surfactants were applied as aqueous coatings over the semiconductor films and dried under a heat lamp. Ammonia was added to the films by passing NH_3 gas over units in an ice bath at about 0°C. Comparative performances of surface-treated GAD's are shown in Table I.

Source and drain electrodes.—A necessary condition for best GAD performance is unhindered electron flow through the source-semiconductor and drain-semiconductor interfaces. In addition to being "ohmic," the deposited electrodes need to be highly conducting, nonreactive with the other layers, and stable with time and temperature.

The many conducting silver and carbon preparations commercially available proved to be nonohmic with the CdS:CdSe layer. Several metals, *viz.* indium, tin, and aluminum, were empirically found to have suitable electrical properties, but simple air-drying inks based on these gave poor registry and line definition and were not particularly useful.

One means for obtaining satisfactory source-drain electrodes on the CdS:CdSe layer made use of a 90% Hg-10% In amalgam. After printing this paste-like mix, the Hg content was lessened by heating in a vacuum at 120°C. The resulting film made good ohmic contact and had solid metallic characteristics. Another

Table I. Representative GAD's and their performances. Transconductances are obtained by dividing the modulated current by the change in gate voltage $\Delta V_g = 18v$.

Unit	CdS:CdSe semiconductor layer type	Dielectric layer	Contact material	Special treatments	Current modulated *vs.* frequency 0.1 cps, ma	1.0 cps, ma	10 cps, ma	100 cps, ma	1000 cps, ma
6323-25#4	Ink	Collodion	In-Hg	None	5.5	3.5	0.72	0.12	0.014
6323-25#8	Ink	Collodion	Evaporated In	None	5.2	3.2	0.64	0.10	0.02
6433-117#10	Ink	GMS	Sn-Ga	None	0.26	0.22	0.14	0.028	0.005
6433-97#14	Ink	GMS	In-Hg	NH_3 surfactant	2.0	1.4	0.70	0.14	0.02
6683-95#7	Ink	Cement† + $BaTiO_3$	Sn-Ga	None	2.0	1.5	1.4	0.5	0.2
6433-61#1	Ink	Cement‡	In-Hg	NH_3 surfactant	1.7	1.6	1.1	0.16	0.02
6433-97#16	Ink	Molten GMS	In-Hg	GMS surfactant	2.4	1.4	0.74	0.09	0.01
6433-97#11	Ink	Molten TALS	In-Hg	TALS surfactant	1.4	1.2	0.65	0.12	0.015
6433-117#1	Ink	Cement‡	Sn-Ga	None	0.71	0.58	0.10	0.006	0.001
6323-137#6	Ink	Cement‡	In-Hg	Leached CdS:CdSe film	2.0	1.8	1.6	1.2	0.350
6683-113#4	Ink	$BaTiO_3$*	Sn-Ga	None	0.0020	0.0024	0.0025	0.0028	0.0035
6683-129#8	Ink	$BaTiO_3$*	Sn-Ga	Excess $CdCl_2$ in CdS:CdSe	0.075	0.080	0.080	0.080	0.080
6683-116#3	Ink	$BaTiO_3$*	Sn-Ga	$BaTiO_3$ @ 1000°C 16 hr	0.045	0.046	0.050	0.052	0.051
6683-147#4	Ink	$BaTiO_3$*	Sn-Ga	Excess $CdCl_2$ + $BaTiO_3$ 1000°C 16 hr	0.260	0.305	0.345	0.380	0.400
Exp64#10	Pressed pellet	Duco	In	None	7.5	5.0	1.4	0.16	0.009

* American Lava Corporation Type T-183-A.
† Sauereisen Cements Company Type 78.
‡ Sauereisen Cements Company Type P-1.

means for printing source-drain electrodes utilized an alloy of Sn-Ga (5-10% Sn) which remains fluid and has excellent wetability. Good line definition was readily obtained as well as good ohmic contact. The composition of this alloy can be varied to control the fluidity of contact. Though the resulting film remains "wet" it does not tend to flow and can be "locked" in place with the gate-insulator material. A third means for making source-drain electrodes used metallic powders of Sn or In, either sprinkled on or conveyed from transfer tapes onto the CdS:CdSe layer, then rolled to promote intimate contact, and finally sintered near the melting point. Fair to good ohmic contact was achieved, but results were often erratic.

Gold normally makes rectifying contacts to CdS:CdSe, but it was found that if the CdS:CdSe ink was fired onto predeposited Au layers, the resulting electrodes were electrically and mechanically very satisfactory for GAD use. A gold-resinate solution, Hanovia Liquid Brite Gold 7621, would first be deposited onto the alumina substrates and decomposed thermally at 750°C in air to give a metallic film. The source-drain electrodes were formed by diametrically scribing a 1-2 mil wide gap after which the CdS:CdSe ink was screened onto the substrate and fired. This method of making contacts restricted devices to the staggered-structure type since the gold ink could not be fired satisfactorily onto a predeposited CdS:CdSe ink layer.

Table I summarizes performances of various GAD devices prepared with the better source-drain materials that were applied by different means. No systematic superiority of any one contact material and method of application has been evident including evaporated indium electrodes which were used as a control, and it is our conclusion that major limitations to GAD performance are not a consequence of contact phenomena. While at least two or three of the methods described have been adequate and useful, further development work will be required before a simple printable contact ink is realized.

Gate insulator-dielectrics.—The insulating material separating the semiconductor layer and the gate electrode is ideally required to have stable dielectric properties, and its processing must be compatible with the remainder of the device. The number of carriers induced into or removed from the source-to-drain electrical path is a direct function of the capacitance existing between the gate electrode and a pseudo-capacitor plate located somewhere at or near the semiconductor surface. While it is desirable to have large current changes in response to gate voltage fluctuations, a compromise becomes necessary since long charging-times and low input impedance are inherent with large capacitances. Furthermore, any nonconstant properties present in the insulator, such as temperature instability or frequency or voltage dependent polarization, can be expected to appear directly as variances in GAD transconductance. Evidence for this dependence will be discussed later.

Organic dielectrics.—Some 25 solvent-, polymer-, and molten-type organic films were tested with various degrees of success. Most successful to date for routinely printing operational GAD's has been nitrocellulose in the form of Duco (DuPont) or flexible collodion, each producing layers having large relative dielectric coefficients ($> 10^5$). Unfortunately, the magnitude of this coefficient is highly frequency dependent, and the frequency performance of typical GAD's would diminish rapidly at frequencies above 1 cps. Furthermore, these films tended to "dry out" if left unencapsulated. GAD performance would correspondingly cease with this drying but could be restored by exposure to the solvent vapors.

The low-frequency dielectric coefficient in nitrocellulose is surprisingly large. It may be a consequence of molecular polarization either between the many polar groups such as —OH, —NO_2, and —O— or between these groups and the surface states on the CdS:CdSe layer. Alternatively, it is possible that the electric potential across the dielectric causes mobile ions to migrate. Movement of these ions would result in a dipole buildup. Evidence for ionic migration and perhaps some electrochemical action was demonstrated by electrolysis experiments with collodion solutions in which ions were tagged with neutral red indicator. Ions were observed to accumulate at and around both electrodes with H_2 gas being released at the negative platinum electrode.

Glyceryl monostearate (GMS), an animal fat derivative, was the best molten-type gate dielectric material found for GAD use. It is an ester formed between glycerol and stearic acid with numerous polar groups,

—OH and —C—O, present in each molecule. GAD units made with the GMS (which is also a surfactant) showed less frequency falloff than nitrocellulose dielectrics and the other organic materials tested. One major disadvantage of GMS is its low melting point of 60°C, a temperature often reached in a GAD under heavy operating loads. Other useful molten films have been made using triethanol amine lauryl sulfate (TALS) and vinyl polymers (*e.g.*, Tygon).

The major disadvantage of the more promising organic gate insulators in conjunction with the CdS:CdSe ink layer is their rapidly decreasing dielectric coefficient with frequency. Although the organic dielectrics cited would ultimately be unsuitable for printing devices meeting reasonable stability and frequency requirements, much knowledge as to what is needed in a good gate insulator was gained from their use.

Inorganic dielectrics.—The numerous difficulties with organic dielectrics prompted a look at inorganic dielectrics which could be expected to be more stable with respect to temperature and frequency. A problem confronted in their projected use was finding a suitable method of application. Inorganic dielectrics such as mica, $BaTiO_3$ and glasses are normally formed at high temperatures which could not be tolerated directly in GAD fabrication. Thus the search for inorganic gate dielectrics was narrowed to materials and processes involving low-melting temperatures, flame spraying, or chemical curing.

Cements were the most fruitful inorganic dielectrics to be applied by a print-on method. Several types were tested, *viz.*, lime, gypsum, phosphate, and silicate, but only the silicate cements (Sauereisen Cement Company) produced devices with adequate transconductances. However, as with the organic dielectrics, the current modulated decreased rapidly in magnitude at frequencies greater than 1-10 cps. The Sauereisen cements successfully used were No. P-1, No. 78, and No. 63 each containing 85-95% SiO_2 with the remainder being Al and Fe oxides and water of hydration. Water was added to make the cement "spreadable" and it was deposited in a straightforward manner onto the CdS:CdSe layer. The units were then stored in a sealed container for 24 to 48 hr to allow silicate, hydroxide, and hydrate reactions to proceed. When cured at room temperature these cements underwent continuous change lasting many weeks which is attributed to chemical processes proceeding to completion. As a consequence, GAD's would show continuing improvements in transconductances and speeds of response as the cements aged. More rapid stabilization could be instigated by heating canned units to 200°C for 48 hr. Some improvements in transconductance and frequency response in cement-dielectric GAD's were obtained when $BaTiO_3$ powder was added to the cement in a ratio of 1:3 by weight.

Dielectric substrate.—The use of the substrate itself as the gate insulator necessitated that the staggered-type structure, Fig. 1(c), be employed. The semicon-

ductor ink would be first screened over one surface of the substrate and processed, then the source and drain electrodes were applied over the semiconductor layer, and finally the gate electrode was printed and dried on the opposing face of the substrate. Since the substrate has to be relatively thick (in order to withstand both handling during processing and flexing that could cause component fractures), the dielectric coefficient needs to be very large in order to provide sufficient charge-change in the semiconductor layer. Few materials are known to have the required dielectric coefficient, and those that do are inherently inconstant in their properties.

$BaTiO_3$ substrates were superior to all materials tested producing GAD's with stable characteristics to over 1000 cps. The attendant problems with $BaTiO_3$ involved undesired reactions during sintering between the CdS:CdSe layer and the $BaTiO_3$. One effect was a doping of the CdS:CdSe layer making it higher in resistivity and another was poor adhesion caused partly by outgassing. Moderation and/or virtual elimination of these effects was affected by presintering the $BaTiO_3$ blank at 1000°-1250°C in air for 16 hr and increasing the amount of $CdCl_2$ in the CdS:CdSe ink. Either of these two corrective measures alone improved device transconductance and together the results were most impressive as seen in Table I.

Gate electrodes.—The gate electrode material and method of application were determined by the dielectric to which it was applied. Major requirements were that the electrode material be highly conducting and that it not react detrimentally with the dielectric. For organic dielectrics, an aqueous ink was developed containing by weight 5 parts Ag + 2 parts Zein + 4.1 parts 2-methyl 2,4 Pentanediol + 4.1 parts H_2O. The Ag (300 mesh powder) was suspended by ball milling and after application was allowed to dry at 25°C. For cement, ceramic, or inorganic dielectric materials, DuPont's Ag Paint No. 5584 was used. This paint is readily applied and quickly dries with only modest heating in air. It was also used to make conducting paths and connections to the header wires.

Electrical Performances and Interpretation

Devices fabricated in the manners described in this paper are composed entirely of disordered materials and obviously can give rise to extremely complicated behaviors not entirely interpretable by modern carrier transport theory as developed with single crystalline materials. The semiconductor layer, being a conglomeration of fused macroscopic particles, is highly inhomogeneous and contains a very high density of surface and bulk traps which strongly influence free carrier responses to electric fields. The insulator dielectric in contact with the semiconductor layer gives rise to further complications since ionic and polarization effects can and do manifest themselves. In spite of these serious problems, however, it is encouraging that with reasonable control over the materials and their processing, GAD's can be reproducibly printed to exhibit certain basic characteristics in their performances. The following section discusses results observed with literally dozens of GAD variations and several thousand devices. Table I summarizes typical performances of representative units at frequency decades ranging from 0.1 to 1000 cps.

Transconductance and drain current.—Transconductance, g_m, in an active device may be taken as a figure-of-merit of device performance. Two kinds of general transconductance-behavior have been encountered: one wherein g_m diminishes with frequency, and the other wherein g_m is relatively invariant with frequency (up to 1000 cps). The former behavior is found in GAD's processed with gate-insulators of deposited layers while the latter behavior is shown by the $BaTiO_3$ dielectric substrate structure devices. Typical transconductance data for two units, each

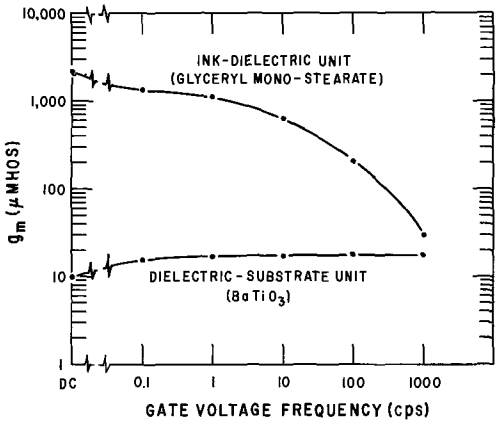

Fig. 2. Mutual transconductance vs. frequency of two representative GAD's.

representative of the behavior noted, are shown in Fig. 2.

The differences observed in g_m magnitude and the variations of g_m with frequency can be in the most part explained by considerations of capacitance data shown in Fig. 3, and simple field effect transistor theory. From Borkan *et al.* (2) the drain current expression is

$$I_d = \frac{\mu C_g}{L^2}\left[(V_g + V_o) - \frac{V_d}{2} \right] V_d \qquad [1]$$

where μ = carrier mobility, C_g = gate capacitance, L = source-to-drain separation, V_g = gate-to-source voltage, V_o = threshold voltage, and V_d = source-to-drain voltage.

It is important to distinguish between total gate capacitance, C_{gm}, as it is measured, and that part of the gate capacitance, C_g, which is effective in adding or subtracting charge carriers in the semiconductor layers. For the two representative devices considered, $C_g \approx C_{gm}/6$, where the factor 6 is calculated from simple area considerations. It follows that transconductance

$$g_m = \left.\frac{\partial I_d}{\partial V_g}\right|_{V_d = \text{constant}} = \mu C_g V_d / L^2 \qquad [2]$$

can be expected to vary directly with C_g, and qualitatively this is what is observed.

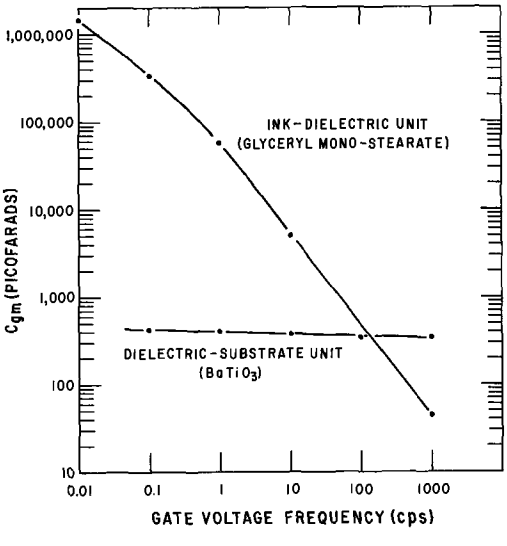

Fig. 3. Measured gate-to-channel capacitance vs. frequency of two representative GAD's. The apparent relative dielectric coefficient is obtained by multiplying the ordinate by 10. The approximate capacitance, C_g, directly interacting with the source-to-drain material can be calculated by dividing the ordinate by 6.

Quantitatively, reasonable agreement between calculated and observed g_m's is obtained for $BaTiO_3$-dielectric substrate units but not for any of the GAD's with film gate-insulators. In the latter type devices, not only does g_m not follow exactly the nearly 1/f proportionality measured for gate capacitance, but the effective relative dielectric coefficient of the dielectrics used turns out to be amazingly large, typically 3×10^6 at 0.1 cps. These data imply the existence of an unusual polarization which is relatively slow in responsiveness. As mentioned earlier, this mechanism very likely involves electric field separation of some type of mobile ionic species and further has associated with it a phenomenon which affects the capacitance as measured but not the capacitance which induces carriers into the semiconductor layer. Two possibilities are: simple battery action, or a combination of electrolysis and polarization. Both of these processes can be expected to absorb electrical energy during part of the dielectric charging cycle and then return some of it during the discharge cycle in a capacitor-like manner. The amount of energy-transfer involved would be strongly dependent upon the inverse of frequency thereby displaying a 1/f capacitance behavior. Furthermore, the charge displacement caused by these processes would not result in equivalent semiconductor carrier-increases because some of the induced carriers would be required to neutralize electrochemical reactions at the interface. The major difficulty with this explanation is accepting that the same kind of polarization-like effect is common to each of the chemically different dielectric species, *viz.*, nitrocellulose, glyceryl monostearate, and silicate cement.

Striking differences observed between GAD performance and that of normal insulated-gate field-effect transistors (IGFET's) is shown in Fig. 4. In a typical IGFET, I_d has a linear or less-than-linear proportionality to V_d, and at some V_d pinchoff (current saturation with increasing V_d) takes place. In the GAD, I_d response is everywhere superlinear with V_d and no pinchoff manifests itself. These differences in device behavior are interpreted as follows.

Pinchoff occurs in normal IGFET's because, as drain voltage increases, an effective voltage is induced across the gate capacitance, C_g, that removes carriers from the conducting channel. In Eq. [1], the terms in the square bracket are proportional to the conducting channel carrier density. The V_o term is proportional to the free carrier density of the semiconductor material itself. The V_g term is directly proportional to the carrier density induced or removed from the channel by gate voltage acting through the dielectric capacitance, C_g. Similarly, the $V_d/2$ term is directly proportional to the carrier density removed from the channel by drain voltage also acting through the gate capacitance. It is the carrier removal represented by the $V_d/2$ term that causes pinchoff in IGFET's. Pinchoff is defined as the point where the slope of the I_d *vs.* V_d curves become ideally zero, *i.e.*, where

$$\frac{\partial I_d}{\partial V_d} = 0 = \frac{\mu C_g}{L^2}\left[(V_g + V_o) - V_d\right] \qquad [3]$$

Pinchoff will not occur when V_d is prevented in some way from influencing the channel carrier density so that the condition of Eq. [3] is not met. The common property suspected to be preventing ink-dielectric GAD's from approaching this condition is the strong frequency dependence of C_g. Equations [1] and [3] do not reveal how this dependency acts to prevent pinchoff because their derivation tacitly assumes no variation of C_g with frequency.

A linear steady-state zero-order analytical accounting for the frequency dependence of gate capacitance can be incorporated into Eq. [1] as follows

$$I_d(\omega_g,\omega_d) = \frac{\mu C_g}{L^2}\left[\left(\frac{V_g}{1 + j\omega_g T_c} + V_o\right) - \frac{V_d}{2(1 + j\omega_d T_c)}\right] V_d \qquad [4]$$

where a gate capacitance time constant, T_c, is defined as the inverse of the angular frequency at which the I_d (or g_m) response to a sinusoidal gate voltage is 0.707 of its d-c value, and ω_g and ω_d are the angular frequencies of applied gate and drain voltages, respectively. The pertinent consequences of Eq. [4] are that not only the transconductances of ink-dielectric GAD's will be frequency dependent but that their pinchoff, as well, will be just as strongly frequency dependent. Pinchoff, of course, will depend on the frequency of applied drain voltage used for measurement rather than the gate voltage frequency. Equation [4] indicates the pinchoff can not occur for $\omega_d >> 1/T_c$. But, as ω_d is reduced, a pinchoff condition will ultimately manifest itself and, furthermore, the pinchoff point will occur at lower and lower drain voltages and currents.

The validity of the foregoing statements in GAD's having different ink-type dielectrics was tested by

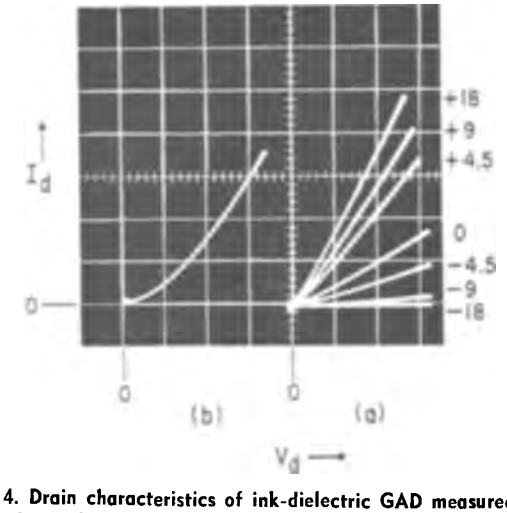

Fig. 4. Drain characteristics of ink-dielectric GAD measured at a drain voltage frequency of 100 cps. (a) Family of characteristics for gate voltages indicated. All curves are somewhat superlinear and pinchoff is not in evidence. Vertical scale = 2 ma/major div; horizontal scale = 5 v/major div. (b) Amplified V_g = — 18v curve showing drain current superlinearity in more detail. Vertical scale = 10 μa/major div; horizontal scale = 5 v/major div.

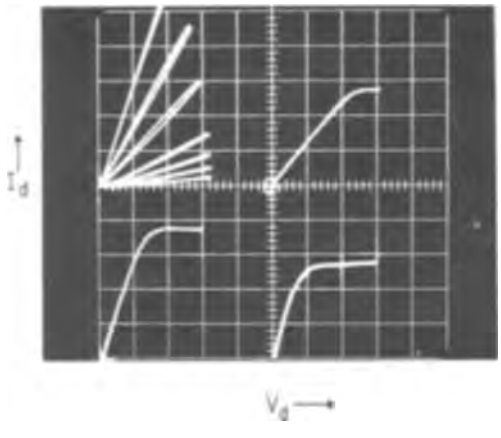

Fig. 5. Drain characteristics of a typical ink-dielectric GAD as a function of frequency showing the frequency dependence of pinchoff. Traces in the upper-left quadrant are a family of characteristics for V_g = 18, 9, 4.5, 0, —4.5, —9, and —18v at a drain voltage frequency of 100 cps. The other quadrants display the V_g = +4.5v curve at lower frequencies: upper right at 10 cps; lower left at 1 cps; and lower right at 0.1 cps. Vertical scales: upper left and right, I = 2 ma/major div; lower left and right, I = 1 ma/major div. Horizontal scales = 5 v/major div. Retraces have been blanked out for purposes of clarity.

varying drain voltage frequency with results from a typical unit pictured in Fig. 5. As drain frequency is decreased a rather well-defined pinchoff appears, thus qualitatively, at least, substantiating the preceding hypothesis. Our normal $BaTiO_3$ dielectric GAD's would not be expected to pinch off for V_d's within their power dissipation limits because V_o, Eq. [1], is too large. However, two specially made units having V_o's of approximately 18v that should have been able to satisfy Eq. [3] for $V_g \leq 0$ were tested and found not to pinch off.

Drain characteristics of one unit are shown in Fig. 6. Lack of pinchoff in conventional IGFET's has been attributed (3) to un-ionized surface donors in the semiconductor at the dielectric interface. Whether this explanation is pertinent to substrate-dielectric GAD's that should pinch off but did not has not been investigated further.

Superlinear volt-ampere characteristics (*i.e.*, $I_d \propto V_d^a$, where $a > 1.0$) are associated with the polycrystalline semiconductor used as channel material. The cause of superlinear characteristics is not completely understood, but it is thought that voltage sensitive intercrystalline boundaries are primarily involved. It is unlikely that superlinearity is due to one-carrier or two-carrier space-charge-limited currents (4, 5) because trap densities are sufficiently high to preclude the trap-filled condition necessary (6). All polycrystalline materials tested (including CdS pressed pellets, CdS vapor deposited films, and CdS:CdSe sintered inks) exhibited superlinearity with the magnitude of the coefficient ranging between $1 < a < 3$. Higher resistivity materials generally were found to have larger coefficients than lower resistivity materials as long as material deposition and processing remained the same. Contact barrier effects as possible sources of superlinear V-I characteristics were examined, but all contact material diffusion and electrical pulse treatments that are known to reduce superlinearity to ohmic behavior in single crystal specimens were of no avail in polycrystalline samples.

Stability.—Storage tests with $BaTiO_3$-substrate GAD's protected from atmospheric environments have shown only minimal changes in g_m while those exposed to ambients have shown varied but no more than 50% degradation over a period of 12 months. When longevity-tested at power dissipation levels of approximately 150 mw or less, no change in performance has been noted with canned units. However, when operated at higher power levels that caused device heating, permanent reduction of g_m would occur.

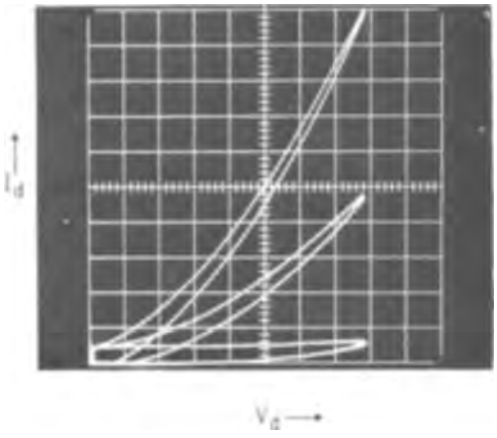

Fig. 6. Drain characteristics of a $BaTiO_3$ dielectric-substrate GAD showing the lack of pinchoff in a device that should meet pinchoff conditions. Vertical scale = 0.5 μa/major div. Horizontal scale = 2 v/major div. Upper, mid, and lower curves were obtained at V_g = +18, 0, and −18v, respectively. Drain voltage frequency = 100 cps. Area in curves due to capacitance of measuring circuit.

Permanent changes invariably would be accompanied by semiconductor conductivity reductions whereas no permanent deterioration in substrate capacitance was ever evidenced.

The $BaTiO_3$ dielectrics used in dielectric-substrate GAD's (Alsimag T-183-A and T-176-A) were moderately temperature sensitive and units would exhibit g_m degradation at elevated temperatures (~60°C) that corresponded with the dielectric coefficient change. This means that use of even higher permittivity materials to achieve greater g_m response has temperature-performance implications for, as far as is known, high permittivity materials have the greatest temperature coefficients. High-permittivity dielectrics are also voltage sensitive; however, the low-voltages employed in normal GAD operation would produce only minimal variations in substrate capacitance.

The shelf-life behavior of GAD's with organic and inorganic ink-dielectric films are qualitatively similar but, in general, exhibit greater instabilities than dielectric-substrate units. Some units of each species more than one year old still operate. Several that were longevity tested under load have been relatively stable at room temperature from one longevity measurement to another but the majority have exhibited varying g_m's that involve the dielectric primarily. Semiconductor material property changes, except for temperature-caused variations, have been found insignificant relative to dielectric changes.

Observed gate-capacitance decreases with time are attributed to solvent evaporation or hydrolysis and the consequent loss of ions from the polarization process. This conclusion is based on observations that canned units invariably had much longer shelf-lives than uncanned units, and on the evidence that replacement of lost solvents would restore C_{gm} and g_m in defunct devices. In some cases these parameters, after solvent additions, were greater than those originally measured. Nonsolvent ink-dielectric GAD's have shown virtually no capacitance changes with time as they contain no time-dependent constituents or lingering chemical reactions.

As might be expected, GAD's printed with any of the successfully deposited dielectrics are sensitive to changes in ambient temperature. Typically, a 100 times increase in g_m occurs as device temperature is raised from 0° to 50°C. This change is attributed mainly to increase in density and mobility of the ion species associated with the polarization (gate capacitance correspondingly increases) and partly to increases in semiconductor conductance.

Concluding Remarks

Producing active devices, having power gain, by serial deposition of particulate "inks" has been demonstrated. Four basic types of insulated-gate field-effect transistors have been processed without recourse to vacuum evaporation, and these have been examined for characteristic performance. Device behavior is largely determined and limited by the properties of the gate dielectric and the dielectric-semiconductor interface. Best stability has been achieved with $BaTiO_3$-substrate GAD's but lack of drain-current pinchoff remains an interesting anomaly.

In this feasibility study, we do not consider the materials and processes that have been developed as anything more than preliminary solutions to a variety of problems involving compatibilities of inks and their interactions with each other. At this time a more systematic evaluation of better materials and printing processes is in order and needs to be carried out. Ideally, it would be desirable to produce entire circuitry at speeds approaching modern newsprint rates in order to achieve the ultimate in low cost manufacturing. Our ink processing times presently preclude achieving this ideal objective. However, the processing times and printing surfaces employed are comparable to those now used in producing thick-film resistor and capacitor combinations. Finally, printed active devices

in their present state of development, are limited in both performance and stability, but improvements are likely to evolve with better understanding of the basic chemical, physical, and electrical processes involved.

Acknowledgments

Acknowledgment is given to Jim Wallis and Don Watson for their efforts in fabricating and testing GAD devices, to Mike Valek who studied rolled contacts, and to Bob Warne for general consultation. Recognition is also given to I. Milt LeBaron for his ideas and general support.

Manuscript received March 30, 1966; revised manuscript Sept. 22, 1966.

Any discussion of this paper will appear in a Discussion Section to be published in the December 1967 JOURNAL.

REFERENCES

1. P. K. Weimer, F. V. Shallcross, and H. Borkan, *RCA Rev.*, **24**, 661 (December 1963).
2. H. Borkan and P. K. Weimer, *ibid.*, **24**, 153 (June 1963).
3. J. E. Johnson, *Solid State Electronics*, **7**, 861 (1964).
4. M. A. Lampert and F. Edelman, *J. Appl. Phys.*, **35**, 2971 (1964).
5. A. Rose, *ibid.*, **35**, 2664 (1964).
6. D. J. Page, A. A. Kayali, and G. T. Wright, *Proc. Phys. Soc.*, **80**, 1133 (1962).

Growth Mechanism of Vapor Deposited Germanium Films

M. S. Seltzer, N. Albon[1], B. Paris, and R. C. Himes

Battelle Memorial Institute, Columbus Laboratories, Columbus, Ohio

ABSTRACT

Direct microscopic observation of the movement of growth steps during chemical vapor deposition of epitaxial layers of germanium on germanium substrates, in an open tube reactor, has been employed to study growth mechanisms operative in this system. The reaction studied was the disproportionation of germanium diiodide: $2GeI_2(g) = Ge(s) + GeI_4(g)$. Rate of step movement has been measured as a function of step height, substrate temperature, iodide pressure, gas flow rate, and other growth variables. In addition, transpiration measurements have been made to determine the actual partial pressures for gaseous species produced at various sites in the open-tube flow system. The predominant stepped growth features observed on (111) planes were triangular pyramids. They are shown to be quite minor deviations from the (111) plane, the slope of the side for a typical pyramid being at most 1 in 30. A maximum in rate of step movement has been found with the germanium seed near 360°C, and observable step movement was detected in a narrow temperature range about this optimum temperature. From the observed influence of step height and iodide pressure on rate of step movement it is suggested that growth depends on processes occurring directly at step sites. At high iodide pressure two-dimensional nucleation of germanium on terrace portions may occur, resulting in an increased concentration of crystalline defects.

In recent years the use of epitaxially grown, single-crystal films in the fabrication of semiconductor devices has become widespread. Among the more attractive methods for preparation of epitaxial deposits are those involving formation of films by chemical reaction, either dissociation or reduction. The utilization of chemical vapor deposition (cvd) techniques for the purpose of obtaining epitaxial semiconductor films has been hampered, however, by a lack of fundamental information concerning the influence of the several variables involved on the growth and perfection of the films formed. In particular there have been few attempts to arrive at a basic understanding of the mechanisms for epitaxial growth of these covalently bonded materials in a cvd system. For many cases, growth of imperfect crystals containing spiral dislocations can be adequately described in terms of the mechanism proposed by Burton, Cabrera, and Frank (1), which consists of surface diffusion of adsorbed species to ledges on low-index terraces, and movement along the ledge to kinks where incorporation of the species into the deposit occurs. This model, although very general, was derived mainly for growth by a process of physical vapor deposition or condensation of monomers at low supersaturation. It was the objective of this investigation to study the process of growth of semiconductor materials by chemical vapor deposition and to determine the degree of applicability of current crystal-growth theory to these rather complex systems. The principal experimental method chosen to attain this objective was direct microscopic observation of the behavior of growth steps in a deposition cell. In order to obtain a satisfactory understanding of crystal growth it is necessary to establish the manner in which growth steps move and the kinetics of this process. Thus, rate of step movement has been measured as a function of step height, substrate temperature, and other growth variables in order to identify rate-controlling processes. Although the movement of growth steps on semiconductor crystals had not been measured previously, the sensitivity of procedures involved in such measurements makes step-movement determination an extremely useful tool for study of crystal growth. The weight of material deposited during an observation on step movement may be many orders of magnitude less than that required when studying growth by more conventional means.

The growth of germanium films on germanium substrates by dissociation of the diiodide in an open-tube flow system was chosen for study in this investigation. There are considerable data available on this system, and precise control of growth conditions, purity, and substrate perfection is possible. Furthermore, the low deposition temperature (350°-400°C) facilitates microscopic observations and measurement of step movement. This low deposition temperature is one of the most significant of the possible advantages to be gained from the use of cvd methods since higher purity deposits may be achievable, with lower point-defect concentrations than are found in material prepared at elevated temperatures.

The design and operation of the apparatus used to study crystal growth in this investigation have been described previously (2). The equipment consists of a

[1] Present address: Unilever Limited, Welwyn, Herts., England.

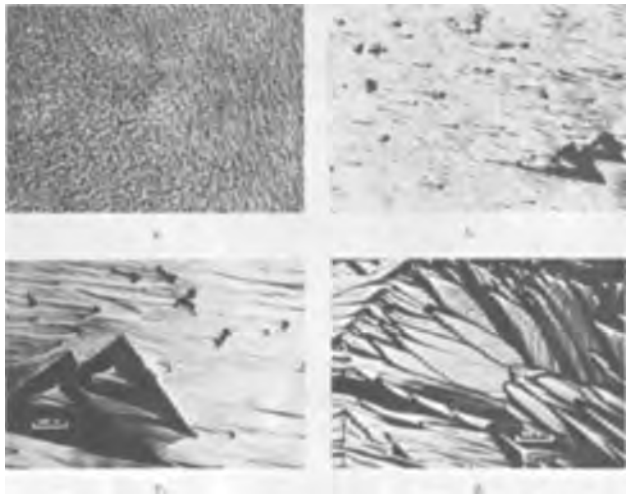

Fig. 1. Various surface features during deposition on the germanium (111) face.

system for carrier gas-flow control and purification, a multistage furnace where formation of gaseous GeI_2 occurs, a deposition cell, and a microscope for observation of growth features. In the following sections we present the experimental observations and results, discussion of step movement data, and conclusions.

The partial pressures for gaseous species produced at various sites in the open-tube reactor employed in this study could not generally be calculated on the basis of equilibrium conditions; instead, a series of transpiration measurements was required to determine the conditions under which equilibrium is achieved at these critical sites. The results of this auxiliary work are discussed in some detail in the Appendix.

Experimental Observations

Various features found during deposition on a (111)-type surface are shown in Fig. 1. A typical surface before deposition is shown in Fig. 1a. When growth commenced, numerous features became visible. Later, these became more pronounced and most of the surface had the appearance shown in Fig. 1b. Still later, two triangular growth hillocks were formed as shown in Fig. 1c. These are similar to features observed by other investigators (3-7) who have studied growth of germanium by the disproportionation reaction. One small area of the deposit displayed a somewhat different appearance as shown in Fig. 1d, which reveals well-defined growth steps on a planar area. It was the movement of such growth steps,

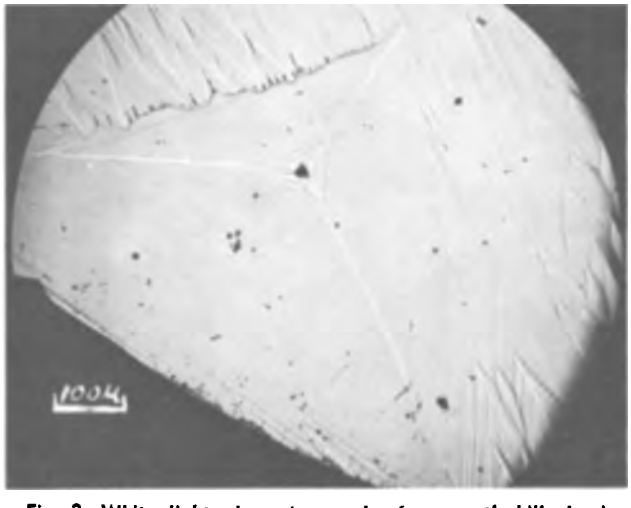

Fig. 2. White light photomicrograph of a growth hill showing many small steps.

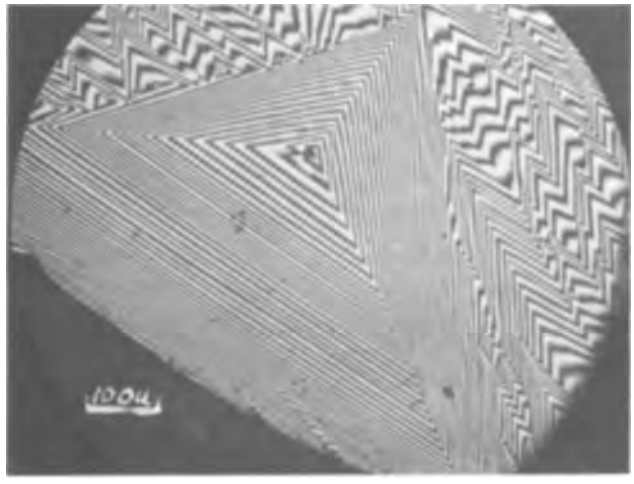

Fig. 3. Same growth hill as shown in Fig. 2 observed under interference lighting.

either on growth pyramids or on planar regions, that was measured during crystal growth. Measurements on planar surfaces were preferred because steps of various heights could be observed better than on hillocks, and their comparative movements measured. In addition, a particular step could be observed for a relatively long period of time. This permitted measurements on the same step under different growth conditions.

The topography of selected growth hillocks was established by utilization of interference microscopy, as exemplified in Fig. 2 and 3. A growth hill is shown under white light in Fig. 2 and under interference lighting in Fig. 3. Many steps can be seen in Fig. 2. As the fringes in Fig. 3 represent a vertical distance of 0.27μ, the height of the hills can be determined. In this example the profile obtained indicated a height of 6.2μ, and the length of each side is 200μ. A rate of step movement of 4 μ/min represents a rate of film thickening at the hillock of 7.5 μ/hr. Although these hills appear prominent, they are quite minor deviations from the (111) plane, the slope of the side being at most 1 in 30. [Seed orientation is such that the exposed surface is, to good approximation, a (111) plane.]

The influence of impurity contamination during deposition has been observed in two ways. First, it has been found that steps often appear to become complex in form, with oxide patches visible on the germanium seed, when undiluted helium is used as the carrier gas. This is probably due to deficiencies in removal of oxygen and water vapor from the helium and source materials.

Second, the problem of incipient doping of the gas stream with moisture has been observed even with hydrogen present, if the experimental procedure did not include preoutgassing of the iodine source. This effect of doping on step movement was observed qualitatively; after the iodine source temperature was increased, the steps moved at a lower rate than expected for the corresponding I_2 pressure. After sufficient time, about 20-30 min, normal step rate was generally resumed. The amount of H_2O in I_2 was small, for no oxide was visible on the seed. No evidence of oxide was observed on the source germanium at 500°C.

Experimental Results

Measurements of rate of step movement were made as a function of seed temperature, step height, GeI_2 pressure, carrier-gas flow rate, and gas composition.

The influence of step height on the rate of step movement was investigated under a variety of conditions. It was determined that at low iodide pressures steps of various heights (greater than 100Å) moved at the same rate, while under higher iodide pressures,

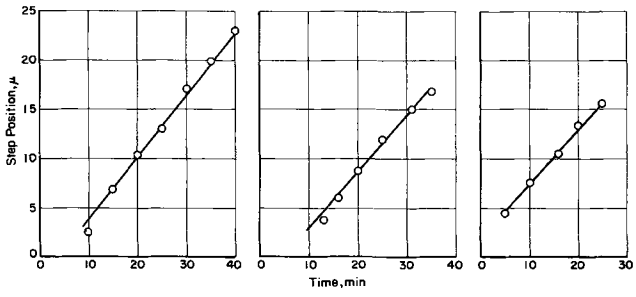

Fig. 4. Step movement for steps of varying height: hydrogen flow 1½ l/min; iodine source temperature 54°C; seed temperature 349°C.

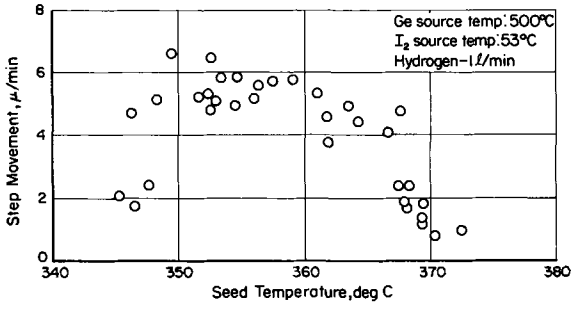

Fig. 5. Rate of step movement with seed temperature

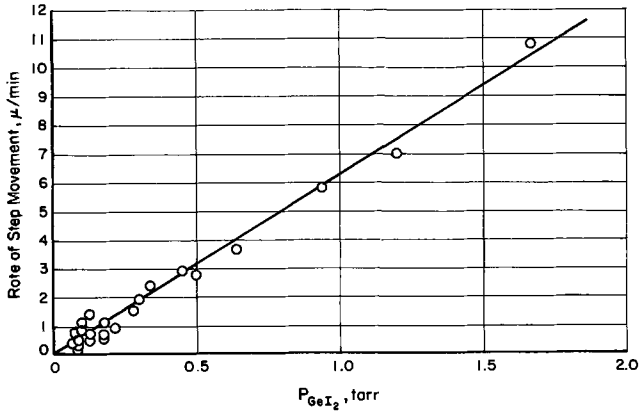

Fig. 6. Rate of step movement plotted as a function of experimentally obtained pressures of GeI_2. Germanium source at 500°C, germanium seed at 354°C, and hydrogen flow rate of 1 l/min.

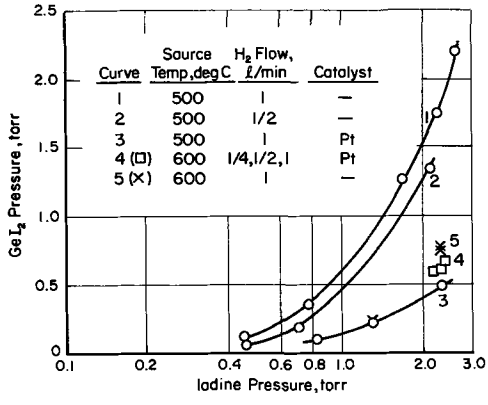

Fig. 7. Vapor pressures of GeI_2 obtained from the weight-loss experiments.

above 2 Torr, larger steps were measured to move at a rate as much as 50% faster than the small steps.

Figure 4 shows step position plotted against time, for three steps of different heights measured during one experiment, where the GeI_2 partial pressure was about 1.8 Torr. The differences in height as determined from contouring of the growth hills with interference fringes were estimated to be at least a factor of ten. The rate of step movement for the three steps is seen to be essentially independent of step height, the slopes varying from 3.0 to 3.1 μ/min, which is within the acceptable range of accuracy, 10%, for these measurements.

An extensive series of measurements was made of the variation of the rate of step movement as a function of seed temperature. These measurements were made at selected iodine pressures and with hydrogen and a mixture of hydrogen and helium as carrier gases. The results presented in Fig. 5, showing the rate of step movement *vs.* germanium seed temperature under the conditions given in the figure, are typical for this series of experiments. Measurable rates of step movement are seen to occur over a narrow temperature range. Changing the iodide pressure or the H_2/He ratio serves to alter the rate of step movement but does not influence the range of seed temperatures over which measurable step movement occurs.

An attempt was made to correlate step movement with the partial pressure of GeI_2, leaving the germanium source, by calculating the equilibrium pressure of GeI_2 under experimental conditions. However, when the results of the transpiration study (Appendix) were obtained, it became apparent that the partial pressures for the various gaseous species could not generally be calculated on the basis of equilibrium conditions, but rather the experimental pressures determined from weight-loss measurements were required. By selecting values for the experimentally determined GeI_2 pressure from curve 1 of Fig. 7, it was possible to replot step velocity (μ/min) *vs.* p_{GeI_2} (Torr), as shown in Fig. 6. The step rates had been determined with germanium source at 500°C, hydrogen flow rate of 1 l/min, seed temperature of 354°C, and with germanium and I_2 source beds equivalent to those used in the weight-loss study. The step velocity in Fig. 6 is seen to be a linearly increasing function of the GeI_2 pressure over the entire range of pressures studied, with possible small deviations at low pressures. Although these deviations at low pressure may be attributed to impurity effects, more likely causes are the variations in experimental conditions which occur during the long periods of time required to obtain step-movement data under low supersaturation.[2]

A cursory investigation of step movement as a function of hydrogen gas flow rate indicated that the rate of step movement increased with gas flow rates up to approximately 1 l/min. Above this flow rate, little increase in step rate was observed. This behavior is compatible with the transpiration results presented in Fig. 8, which showed that the GeI_2 pressure increased with increasing flow rate in the range 250-1000 cm³/min. Possible reasons for this effect are discussed in the Appendix.

Step movement studies complementary to the weight-loss work were performed by measuring step velocity under conditions which assured complete conversion to HI of all iodine entering the germanium source bed. This was accomplished by placing a quantity of platinum wool between the iodine and germanium source beds at a temperature in excess of 300°C. It was apparent from initial experiments in which the platinum catalyst was utilized that considerably less GeI_2 was produced than in similar experiments which did not include use of a catalytic agent. Step velocities were substantially depressed as compared with rates obtained under similar conditions (germanium source at 500°C, iodine source at

[2] Another possibility, suggested by the reviewer, is that the growth rate at seed is diffusion and/or mass transport controlled in the gas phase which can be minimized by increasing the flow rate.

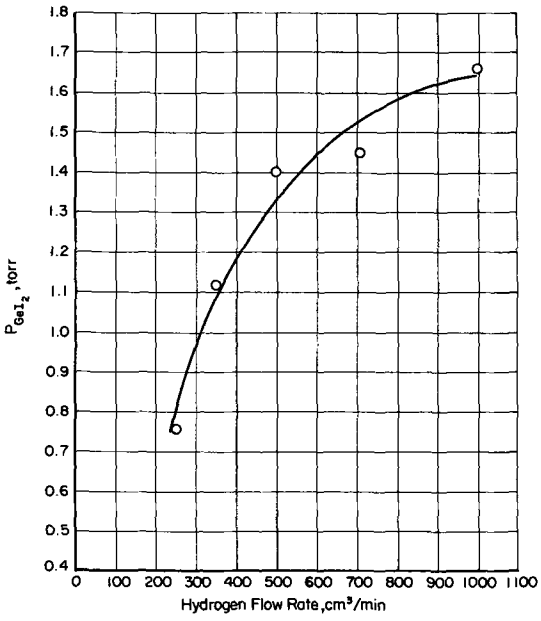

Fig. 8. Partial pressure of GeI_2 as a function of hydrogen flow rate.

50°C, hydrogen flow rate of 1 l/min, and seed at 354°C) but without a catalytic agent placed in the system. This result would be predicted from the data obtained in the weight loss-experiments. Comparison of curves 1 and 3 in Fig. 7 shows that the presence of platinum catalyst reduces the available GeI_2 concentration by a factor of four at iodine pressure corresponding to a source temperature of 50°C.

Discussion of Step-Movement Data

It was shown above that, under the conditions of these experiments, step velocity was independent of step height with low gas pressure and increased slightly with increasing height at high GeI_2 partial pressure. These results suggest that surface diffusion of adsorbed species to kink sites is not the rate-controlling process for growth since they are contrary to the behavior expected according to the BCF surface-diffusion-limited theory of crystal growth. It is suggested, rather, that in this study, the growth of germanium by dissociation of the diiodide is controlled by processes occurring directly at the step.

Calculation of the rate of impingement of GeI_2 molecules directly onto the growth step, based on typical conditions of $p_{GeI_2} = 1.0$ Torr with seed temperature of 354°C and step velocity of 6.2 μ/min shows that the rate of step movement can easily be accounted for by dissociation of those molecules which impinge directly on the step.

This suggestion is similar to that proposed for certain examples of whisker growth (8), in which case reaction is assumed to occur only at ledges on the tip where a spiral dislocation emerges. In the case of growth of copper whiskers by hydrogen reduction of CuI, it was assumed that reduction did not occur in the vapor phase, but that catalytic reduction of absorbed iodide occurred at the whisker tip. For the case of germanium growth, it may be supposed that the reaction at the growth step involves reduction

$$H_2(g) + GeI_2(g) \rightarrow Ge(s) + 2HI(g) \qquad [1]$$

or disproportionation

$$2GeI_2(g) \rightarrow GeI_4(g) + Ge(s) \qquad [2]$$

The step velocity has been shown to be directly proportional to the GeI_2 concentration (Fig. 6) as would be expected either from reaction [1] or [2], where, for example, the rate-controlling step may involve association of a GeI_2 molecule with one previously adsorbed on the step to yield germanium and the tetraiodide. It should be possible to distinguish between the predominance of reactions [1] or [2] by determination of rate of step movement at fixed GeI_2 pressure under varying hydrogen flow rates.

A number of factors may have contributed to limit the temperature range over which appreciable germanium deposition occurred. The results of some thermodynamic calculations (9) based on an assumed model for the experiment indicate that in the disproportionation reaction the pressure of GeI_2 becomes equal to its saturation pressure between 300° and 350°C, resulting in the formation of solid GeI_2. Therefore the inability to produce observable germanium growth below 345°C may have been due to a lack of available germanium in the gas phase at the lower temperatures. Furthermore, it was shown that under equilibrium conditions the amount of germanium (all species) in the gas phase for the system Ge-I_2-H_2 increases as the temperature is lowered from 500° to 323°C. This increase would have to be at the expense of the seed crystal. Of course, growth has been observed above 345°C, indicating that equilibrium is not achieved at the seed under the experimental conditions, but a tendency toward limited or negative growth at low temperature is suggested from the thermodynamic analysis.

Figure 5 shows that the rate of step movement approaches a pronounced maximum near 360°C, leveling off to gradually decreasing values above 370°C. This behavior may be explained in terms of the amount of germanium available for deposition, as determined in the thermodynamic analysis. Under equilibrium conditions the Ge/I_2 ratio at the seed temperature slowly approaches the value obtained at the source temperature (500° to 600°C) with increasing seed temperature. This might lead to the results obtained for seed temperatures above 370°C.

Although not explicitly discussed in the previous sections presenting details of the research, some attention should be given to the changes in appearance of growth features with increasing GeI_2 pressure. As the partial pressure of diiodide is raised, the small, straight steps are seen to become ragged, with large steps overtaking smaller ones. A possible explanation of this effect is that the steps become unstable because the concentration of unreacted GeI_2 on the surfaces is high enough for projections to be stable. Thus two-dimensional nucleation may be possible between the steps, leading to the formation of germanium crystallites and ragged growth. This observation of fundamental change in the growth mechanism is particularly significant in relation to the perfection of deposits. It is anticipated that films grown under conditions where nucleation occurs would have increased concentrations of crystalline defects such as stacking faults.

Summary and Conclusions

The low-temperature vapor deposition of germanium was studied by microscopic measurement of step movement as a function of iodide pressure, gas flow rate and composition, seed temperature, and growth-step height. In conjunction with the information obtained from a thermodynamic analysis and the source weight-loss study, these results obtained for rate of step movement were considered, and the following conclusions were reached.

1. The predominant stepped growth features observed on (111) planes were triangular pyramids. The hillocks were shown to be quite minor deviations from the (111) plane, the slope of the side for a typical pyramid being at most 1 in 30.

2. Generally, rate of step movement appears to be nearly independent of step height. Under high partial pressures of GeI_2 step velocity may increase with increasing step height. It is suggested that the rate of step movement depends on processes occurring directly at step sites rather than on surface diffusion of adsorbed species to the steps.

3. Step velocity has been shown to be directly proportional to $GeI_2(g)$ pressure, as would be expected from consideration of the reactions by which deposition might occur. From measurements of GeI_2 pressure *vs.* rate of step movement an estimate of the relation between impinging GeI_2 and rate of addition of germanium atoms could be made. It was found that the rate of step movement could be accounted for by dissociation of these molecules which are adsorbed directly on the step.

4. A maximum in rate of step movement has been found with the germanium seed temperature near 360°C, and observable step movement was detected in a narrow temperature range about this optimum temperature. This behavior was obtained for several different iodine pressures and carrier-gas compositions.

5. With increasing $GeI_2(g)$ pressure, small, straight growth steps were observed to change in appearance, first to dark bands, and then into ragged, nonlinear arrays. A possible explanation of this effect is that two-dimensional nucleation occurs on the epitaxial surface as the concentration of unreacted GeI_2 on the surfaces is increased.

Acknowledgment

This research was supported by the sponsoring companies of the Chemical Vapor Deposition Research Group, at Battelle Memorial Institute.

Manuscript received Dec. 20, 1965; revised manuscript received Sept. 10, 1966.

Any discussion of this paper will appear in a Discussion Section to be published in the December 1967 JOURNAL.

REFERENCES

1. W. K. Burton, N. Cabrera, and F. C. Frank, *Phil. Trans. Soc. London*, Ser. A, **243**, 299 (1950).
2. M. S. Seltzer, N. Albon, B. Paris, and R. C. Himes, *Rev. Sci. Instr.*, **36**, 1423 (1965).
3. J. C. Marinance, *IBM J. Res. Dev.*, **4**, 248 (1960).
4. W. J. Heinecke and S. Ing, Jr., *J. Appl. Phys.*, **32**, 1498 (1961).
5. M. Takabayashi, *Japan, J. Appl. Phys.*, **1**, 22 (1962).
6. G. A. Kurov, *Soc. Phys.-Cryst.* (English transl.), **7**, 6 (1962).
7. R. C. Newman and J. Wakefield, *Solid State Phys. Electron. Telecommun, Proc. Int. Conf., Brussels, 1958*, **1**, 160 (pub. 1960).
8. S. S. Brenner, in "The Art and Science of Growing Crystals," Chap. 2, pp. 30-54, J. J. Gilman, Editor, John Wiley & Sons, Inc., New York (1963).
9. This analysis is due to J. Droege (Seventh Quarterly Progress Report to Chemical Vapor Deposition Group Research Sponsors) Feb. 15, 1964.
10. A. Reisman, M. Berkenblit, and S. A. Alyanakyan, *This Journal*, **112**, 241 (1965).
11. A. Reisman and S. A. Alyanakyan, *ibid.*, **111**, 1154 (1964).
12. A. Reisman and M. Berkenblit, *ibid.*, **112**, 315 (1965).
13. A. Reisman and M. Berkenblit, *ibid.*, **113**, 146 (1966).
14. F. Jona, *J. Chem. Phys.*, **43**, 1025 (1965).

APPENDIX

Transpiration Studies

In order to determine the operating conditions under which equilibrium is achieved in the open-tube flow system used in this work a transpiration study was initiated whereby weight-loss measurements were employed to determine the pressures of various gaseous species formed at the iodine and germanium sources for the system $Ge\text{-}I_2\text{-}H_2$. A number of studies of systems including $Ge\text{-}I_2\text{-}H_2\text{-}He\text{-}HI$ have been made (10-14), but the results of these studies are not necessarily applicable to the physical system employed in the present investigation. Measurements were made as a function of iodine and germanium source temperatures and gas flow rate.

Experimental Procedure

A technique for easy disassembly of the reaction train was required for an extensive program of weight-loss determinations. At the same time, it was desirable to maintain in the germanium and iodine source chambers the physical dimensions of the beds used in the step-movement study. The following arrangement proved satisfactory and was of sufficient simplicity to ensure a maximum number of transpiration experiments.

A U-shaped iodine source chamber was designed which could be immersed in a constant-temperature water bath containing a mechanical stirrer. Teflon stopcocks, placed on either side of the U-shaped chamber, could be fixed so that the incoming hydrogen, purified by the palladium-diffusion process, flushed the germanium source and bypassed the iodine charge during heatup. The problem of channeling in the iodine was minimized by the vertical position of the source and by vigorous shaking of the entire chamber after each run.

The container for the germanium source was a Vycor test tube, 2.6 cm in ID and 17.5 cm long. Gas flow through the bed was provided for by perforations in the closed end of the tube. The charge itself consisted of a uniform distribution of irregularly shaped particles whose weight varied from 0.2 to 2.0g. The packed chamber was placed, open end toward the iodine supply, within a close-fitting 30-mm quartz tube and pushed against a tapered section to form a seal. For some runs, to ensure complete conversion of I_2 to HI, platinum wool (fibers 0.001-0.004 in. in diameter) in the form of a plug 1.8 cm in diameter and 8.7 cm long was positioned between the iodine and germanium source beds and maintained at a temperature greater than 300°C.

A run consisted of bringing the source beds to the desired temperatures and allowing a known flow of purified hydrogen to pass through the system for a predetermined time. At the end of a run the hydrogen was allowed to bypass the iodine chamber, and the entire system was brought to room temperature. Both source beds were then weighed on a balance accurate to 1 mg with a 5-kg capacity.

Experimental Results and Discussion

The following assumptions were made in interpretation of results obtained from weight-loss measurements.

1. The formation of GeI_4 may be neglected for germanium source temperatures above 500°C, and therefore all germanium consumed at the source bed is in the form of GeI_2.
2. All iodine not associated with germanium reacts with hydrogen gas and leaves the germanium source as HI.
3. Partial pressures of GeI_2 and HI can be determined from the ideal gas equation.

The experimental variables include time, gas flow rate, germanium- and iodine-source temperatures, and the absence or presence of a platinum catalyst. It was found that in all cases the sum of the p_{GeI_2} and $\frac{1}{2}\, p_{HI}$ was approximately equal to the equilibrium vapor pressure of I_2 at various iodine source temperatures employed. This suggests that the equilibrium iodine concentration was removed from the iodine source bed for the various hydrogen flow rates used.

In Fig. 7, the partial pressure of the volatile halide, GeI_2, is plotted as a function of the iodine pressure for a series of experiments in which other variables were maintained at the values given in the figure. Curve 1 is drawn through points which represent data obtained with a germanium source at 500°C and a hydrogen flow rate of 1 l/min. The GeI_2 pressure is seen to be a rapidly increasing function of the iodine pressure under these conditions. A similar pressure dependence is observed when the hydrogen flow rate is reduced to ½ l/min as can be seen from examination of curve 2. It is noted, however, that when the flow rate is reduced to one-half of the previous value, lower GeI_2 pressures are obtained. Comparison of curves 1 and 3 reveals a dramatic decrease in GeI_2 formation (especially for high iodine pressures), when a platinum catalyst is placed in the reaction system. The number 4 represents data indicated by the squares. These were obtained with the germanium source at 600°C, a platinum catalyst in the system, and hydrogen flow rates of 1, ½, and ¼ l/min. Flow rate seems to have little influence on GeI_2 pressure

under these conditions. The points (x) designated by 5 are those resulting from data obtained with a source temperature of 600°C, flow rate of 1 l/min and no platinum catalyst in the system. The excellent agreement obtained for p_{GeI_2} from these two runs, and the lack of deviation of experimental points from curves 1, 2, and 3 of Fig. 7 are a measure of the reproducibility of the weight-loss measurements.

The following observations can be made from examination of the experimental data presented in Fig. 7.

1. It is evident that H_2-I_2-HI equilibrium is not achieved under the conditions represented by curves 1 and 2 when compared with curve 3, which represents the case where an active catalyst is known to convert all of the I_2 to HI. Thus, for cases 1 and 2, a large amount of free iodine vapor is allowed to enter the germanium source chamber and react to form GeI_2.

2. From comparison of curves 1 and 2 it would appear that germanium is a poor catalyst for the reaction $H_2(g) + I_2(g) \rightleftharpoons 2HI(g)$ at 500°C. Lowering the flow rate to increase the residence time of the gaseous species over the germanium bed has little effect on the amount of GeI_2 formed.

3. The formation of GeI_2 is critically dependent on iodine pressure for the conditions represented by curves 1 and 2. For an iodine pressure of 2 Torr, the pressure of GeI_2 formed changes by 0.1 Torr for a 2°-change in iodine source temperature. This factor may be an important cause of fluctuations in step-movement measurements, although inconstancy of supply of iodine vapor due to channeling in the iodine bed may also be a significant factor here.

4. From examination of curve 3, it is seen that formation of GeI_2 is less sensitive to variations in iodine pressure when a platinum catalyst is employed in the system. However, the transport efficiency, in terms of GeI_2 formed, is considerably reduced when complete conversion of free iodine to HI is accomplished. Thus, for a system using hydrogen as a carrier gas, transport of germanium is increased with increasing free-iodine concentration, but the more rapid step movement which results may be obtained at the expense of reproducible crystal growth rates.

5. Weight-loss measurements from runs with the germanium source at 600°C and a platinum catalyst present show that a higher yield of GeI_2 is obtained as compared with that obtained in similar experiments in which a lower germanium source temperature was employed (compare 3 and 4 in Fig. 7). This result is attributed to an increase in reaction rate with increasing temperature for

$$2HI(g) + Ge(g) \rightleftharpoons H_2(g) + GeI_2(g) \qquad (A)$$

It has already been mentioned that flow rate has little effect on GeI_2 formation at 600°C. Furthermore, comparison of 4 and 5 in Fig. 7 indicates that presence of a platinum catalyst has little influence on GeI_2 formation at 600°C. Thus it may be tentatively concluded that for hydrogen flow rates less than 1 l/min and iodine pressures below 2.5 Torr, equilibrium is achieved at 600°C for the system Ge-I_2-H_2-HI.

In Fig. 8, the partial pressure of the volatile halide, GeI_2, is plotted as a function of hydrogen flow rate for a series of experiments in which the germanium source was held at 500°C while the iodine source was maintained at 50°C. It is seen that the GeI_2 pressure is strongly dependent on gas flow rate over the range 250-1000 cm^3/min and that the experimental partial pressure of GeI_2 tends to level off as the flow rate is increased.

It is believed that these results may be explained in terms of the equilibrium or lack of attainment of equilibrium in the open-tube flow system employed in this study. At the lowest carrier-gas flow rates (lower than those employed in this study), it is presumed that the reaction of hydrogen with iodine to form hydrogen iodide goes nearly to completion. Then the reaction controlling the formation of GeI_2 at the germanium source is given by

$$2HI(g) + Ge(s) \rightleftharpoons GeI_2(g) + H_2(g) \qquad (B)$$

as discussed above. Thus, for some range of low carrier-gas velocities it is expected that the partial pressure of GeI_2 formed will be independent of flow rate.

Increasing the hydrogen flow rate decreases the residence time for the carrier gas over the sources with the result that the reaction

$$H_2(g) + I_2(g) \rightleftharpoons 2HI(g) \qquad (C)$$

does not go to completion. In this case a quantity of free iodine is available for direct reaction with germanium to form GeI_2 according to

$$Ge(s) + I_2(g) \rightleftharpoons GeI_2(g) \qquad (D)$$

Thus the partial pressure of GeI_2 is found to increase with increasing flow rate in some intermediate range of hydrogen flow rates, which includes those given in Fig. 8.

Finally, at very high flow rates (somewhat above 1 l/min), the hydrogen acts simply as an inert carrier in the system and the partial pressure of GeI_2 formed might approach that of the elemental iodine formed at the iodine source, 2.18 Torr. Complications may be introduced at high carrier-gas flows, however, if the equilibrium concentration of iodine is not removed from the iodine source, or if some germanium leaves the germanium source as GeI_4.

Technical Notes

Segregation Coefficients of the Rare Earth Niobates in $CaMoO_4$

L. H. Brixner

Pigments Department, Experimental Station,

E. I. du Pont de Nemours & Company, Inc., Wilmington, Delaware

In an earlier paper (1), the segregation coefficients of the $LnNbO_4$-type rare earth niobates have been reported for the $SrMoO_4$ host. Because of the deviation of the ionic radii of the smaller rare earths from that of Sr^{+2}, only a limited number of single crystals could be grown. Since none of the rare earth ion radii (except Sc^{+3}) deviates more than 15% from that of Ca^{+2}, all rare earths should fit substitutionally in the calcium site in $CaMoO_4$; therefore a more complete study of their distribution characteristics can be done in this host. Nassau (2) has already incorporated the rare earths in $CaWO_4$, using both $LnNa(WO_4)_2$ as well as $Ln_2(WO_4)_3$ as dopants, and a limited list of segregation coefficients for some $LnNbO_4$ compositions in $CaMoO_4$ has been reported (3).

This note reports the distribution coefficients of all rare earth niobates in $CaMoO_4$ and points out some relationships of these parameters as a function of the ion size deviation from that of the host. In addition, some previously unreported absorption spectra and structural parameters are presented.

All crystals were grown by the Czochralski technique. Particular care was taken to keep the pulling speed (½ in./hr), the rotation rate (20 rpm), and the shape of the crystal (½ in. diameter, c-axis) as identical as possible from run to run. Generally, 50 ± 5% of a 100g charge was grown into single crystalline material. The rare earth niobates were charged in the form of their constituent components according to

$$0.99CaMoO_4 + 0.005Ln_2O_3 + 0.005Nb_2O_5 \rightarrow$$

$$Ca_{0.99}Ln_{0.01}Mo_{0.99}Nb_{0.01}O_4$$

Since the segregation coefficient for all rare earth niobates in $CaMoO_4$ is greater than 1, this resulted in an actual rare earth concentration of slightly more than 1 mole % in the growth crystal.

All analytical information was obtained by x-ray fluorescence techniques. The analytically determined ratio of Ln_2O_3:Nb_2O_5 in no case fell below 1:0.95 or exceeded 1:1.15. No particular trend or shift of this ratio as a function of growth rate could be detected (it went up in 6 cases, down in 8, and stayed the same in 1); therefore, the stoichiometry of the rare earth niobates in $CaMoO_4$ fluctuates only slightly around the theoretical 1:1.00 ratio. The computed segregation coefficients, together with the ion size deviation and the color of the crystals, are summarized in Table I. We can see that Sc^{+3} is the only element which deviated in size more than 15% from Ca^{+2}, and repeated attempts to grow a single crystal with Sc^{+3} invariably failed. The only crystal in this series differing in color from those of the $SrMoO_4$ group was that containing Ce, which had a much more intense color. Although it is not reflected in the value of the segregation coefficient, it is suspected that in the $CaMoO_4$ host an even higher concentration of Ce^{+4} is present than in $SrMoO_4$. Due to the fact that the Ce^{+4}/Ca^{+2} difference (0.05Å) is smaller than the Ce^{+3}/Ca^{+2} (0.08Å) difference, it could be understood how some Ce^{+4} is stabilized in the Ca^{+2} site. The best qualitative colorimetric technique (4) failed, however, to show the presence of Ce^{+4}. In an ESR experiment, the crystal did exhibit strong paramagnetic absorption, indicating the presence of a predominant amount of Ce^{+3}. In the europium case, the crystal again grew deep red, but was readily oxidized to the colorless trivalent state of Eu^{+3}. This in sharp contrast to the $SrMoO_4$ case where such an oxidation was impossible. The $EuNbO_4$ segregation coefficient deviates significantly in the direction of larger ions (because of Eu^{+2} content) as can be seen in Fig. 1. All other rare earth niobates fall on the curve in Fig. 1 within the analytical error of the determination of k. This error was taken as the maximum deviation experienced in many repeated analyses on the same as well as on different crystals grown under the same conditions. It corresponds to ±0.02 points of k or roughly ±2%. Basically, the top part of the curve corresponds to the plot presented earlier (1) for the $SrMoO_4$ case. However,

Table I. Segregation coefficients for the $LnNbO_4$-type rare earth niobates in $CaMoO_4$

Ln^{+3}	Ionic radius in Å	% Deviation from Ca^{+2} (0.99Å)	Color of crystal	k
Sc	0.81	−18.2	—	—
Y	0.92	−7.1	Colorless	1.35
La	1.14	+15.2	Colorless	1.01
Ce	1.07	+8.1	Orange-Red	1.19
Pr	1.06	+7.1	Green	1.24
Nd	1.04	+5.1	Blue	1.30
Sm	1.00	−1.0	Light Tan	1.38
Eu	0.98	−1.0	Colorless	1.34
Gd	0.97	−2.0	Colorless	1.40
Tb	0.93	−6.1	Colorless	1.36
Dy	0.92	−7.1	Light Yellow	1.35
Ho	0.91	−8.1	Tan	1.34
Er	0.89	−10.0	Pink	1.28
Tm	0.87	−12.1	Colorless	1.22
Yb	0.86	−13.1	Colorless	1.18
Lu	0.85	−14.1	Colorless	1.13

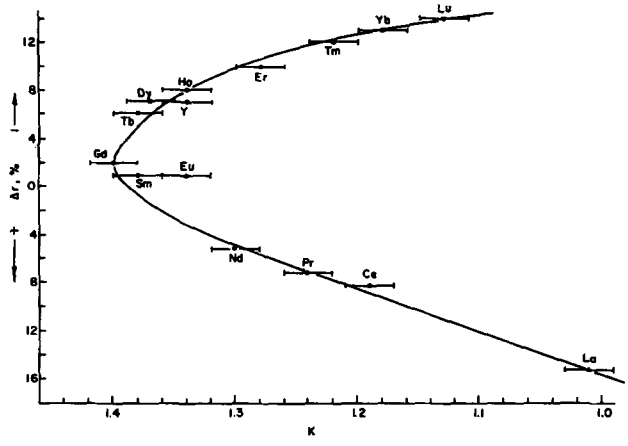

Fig. 1. Segregation coefficients, k for $LnNbO_4$ in $CaMoO_4$ as a function of differential cation radii.

since in the $CaMoO_4$ case we have an almost equal number of rare earths deviating on the positive side of Ca^{+2}, the lower part of the curve is new. Fundamentally, this plot reflects the fact that the rare earths with the best fit (near 0 deviation in the curve) exhibit the largest segregation coefficient,[1] $k = c_s/c_l$, since the solubility in the solid, c_s, is greatest. Deviation to either side decreases the solubility in the solid and results in a smaller k. Although this relationship was by no means evident from the few segregation coefficients reported in (3), the agreement with those earlier data is fairly good. If one examines Nassau's (l.c.) data in view of this relationship, one can also detect the same curve, although on first glance the data seem to reflect only scatter around a basic number. The three key points, Lu, Sm, and La, are in good agreement and show the same spread of k on a different scale (0.23, 0.50, 0.22 as compared to 1.13, 1.38, 1.01).

The greatest difference compared with the $SrMoO_4$ series is the fact that all segregation coefficients in $CaMoO_4$ are greater than 1. This prompted us to study some mixed Ca-Sr molybdates as hosts for Nd^{+3} only. Four crystals were grown with the host composition $Ca_{0.99-x}Sr_xMo_{0.99}Nd_{0.01}Nb_{0.01}O_4$, where x varied from 0.195, 0.09, 0.04 to 0.01. In the first case, the crystal melted 50°C under the normal melting point of 1490°C, indicating the formation of a eutectic. It also cracked repeatedly. The segregation coefficient for $NdNbO_4$ was 0.68. The second crystal also cracked and gave a segregation coefficient of 1.31. The third and fourth grew without cracking and gave segregation coefficients of 1.35 and 1.27, respectively. Since the segregation of Sr^{+2} in these mixed hosts is opposite to that

[1] The segregation (or distribution) coefficient k is defined as the ratio of the concentrations of the active (or impurity) element in the solid (c_s) over the concentration in the liquid (c_l).

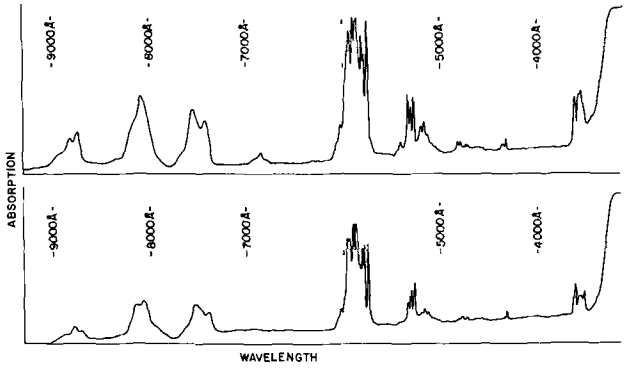

Fig. 2. Absorption spectra of $Sr_{0.01}Ca_{0.98}Nd_{0.01}Mo_{0.99}Nb_{0.01}O_4$ (top) and $Ca_{0.99}Nd_{0.01}Mo_{0.99}Nb_{0.01}O_4$ (bottom).

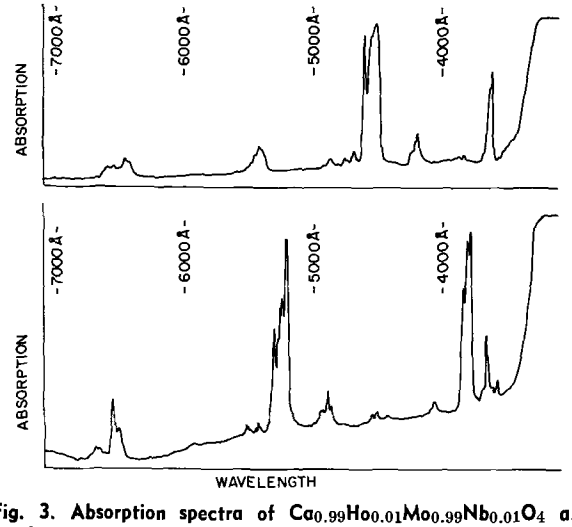

Fig. 3. Absorption spectra of $Ca_{0.99}Ho_{0.01}Mo_{0.99}Nb_{0.01}O_4$ and $Ca_{0.99}Er_{0.01}Mo_{0.99}Nb_{0.01}O_4$.

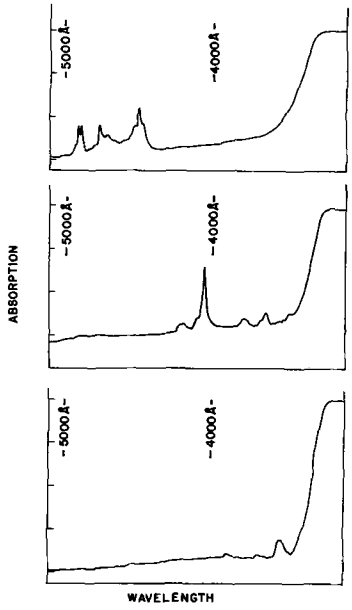

Fig. 4. Absorption spectra of $Ca_{0.99}Pr_{0.01}Mo_{0.99}Nb_{0.01}O_4$, $Ca_{0.99}Sm_{0.01}Mo_{0.99}Nb_{0.01}O_4$, and $Ca_{0.99}Dy_{0.01}Mo_{0.99}Nb_{0.01}O_4$.

of both Nd^{+3} and Nb^{+5}, the only advantage we can see is in a more perfect valence compensation throughout the length of the crystal as indicated by a Nd_2O_3:Nb_2O_5 ratio of 1:0.98 on top and 1:1.04 on the bottom of a 3-in. crystal. It is also interesting to note that despite the small concentration of Sr^{+2} in $Ca_{0.98}Sr_{0.01}Nd_{0.01}Mo_{0.99}$-$Nb_{0.01}O_4$ the crystal had the more reddish-blue color typical of the pure $SrMoO_4$ host. This difference can easily be seen in a comparison of the absorption spectra in Fig. 2. All spectra were determined at room temperature on single crystal slices, 0.25-0.50 mm thick. A CARY Model 14 spectrograph was used with a standard scanning speed of 25 Å/sec. Figures 3 and 4 represent the absorption spectra of the other colored rare earths. The rest of the crystals were colorless with a u.v. cut-off at 0.33μ, except the cerium sample which cut-off at 0.43μ. All spectra were run up to 2.1μ in the infrared and the noteworthy absorption characteristics are summarized in Table II.

In a structural characterization, we determined the lattice parameters of the top portions of an undoped $CaMoO_4$, a $LaNbO_4$, and a $LuNbO_4$ doped crystal. These data are summarized in Table III. The small parameter and cell volume differences reflect the size changes due to the two rare earths differing most from Ca^{+2} toward each extreme.

In summary, we can state that the Ca^{+2} site in $CaMoO_4$ afforded a unique opportunity to study the substitution characteristics of all rare earths whose ion radii deviate just about up to ±15% to either side of the calcium ion radius. The segregation coefficient for

Table II. IR-spectral characteristics of the $LnNbO_4/CaMoO_4$ crystals

Ln	Transparency range or absorption peaks
La	0.7-2.1μ
Ce	0.7-2.1μ
Pr	1.528, 1.533, 1.565, 1.581, 1.932, 1.964, 1.987μ
Nd	0.740, 0.752, 0.807, 0.814, 0.870, 0.878μ
Sm	1.091, 1.246, 1.261, 1.395, 1.406, 1.442, 1.498, 1.513, 1.567, 1.584, 1.630μ
Eu	0.7-2.1μ
Gd	0.7-2.1μ
Tb	0.7-2.1μ
Dy	1.265, 1.277, 1.298, 1.300μ
Ho	0.7-2.1μ
Er	1.497, 1.503, 1.511, 1.524μ
Tm	0.795, 1.183, 1.211, 1.265, 1.691, 1.734, 1.742, 1.752, 1.793μ
Yb	0.930, 0.954, 0.968, 0.976μ
Lu	0.7-2.1μ

Table III. Lattice parameters of doped and undoped $CaMoO_4$ single crystals

Composition	a_t, Å	c_t, Å	Cell volume, Å^3
$La_{0.01}Ca_{0.99}Mo_{0.99}Nb_{0.01}O_4$	5.229 ± 0.001	11.426 ± 0.003	312.4
$CaMoO_4$	5.226 ± 0.001	11.430 ± 0.003	312.1
$Lu_{0.01}Ca_{0.99}Mo_{0.99}Nb_{0.01}O_4$	5.224 ± 0.001	11.429 ± 0.003	311.9

the $LnNbO_4$ compounds in $CaMoO_4$ does not show a direct dependence as a function of the Ln^{+3} ion size, but rather goes to a maximum at the point of least deviation from the host ion's size and decreases again as the deviation proceeds in the opposite direction. Knowledge of this behavior and the establishment of the dependence in a graphical plot will permit predicting segregation coefficients of any one Ln^{+3} ion in the Ca^{+2} site of the $CaMoO_4$ host. In other hosts, the determination of k for 2 or 3 key compositions should therefore also permit the prediction of the segregation coefficient of all the other rare earths.

Manuscript received June 1, 1966; revised manuscript received Sept. 27, 1966.

Any discussion of this paper will appear in a Discussion Section to be published in the December 1967 JOURNAL.

REFERENCES

1. L. H. Brixner, *This Journal*, **113**, 621 (1966).
2. K. Nassau, *J. Appl. Phys.*, **33**, 3064 (1962).
3. L. H. Brixner, *This Journal*, **11**, 690 (1964).
4. E. B. Sandell, "Colorimetric Determination of Traces of Metals," p. 252, Interscience Publishers, New York (1950).

Carrier-Concentration Profiles of N-Type Sn and Te Doped Epitaxial GaAs Films

R. R. Moest and D. T. Lassota

Bell Telephone Laboratories, Incorporated, Murray Hill, New Jersey

Carrier concentration profiles of n-type doped epitaxial GaAs films grown by the HCl/H_2 transfer technique have been studied. The growth system is the same as reported earlier for the growth of undoped films (1). Because of the anomalous results obtained on {111} oriented substrates with undoped epitaxial films, the substrates used in this study were almost exclusively (100) oriented. The GaAs substrates had net carrier concentrations of 2 x 10^{18} and 6 x 10^{18} as determined by Hall measurements and were Te- or Se-doped, respectively. Only readily available Te- or Sn-doped GaAs source material was used with the net carrier concentration ranging from 2 x 10^{16} to 5 x 10^{18}. The carrier concentration profiles in the films were determined by the differential capacitance-voltage method on gold surface barrier diodes (1, 2).

Results

The surfaces of the epitaxial films were microscopically smooth and free of growth patterns and were obviously not affected by the high impurity concentration of the films. The net carrier concentrations of the doped films depend on the concentration as well as on the kind of dopants in the source material: tin or tellurium.

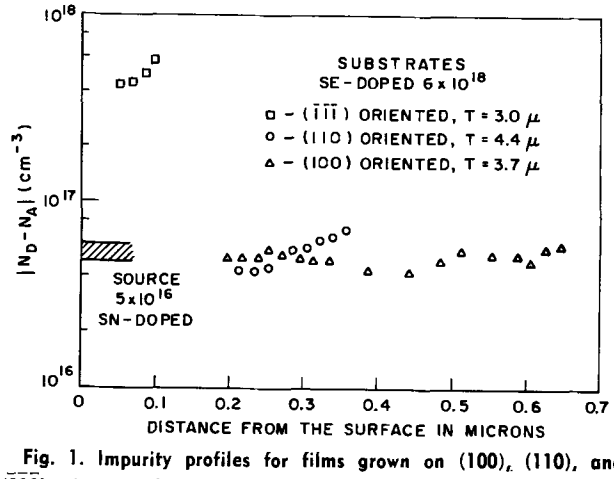

Fig. 1. Impurity profiles for films grown on (100), (110), and (1̄1̄1) oriented substrates from 5x10^{16} Sn-doped source.

Sn-*doped* GaAs *source*.—The Sn-doped GaAs source materials used in these experiments had net carrier concentrations of 5 x 10^{16}, 2 x 10^{17}, 3 x 10^{18}, and 5 x 10^{18}. Initially some epitaxial films were grown on n^+-type substrates of (1̄1̄1) and (110) orientations from 5 x 10^{16} Sn-doped source material. Results are shown in Fig. 1. The impurity profile for the (100) film at approximately 5 x 10^{16} is essentially flat over the thickness measured. The impurity concentration of the (1̄1̄1) films is well above the level of the dopant concentrations of the source material and is identical with the anomalous profiles obtained from undoped source material, observed in a previous study (1). Figures 2B, 3A and 2A show impurity profiles of (100) films grown from different source materials: tin doped 2 x 10^{17}, 3 x 10^{18}, and 5 x 10^{18}, respectively. The data scattering on films with impurity concentrations above 2 x 10^{18}, as indicated in Fig. 2A and 3A, are due to the rather poor quality of the surface barrier diodes on such highly doped material. Figures 3A and 3B show

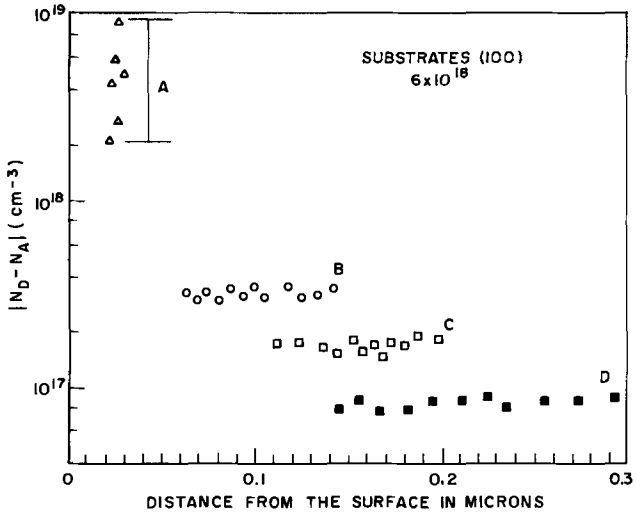

Fig. 2. Impurity profiles for films grown on (100) Se- or Te-doped substrates from different sources: A, GaAs, Sn-doped 5x10^{18}; B, GaAs, Sn-doped 2x10^{17}; C and D, GaAs, Te-doped 2x10^{18}. C = upstream, D = downstream sample.

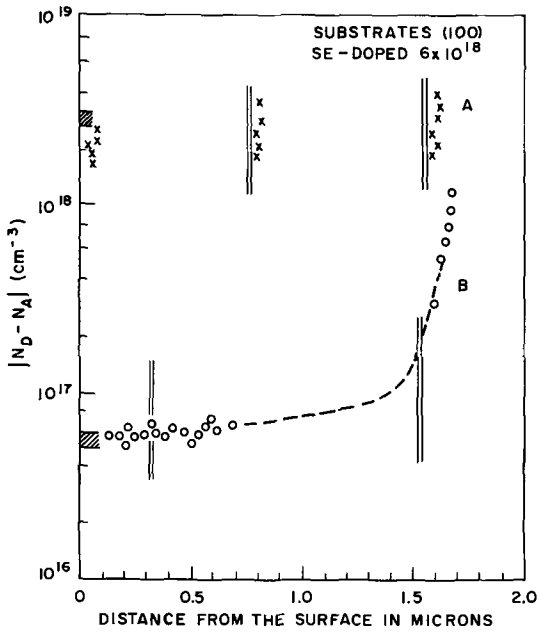

Fig. 3. Impurity profiles for films grown on (100) oriented substrates from A, GaAs, Sn-doped $3x10^{18}$; B, GaAs, Sn-doped $5x10^{16}$.

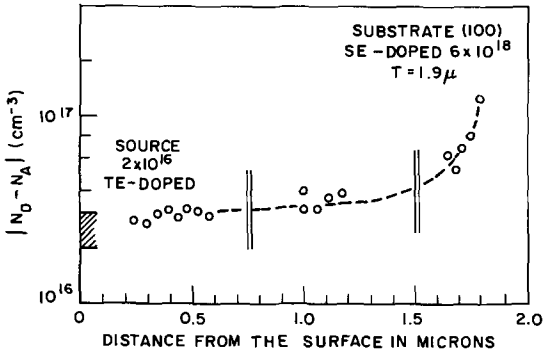

Fig. 4. Impurity profile for step etched (100) film grown from $2x10^{16}$ Te-doped source.

the impurity profiles of Sn-doped films after step etching. Several terraces had been etched in the epitaxial films prior to the evaporation of 10 mil gold dots. The results in Fig. 3A indicate that, within the accuracy of the measurements, the doping concentration remains fairly constant throughout the thickness of the epitaxial films. For all tin-doped source material studied with carrier concentrations from 5 x 10^{16} to 5 x 10^{18}, the experimental results indicate a net carrier transfer ratio of 1:1.

The reverse bias breakdown voltages for 10 mil diameter surface barrier diodes varied with the doping level of the film; 10v for 5 x 10^{16}, 3-4v for 2 x 10^{17}, and 0.7-1.5v for 5 x 10^{18} were measured on 2-3μ thick (100) films.

Te-*doped* GaAs *source*.—The Te-doped GaAs source materials had net carrier concentrations of 2 x 10^{16}, 5 x 10^{16}, 2 x 10^{17}, 4 x 10^{17}, and 2 x 10^{18}. Only (100) oriented substrates were used and the results of these experiments are shown in Fig. 2C, 2D, 4, 5, 6, and 7. Figures 4 and 5 depict the doping profiles of films grown from 2 x 10^{16} and 5 x 10^{16} Te-doped source materials, respectively. Within this doping range, an impurity transfer ratio of approximately 1:1 is observed. However, a downstream impurity depletion in the GaAs deposition zone becomes noticeable. This effect is also observed with Sn-doped source material although not to such an extent.

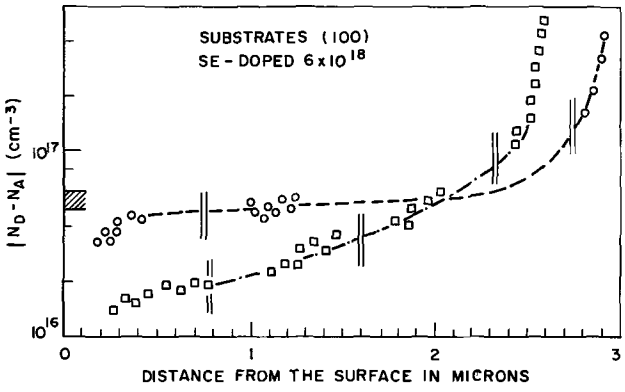

Fig. 5. Impurity profiles for step etched (100) films grown from $5x10^{16}$ Te-doped source.

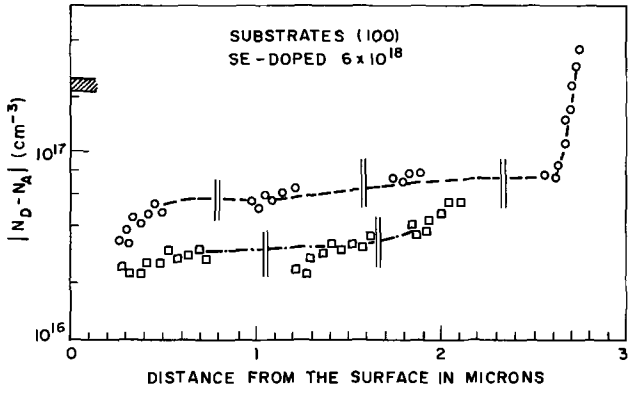

Fig. 6. Impurity profiles for step etched (100) films grown from $2x10^{17}$ Te-doped source.

Figures 5, 6, 2C and 2D show the respective impurity profiles for pairs of substrates positioned less than 1 cm apart from each other and at a uniform temperature of 750° ± 3°C. The impurity profiles of the upstream substrates appear generally flat whereas the downstream samples seem to have more graded doping profiles. The film-substrate interfaces are abrupt and approach an infinite slope, even on downstream samples. The downstream dopant depletion effect becomes noticeable even on single, large wafers exceeding the usual substrate size of approximately 1 cm^2. In these cases, it has been observed that the film doping level was higher on the upstream and lower on the downstream portion of one wafer. This effect is again much more pronounced with Te- than with Sn-doped source material.

The Te-doped films were step-etched as described earlier; in Fig. 4, 5, 6, and 7 these terraces are indicated by double bars intersecting the impurity profiles. If the Te-doping concentration of the source material exceeds approximately 1 x 10^{17}, the apparent impurity transfer ratio changes and less tellurium seems to be transferred to the substrates. This effect is demon-

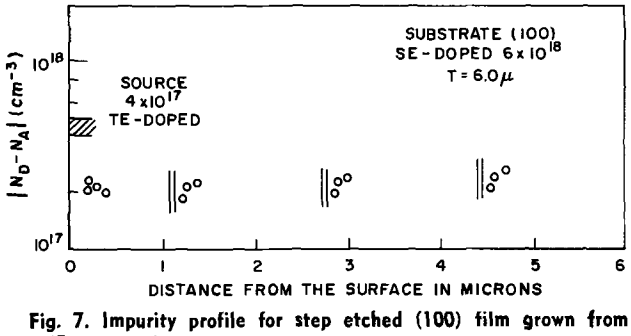

Fig. 7. Impurity profile for step etched (100) film grown from $4x10^{17}$ Te-doped source.

strated by the profiles in Fig. 6, 7, 2C and 2D. It appears that a maximum doping transfer of tellurium is approached at approximately 2 x 10^{17}, even if the Te concentration of the source material is as high as 2 x 10^{18}. This result is vastly different from the one observed with Sn-doped source material where the apparent transfer ratio of 1:1 is maintained up to a carrier concentration of approximately 5 x 10^{18}.

The maximum net carrier concentration for Sn-, or Te-doped, pulled, or boat grown GaAs is approximately 5 x 10^{18} (3). This imposes an upper limit for the impurity concentration of the epitaxial films grown from Sn-doped GaAs source material. Williams (3) reported, however, that net carrier concentrations of 1 to 2 x 10^{19} can be obtained in epitaxial films by using elemental Sn, Te, or Se as dopants in a stream of HCl at elevated temperatures. For films with carrier concentrations higher than those reported in this paper, the use of additional dopants is necessary.

Acknowledgment

The authors are indebted to Mr. B. Schwartz for his sustained interest in this work.

Manuscript received July 5, 1966; revised manuscript received Sept. 12, 1966.

Any discussion of this paper will appear in a Discussion Section to be published in the December 1967 JOURNAL.

REFERENCES

1. R. R. Moest, *This Journal*, **113**, 141 (1966).
2. C. O. Thomas *et al.*, *ibid.*, **109**, 1055 (1962).
3. F. V. Williams, *Solid State Electronics*, **7**, 833 (1964).

ELECTROCHEMICAL SCIENCE

A Coulogravimetric Study of the Sintered Silver Electrode in 1 Molar Potassium Hydroxide

A. Langer and J. T. Patton

Research Laboratories, Westinghouse Electric Corporation, Pittsburgh, Pennsylvania

ABSTRACT

Weighing of a sintered silver electrode while immersed in electrolyte during cathodic and anodic reaction reveals breaks in the weight change-coulomb curves. The different slopes can be explained by the volume change during phase transformation, affecting the buoyancy of the electrode. These breaks coincide with the potential changes of the plate, measured against a reference electrode.

The silver electrode in alkali electrolyte has gained considerable prominence in the construction of batteries offering high discharge rates and high energy densities per unit weight and volume. The outstanding properties of this electrode have long been recognized (1-4), but a complete understanding of its behavior is still lacking (5,6). Moreover, since efficient electrodes are usually of the porous type, an exhaustive interpretation of their behavior requires an understanding of the many factors affecting this type of electrode. Among these are the expansion and contraction of the active mass.

This volume change affecting the buoyancy is studied by weighing continuously the porous silver electrode in 1.0M potassium hydroxide as electrolyte during the complete cathodic and anodic cycle. Simultaneously, the corresponding number of coulombs involved is determined, and the potential of the electrode is recorded against a suitable reference electrode and correlated with the change in weight. A similar procedure was used by Schoop (7) at the turn of the century, but it has not been practiced frequently since (8, 9).

Theory

If a silver plate suspended in the electrolyte is oxidized anodically to silver oxide, the change in the weight of the immersed electrode is the algebraic sum of several related effects, principally (*i*) a weight increase due to the added mass of reacted oxygen, and (*ii*) an altered buoyancy lift due to the volume change of the electrode by the newly formed compound. There is still another factor affecting the buoyancy of the sample considered to be minor. The density of the electrolyte around the electrode is changing, due to the consumption of ions at the interface and the heat that is generated by the passage of the current.

In the following discussion we assume that minor effects can be neglected, provided low current densities are used, so that concentration differences in the electrolyte are small since equalized by diffusion. Additionally, for these conditions, the density gradients are not large enough to produce convection of the electrolyte which may still further influence the weight of the sample. The reaction must be carried out at potentials where no gas evolution will occur since small bubbles formed in or adhering to the electrode will alter its true weight. We also assume that the reaction products are only sparingly soluble in the electrolyte.

Under these conditions we can derive an equation for the weight change of the electrode in the electrolyte. Let a mass of silver m_{Ag} and density d_{Ag} be immersed in a liquid electrolyte of density d_s. The weight of the silver in the solution $m_{Ag}{}^s$ will be

$$m_{Ag}{}^s = m_{Ag}\left(1 - \frac{d_s}{d_{Ag}}\right) \quad [1]$$

If the silver is converted to an oxide, for example AgO, the weight of the oxide in the electrolyte will be

$$m_{AgO}{}^s = m_{AgO}\left(1 - \frac{d_s}{d_{AgO}}\right) \quad [2]$$

If the metal were oxidized and weighed in air, the weight increase would be

$$m_{AgO} - m_{Ag} = m_O \quad [3]$$

or simply the mass of oxygen reacted with the specimen. In the electrolyte we will register a change m^s due to both mass increase and volume change, given by the equation

$$m^s = m_{AgO}\left(1 - \frac{d_s}{d_{AgO}}\right) - m_{Ag}\left(1 - \frac{d_s}{d_{Ag}}\right) \quad [4]$$

In an electrochemical process without any side reaction, the mass of the reaction products produced by a current I in a time t is given by Faraday's law

$$m = \frac{It\,M}{nF} = Eq \cdot Q \quad [5]$$

Here $Q = It$ is the number of coulombs passed, $Eq = (M/nF)$ is the electrochemical equivalent of the species of molecular weight M, F is the Faraday, and n is the number of electrons per molecule taking part in the reaction. A line should result if the weight change m^s of the electrode in the electrolyte is plotted against the number of coulombs used. The slope of this line can be expressed by substituting [5] into [4]

$$\frac{m^s}{Q} = Eq_{AgO}\left(1 - \frac{d_s}{d_{AgO}}\right) - Eq_{Ag}\left(1 - \frac{d_s}{d_{Ag}}\right) \quad [6]$$

If a constant reaction rate is maintained by charging (or discharging) the electrode with a constant current, then Q is calculated by measuring the elapsed time.

In cases where the density of the electrolyte is not altered, a change in the slope of m^s *vs.* Q represents a variation in the density of the active mass formed. Information can be obtained concerning the density of the products by utilizing Eq. [6] and the experimentally determined value of the slope.

Electrode Reactions

Ever since the earliest investigations on the silver electrode, it has been apparent that charging and discharging processes in an alkaline solution proceed in steps that have been associated with the formation of the oxides Ag_2O and AgO.

The formation of these oxides seems to be well established and verified by x-ray diffraction (10-13)

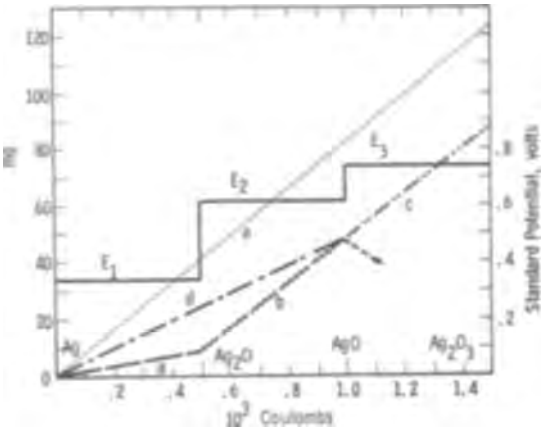

Fig. 1. Ideal weight change-coulomb relations, silver electrode of 10^3 coulomb total capacity.

Reaction	Weighing in electrolyte $d_s = 1.050$ line	slope mg/kQ	Weighing in air line	slope mg/kQ
$2Ag + ½ O_2 \rightarrow Ag_2O$	a	18.4	e	82.9
$Ag_2O + ½ O_2 \rightarrow 2AgO$	b	78.2	e	82.9
$Ag + ½ O_2 \rightarrow AgO$	d	48.0	e	82.9
$2AgO + ½ O_2 \rightarrow Ag_2O_3$	c	—	e	82.9

although the true nature of the AgO is still disputed (14). It has been shown that AgO can take up additional oxygen electrochemically (15). However, in the charging process, oxygen gas is liberated on the electrode after the AgO level has been reached. Other reactions of the silver electrode have been advanced (16, 17), especially the direct conversion of silver to AgO, but their importance is not well established. The main reactions are accompanied by definite potential plateaus.

Using the density of the involved species, $d_{Ag} = 10.5$, $d_{Ag_2O} = 7.14$, and $d_{AgO} = 7.44$ g/cm^3 (18), in Eq. [6], and assuming that silver will convert first completely to the Ag_2O oxide of bulk density and then completely again to AgO, we can calculate the weight change curves. Figure 1 represents the idealized theoretical behavior of a silver plate of 10^3 coulombs (1 kQ) total capacity up to the AgO level. The plate is immersed in approximately 1.0M KOH electrolyte of density $d_s = 1.050$ at room temperature.

Line a represents the weight increase of the electrode for formation of Ag_2O. Because of the large difference in density between silver and this oxide, there is a considerable buoyancy correction, causing the slope m^s/Q to be 18.4 mg/kQ, rather than the 82.9 mg/kQ slope that would be obtained if the weighing were performed in air. The weight change curve in air is represented by line e. As the oxidation proceeds from Ag_2O to AgO, the change in density should be relatively small, resulting in only a minor buoyancy influence. The calculated slope of 78.2 mg/kQ, as represented by line b, is therefore almost parallel to the line representing the weighing in air. The possible weight change curve for formation of Ag_2O_3 cannot be predicted with any certainty since the density of the compound is unknown. In case silver is directly converted to the AgO, the weight increase should follow line d with a slope of 48 mg/kQ.

The potential-coulomb curve should follow lines E_1-E_3, representing the standard potentials of the reactions. In actual charging E_c and discharging E_d, the effect of overvoltage for the particular current density must be considered.

How an actual sintered electrode follows this predicted scheme was tested on the following experimental arrangement.

Experimental

The apparatus used is shown schematically in Fig. 2. It consists of an analytical balance, with small mercury-filled cups attached to the balance support and to one of the pans. Platinum wires, fastened to the middle and end of the balance beam, were bent to dip very slightly into the mercury. In this way, electrical connection could be maintained through the balance arm without impairing its free movement. The automatic weighing was done with a permanent magnet and solenoid restoring element, balanced by a dual photocell (19). The weight change was recorded on a pen recorder. The speed of the recording paper (1 in. in 10 min) gave the time base for the reactions studied. The sensitivity was adjusted so that 1 mg gave ½ in. on the chart. Weight fluctuations due to amplifier noise were about 0.2 mg.

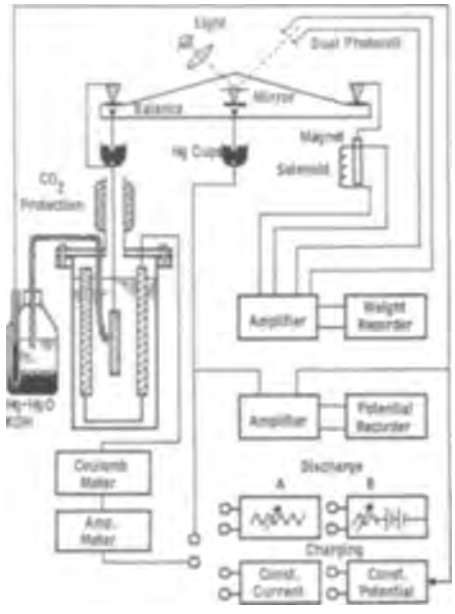

Fig. 2. Continuous coulogravimetric arrangement

The electrodes were enclosed in a plastic box with a small opening for the wire suspending the working electrode. The wire was also passed through an attached perforated tube surrounded by solid KOH. It was hoped to minimize in this way the influence of atmospheric CO_2 on the electrolyte, as carbon dioxide seems to affect adversely the extended operation of silver electrodes. As the negative electrodes, two commercial sintered cadmium plates were used; each was about 5 times the physical size of the silver electrode. The cadmium electrodes were wrapped in two layers of wettable cellophane of the type used to wrap silver electrodes. This was done to retard the possible deposition of silver on these plates. An external 1.0M KOH mercury-mercury oxide electrode was used as reference. The capillary was made of polyethylene tubing filled with a purified asbestos string. The potential was recorded by a high impedance chart recorder driven synchronously with the weight recorder.

The current passed through the cell was registered on a calibrated multirange ampere meter. An ampere-hour meter (Danubia-Wien, Austria), accurate to 0.001 amp-hr, was used as a check, to record the total number of coulombs. Reversing switches were used to operate these instruments during charge and discharge cycles.

The electronically regulated, constant-current power supply allowed charging currents up to 400 ma. The constant current discharges were made by manually regulating the current with a decade resistance box. To obtain very deep discharge, or to help stabilize the discharge current, a 12v storage battery was sometimes used in series with the test cell.

The working electrode consisted of a piece of sintered silver plate, cut to about 3.1 x 3.1 cm and 0.05 cm thick, and attached to the balance by a silver wire. As an electrolyte, a 1M solution was prepared from

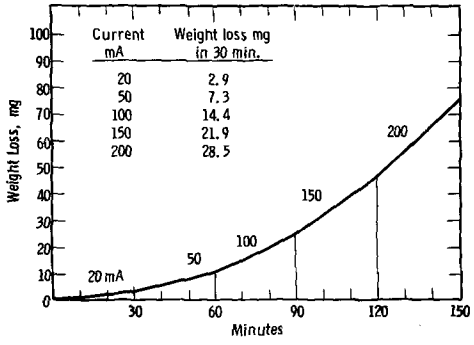

Fig. 3. Weight loss-time relation, porous silver electrode of 16 cm^2 area; electrolyte 1.0M KOH d_s = 1.05 g/cm^3. Discharge at the Ag_2O level at different current densities.

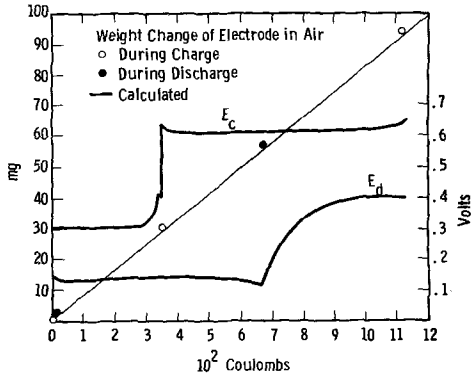

Fig. 4. Efficiency test of silver electrode reactions. Weight change-coulomb relations.

chemically pure KOH and boiled water that had been cooled under N_2. Although the solution was handled as little as possible in air, it could have absorbed unknown amounts of CO_2. All experiments were performed at about 25°C with some shielding against light.

Results

Before proceeding with the experiments, the validity of Eq. [1] was tested by electroplating copper from a copper sulfate solution onto a copper strip. The corrected weight in the electrolyte, the weight in air after washing and drying, and the weight calculated from the number of coulombs all agreed within 2%.

The assumption that the electrolyte in the pores and around the electrode interchanges rapidly with the bulk of the solution was tested in the following way. An approximately 4 x 4 cm, 0.05 cm thick, sintered and previously cycled silver plate was first fully charged and then drained at the Ag_2O voltage plateau, using discharge rates ranging from 20 to 200 ma for the whole plate. Figure 3 shows straight sections of different slopes in the weight loss-time coordinate system. For the same number of coulombs passed, the weight loss was equal for all of the current densities used. This result indicates that no appreciable concentration polarization could occur at these current densities, and that there was no deficiency in transport of the proper ions to sustain the reaction. This conclusion was also substantiated by the observation that the different rates were established without any noticeable time delay on the graphs.

To verify that the Faradic efficiency of the reactions was close to 100% under the prevailing conditions, direct weighings of the electrode were performed in air at different stages in the charge and discharge cycle (11). The electrode was removed from the electrolyte and soaked in fresh water four times for a period of at least 1 hr each. After rinsing with alcohol, the electrode was dried to a constant weight in a desiccator. The weighings were made in the region where the potential plateaus changed. The results are shown in Fig. 4. These points coincide quite well with the calculated values for m_O. We conclude, in addition, that the compounds formed in the reaction are stable enough to withstand this analytical procedure.

The actual weighings of the electrode during the charge-and-discharge cycle has indicated that the silver electrode behaves similarly to predictions from the theoretical equation. Typical experimental results are plotted on Fig. 5.

When an unused, sintered silver electrode is charged at constant current, the measured potential settles down to an almost constant value E_1 after an initial potential rise in the first few seconds. This steady potential is designated as the Ag-Ag_2O level. With the 10 cm^2, 0.05 cm thick electrode charged at a 100 ma total current rate, the measured weight-change/coulomb slope was 36 mg/kQ as shown in dashed line

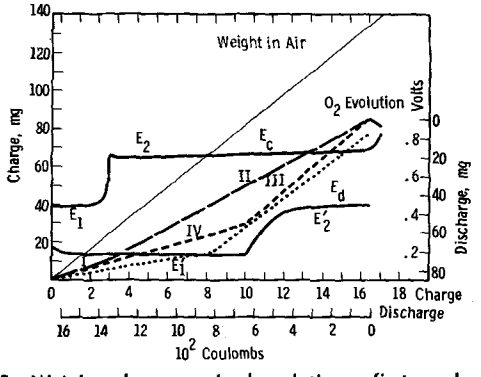

Fig. 5. Weight change-coulomb relations, first cycle; porous silver electrode 3.1 x 3.1 cm, 0.5 mm thick, in KOH electrolyte of d_s = 1.050 g/cm^3 at 25°C; charge and discharge current 100 ma; slope of segments in mg/kQ. Charging I = 36, II = 56, discharge III = 83, IV = 29.

segment I. This slope is almost twice as large as the predicted 18.4 mg/kQ (dotted line), but it is much lower than would be expected if no volume change had taken place. One can conclude that the density of the compound formed in the experiment must be around 8 g/cm^3.

At a later stage, the potential-coulomb curve starts to rise, slowly at first and then suddenly, until a new higher level E_2 is reached. This level is assigned to the formation of AgO. Figure 5 shows that more silver is oxidized on this level than on the previous one. It is interesting to observe that the point of sudden increase in potential coincided with a change in the slope of the weight-change/coulomb curve, the new slope being close to 56 mg/kQ as shown by dashed line segment II. This value is not as high as the predicted 78.2 mg/kQ for the conversion of Ag_2O to AgO and indicates that the active mass is expanding more than expected, so that a larger buoyancy correction is still in play. Actually, the slope of 56 mg/kQ is closer to the value of 48 mg/kQ that would indicate the direct conversion of silver to AgO.

Whether these data represent a gradual expansion of the existing lattice, or the formation of new distinct crystals as revealed by some x-ray diffraction studies (19) cannot be decided.

After a lengthy plateau region, during which the potential rises only slightly, there is a sudden increase with a corresponding change in the weight-change curve. The curve becomes erratic, levels for a short period, and then decreases quite rapidly. An inspection of the electrode at this point reveals that the gassing stage has been reached and the decrease in weight is caused by gas bubbles clinging to the surface of the electrode.

Several minutes are allowed for the gas to be dispelled before starting the discharge process. At the same current density of 100 ma/plate, one finds that

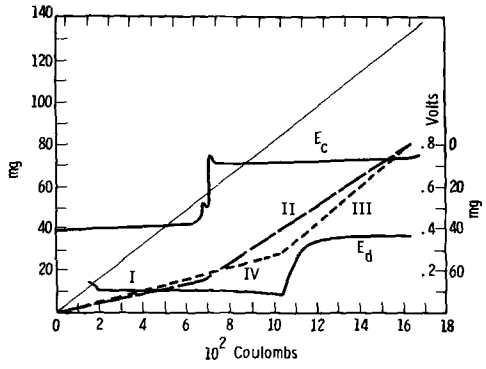

Fig. 6. Weight change-coulomb relations, second cycle; slope of segments in mg/kQ. Charging I = 23, II = 68, discharge III = 83, IV = 29.

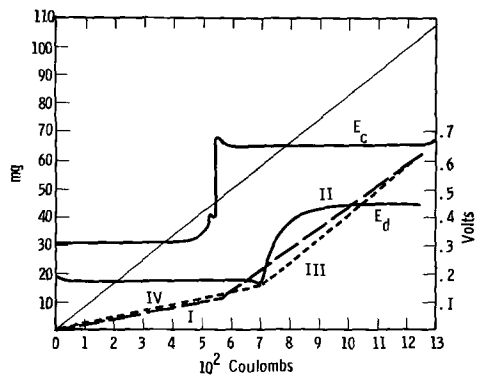

Fig. 7. Weight change-coulomb relations, fourth cycle; slope of segments in mg/kQ. Charging I = 20, II = 74, discharge III = 82, IV = 22.

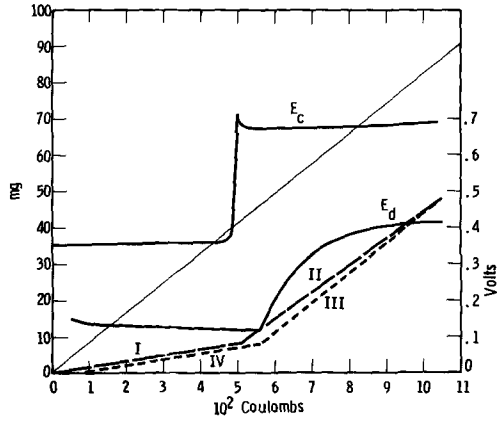

Fig. 8. Weight change-coulomb relations, sixth cycle; slope of segments in mg/kQ. Charging I = 16, II = 72, discharge III = 80, IV = 17.

the discharge proceeds at a potential E_2'. This potential decreases slowly at first, then gradually faster, but never is the change as rapid as during the charging process. The weight decreases rather fast at a rate of 83 mg/kQ, as shown by shortly dashed line III. (The discharge curves on all the graphs are plotted backwards from the charge curves. The new origin for the weight-change and number of coulombs is the maximum value reached during charging as indicated by the double scale in Fig. 5 but omitted in succeeding graphs.) This rapid change in weight is nearly what the plate would suffer if the weighings were made in air. This may mean that the volume of the electrode remains unchanged during the higher potential plateau of the discharge cycle. The slight contraction that should occur in this region should give a slope of 78.2 mg/kQ.

After the potential reaches the second discharge plateau, E_1', the potential remains almost constant until the silver oxide is close to exhaustion. In a self-sustained discharge, the potential begins to rise with the rapidly falling current output. In most cases tested, the current sank so low, even with the resistance box shorted, that a complete exhaustive discharge was not achieved. Shorting of the cell for many hours was not attempted. In this region, the weight curve followed the line IV with a slope of 29 mg/kQ, as compared to a slope of 36 mg/kQ in the charging portion, but not as low as the expected slope of 18.4 mg/kQ.

The data clearly show the large "hysteresis loop" created by the weight-change, coulomb charge and discharge curves. The rather short charging branch on the Ag_2O level represents only 18% of the total charge taken up, while the corresponding branch on discharge amounts to about 60% of the total charge released.

As early as the second cycle, Fig. 6, the Ag_2O charging branch becomes considerably extended. The slope was now 23 mg/kQ. Assuming a start from the silver level, this slope would represent the formation of an oxide of 7.3 g/cm^3 density. This density is very close to 7.25, the x-ray density of Ag_2O.[1] The weight change for the AgO plateau was 78 mg/kQ on charging, and again 83 mg/kQ during discharge. Figure 6 also shows that a slope of 29 mg/kQ was obtained during discharge at the Ag_2O level. The difference between the charge and discharge behavior became less pronounced.

A potential overshoot is usually noticed on charging during the transition from the Ag_2O to the AgO level. This overshoot has been the subject of several investigations, and different causes have been assigned for its appearance (16, 21). It can be seen in Fig. 6 that an additional small peak preceded the main one. In other runs, such peaks sometimes followed the main one.

Figures 7 and 8 represent the response of the same electrode in the fourth and sixth cycle. The cathodic and anodic behavior become even more similar, with weight change per coulomb values approaching the predicted values, and both plateaus in the charging and discharging cycle of almost the same length. But another factor became more apparent, namely, the total capacity of the plate decreased progressively during cycling. The first cycle gave 1650 coulombs, and the sixth only about 1050 coulombs. Taking into account the weight of the active silver in the electrode, by subtracting the weight of the reinforcing grid, the electrode was about 50% efficient in the first cycle, considering the conversion to AgO. The departure from higher efficiencies obtained in actual batteries might be attributed to the difference in electrolyte concentration. The decrease in capacity represents a calculated loss of 335 mg of active silver.

These experiments were repeated with new electrodes and electrolyte several times. The behavior was not completely identical although the general features were the same. One factor became disturbing during cycling. The electrolyte acquired a dark brown color, and some sediment appeared at the bottom of the cell, indicating considerable solubility of the active compounds in the electrolyte. Taking the solubility of the silver oxides in 1M KOH as 2.10^{-4}M Ag (22, 23), the silver in the 200 ml of electrolyte amounts to only 4.3 mg. The residue formed in cycling which settled at the bottom of the cell was less than 50 mg. The combined weight loss and solubility alone cannot account for the large loss in capacity of the silver electrode.

Conclusions

The coulogravimetric experiments confirm the proposition that the silver electrode undergoes a large volume change, mainly during the transition from Ag to Ag_2O phase. This change occurs in both the

[1] Data of x-ray density were kindly indicated by one of the reviewers.

cathodic and anodic reaction. Changes in the weight-coulomb relation coincide with the changes in potential-coulomb curves. Differences in coulombic efficiencies of the two potential-coulomb plateaus were found mainly during the first few charging and discharging cycles. More silver was being oxidized on the second AgO plateau than the amount converted in the initial step. On the contrary more oxide was reduced on the Ag_2O level than at the higher oxide one. These differences became less pronounced during repeated cycling.

The loss of electrode capacity during cycling cannot be explained solely by the dissolution of the silver oxides in the electrolyte or shedding of the active mass. The loss in capacity might be due to sealing up of capillary passages in the sintered electrode, reducing the available active area in the next cycle or the influence of increasing carbonate concentration.

Manuscript received March 30, 1966; revised manuscript received Nov. 10, 1966.

Any discussion of this paper will appear in a Discussion Section to be published in the December 1967 JOURNAL.

REFERENCES

1. E. W. Junger, DPR, 110210, 1899.
2. W. Morrison, U. S. Pat. 978,980 (1910).
3. F. Jirsa, *Z. Elektrochem.* **33**, 129 (1927).
4. H. Andre, *Bull. soc. franc. electriciens*, **1**, 132 (1941).
5. T. P. Dirkse, *This Journal*, **106**, 453 (1959).
6. J. A. McMillan, *Chem. Rev.*, **62**, 65 (1962).
7. M. U. Schoop, *Electrochem. Industry*, **2**, 279 (1904).
8. G. W. Vinal and L. M. Ritchie, *Technol. Papers Bur. Stand.*, **17**, 117 (1922).
9. H. Winkler, *Elektrotechnik*, **6**, 355 (1952); **9**, 300 (1955).
10. R. Luther and F. Pokorny, *Z. anorg. u. allgem. chem.*, **57**, 290 (1908).
11. T. P. Dirkse, *This Journal*, **106**, 920 (1959).
12. I. A. Denison, *Trans. Electrochem. Soc.*, **90**, 387 (1946).
13. C. P. Wales and J. Burbank, *This Journal*, **106**, 885 (1959).
14. V. Scatturin and P. L. Bellon, *ibid.*, **108**, 819 (1961).
15. B. D. Cahan, J. B. Ockerman, R. F. Amlie, and P. Rüetschi, *ibid.*, **107**, 725 (1960).
16. T. P. Dirkse and G. J. Werkena, *ibid.*, **106**, 88 (1959).
17. T. P. Dirkse and D. B. DeVries, *J. Phys. Chem.*, **63**, 107 (1959).
18. N. A. Lange, "Handbook of Chemistry," p. 304, Handbook Publ. Inc., 1956.
19. F. A. Mauer, *Rev. Sci. Instr.*, **25**, 598 (1954).
20. P. Jones, H. R. Thirsk and W. F. K. Wynne-Jones, *Trans. Faraday Soc.*, **52**, 1003 (1956).
21. P. C. Wales and J. Burbank, *This Journal*, **112**, 13 (1965).
22. R. F. Amlie and P. Rüetschi, *ibid.*, **108**, 813 (1961).
23. T. P. Dirkse and B. Wiers, *ibid.*, **106**, 284 (1959).

A Kinetic Study of the Heterogeneous Reactions of Metallic Sodium with Chlorine and Bromine

M. J. Dignam and D. A. Huggins[1]

Department of Chemistry, University of Toronto, Toronto, Ontario, Canada

ABSTRACT

Data on the chlorination and bromination of sodium in the temperature range of 238°-323°K have beeen obtained for evaporated sodium films by following the change in optical density of the metal films. The chlorination data corresponding to the first few minutes of reaction have been found to be in accord with an equation of the form of that predicted by Mott and Cabrera for the growth of very thin oxide films on metals, while the bromination data for 273°K and below are in accord with a direct logarithmic law. Following longer reaction periods for chlorination, and above 273°K for bromination, the behavior is complex, being influenced in the case of bromination, for example, by illumination with light.

Stimulated by the practical problems of corrosion, fundamental research in the field of anodic and air oxidation of metals has gained increasing attention in recent years. Whereas early studies were concerned primarily with the formation of thick films (>1000Å) recent studies have examined more closely the kinetics and morphology of thin film formation. The material reported herein falls into this latter category.

Many metals, perhaps all which oxidize readily, show very similar behavior when exposed to oxygen at sufficiently low temperatures. The oxidation rate is initially very rapid, but drops off to a low or negligible value, a stable film of the order of 20-200Å being formed (1). Theories which have been applied to these low-temperature, thin film conditions have been based on a model involving a continuous adherent and homogeneous film. The rate-controlling process has been assumed variously to be electron transport (1-5); ion transport under the influence of the high electrostatic field produced by equilibration of electrons between the metal and surface levels at the film-oxidant interface (6, 7); chemisorption or incorporation of the oxidant at the film oxidant interface (8); combinations of some of the above allowing for space charge in the film; and finally film recrystallization and related phenomena (9, 10).

Differentiation between some of these theoretical approaches from experimental data is difficult, since many of them lead to the same or a similar form for the rate law. It is for this reason that we chose to investigate the halogenation of the alkali metals, which apart from providing a unique series of reactions, involves reactants and products which are sufficiently simple to make possible calculations of the rate constants from other data. In this manner, an unequivocal choice between alternate theories should be possible. At present one cannot say what information, if any, gained in the study of these systems may be readily related to more conventional metal oxidation reactions. It appears almost certain, however, that a thorough experimental and theoretical investigation of these systems will provide considerable insight into conventional oxidation studies. In addition, the investigation has intrinsic interest.

The present paper presents data on the reactions of metallic sodium with chlorine and bromine in the temperature range 230°-320°K. The chlorination reaction appears to be in accord with the Mott-Cabrera (7)

[1] Present address: J. Roy Gordon Research Laboratories, Sheridan Park, Clarkson, Ontario, Canada.

mechanism for film growth in the very thin film region. Good agreement between the data and the theoretical equation has been obtained over five decades of time and for up to a sevenfold increase in the film thickness.

The bromination data show some very interesting effects. The rate law is not that obeyed for the chlorination reaction, but instead takes the form

$$X = K \log t + K'^{2}$$

where for the lower temperatures, K is independent of temperature. Limitations of the data prevented the temperature coefficient of K' from being ascertained. It appears, however, to be fairly small or zero. At higher temperatures the value of K is smaller, the change in K' being once again uncertain. Irradiation with light of wavelength 5461Å has no effect on the rate at low temperatures, but at the higher temperatures it increases K to the value observed at low temperatures.

Experimental

As the apparatus employed for the present investigation is now being replaced, the description of it will be kept to a minimum. An outline of the experimental procedure follows, with further details given in subsequent sections.

Distilled sodium metal was evaporated in a stainless steel system at a rate of about 4 Å/sec, to form a film approximately 1000Å thick on a quartz slide cooled to near liquid nitrogen temperatures. The evaporation process was stopped by introducing purified argon to a pressure of about 1 atm.

The quartz slide was mounted on the end of a stainless steel tube which could be manipulated through a double "o" ring vacuum seal. Following film deposition the sample was transferred into the reaction chamber, which was then isolated from the evaporation unit.

The film was annealed at 60°C, the argon pumped out of the reaction chamber, and a predetermined pressure of halogen introduced through a pneumatically operated valve. The rate of the reaction was then followed by measuring the change in the intensity of the beam of monochromatic light (Hg 5461Å line) transmitted through the film. This change arises from the decrease in optical density of the film, since the metal with a high extinction coefficient reacts to give an essentially transparent halide layer. The output from the photocell unit, to be described later, was connected to an oscilloscope with camera and to a recording potentiometer.

The switch that controlled the pneumatic valve also triggered the oscilloscope, and thus the course of the reaction could be followed from times as short as a few milliseconds up to many hours or even days. It is primarily the speed of measurement which recommends this optical method for the study of thin film formation.

Evaporation unit and reaction vessel.—Figure 1 is a scale drawing, somewhat simplified, of the apparatus labelled to indicate the function of the various components. It was constructed entirely from stainless steel, the vacuum seals being formed with "o" rings of compound number 17507, Precision Rubber Products (a fluorocarbon polymer of high chemical inertness and stable to temperatures in excess of 150°C). As the diagram is largely self-explanatory, little will be added except to point out the various functions of the sample support tube which supports at one end the quartz slide on which the metallic sodium was deposited. Its principal function was to transport the slide from the sodium evaporation chamber to the reaction chamber while maintaining high vacuum or controlled atmosphere conditions. At the same time, however, a flange on this tube sealed the evaporation chamber from the reaction chamber when the slide

[2] By log y shall be meant $\log_{10} y$.

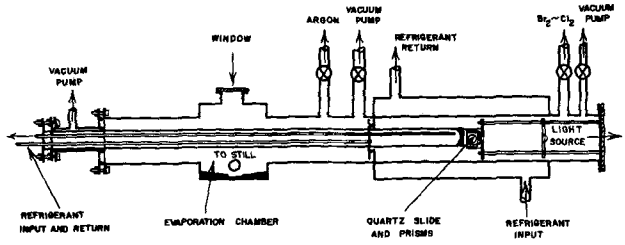

Fig. 1. Evaporation unit and reaction vessel

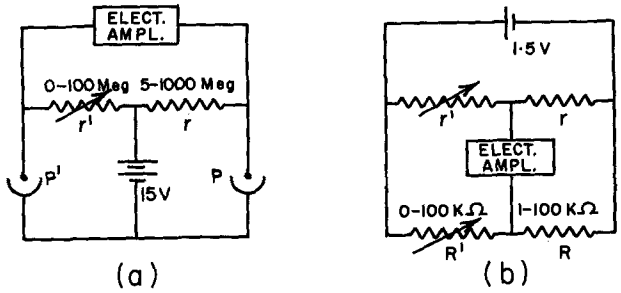

Fig. 2. Photometer circuit diagram and related circuit

was positioned in the latter, thus preventing contamination of the sodium in the evaporation chamber during the reaction. Within the main sample support tube were smaller tubes through which thermostated fluids or liquid nitrogen could be circulated to control the temperature of the quartz slide. The window in the evaporation chamber was used to observe the sodium film during deposition.

Following bakeout at about 150°C, the apparatus could be evacuated to a pressure of better than 3 x 10^{-7} Torr.

Photometric measurements.—A mercury arc lamp (General Electric AH100A) in conjunction with filters to isolate the 5461Å line (Kodak interference filter 540 and gelatin filter number 77), collimating lenses, first surface mirrors, and prisms made up the optical part of the photometric equipment. A beam splitter was used, and the intensity of the beam transmitted through the metal film was compared to that of the reference beam using circuits (Fig. 2) similar to those described by Dignam, Forbes, and Le Roy (11). Figure 2a consists of a Wheatstone bridge in which two adjacent resistance elements are replaced by 1 P37 vacuum photocells (P and P') whereas Fig. 2b is a simple Wheatstone bridge used to obtain the value of the resistance ratio r/r' in terms of the precision resistors R and R'. The electrometer amplifier was a Keithley Model 603 instrument (input impedance 10^{15} ohms), the output for which was connected to a recording potentiometer and to an oscilloscope with camera.

In addition to the circuits illustrated in Fig. 2, two other circuits could be selected which enabled the voltages across the resistors r' and r to be measured independently. Under experimental conditions the photocell dark currents were about 2 x 10^{-11} amp, with the lowest value for the light current being about 5 x 10^{-10} amp. In some runs, therefore, correction for the dark current was required.

Changes in the optical density of the metal film were measured as follows. The experimentally determined quantities are the voltages across the resistors r and r' and the ratio R/R' when circuit b is in balance. Associating P' with the reference beam, and P with the transmitted beam, the following symbols are defined in connection with the transmitted beam: V, voltage across r; i, total photocurrent; i_d, dark current; i_L, $i - i_d$; I, light intensity incident on photocell P. An identical set of primed symbols are defined in connection with the reference beam.

From Fig. 2a, $i = V/r$ and $i' = V'/r'$, and from Fig. 2b, at balance, $r/r' = R/R'$ so that

$$i/i' = (R'/R)(V/V')$$

or

$$\frac{i}{i'} = \frac{R'}{R}\left[1 + \frac{\Delta V}{V'}\right] \qquad [1]$$

where $\Delta V = V - V'$.

The dark current could always be neglected in connection with the reference beam, but not always in connection with the transmitted beam. Therefore $i = i_L + i_d$ and $i' = i'_L + i'_d \simeq i'_L$ so that [1] becomes

$$\frac{i_L}{i'_L} = \rho - \rho_d \qquad [2]$$

where

$$\rho = \frac{R'}{R}\left[1 + \frac{\Delta V}{V'}\right] \qquad [3]$$

and ρ_d is the value of ρ when $i = i_d$ (*i.e.*, the value of ρ measured with $I = 0$). Since $I \propto i_L$ and $I' \propto i'_L$[3] we may write

$$I/I' \propto (\rho - \rho_d)$$

The change in optical density from time zero to time t

$$\Delta\alpha = \log \frac{I(t=0)}{I(t)} \qquad [4]$$

is therefore given by

$$-\Delta\alpha = \log\left(\frac{\rho(t) - \rho_d}{\rho(t=0) - \rho_d}\right) \qquad [5]$$

During any given run, the value of r was held constant, as was the intensity of the lamp, so that I' remained constant. Thus $V' \propto I'r' = I'r(R'/R)$ so that we may set $V' = v(R'/R)$ where v is a constant for any given run.

The equation for ρ now becomes

$$\rho = \frac{R'}{R} + \frac{\Delta V}{v} \qquad [6]$$

Prior to beginning a run, r and r' were adjusted to make ΔV close to zero, and v was determined. ΔV was then recorded continuously during the run, with r' (and hence the ratio R'/R) adjusted from time to time to keep ΔV within the recorder scale. In Eq. [6], the second term, $\Delta V/v$, arises from the off-balance of the bridge circuit (Fig. 2a). By maintaining $\Delta V/v$ small compared with R'/R, fluctuations in the lamp intensity have only a small effect on the values of ρ determined. With this circuit it was possible to detect changes in the transmitted light intensity as small as 1 part in 3000, although such sensitivity was rarely required.

The thickness of the halide film may now be related to the change in optical density, $\Delta\alpha$, in the following way. If we let I_o be the light intensity incident on an element of area, dA, of the metal film system, then on neglecting multiple reflections within the films the element of transmited light, dI, is given by

$$dI = dA\, I_o\, 10^{-\epsilon X_m} \qquad [7]$$

where ϵ and X_m are the decadic extinction coefficient and thickness of the metal film. We shall assume that I_o and X_m are in general dependent on the position on the surface, but that ϵ and the halide film thickness, or thickness of metal consumed, ΔX_m, are independent of position. Substituting $X_m = X^o_m - \Delta X_m$ in the above equation, where X^o_m is the metal film thickness before reaction, and integrating over the entire illuminated surface, we obtain the following expression

$$I = \int_{\text{Area}} dA\, I_o\, 10^{-\epsilon(X^o_m - \Delta X_m)} \qquad [8]$$

[3] In the intensity range employed, 1P37 vacuum photocells have a linear response according to tube specifications.

Since ΔX_m is constant at any given time, and is zero at time zero, it follows immediately from [8] that

$$\frac{I(t)}{I(t=0)} = 10^{\epsilon\Delta X_m} \qquad [9]$$

and hence from [4], [5], and [9]

$$\Delta X_m = \frac{1}{\epsilon}\log\frac{\rho(t) - \rho_d}{\rho(t=0) - \rho_d} \qquad [10]$$

The thickness of the halide film, X, can be calculated from [10] and the relation

$$X = (\Omega/\Omega_m)\Delta X_m \qquad [11]$$

where Ω and Ω_m are the volumes per metal atom in the halide and metal, respectively.

The extinction coefficient, ϵ, was calculated from the optical constants[4] for evaporated sodium films measured by Ives and Briggs (12), the value for 5461Å radiation being given by $\epsilon = 2.32 \times 10^{-3}$ Å^{-1}.

The effect of neglecting multiple internal reflections within the metal and halide films will now be examined. Multiple reflections within the metal film can, of course, be entirely neglected because of the extremely high rate of attenuation of amplitude in this medium. Interference effects arising from multiple reflections within the halide film are, however, significant. Thus, a NaBr film (refractive index 1.62) 500Å thick, will cause a reduction in the transmitted intensity of about 6%, which in turn corresponds to an error in the halide film thickness determination of about 10Å. For thinner films, the error is less, going to zero at zero film thickness. The errors for NaCl films are somewhat less for the same thickness owing to the smaller value for the refractive index (1.50). In both cases, the errors introduced by neglecting multiple reflections, although not insignificant, are of the same order or smaller than random errors arising from other sources, principally light scattering, a phenomenon which is discussed later.

As the properties of thin metal film are known to depend appreciably on film thickness for sufficiently thin films, care was taken to make sure that the metal film thickness never fell below about 300Å during the run.

Materials.—Analar grade sodium was melted in a Pyrex vessel under vacuum, filtered, then outgassed, and finally transferred in an argon atmosphere to a stainless steel still connected to the sodium evaporation chamber. It was further outgassed here under high vacuum conditions and finally distilled at about 375°C into the evaporation chamber, the background pressure being never higher than 10^{-5} Torr. According to Horsley (13) this should produce sodium of 99.9995% purity, apart from gas content.

Argon was purified as required by bubbling it through a column of liquid sodium.

Commercial tank chlorine was condensed into a Pyrex trap and subjected to ten trap-to-trap distillations while pumping. On the final distillation, the background pressure did not rise above 2×10^{-6} Torr.

Bromine was treated in a similar manner.

Results

Chlorination.—Chlorination results obtained for metal films deposited under conditions where the background pressure during deposition was much in excess of 10^{-6} Torr were irreproducible. Only results obtained for films deposited at background pressures of 7×10^{-7} Torr or less are reported herein. The apparatus is being replaced by an ultrahigh vacuum system, capable of sustaining vacuums of the order of 10^{-10} Torr, in order to overcome the above difficulty.

For a number of runs, the expected behavior of the transmitted light intensity with time was not ob-

[4] The familiar chemical extinction coefficient is related to the fundamental optical extinction coefficient k' (which is the imaginary part of the complex refractive index) by the equation $\epsilon = 4\pi k'/\lambda_o$ 2.303, where λ_o is the wavelength of the light *in vacuo*.

served. Instead, the transmitted light first appeared to decrease in intensity, followed ultimately by the expected increase with time. The anomalous behavior arose almost certainly as a result of the scattering of the light beam at the sodium-halide-halogen interfaces, brought about presumably by the roughening of the surface during the initial period of reaction. This extremely undesirable effect was reduced very substantially by having the light beam incident on the bare surface of the quartz slide rather than on the halide surface. The effect appeared to be entirely absent for several runs, suggesting that the initial roughening of the surface probably took place as a result of surface contamination prior to introducing the halogen gas. However, no reaction could be detected prior to introducing the halogen, despite the fact that reaction of about 1/10 of the sodium atoms on the surface should produce a detectable change in optical transmission.

The above problem constitutes the major limitation of the data and the principal incentive to abandon the apparatus in favor of one which overcomes this difficulty. Nevertheless, the present data, despite this limitation, provide some interesting information concerning the kinetics of halogenation of sodium.

The chlorination data, plotted as chloride film thickness *vs.* the logarithm of the reaction period, are presented in Fig. 3 to 6, the circles representing the experimental values. The runs at 237° and 255°K (Fig. 3) were the only ones which showed no evidence of the light scattering effect mentioned above. The points for these two runs were calculated using Eq. [10] and [11], no correction for scattering being applied. Five further runs, (Fig. 4-6) although they showed a light scattering effect, were otherwise acceptable in that the background pressure during film deposition was less than 7×10^{-7} Torr. Of these five, all but one (curve a, Fig. 5) gave results reasonably consistent with the above two for reaction periods greater than 10 sec on applying an additive correction, X_0, to the film thickness calculated from [10] and [11]. If the fraction of light scattered remained constant after about 10 sec of reaction, such an additive correction should indeed apply. The method of choosing the values for the correction thickness, X_0, will be dealt with shortly.

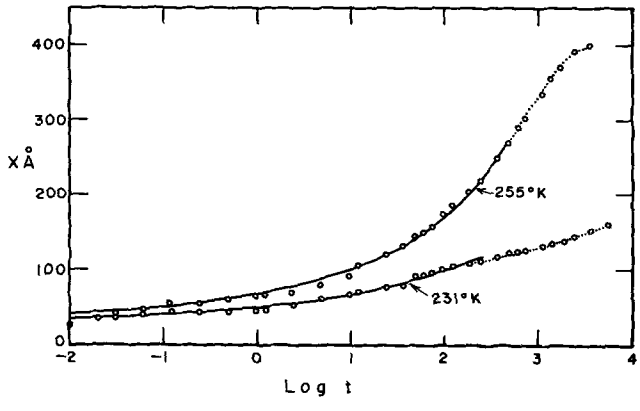

Fig. 3. Results for the chlorination runs which showed no evidence of the light scattering effect. Time in sec; chlorine pressure 3.86 Torr at 331°K, 3.90 Torr at 255°K.

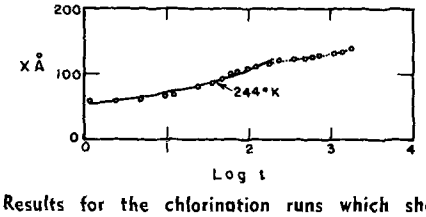

Fig. 4. Results for the chlorination runs which showed light scattering, corrected for light scattering as discussed in paper. Time in sec; chlorine pressure 4.60 Torr.

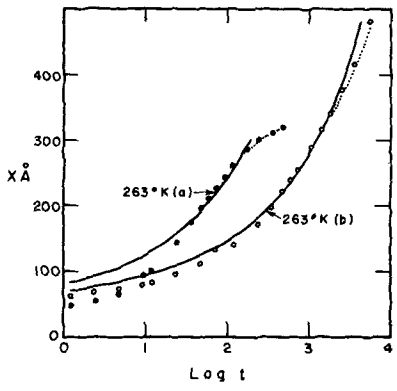

Fig. 5. Results for the chlorination runs which showed light scattering, corrected for light scattering as discussed in paper. Time in sec; chlorine pressure 5.48 Torr curve a, 6.90 Torr curve b.

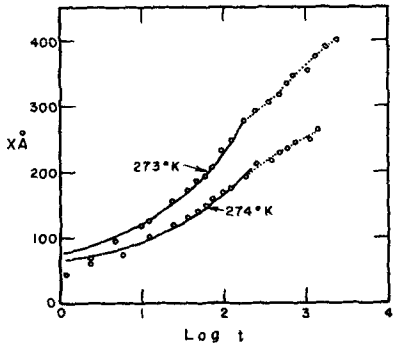

Fig. 6. Results for the chlorination runs which showed light scattering, corrected for light scattering as discussed in paper. Time in sec; chlorine pressure 4.61 Torr at 273°K, 4.90 Torr at 274°K.

An experiment to determine the pressure dependence of the reaction rate, although not entirely conclusive, indicated that the rate was proportional to the chlorine pressure to the power of approximately 0.3 (see Fig. 7).

Bromination.—As the data for the bromination of sodium were found under certain conditions to be affected by the 5461Å radiation used in the optical transmission measurements, the majority of these runs were carried out under conditions of intermittent illumination, the sample being illuminated only long enough to make the individual measurements (about 1 sec).

As was the case for the chlorination, only results for metal films deposited at background pressures of 7×10^{-7} Torr or less are reported. Furthermore, all

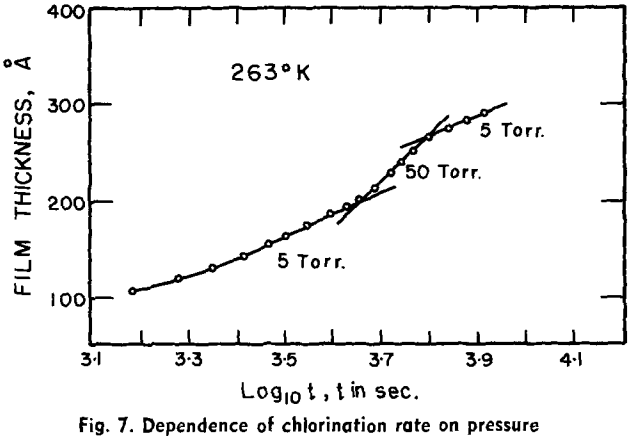

Fig. 7. Dependence of chlorination rate on pressure

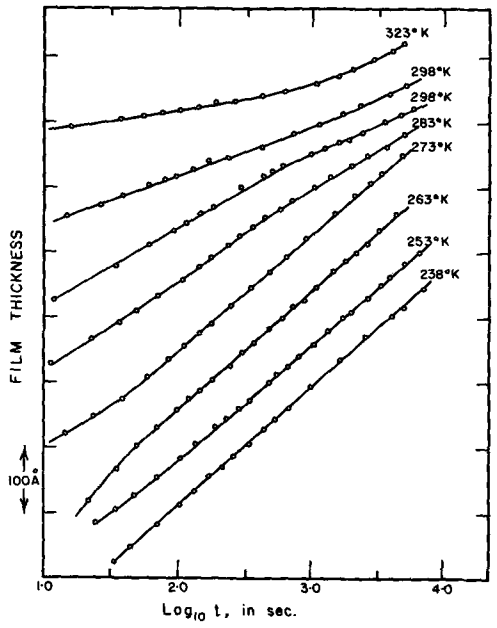

Fig. 8. Bromination results

the runs showed the light scattering effect, making it impossible to determine the absolute thicknesses of the bromide films. The change in thickness following the first few seconds of reaction could be determined as before, however, provided the fraction of scattered light remained independent of film thickness and time (*i.e.*, provided the degree of roughness of the halide-halogen interface remained essentially constant).

The data are presented in Fig. 8, the positioning of the curves with respect to translation along the "Film Thickness" axis being arbitrary. As far as could be determined, however, there appeared to be no systematic change in intercept with temperature for the temperature range 238°-273°K. indicating only a small or zero temperature coefficient for the reaction rate in this temperature range. It is clear from Fig. 8 that above 273°K, the behavior is somewhat different.

Illumination with 5461Å radiation was found to have an effect on the rate only for runs at the higher temperatures (*i.e.*, above 273°K). The influence of continuous irradiation on the rate is illustrated in Fig. 9.

Combined bromination, chlorination runs.—A few runs were carried out under conditions of intermittent illumination in which the sodium film was first reacted with bromine, then the bromine removed and chlorine

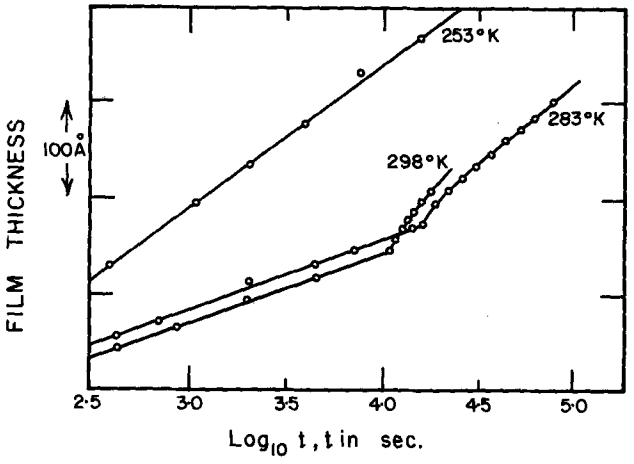

Fig. 9. Effect of illumination with 5461Å radiation on bromination rate.

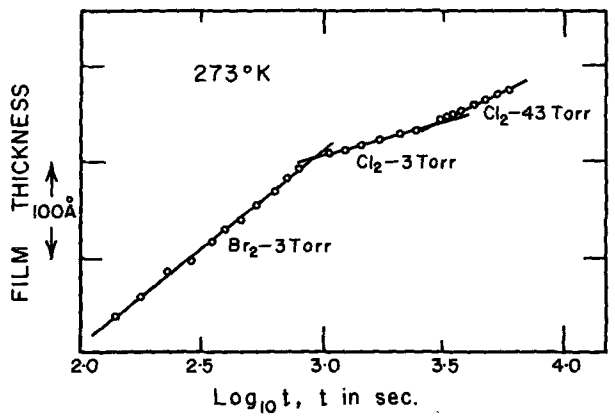

Fig. 10. Effect on rate of metal consumption of replacing bromine with chlorine following bromination.

introduced. The results for one such run are presented in Fig. 10.

Discussion

Chlorination results.—The data for the chlorination of sodium were fitted to a slightly modified form of the Mott-Cabrera theory (10) for the growth of thin and very thin films. The equation, which is discussed in some detail by Dignam, Fawcett, and Böhni (14), is given below

$$dX/dt = 2A \sinh (B/X) \qquad [12]$$

$$A = \Omega\nu\, an \exp (-U/kT) = A_o \exp (-Q/kT) \qquad [13]$$

$$B = \mu^* V/kT \qquad [14]$$

where the symbols are defined as follows: n, volume concentration of mobile species, in general a function of temperature; U, zero field activation energy associated with movement of the species; ν, usual frequency term associated with the movement of the species; a, distance travelled per activation, or the jump distance; Ω, volume of product per cation or anion (depending on whether transport is cationic or anionic); μ^*, charge-activation distance produced (activation dipole) associated with movement of the species; V, potential drop across the product film arising from equilibration of electrons in the metal with those in surface states at the film-gas interface. Equation [12] may be re-written in the following integrated form

$$\int_{B/X}^{\infty} \frac{(1/2)\ \mathrm{csch}\ u}{u^2}\, du = \frac{A}{B} t \qquad [15]$$

where the boundary condition $X = 0$ at $t = 0$ has been used. The data in Fig. 3 where fitted to Eq. [15] using a 7094 IBM computer and a procedure outlined previously. The solid curves shown were calculated for values of B and A which minimized the variance in each case. From the values of B, μ^*V was calculated to be $7.2_2 \pm 0.3_3$ and $7.7_7 \pm 0.2_6$ eÅv for the runs at 231° and 255°K, respectively. Since the two values agree within their combined standard deviations, μ^*V was taken to be temperature independent, the weighted mean value and the standard deviation of the mean being given by: $\mu^*V = 7.5_7 \pm 0.2_1$.

As the remaining data (Fig. 4-6) involve light scattering effects, as mentioned previously, they were analyzed in a slightly different manner. In Eq. [15], X was replaced by $X' + X_o$ where X' is the apparent film thickness calculated from [10] and [11], and X_o the correction term to allow for the attenuation of light arising from scattering. If the fraction of light scattered remains constant after a short period of time, then X_o will be constant following this transition period. For these runs, therefore, B was assumed to be given by [14], using the above value for μ^*V, and

A and X_o chosen to minimize the variance. The computed curves for these runs are also shown as solid lines in Fig. 4-6.

It is clear from the data that following chlorination for a period in the neighborhood of 100-1000 sec, a more or less abrupt break occurs in the plot of film thickness *vs.* log (time), the direction of the break suggesting a fairly sudden decrease in the reaction rate. Apart from this effect, however, which will be discussed later, fairly good agreement between the data and calculated curves is obtained.

Thus, the only two fully reliable chlorination runs (Fig. 3) fit Eq. [12] or [15] over about 4 decades in the chlorination period, and in the case of the run at 255°K, over a factor of 7 in the chloride film thickness. Furthermore, the fit is obtained for essentially the same value of μ^*V. Of the remaining five runs which may be considered, all of which involve light scattering, two (Fig. 4 and 5b) are brought into excellent accord, and two (Fig. 6) into fair accord with [12] or [15] after correcting for scattering on the assumption of a constant fraction of light scattered. Furthermore, the accord is achieved for the same value of μ^*V as above. Again, the values of A determined for the seven runs show the expected temperature dependence (Fig. 11) within experimental scatter. It therefore appears that the chlorination of sodium in the temperature range 231°-273°K takes place initially in accord with [12] (*i.e.*, essentially the Mott-Cabrera theory), a "break-away" occurring to lower rates after a certain period.

Before the Mott-Cabrera theory or any minor modification of it can be accepted even tentatively, however, other common rate laws must be examined. To this end, the data of Fig. 3 (255°K), which do not involve light scattering, and furthermore are the most extensive, were fitted to the most general form of the parabolic and direct logarithmic equations (*i.e.*, $X = K_p(t + t_o)^{1/2}$ and $X = K \log (t + t_o) + K'$, respectively). The results are summarized in Table I, in which the standard deviation of X, σ_X, from the most probable curve is given for the three rate laws. In order that the statistical significance of differences in σ_X can be ascertained, the standard deviation of σ_X, σ_σ, is also given.[5] From these values one can conclude that the chances against the improved fit for the Mott-Cabrera law being accidental are about 20 to 1 on comparison with the logarithmic law and 100 to 1 for the parabolic law. An even more pronounced decision in favor of the Mott-Cabrera law is obtained for run b, Fig. 5. As this run involved light scattering, however, the result is perhaps less convincing than the above. For the remaining runs, the total per cent change in film thickness is insufficient to provide a basis for distinguishing between the three rate laws. On the present evidence we conclude, therefore, that the chlorination data for the initial reaction period are in accord with the Mott-Cabrera law, rather than either the direct logarithmic or parabolic law.

[5] σ_σ was calculated from the relationship $\sigma_\sigma = \sigma_X/[2(n - i)]^{1/2}$ where n is the number of experimental points and i the number of disposable constants in the equation being fitted.

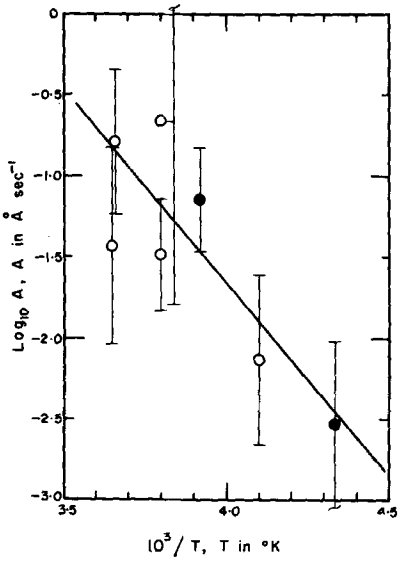

Fig. 11. Temperature dependence of the factor A for chlorination of sodium. The vertical lines represent 95% confidence limits, the diagonal line being the weighted least squares regression line for A. The solid circles represent the results for the runs which did not involve light scattering.

Table I. Comparison of the fit of the data of Fig. 3 (255°K) to the Mott-Cabrera, direct logarithmic and parabolic rate laws

	Mott-Cabrera	Logarithmic	Parabolic
σ_X, Å	6.0	10.6	13.4
σ_σ, Å	0.9	1.6	2.0

From Fig. 11, the temperature dependence of A is given by [13] with log (A_o in Å/sec) = 7.9 ± 2.4, Q = 0.48 ± 0.12 ev where the limits represent one standard deviation. We note that Q is smaller than the activation energy for migration of a cation vacancy in sodium chloride (about 0.8 ev) suggesting that the concentration of cation vacancies in the present case has a negative temperature coefficient. Although a detailed mechanism can support such a proposition, the difference in the activation energies is not sufficiently large compared with the standard deviation in Q, to rule out chance disagreement.

Any explanation of the "break-away" phenomena offered at this stage must be regarded as highly speculative. Bearing this in mind, the accumulation, as the film thickens, of the space charge due to the mobile ionic species would have the effect of reducing the rate below that predicted by [12]. Although this postulate has been tested quantitatively and successfully, further development of the thesis will be delayed until more extensive data are available.

Bromination results.—From Fig. 8 it is clear that for runs at temperatures of 273°K and below, the data are in accord with a direct logarithmic law (*i.e.*, film thickness linear in log time). This is in contrast with the chlorination results which appear to fit the Mott-Cabrera theory of metal oxidation, an approximate integrated form of which is sometimes referred to as the inverse logarithmic law. That reactions which are so very similar in nature should follow different kinetic rate laws is somewhat surprising. We note, however, that the chlorination data fit the Mott-Cabrera theory only for sufficiently short time periods. It is possible that the bromination data for sufficiently short time periods would also fit this law. The light scattering effect mentioned previously thwarted attempts to obtain such data.

A further interesting result is that the decadic rate constant is temperature-independent below 273°K (although it cannot be said with any degree of certainty that the intercept on a thickness *vs.* log t graph is likewise temperature-independent) and decreases as one proceeds to higher temperatures (see Fig. 8). Furthermore, illumination with 5461Å radiation, while having no measurable effect on the decadic rate below 273°K, above this temperature it causes the decadic rate to increase to the value found below 273°K (see Fig. 9). A tentative explanation for these observations follows.

It is possible that for sufficiently thin films the rate is controlled by ion transport through the film. In the absence of space charge effects this will lead to data in accord with the Mott-Cabrera theory (*i.e.*, inverse logarithmic law). If space charge effects are important, however, then a kinetic law approximating to a direct logarithmic law might perhaps be expected (15). As the film thickens, the rate might become controlled by

electron transport through the film rather than ion transport. Assuming the mechanism of electron transport to involve Schottky emission, this mechanism will also lead to a kinetic rate law approximating to a direct logarithmic law (16). Illumination of the brominating sample with light would be expected to have little if any effect on the rate of ion transport through the film, but would alter very substantially the rate of emission of electrons. Thus, at the higher temperatures where the electron transport mechanism is presumably operative, illumination with 5461Å radiation could stimulate electron transport through the film to such an extent that the rate-controlling process becomes ion transport once more. No such effect is expected at the lower temperatures where the rate-controlling process is presumably already ion transport. These considerations must be regarded at present as highly speculative.

Results for combined bromination chlorination runs. —The significance of these results (Fig. 10) concerns the fact that most of the reaction conditions remain unaltered as one proceeds from a point just before that at which the bromine was removed to a point immediately after the reaction was recommenced with chlorine present. In particular, the temperature, metal, and film materials are the same in both cases as well as the film thickness. The only change in the system, therefore, concerns the nature of the film-gas interface. We note that the rate of reaction on replacing the bromine with chlorine is reduced very substantially despite the fact that the free energy decrease for the reaction of sodium with chlorine is greater than that with an equivalent pressure of bromine at the same temperature. We must conclude, therefore, that the detailed structure of the film-gas interface is extremely important in the over-all kinetic process. Presumably the reduction in rate arises from the fact that chlorine atoms can be less readily chemisorbed on sodium bromide than can bromine atoms. Further investigation along these lines should provide interesting results.

Summary and Conclusions

Preliminary data on the chlorination and bromination of sodium have been obtained in the temperature range 238°-323°K. The results may be summarized as follows.

The initial chlorination data are in accord with an equation of the form

$$dX/dt = p^m \gamma \sinh (B/X)$$

where

$$m \approx 0.3,\ \gamma \simeq 2 \times 10^8 \exp (0.5/kT \text{ (ev)})$$

$$B = \mu^* V/kT,\ \mu^* V = 7.6 \text{ eÅv}$$

After a few minutes reaction time, however, the rates fall below those predicted by this equation. At 255°K, the results adhered to this equation over a range corresponding to more than 4 decades in the time and to an increase in the film thickness of more than a factor of 7. The film thicknesses achieved after about 1 hr reaction time range from about 150 to 420Å over the temperature range 231°-273°K.

For temperatures of 273°K and below, the data which correspond to bromination periods of 10 sec or more are in accord with an equation of the form

$$X = K \log t + K'$$

where K, the decadic rate constant, is independent of temperature in this region and has a value of 180Å per decade of time. The temperature dependence of the intercept, K' is uncertain, but appears to be small. Above 273°K, the decadic rate constant decreases with increasing temperature, however on illumination with 5461Å radiation, the decadic rate is increased to match that found below 273°K.

On interrupting a bromination run by replacing the bromine with chlorine at the same pressure, the rate is found to decrease very substantially, indicating that the processes occurring at the film oxidant interface play an important role in the over-all kinetic behavior.

The present data, though preliminary in nature, already show promise in providing information for the critical evaluation of mechanisms of growth of thin continuous films on metals. Further calculations will be postponed, however, until more extensive and more precise data are available.

Acknowledgments

The authors are grateful to the National Research Council of Canada for supporting this research and for a scholarship (D.A.H.). They also wish to express their thanks to Miss W. Y. Shiu and Mr. D. Goad for assistance in carrying out the calculations.

Manuscript received July 18, 1966; revised manuscript received Nov. 10, 1966. This paper was presented at the Philadelphia Meeting, Oct. 9-13, 1966.

Any discussion of this paper will appear in a Discussion Section to be published in the December 1967 JOURNAL.

REFERENCES

1. N. F. Mott, *Trans. Faraday Soc.*, **35**, 1175 (1939).
2. N. F. Mott, *ibid.*, **36**, 472 (1940).
3. H. H. Uhlig, *Acta Met.*, **4**, 541 (1956).
4. A. T. Fromhold, Jr., *Nature*, **200**, 1309 (1963).
5. A. T. Fromhold, Jr., *J. Phys. Chem. Solids*, **24**, 1309 (1963).
6. T. B. Grimley, *Discussions Faraday Soc.*, **28**, 223 (1959).
7. N. Cabrera and N. F. Mott, *Rep. Prog. Phys.*, **12**, 163 (1948).
8. D. D. Eley and P. R. Wilkinson, *Proc. Roy. Soc. (London)*, Ser. A, **254**, 326 (1960).
9. R. W. Bartlett, *This Journal*, **111**, 903 (1964).
10. M. J. Dignam and W. R. Fawcett, *This Journal*, **113**, 663 (1966).
11. M. J. Dignam, W. G. Forbes, and D. J. Le Roy, *Can. J. Chem.*, **35**, 1341 (1957).
12. H. E. Ives and H. B. Briggs, *J. Opt. Soc. Amer.*, **27**, 181 (1936).
13. G. W. Horsley, A.E.R.E. Report M/R 1152 (1953).
14. M. J. Dignam, W. R. Fawcett, and H. Böhni, *This Journal*, **113**, 656 (1966).
15. M. J. Dignam, *ibid.*, **109**, 192 (1962).
16. E. L. Cook and A. T. Fromhold, Jr., Paper presented at Southeastern Sectional Meeting of the American Physical Society, November, 1965.

Oxide Growth and Capacitance on Preirradiated Zircaloy-2 and Zirconium

R. J. Davis

Reactor Chemistry Division, Oak Ridge National Laboratory, Oak Ridge, Tennessee

ABSTRACT

Previous work has demonstrated a large enhancement of corrosion of Zircaloy-2 by oxygenated aqueous solution during bombardment by fast neutrons. Measurements of oxide growth and of film impedance were made on specimens preirradiated with fast neutrons in order to determine whether the irradiation damage important to corrosion occurs in the oxide film or in the metal substrate. A small enhancement of corrosion was observed with some specimen pretreatments. The results indicate that some corrosion enhancement results from irradiation of the substrate metal and that dissolved oxygen is required for the effect.

It has been demonstrated that corrosion of Zircaloy-2 in oxygenated aqueous media under heavy particle irradiation occurs at constant rates. If the heavy particles are fission fragments, the corrosion rate R (mils per year) depends on the fission power density in solution, P (watts per ml). At high power densities (greater than several w/ml) the rates also depend on temperature according to (1-3)

$$1/R = 2.3/P + 2.25 \times 10^{-11} \exp^{11,500/T} \quad [1]$$

If the heavy particles are fast neutrons and the flux, ϕ is 10^{13} (n/cm^2/sec $>$ 1 Mev) or less, the rate increases with fast neutron flux according to (4)

$$R = 4.3 \times 10^{-13} \phi \quad [2]$$

It was hypothesized that the radiation damage which affected corrosion, with both types of heavy particles, was the production of interstitials and vacancies (4). The rate equations were roughly correlated (*i.e.*, as well as the uncertainty of the estimation of the number of defects per fission would allow). This indicated that in terms of the rates of atom displacement D (no/cm^3/sec)

$$R \cong 10^{-15} D$$

These efforts did not establish the mechanism of the radiation effect. It is the purpose of this study to determine one feature of the mechanism, namely, where the important damage occurs.

Experimental

In outline the experimental proposal was to prepare pairs of specimens with and without oxide film, to irradiate one specimen of each pair and retain the other for a control and to corrode both specimens in an oxygen-steam environment and compare rates of weight gain and film impedance. The weight gain data were to provide a measure of corrosion rates and the film impedances an empirical indication (5) of the protective quality of the film. It can be shown that such data would in principle distinguish between three conceivable situations: (*i*) the primary radiation damage is in the oxide; (*ii*) the primary damage is in the metal which results in inferior oxide; or, (*iii*) the damage is in the metal, but the oxide is not changed.

Table I. Preirradiation treatments

Prefilmed:	Pickle in HF-HNO_3; oxidized in 300°C H_2O-O_2 (50-50 volume % mixture at 1 atm); seal in He-filled Zr-2 autoclave.
Film free:	Pickle in HF-HNO_3; seal in He-filled Zr-2 autoclave;[1] heat at 500°C 16 hr.
Film-free, fluoride-free:	Pickle in HF-HNO_3, vacuum anneal at 700°C 4 hr; oxidize in 300°C H_2O-O_2 (50-50 volume % mixture at 1 atm) for 1 hr; seal in He-filled Zr-2 autoclave; heat at 500°C 16 hr.
Low oxygen content:	Pickle in HF-HNO_3; seal in He-filled Zr-2 autoclave; heat at 800°C 16 hr.

[1] In one experiment the interior of the autoclave was pickled. (In all other experiments the autoclave surfaces were as machined.)

Two sets of prefilmed specimens were prepared as indicated in Table I; one set was preoxidized for 1 hr and the other set for four days. Two sets of film-free Zr-2 specimens were also prepared (Table I); the 500°C heating in helium was employed to dissolve into the metal (6) the small amount of oxide left by pickling. (In the film-free specimen experiment, number 2, the interior of the autoclave was pickled; in all other experiments the autoclave interiors were as machined.)

The results of the first experiments led to other specimen preparations as indicated below. There was some indication of an effect due to fluoride left in pickling; also the possibility was raised that the effect found was due to the additive elements in Zircaloy-2. For these reasons a set of crystal-bar zirconium specimens was prepared to be film-free and fluoride-free but in a manner to provide some dissolved oxygen in the substrate metal. This is the film-free, fluoride-free preparation in Table I. The 700°C vacuum anneal was done in a large, zirconium foil-lined, quartz furnace. Any fluoride was expected to be volatilized as ZrF_4 by the treatment.

A set of specimens was prepared, as indicated in Table I, in a way to provide not only a film-free surface but a surface with a low dissolved oxygen content in the substrate metal. The low oxygen content was achieved by heating in helium at 800°C which is expected to dissolve into the metal the small amount of oxide left by pickling and disperse it almost uniformly through the metal (6).

The irradiations were made with the specimens still in the autoclaves which were canned as shown in Fig. 1, with a layer of boron-10 around them to reduce the thermal neutron flux and hence the activation of the zirconium. The irradiations were done at 100°C at a fast flux (>1 Mev) of 10^{13} for ten days. The control specimens were held at 100°C in an oven for a similar period.

The postirradiation oxidations were made in a furnace which provides a stream of a 50-50 mixture of oxygen and steam at 300°C and 1 atm. This environment was chosen for two reasons: (*i*) it contains water and oxygen, the chemical constituents of the media in which irradiation enhancement of corrosion has been seen (1, 2), and (*ii*) it is a convenient system. The notable feature of this furnace is the rapid heat-up device. By appropriate manual interchanges of the two portable furnaces shown on the left (Fig. 2), specimens were heated to 300°C in 30 sec and

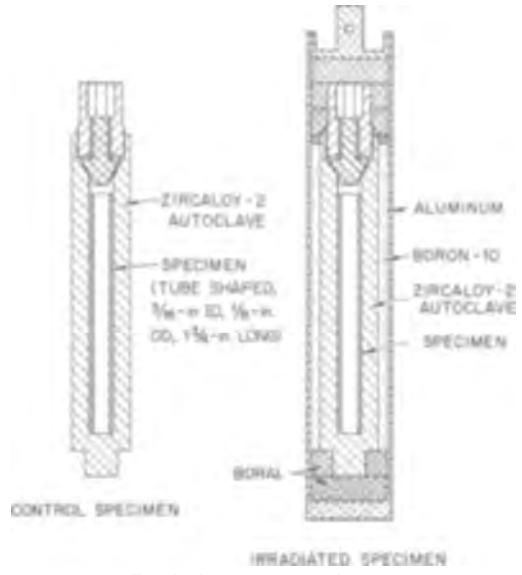

Fig. 1. Specimen autoclaves

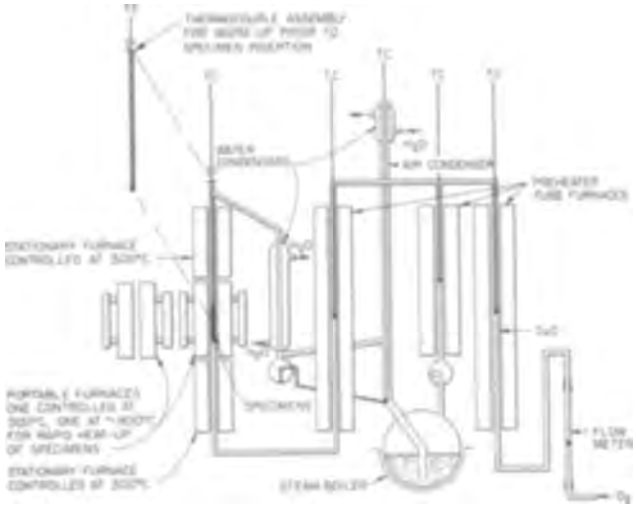

Fig. 2. Steam-oxygen furnace

meaningful exposures of as short as 5 min were made. Periodic rapid heat-ups were shown not to affect subsequent corrosion.

The impedance measuring devices are shown in Fig. 3. All but the cell are conventional equipment. The electrolyte was 1M NH_4NO_3. NH_4NO_3 was chosen because it decomposes at 210°C to volatile products; therefore traces of the electrolyte should not affect subsequent corrosion.

The measured impedances include the impedance of the platinized platinum surface, the electrolyte, and the ZrO_2 film. The impedance of the platinum surface is negligible, the electrolyte resistance is small and is known both by observation and calculation and can therefore be subtracted out. The impedance of the ZrO_2 film can therefore be measured (9).

The novel feature of this cell is the use of Teflon sleeves to demark the area over which the impedance is observed. Previous workers have used various sealing waxes (10). The important advantage of Teflon is that the impedance measurements do not affect the specimen weight or subsequent corrosion.

Several measurements were made to demonstrate the reliability of the impedance measurements. Reported film capacities on anodized films (10) have been reproduced. It was demonstrated that the same impedance is measured using Teflon as using Apiezon

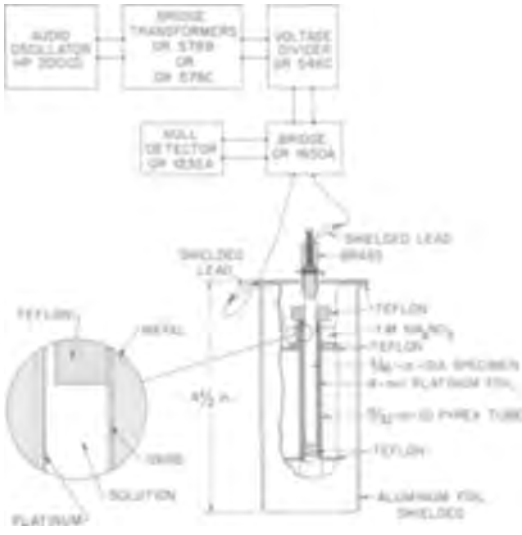

Fig. 3. Capacitance cell

W sealing wax. It was also shown that a γ-field of intensity similar to that from induced radioactivity in an irradiated specimen does not affect the measured impedance. The impedances reported were all measured at 1 kc. Weight gains were measured on a microbalance with a precision of about 0.3 $\mu g/cm^2$.

Results

The weight-gain *vs.* time data for the film-free specimens (Fig. 4) show that a small increase (x 1.5-2 in corrosion rates occurred due to the irradiation. (The film-free specimen which was pretreated and irradiated in the autoclave which had been pickled showed a smaller radiation effect.) The corrosion of the irradiated specimen was continuously faster than the controls from essentially the start to the end of the postirradiation exposures. The crystal-bar specimen with the minimized surface fluoride showed the same behavior as the others.

The weight-gain data for the prefilmed specimens (Fig. 5) show no acceleration of corrosion due to irradiation; in fact the data suggest a small and temporary retardation of corrosion. [The prefilmed control specimens corroded more rapidly than the film-free controls. This is attributed to the 100°C treatment in He for 10 days. Others (7, 8) have found that heating a corrosion film in an inert environment at as low as 150°C (8) enhances subsequent corrosion.]

The low-oxygen specimen (Fig. 6) showed no effect as a result of irradiation.

The impedance data are given in Fig. 7-9. The data taken from the impedance bridge were equivalent series capacitance and loss tangent (tan δ) across the cell for about 0.5 cm^2 areas. The observed values were corrected for the solution resistance (~1 ohm-cm) and

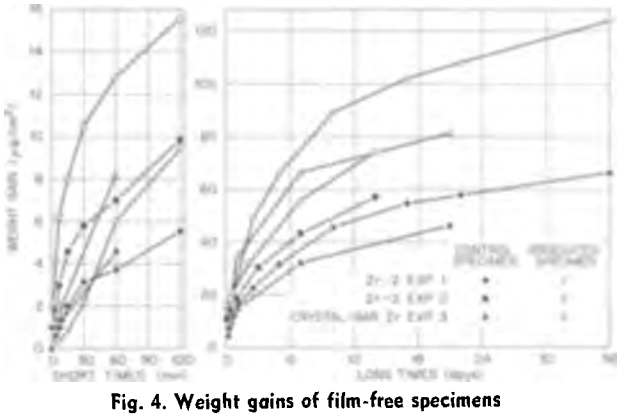

Fig. 4. Weight gains of film-free specimens

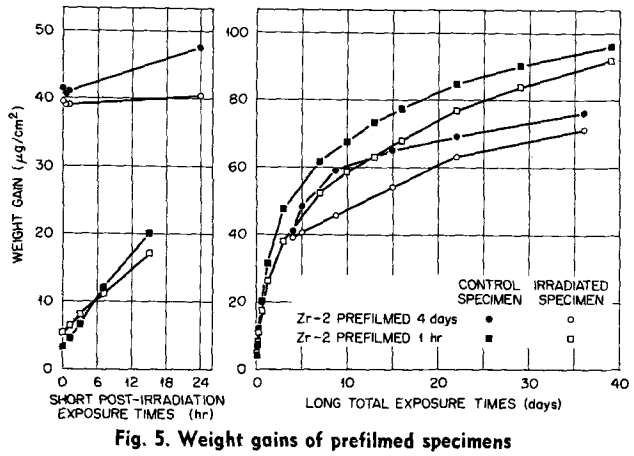

Fig. 5. Weight gains of prefilmed specimens

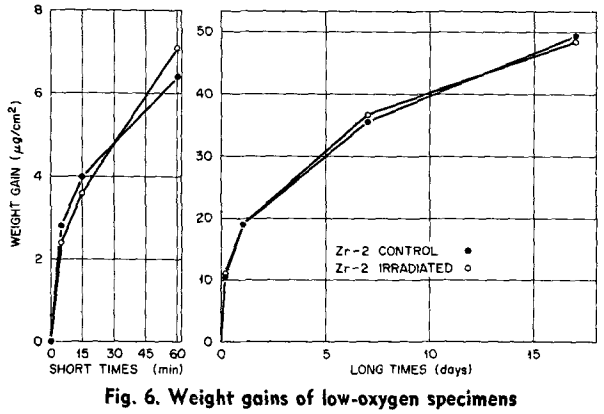

Fig. 6. Weight gains of low-oxygen specimens

the capacitances were converted to equivalent parallel capacitances per unit area. Both corrections are small. The data are plotted as reciprocal of capacitance per unit area and tan δ, both as a function of weight gain. For uniform growth of a homogeneous oxide film, reciprocal capacitance *vs.* weight gain should plot as a straight line through the origin. The slope of the line is inversely proportional to the dielectric constant of the oxide. Tan δ, for a homogeneous insulating material, is a property of the material, independent of thickness.

The impedance data (Fig. 7-9) generally show two deviations from the simple behavior expected for uniform growth of homogeneous material. In some cases the reciprocal capacitance (Fig. 7) remained very low up to weight gains as high as 20 μg/cm². In most cases (Fig. 7, 8, and 9), tan δ was lower (in one case higher) during the first 20 μg/cm² of weight gain than the approximately constant value observed thereafter. Neither of these effects were peculiar to irradiated specimens.

The impedance data for film grown on film-free specimens (Fig. 7) show no significant effect due to irradiation on either tan δ or reciprocal capacitance. (A possible exception is the reciprocal capacitance of the crystal-bar specimen, however neglecting the first 20 μg/cm² weight gain) the slopes of these two plots on Fig. 7, are similar.)

The impedances of the prefilmed specimen, after postirradiation oxidation are given in Fig. 8. Here we find no significant effect on tan δ but the reciprocal capacitances were less (or the dielectric constant greater) for the irradiated specimens. The differences were about 15% for the four day prefilmed specimens and almost 30% for the 1-hr prefilmed specimen.

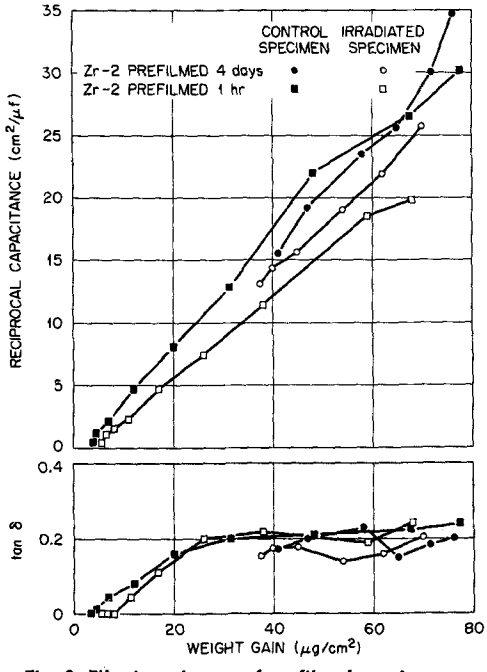

Fig. 8. Film impedances of prefilmed specimens

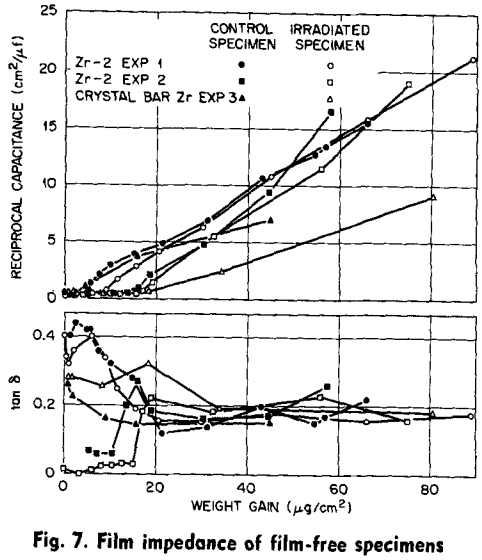

Fig. 7. Film impedance of film-free specimens

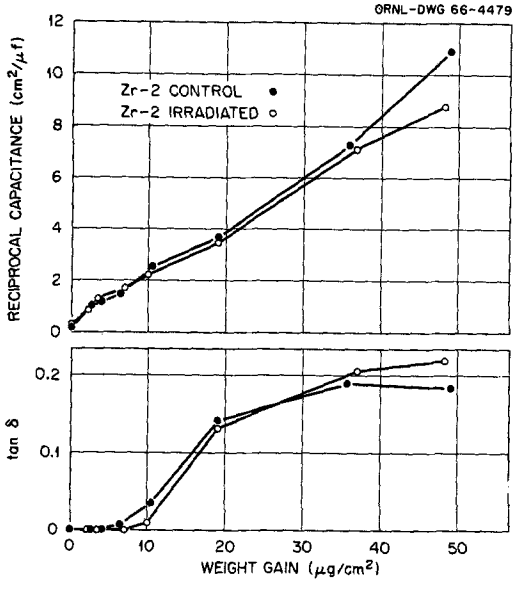

Fig. 9. Film impedances of low-oxygen specimens

The low oxygen specimen (Fig. 9) showed no effects due to irradiation.

Discussion

A small and continuing enhancement of postirradiation corrosion due to irradiation was found with certain pretreatments and not with others. Corrosion enhancement due to irradiation was observed with specimens pretreated to be free of oxide film, showing that the irradiation damage was in the metal. The pretreatments which would provide an oxygen-rich layer of metal at the surface resulted in irradiation enhancement of corrosion. These pretreatments included: (*i*) the Zr-2 pickled then heated in helium at 500°C and (*ii*) the X-bar Zr pickled, annealed, briefly prefilmed, then heated in helium at 500°C. The pretreatments which would lead to a nearly oxygen-free metal layer at the surface resulted in no enhancement of corrosion by irradiation. These include the pickle followed by heating in helium at 800°C, and prefilming at 300°C. These results indicate that the irradiation damage in the metal, which affects corrosion, is associated with dissolved oxygen although other interpretations, related to effects in the metal as a result of the various heat treatments, may be possible. The small irradiation enhancement was observed with the fluoride-free X-bar Zr, which is taken to indicate that neither fluoride nor the additive elements in Zr-2 are required for the irradiation effect.

The film impedances were measured to provide an empirical indication of protective quality. It was presumed that oxide of lower apparent dielectric constant would be more protective. (In terms of the weight gain, w, and reciprocal capacitances, 1/c, and where K is an appropriate constant, the apparent dielectric constant is given by: $\epsilon = K\frac{d(w)}{d(1/c)}$. In the case of an irradiation effect in the metal, it was anticiated that film impedances would distinguish between two possibilities: first, that the damaged metal was more chemically reactive, and second, the metal damage resulted in poor quality oxide.

The apparent dielectric constants of film grown on those specimens which show the small corrosion enhancement, was not significantly different from the controls. However, it is not clear how the apparent dielectric constant relates to protective quality. In the case of the prefilmed specimens, the slight retardation of corrosion was accompanied by a significant increase in apparent dielectric constant, which is opposite to the relation expected (5). The film impedances therefore do not distinguish between the possibility that poor oxide grows on irradiated metal from the possibility that the damaged metal is more chemically reactive.

As indicated in the introduction, simultaneous exposure of Zircaloy-2 to oxygenated aqueous media at 300°C with irradiation to a fast neutron flux of 10^{13} n/cm^2/sec results in linear corrosion at a rate of 4.3 mils/year (metal consumption) or about 3 μg/cm^2/hr (weight gain). The question of whether this phenomenon and the enhancement of postirradiation corrosion reported in this paper are indeed ramifications of the same kind of irradiation damage cannot be completely resolved.

Although not related to irradiation effects, it is of incidental interest to take note of the two phenomena regarding the impedances of thin films. Up to 20 μg/cm^2 weight gain, very low reciprocal capacitances were observed for several specimens, perhaps due to short circuits through the film. Also low (and in one case high) tan δ values were observed for thin films on Zr-2 specimens; this indicates a change in the nature of the material at about 20 μg/cm^2 weight gain.

It is concluded that a small enhancement of corrosion of Zircaloy-2 results from prior irradiation of film-free surfaces prepared in certain ways. The data indicate that the damage occurs in the metal and is probably related to dissolved oxygen.

Cox (11) has found that Zircaloy-2 corrosion in steam is accelerated by inhomogeneously distributed oxygen in the metal surface, and particularly in the limiting case where oxygen is present as particles of ZrO_2 in the metal. Fast neutron irradiation has been found to precipitate carbon (12) and nitrogen (13) in iron as the carbide and nitride, respectively. A possible mechanism of the irradiation effect on corrosion is therefore suggested: during the process of corrosion the outermost layers of metal are supersaturated with dissolved oxygen. Fast neutrons cause the precipitation of this dissolved oxygen as zirconium oxide particles, and these precipitated particles enhance corrosion.

Manuscript received July 1, 1966; revised manuscript received Oct. 17, 1966. This research was sponsored by the United States Atomic Energy Commission under contract with the Union Carbide Corporation.

Any discussion of this paper will appear in a Discussion Section to be published in the December 1967 JOURNAL.

REFERENCES

1. G. H. Jenks, "Fluid Fuel Reactors," pp. 232-245, J. A. Lane, H. G. MacPherson, and Frank Mason, Editors, Addison-Wesley Co., Inc., Reading, Mass. (1958).
2. G. H. Jenks, "Corrosion of Zirconium Alloys," ASTM Special Tech. Pub. No. 368, Philadelphia, Pa., 1963, pp. 101-117.
3. B. Cox, K. Alcock, and F. W. Derrick, *This Journal*, **108**, 129 (1961).
4. G. H. Jenks and R. J. Davis, To be published.
5. J. N. Wanklyn and D. R. Sylvester, *This Journal*, **105**, 647 (1958).
6. J. P. Pemsler, *ibid.*, **105**, 315 (1958).
7. S. Kass and D. B. Scott, *ibid.*, **109**, 92 (1962).
8. D. W. Shannon, *Corrosion*, **19**, 414 (1963).
9. L. Young, "Anodic Oxide Films," pp. 150 *et seq.*, Academic Press, Inc., London and New York, (1961).
10. A. B. Reidinger, "The Corrosion Behavior of Zircaloy," MS Thesis, Union College, Schenectady, N. Y., May 1958.
11. B. Cox and B. R. Harder, *This Journal*, **110**, 1110 (1963).
12. F. E. Fujita and A. C. Damask, *Acta Meta.*, **12**, 331 (1964).
13. J. T. Stanley, "Diffusion in Body Centered Cubic Metals," J. A. Wheeler and F. R. Winslow, Editors, Chap. 26, p. 349, ASM, Metals Parks, Ohio (1965).

Electrodeposition of Tc^{99} from Aqueous Solution

Roger E. Voltz[1] and M. L. Holt

Chemistry Department, University of Wisconsin, Madison, Wisconsin

ABSTRACT

A study has been made to determine the optimum conditions necessary for the electrodeposition of macro amounts of technetium (Tc^{99}) from an aqueous bath containing about 0.018 mole of NH_4TcO_4 and 1 mole of $(NH_4)_2SO_4$ per liter of solution with H_2SO_4 added to *p*H about 1. Electrolysis of this solution at 1 to 2 amp/dm^2 and room temperature gives a bright, metallic appearing deposit of Tc with a cathode current efficiency of up to 30%. Included in this study are the effects on CCE of such factors as current density, bath *p*H, concentrations of the various reagents, temperature, and the colored cathode reduction product. Tests made to determine the nature of the deposit showed it to be essentially metallic; however, annealing is necessary to produce metallic crystals. During electrolysis a light pink reduction product forms in the bath; as electrolysis continues this reduction product becomes darker and appears to poison the bath. Addition of small amounts of H_2O_2 to the bath during electrolysis can prevent the colored reduction products from forming.

Technetium, the first artificial element to be synthesized (1), can be purchased from Oak Ridge National Laboratory as the salt NH_4TcO_4 for about $90 per gram of activity. This availability suggested to the authors that a study of the electrodeposition of technetium on a macro scale from aqueous solution would be a worthwhile addition to the already extensive literature dealing with the electrochemistry of the element and its compounds. An excellent review article by Boyd (2) and a book by Colton (3) gives information about the production and properties of Tc so detailed information will not be repeated here.

Tc^{99} has a half life of about 2.12×10^5 years and emits weak beta rays with a maximum energy of 0.32 Mev (4); thus the walls of ordinary laboratory glassware give sufficient radiation protection when Tc and its compounds are being used. Since information about the physiological effects of Tc is still incomplete, great care should be taken to protect the worker as well as the laboratory from contamination. Several sources of information describing the handling of Tc and its salts (3, 5) are available. Use of rubber gloves, protective clothing, a "film badge," a well-ventilated hood [$HTcO_4$ is fairly volatile (6)], and a covered plating cell are mandatory protections for the laboratory worker.

A number of reports of the electrodeposition of technetium from aqueous solutions have appeared in the literature, but most of them necessarily deal with dilute baths in the order of 10^{-12} to 10^{-5} m/l (mole per liter). The discoverers of Tc, Perrier and Segré, reported the deposition of a thin layer on a platinum wire from a very dilute acid solution (7). Other investigators (8) obtained bright cathode deposits from solutions of NH_4TcO_4 in 2*N* H_2SO_4 and NH_4HF_2. Black or brown cathode deposits were obtained when various pertechnetate salts in H_2SO_4 were electrolyzed (9, 10). Lietzke and Stoughton (11) obtained semi-quantitative data on the electrodeposition of Tc on Pt and Hg cathodes indicating that up to 97% of the Tc could be removed from an acid bath but not necessarily as the pure metal. An alkaline bath containing a Tc salt in 2*N* NaOH produced dark deposits (12). Polarographic studies have indicated the reduction of TcO_4^- to the metal or even to the hydride (13-15).

A survey of the literature suggested that two plating baths producing macro electrodeposits of Tc should be tried before further work was undertaken. The first was the bath reported by Eakins and Humphries (16) which contained NH_4TcO_4 in 2*N* H_2SO_4 with H_2O_2 added to prevent formation of a colored reduction product. We found that electrolysis of this bath at the conditions recommended by the authors gave a metallic appearing plate with a CCE of about 10%. The second macro bath developed by Box (17) uses various minimum amounts of H_2SO_4 (depending on the metal used as a cathode) with ammonium pertechnetate in 0.7M ammonium oxalate and a specially designed electrolysis cell. Plates up to 18 mg/cm^2 were reportedly obtained from this bath at a current density of 130 amp/dm^2, and no H_2O_2 was needed. We were not able to duplicate exactly these results in our electrolysis set-up which consisted of small (1 cm^2) cathodes and anodes in 50-100 ml of plating solution contained in a 150 ml beaker. We found that a light green reduction product formed when the NH_4TcO_4 concentration was about 1 g/l although the bath continued to plate at a low efficiency (about 2%). The extremely high C.D. makes it necessary to take special precautions, and apparently it is necessary to use the plating cell described in the article in order to operate this bath effectively.

Both of these reports indicate that virtually 100% of the Tc can be removed from the plating solutions as what appears to be metallic Tc. Neither of these baths was studied in detail. The first seemed unsuitable for our purpose because of the variation in CCE with each addition of H_2O_2 and the rapidity with which the bath darkened if H_2O_2 was not added. The second was unsuitable for our purpose because of the low CCE and because we were unable to obtain consistent results in our electrolysis set-up. For example, five different baths containing 1-2 g/l of NH_4TcO_4, made according to directions (17), were electrolyzed using both gold and copper cathodes. The deposits on the gold were very loose but metallic gray in appearance whereas those on copper were dark and obviously heavily oxided. All of these baths containing 1-2 g/l of NH_4TcO_4 turned light green after 15 min of electrolysis.

Experimental Methods

The source of Tc in all plating solutions was NH_4TcO_4. Boiled, distilled water was used for making the solutions. One hundred ml of bath was used for each plating run. The electrolysis cell, a 150 ml beaker, was fitted with two 3 x 3 cm Pt anodes and either a gold, copper, or stainless steel cathode of the same size. Direct current was supplied by a variable voltage rectifier. Cells were covered during electrolysis by specially fitted hard plastic plates, and all runs were made in a well ventilated hood. All *p*H determinations were made with a Beckman, battery operated *p*H meter. When semi-quantitative results were required a copper coulometer was used in series with the plating cell. The bus bars were arranged so that the coulometer electrodes and the plating cell elec-

[1] Chemistry teacher, East High School, Wauwatosa, Wisconsin. National Science Foundation Fellow.

trodes could be removed simultaneously from their respective cells. In cathode current efficiency calculations, the equivalent weight of Tc was assumed to be 14.4g (99/7). Shielding and possible spillage or spattering were monitored with a model 107C Professional Geiger Counter.

Preliminary observations.—A number of different plating solutions each containing 0.006 mole of NH_4TcO_4 per liter of solution were electrolyzed at room temperature for about 15 min with a cathode current density (CCD) of about 4 amp/dm^2, and the results are given in Table I.

The results given in Table I indicated that the sulfuric acid bath containing $(NH_4)_2SO_4$ was quite promising. Hull cell tests showed a plating range of approximately 0.6 to 15 amp/dm^2 for a pH 1.0 solution of this bath compared to about 0.1 to 4.0 amp/dm^2 for the acid solutions without $(NH_4)_2SO_4$. Also, this bath had a higher CCE (about 18%) than a comparable bath containing NH_4HF_2 (about 12%). Both the K_2SO_4 and Na_2SO_4 baths gave CCE's (16 and 17%, respectively) comparable to the ammonium sulfate bath, but the solubilities of these salts limited a study of their concentration effects. Thus all additional experimental results were obtained using the NH_4TcO_4-$(NH_4)_2SO_4$-sulfuric acid bath.

Experimental Results

The bath used to obtain the following experimental results contained (unless otherwise stated) 1 mole of $(NH_4)_2SO_4$ and 0.006 mole of NH_4TcO_4 per liter of solution with H_2SO_4 added to give the desired pH. Electrolysis resulted in a pink or brown solution; this was shown to be a cathode reduction product when the cathode was placed in a porous cup during electrolysis runs. The solution in the cup became black and heavy with precipitate while the solution outside the cup remained clear and colorless. The effect of this precipitate on the electrolysis is indicated by the low CCE of these runs (about 3%). Addition of small amounts of H_2O_2 removed the color and dissolved the precipitate. If the bath was to be restored to its former plating efficiency, it was necessary to decompose the excess H_2O_2 by heating with Pt black. Failure to do so resulted in a plating solution that gave a lower CCE.

Cathode current density and CCE.—The results of this study are given in Table II and show that CCE decreased as CCD increased and that a CCD of about 1-2 amp/dm^2 was satisfactory.

Bath pH and CCE.—H_2SO_4 was used to vary the pH. The results given in Table III indicate that a pH range of 0.5-1.5 is satisfactory for producing metallic appearing plates, and thus a bath pH of 1.0 was used for additional work.

Bath temperature and CCE.—Although most electrolyses were made at room temperature, the results given in Table IV show that a higher CCE is obtained at elevated temperatures.

It was noted that the plate taken from the bath at 90°C was much duller and darker than those from lower temperature baths, probably indicating deposit of some oxide and accounting for the apparently much higher CCE. It was also noted that the baths darkened much faster at elevated temperatures than they did at room temperature.

NH_4TcO_4 *concentration and CCE.*—A series of runs were made with baths containing larger amounts of NH_4TcO_4. Table V shows that at about 0.018M NH_4TcO_4 the CCE begins to level off.

All plates were bright and metallic in appearance. Two further runs were later made on fresh baths at 0.030 and 0.036M NH_4TcO_4 concentration. They produced CCE's of 32 and 33%, respectively, again showing the tendency for the CCE to level off at a maximum near 30%.

$(NH_4)_2SO_4$ *concentration and CCE.*—The results, shown in Table VI, indicate that any concentration of $(NH_4)_2SO_4$ above 1 m/l produces a darker plate. For all subsequent studies, the concentration of $(NH_4)_2SO_4$ was 1 m/l.

Table I. Electrolysis of 0.006M NH_4TcO_4 solutions; room temperature; 15-min runs at 4 amp/dm^2

Solution	pH	Appearance of cathode deposit	Remarks
NH_4TcO_4 aqueous	6.0	Shiny, metallic	Poor conductivity
NH_4TcO_4 + H_2SO_4	2.0	Dark, loose	Bath darkened
NH_4TcO_4 + H_2SO_4	1.0	Shiny, metallic	Bath darkened
NH_4TcO_4 + 1M H_2SO_4	—	Shiny, metallic	Bath darkened
NH_4TcO_4 + 2M H_2SO_4	—	Shiny, metallic	Bath darkened
NH_4TcO_4 + H_2SO_4 + NH_4HF_2	1.0	Shiny, metallic	Bath darkened
NH_4TcO_4 + citric acid + H_2SO_4 or NH_4OH	2 to 9	All black	Bath darkened
NH_4TcO_4 + $(NH_4)_2SO_4$ + H_2SO_4	0.5 to 1.5	Shiny, metallic	Bath turned light pink
NH_4TcO_4 + Na_2SO_4 + H_2SO_4	1.0	Shiny, metallic	Light pink
NH_4TcO_4 + K_2SO_4 + H_2SO_4	1.0	Shiny, metallic	Light pink
NH_4TcO_4 + NaOH	12.0	Black	Bath dark

Table II. Effect of CCD on CCE; pH 1.0; room temperature; fresh bath for each 15-min run

CCD, amp/dm^2	Wt of deposit,* g	CCE, %
1	0.0050	27
2	0.0075	18
3	0.0103	14
4	0.0101	11

* All deposits were shiny and metallic in appearance.

Table III. Bath pH and CCE; room temperature; 2 amp/dm^2; fresh bath for each 15-min run

Bath pH	Wt of deposit, g	CCE, %	Deposit appearance
0.5	0.0080	13	Bright
1.0	0.0075	18	Bright
1.5	0.0096	21	Bright
2.0	—	—	Dark, loose

Table IV. Bath temperature and CCE; pH 1.0; 2 amp/dm^2; fresh bath for each 15-min run

Bath temperature, °C	Wt of deposit, g	CCE, %	Deposit appearance
25	0.0075	18	Bright
40	0.0089	19	Bright
55	0.0101	24	Bright
70	0.0145	26	Bright
90	0.0166	37	Dull

Table V. Effect of NH_4TcO_4 concentration on CCE: room temperature; pH 1.0; 2 amp/dm^2; fresh bath for each 15-min run

NH_4TcO_4, mole/liter	Wt of deposit, g	CCE, %
0.006	0.0075	18
0.012	0.0126	27
0.018	0.0153	30
0.024	0.0163	32

Table VI. Effect of $(NH_4)_2SO_4$ concentration on CCE; room temperature; pH 1.0; 2 amp/dm^2; fresh bath for each 15-min run

Concentration of $(NH_4)_2SO_4$, m/l	Wt deposit, g	CCE, %	Deposit appearance
0.0	0.0062	14	Bright
0.5	0.0065	14	Bright
1.0	0.0077	18	Bright
2.0	0.0096	20	Dark on edges
3.0	0.0076	17	Dark on edges
4.0	0.0080	17	Dark and dull

Table VII. Effect of consecutive runs on CCE; 0.012 m/l NH_4TcO_4 in first 15-min run; room temperature; pH 1

Consecutive run	Wt deposit, g	CCE, %
1	0.0126	27
2	0.0095	21
3	0.0078	17
4	0.0062	12
5	0.0055	11

Continued electrolysis and CCE.—A plating solution originally containing 0.012 m/l of NH_4TcO_4 was used in a series of 15-min runs with no treatment between consecutive runs. A dark precipitate gradually formed in the bath and, as shown in Table VII, the CCE decreased. All plates, however, remained shiny and metallic in appearance.

After this series of runs, a small amount of H_2O_2 was added to the solution to oxidize the black reduction product back to the colorless TcO_4^-. The solution was then warmed with Pt black to decompose the excess H_2O_2. The resulting solution, made up to 100 ml and pH 1.0, on electrolysis gave a CCE only slightly (2%) less than the original solution. A bath originally containing 0.03 m/l of NH_4TcO_4 gave similar results with 12 consecutive 15-min runs, and H_2O_2 treatment also restored this bath so that on electrolysis it gave almost its original CCE (29 instead of 32%).

Nature of the Cathode Deposit

The cathode deposit obtained from the ammonium pertechnetate-ammonium sulfate-sulfuric acid bath at pH 0.5-1.5 appeared very metallic. It was not attacked by HCl and only slowly by concentrated H_2SO_4. It was attacked readily by HNO_3 of various concentrations and also by H_2O_2 in either sulfuric acid or ammonium hydroxide, as others have reported (18). When the bath pH was 2.0 or higher, the deposit became dark and quite loose. Accordingly, the possibility that the deposit was an oxide of technetium existed. Three series of tests were developed to explore this possibility. These were hydrogen reduction studies, precipitation studies, and x-ray diffraction studies. Other methods for quantitative determination of Tc are summarized by Colton (3).

Cathode deposits for these studies were obtained from 100 ml of the $(NH_4)_2SO_4$-H_2SO_4 bath containing 0.012 mole of NH_4TcO_4 per liter (pH 1.0, C.D. 2 amp/dm^2) on gold, platinum, and stainless steel cathodes. Before electrolysis, cathodes were rinsed with distilled water and then alcohol and dried to constant weight in an evacuated dessicator and after the plating run was completed, the plated cathodes were treated in the same manner.

Hydrogen reduction.—Ten plated cathodes, along with the control plates (unused stainless steel cathodes), were heated in a hydrogen atmosphere at 350°-400°C (10, 15) for 2 hr. They were then allowed to cool to room temperature, with the hydrogen still passing over them, before reweighing. Calculations, based on the stoichiometry: $Tc + TcO_2 \cdot 2H_2O + 2H_2 \rightarrow 2Tc + 4H_2O$, showed the deposit to be 92 ± 5% metallic Tc. Allowance was made for standard weighing deviations and control plate weight loss (average 0.0001g), but there was no way to measure the weight loss involved in the mere handling of this deposit that was not very adherent. Hence the evidence from this study can only be interpreted as indicating that the plate is essentially Tc metal.

Precipitation studies.—Three cathode deposits, whose weights had been previously determined, were dissolved in HNO_3 to remove the deposit from the gold cathodes and the solution adjusted to pH 8.0 with NH_4OH. Tetraphenylarsonium chloride was then used as the precipitating agent using the procedure described in the literature (19). Preliminary tests on this procedure had indicated a recovery of Tc was 98-100% which was in accord with the results of other investigators (20) and well within our standard weighing deviations. After drying the tetraphenylarsonium pertechnetate to constant weight, calculations were made based on the stoichiometry: $Tc + TcO_2 \cdot 2H_2O + 10\ HNO_3 + 2NH_4OH + 2(C_6H_5)_4AsCl \rightarrow 2(C_6H_5)_4AsTcO_4 + 2NH_4Cl + 10\ NO_2 + 8H_2O$. The results obtained showed the deposit to be 100 ± 2% Tc metal.

X-ray diffraction studies.—It was felt that three comparison values were needed in order to pursue this investigation: (*i*) A diffraction study of pure Tc metal. The Tc metal was prepared by electrodepositing Tc on stainless steel cathodes and subjecting these deposits to hydrogen reduction at 400°C until no further weight loss was noted. The deposits were then scraped (with great difficulty) from the stainless steel. (*ii*) A diffraction study of technetium dioxide. The oxide was deposited from a high pH (9.0) bath and dried to constant weight at 100°C. (*iii*) A diffraction study of the cathode deposit taken from the bath being studied. The cathode deposit taken from the bath described above was dried and easily scraped from the stainless steel cathode. Each of these prepared samples was then submitted for an x-ray diffraction study. The pure Tc metal prepared as above, showed only the lines of Tc, as reported in the literature (21), and no other lines; but neither the oxide nor the cathode deposit scrapings showed any lines capable of evaluation. Both were judged as being amorphous. A search of the literature revealed that others had experienced the same difficulty in evaluating a plate taken from a slightly acid ammonium sulfate-ammonium pertechnetate bath (22) and found that further annealing was necessary to develop the crystalline nature of the plate. Their study showed that from their higher pH bath, both Tc and Tc in an oxidation state of 4 were present.

We obtained several more cathode plates and collected more oxide and annealed both in an argon atmosphere for 2 hr. It was found that a temperature in excess of 200°C was needed to bring out the lines in the oxide while a temperature of 350°-400°C was required to anneal the plate material.

Seven fresh cathode plates were then prepared from the bath and the weights determined as described previously. The plates, along with control plates, were then annealed in an argon atmosphere for 2 hr at 400°C and the weight loss noted. In all cases, the weight losses were well within the standard weighing deviation. Annealing made the deposit extremely adherent and difficult to remove from the basis metal.

The scrapings from the plates were submitted to x-ray and in all cases showed only the lines of Tc and no other lines. At the annealing temperature we would expect any hydrated technetium oxide to have released its water of hydration with the stoichiometry:

$$Tc + TcO_2 \cdot 2H_2O \xrightarrow{400°C} Tc + TcO_2 + 2H_2O \quad (23).$$

Since the weight losses were well within the standard weighing deviations and since no lines other than pure Tc metal were discernible in the x-ray diffraction pattern, it appears that the amorphous plates, produced under the bath conditions described, were metallic within the limits of our investigation. Thus, all three studies tend to support the conclusion that the plate is certainly not oxide and is probably about 100% metallic.

Alloys

Attempts to electrodeposit a Ni-Tc (TcO_4^- added to a Watts bath) and a W-Tc alloy ($TcO_4^- + Na_2WO_4$ solution) were not successful. There was some evidence, however, that it might be possible to codeposit Re and Tc from a solution containing ReO_4^- and TcO_4^-.

Conclusions

The results presented show that Tc can be deposited in macro amounts as the bright metal from various

aqueous solutions. The $(NH_4)_2SO_4$-NH_4TcO_4-H_2SO_4 bath described here gives good CCE, is reasonably stable, can be readily rejuvenated by H_2O_2, and with reasonable precautions can be used safely in ordinary laboratory equipment. A bath containing 1M $(NH_4)_2SO_4$ and from 0.006 to 0.024M NH_4TcO_4 with H_2SO_4 added to give a *p*H of about 1.0, can be electrolyzed at 1-2 amp/dm^2 to produce a metallic cathodic deposit of Tc with a CCE range of 18-30%.

Electrodeposited Tc metal has few uses at the present time outside of medicine (24). However, its superconductivity at low temperatures as a metal (25) and as an alloy may find value in the rocket guidance systems and computer systems at a future time (26). Certainly, the possibility of plating an alloy of Tc deserves consideration.

Acknowledgment

The authors express their thanks to Dr. Chin-Hsuan Wei, of this department, who gathered and interpreted the x-ray diffraction data. One of us (REV) is grateful to NSF for financial support that made this work possible.

Manuscript received Sept. 8, 1964; revised manuscript received Sept. 9, 1966.

Any discussion of this paper will appear in a Discussion Section to be published in the December 1967 JOURNAL.

REFERENCES

1. C. Perrier and E. Segré, *J. Chem. Phys.*, **5**, 712 (1937).
2. G. Boyd, *J. Chem. Ed.*, **36**, 3 (1959).
3. R. Colton, "The Chemistry of Rhenium and Technetium," John Wiley & Sons, Inc., London (1965).
4. S. Fried, A. Jaffey, N. Hall, and L. Glendenin, *Phys. Rev.*, **81**, 741 (1951).
5. U. S. Dept. of Commerce, Nat. Bur. of Stand. Handbook 42, Sept. 1949, "Safe Handling of Radioactive Isotopes."
6. W. Smith, Jr., J. Cobble, and G. Boyd, *J. Am. Chem. Soc.*, **75**, 5773 (1953).
7. C. Perrier and E. Segré, *J. Chem. Phys.*, **7**, 155 (1939).
8. E. Motta, Q. Larson, and G. Boyd, ORNL Declassified Report, Mon-C-99, April, 1947, p. 22., (cited from ref. 2).
9. G. Cartledge and W. Smith, Jr., *J. Phys. Chem.*, **59**, 1111 (1955).
10. J. Cobble, C. Nelson, G. Parker, W. Smith, Jr., and G. Boyd, *J. Am. Chem. Soc.*, **74**, 1852 (1952).
11. M. Lietzke and R. Stoughton, Private communication.
12. N. Matuura and M. Yumoto, *Radioisotopes*, **8**, 28 (1959); *C. A.*, **53**, 21272 (1959).
13. G. Salaria, C. Rulfs, and P. Elving, *J. Chem. Soc.*, **1963**, 2479.
14. G. Salaria, C. Rulfs, and P. Elving, *Anal. Chem.*, **35**, 979 (1963).
15. R. Colton, J. Dalziel, W. Griffith, and G. Wilkinson, *J. Chem. Soc.*, **1960**, 71.
16. J. Eakins and D. Humphries, *J. Inorg. Nucl. Chem.*, **25**, 737 (1963).
17. W. Box, *Nucl. Applic.*, **1/2**, 155 (1965).
18. R. Colton and R. Peacock, *Quart. Rev.*, **16**, 299 (1962).
19. F. Jasim, R. MaGee, and C. Wilson, *Talanta*, **4**, 17 (1960).
20. C. Parker and W. Martin, U.S. At. En. Com. Document, ORNL-1116, 26 (1952).
21. R. Mooney, *Acta. Cryst.*, **1**, 160 (1948).
22. V. Spitsyn, A. Kuzina, N. Zamoshnikova, and A. Oblova (USSR), A/Conf. 28/p. 349, May 1964. Nuc. Abs. 18: 37108 (1964).
23. C. Nelson, G. Boyd, and W. Smith, Jr., *J. Am. Chem. Soc.*, **76**, 348 (1954).
24. W. Box, *Nucl. Applic.*, **1/2**, 157 (1965). Private communications of E. Christenberry.
25. J. Daunt and J. Cobble, *Phys. Rev.*, **92**, 507 (1953).
26. A. Pozdnyakov, *Rus. Chem. Rev.*, **2**, 129 (1965).

Determination of the Composition of Complexes and Their Instability Constant by Calorimetry

II. The Complex in Fused Potassium Chloride and Cadmium Chloride

William H. Metzger, Jr., Abner Brenner, and Harry I. Salmon

National Bureau of Standards, Washington, D. C.

ABSTRACT

A new method of determining the composition of complexes in solution and their equilibrium constant has been developed which is based on the determination of the partial molal heat effect developed when a small increment of each salt is added in turn to a series of mixtures covering the range of composition from 0 to 100%. The method was applied to the molten KCl-$CdCl_2$ system. The data show that the system contains the 1:1 complex with an instability constant of 0.32 at temperatures of 600° and 780°C. A calorimeter is described which permits the addition of the increments of salt to the molten mixture while the latter is stirred continually.

In a previous publication (1) a general method was described for determining the composition of complexes and their instability constant by calorimetric measurements. The experimental procedure consisted in adding a small amount of one reactant to a mixture of the reactants and determining the heat effect. From the latter the partial molal heat effect was obtained. The purpose of adding only a small amount of reactant was to determine the resultant heat effect without changing the composition of the mixture by more than a per cent. Thus, the heat effect is a function of the composition of the mixture. This procedure was repeated with one or preferably with both reactants over the range of composition of mixtures from 0 to 100%. In the aforementioned paper the method was applied to the determination of the composition and instability constant of two of the copper cyanide complexes. These measurements involved the addition of about 1g of sodium cyanide to solutions of cuprocyanide covering a range of composition.

The partial molal heat effect can be considered as the heat effect resulting from the addition of one mole of reactant to an infinite amount of mixture. It can be seen qualitatively that the heat effect is a function of the composition of the mixture by the following example: Let the complex formed from the two reactants A and B be AB_2. If small increments of A are added to a series of mixtures, starting with pure B

and then proceeding through intermediate steps to the composition AB_2 and beyond to pure A, it would be found that the maximum heat effect would occur when the addition of A is made to pure B. If the instability constant is small (less than 10^{-2}), the molal heat effect would be approximately equal to the heat of formation of the compound AB_2. The heat effect would diminish only slightly with succeeding mixtures until the composition AB_2 is approached. At the stoichiometric point the partial molal heat effect would rapidly decrease and beyond this point would have a small value. The partial molal heat effect of adding pure B to an infinite amount of pure A would be only half of that obtained by adding A to an infinite amount of B because only ½ mole of complex is formed per mole of B.

Assume that almost complete reaction occurs when a small amount of A is added to an infinite amount of B, and let this maximum heat effect (which is approximately the heat of reaction) be designated by θ_A per mole of A. Then the ratio of the partial molal heat effect $\Delta\overline{H}$ (obtained by adding a mole of A to an infinite amount of a mixture of A and B) to θ_A represents the fraction of a mole of AB_2 formed. For example, if θ_A is 10 kcal and $\Delta\overline{H}$ for a mixture just beyond the stoichiometric point is 0.5 kcal, this would mean that the addition of one-mole of A to an infinite amount of mixture of that composition results in the formation of only 1/20 mole of complex. This ratio, which is the fraction of a mole formed in the reaction, will be called the "fraction of reaction."

The fraction of reaction is the quantity which is experimentally determined. It can vary from zero to unity. This fraction is a partial derivative and is related to the mass action expression. If dy is the increment of A added to a mixture of any composition and $d\bar{a}$ is the amount of the product AB_2 formed, then the fraction of reaction is $\partial\bar{a}/\partial y$. Similarly, if dx denotes the increment of B that is added to a mixture, then $\partial\bar{a}/\partial x$ also is the fraction of reaction, and it cannot be larger than ½.

The two partial derivatives will be denoted by $\bar{a}'_x$ and $\bar{a}'_y$ or simply $\bar{a}'$ when only one independent variable is used throughout the discussion. They are derived mathematically from the expression for the mass action law by differentiation. If the reaction is $rA + sB \rightarrow A_rB_s$, the general expression for the mass action law for fused salts written in terms of mole fraction is

$$\frac{\left[\frac{y-r\bar{a}}{f}\right]^r\left[\frac{x-s\bar{a}}{f}\right]^s}{\frac{\bar{a}}{f}} = k \qquad [1]$$

where y and x represent the initial moles of A and B, respectively, used in making up the mixture, $\bar{a}$ represents the moles of A_rB_s formed at equilibrium. r and s are the coefficients of A and B in the chemical reaction, and f is the total number of moles present, $f = x + y + \bar{a}(1-r-s)$.

The formulas and the methods of determining the composition and the instability constant of a complex were derived in a former publication (1).

The cadmium chloride-potassium chloride system was chosen for study mainly to explore the applicability of the partial molal heat method to a fused salt system. This system had received extensive investigation (3-17) but the complexes present in the molten mixture had not been determined with certainty. We studied the system at a temperature of about 780°C so that it would be above the melting point of the highest melting component, potassium chloride (mp 772°C). This permits the introduction of increments of either salt in the molten form, hence there is no complication owing to heat of fusion of a solid. This temperature was higher than that used by most of the previous workers.

Apparatus

The determination of the heats of reaction in the fused salt bath requires the construction of a calorimeter which is operable at temperatures up to 900°C. The literature contains descriptions of several high temperature calorimeters, but experience with them has been so limited that no one design has emerged as the best. A description of the various high temperature calorimeters which have been constructed would be too much of a digression here. However, none of them have the two features which we consider essential for the success of the measurements. The two features are (*i*) continuous stirring of the reaction mixture while an increment of a reactant is added, and (*ii*) the complete submersion of the ampoule containing the increment below the surface of the fused salts, so that it is exactly at the temperature of the reaction mixture at the time that the ampoule is broken. Otherwise the construction of the furnace and calorimeter is conventional.

The construction of the calorimeter is shown in Fig. 1. It consists of a stainless steel jacket about 40 cm in diameter and 75 cm high, surrounded by a 5 cm thick layer of thermal insulation. Internally, the loss of heat is diminished by seven radiation shields made of stainless steel. The heating system consists of two wire wound concentric heaters and a third flat heater placed horizontally on the bottom below the other two. The outer and the bottom heaters are operated at a con-

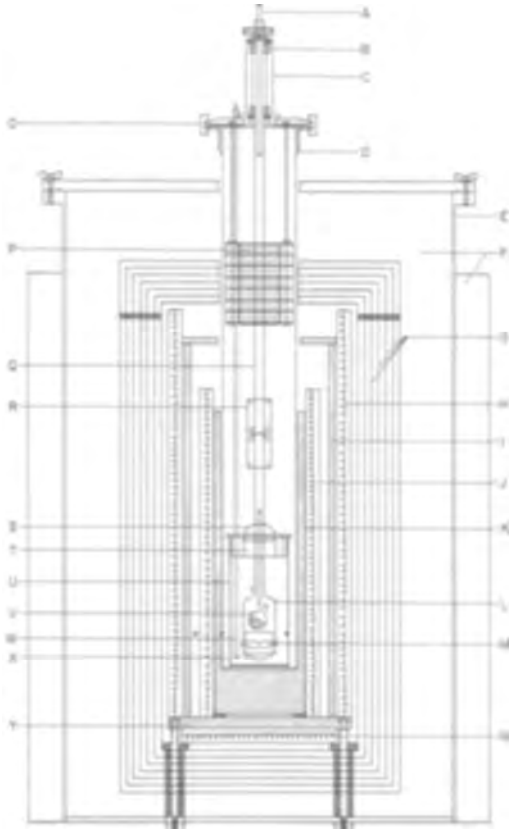

Fig. 1. Diagram of furnace and calorimeter. A, Tungsten rod for breaking ampoule; B, graphite-Teflon sleeve bearing; C, bearing holder; D, silicone adhesive; E, furnace jacket, stainless steel; F, zirconia wool-filled space; G, radiation barrier shields, stainless steel; H, outer circumferential heater; I, heat sink, silver; J, inner circumferential heater; K, heat sink, silver; L, perforated dispenser device, Pt-Ir alloy; M, bar against which ampoule is crushed; N, bottom heater; O, split-ring clamp; P, middle bearing; Q, dispenser-stirrer shaft, nickel tube; R, shaft coupling, nickel; S, bottom bearing, Vycor; T, calorimeter cap, machined of fused silica; U, calorimeter, Pt-Rh alloy; V, loaded ampoule of fused silica; W, Vycor tube containing the platinum heater used for calibrations; X, retainer cup, Pt-Ir alloy; Y, heat sink, silver. * Thermocouple locations.

stant current, such that a temperature slightly below the desired temperature is maintained in the center of the furnace. The inner heater is controlled by an automatic device which obtains its input signal from two chromel alumel thermocouples connected in series and located in the heart of the furnace near the reaction vessel. Most of the emf of these thermocouples is annulled by a potentiometer as the controller can handle a maximum input of only 7 mv. This method of obtaining the emf-change only as a difference increases the sensitivity of the control system. Over a period of 10 min the temperature of the inner vessel holds constant to about 0.01°C, but over a period of a day the temperature varies about 0.5°C. However, since the reaction is complete in about 15 to 30 sec, constancy for only a short time is adequate. The heaters have a total maximum power capacity of 5 kva.

To improve the uniformity of temperature, the furnace is provided with two concentric cylinders of silver about 1 cm thick, having a total weight of about 30 kg.

The inner vessel consists of a mullite tube, 8 cm in diameter and 60 cm long which is closed at the lower end. The upper end carries a brass flange which is cemented to the tube by an air cured silicone plastic material. The end projects sufficiently above the furnace so as not to be heated higher than 200°C. Another reason for having the open end of the tube project above the level of the furnace is to prevent corrosive halide vapors from damaging the heating elements.

The fused salt is contained in a platinum-rhodium vessel measuring 6.5 cm in diameter and 14 cm high. About 600 to 800g of salt are used for an experiment and the liquid level generally comes to within 5 cm of the top of the vessel. It is essential to construct the vessel of a platinum alloy as ceramic vessels frequently break when the fused salts solidify in them.

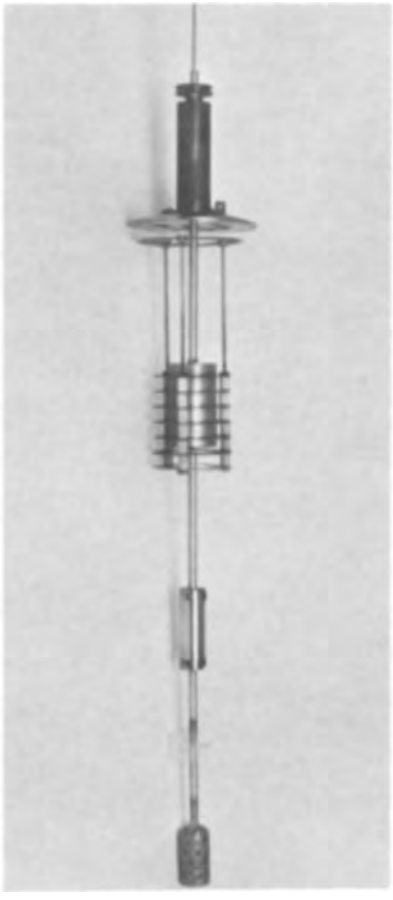

Fig. 2. Dispenser-stirrer unit, fully assembled with bearings and removable radiation shields.

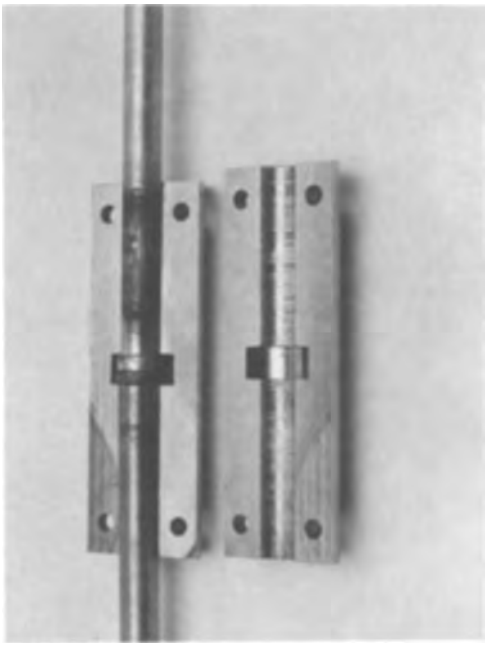

Fig. 3. Shaft coupling of the dispenser-stirrer; open view.

Fig. 4. Dispenser-stirrer: exploded view of the dispenser with loaded ampoule.

The most time-consuming part of the investigation was the development of a satisfactory device hereafter referred to as "dispenser-stirrer" for stirring the molten salt and for adding the increment. This part of the apparatus is shown in Fig. 2-4 in both an assembled and exploded photographic view. The dispenser-stirrer body is constructed of a platinum-iridium alloy, as ceramic vessels which were tried were not rugged enough and caused the loss of many experiments through breakage. The platinum alloy basket holds the ampoule, retains the broken fragments of the ampoule, and prevents them from catching in the thermocouples or the heater used for calibration. The notched platinum alloy bar with tabs holds the basket and ampoule in place and in addition acts as an anvil for breaking the ampoule. The pointed tungsten rod located inside of the shaft is used for breaking the ampoule containing the increment of salt. The stirring shaft is a nickel tube connected to the

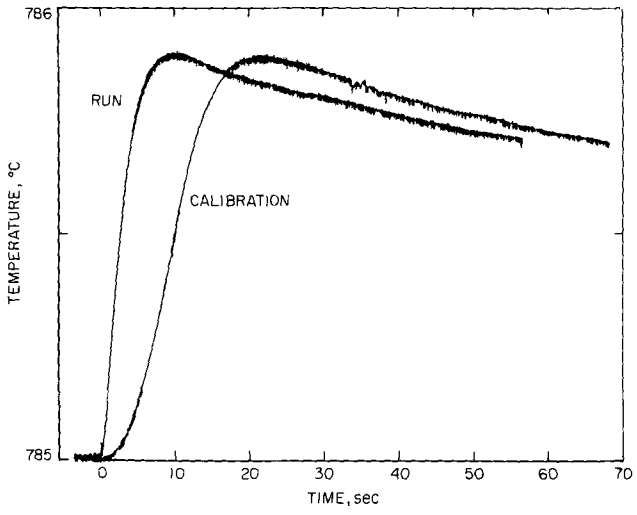

Fig. 5. Typical curves of temperature vs. time obtained with the recording potentiometer.

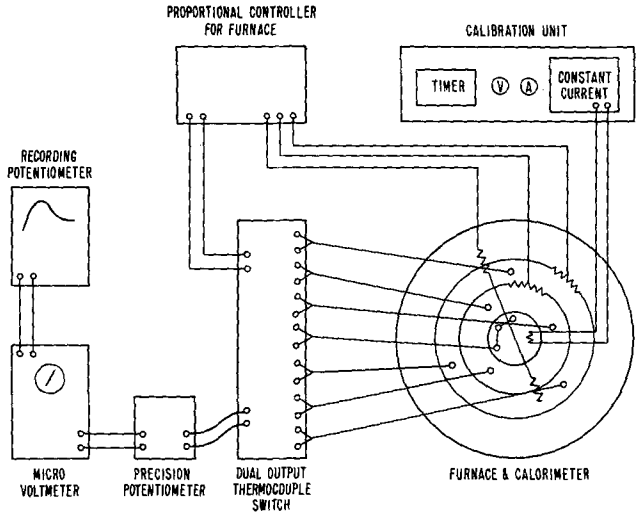

Fig. 6. Block diagram of apparatus

upper tubular part of the dispenser-stirrer by the coupling shown in Fig. 3. This construction allows for interchange of parts and permits the tungsten rod to move freely up and down in the shaft while the assembly is rotating.

The ampoules are made of fused silica. They are thin-walled and about 2 cm in diameter. They are easily broken by punching with the tungsten rod while stirring is in progress. The end of the neck of the ampoule is either bent or enlarged with a piece of fused silica to prevent the neck from protruding through the holes in the dispenser and snagging a thermocouple.

The temperature rise in the reaction vessel is measured by three commercial chromel alumel thermocouples connected in series. These are only 1.5 mm in diameter and require very little space. Furthermore, because of their small size they react to the temperature changes in a second. A temperature change of 0.01°C gives an indication slightly more than 1 μv. The average temperature rise in the experiments is about 1°C and the largest temperature rise is about 3°C.

The temperature increase during an experiment is measured by a microvoltmeter in series with an output voltage from a microvolt potentiometer. This arrangement made it posible to balance the thermocouple emf with the potentiometer immediately prior to the breaking of the ampoule and thus read the emf change on the microvoltmeter. The temperature rise is measured on the microvoltmeter, usually on the 100 μv scale. The voltage *vs.* time trace is recorded on a recording potentiometer connected to the microvoltmeter shown in Fig. 5. Readings are made to 1 μv.

For purposes of accurate temperature measurement and stability, the thermocouples used in the body of the furnace consist of platinum, platinum-10% rhodium alloy. These thermocouples are placed in tubes of pure aluminum oxide. At a temperature of 800°C the resistance between a thermocouple and ground is about 20 megohms. The proper insulation of the thermocouples is a matter of considerable importance.

In our first experiments the thermocouples were placed in mullite tubes, and they operated satisfactorily up to a temperature of about 600°C. But at 800°C the mullite tubes became too conductive and the thermocouples picked up stray voltages which prevented accurate readings being taken with the microvoltmeter. The block diagram for the thermocouples and associated measuring instruments is shown in Fig. 6.

Procedure

The furnace is allowed to come almost to temperature by being left on at a steady current over night. The furnace is put on automatic temperature control in the morning. The salt mixture is placed in the platinum-rhodium reaction vessel and melted in a pot furnace. It is then quickly transferred to the calorimeter furnace. The preliminary heating of the mixture reduces the time required for the setup to come to thermal equilibrium, and in so doing also reduces the loss of cadmium chloride by volatilization.

Next, the dispenser-stirring device is loaded with an ampoule of salt, the latter weighing usually from 1 to 3g (usually about 0.02 mole of salt is added to about 4 moles of salt mixture). The entire unit shown in Fig. 2 is locked into place with a split ring-clamp at the top of the ceramic tube. Stirring is started and after about ½ hr thermal equilibrium attained. This is considered to be the case when the temperature does not change more than 0.01°C/min. On breaking the ampoule, the reaction is completed in about 15 sec, as indicated by the maximum in the temperature rise.

The calibration of the calorimeter is performed at least twice for each determination, usually before and after the introduction of the increment of salt. An electric current of about 4 amp at 14v is passed through the platinum alloy heater coil (the latter being enclosed in a fused silica tube) for 10 to 20 sec. The high current and short period of heating is necessitated by the need to duplicate the heating rate of the chemical reaction. This is not achieved exactly, as the time of heating would have to be too short and the current too large for convenience in measuring. Although the interval of calibration may vary from 10 to 20 sec, it is accurately read on an electric timer accurate to 0.01 sec. The current is delivered by a constant current device, consequently, only one reading of current needs to be made during the calibration. The voltage, however, varies from about 13 to 14v during the calibration. Readings are therefore taken at intervals of about 2 or 3 sec on a voltmeter accurate to 0.5% and averaged. The heat capacity of the calorimeter, including the fused salt, is about 1 cal/μv or about 120 cal/degree.

In calculating the heats of reaction, no correction is made for the heat leak. The temperature rise is taken as the peak of the curve. This probably does not represent the true equilibrium temperature, but since the calibration is made in the same manner, most of the error is annulled. Since the heat leak is mostly a result of radiation, a simple correction cannot be made, as in calorimetry which is done at room temperature. This is because the rate of heat leak is not directly proportional to the temperature head. A graphical method of correcting for heat leak, which is based on the cooling curve, is given in the appendix. This correction for heat leak was not considered to be practicable in our work, because the calorimeter did not maintain a sufficiently constant temperature over

the period of 10-30 min that would be required to establish the cooling curve.

The filling of the ampoule presented a special problem, because the presence of a trace of moisture in the salt caused some of them to explode in the furnace. The following procedure is successful. After the required amount of salt is placed in the ampoule, it is placed in a furnace at 650°C for an hour to remove moisture. Then after cooling in a desiccator the ampoule is evacuated and sealed.

To expedite the measurements, two complete dispenser-stirring units are used. This permits another run to be made as soon as one unit is removed from the calorimeter. Four complete runs can be made in one day, including the necessary number of calibrations. The largest amount of time is spent in waiting for the system to come to thermal equilibrium.

Results

Although the precision of measuring the temperature rise in most of the experiments was about 1%, the precision of the measurements of the heat capacity of the system was about 3%. The over-all precision of the measurement of the partial molal heat effects was about 5% or 200 cal, whichever was the larger.

As an over-all check on the accuracy of the measurements, the heat of fusion of potassium chloride was measured. This was done by adding about 3g of potassium chloride to 450g of a melt consisting of about 95 mole % potassium chloride and 5 mole % cadmium chloride. Additions of solid potassium chloride were made at about 8° below its melting point. We found that the heat of solution (cooling) of the solid potassium chloride was 6380 cal/mole (1 cal = 4.18 Joules). The heat of mixing of the molten potassium chloride, determined at 780°C in the same melt, was small and positive, about 180 cal/mole. The heat of fusion of potassium chloride was 6560 ± 160 cal/mole. This result is about 5% higher than the value of 6274 cal/mole obtained by the drop method of calorimetry (2).

The experimental results for the $CdCl_2$-KCl system were obtained in the form of a heat effect for the increment of potassium chloride or cadmium chloride added to the melt. From this effect was computed the heat effect per mole of added salt, that is, the partial

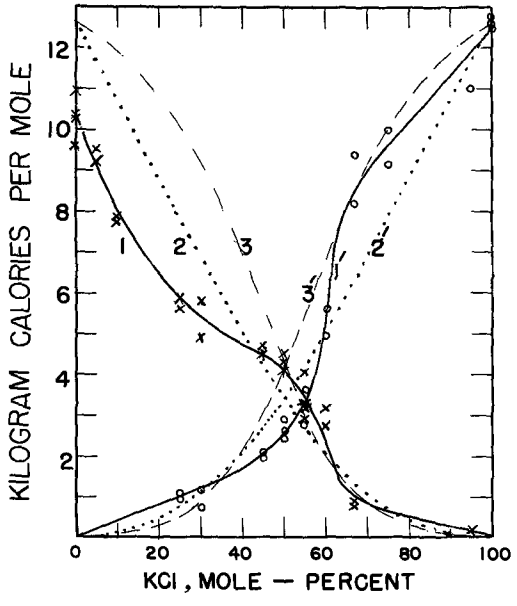

Fig. 7. Partial molal heat effects obtained at 780°C. by adding either potassium chloride (curve 1) or cadmium chloride (curve 1') in the molten state to molten mixtures of potassium and cadmium chloride. Curves 2 and 3 represent theoretical curves for the addition of potassium chloride and curves 2' and 3' represent the corresponding curves for cadmium chloride.

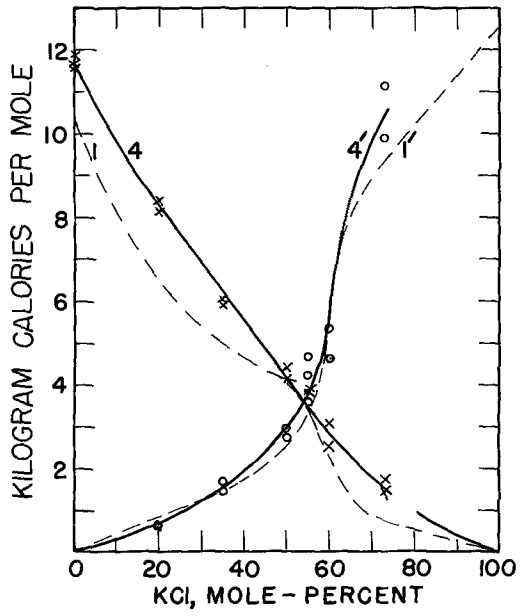

Fig. 8. Partial molal heat effects obtained by adding either potassium chloride (curves 1 and 4) or cadmium chloride (curves 1' and 4') to molten mixtures of potassium chloride and cadmium chloride. Curves 1 and 1' are the same as the like-numbered curves in Fig. 7 and refer to a temperature of 780°C. Curves 4 and 4' represent the data obtained at 600°C with cadmium chloride and potassium chloride.

molal heat effect, $\Delta\bar{H}$. These data are graphed in Fig. 7 and 8 against mole per cent of potassium chloride in the melt.

Even without any mathematical analysis, the data show that the complex consists of equal moles of $CdCl_2$ and KCl. This follows from the approximately equal heat of reaction for an increment of KCl added to pure $CdCl_2$ and an increment of $CdCl_2$ added to pure KCl. Further evidence is that the curves cross at 55 mole % which is close to the stoichiometric 50 mole % point. No other complex appears to exist at the temperature of 780°C.

The mass action expression, in terms of the mole fraction, is

$$(x-\bar{a})(y-\bar{a}) = \bar{a}k(x+y-\bar{a}) \qquad [2]$$

where x and y are the initial number of moles of reactants, $\bar{a}$ is the moles of complex formed, and $(x + y - \bar{a})$ is the total number of moles present at equilibrium.

The instability constant may be calculated either from the fraction of reaction $\bar{a}'$, or from the slope of the curves at their intersection. The former method is less satisfactory than the latter if the instability constant is small, but in the present case it is equally satisfactory. The value of $\bar{a}'$ is obtained for the point of intersection of the two curves, where $\Delta\bar{H}$ = 3400 cal/mole. Hence, $\bar{a}'$ = 3400/12,600 = 0.27. (The value of 12,600 cal/mole is the heat of reaction derived from our experiment of adding an increment of molten cadmium chloride to molten potassium chloride, as shown in Fig. 7 for the abscissa: KCl, 100%.) This value is substituted into the following equation [see Eq. 33 of ref. (1)]

$$k = \frac{(1-2\bar{a}')^2}{4\bar{a}'(1-\bar{a}')} = \frac{(1-0.54)^2}{4(0.27)(0.73)} = 0.27 \qquad [3]$$

To use the second method, $\bar{a}''$ is found at the point of the intersection of the curves, from the slope of the curves. Since the intersection should have occurred at the stoichiometric point, consider $x = y = 1$ at the point of intersection.

$$\bar{a}'' = \frac{\partial \bar{a}'}{\partial x} = \frac{1}{\theta} \cdot \frac{\partial \Delta \bar{H}}{\partial x} \quad [4]$$

Since the abscissa represent the mole per cent, $\frac{x}{x+y} \times 100$, of the components weighed out, that is the initial composition of the melt, the slope of the curve at the stoichiometric point is with respect to the mole per cent (or mole fraction) and must be converted to a function of x as follows

$$\frac{\partial \Delta \bar{H}}{\partial x} = \frac{y}{(x+y)^2} \cdot (\text{Slope}) \quad [5]$$

$$\bar{a}'' = \frac{1}{\theta} \cdot \frac{y}{(x+y)^2} \cdot (\text{Slope})$$

$$= \frac{1}{12{,}600} \cdot \frac{1}{4} (-18{,}500) = -0.367 \quad [6]$$

if $x = y = 1$

The instability constant is calculated from the following equation [see Eq. 37 and 38 in Ref. (1)]

$$k = \left[\frac{\bar{a}'}{2\bar{a}''y}\right]^2 \cdot \left[\frac{1-\bar{a}'}{\bar{a}'}\right]$$

$$= \left[\frac{0.27}{2(-0.367)}\right]^2 \cdot \frac{(1-0.27)}{0.27} = 0.137 \times 2.7 = 0.37 \quad [7]$$

This result of 0.37 calculated from the slope of the curves agrees fairly well with value of 0.27 calculated from the ordinate of the curve. The average value of 0.32 will be used in following discussions.

Another possibility for the composition of the complex presents itself for consideration on the basis that the curves cross at 55 mole per cent potassium chloride. This composition represents a compound having the formula $6KCl \cdot 5CdCl_2$ which has a mole percentage of KCl of 6/11 x 100 = 54.5% or a mole ratio of cadmium chloride to potassium chloride of 0.83. This possibility seems to derive support from the differing values of the partial molal heat effects for the addition of $CdCl_2$ to pure KCl ($\Delta\bar{H}$ = 12,600 cal) and KCl to pure $CdCl_2$ ($\Delta\bar{H}$ = 10,300 cal) which give a ratio of 0.82, a result very close to the ratio obtained from the point of intersection of the curves. However, this possibility has been discounted because the calculation of the instability constants from the ordinate, a', of the curve [see formula 33 of reference (1)] gives a value of $k = 1.0 \times 10^{-3}$, whereas the calculation from the slope of the curve, via $\bar{a}''$, [see formula 37 of reference (1)] gives the greatly different value of $1.0 \times 10^{+3}$.

Returning now to a consideration of the simple complex, $KCl \cdot CdCl_2$, since it has a relatively large instability constant, this means that the complex is moderately dissociated. At the stoichiometric point the melt contains about 50% of the constituents in the form of complex. (This follows from the relation that the amount of complex formed by adding 1 mole of A and then 1 mole of B to an infinite amount of 1:1 mixture is $(1 \times \bar{a}'_x) + (1 \times \bar{a}'_y) = 0.27 + 0.27 = 0.54$.) It is rather surprising that the complex is dissociated even in the presence of a large excess of either one of its components. This follows from the mass action law which shows that on adding an increment of salt to an infinite amount of the other constituent, the whole increment is not converted into complex, that is to say, the fraction of reaction, $\bar{a}'$, is appreciably less than unity

$$a'_x = \frac{\bar{a}(1+k) - y}{(1+k)(2a - x - y)} \quad [8]$$

As the content of y in the melt becomes infinite with respect to both the increment x and the complex $\bar{a}$, the value of $\bar{a}'_x$ approaches the limit

$$\bar{a}'_x = \frac{1}{1+k} = \frac{1}{1+0.32} = 0.76$$

On this basis the true heat of reaction of potassium chloride and cadmium chloride to form a mole of complex must be larger than the observed value of 12,600 cal and have the value of 12,600/0.76 = 16,600 cal. With this derived value for the heat of reaction and with the value of k = 0.32 two curves were drawn, 3 and 3′ (see Fig. 7) for comparison with the two experimentally determined curves. The agreement is fair. It will be noted, however, that the derived curves cross at a value of $\Delta\bar{H}$ = 4300 cal instead of the experimentally determined value of 3400 cal, because of the higher value of the heat of reaction used in the computation.

Probably the best fit of derived curves with the experimental data is obtained if the curves are chosen so as to intersect at 3400 cal and to have the value of 12,600 cal at the right and left sides of the graph. Calculation yielded the result that the value of k would be 2.7 and the value of the true heat of reaction would be 46,620 cal. These derived curves are shown in Fig. 7 as dotted lines 2 and 2′. These fit the experimental data better, but it is doubtful that such a large extrapolation is meaningful in view of the probable experimental error of the data, hence, we reject this interpretation. A value of k = 2.7 leads to the result that the reaction mixture contains only about 15% of complex at the stoichiometric point and that only about 27% of an increment is converted into complex when added to the pure salts.

The feature of the experimental data for which we have no explanation at present is the intersection of the curves at a mole fraction of about 55 mole per cent instead of the stoichiometric value of 50%. With a melt of stoichiometric composition, an increment of either salt should yield the same partial molal heat effect. A difference in activity coefficients is not an acceptable explanation, since the same reaction mixture (hence, the same activities) is used for both increments. Perhaps the discrepancy can be explained on the basis of the formation of another complex which is too dissociated to yield a definite inflection in the curves.

The heat of reaction (12,600 cal) resulting from the addition of $CdCl_2$ to KCl is larger than that (10,300 cal) obtained by adding KCl to molten $CdCl_2$, whereas on the basis of simple considerations they are expected to be equal. The difference might be due either to a lower activity of cadmium chloride in the mixture in comparison with potassium chloride, or to the formation of a small amount of a higher complex, for

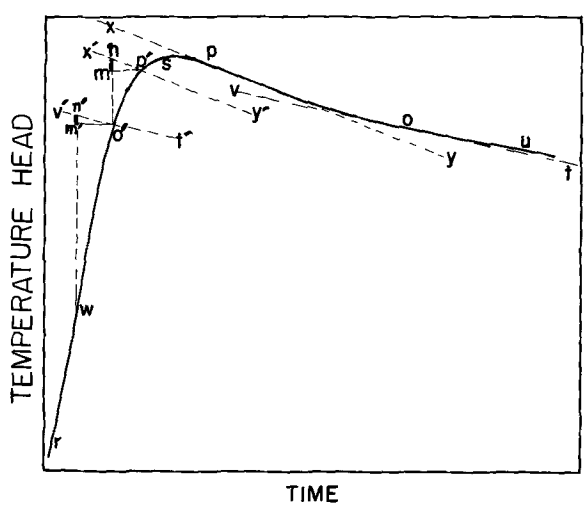

Fig. 9. Method of using the cooling curve, sou, for correcting the heat lost during the period of temperature rise, rws.

example, $2KCl \cdot CdCl_2$, when $CdCl_2$ is added to molten KCl.

The cadmium chloride-potassium chloride system was also investigated at a temperature of 600°C. At this temperature potassium chloride is solid, and consequently all the experiments with increments of KCl had to be corrected by the heat of fusion of KCl, for which purpose we took the round number of 6500 kcal. The melt becomes solid at about 75 mole % potassium chloride, hence, our data was extended only to a melt of 73 mole % KCl. In Fig. 8 the curves 4 and 4′ for the 600°C determination are compared with the curves 1 and 1′ obtained at 780°C. The data for the 600°C determinations yielded about the same instability constant as the data for 780°C. This follows because the curves 4 and 4′ cross at about the same point as curves 1 and 1′ and the slopes are not very different for these two pairs of curves at the points of intersection.

Discussion of the Literature

There are a number of publications in the literature dealing with the nature of the molten cadmium chloride-potassium chloride system. The constitutional diagram of the system, first investigated by Brandt (3) shows the existence of the congruently melting compound $KCl \cdot CdCl_2$ and the incongruently melting compound, $4KCl \cdot CdCl_2$. However, the existence of a solid compound does not prove its existence in a melt.

Attempts have been made to determine the composition of the complex in the molten system by means of various physical measurements. The rationale behind these studies is that the deviation of a physical property from an additive or ideal value based on the properties of the parent compounds would be greatest at the stoichiometric point. However, since both positive and negative deviations from ideal behavior occur for mixtures of fused salts that are known not to form complexes, these measurements do not generally lead to an unequivocal conclusion.

The physical property of the system that has been investigated most is electrical conductivity. This was first measured by Sandonnini (4) whose data on specific conductivity showed a slight minimum at 40 mole % potassium chloride. Mulcahy and Heymann (5) computed the equivalent conductivities from Sandonnini's data. Finding the greatest departure from additivity at 65 mole % potassium chloride, they suggested the formula, $2KCl \cdot CdCl_2$. Bloom and Heymann (6) found that the equivalent conductivity of the mixture was at a minimum between 55 and 60 mole % potassium chloride (their specific conductivities did not show a definite minimum) and that the temperature coefficient of the conductivity was a minimum at 50 mole %. The electrical conductivity of the system was also investigated by Sakai (7).

Several other physical properties of the system have been investigated. Harrap and Heymann (8) found that the viscosity of the system at 650°C was at a minimum between 50 and 60 mole % potassium chloride. Measurement of the densities and molar volumes of the system by Boardman, Dorman, and Heymann (9) showed that the system had large positive deviations from additivity. The measurement of surface tension by Boardman, Palmer, and Heymann (10) showed a negative deviation from ideal behavior, but no well defined minimum that would unambiguously define a compound. Barton and Bloom (11) measured the vapor pressure of the system and calculated activity coefficients for 900°C. Their discussions of the composition of the complex were speculative. Bloom, Davis, and James (12) investigated the surface tension and surface heat of the system and had this to say: "This method, in common with results of electrical conductivity, viscosity, molar volume, etc., do not lead unequivocally to the stoichiometric composition of such complex ions, although there is general acceptance of their presence in certain systems."

The Raman spectra of the system have also been investigated. Bues (13) favored the $CdCl_3^-$ complex ion on the basis of his measurements, but Bredig and Van Artsdalen (14) claim that Bues' data could better be interpreted to prove the existence of the $CdCl_4^{2-}$ complex. Bredig (15) backed up his assertion in a subsequent publication dealing with Raman spectra and electrical conductivity, and in a paper published the following year (16) claimed that the measurement of activity coefficients that had been published by Russian investigators supported his view.

Bockris and co-workers also entered the discussion. On the basis of the measurement of the self-diffusion of Cd^{++} ion in the molten mixture, Bockris and Angell (17) found the maximum rate to occur at the composition corresponding to $KCl \cdot CdCl_2$. Tanaka, Balasubramanyam, and Bockris (18) also measured the Raman spectra of the system and considered that the data indicated that the complex ion was $CdCl_3^{-1}$ and thus supported Bues instead of Bredig. However, they differed from the former in finding that the complex was pyramidal, whereas Bues had found it to be a planar triangle. The arguments of Tanaka, Balasubramanyam, and Bockris were somewhat tenuous as they were not based entirely on experimental findings, and some of the Raman lines were very weak.

Summary

The foregoing discussion indicates that measurements of the physical properties of the system did not lead to a decisive determination of the composition of the complex ion in the melt and none of the methods led to a value for the instability constant. The method of partial molal heat effect, in contrast, has led to an unambiguous determination of the composition of the complex, as well as to an approximate value of the instability constant. The fundamental reason that the calorimetric method has been more successful is that it involves measurements on the chemical reaction itself, and in this way it is unique. It leads to a determination of the "fraction of reaction." It requires no prior knowledge of the physical constants of the components or of the complex, whereas the other methods depend on deducing the existence or the concentration of a complex by comparing physical properties of static systems.

Acknowledgment

The authors wish to thank the Division of Research, Chemistry Branch, Atomic Energy Commission, for the continuing support of our projects on calorimetry.

Manuscript received June 13, 1966; revised manuscript received Sept. 6, 1966.

Any discussion of this paper will appear in a Discussion Section to be published in the December 1967 JOURNAL.

REFERENCES

1. A. Brenner, *This Journal*, **112**, 611 (1965).
2. Thomas B. Douglas, National Bureau of Standards, Private communication.
3. H. Brand, *Neues Jahrb. Mineral., Geol.*, **32**, (B1), 627 (1911). Data reproduced in "International Critical Tables," Vol. IV, p. 55, McGraw-Hill Publishing Co., New York (1928).
4. C. Sandonnini, *Gazz. chim. ital.*, **50**, 289 (1920).
5. M. F. R. Mulcahy and E. Heymann, *J. Phys. Chem.*, **47**, 485 (1943).
6. H. Bloom and E. Heymann, *Proc. Roy. Soc.*, **A188**, 392 (1947).
7. Kaoru Sakai, *J. Chem. Soc. Japan* (Pure Chem Sect.) **75**, 182 (1954); *Nippon Kagaku Zasshi*, **77**, 1172 (1956); *ibid.*, **78**, 1257 (1957).
8. B. S. Harrap and E. Heymann, *Trans. Faraday Soc.*, **51**, 268 (1955).
9. N. K. Boardman, F. H. Dorman, and E. Heymann, *J. Phys. Chem.*, **53**, 375 (1949).
10. N. K. Boardman, A. R. Palmer, and E. Heymann, *Trans. Faraday Soc.*, **51**, 277 (1955).
11. J. L. Barton and H. Bloom, *ibid.*, **55**, 1792 (1959).
12. H. Bloom, F. G. Davis, and D. W. James, *ibid.*, **56**, 1179 (1960).

13. W. Bues, *Z. anorg. Chem.*, **279**, 104 (1955).
14. M. A. Bredig and E. R. Van Artsdalen, *J. Chem. Phys.*, **24**, 478 (1956).
15. M. A. Bredig, *Electrochim. Acta*, **5**, 299 (1961).
16. M. A. Bredig, *J. Chem. Phys.*, **37**, 451 (1962).
17. J. O'M. Bockris and C. A. Angell, *Electrochim. Acta*, **1**, 308 (1959).
18. M. Tanaka, K. Balasubramanyam, and J. O'M. Bockris, *ibid.*, **8**, 621 (1963).

APPENDIX

Graphical Method of Correcting for Heat Leakage in Calorimetry

In Fig. 9, rws is the temperature-time curve resulting from the reaction and st is the cooling curve.—The graphical correction involves no assumption other than that the rate of heat leakage is a function of temperature head. Thus, for any given temperature head while the temperature of the reaction vessel is rising (point p', for example) the rate of loss of heat is the same as that noted at the same temperature (point p, for example) while the reaction vessel is cooling. Thus p and p' (and O and O') are characterized by the same temperature head and, therefore, by the same rate of heat loss. The heating effect of stirring is neglected.

Divide the curve rs into a number of segments, such as wo' and o'p'. The correction is applied to each segment, then summed. The segments need not be of the same length.

Example of graphical method: Draw tangent xy at p and with triangle and straight edge reproduce same slope x'y' at p'. Draw line nmo'. The length of mn is the correction. Repeat performance for each segment, such as wo'. The correction is the sum of the lines such as mn and m'n'. These can be summed up by marking off the lengths on the edge of a sheet of paper.

The reason that mn is the temperature correction, ΔT, for the segment between o' and p' is that the slope of xy gives the rate of temperature change, dT/dt for that temperature head. mp' represents the time, dt, that the system was at that approximate temperature head during the heating period.

$mn = dT/dt \times dt = \Delta T$.

Phenomena at an Electrode Covered with an Electrolyte Film

F. G. Will

General Electric Research and Development Center, Schenectady, New York

ABSTRACT

The anodic oxidation of hydrogen is studied on a large horizontal electrode covered with an electrolyte film of millimeter thickness. Polarization curves and the potential distribution in the film are obtained for various film thicknesses and electrolyte concentrations. Concentration gradients in the film electrolyte are measured and found to be very small. Convection in the film and water transport above the film are shown to exist. Both phenomena appear to be significant factors in keeping the concentration gradients small. Theoretical considerations suggest that the convection is induced by surface tension gradients. The convection is formally taken into account in an analysis of the rate-controlling transport of the reacting gas through the film. This involves the introduction of a diffusion layer thickness as parameter. Excellent agreement is found between experimental and calculated polarization curves and potential distribution. The phenomena occurring at the model electrode are believed to represent similar phenomena occurring at actual gas diffusion electrodes. Certain ramifications also exist with regard to wet corrosion.

The transport of reacting gases through thin films of electrolyte covering a metal surface plays an important role in many fuel cell and battery electrodes and in metal corrosion. In the case of fuel cell electrodes operating on gases like hydrogen, hydrocarbons, and oxygen, it is very likely (1-9) that the reacting gas passes through a thin electrolyte film covering the pore walls or the catalyst particles prior to reacting at the electrode surface. Likewise, in hermetically sealed batteries, oxygen and hydrogen that are evolved especially during overcharge are expected to diffuse through thin electrolyte films before reacting on one of the battery plates or an auxiliary electrode (10-12). "Wet" metal corrosion often involves the simultaneous anodic dissolution of the metal and cathodic reduction of oxygen from the air. The rate at which oxygen diffuses through the liquid layer covering the metal surface (13) often controls the rate of corrosion.

A previous experimental study (2) of the oxidation of hydrogen on a platinum electrode partially immersed in sulfuric acid had strongly suggested gas transport through a thin electrolyte film as rate-controlling reaction step. This mechanism was further supported by the good agreement between experimental polarization curves and curves resulting from a mathematical analysis (3). The analysis was made under the assumptions of diffusion control without convection in the film and of constant electrolyte concentration throughout the length of the film. Furthermore, the analysis contained the film thickness as an adjustable parameter.

However, we might expect a substantial increase of the electrolyte concentration in the film due to the formation of hydrogen ions and the migration of anions in the film (14, 15). If, on the other hand, concentration gradients exist, we expect convection in the film electrolyte, caused either by evaporation and condensation of water vapor, or by gradients in surface tension (13, 16-19).

It is the aim of this paper to test the assumptions of the previous analysis experimentally and to verify the predicted potential and current distribution in the film. This information cannot be obtained by direct measurements on porous electrodes or partially immersed electrodes, owing to the small thickness of the electrolyte film (20) and the short length of the reaction zone. Hence, measurements were carried out on a scale-up model of an electrode covered with a thin film of electrolyte.

The results obtained on such an experimental model have important ramifications regarding a better understanding of the gas transport phenomena occurring in many porous electrodes and in corrosion. To which extent information obtained on the model can be transferred to actual systems depends on the extent of hydrodynamic similarity (19) between model and system and has to be decided from case to case.

Experimental

The scale-up model used in the following study consists of a horizontal platinum foil, 40 cm long, 2.42 cm wide, and 50μ thick that has been cemented to a plane-

parallel glass bar of equal length and width. Acid-resistant, high-temperature cure epoxy resin was used for cementing. The cemented foil proved to be flat within $\pm 10\mu$. The glass bar with foil is tightly fitted on three sides into the rectangular depression of a Teflon bar. A small rectangular reservoir for the electrolyte borders on the fourth side of the glass bar. The top edges of the Teflon vessel rise 1 mm above the top of the platinum foil. The Teflon vessel with glass bar and foil is contained in a glass cell. A platinum foil counter electrode and a platinum screen reference electrode are introduced into the reservoir through a glass joint. This part also has provisions for introducing gas and electrolyte. The gas leaves the cell through a water trap. Platinum wire probes of 0.5 mm diameter are introduced through glass joints in the top of the glass cell. The probes are located in the center line of the foil and spaced 2 cm apart from each other. Their flat ends are spaced at an accurate height of 0.25 mm above the foil. Counter electrode, reference electrode, and the tips of all probes are platinized. The electrolyte, contained in the reservoir, spreads over the platinum foil, forming a film of uniform thickness. A steady stream of hydrogen was blown over the electrolyte film at a rate of about 10 cm^3/min. To minimize evaporation of the film, the hydrogen, before entering the cell, was blown through two gas wash bottles containing sulfuric acid of the same concentration as used in the experiment. These concentrations were 8*N*, 1*N*, 0.4*N*, 0.1*N*, and 0.02*N*. All experiments were carried out at a controlled room temperature of 25° ± 1°C.

Electrolyte films of thicknesses 2, 1, and 0.5 mm were applied. The film thicknesses were measured mechanically to a precision of $\pm 25\mu$. A platinum tube with a flat end, rigidly mounted on a precision cathetometer, was lowered through a glass joint after removing the respective probe. An ohm-meter was connected between the platinum tube and the platinum foil. The moments that the platinum rod first touched the electrolyte surface and then the platinum foil could be precisely determined by the changes in the deflection on the ohm-meter.[1]

A block diagram of the electrical setup is shown in Fig. 1. The lower part of the diagram contains a schematic of the electrolytic cell with the grounded test electrode (platinum foil) T, counter electrode C, reference electrode R, and probes P1 to P20. Potentials E_a' between 0 and 0.8v are applied between R and T by means of a potentiostat, and the cell current I through C and T is measured as a function of E_a'. In all plots and equations, the corrected applied potential E_a occurs instead of E_a'. E_a is identical to the potential measured between probe 1 and test electrode T and is related to E_a' by

$$E_a = E_a' - E_{1R} \qquad [1]$$

where E_{1R} is the ohmic voltage drop between probe 1 and reference electrode R. The local electrode potentials $E(x)$, *i.e.*, the potential distribution, are measured as the potentials between the various probes P1 to P20 and T. The impedances between the various probes and T were measured at frequencies of 1 and 10 kHz using an impedance bridge. A 1 μF capacitor effectively prevented the bridge circuit from interfering with the d-c measurements. Thus, the impedances could be measured while different d-c potentials E_a' were being applied. At 10 kHz, the ohmic component of the measured impedance is essentially identical to the electrolyte resistance between the particular probe and the test electrode. After calibration with known electrolyte concentrations, the magnitude of this resistance is an accurate measure for the concentration of the electrolyte in the vicinity of that particular probe.

[1] The suggestion of this simple and precise method by J. D. Livingston of our laboratory is gratefully acknowledged.

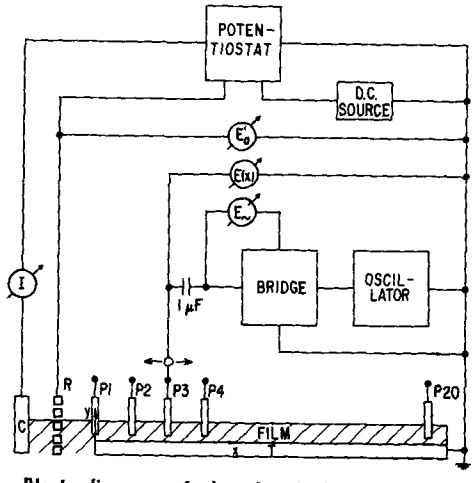

Fig. 1. Block diagram of the electrical setup and electrolytic cell: T, test electrode; C, counter electrode; R, reference electrode; P1 to P20, probes.

Results

Current-potential curves.—Polarization curves for different concentrations of sulfuric acid and different film thicknesses are shown in Fig. 2. The cell current per centimeter width of the electrode, I/W, is plotted against a square root expression containing the applied potential E_a and an exponential of E_a. The reasons for plotting the polarization curves in this particular way will become apparent in the Discussion section.

The following features of the polarization curves are noted: (*i*) The effect of the film thickness on the slope of the polarization curves is relatively small. (*ii*) Decreasing the concentration of the sulfuric acid decreases the slope of the curves drastically, *i.e.*, increases the polarization for fixed current drastically. (*iii*) A limiting current is obtained for 8*N* H_2SO_4. The limiting current is considerably larger for 1 mm than for 2 mm film thickness.

Potential distribution.—Figure 3 shows a linear plot of the local electrode potentials against the distance

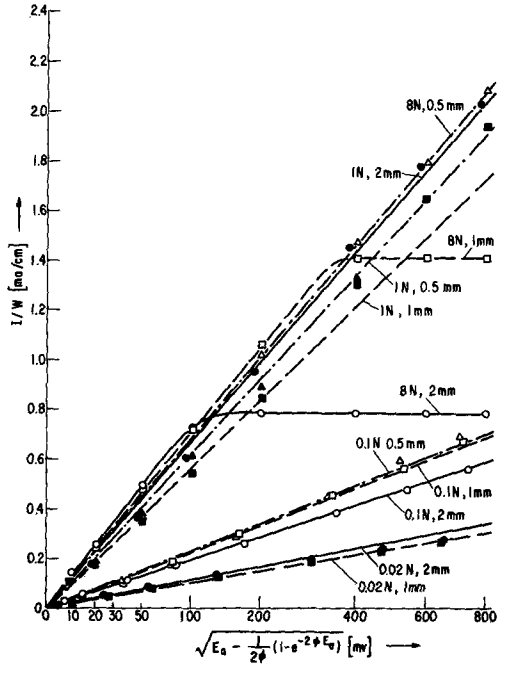

Fig. 2. Polarization curves for various acid concentrations and film thicknesses: I/W, cell current per unit width of electrode; E_a, applied potential; Ψ, F/RT.

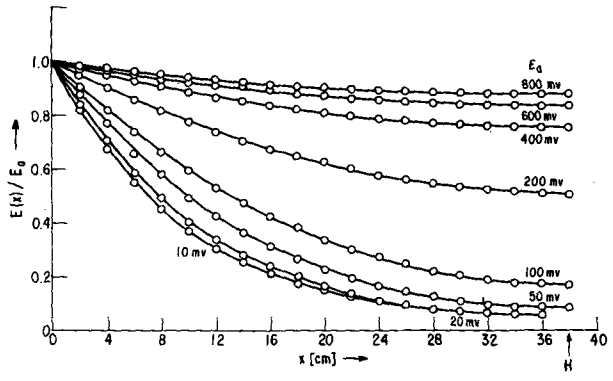

Fig. 3. Potential decay for 8N H_2SO_4 and 2 mm film thickness with applied potential E_a as parameter.

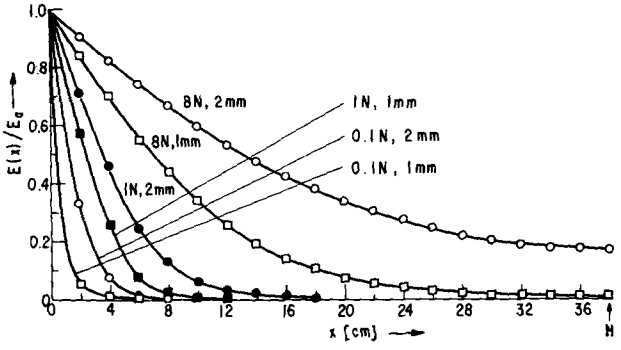

Fig. 4. Potential decay for fixed applied potential E_a = 100 mv with the concentration and film thickness as parameters.

x for 8N H_2SO_4 and 2 mm film thickness with the applied potential E_a as a parameter. $E(x)$ is plotted in dimensionless units as ratio $E(x)/E_a$. The distance x along the film is counted from the beginning of the film at probe 1. We find that the potential decay is quite small for the larger applied potential and that the rate of decay is substantially increased as the applied potential is decreased. This finding applies to all acid concentrations and film thicknesses.

The effect of the acid concentration and the film thickness on the potential decay for a fixed applied potential of 0.1v is shown in Fig. 4. As expected, the potential decays much more rapidly as the acid concentration or the film thickness are decreased. In 0.02N H_2SO_4, and for δ = 2 mm the potential decays to 2% of the applied value between probe 1 and 2 and to less than 1% for δ = 1 mm.

Concentration changes.—The impedances between the various probes and the test electrode were measured in 0.4N H_2SO_4 at a film thickness of 1 mm. The flow rate of hydrogen was decreased to about 1 cm^3/min to minimize evaporation of the film. For a fixed applied potential of 100 ± 0.5 mv, the current, the potential distribution, and the impedances were measured as a function of time over a period of 240 hr.

During this period, the film thickness decreased from 1.0 to 0.9 mm and the current from 0.84 to 0.82 ma. Concurrently, the potential decay became slightly larger, as shown in Fig. 5. The maximum change amounted to less than 5%.

The electrolyte resistances at t = 0 between the various probes and the test electrode fell in the range 18.7-24.4 ohms. The spread in resistance values is caused by the nonuniformity of the vertical spacing of the probes above the test electrode. After 240 hr, the resistances varied from 18.4 to 25.4 ohms. The changes of the resistances, ΔR, at the various probes, in per cent deviation from their original values, are plotted in Fig. 5. We note that the resistances have become slightly larger near the reservoir, at probe 1 and 2, and near the film end. Between probes 3 and 13, on the other hand, the resistances have become

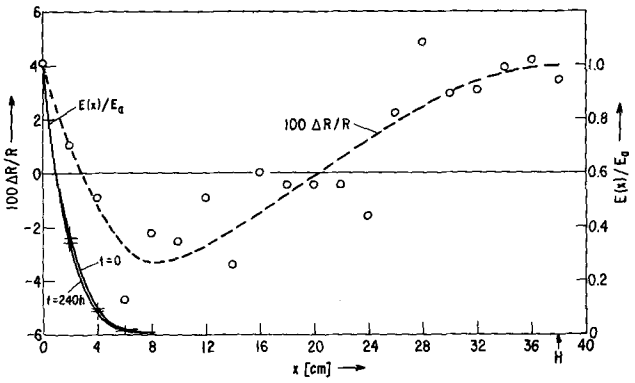

Fig. 5. Resistance changes in per cent deviation from original values after 240-hr polarization at 100 mv in 0.4N H_2SO_4. Also potential distribution at t = 0 and t = 240 hr.

slightly smaller. This reflects a tendency of the acid concentration to become slightly smaller in the reservoir and near the film end and slightly larger in the regions of the film where the oxidation of the hydrogen occurs. However, the effect is quite small, the changes of the acid concentration amounting to less than ±5% along the whole length of the film.

Water vapor transport.—Water vapor may be transported above the film from areas of the film with low electrolyte concentration to those with higher concentration. The rate of vapor transport would then be expected to have an effect on the magnitude of the concentration changes and, hence, the electrolyte resistance.

The possible effect of vapor transport was studied by decreasing the rate of vapor transport perpendicular to the film relative to the rate of hydrogen transport. This was effectively done by floating a Teflon membrane of 3μ thickness on the 1 mm thick film of 0.4N H_2SO_4. Hydrogen permeates through Teflon membranes roughly 30 times faster than water vapor.[2] The probes were inserted through small holes in the Teflon membrane. The current for E_a = 100 mv was 15% smaller (0.71 ma) than without the Teflon membrane (0.84 ma) due to the limited rate of permeation of hydrogen through the membrane. The electrolyte resistances between x = 0 and 20 cm changed in a manner similar to that shown in Fig. 5 which applies to the case without membrane. However, the relative changes were approximately double as large as without the membrane. Hence, the concentration gradients between x = 2 and 20 cm were about double as large as without membrane. For x > 20 cm, the concentration changes amounted to less than 1%.

Convection of film electrolyte.—Possible convection of the film electrolyte was tested for by adding a small amount of red pigment to the electrolyte. The electrode was covered with a 1 mm film of 1N H_2SO_4. A potential of 800 mv was applied. The current of 4.6 ma did not change on addition of the pigment through the glass joints in the top of the cell. The pigment quickly conglomerated to form particles of a few tenths of a millimeter diameter which floated in the film electrolyte. Within a few minutes, these particles moved from near the center of the film to the vicinity of the film edges. This motion proved to be independent of any applied potential. The cell was then left standing for 12 hr without a potential applied. The particles remained essentially motionless during this time. A potential of 800 mv was now applied and the motion of several particles monitored with markers. The particles in the film between probe No. 1 (x = 0) and probe No. 6 (x = 10 cm) showed a distinct motion in the direction of the reservoir while the particles closer to the film end (x > 20 cm)

[2] Private communication by W. L. Robb of the General Electric Research and Development Center.

remained essentially motionless. As soon as the applied potential was turned off ($E_a = 0$), the particles stopped moving. With a potential applied again, the particles started moving again. The velocity of the particles near probe No. 4 ($x = 6$ cm) was determined in repeated runs as $1.3 \cdot 10^{-3}$ cm/sec $\mp$ 10%.

Discussion

Concentration changes and convection.—If there were no convection in the film electrolyte, we would expect an exponential increase of the electrolyte concentration in the film over that in the reservoir (14, 15). In this case, the steady-state current would be due to migration and diffusion of hydrogen ions.

The finding that the electrolyte concentration changes very little indicates the presence of convection in the film electrolyte. Indeed, convection was proved to exist by observing the motion of particles added to the film electrolyte.

We suggest two effects that are likely to cause the observed convection: (*i*) motion induced by gradients of the surface tension in the electrolyte and (*ii*) motion induced by water vapor transport above the electrolyte.

Motion induced by surface tension.—The formation of hydrogen ions at the electrode surface is expected to give rise to concentration gradients in the film parallel to the surface and also perpendicular to the surface. The concentration gradients, in turn, cause gradients of the surface tension in the electrolyte which are known to set the liquid in motion if certain instability criteria are fulfilled.

A number of papers have dealt with convection cells or Bénard cells (21) driven by surface tension gradients (18) and established the criteria for convective instability in liquid films (22-26). Pearson (22) derived a characteristic dimensionless constant B, whose value determines the onset of convective instability. If the driving forces are concentration gradients in the film rather than temperature gradients, one obtains

$$B = (\delta^2/\mu D_+)\ (\partial\sigma/\partial c_+)\ (\partial c_+/\partial y) \qquad [2]$$

δ = film thickness, μ = viscosity, c_+ = concentration, D_+ = diffusivity of electrolyte, σ = surface tension, y = coordinate perpendicular to the film. For the case of constant flux at the bottom of the film ($y = 0$), Pearson calculates a critical value $B_{crit} = 48$. $B > B_{crit}$ characterizes the onset of convective instability. Using Eq. [2] we find that for a 1 mm thick film of $1N$ H_2SO_4 a concentration gradient of only 10^{-3} mole/l/cm is required to cause convective instability.

It is important to note that convective instability caused by density gradients is governed by a dimensionless constant, called Rayleigh number (27), which is proportional to δ^4 and that the critical Rayleigh number is more than an order of magnitude larger than B_{crit}. Thus, in films of 1 mm thickness and thinner, convective instability can confidently be attributed to the surface tension rather than the buoyancy mechanism (22).

In contrast to cellular motion, Levich (19) treated gross motion of the film electrolyte parallel to the surface induced by surface tension gradients which are caused by temperature or concentration gradients in the x-direction. He derived a parabolic velocity distribution

$$v_x = (3/4\delta\mu)\ [(y-\delta/3)^2 - (\delta/3)^2]\ \partial\sigma/\partial x \qquad [3]$$

where v_x = x-component of the velocity of the liquid. Equation [3] predicts a motion of the electrolyte in the direction of the surface tension gradient near the electrode surface (lower 2/3 of film thickness) and in the opposite direction near the film surface (upper 1/3 of film thickness). The surface tension of sulfuric acid increases with increasing concentration in the range of 0-50% by weight (28). The change amounts to about 1 dyn/cm/mole/l. The observed change of the electrolyte resistance in $0.2M$ H_2SO_4 for $0 < x < 8$ cm (see Fig. 5) corresponds to a concentration gradient of $2.5 \cdot 10^{-3}$ mole/l/cm. Using this value, we calculate from Eq. [3] an average velocity in the lower 2/3 of the film of $0.7 \cdot 10^{-3}$ cm/sec. This is about one half the observed velocity of the suspended particles ($1.3 \cdot 10^{-3}$ cm/sec) and suggests that surface tension gradients are likely to be a significant factor in causing convection in the film electrolyte and thereby reducing concentration gradients.

Water vapor transport.—A rough calculation of convective transport of water vapor above the film shows that a flow velocity of only $2 \cdot 10^{-2}$ cm/sec is sufficient to keep the concentration gradient of the electrolyte near the film surface at the low observed value. The fact that the concentration gradient is roughly doubled when a Teflon membrane is used also suggests that water vapor transport is significant in reducing concentration gradients. The evaporation and condensation of water vapor are expected to cause convection in the film electrolyte due to capillary and gravity forces.[3]

Diffusion layer thickness.—Since the film electrolyte is in motion, the reacting gas (hydrogen) is carried to the electrode surface by convective diffusion. The gas flux and, hence, the current density is larger than for pure diffusion through the electrolyte film. Mathematically, the treatment of this problem is very complicated because it involves the introduction of the velocity of the electrolyte as a function of x and y into the convective diffusion equation. A specific case of this general problem was treated by Levich (19), but is not applicable to the present problem. In general, the flux in a convective diffusion regime can be expressed in terms of Fick's law of diffusion by introducing a diffusion layer which is a function of the coordinate x and contains various material constants (19).

Lacking a theory that would allow us to express the diffusion layer thickness in this way, we introduce a diffusion layer thickness δ' formally as an adjustable parameter.

The previous analysis (3) of electrochemical reactions involving the slow diffusion of a reacting gas through the electrolyte film was made under the assumption of no convection and constant concentration in the film electrolyte. The analysis will now be modified in terms of a diffusion layer thickness δ', which, due to convection, is only some fraction of the actual film thickness δ.

Current-potential curves.—For penetrations of the electric field small compared to the length of the film, *i.e.*, if the potential at the film end, E_H, is essentially zero, the expression

$$I/W = 2\sqrt{\delta/\delta'}\ \sqrt{FDc_0\kappa}\ \sqrt{E_a - (1-e^{-2\Phi E_a})/2\Phi} \qquad [4]$$

results for the current-potential curve. W is the width of the electrolyte film, D and c_0 the diffusion coefficient and the solubility of hydrogen in sulfuric acid, respectively; κ is the conductivity of the electrolyte, and $\Phi = F/RT$. It is interesting to note that the current in the original expression (3) is independent of δ.

For $E_a >> RT/F$ and penetrations of the electric field large compared to the length of the film, *i.e.*, for $E_H \lessapprox 50$ mv, the concentration of molecular hydrogen at the surface of the test electrode approaches zero along the whole length of the film. Under these conditions, a maximum diffusion current

$$I_m/W = 2\ (\delta/\delta')\ FDc_0/\delta \qquad [5]$$

should be obtained.

The value of the applied potential, E_m, for which the maximum diffusion current at any given value of $(H/\delta)_m$ is obtained, can be calculated from

[3] The possible significance of vapor transport was also suggested by Bennion and Tobias (29).

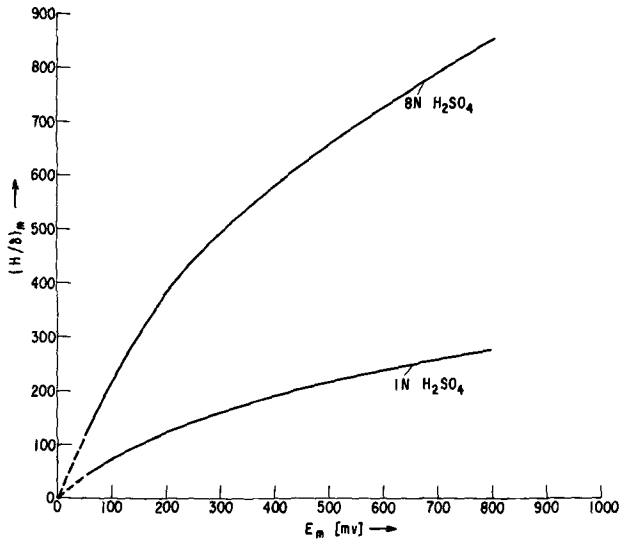

Fig. 6. Values of the ratio film length H to film thickness δ for which the applied potentials E_m produce the maximum diffusion current in 8N and 1N H_2SO_4.

$$E_m - E_H = (FDc_0\,\delta/\delta'\kappa)\ (H/\delta)^2_m \qquad [6]$$

where $E_H = 0.05$v. An increase of H/δ beyond $(H/\delta)_m$ produces essentially no increase of the current. Figure 6 correlates values of $(H/\delta)_m$ and E_m over a wide range of potentials for 8*N* and 1*N* H_2SO_4.

According to Eq. [4], straight lines should result in a plot of I/W against $\sqrt{E_a - [1 - \exp(-2\Phi E_a)]/2\Phi}$. Equation [5] predicts a maximum diffusion current for 8*N* H_2SO_4 whose magnitude is inversely proportional to δ. According to Eq. [6] and Fig. 6, the maximum diffusion current should start at lower potentials for the larger film thicknesses. It is seen from Fig. 2 that the experimental curves follow the predicted behavior. A good quantitative fit between experimental and theoretical curves is obtained for the values of δ/δ′ shown in Table I. Also tabulated are the experimental values for the slopes of the curves in Fig. 2, the maximum diffusion currents and the values for E_m. For all acid concentrations, the values of δ/δ′ lie between 1.8 and 2.9, *i.e.*, the diffusion layer thickness is only about 1/2 to 1/3 of the film thickness.

Potential distribution.—For small values of the applied potential, *i.e.*, $E_a << RT/F$, the local electrode potential can be written as

$$E(x)/E_a = \exp\left(-2\sqrt{F^2Dc_0/\kappa RT}\,\sqrt{\delta/\delta'}\,x/\delta\right) \qquad [7]$$

Figure 7 shows a plot of the logarithm of $E(x)/E_a$ against x/δ for $E_a = 10$ mv and different acid concentrations and film thicknesses. As predicted by Eq. [7], the experimental points lie on straight lines. Their slopes can be matched with the theoretical slopes

$$2\sqrt{F^2Dc_0/\kappa RT}\,\sqrt{\delta/\delta'}$$

for the values of δ/δ′ given in Table II. While two of these values (2.30 and 1.90) agree well with the values given in Table I, the other three values are by some 25 to 35% smaller than those in Table I.

Table II. Values of δ/δ′

	8*N*		1*N*		0.1*N*
	2 mm	1 mm	2 mm	1 mm	2 mm
δ/δ′	2.30	1.50	2.20	1.40	1.90

For large values of the applied potential, *i.e.*, $E_a >> RT/F$, and large penetrations of the electric field, *i.e.*, $E_H \gtrapprox 50$ mv, one obtains

$$\psi(x) = E_a - E(x) = (FDc_0\,\delta/\delta'\kappa)\ \{(H/\delta)^2 - [(H-x)/\delta]^2\} \qquad [8]$$

The potential decays less rapidly than the exponential decay given by Eq. [7]. We expect straight lines in a plot of the ohmic potential drop $\psi(x)$ in the electrolyte film against $(H/\delta)^2 - [(H-x)/\delta]^2$. Their slopes are given by $FDc_0\,\delta/\delta'\kappa$ and should depend on the film thickness δ only insofar as δ enters through the correction factor δ/δ′ with values between 2 and 3. Figure 8 shows that these predictions are fulfilled very well for 8*N* H_2SO_4 and $\delta = 2$ and 1 mm. The four top curves, shown in Fig. 3 for $E_a = 200$, 400, 600, and 800 mv, all fall on one straight line when plotted as in Fig. 8. The same is true for all potentials between $E_a = 400$ and 800 mv in the case of $\delta = 1$ mm. For the other concentrations and film thicknesses, the condition $E_H \gtrapprox 50$ mv is not fulfilled. Hence, Eq. [8] cannot be applied. A quantitative fit between the

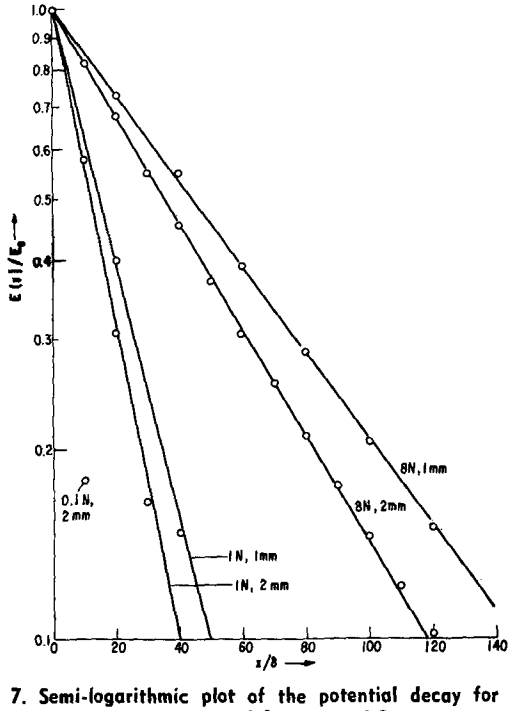

Fig. 7. Semi-logarithmic plot of the potential decay for E_a = 10 mv at various normalities, and δ = 1 and 2 mm.

Table I. Values of δ/δ′

	8*N*			1*N*			0.1*N*			0.02*N*	
	2 mm	1 mm	0.5 mm	2 mm	1 mm	0.5 mm	2 mm	1 mm	0.5 mm	2 mm	1 mm
S_{exp}, ma/cm $\sqrt{V}$	2.56	2.44	2.36	2.30	1.96	2.14	0.67	0.77	0.79	0.39	0.34
S_{th}, ma/cm $\sqrt{V}$	1.71	1.71	1.71	1.34	1.34	1.34	0.50	0.50	0.50	0.25	0.25
$\delta/\delta' = (S_{exp}/S_{th})^2$	2.24	2.04	1.91	2.94	2.14	2.55	1.80	2.37	2.50	2.50	1.92
$I_{m\ exp}/W$, ma/cm	0.79	1.41									
$I_{m\ th}/W$, ma/cm	0.35	0.69									
δ/δ′	2.26	2.04									
$E_{m\ exp}$, mv	130	350									
$E_{m\ th}$, mv	85	200									
δ/δ′	2.28	2.00									

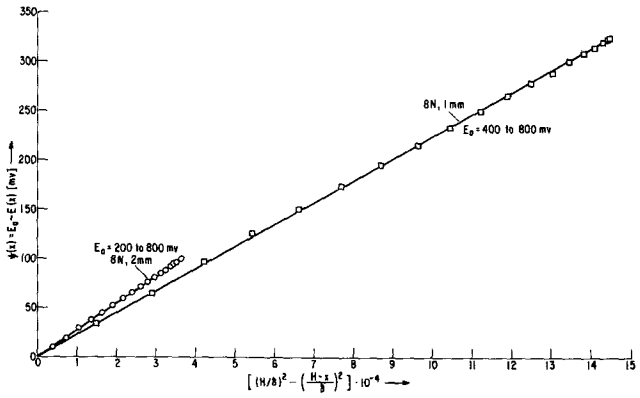

Fig. 8. Ohmic potential drop in the electrolyte as a function of the distance in a square plot for large E_a in 8N H_2SO_4 for $\delta = 1$ and 2 mm.

slopes of the straight lines in Fig. 8 and the slopes calculated from Eq. [8] is obtained with $\delta/\delta' = 2.63$ for $\delta = 2$ mm and $\delta/\delta' = 2.18$ for $\delta = 1$ mm. These values agree moderately well with those given in Table I.

Hydrodynamic similarity between model and gas electrodes.—The degree of hydrodynamic similarity between the model electrode and actual gas electrodes can strictly be obtained only by a rigorous analysis with dimensionless quantities. Such an analysis leads to a system of second order partial differential equations. These can be solved only in special cases and with approximations which are often so stringent that the case treated no longer represents the original problem. Levich (19) treated a special case of convective diffusion of a gas through a liquid film with surface tension-induced motion. However, he did not concern himself with concentration gradients in the liquid and ionic motion due to migration, diffusion and convection. He derived a Reynolds number for the film which is

$$Re = (\delta^2\rho/4\mu^2)\ (\partial\sigma/\partial c_+)\ (\partial c_+/\partial x) \qquad [9]$$

when written in terms of a concentration gradient as driving force. The dependence of Re on δ^2 and on the concentration gradient is the same as that of Pearson's dimensionless constant B in Eq. [2]. Own unpublished calculations show that $\partial c_+/\partial x$ is, to a first approximation, inversely proportional to δ^2. This means that the film Reynolds number and Pearson's constant B are independent of the film thickness and would indicate hydrodynamic similarity between model and actual gas electrode. We stress that this conclusion is based on an approximate solution of the problem and not the result of a rigorous analysis.

Before we can establish similar arguments with regard to the significance of water vapor transport in gas electrodes we have to obtain knowledge about the thickness of films as a function of the pore radius. A rough calculation shows, however, that vapor transport in pores of 4μ diameter with 0.1μ thick films is a feasible mechanism.

Experimental results show that good hydrodynamic similarity must exist between the millimeter thick films on the model electrode and the micron thick films (2, 3, 20) on partially immersed electrodes under diffusion control. The current-potential curves in both cases are essentially identical and follow the behavior predicted for electrodes under diffusion control in the absence of concentration gradients in the film electrolyte. For the case of the large concentration gradients expected (14, 15) in the absence of convection and vapor transport, the predicted current-potential curves are quite different (30) from the experimental curves.

Several experimental facts also suggest that fair hydrodynamic similarity exists between the model electrode and actual gas electrodes under diffusion control. Polarization curves obtained on actual hydrogen (4) and oxygen diffusion electrodes (4, 5), the latter at higher current densities, show the same typical behavior as those obtained on the model electrode and as predicted by Eq. [4].

Conclusions

Polarization curves obtained on the model electrode, which is completely covered with an electrolyte film of precisely known thickness, display a dependence of the current on the square root of the potential and an exponential of the potential. This dependence is predicted by an analysis of rate-controlling diffusion of the reacting gas through the film under the assumption of constant concentration of the film electrolyte. Experimental evidence for convection in the film and transport of water vapor above the film is presented, and both phenomena are made responsible for the observed lack of substantial concentration gradients in the film electrolyte. Theoretical considerations suggest that the motion of the film electrolyte is induced by surface tension gradients. A diffusion layer thickness δ' is formally introduced in the analysis which, due to the convection, is only a fraction of the film thickness δ. For values of δ'/δ between 1/3 and 1/2 a quantitative fit between observed and calculated polarization curves is obtained. The measured potential distribution also follows closely the predicted behavior, namely, the potential decays exponentially for small polarizations and less steeply, as the square of the distance x, for large polarizations.

Polarization curves obtained on partially immersed electrodes and on actual gas electrodes often display the same typical behavior as the curves obtained on the model electrode. We conclude from this fact that a good degree of hydrodynamic similarity exists between these different systems. This conclusion is also borne out by theoretical considerations. Hence, we expect the phenomena observed on the model electrode to be fairly representative for similar phenomena occurring on actual gas electrodes.

Acknowledgments

The author gratefully acknowledges the active help of Mr. F. R. Landsberger in the experimental part and valuable discussions with Dr. D. J. BenDaniel.

Manuscript received Dec. 20, 1965; revised manuscript received Sept. 23, 1966. This paper was presented at the Buffalo Meeting, Oct. 10-14, 1965.

Any discussion of this paper will appear in a Discussion Section to be published in the December 1967 JOURNAL.

REFERENCES

1. H. C. Weber, H. P. Meissner, and D. A. Sama, *This Journal*, **109**, 884 (1962).
2. F. G. Will, *ibid.*, **110**, 145 (1963).
3. F. G. Will, *ibid.*, **110**, 152 (1963).
4. F. G. Will, Paper presented at the Pittsburgh Meeting of the Society, April 1963, Abstract No. 181.
5. P. Ruetschi and J. B. Ockerman, Private communication.
6. R. P. Iczkowski, *This Journal*, **111**, 605, 1079 (1964).
7. Yu. V. Alekseev and Yu. A. Popov, *Soviet Electrochem.*, **1**, 363 (1965).
8. A. G. Pshenichnikov, G. I. Shnaider, and R. Kh. Burshtein, *ibid.*, **1**, 367 (1965).
9. T. Katan and S. Szpak, *This Journal*, **112**, 1166 (1965).
10. A. Dassler, U. S. Pat. No. 2104973, Jan. 1938; A. E. Lange, E. Langguth, E. Breuning, and A. Dassler, U.S. Pat. No. 2131592, September 1938.
11. G. Neumann and U. Gottesmann, U. S. Pat. No. 2571927, Oct. 1951.
12. K. Dehmelt and H. von Dohren, *Proc. 13th Ann. Power Sources Conf.*, **13**, 85 (1959).
13. I. L. Rosenfeld and K. A. Zhigalova, *Dokl. Akad. Nauk SSSR*, **104**, 876 (1955).
14. K. J. Vetter, "Elektrochem. Kinetik," p. 151, Springer, Berlin (1961).

15. J. A. Rockett and R. Brown, *This Journal*, **113**, 207 (1966).
16. J. Thomson, *Phil. Mag.*, Ser. 4, **10**, 330 (1855).
17. A. V. Hershey, *Phys. Rev.*, **56**, 204 (1939).
18. M. J. Block, *Nature*, **178**, 650 (1956).
19. V. G. Levich, "Physicochemical Hydrodynamics," (translated from Russian), p. 384, Prentice Hall, Englewood Cliffs (1962).
20. R. H. Muller, Paper presented at the Washington Meeting of the Society, Oct. 1964, Abstract No. 4.
21. H. Bénard, *Am. Chim. Phys.*, **23**, 62 (1901).
22. J. R. A. Pearson, *J. Fluid Mech.*, **4**, 489 (1958).
23. E. Palm, *ibid.*, **8**, 183 (1960).
24. L. E. Scriven and C. V. Sternling, *ibid.*, **19**, 321 (1964).
25. J. C. Berg and A. Acrivos, *Chem. Eng. Sci.*, **20**, 737 (1965).
26. L. E. Scriven and C. V. Sternling, *Nature*, **187**, 186 (1960).
27. Lord Rayleigh, *Phil. Mag.*, **32**, 529 (1916).
28. Gmelins Handbuch der anorganischen Chemie, "Schwefel," p. 661, 8. edition B2, Verlag Chemie, Weinheim (1960).
29. D. N. Bennion and C. W. Tobias, Paper presented at the Washington Meeting of the Society, October 1964, Abstract No. 5.
30. F. G. Will, Unpublished calculations.

Technical Notes

Fuel Cell Performance as a Function of Catalyst Surface Area

Harold I. Zeliger[1]

Union College, Schenectady, New York

In order to study the relationship between specific platinum surface area and fuel cell performance, it is necessary to have electrodes which are prepared similarly and which contain catalysts that are similar but with varying platinum content and specific platinum surface area. In the work described below the dependence of fuel cell performance on the surface area of the catalyst was demonstrated.

Platinized asbestos samples with varying platinum content were prepared by repeated (6 cycle) platinization (1) of a single starting batch of asbestos as follows.

Asbestos (5g) was impregnated with a 3% solution of chloroplatinic acid and the excess solution was filtered off. The moist impregnated asbestos was dried and reduction was carried out with hydrogen at 100°C. The platinization was repeated 5 more times, with samples taken at the end of each cycle. Platinized asbestos samples with 1, 2, 3, 4, 5, and 6% platinum were prepared in this manner from a single starting batch of asbestos. A 3% solution was used because it was found empirically that this added 1% of platinum per cycle.

The electrodes used in this study were modified Neidrach-Alford (2) electrodes. They consisted of a mixture of catalyst, Teflon binder, and conducting graphite diluent (which was required in these electrodes because of the small quantities of platinum present) pressed into a supporting platinum screen which also served as a current collector. A porous Teflon film on the gas side of the electrode provided for proper electrode wetting so that both the electrolyte and reacting gas had satisfactory access to the catalyst incorporated into the structure. This electrode structure provided for high electronic conductivity and rapid input and removal of reactants and products.

All the electrodes prepared were evaluated as oxygen cathodes in standard test fuel cells. The test cells contained the test electrode, a Teflon-bonded (2) hydrogen counter electrode with 34 mg platinum per cm^2, and 5*N* sulfuric acid electrolyte.

Fuel cell performance data were obtained under the condition of steady d-c drain. The cells tested were discharged through a resistive load. IR free potentials were obtained by interrupting the flow of current (sweep speeds of 100 μsec/division were adequate) and monitoring the voltage change on an oscilloscope.

Specific platinum surface areas were determined by measuring the dissociative chemisorption of hydrogen on platinum (3), using the apparatus of McKee (4).

Platinum contents and specific platinum surface areas of the six samples of platinized asbestos prepared are given in Table I.

Table I. Properties of catalysts prepared through stepwise platinization

Catalyst	% Pt	Specific Pt surface area in m^2/g
A	1.0	46
B	2.0	42
C	3.0	37
D	4.0	32
E	5.0	28
F	6.0	23

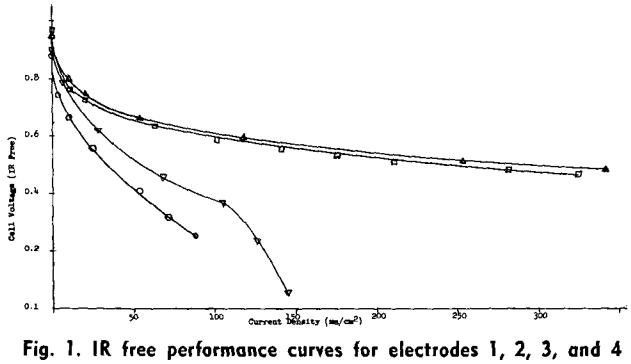

Fig. 1. IR free performance curves for electrodes 1, 2, 3, and 4 on oxygen at ambient temperature, obtained via direct d-c discharge method. Anodes, standard electrodes with 34 mg Pt/cm^2; cathodes, test electrodes with varying Pt content; electrolyte, —5N H_2SO_4, ⅜ in. electrolyte gap. ○, Electrode 1 (0.17 mg Pt/cm^2); ▽, electrode 2 (0.33 mg Pt/cm^2); □, electrode 3 (0.66 mg Pt/cm^2); △, electrode 4 (1.0 mg Pt/cm^2).

[1] Present address: Avco Space Systems Division, Lowell, Massachusetts.

Table II. Data for comparison of current density obtained per unit area of platinum

Electrode No. and catalyst	Mg Pt per electrode	Specific Pt surface area in m^2 per g	Total Pt area in m^2	Current density at 0.7v IR free in ma/cm^2	Current density per unit area at 0.7v IR free, in $ma/cm^2/m^2$
1-A	3.0	46	0.139	7.9	57.0
2-B	6.0	42	0.252	14.9	59.0
3-D	12.0	32	0.392	22.8	58.0
4-F	18.0	23	0.414	25.0	61.0

Electrodes 1, 2, 3, and 4 were prepared incorporating catalysts A, B, D, and F, respectively, and containing 0.17, 0.33, 0.66, and 1.0 mg Pt/cm^2. The electrodes were evaluated as cathodes in fuel cells. Oxygen rather than hydrogen was used for the evaluation, because hydrogen is such a good fuel that it gives excellent performance with very small amounts of platinum catalyst. IR-free polarization curves for the four electrodes are given in Fig. 1.

Comparison of fuel cell performance with specific platinum surface area was made by measuring the current density produced per unit area of platinum at a 0.7v potential for each of the test electrodes. Table II summarizes the data. As can be seen from the data in Table II, there is an excellent correlation between surface area and performance. All four electrodes, each with a different platinum content, gave between 0.057 and 0.061 $ma/cm^2/m^2$ of platinum area at 0.7v.

It is believed that the interior of a metal catalyst does not contribute to the catalytic process. The above described work supports the conclusion that this is indeed the case for the electrocatalytic reduction of oxygen in fuel cells.

Acknowledgments

The author is indebted to Professor K. V. Nahabedian of Union College and L. W. Niedrach of the General Electric Research and Development Center for their guidance and assistance in this work. The author also wishes to gratefully acknowledge the assistance of D. W. McKee of the G. E. R&D Center for his assistance in determining surface areas. H. A. Liebhafsky, Manager Electrochemistry Branch of General Electric R&D Center, is sincerely thanked for making available the facilities with which the experimental work was carried out.

Manuscript received Sept. 1, 1966; revised manuscript received Oct. 12, 1966. The information reported in this paper is part of an M.S. thesis submitted to Union College.

Any discussion of this paper will appear in a Discussion Section to be published in the December 1967 JOURNAL.

REFERENCES

1. D. A. Richards, *Phil. Mag.*, **16**, 778 (1933).
2. L. W. Niedrach and H. R. Alford, *This Journal*, **112**, 117 (1965).
3. G. C. Bond, "Catalysis by Metals," Chap. 8, Academic Press, London and New York (1962).
4. D. W. McKee, Unpublished results.

The Anodic Oxidation of Alloys

G. C. Wood, C. Pearson, A. J. Brock, and S. W. Khoo

Corrosion Science Division, Department of Chemical Engineering,

The University of Manchester Institute of Science and Technology, Manchester, England

Surprisingly little previous work on anodic film growth on alloys, either of a fundamental or practical nature, has appeared in the open literature. This is true even for dilute alloys but is particularly so for compositions far removed from those of the pure "valve" metals. Investigations are in progress to elaborate the theory of film growth on binary alloys between valve metals, and between valve metals and metals which do not themselves form this type of film, and to pursue possible applications of such films in the fields of corrosion-resistant materials, capacitors, and catalysts. The present communication presents results and theories principally for niobium-base alloys, but certain concepts introduced are considered of much more general significance.

Experimental

Specimens cut from sheet or spark-machined as slices from rod were prepared from zone-refined niobium, electron-beam-melted niobium, and from binary alloys of niobium containing, respectively, nominally 5, 20 and 50 a/o (atomic per cent) zirconium, titanium, tungsten, vanadium, or molybdenum. Additional experiments were conducted on Nb-V, Ti-V, Nb-Mo, and Ti-Mo alloys containing 70, 85, or 95 a/o of vanadium or molybdenum. The alloys were generally made from electron-beam-melted or comparable purity metals. After chemical polishing, followed by a 10-sec etch in 40% HF, the samples containing up to 50 a/o alloying element were anodized at 10 ma/cm^2 or at 100 $\mu a/cm^2$ to an appropriate cell voltage, followed by current decay, in 3% W/V ammonium tartrate solution (*p*H adjusted to 7) at 25°C. The alloys richer in vanadium or molybdenum were prepared only at 10 ma/cm^2 with current decay in this electrolyte or alternatively in the nonaqueous electrolyte of 20% W/V ammonium pentaborate in ethylene glycol.

After visual examination for adhesion, compactness, and color, the frequency dispersions of balancing series capacitance and dissipation factor of films were measured in 1M sodium chromate solution (*p*H adjusted to 7.2) at 25°C using a General Radio capacitance measuring assembly type 1610-B with a 50-mv p-p signal. These data also permitted the calculation of average a-c resistivities, on the assumption of the validity of a simple electrical analogue for the film of a resistor in parallel with a capacitor at any one frequency. It was also assumed that the Å/V ratio of 23 and dielectric constant of 41.4, which refer to Nb_2O_5 films on pure niobium, held. Although this is not strictly true, any errors involved in the assumption do not greatly affect the subsequent argument. It should be noted that resistivities measured in chromate solution cannot be compared directly with those measured for films on pure metals in tartrate solution (1). This is because of the influence of the double layer impedance on the measured film impedance, for reasons (2) that will be explained elsewhere.

Results

Thick, relatively good quality films were readily produced on niobium and the alloys containing up to 50 a/o additions, with approximate current efficiencies of 100% at 10 ma/cm^2 and 64-72% at 100 $\mu a/cm^2$. Current decay performed at the end of the main anodizing run had little effect on the film properties, but enabled reproducible film thicknesses to be obtained. These were 230, 1150, and 2300Å, respectively, for pure niobium, but films on the alloys were ap-

parently a little thicker except for tungsten alloys where they were a little thinner. Deviations from the above thicknesses for 50 a/o alloys were never greater than 20-30% from capacitance measurements and were generally less than this when compared with an optical step gauge constructed with Nb_2O_5 films on niobium, and from considerations of the charge required to form films to a given cell voltage. Thus, although there was undoubtedly some error in defining the film thicknesses and consequently in calculating resistivities, this was not sufficient to invalidate the comparisons of alloy behavior seriously. It is very important to note that all these films appeared of comparable quality, although it is likely that there were minor differences in compactness, solubility, etc. This contrasts strongly with experiments on pure metals in tartrate electrolyte where it was found (1, 2) that only niobium and zirconium gave good films. Film formation on titanium was limited by extensive oxygen evolution and on tungsten by film solubility, and it was impossible to anodize vanadium or molybdenum. It is the authors' experience that even films formed on vanadium or molybdenum in nonaqueous electrolytes are nonadherent and of poor quality. All the present films were insoluble in tartrate or chromate solutions, even after several days. Clearly their solubilities in more severe electrolytes will vary and further work is progressing to pursue this aspect.

Figures 1a and 1b, giving the frequency dispersions of dissipation factor for films formed to 10 and 100v, respectively, on niobium and its alloys, show that in general alloying increased the dielectric loss of the films. Additionally, it tended to increase the slopes of plots of series capacitance against frequency (which have been omitted in the interests of brevity).

Figures 2a and 2b illustrate the frequency dispersions of average a-c resistivity for films approximately 230 and 2300Å thick on niobium and the 50 a/o alloys, derived from Fig. 1a and 1b as mentioned earlier. The values were largely independent of whether the initial current density of formation was 10 ma/cm² or 100 μa/cm². The results were identical, within experimental error, for films on the two purities of niobium. The average resistivities and frequency dispersions of resistivity were greater for the oxide on niobium than on any of the alloys. The various curves

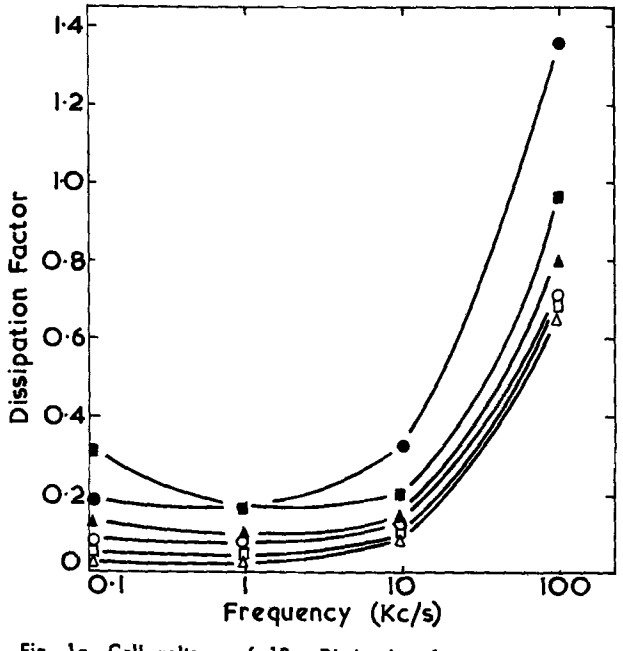

Fig. 1a. Cell voltage of 10v. Dissipation factor vs. frequency (kc/s) for films formed on niobium and Nb-50 a/o alloys. △, Niobium; □, Nb-Zr; ○, Nb-Ti; ▲, Nb-Mo; ■, Nb-V; ●, Nb-W. The symbols are the same for Fig. 1 and 2.

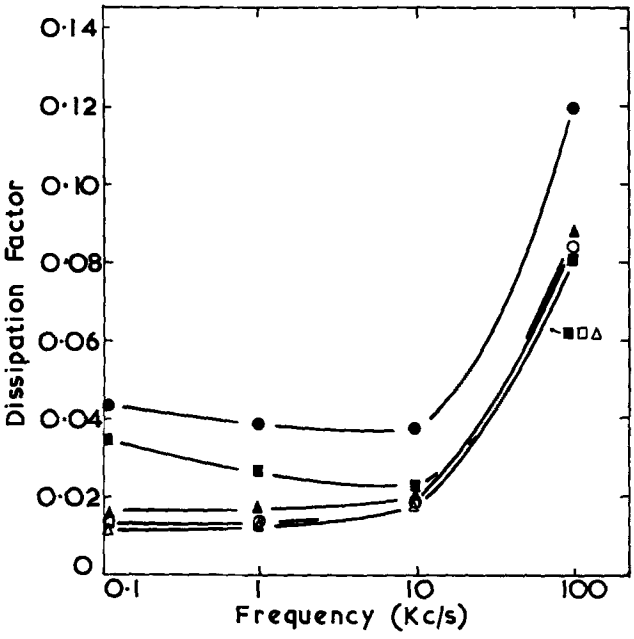

Fig. 1b. Cell voltage of 100v.

almost converge at 100 kc/s with the exception of those for Nb-50 a/o W, probably because the latter were somewhat thinner. At lower frequencies the resistivity was always lower with alloy addition, the effect generally increasing in the order zirconium, titanium, molybdenum, vanadium, and tungsten. This

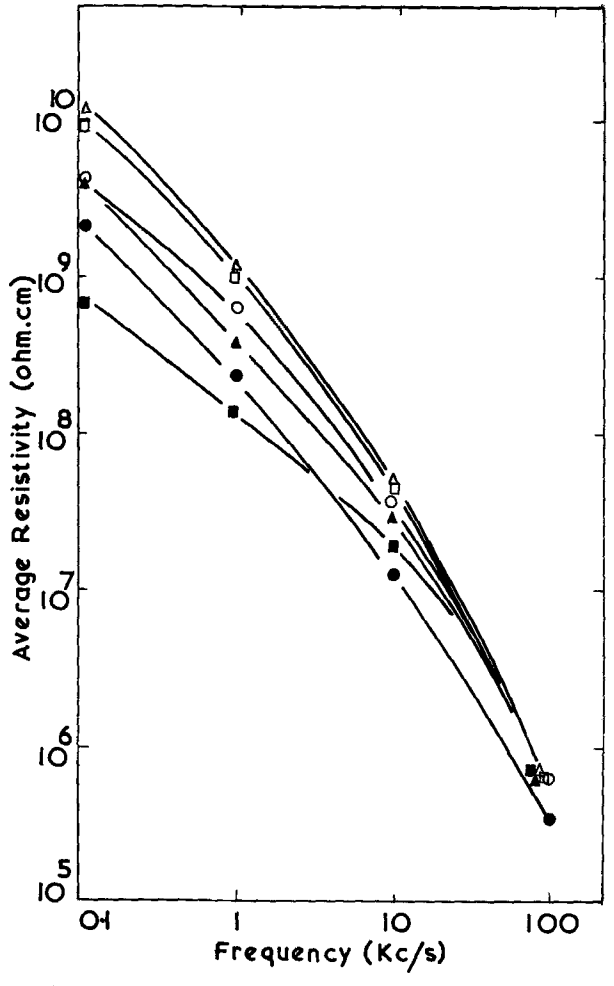

Fig. 2a. Approximately 230Å films; average resistivity (ohm cm) vs. frequency (kc/s) for films on niobium and Nb-50 a/o alloys.

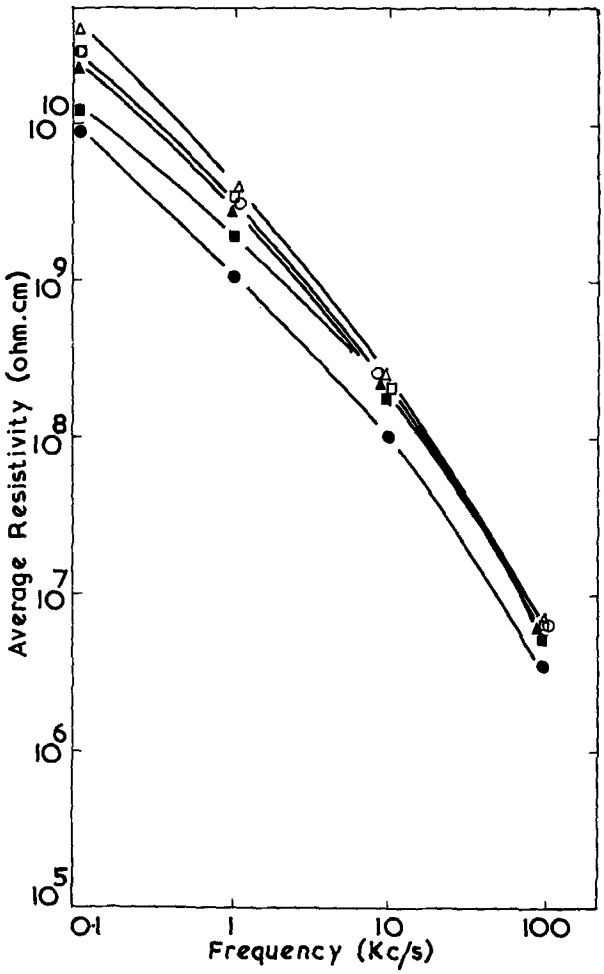

Fig. 2b. Approximately 2300Å films

result appears to be a general one with all the alloy systems that the authors have studied. Curves for films on the more dilute alloys lay in the anticipated order between those for the pure metal and the 50 a/o alloys.

Thus, with the apparent exception of tungsten, the addition of a valve metal to niobium led to higher resistance films than did the addition of vanadium or molybdenum, which do not themselves normally develop typical thick anodic films. An important observation was that the effect of the alloying additions studied in reducing the resistivity of films on niobium was most pronounced for the thinner films. The film capacitances were also relatively larger and showed a greater frequency dispersion. Particularly with Nb-50 a/o V and Nb-50 a/o Mo the thicker films appeared of much better quality; indeed for 2300Å films it is remarkable to observe that the curve for the film on Nb-50 a/o Mo alloy is little lower than that for the film on pure niobium. The reason for this consistent result will be evident later. By analogy with previous results for films on the niobium and zirconium (1), it might have been expected that the curve for Nb-50 a/o Zr would lie above that for pure niobium. Presumably this is not so because the alloy is two-phase and oxide above the niobium-rich regions, which predominates, will produce the dominant dielectric loss. It should also be noted that for all alloys the trend of the thicker the film the higher its average resistivity held at all frequencies. The spaces between curves increased as alloying element was added in the order zirconium, titanium, molybdenum, and vanadium because the improvement of film quality with increased thickness increased in this order.

Electron probe microanalysis at low kilovoltages of stripped and attached films examined in plan proved that tungsten and titanium were incorporated into 2300Å films on 50 a/o alloys in their alloy proportions, and the slight apparent enrichment of vanadium and depletion of molybdenum in the appropriate films were probably insignificant. Similar conclusions were recently reached for copper and zinc entry into films on aluminum alloys (3).

With progressive alloying additions greater than 50 a/o vanadium or molybdenum to niobium or titanium there was a gradual transition from films with good properties to insignificant film formation. On Nb-70 a/o V and Nb-70 a/o Mo films were formed, at rather lower current efficiencies than those given earlier, to voltages of 10, 50, or 100v (corresponding to 230, 1150, and 2300Å films, respectively, on pure niobium). They may in fact have been somewhat thicker than these figures indicate, with a porous outer layer and most of the voltage concentrated across an inner barrier layer, but this remains to be determined. The films were of the usual visual appearance, displaying interference colors and were insoluble or dissolved only very slowly in tartrate, chromate, or distilled water. Films of 10v (nominally 230Å) gave very high capacitances, close to values expected for the double layer capacitance, probably indicating a high degree of microporosity. As the film thickness was increased the impedance characteristics progressively improved until at 100v (nominally 2300Å) the capacitances were relatively low and the frequency dispersion of capacitance was only slightly greater than that expected for a top quality anodic film. The resistivities of these films were sufficiently high to suggest that they may be useful practically, but were several times lower than for the 50 a/o alloys or pure niobium. On Nb-85 a/o V and Nb-85 a/o Mo films could also be formed to high voltages at an even lower current efficiency, but viscous dissolution products could be seen streaming away from the anode, reminiscent of electropolishing. These films, especially when only formed at 10 or 50v, continued to dissolve in the forming electrolyte, in chromate solution, or in distilled water. Films formed at 100v tended to persist in an adherent form for long periods, but showed low impedances which fell with time, indicative of continued dissolution. Nb-95 a/o V and Nb-95 a/o Mo could not be anodized in the aqueous tartrate but films could be formed on the former alloy in the almost "nonaqueous" borate electrolyte (as indeed they could on the other alloys). However, these were soluble in water or in aqueous solutions. The same general pattern was true of Ti-V and Ti-Mo alloys except there was a greater tendency to poorer and more soluble films, as would be expected from the poorer film-forming properties of titanium itself.

Discussion

In attempting to explain the above results it is worthwhile initially demonstrating briefly that analogous concepts developed for the thermal oxidation of alloys appear inapplicable.

1. There is little, if any, preferential oxidation effect, as in thermal film growth, during which one alloying constituent is preferentially incorporated into the film. Thus, a mixed oxide must be considered, although it is not yet known how alloying elements are distributed through the film. From the ability to form films on alloys containing only small concentrations of niobium, it might have been postulated that this element would be expected toward the exterior of the film. Work on the analogous case of InSb, using a sensitive chemical analysis method (4) however, indicated that this is perhaps unlikely because the film contained a uniform distribution of both elements through its thickness, except for the outer 100Å where the concentration of the soluble component, antimony, fell almost to zero.

2. Since all the added ions, whether of higher or lower valency than five, reduce the a-c resistivity of the film, it is apparent that Hauffe's valency rules are of little application to anodic films, whether the a-c

conduction process occurring during impedance measurements be related to d-c electronic conductivity, electronic relaxation processes due to anion vacancies and their associated electrons, or to ionic relaxation processes associated with anion vacancies or interstitial cations. It is possible that all additions to the cation lattice make a more disordered structure, promote ionic relaxation effects, and thus reduce the low frequency resistivity.

3. Consideration of the effect of the addition element on the Pilling-Bedworth ratio in altering the degree of compactness of the oxide has proved useful in thermal oxidation, but the criterion does not apply here, if ionic sizes are considered.

The most useful approach is to compare the properties of these mixed anodic alloy oxide films, such as their solubilities, with those of metallic alloys interacting with electrolytes. Thus the "theory of parting limits" indicates that a noble metal will tend to prevent the selective dissolution of a base metal with which it is alloyed, even when present in only relatively low concentrations. The precise parting limit, often in the range 50-70 a/o of the soluble element, may be sharp or diffuse depending on the alloy and the solution. In certain alloys the base metal is leached out leaving a skeleton rich in the more noble metal. This concept is of course much related to electrochemical processes and does not specifically refer to oxides. In the analogous situation with anodic films, ions of the valve metal, such as Nb^{5+}, effectively play the part of the noble metal and tend to suppress the dissolution of V^{5+}, W^{6+}, or Mo^{6+} ions and their associated oxygen ions from the film.

The experiments described earlier suggest that there is a diffuse transition between solubility and insolubility of anodic films. The "useful" parting limit will depend on the alloy, the electrolyte, and the application. Thus, for the V-Nb system it would be in the range 70-80 a/o V for exposure to certain neutral electrolytes, but less vanadium in the alloy would be permissible in certain severe environments and more if forming were conducted in a nonaqueous electrolyte and the film kept dry subsequently. Similar considerations apply to the other alloy systems.

A film model may be envisaged in which there is an outer porous layer and an inner more compact layer. The precise nature of the "pores" cannot yet be stated, although preliminary electron microscopial examination confirms their existence; they will probably be extremely fine for the more dilute alloys and coarser in alloys rich in soluble component. The degree of this porosity will fall progressively from the oxide/electrolyte interface to the alloy/oxide interface. In certain cases, *e.g.*, in the 50 a/o alloy, it appears that it terminates after only a short distance into the film (perhaps about 100Å), when there is no longer a feasible continuous path of soluble material connecting with the electrolyte. This penetration would be approximately constant for all greater film thicknesses. In other alloys, such as the Nb-85 a/o V and Nb-85 a/o Mo alloys it is more extensive, as witnessed by the continuous stream of soluble material leaving the anode. Such a model is in agreement with the observation that thicker films have generally better properties and superior impedance characteristics. This would be expected because the thicker films would possess much thicker compact regions adjacent to the alloy protected from dissolution.

In view of the above considerations, it is tempting to suggest that the dielectric properties, particularly at low frequencies, of even good quality films on certain valve metals may be modified by hydrated or electrolyte anion-rich regions between the film crystallites. There are instances where impedances of films, *e.g.*, on aluminum, are modified by the anion type and *p*H of the electrolyte, and the authors will return to these matters elsewhere.

The general conclusion is therefore that metals such as molybdenum and vanadium, which cannot themselves normally be anodized, can be made to produce films by alloying with relatively low proportions of valve metals such as niobium and titanium. Zirconium, aluminum, and possibly tungsten would probably afford similar protection. Also the properties of films on metals such as titanium and tungsten, which are relatively poor, can be improved by alloying with metals giving superior films.

Acknowledgments

The authors thank Professor T. K. Ross for providing facilities and for his interest and the Science Research Council and the Commonwealth Scholarship Fund to two of the authors (C. P. and S. W. K. respectively). They are indebted to Dr. A. G. Knapton and Dr. T. Raine of Associated Electrical Industries Ltd., Power Division, for making the alloys.

Manuscript received Aug. 22, 1966; revised manuscript received Oct. 21, 1966.

Any discussion of this paper will appear in a Discussion Section to be published in the December 1967 JOURNAL.

REFERENCES

1. G. C. Wood and C. Pearson, *Nature*, **208**, 547 (1965).
2. C. Pearson, Ph.D. Thesis, Univeristy of Manchester, 1966.
3. G. C. Wood and A. J. Brock, *Nature*, **209**, 773 (1966).
4. J. F. Dewald, *This Journal*, **104**, 244 (1957).

SOLID STATE SCIENCE

Analysis of N-Type GaAs with Electron-Beam-Excited Radiative Recombination

H. C. Casey, Jr., and R. H. Kaiser

Bell Telephone Laboratories, Incorporated, Murray Hill, New Jersey

ABSTRACT

The study of spontaneous emission for n-type GaAs has shown that the spectral shape and peak position may be utilized to determine the free electron concentration within ±15% near concentrations of 5 x 10^{17} cm^{-3} and ±7% at 5 x 10^{18} cm^{-3}. Excitation of the sample with a 1μ diameter electron beam gives such sensitivity with a 3-6μ spatial resolution. This sensitivity and spatial resolution are sufficient for investigating sample inhomogeneities that are related to the spatial variations in the quantum efficiency.

Several investigations (1, 2) of radiative recombination in heavily doped GaAs have shown that the photoluminescent peak shifts to higher energy as the donor concentration is increased above 5 x 10^{17} cm^{-3}. Cusano (3) has reported data demonstrating the dependence of the cathodoluminescent (electron-beam excitation) peak energy and the spectral half-width on the donor concentration. For n-type GaAs, the average distance between impurity atoms is close to the diameter of the Bohr orbit of a donor electron in the crystal for concentrations in excess of 5 x 10^{17} cm^{-3}, and the density of states becomes a function of the substitutional impurity concentration (4). Since the spontaneous emission is given by an integral containing the conduction and valence band density of states and their corresponding occupation probabilities (5), the spectral shape will depend on the impurity concentration. Therefore, the observed dependence of the spectral shape on free electron concentration is also suggested by fundamental theoretical arguments. This paper explains how the dependence of the spectral shape on the free electron concentration may be used to determine the donor concentration in micron-sized regions. No attempt will be made to calculate the density of states and then the spectral shape to demonstrate explicitly the dependence of spectral shape on impurity concentration. However, the spectral shapes presented here may permit comparison of the various models for the density of states and indicate which approach best describes n-type GaAs in the 0.5 to 5 x 10^{18} cm^{-3} impurity range.

There are many nondestructive techniques for determining the electrically active impurity concentration; however, only electron-beam excitation offers micron-sized resolution. Hall measurements are the most sensitive and accurate, but give an average value for the entire sample and cannot be used on layered structures of the same conductivity type. Optical methods [photoluminescence or Reststrahlen-band minimum (6)] normally require excitation of a thin layer of a large cross section, and therefore spatial variations will not be resolved. Schottky barrier diodes (7) can be used for thin layers with 50-100μ diameter spots, but at donor concentrations in excess of 5 x 10^{17} cm^{-3} the high conductance makes the capacitance measurements difficult. Most applications for electroluminescent GaAs devices require free electron concentrations in the decade of 5 x 10^{17} to 5 x 10^{18} cm^{-3}, and it is in this concentration range where the spectral shape may be utilized to determine the substitutional donor concentration. This concentration determination is confined to a hemispherical volume whose radius can be approximated by the sum of the electron-beam radius, the depth of electron penetration, and the diffusion length for holes. A total radius on the order of 4-6μ would be expected for a 40-kev beam voltage in n-type GaAs. At lower beam energies, features as small as 3μ have been resolved in the cathodoluminescence.

The quantum efficiency η_q of n-type GaAs for electron-beam excitation has a strong dependence on free electron concentration n_o (3, 8). The quantum efficiency initially increases as n_o increases, and then η_q decreases rapidly when n_o exceeds about 5 x 10^{18} cm^{-3}. Also, the quantum efficiency for a given wafer can vary greatly over a distance of only a few microns (9, 10). Therefore, it is extremely useful to have an analytical tool with a spatial resolution of the same order of magnitude as the macroscopic crystal variations. By procedures discussed in this paper, it is possible to investigate the variations in quantum efficiency and consider the possibility that these variations correspond to free electron variations or compensation.

Experimental Procedure

The samples used in this study were single-crystal, <100> oriented, Te-doped, floating-zone wafers prepared at Bell Telephone Laboratories. The electron concentrations, 0.2 to 8 x 10^{18} cm^{-3}, were measured on each wafer investigated. The wafers were polished to provide a damage-free surface with a bromine-methanol etch described by Sullivan and Kolb (11). In fact, the usual preparation of a wafer for device fabrication, one which gives a planar damage-free surface, satisfies all the requirements of sample preparation for cathodoluminescence.

The electron-beam-excitation system is an electron probe microanalyzer, the Cambridge Microscan, in which a light pipe has been inserted to transmit the recombination radiation through the specimen chamber exit port. This excitation system is shown schematically in Fig. 1. The finely focused electron beam at A is deflected synchronously with the display cathode-ray tube. The electron beam strikes the GaAs wafer at B and creates one hole-electron pair for each 4.5 ev of beam energy (12). A small fraction of these generated carriers produces infrared radiation by recombining radiatively. This radiation is

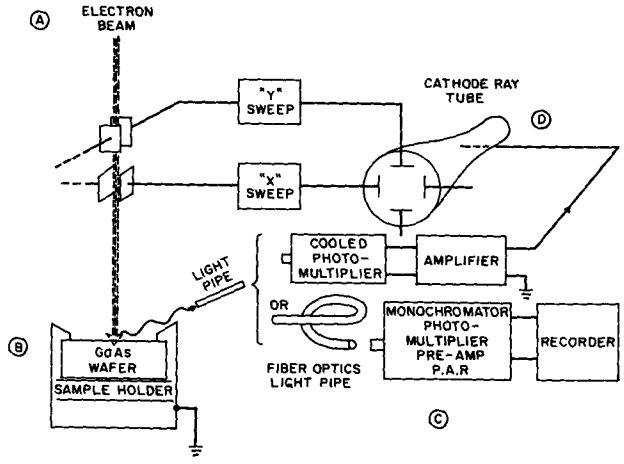

Fig. 1. Schematic representation of the electron-beam excitation system and the infrared detection systems.

transmitted outside the specimen chamber by the light pipe that views the sample at 70° from the surface normal with a solid angle of approximately 3 x 10^{-2} steradians. For display of spatial variations in the radiative-recombination intensity, a dry-ice cooled Amperex 150 CVP (S-1 response) photomultiplier detects the radiation transmitted through the light pipe as shown at C; after amplification this photomultiplier signal serves to intensity-modulate the cathode-ray tube D. In this manner recombination radiation intensity variations over approximately 300 x 300μ areas may be observed at magnifications of several hundred times in the television-type picture that appears on the cathode-ray tube. Wittry and Kyser (9, 10) have described some features of the spatial variations; further elaboration on the features in the scanning-infrared images, especially precipitation and dislocations, is given in the next paper (13).

In the place of the photomultiplier, a fiber optics light pipe may be used to transmit the radiation to a Leiss double-prism monochromator (resolution = 4 mev) in order to resolve the spectral shape. The infrared radiation, chopped at 37.5 Hz, is detected at the exit of the monochromator by the cooled photomultiplier, and the resulting signal amplified by a Princeton Applied Research lock-in amplifier which drives a recorder. The electron-beam accelerating voltage was generally 40 kev, and the beam current could be varied from 2.0 to as low as 0.07 μa with a beam diameter of 2μ or less and obtain resolvable spectra. During measurements of spectral shape the beam current was held constant at 0.5 μa or less, and the beam was generally stationary rather than scanning a line or area. The temperature of the excited region (14) was approximately (30 + 80I_B) °C where I_B is the beam current in microamperes.

Experimental Spectra

A typical cathodoluminescent spectrum is shown in Fig. 2 for a sample containing 1.75 x 10^{18} electrons/cm^3. The electron-beam voltage was 40 kev and the beam current was 0.3 μa. The low-energy side of the spectrum appears exponential and can be represented by $I = I_0 \exp(\beta h\nu)$, where I is the intensity, β the low-energy tail slope, and $h\nu$ the emission energy. At lower intensities the emission is dominated by a deep level as shown. In more lightly doped material and at temperatures below room temperature, this deep level becomes more dominant and can prevent an accurate determination of the low-energy tail slope. The width of the spectrum at one-half the maximum intensity and the energy of the maximum intensity $h\nu_p$ are also shown.

The spectral shapes for a series of samples containing 0.2 to 5 x 10^{18} electrons/cm^3 have been summarized in Fig. 3, 4, and 5 by plotting the low-energy tail slope, the energy of the maximum intensity $h\nu_p$, and the half-width as a function of the free electron concentration. (The technique described here still applies above 5 x 10^{18} cm^{-3}, but the drastic decrease in quantum efficiency made it difficult to resolve the spectral shape.) The thermal equilibrium free electron concentration is used rather than the donor concentration because n_o is the quantity determined by

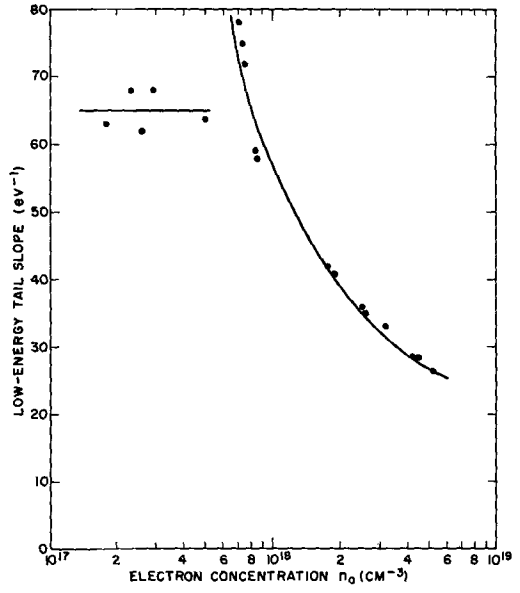

Fig. 3. Low-energy tail slope as a function of the free electron concentration.

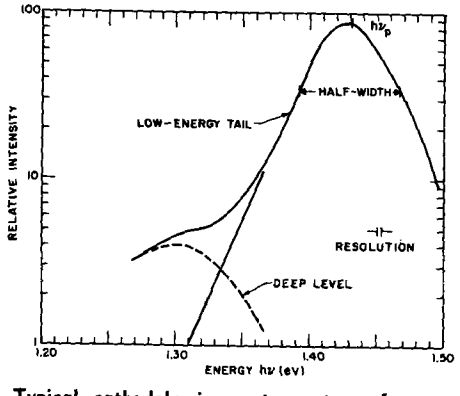

Fig. 2. Typical cathodoluminescent spectrum for n-type GaAs containing 1.75×10^{18} electrons/cm^3. The electron beam voltage was 40 kv and the beam current was 0.3 μa.

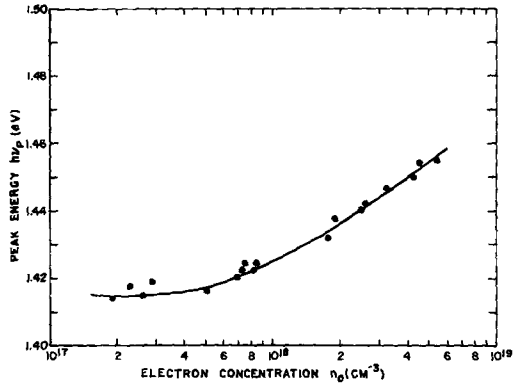

Fig. 4. Peak energy as a function of the free electron concentration.

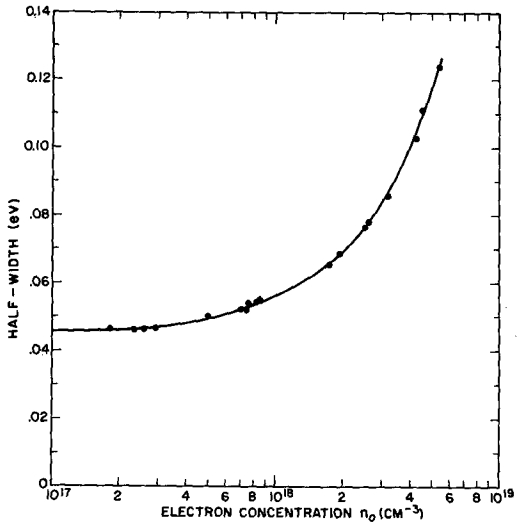

Fig. 5. Half-width as a function of the free electron concentration.

Hall measurements [see Discussion, ref. (13)]. In Fig. 3 the slope of the low-energy tail appears to be constant until a concentration of about 5 x 10^{17} cm^{-3} is reached, then a discontinuity occurs which is followed by a smooth decrease in slope as the electron concentration becomes larger. The slopes at the lower concentrations are influenced by emission from the deep level and are subject to increasing uncertainties. Therefore, without additional study no significance should be placed in the discontinuity shown near a concentration of 5 x 10^{17} cm^{-3}. The peak energy is shown by Fig. 4 to shift to higher energies as the electron concentration exceeds 5 x 10^{17} cm^{-3}. The half-widths summarized in Fig. 5 show a change of 2.5 times over the decade of concentration from 5 x 10^{17} to 5 x 10^{18} cm^{-3}, and the experimental data show very little scatter. From these three figures it should now be obvious that from the spontaneous emission spectral shape it is possible to determine if a sample contains more or less than 5 x 10^{17} electrons/cm^3, and if more, the concentration value.

Since the emission intensity was observed to vary across the sample (9, 10), it was necessary to resolve the spectra in regions that differ in total emission intensity. No variations in spectral shape between regions of differing quantum efficiency were observed for any floating-zone sample. This lack of variation in spectral shape between regions of varying emission intensity suggests two possibilities: either the free electron concentration does not vary between regions, or the sensitivity of spectral shape to variations in n_o is insufficient to resolve possible differences in n_o. To separate these possibilities it is necessary to determine the sensitivity of this technique, the dependence of quantum efficiency on n_o, and the variations in Te concentration between regions differing in emission intensity. The sensitivity of this technique is considered in the next section, while the dependence of quantum efficiency on n_o and the magnitude of the Te concentration variations that could lead to variations in n_o are considered in the following paper (13) on inhomogeneities in GaAs.

Discussion

Figures 3, 4, and 5 show that the spectral shape depends on n_o only above about 5 x 10^{17} cm^{-3}. Of the three spectral shape properties, the low-energy tail slope is the least reliable. This difficulty results from the distortion of the low-energy tail that can occur because of the deep level shown in Fig. 2, as previously discussed. Also, for the lightly doped samples the slopes are quite steep, and any slow responses in the detection and recording system can introduce sizable errors. The build-up of a carbon contamination spot[1] on the sample due to the electron beam was found to reduce the emission intensity. This effect was minimized by using only as large a beam current as necessary to detect the spectral shape and by using a cold finger cooled by liquid nitrogen. At heavier doping levels the emission peak tends to flatten out, and the exact value of $h\nu_p$ can be difficult to determine. Even though the exact energy of the peak intensity is difficult to measure, the value of the peak intensity is rather obvious. Therefore, the spectral width at half the maximum intensity is an accurate and easy quantity to determine. The lack of data scatter in Fig. 5 as compared with Fig. 3 and 4 demonstrates the greater inherent ease in determining the half-width. For these reasons, the half-width will be used as the primary means of determining n_o, and the low-energy tail slope and peak energy will be considered as supplementary data. Taking ±0.005 ev as the resolvable difference in half-width results in a sensitivity of ±0.3 x 10^{18} cm^{-3} for the concentration range covered in Fig. 5.

The sensitivity of ±0.005 ev is a very conservative quantity. For example, the ±0.3 x 10^{18} cm^{-3} sensitivity would suggest that at 7 x 10^{17} cm^{-3} it would not be possible to tell the difference between 5 and 7 x 10^{17} cm^{-3}, while Fig. 5 shows that this distinction is readily made. Therefore, a sensitivity of ±15% at the lower concentrations and ±7% at the higher concentrations might be more reasonable. As mentioned in the introduction, the spatial resolution for this sensitivity depends on the beam voltage and is typically 3-6μ.

Several experimental factors can influence the spectral shape. If the steady-state minority carrier density becomes large enough, a superlinear peak will emerge on the low-energy side of the peak (15). For excitation densities below this level, the spontaneous emission at these impurity concentrations has a linear dependence on the beam current. Also, the effect of self-absorption on the spectral shape must be considered. A detailed analytical treatment of self-absorption cannot be made for the case of a finely focused beam for two basic reasons: (*a*) presently available models for the energy loss of energetic electrons are not adequate for properly describing the carrier generation rate in two independent spatial coordinates, and (*b*) the experimental absorption coefficients for heavily doped GaAs have not been measured for absorption coefficients above 10^3 cm^{-1}, the range where self-absorption might be significant. By making certain reasonable approximations it is possible to consider qualitatively what quantities contribute to self-absorption and their effect on spectral shape.

For description of the variation of electron penetration with beam voltage, the carrier generation rate may be approximated by neglecting the lateral scattering and representing the energy loss by Lenard's law (16)

$$I/I_o = \exp(-\alpha_e x) \qquad [1]$$

where I/I_o is the fraction of the electron flux transmitted, α_e the electron linear absorption coefficient, and x the distance measured from the sample surface. The advantage of using Lenard's law is that it is simple mathematically and analogous to the more familiar expression for optical absorption. The disadvantage is that it does not completely fit the experimental results. The absorption coefficient in Lenard's law depends on beam voltage and can be represented by (17)

$$\alpha_e = 1.9 \times 10^{11} \rho Z^{1/2} E_o^{-2} \qquad [2]$$

where ρ is the sample density, Z the atomic number, and E_o the beam voltage. For a density of 5.32 g-cm^{-3}

[1] A representative presentation of carbon contamination which also occurs in electron microscopes: Hans Gunther Heide, "*Electron Microscopy*," Vol. 1, p. A-4, Sydney S. Breese, Jr., Editor, Academic Press, New York (1962).

and Z of 32, α_e decreases from 1.4 x 10^4 cm^{-1} at 20 kv to 3.6 x 10^3 cm^{-1} at 40 kv. Therefore, the carrier generation rate will vary exponentially in depth as given in Eq. [1], and generation of carriers deeper in the sample will occur as the beam voltage increases.

The distribution in depth of the steady-state minority carrier density depends not only on the generation rate, but also on the diffusion length for holes L_p. This dependence is shown by solution of the continuity equation (neglecting lateral scattering) with suitable boundary conditions. For surface recombination velocities equal to the thermal velocity, an approximate expression for the minority carrier density may be written as

$$p(x) = KE_o[\alpha_e\tau_{nr}/(\alpha_e^2L_p^2 - 1)] [\exp(-x/L_p) - \exp(-\alpha_e x)] \quad [3]$$

where K is a spatially independent factor and τ_{nr} the over-all lifetime which is dominated by the nonradiative lifetime. The generated spectral shape will be uniform in depth and have an intensity proportional to $p(x)$. [Wittry recently presented a more complex analysis for the steady-state minority carrier density. The distribution in depth depends on L_p and the penetration of the beam into the sample, but not as simple exponentials (18)]. At 40 kv and for an L_p of 1.25μ, about 50% of the emission occurs within 3μ of the surface and 95% within 10μ. Emission from a given depth x will be observed after being attenuated by a factor of exp $[-\alpha(h\nu)x_1]$ where $\alpha(h\nu)$ is the optical absorption coefficient at the energy $h\nu$, and x_1 the distance traversed in the solid ($x_1 = x/\cos 70°$). When the $\alpha(h\nu)x_1$ product is the order of unity or larger, significant self-absorption will occur.

The effect of self-absorption on spectral shape really becomes the question of what effect changes in L_p for samples of the same free electron concentration will have on the spectral shape. Reference to the available absorption coefficient data reveals that significant self-absorption is to be expected only above the peak energy. Studies of absorption and photoluminescence by Lucovsky *et al.* (19) have shown that the spontaneous emission peak occurs where the logarithmic slope of the absorption coefficient is $(kT)^{-1}$, where k is Boltzmann's constant and T the temperature. From Fig. 4 and Hill's absorption data (2) the emission peak is found to occur at an absorption coefficient of approximately 10^3 cm^{-1}. Above the peak energy the absorption coefficient will approach a value slightly greater than 10^4 cm^{-1}. For the nominal values of α_e and L_p previously considered in Eq. [3], the emission will occur within less than 10μ of the surface so that the self-absorption, as represented by the $\alpha(h\nu)x_1$ product approaching or exceeding unity, will occur only for emission on the high-energy side of the peak. It is certainly not readily possible to demonstrate experimentally at a given n_o the variation of spectral shape with L_p, but a change in electron penetration can have a similar effect to variations in L_p. Therefore, the dependence of spectral shape on the steady-state hole distribution in depth may be illustrated by varying the beam voltage.

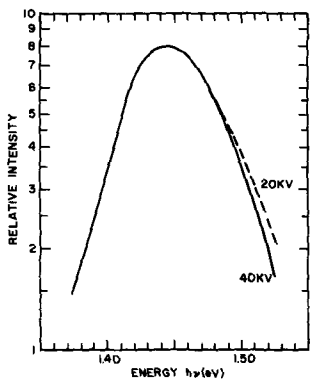

Fig. 6. Demonstration of the effects of self-absorption in a sample of $n_o = 3.2\times10^{18}$ electrons/cm^3. The deeper penetration of electrons at 40 kv may be seen to result in greater self-absorption only at energies above the peak energy.

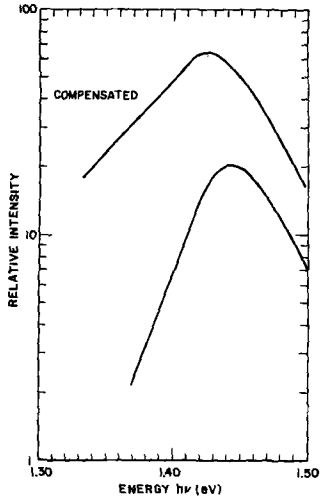

Fig. 7. Comparison of the spectrum for compensated (upper curve) and uncompensated (lower curve) samples with the same n_o of 2.6×10^{18} electrons/cm^3. The relative quantum efficiencies of the uncompensated and compensated samples do not significantly differ. They are displaced in intensity only to clearly illustrate their spectral shapes.

Figure 6 shows the spectra at 40 and 20 kv for a sample containing 3.2 x 10^{18} electrons/cm^3. The spectrum at 20 kv was normalized to the 40 kv spectrum by setting the intensities equal at 1.400 ev. The two spectral shapes diverge only well above the peak intensity. The difference in penetration, as represented by a change in α_e by a factor of 4, leads to no change of the low-energy tail slope or peak position, but changes the half-width by 0.005 ev. Because changes in the electron penetration and L_p have a similar effect on the steady-state minority carrier density, Fig. 6 suggests that variations in L_p by a factor of 2 or more at a given n_o would be necessary to change the half-width an observable amount. Fortunately, significant optical absorption coefficients occur at emission energies greater than the peak energy, and the effect of self-absorption is minimized.

By use of the calibration curves, it is possible to identify compensated samples. The spectrum for a compensated sample with a net free electron concentration of 2.6 x 10^{18} cm^{-3} is shown in Fig. 7 along with the spectrum of an uncompensated sample of the same n_o (see figure caption). Reference to Fig. 3, 4, and 5 shows that the half-width of the compensated sample corresponds to an n_o larger than 2.6 x 10^{18} cm^{-3}, while the peak position corresponds to a smaller concentration. In addition, the low-energy tail slope corresponds to a larger n_o by an order of magnitude. Thus, a compensated sample is characterized by a peak position that is too low for the n_o indicated by the half-width, and also a low-energy tail slope much less than expected for its half-width. By considering the effect of compensation on the edge absorption coefficient and the resulting spontaneous emission in the manner described by Lucovsky *et al.* (19), it can be seen that the decreased slope and peak energy are consistent with compensation effects. Comparison of Fig. 6 and 7 illustrates the manner in which self-absorption and compensation influence the spectral shape and shows the variation in L_p at a given n_o cannot lead to spectra representative of compensation.

Conclusions

The spontaneous emission spectral shape, characterized by half-width, peak energy, and logarithmic slope of the low-energy tail, depends uniquely on the

free electron concentration above concentrations of about 5 x 10^{17} cm^{-3}. A sensitivity of ±15% may be expected near 5 x 10^{17} cm^{-3} and ±7% at 5 x 10^{18} cm^{-3} with a spatial resolution of 3-6μ. The spectral shape also readily identifies compensated samples. This technique of measuring the free electron concentration from the spectral shape may also be applied to photoluminescence which is generally simpler experimentally; however, most bulk or layered samples are often inhomogeneous, and the small spatial resolution of electron-beam excitation is necessary for investigation of these features. The technique presented here should be applicable to p-type GaAs, but the concentration at which the spectral shape begins to depend on the acceptor concentration will probably be about a factor of 10 higher because of the larger effective mass of holes.

Acknowledgments

The authors are indebted to R. G. Sobers and K. L. Lawley for growing the floating-zone crystals and to F. Ermanis for making the many Hall measurements.

Manuscript received July 18, 1966. This paper was presented at the Cleveland Meeting, May 1-6, 1966.

Any discussion of this paper will appear in a Discussion Section to be published in the December 1967 JOURNAL.

REFERENCES

1. M. I. Nathan, Gerald Burns, S. E. Blum, and J. C. Marinace, *Phys. Rev.*, **132**, 1482 (1963).
2. D. E. Hill, *Phys. Rev.*, **133**, A866 (1964).
3. D. A. Cusano, *Solid State Comm.*, **2**, 353 (1964).
4. B. I. Halperin and Melvin Lax, *Phys. Rev.*, **148**, 722 (1966).
5. Gordon Lasher and Frank Stern, *ibid.*, **133**, A553 (1964).
6. W. G. Spitzer and J. M. Whelan, *ibid.*, **114**, 59 (1959).
7. H. K. Henisch, "Rectifying Semiconductor Contacts," p. 214, Oxford University Press, New York (1957).
8. H. C. Casey, Jr., *Bull. Am. Phys. Soc.*, **10**, 1199 (1965).
9. D. B. Wittry and D. F. Kyser, *J. Appl. Phys.*, **35**, 2439 (1964).
10. D. F. Kyser and D. B. Wittry, "The Electron Microprobe," T. D. McKinley, K. F. J. Heinrich, and D. B. Wittry, Editors, p. 691, John Wiley & Sons, Inc., New York (1966).
11. M. V. Sullivan and G. A. Kolb, *This Journal*, **110**, 585 (1963).
12. W. Czaja, *Helv. Phys. Acta*, **34**, 760 (1961).
13. H. C. Casey, Jr., *This Journal*, **114**, 153 (1967).
14. J. Vine and P. A. Einstein, *Proc. IEE*, **111**, 921 (1964).
15. H. C. Casey, Jr., and R. H. Kaiser, *Appl. Phys. Letters*, **8**, 113 (1966).
16. P. Lenard, *Ann. Phys. Chem.*, **56**, 255 (1895).
17. V. E. Cosslett and R. N. Thomas, *Brit. J. Appl. Phys.*, **15**, 883 (1964).
18. D. B. Wittry, The Electron Probe Microanalysis Conference, May 6, 1966, College Park, Md.
19. G. Lucovsky, A. J. Varga, and R. F. Schwarz, *Solid State Comm.*, **3**, 9 (1965).

Investigation of Inhomogeneities in GaAs by Electron-Beam Excitation

H. C. Casey, Jr.

Bell Telephone Laboratories, Incorporated, Murray Hill, New Jersey

ABSTRACT

Striations concentric with the growth axis, which are usually considered as impurity fluctuations, represent the inhomogeneity most frequently encountered in GaAs. Images of such striations were obtained by scanning-electron-beam-excited recombination radiation (SEBERR) and displayed on a cathode-ray tube. The samples investigated were Te-doped, floating-zone GaAs containing 2 x 10^{17} to 8 x 10^{18} free electrons-cm^{-3}. The spectral shape of recombination radiation demonstrated that any variation in free electron concentration within a cross section normal to the growth axis must be less than about 10%. In addition, the spectral shape showed that compensation is not the reason for the difference in the Te concentration and the free electron concentration. Precipitation of a Te-rich ternary solid solution with a crystal structure other than GaAs may be the most consistent explanation for the striation inhomogeneity and also may account for the cathodoluminescent features associated with dislocations.

In GaAs many techniques have shown the presence of concentric striations normal to the crystal growth axis. These striations represent fluctuations or inhomogeneities in several properties of the semiconductor crystal. Since the striations are readily revealed by etching (1), they obviously affect the rate of many etches. They also have been reported to cause variations in the infrared transmission (2). Schlieren imaging (3, 4) shows that the striations give fluctuations in the index of refraction and that no significant strains are associated with the striations (4). In the images produced by scanning-electron-beam-excited recombination radiation (SEBERR) and displayed on a cathode-ray tube, bands of decreased intensity were observed (5, 6); these bands will be shown to be the striations which can be revealed by etching. This variation in emission intensity indicates that the striations affect the radiative recombination. Striations have been observed also by x-ray diffraction microscopy in silicon (7) and by resistivity probing in germanium (8). Light emission from reverse-biased GaP p-n junctions clearly reveals striations and their effect on reverse breakdown (9). Because of striations, it is necessary, when preparing wafers for epitaxial growth, to use etching techniques that are not sensitive to these inhomogeneities (10); it is also necessary to consider the effect of these inhomogeneities on diffusion and p-n junction lasers (2, 3, 11,12).

Such an effect which causes variations in so many semiconductor properties has stimulated numerous investigations of both the origin and the nature of striations. Recent studies of InSb single crystals have shown that the formation of striations is the result of temperature fluctuations at the solid-liquid interface due to sharp temperature gradients in the growing crystal near the interface (13). For Te in GaAs, striations were shown by autoradiograms (14) and

electron probe microanalysis (15) to be Te concentration variations. These measurements of Te concentration also revealed that the average Te concentration exceeds the free carrier concentration as determined by Hall measurements. A transmission electron microscope study showed the striations in the particular crystals studied to contain bands of very fine precipitates (16). The result of using the Schlieren technique suggests the striations are variations in the index of refraction due to free electron concentration variations or band-gap changes (4). A number of reasons for the variations in the crystal properties and the difference in the total Te and free electron concentration have been proposed: (*a*) un-ionized Te, (*b*) fluctuations in free electron concentration, (*c*) compensation, (*d*) band-gap changes, and (*e*) precipitation.

Of the many techniques just described for observing the striations, none discriminates entirely between the proposed reasons for the variations. For example, the transmission electron microscope shows precipitation, but does not rule out other possibilities such as variations in free electron concentration. This paper explains how electron-beam excitation may be utilized to observe and investigate the striations and also to discriminate between the proposed reasons for the variations. Another benefit of SEBERR is that the range of magnification and resolution permits observation of such interesting features as dislocations and the discrete nature of some striations. The other techniques, although very useful, are generally limited to low magnifications where the fine features are not resolved or to such extremely high magnifications that the large-scale variations are lost and do not directly demonstrate the effect of the inhomogeneities on radiative recombination.

As previously reported (17), the spontaneous emission spectral shape and peak position may be used to determine the free electron concentration within $\pm 15\%$ near concentrations of 5×10^{17} cm^{-3} and $\pm 7\%$ at 5×10^{18} cm^{-3}, or to determine if a sample is compensated. These concentrations cover the range where the striations are most pronounced and also the range most useful for electroluminescent devices. In addition, the characteristic x-rays generated by the electron beam permit quantitative measurement of the impurity concentration if the spectrometer system has sufficient sensitivity. A Cambridge Microscan can detect Te concentrations only above about 10^{20} cm^{-3}, but by using a fully focusing spectrometer Wittry (15) was able to achieve a sensitivity in the low 10^{18} cm^{-3} concentration range. The spatial resolution for cathodoluminescence (CL) is 3-6μ and 2-3μ for x-rays. This paper is concerned only with CL, but Wittry's x-ray results (15) for Te variations will be discussed in order to describe the striations properly.

Relationship between Cathodoluminescent and Etching Features

It is beneficial first to consider the factors that contribute to the observed contrast in SEBERR images. For a sample scanned by a constant-current beam at a fixed-beam voltage, the measured intensity of the recombination radiation is proportional to the quantum efficiency η_q in a material of uniform generation rate times a factor which accounts for nonradiative surface recombination. This factor F_s will depend on surface-recombination velocity, minority carrier diffusion length, and beam voltage. At a fixed-beam voltage and a constant surface-recombination velocity, the principal effect of F_s on the observed intensity will be due to the diffusion length L_p or the over-all lifetime τ, since $L_p = \sqrt{D\tau}$ where D is the diffusion constant for holes. Wittry's results (18) indicate that τ becomes smaller at the higher impurity concentrations, and thus the factor due to nonradiative surface recombination F_s has a functional dependence on the free electron concentration n_o, $F_s \propto f(n_o)$. The quantum efficiency is simply the ratio of the hole-electron pairs that recombine radiatively to the total that recombine. This relationship is expressed as (19)

$$\eta_q = \frac{C}{n_i^2} \tau_{nr} n_o \int_0^\infty \alpha(h\nu) \exp(-h\nu/kT)\, d(h\nu) \quad [1]$$

where C is a collective constant, n_i^2 the thermal equilibrium electron-hole density product, τ_{nr} the over-all lifetime which is dominated by the nonradiative lifetime, and $\alpha(h\nu)$ the absorption coefficient at the energy $h\nu$. The absorption coefficient has a strong dependence on n_o at the concentrations being considered (20) and will cause the integral in Eq. [1] to decrease above concentrations of 10^{18} cm^{-3}. No data are now available to describe the concentration dependence of n_i^2, but some preliminary calculations based on a model by Halperin and Lax (21) suggest that the dependence will be small. The dependence of τ_{nr} on n_o has not been established, but τ_{nr} can depend on both the concentration of other impurities serving as traps and also on the lattice imperfections. For the present argument, the surface recombination factor F_s will be neglected and the observed intensity taken as η_q. Therefore, contrast in CL shows variations in the minority carrier generation rate, or for a uniform generation rate it measures variations in free electron concentration, unknown impurities, and/or lattice defects.

For comparison of the CL and the preferentially etched surface features over a reasonable portion of a wafer, an area was defined on a <111> oriented wafer containing 2.2×10^{18} cm^{-3} electrically active Te atoms. A smooth surface was obtained by chemically polishing by a procedure using a bromine-methanol etch and intensive stirring (22). Then a "home-plate" shaped mesa with a 0.060 in. base was produced by masking and etching the surrounding material to a depth of 10μ. Areas on this mesa of approximately $300 \times 300\mu$ were scanned by a 40-kv, 0.05-μa electron beam, and the SEBERR pictures were obtained from the cathode-ray tube as previously reported (17). The only optically observable surface irregularities were scratches that occurred during processing. The cathodoluminescent picture of the mesa, made by joining the many pictures of the scanned areas, is shown in the left half of Fig. 1. The sample was then etched with a solution known to reveal dislocations (23); the resulting optical photomicrograph is shown in the right half of Fig. 1. The cathodoluminescent and optical pictures are shown as mirror images so that features found at a certain distance to the right of the center line may be compared with the features at the same distance to the left.

There are a number of features with a unique correspondence between the etched and cathodoluminescent pictures. The irregular, roadlike lines are surface scratches obtained in processing the sample and are actually necessary to align and join the many pictures properly in the composite picture. The dark spots in the cathodoluminescence surrounded by bright regions about 100μ in size correspond uniquely to pits surrounded by smooth regions in the etch portion of the figure. Increased magnification readily identifies the pits as dislocation etch pits. The slightly curved vertical bands of decreased infrared emission spots appear as striations or bands of irregular, overlapping pits. A careful comparison of the left and rights sides of Fig. 1 conclusively demonstrates that the features of dislocations and striations seen by etching are completely reproduced in cathodoluminescence.

General Cathodoluminescent Characteristics of Striations and Dislocations

Examination of SEBERR pictures of samples taken from several Te-doped, floating-zone GaAs ingots reveals typical properties of striations and dislocations which are described in this section. This information

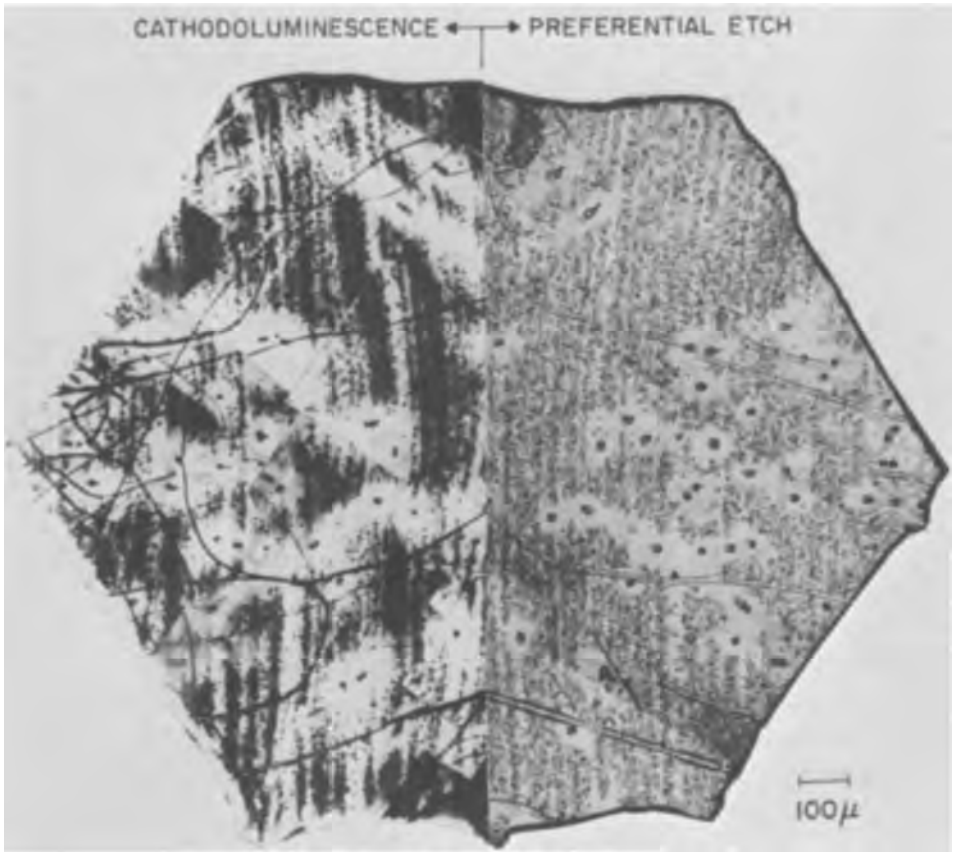

Fig. 1. Comparison of the cathodoluminescent and preferential etch features in GaAs. The free electron concentration is 2.2×10^{18} cm^{-3}.

will be utilized in the next section to infer the nature of the inhomogeneities.

The wafers in Fig. 2 cover a decade in free electron concentration, and for this figure as well as Fig. 3 the wafers were cut normal to the growth axis resulting in <100> orientation. In parts (a) and (b) of Fig. 2, the concentric, circular nature of the striations may be seen. The sample in Fig. 2(c) has a very large dislocation density, and the concentric nature of the striations is not recognizable in a picture of an area this small. The free electron concentrations of the samples in Fig. 1 and Fig. 2(c) are about the same; however, the striation regions of decreased recombination radiation in Fig. 1 are discrete, small, overlapping spots, while in the other wafer these regions appear continuous. Three samples from the same ingot are shown in Fig. 3 to further illustrate this property. Figure 2(b) is representative of most samples up to free electron concentrations of 6×10^{18} cm^{-3}. At higher concentrations the quantum efficiency rapidly decreases, and variations, if present, would be lost in the detector and amplifier system noise.

The dark spots at dislocations have the unique feature of usually being surrounded by a radially symmetrical region of increased emission intensity even in the dark band of the striations. In Fig. 1, 2, and 3 these regions have a radius of approximately 10-50μ. Often, as in Fig. 1, this high-intensity region surrounding a dislocation has the same quantum efficiency as the bright bands between the dark striations. The size of the dark spot at the dislocation is usually at least twice as large as the resolution of this technique (about 3-6μ), and therefore the contrast must be caused by more than just the line associated with the extra plane of atoms.

The three pictures in Fig. 3 show that an interesting and consistent relationship exists between the occurrence and size of discrete spots in striations, and the size of the dislocation spot and its surrounding bright region. Samples shown in Fig. 3 are from the same ingot and have free electron concentrations of 1.7, 2.5, and 3.2×10^{18} cm^{-3}, respectively. The approximate diameters of a dislocation and a bright region, and the size of the striation spot in Fig. 3 are summarized in Table I. This table shows that the larger striation spots occur with the larger dislocation spots and bright regions.

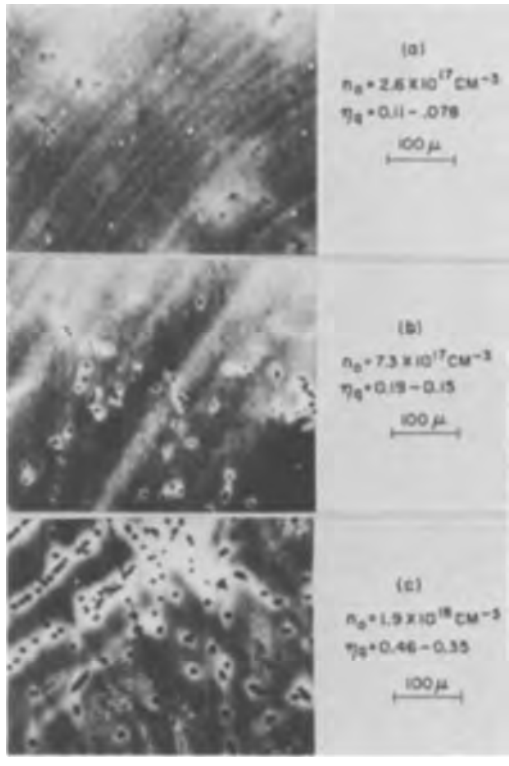

Fig. 2. Typical properties of the inhomogeneities in GaAs as illustrated by SEBERR pictures. The relative quantum efficiency η_Q is given for the bright region surrounding the dislocation (dark spots) and the dark bands in the striations.

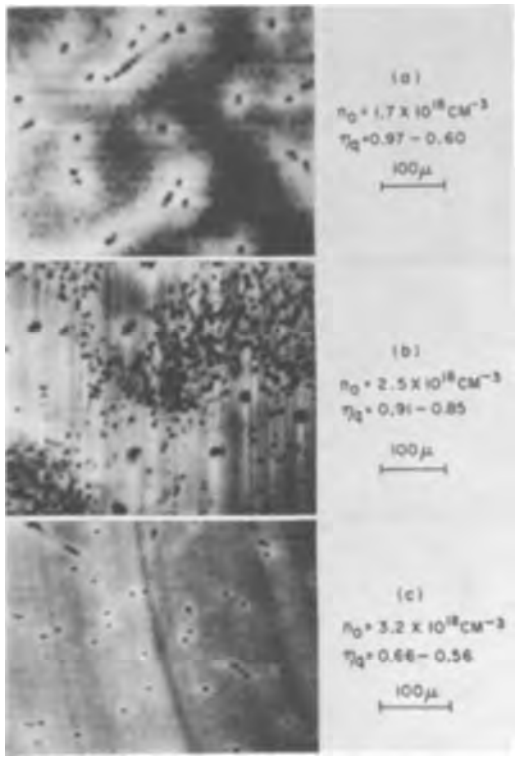

Fig. 3. SEBERR pictures demonstrating the size relationships of the dark spots at the dislocation, the radially symmetric bright region surrounding the dislocation, and the discrete nature of striations.

Since the contrast displayed on a cathode-ray tube can be deceptive, it is necessary to obtain the magnitude of the relative quantum efficiency variations by measuring the relative output voltage of the photomultiplier. The resulting efficiencies for bright regions near dislocations and the dark striation bands are plotted as open and closed circles respectively in Fig. 4. The efficiency limits for these wafers show the same general dependence on free electron concentration as the average values given by Cusano (24) and Kyser and Wittry (6). The rapid decrease in quantum efficiency above about 5 x 10^{18} electrons-cm^{-3} may be attributed partly to movement of the absorption edge to higher energies as described by the Burstein (25) shift which reduces the integral in Eq. [1] (19).

The spontaneous emission spectral shapes were resolved for the samples summarized in Fig. 4. Both the bright areas near dislocations and the dark striations were considered, but no differences in spectral shape were found on any wafer. This result means that the free electron concentration fluctuations must be less than ±15% near 5 x 10^{17} cm^{-3} and ±7% near 5 x 10^{18} cm^{-3} (17). These limits of uncertainty are rather conservative, and with extreme care the uncertainty will be half the above values. Also, spectral shapes which are characteristic of compensation (17) were not observed in the striations.

Discussion of Results

Initially, it is necessary to examine the relationship between the free electron concentration and the donor concentration. At Te concentrations above 10^{17} cm^{-3},

Table I. Size relationships of cathodoluminescent features

Figure	Diameter of dislocation spot, μ	Diameter of bright region, μ	Striation spot size, μ
3(a)	12	60	4-6
3(b)	20	100	10-12
3(c)	6	25	Continuous

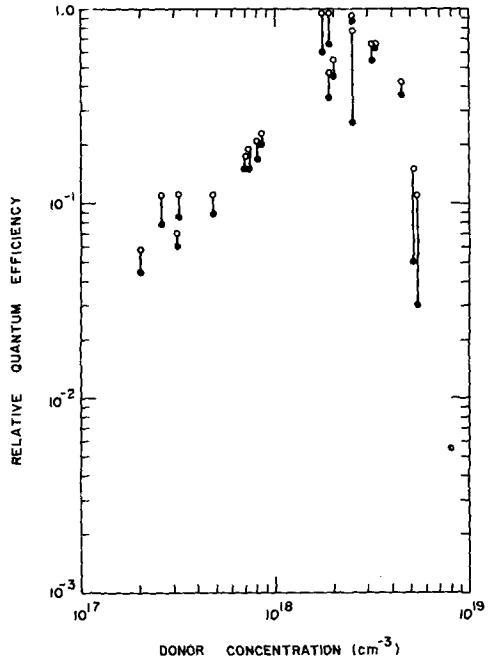

Fig. 4. Relative quantum efficiency as a function of free electron concentration. The open circles represent the efficiency in the bright regions near dislocations and the solid circles represent the efficiency in the dark bands of the striations.

the average distance between impurity atoms is close to the diameter of the Bohr orbit of a donor electron in a crystal, and Hall measurements reveal conduction by carriers in impurity bands or band tails (26). Under these conditions the free electron concentration no longer has any temperature dependence. This result indicates that for concentrations above 10^{17} cm^{-3} each donor atom located substitutionally in an As site contributes one free electron, and substitutional donors do not exist in a neutral or un-ionized state which would demand a temperature dependence of the free electron concentration. The possibility of the compensation as an explanation for the differences between n_o and the Te concentration or for the CL contrast can readily be eliminated since none of the spectral properties related to compensation (17) was observed.

The striations have been shown to be Te fluctuations by Wittry's (15) electron probe microanalysis and autoradiograms by Cronin *et al.* (14). Bands of increased Te concentration showed a decrease in CL intensity (15), which means the dark bands (and presumably the dark spots at the dislocations) in Fig. 1, 2, and 3 are the regions of greater Te concentration. Not only are Te fluctuations present, but the average Te concentration was significantly greater than n_o (14, 15). For example, in a sample containing 5.2 x 10^{18} electrons-cm^{-3}, the average Te concentration was approximately 7 x 10^{18} cm^{-3} (15), and chemical analysis of one of our samples with n_o = 8 x 10^{18} cm^{-3} showed it contained 1.5 x 10^{19} Te atoms-cm^{-3}. This discrepancy between the impurity concentration and the free electron concentration was also observed for Se (27) (results of numerous other papers suggest this is a general effect), but the differences are larger at a given Se concentration than observed for Te. Clearly, Te must be present in a form other than as a substitutional donor on an As site.

A variation of the free electron concentration would be expected because the striations are Te concentration fluctuations. However, the lack of any observable variations in spectral shape between bright and dark bands in the striations limits the possible range of variation to approximately 10%. With 30% Te fluctuations, Wittry (15) was also unable to find any spectral shape variations. In general, at high concentrations n_o does not follow the Te concentration;

in fact, Vieland and Kudman (27) found that n_o varied as $(Se)^{1/3}$ above concentrations of 4×10^{18} cm^{-3}. This dependence of n_o on the Te concentration suggests that the bands of greater Te concentration would not be accompanied by a comparable n_o change. The spectral shape technique does limit the possible variation in n_o, but cannot demonstrate a complete absence of n_o variation.

Equation [1] can be used for showing that differences in quantum efficiency between the bright regions and the dark bands of the striations, if attributed to differences in free electron concentration alone, will lead to an inconsistent result. Since the SEBERR pictures show dislocations as dark spots surrounded by bright regions of the same intensity as the bright striation bands throughout the n_o concentration range studied, it will be assumed that the dark bands in low concentration samples are bands of greater Te concentration as found for the more heavily doped samples. Below concentrations of 10^{18} cm^{-3}, the absorption coefficient is constant at a given $h\nu$, and with a constant τ_{nr} and n_i^2 Eq. [1] becomes

$$\eta_q = C_1 n_o \qquad [2]$$

where C_1 is a constant containing the various constant factors. From the data in Fig. 4, the dark striations would be predicted to contain a smaller concentration than the bright regions: $n_o(\text{dark}) < n_o(\text{bright})$. At higher concentrations, α at a given $h\nu$ decreases rapidly, and small changes in n_o cause a larger change in the integral in Eq. [1] than the linear dependence on n_o. In this case Eq. [1] becomes

$$\eta_q = C_2 \int_0^\infty \alpha(h\nu) \exp(-h\nu/kT)\, d(h\nu) \qquad [3]$$

with the various constants represented by C_2. At concentrations above 10^{18} cm^{-3} the dark regions in Fig. 4 would be due to a smaller α at a given energy, and hence $n_o(\text{dark}) > n_o(\text{bright})$, which is inconsistent with the previous inequality. Inclusion of the nonradiative surface recombination will lead to more complex expressions than Eq. [2] and [3], but will not change the above inequalities between concentrations in the bright and dark regions. Thus, any possible variation in the free electron concentration, which has been limited to about 10%, will not be the principal source of contrast or inhomogeneity seen in cathodoluminescence.

From the above discussion, the most probable source of contrast seen in the SEBERR pictures is the nonuniform distribution of the precipitated Te-rich phase or complex associated with the difference between Te concentration and n_o. Whether the inhomogeneities are band-gap variations will depend entirely on the nature of the precipitation. The contrast would be interpreted in terms of Eq. [1] as τ_{nr} variations. The spatial characteristics are more fully described in Table I by comparing the diameter of the dark spots at dislocations and the surrounding bright regions along with the size of the spots in the striations for the samples shown in Fig. 3. In general, this difference in Te concentration and n_o can be described as a Te-rich ternary solid solution with a crystal structure other than GaAs, but a more explicit description would only be speculation. For example, a solid solution of GaAs-Ga_2Te_3 can form as the crystal cools below 827°C (28). However, to explain the size of the bright regions around the dislocations requires diffusion of Te (at 827°C or lower) from the dark bands to the "dislocation" at very much larger diffusion rates than observed for donors in GaAs (29). Therefore, the Te-rich phase or complex must either be grown into the crystal or be formed by a species which is capable of extremely rapid diffusion.

Vacancies diffuse rapidly, and Vieland and Kudman (27) have suggested a complex involving a Ga vacancy and three Se atoms to describe the cube root dependence of n_o on the Se concentration. Mass action relations were written to describe the cube root dependence; however, mass action relations only mathematically describe equilibrium reactions and do not necessarily prove the existence of the assumed reactants. Acceptors also diffuse rapidly, but there is no evidence of any significant amount of compensation in these highly doped crystals.

The experimental observation that the free electron concentration is consistently less than the chemical donor concentration seems to be a general relationship for GaP (30) as well as GaAs. A fundamental understanding of this phenomenon is lacking at the present time.[1] Electron-beam excitation may be useful as a quantitative measurement technique in experiments intended to study this effect. This technique of studying inhomogeneities in bulk crystals should be applicable to many other compounds, especially the III-V mixed crystals. The only requirements are that the energy of the radiative recombination must exceed about 1.2 ev to permit detection with photomultipliers, and the quantum efficiency be not less than about 10^{-5}.

Conclusions

The features in SEBERR pictures were found to have a complete correspondence to those seen in photomicrographs of preferentially etched surfaces. These features included both dislocations and striations. Dislocations are characterized by 6-12μ dark spots that are usually surrounded by 25-100μ bright regions. The striations appear as either continuous bands or bands of discrete spots of decreased radiative recombination. In previously published results, the striations were found to contain Te concentrations in excess of the free electron concentration. Hall measurements and theoretical considerations show that Te atoms located substitutionally in the lattice cannot exist at these concentrations in an un-ionized form. Other techniques readily demonstrate the presence of inhomogeneities, but do not discriminate between the various reasons suggested for the variations in crystal properties. The infrared emission spectral shape demonstrates that compensation is not present in the striations, nor can very large free carrier variations be present. The contrast in cathodoluminescence and the difference between the total Te concentration and the free electron concentration are therefore accounted for by precipitation of a Te-rich solid solution or complex.

Acknowledgments

The author is indebted to several people for contributions to this paper. The floating-zone crystals were grown by R. G. Sobers, and the Hall measurements were made by F. Ermanis. R. H. Kaiser assisted in the spectral shape measurements, K. L. Lawley aided in the etching studies, and M. B. Panish provided information on the Ga-As-Te phase diagram.

Manuscript received July 18, 1966. This paper was presented at the Cleveland Meeting, May 1-6, 1966.

Any discussion of this paper will appear in a Discussion Section to be published in the December 1967 JOURNAL.

REFERENCES

1. T. S. Plaskett and A. H. Parsons, *This Journal*, **112**, 954 (1965).
2. G. Ziegler and H.-J. Henkel, *Z. Angew. Phys.*, **19**, 401 (1965).
3. H. Salow and K.-W. Benz, *ibid.*, **19**, 157 (1965).
4. M. E. Drougard, *J. Appl. Phys.*, **37**, 1858 (1966).
5. D. B. Wittry and D. F. Kyser, *ibid.*, **35**, 2439 (1964).
6. D. F. Kyser and D. B. Wittry, "The Electron Microprobe," p. 691, T. D. McKinley, K. F. J. Heinrich, and D. B. Wittry, Editors, John Wiley & Sons, Inc., New York (1966).
7. G. H. Schwuttke, *J. Appl. Phys.*, **34**, 1662 (1963).
8. J. A. M. Dikhoff, *Solid-State Elec.*, **1**, 202 (1960).
9. M. Gershenzon and A. Ashkin, *J. Appl. Phys.*, **37**, 246 (1966).
10. R. R. Moest, *This Journal*, **113**, 141 (1966).

[1] Note added in proof: A recent paper, G. Schottky, *J. Phys. Chem. Solids*, **27**, 1721 (1966), considers the Ga vacancy-donor atom complex in considerable detail.

11. J. C. Marinace, *ibid.*, **110**, 1153 (1963).
12. M. H. Pilkuhn and H. Rupprecht, *Trans. Met. Soc.*, **230**, 296 (1964).
13. K. Morizane, A. F. Witt, and H. C. Gatos, *This Journal*, **113**, 51 (1966).
14. G. R. Cronin, G. B. Larrabee, and J. F. Osborne, *ibid.*, **113**, 292 (1966).
15. D. B. Wittry, *Appl. Phys. Letters*, **8**, 142 (1966).
16. E. S. Meieran, *J. Appl. Phys.*, **36**, 2544 (1965).
17. H. C. Casey, Jr., and R. H. Kaiser, *This Journal*, **114**, 149 (1967).
18. D. B. Wittry, Electron Probe Microanalysis Conference, May 6, 1966, College Park, Md.
19. H. C. Casey, Jr., *Bull. Am. Phys. Soc.*, **10**, 1199 (1965).
20. D. E. Hill, *Phys. Rev.*, **133**, A866 (1964).
21. B. I. Halperin and Melvin Lax, *ibid.*, **148**, 722 (1966).
22. M. V. Sullivan and G. A. Kolb, *This Journal*, **110**, 585 (1963).
23. M. S. Abrahams and C. J. Buiocchi, *J. Appl. Phys.*, **36**, 2855 (1965).
24. D. A. Cusano, *Solid State Comm.*, **2**, 353 (1964).
25. E. Burstein, *Phys. Rev.*, **93**, 632 (1954); see also T. S. Moss, *Proc. Phys., Soc. (London)*, **B67**, 775 (1954).
26. D. N. Nasledov, *J. Appl. Phys.*, **32**, 2140 (1961).
27. L. J. Vieland and I. Kudman, *J. Phys. Chem. Solids*, **24**, 437 (1963).
28. M. B. Panish, *This Journal*, **114**, 91 (1967).
29. R. W. Fane and A. J. Goss, *Solid-State Elec.*, **6**, 383 (1963).
30. F. A. Trumbore, H. G. White, M. Kowalchik, R. A. Logan, and C. L. Luke, *This Journal*, **112**, 782 (1965).

Textural and Electrical Properties of Vacuum-Deposited Germanium Films

J. D. Williams and L. E. Terry[1]

Solid State and Thin Film Devices Division, Sandia Corporation, Albuquerque, New Mexico

ABSTRACT

An investigation has been conducted to determine the effect of condensation rate and substrate temperature on the textural and electrical properties of germanium films vacuum-deposited on amorphous substrates. All films deposited were either amorphous or polycrystalline. Regions in the condensation rate-substrate temperature plane exist which exhibit very high degrees of preferred orientation of the polycrystalline films. It was confirmed that substrate temperature influences the textural properties of the films. Also, for large variations in condensation rate, different preferred orientations were obtained for a constant substrate temperature. This demonstrates that film structure is a function of both the substrate temperature and the deposition rate.

Thin-film semiconductor research activity has been greatly stimulated by the need for improvement in one or more of the aspects of lower cost, smaller size, greater reliability and radiation resistance in electronic components and circuits. The electrical properties of semiconducting films are intimately related to their textural properties; therefore, this investigation of germanium films has been conducted to determine the effect of condensation rate and substrate temperature on the textural and electrical properties of the films. Two papers reporting textural properties of vacuum-deposited germanium films on heated amorphous substrates produced seemingly contradictory results. Davey (1) working with condensation rates on the order of 1 Å/sec, reported [110] texture for substrate temperatures in the 175°-350°C range. He found that a competition for growth occurs in the 350°-575°C range and that the texture varies principally between being powder, [110] and [111]. Above 575°C he found that the [111] texture became dominant. Via and Thun (2), working at 80 Å/sec, reported practically amorphous films at substrate temperatures up to 400°C. In the 400°-500°C range, they found mixed orientation of [110] and [100]. At approximately 500°C, the [100] orientation disappears and a mixture of [110] and [111] is found. At temperatures above 600°C, they found that the preferred [110] is by far predominant.

Sloope and Tiller (3), investigating vacuum-deposited germanium films on heated single-crystal substrates, found that the tendency of a film to exhibit epitaxy increases with increasing substrate temperature. Krikorian and Sneed (4) reported a similar observation in their investigation of sputtered germanium films deposited on heated single-crystal substrates. These observations, plus our own preliminary findings, led us to expect that a given preferred orientation obtained on heated amorphous substrates at low condensation rates and low temperatures could also be obtained at higher substrate temperatures and condensation rates.

During the course of our work, Davey *et al.* (5), published another paper which stated that, for thicknesses of germanium films greater than 500Å, the [110] texture was independent of all the other deposition parameters. A careful examination of Davey's data revealed that, for a constant substrate temperature, 240°C, the deposition rate was varied between 1 and 100 Å/sec. Likewise, for a constant deposition rate of 8.25 Å/sec, the substrate temperature was varied between 225° and 600°C. Therefore, we have chosen to investigate the textural properties of germanium films formed in an extended portion of the rate-temperature range.

Experimental Procedure and Equipment

Two hundred germanium films were vacuum-evaporated onto glazed alumina ceramic and Corning No. 7059 glass substrates with the following range of deposition parameters: (*a*) substrate temperature 25° to 700°C, (*b*) condensation rate 0.5 to 380 Å/sec, (*c*) deposition pressure 10^{-8} to 5 x 10^{-6} Torr, and (*d*) thickness 800 to 50,000Å. The vacuum evaporations were performed with the fixtures and bakeable ion-pumped system shown in Fig. 1. The molybdenum and 304 stainless steel fixture permitted seven samples to be prepared in one pumpdown cycle. Magnetic rotary motion feedthroughs allowed a selection of groups of 2-3-2 substrates for a choice of temperature and condensation rates. The 0.1-ohm centimeter n-type germanium source material was heated to evaporation temperatures with a Varian electron gun. Open cylindrical alumina and quartz crucibles, resistance-

[1] Present address: Motorola Inc., Phoenix, Arizona.

Fig. 1. Substrate holder and heater

heated by helical tungsten baskets and heavy tungsten coils with no inserts, were used as evaporation sources to obtain condensation rates above 100 Å/sec. Substrate heating was accomplished by two methods: (*i*) A molybdenum or stainless steel block, with heater wire imbedded in it, was placed in intimate contact with the substrate; (*ii*) The substrates were placed in a cylindrical oven. The contact heater was capable of raising the substrate temperature to approximately 600°C, and the oven was capable of producing substrate temperatures up to at least 800°C. Construction details of the contact heater are shown in Fig. 2.[2] Substrate temperatures were monitored by chromel-alumel thermocouples in contact with the back of the substrates. A considerable temperature differential is created between the front and back surfaces of the substrates when they were heated by the contact heater. In some cases this temperature difference is as much as 250°C. These differences were carefully correlated with the back surface temperatures by attaching thermocouples to both front and back surfaces and simulating the evaporating conditions. All temperatures in this report refer to the front surface of the substrate.

[2] The imbedded heater wire was Thermocoax manufactured by the Amperex Corporation, Hicksville, New York.

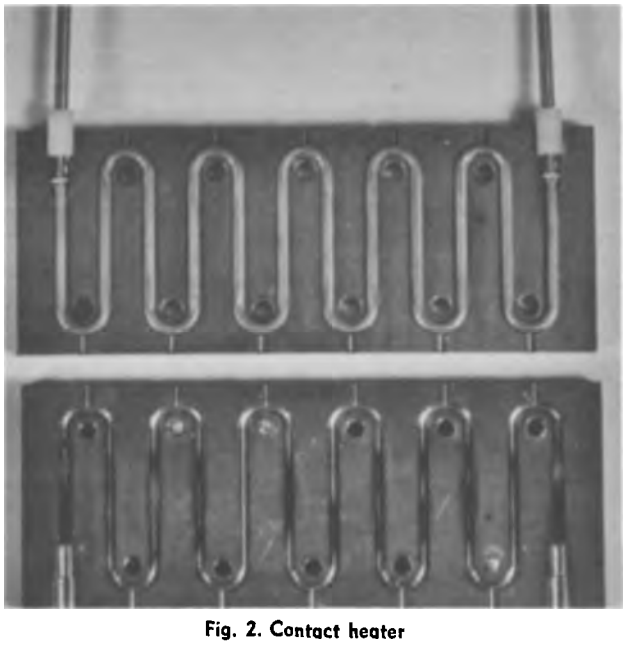

Fig. 2. Contact heater

The substrates were cleaned by the following procedure[3]: (*i*) 15-min ultrasonic bath in Alconox (3 g/liter distilled H_2O), (*ii*) 15-min ultrasonic rinse in room temperature distilled water, (*iii*) 10-min immersion in a boiling 10% solution of H_2O_2, (*iv*) boiling in ultrasonic rinse in distilled water, (*v*) drying in ethanol vapor, and (*vi*) storing in jars with ground glass seals.

The deposition parameters were varied by controlling the electron-gun beam current, the power delivered to the tungsten coil, and/or the deposition time. The source dimple of the electron gun was always filled with approximately 2*g* of germanium. The source material was slowly outgassed and the evaporation conditions allowed to reach equilibrium before the shutter was opened. Since the source material was never depleted by more than a few per cent during any evaporation, the effective source area and volume remained nearly constant, resulting in uniform condensation rates. Films were measured for thickness on a Zeiss interference microscope with the exception of a few of the very high substrate temperature films which exhibited rather rough surfaces. A beta-ray backscattering instrument was used to measure the average thickness of these films.

All samples were analyzed by x-ray diffraction on a General Electric XRD-6 diffractometer unit. The Bragg reflection peaks from the (111), (220), (311), and (400) planes were scanned at 4° and 0.4°/min. The method of determining the degree of preferred orientation of the films and a description of the crystallographic notation is given in Appendix A.

Results and Discussion

Crystallite orientation.—All films deposited on amorphous substrates were either amorphous or polycrystalline. Films deposited in the 1-100 Å/sec condensation rate and 25°-150°C substrate temperature range were all amorphous. Polycrystallinity was observed between 150° to 200°C but consistent, repeatable results were not obtained until the substrates were heated to above 200°C. A composite plot showing regions of preferred orientation in the substrate temperature-condensation rate plane is given in Fig. 3. Additional information pertinent to the data pre-

[3] This is cleaning procedure No. 1 reported in "A Comparison of Substrate Cleaning Procedures," J. D. Williams and J. N. Shafer, presented at the San Francisco Meeting of the Electrochemical Society, May 1965, Abstract No. 115.

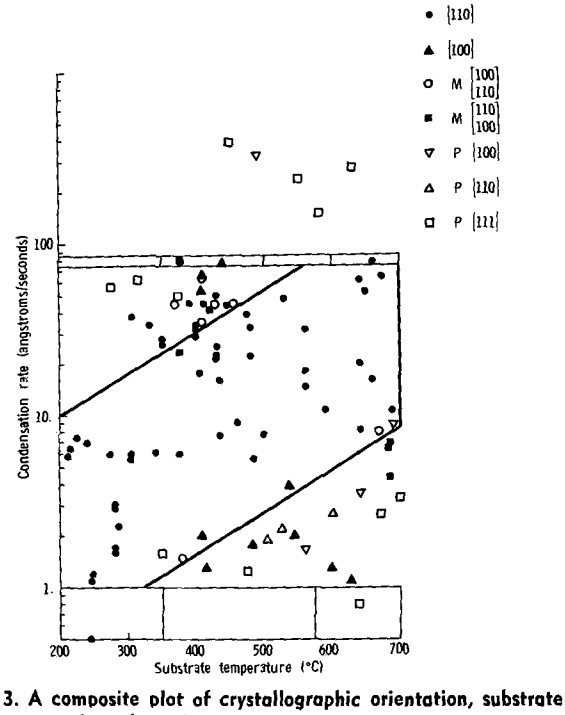

Fig. 3. A composite plot of crystallographic orientation, substrate temperature and condensation rate.

Table I. Additional data relative to Figure 3

Film number	Thickness (Angstroms)	Rate (Å/sec)	Substrate temp (°C)	Orientation	R_{220} (R_{111} always = 1)	R_{311}	R_{100}
2-3-2	800	1.65	350	P[111]	0.505	0.1	0.02
2-12-1	900	1.25	475	P[111]	0.58	0.8	0.94
3-4-1	1,100	0.8	640	P[100]	0.74	0.71	1.36
2-12-3	900	1.25	410	[100]	1.25	0.01	2.7
4-11-2b	1,400	0.5	245	[110]	97	0.1	0.7
2-13-2	2,200	1.83	485	[100]	0.95	0.1	3.2
2-24-1	2,430	2.7	600	P[110]	1.32	0.47	1.2
3-2-1	2,160	3.6	640	P[100]	0.88	0.9	1.76
3-4-2	1,620	1.08	620	[100]	0.8	0.5	3.1
3-4-3	1,900	1.25	600	[100]	1.02	0.76	3.9
3-14-2c	2,160	36	410	M[100/110]	2.0	0.1	2.8
4-9-3	2,430	8.1	670	M[100/110]	0.4	0.01	1.64
2-10-1	2,700	5.6	485	[110]	5.6	0.13	0.01
2-13-1	2,700	2.2	525	P[110]	1.69	0.94	1.5
2-18-1	2,530	1.7	560	P[100]	1.13	0.65	1.3
2-26-1	2,600	1.73	560	P[100]	1.22	1.18	1.28
2-26-2	2,600	2.06	545	[100]	1.3	0.92	2.4
2-26-3	2,600	1.88	505	P[110]	1.24	0.425	0.465
3-14-1a	2,700	45	430	M[100/110]	4.28	0.7	4.6
3-14-2a	2,700	45	410	[110]	3.89	0.35	2.52
3-14-3a	2,700	45	370	M[100/110]	2.33	0.26	3.18
3-14-3b	2,700	45	390	[110]	3.58	1.51	2.13
3-16-2c	3,240	54	410	[100]	1.98	0.3	3.44
3-7-2	2,700	1.5	380	M[100/110]	1.9	0.5	2.1
3-7-1	3,590	2	410	[100]	1.5	0.2	3.6
2-24-2	3,510	3.9	535	[100]	2.1	0.47	3.12
3-11-1b	5,400	22.5	430	[110]	7.62	0.69	3.4
3-16-1a	4,600	76.8	440	[100]	2.1	0.6	3.97
3-16-1b	4,730	79	440	[100]	1.4	0.65	4.1
3-16-2a	3,920	65	410	[100]	3.1	0.72	5.9
3-16-2b	3,780	63	410	M[100/110]	3.2	0.6	3.77
3-16-3a	5,000	83.5	375	M[110/100]	3.74	0.5	3.17
3-16-3b	5,000	83.5	375	[110]	5.0	0.6	3.97
3-17-1a	5,570	44	445	[110]	5.1	1	2.3
3-17-2b	5,130	42.8	420	M[110/100]	5.03	0.64	4.78
3-17-3a	4,590	38	305	[110]	6.5	0.3	4.55
3-17-3b	4,050	33.7	330	[110]	13.7	0.8	4
3-20-2a	5,120	21.3	430	[110]	6.49	0.7	2.3
3-23-2a	5,400	18	560	[110]	5	0.78	1.78
3-23-2b	4,860	16.2	660	[110]	2.7	0.43	1.1
3-23-2c	4,460	14.7	560	[110]	4.3	0.45	0.7
3-23-3a	5,400	22.5	480	[110]	7	0.4	3.5
3-25-1a	5,400	9	460	[110]	5.2	0.42	1.91
4-1-2	4,600	6.4	685	M[110/100]	2.02	0.615	1.45
4-9-1	4,050	3.4	700	P[111]	0.8	0.43	0.7
4-11-1a	3,920	1.2	245	[110]	25	0.7	1.84
4-11-1b	3,650	1.1	245	[110]	55	0.8	1.95
4-10-3a	4,580	1.7	280	[110]	40	0.6	2.1
4-10-3b	4,330	1.6	280	[110]	45	0.7	1.9
Ge-x-13	4,100	65	675	[110]	2.9	0.3	0.45
3-20-3a	5,670	23.6	375	M[110/100]	3.6	0.43	3.4
3-25-3b	5,800	16	435	[110]	10.2	0.4	0.48
4-13-3a	5,800	6.5	215	[110]	117	1.4	2.5
4-13-3b	5,800	6.5	215	[110]	146	1.14	1.7
3-11-1a	6,075	25.3	430	[110]	7.31	0.69	3.4
3-25-3a	6,350	17.6	405	[110]	9.3	0.46	0.55
3-25-2c	6,900	7.7	435	[110]	2.1	0.43	0.71
3-11-2c	7,020	29.2	400	[110]	5	0.576	3.15
3-25-2b	7,030	7.8	500	[110]	3.78	0.38	0.2
3-11-2b	7,840	32.6	400	[110]	14	0.78	5.2
3-11-2a	8,100	33.8	400	[110]	15	0.574	3.27
3-13-1a	8,640	48	530	[110]	6.1	0.52	1.76
3-13-2c	9,450	39	475	[110]	7	0.265	2.2
3-20-1a	8,900	33	480	[110]	7	0.24	2.1
3-20-1b	8,630	32	560	[110]	3.4	0.42	2.1
3-23-1a	7,830	10.8	590	[110]	5.5	0.425	2.0
3-23-1b	7,830	10.8	690	[110]	2.7	0.52	1.5
4-2-1	8,100	9	690	P[100]	1.1	0.87	1.5
4-10-1a	8,240	2.3	285	[110]	146	0.94	0.16
4-10-1b	8,100	2.25	285	[110]	53	0.37	0.35
4-10-2a	8,240	3.05	280	[110]	146	0.93	0.01
4-10-2b	8,100	3.0	280	[110]	135	1.2	0.17
4-10-2c	7,840	2.9	280	[110]	250	1	0.38
3-6-2	74,900	20	640	[110]	2.9	0.74	1.74
3-11-3a	10,120	28.2	350	[110]	10.2	0.915	5.3
3-11-3b	9,720	27	350	[110]	11.1	0.8	5.5
3-13-2a	10,800	45	455	M[100/110]	7.62	0.35	5.08
3-13-3a	12,150	50	430	[110]	3.7	0.3	2.1
3-13-3b	12,150	50	430	[110]	3.67	0.27	2.2
3-26-1a	11,080	6.15	340	[110]	250	0.7	4.2
3-26-1b	10,800	6	375	[110]	241	0.7	5.6
3-26-2a	11,200	6.2	275	[110]	53	0.8	0.4
3-26-2b	10,800	6	305	[110]	40	0.82	0.3
3-36-2c	10,100	5.6	305	[110]	23.8	0.85	0.2
3-26-3a	13,500	7.5	225	[110]	159	0.9	0.3
3-26-3b	12,550	7.0	240	[110]	121	0.33	0.35
3-31-1	16,000	53	650	[110]	6.5	0.55	3.56
3-31-2	11,000	61	640	[110]	7.31	0.44	4.2
3-31-3	12,500	8.3	640	[110]	6.7	0.58	1.01
4-2-2	12,150	6.75	685	M[110/100]	2.4	0.52	1.82
4-2-3	10,800	4.5	685	M[110/100]	1.75	0.535	1.48
Ge-x-3	19,000	61	315	P[111]	0.45	0.4	0.31

Table I (Continued)

Film number	Thickness (Angstroms)	Rate (Å/sec)	Substrate temp (°C)	Orientation	R_{220} (R_{111} always = 1)	R_{311}	R_{100}
Ge-x-2	17,000	58	275	P[111]	0.05	0.6	1
Ge-x-4	22,000	46	395	P[111]	0.5	0.2	0.22
Ge-x-6	43,000	240	550	P[111]	0.8	0.66	0.68
Ge-x-7	23,000	147	580	P[110]	1.04	0.723	0.832
Ge-x-8	39,000	390	450	P[111]	0.94	0.6	0.511
Ge-x-9	40,000	330	490	P[100]	0.11	0.66	1.92
Ge-x-11	50,000	280	630	P[111]	0.9	0.74	0.945

sented there is given in Table I. In Fig. 4 the three regions of the substrate temperature condensation rate plane previously investigated by Davey and Via and Thun are outlined. Three broader regions designated A, B, and C are also labeled to aid in the discussion of the figure.

Davey's first results are shown in the lower portion of Fig. 4. He found [110] texture[4] for low substrate temperatures (175°-350°C) and [111] texture for high substrate temperatures (525°-650°C) with the indicated mixed orientations in between. Via and Thun's results are shown near the top of the figure. Their films were all deposited at a condensation rate of 80 Å/sec. Polycrystallinity was first observed at 350°C. Mixed orientation was found up to 600°C, and the [110] texture was by far predominant above 600°C. The results of the present work extend into both regions and clearly indicate that a continuous range exists which connects the two regions of [110] texture. This is shown as region B in Fig. 4. In these polycrystalline films, a certain crystallographic plane of each crystallite is arranged parallel to the substrate surface, but we expect that the orientation is random in the other two directions. Two possible factors which influence the texture are: (*i*) that a larger binding energy exists between the condensing atoms than between the film atoms and the substrate surface, and (*ii*) the surface mobility of the atoms is an increasing function of the substrate temperature. According to a generalization of Bravais, the bounding planes which develop in growth are likely to be those which are parallel to the crystallographic planes of densest packing. There are many exceptions to this, but in the diamond structure the [110] is the most dense plane. In order to maintain similar conditions on the sub-

[4] The word texture is used to denote preferred orientation of crystallite faces parallel to the plane designated by the smallest integer Miller indices. For germanium the x-ray peaks are actually from the (111), (220), (311), and (400) reflections.

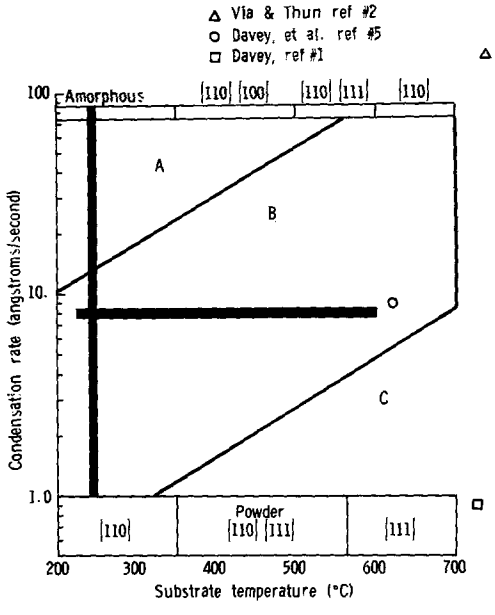

Fig. 4. Regions of special interest of the composite plot

strate surface, the surface mobility of atoms must be increased as the deposition rates increase, to keep successively arriving atoms from burying the preceding atoms which have not had time to form an appropriate lattice.

In general, the textures other than [110] reported by Davey, Via, and Thun are also confirmed by our investigation. The differences found probably result from different definitions of preferred orientation. For example, we actually classed as [100] the region designated by Davey as [111]. But if only the first three reflection planes were used for comparison, then we also would have obtained the [111] texture there. All condensation rates in the range 100-380 Å/sec in the substrate temperature range 250°-600°C caused the random powder orientation which probably results from the burying effect mentioned earlier. For substrate temperatures greater than 650°C and condensation rates of 10 Å/sec or less, the films are very granular. All of these films exhibit either the random powder orientation or a mixed orientation, probably because the evaporant atoms are not arriving fast enough to permit any orderly bonding arrangement.

Table I also contains values of R_{111}, R_{220}, R_{311}, and R_{400} calculated by the method outlined in Appendix A. In the left center portion of region B, values of R_{220} as high as 250 were obtained, indicating very strong [110] texture. For some specially selected rates and temperatures outside region B, [110] texture can also be obtained; but, in general, in regions near the indicated borders, the competition for growth results in a mixed texture.

The theory of nucleation on amorphous substrates is not well understood. Many and widely different theories and models have been proposed even when the experiments performed have been conducted on cleaved or ultraclean single-crystal substrates. For example, lattice constants of the parent crystal and the growth film were once expected to be within 15% for epitaxy to occur (6). A new concept, pseudomorphism, has been developed to explain the fact that oriented overgrowth has been observed for even greater differences in lattice constants. Such variables as substrate temperature and condensation rate are often of greater significance than the amount of lattice misfit (7, 8). The glass substrates used in our experiments, even though ultraclean, do not exhibit the ordered surface of a single-crystal substrate. Therefore, they do not lend themselves readily to conventional epitaxial theories.

The diamond structures of germanium can be considered as two interpenetrating face-centered cubic lattices. Because of the complicated covalent bonding of the diamond-type semiconductor structure, a rigorous treatment of the dependence of crystallographic formation on the substrate temperature is not given. However, a heuristic argument, following a development of Rhodin and Walton (9), is presented to offer a qualitative understanding of the changes in orientation with temperature and rate.

Rhodin and Walton considered the formation of a deposit of a face-centered cubic metal as a function of substrate temperature at a constant incident rate. At the low-temperature limit, the critical nucleus is a single atom, and the nucleation rate, I, can be expressed as

$$I_1 = R\left(\frac{R}{\nu N_0}\right)\exp\left[\frac{(2Q_{ad}-Q_D)}{kT}\right] \quad [1]$$

which is obtained from a general expression

$$I_n = R\left(\frac{R}{\nu N_0}\right)^n \exp\left[\frac{(n+1)Q_{ad}+E_n-Q_D}{kT}\right] \quad [2]$$

where n = number of atoms in the critical nucleus, E_n = dissociation energy of the critical nucleus ($E_1 = 0$), R = rate of incidence of vapor atoms, N_0 = density of adsorption sites, ν = a frequency term of the order of 10^{12}/sec, Q_{ad} = heat of adsorption of adsorbed atom, Q_D = activation energy for surface diffusion, k = Boltzmann constant, and T = absolute temperature.

At the low-temperature limit, the critical nucleus should be a single atom. Therefore, each time that a pair is formed it will usually grow, rather than decay into two single atoms. As the supersaturation is decreased, either by increasing substrate temperature or by decreasing incidence rate, a supersaturation point is reached where the probability of a pair decaying is equal to the probability of its growing. Below this point of supersaturation, a pair will be a critical nucleus until supersaturation is reached where the stable configuration formed by adding a single atom to the pair becomes unstable. Then the three-atom cluster becomes the stable nucleus.

As the substrate temperature is increased, a temperature is reached at which the pair is no longer stable (Eq. [2]). The next smallest cluster (three-atom) is one that has a minimum of two bonds per atom. One way of achieving a minimum of two bonds per atom is to have three atoms arranged in a triangle. The critical nucleus is the pair and the nucleation rate is

$$I_2 = R\left(\frac{R}{\nu N_0}\right)^2 \exp\left[\frac{(3Q_{ad}+E_2-Q_D)}{kT}\right] \quad [3]$$

where E_2 is the dissociation energy of the pair.

Another way of achieving a minimum of two bonds per atom is to have four atoms arranged in a square. The critical nucleus for this arrangement can be taken as three atoms in a capital L arrangement, and the nucleation rate is

$$I_3 = R\left(\frac{R}{\nu N_0}\right)^3 \exp\left[\frac{(4Q_{ad}+E_3-Q_D)}{kT}\right] \quad [4]$$

where E_3 is the dissociation energy of the three atoms in the critical nucleus.

The three-atom smallest stable cluster leads to an orientation in which the [111] plane is parallel to the substrate. The four-atom configuration leads to the [100] orientation. Therefore, Eq. [4] applies where the [100] is the first orientation to be observed, and Eq. [3] when the [111] orientation is first observed. Similarly, other orientations can also be observed. To obtain the temperature, T_1, at which the smallest stable cluster of one bond per atom changes to the two bond per atom (a triangular arrangement), one need only to equate Eq. [1] and [3] to obtain

$$T_1 = \frac{-(Q_{ad}+E_2)}{k\ln\left(\frac{R}{\nu N_0}\right)} \quad [5]$$

Likewise, the temperature, T_2, at which the smallest stable cluster of one bond per atom changes to the two bond per atom (a square arrangement), is obtained by equating Eq. [1] and [4]. This yields the following expression for T_2

$$T_2 = \frac{-(Q_{ad}+E_3/2)}{k\ln\left(\frac{R}{\nu N_0}\right)} \quad [6]$$

The preceding discussion, for the simple faced-center cubic metal, illustrates, at least for the initial stages of growth, that the type of orientation obtained for a given deposit is a function of substrate temperature. Since the nucleation rate is also dependent on the incidence rate of vapor atoms, the number of atoms in a critical nucleus is dependent on the condensation rate as well as the substrate temperature.

The preceding development would be more plausible if the complete films were formed as successive complete monolayers. The experimentally observed orientation rate and temperature dependence could then be

described by heterogeneous nucleation rate theory. However, monolayer formation does not seem to be the normal mode of growth for alkali halides and various metals previously studied (10). Since it is more likely that the germanium nuclei are experiencing three-dimensional growth, it therefore appears that a combination of heterogeneous and homogeneous nucleation is occurring.

Crystallite sizes.—When the size of the individual crystal is approximately 2000Å or less, one may use information obtained from diffractometer line broadening in estimating crystallite sizes. The extent of line broadening is given by the Scherrer formula

$$t = \frac{K\lambda}{(B_M^2 - B_S^2)^{1/2} \cos\theta} \qquad [10]$$

where B_M = width of diffraction line measured at half its maximum intensity, B_S = width from standard of crystallite size larger than about 2000Å, t = diameter of the crystal particle, K is a constant taken to be equal to 0.9, θ the Bragg angle, and λ is the wavelength of characteristic x-ray target material. All diffraction lines have a measurable breadth because of divergence of the incident beam and width of the x-ray source in diffractometers. The expression $B_M^2 - B_S^2$ assumes a Gaussian distribution of the counts and is essentially zero whenever the particle size exceeds approximately 2000Å. A standard half-width B_S was obtained for the XRD-6 unit by scanning the peaks from 40μ germanium powder samples. Six calibration samples of 40μ powder yielded an 8.8-min resolution width for the (111) peak and 11.6-min for the (220) peak.

Half widths for the (111) and (220) peaks were measured and are presented in Fig. 5 as a function of the substrate temperature. The data represented here covers deposition rates from 0.2 to 80 Å/sec and thicknesses from 2500 to 15,000Å. The data were grouped in temperature increments of 25°C, and the peak widths averaged within this temperature increment. Thus, each point represents approximately eight samples whose peak widths normally varied less than 2 min. The (111) and (220) crystallite size increases with temperature and, in agreement with Davey (5), the (220) crystallite sizes are larger than the (111) crystallites over the whole temperature range. Crystallite sizes calculated from the peak half-width data are also presented in Fig. 5. Some individual films from region B over the complete temperature range were also checked for crystallite size. It was found that the crystallite sizes of individual films followed the average data of Fig. 5 very closely. Thus, even though R_{220} peaks in the 250°-350°C range, the crystallite sizes are increasing functions of temperature. The [110] crystallite films in the 275°-280°C temperature range were also investigated for changes in crystallite size as a function of deposition rate. It was found that at a substrate temperature of 280°C when the condensation rate was increased from 1-8 Å/sec the [110] crystallites increased from 800 to 1200Å in average size.

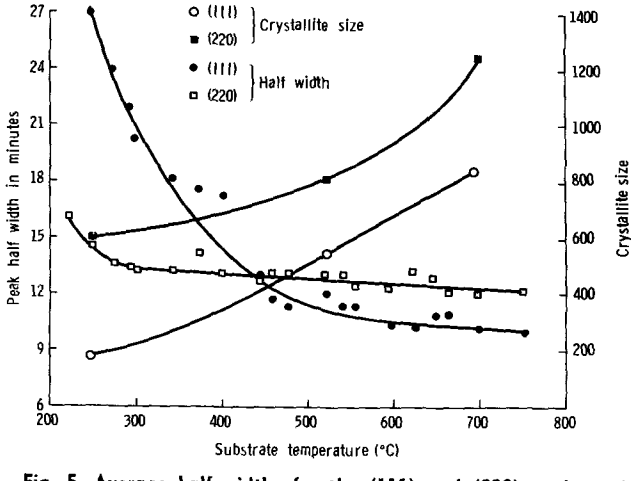

Fig. 5. Average half widths for the (111) and (220) peaks and crystallite size vs. substrate temperature.

Electrical properties.—In single-crystal semiconductor technology the most important parameters are resistivity, conductivity type, carrier mobility, carrier concentration, and lifetime of injected carriers. Because most single-crystal devices are minority carrier devices, the quantities mentioned above are those most pertinent to minority carrier devices. Vacuum-deposited semiconductor films presently produced on amorphous substrates are no more than polycrystalline films with large (>1000Å) diameter crystallites which may or may not exhibit a preferred crystallographic orientation. The most successful use of these semiconductor films has been in majority carrier devices. In polycrystalline films, the parameters mentioned are not always as meaningful as they are in single-crystal materials; however, they do form a basis of comparison and are widely used in thin-film research. The electrical parameters measured for these films are the conductivity type, the resistivity, and the Hall coefficient. All measurements were made at room temperature.

Lattice defects, grain boundaries, and other film imperfections found in polycrystalline films exhibit acceptor-type characteristics. Therefore, in these films the apparent doping level is shifted, in general, from source to film in the direction of higher p-values. All of the films deposited exhibited p-type conductivity, although the source material was n-type.[5]

Figure 6 shows the resistivity of the films *vs.* substrate temperature as measured with a four-point probe.[6] The data was also grouped in temperature increments and averaged. A few values of mobility are shown at key points in Fig. 6. Although the resistivity again increases slightly at temperatures above 400°C, the mobility of crystallite sizes continue to increase. Rectifying grain boundaries in polycrystalline material will cause fluctuation in the electric field intensity. Therefore, the resistivity will register higher values than in similarly doped single-crystal material.

[5] The film conductivity type was checked by a thermoelectric probe and by observing the sign of the Hall voltage. The film conductivity type was checked immediately after the films were removed from the vacuum chamber.

[6] For films less than 10^5Å thick $\rho = 4.532 \times 10^{-8}\ V/I\ W$, where V is in volts, I in amperes, and W in angstroms.

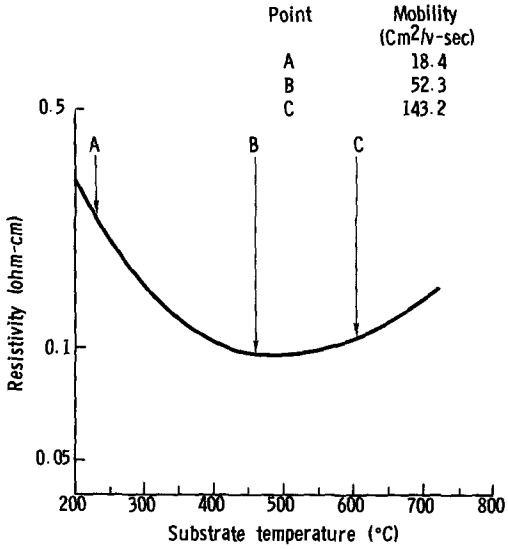

Fig. 6. Resistivity vs. substrate temperature

Conclusions

For large variations in condensation rate, different preferred orientations can be obtained for a constant substrate temperature. This fact, combined with the well-known variations in textural properties with changes of substrate temperature, suggests that film structure is a function of both the substrate temperature and the deposition rate. The [110] textural characteristics produced at low-substrate temperatures and low-condensation rates can be extended through higher substrate temperatures if the condensation rate is increased. Thus, since the results of Davey and Via and Thun fall at opposite ends of a continuous substrate temperature condensation rate region they are basically in agreement rather than contradictory.

From x-ray diffraction line broadening, the crystallite sizes increase with substrate temperature. The crystallites of [110] texture are always larger than the [111] oriented crystallites. The ratio R_{220}, which gives a quantitative measure of the degree of preferred orientation, peaks in the 250°-350°C, 2-7 Å/sec portion of region B. Crystallite sizes were also observed to increase with condensation rate. A 50% increase in crystallite size could be observed by increasing the temperature or by increasing the condensation rate across the ranges of region B.

The resistivity and Hall mobility of the films are dependent on the substrate temperature during deposition. The resistivity varies down to a minimum of approximately 0.1 ohm-cm near a substrate temperature of 500°C. The Hall mobility increases with substrate temperature. Values from 1 to 150 cm^2/sec were obtained. The resistivity values seem to depend on the number of crystallites oriented, since they pass through a minimum soon after the degree of preferred orientation peaks. The mobility continues to increase and therefore must depend on the average crystallite size.

Manuscript received May 10, 1965; revised manuscript received Aug. 29, 1966. This paper was presented at the Toronto Meeting, May 3-7, 1964. This work was supported by the United States Atomic Energy Commission.

Any discussion of this paper will appear in a Discussion Section to be published in the December 1967 JOURNAL.

REFERENCES

1. John E. Davey, *J. Appl. Phys.*, **32**, 877 (1961).
2. G. C. Via and R. E. Thun, *8th Nat. Vacuum Symp. Trans.*, October 1961, p. 950.
3. B. W. Sloope and C. O. Tiller, *10th Nat. Vacuum Symp. Trans.*, October 1963, p. 339.
4. E. Krikorian and R. J. Sneed, *10th Nat. Vacuum Symp. Trans.*, October 1963, p. 368.
5. J. E. Davey, R. J. Tiernan, T. Pankey, and M. D. Montgomery, *Solid-State Electron*, **6**, 205 (May-June 1963).
6. F. L. Frank and J. H. van der Merwe, *Proc. Roy. Soc.*, **A198**, 205 (1949).
7. S. A. Semiletov, *Kristallograiya*, **I**, No. 5, 542 (1956).
8. G. A. Bassett, J. W. Menter, and D. W. Pashley, in "Structure and Properties of Thin Films," Neugebauer, Editor, p. 11, John Wiley and Sons, New York (1959).
9. T. N. Rhodin and Derek Walton, "Metal Surfaces," Proc. ASM Meeting, October 27, 28, 1962, pp. 259-286.
10. D. W. Pashley, "Thin Films," p. 62, Amer. Soc. for Metals, Metals Park, Ohio (1964).

APPENDIX A

Determination of Preferred Orientation

A standard definition of what is meant by "preferred orientation" of polycrystalline films does not exist. The following definition was developed and used in this paper. A ratio that provides a quantitative measure of the relative amount of preferred orientation is defined as follows

$$R_{ijk} = \frac{h_{ijk}^{s}}{h_{111}^{s}} \frac{h_{111}^{Ps}}{h_{ijk}^{Ps}}$$

where h_{ijk}^{s} = height of (ijk) plane reflection peak, above noise, for sample being measured; h_{ijk}^{Ps} = height of (ijk) plane reflection peak, above noise, for powder standard (for germanium $h_{111}^{Ps} = 1$, $h_{220}^{Ps} = 0.57$, $h_{311}^{Ps} = 0.39$, $h_{400}^{Ps} = 0.07$); h_{111}^{s} = height of (111) plane reflection peak, above noise, for sample being measured; and h_{111}^{Ps} = height of (111) plane reflection peak, above noise, for powder standard.

Thus, for example, we have

$$R_{220} = \frac{h_{220}^{s}}{h_{111}^{s}} \cdot \frac{h_{111}^{Ps}}{h_{220}^{Ps}}$$

and

$$R_{400} = \frac{h_{400}^{s}}{h_{111}^{s}} \cdot \frac{h_{111}^{Ps}}{h_{400}^{Ps}}$$

It is apparent then that if

$$R_{220} = 1$$

then the height of the (220) plane reflection peak in the sample and the height of the (111) reflection peak in the sample are in the same ratio as these two peaks in the powder standard. However, if

$$R_{220} > 1$$

then the ratio of the height of the (220) plane reflection peak to that of the (111) plane reflection peak for the sample is larger than the corresponding ratio for the powder standard. Thus we have preferred orientation of (220) over the (111) in the sample.

Similarly, if

$$R_{220} < 1$$

then the (111) is preferred over the (220).

It is apparent that all the ratios are normalized to the (111) plane. Therefore, if we have $R_{400} > R_{220}$ then the (400) plane is preferred over the (220) plane.

If a particular plane exhibited a relative ratio of at least one greater than the next highest ratio, the sample was considered to exhibit preferred orientation in that direction. If no more than three of the peaks exhibited ratios within one of each other, the preferred orientation of the sample was considered mixed between the two highest ratios; and if all four ratios were within one of each other, the sample was considered to exhibit the random powder orientation. The above criterion can be used for all evaluations except those in which the (111) reflections are predominant. In these cases, all ratios are one or less; therefore the criterion becomes one-half below rather than one above: *i.e.*, the (111) direction is preferred if $R_{111} = 1$ and all other R_{ijk}'s are below one-half; mixed orientation between the two highest reflections is obtained if no more than three of the peaks exhibit ratios within one-half of each other; and if all four ratios were within one-half of each other, the sample was considered to exhibit the random powder orientation. If no peaks were observed, the sample was considered to be amorphous. The notation used throughout this paper is as follows: [111] =preferred orientation or texture; $M\begin{pmatrix}111\\110\end{pmatrix}$ = mixed orientation with $R_{111} > R_{220}$; and P[111] = powder orientation with $R_{111} >$ the other R_{ijk}.

Preparation of Epitaxial $Ga_xIn_{1-x}As$

R. W. Conrad, P. L. Hoyt, and D. D. Martin

Texas Instruments Incorporated, Dallas, Texas

ABSTRACT

Single-crystal, epitaxial $Ga_xIn_{1-x}As$ alloys have been prepared on (100), semi-insulating GaAs substrates, using an open-tube, vapor phase deposition system. High-purity elemental gallium, indium, and arsenic were used as source materials. Severe distortion of substrate and deposit was observed when thin substrates (less than *ca.* 11 mils) were used. This was attributed to the large lattice mismatch between deposit and substrate. The electron Hall mobility showed a pronounced minimum for alloys in the middle of the composition range, in agreement with earlier results.

In contrast to the $GaAs_xP_{1-x}$ alloy system, relatively few studies of the preparation and properties of $Ga_xIn_{1-x}As$ alloys have been reported. Abrahams *et al.* (1) prepared polycrystalline $Ga_xIn_{1-x}As$ alloys by gradient freeze and zone-leveling techniques. The variations of lattice thermal conductivity, electron mobility, and band gap were determined as a function of alloy composition. Woolley *et al.* (2) apparently prepared more homogeneous polycrystalline alloys by directional freezing. The variation of energy gap with composition was found to be linear up to about 80 mole % GaAs. At higher GaAs contents, a more rapid increase in energy gap was observed. Hall measurements of these alloys gave mobilities lower than obtained by Abrahams *et al.* when single-carrier treatment of the data was used. This was attributed to mixed conduction. Homogeneous polycrystalline alloys were recently prepared by Hockings *et al.* (3) by zone-leveling. Thermal conductivity, Seebeck coefficient, and electrical resistivity were measured as functions of temperature, impurity concentration, and alloy composition. Electron mobilities were reported for several samples with $x = 0.3$ and 0.7. However, these samples were very highly doped with selenium (from 7×10^{17} to $4 \times 10^{18}/cm^3$). Sirrine (4) briefly described the nonseeded growth of several single crystals of $Ga_xIn_{1-x}As$ using halogen vapor transport in a closed system. Minden (5) reported on the preparation of single-crystal $Ga_xIn_{1-x}As$ alloys, both unseeded by a closed tube method, and epitaxial on GaAs substrates using an open-tube system. Minden's open-tube system employed sources of elemental arsenic and gallium-indium solutions. Considerable fractionation of the gallium-indium source occurred, making control of composition difficult. Electrical properties were not reported.

The present investigation further deals with the open-tube preparation and properties of epitaxial $Ga_xIn_{1-x}As$ alloys on GaAs substrates. Instead of mixed gallium-indium solutions as a source material, separate reservoirs of gallium and indium are used.

Experimental

Materials preparation.—Initially, a deposition system employing separate reservoirs of crushed GaAs and InAs was tried. Transport of the gallium- and indium-halides and introduction of arsenic were accomplished by passing $AsCl_3/H_2$ mixtures over the heated source materials. Control of alloy composition in this system however was not straightforward in that InAs and alloys with greater than about 50 mole % InAs were difficult to prepare. For this reason and for reasons of economy, flexibility, and purity, a different type of system was devised.

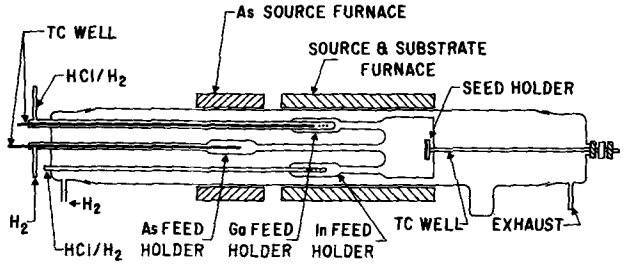

Fig. 1. Open-tube vapor deposition system for epitaxial $Ga_xIn_{1-x}As$ alloy preparation.

The open-tube deposition system used in this work is shown schematically in Fig. 1, and is constructed of fused quartz. Purified H_2 was passed over heated elemental arsenic[1] to transport arsenic vapor to the deposition zone. Mixtures of purified H_2 and HCl (prepared by H_2 reduction of $AsCl_3$) were passed through the heated gallium[1] and indium[1] reservoirs to transport the volatile gallium and indium chlorides to the deposition zone. (The concentration of HCl in the gas mixture is fixed at about 6 v/o by the vapor pressure of $AsCl_3$, which is maintained at 25°C.) The compositions of the deposited alloys were primarily controlled by the relative flow rates of the gas mixture through the gallium and indium reservoirs. These could be varied continuously from 0 to about 70 cc/min. An additional flow of H_2 of about 30 cc/min was introduced into the outer reactor tube to prevent back-diffusion and to aid in sweeping out the reaction products.

A two-zone resistance furnace was used to provide temperature control of the arsenic, gallium, indium, and substrate. One zone controlled the arsenic temperature (typically 440°C). The second zone controlled the gallium and indium reservoirs simultaneously (at 865°-870°C) since they are side-by-side. Control of the substrate temperature (745°-750°C) was accomplished by placing the substrate on a movable holder and positioning it at the proper location in the temperature gradient at the end of the gallium-indium source zone. The substrate had to be held in a vertical position because of the steepness of the temperature gradient. With care, all temperatures were maintained at ± 2°C.

Substrates used in this investigation were (100)-oriented wafers cut (30 mils thick) from chromium-doped GaAs pulled crystals. Room temperature resistivities of such crystals were about 10^8 ohm-cm. The wafers were chemically polished using the method of Reisman and Rohr (6), and etched in 5:1:1 $H_2SO_4:H_2O_2:H_2O$ immediately prior to use.

Materials evaluation.—The alloy layers were shown to be epitaxial by x-ray diffraction. Epitaxial layer thicknesses were determined by bevel-lap and stain techniques. A good stain for delineating the junction in GaAs and GaAs-rich alloys was the $Fe\text{-}HNO_3\text{-}H_2O$ stain (7). For InAs and InAs-rich alloys, a brief treatment with 1.5% NaOCl in H_2O provided sharp contrast between substrate and layer (8).

Compositions were determined by x-ray diffraction techniques, assuming a linear variation of lattice

[1] 99.9999% pure.

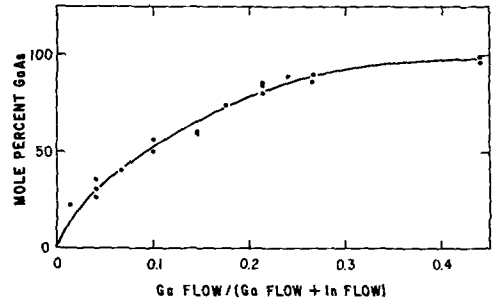

Fig. 2. Variation of composition of epitaxial $Ga_xIn_{1-x}As$ alloys with change in fractional $HCl-H_2$ mixture flow through gallium reservoir.

constant with alloy composition. The sharpness of the alloy diffraction peaks also provided a qualitative measure of deposit homogeneity.

Hall and resistivity measurements were made on ultrasonically cut six-armed specimens with indium solder contacts, using either a-c or d-c techniques, depending on whether the sample resistance was low or high.

Results and Discussion

Physical properties.—Deposition rates obtained with this system ranged from 20 to 35 μ/hr, essentially independent of substrate temperature over the range 720°-760°C, and also independent of alloy composition. These results are in contrast with the observation (5) that InAs deposition occurs efficiently only at temperatures below 700°C.

Alloy composition could be varied in a straightforward fashion by changing flow rates over the gallium and indium sources. This relation is shown in Fig. 2. The abscissa is the ratio of the flow rate of the $HCl-H_2$ mixture over the gallium source to the total flow rate of the $HCl-H_2$ mixture over both gallium and indium sources. This is similar to the variation of alloy composition with source composition found by Minden (5). In contrast, however, we have experienced no difficulty in fabricating alloys with less than 10 mole % InAs. The relationship shown in Fig. 2 is unusual in view of the fact that deposition rate is essentially independent of alloy composition even though GaAs appears to deposit preferentially. We have no explanation for this at present.

The homogeneity of alloys produced in the deposition system using compound source materials has been described previously (9). Material produced in the present system was similarly examined using reflectivity and absorption methods and found to be homogeneous within the limits of resolution of the analytical methods (about ± 3% absolute).

Often the alloy layers had macroscopically smooth, shiny surfaces and sharp substrate-deposit interfaces. Occasionally, for reasons not yet clear, physical defects of the "hillock" type were obtained in the more GaAs-rich alloys. These generally were protrusions with apparently (100) facets. For InAs-rich alloys, defects took the form of short line imperfections oriented along <110> directions. These line imperfections appear to be (100) analogs of the (111) stacking faults in epitaxial GaAs described by Gabor (10).

The hillock imperfections appeared to be connected with substrate quality, since some substrate crystals yielded higher hillock densities than others. The line imperfections, however, did not appear to be closely connected with the substrates. Since such line imperfections were only observed in InAs-rich alloys, they may be related to the large lattice mismatch (InAs, 6.06Å; GaAs, 5.65Å).

When alloys were deposited on very thin GaAs substrates (less than about 11 mils thick), the samples were severely plastically distorted. Figure 3 shows a

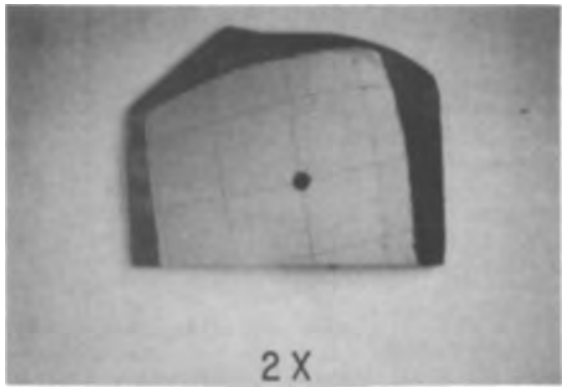

Fig. 3. Distorted epitaxial $Ga_{0.75}In_{0.25}As$ sample obtained by deposition on a 10 mil thick (100) GaAs substrate.

39μ thick layer of $Ga_{0.75}In_{0.25}As$ on a substrate 10 mils thick. (The sample was photographed through a hole in a piece of graph paper to illustrate the curvature.) Surface contour measurements showed this sample to be symmetrically curved about its center point with a radius of curvature of 12 cm. A detailed study of this phenomenon was not performed. However, we did ascertain that (*i*) the effect was caused by alloy deposition since heat-treatment of a thin substrate under conditions similar to those used during a deposition did not produce bending, and (*ii*) qualitatively the effect appears to become more severe as the InAs content of the alloy is increased. Since the thermal expansion coefficients of InAs and GaAs are not very different over the temperature range 50°-700°C (11), the distortion is attributed to the considerable mismatch of lattice constants.

Electrical properties.—The initial investigations of the electrical properties of the $Ga_xIn_{1-x}As$ system were at the end points of the alloy range, *i.e.*, GaAs and InAs. Table I shows the electrical properties of the better deposits. Next, alloys of various compositions were prepared and evaluated. Generally, deposits were n-type with excess carrier concentrations in the 10^{15}-10^{16} cm^{-3} range. However, we observed that use of low arsenic reservoir temperatures (<*ca.*400°C) invariably produced p-type, high-resistivity layers (10^4-10^5 ohm-cm at 300°K) for GaAs and alloys with less than about 70 mole % InAs. The resistivities of such deposits were essentially independent of alloy composition. The nature of the impurity or defect causing such behavior is not known; however, the invariance of resistivity with composition implies an acceptor level which stays approximately a fixed distance from the valence band through the alloy range. This has been partially confirmed by conductivity measurements as a function of temperature for several such samples. The activation energy of con-

Table I. Hall and resistivity data on InAs and GaAs layers on (100) GaAs substrates

Sample No.	Layer thickness, μ	300°K Mobility, cm^2/v-sec	300°K Excess carrier conc, cm^{-3}	77°K Mobility, cm^2/v-sec	77°K Excess carrier conc, cm^{-3}
		InAs			
−128	24	2.1×10^4	1.1×10^{16}	5.9×10^4	7.6×10^{15}
−124	16	2.0×10^4	1.7×10^{16}	4.8×10^4	1.2×10^{16}
−52	14	1.9×10^4	1.5×10^{16}	5.3×10^4	9.8×10^{15}
−50	20	2.3×10^4	8.7×10^{15}	7.0×10^4	6.1×10^{15}
66-280	28	1.7×10^4	4.2×10^{15}	5.9×10^4	2.5×10^{15}
		GaAs			
15	12	6.6×10^3	5.5×10^{15}	2.6×10^4	4.4×10^{15}
114	9	6.4×10^3	1.2×10^{16}	2.3×10^4	8.9×10^{15}
94	12	6.6×10^3	2.5×10^{15}	3.2×10^4	1.8×10^{15}
129	19	7.0×10^3	1.4×10^{15}	2.6×10^4	1.2×10^{15}
133	16	8.0×10^3	8.3×10^{14}	3.5×10^4	7.5×10^{14}

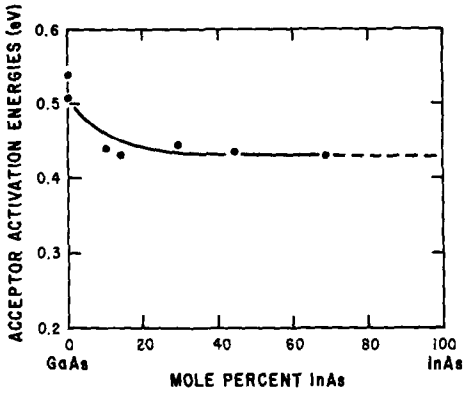

Fig. 4. Activation energy in electron volts for conduction of unknown acceptor impurity or defect as a function of $Ga_xIn_{1-x}As$ alloy composition.

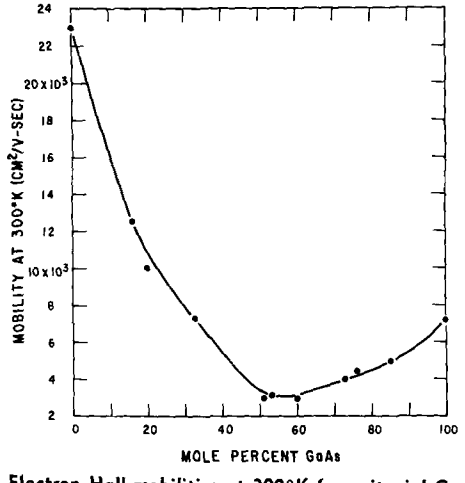

Fig. 5. Electron Hall mobilities at 300°K for epitaxial $Ga_xIn_{1-x}As$ alloys on (100) GaAs substrates.

duction (ΔE) as a function of alloy composition is shown in Fig. 4. The ΔE values shown are uncorrected for variations of mobility and densities of states with temperature. However, in all cases the variation of the logarithm of conductivity with reciprocal absolute temperature was linear over a large temperature range (from 100° to 300°K). The energy level of the unknown acceptor appears to become deeper than $E_g/2$ at about 70 mole % InAs. This is consistent with our observation that p-type high resistivity alloys with more than 70 mole % InAs could not be obtained. The electrical properties (at 300°K) of alloys with more than 70 mole % InAs prepared at excessively low arsenic temperatures (less than about 400°C) were typically < about 10^{15} electrons/cm^3 with very low mobilities (< about 2000 cm^2/volt-sec). This is consistent with an acceptor deeper than $E_g/2$.

The reason for the change from p-type high resistivity to n-type, low resistivity with increasing arsenic temperature is not clear. Three likely explanations of such behavior however are (*i*) a strong dependence of an impurity vapor-solid segregation coefficient on arsenic pressure, (*ii*) increased shallow donor impurity contamination from the arsenic at the higher temperatures, (*iii*) a physical defect whose concentration is dependent on the arsenic pressure. Unfortunately very little is known about the influences of items (*i*) and (*iii*) on epitaxial film growth, and we cannot definitely eliminate the possibility of (*ii*).

The variation of electron Hall mobility (at 300°K) of our best samples with alloy composition is shown in Fig. 5. (The excess electron concentrations of these samples, determined from Hall measurements, are all in the range 1-8 × 10^{15}/cm^3, except for the GaAs sample, which was 8 × 10^{14}/cm^3.) These mobilities are similar to those observed by Abrahams *et al.* (1) for polycrystalline alloys with higher excess electron concentrations. Invariably, the mobilities of the alloys decreased with decreasing temperature, in contrast to the temperature variation of mobility of GaAs and InAs. This implies scattering from a charged center of some type. Since the mobilities of the GaAs and InAs samples prepared in this system compare favorably with published values, we suspect that alloy formation *per se* may be responsible in part for the low mobilities. However, alloy scattering of the kind described by Brooks (12) does not appear to be applicable in this case, since a negative temperature dependence of mobility is predicted.

Conclusion

An open-tube system employing separate reservoirs of gallium, indium, and arsenic is a satisfactory method for fabricating epitaxial layers of $Ga_xIn_{1-x}As$ alloys on GaAs substrates with good physical properties. There appears to be considerable strain associated with lattice mismatch. However, InAs, for which lattice mismatch is greatest, can be prepared with electrical properties comparable to bulk material.

The electrical properties (primarily electron mobility) of the alloys prepared in such a system are not improved over polycrystalline alloys prepared by gradient freeze and zone-leveling techniques. However, the versatility of the open-tube system permits fabrication of material suitable for device fabrication and investigation.

Acknowledgments

The authors wish to thank L. G. Bailey for his informative discussions and W. Neff and M. Jeffcoat for assistance in materials synthesis.

This work was supported by the Electronics Technology Division of the Air Force Avionics Laboratory under Contract AF 33(615)-1272.

Manuscript received July 15, 1966; revised manuscript received Sept. 20, 1966.

Any discussion of this paper will appear in a Discussion Section to be published in the December 1967 JOURNAL.

REFERENCES

1. M. S. Abrahams, R. Braunstein, and F. D. Rosi, *J. Phys. Chem. Solids*, **10**, 204 (1959).
2. J. C. Woolley, C. M. Gillett, and J. A. Evans, *Proc. Phys. Soc. London*, **77**, 700 (1961).
3. E. F. Hockings, I. Kudman, T. E. Seidel, C. M. Schmelz, and E. F. Steigmeier, *J. Appl. Phys.*, **37**, 2879 (1966).
4. R. Sirrine, *This Journal*, **111**, 750 (1964).
5. H. T. Minden, *ibid.*, **112**, 300 (1965).
6. A. Reisman and R. Rohr, *ibid.*, **113**, 296 (1966).
7. P. L. Hoyt and R. W. Haisty, *ibid.*, **113**, 296 (1966).
8. G. R. Cronin, R. W. Conrad, and S. R. Borrello, *This Journal*, **113**, 1336 (1966).
9. R. W. Conrad, C. E. Jones, and E. W. Williams, *ibid.*, **113**, 287 (1966).
10. T. Gabor, *ibid.*, **111**, 817 (1964).
11. L. Bernstein and R. J. Beals, *J. Appl. Phys.*, **32**, 122 (1961).
12. H. Brooks, Unpublished work.

Transport Processes in the Thermal Growth of Metal and Semiconductor Oxide Films

F. C. Collins and T. Nakayama

Polytechnic Institute of Brooklyn, Brooklyn, New York

ABSTRACT

The transport problems involved in the thermal growth of thick oxide films are reexamined on the basis of a semiconductor model of the oxide film, in which the electron and hole concentrations are assumed to be in local thermodynamic equilibrium. The coupled transports of ions and of electrons or holes required in the Wagner electrochemical model of film growth are related separately to the electrostatic and Fermi potential gradients in the oxide film. The electrostatic potential difference across the oxide film is shown to be fixed by the free energy of formation of the oxide and by the transport coefficients of the several migrating species. The effect of externally applied fields on the thermal growth process is discussed. Anomalies pointed out by Raleigh are shown not to be inconsistent with the electrochemical model of film growth. The question of local electroneutrality in the film relative to the parabolic growth law is also examined.

Interest in the theoretical aspects of the thermal growth of oxide films has been greatly stimulated by recent experimental studies particularly by the intensive investigations of the growth of amorphous silicon dioxide films on single crystals of silicon (1). The work of Jorgensen (2) in this connection is of special interest particularly his finding that the thermal growth rate can be altered by the application of an external electric potential. This indicates that film growth involves ionic migration in agreement with the electrochemical model of film growth of Wagner (3), Mott (4), and Cabrera and Mott (5).

The electrochemical model assumes the transport of charged species, rather than neutral molecules, across the growing oxide film with counterflow of electrons and holes to maintain electrical neutrality. Whether the growth of a particular oxide film is supported by the transport of a metal cation or an oxygen anion may be established by a marker experiment. In the case of most metal oxides, the metal cation is the dominant species transported. However several investigators (6) have found that an oxygen anion is the species transported in the case of the growth of silicon dioxide films.

In the interests of an explicit presentation, the electrochemical model will be discussed within the framework of the case of the silicon dioxide thermal growth, which is selected because of the relatively large amount of published experimental data for this system. The general concepts outlined may be extended to other thermal oxides without difficulty. The possible species transported and the corresponding electrode reactions at the opposite interfaces of the silicon dioxide film are shown in Fig. 1. The nonelectrochemical case of the diffusion of neutral oxygen molecules which react at the silicon-silicon dioxide surface is also illustrated. It will be treated later in the discussion of alternatives to the electrochemical model.

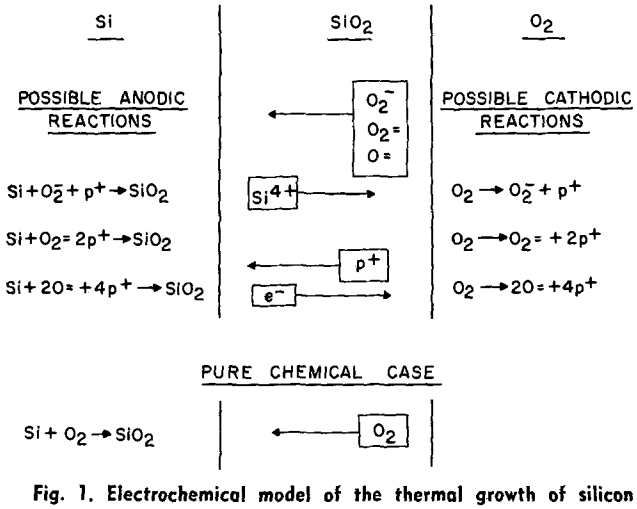

Fig. 1. Electrochemical model of the thermal growth of silicon dioxide films in a pure oxygen ambient.

It is clear that the transport of an ionic species must be balanced by the transport of an equivalent number of electrons or holes in order to prevent build-up of charge on the opposite sides of the film. However the counterflows of ions and of electrons and holes do not necessarily bring about local electroneutrality in the oxide film.

In most ionic crystals, first-order electroneutrality is provided for in that the current-carrying ionic defects are generally present as oppositely charged pairs. Thus in SiO_2, anionic conduction could occur by anti-Frenkel defects (equal concentrations of oxygen interstitials and vacancies) or by oxygen anionic defects compensated by cations of some impurity. Electroneutrality then requires that the electronic carrier concentration compensate the difference in the concentration of the two kinds of ionic defects at every point in the oxide film. This condition will not necessarily be established by balance of the ionic and electronic currents.

Fromhold (7) has shown that the generally observed parabolic law of growth requires local neutrality throughout the bulk of the film. Thus the transport processes must be subject to some additional constraint in order to provide local electroneutrality.

Raleigh (8) has recently cast some doubt on the interpretation of the Jorgensen experiments in terms of the simple variation of the drift rate of diffusing ions under the externally applied potential. He points out that the application of an external field in the direction which accelerates growth will retard the flux of holes and electrons while promoting the migration of ions. He explains the Jorgensen results on the basis of an electrolysis superposed on the normal diffusion-controlled oxide film growth.

The present paper attempts the resolution of these questions on the basis of the electrochemical model of film growth.

Semiconductor Model of Oxide Films

The substrate in oxide film thermal growth problems may be generally treated as metallic. This is true even in the case of semiconductor substrates such as

silicon, which will be degenerate at the temperatures encountered in thermal growth. On the other hand, even those oxide films which have wide band gaps and are insulators at room temperature will behave as semiconductors at the temperatures at which thermal growth occurs. For example, amorphous intrinsic silicon dioxide with an optical absorption edge of about 1900Å has a carrier density at 1000°C at least equal to that of an intrinsic semiconductor with a band gap of 1.5 ev at room temperature.

It is to be expected that the electron and hole densities in oxide films undergoing thermal growth will correspond to conditions of thermal equilibrium except for some slight perturbation due to the small flux of holes and electrons involved in the growth process. The presence of ionic species and structural disorders may cause the oxide film to behave as an extrinsic semiconductor, apart from the question of the effect of the space charge of ionized impurities on local electron and hole densities. However in any case the electron and hole densities are fixed by thermodynamic considerations other than satisfaction of an electroneutrality condition. The semiconductor model of the oxide film requires that the Fermi or electrochemical potential for holes and electrons be explicitly distinguished from the electrostatic field acting on all charged species. This distinction appears not to have been brought out in previous treatments. The transport of holes and electrons is most conveniently formulated in terms of the gradient of the Fermi potential, but the latter is largely irrelevant to the transport of ions which drift under the gradient of the electrostatic potential. In the next section of this paper, it will be shown that the requirement of conservation of charge in the transport process leads to a formulation of the Fermi potential difference across the film in terms of the free energy change involved in the oxidation reaction and of the transport coefficients. In the present section, the principles of transport of holes and electrons will be reviewed for later reference.

The equilibrium concentrations of holes p and that of electrons n in a semiconductor are given by the well-known equations

$$\mathrm{p} = \mathrm{n_i}\, e^{q(\phi - V)/kT} \qquad [1]$$

$$\mathrm{n} = \mathrm{n_i}\, e^{q(V - \phi)/kT} \qquad [2]$$

where $\mathrm{n_i}$ is the concentration of electrons in the intrinsic material, ϕ is the Fermi potential, V is the electrostatic potential, and the other symbols have their usual significance. The fluxes of holes J_P and that of electrons J_n are given by the generalized Fick's first laws

$$J_p = -\frac{kT}{q}\mu_p \frac{dp}{dx} - \mu_p \mathrm{p}\frac{dV}{dx} \qquad [3]$$

$$J_n = -\frac{kT}{q}\mu_n \frac{dn}{dx} + \mu_n \mathrm{n}\frac{dV}{dx} \qquad [4]$$

where μ_p and μ_n are the respective mobilities, x is the position coordinate in the film, and Einstein's relation $D = \mu q/kT$ has been used. On differentiating Eq. [1] and [2] and inserting the results into Eq. [3] and [4] we obtain

$$J_p = -\mu_p \mathrm{p}\frac{d\phi}{dx} \qquad [5]$$

$$J_n = \mu_n \mathrm{n}\frac{d\phi}{dx} \qquad [6]$$

where the fluxes are formally proportional to the gradient of the Fermi potential. The total electronic current is given as usual by

$$I = q\,(J_p - J_n) = -\,q\,(\mu_p \mathrm{p} + \mu_n \mathrm{n})\frac{d\phi}{dx} \qquad [7]$$

$$= -\,\sigma_e \frac{d\phi}{dx}$$

where σ_e is the electronic conductivity as ordinarily defined.

The flux J_i of the i_{th} ionic species across the growing oxide film is given by

$$J_i = -D_i\frac{dc_i}{dx} - D_i\frac{\alpha_i q}{kT}c_i\frac{dV}{dx} \qquad [8]$$

where D_i is the diffusion coefficient of the i^{th} species, c_i its concentration, and α_i the number of electronic charges on it, taken with due regard to sign. A steady value of electrostatic potential across the film requires that

$$I + \sum_i \alpha_i q J_i = 0 \qquad [9]$$

The growth rate of the film is proportional to the sum of the flux terms where all migrating species are assumed to contribute to growth and may be represented as

$$\frac{dX}{dt} = S\sum_i |\alpha_i| J_i \qquad [10]$$

Here, if J_i is given in terms of number flux

$$S = \frac{M/\beta}{\rho N_o} \qquad [11]$$

where M is the molecular weight of the oxide, β is twice the number of oxide ions in the molecular formula of the oxide, ρ is the density, and N_o is Avogadro's number.

The growth rate is then related to the electronic current by

$$\frac{dX}{dt} = -\frac{SI}{q} \qquad [12]$$

The Fermi Potential Profile

The further development of the problem requires the calculation of the Fermi potential as a function of position within the oxide film. The standard cell potential E^o corresponding to the oxidation process is given by the thermodynamic equation

$$E^o = -\Delta G^o/\alpha q \qquad [13]$$

where ΔG^o is the free energy change of the redox reaction expressed in electron-volts and α is the number of electrons involved in the oxidation. The Fermi potential difference $\Delta\phi$ across the film at infinite electronic impedance is given by

$$\Delta\phi = \phi(\mathrm{X}) - \phi(\mathrm{O}) = E^o \qquad [14]$$

where the metal-oxide interface has been selected as the origin of the coordinate system, and X is the outer surface of the film. Under the condition of infinite electronic impedance, there is no electrostatic potential difference across the film, the charges balancing separately in each of the electrical double layers at the surfaces of the oxide film.

If electric current is transported across the film by electron and hole conduction at a finite rate, the Fermi potential is lowered accordingly and is given by

$$\Delta\phi = E^o + \Delta V \qquad [15]$$

In the limit of very small electronic impedance, $\Delta\phi$ approaches zero[1] and

$$\Delta V = -E^o \qquad [16]$$

This is analogous to the well-known situation in a semiconductor p-n junction.

In the further development of this discussion, the mathematical handling of the general case of several

[1] Cabrera and Mott (5) present a detailed discussion of the background of Eq. [14] and [16].

ionic diffusing species with arbitrary charges and the transport of both holes and electrons becomes unwieldy. We shall therefore restrict the present treatment to that of the migration of a univalent anion in a p-type oxide. The treatment may be extended to other specific situations by analogy.

We shall also simplify matters by assuming electroneutrality throughout the oxide film. This could be brought about by complete compensation of the anions by immobile cationic defects. The maximum deviations from electroneutrality consistent with a parabolic law of growth will be presented in a subsequent section of this paper, together with an exploration of the considerations tending to produce electroneutrality.

Let us first examine the situation with respect to electronic transport. By combining Eq. [1] and [5] and making use of $V(x) = x\ \Delta V/X$, where the latter is a consequence of electroneutrality, we obtain

$$J_p e^{qx\Delta V/kTX} dx = \mu_p n_i\, e^{q\phi/kT} d\phi \qquad [17]$$

which may be integrated between the points $x = 0$ and $x = x$ to yield

$$J_p = \frac{\Delta V}{X} \mu_p n_i \frac{(e^{q\phi_o/kT} - e^{q\phi/kT})}{(e^{qx\Delta V/kTX} - 1)} \qquad [18]$$

where ϕ_o is the Fermi potential at the point $x = 0$. Because of the large excess of electrons in the metal compared to the semiconductor oxide film and its adsorbed oxygen layer it may be presumed that the Fermi level in the semiconductor is pinned to that of the metal at the metal interface. Equation [18] then gives the profile of the Fermi potential $\phi(x)$ in terms of the electrostatic potential difference across the oxide film and the hole concentration

$$p(O) = n_i e^{q\phi_o/kT} \qquad [19]$$

in the semiconductor at its interface with the metal.

Equation [8] for the flux J of univalent anions may be put into the form

$$J e^{-qx\Delta V/kTX} = -D \frac{d}{dx} (c e^{-qx\Delta V/kTX}) \qquad [20]$$

which may be integrated to yield[2]

$$J = \frac{Dq\Delta V}{kTX} \frac{[c(O)\, e^{q\Delta V/kT} - c(X)]}{(e^{q\Delta V/kT} - 1)} \qquad [21]$$

For the special case of holes and univalent anions, Eq. [9] simplifies to

$$J_p = J \qquad [22]$$

If now Eq. [18] is evaluated at the point $x = X$ and combined with Eq. [19], [21], and [22], we obtain

$$\frac{Dq}{kT} [c(O)\, e^{q\Delta V/kT} - c(X)] = \mu_p p\ (O)\ (1 - e^{q\Delta\phi/kT}) \qquad [23]$$

The Fermi level difference $\Delta\phi$ may be obtained explicitly by introducing Eq. [15]

$$e^{q\Delta\phi/kT} = \frac{\mu_p p\ (O) + \frac{Dc}{kT} c(X)}{\mu_p p\ (O) + \frac{Dq}{kT} c(O) e^{-qE_o/kT}} \qquad [24]$$

The unknowns in Eq. [23] and [24] may be taken as the electrostatic potential difference ΔV and the boundary concentrations $c(O)$ and $c(X)$, if we assume that the transport coefficients $\sigma_p = q\,\mu_p p_o$ and D are available in principle. It may be readily confirmed that the boundary concentrations in the growing oxide film are not those corresponding to the equilibrium concentrations of the Nernst equation

$$\Delta\phi = E^o - \frac{kT}{q} \ln \frac{c(O)}{c(X)} \qquad [25]$$

as in this case Eq. [21] yields a value of $J = 0$. Possible experiments would be the measurement of the Fermi level difference $\Delta\phi$ by an electrometer. With this information, Eq. [23] and [24] may be solved for the ratio of the unknown boundary concentrations $c(O)$ and $c(X)$. Measurement of the growth rate enables the two boundary concentrations to be determined separately by use of Eq. [10] and [21].

Deviations of the Oxide Film from Electroneutrality

Here we shall investigate quantitatively the magnitude of the maximum space charge in the oxide film which is consistent with a parabolic growth law within the ordinary experimental errors encountered in this type of measurement. Let us commence with some arbitrary distribution of space charges $C(x)$ which will be taken to be positive and univalent for the sake of convenience. The potential distribution is then obtained from Poisson's equation

$$\frac{d^2V}{dx^2} = -\frac{qC(x)}{\epsilon} \qquad [26]$$

where ϵ is the permittivity of the oxide.

A single integration with the boundary condition $(dV/dx)_o = -\mathcal{E}_o$ yields

$$\frac{dV}{dx} = -\mathcal{E}_o - \frac{q}{\epsilon} \int_o^x C(x')\, dx' \qquad [27]$$

A second integration with the boundary condition, $V(O) = 0$, leads to

$$V = -\mathcal{E}_o\, x - \frac{q}{\epsilon} \int_o^x \int_o^{x'} C(x'')\, dx''dx' \qquad [28]$$

The ionic flux is then obtained in terms of a differential equation by rearranging Eq. [8]

$$J e^{qV(x)/kT} = -D \frac{d}{dx} [c(x) e^{qV(x)/kT}] \qquad [29]$$

Particular note is to be taken that the concentration of the diffusing species c is not necessarily equal to the net concentration C of the defects responsible for space charge in Eq. [26]. Integration using the boundary conditions $V(O) = 0$ and $V(x) = \Delta V$ yields

$$J = -\frac{D\,[c(X) e^{q\Delta V/kT} - c(O)]}{\int_o^x e^{-[E_o x + w(x)]q/kT}\, dx} \qquad [30]$$

where

$$w(x) = \frac{q}{\epsilon} \int_o^x \int_o^{x'} C(x'')\, dx''dx' \qquad [31]$$

Further progress cannot be made without introducing assumptions concerning the magnitude and nature of the distribution $C(x)$. Let us determine the effect of a small arbitrary space charge on the ionic flux J. Expanding the exponential in the denominator of Eq. [30] we obtain

$$\int_o^x e^{-qE_o x/kT} \left[1 - \frac{qw(x)}{kT}\right] dx = \frac{kT}{q\mathcal{E}_o} [1 - e^{-qE_o X/kT}] - W(X) \qquad [32]$$

where

$$W(X) = \frac{q}{kT} \int_o^X w(x) e^{-qE_o x/kT}\, dx \qquad [33]$$

Introducing Eq. [32] into [30], we obtain

$$J = -\frac{D[c(X) e^{q\Delta V/kT} - c(O)]}{\frac{kT}{q\mathcal{E}_o} [1 - e^{-qE_o X/kT}] - W(X)} \qquad [34]$$

[2] Equation [18] is equivalent to one previously derived by Fromhold (9).

It may be expected that the term $W(X)$ will cause the growth behavior to deviate from the parabolic law.

Under the condition of a uniform charge density so that $C(x) = C$, Eq. [32] is readily integrated and yields

$$w(x) = \frac{qC}{2\epsilon} x^2 \qquad [35]$$

Equation [33] may likewise be now integrated

$$W(X) = \frac{-q^2C}{2kT_\epsilon}\left\{e^{-qE_0\,X/kT}\left[\frac{kT}{q\mathcal{E}_0}X^2 + 2\left(\frac{kT}{q\mathcal{E}_0}\right)^2 X + 2\left(\frac{kT}{q\mathcal{E}_0}\right)^3\right] - 2\left(\frac{kT}{q\mathcal{E}_0}\right)^3\right\} \qquad [36]$$

The boundary field $\mathcal{E}_0$ may be evaluated from Eq. [28] and is

$$-\mathcal{E}_0 = \frac{\Delta V}{X} + \frac{qCX}{2\epsilon} = \frac{\Delta V}{X}\left(1 + \frac{qCX^2}{2\epsilon\Delta V}\right) \qquad [37]$$

In the field migration case, $(q\Delta V/kT) >> 1$, enabling considerable simplification of the problem. The ratio $q\Delta V/kT$ will ordinarily be of the order of 10. The expansion of the denomination of Eq. [30] places an upper limit on $w(x)$ of the order of 0.01V. Further for the case of relatively small space charge density C, we may approximate

$$-\frac{1}{\mathcal{E}_0} = \frac{X}{\Delta V}\left(1 - \frac{qCX^2}{2\epsilon\Delta V}\right) \qquad [38]$$

With the use of the above, together with Eq. [36], Eq. [34] takes the following limiting form with neglect of terms higher than first order in $qCX^2/2\epsilon\Delta V$ and $kT/q\Delta V$

$$J\left\{\frac{kTX}{q\Delta V} - \frac{qCX^3}{2\epsilon\Delta V}\right\} = Dc(X) \qquad [39]$$

Upon making use of Eq. [10] formulated for a single univalent anionic diffusing species and rearranging, we have

$$\frac{dX}{dt}\left(X - \frac{q^2CX^3}{2kT\epsilon}\right) = SD\frac{q}{kT\epsilon}c(X) \qquad [40]$$

Integration yields

$$\frac{X^2}{2} - \frac{q^2CX^4}{8kT\epsilon} = k_2 t \qquad [41]$$

The coefficient $q^2C/8kT\epsilon$ could be determined experimentally from a plot of t/X^2 *vs.* X^2. Alternatively, the space charge density C corresponding to a stated deviation δ, say 2%, from the parabolic growth law may be evaluated. For the interesting case of a silicon dioxide film of 5000Å thickness, and dielectric constant of 4, thermally grown at 1000°C, we obtain

$$C = \frac{4kT\epsilon\delta}{q^2X^2} = 1.25 \times 10^{13}\ \text{cm}^{-3} \qquad [42]$$

with

$$\sum = \int_0^x C\,dx = 1.25 \times 10^8\ \text{cm}^{-2}$$

This order-of-magnitude value of the space charge density indicates that charge compensation of the diffusing ions in the case of the silicon dioxide film need not be fully complete in order to yield an apparent parabolic growth law from the experimental point of view.

Partial or complete compensation of diffusing anions may be brought about by holes, if the oxide is p-type, or by immobile cations. Let us examine the situation of complete compensation via the first of these cases. This corresponds to the introduction of the additional condition that

$$p(x) = c(x) \qquad o \leq x \leq X \qquad [43]$$

in addition to the balance of the hole and anionic fluxes previously considered, Eq. [9].

The boundary concentrations are then immediately given by

$$c(X) = c(O)\ e^{qE_0/kT}$$

with the aid of Eq. [1] and [15]. The electrostatic potential difference ΔV following rearrangement of Eq. [23] is given by

$$e^{q\Delta V/kT} = \frac{R + e^{qE_0/kT}}{Re^{qE_0/kT+1}} \qquad [44]$$

where

$$R = \frac{\mu_p}{Dq/kT}$$

The transport coefficients may be individually evaluated from experiment by the use of Eq. [21], [43], and [44]. The validity of the assumed condition of Eq. [43] may then be tested by comparing the transport coefficients above calculated with those obtained by independent measurement.

Compensation of the diffusing anions by immobile cations implies the condition that

$$c_-(x) = c_+(x) \qquad [45]$$

where c_- and c_+ are the concentrations of anions and cations, respectively. From Eq. [20] and [21] we obtain

$$c_-(x) = c_-(O)\,e^{qx\Delta V/kTX} - J\frac{kTX}{Dq\Delta V}\left(e^{qx\Delta V/kTX} - 1\right) \qquad [46]$$

where the final term represents the perturbation of the Boltzmann distribution by the transport process. It is now easily established that the cation distribution corresponding to Eq. [46] is such that if the cations were mobile, the free diffusion term of Eq. [8] would be of a direction to oppose the growth of the oxide film while the field term will contribute to the growth. Thus it would appear that complete compensation of diffusing anions by diffusing cations is generally inconsistent, with the following exception: where $q\Delta V/kT >> 1$, then Eq. [21] assumes the limiting form

$$J_- = \frac{Dq}{kT}c(x)\frac{\Delta V}{X} \qquad [47]$$

with the concentrations of anions and cations uniform throughout the film.

Raleigh Electrolysis Theory

Raleigh (8) has suggested that in consequence of the conservation Eq. [9] an externally applied electric field of itself should have no effect upon the growth rate because, if the field promotes the migration of the ions supporting the growth of the film, it must hinder the migration of the electrons or holes, the transport of which is required to maintain over-all electrical neutrality. He proposes that the effect of the applied potential in the Jorgensen experiments in accelerating or retarding the thermal growth of the silicon dioxide film is due to an electrolytic cell process superposed on the normal thermal growth. It is the purpose of this section to formulate this proposal in more detailed terms and to show that it is consistent with the Wagner electrochemical model of film growth.

In terms of the diffusion of neutral molecules, the oxidation of silicon may be represented as in Fig. 1 with the chemical reaction $Si + O_2 \rightarrow SiO_2$ occurring at the silicon-silicon dioxide interface. If no ionization of the oxygen occurs, its transport in the film occurs solely by free diffusion, thus

$$J = -D\frac{dc}{dx} \qquad [47]$$

where c here refers to the effective concentration of the species O_2 in the film. In the steady state J is constant implying that

$$\frac{dc}{dx} = \frac{c(X) - c(O)}{X} \quad [48]$$

which leads to the parabolic growth law as earlier noted.

As pointed out by Raleigh, the neutral species O_2 may be in thermodynamic equilibrium with ionized forms. Examples of possible equilibria for the case of silicon dioxide growing in a perfectly dry oxygen ambient are shown in Fig. 1. For the sake of simplicity, let us consider just the first of these equilibria which may be formulated in terms of the equilibrium constant

$$K = \frac{[O_2^-]p}{[O_2]} \quad [49]$$

on introducing Eq. [49] into Eq. [47], we obtain

$$J = -D\frac{p}{K}\frac{d[O_2^-]}{dx} + \frac{Dq}{kT}\frac{p}{K}[O_2^-]\frac{\Delta V}{X} - \frac{Dq}{kT}\frac{[O_2^-]}{K}p\frac{d\phi}{dx} \quad [50]$$

where Eq. [1] had been specialized to the case of electroneutrality. The last term of Eq. [50] represents the contribution of hole flux to the net transport of the oxygen molecules. Upon again making use of Eq. [49], Eq. [50] takes the form

$$J = -D\frac{[O_2]}{[O_2^-]}\frac{d[O_2^-]}{dx} - \frac{Dq}{kT}[O_2]\left[\frac{d\phi}{dx} - \frac{\Delta V}{X}\right] \quad [51]$$

Let us now consider the case that an external field E is applied across the oxide film by insulated electrodes so that no transport of holes takes place externally. The electrostatic potential gradient and the Fermi potential gradient are each increased by the amount E. It is clear from Eq. [51] that no increase of the flux J will occur, in complete agreement with the discussion of Raleigh.

The situation is completely altered if the field is applied by means of electrodes which are in ohmic contact with the oxide film. Here hole transport through the external circuit takes place, and the Fermi potential differences across the film is fixed by the potential ΔU applied by the external source. The treatment developed in this paper remains applicable with $\Delta\phi$ replaced by $\Delta\phi + \Delta U$ throughout. The application of an anodic potential is then tantamount to the situation which would exist in an oxidation reaction with a higher free energy change but with all other physical variables remaining the same.

Acknowledgment

The authors are indebted to Dr. Raleigh for kindly furnishing them with a preprint of his paper and for helpful discussion. They are also grateful to Dr. R. N. Hall for useful discussion of the problem.

Manuscript received Feb. 21, 1966; revised manuscript received Sept. 9, 1966.

Any discussion of this paper will appear in a Discussion Section to be published in the December 1967 JOURNAL.

REFERENCES

1. T. Nakayama and F. C. Collins, *This Journal*, **113**, 706 (1966). (This paper contains a list of 24 references to the prior work on the thermal growth of silicon dioxide films.)
2. P. J. Jorgensen, *J. Chem. Phys.*, **37**, 874 (1962).
3. C. Wagner, *Z. Phys. Chem.*, **B21**, 25 (1933); **B32**, 447 (1956); *Trans. Faraday Soc.*, **34**, 851 (1938); C. Wagner and K. Grunewald, *Z. Phys. Chem.*, **B40**, 455 (1938).
4. N. F. Mott, *Trans. Faraday Soc.*, **36**, 472 (1940); **43**, 429 (1947).
5. N. Cabrera and N. F. Mott, *Rept. Progr. Phys.*, **12**, 163 (1948).
6. W. G. Spitzer and J. R. Ligenza, *J. Phys. Chem. Solids*, **17**, 196 (1961); N. Karube, K. Yamamoto, and M. Kamiyama, *Japan J. Appl. Phys.*, **2**, 11 (1963); W. A. Pliskin and R. P. Gnall, *This Journal*, **111**, 872 (1964); P. Balk, C. Aliotta, and L. V. Gregor, *Trans. Metall. Soc. AIME*, **233**, 563 (1965).
7. A. T. Fromhold, Jr., *J. Chem. Phys.*, **40**, 335 (1964); *J. Phys. Chem. Solids*, **25**, 1129 (1964).
8. D. O. Raleigh, *This Journal*, **113**, 782 (1966).
9. A. T. Fromhold, Jr., *J. Phys. Chem. Solids*, **24**, 1081 (1963).

Studies of the Defect Structure of Nonstoichiometric Rutile, TiO_{2-x}

R. N. Blumenthal, J. Baukus, and W. M. Hirthe

Metallurgy and Materials Science, Department of Mechanical Engineering, College of Engineering, Marquette University, Milwaukee, Wisconsin

ABSTRACT

The electrical conductivity of single crystals of rutile was measured in the "c" and "a" directions over the temperature range 1000°-1500°C and from 1 to 10^{-15} atm of oxygen. Based on the excellent fit observed between the theoretically derived relation

$$\sigma^5 = (A\sigma + B)P_{O_2}{}^{-1} + I'\sigma^3$$

and the experimental conductivity data, the nonstoichiometric defect structure of rutile was rationalized in terms of quasi-free electrons and both triply and quadruply ionized titanium interstitials. In addition, this equation satisfies a contribution due to impurity conduction where I' is proportional to a temperature dependent concentration of ionized impurities or a contribution due to intrinsic conduction where I' is proportional to a temperature dependent concentration of holes in the valance band.

The standard enthalpy of formation for the following defect reactions in rutile

$$\mathrm{Ti} + 2\,\mathrm{O} = \mathrm{O_2(g)} + \mathrm{Ti_i}^{+3} + 3e; \qquad \Delta H_a{}^o = 9.6 \pm 0.2 \text{ ev} \qquad (a)$$

$$\mathrm{Ti} + 2\,\mathrm{O} = \mathrm{O_2(g)} + \mathrm{Ti_i}^{+4} + 4e; \qquad \Delta H_b{}^o = 10.8 \pm 0.2 \text{ ev} \qquad (b)$$

$$\mathrm{Ti_i}^{+3} = \mathrm{Ti_i}^{+4} + e; \qquad \Delta H_c{}^o = 1.2 \pm 0.4 \text{ ev} \qquad (c)$$

$$I = I^{+} + e; \qquad \Delta H_d{}^o = 3.7 \pm 0.2 \text{ ev} \qquad (d)$$

were determined from the temperature dependence of A, B, and I' obtained from the above relation and from the experimental expression for the temperature dependence of electron mobility. The values of $\Delta H_a{}^o$, $\Delta H_b{}^o$, and $\Delta H_c{}^o$ are in agreement, within experimental error, with those obtained in an earlier investigation based on conductivity measurements in the c direction only. If impurity conduction is involved, $\Delta H_d{}^o$ is equal to the standard enthalpy of formation for the ionization of an impurity. If intrinsic conduction is involved, $\Delta H_d{}^o$ is equal to the band gap energy which is thought to be between 3 and 4 ev for rutile. The ratio of electrical conductivities for the c and a direction is essentially independent of oxygen pressure above 1100°C; but at the lower temperatures, 1000° and 1100°C, the ratio is dependent on pressure in contradiction to the initial assumption that mobility is a function of temperature only.

Nonstoichiometric rutile may be classified as a metal-excess, n-type semiconductor on the basis of experimental observations (1, 2). Recent investigations (3-5) have favored a defect model consisting of quasi-free electrons and titanium interstitials in one or more states of ionization. In an earlier investigation in this laboratory (5) the nonstoichiometric defect structure of rutile was rationalized in terms of a defect model involving quasi-free electrons and both triply and quadruply ionized titanium interstitials.

The investigation reported here was initiated to obtain additional conductivity data for the *c* direction, particularly in the oxygen pressure range 10^{-2} to 10^{-9} atm, in order to account for the marked temperature dependence of the term in the electroneutrality equation attributed to the concentration of ionized impurities revealed in subsequent analyses of the experimental data and to refine calculations of the parameters in the theoretically derived relation. In addition, the conductivity was measured in the a direction over the same range of temperature and oxygen partial pressure in order to determine the validity of this type of relation and the dependence of conductivity on crystallographic direction.

Experimental Procedure

Single crystal specimens of dimensions 0.15 x 0.25 x 1 in. with the longitudinal axis parallel to the c or a direction were cut from a boule obtained from the National Lead Company. The apparatus and techniques employed were essentially the same as those described in the earlier investigation (5). The electrical conductivity was measured over the range 1000°-1500°C and from 1 to 10^{-15} atm of oxygen. This range of oxygen pressure effectively covers the stability limit of rutile (6, 7), TiO_{2-x}, at 1500°C, and includes the major portion of the phase field at 1000°C where the pressure corresponding to the stability limit is about 7×10^{-19} atm.

Results and Discussion

Isobaric plots of the logarithm of electrical conductivity *vs.* the reciprocal of absolute temperature for oxygen partial pressures from 1 to 10^{-3} atm are shown in Fig. 1 and 2 for the c and a direction, respectively. The experimental technique utilized in this investigation was substantiated by the excellent agreement between the conductivity measured in both c and a directions from 1000° to 1500°C in 1 atm of air and the data of Cronemeyer (8).

In order to analyze the data, experimental plots of log σ *vs.* log P_{O_2} were obtained in the following manner. Values of the conductivity were selected at 100°C intervals between 1000° and 1500°C from the plots of log σ *vs.* $1/T$. For the isobaric plots, Fig. 1 and 2, the values of conductivity at 1000° and 1100°C were taken from the straight line extrapolated from higher temperatures rather than the measured conductivity data for a few of the points. Justification for this treatment lies in the fact that the previous investigation (5) revealed that the appearance of a two-slope behavior in this range of temperature is the result of contamination of the specimens *in situ* during the period of time the measurements are being taken. The partial pressure of oxygen corresponding to the above values of conductivity for various atmospheres was

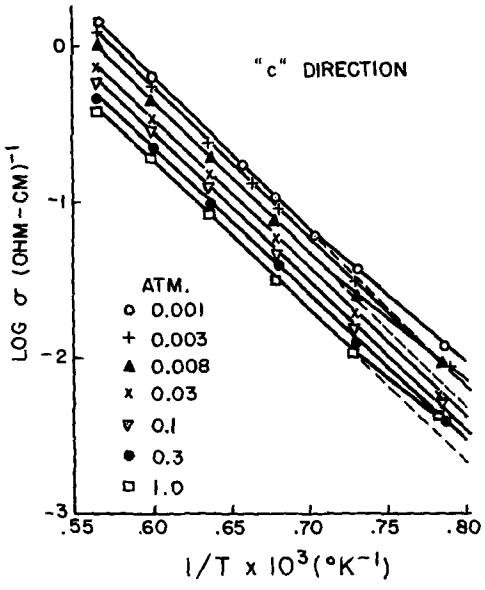

Fig. 1. Logarithm of electrical conductivity of rutile single crystal in the c direction vs. the reciprocal of absolute temperature for oxygen partial pressures from 1 to 10^{-3} atm.

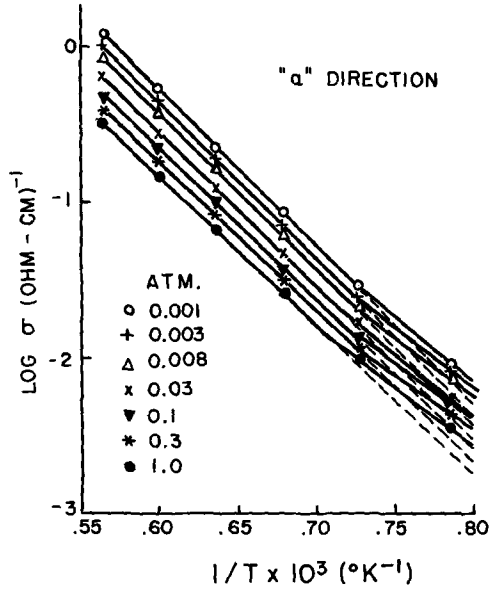

Fig. 2. Logarithm of electrical conductivity of rutile single crystal in the a direction vs. the reciprocal of absolute temperature for oxygen partial pressures from 1 to 10^{-3} atm.

calculated and combined with the respective conductivity to obtain the isothermal plots at 100°C intervals between 1000° and 1500°C of log σ *vs.* log P_{O_2} shown in Fig. 3 and 4 for the c and a directions, respectively. The curvature of the 1000°C isotherms at the low pressure end of the plots was verified experimentally by subjecting the specimen to partial pressure less than 10^{-15} atm followed by a return to 10^{-15} atm. The conductivity values before the further reduction and after the increase to 10^{-15} atm were the same indicating that the curvature is representative of the equilibrium situation.

The objection to the analysis presented in the earlier investigation lies in the fact that it does not account for the temperature dependence of the third term in the electroneutrality equation revealed in subsequent analyses of the experimental conductivity data. Therefore, an electroneutrality expression of the following type

$$n = 3(\mathrm{Ti}_i^{+3}) + 4(\mathrm{Ti}_i^{+4}) + I^+ \qquad [1]$$

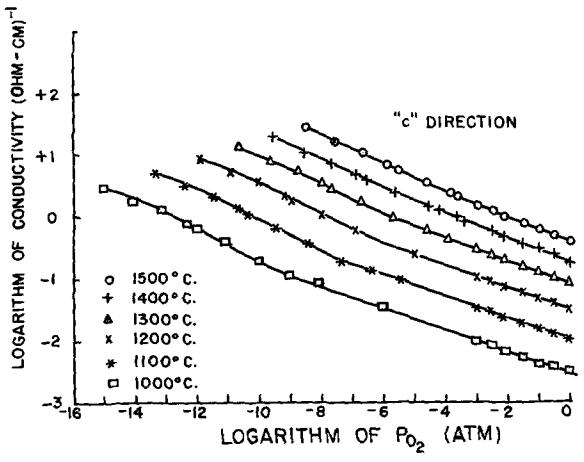

Fig. 3. Isothermal relation between the logarithm of electrical conductivity in the c direction and the logarithm of partial pressure of oxygen in the range 1000°-1500°C.

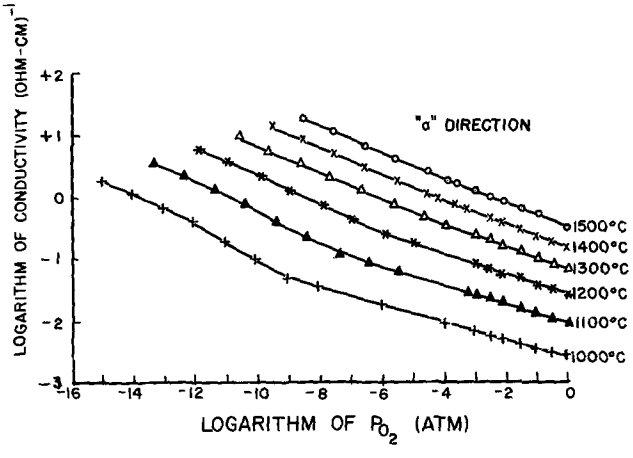

Fig. 4. Isothermal relation between the logarithm of electrical conductivity in the a direction and the logarithm of partial pressure of oxygen in the range 1000°-1500°C.

where (Ti_i^{+3}) is the concentration of triply ionized titanium interstitials, (Ti_i^{+4}) is the concentration of quadruply ionized titanium interstitials, and I^+ is the temperature dependent concentration of ionized impurities which act as donors, was employed to obtain a quantitative relation between σ and P_{O_2}. The relation for the ionization of the impurity is

$$I = I^+ + e \qquad [2]$$

and from the law of mass action the equilibrium constant can be written as

$$K_6 = \frac{I^+ n}{I} \qquad [3]$$

If the assumption is made that $I >> I^+$, the expression for the conductivity as a function of oxygen partial pressure may be obtained by combining Eq. [1], the mass action equations for defect equilibrium, and the equation for extrinsic electron conduction

$$\sigma^5 = (A\sigma + B)P_{O_2}{}^{-1} + I'\sigma^3 \qquad [4]$$

where

$$A = 3K_4'C^4; \quad B = 4K_5'C^5; \quad I' = IK_6C^2 \qquad [5]$$

It should be pointed out at this time that Eq. [4] will also apply for the case of intrinsic conduction where I^+ is the temperature dependent concentration of holes in the valence band. The corresponding equation for conduction involving holes and electrons is

Table I. Calculated values of the parameters A, B, and I' in the expression $\sigma^5 = (A\sigma + B) P_{O_2}^{-1} + I' \sigma^3$ and the standard error (95% confidence limit) in the calculation of these parameters at 100°C intervals from 1000° to 1500°C:

Temperature, °C	A	Standard error of A (±)	B	Standard error of B (±)	I'	Standard error of I' (±)
			c Direction			
1000	8.64×10^{-14}	7.68×10^{-15}	4.82×10^{-14}	6.53×10^{-15}	9.41×10^{-6}	1.27×10^{-6}
1100	4.20×10^{-11}	3.54×10^{-12}	3.22×10^{-11}	5.64×10^{-12}	1.22×10^{-4}	2.04×10^{-5}
1200	7.59×10^{-9}	4.92×10^{-10}	1.12×10^{-8}	1.38×10^{-9}	8.03×10^{-4}	1.84×10^{-4}
1300	8.32×10^{-7}	4.16×10^{-8}	1.63×10^{-6}	1.95×10^{-7}	4.76×10^{-3}	1.35×10^{-3}
1400	3.47×10^{-5}	8.40×10^{-7}	1.67×10^{-4}	6.21×10^{-6}	8.61×10^{-3}	3.22×10^{-3}
1500	1.33×10^{-3}	3.42×10^{-5}	7.94×10^{-3}	3.78×10^{-4}	6.66×10^{-4}	1.89×10^{-2}
			a Direction			
1000	8.23×10^{-15}	1.99×10^{-15}	4.85×10^{-15}	9.93×10^{-16}	7.14×10^{-6}	3.61×10^{-7}
1100	5.17×10^{-13}	7.63×10^{-13}	5.17×10^{-12}	7.70×10^{-13}	8.82×10^{-5}	5.38×10^{-6}
1200	1.13×10^{-9}	1.17×10^{-10}	2.40×10^{-9}	2.28×10^{-10}	6.53×10^{-4}	5.81×10^{-5}
1300	1.15×10^{-7}	8.05×10^{-9}	4.79×10^{-7}	2.85×10^{-8}	3.68×10^{-3}	3.67×10^{-4}
1400	6.17×10^{-6}	3.03×10^{-7}	4.63×10^{-5}	1.55×10^{-6}	1.64×10^{-2}	1.36×10^{-3}
1500	2.87×10^{-4}	8.38×10^{-6}	2.23×10^{-3}	6.90×10^{-5}	3.48×10^{-2}	6.67×10^{-3}

$$\sigma = nq\mu + pq\mu' \quad [6]$$

where p is the concentration of holes and μ' is the hole mobility. However, previous investigations (2, 9, 10) of the thermoelectric power of rutile have suggested that

$$\mu >> \mu' \quad [7]$$

Consequently, Eq. [6] reduces to the relation for extrinsic electron conduction, and Eq. [4] also represents the conductivity as a function of the partial pressure of oxygen for a defect model based on both triply and quadruply ionized titanium interstitials and intrinsic conduction.

A computer program was written for Eq. [4], and the calculated values of the parameters in this equation and their standard errors are tabulated in Table I. It is apparent from the values of the standard error as the parameter shown in Table I that Eq. [4] represents an acceptable fit of the experimental data for both the c and a directions. Thus the excellent agreement between Eq. [4] and the experimental data for the electrical conductivity in both the c and a direction provides a quantitative confirmation of a defect model involving both triply and quadruply ionized titanium interstitials and a third term in the electroneutrality equation which is dependent on temperature.

Plots of the logarithm of the parameters A, B, and I' *vs.* the reciprocal of absolute temperature yield straight lines for both c and a directions. The standard enthalpies of formation for the reactions

$$\mathrm{Ti} + 2\,\mathrm{O} = \mathrm{O_2(g)} + \mathrm{Ti_i^{+3}} + 3e; \quad \Delta H_a^\circ \quad [8]$$

$$\mathrm{Ti} + 2\,\mathrm{O} = \mathrm{O_2(g)} + \mathrm{Ti_i^{+4}} + 4e; \quad \Delta H_b^\circ \quad [9]$$

$$I = I^+ + e; \quad \Delta H_d^\circ \quad [2]$$

can be calculated from the slopes of these lines by assuming (2) that the electron mobility is proportional to the exp (0.1 (ev)/kT). In addition, the standard enthalpy of formation for the ionization reaction

$$\mathrm{Ti_i^{+3}} = \mathrm{Ti_i^{+4}} + e; \quad \Delta H_c^\circ \quad [10]$$

can be calculated from the equation

$$\Delta H_c^\circ = \Delta H_b^\circ - \Delta H_a^\circ \quad [11]$$

The results of these calculations for both c and a direction data are shown in Table II and compared with data of the previous investigation. The good agreement in ΔH_a°, ΔH_b°, and ΔH_c° between these investigations based on c direction data indicates that the interpretation of the nonstoichiometric defect structure is independent of the physical significance given to the third term on the right-hand side of the electroneutrality equations. The agreement in these values of enthalpies based on c and a direction conductivity further substantiates the validity of the proposed nonstoichiometric defect structure since these thermodynamic quantities should be independent of crystallographic direction. The values of ΔH_d° based on c and a direction data are independent of direction, and this is consistent with the concept of an impurity ionization energy or intrinsic conduction. However, the magnitude of ΔH_d°, 3.7 ev, suggests intrinsic conduction because the intrinsic band gap energy is thought to be between 3 and 4 ev as the result of numerous optical and thermal measurements (1).

In order to substantiate further the validity of Eq. [4], the parameters A, B, and I' were extrapolated to 600°C, and the conductivity was calculated as a function of temperature in the range 1500° to 600°C for 1 atm of air. A comparison of the temperature dependence of the conductivity as calculated from Eq. [4] with the data of Cronemeyer over the same range of temperature in air is shown in Fig. 5 and 6 for the c and a directions, respectively. It is significant to note that Eq. [4] yields the well-known two-slope behavior for a plot of log σ *vs.* $1/T$. The agreement in the magnitude of the conductivity is good in the high-temperature regions, but there is some discrepancy in the low-temperature regions. This discrepancy can be accounted for in Eq. [4] if I' is assumed to be proportional to the number of impurities which act as donors when ionized. For this case, the magnitude of the conductivity and the experimental activation energy will depend on the nature and concentration of impurities present in the crystal employed in the particular investigation.

Since only conductivity data was taken in this investigation, the electron mobility could not be determined. However, the ratio of electron mobility in the c to the mobility in the a direction was determined by

Table II. Standard enthalpies of formation calculated for both c and a direction data

	ΔH_a° c	ev a	ΔH_b° c	ev a	ΔH_c° c	ev a	ΔH_d° c	ev a
Previous investigation (5)	9.3	—	10.7	—	1.4	—	—	—
This investigation	9.5	9.8	10.7	11.0	1.2	1.2	3.7	3.7
Error*	±0.2	±0.2	±0.2	±0.2	±0.4	±0.4	±0.2	±0.2

* Estimate of error includes experimental error as well as the error in the assumed value of the temperature dependence of electron mobility.

Table III. Comparison of the ratios of the experimental conductivity with the calculated parameters of Eq. [4] raised to the appropriate power

Temperature, °C	σ_c/σ_a	$(A_c/A_a)^{1/4}$	σ_c/σ_a	$(B_c/B_a)^{1/5}$	σ_c/σ_a	$(I_c'/I_a')^{1/2}$
1000	1.64	1.80	2.03	1.58	1.20	1.15
1100	1.51	1.69	1.64	1.44	1.23	1.18
1200	1.53	1.61	1.44	1.36	1.23	1.11
1300	1.50	1.64	1.30	1.28	1.22	1.14
1400	1.46	1.54	1.20	1.29	—	—
1500	1.41	1.47	1.25	1.29	—	—

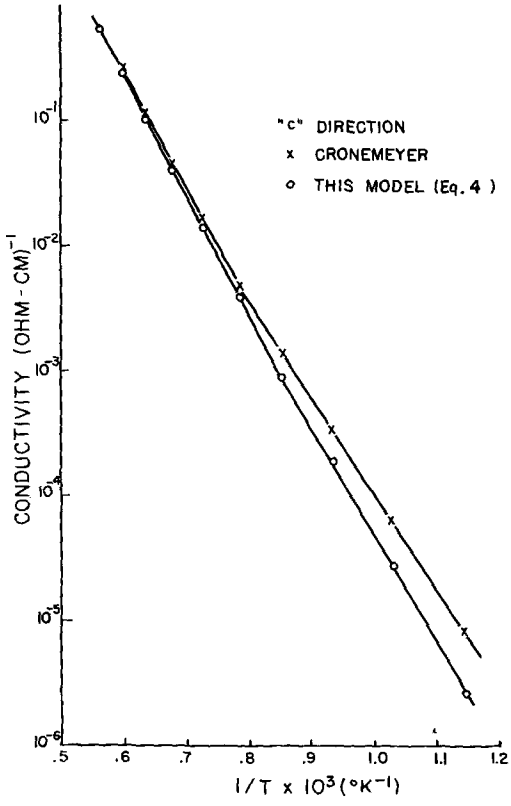

Fig. 5. Comparison of the temperature dependence of electrical conductivity in the c direction as calculated from Eq. [4] with the data of Cronemeyer over the same range of temperature in air.

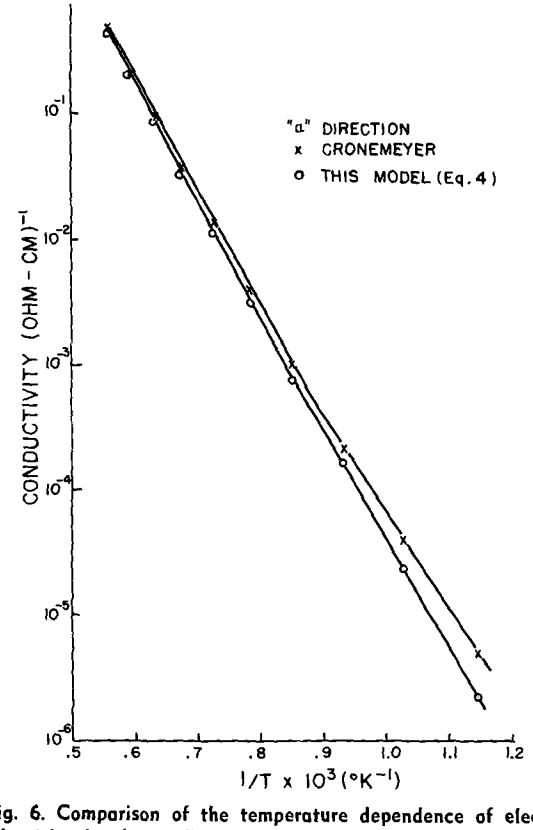

Fig. 6. Comparison of the temperature dependence of electrical conductivity in the a direction as calculated from Eq. [4] with the data of Cronemeyer over the same range of temperature in air.

plotting the ratio of the conductivities as a function of the logarithm of partial pressure of oxygen at 100° intervals between 1000° and 1500°C as shown in Fig. 7. From Fig. 7 it can be seen that the mobility is essen-

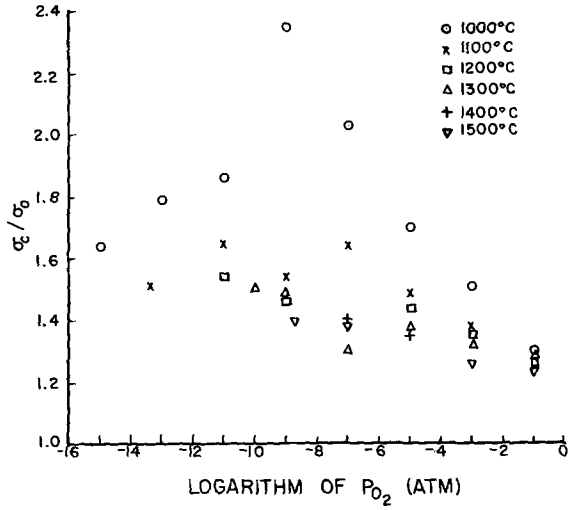

Fig. 7. Isothermal relation between the ratio of electrical conductivity and the logarithm of partial pressure of oxygen in the range 1000°-1500°C.

tially independent of pressure at the higher temperatures within the limits of experimental error. At the lower temperatures, 1000° and 1100°C, the ratio of the mobilitites is dependent on pressures in contradiction to the initial assumption that the mobility was dependent on temperature only. In general, the ratio of the mobilities decreases with increasing temperature in the range of this investigation. This plot clearly indicates the limitation of the technique employed in this investigation and the need for electron mobility data in order to understand the nature of the transport mechanisms in rutile below 1000°C.

As a check on the internal consistency of the data, the ratios of the experimental conductivities are compared with the ratios of the calculated parameters of Eq. [4] raised to the appropriate power in Table III. The corresponding values of conductivity ratio and parameter were selected in the oxygen pressure range where the particular defect was the major contributor to the concentration of conduction electrons, n, in the electroneutrality equation. The variation in these values with temperature can be explained in terms of the temperature dependence of the mobilities in the c and a direction. If these dependencies are not the same, some variation with temperature is reasonable.

Conclusions

The nonstoichiometric defect structure of rutile is rationalized in terms of quasi-free electrons and both triply and quadruply ionized titanium interstitials. In addition, there is a contribution to the electrical conductivity due to impurity conduction or intrinsic conduction. The experimental confirmation of this model is based on the excellent agreement between the theoretical relation

$$\sigma^5 = (A\sigma + B)\, P_{O_2}{}^{-1} + I'\sigma^3$$

and the c and a direction conductivity data measured over the temperature range 1000° to 1500°C over the oxygen partial pressure range 1 to 10^{-15} atm.

The standard enthalpy of formation for the following defect reactions in rutile

$$\mathrm{Ti} + 2\,\mathrm{O} = \mathrm{O_2(g)} + \mathrm{Ti_i^{+3}} + 3e; \quad \Delta H_a^\circ = 9.6 \pm 0.2\text{ev} \text{ (a)}$$

$$\mathrm{Ti} + 2\,\mathrm{O} = \mathrm{O_2(g)} + \mathrm{Ti_i^{+4}} + 4e; \quad \Delta H_b^\circ = 10.8 \pm 0.2\text{ev} \text{ (b)}$$

$$\mathrm{Ti_i^{+3}} = \mathrm{Ti_i^{+4}} + e; \quad \Delta H_c^\circ = 1.2 \pm 0.4\text{ev} \text{ (c)}$$

$$I = I^+ + e; \quad \Delta H_d^\circ = 3.7 \pm 0.2\text{ev} \text{ (d)}$$

where determined from the temperature dependence

of A, B, and I' obtained from the above relation and from the experimental expression for the temperature dependence of electron mobility. The values of ΔH_a°, ΔH_b°, and ΔH_c° are in agreement, within experimental error, with those obtained in the previous investigation based on conductivity measurements in the c direction only. If impurity conduction is involved, ΔH_d° is equal to the standard enthalpy of formation for the ionization of an impurity. If intrinsic conduction is involved, ΔH_d° is equal to the band gap energy which is thought to be between 3 and 4ev for rutile.

Values of the electrical conductivity calculated from the above equation yield the well-known two slope behavior on a plot of logarithm of electrical conductivity vs. reciprocal of absolute temperature. The calculated values agree in magnitude with the data of Cronemeyer for the same range of temperature, 600°-1500°C, and a pressure of 1 atm of air. The ratio of electrical conductivities in the c and a direction is essentially independent of oxygen partial pressure above 1100°C; but at the lower temperatures, 1000° and 1100°C, the ratio is dependent on pressure in contradiction to the initial assumption that mobility is a function of temperature only. In general, the ratio of conductivities, *i.e.*, mobilities, decreases with increasing temperature in the range of this investigation.

Acknowledgments

The authors gratefully acknowledge the assistance of Mr. Joseph Zuercher and the support of Aerospace Research Laboratories, Office of Aerospace Research, United States Air Force, Contract No. AF 33(615)-1244.

Manuscript received June 16, 1966; revised manuscript received Sept. 19, 1966.

Any discussion of this paper will appear in a Discussion Section to be published in the December 1967 JOURNAL.

REFERENCES

1. F. A. Grant, *Rev. Mod. Phys.*, **31**, 646 (1959).
2. H. P. R. Frederikse, *J. Appl. Phys.*, **32**, 2211 (1961).
3. T. Hurlen, *Acta Chem. Scand.*, **13**, 365 (1959).
4. D. S. Tannhauser, *Solid St. Commun.*, **1**, 223 (1963).
5. R. N. Blumenthal, J. Coburn, J. Baukus, and W. M. Hirthe, *J. Phys. Chem. Solids*, **27**, 643 (1966).
6. R. N. Blumenthal and D. H. Whitmore, *This Journal*, **110**, 92 (1963).
7. L. Porter, Private communication.
8. D. C. Cronemeyer, *Phys. Rev.*, **87**, 876 (1952).
9. H. P. R. Frederiske and W. R. Hosler, "Properties of Rutile, I. Electrical Conductivity and Thermoelectric Power," NBS Rpt. No. 6585, Nov. 1, 1959.
10. J. Rudolph, *Z. Naturforschg.*, **14a**, 727 (1959).

Germanium Oxidation in Nitric Acid

Ernest W. Valyocsik

Research Laboratories, General Motors Corporation, Warren, Michigan

ABSTRACT

The oxidation in nitric acid of single crystal Ge (100) surfaces and of polycrystalline Ge (111) surfaces has been studied at 27.5°C over the concentration range 7.0-15.6N HNO_3. The surface oxide growth rate decreases smoothly with time and is not described by simple film growth laws. The average oxide nuclei size at saturation thickness decreases with increasing acid concentration, and more rapid surface saturation occurs with increasing acid concentration. No induction period for surface oxide growth was observed over the range of concentrations studied. The oxide films which grew on the Ge surfaces had saturation thicknesses inversely dependent on acid concentration, and the saturation thickness was also observed to be dependent on the crystallographic orientation of the Ge surface. Structural studies of the oxide layers by infrared, x-ray, and electron diffraction techniques indicate that the surface oxide grown under these conditions is crystalline hexagonal germanium dioxide.

Etching solutions in practice contain strong oxidizing agents which attack a semiconductor surface with subsequent dissolution of the products in the bulk solution. One such commonly employed oxidizing agent is nitric acid. Even after etching in dilute solutions, Ge surfaces still retain a thin oxide layer. At higher concentrations the removal of the reaction products from the solid-liquid interface into the bulk liquid is restricted to such an extent that the growth of thick oxide films is promoted on the semiconductor surface (1-4).

The object of the present work was to study the kinetics of oxide growth and the nature and structure of the oxide layers grown on Ge surfaces over an extended range of nitric acid concentrations. Measurements were made on the oxide films by several techniques in an effort to determine the crystallographic structure of the films grown under these conditions. It is the purpose of this paper to report the results of a study of Ge surface oxidation in concentrated nitric acid solutions.

Experimental Method

Materials.—Samples of Ge for oxidation were in the form of rectangular slabs. The Ge was obtained from two sources: (*A*) Polycrystalline samples (n-type, resistivity 2.5 ohm-cm) of size 1.4 x 9.0 x 15.8 mm were cut from Ge crystals grown in our laboratory by the Czochrolski method. Many of the samples possessed low-angle grain boundaries. The principal orientation of the largest faces of the rectangular slabs was parallel to the (111) planes to within 10° as determined by x-ray techniques. (*B*) Single crystal samples (n-type, arsenic doped; resistivity range 13-24 ohm-cm) of size 0.43 x 4.9 x 15.0 mm were cut from a boule of zone-refined Ge. The orientation of the largest faces was parallel to the (100) planes.

All chemicals used in this study were of reagent grade quality. Normalities of the nitric acid solutions were determined by standard titrimetric methods and ranged from 7.0 to 15.6N. It has been shown by Cretella and Gatos (1) that the dissolution rate of Ge in HNO_3 reaches a maximum at 6N. Ge oxidation was not studied in solutions of concentration less than 7.0N.

Surface treatment.—The rectangular Ge slabs were attached to the faces of glass plates with low-melting wax and lapped with a water slurry of 800 mesh silicon carbide. This was followed by lapping the surfaces to a shiny finish with ~1μ alumina. The samples were then removed from the glass plates and washed free of wax with boiling methanol.

Prior to reaction the Ge slabs were etched for 2 min at room temperature in 30% H_2O_2 (one part by volume) 49% HF (one part by volume) and de-ionized water (one part by volume). After etching, the

surfaces were visibly bright and shiny although they are known not to be "oxide free."

Apparatus.—Reactions were carried out in a thermostat controlled at 27.50° ± 0.05°C. All weighings were made to an accuracy of ± 4 μg.

Procedure.—Before reaction the samples were weighed, and all exposed areas of the rectangular Ge slabs were measured.

Nitrogen gas was bubbled through the solution for about 1 hr prior to placing the Ge into the solution in order to sweep the solution free of dissolved oxygen gas. The solutions were covered but not stirred during reaction. Samples were removed at given time intervals, placed in methanol, and boiled for 15 min. After removal from the methanol, the samples were rinsed several times with fresh methanol and dried before reweighing. The weight change of each sample was the net difference between the weight lost by Ge dissolution and the weight gained by surface oxide growth during the reaction time interval.

In the first few experiments the oxide thickness was determined by dissolution of the oxide in 49% HF at room temperature. There was no additional detectable weight loss of the sample after 5 min in 49% HF at room temperature. Ge is not soluble in HF at these conditions. Thus, it is assumed that the HF treatment removed the oxide only.

Following oxide removal, the samples were reweighed, and the oxide thickness was calculated. Since this method of thickness determination destroyed the sample for further studies, a technique was developed (5) whereby infrared absorption (6) was used to measure oxide film thickness *in situ*.

Lippincott and co-workers (6) have observed a strong fundamental absorption at 11.5μ (attributed to the Ge-O stretching mode) and a somewhat weaker set of fundamental absorption bands at about 17, 18, and 19μ. Combination or overtone bands due to the lattice vibration at about 7.50, 6.90, and 6.55μ, which are much weaker in strength relative to Lippincott's set at 17-19μ, have also been observed in our laboratory (5). Depending on the oxide thickness range, one or other of these bands can be used to measure the oxide thickness. The weaker bands are more appropriate for the thicker oxide layers. Film thickness measurements were made on a Perkin-Elmer Model 21 Infrared Spectrometer equipped with a scale expansion accessory. A weighed, oxidized sample was placed in one beam of the spectrometer with an unoxidized Ge sample in the reference beam and the spectrum scanned. The oxidized sample was then placed in water and part of the surface oxide dissolved. The sample was dried, then carefully reweighed, and the infrared absorption measurement repeated. This procedure was continued until all detectable oxide was removed. The integrated intensities corresponded to the peak heights so that after calibration the peak heights were measured to determine the oxide thickness of the samples. A calibration curve for oxide thickness *vs.* infrared absorption of the 18μ band is reproduced in Fig. 1.

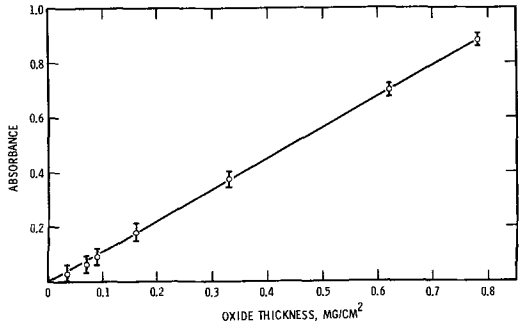

Fig. 1. Infrared absorption measurement of oxide film thickness

Results and Discussion

Nucleation of surface oxides.—On immersion of a Ge sample in nitric acid the surface is rapidly oxidized with some dissolution of the oxidized Ge. Dissolution decreases with continuing reaction presumably because of local saturation at the solid-liquid interface. Cretella and Gatos (1) had observed that in stirred concentrated HNO_3 solutions the behavior of Ge is similar to that in nonstirred solutions except that higher concentrations or longer times were required to achieve saturation of the surface by the oxide. Due to the rapid decrease in solubility of germanium oxide (7) with increasing nitric acid concentration, supersaturation of the interface takes place more rapidly at the higher acid concentrations. As the solubility limit is approached, the oxide can nucleate to produce crystalline particles on the Ge surface. The effect of an oxide-saturated interface on Ge dissolution was tested by preparing HNO_3 solutions containing dissolved hexagonal GeO_2 powder. These solutions were prepared by vigorously stirring the HNO_3 with excess GeO_2 powder over night at the temperature of the bath. After stirring was terminated, the excess GeO_2 powder settled to the bottom of the beaker. The solutions were ready for reaction after bubbling N_2 through them. A comparison run was conducted for Ge reaction in pure 7.5*N* HNO_3 and in 7.5*N* HNO_3 saturated with GeO_2. Referring to Fig. 4, one sees that the maximum Ge weight loss in 7.5*N* HNO_3 occurs at approximately 1.5 hr after reaction starts. Single crystal Ge (100) samples were removed from solution after 1.7 hr of reaction time. This was done to check the effect of solution saturation at the maximum weight loss point. The results showed that the Ge sample in pure 7.5*N* HNO_3 lost 3.18 mg/cm² while the sample in 7.5*N* HNO_3 saturated with GeO_2 lost 2.69 mg/cm² of weight. The oxide thicknesses at these times were 1.78 mg/cm² for reaction in pure acid as compared to 2.61 mg/cm² for the oxide saturated acid. These values are the averages for three Ge samples in each solution. There was a definite decrease in the dissolution of the Ge sample and an increase in the surface oxide thickness with the GeO_2 present in solution prior to reaction. The magnitude of the dissolution did not approach that characteristic of 10.2*N* HNO_3 (Fig. 4). Two alternatives can be considered: (*a*) the solution was not equilibrated with the GeO_2 prior to reaction, or (*b*) saturation of the interface may not be the controlling factor in Ge dissolution or surface oxide growth. In their work Brauer and Müller (7) found that solutions of 2-5*N* HNO_3 had equilibrated with GeO_2 within 10 hr at 25°C. Solutions far from equilibrium could not easily account for the magnitude of the effect on the dissolution of the Ge sample. The oxide layers grown in the 7.5*N* HNO_3 containing GeO_2 did appear more uniform than those grown in the pure acid. The fact that dissolution of the Ge in the oxide saturated acid was not entirely eliminated may be related to factors other than interface saturation which are important in controlling the sample dissolution and oxide nucleation rate. Reactions of single crystal Ge (100) surfaces with pure 15.6*N* HNO_3 and GeO_2 saturated 15.6*N* HNO_3 after 1.7 hr showed sample weight gains of 0.204 mg/cm² and 0.221 mg/cm² for the pure and oxide saturated acid, respectively.

Figure 2 shows photomicrographs of Ge (111) surfaces oxidized in 7.0*N* HNO_3 for 1 and 3 hr. The oxide nuclei are seen to have a definite crystalline structure and appear to have a random surface orientation. Konorov and Romanov (4) have also observed the growth of definite hexahedral crystals of ~10μ dimensions on the Ge surface in 7*N* HNO_3. The growth of these oxide nuclei on Ge surfaces is similar to the growth of As_2O_3 nuclei that takes place on GaAs surfaces oxidized in concentrated nitric acid solutions (8, 9). In the early stages of oxidation at the lower

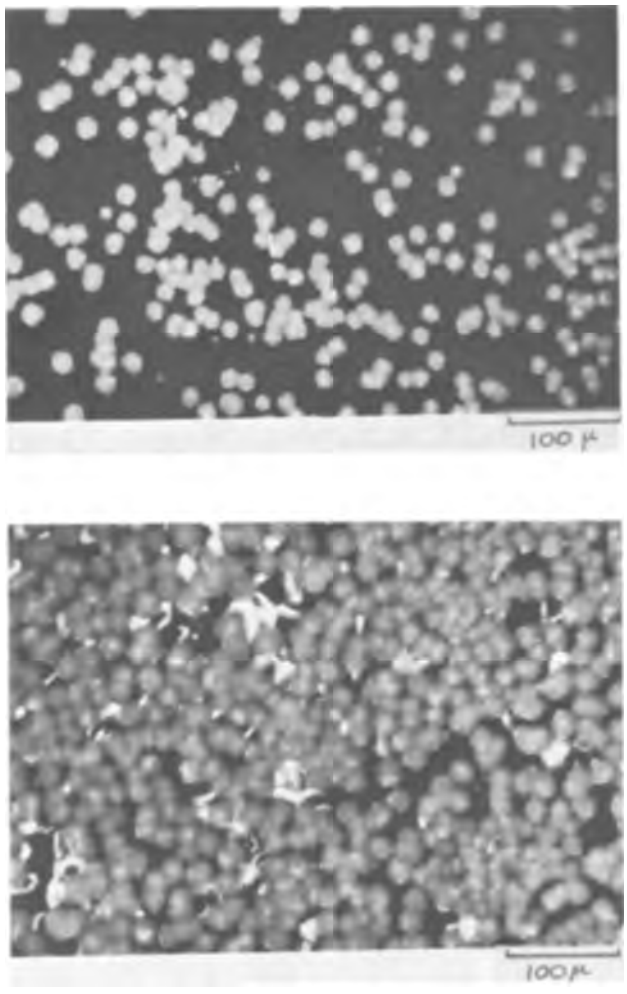

Fig. 2. Ge (111) surfaces oxidized in 7.0N HNO_3 for (a) (top) 1 hr and (b) (bottom) 3 hr.

acid concentrations the oxide nucleates and grows in patches on the surface, accompanied by severe surface etching. With continued oxidation the nuclei grow, with additional nucleation occurring, presumably at points of high local saturation, until the surface is completely covered. Thus, a protective oxide layer forms; that is, the oxide layer grows to a limiting thickness and then stops, with no further reaction taking place. These oxide nuclei adhere strongly to the surface, but for Ge samples left for long times in the less concentrated solutions the chemical attack may be so severe that, on occasion, spalling of the oxide film takes place.

At the higher acid concentrations (greater than 11*N*) nucleation occurs very rapidly at many random sites, and the surface density of nuclei is very large. This observation is in agreement with the results of Faust (3). The nucleation rate of the oxide particles on the surface is so high and the surface density so great that the nuclei do not grow to large sizes. The protective effect of the oxide layer was also noted by Cretella and Gatos (1) and Miuller and co-workers (2).

Figure 3 is a photomicrograph of a Ge (111) surface oxidized for 30.2 hr in 11.9*N* HNO_3 at 27.5°C. This surface can be compared with those oxidized in 7.0*N* HNO_3 as shown in Fig. 2. The oxide nuclei sizes are noticeably smaller than those grown at lower acid concentrations.

Oxide film growth.—In Fig. 4 are plotted the data at 27.5°C for the weight change, in mg/cm^2, of polycrystalline Ge samples (each point a separate sample) as a function of time in solution with no stirring. For solutions with concentration 10.2*N* and less we observed an initial net sample weight loss since the weight lost by Ge dissolution exceeds the weight gained by surface oxide growth. After a time interval, the sample weight gain from oxide film growth overtakes the weight lost by dissolution. For concentrations greater than 10.2*N*, a net sample weight gain is noted from the beginning. All of the weight change curves approach limiting values.

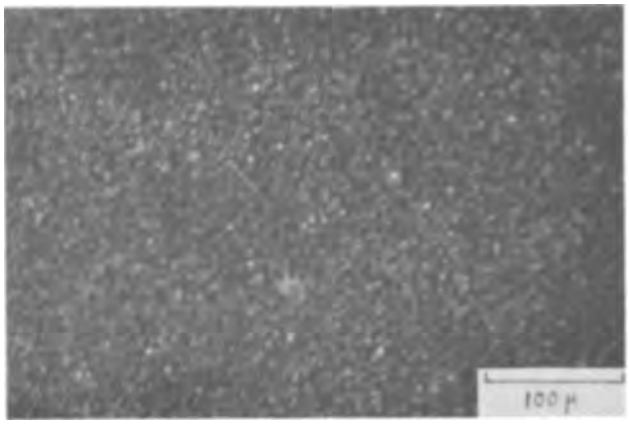

Fig. 3. Ge (100) surface oxidized for 30.2 hr in 11.9N HNO_3 at 27.5°C. Oxide nuclei sizes are notably smaller than those grown in 7.0N HNO_3.

The data for oxide film growth on Ge (111) surfaces at 27.5°C in varying HNO_3 concentration are given in Fig. 5. No induction period for oxide growth was observed at any acid concentration in the range studied although Cretella and Gatos (1) report an induction period to oxide growth at 7.5*N* HNO_3. This is probably due to differences in the preparation of the samples. The initial growth rate of the film is high, but, as the protective oxide film builds up on the Ge surfaces, the growth rate decreases, and the film thickness approaches a maximum value. This saturation value for films grown in 7.0*N* HNO_3 (Fig. 5) is seen to be on the order of five times the value for films grown in 15.6*N* HNO_3 solutions. As was discussed above, the high nucleation rate of surface oxides at the high acid concentration produces rapid saturation of the Ge surface with a protective layer. A similar trend was noted by Cretella and Gatos (1). The average oxide thickness, in microns, was calculated by assuming that the density of the surface oxide was that of the bulk hexagonal GeO_2, 4.228 g/cm^3 (10). The basis for this assumption is discussed in the next section.

The surface oxide layer was observed to improve in uniformity with increasing acid concentration. Figure 6 is a comparison of single crystal Ge (100) surfaces oxidized for 12 hr in 7.5, 10.2, 11.9, and 15.6*N* HNO_3. At 7.5*N* HNO_3 the oxide layer is "patchy" while the

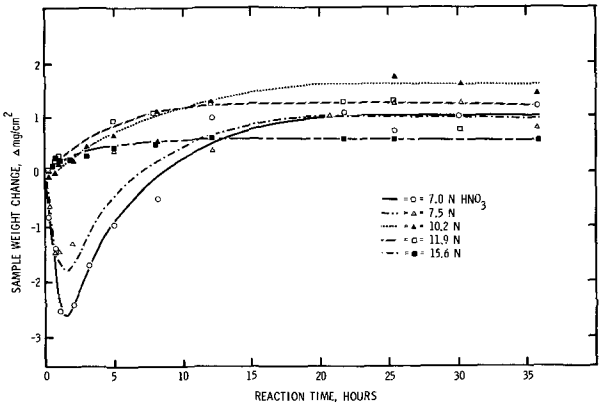

Fig. 4. Weight change of polycrystalline Ge samples with time at 27.5°C. At lower HNO_3 concentrations a net sample weight loss occurs initially.

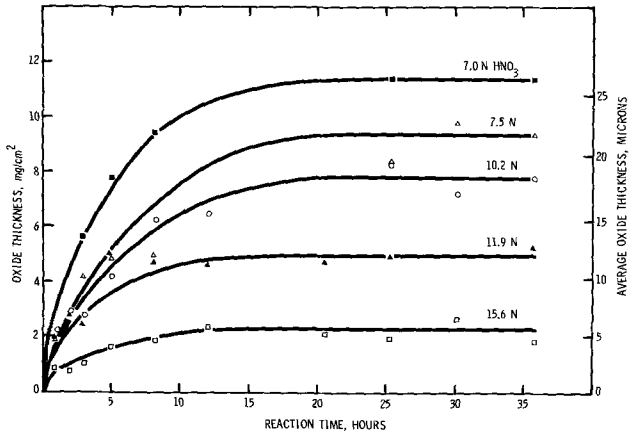

Fig. 5. Oxide growth on polycrystalline Ge (111) surfaces at 27.5°C. Film thicknesses approach saturation values.

most uniform layers are grown in 15.6*N* HNO_3. The variation in the appearance of the samples from dark to white results from the variation in visible light reflection from the surfaces with change in oxide thickness. An electronmicrograph of a Ge (100) surface oxidized for 2 hr in 15.6*N* HNO_3 at 27.5°C is reproduced in Fig. 7. The oxide nuclei density for layers grown in 15.6*N* HNO_3 is seen to be much greater than that for layers grown in 7.0*N* HNO_3 (Fig. 2).

Temperature dependence studies were not pursued to any extent since the contiguity of the oxide layers showed no marked improvements in a preliminary study. Hot nitric acid produced a layer with a higher density of fine-grained oxide nuclei than the layers grown at room temperature (9a). Faust (3) also had noted this. For long reaction times at high temperatures the acid concentration became less certain as a result of loss of nitrogen oxides. A fine-grained oxide layer was observed to grow at lower temperatures when the Ge surface was oxidized in contact with an inert surface such as polyethylene (9a).

Surface oxide characterization.—Germanium dioxide is known to exist in at least three polymorphic forms (10, 11): (*a*) hexagonal crystalline, (*b*) tetragonal crystalline, and (c) amorphous GeO_2. At ordinary temperatures tetragonal GeO_2 is the thermodynamically stable modification (12), but, when Ge is oxidized, the normally occurring forms are the hexagonal or amorphous GeO_2, depending on conditions. Tetragonal GeO_2 can be formed by conversion from hexagonal GeO_2 by using a fluxing agent (13). The phase diagram of the Ge-GeO_2 system has been determined (14, 15), and the transition temperature for the tetragonal to hexagonal crystalline modification has been measured to be 1033°C (12).

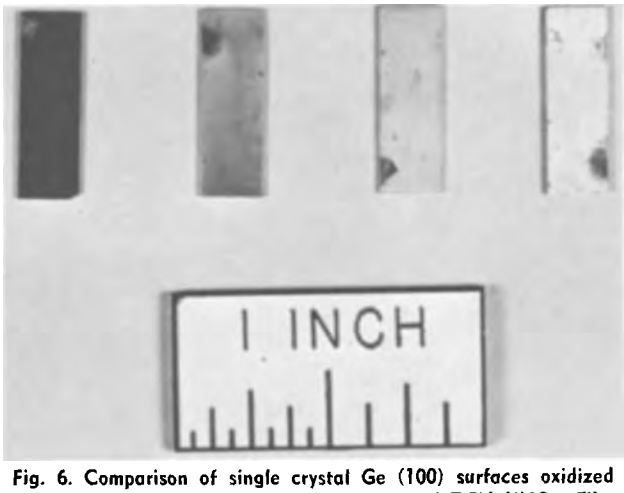

Fig. 6. Comparison of single crystal Ge (100) surfaces oxidized for 12 hr in (l. to r.) 15.6N, 11.9N, 10.2N, and 7.5N HNO_3. Film uniformity improves with increasing acid concentration.

Fig. 7. Electronmicrograph of a Ge (100) surface oxidized for 2 hr in 15.6N HNO_3 at 27.5°C. The oxide layer is seen to be composed of densely packed crystalline oxide nuclei.

In order to determine the form assumed by the oxide in the nitric acid oxidation studies, structural studies were performed on the surface oxide layers by three techniques: (*a*) infrared absorption, (*b*) x-ray diffraction, and (c) electron diffraction. The method used for infrared absorption measurements has already been described. The spectra were compared to those published (6) on the polymorphs of GeO_2. The results indicated that the oxide layers grown in 7.0-15.6*N* HNO_3 on Ge surfaces are composed of hexagonal GeO_2. Infrared spectra characteristic of amorphous (16) and tetragonal GeO_2 were not detected.

X-ray diffraction studies were undertaken to characterize the surface oxide further. Oxidized samples were mounted in a General Electric XRD-5 unit, and diffraction patterns of the surface oxide were obtained using chromium Kα radiation. Measured d-values for the surface GeO_2 were compared to published values (17, 18). Only hexagonal GeO_2 lines were identified. No lines characteristic of tetragonal GeO_2 were detected.

Thin layers of surface oxide, grown for short periods in HNO_3, were prepared for electron diffraction studies in a Siemens Elmiskop I in an effort to determine the nature of the oxide at the Ge-GeO_2 interface. 100 kev electrons were diffracted from the thin oxide layers at low angles (1°-2°) of incidence, and measured patterns were compared with published results for GeO_2 (19). Hexagonal GeO_2 was identified, but, again, no tetragonal GeO_2 was detected in the surface oxide layers. The results of these structural studies indicate that the surface oxide layers grown on Ge surfaces in concentrated HNO_3 are crystalline hexagonal GeO_2..

Orientation effect.—The growth of oxide layers on Ge surfaces in concentrated HNO_3 appears to be affected by the crystallographic orientation of the Ge surface. Figure 8 is a photomicrograph of a grain boundary on a polycrystalline Ge (111) surface oxidized for 30.2 hr in 11.9*N* HNO_3. Faust (3) also noted a dependence of oxide film growth on the Ge surface

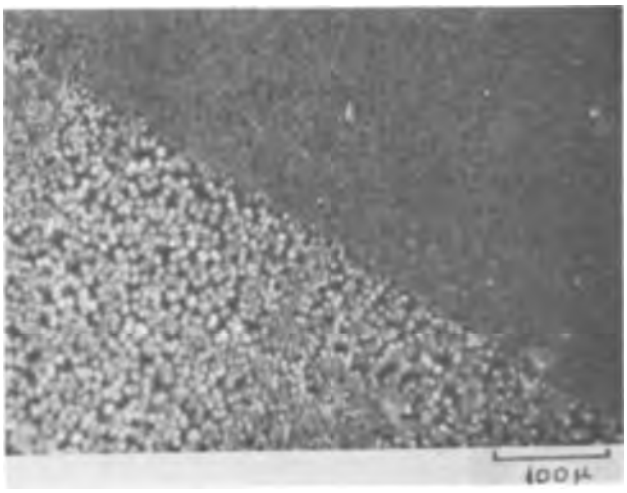

Fig. 8. Oxidation of a grain boundary on a polycrystalline Ge (111) surface after 30.2 hr in 11.9N HNO_3 at 27.5°C. An orientation effect on oxide film growth is visible.

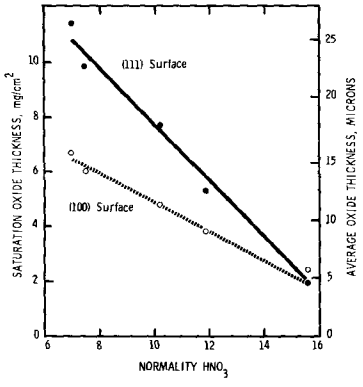

Fig. 9. Dependence of saturation oxide film thickness on HNO_3 concentration at 27.5°C. The surface orientation becomes less important with increasing acid concentration.

orientation, but quantitative data were lacking. Our study considered film growth on Ge (111) and Ge (100) surfaces. Saturation oxide layer thickness, measured by infrared absorption, is compared in Fig. 9. Two interesting features are readily apparent from the data of Fig. 9: (*a*) saturation oxide film thickness is inversely dependent on HNO_3 concentration, and (*b*) oxide film thickness is orientation dependent. The difference in film thickness with Ge surface orientation is seen to decrease with increasing acid concentration. It is interesting to note that the etching rate decreases with increasing acid concentration (1, 2), while the oxide nucleation rate increases with increasing acid concentration. An orientation effect on the etching rate of Ge in solution has been detected by others (20-22). Harvey and Gatos (21) observed that the dissolution rates were (100) > (110) > (111) for the three principal crystallographic orientations at 30°C while Camp (20) found that the order of (100) and (111) was reversed below 25°C. Schwartz and Robbins (22) studied the etching rates of Ge in HNO_3 solutions containing low concentrations of HF. Their results show that the rate dependence on orientation is (110) > (111) > (100). Miuller and co-workers (2) also noted a reduced etching rate for (100) and (110) compared to (111) surfaces. These data indicate that at the lower HNO_3 concentration the etching rate of the Ge surface may be the rate-controlling factor, while at the higher acid concentrations the nucleation rate may be the dominant factor so that the orientation of the surface becomes less important (Fig. 9). As a result, it is difficult to apply a simple diffusion model, proposed for silicon (23), to the oxidation behavior of Ge in solution.

The dissolution of Ge is evidently a complex heterogeneous reaction with simultaneous oxidation of Ge surface atoms and hydration of oxidation products followed by their transfer into solution. Nitric acid as the oxidizing agent complicates the interpretation because of the complex kinetic relationship of nitric acid with its various reaction products (24, 25). Briner and co-workers (26, 27) have shown that the oxidizing power of HNO_3 in concentrated solutions depends on the undissociated species. Cretella and Gatos find that the rate of oxidation of Ge is proportional to the product of HNO_2 and undissociated HNO_3. Their reasoning is based on the mechanism proposed by Vetter (24)

$$HNO_2 + HNO_3 = N_2O_4 + H_2O \quad \text{slow} \quad [1]$$

$$N_2O_4 = 2NO_2 \quad \text{fast} \quad [2]$$

$$NO_2 + e^- = NO_2^- \quad \text{fast} \quad [3]$$

Miuller and co-workers (2) also consider the active species to be NO_2. The apparent over-all rate of oxidation, as deduced from the observed weight changes, is related to the exposed Ge surface area. As this area decreases with the build up of a protective oxide layer, the apparent growth rate of the surface oxide decreases, and the oxide thickness approaches a saturation value. A lack of detailed knowledge of the oxidizing agent and of the exact nature of the possible oxidation products (H_2GeO_3, $HGeO_3^-$, GeO_2, . . .) that are diffusing through the surface-liquid interface, precludes a quantitative model of the oxide growth process at the present time.

Some qualitative remarks can be made however. The rate limiting process cannot be purely a diffusion process as evidenced by the orientation dependence and the way the dissolution kinetics are affected by saturating the HNO_3 with GeO_2 prior to sample oxidation. Miuller and co-workers (2) propose a chemical oxidizing-hydrating mechanism of Ge atom transfer into solution where the rate of the process is limited by the chemical heterogeneous reaction and the accompanying diffusion into solution. Their proposed mechanism follows several steps: (*i*) the exposed Ge surface atom, with an individual pair of electrons, bonds with the oxygen atom from NO_2; (*ii*) a surface dipole is formed; (*iii*) coordination bonds can be formed between protons and the oxygen atom in acid solution, Ge retains a positive charge; (*iv*) the molecule $GeO(OH)_2$ is separated from the surface as a result of hydrolysis and can react with a second NO_2 molecule; (*v*) a new surface of Ge atoms with unshared electron pairs is exposed after the oxide has gone into solution, and the cycle starts anew. The relative importance of each of these steps (plus others, perhaps) in limiting the oxide growth rate is, for the moment, speculative. Additional work on the kinetics of oxide growth will be necessary in order to establish, with any certainty, the chemical mechanism which dominates the oxidation process. Presumably, the temperature dependence studies, under consideration in our laboratory, may provide a more complete view of the reaction mechanism involved. The higher acid concentrations used in our study did not reveal any gross differences from the results published for Ge oxidation at lower acid concentrations (1, 2, 4).

Summary and Conclusions

The study of Ge oxidation in HNO_3 has been extended to high acid concentrations. Thick oxide layers can be grown on Ge surfaces in the concentration range 7.0-15.6*N* HNO_3. Film uniformity improves with increasing acid concentration. No induction period for oxide growth was observed over the acid concentration range studied. The oxide growth rate decreases smoothly with time and is not described by simple film growth laws. Saturation film thickness was observed to be inversely dependent on acid concentration. The oxide nuclei sizes at saturation film thickness decrease markedly with increasing acid concen-

tration. The saturation film thickness was found to be dependent on the crystallographic orientation of the Ge surface. This result indicates that the rate limiting step in oxide growth is probably not purely diffusion controlled. Structural studies, by infrared, x-ray and electron diffraction techniques, of the oxide layers grown on Ge surfaces in concentrated HNO_3 solutions indicate, unambiguously, that the surface oxide is crystalline hexagonal GeO_2.

Acknowledgments

The author would like to express his gratitude to D. E. Swets for the polycrystalline Ge crystals and P. A. Gudaitis for technical assistance. T. R. McKinney performed electron diffraction analyses, and Miss A. Forster performed x-ray analyses on oxidized samples. Discussions with W. A. Albers, Jr., C. E. Bleil, R. N. Hollyer, Jr., and P. V. Mohan were of much benefit to the author.

Manuscript received June 17, 1966; revised manuscript received Sept. 1, 1966.

Any discussion of this paper will appear in a Discussion Section to be published in the December 1967 JOURNAL.

REFERENCES

1. M. C. Cretella and H. C. Gatos, *This Journal*, **105**, 487 (1958).
2. R. L. Miuller, T. P. Markova, and S. M. Repinskii, *Leningr. Univers., Vestnik* (16): 106 (1959).
3. J. W. Faust, Jr., *Acta. Met.*, **11**, 1077 (1963).
4. P. P. Konorov and O. V. Romanov, *Sov. Phys.—Solid State*, **5** [10], 2225 (1964).
5. P. V. Mohan and W. A. Albers, Jr., Private communication.
6. E. R. Lippincott, A. Van Valkenburg, C. E. Weir, and E. N. Bunting, *J. Research Nat. Bur. Stand.*, **61**, 61 (1958).
7. G. Brauer and H. Müller, *Z. anorg. u. allgem. Chem.*, **287** [1-2], 71 (1956).
8. D. F. Kyser and M. F. Millea, *This Journal* **111**, 1102 (1964).
9. M. E. Straumanis and C. D. Kim, *ibid.*, **111**, 1186 (1964).
9a. W. A. Albers, Jr., and P. V. Mohan, Unpublished data.
10. A. W. Laubengayer and D. S. Morton, *J. Am. Chem. Soc.*, **54**, 2303 (1932).
11. J. H. Müller and H. R. Blank, *ibid.*, **46**, 2358 (1924).
12. J. I. Carasso and M. M. Faktor, "The Electrochemistry of Semiconductors," pp. 216-219, P. J. Holmes, Editor, Academic Press, New York (1962).
13. W. A. Albers, Jr., E. W. Valyocsik, and P. V. Mohan, *This Journal*, **113**, 196 (1966).
14. V. O. Candidus and D. Tuomi, *J. Chem. Phys.*, **23**, 588 (1955).
15. F. A. Trumbore, C. D. Thurmond, and M. Kowalchik, *J. Chem. Phys.*, **24**, 1112 (1956).
16. P. V. Mohan, Private communication.
17. W. Zachariasen, *Z. Krist*, **67**, 226 (1928).
18. V. M. Goldschmidt, *Z. physik Chem.*, **17B**, 172 (1932).
19. ASTM Powder Diffraction File; Data Cards 9-379, 4-0497, 4-0498.
20. P. R. Camp, *This Journal*, **102**, 586 (1955).
21. W. W. Harvey and H. C. Gatos, *ibid.*, **105**, 654 (1958).
22. B. Schwartz and H. Robbins, *ibid.*, **111**, 196 (1964).
23. H. Robbins and B. Schwartz, *ibid.*, **107**, 108 (1960).
24. K. Vetter, *Z. phys. Chem.*, **194**, 199 (1950); *Z. anorg. Chem.*, **260**, 242 (1949).
25. E. Abel, *Monatshefte fur Chem.*, **89**, 74 (1958).
26. E. Briner, *Helv. Chim. Acta.*, **18**, 363 (1935).
27. E. Briner and P. Bolle, *ibid.*, **18**, 368 (1935).

Precipitates Induced in GaAs by the In-Diffusion of Zinc

J. F. Black and E. D. Jungbluth

The Bayside Laboratory, research center of

General Telephone & Electronics Laboratories Incorporated, Bayside, New York

ABSTRACT

Imperfections in GaAs due to the in-diffusion of zinc at temperatures in the range of 700°-1100°C have been investigated by means of x-ray diffraction topography, optical microscopy, and infrared transmission microscopy. The imperfections, which were generated in the diffused layer, were identified as submicroscopic precipitates. Precipitation was almost unavoidable when metallic zinc was used as the diffusant source. Although precipitation could be prevented when $ZnAs_2$ was used as a source, prolonged diffusion always resulted in precipitation. It was concluded that diffusion-induced dislocations plus precipitation, or diffusion-induced precipitation alone, was occurring in our samples.

The study of defects generated in semiconductors by the in-diffusion of p- or n-type impurities has achieved considerable impetus in recent years. In particular, the generation of dislocations due to the diffusion of phosphorus or boron into silicon has been extensively investigated (1). The documentation of diffusion-induced defects in silicon is in contrast to the small amount of published information on these effects in the compound semiconductor GaAs. Recent work (2-4) has shown that surface layers with a high content of structural defects can be produced in GaAs by the vapor phase in-diffusion of zinc. Zinc is widely employed as a p-diffusant in GaAs; therefore it is imperative to define the conditions that give rise to these defects so that their occurrence may be controlled.

This paper presents some results of an investigation of zinc-diffusion-induced imperfections in GaAs. Diffused samples were examined by x-ray anomalous transmission, by infrared transmission microscopy, and by optical microscopy of etch structures. Previous indications (2) of severe lattice damage by diffusion of zinc into GaAs were confirmed, and it was established that this damage was largely due to submicroscopic precipitation in the diffused layer. It was further established that precipitation and its consequent lattice damage in the diffused GaAs could be avoided by proper control of diffusion conditions.

Experimental Techniques

Sample preparation.—The starting material was commercially available single crystal GaAs, boat-grown by the gradient freeze technique. The single crystals displayed dislocation densities ranging from about $10^2/cm^2$ to $10^5/cm^2$, as determined by etch pit counts. Wafers 0.5-1.5 mm thick were cut from these crystals and were then chemically etched or chemically polished to remove all traces of damage resulting from cutting and grinding operations. All diffusions were made by a standard technique; the GaAs samples were contained along with 1g of GaAs powder

and 10 mg of pure zinc (or in some cases with only 10 mg $ZnAs_2$) in evacuated quartz ampoules of 50 cm^3 volume. Each diffusion was carried out with one or more low dislocation density samples in the capsule in addition to other samples of high dislocation density and of differing n-doping level. The low-dislocation-density samples were required for x-ray anomalous transmission topographs, while the high-dislocation-density samples allowed evaluation of the effects of initial crystal perfection. The samples of differing n-doping level made it possible to estimate the zinc penetration profile (p-n junction depth *vs.* n-doping level) for each diffusion run. Diffusion was carried out at temperatures ranging from 700° to 1100°C for a period of 2 hr with GaAs powder and pure zinc in the capsule, unless otherwise noted. All diffusions were carried out so that the end of the capsule containing the diffusant source was maintained at a temperature 10°C below the diffusion temperature. After diffusion the ampoule was cooled by gradually withdrawing it from the furnace over a period of 2 min and then immersing it in water. In this way the contents of the capsule were cooled to room temperature within 3 min. A few diffusion runs were terminated by rapid quenching and a few by slow cooling in the furnace. Rapid quenching was accomplished by withdrawing the capsule from the furnace, plunging it into a bucket of water and crushing with a long-handled pliers. It is estimated that in this way samples were cooled to room temperature within 5 sec.

Examination of samples.—Large-area x-ray diffraction topographs of starting material with low dislocation densities were recorded by the anomalous transmission method (5). This method is highly sensitive to the perfection of the material. Highly imperfect crystals strongly attenuate the x-ray transmission, especially in the immediate vicinity of imperfections. Thus crystal imperfections are revealed as areas of reduced x-ray intensity within the x-ray topographs.

GaAs wafers studied with this x-ray method were oriented in <111> directions. The diffused junctions on the As face were always removed by chemical etching prior to recording x-ray topographs. Since defects confined to shallow surface layers, such as occur in diffused junctions, appear sharpest where the x-ray beam leaves the crystal, the wafers were always positioned so that the Ga face corresponded to the exit surface of the beam on the crystal (6). This allowed etch pit studies, which were carried out on the Ga face, to be correlated with defects shown in x-ray topographs. In many of the samples studied, the diffusions resulted in very strong x-ray absorption by the crystal, and crystal wafers were defined as being opaque to x-rays when no diffracted image could be obtained. Pictures of the diffraction topographs are photographic negatives; consequently, highly imperfect regions appear dark.

In addition to anomalous transmission studies, etch structures were also examined to reveal the presence of crystalline defects. The etch structures were developed on a Ga (111) surface by swabbing the surface with a freshly prepared mixture of one part 30% H_2O_2 and five parts 2% NaOH for 2 to 5 min. This etchant was selective to surface orientations near a (111) Ga surface and developed small pits with a well-defined triangular shape. The pits could be developed over a range of orientations, although with distortion in symmetry, as much as 10° from <111> Ga direction, thus obviating preparation of accurately oriented samples. At sample orientations more than a few degrees from <111>, however, the number of pits produced in a given sample was reduced, so all etching was carried out on surfaces within 2° of an (111) Ga surface. Etch pit counts obtained on a well-oriented wafer were in substantial agreement with etch pit counts obtained with a known GaAs dislocation etch (1 conc. $NHO_3 - 2H_2O$ solution).

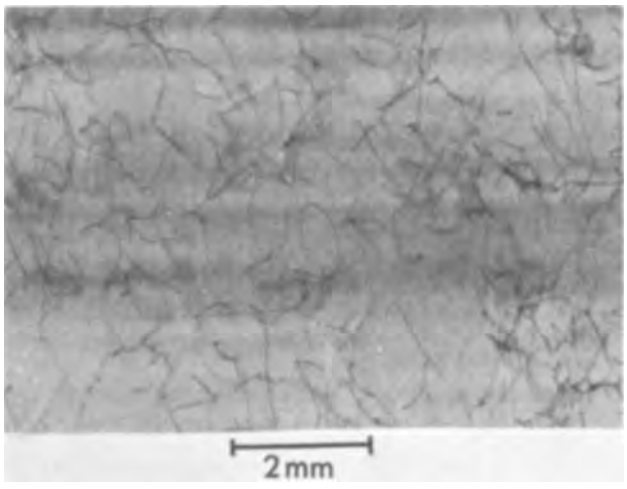

Fig. 1. X-ray topograph of low dislocation density GaAs

Infrared transmission microscopy was accomplished by means of a commercially available image converter adapted to the occular of an inverted stage microscope. Infrared photomicrographs were recorded on Eastman Kodak Type I-M 4 x 5-in. spectrographic plates.

Results

Description of the defect structure.—The dislocation density of the samples used for most of the x-ray anomalous transmission studies was no more than 200/cm^2 (by etch pit count). Figure 1 shows an x-ray topograph typical of this material. After standard diffusions at 700° and 725°C such material showed a slight reduction in the anomalous transmission intensity, but no change in the appearance or in the number of the dislocations occurred. Furthermore, no additional defects, such as misfit dislocation networks, could be detected in the x-ray topographs. At 750°C the intensity due to anomalous transmission was reduced about 20% by the in-diffusion of zinc, and there was still no change in the dislocation structure. Standard diffusions at temperatures higher than 750°C resulted in complete x-ray absorption by the sample, indicating that a high degree of crystal lattice imperfection had been produced. The fact that the transmitted x-ray intensity was reduced (resulting in ultimately opaque samples), while the original dislocation structure was preserved indicates that the diffusion process has produced a substantially uniform microscopic strain in the crystals. Patel and Batterman (7) have reported a similar kind of reduction in anomalous x-ray transmission through silicon, caused by annealing single crystals contaminated with oxygen. These authors established the presence of microscopic strains resulting from the formation of Si-O clusters in the early stages of the precipitation of silicon oxides. This connection of microscopic strain with precipitation is significant because in the present work other evidence of precipitation, *i.e.* high densities of etch pits, appeared in the diffused layer, concomitant with the reduction in anomalous x-ray transmission.

Figure 2 shows three photomicrographs of etched cross sections of diffused samples mounted and polished to produce a (111) Ga plane of section. In an investigation of the precipitation of Cu_2O in copper single crystals Young (8) has described etch structures strikingly similar to those of Fig. 2a. Young observed triangular pit etch structures in oxygen-doped copper single crystals annealed to cause small Cu_2O particles to form. Each particle, even when submicroscopic in size, gave rise to a surrounding cluster of densely packed etch pits, which was interpreted to be due to dislocations produced by plastic deformation which accompanied the formation and growth of the precipitate particles. The dense pitting that is observed throughout the surface layer of the

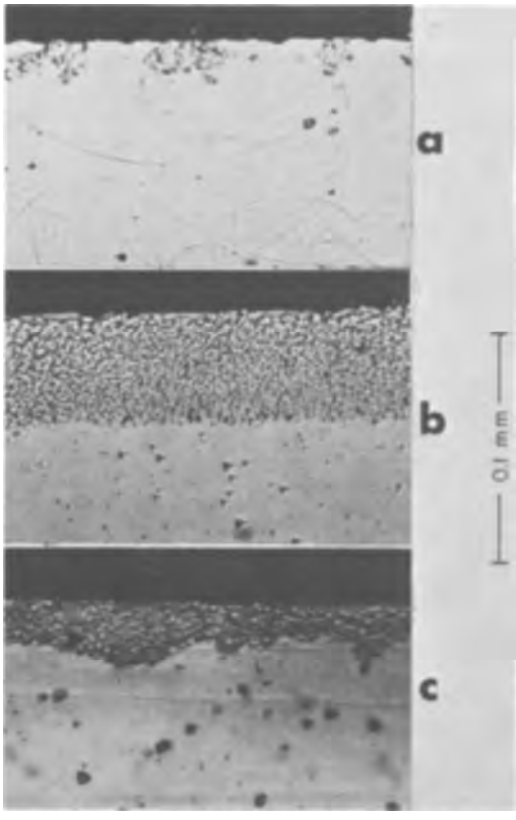

Fig. 2. Etched cross sections of GaAs wafers diffused from a pure zinc source: a, 2 hr at 750°C; b, 2 hr at 800°C; c, 24 hr at 700°C.

sample diffused at 800°C is therefore consistent with the complete x-ray opacity of the GaAs slices that were subjected to standard diffusions at temperatures greater than 750°C. Additional data and pertinent comments for diffusions performed with pure zinc as a source are contained in Table I.

The etched cross sections of samples diffused at a temperature of 700°C showed no evidence of imperfections in the diffused layer even though there had been appreciable diffusion of zinc into these samples (attested by the development of a p-n junction 8μ deep in samples of $n = 5.9 \times 10^{18}/cm^3$). There was, nevertheless, a defect structure layer present that was so thin (1 or 2μ) that it was difficult to develop a clearly defined etch structure in cross section. This layer was detected by carefully etching the diffused surface of the samples. The fact that such a layer, however thin, was detected is again consistent with the reduction in transmitted x-ray intensity noted for these samples. These results suggest a pre-precipitation

Table I. Data on diffusions for 2 hr from a pure zinc-powdered GaAs source

Temp, °C	Depth of p+p junction, μ	Comments
700	7	Slight reduction in x-ray transmission, no change in etch structure
725	10	Slight reduction in x-ray transmission, no change in etch structure
750	20	20% reduction in x-ray transmission, scattered etch pit clusters in p+ layer, sample still transparent to IR
775	35	Completely opaque to x-rays, high etch pit density in p+ layer
800	50	Completely opaque to x-rays, nearly opaque to IR, high etch pit density in p+ layer
900	110	Completely opaque to x-rays, completely opaque to IR, high etch pit density in p+ layer
1000	125	Completely opaque to x-rays, completely opaque to IR-high etch pit density in p+ layer
1100	125	Completely opaque to x-rays, completely opaque to IR, high etch pit density in p+ layer

incubation period of about 2-hr duration in 700°C standard diffusions. At diffusion times longer than two hours at low temperatures, *e.g.*, 24 hr at 700°C, deep zinc penetration was achieved, and the diffused layers were again so highly defective as to be opaque to x-rays. Such a layer is shown in cross section in Fig. 2c.

The infrared absorption increased along with the x-ray absorption, but was not nearly as sensitive a measure of diffusion-induced damage. For instance, the sample of Fig. 2c, though completely opaque to x-rays was still somewhat transparent to IR radiation; the sample of Fig. 2b was opaque to x-rays and very nearly opaque to IR; while a sample with structure like that of Fig. 2b but diffused at 900°C was opaque to both x-rays and IR. In no instances were structures such as decorated dislocations revealed by IR transmission microscopy. Note that the starting dislocation density (etch pit density) is preserved in the region below the diffused layer of Fig. 2c. The only difference apparent between damaged layers produced at low diffusion temperatures (700°C) and those produced at higher temperatures (800°C) was that the boundaries of the layers produced at the lower temperatures were more irregular. This probably is related to the fact that the diffusion-induced damage begins in isolated regions of these samples (see Fig. 2a). These regions, indicated by the etch pit clusters, spread out and penetrate more deeply with time. Until the diffusion depth is large compared with the mean distance between clusters, however, we continue to see evidence of the heterogeneous beginnings of the diffusion-induced damage in the uneven boundary of the defect structure layer.

The samples shown in Fig. 2 had initial dislocation densities of $10^3/cm^2$ to $10^4/cm^2$ by etch pit count. The starting dislocation density did not have a strong effect on the occurrence of highly defective layer structures; the defect structure could be equally well developed in samples with starting dislocation densities of $200/cm^2$ and $100{,}000/cm^2$. This indicates that the diffusion-induced damage was not critically dependent on the presence of existing dislocations, as would have been the case, for example, if the damage were due to decoration of existing dislocations. Clustering of etch pits such as is seen in the sample diffused at 750°C in Fig. 2a was specially prevalent in the early stages of diffusion at temperatures in the range 700°-750°C. Again, if the production of diffusion induced damage was heterogeneous, it would be most apparent in the early stages of its occurrence.

When $ZnAs_2$ was used as the source of zinc, it was possible to preserve the crystal perfection in the diffused layers if the diffusions were not too deep and were not made at too high a temperature. For example, samples diffused for ½ hr at 800°C from a pure zinc-powdered GaAs source developed 25μ deep layers that were opaque to x-rays, while samples diffused for eight hours at 800°C from a $ZnAs_2$ source developed 25μ deep layers with no measurable reduction in anomalous transmission. This was most interesting because of the experience that some workers have reported in fabricating efficient light-emitting diodes (9). Diffusions from a $ZnAs_2$ source were found to yield better GaAs electroluminescent and laser diodes than diffusion from a pure zinc source. It would appear that these results can partly be explained by the differences in defect structure between p-layers prepared from pure zinc source and p-layers produced from $ZnAs_2$.

At diffusion temperatures higher than 800°C or for long diffusion times at 800°C (24 hr), diffusion from a $ZnAs_2$ source ultimately developed highly imperfect layers. One of the effects of using $ZnAs_2$ as a diffusant source is a lengthening of the incubation period before the onset of diffusion damage. The distribution of etch pits in the defect layer was found to be quite different from that observed for pure zinc diffusions. A good example of the structure produced by a $ZnAs_2$ diffu-

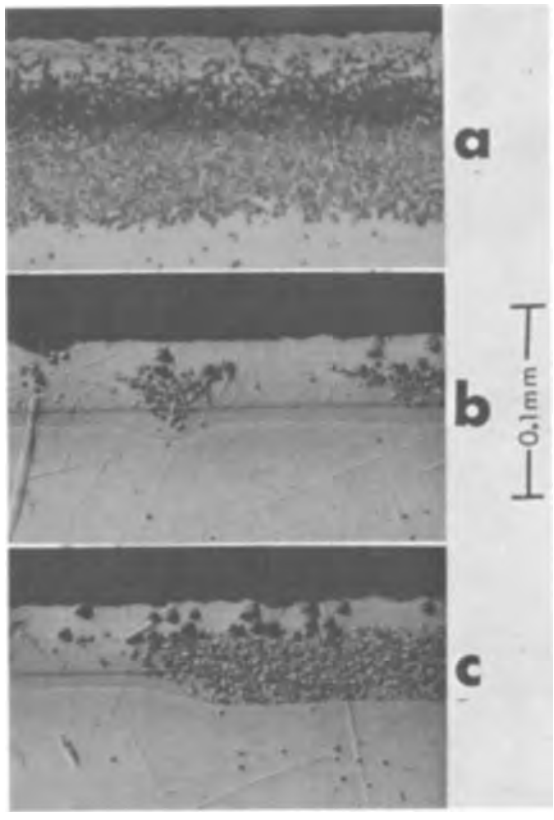

Fig. 3. Etched cross sections of GaAs diffused from $ZnAs_2$ source: a, 8 hr at 900°C; b and c, 24 hr at 800°C.

sion is shown in Fig. 3a. Although a detailed explanation of why the etch pit distribution is so different for $ZnAs_2$ cannot be given at this time, it is probably a result of the much less steep penetration profile produced by diffusion from $ZnAs_2$ (9).

A particularly good example of clustering of defects was observed in a sample diffused from $ZnAs_2$ and is shown in Fig. 3b and 3c. This sample has been etched with a p-n junction etch as well as with the hydroxide-peroxide defect structure etch. It can be clearly seen in Fig. 3b that clustering of etch pits is closely associated with a deeper penetration of the p-n junction. The heavy dark line just above the p-n junction was seen in p-type samples as well as in n-type samples and was identified as a p^+-p boundary by previous studies (10). By comparison with companion samples doped with tellurium to various levels of free electron concentration, the zinc concentration at the p^+-p boundary in the samples of Fig. 3b and 3c was estimated to be $6 \times 10^{18}/cm^3$, and at the p-n junction $3.0 \times 10^{17}/cm^3$. The deeper penetration of the p-n junction in regions of etch pit clusters suggest that the diffusion process induces defects to appear first in regions where there is already some kind of lattice disturbance in the crystal. This is also in line with our observation that clustering was more prevalent in samples of initial high imperfection. However, the kind of defect assumed to be inherent in the host matrix was not evident by x-ray contrast methods before the diffusion cycle. It would be expected that regions of imperfect lattice structures would show enhanced mobility of a diffusant (deeper penetration of p-n junction). Pilkuhn and Rupprecht (9) have shown similar evidence of enhancement in p-n junction depth in regions of crystal defects in GaAs. Evidence that these diffusion-induced defects can seriously affect device properties is shown in Fig. 3c, where the defects extend all the way to the p-n junction.

Optical micrographs of etch structures of a diffused sample are correlated with x-ray topographs in Fig. 4. Dense clustering of defects which occurred in this

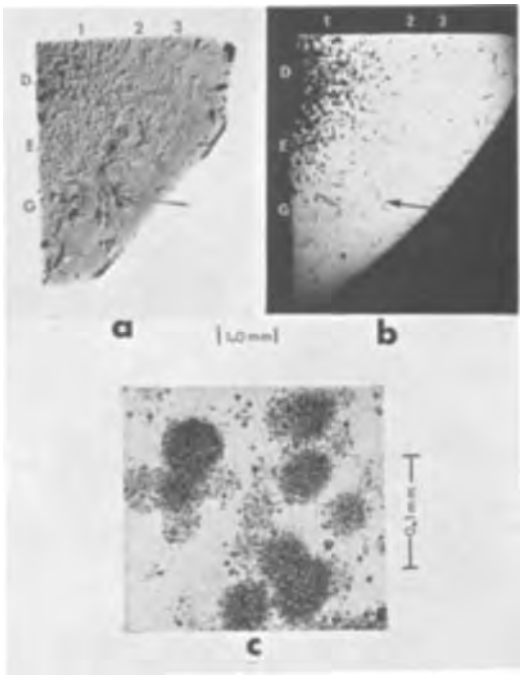

Fig. 4. a, X-ray topograph of clustered defect structure; b, corresponding etch structure; c, details of etch pit clusters.

sample, diffused at 750°C, is evident in Fig. 4a and b within region D1. More clustered defects are seen in the x-ray topograph than the etched surface, which is the plane of diffusion, because only the clusters that intersect the surface are seen by etching, while all of the clusters are seen by x-ray transmission. The clusters were also areas of reduced IR transmission, but the optical contrast was so slight that it could not be clearly registered on our IR sensitive plates. An enlarged view (Fig. 4c) shows that the defect clusters are composed of triangular type pits. These clusters of etch pits have the same structure as those shown in cross-section in Fig. 2a. The dark broad images in the diffraction topograph, such as are indicated by the arrows, are scratches introduced after the diffusion.

Figure 5 shows x-ray topographs of a sample before and after an 800°C diffusion. The sample was initially 1.0 mm thick and was diffused to a depth of 50μ. Because the diffused layers were opaque to x-rays, it was necessary to remove the diffused layer from the B side (the As side) and then angle lap and etch away nearly the entire layer on the A side to obtain the topograph shown in Fig. 5b. Notice that where the diffused layer has been completely removed, Fig. 5c, and region C in Fig. 5b, the original dislocation structure has been preserved. The original structure is still reflection dependent; hence no precipitation along dislocations has occurred in the bulk of the wafer. A clear line of demarcation separates what remains of the defective diffused layer on the A side from the underlying undisturbed material. The diffraction contrast at this boundary resembles the contrast seen in the clusters of Fig. 4. By means of control runs, *i.e.*, runs in which the treatment of samples was identical except that there was no zinc (or $ZnAs_2$) present in the capsule, it was established that only when zinc was indiffused did defect structures appear. This confirmed that these effects were due to zinc and not to thermal stresses, or the precipitation of impurities independent of the presence of zinc.

There was good reason to believe that these defects were due to precipitation, presumably a zinc-complex. A detailed argument and analysis of the data to justify this belief will be presented in the Discussion section, but we mention it at this point because the experiments to be described in the next three paragraphs were performed to confirm whether pre-

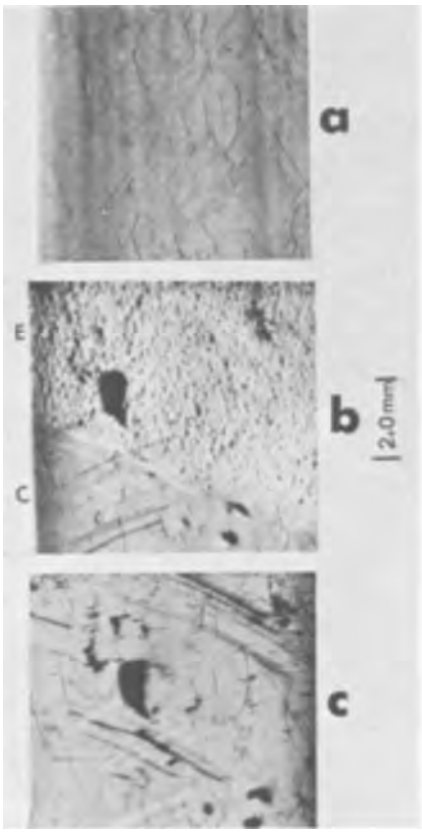

Fig. 5. X-ray topographs of zinc diffused GaAs: a, original sample; b, sample after diffusion at 800°C with B layer removed and A layer partially removed, region E indicates the A layer remaining and region C is the original bulk material; c, sample after removal of additional 30μ from A side. The dark spots are due to deep damage.

cipitation was responsible for the defect structures we had observed.

Experiments with zinc (melt) doped GaAs.—Electron probe analysis of several standard diffused samples established that the concentration of zinc at the boundary of the layer of high etch pit density was about 5 x 10^{18}/cm^3. This agreed with the observation that the boundary of this layer usually coincided with the p^+-p junction (Zn = 6 x 10^{18}/cm^3) in standard samples.

On samples melt-doped with zinc up to 3.7 x 10^{19} atoms/cm^3 (free hole concentration equal to zinc concentration within 10%) no trace of defects besides grown in dislocation tangles (about 5 x 10^3/cm^2) could be observed either by etching or by x-ray analysis. Even when the melt-doped samples were additionally annealed (in the presence of their own powder) under conditions of time and temperature where defects consistently occurred by diffusion into undoped GaAs, the zinc-melt-doped samples remained unaffected. However, when the zinc-melt-doped samples were subjected to a standard zinc diffusion at 1000°C the samples developed a defect layer structure and became opaque to x-rays and IR radiation.

The attenuation of optical transmissions was far stronger in diffused samples than in melt-doped samples for material of equal thickness, even though the concentration of zinc in the diffused samples was less than that in the melt-doped samples. For example, for a 100μ thick diffused layer with a zinc concentration ranging from 4 x 10^{19} atoms/cm^3 to 5 x 10^{18} atoms/cm^3(p^+-p boundary), optical transmissions over the range of wavelengths from 0.9 to 1.2μ (s-1 image convertor) were nil, while a 100μ thick wafer of the zinc-melt-doped GaAs was transparent in the same spectral region. If the diffusion-induced damage were largely a result of precipitation, this result might be expected except that the intensity of the IR attenuation implies a rather large amount of precipitate ($>>$ 10^{18} atoms/cm^3).

To ascertain whether the defects were due to some impurity unknowingly introduced during the preparation and diffusion processes, samples were analyzed by emission spectroscopy both before and after diffusion. Only three impurities were detected Cu 3-6 ppm, Mg 5-15 ppm, and Si 10-50 ppm, and their concentrations were unchanged by the diffusion process. It is possible that the residual impurities or that undetected impurities, such as oxygen, are responsible for the diffusion damage, but whatever the nature of the defect structures, they occurred only when zinc was indiffused.

Quenching experiments.—We found that the defect structure that appeared in zinc-diffused GaAs was identical whether samples were quenched from the diffusion temperature to room temperature in a matter of seconds or whether they were slowly cooled in the diffusion furnace over a period of many hours. The character of the defect structure was inspected by etching within 15 min of quenching, and by x-ray anomalous transmission within 30 min after quenching. In both instances the defect structure was fully developed. It was therefore concluded that the defects were occurring during the in-diffusion of zinc or were occurring extremely rapidly during cooling.

In a study of zinc diffused GaP, Gershenzon and Mikulyak (16) observed precipitate structures which they tentatively identified as zinc-rich. They likewise were not able to quench their samples fast enough to prevent the occurrence of these precipitates. It was concluded that the precipitation was occurring during the diffusion period and, furthermore, thermodynamic considerations then implied that the precipitate phase could not be pure zinc. These considerations apply in the present circumstances as well.

Free carrier concentration vs. zinc concentration.—The reduction in the free carrier concentration is a frequently used measure of the progress of precipitation in semiconductors (11). Thus the free carrier concentration was compared with the zinc concentration (average zinc concentration $\geq$ 5 x 10^{18} atoms/cm^3) in diffused samples known to contain well-developed defect (precipitate) structures. These samples were opaque to IR radiations as well as to x-rays. We did find samples which exhibited a free carrier (hole) concentration less than the zinc concentration, but we also found samples which showed agreement (within $\pm$30% spectroscopic analysis accuracy) between the free hole concentration and the zinc concentration. The ratio of free charge carriers to zinc depended in a systematic way on the exact diffusion conditions for each sample. These results are, however, the subject of a separate investigation (12) and they will not be described further in this paper.

The occurrence of these defects did not depend critically on the purity of the GaAs or on the particular method of crystal growth. It was induced in many different crystals, p-doped to 4 x 10^{19}/cm^3, n-doped to 6 x 10^{18}/cm^3 and undoped n = 1.2 x 10^{16}/cm^3, μ = 5,000 cm^2/v-sec, grown by the gradient freeze method in quartz boats, in crystals taken from ingots zone refined in graphite boats, and in crystals pulled from graphite, alumina, or boron nitride crucibles.

Discussion

The introduction of an impurity atom into a crystal by vapor phase diffusion can have two distinct but not necessarily separate effects on the lattice perfection: (*i*) the diffusion can cause dislocations to be introduced to accommodate lattice deformation effects of the solute atom; (*ii*) the diffusion can cause precipitates to appear. Solute atom deformation of the host lattice usually results in highly regular networks of dislocation lines. Diffusion induced precipitation

can be of several kinds and can occur (*a*) during cooling, because of reduced solubility of the diffusant at low temperatures; (*b*) during diffusion because of formation of stable compounds between the diffusant and the constituents of the host lattice; (*c*) during diffusion because of exolution of residual impurities, similar to the "common ion effect" which is well known in solution chemistry. We believe that the clusters and layers of high etch pit density produced in our samples by the in-diffusion of zinc are areas in which submicroscopic precipitation has occurred. No individual precipitate particles could be observed at magnifications up to 1000X. Although it seemed very likely that the diffusion induced precipitate was zinc, or some substance containing zinc as a major constituent, the experimental data were not sufficient to permit us to describe the precipitate in any detail.

The appearance of diffusion-induced dislocations will not automatically cause the appearance of precipitate structures, but if there are species present which are liable to precipitate, diffusion-induced dislocations will hasten their appearance. If precipitation occurs during in-diffusion or during a slow cool, dislocations of a type other than solute deformation dislocations will occur. These dislocations will be due to differences in the specific volume of the precipitate phase and the matrix phase and will be more localized and more intense than diffusion-induced dislocations.

In the following sections our data will be analyzed to show that both diffusion-induced dislocations with precipitation or precipitation alone are occurring. None of our results indicate the production of diffusion-induced dislocations alone.

The case for precipitation alone.—In samples diffused from pure zinc at temperatures below 775°C ($ZnAs_2$ source at temperatures below 850°C) there was no evidence of the regular networks of dislocation traces that are so characteristic of solute-induced lattice deformation. The x-ray topographs do, however, show that for diffusions from pure zinc the crystal perfection is being uniformly degraded (x-ray absorption is being increased). Such behavior is characteristic of the early stages of precipitation in highly perfect crystals (7). The heterogeneous nature of the defect structures observed in the early stages of their formation is characteristic of precipitation but not necessarily of diffusion induced dislocations. Also the distinct incubation period that is observed before damage to the crystal structure appears and the fact that this period is inversely proportional to both the temperature and the partial pressure of zinc (concentration of zinc), is consistent with a precipitation reaction. Furthermore the strong IR absorption which was observed in the defect structures is to be expected if precipitation is occurring but not if dislocations alone are present.

For those samples subjected to standard diffusions from a pure zinc source at 800°C or above, it was not possible to quench the precipitation. If the precipitation were supposed to have occurred during the diffusion period, this result is understandable. If the precipitation were supposed to have occurred after the diffusion, *i.e.*, during the cooling period, it is difficult to argue for a pure precipitation reaction unless the samples had initial high dislocation densities. The fact is that these samples had initial dislocation densities as low as 100/cm^2. For the moment we shall defer the question of precipitation during diffusion to pursue the argument for diffusion-induced dislocations with precipitation.

The case for diffusion-induced dislocations with precipitation.— If dislocations were generated during standard diffusions from pure zinc at 800°C and higher we could, at least qualitatively, explain the failure to quench the precipitation by citing the strong effects that dislocations are known to have in accelerating solid-state precipitation reactions (13, 14). The important question of whether or not dislocations are actually generated in GaAs by the in-diffusion of zinc has been answered by the recent work of Schwuttke and Rupprecht (4). They showed that under certain conditions the diffusion of zinc into GaAs can cause the regular arrays of dislocations characteristic of lattice solute deformation. For prolonged diffusion, however, a layer of intense crystal damage was produced. Although this may have been a layer of submicroscopic precipitation similar to the layers we have observed, it would be necessary to verify this by other techniques. For those samples of the current investigation in which we could have observed dilatational dislocations, had they occurred, the diffusion conditions were sufficiently different from those of Schwuttke and Rupprecht to explain the absence of dislocations. In those samples in which solute dilation dislocations should have been observed we are prevented from confirming their occurrence because of the high density of microprecipitation.

It must be emphasized that at high defect concentrations it is not possible to distinguish between crystal imperfections due to lattice solute deformation, *i.e.*, misfit dislocations, and crystal damage due to precipitation. The rather dramatic onset of the defect structure between 725° and 775°C (see Table I) is, nevertheless, consistent with the introduction of dislocations during the diffusion process. It has long been known that, at a temperature close to 2/3 T_m (15), where T_m is the absolute melting temperature, many of the so-called intermetallic compounds, including the III-V zinc blend type semiconductors, undergo a change in mechanical properties from brittle to ductile behavior. For GaAs 2/3 T_m is equal to 738°C, which is within the temperature range where our experiments suggest that dislocations are introduced. Whether precipitation occurred during in-diffusion or during cooling, diffusion-induced dislocations would be expected to enhance the rate of precipitation.

There are cases known, especially involving high dislocation densities ($> 10^6$/cm^2) (13) where precipitation reactions occur with time constants of a second or so, *i.e.*, fast enough to make quenching very difficult. However, the amount of precipitant exsolved within this second or so is only a few parts per million. There are no cases extant of nearly instantaneous precipitation of relatively large amounts of material (> 100 ppm) in the solid state. Although precipitation of a few parts per million of an impurity is sufficient to explain the strong attenuation of x-rays (7) it does not seem to be nearly enough to account for the strong IR absorption and scattering in our samples.

For example, the precipitation in the zinc-diffused regions of the crystals was sufficient to render these regions (only several thousandths of an inch thick) quite opaque to optical transmission as viewed through an IR image convertor (0.9 to 1.2μ wavelength). The average absorption coefficient of such a diffused layer containing between 4 x 10^{19} and 5 x 10^{18} zinc atoms/cm^3 (800-100 ppm, respectively) was greater than 500 cm^{-1}. The average free-carrier concentration p = 2.0 x 10^{19}/cm^3 agreed with the average zinc concentration within 30% which means that no more than about 6 x 10^{18} zinc atoms/cm^3 could have been precipitated. The average free-carrier absorption coefficient for p-type GaAs in the 0.9-1.2μ spectral interval for a carrier concentration range from 5 x 10^{18}/cm^3 to 4 x 10^{19}/cm^3 is only about 200 cm^{-1} (20). Thus we must account for an excess "absorption" amounting to more than 300 cm^{-1}, apparently with a precipitate structure involving no more than 6 x 10^{18} zinc atoms/cm^3 (120 ppm). Gershenzon and Mikulyak (16) have published optical measurements of zinc diffused GaP which indicate an excess absorption of 20 cm^{-1} in a sample containing precipitates and in which $\bar{p}$ = 2 x 10^{18} holes/cm^3. No information was provided on the actual zinc concentration present in these samples, but the conditions of diffusion indicates an average zinc content of at least 5 x 10^{18} atoms/cm^3. Therefore the excess absorption of 20 cm^{-1} appears to be due

to more than 3 x 10^{18} atoms/cm^3 of precipitated zinc. These measurements of zinc diffused GaP suggest that we need considerably more than 6 x 10^{18} zinc atoms/cm^3 (precipitated) to explain an excess IR attenuation of 300 cm^{-1} in GaAs. Nevertheless, we cannot be certain that 6 x 10^{18}/cm^3 or even 1 x 10^{18} atoms/cm^3 of precipitated zinc is not enough to explain the observed effects. A firm description of the sizes, distribution, and composition of the precipitate particles necessary to explain a given degree of particulate attenuation is required to calculate the corresponding zinc concentration. The authors could find no experimental papers in the literature that could provide an unqualified answer to this problem. The pursuit of a solution to this problem can be conducted on theoretical grounds, but this is not within the scope of this paper.

Let us return, now, to discussion of the case for precipitation during the diffusion period with or without help from diffusion-induced dislocations. The results of several investigations (17) of zinc doped GaAs have shown that the solubility of zinc in solid GaAs is greater than 7 x 10^{19} atoms/cm^3 at temperatures in the range of 700°-1100°C. How, then, can we explain the occurrence of precipitates in GaAs diffused with much less than 7 x 10^{19} atoms/cm^3 of zinc at these temperatures. The exsolution of residual impurities or the undetected introduction of other impurities during the diffusion offers a ready explanation. The question of the exsolution of residual impurities is a difficult one to answer experimentally, but the question of the introduction of impurities during diffusion is one that can be answered by experiment. Because the quartz capsules that we used were not of the highest purity, it was possible that undetected impurities had been leached out of the quartz to contaminate our samples during the diffusion period. For example, impurities such as Li, Na, and Ca, which are difficult to detect by the usual emission spectroscopy techniques, are known to be present in the range of 5-10 ppm in ordinary quartz. To check the possibility that impurities were being leached from the quartz, several GaAs wafers were diffused in Spectrasil capsules. Spectrasil is a highly pure grade of quartz, but nevertheless the zinc diffused samples still developed the usual precipitate structures. The fact that the free-carrier concentration was substantially equal to the zinc concentration in many samples with well-developed precipitate structures supports the premise that the precipitates are composed of an element other than zinc. On the other hand the fact that some samples do show much less free carriers than zinc is evidence that zinc eventually does precipitate. It must be remembered, too, that because of problems in attaining a better degree of accuracy in the zinc analysis, *i.e.*, better than 30% accuracy, those samples which showed agreement of zinc analysis and free carrier concentration, still could have had, at the very least, 1.5 x 10^{18} zinc atoms/cm^3 tied up in the precipitate structure.

Although, the occurrence of crystal damage due to precipitation does not depend critically on the identity of the precipitating species, the identification of the species is critical, if we wish to understand the precipitation processes.

Conclusions

None of the recent experimental-theoretical investigations (18, 19) of the diffusion of zinc into GaAs take account of the possibility of diffusion induced damage, especially precipitation. Clearly, the current investigation shows that one must qualify such investigations: (*i*) by establishing the absence of such precipitation; (*ii*) by demonstrating that precipitation is of no consequence to the diffusion processes; or (*iii*) by modifying the transport equations to take account of precipitation. In particular it would be interesting to determine if the isoconcentration diffusion studies of Chang and Pearson (19) were conducted in the presence of diffusion-induced defects since these investigators employed vapor phase in-diffusion of zinc to prepare zinc-doped GaAs wafers for subsequent isoconcentration diffusion with radioactive zinc.

Acknowledgments

The authors wish to express their thanks to R. J. Modena, J. Daly, and J. Hurley for their technical assistance in various phases of the experimental work. They also wish to acknowledge the support and encouragement of Dr. B. Smith and Mr. D. J. Bracco in carrying out this investigation.

Manuscript received March 24, 1966; revised manuscript received Aug. 5, 1966.

Any discussion of this paper will appear in a Discussion Section to be published in the December 1967 JOURNAL.

REFERENCES

1. S. Prussin, *J. Appl. Phys.*, **32**, 1876 (1961); G. H. Schwuttke and H. J. Queisser, *ibid.*, **33**, 1540 (1962); M. L. Joshi and F. Wilhelm, *This Journal*, **112**, 185 (1965).
2. J. Black and P. Lublin, *J. Appl. Phys.* **35**, 2462 (1964); E. D. Jungbluth and J. Black, *Bull. Am. Phys. Soc.*, **10**, 581 (1965).
3. E. D. Jungbluth, *This Journal*, **112**, 580 (1965).
4. G. H. Schwuttke and H. Rupprecht, *J. Appl. Phys.*, **37**, 167 (1966).
5. H. Barth and R. Hoseman, *Z. Naturforsch.*, **13a**, 792 (1958).
6. E. D. Jungbluth, *Appl. Phys. Letters*, **7**, 302 (Dec. 1, 1965); V. Gerold and F. Meier, *Z. Physik*, **155**, 387 (1959).
7. J. R. Patel and B. W. Batterman, *J. Appl. Phys.*, **34**, 2716 (1963).
8. F. W. Young, Jr., "On the Formation of Dislocations Around Precipitate Particles of Cu_2O in Cu," p. 103, "Direct Observation of Imperfections in Crystals," Newkirk and Wernick, Editors, Interscience Publishers, Inc., New York (1962).
9. H. Rupprecht and C. Z. LeMay, *J. Appl. Phys.*, **35**, 1970 (1964); M. H. Pilkuhn and H. Rupprecht, *Trans. AIME*, **230**, 296 (1964).
10. J. Black, *This Journal*, **111**, 924 (1964); J. Marinace, *ibid.*, **110**, 1153 (1963).
11. H. Reiss and C. S. Fuller, "Diffusion Processes in Germanium and Silicon," Chap. 6, "Semiconductors," N. B. Hannay, Editor, Reinhold Publishing Co., New York (1959).
12. J. Black, To be published.
13. A. G. Tweet, *J. Appl. Phys.*, **30**, 1244 (1959).
14. J. N. Hobstetter, "Effect of Imperfections on Germanium and Silicon," Chap. 12, "Semiconductors," N. B. Hannay, Editor, Reinhold Publishing Co., New York (1959).
15. "Mechanical Properties of Intermetallic Compounds," J. H. Westbrook, Editor, John Wiley & Sons, Inc., New York (1960).
16. M. Gershenzon and R. M. Mikulyak, *J. Appl. Phys.*, **35**, 2132 (1964).
17. M. S. Panish, *J. Phys. Chem. Solids*, **27**, 291 (1966); L. L. Chang and G. S. Pearson *ibid.*, **25**, 23 (1964).
18. D. L. Kendall, Doctoral Dissertation Stanford University, Department of Materials Science Report No. 65-29 (1965).
19. L. L. Chang and G. S. Pearson, *J. Appl. Phys.*, **35**, 1960 (1964).
20. D. E. Hill, *ibid.*, **36**, 3405 (1965).

Decorated Dislocations and Sub-Surface Defects Induced in GaAs by the In-Diffusion of Zinc

J. F. Black and E. D. Jungbluth

The Bayside Laboratory, Research Center of

General Telephone & Electronics Laboratories Incorporated, Bayside, New York

ABSTRACT

The diffusion of zinc into GaAs can, under certain conditions, cause defects to appear in the diffused crystal. These diffusion-induced crystal imperfections have been investigated by means of x-ray anomalous transmission topography, optical microscopy, and infrared transmission microscopy. There were three kinds of defects observed: submicroscopic precipitation in the diffused surface layer, decorated dislocations below the diffused surface, and an unidentified defect structure which extended throughout the undiffused region of the wafers. Diffusion-induced decoration of dislocations initially present in samples was observed in crystals previously melt doped with zinc, but not in undoped or in n-doped crystals. The unidentified deep-lying imperfections occurred only in wafers with very intense precipitation in the diffused surface layer.

In a recent publication (1) the authors showed that the diffusion of zinc into GaAs could induce submicroscopic precipitation in the diffused layer. This precipitation was always accompanied by severe crystal damage in the diffused layer and in many cases there was sufficient precipitation to cause strong attenuation of optical transmissions. This paper presents the results of further investigations of zinc-diffused GaAs in which visible precipitate structures and damage to the underlying crystal were observed in addition to submicroscopic precipitation in the diffused surface. The visible precipitates, which were composed of submicroscopic particles condensed onto curvilinear dislocations initially present in the crystals, caused high attenuation of x-ray anomalous transmission and high attenuation of infrared (IR) transmissions. Zinc-diffusion-induced damage to the underlying crystal caused high attenuation of x-rays, but had little effect on transmission of optical radiations.

Experimental Techniques

Sample preparation.—The starting material was single crystal GaAs grown in quartz boats by the gradient freeze technique. Dislocation densities, by etch pit count, ranged from 50/cm^2 to 50,000/cm^2. Wafers cut from the crystals were ground flat and parallel and were then chemically polished in a Br_2-methanol solution to remove the crystal damage resulting from cutting and grinding operations. The final thickness of the wafers ranged from 0.5 to 1.5 mm. Unless otherwise indicated, the diffusions were carried out according to the following conditions: 10 mg of pure zinc 1g of GaAs powder in evacuated quartz capsules of 50 cm^3 volume (ordinary grade quartz); the diffusion time was 2 hr at a fixed temperature ranging from 800° to 1000°C. These diffusions are referred to as standard diffusions. Each diffusion included several samples of differing n-doping level in addition to the samples used for study of diffusion-induced defects. The purpose of the n-doped samples was to allow an estimate of the zinc penetration profile for each diffusion run, by measurements of p-n junction depth *vs.* n-doping level. At no time during the diffusion cycle was the temperature of the end of the capsule initially containing the diffusant source allowed to rise above that of the region containing the GaAs powder and the samples. The samples, which were laid flat in the boat with the Ga face up, were separated from the powder by a quartz partition. All diffusions were terminated by gradually withdrawing the ampoule from the furnace over a period of 2 min and then immersing it in water. It is estimated that by this procedure the contents of the capsule were cooled to room temperature within 3 min.

Examination of samples.—X-ray diffraction topographs were recorded by the anomalous transmission method (2) using Cu radiation. Highly imperfect regions of crystals strongly attenuate the x-ray transmission, especially in the immediate vicinity of the imperfections. Such regions show up as dark areas in the topographs of Fig. 2, 4, and 6. The GaAs wafers studied by the x-ray anomalous transmission technique were oriented in <111> directions. The diffused layers on the As face were always removed by chemical etching prior to examination by x-rays, and the wafers were positioned so that the Ga face corresponded to the exit surface of the x-ray beam. Because defects in shallow surface layers, such as occur in diffused samples, appear sharpest where the x-ray beam leaves the crystal (3), this procedure allowed etch structures produced on the Ga face to be correlated with defects shown in x-ray topographs.

Etch structures were developed on the Ga (111) surface by swabbing the surface with a freshly prepared mixture of one part 30% H_2O_2 and five parts 2% NaOH solution for several minutes. This etchant was selective to surface orientations within 10° of a (111) Ga surface and developed small pits with a well-defined triangular shape. Etch pit counts on a <111> Ga oriented wafer were in agreement with counts of etch pits developed by 1 part concentrated HNO_3 — 2 parts H_2O, a well-known dislocation etchant for GaAs. All etching with the NaOH-H_2O_2 defect etch was carried out on surfaces within 2° of a (111) Ga surface.

Infrared transmission microscopy was accomplished by means of a commercially available image convertor adapted to the ocular of an inverted stage microscope. Infrared photomicrographs were recorded on Eastman Kodak Type I-M 4x5 in. Spectrographic Plates.

Experimental Results and Discussion

Unless the diffusion of zinc into GaAs is properly controlled, intense submicroscopic precipitation will occur in the diffused layer. This precipitation will cause the appearance of an etch structure like that shown in Fig. 1b. In addition, such precipitation causes strong attenuation of x-ray anomalous transmission wavelengths and strong absorption (in excess of that corresponding to the free carrier absorption) of near-infrared radiation. A detailed description and discussion of these structures can be found elsewhere (1).

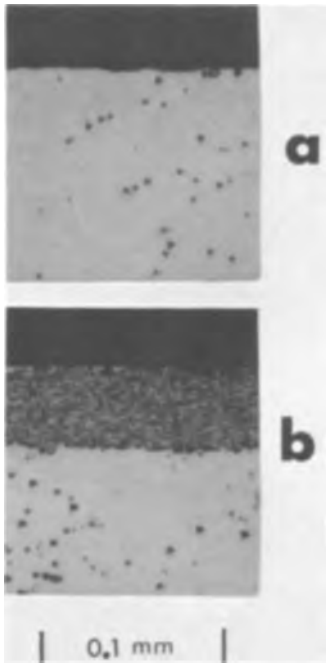

Fig. 1. Etch structure of GaAs sample: (a) initial etch structure, (b) after sample was subjected to a standard diffusion (see text) at 800°C. The plane of section is a (111) Ga plane normal to the surface of the sample. The layer of high etch pit density is a region containing submicroscopic precipitation.

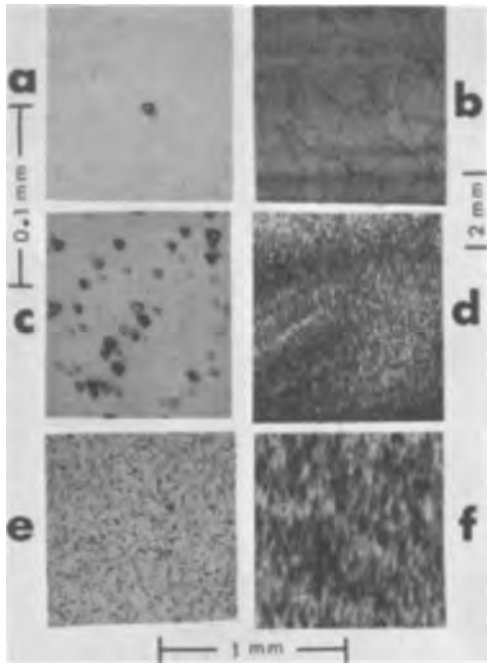

Fig. 2. Etch structures (on the left) and x-ray topographs (on the right) of a GaAs sample. Note the difference in scale between (a), (c) and (b), (d). (a) Initial etch structure, (b) initial x-ray structure, (c), (e) and (d), (f) etch structure and x-ray structure, respectively, of the crystal after it was subjected to a standard diffusion and after removing the damaged precipitate containing layer.

It is important to note here, however, that in samples in which submicroscopic precipitation had occurred it was found that the concentration of zinc along the sub-surface boundary of the precipitate containing layer was usually close to 1×10^{19} atom/cm^3. In crystals diffused under standard conditions at temperatures of 800°C or lower in which such precipitation had occurred, the careful removal of the damaged precipitate-containing layer was found to yield the underlying crystal essentially in its original state of crystal perfection (1). In standard diffusions performed at temperatures of 900°C or higher the crystal damage was not confined to the diffused layer but extended throughout the bulk of the wafer. The character of this subsurface damage was, however, different from the damage induced in the diffused surface layer.

An example of damage below the diffused layer is seen in the photographs of Fig. 2. A 1-mm thick wafer whose initial etch pattern is shown in Fig. 2a, and whose x-ray topograph is shown in Fig. 2b was diffused with zinc to a measured depth of 120μ. The initial etch pit count was 150/cm^2. After diffusion, 320μ were removed from each face, and the etch structure and x-ray topograph of the zinc-free substrate was recorded, Fig. 2c and 2d. The etch pit count after diffusion was $\sim$ 250,000/cm^2. Figure 2e and 2f compare the x-ray topograph and the etch structure of the zinc-free substrate on the same scale. As expected from the high etch pit count, the sample is nearly opaque to x-rays. A crystal which is opaque to x-rays is defined as a crystal whose anomalous transmission properties are so much reduced due to regions of imperfect lattice structure that no diffracted image can be obtained. Examination of the sample under IR transmission (0.9 to 1.2μ wavelength) showed little change in the IR transmissivity and no IR absorption structure like that suggested by the x-ray topograph. It is clear that diffusion has caused an increase of more than three orders of magnitude in the defect concentration of the crystal lattice below the diffused layer.

Because these defects occurred in a region that was essentially free of zinc ($<$ 5 ppm), and because the defects did not show up under IR microscopy, they cannot be submicroscopic precipitates of the type found in the diffused layer. This raises the question of the nature and the origin of these subsurface defects. One possibility is that we are observing precipitation, but in such an early stage of development that it is detectable by x-ray topography but not by IR transmission microscopy. The concentration of these subsurface defects was, however, too high to determine whether they were dislocations or precipitates by observation of the reflection dependence of individual defects in the x-ray topograph of Fig. 2d. If we suppose that these defects are due to precipitation, then we must explain how the presence of high concentrations of zinc and/or the presence of precipitates in the surface layer can cause precipitation deep in the interior of the crystal. For example, to what impurity can we attribute such precipitation? Spectroscopic analysis before and after diffusion showed no increase in residual impurities nor any (spectroscopically detectable) additional impurities. Though the nature of these deep-lying defects was not clearly established, the occurrence of dislocations in crystal material underlying a severely damaged surface layer is not inconsistent with the formation of such a layer. The existence of precipitation in the zinc-diffused layer is concomittant with the presence of high internal stresses in this layer. The more intense the precipitation the stronger the surface layer becomes and the higher the surface stresses become. Eventually these surface layer stresses exceed the yield strength of the interior GaAs crystal and dislocations are introduced. This would explain why interior defects were not produced by all diffusion runs; they only occur when the precipitation is sufficiently intense to cause stresses in the interior crystal lattice exceeding the yield strength. In this respect it is significant that in most of the crystals with interior crystal damage the precipitation in the surface layer was great enough to render this layer completely opaque to IR transmissions.

Further evidence that considerable stresses can be produced by the diffusion of zinc into GaAs is shown in Fig. 3. These are photomicrographs of diffused GaAs crystals that were cleaved normal to the diffused layer

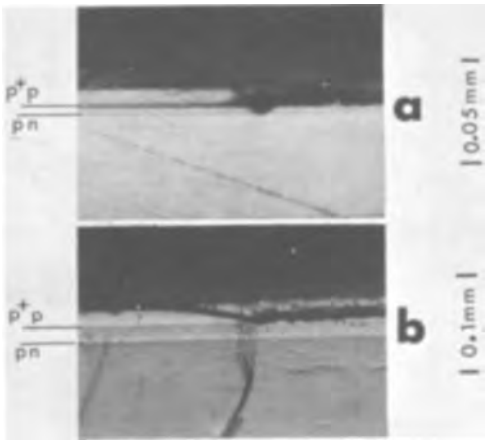

Fig. 3. Etched cross-sections of diffused and cleaved GaAs. (a) 800°C pure zinc source for 10 min, n(Te) = 3.1 x 10^{17}/cm^3, sample has been mounted and polished after cleaving, (b) $ZnAs_2$ source 800°C for 1 hr, n(Te) = 1.1 x 10^{18}/cm^3, curved lines are cleavage steps.

in the process of fabricating injection electroluminescence devices. The material, which was <111> oriented, showed a tendency to fracture parallel to the plane of diffusion along the p$^+$-p boundary, indicating the presence of residual stress at this boundary. Such behavior would be expected of diffused zinc-blende-type crystals in which stresses were built up by the diffusion process. Diffusion-induced stresses become locked-in along the diffusion boundary when the sample is cooled from the diffusion temperature. This occurs because the yield strength of zinc-blende-type semiconductor crystals increases rapidly as the temperature is lowered and eventually exceeds the diffusion stresses. The diffusion stresses can then no longer be relieved by slip in the crystal and become locked-in. X-ray extinction contrast topographs of profile sections of zinc-diffused samples, published recently by Schwuttke and Rupprecht (4), also show regions of high residual stress immediately beneath a heavily damaged surface layer.

To determine whether precipitation could be made to occur in samples already doped with more than 5 x 10^{18}/cm^3 zinc, some melt-doped samples were subjected to annealing treatments. The samples were annealed in the presence of their own powder to prevent both out-diffusion of zinc and the decomposition of the sample. Figure 4 shows an x-ray topograph of a zinc-doped wafer before the annealing treatment. The dislocation density is about 5000/cm^2 by etch pit

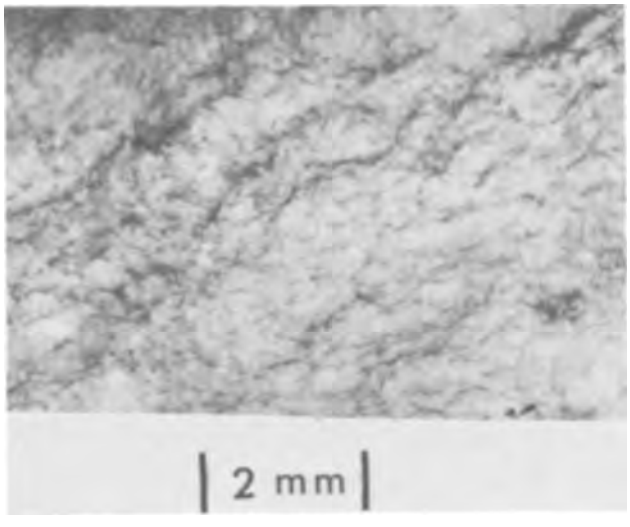

Fig. 4. X-ray topograph of zinc-(melt)-doped GaAs before diffusion.

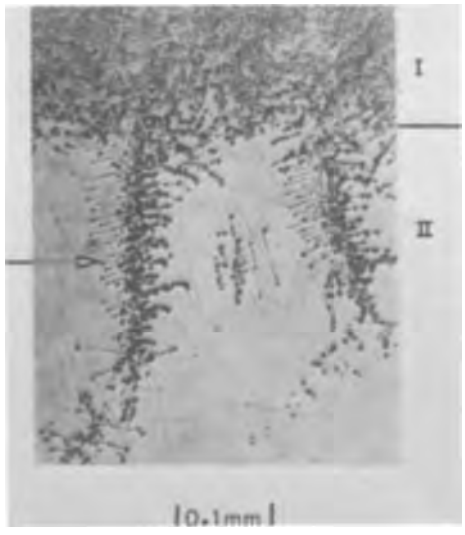

Fig. 5. Etched cross-section of zinc-(melt)-doped GaAs after standard zinc diffusion at 1000°C. I, region of general microprecipitation, opaque to x-rays; II, region of decorated dislocations (arrows).

count and consists of individually resolved and tangled curvilinear dislocations. Although the zinc content of the melt doped samples was 3.7 x 10^{19} atoms/cm^3 (which was considerably more than the zinc concentration at which precipitation occurred in standard diffused samples), annealing of the samples for 2 hr at 1000°C had no effect on the crystal perfection. Contrary to expectations, there was no reduction in x-ray anomalous transmission nor in IR transmissivity; neither was there any change in the x-ray topograph (dislocation contrast), etch structure, or IR transmission structure. However, when a melt-doped sample was zinc diffused at 1000°C for 2 hr, it became opaque to x-rays and a precipitate structure was developed. This structure is shown in cross section in the photomicrograph of Fig. 5. In addition to the layer of submicroscopic precipitation and high etch pit density (region I), usually generated in GaAs by such a diffusion treatment, there was a region (II) about 200μ thick just ahead of this layer in which other more distinctive types of etch structures were seen. These etch structures were best correlated with x-ray anomalous transmission topographs and with infrared transmission microscopy in a sample sectioned parallel to the diffused layers. Thus the structures seen in Fig. 6a, 6b, and 6c were recorded after the diffused layers had been removed from both the A and B faces of a sample and after the sample had been further lapped and polished down to 100μ thickness in the region designated II in Fig. 5. To obtain good infrared transmission photomicrographs it was necessary to make the sample thin in order to minimize the optical absorption due to the high background zinc level. Notice that the dislocation structure in Fig. 6a is no longer visible as fine lines (compare with Fig. 4), but in place of the individual curvilinear dislocations and tangles, broad diffraction contrast images now appear. The very strong infrared absorption of these structures indicates that they too are precipitates of some kind. Examination of carefully polished samples as well as lightly etched samples at magnifications of 1000X failed to show any trace of sharp boundaries around these structures such as would have been present if a precipitate phase of microscopic dimensions had formed. This is the result expected if these structures have been formed by the decoration of dislocations, since this process leads to condensation of particles of submicroscopic size onto the dislocation line.

In Fig. 7 an area of the sample is shown at higher magnification to resolve details of the precipitates by

Fig. 6. Defects in region II, (see Fig. 5) sample preparation described in text. (a) X-ray topograph, (b) IR transmission photomicrograph, (c) etch structure of the area shown in (b).

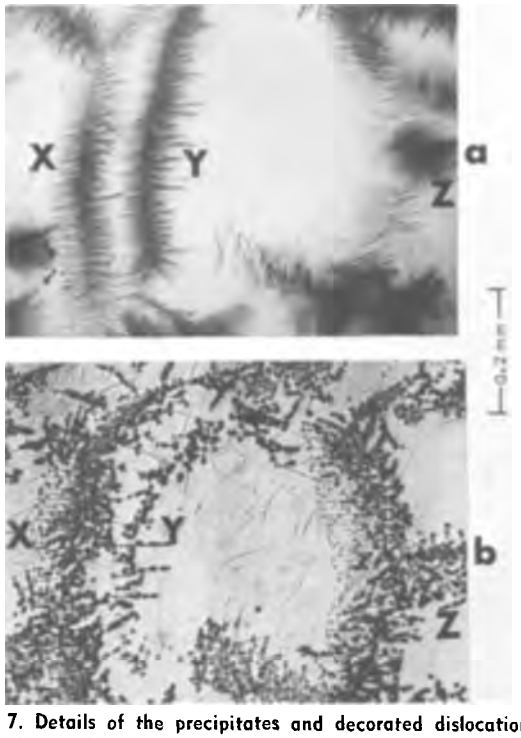

Fig. 7. Details of the precipitates and decorated dislocations in region II. (a) IR transmission structure, (b) etch structure of the area shown in (a).

infrared transmission and visible reflection microscopy. Figure 7a is the infrared transmission photomicrograph of the sample before etching, and Fig. 7b is the photomicrograph of the etch structure of the same region. The curved centipede-like configurations are the broad images seen at low magnification in Fig. 6a and are very similar to decorated dislocations that are revealed in silicon by the Dash method of Cu precipitation (5). The dislocation marked Y in the infrared photo is only partially visible in the etched sample because it is not as close to the plane of section, as for example, the dislocation at X. Infrared absorption not associated with decorated dislocation lines but associated with clusters of etch pits (microprecipitation) can be seen at locations such as Z in the figure. A very close correspondence exists between the infrared transmission structure and the etched structure.

There are several features of the defect structures in Fig. 6 and 7 that merit further discussion. The direction of the dislocations is more or less random, but the direction of the decorating spikes is quite regular and in fact lies almost normal to the direction of the dislocation. Most of the spikes lie along two of three directions the projections of which are 120° apart on the (111) plane, which is the plane of polish as well as the plane of diffusion. On a given dislocation practically all of the decorating spikes lie along the same direction. Also, in curvilinear dislocations long enough to show changes in direction greater than 10° or 15°, such as X and Y in Fig. 7a, the decoration becomes less intense as the direction of the dislocation line approaches the direction of the spikes. This is in agreement with observations of dislocations in GaP decorated by indiffusion of zinc (6). Very similar effects are observed in Cu decorated silicon (5, 7) where it has also been established that precipitate needles are oriented in <110> directions perpendicular to the Burgers vector of the particular dislocation or dislocation segment they decorate. This could also be the case in the present instance, though more detailed data are necessary to make definite conclusions. Abrahams and Buiocchi (8) have recently described etch structures in GaAs essentially the same as those associated with the precipitate spikes in Fig. 7. They identified their etch structures as decorated dislocations from etching behavior alone. Our observations, while confirming the conclusions of Abrahams and Buiocchi, provide more convincing evidence that these etch structures are due to decorated dislocations.

The appearance of a decorated dislocation structure, such as shown in Fig. 6 and 7, was unique to the diffused zinc-melt-doped GaAs samples. Despite diligent examination of many other zinc diffused samples, which were initially undoped or n-doped not a trace of similar structures was found. A comparison of spectroscopic analysis of the zinc-doped material before and after diffusion showed no new (spectroscopically detectable) impurities after the diffusion and no increase in the impurities initially present. There were only three impurities detected; Cu (4 ppm), Mg (5 ppm), and Si (30 ppm).

To determine if the regions containing precipitates were of significantly different composition than the surrounding crystal, electron probe microanalysis was conducted in region I and along the backbone of the centipede-like structures in region II. Since precipitation was observed only after the indiffusion of zinc, it was expected that more zinc would be found in the precipitates than elsewhere in the diffused crystal. However, zinc content in regions of precipitation was found to be no higher than in the surrounding precipitate-free material (where Zn = 4.0×10^{19} atoms/cm^3). Only near the surface of the diffused layer (about 50μ below the surface in region I) did the zinc concentration rise above that of the initial zinc doping level. This, in fact, was the only evidence that zinc had actually been diffused into the crystal.

Residual impurities were the next most likely precipitants. The Cu content was also determined to be no higher at the precipitates than in the surrounding regions. The limit of detection for Cu in GaAs was estimated to be the same as that for Zn in GaAs which is about 100 ppm. Electron probe microanalysis for Si and Mg, the other (known) residual impurities,

failed to show concentration of these elements at precipitates either. The Si and Mg analysis are not too meaningful though, since the limits of detection for these elements in GaAs were quite high (> 1000 ppm).

It has recently been shown (9) that submicroscopic precipitation in zinc-diffused GaAs is definitely zinc rich. Moreover, it has been established (1) that the critical concentration of diffused zinc necessary for the appearance of these precipitates is about 5 x 10^{18} atoms/cm^3. Thus the failure to observe a zinc concentration in excess of the background (initial) zinc concentration in the precipitates of regions I and II can be explained as follows. Since we need only 5 x 10^{18} zinc atoms/cm^3 (diffused) to form precipitates, the total zinc concentration at precipitates in the diffused melt-doped crystal need only be 4.5 x 10^{19} atoms/cm^3, not much different from the background zinc doping (4.0 x 10^{19} atoms/cm^3) in the crystal. Such a difference could not have been clearly distinguished by the electron probe since this was just about the limit of the analytical precision for zinc in this concentration range. If there had been much more than 5 x 10^{18} atoms/cm^3 excess zinc, say at least 1 x 10^{19} atoms/cm^3, it would have shown up in the probe analysis. It appears that only indiffused zinc is capable of decorating these dislocations initially present in the zinc-doped GaAs.

Acknowledgments

The authors wish to express their thanks to R. J. Modena, J. Daly, and J. Hurley for assistance in various phases of the experimental work. They also wish to acknowledge the support and encouragement of Dr. B. Smith and Mr. D. J. Bracco in carrying out this investigation.

Manuscript received Aug. 23, 1966.

Any discussion of this paper will appear in a Discussion Section to be published in the December 1967 JOURNAL.

REFERENCES

1. J. F. Black and E. D. Jungbluth, *This Journal*, **114**, 181 (1967).
2. H. Barth and R. Hoseman, *Z. Naturforsh.*, **13a**, 792 (1958).
3. E. D. Jungbluth, *App. Phys. Letters*, **7**, 302 (1965); V. Gerold and F. Meier, *Z. Physik*, **155**, 387 (1959).
4. G. H. Schwuttke and H. Rupprecht, *J. Appl. Phys.*, **37**, 167 (1966).
5. W. C. Dash, *ibid.*, **27**, 1193 (1956).
6. M. Gershenzon and R. M. Mikulyak, *ibid.*, **35**, 2132 (1964).
7. L. Fiermans and J. Vennik, *Phys. Stat. Sol.*, **12**, 277 (1965).
8. M. S. Abrahams and C. J. Buiocchi, *J. Appl. Phys.*, **37**, 1973 (1966).
9. J. Black, *This Journal*, **113**, 163C (1966).

Preparation and Properties of Epitaxial Gallium Phosphide

G. S. Kamath and D. Bowman

Xerox Corporation, Webster, New York

ABSTRACT

Gallium phosphide has been grown epitaxially by open tube vapor transport using Ga and PCl_3 as starting materials. The over-all reaction for the process can be represented by $5Ga + 2PCl_3 \rightarrow 2GaP + 3GaCl_2$. The undoped GaP obtained is p-type with carrier concentration ~10^{14} cm^{-3} and mobilities up to 150 cm^2 v^{-1} sec^{-1} at 300°K. The transport properties as well as the mass spectroscopic analysis are presented and demonstrate the high purity of the GaP. The addition of water vapor to the hydrogen carrier gas progressively raises the resistivity of the p-type epitaxial layer. Semi-insulating GaP has been produced by this method with resistivities over 10^{10} ohm cm.

Gallium phosphide has been grown by many variations of the vapor transport process starting from the presynthesized polycrystalline form (1) as well as from the elements, Ga and P, themselves (2). In the present investigation Ga and PCl_3 were used as starting materials.

The two major objectives were to ascertain the over-all mechanism of the process and to study the influence of water vapor in the carrier gas on the nature of the epitaxial deposit.

Experimental Procedure

The apparatus used is shown schematically in Fig. 1 and is similar to the one reported by Oldham (3). Some innovations of special significance are the use of an Engelhard palladium diffusion purifier for the hydrogen carrier gas and the fully glass-enclosed solenoid-operated valves which eliminate all greased joints and valves for controlling gas flow. Low flow rates of hydrogen (30-80 cm^3 min^{-1}) plus the use of a bubbler in the gallium boat ensure thorough mixing of PCl_3 and Ga at the source temperature. The temperature profile was optimized to grow pure gallium phosphide. The source and substrate temperatures were comparatively low and gave GaP with minimum contamination from the GaAs substrate and the quartz reaction tube. The graded junction normally formed between GaAs and GaP was held to a minimum even though this resulted in some strain in the epitaxial layer. The minimum temperature for epitaxy at a practical growth rate (~10 μ/hr) was found to be about 780°C. The flow rates used were about 35 cm^3/min. H_2 through PCl_3 kept at 0°C. The ice point was chosen because the vapor pressure of PCl_3 is a rapidly varying function of the temperature and accurate control of this parameter is essential to maintain steady growth conditions at the substrate. The (111) A face of n-type GaAs was used for deposition as it proved to be the best suited for rapid growth of a

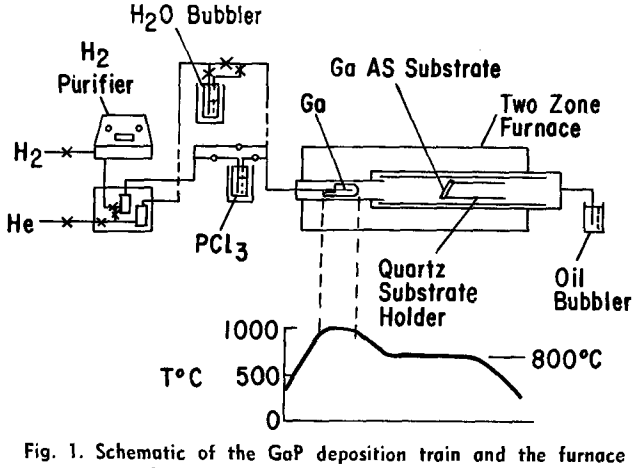

Fig. 1. Schematic of the GaP deposition train and the furnace temperature profile.

homogeneous epitaxial layer. The deposition rates were about 40 μ/hr and layers grown varied from 200μ to a few millimeters in thickness.

After deposition, the GaAs was removed with aqua regia and the side of the epitaxial layer adjacent to the GaAs lapped to remove any graded junction. This procedure yielded single crystals of GaP with arsenic contamination of only a few hundred ppm. Previous studies report an arsenic impurity in the per cent range (4, 9). Another important observation singular to the present work is that p-type GaP was invariably obtained in the normal undoped runs. Comparable experiments in the literature report low resistivity n-type deposits (3, 4), presumably due to sulfur or other impurities.

X-ray Laue patterns as well as etching and polishing studies confirm the epitaxy of the GaP, and optical absorption measurements from 0.4-10μ indicate the material to be pure with no detectable GaAs contamination. The purity of the samples is further confirmed by mass spectroscopic analysis, the results of which are given in Table III.

A slight modification of the apparatus was made to study the effect of water vapor on the deposit. Figure 1 shows the side arm with the water bubbler at a controlled temperature. It permits the addition of known amounts of water vapor into the carrier gas.

Electrical resistivity and the Hall coefficients were measured on several representative samples as a function of temperature. The contacts used were mainly pressure type to gallium dots ultrasonically applied to the clean GaP surface. When properly prepared, these contacts were found quite satisfactory for p-type material, i.e., ohmic and low resistance.

Results and Discussion

The over-all reaction.—The three possible reactions that should be considered are the following.

$$2Ga + PCl_3 \rightarrow GaP + GaCl_3 \quad [1]$$

$$5Ga + 2PCl_3 \rightarrow 2GaP + 3GaCl_2 \quad [2]$$

$$4Ga + PCl_3 \rightarrow GaP + 3GaCl \quad [3]$$

It must be emphasized that only the over-all reaction is being considered in its simplest form. The data now available does not warrant a discussion of the many complex intermediate steps.

Even the actual reaction probably involves more than one of these, but it was hoped one would be dominant. It has been assumed in the literature (5) that [1] is the most probable from analogy with the comparable GaAs reaction and because $GaCl_3$ is the most stable chloride. Preliminary results from the present investigation were inconsistent with this postulate, and this led to a systematic study of the over-all reaction mechanism. The pertinent data given in Table I covers over 50 deposition runs.

Column 3 shows the agreement between calculated and observed values for the amount of PCl_3 used to transport 50g of gallium. This quantity can be measured accurately by difference in volume before and after the run. On the contrary, the amount of gallium phosphide formed (column 4) is difficult to determine since it is in large part deposited on the quartz tube and cannot be removed completely. Both values are

Table I. Characteristics of the three principal reactions

Reaction No.	Efficiency,* %	PCl_3 used: cm^3/50g calc.	PCl_3 used: Ga obs.	GaP formed: g/50g calc.	GaP formed: Ga obs.	End prod. Ga (cl)x
1	50	31		36		$GaCl_3$
2	40	24.6	23-25	28	20-28	$GaCl_2$
3	25	15.4		17		GaCl

* Efficiency: Ga converted to GaP/Ga used up. All calculations made assuming 50g Ga source being used up in the reaction.

Table II. Influence of water vapor on the resistivity of the epitaxial GaP layer

No. of runs	p_{H_2O}, mm Hg	ρ, ohm cm	p_{O_2} calc., mm Hg
15	0	10^2-10^5	
5	0.1	10^2-10^5	10^{-14}
5	0.1-0.5	10^3-10^8	10^{-13}
10	1	10^8	10^{-13}
4	10	10^{10}	10^{-12}

seen to be in good agreement with those predicted by reaction [2]. Further, the grayish halide deposited at the cool exit side of the reaction tube can be shown to be $GaCl_2$, with properties (such as the melting point) described by Laubengayer and Schirmer (6). The dichloride invariably shows some dissociation into Ga + $GaCl_3$. These results suggest that [2] is the dominant over-all reaction under the conditions of transport.

Water vapor experiments.—The addition of small amounts of water vapor to the carrier gas affects the properties of the epitaxial layer drastically as can be seen from Table II.

The resistivity of the layer rises with increasing partial pressure of water vapor in the carrier gas. The role of oxygen in raising the resistivity of III-V compounds in general is well known (7). As the effect here is quite similar, it was assumed that the water vapor acts as a source of oxygen in the reaction zone. This led to the rough estimate of the oxygen present in the gas as follows. The concentration of water vapor in the carrier gas was determined from the flow rate of hydrogen through the water bubbler. Using the dissociation constant of water (18), the equivalent partial pressure of oxygen was calculated for the highest temperature in the reaction zone. This was used for making a qualitative comparative estimate of the amount of oxygen in the reaction zone. The complicated nature of the various reactions in the total process precludes any refined quantitative approach. The point of interest is that the use of water vapor allows the addition of oxygen to the hydrogen in concentrations less than 1 ppm. The values obtained appear in column 4, Table II.

Over thirty runs were made with controlled addition of water vapor into the hydrogen carrier gas. The results show that, with increasing water vapor concentration, the epitaxial layer stays p-type until extensive gallium oxide formation takes place. There is a systematic and reproducible variation in the resistivity of the GaP epitaxial layer as a function of the partial pressure of water vapor (p_{H2O}). In electrical characteristics, the acceptor level changes from 0.4 to 0.9 ev with increased p_{H2O}. The result is in agreement with the observations of D'Yakanov and coworkers (9).

The exact role of oxygen is not clear, and several possibilities suggest themselves. Oxygen may interact with the 0.4 ev level p-type impurity in two ways. (*i*) It may react with the impurity in the gas phase and prevent it from reaching the GaAs substrate or, (*ii*) it may be incorporated in the epitaxial layer and interact with the 0.4 ev level.

Mass spectroscopic analysis results show that if (*i*) is the mechanism, the variation in resistivity is not due to interaction of oxygen with Si as has been suggested for GaAs (10), since Table III shows that similar amounts of Si are present in both high and low resistivity samples. It can also be seen from the data that there is no systematic variation of any detectable impurity with the resistivity of the layer. The possibility remains that the impurity concerned may be one below detection limits.

The alternative (*ii*) is more complicated. As a donor, oxygen could act as a compensating n-type impurity. Gershenzon and co-workers (8) indicate a 0.47 ev donor level for oxygen. Such a level should give rise to n-type conductivity when the oxygen concen-

Table III. Results of mass spectroscopic analysis and electrical measurements on the epitaxial GaP

Sample No.	Si*	As*	B*	Al*	ρ, ohm cm	μ, cm v^{-1} sec^{-1}	n, cm^{-3}
A32	1.6	?	0.9	0.9	1.1×10^{3}	60	1×10^{14}
A38	8.2	400	0.07	1.5	4×10^{3}	140	1.2×10^{13}
A49		80	0.3	2.0	3×10^{3}	80	3×10^{13}
B9	6.0	2400	0.08	18.5	3×10^{3}	62	4×10^{13}
B10	0.3	2000		0.02	1×10^{3}	90	6×10^{13}
B11	6	2000	0.06	17	3×10^{10}	40	5×10^{6}
B60		80	0.2	6.0	5×10^{10}	40	3×10^{6}

* All values for impurity concentrations are in parts per million. Detection limits for most impurities 0.01-0.1 ppm.

tration is progressively increased. No such change has been observed which might indicate that the oxygen level, if present, is much deeper. If the oxygen level were deeper than the 0.9 ev acceptor level, it could compensate the 0.4 ev acceptor level, but never achieve high enough electron concentration to yield n-type samples. Alternatively the solubility of the oxygen may be governed by the concentration of the acceptor impurity at the 0.4 ev level. Identification of, and controlled doping experiments with, the acceptor and oxygen are necessary to determine which of these alternatives is the controlling factor in producing high resistivity GaP layers. Until such studies are available, the above models will have to be tentative suggestions only.

Several samples were analyzed by mass spectroscopic methods, and the results appear in Table III. The classic impurities in III-V compounds like groups II and VI and copper are below detection limits. The absence of several of these with shallow levels in the forbidden band, especially the group VI, is further confirmed by the transport properties given in the next section. The group III and V impurities present should be electrically neutral. The main impurity detected, silicon, does not seem to play the role generally allocated to it. Previous results (11, 12) report it to be a net shallow donor. At least at concentrations below $10^{17}/cm^3$ this is in disagreement with the present data. In this region silicon would have to be either self compensating or a net acceptor. Recent results on electroluminescence (13) in gallium phosphide infer the possibility of Si having a p-type level in GaP. Only a much more detailed study can lead to an unequivocal solution to this problem.

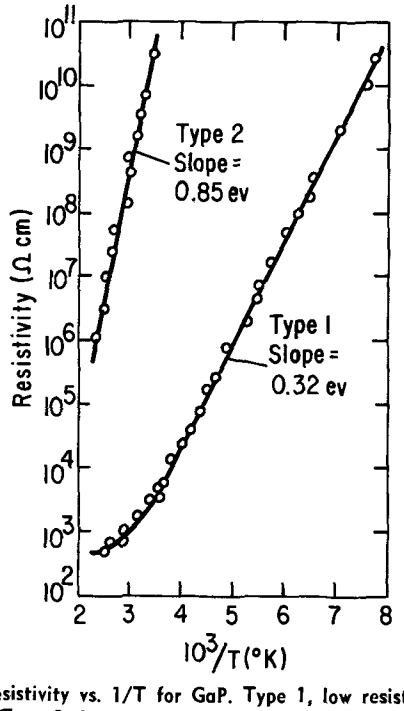

Fig. 2. Resistivity vs. 1/T for GaP. Type 1, low resistivity p-type (undoped); Type 2, high resistivity p-type (doped).

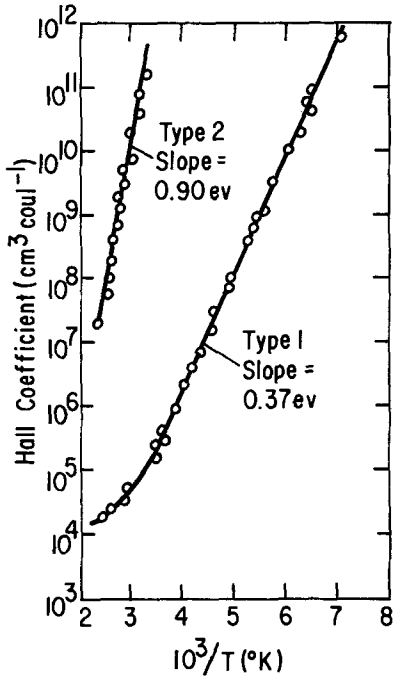

Fig. 3. Hall coefficient vs. 1/T for GaP, type 1* and type 2* (* see Fig. 2).

Transport properties.—Figure 2 shows the resistivity as a function of temperature for two types of samples; type 1, undoped low-resistivity p-type; and type 2, high-resistivity material grown at $P_{H_2O} > 0.1$ mm Hg (vide Table II). Type 1 ranged up to 10^6 ohm cm (300°K) in resistivity whereas type 2 exceeded 10^7 ohm (300°K).

Figure 3 gives the Hall coefficient as a function of temperature for the same samples. Since the Hall coefficient has a linear variation over six orders of magnitude a one-carrier system is assumed and the Hall mobility is then given by $R_H\sigma$.

Figure 4 represents the Hall mobility as a function of temperature for the two sets of samples. All type 1 samples show a similar variation in resistivity and Hall coefficient over a wide range of temperature. Type 2 samples could only be studied over a small

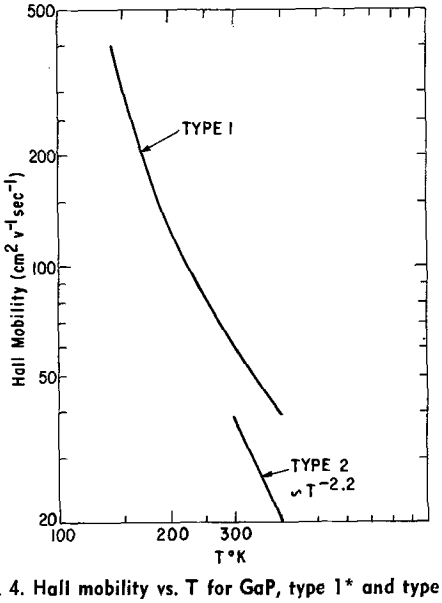

Fig. 4. Hall mobility vs. T for GaP, type 1* and type 2*

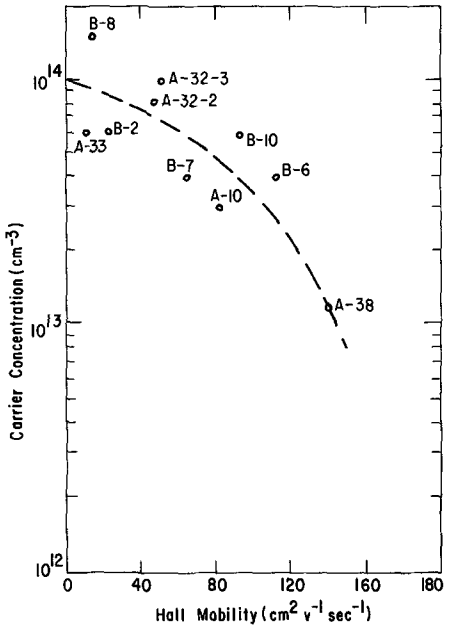

Fig. 5. Carrier concentration vs. Hall mobility at 300°K

range of temperature due to their high resistivity. The $T^{-2.2}$ dependence observed, consequently, has limited significance.

It is instructive to compare the results on type 1 samples with those in the literature. Alfrey and Wiggens (14) reported some results on p-type material with a carrier concentration $\sim 10^{17}$ cm^3 and mobility $\mu \sim 70$ $cm^2\ v^{-1}\ sec^{-1}$. They found that μ varied as $T^{-3/2}$ above 100°K and attributed this to acoustic mode scattering. Below 100°K their data indicated a dominance of impurity scattering. Their acceptor impurity was a shallow one at 0.04 ev and was not identified. Essentially similar results were reported by Nasledov and Slobodchikov (15) and Allen and Cherry (16) for p-type material. Using a largely empirical and semi-qualitative approach Allen and Cherry also postulated a limiting mobility of ~ 250 $cm^2\ v^{-1}\ sec^{-1}$ and an effective mass ratio for holes ~ 0.5.

The present data for type 1 samples gives an exponential μ *vs.* T dependence below room temperature. Such a behavior indicates screened polar scattering following Ehrenreich's (17) calculations for III-V compounds, although the magnitude of the mobilities can be explained fully only by assuming some other form of scattering also to be present.

Figure 5 shows the carrier concentration as a function of Hall mobility at 300°K for a number of type 1 samples. Although the scatter is quite large, and only one high mobility, low carrier concentration point is shown, it is felt that the dashed line shows a general trend indicating a limiting Hall mobility of the order of 180 $cm^2\ v^{-1}\ sec^{-1}$. Therefore, using arguments similar to those advanced by Allen and Cherry, a hole effective mass ratio somewhat less than their value of 0.5 is likely. This lower value would be in agreement with a greater predominance of optical polar scattering which has been observed.

In summary, the present study has helped establish the over-all reaction for the open tube transport process for the synthesis of GaP from Ga and PCl_3. It also provides a method for growing epitaxial layers of GaP with controllable resistivities in the range 10^2-10^{11} ohm cm by incorporating known levels of water vapor into the carrier gas. Results on the electrical and transport properties of single crystal epitaxial GaP obtained are reported.

Manuscript received April 5, 1966; revised manuscript received Aug. 17, 1966.

Any discussion of this paper will appear in a Discussion Section to be published in the December 1967 JOURNAL.

REFERENCES

1. C. J. Frosch and P. W. Foy, *This Journal*, **108**, 177C (1961).
2. W. F. Finch and E. W. Mehal, *ibid.*, **111**, 814 (1964).
3. W. G. Oldham, *J. Appl. Phys.*, **36**, 2887 (1965).
4. 3 above and H. Flicker, B. Goldstein, and P. A. Hoss, *ibid.*, **35**, 2959 (1964).
5. D. Effer and G. R. Antell, *This Journal*, **107**, 252 (1960).
6. A. W. Laubengayer and F. B. Schirmer, *J. Am. Chem. Soc.*, **62**, 1578 (1940).
7. Otfried Madelung, "Physics of III-V Compounds," p. 263ff, John Wiley & Sons Inc., New York (1964).
8. M. Gershenzon, F. A. Trumbore, R. M. Mikulyak, and M. Kowalchik, *J. Appl. Phys.* **36**, 1528 (1965).
9. L. I. D'yakonov, V. N. Maslov, and B. A. Sakharov, *Soviet Phys.—Doklady*, **10**, 650 (1966).
10. J. F. Woods and N. G. Ainslie, *J. Appl. Phys.*, **34**, 1469 (1963).
11. M. Rubenstein, *This Journal*, **112**, 1010 (1965).
12. F. A. Trumbore, H. G. White, M. Kowalchik, C. L. Luke, and D. L. Nash, *ibid.*, **112**, 1208 (1965).
13. M. R. Lorenz and M. Pilkuhn, *Bull. Am. Phys. Soc. Meeting*, New York, Jan. 1966, Abstract C.D. 12.
14. G. F. Alfrey and C. S. Wiggins, *Z. Naturforsch*, **15. a**, 267 (1960).
15. D. N. Nasledov and S. V. Slobodchikov, *Soviet Phys.—Solid State*, **4**, 2021 (1963).
16. J. W. Allen and R. J. Cherry, *J. Phys. Chem. Solids*, **23**, 163 (1962).
17. H. Ehrenreich, *ibid.*, **8**, 130 (1959).
18. F. D. Richardson and J. H. E. Jeffes, *J. Iron Steel Inst.*, **160**, 261 (1948).

Tracer Evaluation of Hydrogen in Steam-Grown SiO_2 Films

P. J. Burkhardt

Components Division, International Business Machines Corporation,

East Fishkill Facility, Hopewell Junction, New York

ABSTRACT

Silicon wafers were oxidized in capsules at 1000°C with 1 atm of tritium-tagged steam. The oxide films formed were investigated by conventional tritium counting techniques. The hydrogen profile suggested a complementary error function type in-diffusion of water, giving a C_o of 4 x 10^{19} molecules of H_2O per cm^3. The profile had a minimum value at around 600Å oxide thickness. The location of this value was independent of original oxide thickness. Following this minimum, the concentration again increased as the Si/SiO_2 interface was approached. The concentration of hydrogen near this interface was greater for the thinner oxide films. This observation led to the conclusion that either a hydrogen-containing intermediate is formed by the reaction between water and silicon and that the concentration of this intermediate is dependent on the oxidation rate or that a transition region exists in the oxide film which permits segregation of the diffusant near the Si/SiO_2 interface. Thermal biasing experiments followed by surface charge measurements and autoradiograms showed that mobile positive charge was present in the oxide near the Si/SiO_2 interface. However, this mobile charge was not hydrogen or a hydrogen-containing species. Out-diffusion experiments yielded an activation energy of 15.7 kcal/mole for the tritium species.

The rapid development of planar transistor and surface field effect transistor technology has brought with it an increasing demand for a better understanding of the insulator films that are used for diffusion masks and surface passivation, as well as for electrical insulators. In silicon technology, a film of thermally grown silicon dioxide has proven to be both effective and convenient. These films, originally suggested by Atalla *et al.* (1) are normally grown at temperatures of 1000°-1200°C in ambients of dry oxygen, pure steam, or oxygen-containing water vapor. Steam oxidation is the faster method and is therefore quite popular. The steam cycle is usually preceded by a period in either oxygen or inert gas to allow the silicon to come to temperature. Following the steam cycle, a final period in a dry ambient is sometimes used to "dry out" the oxide.

Kuper and Nicollian (2) have made a study of steam-grown oxides formed on ring-dot diodes and have noted that an n-channel is formed after steam oxidation. Treatment of these devices in a dry ambient at elevated temperatures tended to reduce the channel. Olmstead *et al.* (3) studied surface inversion under an oxide film by measuring channel resistance and found that annealing in forming gas produced an n-channel. Subsequent etching experiments showed that the region of oxide responsible for the channel was within 400Å of the Si/SiO_2 interface.

Balk (4) has found by electron spin resonance (ESR) studies of thermal oxides that an ESR peak occurs only when the final preparatory step does not include a hydrogen-containing species. Thus, steam oxides have no unpaired spins while steam oxides subjected to a period in dry oxygen do. Recently, Nishi (5) reported ESR studies which appeared to contradict Balk's findings. He reports resonance absorption centers produced by hydrogen annealing which can be removed by subsequent annealing in dry oxygen. Balk (6) also found that annealing of dry-oxygen-grown oxides in hydrogen increased the field effect mobility of electrons at the silicon surface. The field effect mobility of devices made using steam-grown oxides was higher than that for dry-oxygen-grown oxides. He further concluded that the primary effect of hydrogen was the annihilation of fast surface states. The fixed charge in the oxide played only a secondary role. The degree of reduction of the fast surface state density depended on the amount of hydrogen in the film, and, consequently, the field effect mobility of devices annealed in pure hydrogen was greater than that of devices annealed in forming gas or unannealed steam-grown oxides. These surface states are probably singly occupied nonbonding orbitals on silicon atoms which also give rise to the ESR peak and can be removed easily by the formation of highly covalent bonds with hydrogen atoms.

This study using oxides grown with tritium-tagged steam was undertaken to observe the disposition of hydrogen and perhaps to shed more light on the mechanism of steam oxidation.

Experimental

Sample preparation.—The oxidations were carried out in fused silica capsules. Each capsule contained several vapor-polished 2-10 ohm-cm p-type silicon wafers that were spaced apart by small indentations in the capsule wall. Each capsule also contained an amount of T_2O-enriched water which would produce 1 atm of vapor when the capsule was placed into a 1000°C furnace. The capsules, of course, were large enough so that the consumption of water vapor by the wafers and walls did not significantly reduce the partial pressure of water vapor in the ambient.

The loading of the capsules with a controlled amount of water was done with the apparatus shown in Fig. 1. The source water, obtained from the New England Nuclear Corporation, contained a T_2O enrichment of 0.5 Curie/g. The ampoule in which it was received was placed in liquid nitrogen to freeze the water, and then scored, opened, and dropped into the

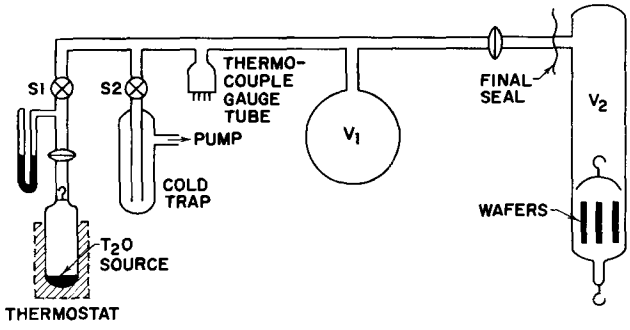

Fig. 1. Apparatus for loading fused silica capsules with tritium-tagged water.

source flask which was immediately connected to the rest of the apparatus. The water was again frozen in the source flask with liquid nitrogen, and the entire system was evacuated with an oil pump to a pressure of about 10μ. Next the source flask was thermostated slightly below room temperature (to avoid condensation in the rest of the system) and the source water vapor expanded into the entire apparatus until the equilibrium vapor pressure, determined by the thermostat temperature, was reached. Volume V_1 was chosen so that the amount of water in the entire system at the vapor pressure was the correct amount for subsequent condensation into the oxidation capsule.

The oxide thicknesses obtained by these capsule oxidations were within 5% of those obtained in a conventional flow system using 1 atm of steam.

Each capsule contained some 10 microcuries and had to be handled with care. The individual wafers however had less than 0.01 microcuries and could be handled conveniently. For the profiling and diffusion experiments, square sections having areas of about 0.6 cm^2 were cut. The oxide on the unpolished side was etched off with HF. Counting was done with a Nuclear-Chicago Model 6810 scintillation counter using a napthalene-dioxane base scintillant. Two counting methods were used in this investigation. The first involved counting the oxide directly on the wafer. For this method, a small aluminum pedestal was fastened to the base of the scintillant vial. The wafer section was placed on this pedestal, which located it near the middle of the vial. A guide edge was provided on the pedestal top so that the wafer section could be located precisely with respect to the counting phototubes. Finally, the vial was filled with scintillant and counted. Next, the wafer section was removed, rinsed in methanol, and placed in an etchant known as p-etch (7). This etchant, prepared by adding 15 ml of 49% hydrofluoric acid and 10 ml of 70% nitric acid to 300 ml of distilled water, removed SiO_2 at the rate of 2Å/sec at 24.7°C. To insure accurate etch rates, the etchant was thermostated in a water bath at 24.7° ±0.2°C. Following the etching, the thickness of the remaining oxide was checked with an SiO_2 step gauge calibrated by the VAMFO technique (8). Finally, the wafer section was again counted as before, and the process was repeated until the oxide had been completely removed. Below 1000Å, where the gauge was ineffective, the etch rate alone was used as the thickness criterion. In some instances where greater accuracy was required, the VAMFO technique was used. Steps ranging in thickness from 100 to 500Å were used, depending on the initial thickness of the oxide. This counting method produced smooth and relatively scatter-free curves, but was greatly affected by attenuation of the low energy betas in thick oxide films. This problem will be discussed later.

The second method involved counting of the etchant. Fifteen 3-cm-long polypropylene tubes 1 cm in diameter fastened onto a metal base with epoxy cement were used to contain 2 ml of the etchant. This entire assembly was thermostated, and etching proceeded by dipping the wafer section into a vial for a predetermined length of time. Between etches, the section was rinsed and, if possible, the remaining thickness was measured. In some instances, the section was also counted between etches. When etching was complete, a 1-ml aliquot was pipetted from each etchant vial into 15 ml of scintillant and counted. Because the counting sensitivity was extremely low, particularly when small steps were used, it was necessary to use this small volume of etchant to reduce the dilution factor.

Calibration of the scintillation counter for the etchant counting was done by comparison of the experimental count rates with that of a tritium water standard. Because small quantities of water in the scintillant tended to quench the light produced by the betas, calibration curves were prepared with varying amounts of added water and etchant. Quenching produced by the etchant was much more severe than that produced by water alone.

For the profiling of the SiO_2 films, both counting methods were used and interpreted according to their relative merits.

In another set of experiments, the rate of out-diffusion of the protonic species was investigated by baking wafer sections at constant temperature and observing the decrease of count rate with time. For these measurements, the wafer counting technique alone was used. Baking was done in a conventional tube furnace with a dry nitrogen flow of 250 cm^3/min.

Finally, the response of the protonic species to an electric field was observed by evaporating an array of 20-mil-diameter aluminum electrodes on the oxide surface. The MOS devices thus formed were thermally biased at 200°C with a d-c field of 2 x 10^5 v/cm for ½ hr. Both positive and negative biases were used. Capacitance-voltage curves were measured before and after biasing. [For a more detailed description of these techniques see ref. (9) and (10).] Following the thermal-bias treatments, the electrodes were removed with a nitric acid aluminum etch, and the oxide was etched down to 1000Å or less with p-etch. Kodak KK x-ray film was then applied, and autoradiograms were made. The exposure times of these autoradiograms ranged from two weeks to one month.

Results and Discussion

For the profiling experiments, the greatest precision was obtained by the wafer counting technique. This method provided smooth scatter-free curves, as shown in Fig. 2 and 3. Because the tritium betas are of such low energies, attenuation becomes a serious problem in films thicker than 1000Å.

When the oxide is sufficiently thin, betas from the entire oxide contribute to the count and, consequently,

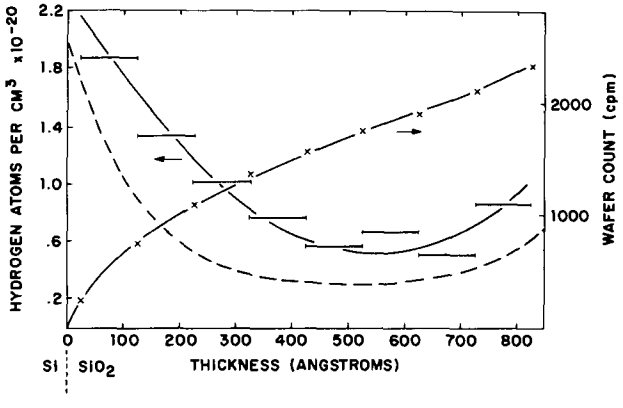

Fig. 2. Wafer count rate vs. thickness and etchant count profile for an 820Å SiO_2 film. The dashed line represents the derivative of the wafer count curve on an arbitrary scale.

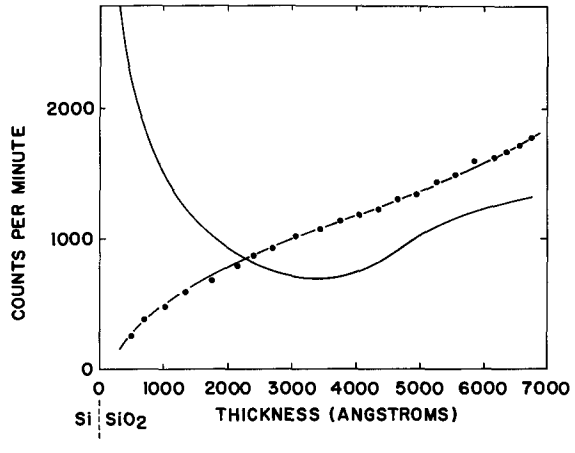

Fig. 3. Wafer count rate of a 6750Å SiO_2 film. The solid line represents the derivative of the count rate curve.

the derivative of the wafer count curve is proportional to the proton concentration in the removed section. To determine the maximum thickness of oxide in which attenuation effects are negligible, it was necessary to calibrate carefully the scintillation counter in terms of beta particle energies and to determine what portion of the beta energy spectrum the counter was capable of measuring. This was done by counting a solution of tritium-tagged water in scintillant at progressively widening energy windows. The lower limit of the energy window remained fixed. The count intensity difference between adjacent windows was taken to be representative of the density of betas having energies equal to those just above the energy maximum of the smaller window. As the window was gradually opened, the count rate increased with decreasing rapidity until finally further expansion of the window produced no more increase in count rate. At this width, betas of all energies were counted, including the highest energy, which was used as a reference calibration. This maximum energy is 18.6 kev (11). Figure 4 shows the beta energy spectrum as determined by this method. The voltage scale represents the counter discriminator voltages that are proportional to the beta energies by a constant determined from the maximum energy of 18.6 kev, which was taken to be at the position shown in Fig. 4. From this calibration, it was found that the lower cut-off limit of the counter was about 1.5 kev. An effort to locate the maximum energy by counting from a low voltage to infinity and continually raising the lower limit of the energies counted was unsuccessful because, as the lower limit was increased, it was necessary to use higher and higher concentrations of tritium in order to maintain a measurable counting rate. This increase, in turn, led to interference from coincidence counting.

It is obvious from Fig. 4 that an accurate energy calibration point for the scintillation counter could not be obtained by using the maximum beta energy of tritium alone. To verify the calibration, a sample of $_{27}Co^{57}$ was used to give another calibration point. This isotope decays to $_{26}Fe^{57}$ by electron capture and gamma emission. The electron capture results in the emission of a 6.4 kev x-ray (12). The three gammas released to relieve the nucleus from its excited state

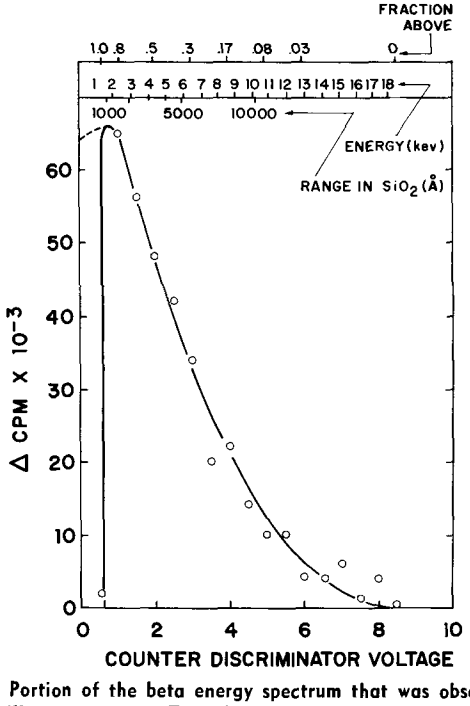

Fig. 4. Portion of the beta energy spectrum that was observed by the scintillation counter. The three scales at the top represent, respectively, the fraction of betas having energies above a certain point, the actual beta energy, and the effective range in SiO_2.

have energies of 14.4, 121.9, and 136.3 kev (13). By examining the spectrum of this isotope in the region of interest, peaks from the 6.4-kev x-ray and the 14.4-kev gamma could produce calibration points. The 14.4-kev gamma peak was found to yield a threshold energy of 1.7 kev for the tritium betas, which is in good agreement with the previous estimate.

The fraction scale in Fig. 4 represents that portion of the total observed tritium betas which have energies greater than that indicated by the same point on the energy scale. This was obtained by integrating the area under the curve. Thus, for example, about 50% of the observed betas have energies greater than 4 kev.

The next problem to be considered is that of the effective range of monoenergetic electrons in silicon dioxide films. For this we refer to the work of Holliday and Sternglass (14), who have made range measurements and who also present data from other authors. In their Fig. 5 they show a nearly linear relationship of the logarithm of effective range (in mg/cm^2) and the logarithm of the primary electron energy from about 1 to 10 kev. Assuming this linear relationship and using a density of 2.2 g/cm^3 for silicon dioxide (15), one obtains a relationship between range in SiO_2 and initial electron energy of

$$d = 5 \times 10^{-6} E^{1.29} \quad [1]$$

where d is the range in cm and E the energy in kev. Recent measurements of effective range of monoenergetic electrons in SiO_2 films by the back-scatter technique indicate that the constant 5×10^{-6} in [1] is slightly low (16). The range in SiO_2 for various energies obtained by using [1] is shown by the range scale in Fig. 4. This scale takes into account the fact that a beta coming out of the SiO_2 film must have an energy of at least 1.5 kev to be counted. Examination of these scales indicates that about 90% of all the tritium betas are capable of penetrating a SiO_2 film 1000Å thick and being counted. Thus, the count rate profile for the 820Å film shown in Fig. 2 may be translated directly into concentration units by plotting the derivative of the curve. This derivative is shown in arbitrary units by the dashed line in the figure. What is immediately apparent from this figure is that the concentration of protonic species increases markedly very near the Si/SiO_2 interface.

The profile for this oxide, obtained by etchant counting, is also shown in Fig. 2. The thicknesses of the etch steps taken here were determined by the etch rate alone. For very thin oxide films, the etch rate is reputed to be somewhat faster than for thicker films (17). This factor was taken into account in determining the thicknesses of the very thin films. The appearance of hydrophobicity also served as an indication of oxide removal. Again, by etchant counting, it was found that the concentration of hydrogen increased near the Si/SiO_2 interface.

The wafer counting data for a thick oxide film (6750Å) is shown in Fig. 3. Also included in the figure is the derivative of the count curve which, of course, does not represent the concentration profile accurately. The increase of this curve toward the Si/SiO_2 interface does not represent an increase in tritium content in this direction but rather represents a decrease in attenuation effects. The etch count profile for this particular oxide is shown in Fig. 5 along with the corresponding profiles for 820 and 4400Å oxides. Note that in all cases we find what appears to be a normal in-diffusion profile over the bulk of the oxide. Assuming a complementary error-function diffusion profile, one may compute a diffusion coefficient. This coefficient, however, turns out to be much smaller than that obtained for water diffusion in SiO_2 (18). This may be due to the distortion of the profile during the cooling of the wafers following oxidation. Note that the hydrogen atom concentration near the outer surface of the oxides is about 8×10^{19} atoms/cm^3, which corresponds to 4×10^{19} water molecules/cm^3. This value is in good agreement with the value of 3.0×10^{19}

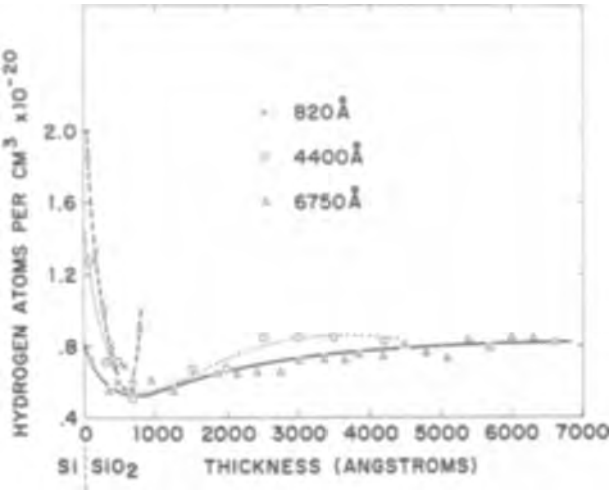

Fig. 5. Etchant count profiles for SiO_2 films of varying thickness

molecules/cm³ obtained for the solubility of steam oxidizing species in SiO_2 at 1000°C by Deal and Grove (19). Moulson and Roberts' (18) infrared value, also given by Deal and Grove, is 3.4 x 10^{19} molecules/cm³.

The data in Fig. 5 represent typical etch count profiles of oxides of various thicknesses. In all cases, the proton concentration began to rise again as the Si/SiO_2 interface was approached. The minimum always occurred in the neighborhood of 600Å no matter how thick the oxide was, indicating that the protonic species in this region was associated with the interface and not the diffusion. It is interesting to note here that the charged species observed by Olmstead *et al.* (3), which was responsible for producing n-channels in the silicon, was located in the region below 400Å. Possibly, it is an intermediate in the reaction between water and silicon. It thus remains near the reaction front until the reaction goes to completion and the product hydrogen then diffuses out rapidly. A potential gradient may also assist in confining the material in this region. This could also be affected by the doping. The steady-state amount of this intermediate behind the reaction front will depend on the rate at which the diffusant reacts with the silicon at the interface, which for practical purposes should be the same as the oxide growth rate. During the early stages of oxidation, the growth rate is very large and is determined by the concentration of oxidant in the gas phase. As the film thickens, the growth rate decreases parabolically. The amount of intermediate will then be greater in the thinner films, which were quenched when the growth rate was the greatest. Comparison of the three curves in Fig. 5 shows that this is indeed the case. The presence of a transition layer in the oxide at the Si/SiO_2 interface could also cause the segregation of the diffusant species in the region below 600Å as well as result in a greater concentration of hydrogen in this region for the thinner oxides. If this transition layer exists, other species could be made to segregate in this region.

A 5-min bake at 1000°C of a 4400Å oxide in a nitrogen ambient was sufficient to reduce the beta count to background level. To make sure that the protonic species near the Si/SiO_2 interface had been removed by this treatment, half of the oxide was etched off and the wafer recounted. No activity was detected. The lower limit of detection for these experiments was estimated to be about 10^{17} hydrogen/cm³. To obtain some rate data on the removal of hydrogen containing species from the oxide film, a number of baking experiments were done in the temperature range of 500°-650°C. In this range, the wafer activity decayed at a conveniently measurable rate. The simplest physical process relating to this situation is the out-diffusion of material from a slab of thickness d into a large, well-stirred, ambient. The solution to this problem (20), where the initial concentration is uniform and one side of the slab is impermeable, is given by

$$M_t/M_o = 8/\pi^2 \sum_{n=0}^{\infty} \frac{1}{(2n+1)^2} \exp - \left[\frac{(2n+1)^2 \pi^2 Dt}{4d^2} \right] \quad [2]$$

where M_t is the amount of material remaining in the slab at time t, M_o the initial amount, and D the diffusion coefficient. For sufficiently long times, this series may be approximated by its first term, leading to an exponential decay of M_t/M_o with time.

The slope should yield the diffusion coefficient if the thickness is known. The situation which we encounter here deviates from the ideal case in two respects: (*i*) the concentration is not uniform, although it does not vary greatly, and (*ii*) the wafer counting method that had to be used does not measure all of the material in a thick film because of attenuation.

The data obtained by baking out oxides of various thicknesses did indeed follow the pattern suggested by [2]. If we consider only the first term in [2], we have

$$M_t/M_o = (8/\pi^2) e^{-t/\tau} \quad [3]$$

where

$$\tau \equiv (4d^2)/(\pi^2 D) \quad [4]$$

Figure 6 illustrates the data for a number of runs on different oxides plotted against t/τ. Normalizing the data to $1/\tau$ has the effect of eliminating dependence on D and d. However, from [3] it is expected that the intercept of the line in Fig. 6 should be at log $8/\pi^2$ = log 0.812, which is not the case. Instead the intercept occurs at the lower value of log 0.59. One explanation for this would be the presence of another protonic species which was in the oxide at time zero, but diffused out very rapidly during the first bake. This situation would lead to an anomalously high value for M_o. If this were the case, the fast species concerned could not be the species located near the Si/SiO_2 interface. The reason for this is that this species could not contribute significantly to M_o, particularly in the thicker oxides, because of attenuation. Efforts to remove any fast species by prebaking at 200°C for ½ hr had no significant effect on the intercept. Consequently, a second fast species must be ruled out as the cause of the intercept deviation. The fact that the distribution of protons is nonuniform will alter the boundary conditions of the diffusion problem, which might lead to a different intercept.

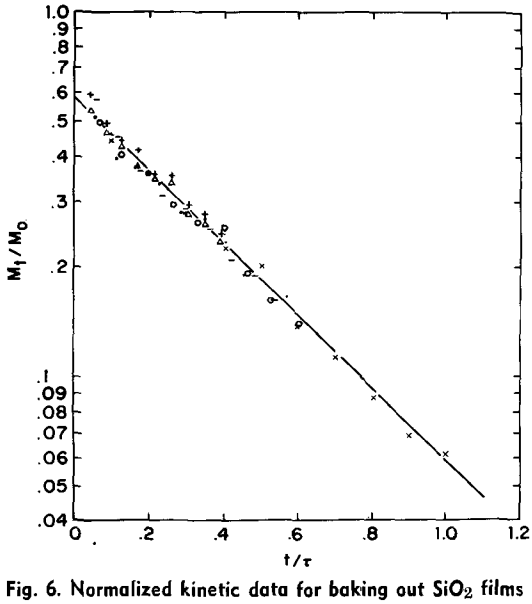

Fig. 6. Normalized kinetic data for baking out SiO_2 films

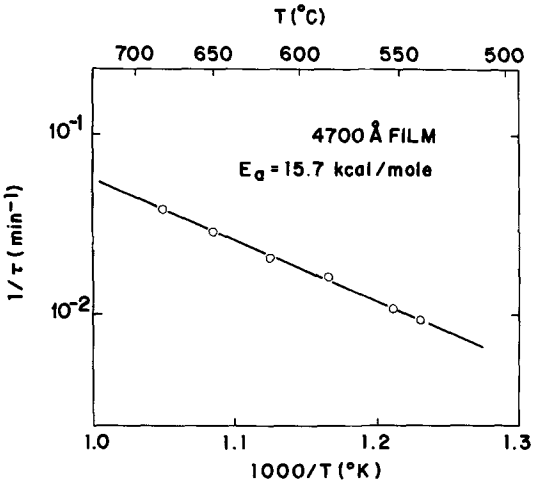

Fig. 7. Activation energy plot for a 4700Å SiO_2 film

From [4], one would expect an exponential temperature dependence of $1/\tau$ by virtue of the diffusion coefficient. The values of $1/\tau$ for a 4700Å oxide at various temperatures are presented in Fig. 7. The activation energy obtained from the slope of this line is 15.7 kcal/mole, which agrees well with that obtained by other authors. Table I gives the values of the activation energy and the pre-exponential of the diffusion coefficient obtained by several methods. The pre-exponential obtained by this work is some two orders of magnitude too low. This may be due in part to an isotope effect, especially if tritons are involved in the diffusion process.

The oxides which were electroded showed a large negative flat-band voltage from the C(V) trace corresponding to a negative surface charge in the silicon of 5×10^{12} charges/cm^2. Normally, oxides grown in a flow system with steam or by the dry-wet-dry method have surface charges of about 3×10^{11} per cm^2. We found that this initial large C(V) offset was characteristic of a capsule-grown steam oxide. Thermal biasing at 200°C for ½ hr showed a reduction of surface charge to about 1×10^{12} charges/cm^2 with negative bias on the aluminum electrode and only a very slight increase with positive bias. This indicates that a large amount of positive charge initially resides in the oxide near the Si/SiO_2 interface. During negative bias, this charge migrates away from the silicon. Positive bias has no significant effect.

It was expected that, if the migrating charge were associated with a hydrogen-containing species, the autoradiograms on the etched oxides would show the outlines of the electrodes for the negatively biased devices. However, the film appeared to be uniformly exposed, with no discernible electrode circles. This result suggests either that the positive charge initially in the oxide was not hydrogen associated or that it was initially on a proton, hydronium ion or some reaction intermediate and subsequently transferred to a silicon atom as follows

$$(\equiv Si - O - Si \equiv) + [RH]^+ \rightarrow (\equiv Si - OH) + [\equiv Si]^+ + R \quad [5]$$

Table I. Diffusion coefficient of water in silicon dioxide

Method	Author	E_a, kcal	D_o, cm^2/sec
Steam oxidation	Pliskin (21)	16.0	2×10^{-7}
Steam oxidation	Edagawa *et al.* (22)	23.0	1×10^{-6}
Wet oxygen oxidation	Deal (19)	16.3	2×10^{-7}
In-diffusion of H_2O	Moulson and Roberts (18)	18.3	1×10^{-6}
Out-diffusion of H_2O	Moulson and Roberts (18)	17.3	2.7×10^{-7}
Out-diffusion of T_2O	This work	15.7	2×10^{-9}

The formation and migration of the charged defect $[\equiv Si]^+$ is discussed in another paper (23).

Another method of charge transfer could be the replacement of a bound sodium ion by a proton, thereby rendering the sodium ion mobile. Such a possibility has been suggested (24) and can be described by

$$(\equiv Si - O - Na) + H^+ \rightarrow (\equiv Si - OH) + Na^+ \quad [6]$$

The presence of significant quantities of sodium in thermally grown SiO_2 films has been observed by neutron activation analysis (25).

Conclusions

The profiling experiments on steam-grown oxides of various thicknesses have suggested the possible existence of a reaction intermediate located in the oxide directly behind the reaction front. The concentration of this intermediate depends on the oxidation rate. Thus, the concentration is greater near the Si/SiO_2 interface in thinner films. Thermal biasing experiments suggest a positively charged species located near the Si/SiO_2 interface. Balk (4) has found that thinner oxides have greater surface charge than thicker ones, thus correlating the positively charged species with the hydrogen-associated species. Our autoradiograms suggested that the charged species which migrates at 200°C is not hydrogen associated. This could only be possible if (*i*) the positively charge species and the hydrogen associated species occur concurrently, as would be the case where a transition phase caused segregation of two species or (*ii*) the positively charged species and the hydrogen-associated species are initially one and the same and a charge transfer like that described by [5] or [6] takes place.

Burgess and Fowkes (26) have recently reported similar experiments using oxides grown with tritium-tagged steam in a flow system. They, too, have found that the hydrogen does not respond to an electric field. The results which are reported here for capsule-grown steam oxides are for the most part compatible with those of Burgess and Fowkes (26) for flow system oxides. There is a marked difference, however, with respect to the out-diffusion of hydrogen. Whereas we found an activation energy of 15.7 kcal/mole using the model described by [2], Burgess and Fowkes obtained an energy about twice as large from a first-order decay law.

Acknowledgment

The author wishes to express his gratitude to Dr. B. J. Masters for his assistance with the radiochemical techniques and to Mr. E. F. Roginsky for much of the experimental work.

Manuscript received May 25, 1966; revised manuscript received Sept. 28, 1966. This paper was presented at the Cleveland Meeting, May 1-6, 1966.

Any discussion of this paper will appear in a Discussion Section to be published in the December 1967 JOURNAL.

REFERENCES

1. M. M. Atalla, E. Tannenbaum, and E. J. Scheibner, *Bell Sys. Tech. J.*, **38**, 749 (1959).
2. A. B. Kuper and E. H. Nicollian, *This Journal*, **112**, 528 (1965).
3. J. Olmstead, J. Scott, and P. Kuznetzoff, *IEEE Trans. Elec. Dev.*, **ED-12**, 104 (1965).
4. P. Balk, Private communication.
5. Y. Nishi, *Japan. J. Appl. Phys.*, **5**, 333 (1966).
6. P. Balk, Paper presented at the San Francisco Meeting of the Society, May 9-13, 1965, Abstract No. 109.
7. W. A. Pliskin and R. P. Gnall, *This Journal*, **111**, 872 (1964).
8. W. A. Pliskin and E. E. Conrad, *IBM J. Res. Dev.*, **8**, 43 (1964).
9. D. R. Kerr, *ibid.*, **8**, 385 (1964).
10. A. S. Grove, B. E. Deal, E. H. Snow, and C. T. Sah, *Solid State Elect.*, **8**, 145 (1965).
11. F. T. Porter, *Phys. Rev.*, **115**, 450 (1959).

12. "Handbook of Chemistry and Physics," Chemical Rubber Pub. Co., Cleveland, Ohio, 45th Ed. (E-74).
13. D. Strominger, J. M. Hollander, and G. T. Seaborg, *Revs. Mod. Phys.*, **30**, 630 (1958).
14. J. E. Holliday and E. J. Sternglass, *J. Appl. Phys.*, **30**, 1428 (1959).
15. E. H. Snow and B. E. Deal, *This Journal*, **113**, 263 (1966).
16. R. Kontrimas, Private communication.
17. W. A. Pliskin, To be published.
18. A. J. Moulson and J. P. Roberts, *Trans. Faraday Soc.*, **57**, 1208 (1961).
19. B. E. Deal and A. S. Grove, *J. Appl. Phys.*, **36**, 3770 (1965).
20. See, for example, W. Jost, "Diffusion," pp. 35-42, Academic Press, New York (1952); J. Crank, "The Mathematics of Diffusion," pp. 52-56, Clarendon Press, Oxford (1956); H. Scholze and H. O. Mulfinger, *Glastechn. Ber.*, **32**, 381 (1959).
21. W. A. Pliskin, *IBM J. Res. Dev.*, **10**, 198 (1966).
22. H. Edagawa, Y. Morita, and S. Maekawa, *Japan. J. Appl. Phys.*, **2**, 276 (1963).
23. P. J. Burkhardt, *IEEE Trans. Elec. Dev.*, **ED-13**, 268 (1966).
24. G. Hetherington, K. H. Jack, and M. W. Ramsey, *Phys. Chem. Glasses*, **6**, 6 (1965).
25. E. Yon, W. H. Ko, and A. B. Kuper, *IEEE Trans. Elec. Dev.*, **ED-13**, 276 (1966).
26. T. E. Burgess and F. M. Fowkes, Paper presented at the Cleveland Meeting of the Society, May 1-6, 1965, Abstract No. 55.

Chemical Vapor Deposition of Mo onto Si

J. J. Casey, R. R. Verderber,[1] and R. R. Garnache[2]

Research and Development Laboratories, Sprague Electric Company, North Adams, Massachusetts

ABSTRACT

Molybdenum has been deposited on single crystal silicon substrates by the vapor phase decomposition of molybdenum chlorides. The thickness, alloy phase, and crystalline nature of the films were studied as functions of substrate temperature, substrate orientation, and source material, using electron microscopy and reflection electron diffraction.

The present study, which originated from work on the deposition of thin film metal layers for the base region of hot electron devices (1), describes the composition and structure of thin layers of molybdenum and molybdenum-silicon phases formed by chemical vapor deposition on single crystal silicon. The fabrication parameters investigated were source material, substrate temperature, and crystal orientation of the substrate.

Previous studies of the molybdenum-silicon system have been mostly concerned with the forming of the disilicide to obtain high temperature corrosion resistant coatings. A monograph (2) on the binary silicides is available which describes the uses, properties, and formation of molybdenum-silicon phases and includes an extensive literature survey.

Experimental

Three series of depositions were made at various substrate temperatures in the range from 600° to 1350°C. Two of these series used molybdenum pentachloride as the source for the molybdenum deposition on (111) and (100) oriented silicon single crystals. The other series utilized a molybdenum oxychloride (MoO_2Cl_2) source on a (100) oriented silicon substrate. The system used to deposit the films is shown in Fig. 1.

A lapped, mechanically polished, and cleaned silicon wafer was placed on the pedestal in the reaction chamber and the system was purged with nitrogen. The wafer was then heated 10 min at 1250°C in a purified hydrogen flow of 1.5 l/min to remove oxides. An epitaxial layer of silicon was then deposited at 1200°C by the hydrogen reduction of silicon tetrachloride. This presented a fresh silicon surface to the molybdenum deposit. The molybdenum was then deposited by the decomposition of the molybdenum pentachloride or oxychloride for 20 min at the various substrate temperatures. The source material was heated in the reservoir chamber to 35°C and transported to the reaction chamber by the purified hydrogen flowing at 1.5 l/min.

[1] Present address: Standard Telecommunications Laboratories, Harlow, Essex, England.

[2] Present address: Tibbitts Research Laboratories, Camden, Maine.

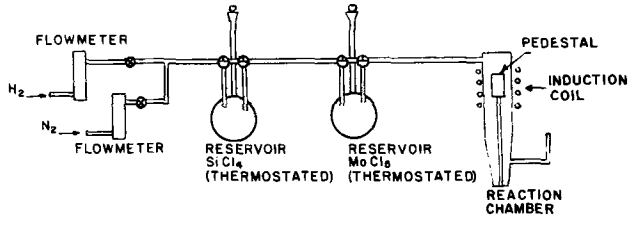

Fig. 1. Deposition system

Measurements

The crystal orientation of the substrates was known and the alloy phases and crystalline nature of each deposit were determined from the reflection electron diffraction data. For deposits that were single crystals, several diffraction patterns were taken at different azimuth angles to obtain the necessary data. Shadowed replicas were made of the surfaces to examine the morphology by electron microscopy.

The effective molybdenum thickness of the deposited molybdenum or molybdenum-silicon alloy was determined by the electron microprobe. The thickness was calculated from the ratio of intensities of MoL_α radiation measured for the film and for bulk molybdenum. The intensity ratio was corrected for x-ray absorption, the nonlinear trajectory of the primary exciting electrons, and the excitation by electrons backscattered from the substrate as described by Hutchins (3). The calibration factor was determined empirically by measurements of films of known thickness and also by interpolation of data for other elements.

For film thicknesses less than 10% of the total electron penetration depth, the corrections are small and the x-ray intensity is a nearly linear function of film thickness. The electron penetration may be controlled by adjusting the beam voltage. At 20 kv the MoL_α intensity is nearly linear up to a thickness of 1000Å of molybdenum.

The excellent sensitivity of the method is most easily demonstrated with an example of representative data (Table I). Relative accuracy depends primarily on counting statistics; absolute error depends primarily on the error in the calibration factor which may be as large as 10%. The measurement gives mass thick-

Table I. Representative data for molybdenum on silicon at 20 kv

Film thickness, Å	Peak counts/ 100 sec	Background counts/ 100 sec	Pk-bgd	Statistical error†	Calibration error*
100	31436	9074	22362	402 (1.8Å)	1118 (5Å)
2	9065	8614	448	265 (1.2Å)	22 (0.1Å)
500	124007	11842	112165	1166 (5.2Å)	5608 (25Å)

†Twice standard deviation 95% confidence.
* Estimated as 5%.

Table II. Properties of phases deposited on (100) Si substrate by H_2 reduction of an $MoCl_5$ source

Substrate temp, °C	Alloy phase	Structure	Thickness, Å, Microprobe
600	Mo	Polycrystalline	190 (as Mo)
700	Mo	Polycrystalline	147 (as Mo)
800	Mo + Mo_3Si	Polycrystalline	104 (as Mo)
900	Mo_3Si	Polycrystalline	52 (as Mo)
1000	Mo_3Si + $MoSi_2$	Polycrystalline and Monocrystalline	64 (as Mo)
1100	$MoSi_2$	Monocrystalline	21 (as $MoSi_2$)
1200	$MoSi_2$	Polycrystalline	16 (as $MoSi_2$)
1300	$MoSi_2$	Polycrystalline	32 (as $MoSi_2$)
1350	$MoSi_2$	Polycrystalline	26 (as $MoSi_2$)

ness; the theoretical bulk density has been used to calculate linear thickness in angstroms.

Results

$MoCl_5$ *Source and (100)* Si *Substrate.*—Table II lists the alloy composition, thickness, and crystalline nature of the layers deposited at the designated temperatures. At 800°C molybdenum-silicon alloys are formed which are molybdenum rich; at more elevated temperatures the deposited layers become more silicon rich until, at 1000°C, molybdenum disilicide is formed.

Deposits below 1000°C are all polycrystalline and have, at most, a small degree of orientation similar to a fiber aggregate (4). At 600°C the orientation is $(100)_{Mo} \parallel (100)_{Si}$ and at 700°C it is $(110)_{Mo} \parallel (100)_{Si}$. All other polycrystalline phases are randomly oriented. A single crystal phase appears at 1000°C and becomes highly developed at 1100°C, Fig. 2. The alloy phase of the 1100°C layer is molybdenum disilicide, and its orientation with respect to the silicon substrate can be described as $(001)_{MoSi_2} \parallel (100)_{Si}$ with $(110)_{MoSi_2} \parallel (010)_{Si}$. At 1200°C the film consists of large unoriented crystallites as evidenced by the occurrence of the diffraction spots on the diffraction rings of a molybdenum disilicide pattern, Fig. 2. These diffraction patterns also show Kikuchi lines typical of the silicon substrate.

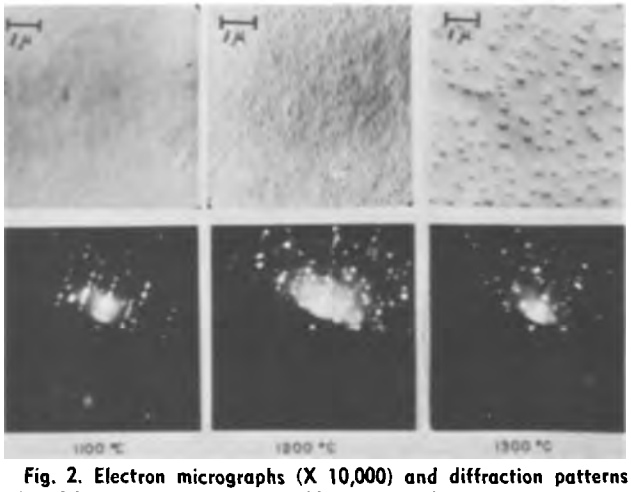

Fig. 2. Electron micrographs (X 10,000) and diffraction patterns of molybdenum deposited on (100) silicon substrate.

Table III. Properties of cylindrical growths obtained on (100) Si substrate using $MoCl_5$ source

Temperature, °C	Diameter, Å	Density, per cm^2	Height, Å	Avg. thickness of $MoSi_2$ (Å), Microprobe Calculated	Measured
1100	250	320×10^8	27	4	21
1200	500	42×10^8	41	3	16
1300	1000	8×10^8	68	4	32
1350	1500	4×10^8	130	9	26

Table IV. Properties of phases deposited on (111) Si substrate by H_2 reduction of an $MoCl_5$ source

Substrate temperature, °C	Alloy phase	Structure	Thickness, Å, Microprobe
800	Mo + $MoSi_{12}$(?)	Polycrystalline	191 (as Mo)
850	Mo + $MoSi_{12}$ (?) + $MoSi_5$ (?)	Polycrystalline	100 (as Mo)
900	Mo_5Si_3	Polycrystalline and Monocrystalline	24 (as Mo)
950	Mo_3Si	Monocrystalline and Polycrystalline	27 (as Mo)
1000	Mo_3Si	Monocrystalline and Polycrystalline	72 (as Mo)
1025	Unidentified	Monocrystalline	15 (as Mo)
1050	Unidentified	Monocrystalline	17 (as Mo)
1074	Unidentified	Monocrystalline	14 (as Mo)

The surfaces of the films are initially smooth and become rougher at higher substrate temperatures. From 1100° to 1350°C one observes cylindrically shaped growths protruding from a very smooth surface (Fig. 2). From the micrographs one can estimate the average size of the growths and the number per unit area can be counted. If one assumes that these growths represent the total $MoSi_2$ present, the average film thickness can be calculated and compared with the measured thickness. Pertinent data are presented in Table III.

The thickness data from the microprobe measurements are based on the assumption that all of the molybdenum determined by the probe is present as molybdenum disilicide, the equivalent thickness of which can be then calculated. Since the measured thickness values are several factors larger than the calculated ones, it must be assumed that either the growths do not represent all of the disilicide, or that some molybdenum has diffused into a thin surface layer of the bulk silicon, or that some other molybdenum-silicon phase is present, which does not contribute to the electron diffraction pattern under the experimental conditions. Insufficient data are available to allow unequivocal choice among these possibilities.

$MoCl_5$ *source and (111)* Si *substrate.*—The results from the experiments for the deposition on the (111) silicon substrate are listed in Table IV.

Molybdenum-silicon alloys initially form at 800°C. The alloys formed are metastable phases and have been tentatively identified as $MoSi_5$ and $MoSi_{12}$ by isomorphism (5) with the molybdenum-aluminum system (6). The structure of the phase tentatively identified as $MoSi_5$ has been determined from the diffraction pattern to be bcc with a_o equal to 7.6Å. The alloys formed become more molybdenum rich at higher substrate temperatures, finally becoming Mo_3Si. Above 1000°C the diffraction patterns (Fig. 3) become rather complex, and the corresponding alloy phases have not yet been identified.

The films deposited below 900°C are polycrystalline and randomly oriented. At 900°C epitaxial growth occurs and well-ordered single crystals are obtained at 950° and 1000°C (Fig. 3). However, a polycrystalline Mo_3Si phase is also present. The orientation of the single crystal phase with respect to the substrate can be described as $(110)_{Mo_3Si} \parallel (111)_{Si}$ with $[335]_{Mo_3Si} \parallel$

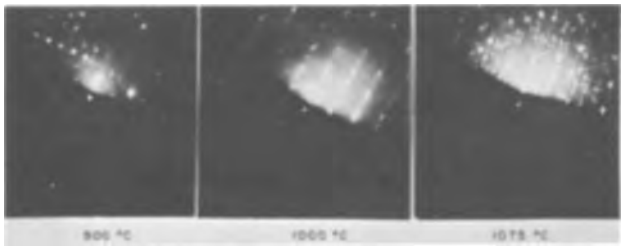

Fig. 3. Electron diffraction patterns of molybdenum deposited on (111) silicon substrate.

$[10\bar{1}]_{Si}$. At higher temperatures, the film consists of large crystals sufficiently disordered to result in a complex diffraction pattern (Fig. 3), and the alloy phase could not be determined.

The electron micrographs of these layers showed no peculiar growths as seen on the (100) silicon substrate and the layers could be described as having slightly rough surfaces.

MoO_2Cl_2 *source on (100) Si substrate.*—Table V lists the results for the series of depositions using the molybdenum oxychloride source material.

The deposits at 650° and 750°C were shown to contain molybdenum by microprobe analysis. Since they are amorphous, however, they cannot be positively identified. By analogy with the results in Table I, which show no silicide formation on (100) silicon at 600° and 700°C, it seems likely that these deposits are molybdenum, but this is not certain.

Discussion

The different alloy phases which are formed on the (100)- and (111)-oriented silicon substrates under similar experimental conditions indicate that the mechanism for alloy formation is different for the two orientations. At 850°C, a stable, molybdenum-rich alloy, Mo_3Si, is formed on the (100) surface, while unstable, silicon-rich alloys along with excess molybdenum are formed on the (111) surface. This difference can be accounted for by the different reactivities of the silicon surfaces which arise from the difference in atom densities. It is well known, for example, that the densely populated (111) silicon surface offers more resistance to chemical etching agents than the less populated (100) surface. A slow rate of reaction on the (111) surface could account for the initial formation of alloys deficient in molybdenum and for the presence of unreacted molybdenum in the deposited layer. In most cases 200Å films of molybdenum deposited at 800°C were found to be metallic, as determined by the attenuation of microwaves through the sample. These films, however, showed a 4-probe resistivity comparable to the silicon substrate. Furthermore, the line widths for the electron diffraction pattern for this specimen indicate that the molybdenum crystallite size is much less than 100Å. It is suggested that the phase tentatively identified as $MoSi_{12}$, unlike $MoSi_2$, Mo_3Si, and Mo_5Si_3, is nonmetallic, and that the whole layer consists of very small molybdenum crystallites in a $MoSi_{12}$ matrix. Further alloys are then formed with an excess of molybdenum available and become more molybdenum rich at the elevated temperatures. This explains the formation of Mo_3Si instead of the disilicide observed in the case of the (100) substrate. Studies of the kinetics of the formation of molybdenum silicides (7) show that Mo_3Si can be formed in a molybdenum-silicon system with excess molybdenum available by annealing at suitable times and temperatures.

Table V. Properties of phases deposited on (100) Si substrate by H_2 reduction of MoO_2Cl_2

Substrate temperature, °C	Alloy phase	Structure	Thickness, Å, Microprobe
650	Unidentified	Amorphous	85 (as Mo)
750	Unidentified	Amorphous	80 (as Mo)
850	Mo_3Si	Polycrystalline	77 (as Mo)
900	Mo_3Si	Polycrystalline	41 (as Mo)
1100	$MoSi_2$	Polycrystalline	10 (as $MoSi_2$)
1200	$MoSi_2$	Monocrystalline	21 (as $MoSi_2$)

The results show that the epitaxial growth is dependent on the substrate temperature, substrate orientation, and source material. As for any type of oriented overgrowth, a minimum temperature must be exceeded to obtain single crystal layers. The temperature is 1000°C for the $MoSi_2$-(100) silicon deposit-substrate pair and 900°C for the Mo_3Si-(111) silicon deposit-substrate pair. However, after a temperature is reached at which the films become well oriented, the orientation of films deposited at still higher temperatures deteriorates, and in the case of the (100) substrate the orientations are random. This indicates other factors are affecting the oriented growth.

The thickness data indicate a limiting deposit thickness at high substrate temperatures. Some clarification of this phenomenon was obtained when attempts were made to deposit molybdenum disilicides at 1200°C on the surface of silicon areas exposed by photoresist techniques on a thermally oxidized silicon surface.

Figure 4 is a photograph of a section of the surface polished on a bevel of 3°. The edge of the beveled section intersects two circular silicon areas on the otherwise oxidized surface. The surface of these areas, having a very thin layer of $MoSi_2$ after the reaction, is seen to lie below the level of the original silicon surface. It can be concluded that the silicon is slowly etched away by the hydrogen chloride and other chlorine-containing species in the reaction ambient. [The reaction of silicon with hydrogen chloride at elevated temperatures has been studied by many authors, among them Lang and Stavish (8).] The thin layer of disilicide deposited may be the result of a steady-state reaction, or it is possible that it is not deposited at all at the high temperature, but only during the cooling period as a result of the desorption of some molybdenum-containing species from the walls of the reaction chamber and subsequent reaction with the exposed silicon surface.

The occurrence of the cylindrical growths on the top (100) silicon surface and their variations in characteristics with temperature are interesting. The formation of a lower density of nuclei on the (100) surface than on the (111) surface is indicated, implying a high mobility of molybdenum atoms on the (100) surface compared to that on the (111) surface. This is particularly true at the higher temperatures, where the growths are larger and less numerous. These

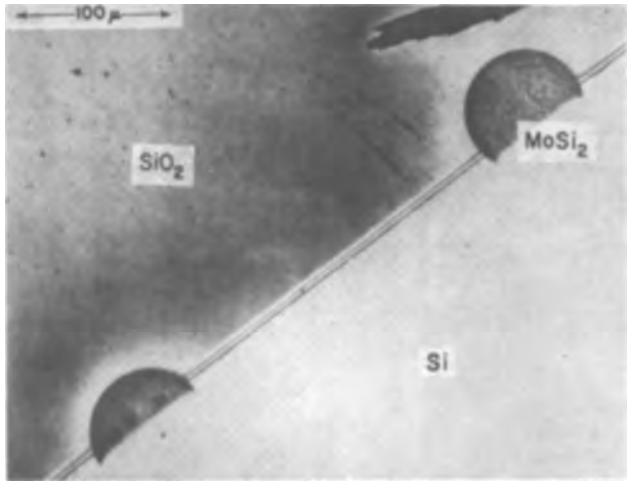

Fig. 4. Beveled section of molybdenum deposited on a masked silicon wafer showing the metal deposit below the initial silicon surface.

phenomena appear to be consistent with Haneman's (9) concepts of the atom arrangements and bonding characteristics on clean surfaces of semiconductors with the diamond structure, arrived at through interpretation of low energy diffraction studies of such surfaces after ion bombardment and vacuum anneal. Freshly formed epitaxial silicon surfaces such as those used as substrates in the present experiments can approach a high degree of perfection and cleanliness and might, therefore, be similar in character to the surfaces studied by Haneman, particularly at high temperatures, where a minimum of gaseous ambient would be adsorbed to the surface. Haneman's model of the (111) surfaces gives s-type bond character to the dangling bond on every other silicon atom in every other row of atoms, and also raises it slightly above the surface, while the dangling bonds on the remainder of the silicon atoms have p-character. Maximum overlap with the orbitals of approaching molybdenum atoms would be offered by the dangling s-bonds, providing a high uniform density of energy minima, which could tend to initiate a high density of nuclei and would result in a very smooth surface, as observed experimentally. The structural model proposed by Haneman for the (100) surface can be interpreted as resulting in dangling bonds which are mostly p-type in character, offering little overlap for the orbitals of approaching molybdenum atoms. The mobility of the molybdenum atoms would be unimpeded, and a smaller number of nuclei would be formed resulting in the type of growth observed in the (100) surface. The nucleation on these surfaces could arise more at the sites of impurity centers and micro-irregularities, which are generally accepted requirements for the initiation of epitaxial growth nuclei, and the high mobility would account for the growth of larger deposits at the higher temperatures. This model is in accord with concepts expressed by Pashley in his reviews on epitaxial growth (10, 11).

The effect of oxides on the crystalline growth is readily seen from the results using the molybdenum oxychloride source. The crystalline nature of the film is considerably poorer over the entire range of substrate temperatures, indicating that oxide contaminants inhibit the formation of a single crystal thin film.

Summary

This study shows that molybdenum can be deposited on a silicon substrate by the decomposition of $MoCl_5$ or MoO_2Cl_2. Under suitable conditions of temperature and source purity, highly oriented thin films can be grown. The process of alloy formation is critically dependent on the orientation of the substrate, and the thickness of the deposit is limited by an etching process occurring at high substrate temperatures.

Acknowledgments

The authors gratefully acknowledge the efforts of A. Harvin for her contribution in supplying the electron diffraction and electron microscopy data and determining the alloy phases, and Mrs. G. Hutchins for microprobe determination of film thicknesses.

This work was partially supported by government funds under Contract No. DA 28-043 AMC-00169(E).

Manuscript received Feb. 3, 1966; revised manuscript received Sept. 14, 1966.

Any discussion of this paper will apear in a Discussion Section to be published in the December 1967 JOURNAL.

REFERENCES

1. J. L. Sprague, J. Lindmayer, R. R. Garnache and J. J. Casey, 23rd Annual Conference Physical Electronics, March 1963, pp. 210-217, MIT, Cambridge, Mass.
2. A. S. Berezhnoi, "Silicon and its Binary Systems," (Academy of Sciences of the USSR, Kiev, 1958. English translation published by Consultants Bureau, New York, 1960) pp. 167-183.
3. G. A. Hutchins, "The Electron Microprobe," McKinley, Heinrich, Wittry, Editors, pp. 390-404, John Wiley & Sons, Inc., New York (1966).
4. J. M. Bijvoet, N. H. Kolkmeyer, and C. H. MacGillavry, "X-Ray Analysis of Crystals," Ist English Edition, translated by H. L. Furth, Interscience Publishers, New York (1951).
5. H. P. Klug and L. E. Alexander, "X-ray Diffraction Procedures," p. 405, John Wiley & Sons, Inc., New York (1954).
6. W. B. Pearson, "Lattice Spacings and Structure of Metals and Alloys," p. 376, Pergamon Press, New York (1958).
7. R. W. Bartlett, P. R. Gage, and P. H. Larssen, *Trans. Met. Soc. AIME*, **230**, 1528 (1964).
8. G. A. Lang and T. Stavish, *RCA Rev.*, **24**, 488 (1963).
9. D. Haneman, *Phys. Rev.*, **121**, 1093 (1961).
10. D. W. Pashley, *Advances in Physics*, **5**, 173 (1955).
11. P. W. Pashley, "Metallurgy of Adv. Elect. Mat.," **19**, pp. 175-207, John Wiley & Sons, New York (1962).

Technical Note

Gas Phase Etching of Sapphire with Sulfur Fluorides

H. M. Manasevit and F. L. Morritz

Autonetics, A Division of North American Aviation, Inc., Anaheim, California

The quality of epitaxial films of silicon grown on sapphire is greatly affected by the quality of the substrate surface (1-3). Processing with diamond has been, generally, a practical requirement for cutting and polishing sapphire substrates. Unless, however, stringent care is taken to polish the surface properly, various size scratches will remain. These scratches affect the nucleation mechanism and, consequently, the silicon overgrowth. Some success in "fine scratch" removal can be effected by a final alumina buff, but the fine powder frequently fills deep scratches and leaves a surface that appears optically to be scratch-free. The usual high-temperature etching prior to deposition can remove this material and expose a rather poor surface for the epitaxial growth of silicon.

Attempts at scratch removal using "wet" chemical techniques appear to have been only partially successful (3, 4). The usual etchants for sapphire (orthophosphoric acid, sodium borate, potassium carbonate, sodium hydroxide, potassium hydrogen sulfate, lead (II) fluoride, and potassium tetrafluoroaluminate) tend to be quite sensitive to orientation and temperature. Usually, polishing can be effected by these agents, but rates cannot be controlled sufficiently to provide the smooth, flat surfaces desired for epitaxial growth.

In addition, any residual surface contamination due to the etchants, even if not optically visible after polishing, can affect the epitaxial process. Furthermore, other wafers in the same system can be contaminated by transfer of residual material. For these reasons, it was thought advisable to study the feasibility of gas phase etchants for sapphire removal. Hydrogen gas has been used (1, 3, 5, 6) to treat sapphire in the reactor prior to deposition, but the etch rate is very low below 1500°C. Its "cleaning" capability is probably due, for the most part, to removal of the polycrystalline alumina residue remaining after optical polishing of the sapphire. Hydrogen chloride (HCl) reacts with sapphire (7) and was found to be a polishing etchant for sapphire at pedestal temperatures exceeding about 1400°-1450°C (8), but the low attendant etch rate of 0.1 μ/min may not be considered practical for removal of considerable surface work damage (or deep scratches).

This paper reports on the successful use of sulfur fluorides as polishing etchants for sapphire. Reactivity of the sulfur fluorides with other oxides had been established at room temperature and below (9, 10), but their use as etchants for aluminum oxide and other oxides at high temperatures has not been reported previously.

Experimental

Apparatus.—A vertical-reactor system similar to that used in our research laboratories for epitaxial growth (11) was used in performing the etching studies. Palladium-diffused hydrogen and a commercial grade helium were used in the studies. Sulfur tetrafluoride (nominally 90-94% pure) and sulfur hexafluoride (nominally 99.99% pure) were used without further purification.

The experiments were usually performed on 0.5-in. diameter sapphire windows, 0.010-in. thick, with $(1\bar{1}02)$ and $(11\bar{2}3)$ orientations. Substrates were heated indirectly while resting on a 3-mm thick alumina spacer which rested on an inductively heated carbon pedestal (except where indicated). The spacer minimized interaction between the substrate and pedestal and provided an even heat distribution. The etching gases were monitored on No. 600 Matheson flowmeters (a sapphire float for SF_4; a Pyrex float for SF_6), and the gases were introduced directly into the flowing H_2 or He ambient at approximately 1 atm total pressure. Carrier gas flow rates were arbitrarily set at 2.5 l/min. Pedestal temperatures were measured with an optical pyrometer, and uncorrected values are reported. They are estimated to be 50°-100° higher than the actual substrate temperature.

Results and Discussion

With SF_4.—Small amounts of SF_4 (less than 1 mole %), diluted with H_2 or He, effectively etched sapphire. After etching at silicon pedestal temperatures of about 1150°C (observed), fluorine compounds were detected on the sapphire surface by electron microprobe induced x-ray fluorescence. AlF_3 formation [presumably epitaxial because of its oriented nature on $(1\bar{1}02)$ sapphire] was suggested by the two-dimensional distribution of aluminum and fluoride which were obtained by electron microprobe techniques (Fig. 1). However, this growth was not observed when gas-phase etching was performed at about 1300°C. Presumably at this temperature the vapor pressure of the material was high enough so as not to interfere with the etching process. Etch rates of about 2 μ/min at carbon pedestal temperatures of 1450°C left highly polished scratch-free surfaces on good quality substrates. Major grain boundaries in sapphire were accentuated by the etching process (see Fig. 2).

With SF_6.—Since pyrolysis of the SF_4 produces sulfur and sulfur hexafluoride (10), the use of the latter was investigated to determine if, indeed, its *in situ* formation might be an important factor. It was found that SF_6 etched sapphire considerably when helium was the diluent gas and almost not at all when hydrogen was used as the carrier under otherwise comparable conditions. Representative removal rates with SF_6 are presented in Fig. 3 through 5 for different temperatures and concentrations. Figure 6 shows the effect of etch-polishing sapphire at 1350°C (ped. temp.) with different SF_6 concentrations so that equivalent amounts of sapphire were removed. The lower concentration produced a smoother sapphire surface.

Success in etching sapphire at reasonable rates by the above processes enhanced the possibility of applying the sulfur fluoride etch process to lapped sapphire surfaces as well as to diamond polished surfaces. The successful gas-phase polishing of lapped surfaces would minimize work damage attributed to mechanical polishing. Experience has indicated that a 10-min exposure of a polished sapphire to SF_6 at 0.22 mole %

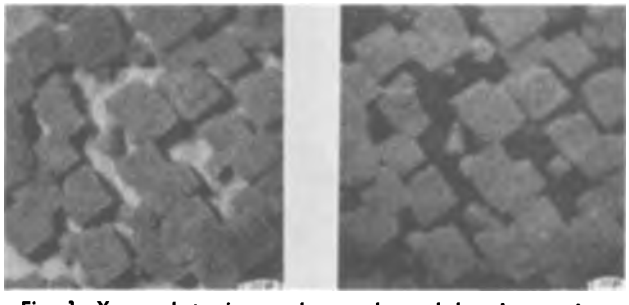

Fig. 1. X-ray photomicrographs as observed by electron beam scanning of the growth on sapphire obtained during etching with SF_4 at 1150°C: (a) (left) due to aluminum; (b) (right) due to fluorine.

Fig. 2. Grain boundaries in sapphire as displayed by SF_4 etching

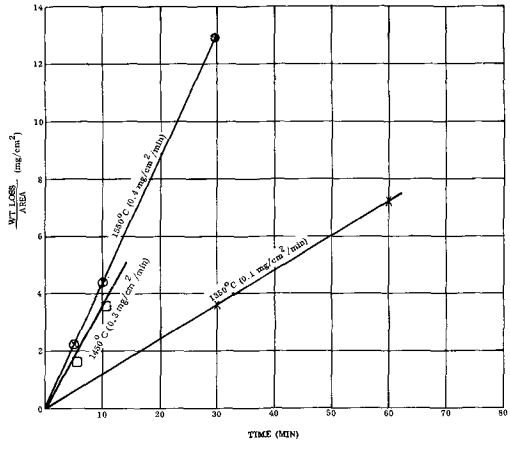

Fig. 3. Etching data with 0.22 mole % SF_6

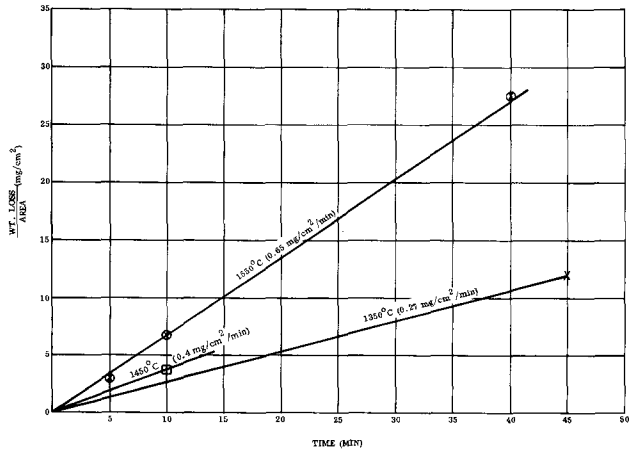

Fig. 4. Etching data with 0.34 mole % SF_6

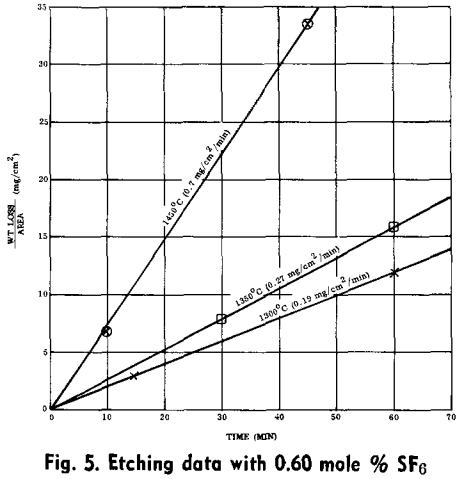

Fig. 5. Etching data with 0.60 mole % SF_6

in He flowing at 2.5 l/min at 1550°C (ped. temp.) will suffice to remove essentially all the surface scratches present due to normal optical polishing techniques. After a 30-min etch under the above flow and temperature conditions, a lapped ($1\bar{1}02$) sapphire slice had a reasonably smooth surface, as indicated in Fig. 7a. Figure 7b shows the surface of a sequential slice (from the boule) which was cut, mechanically polished and processed in the reactor simultaneously with the slice shown in Fig. 7a. The same grain boundary is depicted.

During preliminary experiments in which substrates rested directly on the heated pedestal, it was observed that the carbon pedestal was attacked by the sulfur fluorides. Examination of the substrate surface showed pitting of the type shown in Fig. 8, especially when low carrier gas flow conditions were used. The pits appear to have a definite orientation. Similar patterns are obtained after carbon particles were deliberately rubbed onto the sapphire surface which then was etch-polished. Molybdenum and silicon were also used as pedestal materials; however, a substantial amount of reaction occurred with the etching gases, producing deposits of undesirable byproducts throughout the reactor.

The results of the etching study with SF_6 indicate that it is selective in its etch-polishing capability for different orientations of sapphire. Under identical conditions, at relatively high SF_6 concentrations, optically polished ($1\bar{1}02$) sapphire will usually etch and roughen while ($11\bar{2}3$) sapphire will polish further. At very low concentrations of SF_6 (less than 0.2 mole %) ($1\bar{1}02$) sapphire seems to polish rather than etch at rather appreciable removal rates. Reasonably polished ($1\bar{1}02$) surfaces have been obtained on good quality

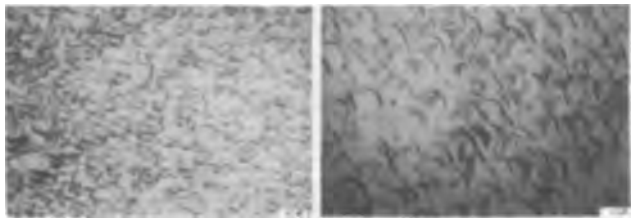

Fig. 6. Surface characteristics ($1\bar{1}02$) sapphire after SF_6 etching: (a) (left) for 30 min at 1350°C with 0.60 mole % SF_6; (b) (right) for 60 min at 1350°C with 0.22 mole % SF_6.

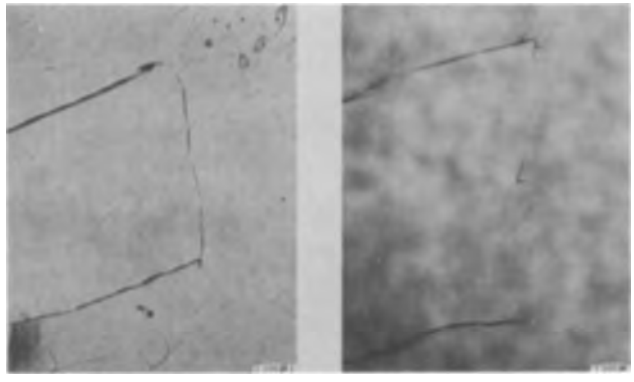

Fig. 7. Structure observed when SF_6 is used to etch ($1\bar{1}02$) sapphire with a (a) (left) lapped ($1\bar{1}02$) surface, and (b) (right) polished surface.

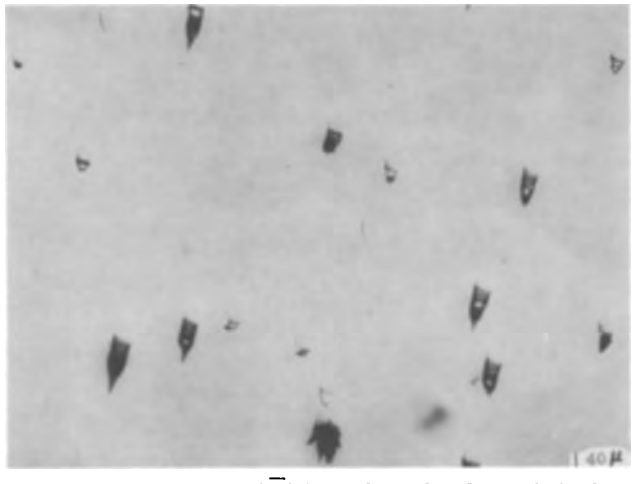

Fig. 8. Pits observed on ($1\bar{1}02$) sapphire after SF_6 etch (carbon pedestal used).

sapphire at removal rates of up to 0.4 mg/cm²/min at 1550°C (obs. ped. temp.) while optically polished surfaces oriented to the ($11\bar{2}3$) have retained a polish at etch rates of 0.7 mg/cm²/min at 1450°C. Single crystal silicon deposits were obtained on SF_4 or SF_6 polished sapphire surfaces.

Conclusion

The polishing of sapphire by the sulfur fluorides seems to offer a distinct advantage over the wet chemical techniques now available. Experience will dictate if the process is to be preferred over HCl polishing, which is considerably slower at comparable temperatures. Since it has been shown that SF_6 (or SF_4) will etch-polish a lapped (or ground) sapphire substrate, its potential as a means for eliminating optical polishing of sapphire is worth consideration.

Acknowledgments

The authors wish to express their appreciation to W. I. Simpson and J. E. Coker for their valuable as-

sistance in the etching studies, to C. C. Nealey and C. W. Laakso for the electron microprobe work, and to the Linde Company for their cooperation in supplying the Czochralski wafers used in the etching study.

Acknowledgment is hereby given to the Bureau of Ships for their support under Contract NObsr No. 93145.

Manuscript received Sept. 19, 1966; revised manuscript received Nov. 7, 1966. This paper was presented at the Cleveland Meeting, May 1-6, 1966.

Any discussion of this paper will appear in a Discussion Section to be published in the December 1967 JOURNAL.

REFERENCES

1. H. M. Manasevit and W. I. Simpson, *J. Appl. Phys.*, **35**, 1349 (1964).
2. H. M. Manasevit, Arnold Miller, F. L. Morritz, and R. L. Nolder, *Trans. AIME*, **233**, 540 (1965).
3. P. H. Robinson and C. W. Mueller, *ibid.*, **236**, 268 (1966).
4. "Single Crystal Silicon Films on Insulating Substrates," Contract NObsr 93145, Autonetics, Anaheim, Calif., First Interim Report, 1 May-31 July, 1965.
5. T. A. Voruz, R. P. Jewett, O. E. Accountius, *J. Amer. Ceram. Soc.*, **46**, 459 (1963).
6. D. W. Readey and G. C. Kuczynski, *ibid.*, **49**, 26 (1966).
7. J. V. Kerrigan, *J. Appl. Phys.*, **34**, 3408 (1963).
8. "Deposition of Silicon on Insulating Substrates," Contract AF19(628)-4220, Westinghouse Research Labs., Pittsburgh, Pa., Scientific Report No. 1, 1 July-31 Dec. 1964.
9. R. J. Brotherton, A. L. McCloskey, and H. M. Manasevit, *Inorg. Chem.*, **2**, 41 (1963).
10. E. L. Muetterties, E. I. du Pont de Nemours and Co., U. S. Pat. No. 2, 883,267, April 21, 1959.
11. H. M. Manasevit, D. H. Forbes, and I. B. Cadoff, *Trans. AIME*, **236**, 275 (1966).

Brief Communication

Travelling Solvent Defects on Silicon Wafers

E. Biedermann

IBM Laboratories, Boeblingen, Germany

In the usual planar silicon technology, the growth of an epitaxial Si layer on a single crystalline substrate wafer at a temperature of 1100°-1200°C is a basic process step. A variety of perturbations and defects can occasionally be observed on these epitaxial surfaces.

In Fig. 1, we show a special type of surface defect which occurs now and then, and which to our knowledge has not yet found its proper explanation. From its optical appearance in Fig. 1, we called it the "nail defect." These nails, achieving sometimes a length of a millimeter and more, can, under proper illumination, easily be observed even with the naked eye. The most obvious characteristic properties of these nails can be summarized as follows:

1. The distribution of the nails over the wafers is completely statistical.
2. Neighboring nails have almost identical length, shape, and orientation, without correlation to the crystal structure of the Si wafer, the orientation of the gas stream, or the direction of the gravitational force. (The exception of unusually short "incomplete" nails will be treated below.)
3. Length, shape, and orientation of the nails can vary strongly from one region of a wafer to another.
4. Under higher magnification (500X), head and shaft of the nails lose all their contrast, indicating that the nails consist of nothing but a slight profiling in the wafer surface (Fig. 2, 3)
5. Only in the uttermost tip of most of the nails, a sharp defect is found under high magnification. (Fig. 3)

These defects have been identified as small impurity pellets which, liquid at the temperature of the epitaxial process, travel over the wafer surface under the influence of the incidental temperature gradients thereon, just as does the liquid zone in the well-known travelling solvent processes (1). Thus the shafts of the "nails" are nothing but the traces of these traveling pellets. The small kinks in these traces can clearly be correlated to the change from preheating cycle to epitaxial growth period to postheating and cooling cycle. The behavior of the travelling pellets is apparently not much influenced by the epitaxial growth process itself, and the growth of a 10μ epitaxial layer

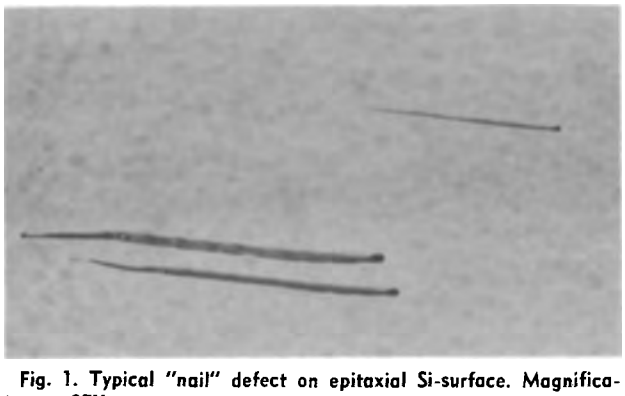

Fig. 1. Typical "nail" defect on epitaxial Si-surface. Magnification ca. 37X.

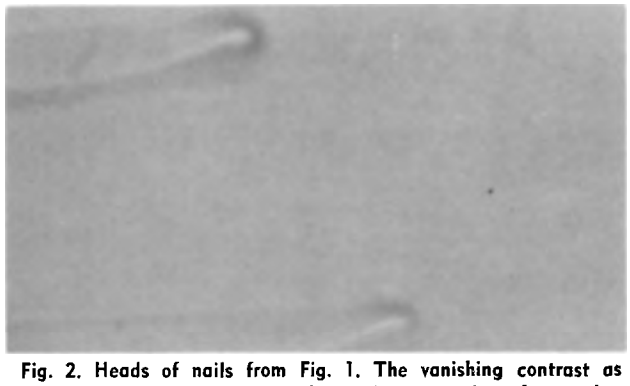

Fig. 2. Heads of nails from Fig. 1. The vanishing contrast as compared to Fig. 1 indicates the nails to consist of a rather smooth surface profiling. Magnification ca. 365X.

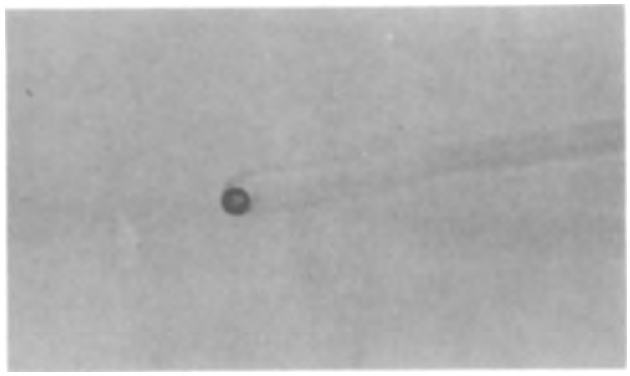

Fig. 3. Tip of nail from Fig. 1 with impurity pellet. Magnification ca. 365X.

does not effect a noticeable levelling out of these traces.

The occurrence of unusually short nails in the neighborhood of longer ones (like the one in Fig. 1) is also easily explained. They never contain a pellet in their tip. Here the impurity material has been used up before the end of the heating cycle by solution in the silicon wafer, respectively by evaporation.

By observation in a high-temperature microscope under pure H_2-atmosphere, the melting point of the pellets has been determined to be about 1000°C and the travelling direction and speed could qualitatively be correlated to the temperature gradient on the wafers.

Electron microprobe analysis showed the pellets to contain the elements Fe, Cr, and Ni in a ratio corresponding approximately to the composition of stainless steel: 70 pt Fe, 20 pt Cr, and 8 pt Ni. Besides these metals an appreciable content of Si was found in the pellets, as is to be expected from the formation of essentially the Fe-Si eutectic with about 25% Si.

Evidently, the vapor pressure of these metals over the eutectic melt and their solubility in the solid silicon are low enough to guarantee the astonishingly long lifetime of these pellets on the silicon surface even in the chlorine-containing ambient of the epitaxial process.

Quite similar nails are easily produced in a pure hydrogen atmosphere on a silicon surface by seeding it with small pellets of other metals such as Cu, Ag, Cr, Ni, Pd, Pt, and heating it in an inert atmosphere like hydrogen to a temperature somewhat above the respective eutectic point. All these metals also have a low solubility in solid silicon at the temperature of their eutectic melt with Si.

From these findings the nails on the Si wafers appear as one example of a quite basic process which may just as well be observed on any other solid surface under appropriate conditions.

Manuscript received Aug. 4, 1966; revised manuscript received Nov. 2, 1966.

Any discussion of this paper will appear in a Discussion Section to be published in the December 1967 JOURNAL.

REFERENCE

1. W. G. Pfann, *Trans. AIME*, **203**, 961 (1951).

ELECTROCHEMICAL SCIENCE

Fused-Organic Electrolytes for Thermal Cells

Richard A. Wallace[1] and Paul F. Bruins

Department of Chemical Engineering, Polytechnic Institute of Brooklyn, Brooklyn, New York

ABSTRACT

The low-melting (<200°C) fused electrolytes tested were salts of organic acids, substituted pyridinium halides, and acetamide salt solutions. Methylpyridinium bromide and several alkali acetates were found to be thermally stable and good conductors, but they entered into spontaneous reactions with cathodic oxidants. Salts in molten acetamide, however, made suitable low-melting electrolytes for organic thermal cells. Potentials of some fused-acetamide cells were measured as a function of temperature, and the behavior on discharge was observed.

An organic fused-salt cell is a reserve-type thermal cell which produces electrical energy of long duration on application of a requisite amount of heat. The organic electrolyte of this cell is solid and nonconducting at ordinary temperatures, but, on activation, the heat rapidly applied to the cell causes the electrolyte to melt and become conducting.

Organic thermal cells have not been studied thoroughly in the past, chiefly because of a lack of reliable data of the physical and electrochemical behavior of suitable low melting salts. The literature on fused-salt thermal cells relates chiefly to inorganic ones of the type reported by Hamer and Schrodt (1) and Goodrich and Evans (2). Special inorganic types have been treated by Rubin and Malmberg (3), McKee (4), Doan (5), Selis (6), and Jennings (7). Panzer (8) carried out exploratory test surveys on a wide variety of organic and inorganic salts for possible application as suitable electrolytes in fused-salt thermal cells. Unfortunately, most fused-salt cell studies are largely qualitative in nature.

The three most important disadvantages of current inorganic thermal cells are (*a*) high operating temperatures (400°-600°C), (*b*) cell life limited to 5-10 min, and (c) marked cathodic polarization.

Organic electrolytes can be divided into two classes. The first is organic salts that conduct electrolytically in the molten state, *e.g.*, the sulfonates, formates, acetates, and substituted pyridinium salts. The second class includes solutions of salts in organic solvents, *e.g.*, molten acetamide salt solutions (9).

Experimental

Reagents.—Methylpyridinium chloride was prepared by the method of Rozhdestvenskii (10). The hygroscopic crystalline solid melted at 138°C, in agreement with that reported in the literature. On melting, the salt forms a clear, water-white melt that did not decompose up to 200°C for 2 hr. This chloride salt was extremely hygroscopic and difficult to obtain in high yields. On the other hand, the corresponding bromide pyridinium salt was appreciably less hygroscopic and was obtainable in yields greater than 80%.

Methylpyridinium bromide was prepared by passing excess methyl bromide into a mixture of equal volumes of pyridine and benzene at room temperature. After about 4 min, the exothermic addition reaction between pyridine and methyl bromide occurred. At this time the addition reaction was stopped, and the resulting white slurry removed and washed with large volumes of benzene to ensure removal of trace amounts of pyridine adsorbed on the salt. The salt was purified further by crystallization from anhydrous ethyl alcohol at —40°C. This purification procedure was repeated three times. The salt was vacuum-dried for two days; its melting point is 150°-151°C. The bromide salt forms a clear, water-white melt that did not char or otherwise decompose up to 200°C for several hours.

Acetamide crystals (Mallinckrodt analytical reagent) were further purified by recrystallization from pure benzene and then vacuum-dried for two days. The salts $MgCl_2$, $AlCl_3$, $ZnCl_2$, and $CdCl_2$ (Baker and Adamson reagents) were used without further purification; they were dried at about 200°C and kept in a desiccator.

Metal rod electrodes (Fisher Scientific) were at least 99.5% pure. Silver-silver chloride electrode was prepared electrolytically. Cathodic oxidants such as $CaCrO_4$ and K_2CrO_4 were supplied by Eagle-Picher. All electrode materials were washed with acetone and dried at 120°C prior to use in cells.

Electrolytic cell.—Figure 1 depicts the electrolytic cell used to measure the potentials of organic fused-salt cells as a function of temperature. The cells were constructed of Pyrex glass unless noted otherwise. All

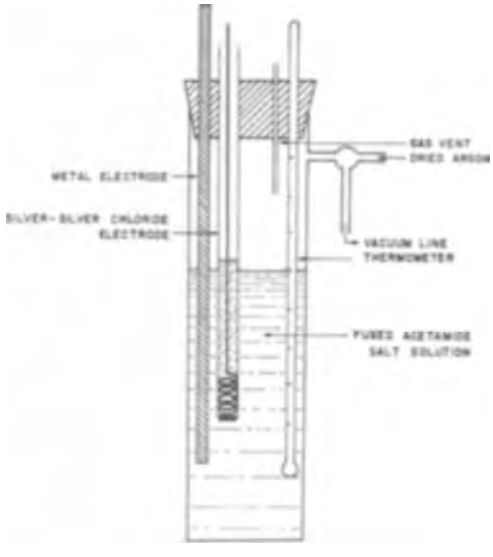

Fig. 1. Fused-acetamide salt cell

[1] Present address: Department of Chemical Engineering, University of California, Berkeley, California.

negative electrodes were ⅛-in. commercially pure metal rods. The positive electrode was nickel mesh with $CaCrO_4$ or K_2CrO_4 oxidants for fused acetate and pyridinium cells. For fused acetamide salt cells, a 1/16-in. Ag/AgCl rod immersed in 0.10M KCl-Acetamide and contained in a fritted glass tube, shown in Fig. 1. A positive liquid head was maintained in the tube compartment of this Ag/AgCl electrode to prevent contamination of the acetamide salt solution. Interelectrode distance was about 1.0 cm. Approximately 100g of a tenth molal metal chloride solution was placed in the cell, immersed in a thermonitor-controlled oil bath by Sargent.

Upon fusion of the organic salt mixture, the cell was vacuum-pumped for 2 hr through the side arm to remove water vapor from the electrolyte. Then dry argon gas was allowed to enter, bringing the system to atmospheric pressure. Argon was continuously maintained above the organic melt and allowed to escape via a small exit tube in the stopper. Once constant temperature was attained, the emf of the system was measured with an L&N K-3 potentiometer.

Results and Discussion

Potassium methylsulfonate and the sodium salts of benzene and p-toluene sulfonic acids all failed to melt. Molten sodium formate did not decompose for several hours at 270°C, but readily reduced AgCl, $CaCrO_4$, and K_2CrO_4 cathodic reactants.

A eutectic mixture (11) of sodium, potassium, and lithium acetates (37.5/11.9/50.6 w/o) melted at 157°C and remained thermally stable and conductive at 200°C for 5 hr. The fused acetate eutectic also reacted spontaneously with $CaCrO_4$ and K_2CrO_4. The cell Mg/alkali acetate eutectic/$CaCrO_4$,Ni failed to deliver useful amounts of current at 250°C.

Substituted pyridinium halides have better thermal and conductive properties than unsubstituted pyridinium halides (12). Methylpyridinium chloride and bromide were thus synthesized and evaluated as molten electrolytes for organic thermal cells. Figure 2 presents the electrical conductivity of molten methylpyridinium bromide. Clearly, this salt conducts very well in the molten state.

The organic salt cell, Mg/methylpyridinium bromide/$CaCrO_4$,Ni gave an open-circuit potential of 1.15v at 200°C. Appreciable currents, however, were not obtained when this cell was under load. At the magnesium electrode, two reactions took place during discharge: the electrochemical cell reaction and the redox reaction between magnesium and methylpyridinium bromide.

Potential-temperature data of several fused acetamide salt systems were measured in our experimental

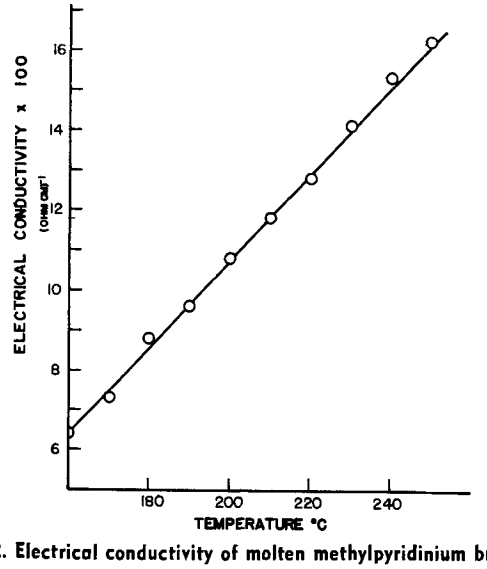

Fig. 2. Electrical conductivity of molten methylpyridinium bromide

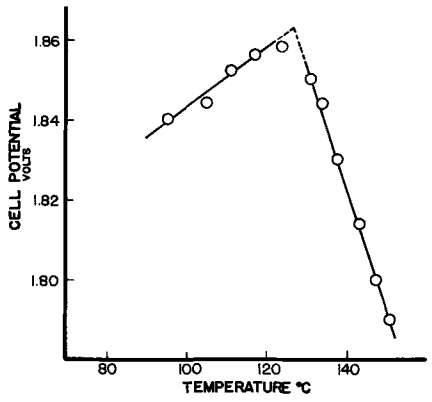

Fig. 3. Cell potential of Mg/0.10M $MgCl_2$-acetamide/AgCl,Ag. Hydrogen was evolved above 125°C.

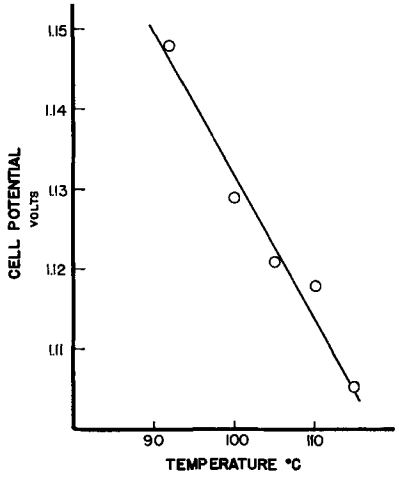

Fig. 4. Cell potential of Al/0.10M $AlCl_3$-acetamide/AgCl,Ag. Hydrogen was evolved both on open circuit and discharge.

cell. Calcium is not included here because of its vigorous reaction with fused acetamide to generate hydrogen. Conductance data for several alkali and alkaline earth chlorides in molten acetamide are given by Wallace (9) and Winkler (13).

Magnesium.—The open-circuit potential of Mg/0.10*M* $MgCl_2$-acetamide/AgCl,Ag cell is shown in Fig. 3 as a function of temperature. The potential (1.835v at 90°C) increased with temperature up to about 125°C (1.860v) where hydrogen evolution began. Above 125°C the cell potential rapidly decreased. The extent of magnesium corrosion with molten acetamide increased slowly up to 125°C and then accelerated in an exponential-like manner with rising temperature.

Much hydrogen gassing occurred in these cells when placed on discharge. On replacing chloride solutions with bromide salt solutions in magnesium-acetamide thermal cells, however, hydrogen evolution was reduced markedly.

Aluminum.—The open-circuit potential of Al/0.10*M* $AlCl_3$-acetamide/AgCl,Ag cell was measured as a function of temperature. Figure 4 shows the cell potentially (1.150v at 90°C) falling sharply with increasing temperature. Hydrogen evolution occurred rapidly with aluminum due chiefly to the high acidity of molten $AlCl_3$-acetamide. When aluminum-acetamide cells were placed on discharge, very vigorous hydrogen evolution was noted.

Zinc.—The equilibrium voltage of Zn/0.10*M* $ZnCl_2$-acetamide/AgCl,Ag decreases linearly with increasing temperature, as shown in Fig. 5. The potential of the cell reaction: $Zn + 2AgCl = ZnCl_2$ (0.10*M*) $+ 2Ag$ with a zinc chloride concentration of 0.10*M* in molten

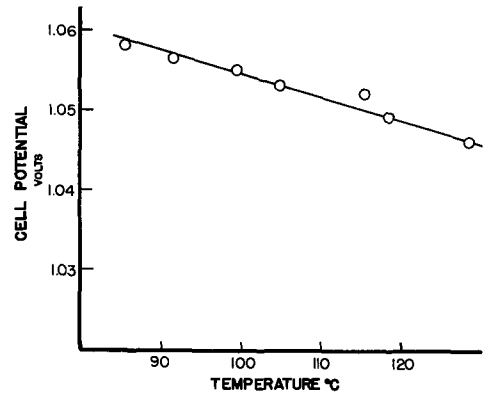

Fig. 5. Cell potential of Zn/0.10M $ZnCl_2$-acetamide/AgCl,Ag

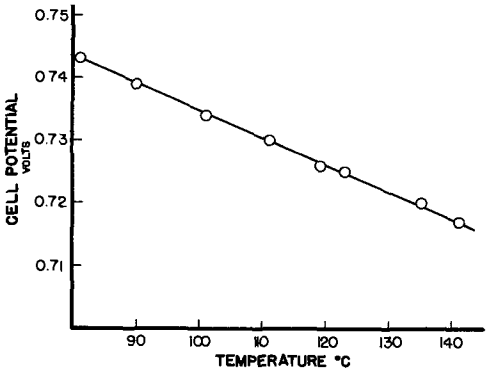

Fig. 6. Cell potential of Cd/0.10M $CdCl_2$-acetamide/AgCl,Ag

acetamide is 1.058v at 90°C. By use of the Gibbs-Helmholtz relation, the heat of reaction is calculated to be —56.3 kcal/mole and entropy change, —25.3 e.u. For comparison, ΔH of —55.6 kcal/mole and ΔS of —34.5 e.u. are recorded at 25°C for the aqueous cell reaction: Zn + 2AgCl = $ZnCl_2$ (a = 1) + 2Ag with unit zinc chloride activity in water (14).

The discharge behavior of this galvanic cell system was determined at 90° and 130°C. Several silver chloride-zinc cells were held at these temperatures for 8 hr before discharging. No harmful effects or cell deterioration was observed. Even under maximum current drains, the zinc electrode did not gas. The initial maximum current output from these cells were largely limited by the resistance offered by the molten electrolyte. Values for the conductivity of molten 0.10*M* $ZnCl_2$-acetamide were 0.5 x 10^{-3} ohms-cm^{-1} at 90°C and 0.9 x 10^{-3} ohms-cm^{-1} at 130°C. Discharge cell performance and limitations for silver chloride-zinc cells are presented in another paper (15).

Cadmium.—In Fig. 6 is given the equilibrium cell potential of Cd/0.10*M* $CdCl_2$-acetamide/AgCl,Ag cell as a function of temperature. The potential of the cell reaction: Cd + 2AgCl = $CdCl_2$ (0.10*M*) + 2Ag with a cadmium chloride concentration of 0.10*M* in molten acetamide is 0.739v at 90°C. The heat of reaction is calculated to be —42.3 kcal/mole and entropy change, —23.0 e.u. For comparison, ΔH of —36.5 kcal/mole and ΔS of —26.1 e.u. are recorded at 25°C for the aqueous cell reaction: Cd + 2AgCl = $CdCl_2$ (a = 1) + 2Ag with unit cadmium chloride activity in water (14).

The discharge behavior of this galvanic cell system was also determined at 90° and 130°C. No cell deterioration or gassing was noted on discharge. Likewise, maximum current output from these silver chloride-cadmium thermal cells were initially limited by the conductivity of 0.10*M* $CdCl_2$-acetamide melt, 0.3 x 10^{-3} ohms-cm^{-1} at 90°C, and 0.7 x 10^{-3} ohms-cm^{-1} at 130°C. Discharge behavior of these cells was similar to silver chloride-zinc thermal cells.

Acknowledgments

The authors wish to thank the Sandia Power Sources Laboratory in Albuquerque, New Mexico, for their sponsorship. Thanks are due to Dr. Charles Jennings and Dr. Frank Hudson for stimulating discussions.

Manuscript received Aug. 12, 1966; revised manuscript received Oct. 12, 1966. This paper was delivered before the New York Meeting Oct. 1-3, 1963. This work was done in partial fulfillment of the requirements for the Ph.D. degree at Polytechnic Institute of Brooklyn by R. A. Wallace.

Any discussion of this paper will appear in a Discussion Section to be published in the December 1967 JOURNAL.

REFERENCES

1. W. J. Hamer and J. P. Schrodt, *J. Am. Chem. Soc.*, **71**, 2347 (1949).
2. R. B. Goodrich and R. C. Evans, *This Journal*, **99**, 207 (1952).
3. B. Rubin and M. S. Malmberg, National Bureau Standards Report 3081, Washington, D. C. (1954).
4. E. S. McKee, Proc. Tenth Annual Battery Conference, Power Sources Div., Signal Corps Engineering Lab., Fort Monmouth, N. J. (1956).
5. D. J. Doan, Proc. Eleventh Annual Battery Conference, Power Sources Div., Signal Corps Engineering Lab., Fort Monmouth, N. J. (1957).
6. S. M. Selis, Proc. Twelfth Annual Battery Conference, Power Sources Div., Signal Corps Engineering Lab., Fort Monmouth, N. J. (1958).
7. C. W. Jennings, *This Journal*, **103**, 531 (1956).
8. R. E. Panzer, Technical Memorandum 44-7, U. S. Naval Ordnance Laboratory, Corona, Calif. (1960).
9. R. A. Wallace, Dissertation, Investigation of Organic Fused-Salt Cells, Polytechnic Institute of Brooklyn, New York (1963).
10. M. S. Rozhdestvenskii and L. M. Broude, *J. Appl. Chem. (USSR)*, **10**, 722 (1937).
11. N. M. Sokolov, *J. Russian General Chem.*, **24**, 1145 (1954).
12. R. C. Elderfield, "Heterocyclic Compounds," Vol. 1, p. 414, John Wiley & Sons, Inc., New York (1950).
13. G. Winkler in "Chemistry in Nonaqueous Ionizing Solvents," G. Jander, H. Spandau, and C. Addison, Editors, Vol. IV, Part 3, Vieweg and Sohn, Braunschweig, Germany (1963).
14. W. M. Latimer, "Oxidation Potentials," Prentice-Hall, New York (1953).
15. R. A. Wallace and P. F. Bruins, *This Journal*, **114**, 212 (1967).

Fused-Acetamide Thermal Cells

Richard A. Wallace[1] and Paul F. Bruins

Department of Chemical Engineering, Polytechnic Institute of Brooklyn, Brooklyn, New York

ABSTRACT

Low-temperature (<200°C) fused-acetamide thermal cells, using highly porous cathodes, furnish appreciable electrical energy on discharge. The cell, Zn/2.5% KCl-acetamide/AgCl,Ag had an average discharge voltage of 0.970v (at 2.0 ma/cm^2 and 100°C) for 360 min. Cathodic polarization was principally responsible for termination. Voltage regulation and uniform discharge depended to a very large degree on silver chloride electrode. Effects of charge rate and addition of small amounts of water on cell discharge were also measured.

In the previous paper (1) we reported that low-temperature (<200°C) organic thermal cells generated appreciable electrical energy on discharge and molten acetamide salt solutions made good cell electrolytes. In this paper, the fused acetamide cell, Zn/2.5% KCl-acetamide/AgCl,Ag has been studied.

Existing information on the physical and chemical properties of solid and molten acetamide has been reviewed by Winkler (2) and Wallace (3). In 1957 Jander and Winkler (4) made careful potentiometric and conductometric titrations of a relatively large number of acid-base neutralization reactions in molten acetamide. Early in 1960, Wallace (3) measured several physical and electrochemical properties of molten KCl-acetamide and KBr-acetamide systems over their full solubility and temperature ranges and reported their use as low-temperature thermal cell electrolytes. We found that molten saturated KCl-acetamide meets most of the basic criteria set down for a suitable electrolyte for organic fused-salt cell usage (1). Its effective liquid range, and hence the temperature range of the cells, lies between 77°C (melting point) and 180°C (200 mm Hg vapor pressure).

Acidic (H_2SO_4) and basic (KOH) solutes are not suitable for cell usage because they decompose acetamide. A nonhygroscopic, neutral salt having good solubility and conductance in molten acetamide is needed and KCl was found suitable. The molten acetamide salt solution (see Fig. 1) should be nearly saturated (2.5g KCl/100g acetamide or 0.33*M*). Such a KCl-acetamide solution is preferred because it provides maximum conductance while still assuring complete solution of KCl at any temperature.

Silver chloride was selected as the cathodic reactant. Preliminary experiments showed that it provides excellent voltage stability and an unusually flat discharge curve in working acetamide cells. Also, it is slightly soluble in saturated KCl-acetamide solutions.

Zinc was the most convenient working anode for a study of fused-acetamide salt cells under discharge for long periods (hours) at moderately high current drains. Zinc did not gas in the organic thermal cell, Zn/KCl-acetamide/AgCl,Ag on dicsharge. It has a high electrochemical capacity (49.2 amp-min/g), and $ZnCl_2$ is highly soluble in molten acetamide.

Experimental

Reagents.—Acetamide crystals (Mallinckrodt analytical reagent grade) were further purified by recrystallization from pure benzene. Recrystallized acetamide was vacuum-dried for two days and then kept in a desiccator. The salts KCl and $ZnCl_2$ (Baker and Adamson reagents) were used without further purification; the salts were dried at about 150°C and the dried salts kept in a desiccator. Dry argon gas was used to minimize dissolved oxygen in fused acetamide. Zinc sheet (N. J. Zinc) was 99.95% containing less than 0.005% Cu, 0.005% Fe, 0.005% Cd, the major impurity being Pb. Rectangular sheets of high-purity, fused AgCl electrodes with a surface skin of Ag to make electronic contact were supplied by Eagle-Picher. Our analysis showed these electrodes contained 99.5% AgCl and 0.5% Ag.

Reference electrode.—The Ag/AgCl/Cl^- reference electrode has been used successfully in both aqueous and molten salt electrochemistry and found by Wallace (3) to be a stable and reproducible reference electrode in molten acetamide systems. The Ag/AgCl/Cl^- reference electrode is described in Fig. 2. The glass container for this reference electrode (Fig. 2) was a small glass tube of about ½-in. diameter with a fritted glass bottom (medium porosity) that acted as a salt bridge between the reference electrode and test cell electrodes. The electrode proper was prepared by chloridizing a 1.6 mm silver wire in 1*N* HCl at 25°C for 2 hr at 10 ma/cm^2 current density. The lower portion of the electrode was wound spirally to provide not only greater electrolytic contact area, but also a snug fit with the inside of the tube, thereby fixing the position of the electrode. Excess solid KCl was added to the tube compartment in order to keep the chloride activity constant.

Conductometric measurements.—Conductances of molten electrolytes were measured with an industrial instrument (model RC-16B2) conductivity bridge using a dip-type cell with a 0.630 cell constant. The measurements were made at a frequency of 1000 Hz; preliminary runs showed that electrolyte resistances were independent of frequency.

Temperatures of molten acetamide solutions were controlled to 0.3°C by a forced-draft electric furnace. A period of 20 min was allowed after each salt addition before a resistance reading was taken. During this period the melt was shaken to ensure complete solution of the added salt and to hasten equilibrium.

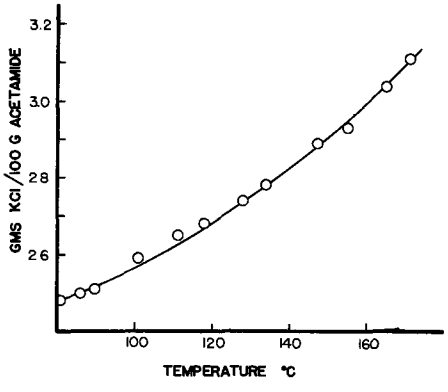

Fig. 1. Solubility of KCl in molten acetamide

[1] Present address: Department of Chemical Engineering, University of California, Berkeley, California.

Cell design and testing.—Experimental acetamide cells consisted of a Ag-AgCl rectangular cathode (3.3 x 3.3 x 0.091 cm) sandwiched between two parallel zinc anodes (3.3 x 3.3 x 0.059 cm). Electrode separation was effected by four tiny glass strips (0.80 cm long and 0.40 cm wide) cemented to the top and bottom edges of each electrode with a high-temperature epoxy adhesive. The parallel-electrode arrangement (Fig. 2) was used because it was simple in geometrical design, provided as nearly uniform current density as possible over the surfaces of the plane electrodes, and allowed the acetamide melt to circulate freely between working electrodes. Electrical contact was made by soldering a thin Zn tab to the two outside Zn sheets and by silver-soldering a thin Ag wire to the silver-coated AgCl electrode, or in the case of electroformed Ag-AgCl, to the Ag mesh screen itself. This sandwich cell was sturdy and did not buckle under thermal stresses produced during testing.

More porous Ag-AgCl cathodes were also prepared by chloridizing spongy silver sheets, incorporated on silver grids of about 50 by 50 mesh supplied by Eagle-Picher. Silver was electrolytically converted into active AgCl by chloridizing in a 1*N* HCl at 25°C and a current density of 10 ma/cm². Formation was continued until the remaining silver was reduced to about one-half its original thickness.

All cells were immersed in a 400 ml Pyrex beaker containing 2.5% KCl-acetamide solution maintained at a constant temperature in an electric oven. Cell voltages were measured with a Sargent (Model MR) multirange potentiometric recorder, calibrated periodically against a Weston standard cell whose emf was 1.0193v. These cells were discharged at a constant current by manually adjusting the load. Charging of the cells was done either on an automatic constant current charger supplied by Ray-O-Vac, Division of Electric Storage Battery Company, or manually.

Electrode polarization.—Polarization potential of the working electrodes were measured at 100°C by means of the reference electrode in the same acetamide electrolyte. Included in these polarization potentials was the ohmic drop in the electrolyte between the reference electrode and the surface of the working electrode. To minimize this voltage drop, the reference electrode was placed in close proximity to the outer edge of both working electrodes, a region where the current flux is minimal.

Results and Discussion

A systematic conductometric analysis of the role and influence of $ZnCl_2$ in molten $KCl_{(sat.)}$-acetamide was made by Wallace (3). In Fig. 3 is presented the specific electrical conductance of $ZnCl_2$-$KCl_{(sat.)}$-acetamide solutions, as a function of zinc salt concentration and temperature. When added in small amounts, $ZnCl_2$ markedly diminished the conductivity of the molten KCl-acetamide electrolyte. On further additions, the conductivity reached a minimum and then increased fairly rapidly thereafter until it attained a maximum value occurring in the 1-3*M* zinc salt region.

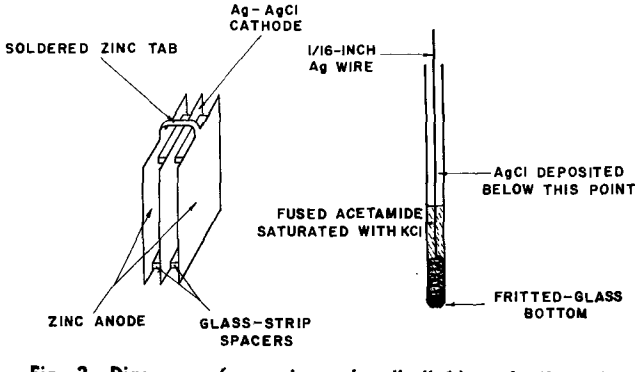

Fig. 2. Diagrams of experimental cell (left) and silver-silver chloride reference electrode (right).

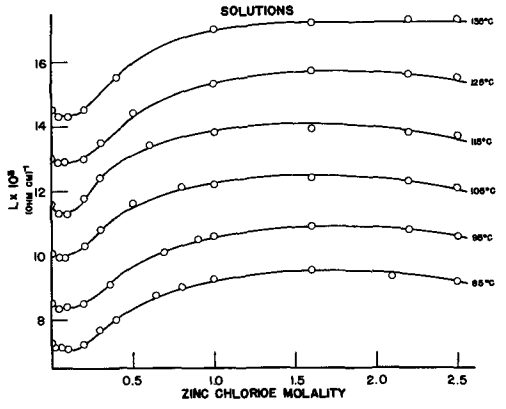

Fig. 3. Specific conductance of molten $ZnCl_2$-$KCl_{(sat.)}$-acetamide solutions.

These conductance deviations were attributed to the formation of chlorozinc complex and coordination molecules in the saturated KCl-acetamide melt; these effects resulted in minimum-maximum curves. The precise location of the minima and maxima points depend upon the temperature and amount of KCl in acetamide. In Fig. 3 it is of interest to point out that the large temperature coefficient of conductance may be due to two factors: (*i*) less stability of chlorozinc complexes with increasing temperature, putting more chloride ions in solution, and (*ii*) increased KCl solubility with temperature, putting more potassium and chloride ions in solution.

Cell performance.—The performance characteristics of experimental Zn/2.5% KCl-acetamide/AgCl,Ag cells were measured with temperature, electrode spacing, and discharge current density as parameters. Typical performance curves for cells using fused Ag/AgCl cathodes are shown in Fig. 4. On applying a load, the cell voltage falls almost instantaneously to a steady value and remains fairly constant throughout discharge.

The magnitude of the maximum current drains increased with an increase in operating temperature and, to a lesser extent, with a decrease in electrode spacing. Discharge current densities exceeding 30 ma/cm² could not be obtained from these experimental cells, although it is likely that higher current densities could be attained in cells using more porous cathodes, operating at higher temperatures with closer electrode spacings.

Temperature effect.—In all experimental cells, the cell voltage and maximum current output increased

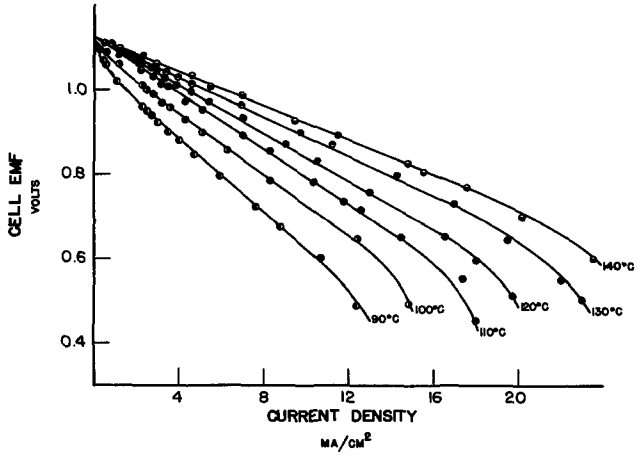

Fig. 4. Performance of Zn/KCl-acetamide/AgCl,Ag cells (0.312 cm electrode spacing) at various temperatures.

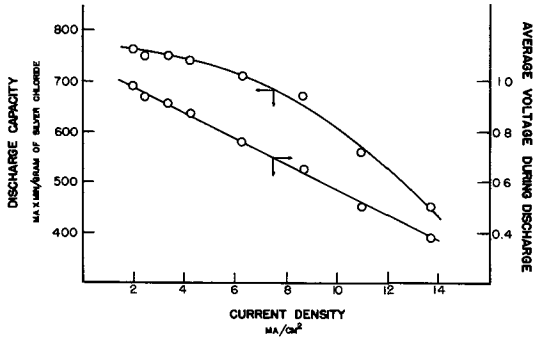

Fig. 5. Discharge capacity and average voltage of acetamide cells on discharge at 100°C.

materially with temperature. Figure 4 illustrates the large temperature effect on cell output.

Discharge capacity.—The discharge capacity, in milliamps-minutes per gram of fused AgCl, was calculated from cell performance curves and given in Fig. 5 as a function of current density. Also included in Fig. 5 is the variation of the average cell voltage with current density. Figure 5 points out that Zn/2.5% KCl-acetamide/AgCl,Ag cells do not furnish as great a capacity when discharging at high current densities as when discharging at low densities.

A more porous, electroformed silver chloride cathode was fabricated and tested. Approximately 1.40g of AgCl was electrolytically formed on the silver mesh grid (22 cm^2 exposed geometric surface area). Several Zn/2.5% KCl-acetamide/AgCl,Ag cells, with this electroformed AgCl were discharged at 100°C at a current density of 2 ma/cm^2. These cells had a 0.970 average discharge voltage and a 360-min cell life, which is equivalent to 1.3g of converted AgCl. In comparing cells using fused AgCl electrodes with an average cell capacity of only 0.762 amp-min/g AgCl with electroformed AgCl electrodes with a cell capacity 11.1 amp-min/g AgCl, a striking increase in cell capacity is revealed. It should be pointed out that this higher cell capacity is close to the theoretical capacity of 11.2 amp-min/g. AgCl. Longer discharge times were also obtained by electroforming even greater amounts of AgCl on silver grids.

Individual electrode behavior.—For the purpose of pinpointing the cause of cell termination and improving performance, individual electrode polarizations were measured at 100°C at a variety of discharge rates. Generally, the current drain had much more effect on cathodic than on anodic polarization. Cathodic polarization increased with time much more rapidly under high current drains and was principally responsible for discharge termination.

Anodic polarization, on the other hand, was comparatively small and did not significantly alter cell performance. The magnitude of anodic polarization was in the 5-15 mv range and increased with an increase in current drain, and only slightly with length

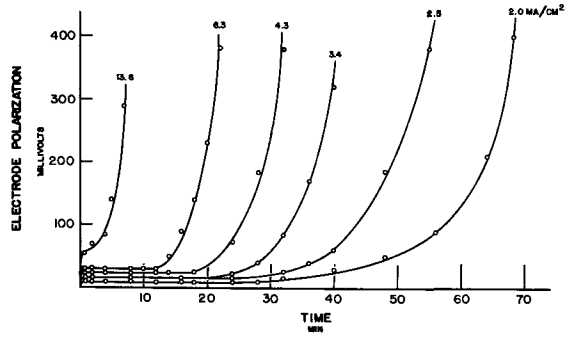

Fig. 6. Fused AgCl cathodic polarization in discharging acetamide cells at 100°C.

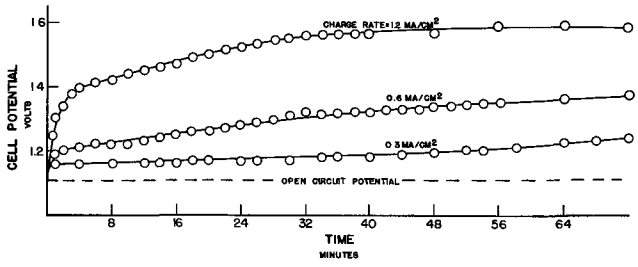

Fig. 7. Performance of Zn/KCl-acetamide/AgCl,Ag cells (0.12 cm electrode spacing) on charging at 100°C.

of discharge. This was attributed entirely to concentration polarization effects.

Cathodic polarization results in Fig. 6, clearly point out that the silver chloride cathode contributes most to cell termination. The polarizations remain fairly constant over much of the discharge until, at the inverted knee of the curve, there is a sudden large increase.

At the end of cell discharge, the AgCl on the cathode surface was observed to be reduced to spongy silver. Chloride ions must diffuse from within this dense, fused AgCl electrode. As a result, severe polarization took place. At current drains greater than 15 ma/cm^2, cell output was virtually dependent on the amount of KCl in immediate contact with active layers of AgCl. These polarization results accentuate the need to use a cathode of high porosity for usage in fused-acetamide thermal cells.

Charge rate.—Figure 7 shows the effect of charge rate on cell performance at low current densities at 100°C. These cells consisted of a zinc sheet (17.0 cm^2 exposed surface area) and a silver grid of the same area. On charge, their terminal cell voltage increased sharply. This abrupt rise in charge voltage was caused by the sudden drop in KCl concentration at the silver electrode and by hydrogen evolution coming from the zinc electrode. All cells were arbitrarily charged for 72 min and then discharged at 4.0 ma/cm^2 current density; on the average, about 60-70% charge was recovered. These experiments demonstrate that Zn/KCl-acetamide/AgCl,Ag molten acetamide cells are capable of being recharged.

Water addition.—Water is completely miscible with molten acetamide and allows the slightly aqueous acetamide to dissolve greater amounts of salt. The effect of water on melting point of solid 2.5% KCl-acetamide solution is recorded in Fig. 8.

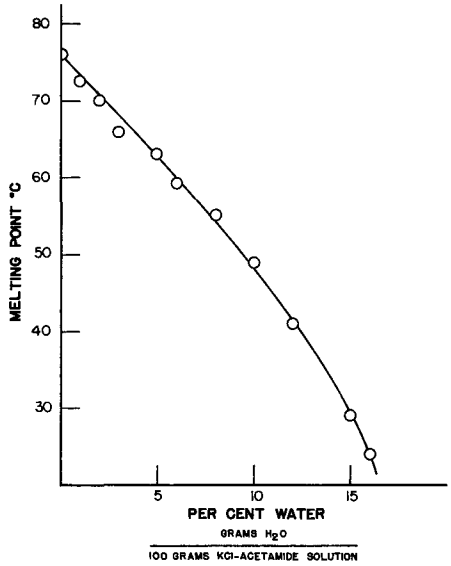

Fig. 8. Effect of water on melting point of solid 2.5% KCl-acetamide solution.

Addition of small amounts of water permitted the operating temperatures of acetamide thermal cells to be extended downwards. For example, three acetamide cells were discharged at 80°C in saturated KCl-2% H_2O-acetamide, melting point 70°C. The discharge performance of these cells at 80°C were similar to anhydrous cells at 100°C.

Acknowledgments

The authors wish to express their thanks to the Sandia Power Sources Laboratory in Albuquerque, New Mexico for their sponsorship, and to Dr. Charles Jennings and Dr. Frank Hudson for stimulating discussions.

Manuscript received Aug. 12, 1966; revised manuscript received Oct. 12, 1966. This paper was delivered before the New York Meeting, Oct. 1-3, 1963. This work was done in partial fulfillment of the requirements for the Ph.D. degree at Polytechnic Institute of Brooklyn by R. A. Wallace.

Any discussion of this paper will appear in a Discussion Section to be published in the December 1967 JOURNAL.

REFERENCES

1. R. A. Wallace and P. F. Bruins, *This Journal*, **114**, 209 (1967).
2. G. Winkler in "Chemistry in Nonaqueous Ionizing Solvents," G. Jander, H. Spandau, and C. Addison, Editors, Vol. IV, Part 3, Vieweg and Sohn, Braunschieveig, Germany (1963).
3. R. A. Wallace, Dissertation, Investigation of Fused-Organic Salt Cells, Polytechnic Institute of Brooklyn, New York (1963).
4. G. Jander and G. Winkler, *J. Inorg. Nuclear Chem.*, 2, 24 (1959).

Infrared Spectroscopic Investigation of Charged Nickel Hydroxide Electrodes

Frederick P. Kober

General Telephone & Electronics Laboratories Incorporated, Bayside, New York

ABSTRACT

Through the use of deuterated samples of $Ni(OH)_2$ electrodes at various stages of charge, it has been possible to make definitive band assignments for the structures of the active material. The relative intensity of the band due to hydrogen bonding in the charged state is shown to be a measure of the electrochemical capacity of the system. The charging reaction gives rise to the formation of active oxygen sites (as defined by Aia) through a site alteration mechanism in addition to the formation of hydrogen bonded sites within the charged phase. The mechanistic and structural implications of these spectral data are discussed in detail.

In a previous publication (1), the characteristic structural changes which occur in the hydrated nickel-oxide electrode during charge-discharge were examined. It was shown that the discharged state is characterized by nonhydrogen bonded hydroxyl groups whereas the charged state is a hydrogen bonded structure. In addition, Labat (2) and more recently Aia (3) have demonstrated the role of active oxygen[1] in the electrochemical capacity of the charged state. In fact, there is quantitative agreement between the equivalents of active oxygen "stored" in the higher oxide structure and the observed electrochemical capacity (3).

The nickel hydroxide electrode reaction, particularly the charged state, has been re-examined using high resolution infrared spectroscopy. By means of deuterium substitution, more definitive band assignments are made for the structure of the active materials. The formation of active oxygen which accompanies the charging reaction is shown to be closely associated with the formation of hydrogen bonding within the solid phase. The relative intensity of the absorption band due to hydrogen bonded groups is found to be proportional to the electrochemical activity of the higher oxide and, hence, its active oxygen content.

Experimental Procedure

Preparation of sintered electrode samples for infrared analysis is given in detail elsewhere (1). For this particular study, Nujol mulls were employed throughout. In the region from 4000 to 2500 cm^{-1} both CaF_2 and Irtran II windows were used, whereas polyethylene windows were used for the far infrared measurements (600-280 cm^{-1}). All measurements were made using a Beckman IR-7 double-beam instrument equipped with CsBr optics.

[1] The concept of active oxygen formation resulting from the anodic polarization of $Ni(OH)_2$ is discussed by Labat (2) and by Aia (3).

Deuteration of the discharged electrode material was accomplished by washing ground samples several times with D_2O (99.99%) using the method of Cabannes-Ott (4). This method takes advantage of the rapid exchange of hydrogen with deuterium in the $Ni(OH)_2$ system (5). When applied to the charged electrode material, this method of deuteration proved unsuccessful. Deuteration was achieved by immersing the discharged electrode in 31% KOD (D_2O), cycling several times, and subsequently washing the charged electrode in D_2O. This result indicates that protons are considerably more tightly bound in the higher oxide thus limiting exchange with D_2O.

The spectra of deuterium-free samples were measured against pure Nujol placed in the reference beam. In order to clearly discern spectral shifts due to deuteration, it was necessary to place undeuterated samples in the reference beam. The necessity of this differential technique was a consequence of the fact that the deuteration procedures employed yielded only partial exchange with hydrogen.

Results and Discussion

4000-2500 cm^{-1} Region.—Deuteration of the discharged electrode caused the sharp intense band observed at 3650 cm^{-1} to shift to 2705 cm^{-1}. This result is in agreement with that of Cabannes-Ott (4) and is illustrated in Fig. 1. These frequencies are in the ratio 1.35 substantiating the assumption that this absorption is the stretching fundamental of the nonhydrogen bonded hydroxyl groups.[2] During charging, the stretching fundamental is replaced by a broad diffuse absorption having a center at approximately 3450 cm^{-1} and attributed to hydrogen bond forma-

[2] To a first approximation, the frequency in wave numbers of a classical harmonic oscillator is given by $\gamma\ (cm^{-1}) = (1/2\pi C)\ (k/\mu)^{1/2}$ where k is the Hook's law force constant and μ is the reduced mass. Consequently, the ratio of frequencies will be inversely proportional to the square-root of the ratios of reduced masses. The theoretical ratio $(\mu_{OD}/\mu_{OH})^{1/2}$ is found to be 1.36.

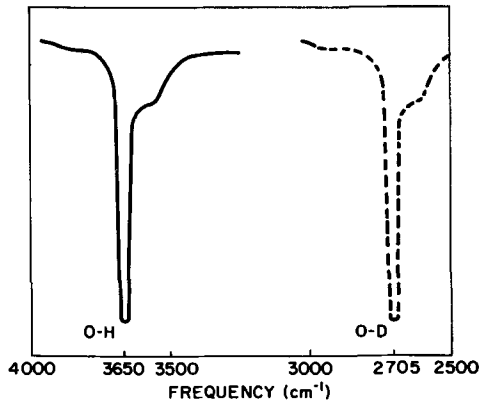

Fig. 1. Shift in OH stretching fundamental due to deuterium substitution.

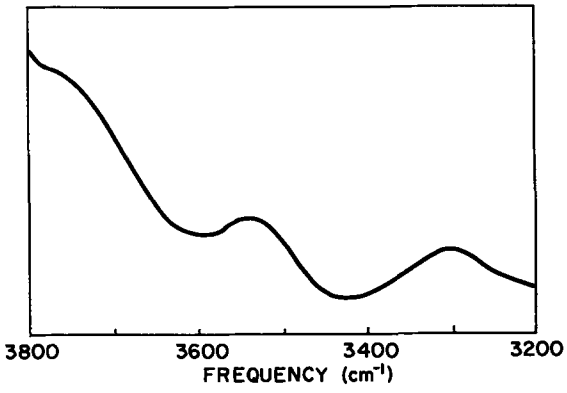

Fig. 2. Spectrum of charged Ni-O electrode in 3μ region

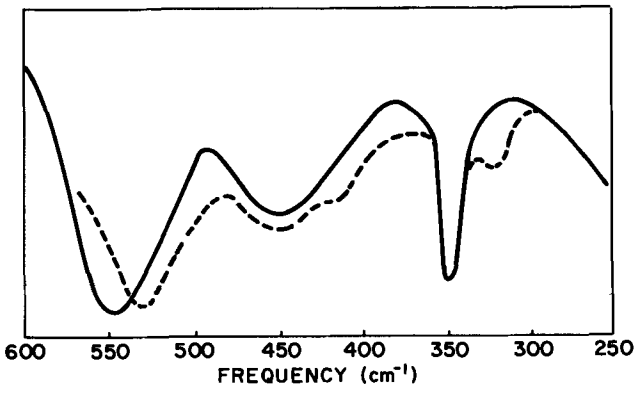

Fig. 3. Spectra of discharged Ni-O electrodes in the region 600 to 250 cm^{-1}; —$Ni(OH)_2$, - - - - $Ni(OD)_2$.

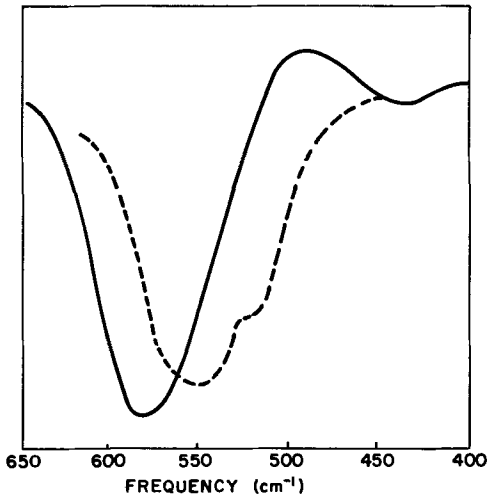

Fig. 4. Spectra of charged Ni-O electrodes in the region 650-400 cm^{-1}; —Ni-O(H); - - - Ni-O(D).

tion (1). Examination of this band under high resolution (greater than 1 cm^{-1}) reveals that, in fact, two or perhaps three bands are superimposed. These bands are shown in Fig. 2. Due to the nature of the samples, it was not possible to achieve better resolution of these absorptions even with deuterium substitution.

The broad diffuse nature of these bands suggests that they arise from lattice modes of the hydrogen bonded hydroxyl layers. Similar spectral features in the three micron region are observed for the minerals boehmite (γ-AlOOH) (6) and lepidocrocite (γ-FeOOH). These minerals are hydrogen bonded layer structures in which the central cations are surrounded by distorted octahedra of oxygens, the over-all symmetry being orthorhombic. Although the spectrum of the charged nickel-oxide electrode is not truly definitive with regard to structure, there is indication that similarities exist between the structure of the higher nickel oxides and that of boehmite (or lepedocrocite).

650-250 cm^{-1} Region.—The spectra, in this region, of both discharged and charged electrodes have been reported previously (1). Upon deuterium substitution, several frequency shifts are observed. These shifts are illustrated in Fig. 3. The band at 325 cm^{-1} in the deuterated sample is associated with the librational mode at 350 cm^{-1}.[3] In addition to the absorption at 325 cm^{-1}, there are bands observed at 415 and 525 cm^{-1}. Since the absorption at 450 cm^{-1} in the undeuterated sample is due to the nickel-oxygen lattice mode and does not involve proton vibration (1), the two vibrations observed for deuterated electrodes must be associated with shifts in the band having a center at 540 cm^{-1}. Consequently, this absorption is actually the superposition of two vibrations. From group theoretical considerations (7), the band at 540 cm^{-1} appears to arise from the singly degenerate lattice vibration associated with the motion of hydroxyl groups along the 001 direction relative to the nickel ion sites. The shift from 550-540 to 525 cm^{-1} is a manifestation of this assignment. Superimposed on this lattice mode is the torsional mode of the weakly bound lattice water also having a band center at 550-540 cm^{-1} (1). Upon deuteration, a shift to 415 cm^{-1} is observed.

The spectral changes which result from charging of the electrode have also been discussed in ref. (1). The broad but intense band having a center at 575-580 cm^{-1} was shown to arise from hydrogen bonding of the hydroxyl groups. For deuterated samples, this band shifts to 540-550 cm^{-1} with the appearance of a shoulder at approximately 520 cm^{-1}. These shifts are illustrated in Fig. 4. The ratios of these frequencies indicate that the 580 cm^{-1} absorption is a lattice mode(s) caused by the motion of hydrogen bonded linkages, *i.e.*, ---H–O–H––, relative to the nickel sites. This band is discussed in greater detail below. All frequencies together with possible assignments are listed in Table I.

580 cm^{-1} Band.—This band, which arises from the motion of hydrogen bonded linkages, appears to be characteristic of the charged state. As was shown by Aia (3), the charging reaction is accompanied by the continuous formation of active oxygen, the equivalents being in quantitative agreement with the electrochemical capacity. Thus, it is not unlikely that hydrogen bond formation is a consequence of structural changes brought about by the formation of active oxygen sites during the charging reaction. This suppo-

[3] The assignment in ref. (1) for the band at 350 cm^{-1} as a combination band arising from an interaction of the nickel-oxygen lattice mode with a low frequency librational mode (<100 cm^{-1}) now appears to be incorrect. Reconsideration of the data leads to the conclusion that the band at 350 cm^{-1} is, in fact, the true librational mode of the free OH groups. For a theoretical discussion of the OH librational mode in nonhydrogen bonded hydroxides see: C. K. Coogan, *J. Chem. Phys.*, 43, 823 (1965).

Table I. Infrared active vibrations (cm^{-1}) of nickel-oxide electrodes

Discharged electrode, $Ni(OH)_2$	$Ni(OD)_2$	Charged electrode	Deuterated charged electrode	Frequency assignments (8)
3650, sh	2705, sh			OH stretching fundamental
		3580, br 3450, str, br	— —	Lattice modes of H-bonded hydroxyl layers
540-550, int.	415, w			Lattice water libration
	525, br, int.			Hydroxyl group lattice mode
		580, br, int.	545 (525)	Lattice mode(s) of H-bonded linkages
450, br	450	450, v. dif.	450, v. dif.	Ni-O lattice mode
350, sh, int.	325			Free hydroxyl libration

sh—sharp, Int.—intense, br—broad, w—weak, v. dif.—very diffuse.

sition is supported by the fact that the formation of hydrogen bonding is also found to be a continuous function of charge (1). Consequently, any change in active oxygen content should manifest itself as a change in intensity of the band at 580 cm^{-1}.

Thermal decomposition of charged electrodes at various temperatures is accompanied by a loss of active oxygen, leading to a loss in electrochemical capacity (3). This loss of active oxygen does indeed result in a decrease in relative intensity of the absorption due to hydrogen bonded linkages at 580 cm^{-1} (Fig. 5). In fact, this decrease in relative intensity is a direct measure of the remaining electrochemical activity of the electrode.

If we assume that the intensity of the 580 cm^{-1} band for an electrode dried at 25°C represents 100% capacity, the relative intensity of this band as a function of drying temperature is then a measure of the remaining capacity (active oxygen content) after thermal treatment. These data are plotted in Fig. 6 together with actual capacity measurements of charged electrodes thermally treated at various temperatures. The excellent agreement between the capacity values predicted from infrared data with those measured experimentally strongly indicates that the formation of active oxygen is associated with the formation of hydrogen bonding. This conclusion is further supported by the thermal and stoichiometric results of Aia (3).

Mechanistic Implications

It has been demonstrated that the local site of electrochemical activity in the $Ni(OH)_2$ structure is at adjacent nonhydrogen bonded hydroxyl groups (8). Also, from the above results we see that the formation of active oxygen sites (electrochemical capacity) during charging of the electrode causes hydrogen bonding to occur within the solid phase. These data imply the following mechanistic steps.

The charging reaction involves the interaction of a "free" hydroxyl group with the electrolyte, resulting in an alteration of the electron density (electronic structure) at that given hydroxyl site. Since the reaction is initiated at the hydroxyl sites any change in the electronic structure of the nickel ion sites must be the result of electron transfer across the nickel-to-oxygen bonds. The change in the d^8 electronic configuration of the nickel sites brought about in this manner results in the formation of a hydrogen bonded structure possessing an over-all symmetry lower than D_{3d}. Thus, the appearance of active oxygen is a manifestation of a change in electronic structure at a hydroxyl site. A theoretical treatment of the changes in electronic structure which occur at the hydroxyl and nickel ion sites as a result of the interaction of a free hydroxyl site with the electrolyte will be presented in a subsequent paper.

The magnetic susceptibility data of Labat (2) clearly demonstrates that the charging reaction causes a decrease in electron-spin density about the nickel ion sites, thus effecting a change in electronic structure. Since the charging reaction alters the electronic structure of both the hydroxyl and nickel ion sites, a resulting change in crystal structure is anticipated. This over-all change in symmetry of the OH groups about the nickel ion sites has been discussed by Aia (3). Infrared data observed for the charged state in the 3μ region suggests that similarities exist between the structure of the higher oxide and that of boehmite (or lepidocrocite). This possibility is indeed compatible with the mechanistic implications discussed above. The beohmite structure is a hydrogen bonded layer lattice comprising brucite-type subunits linked through the sharing of oxygen atoms at the corners

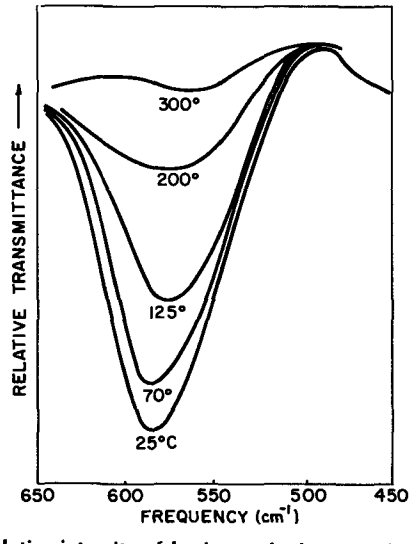

Fig. 5. Relative intensity of lattice mode due to hydrogen bonded linkages as a function of drying temperature.

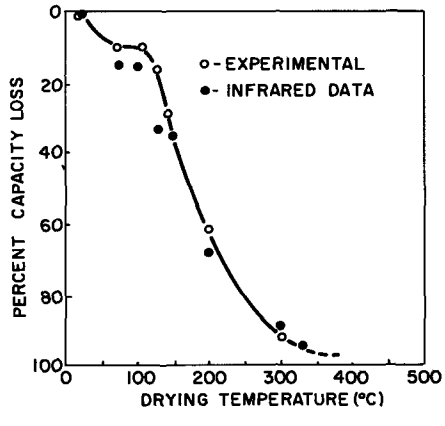

Fig. 6. Predicted and experimental electrochemical capacity remaining after thermal treatment at various temperatures.

of MO_6 octahedra (9). The fact that the nickel-to-oxygen coordination remains essentially octahedral upon charging has been previously shown (1, 8). It is not difficult to envision the conversion of the $Ni(OH)_2$ brucite-type structure into the orthorhombic boehmite-type structure via a change in symmetry at the hydroxyl sites.

Acknowledgment

The author wishes to thank M. Fucci for his aid with the experimental work and M. A. Aia for stimulating discussions concerning this work.

Manuscript received Sept. 14, 1966; revised manuscript received Nov. 21, 1966.

Any discussion of this paper will appear in a Discussion Section to be published in the December 1967 JOURNAL.

REFERENCES

1. F. P. Kober, *This Journal*, **112**, 1064 (1965).
2. J. Labat, Thesis, Univ. Bordaux, *Ann. Chim. (Paris)* **9**, 399 (1964); A. Pacault and J. Labat, *Compt. rend.*, **258**, 541 (1964).
3. M. A. Aia, Ext. Abstracts, Battery Div., Philadelphia Meeting of the Society (1966).
4. *Mme.* C. Cabannes-Ott, *Ann. Chim. (Paris)*, **5**, 905 (1960).
5. For an analysis of the exchange kinetics of H with tritium in $Ni(OH)_2$ see W. Feitknecht, A. Wyttenback, and W. Buser, Proc. 4th Inter. Symp. Reactivity of Solids, Amsterdam (1960), pp. 234-239.
6. L. D. Fredrickson, Jr., *Anal. Chem*, **26**, 1883 (1964); K. A. Wickersheim and G. K. Korpi, *J. Chem. Phys.*, **42**, 579 (1962); E. Schwatzmann, *J. Anorgan. Chem.*, **317**, 176 (1962).
7. For a complete group theoretical analysis of the brucite-type structure see S. S. Mitra, *Solid State Phys.*, **13**, 1 (1962).
8. F. P. Kober, Proc. 5th Internat. Battery Symp., Brighton, September (1966).
9. A. F. Wells, "Structural Inorganic Chemistry," pp. 556-560, Oxford University Press, London (1962).

Kinetics of the Fluorination of Iron

Patricia M. O'Donnell

Lewis Research Center, National Aeronautics and Space Administration, Cleveland, Ohio

ABSTRACT

The effect of temperature and pressure on the reaction of fluorine gas on solid iron samples was studied at various pressures up to 200 Torr over the temperature range of 225° to 525°C. The reaction was found to follow the logarithmic rate law, and logarithmic rate constants are reported. The probable mechanism of film growth is movement of fluorine through defects in the fluoride film to the iron surface.

The purposes of this report are (*i*) to present the results of a kinetic study of the fluorination of iron in the temperature range of 225°-525°C and (*ii*) to propose a mechanism for this reaction. The kinetics of this reaction are interesting since the only data available in the literature are the corrosion type where the reaction of fluorine on iron has been observed by taking a few measurements at long incremental time periods and linearly extrapolating them to give results reported as inches of penetration per month or per year at varying temperatures (1). A linear extrapolation of this type does not give a detailed picture of the reaction but merely defines maximum gross effects. This kinetic study was, therefore, undertaken in order to observe the details of the reaction of fluorine on iron. A few detailed studies of the reaction of fluorine gas with other metals have been reported. By studying the reaction between copper powder and fluorine gas from room temperature up to 250°C and at pressures up to 60 Torr, Brown, Crabtree, and Duncan (2) found that the reaction obeys a logarithmic rate law and is not pressure dependent. This law is widely applicable to corrosion kinetics (3) and relates the amount of reaction y with time t by

$$y = K \log (at + 1) \qquad [1]$$

and where K and a are constants for a given system and temperature. In a study of the reaction of fluorine on plate copper (4, 5), it was found that the reaction followed a logarithmic law above 538°C, but that below that temperature a simple power law was applicable. The reaction was observed to be pressure dependent. Other studies have been made of the reaction kinetics of fluorine with copper (6), nickel (7), and zirconium compounds (8) under various conditions. Although there have been extensive kinetic studies of the rates of oxidation of iron, there are no similar studies on the rates of the fluorination of iron.

Experimental

The vacuum apparatus used to measure the rate of fluorination of iron has been described previously (5).

The general experimental method used to determine the rate of fluorine consumption by iron was to measure the pressure decrease in a vessel of known volume containing the iron sample. In order to maintain approximately constant fluorine pressure, the pressure was allowed to drop only about 2 Torr, whereupon additional fluorine was admitted to return the pressure to its initial value. The perfect gas law was used to calculate the amount of fluorine consumed after each of these steps, from the incremental pressure drop, the vessel volume, and the temperature. Fluorine consumed was expressed in milliliters at standard temperature and pressure. Standard volumetric procedures were used to calibrate the volume of the furnace, storage vessel, and connecting lines. The glass system was passivated by introducing fluorine at increasing pressures and temperatures until further reaction of fluorine with the system was insignificant. The blank after passivation represented a correction of less than 1%.

To determine the temperature gradient along the iron strip, a special strip was made with eight Chromel-Alumel thermocouples attached along it. The leads came through a special end plug to a recording system. The temperature profile along the strip varied ±0.5°C at the low temperatures and ±3° for the 525°C temperature in a nitrogen atmosphere.

The iron samples were machined from spectrographically pure iron having the following impurities in parts per million: manganese, 2; silicon, 2; magnesium, 1; nickel, 1; silver, 1; and copper, 1. The samples were 1.27 x 15.24 x 0.012 cm with a 0.5-cm hole drilled in one end to facilitate handling. All samples were degreased in trichloroethylene, cleaned in 20% hydrochloric acid for 3 min, and washed in distilled

water, acetone, and alcohol. Samples were immediately inserted into the furnace under flowing argon and were positioned the same for each run. The system was sealed and pumped down to about 0.1μ pressure. All samples were preheated 0.5 hr at 525°C under vacuum before running. After the pretreatment, the temperature was adjusted to the operating temperature, and fluorine was introduced to the desired pressure. The recorder plotted the amount of fluorine consumed on a continuous time trace. Some experimental points from the traces are shown on Fig. 1 and 2. When the consumption of fluorine had decreased to a negligible value, the heaters were turned off, the system was allowed to cool to 25°C, and the fluorine was pumped out of the system through the soda lime traps. The test sample was removed to a glass tube holder, which was attached to the end of the reaction section, and was sealed under flowing argon for later visual and instrumental analysis. Some of the films scraped from the strips were analyzed by x-ray diffraction.

For cross-sectional analysis, samples were embedded in plastic, cut, and polished. They were then examined on a metallograph and photographed. The cross section was etched and dyed in order to determine if there was any grain boundary attack. Microscopic analysis was performed to reveal the topology of the samples.

Results and Discussion

The fluorine consumption by the iron samples was measured at several temperatures and pressures (Table I). Figures 1 and 2 illustrate the results; the milliliters of fluorine consumed per square centimeter of iron surface are plotted against the time in minutes. Some duplicate runs (solid symbols) have been plotted in order to show the reproducibility of the data. The effect of temperature on the reaction is shown in Fig. 1 where the data are plotted at temperatures from 225° to 525°C at a constant pressure of 60 Torr. Figures 2(a) and (b) show the effect of pressure on the reaction. In Fig. 2(a) the pressure effect is plotted at a constant temperature of 225°C and in Fig. 2(b) at a constant temperature of 525°C. In Fig. 1 the runs at 375° and 425°C cross at t = 90 min. Similar behavior is noted in Fig. 2 where the runs at 60 and 100 Torr at 525°C cross at t = 70 min. This type of crossover phenomena has also been observed in the oxidation of iron (9). In the 525°C 15-Torr run [Fig. 2(b)], the fluorine was pumped out after 125 min while the sample was kept at 525°C in order to determine the effect of heat and vacuum on the reaction. New fluorine was introduced to 15 Torr (point B), and the reaction appeared to start again. Copper plate and fluorine showed similar behavior (5); however, the reaction between copper powder and fluorine did not start again under similar conditions (2).

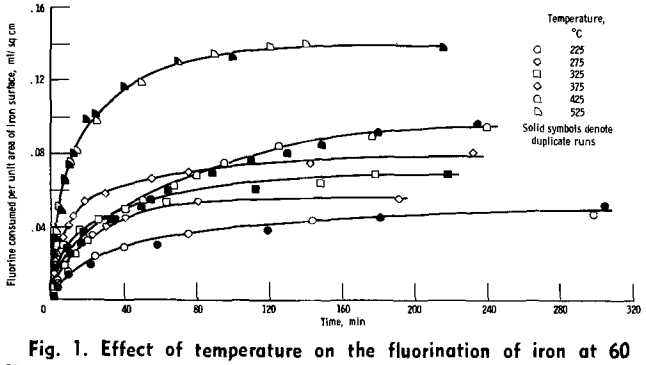

Fig. 1. Effect of temperature on the fluorination of iron at 60 Torr.

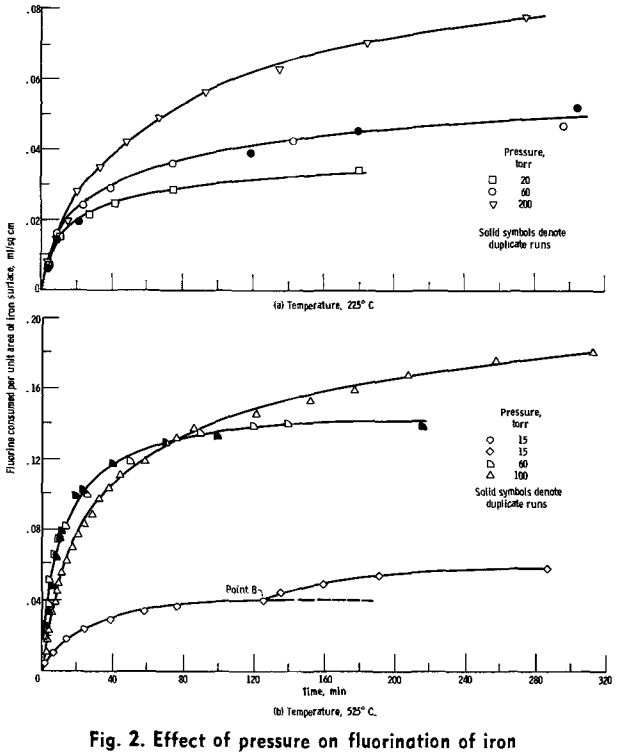

Fig. 2. Effect of pressure on fluorination of iron

Table I. Summary of temperature and pressure conditions and calculated logarithmic rate constants

Temperature, °C	Pressure, Torr	Logarithmic rate constant, ml/cm²
225	60	0.024
275	⏐	0.026
325	⏐	0.029
375	⏐	0.031
425	⏐	0.057
525	↓	0.064
225	20	0.016
225	60	0.024
225	200	0.046
525	15	0.022, 0.013
525	60	0.064
525	100	0.089

Product identification and volume ratio.—X-ray diffraction patterns were run on both the low and high temperature films and the product was identified as ferric fluoride (FeF_3); no ferrous fluoride (FeF_2) was detected. The over-all reaction may be described by

$$2Fe + 3F_2 \rightarrow 2FeF_3 \qquad [2]$$

In this reaction, the fluoride occupies a larger volume than the metal destroyed. The volume ratio (10) is defined as $\Phi = Wd/wD$ where W is the molecular weight of the film formed, w the formula weight of the metal, D the density of the film formed, and d the density of the metal. The volume ratio Φ for this reaction has a value of 4.9 at 25°C.

Logarithmic equation.—The data from Fig. 1 and 2 are replotted in Fig. 3 and 4 on a log time as a function of fluorine consumed basis. The straight lines shown on Fig. 3 and 4 fit a logarithmic equation that is similar to Eq. [1]. This equation is

$$y = K(\log at) + c \qquad [3]$$

where y is the fluorine consumed (at STP), ml/cm²; t time, min; K the logarithmic rate constant; a the constant with dimensions of reciprocal min; and c the intercept. The constant a is unity for the lines drawn on Fig. 3 and 4. Figure 3 shows the data at constant pressure of 60 Torr for various temperatures. In Fig. 4(a) the 225°C data are plotted at 20, 60, and 200 Torr, and in Fig. 4(b) the 525°C data are plotted at 15, 60, and 100 Torr showing the effect of pressure at constant temperature. It can be seen that the logarithmic equation fits all the data within the experimental error except at short times. Figure 2 indicates that heat and vacuum have an effect on the passivity of the metal strip. At point B the metal strip had reached a point

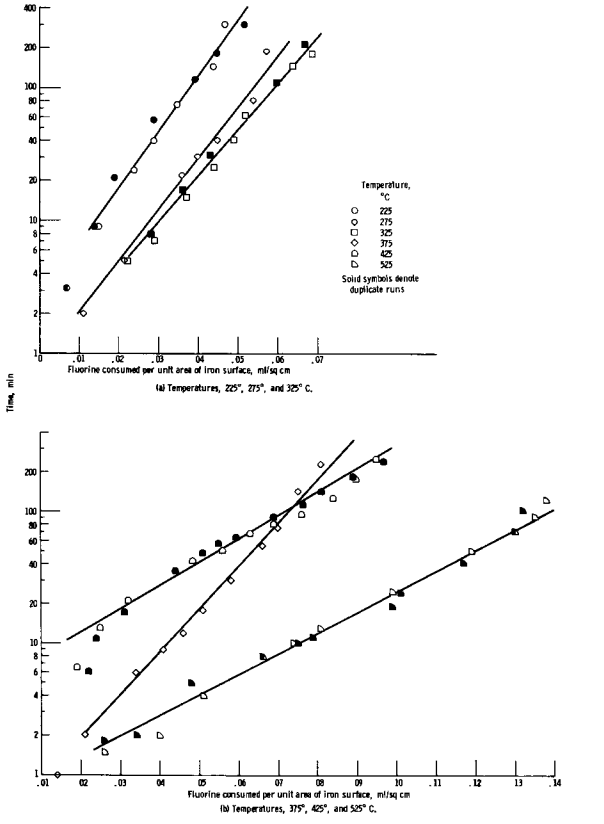

Fig. 3. Temperature effect at 60 Torr

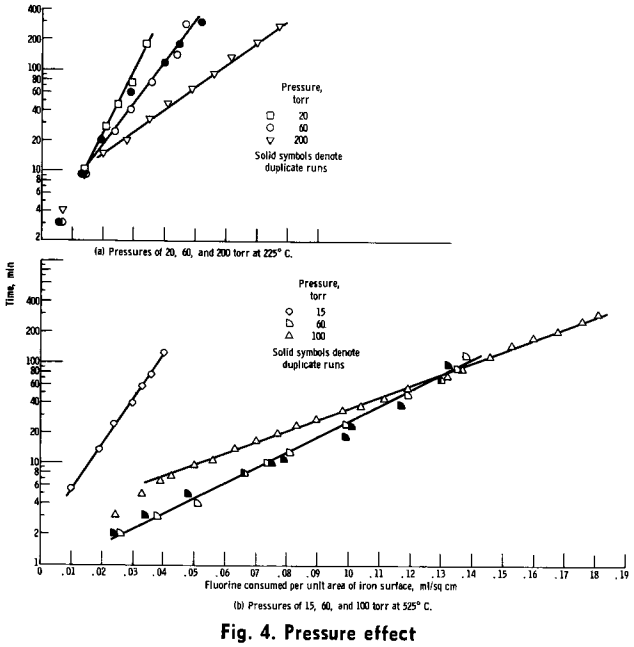

Fig. 4. Pressure effect

of negligible reactivity (passivation), however, when subjecting it to heat and vacuum for a period of approximately ten minutes and then to fluorine again it appears to lose some of its passivation. Figure 5 shows both parts of the 525°C run at 15 Torr plotted according to the logarithmic equation. The two lines on Fig. 5 were obtained by plotting the fluorine consumption against log time from point B on by considering the fluorine consumption for this second part of the reaction as the difference between reaction 1 (dashed line) and reaction [2] and B as the zero time point for reaction [2]. The rate for this second reaction is, however, lower than the original rate. The values of K for these reactions are 0.022 and 0.013 ml/cm^2, respectively, and are listed in Table I along with the values of the other rate constants.

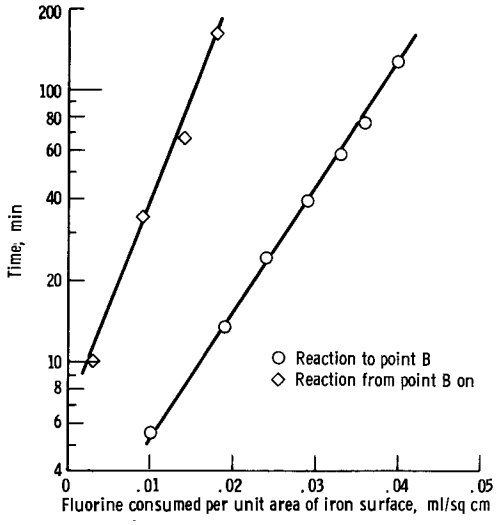

Fig 5. Interrupted fluorination of iron at 525°C and 15 Torr

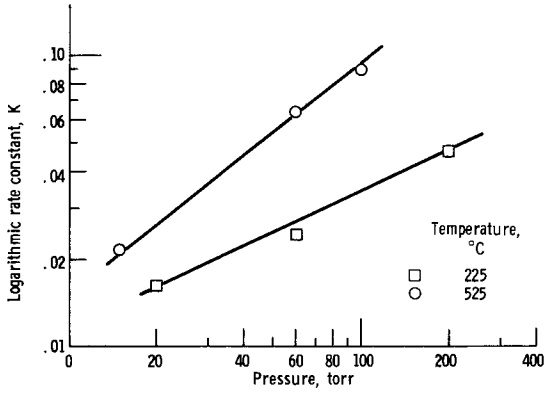

Fig. 6. Effect of pressure on rate constant

From the data of Fig. 1 and 2, the reaction between iron and fluorine is seen to be both temperature and pressure dependent. The effect of pressure on the logarithmic rate constant is shown in Fig. 6 where the log of this constant is plotted as a function of pressure at constant temperature according to the equation $\log K = m \log P + B$. The slope m is the order of the reaction with respect to the fluorine pressure. At 225°C, m has a value of 0.87, and at 525°C m is 0.48.

Metallographic studies.—Cross sections of the fluorine-corroded iron strips were prepared by standard metallographic techniques. Photomicrographs of typical cross sections are shown in Fig. 7. These photographs show that the boundary between the fluoride and the iron is very sharply defined. The fluoride film does not grow preferentially along grain boundaries in the iron. This was confirmed by etching and staining of polished cross sections. Near the iron-fluoride interface, the fluoride appears to be uniformly dense. Near the surface of the fluoride film, the fluoride appears somewhat broken and imperfect. This is to be expected, since the fluoride film occupies a volume 4.9 times larger than the iron from which it is formed, and this volume expansion must result in stresses which can fracture the film when it is thick enough.

Mechanism of fluorine attack.—The rate-determining process in growth of corrosion films on metals can be deduced by consideration of the growth law of the film. For example, if the film grows by diffusion of lattice vacancies through the film, the film thickness will increase with the square root of time. In the experiments reported here, the fluorine uptake, and hence the film thickness, varied directly with the logarithm of time except at short times, where the

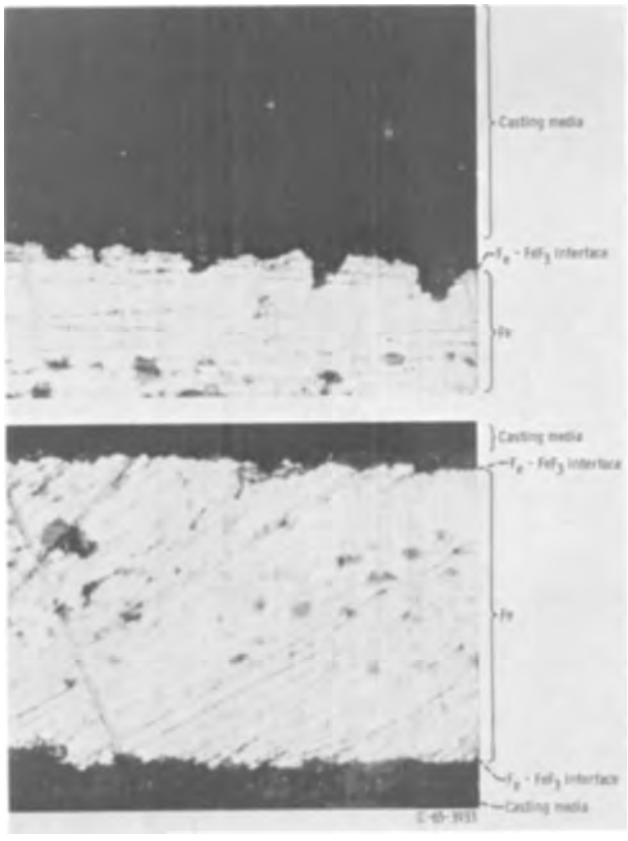

Fig. 7. Cross-section views (Fe + F_2 at 500°C). X500

film thickness is less than about 350Å. Theoretical analyses (3) have shown that such a direct logarithmic dependence can arise from either of two mechanisms: (*i*) when the growth rate is controlled by tunneling of electrons through the film, or (*ii*) when the growth rate is controlled by passage of gas through pores or other defects in the film to the metal surface. Tunneling is important only for films thinner than a few hundred angstroms. The film thicknesses in this research were much larger, so that this mechanism can be discarded. The second mechanism, that of passage of gas through pores in the film, is the most likely process. The pores through which the gas moves may be the intersection of three grains, the intersection of two slip-planes, screw, and edge dislocations, or simply fractures in the film. When the compressional stress in one pore exerts a pressure on neighboring pores, some of these will be blocked as the film grows. This is the case of mutually blocking pores and leads to the direct logarithmic growth law as found in this research. At low temperatures, the logarithmic law is found to be obeyed for the oxidation of iron and copper, where the expansion which occurs when metal is transformed to oxide tends to close up neighboring pores. In this research, the fluoride occupies a volume 4.9 times that of the metal from which it is formed, so that mutual blockage by compression can be expected. It is concluded that above a film thickness of about 350Å the fluoride film on the iron grows by passage of fluorine through pores in the film, and that these pores tend to block one another as the film thickness increases.

Manuscript received June 20, 1966; revised manuscript received Nov. 22, 1966.

Any discussion of this paper will appear in a Discussion Section to be published in the December 1967 JOURNAL.

REFERENCES

1. E. Skinner, *Chem. Eng.*, **65**, 137 (1958).
2. P. E. Brown, J. M. Crabtree, and J. F. Duncan, *J. Inorg. Nuclear Chem.*, **1**, 202 (1955).
3. U. R. Evans, "The Corrosion and Oxidation of Metals: Scientific Principles and Practical Applications," St. Martin's Press, Inc. (1960).
4. P. M. O'Donnell and A. E. Spakowski, Reaction of Copper and Fluorine from 800° to 1200°F, NASA TN D-768, 1961.
5. P. M. O'Donnell and A. E. Spakowski, *This Journal*, **111**, 633 (1964).
6. Yu. A. Luk'yanychev, N. S. Nikolaev, I. I. Astakhov, and V. I. Luk'yanycheva, *Dokl. Akad. Nauk. SSSR*, **147**, 1130 (1962).
7. R. L. Jarry, J. Fischer, and W. H. Gunther, *This Journal*, **110**, 346 (1963).
8. A. K. Kuriakose and J. L. Margrave, *J. Phys. Chem.*, **68**, 290 (1964).
9. E. A. Gulbransen, *Trans. Electrochem. Soc.*, **81**, 327 (1942).
10. N. B. Pilling and R. E. Bedworth, *J. Inst. Metals*, **29**, 529 (1923).

Electrochemical Aspects of the Interaction Between Materials and Blood

Dennis B. Matthews and Avery Catlin

Department of Materials Science, School of Engineering and Applied Science, University of Virginia, Charlottesville, Virginia

ABSTRACT

Electrolysis of human plasma, collected under various conditions, and of bovine fibrinogen (a protein normally present in blood) was carried out in order to verify conclusions made by earlier investigators. Electrolysis of recalcified plasma, ACD-plasma (plasma to which an acid solution of dextrose and sodium citrate has been added), citrated-plasma (plasma to which sodium citrate has been added), and heparinized plasma (plasma containing heparin anticoagulant) in glass, plastic, and silvered tubes did not support the conclusion that electrolysis produced inhibitors of, or catalysts for, the enzymatic blood coagulation reaction. The results were interpreted in terms of the effect of *p*H on the rate of coagulation.

Blood, withdrawn from a human and placed in contact with various materials, clots at a rate dependent on the material with which it is in contact. The rate of clotting is a maximum for such materials as glass, kaolin, celite (diatomaceous silica), and barium carbonate; it is a minimum for such materials as the normal vascular endothelium (the inside lining of blood vessels), paraffin, plastics including cellophane, and siliconized glass. For use as vascular prostheses such as artificial arteries, heart valves, and hearts, a

material must, besides other requirements, not initiate blood coagulation.

The intrinsic enzyme mechanism of blood coagulation, initiated by contact with a foreign surface, is fairly well documented, and the mechanism currently accepted by a large number of the workers in this area is shown below.

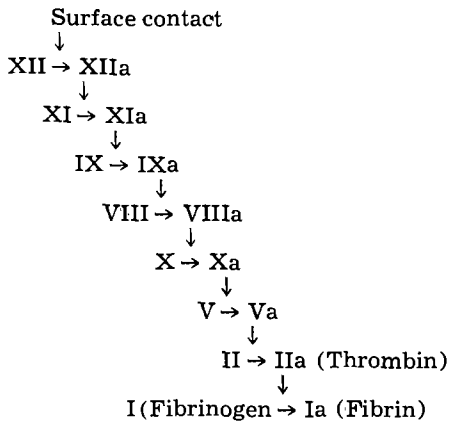

This enzyme cascade (1, 2) sequence or bioamplifier (3, 4) system is believed to be initiated by adsorption of factor XII (Hageman factor). The adsorbed factor XII is in an active state, designated as XIIa and capable of activating factor XI to give XIa which in turn activates factor IX, and so on, until the enzyme IIa (thrombin) attacks factor I (fibrinogen), converting it to fibrin which polymerizes, both end-to-end polymerization and crosslinking occurring, forming a net which enmeshes blood cells and serum.

There exists at present in the literature sufficient evidence to be able to conclude that electrical and possibly electrochemical factors play a role in the interaction between materials and blood, both "*in vitro*" and "*in vivo*" (21, 25).

This paper is concerned with the analysis of existing data in the light of some new results reported herein.

Despite the fact that the dependence of blood coagulation on electrolysis was observed as early as 1824, the first significant and systematic work on this subject was not carried out until 1953. In 1953, Sawyer, Pate, and Weldon (5, 7) observed that the potential difference across the canine artery wall changed sign upon injury being −3 to −15 mv (inside negative with respect to the outside) before injury and +1 to +10 mv after injury. The current flowing across the artery wall was also observed to change its sign and magnitude upon injury. The reversal of sign of the potential difference and the appearance of an "injury current" was accompanied by the formation of a thrombus, or blood clot, within the injured artery. A similar result was reported by Sawyer and Pate (6, 7) for the canine aorta.

Electrolysis of heparinized or citrated canine blood between platinum electrodes in a glass tube at 0.2-10 ma for 30 min resulted in the formation of a precipitate at the anode (8). The precipitate contained platelets, red blood cells (erythrocytes), and white blood cells (leukocytes). In the case of heparinized blood, fibrin strands were also reported to be part of the precipitate. No precipitate was formed at the cathode. It was demonstrated by Sawyer and Pate (8) that this precipitate was not caused by gross changes in *p*H. As the anode and cathode were situated in the same vessel separated only by 1 cm of solution it is not surprising that no gross changes of *p*H were observed.

The results of Sawyer and Pate (8) have been repeated by Lamb *et al.* (14) who used platinum wires 5 mm apart in the electrolysis of heparinized whole blood and plasma. The nature and amount of deposit formed on the anode was noted for various potentials between the anode and cathode and for various quantities of charge passed.

Passage of current across a blood vessel wall or across the blood vessel *in vivo* was also found to produce a deposit, or thrombus, on the vessel wall nearest the anode. On the basis of these experiments it was postulated by Sawyer, Deutch, and Pate (9) in 1955 that reversal of the normal potential difference across the canine blood vessel wall results in an electrophoretic migration of platelets, other cellular elements, and negatively charged proteins to the injured vascular wall thus precipitating a thrombus (blood clot). In later years, however, Sawyer (15) has concluded that electrolysis interferes with the intrinsic enzyme mechanism of blood coagulation.

In 1956 the investigations proceeded one step further when it was found by Sawyer and Deutch (10) that thrombosis (blood clot formation) was delayed at the cathode during electrolysis. Currents greater than 30 μa, when passed between a platinum cathode, placed around crushed canine arteries and veins, and an anode located at a distant position in the dog, were able to delay thrombosis compared to a control experiment where no current was passed.

These results were confirmed in 1959 by Schwartz (11) who observed *in vivo* thrombosis at the anode during electrolysis and who found that cathodic polarization was able to delay thrombin-induced thrombosis. Several other workers (12, 13, 16, 17) have since been able to produce *in vivo* thrombi by anodic polarization.

The experiments of Sawyer and Pate (8) were repeated by Sawyer, Dennis, and Wesolowski (15) with platinum electrodes in separate glass tubes connected by a salt bridge. Currents of 0.1-1.0 μa were found to produce a deposit on the anode in heparinized or citrated blood. A solution of fibrinogen in sodium chloride was also electrolyzed, and a deposit was observed at the anode. This deposit was thought to be fibrin produced from fibrinogen by electrolysis. It was conjectured that electrolysis can cause blood coagulation by bypassing all but the final steps in the intrinsic enzyme clotting mechanism.

In all the above *in vitro* experiments the blood was heparinized or citrated. The intrinsic blood coagulation mechanism was thus checked; in particular, the activation of factor IX is inhibited under these conditions.

In 1964 Naumovski and Dejanov (21) reported some results on the effect of electrolysis on *in vitro* clotting. Currents of 1.6 ma were passed through citrated plasma for 1 hr. At the cathode the plasma was found to have a markedly prolonged recalcification time, more than 80 times the average spread. The plasma *p*H was 9.6-9.8. Diluting the cathode plasma by imadazole buffer (*p*H 7.4) did not change the anticoagulant effect. Plasma at the anode changed negligibly, and the *p*H was 6.6-6.8.

On the other hand, Lavelle (21) concluded that direct electric current does not appear to initiate, or accelerate, the enzymatic coagulation system in circulating native blood. Lavelle's work, however, suffered from the disadvantage that the anode and cathode were not in separate chambers. Any material oxidized at the anode may well have been reduced at the cathode. In 1964 Sawyer, Brattain, and Boddy (18) observed that erythrocytes and leukocytes in Krebs solution (an electrolyte of ionic composition similar to that of blood) at *p*H 7.4 migrate and adhere to a platinum electrode at potentials greater than or equal to +0.33v (against NHE). Decrease of this potential led to desorption of the blood cells.

A similar behavior was observed with platelet suspensions (19) except that the adsorption of platelets was irreversible, the platelets visibly disintegrating at the electrode. Fibrinogen in buffer solution, however, was not found to deposit under these conditions (20).

The above results obtained by Sawyer and his coworkers and by others have led Sawyer to believe (21) that electrolysis is capable of interfering with the in-

trinsic enzyme mechanism of blood coagulation, the rate of blood coagulation being catalyzed at an anode and an inhibitor being produced at the cathode.

It was the aim of the present work to substantiate if possible the above viewpoint by repeating the *in vitro* experiments of Sawyer and co-workers under conditions where the intrinsic enzyme mechanism of coagulation is operative.

Experimental

Blood was collected in 450 ml quantities from healthy male donors. The blood was withdrawn under vacuum into a double plastic pack containing acid citrate-dextrose (ACD) anticoagulant. In some experiments sodium citrate or heparin anticoagulant was used in the place of ACD. The blood was centrifuged at either 1000g (platelet poor plasma, p.p.p.) or 300g (platelet rich plasma, p.r.p.) for 30 min to remove red cells and white cells. The plasma was squeezed off from the packed cells into the second plastic pack. Aliquots of about 4 ml were gravity fed from the pack into siliconized glass or polystyrene tubes, sealed and stored at either 4° or −20°C. Immediately prior to an experiment a plasma aliquot was thermostatted in a water bath at 37°C. In the case of plasma stored at −20°C, this procedure disrupts the platelets, producing lysed plasma.

To initiate clotting, 0.20 ml of 0.25M $CaCl_2$ was added to 2 ml of plasma. The rate of coagulation was followed with a photometric system (23). Light from a voltage regulated 0.25 amp 6-volt lamp was passed through the sample, contained in a block of aluminum thermostated at 37° ± 0.5°C, and the transmitted light was monitored with a CdS photocell. The resistance of the photocell was measured with a Wheatstone bridge, and the change of resistance with time was continuously recorded with a potentiometric recorder. The measuring system is shown in Fig. 1. The type of recording obtained is idealized in Fig. 2. The times t_0 and t_1 mark the onset and completion of fibrin polymerization, respectively. The shape of the curve obtained depended on the experimental conditions. In the case of a simple sigmoidal curve the time $t_{1/2}$ was used as a measure of the rate of coagulation. For more

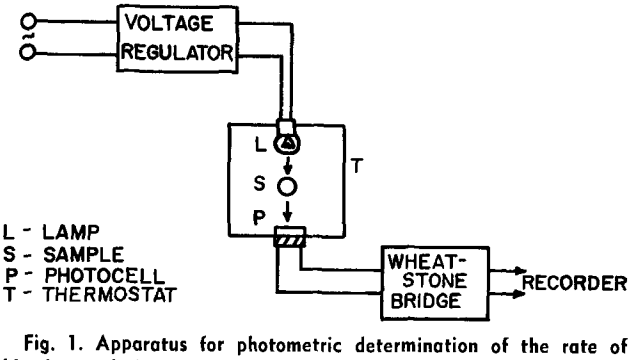

Fig. 1. Apparatus for photometric determination of the rate of blood coagulation.

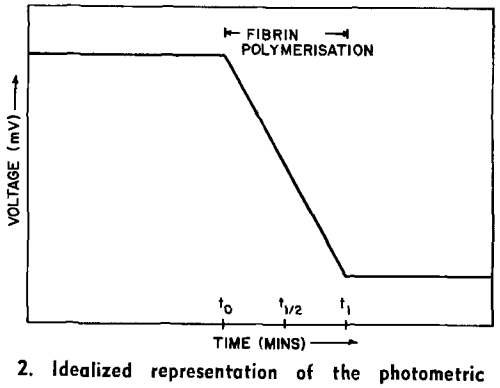

Fig. 2. Idealized representation of the photometric clotting curve.

Table I. Effect of electrolysis on the rate of coagulation of human plasma at 37°C

Polarity	Current, ma	Platelet content	Anti-coagulant	Storage temper-ature, °C	t_0, min
Control	0	Poor	Na citrate	−20	3.2 ± 0.2
Cathode	0.5	Poor	Na citrate	−20	3.5 ± 0.3
Anode	0.5	Poor	Na citrate	−20	3.1 ± 0.2
Control	0	Poor	ACD	−20	2.2 ± 0.1
Cathode	2.0	Poor	ACD	−20	2.7 ± 0.1
Anode	2.0	Poor	ACD	−20	2.4 ± 0.1
Control	0	Poor	ACD	4	6.9 ± 0.7
Cathode	2.0	Poor	ACD	4	6.4 ± 0.1
Anode	2.0	Poor	ACD	4	6.5
Control	0	Rich	ACD	4	3.9 ± 0.4
Cathode	2.0	Rich	ACD	4	3.4 ± 0.4
Anode	2.0	Rich	ACD	4	4.2 ± 0.2
Control	0	Rich	ACD	4	5.6 ± 0.3
Cathode	1.0	Rich	ACD	4	4.8 ± 0.1
Anode	1.0	Rich	ACD	4	6.3 ± 0.3
Control	0	Poor	Na citrate	4	4.9 ± 0.3
Cathode	1.0	Poor	Na citrate	4	4.2 ± 0.7
Anode	1.0	Poor	Na citrate	4	5.1 ± 0.2

complex curves. *e.g.*, double sigmoidal, linear + sigmoidal, the times t_0 and t_1 were tabulated.

Electrodes used were, except where otherwise indicated, platinum wire spirals approximately 1 cm^2 in area. The cathode and anode were placed in separate tubes connected by a saturated KCl-gelatin salt bridge. The salt bridge was constructed either of siliconized glass tubing or of polyethylene tubing. The platinum electrodes were cleaned in 1:1 mixture of concentrated HCl-concentrated H_2SO_4, rinsed with distilled water, and heated to red heat in a flame.

Bovine fibrinogen obtained from Warner-Chilcott was dissolved by standing at 37°C with distilled water.

All pipettes and other glassware used in handling plasma were siliconized with Clay-Adams Siliclad. Test tubes were discarded after use, fresh tubes being used in each test.

Polystyrene tubes were silver coated according to a well-known procedure (22) and dried at 60°C for 5 hr or more.

Results

The effect of electrolysis, after recalcification, of various types of plasma, collected and stored under various conditions, is summarized in Table I and Fig. 3. The tests were carried out in glass tubes at 37°C. In these experiments the plasma was in contact with both glass and an electrode.

In order to eliminate uncertainties brought about by contact with glass, a polystyrene tube coated internally with electrically conducting silver was used both as container and cathode. The effect of cathodic electrolysis was tested in these tubes by electrolyzing citrated plasma for a given time, t_a, and then transferring the plasma to a polystyrene tube containing $CaCl_2$. The experiments were carried out at 37°C with

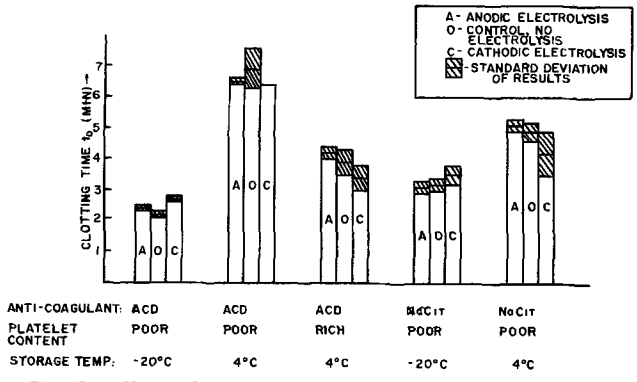

Fig. 3. Effect of electrolysis on the rate of coagulation of human plasma in glass at 37°C.

Table II. Effect of electrolysis at a silver cathode on the rate of coagulation of platelet poor lysed plasma at 37°C

t_d, min	Current, ma	$t_{1/2}$, min
5	0	8.1 ± 0.1
5	2	6.8 ± 0.1
5	0	7.8 ± 0.7*
5	2	6.6 ± 0.4*
12	0	7.6 ± 0.9
12	2	5.6 ± 0.9

* Plasma was deaerated with nitrogen.

platelet poor plasma (lysed) collected in ACD. Results are given in Table II.

The experiment of Sawyer, Dennis, and Wesolowski (15) on the electrolysis of fibrinogen was repeated. Purified bovine fibrinogen (2.0 ml) was electrolyzed with platinum electrodes in separate glass tubes connected by a salt bridge. At 1 ma a deposit formed on the anode within 25 sec. The deposit consisted of a white precipitate mixed with bubbles of O_2 causing the precipitate to adhere to the anode. No reason was seen for believing the deposit to be fibrin rather than fibrinogen. Addition of sodium citrate to fibrinogen was found to inhibit the formation of a deposit. Only after 15 min of electrolysis at 1 ma did a very fine precipitate form, and this tended to remain in suspension. Electrolysis of citrated plasma itself, which contained the same concentration of fibrinogen as in the above experiments, resulted in the formation of a very fine precipitate only after 15 min of electrolysis at 1 ma. The possibility of fibrinogen being precipitated by a decrease in pH of the solution in the anode compartment was checked both by calculation and actual measurement of the pH change. In the absence of buffer the pH changed from 6.00 to 3.61 after 1 min of electrolysis at 1 ma, while in the presence of sodium citrate the pH change was from 8.16 to 7.58.

The experiments of Naumovski and Dejanov on the electrolysis of citrated plasma were repeated using platelet poor plasma. Electrolysis was carried out at 1.6 ma with 10 ml of plasma in polystyrene tubes using Pt electrodes. After 60 min electrolysis the plasma was thermostatted at 37°C and 2 ml recalcified in glass tubes at 37°C. Results obtained are shown in Table III. Both cooled and lysed plasma were tested.

The above experiments were repeated with heparinized platelet poor plasma. Electrolysis was conducted in polystyrene tubes at 3.2 ma for 30 min using 10 ml of fresh plasma. After electrolysis 2 ml of the sample was contacted for 10 min in glass tubes at 37°C, 0.20 ml of protamine sulfate was then added to neutralize the heparin. This experiment was repeated with a 1:1 sample of fresh plasma and veronal buffer (pH = 7.5),

Table III. Effect of prolonged electrolysis on the rate of clotting of citrated platelet-poor plasma at 37°C

Electrolysis carried out for 60 min at 1.6 ma in polystyrene tubes with Pt electrodes. Vol. of plasma = 10 cc. Plasma recalcified in glass tubes.

A. Fresh plasma

Electrode	pH	t_0, min
Anode	6.59	16.7 ± 2.3
Cathode	7.29	7.7 ± 0.2

B. Lysed plasma

Electrode	pH	t_0, min
Anode	6.47	9.0 ± 0.5
Cathode	7.35	3.7 ± 0.5
No current	7.01	4.7 ± 0.2

Table IV. Effect of prolonged electrolysis on the rate of clotting of heparinized platelet-poor fresh plasma at 37°C

Electrolysis carried out for 30 min at 3.2 ma in polystyrene tubes with Pt electrodes. Volume of plasma = 10 cc. Plasma contacted with glass for 10 min. Heparin neutralized with protamine sulfate.

Polarity	pH	$t_{1/2}$, min
A. Unbuffered		
Control, no current	7.66	5.5 ± 0.4
Cathode	8.20	8.9 ± 0.2
Anode	7.25	6.2 ± 0.1
B. Buffered		
Control, no current	7.52	6.3 ± 0.4
Cathode	7.90	5.6 ± 0.3
Anode	7.18	6.7

in order to inhibit the pH changes brought about by electrolysis. The results of the experiments with heparinized plasma are given in Table IV.

Discussion

Table I shows that for plasma collected in either ACD or sodium citrate there is little effect of electrolysis either on t_0 or t_1. This result is independent of whether the plasma was platelet rich or platelet poor and whether or not the platelets were lysed by freezing and thawing. The variations in clotting time as a function of platelet concentration and platelet condition are not meaningful since each set of results refers to a different batch of plasma. Variations in plasma obtained from different donors or from the same donor on different days are such as to allow comparison only between results obtained within a given batch of plasma. Such experiments yield the result that the clotting time t_0 is less for platelet rich than for platelet poor plasma. With platelet rich plasma clot retraction was very pronounced and prevented determination of t_1. Platelet lysis led to a decrease in clotting times t_0 and t_1, but the decrease in t_0 was almost independent of the original platelet concentration indicating the release of an enzyme from the platelets. The decrease in t_1 was dependent on the original platelet concentration, but when the platelet fragments were removed by centrifugation at 2500g then lysis caused no change in $t_1 - t_0$.

A small increase in the rate of clotting was produced by cathodic electrolysis, but this effect is much smaller and of opposite sign to that previously reported for plasma and whole blood containing anticoagulant. Moreover, in the presence of anticoagulant (ACD), Table II shows that electrolysis in silvered tubes did not inhibit the formation of contact factor (factor XIa) nor did it produce an inhibitor to clotting, rather, a small increase in coagulatibility was observed.

Electrolysis of fibrinogen in unbuffered solutions was shown to produce a rapid and large decrease of pH in the anode compartment with the resultant precipitation of fibrinogen.

Prolonged electrolysis of plasma in polystyrene tubes with Pt electrodes did not produce an inhibitor in the plasma. The recalcification time was not greatly increased by cathodic electrolysis contrary to the observation of Naumovski and Dejanov, rather, the clotting time for ACD-plasma was slightly decreased by cathodic electrolysis. Anodic electrolysis caused an increase in clotting time compared to unelectrolyzed ACD-plasma. These results may be attributed to the pH changes produced in the plasma by electrolysis. It is well known (24) that the clotting time for blood is a minimum at pH = 7.5 and increases rapidly with either increase or decrease of pH. Inspection of Table III for lysed plasma shows that cathode plasma with pH 7.35 has the smallest clotting time. Unelectrolyzed plasma of pH 7.01 (due to presence of ACD) has a slightly larger clotting time and anode plasma with pH 6.47 has a much larger clotting time. Similar effects were noted on electrolysis of heparinized plasma.

The present results on the electrolysis of human plasma and bovine fibrinogen indicate no interference with the intrinsic enzyme mechanism of blood coagulation, and it is concluded that the results of Sawyer and others on the electrolysis of blood were caused by an electrophoresis mechanism, negatively charged erythrocytes, leukocytes and platelets migrating in the field between the anode and the cathode.

The results do not exclude the possibility of electrochemically influencing the intrinsic enzyme mechanism of blood coagulation. One might reasonably hope to influence the adsorption of Hageman factor (factor XII) on a given material by altering the charge on the material. However, the conditions under which specific proteins are adsorbed and desorbed are by no means obvious and information is required on factors which influence protein adsorption at the solid-liquid interface. Such information would be of great value not only to the study of blood-materials interaction but to the general area of compatability of prosthetic materials and the human body.

Acknowledgments

This work was supported by the National Institute of Dental Research, Grant DE-2111-02. The authors acknowledge the cooperation of the University of Virginia Medical Center and, in particular, the continued interest and assistance of Doctors Oscar A. Thorup, Jr., Phillip M. Allen, and Mary Lou Abram.

Manuscript received Aug. 16, 1966.

Any discussion of this paper will appear in a Discussion Section to be published in the December 1967 JOURNAL.

REFERENCES

1. R. G. Macfarlane, *Nature*, **202**, 498 (1964).
2. E. W. Davie and O. D. Ratnoff, *Science*, **145**, 1310 (1962).
3. G. Wald, *ibid.*, **150**, 1028 (1965).
4. S. N. Levine, *ibid.*, **152**, 651 (1966).
5. P. N. Sawyer, J. W. Pate, and C. S. Weldon, *Am. J. Physiol.*, **175**, 108 (1953).
6. P. N. Sawyer and J. W. Pate, *ibid.*, **175**, 113 (1953).
7. P. N. Sawyer and J. W. Pate, *Surgery*, **34**, 491 (1953).
8. P. N. Sawyer and J. W. Pate, *Am. J. Physiol.*, **175**, 103 (1953).
9. P. N. Sawyer, B. Deutch, and J. W. Pate, Thrombosis and Embolism, Proceedings of the first *International Conference*, 1954, Basil, Switzerland, Schwabe (1955).
10. P. N. Sawyer and B. Deutch, *Am. J. Physiol.*, **187**, 473 (1956).
11. S. I. Schwartz, *Surg. Gyn. Obst.*, **113**, 324 (1961).
12. R. D. Williams and L. C. Carey, *Annals Surgery*, **149**, 381 (1959).
13. R. R. Bradham, *Surg. Gyn. Obst.*, **113**, 324 (1961).
14. J. C. Lamb, J. P. Isaacs, W. L. Bloom, and D. S. Harmer, *Am. J. Physiol.*, **208**, 1006 (1965).
15. P. N. Sawyer, C. Dennis, and S. A. Wesolowski, *Ann. Surg.*, **154**, 556 (1961).
16. J. W. Richardson and S. I. Schwartz, *Surgery*, **52**, 636 (1962).
17. S. I. Schwartz, *Surg. Forum, Am. Coll. Surgeons*, **12**, 46 (1961).
18. P. N. Sawyer, W. H. Brattain, and P. J. Boddy, *J. Proc. Nat. Acad. Sci.*, **51**, 428 (1964).
19. P. N. Sawyer, J. H. Reardon, and I. C. Oganiak, *ibid.*, **53**, 200 (1965).
20. J. C. Oganiak and P. N. Sawyer, *ibid.*, **53**, 572 (1965).
21. "Biophysical Mechanisms in Vascular Hemostasis and Intravascular Thrombosis," P. N. Sawyer, Editor, Appleton-Century-Crofts, New York (1965).
22. "Handbook of Chemistry and Physics," 39th ed., p. 3051, Chemical Rubber Publishing Co. (1957-58).
23. H. W. Hanover and D. L. Brook, *Ann. Surgery*, **160**, 870 (1964).
24. "Blood Coagulation, Hemorrhage and Thrombosis," L. M. Tocantins and L. A. Kazal, Editors, Grune and Stratton, New York (1964).
25. S. I. Schwartz, *Monographs of the Surgical Sciences*, **2**, 159 (1965).

Surface Tensions of Co-Ce and Pu-Co-Ce Alloys as Determined from Frozen Menisci

John C. Biery

University of California, Los Alamos Scientific Laboratory, Los Alamos, New Mexico

ABSTRACT

The surface tensions of three Pu-Co-Ce and three Co-Ce alloys at their freezing point were determined from their frozen menisci. A new calculational procedure was used in which calculated menisci were compared with the experimental menisci. The meniscus shapes were calculated by numerically integrating the Laplace-Young equation. The best surface tension for a given meniscus was found by comparing the computed and experimental menisci at 25 points across the meniscus and by varying the surface tension and contact angle at the outside of the meniscus section until various restraints were satisfied. The meniscus comparing techniques satisfactorily detected and discarded distorted menisci. Of the 28 menisci studied, 15 were found to be acceptable.

Molten plutonium alloys with cobalt and cerium were tested as possible fast nuclear reactor fuels. These studies indicated that unusual phenomena occur at and above the liquid/gas interface of the molten fuel when it is contained in tantalum capsules. Since some of these phenomena may be associated with the energy in the interface, the surface tensions of these alloys should be known to understand the systems better. The usual methods of determining surface tension such as capillary rise, pendant drop, sessile drop, and bubble pressure require expensive and time-consuming experiments when plutonium is involved. Therefore, a technique was developed to generate surface tensions from photographs of menisci since in many cases well-formed menisci are observed in sectioned capsules containing the Pu-Co-Ce alloys. The initial mathematical and numerical techniques for making these determinations from menisci and the test of the method with mercury and water are reported elsewhere (1). Here, the results from analyzing frozen menisci of Co-Ce, Pu-Co-Ce, and Ni-Ce/NaK are presented.

The previously published geometrical and computational methods (1) were tested experimentally with liquid menisci. An important objective of this paper is to test the applicability of the methods as applied to frozen menisci. The tests of the methods were made by (*i*) processing many capsules and comparing the

acceptable results from capsules with similar radii, (*ii*) comparing results from menisci formed in capsules with significantly different radii, and (*iii*) comparing results for Pu-Co-Ce with one value obtained from a capillary rise experiment.

Experimental and Calculational Procedure

The frozen menisci were analyzed by an experimental and calculational procedure that has been previously described in detail (1). Below are summarized the important features of the analysis.

Experimental procedure.—The capsule containing the frozen alloy is sectioned longitudinally and is then polished to the centerline position.[1] For best results the void space above the alloy should be filled with epoxy resin. The meniscus is then photographed, and the photograph is enlarged to 25 cm across the diameter of the tube. Meniscus heights at 25[2] positions across the radius are read from a graph onto which the meniscus curve had been traced. These heights are replotted on a graph of expanded scale, and a smooth curve is drawn through the points. Values from this curve are read into the computer for comparison with the computed curves.

Also, from the experimental heights, the sine of the tangent angle at the outside of each radial increment is calculated. A smooth curve is drawn through these points. This "adjusted" sine curve is positioned after calculations have been made to produce a constant surface tension when these sines are used as boundary conditions in the calculations.

Calculational procedure.—The analysis as developed includes a mathematical procedure for calculating the meniscus curve and a method for comparing the computed and experimental curves. The comparison is made in such a manner as to produce the best surface tension value and to throw out the distorted menisci. The meniscus curve is generated by numerically solving a modified form of the Laplace-Young equation shown below.[3]

$$z = \frac{\gamma}{rg(\rho_1 - \rho_2)} \frac{\partial}{\partial r} (r \sin \theta) \qquad [1]$$

The determination of the surface tension and the testing of the distortion of the meniscus involves the selection of γ and ϕ to produce a best fit between the computed and experimental meniscus curves. The procedure involves the following steps:

1. A $\gamma_{optimum}$ *vs.* $\sin\phi$ curve is calculated for portions of the meniscus out to radial increments 21 through 25.[4] The range of $\sin\phi$ for each sized meniscus is determined by a ± 0.015 range about the smoothed experimental $\sin\theta$ curve. For each $\sin\phi$, $\gamma_{optimum}$ is found by satisfying the "sum of mass restraint." A series of menisci are calculated with various surface tension values, γ_{as}, for each $\sin\phi$. The capillary rise, z_o, calculated at the center of the capsule for each γ_{as}, when combined with the experimental meniscus curve, allows a γ_{cal} to be calculated by equating the net weight of fluid between the meniscus and the datum plane to the peripheral surface tension force. When the γ_{as} and γ_{cal} agree, this common value is the desired surface tension which satisfies the "sum of mass restraint" for the chosen $\sin\phi$.

2. An "adjusted" experimental $\sin\theta$ curve is drawn to fit the experimental $\sin\theta$ points best and to give the same value of surface tension for the calculations at increments 21 through 25. The $\gamma_{optimum}$ *vs.* $\sin\phi$ curves calculated in 1 above are used to determine the surface tension at each radial position.

3. For each calculation, standard deviations, s and s_7, between the calculated and experimental meniscus heights are calculated. For an undistorted meniscus at the correct values of γ and ϕ, these standard deviations should be a minimum and should have a value less than 0.0015 cm. If such a minimum occurs with $\sin\phi$ within a ± 0.015 range of the "adjusted" experimental sine curve, then this surface tension is allowed as an acceptable value.

Thus, the primary test as to whether or not a meniscus is undistorted and the surface tension value is acceptable is that the s and s_7 standard deviation values calculated at the conditions where the "sum of mass restraint" is satisfied have minima which are less than some arbitrarily chosen value. Also, the $\sin\phi$ values at these minima in s and s_7 must be within ± 0.015 range of the "adjusted" experimental sine curve. Averaging methods 1, 2, 3 as listed below are versions of this set of requirements with increasing limits on the maximum allowable values of s and s_7 at the minima. In the original formulation of the averaging methods, additional less stringent requirements were proposed as methods 4 through 9. These methods were tested in the present study but are not listed below. Their requirements can be formed elsewhere (1).

Method 1.[5] Average of all surface tension values as determined by the "sum of mass restraint" and a minimum in s or s_7 where $|(\sin\phi_{min} - \sin\phi_{adj})| < 0.015$ and s and $s_7 < 15 \times 10^{-4}$ cm.

Method 2.[5] Same as method 1 except s and $s_7 < 25 \times 10^{-4}$ cm.

Method 3. Same as method 1 except s and $s_7 < 35 \times 10^{-4}$ cm.

The above restricting procedures were designed to separate the undistorted from the distorted menisci. The possible sources of distortion in both liquid and frozen menisci that require detection are as follows: (*a*) optical distortion when meniscus is viewed through a cylindrical surface; (*b*) distortion produced by local wetting such that the meniscus is not a surface of revolution; (c) variation of the surface with time where wetting conditions or temperature conditions are not stabilized to produce an equilibrium meniscus; and (*d*) errors introduced by sectioning of a frozen meniscus where the cut may be off center or not parallel to the axis of the cylinder.

Specific tests in the initial paper (1) or in this paper have not been performed to determine specifically the limits of distortion which the various restricting techniques detect. In both cases the applicability of the methods is inferred by the comparison of numerical results from a number of menisci and the comparison of surface tensions with known values as determined by other methods.

[1] Most of the capsules utilized in this study were not carefully polished to the centerline position since the sectioning was done for metallographic purposes in conjunction with another project.

[2] The value of N, the number of increments across the radius of the tube, is arbitrary and should be chosen small enough to limit computation time but large enough to allow accurate reproduction of the highly curved section of the meniscus near the wall. For the present system with surface tensions in the 600 to 1000 d/cm range, densities near 10 g/cc, and tube radii between 0.45 and 1.2 cm, the choice of N equal to 25 was found to give good results. However, with larger capsules N should be increased to insure that the highly curved section near the wall is divided into at least 5 and preferably 10 increments. Also, with a smaller ratio of $\gamma/(\rho_1 - \rho_2)$ and a resulting flatter meniscus, more increments may have to be used.

[3] See Nomenclature at end of paper.

[4] In all of the calculations and comparisons, the section of the meniscus used was that portion from the centerline out to some arbitrary radial position less than or equal to the radius of the tube. The effect of utilizing successively smaller portions of the meniscus was studied by discarding increments of the meniscus at the outside perimeter. As each increment was discarded and the comparison between computed and experimental data was made, a better or worse value of surface tension was obtained. The change depended on whether or not the discarded increment was more or less distorted than the remaining inside portion of the meniscus. Many calculations were run with 21, 22, 23, 24, and 25 increments retained when the radius was divided into 25 increments. The results indicated that the 25th increment, which was next to the tube wall, was many times distorted and that the most consistent data were obtained when the calculations were made for 24/25 or 23/25 of the total meniscus. Because of the increased curvature near the wall, the most readily detectable surface tension data were contained in the outside 10/25th of the meniscus. Therefore, the quality of the surface tension results deteriorated when as many as 4 increments were discarded.

[5] The limits on methods 1 and 2 were revised somewhat as compared to those used in the Hg, water calculations (1). The changes were made to make methods 1, 2, and 3 consistent. In these three methods the limit on the sines is held constant while the restraint on s and s_7 is progressively relaxed.

Surface Tensions of Co-Ce Alloys from Frozen Menisci

The surface tensions of 6, 12, and 18 w/o Co in Co-Ce alloys were determined from their frozen menisci. A total of 12 menisci were analyzed, and of this number 7 produced minima in the s and s_7 curves that met the demands of methods 1, 2, or 3. The best data came from the 12 w/o Co-Ce melts. For this composition, 6 samples were run, and four of them gave acceptable s and s_7 minima.

In Tables VII and VIII in the Appendix,[6] are compiled the physical properties and chemical analyses of the alloys, characteristics of the menisci, and the computation data for the three alloys. The densities at melting of the alloys were obtained from a paper by Perkins *et al.* (2). These density studies show the 12 and 18 w/o Co-Ce alloys to be near eutectics and to melt at nearly constant temperatures of 425° and 440°C. The 6 w/o alloy is not a eutectic and melts over a range from 420° to 625°C. Therefore, the surface tension for the 6 w/o material does not accurately represent the surface tension of the alloy, but probably shows the properties of a melt near 12 w/o Co which is the last material to solidify at 420°C.

All of these alloys expand on freezing. Thus, the shape of the meniscus is quite well preserved since a crust tends to form first over the meniscus and excess liquid is squeezed upward by the freezing action and usually escapes up on the meniscus crust through cracks. The upward pressure of the unsolidified melt does not seem to distort the meniscus unduly. The characteristics of each alloy and its surface tension determination are discussed below.

6 w/o Co-Ce alloy.—The surface tensions for the 6 w/o alloy are shown in Table I. Because of a large s value greater than 0.0025, only those methods that did not include or relaxed the s and s_7 size restrictions gave any useful results. Acceptable minima in s were obtained when s was allowed to be as large as 0.0035 cm in method 3, and the average surface tension, 685 ± 38.2 dynes/cm, obtained with these restrictions had the smallest 95% confidence intervals. Methods 8 and 9 gave comparable results, 677 dynes/cm, but with a larger confidence interval of ±96.8 dynes/cm.

In these determinations the radius of the capsule ranged from 0.47 to 0.57 cm. The meniscus in this sized capsule had maximum heights above the meniscus bottom of 0.32 cm, and the calculated capillary depression varied between 0.23 and 0.29 cm for the two acceptable menisci. In Table X in the Appendix, is tabulated a summary of the computation results for the three menisci.

12 w/o Co-Ce alloy.—The analyses of the 12 w/o Co-Ce menisci gave the best and most consistent results. Six menisci were studied, and these were formed in three different size tubes of 0.46, 0.57, and 1.2 cm radii. Acceptable minima in the s and s_7 curves were obtained from all three sizes of menisci. These menisci produced surface tensions with an average value of 644.5 dynes/cm with a 95% confidence interval of ±7.7 dynes/cm. The menisci with the largest radius were most easily analyzed. The minima in s and s_7 were much sharper, and the surface tension was much more insensitive to changes in $\sin\phi$. Also, in the larger radius capsules the value of z_0 was smaller, and its influence on the total calculation was less.

The results from the 12 w/o Co-Ce menisci gave the best indication that distortion was not significant when the criteria of method 1 were satisfied. Menisci from three different radii tubes were analyzed, and the results from all three agreed very satisfactorily. Since the cooling histories of the melts in the capsules were considerably different, the probability of all menisci distorting in such a manner to meet the demands of method 1 and still give the same value of surface tension is quite small. In Fig. 1 and 2 are shown the menisci for capsule 3 (1.21 cm radius) and capsule 277 (0.459 cm radius), both of which produced surface tensions which met the requirements of method 1. The large diameter capsule exhibited distortion in the center. However, the outside portions of the meniscus were undistorted and produced acceptable values of surface tension. Capsule 277 meniscus appears visually to be undistorted, and the computations supported

[6] The Appendix has been deposited as Document No. 9231 with the American Documentation Institute Photoduplication Service, Library of Congress, Washington 25, D. C., and may be obtained for $3.75 for photoprints or $2.00 for 35 mm microfilm.

Table I. Summary of surface tension data

Type of av	No. of menisci in av	No. of surface tension determinations in av	Range of surface tensions in av, dynes/cm	95% Confidence interval for av value of surface tension, dynes/cm	Av value of surface tension, dynes/cm
		6 w/o Co-94 w/o Ce			
1	None	—	—	—	—
2	None	—	—	—	—
3	2	2	628-688	±38.2	685.0
4	None	—	—	—	—
5	1	1	699	—	699
6	1	1	632	—	632
7	None	—	—	—	—
8	2	3	632-700	±96.8	677.0
9	2	3	632-700	±96.8	677.0
		12 w/o Co-88 w/o Ce			
1	4	10	628-660	±7.7	644.5
2	Ditto				
3	Ditto				
4	3	3	617-668	±65.9	646.7
5	5	5	617-1029	±219.0	719.2
6	6	6	617-1029	±175.8	744.0
7	4	9	617-669	±16.5	647.7
8	5	12	617-880	±56.3	682.6
9	4	9	617-669	±16.5	647.7
		18 w/o Co-82 w/o Ce			
1	1	2	897-943	±293	920.0
2	Ditto				
3	Ditto				
4	None	—	—	—	—
5	1	1	872	—	872
6	2	2	872-880	±51.0	876
7	None	—	—	—	—
8	None	—	—	—	—
9	None	—	—	—	—

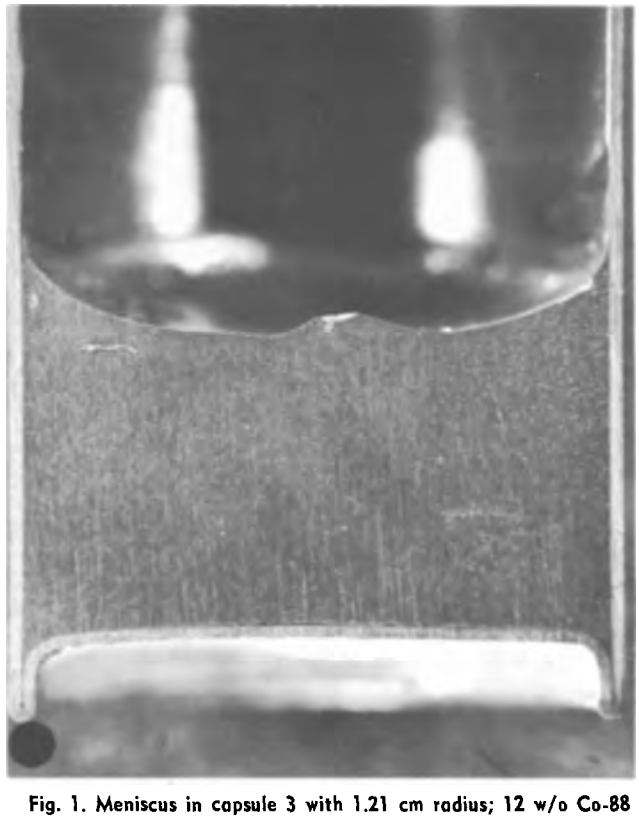

Fig. 1. Meniscus in capsule 3 with 1.21 cm radius; 12 w/o Co-88 w/o Ce.

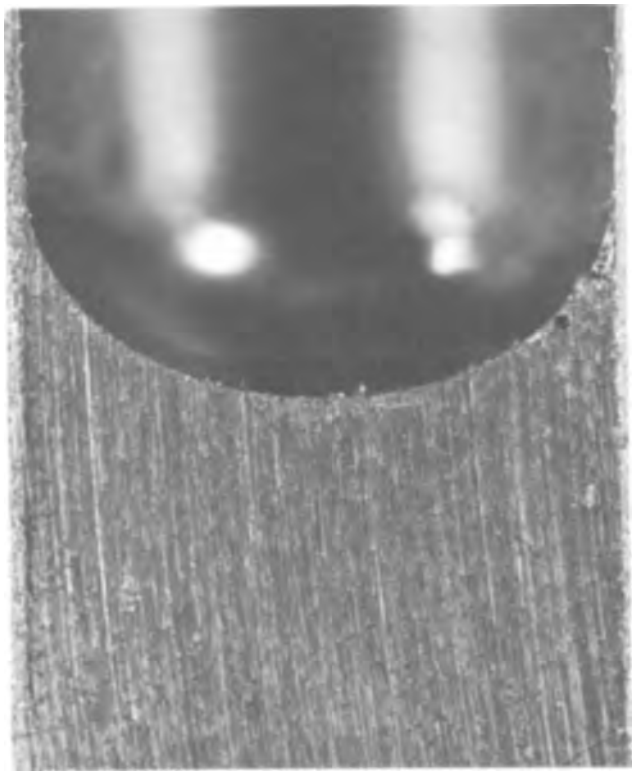

Fig. 2. Meniscus in capsule 277 with 0.459 cm radius; 12 w/o Co-88 w/o Ce.

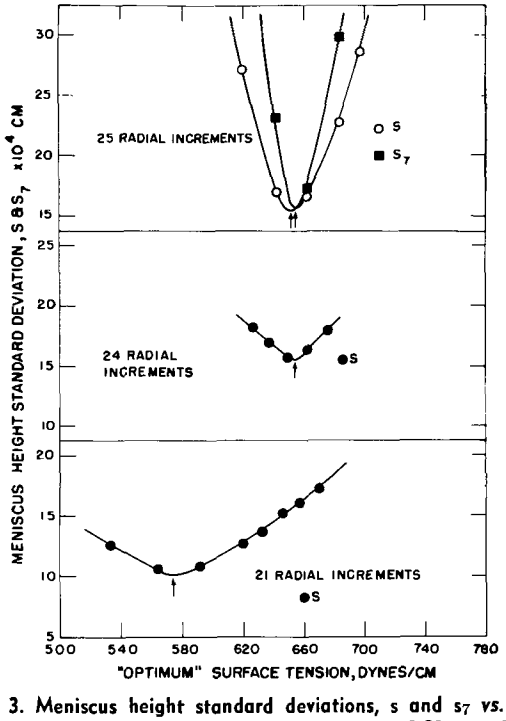

Fig. 3. Meniscus height standard deviations, s and s_7 *vs.* "optimum" surface tension for capsule 3; radius = 1.21 cm, 12 w/o Co-Ce.

this contention. In Fig. 3 and 4 are shown the s and s_7 curves for these two capsules.[7] The "adjusted" and experimental sine curves for these two capsules are shown in Fig. 5 and 6. Visual comparison of Fig. 3 *vs.* 4 and of Fig. 5 *vs.* 6 indicates that the methods used to treat the data permit satisfactory results to be obtained from both symmetric and distorted menisci provided only that the region of obvious distortion is not in the curved section near the outside perimeter of the meniscus.

In Table X in the Appendix are summarized the computational results for the 12 w/o Co-Ce alloys.

18 w/o Co-Ce *alloy.*—The surface tension results for the 18 w/o Co-Ce melts are summarized in Table I. Only one of the three menisci gave acceptable minima in the s and s_7 curves. However, the limitation of method 6 allowed two results from two capsules to be averaged and gave a result of 876 ± 51 dynes/cm. The two acceptable menisci for method 6 had significantly different radii of 0.57 and 1.21 cm. The computational

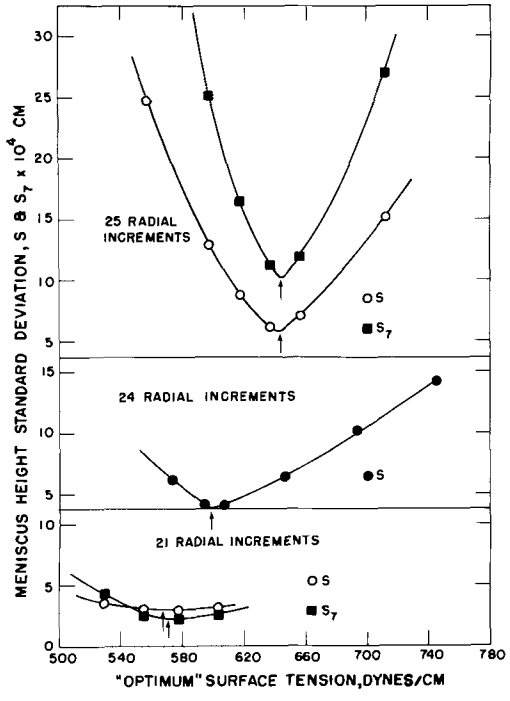

Fig. 4. Meniscus height standard deviations, s and s_7 *vs.* "optimum" surface tension for capsule 277; radius = 0.46 cm; 12 w/o Co-Ce.

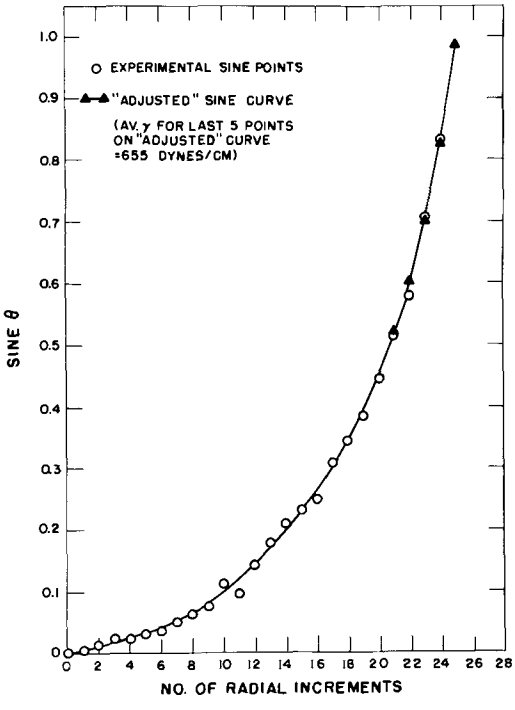

Fig. 5. Experimental and "adjusted" sine curve for capsule 3; radius = 1.21 cm, 12 w/o Co-Ce.

[7] In each case the radius was divided into 25 increments. Three calculations are shown for the cases where the inside 21, 24, and 25 increments are retained in the comparison.

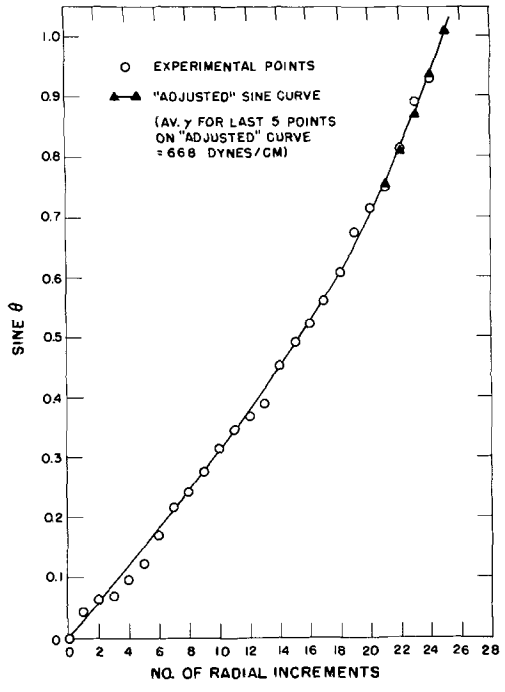

Fig. 6. Experimental and "adjusted" sine curve for capsule 277; radius = 0.46 cm; 12 w/o Co-Ce.

and comparison results for the 18 w/o Co-Ce alloys are presented in Table XI in the Appendix.

Surface Tensions of Pu-Co-Ce Alloys

The Pu-Co-Ce system forms a series of low melting alloys in which the plutonium concentration can be varied over a wide range of concentrations without significantly changing the melting temperature. These alloys are of interest in a liquid metal nuclear reactor because of the possibility of changing the plutonium concentration and the power density without changing the temperature requirements of the coolant system. Alloys from this system have been extensively tested as to their corrosion characteristics in tantalum containers, and some usable menisci were observed when photomicrographs were made from the sectioned capsules. The three alloys of interest are the 3, 5, and 8g Pu/cc concentrations. The nominal weight per cent compositions for the three alloys are listed in Table II. Also, listed are the melting ranges of these materials. These alloys are not true ternary eutectics, but their compositions do reside near the bottom of a temperature trough running through the ternary diagram. Therefore, the 3 and 5g Pu/cc materials do melt over a very narrow range of 10°C while the 8 g/cc melts over a 25°C range.

The data reported here were obtained from various capsules that were run for other purposes. As a result, many menisci were asymmetrical and distorted from not being in an exact vertical position on freezing. Also, no great care was taken to section the capsule exactly in the center. However, the number of undistorted menisci was sufficiently large to give reasonable estimates of the surface tension of the melts on freezing. In Tables XII and XIII, in the Appendix, are listed the chemical analyses for many of the melts tested. Also, the physical properties of the menisci and the computation requirements for the three alloys are tabulated in Table XIV of the Appendix.

Table II. Nominal compositions and melting ranges for Pu-Co-Ce alloys

Alloys Pu conc., g/cc	Nominal composition, w/o Pu	Co	Ce	Melting range, °C
3	33.5	10.2	56.3	436 ± 5
5	49.3	9.9	40.8	440 ± 5
8	68.1	8.3	23.6	420-445

Table III. Summary of surface tension data

Type of av	No. of menisci in av	No. of surface tension determinations in av	Range of surface tensions in av, dynes/cm	95% Confidence interval for av value of surface tension, dynes/cm	Av value of surface tension, dynes/cm
			3 g/cc Pu-Co-Ce		
1	2	10	628-687	±14.9	653.6
2	Ditto				
3	Ditto				
4	2	2	616-648	±415	648.5
5	3	3	616-1124	±663	807.0
6	3	3	616-1124	±663	807.0
7	3	8	615-1124	±144	704.0
8	5	13	397-1124	±143	728.8
9	5	10	397-1124	±130	662.6
			5 g/cc Pu-Co-Ce		
1	None				
2	2	8	927-1340	±151	1125.3
3	Ditto				
4	1	1	1148.0		1148.0
5	2	2	979-1148	±1074	1063.5
6	3	3	629-1148	±633	918.7
7	2	5	977-1148	±115.6	1079.8
8	4	8	629-1279	±164.8	1035.8
9	3	7	629-1148	±171.4	1001.0
			8 g/cc Pu-Co-Ce		
1	None				
2	None				
3	3	5	935-1135	±117.5	1019.0
4	None				
5	1	1	918.0		918.0
6	3	3	918-1184	±334.0	1041.0
7	None				
8	3	5	918-1187	±163.6	1044.0
9	3	4	918-1187	±205.5	1076.3

3 g/cc Pu-Co-Ce *alloy.*—Five menisci were analyzed for the 3 g/cc alloy; the results are shown in Table III. Two of the menisci produced acceptable minima in the s and s_7 curves as required by method 1, with a resulting average surface tension of 653.6 ± 14.9 dynes/cm. For this alloy only methods 1, 2, and 3 produced averages with small enough confidence intervals to be meaningful.

One of the 5 menisci was obtained by radiographing a sealed capsule in which the meniscus was frozen. Added uncertainty was produced by the fuzzy nature of the radiograph, and the resulting s and s_7 values were excessively large. However, the average γ from the "adjusted" sine curve was 598 dynes/cm which compares surprisingly well with the 654 dynes/cm value from the two acceptable mensici. A summary of the computational and comparison results for the 3 g/cc alloy is presented in Table XV of the Appendix.

5 g/cc Pu-Co-Ce *alloy.*—Five menisci from the 5 g/cc alloy were studied, and two of the menisci produced minima acceptable by method 2. However, in this case the range of the surface tensions from these minima was very large, 927 to 1340 dynes/cm. The average surface tension from method 2 was 1125 ± 151 dynes/cm. Method 7 actually produced an average with a smaller confidence interval, 1079.8 ± 116 dynes/cm. This wide confidence interval indicates that some distortion was being allowed in method 2 and that more menisci should be studied as they become available. The tabulation of comparison results is given in Table XVI in the Appendix.

The radiographed meniscus again had very large s values. The average value from the adjusted sine curve was 629 dynes/cm which does not compare favorably with the above averages.

8 g/cc Pu-Co-Ce *alloy.*—The average surface tensions found for the 8 g/cc alloy are presented in Table III. Of the 5 menisci tested none met the requirements of methods 1 and 2. However, the minima in s and s_7 were acceptable from three of the menisci when the size restriction of s and s_7 was relaxed to

35 x 10^{-4} cm in method 3. This result of 1019 ± 118 dynes/cm had the smallest 95% confidence interval for all of the 9 averaging methods. All other restricting methods had confidence limits of ±164 dynes/cm or greater. Table XVII in the Appendix contains the computational and comparison results for the various menisci.

The radiographed capsule had very large s and s_7 values and gave an average surface tension of 740 dynes/cm. The fuzziness of the radiograph produced some of the distortion indicated by the size of the s and s_7.

Capillary rise surface tension determination.—The surface tensions of these alloys have not been determined by other methods in experiments designed for such determinations. However, one independent calculation of the surface tension of 6.2g Pu/cc Pu-Co-Ce (57.7 w/o Pu-9.4 w/o Co-32.8 w/o Ce) was made possible from a radiograph of the fluid contained in an electromagnetic pump experimental apparatus (3). The reservoir and manometer legs provided a system in which capillary rise in the legs could be measured. At 530°C the rise in the manometer tube along with the assumption of 0° contact angle gave a surface tension of 1050 dynes/cm. This value compares very favorably with the values of 1125 ± 151 and 1019 ± 118 dynes/cm for the 5 and 8g Pu/cc Pu-Co-Ce alloys.

Interfacial Tension of a Co-Ni Alloy Covered with NaK

In density studies made with a NaK volumeter (2) the density specimen is held in direct contact with the indicating NaK fluid. Many of the specimens formed well-shaped concave menisci between the alloy and the NaK. At this time one of these menisci from an 18 w/o Ni-Ce alloy has been analyzed. The results presented in Table IV indicate that the meniscus was relatively undistorted since acceptable minima in s and s_7 at three of the four radial increments tested were obtained. The best result came from method 3 where a tension of 421.3 ± 16.1 dynes/cm was produced. Since only one sample was run, most of the analyzing methods could not give a 95% confidence interval. The physical data for the mensicus and the computation times are given in Table XIX in the Appendix. The computation results for each radial increment are included as Table XX in the Appendix. As indicated in Table XVIII the Ni-Ce alloy melted over a temperature range of 450°-490°C and is not a true eutectic. A complete tabulation of the experimental meniscus heights for all of the menisci studied are presented in Table XX in the Appendix.

Results and Conclusions

Surface tensions of 6, 12, and 18 w/o Co-Ce, 3, 5, and 8g Pu/cc Pu-Co-Ce alloys, and the interfacial tension of 18 w/o Ni-Ce/NaK were determined from frozen menisci of the alloys. A total of 28 menisci were analyzed and, of this number, 15 produced minima in the standard deviations, s and s_7, that met the limitation of size of s and s_7 and of deviation in $\sin\phi$, as required by averaging methods 1, 2, and 3. Nine methods of testing the surface tension data for distortion were tested on the menisci, and methods 1, 2, and 3 which require acceptable minima in s and s_7 were consistently the best. Of the more liberal restricting techniques, methods 7, 8, and 9 most consistently produced results that agreed with methods 1, 2, and 3. These last restrictive methods invariably had 95% confidence intervals that were from 1½ to 10 times as large as those from methods 1, 2, and 3. In one case, for 18 w/o Co-Ce, method 6 which only requires that experimental and adjusted sine curves be nearly parallel gave the most acceptable results with the smallest 95% confidence interval. The surface tensions obtained from the analyses are summarized in Table V.

The surface tension calculation and restriction procedure was designed such that if averaging method 1 was satisfied the meniscus could be assumed to have no significant distortion from freezing. Averaging methods 2 and 3 also should minimize the possibility of distortion, but because of the larger allowable standard deviation in meniscus differential heights, more distortion is permitted. The analysis of the 28 menisci in this study indicate that the restrictions of method 1 are sufficient to eliminate distorted menisci. Methods 2 and 3 with their relaxation on the size of the standard deviation also give good results in general. Three tests of the restricting procedures were possible from the computations. Comparisons of surface tensions from capsules of similar size could be made. Also, surface tension comparisons from capsules with significantly different radii were possible. And finally, one independent surface tension determination was available for comparison.

In the first test, the surface tension of a given alloy was determined from a number of capsules of approximately the same diameter, and these values were compared. Since the cooling histories of the capsules were probably dissimilar, the surface tension values from the capsules could be significantly different if distortion were allowed to influence the results. Also, the values from the various capsules could vary from asymmetries resulting from nonvertical freezing and noncenterline cutting. The minima methods were designed to detect and discard nonmeniscus type of shapes. Thus, if the methods are operating satisfactorily, the remaining acceptable menisci should produce comparable values of surface tension. In Table VI are summarized the data obtained from capsules of comparable size for the alloys tested. The surface tensions of the capsules accepted and from those rejected are noted. Also, the type of minima method used is listed. Three sets of capsule pairs from two alloys met the requirements of method 1. The range of the dual values was for each set within ±1.8, ± 1.2, and ± 0.23% of the average for the two capsules. As the magnitude of the standard deviations, s and s_7, was relaxed in methods 2 and 3, the spread in surface tensions became greater. For the 5g Pu/cc Pu-Co-Ce with method 2, the range was ± 13.4%. Method 3 gave very good results for 6 w/o Co-Ce with a range of ± 0.43%. However, the range with method 3 for 8g Pu/cc Pu-Co-Ce was ± 10.5%. These results tend to indicate that method 1 is sufficiently stringent to insure that the shape being studied was formed by surface tension forces. However, some dis-

Table IV. Summary of interfacial tension data
18 w/o Ni—81 w/o Ce/78 w/o NaK

Type of av	No. of menisci in av	No. of surface tension determination in av	Range of surface tensions in av, dynes/cm	95% Confidence interval for av value of surface tension, dynes/cm	Av value of surface tension, dynes/cm
1	1	4	408.0-440.0	±22.8	423.0
2	Ditto				
3	1	5	408.0-444.0	±16.1	421.4
4	None				
5	1	1	423.1		423.1
6	1	1	423.1		423.1
7	1	1	423.0		423.0
8	1	1	423.0		423.0
9	1	1	423.0		423.0

Table V. Summary of surface tensions obtained from frozen menisci

Material	Method No.	Surface tension, dynes/cm	95% Confidence interval
6 w/o Co-94 w/o Ce	3	685.0	±38.2
12 w/o Co-88 w/o Ce	1	644.5	±7.7
18 w/o Co-82 w/o Ce	6	876	±51
3 g/cc Pu-Co-Ce	1	653.6	±14.9
5 g/cc Pu-Co-Ce	2	1125	±151
8 g/cc Pu-Co-Ce	3	1019	±118
18 w/o Ni-82 w/o Ce/NaK	1	423.0	±22.8

Table VI. Comparison of surface tension values from capsules of comparable size which satisfy averaging methods 1, 2, and 3

Material	No. of menisci tested with similar radii	Radius range, cm	No. of menisci acceptable	Averaging method used	Average values of surface tension for each capsule accepted	Average values of surface tension for each capsule not accepted
6 w/o Co-94 w/o Ce	3	0.47-0.57	2	3	682, 688	405
12 w/o Co-88 w/o Ce	4	0.46-0.57	2	1	645, 642	853, 1073
	2	1.21	2	1	654, 637	
18 w/o Co-82 w/o Ce	1	0.57	1	1	920	
	2	1.21	0	—	—	808, 541
3 g Pu/cc-Pu-Co-Ce	5	0.46-0.48	2	1	668, 644	303, 1360, 412
5 g Pu/cc-Pu-Co-Ce	5	0.46-0.48	2	2	1260, 962	1279, 629, 1137
8 g Pu/cc-Pu-Co-Ce	5	0.47-0.48	3	3	1121, 985, 937	510, 735

tortion in the meniscus can be expected if methods 2 or 3 are used.

A second test of averaging method 1 was made available by the data from the 12 w/o Co-Ce menisci. Here two sets of capsules with significantly different radii met the requirements of method 1. The shapes of these menisci were quite different as indicated in Fig. 1 and 2, and their thermal cooling histories had to be very different because of the different radii. As shown in Table VI, the average values for these two sets of capsules were 643 and 645 dynes/cm.

Finally, a surface tension value was obtained by a capillary rise experiment for the 6.2g Pu/cc Pu-Co-Ce fuel. This value was 1050 dynes/cm which falls right between the values obtained for the 5 and 8g Pu/cc fuels as determined by methods 2 and 3.

These calculational and experimental results show that good surface tension values can be obtained from frozen menisci with the comparison and restricting procedures utilized. However, the less stringent averaging procedures, methods 4 through 9, should be used with care and should be utilized only to indicate the general range of the surface tension for a given liquid metal.

Acknowledgment

The author wishes to thank Carl R. Cushing and John M. Oblak for their help in obtaining and preparing the experimental data. Also, the efforts of Marguerite Coleman and Doreen Bourne in preparing the manuscript are greatly appreciated.

This work was performed under the auspices of the United States Atomic Energy Commission.

Manuscript received March 7, 1966; revised manuscript received Oct. 31, 1966. This paper was presented at the Washington Meeting, Oct. 11-15, 1964.

Any discussion of this paper will appear in a Discussion Section to be published in the December 1967 JOURNAL.

REFERENCES

1. J. C. Biery and J. N. Oblak, *Ind. & Eng. Chem. Fundamentals*, **5**, 121 (1966).
2. R. H. Perkins, L. A. Geoffrion, and J. C. Biery, *Trans. Met. Soc. AIME*, **233**, 1703 (1965).
3. G. L. Caldwell, "An Experimental dc Electromagnetic Pump for a Molten Plutonium Alloy," Los Alamos Scientific Lab. LA-3240, Dec. 9, 1965.

NOMENCLATURE

g	acceleration due to gravity, cm/sec^2
s	sample standard deviation between calculated and experimental heights at all N radial positions, cm
s_7	sample standard deviation between calculated and experimental meniscus heights at outside seven radial positions, cm
z	height of meniscus above datum plane at radial position r, cm
z_o	height of meniscus above datum plane at $r = 0$, cm
$z'_{m-1/2(\text{exp})}$	experimental meniscus height above horizontal tangent plane, cm
$z'_{m-1/2(\text{num})}$	numerically calculated meniscus height above horizontal tangent plane, cm
ρ_1	density of fluid, below meniscus, g/cc
ρ_2	density of fluid, above meniscus, g/cc
θ	angle between tangent to surface tension curve and horizontal line at radial position r, radians
θ_{exp}	experimental angles calculated from $z'_{m-1/2(\text{exp})}$, radians
θ_{adj}	values of θ on a smoothed curve through $\sin\theta_{\text{exp}}$ points. Values from this curve when used for boundary condition of $\sin\phi$ give approximately a constant value of γ at all radial positions tested
ϕ	angle of tangent to meniscus curve at outside of meniscus. This is the boundary condition required in the numerical computation, radians
ϕ_{min}	value of ϕ at minimum in s or s_7, radians
ϕ_{as}	external tangent angle assumed for a computation, radians
γ	surface tension, dynes/cm
γ_{as}	surface tension assumed for a computation, dynes/cm
γ_{cal}	surface tension calculated with sum of mass restraint dynes/cm
γ_{optimum}	surface tension calculated with sum of mass restraint where $\gamma_{\text{as}} = \gamma_{\text{cal}}$, dynes/cm

Technical Notes

The Application of Ultraviolet Analytical Techniques to Lead Acid Systems

Thomas F. Sharpe

Research Laboratories, General Motors Corporation, Warren, Michigan

The use of ultraviolet (uv) spectrophotometric techniques to clarify the role of organic additives in electrolytic systems has been restricted to some extent because portions of the spectra of the organic materials have been obscured. In studies of adsorption at copper, nickel, and silver electrodes, Barradas and Conway reported (1) that traces of metal ions and/or complexes formed between the metal ion and the organic compounds tended to distort the uv absorption bands of the organic adsorbate. To minimize these effects, the study was confined to alkaline and weakly acidic solutions at electrode potentials near the reversible hydrogen potential for the given solution.

Similarly, the application of uv methods for studying the reactions of conjugated organic compounds in experimental lead-acid battery systems is limited because of inorganic uv-absorbing materials in the electrolyte.

This paper reports on attempts to characterize the various inorganic uv-absorbing constituents in lead-acid cells to find ways to minimize their interference with the evaluation of concentration and structural changes of the organic materials. The experimental approach was to measure the uv absorbance of sulfuric acid solutions exposed to lead surfaces on open circuit and during polarization, and then to compare these results with the absorbance exhibited by lead and lead-antimony corrosion products added to the acid as the reagent grade chemicals. Absorbance measurements were made with a dual beam spectrophotometer[1] using distilled water as a reference. The sulfuric acid solutions were prepared by diluting the reagent grade acid to the desired specific gravity with distilled water. The absorbance exhibited by these solutions was negligible throughout the range 350-210 mμ.

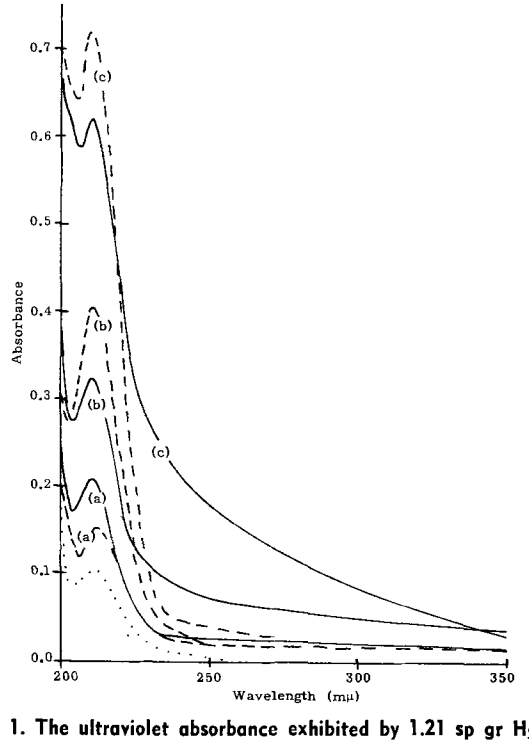

Fig. 1. The ultraviolet absorbance exhibited by 1.21 sp gr H_2SO_4 solutions containing: ——— lead power, (a) 10 g/liter, (b) 100 g/liter, and (c) 500 g/liter; — — — PbO_2, (a) 1 g/liter, (b) 10 g/liter, and (c) 100 g/liter; and . . . . $PbSO_4$ (saturated).

The absorption spectra presented in Fig. 1 were obtained following the additions of pure lead powder, lead sulfate ($PbSO_4$), or lead dioxide (PbO_2) to 1.21 sp gr H_2SO_4. To insure equilibrium, the solutions were stirred thoroughly for several hours; then the excess solid material was allowed to settle before making the absorbance measurements.

The magnitude of absorbance exhibited by the $PbSO_4$ is attributed to the sparingly soluble Pb^{2+} ion, since quantities of $PbSO_4$ greater than those required for saturation did not affect the absorbance. Increasing the amount of excess PbO_2, however, caused an increase in absorbance. Since PbO_2 can oxidize the water in the solution, the absorbance may be caused by Pb^{2+} ion present in greater quantity than normal saturation, or by the formation of an oxygen-containing complex, such as $PbO \cdot PbSO_4$. The absorbance of the acid exposed to the pure lead powder reached its maximum in 18 hr and is similar to that resulting from additions of PbO_2.

Since the increase in absorbance of H_2SO_4 solutions exposed to the lead may be caused by the reaction of lead with oxygen, some experiments were conducted in nitrogen stirred solutions to determine whether the absorbance was minimized. Electrodes (3.0 x 4.0-cm portions of a lead-3% antimony gauze) were polarized in an H-type cell whose two electrode compartments were separated by a glass frit. Figure 2 shows the effect of both anodic and cathodic polarization on absorbance of the acid determined by sampling the appropriate compartment of the H-cell for spectrophotometric analysis.

No increase in absorbance was found after an 18-hr open-circuit exposure of the electrodes in nitrogen stirred solution. However, anodic polarization in nitrogen stirred solution, even at very low current densities, gave measurable increases in absorbance.

Prolonged cathodic polarization in nitrogen stirred solution at low current density gave no increase in absorbance. However, when nitrogen stirring was replaced by air stirring (without interrupting the current), the absorbance increased in a manner similar to that found in the solution from the anode compartment. In the presence of air, the absorption con-

[1] Cary Model 15, Applied Physics Corporation, Monrovia, California.

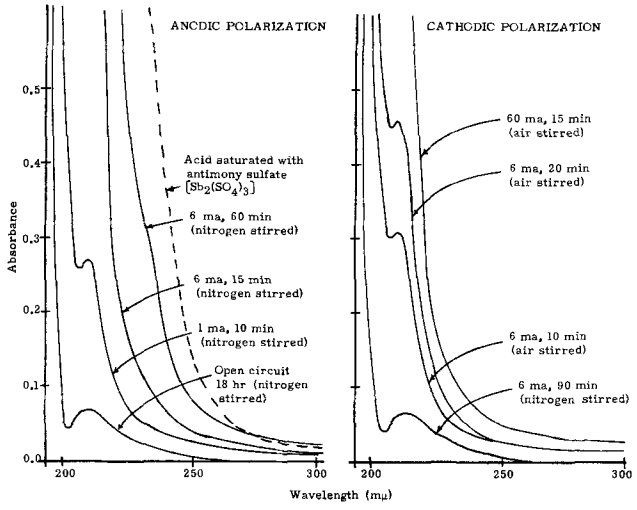

Fig. 2. Effect of anodic and cathodic polarizations of lead-3% antimony electrodes on the absorbance of 1.30 sp gr H_2SO_4. (Acid saturated with $PbSO_4$ before test.)

tinued to increase even at much higher cathodic current densities.

The spectrum (broken line in Fig. 2) resulting from the addition of antimony sulfate [$Sb_2(SO_4)_3$] to the acid suggests that a substantial portion of the absorbance shown in Fig. 2 was because of dissolution of the antimony. It appears that in nitrogen stirred solutions the electrode potential is sufficiently noble so that there is no metal dissolution. However, in the presence of oxygen (air), even when applying a low cathodic current, the potential is sufficiently active to allow metal dissolution to take place.

It has been suggested that an additional cause for absorption is the possible formation of hydrogen peroxide (H_2O_2) by reduction of oxygen (2) at the cathode. Small quantities of H_2O_2 in H_2SO_4 give uv absorbance patterns similar to those shown by the acid exposed to the lead surfaces. The minimum quantity of H_2O_2 detectable by the uv method is 0.001%, which was established by measuring the absorbance of H_2SO_4 solutions containing known quantities of H_2O_2. During the experiment represented in Fig. 2, quantities of solution in the cathode compartment were checked periodically for H_2O_2. Using the standard peroxytitanic acid test (3), the presence of H_2O_2 was not indicated. Since this test is sensitive to $< 0.001\%$ H_2O_2, it appears that H_2O_2 is not a contributor to absorption in these experiments. The absence of H_2O_2 in lead-acid systems is not surprising, however, since lead surfaces are reported (4) to be excellent peroxide decomposers.

To summarize, these experiments indicate that when ultraviolet techniques are applied to lead-acid systems, conditions should be maintained to minimize buildup of corrosion products of lead and lead-antimony alloys. Therefore, the reactions of conjugated organic compounds at lead surfaces should be studied in nitrogen stirred solutions at potentials more cathodic than the corrosion potential of the lead surface.

Manuscript received Nov. 1, 1966; revised manuscript received Dec. 7, 1966.

Any discussion of this paper will appear in a Discussion Section to be published in the December 1967 JOURNAL.

REFERENCES

1. R. G. Barradas and B. E. Conway, *J. Electroanal. Chem.*, **6**, 314 (1963).
2. M. Taube, *Ber. Chem. Deutsch. Ges.*, **15**, 2434 (1882).
3. G. M. Eisenberg, *Ind. Eng. Chem.*, **15**, 327 (1943).
4. W. C. Schumb, C. N. Satterfield, and R. W. Wentworth, "Hydrogen Peroxide," pp. 168, 402, Reinhold Publishing Corp., New York (1955).

Studies of Hydrocarbon Fuel Cell Anodes by the Multipulse Potentiodynamic Method

IV. Effect of Various Electrolytes on the Behavior of Hydrocarbons on Conducting Porous Teflon Electrodes

L. W. Niedrach and M. Tochner[1]

General Electric Research & Development Center, Schenectady, New York

Important variables in fuel cell studies are the electrocatalyst, electrode structure, electrolyte, and fuel structure. A systematic study of these variables using the multipulse potentiodynamic (MPP) method has been under way in this Laboratory (1-5). Previous papers in the present series have dealt with the behavior of methane, ethane, and propane on Teflon bonded platinum black electrodes with a perchloric acid electrolyte (3, 4) and with methane through butane with a phosphoric acid electrolyte (5).

Recent observations in fuel cell studies that higher current densities can be sustained by hydrocarbons with a hydrofluoric acid azeotrope electrolyte than a concentrated phosphoric acid electrolyte (6) initiated the present examination of the effects of various electrolytes. Of particular interest was any difference in behavior that could account for the higher, steady-state current densities that can be supported in hydrofluoric acid cells without the appearance of voltage decay and oscillations. The electrolytes that were compared in this study were H_3PO_4, $HClO_4$, and HF at 60°C. Ethane served as the model hydrocarbon for the comparison.

Experimental

A three-compartment Teflon cell described elsewhere (3) was used in these experiments. A miniature version (0.2 cm diameter) of a previously described (7) conducting-porous "Teflon" fuel cell electrode containing platinum black as the catalyst was employed. That used in this work was designated as ME-16.

Both the hydrogen reference and counter electrodes were platinized platinum flags. The hydrogen reference communicated with the working electrode by a Luggin capillary. All potentials are referred to this electrode. The cell was operated in an air thermostat enabling control of the temperature to within 0.1°C.

The acids employed in the study were 4.3*N* perchloric acid, 5*N* phosphoric acid, 36*N* (75%) phosphoric acid, and 22*N* (azeotrope) hydrofluoric acid. All were prepared by diluting reagent grade acids with quartz distilled water. Electrolytic grade hydrogen was used in the reference electrode chamber, and

[1] Present address: Silicone Products Department, General Electric Company, Waterford, New York.

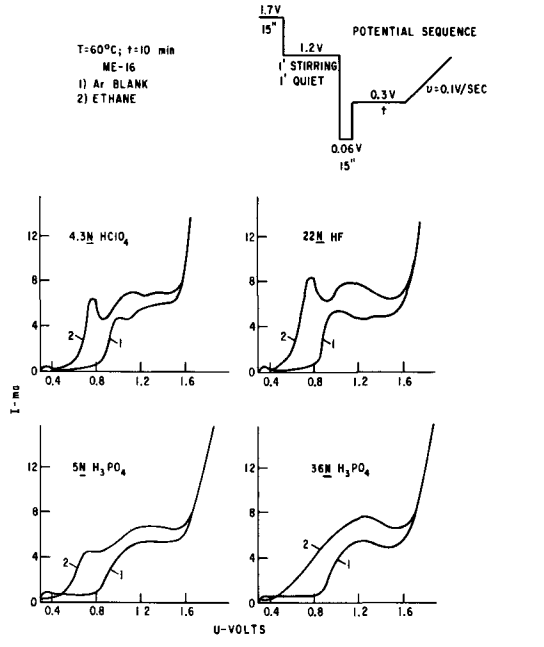

Fig. 1. Current-potential (time) traces for adsorbed ethane with various electrolytes.

Phillips research grade ethane was used as the fuel. Tank argon deoxygenated by passage over heated copper turnings was substituted for the fuel for obtaining solvent blanks. Tank argon was also used for degassing the electrolyte.

As in the earlier work linear anodic sweeps were applied to the electrode to determine the behavior of the ad-layer as well as the amount of fuel adsorbed after equilibrations at various potentials for varying times. Prior to each equilibration the electrode was pretreated with a series of potential steps which have previously been found to result in reproducible conditions. The sequence of steps is shown in Fig. 1 and the details are discussed elsewhere (3).

Briefly, oxidizable impurities are removed from the electrode during the period at 1.7v. During the step at 1.2v, oxygen evolution ceases, and free oxygen is removed from the vicinity of the electrode. Adsorption of fuel is blocked at this time by "adsorbed oxygen" on the electrode. The brief excursion to 0.06v results in reduction of the "adsorbed oxygen" layer at a potential at which hydrocarbons are themselves not adsorbed. The potential is then stepped to that at which adsorption and performance data are required. After the desired equilibration time a linear anodic sweep is applied in order to determine the number of coulombs associated with oxidation of the carbonaceous ad-layer. This information is obtained by integrating the area between the trace for the equilibrated electrode and that obtained when argon is substituted for the fuel. In the latter case the wave starting at about 0.8v corresponds to the formation of the adsorbed oxygen layer. When fuel is present on the electrode some ad-species may be oxidized prior to the formation of the oxygen ad-layer while others may be oxidized concurrently over the same potential range. In the latter case, the wave obtained over the potential range 0.8-1.6v is enhanced over that obtained during an argon blank. The final sharp rise in all of the traces marks the onset of oxygen evolution.

Polarization curves were obtained by measuring the currents during the longer equilibrations just prior to application of the linear anodic sweeps. These curves, of course, differ in form from the current-voltage traces obtained during linear anodic sweeps. The former reflect quasi steady-state performance while the latter are associated with complete oxidation of all of the ad-species on the surface. It is to be noted that the steady-state currents are much smaller than those flowing during the linear anodic sweeps. They therefore introduce a negligible error in the determination of the charge associated with oxidation of the ad-layer.

Results and Discussion

The general form of the current-voltage traces obtained with linear anodic sweeps for adsorbed ethane in the presence of the four electrolytes is shown in Fig. 1 after 10-min equilibrations at 0.3v. Traces obtained after shorter and longer equilibrations were of the same form. In all cases the ad-layer is oxidized over a range of potentials. With the perchloric and hydrofluoric acid electrolytes two distinct waves can be detected. The first occurs at potentials below those (approximately 0.8v) at which the surface itself is normally oxidized. The second wave exhibits a flat maximum which extends from 0.8v to oxygen evolution potentials. In the case of the perchloric acid electrolyte the first wave has been attributed to the oxidation of C_1 species and the second to C_2 species (1-4).

With the phosphoric acid electrolytes oxidation of the ad-layer is again initiated at potentials below those required for platinum surface oxidation, but the resolution of two discrete waves is less pronounced than with the other electrolytes. It has been noted, however, that at higher temperatures resolution of the two waves occurs (5).

As the equilibration potential is increased from about 0.2v the magnitudes of both waves decline, indicating that the surface coverage with the assorted species decreases (3, 5). This occurs in order that the rate of adsorption may keep pace with the increasing steady-state currents being drawn from the electrode as the potential increases (1-5). The change in coverages with equilibration potential, as reflected by changes in Q_{E1} and Q_{Etot}, the charges required for oxidation of the species of wave 1 and the entire ad-layer, respectively, are illustrated in Fig. 2 through 5. Because of the incomplete identification of the precise oxidation states of the species involved, it is not possible to relate these data to the actual number of surface sites obscured. The values of Q_{Etot} were obtained from linear anodic sweeps by integrating the area between the ethane trace and that of the argon blank as described above. Q_{E1} was obtained by a similar integration to the left of a perpendicular at about 0.85v. In the cases of the perchloric and hydrofluoric acid electrolytes this potential corresponded to the minimum on the fuel oxidation trace.

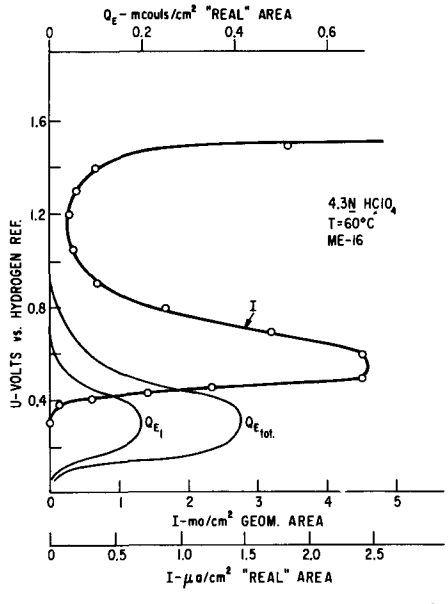

Fig. 2. Polarization and surface charge curves for ethane with a perchloric acid electrolyte.

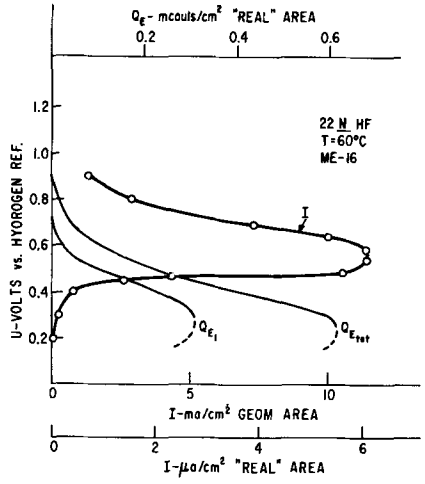

Fig. 3. Polarization and surface charge curves for ethane with a hydrofluoric acid electrolyte.

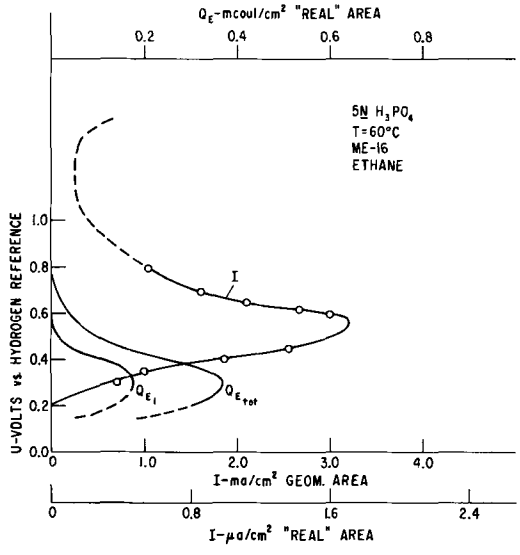

Fig. 4. Polarization and surface charge curves for ethane with a 5*N* phosphoric acid electrolyte.

Also shown in Fig. 2 through 5 are polarization curves for the four electrolytes. The form of the polarization curves is similar for the four electrolytes. However the maximum currents vary strongly among them as shown by the data in Table I. In all cases the maximum currents occur at potentials at which there is still adsorbed fuel on the electrode surface. Maximum surface coverage of the electrode occurs at 0.2-0.3v in all cases.

Table I. Effect of electrolyte on maximum current

Electrolyte	Maximum current density	
	ma/cm² (geom.)	Relative
4*N* $HClO_4$	4.6	1.0
22*N* HF	11.4	2.5
5*N* H_3PO_4	3.2	0.7
36*N* H_3PO_4	1.5	0.3

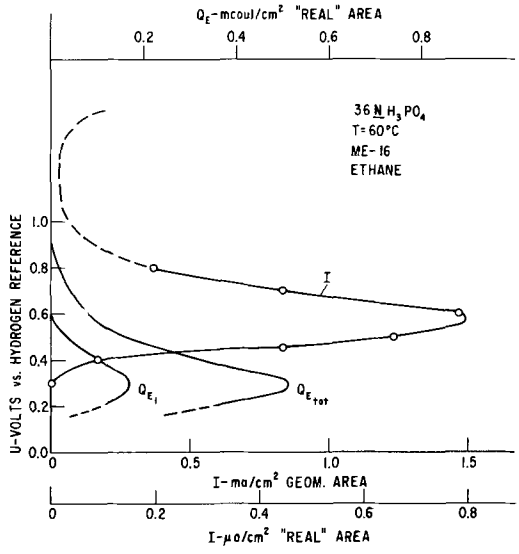

Fig. 5. Polarization and surface charge curves for ethane with a 36*N* phosphoric acid electrolyte.

Summary and Conclusions

Linear anodic sweep data obtained with ethane as a model hydrocarbon with perchloric acid, hydrofluoric acid, and phosphoric acid electrolytes indicate that in a qualitative sense the behavior is similar with all of the electrolytes. In view of the similarities of the behaviors of ethane, propane, and butane in previous studies (3,5) it is anticipated that the present observations with ethane will extend to higher hydrocarbons as well. Quantitative effects therefore appear to account for the differences in performance of hydrocarbons in fuel cells employing different acidic electrolytes. These are probably associated with changes in the double layer structure and may also reflect differences in the solubility of the hydrocarbons in the various electrolytes.

Acknowledgment

This work is a part of the program under contracts DA-44-009-AMC-479(T) and DA-44-009-ENG-4909, ARPA Order No. 247 with the U.S. Army Engineer Research and Development Laboratories, Fort Belvoir, Virginia, to develop a technology which will facilitate the design and fabrication of practical military fuel cell power plants for operation on ambient air and hydrocarbon fuels.

Manuscript received March 15, 1966; revised manuscript received Dec. 1, 1966.

Any discussion of this paper will appear in a Discussion Section to be published in the December 1967 JOURNAL.

REFERENCES

1. S. Gilman, *Trans. Faraday Soc.*, **61**, 2546, 2561 (1965).
2. S. Gilman in "Hydrocarbon Fuel Cell Technology," B. S. Baker, Editor, p. 349, Academic Press, New York (1965).
3. L. W. Niedrach, S. Gilman, and I. Weinstock, *This Journal*, **112**, 1161 (1965).
4. L. W. Niedrach, *ibid.*, **113**, 645 (1966).
5. L. W. Niedrach and M. Tochner, *ibid.*, **114**, 17 (1967).
6. E. J. Cairns in "Hydrocarbon Fuel Cell Technology," B. S. Baker, Editor, p. 465, Academic Press, New York (1965).
7. L. W. Niedrach and H. R. Alford, *This Journal*, **112**, 117 (1965).

A New Air Electrode for Fuel Cells

Harold I. Zeliger[1]

General Electric Research & Development Center, Schenectady, New York

It is believed that a porous structure will allow better mass transport of reactant gases to the active sites of fuel cell electrodes and thereby give higher performances. With the thought that the incorporation of high surface area inert material would yield a highly porous structure, electrodes containing silica were prepared and evaluated in fuel cells.

Standard Teflon bonded electrodes (1) (pressed at 350°C) were prepared incorporating silica. These electrodes were extremely hydrophobic, showed no porosity when placed in fuel cells, and would not perform on hydrogen. They apparently were impervious to hydrogen. Leaching them with sodium hydroxide or hydrofluoric acid for periods of up to 3 days improved their fuel cell performances only slightly. (Apparently the Teflon protected the silica from the leaching media.)

If, however, the electrodes were pressed cold (room temperature) the resulting structures were highly porous and readily wetable, and the electrodes showed moderate fuel cell performance. Further experimentation led to an electrode fabrication procedure which gave very high performance electrodes. It is as follows:

A mix was prepared consisting of 0.15g John Cabot Cab-O-Sil silica (surface area: 175-200 m^2/g), 0.15g graphite,[2] 0.12cc Dupont T-30 Teflon suspension (0.108g Teflon), 5 drops Rohm and Haas Triton X-100 wetting agent, the appropriate quantity of chloroplatinic acid (from Engelhardt Industries, 40% platinum), and sufficient water to give a free flowing slurry. The slurry was applied on alternate sides of a 17.7 cm^2 (1⅞ in. diameter) 45 mesh platinum screen (woven from 8 mil wire) with a single quill camel's hair brush or medicine dropper and dried above a 350°C hot plate after each application. Four or five applications were required on each side to get all the material onto the screen. After each application the material was pressed into the screen by rolling a glass rod over it with a firm hand. Drying was carried out at 350°C so that it could be accomplished quickly thereby preventing the Teflon from settling out of the mix.

A 1.6 mg/cm^2 waterproofing Teflon film was sprayed onto one side of the electrode (1). Finally, the chloroplatinic acid was reduced under a stream of hydrogen at room temperature for 2 hr.

By initially incorporating chloroplatinic acid rather than platinum black into the electrode, the catalyst was not subjected to high temperatures which could cause sintering. A second advantage of adding the platinum in solution is that more uniform distribution of catalyst in the final electrode structure is assured than if materials of varying densities were mixed together.

Electrodes with varying platinum content[3] were prepared and evaluated on hydrogen, oxygen, and air in ambient temperature, 5*N* sulfuric acid electrolyte fuel cells. A Kordesch-Marko (2) interrupter bridge was employed to monitor performance.

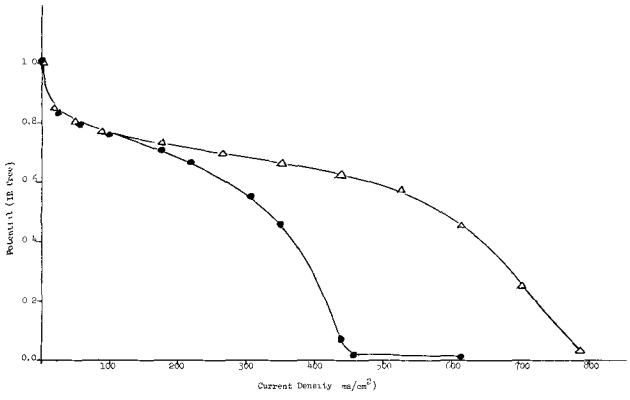

Fig. 1. IR free performance curves for standard and new silica containing electrodes on air at ambient temperature. Anodes, standard electrodes with 34 mg Pt/cm^2; cathodes, △ = new silica containing electrode with 10 mg Pt/cm^2, • = standard electrode with 34 mg/cm^2; electrolyte: 5*N* H_2SO_4.

Excellent performances (0.8v IR free at 350 ma/cm^2) were obtained on hydrogen with platinum loadings of 1.0 mg/cm^2, and on oxygen with platinum loadings of 4.0 mg/cm^2. It was, however, as air electrodes that these new electrodes showed superiority. Figure 1 shows the IR free polarization curves for a test electrode with 10 mg platinum/cm^2 (also containing 0.15g silica, 0.15g graphite, and 0.12 cc T-30) and for a representative standard electrode (1) containing 34 mg platinum/cm^2. At low current densities (up to 100 ma/cm^2) performance of the test electrode paralleled those of standard electrodes, while at higher current densities the performance of this electrode, was significantly better. This electrode had a limiting current density of 800 ma/cm^2.

At current densities where standard electrodes show major polarization attributed to mass transport limitations, this new electrode, with less than one third the catalyst content, showed very little polarization. At 450 ma/cm^2 the IR free difference in potential between the two electrodes was 0.6v.

This improved performance is most probably attributable to a very highly porous electrode structure which allows for rapid mass transport of air to the catalytically active sites. Incorporation of a high surface area material such as silica into a fuel cell electrode makes the attainment of such a structure possible.

Manuscript received Oct. 14, 1966.

Any discussion of this paper will appear in a Discussion Section to be published in the December 1967 JOURNAL.

REFERENCES

1. L. W. Niedrach and H. R. Alford, *This Journal*, **112**, 117 (1965).
2. K. Kordesch and A. Marko, *ibid.*, **107**, 480 (1960).

[1] Present address: Avco Space Systems Division, Avco Corporation, Lowell, Massachusetts.

[2] The graphite served the dual purpose of imparting structural stability and conducting current in electrodes with low platinum contents.

[3] With lower platinum loadings (<6 mg/cm^2) more graphite was used, *e.g.*, electrodes with 1.0 mg Pt/cm^2 contained 0.3 g graphite.

Further Observations on the Oxidation of Zirconium in Dry Oxygen

E. Hillner

Bettis Atomic Power Laboratory, Westinghouse Electric Corporation, Pittsburgh, Pennsylvania

In a previous investigation on the high-temperature oxidation performance of pure zirconium, it was demonstrated that crystal bar (iodide process) zirconium will exhibit a transition in rate kinetics from cubic to parabolic behavior after extended exposure periods whereas high-grade sponge material undergoes a cubic-to-linear change under these same conditions (1). Both materials were found to behave in almost an identical manner in all other aspects of the oxidation reaction. Further investigations were undertaken at this laboratory in an attempt to substantiate the previously observed variance in posttransition behavior between sponge and crystal bar zirconium, and to initiate a limited parametric study involving the possible origins of this deviation.

Experimental

The primary concern associated with the initial study (1) involved the choice of specimen geometry (0.05 cm diameter wire). The present investigation employed platelet specimens of both materials, ~2.5 x 1.25 x 0.38 cm. Due to the size and weight of these coupons, the constant modulus helical spring balance employed in the first study could not be used; instead, the new specimens were placed in a molybdenum boat, in the center of a tubular zircon vacuum chamber, which in turn was externally heated with the aid of a horizontally mounted, split-tube, resistance-wound furnace. The loading and weighing of specimens was performed by two different schedules. In the first scheme, four specimens (two sponge and two crystal bar zirconium) were loaded into the boat, evacuated to below 10^{-5} Torr, heated in 400 Torr predried oxygen for a specified length of time, cooled to room temperature, weighed on a Mettler semi-automatic microbalance, and returned to the vacuum chamber for additional exposure. Thus, this method of collecting kinetic data involved the repeated heating, cooling, and weighing of the same specimens after various exposure times. Specimens handled in this manner are henceforth designated as having undergone "discontinuous weight determinations." In the second schedule, the specimens were exposed for only one time cycle, cooled, weighed and then discarded. A freshly prepared group of platelets was then employed for the next exposure time, etc. Data from this latter group are indicated by the term "continuous weight determinations." In order to expedite the comparison of the current information with that presented in (1), all test results generated in this study have been obtained at the highest test temperature of the referenced experiments, *i.e.*, 850°C. Oxygen pressure was maintained at 400 Torr for each exposure, and at least two experimental runs were carried out for each test condition. Detailed chemical analyses of the two zirconium materials are presented in (1).

Results

The kinetics of oxidation can be described by the empirical equation

$$(\Delta W)^n = kt$$

where ΔW is the weight gain per unit area of original surface, t is the time, n and k are constants for a given temperature. To determine the applicable rate equation from weight gain data, the empirical equation is more conveniently used in its logarithmic form

$$\log \Delta W = 1/n \log k + 1/n \log t$$

in which case, a plot of ΔW against t on logarithmic coordinates yields a straight line having a slope of $1/n$. The average results for each test condition are plotted in this manner in Fig. 1. The open symbols represent specimens that were chemically polished in

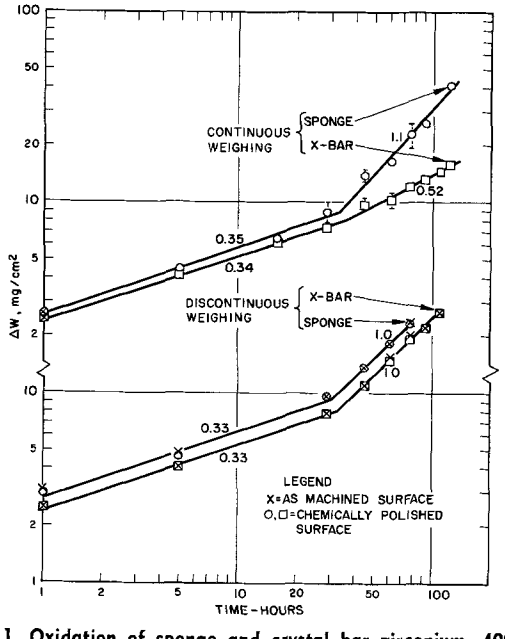

Fig. 1. Oxidation of sponge and crystal bar zirconium, 400 Torr O_2, 850°C, 0.38 cm thick specimens.

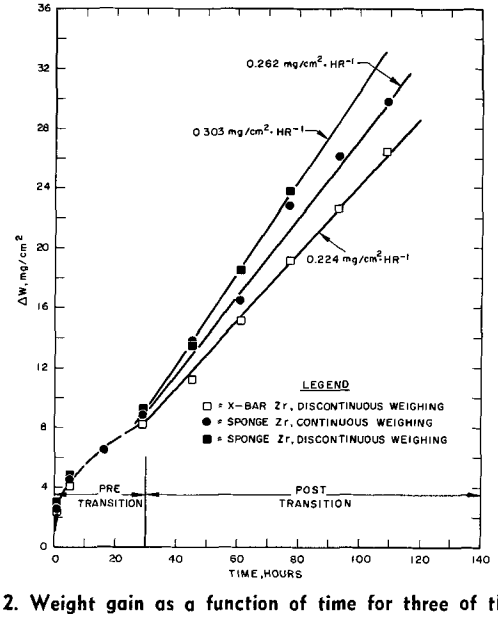

Fig. 2. Weight gain as a function of time for three of the four curves depicted in Fig. 1.

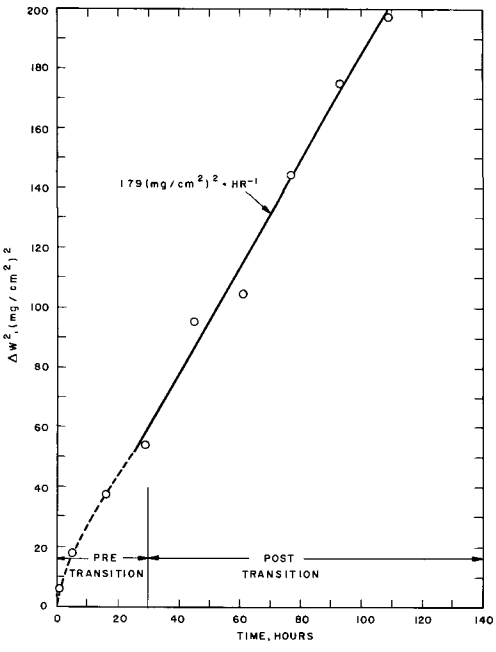

Fig. 3. Square of the weight gain as a function of time; continuously weighed X-bar specimens.

solutions of 45 v/o HNO_3 + 5 v/o HF + 50 v/o H_2O prior to exposure whereas the "X"'s indicate the data generated with specimens whose surfaces were machined to a 64 rms finish, degreased and rinsed in ethyl alcohol before each test. The numerical values indicate the calculated slopes on the log-log plot. Values for n in the pretransition kinetic region were obtained directly from Fig. 1; k_c was determined from a plot of the cube of the weight gain against time. The corresponding values for posttransition oxidation performance were obtained by replotting the data on linear coordinates (Fig. 2, 3). (One group of data, X-bar under continuous weighing conditions, required a replot of the square of the weight gain against time.) Table I compares the results generated in this limited study with those of the parent investigation.

Discussion and Conclusions

The data shown in Table I appear to indicate no significant alteration in the oxidation characteristics of the two materials as a consequence of the change in specimen geometry. At first glance it may appear that the pretransition rate constants (k_c) cluster into two groups; one group with an average value of 0.28, the other at approximately 0.47. It should be recalled, however, that the cubic rate constant is obtained from the cube of the weight change ($\Delta W^3 = k_c t$); a variation in the weight gain data of ~12% can account for the differences noted in the pretransition rate constants. Thus, the observed values are within the uncertainty band associated with data acquisition since it has been established previously (1) that the reproducibility in weight gain data in this series of experiments was no better than 10-15%. The same discussion can be applied to the apparent variations noted in the two posttransition parabolic rate constants (k_p) determined from the square of the weight gain. A weighing bias of ~14% can account for the observed differences in the latter values.

Once again, it has been demonstrated that for the method of continuous weight gain determination, the pretransition oxidation performances of high-grade sponge zirconium and crystal bar zirconium are alike in all respects. It has also been substantiated that, for continuously weighed specimens, the posttransition kinetics of sponge zirconium will follow a linear rate equation whereas crystal bar zirconium exhibits parabolic rate behavior. It has been postulated previously that this disparity in posttransition oxidation behavior may be related to the initial oxygen level of the two materials (1). Since the data generated in ref. (1) were obtained in 50 Torr oxygen pressure and those of the present study in 400 Torr oxygen, the oxidation performance of either grade of zirconium appears insensitive to oxygen pressure in the range 50-400 Torr. These results confirm the work of other investigators who found no pressure effect on zirconium oxidation (2, 3).

The major conclusion drawn from this limited study involves the sensitivity of crystal bar zirconium in the posttransition kinetic region to the method of obtaining weight change information. Thus, the information presented in Table I and Fig. 1 clearly shows that crystal bar zirconium will oxidize in accordance with a posttransition parabolic rate equation when weight gain information is obtained by either continuous measurements at test temperature (1) or by employing different specimens for each datum point. When a fixed group of identical specimens was used to obtain the entire kinetic curve by means of interrupted weight determinations on the same samples, linear posttransition behavior was observed. The crystal bar pretransition region and the entire kinetic behavior of sponge zirconium appears unaffected by the mode of weight change measurement. A possible explanation for this behavior may involve the enhanced susceptibility to oxide film breakdown due to the thermal cycling imposed on those specimens subjected to repeated heating and cooling during interrupted weight gain determinations.

Table I. Comparison of the oxidation behavior of high-grade sponge and crystal bar (iodide) zirconium at 850°C

Parameter	Units	Type of weight gain determination	Sponge Zr**		X-Bar Zr**	
			0.056 cm dia Wire (1)	0.38 cm Thick plate	0.056 cm dia Wire (1)	0.38 cm Thick plate
n (pretrans)*	—	Continuous	3.1	2.9	3.0	2.9
n (pretrans)*		Discontinuous	—	3.0	—	3.0
k_c (pretrans) cubic	$(mg/cm^2)^3 \cdot min^{-1}$	Continuous	0.55	0.29	0.41	0.26
k_c (pretrans) cubic	$(mg/cm^2)^3 \cdot min^{-1}$	Discontinuous	—	0.45	—	0.28
ΔW_{Trans}‡	mg/cm^2	Continuous	9.0	8.8	8.7	8.0
ΔW_{Trans}‡	mg/cm^2	Discontinuous	—	9.2	—	8.0
t_{Trans}‡	hours	Continuous	35	34	32	34
t_{Trans}‡	hours	Discontinuous	—	32	—	33
n' (posttrans)*	—	Continuous	1	1	2	2
n' (posttrans)*		Discontinuous	—	1	—	1
k_L (posttrans linear)*	$mg/cm^2 \cdot hr^{-1}$	Continuous	0.29	0.26	N/A	N/A
		Discontinuous	—	0.30	—	0.23
k_p (posttrans parabolic)*	$(mg/cm^2)^2 \cdot hr^{-1}$	Continuous	N/A	N/A	3.8	1.8
		Discontinuous	—	N/A	—	N/A

* For pretransition: $\Delta W^n = k_c t$.
For posttransition, $\Delta W^{n'} = k_L t$ (when $n' = 1$) or $\Delta W^{n'} = k_p t$ (when $n' = 2$).
** All chemically etched surfaces.
‡ Trans—at transition.
N/A = not applicable.

As a final observation, it can be seen from Fig. 1 and Table I that the quantity of residual fluorides or other contaminants that may be associated with the chemical polishing of zirconium surfaces does not affect the subsequent long-term oxidation behavior of the metal to any significant degree.

Acknowledgment

The author greatly appreciates the kind encouragement of and helpful discussions with Doctors B. Lustman, J. Hino, and J. N. Chirigos. This work has been performed under AEC Contract AT-11-1-GEN-14.

Manuscript received Sept. 30, 1966.

Any discussion of this paper will appear in a Discussion Section to be published in the December 1967 JOURNAL.

REFERENCES

1. E. Hillner, *Electrochem. Technol.*, **4**, 132 (1966).
2. H. A. Porte, J. G. Schnizlein, R. C. Vogel, and D. F. Fischer, *This Journal*, **107**, 506 (1960).
3. R. E. Westerman, *ibid.*, **111**, 140 (1964).

Brief Communications

The Diffusion Layer on a Rotating Disk Electrode

John Newman

Inorganic Materials Research Division, Lawrence Radiation Laboratory, and Department of Chemical Engineering, University of California, Berkeley, California

In a recently published work (1), the author treated the current distribution on a rotating disk under conditions where ohmic potential drop, surface overpotential, and concentration variations near the electrode must all be taken into account. The diffusion layer, which is then characterized by a nonuniform current density and concentration at the surface, was handled by a power-series expansion in r, the radial distance from the axis of rotation

$$c = c_\infty \left[1 + \sum_{m=0}^{\infty} A_m (r/r_o)^{2m} \theta_m(\zeta) \right] \qquad [1]$$

where c is the concentration of the reactant, c_∞ is the bulk concentration, r_o is the radius of the electrode, and θ_m represents functions of $\zeta = y(a\nu/3D)^{1/3}\sqrt{\Omega/\nu}$, where y is the normal distance from the disk, $a = 0.51023$, ν is the kinematic viscosity, D is the diffusion coefficient, and Ω is the rotation speed of the disk.

The functions θ_m and, in particular, the derivatives $\theta_m'(0)$ at the surface were obtained by a finite-difference solution of the differential equations

$$\theta_m'' + 3\zeta^2\theta_m' - 6m\zeta\theta_m = 0 \qquad [2]$$

subject to the boundary conditions

$$\theta_m = 1 \text{ at } \zeta = 0 \text{ and } \theta_m = 0 \text{ at } \zeta = \infty$$

Subsequent numerical difficulties were encountered which required accurate values of the derivatives $\theta_m'(0)$.

As suggested by the work of Rosner (2), one can use the equations in section 58 of Levich's book (3) to obtain the concentration at the surface in terms of an integral over the concentration derivative at the surface

$$c(r,o) = c_o(r) = \frac{1}{\Gamma(2/3)} \int_o^r \frac{J(r')r'\,dr'}{(r^3 - r'^3)^{2/3}} \qquad [3]$$

where $J(r) = -\partial c/\partial\zeta$ at $\zeta = 0$. Substitution of a power-series expansion for c into Eq. [3] yields an expression for $\theta_m'(0)$

$$\theta_m'(0) = -\frac{3\Gamma\left(\frac{5}{3}\right)\Gamma\left(\frac{2m+3}{3}\right)}{2\Gamma\left(\frac{4}{3}\right)\Gamma\left(\frac{2m+2}{3}\right)} \qquad [4]$$

The gamma functions necessary to evaluate $\theta_m'(0)$ from Eq. [4] are given (4) to 15 significant figures. Values of $\theta_m'(0)$ are in satisfactory agreement with those tabulated in Table I of ref. (1). At the same time direct use of Eq. [3] or its inverse (2) provides a possibility of avoiding the numerical difficulties encountered in the earlier work (1).

Acknowledgment

This work was supported by the United States Atomic Energy Commission.

Manuscript received Dec. 6, 1966.

Any discussion of this paper will appear in a Discussion Section to be published in the December 1967 JOURNAL.

REFERENCES

1. John Newman, *This Journal*, **113**, 1235 (1966).
2. D. E. Rosner, *ibid.*, **113**, 624 (1966).
3. V. G. Levich, "Physicochemical Hydrodynamics," Prentice-Hall, Inc., Englewood Cliffs, N. J. (1962).
4. "Handbook of Mathematical Functions," Milton Abramowitz and I. A. Stegun, Editors, p. 3, National Bureau of Standards, Washington (1964).

Large Amplitude A-C Polarography of Aqueous Cd(II)

J. D. McLean and Andrew Timnick

Department of Chemistry, Michigan State University, East Lansing, Michigan

Theoretical treatment of a-c polarographic data has been limited to the condition that the amplitude of the applied a-c voltage, $\Delta E_{p\text{-}p}$, be no larger than $16/n$ mv peak to peak, n being the number of electrons transferred in the reduction process (1). Several formulas have been derived for large amplitudes for the special case of very small frequencies ($k_h >> \omega D$), but these are of very limited use (2). Here, k_h is the heterogeneous rate constant for electron transfer, ω is the angular frequency of the applied alternating

potential, and D is the diffusion coefficient. Recently, Smith extended the theoretical treatment to $70/n$ mv p-p and derived an expression by which currents and phase angles could be calculated (3). No experimental verification was presented.

The work reported in this note was in progress when the most recent information appeared (3). Even though this work does not directly test Smith's equations it was undertaken to test the extent of applicability of existing equations developed for low amplitudes, by determining the effect of large amplitudes on experimentally determined k_h values for aqueous solutions of Cd(II).

All data were obtained at $E_{1/2}{}^R$, the reversible d-c half-wave potential, since maximum deviation in quantities measured to evaluate k_h would be expected at this d-c potential. Several supporting electrolytes were employed, to obtain a variation in the value of k_h.

The solutions used were prepared from A.C.S. reagent grade chemicals without further purification. A 0.0100M Cd(II) stock solution was prepared from $Cd(NO_3)_2 \cdot 4H_2O$ and standardized by EDTA titration (4).

Current and phase-angle measurements were obtained at maximum drop size, with an a-c polarograph constructed in this laboratory using the circuits of Smith (5) with modifications in the phase-angle detecting circuit (6). A Hewlett-Packard Model 202A signal generator provided all a-c potentials. A Sargent S-30260 potentiometer was employed to measure all d-c potentials applied to the cell. A Tektronix Model 502 oscilloscope was employed to measure the amplitude of the alternating potential applied to the cell. A Sargent Model S.R. recorder was employed to measure the d-c currents, rectified a-c currents, and signals proportional to the phase angle.

Phase angles were corrected for the uncompensated solution resistance and double-layer charging current of the supporting electrolytes according to the method of Bauer and Elving (7).

The polarographic cell was constructed so that prepurified nitrogen, which had been further purified by bubbling through an acid vanadous column, could be either bubbled through the solution by way of a coarse frit at the cell bottom or blown over the top of the solution. The cell was equipped with three electrodes: dropping mercury electrode, saturated calomel electrode, and a platinum wire auxiliary electrode. The side arm of the reference electrode was separated from the polarographic solution by an isolation compartment with a fine frit. The auxiliary electrode was also separated from the polarographic solution with a similar isolation compartment. The isolation compartments contained the supporting electrolyte.

All measurements were made in a constant temperature room which had an ambient temperature of 24 ± 1°.

Instrument performance was tested at large amplitudes through the frequency range 30-1200 Hz by determining the resistance and capacitance values for known value components of a dummy cell. Tests were run at 10, 50, and 100 mv peak to peak, and all results were within an experimental error of the order of 3%. The double-layer capacity, C_{dl}, and uncompensated solution resistance, R_t, for the supporting electrolytes 1.0M Na_2SO_4, 1.0M H_2SO_4, and 1.0M KNO_3 were determined at both 10 and 100 mv. The resistances and double-layer capacitances measured at 10 mv for the individual supporting electrolytes did not vary by more than 3% from those measured at 100 mv over the frequency range investigated. The values measured at 10 and 100 mv are listed in Table I, as well as the half-wave potentials at which they were measured. The $E_{1/2}{}^R$ for Cd(II) in each supporting electrolyte was determined from the log = 0 intercept of a log $(i_d - i)/i$ *vs.* $E_{d\text{-}c}$ plot. The diffusion coefficients listed in Table I were determined in this laboratory during a previous study (6) and were calculated by the Lingane-Loveridge equation (9).

Table I. Experimental constants for evaluation of k_h in various supporting electrolytes

Supporting electrolyte	$E_{1/2}{}^R$ *vs.* SCE, v	$C_{a.l.}$, μf		R_t, ohms		$D \times 10^6$, cm²/sec*
		10 mv	100 mv	10 mv	100 mv	
1.0M Na_2SO_4	−0.606	0.833	0.834	77.2	78.7	5.51
1.0M H_2SO_4	−0.597	0.952	0.956	58.9	60.4	7.03
1.0M KNO_3	−0.585	1.14	1.14	76.4	78.0	10.20

* $D = D_0{}^{\beta} D_R{}^{\alpha}$ where α and β are transfer coefficients.

Table II. Variation of heterogeneous rate constant with changing amplitude of applied a-c potential for 5.0 x 10^{-4}M Cd (II) in various supporting electrolytes evaluated at $E_{1/2}{}^R$

$E_{p\text{-}p}$, mv	1.0M Na_2SO_4		1.0M H_2SO_4		1.0M KNO_3	
	slope × 10^2	k_h, cm/sec	slope × 10^2	k_h, cm/sec	slope × 10^3	k_h, cm/sec
10	2.62	0.06	1.32	0.14	3.35	0.67
20	2.32	0.07	1.36	0.14	2.27	1.00
30	2.40	0.07	1.47	0.13	2.51	0.90
40	2.30	0.07	1.41	0.13	2.48	0.91
50	2.32	0.07	1.39	0.13	2.50	0.90
60	2.24	0.07	1.28	0.15	2.20	1.03
70	2.24	0.07	1.20	0.16	1.82	1.24
80	2.15	0.08	1.23	0.15	1.46	1.55
90	2.10	0.08	1.19	0.16	1.50	1.51
100	2.11	0.08	1.06	0.18	1.13	2.00

The dependence of the heterogeneous rate constant on the applied a-c potential is tabulated in Table II, for various supporting electrolytes. The heterogeneous rate constants were obtained by use of the expression

$$\cot \Phi = 1 + \frac{1}{k_h} (D\omega/2)^{1/2} \qquad [1]$$

where Φ is the corrected phase angle (8). This is the correct expression for the special case when $E_{d\text{-}c} = E_{1/2}{}^R$ and under the restriction that the amplitude of the applied alternating voltage be less than $16/n$ mv p-p. By plotting cot Φ *vs.* $\omega^{1/2}$ (see Fig. 1 and 2), one can readily calculate k_h from the slope of the linear

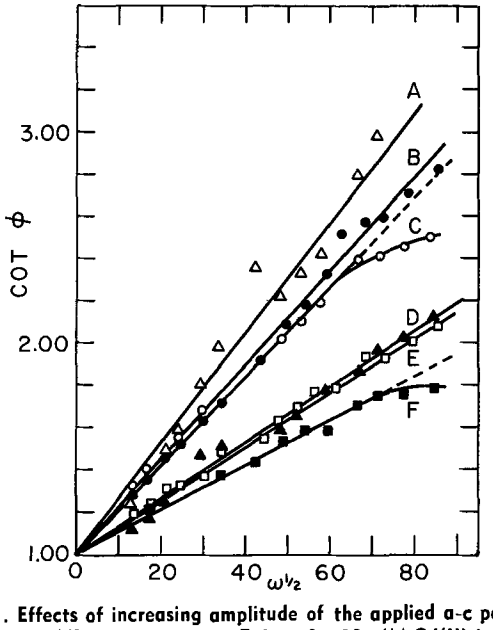

Fig 1. Effects of increasing amplitude of the applied a-c potential on cot Φ vs. $\omega^{1/2}$ evaluated at $E_{1/2}{}^R$ for 5.0 x 10^{-4}M Cd(II) in sulfate media. Curves A, B, and C are for 1.0M Na_2SO_4: A, $\Delta E_{p\text{-}p}$ = 10 mv; B, $\Delta E_{p\text{-}p}$ = 60 mv; C, $\Delta E_{p\text{-}p}$ = 100 mv. Curves D, E, and F are for 1.0M H_2SO_4: D, $\Delta E_{p\text{-}p}$ = 10 mv; E, $\Delta E_{p\text{-}p}$ = 60 mv; F, $\Delta E_{p\text{-}p}$ = 100 mv.

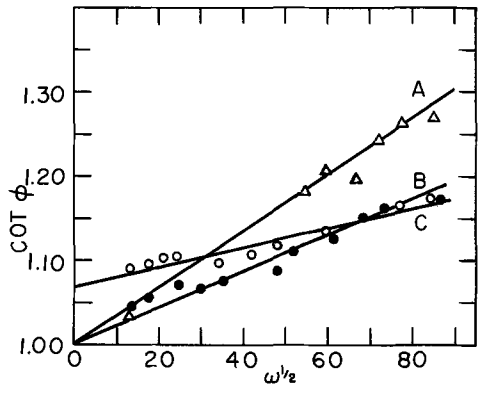

Fig. 2. Effects of increasing amplitude of the applied a-c potential on plots of cot Φ *vs.* $\omega^{1/2}$ evaluated at $E_{1/2}{}^{R}$ for 5.0 x 10^{-4}M Cd(II) in 1.0M KNO_3. A, $\Delta E_{p\text{-}p}$ = 10 mv; B, $\Delta E_{p\text{-}p}$ = 60 mv; C, $\Delta E_{p\text{-}p}$ = 100 mv.

portion of the plot, if a value for $D^{1/2}$ is known. The values used for the plots were obtained by making phase-angle measurements on 5.0 x 10^{-4} M Cd(II) in various supporting electrolytes at fourteen different frequencies between 30 to 1200 Hz and at the d-c potential equal to $E_{1/2}{}^{R}$.

From Table II it can be seen that, if k_h is between 0.05 and 0.20 cm/sec, its value, as determined by the low amplitude equation, does not vary markedly to the limit of amplitudes tested up to a frequency of 800 Hz. Although the k_h values show good agreement, some deviations in the data become apparent above 60 mv as is shown in Fig. 1. These deviations occur as a distinct falling off from linearity of the cot Φ *vs.* $\omega^{1/2}$ plots at frequencies above 800 Hz, with the magnitude of the error increasing directly with the frequency. In all of these plots, the intercept is cot Φ = 1 at 0 frequency, as is predicted by Eq. [1].

In a recent monograph (3), Smith presents theoretical a-c polarograms and a-c polarographic phase angles for a specific hypothetical system for $\Delta E_{p\text{-}p}$ of 10, 40, 60, and 80 mv. He demonstrates that cot Φ should decrease with increasing values of $\Delta E_{p\text{-}p}$ at the d-c potential equal to $E_{1/2}{}^{R}$. Although the magnitudes of these changes cannot be compared directly with our experimental values due to differences in constant parameters involved, one can see that the changes follow the same pattern. Smith's theoretical figures as well as our experimental data indicate that the changes are relatively small if the heterogeneous rate constant is in the range 0.01 to 0.20 cm/sec as is the case for Cd(II) in sulfate media.

Heterogeneous rate constants for Cd(II) in 1.0M KNO_3 calculated from slopes obtained from Fig. 2 show much greater variation than the values obtained in sulfate media. This is primarily due to the fact that the heterogeneous rate constant in this medium is considerably faster, and thus changes in the slope produce a much greater change in the value of k_h. Rate constants of the order of 1.0 cm/sec or faster are difficult to determine accurately by the a-c method we employ. Figure 2 data were included to demonstrate what might be expected if large amplitudes are employed on these systems. Although the values of k_h show deviation as $\Delta E_{p\text{-}p}$ increases, no deviation from theoretical behavior, that is linearity of the plot of cot Φ *vs.* $\omega^{1/2}$ and intercept of cot Φ = 1 as $\omega \rightarrow 0$, is observed until $\Delta E_{p\text{-}p}$ exceeds 60 mv. At this point, the cot Φ intercept at $\omega \rightarrow 0$ becomes greater than 1.00 in violation of theory. Again, the error becomes increasingly large as $\Delta E_{p\text{-}p}$ increases.

The results obtained for the aqueous Cd(II) system indicate that if the heterogeneous rate constant for the electron transfer is between 0.05 and 0.20 cm/sec, low amplitude equations can be used to calculate k_h values for $\Delta E_{p\text{-}p}$ up to 70 mv, which is considerably beyond the previously predicted limit of $\Delta E_{p\text{-}p} = 16/n$ mv, which would be 8 mv for Cd(II).

Acknowledgment

The authors are grateful to the Socony Mobil Oil Company and The Electrochemical Society for the support of this work.

Manuscript received Nov. 21, 1966.

Any discussion of this paper will appear in a Discussion Section to be published in the December 1967 JOURNAL.

REFERENCES

1. H. Matsuda, *Z. Elektrochem.*, **62**, 977 (1958).
2. B. Breyer and H. H. Bauer, "Alternating Current Polarography and Tensammetry," Chap. 2, Interscience Publishers, New York (1963).
3. D. E. Smith, "Electroanalytical Chemistry," Vol. I, Chap. I, A. J. Bard, Editor, Marcel Dekker, Inc., New York (1966).
4. G. Schwarzenbach, "Complexometric Titration," Interscience Publishers, New York (1957).
5. D. E. Smith, *Anal. Chem.*, **35**, 602 (1963).
6. J. K. Frischmann, Ph.D. thesis, Michigan State University, East Lansing, Mich. (1966).
7. H. H. Bauer and P. J. Elving, *J. Am. Chem. Soc.*, **82**, 2091 (1960).
8. R. Tamamushi and N. Tanaka, *Z. Physik. Chem.*, **21**, 89 (1959).
9. J. J. Lingane and B. A. Loveridge, *J. Am. Chem. Soc.*, **72**, 439 (1950).

Recrystallization of Supported Platinum

J. F. Connolly, R. J. Flannery, and B. L. Meyers

Research and Development, American Oil Company, Whiting, Indiana

Measurements of surface areas electrochemically (1) and by x-ray diffraction show that supported platinum crystallites grow rapidly when in contact with a conducting solution. This effect indicates that the type of dispersion necessary to make platinum an economic direct-hydrocarbon-fuel-cell catalyst may be difficult to maintain.

The crystallite growth was first observed during attempts to extend the conditions for electrochemical platinum-area measurements (1) to higher temperatures. Results are summarized in Table I. Platinum area losses range from 5 to 90% of the initial area depending on such factors as initial crystallite size, temperature, and type of support.

Area losses are not due to poisoning because they are detected in roughly the same measure by both x-rays and the electrochemical method. Furthermore, they cannot be attributed to permanent platinum dissolution because: platinum determinations made before and after treatment usually agreed within the reproducibility of the method (2%); analyses of the soaking liquids after the highest temperature runs showed a pickup of only 0.1% of the platinum originally in the samples; integrated x-ray diffraction intensities increased in all cases where they were measured.

There are no detectable area losses due to heating in air or argon at these temperatures, or even 100°C

Table I. Summary of results

Support[j]	Support area, m^2/g	Wt, % Pt	Initial x-ray cryst. size,[k] Å	Initial electrochem. Pt area, m^2/g Pt	% Pt area lost x-ray[l]	% Pt area lost electrochemical[m]
ACG	11	4.1	30	45	80[a]	60[a]
ACG	11	8.6	40	45	65[a]	70[a]
ACG	11	8.6	40	45	5[e]	10[e]
ACG	11	8.6	40	45	70[f]	90[f]
ACG	11	8.6	40	45	15[g]	10[g]
ACG	11	16.6	30	25	75[a]	60[a]
ACG	11	16.6	30	25	85[b]	80[b]
ACG	11	16.6	30	25	80[c]	75[c]
ACG	11	16.6	30	25	90[d]	90[d]
ACG	11	5.2	45	—	50[i]	—
ACG	11	8.9	100	35	10[a]	30[a]
ACG	11	8.9	100	35	20[h]	30[h]
ACG	11	8.9	100	35	20[b]	40[b]
SB	60	9.7	30	40	75[a]	55[a]
PC62	200	8.7	60	70	10[a]	5[a]
PC62	200	8.7	60	70	20[b]	15[b]
B_4C	11	11.1	30	25	55[a]	45[a]
SiC	<1	1.2	125	—	10[c]	—
SiC	<1	1.2	125	—	15[d]	—
Al_2O_3	2	2.1	145	—	40[c]	—
Al_2O_3	2	2.1	145	—	55[d]	—
Al_2O_3	15	9.0	140	—	30[c]	—
Al_2O_3	15	9.0	140	—	40[d]	—
Al_2O_3	85	1.2	40	—	40[c]	—
Al_2O_3	85	8.9	80	—	55[c]	—
Al_2O_3	85	8.9	80	—	55[d]	—

[a] Open circuit in 95% H_3PO_4 at 150°C for 60 hr.
[b] Open circuit in 95% H_3PO_4 at 190°C for 60 hr.
[c] Open circuit in 50% $CaCl_2$ at 150°C for 60 hr.
[d] Open circuit in 50% $CaCl_2$ at 190°C for 60 hr.
[e] Open circuit in 90% H_3PO_4 as 105°C for 60 hr.
[f] Open circuit in 65% $CaCl_2$ at 150°C for 60 hr.
[g] Open circuit in H_2O (150 μmho/cm) at 165°C for 60 hr.
[h] Open circuit in 95% H_3PO_4 at 150°C for 480 hr.
[i] 0.10-1.0v in 85% H_3PO_4 at 145°C for 6 hr. This sample was bonded with 40% Teflon. All other samples are in powdered form.
[j] ACG → Am. Cyanamid graphite (3), SB → Schawinigen Black, PC → Stackpole Carbon Co., B_4C → Boron carbide from Norton Co., NC → National Carbon Co.
[k] Dimension perpendicular to 111 plane, calculated from the Scherrer equation, employing the Warren method for instrumental broadening (2). The dimension perpendicular to the 200 plane, as measured for a few samples, was about 20% less. The 311 plane was used for the 1.2% Pt on Al_2O_3 sample.
[l] 100 [1-(initial crystallite size)/(final crystallite size)].
[m] 100 [1-(final electrochemical area)/(initial electrochemical area)].

higher. Thus, the rate of area loss is orders of magnitude higher than that of the losses experienced in "sintering." A possible mechanism would be "electrorecrystallization," *i.e.*, local cells may be formed between large and small platinum crystallites, with the smaller crystallites acting as anodes because of their higher surface energies. Complex platinum ions would then be transported through the solution while electrons pass through platinum-platinum contacts, or through a conducting support, or through both. The transport of platinum complexes through the solution with no necessity for electron flow between crystallites would also be conceivable.

Experimental

The technique for making electrochemical measurements of the surface area of carbon-supported platinum (1) has been simplified by using powdered rather than Teflon-bonded samples, and by substituting a charge measurement in the "double layer" region for the oxide arrest as a measure of the support effect.

Teflon bonding of powders, in addition to being tedious, requires that they be subsequently anodized extensively (1) to reactivate the platinum surface. We have found that tightly confining a powdered sample between porous tantalum plates (Kennametal) in a tantalum holder gives reproducible results for samples with supports like NC60[1] and ACG.[1] Hard supports like PC62[1] and B_4C may be used in the same way, so long as a three- or fourfold dilution with a low-surface-area graphite like NC60 is used to promote electrical contact. The NC60 has practically no effect on the measurement. Because the holder exposes only 0.8 cm^2 of the porous tantalum plates (Fig. 1) the currents

[1] See Table I footnote j.

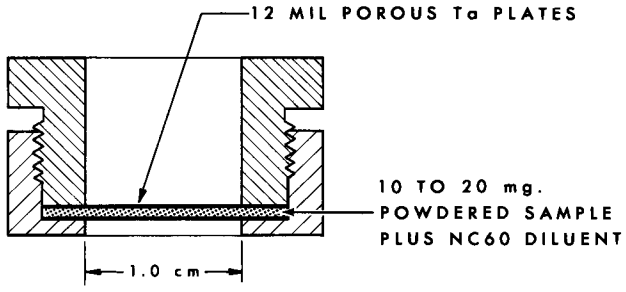

Fig. 1. Tantalum holder for powdered samples

must be held below 20 ma to avoid excessive IR drops. IR drops are further minimized by drawing 0.1-0.2 cc of electrolyte through the holder after assembly to thoroughly wet the sample and porous tantalum plates.

The change from Teflon-bonded to powdered electrodes resulted in the higher area carbons giving somewhat more O_2 evolution activity at 1.3-1.4v (*vs.* a reversible hydrogen electrode in the same solution) than is desirable. Therefore, as a measure of the support contribution, the charge consumption from 0.55 to 0.35v was substituted for the charge consumption in the oxygen arrest.[2] We then obtain equations for platinum surface area analogous to Eq. [5] and [6] of ref. (1), *i.e.*,

$$r' = Q_{C,D}/Q_{C,H} \quad [1]$$

$$A_{Pt} = (r'Q_{T,H} - Q_{T,D})/(r'k_H - k_D) \quad [2]$$

where A_{Pt} is the platinum area in contact with solution, $Q_{C,D}$ and $Q_{C,H}$ are charges consumed on the carbon support from 0.55 to 0.35v and 0.05 to 0.30v, $Q_{T,D}$ and $Q_{T,H}$ are the total charges consumed on the electrode from 0.55 to 0.35v and 0.05 to 0.30v, and k_D and k_H are constants which give the charge consumption on platinum per square centimeter of platinum from 0.55 to 0.35v and 0.05 to 0.30v. The quantities $Q_{C,D}$ and $Q_{C,H}$ are measured at the same dv/dt (usually 10 to 20 mv/sec) on the nonplatinized carbon support while $Q_{T,D}$ and $Q_{T,H}$ are similarly measured on the platinized electrode; k_D and k_H are measured on bright platinum of known roughness.

For the supports listed in Table I, $r' = 1.00 \pm 0.05$. Using this value for r' and $k_H = 0.19$ mc/cm^2 and $k_D = 0.005$ mc/cm^2 reduces Eq. [2] to

$$A_{Pt} \cong 5.4(Q_{T,H} - Q_{T,D}) \quad [3]$$

Equation [3] was used to calculate the electrochemical areas in Table I. The potential-time sequence for each measurement is shown in Fig. 2.

There is a misprint in ref. (1). The equations for calculating the fractions of the total charge consumptions which are due to the carbon support should be

[2] Of course, in those cases where oxide stripping is suitable and the hydrogen arrest is unuseable (*e.g.*, palladium area measurements on moderate area carbons), then a charge measurement in the double layer region can correct for the support contribution in the oxide reduction arrest.

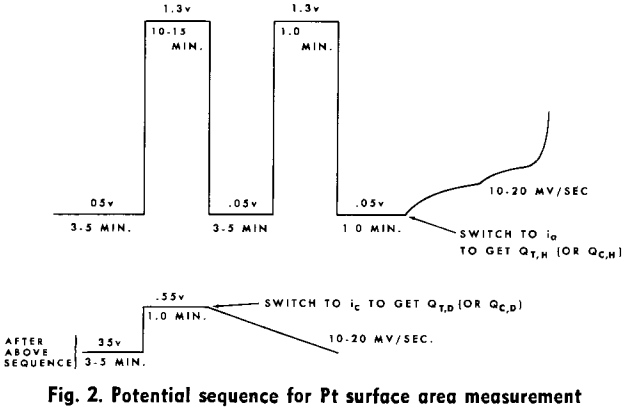

Fig. 2. Potential sequence for Pt surface area measurement

$$\frac{Q_{C,O}}{Q_{T,O}} = r\left(1 - \frac{k_0}{k_H}\frac{Q_{T,H}}{Q_{T,O}}\right) \Big/ \left(r - \frac{k_0}{k_H}\right) \quad [4]$$

$$\frac{Q_{C,H}}{Q_{T,H}} = \left(\frac{Q_{T,O}}{Q_{T,H}} - \frac{k_0}{k_H}\right) \Big/ \left(r - \frac{k_0}{k_H}\right) \quad [5]$$

For the simplified procedure used in this note Eq. [4] has little meaning, while Eq. [5] reduces to

$$\frac{Q_{C,H}}{Q_{T,H}} \cong \frac{Q_{T,D}}{Q_{T,H}}$$

Reference (1) also contains the doubtful claim: "there should be no lower limit on the size of the platinum crystallites which can be detected." However, very small crystallites probably grow at rates large enough to interfere with electrochemical surface-area measurements made at room temperature.

Acknowledgment

The authors thank L. Granatelli for making the platinum analyses and R. F. Waters for platinizing the electrodes.

Manuscript received Oct. 20, 1966; revised manuscript received Dec. 9, 1966.

Any discussion of this paper will appear in a Discussion Section to be published in the December 1967 JOURNAL.

REFERENCES

1. J. F. Connolly, R. J. Flannery, and G. Aronowitz, *This Journal*, **113**, 577 (1966).
2. H. P. Klug and L. E. Alexander, "X-Ray Diffraction Procedures," p. 506, John Wiley & Sons, Inc., New York (1954).
3. R. G. Haldeman, W. P. Colman, S. H. Langer, and W. A. Barber, "Fuel Cell Systems," p. 106, American Chemical Society, Washington, D. C. (1965).

SOLID STATE SCIENCE

Manganese-Activated Luminescence in the $MgO-Al_2O_3-Ga_2O_3$ System

Jesse J. Brown

Chemical and Metallurgical Division, Sylvania Electric Products Inc., Towanda, Pennsylvania

ABSTRACT

Manganese-activated phosphors were prepared by solid state reactions throughout the spinel crystalline solution region in the $MgO-Al_2O_3-Ga_2O_3$ system. The best ultraviolet-excited phosphor examined, $(Mg_{0.90},Mn_{0.01})Ga_{2.06}O_4$, is characterized by a peak emission wavelength at 512 nm, a 50% peak intensity band width of 36 nm, and a quantum efficiency equivalent to that of Zn_2SiO_4:Mn. Al^{3+} for Ga^{3+} substitutions in $MgGa_2O_4$ lead to phosphors with improved cathodoluminescence, decreased photoluminescence, longer peak emission wavelength, and longer cathodoluminescence decay characteristics. These data are discussed in view of temperature, crystal structure, and related literature.

The mineral spinel, $MgAl_2O_4$, is only one of a large class of isostructural AB_2O_4 compounds that have become known as spinels. Ideally the spinel structure consists of a face-centered cubic close-packed array of oxygen anions with metal cations filling the interstices. The unit cell contains 32 oxygen ions or eight AB_2O_4 molecules. This gives rise to 96 interstices per unit cell of which 32 are octahedral (B) sites and 64 tetrahedral (A) sites. Normally only 16 of the B and 8 of the A sites are filled with cations. There are three general classifications of spinels, the normal spinel in which the A ions are in tetrahedral sites and the B in octahedral, the random or intermediate spinel in which the A and B ions are randomly distributed in the 8 tetrahedral and 16 octahedral sites, and the inverse spinel in which the 8 tetrahedral sites are occupied by B ions and the 16 octahedral sites occupied randomly by A and B ions. It is well established that the equilibrium cation distribution in spinels is dependent on temperature and pressure as well as composition.

Originally it was the purpose of this investigation to attempt to incorporate Mn^{2+} selectively in octahedral and tetrahedral sites in basically the same spinel compound. A logical choice for this study was the crystalline solution series between the compounds $MgGa_2O_4$ and $MgAl_2O_4$ in the $MgO-Al_2O_3-Ga_2O_3$ ternary system since Mn^{2+} has an octahedral site preference larger than Ga^{3+} but smaller than either Mg^{2+} or Al^{3+}. However, when the intense uv-excited green luminescence of $MgGa_2O_4$:Mn was observed, major emphasis was shifted to the empirical optimization of formulation variables and characterization of spectral properties of phosphors throughout the ternary system.

Literature

Moller and King (1) prepared various gallate compounds, including $MgGa_2O_4$ spinel, and presented characteristic x-ray diffraction data. More recently Schmalzried (2) established the phase relationships in the $MgO-Ga_2O_3$ system. Twenty mole % Ga_2O_3 and 2 mole % MgO were found to be soluble in $MgGa_2O_4$ at 1200°C. At 1000°C, the solubility of Ga_2O_3 decreased to 10% and of MgO to about 1%. The population of Mg^{2+} in octahedral sites in $MgGa_2O_4$ was found to vary from 0.90 at 900°C to 0.84 at 1400°C, indicating the influence of temperature on cation distribution in this spinel compound. More recently Weidenborner *et al.* (3) determined the detailed structure of magnesium gallate from single crystals grown from a molten lead-oxygen-fluoride melt. Their results confirmed the partially inverted nature of $MgGa_2O_4$, that it belongs to the space group Fd3m with $a_o = 8.286 \pm 0.003$Å, and that 16 ± 2% of the Mg^{2+} are in tetrahedral sites and 81 ± 1% in octahedral. Since the single crystals used in this study were annealed slowly from 1200° to 850°C, the data must be assumed to correspond to a temperature of 850°C or slightly higher.

The $MgO-Al_2O_3$ phase relations have been studied by several people (4-7). This system resembles the $MgO-Ga_2O_3$ system in that considerable Al_2O_3 is soluble in $MgAl_2O_4$ spinel, but only trace amounts of MgO. Datta and Roy (8,18) have reported that the cation distribution in $MgAl_2O_4$ is a function of temperature and pressure and becomes more normal at high temperatures. Saalfeld (9) has found that the vacancies associated with the $MgAl_2O_4$ crystalline solution series in the $MgO-Al_2O_3$ system prefer to locate on octahedral cation sites. Hummel and Sarver (10) prepared cathodoluminescent phosphors by activating $MgAl_2O_4$ by Mn^{2+} and isoelectronic Fe^{3+}.

Hill *et al.* (11) established the phase relationships in the $Ga_2O_3-Al_2O_3$ system which showed extensive crystalline solution at high temperatures and the formation of an intermediate solid solution series below 800°C. Katz and Roy (12) studied the phase relationships in the $MgAl_2O_4-Ga_2O_3$ binary join and found extensive crystalline solution of Ga_2O_3 in $MgAl_2O_4$. These data were used to estimate the extent of crystalline solution within the ternary system.

Based on the above references, the probable phase relationships in the $MgO-Al_2O_3-Ga_2O_3$ system were constructed as shown in Fig. 1.

Green-emitting $ZnGa_2O_4$:Mn is the only gallate compound reported by Leverenz (13) in his extensive treatment of luminescent materials.

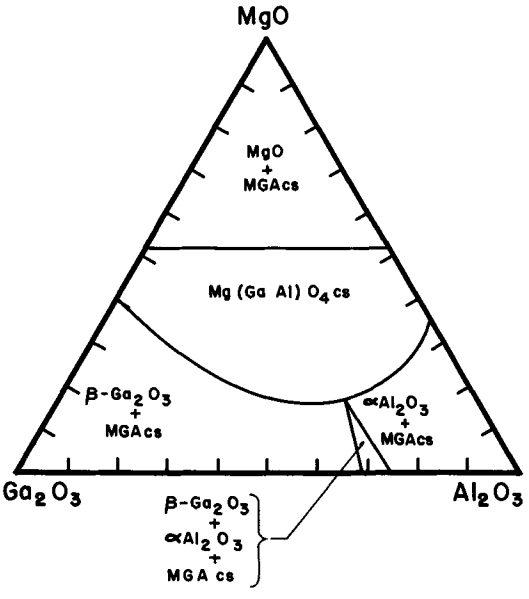

Fig. 1. (a, b, c, d). 1400°C isothermal section of the MgO-Ga_2O_3-Al_2O_3 ternary system and probable T-X diagrams of associated binary systems (2, 4, 5, 6, 7, 11, 12).

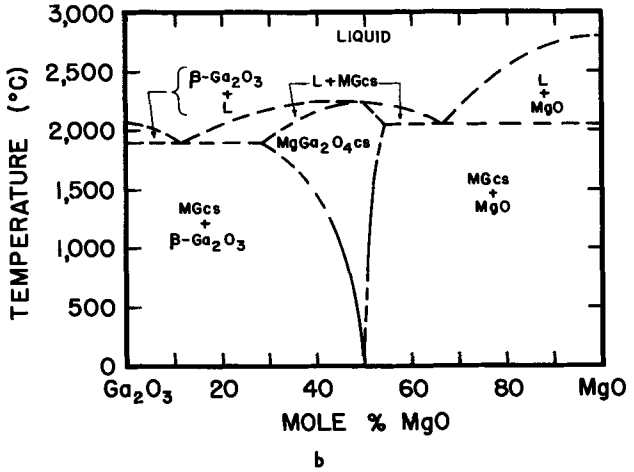

b

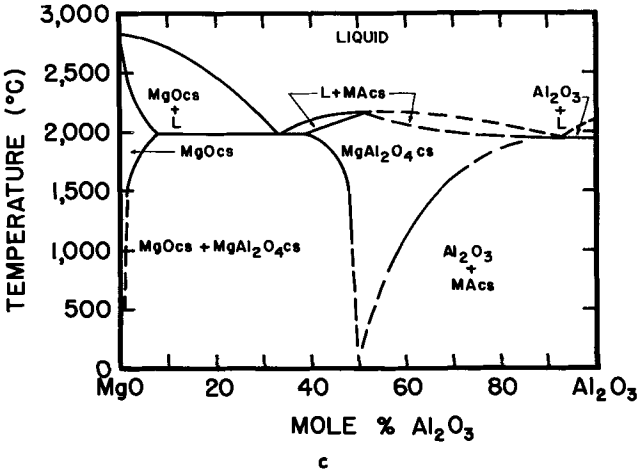

c

Experimental Procedure

Sample preparation.—The raw materials used in this investigation consisted of luminescent grade basic magnesium carbonate, $MgCO_3 \cdot Mg(OH)_2$, and manganese carbonate, $MnCO_3$, aluminum hydroxide, $Al_2O_3 \cdot nH_2O$, and 99.999% pure gallium oxide, Ga_2O_3. Weight loss measurements were conducted on the magnesium

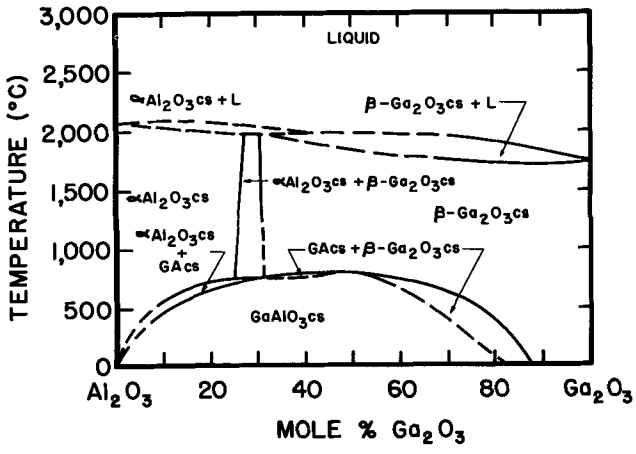

d

and aluminum compounds in order to compensate batch calculations for sorbed water. Appropriate proportions of the raw materials were weighed to an accuracy of ±0.1 mg on an analytical balance. Each preparation was hand mixed under acetone in a glass mortar and pestle for 10 to 20 min and allowed to air dry. Samples to be used for subsolidus equilibria studies were heat treated twice in air at the desired temperature for 17 hr each, with an intermediate light mixing. This procedure was necessary to insure complete reaction and homogeneity. Preparations used for luminescence studies were heat-treated only once in air at the desired temperature for 8 to 17 hr, then reheated at a slightly lower temperature for 1 hr in a very mildly reducing atmosphere. In all cases, fused silica or sintered alumina crucibles were used. Noble metal containers were unsatisfactory because the gallium tended to amalgamate with the crucible metal.

Compositions were periodically analyzed quantitatively by atomic absorption and wet chemical methods in order to confirm the formulated compositions. A typical result is shown in Table I.

A Norelco x-ray diffractometer employing nickel-filtered CuKα radiation, operating at 40 kv and 15 ma was used with a scanning rate of 1°-2θ/min for routine phase identification and 1/8°-2θ/min for more precise lattice parameter measurements.

Luminescence.—All fluorescence excitation and emission spectra and peak height measurements were obtained with a Perkin-Elmer spectrofluorimeter as previously described (14).

Cathodoluminescence spectra were obtained using a demountable cathode-ray tube operating at 12 kv anode potential and 6 μa beam current over a standard scan TV raster of 1 in.^{2} area. Brightness under these conditions were measured with an eye-corrected Weston foot-Lambert meter.

Experimental Results

The MgO-Ga_2O_3 *system.*—Table II lists the compositions, x-ray diffraction, and luminescence data for preparations throughout the MgO-Ga_2O_3 system. In all cases the samples were heat-treated in two steps. The first heat-treatment at 1400°C/17 hr in air formed the host lattice with manganese incorporation. Qualitative data indicated that the highest practical

Table I. Comparison of formulated and analyzed ingredients in a typical preparation

Element	Formulated	Weight per cent Atomic absorption	Chemical analysis
Mg	9.5	10.0	10.18
Ga	62.5	62.0	63.42
Mn	0.25	0.25	No data

Table II. Phase equilibria and luminescence data of phosphors prepared throughout the MgO-Ga_2O_3 system

Composition, mole % MgO	Ga_2O_3	MnO	Phase assemblages	a_o of $MgGa_2O_4$ spinel phase, Å	Relative fluorescence peak height	Cathodoluminescence Brightness, ft-L	Color coordinates x	y
—	99	1	β-Ga_2O_3	—	—			
9	90	1	β-Ga_2O_3 + $MgGa_2O_{4cs}$	8.27	3			
19	80	1	β-Ga_2O_3 + $MgGa_2O_{4cs}$	8.274	18			
29	70	1	β-Ga_2O_3 + $MgGa_2O_{4cs}$	8.272	39			
39	60	1	β-Ga_2O_3 + $MgGa_2O_{4cs}$	8.271	75			
44	55	1	β-Ga_2O_{3tr} + $MgGa_2O_{4cs}$	8.272	89	8.0	0.103	0.664
45	54	1	$MgGa_2O_{4cs}$	8.275	95	8.0	0.101	0.671
46	53	1	$MgGa_2O_{4cs}$	8.277	100	7.0	0.111	0.671
47	52	1	$MgGa_2O_{4cs}$	8.279	92	7.0	0.112	0.678
49	50	1	$MgGa_2O_{4cs}$	8.282	70	5.5	0.112	0.678
59	40	1	$MgGa_2O_{4cs}$ + MgO	8.288	13			
69	30	1	$MgGa_2O_{4cs}$ + MgO	8.289	11			
79	20	1	$MgGa_2O_{4cs}$ + MgO	8.290	9			
89	10	1	$MgGa_2O_{4cs}$ + MgO	8.292	5			
99	—	1	MgO	—	—			

reaction temperature eventually provided the brightest phosphors. Typical preparations at this point had a pink body color and very weak green and red emission bands when excited by 253.7 nm radiation.

The second heat-treatment, carried out at 1200°C/1 hr in a 2% H_2 — 98% N_2 by volume gas mixture, provided preparations with a white body color and bright blue-green luminescence. For maximum phosphor brightness, it was found necessary to cool the samples to below 500°C in the protective atmosphere. Brightness was found to be dependent on the time, temperature, and atmosphere of the second heat-treatment, with the conditions specified above being optimum for 25g samples.

It is evident from Table II that magnesium gallate crystalline solution is the phase responsible for the luminescence in the MgO-Ga_2O_3 system. Manganese-activated MgO and β-Ga_2O_3 are nonluminescent under these conditions of preparation. It is also evident from Fig. 2 and Table II that these phosphors are efficiently excited only by 253.7 nm radiation. Cathodoluminescence measurements indicated typical light outputs of about 7.0 ft-L and color coordinates of $x \cong 0.110$ and $y \cong 0.670$.

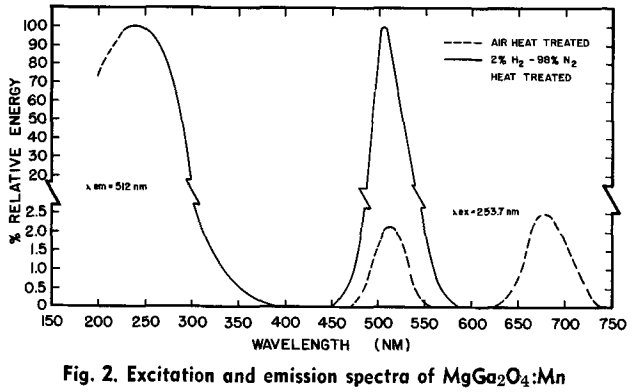

Fig. 2. Excitation and emission spectra of $MgGa_2O_4$:Mn

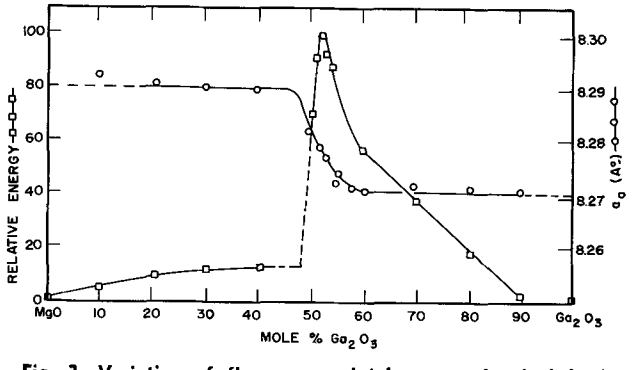

Fig. 3. Variation of fluorescence brightness and spinel lattice parameter a_o with composition in the MgO-Ga_2O_3 system.

Table III. Comparison of fluorescence characteristics and efficiency of $MgGa_2O_4$:Mn with Zn_2SiO_4:Mn and $MgWO_4$

	Zn_2SiO_4:Mn NBS 1028	$MgWO_4$ NBS 1027	$MgGa_2O_4$:Mn
Peak wavelength, nm	536	501	512
Band width at ½ I_{max}, nm	45	152	36
Relative peak height	253	100	326
Color coordinates			
x	0.277	0.234	0.116
y	0.686	0.320	0.679
% Absorption at 253.7 nm	94.2	96.0	84.7
Relative quanta × 10^{-6} [eg $\int \lambda_o I_o d\lambda$]	2.78	7.57	1.93
Emitted energy [eg $\int \rho(\lambda) d\lambda$]	1.12	3.58	0.87
Energy efficiency	35	43 (19)	34
Quantum efficiency	81	85 (19)	81

The excitation and emission spectral energy distribution curves for $MgGa_2O_4$:Mn are shown in Fig. 2. It can be noted that the excitation spectrum peaks near 253.7 nm making this phosphor especially suited for application in fluorescent lamps. The emission peaks sharply at 512 nm with a half width of 36 nm. Following the method of Palumbo and Wisnieski (16), the fluorescence quantum efficiency of $MgGa_2O_4$:Mn was found to be equivalent to that of NBS 1028 zinc orthosilicate (with high manganese concentration) as shown in Table III. Also shown in Fig. 2, for sake of comparison, are the emission bands present prior to the second heat-treatment. The green emission is increased about 50 times by mild reduction, whereas the red band completely disappears.

Figure 3 shows the variation of the spinel a_o lattice parameter and fluorescence peak height with composition. The abrupt breaks in both curves near 48 and 62 mole % Ga_2O_3 signify the limits of $MgGa_2O_4$ crystalline solution. These are in good agreement with Schmalzried's (2) data when one realizes that the preparations of the present study contain 1 mole % manganese activator. Optimum fluorescence is obtained within the crystalline solution region at approximately 53 mole % Ga_2O_3. Crystalline solution of MgO in $MgGa_2O_4$ decreases the fluorescence more markedly than Ga_2O_3 substitutions. The brightness curves outside of the crystalline solution region approximates linearity because of dilution effects from the second phase.

Table IV and Fig. 4 show the effect of manganese concentration on phosphor brightness and peak emis-

Table IV. Effect of Mn^{2+} variations on $MgGa_2O_4$ phosphor

Sample No.	Composition, moles MgO	Ga_2O_3	MnO	Moles MnO / Moles MgO + MnO	% Relative peak height	Peak wavelength, nm	% Peak height decrease at 100°C
1	100	100	—	—	—	—	—
2	99	100	0.1	0.001	80	510.5	—
3	98	100	0.5	0.005	96	510.5	8.5
4	97	100	1.0	0.010	100	510.5	11.0
5	96	100	2.0	0.020	77	513.5	19.0
6	94	100	3.0	0.030	53	514.5	>20
7	93	100	4.0	0.040	42	515.5	—
8	92	100	5.0	0.050	29	516.5	—

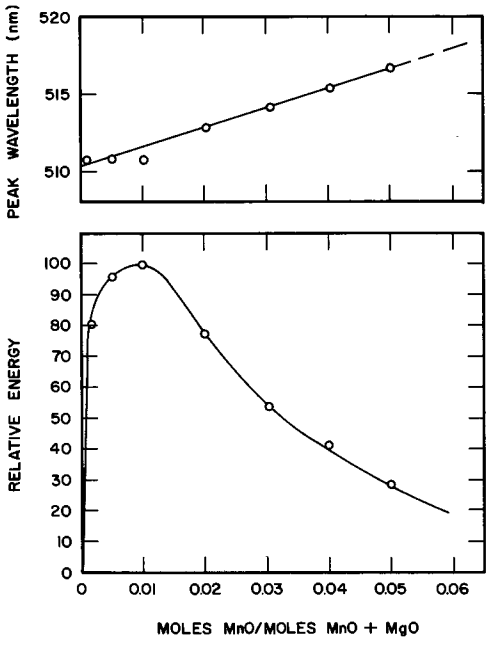

Fig. 4. Variation of peak wavelength (top) and brightness (bottom) with manganese concentration in $MgGa_2O_4$.

sion wavelength. Compositions were adjusted for manganese additions so that the Mn^{2+} could substitute for Mg^{2+} (or Ga^{3+}) and maintain the same approximate vacancy concentration. The top curve in Fig. 4 shows the variation of peak wavelength with increasing manganese additions. The apparent linear relationship is not surprising in view of the isomorphous $MgGa_2O_4$ and $MnGa_2O_4$ structures. The bottom curve shows the variation of peak intensity with manganese content. Concentration quenching, common to many Mn^{2+}-activated phosphors can be observed. Optimum fluorescence brightness is obtained at approximately 0.01 moles MnO.

The extreme right-hand column of Table IV shows the per cent peak height decrease observed between 25° and 100°C. This property was obtained by mounting a small furnace in the sample chamber of the spectroradiometer. These data confirm the general knowledge that low Mn^{2+} levels usually improve the temperature dependence of a phosphor. A very slight emission broadening and peak wavelength shift (towards shorter wavelengths) was observed, especially at high manganese levels.

Figure 5 shows the temperature dependence of $MgGa_2O_4$:Mn (sample 4, Table IV) measured up to 400°C with a HPMV plaque tester (17). The curve was found to be completely reversible up to at least 250°C, eliminating the possibility of the brightness decrease being caused by a chemical reaction.

These high-temperature data are important because they indicate that this phosphor, correctly formulated, can be used in fluorescent lamps (which generally operate below 100°C) without significant changes in brightness or other spectral characteristics.

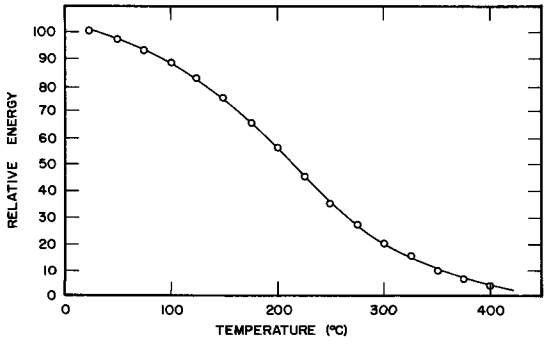

Fig. 5. Temperature dependence of $MgGa_2O_4$:Mn

Table V. Compositions and luminescence and x-ray data for preparations throughout the spinel crystalline solution series in the MgO-Ga_2O_3-Al_2O_3 systems

No.	Composition, mole % MgO	Al_2O_3	Ga_2O_3	MnO	253.7 nm Excited Pk ht	Peak λ	CR excited Ft-L	x	y	Lattice parameter a_o, Å
1	50	—	50	0.5	100	510.0	5.5	0.116	0.673	8.279
2	45	—	55	0.5			4.0	—	—	
3	40	—	60	0.5			3.7	0.102	0.631	
4	35	—	65	0.5			3.0	—	—	
5	30	—	70	0.5			3.0	0.101	0.609	
6	50	10	40	0.5	64	512.0	9.5	0.134	0.706	8.249
7	45	12.5	42.5	0.5			8.8	0.123	0.692	
8	40	15	45	0.5			7.5	—	—	
9	35	17.5	47.5	0.5			6.0	0.106	0.682	
10	30	20	50	0.5			4.5	—	—	
11	25	22.5	52.5	0.5			4.5	—	—	
12	20	25	55	0.5			2.3	0.122	0.697	
13	50	25	25	0.5	31	517.5	9.5	0.148	0.712	8.160
14	45	27.5	27.5	0.5			10.0	—	—	
15	40	30	30	0.5			10.2	0.146	0.714	
16	35	32.5	32.5	0.5			10.0	—	—	
17	30	35	35	0.5			10.0	0.132	0.696	
18	25	37.5	37.5	0.5			8.0	—	—	
19	20	40	40	0.5			8.5	0.136	0.702	
20	50	40	10	0.5	7	523.0	8.8	0.173	0.727	8.122
21	45	42.5	12.5	0.5			8.8	—	—	
22	40	45	15	0.5			9.0	0.166	0.720	
23	35	47.5	17.5	0.5			9.0	—	—	
24	30	50	20	0.5			9.0	0.162	0.721	
25	25	52.5	22.5	0.5			10.0	—	—	
26	20	55	25	0.5			9.9	0.145	0704	
27	50	50	—	0.5	—	—	8.0	0.225	0.724	8.083
28	45	55	—	0.5			8.9	0.216	0.730	
29	40	60	—	0.5			7.1	—	—	
30	35	65	—	0.5			7.3	0.222	0.730	
31	30	70	—	0.5			6.9	—	—	

The MgO-Al_2O_3 *binary system.*—Phosphors prepared throughout the spinel crystalline solution region of this system were excited only by cathode rays. The results of samples prepared at 1400°C are shown in Table V. Brightness appears to be maximum at approximately $(Mg_{0.90},Mn_{0.01})Al_{2.06}O_4$, and there is little change in color coordinates throughout the series. In general, these data are in agreement with those of Hummel and Sarver (10).

The Al_2O_3-Ga_2O_3 *binary system.*—Manganese-activated phosphors were prepared throughout the Al_2O_3-Ga_2O_3 system at 1400°C. Significant luminescence was not observed. X-ray diffraction powder data agreed essentially with the phase diagram of Hill *et al.* (11). Compositions in the intermediate crystalline solution region were not prepared because of their low-temperature stability range.

The MgO-Al_2O_3-Ga_2O_3 *ternary system.*—The compositions, lattice parameters, fluorescence, and cathodoluminescence data for preparations throughout the

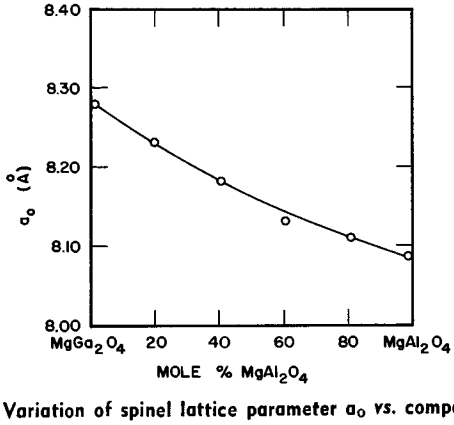

Fig. 6. Variation of spinel lattice parameter a_o vs. composition on the $MgGa_2O_4$-$MgAl_2O_4$ join.

spinel crystalline solution region in the MgO-Al_2O_3-Ga_2O_3 ternary system are listed in Table V. All compositions were heat-treated at 1400°C/17 hr in air and second fired at 1200°C/1 hr in a 2% H_2-98% N_2 atmosphere. The data plotted in Fig. 6 illustrate the variation of the a-axis of the spinel unit cell with composition throughout the $MgGa_2O_4$-$MgAl_2O_4$ join. The continuous variation of this parameter confirms the existence of a crystalline solution series. The decrease of a_o from 8.279Å for $MgGa_2O_4$ to 8.083Å for $MgAl_2O_4$ reflects the relative sizes of the trivalent cations, *e.g.*, the Goldschmidt radius of Ga^{3+} is 0.62Å and Al^{3+} is 0.57Å. The following luminescence results were obtained:

1. Photoluminescence.—As Al^{3+} replaces Ga^{3+} in the spinel structure, the manganese-activated ultraviolet excited peak wavelength increases and brightness decreases (Fig. 7). Magnesium aluminate is practically inert.

2. Cathodoluminescence.—The general trend of peak wavelength observed for ultraviolet excitation is also evident for cathode-ray excitation. (Brightness data are too erratic for a trend to be observed.)

Figure 8 illustrates the variation of brightness (ft-L) and chromaticity coordinates (x,y) throughout the ternary crystalline solution region. These results indicate (*i*) brightness is maximum near the center of the region (*e.g.*, near 40MgO, $30Ga_2O_3$, $30Al_2O_3$), and (*ii*) x and y increase as the Al^{3+} content increases.

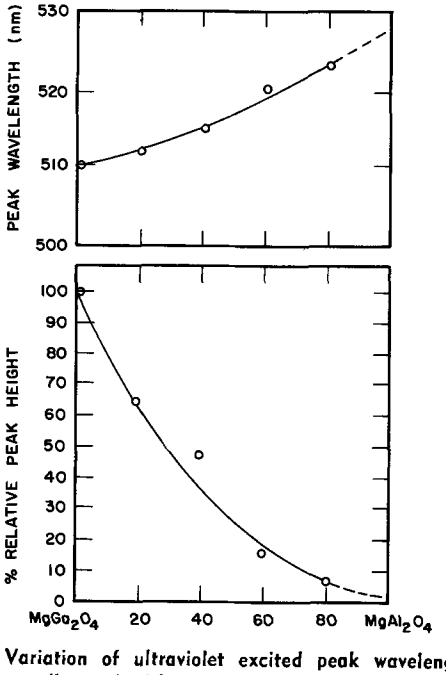

Fig. 7. Variation of ultraviolet excited peak wavelength (top) and brightness (bottom) with composition on the $MgGa_2O_4$-$MgAl_2O_4$ join.

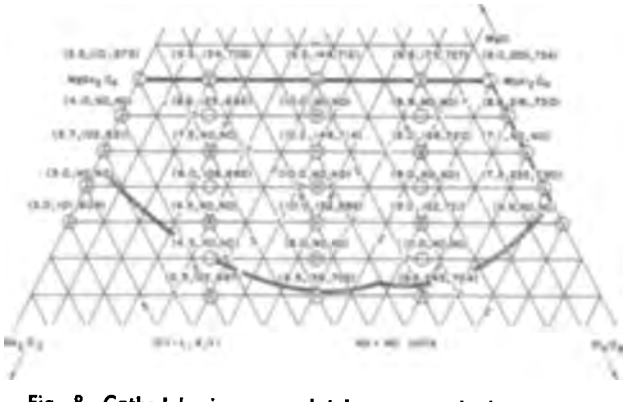

Fig. 8. Cathodoluminescence brightnesses and chromaticity coordinates of phosphors prepared throughout the spinel crystalline solution region in the MgO-Al_2O_3-Ga_2O_3 system.

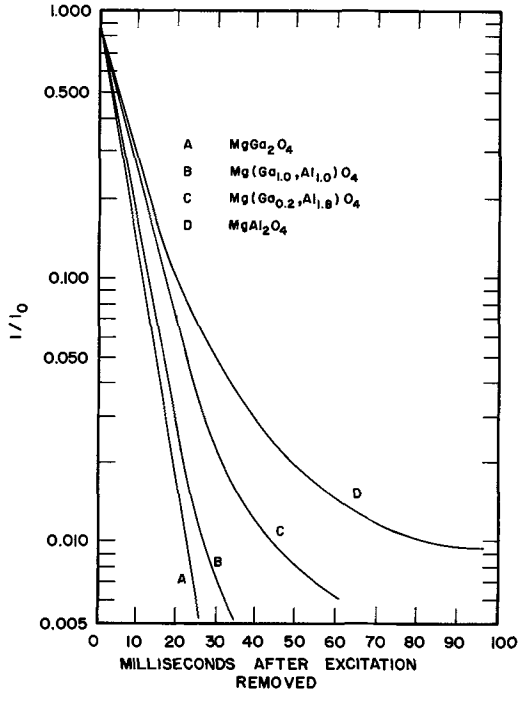

Fig. 9. Cathodoluminescence decay of phosphors throughout the $MgGa_2O_4$-$MgAl_2O_4$ join.

Figure 9 illustrates the effect of increasing $MgAl_2O_4$ concentrations on the decay characteristics of this phosphor. A persistent "tail" develops at about 50% $MgAl_2O_4$ and becomes progressively longer at higher $MgAl_2O_4$ concentrations. These decay curves were found to vary somewhat depending on the composition of the atmosphere of the second heat-treatment.

Discussion

Although both $MgGa_2O_4$ and $MgAl_2O_4$ crystallize with the spinel structure, they differ in their cation distributions as previously pointed out. The green emission of manganese in both of these compounds suggest tetrahedral oxygen coordination of Mn^{2+}. Furthermore, the pink body color and absence of luminescence after only air heat-treatments of $MgGa_2O_4$ suggest the possibility of manganese entering the structure as Mn^{3+}. The presence of Mn^{3+} after air heat-treatment is strengthened by the reflectance spectra of $MgGa_2O_4$:Mn measured before and after reduction as shown in Fig. 10. The broad absorption band in the blue-green region of the spectrum present only in the air-fired sample appears to be similar to

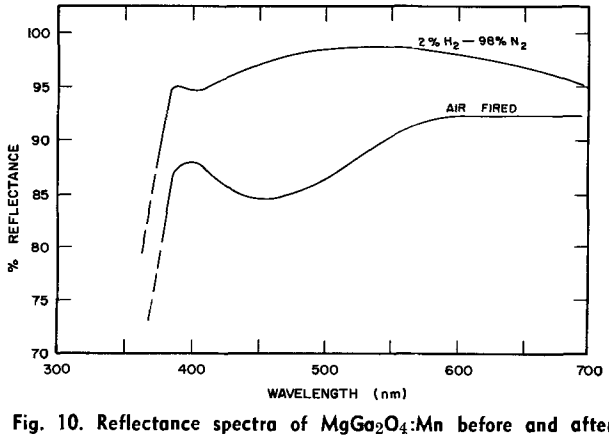

Fig. 10. Reflectance spectra of $MgGa_2O_4$:Mn before and after reduction.

that shown by Rabatin and Gillooly (15) to be characteristic of Mn^{3+}. Another qualitative indication of this mechanism was the significant green fluorescence developed after only air heat-treatments in preparations where small amounts of Si^{4+} or Ge^{4+} were substituted for Ga^{3+}. This probably resulted from the tetravalent cations forcing more of the manganese into the divalent state in order to balance the electrostatic charges.

Jagodzinski and Saalfeld (4) have shown that vacancies are distributed only over octahedral sites in $MgAl_2O_4$. If it is assumed that this is also the case for $MgGa_2O_4$, and that the population of Mg^{2+} ions in octahedral sites is about 0.84 at 1400°C (2), then the optimum phosphor composition can be approximated as follows

$$(Mg^{2+}_{0.06},Ga^{3+}_{0.93},Mn_{0.01})^{IV}\ (Mg^{2+}_{0.84},\square_{0.03},Ga^{3+}_{1.13})^{VI}\ O_4$$

Summary

1. Magnesium gallate activated by divalent manganese has been found to be an efficient ultraviolet excited phosphor with a peak emission wavelength at 512 nm. The optimum phosphor composition was determined to be $(Mg_{0.90},Mn_{0.01})(Ga_{2.06})O_4$.

2. Al^{3+} for Ga^{3+} substitutions in the spinel lattice rapidly decrease the fluorescence brightness, but increase the cathodoluminescence light output. The peak emission shifts from 512 to 525 nm and the decay characteristics become increasingly longer with Al^{3+} substitutions.

Acknowledgments

The author wishes to thank Mr. D. T. Palumbo and Dr. R. W. Mooney for many stimulating discussions during the course of this investigation. X-ray diffraction data were obtained by Dr. C. W. W. Hoffman. Procedures for the quantitative analyses of Mg, Ga, and Mn in magnesium gallate by wet chemistry methods were developed by Mrs. A. R. Mikus and by atomic absorption methods by Mr. J. L. Seeley. Sample preparations were carried out with the assistance of Messrs. J. D. Deysher and O. B. Bullock.

Manuscript received Aug. 25, 1966; revised manuscript received Oct. 14, 1966. This paper was presented at the Cleveland Meeting, May 1-6, 1966.

Any discussion of this paper will appear in a Discussion Section to be published in the December 1967 JOURNAL.

REFERENCES

1. T. Moller and G. L. King, *J. Am. Chem. Soc.*, **75**, 6060 (1953).
2. H. Schmalzried, *Z. physik. Chem.*, **28**, 203 (1961).
3. J. E. Weidenborner, N. R. Stemple, and Y. Okaya, *Acta Cryst.*, **20** [6], 761 (1966).
4. H. Jagodzinski and H. Jagodzinski, *Z. Kristallogr.*, **110**, 197 (1958).
5. H. Saalfeld and H. Jagodzinski, *ibid.*, **109**, 87 (1957).
6. A. M. Alper, R. N. McNally, P. G. Rebbe, and R. C. Doman, *J. Am. Ceram. Soc.*, **45** [6], 263 (1962).
7. D. M. Roy, R. Roy, and E. F. Osborn, *Am. J. Sci.*, **251**, 337 (1953).
8. R. K. Datta and R. Roy, *Nature*, **191**, 169 (1961).
9. H. Saalfeld, *Ber. Dtsch. Keram. Ges.*, **39**, 52 (1962).
10. F. A. Hummel and J. F. Sarver, *This Journal*, **111** [2], 252 (1964).
11. V. G. Hill, R. Roy, and E. F. Osborn, *J. Am. Ceram. Soc.*, **35** [6], 136 (1952).
12. G. Katz and R. Roy, *ibid.*, **48**, 450 (1965).
13. H. W. Leverenz, "An Introduction to Luminescence of Solids," John Wiley & Sons, Inc., New York (1950).
14. W. Slavin, R. W. Mooney, and D. T. Palumbo, *J. Opt. Soc. Am.*, **51**, 93 (1961).
15. J. G. Rabatin and G. R. Gillooly, *This Journal*, **111** [5], 542 (1964).
16. D. T. Palumbo and R. J. Wisnieski, "Efficiencies of Lamp Phosphors," In press.
17. R. W. Mooney, *This Journal*, **105**, 456 (1958).
18. R. K. Datta and R. Roy, Geol. Soc. Amer., Special paper No. 68, 159 (1961).
19. A. Bril and W. Hoekstra, *Philips Research Rept.*, **16**, 356 (1961).

Fluorescence of Eu^{3+}-Activated Garnets Containing Pentavalent Vanadium

G. Blasse and A. Bril

Philips Research Laboratories, N. V. Philips' Gloeilampenfabrieken, Eindhoven-Netherlands

ABSTRACT

$NaCa_2Mg_2V_3O_{12}$ has garnet structure and shows a broad emission band with a maximum at about 500 nm under short-wave uv excitation. Eu^{3+} is introduced according to the substitution $Ca^{2+} + Mg^{2+} \rightarrow Eu^{3+} + Li^+$. Unlike the emission of the usual Eu^{3+}-activated garnets (like YAG) the Eu^{3+} emission shows strong $^5D_0$-$^7F_2$ transitions in this case. The energy transfer from the vanadate group to the Eu^{3+} ion is not very efficient. This is ascribed to the small value of the overlap of the Eu^{3+} and V^{5+} orbitals, the V-O-Eu angles being 90° and 120°.

Rare earth activated garnets have been studied extensively. Usually the composition of the host lattice is $A_3B_5O_{12}$ (A = Y,Gd; B = Al, Ga). The formula $\{Y_3\}[Al_2](Al_3)O_{12}$ gives more insight into the crystal chemistry of the garnets: { } represents a dodecahedral site, [ ] an octahedral site, and ( ) a tetrahedral site. Recently Bayer (1) described garnets containing pentavalent vanadium, *e.g.*, $\{Na\,Ca_2\}[Mg_2](V_3)O_{12}$. Since a number of vanadates [*e.g.*, YVO_4 (2) and $Ca_3(VO_4)_2$ (3)] appear to be suitable host lattices for rare earth activated phosphors, we studied the fluorescence of unactivated and Eu^{3+}-activated $NaCa_2Mg_2V_3O_{12}$.

Experimental

Materials with composition $\{NaCa_{2-\delta}Eu_\delta\}[Li_\delta Mg_{2-\delta}](V_3)O_{12}$ were prepared by firing intimate mixtures of Na_2CO_3, $CaCO_3$, Eu_2O_3, Li_2CO_3, $MgCO_3$, and NH_4VO_3 at 750°C in O_2 several times. X-ray powder diagrams were obtained using CuKα radiation.

The performance of the optical measurements has been described in detail elsewhere (4).

Results

Compositions $\{NaCa_{2-\delta}Eu_\delta\}[Li_\delta Mg_{2-\delta}](V_3)O_{12}$ proved to be single-phased garnets up to $\delta = 0.4$. For higher values of δ a second phase with zircon structure was found in the x-ray diagrams. These materials were not studied further. The lattice parameter of the garnet phase did not change more than 0.01Å going from $\delta = 0$ to $\delta = 0.4$ and amounted to a = 12.45Å for $\delta = 0$, in good agreement with Bayer's results (1).

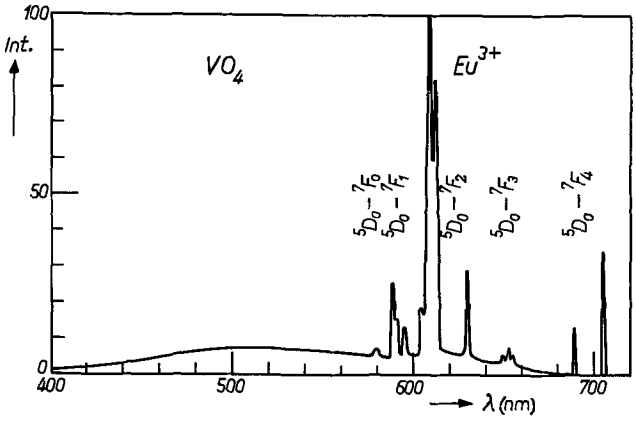

Fig. 1. Spectral emission under short wavelength u.v. excitation of $NaCa_{1.9}Eu_{0.1}Li_{0.1}Mg_{1.9}V_3O_{12}$.

Under short-wave u.v. excitation $NaCa_2Mg_2V_3O_{12}$ shows a white emission at room temperature (quantum efficiency about 30%; this value may be a lower bound due to the low reaction temperature). Even at the highest Eu^{3+} concentration ($\delta = 0.40$), we observed this host lattice emission in addition to the characteristic Eu^{3+} emission. Figure 1 presents the emission for the composition with $\delta = 0.10$. Table I gives the ratio of Eu^{3+} emission to total emission for several values of δ. The excitation spectrum of the fluorescence and the diffuse reflection spectrum for the material with $\delta = 0.10$ are given in Fig. 2. These spectra do not change with the activator concentration.

Discussion

Emission.—Figure 1 shows the host lattice emission as well as the activator emission. The former consists of a very broad band extending from approximately 400 to 700 nm with a maximum at roughly 500 nm, which must be due to transitions in the vanadate group. Vanadate emission at room temperature has been reported earlier for compounds of the type $M_2V_2O_7$ (M = Mg, Zn, Cd, Ca, Sr, Ba) (5).

The emission of the Eu^{3+} ion consists of the well-known transitions from $^5D_0$ down to the ^7F manifold. It is interesting to note that in the vanadium garnet the red lines ($^5D_0 - {}^7F_2$) have the strongest intensity. In the aluminum and gallium garnets (*e.g.*, YAG), however, the red and orange lines ($^5D_0 - {}^7F_1$) have comparable intensity (6), which is not surprising, because the Eu^{3+} ion occupies a site which has an approximate center of symmetry, if only the nearest neighbors, *viz.*, the eight O^{2-} anions are considered. For a strict center of symmetry the red fluorescence due to the $^5D_0 - {}^7F_2$ transition is forbidden. Blasse, Bril, and Nieuwpoort (7) have noticed that the intensity ratio of the red and orange lines can be drastically changed by chemical variations of the next-nearest neighbors of the Eu^{3+} ion. The present results are another example of this effect. Contrary to the situation with the anions, the cation neighbors of the dodecahedral site in the garnet structure of $Y_3Al_5O_{12}$ lack inversion symmetry. In $NaCa_2Mg_2V_3O_{12}$, where the tetrahedral Al^{3+} ions are replaced by V^{5+} ions and the octahedral Al^{3+} ions by Mg^{2+} ions, this lack of inversion symmetry seems to be of more importance.

Table I. Ratio of the quantum efficiency of the Eu^{3+} emission to the total quantum efficiency for materials $NaCa_2Mg_2V_3O_{12}$: Eu, Li

Composition	Ratio
$NaCa_2Mg_2V_3O_{12}$	0
$NaCa_{1.96}Eu_{0.04}Li_{0.04}Mg_{1.96}V_3O_{12}$	0.1
$NaCa_{1.9}Eu_{0.1}Li_{0.1}Mg_{1.9}V_3O_{12}$	0.2
$NaCa_{1.8}Eu_{0.2}Li_{0.2}Mg_{1.8}V_3O_{12}$	0.4
$NaCa_{1.6}Eu_{0.4}Li_{0.4}Mg_{1.6}V_3O_{12}$	0.6

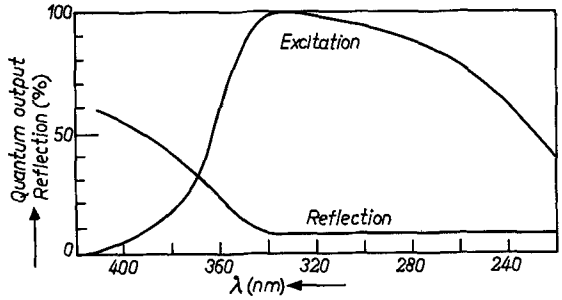

Fig. 2. Relative excitation spectrum of the fluorescence and diffuse reflection spectrum of $NaCa_{1.9}Eu_{0.1}Mg_{1.9}V_3O_{12}$.

This is an indication again that the intensity alterations seem to be dependent on the state of polarization of the oxygen ions, as noted earlier (7): in $NaCa_2Mg_2V_3O_{12}$ the anions are much more strongly polarized than in YAG because in $NaCa_2Mg_2V_3O_{12}$ each O^{2-} ion has one highly charged and small V^{5+} ion as one of its neighbors. The crystal field splittings are not strongly influenced by this effect, as follows from a comparison of the Eu^{3+} emission of YAG : Eu (6) and $NaCa_2Mg_2V_3O_{12}$: Eu, Li. The $^5D_0 - {}^7F_1$ transition contains three lines and the $^5D_0 - {}^7F_2$ transition four lines in both cases. The splittings are of the same order of magnitude.

In this connection we note that the anomalous behavior of the Curie temperature of V^{5+}-substituted yttrium iron garnet (the Curie temperature does not change if the paramagnetic ions are replaced by diamagnetic ions) has also been ascribed to an influence of the V^{5+} ions on the chemical bonding (8).

Excitation and reflection.—Since the reflection spectra do not change very much in the investigated region of δ(0-0.4), the absorption in the u.v. region is ascribed to the vanadate groups of the host lattice. The excitation is most efficient at the wavelength of the absorption edge (see Fig. 2). From Table I it is seen that the energy transfer from vanadate group to Eu^{3+} activator is not very efficient. This is contrary to the energy transfer from vanadate group to Eu^{3+} ion in Eu^{3+}-activated YVO_4 and $Ca_3(VO_4)_2$, where the transfer is very efficient (2, 3). Elsewhere we have argued that transfer of this type is exchange-regulated and therefore strongly dependent on the crystal structure, the O^{2-} ions playing a role (9). Unfortunately the structure of $Ca_3(VO_4)_2$ is not known. In YVO_4 : Eu the V-O-Eu angle is 170°, whereas in $NaCa_2Mg_2V_3O_{12}$: Eu,Li the V-O-Eu angle is 90° or 120° (10). This means that the wave function overlap of the vanadium and europium ions is larger in YVO_4 than in $NaCa_2Mg_2V_3O_{12}$, σ-bonding being involved in the 180° case and π-bonding in the 90° case. Therefore the vanadate → Eu^{3+} ion transfer should be more efficient in YVO_4 than in $NaCa_2Mg_2V_3O_{12}$, in agreement with the experimental results. That there is still considerable energy transfer from vanadate group to Eu^{3+} ion in the garnet may be due to direct overlap of the orbitals of the V^{5+} and Eu^{3+} ion. Each V^{5+} ion is surrounded by six dodecahedral ions, of which two are at a distance equal to one quarter of the cell edge, *i.e.*, only 3.1Å in the present case. Direct overlap is a well-known phenomenon in magnetic exchange theories as is the angle-dependence of the overlap of wave functions of cations separated by anions (11). The strong magnetic interaction between Cr^{3+} ions in $ZnCr_2O_4$, for instance, is ascribed to direct overlap of t_{2g} wave functions of the Cr^{3+} ions ($Cr^{3+} - Cr^{3+}$ distance 2.9Å).

Manuscript received Aug. 8, 1966; revised manuscript received Oct. 17, 1966.

Any discussion of this paper will appear in a Discussion Section to be published in the December 1967 JOURNAL.

REFERENCES
1. G. Bayer, *J. Am. Chem. Soc.*, **48**, 600 (1965).
2. F. C. Palilla, A. K. Levine, and M. Rinkevics, *This Journal*, **112**, 776 (1965).
3. L. H. Brixner and P. A. Flournoy, *ibid.*, **112**, 303 (1965).
4. A. Bril and W. L. Wanmaker, *ibid.*, **111**, 1363 (1964).
5. Y. Kotera and T. Sekine, *Bull. Chem. Soc. Japan*, **27**, 13 (1954).
6. L. G. Van Uitert, R. C. Linares, R. R. Soden, and A. A. Ballman, *J. Chem. Phys.*, **36**, 702 (1962); J. A. Koningstein, *Phys. Rev.*, **136**, A717 (1964).
7. G. Blasse, A. Bril, and W. C. Nieuwpoort, *J. Phys. Chem. Solids*, Int. Conf. on Luminescence, Budapest, 1966.
8. S. Geller, G. P. Espinosa, H. J. Williams, R. C. Sherwood, and E. A. Nesbitt, *J. Appl. Phys.*, **35**, 570 (1964); *Appl. Phys. Letters*, **3**, 60 (1963).
9. G. Blasse and A. Bril, *J. Chem. Phys.*, In press; G. Blasse, *J. Chem. Phys.*, In press.
10. S. Geller and M. A. Gilleo, *J. Phys. Chem. Solids*, **3**, 30 (1957).
11. J. B. Goodenough, "Magnetism and the Chemical Bond," p. 202, Interscience Publishers, New York (1963).

Fluorescence and Cathodoluminescence of Eu^{+3} in Some Alkali and Alkaline Earths-Yttrates and Gadolinates as Hosts

L. H. Brixner

Pigments Department, Experimental Station,

E. I. du Pont de Nemours & Company, Wilmington, Delaware

ABSTRACT

Efficient fluorescence of Eu^{+3} was measured in alkali yttrate and gadolinate hosts of the type ABO_2, where A is Li or Na; B, Y or Gd, under both ultraviolet and electron excitation. The optimum Eu^{+3} concentration was determined for each host; the concentration *vs.* fluorescent intensity curves are presented, as well as some fluorescent emission spectra. Some alkaline earth compounds were also studied as hosts.

Although the fluorescence of Eu^{+3} in such hosts as Gd_2O_3 and $CaWO_4$ was studied as early as 1909 by Urbain (1), it was not until the advent of the laser concept that europium has been more extensively investigated in all conceivable solid hosts as well as in liquid systems. Stimulated emission was first observed from Eu^{+3} in a chelate (2) and later also in Y_2O_3 (3) as a solid state host. In some of our own experiments (4), we failed to observe laser action from Eu^{+3} in $Ca_3(VO_4)_2$, despite the fact that energy exchange between the host lattice and Eu^{+3} was demonstrated. Van Uitert (5) showed that energy exchange also occurs in the host $GdVO_4$. This composition, or rather the isostructural YVO_4, became of interest recently when Levine *et al.* (6) found that europium in this type of host also shows very efficient cathodoluminescence. It was probably this finding which initiated a renewed search for other novel host structures for Eu.

Most previous work was either done with compositions where the rare earths (Y or Gd for instance) have a cationic function (vanadates, molybdates, tungstates, etc.) or with the rare earth oxide itself. A number of rare earth compounds where the rare earth constitutes the anionic portion, such as SrY_2O_4 (7) or $LiYO_2$ (8), have been described recently, and it was the purpose of this study to investigate these compounds as hosts for Eu^{+3}.

Experimental

The constituent components were generally of the best commercially available purity and were given no further purification treatment. The preparation techniques were essentially identical to those described in detail in (9). Occasional analytical checks were carried out for compositions after complete reaction employing x-ray fluorescence techniques. X-ray powder patterns were taken to confirm the structures obtained with those well documented in the literature; only minor lattice parameter deviations could be observed when appreciable portions of Y^{+3} were substituted by Eu^{+3}. For the Gd hosts, the parameters were essentially unchanged when Eu was introduced. The procedures for obtaining the spectra upon optical excitation have already been described (9). To study the emission characteristics under electron excitation we used an available electron microprobe analyzer. The advantage here was the fact that as many as 11 samples could be excited and studied under absolutely identical conditions. These were generally an excitation current of 0.002 μA, a voltage of 20 kv, using a S-11 response-type detector tube (No. 6199) together with a red filter. The samples were powder compacts pressed into 1/8 diameter holes of a 1 in. diameter brass support plate. The inspection area was approximately 540 μ^2.

The first system which was studied in detail was $LiY_{1-x}Eu_xO_2$. As can be seen from Fig. 1, the optimum fluorescent emission occurred around 6 mol % Eu^{+3} for both ultraviolet and electron excitation. Although different in gradients, the two curves show

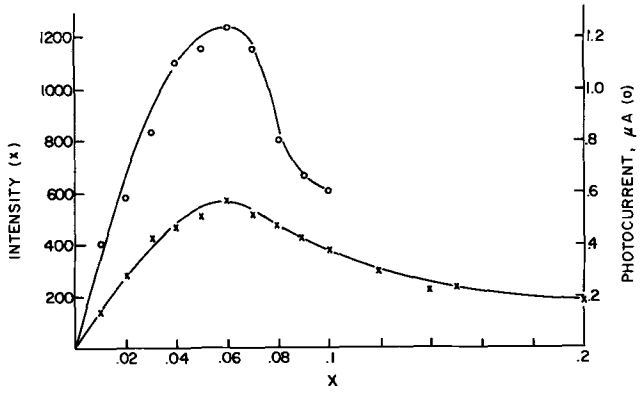

Fig. 1. Intensity of fluorescent emission on electron excitation (o) and on u.v. excitation (x) as a function of X for the $LiEu_xY_{1-x}O_2$ system.

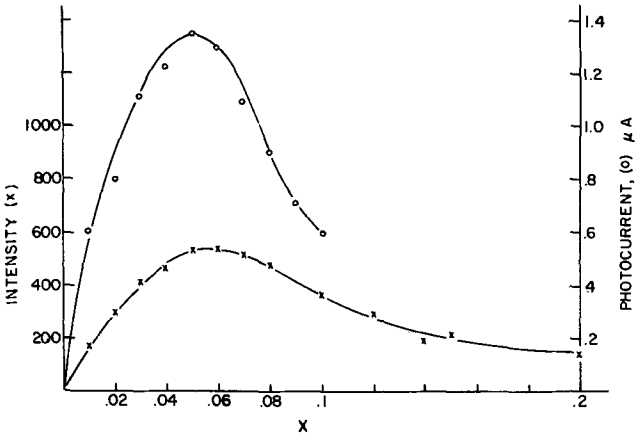

Fig. 2. Intensity of fluorescent emission on electron excitation (o) and on u.v. excitation (x) as a function of X for the $LiEu_xGd_{1-x}O_2$ system.

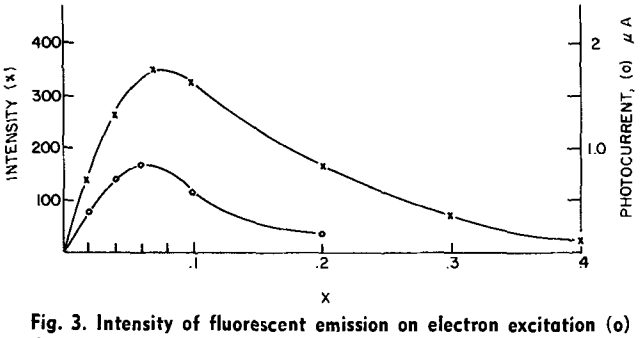

Fig. 3. Intensity of fluorescent emission on electron excitation (o) and on u.v. excitation (x) as a function of X for the $Eu_xY_{1-x}NaO_2$ system.

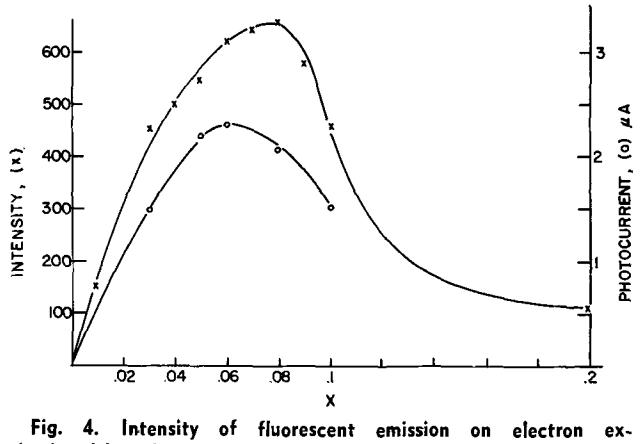

Fig. 4. Intensity of fluorescent emission on electron excitation (o) and on u.v. excitation (x) as a function of X for the $NaEu_xGd_{1-x}O_2$ system.

fundamentally the same characteristics of a steep rise to the optimum emission point and then gradual drop of emission intensity until eventually complete concentration quenching occurs. Figures 2, 3, and 4 show the same results for the corresponding systems: $LiGd_{1-x}Eu_xO_2$, $NaY_{1-x}Eu_xO_2$, and $NaGd_{1-x}Eu_xO_2$. All attempts to prepare any compositions between both Y_2O_3 and Gd_2O_3 and the alkali oxides of K, Rb, and Cs failed completely.

For the purpose of a comparison, the peak intensities of the investigated compositions are summarized in Table I. In the last column marked Lum/o, we have something of a "Figure of Merit," giving the efficiency based on the equivalent Eu concentration. The term is derived from the over-all intensity divided by the % Eu present in this composition. The

Table I. Comparison of peak emission for some Li and Na yttrates and gadolinates

Composition	Opt. inten. under uv excitation (2537Å)	Opt. inten. under electron excitation	% Eu	Lum/o
$LiEu_{0.06}Y_{0.94}O_2$	570	1.24	6.93	82.25
$LiEu_{0.05}Gd_{0.95}O_2$	540	1.35	3.88	139.20
$NaEu_{0.07}Y_{0.93}O_2$	350	0.85	7.17	48.81
$NaEu_{0.08}Gd_{0.92}O_2$	660	2.30	5.74	115.00

location of the peak emission of all compounds is at about 613 mμ as specifically demonstrated for $LiEu_{0.07}Y_{0.93}O_2$ in Fig. 5. The halfwidth of the predominant 613 mμ line narrowed to 3Å at 77°K.

Concerning ternary compositions between the alkaline earth oxides and Y_2O_3 and Gd_2O_3, Schwarz (7) had already demonstrated that only SrO and BaO formed compounds of the types AB_2O_4 (A = Sr^{+2}, Ba^{+2}; B = Y^{+3}, Ln^{+3}). In our own experiments, we also failed to form compounds with CaO or with MgO, ZnO, and CdO. For these reasons, we studied only SrY_2O_4 and BaY_2O_4 as host compositions for Eu^{+3}.

Although the substitutional elements are the same as in the previously discussed compounds, due to the different environmental symmetry as well as the different crystal field influence on the Stark splitting, the fluorescent emission spectra for Eu^{+3} in these hosts could be expected to be different and therefore it seemed of interest to study it. The most striking difference becomes apparent in Fig. 6, where a complete reversal of the intensity in the 590 and 610 mμ region can be observed. Such shifts of the bulk of the emission intensity are, of course, associated with the corresponding change of symmetry. Unfortunately the structures of neither host are well enough known to establish from group theory the number of possible components which each transition would be allowed to have. Under monoclinic symmetry the $^5D_0 \rightarrow {}^7F_1$

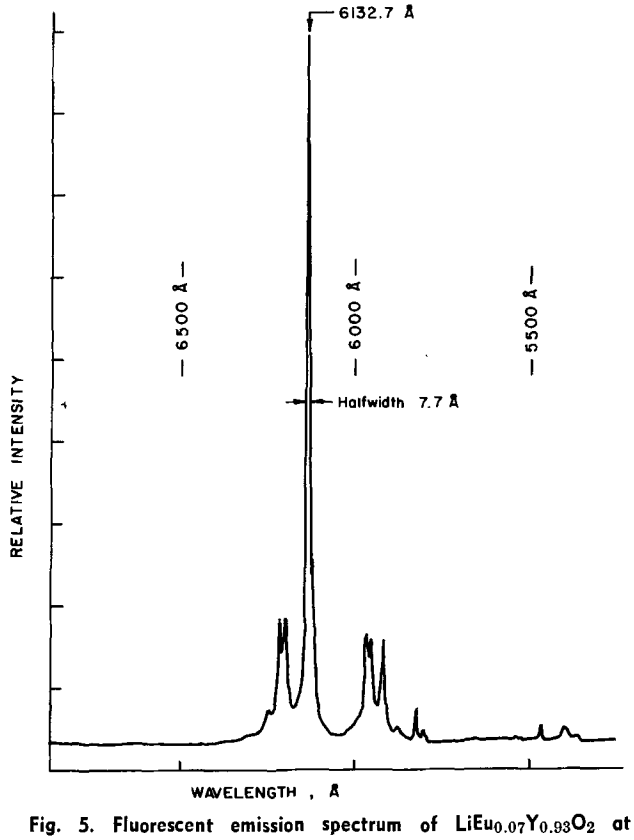

Fig. 5. Fluorescent emission spectrum of $LiEu_{0.07}Y_{0.93}O_2$ at 300°K.

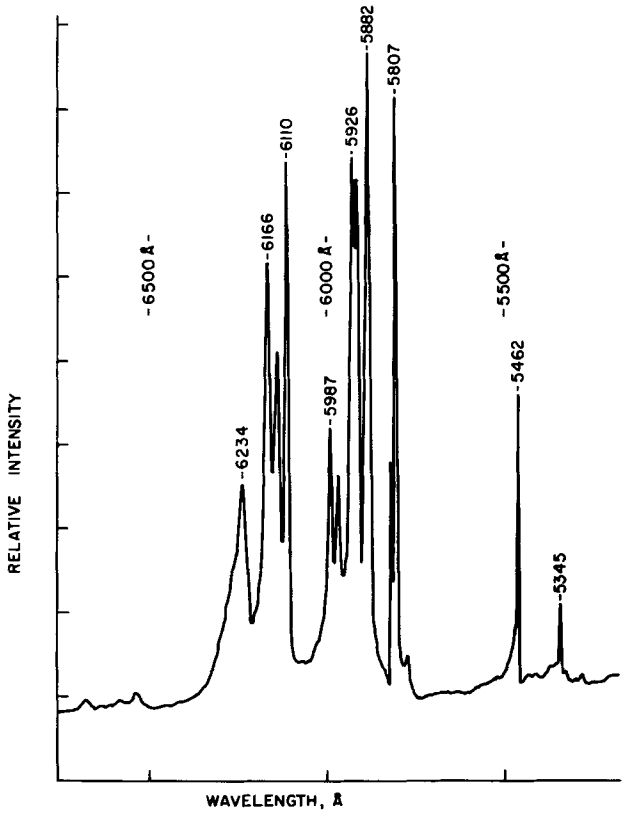

Fig. 6. Fluorescent emission spectrum of $SrEu_{0.20}Y_{1.80}O_4$ at 300°K.

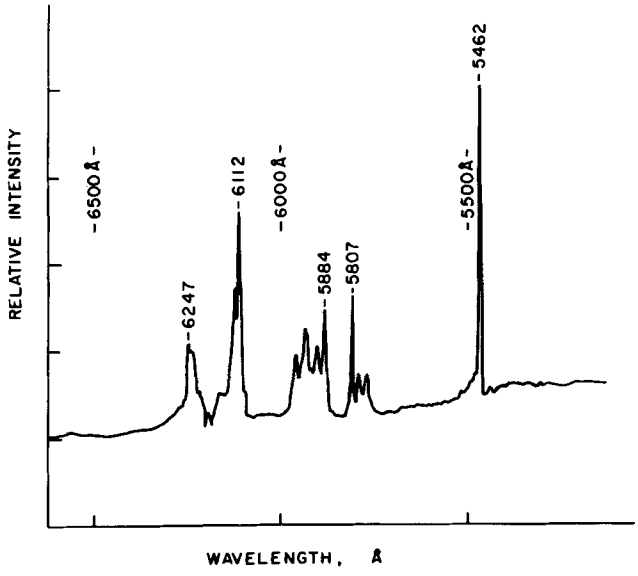

Fig. 7. Fluorescent emission spectrum of $BaEu_{0.14}Y_{1.86}O_4$ at 300°K.

transition can, for instance, exhibit a maximum of three components, all of which are clearly resolved in the spectrum of $Gd_{0.5}Eu_{0.5}NbO_4$ (10). For this case, the bulk of the emission also shifts from the $^5D_0 \rightarrow {}^7F_2$ transition to the $^5D_0 \rightarrow {}^7F_1$ transition in going to the more symmetrical $Ba_2La_{0.9}Eu_{0.1}NbO_6$. Similar observations have also been made for organic Eu compounds (11). Figure 7 shows the corresponding spectrum for $BaEu_{0.14}Y_{1.86}O_4$ where the same type of reversal can be seen. The over-all intensities were also much weaker than in the alkali-rare earth oxide hosts. For the purpose of a comparison we did determine the complete fluorescent emission characteristics as a function of the Eu concentration in both hosts. In $BaEu_xY_{2-x}O_4$, the optimum occurred at $x = 0.14$, and in $SrEu_xY_{2-x}O_4$, at $x = 0.20$. The observed intensities of emission at the optimum x were 78 for the Ba and 52 for the Sr compounds, compared with 570 for $LiEu_{0.06}Y_{0.94}O_2$.

In summary, we can state that the Li and Na rare earth oxides of Y_2O_3 and Gd_2O_3 make interesting and efficient hosts for Eu^{+3}, but the location of the emission prevents them from being useful as good red phosphors. The alkaline earth compounds SrY_2O_4 and BaY_2O_4 showed completely different fluorescent emission characteristics and were furthermore substantially less efficient as hosts for Eu^{+3}.

Manuscript received June 3, 1966; revised manuscript received Oct. 24, 1966.

Any discussion of this paper will appear in a Discussion Section to be published in the December 1967 JOURNAL.

REFERENCES

1. G. Urbain, *Am. Chem. Phys.*, **18**, 293 (1909).
2. H. Samelson and A. Lempicki, *Applied Phys. Letters*, 5, 173 (1964).
3. N. C. Chang, *J. Appl. Phys.*, **34**, 3500 (1963).
4. L. H. Brixner and P. A. Flournoy, *This Journal*, **112**, 303 (1965).
5. L. G. van Uitert, R. R. Soden, and R. C. Linares, *J. Chem. Phys.*, **36**, 1793 (1962).
6. A. K. Levine and F. C. Palilla, *Appl. Phys. Letters*, 5, 108 (1964).
7. H. Schwarz, *Z. Naturforsch.*, **19B**, 955 (1964).
8. K. S. Vorres, Rare Earth Conferences II, 147 (1964).
9. L. H. Brixner, *This Journal*, **111**, 690 (1964).
10. L. H. Brixner, International Conference on Luminescence, Budapest (1966), Preprints, Section D-9, p. 3.
11. N. J. Rose and E. Abramson, *J. Chem. Phys.*, **42**, 1849 (1965).

Resistivity Inhomogeneities in Silicon Crystals

R. G. Mazur

Research Laboratories, Westinghouse Electric Corporation, Pittsburgh, Pennsylvania

ABSTRACT

The extent of small-scale radial resistivity inhomogeneity in several n-type silicon crystals has been quantitatively determined with high spatial resolution by the spreading resistance resistivity measurement technique. Typical results for Czochralski, float-zone refined, crucible-less, web-grown and vapor-deposited epitaxial silicon are given, showing that appreciable nonuniformity in local resistivity exists in many crystals. The usefulness of the spreading resistance technique in rapid evaluation of the degree of resistivity inhomogeneity of individual silicon samples is illustrated.

In the last few years a number of publications have dealt with a variety of microdefects and inhomogeneities in silicon single crystals. This work has recently been reviewed by John, Faust, and Stickler (1). The various crystallographic defects have been extensively studied with high spatial resolution by several techniques. Optical and infrared microscopy, scanning electron microscopy, and x-ray diffraction microscopy have given a linear spatial resolution on the order of 10^{-4} cm, while transmission electron microscopy has utilized a much higher spatial resolution capability of about 10^{-7} cm.

Resistivity or impurity concentration inhomogeneities have also been observed qualitatively with 10^{-4} cm linear resolution using several preferential etching and plating techniques. However, quantitative measurements on electrically active inhomogeneities have been limited by the spatial resolution of the standard potential probe resistivity measurement techniques. While certain situations allow a high linear spatial resolution through a one-dimensional approach, *e.g.*, the study of diffusion profiles by incremental etch and four-point probe (2), the general case is strongly affected by the fact that resistivity is a volume property. Standard potential probe limitations are most obvious when minimum volumes sampled are compared with those of the "visual" techniques mentioned above. Light microscopy, scanning electron microscopy, and x-ray diffraction microscopy all provide a volume resolution of ca. 10^{-12} cm^3 and transmission electron microscopy utilizes a volume resolution of 10^{-18} cm^3 or better. In contrast, the incremental anodic oxidation, etch and four-point probe technique involves a minimum volume of about 5×10^{-8} cm^3. The one- or two-point potential probe technique requiring a bar-sample of at least $5.0 \times 10^{-2} \times 10^{-2}$ cm^2 cross-sectional area gives an average resistivity over a volume of 5×10^{-7} cm^3, if the probes are moved in 1×10^{-3} cm increments along the length of the bar. There is obviously a difference of several orders of magnitude in the spatial resolution of resistivity fluctuations by the standard methods as opposed to the essentially visual techniques. Recent developments in the spreading resistance resistivity measurement technique (3) have enabled us to begin a study of fine-scale resistivity fluctuations in silicon with a sampling volume of 10^{-10} cm^3 or less. This paper provides preliminary data on fine-scale resistivity inhomogeneities observed in typical Czochralski, float-zone refined, crucible-less, web-grown and vapor-deposited epitaxial silicon, showing that significant variations do exist in many crystals. The data also suggest a tentative procedure for assessing the microscale quality of silicon by the spreading resistance technique.

The data reported are not considered extensive enough for a judgment of the relative worth of material produced by the various growth processes as the total number of samples examined to date is small and the degree of correlation between raw material fine-scale resistivity homogeneity and final device performance is not accurately established.

Experimental

All of the material examined to date has been n-type silicon. The samples used were not especially selected in any way so that, aside from their limited number, they represent a good cross section of single crystal silicon commonly available. Sample resistivities ranged from a few tenths of an ohm-centimeter to several hundred ohm-centimeters. This initial study has been limited to radial resistivity variation as much as it is possible to do so on the scale involved.

Spreading resistance resistivity measurements can be made by measuring the resistance between a pair of probe-contacts (obviating the need for any other contacts to the sample) or with a single spreading resistance probe and some form of relatively large-area contact to the sample for current return. This latter mode provides maximum spatial resolution, and all data reported here were obtained with a single probe. The base contact used was ultrasonically soldered tin-indium (50:50). Base contact resistance was separately checked for each sample to insure that it was negligibly small compared to the spreading resistance on that sample.

Each sample was polished with 0.3μ alumina in a water slurry on a rough glass plate to produce the surface finish for which the calibration curve relating spreading resistance and sample resistivity had been previously established. Certain samples were also checked after several minutes etching in CP4A.[1]

After preparation each sample was probed radially at intervals of 0.1 mm over a span of 5.0 mm located approximately midway between the center and edge of the crystal. A second set of measurements was then made, covering a 0.5 mm interval midway in the first 5 mm span in steps of 0.01 mm. The raw values of measured spreading resistance were then computer processed to

(*i*) convert the local spreading resistance values to local resistivities (ρ_i), using a predetermined calibration curve;

(*ii*) calculate the average resistivity of each set of measurements ($\bar{\rho}_i$);

(*iii*) calculate the standard deviation ($s = \sqrt{\Sigma^n_{i=1}(\bar{\rho}_i - \rho_i)^2/n-1}$) of the n individual values of resistivity ρ_i about the average $\bar{\rho}_i$;

(*iv*) tabulate the individual deviations of the ρ_i from $\bar{\rho}_i$;

(*v*) reject any raw data which led to a deviation ($\bar{\rho}_i - \rho_i$) greater than 4s;

(*vi*) if such rejection of "spurious" data was necessary, the amended data was reprocessed through steps (*i*) to (*iv*);

[1] 120 cc 40% HF, 120 cc acetic acid, 200 cc HNO_3.

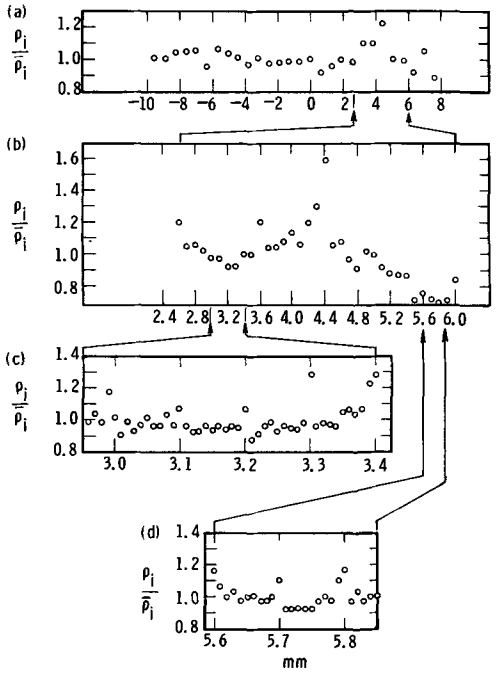

Fig. 1. Typical radial resistivity inhomogeneity in float-zone silicon, plotted as $\rho_i/\bar{\rho}_i$ vs. relative radial position, where $\bar{\rho}_i$ is in each case the local average resistivity. (a) Standard potential probe profile; (b), (c), (d), spreading resistance probe profiles; (b) 0.1 mm scale; (c) and (d) 0.01 mm scale.

(*vii*) calculate values of the ratio of local resistivity, ρ_i, to the average resistivity, $\bar{\rho}_i$, for each point probed (in order to allow direct comparison of resistivity fluctuations in samples of varying nominal resistivity); (*viii*) plot these values of ρ_i/ρ_i *vs.* the radial position (*ix*) calculate $s/\bar{\rho}_i$ for each sample, in an attempt to characterize the various materials checked by a single quantitative parameter as well as by the pictorial results produced by the digital plotter.

Results and Discussion

Figure 1 is an illustration of some results obtained with the procedure described above. The sample is a rather typical float-zone crystal of 1 ohm-cm average resistivity. Figure 1a is a radial resistivity profile obtained by a standard one-point traveling potential probe technique covering a span of 18 mm more or less centered on the crystal. The potential probe was moved in 0.5 mm increments. The average resistivity of these 0.5 mm sections is seen to vary from about 0.9 to 1.2 times the over-all average resistivity of the crystal. Figure 1b gives a spreading resistance-derived resistivity profile on the same sample as in Fig. 1a. The arrows indicate the section of the 1a sample examined. The spreading resistance probe measurement was made at intervals of 0.1 mm. The resulting values of $\rho_i/\bar{\rho}_i$ show that the resistivity fluctuations in this material are more extreme than was indicated by the standard traveling probe potential profile, with local resistivities ranging from 0.7 to > 1.3 times the average resistivity of the material probed in Fig. 1b. Figure 1c and 1d are plots of $\rho_i/\bar{\rho}_i$ of two separate sections of the material covered in Fig. 1b, now at intervals of 0.01 mm.

Figure 2a is a plot of $\rho_i/\bar{\rho}_i$ for a 10 ohm-cm Czochralski crystal, probed at 0.1 mm intervals over a span of 5 mm. It can be seen that the local resistivity varies from about 0.85 to about 1.15 times the average resistivity of this 5 mm section of the crystal. For the data in Fig. 2a, $s/\bar{\rho}_i = 0.067$. Thus, local resistivities 6.7% greater or less than the average resistivity in this 5 mm section of silicon have a probability of occurrence of 0.32; with 1% of the volumes sampled then having a probable resistivity 2.5 ($s/\bar{\rho}_i$) or about

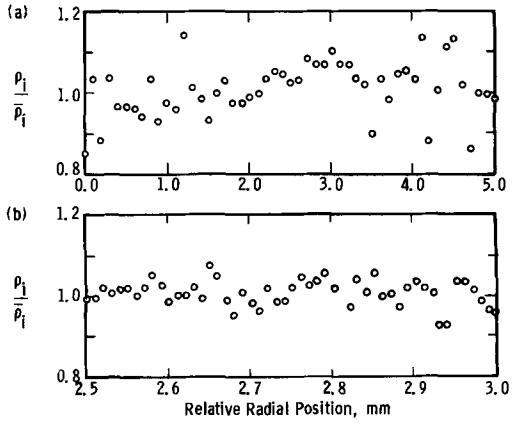

Fig. 2. $\rho_i/\bar{\rho}_i$ vs. relative radial position in a 10 ohm-cm Czochralski crystal. (a) 0.1 mm scale, $s/\bar{\rho}_i = 0.067$; (b) 0.01 mm scale, $s/\bar{\rho}_i = 0.031$.

17% greater or less than the sample's average resistivity.

Figure 2b gives the values of $\rho_i/\bar{\rho}_i$ measured in the central region of the 2a sample with a 0.01 mm spacing. The local resistivity variation on this finer scale is seen to be less than that observed on the 0.1 mm scale. The lesser range of local resistivity values on the 0.01 mm scale is reflected in a smaller value of fractional standard deviation of 0.031 for the data in Fig. 2b.

Another Czochralski crystal, a 14 ohm-cm (average resistivity) sample, clearly illustrates in Fig. 3 several features of this type of measurement. While the fine-scale data of Fig. 3b, as well as the point-to-point variation of $\rho_i/\bar{\rho}_i$ in Fig. 3a, show the material to be relatively uniform on the fine-scale, a long-period and very large variation in resistivity is apparent from the data of Fig. 3a, which shows a variation of almost a factor of two in resistivity over a 4 mm span of this crystal. This type of profile is also indicated nonpictorially by the relative values of fractional standard deviation, these being 0.024 for the 0.01 mm scale data of Fig. 3b and 0.185 for the 0.1 mm data in Fig. 3a, a ratio of $s/\bar{\rho}_i$ (0.1 mm) to $s/\bar{\rho}_i$ (0.01 mm) of about 8.

An interesting point illustrated by the sample depicted in Fig. 3 is that, while the fractional standard deviation obviously fails to characterize accurately the material in detail completely, it fails safe; that is,

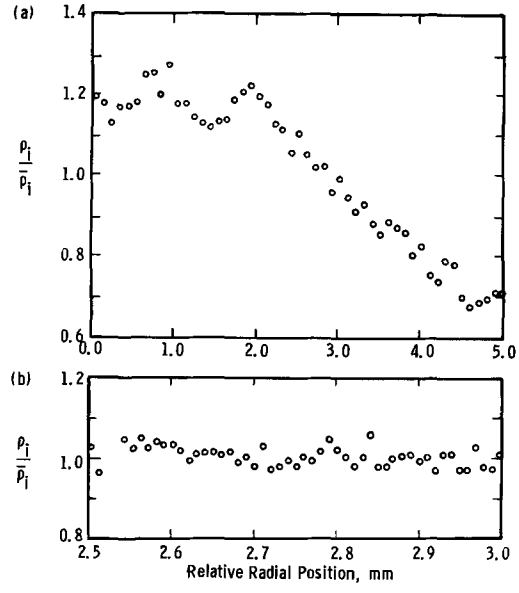

Fig. 3. $\rho_i/\bar{\rho}_i$ vs. relative radial position in a 14 ohm-cm Czochralski crystal with a long-term resistivity gradient. (a) 0.1 mm scale, $s/\bar{\rho}_i = 0.185$; (b) 0.01 mm scale, $s/\bar{\rho}_i = 0.024$.

the material is clearly indicated to be defective or questionable in some way by a high value of $s/\bar{\rho}_i$ on any scale.

Figure 4 is a plot of fine-scale (0.01 mm probe intervals) made on a sample of 175 ohm-cm Czochralski crystal before and after etching the sample for several minutes in CP4A. The purpose of this experiment was to determine how much of the fine-scale, point-to-point spreading resistance variation was due to inherent fluctuations in resistivity in the material and how much was the result of scratches or other polishing artifacts on the alumina-polished surface. Figure 4a (the polished surface) apparently has the same scatter as that of the etched sample (Fig. 4b). The quantitative measure of homogeneity, the fractional standard deviation, bears out the qualitative picture: values of $s/\bar{\rho}_i$ of 0.038 (for the polished surface) and 0.032 (for the etched surface) are not significantly different. Thus, the observed fine-scale fluctuations in resistivity are not due to the surface finish.

Figure 5 shows some results obtained on a 0.7 ohm-cm float-zone crystal. Figure 5a is the 0.1 mm scale

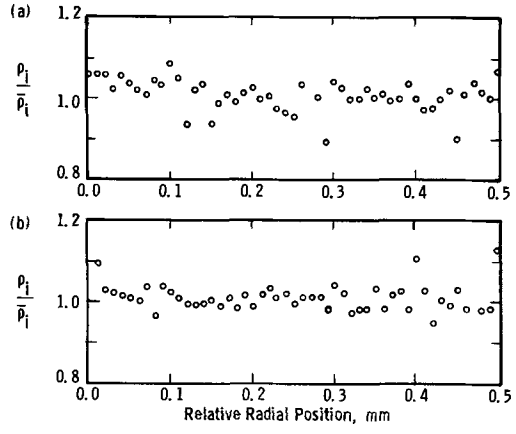

Fig. 4. $\rho_i/\bar{\rho}_i$ vs. relative radial position in a 175 ohm-cm Czochralski crystal as a function of surface finish. (a) alumina-polished surface, 0.01 mm scale, $s/\bar{\rho}_i = 0.038$; (b) chemically polished surface, 0.01 mm scale, $s/\bar{\rho}_i = 0.032$.

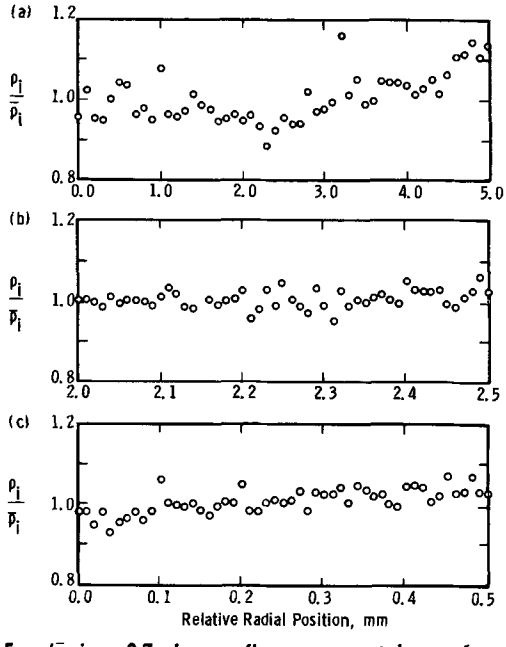

Fig. 5. $\rho_i/\bar{\rho}_i$ in a 0.7 ohm-cm float-zone crystal as a function of relative radial position and surface finish. (a) 0.1 mm scale, alumina-polished surface, $s/\bar{\rho}_i = 0.060$; (b) 0.01 mm scale, alumina-polished surface, $s/\bar{\rho}_i = 0.022$; (c) 0.01 mm scale, chemically polished surface, $s/\bar{\rho}_i = 0.029$.

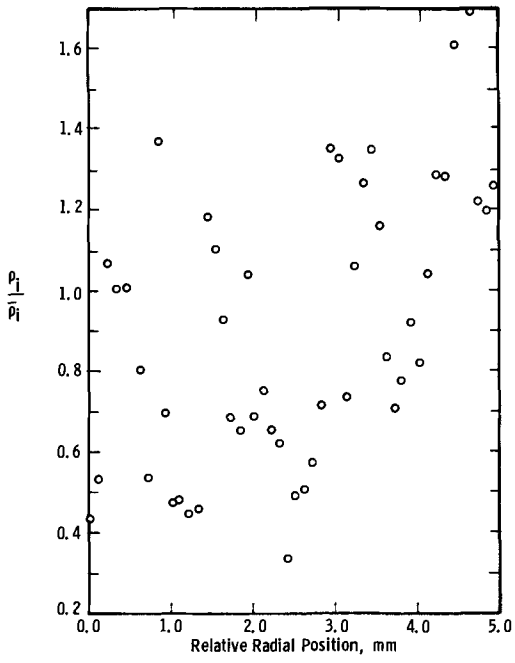

Fig. 6. $\rho_i/\bar{\rho}_i$ vs. relative radial position in a 250 ohm-cm float-zone crystal, 0.1 mm scale, $s/\bar{\rho}_i = 0.37$.

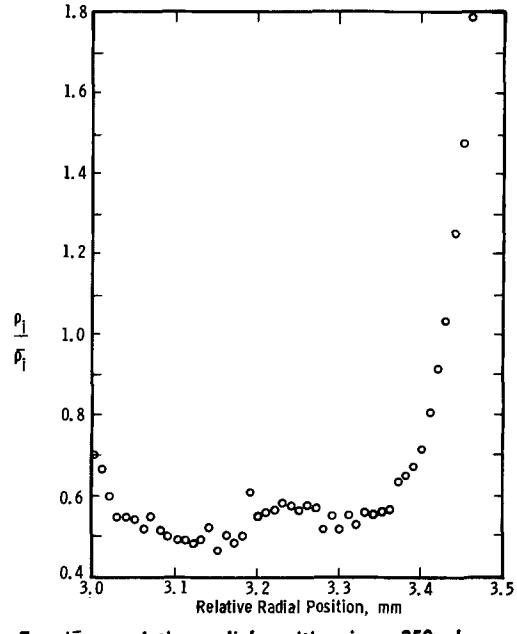

Fig. 7. $\rho_i/\bar{\rho}_i$ vs. relative radial position in a 250 ohm-cm float-zone crystal, 0.01 mm scale, $s/\bar{\rho}_i = 0.42$.

data, with $s/\bar{\rho}_i = 0.06$; Fig. 5b gives the 0.01 mm scale data on the center section of the polished sample shown in Fig. 5a, with $s/\bar{\rho}_i = 0.022$; Fig. 5c shows 0.01 mm scale data on a sample of this same material etched for several minutes in CP4A. The value of $s/\bar{\rho}_i = 0.029$ for the etched sample of Fig. 5b again demonstrates that the variations in resistivity observed in this work are real and do not reflect a variable surface finish.

Figure 6 illustrates an extreme situation. This is a 250 ohm-cm float-zone crystal which has a 0.1 mm scale fractional standard deviation of 0.37; with a corresponding range of local resistivities varying by a factor of about 6. Figure 7 shows a small section of this material on the 0.01 mm scale. While the resistivity fluctuation over distances of a few tenths of a millimeter is quite small, the beginning of a high ρ region at the end of the section shown leads to an over-all value of $s/\bar{\rho}_i = 0.42$. As before, it is apparent

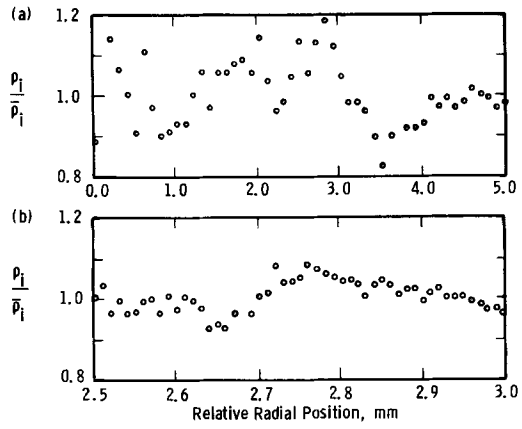

Fig. 8. $\rho_i/\bar{\rho}_i$ vs. relative radial position in a 44 ohm-cm crucible-less pulled silicon crystal. (a) 0.1 mm scale, $s/\bar{\rho}_i = 0.079$; (b) 0.01 mm scale, $s/\bar{\rho}_i = 0.037$.

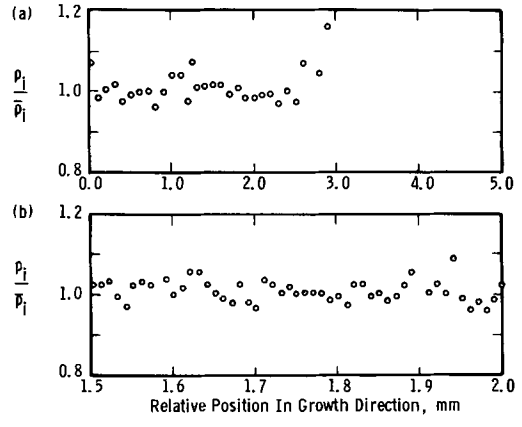

Fig. 9. $\rho_i/\bar{\rho}_i$ vs. relative position in growth direction in a 0.31 ohm-cm silicon web: (a) 0.1 mm scale, $s/\bar{\rho}_i = 0.039$; (b) 0.01 mm scale, $s/\bar{\rho}_i = 0.027$.

that the value of the fractional standard deviation of ρ_i is a "fail-safe" parameter in evaluating crystal quality in that it is necessary for the material to be uniform on both the macroscopic and microscopic scale to satisfy the condition $s/\bar{\rho}_i << 1$.

Figure 8 shows a sample of crucible-less silicon with a resistivity of 44 ohm-cm. Here the fractional standard deviation of the 0.1 mm scale data is 0.079. The fractional standard deviation of the 0.01 mm scale data (Fig. 8b) is 0.037. From this and other specimens, it is apparent that the crucible-less silicon, in this respect, as in many others, is often midway between the float-zone and Czochralski crystals.

Figure 9 shows a web sample with a resistivity of 0.31 ohm-cm. Figure 9a shows a 3 mm section of the material probed at 0.1 mm intervals, with a fractional standard deviation in the resistivity values of 0.039. Figure 9b shows the fine-scale data taken at 0.01 mm intervals with a fractional standard deviation of 0.027. These data indicate that this web material is at least

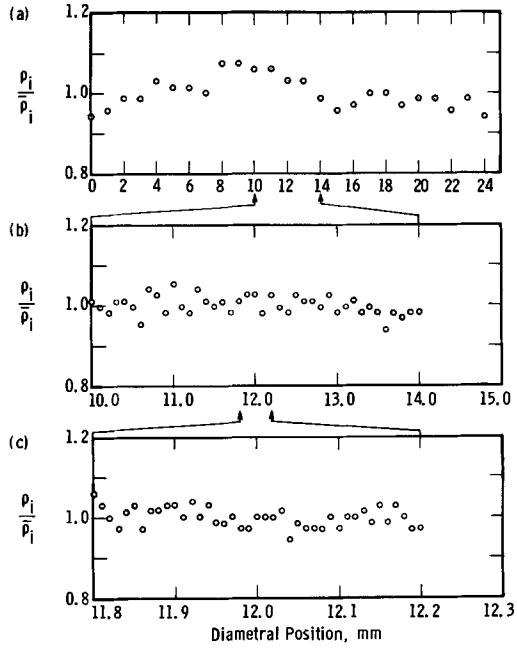

Fig. 10. $\rho_i/\bar{\rho}_i$ vs. diametral position coordinate in a 28 ohm-cm vapor-deposited epitaxial crystal: (a) 1.0 mm scale, $s/\bar{\rho}_i = 0.039$; (b) 0.1 mm scale, $s/\bar{\rho}_i = 0.023$; (c) 0.01 mm scale, $s/\bar{\rho}_i = 0.025$.

as uniform as the float-zone material on the coarse scale and is as uniform or more uniform than either float-zone or Czochralski material on the fine-scale. Note also the near unity value of the ratio $s/\bar{\rho}_i$ (coarse) to $s/\bar{\rho}_i$ (fine-scale).

Figure 10 shows a sample of 28 ohm-cm, n-type epitaxial silicon produced in our laboratories. It may be seen that the epitaxial sample, at least produced under the conditions used here, is very uniform in resistivity, both across the whole of the diameter of a 25 mm slice, and on the fine-scale as well, with the total scatter of all of the resistivity values lying in the range of plus or minus 7%.

Where a comparison may be made, these results agree with those of Benson (4) relating to radial resistivity variations in Czochralski crystals. They also provide experimental support for a model involving convection currents in the liquid as the primary cause of resistivity inhomogeneities in melt-grown silicon (5). If this model is indeed an accurate one, the greater resistivity homogeneity of silicon web and epitaxial silicon may be then understood as the result of the rapid growth rate of web from its supercooled melt and, in the case of the vapor-grown epitaxial material, as due to the complete absence of a liquid phase.

Summary and Conclusions

The quantitative results of these measurements are summarized in Table I. Note especially the values given for the ratio s (0.1 mm scale) to s(0.01 mm scale). The tabulated data suggest that two parameters

Table I. Quantitative results of measurements

Growth process	Over-all average resistivity, $\bar{\rho}$ (ohm-cm)	s/ρ_i, 0.1 mm scale	s/ρ_i, 0.01 mm scale	Surface finish	s, 0.1 mm scale / s, 0.01 mm scale
Czochralski	10	0.067	0.031	Alumina polish	2.2
Czochralski	14	0.185	0.024	Alumina polish	7.7
Czochralski	175		0.038	Alumina polish	—
Czochralski	175		0.032	Chemical polish	—
Float-zone	0.7		0.029	Chemical polish	—
Float-zone	0.7	0.060	0.022	Alumina polish	2.7
Float-zone	250	0.37	0.42	Alumina polish	0.88
Crucible-less	44	0.079	0.037	Alumina polish	2.1
Web	0.31	0.039	0.027	Alumina polish	1.4
Vapor-deposited	28	0.023	0.025	Alumina polish	0.92

may be conveniently used to establish crystal quality insofar as resistivity inhomogeneity is concerned. These are the fine-scale (0.01 mm scale) fractional standard deviation of resistivity and the ratio of the coarse-scale value of fractional standard deviation to the fine-scale value. With these parameters determined in accordance with the procedures used in this work, a low value of $s/\bar{\rho}_i$ (0.01 mm scale) and a near-unity value of the ratio of $s/\bar{\rho}_i$ (0.1 mm) to $s/\bar{\rho}_i$ (0.01 mm) indicates uniform resistivity silicon. It is essential to note that both criteria must be met to rate material as truly homogeneous.

In conclusion, while this work cannot support a final judgment of the relative worth of material produced by the various growth processes, it does show that significant variations in local resistivity do exist in at least some silicon samples and that the spreading resistance technique may be used to advantage in investigating the problem of resistivity inhomogeneity in silicon. Further work must be done, especially in comparing device yields to crystal "quality" as defined above, to determine the real importance of these measurements.

Manuscript received Aug. 18, 1966; revised manuscript received Oct. 24, 1966. This paper was presented at the Cleveland Meeting, May 1-6, 1966.

Any discussion of this paper will appear in a Discussion Section to be published in the December 1967 JOURNAL.

REFERENCES

1. H. F. John, J. W. Faust, Jr., and R. Stickler, *IEEE Trans. Parts, Materials and Packaging*, September 1966.
2. E. Tannenbaum, *Solid-State Electron*, **2**, 123 (1961).
3. R. G. Mazur and D. H. Dickey, *This Journal*, **113**, 255 (1966).
4. K. E. Benson, *Electrochem. Tech.*, **3**, 332 (1965).
5. A. Mueller and M. Wilhelm, *Z. Naturforschung*, **19a**, 254-263 (1964).

The Solidification of Bi_2Te_3 and Its Solid Solutions with Bi_2Se_3 and Sb_2Te_3 under the Influence of Ultrasonic Agitation

H. E. Bates and Martin Weinstein

Tyco Laboratories, Inc., Waltham, Massachusetts

ABSTRACT

The effect of ultrasonic agitation during solidification was studied for three systems: Bi_2Te_3, 0.8 Bi_2Te_3-0.2 Bi_2Se_3, and 0.25 Bi_2Te_3-0.75 Sb_2Te_3. Reduction in grain size was most pronounced in 0.8 Bi_2Te_3-0.2 Bi_2Se_3; the other compositions showed relatively little refinement. A definite tendency for alignment of acicular grains with low intensities of ultrasonic irradiation was noted in all three systems. Compressive fracture stress was increased by agitation for all three systems with considerable anisotropy of strength, relative to the growth direction, occurring in agitated and unagitated material. Highest fracture strength was found in 0.8 Bi_2Te_3-0.2 Bi_2Se_3, 7000 *vs.* 5000 psi for unagitated material. Reduction in length was about equal at 3%. Seebeck coefficient and resistivity were measured as functions of temperature and found to exhibit a difference between agitated and unagitated material which correlated with the amount of grain refinement observed. This is a result of the crystallographic anisotropy of electrical properties in Bi_2Te_3 alloys, reflected by the degree of misorientation caused by ultrasonic agitation.

During the course of investigating the effects of ultrasonic energy on the solidification of thermoelectric materials (1, 2), experiments were carried out with Bi_2Te_3 and some of its technologically interesting alloys. It was of specific interest to observe the effect of ultrasonic agitation on the solidification behavior of these materials because of their highly anisotropic nature.

Other investigators (3-5) have observed coarsening of acicular crystallites in solidified eutectic structures with sonic and ultrasonic vibrations. These are the only instances of the effects of vibration on the solidification of crystals having strong acicular growth habits. In addition Bi_2Te_3 alloys are susceptible to segregation during freezing, requiring either elaborate zone-leveling techniques to produce homogeneous ingots or preparation of thermoelements by powder metallurgical techniques which introduce a number of difficulties with contamination (6) and sintering and grain size effects (7, 8). The results of our investigations with PbTe materials indicated the possibility of considerably enhancing the mechanical properties and improving the homogeneity of cast ingots of Bi_2Te_3 and related alloys.

Thus, the purpose of the present work was to explore the effect of ultrasonic agitation during solidification of a class of alloys exhibiting highly anisotropic growth and to observe the consequences of this method of preparation on the mechanical and electrical properties of these alloys.

Experimental

The experimental procedures and apparatus have been described in detail previously (1, 2). The assembly used to solidify the melts with ultrasonic agitation is shown in Fig. 1.

A charge of 50-75g was sealed under vacuum in the quartz tube. A resistance furnace was lowered over the tube and heated until the charge had melted, as indicated by a thermocouple attached at the base of the tube. After a short period at a temperature 30°-40° above the melting point, the piezoelectric transducer, epoxied to the base of the quartz pedestal, was energized. The furnace was then raised by a motorized hoist so that solidification proceeded upward from the bottom of the ingot at a rate defined by the rate of removal of the furnace. As the freezing interface moved upward, the input frequency to the piezoelectric crystal was varied slightly to maintain a resonant condition. The input power was also increased gradually to compensate for increasing attenuation of the ultrasonic energy in the solidified portion of the

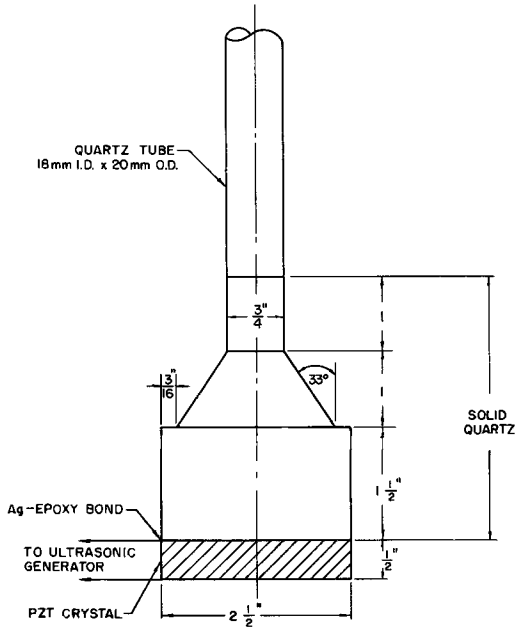

Fig. 1. Piezoelectric transducer, quartz concentrator, and crucible assembly.

melt. Energy intensities varied from 1-9 w/cm^2 at frequencies of approximately 21 and 33-35 kc. Solidification rates were varied from 6.3 x 10^{-3} to 14.1 x 10^{-3} mm/sec.

Results

The effect of ultrasonic agitation during solidification was to cause some reduction in grain size in all three materials. The most interesting result was the varying responses to agitation of three materials of identical structure. Bismuth telluride is rhombohedral with atoms arranged in a sequence Te-Bi-Te-Bi-Te . . . Te with adjacent Te atoms probably bonded only by van der Wall's forces (9). This structure accounts for the anisotropic transport processes and easy cleavage of Bi_2Te_3. Bismuth selenide and antimony telluride form complete isomorphous pseudobinary solid solutions with Bi_2Te_3.

Macrophotographs (Fig. 2) show the gross structure of two ingots of 0.8 Bi_2Te_3-0.2 Bi_2Se_3, the one on the left directionally solidified, the one on the right directionally solidified with 8 watts/cm^2 of ultrasonic agitation for approximately two-thirds of its length. Both were grown at the same rate of 1.1 iphr. The coarse acicular grain structure of the unagitated ingot is plainly visible, while in the lower half of the

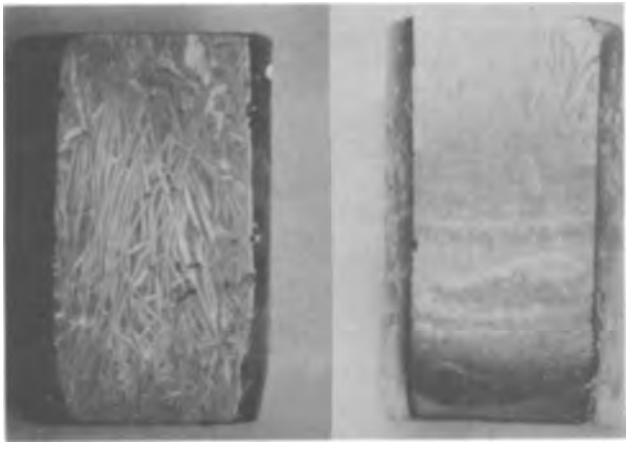

Fig. 2. Macrostructure of 0.8 Bi_2Te_3-0.2 Bi_2Se_3 ingots: (a) directionally solidified; (b) directionally solidified with ultrasonic agitation. Magnification 1½X.

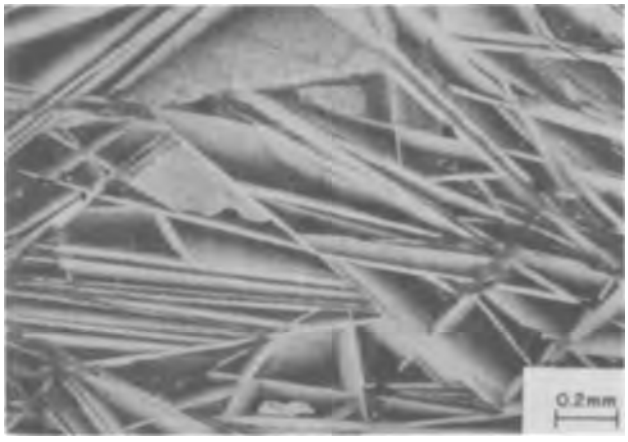

Fig. 3. Microstructure of directionally solidified 0.8 Bi_2Te_3-0.2 Bi_2Se_3. Magnification *ca.* 35X.

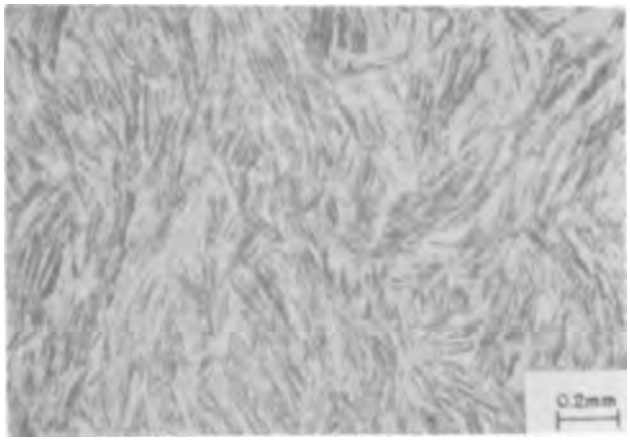

Fig. 4. Ultrasonically agitated 0.8 Bi_2Te_3-0.2 Bi_2Se_3. Magnification *ca.* 35X.

agitated ingot the grains cannot be resolved. The various bands in the agitated ingot are the result of changes in the frequency of the ultrasound to maintain resonance and of turning off the ultrasonic input for a short period at one point. The microstructures of these ingots are shown in Fig. 3 and 4. It is interesting to note here that the very finest grains found in the agitated material were still basically acicular. Figure 3 is not truly representative of the structure of the unagitated material since none of the very large grains are shown. The bismuth telluride-bismuth selenide showed the greatest reduction in grain size of all three systems. The average grain size (length) in the agitated material was approximately 30 times less than that of the unagitated, directionally solidified material.

The structure of the unagitated Bi_2Te_3 was virtually identical to that of the Bi_2Te_3-Bi_2Se_3 shown in Fig. 3. A transverse section at the bottom of an agitated ingot of Bi_2Te_3 is shown in Fig. 5. The ultrasonic energy intensity was approximately 6 w/cm^2 and growth rate 1.1 iphr. It is obvious that while the grains here are fairly long, they are considerably more "blocky" than those in the Bi_2Te_3-Bi_2Se_3. The top of an ingot similarly prepared is shown in Fig. 6; the grains are very needle-like here. The top ends of the ingots, which were 1.5 to 1.75 in. long, received substantially less agitation than the bottom portions because of increased attenuation in the solidified portion of the ingot. The intensity applied to the top section may have been about 1w/cm^2 or less. This is a clear example of the application of increasing ultrasonic energy tending to promote an increasingly equiaxed structure. Grain size reduction in the lower portions of agitated ingots was of the order of 10 or 12:1. An

Fig. 5. Microstructure of Bi_2Te_3 solidified with ultrasonic agitation; bottom section of ingot. Magnification *ca.* 35X.

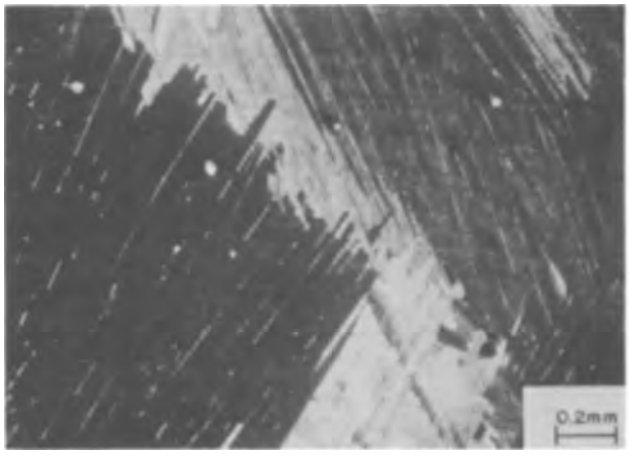

Fig. 6. Microstructure of top section of Bi_2Te_3 of Fig. 5, transverse section. Magnification *ca.* 35X.

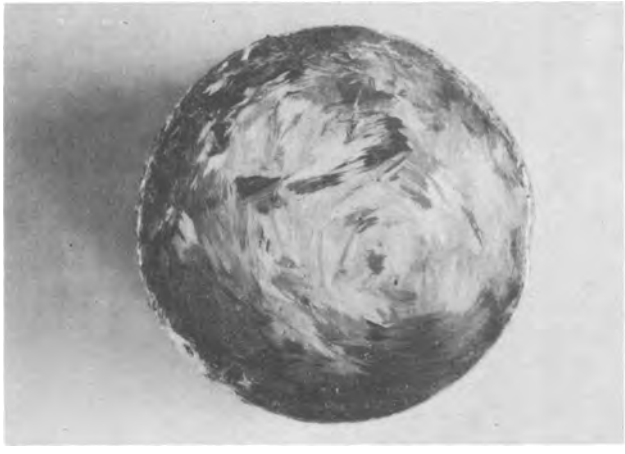

Fig. 7. Macrostructure of Bi_2Te_3 ingot showing crystallite alignment by low intensity vibrations in top section. Magnification 1½X.

interesting phenomenon was observed in the top sections of agitated ingots of all three materials. particularly bismuth telluride and bismuth-antimony telluride. An example from Bi_2Te_3 is shown in Fig. 7. The grains in this case tend to line up with their long axes roughly parallel to the circumference thus giving the somewhat spiral appearance to the gross structure. This was apparently the result of low intensity radial vibrations of the system. Such an effect of low intensity vibrations could be of benefit in producing an oriented structure in the materials so as to take advantage of the anisotropic thermoelectric properties.

Bismuth-antimony telluride, when solidified quickly, grows in acicular grains which are severely segregated

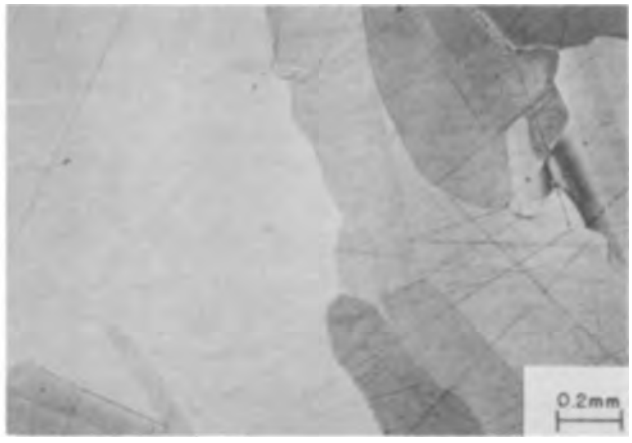

Fig. 8. Microstructure of directionally solidified 0.25 Bi_2Te_3-0.75 Sb_2Te_3. Magnification *ca.* 35X.

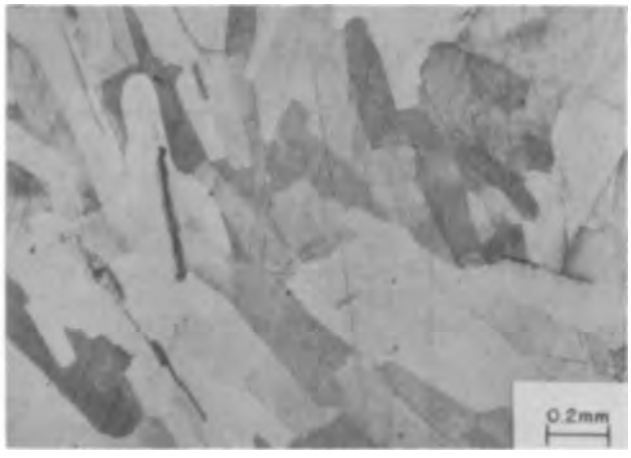

Fig. 9. Ultrasonically agitated 0.25 Bi_2Te_3-0.75 Sb_2Te_3. Magnification 35X.

on a microscale. We found this in water-quenched material and to some extent in ingots grown at more than two inches/hr. Solidification at 0.9 iphr produced the microstructure of Fig. 8. This unagitated ingot exhibited a wide range of grain sizes, the majority tending to a length/diameter (l/d) ratio of about three. Significant grain refinement was difficult to achieve in this system. Figure 9 shows the microstructure of the agitated material. (Ultrasonic energy intensity was 8-9 w/cm^2.) The grains retain approximately the same l/d ratio, while a reduction in average size of about 6-8:1 has occurred. A tendency to greater ratios of length to width in the grains of the top section was found in both agitated and unagitated ingots. The grains of the agitated ingots showed an alignment with the side of the crucible similar to that in Bi_2Te_3.

Compressive strength.—The compressive fracture strengths were measured on samples cut parallel and perpendicular to the growth direction of the ingots as shown in Table I. Samples were mainly in the shape of rectangular blocks about 0.25 in. on a side by 0.4-0.5 in. long. A Hounsfield Type W Tensometer was used for the tests. The agitated material showed

Table I. Compressive fracture strength parallel to growth direction

Material	Compressive fracture strength, psi	Total strain at fracture, in/in
Bi_2Te_3 (agitated)	3,500	0.03
Bi_2Te_3 (unagitated)	2,500	0.02
0.8 Bi_2Te-0.2 Bi_2Se_3 (agitated)	7,000	0.030
0.8 Bi_2Te_3-0.2 Bi_2Se_3 (unagitated)	5,000	0.026
0.25 Bi_2Te_3-0.75 Sb_2Te_3 (agitated)	6,500	0.016
0.25 Bi_2Te_3-0.75 Sb_2Te_3 (unagitated)	2,300	0.08

a definite increase in strength over the unagitated for all three materials.

Considerable anisotropy of strength was found in all the materials. Fracture strength perpendicular to the growth direction was 50-60% of that parallel to the growth direction in unagitated samples. In the agitated samples strength perpendicular to the growth direction was 70-80% of that parallel. Grains grow in these materials as a rule with their cleavage planes parallel to the heat flow. In the unagitated, directionally solidified ingots the grains were generally aligned with the growth direction. Thus, compression parallel to the growth direction was also parallel to the cleavage plane.

Compression perpendicular to the growth direction is averaged over all angular orientations of the cleavage plane with respect to the compression direction. Thus in compressing perpendicular to the growth direction some favorably oriented grains reach the critical shear stress for slip or cleavage in the basal plane at a fairly low over-all stress level. In compressing parallel to the growth direction, where the cleavage planes are essentially all parallel to the stress axis, the over-all stress level must approach the critical shear stress for slip and/or cleavage. The samples of agitated material, however, with decreased orientation of the grains with the growth direction, exhibit strengths more nearly equal in the two directions. That the agitated materials showed generally higher strengths may be attributed to their finer grain sizes. A fine grain size increases the strength by limiting the propagation of slip or cleavage in any given grain through the interference of the more numerous grain boundaries.

Electrical properties.—Measurements of the Seebeck coefficient and resistivity as functions of temperature were made parallel to the growth direction on all ingots. The results of these measurements are shown as α^2/ρ (volt^2/°C — ohm cm) in Fig. 10-12 for 0.8 Bi_2Te_3 — 0.2 Bi_2Se_3 + 0.04% CuBr (n-type), Bi_2Te_3 + 0.04% Pb (p-type), and 0.25 Bi_2Te_3 — 0.75 Sb_2Te_3 + 0.05% Pb + 0.03% Cd (p-type). The values shown are in generally good agreement with those reported by most other authors for these materials.

The curves reflect the effect of the ultrasonic agitation in disturbing the orientation of the grains with the growth direction. With the cleavage planes generally oriented in the growth direction, the unagitated materials exhibit higher electrical efficiency factors. Madigan (10) predicted a reduction of 28% in the figure of merit of randomly oriented polycrystalline rods of Bi_2Te_3 *vs.* oriented single crystals, while Piwkowski (8) finds differences of 25-60% in

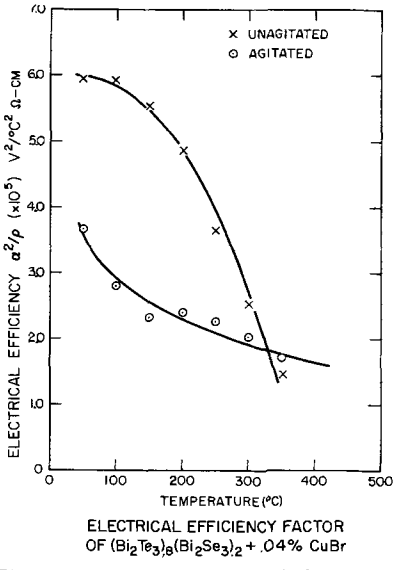

Fig. 10. Electrical efficiency factor of 0.8 Bi_2Te_3-0.2 Bi_2Se_3 measured parallel to growth direction.

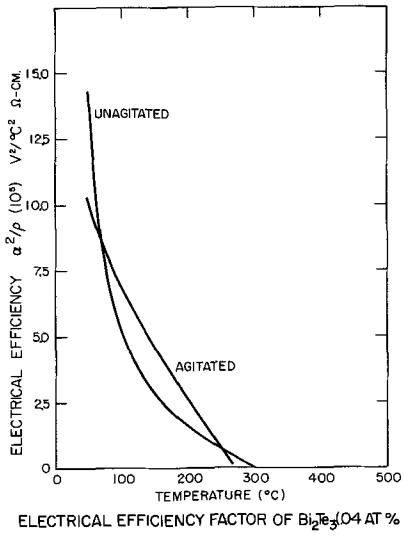

Fig. 11. Electrical efficiency factor of Bi_2Te_3 (0.04 a/o Pb) measured parallel to growth direction.

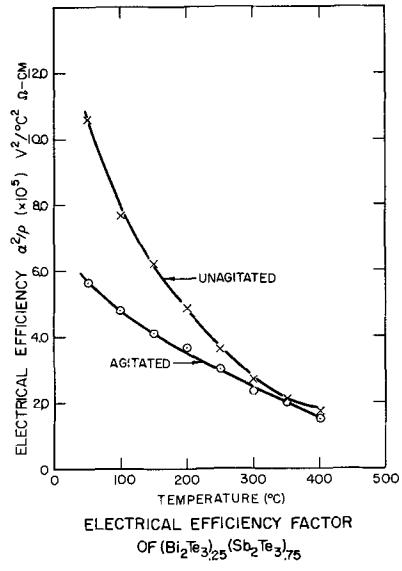

Fig. 12. Electrical efficiency factor of 0.25 Bi_2Te_3-0.75 Sb_2Te_3 measured parallel to growth direction.

the figure of merit of single crystal compared with pressed and sintered Bi_2Te_3.

The sharper decrease of α^2/ρ with increasing temperature for the unagitated Bi_2Te_3 — Bi_2Se_3 and Bi_2Te_3 —Sb_2Te_3 can be attributed to somewhat poorer chemical homogeneity than the agitated material. This is ultimately reflected in a less regular behavior than that exhibited by the agitated material.

Conclusions

1. Significant grain refinement was obtained in the Bi_2Te_3 — Bi_2Se_3 system by ultrasonic agitation of the melt during solidification. Little refinement was observed in the Bi_2Te_3 and Bi_2Te_3 — Sb_2Te_3 systems.
2. A tendency for alignment of acicular grains parallel to the crucible wall was noted at low ultrasonic intensities.
3. The Seebeck coefficient and resistivity as a function of temperature exhibit a difference between agitated and unagitated material which correlates with the amount of grain refinement. This is a result of the crystallographic anisotropy of electrical properties in Bi_2Te_3 alloys, reflected by the degree of misorientation caused by ultrasonic agitation.

Acknowledgments

The authors wish to thank Mr. E. J. Sherwin for his expert experimental aid. This work was performed

under Contract NObs-86015 for the Bureau of Ships, Department of the Navy.

Manuscript received Aug. 18, 1966. This paper was presented at the Cleveland Meeting, May 1-6, 1966.

Any discussion of this paper will appear in a Discussion Section to be published in the December 1967 JOURNAL.

REFERENCES

1. M. Weinstein, *Trans. AIME*, **230**, 321 (1964).
2. H. E. Bates and M. Weinstein, *This Journal*, **112**, 693 (1965).
3. M. J. Berger and W. Rostoker, *Foundry*, **81** [7], 100 (1953).
4. R. S. Richards and W. Rostoker, *Trans. ASM*, **48**, 884 (1956).
5. R. G. Garlick and J. F. Wallace, *Trans. AFS*, **67**, 366 (1959).
6. R. A. Horne, "Direct Conversion of Heat to Electricity," J. Kaye and J. Walsh, Editors, John Wiley & Sons, Inc., New York (1960).
7. C. Kolm and J. J. Giacalone, "Properties of Elemental and Compound Semiconductors," H. C. Gatos, Editor, Interscience Publishers, New York (1960).
8. T. R. Piwkowski, *Adv. Energy Conv.*, **4**, 247 (1964).
9. M. H. LaChance and E. E. Gardner, *ibid.*, **1**, 133 (1961).
10. J. R. Madigan, *J. Appl. Phys.*, **33**, 3564 (1962).

Nucleation and Growth of Crystals in Gels

J. Dennis and H. K. Henisch

Materials Research Laboratory, The Pennsylvania State University, University Park, Pennsylvania

ABSTRACT

Because the crystals in any one-growth system grow competitively, nucleation control is one of the keys to the practical exploitation of the gel-growth technique. The paper discusses some of the principal factors on which nucleation in gels depends and shows how nucleation can be controlled by programming of the reagent concentrations, by trace impurities, and by varying the gel structure. Multiple reseeding procedures are described which permit the growth of larger crystals than can be obtained with single growth stages.

Studies of nucleation have in the past been hampered by the lack of sufficiently simple systems on which meaningful experiments could be performed and by the general difficulty of controlling the processes involved. For such studies, the gel method (1, 2) offers new opportunities. The crystals grow within the gel, in the same localities in which they nucleate and in chemical environments which can be locally analyzed. Once nucleation has taken place, the growth has been shown to be diffusion controlled (2). This paper describes the results of nucleation experiments and shows how they can be at least qualitatively understood in terms of critical radius theory. It also provides an explanation for the photonucleation phenomena previously reported (1) and describes procedures which promote orderly growth through nucleation control.

The growth procedures are simple, even though the associated chemical and diffusion processes are not. Gels of 1.06 g/cm^3 density are made from solutions of sodium metasilicate, in the presence of varying acid concentrations. The acid in question may be one of the reagents participating in the formation of the crystal material. The other reagent is placed as a solution on top of the gel and allowed to diffuse. Alternatively, a nonacid reagent may be added to the sodium silicate solution before gelling, in addition to an acid which then serves only to adjust the pH. There are various possibilities, as the following examples will make clear:

(*a*) Growth of calcium tartrate crystals:
Present in the gel: tartaric acid, (initially pH 2.7), Diffusing into the gel: calcium chloride (initially 1*N*).

(*b*) Growth of lead iodide crystals, PbI_2:
Present in the gel: lead acetate and acetic acid, (initially pH 4.0), Diffusing into the gel: potassium iodide (initially 0.1*N*, increasing to 0.5*N*).

(c) Growth (3) of lead hydroxy iodide crystals, PbI(OH):
Present in the gel: acetic acid and potassium iodide (initially pH 8.5), Diffusing into the gel: lead acetate (initially 0.2*N*).

It has already been shown that a variety of crystals suitable for solid-state experimentation can be produced in similar ways. The method is especially useful for substances which, because of their low solubilities or low dissociation temperatures (or both) cannot readily be grown by other methods. Since the crystals in any one growth system grow competitively, control of the nucleation process is in many cases a key to the practical utility of the method.

Heterogeneous and Homogeneous Nucleation

The most readily accountable form of nucleation is "heterogeneous," in the sense that it depends on the presence of foreign substrates. It is easy to demonstrate (*e.g.*, by dispersing inert crystalline powders) that it can take place in a gel. There is no reason for expecting heterogeneous nucleation in a gel to be generically different from corresponding process in simple solution, but the frequency of its occurrence is not the same. Thus, most of the accidentally present dust grains which would ordinarily be eligible as nuclei in solution are immobilized by the presence of the gel, perhaps because they are embedded in small cells. In such circumstances, very thin layers of crystal may grow on them, but insufficient material would be available to permit growth beyond submicroscopic size. Alternatively, since the gelling process itself is believed to depend on the presence of foreign nucleation centers, most of the available substrates may be used up by the time gelling is complete. What ever the mechanism, the immobilization of unwanted nucleation centers is believed to be one of the important factors governing the success of the gel method.

Heterogeneous nucleation can be utilized for epitaxial growth and may become important in connection with the growing interest in heterojunctions. In passing, heterojunctions of PbI_2/PbI(OH) and $CaC_4H_4O_6/CuC_4H_4O_6$ have been gel-grown in this way.

There are, however, reasons for believing that much and sometimes most of the nucleation observed in reasonably low dust content gel media is "homogeneous," *i.e.*, that it depends on the formation of critical

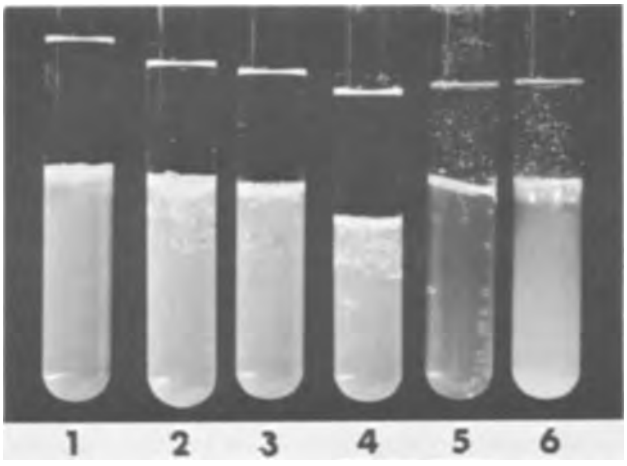

Fig. 1. Experiments on nucleation control: 1, 2, 3, 4, calcium tartrate, 5, 6, lead iodide; 1, 2, pH 3.5; 3, pH 2.5; 4, pH 2.8; 5, 6, pH 4.1. Artificial nuclei present in tubes 2, 3, 4 and 6; the round objects in tube 5 are bubbles.

nuclei. This follows in part from the enormous supersaturations which prevail in the gel, from the distribution of crystals in any given growth system, and from the time-sequence of their appearance. If nucleation were heterogeneous, the final distribution should in the normal way be uniform, corresponding to a uniform dust-distribution, but this is not in fact observed. There is, in principle, the possibility (4) that the diffusing reagent may create its own foreign substrates by reacting with impurities in the resident reagent, thereby creating a nonuniform distribution of nuclei. However, this would involve rather specialized conditions and, as a general mode of operation, seems unlikely. Epitaxial growth on a foreign substrate generally calls for lower supersaturations than homogeneous nucleation, and a corresponding demonstration is shown on Fig. 1. Tubes 1 and 2 contain, above the gel, the same solution of $CaCl_2$. The gel in tube 1 is free of deliberately added foreign nuclei and is seen not to support any crystal formation because the $CaCl_2$ concentration is too low. Some accidental unwanted dust grains are undoubtedly present but are evidently immobilized by the gel. Tube 2 contains heterogeneous nuclei in the form of fine titanium dioxide dust and supports copious nucleation. The number of crystals formed is still much smaller than the total number of TiO_2 grains present, showing that, in the presence of very high dust concentrations, the gel cannot immobilize all the potential nucleation centers. Tubes 5 and 6 provide the same demonstration for PbI_2. A similar difference can be observed by varying the pH in the gel. One would expect the homogeneous nucleation of calcium tartrate to be sensitive to the acidity of the gel, considering that the material is appreciably soluble in tartaric acid. In fact, crystal formation in a clean system is rare below pH 3. In the presence of artificial nuclei, pH is still an important factor but crystals appear in gels which are considerably more acidic. Tubes 3 and 4 on Fig. 1 show this, the acidities being 2.5 and 2.8, respectively.

Nucleation Control through Concentration Programming

The above considerations lead (in low dust-content gel media) to a simple method of nucleation control. The concentration of the diffusing reagent is initially kept below the level at which nucleation is known to occur. It is then increased in a series of small steps, which can be optimized for any system as regards magnitude and timing. At some stage, a few nuclei begin to form. As the concentration of the diffusant increases, these nuclei act as sinks, and the resulting establishment of radial diffusion patterns reduces concentrations and appears thus to inhibit the formation of additional nuclei. Subsequent increases of reagent concentration lead to faster growth but not, in general, to new nucleation. The existing crystals are thus able to grow noncompetitively and their quality is correspondingly good. It has been found empirically that frequent small steps are more beneficial than a few large concentration increases. The method has been successfully applied to the control of nucleation in several systems (Table I), and has yielded crystals of larger size and a higher degree of perfection than those produced without programming. The size increase amounts to approximately a factor of 3, except for calcium tartrate for which nucleation is rare enough even without programming to reduce the importance of the competitive growth limitation.

Table I. Effect of concentration programming on crystal size

Crystal	Typical sizes: largest linear dimensions, mm	
	Without programming	With programming
Calcium tartrate	~12	~12
Cuprous tartrate	1	3
Lead iodide	3	15
Thallium iodide	0.5	1.5
Calcium carbonate (aragonite spherulites)	0.5	1.5
Cadmium oxalate	2	5

It remains to be shown that the method can be more generally applied, the present indications being that it can.

Effect of Trace Impurities and Molecular Volume

The theory of homogeneous nucleation via critical nucleus formation in solution is still only imperfectly understood (5, 6). Under the simplifying assumptions envisaged by the Kelvin equation and the Gibbs-Duhem relationship, the radius r_c of the critical nucleus forming in a solution would be given by

$$r_c = \frac{2\sigma V_s}{kTS}$$

where V_s is the molecular volume of the solute, S the supersaturation, and σ the surface energy per unit area (closely related to the surface tension and identical with it under simplest conditions). By analogy with other interface parameters, σ is expected to be selectively sensitive to the presence of contaminants, especially since the free energy of nucleus formation (7) depends on σ^3. It is certainly true that solution processes can be affected sensitively by the presence of contaminants in the low ppm range (8). For the calcium tartrate system, the most potent contaminant

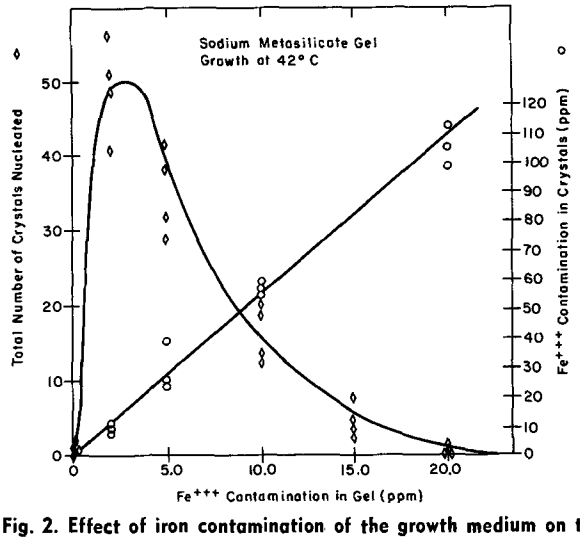

Fig. 2. Effect of iron contamination of the growth medium on the nucleation and composition of calcium tartrate crystals.

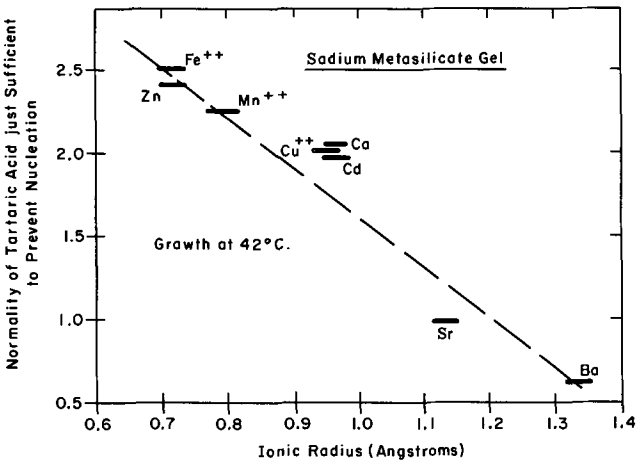

Fig. 3. Effect of molecular volume on critical nucleus formation of tartrates.

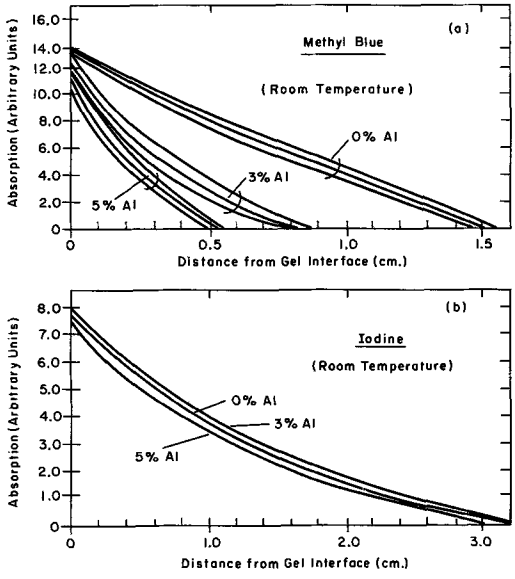

Fig. 4. Effect of alumina content on the diffusion of methyl blue and iodine in sodium metasilicate aluminate gels, assessed by optical absorption measurements.

was found to be iron. Results which show its effect are given in Fig. 2 and the relationship is evidently not simple. A very small concentration of ferric ions promotes nucleation; larger concentrations inhibit it, whereas the uptake of iron by the crystal itself (spectroscopically determined) increases uniformly as expected. That the growing crystals become enriched in contaminant appears to be a peculiarity associated with iron. There is, of course, infinite scope for investigations of this kind, using different combinations of crystals and potential contaminants. General predictions cannot as yet be made.

The previously reported observations of photonucleation can, in all likelihood, be understood in similar terms, *i.e.*, as an indirect effect of light on σ. It has long been known (9) that light (especially uv) dissociates tartaric acid with the production of CO_2, which can easily be shown to enhance the nucleation of calcium tartrate crystals. This can be demonstrated convincingly by comparing a series of growth systems, maintained in darkness, but with different amount of CO_2 additive in the gel.

In a manner similar to that demonstrated above, a correlation can be established between nucleation frequency and the molecular volume of the solute, as suggested by the approximate calculation of the critical radius. For this purpose it is actually convenient to use, as an index of comparison, not the probability of nucleation as such, but the normality of the acid on the gel which is just sufficient to suppress nucleation. Its correlation with the ionic radius of the metal is shown in Fig. 3 for a series of tartrates grown under otherwise identical conditions. The radius may be taken as a relative measure of molecular volume.

Effect of Gel Structure

If the views expressed above are correct, then one would expect nucleation to be more difficult in gels of smaller cell size. In order to test this, it is necessary to have some method whereby gels can be compared from this point of view, at least in a semiquantitative manner. Quantitative work on hydrogels is, of course, hampered by their complicated structure and, in particular, by the fact that not only the mean cell dimensions but also the size distribution about this mean can vary. However, by allowing a compound of large molecular volume to diffuse, an empirical relative measure of effective cell size can be obtained. In the present case, this was done by observing the diffusion of methyl-blue in gels of varying Si:Al ratio. The diffusion process is monitored by making light absorption measurements as a function of distance from the gel surface. As Fig. 4 shows, diffusion becomes more difficult as the amount of Al increases, and it is reasonable to conclude that this is due to progressively diminishing cell sizes. Al certainly has this effect on the cell dimensions of dehydrated gels, as Plank and Drake (10) have demonstrated.

Table II shows how, under a standard set of conditions, the number of crystals nucleated depends on gel composition and thus evidently on the cell size. The expected correlation is observed and Table II, incidentally, gives an impression of the extent to which the results vary between growth tubes of the same composition and thermal history. It is, however, necessary to check that the various gels used do not present different diffusion conditions to the reagents involved in crystal formation. When the diffusants are very small compared with the cell size, the cell size should have no material effect on the diffusion process. Figure 4 shows that (for iodine) this is indeed correct, and the comparison implied by Table II is therefore valid.

Reseeding Procedures

Once nucleated, the crystals grow until they reach a constant size. It has already been shown that this size is determined by the progressive exhaustion of the reagents (1). Replenishment of at least one (the diffusing) reagent is a simple matter, but the removal of the waste products of the reaction is not. If, therefore, a crystal of larger size is required, it must be reseeded into another gel. This is done first by gelling a small amount of sodium metasilicate in a tube, resting the seed on the gel surface thus formed, and covering it first with additional sodium metasilicate solution and, after second gelling, with the diffusing reagent. In the course of transferring the crystal from one growth system to another, its surfaces are generally damaged and possibly contaminated, resulting in polycrystalline growth. To prevent this, the temperature is

Table II. Standard set of conditions.

Crystal	0% Al	3% Al	5% Al	6% Al	8% Al
Calcium tartrate	65, 75, 107, 93	30, 14, 19, 24	7, 0, 13, 6	13, 5, 44, 22	0, 0, 0, 2
Copper tartrate	536, 324, 342, 441	67, 57, 78, 30			
Lead iodide	8, 7, 7, 10	3, 4, 0, 0	0, 0, 0, 0		0, 0, 0, 0

Table III. Weights of three crystals each of calcium and copper tartrate after re-seeding

Crystal	Initial	Weight in mg 1st Seeding	2nd Seeding	3rd Seeding	4th Seeding
Calcium tartrate	137.2	354.0	820.5	939.2	1104.0
	175.6	401.4	873.5	1083.1	1204.1
	139.4	347.0	685.4	803.1	952.3
Copper tartrate	21.2	43.3	63.5	78.4	96.3
	18.7	37.8	69.6	84.4	101.1
	18.4	30.2	66.0	81.7	103.4

raised immediately after reseeding in order to dissolve a portion of the seed, as is usual in all seeding procedures. When the temperature is subsequently lowered, growth proceeds in the normal way until the reagents are once again exhausted. The process can then be repeated. In a series of steps it is thus possible to grow considerably larger crystals than can ordinarily be obtained in a single growth system. The method has not yet been widely applied, but the principle is illustrated below on the basis of calcium and copper tartrate. Table III shows the weights of particular crystals after successive reseeding stages. With care, their high degree of optical perfection can be fully maintained throughout this procedure.

Acknowledgment

This work was supported by contract No. DA 49-083 OSA-3140 with the Advanced Research Projects Agency.

Manuscript received Oct. 12, 1966.

Any discussion of this paper will appear in a Discussion Section to be published in the December 1967 JOURNAL.

REFERENCES

1. H. K. Henisch, J. Dennis, and J. I. Hanoka, *J. Phys. Chem. Solids*, **26**, 493 (1965).
2. H. K. Henisch, J. I. Hanoka, and J. Dennis, *This Journal*, **112**, 627 (1965).
3. H. K. Henisch and J. Dennis, *This Journal*, **112**, 1240 (1965).
4. V. Vand, Private communication.
5. J. W. Gibbs, "Collected Works," p. 78, Longmans Green, Inc., London (1928).
6. D. Turnbull, *Solid State Phys.*, **3**, 225 (1956).
7. A. Van Hook, "Crystallization," p. 107, Reinhold Publishing Corp., New York (1961).
8. M. B. Ives and J. J. Plewes, *J. Chem. Phys.*, **42**, 293 (1965).
9. H. A. Spoehr, *Biochem. Z.*, **57**, 95 (1914).
10. C. J. Plank and J. C. Drake, *J. Coll. Sci.*, **2**, 399 (1947).

Characteristics of the Surface-State Charge (Q_{ss}) of Thermally Oxidized Silicon

B. E. Deal, M. Sklar, A. S. Grove, and E. H. Snow

Research and Development Laboratories, Fairchild Semiconductor, Palo Alto, California

ABSTRACT

The nature of the surface-state charge (Q_{ss}) associated with thermally oxidized silicon has been studied experimentally using MOS structures. The effects of oxidation conditions, silicon orientation, annealing treatments, oxide thickness, and electric field were examined, as well as the physical location of the surface-state charge. The results indicate that the surface-state charge can be reproducibly controlled over a range 10^{10}-10^{12} cm^{-2}, and that it is an intrinsic property of the silicon dioxide-silicon system. It appears to be due to an excess silicon species introduced into the oxide layer near the silicon during the oxidation process.

In much of the early work on the properties of semiconductor surfaces, experimental results were interpreted within the framework of two quantities: fast and slow surface states (1). "Fast surface states" are electronic states within the forbidden gap of the semiconductor, located at the surface, which are in good electrical communication with the semiconductor bulk. Because of this, they can act as surface recombination centers. Their density per unit area for both clean germanium and silicon surfaces has been generally found to be of the same order as the surface atom density. If the semiconductor is covered by an adsorbed layer, or an oxide, the density of fast states has been found to decrease to 10^{11}-10^{12} cm^{-2}. "Slow states," in contrast, have been attributed to ionic contamination within an oxide covering the semiconductor surface. Because of their relatively large distance from the semiconductor, they are in poor electrical communication with it. Their density is a strong function of the ambient and surface treatment of the sample, but generally ranges in the neighborhood of 10^{12}-10^{13} cm^{-2}.

In the past several years, the thermally oxidized silicon surface has been investigated very intensively, partly due to its extreme technological importance and partly to the ease with which its characteristics can be studied (2). As a result of these investigations, a detailed picture of this system has emerged which is not explainable strictly within the framework of fast and slow surface states.

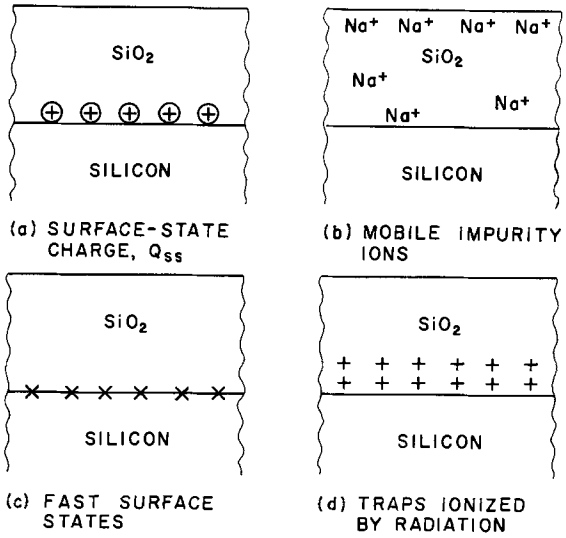

Fig. 1. Charges or states associated with the silicon dioxide-silicon system.

An idealized representation of the current picture of the thermally oxidized silicon system is depicted in Fig. 1. Fast surface states have been identified, but in many cases their density has been found to be less than 5 x 10^{10} cm^{-2} (3), considerably lower than in other systems, thus leading to the low surface recombination velocity of passivated silicon devices (4). While slow surface states, in the customary sense, have not been evident, ionic space charges within the oxide have been observed. These were found to result from either contamination by relatively mobile ions such as sodium (5, 6), or from exposure to ionizing radiation (7). They are evidently in poor electrical contact with the underlying silicon even when located very near the oxide-silicon interface.

These charges within the oxide, which have generally been found to be positive, induce a negative charge in the silicon, and thereby lead to the tendency of thermally oxidized silicon surfaces to be n-type, as observed already in the earliest experiments (8). On the other hand, it has been shown (3) that even oxides grown in such a manner that ionic contamination was precluded are characterized by a positive charge, apparently located in the oxide, near the oxide-silicon interface. This charge, which has been designated the surface-state charge, and whose density per unit area is denoted by Q_{ss} (3), is the subject of the present paper.

The characteristics of the surface-state charge as established in the earlier study, were the following: (*i*) Its density Q_{ss} is reproducible. For one particular set of conditions [oxidation at 1200°C, in dry O_2; (111) silicon orientation] its density is ~2 x 10^{11} cm^{-2}. (*ii*) Its density is independent of the impurity concentration in the silicon, and of the oxide thickness over a wide range. (*iii*) Its density is independent of the band bending or surface potential in the silicon over at least the middle 0.7 ev of the energy gap. (*iv*) Its density is stable under elevated temperature—bias test conditions of the kind that would lead to rearrangement of sodium contamination in the oxide, or to annealing of radiation-induced space charges.

These characteristics are difficult to reconcile with the conventional picture of slow and fast states at a semiconductor surface. Therefore, a study was undertaken to examine in detail the nature of the surface-state charge. The present paper contains a summary of an extensive experimental investigation dealing with the effect of oxidation conditions, silicon orientation, annealing treatments, oxide thickness, and electric fields on Q_{ss} and with its spatial distribution in the oxide. The primary means of evaluation was the capacitance-voltage method of analysis using metal-oxide-semiconductor (MOS) structures.

Experimental

Materials.—Silicon used in these studies was single crystal Czochralski type. It was obtained from the Kollstan Semiconductor Elements Company of Westbury, New York, in the form of circular slices approximately 2 cm in diameter and lapped on both sides to a thickness of 250μ. Dislocation count was specified to be less than 100 cm^{-2}. Both p- and n-type dopants (boron and phosphorus) were included, the concentrations being ~10^{16} cm^{-3} for most of the experiments. Various surface orientations were studied, including (111), (110), and (100).

Aluminum used for field plates and back contacts was obtained from Cominco Products, Inc., Spokane, Washington, and was specified as 99.9999% pure. A separate analysis indicated the sodium content was 1 ppm or less. Gases used for oxidation and annealing (O_2, N_2, and argon) were obtained in a liquid form from Air Reduction Company, Richmond, California. Total water content was less than 5 ppm in each gas. Special tests indicated other impurities such as hydrocarbons or hydrogen were extremely low, *i.e.*, less than 2 ppm. A molecular sieve trap was used to remove any excess water or hydrocarbons in all gases. Deionized water used for rinsing samples and for wet oxidations had a resistivity at 25°C of 16 megohm-cm and an initial sodium content of less than 0.002 ppm. Although this latter value increased upon storage in the Pyrex or quartz bubbling flask, the analysis of the distillate from the exit end of the oxidation tube indicated 0.030 ppm Na or less.

Procedure.—Immediately prior to oxidation, the silicon slices used for MOS device fabrication were cleaned in both organic and inorganic solvents using ultrasonic agitation. They were then chemically polished in a 4HF: 10HNO_3 solution followed by a quench in acetic acid. Approximately 50μ per side were removed during this operation. Appropriate deionized water rinses were used between the various cleaning and polishing steps. Samples used for thickness measurements were mechanically polished resulting in the removal of 30μ per side. The same cleaning as mentioned above was carried out following mechanical polishing.

The oxidation procedure was essentially the same as described earlier (9). Slices were placed flat on a thin quartz boat and inserted in a tube furnace with separate systems being used for n- and p-type samples. Either dry oxygen or wet oxygen (oxygen bubbled through 95°C H_2O) was used as the oxidizing ambient, with the time and temperature of oxidation depending on the specific experiment. Various pulling rates were employed, the standard one being very rapid (less than 3 sec through the 50 cm from the center of the furnace to the end of the tube).

In certain cases, the samples were annealed in either nitrogen or argon following oxidation. Each oxidation contained a slice for thickness evaluation in addition to those samples used for MOS device fabrication and evaluation. Oxide thicknesses were determined on the special test slices using multiple beam interferometry (10). Accuracy of this method was found to be ±40Å for oxides greater than 2000Å and ±20Å for thicknesses less than 2000Å. After oxidation or annealing, the back oxide was removed from selected samples and MOS capacitance-voltage plots obtained using a gold pressure contact probe. The other samples were metallized with aluminum on the top surface after first removing 50-100Å of oxide in a 10:1 H_2O:HF solution to eliminate contamination. The thickness of the aluminum field plate was 2000-5000Å. The back oxide was then removed and aluminum evaporated on the bare silicon. Top field plates 375μ in diameter on 1250μ centers were then prepared by photoresist operations. Finally, the slices were heat treated at 550°C for 2-5 min in dry nitrogen. Most electrical measurements were made on the slice but in certain cases the slices were scribed and broken into individual dice 1250μ square.

Evaluation.—The majority of the electrical evaluations in this investigation involved the determination of the surface-state charge density Q_{ss}. This measurement was accomplished by determining the shift of an experimental MOS capacitance-voltage curve along the voltage axis from the ideal theoretical curve calculated on the basis of assuming no fast surface states or oxide charges and no work function difference between metal and semiconductor. The resulting voltage shift ΔV is related to Q_{ss} by the expression (3)

$$\Delta V = Q_{ss}\frac{x_o}{K_o\epsilon_o} - \Phi_{MS}$$

where Q_{ss} is the surface-state charge density per unit area, $K_o\epsilon_o/x_o$ is the oxide capacitance per unit area, and Φ_{MS} is the metal-semiconductor work function or barrier energy difference. The latter value for aluminum/SiO_2/n-type silicon (10^{16} cm^{-3}) is —0.25v, while for aluminum/SiO_2/p-type silicon (10^{16} cm^{-3}) it is —0.95v (11). In the majority of the experiments, the experimental C-V curve was identical in shape to the theoretical curve so that the shift along the voltage axis was parallel within experimental error.

In general, C-V plots were obtained on a number of units from each slice. The measurements were made by automatically plotting capacitance *vs.* voltage on an X-Y recorder. Capacitance measurement frequency was about 100 kc and measurements were at 25°C. Reproducibility of Q_{ss}/q values was always better than 5 x 10^{10} cm^{-2} for a particular condition of sample preparation.

Results

Oxidation conditions.—The temperature of oxidation in dry oxygen was found to affect the value of Q_{ss} significantly. A certain reproducible value of Q_{ss} was obtained at any given temperature. This was the case whether the oxide was prepared at that particular temperature, e.g., 1000°C, or prepared at another temperature and then given a final treatment in dry oxygen at 1000°C. This effect was observed with both n-type and p-type silicon.

Typical MOS C-V plots for samples prepared by dry O_2 oxidation of n-type silicon at four different temperatures are shown in Fig. 2. The effect of oxidation temperature on Q_{ss} is clearly demonstrated by the displacements of the different plots from the theoretical curve. More complete data showing the effect of temperature on Q_{ss} are shown in Fig. 3. Both n-type and p-type values are included for temperatures ranging from 550° to 1250°C. All oxide thicknesses for this particular graph are 0.20μ. Above 920°C, the oxides were prepared at the temperature indicated. Below 920°C, the oxides were first prepared at 1200°C and

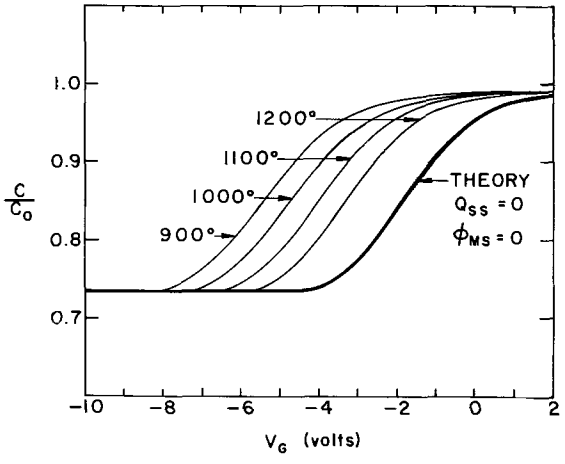

Fig. 2. Capacitance-voltage characteristics of MOS structures prepared by oxidation in dry oxygen at various temperatures [x_o = 0.20μ; N_D = 1.4 x 10^{16} cm^{-3}; (111) orientation].

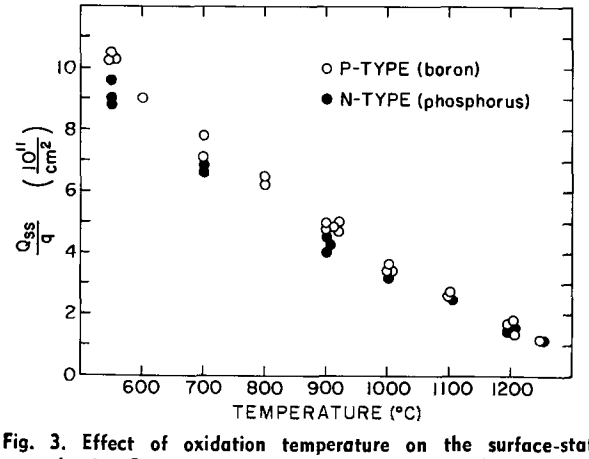

Fig. 3. Effect of oxidation temperature on the surface-state charge density Q_{ss}—dry oxygen [x_o = 0.20μ; N_A, N_D = 1.4 x $10^{16}$$cm^{-3}$; (111) orientation].

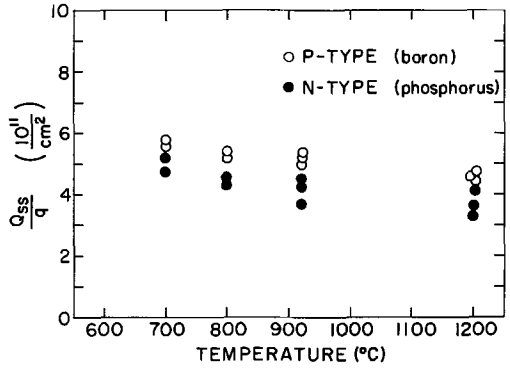

Fig. 4. Effect of oxidation temperature on the surface-state charge density Q_{ss}—wet oxygen (95°C H_2O) [x_o = 0.20μ; N_A, N_D = 1.4 x 10^{16} cm^{-3}; (111) orientation].

then immediately subjected to the lower temperature for a sufficiently long time (previously determined) that the steady state value of Q_{ss} was reached. This time varied from less than 10 min at 900°C to nearly 1 hr at 550°C. It should be re-emphasized that the values presented in Fig. 3 were obtained by quenching the oxidized silicon slice from the oxidation temperature as described previously.

The effect of oxidation temperature on Q_{ss} for the case of oxides prepared in wet oxygen (95°C H_2O) was not nearly so pronounced: Q_{ss} was found to be nearly unchanged between 700° and 1200°C, increasing only slightly with decreasing temperature. Typical data are shown in Fig. 4. Note that at the higher temperatures the Q_{ss} values for wet O_2 are considerably higher than those for dry O_2 oxides, but dry O_2 values are higher below 900°C. Results identical to those shown in Fig. 4 were obtained by oxidation in wet argon (95°C H_2O). By oxidizing under bias in order to exclude contamination, Goetzberger (12) found $Q_{ss}/q = 4$ x 10^{11} cm^{-2} for 1000°C, steam oxidation, in agreement with these data.

The increased values of Q_{ss} at lower oxidation temperatures (for dry O_2 oxidation) are directly related to another effect, namely, the dependence of Q_{ss} on pull rate from the oxidation furnace. Typical data are given in Table I for various pull rates from a 1200°C oxidation in dry oxygen. It is evident that the slower the rate of pull, the higher the Q_{ss} value. These observations are easily explained by the fact that the slower the rate of pull, the more time the sample is exposed to oxygen in the lower temperature range, which results in increased Q_{ss} values. The rapid pull (t < 3 sec) evidently does not permit sufficient exposure of the samples to oxygen in this temperature range and therefore results in the Q_{ss} value corresponding to the oxidation temperature.

Silicon orientation.—It has been shown (13-15) that silicon orientation affects the surface-state charge density Q_{ss} of MOS devices, *i.e.*, the value of Q_{ss} decreases in the order (111)>(110)>(100). Results obtained in the present study, which are in agreement

Table I. Dependence of surface-state charge density (Q_{ss}) on pull rate in dry O_2 following thermal oxidation

(Samples were oxidized at 1200°C for 60 min. x_o = 0.2μ. Silicon was p-type, boron doped, C_B = 1.4 x 10^{16} cm^{-3}, (111) orientation. Distance from center to end of tube was 54 cm.)

Pulling time (min)	Pulling rate (cm/min)	Q_{ss}/q (cm^{-2})
<0.05	>1065	1.9 x 10^{11}
0.167	319	2.8
0.50	106	5.6
1.0	53.3	7.3
2.8	19.0	8.9
34.0	1.6	9.8

Table II. Dependence of the surface-state charge density and the linear oxidation rate constant on silicon orientation

Oxide type	Temp (°C)	Silicon orientation	Q_{ss}/q (cm^{-2})	B/A (μ/hr)
Dry O_2	1200	(111)	1.7×10^{11}	1.12
		(110)	0.6	0.90
		(100)	0.2	0.56
Dry O_2	920	(111)	4.7	0.021
		(110)	2.1	0.018
		(100)	1.7	0.012
Wet O_2 (95°C H_2O)	1200	(111)	4.0	14.40
		(110)	1.7	12.0
		(100)	1.2	7.2
Wet O_2 (95°C H_2O)	920	(111)	5.6	0.406
		(110)	3.6	0.37
		(100)	3.4	0.21

with those of ref. (13-15), are summarized in Table II, for both dry and wet O_2 oxidation at 1200° and 920°C.

A similar effect of orientation on oxidation kinetics was noted in earlier investigations (9, 16). In particular, it is now known (17) that the silicon orientation influences the linear rate constant B/A, which is proportional to the chemical reaction rate constant at the oxide-silicon interface (17-19). This effect is also indicated in Table II. It is evident that the values of B/A and of Q_{ss} for the three orientations follow similar trends.

Annealing treatments.—A wide variety of annealing effects on the surface condition of thermally oxidized silicon has been reported (20-25).

The effect on Q_{ss} due to annealing in oxygen at temperatures other than that of initial oxidation was already described above. This effect is summarized in Part A of Table III. Here, values of Q_{ss} are listed for three conditions of oxygen anneal after 1200°C oxidation: slow pull in O_2, anneal at 900° and at 550°C. These results are compared with the 1200°C standard. Both (111) and (100) orientations are included. It can be inferred from earlier work (21, 24) that the higher Q_{ss} values resulting after certain oxidation conditions can be significantly reduced by annealing in an inert ambient. The inert ambient effect is shown in Part B of Table III. Data are presented for both wet and dry oxygen oxidations followed by inert ambient anneals for two silicon orientations. It can be noted that regardless of the original oxidizing ambient, the final Q_{ss} value will be approximately that of 1200°C dry O_2 if the sample is subsequently annealed in dry argon or nitrogen.

Part C of Table III also demonstrates the fact that the final oxidation or annealing treatment determines the Q_{ss} value. In this case samples have been given combination oxidation treatments, *i.e.*, first dry O_2 followed by wet O_2 or conversely wet O_2 and then dry O_2. Standard dry O_2 and wet O_2 data are also included for comparison. In each case the value of Q_{ss} was characteristic of the final oxidizing ambient.

These results are best summarized by reference to the "dry oxygen triangle" illustrated in Fig. 5. Here

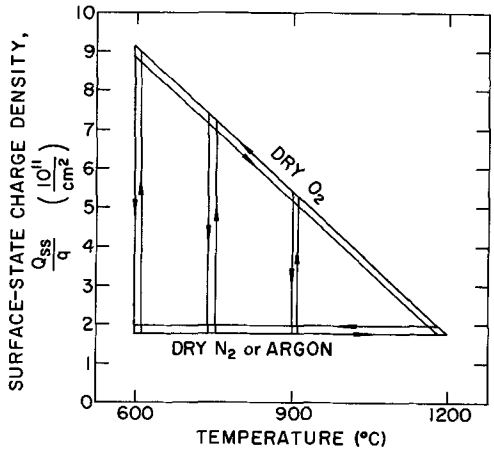

Fig. 5. Illustration of the reversibility of heat treatment effects on the surface-state charge density Q_{ss}.

Q_{ss} is plotted against oxidation temperature. As temperature decreases, Q_{ss} increases and we may move in either direction along the diagonal line labeled "dry O_2." Thus, an oxidized sample may be prepared at any temperature and then subjected to dry oxygen at any other temperature, with the resulting value of Q_{ss} being that associated with the final temperature. The time required for attaining steady state increases with decreasing temperature, being less than 5 min at 1200°C and approximately 1 hr at 550°C.

Another characteristic of the "dry oxygen triangle" is that associated with annealing in an inert ambient. As is indicated in the figure by the lower plot marked "N_2 or Argon", any Q_{ss} value resulting from a previous oxidation at a given temperature can be reduced to a constant value approximating that af 1200°C dry oxygen. This is accomplished by subsequently annealing the structure in dry high purity nitrogen or argon for times characteristic of the particular temperature. These times are similar to those mentioned above for oxygen. Both of these effects are reversible.

The lines shown in Fig. 5 are based on data for (111) p-type silicon; the effect with n-type silicon is approximately the same. A similar relationship exists for (100) silicon, where the Q_{ss} values are reduced by a factor of 2-3 from that of an MOS structure prepared from (111) silicon under identical conditions.

The purity of the gases used in the annealing experiments was found to be extremely critical, especially in the case of the inert ambients argon or nitrogen. For instance, gaseous sources of argon gave nonreproducible increases of Q_{ss} values at the lower temperatures. This was believed to be due to contamination of the gas, although the impurities involved were not identified. Only by use of freshly evaporated liquid argon were reproducible results obtained.

Table III. Dependence of surface-state charge density on annealing treatments and silicon orientation

	Oxide type	Oxidation temperature (°C)	Annealing ambient	Annealing temperature (°C)	Annealing time	Q_{ss}/q (cm^{-2}) (111)	(100)
(A)	Dry O_2	1200	—	—	Std. fast pull (<3 sec)	1.7×10^{11}	0.2×10^{11}
	Dry O_2	1200	O_2	—	Slow pull (2 min)	7.4	2.0
	Dry O_2	1200	O_2	900	10 min	4.6	1.7
	Dry O_2	1200	O_2	550	90 min	10.0	4.2
(B)	Dry O_2	1200	—	—	Std. fast pull	1.7	0.2
	Dry O_2	1200	N_2	1200	10 min	1.8	0.0
	Dry O_2	920	—	—	Std. fast pull	4.7	1.7
	Dry O_2	920	Argon	920	30 min	1.9	0.7
	Wet O_2	920	—	—	Std. fast pull	5.6	3.4
	Wet O_2	920	N_2	920	20 min	2.0	0.8
(C)	Dry O_2	1200	—	—	Std. fast pull	1.7	—
	Dry O_2	1200	Wet O_2	1200	1 min	5.0	—
	Wet O_2	1200	—	—	Std. fast pull	4.7	—
	Wet O_2	1200	Dry O_2	1200	20 min	2.1	—

Table IV. Values of Q_{ss} for various thickness of dry O_2 oxides prepared at 1200° and 920°C

Two orientations, (111) and (100) for both p- and n-type silicon (10^{16} cm^{-3}) are included.

Silicon type	Oxidation temperature (°C)	(111) Orientation: Oxide thickness (μ)	(111) Orientation: Q_{ss}/q (cm^{-2})	(100) Orientation: Oxide thickness (μ)	(100) Orientation: Q_{ss}/q (cm^{-2})
p-type	1200	0.205	1.7×10^{11}	0.195	0.2×10^{11}
		0.415	1.9	0.410	0.2
		0.635	1.8	0.630	0.1
p-type	920	0.061	4.0×10^{11}	0.030	0.9×10^{11}
		0.100	4.6	0.080	1.4
		0.205	4.7	0.161	1.4
		0.263	4.7	0.201	1.7
		0.331	4.6	0.258	1.6
n-type	1200	0.200	1.4×10^{11}	0.195	0
		0.405	1.7	0.400	0
		0.620	1.8	0.610	0
n-type	920	0.205	3.8×10^{11}	0.154	0.4×10^{11}

Table V. Values of Q_{ss} for various thicknesses of wet O_2 (95°C H_2O) prepared at 1200° and 920°C

Two orientations, (111) and (100), for both p- and n-type silicon (10^{16} cm^{-3}) are included.

Silicon type	Oxidation temperature (°C)	(111) Orientation: Oxide thickness (μ)	(111) Orientation: Q_{ss}/q (cm^{-2})	(100) Orientation: Oxide thickness (μ)	(100) Orientation: Q_{ss}/q (cm^{-2})
p-type	1200	0.200	4.0×10^{11}	0.180	1.1×10^{11}
		0.410	4.5	0.400	1.7
		0.620	5.3	0.600	1.4
p-type	920	0.082	4.5×10^{11}	0.056	1.9×10^{11}
		0.170	5.4	0.120	2.6
		0.345	6.7	0.245	3.6
		0.550	6.6	0.415	3.5
n-type	1200	0.200	3.3×10^{11}	0.190	0.6×10^{11}
n-type	920	0.185	3.7	0.127	1.7×10^{11}

Oxide thickness.—Measurements of the effect of oxide thickness on Q_{ss} were extended to include samples prepared in both dry and wet oxygen at 1200° and 920°C, and for (111) and (100) oriented p- and n-type silicon. Oxide thicknesses ranged from less than 0.01μ to over 0.6μ. The resulting Q_{ss} values are given in Tables IV and V. It can be noted that the values of Q_{ss} are relatively constant over the entire thickness range.

The orientation effect is again quite evident from the data in Tables IV and V, with the Q_{ss} ratio between (111) and (100) samples being approximately 2-3:1 for any given condition.

It should be emphasized that unless the correction for work function difference Φ_{MS} is made, an erroneous dependence of Q_{ss} on thickness would be obtained. That this correction is necessary is evident from Fig. 6 where the voltage shift ΔV is plotted as a function of oxide thickness for four different oxidation conditions. It is evident that conditions (A), (B) and (D) have widely different slopes reflecting the different Q_{ss} values, but that they have identical intercepts, *i.e.*, Φ_{MS} values. Conditions (B) and (C) have identical slopes, *i.e.*, Q_{ss} values, but different intercepts, reflecting the difference in Φ_{MS} for p- and n-type silicon (11). These results are in close agreement with data presented by Ko and Locher (26) who demonstrated the constancy of Q_{ss} with oxide thickness and the effect of metal work function in a similar manner.

Electric field[1].—It has been shown that ionic contamination within the SiO_2 layer can be rearranged in minutes at 150°C (5). On the other hand, the characteristics of MOS structures prepared as described above have been demonstrated to be stable at 150°C, under applied fields of ± 75 v/μ for 3600 hr (3), and also under various other test conditions (27). Recently, an apparent increase in Q_{ss} has been reported (28, 29) due to application of negative fields (metal negative) at higher temperatures. This effect was investigated in further detail.

[1] The phenomenon discussed in this section has locally been referred to as Drift VI.

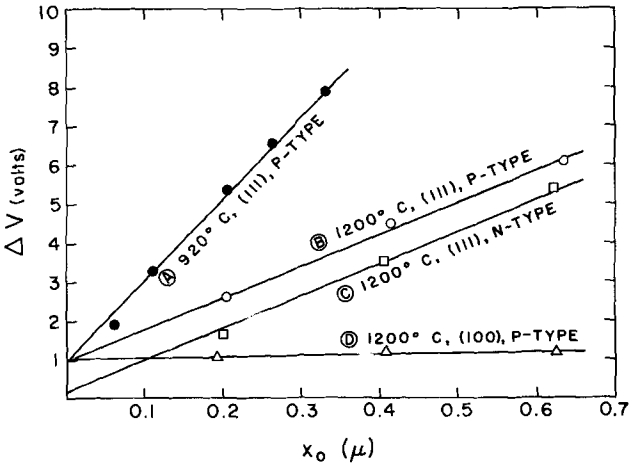

Fig. 6. Displacement ΔV between experimental and theoretical capacitance-voltage characteristics as a function of oxide thickness x_o. In each case the slope is proportional to Q_{ss} while the intercept equals $-\Phi_{MS}$.

Negative fields of 50 to 275 v/μ were applied across the oxide at temperatures of 300°-450°C for times of 2 min or more. Typical results are shown in Fig. 7, where the plots in Fig. 7(a) are for a 0.2μ dry oxide on p-type silicon, while Fig. 7(b) is for the same type of oxide on n-type silicon. In each case, the theoretical curve is labeled (A), the original experimental curve is labeled (B) while the curve resulting after application of the negative field is labeled (C). It can be noted that for each conductivity type the resulting curve displays a sharp break near the intrinsic point. Other experiments using current-voltage measurements on gate-controlled p-n junction diodes (4) have definitely related this phenomenon to an increase in fast surface state density N_{st}. The approximate N_{st} values can be estimated as indicated in Fig. 7 to be about 5×10^{11} cm^{-2}, while the resulting increase in Q_{ss} values are about $5\text{-}7 \times 10^{11}$ cm^{-2}. If no fast states were observed after application of the negative field, the resulting curves (due only to a change in Q_{ss}) would be represented by the dotted lines in Fig. 7, labeled (D).

Several interesting observations were made concerning the effect of negative fields on the C-V characteristics of MOS structures. These effects were similar for p- or n-type silicon with (111) or (100) orientations, and for wet or dry oxides prepared at high or low temperatures. First, an increase in Q_{ss} was generally accompanied by an increase in N_{st} of about equal magnitude. Second, the total change of C-V characteristics would saturate in 1 to 3 min at 400°C for a given applied field. At 300°C, the time required to reach the same saturated or steady-state value was about 8 hr. These times are about four orders of magnitude longer than those required for the rearrangement of sodium contamination. Third, the total change in C-V characteristics at a given field was proportional to the initial Q_{ss} value. Finally, the results obtained with different oxide thicknesses show the effect to be proportional to the applied field rather than the applied voltage.

Examples of some of the above observations are indicated in Fig. 8 and 9. In Fig. 8, the steady state values of $Q_{ss}/q + N_{st}$, corresponding to the total displacement of the midpoints of the C-V plots from the

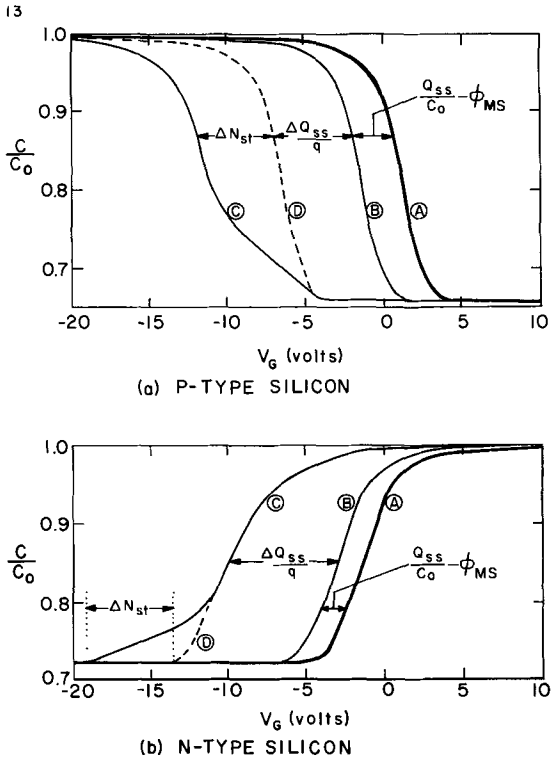

Fig. 7. Illustration of the effect of heat-treatment under negative gate bias on the capacitance-voltage characteristics [—200 v/μ for 2 min at 400°C].

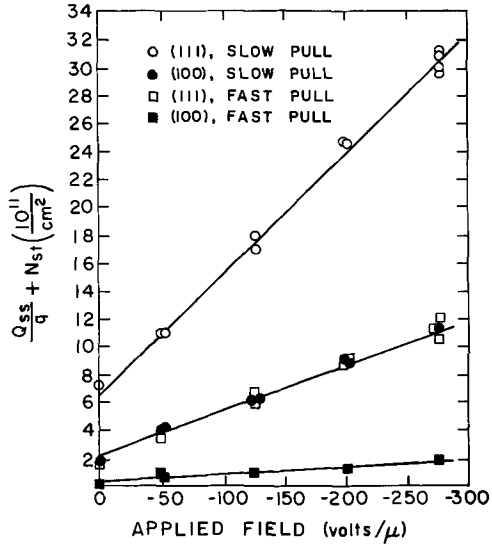

Fig. 8. Steady-state values of $Q_{ss}/q + N_{st}$ as a function of applied field for four different MOS structures with various initial Q_{ss} values [1200°C dry O_2 oxidation; $x_o = 0.20\mu$; p-type, $N_A = 1.4 \times 10^{16}$ cm^{-3}].

theoretical value [see Fig. 7 (a)] are shown for four structures as a function of applied field. The linear dependence of change in the C-V curve with applied field is readily seen, as well as the dependence on the initial Q_{ss} value. In Fig. 9, similar plots are shown for oxides of three different thicknesses on n-type silicon. Here the total change in C-V characteristics reflects only ΔQ_{ss}, but the ΔN_{st} term would just double the change. It is obvious from this plot that the change is dependent on field, not voltage, across the oxide.

An attempt was made to move the charge in the opposite direction by application of a positive field. Small decreases in Q_{ss} were indeed noted, even on structures with low initial Q_{ss} values. It was also noted that in cases where the C-V characteristics had

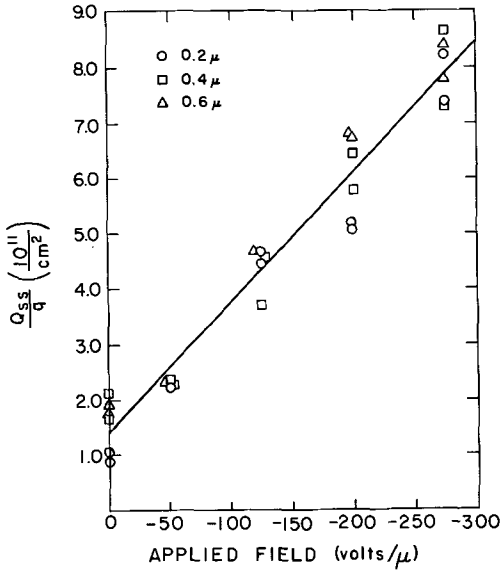

Fig. 9. Steady-state values of Q_{ss}/q as a function of applied field for MOS structures with various oxide thicknesses [1200°C dry O_2 oxidation; (111) orientation; n-type, $N_D = 1.4 \times 10^{16}$ cm^{-3}].

been shifted by a negative field, they could be partially recovered toward the original value by the application of a positive voltage or by shorting the field plate to the silicon at 400°C.

Spatial distribution of Q_{ss}.—The spatial distribution of Q_{ss} within the oxide can be inferred from etching experiments in which the conductance of an inverted surface is measured as a function of the amount of oxide removed.[2] However, one must use great care in the interpretation of these experiments. In particular, it should be noted that the inversion layer conductance will decrease as the oxide is removed even if Q_{ss} is located entirely at the oxide-silicon interface. The reason for this is that, because of the finite width of the surface depletion region in the silicon, Q_{ss} will induce part of its image charge on the outer surface of the oxide and only part in the silicon. As the oxide becomes thinner compared to the depletion region width, more and more of the image charge will be induced on the outer surface and correspondingly less in the silicon. This is clearly true in the case of a metallized surface where the charge at the outer surface is in the form of electrons in the metal. In the case of a bare oxide, it is reasonable to assume that the charge at the outer surface is in the form of ions adsorbed onto the surface from the etch solution.

If we assume Q_{ss} to be uniformly distributed over some finite width d near the oxide-silicon interface, then the charge distribution in an oxidized, high resistivity p-type silicon surface will be as shown in Fig. 10 where Q_G is the charge per unit area induced on the outer surface of the oxide, Q_n is the charge per unit area in the inversion layer,[3] Q_B is the charge per unit area in the surface depletion region and $x_{d\,max}$ is the depletion region width. The condition of charge neutrality requires that

$$Q_G + Q_{ss} + Q_n + Q_B = 0$$

and the condition of zero voltage drop across the system requires that

$$\frac{Q_G x_o}{K_o} + \frac{Q_{ss} d}{2K_o} - \frac{Q_B x_{d\,max}}{2K_s} = 0$$

[2] Similar experiments have been used to determine the spatial distribution of sodium ions (5) and of radiation-induced space-charge (30).

[3] Most of the inversion layer charge will be within a distance from the Si-SiO_2 interface of the order of $(^\circ KT/q)E_s$ where $E_s = Q_s/K_s\epsilon_o$ is the surface field. For the case considered, this distance is about 30Å and is therefore negligible.

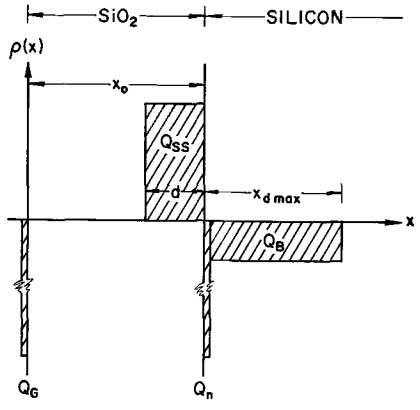

Fig. 10. Charge distribution due to Q_{ss} in a thermally oxidized, p-type silicon structure.

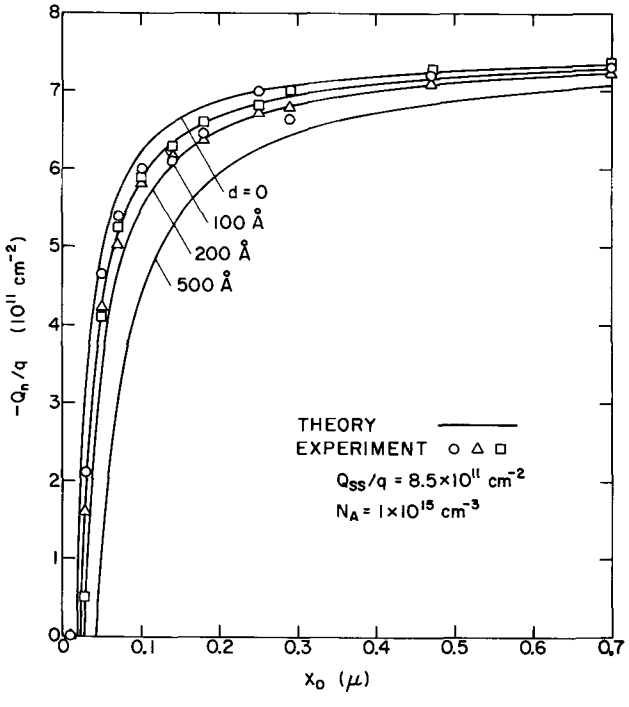

Fig. 11. Inversion layer charge density as a function of remaining oxide thickness. Theory is based on various assumed spatial distributions of Q_{ss}; experimental points are based on channel conductance measurements.

If Q_G is eliminated between these two equations, we obtain for the charge in the inversion layer

$$-Q_n = Q_{ss}\left(1 - \frac{d}{2x_o}\right) + Q_B\left(1 + \frac{K_o x_{d\,max}}{2K_s x_o}\right)$$

Since Q_B and $x_{d\,max}$ can be calculated for any given doping level (3), one can plot a family of theoretical curves of $-Q_n$ *vs.* x_o with d as a parameter. This is done in Fig. 11 for the case of $Q_{ss}/q = 8.5 \times 10^{11}$ cm^{-2} and $N_A = 10^{15}$ cm^{-3}.

Experimentally, Q_n can be determined directly by measuring the small-signal source-drain conductance of an MOS transistor which is given by $g = -\mu_{eff} Q_n Z/L$, where Z/L is a known geometrical factor and μ_{eff} is the effective inversion layer mobility which has been previously determined (31). Experiments have been performed in which Q_n was measured as the oxide was etched away in steps. Some typical results are plotted in Fig. 11 along with the corresponding theoretical curves. By comparing experiment and theory it can be concluded that d lies between 0 and 200Å, although the method is not sufficiently sensitive to allow a more precise determination.

Similar results were obtained on other samples with Q_{ss}/q values ranging between 2 x 10^{11} and 1 x 10^{12} cm^{-2}. These findings are not in agreement with the results of a similar experiment by Lindmayer (25). The discrepancy appears to be due to his neglecting the factors discussed above.

Discussion

On the basis of the above experimental results, it is possible to enumerate certain characteristics of the surface-state charge.

Its density Q_{ss} is independent of the band bending or surface potential over at least the middle 0.7 ev of the energy gap. This can be concluded from the fact that experimentally observed capacitance-voltage characteristics are displaced in a parallel manner from the ideal theoretical characteristics (3).

Its density is stable under moderate temperature-bias tests (3).

Its density is practically independent of the impurity type and concentration in the silicon in the range 10^{14} to 10^{17} cm^{-3} (3), although n-type Si shows a slightly lower density than p-type (see Fig. 3 and 4).

Its density is independent of the oxide thickness for a given preparation condition (see Tables IV and V and Fig. 6).

Most of the charge is located within not more than 200Å of the oxide-silicon interface as demonstrated by etching experiments (see Fig. 11).

Its density can be significantly, reproducibly, and reversibly varied by changing the ambient (*i.e.*, dry oxygen or water vapor) and temperature of oxidation. The surface-state charge density is dependent only on the final oxidation step (see Fig. 5).

Heat treatment in inert ambients reduces Q_{ss} to approximately its lowest value, that found after oxidation in dry oxygen at 1200°C (see Fig. 5).

The orientation of the silicon influences Q_{ss} significantly (13-15). The variation follows approximately the variation of the surface reaction rate constant for oxidation (see Table II).

Under negative fields applied at temperatures well in excess of that required to move sodium contamination in the oxide, Q_{ss} can be increased (28-29). This increase saturates at a value proportional to both the initial Q_{ss} and the applied field (see Fig. 8 and 9); and it is also accompanied by an apparent increase in the density of fast surface states (see Fig. 7).

The most important conclusion that can be made on the basis of these facts is that the surface-state charge is not an extraneous contamination, such as sodium ions, but is a phenomenon intrinsically connected with the silicon dioxide-silicon interface. This is supported by the relative immobility of the surface-state charge, and more importantly, by its high degree of reproducibility.

The lack of variation of this charge with surface potential taken together with the observation that the charge is located within 200Å of the interface indicates that this charge must be related to energy levels which are outside of the middle 0.7 ev of the silicon energy gap. It is quite possible, in fact, that the energy levels are outside of the entire silicon energy gap, but are located within the forbidden gap of the silicon dioxide as illustrated in Fig. 12.

The fact that the charge is practically independent of doping type and concentration rules out the possibility that it is due to doping impurities from the silicon being incorporated into the oxide during its formation. On the contrary, the silicon orientation dependence strongly suggests that it is a silicon species in the oxide that is responsible for the surface-state charge.[4]

[4] For the purposes of this discussion, we make no attempt to distinguish between an excess of silicon and a deficit of oxygen. It should be noted that oxygen vacancies generated as a result of reaction between the metal gate electrode of an MOS structure and the silicon dioxide layer have been proposed in an entirely different context as an explanation for the low temperature instability (32).

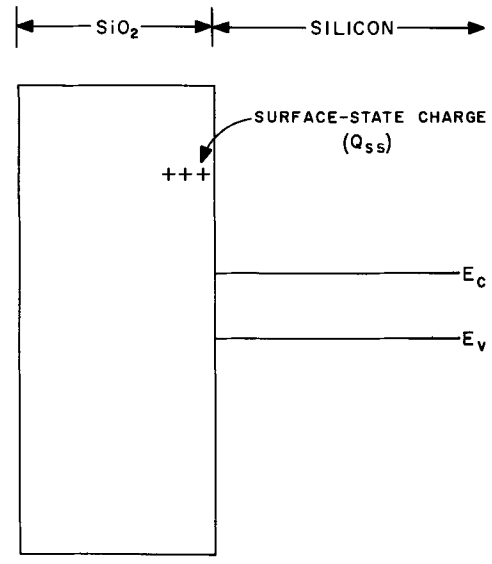

Fig. 12. Energy band structure of the Si-SiO_2 system, in flat-band condition, showing proposed energy levels associated with the surface-state charge.

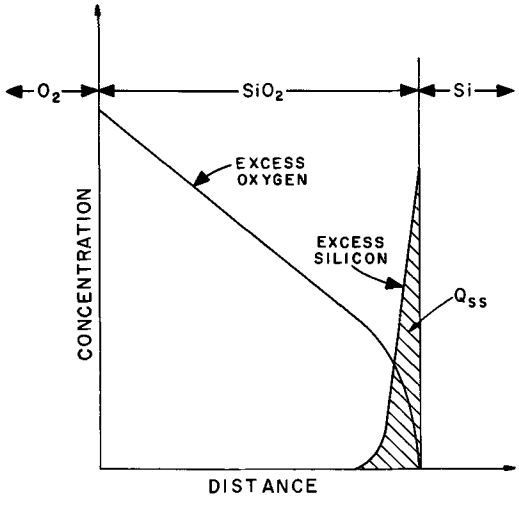

Fig. 13. Schematic illustration of the proposed distribution of excess species in an oxide film during formation.

This possibility is further supported by the fact that the strongest effect on Q_{ss} is due to variations in the oxidation conditions. Although it is well known that thermal oxidation of silicon proceeds by the inward motion of an excess of the oxidizing species, there must be an excess of silicon present near the oxide-silicon interface in order to react with the oxidant. Should this excess silicon be ionic,[5] it could indeed lead to a positive charge near the interface with many of the observed characteristics.

This possibility makes the variation of Q_{ss} with oxidation conditions plausible. It is also consistent with the observed increase in surface-state charge density on application of a negative field at high temperatures: it is known (35) that during anodic oxidation it is the silicon species that moves, under the influence of negative fields, toward the outer oxide surface. It might be then that in this case also, the negative field near the interface aids the entry of excess silicon into the oxide. This would be consistent also with the resulting increase in fast surface state density: vacancies in bulk silicon are known to act as recombination centers. Thus, should silicon be injected from the interface into the oxide, an enhanced concentration of vacancy-like irregularities would result which might lead to increases in surface recombination rates and in fast surface state densities.

It is interesting to note that a similar hypothesis has been advanced by Brody and Handy (36) in order to resolve discrepancies in measurements on tunnel sandwiches involving the Al-Al_2O_3 interface. Also, Heine and Sperry (37) have shown evidence for the existence of excess ionic aluminum incorporated into the aluminum oxide near the oxide-metal interface.

Thus, in summary, it appears that the surface-state charge (Q_{ss}) can best be explained as being due to excess silicon ions in a narrow region next to the silicon, which are introduced into the oxide, as illustrated schematically in Fig. 13, during the process of oxidation.

[5] Ionized silicon was one of several possibilities suggested in this context by Donovan (2) and by Revesz (33). Without specifying the species leading to the surface-state charge, Lindmayer (34) developed a model which treats the interface between oxide and silicon as a heterojunction. This model, although appealing, seems inconsistent with the experimental results; the heterojunction picture leads to the conclusion that the charge transfer from oxide to silicon should be a function of the impurity concentration and type in the silicon much as is the case in an ordinary p-n junction. This, however, is in contradiction to the experimental observations.

Acknowledgment

The authors wish to thank P. J. Fleming for his assistance with the measurements and G. E. Moore for his continued suggestions and encouragement throughout this investigation.

Manuscript received Aug. 19, 1966.

Any discussion of this paper will appear in a Discussion Section to be published in the December 1967 JOURNAL.

REFERENCES

1. See Chap. 9 in A. Many, Y. Goldstein, and N. B. Grover, "Semiconductor Surfaces," John Wiley and Sons, New York (1965).
2. For a comprehensive review of silicon oxidation studies prior to 1965 see "Integrated Silicon Device Technology, Volume VII. Oxidation," Technical Report No. ASD-TDR-63-316, Research Triangle Institute, June (1965).
3. A. S. Grove, B. E. Deal, E. H. Snow, and C. T. Sah, *Solid-State Electronics*, **8**, 145 (1965).
4. A. S. Grove and D. J. Fitzgerald, *ibid.*, **9**, 783 (1966).
5. E. H. Snow, A. S. Grove, B. E. Deal, and C. T. Sah, *J. Appl. Phys.*, **36**, 1664 (1965).
6. E. Yon, W. H. Ko, and A. B. Kuper, *IEEE Trans. Electron Devices, ED-13*, 276 (1966).
7. For a review of radiation effects on surfaces, see J. P. Mitchell and D. K. Wilson, *Bell Syst. Tech. J.*, **46**, 1 (1967).
8. M. M. Atalla, E. Tannenbaum, and E. J. Scheibner, *ibid.*, **38**, 749 (1959).
9. B. E. Deal, *This Journal*, **110**, 527 and 1292 (1963).
10. S. Tolansky, "Multiple-Beam Interferometry of Surfaces and Films," Clarendon Press, Oxford, England (1948).
11. B. E. Deal, E. H. Snow, and C. A. Mead, *J. Phys. Chem. Solids*, **27**, 1873 (1966).
12. A. Goetzberger, *This Journal*, **113**, 138 (1966).
13. Y. Sasaki, Private communication, Nov. 11, 1964.
14. J. F. Delord, D. G. Hoffman, and G. Stringer, *Bull. Am. Phys. Soc.*, **10**, 546 (1965).
15. P. Balk, P. J. Burkhardt, and L. V. Gregor, *Proc. IEEE*, **53**, 2133 (1965).
16. J. R. Ligenza, *J. Phys. Chem.*, **65**, 2011 (1961).
17. W. A. Pliskin, *IBM, J. Research Dev.*, **10**, 198 (1966).
18. B. E. Deal and A. S. Grove, *J. Appl. Phys.*, **36**, 3770 (1965).
19. P. J. Burkhardt and L. V. Gregor, *Trans. Met. Soc. AIME*, **236**, 299 (1966).
20. H. S. Lehman, *IBM J. Research Dev.*, **8**, 422 (1964).
21. A. B. Kuper and E. H. Nicollian, *This Journal*, **112**, 528 (1965).
22. P. Balk, Paper presented at the San Francisco Meeting of the Society, Abst. No. 109, May 9-13, 1965.
23. E. Kooi, *IEEE Trans. Electron Devices, ED-13*, 238 (1966).
24. A. G. Revesz and K. H. Zaininger, *ibid.*, 246 (1966).
25. J. Lindmayer, *Solid-State Electronics*, **9**, 225 (1966).
26. W. H. Ko and R. Locher, "Recent News" Paper

presented at the Cleveland Meeting of the Society, May 1-6, 1966.
27. P. Lamond, J. Kelley, and M. Papkoff, Paper Presented at the Washington, D. C., Meeting of the IEEE Electron Device Group, Oct. 1964.
28. Y. Miura and Y. Matukura, *Jap. J. Appl. Phys.*, **5**, 180 (1966).
29. A. Goetzberger, "Recent News" Paper presented at the Cleveland Meeting of the Society, May 1-6, 1966.
30. A. S. Grove and E. H. Snow, *Proc. IEEE*, **54**, 894 (1966).
31. O. Leistiko, Jr., A. S. Grove, and C. T. Sah, *IEEE Trans. Electron Devices, ED-12*, 248 (1965).
32. J. E. Thomas and D. R. Young, *IBM J. Research Dev.*, **8**, 368 (1964).
33. A. G. Revesz, *IEEE Trans. Electron Devices, ED-12*, 97 (1965).
34. J. Lindmayer, *Solid-State Electronics*, **8**, 523 (1965).
35. E. A. Benjamini, E. F. Duffek, C. A. Mylroie, and F. Schulenburg, "Recent News" Paper presented at the New York Meeting of the Society, Oct. 1-4, 1963.
36. T. P. Brody and R. M. Handy, "Hot Electron Emission Controlled by Bolometric Layers," Fourth Quarterly Report, Contract No. DA-44-009-AMC-357(x), Sept. 30, 1964.
37. M. A. Heine and P. R. Sperry, *This Journal*, **112**, 359 (1965).

A Nitric Oxide Process for the Deposition of Silica Films

Myron J. Rand

Bell Telephone Laboratories, Inc., Allentown, Pennsylvania

ABSTRACT

A new process for vapor depositing thin films of silica on a heated substrate is described. The reagents are hydrogen (≧95%), nitric oxide (1-4%), and silicon tetrachloride or tetrabromide (0.1-1%). The chloride system is useful at 950°-1200°C and the bromide at 775°-950°C, so that the latter may serve to coat Ge as well as Si. The over-all reaction is believed to be $2NO + 2H_2 + SiX_4 \rightarrow SiO_2 + N_2 + 4HX$ and is probably mostly homogeneous. For the more commonly used film thicknesses the nitric oxide process is three to five times more rapid than either the steam or carbon dioxide reactions. Rate curves are presented for various temperatures and concentrations. The apparent temperature coefficient of deposition rate decreases markedly in the upper part of the temperature range for both the Cl and Br systems. Improved film thickness uniformity may be obtained as a practical result. The films produced are transparent, vitreous, smooth, and tightly adherent. Physical tests indicate they are amorphous silica with less short-range order than in thermal oxides. Films from the chloride system regularly produce Si surface charges of 3-6 x $10^{11}/cm^2$ in MOS capacitor tests. Breakdown voltages equal those of steam oxides. Limited bias-aging experiments have shown shifts similar to those of steam oxides. The films are satisfactory masks for boron and phosphorus diffusions; Kodak Photoresist adheres very well.

In principle, deposition of silicon dioxide films from the vapor phase has several advantages in planar semiconductor device processing over the more conventional thermal oxide formation by reaction of a silicon substrate surface with steam or wet oxygen. Since no silicon is consumed, junction movement is minimized, as is pileup or depletion of dopants at the substrate-oxide interface. It is easier to produce thick films by vapor deposition, since the rate is not diffusion-limited. The process is also more practical for producing doped films for diffusion sources. Finally, materials other than silicon may be coated; an example is the deposition of silica for an etching mask with nonfluoride-containing etches.

Nevertheless, deposited oxide film processes are uncommon in device production, with the exception of low-temperature pyrolytic oxides from organosilanes used by necessity for germanium coating. Recently there has been experimental-scale interest in oxides from the hydrogen-carbon dioxide-silicon tetrahalide system (1-4). The slow acceptance of deposited oxides from this (and other) systems appears to arise from the difficulties of producing uniform thicknesses, the fact that growth rates are not significantly faster than for thermal oxides for the more useful film thicknesses, the possibility of introducing carbon into the film or substrate, the evidence for some substrate etching reaction occurring, and unfamiliarity with film quality.

This paper presents a novel system for silica film deposition from mixtures of hydrogen, nitric oxide, and silicon tetrachloride or tetrabromide. It was originally devised to improve two of the five conditions mentioned above, those of growth rate and possible carbon contamination. As it happens, the other three are affected favorably also. This report summarizes some sixty runs in apparatus ranging from a single-slice vertical-flow tube to a ten-slice machine with provision for continuous rotation of each substrate independently. Films up to 1.5μ thick have been deposited.

The $NO-H_2$ *System*

Silica vapor deposition employing oxides of nitrogen was investigated primarily because of the large free energy change available to drive the reaction. In addition, any trace codeposition of silicon nitride which may occur should be tolerable, since it is a good insulator and diffusion barrier also. Nitric oxide, rather than N_2O or NO_2, was chosen for superior thermal stability to confine the reaction to a zone very close to the heated substrate and thus avoid deposition of particulate silica both on the slice and in the cooler parts of the system. NO has an additional advantage: it is a good intermediate in chain reaction mechanisms because it is readily either oxidized or reduced. As an example, it is known that NO may transform the chain initiation or termination steps in the H_2-Cl_2 reaction from heterogeneous to homogeneous (5).

The standard free energy change for the NO process is shown in Fig. 1, with the corresponding reactions for the CO_2 process included. At all temperatures the NO process has much greater driving energy. The reaction as written assumes that the ultimate reduction product of the NO is nitrogen. Other possibilities are N_2O, hydroxylamine, ammonia, and hydrazine; in ≧95% hydrogen ambient at the 800°-1200°C used in this work only ammonia is considered a rea-

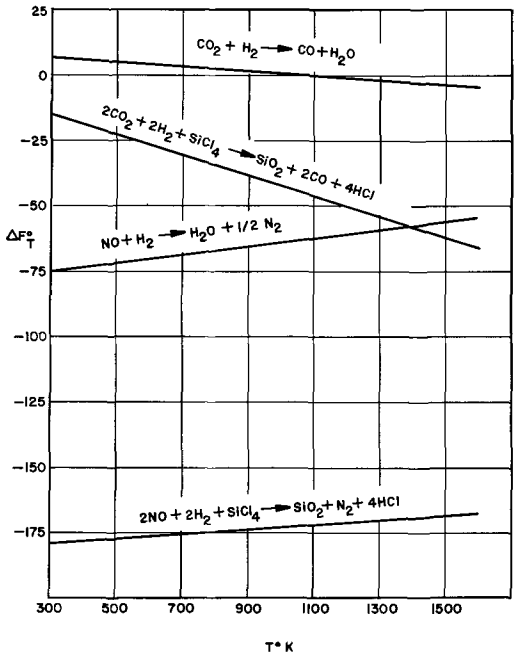

Fig. 1. Standard free energies of nitric oxide and carbon dioxide process reactions at various temperatures.

sonable alternative to nitrogen, and even ammonia is extensively dissociated at equilibrium at these temperatures.

The NO-H_2 reaction has been investigated at temperatures below 500°C (6, 7), where it must be catalyzed and where substantial amounts of ammonia may be formed. At the other extreme it has been studied extensively under conditions providing an abundance of atomic hydrogen, in flames (>1500°C) or with mercury photosensitization; here the reaction is homogeneous. The only recent study of the intermediate zone is that of Graven (8) in the range 850°-1060°C. The reaction was predominantly homogeneous; a complex rate expression was proposed, but the reaction mechanism could not be determined unequivocally.

The multislice deposition apparatus used for much of the work reported here employed an r.f.-heated molybdenum susceptor as the major hot surface. By monitoring the moisture content of the exhaust gases, the reaction between hydrogen and 2% NO in this apparatus was observed to begin at 400°-500°C and increase steadily as the temperature was raised. At 1000°C, at a flow rate which would displace the reactor volume about once a minute, the moisture content of the exhaust was 5000 ppm, or a reaction "efficiency" of 25%. By scrubbing the exhaust gas with dilute HCl and back-titrating it was established that less than 2% of the NO present was reduced to ammonia.

At present we believe that in excess hydrogen NO reacts at 800°-1200°C to produce nitrogen and water; that the reaction is mostly homogeneous, with some surface catalysis possible in the lower part of the range; and that it is a chain reaction of unknown mechanism, proceeding by unstable intermediates probably including atomic hydrogen, N_2O, nitroxyl (HNO), and perhaps HO_2. Needless to say, the addition of the silicon tetrahalide multiplies the complexity. The nitric oxide process for silica film deposition may be regarded as

$$2\left[NO + H_2 \rightarrow \frac{1}{2}N_2 + H_2O\right] \qquad [1]$$

$$2H_2O + SiX_4 \rightarrow SiO_2 + 4HX \qquad [2]$$

only if it is borne in mind that there are many possible routes to SiO_2 other than reaction [2]

Nothing in the foregoing discussion should limit the process to silicon halides; it should be adaptable to oxide deposition in any system with volatile metal halides. To date only silica deposition has been attempted.

Experimental

The deposition area of the apparatus most frequently used has already been described (4); in any event, the reactor design is not important to the success of the process. Each apparatus geometry has different gas dynamics and should be calibrated for the effect of total flow rate. Nitric oxide (Matheson Company) contained ~0.1% each of N_2, N_2O, and NO_2. When passage through Ascarite (which removes NO_2) and a −78° trap did not influence deposition rates the gas was thereafter used without purification. Reactant concentrations ranged from 0.25% NO-0.05% SiX_4 to 4.2% NO-1.0% SiX_4. Total flow rates were such as to displace the reactor volume about once a minute. The bromide system was studied over the range 790°-950°C, the chloride system 950°-1200°C. Substrates coated include Si and Ge of various resistivities, Mo, Ta, and fused silica.

Instead of bringing the substrates to temperature in hydrogen and then introducing the other reactants, it was found advantageous to adjust the gas ambient first and then heat the substrate. Using this method the substrate etching which often plagues the carbon dioxide process was not observed. There are several possible etching reactions, but at temperatures at which their rates become significant the nitric oxide process has already sealed the surface with a continuous silica film. With any method of ambient adjustment, however, the NO process definitely gives less trouble with etching than the CO_2 process.

Deposition Rates

Figures 2 and 3 are Arrhenius plots showing rates of silica film deposition for typical reactant concentrations for the chloride and bromide systems. Rates for the CO_2 process from ref. (1, 2, 4) are included also. Activation energy for the Cl system is 65 kcal (2.8 ev)/mole, and for the Br system 55 kcal (2.4 ev)/mole. Since activation energies for the NO-Cl and CO_2-Cl processes are about the same, it is possible that the rate-determining slow step for the two is the same. If so, this could only be the gas-phase hydrolysis of $SiCl_4$. It would then be a mistake to assume that this reaction, at elevated temperature, is very rapid simply because it is rapid in the liquid phase at room temperature.

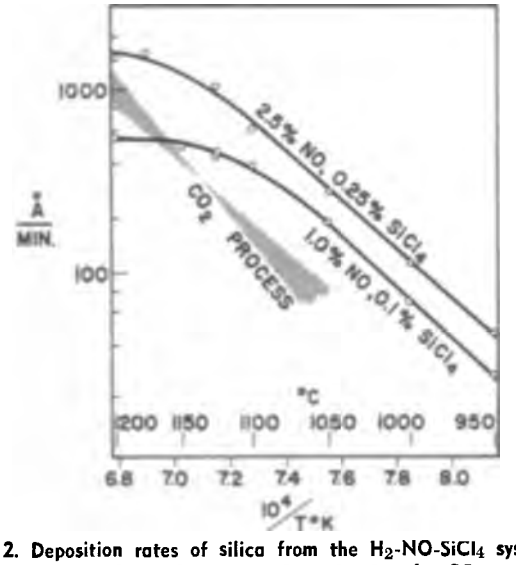

Fig. 2. Deposition rates of silica from the H_2-NO-$SiCl_4$ system. The shaded area shows the range of results for the CO_2 process from ref. (1), (2).

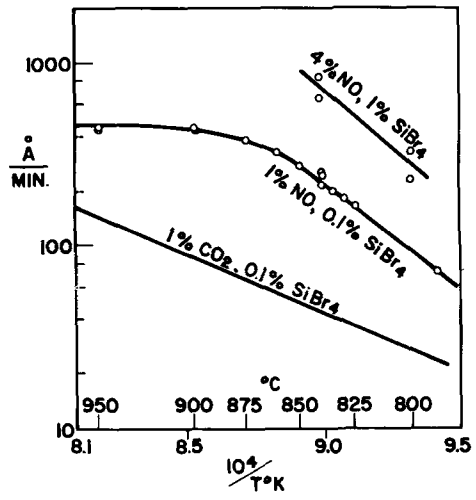

Fig. 3. Deposition rates of silica from the H_2-NO-$SiBr_4$ system

Table I compares the time required to grow a 5000Å film by steam, CO_2, and NO processes at various temperatures. The NO process has a speed advantage of 3 to 5 times over competing processes under usual operating conditions.

The shape of the Arrhenius plots requires comment. In the lower parts of the temperature ranges studied the expected linear dependence of log rate *vs.* $1/T$ is found. Results are little affected by transport rate, *i.e.*, total flow rate, and should thus be close to true kinetic rates. However, at higher temperatures the deposition rate levels off to an extent which is influenced by concentration. Here there is evidently serious depletion of silicon halide in the reaction zone, and the reaction is becoming diffusion-controlled. At still higher temperatures the apparent rate actually decreases, and particulate silica is embedded in the deposited films. The interpretation is that now the reaction zone has moved out far enough from the substrate to allow some of the silica formed to escape deposition and instead be carried away by the gas flow.

The tendency of the deposition rates to level off may be used to advantage in improving the thickness uniformity of oxides from the NO system. If nonuniformity is due to temperature inhomogeneity of the substrate, it may be minimized by operating under conditions where the apparent temperature coefficient of deposition rate is low. An oxide thickness variation of only ±5% across a 1 in. diameter slice may be obtained, for example, at 950° in the bromide system. The same equipment, used for the CO_2 process under identical conditions, produced ±17% variation in oxide thickness. The deposition of particulate silica imposes an upper temperature limit to the use of this expedient. Film uniformity is also aided by high total flow rate and by low reactant concentrations.

Film Properties

The nitric oxide process reliably produces clear, vitreous, tightly adherent silica films which are amorphous by electron diffraction. Electron microscopy shows fewer surface features than with any other process yet examined; the NO-Br system film appears particularly smooth.

Table I. Time (minutes) required for a 5000Å SiO_2 film

Temperature, °C	Steam	CO_2-$SiCl_4$	2.5% NO - 0.25% $SiCl_4$	1% CO_2-0.1% $SiBr_4$	1% NO-0.1% $SiBr_4$
825	—	—	—	143	30
900	—	—	—	58	12
950	112	>350	114	38	11
1050	44	83	17	—	—
1100	35	28	7	—	—
1200	19	5	3.2	—	—

Some other film properties are given in Table II. The etch rate and residual halogen content are of the same order as those of CO_2 process oxides. The slightly high refractive index, considered along with the absorption spectrum, opens the possibility that the films are slightly oxygen-deficient. (The high refractive index of the NO-Br system film can be accounted for by its Br content, however.) The SiO stretching vibration appears at a frequency lower than in thermal oxides, and the absorption band is considerably broadened. The NO oxide is evidently more truly amorphous, *i.e.*, has less short-range order. Instead of oxygen deficiency, an alternative explanation is that the films contain small amounts of codeposited silicon nitride. The absorption maximum of the nitride is ~850 cm^{-1}, and its refractive index near 2.0.

No hydroxyl has been detected in the Cl system films; small amounts are sometimes seen in the Br system films, but this is common in films made at 850° by any deposition process where water is a possible product.

Kodak KPR Photoresist adheres very well to NO process oxides. Patterns etched in the silica and examined at 500X have shown no evidence of resist-film lifting at the edges.

The electrical properties given in Table II have been measured on three MOS capacitors on each of 16 slices, these made in ten separate runs. The NO-Cl oxides, as made, produce a lower Si surface charge than does routinely produced steam oxide. NO-Br oxides run about twice as high as steam; these have not yet been subject to experiments on treatments to reduce the charge. Both systems produce films with acceptable insulating properties. Breakdown voltage is not polarity-dependent, and is usually sharp. A few capacitors showed "channels" (current limiting) which did not then break down further up to 2 x 10^7 v/cm.

Tests as masks against boron and phosphorus diffusion have been made with patterns etched in 0.4-0.5μ thick films made with 1% NO-0.1% $SiCl_4$ at 1100°. Conditions for the B diffusion were: B_2O_3 predeposition 18 min, 870° in N_2, later followed by 135 min drive-in at 1200° in 90% N_2-10% O_2. For phosphorus P_2O_5 in O_2 for 45 min at 1040° was used. Junctions were delineated by angle-lapping and staining. There was no instance of dopant leaking through the film, or of any mechanical film failure.

Planar transistors made with the NO process film as the first oxide were indistinguishable from those with

Table II. Properties of NO-process silica

	Steam, 1050°	NO-$SiCl_4$, 1100°	NO-$SiBr_4$, 850°
Relative etch rate, P etch*	1	1.8	3.8
Halogen content, %	0	0.5	2.6
Refractive index, 546 mμ	1.455-1.460	1.48-1.50	1.49-1.51
Water contact angle	35-40°	40°	55°
I.r. transmission minimum, cm^{-1}**	1089	1065	1064
Half-band width, cm^{-1}	85	110-170	113-121
MOS capacitor results:			
Surface charge/cm^2***	5-8 x 10^{11}	3-5 x 10^{11}	1-2 x 10^{12}
Av. dielectric constant 0.5 mc	3.9	3.7	3.8
Breakdown v/cm	6-8 x 10^6	5-10 x 10^6	5-7 x 10^6

* Ref (9).
** 0.6μ thick film.
*** As made, *i.e.*, no subsequent heat-treatment.

conventional processing in such tests as breakdown voltages, leakage currents, gain, capacitance, frequency cutoff, and saturation voltage. Extended aging tests are not yet available. A limited study of drift in films 1700-2100Å thick was made using MOS structures. After 1 hr at 100°C with a field of 10^6 v/cm (field plate positive), the surface charge density was increased by 2-4 x 10^{11}/cm^2. Freshly grown 1050° steam oxides with field plates deposited in the same evaporation equipment showed increases of 3-4 x 10^{11}/cm^2 under the same drift conditions.

Acknowledgment

The aid of J. Drobek and H. E. Nigh in the physical evaluation of the films is acknowledged with thanks.

Manuscript received Aug. 1, 1966; revised manuscript received Oct. 17, 1966. This paper was presented at the Philadelphia Meeting Oct. 9-14, 1966.

Any discussion of this paper will appear in a Discussion Section to be published in the December 1967 JOURNAL.

REFERENCES

1. W. Steinmeier and J. Bloem, *This Journal*, **111**, 206 (1964).
2. S. K. Tung and R. E. Caffrey, *Trans. Met. Soc. AIME*, **233**, 572 (1965).
3. K. H. Maxwell and L. H. Rabouin, *Electrochem. Tech.*, **3**, 37 (1965).
4. M. J. Rand and J. L. Ashworth, *This Journal*, **113**, 48 (1966).
5. P. G. Ashmore and J. Chanmugam, *Trans. Faraday Soc.*, **49**, 254 (1953).
6. S. Sourirajan and J. L. Blumenthal, *Int. J. Air Water Pol.*, **5**, 24 (1961).
7. R. J. Ayen and M. S. Peters, *Ind. Eng. Chem. Process Design Develop.*, **1**, 204 (1962).
8. W. M. Graven, *J. Am. Chem. Soc.*, **79**, 3697 (1957).
9. W. A. Pliskin and R. P. Gnall, *This Journal*, **111**, 872 (1964).

Physical Description of the Anisotropic Stress Effect in the Silicon P-N Junction Cantilever Transducer

Lewis K. Russell and Wilhelm H. Legat

Components Division, Semiconductor Operation, Raytheon Company, Mountain View, California

ABSTRACT

A silicon p-n junction device using the anisotropic stress effect has been constructed. The device exhibits a change in reverse leakage current on application of a bending force. The device consists of a narrow bar of silicon into which a sharp notch is cut electrolytically. On the opposite surface, a shallow p-n junction is produced by diffusion. Sensitivity to bending is achieved when mechanical damage is produced at the surface of the shallow junction in a controlled fashion. The corresponding change in the forward and reverse characteristics of the device after scribing is described. Methods of testing the device and changes in operating characteristics are discussed.

A theory of device operation is proposed. This theory presents a model of generation of dislocation loops from Frank-Read sources produced during the plastic deformation phase. The dislocation loops, on application of stress, enter the depletion region of the junction creating a generation current according to the Sah-Noyce-Shockley generation-recombination theory. A mathematical model of the device is developed. Operating characteristics are then compared with the mathematical model. The sensitizing operation produces noise sources within the device. The spectrum of these sources is described and the intensity is compared to device sensitivity during the scribing operation. Device noise is reduced by a decrease in the emitter perimeter. Operating characteristics of the device are discussed. These include linearity of the stress-leakage current curve, change of sensitivity with voltage, deflection with applied force, a-c impedance, junction capacity, mechanical stiffness, effective minority carrier lifetime, and fundamental vibration frequency.

In 1962, Wilhelm Rindner reported extreme changes in the electrical characteristics of p-n junctions when they were anisotropically stressed by a diamond stylus (1). He called the effect "the anisotropic stress effect" (ASE). Similar stress on the emitter-base junction of transistors will drastically modify the collector characteristics causing a large decrease in current gain (2). Indeed, any solid-state device wherein a shallow junction is anisotropically stressed will show changes in operating characteristics. Besides transistors, the devices which have been investigated include: 4-layer diodes (3) and avalanche transistors which showed changes in their negative resistance regions, field-effect transistors (3) where large impedance and transconductance changes were seen, and tunnel diodes (4) where large excess current changes were observed.

A distinct and separate stress effect was reported by Goetzberger and Finch (5) who observed a reversible change in diode breakdown voltage when the shallow junction was stressed by a stylus of material softer than silicon. Like Rindner, Goetzberger and Finch used a stylus to apply force to the junction.

Description of the Device

Figure 1 shows a sketch of a stress transducer that does not require the use of a stylus but depends entirely on the stress created at the junction by bending the device about a sharp notch running beneath the

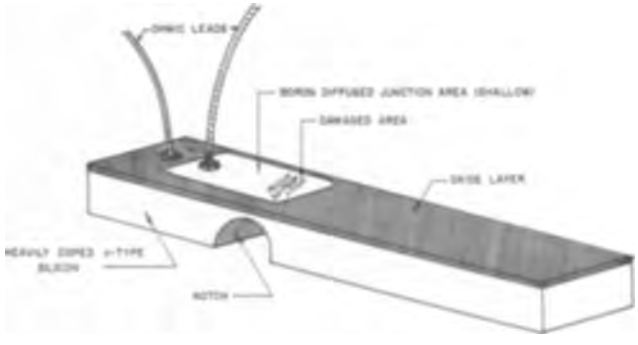

Fig. 1. Structure of the silicon p-n junction stress transducer

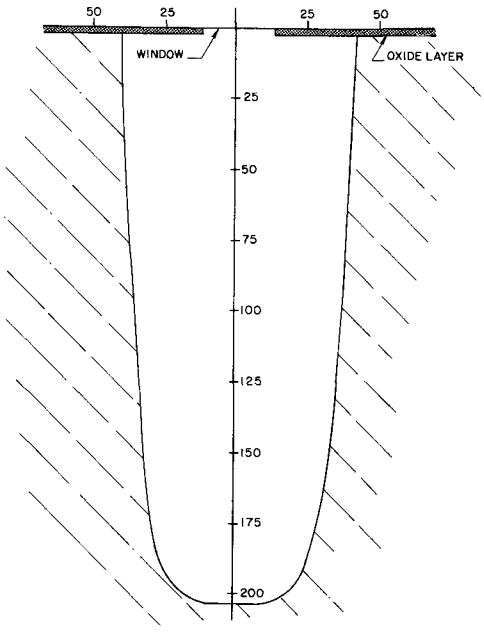

Fig. 2. Typical notch profile, in microns.

junction area. When one fastens one end of the device and bends the free end down, tension will be created at the shallow junction, ($\lesssim 0.5\mu$ deep). Bending in the opposite direction will create compression at the junction. Experimentally, it was seen that the bending occurred only in the vicinity of the notch. The high stress necessary for the anisotropic stress effect is thus produced. The range of reverse-bias operation of the device is controlled completely by the choice of starting material resistivity. If a low voltage device is desired which has voltage variations about a reference level of 1-2v, a material resistivity of about 0.01 ohm-cm is necessary as indicated in Fig. 1. Other devices were made having material resistivities as high as 50 ohm-cm. These devices were better suited for study of the effect whereas the low resistivity devices have better noise properties and are better suited for practical applications. A complex relationship exists between device sensitivity (current change per unit bending moment), applied voltage, and substrate resistivity; it has been determined empirically from measurement of many samples to be $S = 2.4V^{155}\ \rho^{-0.8}$ where S is sensitivity in μa/gcm, V is in volts, and ρ is resistivity in ohm-cm.

The junction was formed by diffusing phosphorus into n-type silicon or boron into p-type silicon to a depth of roughly $\frac{1}{2}\mu$. Suitable metallic contacts were sintered into the n- and p-regions to form ohmic contacts. Gold wires of roughly 1 mil diameter were ball-bonded onto the metal contacts leaving enough lead-length to permit easy testing.

The bridge of silicon running above the apex of the notch is typically 25μ thick. This thickness and even the notch shape may be varied to meet the demands of sensitivity and mechanical stiffness. A typical notch shape is shown in Fig. 2. Depth to width ratios of 2.5 are easily obtained by electrolytic etching. One can see in the figure the presence of a thin oxide layer with a 25μ window. Etching occurs through this window which acts as a virtual cathode in that all ionized particles must pass through this window. By varying the electrical field intensity one may vary the notch shape. The notch shape may also be varied by changing the window size and the length of time of etching.

Sensitization

Early in our work to develop the intrinsic stress transducer, we discovered that no measurable anisotropic stress effect could be produced by stress concentration alone (6). At about the same time it was discovered that physical damage occurred to the surface of p-n junctions that were stressed by diamond stylii. It thus seemed reasonable that some method of sensitization was required to produce the desired effect. Various methods of treating the surface of the junction were attempted, including damage by high-speed electrons, damage by sandblasting, damage by ultrasonic scribing, and damage by scribing with a diamond stylus under a controlled pressure. Of these four methods the last was most satisfactory and most controllable.

The damaged area shown in Fig. 1 is produced by scribing with a diamond stylus under a controlled pressure while displaying the characteristics of the diode on a Tektronix 575 curve-tracer. Scribing is continued until a given degradation of the reverse characteristic of the diode is obtained. Figure 3 shows a drawing of the reverse characteristic of a typical diode with a high resistivity before and after

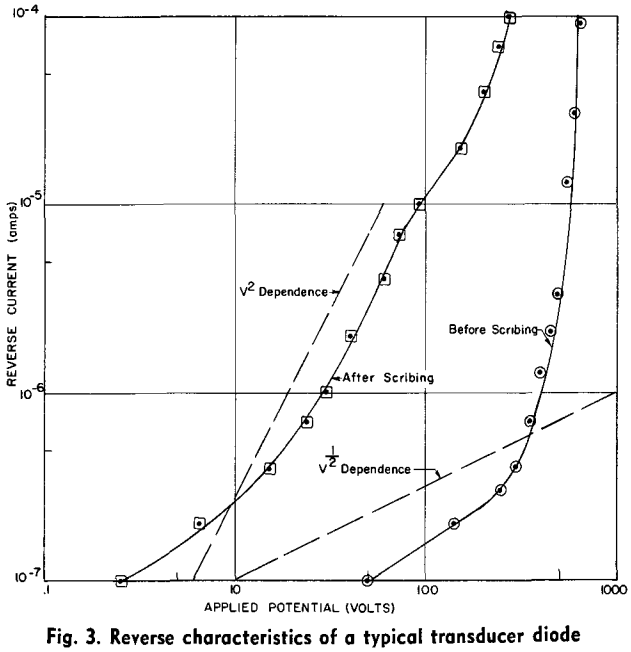

Fig. 3. Reverse characteristics of a typical transducer diode

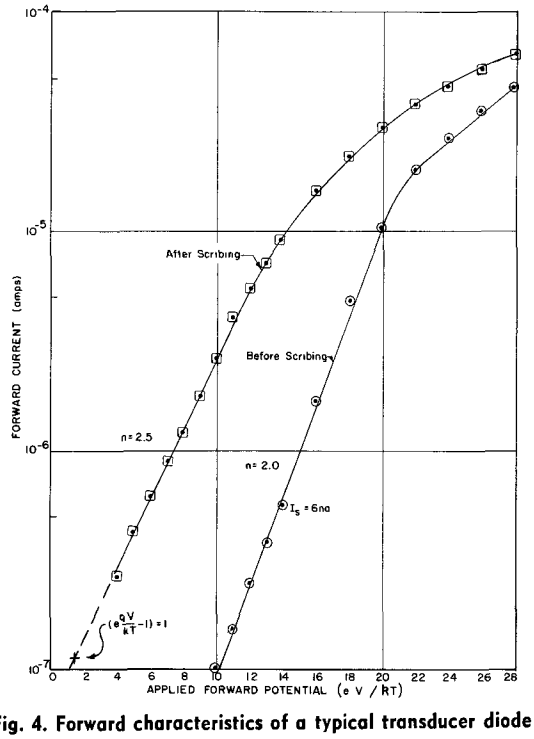

Fig. 4. Forward characteristics of a typical transducer diode

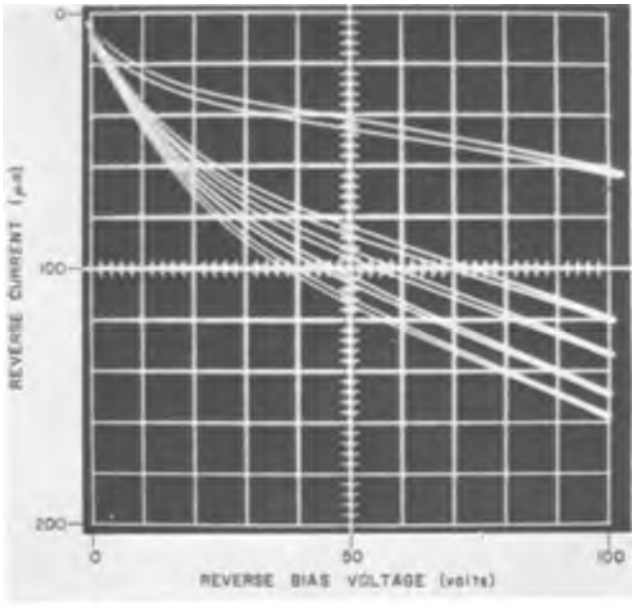

Fig. 5. Multiple exposure oscillograph of the reverse characteristics of a transducer diode under forward loads of 0, 9,000, 12,000, 14,500, and 17,000 dynes at a distance of 2 mm from the notch.

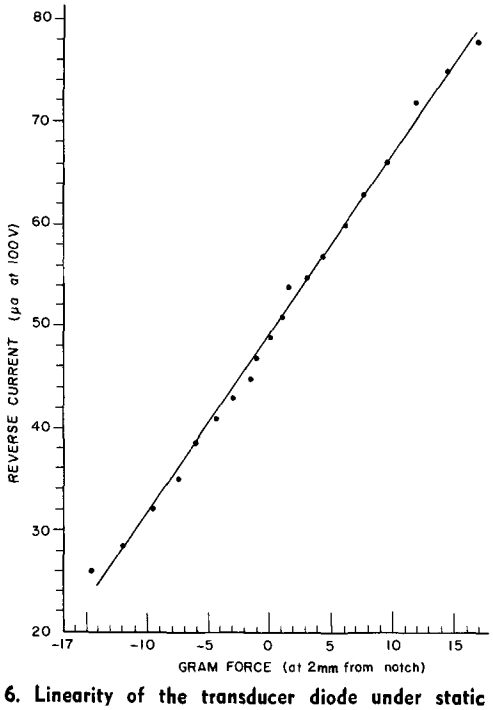

Fig. 6. Linearity of the transducer diode under static test.

scribing. Before scribing the leakage current is very small; after scribing a large leakage current is seen. We have deliberately destroyed some of the rectifying properties of the diode, principally, the high impedance in the reverse bias condition. Figure 4 shows that the forward current increased by about an order of magnitude up to an applied forward potential of about 15 ev/kT. In both forward and reverse bias conditions, the amount of change is proportional to the amount of damage sustained by the junction. With little damage, there would be little change in the operating characteristics.

Response

Figure 5 shows a multiple exposure oscillograph of a typical transducer under forward loads of from 9,000 to 17,000 dynes. The top curve is the zero load curve. Forward load refers to the fact that bending occurs in such a way as to produce compression at the junction. Under reverse load, tension would be created at the junction, and the characteristics of the device under load would fall above the zero load line. Thus, forward load produces an increase in reverse current and reverse load produces a decrease in reverse current. Figure 6 best illustrates the difference. Here, reverse current is plotted against gram force at a distance of 2 mm from the notch. One notices that a reverse current of 50 μa at 100v bias is obtained when the device is unstressed. At a forward load of 9800 dynes, reverse current has risen to 67 μa. The corresponding reverse load produces a reverse current of 32 μa.

In the earliest devices made, we could obtain an initial sensitivity of about 2 μa/dyne-cm. Under testing and high current heating, this sensitivity dropped to about 0.86 nanoamp/dyne-cm. This represents a factor of 2000 change. At this final sensitivity little further sensitivity degradation of the device was seen. More recent devices have not shown this much decrease of sensitivity, but some annealing is observed after the sensitizing process. We have also seen experimentally that temperatures on the order of 500°C will accelerate this annealing process. Complete annealing, however, is not possible even at temperatures up to 800°C, and usually 0.17% of the initial sensitivity remains at this temperature.

Figure 7 shows a typical graph of the reduction of reverse leakage current over a period of continuous testing at high dissipation levels. The device was reverse biased at 100v. The top curve shows the initial current-force characteristic. The slope of this curve from 1 to 3½g force shows a 25 μa/g sensitivity. The 40 mw dissipation is shown by the arrow. After 2 hr of testing, the sensitivity dropped to 16 μa/g. The 20 mw power dissipation point is shown by the arrow on this curve. After 6 hr of continuous testing, the sensitivity had dropped to 5 μa/g. After 10 hr, the sensitivity was 2 μa/g, and further reduction of device stress sensitivity was slight. The 5 mw point is shown on the diagram.

This sensitivity degradation or annealing of the anisotropic stress effect was at first considered to be a serious flaw in the device design. However, after the initial annealing is accomplished, the characteristics remain stable over long periods of time. This type of Joule heat annealing has also been shown to exist in germanium tunnel diodes which were degraded by indentation with a stylus and by 2 Mev

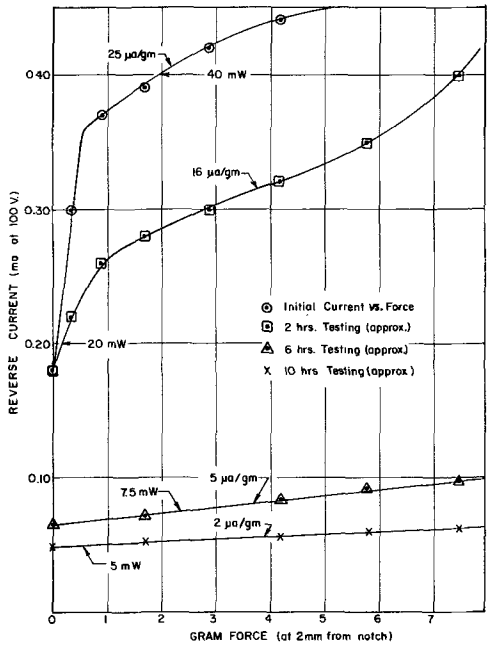

Fig. 7. Decrease of reverse current sensitivity over a period of continuous testing at high dissipation levels (100v reverse bias).

electrons (7). Stability was tested by bending the device in forward and reverse directions continuously at 120 Hz for a period of 11 months. During this time further degradation of the device characteristics was not observed. This test was performed at room temperature. Temperatures up to 100°C did not seem to cause further deterioration of the device characteristics, *i.e.*, sensitivity.

Theory of Device Operation

Several models of the anisotropic stress effect have been proposed up to this time (4, 8, 9). These models include piezoresistance, internal field emission, band bending, and generation-recombination. These models have all been examined in detail by Rindner (3, 10). The piezoresistance and internal field emission models predict a reverse current change with applied force having the wrong temperature dependence, whereas band bending has been shown (9) to produce a smaller effect in the reverse bias condition of silicon (111) diodes than is seen experimentally. As stated earlier, no stress sensitivity was detected by using the notch alone; sensitivity was seen only after the sensitization was accomplished. The fact that ASE sensitivity can be annealed out strongly suggests that the major mechanism contributing to the effect is one that is also affected by high temperature. The best model having the correct temperature dependence and strong stress sensitivity is the generation-recombination model. This model was first proposed by Rindner in 1963 (8) and is the model which best describes the results obtained with the present transducer.

In the early work using the diamond stylus visible damage was seen on the surface of the semiconductor even at very low forces. Rindner, in his discussion of stylus type anisotropic effect, also indicates a limit to complete reversibility of the effect, *i.e.*, when a certain load on the stylus was exceeded, the zero stress curve had shifted in the direction of increasing current. Thus the junction and the electrical characteristics of the junction show permanent deterioration. Surface damage of this type is very likely to produce dislocations which extend deep into the body of the semiconductor material. These dislocations have been postulated to be loops which are pinned to the damage at the surface or to internal defects. Annealing of the damaged surface at the plastic flow temperature and subsequent etching with CP4 shows the typical rosette pattern of dislocation loops attaching to pinning points at the surface (11). These rosette patterns have long been known to exist in lithium fluoride crystals which have been indented by small particles (12).

Pariiski, Landau, and Startsev investigated the jumping of dislocation loops in LiF single crystals when the pinning points were etched away (13). They found that energy was stored in the dislocation loops, and when the pinning points were removed the loops would reduce in size, collapsing toward the center, until the loop intersection with the surface encounters another pinning point or blocking point which retards further jumping. Jumping occurs with subsequent etchings until the dislocation loop completely annihilates itself. These specimens were etched at room temperature without application of any external load to the crystal. These researchers determined a lower limit of the dislocation velocity during the jump. This minimum velocity was given as about 500 μ/sec. They conclude that the velocity might be much higher than this.

Chaudhuri *et al.* (14) have investigated the velocity of dislocations in semiconductors. They propose an activation energy for dislocations in silicon of 2.17 ev which appears to be independent of stress level and temperature. Using the equation for the velocity of a dislocation held by pinning points (locks) proposed by van Bueren (15) and reasonable stress values, one would predict velocities of from 3 to 3000 cm/sec at room temperature. For example, a loop 1000Å in length and a stress level of 1.075×10^8 dynes/cm^2 (less than two orders of magnitude below the theoretical yield strength of silicon) would produce a velocity of 250 cm/sec. Detailed calculation of dislocation velocity using van Beuren's equation may be found in the appendix.

Direct experimental measurement of these velocities are made extremely difficult because the loops are, first of all, quite small, and second, they encounter obstacles in the form of other loops and flaws which again pin the moving loop and retard or stop its forward motion. Celli *et al.* (16) have proposed a model of dislocation motion which considers the effect of dragging points. With reasonable assignment of parameters the theory is able to agree with experimental values of dislocation velocity. Although dislocation velocities of the magnitude proposed here have not been observed by direct experiment, some indirect evidence does exist that very high dislocation velocities are achieved in crystals at room temperature, *e.g.*, in LiF. The experimental difficulties of growing sufficiently pure dislocation free silicon crystals have restricted all experiments to crystals having a high density of dragging points and hence quite low dislocation velocities. Since we have been unable to detect any significant ASE due to bending stress alone, we have been forced to conclude that damage, and hence dislocations, have a key role in the effect. To our knowledge we know of no other experiments wherein anisotropic stress has been applied to a shallow p-n junction in the absence of damage and where the ASE has been demonstrated. If one now assumes the existence of such dislocation loops pinned to the surface at the damaged region created by the scribe line (the results of Rindner seem to indicate this is possible), one may extend or diminish the loop size by compressing or extending the material between the pinning points as shown in Fig. 8. Kabler (17) has indicated that the loop is probably a half-hexagon where loop growth is accomplished by motion parallel to the surface of the 60° segments and motion perpendicular to the surface of the bottom segment. In Fig. 8, 9, and 10 the depletion layer is shown as roughly symmetrical about the junction. This corresponds to the low-voltage transducer design wherein a shallow diffusion is made into an already heavily doped crystal. The dimensions are not accurate since the figures are intended to illustrate the dislocation motion only.

Another mechanism by which dislocations may enter the depletion region is as follows. Deformation

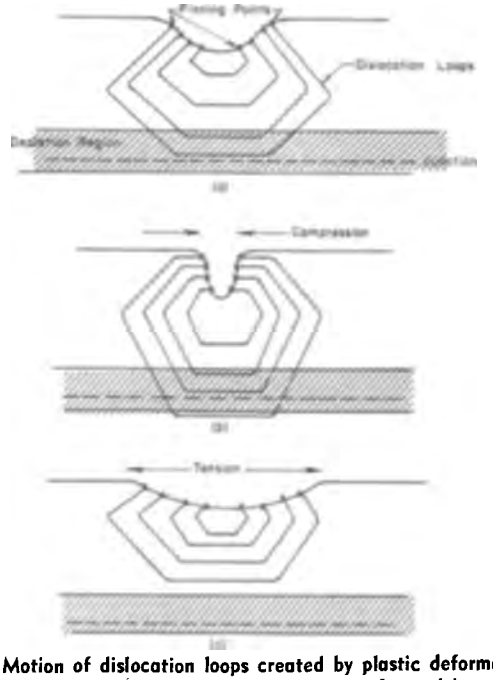

Fig. 8. Motion of dislocation loops created by plastic deformation (scribing): (a) no stress; (b) compression at surface; (c) tension at surface.

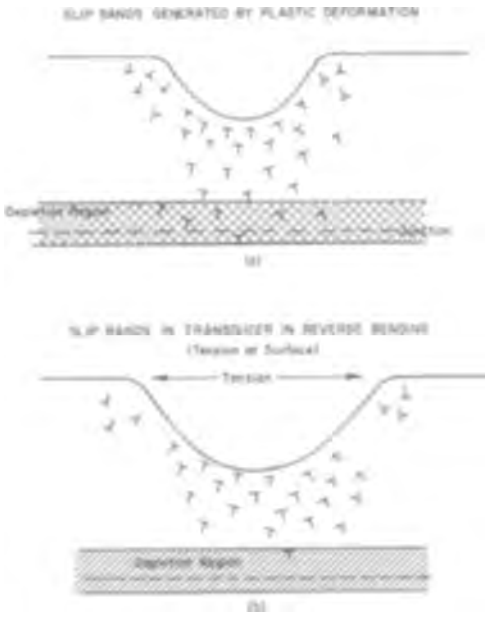

Fig. 9. Motion of slip bands created by plastic deformation: (a) no stress; (b) tension at surface.

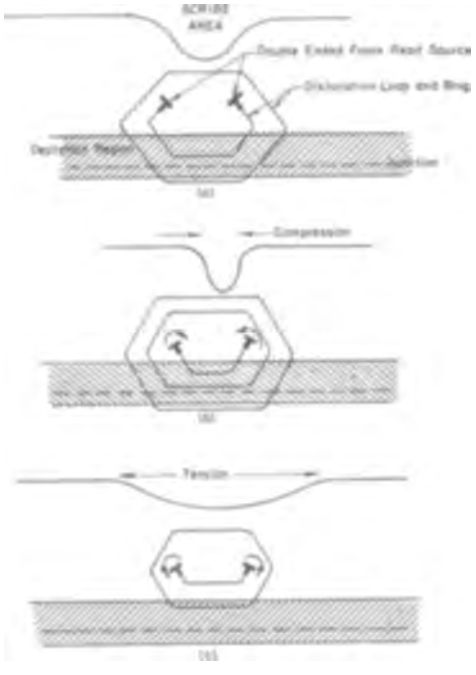

Fig. 10. Motion of dislocation loops and rings emanating from a double-ended Frank-Read source: (a) no stress; (b) compression at surface; (c) tension at surface.

bands are known to be generated by plastic deformation. These bands are formed mostly in crystals by compression or tension rather than in bending or twisting. Slip bands are formed across the deformation bands without interruption apart from bending to follow the curvature of the lattice as shown diagramatically in Fig. 9. On forward bending, compression is created at the surface, and the slip bands, under compression, migrate deeper into the body of the material. Thus more dislocations enter the depletion region of the p-n junction. Reverse bending causes tension at the junction as shown. The slip bands migrate toward the surface pulling the dislocation lines out of the depletion region. As seen in Fig. 9, the number of dislocations at any point is proportional to the radius of curvature at that point. An increase in the radius of curvature at the surface will cause the dislocations to pull in toward the scribe line.

The two theories of reversible movement of dislocations in and out of the depletion region may not be the only ones possible. In creating the anisotropic stress effect, both theories of dislocation movement may apply. The movement of dislocation lines and loops is further complicated by Frankel defects and foreign atoms lying inside the crystal bulk. Thus the theories presented here are not complete answers but merely steps toward solving a complicated phenomenon. A third theory involves a merging of the two previous theories. In Fig. 9 the parallel dislocation lines may, under stress, rotate forming dislocation loops. Pairs of dislocation lines may act as double-ended Frank-Read sources (18). After plastic deformation, dislocation loops may already have been generated by the dislocation line pairs. Many of these loops enter the depletion region causing the degraded reverse characteristic. Figure 10 shows a diagram illustrating the process. Under compression the loops radiate further outward and more loops are formed by the line pairs. When the compression is relieved, the dislocation loops collapse toward the Frank-Read sources as in the diagram. Tension causes further collapse of the loops and even the collapse of rings that have been formed. This pulls more loops and rings out of the depletion region. This effect is known as the Bauschinger effect (19). When the device is under forward pressure, compression is applied to the scribed area and an increase in reverse leakage current is observed. This corresponds to an increase in the number of dislocation loops in the depletion region. In Fig. 10 only one double-ended Frank-Read source is shown. In reality, there may be many Frank-Read sources packed close together under the scribe line, the density of sources being proportional to the amount of plastic damage sustained by the crystal during the sensitizing process. One must recognize that this theory is very incomplete and has not been proven by an extensive program of metallurgical experiments.

We have endeavored, using x-ray diffraction studies, to determine whether room temperature scribing with a diamond stylus would produce any dislocations in silicon. The silicon slices were cut from an ingot doped with antimony to a resistivity of roughly 0.01 ohm-cm. They were lapped to 15 mils thickness and chemically polished to a final thickness of 11 mils. Scribing was performed in the $(1\bar{1}0)$ direction and perpendicular to the $(1\bar{1}0)$ direction with forces of 2000, 4000, and 8000 dynes. X-ray micrographs were taken following scribing with the diffracting plane lying in the $(1\bar{0}1)$, $(1\bar{1}0)$, and the $(0\bar{1}1)$ planes of the slice. If the Burgers vector of a generated dislocation lies in the diffracting plane it will almost disappear from the micrographs, whereas if it is perpendicular to the dif-

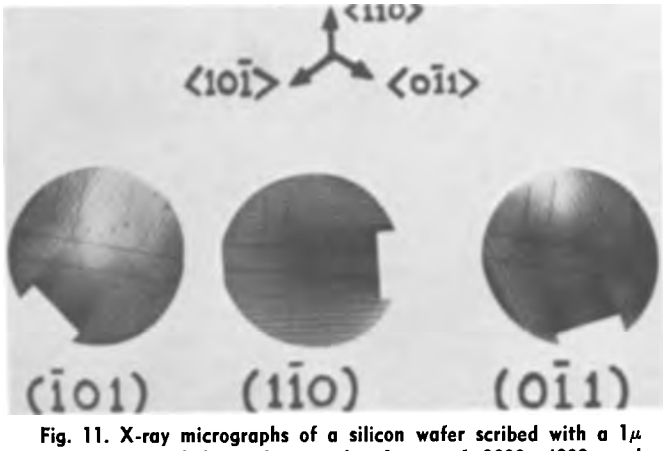

Fig. 11. X-ray micrographs of a silicon wafer scribed with a 1μ diameter diamond hemisphere under forces of 2000, 4000, and 8000 dynes along the <111> direction and perpendicular to the <111> direction. Diffractiongraphs were taken with the plane of diffraction parallel to the $(\bar{1}01)$, $(1\bar{1}0)$, and $(0\bar{1}1)$ planes of the crystal.

fraction plane it will exhibit maximum contrast. Figure 11 shows the existence of dislocations due to room temperature scribing. In the center micrograph the short 2000 dyne/cm^2 line has all but disappeared. The diffraction plane is here almost parallel to the dislocation Burgers vector. In the two side micrographs the diffraction plane lies at 30° to the Burgers vector of the long lines. Here the 2000 dyne/cm^2 line shows much reduced contrast. Further diffraction experiments have been completed and will be reported in the near future (20).

It is known that dislocations act as acceptors in silicon producing trapping levels in the forbidden region between the valence band and the conduction band. Depending on the position of the Fermi level, the acceptor sites are filled to some degree, and the dislocation line is negatively charged. This negative line charge is neutralized by a cylindrical space charge of fixed donors around the dislocation. It has been confirmed (21) that dislocations produce recombination centers in germanium and that the minority carrier lifetime is drastically decreased by the existence of these recombination centers. Indeed, at room temperature, p-type germanium has a lifetime of $\tau=0.7/N_d$. In n-type, the lifetime is $\tau=2.5/N_d$ where N_d is the dislocation density. One would expect similar relationships to exist for silicon.

Up to now the argument has been to link the reversible motion of dislocation loops with reversible changes in the leakage current of the back biased diode. Justification for this linkage can be made by using the Sah-Noyce-Shockley model of carrier generation and recombination in p-n junctions and its effect on p-n junction characteristics (22). for medium to large reverse bias ($V > kT/q$) the generation current is given by Eq. [1].

$$J_{gr} = \frac{qn_i W}{2\sqrt{\tau_{no}\tau_{po}}} \left[\cosh\left\{\left(\frac{E_t - E_i}{kT}\right) + \ln\sqrt{\frac{\tau_{po}}{\tau_{no}}}\right\}\right]^{-1} \quad [1]$$

where W is the space charge layer width, τ equals minority carrier lifetime, E_t the energy level of the traps, and E_i the energy of the intrinsic Fermi level. τ_{no} and τ_{po} are the electron and hole minority carrier lifetimes. When the trap levels lie at mid-band the first term in the hyperbolic cosine is 0 and the term in square brackets is given by expression [2].

$$\cosh\left\{\ln\sqrt{\frac{\tau_{po}}{\tau_{no}}}\right\} = 1/2\left(\exp\left[\ln\sqrt{\frac{\tau_{po}}{\tau_{no}}}\right] + \exp\left[-\ln\sqrt{\frac{\tau_{po}}{\tau_{no}}}\right]\right) = 1/2\left(\sqrt{\frac{\tau_{po}}{\tau_{no}}} + \sqrt{\frac{\tau_{no}}{\tau_{po}}}\right) \quad [2]$$

As a simplifying assumption, let us consider this to be true (Rindner has found the effective trapping level in germanium to be 0.09 ev from the intrinsic Fermi level). Using this simplifying assumption, Eq. [1] now becomes

$$J_{gr} = +\frac{qn_i W}{4}\left(\frac{1}{\tau_{po}} + \frac{1}{\tau_{no}}\right) \quad [3]$$

We see that the generation recombination current is dependent upon depletion layer width and lifetime. Investigators of ASE in Japan have been successful in demonstrating up to a 30% decrease in minority carrier lifetime under both uniaxial and anisotropic stress for both germanium and silicon (23, 24). They attributed the reduction in lifetime to strain fields and expressed total lifetime as a function of two components, the stress independent and the stress dependent lifetimes, in the following fashion:

$$\frac{1}{\tau_n} = \frac{1}{\tau_{no}} + \frac{1}{\tau_\sigma}$$

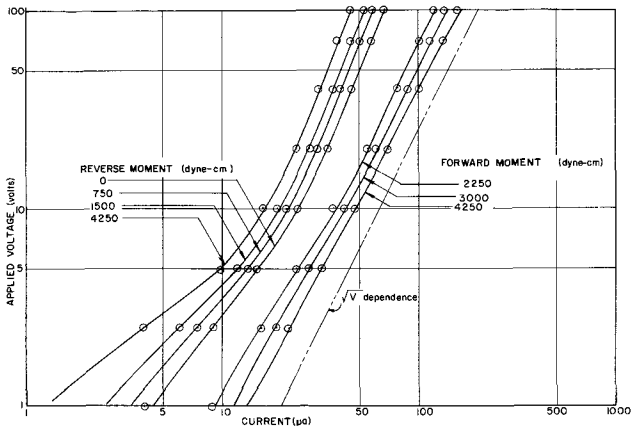

Fig. 12. Reverse characteristics of a typical transducer diode under stress.

where τ_σ has the following dependence

$$\tau_\sigma = \frac{1}{vAN}$$

where v is the thermal velocity of minority carriers, cm/sec^{-1}, A the capture cross section for minority carriers, cm^2, and N the number of recombination centers, cm^{-3}.

Assuming v and A constant throughout our measurements we may obtain J_{gr} as a function of N. Thus for an N-type substrate with a p-type diffusion the lifetime of minority carriers in the surface layer will be

$$\tau = \left[\frac{1}{\tau_{no}} + vAN\right]^{-1}$$

Since the p-n junction is formed by using a constant impurity source high-temperature diffusion for a very short time, it will closely approximate a step junction, especially at the higher voltages and for shallow junctions. For a 0.5μ junction the voltage at which the cube root dependance becomes a square root dependance is about 2v (26). Using the step-function equation for depletion layer width given by Eq. [4]

$$W = \left[\frac{2\kappa\epsilon_0 V'}{q(N_D - N_A)}\right]^{1/2} \quad [4]$$

and considering only the effect of the change of minority carrier lifetime given by the equation above we have

$$J_{gr} = \frac{qn_i}{4}\left[\frac{2\,\kappa\epsilon_0 V'}{q(N_D - N_A)}\right]^{1/2}\left(\frac{l}{\tau_{no}} + vAN\right) \quad [5]$$

where V' is the applied voltage plus the built-in voltage.

Thus, for reverse voltages greater than kT/q the generation-recombination current is proportional to the density of recombination centers in the depletion region and proportional to the square root of the applied voltage. Figure 12 shows the square root voltage dependence for our device under various forward and reverse load conditions and for reverse bias. Figure 6 shows clearly that the current-force relationship was quite linear which would suggest that recombination center density is linearly proportional to the applied bending moment. Note that an approxi-

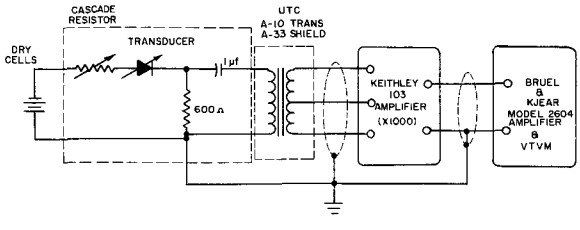

Fig. 13. Transducer noise measurement set-up

mate square-root voltage dependence is maintained for both forward and reverse bending moment for voltages above 5v. Below this voltage the slope changes somewhat for the reverse moment curves in the direction of lower resistance approaching an inverse cube-root dependence.

For the moment it is not clear whether the change in τ_σ is due to a change in A or a change in N. Certainly a strain field would change A, but on the other hand dislocation loops have been shown to exist in silicon, they have been shown to move rapidly as a function of the motion of the pinning points in LiF, and we show here that ASE is seen in the bending mode only when damage is present. With this assemblage of facts it does not seem too unreasonable to postulate that the change in $1/\tau_\sigma$ is due to N, and that the change in N is due to the reversible movement of dislocation loops into the depletion region as previously discussed.

Noise

Electrical noise generated at the junction was investigated using the apparatus shown in Fig. 13. The transducer diode was biased at its normal operating voltage (around 1.0v for the low-voltage variety and 45.0v for the high-voltage type). Using this set-up the noise current-frequency spectrum was found to be approximately (1/f) from 1 to 100 kHz both before and after the sensitizing operation although scribing increased the noise current over the entire range by roughly a factor of 10 as shown in Fig. 14. Indeed, scribing changes the noise current from about 6 na to about 60 na on typical units as may be seen from Fig. 15. The oxide layer offers some protection as can be seen by the increase of noise after oxide removal. Much of the noise eliminated by the oxide layer is below 100 Hz and is due to slow states in the thin air grown oxide present after the removal of the thermal oxide. The noise current generated by scribing is (1/f) flicker noise due to reverse leakage current. As was mentioned earlier, scribing degrades the reverse characteristic lowering the resistance, and increasing the leakage. Fonger (27) has shown that this type of noise current is directly proportional to leakage current. We have observed this type of behavior as may be seen from Fig. 16.

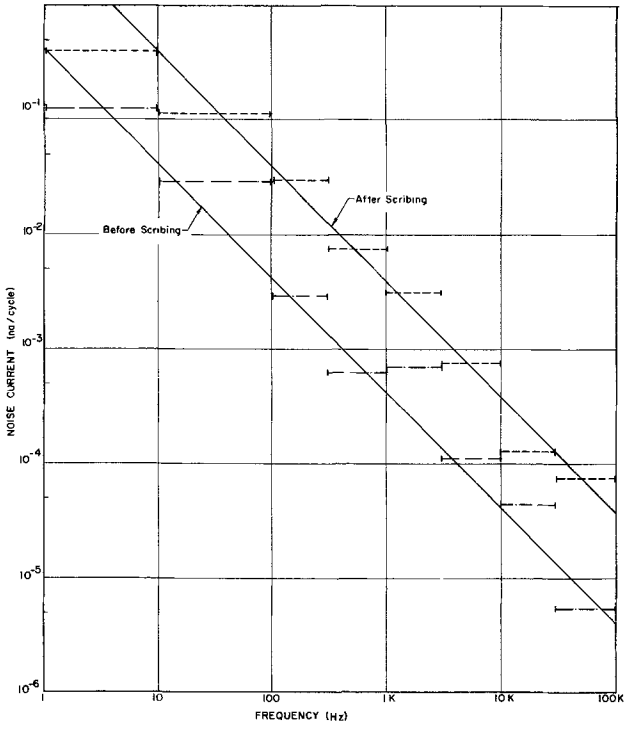

Fig. 14. Noise current spectrum of a typical transducer diode

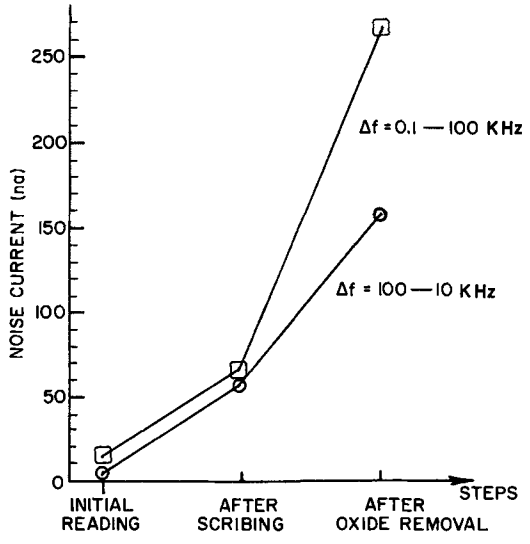

Fig. 15. Noise current increase in the transducer diode after scribing and oxide removal.

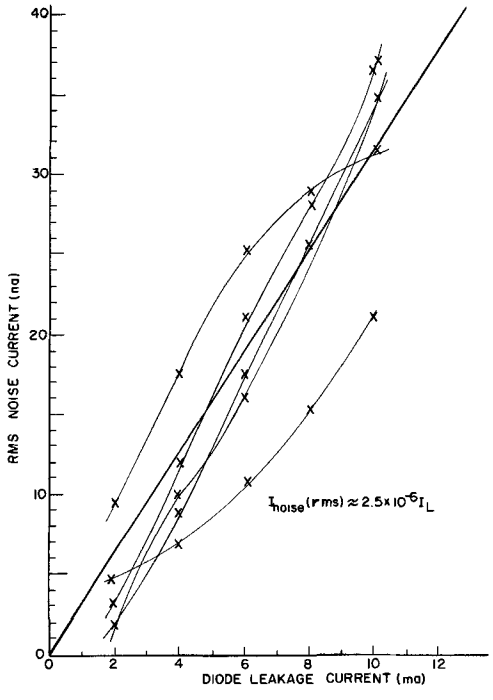

Fig. 16. Variation of diode noise current with reverse leakage current.

With the protective oxide present the transducer is insensitive to gaseous ambients. Gas cycles using dry N_2, wet N_2, O_2, and air were applied to the surface without a change in noise current. CCl_4 was also tried as an atmosphere, but it did not change the (1/f) spectrum or intensity. Contact noise has been shown to be responsible for flicker noise by Montgomery (28).

An experiment involving four ohmic contacts on the diode showed that contact noise was responsible for only 20% of the total (1/f) noise. About half of the total noise is located at the perimeter of the junction where it intersects the oxide layer. Reduction of this perimeter correspondingly reduced the (1/f) noise. This noise is also leakage noise generated by channeling under reverse bias.

Since the sensitivity of the transducer increases with scribing as well as the noise it was at first thought that the signal-to-noise-current ratio might remain

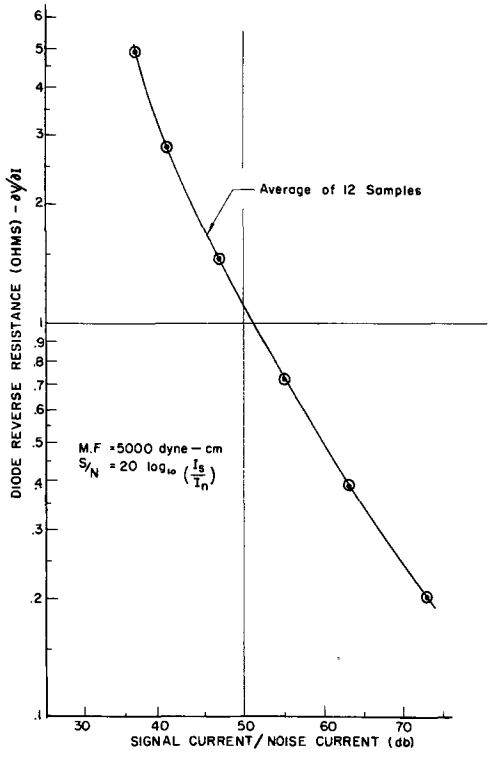

Fig. 17. Change in signal-to-noise ratio as a function of diode reverse resistance.

constant during the process. However, an experiment revealed that the signal-to-noise ratio actually slowly increased with scribing as shown in Fig. 17. In the figure the reverse resistance is the slope of the reverse-biased current-voltage trace taken at the operating voltage. The increase in S/N ratio is perhaps due to the relative decrease in importance of nonscribe-related noise sources. A device with 75db signal-to-noise ratio was obtained under a 5000 dyne-cm variation.

An analysis of stress created at the junction in a direction parallel to the surface and perpendicular to the notch indicates a stress maximum of 3.6×10^9 dynes/cm^2 for a bending moment of 5000 dyne-cm. Beyond this stress the more fragile units would fracture. The pressure and shape of the notch seriously complicates an analysis of the stresses at the junction itself although methods of analysis exist (29). A typical notch had a mechanical stiffness of 3.3×10^5 dynes/cm.

A recent analysis of dislocation velocity (14) in silicon indicates a room temperature velocity for these stress levels above 100 cm/sec. For a movement of 0.1μ a frequency of 10 MHz is theoretically possible. The maximum frequency of vibration of the free end of the transducer is however related to the geometry of the device. Typical units had a 10 kHz self-resonance, and no attempt was made to increase this value. Mechanical stiffness for the 10 kHz resonance was about 3×10^5 dynes/cm.

Effective junction lifetime using the method of Lederhandler and Giacolleto (30) was found to be in the range of 1 μsec before stress was applied. One must remember here that this already represents the lifetime of a seriously degraded junction. This lifetime corresponds to that obtained by Matsuo (31) using a stylus pressure of almost 30g. A simple equivalent circuit of the diode under reverse bias is a variable resistor with a zero-stress resistance of 500 ohms in parallel with a capacitor of about 200 pf capacity. Impedances calculated using this model are in close agreement to measurements taken on a typical transducer diode from d.c. to 1 MHz.

Manuscript received Nov. 22, 1965; revised manuscript received Oct. 14, 1966. This paper was presented at the San Francisco Meeting, May 9-15, 1965.

Any discussion of this paper will appear in a Discussion Section to be published in the December 1967 JOURNAL.

REFERENCES

1. W. Rindner, *J. Appl. Phys.*, **33**, 2479 (1962).
2. W. Rindner and R. Nelson, *Proc. IRE*, **50**, 2106 (1962).
3. W. Rindner, G. Doering, and R. Wonson, *Solid State Electronics*, **8**, 227 (1965).
4. W. Bernard, W. Rindner, and H. Roth, *J. Appl. Phys.*, **35**, 1860 (1964).
5. A. Goetzberger and R. H. Finch, *ibid.*, **35**, 1851 (1964).
6. W. H. Legat and L. K. Russell, *Solid State Electronics*, **8**, 709 (1965).
7. W. Rindner, H. Roth, and W. Bernard, *J. Appl. Phys.*, **36**, 3625 (1965).
8. W. Rindner and I. Braun, *ibid.*, **34**, 1958 (1963).
9. R. Edwards, Trans. IEEE-ED11, 286 (1964). J. J. Wortman, J. R. Hauser, and R. M. Burger, *J. Appl. Phys.*, **35**, 2122 (1964).
10. W. Rindner, *J. Appl. Phys.*, **36**, 2513 (1965).
11. W. Rindner and R. F. Tramposch, *ibid.*, **34**, 758 (1963). R. F. Tramposch and W. Rindner, *Appl. Phys. Letters*, **3**, 42 (1963).
12. J. J. Gilman and W. G. Johnston, "Dislocations and Mechanical Properties of Crystals," J. Wiley & Sons, Inc., New York (1957).
13. Z. B. Pariiski, A. I. Landau, and V. E. Startsev, *Soviet Phys. Solid State*, **5**, 1002 (1963).
14. A. R. Chaudhure, J. R. Patel, and L. G. Rubin, *J. Appl. Phys.*, **33**, 2736 (1962).
15. H. G. van Bueren, "Imperfections in Crystals," North-Holland Publishing Co. (1960).
16. V. Celli, M. Kabler, T. Ninomiya, and R. Thomson, *Phys. Rev.*, **131**, 58 (1963).
17. M. N. Kabler, *ibid.*, **131**, 54 (1963).
18. A. H. Cottrell, "Dislocation and Plastic Flow in Crystals," Oxford Press (1953).
19. N. F. Mott, "Dislocations and Mechanical Properties of Crystals," Lake Placid Conference, John Wiley & Sons, Inc., New York (1957).
20. E. M. MacKenna, W. H. Legat, and L. K. Russell, To be published.
21. G. K. Wertheim and G. L. Pearson, *Phys. Rev.*, **107**, 694 (1957).
22. C. T. Sah, R. N. Noyce, and W. Shockley, *Proc. IRE*, **45**, 1228 (1957).
23. Y. Matukura, *Japanese J. Appl. Phys.*, **3**, 256 (1964).
24. T. Imai, M. Uchida, H. Sato, and A. Kobayashi, *ibid.*, **4**, 102 (1965).
25. Y. Matukura and Y. Miura, *ibid.*, **4**, 72 (1965).
26. "Integrated Silicon Device Technology—Vol. II" AD423148-Defense Documentation Center (unclassified).
27. W. H. Fonger, "Transistors L" RCA Laboratories, Princeton (1956).
28. H. C. Montgomery, *Bell Syst. Tech. J.*, **31**, 950 (1952).
29. H. Neuber, "Kerbspannungslehre," J. Springer, Berlin (1958).
30. S. R. Lederhandler and L. J. Giacoletto, *Proc. IRE*, **43**, 477 (1955).
31. K. Matsuo, *J. Phys. Soc. Japan*, **19**, 1490 (1964).

APPENDIX

Calculation of dislocation velocities at room temperature under high stress.—Van Bueren has derived an expression for the velocity of a dislocation line pinned between two points in a crystalline lattice (15). The resulting expression is given below.

$$v = \nu_0 b \exp(-E/kT) \sinh(\tau b^2 l/kT)$$

where ν_0 is the lattice vibrational frequency, b the distance of line travel (minimum of one lattice constant), τ stress level, l length of dislocation line between pinning points, and E activation energy for the motion of a dislocation; k and T have their usual meaning.

When $b^2 l >> kT$ we have $\sinh(\tau b^2 l/kT) \approx \frac{1}{2} \exp(\tau b^2 l/kT)$ and our equation becomes

$$v = \frac{\nu_0 b}{2} \exp\left(\frac{\tau b^2 l}{kT} - \frac{E}{kT}\right)$$

Consider a dislocation loop 1000Å long between the two pinning points. If we subject the loop to a stress of 10^8 dynes/cm^2 the resulting dislocation velocity should be found as shown below:

for $b = 5.4 \times 10^{-8}$ cm; $b^2 = 2.916 \times 10^{-15}$ cm^2
$\nu_0 = k\theta_0/h = 1.376 \times 10^{13}$ (sec)$^{-1}$ (θ_0 = Debye temperature)
$k = 1.38 \times 10^{-16}$ ergs/°K $= 8.625 \times 10^{-5}$ ev/°K
$T = 300$°K; $kT = 4.14 \times 10^{-14}$ dyne-cm $= 0.0258$ ev
$E = 2.17$ ev (14)

Since $\tau b^2 l/kT = 70.42$ and $E/kT = 83.86$, the exponential term equals 8.23×10^{-5}.

Also $\nu_0 b/2 = 3.72 \times 10^5$ which yields $v = 3.06$ cm/sec.

If we increase the stress level slightly (say by only 1%) a large increase in dislocation velocity results.

We now have

$$\tau = 1.01 \times 10^8 \text{ dynes/cm}$$
$$\tau b^2 l/kT = 71.121$$

and the exponential term becomes 8.83×10^{-6}. This gives a resultant $v = 3.28$ cm/sec, *i.e.*, almost a 10% increase in velocity. Calculations of 5, 7.5, and 10% increases in stress yield velocities as shown below:

% Increase	Velocity, cm/sec
1.0	3.28
5.0	18.0
7.5	250.0
10.0	3.120.0

Since τ and l exhibit the same behavior in the equation, a slight change in the length of the dislocation loop would produce the same effect on the dislocation velocity. We also observe that the distance of travel of the loop (b) profoundly affects the dislocation velocity. The distance of travel will of course be limited by crystalline imperfections preventing its forward travel. When such an imperfection is encountered by a loop, a great deal more energy is needed to overcome this barrier than is necessary for simple unhindered forward travel.

The velocity calculated above is instantaneous velocity between imperfections as opposed to average velocity taken over large distances and times. Average velocity is the quantity reported in experiments on various materials. Chaudhuri *et al.* (14) report that the distances over which the dislocations accelerate before encountering imperfections are small compared to the distances necessarily involved in making an experimental measurement of dislocation velocity.

Chemical Etching of Germanium in the System HF-H_2O_2-H_2O

B. Schwartz[1]

Bell Telephone Laboratories, Incorporated, Murray Hill, New Jersey

ABSTRACT

The etching of germanium in the system HF-H_2O_2-H_2O has been studied, and comparisons are made with results obtained from the HF-HNO_3-H_2O system. Strong crystal-orientation influences and relatively high apparent activation energies are observed; surface reactivity and subsequent removal of reaction products are consequently proposed as rate limiting in the etching reaction. On the basis of equilibrium in the adsorption-dissociation steps, an equation is derived which describes the rate data obtained over the entire concentration and temperature ranges studied. Evidence is presented to show that divalent germanium is the prime oxidation state leaving the (100) and (111) surfaces. $GeOF_2$ is postulated as one of the reaction products leaving the (110) surface.

The use of semiconductor materials in the fabrication of active electronic devices has resulted in much work on the chemistry of these materials. Most of the effort has been spent on the problems of impurity content, stoichiometry, and thermodynamics in the formation of single crystals of these materials (1-3). Another important aspect is the etching of the single crystals to obtain the desired electrical and geometrical characteristics (4).

When an elemental semiconductor is etched in an aqueous system, somewhere in the process oxidation of the element must occur in order to produce a removable product. For that reason, an oxidizing agent is always present in the solution[2] when either silicon (6, 7) or germanium (8-11) is etched. In most cases nitric acid is used as the oxidizing agent and hydrofluoric acid is added as the means of forming a soluble or gaseous reaction product (6, 8, 11). However, the etching of germanium in the system HF-HNO_3-H_2O is beset with many difficulties, such as uncontrollable induction periods and passivating films (9, 11). Another etching system for germanium that has found practical application is HF-H_2O_2-H_2O (10). This paper reports the results of a study of the etch rate of single-crystal germanium in aqueous solutions of HF and H_2O_2 as a function of the composition and temperature of the etchant. The influence of crystallographic orientation and conductivity type of the germanium specimens on the etch rate is discussed. A kinetic model is developed, based on adsorption-dissociation isotherms, which describes mathematically the etch-rate data obtained. A comparison is made of equilibrium constants for both peroxide and fluoride adsorption and dissociation reactions. From the order of the reaction, relative to H_2O_2 and HF concentrations, postulations of the desorbing species are made.

Experimental Procedure

The etch rates were determined by measuring the decrement in thickness of both n- and p-type germanium dice of approximately 3 ohm-cm resistivity after subjecting them to the etchant under the chosen conditions of time and temperature. The thickness of each die was measured at its center with a double-pointed micrometer that could be read to ±0.0001 in., and the reading was estimated to the next decimal place. Three dice were etched simultaneously in each

[1] The data used in this paper were obtained while the author was employed at Hughes Aircraft Company.

[2] Although it has been observed that water will dissolve germanium, Harvey and Gatos (5) determined that it was necessary to have dissolved oxygen in the water or the etching would not proceed.

experiment; all three were of the same conductivity type, but the major faces of each displayed only one of the three low-index planes. All of the dice were approximately 0.025 in. thick, but the surface areas were 1.25×10^{-2}, 1×10^{-2}, and 1.6×10^{-2} in.^{2} for the (111)-, (110)-, and (100)-oriented samples, respectively. All dice were pre-etched in a solution of HF-HNO_3-H_2O-$HC_2H_3O_2$ to produce a specular surface free of work damage.

The etching solutions were prepared by weighing out the required amounts of the reagents in polyethylene bottles. Although it has been found that solutions so made and stored are stable (8), no solutions were allowed to stand overnight, and all solutions were used within ½ hr to 4 hr after preparation. In order to ensure an adequate supply of reagents of constant concentration, several 1-lb bottles of the specific reagent (HF or H_2O_2) were thoroughly mixed in a large container. The concentrations of these master batches were determined, and the original bottles were then refilled from these master batches.

Since H_2O_2 is catalytically decomposed by many metals and metallic ions, it was considered necessary to take precautions to exclude these from contact with the etching solutions. Thus neither platinum nor stainless-steel equipment could be used, and all experiments were conducted in polyethylene ware. The etchant was allowed to equilibrate thermally in a constant temperature bath before any samples were introduced. The quoted temperature was the initial temperature of the solution and, unless otherwise stated, was 25°C. Because of the poor heat-transfer characteristics of polyethylene beakers, the experiments were run under essentially adiabatic conditions.

All of the samples were contained in a small, perforated basket, which was agitated violently while immersed in the etching solution. Quenching was achieved by rapidly transferring the basket to a large beaker containing 250 ml of water. Approximately 20 ml of etchant was used for each measurement and was discarded immediately afterward; fresh solution was used for each determination. The conditions of etching were chosen such that the concentrations of reagents in the etching solution were depleted to a negligible extent.

Experimental Results

Figure 1, a plot of thickness change as a function of time, using differently oriented specimens, shows that there are no apparent induction periods in this system; thus, explicit etch-rate numbers can be quoted. In general, the rate numbers obtained in this work were comparable, to within ±5%, to the numbers obtained by Bloem and van Vessem (10).

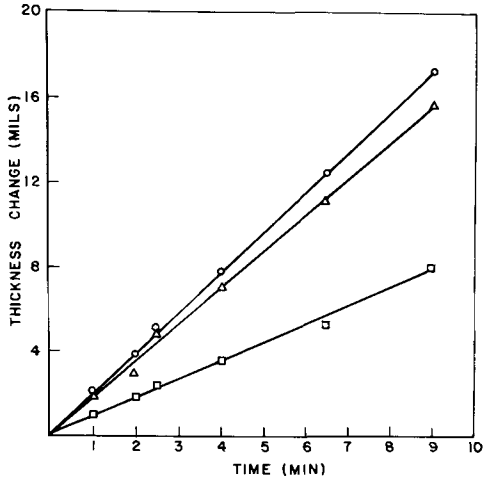

Fig. 1. Thickness change as a function of time, using a solution of 50% HF, 50% H_2O_2. The samples were n-type and were □ (100), ○ (110), and △ (111)-oriented, respectively. The solutions were made using 49.05% HF and 29.0% H_2O_2.

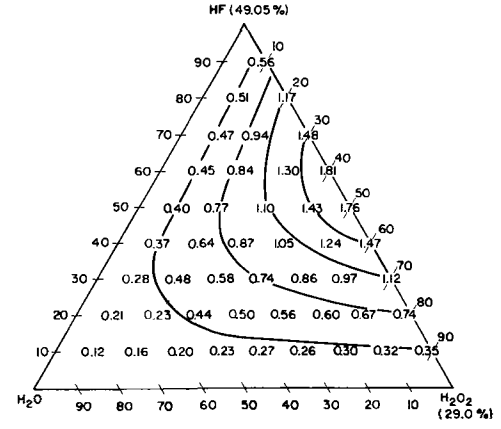

Fig. 2. Etch rate, in mils/min, as a function of etch composition. Samples were n-type, (111)-oriented, and the initial temperature was 25°C.

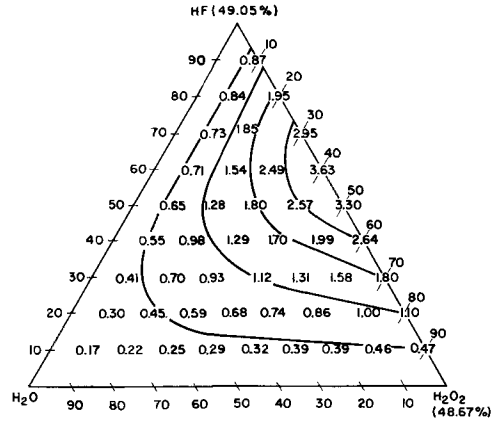

Fig. 3. Etch rate, in mils/min, as a function of etch composition. Samples were n-type, (111)-oriented, and the initial temperature was 25°C.

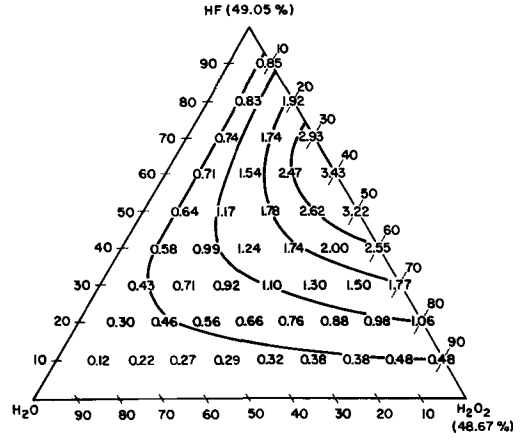

Fig. 4. Etch rate, in mils/min, as a function of etch composition. Samples were p-type, (111)-oriented, and the initial temperature was 25°C.

Figures 2, 3, and 4 are triaxial plots of etch rates at 25°C as a function of etchant composition, using (111)-oriented specimens. For ease in displaying the data,[3] the axes were left in weight-per cent units and normalized to 100% of the concentrated solutions used. The H_2O axis represents added water, not total water in the system. Also it should be noted that both standard-concentrated H_2O_2 (29.0% in Fig. 2) and

[3] Conversion of the scales to mol fraction units compresses the region of representation considerably but yields basically the same isoetch-rate contours.

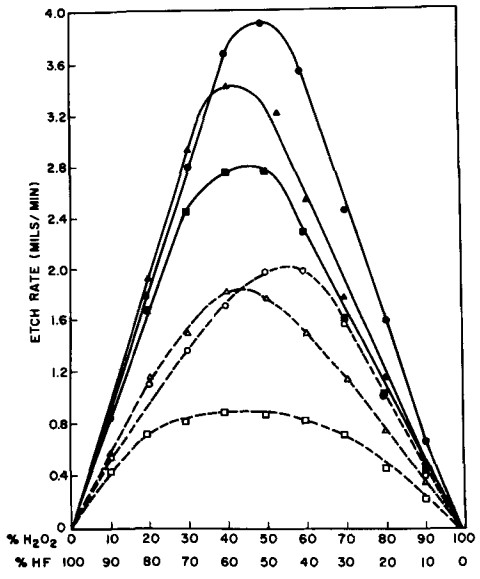

Fig. 5. Etch rates *vs.* normalized etch composition, using only the zero-added-water data. The solid curves were obtained using 49.05% HF, 48.67% H_2O_2 solutions, and the dashed curves were obtained with 49.05% HF, 29.0% H_2O_2 solutions. Orientations were ○ (110), □ (100), △ (111), and all samples were p-type.

special high-concentration H_2O_2 (48.67% in Fig. 3 and 4) were used as reagents for this study. Figures 2 and 3 show that a change from 29 to 49% H_2O_2 had practically no effect on the isoetch-rate contour but changed only the magnitude of the etch rates. A comparison of the data in Fig. 3 and 4 shows that, within experimental error, n- and p-type germanium of the same crystallographic orientation etched at the same rate in comparable etching solutions.

When all of the triaxial plots are examined, it is seen that in the regions of high H_2O_2 concentrations the isoetch-rate curves are essentially parallel to constant HF lines. Conversely, in regions of high HF concentrations the isoetch-rate curves indicate that the H_2O_2 concentration is the important rate-controlling factor.

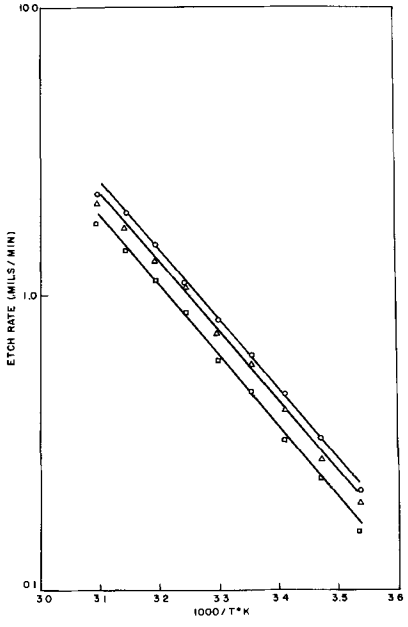

Fig. 6. Influence of temperature on the etch rate of n-type samples. The curves were obtained using 10% HF, 90% H_2O_2. The solution was made from 49.05% HF and 48.67% H_2O_2. Orientations were ○ (110), □ (100), and △ (111).

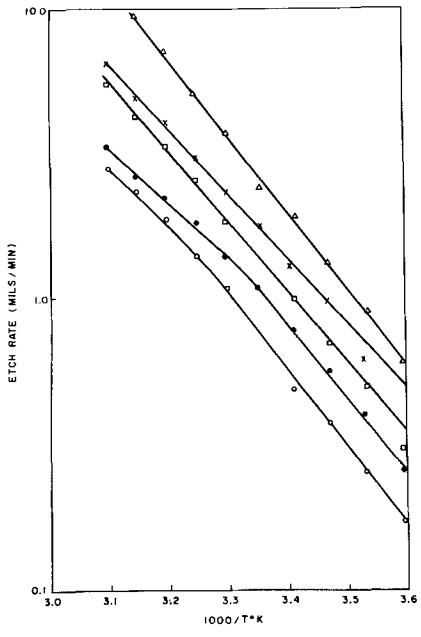

Fig. 7. Influence of temperature on the etch rate of (100)-oriented, n-type samples. Solution concentrations were: ○, 15% HF-55% H_2O_2-30% H_2O; ●, 55% HF-15% H_2O_2-30% H_2O; □, 20% HF-80% H_2O_2; X, 80%HF-20% H_2O_2; △, 35% HF-65% H_2O_2. Solutions were made using 49.05% HF and 48.67% H_2O_2.

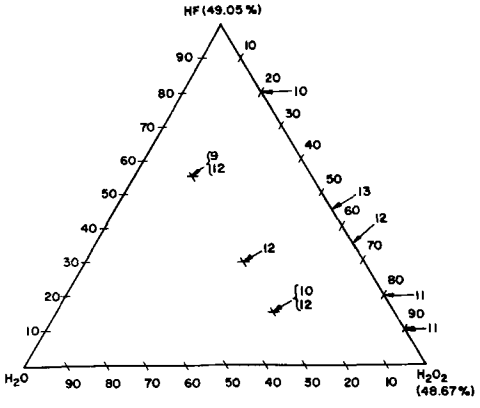

Fig. 8. Temperature dependences, in kcal/mol, as a function of solution composition.

Whereas Fig. 3 and 4 show that conductivity type had no apparent effect on the etch rate, Fig. 5 shows that orientation influences the etch rate strongly in both the 49 and the 29% H_2O_2 systems.

A study of the influence of temperature on the etch rate yielded curves shown in Fig. 6 and 7. Although the different orientations etch at different rates, the slopes of the lines drawn through the points in Fig. 6 are essentially the same. The breaking curves of Fig. 7 are typical of data obtained when there appears to be a shift in the rate-controlling step. A summary of the "apparent" activation energies as a function of etch composition is given in Fig. 8. The magnitude of the temperature dependences (9-13 kcal/mol) and the effect of orientation on the etch rates, together with the fact that etch rates in this system are much lower than in the HNO_3 system (11), suggest that over the entire composition region the etching reaction is surface controlled and not diffusion controlled.

Figure 9 is a plot of the effect of dilution with water on the etch rate of (110)-oriented dice; it is a two-dimensional representation of the three-dimensional etch-rate surface obtained with these reagents. The line drawn is the curve of 2:1 mol ratio of HF to

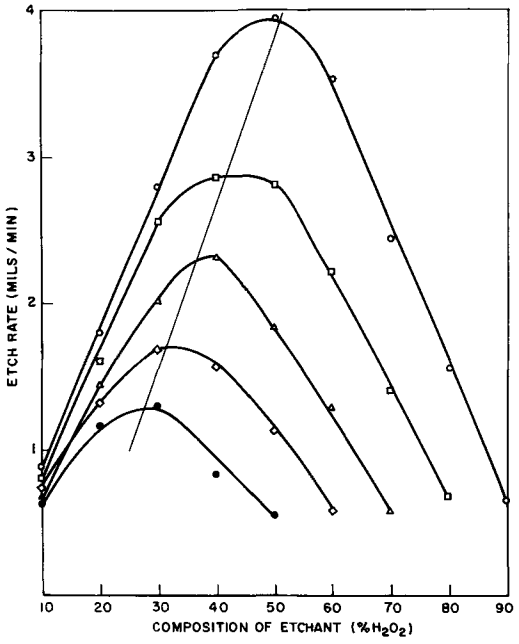

Fig. 9. Influence of added water on the etch rate of p-type, (110)-oriented germanium. Dilutions were ○, zero; □, 10%; △, 20%; ◇, 30%; and ●, 40% added water. Reagent concentrations were 49.05% HF and 48.67% H_2O_2.

H_2O_2, and it appears to agree very well with the etch-rate maxima. This might indicate the following stoichiometry

$$Ge + 2HF + H_2O_2 \rightarrow GeF_2 + 2H_2O \quad [1]$$

or

$$Ge + 4HF + 2H_2O_2 \rightarrow GeF_4 + 4H_2O \quad [2]$$

as the over-all reaction equation. However, as can be inferred from Fig. 5, the line that could be drawn through the maxima of the (111) and (100) etch rates would be displaced to mol ratios greater than 2:1. An analysis of the raw data showed that the ratios could be as high as 3:1, as indicated by Bloem and van Vessem (10). This ratio would then suggest the stoichiometry

$$Ge + 6HF + 2H_2O_2 \rightarrow H_2GeF_6 + 4H_2O \quad [3]$$

Miuller and his co-workers (12), studying the dissolution of germanium in acidic and basic solutions of hydrogen peroxide, found that the etching rate increased with increasing acid or base concentration. The dissolution rate passed through a maximum and then decreased as more additive was put in the etching solution. In fact, if enough acid or base was added to the solution, the etching action would cease. Supin (13) has also studied the dissolution of germanium in hydrogen peroxides of various *p*H and found similar effects.

In order that the influence of an acid diluent on the etch rate in this system might be seen, a comparison was made between the etching rates of n-type (110)-oriented germanium in solutions that were diluted with pure water, glacial acetic acid, or concentrated sulfuric acid. Figure 10 shows the results of these experiments: curve I resulted when 20% acetic acid was added; curve II shows the effect when 20% sulfuric acid was added; and curve III indicates the effect of 20% added water; curve IV shows the effect of adding only 10% water, and curve V is the etching rate with no added diluent. Note the similarity of curves II and V; the etch rate appears to remain the same whether the solution was diluted with H_2SO_4 or not. However, dilution with acetic acid results in a definite increase in the etch rate. In both cases of dilution in acid, though, more etching was achieved than with an equivalent water-diluted system. It appears

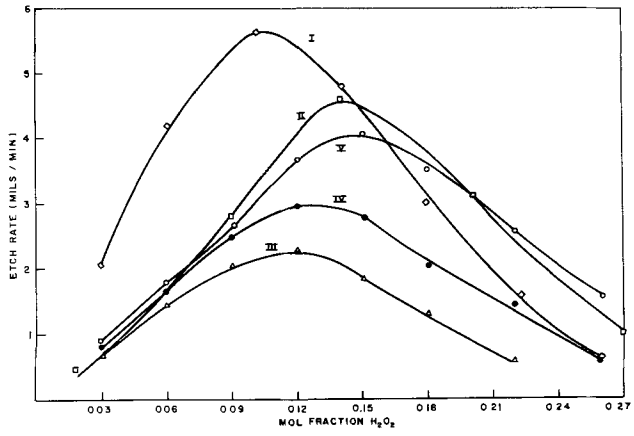

Fig. 10. Influence of acid diluent on the etch rate of (110)-oriented, n-type samples. Curve I, 20% added glacial $HC_2H_3O_2$; II, 20% added concentrated H_2SO_4; III, 20% added H_2O; IV, 10% added H_2O; V, zero added H_2O. Reagent concentrations were 49.05% HF and 48.67% H_2O_2.

that the etch-rate surface generated by the composition-rate plot for acid-diluted HF-H_2O_2 etches would probably have less of a gradient in the direction of the diluent until critical added-acid concentrations were reached. Then a very marked decrease in etch rates would occur owing to the presence of large concentrations of diluent in the system.

Discussion of the Kinetics Model

In the introduction it was noted that dissolution of an elemental semiconductor proceeds in stepwise fashion: oxidation of the element followed by complexing of the oxidized form. Laidler (14) points out that a heterogeneous reaction occurring on a solid surface involves five consecutive steps:

1. Diffusion of the reacting molecules to the surface.
2. Adsorption of the reactants on the surface.
3. Reaction on the surface.
4. Desorption of the products.
5. Diffusion of the desorbed products into the main body of the surrounding medium.

Since the present study deals with the dissolution of a solid in a liquid, these five steps must be considered. In the system Si-HF-HNO_3-H_2O it was shown (6, 7) that, in a specific etchant-composition region, diffusion was the dominant kinetic factor in the dissolution. In the system Ge-HF-HNO_3-H_2O it was observed (11) that control by diffusion was only of secondary importance, and it was postulated that step 4 was the most important part of the sequence. In the system Ge-HF-H_2O_2-H_2O the high-temperature dependence and strong crystallographic orientation effects clearly indicate that, over the entire composition region studied, the rate-controlling factors are involved in one or more of steps 2, 3, and 4, while steps 1 and 5 play only minor roles.

Camp (8) considered the system of r-sequential steps involved with rate control at a Ge-HF + H_2O_2 solution interface and derived a relationship which fitted his temperature data quite well

$$R = \frac{1}{\sum_{1}^{r} \frac{e^{E_i/kT}}{a_i C_i^{p_i}}} \quad [4]$$

where R = etch rate, E_i = activation energy of i^{th} step, C_i = concentration of reagent involved in i^{th} step, p_i = power to which C_i enters i^{th} reaction, a_i = constant associated with i^{th} reaction, k = Boltzmann constant, T = absolute temperature. For his derivation Camp used the expression

$$R_j = \theta_j a_j C_j^{p_j} \exp(-E_j/kT) \quad [5]$$

where θ_j was the fraction of the surface on which the j^{th} or rate-limiting reaction took place; he assumed rate control by only one reagent at a time.

It was found that Eq. [4] qualitatively fitted the temperature data shown in Fig. 6 and 7 and also the data displayed in Fig. 5, which were obtained by varying the reagent concentrations and holding the temperature constant. However, if the data of Fig. 2, 3, and 4 are converted to mol fraction or molality units and replotted as a function of varying only one reagent at a time (Fig. 11 and 12), then Eq. [4] no longer describes the shapes of the curves obtained.

Laidler (14) has considered the case where a diatomic molecule is first adsorbed and then dissociated on a surface

$$A_2 + 2S \rightleftharpoons 2(S-A) \qquad [6]$$

He found that at equilibrium the fraction of surface sites covered, θ, was

$$\theta = \frac{a_\theta C_{A_2}{}^{1/2}}{1 + a_\theta C_{A_2}{}^{1/2}} \qquad [7]$$

where a_θ = constant of proportionality. His analysis can be extended so that if there are two diatomic molecules simultaneously in equilibrium with activated surface sites, *i.e.*

$$X_2 + 2S \overset{K_X}{\rightleftharpoons} 2(S-X) \qquad [8]$$

$$Y_2 + 2S \overset{K_Y}{\rightleftharpoons} 2(S-Y) \qquad [9]$$

then the fractions of the surface covered by each activated species would be

$$\theta_X = \frac{K_X{}^{1/2} C_{X_2}{}^{1/2}}{1 + K_X{}^{1/2} C_{X_2}{}^{1/2} + K_Y{}^{1/2} C_{Y_2}{}^{1/2}} \qquad [10]$$

$$\theta_Y = \frac{K_Y{}^{1/2} C_{Y_2}{}^{1/2}}{1 + K_X{}^{1/2} C_{X_2}{}^{1/2} + K_Y{}^{1/2} C_{Y_2}{}^{1/2}} \qquad [11]$$

and the fraction of unoccupied sites would be

$$(1 - \theta_X - \theta_Y) = \frac{1}{1 + K_X{}^{1/2} C_{X_2}{}^{1/2} + K_Y{}^{1/2} C_{Y_2}{}^{1/2}} \qquad [12]$$

Laidler (14) also considered the generalized bimolecular surface-catalyzed gas-phase reaction

$$A + B + S_2 \rightleftharpoons ABS_2 \rightarrow \text{reaction products} \qquad [13]$$

and he arrived at the expression

$$R = k' C_A C_B C_{S_2} \qquad [14]$$

where k' = rate constant, C_A = concentration of reagent A, C_B = concentration of reagent B, C_{S_2} = concentration of bare dual sites at adsorption-desorption equilibrium.

The following is an attempt to apply the surface adsorption-dissociation concepts to the aqueous system under study here. If we assume an n-component system in steady state with the surface reaction or desorption step as rate limiting, then an equation analogous to Laidler's expression for the j^{th}, or rate-controlling, step can be written as

$$R_j = a_j e^{-E_j/kT} C_{S_m} \prod_1^n C_i{}^{p_i} \ [4] \qquad [15]$$

where C_i = concentration of each of the reagents in solution, p_i = stoichiometry with which each of the reagents is involved in the rate-limiting step, C_{S_m} = a surface-concentration function that describes the nature of the surface on which the j^{th} reaction takes place (the adsorption and dissociation steps on the surface are assumed to be in equilibrium with the reagents in solution).

For the system Ge-HF-H_2O_2-H_2O, Eq. [15] becomes

$$R = a'[H_2O_2]^{p_1}[HF]^{p_2} C_{S_m} \qquad [16]$$

where a' contains the water and the activation terms, which are assumed to be constant factors at constant temperature. Note that Eq. [15] reduces to Camp's original expression, Eq. [5], if indeed the reaction steps are sequential and the rate-controlling step involves only one reagent. Therefore Laidler's surface-concentration function should be Camp's fraction of the surface on which the rate-limiting reaction can proceed and

$$R = \theta a'[H_2O_2]^{p_1}[HF]^{p_2} \qquad [17]$$

Let us assume that X_2 and Y_2 in Eq. [8] and [9] represent the peroxide and fluoride reagents, respectively; the pair of adsorption and dissociation steps might then be

$$H_2O_2 + 2Ge \overset{K_1}{\rightleftharpoons} 2(Ge-OH) \qquad [18]$$

and

$$HF_2^- + 2Ge \overset{K_2}{\rightleftharpoons} (2Ge \cdot HF_2)^- \ [5] \qquad [19]$$

For constant [HF], and if we assume that H_2O_2, the rate-limiting reagent, acts only on the unoccupied surface sites, then Eq. [17] becomes

$$R = (1 - \theta_1 - \theta_2)\, a''[H_2O_2]^{p_1}[HF]^{p_2} \qquad [20]$$

Substitution of corrected Eq. [12] into Eq. [20] results in

$$R = \frac{a''[H_2O_2]^{p_1}[HF]^{p_2}}{1 + K_1{}^{1/2}[H_2O_2]^{1/2} + K_2{}^{1/2}[HF]^{1/2}} \ [6] \qquad [21]$$

For constant [H_2O_2] and if we assume that HF, the rate-limiting reagent, acts only on the oxidized surface sites, then Eq. [17] becomes

$$R = \theta_1 a'''[H_2O_2]^{p_1}[HF]^{p_2} \ [7] \qquad [22]$$

Substitution of corrected Eq. [10] into [22] results in

$$R = \frac{a'''K_1{}^{1/2}[HF]^{p_2}[H_2O_2]^{p_1+1/2}}{1 + K_1{}^{1/2}[H_2O_2]^{1/2} + K_2{}^{1/2}[HF]^{1/2}} \qquad [23]$$

Although Eq. [15] is the general rate expression governing the over-all system, the assumption that there are two different rate-limiting situations results in two specific rate equations. In that part of the etchant composition region where [H_2O_2] is rate limiting, it is the oxidation of bare germanium that is assumed to be the important step and Eq. [21] is believed to be the rate expression describing the situation. When [HF] is rate determining, Eq. [23] is believed to be the appropriate rate expression. One approach to the generation of a single relationship which describes the entire system is to use the mathematical technique of linear combination of the component parts. This results in

$$R = \frac{b[H_2O_2]^{p_1}[HF]^{p_2}}{1 + K_1{}^{1/2}[H_2O_2]^{1/2} + K_2{}^{1/2}[HF]^{1/2}} + \frac{b'K_1{}^{1/2}[H_2O_2]^{p_2+1/2}[HF]^{p_2}}{1 + K_1{}^{1/2}[H_2O_2]^{1/2} + K_2{}^{1/2}[HF]^{1/2}} \qquad [24]$$

or

$$R = (b + b'K_1{}^{1/2}[H_2O_2]^{1/2}) \frac{[H_2O_2]^{p_1}[HF]^{p_2}}{1 + K_1{}^{1/2}[H_2O_2]^{1/2} + K_2{}^{1/2}[HF]^{1/2}} \qquad [25]$$

[4] It should be noted that $a_j \exp(-E_j/kT)$ is equivalent to k' of Eq. [14] by the Arrhenius equation.

[5] According to Sidgwick (16), the predominating anionic species in hydrofluoric acid solutions is HF_2^-. The symbol $(_2Ge \cdot HF_2)^-$ is to be regarded as an abbreviation for a possible bridged structure of the form Ge·F-H-F·Ge⁻.

[6] Note that [HF] has been used in the denominator in order to simplify the analysis. The fluoride species of importance is not really known. A more rigorous derivation might require use of $[HF_2^-]$ or $[H_2F_2]$, but this would merely be a correction of K_2 by a factor of 20 or 2, respectively. The former number comes from the fact that the concentration of the bifluoride ion is approximately 5% of the total hydrogen fluoride in solution.

[7] The reason a'' and a''' are used and are to be distinguished from the generalized a' is that now two different rate-controlling reagents are being considered separately and the specific rate constants for these reactions do not necessarily have to be equal.

Let us now consider the results of applying some specific sets of conditions to Eq. [25].

Case I.—If [HF] is held constant at different parametric values and $[H_2O_2]$ is considered to be the independent variable, then

(*A*) when

$$1 + K_1^{1/2}[H_2O_2]^{1/2} << K_2^{1/2}[HF]^{1/2} \quad [26]$$

and if $b'\sqrt{K_1[H_2O_2]}$ is also small then

$$R \propto [H_2O_2]^{p_1} \quad [27]$$

(*B*) when

$$1 + K_2^{1/2}[HF]^{1/2} << K_1^{1/2}[H_2O_2]^{1/2} \quad [28]$$

and if b' is small then

$$R \propto [H_2O_2]^{p_1 - 1/2} \quad [29]$$

Case II.—If $[H_2O_2]$ is held constant at different parametric values and [HF] is considered to be the independent variable, then

(*A*) when

$$1 + K_2^{1/2}[HF]^{1/2} << K_1^{1/2}[H_2O_2]^{1/2} \quad [30]$$

then

$$R \propto [HF]^{p_2} \quad [31]$$

(*B*) when

$$1 + K_1^{1/2}[H_2O_2]^{1/2} << K_2^{1/2}[HF]^{1/2} \quad [32]$$

then

$$R \propto [HF]^{p_2 - 1/2} \quad [33]$$

Application of the Kinetics Model

It is readily seen that the curves in Fig. 11 can be expressed by the relationships shown in Eq. [26] through [29] if p_1 is unity. Similarly, the curves of Fig. 12 can be expressed by the relationships shown in Eq. [30] through [33] if p_2 is greater than unity but less than 2.[8] And finally, the data in Fig. 5 can be described by Eq. [25] since, when the concentration of either of the reagents is zero, the rate is zero.

Consideration of the appropriate data on all three orientations studied made possible an evaluation of p_1 and p_2 as a function of orientation; the results are shown in Table I.

[8] When the data in curves IV, V, and VI of Fig. 12 are used, p_2 appears to be about 1.3.

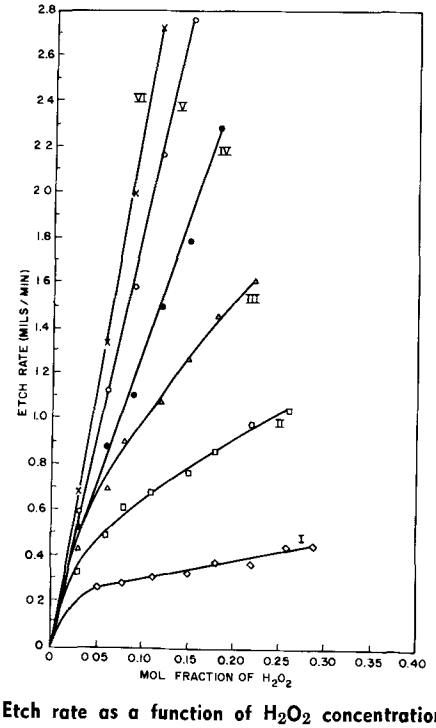

Fig. 11. Etch rate as a function of H_2O_2 concentration at constant HF concentration. The HF mol fractions were: I, 0.05; II, 0.09-0.11; III, 0.14-0.16; IV, 0.18-0.21; V, 0.23-0.26; and VI, 0.28-0.31. Samples were p-type, (100)-oriented.

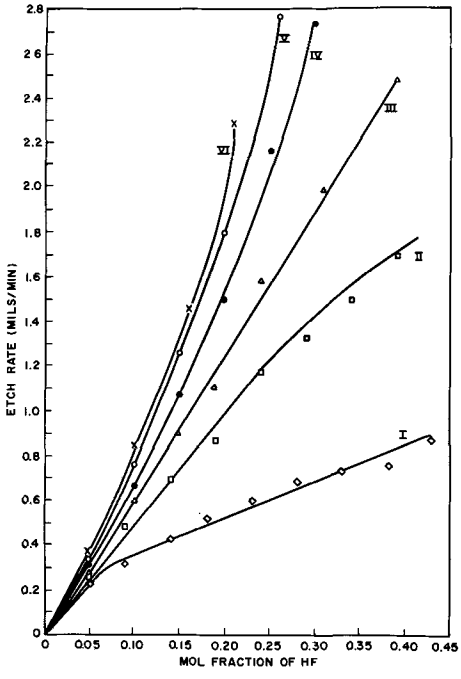

Fig. 12. Etch rate as a function of HF concentration at constant H_2O_2 concentration. The H_2O_2 mol fractions were: I, 0.03; II, 0.06; III, 0.08-0.09; IV, 0.11-0.12; V, 0.15; and VI, 0.18. Samples were p-type, (100)-oriented.

Equation [29] and the data from Table I lead to the prediction that at low [HF] and relatively high $[H_2O_2]$ the etch rate for the (100) surface should vary as the square root of the peroxide concentration. When the data from curves I and II of Fig. 11, which are an approximation to these reagent concentration conditions, are used, the predicted square-root dependence is indeed obtained. In a similar manner, Eq. [33] predicts a $(p_2 - 1/2)$ dependence of the etch rate on [HF] at low $[H_2O_2]$. From curve I of Fig. 12, the etch rate is found to be dependent on [HF] to the 0.7 power, in excellent agreement with the value predicted using the (100)-data in Table I.

Although Eq. [25] appears to express the over-all etching situation, it contains at least four parameters that can be manipulated in any attempt at a detailed quantitative evaluation. Since the raw data are limited in quantity and precision, it is simpler to take Eq. [21] and [23] and attempt order-of-magnitude calculations to determine if the assumptions made in the analysis are reasonable. With each of the two equations considered separately as the working relationship, the etch-rate data for all three orientations of the p-type series were analyzed using an IBM 7094 computer[10] to determine the best values for a, K_1, and K_2. The computer analysis consisted of determining the root-mean-squared deviation of calculated from measured etch rates for each of the experimental con-

Table I. Results of evaluation[9]

Orientation	p_1	p_2
(100)	1	>1
(111)	1	>1
(110)	>1	>1

[9] In most cases the value for p_2 was approximately 1.2 – 1.3. For the (110) orientation p_1 is identical to p_2. When both HF and H_2O_2 concentrations were simultaneously high, it was observed that p_2 could go as high as 1.9.

[10] The entire computer program and analysis were developed by M. Yamin.

Table II. Summary of results

Orientation	From use of Eq. [21] a''	From use of Eq. [21] K_1/K_2	From use of Eq. [23] a'''	From use of Eq. [23] K_1/K_2
(100)	2×10^4	3	1×10^2	10
(111)	2×10^4	3	1×10^2	10
(110)	2×10^4	3	2×10^2	5

ditions. This computation was performed for 1000 combinations of a, K_1, and K_2, covering a predetermined range for each constant. The particular combination of a, K_1, and K_2 which minimized the root-mean-square deviation was selected. The parameter ranges were determined initially by a hand calculation where the data from two experimental points were used in solving a pair of simultaneous equations. Table II summarizes the results of the computer analysis. These results show that in all cases the peroxide adsorption reaction is favored over the fluoride adsorption reaction. It is also seen that $a'' >> a'''$ by two orders of magnitude, and this is consistent with the assumption that $b >> b'$.

The agreement between experiment and theory can be seen in Fig. 13 and 14, which are computer-generated plots of calculated *vs.* measured etch rates for the (111)-oriented specimens using Eq. [21] and [23], respectively. On the basis of any normal standards for predicting rates in heterogeneous kinetics, this is a surprisingly good correlation, considering that all 45 points covering the entire composition region studied are being examined in each case. The predicted rate is less than a factor of two away from the experimentally measured value at any given point.

The data of Table I indicate that for the (100) and (111) orientations the etch rate is first order with respect to the hydrogen peroxide concentration. This means that the rate-controlling step involves formation or removal of divalent germanium on or from the surface, as described, for example, in Eq. [1]. For the (110) orientation, the superlinearity, evidenced by the higher value of p_1, indicates that some tetravalent germanium is also being formed. However, the fact that for the (110) orientation p_1 and p_2 were equal and greater than 1 but less than 2 leads to the postulation of the reaction stoichiometry

$$Ge + 2HF + 2H_2O_2 \rightarrow GeOF_2 + 3H_2O \qquad [34]$$

GeF_2 as a chemical entity has been isolated and identified (16, 17), but the existence of $GeOF_2$ has never been demonstrated; the analogous $GeOCl_2$ has been obtained (17). In all cases it is believed that once the reaction product leaves the surface of the solid and diffuses into the bulk of the solution, continued fluoridation to the GeF_4 or H_2GeF_6 form takes place.

Earlier in this paper, in discussion of Fig. 9, comments were made about reaction stoichiometry based on the maximum etch rate and solution concentration. Although at first it would appear that these results were being contradicted by the stoichiometries resulting from the kinetics analysis, in reality they are two different situations. The former relationship is the efficiency of the system as a function of concentration. The latter relationship is the rate-limiting process taking place only on the surface and therefore should be considered as truly kinetics limiting.

It has been shown that Eq. [15] can be reduced to Camp's original expression, Eq. [5]. Using an analysis similar to his, it is possible to obtain a temperature-dependence relationship of the form

$$R = \frac{1}{\sum_{1}^{r} \frac{e^{E_i/kT}}{a_i \prod_{1}^{n} C_h^{p_h}}} \qquad [35]$$

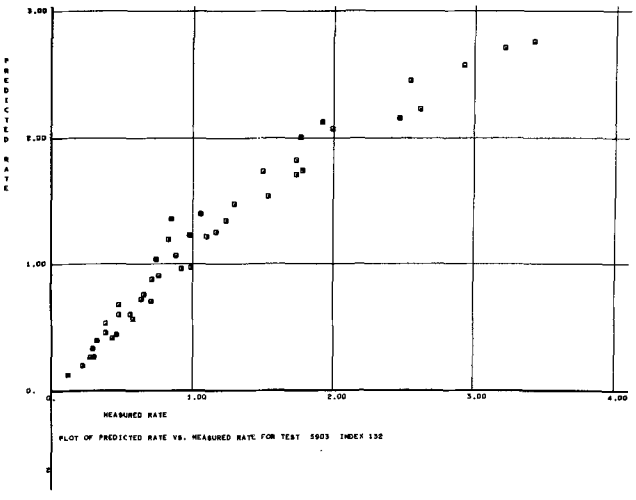

Fig. 13. Computer-generated plot of calculated etch rate *vs.* measured etch rate for (111)-oriented, p-type specimens with Eq. [21] as the generating function. Both coordinates are in units of mils/min.

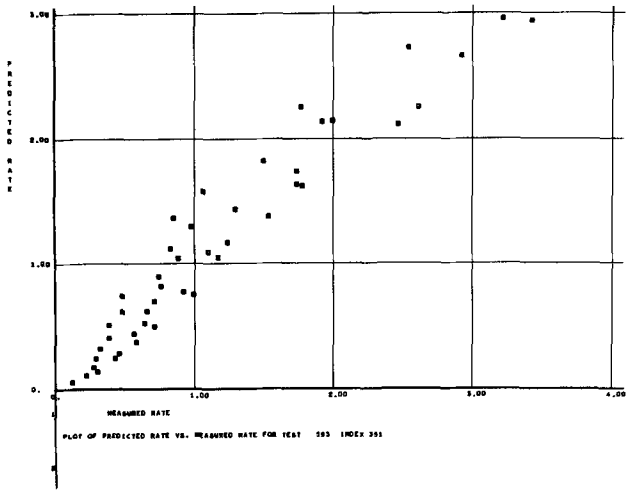

Fig. 14. Computer-generated plot of calculated etch rate *vs.* measured etch rate for (111)-oriented, p-type specimens with Eq. [23] as the generating function. Both coordinates are in units of mils/min.

Although the j^{th} reaction may be the rate-limiting step at a given temperature, it does not necessarily hold that this step is rate limiting at all temperatures. In fact, another step in the sequence could become the slow step at an elevated temperature and the rate limitation would shift from the j^{th} to the k^{th} step. In order for this to occur there would have to be a higher activation energy[11] associated with the k^{th} step than with the j^{th} step, and breaking curves of the form observed by Camp and also seen in Fig. 7 would then result.

Reaction Mechanism

The question naturally arises as to what is the actual mechanism by which the above-described surface reactions take place. Unfortunately, no answers can be provided at this time. In fact, the existence of the intermediate reaction products hypothesized above still needs to be verified experimentally. It is interesting to speculate, however, about certain aspects of the mechanism implied by the kinetics postulated. Why is the "adsorbed fluoride" not the final form of

[11] It is interesting to note the relationship between rate and activation energy in Eq. [35]. Because of the inverse-sum effect, the temperature dependence of the rate becomes low when the activation energy is high. This is a good example of how dangerous it is to attempt to get a true activation energy from a semi-logarithmic plot of rate *vs.* reciprocal of temperature.

the intermediate? A suggested answer (18) might be that ultimately at least two fluorine atoms are needed on each germanium atom and the adsorption of the charged anionic form of the fluoride reduces the possibility that a second fluorine may come to that site. If this is so, then it is possible that the acid-dilution effects seen in Fig. 10 are in reality merely influencing the concentration of HF_2^- ions, which in turn influence the concentration of "inactive" sites on the surface. However, this approach to the possible reaction mechanism still does not give any understanding of why the particular orientations act the way they do.

Conclusions

The major conclusion reached in this study is that the Ge-HF-H_2O_2-H_2O etching system is etch-rate limited by a surface-reaction or product desorption step. The application of Laidler's gas-phase adsorption-dissociation isotherm concepts to this liquid system yields results qualitatively in agreement with the experimental data, and consistent with the relationships previously obtained by Camp.

Evidence has been presented which shows that divalent germanium is the major reaction product leaving the surface. There is also strong kinetic evidence for postulating the formation of $GeOF_2$ as a reaction product leaving the (110) surface. However, it is believed that the ultimate reaction product found in solution would probably be GeF_4 or H_2GeF_6.

A comparison of the equilibrium constants for the peroxide and bifluoride adsorption-dissociation reactions shows that the peroxide reaction is favored over the bifluoride reaction.

Although different orientations appear to have different reaction stoichiometries, no firm mechanism explaining these results can be presented at this time.

Acknowledgments

The author would like to express his appreciation to Mr. J. Estlick and Miss J. Werner, of the Hughes Aircraft Company, for their assistance in obtaining the rate data; and his deep indebtedness to Mr. H. Robbins, of the Bell and Howell Company, for the time and effort which he spent on this problem. Also, stimulating discussions with many of his colleagues, D. L. Klein, M. Yamin, P. C. Milner, B. G. Cohen, J. Klerer, K. L. Lawley, and I. Amron, to name only a few, were of invaluable assistance.

After this paper was accepted for publication, one of the reviewers questioned the legitimacy of using the technique of linear combinations in going from Eq. [21] and [23] to Eq. [24]. Since we have assumed that the system is in steady state, by definition

$$R = R_1 = R_2 = R_3 = \ldots = R_r \quad (a)$$

Therefore, also by definition

$$R = \frac{1}{r}\sum_{1}^{r} R_i \quad (b)$$

which is a linear combination of the component reactions. For Eq. [24] I have chosen to use only two terms of the sum and the $1/r$ factor is included in the constants b and b^1.

Manuscript received May 31, 1966; revised manuscript received Nov. 2, 1966. This paper was presented in part at the Houston Meeting, Oct. 9-13, 1960.

Any discussion of this paper will appear in a Discussion Section to be published in the December 1967 JOURNAL.

REFERENCES

1. B. Schwartz, "Vapor Deposition," C. F. Powell, J. H. Oxley, and J. F. Blocher, Jr., Editors, John Wiley & Sons, Inc., New York (1966).
2. "Semiconductors," N. B. Hannay, Editor, Reinhold Publishing Corp., New York (1959).
3. R. K. Willardson and H. L. Goering, Editors, "Compound Semiconductors," Reinhold Publishing Corp., New York (1962).
4. P. J. Holmes, Editor, "The Electrochemistry of Semiconductors," Academic Press Inc., New York (1962).
5. W. W. Harvey and H. C. Gatos, *This Journal*, **105**, 654 (1958).
6. B. Schwartz and H. Robbins, *ibid.*, **106**, 505 (1959).
7. D. L. Klein and D. J. D'Stefan, *ibid.*, **109**, 37 (1962).
8. P. R. Camp, *ibid.*, **102**, 586 (1955).
9. M. C. Cretella and H. C. Gatos, *ibid.*, **105**, 487 (1958).
10. J. Bloem and J. C. van Vessem, *ibid.*, **109**, 33 (1962).
11. B. Schwartz and H. Robbins, *ibid.*, **111**, 196 (1964).
12. R. L. Miuller, A. V. Danilov, T. P. Markova, V. N. Mel'nikov, A. B. Nikol'skii, and S. M. Repinskii, *Leningr. Universitet, Vestnik, Ser. Fiz. i. Khim*, **15**, 80 (1960).
13. G. S. Supin, *Zhur Prikl. Khim.*, **32**, 478 (1959).
14. K. J. Laidler, "Chemical Kinetics," McGraw-Hill Book Co., New York, (1950).
15. S. Glasstone, "Textbook of Physical Chemistry," D. Van Nostrand Co., Inc., Princeton (1946).
16. N. V. Sidgwick, "The Chemical Elements and their Compounds," Clarendon, Oxford (1950).
17. O. H. Johnson, *Chem. Rev.*, **51**, 431 (1952).
18. D. L. Klein, Private communication.

Reflection X-Ray Topography of GaAs Deposited on Ge

Eugene S. Meieran

Fairchild Semiconductor, Division of Fairchild Camera & Instrument Corporation, Palo Alto, California

ABSTRACT

Reflection x-ray topography is well suited to the study of defects in epitaxial films deposited on single crystal substrates. In particular, since GaAs and Ge have lattice parameters that are almost, but not quite equal, certain reflecting planes can be used with suitable radiation to allow separate topographs of the GaAs epitaxial film and Ge substrate to be taken. In this way, the various types of defects appearing in the epitaxial film can be analyzed to show whether or not they were influenced by growth conditions or by substrate preparation. During our investigation, growth pyramids due to imperfections or contamination in the substrate, and dislocation networks, probably due to mismatch between film and substrate lattice parameters, were observed. The latter were observed in both the film and substrate, but occurred only for films more than about 2μ thick.

Germanium is structurally an ideal substrate material for the epitaxial deposition of GaAs, since single crystal Ge is relatively inexpensive, the technology of wafer preparation is well known, and the lattice parameter is within 0.1% of that of GaAs. Several types of epitaxial reactors for such deposition have been described in the literature (1, 2). In addition, studies by means of optical microscopy of the perfection of the GaAs layer have been conducted (3). It is the purpose of this paper to describe how x-ray topography, using reflection Berg-Barrett geometry (4), can be used to characterize, separately and nondestructively, both the substrate Ge and the epitaxial GaAs film. The comparison of topographs of the film and substrate can aid in understanding the propagation of defects into the film from the substrate, or the formation of defects in the film or substrate separately.

Experimental

Sample preparation.—The GaAs films were grown by the water transport method (5) on chemically polished (111) Ge wafers, doped with As to a carrier

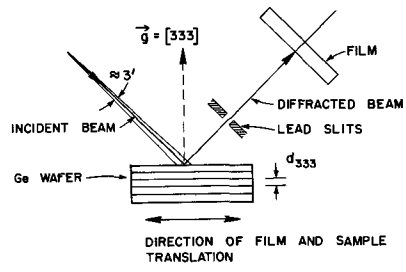

a) (333) reflection, Cu $K\alpha_1$ radiation

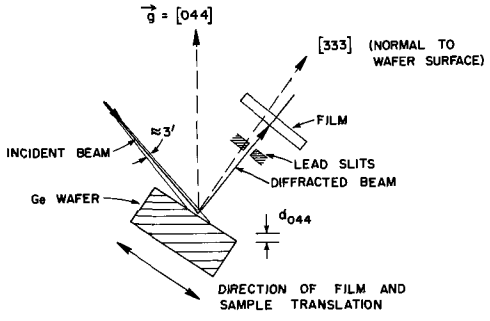

b) (044) reflection, Cu $K\alpha_1$ radiation

Fig. 1. Crystal alignment for taking (333) and (044) topographs

concentration of about 1 x 10^{19}/cc. All films described in this paper were doped to about 1 x 10^{18} carriers/cc and ranged between 1 and 15μ thick. The surface of the wafer after deposition consists of a central region covered with single crystal GaAs deposition, a narrow surrounding region covered with polycrystalline GaAs, and pure Ge on which no deposition took place.

X-ray technique.—The difference in lattice parameters a_o between GaAs and Ge, 5.6576 *vs.* 5.6534Å, is the important parameter in the x-ray technique. According to Bragg's law

$$\lambda = 2d \sin\theta$$

so

$$\frac{\Delta\theta}{\tan\theta} = \frac{\Delta d}{d} = \frac{\Delta a}{a_o}$$

and transposing

$$\Delta\theta = \frac{\Delta a}{a_o}\tan\theta = \frac{0.0042}{5.65}\tan\theta = 7.42 \times 10^{-4}\tan\theta$$

where d is the interplanar spacing of the crystal and 2θ the angle between incident and diffracted beams. Consequently, for any particular set of reflecting planes, in order to take separate topographs of Ge and GaAs, $\Delta\theta$ should be as large as possible. For this reason, and because surface defects only rather than bulk defects are to be studied, Cu$K_{\alpha 1}$ radiation is used with reflection geometry. For convenience in comparing the topographs to normal optical micrographs, the topographs should be as undistorted as possible, while for maximum resolution, the diffracted beam should be normal to the recording film. For all these reasons, (333) symmetric and {044} asymmetric reflections are useful. All the pertinent data for these two reflections are given in Table I, and the geometries involved for (111) wafers are shown in Fig. 1. The geometries necessary for other wafer orientations, such as {100} or {110}, can be derived similarly. For intensity purposes, the (333) reflection is more useful and allows faster topographs to be taken, while from the point of distortion, the {044} is more useful.

It is seen from Table I that a beam divergence of less than 5 min of arc is needed to resolve the four peaks due to the $K_{\alpha 1}$ $K_{\alpha 2}$ doublets from both GaAs and Ge. Therefore, the divergence slits were set to 3 min of arc. Then, in order to examine large regions of the sample, both the sample and recording film (film firmly attached to the sample) were translated through the direct beam, in a manner similar to Lang scanning (6).

The actual apparatus used was a Lang camera, modified for taking reflection topographs. Since the counter window used for aligning the sample is wide, the 2θ setting of the counter arm need only be approximate. However, the actual sample setting is critical and must be set to within a few seconds of arc. The alignment of the wafer for (333) reflections does not depend on the rotation of the wafer about its normal, since the reflecting planes are parallel to the wafer surface. However, for asymmetric reflections, where the reflection planes must be rotated to the vertical position, a Laue photograph is useful. For the purposes described here, a 100μ spot focus and Cu target of a Jarrell Ash Microfocus x-ray unit was used, operating at 35 kv and 6.5 ma. The beam divergence slits were set to 0.5 mm wide, and were placed 50 cm from the focal spot of the x-ray tube. Ilford nuclear plates emulsion L-4, 50μ thick, were used and required an exposure time of about 1 hr for 1-cm scan.

Results

The optical micrograph of a thick film chosen to illustrate some of the defects observed is seen in Fig. 2a. Pyramidal defects and "fish scale" are seen, as is the polycrystalline boundary between the single crystal film and the film free region. The film-free area at the bottom of the micrograph is almost defect free. Figure 2b shows the (333) reflection topograph using only the beam diffracted from the Ge, while Fig. 2c shows the (333) reflection topograph using only the GaAs. The polycrystalline boundary region between the single crystal GaAs and the undeposited region is clearly seen in both Fig. 2b and 2c, as are the pyramidal defects which appear as white dots. As reported elsewhere for Si (7, 8), it appears that the pyramids nucleate at the epitaxial film-substrate interface and grow larger as the film grows thicker. Also seen in both topographs is evidence of slip in the Ge and GaAs along the three <110> directions in the (111) surface plane. (The <110> directions do not seem to meet at 60° due to distortion in angles, as seen in Fig. 1a.) None of this slip corresponds to the "fish scale" of Fig. 2a. The region of Ge free from film appears defect free, in agreement with Fig. 2a.

For comparison purposes, Fig. 2d is an (044) topograph of the same region of the sample. For this topograph, the divergence slits were opened slightly so that both the GaAs and Ge peaks record simultaneously. Again, the various types of defects mentioned above are visible. As schematically shown in Fig. 1b, there is very little angular distortion in this topograph.

The question of whether the strain field in the Ge is plastic, due to slip in the Ge, or elastic, due to the slip in the GaAs and the adherence of the GaAs to the Ge, can be answered by Fig. 3. Figure 3a shows the surface of a Ge wafer from which the deposited GaAs film was etched away in a small region. Again, numerous pyramidal type defects can be seen both

Table I. Interplanar spacings and 2θ values for (333) and (044) reflections from Ge and GaAs, for Cu$K_{\alpha 1}$ and Cu$K_{\alpha 2}$ radiation

	a_o	d_{333}	$2\theta_{333}$, K_{α_1}	$2\theta_{333}$, K_{α_2}	d_{044}	$2\theta_{044}$, K_{α_1}	$2\theta_{044}$, K_{α_2}
GaAs	5.6534	1.0880	90° 8.3'	90° 25.3'	0.9994	100° 50.4'	101° 10.8'
Ge	5.6576	1.0888	90° 3.1'	90° 20.3'	1.0001	100° 44.4'	101° 4.8'

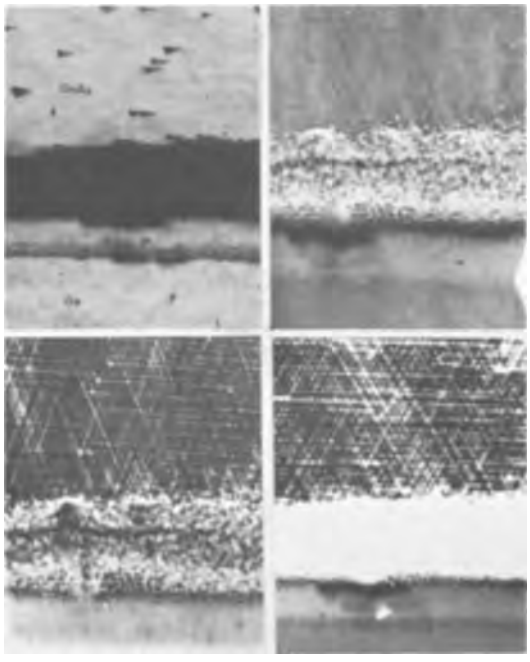

Fig. 2. GaAs deposited on (111) Ge substrates: a (top left) optical micrograph; b (top right) (333) Ge topograph; c (bottom left) (333) GaAs topograph; d (bottom right) (044) GaAs and Ge topograph. Magnification *ca.* 5X.

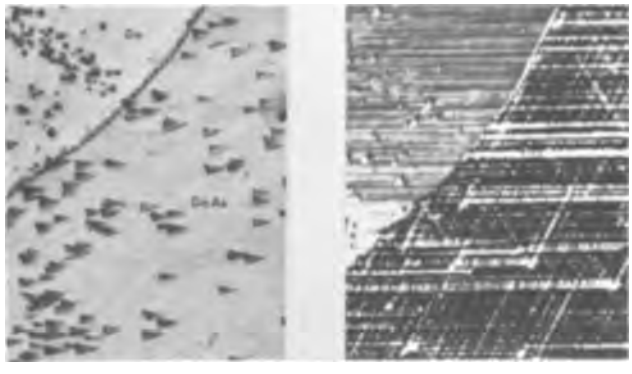

Fig. 3. GaAs deposited on (111) Ge: a (left) optical micrograph; b (right) (044) GaAs and Ge topograph. Magnification *ca.* 5X.

in the remaining film and on the Ge. Figure 3b shows an (044) topograph which records both GaAs and Ge peaks. The strain in the Ge remains even though the GaAs has been removed, and is therefore plastic strain. This is in agreement with the work of Amick (3), who by optical techniques saw strain patterns in the Ge substrate which resembled those seen in Fig. 2 and 3.

The depth of strain field in the Ge was estimated by taking a wafer, removing the GaAs film, and then etching steps about 8μ deep into the Ge itself, as shown in the optical micrograph Fig. 4a. The Ge topograph, Fig. 4b, shows that the strain lines disappear after about 15μ of Ge is removed, so that the depth of the strain in Ge corresponds roughly to the thickness of the epitaxial film, about 15μ thick in this example.

It is apparent that the strain is due to large amounts of plastic deformation or slip that occurs during either film growth or sample cooling from the deposition temperature. The slip is probably due to mismatch in lattice parameters between substrate and film. This was indirectly confirmed by taking x-ray topographs of GaAs deposited on GaAs, where the film and substrate resistivities corresponded roughly to the GaAs on Ge case. No evidence of large-scale slip was observed. Unfortunately, a comparison of theoretical values of dislocation density necessary to accommodate mismatched lattices (10) with experimental observations is not possible. This is due to the lack of resolution of the x-ray technique ($\approx 2\mu$) in comparison to the required theoretical dislocation spacing of less than 0.1μ. However, it can be stated that the dislocations forming the networks observed in Fig. 2, 3, and 4 are spaced much closer than 2μ apart, since individual dislocations cannot be resolved. These latter observations were confirmed by transmission electron microscopy. A sample with a thick GaAs film was etched to remove the film and chemically thinned from the backside to enable transmission samples to be made which showed the strained surface. The electron micrographs showed dislocation clusters in which the dislocations were spaced $\approx 0.1\mu$ apart. The dislocations ran in the <110> directions.

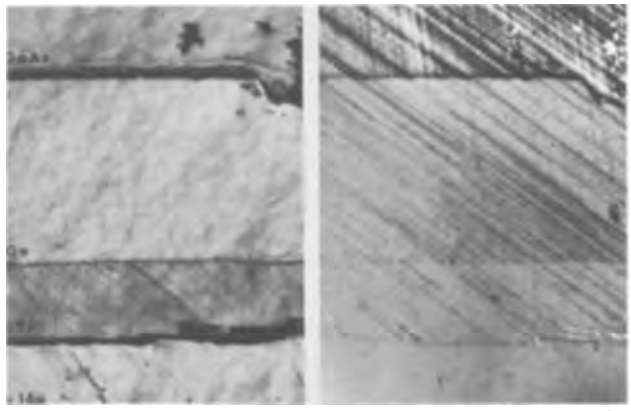

Fig. 4. GaAs deposited on (111) Ge substrate, with GaAs film etched away from part of the sample and steps etched into the Ge. a (left) optical micrograph; b (right) (333) Ge topograph. Magnification *ca.* 15X.

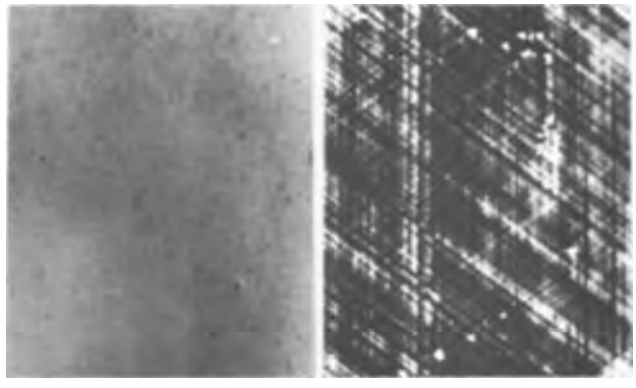

Fig. 5. GaAs deposited on (111) Ge substrate by HCl transport. (333) Ge + GaAs topographs: a (left) 1μ thick film; b (right) 15μ thick film. Magnification *ca.* 10X.

No dislocation networks were observed in films less than about 2μ thick, in agreement with theoretical considerations proposed by Van der Merwe (10). For example, Figs. 5a and 5b are topographs of the GaAs layer deposited on two identical Ge substrates. Figure 5a shows a film about 1μ thick, while Fig. 5b shows a 15μ thick film, made under identical deposition conditions except for duration of deposition. No slip is seen in Fig. 5a while slip similar to Fig. 2, 3, and 4 is seen in Fig. 5b. These two films were deposited by HCl transport rather than H_2O transport, but no structural differences in films have been observed to depend on the transporting medium.

Conclusions

1. Reflection x-ray topography can be used to image separately and nondestructively the GaAs films and the Ge substrates on which they have been deposited.
2. For films thicker than a few microns both the substrate and film contain dislocation networks, probably due to the mismatch between lattice parameters.

3. In cases where slip occurs, the depth of the strain in the Ge is of the same order of magnitude as the thickness of the epitaxial film, about 15μ.

Acknowledgments

The author wishes to thank Dr. Bruce Cairns for growing the epitaxial films; R. Warncke and R. Jiminez for assistance in the laboratory; and Doctors I. Blech and H. Sello for many valuable and interesting discussions.

Manuscript received Aug. 19, 1966; revised manuscript received Oct. 25, 1966.

Any discussion of this paper will appear in a Discussion Section to be published in the December 1967 JOURNAL.

REFERENCES

1. N. Goldsmith and W. Oshinsky, *RCA Rev.*, **24**, 546 (1963).
2. N. Holonyak, Jr., D. C. Jillson, and S. F. Bevaqua, "Metallurgy of Semiconductor Material XV," p. 49, Interscience (John Wiley & Sons), New York (1959).
3. J. A. Amick, *RCA Rev.*, **24**, 555 (1963).
4. C. S. Barrett, "Structure of Metals," McGraw-Hill Book Co., New York (1952).
5. P. H. Robinson, *RCA Rev.*, **24**, 574 (1963).
6. A. R. Lang, *J. Appl. Phys.*, **30**, 748 (1959).
7. J. E. Lawrence and R. Tucker, *ibid.*, **36**, 3095 (1965).
8. G. R. Booker, *Phil. Mag.*, **11**, 1007 (1965).
9. J. A. Amick, "Single Crystal Films," p. 281, Francombe and Sato, Editors, Pergamon Press, New York (1964).
10. J. H. van der Merwe, ref. (9), p. 139.

Technical Notes

Chemical Polishing of Cadmium Sulfide

M. V. Sullivan and W. R. Bracht

Bell Telephone Laboratories, Incorporated, Murray Hill, New Jersey

The usual crystal form of CdS is the wurtzite structure which is in the hexagonal crystal system. When crystal faces, which are perpendicular to the c axis, are examined one notices striking differences in some of the physical, electrical, and chemical properties. These differences may be attributed to the fact that on one face the surface Cd atoms have only three S atoms as nearest neighbors, whereas the S atoms have four Cd atoms as nearest neighbors. On the opposite face the order is reversed. Thus, one face appears to be rich in Cd, whereas the other appears to be rich in S. The Cd-rich face (00.1) is commonly referred to as the A face. The opposite face (00.$\bar{1}$) appears to be rich in S and is referred to as the B face. The difference in etching characteristics of these two faces has been noted many times (1-4). Although several etchants for CdS are described in the literature, none produces a high polish on the B face.

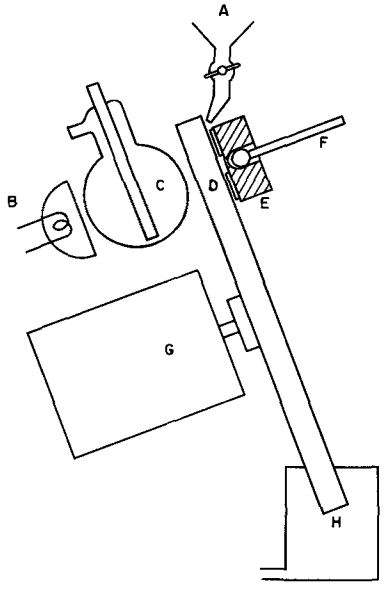

Fig. 1. Schematic arrangement of electropolishing equipment: A, dropping funnel containing etchant; B, light; C, heat absorber; D, rotating disk; E, polishing block holding 3 or more specimens; F, support rod for polishing block; G, motor drive; H, drip pan.

It is well known that stirring of the etchant often influences etching rates. Advantage has been taken of this effect in order to improve the flatness and smoothness of polished semiconductor surfaces (5, 6). A known etchant is selected and fed between the semiconductor being polished and a large flat surface moving parallel to the semiconductor. The result is a stirring action which accelerates the etching on elevated areas of the surface being polished and thus produces a relatively flat, smooth surface. The present work describes the application of this polishing technique to CdS.

Experimental

A schematic drawing of the equipment is shown in Fig. 1. It is similar to that developed for polishing other semiconductors (5, 6). Undoped CdS in the range of 1-10 ohm-cm with a Hall mobility of 300-380 cm^2/v-sec was cut perpendicular to the c axis, producing A (00.1) and B (00.$\bar{1}$) faces, and perpendicular to the a axes producing the six equivalent sides of the hexagonal unit prism. The A and B faces can be distinguished from each other by a 60-sec etch in 50% HCl.[1] This produces a mat finish on the B face and a bright finish on the A face. The slices were mounted on block E as shown in Fig. 1 and lapped with 5μ Al_2O_3. Disk D is 12 in. in diameter and covered with PAN-W Pellon cloth. The HCl etchant is fed at the rate of about 15 cc/min from supply A to the region between the driven disk (rotating about 50 rpm) and the free-running polishing block E. Light, if required, is supplied by a Sylvania Sun Gun, B, and the majority of the radiant heat is removed in the water-filled flask C.

Results and Discussion

The etching rate as a function of concentration is shown in Fig. 2. In the lower range (10-20%) the removal rate was inconveniently slow, and near the upper limit (40-50%) the intensive stirring could not control the rapid etching rate and preferential etch-

[1] All concentrations of HCl are expressed as a volume per cent of the standard 37-38% assay HCl.

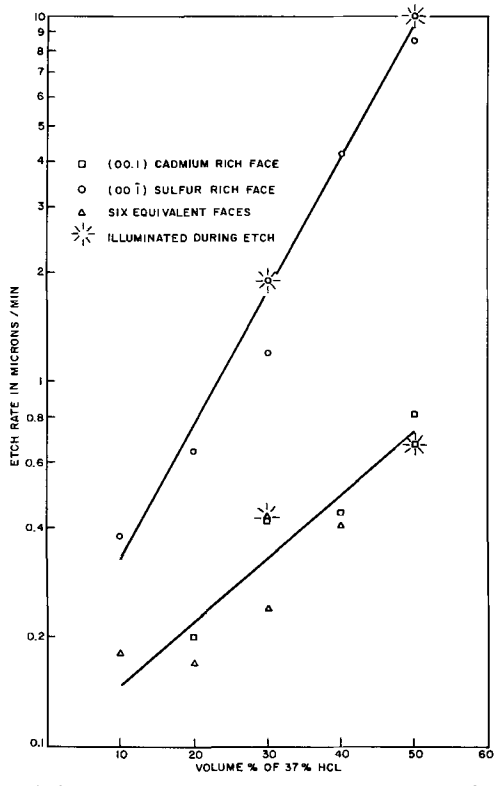

Fig. 2. Etch rate for CdS in various concentrations of concentrated (37-39%) HCl and H_2O.

ing appeared. This preferential etching occurred on the A-face (00.1) at a slightly lower HCl concentration than on the B-face (00.$\bar{1}$) or on any of the six equivalent faces of the hexagonal unit prism. A practical concentration limit for routine work seems to be 30% HCl since this composition can be used on all of the principal faces with excellent results. Figure 3A illustrates an A-face polished in a high concentration of HCl while Fig. 3B is typical of any face polished in the 30% composition.

Figures 4A and 4B are interference photographs of the A and the B face, respectively, of a slice of CdS polished in 30% HCl. A major portion of the surfaces is flat to within ±0.1 mil (±2.5μ). Figures 5A and 5B are profiles of the same surfaces taken on at Talysurf, model 3. Irregularities in the surface of the A-face are consistently less than 500Å and on the B-face less than

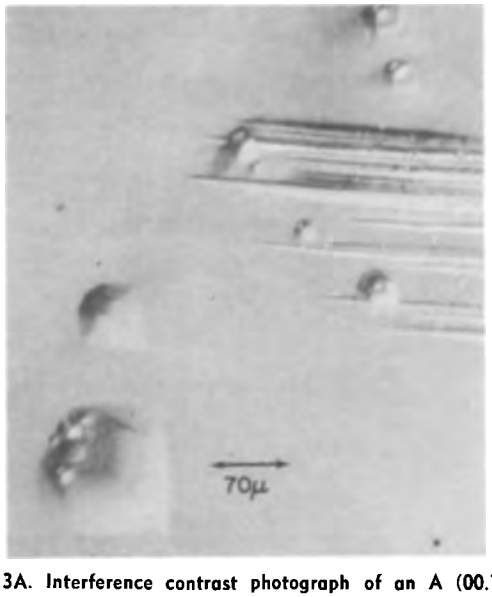

Fig. 3A. Interference contrast photograph of an A (00.1) face polished in 50% HCl. Preferential etching results in poor polishing at this concentration of HCl.

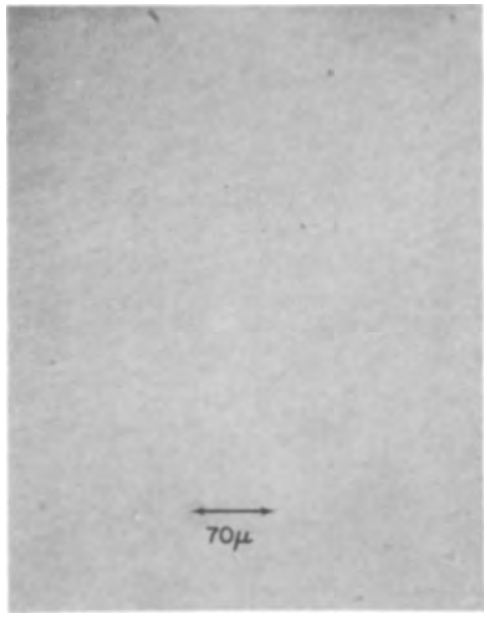

Fig. 3B. The A (00.1) face polished in 30% HCl. The B (00.$\bar{1}$) face and the six equivalent faces of the hexagonal unit prism appear similar to the A (00.1) face when polished in 30% HCl. The field of view in Fig. 3A and 3B is about 0.017 x 0.019 in.

250Å. Occasionally it is more difficult to polish the A-face of a particular crystal of CdS, but only rarely is any difficulty encountered on any other crystal face.

The data in Fig. 2 indicate that there may be a slight effect of light on the etch rate as calculated from thickness measurements. On two faces there was an increase in rate and on the third face a slight decrease. Illumination on the A face appeared to produce a slight beveling effect indicating a greater etch rate at the edges of the slice.

In the chemical polishing of GaAs (6) it was found that the etch rate varied directly with pressure. Since polishing is usually a slow process, this acceleration due to pressure was very desirable. In the case of CdS, any significant increase in pressure over that required to maintain the polishing block close to the wheel

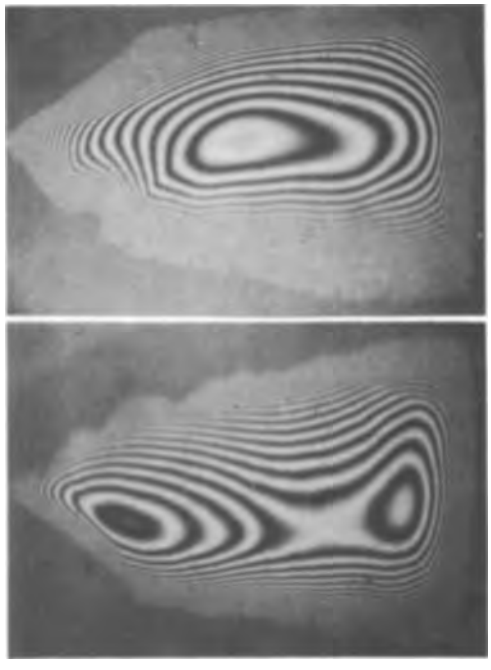

Fig. 4A (top) Interference photograph using thallium light of a polished A (00.1) face. Each fringe represents 2700Å difference in elevation and the field of view is about 0.25 x 0.36 in. Fig. 4B (bottom) Same for the B (00.$\bar{1}$) face.

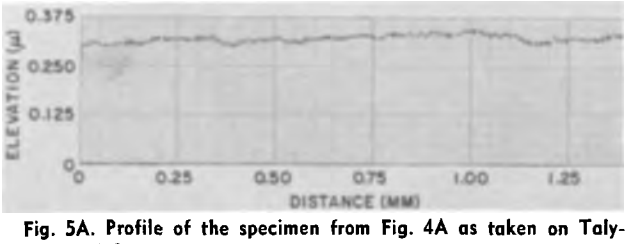

Fig. 5A. Profile of the specimen from Fig. 4A as taken on Talysurf Model 3.

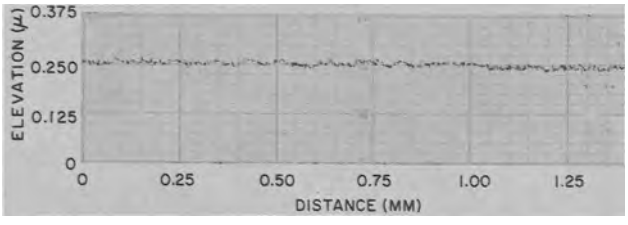

Fig. 5B. Profile of the specimen from Fig. 4B as taken on Talysurf Model 3.

(about 50 g/cm^2) caused scratching of the surface.

The epitaxial films which have been grown on CdS polished in this manner are more perfect than those which have been grown on mechanically polished or chemically polished (HCl without "planar intensive stirring") CdS.

Summary

The chemical polishing of CdS with HCl ordinarily gives a bright surface on the A face and a satin finish on the B face, but neither surface has the "polished" finish which is most desirable for device applications. The addition of planar intensive stirring to the chemical polishing has resulted in smooth, flat damage-free surfaces on all of the principal faces including both the A and the B faces. The recommended polishing solution is 30% concentrated (37-38%) HCl in water.

Manuscript received Oct. 24, 1966; revised manuscript received Nov. 21, 1966.

Any discussion of this paper will appear in a Discussion Section to be published in the December 1967 JOURNAL.

REFERENCES

1. D. Coster, K. S. Knol, and J. A. Prins, *Z. Phys.*, **63**, 345 (1930).
2. D. C. Reynolds and S. J. Czyzak, *J. Appl. Phys.*, **31**, 94 (1960).
3. R. Zare, W. R. Cook, Jr., and L. R. Shiozawa, *Nature*, **189**, 217 (1961).
4. E. P. Warekois, M. C. Lavine, A. N. Mariano, and H. C. Gatos, *J. Appl. Phys.*, **33**, 690 (1962); Erratum, *ibid.*, **37**, 2203 (1966).
5. M. V. Sullivan, D. L. Klein, R. M. Finne, L. A. Pompliano, and G. A. Kolb, *This Journal*, **110**, 412 (1963).
6. M. V. Sullivan and G. A. Kolb, *ibid.*, **110**, 585 (1963).

Addendum to Precipitates Induced in GaAs by the In-Diffusion of Zinc

J. F. Black and E. D. Jungbluth

General Telephone & Electronics Laboratories, Bayside, New York

(Vol. 114, No. 2, pp. 181-187)

The purpose of this communication is to clarify some of the procedures and qualify several of the results described in this recently published paper (1).

The infrared (IR) absorption (more accurately called IR attenuation) of diffused samples was frequently referred to in terms such as "strong IR absorption," or "reduced IR transmission," or "opaque to IR." These phrases were intended to denote IR attenuation over and above that which could be attributed to free carrier absorption.

A progressive increase in (excess) *IR* attenuation was described for several samples listed in Table I of the paper. This increase in IR attenuation was ascribed to increasing degrees of precipitation. Under illumination normal to the plane of diffusion the different thickness of the diffused layers in these samples would, alone, have caused strong differences in IR attenuation. Therefore, in this work comparisons of the IR attenuation were conducted on polished profile sections of equal thickness (75μ) cut from each sample. These comparisons were made with the aid of slotted masks, positioned and fixed under the microscope, over each profile section so that only the diffused layer was exposed to the IR illumination. When these masks were not used, or when they were not properly positioned, the IR radiation passing through the relatively transparent undiffused portion of the section interfered with the observations of IR transmission through the diffused layer. Recent measurements have shown, however, that the concentration of zinc at the boundary of the precipitate containing layers varied significantly from sample to sample (these measurements are described below). Consequently, the variation in IR attenuation through the diffused layers can only be approximately equated with variations in the degree of precipitation in each sample.

Diffused samples were sectioned normal to the diffusion plane for junction delineation by etching. Since etching did not generally produce a sharp line at the p+ p junction (for 600 X magnification), it was usually difficult to resolve a separation as small as 1μ between p+ p and p-n junctions. This meant that even though a p+ p junction occurred at a zinc concentration greater than 1 x 10^{19} atoms/cm^3 in an n-doped sample, if the p+ p junction was no more than 1μ away from the p-n junction it would appear that only one junction was present. In such a case, for example in our 5.9 x 10^{18} n-doped samples, the p+ p junction would be judged to occur at the same concentration as the p-n junction; 5.9 x 10^{18} atoms/cm^3. This amplification of our previous comments shows that our data are consistent with other recent measurements (2) of etched profile sections of p+ p and p-n junctions in zinc diffused GaAs. Extrapolation of these other junction measurements suggests that the p+ p junction in zinc diffused GaAs occurs at a zinc concentration of about 2 x 10^{19} atoms/cm^3.

Additional determinations of diffusion profiles performed with the electron beam microprobe showed somewhat higher zinc values at the p+ p boundary than before. On three additional samples the zinc concentration at the boundary of the layer of high etch pit density was 8 x 10^{18} atoms/cm^3 (24 hr at 700°C), 1.2 x 10^{19} atoms/cm^3, (2 hr at 800°C), and 1.0 x 10^{19} atoms/cm^3 (2 hr at 900°C). On each analysis the instrument "noise" level was equivalent to ± 5 x 10^{18} zinc atoms/cm^3. These analyses were obtained with a Philips Model AMR-3 Electron Probe Microanalyzer using a flexible mica crystal to achieve optimum focussing of characteristic x-rays and a 30 kv beam, at a sample current of 0.18 μa and counting over a period of 100 sec.

The discussion (1) of the excess IR attenuation in the diffused layers led to the conclusion that, for a zinc concentration of 5 x 10^{18} atoms/cm^3 at the boundary of the layer, the excess IR attenuation amounted to more than 300 cm^{-1}. This excess was proposed to be due to the presence of the submicroscopic precipitation. It would appear that the magnitude of this excess absorption must now be revised downward because the boundary zinc concentration may in general be higher than 5 x 10^{18} atoms/cm^3. However, even if the zinc concentration were as high as 2 x 10^{19} atoms/cm^3, which seems possible according to recent measurements, we must still account for excess IR attenuation amounting to about 200 cm^{-1}.

Acknowledgment

The authors wish to express their gratitude to W. J. Sutkowski for the electron probe analysis.

REFERENCES

1. J. F. Black and E. D. Jungbluth, *This Journal*, **114**, 181 (1967).
2. A. Herzog, *Solid-State Elec.*, **9**, 721 (1966).

Brief Communication

Study of Impurity Heterogeneities in InSb by Means of a Permanganate Etchant

A. F. Witt

Department of Metallurgy and Center for Materials Science and Engineering, Massachusetts Institute of Technology, Cambridge, Massachusetts

Heterogeneities of the impurity distribution in semiconductors (coring and striations) can be revealed by several different techniques like autoradiography, resistivity measurements, and etching. Of these, etching is the method most frequently used because of its relative simplicity and the good resolution that can be obtained.

In InSb impurity striations are commonly investigated with dilute or modified CP-4 etchants. This reagent gives good resolution if the semiconductor surface is properly prepared and adequate optical facilities are available. Like most etchants it suffers from a major disadvantage: the etching process is accompanied by gas evolution which frequently leads to severe pitting and demands careful control if optimum resolution is to be obtained. The background of the etched surface is not very smooth and thus requires relatively long exposure times for microphotography with a resulting deterioration of the photographic resolution.

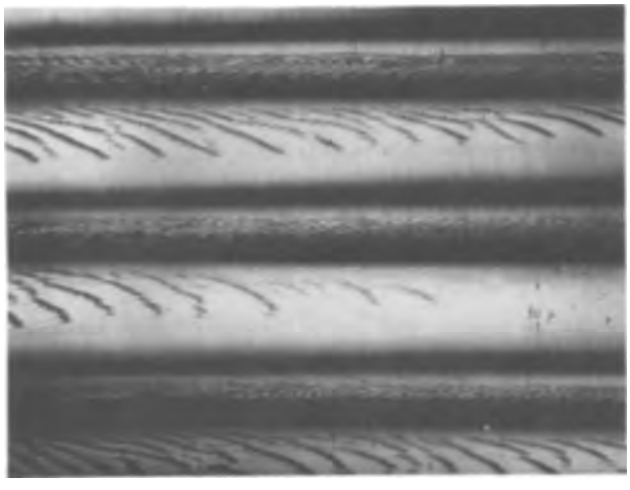

Fig. 1. Vibrational tellurium striations in InSb

A permanganate nongas-evolving etchant was developed (1 HF, 1 CH_3COOH, 1 $KMnO_4$ 0.05M) which has striking advantages over modified CP-4 etchants. For optimum results the semiconductor surface to be investigated is either immersed into the etchant or alternately the etchant is applied with a cotton applicator for a period of 4 to 6 min. (Heating or agitation is not required.) Since the oxidation process with $KMnO_4$ is not accompanied by any gas evolution the etching time is not critical and pitting is completely absent. This particular etching solution leads to a very smooth background and reveals striations with extremely high resolution. From our investigations we conclude that the ultimate resolution of striations is limited by the resolution of the optical system (about 0.2μ) rather than by that of the etchant. As a consequence of the increased reflectivity of the specimen (smoothness) it is possible to decrease the exposure times for microphotography from several minutes to fractional seconds and thus to preserve optimum resolution.

Fig. 2. Impurity striations in InSb as revealed with permanganate etch on a (211) plane.

Figures 1 and 2 show two typical instances of InSb surfaces etched with the new nongas-evolving etchant. Resolution of this magnitude could not be achieved with the standard etchants. It is most likely that the same etchant or some modified composition could be used for other materials.

Manuscript received Dec. 12, 1966.

Any discussion of this paper will appear in a Discussion Section to be published in the December 1967 JOURNAL.

ELECTROCHEMICAL SCIENCE

On the Electrolytic Conductivity of Electrolytes Simulating Those Found in Silver Chloride-Magnesium, Sea Water Activated Batteries

Duane W. Faletti and Michael A. Gackstetter

Applied Physics Laboratory, University of Washington, Seattle, Washington

ABSTRACT

Experimental determinations were made at temperatures of 5°-75°C of the electrolytic conductivity of simulated sea water activated AgCl-Mg battery electrolytes formulated from 4.5 to 19 °/oo (parts per thousand) chlorinity artificial sea water with 0-70g $MgCl_2$ added per liter of sea water.

The Applied Physics Laboratory, University of Washington, is conducting studies of the magnesium-silver chloride electrochemical couple in a sea water electrolyte. Because these studies require a knowledge of the voltage drop resulting from the electrical resistance of the electrolyte, an investigation was made of the electrical conductivity of sea water electrolytes.

If pure magnesium is used as the anode of a magnesium-silver chloride cell, two simultaneous reactions take place during the discharge: the electrochemical reaction

$$2AgCl + Mg \rightarrow MgCl_2 + 2Ag \qquad [1]$$

and the corrosion reaction

$$Mg + 2H_2O \rightarrow Mg(OH)_2 + H_2 \qquad [2]$$

which gives magnesium its anode efficiency of approximately 70%. Therefore, the cell reaction modifies the electrolyte through the addition of soluble $MgCl_2$, particles of insoluble $Mg(OH)_2$, and hydrogen gas.

In order to simulate the electrolyte conditions that occur during normal operation of a sea water activated Mg-AgCl battery, the chlorinity, temperature, and added $MgCl_2$ concentration of the electrolyte were varied. Three basic electrolytes having chlorinities of 4.5, 9.0, and 19.0 °/oo were studied. The solution having a chlorinity of 19 °/oo follows the artificial sea water formula of Lyman and Fleming (1940) taken from ref (1) and presented in Table I.

Since the chlorinity is a measure of the concentration, per kilogram, of the ions found in sea water, the other two basic electrolytes represent dilutions of the 19 °/oo chlorinity by weight factors of 2.111 (19.0 °/oo/9.0 °/oo) and 4.222 (19.0 °/oo/4.5 °/oo) to give chlorinities of 9.0 °/oo and 4.5 °/oo, respectively. The temperature and added $MgCl_2$ concentration of each basic electrolyte were varied over the ranges of 5°-75°C and 0-70g $MgCl_2$ per liter of a base electrolyte at 25°.

Table I. Composition of artificial sea water of 19 °/oo chlorinity

Salt	g/Kg
NaCl	23.476
$MgCl_2$	4.981
Na_2SO_4	3.917
$CaCl_2$	1.102
KCl	0.664
$NaHCO_3$	0.192
KBr	0.096
H_3BO_3	0.026
$SrCl_2$	0.024
NaF	0.003
	34.481

Apparatus and Procedure

The a-c impedance bridge employed in the conductivity program is an Electro-Scientific Industries Corporation Model 250 DA and operates at a frequency of 1000 cps. On the basis of measurements of reference (±0.05%) resistors, the manufacturer's guaranteed accuracy of ±0.3% is considered to be conservative. Compensation for cell reactance was achieved in the usual manner by placing a variable air capacitor in parallel with the variable resistance arm of the bridge.

A dip-type conductivity cell, Industrial Instruments, Inc., Model CEL-H50, was used. By measurement of the standard KCl conductivity solutions of Jones and Bradshaw (2-4), the cell constant was found to be 49.95 ± 0.20 cm^{-1} over a temperature range of 5°-80°C.

All of the electrolytes studied were made up from ACS reagent grade salts and distilled water having a measured conductivity of less than 4×10^{-6} mhos/cm. All weighings were made in air, and, with the exception of $MgCl_2$, all of the salts were weighed out in crystalline form. Since the degree of hydration of $MgCl_2$ is difficult to determine accurately, $MgCl_2 \cdot 6H_2O$ was dissolved in distilled water to form stock solutions which were analyzed for $MgCl_2$ content.

All conductivity measurements were made with the conductivity cell suspended in a Dewar flask containing the electrolyte. Appropriate precautions were observed to avoid contamination or dilution of the electrolyte and to insure temperature equilibrium between the cell and the electrolyte.

Each electrolyte sample was tested first at 25.0° and then consecutively at 5.0°, 50.0°, and approximately 75°C. An immersion heater was used for the 25° runs, and precooling or preheating of the electrolyte in closed containers for the low- and high-temperature runs. In order to minimize evaporation of the solvent water, no attempt was made to allow each preheated electrolyte to approach exactly 75° in the open Dewar flask. Instead, the temperature and cell resistance were recorded as soon as the bridge reading stabilized, indicating temperature equilibrium between the electrolyte and the cell. The temperatures so obtained varied from 71° to 80°C.

All temperature measurements were obtained with calibrated partial immersion mercury thermometers

and with estimated accuracies of ±0.1° at 5°, 25°, 50° and ±0.2° at 71°-80°C.

Tests were made to determine the reproducibility of the measurements and to check for errors in the high-temperature data caused by water evaporation. Reproducibility was determined by testing at 25° several carefully stored electrolytes both at the time of preparation and at intervals up to approximately 40 days after preparation. Errors due to water evaporation were determined by again taking measurements of some electrolytes at 25° after each of the 50° and 75° runs and comparing these with the initial 25° measurements. The results of these tests are discussed in the following paragraphs.

Discussion of Results

The specific conductivities measured for the 4.5, 9.0, and 19.0 °/oo chlorinity electrolyte series ($MgCl_2$ added in amounts of 0-70 g/liter of base electrolyte at 25°C) are given in Tables II, III, and IV, respectively.

It should be noted that the data for high temperatures given in Tables II-IV are reported at 75.0°, whereas the experimental data were taken at temperatures of 71°-80°C. Preliminary plots of measured conductivities vs. temperature were very nearly linear over 50° for each electrolyte. For convenience in reporting the data in tabular form, the 71°-80° data were extrapolated (or interpolated) to 75.0° by utilizing the slopes of the preliminary plots in the region between 75.0° and the experimental temperatures. The error introduced by this procedure is estimated to be less than ±0.1% and is considered to be negligible compared to the other sources of error discussed below.

By means of the tests described above, the 25° data were found to be reproducible to within ±0.3%, and the 50° and 75° data were found to be subject to evaporation errors of zero to +0.3% and zero to +0.7%, respectively.

Uncertainties in measured temperatures and $MgCl_2$ stock solution concentrations lead to estimated maximum errors of ±0.3% and ±0.2%, respectively.

Adding these errors to the ±0.4% for the cell constant and the ±0.3% for the bridge, the over-all maximum possible errors in the reported data are estimated to be ±1.2% at 5° and 25°, +1.5% to −1.2% at 50°, and +1.9% to −1.2% at 75°.

To the authors' knowledge, no other data exist in the literature for sea water with augmented $MgCl_2$ content. However, the agreement with literature values of this study's data for the basic electrolytes (artificial sea water with chlorinities of 4.5, 9.0, and 19.0 °/oo) is well within the estimated experimental error, *e.g.*, they differ from the data of Thomas *et al.* (5) by + 0.7 to −0.4% at 5° and 25°C.

Table II. Specific conductivities of 4.5 °/oo chlorinity electrolyte series*

Grams $MgCl_2$ added per liter at 25°C	Temperature, °C			
	5.0	25.0	50.0	75.0
0	0.875	1.41	2.15	2.95
11.10	2.01	3.21	4.92	6.72
22.23	3.00	4.79	7.32	9.98
36.27	4.15	6.52	10.01	13.69
70.00	6.32	10.03	15.27	20.88

Table III. Specific conductivities of 9.0 °/oo chlorinity electrolyte series*

Grams $MgCl_2$ added per liter at 25°C	Temperature, °C			
	5.0	25.0	50.0	75.0
0	1.66	2.65	4.05	5.51
11.07	2.71	4.31	6.57	8.94
22.21	3.65	5.81	8.84	12.00
36.26	4.72	7.49	11.43	15.50
70.00	6.80	10.77	16.38	22.24

Table IV. Specific conductivities of 19.0 °/oo chlorinity electrolyte series*

Grams $MgCl_2$ added per liter at 25°C	Temperature, °C			
	5.0	25.0	50.0	75.0
0	3.28	5.19	7.93	10.75
10.98	4.19	6.60	10.04	13.54
22.12	5.00	7.88	11.96	16.30
36.15	5.96	9.40	14.26	19.33
70.00	7.78	12.27	18.67	25.28

* The specific conductivities, in mhos/cm times 100, are given in the tables.

Acknowledgment

Mr. J. G. Turbitt and Mr. J. A. Arne of the Quality Evaluation Laboratory, Naval Torpedo Station, Keyport, Washington, carried out certain chemical analyses for this study. Dr. William R. Davis, Assistant Director of the Applied Physics Laboratory, and staff, Mrs. Janna Miles, Mr. William Felton, and Mr. Rodney Lipp contributed to the success of this effort. Their contributions are gratefully acknowledged.

This work was supported by the Bureau of Naval Weapons, U.S. Navy Department, under Contract NOw 65-0207-d.

Manuscript received April 27, 1966; revised manuscript received Nov. 15, 1966.

Any discussion of this paper will appear in a Discussion Section to be published in the December 1967 JOURNAL.

REFERENCES

1. H. V. Sverdrup, M. W. Johnson, and R. H. Fleming, "The Oceans, Their Physics, Chemistry, and General Biology," p. 186, Prentice-Hall, Inc., New York (1946).
2. G. Jones and B. C. Bradshaw, *J. Am. Chem. Soc.*, **55**, 1780 (1933).
3. G. C. Benson and A. R. Gordon, *J. Chem. Phys.*, **13**, 473 (1945).
4. R. F. Chambers, *J. Phys. Chem.*, **62**, 1136 (1958).
5. B. D. Thomas, T. G. Thompson, and C. L. Utterback, *J. du Conseil Perm. Internat. Pour l'Explor. de la Mer*, **9**, 28 (1934).

Solubility and Diffusion of Hydrogen in Strong Electrolytes and the Generation and Consumption of Hydrogen in Sealed Primary Batteries

Paul Rüetschi

Leclanché S.A., Yverdon, Switzerland

ABSTRACT

Experimental means to measure the H_2 generation of negative electrodes are described. Results obtained with Zn electrodes in KOH solution show that H_2 generation is decreased by the addition of K_2ZnO_2 at KOH concentrations above 2N, but is increased at concentrations below 2*N*. These findings are interpreted in terms of ZnO or $Zn(OH)_2$ film formation and dissolution. Electrochemical consumption of hydrogen within the cells may be achieved on catalyzed auxiliary electrodes, held at a suitable voltage level by a regulating device, such as a diode.

A major reason for the deterioration of dry cells on storage is drying out (1). Loss of water by evaporation leads to shrinkage of the immobilized electrolyte and to the creation of cracks and channels, allowing access of air to the zinc electrode. The resulting electrochemical oxidation and dissolution of zinc is accompanied by an equivalent consumption of air-oxygen.

In order to avoid loss of water by evaporation, as well as leakage, during long-term storage or operation the cells must therefore be sealed. For applications in outer space a hermetic seal is imperative. However, those negative electrode materials which have the most desirable characteristics with respect to power output per unit volume and per unit weight, such as zinc or magnesium, are thermodynamically unstable in common aqueous electrolytes and thus evolve hydrogen according to

$$M + 2H_2O \rightarrow M(OH)_2 + H_2 \qquad [1]$$

which leads to pressure build-up within the cell. The rate of reaction [1] increases exponentially with temperature. While the self-discharge of the cell due to reaction [1] can be of insignificant proportions, the associated pressure build-up might become very annoying.

In the past, it has been recognized that the long-term storage of Leclanché-type dry cells (1-5) is closely related to the problem of gassing. A convenient way of measuring the corrosion of zinc due to reaction [1] is by placing an appropriate sample in a closed vessel containing the electrolyte and by following the hydrogen generation volumetrically (6-8).

If complete Leclanché-type dry cells are enclosed in glass or metal containers, analysis of the gas evolved indicates that it consists largely of H_2 and CO_2. Practically no oxygen is found since the latter is consumed by the zinc electrode in a manner corresponding to the "oxygen cycle" in sealed nickel-cadmium cells. The percentage of CO_2 depends strongly on the type of MnO_2 used, electrolytic and chemically activated ores producing a much greater quantity of CO_2. Aufenast and Müller (8) suggest that the CO_2 stems from the oxidation of sugars contained in the starches employed for the pastes. However, some of the CO_2 probably comes from carbonates contained in the ores or electrolytes employed. Some CO_2 evolution is also observed in sealed lead acid batteries as a result of the oxidation of separator material and suspended organic matter. In alkaline cells any CO_2 produced is absorbed by the electrolyte. On the other hand, H_2 evolution might pose a serious problem in sealed alkaline primary cells.

The rate of hydrogen generation is governed by the overvoltage. The extremely strong effects of impurities have long been recognized and investigated (8). In Leclanché-type cells the order of increasing catalytic action on hydrogen evolution is

$$Pb < Mn < Fe < Cu < Mo < As < Sb \qquad [2]$$

To reduce "local action" the technique of amalgamation has been practiced over 100 years. It is particularly effective in reducing hydrogen evolution on zinc electrodes in alkaline electrolytes (9). However, in dry cell electrolytes of *p*H 5-6, particularly at elevated temperatures, amalgamation tends to increase hydrogen evolution.

Organic and inorganic inhibitors have been utilized to decrease hydrogen evolution in dry cells (6). Chromate films on zinc electrodes have found com-

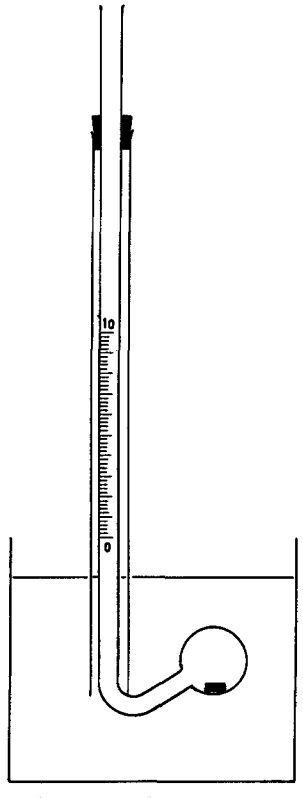

Fig. 1. Cell for the study of hydrogen evolution of negative electrodes.

mercial use as inhibitors (10). The type of starch used in the paste has a strong influence on charge retention. Vinal reports that colloidal proteins, as found in wheat flour, are good inhibitors.

Hydrogen Generation

In the present study the simple, but effective, volumetric device illustrated in Fig. 1 has been used to measure the rate of hydrogen evolution. A sample of the electrode material under study, *e.g.*, amalgamated zinc, was placed in the 20 ml round flask and the electrolyte level adjusted to the zero mark of the 10 ml calibrated capillary. The cell was immersed in a constant temperature bath. The glass tube surrounding the capillary served as thermal insulation. Hydrogen accumulated in the top of the spherical portion and displaced an equivalent volume of electrolyte into the capillary. Readings were corrected for water vapor pressure of the electrolyte, temperature, atmospheric pressure, and hydrostatic head. The gas volumes were expressed in terms of cubic centimeters at STP. Results obtained with this apparatus are shown in Fig. 2-5. These results refer to samples of 0.300g of amalgamated zinc powder in potassium hydroxide electrolyte. The samples were pretreated in the corresponding electrolyte for 2 to 20 hr, depending on the temperatures involved, to achieve steady-state conditions.

Figure 2 demonstrates the well-known effect of amalgamation, substantiating the findings of Snyder and Lander (9).

Of particular interest is the dependence of the hydrogen evolution rate on electrolyte concentration. Figures 3 and 4 illustrate corresponding results at 60°C with and without zinc oxide addition to the potassium hydroxide electrolyte, respectively, after an initial conditioning period of 20 hr. For zincate-free electrolytes the KOH concentration was determined by acidmetry using phenolphthalein as indicator. The carbonate concentration was smaller than 0.55 g/l in

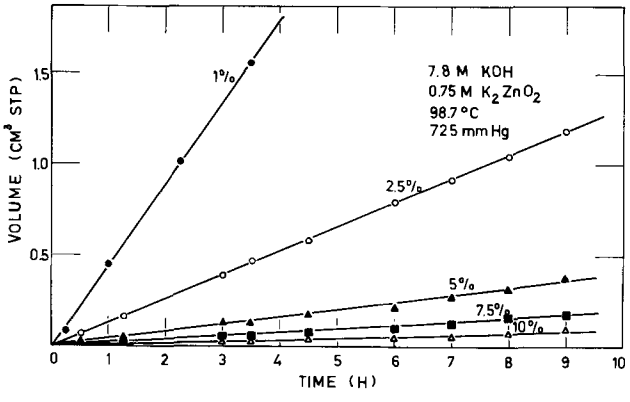

Fig. 2. Effect of amalgamation of zinc electrodes (1, 2.5, 5, 7.5, and 10% Hg) on hydrogen generation in potassium hydroxide at 98.7°C.

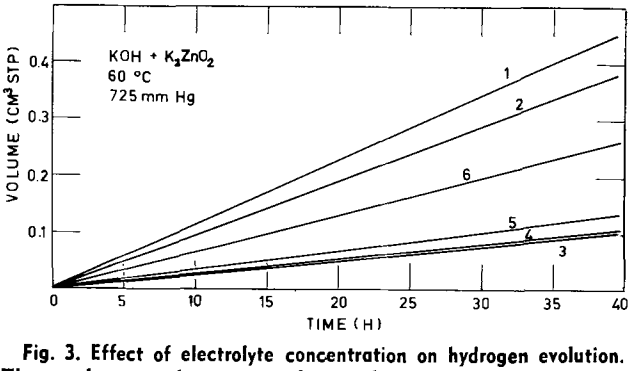

Fig. 3. Effect of electrolyte concentration on hydrogen evolution. The numbers on the curves refer to the electrolyte compositions given in Table I under KOH + K_2ZnO_2.

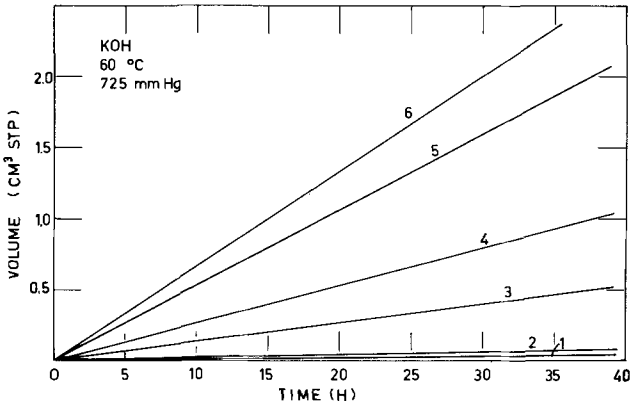

Fig. 4. Effect of electrolyte concentration on hydrogen evolution. The numbers on the curves refer to the electrolyte compositions given in Table I under KOH pure.

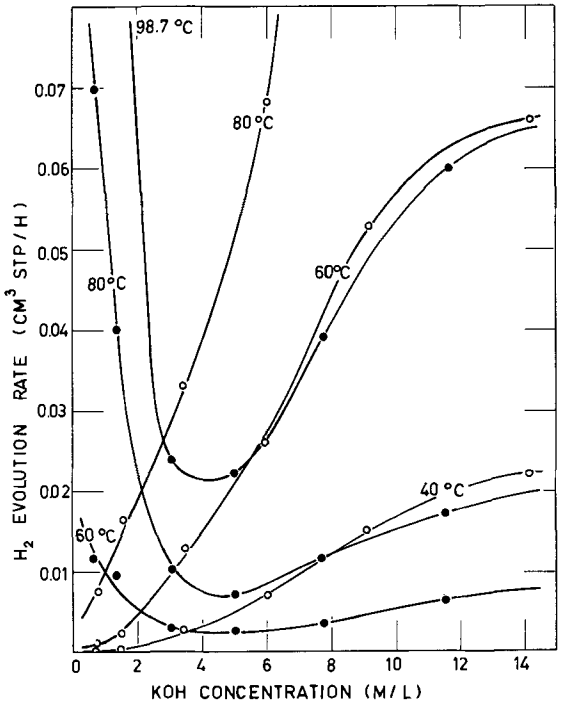

Fig. 5. Hydrogen evolution rate (cm^3 STP/hr) as a function of electrolyte concentration at various temperatures. Black dots refer to solutions containing zincate. Open circles refer to pure KOH solutions. The abscissa is the "free" KOH concentration in all cases.

all cases. For electrolytes containing ZnO, the concentration of "free" KOH was determined by acidimetric titration, using methylorange, and by subtrating the normality of the zincate concentration, as determined by complexometric titration. Compositions of the electrolytes used are listed in Table I. The zinc samples contained 5% Hg. Gassing rates are summarized in Table II.

In Fig. 5 the gassing rate is plotted against the free potassium hydroxide concentration at three different temperatures. It is apparent that in relatively dilute electrolytes, that is below 2*N* KOH, the presence of K_2ZnO_2 increased the gassing rate, whereas above 2*N* KOH, the presence of K_2ZnO_2 strongly decreased the gassing rate. This result is in accord with the practice of alkaline mercury cell manufacture (11), but is at variance with the findings of Snyder and Lander (9).

Under the experimental conditions used by these authors, the electrolyte in the vicinity of the zinc electrodes became saturated with ZnO and its concen-

Table I. Electrolyte compositions at 25°C

KOH pure No.	KOH conc, g/l	KOH conc, M/l	K_2CO_3 conc, g/l
1	42.6	0.760	0.21
2	84.2	1.50	0.21
3	193	3.45	0.14
4	339	6.03	0.41
5	513	9.15	0.41
6	796	14.20	0.55

KOH + K_2ZnO_2 No.	Free KOH conc, g/l	Free KOH conc, M/l	K_2ZnO_2 conc, M/l
1	37.3	0.665	0.0195
2	77.5	1.380	0.0980
3	173	3.08	0.235
4	285	5.08	0.400
5	437	7.80	0.750
6	653	11.60	0.980

Table II. Hydrogen evolution rates (cm^3 STP/hr) of amalgamated Zn (0.3g) in alkaline solutions, Electrolytes 1-6 of Table I

Temperature, °C	No.	KOH + K_2ZnO_2, cc/hr	KOH pure, cc/hr
98.5	1	0.120	
	2	0.095	
	3	0.0237	
	4	0.0222	
	5	0.039	
	6	0.060	
80	1	0.070	0.0075
	2	0.040	0.016
	3	0.010	0.033
	4	0.007	0.068
	5	0.0115	0.14
	6	0.017	0.16
60	1	0.0115	0.001
	2	0.0095	0.002
	3	0.0025	0.013
	4	0.0027	0.026
	5	0.0035	0.053
	6	0.0065	0.066
40	1		0.0001
	2		0.0002
	3		0.0032
	4		0.0070
	5		0.0149
	6		0.0220

tration correspondingly decreased with time in accordance with the process

$$Zn + 2KOH \rightarrow K_2ZnO_2 + H_2 \qquad [3]$$

The results of Fig. 5 indicate that for zincate-free electrolytes the hydrogen evolution rate increases with KOH concentration. The reaction appears to depend on the rate of dissolution of the interfacial ZnO or $Zn(OH)_2$ film, formed by spontaneous reaction between the zinc and the water of the electrolyte. The zinc oxide solubility strongly increases with increasing KOH concentration.

The relatively high evolution rate in dilute KOH solutions containing zincate may then be explained by the presumption that the interfacial ZnO or $Zn(OH)_2$ layer formed on immersion of a fresh zinc electrode in such electrolytes is thinner, or less compact and less protecting (12) than in zincate-free electrolyte.

From a practical point of view it is of importance to consider the question how the hydrogen, once generated, is removed from the negative electrode surface. Bubble formation will occur only if the adjacent electrolyte layer is saturated with hydrogen. At very low evolution rates a substantial portion of the hydrogen will thus be removed by molecular diffusion. The shorter the diffusion path, that is, the thinner the electrolyte layer covering the negative electrode, the higher is the diffusion rate. In ordinary dry cells with immobilized or gelled electrolyte hydrogen removal by diffusion, without bubble formation, is desirable, since evolving hydrogen bubbles may create channels for the access of air to the zinc electrode, resulting in rapid corrosion.

Hydrogen Consumption

For operation of primary batteries in a hermetically sealed condition over prolonged periods of time hydrogen-consuming means within the cell may be employed. While it is known that hydrogen can be oxidized to water by homogeneous reaction with electrolyte solutions containing copper and silver salts (13), it is believed that electrochemical oxidation through heterogeneous reaction at an electrode surface could offer a practical solution. The use of catalytically active electrode surfaces for the removal of hydrogen in sealed cells was first suggested by Dassler (14).

It is known today that electrochemical reactions on diffusion electrodes take place on locations covered with a thin, wetting electrolyte film (15). For the process of hydrogen oxidation to take place, the hydrogen must dissolve in the electrolyte, diffuse across the liquid film, and react electrochemically at the electrode interface. Therefore, both hydrogen solubility as well as diffusion rate may play decisive roles in governing the speed of the over-all process.

The solubility of hydrogen is greatly decreased in strong, concentrated electrolytes, due to salting-out effects. Ions with large hydration shells are particularly effective in salting-out. Hydrogen solubility is therefore lower in KOH than in H_2SO_4 or NH_4Cl.

The solubility of hydrogen, as determined recently (16) is shown as a function of electrolyte concentration in Fig. 6.

The diffusion coefficient of hydrogen may be obtained from limiting diffusion currents to a rotating platinum disk electrode. According to the equation of Levich (17)

$$i_d = 0.62\, nFA\, c\, \nu^{-1/6}\, D^{2/3}\, \omega^{1/2} \qquad [4]$$

where n is the number of electrons, $\mathbf{F}$ the Faraday, A the electrode area, c the concentration (solubility of hydrogen), ν the kinematic viscosity, D the diffusion coefficient, and ω the rotational speed. New results derived in this manner are shown in Fig. 7.

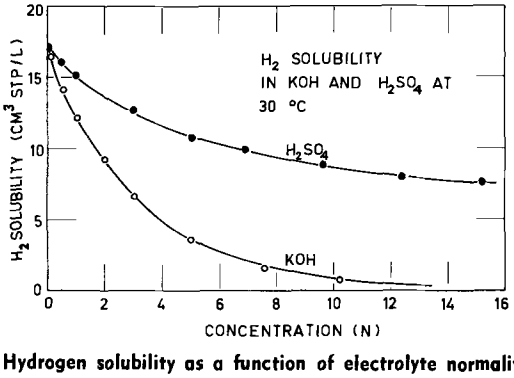

Fig. 6. Hydrogen solubility as a function of electrolyte normality.

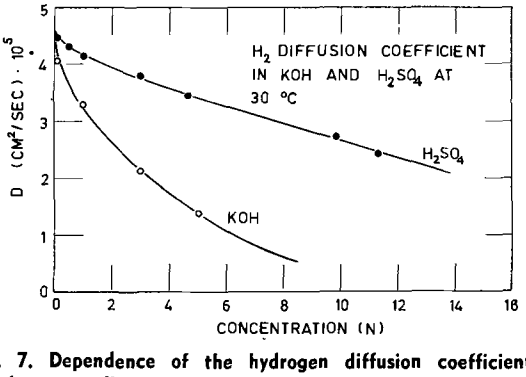

Fig. 7. Dependence of the hydrogen diffusion coefficient on electrolyte normality.

The electrochemical hydrogen ionization rate depends on electrolyte concentration, as demonstrated in Fig. 8, where the exchange current i_o of a platinized platinum electrode is plotted against electrolyte normality. These results were derived from current-voltage plots near the equilibrium potential of high-speed rotating disk electrodes. The decrease of the exchange current at high electrolyte concentration had been noted for alkaline solutions by Vielstich (18). The present result indicates a similar decrease at high acid concentrations.

At highly positive electrode potentials, that is above 500 to 900 mv *vs.* H_2 in the same solution, depending on the nature of the anions present, the electrochemical ionization of H_2 on platinum and similar materials is strongly inhibited by anion or oxygen adsorption (19). Although there has been reported consumption of H_2 on silver oxide electrodes in alkaline solutions at not insignificant rates (20, 21) and on nickel oxide electrodes (22) at very low rates, the results obtained so far with oxide electrodes are erratic (23) and seem to depend on factors which are not yet entirely understood. On the other hand, high rates of hydrogen consumption may be achieved consistently with auxiliary electrodes containing platinum metals, Raney nickel, or other H_2-catalysts, whose potentials are kept at a constant level between +100 and +400 mv with respect to a reversible H_2 electrode in the same solution, by applying voltage regulating means such as diodes (24, 25). An arrangement of this kind is shown for a primary Ag_2O-Zn cell in Fig. 9, where R signifies a high resistance in the order of $10^5/C$ ohm (C being the capacity of the cell in ampere hours) and where D is a forward or backward diode with a voltage drop in the order of 1v. The tiny current flowing through the resistor keeps the voltage of the auxiliary electrode at its working level even if temporarily no hydrogen should be present in the cell.

A practical three-terminal construction of a small sealed cell is indicated in Fig. 10.

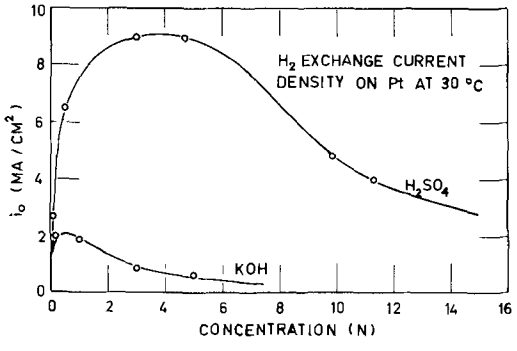

Fig. 8. Exchange current of a Pt-catalyzed hydrogen electrode as a function of electrolyte normality.

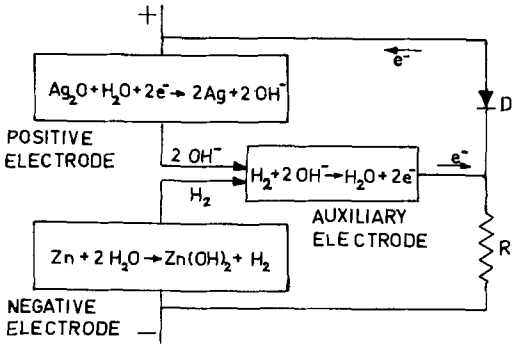

Fig. 9. Schematic representation of the generation and consumption of hydrogen in a sealed silver-zinc primary battery with auxiliary electrode.

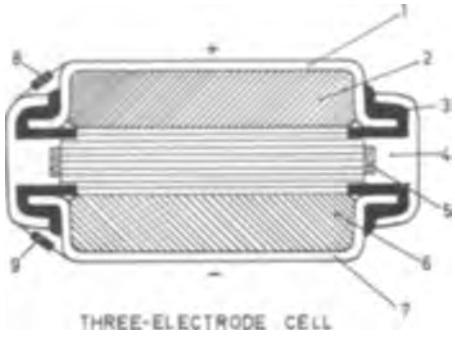

Fig. 10. Construction of a small sealed cell with auxiliary H_2-consuming electrode: 1, positive cell can; 2, positive electrode; 3, grommet seal; 4, side wall serving as auxiliary electrode terminal with crimp-seals; 5, auxiliary porous electrode; 6, negative electrode; 7, negative cell can; 8, diode; 9, resistor.

If the hydrogen-consuming electrode is barely wetted, ohmic drops, caused by ionic current flow in the thin electrolyte films, will cause certain parts of the electrode to exhibit a local potential near that of a reversible H_2 electrode. Anionic inhibition is then less of a problem even at relatively high external anodic potentials.

Under these conditions the following equation applies, up to relatively high anodic potentials, for the case of limiting H_2 diffusion across the thin, wetting film on a porous partly wetted electrode

$$I_a = (2DZ_m\mathbf{F}k_hs^2/\rho)^{1/2}\, p^{1/2}\, \eta_a^{1/2} \qquad [5]$$

where I_a is the current density/cm^2 of projected porous electrode surface; D the diffusion coefficient of H_2; $\mathbf{F}$ the Faraday number; k_h the Henry solubility constant of H_2; s the internal surface area (cm^2/cm^3); ρ electrolyte specific resistance; p partial H_2 pressure; η_a the applied electrode potential with respect to a reversible H_2 electrode in the same solution; and Z_m the electrons required per molecule (2 for H_2).

If the rate is controlled by the speed of electrochemical ionization at the interface, the current becomes

$$I_a = (2\tau_o s^2 k_o k_h/\rho\phi)^{1/2}\, p^{1/2} \exp(\phi\eta_a/2) \qquad [6]$$

where τ_o is the effective electrolyte film thickness, k_o the electrochemical rate constant, and, $\phi = \alpha n\mathbf{F}/kT$. In either case the current is proportional to the square root of internal partial H_2 pressure.

In conclusion, it can be stated that means are available to limit the generation and to accelerate the consumption of hydrogen in primary batteries, allowing the latter to be hermetically sealed.

Manuscript received Sept. 12, 1966. This paper was presented at the Philadelphia Meeting, Oct. 9-14, 1966.

Any discussion of this paper will appear in a Discussion Section to be published in the December 1967 JOURNAL.

REFERENCES

1. G. W. Vinal, "Primary Batteries," p. 126, John Wiley & Sons, Inc., New York (1950).
2. W. J. Hamer, J. P. Schrodt, and J. W. Vinal, *Trans. Electrochem. Soc.*, **90**, 449 (1946).
3. C. G. Birdsall, Proc. 10th Annual Power Sources Conference, p. 1 (1956).
4. A. G. Hellfritzsch, Proc. 11th Annual Power Sources Conference, p. 27 (1957); L. D. Warburton, *ibid., 17th*, p. 138 (1963).
5. J. Davis, "Proceedings of the 4th International Symposium on Batteries," p. 233, Collins, Editor, Pergamon Press, Oxford (1965).
6. C. K. Morehouse, W. J. Hamer, and G. W. Vinal, *J. Research Natl. Bur. Standards*, **40**, 151 (1948).
7. F. G. Stickland, *J. Appl. Chem.*, **1960** 155.
8. F. Aufenast and J. Müller, "Proceedings of the 3rd International Symposium on Batteries," p. 325, Collins, Editor, Pergamon Press, Oxford (1963).

9. R. N. Snyder and J. J. Lander, *Electrochem. Technol.*, **3**, 161 (1965).
10. G. W. Vinal, "Primary Batteries," 3rd ed., p. 97, John Wiley & Sons, Inc., New York (1950).
11. S. Rubens, U. S. Pat. 2,422,045, June 10, 1947.
12. K. Huber, *This Journal*, **100**, 376 (1953); M. Eisenberg, H. F. Bauman, and D. M. Brettner, *This Journal*, **108**, 909 (1961); N. A. Hampton, M. J. Tarbox, J. T. Lilley, and J. P. G. Farr, *Electrochem. Technol.*, **2**, 309 (1964).
13. A. H. Webster and J. Halpern, *J. Phys. Chem.*, **61**, 1239, 1245 (1957).
14. A. Dassler, German Pat. 602,702 (1934); U. S. Pat. 2,104,973 (1938).
15. F. Will, *This Journal*, **110**, 145 (1963); P. Rüetschi and J. B. Ockerman, Submitted for publication.
16. P. Rüetschi and R. F. Amlie, *J. Phys. Chem.*, **70**, 718 (1966).
17. B. Levich, *Zhur. Fiz. Khim.*, **18**, 335 (1944); *Discussions Faraday Soc.*, **1**, 37 (1947); E. A. Aikazyan and A. I. Fedorova, *Dokl. Akad. Nauk.*, **86**, 1137 (1952).
18. W. Yielstich, "Brennstoffelemente," p. 50, Verlag Chemie, Weinheim-Bergstr. (1965).
19. A. N. Frumkin and E. A. Aikazyan, *Dokl. Akad. Nauk. SSSR*, **100**, 315 (1955); *Izv. Akad. Nauk. SSSR*, **2**, 202 (1959).
20. J. J. Lander and J. A. Keralla, Tech. Rept. RTD-TDR-63-4029, Air Force Systems Command, Wright-Patterson, Air Force Base, Ohio, 31 Oct. 1963.
21. F. Bachmann, U. S. Pat. 3,117,033, Jan. 7, 1964.
22. H. B. Lunn and J. Parker, "Batteries," p. 129, Collins, Editor, Symposium Publications Division, Pergamon Press, London (1965).
23. A. Fleischer, "Proc. 13th Ann. Power Sources Conf." USASRDL, p. 78 (1959).
24. P. Rüetschi *et al.*, U.S. Pat. 3,080,440, March 5, 1963.
25. P. Rüetschi and J. B. Ockerman, *Electrochem. Technol.*, **4**, 383 (1966).

Kinetics of the Attack of High-Temperature Molybdenum and Tungsten by Atomic Oxygen

Daniel E. Rosner and H. Donald Allendorf

AeroChem Research Laboratories, Inc., a subsidiary of Ritter Pfaudler Corporation, Princeton, New Jersey

ABSTRACT

Using microwave discharge, fast-flow system techniques coupled with resistance heating and monitoring of the reacting specimens, the true kinetics of metal atom removal for polycrystalline molybdenum and tungsten filaments attacked by atomic oxygen have been obtained in the nominal temperature range 1000°-2200°K at oxygen atom pressures in the range 10^{-3} to 5 x 10^{-2} Torr. Under these conditions the oxides of molybdenum and tungsten essentially volatilize as rapidly as they are formed, leaving the metal surface vulnerable to direct oxygen atom attack at constant (time independent) rates. Reaction probabilities are found to be up to 140 times those for O_2 attacking the same surface, are independent of O-atom partial pressure, and exhibit a much weaker temperature dependence than those for O_2. These observations are in accord with a Rideal-type mechanism in which O atoms from the gas phase strike chemisorbed oxygen, leading either to product formation and desorption, or surface-catalyzed oxygen atom recombination.

Owing to the rapidity of the chemical reactions involved and the desirability of measuring product distributions using existing mass spectrometer techniques, most fundamental studies of the oxidation kinetics of refractory metals that form oxides which are volatile at the reaction temperature have been carried out at very low O_2 pressures, typically much less than 10^{-3} Torr (1-3). Under these conditions one finds that the observed reaction probabilities and product distributions can be understood only in terms of the inferred population of adsorbed *atomic* oxygen (2, 3), *i.e.*, oxygen atoms arriving as part of oxygen molecules which are not dissociatively adsorbed on impact are denied any role in subsequent events leading to product formation-desorption. This being the case, the average reaction probability cannot exceed the "sticking" (dissociative adsorption) probability, which itself can be quite small ($<10^{-2}$) on crystallite surfaces already partially covered with chemisorbed oxygen (4, 5). Clearly the situation is quite different if the attacking gas is already dissociated, and it is of fundamental interest to inquire as to the consequences of prior dissociation on the observed rates of such heterogeneous reactions, particularly at high oxygen pressures.

This question is also timely in view of recent advances in aerospace technology since, as discussed in the Appendix, vehicle speeds are now high enough to cause significant dissociation of diatomic oxygen in the air wetting such vehicles. Yet relevant experimental data and detailed consideration of the role of atomic oxygen in the degradation of high-temperature materials is conspicuously absent from most recent oxidation (or "ablation") studies, a situation which, in part, motivated the present work. In addition, regions of the earth's atmosphere (>100 km) in which atomic oxygen is naturally present due to solar-induced photodissociation are being rocket-probed with increasing frequency, again raising questions about the response of materials in such environments.

Accordingly, the experiments reported herein were designed to provide the first high-temperature data on the attack of polycrystalline molybdenum[1] and tungsten by atomic oxygen under conditions such that the observed reaction rates: (*a*) would not be falsified by reactant or product diffusional limitations and thermal accommodation effects, and (*b*) could be directly compared with oxidation rates for diatomic oxygen attacking the same metal surfaces using the same experimental techniques, at reactant partial pressures of aerospace interest. Despite the rapidity of the O-atom attack, this has been accomplished at surface temperatures up to 2200°K by combining the conditions of low total pressure, high pumping speed, and small specimen size, as described below, using a microwave discharge to dissociate oxygen.

Experimental

The techniques and equipment used here are similar to those developed in connection with our previous

[1] The present work considerably extends (from 1500° to 2600°K) the preliminary results for molybdenum reported by the authors in (6) and presents for the first time the corresponding oxidation behavior for tungsten and some observations on one industrially important alloy of molybdenum (TZM). Extensive results for the reaction order in O_2 are also presented here.

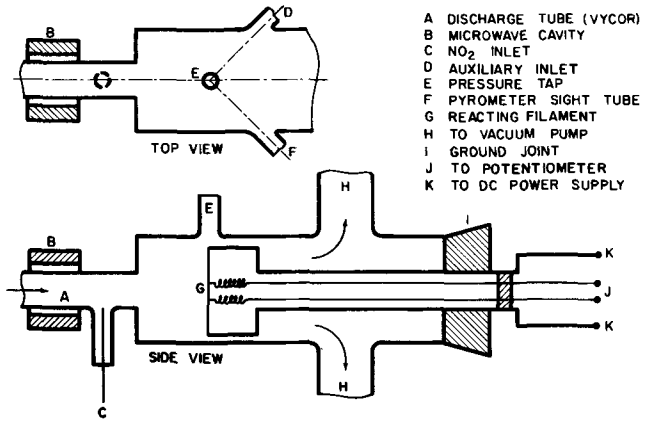

Fig. 1. Filament oxidation apparatus (schematic)

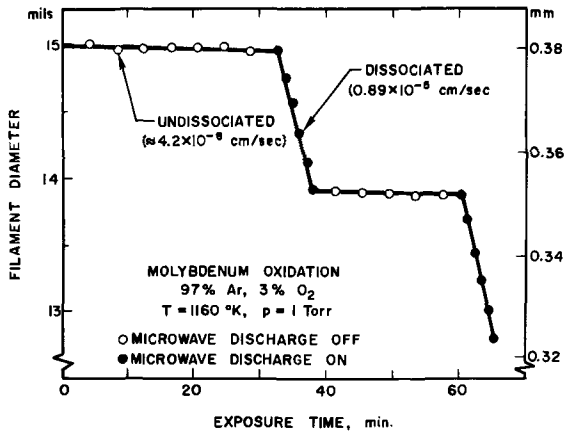

Fig. 2. Effect of dissociation on the oxidation rate of molybdenum

studies of the attack of high-temperature graphite and molybdenum by atomic oxidizers (6-9). Significant details are given here to facilitate an understanding of the results presented below.

Atom production.—As indicated schematically in Fig. 1, the apparatus consists of a Vycor discharge tube-Pyrex vacuum flow system coupled to a pair of mechanical pumps (not shown) providing a maximum capacity of about 25 l/sec. Metered diluent-O_2 gas mixtures (usually Ar/O_2, dilute in O_2) are passed through a 2450 MHz, 125w microwave-powered discharge cavity[2] 28 cm downstream of which the gas encounters the electrically heated filament being studied. Most of the experiments were carried out with the pressure level at the specimen location maintained at 1 Torr (1.316×10^{-3} atm) and the flow rate maintained at 21.7 cc (STP)/sec. This corresponded to a linear velocity of approximately 2×10^4 cm/sec in the discharge tube, or a residence time of 45 μsec/cm. As noted below, experiments at higher total pressures (up to 1 atm), using carrier gases other than argon (*e.g.*, He, N_2) and at various flow rates, were carried out to determine the true reaction order (reactant partial pressure dependence) and to verify the absence of diffusional falsification phenomena.

Reaction rate.—Reaction rates were inferred directly from continuous measurements of the resistance-time curve of electrically heated filaments of circular cross section. Together with current measurements, the voltage drop across the central 0.55 cm of each 3.1 cm long filament was continuously monitored using spring-loaded contacts (*cf.* Fig. 1) leading to a recording potentiometer. During a run the filament surface temperature was maintained constant (to within about ±5°K) by manually altering the direct current in accord with the output of an optical pyrometer, thereby allowing the decrease in filament diameter caused by the reaction (typically less than a total of 0.005 cm for an initial filament diameter of 0.0381 cm) to be calculated.[3] While the optical pyrometer was used to maintain constant filament temperature during an experiment, the absolute value of the surface temperature, which in the present experiments was in the range of 1040°-2600°K, was determined from the initial filament resistance, in accord with its resistivity-temperature relation (11, 12). A typical plot of inferred filament diameter versus time is shown in Fig. 2, in which data for both undissociated and dissociated oxygen are included for comparison. In each case the reaction rate (proportional to the absolute value of the slope) is seen to be constant in time, as expected for heterogeneous reactions forming volatile (nonprotective) oxides. Owing to the large increase in reaction rate on activation of the electrical discharge and the small concentrations of O_2 simultaneously present, except at the highest temperature investigated the observed reaction rate for the dissociated gas condition (discharge on) is dominated by the O-atom contribution, thereby necessitating only small corrections[4] (typically much less than 7%) for the O_2 contribution.

In the absence of the electrical discharge, our technique is similar to that described in an unpublished study (13) of the oxidation kinetics of molybdenum in air at subatmospheric pressures. Indeed, the results of ref. (13) could be reproduced[5] in the present equipment (see Fig. 3), thereby providing a check on a portion of the present methods and, incidentally, demonstrating that the results of ref. (13) were not influenced by oxygen transport (access) limitations.[6]

Atom detection.—Basic to the inference of reaction probabilities is the determination of absolute atom concentrations in the gas mixture emerging from the microwave discharge cavity. This has been accomplished by using the so-called $NO_2(g)$ light-titration technique described in ref. (14) and (15). The method

[2] The cavity used was type 2A (foreshortened ¾ wave coaxial) as described in (10).

[3] Results agreed well with periodic checks of the diameter reduction, as obtained from direct measurements on filaments observed under a microscope.

[4] For this purpose the O_2 reaction was assumed to be independent of the O-atom reaction, merely adding to the net rate. Experimental evidence for this independence is discussed later on.

[5] Slight but systematic departures from simple "power-law" (*i.e.*, constant reaction order) kinetics are now evident at pressures above 10 Torr (see Fig. 3).

[6] In ref. (13) flow rates were left unspecified. The present results, displayed in part in Fig. 3, were verified to be flow-rate independent.

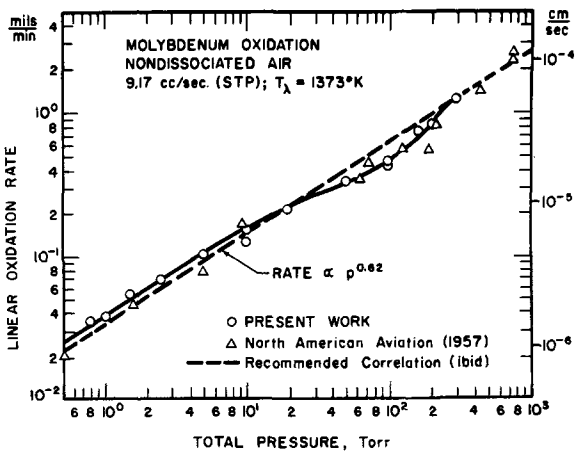

Fig. 3. Pressure dependence of the molybdenum oxidation rate in undissociated air at subatmospheric pressures; comparison with the work of ref. (13).

is a titration in the sense that one adds $NO_2(g)$ to the gas discharge products until the visible radiation (air afterglow) produced by the reaction sequence

$$O + NO_2 \rightarrow NO + O_2 \quad \text{(fast)} \quad [1]$$

$$O + NO \rightarrow NO_2 + h\nu \quad \text{(slow)} \quad [2]$$

vanishes (the titration "end point"). The $NO_2(g)$ flow rate at which this occurs is then an accurate measure of the initial O-atom flux (14, 15). $NO_2(g)$ was added through a retractable, perforated-tip Pyrex tube inserted at point C (see Fig. 1). Flow rates were determined using a critical flow orifice[7] calibrated against actual NO_2 absorption by Indicarb[8] CO_2 absorbent. At the pressure levels and flow rates investigated here, homogeneous O-atom losses by termolecular recombination or ozone production (see Discussion) between the discharge and the filament location can be ruled out on kinetic grounds, thereby eliminating the need for axial spatial resolution in the atom-detection technique. Radial gradients in the O-atom concentration are expected to be small due to the inefficiency of cool Vycor as an oxygen atom recombination catalyst (16). Moreover, the effects of any radial gradients in atom flux are minimized by the fact that only the central portion (0.55 cm) of the reacting specimen is monitored, whereas the upstream discharge tube (see Fig. 1) has an inner diameter of 1.06 cm.

Materials.—All of the data included here were obtained using commercially available polycrystalline materials. The pure molybdenum and tungsten (wolfram) filaments were cut from 0.0381 cm (15 mil) diam, high-recrystallization-temperature, drawn wire previously cleaned to remove surface oxides (Westinghouse Lamp Division, Bloomfield, New Jersey, Type A, Process C3H molybdenum and Type HRE Process C3I tungsten). The titanium-zirconium-molybdenum alloy (TZM) supplied by Sylvania Electric Products Inc., Towanda, Pennsylvania, (designation MT-104) contained 0.50% Ti, 0.099% Zr, and 0.040% C. Extra-dry-grade (Linde) oxygen, prepurified-grade argon (Linde), prepurified-grade nitrogen (Linde), high-purity-grade helium (Linde), and nitrogen dioxide (Matheson) cylinder gases were used without pretreatment.

Results—Molybdenum/Oxygen System

It is instructive to cast all experimental chemical kinetic results in terms of dimensionless reaction probabilities. In our previous work (6-9) and in the present case, this may be done without any assumptions as to the product gas species distribution[9] by introducing the oxidation probability ϵ, defined here as the ratio of the flux of molybdenum atoms (regardless of their chemical state of aggregation) away from the surface to the collision flux of O(g) or $O_2(g)$ with the surface. The molybdenum element flux, $Z''_{(Mo)}$, is obtained from the observed rate of filament radius change, the density of the filament (about 10 g/cc in the temperature range of interest), and the molecular weight of molybdenum (95.95 g/g-mole). The incident O(g) or $O_2(g)$ flux (Z''_O, Z''_{O_2}) is directly proportional to their known partial pressures and is obtained from the Hertz-Knudsen equation evaluated at the filament surface temperature[10] T

$$Z''_i = \frac{p_i}{kT} \cdot \left(\frac{kT}{2\pi m_i}\right)^{1/2} \quad [3]$$

where i = O or O_2, p_i and m_i are the partial pressure and molecular mass of species i, respectively, and k is the Boltzmann constant. It should be noted that if $Z''_{(Mo)}$ is experimentally found to be proportional to the n^{th} power of the oxygen partial pressure, where n is the reaction order, the probability ϵ reported herein will be proportional to the $n - 1$ power of oxygen partial pressure (and, hence, independent of the latter when the reaction is truly first order, *i.e.*, $n = 1$). It is also seen from Eq. [3] that the apparent activation energy locally inferred from an Arrhenius plot of ln ϵ *vs.* $1/T$ will exceed that obtained from a plot of ln $Z''_{(Mo)}$ *vs.* $1/T$ by the amount $\frac{1}{2}RT$, where R is the universal gas constant.[11]

Temperature dependence of the oxidation probability.—Figure 4, which considerably extends and supersedes the preliminary results reported in ref. (6), summarizes our data on the temperature dependence of ϵ for high-temperature molybdenum subjected to O or O_2 attack at comparable partial pressures. Except at the highest temperatures investigated (>2200°K), the O-atom reaction probability is seen to be considerably higher than that for O_2, the factor exceeding 100-fold at surface temperatures less than about 1200°K. The absolute value of the O-atom reaction probability is quite high (greater than 10^{-2} even at temperatures as low as 1040°K). Neither reaction displays simple Arrhenius behavior (constant activation energy), and neither reaction probability passes through a temperature maximum under the conditions investigated ($p_O = 10^{-2}$ Torr, $p_{O_2} = 3 \times 10^{-2}$ Torr, and $1060 < T < 2600$°K. However, as reported earlier (6), in the temperature range below about 1450°K both reaction probabilities exhibit simple Arrhenius behavior, with the O-atom activation energy (≈6 kcal/mole) being smaller than that for O_2 (26 kcal/mole) by a factor of 4.4. While the high-temperature (1680°-2620°K) branch for the O_2 reaction corresponds to an apparent

[7] Owing to the temperature-sensitive equilibrium $2NO_2(g) \rightleftarrows N_2O_4(g)$, the entire critical orifice metering system was kept immersed in a constant-temperature bath (305°K).

[8] Fisher Scientific Company, supplier.

[9] Thus, unless one is only interested in orders of magnitude, the probability ϵ introduced here should be distinguished from the fraction of the incident oxygen atoms or molecules which react. For example, if (as is often done) an author has assumed that molybdenum trioxide is the major reaction product, then ϵ (as defined here) would be larger than the reported fraction of O_2 molecules which react by the factor 3/2. More generally if α $MoO_2(g)$ molecules are produced for every $(1 - \alpha)$ $MoO_3(g)$ molecule, then the fraction of the incident O atoms which react is $[3(1 - \alpha) + 2\alpha]\epsilon$, and the fraction of the incident O_2 molecules which react is $\{[2(1 - \alpha)/3] + \alpha\}\epsilon$.

[10] At 1 Torr total pressure, under the conditions of most of the experiments reported here, the Knudsen number based on filament diameter (*i.e.*, the ratio of mean free path to filament diameter) was about 10^{-1}, the Mach number (ratio of local approach velocity to local acoustic velocity) was less than 0.6, and the Reynolds number based on filament diameter was about 10 (fluid property values are those relevant to the up-stream gas mixture). Under these conditions it is likely that approaching gas atoms or molecules make a sufficient number of collisions with other molecules (whose translational temperature has already been raised by the presence of the hot surface) to be raised to the filament temperature (see also Discussion: Absence of Transport Limitations). It should also be remarked that even if the system were isothermal and gas-phase encounters near the filament could be neglected, at the highest Mach numbers investigated here the average collision rate with the surface would not differ from the Hertz-Knudsen (Eq. [3]) by more than about 15% [see *e.g.*, ref. (7)].

[11] For example, at 2000°K the difference is 1.987 kcal/mole. This may be considerably greater than the scatter of available Arrhenius-type rate data, especially for low-activation-energy reactions.

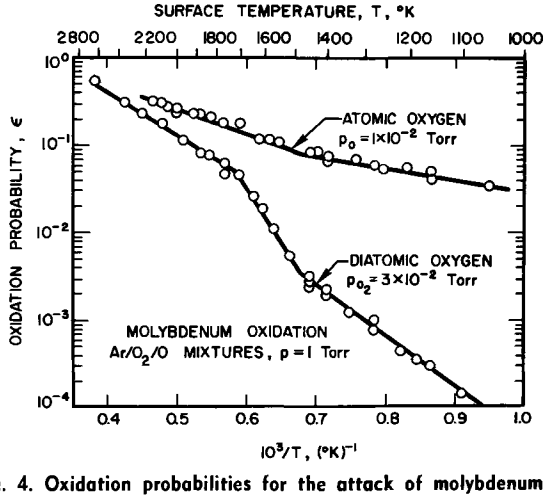

Fig. 4. Oxidation probabilities for the attack of molybdenum by atomic and diatomic oxygen; temperature dependence.

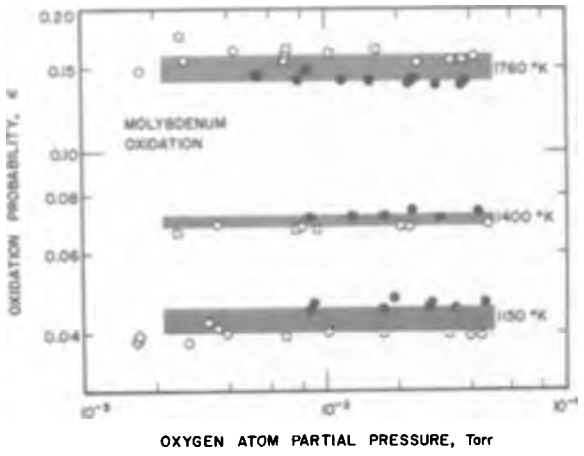

Fig. 5. Oxidation probabilities for the attack of molybdenum by atomic oxygen; oxygen pressure dependence (○ p = 1 Torr; •X_O = const., ◇ O-atoms produced from N + NO).

activation energy of 22 kcal/mole, at intermediate temperatures (≈1480°-1680°K) the apparent activation energy for this reaction is as large as ≈60 kcal/mole.

Kinetic order of the oxidation reactions.—To determine if the molybdenum reaction probabilities displayed in Fig. 4 are dependent on oxygen pressure,[12] an extensive series of constant-filament-temperature experiments was carried out. Interestingly enough, under all conditions investigated (see Fig. 5) the O-atom oxidation probability for molybdenum was found to be independent of O-atom partial pressure,[13] indicating a first-order heterogeneous reaction.

In contrast, the O-reaction probability showed a general tendency to decrease with increased O_2 pressure (see Fig. 6), indicating fractional order (typically between ½ and 1) kinetics. Moreover, the true kinetics display systematic and quite complex departures from simple power-law (straight line on log-log coordinates) behavior[14] (see Fig. 6, Table I, and the discussion below), frequently passing from an intermediate reaction order (0.57-0.66) at low O_2 pressures to a nearly first-order ($n \approx 1.04$) regime at high O_2 pressures, through an intermediate regime of very low (≈0.35) reaction order (see open points, Fig. 6 and Table I) which becomes more extensive at high filament temperatures.

[12] $O_2(g)$ data are also necessary in order to correct the O(g) + $O_2(g)$ data for the $O_2(g)$ contribution.

[13] In these experiments p_O was varied (over about a 30-fold range) in two distinct ways. In Fig. 5, results obtained at constant total pressure (1 Torr) by varying the O-atom mole fraction are shown as open circles; those obtained at constant O-atom mole fraction but variable total pressure are shown as darkened circles. Taking into account reproducibility factors in the absolute rates, the two sets of results are seen to be in substantial agreement, especially as regards reaction order. Our recent results at 1760°K using O-atoms produced from the reaction N + NO → N_2 + O (See Discussion) reveal no significant departures from first order behavior even one-decade lower in O-atom pressure than that shown in Fig. 5.

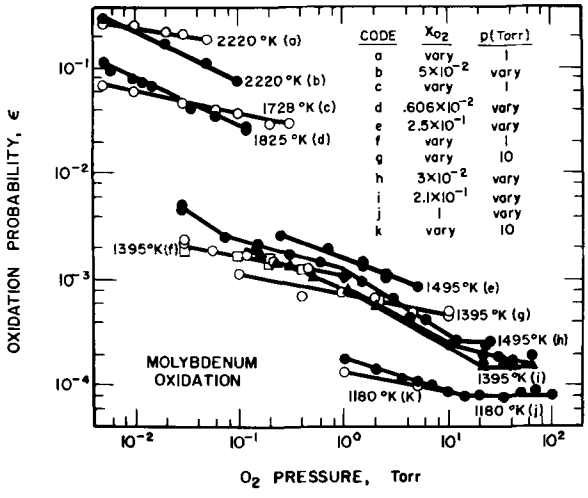

Fig. 6. Oxidation probabilities for the attack of molybdenum by diatomic oxygen; oxygen pressure dependence (open points pertain to constant total pressure; darkened points pertain to constant oxygen mole fraction; circles pertain to the carrier gas argon, triangles: nitrogen, and squares: helium).

Table I. Observed reaction orders; Mo(s)/O_2(g) reaction[a]

T, °K	p, Torr	X_{O_2}	n	Identification[a]
1180	10	0.1 to 1.0	0.80	k
1395	1	0.03 to 1.0	0.80	f
1395	10	0.01 to 1.0	0.81	g
1728	1	0.005 to 0.3	0.80	c
2220	1	0.005 to 0.05	0.82	a
1180	1 to 15	1.0	0.66	j
1395	1 to 10	0.21	0.64	i
1495	1 to 35	0.03	0.67	h
1495	1 to 20	0.25	0.65	e
1825	0.9 to 20	0.00606	0.58	d
2220	1 to 20	0.005	0.57	b
1395	10 to 90	0.21	0.39	i
1495	35 to 450	0.03	0.39	h
1180	15 to 100	1.0	1.04	j
1395	90 to 300	0.21	1.04	i
1495	450 to 760	0.03	1.04	h

[a] cf. Fig. 6.

An important feature of the O-atom results, not obvious from Fig. 5 alone, is that the reaction probability is independent of p_O despite the fact that the ratio p_O/p_{O_2} varied by a factor of about 10 for these experiments (6). Thus, under these conditions, O_2 plays no role in the O-atom oxidation reaction.[15] Interestingly enough, N atoms in amounts up to 1/10 of the O-atom concentration ($p_O = 10^{-2}$ Torr) did not noticeably affect the oxidation rate of 1150° and 1500°K molybdenum filaments.

O-atom attack of TZM alloy.—In view of the practical importance of the refractory metal alloys, exploratory experiments on the O-atom attack of TZM (0.5% Ti-0.1% Zr-molybdenum alloy) were carried out to determine if the oxidation rates are significantly different from those reported above for pure molybdenum. Interestingly enough, in all cases examined ($T \approx$ 1400°K and 2020°K, $p_O = 2.35 \times 10^{-2}$, or p_{O_2} = 1 Torr) the observed oxidation rates were within about 15% of the corresponding rates for pure molybdenum. This implies that unprotected TZM will likewise exhibit significantly reduced oxidation resistance in partially dissociated gaseous environments similar to those investigated here.

Results—Tungsten/Oxygen System

Similar experiments, but over a somewhat more restricted temperature range (≈1400°[16] to 2600°K) have been carried out on the oxidation kinetics of tungsten filaments, again with special emphasis on the effects of oxygen dissociation. In an analogous way, we define the oxidation probability ε as the ratio of the flux of tungsten atoms (regardless of their chemical state of aggregation) away from the surface to the collision flux of O(g) or O_2(g) with the surface. Here we use 19 g/cm³ as the mean density of the W(s)

[14] One interesting feature, discussed briefly in ref. (18) and evident in Fig. 6, is that experiments at constant pressure (variable O_2 mole fraction) lead to higher apparent reaction orders (≈0.80-0.82) than corresponding experiments at variable pressure (constant O_2 mole fraction, as in air; cf. Fig. 3), an effect which seems to be independent of whether the carrier gas is helium, nitrogen, or argon. As noted in ref. (18), this accounts for the apparently discrepant results reported for the Mo(s)/O_2(g) reaction in ref. (13) and by Berkowitz *et al.* (19), and Gulbransen *et al.* (20).

[15] A similar conclusion has been reached by Fryberg (21) for the O-atom attack of platinum.

[16] While filament temperatures lower than 1400°K are well within the pyrometer capability, for this reaction reliable measurements at such temperatures were precluded by the formation of thick tungsten oxide films on the reacting filaments.

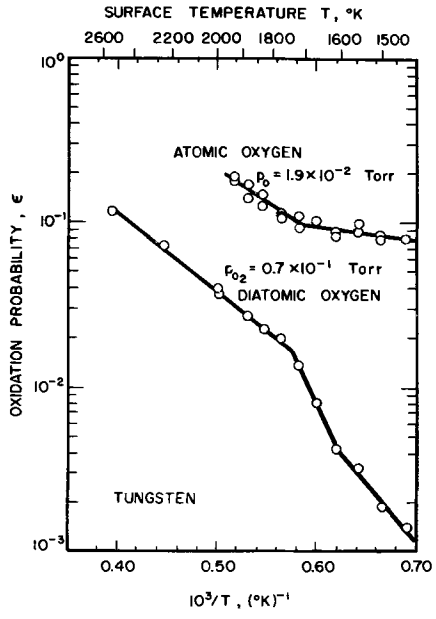

Fig. 7. Oxidation probabilities for the attack of tungsten by atomic and diatomic oxygen; temperature dependence.

filament material in the temperature range of interest and the tungsten molecular weight of 183.92 g/g-mole.

Temperature dependence of the oxidation probability.—An Arrhenius plot of our tungsten oxidation rate data is shown in Fig. 7,[17] which is qualitatively similar to the molybdenum plot shown in Fig. 4. Again, particularly at low surface temperatures (say <1700°K), metal atom removal per O-atom strike is much more likely than for an O_2 strike, the difference attaining a factor of about 56 (if the oxygen pressure were $p_O = 0.7 \times 10^{-1}$ Torr) at 1450°K. In this temperature range the O-atom oxidation probability is seen to be large in absolute value (of the order of 1/10) and weakly temperature dependent (apparent activation energy ≈ 4 kcal/mole). The corresponding apparent activation energy for O_2 below 1600°K is about 32 kcal/mole, in agreement with lower O_2-pressure data of Langmuir (24) and Eisinger (25).[18] Above about 1750°K (in the present case) the O_2 data exhibit a somewhat reduced temperature sensitivity (≈ 24 kcal/mole), in good agreement with data reported by Perkins, Price, and Crooks (28), and Walsh (29) at comparable O_2 pressures and temperatures. The absence of a maximum in the true reaction probability at temperatures below 2600°K when p_{O_2} is as large as 0.7×10^{-1} Torr (see Fig. 7) is also consistent with the observations of these authors and Singleton (see footnote below). As will be discussed (see Discussion Section on Mechanistic Considerations) the enhancement in oxidation rate due to dissociation (Fig. 7) is expected to be greatest at the "high" oxygen pressures[19] employed in the present work.

Kinetic order of the oxidation reactions.—The oxygen-pressure dependence of the tungsten reaction probabilities was investigated with results similar to those already reported for molybdenum. As displayed in Fig. 8, the O-atom attack was found to be first order (ϵ independent of p_O) over more than a decade change in O-atom partial pressure. We conclude that the reaction probabilities shown in Fig. 7 for the case $p_O = 1.9 \times 10^{-2}$ Torr would remain invariant with at least comparable changes in O-atom pressure.[20]

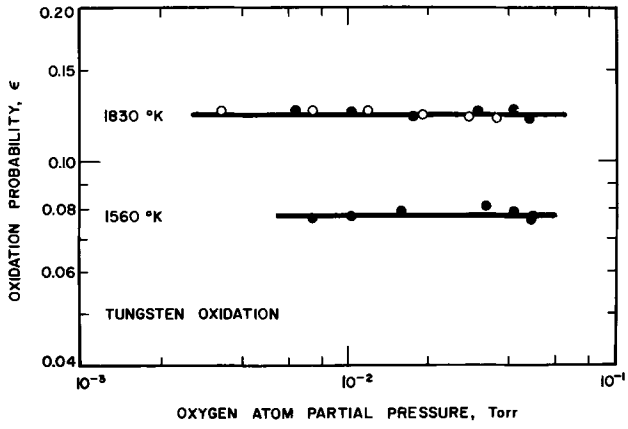

Fig. 8. Oxidation probabilities for the attack of tungsten by atomic oxygen; oxygen pressure dependence (○ p = 1 Torr; •X_O = const.).

Once again, the corresponding O_2 reaction displays fractional-order behavior (see Fig. 9, on which the apparent reaction order for each set of data is given) with complexities similar to those appearing in Fig. 6.[21]

Discussion

Identity of the active species.—Since electronically and vibrationally excited states can be produced in gas discharges, it is essential to prove that our O-atom attack data are not falsified by the enhanced reactivity that might be associated with such excitation. Based on the evidence presented below, we have concluded that the observed reactivity of the oxygen passed through the microwave discharge is due to the presence of ground-state O(^{3}P) atoms.[22]

First, using molybdenum filaments at 1150°K, we have shown that O atoms ($p_O \approx (1.5\text{-}3) \times 10^{-3}$ Torr, as determined by the NO_2 or NO light titration tech-

[19] Preliminary experiments have also been carried out to determine whether the simultaneous presence of N atoms affects the O-atom oxidation probability. No such effect was observed for an 1800°K tungsten filament when $p_O = 0.8 \times 10^{-2}$ Torr, $p_N = 4 \times 10^{-3}$ Torr.

[20] In particular, departures from simple power law (constant reaction order) behavior are observed, and constant-pressure experiments again tend to give higher apparent reaction orders than those carried out at a constant O_2 mole fraction.

[22] Conversely, the use of such filaments or thin films for inferring O-atom concentrations in novel environments is currently under investigation at this laboratory.

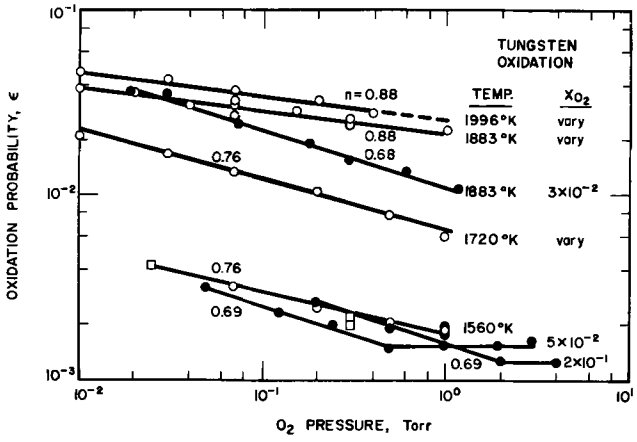

Fig. 9. Oxidation probabilities for the attack of tungsten by diatomic oxygen; oxygen pressure dependence (○ p = 1 Torr; •X_{O_2} = const.; □ carrier gas = helium; n = observed reaction order).

[17] Which corrects and supersedes the corresponding unpublished data reported in ref. (22) and (23).

[18] J. Singleton [J. Chem. Phys., 45, 2819 (1966)] has recently reported an activation energy of 33 kcal/mole at surface temperatures below 1500°K and at O_2-pressures between 10^{-3} and 10^{-5} Torr, in good agreement with ref. (24, 25) and the higher pressure data reported here. Gulbransen *et al.* (26) have reported 14.3 kcal/mole for this reaction; however, it is readily demonstrated that the data contained in ref (26) are subject to appreciable systematic errors due to the presence of diffusional limitations on the observed rates. Oxidation probabilities calculated from the correlation equation suggested in ref. (27) are appreciably lower than the data shown in Fig. 7 for the same reason.

[19] Compared with those which characterize most mass spectrometer studies of oxidation kinetics (<10^{-3} Torr).

nique) produced in two quite different ways yield the same results. One method, already discussed in some detail above, is to pass a microwave discharge through an Ar-O_2 mixture to produce O atoms directly. The second method (30, 31) is indirect in that N atoms are first produced in a pure nitrogen discharge, from which O atoms are produced upon downstream introduction of nitric oxide (via the rapid bimolecular reaction $N + NO \rightarrow N_2 + O$). Experimental results using this indirect technique for producing O atoms are shown as open diamonds (◇) in Fig. 5. Since the concentrations of excited atomic and diatomic oxygen are expected to be totally different in these two environments,[23] it is significant that the resulting oxidation rates agreed to within better than 10%.

Second, we have investigated the possibility of excited-molecule attack by introducing an oxidized silver foil upstream of the molybdenum filament when the microwave discharge was on. This foil recombines the O atoms produced in the discharge but admits electronically excited $O_2(^1\Delta_g$ and $^1\Sigma_g^+)$ molecules (33) (abbreviated hereafter as O_2^*). Similar experiments were carried out using HgO(s) mirrors which, from the work of ref. (33), not only preferentially remove O atoms but actually enhance the O_2^* concentration. Preliminary measurements showed that the reaction probability for O_2^* in the temperature range $1050° < T < 1500°K$ was somewhat greater than for ground-state O_2 but negligible compared to the O-atom probability, thereby validating our previous measurements and their interpretation.

Third, the very fact that the observed oxidation rates of molybdenum and tungsten increased linearily with O-atom partial pressure as inferred from the NO_2 light titration technique (see Fig. 5 and 8) constitutes further evidence (indirect) that excited oxygen molecules play a negligible role in the present work. These experiments cover about a 30-fold range of initial O_2 mole fractions (prior to discharging) and were carried out at microwave power levels from about 30 to 90% of full power. If excited oxygen molecules played a significant role in the observed kinetics, it is unlikely that simple first-order behavior would have been observed over the resulting range of $[O_2^*]/[O]$ ratios.

Finally, as suggested earlier (*cf.* Experimental-Atom Detection Section), the steady-state ozone concentrations resulting from the termolecular reaction $O + O_2 + Ar \rightarrow O_3 + Ar$ followed by $O + O_3 \rightarrow 2O_2$ [rate constants for which have been critically reviewed by Kaufman (14)] are of the order of only one-thousandth of the O-atom concentrations reported here. Hence, ozone production by 1-Torr microwave discharges through dilute O_2/Ar mixtures can be neglected safely.

Absence of transport limitations.—At pressures of technical interest, one of the many pitfalls in kinetic investigations of rapid heterogeneous reactions forming volatile products is that the observed reaction rates may be falsified (34-36) in part by oxygen supply and product molecule escape limitations in the immediate vicinity of (*i.e.*, diffusion "boundary layers" adjacent to) the reacting surface.[24] As demonstrated below, despite the efficiency of the high-temperature molybdenum and tungsten oxidation reactions, these difficulties have been avoided in the present work owing to the combined choice of high flow rates, small specimen size, and subatmospheric total pressure. Consequently, the observed departures of the molybdenum and tungsten oxidation probabilities from simple Arrhenius and power-law behavior are believed to be true kinetic phenomena, characteristic of the temperature and oxygen pressure levels investigated herein, and are not peculiar to this particular reactor configuration or choice of experimental techniques.

Two types of experiments have been used to rule out diffusional phenomena. One type consists of verifying that the observed reaction rates are independent of gas flow rate, as they should be if the kinetically controlled asymptote has been achieved.[25] Checks of this type were made[26] over the entire range of conditions for which data are reported herein, with particular attention to the high-temperature/high-pressure regime.[27] The onset of a flow rate dependence, in fact, dictated the high-temperature cut-off of the O-atom reaction probability data (see Fig. 4 and 7).

The other check for the absence of diffusional limitations, extensively used in the case of the O_2-oxidation reactions, was to verify that the observed oxidation rates were independent of the identity of the carrier gas (helium, nitrogen, or argon). Points appropriate to each of these carrier gases are superposed on Fig. 6 and 9 (see figure caption for coding). Despite the wide differences in molecular weight and effective "size" (cross section) of these molecules, the observed rates are seen to depend only on the O_2 pressure[28] and surface temperature, thereby ruling out transport limitations and demonstrating that these gases are true "inerts" with respect to the interfacial reactions studied herein.

Mechanistic considerations.—To anticipate oxidation rates under dissociated gas and temperature conditions other than those experimentally investigated here and for refractory metals other than molybdenum and tungsten, it is necessary to inquire into the mechanism underlying the striking increase in reactivity upon dissociation observed in the present work. Owing to the qualitative similarities in the results and properties of the two metals, it appears possible to discuss the molybdenum and tungsten oxidation kinetics jointly.

An intriguing feature of the observed kinetics is the comparative simplicity of the O-atom attack reactions, as revealed especially in the reaction order (*cf.* Fig. 5 and 6, 8 and 9). Indeed, the O-atom and O_2 attack data are so different in character one suspects that the two mechanisms have rather little in common. This would be fortunate since the task of rationalizing all kinetic subtleties of the Mo(s)/O_2(g) and W(s)/O_2(g) reactions is formidable and will not be attempted here. Suffice it to say that the O_2 data presented in Fig. 4, 6, 7, and 9 and previous work on the Mo(s)/O_2(g) and W(s)/O_2(g) reactions [1] to [3]; (which includes product distribution measurements) suggest a Langmuir-Hinshelwood-type mechanism (38). This means that product formation-desorption is the result of the mutual encounter of chemisorbed species,[29] the surface population of which is largely

[23] Indeed, O_2 is absent when N + NO technique is used.

[24] A distressing amount of "kinetic" data obtained in low-flow-rate furnace/microbalance devices or on electrically heated specimens located in quiescent (stagnant except for natural convection currents) oxidizing atmospheres are of limited value either because the role of diffusional limitations in determining the true local oxidizer concentration has not been appreciated, or "corrections" have been made based on theoretical models which account for only a fraction of the complicating phenomena (18).

[25] Strictly speaking, this is a necessary but insufficient condition since cases have been recorded in which (local) independence on flow rate (or "stirring") is a peculiarity of the flow system, *e.g.*, due to a drop in stirrer efficiency at high speeds (37).

[26] Double logarithmic (scale) plots must be used for this purpose. It is often argued that flow rate effects are absent based on a plateau-tendency exhibited on linear reaction rate *vs.* flow rate coordinates. However, a fractional power law, which is typical, even for diffusion-controlled reactions, is easily mistaken for a plot showing a true plateau, particularly in view of the scatter inevitable in limited, high flow rate kinetic data.

[27] Incidentally, the absence of flow rate and carrier gas identity effects also constitutes evidence that (owing to a sufficient number of collisions in the gas phase) the gas is brought up to the surface temperature at the time of reaction. The kinetic data reported here are thus relevant to the filament temperature, and not the ambient temperature of the upstream gas.

[28] For the O_2 reaction, however, a systematic dependence on total pressure has been observed (see Fig. 6 and 9, and the corresponding caption footnotes).

[29] Some chemisorbed O atoms are assumed to be strongly bound (*i.e.*, the "first" layer) and some comparatively weakly bound (the "second" layer). The true reaction probability passes through a maximum and decreases with further increases in surface temperature only when the surface has been denuded of the second layer and begins losing its first layer (1-3).

determined by a balance between dissociative adsorption and evaporation processes.

If one retained this view, the observed effect of prior dissociation on the reaction probability could be postulated to be due largely to an increased sticking probability and, hence, increased steady-state adatom coverage, *i.e.*, once an atom is adsorbed, its average residence time on the surface and the remaining elementary events leading to product formation would be similar to those in the O_2 case. While this mechanism cannot be ruled out completely as a contributor, it is difficult to reconcile it with the observed pressure-independent and temperature-insensitive O-atom reaction probability, and hence it is considered unlikely as the dominant mechanism.

Instead, we have postulated (6) that an entirely different route, of the so-called Rideal-type, [see *e.g.* ref. (38)] becomes available in the presence of ambient atomic oxygen, *i.e.*, a mechanism in which the reaction step on the surface involves an oxygen atom coming directly from the gas phase (not chemisorbed at the time of activated complex formation/reaction) striking adsorbed oxygen or metal suboxides. The metal oxide (MO_2, MO_3, . . .) complex thus formed[30] on the surface either evaporates as a stable product molecule (thereby contributing to the oxidation rate) or decomposes on the surface, liberating $O_2(g)$ (equivalent, therefore, to surface-catalyzed atom recombination). This mechanism can produce a high, p_O-independent reaction probability over a wide temperature range (see Fig. 4 and 7), since the dominant processes by which O atoms are removed from the "second" layer (*viz.* reaction or recombination immediately following an O-atom strike) are linear in O-atom pressure, as is the temperature-insensitive chemisorption rate. The adatom concentration is thus maintained at a high level in the presence of O(g), a situation which favors a high probability of sufficiently "direct" hits. In contrast, while the steady-state adatom concentration is also high at the lower temperatures investigated here for the O_2 reaction, the O_2 reaction probability drops sharply at these temperatures due to a combination of low sticking probability and surface mobility-activation energy requirements implicit in any Langmuir-Hinshelwood scheme. Hence, the mechanism described above is consistent with our finding that enhanced reactivity due to dissociation is most noticeable at the lower end of the temperature range (*cf.* Fig. 4 and 7). It is also interesting to note that, according to this mechanism, we would not expect a large oxidation rate enhancement due to dissociation at temperatures and pressures such that the metal surface is relatively bare, for under these conditions the O_2-sticking probability is itself high (3, 4) and, moreover, when O atoms are used as the oxidizer, the chance for "direct" hits by O-atoms on (near) adsorbed oxygen becomes small.[31]

Another interesting implication of the proposed mechanism (6), which warrants further investigation, is that it predicts the likelihood of an intimate relationship between the oxidation and recombination probabilities on the same surface. This is a consequence of the fact that both rate processes should depend on adatom coverage in the same way; hence, one would expect the ratio of ϵ to the recombination probability γ to be temperature dependent only.[32] By comparing the electrical power required to maintain the filament at prescribed temperatures both in the absence and presence of the electrical discharge we have made measurements of the sum of the recombination and oxidation heating of molybdenum filaments in the temperature range 1050°-1500°K, at O-atom pressures between 0.66×10^{-2} and 2.2×10^{-2} Torr. However, until a detailed knowledge of the product distribution[33] (and accurate thermochemical data) become available, calorimetric data alone cannot provide reliable absolute values for the recombination coefficient.

With regard to surface-catalyzed oxygen-atom recombination, which is itself a strongly exothermic process,[34] it should be remarked that the enhanced rate of metal removal in partially dissociated oxygen cannot be due to thermally induced "sputtering"[35] of molybdenum and tungsten due solely to localized heating. Thus, while these same metals also catalyze (to a comparable extent) the recombination of nitrogen atoms (40) [which give up 225 kcal/mole $N_2(g)$ formed] metal removal is negligible when electrically heated filaments are maintained in the presence of an electrical discharge through N_2 or Ar/N_2 mixtures. Metal removal is thus fundamentally associated with the formation of metal-oxygen chemical bonds, which undermine the strength with which the metal atoms involved are held in the lattice at the surface.

Finally, it seems likely that the kinks observed in the Arrhenius diagrams (Fig. 4 and 7) are related to shifts in the identity of the dominant product molecule (1, 2) and/or the state of oxide coverage on the surface[36] as opposed to structural changes in the polycrystalline filament material itself. Thus, while the low-temperature transitions observed for both molybdenum and tungsten happen to be in the recrystallization temperature range for these materials,[37] low-tem-

[30] Here M represents either a molybdenum or tungsten atom.

[31] Indeed, Schissel and Trulson (2) recently reported the results of a preliminary experiment revealing no significant difference in the reactivity of O(g) and $O_2(g)$ on tungsten at pressures below 10^{-4} Torr, presumably at surface temperatures higher than that at which the oxidation probability passes through is maximum. Regarding our postulated mechanism, it should be remarked that if (at sufficiently high temperatures) the monoxide, MO, becomes a significant reaction product, "direct hits" may not be necessary.

[32] While direct measurements of γ have not yet been made on oxidizing filaments, it should be remarked that the present measurements provide an upper bound to γ. This follows from the fact that an incident atom can either react, reflect, or recombine; hence, the sum of these probabilities (when suitably defined) must be unity and γ cannot be larger than the value calculated assuming zero reflection probability. For the case of only metal dioxide and trioxide formation, this leads to the bound:

$$\gamma \leq 1 - [3(1 - \alpha) + 2\alpha]\epsilon$$

which becomes $\gamma \leq 1 - 2\epsilon$ when only the metal dioxide is formed. Since ϵ has already approached ½ for O-atom attack of molybdenum at $\approx$ 2200°K (see Fig. 4), this suggests that oxidation becomes the dominant reaction path at high filament temperatures. Similar data for the C(s)/O(g) reaction (7, 8) and the Mo(s)/Cl(g), Ni(s)/Cl(g) reactions (9) indicate that the tendency for product formation to increase relative to atom recombination at high surface temperatures is common.

[33] The fact that the observed sum of the oxidation and recombination heating increases at low temperatures and then passes through a maximum near 1300°K suggests but does not prove that for the Mo(s)/O(g) reaction there is a transition from the dominant product $MoO_3(g)$ to the less exothermic formation of $MoO_2(g)$ in this temperature range.

[34] The O_2 bond dissociation energy ($\approx$118 kcal) is released on formation of one mole of O_2 from two moles of O atoms. For comparison, the molar heats of sublimation of molybdenum and tungsten are 155.5 kcal and 202.7 kcal, respectively, at 298.16°K (39), although it should be kept in mind that these latter values are not the strengths of individual (single) metal-metal bonds at the surface.

[35] Ordinary metal evaporation, or metal evaporation followed by gas-phase oxidation, is ruled out by the fact that the observed metal removal rates far exceed even the vacuum evaporation rates of these materials (by some 5 decades for molybdenum at 2000°K). These possibilities are also inconsistent with the observed dependence of the metal removal rates on surface temperature and the invariance under changes in gas flow rate (see Discussion, Absence of Transport Limitations).

[36] Initial encouragement for this view came from the fact that for the Mo(s)/O_2(g) reaction the low-temperature break occurs at about the temperature one would expect the product $MoO_3(g)$ to be in equilibrium with $MoO_2(s)$. For this calculation the $MoO_3(g)$ "kinetic" pressure adjacent to the filament was estimated directly from the observed reaction rate, whereas the $MoO_3(g)$ pressure in equilibrium with $MoO_2(g)$ was obtained from the Knudsen cell data of Blackburn *et al.* (41). We have also observed an emittance change at this temperature. However, similar calculations for the Mo(s)/O(g) reaction and the corresponding tungsten oxidations fail to produce similar agreement. In retrospect, even limited agreement is probably fortuitous, since the relevance of thermodynamic data on bulk oxides is open to question when one is dealing with surface oxides of molecular dimensions.

[37] Neither pure molybdenum nor pure tungsten (both body-centered cubic metals) undergo high-temperature phase transitions.

perature oxidation rate data on annealed filaments, *i.e.*, wires heated well above their recrystallization temperature for more than 5 min, failed to show significant filament annealing effects in either O_2 or O atoms. Moreover, it is inherently unlikely that (all else being equal) recrystallization and stress relief would give rise to higher probabilities as observed (see Fig. 4 and 7) on a temperature increase. For the W(s)/O_2(g) reaction it should be remarked that the high-temperature break, *i.e.*, reduction in apparent activation energy, shown in Fig. 7 is quite similar to that reported in ref. (28).

Homogeneous thermal dissociation.—At temperatures as high as 2600°K (see Fig. 4 and 7) and at p = 1 Torr the extent of O_2 dissociation predicted thermodynamically is appreciable. Indeed, based on the equilibrium constant at 2600°K (42): $[p_O p_{O_2}^{-1/2} = 10^{-1.636}$ $(atm)^{1/2}]$, the gas wetting the filament could attain an equilibrium O-atom partial pressure of 4.75×10^{-2} Torr,[38] even in the absence of a microwave discharge. At first sight, this casts doubt on the significance of the data in "undissociated oxygen" at these elevated filament temperatures (see Fig. 4 and 7). However, using reasoning similar to that given in ref. (9), we conclude that, while a sufficient number of collisions occur to ultimately raise the gas temperature to the filament temperature, not enough time is available for appreciable homogeneous O_2 dissociation in the immediate vicinity of the heated filament. Thus, if we compare the average residence time for a molecule within the thermal layer of the filament (at most, of the order of $d^2/D_{O_2\text{-}Ar}$, where d is the filament diameter and $D_{O_2\text{-}Ar}$, is the O_2-Ar Fick interdiffusion coefficient) with the characteristic time $(k_{d,Ar} n_{Ar})^{-1}$ for homogeneous O_2 dissociation (where $k_{d,Ar}$ is the appropriate dissociation rate constant,[39] and n_{Ar} is the argon number density), we find that the residence time is too small by more than six orders of magnitude. It seems reasonable to conclude that, even at the highest filament temperatures investigated here, O atoms were effectively absent as a potential reactant in all oxidation experiments carried out with the electrical discharge off.

Conclusions

Based on the experimental data and the foregoing discussion, the following conclusions may be drawn:

1. Using a microwave-discharge, subatmospheric-pressure, fast-flow system and resistance heating-monitoring of small (filament) specimens, it has been possible to study the true kinetics of rapid molybdenum and tungsten oxidation by both atomic and diatomic oxygen at partial pressures greater than 10^{-3} Torr and at temperatures in the approximate range 1000°-2600°K. Under these conditions the oxidation reactions are not falsified by oxygen transport limitations and proceed at constant (time-independent) rates, as expected for reactions forming volatile (nonprotective) products. Moreover, owing to the occurrence of an adequate number of gas-phase collisions in the immediate vicinity of the specimen, the data pertain to the most important case in which the translational temperatures of the incident (reactant) species and surface are essentially equal.

2. Oxygen dissociation causes a striking increase in the reaction probability, particularly at the lower end of the temperature range investigated here. For molybdenum and TZM alloy the enhancement is greater than two orders of magnitude at temperatures less than about 1200°K. For tungsten the corresponding enhancements are lower, the maximum observed being a factor of about 56 at 1450°K. Consistent with the reduction in apparent activation energy caused by oxygen dissociation, the O and O_2-reaction probabilities tend to become comparable at the highest temperature investigated (>2000°K), where the O_2-reaction probabilities themselves exceed 10^{-1} (see Fig. 4 and 7).

3. Whereas the O_2-attack reactions display a rather complex (fractional order) oxygen partial pressure dependence (see Fig. 6 and 9), the O-atom attack of both molybdenum and tungsten is found to be first order, corresponding to an oxidation probability which is independent of O-atom partial pressure (see Fig. 5 and 8) in the range 10^{-3} to 5×10^{-2} Torr.

4. Experiments in which atomic oxygen is produced in two distinct ways, and in which excited oxygen molecules are preferentially removed or enhanced upstream of the reacting filament, demonstrate that the observed reactivity of microwave-discharged O_2-Ar mixtures is due to the presence of ground state: O(^{3}P) atomic species. O_2 appears to play no essential role in the kinetics of these atom/metal reactions.

5. The large observed reaction probability, reduced activation energy, and first-order kinetics strongly suggest that the enhanced reaction probability exhibited by O-atoms is due to direct attack from the gas phase by a Rideal-type mechanism rather than merely the result of a Langmuir-Hinshelwood mechanism with an increased steady-state oxygen adatom coverage associated with increased sticking probability. Two interesting consequences of this mechanism (route) meriting further investigation are (*a*) an intimate relationship should exist between the oxidation and atom recombination probabilities on the same surface (6) and (*b*) significantly enhanced reactivity due to dissociation should disappear at temperatures and oxygen pressures such that an appreciable portion of the metal surface is bare (zero second layer coverage and partial first layer coverage).

Acknowledgments

It is a pleasure to acknowledge the extensive advice and assistance of Dr. A. Fontijn in the areas of excited species generation/detection/reactivity, the helpful criticism of Dr. S. C. Kurzius and other members of the laboratory staff, the assistance of A. Chiarello and A. D. Freda with a portion of the experiments, and W. W. Brenner with the microwave and other electrical instrumentation. The senior author also wishes to thank Dr. G. C. Fryberg (NASA) and Dr. J. Berkowitz-Mattuck (A. D. Little) for their helpful correspondence and interest in the present work. The authors are especially indebted to the Propulsion Division of the U.S. Air Force Office of Scientific Research for their sustained interest and financial support under Contracts AF 49(638)-1195 and AF 49(638)-1637; Lieutenant Colonel C. J. Donovan, Scientific Officer).

Manuscript received July 2, 1966; revised manuscript received Dec. 15, 1966. This paper was presented at the Philadelphia Meeting Oct. 9-14, 1966.

Any discussion of this paper will appear in a Discussion Section to be published in the December 1967 JOURNAL.

APPENDIX

Oxygen Dissociation Produced by Hypervelocity Motion through the Earth's Atmosphere

While subsonic vehicles (*e.g.*, conventional aircraft) produce negligible chemical changes in the air through which they move, the kinetic energy represented by a hypersonic vehicle (*e.g.*, a reentering spacecraft or ballistic missile) is comparable to the dissociation energy of oxygen and (even) nitrogen molecules present in undisturbed air. As a result, even at low altitudes significant oxygen-atom concentrations are produced by the deceleration of air relative to such vehicles, a fact which must be considered in designing their heat protection systems.

Actual O-atom partial pressures experienced at a vehicle surface depend strongly on the altitude-ve-

[38] Compared to $p_O = 1 \times 10^{-2}$ Torr and 1.9×10^{-2} Torr, used in the molybdenum and tungsten oxidation experiments, respectively.

[39] An upper limit of $k_{d\text{-}Ar} \approx 10^{-17}$ cm^3 molecules^{-1} sec^{-1} can be estimated by extrapolating the 10% O_2-Ar shock tube data of Schexnayder and Evans (43) down to 2600°K.

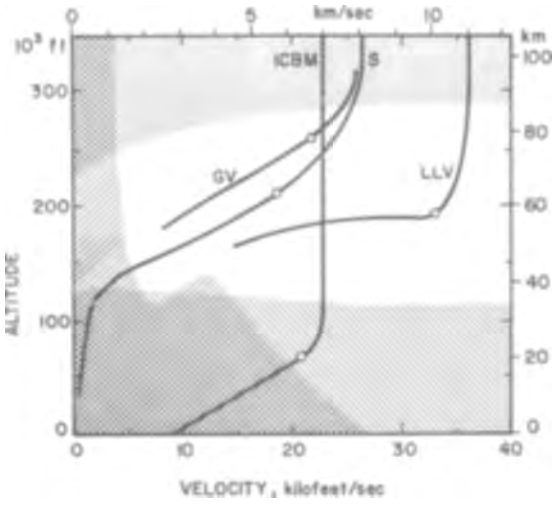

Fig. 10. Oxygen atom nonequilibrium regimes[44] encountered during the reentry of manned and unmanned vehicles into the Earth's atmosphere: ICBM = intercontinental ballistic missile, S = satellite, GV = glide vehicle, LLV = lunar lifting vehicle.

locity history ("trajectory") of the particular vehicle, as well as its over-all size. Typical trajectories for several classes of vehicles are shown in Fig. 10,[40] together with (*a*) (shaded) regions in which one can rule out appreciable O-atom concentrations for various reasons (outlined below) and (*b*) points (open circles) on each trajectory at which the conditions of aerodynamic heating are most severe. In the odd-shaped shaded region to the left (*i.e.*, low velocity), the vehicle kinetic energy is insufficient to thermodynamically produce appreciable oxygen-atom concentrations at the prevailing pressures. In the upper (high-altitude) shaded region the energies are sufficient, but the rates of dissociation are inadequate for bodies in the size range of aerospace interest. In the lower (low-altitude/high-density) shaded region, O atoms produced in the high-temperature regions of the flow undergo a sufficient number of termolecular encounters in the cooler gas regions near the surface to recombine (reforming O_2) in the gas phase. The remaining (unshaded) region is still seen to be quite

[40] This figure, a more detailed version of which is discussed from the point of view of aerodynamic heating in ref. (44), displays the trajectories of two ballistic (without aerodynamic lift) vehicles [earth satellite (S) and intercontinental ballistic missile (ICBM)] and two "lifting" vehicles [glide vehicle (GV) and lunar lifting vehicle (LLV)] differing widely in their initial (entry) speed. As a specific case of interest here, four recent Air Force (ASSET-ASV) glide test vehicles were boosted to altitudes of 196-212 kft at velocities of 16-19.5 kft/sec.

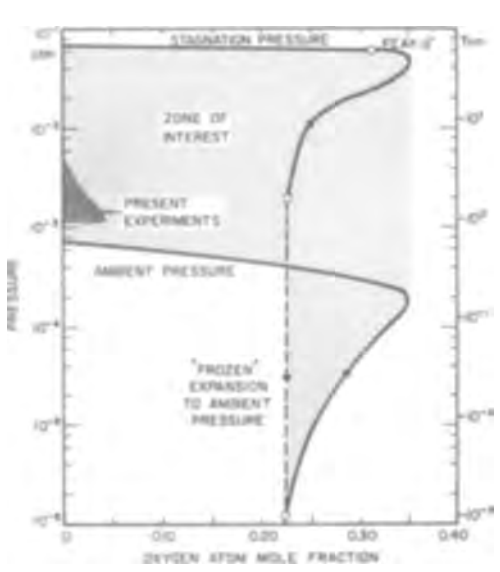

Fig. 11. Pressures and oxygen-atom concentrations simultaneously experienced during the reentry of vehicles with aerodynamic lift.

large, in fact we note that, of the vehicles shown, all but the ICBM experience peak heating rates under conditions such that high nonequilibrium oxygen-atom concentrations will be present.

For definiteness, let us now focus on the glide reentry vehicle (GV) since such vehicles are likely to make extensive use of the refractory metals of interest in the present investigation. Over its trajectory one can estimate the pressures and oxygen atom-mole fractions encountered at various points along the surface. Typical results are displayed in Fig. 11 for two extreme locations, *viz.*, the forward stagnation point or leading edge (at which the highest local pressures are experienced) and a point back along the surface at which the static pressure has dropped to that prevailing in the undisturbed atmosphere. All of the conditions shown shaded[41] are thus experienced at intermediate locations on the surface and hence are also of interest. While the resulting range of O-atom pressures far exceeds the capability of any one experimental technique, it is noteworthy that the techniques exploited in the present work provide true kinetic data within the region of interest (cf. Fig. 11). Moreover, owing to the comparative simplicity of the O-atom kinetics (*cf.*, Fig. 5 and 8) the present results can be extrapolated with respect to reactant partial pressure with greater confidence than those pertaining to O_2. Hence, the present work, and measurements currently in progress, enable rational estimates to be made of the consequences of bare metal exposure (*e.g.*, protective coating failure or deliberate transient use) in the reentry environment.

REFERENCES

1. J. B. Berkowitz-Mattuck, A. Buchler, J. L. Engelke, and S. N. Goldstein, *J. Chem. Phys.*, **39**, 2722 (1963).
2. P. O. Schissel and O. C. Trulson, *J. Chem. Phys.*, **43**, 737 (1965).
3. J. A. Becker, E. J. Becker, and R. G. Brandes, *J. Appl. Phys.*, **32**, 411 (1961).
4. G. Ehrlich, *J. Chem. Phys.*, **31**, 1111 (1959).
5. D. O. Hayward and G. M. W. Trapnell, "Chemisorption," 2nd ed., Butterworths, London (1964).
6. D. E. Rosner and H. D. Allendorf, *J. Chem. Phys.*, **40**, 3441 (1964).
7. D. E. Rosner and H. D. Allendorf, *AIAA J.*, **3**, 1522 (1965).
8. D. E. Rosner and H. D. Allendorf, CARBON, **3**, 153-156 (1965).
9. D. E. Rosner and H. D. Allendorf, *J. Phys. Chem.*, **69**, 4290 (1965).
10. F. C. Fehsenfeld, K. M. Evenson, and H. P. Broida, *Rev. Sci. Inst.*, **36**, 294 (1965).
11. J. L. Everhart, W. E. Lindlief, J. Kanegis, P. G. Weissler, and F. Siegel, "Mechanical Properties of Metals and Alloys," U. S. Natl. Bur. Standards, Circular C447 (Dec. 1, 1943).
12. R. H. Osborn, "Thermophysical Properties of Solid Materials," DDC AD 247 193.
13. *Anon.*, "High Temperature Oxidation of Molybdenum Under High-Altitude Conditions," North American Aviation Inc., Missile Development Division; Report AL-2617, Sept. 1, 1957, ASTIA AD 147 839.
14. F. Kaufman, "Reactions of Oxygen Atoms," "Progress in Reaction Kinetics," G. Porter, Editor, Chap. 1, Vol. 1, pp. 3-39, Pergamon Press, New York (1961).
15. F. Kaufman, *Proc. Roy. Soc.*, A **247**, 123 (1958); See also A. A. Westenberg, and N. deHaas, *J. Chem. Phys.*, **40**, 3087 (1964).
16. J. C. Greaves and J. W. Linnett, *Trans. Faraday Soc.*, **54**, 1323 (1958).
17. A. K. Oppenheim, *J. Aero. Sci.*, **20**, 49-58 (1953).
18. D. E. Rosner and H. D. Allendorf, *This Journal*, **111**, 759 (1964).
19. J. Berkowitz *et al.*, "Kinetics of Oxidation in the Mo-Si System," Aeronautical Systems Division, Dir/Materials and Processes, Metals and Ceramics Lab., Wright-Patterson AFB, Ohio, Rpt. Nr ASD-TDR-62-203; ASTIA AD 278 826, May 1962.
20. E. A. Gulbransen, K. F. Andrew, and F. A. Brassart, *This Journal*, **110**, 952 (1963).

[41] The upper limit of 34.7 mole % atomic oxygen corresponds to the dissociation of every oxygen molecule present in undisturbed air, before the onset of any appreciable nitrogen dissociation. This "sequential" dissociation is very nearly realized in practice owing to the large difference in the bond dissociation energies of the O_2 and N_2 molecules.

21. G. C. Fryberg, *J. Phys. Chem.*, **69**, 3660 (1965).
22. D. E. Rosner and H. D. Allendorf, "Kinetic and Aerodynamic Aspects of the Oxidation of Metals by Partially Dissociated Oxygen," AeroChem (Princeton, N. J.) TN-61; DDC AD 438 927, May 1964.
23. D. E. Rosner and H. D. Allendorf, "Chemical Kinetic Aspects of the Oxidation of Materials by Partially Dissociated Gases," AeroChem (Princeton, N. J.) TP-124, Final Report; DDC AD 628 515, Dec. 3, 1965.
24. I. Langmuir, *J. Am. Chem. Soc.*, **35**, 105 (1913).
25. J. Eisinger, *J. Chem. Phys.*, **30**, 412 (1959).
26. E. A. Gulbransen *et al.*, "Oxidation of Tungsten and Tungsten Based Alloys," Aeronautical Systems Division, Dir/Materials and Processes, Metals and Ceramics Lab., Wright-Patterson AFB, Ohio, Rpt Nr WADC-TR-59-575, Final Report, July 1962.
27. R. A. Perkins and D. D. Crooks, *J. Metals*, **13**, 490 (1961).
28. R. A. Perkins, W. L. Price, and D. D. Crooks, "Oxidation of Tungsten at Ultra-High Temperatures," Oxidation of Tungsten and Other Refractory Materials (Proc. Joint AIME/Air Force Materials Laboratory Symposium 1962), Technical Doc. Report ML TDR 65-162, April 1965, pp. 125-150.
29. P. Walsh *et al.*, "Principles Governing the Behavior of Solid Materials in Severe, High Temperature Environments," Union Carbide Research Inst. (Tarrytown, N. Y.) Final Report UCRI 388, May 31, 1966.
30. J. E. Morgan, L. Elias, and H. I. Schiff, *J. Chem. Phys.*, **33**, 930 (1960).
31. J. E. Morgan and H. I. Schiff, *ibid.*, **38**, 1495 (1963).
32. L. Elias, E. A. Ogryzlo, and H. I. Schiff, *Can. J. Chem.*, **37**, 1680 (1959).
33. M. A. A. Clyne, B. A. Thrush, and R. P. Wayne, *Nature*, **199**, 1057 (1963); see also, L. W. Bader and E. A. Ogryzlo, *Discussion Faraday Soc.*, **37**, 46 (1964).
34. D. E. Rosner, *AIAA J.*, **2**, 593 (1964).
35. D. E. Rosner, "Convective Diffusion Limitations on the Rates of Chemical Reactions at Solid Surfaces-Kinetic Implications," AeroChem TP-129, March 8, 1966; invited paper to appear in the *Eleventh Symposium (International) on Combustion* (The Combustion Institute, Pittsburgh, Pa.) ca. 1967.
36. D. E. Rosner, "Effects of the Stefan-Nusselt Flow on the Apparent Kinetics of Heterogeneous Chemical Reactions in Forced Convective Systems," AeroChem (Princeton, New Jersey) TP-111, April 1965; Int. J. Heat Mass Transfer **9**, 1233 (1966).
37. D. A. Frank-Kamenetskii, "Diffusion and Heat Exchange in Chemical Kinetics," Translated by N. Thon, 1955, Princeton University Press, Princeton, N. J.
38. P. G. Ashmore, "Catalysis and Inhibition of Chemical Reactions," Butterworths, London (1963).
39. T. L. Cottrell, "The Strengths of Chemical Bonds," Butterworths, London (1958).
40. H. H. Ammann, "Heterogeneous Recombination and Heat Transfer with Dissociated Nitrogen," PhD. Dissertation, Purdue University, January 1964.
41. P. E. Blackburn, M. Hoch, and H. L. Johnston, *J. Phys. Chem.*, **62**, 769 (1958).
42. JANAF Thermochemical Tables, The Dow Chemical Co., Midland, Mich., ASTIA AD 248 425 (1963).
43. C. J. Schexnayder, Jr., and J. S. Evans, "Measurements of the Dissociation Rate of Molecular Oxygen," NASA TR R108 ((1961).
44. D. E. Rosner, *AIAA J.*, **1**, 1550 (1963).

Contribution to the Mn-O Phase Diagram at High Temperature

A. Z. Hed[1] and D. S. Tannhauser

Department of Physics, Technion—Israel Institute of Technology, Haifa, Israel

ABSTRACT

Part of the phase diagram of the system Mn-O was determined in the temperature range 1100°-1800°C, and the range of oxygen partial pressure 1 atm $\leq P(O_2) \leq 10^{-19}$ atm. Data are presented of the ratio O/Mn within the MnO phase and of some of the boundaries of this phase. The data are based on a combination of thermogravimetric and electrical measurements and on direct observation of the melting oxide in the furnace.

Numerous investigations have been reported dealing with various aspects of the Mn-O system; however, none of them give a comprehensive account of the temperature-pressure-composition relations in the system Mn-O.

MnO, Mn_3O_4, Mn_2O_3, and MnO_2 are known to exist as stable crystalline phases and can be converted into each other by a suitable choice of temperature and oxygen partial pressure. Our work is concerned only with the oxides MnO and Mn_3O_4. MnO is generally assumed to deviate from stoichiometry, but there are large discrepancies between the quantitative data available for the various equilibria. This may be due partly to the fact that the equilibria states have been estimated by the combination of heat of formation and entropy data, each of which has a considerable limit of error, and partly to the fact that all data pertaining to the high-temperature region were measured after quenching the samples to room temperature.

Millar (1), Le Blanc and Wehner (2), Shomate (3), Moore, Ellis, and Selwood (4), and Hahn and Muan (5) investigated the composition of Mn_3O_4. Le Blanc and Wehner found Mn_3O_4 near 400°C to deviate considerably from stoichiometry, it being an excess oxygen compound. The other investigators who studied Mn_3O_4 at $T \geq 1000$°C found that it is practically stoichiometric.

The MnO phase was studied by Davies and Richardson (6) and in ref. (2, 4, 5). Davies and Richardson give quantitative data, while the other authors concluded only that the composition varied with the condition of preparation without quoting numbers.

The melting point of Mn_3O_4 has been reported by Hahn and Muan (5) as 1540°C in equilibrium with MnO and as 1567°C in air. Wartenberg *et al.* (7) reported the mp as 1590° ± 20°C, without specifying the atmosphere.

No measurements of the melting point of MnO as function of oxygen partial pressure were made. However, Singleton *et al.* (8) reported the value 1815° ± 7°C as the melting point of MnO in purified helium, and Glasser (9) deduced a melting point of 1850°C by extrapolation from the system MnO-SiO_2.

Experimental Technique

Two samples of manganese metal in the form of thin plates (Johnson-Matthey spectrographic stand-

[1] Present address: Battelle Memorial Institute, Columbus, Ohio.

ard), chemically thinned to 0.3 mm, were suspended in a vertical furnace. One sample was used to measure the electrical conductance, G, of MnO; the other, which weighed about 1g, served to determine the deviation from stoichiometry through thermogravimetric measurements. Mixtures of either O_2 and argon or CO_2 and CO flowed through the furnace at 0.7 cm/sec, the partial pressures of oxygen, $P(O_2)$, being calculated from the free energies of formation given by Coughlin (10). The manganese metal was oxidized for more than 12 hr at 1100°C in a flowing mixture of 100 parts CO_2 to 1 part CO, and the samples were then fired in various atmospheres

$$\left(20 \leq \frac{P(CO_2)}{P(CO)} \leq 100\right)$$

at 1550°C for 2 hr. The oxidation temperature was chosen to prevent melting of the metal [mp 1244°C (11)] before oxidation. At temperatures higher than 1350°C equilibrium of the samples with the atmosphere was established in less than 10 min after $P(O_2)$ was changed. The equilibrium times at temperatures lower than 1200°C were longer than 1 hr. Constancy of the resistance of the samples indicated the equilibrium state.

The conductance G was measured by a four-probe method with an a-c bridge described by Dauphinee and Mooser (12). The four Pt 10% Rh wires, which served as electrodes, were attached tightly to the sample through holes of 0.5 mm ϕ pierced by a concentrated jet of fine alumina powder (S. S. White Industrial "Airbrasive" unit).

For the gravimetric measurements we used a Cahn electrobalance, mounted on the furnace. The balance was used as a differential weighing device, since absolute weighing of the samples was not possible. The apparent weight of the sample is composed of its real weight, the weight of the hanging wires, and a fictitious weight caused by the hot flowing gases in the furnace. This fictitious weight depends on the geometry of the samples, temperature, molecular weight, and velocity of the gas mixture flowing in the furnace. Differential weighing along an isotherm keeping the gas velocity constant is affected only by changes of the molecular weight of the gas. This effect was measured on a dummy alumina sample and was estimated to be less than 100 μg over the range of our measurements.

The balance was used in the range of 100 mg with a sensitivity of 10 μg. This sensitivity was good enough, since turbulence caused random fluctuation of $\pm$ 50 μg in the apparent weight of the sample. The suspending wire was composed of two parts; the upper one in the less hot region of the furnace was a platinum wire. In the hottest part of the furnace we used a sapphire single crystal (Linde division of Union Carbide Corporation), which can be used up to 1520°C, the eutectic point of the system MnO-Al_2O_3 (13). For later experiments, which extended above 1520°C, we used iridium as a suspending wire.

The two samples were very close to each other, and a Pt/Pt 10% Rh thermocouple measured their temperature. Since the temperatures reached were very high, the thermocouple could not be relied on as being accurate for long periods, and it was often replaced and periodically checked against the melting point of palladium (1552°C).

For the visual determination of the melting point of the oxides we used thin (0.2-0.3 mm thick) oxide sheets suspended in the furnace by an iridium hook, so that their large face was horizontal. A palladium calibration wire was used near the sample in each run, in addition to the Pt/Pt 10% Rh thermocouple, for a better determination of the temperature. We heated the furnace at a rate that did not exceed 5°C/min, the sample being in a constant $P(O_2)$. The deformation of the sample indicated its melting point.

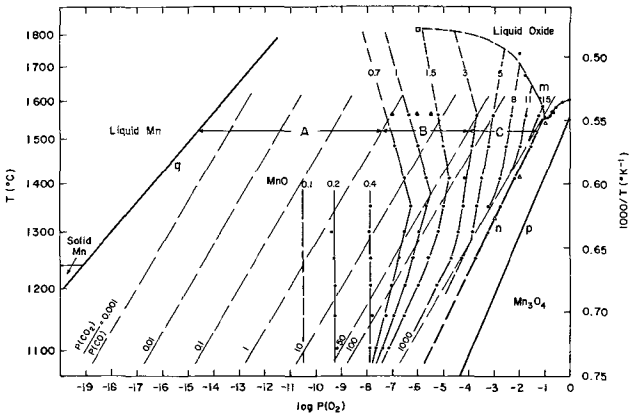

Fig. 1. Temperature pressure diagram of the system Mn-O in the temperature range 1100°-1800°C. In the MnO field experimental lines of constant composition are given with the value of their molar excess of oxygen, x, multiplied by 10^2. The boundary lines q and p are calculated according to Coughlin (10). The boundary n and part of m (•) are determined in this work, the point □ at 1815°C is taken from the work of Singleton *et al.* (8). The division into regions A, B and C is according to Fig. 3. For comparison representative points (▲) taken from Fig. 1 of ref. (6) are given for $x.10^2$ = 0.7, 1 and 1.5. Representative points (△) on the boundary n and n are taken from ref. (5). Lines of constant p $(CO_2)/P(CO)$ are superimposed (thin dashed lines).

It is obvious that this determination does not define a liquidus or a solidus line, but some value between these lines.

Results

Figure 1 shows the temperature-pressure diagram of the system Mn-O. The phase boundary Mn-MnO (q) is calculated from the free energies of formation given by Coughlin (10). We did not extend our measurements to these low oxygen partial pressures because Mn quickly evaporates from the oxide at these pressures. This made the determination of the deviation from stoichiometry very difficult. The manganese vapor also attacked the Pt 10% Rh electrodes, thus preventing electrical measurements in this range.

The MnO-Mn_3O_4 boundary (n) was determined by the sudden increase in weight of the sample as the oxygen partial pressure was slightly increased.

The melting point of Mn_3O_4 was found to decrease from 1600° $\pm$ 8°C at $P(O_2)$ = 1 atm to 1555° $\pm$ 5°C at about $P(O_2) = 10^{-1}$ atm. Maun and Hahn (5) reported an eutectic point in the system Mn-O at $P(O_2) = 10^{-1}$ atm, but mentioned 1540° $\pm$ 6°C as the mp at the eutectic composition. However, the calibration palladium wire used in each of our runs always melted before the deformation of the oxide, and we conclude therefore that the lowest mp in that system is not lower than 1552°C. The limit of error given above is slightly more liberal because of the possibility that the oxide sample with the higher heat content might be at a slightly lower temperature than that of the thermocouple.

The melting point of MnO as function of $P(O_2)$ was determined down to $P(O_2)$ = 0.01 atm, where the mp was found to be 1734° $\pm$ 10°C. We did not measure the mp at lower $P(O_2)$, since the thermocouple is not reliable at such a high temperature, and because the maximum operating temperature of our oven was 1800°C. However, we drew in Fig. 1 a curved line up to 1815°C, the melting point of MnO in purified helium determined by Singleton *et al.* (8). We estimated that the purified helium around their samples is equivalent to $P(O_2) = 10^{-6}$ atm. We did not take into account the value 1850°C mentioned by Glasser (9), since this value is an extrapolated one and not a measured value, as that of Singleton *et al.*

The calculation of x given near the lines of constant composition in Fig. 1 (see Fig. 2) requires knowledge

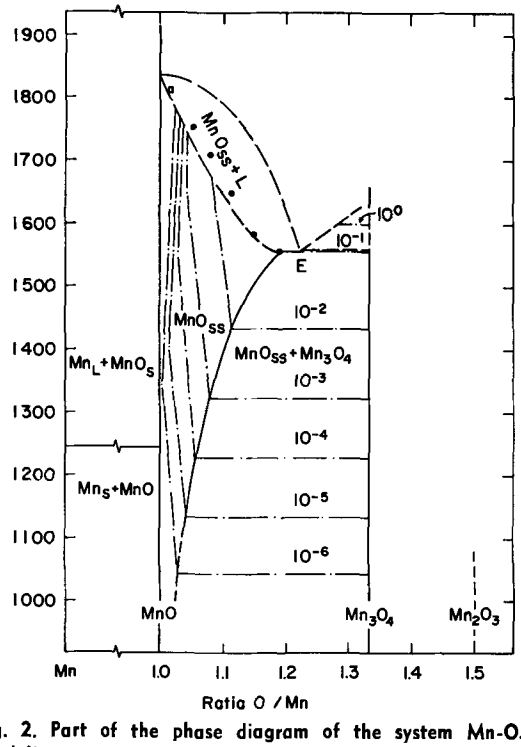

Fig. 2. Part of the phase diagram of the system Mn-O. Dot-dashed lines are oxygen isobars. Dashed lines are hypothetical solids and liquidus lines. The abscissas of the points in the MnO_{ss} + liquid field are based on extrapolation of the constant composition lines in Fig. 1. The abscissa of the eutectic point E is hypothetical. The point □ is taken from Fig. 1.

of the weight of MnO at stoichiometry (see Eq. [4] below). Since the gravimetric measurements were performed by a differential method, the stoichiometric weight of samples could not be determined directly, but was determined with the aid of the electrical measurements by the method of Fisher and Tannhauser (14).

Figure 3 shows isotherms of the conductivity G *vs.* log $[P(CO_2)/P(CO)]$. It is seen that the conductivity of MnO behaves differently in three regions, which are labelled A, B, C, respectively. In those parts of regions A and B which are not too close to the minimum in G, G can be expressed in the general form

$$G = K(T)\,[P(CO_2)/P(CO)]^{1/s} \qquad [1]$$

or, using the relation $P(O_2) = K'(T)\,[P(CO_2)/P(CO)]^2$, in the form $G = K''(T)P(O_2)^{1/2s}$ where s is negative in region A and positive in region B.

In this article only region B is discussed, since it is needed for the determination of the stoichiometric point. Region B is characterized by the value $s = 3.0 \pm 0.1$. This value fits the model proposed by Smyth (15), namely, that the dominant defects in region B are doubly ionized manganese vacancies. That this model gives the relation [1] with $s = 3$ can easily be proved (16) by applying the mass action law to the reactions

$$\tfrac{1}{2}O_2\ (\text{gas}) \rightleftharpoons O\ (\text{Lattice}) + V_M$$

$$V_M \rightleftharpoons V'_M + \oplus$$

$$V'_M \rightleftharpoons V''_M + \oplus$$

with the condition $[V''_M] >> [V'_M]$ and the assumption that the mobility, μ, of the positive free charge carriers, $\oplus$, does not depend on $P(O_2)$. $[V_M]$, $[V'_M]$, $[V''_M]$ are the molar fractions of manganese vacancies, nonionized, singly, and doubly ionized, respectively.

The molar excess of oxygen, x, defined by the formula MnO_{1+x}, which is equivalent to $Mn_{1-x}O$ at low x, is given by

$$x = [V_M] + [V'_M] + [V''_M] \qquad [2]$$

If now, in addition to $[V''_M] >> [V'_M]$, the relation $[V''_M] >> [V_M]$ holds as proposed by Smith (15), Eq. [2] will read $x = [V''_M]$ and the concentration of charge carriers p will be given by

$$p = [V'_M] + 2\,[V''_M] = 2\,[V''_M] = 2x \qquad [3]$$

A plot of $G = C\mu ep$ *vs.* x will be linear if the last relation holds. Such plots are shown in Fig. 4, and are seen to be linear in region B, a fact that supports the above assumptions.

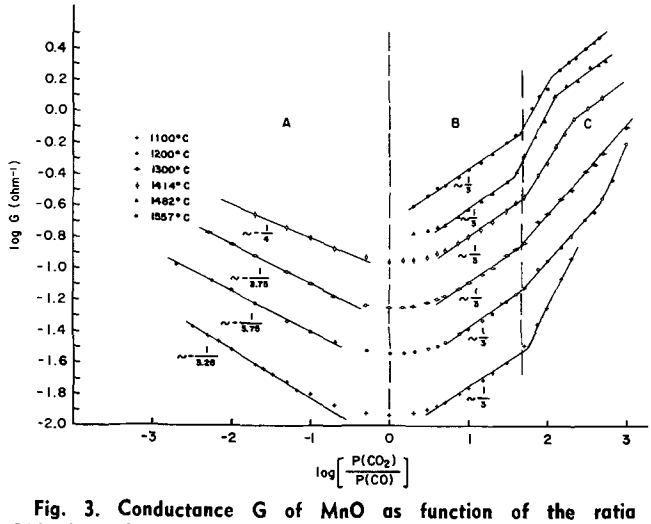

Fig. 3. Conductance G of MnO as function of the ratio $P(CO_2)/P(CO)$, at constant temperatures. The value of $P(CO_2)/P(CO)$ in the figure is the actual ratio of the gases in the furnace under equilibrium conditions, when mixtures of CO and CO_2 are used. When mixtures of Ar and O_2 are used, the ratio $P(CO_2)/P(CO)$ is calculated to give the correct oxygen partial pressure. A and B are regions where G behaves according to formula 1. The numbers give the values of 1/s. C is a region where the behavior of G is not well understood. The inaccuracy in the isotherm 1414°C may be ± 15°C, while the inaccuracy in the others does not exceed ± 5°C.

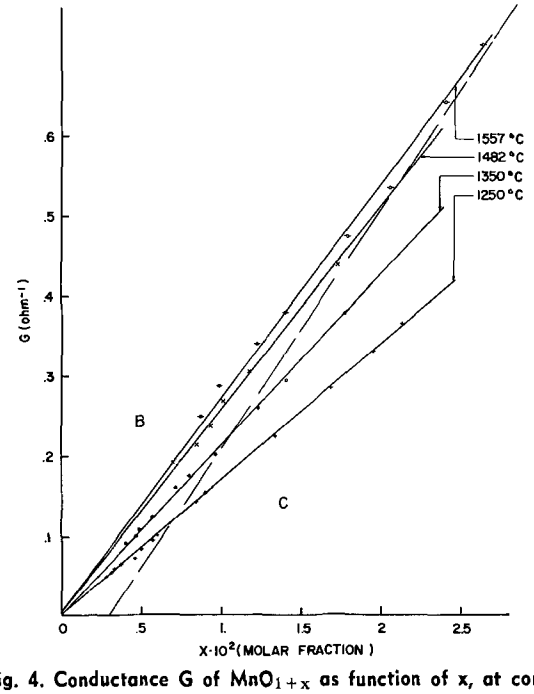

Fig. 4. Conductance G of MnO_{1+x} as function of x, at constant temperature, for low values of x. The line separating regions B and C is taken from Fig. 3 (see text).

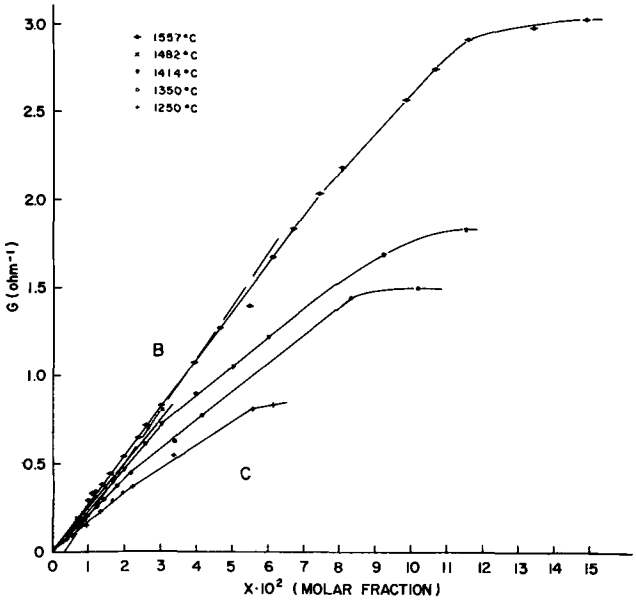

Fig. 5. Conductance G of MnO_{1+x} as function of x at constant temperature over the whole range of existence of the phase. The line separating regions B and C is taken from Fig. 3 (see text).

In Fig. 4 we drew the line that separates regions B and C in Fig. 3; no breaks in G *vs* x occur at that line. However, in Fig. 5, where the regions B and C are given in full, the expected breaks are seen. The fact that these breaks do not occur at the transition points indicated in Fig. 3, but at higher x (and therefore higher $(P(CO_2)/P(CO)$ ratios) is not well understood.

The zero point in Fig. 4 was determined by extrapolation of G *vs.* $M(x)$, the apparent weight at a composition MnO_{1+x}, to zero conductivity. Since from Eq. [3] we have $x = 0$ for $G = 0$, we will read on a graph of G *vs.* $M(x)$ for $G = 0$ $M = M(o)$, the apparent sample weight at the stoichiometric composition. x can then be calculated from the relation

$$x = \frac{[M(x) - M(o)] \times 54.94}{16\, M(Mn)} \qquad [4]$$

where 54.94 and 16 are the atomic weights of manganese and oxygen, and $M(Mn)$ is the weight of manganese contained in the oxide; this weight is determined separately before the oxidation of the specimens.

The errors in the determination of x arise principally from two causes: the systematic errors mentioned above, and the indeterminancy of the stoichiometric point caused by the scatter of the points in Fig. 4. The total error is estimated to be $\Delta x = \pm 10^{-3}$.

Another source of error is the extrapolation procedure; since at $x = 0$ G is not exactly zero, due to intrinsic conductivity. However, we could show by detailed analysis of the conductivity that this error is much smaller than the $\Delta x = \pm 10^{-3}$ mentioned above.

Breaks occur in the lines of constant x near the transition from region B to region C, and are probably due to the change of the ionization state of the manganese vacancies. The fact that the slopes of the lines of constant composition undergo a sharp change near 1375°C might be explained by a phase transition in the oxide. Some evidence for such a phase transition was found also in the electrical properties of MnO and will be reported later.

The composition of the MnO phase corresponding to the eutectic point was estimated by extrapolation to be near $MnO_{1.18}$, but it was not determined separately.

Measurements of the deviation from stoichiometry in region A are extremely difficult, since evaporation of manganese from the samples made the determination of weight change uncertain. At temperatures higher than 1400°C the evaporation is so severe that the platinum electrodes of the samples are attacked by the manganese vapor and destroyed, preventing continuous measurements of both x and G in region A.

For $T < 1400$°C we could however show experimentally, by taking the samples back and forth between regions A and B, that almost all the change in the apparent weight in region A was due to evaporation: only near 1400°C was a definite change of x in region A distinguishable. In Fig. 1 we draw a dashed line with $x = 0.001$, which shows approximately the lowest x definable by our method. For lower $P(O_2)$ MnO is practically stoichiometric (within the experimental error $x = \pm 0.001$). The fact that the conductivity in region A rises to fairly high values in spite of very small deviation from stoichiometry is probably due to very high mobility electrons and will be discussed in a later publication.

For the sake of completeness we drew from our results a phase diagram of the system Mn-O, given in Fig. 2. The Mn-MnO boundary is given by a straight line, since MnO practically reaches stoichiometric composition.

The Mn_3O_4 field is also a straight line, since no deviation from stoichiometry was found in that compound. The exact position of the eutectic point E is not determined in this work; its position in Fig. 2 is only hypothetical.

The temperatures at which deformations occur are not on the solidus line, but somewhat higher; we therefore drew a solidus line somewhat lower than our measured points.

The liquidus lines were not determined in this work, and in Fig. 2 they are hypothetical.

Discussion

Previous work on the system Mn-O was based mainly on measurements made after the sample was brought to room temperature, while the measurements in this work were made at the equilibria states themselves, giving us the advantage of direct observation of these equilibria.

In Fig. 1 we give the MnO-Mn_3O_4 phase boundary as measured in this work, and as calculated from the free energies of formation given by Coughlin (10).

Our measurements agree fairly well with the results of Hahn and Muan (5). The fact that the values calculated from the free energies of formation do not fit our experiments is probably due to the large deviation from stoichiometry of MnO near the boundary. In the calculation of that boundary we assumed the activity of MnO to be unity, an assumption not justified when dealing with nonstoichiometric compounds.

On the other hand, the Mn-MnO phase boundary, which is calculated from the free energies of formation of MnO given by Coughlin (10), is probably reliable, since, as we have shown above, MnO is practically stoichiometric in our region A (Fig. 1) to very low oxygen pressures, and it is therefore fairly safe to assume that it is stoichiometric at the boundary itself.

Mn_3O_4 was found to be practically stoichiometric, up to 1 atm oxygen, this again agreeing with the measurements of Hahn and Muan (5). The deviation from stoichiometry found by Le Blanc and Wehner (2) was probably due to the metastable condition of their experiments.

The highest measured deviation from stoichiometry was 15% excess oxygen, corresponding to $MnO_{1.15}$. Davies and Richardson (6) found the maximum deviation to be 4.4% and found a completely different dependence on $P(O_2)$ in the range $P(O_2) > 10^{-5}$ atm. This may be due to two different causes: (*a*) flushing of their oven with nitrogen before quenching the samples, (*b*) the quenching process itself.

Davies and Richardson equilibrated their samples in the temperature range 1500°-1650°C, where equilibria are quickly established. The partial pressure of oxygen in nitrogen, which is determined by impurities like O_2, H_2O, or CO_2, is usually very low, and may easily reduce the oxygen contents of the oxide at these elevated temperatures. As to the quench procedure, Davies and Richardson mention precipitation of Mn_3O_4, when they quenched samples equilibrated at $P(O_2) > 10^{-2}$ atm. This feature is known also in the system FeO (14), but it does not mean that at these oxygen pressures MnO does not exist at high temperature. At $P(O_2) < 10^{-6}$ atm, our results coincide with the results of Davies and Richardson (6), as shown in Fig. 1. In this case, the remark of Davies and Richardson, that only small amounts of gases pass over the sample, and therefore no further oxidation of the MnO sample is expected, applies.

The melting points of Mn_3O_4 found in this work are in good agreement with earlier workers. Our value of 1600°C at $P(O_2) = 1$ atm agrees with Wartenberg's (7) value of 1590° ± 20°C, and the values we found in air and at $P(O_2) = 0.1$ atm agree fairly well with those of Hahn and Muan (5) (see Fig. 1).

Acknowledgment

The authors wish to thank Mr. I. Dubner for his valuable technical help.

This work was partially sponsored by the Aerospace Research Laboratories under Contract No. AF 61(052)-825 with the European Office of Aerospace Research, United States Air Force.

Manuscript received April 13, 1966; revised manuscript received Dec. 19, 1966. This work constitutes part of the thesis submitted by one of the authors (A.Z.H.) to the Senate of the Technion in partial fulfilment of the requirements of the D.Sc. degree.

Any discussion of this paper will appear in a Discussion Section to be published in the December 1967 JOURNAL.

Note added in proof: Two new works dealing with the system Mn-O have recently been published. The electrical conductivity of MnO as a function of the oxygen partial pressure was measured by N. G. Eror (Dissertation Abstr., vol. 26, p. 3225 (1965-66)) between 900° and 1200°C. Eror found three different regions as in the present work, and he pointed out that the conductivity of MnO is anomalous at high oxygen partial pressure, in the sense that the conductivity decreases with increasing temperature at constant $P(O_2)$. This anomaly is well explained in the present work by the decrease of concentration of the cation vacancies (see Fig. 2, region C) when increasing the temperature at constant $P(O_2)$.

D. Q. Kim, Y. Wilbert, and F. Marion [*Compt. rend.*, 262C, 756 (1966)] found the different phase boundaries in the system Mn-O, and the position of the boundary MnO-Mn_3O_4 agrees qualitatively with the present work at high temperatures.

REFERENCES

1. R. W. Millar, *J. Am. Chem. Soc.*, **50**, 1875 (1928).
2. M. Le Blanc and G. Wehner, *Z. Physikal. Chem. Abt. A.*, **168**, 59 (1934).
3. C. H. Shomate, *J. Am. Chem. Soc.*, **65**, 785 (1943).
4. T. E. Moore, M. Ellis, and P. W. Selwood, *ibid.*, **72**, 856 (1950).
5. W. C. Hahn, Jr., and A. Muan, *Am. J. Sci.*, **258**, 66 (1960).
6. M. W. Davies and F. D. Richardson, *Trans. Faraday Soc.*, **55**, 604 (1959).
7. H. V. von Wartenberg, H. J. Reusch, and E. Saran, *Z. anorg. u. allgem. Chem.*, **230**, 256 (1937).
8. E. L. Singleton, L. Carpenter, and R. V. Lundquist, U. S. Bur. Mines. Rept. of Invest. No. 5938.
9. F. P. Glasser, *Am. J. Sci.*, **256**, 398 (1958).
10. J. P. Coughlin, Bull. 542 U. S. Bureau of Mines.
11. A. H. Sully, "Manganese," Butterworth Scientific Publications, London (1955).
12. T. M. Dauphinee and E. Mooser, *Rev. Sci. Instr.*, **26**, 660 (1955).
13. R. Hay, J. White, and A. B. McIntosh, *J. West. Scot. Iron Steel Inst.*, **42**, 99 (1934).
14. B. Fisher and D. S. Tannhauser, *This Journal*, **111**, 1194 (1964).
15. D. M. Smyth, *J. Phys. Chem. Solids*, **19**, 167 (1961).
16. F. A. Kroger and H. J. Vink, "Solids State Physics," vol. 3, Seitz and Turnbull, Editors, Academic Press Inc., New York (1956).
17. A. von Hoffman, *Z. Elektrochem.*, **2**, 207 (1959).

Mechanism of the Absorption Induced Electrode Potential Cells

I. Nature of the Potential

Henri L. Rosano, Charles J. Cante, and Evan Morgan

Department of Chemistry, The City College of The City University of New York, New York, New York

ABSTRACT

Previous experiments have shown that by using different electrode pairs and electrolytes, cells comprised of a wettable exposed electrode/electrolyte/immersed electrode may be sensitive to either ionizable or nonionizable vapors. When air containing a vapor was injected with syringes into the carrier gas stream entering a cell of the type described above, changes in cell potential or cell current were recorded. It was noted that the potential changes, as well as the current changes, obtained from the absorption induced electrode potential cells depended on the presence of a meniscus (solid/liquid and liquid/gas interfaces) on the exposed electrode. In the present paper the case of an ionizable vapor, hydrogen chloride, injected into the carrier gas stream entering a Ag/AgCl (exposed blade)/HCl aqueous/Ag/AgCl (immersed wire) cell has been investigated. It was concluded that (*i*) the absorption of vapor on the exposed electrode creates a momentary concentration cell with transference and (*ii*) the great sensitivity of these types of electrochemical cells can be attributed to an active zone located at the upper part of the meniscus.

In a previous paper (1), it was reported that a galvanic cell consisting of a platinum gauze electrode, which was partially immersed in a nitrochromic acid oxidizing mixture (70.3% HNO_3 saturated with 99.1% CrO_3), and a graphite electrode, which was completely immersed in the same electrolyte, responded to organic vapors. Introduction of short chain alcohol vapors into the system resulted in the production of a current which was recorded as a function of time. This was essentially a Berton cell (2-4).

Rosano and Scheps (1, 5) studied only the currents produced by organic vapors in an oxidizing electrolyte. In view of the complexities encountered with the nitrochromic electrolyte, it was decided to use different cells with simpler electrolytes in the investigation of the nature of the potential produced by absorption induced electrode potential (AIEP) cells.

Experimental Procedure

The electrolytes used in these investigations were aqueous solutions of potassium chloride and hydrochloric acid. The exposed electrodes were either (*i*) a Ag/AgCl blade (2.25 x 1.0 x 0.05 cm) or (*ii*) a semi-silvered, sand-blasted, glass blade and the immersed counter electrode was a Ag/AgCl wire (0.06 cm in diameter). Sand-blasted glass slides were covered with silver by sucrose reduction of a silver ammonia complex. The lower half of the blade was again sand-blasted to remove the silver on that section. Sand-blasting insures the wettability of the electrode. The vapor was hydrogen chloride. The carrier gas, nitrogen or air, continuously flowed through the cell. The effect of the air stream was negligible compared with the effect of HCl. The carrier gas was passed through a series of filters (anhydrous calcium chloride, potassium hydroxide, and charcoal) before entering the cell at a controlled flow of 60 cc/min. The basic cell design in all experiments is shown in Fig. 1. The glass container (internal diameter 3.6 cm) of the cell has a total volume of 60 cc. The volume of electrolyte used in all experiments was 15 cc.

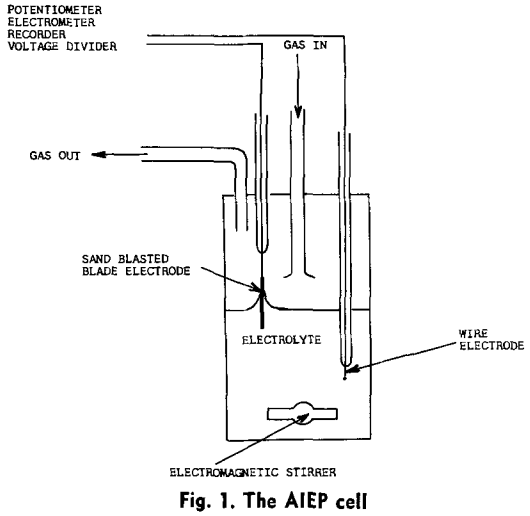

Fig. 1. The AIEP cell

A hydrochloric acid solution in a closed Erlenmeyer flask was allowed to reach equilibrium with its own vapor. A given volume of the HCl vapor was then withdrawn from the flask with syringes and subsequently injected into the carrier gas stream. All chemicals were reagent grade, and distilled water was used in the preparation of all solutions. The various electrolytes were uniformly stirred by a magnetic stirrer. These experiments were performed at room temperature (26° ± 1°C).

Measurement of cell potential.—Given volumes of HCl vapor were injected into a regulated stream of nitrogen entering a Ag/AgCl (exposed blade)/HCl or KCl (aqueous)/AgCl/Ag (immersed wire) cell. Two different experiments were performed: (*i*) for a fixed bulk concentration of KCl or HCl, the change in cell potential was recorded as a function of the volume of HCl vapor injected, and (*ii*) the change in cell potential was recorded when the bulk electrolyte concentration was varied while the volume of HCl vapor injected was kept constant. An electrometer (D.C. Multimeter, Model MV77B, Millivac Instruments) was used to measure the maximum potential changes which were recorded (Sargent Model SR Recorder) as a function of time. In order to justify the use of the recorder (balancing speed: 1 sec for full scale travel), it was necessary to determine the duration of the potential rise in a measurement of emf *vs.* time. An oscilloscope (Hewlett-Packard, Model 130C with Dumont Camera attachment) was used in place of the recorder. The time of the potential rise was found to

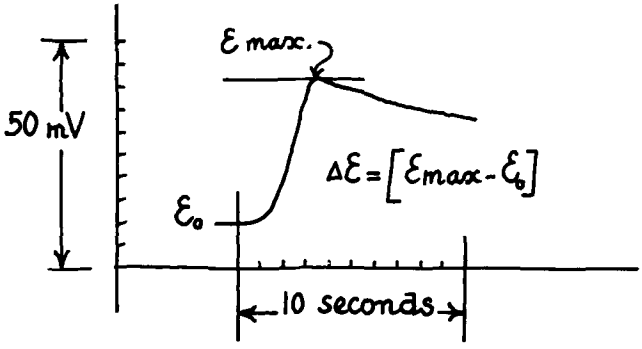

Fig. 2. Potential as time curve for the injection of HCl vapor into a Ag/Ag/Cl (exposed blade)/1M HCl/AgCl/Ag immersed wire cell illustrating the decay of the transient potential.

be of the order of 3-6 sec depending on the volume of vapor injected. Therefore, for convenience, the recorder was used in all our experiments. After injection of HCl vapor into the cell, the cell emf increases immediately to a maximum value (see Fig. 2). With time, the cell emf decays to its initial value. After repeated injections of HCl vapor, the cell emf does not return to its initial value but levels off at some higher emf due to the change in the bulk electrolyte concentration. The difference between the maximum instantaneous emf and the initial emf was selected as the parameter to be reported.

EMF of HCl *concentration cells with transference.*—The emf of HCl concentration cells with transference with measured (*e.g.*, Ag/AgCl/HCl, 1M // HCl, xM / AgCl/Ag where 1M — xM — 12M).

A priori it was postulated that the absorption of HCl vapor at the level of the meniscus formed on the exposed electrode would create a momentary concentration cell with transference between the exposed blade and the immersed wire electrodes of the absorption induced electrode potential cell. In order to estimate the maximum momentary concentration of HCl on the exposed electrode of the AIEP cell, the emf's obtained with the cell were compared to the emf's of a classical concentration cell with transference. According to our hypothesis, for the same emf's the difference in concentrations must be comparable for the two systems.

Influence of the dimensions of the exposed blade electrode on the cell emf.—2cc of HCl vapor were injected into the AIEP cell described above. The dimensions of the exposed blade electrode were changed in order to determine their effects on the emf obtained with a given injection. Experimentally, the emf is practically independent of the width of the blade. It is dependent on the relative position of the bottom of the blade with respect to the plane of the electrolyte (see Fig. 3).

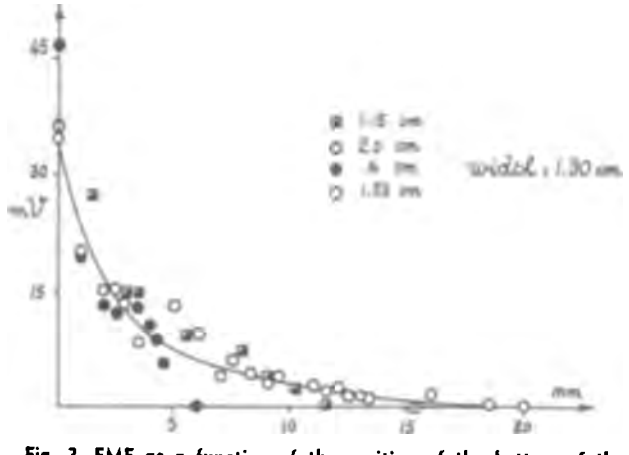

Fig. 3. EMF as a function of the position of the bottom of the blade electrode below the liquid-gas interface for a solid silver blade.

Influence of the position of the bottom of the exposed electrode at different levels in the meniscus.—Practically, the bottom of the Ag/AgCl blade cannot be above the plane of the solution otherwise the blade will not support a meniscus. Instead a sand-blasted, semisilvered, glass blade electrode was used. With this electrode it is possible to position the silvered part of the blade at any level in the meniscus; the bottom half of the electrode (sand-blasted glass) supports the meniscus (position measured with Gaertner cathetometer).

Results

Influence of the volume of HCl *vapor injected on the cell emf.*—In the first series of experiments the bulk electrolyte concentration was fixed at 1M so that data were obtained for the changes in emf as a function of the volume of HCl vapor injected. The experimental results are shown in Fig. 5. The upper abscissa of Fig. 5 represents the volume (cc's) of HCl vapor injected on a log scale. A curve was traced through the experimental points.

EMF's of concentration cells with transference.—The emf's of the concentration cells with transference were plotted on the ordinate of Fig. 5. A horizontal line, intersecting the experimental curve, was drawn for each measured emf. The intersections of these horizontal lines and the previously traced curve deter-

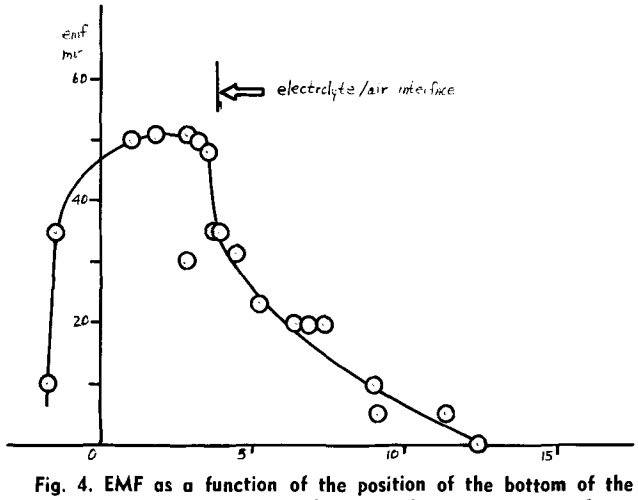

Fig. 4. EMF as a function of the position of the bottom of the exposed electrode relative to the electrolyte-air interface for a semisilvered, sand-blasted, glass blade electrode.

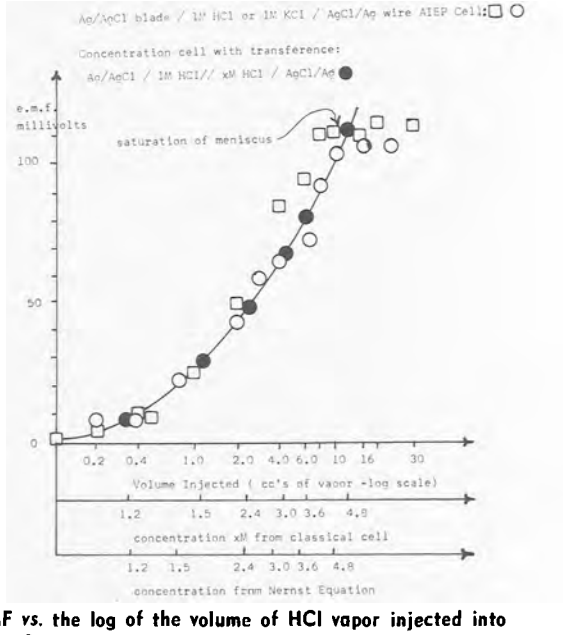

Fig. 5. EMF *vs.* the log of the volume of HCl vapor injected into the cell of Fig. 1.

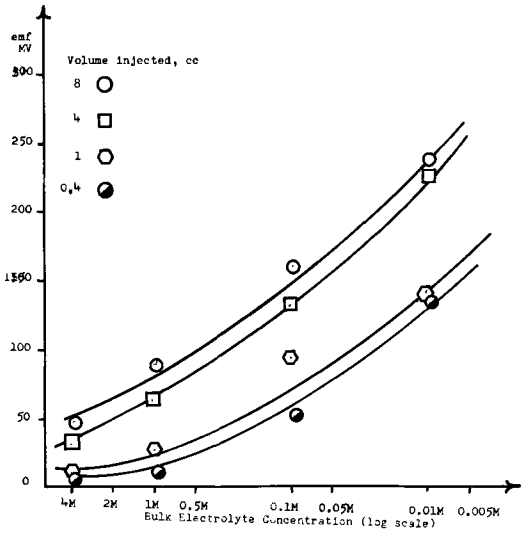

Fig. 6. EMF *vs.* the log of the bulk electrolyte concentration for a fixed injected volume of HCl vapor.

mined the position of the values of xM on the middle abscissa of Fig. 5.

Variation of Cell emf as a function of the bulk electrolyte concentration for a given injected volume of HCl *vapor.*—A fixed volume of HCl vapor was injected into the carrier gas stream entering a Ag/AgCl (exposed blade)/HCl (aqueous)/AgCl/Ag (immersed wire) cell. The maximum changes in emf for various concentrations of the electrolyte were measured. Results are shown in Fig. 6. In the potential measurement experiments no visible physical changes of the silver-silver chloride electrodes were observed.

Influence of the position of the bottom of the exposed blade electrode vs. the plane of the liquid-air interface.—Figure 4 is a representative experiment of the emf response *vs.* the relative position of the bottom of the silvered segment of the semisilvered electrode with respect to the maximum upper meniscus boundary. The surface tension of the electrolyte was measured before and after each experiment. The maximum height of the meniscus was calculated and taken as the origin on Fig. 4. An arrow indicates the vertical distance between the top of the meniscus and the horizontal plane of the electrolyte.

Discussion

Apparent HCl *concentration in the meniscus.*—When HCl vapor penetrates into a Ag/AgCl (blade)/HCl or KCl (aqueous)/AgCl/Ag (immersed wire) cell, it can be assumed that the concentration of chloride ion around the exposed electrode increases suddenly. The difference in chloride ion activity between the exposed and immersed electrodes suggests, as we have already mentioned, a concentration cell with transference. The maximum apparent concentration of HCl in the meniscus was estimated theoretically and experimentally.

The theoretical approach is the application of the Nernst equation (Eq. [3]) for concentration cells with transference (utilizing activity coefficients and transference numbers cited in the literature) and fitting the emf's corresponding to the various calculated concentrations to the experimental curve.

If the chloride ion concentration in the meniscus is the sum of the bulk chloride concentration and the contribution made by the injected HCl vapor which absorbed at the liquid-air interface, it can be written: $C_M = C_B + X$ (where C_M and C_B are the meniscus and bulk chloride ion concentrations, respectively, and X is the contribution of the absorbed HCl). Assuming that the expression for the emf of a concentration cell with transference (6) is applicable in our case it follows that

$$E \text{ (millivolts)} = \frac{2t_+RT}{n\mathbf{F}} \ln \frac{a_M}{a_B} \quad [1]$$

$$a_M = f_M C_M = f_M [C_B + X] \text{ and } a_B = f_B C_B \quad [2]$$

$$E \text{ (millivolts)} = \frac{2t_+RT}{n\mathbf{F}} \left[\ln \frac{C_M}{C_B} + \ln \frac{f_M}{f_B} \right] \quad [3]$$

Equation [3] can be rewritten as

$$E = \frac{2t_+RT}{n\mathbf{F}} \left[\ln \frac{f_M}{f_B} + \ln \frac{C_B + X}{C_B} \right] \quad [4]$$

where R is the gas constant, T was 299°K, $\mathbf{F}$ is the value of the Faraday-96,500 coulombs/equivalent, t_+ is the transference number of the hydrogen ion, a_M and a_B are the activities of the chloride ion in the meniscus and the bulk electrolytes respectively, C_M and C_B are the concentrations of the chloride ions in the meniscus and bulk, respectively, and f_M, f_B are the activity coefficients obtained from the literature (7). The results are presented on the bottom abscissa of Fig. 5.

The experimental approach, as was previously mentioned, has been to assume that identical emf's obtained with an AIEP cell and a classical concentration cell with transference must correspond to comparable concentration differences. Therefore, the variable concentration of the classical cell with transference is plotted on the middle abscissa of Fig. 5 to fit the experimental curve, emf *vs.* volume injected (cc's), obtained with the AIEP cell. The correspondence between the concentrations on the two lower abscissae is fairly good. The middle abscissa represents the apparent HCl concentration in the meniscus. Figure 5 therefore has three abscissae which represent from top to bottom: (*i*) the volume of HCl vapor injected into the cell, (*ii*) the HCl concentrations (xM) of the concentration cell with transference, and (*iii*) the calculated apparent meniscus concentration using the Nernst equation with transference. The two approaches are equivalent.

Respective contributions of the sheath of wetting and the meniscus of the exposed electrode to the cell emf.—Experimentally, the exposed electrode must be wettable by the electrolyte and form a meniscus in order to have a sensitive cell. The Laplace equation of capillarity (Eq. [5]) allows the determination of the height of a meniscus if the surface tension and density of the liquid are known (8).

$$h = (2\gamma/\rho g)^{1/2} \quad [5]$$

where h is the meniscus height (cm), g is the acceleration of gravity (cm/sec^2), ρ is the density of the liquid (g/cm^3) and γ is the surface tension (dynes/cm). For a liquid with γ = 72 dynes/cm (*e.g.*, water) h is 0.384 cm. Table I presents a few typical values of h calculated using Eq. [5] and experimental values of γ and ρ. When a wettable blade is vertically withdrawn from a liquid surface, it forms a meniscus. Beyond a certain height h, the maximum height of the meniscus, any further extension of the blade will only increase the sheath of wetting covering the blade above the top of the meniscus. If the blade is situated in an atmosphere saturated with water vapor, the sheath of wetting will cover the entire blade. Eventually, the sheath of wetting will slowly thin out due to drainage. On the other

Table I. Values of *h* from experimental data

Electrolyte	ρ density, g/cm^3	γ surface tension, dynes/cm	h, maximum meniscus height, cm
HCl, 1M	1.0156	72.4	0.381
Igepal, CO-630 in 1M HCl	—	30.8	0.267
Igepal, CO-730 in 1M HCl	—	35.4	0.249
KCl, 1M	1.0467	74.3	0.380

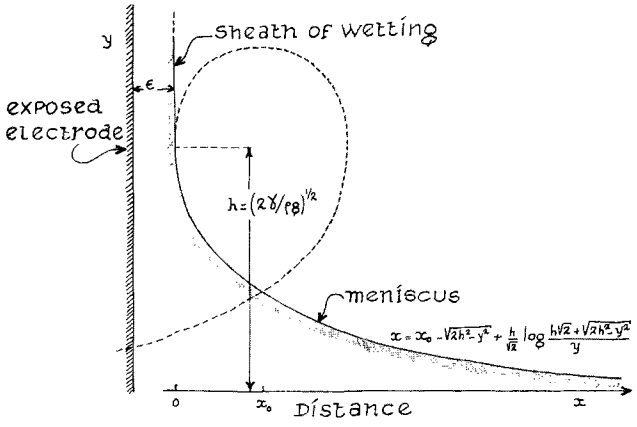

Fig. 7. Relationship between a wettable exposed electrode surface, sheath of wetting, and the meniscus formed on the exposed electrode.

hand, if the blade is situated in a continuously replenished atmosphere, as in our experiments, the sheath of wetting will evaporate down to a position relatively close to the upper boundary of the meniscus. The thickness of the sheath of wetting is determined by the electrolyte and the surface of the electrode. It represents the minimum possible liquid thickness of the electrode, (see Fig. 7).

Let us consider two cases in which: (*i*) the meniscus and the sheath of wetting are taken into account and (*ii*) the existence of the meniscus is disregarded and replaced by a film of thickness, ϵ, which forms a right angle boundary with the bulk electrolyte at the liquid-gas interface.

Let us assume, for the first case, that n moles of HCl vapor enter the cell and are absorbed into a volume $A \times \epsilon$ (where A is the total liquid-gas interface; 10.8 cm^2 in our case and ϵ is a thickness). The area of the meniscus and adjacent film can be estimated to be 10% of the total liquid-gas area or $0.1A$. As an example, when 1 cc of HCl vapor was injected into the carrier gas stream entering a Ag/AgCl (exposed blade)/1M HCl/AgCl/Ag (immersed wire) cell, the emf changed by 20.2 mv. From Fig. 5 (middle abscissa) the maximum apparent HCl concentration in the surface volume $A \times \epsilon$ should be 1.4×10^{-3} moles/cc. The increase in the number of moles of HCl after injection was 36.4×10^{-7} moles. This increase was determined by injecting the stated volume of vapor into an equivalent system in which the HCl electrolyte was replaced by distilled water. By measuring the *p*H of the distilled water before and after the injection of vapor, the increase in the number of moles of HCl was calculated. Of these moles, 3.64×10^{-7} were in a volume $0.1A \times$ cc's with an apparent concentration of 1.4×10^{-3} moles/cc. Therefore

$$\epsilon = \frac{3.64 \times 10^{-7}}{1.08 \times 1.4 \times 10^{-3}} \approx 2.4\mu$$

For the second case, let us assume that: (*i*) a film of uniform thickness, ϵ, exists in place of a meniscus, and (*ii*) that only 10% of the total moles of HCl entering the cell are absorbed into the volume: $2 \times L \times H \times \epsilon$, where L is the length of the blade along the liquid-gas interface, H is the height of the blade, and ϵ is the thickness of the sheath of liquid on the blade. For the experiment cited in case (*i*), the blade was 2.25 cm long by 0.6 cm high, therefore for case (*ii*)

$$\epsilon = \frac{3.64 \times 10^{-7}}{2 \times 0.6 \times 2.25 \times 1.4 \times 10^{-3}} \approx 1\mu$$

Mathematically the shape of the meniscus on a vertical planar surface is represented by

$$X = X^o - (2h^2 - y^2)^{1/2} + (h/\sqrt{2}) \ln \left[\frac{(h\sqrt{2} + \sqrt{2h^2 - y^2})}{y} \right] \quad [6]$$

where h is given by Eq. [5], y is the vertical height along the meniscus, X^o is a constant of integration, and X is the horizontal distance from the vertical surface. By substituting for X the calculated values of ϵ, 1, and 2.4μ, the corresponding values of y are $\sim h$, *i.e.*; right at the top of the meniscus (upper 0.2 mm). Therefore, the main contribution to the emf comes from the very top of the meniscus and from the sheath of wetting which extends vertically from the boundary of the meniscus. The fact that for a given injection of HCl vapor the emf obtained is the same regardless of the blade height above the meniscus line (Fig. 3 indicates that a blade 0.6 cm high and one 2 cm high give similar emf's when their bottoms are in the plane of the liquid-gas interface) demonstrates that the sheath of wetting on silver cannot extend vertically much more than 1 or 2 mm. In addition, by using a semisilvered, sand-blasted, glass electrode we were able to probe from the bottom to the top of the electrolyte meniscus and beyond. When the bottom edge of the silvered segment is placed at the top of the meniscus (the lower portion of the electrode is glass and is supporting the meniscus), the emf drops abruptly. If the silvered edge is raised beyond the top of the meniscus, the emf drops off to zero indicating that contact with the electrolyte has been broken—measurement of the electrical resistance further indicates that there is no longer any electrical contact (see Fig. 4). This fact further supports the above conclusion.

According to the previous argument, it was expected that a maximum emf would be obtained when the bottom of the blade was at the maximum height of the meniscus and even slightly above (in the sheath of wetting). At least thirty experiments similar to the one shown on Fig. 4 were performed. The maximum emf measured was generally obtained when the bottom of the exposed blade electrode had not yet reached the top of the meniscus.

This apparent contradiction between the experimental results and our prediction can be explained by assuming that the height of the meniscus can change instantaneously on the arrival of vapor (transient lowering of the surface tension and consequent decrease in the maximum height of the meniscus during the process of absorption). In addition, within 0.2 mm, 1 mm below the maximum meniscus height, the sheath of wetting is constant.

Essentially our conclusion is similar to the conclusion of Will (9), who studied the electrochemical oxidation of hydrogen on partially immersed platinum electrodes. He concluded that the electrode surface above the intrinsic meniscus is covered with a thin electrolyte film of a thickness comparable to or smaller than the surface roughness. The electrochemical process occurs almost exclusively at the upper edge of the meniscus and adjacent film close to it.

In a numerical example given by Will (9), the narrow band (active region) is 0.35 mm of the meniscus and 0.38 mm of the adjacent film with a film thickness of 1.0μ for the case of $8N$ H_2SO_4 electrolyte and an applied potential of 400 mv. The active region is responsible for 98% of the total response. Other recent works (10-15), have established similar behavior for several systems involving a partially immersed electrode.

EMF variation as a function of bulk electrolyte concentration for a fixed injected volume of HCl *vapor.*— In the case of HCl vapor, the exposed electrode is the anode. However, a mixed potential exists on the blade electrode when HCl vapors are injected into the cell. As a result, the blade electrode senses a whole range of HCl concentrations from the meniscus-sheath of wetting zone down to the bottom of the blade (which is positioned in the bulk of the meniscus). Reduction

must therefore occur at the bottom of the blade. In conclusion, the use of the Nernst equation allows only the calculation of the apparent instantaneous HCl concentration in the meniscus for a given volume of injected vapor. The solid lines on Fig. 6 have been calculated using equation 4 and the X values obtained from Fig. 5. It can be seen that the agreement with the experimental results is quite good. This agreement indicates that by using the Nernst equation we are in fact calculating an apparent HCl concentration which corresponds to a uniform concentration along the exposed electrode. However, in reality there is a gradient of concentration from the top to the bottom of the meniscus.

Conclusion

In the case of an ionizable vapor (HCl) and an absorption induced electrode potential cell with reversible electrodes, it is concluded that the emf response can be described as that of a concentration cell with transference. Moreover, the sensitivity of the cell (Δ mv) depends primarily on the presence of a meniscus on the exposed electrode. Although a mixed potential is set up on the exposed electrode when HCl vapor is injected into the cell, the emf between the exposed and immersed electrodes can be thought of as a concentration cell with transference.

This study also shows the unusual fact that the great sensitivity of this type of electrochemical cell is solely due to the active zone formed by the upper part of the meniscus and the lower part of the adjacent film.

Acknowledgments

This research was supported in part by the City College Alumni Fund and the National Science Foundation College Teacher's Summer Institute.

The authors are indebted to Professor Louis Meites for his useful comments.

APPENDIX

The constant of integration, X^o, in the mathematical description of a meniscus on a vertical planar surface is given by

$$X^o = 0.377\ (\gamma/\rho g)^{1/2} \qquad [A\text{-}1]$$

where γ, ρ, and g have been defined in the text and $X = X^o - \sqrt{2h^2 - y^2} + (h/\sqrt{2})$ ln

$$\left[\frac{(h\sqrt{2} + \sqrt{2h^2 - y^2})}{y}\right] \qquad [6] \text{ text}$$

Manuscript received Aug. 12, 1966; revised manuscript received Dec. 27, 1966.

Any discussion of this paper will appear in a Discussion Section to be published in the December 1967 JOURNAL.

REFERENCES

1. H. L. Rosano and S. Q. Scheps, *Ann. N. Y. Acad. Sci.*, **116**, 590 (1964).
2. A. Berton, *J. Chim. Anal.*, **45**, 585 (1963).
3. A. Berton, *ibid.*, **41**, 351 (1959).
4. M. Guillot and A. Berton, *Compt. rend*, **250**, 1857 (1960).
5. H. L. Rosano, "4th International Congress on Surface Activity; Brussels," September 1964, pp. 10-17.
6. S. Glasstone, "Introduction to Electrochemistry," D. van Nostrand Co., Inc., New York (1942).
7. G. F. Kortum and J. O'M. Bockris, "Textbook of Electrochemistry," vol 2, Elsevier, New York (1951).
8. R. Matalon, Thesis 1948, University of Lyons, France.
9. F. Will, *This Journal*, **110**, 145 (1963).
10. D. N. Bennion and C. W. Tobias, *ibid.*, **113**, 589 (1966).
11. A. T. Hartner, *et al.*, Effect of Oxygen Partial Pressure on Fuel Cell Cathodes, presented before the Division of Fuel Chemistry, American Chemical Society, New York, N. Y. September 8-13, 1963.
12. E. N. Lightfoot, *This Journal*, **113**, 614 (1966).
13. H. J. R. Maget and R. Roethlein, *ibid.*, **112**, 1034 (1965).
14. H. J. R. Maget and R. Roethlein, *ibid.*, **113**, 581 (1966).
15. H. C. Weber, H. P. Meissner, and D. A. Sama, *ibid.*, **109**, 884 (1962).

Solid-State Electrochemical Cells Based on Charge Transfer Complexes

F. Gutmann,[1] A. M. Hermann, and A. Rembaum

Jet Propulsion Laboratory, California Institute of Technology, Pasadena, California

ABSTRACT

Solid-state electrochemical cells have been devised using a variety of metals as anodes and electronically conducting charge-transfer complexes as cathodes. The product of the electrochemical reaction, the electrolyte, was formed *in situ*. Data are reported for halogen complexes as well as for complexes containing nitrogen compounds as acceptors. It is shown that the voltage-producing electrochemical reaction is the formation of the corresponding metal salt. Open-circuit voltages of 1.5-2.5v per cell were attained with magnesium or calcium anodes, and short-circuit current densities of up to 25 ma/cm^2 were found. Current-voltage characteristics have been studied as a function of temperature, and constant-load discharge curves are shown. Maximum power densities of one watt per pound and useful energy densities of 1 whr/lb are reported. An analysis based on irreversible thermodynamics is presented, and possible applications are suggested.

This paper reports the results of studies intended to explore the characteristics of a solid-state electrochemical cell. The aim is the direct conversion of chemical energy into electrical energy without the use of liquid or fused electrolytes at elevated temperatures, although permitting operation at such temperatures.

While devices have been described previously using silver anodes and silver halides as the electrolytes (1, 2), the voltages attained were of the order of 0.2-1.0v and the maximum current densities of 1-2 ma/cm^2, unless operated at relatively high temperatures.

[1] Department of Physical Chemistry, University of New South Wales, Sydney, Australia.

In this paper we report a greatly improved solid-state cell in which the electrolyte is formed *in situ* and the cathode is an electronically conducting charge-transfer complex.

The present results are to be construed as preliminary findings; the justification of this report rests primarily on the exciting commercial implications of the cell characteristics, *i.e.*, open-circuit voltages of up to 2.5v and short-circuit current densities of up to 25 ma/cm^2.

It will be useful to define a number of terms before presenting the data and the interpretation of results. A charge-transfer complex can be briefly defined in the Mulliken sense as a system involving the partial transfer of one or more electrons from a donor (typically, an aromatic hydrocarbon) to an acceptor (typically, a halogen or an organic compound of high electron affinity) (3).

One of the characteristics of charge-transfer complexes pertinent to the discussion of their use in power sources is their high electronic conductivity, greatly enhanced over that of either donor or acceptor. In the electrochemical cells discussed below, a metal halide or salt is produced but is not involved in the cell assembly; it will be designated nevertheless as the electrolyte in conformity with the traditional terminology, and the charge-transfer complex will be called the cathode. The term "inert electrode" will be used to designate an electrode on the cathode side of the complex whose free energy of formation with the acceptor of the complex is small (or zero) in comparison with that of the anode with the acceptor. The term "matched load" will be used to designate the resistance of a suitable external resistor in series with the cell in order to produce a terminal voltage equal to half of its open-circuit value. Other terms of an electrochemical nature (including polarity) maintain their normal usage. Definitions can be found in the references (4).

Experimental Technique

The energy producing reaction is the formation of either the metal halide from the elements or, as in the case of the tetracyanoquinodimethane (TCNQ) compounds as acceptors, of the metal salt. Thus, for example, the reaction of iodine with magnesium gives rise to magnesium iodide with the liberation of energy. In contrast to the cells cited in the references, the authors did not physically include the halide (or salt) in assembly of the cells, but merely allowed it to form at room temperature *in situ*. Thus a metal halide layer is formed on the surface of the anode and is permeable to ion motion, but seems to constitute an electronic insulator which prevents complete internal short-circuiting.

The chemicals used in complex preparation ranged from high-purity materials to that of reagent grade. Cell performance was found to be independent of fluctuations in purity level within this range. High molecular weight poly-N-vinylcarbazole of intrinsic viscosity in benzene = 0.84 dl/g, was obtained from the Borden Chemical Company; it was purified by precipitating it twice from a benzene solution with methanol and dried in a vacuum oven at 50°C. Resublimed iodine was used as received. Reagent grade perylene was kept in the presence of $CaCl_2$. Other chemicals were used as received with the exception of poly-2-vinylquinoline, which was prepared by anionic polymerization of 2-vinylquinoline in benzene using butyllithium as initiator. Carbon black was purchased from Cabot Corporation (Vulcan XC72R).

The following methods were used for complex preparations: (*i*) mixing of the components in an inert solvent (*e.g.* dichloromethane), the solvent being subsequently removed in high vacuum at 0°C; (*ii*) grinding in a mortar or melting the components together in cases where the melting point of the charge-transfer complex was relatively low. The method of preparation seemed to have little effect on the cell characteristics.

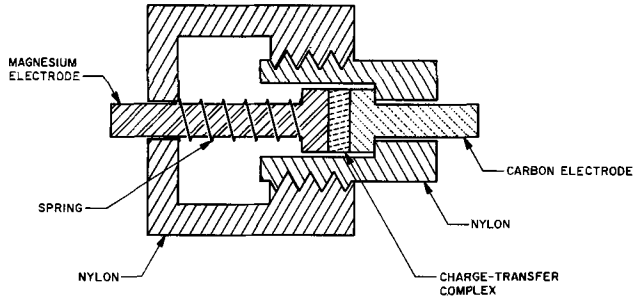

Fig 1. Sketch of test jig

The anode material was degreased and surface oxides were removed by abrasion or acid washing, followed by an acetone rinse and drying. Either technique seems suitable, the key feature being the necessity of assembly in a dry atmosphere to achieve reproducible results (see section on Experimental Results, below).

The complex was compacted in a hydraulic press under a pressure of about 100,000 lb/in.^{2}, yielding a pellet of ½ in. diameter and approximately 0.04 in. thickness. The metals were formed into disks of the same diameter, and the resulting sandwich was assembled in a Nylon or Teflon jig under small positive spring pressure (see Fig. 1). All currents quoted in this report refer to an area therefore of 1.26 cm^2.

Voltages and currents were measured with a Hewlett Packard 412A VTVM and a Keithley 610A electrometer.

Experimental Results

Cell composition.—Metal pure iodine systems.—In order to explore the suitability of anodes other than silver, a number of metals were tested, under standardized conditions, using a compacted pellet of pure iodine as the electrolyte and Pt, graphite, or Au as the counter electrode, thus forming a simple, well-defined system. Preliminary tests have shown that Pt as well as graphite and Au form good inert contacts to iodine. Results are summarized in Table I.

It is seen that the voltages previously reported for Ag (1) have been reproduced, but that considerably higher voltages are obtainable for Ba, Ca, and Mg in agreement with the high heat of formation of their iodides (5). This quantity is listed in Table I rather than the free energy of formation because of lack of data on the latter.

The system Mg/*iodine charge-transfer complex*/Pt *or* C.—A number of such systems were prepared and studied; results are summarized in Table II. Most of the complexes (*e.g.*, perylene-iodine, phenothiazine-iodine) were of sufficiently high conductivity to give a low internal impedance. A few of the complexes (*e.g.*, polyvinylpyridine-iodine) were characterized by relatively low conductivity; to those designated as such, a small percentage of carbon black (3-10% by weight)

Table I. Variation of the open-circuit voltage with the heat of formation of the metal iodide for cells of the type metal/I_2/Pt, C, or Au

Metal 1	Open-circuit voltage, v	Metal 2	Heat of formation of the metal-iodide[2], kcal-mole^{-1}
Ba	2.25	Au	−144
Ca	2.20	Pt	−127
Mg	1.85	Pt	−86
Al	0.82	Pt	−75
Ag	0.66	Pt or C	−15
Sn	0.23	Pt	
Fe	0.006	Pt	−30
Pt	0	Pt	0

Table II. Variation of the open-circuit voltage and short-circuit current with donor for cells of the type Mg/I_2-complex/Pt, C, or Au

Electrolyte, I_2 complexed with:*	Open-circuit voltage, v	Short-circuit current, μa
- - - 100% Iodine	1.85	1
Poly-N-vinylcarbazole	1.45	105
Poly-2-vinylquinoline	1.45	500
Poly-N-vinylcarbazole + carbon black	1.72	1000
Perylene	1.45-1.85	1100-16,000
Carbon black	1.4	1000
Polypropylene-carbon black	1.6	2300
Polyvinylpyridine-carbon black	1.75	1000-30,000
Phenothiazine-iodine	1.75	6500

* Approximately 50% I_2 by weight.

was added; the resulting cell performance is shown to be similar.

The heat of formation of MgI_2 predicts a reversible, open-circuit potential of 1.85v against an inert electrode (see discussion below). The deviations from this value are thought to be caused by imperfect formation of the magnesium iodide layer resulting in a small degree of internal short-circuiting.

From the Gibbs-Helmholtz equation we may write

$$E = \frac{\Delta H}{z\mathbf{F}} + T\frac{dE}{dT} \qquad [1]$$

where ΔH is the enthalpy change, *viz.*, −86 kcal/mole, z the number of electrons involved in the reaction, **F** the Faraday, E the open-circuit voltage, and T the absolute temperature.

For the MgI_2 reaction described in Eq. [1], $z = 2$. If one retains the first term only (Eq. [1]) and neglects the entropy contribution, one obtains the Helmholtz-Thomson equation which yields $E = 1.85$v. Direct measurement of dE/dT showed that it is negligible in the vicinity of room temperature. At temperatures above 45°C a value of about -5×10^{-4} v/deg was obtained. Since ΔH is negative, the voltage tends to drop with increasing temperature.

A value of 1.81v is obtained from the reverse (charging) current-voltage characteristics shown in Fig. 2. These curves refer to two different complexes both using Mg anodes and inert Pt counter electrodes.

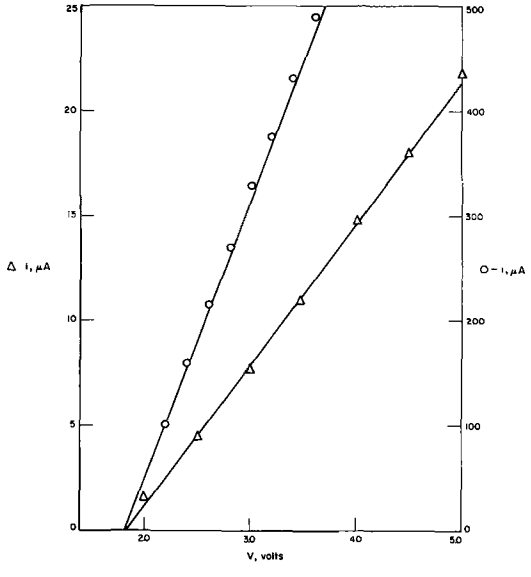

Fig. 2. Reverse (charging) characteristics. Points marked ⊙ refer to the system Mg/I_2-graphite complex/Pt, use right-hand scale for ordinates; points marked △ refer to Mg/I_2-poly-N-vinylcarbazole/Pt, use left-hand scale for ordinates.

In both cases it is seen that the relation is linear at higher values of applied voltage of reverse polarity and that extrapolation yields the potentiometric, zero-current voltage of 1.81v. Bromine complexes behave in a similar manner.

The short-circuit currents listed in Table II are limited by the resistance of the complex only in the first three cases; for pure iodine, for the poly-N-vinylcarbazole-iodine, and for the poly-2-vinylquinoline-iodine complex. The resistance of the complex for the other cells is of the order of 1-100 ohms, well below the value of the internal impedance. The large fluctuations from cell to cell in the short-circuit current have been found to be caused primarily by lack of controlled low humidity, leading to the formation of variable amounts of magnesium hydroxide [the formation of magnesium hydroxide on magnesium anodes has been studied in detail (6)]. When cells were assembled under 2% relative humidity, short-circuit currents of the order of 6-16 ma/cm² were obtained. This is thought to constitute a reasonable reproducibility in view of the crudeness of the contact method. However, it is felt that vacuum deposited anodes will further improve reproducibility.

It is appropriate to point out the effect of excess moisture in the complex or at the Mg/complex interface. With water in the complex in quantities of 5-20% by weight, or with a wet magnesium anode used in the cell assembly, initial performances of the cells were improved (current densities as high as several hundred ma/cm² were attained). However, the final values (reached after several minutes) of both the open-circuit voltages and the short-circuit currents were well below those presented in Table II. It appears that a controlled supply of water, by itself or in some suitable medium, may improve significantly the long-range cell characteristics. The effect of minute amounts of water on cell performance is unknown at this time and is subject of a present investigation.

Other iodine complex systems.—The results of a preliminary study of a number of other systems using iodine complexes and metals other than magnesium are listed in Table III.

The prior remarks about humidity seem pertinent to the barium and calcium cells. Calcium in particular was found to exhibit short-circuit current densities of the order of 3-4 ma/cm² in every case when the cells were assembled in a 2% relative humidity environment.

Noniodine systems.—The presence of iodine or, more generally, of halides is by no means a necessary condition for the electrochemical generation of useful electrical power, as seen from Table IV. Thus, the charge transfer complex between the donor graphite and the acceptor tetracyanoquinodimethane (TCNQ) yields a voltage of the same order and a current about 1 to 2 orders of magnitude below those obtained with the best of the iodine systems. Bromine complexes gave results comparable to those obtained with the iodine complexes, the voltages attainable being even higher,

Table III. Variation of the open-circuit voltage and short-circuit current with the anode metal for cells of the type metal/iodine-complex/inert electrode

Metal 1	Metal 2	Donor*	Open-circuit voltage	Short-circuit current, μa
In	Ni	Perylene	0.05	820
Cd	Pt	Perylene	0.008	2
Ba	Ni	Perylene	2.4	0.24-10
Ca	Ni	Perylene	2.5	1-4000
Ag	SnO	Poly-N-vinylcarbazole	0.66	0.2
Ca	Ni	Phenothiazine	1.8	2800-8000*

* Approximately 50% I_2 by weight, except for the phenothiazine cell whose composition was 2 to 1 by weight of iodine.

Table IV. Variation of the open-circuit voltage and short-circuit current with various iodine-free complexes for cells of the type Mg/iodine-free complex/Pt

Metal 1	Metal 2	Complex	Open-circuit voltage	Short-circuit current, μa
Mg	Pt	Poly-N-vinylcarbozole-Br_2-graphite	1.9	150
Mg	Pt	Poly-N-vinylcarbozole-$SbCl_5$	0.62	0.5
Mg	Pt	TCNE-graphite*	1.5	4
Mg	Pt	TCNQ-graphite**	1.50	150

* TCNE: tetracyanoethylene.
** TCNQ: tetracyanoquinodimethane.

in agreement with the higher heat of formation of $MgBr_2$.

It should be pointed out that the presence of a metal electrode is not a prerequisite for the electrochemical generation of useful power; however, an ionic concentration gradient across a potential barrier is essential. Thus, it was found possible to devise a wholly nonmetallic battery, based entirely on organic compounds. Work along these lines is proceeding.

Other variables: current-voltage relationships as a function of temperature and time.—A number of systems of the type Mg/I iodine complex have been discussed (see Table II). Typical current-voltage curves are shown in Fig. 3 and 4.

It has been shown that for cell assembly in uncontrolled humidity environments there was an improvement of cell characteristics with time. This "aging" effect has been observed with magnesium anodes in other types of cells (6). It is probably associated with the processes governing the formation and dissociation of the magnesium hydroxide layer mentioned previously. Figures 3 and 4 show quantitatively how aging improves cell characteristics. This effect is not observed for cell assembly in low humidity environment.

The overvoltage (Fig. 3 and 4) is taken as the difference between the (reversible) open-circuit potential, and the voltage actually obtained for a given current drain. Thus, the figures show two abscissae, actual terminal voltage and overvoltage; the latter is zero by definition when the current vanishes.

Figure 5 shows the temperature dependence of the current voltage characteristics of iodine complexed with poly-2-vinylpyridine and carbon black. Two features to be noted from this figure are that the cell es-

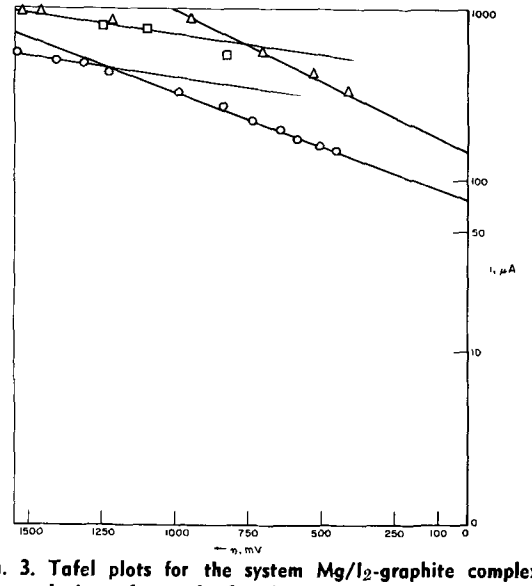

Fig. 3. Tafel plots for the system Mg/I_2-graphite complex/Pt. Points marked ⊙ refer to the freshly prepared cell, the other points refer to the same cell after three days' aging; △ were obtained on increasing the current and points □ on lowering the current. The abscissae here represent overvoltages.

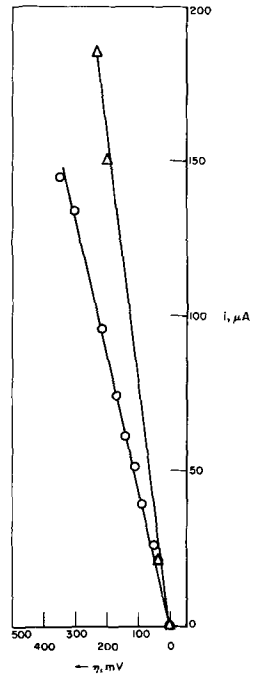

Fig. 4. Low overvoltage current-voltage characteristics. These data represent the low current region, continuing Fig. 3, but on a linear scale; they refer to the same system. Points marked ⊙ were obtained with the freshly prepared and points △ with the same cell aged for three days. The abscissae again reads overvoltages.

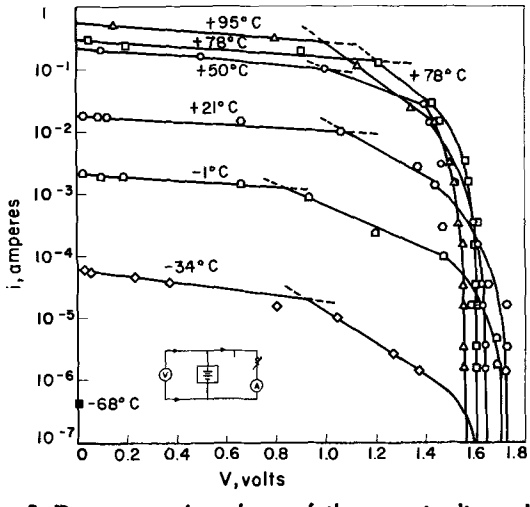

Fig. 5. Temperature dependence of the current-voltage characteristics for the system

Mg	Poly-2-vinylpyridine	40% by wt	C
	Iodine	50% by wt	
	Graphite	10% by wt	

sentially ceases operation below −68°C, and that the short-circuit current increases with increasing temperature, reaching 0.7 amp at 95°C. This dramatic increase of the current in the Tafel and diffusion regions can be analyzed by plotting the variation of the short-circuit current with reciprocal temperature. A plot of this type gives an excellent straight line below 50°C, whose slope corresponds to an activation energy of 15.6 kcal/mole and straight line above 50°C, whose slope corresponds to an activation energy of 5.99 kcal/mole. This particular cell was also cooled to 80°K for 10 min, recovering fully upon warming to room temperature.

Figure 6 shows discharge curves for the perylene-iodine complex (weight ratio 1:2) at various constant loads. The voltage drop rates have been determined in

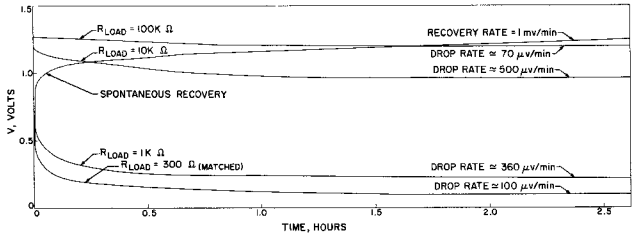

Fig. 6. Discharge curves at room temperature for the system Mg/perylene-iodine/Pt at various fixed loads. Also plotted is the spontaneous open-circuit voltage recovery measured after the discharge data were recorded.

the region designated in the figure; these rates decrease with increasing time. A spontaneous recovery curve is also recorded in Fig. 6; this plot was made by recording the time dependence of the open-circuit voltage immediately after the last of the discharge curves was completed. It can be inferred from the recovery curve that the decrease in current with time is due primarily to a nonequilibrium distribution of ions in the cell, and only in part due to the formation of the magnesium iodide layer (and consequent reduction in ion diffusion). The information that can be obtained from Fig. 6 (using cell weights of 0.5 g, including complex and electrode contributions) is summarized as follows: open-circuit voltage, 1.4v; initial, matched load, current density, 2.0 ma/cm^2; maximum power density (under matched load, initial time conditions): ~ 1 watt/lb; useful energy density (for 100 kohm, load assuming that a voltage below one half the open-circuit value is not useful): ~ 1 watt hr/lb. Further discharge data are being gathered to determine the energy efficiency of the cell.

Figure 7 shows a current-voltage characteristic of a cell using a poly-N-vinylcarbazole-iodine complex as the cathode. This is a system with a relatively high cathode resistance; the current is seen to remain limited by this IR drop and the Tafel region cannot be reached. The dynamic resistance of the system is 54,000

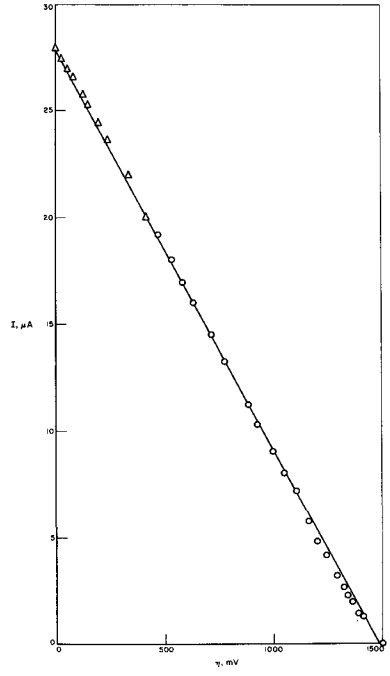

Fig. 7. Current voltage characteristic of the system Mg/I_2-poly-N-vinyl-carbazole complex/Pt. Points ⊙ and △ were taken at different times. The abscissae read overvoltages. The overvoltages are seen to be entirely determined by the ohmic series resistance of the cell.

ohm; while one can, formally, calculate an exchange current from this curve, little significance may be attached to it since the system does not operate under activation control. With this proviso, a value of i_o = 6 x 10^{-7} amp/cm^2 is reported.

Analysis: Thermodynamics of the Mg/I_2-C System

The room temperature current-voltage characteristics (Fig. 3 and 4) show that the Tafel equation is obeyed at current densities in excess of a few 100 μa/cm^2. At low current densities and correspondingly low values of overvoltage, the current is proportional to voltage. The current then obeys the relation approximately valid (7) for this region

$$i = \frac{i_o \eta \mathbf{F}}{RT} \qquad [2]$$

where i is the current corresponding to an overvoltage η, and i_o is the exchange current; R, T, and $\mathbf{F}$ have the usual meaning. From the slope, a dynamic resistance of 2300 ohms/cm^2 for freshly prepared Mg/I_2-C complex/Pt cell is obtained, valid up to about 156 μa/cm^2. This resistance corresponds to an exchange current density of 9.4 x 10^{-6} amp/cm^2. At higher current densities and thus higher overvoltages, a Tafel slope of —0.714 results; the exchange current density then follows by extrapolation as 58.3 μa/cm^2 which is not too different from the value obtained or the low current region.

The stoichiometric number γ of the rate-determining step represents the number of times this reaction has to occur for the over-all reaction to advance by one DeDonder unit. A value for γ may be obtained from the low current-density versus η plot, using the relation (8)

$$\gamma = \left| \frac{z\mathbf{F}i_o}{RT} \left(\frac{\partial \eta}{\partial i} \right)_{\eta \to 0} \right| \qquad [3]$$

This yields γ = 2.12, *i.e.*, practically 2, meaning that the rate-determining step must occur twice in order for the over-all reaction to be advanced by one unit. It is also assumed that there is no change in the rate-determining mechanism between the reversible region and the region of activation control.

From the slope of the current-voltage curve shown in Fig. 3, a value for the Tafel coefficient β_a = 0.018, valid for the region of activation control, is obtained for the freshly prepared Mg/I_2-C/Pt system. The electrochemical information thus available on this system is the following: number of electrons involved in the over-all reaction, z = 2; stoichiometric number, γ = 2; Tafel coefficient, β_a = 0.018; exchange current density, i_o = 9.4 μa/cm^2. We shall also assume that the affinity factor δ of the rate-determining step has a value very close to unity (9); the affinity factor is defined (9) as the number of electrons involved in one single rate-determining event.

In these solid-state electrochemical cells, we consider one reaction, in the present case, the formation of magnesium iodide. For the region of activation control, we may write

$$I = I_o \left(e^{\alpha_a \mathbf{F}\eta/RT} - e^{-\alpha_c \mathbf{F}\eta/RT}\right) \qquad [4]$$

where the first term refers to the forward and the second term to the reverse reaction. The transfer coefficients α_a for the forward and α_c for the reverse reaction must add up to unity

$$\alpha_a + \alpha_c = 1 \qquad [5]$$

We may also write (4)

$$\left.\begin{aligned} \beta_a + \beta_c &= (\alpha_a + \alpha_c)\frac{z\delta}{\gamma} \\ \alpha_a &= \beta_a/(\beta_a + \beta_c) \end{aligned}\right\} \qquad [6]$$

For the linear, low overvoltage region, we may also approximate

$$I \simeq I_o \frac{(\beta_a + \beta_c)\mathbf{F}\eta}{RT} \quad [7]$$

Since $\delta \simeq 1$, it follows that $\beta_a + \beta_c = 1$, so that

$$\begin{aligned} \beta_c &= 0.982 \\ \alpha_a &= \beta_a = 0.018 \\ \alpha_c &= \beta_c = 0.982 \end{aligned} \quad [8]$$

In irreversible thermodynamics

$$\gamma \tilde{A}^o = \delta \tilde{A} \quad [9]$$

Here, $\tilde{A}^o$ stands for the electrochemical affinity of the rate-determining step and $\tilde{A}$ for the total electrochemical affinity of the over-all reaction, given by

$$\tilde{A} = z\mathbf{F}\eta \quad [10]$$

The electrochemical affinity of the rate-determining step thus follows as

$$\begin{aligned} \tilde{A}^o = z\mathbf{F}\eta\delta/\gamma &= 6.9 \times 10^4 \text{ volt-coul/mole} \\ &= 16.5 \text{ kcal/mole} \end{aligned} \quad [11]$$

for the same cell operating under matched load conditions, $\eta = 750$ mv.

The increase in the degree of advancement (10) of the over-all, energy producing cell reaction, $d\xi/dt$, which may be equated to the conventional reaction rate v, is given by

$$i = z\mathbf{F}\frac{d\xi}{dE} = z\mathbf{F}v \quad [12]$$

Under matched load conditions a current density of about 500 μa/cm^2 is obtained using a Mg anode and an I_2-C complex as a cathode. Two electrons being involved, a reaction rate of 2.5 x 10^{-9} moles-cm^{-2} results. This may be inserted into the equation (11)

$$v = d\xi/dt = \left[\tau\frac{KT}{h}\exp\left(\frac{-\Delta\bar{G}^{\#}}{RT}\right)\right][C_s(1-\theta)] \quad [13]$$

where τ is a transmission coefficient, $\Delta\bar{G}_o^{\#}$ the electrochemical standard free energy of activation, C_s the concentration of the reactant at the Mg-electrolyte interface, and $(1-\theta)$ gives the specific fractional area available for the discharge of additional molecules at the surface. $\theta = f(v)$ and thus represents the fraction of the surface area covered with reaction product (MgI_2) at the given current. Generally, $\tau \simeq 1$. Direct measurement of the current at 20° and at 135°C showed an increase by a factor of 300; thus, $\Delta\bar{G}_o^{\#}$ = about 12.4 kcal/mole. At 300°K, the quantity in the square brackets, representing an effective surface concentration, results as 4 x 10^{-13} moles/cm^{-2} = 2.4 x 10^{11} molecules of I_2 per cm^2 area. Since a monolayer of I_2 contains about 5.2 x 10^{14} molecules cm^{-2}, this shows a coverage of about 4.6 x 10^{-4} of the total electrode area; $(1-\theta)$ = 4.6 x 10^{-4}. Thus only a minute fraction of the total electrode area is available for further internal discharge; most of the area is covered with the MgI_2 produced by the reaction.

Under reversible conditions, about 1/7th of a monolayer participates in the electrochemical reaction if the exchange current value of 1.4 x 10^{-5} amp/cm^2, valid for a freshly prepared cell, is used. The highest exchange current in well-aged cells, valid in the Tafel region before the onset of diffusion limitation, is 1.8 x 10^{-4} amp/cm^2. Then, about one-half of a monolayer is seen to participate in the electrochemical reaction. Thus, as soon as higher current densities are demanded from the system, the effective electrode area, available for the electrochemical process, tends to shrink rapidly until the previously calculated fraction of about 4.6 x 10^{-4} of the total electrode area is reached; "polarization" thus is due to the cumulative poisoning of the electrode surface by the accumulation of reaction product.

At high current densities and overvoltages, the slope of the Tafel plots in the I/V characteristics is seen to change, the current tending to saturate. It is seen from Fig. 3 that the slope of these lines is the same irrespective of aging and, indeed, the same for different samples. Thus, it is very likely that in this region the current is limited by diffusion and no longer is activation controlled. The limiting, diffusion current i_L is about 1 ma/cm^2. This may be written

$$i_L = Dz\mathbf{F}a/sn \quad [14]$$

where D is the diffusion coefficient of the reactant, a its effective surface activity, s the thickness of the diffusion layer, and n stands for the sum of the transport numbers of all the ion species engaged in the electrochemical reaction. Taking $n = 1$, and using concentration instead of the activity, we obtain, inserting the value for the effective surface concentration obtained before, *viz.*, 2.4 x 10^{11} molecules/cm^2, corresponding to 5.43 x 10^{17} molecules/cm^3, s = 0.046 cm. The thickness of the diffusion layer being about 0.5 mm, it follows that there is little or no virtue in using cathode layers much thicker than, say 1 mm or so (neglecting lifetime considerations). A value of D = 10^{-5} cm^2 sec^{-1} has been used, this being a reasonable value.

The instantaneous efficiency of energy conversion, H, may be calculated from irreversible thermodynamics using an equation derived by van Rysselberghe (12)

$$H = 1 - z\mathbf{F}(\Sigma\eta)/A \quad [15]$$

where $\Sigma\eta$ is the sum of all overvoltages and A the (instantaneous) chemical affinity of the cell reaction, $A = -(\partial G/\partial\xi)_{T,P}$. Using the value for the heat of formation of MgI_2 listed in Table I for A instead of the free energy change, which latter value is not available, yields H = 78%.

Reaction Mechanisms

Since the open-circuit voltages of a given metal are virtually the same with pure iodine and with iodine complexes as with the electrolyte, it appears that the energy producing reaction is the formation of the metal-iodide from the elements. This is further supported by the excellent agreement between the values of the open-circuit voltage and the energy of formation, see Table I. Two electrons are thus involved in the over-all reaction, and the value obtained for $\gamma = 2$ requires that the rate-determining reaction must be carried through twice for the over-all reaction to advance by one unit, *i.e.*, for the formation of 1 mole of MgI_2. Several reaction mechanisms may be devised to agree with these requirements. Thus, *e.g.*, the following mechanism is compatible with $z = 2$ and $\gamma = 2$

$$\left.\begin{array}{l} 2[Mg + I^- \rightarrow MgI + e^-] \\ 2MgI \rightleftarrows MgI_2 + Mg \\ \hline Mg + 2I^- \rightarrow MgI_2 + 2e^- \end{array}\right\} \quad [16]$$

The first step is the rate-determining one, while the second step involves a reaction at or near equilibrium. There must be, linked with the above reaction scheme, a further reaction as a source of I^- ions; this could well be

$$I_2 + 2e^- \rightleftarrows 2I^- \quad [17]$$

The reaction involved in the case of the halide-free electrolytes, viz., TCNQ-C and TCNE-C complexes, is less clear, Both TCNE and TCNQ are good electron acceptors, readily forming ions $TCNQ^-$ or $TCNE^-$. The electrode reaction then is likely to be

$$Mg \rightleftarrows Mg^{++} + 2e^-$$

$$2TCNQ + 2e^- \rightleftarrows 2TCNQ^-$$

$$Mg^{++} + 2TCNQ^{-} \rightleftarrows (TCNQ^{-}\_\_Mg\_\_TCNQ^{-})$$

$$Mg + 2TCNQ \rightleftarrows (TCNQ^{-}\_\_Mg^{++}\_\_TCNQ^{-}) + \text{energy} \quad [18]$$

This seems reasonable since the $Mg^{++}(2TCNQ)^{-}$ is known to exist.

Advantages and Practical Applications

These cells operate at room temperatures, but will stand elevated temperatures at least up to 130°C; thus, they are likely to be heat sterilizable. These are true solid-state devices; thus, they may be encapsulated and made as small as desired. They could be used for energizing microelectronic circuits where they may become an integral part of the circuit; the cell may be produced by sequential deposition processes occupying a minimum of space. They also should lend themselves very well for a variety of electromedical applications.

The energy density of the prototypes thus far studied is below the requirements for space vehicle power devices. It is certain however, that proper engineering and improvements due to further studies will improve present performance substantially. The iodine-complexes are known to be stable; the shelf-life may be limited, therefore, only by internal short-circuiting. The recovery even after prolonged short circuiting is very fast, usually within minutes. The cells lend themselves particularly well for the powering of firing mechanisms for pyrotechnic devices, like squibs, where a capacitor is charged from the primary power source.

Acknowledgments

The authors are greatly indebted to Professor Pierre van Rysselberghe, of Stanford University, for his constructive comment and criticism.

This paper represents one phase of research performed by the Jet Propulsion Laboratory, California Institute of Technology, sponsored by the National Aeronautics and Space Administration, NAS7-100.

Manuscript received May 24, 1966; revised manuscript received Dec. 15, 1966.

Any discussion of this paper will appear in a Discussion Section to be published in the December 1967 JOURNAL.

REFERENCES

1. K. Lehovec and J. Broder, *This Journal*, **101**, 208 (1954); J. D. Broder, US Pat. 2,690,465 (Sept. (1954); K. Lehovec, US Pat. 2,689,876. See also, N. Mrgudich in Encyclopedia of Electrochemistry, p. 84, Reinhold, N. Y. (1964).
2. T. Takahashi and O. Yamamoto, *Electrochim. Acta*, **11**, 779 (1966).
3. For a more detailed discussion, see F. Gutmann and L. E. Lyons, "Organic Semiconductors," John Wiley & Sons, Inc., New York (1966).
4. *Electrochim. Acta*, **5**, 28 (1961); **8**, 543 (1963).
5. "Handbook of Physics & Chemistry," p. 1691, Chemical Rubber Publishing Co., 38th ed., Cleveland (1956/57).
6. J. L. Robinson and P. F. King, *This Journal*, **108**, 36 (1961).
7. F. Gutmann and P. van Rysselberghe, *Electrochim. Acta*, **10**, 107 (1965).
8. B. E. Conway, "Theory and Principles of Electrode Processes," p. 264, Ronald Press Co., New York (1965).
9. J. O'M. Bockris and E. C. Potter, *This Journal*, **99**, 169 (1952).
10. P. van Rysselberghe, "Thermodynamics of Irreversible Process," Hermann, Paris (1963); P. van Rysselberghe, *Electrochim. Acta*, **8**, 583, 709 (1963); **9**, 1547 (1964).
11. B. E. Conway, "Theory and Principles of Electrode Processes," p. 264, Ronald Press Co., New York (1965).
12. P. van Rysselberghe, *Electrochim. Acta*, **11**, 125 (1966).
13. H. Akamatu, H. Inokuchi, and Y. Matsunga, *Bull. Chem. Soc. Japan*, **29**, 213 (1956).

The Effect of Pressure on the Dissociation of Carbonic Acid from Measurements with Buffered Glass Electrode Cells

The Effects of NaCl, KCl, Mg^{++}, Ca^{++}, $SO_4^{=}$, and of Boric Acid with Special Reference to Sea Water

A. Distèche and S. Distèche

Laboratory of General Biology, Zoology Institute, University of Liège, Liège, Belgium

ABSTRACT

The effect of pressure on the dissociation of carbonic acid has been investigated over a wide range of pH (*pa*H 5.1-9.6) and ionic strength (0-1.0) in NaCl and KCl, using junctionless glass electrode cell measurements. At 22°C, $\Delta V_1^\circ = -25.4$ cm^3 mole^{-1} and -25.6 cm^3 mole^{-1} for the first and second ionization steps, respectively. The directly measured *pm*H or *pc*H shifts induced by pressure in sea water between *pa*H$_1$ 5.1 and 9.1 are explained by the enhanced dissociation of H_2CO_3, HCO_3^-, $CaCO_3$, and $MgCO_3$, the effect of $SO_4^=$ and the interference of boric acid ($\Delta V_1^\circ = -32.1$ cm^3 mole^{-1}). Values of the ionization functions $k'_{(1)} = [H^+][HR^-]/[H_2R]$ and $k'_{(2)} = [H^+][R^=]/[HR^-]$ of carbonic acid, valid in natural seawater, have been determined at 22°C, at 1 atm and at 1000 bars together with the apparent dissociation constants ($pK''_{(1)}$ and $pK''_{(2)}$ used in oceanography to calculate $[CO_3^=]_{total}$, $[HCO_3^-]_{total}$ from *in situ pa*H values. Corrections are given for different types of reference half-cells, and an approach toward the absolute values of $pk_{(1)}$ and $pk_{(2)}$ in sea water is indicated.

The effect of pressure (p) on the dissociation constant (K) of a weak electrolyte (HR) is related to the corresponding volume change (ΔV) for the ionization reaction $HR \rightleftharpoons H^+ + R^-$ by the equation

$$\left(\frac{\partial \ln K}{\partial p}\right)_{m,T} = \frac{-\Delta V}{RT} \qquad [1]$$

Data are available for ΔV_1° at atmospheric pressure, zero salt concentration, and zero weak electrolyte concentration for carbonic acid calculated from density measurements, conductivity, and glass electrode determinations:

Reaction	Density, 25°C $-\Delta V_p^\circ$ (p = 1 atm) cm^3 mole^{-1}	Conductivity, 25°C $-\Delta V_p^\circ$ (p = 1 atm) cm^3 mole^{-1}	Glass electrode, 22°C $-\Delta V_p^\circ$ (p = 1 atm) cm^3 mole^{-1}
$H_2CO_3 \rightarrow HCO_3^- + H^+$	29.0 (1)	26.5 (2)	26.6 (3) (unbuffered cell) 25.5 (3) (buffered cell) 25.4 (this paper; buffered cell)
$HCO_3^- \rightarrow CO_3^= + H^+$	27.8 (1)	—	25.6 (this paper; buffered cell)

The ΔV_1° values from glass electrode measurements published in our earlier papers (3, 4) were obtained by extrapolation of ΔV_1 to zero KCl concentration over a limited ionic strength range (0-0.1).

In view of the interest in precise knowledge of the effect of pressure on the dissociation of carbonic acid for oceanographic work, the present paper deals with the determination between 1 and 1000 atm of the dissociation constants $K_{(1)}$ and $K_{(2)}$ and the ionization functions $k_{(1)}$, $k_{(2)}$ ($k_{(1)} = [H^+][HCO_3^-]/[CO_2]$, $k_{(2)} = [H^+][CO_3^=]/[HCO_3^-]$) in presence of NaCl or KCl, over a wide ionic strength range (0-0.8), at various buffer ratios (*pa*H 5.1-9.6). The effect of Ca^{++}, Mg^{++}, and $SO_4^=$ ions and boric acid is investigated to interpret the data obtained with natural sea water samples (4) and from direct in situ determinations (5, 6).

Theoretical

The theory underlying the determination of dissociation constants as a function of pressure has been discussed in previous papers (3, 4).

The buffered cell used for the present determinations is of the type:

Ag — AgCl	Ref. compartment HCl (0.01) MCl (m_3 — 0.01)	glass	x compartment HR(m_1) + MR(m_2) MCl (m_3)	AgCl — Ag

where M represents Na or K.

The emf (E) at pressure 1, or p, is expressed by:

$$E_{1,p}\,\mathbf{F}/2.3\,RT = \log (m_{H^+})^{ref}{}_{1,p} - \log (m_{H^+})^{x}{}_{1,p} + 2 \log \frac{(\gamma_{HCl})^{ref}{}_{1,p}}{(\gamma_{HCl})^{x}{}_{1,p}} \qquad [2]$$

For an acid HR of the strength of carbonic acid $\log K^m = \log (m_{H^+} m_1/m_2) + 2 \log \gamma_A$; $2 \log \gamma_A = \log (\gamma_{H^+} \gamma_{R^-}/\gamma_{HR})$; $m_{H^+} m_1/m_2 = k^m$ and:

$$(E_1 - E_p)\mathbf{F}/2.3\,RT = \log \frac{K^m{}_p}{K^m{}_1} + 2 \log \frac{\gamma_{A1}}{\gamma_{Ap}} + 2 \log \frac{(\gamma_{HCl})^{ref}{}_1}{(\gamma_{HCl})^{ref}{}_p} - 2 \log \frac{(\gamma_{HCl})^{x}{}_1}{(\gamma_{HCl})^{x}{}_p} \qquad [3]$$

The terms in γ_{HCl} cancel each other at infinite dilution of the weak electrolyte, but if m_1 and m_2 are small and if the salt effect of the weak acid is small, cancellation practically occurs for finite values of m_1 and m_2.

Equation [3] then simplifies to

$$(E_1 - E_p)\,\mathbf{F}/2.3\,RT = \log \frac{K^m{}_p}{K^m{}_1} + 2 \log \frac{\gamma_{A1}}{\gamma_{Ap}} = \log \frac{k'^m{}_p}{k'^m{}_1} \qquad [4]$$

the primes indicating that k' is only known approximately because of the former assumptions.

In the case of carbonic acid, extrapolation of $(E_1 - E_p)\,\mathbf{F}/2.3\,RT$ as a function of $\sqrt{\mu}$ leads easily to log $K^m{}_p/K^m{}_1$ and a double extrapolation first to zero weak acid concentrations at a given μ, and then to zero KCl or NaCl concentration, is not required.

It can be shown (7) that $\Delta V_1 = 1.016 \times (E_1 - E_{1000})$ if ΔV_1 is expressed in cm^3 mole^{-1}, E in millivolts, p in kg. cm^{-2}. E_{1000} is measured on the tangent of $E_1 - E_p = f(p)$ drawn through $p = 1$ atm. For carbonic acid, $E_1 - E_p = \Delta E_p$ is a linear function of p up to 1000 kg. cm^{-2}, so that E_{1000} corresponds to the emf effectively measured at 1000 kg. cm^{-2}.

Concentrations (m) and activity coefficients (γ) are given on the molal scale (mole per kg of pure solvent) in Eq. [1]-[4].

If the concentrations are expressed on the molar scale (mole per liter solution, c) the following classical equations ([5]-[10]) can be used to relate c, m, the corresponding activity coefficients, y and γ, the density (d) of the solution and of pure water (d_o), M_i the molecular weight of solute i. the dissociation constants and ionization functions K^c, k^c, K^m, k^m

$$m_i = c_i/(d - \Sigma c_i M_i/1000) \qquad [5]$$

$$c_i = m_i d/(1 + \Sigma m_i M_i/1000) \qquad [5']$$

$$\gamma = y[(d - \Sigma c_i M_i/1000)/d_o] \qquad [6]$$

$$m\gamma d_o = cy \qquad [7]$$

$$K^m = K^c/d_o;\; k^m = k^c(1 + \Sigma m_i M_i/1000)/d \qquad [8]$$

$$\log K^m{}_p/K^m{}_1 = \log K^c{}_p/K^c{}_1 - \log d_{op}/d_{o1} \qquad [9]$$

$$\log k^m{}_p/k^m{}_1 = \log k^c{}_p/k^c{}_1 - \log d_p/d_1 \qquad [9']$$

Combining [7] and [2] gives

$$\frac{(m\gamma)^{\mathrm{ref}}{}_{1,p}}{(m\gamma)^{x}{}_{1,p}} = \frac{(cy)^{\mathrm{ref}}{}_{1,p}}{(cy)^{x}{}_{1,p}} \qquad [10]$$

If the activity coefficients can be made to cancel in both ref and x compartments of the glass electrode, $(E_1 - E_p)\mathbf{F}/2.3\,RT$ will be equal to log $k'^m{}_p/k'^m{}_1$ and extrapolate to log $K^m{}_p/K^m{}_1$ as a function of μ (Eq. [4]) whatever the concentration scale used.

In aqueous solutions $d_p/d_1 = d_{op}/d_{o1} = 1.04$ at 1000 atm, log $d_{1000}/d_1 = 0.017$, and it is thus easy to use $(E_1 - E_{1000})$ to calculate the ratios of the dissociation constants and ionization functions either on the c or the m scale.

When the absolute values of $k'^m{}_1$, $k'^c{}_1$ are required, Eq. [5], [5'], and [6] can be used to calculate either ionization function from the results obtained on the c or the m scale, respectively.

In practice, if the highest precision is not required, $c \simeq m$ at 0.1M. At concentrations where the correction to calculate m from c is more important, the densities in the x and ref compartments of the glass electrode are nearly equal when the buffer concentration is small compared with the NaCl or KCl concentrations, and only m_{H+} needs be computed in the reference solution, since $m_{Cl^-}{}^{x} = m_{Cl^-}{}^{ref}$.

In the present paper, concentrations referring to the gross composition of the solutions are indicated on the molar scale, and to simplify the symbol M referring to molarity is omitted (0.5 NaCl means 0.5M NaCl). The hydrogen ion stoichiometric concentration [H$^+$] is represented by pcH = −log [H$^+$] on the c-scale and pmH on the m-scale, the hydrogen ion activity a_{H+} by paH = −log a_{H+} and if the distinction between pcH, pmH, paH is irrelevant, the symbol pH is used; subscripts p, 1, 1000 indicate pressure p, 1 atm, 1000 kg. cm^{-2} (ex. : pmH$_1$, pmH$_{1000}$); $\Delta E_{1000} = E_1 - E_{1000}$ in millivolts (mv).

Experimental

The equipment described in 1962 (7) is used. It is important in the experiments involving equilibration with either pure CO_2 or mixtures of CO_2 and nitrogen to saturate the silicone oil used in the glass electrode cell and to fill the cell with pipettes containing a controlled gas phase (3).

The glass electrode is made from Corning 015 glass, when no sodium error is to be expected. A commercial electrode, E.I.L.[1] n° 18331 unsensitive toward Na^+ at alkaline pH is used whenever necessary.

Corrections for asymmetry potential shift with pressure is made as described earlier (3, 4, 7). When both cell compartments contain the same solution ΔE_{1000} is generally between 0 and ±1.0 mv. Higher values indicate defective Ag-AgCl electrodes.

Highest grade reagents (Merck) and air-free bidistilled water (Pyrex) are used.

Results

First ionization function and first dissociation constant of carbonic acid in bicarbonate buffer in presence of NaCl *or* KCl, *at $p = 1$ atm and $p = 1000$ kg. cm^{-2}.*—Figure 1 shows ΔE_{1000} in mv as a function of $\sqrt{\mu}$ for various bicarbonate buffers at different buffer ratios, in presence of NaCl or KCl. Extrapolation to zero ionic strength gives 25.0 mv corresponding to $-\Delta V_1{}^o = 25.4$ cm^3 mole^{-1}, in agreement with our previous experiments (4).

Figure 2 gives the ionization function $pk'^c{}_{(1)} = -\log k'^c{}_{(1)}$ and $pK'^c{}_{(1)} = -\log K'^c{}_{(1)} = pk'^c{}_{(1)} + \dfrac{1.01\sqrt{\mu}}{1+\sqrt{\mu}}$ as a function of μ at $p = 1$ atm and $pK'^c{}_{(1)p} + \log d_p/d_1$ at $p = 1000$ kg. cm^{-2} (log $d_p/d_1 = 0.017$).

The absolute values of $pK^c{}_{(1)}$ (6.38) and $pk'^c{}_{(1)}$ are in good agreement with the data of Harned and Davis (8) and of Harned and Bonner (9) ($pK^m{}_{(1)} = 6.3809$ at 20° and 6.3519 at 25°C).

The concentration ratios $[HCO_3^-]/[CO_2]$ are computed from the equations of these authors and the same extrapolation function is found to fit our results and theirs. The 2 log $(y_{HCl})^{ref}/(y_{HCl})^x$ term in Eq. [1] (c scale) is calculated from the values of γ_{HCl} in NaCl and KCl taken from Harned and Owen (10). It is assumed that γ_{HCl} in the x compartment is only affected by the ionic strength, and the ratio of the activity coefficients is also supposed to be valid on the molar scale. At $\mu \geq 0.5$, γ_{HCl} practically cancels in both compartments.

At $\mu = 0.75$, $pk'^m{}_{(1)} = pk'^c{}_{(1)} - 0.007 = 5.995$. The correction is −0.005, −0.0057, −0.0065, −0.0073,

[1] Electronic Instruments Limited, Richmond, Surrey, England.

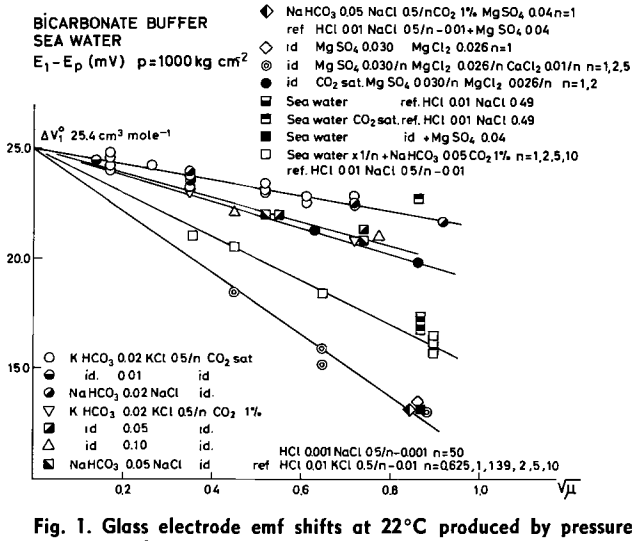

Fig. 1. Glass electrode emf shifts at 22°C produced by pressure (1000 kg.cm^{-2}), in bicarbonate buffers, at different buffer ratios, as a function of $\sqrt{\mu}$, in NaCl, KCl, in presence of Mg^{++}, Ca^{++}, $SO_4^=$ ions, and in sea water.

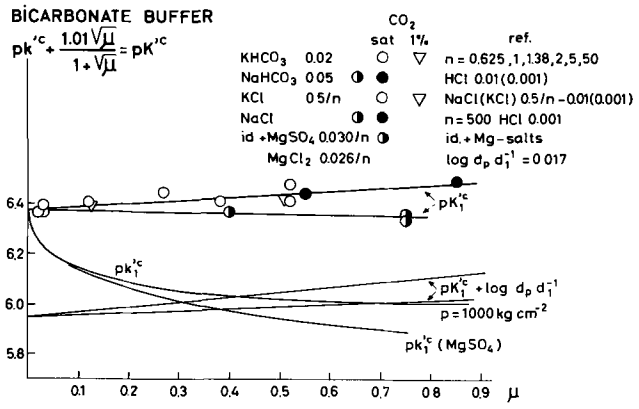

Fig. 2. First ionization function ($k'^c_{(1)}$) of carbonic acid and as a function of μ at atm pressure and 1000 kg.cm^{-2} in NaCl and KCl at 22°C. Effect of $MgSO_4$ + $MgCl_2$.

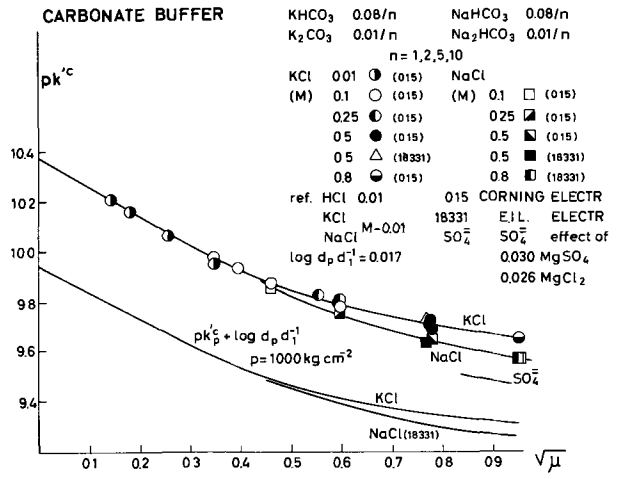

Fig. 4. Second ionization function ($k'^c_{(2)}$) of carbonic acid as a function of $\sqrt{\mu}$ at atm pressure and 1000 kg.cm^{-2} in NaCl and KCl at 22°C. Sulfate effect of 0.030 $MgSO_4$ (+0.026 $MgCl_2$).

−0.0081, −0.009 at μ0.5, 0.6, 0.7, 0.8, 0.9, 1.0, respectively (calculated from the density of NaCl solutions), and at $\mu = 0$, it is equal to −0.001.

Second ionization function and second ionization constant of carbonic acid in carbonate buffer in presence of NaCl *or* KCl, *at p = 1 atm and p = 1000 kg. cm^{-2}.*—Figure 3 gives ΔE_{1000} in mv, as a function of $\sqrt{\mu}$ for carbonate buffer in presence of NaCl or KCl.

Extrapolation to zero ionic strength gives 25.1 mv or $-\Delta V_1^o$ = 25.6 cm^3 mole^{-1}, which is practically the same result obtained in bicarbonate buffers. The value calculated by Owen and Brinkley (1) from density determinations is 27.8 cm^3 mole^{-1}.

Figure 4 shows the ionization function $pk'^c_{(2)}$ as a function of $\sqrt{\mu}$ at p = 1 atm, $pk'^c_{(2)p}$ + log d_p/d_1 at p = 1000 kg. cm^{-2}; the results in 0.5 and 0.8 NaCl do not depend on the buffer ratio and are identical either with $NaHCO_3$ 0.08 + Na_2CO_3 0.01 or with $NaHCO_3$ 0.025 + Na_2CO_3 0.025. $pK^c_{(2)}$ = 10.37 corresponds to the values published by Harned and Scholes (11) ($pK^m_{(2)}$ = 10.377 at 20°C, 10.329 at 25°C) who extrapolate their data between μ = 0.15 and 0.

At μ = 0.75, $pk'^m_{(2)1}$ = 9.60 − 0.007 in NaCl.

Effect of buffer ratio on the ionization of carbonic acid at 1000 kg. cm^{-2} in NaCl *and* KCl *solutions.*—Figures 1 and 3 show that, at a given buffer ratio, ΔE_{1000} extrapolates linearly to the same value at μ = 0, and that a change in the buffer concentration has the same effect as the corresponding μ change produced by an increase of the NaCl or KCl concentration. It is therefore easy to obtain a graphical estimate of ΔE_{1000} at a chosen ionic strength, even from isolated values measured at another ionic strength.

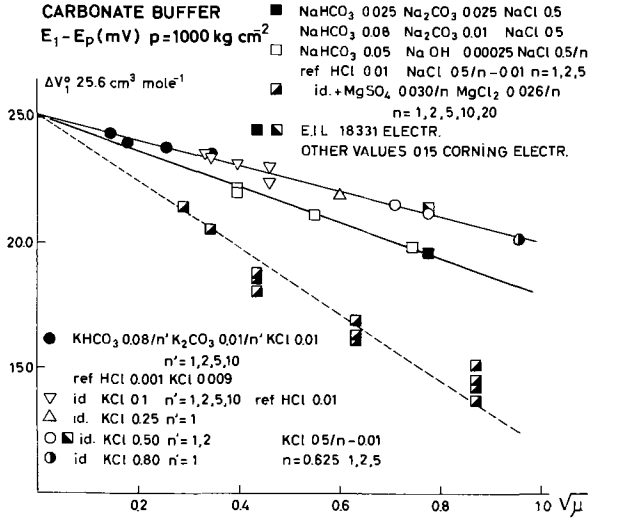

Fig. 3. Glass electrode emf shifts at 22°C, produced by pressure (1000 kg.cm^{-2}) in carbonate buffers, at different buffer ratios, as a function of $\sqrt{\mu}$, in NaCl or KCl, in presence of Mg^{++}, Ca^{++}, $SO_4^=$, and in sea water.

Curves 1 and 1′ from Fig. 5 give ΔE_{1000} at μ = 0.75 (ionic strength of sea water at Cl‰ = 20.0) as a function of pmH_1, in NaCl and KCl. The emf shifts depend only slightly on the total CO_2 concentration in the range investigated ($[HCO_3^-] + [CO_3^=]$ between 0.09 and 0.0025; arrows indicate the values at 0.0025 in Fig. 5).

The reason for the difference between the results in NaCl and KCl at $pmH_1 \geqq 8.5$ is, we believe to be correlated with the fact that, at 1 atm, the curves giving $pk'_{(2)}$ as a function of $\sqrt{\mu}$ (Fig. 3) demonstrate the greater tendency for carbonate ions to associate with Na than with K. Ion pairs like $Na^+ - CO_3^=$ or $Na^+ - NaCO_3^-$ will dissociate under pressure, and free $CO_3^=$ ions, hitherto masked for the carbonic acid equilibrium, will modify the buffer ratio, so that the pmH shift induced by pressure can be expected to be smaller than in a medium where association is less important or inexistent. We will see that magnesium and calcium ions which have a much larger tendency to form ion pairs with $CO_3^=$ than sodium ions also have a much larger lowering effect on the emf changes produced by pressure in carbonate buffers.

Since K^+ or Na^+ may also form ions pairs with HCO_3^-, a complete analysis of curves 1 and 1′ appears to be far from easy and would require the knowledge of $pk'_{(1)(2)}$ and $\Delta pk'_{(1)(2)}/\Delta p$ in absence of any ionic association; the dissociation constants of $NaCO_3^-$ and $NaHCO_3$ would have to be taken into account and also the equilibrium $2HCO_3^- \leftrightharpoons CO_3^= + H_2CO_3$, which is displaced when $CO_3^=$ or HCO_3^- is released in the solution. Besides the salt effect of NaCl or KCl would have to be known.

There is however no difficulty in considering that in the ionization functions $k'_{(1)}$ and $k'_{(2)}$, determined at atmospheric pressure or at 1000 kg. cm^{-2}, $[CO_3^=]$ and $[HCO_3^-]$ refer to the total concentration of $CO_3^=$ of HCO_3^-, ions present either as free ions or forming ion pairs with Na or K.

In the pmH_1 interval 8.5-9.5 the thus defined $pk'_{(2)1000}$ can be measured without ambiguity from curves 1 and 1′ of Fig. 5 since ΔE_{1000} is constant. The buffer ratio and the term 2 log γ_{A1}/γ_{Ap} in Eq. [3] are constant, the mean activity coefficient being referred to the total concentrations of free and masked ions. Log $k'^m_{(2)1000}/k'^m_{(2)1}$ is therefore equal to 0.315 (ΔE_{1000} = 19.0 mv) and 0.350 (ΔE_{1000} = 20.8 mv) in NaCl and KCl, respectively.

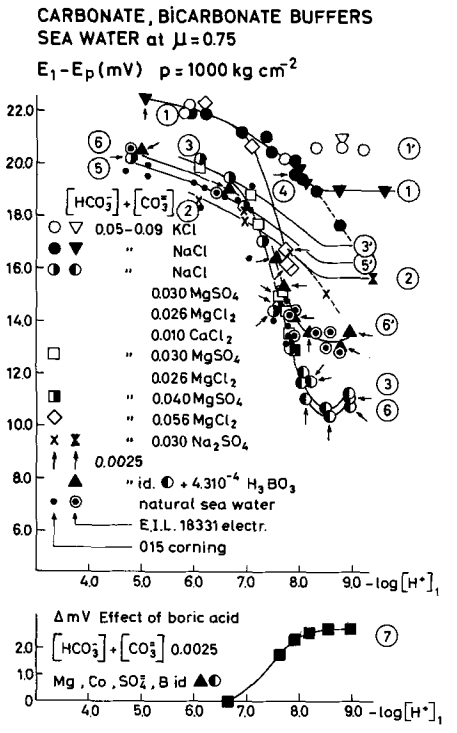

Fig. 5. Glass electrode emf shifts at 22°C produced by pressure (1000 kg.cm^{-2}) in bicarbonate, carbonate buffers, and sea water at $\mu = 0.75$, as a function of $pmH = -\log m_H$ measured at atm pressure. Curve 1, $NaHCO_3$, Na_2CO_3, CO_2 ($[HCO_3^-] + [CO_3^=]$ 0.05 — 0.09 and 0.0025 (arrow) in 0.5 NaCl. Curve 1', $KHCO_3$, K_2CO_3, CO_2 ($[HCO_3^-] + [CO_3^=]$ 0.05 — 0.09) in 0.5 KCl. Curve 2, $NaHCO_3$, Na_2CO_3, CO_2 ($[HCO_3^-] + [CO_3^=]$ 0.05 — 0.09) in 0.5 NaCl; effect of Na_2SO_4 (0.030). Curve 3, $NaHCO_3$, Na_2CO_3, CO_2 ($[HCO_3^-] + [CO_3^=]$ 0.05 — 0.09) in 0.5 NaCl; effect of $MgSO_4$ (0.030), $MgCl_2$ (0.026), $CaCl_2$ (0.01) (Precipitates are obtained at pH > 8.0). Arrows indicate results for $[HCO_3^-] + [CO_3^=] = 0.0025$ (see also curve segments 6). Curve 3', $NaHCO_3$, Na_2CO_3, CO_2 ($[HCO_3^-] + [CO_3^=]$ 0.05 — 0.09) in 0.5 NaCl; $SO_4^=$ effect of $MgSO_4$ (0.030). Curve 4, $NaHCO_3$, Na_2CO_3, CO_2 ($[HCO_3^-] + [CO_3^=]$ 0.05 — 0.09 and 0.025 (arrows); effect of $MgCl_2$ (0.056). Curve 5, Natural sea water Cl $‰_0 \simeq 19.5$ (Atlantic), corrected at Cl$‰_0$ 20.0 ($\mu = 0.75$). Curve 5', Natural sea water; $SO_4^=$ effect. Curve 6, Artificial sea water: $[HCO_3] + [CO_3^=] = 0.0025$; 0.030 $MgSO_4$, 0.026 $MgCl_2$, 0.010 $CaCl_2$, 0.5 NaCl (with or without boric acid in the acid range). Curve 6', Artificial sea water with boric acid (4.3 10^{-4}) (alkaline range). Curve 7, Effect of boric acid; smoothed difference in mv between ($E_1 - E_{1000}$) in artificial sea water without boric acid (see curves 3 and 6) and ($E_1 - E_{1000}$) in the same with 4.3 10^{-4} boric acid (see curves 6 and 6').

Inspection of curve 1 further indicates that the results at $pmH_1 \leq 7.00$ are identical in KCl and NaCl. If one again assumes that the bicarbonate concentration corresponds to the sum of the free HCO_3^- ions and the undissociated sodium or potassium bicarbonate, log $k'^m_{(1)1000}/k'^m_{(1)1}$ is equal to 0.359 ($\Delta E_{1000} = 21.0$ mv) at pmH_1 7.0, 0.376 at pmH_1 6.0, and 0.385 at pmH_1 5.0. Here the term 2 log $\gamma_{A_1}/\gamma_{A_p}$ in Eq. [3] is not constant and depends on the buffer ratio.

The question that remains to be answered concerns the choice of suitable values for $pk'_{(1)1000}$ and $pk'_{(2)1000}$ in the pmH_1 range 7.0-8.5, where the emf changes induced by pressure depend on both ionization functions.

If we consider a solution containing NaCl and $NaHCO_3$ at atmospheric pressure, its $pmH_1 = \frac{1}{2}(pk'^m_{(1)1} + pk'^m_{(2)1})$; at $\mu = 0.75$, one finds $pmH_1 \simeq 7.8 = \frac{1}{2}$ (6.0 + 9.6) and $[CO_2] = [CO_3^=]$. At $pmH_1 = 7.8$, $\Delta E_{1000} = 20.0$ mv, and simple considerations show that $[CO_2]$ will remain equal to $[CO_3^=]$ if 2.3 $RT/\mathbf{F}$ log $k'^m_{(1)1000}/k'^m_{(1)1}$ and 2.3 $RT/\mathbf{F}$ log $k'^m_{(2)1000}/k'^m_{(2)1}$ are taken symmetric with respect to $\Delta E_{1000} = 20.0$ mv. For instance, 21.0 and 19.0 mv read at pmH_1 7.0 and 8.5 on curve 1 of Fig. 5. In that case the equilibrium $2HCO_3^- \rightleftharpoons CO_3^= + H_2CO_3$ is shifted. Thus, at $pmH_1 = 7.8$, if $[HCO_3^-] + [CO_3^=] = 0.05$, 6.10^{-5} HCO_3^- is formed at 1000 kg. cm^{-2} at the expense of 3.10^{-5} CO_2 and 3.10^{-5} $CO_3^=$, which corresponds to a 4% change of the initial CO_2 and $CO_3^=$ concentrations. At pmH_1 7.0 and 8.5, the change of either $[CO_2]$ and $[HCO_3^-]$ or $[CO_3^=]$ and $[HCO_3^-]$ is negligible when pressure is applied. If one could assume 2.3 $RT/\mathbf{F}$ log $k'^m_{(1)1000}/k'^m_{(1)1}$ and 2.3 $RT/\mathbf{F}$ log $k'^m_{(2)1000}/k'^m_{(2)1}$ to be equal to ΔE_{1000} read on curve 1 at any pmH_1 between 5.0 and 9.0, the CO_2, HCO_3^-, $CO_3^=$ concentrations would remain constant at any pressure. This is what happens at infinite dilution where $\Delta V^o_{(1)1} = \Delta V^o_{(2)1}$.

In KCl, if one neglects the slight minimum at pmH_1 7.8, 2.3 $RT/\mathbf{F}$ log $k'^m_{(1)1000}/k'^m_{(1)1}$ and 2.3 $RT/\mathbf{F}$ log $k'^m_{(2)1000}/k'^m_{(2)1}$ are equal within ± 0.25 mv over the range 7.0-9.0. However, this is an oversimplification since the minimum at 7.8 could be explained by the release of $CO_3^=$ and HCO_3^- from ion pairs. HCO_3^- behaves as a base at $pmH_1 < 7.8$ and as an acid at $pmH_1 > 7.8$, whereas the release of $CO_3^=$ always results in lowering the hydrogen ion concentration.

The choice of the values of $pk'^m_{(1)1000}$ at pmH_1 7.0 and $pk'^m_{(2)1000}$ at pmH_1 8.5 to be used in the pmH_1 interval 7.0-8.5 remains questionable, even in KCl, but there is no other alternative unless reliable values for $pk'^m_{(1)}$ and $pk'^m_{(2)}$ become available in absence of any ionic association. However, at the alkaline end of the pmH_1 interval 7.0-8.5, $pk'^m_{(1)}$ needs not to be known with great precision to calculate $[HCO_3^-]$ or $[CO_3^=]$. At pmH_1 8.0, an error of 0.02 ($\Delta E \simeq 1.2$ mv) in $pk'^m_{(1)1000}$ affects $[CO_2]$ by 2% and $[HCO_3^-]$ and $[CO_3^=]$ by only 0.1%.

The separate salt effect of NaCl on 2.3 $RT/\mathbf{F}$ log $k'^m_{(1)1000}/k'^m_{(1)1}$ can be estimated at $pmH_1 < 5.0$ since curve 1 in Fig. 5 seems to reach a plateau in the acid range and since ΔE_{1000} is known at 0 ionic strength (25.0 mv). Thus, for the salt effect, one finds 25.0 — 22.6 = 2.4 mv. This value fits with the fact that 2 ΔE_{1000} = 23.6 mv at $\mu = 0.75$ in a solution containing only NaCl and saturated with CO_2. At $\mu = 0$, 2 ΔE_{1000} = 26.2 mv (3) and the difference 26.2 — 23.6 = 2.6 mv.

It seems reasonable to assume that the difference between ΔV^o_1 found in pure CO_2 solutions and in bicarbonate buffer at 0 ionic strength might be related to the existence of $NaHCO_3$ ion pairs even when the concentration of $NaHCO_3$ becomes very small. The same effect occurs in other buffer systems investigated with the glass electrode technique: ΔV^o_1 is always found to be smaller in buffers than in the corresponding pure acid (3), and the explanation given above might be general.

Finally, one will notice (Fig. 5, dotted part of curves 1 and 2) that Corning 015 electrodes display an alkaline error in presence of NaCl at 1000 kg. cm^{-2} at $pmH_1 > 8.25$, although no such error can be detected even at 8.75 at atmospheric pressure.

Ionization of carbonic acid in presence of Mg^{++}, Ca^{++}, *and* $SO_4^=$ *in* NaCl *solutions, at concentrations found in sea water, at 1 atm and 1000 kg. cm^{-2} and at different buffer ratios ($\mu = 0.75$).*—When Ca or Mg salts are added to carbonate and bicarbonate buffers, it is well known [see Garrels, Thompson, and Siever (12)] that $MgCO_3$ and $CaCO_3$ ion pairs are formed and that the trapping of HCO_3^- ions is also to be considered. The dissociation of carbonic acid can still be described by the ionization functions $k'_{(1)}$ and $k'_{(2)}$ where $[CO_3^=]$ and $[HCO_3^-]$ refer to the free carbonate and bicarbonate ions (plus those bound to Na as seen in the preceding section), but it is also useful to define apparent ionization functions $k''_{(2)} = [H^+]\,[CO_3^=]_T/[HCO_3^-]_T$, $k''_{(1)} = [H^+]\,[HCO_3^-]_T/[CO_2]$ where $[CO_3^=]_T$ and $[HCO_3^-]_T$ correspond to the total amount of carbonate and bicarbonate. We will call $k'_{(2)}$ and $k'_{(1)}$ true ionization functions.

True and apparent ionization functions of carbonic acid in presence of Mg^{++}, Ca^{++} *and* $SO_4^=$, *in* NaCl *solutions at 1 atm* ($\mu = 0.75$).—Figure 6 gives the pmH_1 changes (in mv) produced when $MgCl_2$, curve 4; $MgCl_2 + MgSO_4$, curve 3; $MgCl_2 + MgSO_4 + CaCl_2$, curve 2; Na_2SO_4, curve 1 are added to bicarbonate and carbonate buffers at atmospheric pressure, as a function of pmH_1 measured in the solutions containing the added salts. The reference 0.01 HCl + 0.49 NaCl solution has the same salt composition as the buffer under test it is assumed that $m_{H+} = m_{HCl}$ and that the mean activity coefficient of HCl is the same in both compartments. The added salts are tested at concentrations normally found in sea water (Cl‰ = 20.0).

Effect of $SO_4^=$ *on the true ionization functions* $k'_{(1)1}$ *and* $k'_{(2)1}$.—Inspection of Fig. 6 shows that the effect of $SO_4^=$ ions can be distinguished from the effect of Ca and Mg.

$MgCl_2$ at $pmH_1 < 6.0$ obviously does not modify $k'^c_{(1)1}$ which is thus the same as in pure bicarbonate solutions at the same ionic strength. The ordinate difference between curves 3 and 4 in Fig. 6 shows but little variations over the pmH_1 interval considered and allows one to calculate $pk'^c_{(1)1}$ and $pk'^c_{(2)1}$. Thus for the investigated buffers ($MgSO_4$ 0.030, $[HCO_3^-] + [CO_3^=]$ between 0.0025 and 0.09) $pk'^c_{(1)1} = 5.89$ and $pk'^c_{(2)1} = 9.49$ at $\mu = 0.75$ (see Fig. 2 and curve segment in Fig. 4); $pk'^m_{(1)1} = 5.89 - 0.005$ and $pk'^m_{(2)1} = 9.49 - 0.005$. The correction for the change of concentration scale is somewhat smaller than in pure NaCl solutions and is based on a total salt content of 36.4g and the corresponding density of sea water 1.025 at 22°C (13).

Effect of Ca *and* Mg *and the apparent ionization functions* $k''_{(1)}$ *and* $k''_{(2)}$.—The shape of the curves of Fig. 6 which give the emf shifts resulting from the addition of Ca and Mg salts to bicarbonate and carbonate buffers can be understood if one bears in mind that removing a constant amount of $CO_3^=$ produces a pmH shift which is maximum at $pmH = \frac{1}{2}(pk'^m_{(1)} + pk'^m_{(2)})$. When the trapped $CO_3^=$ is a function of the initial $CO_3^=$ concentration, the maximum is broadened and shifted toward a more alkaline pmH. Removing HCO_3^- produces no shift at $pmH = \frac{1}{2}(pk'^m_{(1)} + pk'^m_{(2)})$, but results in an acidification or an alkalinization at more acid or more alkaline pmH values; HCO_3^- trapping is evident in Fig. 6 in the acid range especially when $CaCl_2$ is added to the more concentrated buffers already containing $MgSO_4$ and $MgCl_2$, but the same operation produces a precipitate at $pmH > 8.1$. No precipitates are observed in the diluted buffers. The data gathered in Fig. 6 can be used to calculate the dissociation constants of $MgCO_3$, $CaCO_3$, $MgHCO_3^+$, and $CaHCO_3^+$ as Garrels *et al.* (12) have done from paH determinations on bicarbonate and carbonate buffers before and after addition of $CaCl_2$ and $MgCl_2$. This problem, which involves lengthy calculations, is quite beyond the scope of the present paper and will not be dealt with.

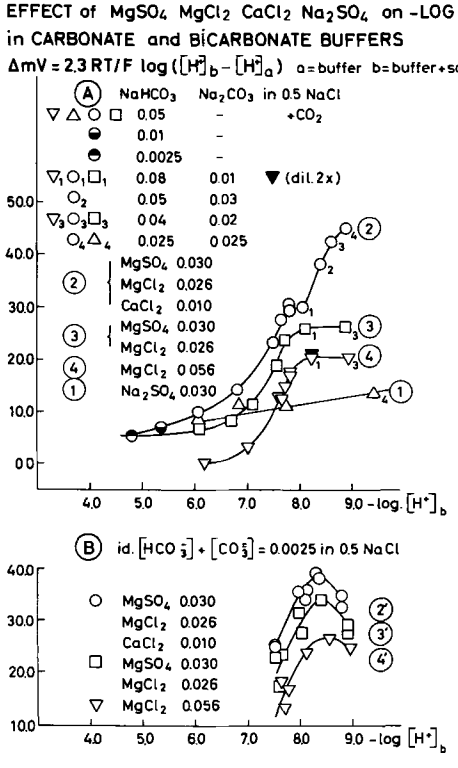

Fig. 6. Glass electrode emf shifts produced by the addition of $MgSO_4$, $MgCl_2$, $CaCl_2$, Na_2SO_4 to bicarbonate and carbonate buffers at atmospheric pressure. A. $[HCO_3] + [CO_3^=]$ 0.05 — 0.09 in 0.5 NaCl: Curve 1, effect of Na_2SO_4 (0.030); Curve 2, effect of $MgSO_4$ (0.030), $MgCl_2$ (0.026), and $CaCl_2$ (0.010). Precipitates are obtained at points 2, 3, and 4; result at pmH 4.8 corresponds to $[HCO_3^=] + [CO_3^=]$ 0.0025; Curve 3, effect of $MgSO_4$ (0.030) and $MgCl_2$ (0.026); Curve 4, effect of $MgCl_2$ (0.056). B. $[HCO_3^-] + [CO_3^=] = 0.0025$. (2'), (3'), (4') same as (2), (3), (4).

However, at $pmH_1 \geq 8.0$, Fig. 6 makes it possible to evaluate the apparent second ionization function of carbonic acid, $k''_{(2)}$, in presence of Ca^{++}, Mg^{++}, and $SO_4^=$ ions.

For buffers where $[HCO_3^-] + [CO_3^=] = 0.0025$, the emf shift due to the addition of 0.030 $MgSO_4$, 0.026 $MgCl_2$, and 0.010 $CaCl_2$ is equal to 38.0 mv at $pmH_1 \simeq 8.3$. With $pk'^c_{(2)1} = 9.67$ in the pure buffer, this leads to $pk''^c_{(2)1} = 9.67 - 0.65 = 9.02$ at $\mu = 0.73$; at $\mu = 0.75$, $pk''^c_{(2)1} = 9.015$.

More refined calculations taking into account the true ionization functions $k'^c_{(1)}$ (5.89) and $k'^c_{(2)}$ (9.49), the equilibrium $2HCO_3^- \leftrightharpoons CO_3^= + H_2CO_3$ which is displaced when $CO_3^=$ is removed, give a mean value of 9.015 ± 0.015 at $\mu = 0.75$ in the pmH_1 interval 7.9-8.5, with a minimum at 8.3 where $pk''^c_{(2)1} = 9.00$. On the molal scale $pk''^m_{(2)} = 9.015 - 0.005$, again at $\mu = 0.75$.

The agreement between the directly evaluated value of $pk''^c_{(2)1}$ and the calculated one, implies that, in first approximation, HCO_3^--trapping by Mg^{++} and Ca^{++} must be very small at $pmH_1 \geq 8.0$. Trapping of HCO_3^- to a greater extent than Na ions do, would lead to an apparent lowering of $pk'^c_{(1)}$ and also affect $pk''^c_{(2)1}$ but in a more complicated way, depending on pH. This problem will not be discussed here, and it will be assumed that between pmH_1 7.9 and 8.5 it is not necessary to introduce a first apparent ionization function, or that $pk''^c_{(1)} = pk'^c_{(1)}$ in buffers where $[CO_3^=] + [HCO_3^-] = 0.0025$.

Since $pk''^c_{(2)1} - pk'^c_{(2)1} = 0.48$, $[CO_3^=]_T \simeq 3\,[CO_3^=]$ and $[Mg - CaCO_3] \simeq 2\,[CO_3^=]$. At pmH_1 8.0 $[HCO_3^-] + [CO_3^=] = 0.0025$, $[CO_3^=] = 7.34\ 10^{-5}$, $[Mg - CaCO_3] = 1.45\ 10^{-4}$ or 0.22% of the total Ca and Mg concentrations, which is of the order of magnitude (0.28%) given by Garrels *et al.* (12, 15).

In buffers where $[CO_3^=] + [HCO_3^-] = 0.09$, $pk''^c_{(2)1}$ at pmH_1 8.1 is found equal to 9.12 when directly evaluated from curve 2, Fig. 6A, and equal to 9.10 when calculated at $\mu = 0.84$, taking reaction $2HCO_3^- \leftrightharpoons CO_3^= + H_2CO_3$ into consideration and neglecting the possibility of HCO_3^- trapping in the alkaline range. The apparent ionization function $pk''^c_{(2)1}$ is thus not only dependent on pH but also on the concentration of the buffering species. This remark is important and needs be taken into consideration when dealing with data to be valid in natural sea water.

True and apparent ionization functions of carbonic acid, in presence of Mg^{++}, Ca^{++}, *and* $SO_4^=$, *in* NaCl *solutions at 1000 kg. cm*$^{-2}$ ($\mu = 0.75$).—Comparison of curves 1 and 2 in Fig. 5 shows that ΔE_{1000} observed in pure buffer solutions is reduced by a constant amount in the presence of 0.030 Na_2SO_4, between pmH_1 6 and 9.5 (the reference 0.01 HCl + 0.49 NaCl solution has

again the same salt composition as the buffer under test and m_{H+} is assumed to be equal to m_{HCl}).

Curve 3 indicates that ΔE_{1000} drops progressively from 20.0 mv at $pmH_1 = 6.0$ to 13.1 mv at $pmH_1 = 7.90$ in 0.05 $NaHCO_3$ + 0.5 NaCl solutions containing 0.030 $MgSO_4$, 0.026 $MgCl_2$, and 0.010 $CaCl_2$ at various concentrations of CO_2.

At pH > 8.1 pressure has been applied to the solutions containing the precipitate (see p. 334). The reported emf shifts correspond to the measurements made during the second or third pressure run. The first run generally gives rather unstable values.

Nearly the same emf shifts are observed at pmH_1 7.8-7.9 with 0.04 $MgSO_4$ or 0.030 $MgSO_4$ + 0.026 $MgCl_2$ with or without 0.010 $CaCl_2$ (also see Fig. 1 and 3). Lowering of the total CO_2 concentration has not a great effect either. At $[CO_3^=] + [HCO_3^-] = 0.0025$, where no precipitates are observed, the results (indicated by arrows and curve segment 6 in Fig. 5) are about 0.3-0.4 mv lower than those obtained with buffers where $[CO_3^=] + [HCO_3^-]$ is between 0.09 and 0.05.

When both NaCl and Mg-Ca salt concentrations are reduced it can be seen from Fig. 1 and 3 that extrapolation to $\mu = 0$ again gives $-\Delta V^o_1 = 25.4$ cm^3 mole^{-1}. The scattering of the results can be explained by the large pH dependence of ΔE_{1000} in the alkaline range.

Adding 0.056 $MgCl_2$ alone to 0.5 NaCl + 0.05 $NaHCO_3$, saturated with CO_2, has no or little effect on ΔE_{1000} observed in pure bicarbonate buffer (Fig. 5, curve 4). Between pmH_1 6.2 and 7.85, ΔE_{1000} falls from 22.3 mv to 16.0 mv. The 6.3 mv difference is nearly the same as the 6.5 mv value obtained with 0.030 $MgSO_4$ + 0.026 $MgCl_2$ for the same pmH_1 interval. The difference between curve 3 and 4 is obviously due to the sulfate ions, since the total Mg concentration is kept constant.

We already have noticed a similar effect of $SO_4^=$ when 0.030 Na_2SO_4 is added to pure bicarbonate buffers (curves 1 and 2 in Fig. 5). The fact that $MgSO_4$ is less dissociated than Na_2SO_4 probably explains the difference in magnitude between the effects of 0.030 Na_2SO_4 and 0.030 $MgSO_4$. Since the ordinate difference between curve 4 and 3 is nearly constant, the $SO_4^=$ effect of $MgSO_4$ practically must be constant over the whole pmH_1 range. This observation allows one to extrapolate curve 3 parallel to curves 2 and 1 in the alkaline range (curve 3') and to dissociate the $SO_4^=$ effect from the more complicated Mg-Ca effect observed between 6.5 and 9.0.

To interpret the Mg-Ca effect, we will assume that the $MgCO_3$ and $CaCO_3$ ion pairs, formed at atmospheric pressure, further dissociate at higher pressures, liberating $CO_3^=$ ions which alter the $[CO_2]/[CO_3^=]$ ratio of the buffer, eventually shift reaction $2HCO_3^- \rightleftharpoons CO_3^= + H_2CO_3$, and thus oppose the acidification induced by pressure and caused by the dissociation constants shifts. This assumption leads to the admission that log k'^m_{1000}/k'^m_1, in presence of $MgCl_2$ has the same value, for each true ionization function, as found in pure bicarbonate buffer at the same pmH_1 and ionic strength, not only between pmH_1 5.5 and 7.0, but throughout the whole pmH_1 range. When $MgSO_4$ is substituted for part of the $MgCl_2$, log k'^m_{1000}/k'^m_1 is lowered by an amount corresponding to the $SO_4^=$ effect. One can then use the same arguments developed above and measure $pk'_{(1)}$ and $pk'_{(2)}$ at pmH_1 7.0 and 8.5, respectively, on curve 3 and 3'.

One thus finds that at $\mu = 0.75$, $[CO_3^=] + [HCO_3^-] = 0.0025$, log $k'^m_{1000}/k'^m_1 = 0.316$ (18.5 mv) for $k'_{(1)}$ and 0.283 (16.5 mv) for $k'_{(2)}$. In more concentrated buffers, these values become 0.325 (19.0 mv) and 0.290 (17.0 mv) at the same ionic strength and pmH_1.

At pmH_1 8.5, Fig. 5 further allows to obtain a direct estimate of the effect of pressure on the apparent ionization function $pk''_{(2)}$. At $[HCO_3^-] + [CO_3^=] = 0.0025$, log $k''^m_{(2)1000}/k''_{(2)1} = 0.178$ ($\Delta E_{1000} = 10.4$ mv). A more elaborate treatment using $pk'^m_{(1)1000}$ and $pk'^m_{(2)1000}$, taking into account the equilibrium $2HCO_3^- \rightleftharpoons CO_3^= + H_2CO_3$, the amount of $MgCO_3$ formed at atmospheric pressure, shows that log $k''^m_{(2)1000}/k''^m_{(2)1}$ increases from 0.178 at pmH_1 8.5, to 0.187 at 8.0, 0.190 at 7.9, and 0.214 at 7.6. A mean value of 0.183 ± 0.005 can be taken in the pmH_1 interval 8.0-8.5. The same value can be read from Fig. 5 at $pmH_1 = 8.5$ for the more concentrated buffers.

The effect of pressure on $pk''_{(1)}$ needs not be considered in the alkaline range since we have admitted that between pmH_1 7.9 and 8.5, $pk'_{(1)} = pk''_{(1)}$. At $pmH_1 \leq 7.0$, comparison of the curves of Fig. 5 and 6 for the more concentrated buffers, where HCO_3^- trapping by Ca^{++} seems obvious, shows that pressure must have only a very small effect on the dissociation of any trapped HCO_3^- ions.

Dissociation of carbonic acid in natural sea water (Cl = 20‰) at high pressures; effect of boric acid.— The reference compartment of the glass electrode contains 0.49 NaCl, 0.01 HCl, 0.030 $MgSO_4$, 0.026 $MgCl_2$ and 0.010 $CaCl_2$.

The sea water samples come from the Atlantic Ocean (north of Spain, Cl ‰ = 19.5) and have been equilibrated with $CO_2 + N_2$ mixtures, or small amounts of Na_2CO_3 have been added to cover the 5.0-9.0 pmH_1 interval. The emf shifts produced by increasing pressure from 1 atm to 1000 kg. cm^{-2} are corrected in Fig. 5 at $\mu = 0.75$ (Cl ‰ = 20.0). Scattering is higher than with artificial buffers; nevertheless, it is obvious that from pmH_1 5.0 to about 7.25 (curve 5), sea water follows the general pattern observed in bicarbonate buffers with added Mg, Ca, and sulfate ions. The quantitative agreement is good, although the data for natural sea water are about 0.3-0.4 mv below these for artificial sea water (arrows in Fig. 5). Extrapolation of the curve drawn in the acid range (curves 5 and 5'), parallel to curves 1, 2, 3', allows one to obtain log k'^m_{1000}/k'^m_1 for the first and second dissociation step: 0.314 (18.3 mv) and 0.278 (16.3 mv), respectively, at $pmH_1 = 7.0$ and 8.5. This corresponds to the shift of the true ionization functions which are assumed to have the same value at 1 atm as the corresponding functions determined in artificial sea water (see above).

At pH > 7.25, the data for natural sea water progressively depart from the results in artificial sea water containing Mg^{++}, Ca^{++}, and $SO_4^=$. At pH 8.5-9.0, ΔE_{1000} is about 3.0 mv higher in natural sea water and to nearly duplicate these results, 0.43 10^{-3} H_3BO_3 must be added, the pmH_1 being adjusted by the $[HCO_3^-]/[CO_3^=]$ ratio (curve 6', Fig. 5). The ordinate difference between curve 6' and the corresponding emf shifts observed in artificial sea water without boric acid is given by curve 7 which shows the effect of boric acid between pmH_1 6.5 and 9.0.

Preliminary experiments to investigate the effect of pressure on the dissociation of boric acid show that in NaCl 0.1, $\Delta V_1'$ extrapolates to −29.0 cm^3 mole^{-1} at zero borate buffer (H_3BO_3 + borax) concentration, to −30.7 cm^3 mole^{-1} in NaCl 0.01 and to −31.4 cm^3 mole^{-1} in NaCl 0.001; $\Delta V_1^o = -32.1$ cm^3 mole^{-1}. In 0.5 NaCl + 0.030 $MgSO_4$ + 0.026 $MgCl_2$ and 0.010 $CaCl_2$, at pH 7.9, $\Delta V_1'$ is equal to −23.1 cm^3 mole^{-1} (22.7 mv) at zero borate concentration, and the same value can be used at the boron concentration of sea water. Since in sea water $pk'^m_{(1)1} = 8.605$ for boric acid ($pk'^c_{(1)1} - \log y_{H+} = pK''^c_{(1)1} = 8.72$ [Lyman (13)], $pk'^m_{(1)1000} = 8.605\text{-}0.39 = 8.215$. These values correspond fairly well to the pmH_1 at which curve 7 of Fig. 5 reaches a maximum. It is also easy to verify that at $pmH_1 = 8.353$ and $[HCO_3^-] + [CO_3^=] = 0.0025$, the increase in HCO_3^- concentration at 1000 kg. cm^{-2} ($pmH_{1000} = 8.124$), calculated from the values of $pk''^m_{(2)}$ and $pk'^m_{(1)}$ for carbonic acid, obtained in artificial sea water without boric acid, corresponds to the decrease in H_3BO_3 concentration, estimated from $pk'^m_{(1)1}$ and

$pk'^{m}_{(1)1000}$ found for boric acid in sea water ($\Delta[HCO_3^-]_T = 0.39\ 10^{-4}$; $\Delta[H_3BO_3] = 0.38\ 10^{-4}$).

The interpretation of the pH changes induced by pressure in natural sea water is thus far from simple. The enhanced dissociation of carbonic acid observed in NaCl at the corresponding ionic strength is modified by the presence of sulfate ions, by the dissociation of $MgCO_3$ and $CaCO_3$, and by the dissociation of boric acid. The two last effects are pH dependent, and reaction $H_3BO_3 + CO_3^= \leftrightharpoons HCO_3^- + H_2BO_3^-$ must be considered.

Without going into the details of a quantitative analysis, it is immediately clear that the emf shifts observed at $pmH_1 > 8.0$ in artificial sea water containing boric acid or in natural sea water cannot be used for a direct estimation of $\Delta pk''_{(2)}/\Delta p$ for the second apparent ionization function; instead, $pk''_{(2)p}$ has to be taken equal to the corresponding function determined in artificial sea water without boric acid in order to calculate $[CO_3^=]_T$ and $[HCO_3^-]_T$ at pressure p. In artificial sea water, in absence of boric acid, log $k''^{m}_{(2)1000}/k''^{m}_{(2)1} = 0.183 \pm 0.005$ from pmH_1 8.0 to 8.5; in natural sea water, since ΔE_{1000} is somewhat lower, log $k''^{m}_{(2)1000}/k''^{m}_{(2)1}$ will be taken equal to 0.178 ± 0.005 in the same pmH_1 interval. If the greatest precision is required, the pH dependence of log $k''^{m}_{(2)1000}/k''^{m}_{(2)1}$ must be taken into account (see p. 335). The value of $pk''^{m}_{(2)}$ at 1 atm found in artificial sea water without boric acid (9.01, see p. 334) is taken to be the same in natural sea water. The complete set of ionization functions which we believe to be valid in natural sea water at 1 atm and at 1000 bars, within our basic assumptions, is given in Table II.

Some of the results of Fig. 5 have been indicated in Fig. 1 together with data obtained with 0.01 HCl + 0.49 NaCl as reference half-cell, and which are in agreement with our earlier results (4). $\Delta E_{1000} = 16.7$ mv instead of 13.4 mv at pmH_1 7.8; the difference of 3.3 mv is due to the effect of pressure on γ_{HCl} in the presence of $MgSO_4 + MgCl_2 + CaCl_2$ compared to γ_{HCl} in pure HCl or HCl + NaCl (see below). Dilution of sea water leads to erratic pressure-induced emf shifts, but sea water + 0.05 $NaHCO_3$, CO_2 1% can be diluted, and the extrapolation of the results to $\mu = 0$ gives $\Delta V_1^\circ = -25.4$ cm^3 mole^{-1} identical with the value found in pure bicarbonate (Fig. 1).

Apparent values of γ_{HCl}, y_{H^+} *in* HCl + NaCl *in presence of* Mg^{++}, Ca^{++}, $SO_4^=$; *effect of pressure.*— The apparent mean activity coefficient of 0.01 HCl on the molal scale in presence of $0.5/n$ — 0.01 NaCl, $MgSO_4$, $MgSO_4 + MgCl_2$, $MgSO_4 + MgCl_2 + CaCl_2$ is given in Fig. 7 for several values of n assuming $m_{H^+} = m_{HCl}$. The reference half-cell was filled with HCl 0.01, NaCl 0.09. The data for pure NaCl or KCl + HCl solutions are taken from Harned and Owen (10), and control experiments show that our results fit these curves with an error not greater than ± 0.002. From Eq. [6], log y can be calculated from log γ: in NaCl solutions at $\mu = 0.5$ log γ = log y — 0.004; the correction factor is —0.0047, —0.0055, —0.063, —0.0071, —0.008 at $\mu = 0.6$, 0.7, 0.8, 0.9, 1.0, and —0.006 at $\mu = 0.75$. At $\mu = 0.75$ in sea water, the correction becomes —0.004.

$MgCl_2$ alone has a much smaller effect on γ_{HCl}: addition of 0.056 $MgCl_2$ to 0.49 NaCl + 0.01 HCl makes log γ_{HCl} drop from $\bar{1}.864$ to $\bar{1}.849$.

The pressure dependency of γ_{HCl} in 0.01 HCl + 0.49 NaCl containing $MgSO_4$, $MgSO_4 + MgCl_2$ is represented in Fig. 8 either with 0.01 HCl + 0.49 NaCl as reference half-cell or 0.1 HCl. It is clear that $MgSO_4$ is the main cause involved.

In the preceding sections, it has been assumed continuously that γ_{HCl} measured in 0.01 HCl + 0.49 NaCl + 0.030 $MgSO_4$ + 0.026 $MgCl_2$ + 0.010 $CaCl_2$ has the same value in carbonate and bicarbonate buffers containing the same salts, in the range $[CO_3^=] + [HCO_3^-] = 0.09 - 0.0025$. That the specific salt effect

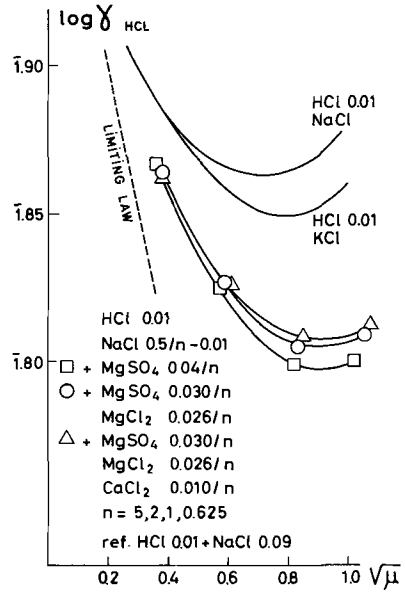

Fig. 7. Mean activity coefficient (γ_{HCl}) of HCl in NaCl, KCl; apparent values in presence of $MgSO_4$, $MgCl_2$, $CaCl_2$ as a function of $\sqrt{\mu}$.

of CO_2, $CO_3^=$, HCO_3^- is small, is demonstrated by Fig. 1, 2, 3, and 4, where it can be seen that changing the buffer concentration (at a given buffer ratio for Fig. 2 and 4) has about the same effect as changing the ionic strength. Comparison of the data of Fig. 5 further shows that lowering the $[CO_3^=] + [HCO_3^-]$ concentration from 0.09 to 0.0025 has only a very small effect on ΔE_{1000} at a given ionic strength (0.75).

Figure 7 also indicates that γ_{HCl} is fairly independent of μ in the region of the ionic strength of sea water. Corrections for salinity differences are thus very small; corrections however have to be made to take into account the eventual difference in Cl^- content between both glass electrode compartments, in order to calculate —log $[H^+]$, assuming γ_{HCl} to be equal in both solutions. Ordinary *pa*H electrodes with liquid junctions at first sight appear to be simpler to use, since the exact composition of the reference glass electrode half-cell does not have to be known with precision. However, conventional *pa*H electrodes display a much more sluggish response and great errors can be introduced

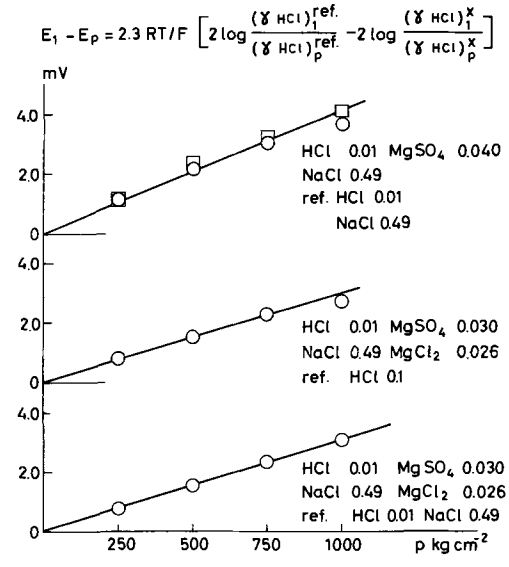

Fig. 8. Effect of pressure on 2 log $(\gamma_{HCl})^{ref}_1/(\gamma_{HCl})^{ref}_p$ — 2 log $(\gamma_{HCl})^{x}_1/(\gamma_{HCl})^{x}_p$ 2.3 $RT/F = E_1 - E_p$, where ref and x correspond to the inner and outer compartment of the glass electrode cell; effect of $MgSO_4$ and $MgCl_2$.

by the liquid junctions. Besides, the effect of pressure on these junctions would have to be taken into account, and the treatment of results based on single ion activity determination is open to criticism.

However, since most of the oceanographic data refer to *pa*H measurements, we have tried to measure *pa*H at atmospheric pressure in mixtures of HCl + NaCl or KCl + $MgSO_4$ + $MgCl_2$ + $CaCl_2$. Saturated KCl agar-agar junctions were used with calomel electrodes as inner and outer electrodes of the glass cell. Stable and reproducible results have been obtained in KCl with 0.01 HCl + 0.09 KCl in the reference compartment. The value indicated on Fig. 9 for log a_{H+} in 0.01 HCl + 0.09 KCl was checked with a hydrogen electrode—calomel electrode cell, and is close to the value reported in Harned and Owen (10), $\bar{3}.898$. The hydrogen ion activity in HCl + KCl was first measured, and the effect of the added salts was investigated either with 0.01 HCl + 0.09 KCl as inner solution or with 0.01 HCl + $0.5/n$ — 0.01 KCl, n being equal on both sides of the glass electrode. Trying to measure a_{H+} in HCl + NaCl with 0.1 HCl as inner solution resulted in erratic information. Reproducible data could only be obtained by systematically using KCl + HCl at the same ionic strength as inner solution.

The curves giving log a_{H+} in HCl + NaCl in presence of Mg and Ca salts have been determined by taking $0.5/n$ NaCl — 0.01 HCl for inner solutions and making n equal in both compartments. If one takes $c_{H+} = c_{HCl}$, log y_{H+} at $\mu = 0.75$ is $\bar{1}.887$ and one then can assume that it nearly has the same value in sea water. Anderson and Robinson (14) estimate log y_{H+} equal to $\bar{1}.880$ in sea water (Cl = 20.0‰) acidified to pH 3.3-3.9 with HCl, which is not too far from our value for log y_{H+}.

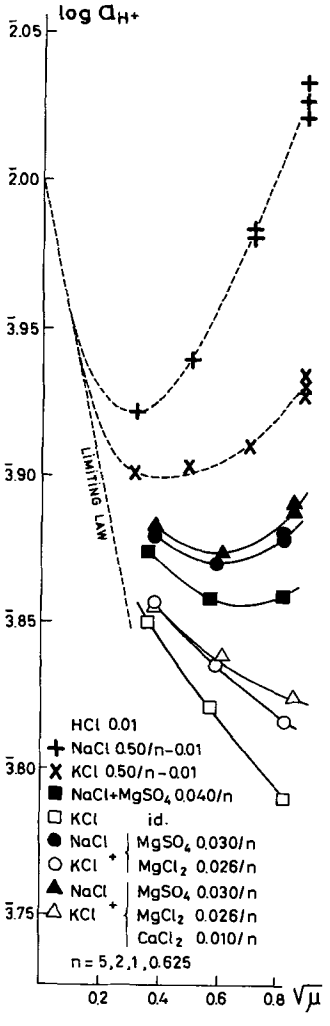

Fig. 9. Hydrogen ion activity (log a_{H+}), in 0.01 HCl + NaCl or KCl, in presence or not of $MgSO_4$, $MgCl_2$, $CaCl_2$ as a function of $\sqrt{\mu}$ (glass electrode with calomel electrodes and sat. KCl agar-agar salt bridges).

Evaluation of apparent dissociation constants $y_{H+}k'^{c}_{(1)} = K''^{c}_{(1)}$ and $y_{H+}k''^{c}_{(2)} = K''^{c}_{(2)}$ of carbonic acid in sea water at 1 atm and 1000 kg. cm^{-2}.—The apparent constants used in oceanography are defined as $K''^{c}_{(1)} = a_{H+} \times [HCO_3^-]_T/[CO_2] = y_{H+}\, k'^{c}_{(1)}$ and $K''^{c}_{(2)} = a_{H+} \times [CO_3^=]_T/[HCO_3^-]_T = y_{H+}k''^{c}_{(2)}$, where T refers to total concentrations. Since $\gamma m = yc/do$ (Eq. [7]) it follows that $pK''^{m}_{(1)(2)} = pK''^{c}_{(1)(2)} - 0.001$ at 1 atm.

According to Lyman (13), $pK''^{c}_{(1)} = 6.00$ and $pK''^{c}_{(2)} = 9.12$ at 22°C, Cl ‰ = 20.0. Taking our values $pk'^{c}_{(1)1} = 5.89$, $pk''^{c}_{(2)1} = 9.015$ valid for artificial sea water in the pmH_1 interval 7.9-8.5, and —log $y_{H+} = 0.11$, gives $pK''^{c}_{(1)} = 6.00$ and $pK''^{c}_{(2)} = 9.125$ which is in good agreement. Since $pk'^{c}_{(1)}$ has been determined at pmH_1 5.0 where obviously HCO_3^- trapping by Mg and Ca is very small or inexistent (see Fig. 6A), but where the effect of $SO_4^=$ can be measured, and since $pk'^{c}_{(1)}$ fits with the $pK''^{c}_{(1)}$ value given by Lyman, one comes to the conclusion that at alkaline pH, HCO_3^- trapping by Mg and Ca must be small in sea water, or that the HCO_3^- bound to Mg or Ca cannot be distinguished from that linked to Na. The problem is however not completely solved since in more concentrated buffers ($[CO_3^=] + [HCO_3^-] = 0.05 - 0.09$) HCO_3^- binding by Ca and Mg is obvious at pmH_1 7.0. Further analysis of these results and more experiments will be needed to decide whether or not HCO_3^- trapping persists in the alkaline range when $CO_3^=$ binding reaches its maximum, and to find out how it depends on the buffer concentration.

To estimate the effect of pressure on pK''_1 and pK''_2, the pressure dependence of γ_{H+} needs be known. It cannot be calculated in media as complex as sea water. Since however this uncertainty affects both pK'' and *pa*H identically, it has no bearing on the determination of the ratios $[CO_3^=]_T/[HCO_3^-]_T$, $[CO_3^=]_T/[CO_2]$ and $[HCO_3^-]_T/[CO_2]$ needed in oceanographic calculations to compute $[CO_2]$, $[HCO_3^-]_T$ $[CO_3^=]_T$ from *pa*H, $pK''_{(1)}$, $pK''_{(2)}$, and $\Sigma CO_2 = [CO_2] + [HCO_3^-]_T + [CO_3^=]_T$. The simplest assumption, which is to neglect the effect of pressure on γ_{H+}, leads to admit that $\Delta pK''^{m}_{(1)(2)}/\Delta p = \Delta pk''^{m}_{(1)(2)}/\Delta p$, so that in natural sea water at 1000 kg. cm^{-2}, $pK''^{m}_{(1)}$ and $pK''^{m}_{(2)}$ would, respectively, be equal to 6.00 — 0.314 and 9.125 — 0.178 (see p. 336) whereas $pK''^{c}_{(1)}$ and $pk''^{c}_{(2)}$ would become : 6.00 — (0.314 + 0.017) and 9.125 — (0.178 + 0.017), between pmH_1 8.0 and 8.5.

According to Buch and Gripenberg (16), the change of $pK''^{m}_{(1)}$ and $pK''^{m}_{(2)}$ with pressure are, respectively, 0.480 and 0.180 at 1000 bars, or 0.470 and 0.176 at 1000 kg. cm^{-2}. Their values were based on $\Delta V_1^\circ = -28.0$ cm^3 mole^{-1} for the first ionization step of carbonic acid and $\Delta V_1^\circ = -10.5$ cm^3 mole^{-1} for the second step assuming that the HCO_3^- ion would behave as acetic acid. Curiously enough our data fit almost exactly for $K''_{(2)}$, although the reasons of the small effect of pressure on $K''_{(2)}$ are completely different from what these authors thought them to be.

As we already indicated, $pk''_{(2)}$ and $pK''_{(2)}$ either on the molar or molal scale, determined in artificial sea water without boric acid at pressure p will give correct estimates for $[HCO_3^-]_T$ and $[CO_3^=]_T$ in the pmH_1 range 8.0-8.5, and it is theoretically possible, taking the boric acid effect into consideration, to calculate the *pm*H, *pc*H, or *pa*H of a given surface sea water sample brought to pressure p, or at the corresponding depth. It is however much more easy to read $\Delta pmH/\Delta p$ from Fig. 5, or to use Table I where we have given the *pa*H shifts on the molar scale in natural sea water

Table I. *pa*H at 1 atm and 1000 bar in natural sea water, molar scale*, Cl ‰ 20.0

*pa*H at 1 atm		7.5	7.6	7.7	7.8	7.9	8.0
*pa*H at 1000 bars							
Buch and Gripenberg (16)		7.15	7.29	7.43	7.55	7.67	7.78
This paper	(*a*)	7.19	7.30	7.41	7.52	7.63	7.74
	(*b*)	7.20	7.31	7.42	7.535	7.65	
*pa*H at 1 atm		8.1	8.2	8.3	8.4	8.5	8.6
*pa*H at 1000 bars							
Buch and Gripenberg (16)		7.89	8.00	8.10	8.20	8.30	—
This paper		7.85	7.95	8.05	8.155	8.255	8.355

* $\log y_{H^+}c_{H^+} = \log \gamma_{H^+}m_{H^+} + 0.016$ at 1000 bars (*c*, molar scale, *m*, molal scale); $\log \gamma_{H^+}$ is assumed not to vary with pressure; $-\log \gamma_{H_1^+} = 0.114$ and $-\log y_{H_1^+} = 0.11$.

predicted on the basis of Buch and Gripenberg's (16) estimates of $pK''_{(2)}$ and $pK''_{(1)}$ at 1000 bars and our experimental rounded off data.

The two series of values from *pa*H 7.5 to 8.0 reflect the scattering of the results of Fig. 5; to obtain set (*a*), 0.3 mv where substracted from curve 6' to take into account the difference between the results in artificial and natural sea water; set (*b*) corresponds to curve 3 between 7.5 and 7.9. To adapt these values to other types of water small corrections will have to be made to take into account differences in salinity, $SO_4^=$, Mg, Ca, and boric acid content.

The set of ionization functions and apparent dissociation constants based on the experiments described in this paper is given in Table II.

It is important to keep in mind that the ionization functions *k'*, *k"*, and also *K"* in Table II, can only be used to interpret emf measurements made with one particular type of reference half-cell. If other cells are used corrections have to be made affecting *pm*H and *pk'* identically.

Conclusions

A coherent set of ionization functions has been established on the molal and the molar concentration scales, from 1 atm to 1000 kg. cm^{-2} and at 22°C for carbonic acid in NaCl (KCl) over a wide range of ionic strengths, in the presence of Mg^{++}, Ca^{++}, and $SO_4^=$ ions, and in sea water. It allows the use of *pm*H or *pc*H measurements with a junctionless glass electrode cell and ΣCO_2 determinations to calculate the concentrations of CO_2, HCO_3^-, $CO_3^=$ (free and bound to Na, Mg, and Ca). Data are also available to take into account the increased dissociation of boric acid in natural sea water at high pressure. Corrections are given for different types of reference half-cells.

*In situ pa*H, pcH, or *pm*H values at any ocean depth have been determined for one type of surface water (Atlantic Cl = 20.0‰) and can simply be read from the experimental curve giving $\Delta pm\text{H}/\Delta p$ as a function of *pm*H, at 1 atm and 22°C, in the *pm*H interval 5.0-9.0. The data can be used at any other temperature if one assumes that the temperature coefficient of the ionization functions is independent of pressure or the pressure coefficient is independent of temperature. This assumption however plausible, remains to be proven experimentally. Small corrections for differences in salinity, sulfate, B, Mg, Ca concentrations will have to be established for other water types.

Detailed calculations will be given in a following paper and will be used for the quantitative interpretation of direct *in situ pc*H or *pm*H measurement at great ocean depths (5, 6).

The apparent mean activity coefficient of HCl has been measured in NaCl solutions in the presence of Mg^{++}, Ca^{++}, and $SO_4^=$ at atmospheric pressure and at 1000 kg. cm^{-2}, and also y_{H^+} at 1 atm. It is thus theoretically possible to calculate $y_{HCO_3^-}$ and $y_{CO_3^=}$ in the various bicarbonate and carbonate buffers investigated including sea water, since y_{CO_2} is known with rather good precision (9, 15).

The determination of y_{H^+} in NaCl in the presence of Mg^{++}, Ca^{++}, $SO_4^=$ allows correlation of the ionization functions obtained with junctionless glass electrode cells with the so-called apparent dissociation constants widely used in oceanography to calculate $[CO_3^=]_{total}$ and $[HCO_3^-]_{total}$. The results show that the apparent second dissociation constant is *p*H dependant with a rather broad minimum between $pm\text{H}_1$ 7.9 and 8.5, where the mean value of $pK''_{(2)}$ is 9.125 at 1 atm and 22°C. Since $pK''_{(1)} = 6.00$ at this temperature and pressure, both these values are in agreement with the data of Lyman (13).

Table II. Ionization functions and apparent dissociation constants for carbonic acid in sea water (Cl 20.0 ‰) at 22° C valid between *pa*H 8.1 and 8.6[a]

	1 atm				1000 bar			
Ionization functions $pk' = -\log \frac{[H^+][R^-]}{[HR]}$	$pk'_{(1)}$		$pk'_{(2)}$		$pk'_{(1)}$		$pk'_{(2)}$	
	c	*m*	c	*m*	c	*m*	c	*m*
	5.89	5.885	9.49	9.485	5.553	5.565	9.19	9.202
	5.89	5.885	9.49	9.485	5.55	5.565	9.19	9.20
Apparent ionization functions[b] $pk'' = -\log \frac{[H^+][R^-]_T}{[HR]_T}$	$pk''_{(1)} = pk'_{(1)}$		$pk''_{(2)}$		$pk''_{(1)} = pk'_{(1)}$		$pk''_{(2)}$	
	5.89	5.885	9.015	9.01	5.553	5.565	8.817	8.829
	5.89	5.885	9.015	9.01	5.55	5.565	8.82	8.83
Apparent oceanogr. dissociation constants $pK'' = -\log \frac{a_{H^+} \times [R^-]_T}{[HR]_T}$	$pK''_{(1)}$		$pK''_{(2)}$		$pK''_{(1)}$		$pK''_{(2)}$	
	6.00	6.00	9.125	9.125	5.663	5.68	8.927	8.944
		(−0.001)		(−0.001)		(−0.001)		(−0.001)
$(pK''^{m}{}_1 = pK''^{a}{}_1 - 0.001)$	6.00	6.00	9.125	9.125	5.66	5.68	8.93	8.94
	$pk'_{(1)}, pk''_{(1)}, pK''_{(1)}$				$pk'_{(2)}$		$pk''_{(2)}, pK''_{(2)}$	
	c	*m*			c	*m*	c	*m*
Ionization functions and dissociation constants shift at 1000 bars	0.320				0.283		0.181	
	+0.017[c]				+0.017		+0.017	
	0.337	0.320			0.300	0.283	0.198	0.181

[a] $\log \gamma_{H^+}$ is assumed not to vary with pressure; the second row of data corresponds to rounded off values; c and *m* indicate the molar and molal concentration scale respectively.
[b] *T* indicates total concentrations.
[c] 0.017 = $\log d_{1000}/d_1$, where *d* is the density.

If one admits that the pressure dependence of γ_{H^+} can be neglected, then the effect of pressure, compared with data from Buch and Gripenberg (16), shows fortuitous agreement for the second apparent dissociation constant in the pmH_1 interval 8.0-8.5 (on the molal scale at 1000 bars, $pK''_{(2)} = 0.181$ against 0.180), but the effect of pressure on the first constant is much less than that predicted by these authors (at 1000 bars, $pK''_{(1)} = 0.320$ instead of 0.480).

The comparison must be considered with caution since we do not know the absolute values of the ionization functions and apparent dissociation constants, but it shows that one cannot simply assume, as Buch and Gripenberg did, that H_2CO_3 dissociates at high pressure in sea water in the same manner as at zero ionic strength and that HCO_3^- behaves as acetic acid.

The reduced effect of pressure on the apparent second dissociation constant of carbonic acid in sea water at $pmH_1 > 8.0$ corresponds to an apparent volume change of -10.6 cm^3 mole^{-1} instead of -25.6 cm^3 mole^{-1} observed at 0 ionic strength. This can be understood by taking into consideration : 1° the effect of NaCl on the pressure dependence of the mean activity coefficient of H_2CO_3 and HCO_3^-; 2° the effect of sulfate ions which does not depend on pH; and 3° the formation of $MgCO_3$ and $CaCO_3$ at atm pressure which dissociate under pressure, liberating $CO_3^=$ ions which alter the buffer ratio, the whole process being pH dependent.

The increased dissociation of boric acid, the result of which is again a function of the hydrogen ion concentration, explains why the pmH or pcH shift observed in sea water is progressively larger from pmH_1 7.0 to 9.0 than that predicted from the effect of pressure on the apparent ionization function of HCO_3^-, measured in artificial sea water without boric acid. Factors 1°, 2°, and 3°, on the contrary, really or apparently depress the effect of pressure on the ionization of carbonic acid. $MgCO_3$ and $CaCO_3$ thus appear to have a buffering action against hydrogen ion concentration changes induced by pressure in sea water although boric acid progressively and partially counteracts this effect at pmH_1 values greater than 7.0.

Starting from these considerations one might imagine that other buffer systems involving ion pairs or complex ions able to liberate anions capable of binding H^+ ions, could be prepared, where $\Delta pmH/\Delta p$ would be very small. Such media would be very useful in, for instance, the study of the specific effect of pressure on biological systems. Furthermore, if the effect of pressure on a given acid-base equilibrium is well known, changes produced by the pressure induced dissociation of added ion pairs offer a way to demonstrate their existence at atmospheric pressure.

The results which we have obtained at 1000 kg. cm^{-2} in pure carbonate and bicarbonate buffers in NaCl or KCl show, for example, that probably more ion pairs exist in NaCl than in KCl, in correlation with the difference observed for the corresponding ionization functions at atmospheric pressure. This observation might prove a clue to interpret the anomalies encountered when $\Delta V_1°$ is computed from glass electrode measurements by extrapolation at zero ionic strength (3). The values obtained in pure acid are always somewhat higher than in the corresponding buffers (-26.5 cm^3 mole^{-1} in H_2CO_3, -25.4 cm^3 mole^{-1} in bicarbonate buffer, for example). This effect could be explained if ion pairs still exist at the highest dilutions which are practical for precise emf determinations.

ADDENDUM[1]

Interpretation of the $SO_4^=$*-effect.*—It has been assumed in the preceding pages that $m_{H^+} = m_{HCl} = 0.01$ in the reference half-cells containing 0.03 $MgSO_4$ and the effect of $SO_4^=$ ions on the observed emf values have therefore been interpreted as a change which affects $k'_{(1)}$, $k'_{(2)}$, γ_{HCl} and γ_{H^+}. This "$SO_4^=$ — effect", observed in presence of NaCl + $MgCl_2$ and $CaCl_2$, is uncommonly large and of the same order of magnitude in each case as shown by the data obtained at $\mu = 0.75$:

	in NaCl	in sol. + $MgSO_4$	Δ
$pk'_{c(1)}$	6.00	5.89	0.11
$pk'_{c(2)}$	9.60	9.49	0.11
2 log γ_{HCl}	$\bar{1}$.734	$\bar{1}$.617	0.117
log γ_{H^+}	0.017	$\bar{1}$.887	0.13

Further, at 1000 kg cm^{-2}, $SO_4^=$ ions apparently increase $pk'_{(1)}$ and $pk'_{(2)}$ by a constant amount which corresponds to an emf shift between 2.0 and 2.7 mv, depending on the buffer concentration (Fig. 5), whereas the effect of the same pressure on the reference half-cell containing $SO_4^=$ is equal to 3.3 mv (Fig. 8). It actually appears that the greatest part of the $SO_4^=$ — effect must find its explanation in the formation of SO_4H^- ions in the reference half-cell, which invalidates the assumption $m_{H^+} = m_{HCl}$ [see Jones and Monk (17)]. Taking $K_{HSO_4^-} = 1.13\ 10^{-2}$, $\gamma_{SO_4^=} = 0.12$ $\gamma_{HSO_4^-} = 0.68$, assuming 54% of the sulfate to be free ions [see the data of Garrels and Thompson for sea water (15)] and $a_{H^+} = 7.7\ 10^{-3}$ ($paH = 2{,}113$, see Fig. 9), one finds $pmH_1 = 2.088$ instead of 2.00, which accounts for 80% of the apparent $SO_4^=$ — effect on $pk'_{(1)}$ and $pk'_{(2)}$ at 1 atm. One will notice that 2 log $\gamma_{HCl} = \bar{1}.698$ in 0.01 HCl + 0.49 NaCl + 0.056 $MgCl_2$ (see p. 336) and that at the same ionic strength, 2 log γ_{HCl} in 0.01 HCl + NaCl is equal to $\bar{1}.730$. Although the salt effects of individual ions are not necessarily additive, the difference 0.032 indicates that the $SO_4^=$ — effect is probably not larger than the calculated value 0.088, since the total effect of $SO_4^=$ and Mg^{++} is equal to 0.117. In other words, pmH_1 in the $SO_4^=$ containing reference solutions is found equal to 2.085 if one assumes that γ_{HCl} in 0.01 HCl + 0.49 NaCl + 0.030 $MgSO_4$ + 0.026 $MgCl_2$ has the same value as that derived from measurements in 0.01 HCl + 0.49 NaCl + 0.056 $MgCl_2$. At 1000 kg cm^{-2}, with $K_{HSO_4^-} = 2.26\ 10^{-2}$, $pmH_{1000} = 2.043$; the difference $pmH_1 - pmH_{1000} = 0.045$ represents equally 80% of the effect of pressure observed in Fig. 8. Further studies on the equilibrium of sulfuric acid will be necessary to verify these estimates, especially since $-\Delta V_1°$ for SO_4H^- is only known from density measurements, with values between 12.0 and 20.6 cm^3 mole^{-1} (Hamann, private communication).

If the above corrections were valid, then the values of pk', pk'', pmH given in this paper would have to be increased by 0.09 at 1 atm; the calculated values of paH_1 in Table I and the values of $pK''_{(1)1}$, $pK''_{(2)1}$ remain unchanged whatever the correction; $\Delta pk'$, $\Delta pk''$ at 1000 kg cm^{-2} and the corresponding ΔpH would have to be increased by 0.045.

These corrections would lead to another coherent set of dissociation functions to calculate the equilibrium of H_2CO_3 in sea water from the corresponding corrected pmH measurements giving exactly the same results as the set of functions of Table II.

Although a precise knowledge of the salt effect of $SO_4^=$ ions is needed for an approach toward the absolute values of $k_{(1)}$, $k_{(2)}$, and pmH in sea water, this search is only of academic interest for most of the oceanographic calculations. Finally, it appears that these could best be made from straight forward pwH $= -\log m_{H^+}\gamma_{H^+}\gamma_{Cl^-}$ determinations at any pressure (using half-cells without $SO_4^=$) and apparent constants defined as $K''\gamma_{Cl^-} = k'\gamma_{H^+}\gamma_{Cl^-}$, thus keeping the advantages of junctionless cells and eliminating the apparent arbitrariness of the different systems of ionization functions. Sufficient data are given in this paper to make this conversion, since the effect of pressure on γ_{HCl} can easily be calculated in pure HCl [see Harned and Owen (10), p. 507].

Acknowledgment

The authors wish to express their gratitude to Dr. R. G. Bates, Chief of Electrochemical Analysis Section, National Bureau of Standards, to Professor B. B. Owen, of the Scripps Institute of Oceanography, to Professor R. Pytkowicz and Dr. Culberson, Oceanography Department, Oregon University, for their help in preparing and discussing the manuscript.

Manuscript received July 5, 1966; revised manuscript received Dec. 14, 1966.

[1] Added on proof.

Any discussion of this paper will appear in a Discussion Section to be published in the December 1967 JOURNAL.

REFERENCES

1. B. B. Owen and S. R. Brinkley, *Chem. Rev.*, **29**, 461 (1941).
2. A. J. Ellis, *J. Chem. Soc.*, **750**, 3689 (1959).
3. A. Distèche and S. Distèche, *This Journal*, **112**, 350 (1965).
4. A. Distèche, *Rev. Sci. Instruments*, **30**, 474 (1959).
5. A. Distèche and M. Dubuisson, *Bull. Inst. Oceanogr. Monaco*, **57**, 1174 (1960).
6. A. Distèche, *ibid.*, **64**, 1320 (1964).
7. A. Distèche, *This Journal*, **109**, 1084 (1962).
8. H. S. Harned and R. Davis, *J. Am. Chem. Soc.*, **65**, 2030 (1943).
9. H. S. Harned and F. T. Bonner, *ibid.*, **67**, 1026 (1945).
10. H. S. Harned and B. B. Owen, "The Physical Chemistry of Electrolytic Solutions," 2nd ed., Reinhold Publishing Co., New York (1958).
11. H. S. Harned and S. R. Scholes, *J. Am. Chem. Soc.*, **63**, 1706 (1941).
12. R. M. Garrels, M. E. Thompson, and R. Siever, *Am. J. Sci.*, **259**, 24 (1961).
13. J. Lyman, Thesis, University of California (1956).
14. D. H. Anderson and R. J. Robinson, *Industr. Engng. Chem. (Anal.)*, **18**, 767 (1946).
15. R. M. Garrels and M. E. Thompson, *Am. J. Sci.*, **260**, 56 (1962).
16. K. Buch and S. Gripenberg. *J. Cons. Int. Explor. Mer*, **7**, 233 (1932).
17. H. Jones and C. Monk, *Trans. Faraday Soc.*, **48**, 929 (1952).

Standard Potentials of the Cl_2/Cl^- Electrode at Various Temperatures with Related Thermodynamic Functions

G. Faita, P. Longhi, and T. Mussini

Laboratory of Electrochemistry and Metallurgy, University of Milan, Milan, Italy

ABSTRACT

The standard potentials of the Cl_2/Cl^- electrode have been redetermined over the temperature range 25°-80°C with an accuracy better than ±0.1 mv. The support for the Cl_2/Cl^- electrode was a tantalum foil coated with a Pt-Ir 45% alloy, which provided complete resistance to corrosion under the experimental conditions. Thermodynamic functions concerning the reactions:

$$Ag + \tfrac{1}{2}Cl_2 = AgCl \text{ and } \tfrac{1}{2}H_2 + \tfrac{1}{2}Cl_2 = H^+ + Cl^-$$

were calculated. Standard entropy values at 25°C for AgCl and Cl^- were obtained which are more accurate than those in the literature.

The present investigation has been carried out to redetermine the standard potential of the Cl_2/Cl^- electrode as accurately as possible over a wide range of temperatures. The data available in the literature refer to 25°C (1-8) excepting those deducible from Gerke's measurements (9) in the range 15°-35°C.

Reversible emf's of the cell

$$-Pt/Ag/AgCl/1.75M\ HCl/N_2 - Cl_2\ 10\%/Pt - Ir\ 45\%, Ta/Pt+ \quad [1]$$

have been measured at temperatures from 25° to 80°C. These emf's are functions of the Cl_2 pressure and are given by

$$E_1 = E^\circ_{Cl_2} - E^\circ_{AgCl} + (RT/2F) \ln p_{Cl_2} \quad [2]$$

where $E^\circ_{Cl_2}$ denotes the standard potential of the Cl_2/Cl^- electrode, and E°_{AgCl} denotes the standard potential of the silver/silver-chloride electrode. As the E°_{AgCl} values are known from the literature (10) and E_1 and p_{Cl_2} are measurable quantities, $E^\circ_{Cl_2}$ can be calculated at any temperature. Taking into account the atmospheric pressure, the solution levels in the electrode vessel and in the guard (see Fig. 1), and the equilibrium partial pressures of H_2O and HCl (11), the reversible emf's of the cell

$$-Pt/Ag/AgCl/1.75M\ HCl/Cl_2,\ 1\ atm/Pt - Ir\ 45\%, Ta/Pt+ \quad [3]$$

were obtained from the corresponding emf's of cell [1]. The emf of cell [3] is given by

$$E_3 = E^\circ_{Cl_2} - E^\circ_{AgCl} \quad [4]$$

so that, using the accurate values of E°_{AgCl} recently redetermined by Bates and Bower (10) over a wide range of temperatures, $E^\circ_{Cl_2}$ can be determined readily from E_3. Values of $E^\circ_{Cl_2}$ thus obtained are collected in Table I with corresponding values of E_3. Among the E°_{AgCl} values of various authors quoted in the literature, Bates and Bower's values (10) were preferred because they were obtained from a comparatively much greater number of measured cells.

The reason for using a low Cl_2 pressure in cell [1] arises from the need to minimize the difference in Cl^- activity in the two half-cells, owing to occurrence of the reaction $Cl_2 + Cl^- = Cl_3^-$ (12) in the chlorine electrode compartments.

Experimental

The structure of the chlorine electrode was as shown in Fig. 1. This structure permitted either bubbling the gas in, or passing it over, the solution. During our

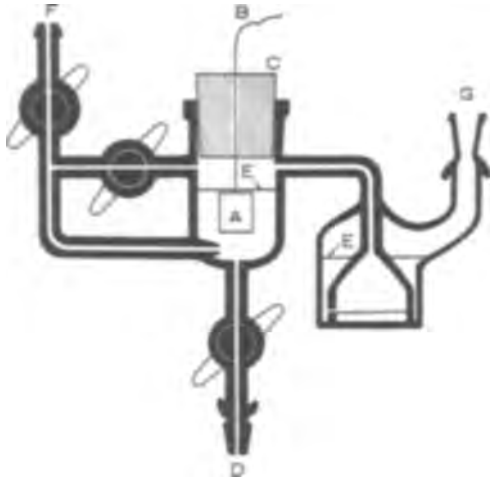

Fig. 1. Structure of the chlorine half-cell: A, electrode substrate consisting of a tantalum foil coated with a Pt-Ir alloy; B, electrical connection to potentiometer; C, polytetrafluoroethylene plug; D, connection to the silver/silver-chloride half-cell; E, solution level; F, chlorine inlet; G, chlorine outlet.

Table I. Emf's E_3 of cell [3], and standard potentials $E°_{Cl_2}$ of the Cl_2/Cl^- electrode at various °C temperatures

T, °C	$E_3 = E°_{Cl_2} - E°_{AgCl}$, abs. volts	$E°_{Cl_2}$, abs. volts
25	1.13596 ± 0.00004	1.35830 ± 0.00005
30	1.13309 ± 0.00004	1.35213 ± 0.00006
40	1.12711 ± 0.00004	1.33919 ± 0.00007
50	1.12110 ± 0.00004	1.32559 ± 0.00007
60	1.11465 ± 0.00004	1.31114 ± 0.00007
70	1.10869 ± 0.00004	1.29651 ± 0.00008
80	1.10231 ± 0.00004	1.28104 ± 0.0001

measurements we checked that, once the solution was saturated and the equilibration of the system was attained, it did not matter whether the gas bubbled into, or simply passed over, the solution. Thus we generally kept the gas bubbling into the solution with the electrode foil almost completely immersed, gas passing over being used occasionally for a check.

The rate of flow of gas is not a critical parameter, within certain limits (*i.e.*, from near to zero up to 5 cm^3/min) if temperature equilibration has been previously attained. Another point that our preliminary experiments showed was that the only permissible materials for the chlorine electrode assembly were glass and polytetrafluoroethylene (PTFE). The system under study was readily poisoned by the use of either polyvinylchloride (PVC), or rubber connections, or silicon-greased stopcocks in the gas circuit. The gas stream, before entering the chlorine electrode compartment, was bubbled into a flask with a large gas chamber and into two Friedrich's saturators, all of them containing a 1.75M HCl solution identical to the one contained in the cell and kept in the same thermostatic apparatus. A large single stock of 1.75M HCl solution was prepared in order to get as many successive runs as required with an identical solution.

For truly accurate determinations of emf's for cell [1] the choice of electrode material for the chlorine half-cell is very important. The chemical nature of the substrate should be such that there is no corrosive attack by the Cl_2-containing solution of HCl. In addition the actual surface area of the electrode and the exchange current at it must be taken into account. The latter factor is of course very important in order to establish the degree of reversibility of any electrode (13).

The electrode metals which have been used mostly are either platinum (1, 7, 8) or Pt-Ir alloys (3, 4, 9) in a compact form. Platinum, however, is not fully appropriate as a substrate for chlorine electrodes because it is subject to corrosive attack by chloride solutions containing Cl_2. Preliminary experiments concerning both the resistance of the electrode materials to chemical attack by Cl_2-containing HCl solutions and the exchange current for the reaction $Cl_2 + 2e^- = 2Cl^-$ have been carried out in this laboratory. These experiments showed that the best material for our purpose was a Pt-Ir alloy with 45% of iridium. However, this alloy, if used as an electrode substrate in the form of a thin foil, would not be adequate because of its small surface. Thus, electrodes of the capillary-imbibition type, based on porous-graphite supports and prepared according to the technique described by Bianchi (16) were first tested. These electrodes, which proved to be very helpful in the study of other gases, were not suitable in the present case due to the slow attainment of the chlorine dissolution equilibrium in the pores of the graphite itself. Electrodes consisting of a foil of an inert substrate (Ti, Zr, Ta) coated with the Pt-Ir alloy according to the procedure described by Beer (15) were then tested. Those based on Ti and Zr gave rise to mixed potentials and were discarded. The tantalum-based electrodes behaved correctly and were selected for use in cell [1] for the systematic measurements of E_1. The method of preparation was as follows. A tantalum foil was scoured with quartz powder, washed, and dried; then it was brushed with a concentrated aqueous solution of H_2PtCl_6 + $IrCl_3$ with addition of isopropyl alcohol. Then it was introduced for 10 min into a furnace heated to 400°C in the presence of NH_3 vapors. This sequence, brushing and heating, was repeated 5-7 times until the quantity of deposited Pt-Ir alloy reached ≈ 1 mg/cm^2; then the electrode was kept for 1 hr in a furnace heated to 450°C in the presence of air, and subsequently chilled in air. Such electrodes did not give rise to any mixed potentials and showed complete resistance to chemical attack even under such drastic and extreme conditions as dipping into azeotropic hydrochloric acid saturated with Cl_2 at atmospheric pressure, at temperatures as high as 80°C. The exchange current, determined in the presence of Cl_2 at atmospheric pressure in 1.75*M* HCl, was 16 ma/cm^2 (apparent geometrical surface) at 25°C, and increased a little with temperature (*e.g.*, 20 ma/cm^2 at 45°C). Four freshly prepared electrodes and one aged electrode, all of them made up as above described, were compared over a period of 10 days at 60°C in 1.75*M* HCl, with Cl_2 bubbling in at atmospheric pressure. The bias potential was 0.01 mv.

The silver/silver-chloride electrode was prepared according to the electrolytic type (14). Its bias potential was 0.01 mv at 25°C, after aging. The stability of the silver/silver-chloride electrode (and that of the chlorine electrode as well) was frequently checked against a capillary-imbibition hydrogen electrode (16), over the experimental temperature range. To prevent any diffusion of dissolved Cl_2 from the chlorine electrode to the silver/silver-chloride electrode, appropriate stopcocks were kept closed between the two half-cells.

For the reversible emf measurements mentioned above, a type K-3 L&N potentiometer was used, having a type 610-B Keithley electrometer as null-point detector. The input resistance of the latter was greater than 10^{14} ohms so that it allowed the measurement of the cell emf's even with the said stopcocks kept closed between the two half-cells.

The temperatures of the system studied were regulated to ±0.02°C by means of a specially designed air-thermostat.

Results and Discussion

When determining the Cl_2/Cl^- electrode potential it is important to consider errors due to the change of activity of Cl^- ions because of the reaction $Cl_2 + Cl^- = Cl_3^-$. Also uncertainty in the Cl_2-N_2 mixture analysis has to be taken into account. The error due to the change in the activity of Cl^- ions at a given HCl molality, decreases by decreasing the Cl_2 fraction in the gas-mixture flow; its value with sign is calculable taking into account the equilibrium constant for the reaction Cl_2, aq. + Cl^-, aq. = Cl_3^-, aq., and making a reasonable assumption about the relevant molal activity coefficients, namely, $\gamma_{Cl_2} = 1$ and $\gamma_{Cl^-} = \gamma_{Cl_3^-}$. From Sherrill and Izard's data (12) this constant can be calculated to be 0.175 (mole/1000g $H_2O)^{-1}$ at 25°C. At temperatures other than 25°C, data for such a constant are unavailable. However, one must expect the value of this equilibrium constant to decrease slightly with increasing temperature from 25° to 80°C, by analogy with the behavior of the corresponding constants in the cases of the Br_3^- ion (17) and of the I_3^- ion (18). In any case, this variation of the equilibrium constant with temperature is a matter of minor importance, as far as the present calculation is concerned; and the value at 25°C was used over the whole range from 25° to 80°C. The chlorine solubility in HCl does decrease greatly with increasing temperature (19) from 25° to 80°C, so that the error in question is much lower at 80° than at 25°C (see below). In addition the effect of any error can be decreased by using chlorine as dilute in admixture with nitrogen as possible, but this must be compatible with good accuracy in analyzing the Cl_2-N_2 mixture. The uncertainty in the analysis of Cl_2-N_2 mixtures by gas

chromatography decreases as the amount of Cl_2 is increased. Thus a compromise must be reached between the low concentration of chlorine needed to minimize the error connected with possible changes in activity of the Cl^- ions and the higher concentrations of Cl_2 needed for accuracy in the analysis of the Cl_2-N_2 mixture. It must also be borne in mind that the concentration of the HCl solution may affect the stability of the potential of the silver/silver-chloride electrode. In fact, at HCl concentrations greater than 4*M*, the solubility of AgCl in HCl to form $(AgCl_{n+1})^{n-}$ complexes would begin to be significant (20) and would in turn affect the Cl^- ion activity. The operative conditions we chose (1.75*M* HCl; N_2 90%-Cl_2 10%) caused: (*i*) an error of +0.025 mv at 25°C, +0.019 mv at 30°C, +0.012 mv at 40°C, +0.006 mv at 50°C, and a negligibly small error (always of positive sign) at 60°, 70°, and 80°C. The values of this error, all of them being of definite and positive sign, were then subtracted from the corresponding emf readings at the appropriate temperatures, and were not included in the evaluation of the cumulative uncertainty; (*ii*) an uncertainty of ±0.013 mv at 25°C, and ±0.015 mv at 80°C, respectively, arising from the gas chromatographic analysis of the chlorine-nitrogen mixture. The chlorine percentage in the mixture was 10.03 ± 0.01.

The uncertainty due to the limits of temperature regulation for the system to be studied (to ±0.02°C) is ±0.012 mv at 25°C and ±0.013 mv at 80°C, since the temperature coefficient of the emf of the cell [3] is −0.60 mv deg^{-1} at 25°C and −0.63 mv deg^{-1} at 80°C, respectively, (see below). It is evident that these limits of uncertainty are nearly constant over the experimental temperature range. Further, if we take into account the previously mentioned bias potentials for the Cl_2/Cl^- electrode and for the silver/silver-chloride electrode, the cumulative uncertainty for the E_3 values is ±0.04 mv over the whole range of temperature of experiment.

The E_3 values quoted in Table I are mean values taken from about a dozen of cell measurements at each temperature, the deviations from the mean being within the limits of the cumulative uncertainty previously described.

Among earlier $E°_{Cl_2}$ values, those deducible from the data of Kameyama, Yamamoto, and Oka (7) are in substantial disagreement with the present work. Kameyama, Yamamoto, and Oka carried out two independent series of measurements at 25°C leading to two final $E°_{Cl_2}$ values (1.3589v and 1.3580v, respectively) which differ from each other by 0.9 mv. No explanation was given for this discrepancy. The cells measured by Kameyama, Yamamoto, and Oka consisted of calomel electrodes combined with chlorine electrodes on platinum substrates, with saturated KCl as supporting electrolyte. Thus, the above discrepancy may possibly be ascribed to two causes: (*i*) use of platinum (instead of an appropriate corrosion-resistant Pt-Ir alloy) as a substrate for the system Cl_2/Cl^-; (*ii*) poor reproducibility as well as erraticity of the calomel electrodes, depending on the method of preparation. Many factors causing unsatisfactory performance of the calomel electrode were recently pointed out by Hills and Ives (21-23) in a critical reexamination of works carried out prior to 1930. The $E°_{Cl_2}$ value deducible from Lewis and Ruppert's work (3) differs from the value in the present investigation by 0.7 mv. This discrepancy can be ascribed to the presence of air in the acid calomel electrode used by Lewis and Ruppert as a reference for the chlorine electrode, as was shown by Randall and Young (3, 22).

The data in Table I have been least-squared with the aid of a type 1620-20K IBM computer, giving the following polynomials for E_3 and $E°_{Cl_2}$ as functions of absolute temperature T

$$E°_{Cl_2} = 1.47252 + (4.82271 \times 10^{-4})T - (2.90055 \times 10^{-6})T^2, \text{ abs. v} \quad [5]$$

$$E_3 = 1.28958 - (4.31562 \times 10^{-4})T - (2.79220 \times 10^{-7})T^2, \text{ abs. v} \quad [6]$$

Both of these expressions fit the tabulated respective data with a maximum deviation of ±0.15 mv.

Introducing the E_3 values and the dE_3/dT temperature coefficients (resulting from the first derivative of Eq. [6]) into the following interrelated equations

$$\Delta G = -n\mathbf{F}E, \quad \Delta S = n\mathbf{F}dE/dT, \quad \Delta H = -n\mathbf{F}E + n\mathbf{F}TdE/dT \quad [7]$$

the values of $\Delta G°$, $\Delta S°$, and $\Delta H°$ for the cell reaction $Ag + \frac{1}{2}Cl_2 = AgCl$ can be readily calculated at every temperature of experiment. Using the same procedure with the $E°_{Cl_2}$ and the $dE°_{Cl_2}/dT$ values (the latter being taken from the first derivative of Eq. [5]), $\Delta G°$, $\Delta S°$, and $\Delta H°$ can also be determined for the chlorine-electrode reaction $\frac{1}{2}Cl_2 + e^- = Cl^-$ at any temperature of experiment. Taking the fundamental convention for which the standard potential $E°_{H_2}$ of the hydrogen electrode is zero at all temperatures (24), it follows that, for the reaction

$$H^+ + e^- = \tfrac{1}{2}H_2 \quad [8]$$

$\Delta G°$, $\Delta S°$, and $\Delta H°$ are zero at all temperatures. Then one obtains also

$$S°_{H^+} = \tfrac{1}{2}S°_{H_2} = 15.6055 \text{ cal deg}^{-1} \text{ mole}^{-1}, \text{ at } 25°C \quad [9]$$

Thus, conventionally, $\Delta G°$, $\Delta S°$, and $\Delta H°$ for the chlorine-electrode reaction are the same as for the reaction

$$\tfrac{1}{2}H_2 + \tfrac{1}{2}Cl_2 = H^+ + Cl^- \quad [10]$$

Table II collects the above mentioned data at 25°C and 1 atm and provides comparison with the corresponding data taken from the standard literature. From $\Delta S°$ for the reaction $Ag + \frac{1}{2}Cl_2 = AgCl$, and taking $S°_{Ag}$ and $S°_{Cl_2}$ from the literature (27, 28), one obtains $S°_{AgCl} = 23.056 \pm 0.004$ cal deg^{-1} mole^{-1}. This value is more accurate than the corresponding value available in literature (26) (*i.e.*, 22.97 cal deg^{-1} mole^{-1}). From $\Delta S°$ for reaction [10], using again the $S°_{Cl_2}$ datum in the literature (27) and taking into account the convention expressed by Eq. [9], one obtains $S°_{Cl^-} = -2.125 \pm 0.006$ cal deg^{-1} mole^{-1}. If one assumes, as customary, the convention $S°_{H^+} = 0.00000$ cal deg^{-1} mole^{-1} (25) instead of the convention [9], one gets the value $S°_{Cl^-} = 13.480 \pm 0.006$ cal deg^{-1} mole^{-1}, which is also more accurate than the corresponding value (*i.e.*, 13.17 cal deg^{-1} mole^{-1}) quoted in the literature. For the calculations involved throughout this paper, the following fundamental constants (17-19) were used: $\mathbf{F} = 23062.4 \pm 0.2$ cal absvolt^{-1} g-equiv^{-1}; $T_{0°C} = 273.16 \pm 0.01$°K, and $R = 1.98719 \pm 0.00008$ cal deg^{-1} mole^{-1}.

Acknowledgment

This investigation has been sponsored by the Consiglio Nazionale delle Ricerche, Rome, Italy.

The authors wish to thank Dr. J. N. Hiddleston of the Gas Council Basic Research Group, Fulham Works, London and Dr. T. S. Light, of the Foxboro Company,

Table II. Comparison of thermodynamic functions at 25°C and 1 atm. Literature data in brackets, with appropriate references.

Reaction	$\Delta G°$, cal mole^{-1}	$\Delta H°$, cal mole^{-1}	$\Delta S°$, cal deg^{-1} mole^{-1}
$Ag + \frac{1}{2}Cl_2 = AgCl$	−26198 ± 1 [−26224] (26)	−30310 ± 2 [−30362] (26)	−13.793 ± 0.002 [−13.88] (26, 27, 28)
$\frac{1}{2}Cl_2 + \frac{1}{2}H_2 = H^+ + Cl^-$	−31326 ± 1 [−31350] (27)	−39903 ± 3 [−40023] (27)	−28.768 ± 0.004 [−29.08] (27)

Foxboro, Massachusetts, for their assistance with the English text and for helpful comments.

Manuscript received Sept. 1, 1966; revised manuscript received Dec. 14, 1966.

Any discussion of this paper will appear in a Discussion Section to be published in the December 1967 JOURNAL.

REFERENCES

1. E. Müller, *Z. physik. Chem.*, **40**, 158 (1902).
2. A. Schmid, *Helv. Chim. Acta*, **7**, 370 (1924).
3. G. N. Lewis and F. F. Ruppert, *J. Am. Chem. Soc.*, **33**, 299 (1911); M. Randall and L. E. Young, *ibid.*, **50**, 989 (1928).
4. G. S. Forbes, S. W. Glass, and R. M. Fuoss, *J. Am. Chem. Soc.*, **47**, 2892 (1925).
5. A. J. de Bethune and N. A. Swendeman Loud, "Table of Standard Aqueous Electrode Potentials and Temperature Coefficients at 25°C" from "Encyclopedia of Electrochemistry," C. A. Hampel, Editor, p. 414, Reinhold Publishing Co., New York (1964).
6. W. M. Latimer, "The Oxidation States of the Elements and Their Potentials in Aqueous Solutions," 2nd ed., p. 53, Prentice-Hall, Englewood Cliffs, N. J. (1959).
7. N. Kameyama, H. Yamamoto, and S. Oka, *J. Soc. Chem. Ind. (Japan)*, **29**, 679 (1926).
8. E. Wilke and O. Kieninger, *Z. physik. Chem.*, **116**, 215 (1925).
9. R. H. Gerke, *J. Am. Chem. Soc.*, **44**, 1684 (1922).
10. R. G. Bates and V. E. Bower, *J. Research Natl. Bur. Standards*, **53**, 282 (1954).
11. "International Critical Tables," Vol. III, p. 301, McGraw-Hill Book Co., New York (1928).
12. M. S. Sherrill and E. F. Izard, *J. Am. Chem. Soc.*, **53**, 1667 (1931).
13. D. J. G. Ives and G. J. Janz, "Reference Electrodes," p. 17, Academic Press, New York (1961).
14. D. J. G. Ives and G. J. Janz, *ibid.*, pp. 204, 207.
15. H. B. Beer, British Pat. 964, 913, July 29, 1964.
16. G. Bianchi, *This Journal*, **112**, 233 (1965); G. Bianchi, A. Barosi, G. Faita, and T. Mussini, *ibid.*, **112**, 921 (1965).
17. T. Mussini and G. Faita, *Ric. Sci.*, **36** (II-A), 175 (1966).
18. M. Davies and E. Gwynne, *J. Am. Chem. Soc.*, **74**, 2748 (1952).
19. A. Seidell, "Solubilities of Inorganic and Metal-organic Compounds," 4th ed. rev. by W. F. Linke, Vol. I, pp. 782, 783, 784, Van Nostrand, New York (1958).
20. G. Akerlöf and J. W. Teare, *J. Am. Chem. Soc.*, **59**, 1855 (1937).
21. G. J. Hills and D. J. G. Ives, *Nature*, **165**, 530 (1950).
22. G. J. Hills and D. J. G. Ives, *J. Chem. Soc.*, **1951**, 311.
23. D. J. G. Ives and G. J. Janz, "Reference Electrodes," pp. 129-133, Academic Press, New York (1961).
24. D. J. G. Ives and G. J. Janz, *ibid.*, p. 11.
25. D. J. G. Ives and G. J. Janz, *ibid.*, pp. 13, 14.
26. "Selected Values of Chemical Thermodynamic Properties," U. S. National Bureau of Standards, Circular 500, p. 224, Washington, D. C. (1952).
27. *Ibid.*, p. 21.
28. *Ibid.*, p. 222.
29. *Ibid.*, p. 1.
30. F. D. Rossini, F. T. Gucker, Jr., H. L. Johnston, L. Pauling, and G. W. Vinal, *J. Am. Chem. Soc.*, **74**, 2699 (1952).
31. R. A. Robinson and R. H. Stokes, "Electrolyte Solutions," 2nd rev. ed., p. XV, Butterworths, London 1965.

Potentiostatic Current-Potential Measurements on a Platinum Electrode in a High-Purity Closed System

Sigmund Schuldiner, Theodore B. Warner, and Bernard J. Piersma[1]

U. S. Naval Research Laboratory, Washington, D. C.

ABSTRACT

In a high-purity closed system, potential regions at which very slow reactions are rate-controlling were accurately separated and measured. Tafel regions and the possible reaction mechanisms on a Pt electrode in helium-saturated 1M H_2SO_4 from the H_2 to the O_2 formation reactions were determined. Effects of dermasorbed H and O atoms on transient and steady-state reaction rates were shown. Maximum oxidizable and reducible impurity levels were quantitatively determined both in solution and as adsorbed species on the working electrode surface. It was shown that the impurity levels were very low. Very small additions of hydrogen or oxygen in the critical transition region from net cathodic to anodic reactions did not appear to have catalytic effects. However, at oxygen partial pressures above 10^{-7} atm, a poisoning effect was apparent.

Recent work from this laboratory (1) has shown that gas-tight, closed electrochemical systems can be devised which will maintain a high degree of solution purity and electrode cleanliness over long periods of time. By maintaining such low levels of impurities it is possible to study reaction mechanisms in the so-called passive regions where reaction rates are so low that trace impurities could easily dominate the potential-current relationships. In order to demonstrate the feasibility of such studies and to explore the reaction mechanisms in the potential region from the gaseous hydrogen to the gaseous oxygen reaction, a potentiostatic investigation of the platinum electrode in 1M H_2SO_4 was undertaken.

[1] National Academy of Sciences Postdoctoral Resident Research Associate at NRL. Present address: Eastern Baptist College, St. Davids, Pennsylvania.

Experimental

The closed electrochemical system, continuously purged with highly purified helium containing less than 1 part in 10^9 O_2, was essentially the same as previously reported (1). It consisted of a gas-tight, glass-pipe system mounted inside a N_2-filled controlled environment box. The main compartment of the cell contained a large Pt gauze electrode (~100 cm^2), a large tightly rolled cylinder of Pt gauze platinized in lead-free platinic acid (geometric area of about 30 cm^2), a Pt wire 5 cm long and 0.064 cm in diameter, and a Pt bead (at the end of a short length of exposed Pt wire) electrode with a true (2) area of 0.190 cm^2. All Pt was 99.99% pure; the beads were formed by melting the end of Pt wire with a hydrogen/oxygen flame. The side arm of the cell (1, 3) con-

tained both a miniature glass electrode and an αPd-H spiral wire electrode which was initially charged with enough hydrogen so that its potential was 75 mv positive to a NHE (normal hydrogen electrode). This αPd-H electrode contains less hydrogen and its potential is positive to the maximum αPd-H electrode (4). The glass electrode was $+0.585 \pm 0.005$v *vs.* NHE. The αPd-H electrode was the reference used to maintain potentiostatic control of the working electrode (Pt bead). The potential of this αPd-H reference was repeatedly checked against the glass electrode during the course of the investigation. The long-term changes in potential difference were ± 5 mv which is attributed to changes in the glass electrode. Short term changes were below the detectable limit of 0.001v.

Potentiostatic control, with a Wenking 61R Potentiostat, between the αPd-H reference and the Pt bead working electrode was maintained using the Pt gauze roll as the counter electrode. The potential between the Pt bead and glass electrode was monitored with a Keithley 610B Electrometer. Current flow between the Pt bead working electrode and the Pt gauze roll counter electrode was measured with a battery-operated Keithley 601 Electrometer and recorded on a Varian G-11A recorder. Necessary precautions were taken and checks made to avoid spurious microcurrents. Such spurious or background currents were in the 10^{-13} amp range.

In the experimental arrangement used, with counter and working electrodes in the same compartment, part of the product generated at the counter electrode might diffuse to the working electrode and yield an erroneously high current reading. A simple analysis shows that if the fraction, K, of the material generated at the counter electrode that reaches the working electrode is less than 1.0, then an unstable positive feedback condition cannot result. If K is ~ 0.1, then the current would be $\sim 11\%$ high. In our case with a tiny working electrode far removed from the counter electrode in a solution stirred with inert gas, K was estimated to be much less than 0.1 with a correspondingly lower error. The validity of this estimate was checked by taking additional data in a two-compartment cell in which the counter electrode was separated from the working by a glass frit, both compartments being continuously purged with He. These data agreed with the single-compartment data. Further, using the simple cell (3) several regions which showed the absence of stirring effects (Fig. 2b) demonstrated the absence of significant cross-diffusion of reactants on the measured currents.

After calibration of the glass electrode against the several Pt/H_2 electrodes, the run was started by stopping the H_2 flow into the cell. This hydrogen line was purged with helium, while being baked, for several hours. The line was then completely disconnected from the system. The environment box was then sealed and filled with N_2. The entire gas purification system and cell were continuously purged with pure helium at a flow rate of about 40 ml/min. For about one month, potential settings which ranged from 0.96 to 1.5v were applied to the Pt bead, wire and gauze electrodes. After this treatment, only the Pt bead was potentiostated at various potentials in the same range for about another month. At this time potential-current density measurements in the very low current density regions settled down and reproducible results were obtained. In the two month purification period the residual amounts of hydrogen and organic impurities were undoubtedly reduced to such a low value that erratic steady-state measurements were no longer obtained.

Normally, applied potentials on the working electrode were changed in such a way that current reversal was avoided. This was to approximate as closely as possible normal slow changes of species at, on, or in the working electrode. In all cases, a given potential was applied to the working electrode long enough so that a steady-state current density was achieved. The required time was strongly dependent on current density at very low current densities. This took a number of days. A current was considered steady-state if there was no monotonic trend in its mean value between successive time periods. Runs up and down the entire potential span were made. In addition, increasing and decreasing potentials were applied in individual Tafel

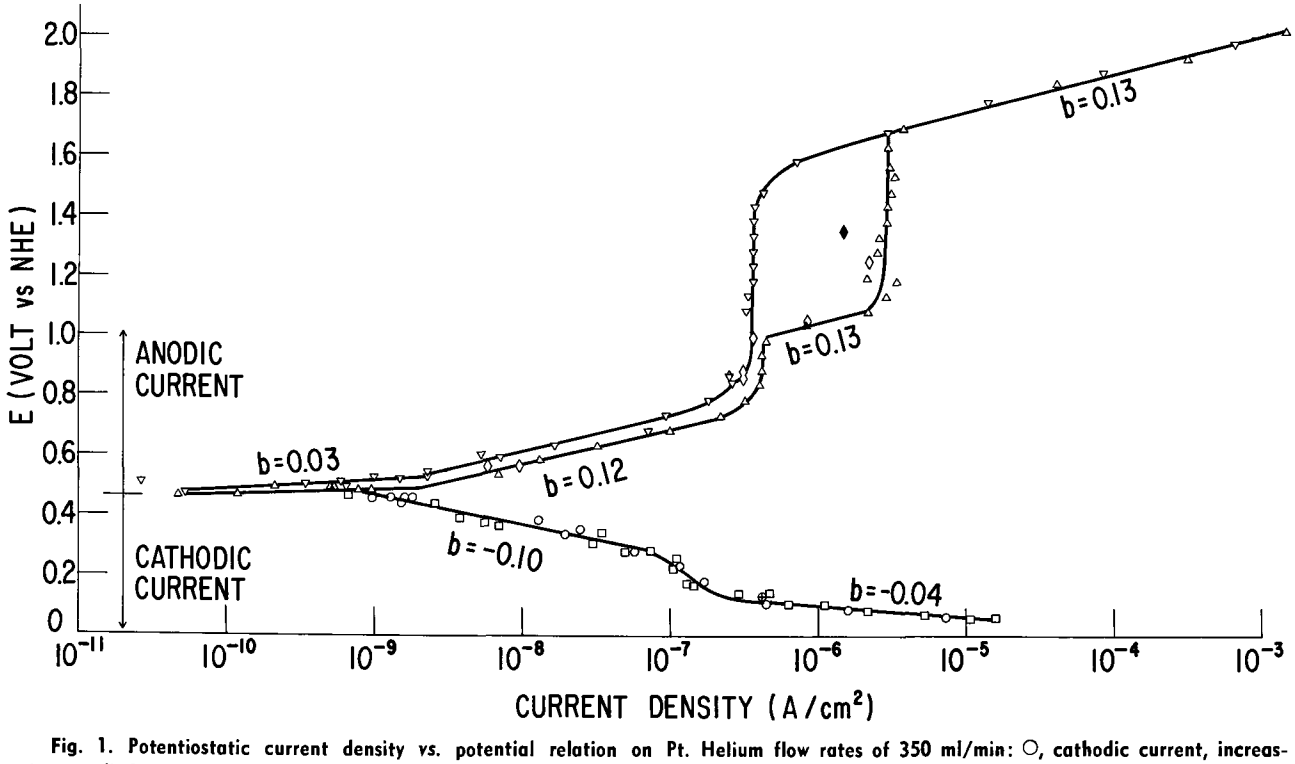

Fig. 1. Potentiostatic current density *vs.* potential relation on Pt. Helium flow rates of 350 ml/min: ○, cathodic current, increasing applied potentials; □, cathodic current, decreasing applied potentials; △, anodic current, increasing applied potentials; ▽, anodic current, decreasing applied potentials; ◇, anodic current, intermediary reversal of applied potential values; ◆, taken under special conditions. See text.

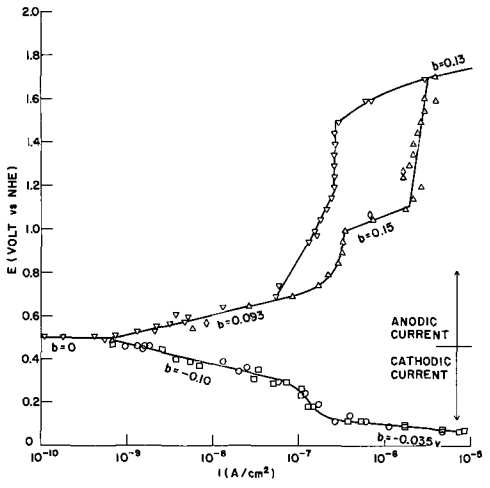

Fig. 2.(a). Potentiostatic current density vs. potential relation on Pt. Helium flow rate of 40 ml/min. Symbols the same as in Fig. 1.

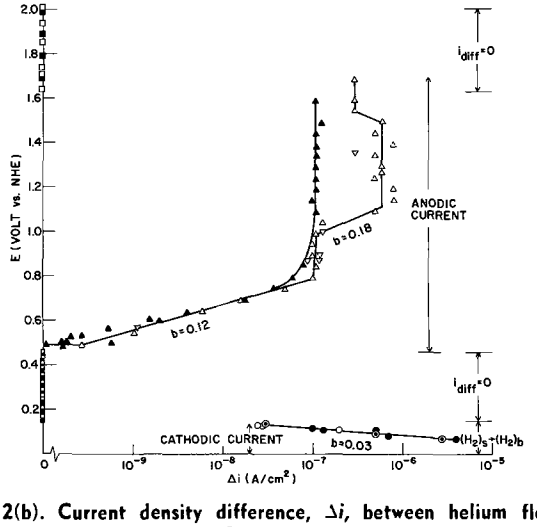

Fig. 2(b). Current density difference, Δi, between helium flow rate at 350 and 40 ml/min: ○, cathodic current, increasing applied potentials; ●, cathodic current, decreasing applied potentials; △, anodic current, increasing applied potentials; ▲, anodic current, decreasing applied potentials; ▽, anodic current, intermediate reversal of applied potentials; □, Δi = 0, increasing applied potentials; ■, Δi = 0, decreasing applied potentials.

regions. Working electrode cleanliness tests (5), based on anodic charging curve linearity in the O_{ad} regions, showed the absence of detectable amounts of impurities. The temperature was 26° ± 2°C. The oxygen content of the environment box normally was about 0.05%.

Results and Discussion

The applied potential *vs.* steady-state current density relations are shown in Fig. 1 and 2. The data in Fig. 1 were taken under rapid stirring conditions (350 + ml/min flow of helium) so that mass transport to and away from the electrode is maximized and the data largely represents kinetic current densities at the set potentials. The data in Fig. 2a were obtained at a He flow of 40 ml/min; and Fig. 2b was obtained at each set potential by subtracting current densities obtained at slow helium flow rates, i_{40}, from the current densities at fast helium flow rates, i_{350}. Steady-state currents at the slower He flow rate were always smaller or equal to those found at faster He flow. Therefore, the data ($\Delta i = i_{350} - i_{40}$) in Fig. 2b represents the increased current densities due to increased diffusion rates at each set potential.

Because of the very low current densities obtained in the potential span studied, it is obvious that net surface processes are relatively slow so that the method used for separation of surface kinetic from solution diffusion controlled currents is accurate. In all cases (except where trace impurities are the primary reactants) the amounts of reactant (hydrogen ion or water) are present in large quantities; therefore, diffusion of these to the surface will not be rate-controlling. In the cases where diffusion of very small amounts of products away from the surface occurs, such mass transport phenomena could affect the currents measured. However, even in these cases surface processes must be slow and are to a large degree controlling.

Cathodic reactions.—The data in Fig. 1 and 2 show two distinct cathodic current regions (which were independent of successively increasing or decreasing potential settings) in the potential range from 0.06 to 0.46v. From 0.06 to 0.13v, Fig. 1 shows a Tafel slope of —0.04 whereas Fig. 2a shows a —0.035 and Fig. 2b a —0.03 slope. Since the datum in Fig. 2b is the current density difference between rapidly and slowly stirred solution, increased diffusion of small amounts of products away from the surface is indicated and the increase in current density is primarily owing to this diffusion. The —0.03 slope undoubtedly indicates that the diffusion of molecular hydrogen away from the electrode surface into solution is rate-controlling. Hence the Knorr (6, 7) mechanism is rate-controlling. On the other hand, the —0.04 slope shown in Fig. 1 confirms and extends the previous work of Schuldiner (8) who showed that when vigorously stirring with an inert gas that the rate-controlling step for the hydrogen formation reaction at very low active H coverages changes from combination of H_{ad} atoms to electrochemical desorption of H_{ad} atoms ($H^+ + H_{ad} + e = H_2$). In the referenced work (8) a —0.04 slope was obtained on Pt at potentials more noble than 0.02v. In Fig. 1, the minimum potential is 0.06v. The intermediate slope of —0.035v shown in Fig. 2a indicates mixed kinetic and diffusion control.

Following a transition region from 0.13 to 0.30v, Fig. 1 shows another Tafel slope of —0.10 which ranges from 0.30 to 0.46v. Figure 2b shows that in the entire potential range from 0.13 to 0.46v that there is no diffusion limiting component. Hence, a reasonable assumption is that in this potential range the Tafel slope of —0.10 indicates a slow discharge of H^+ to H as the rate-controlling step. Evidently under these potential conditions the surface coverage with H_{ad} atoms is so low that the electrochemical desorption mechanism is negligible and the energetics of the surface is such that slow discharge may be controlling. The amounts of H_{ad} formed in this region are so low that only a few monolayers would be involved over the several days in which the measurements were taken.

This is an interesting finding inasmuch as Horiuti and Polyani (9) concluded that as the heat of adsorption of H atoms increases, the rate of the discharge step would increase. Parsons (10) and Gerischer (11), however, showed that after a critical free energy of adsorption of H atoms is reached, the rate of the discharge step decreases. Our results at these very low coverages confirm the Parsons-Gerischer treatment. An examination of their rate equations for the case of very low surface coverage with H atoms and essentially zero H_2 partial pressure favors the possibility of H^+ discharge being rate-controlling under the given conditions. Slow surface diffusion or absorption or desorption steps which would be unaffected by solution stirring rates are possible also, but it is not obvious how these steps would give a —0.10 Tafel slope.

One of the most important aspects of the lack of solution stirring rate dependence in the 0.13-0.46v range is that this shows that the impurity level of reducible substances in our solution must be below a

level to give current densities in the order of 10^{-9} amp/cm^2. More will be said about reactable solution impurities in a later section.

In the vicinity of 0.46v there is a shift from a net cathodic to a net anodic reaction. In principle, in the total absence of reactive trace impurities and with sensitive enough potential control, one should find a potential at which zero current flows. This, of course, is a virtually impossible experimental condition to reach. However, the minimum current density reached in the transition from cathodic to anodic does give an indication of solution purity. Another important conclusion which can be reached is that at about 0.46v, the electrode is virtually completely free of sorbed hydrogen and oxygen. In the course of our experiments, after the Pt bead electrode was potentiostatically kept in the vicinity of 0.46v for many days, the open-circuit potential on this electrode was very close to 0.48v. This further indicates that a Pt electrode free of both hydrogen and oxygen will have a potential close to 0.46v. In other words, the open-circuit rest potential of pure Pt in a helium-saturated 1M H_2SO_4 solution $\approx$ 0.46v *vs.* NHE. The presence of dermasorbed H lowers that potential. Dermasorbed H can control the open-circuit potential down to as low as 0.18v (1).

Anodic reactions.—On the anodic side of the curves shown in Fig. 1, four distinct Tafel regions are obvious. One should further note that there are hysteresis effects except in the potential region above 1.7v. The reason for this hysteresis is most likely due to the dermasorption of atomic oxygen in the Pt skin which takes place at potentials above 1.4v. This always gave lower current densities at a set potential. Changing the potential in either a more positive or negative direction before this voltage is reached does not affect the current density-potential relation. However, once a 1.4v potential is exceeded, hysteresis occurs.

The potential region with the 0.03 Tafel slope is most likely owing to impurities in solution. The diffusion limiting overvoltage was undoubtedly a factor. This would indicate that oxidizable impurities, such as, hydrogen and organic species are present to an amount which can give a maximum current density of about 2 x 10^{-9} amp/cm^2. Thus, we have a very sensitive test for trace oxidizable impurities. Furthermore, the oxygen (or reducible) impurity level is at least an order of magnitude less. This will be discussed further in the next section.

In the Tafel region with a 0.12 slope (Fig. 1), an oxidation reaction is occurring which undoubtedly involves water. The formation of atomic oxygen is unlikely since no hysteresis effects are noted if the potential remains below 1v. The 0.12 slope indicates a one electron slow discharge. Some authors (12) have postulated the formation of hydroxyl radical

$$Pt + H_2O \rightarrow H^+ + Pt - OH + e \qquad [1]$$

At steady-state the level of OH adsorption is maintained constant by OH possibly decomposing to water and O_2. The data in Fig. 1 strongly support such a mechanism; however, it does not prove it. The data in Fig. 2a, b which show effects of diffusion control give essentially the same Tafel slopes. We have no ready explanation of this.

In the potential range from 1.0 to 1.1v (Fig. 1) a Tafel slope of 0.13 is found only when potentials above ~1.4v do not precede this range. Here, again, the slope indicates a one electron rate-controlling mechanism. At these potentials, previous experience at this and other laboratories indicates the formation of O atoms. The mechanism could be

$$Pt - OH \rightarrow Pt - O + H^+ + e \qquad [2]$$

Under steady-state the amount of O associated with the Pt would be constant, excess O being lost possibly by peroxide formation and decomposition. The atomic oxygen can be both dermasorbed in the skin of the Pt and be chemisorbed on the surface. In the 1.0-1.1v range represented by the 0.13 slope, dermasorption most likely occurs to only a small extent. This is indicated by going to a more anodic potential of 1.4v and then decreasing the potential (◈) points with no apparent deviation. The limiting current at about 3 x 10^{-6} A/cm^2 appears to be on Pt fully covered with O_{ad} with only small absorption of O atoms. The surface coverage with atomic oxygen probably varies in the first 0.13 slope range, but full coverage is obtained at values above 1.1v. Only when the potential rises to about 1.7v is there an indication that molecular oxygen is evolved in quantity and that saturation of the dermalayer is complete. This is shown both by the lower current densities on the decreasing potential curve and the fact that after reaching a potential of about 0.9v, a subsequent increase in potential to 1.36v will give a current density (◆, Fig. 1) somewhere between the two branches of the hysteresis loop. The degree of oxygen saturation of the dermalayer thereby appears to be both a function of potential and previous history.

The atomic oxygen formation region (1.0-1.7v) appears to give off a diffusable product as is evident from effects of diffusion currents obtained in Fig. 2a and b. Whether this product is O_2, H_2O_2, or something else is not obvious, although the rate of diffusion does generally follow the same potential independence seen for the kinetic reaction in Fig. 1. This is reasonable since the limiting current densities show that the rates of formation of products are independent of potential. This indicates that dermasorption of O atoms could be rate-controlling. At potentials above ~1.6v, the current density is independent of stirring rate. This shows that the rate-determining step in the oxygen gas formation reaction is so slow that it gives complete kinetic control and that diffusion away of molecular oxygen contributes nothing to the overvoltage.

The potential region above 1.6v is undoubtedly the molecular oxygen generation region, where the Tafel slope of 0.13 again indicates a rate-controlling step involving a one-electron reaction. This slope verifies Hoare's work (13). The total oxygen generating mechanisms may be

$$\left.\begin{aligned} &Pt + H_2O \rightarrow Pt - OH + H^+ + e \\ &Pt - OH \rightarrow Pt - O + H^+ + e \\ &Pt - O + H_2O \rightarrow Pt + H_2O_2 \\ &H_2O_2 \rightarrow H_2O + \tfrac{1}{2}O_2 \end{aligned}\right\} \text{or, } 2Pt - O \rightarrow 2Pt + O_2 \qquad [3]$$

Under these conditions the Pt skin is saturated with dermasorbed O atoms and the current densities are independent of increasing or decreasing potentials.

After the electrode had been taken to potentials above 1.7v, on decreasing the potential to about 0.9v, the transient anodic current density decreased and eventually became cathodic. Under these conditions increasing the rate of He flow decreased the net cathodic current density. This can be explained by the fact that the anodic current increases with increased stirring rate (Fig. 2b). Thus the increased rate of the anodic reaction plus the cathodic reaction gave a lower net cathodic current. This cathodic current persisted for about two days and eventually returned to the anodic current indicated in Fig. 1 at this potential. These decreases in anodic current were undoubtedly due to the oxygen stored primarily in the dermalayer migrating to the surface and being reduced to water. The fact that increased He stirring appears to increase the rate of anodic reaction with little change in the rate of the cathodic reaction bears this out. This further indicates that dermasorbed oxygen is unstable at potentials below 1v, and even though the small hysteresis effects found at potentials below 1v are probably due to small traces of dermasorbed O, the bulk of these dermasorbed O atoms is removed. It is quite possible that at potentials below 1v that at least part of the source of dermasorbed O is from the in-

terior of the metal and this migration is so slow that its removal takes some time. Once the electrode is taken into the cathodic current region and held there for some hours, the potential *vs.* current behavior over the entire anodic current range is essentially the same as shown for the potential increasing values shown in Fig. 1.

Impurity levels in solution.—One of the goals of this investigation was to determine quantitatively the maximum levels of impurities in the solution. As mentioned above, the data in Fig. 1 indicated that the level of impurities which were reducible in the vicinity of 0.46v was below an amount which would give a cathodic current of -10^{-9} amp/cm² on the Pt bead electrode. This was determined by the lack of stirring effects in this region. It also was shown that the maximum amount of oxidizable impurity in the vicinity of 0.49v gave an equivalent of about 2×10^{-9} amp/cm². These current densities give upper limits of the amounts of both oxidizable and reducible impurities which actually react at the working electrode surface.

Since, as will be shown, the level of reducible impurity (most likely O_2) in solution is at least one order of magnitude less than oxidizable impurities (H_2 and organic species) reducible impurities will have an insignificant effect on the anodic current density due to oxidizable impurities. Similarly at cathodic current densities of -10^{-9} amp/cm², and at anodic current densities of 10^{-8} amp/cm², there are negligible impurity effects. To give some idea of how low these impurity levels are, the fraction of Pt surface which reducible impurities (mostly O atoms) contact in one second must be less than 2×10^{-6}; and the fraction of Pt surface which H atoms (or equivalent organic molecules) contact in 1 sec must be not more than 4×10^{-5}. Of course, this tells us nothing about the catalytic effects of these very small amounts of impurities. However, the data which will be given next on the effects of additions of trace amounts of hydrogen and oxygen indicate that at these low impurity levels, increased, but still very small, amounts of these impurities have no apparent catalytic effects.

Because of the very low net currents involved, the potential region from 0.46 to 0.50v is most sensitive to added impurities. By controlling the potential at 0.46 volt, the effects of trace amounts of hydrogen and oxygen[2] on the original net cathodic current is seen in Fig. 3. Controlling the potential at 0.50v gave the data shown in Fig. 4 and 5.

The data in Fig. 3 show that when successive small amounts of either hydrogen or oxygen are added to the helium gas stream to give the partial pressures shown, a detectable change in the cathodic current density is

[2] See ref. (14) for technique used for additions of small partial pressures of hydrogen and oxygen to helium carrier gas.

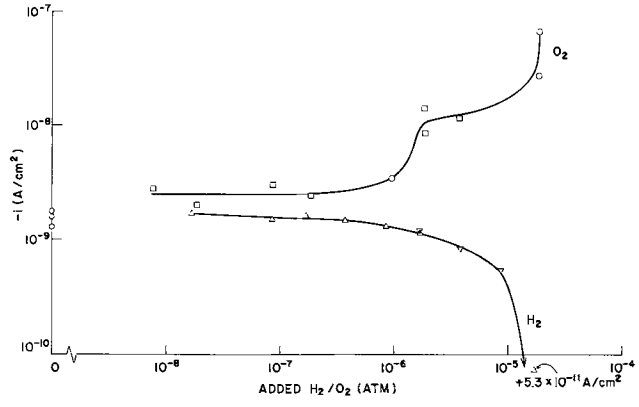

Fig. 3. Changes in net cathodic current density at 0.46v owing to added H_2 and O_2. He flow rate of 40 ml/min: △, added H_2, increasing partial pressures; ▽, added H_2, decreasing partial pressures; ○, added O_2, increasing partial pressures; □, added O_2, decreasing partial pressures.

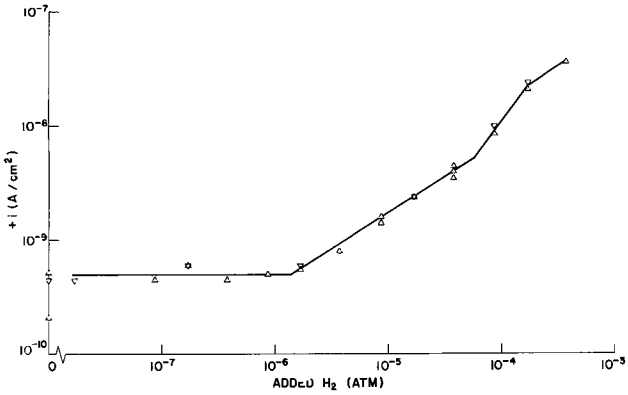

Fig. 4. Increases in the net anodic current density at 0.50v owing to added H_2. He flow rate of 40 ml/min. Symbols the same as in Fig. 3.

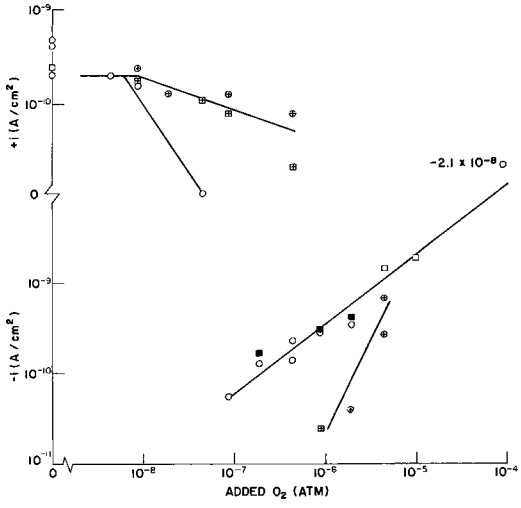

Fig. 5. Decreases in the net anodic current density and transition to net cathodic current density at 0.50v owing to added O_2. He flow rate of 40 ml/min: ⊙ first run, increasing O_2 partial pressure; square with dot, first run, decreasing O_2 partial pressure; ⊕ second run, increasing O_2 partial pressure; square with plus, second run, decreasing O_2 partial pressure; ■ third run, decreasing O_2 partial pressure.

felt between 10^{-7} and 10^{-6} atm of H_2 or O_2. An estimate of the diffusion current that would result if all of the hydrogen or oxygen which reached the surface reacted can be obtained from the Nernst diffusion equation (15)

$$i_{diff} = \tfrac{1}{2}j = \frac{DF(C_o - C_s)}{2 \times 10^3\,\delta} \qquad [4]$$

where j is the calculated diffusion current density in amp/cm² (to put i_{diff} on a true area basis, the roughness factor of the electrode being ~2, j in Eq. [4] is divided by 2), D is the diffusion coefficient, **F** is the faraday, C_o is the concentration in the bulk of the solution in equiv/l, C_s is the concentration at the surface which is zero at steady state, and δ is the "effective thickness" of the boundary layer.

The current due to diffusion of dissolved gases to the electrode may be calculated using $D_{H_2} = 4.87 \times 10^{-5}$ cm²/sec (16), and $D_{O_2} = 1.98 \times 10^{-5}$ cm²/sec (16) and

$$[Co]_{H_2} = \frac{0.0149 \times 1000 \times 2}{22{,}400} P_{H_2}$$

$$= 1.33 \times 10^{-3} P_{H_2} \text{ equiv H/l}$$

$$[Co]_{O_2} = \frac{0.023 \times 1000 \times 4}{22{,}400} P_{O_2}$$

$$= 4.1 \times 10^{-3} P_{O_2} \text{ equiv O/l} \qquad [5]$$

where 0.0149 and 0.023 are the respective Bunsen coefficients [std. cc gas in 1 cc of 1M H_2SO_4 (17)] of H_2 and O_2, respectively, 2 and 4 are the respective number of electrons involved in H_2 oxidation and O_2 reduction, and P is the partial pressure of each gas in atm. Thus,

$$i_{diff,\,H_2} = 3.25 \times 10^{-6} \frac{P_{H_2}}{\delta} \text{ amp/cm}^2$$

$$i_{diff,\,O_2} = -4.06 \times 10^{-6} \frac{P_{O_2}}{\delta} \text{ amp/cm}^2 \qquad [6]$$

Since the changes in current densities found in Fig. 3, 4, and 5 on addition of either hydrogen or oxygen are due to their respective oxidation or reduction and assuming that the changes in current are primarily owing to the rate of diffusion of these gases to the surface

$$i_{res} = i_{meas} - i_{diff} \qquad [7]$$

In Eq. [7], i_{res} is the residual current density in the absence of added hydrogen or oxygen, i_{meas} is the measured current density found in the presence of added hydrogen or oxygen and is taken from Fig. 3, 4, and 5, i_{diff} are the diffusion currents calculated from Eq. [6]. The value of δ was adjusted to give the most constant i_{res} values. This gave a δ for H_2 of 0.035 cm and δ for O_2 of 0.02 cm. These were reasonable values when compared to the data of Ibl (18) for a δ in moderately stirred solution (40 ml He/min). Using these values of δ and Eq. [6] and [7], the results shown in Table I were obtained.

The data in Table Ia show that at 0.46v changes in the partial pressure of hydrogen give a constant i_{res} which is very close to the value found in the absence of added hydrogen. Hence current changes due to hydrogen at this potential are essentially diffusion-controlled. Table Ib at 0.50v also shows hydrogen diffusion control. At P_{H_2} above 1 x 10^{-4} atm a kinetic process is involved since the calculated diffusion current density does not account for all of the current density increase. For some reason at partial pressures above 10^{-4} atm, the rate of the oxidation reaction on the surface increases. This may be owing to changes in the catalytic properties of the surface.

The data in Table Ic and d concerning the effects of oxygen additions, however, cannot be simply attributed to diffusion control. At 0.46 and at 0.50v up to 1x10^{-6} atm added O_2 essentially shows $i_{res} \approx i_{meas}$. This means that i_{diff} is relatively insignificant. Even though the scatter at 0.50v is not too satisfactory diffusion control is apparently unimportant except at $P_{O_2} \geqq 10^{-6}$ atm. Since changes in the measured current density were rather small, the oxygen reduction reaction is relatively slow and even though real effects of added oxygen are apparent in Fig. 5, they are very small.

Table I. Effects of added H_2 and O_2 on i_{res}

(a) at 0.46v

P_{H_2}, atm	$i_{meas} \times 10^9$, amp/cm²	$i_{res} \times 10^9$ δ = 0.035 cm, amp/cm²
5 × 10⁻⁸	−1.6	−1.6
1 × 10⁻⁷	−1.5	−1.5
5 × 10⁻⁷	−1.4	−1.4
1 × 10⁻⁶	−1.3	−1.4
5 × 10⁻⁶	−0.76	−1.2
1 × 10⁻⁵	−0.40	−1.3

i_{res} at P_{H_2} = 0 (Fig. 3) −1.3 to −1.8

(b) at 0.50v

P_{H_2}, atm	$i_{meas} \times 10^{10}$, amp/cm²	$i_{res} \times 10^{10}$ δ = 0.035 cm, amp/cm²
1 × 10⁻⁷	5	4.9
1 × 10⁻⁶	5	4.1
1 × 10⁻⁵	17	7.7
2 × 10⁻⁵	27	9.4
1 × 10⁻⁴	100	7.0
2 × 10⁻⁴	250	64.0
3.5 × 10⁻⁴	360	34.0

i_{res} at P_{H_2} = 0 (Fig. 4) 2 to 5

(c) at 0.46v

P_{O_2}, atm	$i_{meas} \times 10^9$, amp/cm²	$i_{res} \times 10^9$ δ = 0.02 cm, amp/cm²
5 × 10⁻⁸	−2.5	−2.5
1 × 10⁻⁷	−2.5	−2.5
5 × 10⁻⁷	−4.0	−4.0
1 × 10⁻⁶	−6.0	−5.8
5 × 10⁻⁶	−14	−13
1 × 10⁻⁵	−25	−23

i_{res} at P_{O_2} = 0 (Fig. 3) −1.3 to −1.8

(d) at 0.50v

P_{O_2}, atm	$i_{meas} \times 10^{10}$, amp/cm²	$i_{res} \times 10^{10}$ δ = 0.02 cm, amp/cm²
*5 × 10⁻⁹	2	2
*1 × 10⁻⁸	1	2
*1 × 10⁻⁷	−0.6	−0.4
*1 × 10⁻⁶	−3.6	−1.6
*1 × 10⁻⁵	−20	0
**5 × 10⁻⁹	2	2
**1 × 10⁻⁸	2	2
**1 × 10⁻⁷	0.9	0.7
**1 × 10⁻⁶	−0.2	1.9
**1 × 10⁻⁵	−20	0

i_{res} at P_{O_2} = 0 (Fig. 5) 2 to 5
* ⊙ □ ■ curve Fig. 5.
** ⊕ ⊞ curve Fig. 5.

At 0.46v the i_{res} values are not constant at partial pressures above 1 x 10^{-7} atm added oxygen; also, the residual current densities are essentially equal to the measured current densities. Diffusion control is evidently a minor factor. It appears that the oxygen which gets to the surface effectively increases the rate of the hydrogen formation reaction. This appears to be a catalytic effect and may be attributed to the removal of catalytic poisons from the electrode surface by chemical oxidation. These poisons may be trace amounts of organic species or even hydrogen itself.

Even with the scatter found for different runs, it is obvious that the oxygen additions as low as 10^{-8} atm significantly decrease the net anodic current density. This specifically shows that the oxygen impurity must be at least an order of magnitude less than 10^{-8} atm and confirms previous estimates (1) of oxygen impurity in our closed system. Since at 10^{-8} atm, O_2 diffusion will give an $i_{diff,\,O_2}$ of about −2 x 10^{-12} amp/cm² and the actual current density found at O_2 additions of 10^{-8} atm (Fig. 5) is between 1 to 2 x 10^{-10} amp/cm², O_2 is only cancelling out a small part of the oxidizable impurity which must be an amount required to give an equivalent of about 10^{-10} amp/cm². Since the current density attributable to oxidizing impurities at 0.46v was about an order of magnitude more, we can conclude from this and the abnormally high effect of O_2 additions that oxygen is affecting the net anodic current density as a catalytic poison.

The sensitivity of this technique of determining maximum possible anodic and cathodic impurity levels and of the purity of the system used can be better demonstrated if the impurity effects are expressed in normal analytical terms of parts per million (g H_2 or O_2 per g solution). The conversion factors are

$$(2 \times 0.0149/22{,}400 \times 1.06)\, P_{H_2} = 1.25 \times 10^{-6} P_{H_2} \text{ [g } H_2 \text{ per g 1M } H_2SO_4\text{]}$$

and

$$(32 \times 0.023/22{,}400 \times 1.06)\, P_{O_2} = 3.1 \times 10^{-5} P_{O_2} \text{ [g } O_2 \text{ per g 1M } H_2SO_4\text{]}$$

where P_{H_2} and P_{O_2} are the gas partial pressures in atm, 2 and 32 are the respective molecular weights of H_2 and O_2, 0.014 and 0.023 are the Bunsen coefficients of H_2 and O_2 (17), respectively, 22,400 is the number of cubic centimeters of gas in one mole equivalent, and 1.06 is the specific gravity of 1M H_2SO_4. Thus the detection sensitivity is 10^{-7} ppm for O_2 and 10^{-6} ppm for H_2. Since oxidizable impurities could be partly organic species, the level of this impurity could be considerably less on a molecular basis, but would have to be more on a weight basis. The actual impurity levels in solution are easily an order of magnitude less than the maximum impurity levels determined.

The really critical impurity level, from an electrochemical viewpoint, would concern the fraction of available Pt sites covered with impurity. Here again from the data shown in Fig. 1 we have seen that reducible impurities which get to the surface give a current density which must be less than −1 x 10^{-9} amp/cm² and oxidizable impurities a current density of not more than 2 x 10^{-9} amp/cm². This means that less than 10^9 electrons are used in reducible impurities per cm²/sec and not more than 10^{10} electrons are donated by oxidizable impurities per cm²/sec. Since the total number of Pt atoms per cm² is about 1.3 x 10^{15}, then in 1 sec, less than one available Pt surface

site per million can be affected by a reducing impurity reaction and less than one available Pt surface site per 100,000 can be affected by an oxidizing impurity reaction.

Conclusions

1. In the potential range from 0.06 to 0.13v, under rapid stirring with He, the rate-controlling step is

$$Pt - H + H^+ + e = H_2$$

The net increased diffusion of H_2 away from the surface by rapid stirring can be determined by subtracting the current density under slow stirring from the current density under fast stirring. This indicated that the Tafel component due to increased diffusion gave a —0.03 slope. However, at slow stirring rates, diffusion and kinetic control were about equal.

2. A second Tafel region between 0.30 to 0.46v indicated a slow hydrogen ion discharge step.

3. The potential at which no net reduction or oxidation reaction occurs (transition point from net cathodic to net anodic reaction) and at which H and O adsorption is equal to zero is about 0.46v *vs.* NHE.

4. Four distinct Tafel regions were found in the anodic range from 0.46 to > 2v. These were: a region in which oxidizable impurities reacted; a region at which water was probably oxidized to give chemisorbed OH; a region in which chemisorbed and dermasorbed O was formed; a region in which O_2 was generated.

5. A hysteresis effect was found, once significant amounts of O were dermasorbed. This lowered the net reaction rates.

6. Impurity levels both in solution and on the electrode surface were determined. The maximum possible level of reducible impurity was found to be equivalent to an O_2 concentration of 10^{-7} ppm and a maximum oxidizable impurity level equivalent to an H_2 concentration of 10^{-6} ppm. The impurity levels of oxidizable and reducible species on the Pt surface were less than equivalent to 10^{10} and 10^9 electrons/cm^2/sec, respectively. This means that about one available Pt surface site per million per sec is affected by an impurity reaction. In a 10^{-12} Torr vacuum system, N_2 arrives at a surface at about 4 x 10^8 molecules/cm^2/sec (19). The rate of electrode contamination in our system is comparable.

7. Very small additions of hydrogen or oxygen in the critical transition region from net cathodic to net anodic reaction did not have catalytic effects, but when the partial pressure of these gases were above 10^{-7} atm catalytic effects were apparent.

8. Further experimental work is required using transient measurements in conjunction with potentiostatic control to determine the kinetic parameters in each of the Tafel regions to determine surface and dermasorbed layer coverages and other kinetic parameters.

9. This study has demonstrated that highly purified closed systems can give precise information concerning potential regions at which net reaction rates are very slow.

Manuscript received Oct. 21, 1966; revised manuscript received Dec. 15, 1966. This paper will be presented at the Dallas Meeting, May 7-12, 1967.

Any discussion of this paper will appear in a Discussion Section to be published in the December 1967 JOURNAL.

REFERENCES

1. S. Schuldiner, B. J. Piersma, and T. B. Warner, *This Journal*, **113**, 573 (1966).
2. S. Schuldiner and R. M. Roe, *ibid.*, **110**, 332 (1963).
3. S. Schuldiner and R. M. Roe, *ibid.*, **110**, 1142 (1963).
4. S. Schuldiner, G. W. Castellan, and J. P. Hoare, *J. Chem. Phys.*, **28**, 16 (1958).
5. S. Schuldiner and T. B. Warner, *J. Phys. Chem.*, **68**, 1223 (1964).
6. L. Kandler, C. A. Knorr, and C. Schwitzer, *Z. Phys. Chem.*, **A180**, 281 (1937).
7. C. A. Knorr, *Z. Elektrochem.*, **59**, 647 (1955).
8. S. Schuldiner, *This Journal*, **108**, 384 (1961).
9. J. Horiuti and M. Polyani, *Acta Physiocochim. USSR*, **2**, 505 (1935).
10. R. Parsons, *Trans. Faraday Soc.*, **54**, 1053 (1958).
11. H. Gerischer, *Bull. Soc. Chim. Belg.*, **67**, 506 (1958).
12. J. O'M. Bockris, *J. Chem. Phys.*, **24**, 817 (1956); H. Wroblowa, B. J. Piersma, and J. O'M. Bockris, *J. Electroanal. Chem.*, **6**, 401 (1963); J. P. Hoare, *This Journal*, **112**, 602 (1965).
13. J. P. Hoare, *Electrochim. Acta*, **11**, 203 (1966).
14. T. B. Warner and S. Schuldiner, *This Journal*, **112**, 853 (1965).
15. C. V. King, *ibid.*, **102**, 193 (1955).
16. B. E. Conway, "Electrochemical Data," p. 174, Elsevier Publishing Co. Amsterdam, (1952).
17. "International Critical Tables," **3**, 271 (1928).
18. N. Ibl. *Chem.-Ing.-Tech.*, **33**, 69 (1961).
19. G. Erlich, "Advances in Catalysis," Vol. 14, p. 392, Academic Press, New York (1963).

Technical Notes

The Transport of Hydrogen to Cylindrical Anodes in Stirred Electrolytes

Elton J. Cairns[1] and Adrian M. Breitenstein[2]

General Electric Research & Development Center, Schenectady, New York

Although the theory of mass transport has advanced a great deal in the last ten years, making it feasible to predict mass transport rates (limiting current densities) from the properties and geometry of simple systems (1, 2), there is still a strong tendency for electrochemists to use complicated geometries and flow conditions in their experiments. It is, therefore, of interest to determine how well the fundamentals of mass transport can be used in the correlation and prediction of mass transport rates (limiting current densities) in a typical stirred electrochemical cell.

[1] Present address: Argonne National Laboratory, Argonne, Illinois.
[2] Present address: Materials & Processes Laboratory, General Electric Company, 1 River Road, Schenectady, New York.

Experimental

The transport-limited electrode reaction chosen was the anodic oxidation of hydrogen dissolved in aqueous

electrolytes. The anode was a smooth platinum cylinder (0.0762 cm diameter, 2.07 cm long); the electrolytes and temperatures chosen were 1*N* $HClO_4$ at 25°C, 1*N* Cs_2CO_3 at 24°C, and 1*N* Cs_2CO_3 at 80°C. The Cs_2CO_3 was prepared and purified by methods already described (3, 4). The hydrogen was purified by diffusion through a silver-palladium tube. The test-electrode compartment of the cell was very large compared to the distance between the tips of the paddle stirrer blades and the test electrode; hence wall effects were expected to be small. The 2-bladed paddle stirrer measured 3.22 cm tip-to-tip, and the center-line distance between the stirrer shaft and the test electrode was 2.75 cm.

Limiting currents were measured for the anodic oxidation of dissolved hydrogen using two methods which yielded identical results: (*a*) steady-state measurement of the limiting current from the electrode held potentiostatically at 0.4v *vs.* the reversible hydrogen electrode in the same electrolyte at the same temperature (rhe); (*b*) pseudosteady-state limiting current determined from a current-voltage recording during a slow, potentiostatically controlled anodic sweep of 0.2 v/sec. The limiting current was taken at the current plateau in the range 0.4-0.6v *vs.* rhe. The electrode was given a pretreatment of alternate anodic and cathodic potentiostatic pulses before each measurement.

The stirring rate was measured by means of a stroboscope-tachometer, and was constant to within 2%. The range of stirrer speeds covered was 60-1000 rpm. The electrolyte was kept saturated with hydrogen by vigorous bubbling and stirring between limiting-current determinations. Bubbling was stopped during the measurements in order to eliminate any stirring due to the bubbles.

Results and Discussion

It would be very convenient if the limiting current density could be predicted from first principles for a system of the present geometry-transverse flow across a smooth cylinder. However, it has been shown from hydrodynamics, both theoretically and experimentally, that boundary layer separation occurs on the downstream side of the cylinder (5), yielding a problem which is mathematically intractible. The theory of mass transport is still very useful, even in this difficult situation, for predicting the types of functional relationships expected among the variables. Some of the useful relationships have been reviewed by Levich (6) and by Bird, Stewart, and Lightfoot (1). In general, such relationships as

$$\mathrm{Nu} = A\mathrm{Re}^{m}\,\mathrm{Sc}^{n} \qquad [1]$$

are expected, with m being less than unity (7). Extensive experimental studies of mass transport to and from flat plates, spheres, and cylinders, plus theoretical studies, indicate that n should be 1/3 (1, 2, 8).

If the dimensionless mass transport parameter j_D is introduced

$$j_D = \mathrm{Nu}\,\mathrm{Re}^{-1}\,\mathrm{Sc}^{-1/3} \qquad [2]$$

then Eq. [1] takes on the simpler form

$$j_D = A'\,\mathrm{Re}^{m-1} \qquad [3]$$

The simplest initial test of the above expressions for applicability to the present system was to test the behavior of i_L $\left(\text{or } \mathrm{Nu} = \dfrac{i_L D}{\Delta X_A\, CN\mathbf{F}\,\mathcal{D}_{AB}}\right)$ as a function of stirring speed $\left(\text{or } \mathrm{Re} = \dfrac{Dv\rho}{\mu}\right)$. If log i_L is plotted against log (stirrer speed), then the result should be a straight line of slope m. A typical test plot for H_2 in 1*N* Cs_2CO_3 at 24°C is shown in Fig. 1. The slope m is exactly 1/2, similar to results for dissolution of soluble cylinders in water and evaporation of water and other liquids from cylindrical surfaces into air (8). All other conditions tested (1*N* $HClO_4$, 25°C, and 1*N* Cs_2CO_3, 80°C) also yielded $m = 1/2$.

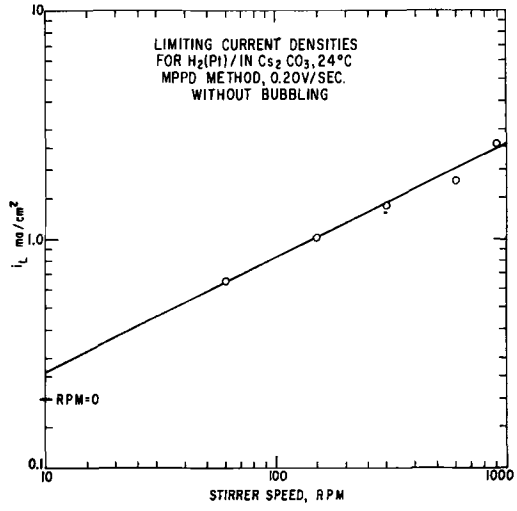

Fig. 1. Limiting current densities for the anodic oxidation of hydrogen in 1*N* Cs_2CO_3 at 24°C, as a function of stirrer speed. The slope is 0.5

In order to test further the applicability of Eq. [1] and [3], it is necessary to have values for all of the properties and variables in the dimensionless groups

$$\mathrm{Re} = \frac{Dv\rho}{\mu} \qquad [4]$$

$$\mathrm{Nu} = \frac{i_L D}{\Delta X_A\, CN\mathbf{F}\,\mathcal{D}_{AB}} \qquad [5]$$

$$\mathrm{Sc} = \frac{\mu}{\rho\mathcal{D}_{AB}} \qquad [6]$$

The characteristic dimension D is the diameter of the cylindrical electrode, 0.0762 cm; v is taken to be the linear velocity of the tip of the stirrer. The values of ρ were determined experimentally using a calibrated pycnometer. Viscosities (μ) were determined with an Ostwald viscometer. The value of $\Delta X_A = X_{A_\infty}$ is the solubility of hydrogen in the electrolyte under the experimental conditions (expressed as mole fraction). The solubility of H_2 in 1*N* $HClO_4$ at 24°C was determined using the value in water and an estimated salting-out constant based on values listed by Harned and Owen (9). For the solubility of H_2 in 1*N* Cs_2CO_3 at 25°C, the value for K_2CO_3 and Na_2CO_3 was used. To obtain the value for 80°C, a curve of log C_{H_2} *vs.* $1/T$ was prepared for H_2 in H_2O, and another for H_2 in 1*N* Cs_2CO_3 was constructed parallel to it, passing through the 25°C value. All solubility values were corrected to the appropriate hydrogen partial pressure.

The diffusion coefficient of H_2 in H_2O (10) was used to calculate values for $\left(\dfrac{\mathcal{D}_{AB}\mu}{T}\right)$ as a function of temperature. These values and the μ values for the electrolytes were then used to calculate $\mathcal{D}_{AB}$ values for hydrogen in the electrolytes. The properties of the systems studied are summarized in Table I. These properties were used to calculate the values of the terms for Eq. [3].

If Eq. [3] adequately represents the behavior of the system with respect to all properties and variables over the ranges investigated, then all data points should lie on a straight line of slope — 1/2 when log j_D is plotted against log Re. The plot in Fig. 2 shows clearly that all of the data for the three sets of experimental conditions are adequately represented by a single straight line having a slope of — 1/2 and a

Table I. Properties of systems used in hydrogen limiting current studies

Electrolyte	C_{H_2}, moles/cm³	$\mathcal{D}_{H_2-m}$, cm²/sec	μ, g/cm sec	ρ, g/cm³	p_{H_2}, atm
1N $HClO_4$, 25°C	8.268×10^{-7}	4.040×10^{-5}	8.926×10^{-3}	1.0550	0.975
1N Cs_2CO_3, 24°C	5.520×10^{-7}	3.482×10^{-5}	1.036×10^{-2}	1.1326	0.975
1N Cs_2CO_3, 80°C	2.816×10^{-7}	7.823×10^{-5}	4.152×10^{-3}	1.0945	0.5565

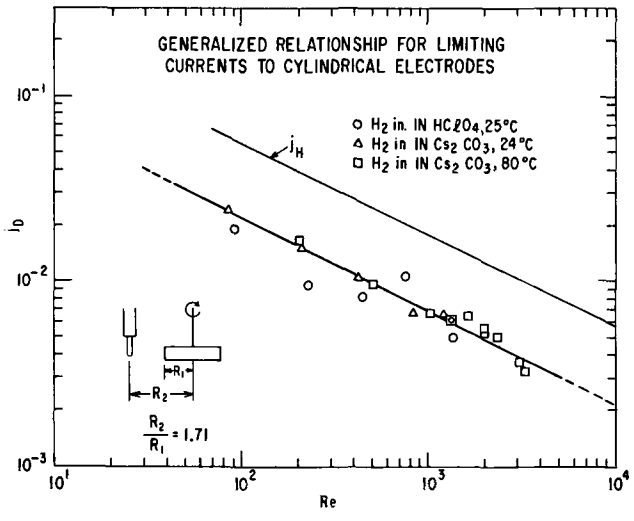

Fig. 2. Mass transport parameter j_D as a function of Reynolds number, for the limiting current of H_2 at a cylindrical anode in a simple paddle-stirred electrochemical cell.

value of A of 0.22 over the Reynolds number range from 80 to about 3500. The fact that a single line represents all of the data is good support for the validity of the relationships expressed by the chosen dimensionless groups, because i_L for a given stirring speed varied by more than 60% from one electrolyte to another. This large variation was caused largely by differences in the hydrogen concentration and diffusion coefficient and the viscosities of the electrolytes.

The line marked j_H represents the results for heat transfer to a cylinder as reported by McAdams (11), where the slope is — 1/2 and A is 0.6. Realizing that the stirrer-tip velocity is actually higher than the velocity of the fluid near the electrode, it is easily shown that a value 20% of the stirrer-tip velocity superimposes the present experimental results on the j_H line.

We can conclude that expressions of the form

$$j_D = A\,\mathrm{Re}^{-1/2}$$

and

$$\mathrm{Nu} = A\,\mathrm{Re}^{1/2}\,\mathrm{Sc}^{1/3}$$

accurately represent the mass transfer, *i.e.*, limiting current, behavior in simple stirred vessels commonly used by electrochemists. Furthermore, a single measurement of the limiting current for any system can be used to determine the value of A for each apparatus. Once the value of A is known, i_L can be calculated for any other set of conditions by substituting the appropriate values of the system properties into the above equations. The sensitivity of the results to the relative positions of the test electrode and the stirrer was not determined. However, it is expected that as long as the electrode-stirrer distance is significantly smaller than the distance of the stirrer and/or electrode from the vessel walls (say a factor of 3), the results will follow the functional dependence found here, but with a different numerical value for the parameter A.

Acknowledgment

It is a pleasure to thank Dr. A. D. Tevebaugh for his participation in the design and construction of the apparatus.

This work is a part of the program under contracts DA-44-009-AMC-479(T) and DA-44-009-ENG-4909, ARPA Order No. 247 with the U.S. Army Engineer Research and Development Laboratories, Ft. Belvoir, Va., to develop a technology which will facilitate the design and fabrication of practical military fuel cell power plants for operation on ambient air and hydrocarbon fuels.

Manuscript received Nov. 7, 1966; revised manuscript received Dec. 30, 1966.

Any discussion of this paper will appear in a Discussion Section to be published in the December 1967 JOURNAL.

Nomenclature

A, A'	constants in Eq. [1] and [3]
C	concentration, moles/cm³
D	electrode diameter, cm
$\mathcal{D}_{AB}$	diffusion coefficient, cm²/sec
$\mathbf{F}$	Faraday's constant, 96,487 coul/equiv
i_L	limiting current density, amp/cm²
j_D	mass transport parameter defined by Eq. [2], dimensionless
m	exponent in Eq. [1], dimensionless
n	exponent in Eq. [1], dimensionless
N	number of equivalents per mole of diffusing species
Nu	Nusselt number, defined in Eq. [5], dimensionless
Re	Reynolds number, defined in Eq. [4], dimensionless
Sc	Schmidt number, defined in Eq. [6], dimensionless
T	temperature, °K
v	velocity of fluid flowing past the electrode, cm/sec
X_A	mole fraction of diffusing species, dimensionless
μ	viscosity of electrolyte, g/cm sec
ρ	density of electrolyte, g/cm³

REFERENCES

1. R. B. Bird, W. E. Stewart, and E. N. Lightfoot, "Transport Phenomena," John Wiley & Sons, Inc., New York (1960).
2. W. M. Kays, "Convective Heat and Mass Transfer," McGraw-Hill Book Co., New York (1966).
3. E. L. Simons, E. J. Cairns, and L. D. Sangermano, *Talanta*, 13, 199 (1966).
4. E. L. Simons, E. J. Cairns, and L. D. Sangermano, *Electrochem. Tech.*, 2, 355 (1965).
5. H. Schlichting, "Boundary Layer Theory," 4th ed., McGraw-Hill Book Co., New York (1960).
6. V. G. Levich, "Physicochemical Hydrodynamics," Prentice-Hall, Englewood Cliffs, N. J. (1962).
7. L. L. Bircumshaw and A. C. Riddiford, *Quarterly Revs.*, 6, 157 (1952).
8. T. K. Sherwood and R. L. Pigford, "Absorption and Extraction," McGraw-Hill Book Co., New York (1952).
9. H. S. Harned and B. B. Owen, "The Physical Chemistry of Electrolytic Solutions," 3rd ed., Reinhold Publishing Co., New York (1958).
10. G. Tamman and V. Jessen, *Z. anorg u. allgem. Chem.*, **179**, 125 (1929); C. A., **23**, 4869 (1929).
11. W. H. McAdams, "Heat Transmission," 2nd ed., p. 221, McGraw-Hill Book Co., New York (1942).

Oxide Dissolution and Its Effect on the Corrosion of 1100 Aluminum in Water at 70°C

Shiro Mori and J. E. Draley

Metallurgy Division, Argonne National Laboratory, Argonne, Illinois

The rate of corrosion of aluminum in water and in many aqueous solutions is generally believed to be limited by a film of oxide produced as corrosion product. If such a film is dissolving at a sufficiently great rate, it is clear that the corrosion rate will ultimately be determined by the dissolution rate. The rate at which dissolution occurs can be expected to depend on the concentration of aluminum oxide in the water. Such dependences have been reported by Dillon (1) and Dickinson (2) for pressurized water and by Hatcher and Rae (3) for in-reactor water well below the boiling point.

In our own research on the corrosion of 1100 aluminum, it has been observed that at 70°C and below, a heavy layer of porous, not significantly protective, bayerite covers a thinner layer (4, 5). This protective layer is believed to be boehmite on the basis of our own (4) and other observations of early formation (6-8). In laboratory exposure to refreshed distilled water, we have seen no evidence that the protective film dissolves or that the corrosion rate is influenced by corrosion product dissolution. In fact, contamination of the water with corrosion product (perhaps alkaline) has increased corrosion. In an effort to resolve these questions specimens have been exposed under circumstances where material balances allow the deduction of the variation of the corrosion product composition with time.

Specimens of 1100 aluminum and exposure conditions were the same (continuously refreshed, $> 10^6$ ohm-cm H_2O, saturated with oxygen) as in a previous investigation (5). Effluent water from the test chamber was accumulated by controlled-level evaporation in a flask to which sulfuric acid was originally added. Periodically, this solution was carefully removed, with acid rinsing, to a platinum dish and evaporated to dryness. The residue was dissolved in molten $KHSO_4$; this was then dissolved and analyzed colorimetrically for aluminum content. Extraneous aluminum was found to come from the source water (1-2 μg/l), from Pyrex glassware, and from the reagents (notably the $KHSO_4$). Correction was made by operating a blank specimen chamber, using the same water supply as for the chamber containing the specimen and making the identical analysis for aluminum. Sometimes the water flow rates were not identical for the two chambers, necessitating a calculated correction based on the concentration of aluminum in the "blank" water. All glass apparatus was leached for several weeks before use.

The amount of metal corroded from a specimen was measured at intervals, using the eddy current gauge developed for the purpose (9). At the same time the dried specimen was weighed, with its adherent corrosion product. The most reproducible drying was obtained overnight at room temperature in a desiccator containing anhydrous calcium sulfate (Drierite). An hour in the constant temperature, constant humidity balance room ensured reproducible readings on the microbalance.

Three quantities were thus available as a function of time: weight gain (G), metal loss by corrosion (L), and the aluminum content of the dissolved corrosion product (ξ). Using the assumption that the adherent corrosion product (as weighed) consisted entirely of boehmite (AlOOH) and bayerite [$Al(OH)_3$], the aluminum contents of these substances on the specimen were calculated from the following

$$b(\text{bayerite}) = \frac{27}{18}G + \frac{60}{18}\xi - \frac{33}{18}L$$

$$a(\text{boehmite}) = L - (b + \xi)$$

The five quantities are shown as a function of time in Fig. 1, for one specimen. The scale of the ordinate is sensitive; various amounts have been subtracted from the quantities in order to make it possible to plot them together. For example, G varied from about 57 to something under 61 mg/dm^2.

It is seen that for a period the amount of corrosion varied with the logarithm of time in accord with previous observations (5); unaccountably, this specimen then deviated from this behavior. The aluminum content of the dissolved corrosion product was much smaller and exhibited a quite different kinetic behavior, as shown on an expanded scale in Fig. 2. After the first 5 days, product dissolved at a constant rate, to provide 11.9 μg Al/dm^2-day in the water (about 0.4 μg Al/l).

The calculated adherent boehmite (Al content) is small and closely follows the metal-corroded curve in Fig. 1. From this it is judged that, predominantly, the

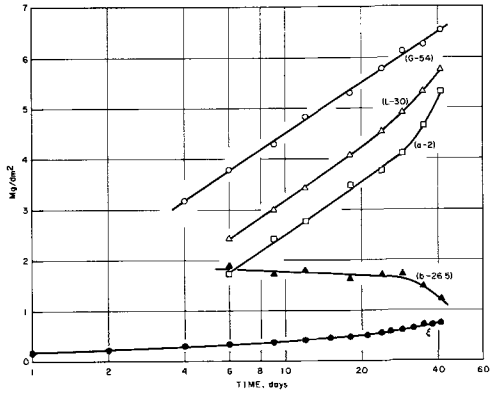

Fig. 1. Summary of corrosion for one specimen of 1100 aluminum in oxygenated water at 70°C.

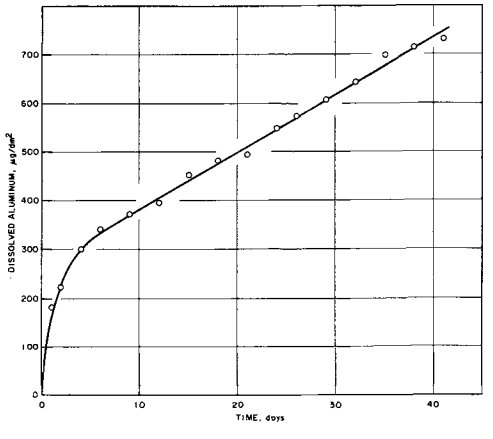

Fig. 2. Corrosion product dissolved from specimen of Fig. 1

corrosion process consists of the formation of boehmite, which is not subsequently lost. The bayerite, all formed within the first day or two of exposure (5), then slowly dissolves. The "b" points in Fig. 1 show too much scatter to judge curve shape. A least squares fit provides an average rate of dissolution of 14 μg Al/dm^2-day. (Compare with analyzed Al pickup of 11.9).

The results do not support these conclusions quite as well as has been suggested. The calculated value of "a" was negative for the first weighing. This is probably the consequence of a few per cent of excess moisture in the adherent corrosion product as weighed. This difficulty cannot be avoided readily; if bayerite is kept in a dry environment, moisture is continually lost past its nominal stoichiometric composition. If corrections are estimated for this factor, little change is made in the slopes of the "a" and "b" curves. It seems clear that within experimental error only boehmite is formed as a corrosion product (after the first few days), and that only the unprotective porous bayerite dissolves.

Similar data are available for two other specimens. Only small variations in behavior were exhibited; all data justify the concluding statement above.

These results obviously are not typical of some situations studied by other investigators. It is important to be aware that oxide dissolution can be important in determining aluminum corrosion rate, even though it is not so under conditions of this investigation.

Manuscript received April 11, 1966; revised manuscript received Dec. 21, 1966. This work was done under the auspices of the United States Atomic Energy Commission.

Any discussion of this paper will appear in a Discussion Section to be published in the December 1967 JOURNAL.

REFERENCES

1. R. L. Dillon, U.S.A.E.C. Report HW-61089, Dissolution of Aluminum Oxide as a Regulating Factor in Aqueous Aluminum Corrosion (1959).
2. D. R. Dickinson, *Corrosion*, **21**, 19 (1965).
3. S. R. Hatcher and H. K. Rae, *Nuclear Science and Eng.*, **10**, 316 (1961).
4. J. E. Draley, Proc. AEC-Euratom, Aqueous Corrosion of Reactor Materials, Brussels, Oct. 14-16, 1959.
5. J. E. Draley, Shiro Mori, and R. E. Loess, *This Journal*, **110**, 622 (1963).
6. R. K. Hart, *Trans. Faraday Soc.*, **53**, 1020 (1956).
7. D. Altenpohl and W. Post, *This Journal*, **108**, 628 (1961).
8. M. Kawasaki, S. Nomura, H. Itami, Y. Kondo, T. Kondo, N. Ito, and C. Akutsu, Proc. Conf. Corrosion of Reactor Materials, Salzburg, Int. Atomic Energy Agency, Vienna, 1962.
9. S. Mori, R. E. Loess, and J. E. Draley, *Corrosion*, **19**, 269t (1963).

The Corrosion of 1100 Aluminum in Water from 50° to 95°C

J. E. Draley, Shiro Mori, and R. E. Loess

Metallurgy Division, Argonne National Laboratory, Argonne, Illinois

After an initial period of a few days duration, the amount of corrosion of 1100 aluminum in water below the boiling point varies with the logarithm of time (1-3). Reproducibility in measured rate constants has not been good. This is felt to be due largely to variation in test parameters such as the water refreshment rate and flow pattern, and the number and position of the specimens in the chamber. Sensitivity to these things has appeared to be maximum during the initial exposure period [cf. ref. (2)].

For purposes of considering reaction mechanisms it is desirable to know the dependence of corrosion behavior on temperature and dissolved oxygen concentration. Because of the variability of past results, it has not been possible to determine reliably the influence of these parameters. The present experiments were therefore run with identical flow rates and specimen disposition in order to provide comparable data.

Materials and general methods were the same as described previously (2). Water resistivity remained well above 1 megohm-cm; it was saturated with cylinder oxygen or helium to provide a choice of two levels of dissolved oxygen, and passed at a low rate (18 cc/min for first 4 days, then 8 cc/min) through the test chamber containing 4 specimens. For those instances where the saturating gas was helium, the oxygen content was monitored with a thallium column (small modification of Industrial Instruments Analyzer type OA-1). For the 50° and 70° tests, the water entering the cell averaged 0.41 mg O_2/l (range: 0.31-0.50); entering the 95° cell dissolved oxygen averaged 0.60 mg/l (range 0.43-1.00). Perhaps 3/4 of this amount would be expected to be lost to the gas phase when the solution was heated to 95°.

Specimens were from the same extruded rod as had been used previously. They were machined, annealed,

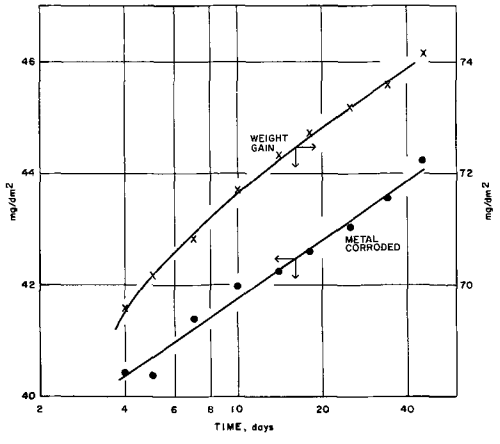

Fig. 1. Corrosion of a single specimen in He-saturated H_2O at 70°C.

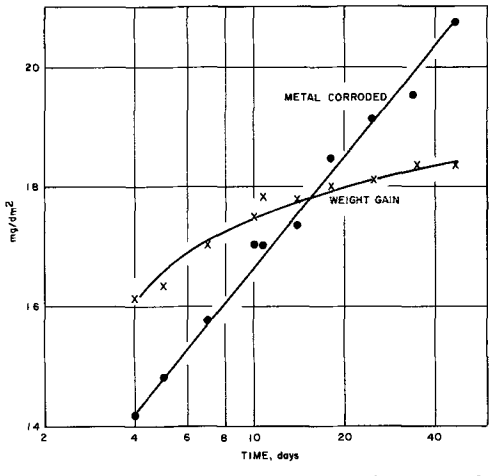

Fig. 2. Corrosion of a single specimen in He-saturated H_2O at 95°C.

Table I. Logarithmic slopes and intercepts for corrosion of 1100 aluminum in water

Temp, °C		O_2-saturated Slope, mg/dm²-cycle	O_2-saturated Intercept, mg/dm²	He-saturated Slope, mg/dm²-cycle	He-saturated Intercept, mg/dm²
50		3.24	37.04	2.80	38.91
		3.13	27.24	2.70	37.65
		3.20	36.60	2.73	38.36
		3.00	35.53	2.26	34.78
	Avg	3.14	36.59	2.62	37.43
70		3.60	38.00	3.72	39.40
		3.79	37.43	3.57	38.25
		3.36	38.00	3.22	38.44
		3.65	36.76	3.42	37.83
	Avg	3.60	37.55	3.48	38.48
95		8.65	7.70	5.75	11.25
		9.30	2.80	4.62	13.32
		7.35	6.13	6.14	10.51
		6.00	6.23	6.13	9.61
	Avg	7.83	5.72	5.66	11.17

and etched under the same conditions as before. They were removed periodically from the test, starting after 4 days' exposure, weighed to ± 10 μg (29 cm² area) after air drying (in the constant temperature and humidity balance room), and the change in the average metal radius determined to a ± 50Å with the eddy current gauge developed for the purpose (4). Gauge corrections for metallurgical change in the specimens at corrosion temperature were required only at 95°. Total test duration was typically 45 days.

Corrosion was approximately logarithmic in all six tests, for the 4-45 day interval. Data for two typical specimens in helium-saturated water are shown in Fig. 1 (70°) and Fig. 2 (95°). Slopes and logarithmic intercepts (extrapolated values at 1 day) of the metal corroded curves are given, for all specimens, in Table I.

There is a consistent increase in rate constant (slope) with increasing temperature, and with increased oxygen concentration. Intercepts are much lower at 95° than at 50° or 70°.

The specimen weight gains increased with time slightly more rapidly than did the metal losses at 50° and 70°, as illustrated in Fig. 1. At 95°, however, it can be calculated from Fig. 2 that (old) corrosion product was being lost to the water more rapidly than new product was being formed during the interval 4 to 47 days.

There is evidence in Table I that precautions were not sufficient to provide rate constants and intercepts which can be compared to obtain accurately the effects of temperature and oxygen content. It is possible, however, to make qualitative comparisons. At 95° there was an inverse relationship between intercept and rate constant. In fact, a continuous trend was observed in these values for specimens from the two tests (oxygenated and low-oxygen). Generally, higher oxygen content resulted in lower intercepts and higher slopes. This is logical in view of: (*a*) known ability of oxygen to diminish the local *p*H increase observed at the specimen surface during the initial stages of corrosion (1, 5), (*b*) the direct dependence of intercept on solution *p*H (1). From these factors, the absence of oxygen can allow the development of a higher *p*H and a thicker oxide (boehmite) film during initial stages; later, when the alkalinity has dispersed, the thicker film might lead to lower corrosion rate.

At 50° the presence of oxygen again generally led to lower intercepts and higher rate constants. Within each test there was correlation opposite to that at 95°: higher rate constants accompanied higher intercepts. At 50° (but not at 95°) a relatively heavy layer of porous bayerite [$Al(OH)_3$] forms during the initial exposure period. It is suggested that, when this layer is heavier, conditions are less favorable beneath the bayerite at what is believed to be the rate-controlling film of boehmite (AlOOH).

An Arrhenius plot of rate constants does not lead to a particularly good straight line. The approximate slope corresponds to the low activation energy of 4 kcal/g-atom. On the basis of the best kinetic model we have to date been able to develop, the corrosion rate is determined by the properties and thickness of a cracked layer of boehmite formed by degradation of the (always thin) primary product, perhaps also boehmite. Variation of the protectiveness (related to porosity) of such a layer with temperature is unknown; if the porosity decreased with increasing temperature, an unusually low temperature coefficient for the corrosion rate constant would be expected.

Manuscript received April 11, 1966; revised manuscript received Dec. 21, 1966. This work was done under the auspices of the United States Atomic Energy Commission.

Any discussion of this paper will appear in a Discussion Section to be published in the December 1967 JOURNAL.

REFERENCES

1. J. E. Draley, Aq. Corr. 1100 Aluminum and of Al-Ni Alloys, Proc. AEC-Euratom Conf., Aq. Corr. Reactor Materials, Brussels, Oct. 14-16, 1959; TID-7585 (AEC), pp. 165-187.
2. J. E. Draley, Shiro Mori, and R. E. Loess, *This Journal*, **110**, 622 (1963).
3. M. Kawasaki, S. Nomura, H. Itami, Y. Kondo, T. Kondo, N. Ito, and C. Akutsu; Work on Corrosion of Aluminum in Water at Japan Atomic Energy Research Institute; Proc. Conf. Corr. Reactor Materials, Salzburg, June 4-8, 1962, Vol. I, pp. 427-475 (Int. At. Energy Agency).
4. S. Mori, R. E. Loess, and J. E. Draley, *Corrosion*, **19**, 269t (1963).
5. S. Mori, R. E. Loess, and J. E. Draley, *ibid.*, **19**, 165t (1963).

Oxide Film Growth over Five Years on Some Aluminum Sheet Alloys in Air of Varying Humidity at Room Temperature

Hugh P. Godard

Aluminium Laboratories Limited, Kingston, Ontario, Canada

The room temperature surface oxidation of aluminum in air has been extensively studied using various techniques (1-9). Vernon *et al.* (10) found that the oxide film growth followed a logarithmic law of the form

$$x = K_1 \log (at + c) \qquad [1]$$

where x is the film thickness at time t, and K_1, a, and c are constants. For dry oxygen, Hart (8) fitted his data to an inverse logarithmic relationship

$$1/x = -K_2 \log (t + t_0) + K_3 \qquad [2]$$

where K_2, K_3, and t_0 are constants. For moist oxygen, the growth law was said to be logarithmic during the first 10 hr and finally inverse logarithmic. Dignam (9) has shown that, if the decrease in specific ionic conduction of the film is taken into account, the anodic overvoltage across the film after exposure to dry oxygen obeys a logarithmic relationship with respect to time. In all instances it was concluded that a maximum

Table I. Composition of metal used

Alcan* alloy	Element, %								
	Cu	Fe	Mg	Mn	Si	Cr	Zn	Ti	Ga
S.P.	0.002	0.002	0.001	—	0.001	—	—	—	—
CA-1S	0.01	0.27	0.001	—	0.011	—	—	—	—
CA-2S	0.01	0.47	0.001	—	0.16	—	—	—	—
CA-3S	0.01	0.38	0.001	1.12	0.27	—	—	—	—
CA-24S-T4	4.52	0.34	1.44	0.63	0.25	<0.10	<0.10	0.01	—
CA-50S-T5	0.02	0.26	0.66	—	0.30	—	—	0.02	—
CA-B54S-O	0.02	0.23	4.19	0.29	0.09	—	—	0.02	—
CA-55S-T6	0.06	0.22	1.40	—	0.65	0.18	—	0.10	—
CA-57S-H34	0.02	0.25	2.35	—	0.10	0.26	—	0.02	—
CA-65S-T6	0.33	0.40	0.99	0.03	0.56	0.24	—	—	—
CA-75S-T6	1.55	0.30	2.46	0.02	0.13	0.16	5.60	0.03	—
S.P. + 0.05% Fe	0.001	0.06	0.001	—	0.001	—	—	—	—
S.P. + 0.10% Fe	0.001	0.11	0.001	—	0.001	—	—	—	—
S.P. + 0.03% Si	0.004	0.003	0.001	—	0.033	—	—	—	—
S.P. + 0.20% Si	0.002	0.002	0.001	—	0.24	—	—	—	—
S.P. + 0.2% Cu	0.19	0.004	0.001	—	0.001	—	—	—	—
S.P. + 1.5% Cu	1.55	0.005	0.001	—	0.002	—	—	—	—
S.P. + 0.5% Mn	0.002	0.003	0.001	0.53	0.002	—	—	—	—
S.P. + 2.0% Mn	0.002	0.003	0.001	2.20	0.002	—	—	—	—
S.P. + 0.3% Zn	0.002	0.004	0.001	—	0.002	—	0.31	—	—
S.P. + 2.0% Zn	0.002	0.004	0.002	—	0.002	—	2.04	—	—
S.P. + 0.02% Ga	0.002	0.003	0.001	—	—	—	—	—	0.021
S.P. + 0.10% Ga	0.002	0.002	0.002	—	—	—	—	—	0.093

* Designation of Alcan Aluminium Limited Alloys.

film thickness was reached and that this value and the rate of oxidation increased as the relative humidity increased.

In this note, we report the rate constants for the oxidation of aluminum and some of its alloys exposed to air at various relative humidities, at room temperature, for periods of five to six years. The oxidation rates were determined from weight gain data.

The 5 x 20 cm coupons were cut from sheet of ten commercial alloys produced by the Aluminum Company of Canada, Limited, Kingston Works. In addition, superpurity (S.P.) sheet (>99.99% Al) and twelve S.P. base experimental alloys containing single additions of Fe, Si, Cu, Mn, Zn, and Ga, prepared in these Laboratories, were included. The compositions are given in Table I.

The coupons were prepared by abrading them on both sides with a dry wire brush until a smooth satin-like texture was produced. Quite arbitrarily, it was assumed that the surface roughness factor was two, and this factor was used in all subsequent calculations of film thickness.

Eight coupons of each alloy were prepared and, after weighing on a microbalance, were stored on edge in desiccators. The relative humidity in the desiccators was 52, 72, 85, and 100%, respectively. The temperature was maintained in the 20°-25°C range over the five to six year period. The coupons were weighed at increasing intervals to two years, then again at five to six years.

Figure 1 is a semilogarithmic plot of the weight gain data for the CA-3S alloy at the four relative humidities. Initially, the weight gain (w) followed a logarithmic law, but as t increased the weight gains exceeded the values predicted by Eq. [1]. Similar curves were obtained for the other alloys. An attempt to fit the results to a log-log plot was no more successful.

Figure 2 shows a plot of $1/w$ vs. log t for the CA-3S alloys. It is obvious that the inverse logarithmic relationship observed by Hart (8) is obeyed in the present work. The data for all the alloys were analyzed by computer. A least squares fit was obtained between the experimental values t_i, w_i, and the line

$$1/w_i = -K \log (t_i + T_0) + K' \qquad [3]$$

Values of K and K' were calculated for a range of the parameter T_0 between 0 and 10 days in increments of 0.5 hr for the first 24 hr, in increments of 1.0 hr for 24 to 120 hr, and in increments of 2 hr for 120 to 240 hr. It was found that in all cases the variance (S^2) was smallest when $T_0 = 0$. Values of K, K', and S^2 for $T_0 = 0$ are given in Table II. These values indicate that the rate of oxidation increases with increasing humidity. It is possible, in view of the method of surface preparation, that the fit of the results to an inverse logarithmic relationship is fortuitous.

The thickness of the oxide films on the coupons after five years was calculated from the expression

$$\text{Thickness (Å)} = \frac{\text{wt gain } (\mu g/dm^2) \times 2.13}{\text{film density} \times \text{surface roughness factor}} \qquad [4]$$

where the atomic mass ratio $Al_2O_3/O_3 = 2.13$. The assumed film density was 3.0 g/cm^3, and the surface roughness factor taken as 2.0. The calculated film thickness (Table III) are included to give an idea of

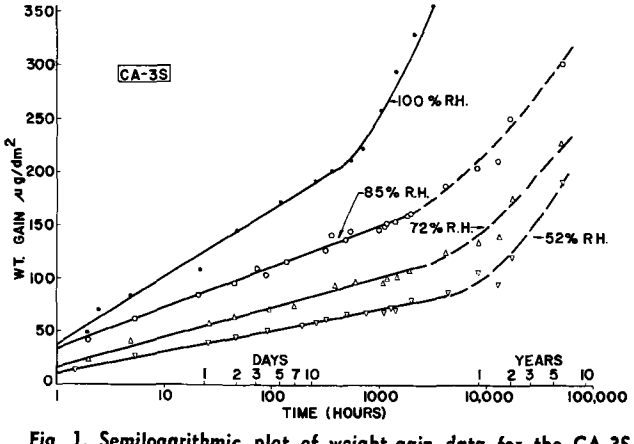

Fig. 1. Semilogarithmic plot of weight-gain data for the CA-3S alloy.

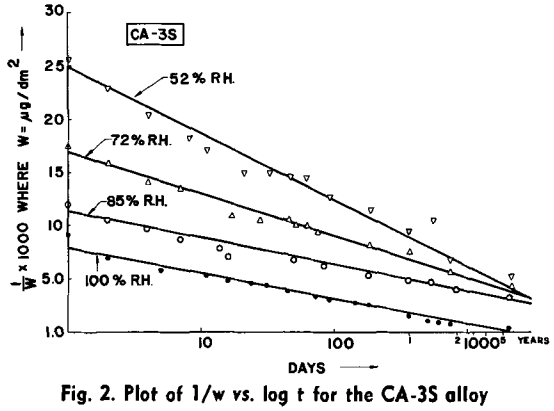

Fig. 2. Plot of 1/w vs. log t for the CA-3S alloy

Table II. Atmospheric oxidation of aluminum alloys at room temperature
(Values of constants in equation $1/w_i = -K \log (t_i + T_o) + K'$ for $T_o = 0$)

Alloy % rel. humidity	$K \times 10^{-2}$ 52	72	85	100	$K' \times 10^{-2}$ 52	72	85	100	Variance $\times 10^{-6}$ 52	72	85	100
S.P.	1.097	0.544	0.454	0.360	4.250	2.215	1.899	1.393	79.6	15.9	6.89	5.51
CA-1S	1.449	0.510	0.439	0.415	6.310	2.493	2.089	1.649	201	13.8	4.82	6.90
CA-2S	0.764	0.390	0.547	0.316	3.664	2.053	2.506	1.300	17.8	2.52	7.34	1.74
CA-3S	1.517	0.653	0.985	0.285	6.107	3.131	2.581	1.263	326	23.0	2.98	0.303
CA-24S-T4	2.074	1.449	0.758	0.504	9.520	6.283	3.237	2.056	314	60.5	24.7	6.12
CA-50S-T5	1.115†	0.490	0.430	0.150	3.701	2.271	1.876	0.627	19.1	5.45	3.49	0.344
CA-B54S-0	0.949	0.845	0.571	0.265	4.409	3.778	2.500	1.037	38.7	8.56	4.48	1.00
CA-55S-T6	7.872*	0.839	0.540	0.252	1.166	3.950	2.474	1.042	39.7	22.0	7.76	0.397
CA-57S-H34	1.040	0.711	0.445	0.353	5.403	3.429	2.183	1.387	16.3	8.94	4.23	1.63
CA-65S-T6	1.353	0.573	0.713	0.599	5.920	2.903	3.191	2.341	61.1	3.01	10.0	9.18
CA-75S-T6	1.439	0.619	0.373	0.369	6.253	3.081	1.980	1.457	157	3.18	2.47	2.17
S.P. + 0.05% Fe	0.524		0.298	0.154	2.558		1.446	0.632	2.29		0.611	0.126
S.P. + 0.10% Fe	0.526	0.407	0.275	0.161	2.540	1.935	1.382	0.681	3.74	4.64	0.647	0.0849
S.P. + 0.03% Si	0.666	0.424	0.278	0.234	3.085	2.088	1.378	0.954	6.49	5.03	0.895	0.424
S.P. + 0.20% Si	0.712	0.436	0.317	0.248	3.599	2.283	1.660	1.013	18.8	2.53	0.945	0.429
S.P. + 0.20% Cu	0.828	0.380	0.462	0.298	3.904	1.945	2.037	1.234	12.2	1.56	8.61	2.74
S.P. + 1.5% Cu	0.747	0.639	0.815	0.335	4.037	3.219	3.600	1.412	9.44	21.7	35.6	1.38
S.P. + 0.5% Mn	0.806	0.439	0.310	0.181	3.943	2.272	1.674	0.828	17.8	6.02	1.86	0.281
S.P. + 2.0% Mn	0.749	0.391	0.297	0.284	3.644	2.102	1.624	1.183	22.8	2.41	1.13	1.98
S.P. + 0.30% Zn	0.663	0.443	0.291	0.338	2.952	2.076	1.376	1.273	4.22	1.36	1.08	1.44
S.P. + 2.00% Zn	0.576	0.449	0.314	0.199	2.795	2.291	1.563	0.830	5.60	1.59	1.71	0.198
S.P. + 0.02% Ga	0.687	0.446	0.259	0.219	3.039	2.084	1.261	0.857	4.80	1.95	0.298	0.256
S.P. + 0.10% Ga	0.690	0.425	0.285	0.209	3.054	1.993	1.321	0.850	9.08	1.31	0.882	0.382

† Based on 6 results. * Based on 4 results.

Table III. Calculated thickness of oxide film on aluminum alloys after five years
(in angstrom units)

Alcan alloy	Relative humidity 52%	72%	82%	100%
S.P.	222	281	378	1710*
CA-1S	73	94	150	2160†
CA-2S	77	109	132	1095†
CA-3S	65	74	105	704†
CA-24S-T4	41	67	112	940†
CA-50S-T5	86	142	161	1620*
CA-B54S-O	65	114†	185†	2060†
CA-55S-T6	46	135	115†	1190†
CA-57S-H34	36	106†	129†	1460†
CA-65S-T6	55	84	94†	835†
CA-75S-T6	40	156†	120†	1120†
S.P. + 0.05% Fe	118	170	257	2170*
S.P. + 0.10% Fe	121	174	228	3080*
S.P. + 0.03% Si	174	138	228	2780†
S.P. + 0.20% Si	61	93	99	1240*
S.P. + 0.20% Cu	91	133	202	482†
S.P. + 1.5% Cu	69	91	117	540†
S.P. + 0.50% Mn	63	90	103	483
S.P. + 2.0% Mn	61	102	117	421†
S.P. + 0.30% Zn	167	194	272	1850*
S.P. + 2.0% Zn	75	93	141	2340†
S.P. + 0.02% Ga	191	205	261	1180*
S.P. + 0.10% Ga	165	209	303	2000*

* Black stains down side or along bottom edge.
† Whitish film along bottom edge.

the magnitude of oxide film growth at the end of five years.

The coupons exposed at 100% R. H. were observed to have dark spotty stains, which developed between two and five years. These spots were originally thought to be caused by droplets of condensation. However, this would be expected to lead to abnormally high weight gains since film growth is much more rapid under water and should give erratic results. On the contrary, the 100% R.H. results showed the smallest variation from the inverse logarithmic function so that the values are believed to be correct. No dark staining was observed at lower humidities, but some coupons exposed at 85% R.H. and 100% R. H. had a narrow band of white film along the edge of the coupon that rested on the desiccator plates.

Manuscript received Dec. 12, 1966.

Any discussion of this paper will appear in a Discussion Section to be published in the December 1967 JOURNAL.

REFERENCES

1. W. H. J. Vernon, *Trans. Faraday Soc.*, **23**, 113 (1927).
2. A. Steinheil, *Ann. Phys. Lpz.*, **19**, 465 (1934).
3. N. Cabrera, J. Terrein, and J. Hamon, *Compt. rend.*, **224**, 1558 (1947).
4. N. Cabrera and J. Hamon, *ibid.*, **225**, 59 (1947).
5. G. Hass, *Optik.*, **1**, 134 (1946).
6. M. Morize and P. Lacombe, *Compt. rend.*, **222**, 658 (1946).
7. M. S. Hunter and P. Fowle, *This Journal*, **103**, 482 (1956).
8. R. K. Hart, *Proc. Roy. Soc. (London)*, **A236**, 68 (1956).
9. M. J. Dignam, *Can. J. Chem.*, **41**, 537 (1963).
10. W. H. J. Vernon, E. Akeroyd, and E. G. Stroud, *J. Inst. Met.*, **65**, 301 (1939).

Preliminary Study of the Chemical Polishing of α-Corundum Surfaces with Vanadium Pentoxide

M. M. Faktor, D. G. Fiddyment, and G. R. Newns

Post Office Research Station, Dollis Hill, London, England

Studies of the epitaxial deposition of thin films of silicon on inert substrates such as α-corundum require polished, clean surfaces free from work damage. Corundum substrates are usually obtained by accurately sawing wafers of the required crystallographic orientation from a large, single crystal. The faces of the wafers are mechanically polished by using diamond powder of diminishing particle size for each successive stage. These processes produce a high degree of polish and flatness, but they introduce work damage such as scratches and associated regions of strain and disorder in the surface. Work damage can be removed by flame-polishing (1, 2), immersion in hot orthophosphoric acid (3-5), and molten salts (1, 5-7), or by reaction

with silicon vapor (8, 9). Attempts to polish corundum wafers by immersion in various molten salts met with limited success, and etched surfaces were usually obtained. Some success was achieved with orthophosphoric acid, but this process was difficult to control and was sensitive to the crystallographic orientation of the corundum wafers. Specimens heated in a vacuum after orthophosphoric acid polishing evolved white fumes in which phosphorus was detected mass spectroscopically (10).

A preliminary examination of molten vanadium pentoxide as a polishing agent gave encouraging results which are reported here, although the investigation is still in progress because of the technological importance of the problem.

The polishing mechanism appears to be independent of crystallographic orientation, since wafers of poorly orientated material (as much as 20° from the basal plane) have been polished successfully.

Specimens were usually 1 cm square wafers of α-corundum cut from a large single crystal grown by the Verneuil process. The wafers were accurately cut, perpendicular to the "c" axis and were approximately 1 mm thick. Each face was lapped and mechanically polished with a final abrasive of 0.5μ diamond dust. Other specimens which were poorly orientated and with an inferior surface preparation (sometimes in the "as-sawn" condition) were also used.

Weighed specimens were suspended vertically in molten vanadium pentoxide by a fine platinum wire. The vanadium pentoxide was contained in a platinum crucible, and heating was carried out in a standard crucible furnace. Specimens normally remained static in the melt, but some specimens were rotated. Specimens were immersed slowly in the melt and allowed to cool slowly after removal from the crucible to avoid thermal shock. The residual solidified vanadium pentoxide was removed from the specimens by immersion in hot concentrated hydrochloric acid. Specimens were washed in distilled water followed by alcohol, and air dried before being reweighed and examined.

For obtaining of kinetic data a fresh charge of vanadium pentoxide was used for each experiment. In other experiments an original melt was sometimes reused, but concentration of alumina in the melt was noted.

Preliminary work was carried out with poorly orientated material having either a 1μ diamond powder final polish or the original sawn surface. Opaque specimens with as-sawn surfaces were rendered transparent by immersion in molten vanadium pentoxide (see Fig. 1).

In a few of these preliminary experiments a pale violet film or bloom appeared on surfaces after immersion in the melt. Immersion in concentrated hydrochloric, nitric or hydrofluoric acids, aqua regia, or a solution of catechol in hydrazine hydrate indicated that the bloom is moderately resistant to chemical attack. Prolonged heating (~24 hr) in air at 1200°C resulted in the complete disappearance of the bloom, but it is not clear whether removal was by evaporation or by diffusion into the specimen as weight changes on heating were insignificant ($< 1 \times 10^{-4}$g).

Blooming also occurred to a lesser degree in later work with well orientated and finished specimens. The majority of specimens did not develop bloomed surfaces after chemical polishing in vanadium pentoxide. As yet the conditions leading to bloomed surfaces and the composition of the bloom have not been elucidated.

Optical and Talysurf assessment was made on material which was well orientated and highly polished and were correlated with alumina weight loss. Figure 2 shows the effect on the surface as material is pro-

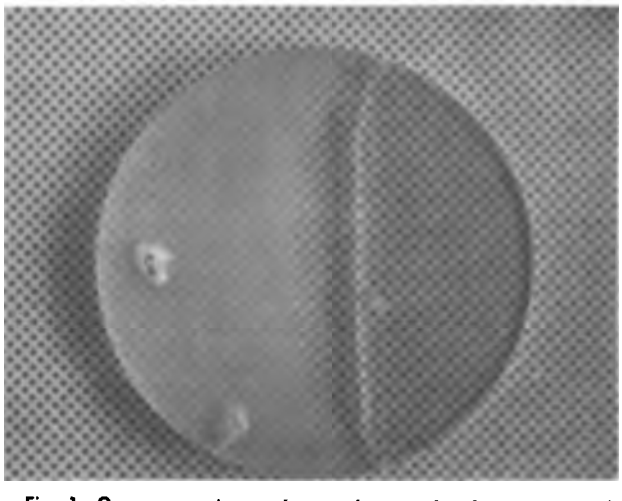

Fig. 1. Opaque specimen of corundum rendered transparent by immersion in molten vanadium pentoxide (15 minutes at 900°C). Magnification x 3.

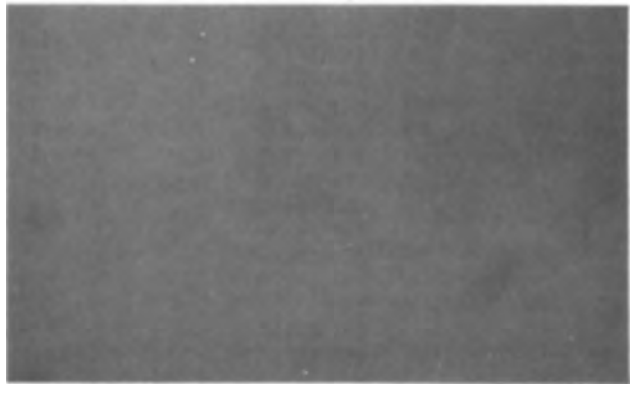

Fig. 2. Effect of progressive removal of material from corundum surfaces. Magnification approximately x 240. Fig. 2a. Original surface (0.5μ diamond dust polish).

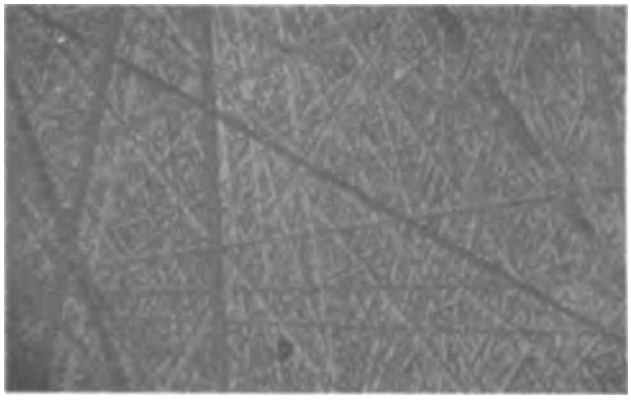

Fig. 2b. After removal of 1.5μ

Fig. 2c. After removal of 10μ

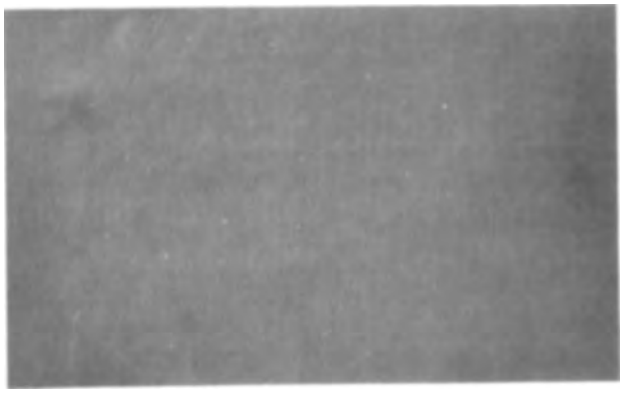

Fig. 2d. After removal of 52μ

Fig. 2e. After removal of 126μ

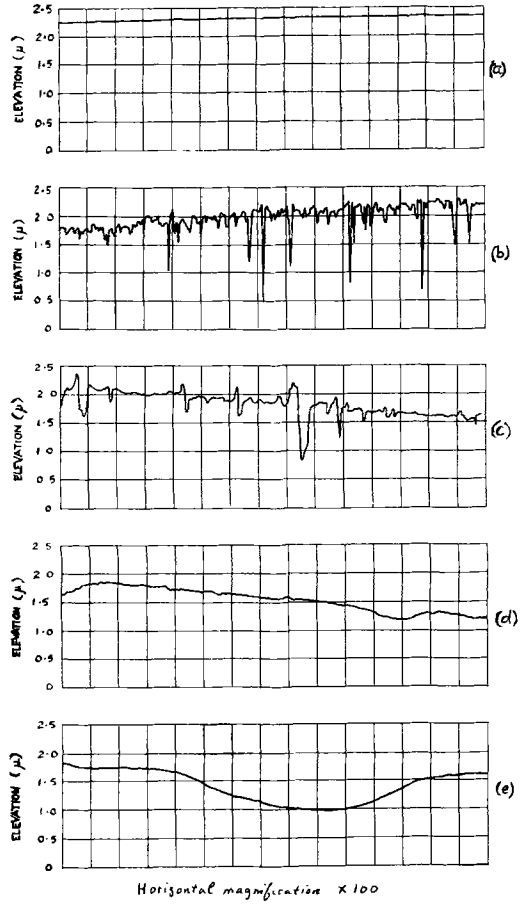

Fig. 3. Talysurf records of corundum surfaces: (a) original surface (0.5μ diamond dust polish); (b) after removal of 1.5μ; (c) after removal of 3.9μ; (d) after removal of 14.7μ; (e) after removal of 33.4μ.

gressively removed. The initial surface is highly polished but possesses numerous scratches. As dissolution occurs the scratches widen and become more marked. Scratches disappear and a substantially featureless surface is obtained when sufficient material has been removed. With further removal of material surfaces become somewhat striated in appearance. Polishing occurred over the whole surface and no significant edge effects were observed.

The Talysurf traces (Fig. 3) of surfaces obtained after different periods of immersion in vanadium pentoxide at 900°C demonstrate a marked smoothing of the surface as material is removed. It should be noted that since the Talysurf instrument had a diamond stylus 2.5μ in diameter, surface features of lesser dimension appear smaller than their actual size. Thus the depth of scratches from 0.5μ abrasive particles is not recorded accurately by Talysurf measurement, and the mechanically polished surface is better observed by the more revealing optical assessment.

Rates of dissolution plotted against time show an initially high rate of dissolution, decreasing as material is removed and eventually levelling out at a fairly constant vaue. Figure 4 shows a typical dissolution rate curve obtained at 800°C, from which the depth of the damaged layer can be estimated as approximately 30μ.

The rate of dissolution increases with temperature. In addition to enhancing the rate of attack, a higher melt temperature also affects the final surface appearance. Thus striations appear if a comparable amount of material is removed at a temperature 100° higher than that producing a featureless surface.

Rotation of a specimen in the melt (at 900°C) resulted in a higher rate of dissolution. The effect of rotation of the specimen on the final surface appearance is clearly seen in Fig. 5. In the absence of stirring a polished surface is obtained usually.

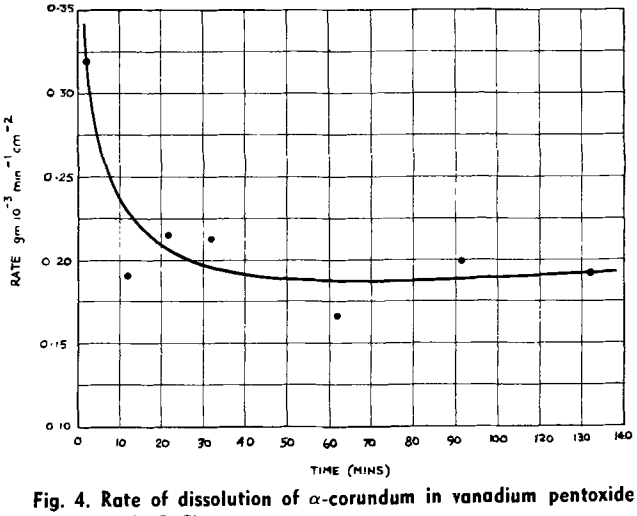

Fig. 4. Rate of dissolution of α-corundum in vanadium pentoxide against time (800°C).

An increase in alumina concentration in the melt lowers the rate of dissolution considerably and also affects the final appearance of a surface. With a melt containing no alumina initially, a high rate of attack occurs (30 μ h^{-1}) whereas in a melt containing originally 1.65% by weight of dissolved alumina only 1.5 μ h^{-1} was removed.

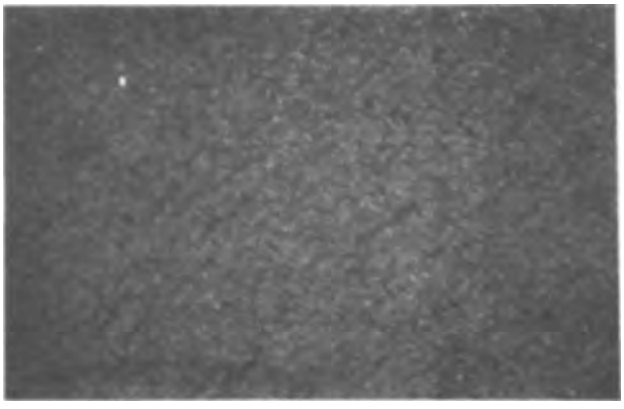

Fig. 5. Effect of stirring on surface appearance. (Magnification x 240). Rotated at 340 rpm 10 min at 900°C. (49μ removed).

Acknowledgment

Acknowledgment is due to the Engineer-in-Chief of the British Post Office for permission to publish this paper.

Manuscript received Nov. 7, 1966; revised manuscript received Jan. 10, 1967.

Any discussion of this paper will appear in a Discussion Section to be published in the December 1967 JOURNAL.

REFERENCES

1. S. K. Popov, in "Growth of Crystals," Vol. 2, p. 103, A. V. Shubnikov and N. N. Sheftal, Editors (Consultants Bureau Inc. New York. Chapman and Hall Ltd. London (1959).
2. F. P. Mallinder and B. A. Proctor, *Phil. Mag.*, **13**, 197 (1966).
3. R. Scheuplin and P. Gibbs, *J. Amer. Ceram. Soc.*, **43**, 458 (1960).
4. N. J. Tighe, *Rev. Sci. Instr.*, **35**, 520 (1964).
5. P. H. Robinson and C. W. Mueller, *Trans. Met. Soc. AIME*, **236**, 268 (1966).
6. M. Seebach, *Neues. Jahrb. Min. Geol.*, **A54**, 420 (1926).
7. W. J. Alford and D. L. Stephens, *J. Amer. Ceram. Soc.*, **46**, 193 (1963).
8. F. H. Reynolds and A. B. M. Elliott, *Phil. Mag.*, **13**, 1073 (1966).
9. J. D. Filby, *This Journal*, **113**, 1085 (1966).
10. R. W. Lawson, Private communication.

Rapid Electronic Switching between Potentiostatic and Galvanostatic Control

Theodore B. Warner and Sigmund Schuldiner

United States Naval Research Laboratory, Washington, D. C.

For a number of applications it is desirable to obtain galvanostatic charging curves on an electrode that is kept under potentiostatic control at all other times. The transition time from one type of control to the other (the "switch time") should be as short as possible, for in this time the electrode potential may be ill-defined. Further, the time between the end of one galvanostatic pulse and the beginning of the next (the "potentiostat time") should be known accurately, and for adsorption rate studies it is desirable that a train of 2 pulses be provided. Existing solutions to this problem have generally involved mercury-wetted relays that have extremely rapid break times, but whose operate times of 3-5 msec make it difficult to reduce switch and potentiostat times much below 1 msec. The circuit described here operates automatically, eliminates the need for active switching circuitry, has an "on" switch time of 0.2 to 1.0 μsec at the beginning of the pulse, and an "off" switch time of from 6 to 20 μsec. The accuracy with which potentiostat time may be defined is limited only by the switch times.

Operation of the circuit, shown in Fig. 1, depends on the fact that the potentiostat, when an off-balance condition exists, will apply up to full output voltage (with about 1 μsec rise time) at the counter electrode until balance is again sensed. This step-change in output is used to back-bias D1 which thus isolates the potentiostat from the cell, prevents it from eliminating the off-balance condition, and keeps it driven to a

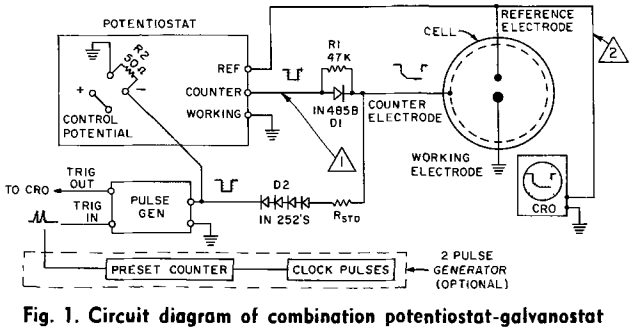

Fig. 1. Circuit diagram of combination potentiostat-galvanostat

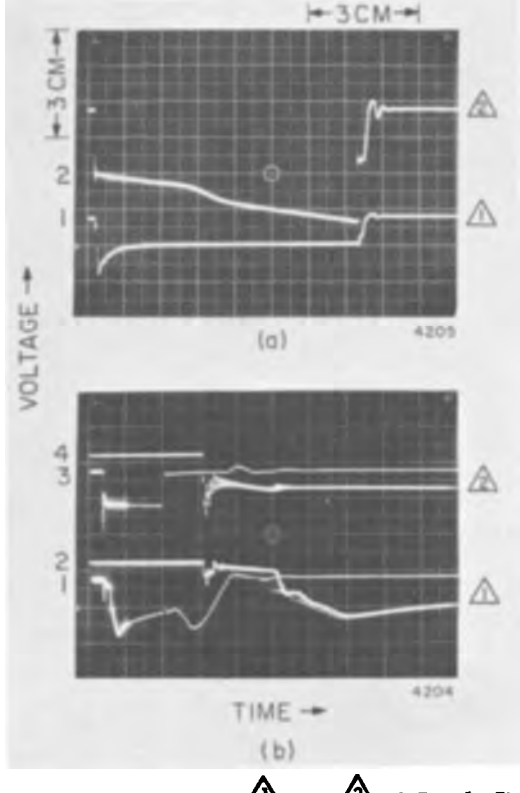

Fig. 2. Potentials at points 1 and 2 of Fig. 1. Fig. 2a: Pulse length 142 μsec, time 20 μsec/cm, voltage 10 v/cm trace 1, 1v/cm trace 2. Fig. 2b: Pulse length 8 μsec, time 5 μsec/cm for traces 1 and 3, 0.5 μsec/cm traces 2 and 4, voltage 10 v/cm traces 1 and 2, 2 v/cm traces 3 and 4. Traces 2 and 4 are expanded presentations of the first 5 μsec of traces 1 and 3, respectively.

limit. The desired off-balance condition is created by injecting the pulse generator output into the potentiostat reference circuit as well as directly into the cell. (The D2 diodes inhibit leakage currents between pulses and R_{std} gives constant current conditions.) The 47K resistor paralleling D1 permits enough current to flow to allow the potentiostat to regain control at the end of the pulse. Its size represents a compromise between degree of isolation desired when D1 is biased off, and the rate of resumption of potentiostatic control after the pulse is removed from the reference circuit.

In operation, the cell is under potentiostatic control except during the time of a galvanostatic pulse. The pulse generator may be used single shot or repetitively pulsed. If the optional apparatus within the dashed lines is included, the generator will provide two pulses whose time separation may be known as precisely as desired depending on the counter or clock generator used.[1]

[1] Any combination of compatible units may be used. In the circuit developed the components used were a Tektronix 547 oscilloscope with 1A1 plug-in, an Electropulse 3450 D pulse generator with 15 nsec rise time, a Wenking Fast Rise 61 RS potentiostat, a Hewlett Packard 5214L Electronic Counter (max. rate 100KC) counting the output from a Tektronix Type 105 Square Wave Generator. The preset counter gives one pulse at the start of counting and one when the preset count is reached. Thus pulses may be spaced a minimum of 10 μsec apart and a maximum of 99,999 times the basic clock rate chosen. Depending on the need for flexibility and time resolution, considerably simpler two-pulse generators may be substituted. Diodes D1 and D2 are noncritical; any of a large number of diodes having suitable power handling characteristics may be used.

Circuit operation is shown in Fig. 2. The working electrode has a real (1) area of 0.21 cm^2, current density was 3.1 amp/cm^2. A typical galvanostatic charging curve appears in trace 2 of Fig. 2a, while trace 1 shows the gating signal appearing at the potentiostat output. In this case the potentiostat was set at ~0.060v (NHE) and the 1*N* H_2SO_4 electrolyte was stirred with He at 10 ml/min. The "off" switch time in such a pulse may be variously considered to be between 6 and 20 μsec depending on how much potentiostat ringing can be tolerated. The "on" switching times are displayed in Fig. 2b, as well as the "off" times for the cases where the electrode is little polarized by the pulse. Traces 2 and 4 show that the working electrode is essentially polarized after 0.2 μsec, but that the potentiostat is not completely gated off until a total of 1 μsec has elapsed. The total "off" switching time is ~10 μsec.

The circuit as described applied negative pulses to the counter electrode which results in anodic working electrode polarization and an inverted display of this, as in Fig. 2a, trace 2. Cathodic polarization will result from using positive pulses and reversing D1 and D2.

Manuscript received Nov. 28, 1966.

Any discussion of this paper will appear in a Discussion Section to be published in the December 1967 JOURNAL.

REFERENCE

1. S. Schuldiner and R. M. Roe, *This Journal*, **110**, 332 (1963).

Brief Communication

Carbon Dioxide Determination during the Galvanostatic Oxidation of Adsorbed Propane Intermediates

W. T. Grubb and M. E. Lazarus[1]

General Electric Research & Development Center, Schenectady, New York

After adsorption of an n-paraffin hydrocarbon at constant potential on a platinum anode in an acidic electrolyte, current peaks due to intermediates have been observed in subsequent oxidation by a linear anodic voltage sweep (1-3). Some of these peaks are not removed by cathodic hydrogenation, and it is supposed that these contain partially oxidized carbon because of their similarity to current peaks from carbon monoxide (3, 4) and reduced carbon dioxide (5). This communication presents confirmatory analytical evidence on this point which has been obtained by combining electrochemical experiments with simultaneous CO_2 analysis in the product gas using extremely high-area platinum-black electrodes.

A Teflon-bonded platinum-black electrode prepared by the method of Niedrach and Alford (6) was mounted in the arrangement shown schematically in Fig. 1 as the working electrode of a half-cell. The counter electrode and reference electrode were hydrogen on platinum black electrodes, the latter communicating with the working electrode through a Luggin capillary not shown. The working electrode was connected to an Anatrol Model 4100 Controller which maintained its potential against the hydrogen reference at a selected constant value. Alternatively, the controller was used as a constant current source by controlling potential across a fixed resistor in series with the cell. Temperature of the cell was maintained at 65° ± 0.5°C by means of a constant-temperature oil bath.

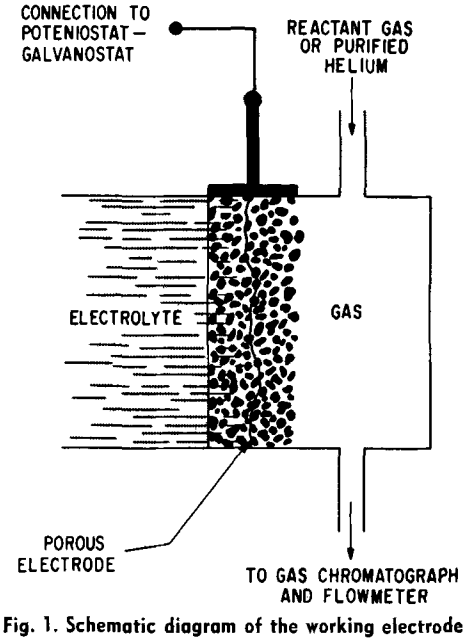

Fig. 1. Schematic diagram of the working electrode

[1] Present address: Knolls Atomic Power Laboratory, General Electric Company, Idaho Test Plant Site, Idaho Falls, Idaho.

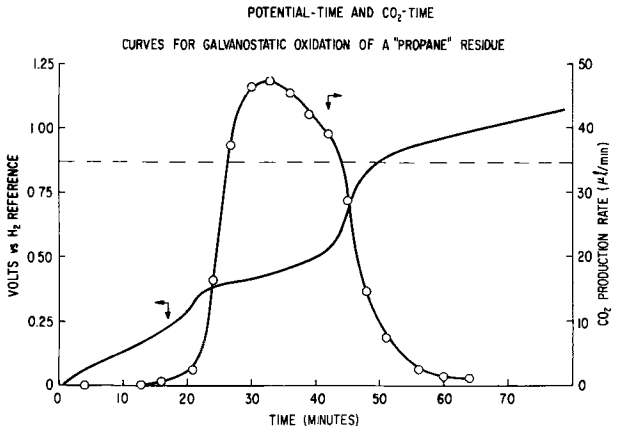

Fig. 2. Plot of CO_2 production rate and voltage *vs.* time for galvanostatic oxidation at 10 ma. The dashed line is the calculated CO_2 production rate for 4-electron oxidation.

Propane was adsorbed at 0.2v *vs.* the hydrogen reference with excess propane flowing through the gas space adjacent to the working electrode. When adsorption was complete, all gaseous propane was swept away with a purified helium purge while maintaining the same potential. The working electrode was then subjected to exhaustive cathodic hydrogenation with the helium purge continuing. The material remaining adsorbed was then oxidized at constant current, and voltage was recorded as a function of time. A voltage arrest or plateau typical of oxidation of carbonaceous species was observed. At the same time, product gas from the cell was swept into a gas chromatograph with a constant, known flow rate of purified helium gas and analyzed for carbon dioxide content. The rate of production of CO_2 from the anode was obtained from the product of the total gas flow rate and the volume fraction of CO_2 present.

Figure 2 shows the superimposed voltage *vs.* time and CO_2 *vs.* time curves. The CO_2 curve obviously coincides with the voltage arrest. Furthermore, the maximum rate of CO_2 production exceeds that which could be produced by a 4-electron oxidation reaction from the total 10 ma galvanostatic current employed (the dashed line in Fig. 2). This could only occur if the surface species contain carbon already partially oxidized, and thus the hypothesis about the nature of the nonhydrogenatable species produced on adsorption of propane is confirmed.

It appears that this type of experiment can provide useful information about hydrocarbon adlayers that is complementary to results obtained on microelectrodes by electrochemical methods.

Acknowledgment

The authors thank Dr. S. Gilman and Dr. L. W. Niedrach for helpful discussions.

This work is a part of the program under contracts DA-44-009-AMC-479(T) and DA-44-009-ENG-4909, ARPA Order No. 247 with the U.S. Army Engineer Research & Development Laboratories, Fort Belvoir, Virginia, to develop a technology which will facilitate the design and fabrication of practical military fuel cell power plants for operation on ambient air and hydrocarbon fuels.

Manuscript received Dec. 30, 1966.

Any discussion of this paper will appear in a Discussion Section to be published in the December 1967 JOURNAL.

REFERENCES

1. L. W. Niedrach, *This Journal*, **113**, 645 (1966).
2. S. Gilman, *Trans. Faraday Soc.*, **61**, 2561 (1965).
3. L. W. Niedrach in "Hydrocarbon Fuel Cell Technology," p. 377, B. S. Baker, Editor, Academic Press, New York, N. Y. (1965).
4. S. B. Brummer and M. J. Turner, *ibid.*, p. 420.
5. J. Giner, *Electrochim. Acta*, **8**, 857 (1963).
6. L. W. Niedrach and H. R. Alford, *This Journal*, **112**, 117 (1965).

SOLID STATE SCIENCE

Kinetics of Tantalum Corrosion in Aqueous Electrolytes, I

K. Lehovec and J. D'Amico[1]

Research and Development Laboratories, Sprague Electric Company, North Adams, Massachusetts

ABSTRACT

The spontaneous growth of thin (6-20Å) oxide films on tantalum immersed into aqueous solutions of H_2SO_4, NaCl, and NaOH has been investigated by means of capacitance and voltage measurements. There is a rather rapid initial oxide growth rate in NaOH until a thickness of about 12Å is reached. Beyond that thickness and over the entire thickness range in the other electrolytes, the oxide thickness increases roughly in proportion to the logarithm of time. There is a small, but well established dependence of "oxide capacitance" on the pH of the electrolyte in which it is measured and a rather large, reversible temperature dependence of the oxide capacitance, which indicate that these thin oxide films do not behave as an ordinary dielectric.

In a previous paper (1) we studied the corrosion of tantalum in aqueous electrolytes while permitting an electric current to flow between the tantalum and the electrolyte through an external circuit.

The external current was monitored as a function of time, and the growth in oxide thickness was followed by means of capacitance measurements between the tantalum substrate and the electrolyte. The results seemed to indicate that for very thin oxide films, *i.e.*, oxide thickness in the range up to about 30Å, (*i*) a significant electron current flows through the oxide in addition to that through the external circuit, and (*ii*) the flow of ions through the oxide does not follow the law encountered in anodic oxidation of thicker oxide films, namely

$$i_I = A \exp BF \qquad [1]$$

where

$$F = (E - V)/d \qquad [2]$$

with V the potential between a standard calomel electrode to the electrolyte and the tantalum; d, the oxide thickness derived from the capacitance between the tantalum substrate and the electrolyte; and E, electromotive force of the reaction.

In the present paper the growth of an oxide film on tantalum immersed in an aqueous electrolyte was studied without permitting an external current to flow. In a subsequent paper an attempt will be described to separate experimentally the voltage and thickness dependencies of the ionic and electronic currents which flow through the oxide during spontaneous corrosion.

[1] Present address: Physics Department, Rensselaer Polytechnic Institute, Troy, New York.

Experimental

Origin and treatment of the tantalum samples used was described in ref. (1). High-purity vacuum annealed tantalum was etched in HF, rinsed for a few seconds in distilled water, and inserted in the aqueous electrolyte in which the spontaneous corrosion was studied. The test cell is shown in Fig. 1 and the test circuit in Fig. 2. The network on the upper right of Fig. 2 is not required for the present investigation, but has been included for reference in a subsequent paper. The counter electrode to the tantalum consisted of two sheets of black platinum spaced 0.5 cm apart from the tantalum. The electrolyte was circulated at a rate of 85-90 ml/min between the cell and a 12-liter constant temperature bath maintained at 20° ± 0.5°C.

Sulfuric acid, sodium hydroxide, and sodium chloride aqueous electrolytes were used. The sulfuric acid

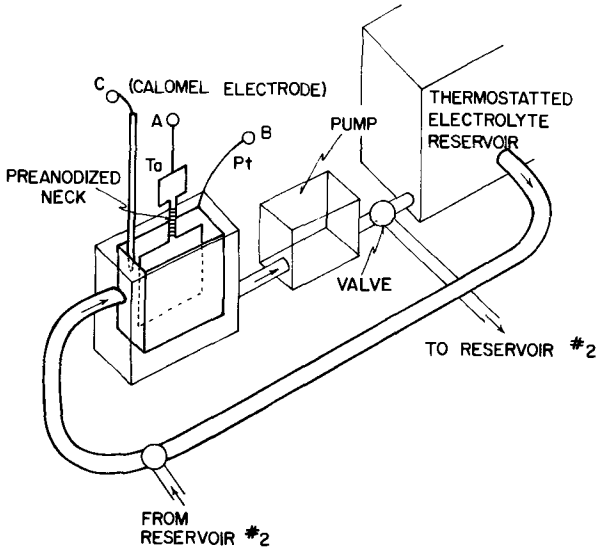

Fig. 1. Experimental arrangement

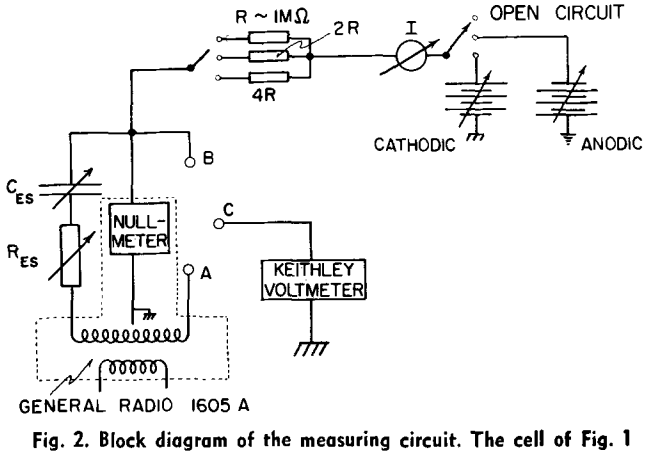

Fig. 2. Block diagram of the measuring circuit. The cell of Fig. 1 is connected to the points marked A, B, and C.

electrolyte had a pH of about unity which was measured with a Beckman Model H2 pH-meter. The pH of the strongly basic sodium hydroxide electrolyte was determined by titration with 1*N* HCl.

A saturated calomel electrode (SCE), Beckman Model 39970, was inserted in the electrolyte and the voltage, V, SCE *vs.* tantalum was measured with a Keithley Model 610BR Electrometer. This voltage is positive for spontaneous corrosion, but eventually becomes negative when anodic oxide is grown by passing an external current.

The a-c impedance, tantalum *vs.* platinum was measured with a General Radio Model 1650A impedance comparator, using a signal voltage of 8.6 mv rms, 100 Hz across the sample. The bridge was balanced by standard capacitors and resistors, indicated by C_{ES} and R_{ES}. The series resistance of the standard capacitor is included in R_{ES}. The time dependence of V and C_{ES} were recorded continuously by use of a Varian Model G22A Dual Channel Recorder.

Open-circuit d-c voltage *vs.* time data taken without the a-c voltage of 8.6 mv applied and the bridge still connected, or else, without the bridge connected at all were identical to those obtained with the small a-c voltage and the bridge connected.

Derivation of oxide thickness from capacitance.— From the equivalent series capacitance, C_{ES}, the quantity

$$d = S\epsilon\epsilon_0/C_{ES} \qquad [3]$$

was calculated using the macroscopic contact area $S = 18.8$ cm^2 between tantalum and electrolyte, the permittivity of free space ϵ_0, and the dielectric constant $\epsilon = 27.6$ (2) for Ta_2O_5. The quantity d will be identified with the "oxide thickness" in what follows.

The use of Eq. [3] to derive the oxide thickness requires justification since: (*a*) there may be contribution to C_{ES} from double layer capacitances at the tantalum oxide-electrolyte and platinum-electrolyte interfaces; (*b*) the "thick" film dielectric constant used might not apply to our "thin" films. (The value $\epsilon = 27.6$ has been determined at 1000 Hz (2), while our measurements were made at 100 Hz. However, the change of ϵ between 100 and 1000 Hz is quite small and not important for our conclusions); (c) the macroscopic sample area, $S = 18.8$ cm^2, might differ from the effective sample area due to a roughness factor $\neq 1$.

To investigate the contribution of solution double layers we proceeded as follows: Equivalent series capacitance and resistance, C_{ES} and R_{ES}, respectively, were measured for the same sample at 100 and 1000 Hz in H_2SO_4, NaCl, and NaOH electrolytes of various concentrations. These measurements were performed during a sufficiently short time and under conditions preventing significant changes of oxide thickness. For each electrolyte, values of the four equivalent circuit parameters of Fig. 3b were calculated from the real and imaginary parts of the measured impedances C_{ES} (f) and R_{ES} (f) of the circuit of Fig. 3a. C_p and R_p represent the capacitance and inverse conductance of the two double layers in the electrolyte at the tantalum oxide and platinum electrodes lumped into only one R_p-C_p combination to simplify the evaluation. C_o is the oxide capacitance. The equivalent parallel resistance R_T of the oxide has been omitted in Fig. 3b, since the time constant R_TC_o is of the order of seconds as concluded from the time constant of the d-c potential transient after passing a small external current through the sample. Thus, R_T should not affect the impedance at frequencies of 100 Hz and larger.

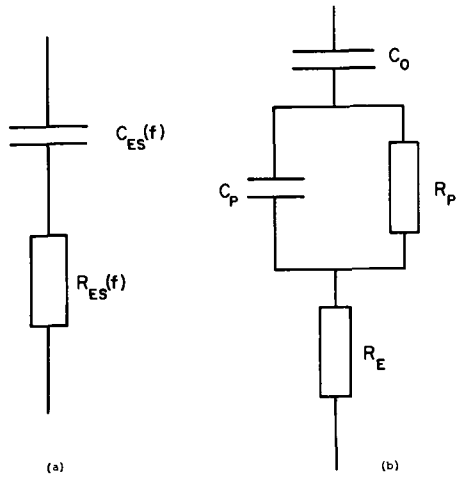

Fig. 3. Measured cell parameters (a) and cell equivalent circuit (b).

Table I gives results of several typical sets of measurements. Values of C_o in electrolytes of the same type, but different concentrations, differ only little. Moreover, at least a portion of these differences can be accounted for by a dependence of oxide capacitance on the pH of the electrolyte, to be discussed in more detail in conjunction with Table II. Thus we consider the near constancy of the values of C_o of Table I as supporting our simplified equivalent circuit Fig. 3b. It can be observed in Table I that for the most conductive electrolytes where $R_{ES} \sim 1$ ohm the oxide capacitance C_o differs from the equivalent series capacitance

Table I. Oxide capacitance measured at 100 and 1000 Hz as a function of the electrolyte

Electrolyte used for capacitance measurements		Approximate oxide thickness, A†	100 Hz		1000 Hz		Components of Fig. 3b		
			R_{ES}, ohm	C_{ES}, μf	R_{ES}, ohm	C_{ES}, μf	C_o, μf	R_p, ohm	C_p, μf
Sulfuric acid	1.1 (pH)	17.9	1.10	251.0	0.94	242.1	256.3	0.27	4286
	1.9		4.30	248.6	4.0	210.3	251.8	0.35	1089
	2.6		26.9	223.1	25.9	163.4	236.4	1.21	495
	1.0	15.4	1.00	293.1	0.82	274.3	298.3	0.23	3257
	1.6		2.15	283.8	1.87	249.2	290.2	0.34	1631
	2.4		11.5	258.8	10.5	193.6	284.2	1.36	583
	1.0*	11.7	0.81	385.1	0.65	344.4	391.0	0.20	3619
	1.8*		3.42	378.5	3.01	294.4	393.0	0.50	1082
	2.4*		11.0	357.9	10.4	238.8	376.0	0.80	583
Sodium hydroxide	13.5 (pH)	22.7	1.21	197.6	1.01	192.4	202.6	0.41	3749
	13.3		1.47	201.3	1.26	193.0	204.9	0.31	3231
	12.9		2.26	206.9	2.04	188.5	209.0	0.28	1735
	12.3		5.46	208.2	4.96	171.9	213.0	0.62	808
	12.0		10.2	206.2	9.32	161.1	217.1	1.11	590
Sodium chloride	3.4 % (wt)	19.1	1.13	235.9	0.92	223.6	240.0	0.27	3165
	1.9		1.47	240.3	1.26	223.3	243.6	0.26	2414
	1.0		2.05	241.0	1.82	216.0	243.0	0.28	1700

† All thickness values computed by Eq. [3] using the C_o values for the electrolyte of lowest R_{ES}.
* 60 μa cathodic current applied during measurement to suppress the oxide growth which would occur otherwise by spontaneous corrosion.

C_{ES} measured at 100 Hz by less than 2%. In Table I we list data obtained with a sulfuric acid electrolyte using three different oxide thicknesses (on three different samples of tantalum). Values of $(C_o - C_{ES})/C_o$ with C_o measured at 100 Hz and for electrolytes of pH $\simeq$ 1 are 2.0, 1.7, and 1.5% for the thicknesses of 17.9, 15.4, 11.7Å, respectively. This suggests that Eq. [3] remains valid even for thicknesses below 11.7Å.

The use of "thick film" values for dielectric constant and density is justified by the following experiment: A known anodic charge was passed through an oxide film. The oxide capacitance, C_o, was calculated by means of the equivalent circuit of Fig. 3b, from impedance measurements at 100 and 1000 Hz. The increment in thickness derived from the C_o values before and after passing the anodic charge was 1.74Å. This value was corrected for the open-circuit oxide growth during the measurements (0.04Å) and for the oxide growth due to the internal electronic current during passage of the anodic charge (0.09Å) assumed to be equal[2] to the open-circuit growth which would have occurred during the same time interval if no anodic current would have been passed. With this correction the increment in oxide thickness resulting from the anodic charge and calculated from the change of C_o becomes 1.61Å compared to the 1.56Å calculated from Faraday's law using

$$\frac{\Delta d}{\int I dt} \simeq \lambda = \frac{M}{2F\rho Sz} = 3.1 \times 10^{-6}\ \text{cm/coul} \quad [4]$$

based on the molecular weight $M = 442$ of Ta_2O_5, the Faraday constant $F = 96{,}500$ coul/g-equivalent, the density (2) $\rho = 7.93$ g/cm^3, and the valence $z = 5$ for the tantalum ions. This good agreement supports the use of Eq. [3] to derive oxide thickness as well as the numerical values used in conjunction with Eq. [3] and [4]. Mutual compensation of several large errors in the constants is possible though unlikely.

In Table II capacitance measurements are listed for samples exchanged between different electrolytes. The data were analyzed in terms of the equivalent circuit of Fig. 3b, with the result that the oxide capacitance C_o depends somewhat on the nature of the electrolyte in a generally reversible manner.

Thicknesses measured in NaCl of 3.44 % wt [pH $\simeq$ 6] and in NaOH of pH $\simeq$ 13.5 are larger than those in H_2SO_4 of pH $\simeq$ 1 by about 2, and 4Å, respectively, in the range of oxide thicknesses 14-23Å. These differences in "oxide thickness" with the type of the electrolyte suggest a dependence of d on the pH. The change of about 4Å from H_2SO_4 of pH $\simeq$ 1 to NaOH of pH $\simeq$ 13.5 corresponds to about 0.3 Å/pH, *i.e.*, a relative change of about 2%/pH. Such a dependence would also account for most if not all of the changes of C_o in Table I in the same electrolyte with pH. Changes of oxide capacitance with pH have been reported by Vermilyea (3).

A further indication of an anomalous behavior of oxide capacitance is the large temperature dependence of C_o. Table III gives values of the apparent "oxide thickness" d derived from capacitance measurements by Eq. [3] when alternating the electrolyte temperature between 41° and 20°C. The oxide film chosen for these measurements was fairly thick (about 22Å) so that the oxide growth rates at these temperatures were only 5.5 x 10^{-4} and 1.6 x 10^{-4} Å/sec, respectively. The "thickness changes" with temperature were corrected for these growth rates and are listed under the heading Δd_{corr}. The resulting change of "oxide thickness" with temperature is −0.04 Å/°C, *i.e.*, −0.2%/°C.

[2] Actually the correction should be somewhat less since an external anodic current has the tendency to suppress the internal electron current.

Table III. Reversible change of oxide thickness, *d*, with temperature

Temperature change	Δd, A	Δd_{corr}, A
From 41 to 20°C	+0.93	+0.84
From 20 to 41°C	−0.72	−0.87
From 41 to 20°C	+0.91	+0.87

Our open-circuit measurements extended over the thickness range from about 5 to 20Å. At the lower thickness limit, the oxide growth rate became so large that balancing the bridge by hand was not possible. At the upper limit, the growth rate became quite slow so that extending the measurements any further was impractical. Film thicknesses in the range discussed here have been determined from capacitance measurements previously by Vermilyea (4) when studying air oxidation of tantalum.

Since there is an open-circuit potential $V_{Pt\text{-}Ta}$ of the order of several tenths of a volt, an anodic charge $C_{ES}V_{Pt\text{-}Ta}$ flows when connecting the bridge circuit to the cell. This corresponds to an increment of oxide thickness, $\Delta d = \lambda C_{ES}V_{Pt\text{-}Ta}$, of about 0.5Å. However, this growth occurs before balancing the bridge. Further growth of this type does not occur during the run since C_{ES} is decreased by switching off sections of the balancing capacitor.

As $V_{Pt\text{-}Ta}$ decreases during the open-circuit growth of the oxide, the standard capacitor is slowly discharged into the oxide capacitor, representing a cathodic bias current of the magnitude $-C_{ES} \cdot \partial V_{Pt\text{-}Ta}/\partial t$ (cathodic bias currents are counted here positive so that the minus has been added since $\partial V_{Pt\text{-}Ta}/\partial t < 0$). However, this cathodic bias current should have no significant effect on the growth rate if it is small compared to the ionic growth current, *i.e.*, if $-\partial V_{Pt\text{-}Ta}/\partial t << I_I/C_{ES}$ or using Faraday's law if $-\partial V_{Pt\text{-}Ta}/\partial d \simeq \partial V/\partial d << I_I[C_{ES}\ \partial d/\partial t]^{-1} = (\lambda\ C_{ES})^{-1}$. In the range investigated by us, the left-hand side of this inequality was two orders smaller than the right-hand side.

Results

Typical data of oxide thickness, d, *vs.* time, for spontaneous corrosion in aqueous H_2SO_4 (pH = 1), NaCl (3.4 % wt), and NaOH (pH = 13.5) solutions are shown in Fig. 4. Time is counted from insertion of the sample into the electrolyte, which is about 5 sec after the extraction from the HF-etch. The data are replotted in Fig. 5 as growth rate $\partial d/\partial t$ *vs.* oxide thickness, d.

After an initial growth period, the oxide thickness increases about linearly with the logarithm of time. This is similar to the observations by Vermilyea (4) on open air oxide growth on tantalum also using capacitance measurements to determine oxide thickness. Oxide growth in sulfuric acid resembles that in

Table II. Change of oxide capacitance with the electrolyte

Oxide grown in	Oxide measured in	at 100 Hz C_{ES}, μf	at 100 Hz R_{ES}, ohm	at 1000 Hz C_{ES}, μf	at 1000 Hz R_{ES}, ohm	Components of Fig. 3b C_o, μf	Components of Fig. 3b R_p, ohm	Components of Fig. 3b C_p, μf	d (Å) by Eq. [3]
H_2SO_4 pH ≃ 1	NaCl 3.44% (wt)	235.9	1.13	223.6	0.92	240.0	0.28	3165	19.1
	H_2SO_4 pH ≃ 1	260.8	1.11	247.6	0.93	265.1	0.24	3608	17.3
H_2SO_4 pH ≃ 1	NaOH pH ≃ 13.5	197.6	1.21	192.4	1.01	202.6	0.41	3749	22.7
	H_2SO_4 pH ≃ 1	227.9	1.08	220.8	0.91	232.6	0.29	4275	19.7
	NaOH pH ≃ 13.5	205.8	1.01	200.4	0.82	210.5	0.35	4091	21.8
NaOH pH ≃ 13.5	NaOH pH ≃ 13.5	251.8	1.02	241.6	0.80	259.9	0.40	3381	17.7
	H_2SO_4 pH ≃ 1	315.7	1.06	299.1	0.85	325.9	0.33	3570	14.1

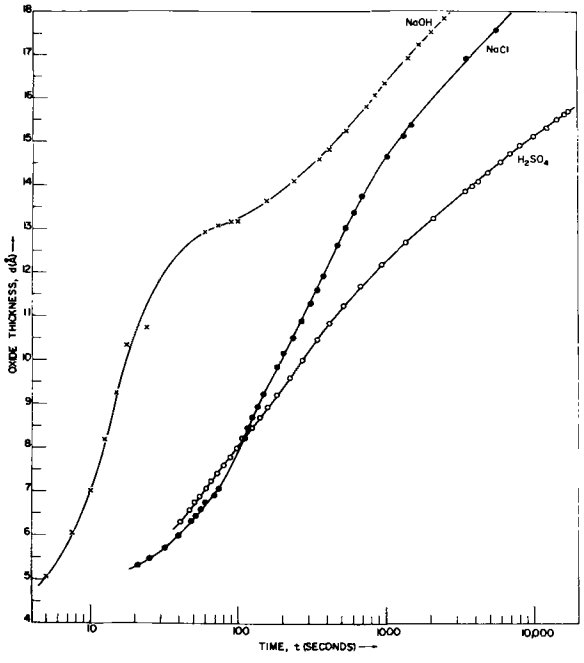

Fig. 4. Oxide thickness *vs.* time during spontaneous corrosion

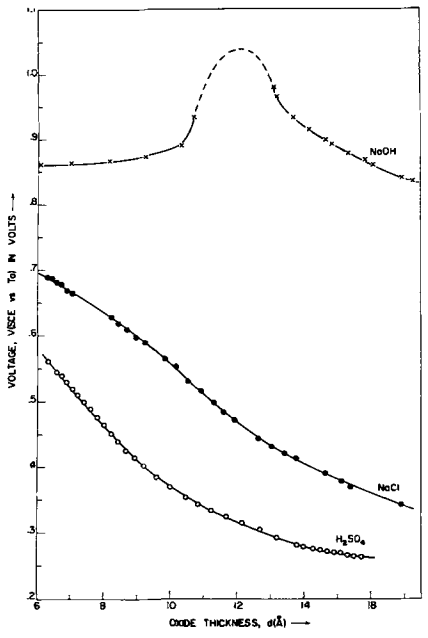

Fig. 6. Voltage, SCE *vs.* tantalum, *vs.* oxide thickness during spontaneous corrosion.

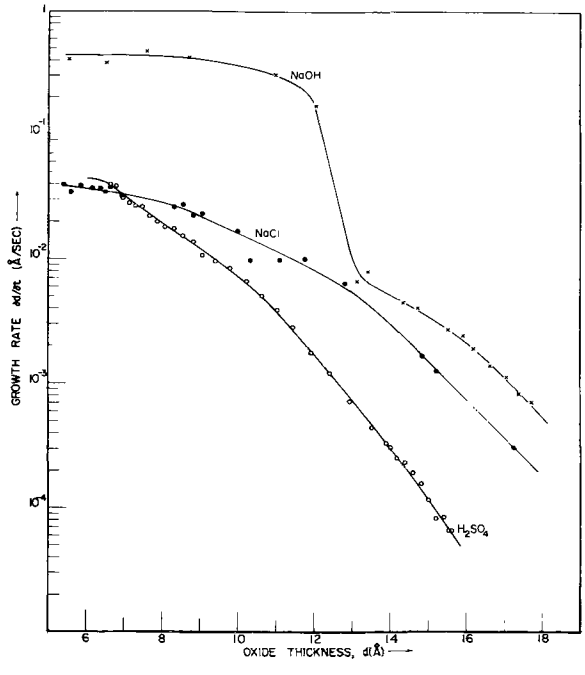

Fig. 5. Growth rate *vs.* oxide thickness during spontaneous corrosion.

sodium chloride electrolytes except that the growth rate is somewhat faster in the sodium chloride solution.

The growth behavior in the sodium hydroxide solution is quite different: After an initial growth at the rapid rate of 0.4 Å/sec (see Fig. 5) up to a thickness of about 12Å, there is a rather abrupt drop of growth rate by about an order of magnitude between 12 and 13Å, followed by a decreasing growth rate similar to that experienced in H_2SO_4 and NaCl solutions. The lateral displacement of the three curves of Fig. 5 may be in part due to the dependence of "oxide thickness" on the electrolyte in which the measurements were taken (see Table II).

Figure 6 shows the voltage (SCE *vs.* tantalum) in the three electrolytes as a function of thickness during open-circuit corrosion for the same runs used in the previous figures. In H_2SO_4 and NaCl electrolytes the voltage decreases in a monotonous fashion with time. In the NaOH-electrolyte the voltage passes through a maximum at the thickness at which the transition from the initial constant growth rate to a growth behavior similar to that in H_2SO_4 and NaCl occurs.

The occurrence of a voltage maximum during spontaneous corrosion in the NaOH electrolyte is an experimental fact which is unrelated to our thickness determination for capacitance measurements and the assumptions thereby made.

Discussion

An inspection of the curves $V(t)$ and $\partial d/\partial t$ *vs.* d for spontaneous corrosion (Fig. 5 and 6) shows that all electrolytes investigated by us behave similarly, except for the rapid initial oxide growth rate in NaOH, which ceases fairly abruptly when a thickness of 12Å (as measured in NaOH) is reached. The nearly constant growth rate of about 0.4 Å/sec corresponds to an ionic current of 65 μa/cm^2 by means of Faraday's law.

The initial growth behavior in the NaOH-electrolyte suggests the mechanism discussed by Mueller (5), *i.e.*, electrolyte transport through pores between the growing anodic film and that at about 12Å the transition occurs to a full coverage of the tantalum by oxide. The occurrence of this growth mechanism might be related to the small but finite solubility of Ta_2O_5 in NaOH.

With the exception of the initial growth in the NaOH electrolyte, the time dependence of oxide thickness is roughly in proportion to the logarithm of time with a proportionality constant $\partial d/\partial \ln t$ of the order of 1 to 3Å.

Observations which shed some doubt on the existence of a well-defined oxide film acting as a dielectric of width d are as follows: (*i*) the dependence of d on the electrolyte in which it is measured (Table II); and (*ii*) the reversible change of d by about 0.04 Å/degree or 0.2% per degree with temperature (Table III). These phenomena may arise by a portion of the oxide being so conducting that it contributes to the equivalent series resistance rather than to the equivalent series capacitance (6, 7). A conducting portion of the oxide may arise from a space charge of electrons in the oxide adjacent to the tantalum metal (8-10), or, more likely, by a space charge of protons in the oxide adjacent to the electrolyte (3). In the latter case, an

increase in the conducting portion of the oxide with H^+ concentration in the electrolyte (*i.e.*, decreasing pH) may be expected, in qualitative agreement with the decrease of "d" with pH of the electrolyte in which capacitance is measured (Table II). The space charges of electrons or protons in the oxide need not necessarily be of such magnitude as to modify significantly the d-c field strength in the oxide.

While the effects described are quite pronounced, the resulting thickness changes of at most 2Å are, nevertheless, very small compared to the total thickness d. It might be hoped, therefore, that identification of d with the total oxide thickness is a justified approximation, and in particular, that the ionic currents determined from $\partial d/dt$ by Faraday's law are not affected significantly.

The driving "force" of the corrosion process is the free energy change of the reaction between tantalum and water to form tantalum oxide. The reaction proceeds by migration of positive tantalum ions and/or oxygen ion vacancies from the tantalum toward the electrolyte, or possibly by migration of negative oxygen ions in the opposite direction. This charge migration tends to charge the tantalum negatively. In the absence of any additional charge flow for charge compensation, a potential equal to the emf of the reaction would rise across the oxide, the field in the oxide would vanish according to Eq. [2], and the ionic charge transport causing oxide growth would cease. Continuing oxide growth thus requires some mechanisms for charge neutralization, usually in the form of flow of electrons or holes. The potential across the oxide establishes itself at a level providing a balance of electronic and ionic flow at the thickness in question. Thus, a theoretical analysis of growth rate would seem to require assumptions on both electronic and ionic charge transports. In a subsequent paper we shall discuss methods by which we attempted to obtain experimental information on the voltage and thickness dependences of electronic and ionic charge transports. These values will then be compared to theoretical concepts of protective oxide film growth such as the Mott-Cabrera (11) mechanism and others.

Conclusions

1. Spontaneous corrosion of tantalum in aqueous electrolytes of H_2SO_4, NaCl, and NaOH is qualitatively similar, except for an initial rapid time-independent corrosion in NaOH which ceases abruptly at about 12Å thickness.

2. The oxide capacitance increases in the sequence H_2SO_4-NaCl-NaOH for a given sample when changing the electrolyte. This sheds some doubt on models treating thin oxide films as a perfect dielectric with a dielectric constant independent of the ambient electrolyte. Furthermore, there are abnormally large reversible changes of oxide capacitance with temperature, which indicate that the oxide does not behave as a perfect dielectric. However, since these changes in oxide capacitance are only a small fraction of the capacitance, the analysis of the measurements based on an "oxide thickness" as determined from capacitance appears to be a valid first order approximation.

Manuscript received Sept. 20, 1966; revised manuscript received Nov. 7, 1966.

Any discussion of this paper will appear in a Discussion Section to be published in the December 1967 JOURNAL.

REFERENCES

1. R. Dreiner, K. Lehovec, and J. Schimmel, *This Journal*, **112**, 395 (1965).
2. L. Young, *Proc. Roy. Soc., A*, **244**, 41 (1958).
3. D. A. Vermilyea, *J. Phys. Chem. Solids*, **26**, 133 (1965).
4. D. A. Vermilyea, *Acta. Met.*, **6**, 166 (1958).
5. J. H. Mueller, "Die Bedeckungs Theorie der Passivitat der Metalle," Verlag Chemie, Berlin (1933).
6. W. Van Geel, "Halbleiterprobleme," I, p. 299, Vieweg and Sohn Brannochweig (1956).
7. L. Young, *Trans. Faraday Soc.*, **51**, 1250 (1955).
8. D. M. Smyth, G. A. Shirn, and T. B. Tripp, *This Journal*, **110**, 1264 (1963).
9. D. M. Smyth and T. B. Tripp, *ibid.*, **110**, 1271 (1963).
10. D. M. Smyth, G. A. Shirn, and T. B. Tripp, *ibid.*, **111**, 762 (1964).
11. N. Cabrera and N. F. Mott, *Rep. Progr. Phys.*, **12**, 163 (1949).

Structure and Luminescence of the Phosphate-Vanadates of Yttrium, Gadolinium, Lutetium, and Lanthanum

Michael A. Aia

General Telephone & Electronics Laboratories Incorporated, Bayside, New York

ABSTRACT

Phosphate-vanadates of Y, Gd, Lu, and La, formed from powders at 1000°C, were solid solutions having the structure of either xenotime or monazite. Compositions containing 25-50 mole % $GdVO_4$, YVO_4, or $LuVO_4$ exhibited intense blue photoluminescence arising from absorption and fluorescence within the vanadate groups. The fluorescence of phosphate-vanadates activated by europium was also investigated and is compared to the fluorescence of the corresponding vanadates.

Reviews of the literature on the structures of the rare earth phosphates (1, 2) and vanadates (1, 3) have been published recently. In general, these compounds have either the xenotime (tetragonal) or the monazite (monoclinic) structure at ordinary pressures. A hexagonal form of $LaPO_4$ is also known (4). Scheelite structures are found in the rare earth vanadates and arsenates at high pressures (3). The cell constants for the phosphates, vanadates, and arsenates having the xenotime structure have been precisely determined (1).

Rare earth-activated luminescence in the phosphates (5, 6) and vanadates of Y, Gd, Lu, and La (7-14) has been actively studied, and YVO_4:Eu is used as the red-emitting component in cathode-ray tubes for color television (9, 14). Weak blue fluorescence is emitted by the unactivated vanadates of Y, Gd, and Lu at room temperature; at —196°C the fluorescence is much more intense (13). In the present work the crystallography and luminescence of solid solutions of unactivated rare earth phosphates and vanadates are examined. It is

shown that the blue emission arising from the vanadate groups is greatly enhanced when the vanadate concentration is diluted by adding a large amount (*e.g.* 75 mole %) of phosphate and firing to produce a solid solution of the vanadate in the phosphate.

Experimental Procedures

Preparation of samples.—Stoichiometric mixtures of $(NH_4)_2HPO_4$, NH_4VO_3, and the appropriate rare earth trioxide were heated in covered silica crucibles; for samples not containing phosphate a 40% excess of NH_4VO_3 was added to insure complete reaction of the trioxide.

Because the phosphates contained large amounts of unreacted rare earth oxide when prepared from solid $(NH_4)_2HPO_4$, they were precipitated at 90°C by slowly adding an excess of 0.4*M* $(NH_4)_2HPO_4$ solution to a 0.4*M* solution of the rare earth nitrate. After washing and oven drying, the phosphates were ground, sieved, and then fired like the other compositions. The powders were heated for 18 hr at 450°C, ground, and reheated for 4 hr at 1000°C, both times starting from a cold furnace. After grinding and sieving 150 mesh the powders were suspended in hot 10% NaOH (to remove unreacted V_2O_5), washed with water, and oven dried at 120°C. Although the purity of the rare earth oxides was alleged by the manufacturer to be 99.9% or better, the Gd_2O_3 contained sufficient Eu^{3+} to produce intense red luminescence in the samples high in $GdVO_4$; the Lu_2O_3 contained sufficient amounts of Tb, Eu, and Tm to produce the luminescence characteristic of those elements (13). Microscopic examination of the finished powders showed that the phosphates were micro-crystalline (particles $<1\mu$), while the vanadates were well crystallized (5-50μ); the phosphate-vanadates were intermediate (2-5μ). More crystalline phosphates have been prepared by using $Pb_2P_2O_7$ as a flux (2) or by hydrothermal treatment with aqueous phosphoric acid (15, 16a).

X-ray diffraction analysis.—A calibrated Philips-Norelco diffractometer was used with Ni filtered CuKα radiation. The scanning rate was one degree 2θ per minute. The d-spacings of the powder patterns were indexed with the help of a computer after starting from the indexing given for YPO_4 (xenotime) and $LaPO_4$ (monazite) in the ASTM Powder Data File (16). The cell parameters were then calculated by the method of least squares.

Luminescence measurements.—Excitation and fluorescence spectra were obtained on a dual-grating Aminco-Bowman spectrophotofluorometer with a xenon lamp as source and either a 1P28 or RCA 6217 photomultiplier as detector, depending on the wavelength region studied. The intensity of the blue luminescence of the compounds was measured relative to that of $CaWO_4$ (Sylvania type No. 2402) and $CaWO_4$:Pb (NBS 1026) using a 1P28 photomultiplier and Corning CS5-61 blue filter. A CS2-63 red filter was used with a 6217 photomultiplier to measure red brightness of samples activated by europium. Photoluminescence was excited by a G4T4 germicidal lamp with principal emission at 253.7 nm after filtering by a Corning 7-54 visible-light-absorbing filter. Cathodoluminescence was measured in a demountable cathode-ray tube after settling the powders uniformly at 5 mg/cm^2 onto Corning EC (electrically-conducting) glass and baking at 450°C; the phosphors were excited using a beam current density of 0.15 μa/cm^2 and an accelerating potential of 15 kv.

Results and Discussion

Unit-cell dimensions calculated from x-ray powder data are summarized in Table I. Values for YPO_4, YVO_4, $GdVO_4$, $LuPO_4$, and $LuVO_4$ are close to those of Schwarz (1). All the compounds of Y, Gd, and Lu had the tetragonal structure except $GdPO_4$ which was monoclinic, like the compounds of La. The addition of

Table I. Structure and lattice parameters for the compounds prepared

Composition	Structure	a_o, A	c_o, A
YPO_4	Xenotime	6.882	6.030
$YP_{0.75}V_{0.25}O_4$	Xenotime (+10% YPO_4)	6.934	6.095
$YP_{0.50}V_{0.50}O_4$	Xenotime	6.980	6.141
$YP_{0.25}V_{0.75}O_4$	Xenotime	7.061	6.230
YVO_4	Xenotime	7.121	6.292
$GdPO_4$	Monazite		
$GdP_{0.75}V_{0.25}O_4$	Xenotime (+10% $GdPO_4$)	7.046	6.189
$GdP_{0.50}V_{0.25}O_4$	Xenotime	7.102	6.236
$GdP_{0.25}V_{0.75}O_4$	Xenotime	7.165	6.283
$GdVO_4$	Xenotime	7.218	6.353
$LuPO_4$	Xenotime	6.816	5.967
$LuP_{0.75}V_{0.25}O_4$	Xenotime (+10% $LuPO_4$)	6.873	6.046
$LuP_{0.50}V_{0.50}O_4$	Xenotime	6.935	6.131
$LuP_{0.25}V_{0.75}O_4$	Xenotime	6.987	6.186
$LuVO_4$	Xenotime	7.038	6.249

Composition	Structure	a_o	b_o	c_o	$\beta°$
$GdPO_4$	Monazite	6.66	6.85	6.29	104.6
$LaPO_4$	Monazite	6.84	7.07	6.46	104.0
$LaP_{0.75}V_{0.25}O_4$	Monazite	6.89	7.14	6.57	103.8
$LaP_{0.50}V_{0.50}O_4$	Monazite	6.95	7.16	6.62	103.6
$LaP_{0.25}V_{0.75}O_4$	Monazite	6.99	7.24	6.67	103.3
$LaVO_4$	Monazite	7.07	7.26	6.69	102.6

25 mole % vanadate to $GdPO_4$ caused the occurrence of xenotime as the major structure. The formation of phosphate-vanadate solid solutions is indicated by the linear increase in the cell dimensions with increasing mole per cent vanadate, as shown on Fig. 1 and 2. Vegard's law is followed except in the case of the c_o parameter of the La compounds where there is a departure from linearity. In general, there was considerable line broadening, indicating lattice strain, in the diffraction patterns of the samples containing 25 mole % vanadate; $GdP_{0.75}V_{0.25}O_4$, $YP_{0.75}V_{0.25}O_4$, and $LuP_{0.75}V_{0.25}O_4$ contained about 10% $GdPO_4$, YPO_4, and $LuPO_4$, respectively.

Inspection under 253.7 nm light at room temperature showed that several of the phosphate-vanadates emitted bright blue fluorescence, similar in color and intensity to that of $CaWO_4$ phosphor. Under 365 nm light the samples were only feebly luminescent. Fluorescence and excitation spectra were obtained at room temperature. Typical uncorrected excitation and fluorescence curves are shown in Fig. 3 where $GdP_{0.75}V_{0.25}O_4$ is compared to both $CaWO_4$ and $CaWO_4$:Pb (NBS 1026). The apparent excitation peaks

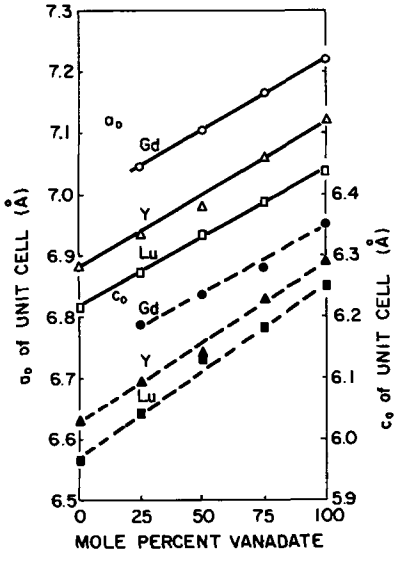

Fig. 1. Unit-cell parameters for the phosphate-vanadates with xenotime structure. Solid lines are a_o parameters; dashed lines are c_o parameters.

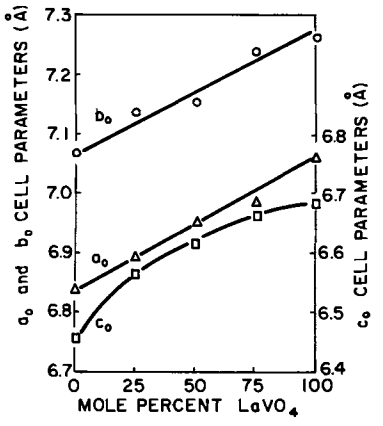

Fig. 2. Unit-cell parameters for the phosphate-vanadates of lanthanum (monazite structure).

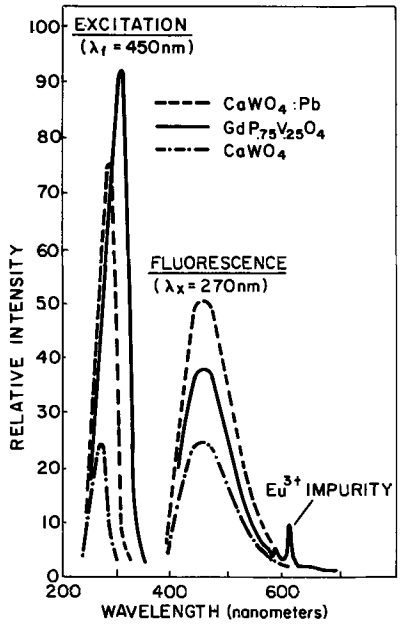

Fig. 3. Comparison of the photoluminescence of $GdP_{0.75}V_{0.25}O_4$ and standard blue phosphors.

of Fig. 3 are exaggerated in sharpness. In agreement with Kroeger (17), the excitation peak of $CaWO_4$:Pb lies at a longer wavelength (285 nm) than that of $CaWO_4$ (270 nm). The excitation peak of $GdP_{0.75}V_{0.25}O_4$ lies near 310 nm, as found for the vanadates of Y, Gd, Lu, and La (13). When excited at the optimum wavelength for $CaWO_4$, the fluorescence of $GdP_{0.75}V_{0.25}O_4$ is much more intense than that of $CaWO_4$, but less than that of NBS 1026. However, when excited at wavelengths from 290 to 320 nm, the $GdP_{0.75}V_{0.25}O_4$ is much brighter than NBS 1026, as can be seen from the excitation spectra.

A summary of the fluorescence and excitation peaks of the phosphate-vanadates is given in Table II. The relative intensities of blue fluorescence were measured under excitation by 253.7 nm light and by cathode rays and compared to $CaWO_4$. These results are also given in Table II. The excitation peak shifts to longer wavelengths as vanadate is combined with phosphate; the biggest changes occur with the first 25 mole % vanadate. Changes in the fluorescence peaks of Table II are due mostly to the effects of rare earth impurities whose luminescence is at longer wavelengths and becomes more pronounced as the vanadate concentration is increased.

In agreement with visual inspection, the brightest host luminescence was obtained at 25-50 mole % vanadate. Although the blue brightnesses in Table II

Table II. Summary of luminescence properties of unactivated phosphate-vanadates at room temperature

Composition	Fluorescence peak, nm	Excitation peak, nm	Intensity of blue fluorescence, % vs. $CaWO_4$: 253.7 nm excitation	Intensity of blue fluorescence, % vs. $CaWO_4$: Cathode ray, 15 kv, excitation
YPO_4	440	270	7	ND*
$YP_{0.75}V_{0.25}O_4$	445	310	108	68
$YP_{0.50}V_{0.50}O_4$	445	312	106	51
$YP_{0.25}V_{0.75}O_4$	445	320	70	44
YVO_4	442	328	46	24
$GdPO_4$	—	270	1	ND
$GdP_{0.75}V_{0.25}O_4$	443	312	131	72
$GdP_{0.50}V_{0.50}O_4$	443	318	92	47
$GdP_{0.25}V_{0.75}O_4$	443	324	55	31
$GdVO_4$	442	328	23	21
$LuPO_4$	440	276	5	ND
$LuP_{0.75}V_{0.25}O_4$	445	296	73	29
$LuP_{0.50}V_{0.50}O_4$	455	308	51	18
$LuP_{0.25}V_{0.75}O_4$	455	312	33	11
$LuVO_4$	455	323	19	12
$LaPO_4$	—	270	3	ND
$LaP_{0.75}V_{0.25}O_4$	—	—	6	4
$LaP_{0.50}V_{0.50}O_4$	—	316	3	3
$LaP_{0.25}V_{0.75}O_4$	—	—	2	1
$LaVO_4$	—	328	2	ND

* ND, not detectable.

peak at 25% vanadate, the over-all brightnesses at 50% vanadate (not shown) were comparable, due to a greater component of emission at longer wavelengths as vanadate content increased. This was especially true for the samples containing Gd since the starting Gd_2O_3 contained an appreciable amount of Eu^{3+} which activates $GdVO_4$ and the phosphate-vanadates very efficiently (*e.g.*, see Fig. 3). Despite Eu^{3+} contamination the brightest blue phosphor was $GdP_{0.75}V_{0.25}O_4$ whose host emission was 31% greater than that of $CaWO_4$ under short uv light. Under cathode-ray excitation the relative intensities *vs.* $CaWO_4$ were lower, which may be partly due to the poor crystallinity of the samples containing phosphate.

Activation of $YP_{0.5}V_{0.5}O_4$ with rare earth ions was investigated. When 0.01 and 0.05 mole Eu, Tb, Ho, or Er were added the blue host emission (due to vanadate ions) was quenched; however, only Eu^{3+} produced an appreciable level of fluorescence at room temperature. Comparison of the fluorescence spectrum of Eu^{3+}-activated $YP_{0.5}V_{0.5}O_4$ with that of Eu^{3+}-activated YVO_4 revealed that the relative intensity of the line group peaking at 595 nm was appreciably greater in the phosphate-vanadate. Similar results were obtained with the Gd and La series containing Eu^{3+}. The red brightnesses of the samples compared to a commercial $Y_{0.95}Eu_{0.05}VO_4$ standard are given in Table III, together with the intensity of emission at 595 nm compared to that of the main emission at 619 nm. Despite smaller particle sizes and generally poorer crystallinity, the phosphate-vanadates activated by Eu^{3+} were comparable in brightness, but were more orange

Table III. Comparison of Eu^{3+} fluorescence in vanadates and phosphate-vanadates of Y, Gd, and La (RCA 6217 Photomultiplier and Corning CS2-63 red filter)

Composition	Average particle size, μ	Relative red brightness, % of std. $Y_{0.95}Eu_{0.05}VO_4$	Relative intensity $I_{595\ nm}/I_{619\ nm}$
$Y_{0.99}Eu_{0.01}P_{0.5}V_{0.5}O_4$	2-5	67	0.28
$Y_{0.99}Eu_{0.01}VO_4$	5-15	79	0.17
$Y_{0.95}Eu_{0.05}P_{0.5}V_{0.5}O_4$	2-5	77	0.29
$Y_{0.95}Eu_{0.05}VO_4$	5-15	85	0.18
$Gd_{0.90}Eu_{0.01}P_{0.5}V_{0.5}O_4$	2-4	57	0.26
$Gd_{0.99}Eu_{0.01}VO_4$	5-15	86	0.18
$Gd_{0.95}Eu_{0.05}P_{0.5}V_{0.5}O_4$	2-4	83	0.27
$Gd_{0.95}Eu_{0.05}VO_4$	5-15	92	0.17
$La_{0.95}Eu_{0.05}P_{0.5}V_{0.5}O_4$	2-4	29	0.52
$La_{0.95}Eu_{0.05}VO_4$	10-50	19	0.36

in emission than their vanadate counterparts. The phosphors containing La were most orange in emission, but lowest in over-all brightness, as found previously (13); they also differ in that they have the monazite structure.

Summary

The unactivated rare earth phosphates-vanadates provide an interesting system in which the interaction of two types of ligand can be deduced, in the solid state, from x-ray and luminescence measurements. Phosphate is a good diluent for vanadate because it can substitute isomorphously in the xenotime structure and does not introduce undesirable absorption bands. Dilution with phosphate leads to considerable enhancement of the vanadate fluorescence which occurs in a broad band that peaks in the blue with the cations Y, Gd, and Lu. As with the undiluted vanadates, the addition of Eu^{3+} diminishes the host emission of the phosphate-vanadates and gives rise to intense emission in the orange and red regions of the spectrum. However, the transition probabilities of the Eu^{3+} fluorescence are altered appreciably by the phosphate ligands and the relative emission at higher energies (*e.g.*, 589 nm) is increased at the expense of the principal emission at 619 nm.

Acknowledgment

The author thanks Steven Barton for his help in programming the computer used in this work.

Manuscript received Aug. 23, 1966; revised manuscript received Nov. 15, 1966.

Any discussion of this paper will appear in a Discussion Section to be published in the December 1967 JOURNAL.

REFERENCES

1. H. Schwarz, *Z. anorg. u. allgem. Chem.*, **323**, 44 (1963).
2. R. S. Feigelson, *J. Am. Ceram. Soc.*, **47**, 257 (1964).
3. V. S. Stubican and R. Roy, *Z. Krist.*, **119** (1963).
4. R. C. L. Mooney, *Acta Cryst.*, **3**, 338 (1950).
5. A. Bril and W. L. Wanmaker, *This Journal*, **111**, 1363 (1964).
6. R. C. Ropp, Papers presented at the Cleveland Meeting of the Society, Abstract Nos. 32 and 33 (1966).
7. L. G. Van Uitert, R. C. Linares, R. R. Soden, and A. A. Ballman, *J. Chem. Phys.*, **36**, 702 (1962).
8. L. G. Van Uitert, R. R. Soden, and R. C. Linares, *ibid.*, **36**, 1793 (1962).
9. A. K. Levine and F. C. Palilla, *Appl. Phys. Letters*, **5**, 118 (1964).
10. L. H. Brixner and E. Abramson, *This Journal*, **112**, 70 (1965).
11. A. Bril and W. L. Wanmaker, *ibid.*, **111**, 1363 (1964).
12. A. Bril, W. L. Wanmaker, and J. Broos, *J. Chem. Phys.*, **43**, 311 (1965).
13. F. C. Palilla, A. K. Levine, and M. Rinkevics, *This Journal*, **112**, 776 (1965).
14. A. K. Levine and F. C. Palilla, *Electrochem. Technol.*, **4**, 16 (1966).
15. Nat. Bur. Standards Circ. 539, **8** (1958).
16. X-ray Powder Data File, Am. Soc. Testing Mater., Philadelphia (1964) (a) Card No. 9-377 (b) Card No. 12-283.
17. F. A. Kroeger, "Some Aspects of the Luminescence of Solids," Elsevier Publishing Co., New York (1948).
18. A. Bril and W. Hoekstra, *Philips Res. Repts.*, **16**, 356 (1961).
19. A. Bril and W. van Meurs-Hoekstra, *ibid.*, **19**, 296 (1964).

An Electronic Paramagnetic Resonance Study of the Chemistry of Mn^{++} during the Formation of Fluorapatite

J. A. Parodi

Lighting Research Laboratory, Lamp Division, General Electric Company, Cleveland, Ohio

ABSTRACT

Electronic paramagnetic resonance (EPR) is used to study the disposition of Mn^{++} among the various phases present during the course of the reaction producing fluorapatite, $Ca_{10-x}Mn_xF_2(PO_4)_6$ where $x = 1.5 \times 10^{-3}$. EPR spectra of Mn^{++} in the various phases are presented. Pertinent spectra of one firing mixture are presented and discussed. The distribution of Mn^{++} between some of the phases, principally calcium oxide and fluorapatite, is determined from relative intensities of EPR lines. The progress of solid solution of Mn^{++} in apatite is followed by the intensity of the apatite:Mn spectrum. In atmospheres of N_2 and $CO/CO_2 = 1/10$ solid solution of Mn^{++} is complete at 1100°. CaO is shown to have a strong affinity, relative to the other phases present, for low concentrations of manganous ion. It has been possible to follow the consumption of $Ca_2P_2O_7$ and CaO during the apatite forming reaction by means of EPR, but not CaF_2.

The chemical reactions involved in the formation of calcium halophosphate phosphor have been the subject of much research activity (1-9). For the most part the experimental methods employed (x-ray diffraction, differential thermal analysis, thermal gravimetric analysis, etc.) have lacked the requisite sensitivity to observe the behavior of manganese, because of its relatively low concentration, during the course of these reactions. Determination of the luminescent properties of halophosphates has been used to study the diffusion of Mn^{++} and also Sb^{+++} into the apatite lattice (10), but this approach gives no information about the presence of manganese in other phases. A method which allows for the direct observation of Mn^{++} in all of the phases which may be present during the course of the apatite forming reaction is that of electronic paramagnetic resonance (11, 12).

The work reported in this paper is an EPR (electronic paramagnetic resonance) investigation of the distribution of manganese among the various phases present during the formation of calcium fluorapatite. The study has been limited to calcium fluorophosphate because the EPR spectrum of Mn^{++} in this material is well defined and of relatively good intensity, whereas the corresponding spectra of chlorapatite and chlorfluorapatite are an order of magnitude weaker and show considerable variation from sample to sample of purportedly equivalent material. Also, in order to avoid a magnetically concentrated condition which would cause spin-spin broadening of the spectral lines

(13), it has been necessary to use about one hundredfold less manganese than is normal in halophosphate production.

Experimental

Preparation of materials.—All firing mixtures were formulated to yield, on completion of the reaction, a product of the composition $Ca_{10-x}Mn_xF_2(PO_4)_6$ where $x = 1.5 \times 10^{-3}$. Raw materials used were lamp phosphor grade $CaHPO_4$, $CaCO_3$, CaF_2, and various compounds containing Mn^{++} which were prepared as follows: (*a*) $CaHPO_4$: 2.5×10^{-4} Mn, by recrystallization of an aqueous slurry of $CaHPO_4 \cdot 2H_2O$ and manganous ion (12); (*b*) $CaCO_3$: 5×10^{-4} Mn, by precipitation from an aqueous solution of Ca^{++} and Mn^{++} with an ammonium carbonate solution; (*c*) CaF_2: 1.5×10^{-3} Mn by treatment of $CaCO_3$: 1.5×10^{-3} Mn with hydrofluoric acid; (*d*) $Ca_9MnF_2(PO_4)_6$ by firing a mixture of $CaHPO_4$, $CaCO_3$, CaF_2, and $MnCO_3$ at 1125°. Manganese was also added to the firing mixture as $Mn(NO_3)_2$ solution. The components of a given mixture were wet blended in acetone either by mortar and pestle or ball mill.

Portions of each of these mixtures were fired at 100° intervals over the range 600°-1200° for 10, 30, and 60 min in atmospheres of both N_2 and $CO/CO_2 = 1/10$. The purpose of the latter gaseous mixture was to provide a mildly reducing atmosphere (14) that would prevent Mn^{++} from oxidizing and at the same time not reduce phosphate.

Electronic paramagnetic resonance.—Electronic paramagnetic resonance of the polycrystalline samples was measured on a Varian Associates EPR spectrometer with a resonant frequency of 9160 MHz and a modulation frequency of 100 kHz. Approximately ¾ in. of powder at one end of a fused quartz sample tube (4 mm OD x 3 mm ID x 6 in. length) was used. The EPR spectra reproduced in this paper are potentiometric recorder tracings of the first derivative of absorption of microwave energy *vs.* the magnetic field, which increases from left to right in the figures.

Preparation of EPR standards.—Some of the raw materials used in the firing mixtures are too poorly crystallized and/or too magnetically concentrated in manganese to be good EPR standards. Differences in the following preparative procedures from those given above were made necessary by the requirements of good crystallinity and sufficient dilution of Mn^{++} to avoid spin-spin broadening.

Precipitated calcium carbonate is generally a mixture of vaterite and calcite. EPR spectra of $CaCO_3$:Mn preparations in which the proportions of vaterite and calcite varied were always the spectrum of Mn^{++} in the crystalline field of calcite only (15), the intensity increasing with calcite concentration. Irreversible transformation of vaterite to calcite occurs at 430°-440° (16), and at 500° the inversion goes rapidly. Precipitated $CaCO_3$: 10^{-4} Mn was heated for 1 hr at 500°, therefore, for use as an EPR standard. CaO: 10^{-4} Mn was made by igniting the carbonate for 1 hr at 1170° in an atmosphere of $CO/CO_2 = 1/10$. CaF_2: 10^{-4} Mn obtained by treatment of $CaCO_3$: 10^{-4} Mn with aqueous HF was heated at 1000° in a stream of nitrogen passed over NH_4HF_2 at 200°. This atmosphere was necessary to prevent the formation of CaO:Mn, which is produced very readily if only a trace of oxygen is available (17). The pyrophosphates were made by the thermal decomposition of $CaHPO_4$: 2.5×10^{-4} Mn.

The distribution of manganese between two or more phases was estimated from relative intensities of their EPR lines by comparison with standard mixtures of the above EPR standards.

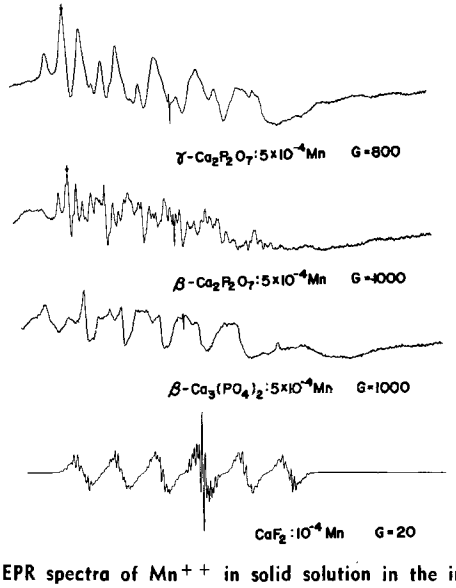

Fig. 1. EPR spectra of Mn^{++} in solid solution in the indicated compounds. G is the relative gain of the spectrometer. H increases from left to right.

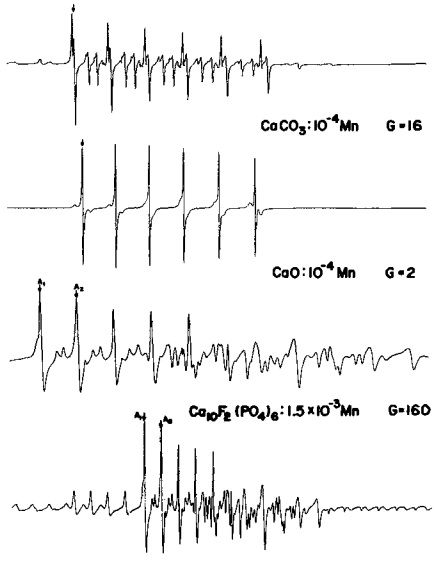

Fig. 2. EPR spectra of Mn^{++} in solid solution in the indicated compounds. G is the relative gain of the spectrometer. H increases from left to right.

Results and Discussion

Compounds that one might expect to be present during various stages of the reaction to form fluorapatite (at temperatures of 600° and greater) are γ-$Ca_2P_2O_7$, β-$Ca_2P_2O_7$, $CaCO_3$, CaO, CaF_2, β-$Ca_3(PO_4)_2$, and $Ca_{10}F_2(PO_4)_6$ (1, 2). EPR spectra of Mn^{++} in solid solution in each of these compounds are given in Fig. 1 and 2. These are the basic spectra that have been used to determine the presence of manganese in these compounds in the fired mixtures. In this connection there are several points that should be discussed. First, it is noted that the first strong line of the apatite spectrum is free of interferences and that the lines of apatite are moderately strong and sharp. It is thus possible to detect low concentrations of apatite in the presence of other phases.[1] The spectral lines of CaO and $CaCO_3$ are much stronger than those of apatite and other phases which are likely to be present, and very low concentrations of these constituents can be detected in mixtures. For example, less than 1% of $CaCO_3$: 10^{-4} Mn in $Ca_{10}F_2(PO_4)_6$: 1.5×10^{-3} Mn and 0.1% of CaO: 10^{-4} Mn in γ-$Ca_2P_2O_7$: 5×10^{-4} Mn are detectable. On the other hand, the predominant spectral lines of γ-$Ca_2P_2O_7$, β-$Ca_2P_2O_7$, and β-$Ca_3(PO_4)_2$ are relatively weak and are not at all well resolved from the strongest apatite lines, so that only relatively large amounts of these compounds are observable in the presence of apatite. The spectrum of CaF_2 has good intensity with one relatively strong, sharp line in the fourth hyperfine group ($m = \frac{1}{2}$), so that even

[1] See Appendix.

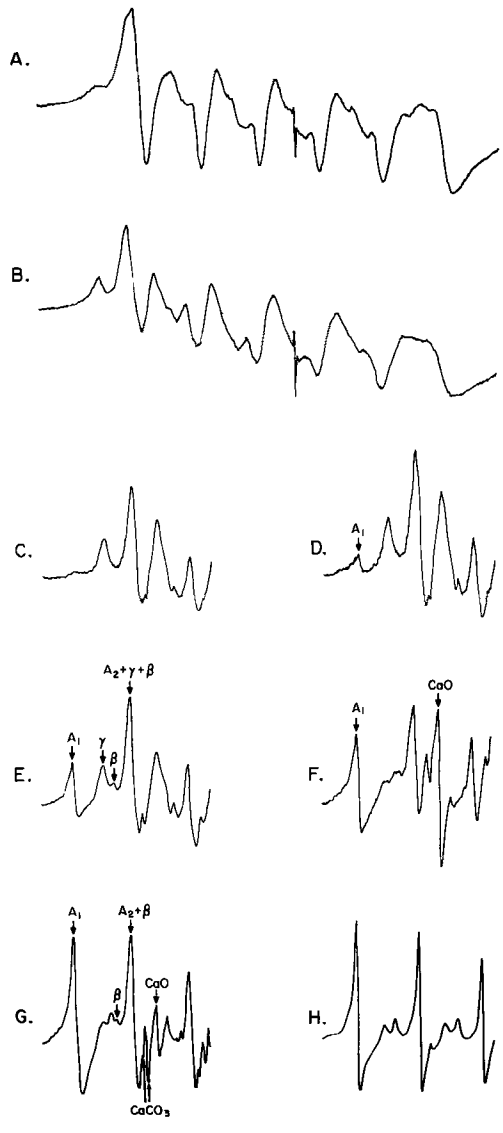

Fig. 3. EPR spectra of the mixture, $6CaHPO_4$:2.5x10^{-4}Mn + $3CaCO_3$ + CaF_2 fired in CO/CO_2 = 1/10:A, unfired mixture; B, 10 min, 500°; C, 60 min, 700°; D, 10 min, 800°; E, 60 min, 800°; F, 10 min, 900°; G, 10 min, 1000°; H, 60 min, 1200°.

though this line falls in a fairly complex region of the apatite spectrum the sensitivity for detection of calcium fluoride in fluorapatite is reasonably good; for example, 2% of CaF_2: 10^{-4} Mn in $Ca_{10}F_2(PO_4)_6$: 1.5×10^{-3} Mn is observable.

It is not practical to reproduce all of the original data, which are potentiometric recorder tracings of EPR spectra, but it will be instructive to present and discuss some of the salient spectra of one set of fired samples. A set which contains most of the spectra that are encountered is that obtained from firings in CO, CO_2 of the mixture, $6CaHPO_4$: 2.5×10^{-4} Mn + $3CaCO_3$ + CaF_2. For the unfired mixture the spectrum is, of course, that of $CaHPO_4$:Mn (Fig. 3a). At 500°, 10 min the dibasic calcium orthophosphate has largely decomposed to γ-$Ca_2P_2O_7$ (Fig. 3b). The spectrum is almost as well developed as that of the firing at 500° and 60 min, conditions which are known to effect complete decomposition. Except for some sharpening of the spectral lines, indicating better crystallinity, there is little change in the spectra over the 500°-700° range. There is probably a trace of apatite appearing at 700°, 60 min (Fig. 3c); this is definite at 800°, 10 min (Fig. 3d). At 800°, 60 min there is evidence for partial conversion of γ-$Ca_2P_2O_7$ to β-$Ca_2P_2O_7$[2] (Fig. 3e). In the presence of even only moderate concentrations of apatite:Mn the detection and estimation of $Ca_2P_2O_7$:Mn becomes difficult, because of factors mentioned earlier. It is possible nevertheless to make a plausible, if not unambiguous, estimate of the distribution of manganese between the pyrophosphates and apatite phases by determining the relative intensity of the first and second strong apatite lines (the first strong line of the pyrophosphates falls directly on the second apatite line) and comparing with standard mixtures. This was done over the range 800°, 10 min through 1000°, 10 min beyond which there is no indication of the presence of $Ca_2P_2O_7$. The spectrum of CaO:Mn first appears at 900°, 10 min, already at its maximum intensity for this set (Fig. 3f). The predominately CO_2 atmosphere has prevented significant decomposition of $CaCO_3$ to this point. Distribution of manganese between CaO and apatite is estimated as indicated in the following paragraph over the range, 900°, 10 min through 1100°, 30 min, above which only the apatite spectrum remains. These distribution coefficients together with those for $Ca_2P_2O_7$, apatite appear in Table I. At 1000°, 10 min (Fig. 3g) manganese is distributed through four phases: CaO, $CaCO_3$, β-$Ca_2P_2O_7$, and $Ca_{10}F_2(PO_4)_6$. A mixture containing 0.3% CaO: 10^{-4} Mn, 1.7% $CaCO_3$: 10^{-4} Mn, 49% β-$Ca_2P_2O_7$: 5×10^{-4} Mn, and 49% $Ca_{10}F_2(PO_4)_6$: 1.5×10^{-3} Mn has an EPR spectrum nearly identical to that of Fig. 3g. From the spectra presented it is clear that the intensity of the apatite spectrum is steadily increasing with firing temperature. Over the temperature range, 800°-1200°, the spectral intensity increase is 60 fold.

Insofar as it is possible to express the data more or less quantitatively, the results of the firings of the various mixtures are presented in Tables I through VI, for which a few words of explanation are desirable. Although the concentration of a paramagnetic species in a given phase is, strictly speaking, proportional to the total area under its EPR absorption curve and hence to the area under one of its absorption lines, it was considered sufficiently accurate for the purposes of this presentation to use the peak to peak distance of the first derivative of an absorption line as a roughly quantitative measure of the manganese concentration, provided it is below the level where line broadening would become a factor. Lines selected for intensity measurement are indicated by arrows in Fig. 1 and 2. The number of moles of manganese in one phase relative to the number of moles of manganese in another phase is called here the distribution coefficient of manganese between the two phases,

$$D \frac{\text{Phase 1}}{\text{Phase 2}}$$

For example,

$$D \frac{\text{CaO}}{\text{Apatite}} = \frac{\text{moles Mn in CaO}}{\text{mole Mn in } Ca_{10}F_2(PO_4)_6}$$

When attempting to get a picture of the relative amounts of manganese in two phases it is wise to determine the distribution coefficient of manganese between the two phases, because a consideration of the EPR line intensities alone can be misleading.

As the incorporation of manganese into fluorapatite is of prime importance let us confine our attention for the moment to the apatite spectral intensities (Table II). The appearance of very weak apatite lines at 700° is the first indication of manganese solid solution in apatite. At this temperature the predominant reaction to form apatite is that given by Montel (18), *viz.*, $18Ca_2P_2O_7 + 14CaF_2 \rightarrow 5Ca_{10}F_2(PO_4)_6 + 6POF_3$ (7). This reaction requires 2.8 moles of CaF_2 for each mole of apatite produced and at 700° goes to about one third of completion in reasonable firing times (19), so

[2] See ref. (12), Fig. 4 for spectra of mixtures of these two phases.

Table I. EPR line intensities and distribution coefficients of manganese for fired apatite mixture: $6CaHPO_4$:2.5×10^{-4}Mn + $3CaCO_3$ + CaF_2

Atmosphere: CO/CO_2 = 1/10

Firing temp, °C	Firing time, min	$I_{\gamma\text{-}Ca_2P_2O_7}$	I_{CaO}	I_{A_1}	I_{CaCO_3}	$D\frac{Ca_2P_2O_7}{Apatite}$	$D\frac{CaO}{Apatite}$	$D\frac{CaCO_3}{Apatite}$
500	10	63						
	30	60						
	60	47						
600	10	46						
	30	50						
	60	69						
700	10	65						
	30	62						
	60	55		0.8				
800	10	66		9		39		
	30	63		23		16		
	60	52		33		9.2		
900	10		95	58		2.1	0.19	
	30		99	88		1.3	0.15	
	60		61	75		0.7	0.12	
1000	10		41	120	39	0.4	0.057	0.02
	30		36	220	15		0.032	0.005
	60		47	270	9		0.033	0.002
1100	10		25	210	13		0.025	0.004
	30		25	530			0.012	
	60			500				
1170	10			430				
	30			560				
	60			440				
1200	10			470				
	30			560				
	60			520				

Table II. Intensity of apatite EPR line, A_1

		Source of manganese and firing atmosphere											
		$CaHPO_4$: 2.5×10^{-4} Mn		$CaCO_3$:5×10^{-4} Mn		$Mn(NO_3)_2$*		CaF_2:1.5×10^{-3} Mn		$Ca_9MnF_2(PO_4)_6$		$Mn(NO_3)_2$*	
Firing temp, °C	Firing time, min	N_2	CO/CO_2	N_2	CO/CO_2	N_2	CO/CO_2	N_2	CO/CO_2	N_2	CO/CO_2	N_2	Air
700	10												
	30						1						
	60	1	0.8				3		2				
800	10	1	9			0.6	8	2	3			3	3
	30	6	23		7	4	20	3	7			8	6
	60	6	33	2	18	9	37	42	10		10	7	6
900	10	6	58	11	30	15	37	24	23	2	6	16	14
	30	44	88	38	44	28	50	34	29	6	17	44	9
	60	85	75	67	50	56	58	88	31	22	32	79	10
1000	10	48	120	90	55	65	67	130	22	38	32	100	18
	30	130	220	240	100	130	130	330	70	110	92	170	35
	60	260	270	270	140	220	140	340	120	170	140	210	50
1100	10	170	210	370	120	110	160	350	95	200	160	210	69
	30	350	530	510	280	390	330	490	300	280	210	210	110
	60	530	500	560	420	460	430	570	430	350	270	220	110
1170	10	490	430	680						260	270	240	210
	30	710	560	870						280	150	180	210
	60	720	440	570	490	300	290	550	250	370	290	210	190
1200	10	660	470										
	30	730	560										
	60	730	520										

* Data of columns 13 and 14 were obtained from a mixture different from that of columns 7 and 8.

that one might expect about 1/10 the formulated amount of apatite to be produced in an hour at 700°. It is seen that the solid solution of manganese in apatite is far less than this, indicating that the driving force for the incorporation of manganese into the apatite lattice is very low at this temperature.

The effect of the ambient atmosphere on the solid solution of manganese in apatite is evident. In the temperature range of 700°-800° the mildly reducing atmosphere of CO, CO_2 promotes greater incorporation of manganese in apatite than the neutral nitrogen atmosphere. Except for the mixture containing CaF_2: Mn, the concentration of manganese dissolved in apatite is about the same for both atmospheres at 900°. At the highest temperatures used manganese incorporation seems to be somewhat better in nitrogen than in the reducing atmosphere. The detrimental effect of an oxidizing atmosphere is underscored by the results of firing one mixture in both N_2 and air. It is seen (last two columns of Table II) that only at 1170° is manganese incorporation as complete in air as in nitrogen. All of these results emphasize the fact that manganese must be in the manganous state before it can substitute for Ca^{++} in apatite. At low and intermediate temperatures it is expected that the Mn^{++} oxidation state would be favored by reducing (CO, CO_2) and neutral (N_2) atmospheres, in that order. For temperatures approaching 1200° the effect of a reducing atmosphere is not so significant, because, as is well known, the equilibria

$$6Mn_2O_3 \rightleftarrows 4Mn_3O_4 + O_2$$

and

$$2Mn_3O_4 \rightleftarrows 6MnO + O_2$$

shift to the right with increasing temperature (20, 21). The reason for better incorporation of manganese at 1100°-1200° in N_2 relative to CO, CO_2 is not clear. Possibly a manganese carbonyl (22, 23), which might be expected to be volatile at these temperatures, is formed in the latter atmosphere. $Mn_2(CO)_{10}$ can only be prepared in reasonable yield by treating a manganous salt suspended in a suitable organic solvent with carbon monoxide at several hundred atmospheres pressure in the presence of a powerful organometallic reducing agent (24, 25). But this does not preclude the possibility that minor amounts of this

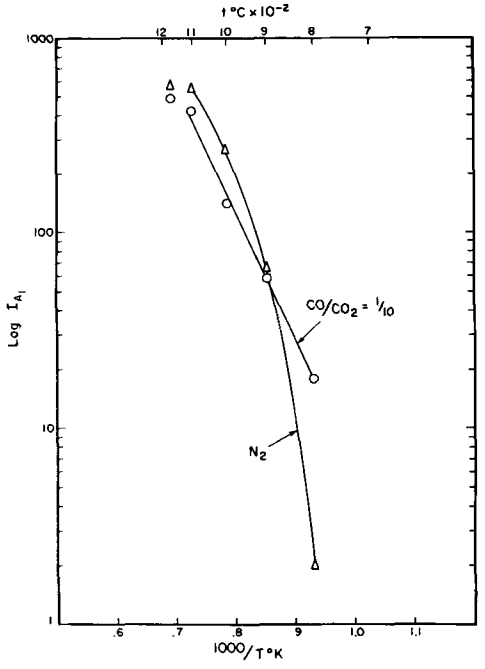

Fig. 4. Arrhenius plot of fluorapatite mixture fired 1 hr in N_2 and in CO/CO_2 = 1/10. Mn added as $CaCO_3$:5x10^{-4}Mn. I_{A_1} is intensity of EPR line of Mn^{++} in apatite (ref. Fig. 2).

compound, or some other combination of manganese and carbon monoxide, could be produced under the conditions described above.

Except for one firing mixture, that containing $CaHPO_4$:2.5 × 10^{-4} Mn [3], the amount of manganese in solid solution in apatite has leveled off at 1100° in both neutral and reducing atmospheres whereas in air a higher firing temperature (*e.g.*, 1170°) is required to bring about an equivalent amount of manganese incorporation. Insofar as solid solution of manganese is concerned, therefore, it should not be necessary to fire a halophosphate phosphor over 1100° in a nonoxidizing atmosphere.

If Arrhenius plots are made of the data of Table II, *i.e.*, log I_{A_1} *vs.* $1/T$, it will be observed that the curves approximate straight lines between 700° and 1100°. Because the EPR line intensity is proportional to the concentration of manganous ion in fluorapatite, it should be possible from this type of plot to determine the activation energy for solid solution of manganese in apatite. There has been no attempt to use the present data for such a purpose, because it is too inaccurate, but sufficient refinement of the measurements could be effected to make meaningful determination of the activation energy possible.

[3] A possible explanation for this is that the dibasic calcium orthophosphate used in this mixture is a laboratory preparation with different crystal shape and size distribution, and therefore different reactivity, from the factory produced $CaHPO_4$ used in all of the other mixtures.

Figure 4, which is presented as a more or less typical example of an Arrhenius plot of the data of Table II, also serves to illustrate two points discussed above. First it is noted that, in the CO, CO_2 atmosphere which has a CO_2 partial pressure of about 670 mm, apatite is produced at 800°. At this temperature the equilibrium partial pressure of CO_2 above $CaCO_3$ is 208 mm (26) and no CaO is produced as is evident from Table IV, so that the major contribution to apatite formation must be the reaction involving only CaF_2 and $Ca_2P_2O_7$. The second point illustrated is that in the reducing atmosphere incorporation of manganese in apatite is greater than in nitrogen at 800°. This brings up a question, however: if $CaCO_3$:5 × 10^{-4} Mn is not decomposing in an essentially CO_2 atmosphere how is the manganese being removed from it so that it may enter into the apatite? A reasonable answer might be that the mobility of manganese is enhanced by the presence of carbon monoxide at this relatively low temperature as well as at higher temperatures as indicated above. Support for this hypothesis is given by the observation of vapor phase transport of manganese at 600° in an atmosphere of water vapor and carbon monoxide (27). This, of course, implies that the necessity for manganese to be divalent is not the whole reason for better incorporation of manganese in apatite at 700°-800° in a CO, CO_2 atmosphere as compared with N_2.

Implicit in the discussion of the results to this point has been the idea of manganese possessing a degree of mobility, increasing with temperature, which enables it to become incorporated in the apatite structure. This is aptly demonstrated by the EPR spectra of the mixture containing $Ca_9MnF_2(PO_4)_6$ as the source of manganese (Table III). At low temperatures the spectrum is a single very broad structureless line of about 400 gauss half width, due to the presence of the magnetically concentrated manganese apatite. At 800° or 900°, depending on the atmosphere, very weak apatite lines superimposed upon the broad peak first appear. These relatively sharp lines gradually increase in intensity with increasing temperature until at about 1100° there is a plateau. Concurrently the broad apatite peak has decreased in strength and disappeared. Manganese has acquired enough mobility to diffuse out of the preformed apatite into the newly produced apatite.

In addition to the diffusion of manganese and its solid solution in the newly formed apatite another interesting phenomenon is occurring. In a nitrogen atmosphere lines of CaO:Mn appear weakly at 700°, increase in intensity to a maximum for 10 min firing at 1000°, and as the CaO is consumed in the apatite reaction disappear after 10 min at 1100°. Although at 800° there is no indication of manganese incorporation in freshly formed apatite, the CaO:Mn spectral

Table III. EPR line intensities and distribution coefficients of manganese for fired apatite mixture: $6CaHPO_4 + 3CaCO_3 + CaF_2 + 1.5x10^{-3}Ca_9MnF_2(PO_4)_6$

Firing temp, °C	Firing time, min	Atmosphere: N_2			Atmosphere: CO/CO_2 = 1/10		
		I_{A_1}	I_{CaO}	$D\frac{CaO}{Apatite}$	I_{A_1}	I_{CaO}	$D\frac{CaO}{Apatite}$
700	60	Broad line	15		Broad line		
800	60	Broad line	140		10	Trace	
900	10	2	180	0.30	6	47	0.082
	30	6	190	0.16	17	39	0.032
	60	22	320	0.11	32	37	0.020
1000	10	38	380	0.089	32	8	0.006
	30	110	170	0.024	92		
	60	170	70	0.009	140		
1100	10	200	10	<0.002	160		
	30	280			210		
	60	350			270		
1170	10	260			270		
	30	280			150		
	60	370			290		

Table IV. EPR line intensities and distribution coefficients of manganese for fired apatite mixture: $6CaHPO_4 + 3CaCO_3{:}5x10^{-4}Mn + CaF_2$

Firing temp, °C	Firing time, min	Atmosphere: N_2 I_{CaCO_3}	I_{CaO}	I_{A_1}	$D\frac{CaO}{Apatite}$	Atmosphere: $CO/CO_2 = 1/10$ I_{CaCO_3}	I_{CaO}	I_{A_1}	$D\frac{CaO}{Apatite}$
600	30	5000							
	60	3800	150						
700	10	3200	64			4300			
	30	2900	460			4200			
	60	2600	1200			4200			
800	10	3100	750			2900			
	30	1800	1700			3100		7	
	60	1500	3000	2		2700		18	
900	10		4500	11	>0.31	*	280	30	0.91
	30		4700	38	0.31	*	260	44	0.73
	60		3800	67	0.22	*	230	50	0.69
1000	10		2700	90	0.19	*	400	55	0.79
	30		1300	240	0.066	*	250	100	0.48
	60		670	270	0.034	*	210	140	0.25
1100	10		360	370	0.018	*	230	120	0.43
	30			510		*	75	280	0.064
	60			560		Trace	30	420	0.024
1170	10			680					
	30			870					
	60			570				490	

* $CaCO_3$:Mn is present, but line intensity is difficult to estimate because of poor resolution.

intensity has already attained one third of its maximum strength. Calcium oxide appears to be removing manganese from $Ca_9MnF_2(PO_4)_6$. Indeed this affinity of calcium oxide for manganese is so pronounced that if one attempts to produce $Ca_{10}F_2(PO_4)_6$:Mn from a mixture containing only a slight excess of CaO he will obtain the EPR spectrum of CaO:Mn only.

Another example of the affinity of calcium oxide for manganese is given by the firings of the mixture containing $CaCO_3{:}5 \times 10^{-4}$ Mn (Table IV). For nitrogen firings the spectrum of CaO:Mn first appears at 600°, reaches a maximum at 900°, and has disappeared at 1100°. As is expected, in an atmosphere which is principally carbon dioxide the decomposition of $CaCO_3$ is delayed until 900° when the spectrum of CaO:Mn is first noted. The intensity of the spectrum remains fairly constant over the 900°-1000° range, drops off at 1100°, and is zero at 1170°. It is observed that the maximum intensity is slightly less than one tenth the maximum intensity of the nitrogen firings. The lines are, however, one and one-half to twofold broader.

These differences are interpreted as follows. In nitrogen the rate of decomposition of $CaCO_3{:}5 \times 10^{-4}$ Mn is already very rapid before apatite formation becomes significant, so that a fairly large amount of unreacted CaO is produced with manganese in solid solution in the approximate molar concentration of 5×10^{-4}. On the other hand for the atmosphere, $CO/CO_2 = 1/10$, the rate of carbonate decomposition is still fairly slow when the formation of apatite becomes appreciable so that much of the calcium oxide is entering into the apatite forming reaction as soon as it is formed. The CaO that does not enter into the apatite reaction combines with a substantial proportion of the manganese produced by the decomposition of the carbonate. The concentration of manganese in calcium oxide is now high enough to cause significant spin-spin interaction evidenced by line broadening. From comparison with CaO:Mn preparations of known manganese content it is estimated that the manganese concentration varies from 7.5×10^{-4} to 8.5×10^{-4}M over the temperature range, 900°-1100°, corresponding to an enrichment of 50-70%.

The affinity of CaO for manganese is very striking in the case of CaF_2, CaO mixtures. When a mixture of CaF_2 with 1% CaO and manganous nitrate in the proportion, $Mn/Ca = 10^{-4}$, is fired for 2 min or longer at 1100° the resulting EPR spectrum is that of CaO:Mn only. Indeed, if CaF_2:Mn is fired for several hours in an atmosphere which contains only a trace of air, the EPR spectrum of CaF_2:Mn disappears and is replaced by that of CaO:Mn. One has to be very careful in preparing CaF_2:Mn for EPR purposes to exclude all traces of CaO and/or air (11, 28).

It must be emphasized that although the affinity of CaO for manganous ion is rather high for low concentrations of the latter such is not necessarily the case for higher concentrations.

There were three reasons for introducing manganese into the reaction mixture in one of a number of different phases. First it was believed that a more uniform dispersion of manganese in the mixture could be obtained by this expedient than by customary procedures. It was also of interest to know whether the ability of manganese to enter into the apatite structure is influenced by its source. As we have seen, except for the mixture containing $CaHPO_4{:}2.5 \times 10^{-4}$ Mn, manganese incorporation in fluorapatite in all cases levels off at 1100°. Finally, one might expect to be able to follow the consumption of a component which is a source of manganese by observing the change in strength of its EPR spectrum. As an example, for nitrogen firings of the mixture containing $CaHPO_4{:}2.5 \times 10^{-4}$ Mn (Table V), it is observed that the spectrum of $Ca_2P_2O_7$, the decomposition product of the acid phosphate, has essentially the same strength over the range 500°-800°, indicating little consumption. Over the 900°-1000° temperature interval the change in distribution of manganese between calcium pyrophosphate and apatite indicates that pyrophosphate is being used up in the apatite forming reaction. At 1100° there is no EPR evidence for the existence of $Ca_2P_2O_7$. This is substantiated by x-ray diffraction analysis.

For mixtures containing $CaF_2{:}1.5 \times 10^{-3}$ Mn as a source of manganese (Table VI), interpretation of the curves is not so readily accomplished. Because it is magnetically concentrated in manganese the spectrum of CaF_2:Mn in these mixtures consists of six broad, structureless lines. In a CO, CO_2 atmosphere these lines progressively diminish in strength between 700°, 10 min, and 800°, 10 min, at the same time picking up a little structure. The spectra for apatite and $CaCO_3$ appear at 800°, 10 min, but they are very weak and can account for only a very small proportion of the manganese which has disappeared from its CaF_2 environment. Thus one cannot infer from the EPR spectra whether CaF_2 is taking part in the apatite reaction or is simply losing its manganese. X-ray diffraction analysis, however, tells us that CaF_2 is being consumed over this firing range; the last CaF_2 is observed at 800°, 60 min. For samples prepared in a nitrogen atmosphere CaF_2:Mn is still observable after 10 min at 700°, but is not seen for longer firing times or higher temperatures. According to x-ray diffraction analysis, however, calcium fluoride is not entirely consumed until after 30 min firing at 1000°. Relatively intense CaO:Mn lines with very broad wings dom-

Table V. EPR line intensities and distribution coefficients of manganese for fired apatite mixture: $6CaHPO_4$:2.5x10^{-4}Mn + $3CaCO_3$ + CaF_2

Atmosphere: N_2

Firing temp, °C	Firing time, min	$I_{\gamma\text{-}Ca_2P_2O_7}$	I_{CaO}	I_{A_1}	$D\frac{Ca_2P_2O_7}{Apatite}$	$D\frac{CaO}{Apatite}$	$D\frac{CaO}{Ca_2P_2O_7}$
500	10	32					
	30	51					
	60	45					
600	10	50					
	30	37					
	60	46					
700	10	41					
	30	56	21				0.0017
	60	50	47	1	150 γ		0.0036
800	10	53	100	1			0.0064
	30	55	330	6		0.22	0.015
	60	45	320	6	39 γ	0.21	0.017
900	10		400	6	>>5.3 γ + β	0.25	
	30		610	44	>5.3 β	0.11	
	60		730	85	2.0 β	0.095	
1000	10		700	48	>5.3 β	0.11	
	30		750	130	1.2 β	0.066	
	60		810	260	0.2 β	0.040	
1100	10		120	170		0.031	
	30		150	350		0.0096	
	60		42	530		0.0036	
1170	10		54	490		0.0024	
	30		19	710		<0.002	
	60		30	720		<0.002	
1200	10		3	660			
	30		3	730			
	60			730			

inate the spectra over the 700°-800° range. Calcium oxide has apparently accelerated the removal of manganese from calcium fluoride and combined with it.

In the case of mixtures containing $CaCO_3$: 5 × 10^{-4} Mn it is relatively easy to follow the decomposition of the carbonate to the oxide and the consumption of the latter during the formation of apatite. In a nitrogen atmosphere, decomposition of $CaCO_3$ seems to be complete for 10 min firing at 900° and calcium oxide is gone after 10 min at 1100°, whereas in the CO, CO_2 atmosphere traces of carbonate appear to persist, along with some calcium oxide, through 60 min of firing at 1100°, after which only the spectrum of apatite remains.

It turns out that the spectrum of calcium oxide, because of its high intensity and the great affinity of this compound for manganese, persists until the apatite reaction is virtually complete. Thus the course of the reaction can be followed by observing the CaO:Mn spectrum, or the distribution of manganese between calcium oxide and apatite.

Finally, it is worth mentioning that in none of the fired mixtures was there any evidence by EPR or x-ray diffraction for the formation of $Ca_3(PO_4)_2$ as an intermediate in the production of apatite. This is in accord with the findings of Rabatin and Gillooly (7).

Summary

Electronic paramagnetic resonance is used to study the disposition of Mn^{++} among the various phases present during the course of the reaction to form fluorapatite. For materials prepared in N_2 or CO/CO_2 = 1/10, solid solution of manganese in fluorapatite is first detected at 700° and is observed to increase exponentially through 1100°, at which temperature incorporation of manganese is virtually complete. Arrhenius plots of the EPR line intensity of Mn^{++} in apatite are approximate straight lines from 700° through 1100°. Over the range 700°-800°, incorporation of manganese in fluorapatite is better in the CO, CO_2 atmosphere than in N_2, whereas the reverse is the case over the range 1000°-1200°. Air inhibits the entry of manganese into the apatite structure, and only at temperatures approaching 1200° is solid solution complete. The differences in solid solution associated with the various atmospheres can be attributed largely to the necessity for manganese to be in the divalent oxidation state. However, in order to explain some of the observed behavior of manganese it is necessary to postulate volatile compound formation involving carbon monoxide. At 800° chemically bound manganese in apatite acquires enough mobility to diffuse into freshly formed apatite originally possessing no

Table VI. EPR line intensities and distribution coefficients of manganese for fired apatite mixture: $6CaHPO_4$ + $3CaCO_3$ + CaF_2:1.5x10^{-3}Mn

		Atmosphere: N_2			Atmosphere: CO/CO_2 = 1/10					
Firing temp, °C	Firing time, min	I_{A_1}	I_{CaO}	$D\frac{CaO}{Apatite}$	I_{A_1}	I_{A_2}	I_{CaO}	I_{CaCO_3}	$D\frac{Ca_2P_2O_7}{Apatite}$	$D\frac{CaO}{Apatite}$
700	10		81							
	30		420							
	60		480							
800	10	2	550	>0.30	3			6		
	30	3	1000	>0.30	7	9		4	3.5	
	60	42	1000	0.14	10	12		7	2.6	
900	10	24	970	0.18	23	19	82	*		0.045
	30	34	1300	0.17	29	26	80	*		0.039
	60	88	1200	0.10	31	29	55	*		0.027
1000	10	130	1200	0.082	22	18	110	*		0.057
	30	330	520	0.030	69	62	150	*		0.031
	60	340	150	0.0094	120	110	110	*		0.017
1100	10	350	45	0.0035	95	85	93	*		0.018
	30	490			300	270	Trace			<0.001
	60	570			430	400				
1170	60	550			250	220				

* Minor amount of $CaCO_3$:Mn is present, but line intensity is difficult to estimate because of poor resolution.

manganese. At various stages of the reaction there is also evidence for the incorporation of manganese into $Ca_2P_2O_7$, $CaCO_3$, and CaO. The most conspicuous of these, from the point of view of frequency of occurrence, intensity, and persistence, is CaO:Mn, due in part to its inherently intense EPR spectrum, but also because of its strong affinity for manganese. It is possible to follow the consumption of $Ca_2P_2O_7$:Mn and CaO:Mn during the reaction by observation of their EPR spectra, but this is not feasible for CaF_2:Mn.

Acknowledgments

The author wishes to thank D. J. Ina and P. A. Hurst for preparation of samples, and L. S. Staikoff and J. R. Cooper for x-ray diffraction analyses. Preliminary work which led into the experiments reported here was conducted with the cooperation of R. L. Hickok and W. G. Segelken, to whom the author is also indebted for many helpful discussions.

Manuscript received Oct. 24, 1966; revised manuscript received Dec. 8, 1966.

Any discussion of this paper will appear in a Discussion Section to be published in the December 1967 JOURNAL.

APPENDIX

It is appropriate to discuss the capabilities and limitations of EPR as a method for studying solid-state reactions. The EPR spectrum of a paramagnetic ion in solid solution in a given crystalline compound is characteristic of that compound. Thus, the presence of a paramagnetic ion in solid solution in a number of different identifiable crystalline phases can, in principle, be detected unambiguously. In practice this is not always possible; *e.g.*, if a paramagnetic ion is in a crystalline field of low symmetry, its EPR spectrum will in all likelihood be a broad characterless line, or for mixtures of compounds containing paramagnetic ions in solid solution the different EPR spectra may interfere with one another so severely that identification of the different constituents is not possible. Although one can detect with certainty the presence of a phase by EPR, one cannot in general use EPR as a criterion for the absence of a phase. Thus, a statement such as, "There is a trace of apatite appearing at 700°, 60 min," is intended to mean that the EPR spectrum of a mixture fired for 60 min at 700° showed the presence of a trace of Mn^{++} in solid solution in apatite, which phase may or may not have been produced at a lower temperature or shorter firing time. The area under the EPR absorption curve of a paramagnetic species is proportional to the number of absorbing ions and therefore the intensity of the EPR spectrum can be related to the amount of a paramagnetic ion in solid solution in a given phase. It should be realized, however, that there is some ambiguity in such a relationship, because, within limits where line broadening is not a factor, it does not distinguish between large and small amounts of the host phase. All that can be said, for example, is that there are Xg of Mn^{++} in solid solution in an unspecified amount of fluorapatite per gram of sample subjected to the resonance conditions. This is the meaning that should be read into the portions of this paper dealing with concentrations of manganese and its distribution among the various phases.

REFERENCES

1. W. L. Wanmaker, A. H. Hoekstra, and M. G. A. Tak, *Philips Research Rept.*, **10**, 11 (1955).
2. W. L. Wanmaker and M. L. Verheyke, *ibid.*, **11**, 1 (1956).
3. S. Kamiya, *Electrochemistry (Denki Kagaku)*, **31**, 246 (1963).
4. K. H. Butler, M. J. Bergin, and V. M. B. Hannaford, *This Journal*, **97**, 117 (1950).
5. D. Robbins, Electrochemical Soc. Electronics Div. Abstracts, **11** [1], 31 (1962).
6. J. L. Ouweltjes and W. L. Wanmaker, *This Journal*, **103**, 160 (1956).
7. J. G. Rabatin and G. R. Gillooly, *ibid.*, **112**, 489 (1965).
8. G. R. Gillooly and J. G. Rabatin, Paper presented at the Cleveland Meeting of the Society, May 1966.
9. J. G. Rabatin, G. R. Gillooly, and J. W. Hunter, *ibid.*
10. W. L. Wanmaker and C. Bakker, "Proceedings of the Fourth International Symposium of Solids, Amsterdam, 1960," pp. 709-717, Elsevier, Amsterdam (1961).
11. P. H. Kasai, *J. Phys. Chem.*, **66**, 674 (1962).
12. J. A. Parodi, R. L. Hickok, W. G. Segelken, and J. R. Cooper, *This Journal*, **112**, 688 (1965).
13. B. Bleaney and K. W. H. Stevens, *Rep. Progr. Phys.*, **16**, 108 (1953).
14. A. Muan, *Am. J. Science*, **256**, 171 (1958).
15. F. K. Hurd, M. Sachs, and W. D. Hershberger, *Phys. Rev.*, **93**, 373 (1954).
16. F. Heide, *Centr. Mineral Geol.*, A **1925**, 198.
17. P. H. Kasai, *J. Phys. Chem.*, **66**, 2719 (1962).
18. G. Montel, Coll. der Sektion f. anorg. Chemie der Internat. Union f. rein u. angew. Chemie, Münster, Sept. 1954, Text der Vorträge u. Disk., Weinhein, Verl. Chemie, 1955, pp. 178-183.
19. J. G. Rabatin, Private communication.
20. W. C. Hahn, Jr., and A. Muan, *Am. J. Science*, **258**, 66 (1960).
21. F. A. Kröger, "Some Aspects of the Luminescence of Solids," pp. 62-64, Elsevier, New York (1948).
22. H. Remy, "Treatise on Inorganic Chemistry," vol. II, p. 352, Elsevier, Amsterdam (1956).
23. P. J. Durrant and B. Durrant, "Advanced Inorganic Chemistry," p. 1076, John Wiley & Sons, Inc., New York (1962).
24. F. A. Cotton and C. Wilkinson, "Advanced Inorganic Chemistry," p. 613, Interscience (1962).
25. R. D. Closson, L. R. Buzbee, and G. G. Ecke, *J. Am. Chem. Soc.*, **80**, 6167 (1958).
26. L. Andrussow, *Z. physik. Chem.*, **116**, 95 (1925).
27. I. L. Smith, Private communication.
28. R. L. Hickok, J. A. Parodi, and W. G. Segelken, *J. Phys. Chem.*, **66**, 2175 (1962).

A Low-Temperature Synthesis of Manganese Activated Zinc Silicate of Superior Crystallinity

Gleb Gashurov and Albert K. Levine[1]

General Telephone & Electronics Laboratories, Bayside, New York

ABSTRACT

A new method for synthesis of manganese activated Zn_2SiO_4 is reported. The method, which is based on the reaction between ZnF_2 and SiO_2 in molten $ZnCl_2$, yields typically well-crystallized rods of 10 by 100μ; activation with manganese can be obtained during or after the synthesis. The fluorescence efficiency of material prepared in this manner is comparable to that of commercial Zn_2SiO_4:Mn phosphors.

Zinc silicate is usually synthesized by a solid-state reaction between ZnO (or $ZnCO_3$) and silicic acid. Typically, as when the manganese activated phosphor is prepared, the reaction between the thoroughly blended ingredients is carried out at 1200°C for about 2 hr. An electronmicrograph of a representative sample of zinc silicate obtained from such a synthesis is shown in Fig. 1. The material is seen to consist of irregularly shaped, often agglomerated and intergrown particles ranging from less than 1μ to several microns in size. The absence of well-developed faces is notable. The use of fluxes to promote crystallization and growth during synthesis is generally objectionable in the case of Zn_2SiO_4, since most common fluxes (*e.g.*, alkali and alkaline earth halides and sulfates) react with silica to form silicates (1). Wilke (2) fluxed $ZnSiO_4$ with small percentages of KCl and Li_2SO_4 at 920°C for 1 hr. His results show no increase in particle size with KCl, while there is an apparent increase with Li_2SO_4. No information is given on the morphology of the individual crystallites.

This paper reports a Zn_2SiO_4 synthesis which proceeds at temperatures considerably lower than those previously reported for solid-state preparation and which produces a material of superior crystallinity. Manganese activation can also be accomplished either during or after the synthesis to produce a green-emitting phosphor, comparable to the commercial product in fluorescence characteristics.

Materials and Measurements

The materials used were Mallinckrodt silicic acid (standard luminescent grade), Fisher $ZnCO_3$ (certified reagent), Fisher $ZnCl_2$ (certified reagent), and Fisher $MnCl_2 \cdot 4H_2O$ (certified reagent). Anhydrous zinc fluoride was obtained from the Chemical and Metallurgical Division of Sylvania Electric Products Inc. Silica was obtained by firing silicic acid in air at 1000°C for 2 hr.

X-ray measurements were made on a Norelco wide range goniometer. Manganese concentration in Zn_2SiO_4 samples was determined by the x-ray fluorescence method. Zinc and silicon were determined gravimetrically; colorimetric analysis was used in fluorine determination.

Present address: Richmond College of the City University of New York, Staten Island, New York.

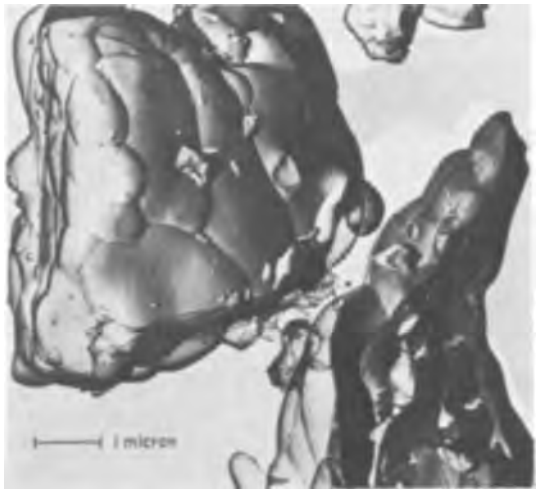

Fig. 1. Electronmicrograph of representative sample of commercially prepared Zn_2SiO_4:Mn phosphor.

Results and Discussion

The sluggishness of the solid-state reaction between zinc carbonate and silicic acid may be demonstrated by the fact that even after 2 hr at 1350°C the reaction is incomplete. The possibility of accelerating the formation of zinc silicate by heating the reactants under high pressure was investigated first. Samples containing an intimate mixture of ZnO and SiO_2 in their stoichiometric ratio were heated in a hot pressing assembly for 1 hr at 900°C under a pressure of 4 tons/in.^{2}. Although this treatment must have led to an improvement in the contact between reactants, the reaction was largely incomplete, and the major crystalline phase of the resulting product was ZnO. In fact, comparison of the various relevant peaks in the x-ray spectrum show that the ratio of ZnO to Zn_2SiO_4 obtained when the synthesis is carried out under pressure is approximately the same as that obtained when the sample is heated at the same temperature and atmospheric pressure. These results indicate that improvement in contact between ZnO and SiO_2 over the degree of contact obtained in normal blending is not a factor in the rate of Zn_2SiO_4 formation. Experiments by Jander and Riehl (3) indicate that the growth of Zn_2SiO_4 by solid-state reaction appears to proceed by the diffusion of ZnO through a zinc silicate layer which forms about a silica particle. In such a case, once a certain minimum degree of contact is established, the rate would be relatively insensitive to pressure.

The synthesis of zinc silicate by the reaction of ZnF_2 and SiO_2 has been described by Lenard, Schmidt, and Tomaschek (4). This method proceeds according to the following stoichiometry

$$2ZnF_2 + 2SiO_2 = Zn_2SiO_4 + SiF_4$$

Lenard *et al.* state that the synthesis is complete after 1 hr at 950°C. Since Lenard *et al.* give no description of the nature of the crystallites, we decided to investigate the synthesis in greater detail. Our results relative to the speed of the reaction agree with those of Lenard *et al.*; as a matter of fact we find that the reaction goes to completion within less than 1 hr at temperatures as low as 750°C. The completeness of the reaction was established by x-ray analysis which showed Zn_2SiO_4 as the only phase. The crystal size of the zinc silicate resulting from the fluoride synthesis is not, however, significantly different from that

obtained by reaction of the oxides; that is, in both cases the crystallites are small and of poor morphology. Nor is there any notable change in either crystal size or crystal habit when the ZnF_2-SiO_2 reaction is carried out at 900°C for longer periods, extending to 24 hr, or at 1200°C for 2 hr. This indicates that ZnF_2 reacts completely with SiO_2 particles in a short time to form small zinc silicate crystals; however, after the SiO_2 is consumed crystal growth proceeds very slowly. Furthermore, in the reaction with ZnF_2, the size of the SiO_2 particles appears to determine the size of the Zn_2SiO_4 crystals which are formed. A similar conclusion has been drawn (5) for the crystals synthesized by the reaction between SiO_2 and ZnO.

Diffusion processes and mass transport are much more rapid in liquid medium than in solid; hence it was decided to carry out the reaction between ZnF_2 and SiO_2 in molten zinc chloride. Zinc chloride was selected because (*i*) it exists in the liquid form over a suitably wide temperature range (318°-732°C); (*ii*) it is quite soluble in water and therefore can be easily separated from Zn_2SiO_4; and (*iii*) it has a common cation with Zn_2SiO_4 which eliminates the possibility of objectionable cation contamination. The initial experiments showed that zinc silicate of excellent crystallinity is obtained when ZnF_2 and SiO_2 are caused to react in molten zinc chloride. However, care must be exercised to insure that all SiO_2 reacts. Thus, for example, when 1.00g of ZnF_2, 0.58g of SiO_2, and 20g of $ZnCl_2$ are maintained at 600°C for 4 hr in a covered platinum crucible, the x-ray analysis of the resulting material after washing in boiling water shows Zn_2SiO_4 as the only crystalline phase. However, microscopic analysis reveals a relatively large number of large, irregularly shaped particles among the smaller well-formed Zn_2SiO_4 rods. The x-ray pattern of the irregular particles, which were separated from Zn_2SiO_4 rods by sieving, showed them to be amorphous, and the particles are presumed to be silica.

Significant reduction of the amount of unreacted silica and larger, more perfect zinc silicate crystallites are obtained when the reaction is carried out near 730°C, the boiling point of $ZnCl_2$. In this case provision must be made to condense $ZnCl_2$ vapor and return it to the system. The boiling also provides sufficient agitation to assist in the reaction. In this procedure an equimolar mixture of ZnF_2 and SiO_2 is placed together with a large excess of $ZnCl_2$ (35g of $ZnCl_2$ to 1g of ZnF_2) into a quartz flask provided with a long narrow neck. The flask is then lowered into a vertical tube furnace maintained at about 600°C. After 15 min the temperature of the furnace is raised, and the mixture refluxed at the boiling point of $ZnCl_2$ (730°C) for about 5 hr. To prevent bumping, the reaction flask is continuously agitated. After completion of the run, the mixture is poured into a quartz beaker, cooled and washed with boiling water to remove $ZnCl_2$. If the ingredients are sufficiently anhydrous, there is only little etching of the quartz flask.

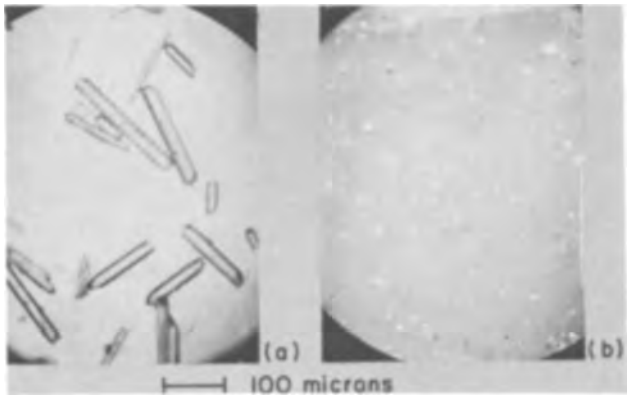

Fig. 2. Photomicrographs of (a) Zn_2SiO_4 prepared by the $ZnF_2/ZnCl_2$ method and (b) commercial Zn_2SiO_4:Mn (Sylvania #161).

Fig. 3. Electronmicrograph of Zn_2SiO_4 prepared by $ZnF_2/ZnCl_2$ method.

Figure 2a shows a photomicrograph of a typical Zn_2SiO_4 sample synthesized by the technique outlined above. For comparison (Fig. 2b), a photomicrograph of a sample of commercial Zn_2SiO_4:Mn phosphor, Sylvania No. 161, is included. One can see that the crystals prepared by the $ZnF_2/ZnCl_2$ method are on the average about 100μ in length and 10μ in cross section. An electronmicrograph (Fig. 3) of these crystals shows them to possess very well-developed faces. Examination under crossed polarizers reveals that most of the particles are strain-free crystals, and x-ray diffraction analysis shows α-Zn_2SiO_4 as the only crystalline phase. Chemical analysis of the synthesis product indicates that it contains some free silica. An assay of a typical product gives 30% by wt SiO_2 and 70% ZnO, whereas the respective stoichiometric values are 27 and 73%.

The following experiment indicates that the growth of Zn_2SiO_4 is controlled by its solubility and diffusion in molten $ZnCl_2$. A stoichiometric mixture of ZnF_2 and SiO_2 was placed at the bottom of a quartz tube, which was then filled to about 50% of its capacity with molten $ZnCl_2$ and heated to 600°C. During the first few minutes silica particles were observed to rise to the surface of the liquid and the solution acquired a gray color. After about 15 min all the particles sank to the bottom of the tube (probably indicating conversion of SiO_2 to Zn_2SiO_4) and the $ZnCl_2$ solution became colorless. Additional molten $ZnCl_2$ was then added to fill the tube to about 80% of its volume. The tube was sealed and placed in an inclined position in a horizontal tube furnace. A temperature gradient was established such that the lower end of the tube was at 690°C while the upper end was at 650°C. After 18 hr the tube was carefully removed, quenched to room temperature, and cut into sections. The quartz tube was only slightly etched, indicating little reaction with its contents. It was found that, while most of the Zn_2SiO_4 was in the hotter end, which had the initial charge, there was a significant amount of Zn_2SiO_4 in the cooler zone. There was, however, a notable difference in the size of the crystals. Figure 4 shows that the crystals grown in the hot zone are on the average a few microns in size, while those grown in the lower temperature region are up to 100μ in length. This result indicates material transport and deposition due to the temperature dependence of the solubility.

Large zinc silicate rods may also be obtained by heating silicon dioxide alone in boiling zinc chloride. The crystals obtained in this way are essentially of the same size and morphology as those prepared by the

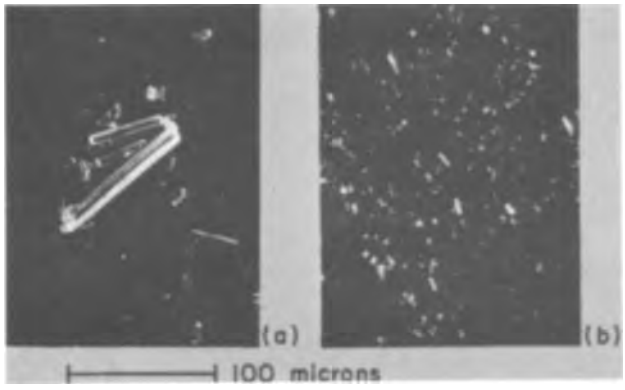

Fig. 4. Photomicrographs of Zn_2SiO_4 crystals grown in (a) the low-temperature zone and (b) the high-temperature zone of $ZnCl_2$ maintained at a temperature gradient.

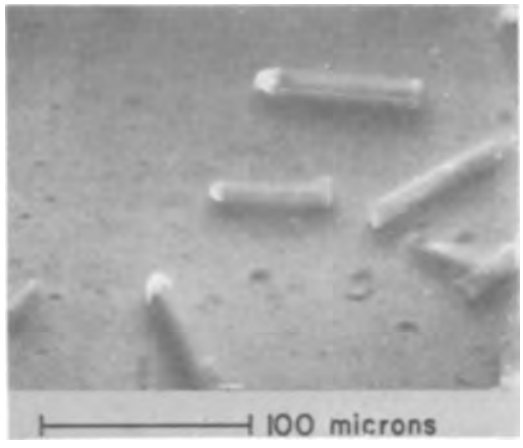

Fig. 5. Photomicrograph of Zn_2SiO_4:Mn crystals illuminated by their own emission when excited with uv radiation.

$ZnF_2/ZnCl_2$ method, although the reaction rate is substantially slower than that in the case of ZnF_2-SiO_2 reaction. For example, refluxing a mixture of SiO_2 and $ZnCl_2$ for 5 hr at 730°C produces Zn_2SiO_4 containing a very large excess of free silica. In a typical case, the composition of the solid phase was 47% SiO_2 by weight and 53% ZnO, whereas the stoichiometric composition of Zn_2SiO_4 is 27 and 73%, respectively. When a mixture of SiO_2 and $ZnCl_2$ was heated at 600°C for 5 hr, no zinc silicate was formed; the solid product after aqueous washing was shown to be amorphous by x-ray diffraction, and its weight was the same as that of the SiO_2 used in the experiment.

Crystallization experiments of the ZnF_2-$ZnCl_2$ type carried out at temperatures below the boiling point of zinc chloride, and in the absence of mechanical agitation, result in Zn_2SiO_4 rods which are mostly smaller than 25μ in length. In such syntheses the amount of unreacted silica is considerably larger than that found when the crystallization is carried out at the boiling point of $ZnCl_2$.

Luminescence of Zn_2SiO_4:Mn

Incorporation of manganese into zinc silicate may be accomplished by either of two techniques: (*i*) An aqueous solution of $MnCl_2$ is added to the Zn_2SiO_4 rods, the slurry is dried at 110°C for several hours and then fired under argon at 1200°C for 2 hr; the amount of manganese added is that which is desired in the final product. (*ii*) $MnCl_2$ is added to the inital reaction mixture, ZnF_2, SiO_2, and $ZnCl_2$, which is then refluxed for 5 hr. In the latter technique a large excess of manganese chloride is required to achieve the desired concentration level in the zinc silicate lattice, because of the miscibility of $MnCl_2$ in $ZnCl_2$ under the synthesis conditions. Table I presents results of photo- and cathodoluminescence measurements made on representative preparations. The output of a low-pressure mercury discharge, rich in 254 nm radiation, was used for uv excitation. Cathodoluminescence measurements were made by settling the materials on glass slides and exciting in a demountable assembly with 15 kv electrons. The light emitted from the phosphors was measured from the irradiated side. To obtain layers suitable for measurement, the rodlike crystals had to be fractured prior to settling. (Grinding was found to reduce the fluorescence efficiency.) This was accomplished by causing the Zn_2SiO_4 crystals to be carried by a high-speed stream of air directed at the wall of a bent quartz tube. The fractured crystals were, on the average, about one-third the length of the original crystals, and are still not well suited for the settling of cathodoluminescent screens. This comminution procedure was found to produce no significant change in the photoluminescence efficiency of the zinc silicate samples. The effect, if any, of the fracturing process on the cathodoluminescence efficiency of the material was not determined because with the large, unfractured rod-shaped crystals it was not readily feasible to form a suitable screen for reproducible measurements.

Table I. Luminescence of Zn_2SiO_4:Mn prepared by the $ZnF_2/ZnCl_2$ method

	Relative fluorescence efficiency	
	Excitation by 254 nm	Excitation by 15 kv electrons
Zn_2SiO_4:Mn (1 mole %), activated by procedure 1	88	93
Zn_2SiO_4:Mn (1.5 mole %), activated by procedure 1	90	90
Zn_2SiO_4:Mn (2.0 mole %), activated by procedure 1	100	92
Zn_2SiO_4:Mn (2.5 mole %), activated by procedure 1	98	89
Zn_2SiO_4:Mn (3.0 mole %), activated by procedure 1	98	86
Zn_2SiO_4:Mn (0.5 mole %), activated by procedure 2	80	75
Zn_2SiO_4:Mn (1.0 mole %), activated by procedure 2	98	84
Zn_2SiO_4:Mn (1.5 mole %), activated by procedure 2	113	85
Zn_2SiO_4:Mn (2.0 mole %), activated by procedure 2	104	78
Sylvania Zn_2SiO_4:Mn #161	100	100

The data show no significant difference in efficiency between samples activated by the two different synthesis procedures. There is, however, some reason to speculate that the intrinsic luminescence efficiency of Zn_2SiO_4:Mn rods may be higher than the values listed above. Because of the relatively smooth crystal surfaces, internal reflection of the fluorescence may be expected to reduce by a significant amount the luminous flux that might otherwise be intercepted by the detector. Comparison of Fig. 1 and Fig. 3, taken with the same magnification, shows the difference in surface smoothness between a particle of commercial Zn_2SiO_4:Mn phosphor and a crystal prepared by the method of this paper. Indeed, as Fig. 5 shows, under uv excitation the fluorescence from the well-crystallized rods is emitted predominantly from their ends which are inclined relative to their major faces.

Acknowledgment

Grateful acknowledgment is made to C. O. Creter for assistance in the experimental work, to R. Weberling and J. Cosgrove for chemical analyses, and to C. F. Tufts for the electron micrographs and for discussions relating to them.

Manuscript received Oct. 5, 1966; revised manuscript received Dec. 12, 1966.

Any discussion of this paper will appear in a Discussion Section to be published in the December 1967 JOURNAL.

REFERENCES

1. H. W. Leverenz, "An Introduction to Luminescence of Solids," p. 235, John Wiley & Sons, Inc., New York (1950).

2. K. T. Wilke, Z. *phys. Chem.*, **224**, 51 (1963).
3. W. Jander and H. Riehl, Z. *anorg. u. allgem. Chem.*, **246**, 81 (1941).
4. P. Lenard, F. Schmidt, and R. Tomaschek, "Phosphoreszenz und Fluoreszenz" in "Handbuch der Experimentalphysik," W. Wien and F. Harms, Editors, Vol. 23, Part 1, p. 456, Akad. Verlag, Leipzig (1928).
5. H. W. Leverenz, Final Report on Research and Development Leading to New and Improved Radar Indicators, p. 185, PB25481, Office Pub. Board, Washington, D. C. 1945.

The Growth and Etching of Si through Windows in SiO_2

W. G. Oldham and R. Holmstrom[1]

Department of Electrical Engineering, University of California, Berkeley, California

ABSTRACT

A theory of the kinetics of vapor deposition and etching through small openings in an oxide layer on Si is developed and compared with experiments. A model that assumes equilibrium at the Si surface and purely diffusive transport through the gas phase is used to derive the concentrations and fluxes of the interesting gaseous species in the neighborhood of the window. The previously reported concave growth surfaces and convex etching surfaces are explained by the constriction of the flow near the edges of the windows. The measured etch rate is in quantitative agreement with theoretical estimates based on this model. Furthermore, the derived concentration profiles explain the appearance and relative size of the band of oxide free from Si overgrowth which surrounds each window in the growth experiments.

Because of the integrated circuit industry's interest in the epitaxial growth of Si on selected areas of Si wafers, some consideration has been given to the scheme of deposition through windows in an SiO_2 layer (1). The results reported thus far have been disappointing; growth on the oxide has been difficult to prevent, and growth in the desired region has usually been uneven (2). A typical result, which illustrates most of the features, is given in Fig. 1. Some important generalizations that may be made for small windows are: (*i*) the Si deposited in the windows is usually smooth and of satisfactory perfection; however, (*ii*) the thickness varies with position, *e.g.*, in the case of deposition without prior gas etching, the deposit is thicker near the edges than in the center; (*iii*) Si crystallites grow more or less uniformly over the surface of the oxide; except that (*iv*) a band of oxide free from crystallites generally surrounds each window.

To identify the important processes responsible for this behavior, some experimental and theoretical studies were made of a typical vapor deposition system. Because of the similarity of etching processes to growth processes and the technological importance of vapor etching, we include as well the investigation of etching through windows in an oxide layer.

In the following we first develop the theory of (*a*) the growth of Si through windows in the oxide, (*b*) the reaction of Si with H_2O, and (c) the growth of Si on the surface of the oxide. Second, we discuss our experiments on each of the above and finally make some conclusions regarding the control of such processes.

[1] Present address: Sprague Electric Company, North Adams, Massachusetts.

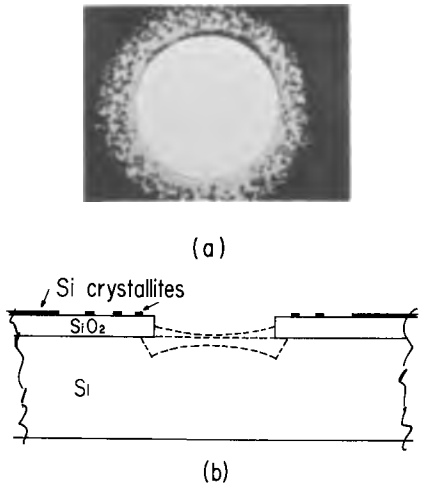

Fig. 1. (a) Typical wafer in the neighborhood of a 16-mil diameter window after Si deposition; (b) cross section (schematic diagram) of a typical wafer. The profile in the bottom of the window depends on the conditions during deposition; three possible profiles are shown.

Theory of Growth and Etching of Si in and around Windows in the Oxide

General considerations.—In this laboratory, the system used for the deposition of Si is the thermal decomposition of $SiCl_4$. It is unnecessary to review the growth mechanisms in Si deposition since they are adequately treated in the literature. In particular, Shepherd (3) treats the kinetics of a typical system and refers to earlier works. Like Shepherd, we use a $SiCl_4$ system with cold reactor walls.[2] In order to discuss selective growth using this type of system quantitatively, it is necessary to determine whether the growth rate is limited by the surface kinetics of a particular reaction or by the mass transfer of some species into (or out of) the region of reaction. A series of experiments was conducted to determine the dependence of growth rate on the temperature of the substrate and on the mole ratio of silicon to hydrogen in the gas stream. A typical set of results is given in Fig. 2, which shows the logarithm of the growth rate plotted *vs.* the reciprocal of the temperature with the mole fraction of $SiCl_4$ in H_2 as a parameter.

The data show that at low temperatures there is little dependence on the amount of silicon; however, at high temperatures the growth rate is nearly proportional to the mole fraction of $SiCl_4$, *e.g.*, at 1270°C, the growth rate is $3.2 \cdot 10^{-4}$ μ/min/ppm $SiCl_4$ over the range 1000 to 8000 ppm $SiCl_4$. Furthermore, the growth rate becomes nearly temperature independent. Thus, both the temperature and concentration dependence of the growth rate indicate that it is possible to work in a regime where growth rate is mass-transport limited. Most of the experiments described here were conducted under such conditions.

Shepherd (3) provides very strong evidence that growth in such a regime as indicated by the left-hand

[2] Details of the apparatus are given in the experimental section.

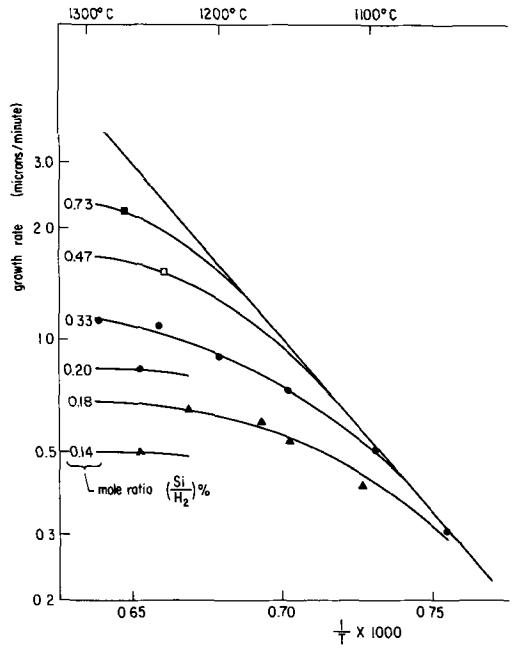

Fig. 2. Deposition rate of silicon for growth over large areas as a function of temperature and $SiCl_4$ concentration in the input stream.

part of Fig. 2 is indeed limited by transport through the gas phase. He calculates the absolute growth rate, assuming purely diffusive transport, and finds good agreement with data obtained in a horizontal reactor configuration. Such a calculation is more difficult for our reactor; however, the calculation becomes again feasible for the case of growth or etching in small windows and is treated in the next section.

Growth of Si through small openings in the oxide.— If we assume diffusion-limited kinetics, a calculation of the most important parameters in the growth process becomes feasible, provided that a sufficiently simple geometry is chosen. A small window in a much larger inactive surface is a tractable geometry if the additional assumption of a stagnant gas phase is made. We shall first calculate the concentrations of the various gaseous species in the neighborhood of the window in the oxide, then apply appropriate boundary conditions, and finally derive the fluxes of pertinent species. The details of the solution are given in the appendix; only an outline and summary of the calculation are given here.

The cylindrical coordinate system used in the calculation is shown in Fig. 3. The height above the surface of the Si wafer is z, and the distance from the z axis is ρ. The thickness of the oxide is assumed to be negligible, and a circular window of radius α is centered about the z axis. In the absence of growth on the oxide, the window acts as a sink in a surface of infinite extent. Furthermore, in the mass-transport limited regime, the window may be assumed to be a surface of equiconcentration. Because the flux through the oxide surface is zero, we may take advantage of the symmetry and solve the problem of a disk-shaped sink in an infinite region, that is, eliminate the oxide surface entirely.

For any gaseous species, we wish to find steady-state solutions to the diffusion equation

$$0 = \frac{\partial \Phi}{\partial t} = D\nabla^2\Phi \qquad [1]$$

subject to the boundary conditions

$$\Phi = \Phi_S \qquad z = 0,\ \rho \leq \alpha \qquad [2]$$

$$\Phi = \Phi_0 \qquad |z| + |\rho| \to \infty \qquad [3]$$

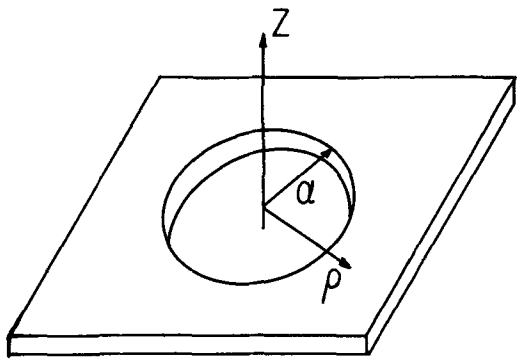

Fig. 3. Cylindrical coordinate system used to derive the concentration profiles. The radial coordinate is ρ and the radius of the window, centered on the z axis, is α.

where Φ denotes the concentration, and D is the diffusivity (assumed constant) of the particular species of interest. Φ_S is the surface concentration (in the Si window), and Φ_0 is the free stream concentration. The validity of applying the second boundary condition at ∞ rather than at a finite distance is established in the appendix. It is shown that as long as the window radius is small compared to effective boundary layer thickness for large area growth, the distance from the surface at which the concentration reaches the free stream concentration is not important and may be set at infinity.

The solution to Eq. [1] applies both to deposition and etching, only the relative magnitudes of Φ_0 and Φ_S are different for the two cases. As shown in the Appendix, the gaseous diffusion problem here is analogous to the electrostatic problem of a charged disk in an infinite three-dimensional space, and the latter has been solved (4). We obtain for the solution to Eq. [1]

$$\Phi(\rho, z) = \frac{\Phi_0 - \Phi_S}{\pi} \cdot 2\cos^{-1}\left[\frac{2\alpha}{\sqrt{(\alpha+\rho)^2+z^2} + \sqrt{(\alpha-\rho)^2+z^2}}\right] + \Phi_S \qquad [4]$$

Equation [4] gives the concentration at any point (z, ρ), and its derivatives give the various components of the flux densities at (z, ρ). We are particularly interested in the flux density incident on the surface of the bare Si magnitude of which is given by

$$\vec{F}(\rho) = -D\nabla\Phi|_{z=0} \qquad [5]$$

Evaluating Eq. [5] in the region $\rho < \alpha$ we have that

$$F(\rho) = D \cdot \frac{2}{\pi}[\Phi_0 - \Phi_S] \cdot \frac{1}{\sqrt{\alpha^2 - \rho^2}} \qquad [6]$$

It is seen that the magnitude of F is largest near the edges, in fact, it approaches ∞ as ρ approaches α. In spite of the singularity of Eq. [6] at $\rho = \alpha$, the total flux F, given by the integral of F over the surface $0 < \rho < \alpha$ is finite and is given by

$$F\ (\text{TOTAL}) = 4\alpha D[\Phi_0 - \Phi_S] \qquad [7]$$

Equation [7], when divided by the area, yields the average growth rate. Expressing the latter in more convenient units, we obtain for the velocity of the growing surface (or etching surface if $\Phi_0 < \Phi_S$)

$$V_{AVG} = 1.55 \times 10^{-20}\frac{D}{\alpha}(\Phi_0 - \Phi_S)\left(\frac{\mu m}{\text{min}}\right) \qquad [8]$$

We have used a molecular weight of 28 and density of 2.3 for Si and assumed that one Si atom is deposited (etched) for each molecule transported. C.G.S. units are used for all parameters. A rough idea of the uniformity of the growth rate over the surface may be

obtained by comparing the average growth rate with the growth rate at the center. If the latter is denoted by V_C, it may be readily verified from Eq. [6] and [7] that

$$V_C = \tfrac{1}{2}V_{AVG}$$

Equations [4]-[8] give the concentrations and fluxes of the various species in terms of the free-stream concentration Φ_o, and the surface concentration Φ_s. The former may be assumed to be equal to the input concentration; however, the latter depends on the thermodynamic properties of the Si surface, as well as on certain properties of the gases. We solve for Φ_s in the usual way, making use of the steady-state requirement of conservation of Cl atoms (or O atoms in the case of transport via SiO). In the case of chloride transport we must decide which species are important because the simultaneous solution for the surface concentrations in the presence of many interacting species is arduous. If the input gas is $SiCl_4$ in low concentrations in H_2, Lever's calculations (5) indicate that the important species present in the temperature range of interest are $SiCl_4$, $SiCl_2$, HCl, and H_2. Consider the growth of Si in such a system. Either $SiCl_4$ diffuses to the Si surface and reacts, or $SiCl_4$ first reacts in the gas phase with H_2 to form HCl and $SiCl_2$. The latter diffuses to the surface, or some combination of the two processes occurs. Fortunately, they give very similar answers for the growth rate, so only the former will be considered here.

We assume a net flux of $SiCl_4$ to the Si surface; the Cl balance is maintained by a flux from the surface of $SiCl_2$ and HCl. The reactions of interest are

$$SiCl_4 + 2H_2 \rightarrow Si + 4HCl \quad [9]$$

and

$$SiCl_2 + H_2 \rightarrow Si + 2HCl \quad [10]$$

The equilibrium constants, denoted respectively by K_9 and K_{10}, may be obtained from the JANAF Tables (6). The order of mangitude of K_9 and K_{10} at 1500°K are 0.01 and 1, respectively; thus we need to consider only the flux of $SiCl_4$ toward the surface and HCl from the surface.[3]

Evaluating Eq. [7] for the two fluxes, we have for the conservation of Cl

$$-D_{HCl}[\Phi_o^{HCl} - \Phi_s^{HCl}] = \tfrac{1}{4}D_{SiCl_4}[\Phi_o^{SiCl_4} - \Phi_s^{SiCl_4}] \quad [11]$$

From Eq. [9] we have, in addition

$$\frac{(\Phi_s^{HCl})^4}{\Phi_s^{SiCl_4}} = K_9/(RT/N_0)^3 \quad [12]$$

in which R is the gas constant, T the temperature, and N_0 Avogadro's number. We assume ideal gas law behavior and constant H_2 pressure of 1 atm.

Equations [11] and [12] are the solutions for the surface concentrations in terms of the input concentrations. Either the pair Φ_o^{HCl} and Φ_s^{HCl} or the pair $\Phi_o^{SiCl_4}$ and $\Phi_s^{SiCl_4}$ may be used in Eq. [8] to obtain the growth rate. We note that the cases of etching and growth are completely symmetric, only the sign of $(\Phi_o - \Phi_s)$ changes. The expected profiles for growth and etching of Si through windows in the oxide, based on the initial rate, are given in Fig. 4. Of course these solutions are valid only when the boundary conditions as formulated are met in the physical system. Thus, as soon as growth or etching progresses to the point where the Si surface is no longer approximated by a flat disk, the solutions are invalid. This effect would modify the shape of the surface for etching in the manner of the dashed line in Fig. 4. An even more severe limitation is that no Si deposition occur on the oxide, at least within a few window radii. In almost all the growth experiments in this laboratory, deposition on the oxide did occur. Thus, in the experimental part

[3] We are interested in the concentration range of Cl in the gas stream of up to at most a few per cent. Thus for 1% HCl, we would have only 0.02% $SiCl_2$ at the surface.

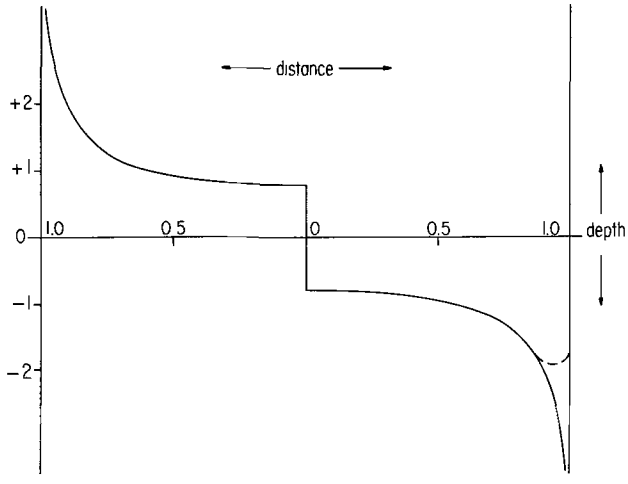

Fig. 4. Expected etching and deposition profiles across the bottom of the window in the oxide; the left half is for growth and the right half for etching. The solid curve is the theoretical prediction based on the initial growth (etch) rate. The actual shape would be modified by the constriction near the edge and for etching might look something like the dashed curve (arbitrarily sketched).

of this paper, we use the etching profile rather than the growth profile to compare with Fig. 4. In the presence of dense growth on the oxide, the growth rate in the window would be constant across the window and the same for all windows, as in normal epitaxy. That this is approximately true, even in the presence of a band of Si-free oxide surrounding the window, may be seen from the following argument. Suppose that the radius out to the edge of the Si-free band is ρ'. The Si from the ring $\alpha \lesssim \rho \lesssim (\alpha + \rho')/2$ is deposited in the window, in addition to the usual share from the region $\rho < \alpha$. The amount of this material is proportional to $\pi\alpha(\rho' - \alpha)$, *i.e.*, it is proportional to both α and the width of the Si-free band. We show in the next section that the width of the band is proportional to α, thus the amount of extra material is proportional to the window area.

Reaction of Si *with* O_2 *and* H_2O.—If oxygen is present in the epitaxial reactor, the etching of the silicon to form silicon monoxide competes with any deposition which may be taking place. In the temperature region of interest, the reaction

$$H_2O + Si \rightleftharpoons SiO + H_2 \quad [13]$$

is driven to the right as long as the concentration of silicon monoxide is less than the equilibrium concentration determined by the reaction

$$Si + SiO_2 \rightleftharpoons 2SiO \quad [14]$$

For silicon monoxide concentrations below the equilibrium value, stable silicon dioxide will not form on the silicon surface.

The oxygen concentration at which the oxide becomes stable may be calculated by considering the net oxygen flux in the system.[4] The dominant oxygen species are assumed to be silicon monoxide and water vapor, because of the hydrogen atmosphere and temperatures in excess of 1100°C. Our experiments to be described indicate that the oxidation of silicon to form silicon monoxide is sufficiently fast that the rate-limiting process is again mass transfer. As in the case of chloride transport, the condition that the net flux of oxygen in the system is zero can be expressed by

$$D_{SiO}\,\Phi_s^{SiO} = D_{H_2O}\,\Phi_o^{H_2O} \quad [15]$$

where D_{SiO} and D_{H_2O} are, respectively, the diffusion

[4] This calculation and its experimental verification have been carried out by Shepherd (7). Wagner made a similar calculation to determine the passivity of molten Si in an oxidizing atmosphere (8).

coefficients of SiO and H_2O in hydrogen, Φ_s^{SiO} is the surface concentration of SiO, $\Phi_o^{H_2O}$ is the concentration of H_2O in the gas stream, and we assume that Φ_o^{SiO} and $\Phi_s^{H_2O}$ are negligible in comparison with Φ_s^{SiO} and $\Phi_o^{H_2O}$, respectively. From Eq. [14] the vapor pressure of SiO over Si when SiO_2 begins to form is given by

$$\Phi_s^{SiO}(MAX) = (K_{14})^{1/2} \quad [16]$$

in which K_{14} is the equilibrium constant for reaction [14]. Combining Eq. [15] and [16], we obtain the maximum permissible water vapor concentration in the gas stream

$$\Phi_o^{H_2O}(MAX) = \frac{D_{SiO}}{D_{H_2O}} (K_{14})^{1/2} \quad [17]$$

Above this concentration, a stable oxide will form. Using 0.6 for the ratio (D_{SiO}/D_{H_2O}) (8) and the data for K_{14} from the JANAF Tables (6), we obtain for the maximum allowable H_2O pressure in the input stream in the neighborhood of 1500°K

$$P_{H_2O}(MAX) = 0.6 \exp\left(\frac{-11{,}300}{T}\right) \quad (\text{Atmos}),$$

about 100 ppm at 1150°C.

As in the case of growth, the reactor geometry prevents an exact calculation of the etch rate over large surfaces, however, the previous calculation, Eq. [1]-[8], apply directly to the etching through small windows. It is only necessary to solve for the surface concentration of SiO and H_2O. Denoting the equilibrium constant for reaction [13] by K_{13}, and making use of Eq. [15]

$$\Phi_s^{H_2O} = \Phi_o^{H_2O} D_{H_2O}/(K_{13} \cdot D_{SiO}) \approx 0 \quad [18]$$

We are justified in assuming that $\Phi_o^{SiO} << \Phi_s^{SiO}$ and $\Phi_s^{H_2O} << \Phi_o^{H_2O}$ because K_{13} is of the order of 100 in the temperature range of interest. Finally, from Eq. [8], the etch rate of Si in small windows of radius α is given by

$$V_{AVG} = 290 \cdot (T/T_0) \cdot \frac{P_{H_2O}}{\alpha} \quad (\mu\text{m/min}) \quad [19]$$

in which we have assumed ideal gas law behavior and used the approximate relationship

$$D_{H_2O} = D_O(T/T_0)^2$$

where $D_O = 0.7$, $T_0 = 273$ (11), and α is the window radius in centimeters.

Growth of Si *on* SiO_2.—As is apparent from Fig. 1, small crystallites of Si are deposited on the oxide, at least under some reactor conditions. In our system, such growth is in fact very difficult to prevent. Alexander and Runyan (2) have made an extensive study of the role of the growth conditions and the cleanliness of the oxide surface in determining the density and size of these crystallites, including purposely contaminated surfaces. We repeated a few of these experiments and made similar conclusions, namely, that any handling or contamination greatly increases the nucleation of Si on the oxide. Exposure to photoresist materials is particularly beneficial in enhancing dense, nonuniform nucleation.

Bicknell *et al.* suggest that oxygen-deficient sites provide locations for the formation of nuclei (9). Oxygen-deficient sites could be produced by the hydrogen reduction of the oxide surface by the reactions

$$SiO_2 + H_2 \rightleftharpoons SiO + H_2O \quad [20]$$

$$SiO_2 + 2H_2 \rightleftharpoons Si + 2H_2O \quad [21]$$

Both of these reactions are thermodynamically favorable at deposition temperatures, but experimental evidence indicates that they are quite slow. We baked wafers for 30 min in hydrogen at 1150°C and found only pinhole formation, but no measurable reduction in over-all oxide thickness. A rough calculation predicts that equilibrium for the reaction would produce a reasonably fast (*i.e.*, 50 Å/min) oxide etch rate under the conditions of the experiment. Our failure to observe such a reduction indicates that either the above reactions are kinetically limited and far from equilibrium under our conditions, or the rapid pinhole formation produces sufficient SiO via reaction [14] that reactions [20] and [21] are suppressed. We consider the former as the more likely explanation as virtually no thickness decrease was observed except in the pinholes.[5]

The apparently very small rate constant for reaction [20], plus the well-established contamination effects indicate that, at least under most reactor conditions, the role of oxygen-deficient sites in nucleation is minimal. In any case we may still draw some quantitative conclusions provided that the nature and density of the nucleation sites may be controlled. Suppose that the free energy change $-\Delta G$ for reaction [9] in the presence of crystalline Si is $\equiv -\Delta G_S$ per atom deposited. Growth on the oxide is inhibited compared to growth on Si if the average free energy change per molecule, $\equiv -\Delta G_0$ is less than $-\Delta G_S$. Clearly, $-\Delta G_0$ is a function of the number of atoms participating, and the nucleation rate is a strong function of the concentration. One might speak of supersaturation then in the sense of some combination of gaseous species sufficiently far from the equilibrium values (determined by $-\Delta G_S$) to drive the reaction to the right and achieve a given nucleation rate. The effect of contamination is to provide sites with $-\Delta G(\equiv -\Delta G_C)$ larger than $-\Delta G_0$ for a given number of atoms participating. Thus the supersaturation to achieve a given nucleation rate is lowered.

If $-\Delta G_C$ or the density of sites cannot be controlled from wafer to wafer, some conclusions may still be drawn by comparing different areas on one wafer, for which such control is considerably easier.

The variables controlling the rate of nucleation during the early stages of growth are of major importance in the explanation of the width of the silicon-free oxide band surrounding the windows. In order for the growth to take place on the oxide, the $SiCl_4$ must be reduced to silicon. We assume for simplicity that $SiCl_4$ does not react in the gas stream but diffuses to the surface before reacting. With this simplification, nucleation may be described in the form of a typical heterogeneous reaction, *i.e.*, (*i*) diffusion of $SiCl_4$ to the surface; (*ii*) adsorption of $SiCl_4$ on the surface; (*iii*) formation of nuclei by reaction of H_2 and $SiCl_4$ to form Si and HCl (this reaction may proceed by intermediate reactions involving other silicon species); (*iv*) desorption of HCl; and (*v*) diffusion of HCl away from the surface. If $SiCl_4$ reacts in the gas stream to form $SiCl_2$ or $SiHCl_3$, the above process will remain unchanged except for a change in the diffusing and reacting species. A similar argument holds if $SiCl_2$ is a reaction product; however, under our conditions HCl is favored as a reaction product.

If one of the steps in the series listed above is slower than the others, it will control the nucleation rate. Steps (*i*) and (*v*) are not rate limiting since before the nuclei are formed, the rate of formation of nuclei is not controlled by diffusion; *i.e.*, no concentration gradients are set up until growth starts. Because of the band of silicon-free oxide, we conclude that the driving force for the rate-limiting step appears to vary as a function of distance from the edge of the window. Because the rates of these processes are concentration dependent, we are interested in evaluating

[5] It is interesting that the rate constant measured by Grove and Deal (10) for the water oxidation of silicon, i.e., the reverse of [21] when combined with the equilibrium constant for [21], predicts an etching rate of less than one monolayer an hour. Of course, such a calculation is open to some criticism as the species involved in the H_2O oxidation of silicon has not been positively identified, and the SiO_2-Si interface is somewhat different than the H_2-SiO_2 interface in our experiments.

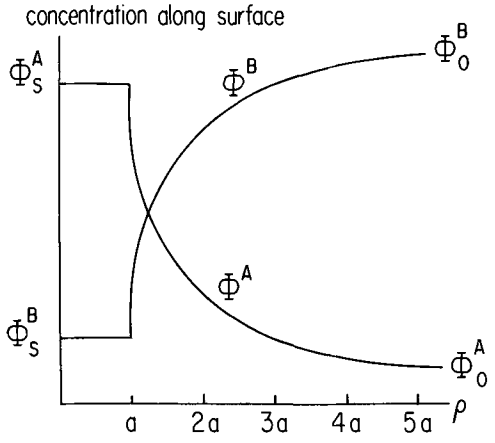

Fig. 5. Concentrations Φ^A and Φ^B of two gaseous species, A and B, along the surface of the oxide. For species A, $\Phi_S{}^A > \Phi_0{}^A$, whereas for species B, $\Phi_S{}^B < \Phi_0{}^B$. The subscript s denotes values on the Si surface, *i.e.*, $\rho \leq \alpha$, and the subscript o denotes the limiting value as $\rho \to \infty$.

the concentrations of the various species in the gas phase along the surface of the oxide. Evaluating Eq. [4] for $z = 0, \rho > \alpha$, we obtain

$$\Phi(\rho) = (\Phi_0 - \Phi_S)\frac{2}{\pi}\cos^{-1}(\alpha/\rho) + \Phi_S \qquad [22]$$

This function is plotted for the two cases $\Phi_0 > \Phi_S$, $\Phi_0 < \Phi_S$ in Fig. 5. In our model, the concentrations of all species follow such curves, only the values Φ_0 and Φ_S vary. The significance of these plots is that some combination of such curves gives the supersaturation. Noteworthy about the function is that the distance at which the value of Φ has decreased (increased) some fraction of its total change is proportional to the window size, and further, Φ drops (increases) from Φ_S most of the way to Φ_0 in a few window radii. Even though the boundary layer thickness for the reactor is on the order of centimeters, effective boundary layer thicknesses vary with window size and are of the order of α.

Experimental

Apparatus and procedures.—The epitaxial growth system used in these experiments is similar to the vertical system used by Theuerer (12). The $SiCl_4$ is held in a Pyrex container suspended in an ice-water bath. This arrangement does not lead to a constant mole ratio of $SiCl_4$ to H_2, hence it is necessary to measure the mole ratio for each run. This is accomplished by bubbling the output gas stream from the reaction chamber through a standard solution of NaOH with a suitable indicator. Airco ultra-high-purity hydrogen (less than 2 ppm impurities) is used without further purification. A rather standard procedure is used, a 5-min reactor purge in H_2 and a 5-min prebake in H_2 at 1200°C, followed by the etching or growth experiment. When oxygen is used, it is added in the form of a 2% oxygen-in-argon mixture prepared in this laboratory. The substrate temperature is measured with an optical pyrometer calibrated at the melting points of silicon and germanium. The thickness of the resulting epitaxial layers is determined by measuring stacking fault size.

Deposition of Si *in windows in the oxide.*—As previously noted (2), the deposition rate in small windows is a function of the window size, although in previous work the ratio of Si area to SiO_2 area rather than window size, has been used as a parameter. Quantitative data are difficult to obtain, however, as growth on the oxide initiates after some short period under deposition conditions. As soon as Si is nucleated on the oxide, our model is invalidated, and no comparison can be made between growth rates, for example in windows of different size. However, the qualitative observations that deposition rate decreases with increasing window size and that the growth rate is higher near the edges of the window, agree with the model. Furthermore, the simple modification of the theory in the presence of growth on the oxide predicts that the growth rate is independent of window size for long growth times. This is in agreement with our observations.

Etching of Si *with* O_2.—For convenience, we introduced O_2, rather than H_2O, into our system for the etching studies. Hence all the water concentrations quoted are effective H_2O input concentrations, equal by definition to twice the actual O_2 input concentrations. If the O_2 is converted into H_2O reasonably far from the wafer surface, then this procedure is correct. If, on the other hand, O_2 diffuses most of the way to the surface before being converted to H_2O, some corrections might seem necessary. Each O_2 molecule transports two Si atoms; however this factor is taken into account in doubling O_2 concentrations to obtain effective H_2O concentrations. Only the difference in diffusion constants produces a difference then and, because the latter would only be expected to be 10-20%, it will be ignored.

The wafers used in this study were all nominally of (111)-plane orientation and had five windows with radii of 1, 2, 4, 6, and 8 mils etched through the oxide by standard photolithographic techniques. The windows were at least 0.25 in. apart in order to minimize interactions. The wafers were subjected to a variety of temperatures and oxygen concentrations. The experimental results for the etch rate in the center of the window are plotted in Fig. 6. The important results to note are that for the larger windows the etch rate is: (*a*) proportional to oxygen concentration, (*b*) inversely proportional to window radius, and (*c*) relatively insensitive but inversely related to temperature.

The theoretical etch rate in the center of the window was calculated with Eq. [19] and is plotted for each concentration in Fig. 6.[6] The theory predicts an etch rate of approximately twice the experimental rate for the larger window sizes.

A possible explanation of the difference between the theoretical and experimental etch rates is the presence of a nonzero background of SiO. Silicon monoxide, in excess of the amount formed by H_2O etching in the windows, is supplied by the oxidation of the silicon covering the susceptor and by the undercutting mechanism (2) at the edges of the windows. The latter source of SiO would explain the larger deviations from the theory at the small windows. If SiO is pro-

[6] The temperature of the substrate is used because of the small effective boundary layer thickness on the order of α.

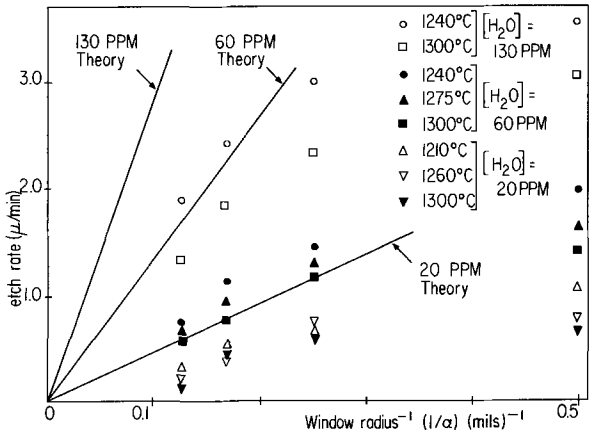

Fig. 6. Etch rate of Si through small windows in the oxide by oxygen. The solid curves give the theoretical etch rates for the three concentrations stated.

duced at a constant rate around the perimeter of each window, then the effect on the etch rate will be larger in the small windows since the ratio of area to perimeter is smaller. Other contributions to the difference between experiment and theory could come from backstreaming of the reaction products from the Si-coated susceptor, from kinetic limitations of the etch rate, and from the significant depth of the holes. The latter mechanism is particularly attractive because it predicts larger deviations for smaller holes as observed.

The experimental temperature dependence is small, but is in the opposite direction of that predicted by either a kinetic or diffusion argument with respect to the primary etching reaction. An excess in the SiO background concentration, either from the perimeter of the window or from the Si susceptor, could cause such a temperature dependence; however we cannot evaluate these or other possibilities.

The profile across the bottom of the window was measured both by a Talysurf and using the limited depth of field of a metallurgical microscope. A typical Talysurf plot is shown in Fig. 7 for 16, 12, and 8 mil windows. The theoretical profiles, from Fig. 4, are shown as dots on the 16 and 12 mil plots for comparison. Similar results were obtained on all samples examined using both methods of measurement. While the general shape of the predicted profile is substantiated, the agreement is not quantitative. The etch rate is too slow near the edges, leading us to conjecture that the production of SiO by the reaction of SiO_2 with Si around the perimeter of the windows is responsible. Jackson has reported the etching of essentially flat-bottomed holes through windows in SiO_2 (13). However, he indicates that the proper combination of temperature, HCl concentration, growth rate, geometry, and orientation are required, indicating that the mass transport regime examined in this paper is not operative.

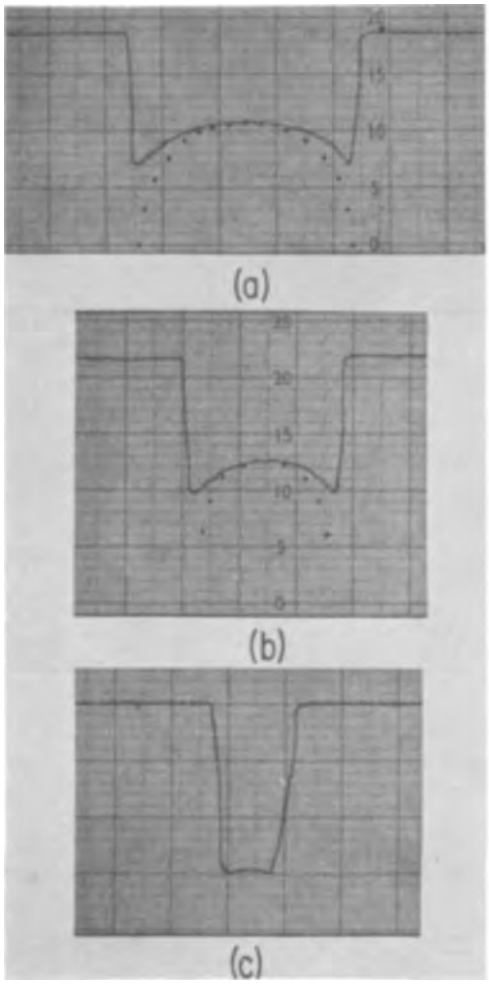

Fig. 7. Profile of the bottom of the window after an O_2 etch. The theoretical prediction, adjusted to match at the center is shown as a series of dots. (a) 16 mil diameter window; (b) 12 mil diameter window; (c) 8 mil diameter window. Vertical scale: 1 μm per division, horizontal scale: 50 μm per division.

Growth of Si *on the oxide.*—As pointed out earlier, the nucleation rate of Si on SiO_2 depends both on reactor environment and previous history of the specimen. Some attempts were made to vary the surface preparation to control the surface properties and determine the most important contaminants, but no information beyond that reported by Alexander and Runyan (2) was obtained. In fact, the rather poor control over the nucleation density was the general rule in our experiments. Nevertheless some experiments were made to try to understand the Si-free band with the hope that the necessary supersaturation for nucleation is nearly constant over a given wafer, however much it might be lowered by contaminants. We made special attempts to prepare several wafers identically in order that some process parameters could be varied and comparisons made between wafers.

We first established that the width of the Si-free band surrounding each window is a characteristic of the reactor and surface condition only and not a strong function of the growth time. In Fig. 8(a) and (b) we demonstrate this for a wafer that has been removed and photographed after 1 min, then placed back in the reactor for 4 min. One notes that the only effect of increasing the growth time by a factor of five is to increase the crystallite size; the density of crystallites in the region close to the window does not increase. This is an important observation, because it implies that the reactor conditions in the very beginning of the growth cycle control nucleation in the neighborhood of the window.

We propose the following model: When deposition is initiated by admitting $SiCl_4$, the bare Si surface remains essentially in equilibrium with the gas stream, but the concentrations of the various chlorides build up over the surface of the oxide. Some time after they exceed the supersaturation required for nucleation, depending on the kinetics, Si begins to nucleate on the oxide. After the Si crystallite density has built up to something less than that indicated by Fig. 8(a), nucleation ceases even on the bare region remaining near

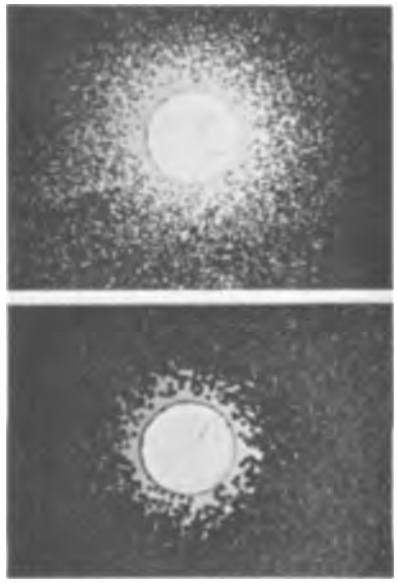

Fig. 8. Comparison of the nucleation rates on the oxide during the initial and later stages of growth. (a) (top) after 1 min of growth. (b) (bottom) the same wafer after 5 min of growth. The diameter of the window is 8 mils.

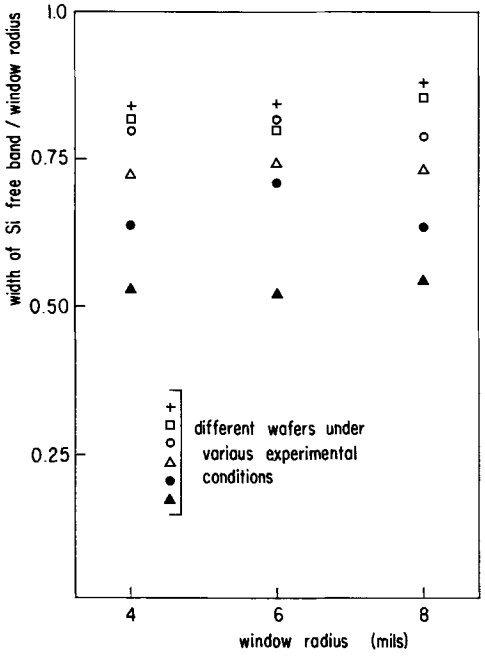

Fig. 9. Ratio of window radius to width of Si-free band for several wafers.

the edge of the window because the large amount of Si present maintains the Si concentration in the gas phase below the supersaturation required for nucleation on the oxide. Hence, the concentration profiles, Eq. [22], control the width of the Si-free band. As noted earlier, Eq. [22] indicates that the ratio of the width of the band to the radius of the window will be constant on a given wafer. Such has been found to be the case over a very wide range of reactor conditions. Typical results are shown in Fig. 9 which, in addition, illustrates the rather large scatter in the data, presumably due to contamination effects. Because these experiments bear out the role of the concentration profiles in determining the bandwidth, we attempted to determine further which species are crucial in determining nucleation rate, and to what power their concentrations appear in the nucleation rate equations. We were successful only in establishing that HCl is not the most important species in controlling the nucleation rate. The addition to the gas stream of concentrations up to one half the input $SiCl_4$ concentration had no effect on the nucleation density. We note that Jackson had success in controlling the nucleation on the oxide with the addition of HCl (13), however the concentrations were not given; therefore the results are not necessarily in contradiction to ours. Varying the $SiCl_4$ pressure, we found that large changes were produced in the nucleation density; however, no quantitative information was possible because of the variations in crystallite size, which made bandwidth comparisons difficult, and because of contamination, which produced large differences between one wafer and another.

These experiments suggest that the rate-limiting process in nucleation is probably adsorption of some silicon chloride species, or its subsequent decomposition reaction. Both processes would be strongly sensitive to foreign substances on the surface and could be independent of the HCl pressure. Much more precise experiments are needed in this area before even these tentative conclusions can be accepted.

In an attempt to test the hypothesis of oxygen-deficient sites (1), various amounts of oxygen were added to the gas stream during deposition. It was found that O_2 decreased the crystallite density for a given growth time, *i.e.*, lowered the nucleation rate. However, the addition of O_2 during the H_2 prebake prior to the deposition, with none present during the deposition, had similar effects. It was found that the most effective procedure was to add O_2 during the 5-min prebake and during the deposition.[7] The effectiveness of a prebake in O_2 suggests that O_2 might simply be an etchant for some of the contaminants on the oxide, *e.g.*, adsorbed hydrocarbons. However, experiments on oxides transported directly from the oxidation furnace to the deposition chamber also showed a reduced nucleation rate with O_2 prebake. Our oxides were not satisfactorily clean even in the latter experiments, however, in comparison with the oxides grown *in situ* by Alexander and Runyan (2). The hypothesis of oxygen-deficient sites cannot be dismissed, but in our laboratory, contaminants are playing a larger role than such sites.

Conclusions

A model has been developed for the concentration profiles in the gas phase around a small opening in an oxide-covered Si surface. The average etch rate of Si using water vapor, as well as the local etch rate across the surface of the window, agree with the predictions of the model. The observations that the growth and etch rates are higher near the edge of the window are explained by the crowding of the flux lines in this region.

The presence of a Si-free band around the window, even when dense nucleation on the oxide occurs, is the consequence of the steady-state profiles derived. The role of oxygen in hindering nucleation on the oxide is still not clear.

If a uniform growth rate across the window surface is intended, deposition under conditions which prevent nucleation on the oxide is not desirable. In fact, one method of assuring uniform growth in the window is to have dense growth on the oxide, eliminating the strong concentration gradients near the edge of the window responsible for the uneven growth. On the other hand, if gas etching is employed prior to deposition, then a clean oxide is mandatory in order that the etched-out volume, deeper at the edges, be exactly refilled by a growth, thicker at the edges, resulting in a flat surface. Any reactor conditions that prevent growth on the oxide, do not result in rough growth, and introduce no kinetic limitations other than diffusion in the gas phase can presumably be used successfully in such an "etch and backfill" process.

Acknowledgments

The authors are indebted to W. H. Shepherd of Fairchild Semiconductor and A. C. English of the University of California for several useful discussions.

The research reported herein was supported wholly by the Joint Service Electronics Program (U.S. Army, U.S. Navy, and U.S. Air Force under Grant AF-AFOSR-139-65/66.

Manuscript received Oct. 17, 1966; revised manuscript received Jan. 2, 1967.

Any discussion of this paper will appear in a Discussion Section to be published in the December 1967 JOURNAL.

APPENDIX

Derivation of the Concentration Profiles

To solve Eq. [1], subject to the boundary conditions given by Eq. [2] and [3], we first solve the easier problem in which the second boundary condition is replaced by

$$\Phi = 0 \quad |z| + |\rho| \to \infty \qquad [23]$$

The problem is the analog of the problem in electrostatics of a charged metallic disk in an infinite medium. By analogy of Eq. [1] with LaPlace's equation, Φ and D are the duals of potential Φ' and dielectric

[7] Of course, the surface of the epitaxial Si suffered because the O_2 does not etch the Si smoothly at these concentrations and temperatures.

constant ϵ, respectively. Further, the gaseous flux density is the dual of the dielectric displacement, and by Gauss's law, the integrated normal component of the flux density over a surface is the dual of the charge enclosed by the surface. We make use of this duality because the electrostatic problem has been solved (4) and has the solution

$$\Phi'(\rho, z) = \frac{Q}{4\pi\epsilon\alpha} \sin^{-1} \frac{2\alpha}{\sqrt{(\alpha+\rho)^2+z^2}+\sqrt{(\alpha-\rho)^2+z^2}} \quad [24]$$

where Φ' is the potential, and Q is the charge residing on the disk. We may express Q in terms of Φ'_s, the potential at $z = 0$, $\rho < \alpha$. Before we write the dual to this equation we may alter the second boundary condition by adding a constant to Φ' everywhere, which allows both a finite potential at ∞ and an arbitrary potential at some finite boundary, independent of Φ_s. This boundary condition permits the potential (concentration) to be specified at a distance equal to the thickness of some boundary layer. In order that the present solution remain valid, we must apply the boundary condition over an equipotential surface of the present solution. These surfaces are ellipsoids that may be specified by the radius ρ_b of the circle formed by their intersection with the plane $z = 0$. Eliminating Q in terms of the surface potential Φ'_s (surface concentration Φ_s) and specifying that the concentration equals Φ_o, the free-stream concentration, over the equiconcentration surface that intersects the plane $z = 0$ in a circle of radius ρ_b, we have for the dual of Eq. [24]

$$\Phi(\rho, z) = \frac{\Phi_o - \Phi_s}{\cos^{-1}(\alpha/\rho_b)} \cos^{-1} \left[\frac{2\alpha}{\sqrt{(\alpha+\rho)^2+z^2}+\sqrt{(\alpha-\rho)^2+z^2}} \right] + \Phi_s \quad [25]$$

In this work we are concerned with very small windows; α is typically 2-16 mils. Typical growth rates such as exhibited in Fig. 2 correspond to effective boundary layer thicknesses of centimeters, the exact value depending on the model that is used. Hence, α is much less than any conceivable boundary layer in our system, and $\cos^{-1}(\alpha/\rho_b)$ will be approximated by $\pi/2$.

REFERENCES

1. B. D. Joyce and J. A. Baldry, *Nature*, **195**, 485 (1962).
2. E. G. Alexander and W. R. Runyan, *Trans. AIME*, **236**, 284 (1966).
3. W. H. Shepherd, *This Journal*, **112**, 988 (1965).
4. J. D. Jackson, "Classical Electrodynamics," p. 89, John Wiley & Sons, Inc., New York (1962).
5. R. F. Lever, *IBM J. Res. and Dev.*, **8**, 460 (1964).
6. JANAF Thermochemical Tables, The Dow Chemical Co., Midland, Mich. (1963).
7. W. H. Shepherd, Personal communication.
8. C. Wagner, *J. Appl. Phys.*, **29**, 1295 (1958).
9. R. W. Bicknell, J. M. Charig, B. A. Joyce, and J. C. Stirland, *Phil. Mag.*, **9**, 965 (1964).
10. B. E. Deal and A. S. Grove, *J. Appl. Phys.*, **37**, 3770 (1965).
11. H. Schafer, "Chemische Transportreaktionen," **28**, Verlag Chemie (1962).
12. H. C. Theuerer, *This Journal*, **108**, 649 (1961).
13. D. M. Jackson, *Trans. AIME*, **233**, 596 (1965).

A Method of Growing CuCl Single Crystals with Flux

Minoru Soga, Rikizo Imaizumi, Yoshihiro Kondo, and Takahiro Okabe

Department of Electronics Engineering, Shizuoka University, Hamamatsu, Japan

ABSTRACT

This report describes a method of growing CuCl single crystals of the zinc blende phase directly from a melt which contains a flux such as $SrCl_2$ or $BaCl_2$. The presence of the flux at 2 mole % depresses the temperature of the melt below 407°C. The melting point of pure CuCl is 422°C, thus making it possible to grow the crystal without going through the phase transition from the wurtzite phase at 407°C. Because of the elimination of the phase transition in the solid, strain-free single crystals of large size, particularly in the direction of growth, can be grown by this method. As a consequence, a very large Pockels effect (maximum phase difference of 240°) can be obtained from a cell made by this method.

Cubic CuCl has a large Pockels effect (1) and can be used for electrooptic light modulators. Optical modulators using cubic crystals such as CuCl have some advantages over dihydrogen phosphate modulators (3).

However, it is difficult to grow strain-free CuCl single crystals of a practical size by the usual Bridgman method, principally because CuCl has a phase transition at 407°C (2).

CuCl crystals have the zinc blende phase in the temperature range below 407°C and the wurtzite phase from 407° to the melting point at 422°C. Therefore, crystals grown from the melt are in the wurtzite phase at first and then convert to the zinc blende phase when cooled below 407°C. This phase transition occurs in the solid state so that there remains in the crystal a heavy strain which can not be eliminated by annealing.

If the melting point of CuCl is depressed below the transition point, however, the solid-state phase transition is eliminated and CuCl should crystallize in the zinc blende phase directly from the melt (3). The crystal thus obtained should be almost free from strain.

Purification.—CuCl is purified first by recrystallizing and then by zone refining as follows: Commercial grade CuCl powder (slightly blue-colored), the purity of which is guaranteed 85% or better, is recrystallized in hydrochloric acid. The recrystallized snow-white leafy CuCl is then washed repeatedly with acetic acid until the hydrochloric acid is completely eliminated before being dried in an air bath at 120°C.

The dried CuCl is put in a clean quartz tube. The air within the quartz tube is flushed out by pure nitrogen gas in order to avoid oxidation of the melted CuCl during the zone refining process. Before the zone refining process, the nitrogen gas is pumped out of the quartz tube while the CuCl is baked at 350°C and the tube is sealed off. The quartz tube loaded with CuCl is passed through a zone refining furnace with a speed of about 100 mm/hr. A colorless transparent CuCl crystal is obtained after some twenty passes of zone refining. The pure CuCl thus obtained is ready for the next process, *i.e.*, single crystal growing.

Crystal growing.—The crystal growing procedure is the same as the usual Bridgman method, except for adding flux. The structure of the furnace and the

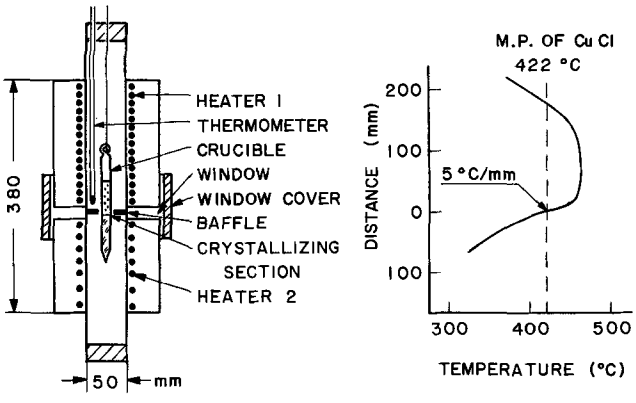

Fig. 1. (a). (left) Structure of the furnace for growing CuCl single crystals; (b). (right) temperature distribution of the furnace.

temperature profile, as measured with the quartz tube not present, are shown in Fig. 1. The voltage applied to the heaters is stabilized within 0.1%, and the temperature fluctuation of the furnace is less than ±1°C throughout the procedure. The temperature gradient of the furnace at the crystallizing section is approximately 5°C/mm.

The purified CuCl and a flux are placed in a quartz tube (8 mm inner diameter) which is used as a crucible. The crucible is sealed off as described in the previous section and then is placed in the furnace. CuCl and the flux are melted and mix themselves during the initial stage of the procedure; then a CuCl single crystal of zinc blende phase begins to grow from the capillary section of the bottom end of the crucible as the crucible moves through the furnace. Our experience shows that a growth rate of 1 mm/hr or less is adequate.

Selection of flux.—Various anhydrous chlorides, each of which was a special grade having 99% or better purity, were further purified by recrystallizing or zone refining for use as fluxes.

The amount of flux required to depress the melting point of CuCl to 407°C was about 1.8 mole % in each case, independent of the valence of the cation. Therefore 2 mole % of flux was added to the CuCl, assuming a small weighing error.

As a result of crystal growing experiments, the fluxes were divided into two groups as shown in Fig. 2, where each chloride used as a flux is represented by a small circle or a group of three circles. Three circles a, b, c, of a group correspond to the lattice constants of the a, b, and c axes of the chloride crystal, respectively. Abscissa and ordinate indicate the radii of the cation (4) and the crystal lattice constants of the corresponding chloride, respectively. A white circle represents a chloride which leaves the CuCl crystal transparent while a black circle represents a chloride which makes the crystal opaque at room temperature, though both depress the melting point of CuCl.

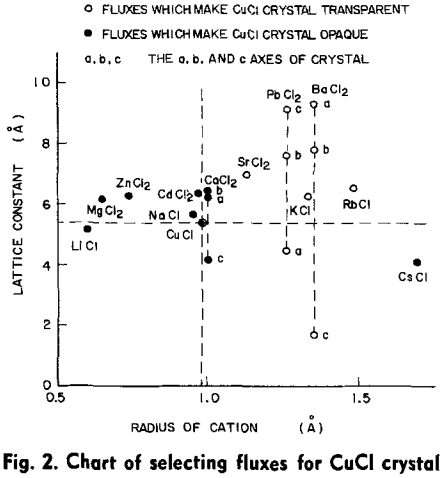

Fig. 2. Chart of selecting fluxes for CuCl crystal

It is seen from Fig. 2 that chlorides whose cation radius and a lattice constant are somewhat larger than those of CuCl, such as $SrCl_2$, $BaCl_2$, and RbCl, are suitable for flux.[1] These chlorides are segregated easily when CuCl crystallizes because of their large cation radius and lattice constant.

As the volume of the melt decreases, the concentration of flux in the melt increases above its initial value of 2 mole % by segregation. When the concentration of flux in the melt reaches about 5 mole %, the crystal becomes opaque, even when such suitable fluxes are used.

It was found that $SrCl_2$ and $BaCl_2$ had a slight tendency to react with the quartz tube, and the crystal grown in the crucible was adherent to the wall.

Preparation of the electrooptic cell.—After being removed from the crucible, the single crystal rod is annealed at 350°C for 24 hr to reduce the strain caused by adherence to the crucible wall. The crystal must undergo another 24-hr annealing at 250°C after the cutting and shaping processes. The surface of the cell becomes less transparent after the second annealing. This, however, can be eliminated by washing it in nitric acid, distilled water, acetic acid, and trichloroethylene, in this order, each for a few seconds. As the final process of the electrooptic cell preparation, electrical contacts are made by conductive paint on the top and bottom surfaces of the cell.

Characteristics.—Characteristics of CuCl single crystals grown by the flux method are shown in Table I, where the corresponding parameters of single crystals grown without flux are also shown for comparison purposes. The methods of measuring these parameters are described in the next section.

The single crystals grown by the flux method have a comparatively small optical strain as shown in Table I. This is due to the elimination of the solid-state phase transition, and the remaining small strain is easily reduced by annealing.

The elimination of the phase transition makes it possible to grow crystals of large size, in particular, in the direction of growth. A strain-free single crystal cube of 5 mm on each edge is easily obtainable by the flux method.

Specific resistance and breakdown field of the crystals grown with $SrCl_2$ or $BaCl_2$ flux are increased. The optical density is somewhat increased by flux which remains in the crystal. However, this slight drawback is not important compared to the marked improvements of the breakdown field and specific resistance. Since this increase of optical density is small, the amount of flux remaining in the crystal seems to be very small.

Because of the high breakdown field, it is possible to apply high electric field to the cell. Consequently, a large electrooptic effect is obtained as shown in

[1] Japanese Patent Pending. This work was sponsored by the Ministry of Education of Japan.

Table I. Characteristics of CuCl single crystals grown by the flux method

Flux, adding 2 mole % to CuCl	Optical strain, per mm	Optical density	Specific resistance, ohm-cm	Breakdown field, kv/mm
$SrCl_2$	0.005	0.20	5×10^8	1.45
$BaCl_2$	0.007	0.19	6×10^8	0.83
$PbCl_2$	—	0.58	1.5×10^8	—
KCl	—	1.1	1×10^6	—
RbCl	—	0.47	9×10^6	—
Growing without flux	0.02	0.12	3.5×10^8	0.58

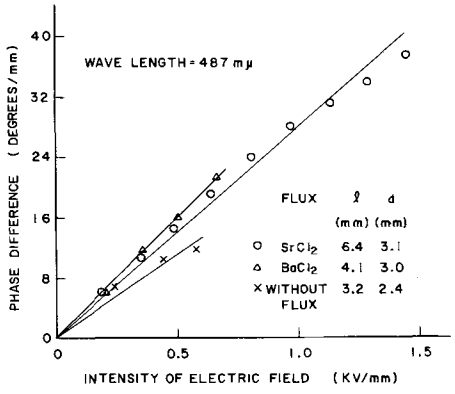

Fig. 3. Electrooptic effect of CuCl single crystals grown by adding fluxes and without flux.

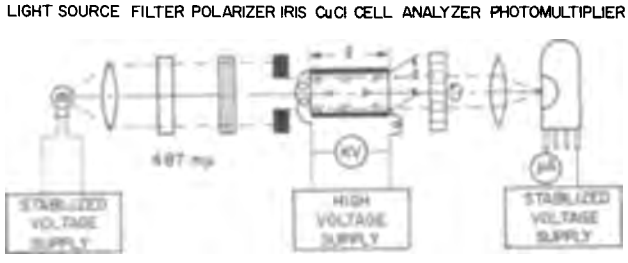

Fig. 4. Optical arrangement for measurement of electrooptic effect and optical strain of the CuCl cells.

Fig. 3. For example, a maximum phase difference of 240° was observed by the cell grown with $SrCl_2$ flux. The size of the cell used in this experiment was 6.4 mm in its axial length and 3.1 mm in its height, which is the distance between the electrodes. The maximum intensity of the applied electric field was 1.45 kv/mm as shown in Fig. 3.

The crystals grown with KCl or RbCl flux have larger optical density and lower specific resistance, which indicate a considerable amount of flux remaining in the crystal. For this reason, KCl and RbCl are inferior to $SrCl_2$ and $BaCl_2$ as flux.

Measurement.—Electrooptic effect.—Figure 4 shows the experimental arrangement for measuring the electrooptic effect. The directions of polarization of the polarizer and the analyzer are crossed. Phase difference can be measured as follows: First, read the transmitted light intensity when a voltage is applied to the cell; Second, with no voltage applied to the cell, rotate the analyzer to obtain the same light intensity as obtained before. Then the phase difference through the cell is given by twice the rotation angle of the analyzer.

Optical strain.—If the cell has no strain, no light is transmitted through the analyzer unless a voltage is applied to the cell. For the case of the actual cell, however, a certain amount of leakage light is transmitted even when no voltage is applied. This is due to the strain remaining in the cell. Therefore, an "optical strain" can be expressed in terms of ratio of the transmitted light intensity with crossed polarizers to the transmitted light intensity through the analyzer when it is parallel to the polarizer.

Conclusions

A method of growing CuCl single crystals of zinc blende phase directly from the melt with a flux has been developed.

Chloride fluxes whose cation radius and a lattice constant are somewhat larger than those of CuCl depress the melting point of CuCl below its transition point and leave the CuCl crystal transparent at room temperature.

It is found that $SrCl_2$ and $BaCl_2$ of 2 mole % are suitable for the flux and a growing rate of 1 mm/hr or less is adequate.

CuCl crystals grown by this method have several advantages; for example, reduction of strain, enlargement of crystal size, and increase of breakdown field and specific resistance.

A large electrooptic effect has been observed on cells made by this method.

Acknowledgment

The authors wish to express their thanks to Dr. S. Mizushina for his kind help. They also wish to express their gratitude for the support by Yashica Company, Ltd., and Hayashi Rika Company, Ltd.

Manuscript received Aug. 29, 1966; revised manuscript received Nov. 14, 1966.

Any discussion of this paper will appear in a Discussion Section to be published in the December 1967 JOURNAL.

REFERENCES

1. C. D. West, *J. Opt. Soc. Am.*, **43**, 335 (1953).
2. M. R. Lorenz and J. S. Prener, *Acta Cryst.*, **9**, 538 (1956).
3. F. Sterzer, D. Blattner, and S. Miniter, *J. Opt. Soc. Am.*, **54**, 62 (1964).
4. L. Pauling, "The Nature of the Chemical Bond," Cornell University Press, Ithaca, N. Y. (1960).

Control of Photoconductive Properties in Cadmium Selenide

Brian Sunners

IBM Components Division, East Fishkill Facility, Hopewell Junction, New York

ABSTRACT

Some aspects of the chemistry of sintered cadmium selenide photoconductors are presented. A tentative scheme is outlined whereby electrical requirements for such photoconductive devices can be used to define the chemistry of the sintered layer. Experimental methods are outlined, and the effects of some process variables on the electrical properties are described. The application of the method is described.

Various aspects of the chemistry of sintered polycrystalline photoconductive layers of group II-VI compounds have been reported in the literature (1-3), but as yet these systems are not completely understood. The available information gives only an indication of the present state of the chemical art and, as such, is not sufficient to define the parameters required to prepare a photoconductor that meets any given set of electrical specifications. Previous approaches have apparently been designed to formulate a chemical description of the system, and no attempt has been made to relate electrical properties quantitatively

with the chemical constitution. In this paper, we will describe this new approach and present a tentative scheme whereby electrical specifications may be used to outline the type and concentration of dopants required to yield cadmium selenide photoconductors with the required range of properties.

As the geometry of the photoconductor system is governed by various mechanical considerations, light sources, interconnections, etc., the electrical requirements for the photoconductor must be related to the properties of known materials on a "per square" basis. The electrical requirements are, usually, the resistance under given conditions of illumination, the dark resistance, and the fall time from the "on" condition to a given resistance level. Also operating temperature limits may be set. As the rise times are usually very fast and therefore acceptable compared to the fall times, they will be neglected in this treatment. In addition, as we have found that a fully compensated binary compound photoconductor of the type considered here has a dark resistance greater than 10^{10} ohms per square, this value also will be considered adequate in all cases. The remaining properties, light resistance and fall time, can be considered in more detail. The photoconductivity (light resistance^{-1}) and the recombination time are related by the equation[1]

$$R_L = (\alpha H \tau e \mu a)^{-1} \qquad [1]$$

where R_L is light resistance, H photons/sec/cm^2, e electronic charge, τ recombination time, μ mobility of majority carrier, a number of squares in parallel, α quantum efficiency. This relationship is derived from the fundamental equation for conductivity

$$\sigma = ne\mu$$

The recombination time τ will be equal to the fall time τ_0 only in the absence of all trapping effects. However, if the time of photocurrent decay is measured only over the initial portion of the decay, then the effects of trapping can be largely discounted. For practical purposes, however, light intensities must be high in order to observe this condition, and, in general, fall times are greater than recombination times by factors dependent on trap distributions and free carrier concentrations (4).

This effect has been used to determine the mobility of current carriers by measurements of photocurrent and fall time to $1/e$ of the maximum value as a function of increasing incident light energy. This measurement gives values for μ as τ_0 approaches τ, and the saturated value of τ_0 gives the mobility value. Of more practical value is the "device" mobility $\mu\tau$, measured under specified conditions of illumination. This is generally lower than the true mobility because light intensities fall below the saturation value and

[1] The author is grateful to Dr. A. S. Miller, now of National Research Corporation, for a discussion of this relationship.

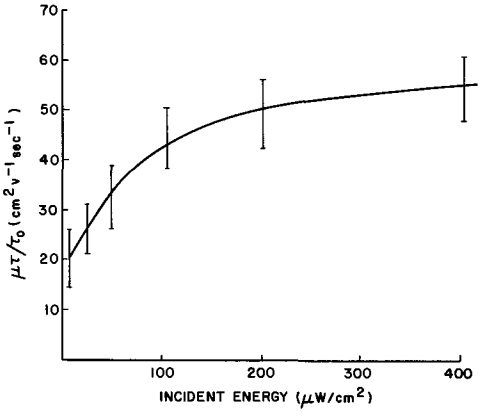

Fig. 1. Determination of mobility

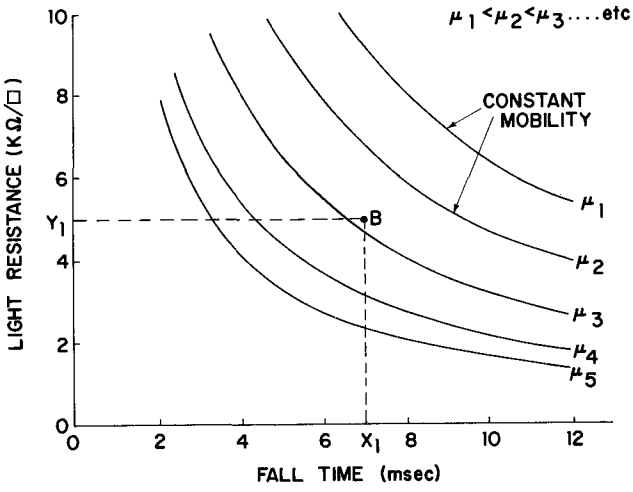

Fig. 2. Relationship between fall time, light resistance, and mobility. Light resistance is measured under 1000 μw/cm² from neon lamp.

appreciable numbers of electrons are trapped. Some values of device mobilities are shown in Fig. 1.

The relationship

$$R_L = (\alpha H \tau e \mu a)^{-1}$$

is illustrated in Fig. 2. In this figure, it has been assumed that the required properties are indicated by X_1 and Y_1. All points within the square Y_1BX_1O therefore lie in specification. Theoretically, material with a carrier mobility of exactly μ_3 can meet the specifications, but, in practice, as the photoresistance and the fall times are temperature sensitive, any increase in the device operating temperature causes an increase in the light resistance and a decrease in the fall time because of thermal desensitization. As the mobility remains relatively constant over small ranges of temperature change, any given set of photoconductor properties will shift along the lines of constant mobility as indicated in the figure. A material with the minimum mobility (μ_3 as shown in Fig. 2) will meet specification only over a very narrow temperature range and, therefore, is not a practical working material. The higher the mobility that can be achieved, the larger the operating temperature range will be. In addition, properties must be selected such that the photoresistance is at a maximum at the highest specified working temperature (along Y_1B) and such that the fall times are at a maximum at the lowest specified working temperature (along X_1B). This effect is shown in Fig. 3, which is taken from data for a large number of photoconductors measured under operating conditions. The contour lines (distribution of properties) represent

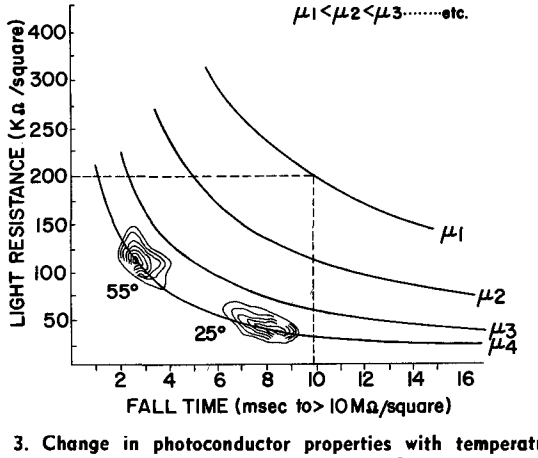

Fig. 3. Change in photoconductor properties with temperature. Light resistance is measured under 1000 μw/cm² from neon lamp.

the spread in the properties at specific temperatures. We can now define the problem as control of carrier mobility; this has been effected by adjusting acceptor and donor impurity concentration and the relative ratio. However, polycrystalline materials (powder or sintered) are usually prepared in such a way as to leave considerable doubt as to the exact concentration and nature of the donors present, particularly in the case of systems involving the use of halide fluxes, and so to determine this number, we have developed a solid-state titration, described below. This enables us to achieve the necessary control of acceptor-to-donor ratio. For maximum sensitivity, the optimum ratio has been quoted as 1.05 (5).

Experimental Methods

Cadmium selenide was mixed with cadmium chloride and dilute solution of copper chloride in the required proportions. Water, glycol, and glycerol were added to form a paste of a consistency suitable for screen printing. This paste was deposited on an aluminum oxide substrate having prefired platinum electrodes and was then carefully air dried. The photoconductors were fired in an atmosphere of flowing nitrogen in a furnace lined with a quartz tube. Typical temperature cycles are shown in Fig. 4. The electrical properties were measured at 10v d.c. and the response to neon light was determined. The effect of varying the light intensity has been explored previously (1, 2) and, in this work (for practical purposes), was maintained at an incident energy level of 300 $\mu w/cm^2$.

Impurity doping.—It should be noted that no "donors" are deliberately added to the above mixture; the chloride (usually described as a donor) is required in this process because of its fluxing action. In fact, chloride probably does enter the lattice as a donor, and selenium vacancies may also occur as donors. Thus to fix the acceptor and donor concentrations as required above, we must determine the total donor concentration and, if possible, distinguish between electrically active impurities and crystal defects as a function of processing variables.

Based on an observation by Avinor (6) that the maximum rate of change of dark current with acceptor concentration in single crystals of CdS occurs when the acceptor and donor concentrations are equal, we have developed a solid-state titration method to determine the concentration of both vacancy and impurity donor centers. A typical titration is carried out by preparing and processing a number of photoconductors, each under identical conditions, with the one exception that the added acceptor (copper) concentration is varied in steps throughout the series. It must be assumed that change in the copper concentration causes no other changes (vacancy concentration, etc.) in the material and that a constant fraction of the added copper enters the lattice as an electrically active species. Reisman and Birkenblit (7) have shown that the first assumption is probably valid but that a $Cu^{+} \rightleftarrows Cu^{++}$ equilibrium probably exists.

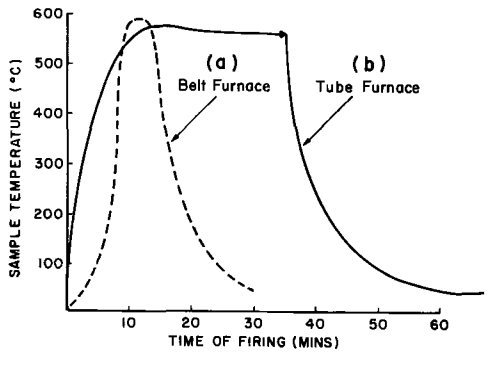

Fig. 4. Photoconductor firing cycle

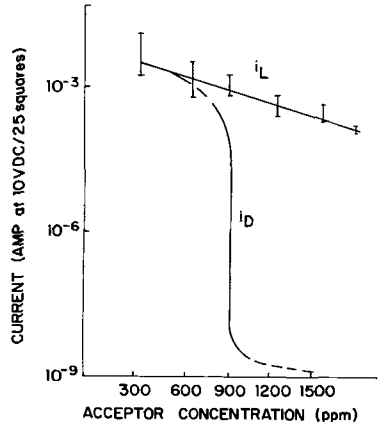

Fig. 5. Change in photoconductor properties with acceptor concentration; light resistance is measured under 300 $\mu w/cm^2$ from a neon lamp.

We must therefore assume that this equilibrium is constant for identical processing conditions. The properties of the resulting photoconductors are strongly dependent on the total copper concentration (Fig. 5); and, by analogy to Avinor's work, the maximum rate of change in dark current is interpreted as the "equivalence point" of the titration. A typical titration curve is shown in Fig. 5. We now have a tool for examining the effect of process variables on the chemistry of the photoconductor and so should be able to proceed to relate such processes to the required electrical properties. Copper "acceptor" concentrations and donor concentrations obtained by titrations are relative and relate, we assume, to the added acceptor concentrations by the position of the equilibrium referred to above; that is, by a constant factor. This simple picture of copper and chloride impurities neglects the possibility of other electronically active centers such as lattice defects and vacancies, or impurities in the starting material. (A typical analysis is shown in Table I.) The existence of selenium vacancies up to 10^4 ppm may be expected (8) and is, in part, confirmed by the effects of the post treatment described below so that we can add selenium vacancies to the list of electronically active centers that can be examined by the titration method.

Post treatment.—If a titration series of nitrogen-fired photoconductors is reheated to 200° or 300°C in nitrogen containing about 2 mm selenium vapor (sulfur vapor may be used), then the titration point decreases typically from 1200 to 300 ppm copper (atom parts per million). We assume that the decrease is due to the loss (filling) of 900 ppm selenium vacancy donors. Support for this assumption is obtained by examining the donor concentration as a function of cadmium chloride flux concentration. Figure 6 shows that the total donor concentration after firing is proportional to the initial flux concentration and extrapolates to about 1000 ppm at zero flux concentration, again presumably due to selenium vacancies. The low value obtained at 2½% (W/W) $CdCl_2$ is probably due to incomplete sintering action at this low flux level. It should be further noted that nonpost-treated photoconductors are not as stable as after post treatment and that some have properties that change even at room temperature

Table I. Spectrographic analysis of cadmium selenide*

Supplier's analysis							
Fe	Cu		Ni	Pb			
2	<0.5		<0.2	2			
IBM analysis							
Fe	Cu	Ni	Pb	Ag	Al	Bi	Mn
2	1	2	3	1	1	2	2

* Supplied by General Electric Company.

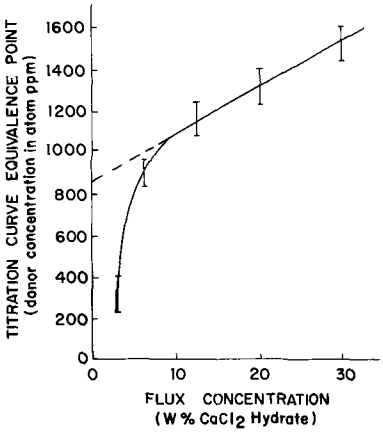

Fig. 6. Effect of flux concentration on concentration of donors

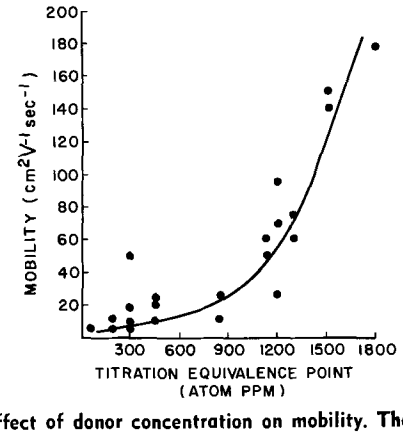

Fig. 8. Effect of donor concentration on mobility. The donor concentration is determined from the equivalence point of a titration curve.

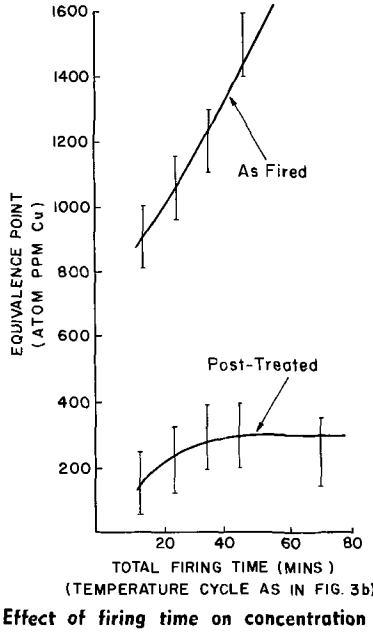

Fig. 7. Effect of *firing time* on concentration of donors

in a direction that parallels the effect of post treatment. The effect of change in firing time at peak temperature, shown in Fig. 7, is not inconsistent with this postulate: the "selenium vacancy" concentration increases with time, whereas the copper concentration appears constant. The effect of temperature on the equivalence point is less marked, but there is a maximum in the photosensitivity of all fully compensated materials between 550° and 575°C, believed to be a result of variation in the chloride concentration. Obviously gas flow velocities are critical in order to achieve reproducible chloride vapor concentrations, and effects are frequently observed due to variations in position when two or more photoconductor stripes are fired together.

It might be argued that the two-step process could be eliminated by firing in an atmosphere containing nitrogen and a critical pressure of selenium; we have explored only the possibility of firing in nitrogen/oxygen mixtures. The photocurrents of such materials are slightly higher than post-treated photoconductors, and the equivalence point is lower, 200 ppm. It is not clear why this should be lower than the usual value (change in the $Cu^+ \rightleftarrows Cu^{++}$ equilibrium may be responsible), but this point has not been pursued because it has been found difficult in air to keep dark currents reproducibly low. This may be due to the formation of cadmium oxide on grain boundaries; in the extreme case of high oxygen concentration (>20%) and long firing time, cadmium oxide can be detected by x-ray diffraction as might be expected.

Carrier mobility.—Measurements of the carrier mobility have been made in materials with a number of different donor concentrations and have shown that the mobility increases with donor concentration (Fig. 8), although it might be initially expected that the mobility would decrease with increasing impurity concentration. However, it is known that carrier mobility also increases with increasing light level, *i.e.*, with increasing number of carriers (9-11) and dependence of a similar nature has been noted by Kroger on cadmium sulfide single crystals (12). Thus, by fixing the donor concentration of a sintered layer by controlled processing, it is possible to select (within limits) the mobility required to meet device design specifications. Values of the speed and sensitivity still have to be fixed so that at room temperature they fall at the slow and sensitive end of the constant mobility lines in Fig. 2. As shown in Fig. 5, the addition of acceptors beyond the equivalence point results in a loss in photosensitivity and a decrease in the fall time; yet the mobility remains constant over a wide range of acceptor concentrations (10). The decrease in fall time may be due to the fact that an uncompensated acceptor forms a recombination center (13). Thus, the acceptor concentration may be adjusted to move the properties to the left or to the right along the constant mobility lines of Fig. 2. This then permits a material to work within its maximum temperature limits without going out of specification.

If in an attempt to decrease R_L, the acceptor concentration must be decreased to such an extent that erratic low dark resistances result, then the mobility is too low for maximum temperature latitude although all other electrical specifications may be met. From this, it might be deduced that in all cases it is desirable to have as high a mobility as possible and to increase the working temperature range of the material by adding acceptors. This, however, is not the case, as other phenomena are observed as the acceptor-to-donor ratio increases. We have already stated that the stability of high donor concentration materials may be less than with lower levels of doping, and Fig. 9 shows another effect, the "fatigue" or short-term photodegradation, arbitrarily defined as i_{30}/i_0, where i_0 is the initial photocurrent and i_{30} is the current after 30 min continuous illumination. The effect of increased acceptor concentration would obviously be undesirable when the device duty cycle involves long "on" times or short recovery times. Thus, the duty cycle must be considered in selecting the appropriate material.

Application.—By taking an arbitrary set of specifications, we can illustrate an application of the above scheme. The conditions of illumination were given as

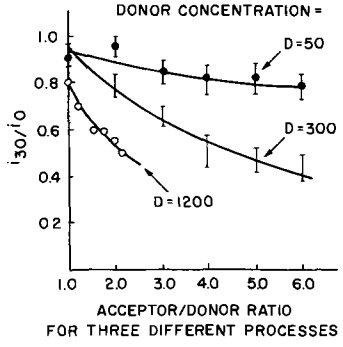

Fig. 9. Effect of acceptor/donor ratio on light fatigue. The acceptor/donor ratio is defined as the added acceptor divided by the titration equivalence point; light resistance is measured under 300 μw/cm^2 from a neon lamp.

1000 μw/cm^2 from a neon bulb, covering approximately a 25 square device. Required are $R_1 \leq 10$ kohm/sq and fall time to 70% $R_L < 5$ msec. Equation [1] gives an approximate value of 50 cm^2 v^{-1} sec^{-1} for the mobility (assuming unit quantum efficiency and ignoring trapping effects); anticipating some device temperature rise and consequent desensitization, we will attempt to utilize a higher mobility material (higher donor concentration) and add excess acceptors to permit sufficient temperature flexibility without conceding device stability (both short and long term). This mobility should require a donor concentration of 1200 ppm (Fig. 8), a number referred to in many of the examples above. However, in these examples, the donor concentration consists of 300 ppm chloride donor ions and 900 ppm selenium vacancies, and thus the material is not as stable as one that has been post-treated to remove (according to our hypothesis) vacancies. Thus the chloride or other donor impurity must be brought up to the 1200 ppm level to obtain a material with sufficient stability. This has been done on a pilot-line scale where the furnace atmosphere is saturated with cadmium chloride vapor. This method has the added advantage of improving uniformity; we lose the end effect by which the first and last units of each substrate are of lower sensitivity or by which the first and last substrates differ from the rest of the run. It is interesting to note that the donor concentration before post treatment is between 1800 and 2100 ppm, showing that the selenium vacancy concentration (600 to 900) is slightly reduced in line with the reduced time at peak temperature in the continuous belt furnace (see Fig. 4 and 7.) Addition of 1500 ppm copper to the material gives the properties outlined in Fig. 3.

Acknowledgments

The author wishes to acknowledge the assistance of his co-workers in this project including Dr. A. S. Miller, Dr. A. H. Mones, D. L. Bowman, and the late Dr. R. S. Schwartz; many of the suggestions and results in this paper have been drawn from their work.

Manuscript received June 9, 1964; first revised manuscript received July 14, 1966; second revised manuscript received Jan. 12, 1967.

Any discussion of this paper will appear in a Discussion Section to be published in the December 1967 JOURNAL.

REFERENCES

1. J. J. B. Thomas and E. J. Zdanuk, *This Journal*, **106**, 964 (1959).
2. R. H. Bube and J. M. Thompson, *Rev. Sci. Instr.*, **26**, 664 (1955).
3. C. P. Hadley and E. Fisher, *RCA Rev.*, **20**, 635 (1959).
4. R. H. Bube, "Photoconductivity of Solids," p. 71, John Wiley & Sons, Inc., New York (1960).
5. R. H. Bube and A. B. Dreeben, *Phys. Rev.*, **115**, 1528 (1959).
6. M. Avinor, Thesis, University of Amsterdam (1959).
7. A. Reisman and M. J. Berkenblit, *This Journal*, **109**, 111 (1962)
8. A. Reisman, M. J. Berkenblit, and M. Witzer, *J. Phys. Chem.*, **66**, 2210 (1962).
9. A. B. Fowler, *J. Phys. Chem. Solids*, **22**, 181 (1961).
10. G. Cheroff and S. Triebwasser, *J. Phys. Chem. Solids*, **22**, 51 (1961).
11. R. H. Bube and H. E. MacDonald, *Phys. Rev.*, **121**, 473 (1961).
12. F. A. Kroger, *Z. Physik. Chem.*, **203**, 1 (1954).
13. R. H. Bube, *Phys. Rev.*, **128**, 532 (1962).

Phase Equilibria in the Cd-Se System

R. A. Burmeister, Jr.,[1] and D. A. Stevenson

Department of Materials Science, Stanford University, Stanford, California

ABSTRACT

A consistent set of temperature-composition and pressure-temperature data has been obtained for the Cd-Se system by combining the results of several previous investigations. It is shown that CdSe vaporizes congruently and that the range of congruent sublimation extends to temperatures in excess of 1200°C. Values of the standard free energy, enthalpy, and entropy of formation of CdSe are derived from the experimental vapor-solid equilibrium data. The activity coefficients of Cd and Se in the liquid phase in equilibrium with solid CdSe are calculated from the experimental data. The liquid is found to exhibit nearly ideal behavior in the region $N_{Se} = 0.0$ to 0.4 for Cd, and $N_{Se} = 0.6$ to 0.77 for Se. The relationship of these data to the attainable concentration ranges of crystalline imperfections is discussed.

Pure binary semiconducting compounds exist over a narrow range of composition by the incorporation of native point defects. The concentrations of these defects may play a dominant role in controlling the electrical and optical properties of these compounds. Because the range of composition is extremely small, it is not operationally feasible to adjust the defect concentration by direct compositional control of the solid. The composition of the equilibrium vapor, however, changes appreciably over the stability range of the solid compound. The control of the component vapor pressure in equilibrium with the solid thus provides a convenient experimental method for adjusting the defect concentration. A description of the high-temperature equilibria between liquid, solid, and vapor phases is essential for this purpose. This information

[1] Present address: Hewlett-Packard Laboratories, Palo Alto, California.

is also important for determining the range of temperature and pressure suitable for crystal growth of the compound. Vapor-solid equilibrium data may be used to evaluate basic thermodynamic properties such as the standard free energy, enthalpy, and entropy of formation of the compound. These thermodynamic properties provide information concerning the nature of the binary system and a quantitative measure of the stability of the compound.

Studies have previously been made of various aspects of phase equilibria in the CdSe system. The minimum vapor pressure has been studied as a function of temperature by several investigators (1-6). The temperature-composition diagram was determined in an independent investigation (7), and recently three-phase (solid-liquid-vapor) equilibrium data have been reported (6). In this paper the data obtained in earlier investigations are combined and revised where necessary to construct a set of temperature-composition (T-X) and pressure-temperature (P-T) diagrams. This information is used to derive thermodynamic data for CdSe and to describe the general behavior of the Cd-Se system.

Solid-Vapor-Equilibria

It is well established that most IIb-VIa compounds sublime according to the equation

$$MX_{(s)} \rightleftarrows M_{(v)} + \tfrac{1}{2}X_{2(v)} \qquad [1]$$

at temperatures well below the maximum melting point (4).

For CdSe, the equilibrium constant corresponding to Eq. [1] is

$$K_p(T) = P_{Cd}P_{Se_2}^{1/2} \qquad [2]$$

At any temperature the total vapor pressure over the solid is the sum of the partial pressures

$$P_T = P_{Cd} + P_{Se_2} \qquad [3]$$

The condition for minimum total vapor pressure is obtained by setting $\partial P_T/\partial P_{Cd} = \partial P_T/\partial P_{Se_2} = 0$, yielding

$$P_{Cd} = 2P_{Se_2} \qquad [4]$$

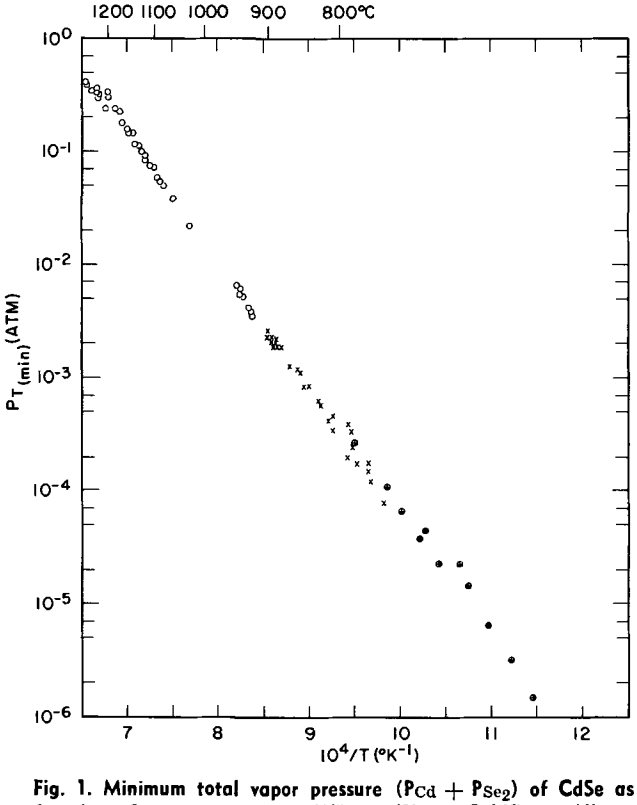

Fig. 1. Minimum total vapor pressure ($P_{Cd} + P_{Se_2}$) of CdSe as a function of temperature: x, Wösten (3); o, Goldfinger (4); o, Shiozawa (6).

Combining Eq. [2], [3], and [4] gives

$$K_p = \frac{2}{3\sqrt{3}} P_{T(min)}^{3/2} \qquad [5]$$

Several different methods have been used to determine $P_{T(min)}$ as a function of temperature, including Knudsen cell (1,4), Bourdon gauge (2), and transpiration techniques (3). Shiozawa (6) employed a novel variation of the "boiling point" method (8) commonly used for liquids. The results of the experimental measurements, shown in Fig. 1, are in good agreement. The measurements of Somorjai (2) have not been included, since they were made using a closed system and therefore do not represent the minimum total pressure (9). Knudsen cell measurements, although corresponding to an effusive steady state which is slightly different from a state of congruent sublimation, give essentially the same value for the minimum total pressure (10).

The standard heats of sublimation corresponding to reaction [1] were calculated from the data of Fig. 1 by use of the Van't Hoff equation, and the values obtained are given in Table I. The corresponding values for the standard entropy of sublimation are shown in Table II. It is not possible to make a Third Law calculation to substantiate the Second Law values given here, since the necessary low-temperature heat capacity data for $CdSe_{(s)}$ are not available.

In order to calculate the standard heat of formation of CdSe at 298°K from the vapor pressure data it is necessary to estimate the heat capacity change for the sublimation reaction. Shiozawa (6) applied Kopp's rule to $CdSe_{(s)}$ using tabulated C_p values for $Cd_{(v)}$ and $Se_{2(v)}$ (11), obtaining an approximate value of $\Delta C_p = 2.8$ cal/deg-mole. Wösten estimated a value of 3 cal/deg-mole for the same reaction. The standard heat of formation of $CdSe_{(s)}$ at 298° from $Cd_{(s)}$ and $Se_{(s)}$ calculated by use of these estimated values of ΔC_p are shown in Table III, together with the results of the emf measurements of Terpilowski *et al.* (12).

The experimental values of the standard entropy of CdSe at 298°K are summarized in Table IV.

Table I. Heat of sublimation of $CdSe_{(s)}$

$\Delta H_s°$, kcal/mole	Temperature range studied, °K	Investigator
78.7	1020-1170	Wösten (3)
73.9	870-1050	Goldfinger *et al.* (4)
77.6	1070-1470	Shiozawa *et al.* (6)

Table II. Standard entropies of sublimation for $CdSe_{(s)}$

$\Delta S_s°$, eu	Temperature range studied, °K	Investigator
47.7	1020-1170	Wösten (3)
46.4	870-1050	Goldfinger (4)
46.8	1070-1470	Shiozawa *et al.* (6)

Table III. Heat of formation of $CdSe_{(s)}$ at 298°K

$\Delta H_f°$, kcal/mole	Investigator	Method
−37.5	Wösten (3)	Vapor pressure data
−32.5	Goldfinger *et al.* (4)	Vapor pressure data
−33.8	Shiozawa *et al.* (6)	Vapor pressure data
−34.6	Terpilowski *et al.* (12)	EMF measurements

Table IV. Standard entropy of $CdSe_{(s)}$ at 298°K

S°, eu	Investigator	Method
18.6	Wösten (3)	Vapor pressure data
23.1	Goldfinger *et al.* (4)	Vapor pressure data
18.6	Terpilowski *et al.* (12)	EMF measurements

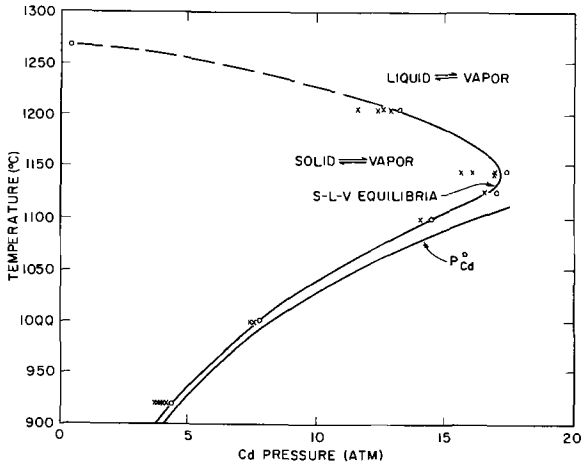

Fig. 2. Solid-liquid-vapor equilibria on the Cd-rich portion of the CdSe system: x, no melting; o, melting observed.

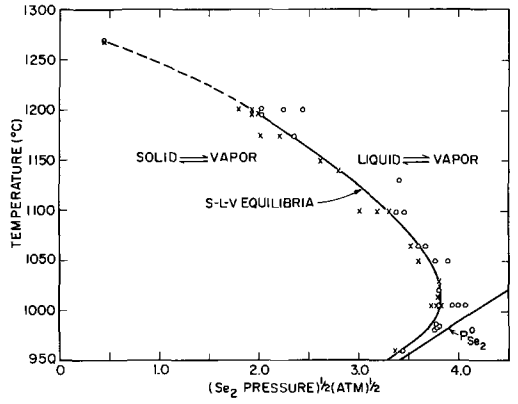

Fig. 3. Solid-liquid-vapor equilibria on the Se-rich portion of the Cd-Se system: x, no melting; o, melting observed.

Solid-Liquid-Vapor Equilibria

Shiozawa (6) has made experimental studies of the solid-liquid-vapor equilibria in the CdSe system. In these experiments, the partial pressure of Cd or Se over a CdSe crystal was fixed by means of a reservoir of the elements held at a lower temperature. The three-phase equilibrium points were determined by noting the points of incipient melting. The vapor pressure of liquid Cd was obtained from the data of Kelley (13), which are in good agreement with the recent measurements of Brebrick *et al.* (10) and Van Gool (14). The data for the three-phase line corresponding to Cd-saturation are shown in Fig. 2. Note that the maximum melting point will in general not correspond precisely to the minimum vapor pressure as shown. The difference in the maximum sublimation point and the maximum melting point cannot be determined precisely due to the lack of experimental data in this region. It is expected that the difference is rather small.

In evaluating the data for the Se-saturated three-phase line, it is necessary to consider the equilibria among the various vapor species of Se. Illarionov and Lapina (15) have shown that the dominant species in selenium vapor are Se_2, Se_4, Se_6, and Se_8 and have determined the relevant equilibrium constants. More recently Brebrick (16) investigated the vapor species over liquid selenium using optical density techniques. These data can be combined with the total pressure measurements of Brooks (17) to give partial pressure of any species as a function of temperature.[2]

In the temperature range investigated by Shiozawa, the dominant species are Se_2 and Se_4.[3] We have corrected that data of Shiozawa for the $Se_{2(v)} \rightleftarrows Se_{4(v)}$ equilibrium and obtained the results shown in Fig. 3. Also shown in the figure is the partial pressure of Se_2 over pure liquid selenium.

The maximum melting point of CdSe was determined by Shiozawa to be 1268° ± 2°C, as compared to the value of 1239°C reported by Reisman *et al.* (7). Part of this discrepancy may be due to the difference in experimental methods employed. Shiozawa employed visual examination of melting of vapor grown single crystals in a sealed quartz ampoule with a relatively large free volume. Reisman used weighed elements in a DTA capsule with a relatively small free volume. In the latter method, an excess pressure of one of the components is more likely with a consequent reduction in melting point in accordance with Fig. 2 and 3.

By combining the data of Fig. 1 through 3 with the T-X diagram it is possible to calculate the activity coefficients of Cd and Se in the liquid phase in equilibrium with solid CdSe, using the following relationships

$$\gamma_{Cd} = \frac{1}{N_{Cd}} \left(\frac{P_{Cd}}{P^{\circ}_{Cd}} \right) \quad [6]$$

$$\gamma_{Se} = \frac{1}{N_{Se}} \left(\frac{P_{Se_2}}{P^{\circ}_{Se_2}} \right)^{1/2} \quad [7]$$

where γ_i denotes the activity coefficient, N_i the mole fraction, P_i the partial pressure, and the superscript $^{\circ}$ denotes the pure component.

The activity coefficients obtained in this manner are plotted in Fig. 4. No values are shown for the region $0.675 \leq N_{Se} \leq 0.995$, since in this region the liquid consists of two phases (7). The activity of Cd in the liquid phase in equilibrium with solids CdSe shows only a slight deviation from Raoult's law in the region $0.0 \leq N_{Se} < 0.4$. Near the region of compound formation there is a very sharp negative deviation from ideality, as expected.

The solid-vapor equilibrium data can be combined with the liquid-solid vapor equilibrium data to construct a pressure-temperature diagram which indicates the limits of solid stability. This diagram is shown in Fig. 5. The ordinate has been expressed in terms of cadmium pressure rather than total pressure, since only one partial pressure can be independently

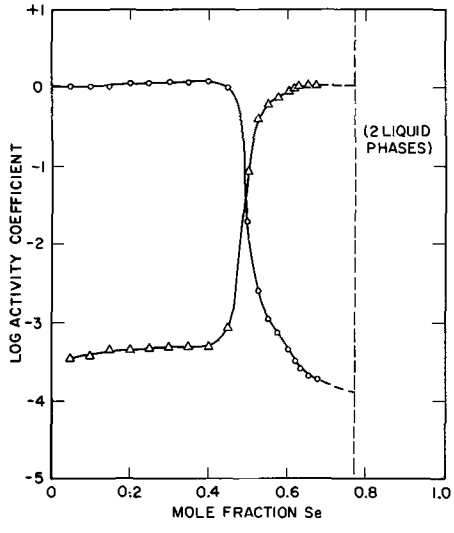

Fig. 4. Activity coefficient of Cd (o) and Se (x) in the liquid in equilibrium with $CdSe_{(s)}$.

[2] Recent measurements of the total pressure of Se vapor over liquid Se by Bonilla and Shulman (18) deviate significantly from those of Brooks, particularly at high temperatures. The reason for the discrepancy is not clear. Since the agreement among the other independent measurements (15, 17) is quite good, we have chosen their data for our calculations.

[3] Shiozawa (6) used the data of Kelley (13), which includes only the Se_2 and Se_6 species.

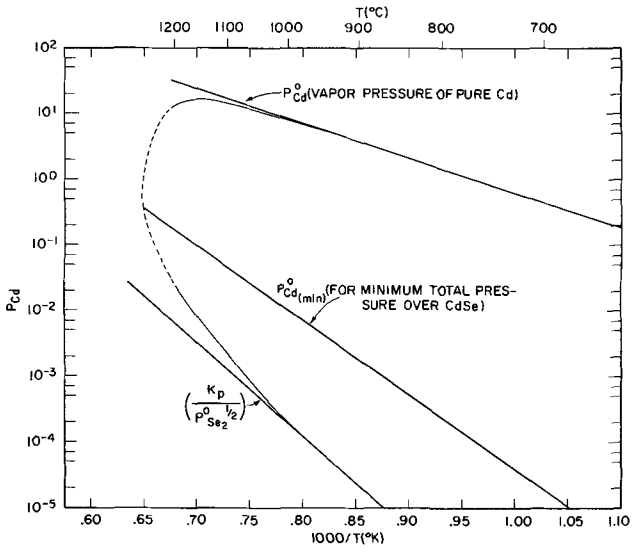

Fig. 5. P-T diagram of the Cd-Se system in the region of CdSe

controlled at a given temperature. The projection of the experimentally determined portion of the three-phase blade onto the *P-T* plane is represented by a solid curved line; the dashed portion is an extrapolation. Also shown on this diagram are the lines representing the vapor pressure of pure cadmium (P°_{Cd}) and that of pure selenium ($P^{\circ}_{Se_2}$). The latter has been expressed as an equivalent cadmium pressure by use of the equilibrium constant data derived from the minimum vapor pressure measurements.

Discussion

It has been suggested previously that CdSe does not exhibit congruent sublimation (7). While this may be true for short transient period at the beginning of the vaporization process, the experimental data summarized in this paper clearly indicate that the steady-state vaporization of CdSe is a two-phase sublimation process in which the solid and the vapor have the same composition. If the vaporization of CdSe proceeded only by a three-phase process, as postulated by Reisman (7), the total pressure over the vaporizing solid would be equal to that of the liquid phase present. At temperatures below ~950°C the vapor pressure of the liquid phase is nearly equal to that of the pure component [see Fig. 1 of ref. (7) and Fig. 2-4 of this paper]. The pressures measured experimentally over the solid during steady-state vaporization, however, are several orders of magnitude smaller than those over the liquid phase. Furthermore, the linear behavior of log $P_{T(min)}$ *vs.* $1/T$ up to 1200°C (Fig. 1) would not be expected if a three-phase vaporization process obtained. Under three-phase vaporization, the liquidus would change composition with temperature in accord with the T-X diagram. This change is reflected in the log *P vs.* $1/T$ diagram [see, for example, the data for HgSe (19)].

Since the concept of congruent sublimation is germane to this discussion, we wish to examine it in more detail. The basic requirement for congruent sublimation in a binary compound MX is that the saturated vapor pressure temperature curves of both components (corresponding to the full width of the solid phase field) overlap. The temperature range of congruent sublimation corresponds to the region of overlap. As a consequence of Gibbs-Konovalow theorem (20), the congruently subliming solid will produce the minimum total pressure at a given temperature. It should be recognized, however, that the congruently subliming solid need not be stoichiometric. The congruent sublimation of a nonstoichiometric compound MX_{1-y} where y denotes the nonstoichiometry and the vapor of X is diatomic, can be represented as

$$MX_{1-y(s)} \rightleftarrows M_{(v)} + \left(\frac{1-y}{2}\right) X_{2(v)} \qquad [8]$$

By following the differentiation procedure outlined in the section on Solid-Vapor-Equilibria, the relationship

$$P_M = \left(\frac{2}{1-y}\right) P_{X_2} \qquad [9]$$

is found for congruent sublimation. Expressions for K_p and P_T can be obtained in a similar manner.

In the case of CdSe, the saturated vapor pressure curves do overlap up to the highest temperatures (1200°C) for which experimental data are available. This can be seen from the data for Fig. 2, 3, and 5. The compound can therefore sublime congruently during steady-state vaporization in this temperature range. This is in distinct contrast to the behavior of III-V compounds such as GaAs and GaP, where congruent sublimation is limited to much lower temperatures (21). The difference in behavior is largely attributable to the magnitude of the difference in vapor pressures of the elemental components, which is small in the case of Cd and Se but large in the case of GaAs and GaP (21). Other II-VI compounds which have comparable elemental vapor pressures and therefore a large degree of overlap of the *P-T* curves should also sublime congruently up to temperatures near the melting point.

A question of central importance is the degree of nonstoichiometry of the congruently subliming solid, since the condition of congruent sublimation pertains in most phase crystal growth processes. The data of Reisman (7) suggest that the congruently subliming solid is nonstoichiometric with an excess of Cd. A quantitative knowledge of the exact composition of the congruently subliming solid as a function of temperature would allow corrections of Eq. [1] through [5] to be made as outlined above. Since the nonstoichiometry is undoubtedly less than 1 a/o, these corrections will be slight.

The pressure-temperature diagram (Fig. 5) is of considerable value in studies of properties of CdSe related to point defect concentrations. At any specific temperature, the attainable values of $P_{Cd_{max}}$ and $P_{Cd_{min}}$ can be ascertained. At a temperature of 900°C, for example, the extremes in pressures for the solid CdSe phase are $P_{Cd_{max}} = 3.8$ atm and $P_{Cd_{min}} = 2.3 \times 10^{-5}$ atm. These data can be used to predict the relative maximum and minimum concentrations for point defects consistent with a given defect equilibrium. A determination of the concentration and charge state of crystalline defects at high temperature obtained, for example, from high-temperature Hall effect measurements as a function of Cd pressure, would accurately define the width and position of the solid phase field on the T-X diagram. This information is required to draw firm conclusions concerning the attainability of p-type conductivity in CdSe by stoichiometry control.

The variation of the activity coefficients with composition along the liquidus (Fig. 4) shows a very small deviation from ideality for Cd on the Cd side of the diagram and for Se on the Se side of the diagram, except in the vicinity of the compound, *viz.*, 40-60 a/o Se, where pronounced negative deviation is observed. This behavior is somewhat different from that found in III-V systems (21). The existence of a wide range of nearly ideal behavior has important implications in predicting the phase equilibria of other II-VI compounds. It is possible, for example, to construct large portions of the P-T diagram by assuming the validity of Raoult's law in the appropriate regions (22).

The fact that the minimum total pressure of CdSe at the melting point is less than 1 atm is of practical importance in crystal growth processes since it indicates that CdSe can be grown from the melt without need for elaborate high pressure apparatus. In experiments of this type it is imperative to achieve an

initial composition close to or equal to the congruently subliming composition, since in a closed system an extremely small amount of excess Cd or Se may produce pressures considerably in excess of one atmosphere at the melting point.

Acknowledgments

The authors are indebted to Mr. L. Shiozawa of the Clevite Corporation for providing much of his experimental data at an early date. They are also grateful to Dr. R. F. Brebrick of Lincoln Laboratories for valuable comments concerning the selenium pressure data. Portions of this work were sponsored by the United States Atomic Energy Commission under Contract AT(04-3)-283.

Manuscript received July 26, 1966; revised manuscript received Dec. 5, 1966.

Any discussion of this paper will appear in a Discussion Section to be published in the December 1967 JOURNAL.

REFERENCES

1. I. V. Korneeva, V. V. Sokolov, and A. V. Novoselova, *Zhur. Neorg. Khim.*, **5**, 241 (1960).
2. G. A. Somorjai, *J. Phys. Chem.*, **65**, 1059 (1961).
3. W. J. Wösten, *J. Phys. Chem.*, **65**, 1949 (1961).
4. P. Goldfinger and Jeunehomme, *Trans. Faraday Soc.*, **59**, 2851 (1963).
5. P. Höschl and C. Konak, *Czech. J. Phys.*, **B13**, 364 (1963).
6. L. R. Shiozawa and J. M. Jost, Reports No. ARL 62-365 (Mar. 1962) and (May, 1965), ARL-65-98, Aerospace Research Lab., U.S.A.F.
7. A. Reisman, M. Berkenblit, and M. Witzen, *J. Phys. Chem.*, **66**, 2210 (1962).
8. A. N. Nesmeyanov, "Vapor Pressure of the Elements", Academic Press, New York (1963).
9. G. A. Somorjai and J. E. Lester, *J. Chem. Phys.*, **42**, 4140 (1965).
10. R. F. Brebrick and A. J. Strauss, *J. Phys. Chem. Solids*, **25**, 1441 (1964).
11. D. R. Stull and G. C. Sinke, "Thermodynamic Properties of the Elements," American Chemical Society, 1956.
12. J. Terpilowski and E. Ratajczak, *Bull l' Acad. Polon. Sci.*, **12**, 355 (1964).
13. K. K. Kelley, U. S. Bureau of Mines Bull. 383 (1935).
14. W. Van Gool, *Proc. Kon. Ned. Akad. Wet.*, **B66**, 209 (1963).
15. B. V. Illarionov and L. M. Lapina, *Dokl. Akad. Nauk. SSSR*, **114**, 1021 (1957).
16. R. F. Brebrick, *J. Chem. Phys.*, **43**, 3031 (1965).
17. L. S. Brooks, *J. Am. Chem. Soc.*, **74**, 227 (1952).
18. C. F. Bonilla and G. Shulman, *Nucleonics*, **22**, 3, 58 (1964).
19. R. F. Brebrick, *J. Chem. Phys.*, **43**, 3846 (1965).
20. I. Prigogine and R. Defay, "Chemical Thermodynamics," p. 282, John Wiley & Sons, Inc., New York (1954).
21. C. D. Thurmond, *J. Phys. Chem. Solids*, **26**, 785 (1965).
22. M. R. Lorenz, *J. Phys. Chem. Solids*, **23**, 939 (1962).

Vacuum Thermal Etching of Germanium and Silicon Surfaces

G. J. Russell and D. Haneman

School of Physics, The University of New South Wales, Sydney, Australia

ABSTRACT

The surface structures formed on {111}, {110}, and {112} surfaces of silicon and germanium heated in the temperature ranges 900°-1380°C for silicon and 650°-937°C (mp) for germanium have been detailed. The changes in topography were found to be markedly dependent on the degree of undersaturation maintained during heating, as well as on the temperature range. The {111} surface of germanium was particularly sensitive to surroundings of the crystal. The proximity and shape of the surroundings influenced the free evaporation rate from the heated surface. Either "worms" or oriented pits formed according to whether the degree of undersaturation was low or high. The various topographical changes are discussed in terms of bond breaking, surface atom mobilities, and free energy minimization.

Surface changes on heat treated germanium and silicon surfaces, under nonoxidizing conditions, have been reported by a number of authors (1-11). The surface changes appear to be diverse in nature. A systematic study has not been made. For surfaces heated to within a few degrees of their melting points geometrical pits were observed (1), each one with a hillock protruding from the center. On partially melted {111} silicon (2) and germanium (3) surfaces, triangular pits were not reported but only hillocks. Differing results have also been reported for silicon and germanium surfaces heated to temperatures well below the mp in high vacuum. The surface changes on the low index surfaces of silicon vary from geometrical thermal pits on all surfaces (4, 5) to an apparently smooth surface containing hillocks on the {111} surface (6) and a "sandblasted" surface structure on the {110} and {100} surfaces (4, 6). These changes are markedly dependent on temperature. However Batdorf and Smits (7) observed that vacuum thermally etched {111} silicon surfaces contain a number of flat-bottomed etch pits for the same temperature range that Hagstrum (6) reported a smooth surface containing hillocks.

For germanium surfaces heated in high vacuum, only observations on the {111} surface have been reported. The initial surface changes reported appear to be inconsistent in that "pocking" of the surface at a temperature of 850°C was first observed by Gatos and Lavine (8) while Gabor (9) found geometrical pits and hillocks as well as straight line pits in the temperature range 570°-850°C. In this latter case, it was found that a number of structures were dependent on the experimental conditions. For temperatures close to 850°C however, a number of authors (8-11) report the presence of "wormlike" structures. According to Haidinger and Courvoisier (10) these "worms" are hillocks which modify their structure with temperature.

The mechanism for the formation of the worm structure on the {111} germanium surface is not fully understood and has been discussed by Haidinger and Courvoisier in terms of surface GeO_2 particles (left after chemical etching) which initiate the worms and by Gatos and Lavine who postulate that surface oxide controls the thermal etching of the surface, the limiting factor being the rate of removal of the oxide present on the surface.

It is desirable to obtain further information on the behavior of the various low index single crystal surfaces of silicon and germanium, both to account for some of the above discrepancies and to provide more complete data to assist in providing explanations for the observed changes.

Experimental

Single crystals of silicon and germanium were cut so that the front surface exposed a {111} plane and the side surfaces exposed {110} and {112} planes, each surface being oriented to within ½ degree by x-ray methods. Several thin silicon and germanium wafers exposing {111} and {$\bar{1}\bar{1}\bar{1}$} planes were also prepared. The surfaces were lapped, polished (0.1μ, Cr_2O_3) and chemically etched before being placed in a high vacuum system for heating. The background pressure was $\sim 10^{-9}$ Torr and pressures in the range 10^{-7}-10^{-8} Torr were maintained during heating.

The silicon surfaces were chemically etched in a solution of 100 : 16 : 44 HNO_3 : HF : CH_3COOH (4) while the germanium surfaces were generally chemically etched in either CP4 or CP4B. In all cases the reaction was stopped with distilled water. The surfaces appeared flat and free of damage under high power optical microscopy, with etch pit (1-6μ) density of the order of 10-200 per cm^2. The crystals were then rinsed in concentrated HF followed by distilled water, and then placed in molybdenum holders, to minimize contamination effects. These were enclosed in an all glass high vacuum system, the front {111} crystal surface being heated by electron bombardment, Fig. 1. Because surroundings were sufficiently far from the crystal surface to remain cool and not return vapor, the conditions correspond to high undersaturation, the percentage ratio R of the crystal evaporation rate to the free evaporation rate being ~100%. (The side {110} and {112} surfaces were heated partly by electron bombardment and partly by conduction from the front surface.)

The surface temperatures of the silicon surfaces were obtained from calibrated optical pyrometer measurements using emissivity data (12) to ±20°C. The temperatures of the Ge surfaces were measured by a combined pyrometer and thermocouple technique, but the temperature could not be given to better than approximately ±25°C in most cases.

The three low index surfaces of germanium were also thermally etched in a second high vacuum system under conditions of low undersaturation. The crystals were placed in a quartz tube under continuous evacuation and heated by an axial oven. The nearness and high temperature of the surrounding walls resulted in appreciable return of germanium vapor (R = <1 − 25%). The surface temperature was measured by a calibrated chromel-alumel thermocouple, the head of which was spaced from the germanium surface by a small, thin molybdenum sheet as germanium attacks the thermocouple material. Measurements were accurate to ± 7°C and the temperature difference across the crystal face was <1°C and along the crystal length ~2°C.

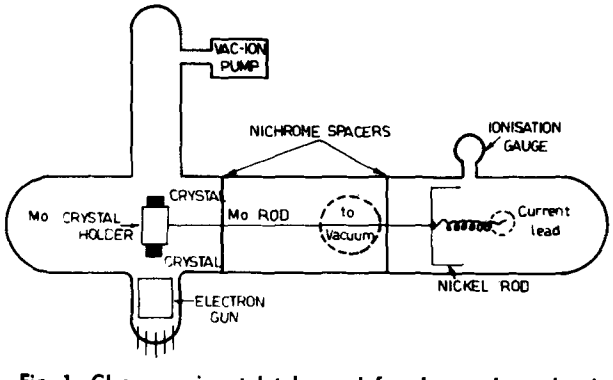

Fig. 1. Glass experimental tube used for electron beam heating of silicon and germanium crystals.

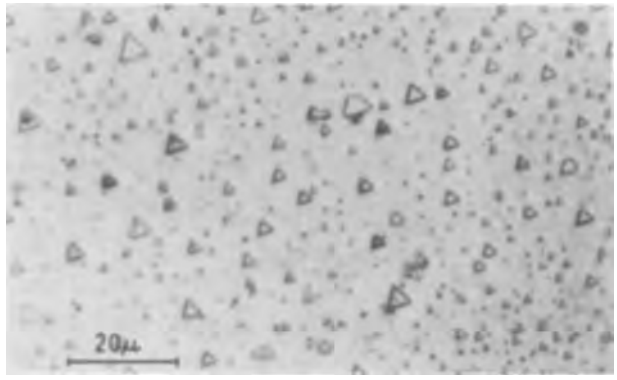

Fig. 2. Triangular thermal pits on the {111} silicon surface, temperature 1080°C; heating time 30 hr.

The surface structures before and after heating were examined at room temperature by high power optical and electron microscopy (shadowed replicas).

Results

The surface topographies observed on the three low index surfaces of silicon and germanium which had been heated in high vacuum under a high undersaturation are summarized in Table I and Table II.

The silicon surfaces were studied in the temperature range 900°-1380°C and for heating times of 2.3-115 hr, while the germanium surfaces were studied in the temperature range 650°C to the melting point (937°C) and for heating times of 0.03-52 hr. In both cases the resultant surface changes were found to be significantly temperature dependent (for observable surface changes), and the observed surface topographies can be approximately correlated to temperature ranges.

The nucleation sites for thermal pit formation on silicon and germanium surfaces appeared to be ran-

Table I. Silicon surfaces, high undersaturation

Surface	Temperature range, °C	Surface structure
{111}	900-1110	Triangular thermal pits exposing {311} planes (mainly 80° with respect to the surface, some 29.5°) and {111} plane, Fig. 2.
	1110-~1250	Transitional surface structure. The triangular pits "deteriorated" at the lower limit and a "scalloped" background with small hillocks formed at the upper limit, Fig. 3.
	~1250-1380 (mp 1412)	Surface covered with hillocks* and a wavy stepped background structure, Fig. 4.
{112}	900-1130	Triangular thermal pits with exposed {111} planes.
	1130-1180	Thermal pits began to "deteriorate" in a way similar to that observed for the {111} surface.
	1180-~1250	A "sandblasted" (4) surface structure is formed which changes to a much smoother background surface structure and hillocks at the upper limit, Fig. 5a.
	~1250-1380	Surface covered with hillocks* and a wavy stepped background structure.
{110}	900-1050	Striation thermal pits and about an equal number of hexagonal thermal pits, both types of pits exposing {111} and {311} planes, Fig. 5b.
	1050-1130	Striation thermal pits and a small number of large hexagonal thermal pits at the lower limit.
	1130-1180	Thermal pits began to "deteriorate" in a way similar to that observed for the {111} surface.
	1180-~1250	A "sandblasted" surface structure is formed which changes to a much smoother background surface structure and hillocks at the upper limit.
	~1250-1380	Surface covered with hillocks* and a wavy stepped background structure.

* The hillocks appeared to be flat-topped, but by careful replication it was found that a small "globule" had formed on each hillock top during heating.

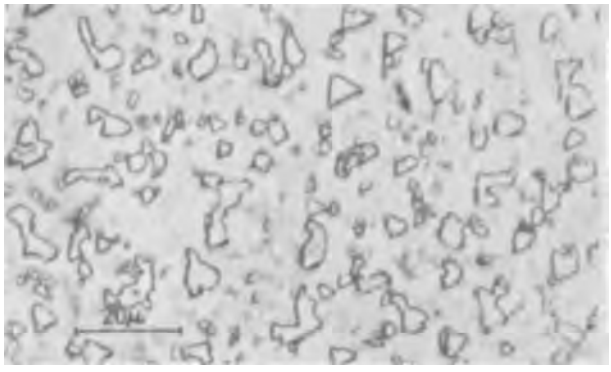

Fig. 3. Deteriorated triangular thermal pits on the {111} silicon surface, temperature 1131°C, heating time 40 hr.

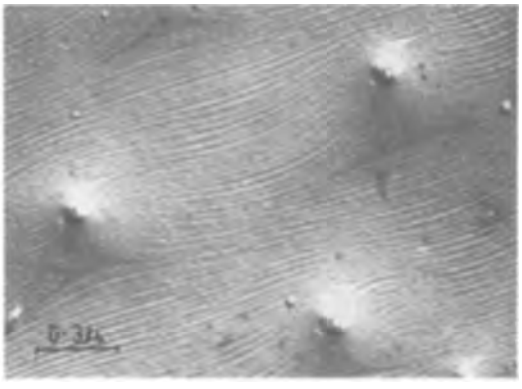

Fig. 4. Hillocks and a wavy stepped surface structure on a {111} silicon surface, temperature 1265°C, heating time 8.5 hr, angle of shadowing ~25°.

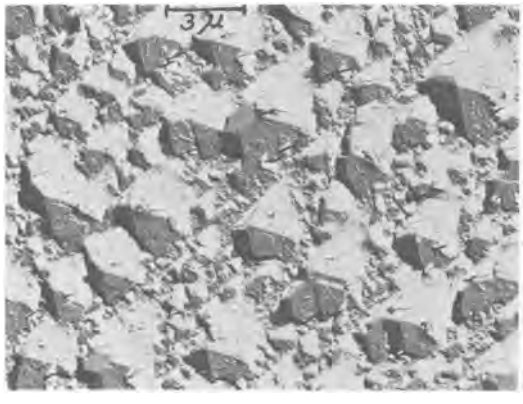

Fig. 5a. Sandblasted surface structure on a {112} silicon surface, temperature ~1200°C, heating time 10 hr, angle of shadowing ~20°.

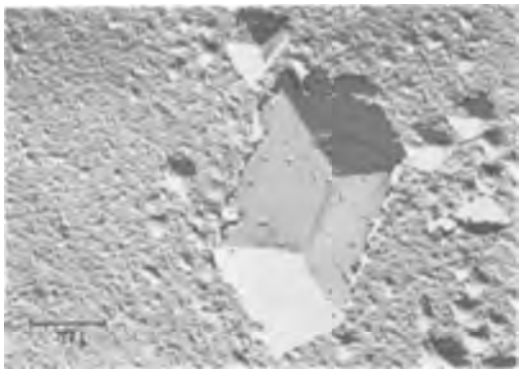

Fig. 5b. Striation and hexagonal thermal pits on a {110} silicon surface temperature 1040°C, heating time 40 hr, angle of shadowing ~25°.

Table II. Germanium surfaces, high undersaturation

Surface	Temperature range, °C	Surface structure
{111}	650-~800	Hexagonal-like thermal pits with exposed {111} and {311} planes. A number of triangular thermal pits exposing {111} planes were also observed, Fig. 6.
	~800-<937 (mp 937)	Triangular thermal pits with exposed {111} planes. A small number of hexagonal-like thermal pits exposing {111} and {311} planes were also observed.
	~937	Surface broken up forming hillocks with an associated pit structure.
{112}	650-<800	Hexagonal-like thermal pit structure with exposed {111} and {311} planes and several triangular pits exposing {111} planes, Fig. 7.
	~800-<937	Triangular thermal pits with exposed {111} planes.
	~937	Surface broken up forming hillocks with an associated pit structure.
{110}	650-~800	Hexagonal thermal pits and several striation thermal pits, both types of pits exposing {111} and {311} planes.
	~800-<937	Striation thermal pits and a large number of very small hexagonal thermal pits, both types of pits exposing {111} and {311} planes.
	~937	Surface broken up forming hillocks with an associated pit structure.

dom. Dislocations intersecting the surface were found to be present at the base of a number of the thermal pits but there existed no one-to-one correspondence.

For {$\bar{1}\bar{1}\bar{1}$} germanium surfaces of thin wafers heated in high vacuum under a high undersaturation by conduction of heat from the electron bombarded front surfaces, the dominant surface features were hexagonal-like and triangular thermal pits as in Table II. However, a wormlike formation was detected after heating to ~725°C and worms were present after temperatures of 900°C. After 725°C heating, a number of

Fig. 6. Hexagonal thermal pit on a {111} germanium surface, temperature 775°C, heating time 43 hr, angle of shadowing ~32°.

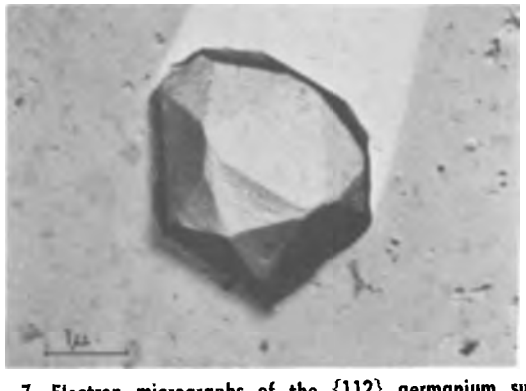

Fig. 7. Electron micrographs of the {112} germanium surface showed that a number of the hexagonal-like thermal pits had eight sides meeting the {112} surface, as above, temperature 650°C, heating time 30 hr, angle of shadowing ~20°.

Fig. 8. Worms on a {111} germanium surface, temperature 861°C, heating time 10 hr.

Fig. 9. Worm on a {111} germanium surface. The hillock in the triangular pit worm-head is prominent; temperature 736°C, heating time 30 hr, angle of shadowing ~30°.

the hexagonal-like (and triangular) thermal pits pointed in the $<2\bar{1}\bar{1}>$ directions due to the increased exposure of {311} planes.

Radiation heating of the low index surfaces of germanium in a high vacuum system giving conditions of low undersaturation caused the formation of a number of somewhat different structures which are summarized in Table III.

The worms were found to be pits, and not hillocks as reported by Haidinger and Courvoisier (10), and to

Table III. Germanium surfaces, low undersaturation

Temperature range, °C	Heating time, hr	R, %	Surface	Surface structure
669-861	10-34	5-10	{111}	Worm formation, Fig. 8.
738-867	10-30	25	{111}	Worm formation and a number of small triangular and hexagonal-like thermal pits.
669-861	10-34	25	{112}*	For temperatures <790°C triangular thermal pits exposing {111} planes and hexagonal-like thermal pits exposing {111} and {311} planes. For higher temperatures triangular thermal pits exposing {111} planes.
792-867	10-30	10	{112}	Triangular thermal pits with one side "deteriorated" and {111} planes exposed.
669-861	10-34	25	{110}*	Striation thermal pits exposing mainly {111} planes, {311} planes also being observed in a number of cases. Several very small hexagonal pits observed for temperatures $\gtrsim$ 750°C.
749	30	10	{110}	Mainly striation pits and a number of very small worm like features.
802-886	5-30	<1	{110}	Worm formation, the worms being relatively small compared with those observed on the {111} surfaces.

* At a temperature of 861°C, heating time 10 hr, several small worms were also observed on these surfaces.

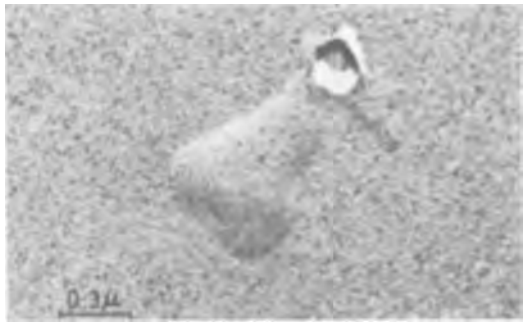

Fig. 10. Pear-shaped worm on a {111} germanium surface; temperature 742°C, heating time 30 hr, electron bombarding voltage 500v, angle of shadowing ~25°.

have the following characteristics: worm formation occurs predominantly on the {111} surfaces; the worms are connected to triangular pits on the {111} surface, as in Fig. 9 (at low temperature $\leq$750°C the triangular pits had either $<\bar{2}11>$ or $<2\bar{1}\bar{1}>$ directions on the same surface while for higher temperatures the pits had only the $<\bar{2}11>$ direction and exposed {111} planes); a small hillock is associated with each worm, generally associated with the triangular worm-head; the shape of the worm is very sensitive to temperature gradients on the surface; the worms increase in length and surface area with increasing temperature and heating time, and a large number of planes are exposed by the worms.

Consideration of the above results indicated that the degree of undersaturation maintained during heating of the germanium surfaces had a profound effect on the surface changes, causing either triangular (and hexagonal) or worm like etch figures at high and low undersaturations respectively. To obtain more detailed information the {111} surface was studied intensively.

Simultaneous electron bombardment (very low power) and radiation heating of {111} germanium surfaces in high vacuum under a low undersaturation ($R \sim$ 5-10%) resulted in a number of surface changes which were voltage dependent. Under various experimental conditions the following surface changes took place; at 200-500v, temperatures 742°-792°C, heating time 30 hr, "pear-worms" (Fig. 10) and several triangular and hexagonal pits formed; at 850v, temperature 807°C, heating time 30 hr, pear-worms, worms, and several triangular and hexagonal pits formed; at 1000v, temperature 780°C, heating time 30 hr the pear-worms were absent, the normal worm formation occurred, and a large number of triangular pits were observed.

In each case where pear-worms were observed, their size was notably smaller than that of normal worms. Their structure consisted of a type of hemispherical head, the planes exposed not being well defined. A hillock associated with each pear-worm was again observed, while very small hillocks were observed on the surface between the pear-worms in several cases.

In a number of cases a "reference" crystal exposing a {111} germanium surface was placed beside the electron bombarded crystal and held at a negative voltage with respect to the rest of the system. The {111} surface of the reference crystal developed worms, but the surface also appeared to have been ion bombarded, the amount of surface damage increasing with electron bombarding voltage (13).

Thus, the different surface structures observed on the {111} germanium surfaces of the experimental crystals can be interpreted in terms of a change in the undersaturation maintained in the experimental tube during heating. The bombarding electrons ionize the germanium vapor atoms, these are then removed at a negative electrode, and the undersaturation is increased. The mechanism for the formation of the pear-worms is not fully understood.

The effect of depositing germanium atoms from a beam onto a hot {111} germanium surface was also studied. The {111} surface was heated resistively, temperature 716°C for 7.5 hr, under free evaporation conditions in high vacuum and hexagonal and triangular thermal pits resulted. A beam of germanium atoms impinging on a hot {111} surface (the beam density being slightly larger than the calculated number of atoms evaporated), temperature 722°C for 7.5 hr, caused almost complete suppression of the thermal pits and worm formation was observed. These conditions correspond to low undersaturation, and confirm the previous conclusion that triangular etch figures are suppressed by returning Ge vapor.

The final experiment consisted of placing a clean molybdenum sheet in front of a {111} germanium surface heated in high vacuum under a low undersaturation. This resulted in the formation of triangular and hexagonal thermal pits and almost complete suppression of worms. The molybdenum sheet reached approximately the same temperature as the {111} surface and the surface of the molybdenum sheet facing the {111} germanium surface was found to have a thin coating of germanium which would increase the undersaturation maintained during heating.

These tests confirmed that the undersaturation maintained during vacuum heating of germanium surfaces is a very important factor in determining surface topography changes.

Discussion

Even though germanium and silicon have the same lattice structure a number of different topographical features formed on corresponding surfaces of the two crystals.

Heating low index surfaces of silicon and germanium under high undersaturation in high vacuum to relatively low temperatures resulted in basically the same surface change. Geometrical pits formed in all cases, the planes exposed by the pits being mainly {111} planes, but in many cases {311} planes were exposed as well. Simple mechanisms based on bond breaking can be postulated for the initial pit formation. The pits of atomic dimensions then grow by various processes. These include preferential evaporation which involves the propagation of steps on the surfaces and the inhibition of lateral motion of steps at the surface-pit kink positions perhaps in part by adsorbed species (14), such as GeO_2, SiO_2 (8). Thus the pits form a geometrical shape. The planes exposed by the pits indicate that there must be sufficient time for the material to be removed by exposing low surface energy crystallographic planes. The variation in facet size of the {311} planes with temperature may be considered as a variation of specific surface free energy with temperature as discussed by Herring (15).

On increasing the temperature, the topographical features on the germanium surfaces appeared not to change even at temperatures close to the melting point; however, for silicon surfaces a number of changes were observed. The most significant change is the formation of hillocks and a stepped surface structure on the {111}, {112}, and {110} silicon surfaces at a temperature of approximately 1250°C. This temperature is similar to that found by a number of workers (1257°-1280°C) to be necessary to "clean" silicon surfaces on the atomic scale by heat-treatment alone. This similarity of temperatures may have some significance. Germanium surfaces do not undergo these surface topographical changes as a function of temperature. It may be noted that germanium surfaces cannot usually be "cleaned" by high vacuum heat-treatment alone, although Jona (16) has reported a chemical treatment for {111} germanium surfaces that leads to clean surfaces after a very long period of heat treatment (~20 hr).

The cause of the hillock formation on the silicon surfaces appears to be the aggregation of refractory surface impurities into "globules" which mask the underlying surface during evaporation. From the work of Newman and Wakefield (17) it appears that silicon carbide precipitates may be the refractory impurities in the globules.

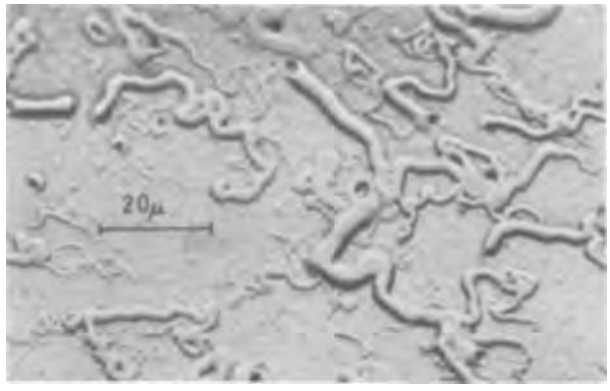

Fig. 11. Worms and hillocks on a {111} germanium surface. Oblique lighting used. The worm-heads have a triangular pit structure; temperature 792°C, heating time 30 hr.

The stepped surface structure can be explained by the nucleation of steps at the crystal edges and the movement of these steps across the surfaces with a mechanism such as time dependent impurity adsorption (18) or pinning by the hillocks to cause the formation of the observed submacroscopic steps. The crystal edges must be protected by "impurities" at the lower temperatures.

The mechanism proposed as an explanation of the worm formation is analogous to that proposed for the formation of surface structures on a partially melted {111} germanium surface. Near the melted region, the surface broke up at random sites, forming hillocks and an associated pit structure. The hillocks are assumed to obtain material for growth from the surrounding pit (1). Close to the melted region the hillocks moved toward the hottest region leaving behind a type of worm pit structure while closer to the melted region the hillocks grew rapidly in size and appeared to move according to the mechanism proposed by Pfann (19) for a two-phase eutectic system.

The above mechanism may be applied to the worm formation which occurs at lower temperatures. The hillocks which are observed could be germanium-impurity aggregates (GeO_2 is probably the impurity) the excess germanium now being supplied by the returning germanium vapor. The favored sites for the initial hillock formation appear to be the thermal pits, Fig. 11. These hillocks migrate from the pits along surface temperature gradients and form the worm structure by preferential evaporation of the surface atoms in the immediate vicinity.

The above mechanisms for worm formation must of course apply to all surfaces of germanium. The reason for the ease with which the {111} germanium surface forms worms can be considered in terms of surface energy criteria. A small increase in the surface energy of the {111} surface during heat-treatment is found (pit formation) and so hillock formation is possible. For the {110} and {112} surfaces, heat-treatment appears to lead to a decrease in the surface energy, whereas hillock formation would increase this energy. Thus, hillock formation on these latter surfaces should be suppressed by preferential reevaporation of the excess germanium from the hillocks.

The topographical changes reported in this work for the {111}, {110}, and {112} silicon and germanium surfaces after heat-treatment in high vacuum show that changes on each surface are dependent on the experimental conditions and the temperature, the heating time being of secondary importance for the ranges studied.

Manuscript received Aug. 3, 1966; revised manuscript received Nov. 3, 1966.

Any discussion of this paper will appear in a Discussion Section to be published in the December 1967 JOURNAL.

REFERENCES

1. G. L. Pearson and R. G. Treuting, *Acta Cryst.*, **11**, 397 (1958).
2. C. H. L. Goodman, *Solid-State Electronics*, **3**, 72 (1961).
3. H. D. Hagstrum, *J. Appl. Phys.*, **32**, 1015 (1961).
4. J. A. Dillon, Jr., and H. E. Farnsworth, *ibid.*, **29**, 1195 (1958).
5. H. E. Farnsworth, R. E. Schlier, and J. A. Dillon, Jr., *J. Phys. Chem. Solids*, **8**, 116 (1959).
6. H. D. Hagstrum, *Phys. Rev.*, **119**, 940 (1960).
7. R. L. Batdorf and F. M. Smits, *J. Appl. Phys.*, **30**, 259 (1959).
8. H. C. Gatos and M. C. Lavine, *Ann. N. Y. Acad. Sci.*, **101**, 983 (1963).
9. T. Gabor, *This Journal*, **111**, 821 (1964).
10. W. Haidinger and J. C. Courvoisier, *Le Vide*, **104**, 141 (1963).
11. J. C. Courvoisier, W. Haidinger, P. J. W. Jochems, and L. J. Tummers, *Solid-State Electronics*, **6**, 265 (1963).
12. F. G. Allen, *J. Appl. Phys.*, **28**, 1510 (1957).
13. R. J. MacDonald and D. Haneman, *ibid.*, **37**, 1609, 3048 (1966).
14. N. Cabrera and D. A. Vermilyea, "Growth and Perfection of Crystals," p. 393, edited by Doremus *et al.*, John Wiley & Sons, Inc., New York (1958).
15. C. Herring, "Structure and Properties of Solid Surfaces," p. 5, edited by Gomer and Smith, University of Chicago Press (1953).
16. F. Jona, *Appl. Phys. Letters*, **6**, 205 (1965).
17. R. C. Newman and J. Wakefield, "Metallurgy of Semiconductor Materials," p. 201, Metallurgical Society Conferences, Vol. 15, edited by Schroeder, Interscience Publishers, New York (1961).
18. F. C. Frank, "Growth and Perfection of Crystals," p. 411, edited by Doremus *et al.*, John Wiley & Sons, Inc., New York (1958).
19. W. G. Pfann, *Science*, **135**, 3509, 1101 (1962).

Technical Notes

Growth of CdS from Liquid Cd Solution

Naim Hemmat and Martin Weinstein

Tyco Laboratories, Inc., Waltham, Massachusetts

Single crystals of the wide-band gap II-VI compounds (CdS, ZnS, CdTe, etc.) have been prepared from the melt and from the vapor phase. Growth from solution, although not applied previously, has many advantages in the specific case of such refractory crystals, since the temperature of growth could be significantly lower than that of the other methods. Such problems at high temperatures as contamination from the crucible and excessive constituent vapor pressures would therefore be minimized. If a proper solvent is chosen, purification may also be accomplished during growth. From a basic standpoint also, solution growth from metallic solution is less susceptible to local uncontrollable temperature fluctuations; therefore, crystals of exceptional perfection and homogeneity can be grown more easily by this technique.

For these reasons an attempt was made to show the feasibility of growing bulk CdS from Cd solution. Cadmium essentially chose itself as the solvent since (*i*) the solubility of CdS in liquid Cd is known (1), (*ii*) Cd solvent extraction has been previously shown to be effective in the purification of CdS (2), and (*iii*) the use of Cd eliminates the need for a third constituent.

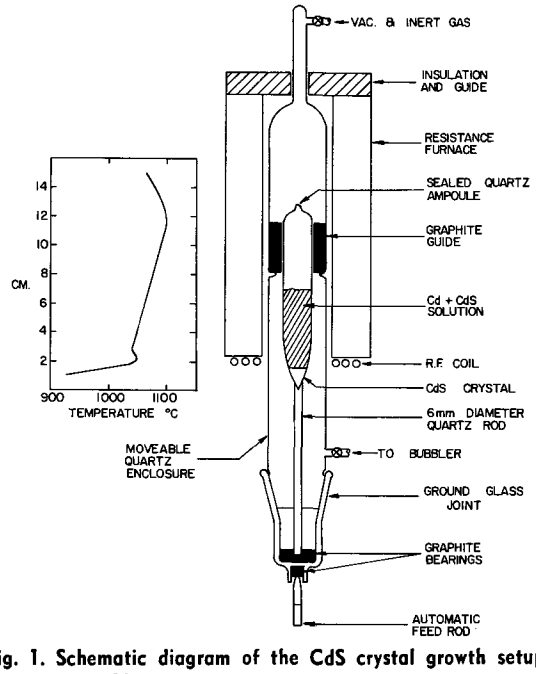

Fig. 1. Schematic diagram of the CdS crystal growth setup and temperature profile.

Procedure

Figure 1 is a schematic diagram of the crystal growth setup and its accompanying temperature profile. Approximately 21g of high-purity Cd (99.9999%) and 2.9g of high-purity sulfur (99.999%) were placed in the quartz ampoule and sealed under vacuum ($\sim 5 \times 10^{-6}$ mm Hg). The S charge was then slowly heated in contact with Cd to form CdS. Care was taken to minimize severe reaction. In this case since such a large excess of Cd was present, little trouble was encountered. The quartz ampoule was 16 mm OD, 2 mm thick, and 5 in. long. The quartz rod served to increase the radiation heat transfer at the initial point of nucleation. As can be seen from the temperature profile, the resistance furnace was controlled so that the maximum temperature (1080°C) was at the top of the ampoule. A pancake rf coil was provided to produce a peak temperature of 1050°C and a sharp thermal gradient at the liquid-solid interface. After the reaction was complete, the quartz ampoule was placed in the furnace with its pointed end at approximately 1020°C. The ampoule was then lowered through the temperature gradient at a rate of 2.5 mm

Fig. 2. Photograph of typical (2.5 cm long) polycrystalline CdS boule grown from Cd solution.

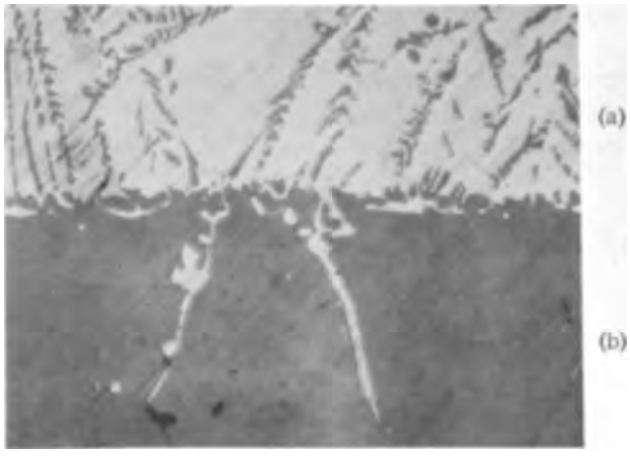

Fig. 3. Longitudinal cross section through a CdS-Cd solvent composite ingot 50 X: (a) Cd; (b) CdS boule.

per day. The growth interface was maintained at approximately 940°C.

Results

Figure 2 is a photograph of a typical 2.5 cm long polycrystalline CdS boule grown from Cd by the above technique. The 5 mm Cd zone is clearly seen on the left. In the best cases the ingots contained single grains of CdS, 4 mm^2 in cross section and 3-4 mm in length. After polishing the surface, the polycrystalline boules appeared yellowish in color and were quite transparent. No preferred growth direction was observed.

Observation of quenched ingots indicated a fairly diffuse boundary between the Cd solvent zone and the polycrystalline boule. Figure 3 is a longitudinal cross section through the CdS boule-Cd solvent composite ingot. As can be seen, a slight amount of Cd is found entrapped in the grain boundaries near the interface. Little, if any, free Cd was found in the first portion of the boule to grow. This may be due to migration of the entrapped Cd after growth took place. CdS dendrites frozen out in the Cd solution can also be seen easily. In some cases hexagonal CdS platelets (Fig. 4) were also found at the upper portion of the Cd solvent zone.

The resistivity of the polycrystalline material was approximately 10^{-1} ohm-cm. The impurity concentration was found to be similar to that of crystals grown from the constituent elements from the vapor phase (3 ppm atomic total) (3).

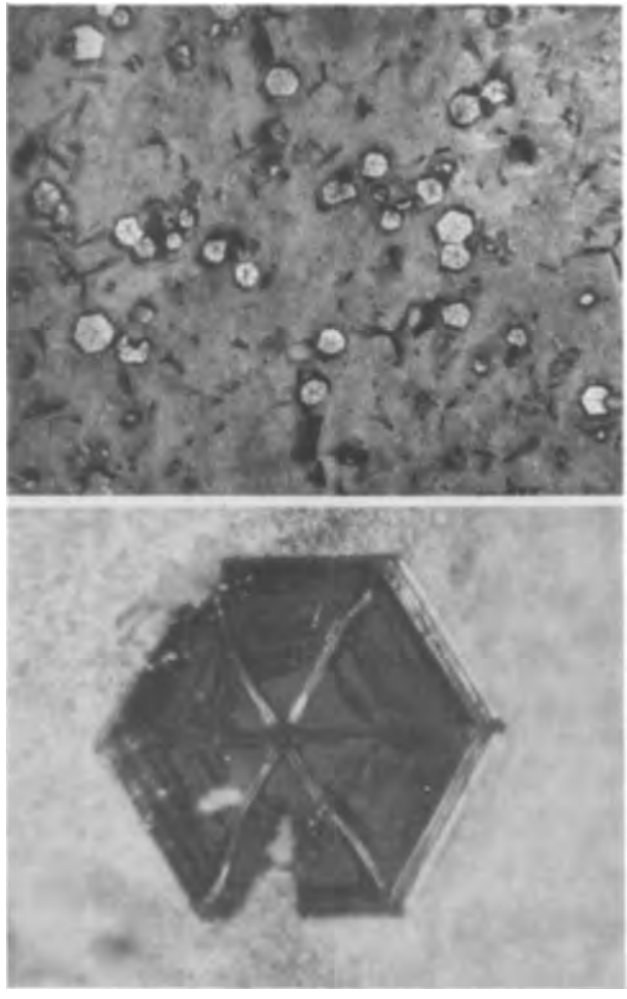

Fig. 4. Hexagonal CdS platelets, on the top surface of the Cd: (a) (top) magnification ca. 30X; (b) (bottom) ca. 260X.

It is clear from this initial attempt that it is feasible to grow crystals of CdS from Cd solution. With proper control of the thermal conditions and with proper seeding, it should be possible to grow well-defined large single crystals of CdS and the other high gap II-VI semiconductors at temperatures significantly below those used for vapor phase and melt growth.

Acknowledgments

The authors wish to acknowledge the experimental assistance of Mr. J. Faiola.

Manuscript received Dec. 5, 1966; revised manuscript received Jan. 11, 1967.

Any discussion of this paper will appear in a Discussion Section to be published in the December 1967 JOURNAL.

REFERENCES

1. H. H. Woodbury, *J. Phys. Chem. Solids*, **24**, 881 (1963).
2. M. Aven and H. H. Woodbury, *Appl. Phys. Lettrs*, **1**, 53 (1962).
3. N. Hemmat and M. Weinstein, To be published.

Anodic Oxide Growth Behavior on Silicon

J. Kraitchman[1] and J. Oroshnik[2]

Westinghouse Electric Corporation, Research and Development Center, Pittsburgh, Pennsylvania

Phosphorous doped anodic oxides grown on silicon have previously been shown to be suitable n-type dopant sources (1). During diffusion drive-in, large out-diffusion losses can occur from these oxides. These out-diffusion losses can be prevented by using a nondoped anodic oxide as a shield (2). The nondoped anodic oxide is grown on top of the original phosphorous doped oxide by reanodizing in a KNO_2-tetrahydrofurfuryl alcohol (THF) solution to about twice the original forming voltage.

We have observed similar large out-diffusion losses during drive-in from boron doped anodic oxides grown on silicon (anodization in polyhedral borane acid-tetrahydrofurfuryl alcohol solutions). These out-diffusion losses from the boron doped oxides were not prevented by the technique used with the phosphorous doped oxides. Moreover, drastically reduced doping levels in the silicon after drive-in were obtained on samples which were reanodized in the KNO_2-THF solution. Experiments, to be described below, indicated that the neutral anodic oxide was growing underneath the boron doped oxide rather than on top of it. This growth behavior appears to be responsible for its failure to prevent out-diffusion losses from the boron doped oxides.

Borane anodic oxides and neutral anodic oxides can be distinguished by their etch rates in a structure-sensitive etch such as p-etch (3).

Experimental

Two types of samples were prepared. Both types of samples were first anodized in the borane acid-THF solution. In type I only part of the borane oxide was reanodized in the nitrite-THF solution. In type II the entire borane oxide plus an unanodized portion of the silicon was reanodized in the nitrite-THF solution.

The oxide regions were etched in a diluted form of p-etch (3 parts HF, 2 parts HNO_3, and 645 parts H_2O). Oxide thickness was determined by visual comparison with known standards. The standards were calibrated by multiple-beam interference techniques. A plot of oxide thickness as a function of total etch time yielded the etch rates, permitting identification and location of the faster and slower etching oxides within the reanodized region.

[1] Present address: Pittsburgh Plate Glass Research Center, Pittsburgh, Pennsylvania.

[2] Present address: Corning Glass Works, Raleigh, North Carolina.

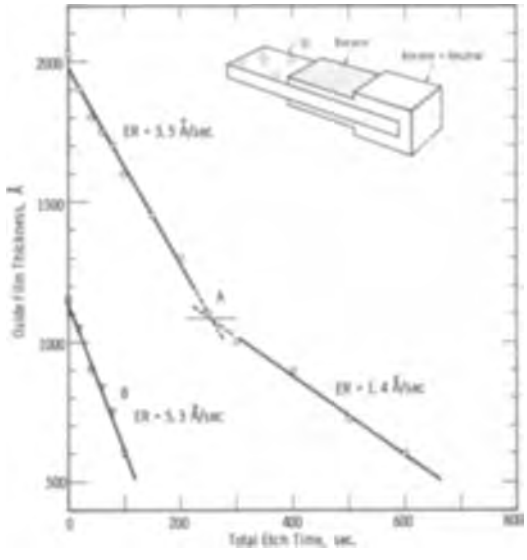

Fig. 1. Etch rate plot of a type I sample

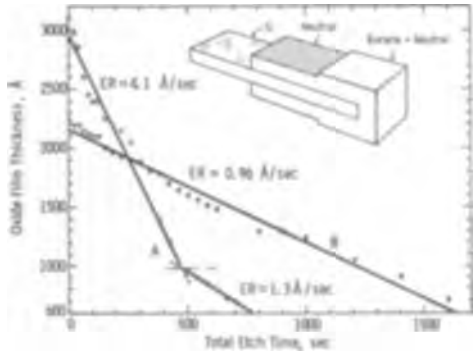

Fig. 2. Etch rate plot of a type II sample

An etch rate plot for a type I sample is shown in Fig. 1. In the reanodized region two different etch rates are readily distinguishable (see curve A). The upper layer has a rapid etch rate of 3.5 Å/sec. The lower layer has a slow etch rate of 1.4 Å/sec. Curve B is an etch rate plot of the region anodized only in the borane-THF solution, which has a rapid etch rate of 5.3 Å/sec.

Figure 2 shows the etch rate plot for a type II sample. This plot shows the same characteristics as the previous one. The upper layer of the reanodized region has a rapid etch rate of 4.1 Å/sec, while the lower layer has a slow etch rate of 1.3 Å/sec (see curve A). Curve B is a plot of the region anodized only in the nondoping solution, which has a slow etch rate of 1.0 Å/sec.

Results and Discussion

Table I is a summary of etch rates determined from rate plots for a number of samples of both types. This tabulation reveals that the etch rates of the oxide layers in the reanodized region lie between the limiting values characteristic of the rapid-etching borane anodic oxide, and the slow-etching neutral anodic oxide. The upper layer always etches somewhat slower than the free borane anodic oxides. Concurrently, the lower layer always etches somewhat faster than the free neutral anodic oxide.

Instead of the anticipated result of a slow-etching upper layer, and a rapid-etching lower layer in the reanodized region, exactly the opposite is obtained. This suggests that during the reanodization, growth

Table I. Summary of etch data on samples of both types

Sample type	Etch rate, Å/sec			
	Free* borane	Upper layer	Lower layer	Free* neutral
I	5.3 ± 0.3	3.5 ± 0.1	1.41 ± 0.06	
I	5.8 ± 0.3	5.1 ± 0.9	1.66 ± 0.07	
I	6.0 ± 0.3	5.2 ± 0.8	1.48 ± 0.07	
II		4.8 ± 0.2	1.85 ± 0.22	0.80 ± 0.02
II		4.1 ± 0.2	1.29 ± 0.04	0.96 ± 0.03

* Free, indicates an independent measurement of a single layer oxide taken simultaneously with the compound region measurements.

is not proceeding at the oxide-electrolyte interface by migration of silicon ions through the oxide. Instead, growth is proceeding at, or close to the oxide-silicon interface by migration of oxygen ions through the boron oxide.

In the boron doped oxides, the mobility of the oxygen diffusing species may be enhanced by the presence of boron. Oxygen migration in these oxides presumably occurs by diffusion of oxygen vacancies. Boron doping would be expected to increase the oxygen vacancy concentration in these oxides and thus increase the diffusion rate of oxygen vacancies.

The etch rate data also suggests that the upper layer is not "pure" borane anodic, and the lower layer is not "pure" neutral anodic oxide. While somewhat oversimplified, the following picture appears to explain the observed results. During reanodization, while oxide growth proceeds primarily by migration of oxygen (or an oxygen-bearing species) through the boron doped layer, some silicon migration also occurs. Thus, some nondoped oxide is grown within the boron doped oxide. Simultaneously, some boron doped oxide is trapped within the growing neutral layer. The result is an upper layer consisting essentially of boron doped oxide admixed with some neutral oxide, and a lower layer consisting essentially of neutral oxide containing a small amount of boron doped oxide.

In summary, etch rate measurements reveal the existence of two distinct layers. In reanodizing to a higher voltage in a nondoping solution "over" a preexistent borane anodic oxide, the nondoped oxide grows between the borane anodic oxide and the silicon. This is possibly the first known instance where anodic oxidation of silicon proceeds at, or close to the oxide-silicon interface. The upper, rapid-etching anodic oxide has been modified during reanodization so that it etches slower than a free borane oxide. The underlying, slow-etching anodic oxide etches somewhat faster than a free nondoped oxide.

Acknowledgments

The authors wish to thank N. J. Roney and W. K. Sheets for assistance in the experimental investigations and T. W. O'Keeffe, for valuable discussions.

This work was supported in part by the Air Force Avionics Laboratory, Research and Technology Division, Air Force Systems Command, Wright-Patterson Air Force Base, Ohio, under Contract Number AF 33(615)-3095.

Manuscript received Aug. 25, 1966; revised manuscript received Dec. 6, 1966.

Any discussion of this paper will appear in a Discussion Section to be published in the December 1967 JOURNAL.

REFERENCES

1. P. F. Schmidt and A. E. Owen, *This Journal*, **111**, 682 (1964).
2. P. F. Schmidt, T. W. O'Keeffe, J. Oroshnik, and A. E. Owen, *ibid.*, **112**, 800 (1965).
3. W. A. Pliskin and R. P. Gnall, *ibid.*, **111**, 872 (1964).
4. L. Young, "Anodic Oxide Films," Academic Press, New York (1961).

Recrystallization of Germanium Thin Films on Insulating Substrates by Electron Beam Zone Melting

C. T. Naber

Research Division, McDonnell Company, St. Louis, Missouri

There is a need in thin film microelectronics for single crystal semiconductor thin films of device quality. Most previous attempts at attaining single crystal thin films on insulating substrates centered on an epitaxial process in which the crystalline properties of the deposited film are strongly dependent on the crystalline properties of the substrate. Recently, techniques of recrystallization of germanium films by electron beam zone melting have demonstrated interesting possibilities for the formation of large area single crystal thin films on both metallic and insulating substrates (1-5). The most successful results in obtaining large area single crystal germanium films on insulating substrates are reported by Maserjian (3) who formed single crystal thin film regions of approximately 0.6 mm^2 on single crystal sapphire substrates. In the research described here, attempts were made to form large area single crystal thin films of germanium on both single crystal and polycrystalline substrates by electron beam zone melting.

Germanium, which was specified intrinsic by the supplier and exhibited n-type conductivity by the hot-point probe technique, was evaporated from a tungsten boat in a vacuum of about 5×10^{-6} Torr onto substrates which were heated to about 500°C. The thicknesses of the films were between 50,000 and 200,000Å. After deposition, the films were placed in an electron beam processor where an electron beam of small cross section and appropriate intensity was scanned across an area of the film in a particular manner so as to create a process of melting and recrystallization. In order to reduce the thermal strains induced during processing, the film and substrate were preheated to about 600°C. A number of substrates were investigated; only polished sapphire and polished alumina were found to be compatible with electron beam zone melting of germanium films.

In one scan pattern investigated the electron beam was oscillated laterally over the film in a triangular wave fashion with a frequency of 0.5 cps and amplitude of about 5 mm and simultaneously swept along the film at slow speeds (0.1 to 1.0 mm/min) perpendicular to the direction of oscillation. The voltage and current of the electron beam were adjusted so that the beam power was sufficient to form a small circular molten zone in the film. Beam currents of about 0.5 ma and beam voltages between 25 and 35 kv were used for most of the films. Figure 1 shows regions of germanium films on sapphire and alumina processed in this manner after etching in WAg (6) along with x-ray back reflection Laue patterns. As can be seen, long slender crystal grains appear in the processed region. The spotty character of the germanium rings in the back reflection Laue pattern indicates the presence of relatively large crystal grains of various orientations. It was found that the size of the crystal grains formed in the processed region increased with increasing temperature of the heated zone during processing. The largest crystal grains were formed when the electron beam parameters were adjusted to heat the film to a temperature just below the value at which the molten zone would break into globules. The largest crystal grains observed were about 0.2 mm wide and 5 mm long.

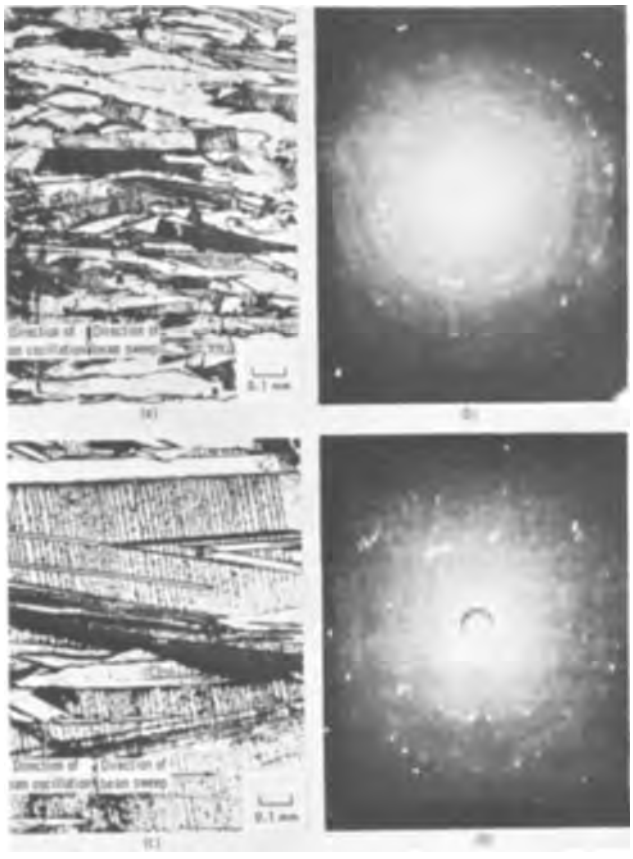

Fig. 1 (a). Photomicrograph of processed region of Ge film on polished alumina; (b) Laue back-reflection photograph of film in (a); (c) photomicrograph of processed region of Ge film on sapphire; (d) Laue back-reflection photograph of film in (c).

After deposition and prior to electron beam processing, all films exhibited p-type conductivity as determined by the hot-point probe technique. After processing, the regions that had relatively large crystal grains exhibited n-type conductivity while the regions that had relatively small grains exhibited p-type conductivity. Photomicrographs of sections of a germanium film on polished alumina after etching in WA_g with grain sizes characteristic of p-type and n-type conductivity are shown in Fig. 2(a) and 2(b). The region of the film shown in Fig. 2(a) which has smaller crystal grains than the region shown in Fig. 2(b) exhibited p-type conductivity while the region shown in Fig. 2(b) exhibited n-type conductivity. There is some question in the literature as to whether the p-type character of vacuum deposited germanium films is due to: (*i*) structural defects (7-10), (*ii*) impurities (11), or (*iii*) surface states (12, 13). Since the conductivity type of the film changed from p-type to n-type when the size of the crystal grains increased and since the regions of the film containing the larger crystal grains certainly have fewer structural defects than the regions containing smaller crystal grains, it appears that structural defects which act as acceptor centers are responsible for the p-type character of the films investigated.

Hall measurements at room temperature were made on a few processed and unprocessed films on sapphire. The Hall mobilities of the processed films ranged from as low as 50 $cm^2/(v\text{-}sec)$ with a charge carrier concentration of about 1.3×10^{17} cm^{-3} to as high as 1200 $cm^2/(v\text{-}sec)$ with a charge carrier concentration of about 6.7×10^{16} cm^{-3}. After the Hall measurements were made, the films were etched and were found to consist of a wide variety of crystal grain sizes. The largest crystal grains were observed in the film which exhibited a mobility of 1200 $cm^2/(v\text{-}sec)$.

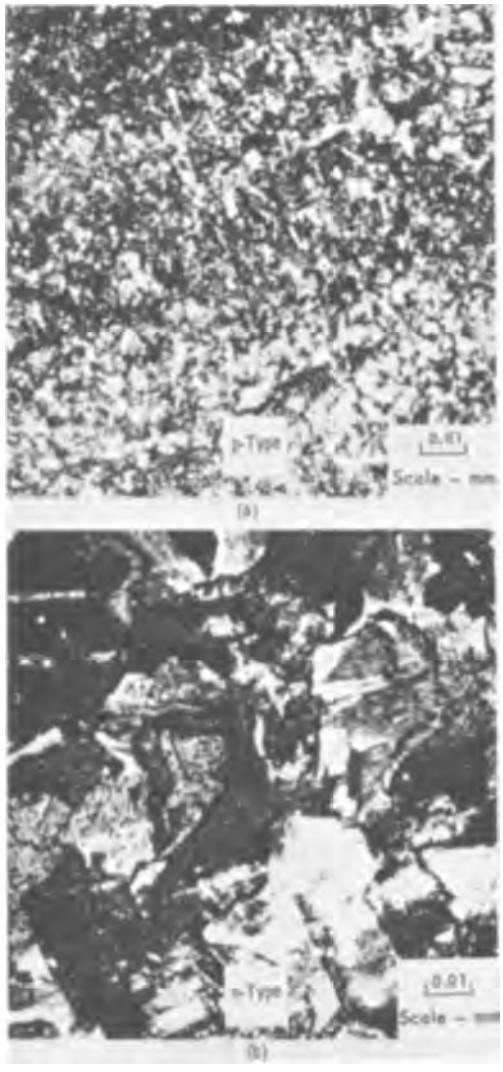

Fig. 2 (a). Photomicrograph of processed region of Ge film on alumina exhibiting p-type conductivity; (b). Photomicrograph of processed region of Ge film on alumina exhibiting n-type conductivity.

In another scan pattern, the electron beam was programmed to sweep across the film in a spiral with a frequency of rotation of about 0.5 cps. Figure 3 is a photomicrograph of a film processed in this manner

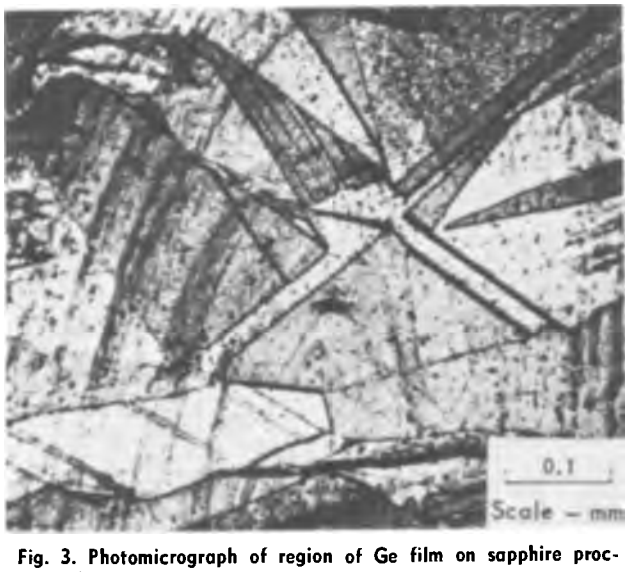

Fig. 3. Photomicrograph of region of Ge film on sapphire processed with spiral pattern.

after etching. As can be seen, relatively large crystal grains appear in the processed region.

The results of this research indicate that recrystallization can be induced in germanium films on insulating substrates by electron beam zone melting. Similar recrystallization effects were observed in germanium films deposited on both single crystal sapphire and polycrystalline alumina. This indicates the recrystallization process is independent of the crystalline properties of the substrate. The principal technological difficulty involved in the process is the maintenance of a stable molten zone through the entire thickness of the film.

Acknowledgment

The author expresses his appreciation to Dr. F. W. Leonhard who originated many of the ideas used in this research and to Mr. R. Wyatt for his technical assistance.

Manuscript received Nov. 9, 1966; revised manuscript received Jan. 11, 1967.

Any discussion of this paper will appear in a Discussion Section to be published in the December 1967 JOURNAL.

REFERENCES

1. G. B. Gilbert, T. O. Poehler, and C. F. Miller, *J. Appl. Phys.*, **32**, 1597 (1961).
2. O. A. Weinreich and G. Dermit, *ibid.*, **34**, 225 (1963).
3. J. Maserjian, *Solid-State Electronics*, **6**, 477 (1963).
4. T. O. Poehler and G. B. Gilbert, "Single Crystal Films," p. 129, The MacMillan Company, New York (1964).
5. S. Namba, *J. Appl. Phys.*, **37**, 1929 (1966).
6. R. H. Wynne and C. Goldberg, *J. Metals*, **197**, 436 (1953).
7. G. A. Kurov, S. A. Semiletov, and Z. G. Pinsker, *Soviet Physics Crystallography*, **2**, 53 (1957).
8. O. Weinreich, G. Dermit, and C. Tufts, *J. Appl. Phys.*, **32**, 1170 (1961).
9. B. W. Sloope and C. O. Tiller, "Transactions of the Tenth National Vacuum Symposium," p. 339, MacMillan Company, New York (1963).
10. J. E. Davey, *Appl. Phys. Letters*, **8**, 164 (1966).
11. E. G. Bylander, J. R. Piedmont, L. D. Shubin, and R. C. Smith, *J. Appl. Phys.*, **34**, 3407 (1963).
12. R. R. Humphris and A. Catlin, *Solid-State Electronics*, **8**, 957 (1965).
13. J. E. Davey, R. J. Tiernan, T. Pankey, and M. D. Montgomery, *ibid.*, **6**, 205 (1963).

Ohmic Contacts to GaAs by a Simple Low Temperature Alloying Process

D. K. Jadus, H. E. Reedy, and D. L. Feucht

Department of Electrical Engineering, Carnegie Institute of Technology, Pittsburgh, Pennsylvania

Standard alloying techniques allow one to make good ohmic contacts to the elemental semiconductors, but they do not work well on gallium arsenide (1-3). In this report a simple low-temperature process is described for making shallow ohmic contacts to n-, ν, or p-type gallium arsenide. The contacts are made by alloying appropriate metallic spheres into bulk GaAs at temperatures between 300° and 450°C in an ambient of argon, hydrogen, and hydrogen chloride gas. The contacts obtained in this manner have very shallow penetration depths and thus offer significant advantages for contacting thin epitaxial layers of GaAs. Similar results using metal-halide fluxes have rerently been reported (4). The results described below show that good ohmic contacts using Sn spheres can be made to n-type GaAs having a bulk resistivity in the range of 0.012 to 10^8 ohm-cm at alloying temperatures as low as 300°C with a resulting penetration depth of less than 0.1μ. Shallow ohmic contacts were also made to p-type GaAs having a bulk resistivity of 0.0065 to 0.33 ohm-cm using Zn, In + 1% Zn and Cd spheres at alloying temperatures near the melting point of the spheres.

The alloying apparatus consists of a carbon strip hot stage with a Pyrex cover and gold or nickel plating on all metal parts in contact with the gas ambient. This gas ambient consists of Ar-15% H_2 gas plus approximately 5% high-purity anhydrous HCl gas,[1] delivered by noncorrodable tubing. The small HCl component serves to clean the spheres and promote wetting. Without HCl the spheres do not wet, adhere well, or make ohmic contact to the GaAs at these low temperatures. It is observed that at a temperature below the sphere's melting point a white haze, almost certainly the metal dichloride, appears on the sphere. This haze disappears abruptly as the sphere melts, and an extremely bright surface on the sphere is observed. It is possible that this process is microscopically identical to that of Schwartz and Sarace (4) in that the metal dichloride is formed and serves as the flux; however, no observable deposit of metal halide remains after the alloying cycle is completed.

To make a contact, the clean GaAs wafer is placed on the carbon strip and one or more clean spheres are placed on the surface to be alloyed. The Pyrex cover is placed over the carbon strip assembly and sealed, and the assembly is purged by flowing about 100 alloy stage volumes of Ar-15% H_2 through the stage. The Ar-H_2 flow is reduced to 1 vol/min and 2-5% by volume of HCl is added to the gas flow. After 5 volumes of flow, the carbon strip temperature is raised quickly to the alloying temperature for 1-5 sec, and then allowed to cool. The HCl is purged, and the sample is removed.

For the alloy contacts reported here, the GaAs was lapped, moderately etched in methanol-0.5% bromine, rinsed in methanol and trichlorethylene, and stored in trichlorethylene until used. The alloy spheres were cleaned in dilute HCl, rinsed in distilled water and methanol and stored in trichlorethylene. Alloy contacts to unetched, but organic solvent cleaned epitaxial GaAs layers yield identical results.

The following characteristics of the alloy contacts were investigated: penetration depth, area wetted by the sphere for a given temperature and substrate orientation, and maximum current density or electric field strength obtainable in the GaAs without departing from an ohmic relation at the contact.

Metallurgical evidence on the penetration depth into commercial GaAs was obtained by preparing alloyed samples under conditions known to result in ohmic contacts, and either sectioning and lapping perpendicular to the direction of alloy penetration or removing the alloy dot from the surface by etching in HCl. A typical Sn contact alloyed at 400°C for 5 sec in the (111)As face of n-type GaAs, is shown sectioned and lapped to a 1μ finish in Fig. 1a. A similar Sn contact alloyed at 300°C in the same (111)As face is shown sectioned and lapped to a 1μ finish in Fig. 1b at a greater magnification. The alloy penetration depth into the sample at 400°C is 7.5μ, but no penetration is apparent for the 300°C case. Figure 2a is a view of the

[1] Precision Gas Products Inc., Linden, New Jersey.

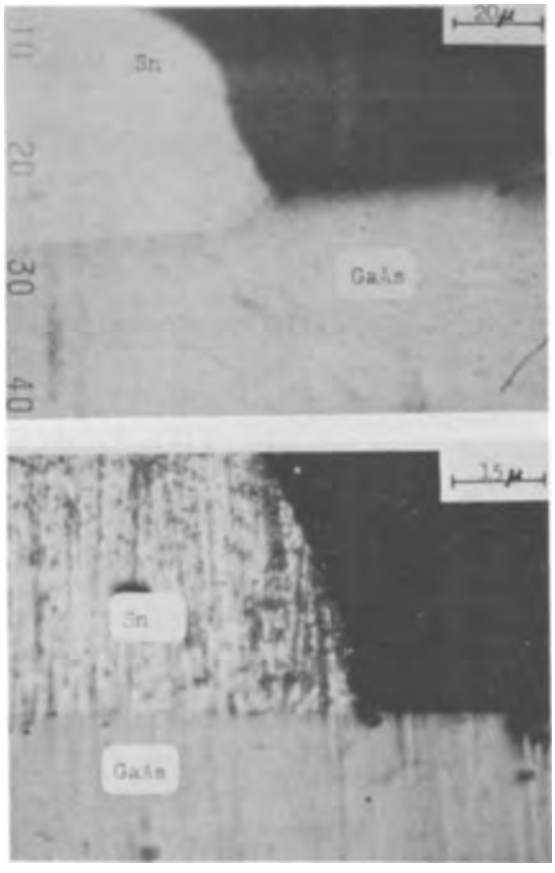

Fig. 1. Cross-section of Sn alloy on (111)As face of GaAs at: a *(top)* 400°C, b *(bottom)* 300°C.

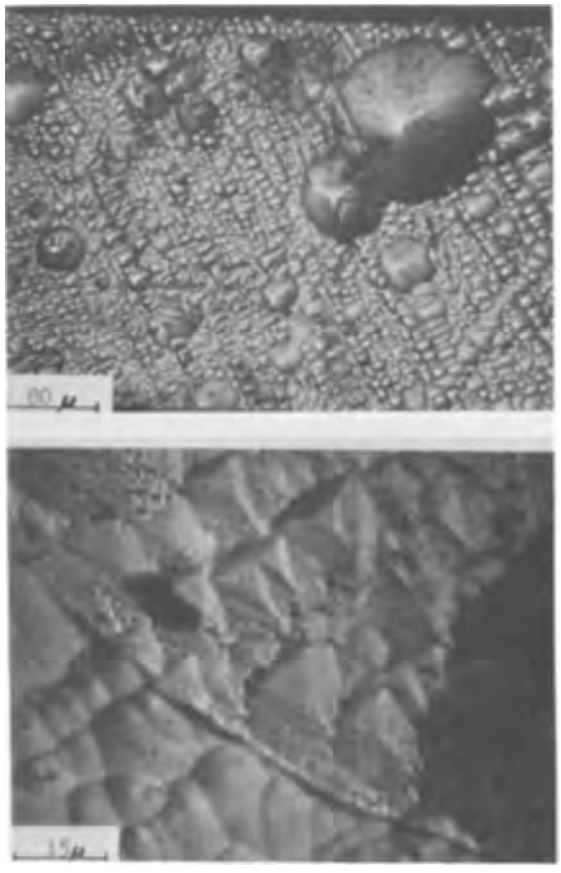

Fig. 2. Surface of (111)Ga face after alloying at 300°C and removal of the Sn dot to show wetted area: a *(top)* 200x, b *(bottom)* 1100x.

(111)Ga face of GaAs after a 300°C alloy and dot removal in acid. The outer ring is the boundary of the area wet by the 10 mil Sn sphere and is approximately 9.7 x 10^{-3} in. in diameter. A section of the region of the alloyed area is shown in greater magnification in Fig. 2b. The portion of this wafer inside the curved line was wetted by the Sn, the exterior was not. The significant observation is that this ohmic contact has not visibly altered the surface structure of the sample. Photographs of the alloyed face prepared as in Fig. 2 for the crystal orientations (111)As, (110), (100), and (111)Ga show that under identical conditions at 300°C a 10 mil Sn sphere wets an area of diameter 15.6, 10.7, 10.7, and 9.7 mils, respectively, with a deviation of less than ±0.5 mils. Holding the contact at these alloying temperatures for several minutes does not visibly increase the wetted areas.

A typical Zn contact alloyed at 430°C for 2 sec to p-type GaAs is shown sectioned and lapped to a 1μ finish in Fig. 3. No alloy penetration is evident, and furthermore there is no perceptible difference in wetted area on the (111)Ga or (111)As faces.

The electrical contact to heavily doped n GaAs was evaluated by determining the maximum current density that was achievable without departing from ohmicity. For 10 mil Sn spheres alloyed at 300°C on the (111) faces of 0.012 ohm-cm GaAs the i-v characteristics of the structure remained linear at a current density of 1.5 x 10^4 amp/cm^2. The measurements were made using 2 μsec pulses on a structure in which the current density was approximately uniform. For Sn spheres alloyed at 250°C the contacts had high resistance and were unreliable.

The electrical contact to n type GaAs in the resistivity range appropriate for Gunn effect devices is described by experiments on 100 ohm-cm GaAs. The nonlinear i-v characteristics and large temperature coefficient of resistance reported (5) and confirmed by our observations for bulk GaAs in this resistivity range necessitated a more careful study of the nature of the contacts. For this investigation the voltage measured at a contact carrying current was compared to the voltage measured at an adjacent noncurrent carrying contact as a function of voltage level. For 5 mil Sn spheres alloyed at 300°C these two voltages were directly proportional up to a field strength in excess of 2000 v/cm in the bulk material. From these measurements it is clear that the voltage drop of the current carrying contact must be quite small compared to the bulk drop. Gunn effect devices have not been made to determine if this contact shows any improvement over present contacts. Similar alloy contacts to 4 ohm-cm GaAs also appeared to be ohmic, although because of heating it was impossible to obtain a large field or high current density in the bulk material.

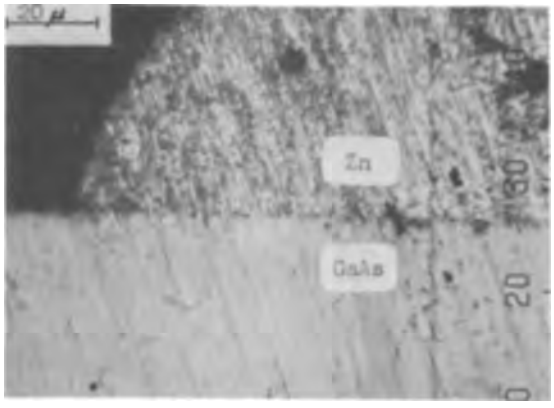

Fig. 3. Cross section of Zn alloy on (111)As face of GaAs at 430°C.

The extent to which an ohmic contact may be made to semi-insulating GaAs was tested using commercial 10^8 ohm-cm material with Sn spheres alloyed on the opposite faces at either 300° or 400°C. The i-v characteristic of such a device is linear up to 10^4 v/cm at room temperature in the dark. When illuminated strongly by a microscope lamp at room temperature the current for a particular voltage is much increased and is related to the voltage by $I = KV^2$ up to 5×10^3 v/cm indicating space charge limited flow. The contact photovoltage due to the same intensity of illumination is less than 5 mv, indicating that the contacts do not add any appreciable voltage drop.

Ohmic contacts to p-type GaAs were obtained by the same alloying technique using Zn, In + 1% Zn or Cd spheres at an appropriate temperature. In order to obtain good ohmic contacts with Zn, it was necessary to alloy the Zn spheres at approximately 430°C (10°C above the melting point) for 1 to 2 sec, in order to limit the formation of Zn_3As_2 (4). Good ohmic contacts, capable of carrying greater than 800 amp/cm^2, on 0.33 and 0.0065 ohm-cm p-type GaAs, were obtained using this technique. Ohmic contacts were also obtained on p-type GaAs by alloying In + 1% Zn spheres at approximately 160°C. Although ohmic contacts may be made to p-type GaAs using Cd spheres they must be alloyed at 400°C (considerably above their melting point) in order to obtain wetting.

GaAs alloy diodes were made using the above techniques on n- and p-type GaAs. When Sn spheres were alloyed to p-type GaAs at 500°C good diodes were obtained on 0.33 ohm-cm material similar to the results of Schwartz *et al.* (4). On 0.0065 ohm-cm p-type GaAs, however, nonlinear resistors resulted. In and In + 1% Zn spheres alloyed into 0.012 ohm-cm n-type GaAs just above their melting points yielded good GaAs diodes also. When using the Zn spheres, however, it was determined that in order to obtain an ohmic contact with Sn following the Zn alloy it was necessary to etch the sample lightly.

Acknowledgments

The research reported in this paper was sponsored in part by, but does not necessarily constitute the opinion of, the Air Force Cambridge Research Laboratories, Office of Aerospace Research under contract AF-19-(628)-5811 and by the U. S. Army Research Office—Durham under contract DA-31-124-ARO(D)-131.

The authors wish to thank IBM and RCA research laboratories for the 100 ohm-cm and 4 ohm-cm GaAs on which many of the measurements were made. The authors also are grateful to Mr. G. Ladd for helpful discussions.

Manuscript received Nov. 21, 1966; revised manuscript received Jan. 16, 1967.

Any discussion of this paper will appear in a Discussion Section to be published in the December 1967 JOURNAL.

REFERENCES

1. J. R. Dale and R. G. Turner, *Solid-State Electron.*, **6**, 388 (1963).
2. J. R. Dale and M. J. Josh, *ibid.*, **7**, 177 (1964).
3. W. A. Schmidt, *This Journal*, **113**, 860 (1966).
4. B. Schwartz and J. C. Sarace, *Solid-State Electron.*, **9**, 859 (1966).
5. S. Knight, *Proc. I.E.E.E.*, **54**, 1004 (1966).

Epitaxial Deposition of GaAs in an Argon Atmosphere

R. C. Taylor

IBM Watson Research Center, Yorktown Heights, New York

Of the several methods currently available for epitaxial deposition of GaAs, the open tube method using Ga and $AsCl_3$ in a hydrogen atmosphere has given material with the best electrical properties to date for applications such as Gunn effect devices (1). In the present investigation, argon was substituted for hydrogen as the carrier gas. There are several potential advantages suggesting the use of argon for the purpose of obtaining better and more reproducible films. Among these are: substitution of an inert species for a reactive one to eliminate at least one reaction from the system, substitution of a heavier carrier gas to minimize the density differential between the carrier and the reacting species and decrease any compositional gradient existing in the gas phase, and elimination of the hydrogen reduction of quartz as a source of silicon contamination to give a purer GaAs deposit.

Experimental

The apparatus and procedures used were similar to those employed by other investigators of the Ga-$AsCl_3$ system (2, 3) the principal difference being the use of argon throughout in place of hydrogen. The main part of the apparatus was a 30 mm ID quartz reactor tube into which was inserted a 25 mm ID quartz liner to facilitate loading and cleaning. The reactor tube extended through a high-temperature (source) zone in which the temperature was uniform to within 1°C for 3 to 4 in., and a downstream low-temperature substrate (deposition) zone in which the temperature gradient was 10°C/in. Pure argon was metered into the reactor through two stainless steel and quartz lines, one line going directly into the reactor and the other through a quartz bubbler containing $AsCl_3$ where saturation of the gas stream took place. Exhaust gases passed out of the reactor at the downstream end through a quartz end cap into an oil bubbler. Source and substrate holders were of quartz, the substrate holders being platforms attached to thermocouple tubes which could be positioned through a Teflon seal in the exhaust cap.

The Ga source temperature was maintained at either 800° or 850°C for the argon runs and at 850°C for comparative hydrogen runs. GaAs substrate temperatures varied with the $AsCl_3$ flow rate but were normally 650°-700°C during argon runs and 700°-750°C during hydrogen runs. The $AsCl_3$ bubbler was at 25°C. Temperatures were controlled to within 1°C during a run. The flow of argon through the $AsCl_3$ was varied over a range which resulted in a flow of 3×10^{-4} to 3×10^{-3} moles/hr of $AsCl_3$. All materials employed in the runs were of a minimum purity of 99.999% and were used without further purification.

After polishing the GaAs substrates (Czochralski crystals, Cr doped), the Ga source and the substrates were weighed and loaded into the reactor which was then flushed with argon at a high flow rate. After flushing, both source and substrates were raised to the source temperature and the substrates were vapor-etched in a high Ar/$AsCl_3$ flow. The flow rate was then lowered to a normal deposition rate and the substrates lowered to deposition temperature. Deposition usually proceeded overnight after which the $AsCl_3$ flow was terminated, the temperatures were measured, and the furnaces shut off. The films were removed at a low temperature. Under the proper conditions, mirror smooth films with thicknesses ranging from 1 to 15 mils were grown with crystallographic quality equal to those grown in hydrogen.

Table I. Effect of substrate temperature on growth rate.

Carrier gas	$AsCl_3$ flow, moles/hr	Substrate orientation	Max. growth rate temp, °C	Max. growth rate, μ/hr	Temp range for epitaxy, °C
Ar	3×10^{-4}	10° off 111A	650	20	540-680
Ar	1.5×10^{-3}	5° off 111B	700	35	580-730
H_2	1.5×10^{-3}	5° off 111B	750	25	640-780

Chemical analysis of the byproduct condensate was performed by dissolving the material in an aqueous 5% sodium hydroxide solution and titrating for Ga with EDTA and for Cl with AgSCN.

Results and Discussion

Effect of substrate orientation and temperature on growth rate.—Substrates with nine different orientations were studied in argon. The growth rate decreased in the order: 10° off 111A, 7 °off 110, 110, 100, 10° off 111B, 5° off 111A, 5° off 111B, 111A, and 111B. Under flow conditions of 3×10^{-4} moles/hr of $AsCl_3$ in 25 cc/min of argon the growth rate at a substrate temperature of 650°C varied from 20 μ/hr on 10° off 111A to 4 μ/hr on 111B. Since the ratio of arsenic in the vapor to the amount of Ga being formed by GaCl disproportionation is 1 : 1, one can expect the growth rate to be fastest on stoichiometric surfaces. This is found to be true with the basic planes of *110*, *100*, and 111. When the orientation is a few degrees off of a basic plane, the high-index plane that results has a surface composed of a large number of small steps. The stepped structure consists of "treads" and "risers" which are made up of the basic planes (4). Deposition on such a surface should be energetically favored with the result that a plane a few degrees off of a basic plane would have a higher growth rate than the basic plane. This is also seen to be true.

Several runs were made to establish the dependence of growth rate on substrate temperature. The results of two argon runs and a comparative hydrogen run are shown in Table I. The source temperature was 850°C. Above the high-temperature limit for epitaxial deposition etching took place, while below the low-temperature limit the film was polycrystalline. In all cases epitaxial growth occurred over about a 150°C temperature range with the temperature of maximum growth rate about 30°C below the high-temperature limit for epitaxy. Increasing the $AsCl_3$ flow rate increased both the growth rate and the temperature for maximum growth rate, and under identical conditions growth in the hydrogen system took place 50°C higher than in argon. Growth rate fell off very rapidly at temperatures above the maximum growth rate temperature due to less supersaturation of the gas phase and possibly some substrate etching or vaporization. It fell off at lower temperatures, but much more slowly, due to a reduced reaction rate of Ga (or GaCl) and As at the substrate surface. The temperature of maximum growth rate was independent of source temperature over the range studied and independent of substrate orientation.

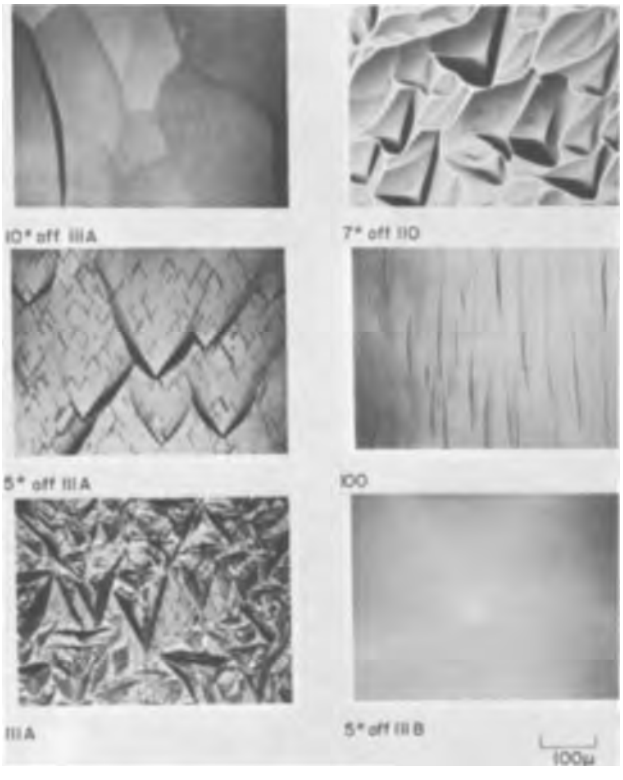

Fig. 1. Effect of substrate orientation on film surface morphology

Effect of substrate orientation and temperature on film surface.—The effect of substrate orientation on the appearance of the deposit was studied for all nine of the aforementioned orientations in the argon system. Films were grown at the maximum growth rate temperature of 650°C at a flow rate of 3×10^{-4} moles/hr of $AsCl_3$. Several of the argon system, as-grown, surfaces are shown in Fig. 1. It can be seen that the pits and stacking faults which are abundant in films deposited on substrates oriented on 111A or 5° off 111A, are not observed in a film deposited on a 10° off 111A substrate. Similar observations were made by Gabor (5) on GaAs films grown on germanium and his explanation of the observations with regard to independent nucleation on two sides of a stacking fault followed by film propagation may apply equally well here. Growth on substrates oriented 5° off 111B resulted in mirror-smooth films which were far superior to those on all other orientations. It is believed that the etching effect of the $AsCl_3$ vapor is the main factor in determining film surface morphology. One would therefore expect some differences in the films grown in hydrogen since in that case the etchant is HCl produced by hydrogen reduction of the $AsCl_3$ (3).

A study was made in the argon system of the effect of substrate temperature on film surface morphology with films of equal thickness on substrates oriented 10° off 111A, grown with an $AsCl_3$ flow of 3×10^{-4} moles/hr. Growth occurred on the substrates over the temperature range of 540°-680°C. At 540°C a grainy, polycrystalline film resulted which converted at a slightly higher temperature to an epitaxial film with severe pitting. As temperature increased, the pits (conical in shape as in Fig. 1, 5° off 111A) diminished in number and increased in size, finally becoming shallow depressions in a fairly smooth film at about 640°C (see Fig. 1, 10° off 111A). At 680°C continuous growth no longer occurred, only occasional epitaxial islands being present. In a similar study made on substrates that were oriented 5° off 111B no pitting occurred, all films being relatively smooth, with mirror like surfaces at the higher temperatures. Apparently the reason for this is that the $AsCl_3$ vapor used in the vapor etch preferentially pits the 111A surface but polishes the 111B. Thus the surface morphology of the film is determined primarily by substrate vapor etching, and the degree of conformity to the substrate surface is determined by the surface mobility of the depositing atoms as a function of substrate temperature.

Transport reactions of the system.—In both the argon and the hydrogen systems, the ratio of the amount of gallium transported from the source to the amount

Table II. Proposed intermediate reactions.

Reaction	Hydrogen	Argon
$AsCl_3$ reduction	$2AsCl_3 + 3H_2 \rightarrow 6HCl + \frac{1}{2}As_4$	
Ga transport	$6HCl + 5Ga \rightarrow GaCl_2 + 4GaCl + 3H_2$	$5Ga + 2AsCl_3 \rightarrow GaCl_2 + 4GaCl + \frac{1}{2}As_4$
Dichloride red.	$GaCl_2 + \frac{1}{2}H_2 \rightarrow GaCl + HCl$	
Disproportionation	$5GaCl \rightarrow 2\frac{1}{2}GaCl_2 + 2\frac{1}{2}Ga$	$4GaCl \rightarrow 2GaCl_2 + 2Ga$
Deposition	$2\frac{1}{2}Ga + \frac{1}{2}As_4 \rightarrow 2GaAs + \frac{1}{2}Ga$	$2Ga + \frac{1}{2}As_4 \rightarrow 2GaAs$

Table III. Electrical properties of GaAs films.

Carrier gas	Resistivity, ohm-cm		Mobility, cm^2/v-sec		Carrier conc, $1/cm^3$	
	298°K	77°K	298°K	77°K	298°K	77°K
H_2	1.6	0.5	6700	32000	6×10^{14}	4×10^{14}
Ar	1.3	0.8	5200	12000	1×10^{15}	6×10^{14}

of $AsCl_3$ introduced into the system was found to be approximately 5/2. To arrive at equations for the over-all reactions, analysis of the byproducts was carried out.

Hydrogen system.—In runs where flow conditions were such that no deposition of GaAs took place, the entire amount of Ga transported from the source was recovered at the exhaust end of the reactor as metallic Ga and as a gallium chloride; 50% was recovered as metallic Ga and 50% as a white chloride. The chloride was identified as the dichloride, $GaCl_2$, rather than the trichloride claimed by other investigators of this system (2, 3). Identification was made from the analytically determined Ga/Cl ratio of 1/2, and by the approximate melting point. The chloride was found to condense as a solid in the temperature range of 150°-200°C. The melting point of the trichloride is 77°C and of the dichloride, 170°C (6). When flow conditions were such that epitaxial deposition of GaAs took place, 50% of the Ga from the source was still recovered as the dichloride, but the amount of metallic Ga byproduct was reduced proportionately to the amount of GaAs deposited. The over-all reaction in the hydrogen system may therefore be expressed as

$$5Ga + 2AsCl_3 + \tfrac{1}{2}H_2 \rightarrow 2\tfrac{1}{2}GaCl_2 + 2\tfrac{1}{2}Ga + HCl + \tfrac{1}{2}As_4 \quad [1]$$

with the gallium and arsenic products that appear in elemental form decreasing as GaAs is formed. It can be seen that there will always be some excess Ga as a byproduct.

Argon system.—In the argon runs there was never any metallic Ga as a byproduct. It always appeared as GaAs. Under all flow conditions, 60% of the Ga removed from the source was recovered as a $GaCl_2$ byproduct. The over-all reaction may be expressed as

$$5Ga + 2AsCl_3 \rightarrow 3GaCl_2 + 2GaAs \quad [2]$$

The amount of GaAs appearing as an epitaxial deposit and the amount appearing as a polycrystalline byproduct was determined by temperature and flow conditions.

Although there is not enough data to establish conclusively the intermediate reactions occurring in the system, nor to preclude the formation of $GaCl_3$ (which could recombine with Ga at a low temperature to form $GaCl_2$), the intermediate reactions leading to the above over-all reactions may be proposed tentatively on the basis of the observations made. They are shown in Table II based on $GaCl_2$ and GaCl as the dominant gallium chloride species. The As_4 vapor initially produced is dissolved by the Ga until saturation occurs. In both systems, the rate of formation and transport of gallium chlorides is constant throughout the runs, both during and after saturation of the Ga with As_4. There might also be additional hydrogen reduction of GaCl at a higher temperature than where disproportionation occurs, accounting for the fact that under equal conditions deposition in the hydrogen system occurs 50°C higher than in the argon system.

Electrical properties.—Electrical properties were measured on the films grown in both the argon and the hydrogen systems. The results are shown in Table III for a 3 mil thick film grown in argon at 700°C and a 5 mil thick film grown in hydrogen at 750°C. Both were grown on semi-insulating GaAs substrates oriented 5° off 111B. The hydrogen system film was grown at a higher $AsCl_3$ flow rate than the argon system film. Considering the differences in growth conditions and the lack of additional purification procedures, the results are comparable. It seems probable that with the higher purity potentially obtainable in the argon system due to lower growth temperature and reduced silicon contamination, the electrical quality of films grown in argon can eventually surpass that of films grown in hydrogen.

Acknowledgment

The author acknowledges the assistance of W. Haag for growing the epitaxial films, Dr. S. Blum for supplying Czochralski crystals, and Dr. J. Woods and Dr. W. Reuter for electrical measurements and chemical analyses.

Manuscript received Dec. 1, 1966.

Any discussion of this paper will appear in a Discussion Section to be published in the December 1967 JOURNAL.

REFERENCES

1. J. Whitaker and D. E. Bolger, *Solid State Communications*, **4**, 181 (1966).
2. W. F. Finch and E. W. Mehal, *This Journal*, **111**, 814 (1964).
3. D. Effer, *ibid.*, **112**, 1021 (1965).
4. R. C. Sangster, "Compound Semiconductors," Vol. 1, Reinhold Publishing Corp., New York (1962).
5. T. Gabor, *This Journal*, **111**, 817 (1964).
6. A. W. Laubengayer and F. B. Schirmer, *J. Am. Chem. Soc.*, **62**, 1578 (1940).

Brief Communications

Determination of Microscopic Rates of Growth in Single Crystals

August F. Witt and Harry C. Gatos

Department of Metallurgy and Center for Materials Science and Engineering, Massachusetts Institute of Technology, Cambridge, Massachusetts

In our studies (1) as in those of others (2) it has become apparent that the various impurity heterogeneities in the form of periodic or random striations or in the form of an impurity "core" in single crystals pulled from the melt are intimately associated with the microscopic rate of growth. No method has been available for the direct determination of the microscopic rates of growth as a function of time and location in the solid-melt interface. The present communication reports on the development of such a method.

We have introduced in the melt high frequency (of the order of 50 Hz) and low amplitude vibrations without altering the growth characteristics of the crystal. Such vibrations are reflected in the crystal in the form of very sharp impurity striations superimposed on the regularly appearing impurity or other heterogeneities. From the known frequency of the vibrations and the separation of the resulting striations one can readily determine the microscopic rates of growth. Appropriately prepared cross sections of the single crystals (or polycrystals) allow the analysis of the growth process in the various parts of the interface as a function of time. By employing suitable etching techniques and interference contrast or dark field microscopy, striations 0.2μ apart can be distinguished. This distance represents the limit of light microscopy resolution. The distance between two striations under the growth conditions of the crystal depicted in Fig. 1 corresponds to growth which has taken place in 1/20 sec. Higher frequencies (of the order of 100 Hz) have been successfully employed. There appears to be no reason for setting an upper limit to the useful frequency range. It is believed that the increased resolution of electron microscopy will lead to a significant decrease in the observable growth time intervals.

We have developed this method employing InSb and pulling from the melt by a Czochralski-type technique. Small amounts of tellurium (of the order of parts per million) were introduced in the melt as the detecting impurity. The high-frequency vibrations were introduced by coupling (contacting) a vibrating rod to the crucible containing the melt. A signal generator and an audio amplifier were used as the source of the known frequencies. Vibrations can also be introduced electrically, eddy currents. Crystals were pulled with and without rotation. By introducing and then discontinuing repeatedly the high frequency vibrations during the growth of a large number of crystals it was shown that the vibrations do not interfere with the growth characteristics under study.

Two typical instances of the use of the high frequency vibrations are shown in Fig. 1 and 2. It is seen in Fig. 1 that the separation of the striations due to the constant frequency of vibrations reaches a maximum between two successive rotational striations in the "off core" region. The separation then decreases, and near the rotational striation no vibrational striations are visible. Obviously, the rotational striations are associated with a very slow microscopic rate of growth and in fact with remelting. It is also apparent from Fig. 1 (immediately before and after each rotational striation) that the microscopic rate of growth is smaller in the "core" region than in the "off core" region. The curved lines on the figure reflect interference of the introduced vibrations with random vibrations present in the experimental arrangement.

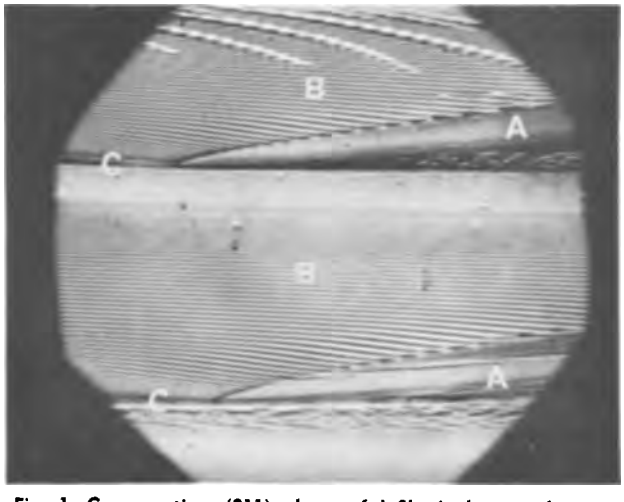

Fig. 1. Cross section, (211) plane, of InSb single crystal grown in the <111> direction. A, "core" region of crystal (see for details Witt and Gatos, *This Journal, 113*, 808 (1966); B, "off core" region of crystal; C, rototional striations (remelt lines). Growth direction is perpendicular to the "core" A. Striations due to the high frequency vibration (20 Hz) are clearly shown. Magnification ca. 600X.

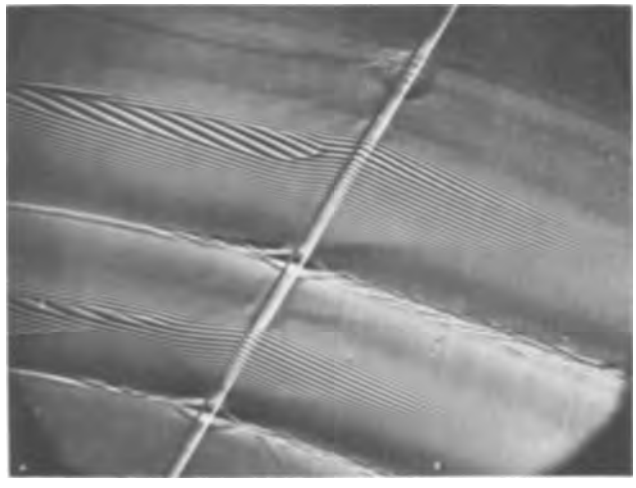

Fig. 2. Cross section, (211) plane, of InSb crystal grown in the <111> direction (orientation as in Fig. 1). Twin boundaries are clearly visible. Magnification ca. 600X.

Figure 2 depicts the presence of a twin in the grown crystal. It should be noted that striking differences in the rate of growth can be seen on either side of the twin boundary and for quite some distance away. No quantitative analysis will be presented here. Although not shown in the figure it is of interest to point out that before the twin appears there is a disturbance in the microscopic rate of growth.

We believe that the present method can serve as a unique tool in observing variations in growth conditions at the solid-melt interface. It can further provide quantitative information regarding the incorporation, distribution of impurities during crystal growth and the formation of crystal defects, orientation effects, and other aspects of the solidification process in general.

Acknowledgment

This work was supported by the Atomic Energy Commission under Contract AT (30-1)-3208.

Manuscript received Dec. 29, 1966.

Any discussion of this paper will appear in a Discussion Section to be published in the December 1967 JOURNAL.

REFERENCES

1. H. C. Gatos, A. J. Strauss, M. C. Lavine, and T. C. Harman, *J. Appl. Phys.*, **32**, 2057 (1961); K. Morizane, A. F. Witt, and H. C. Gatos, *This Journal*, **113**, 51 (1966); A. F. Witt and H. C. Gatos, *ibid.*, **113**, 808 (1966).
2. See for instance K. F. Hulme and J. B. Mullin, *Solid State Electronics*, **5**, 211 (1962).

Observation of Etching of n-Type Silicon in Aqueous HF Solutions

S. M. Hu and D. R. Kerr

IBM Components Division, East Fishkill Facility, Hopewell Junction, New York

This note reports the observation of the etching in silicon in aqueous solutions of hydrofluoric acid. Measurements were made on n-type, 2 ohm-cm wafers of <111> orientation with HCl vapor-etched surfaces. After masking a portion of the surface with wax, wafers were placed in HF solutions at 25°C for periods on the order of 15 hr. In this time sharp steps were obtained which were measurable by Tolansky interferometry to an accuracy of ±50Å after evaporation of aluminum to increase reflectivity. For concentrated (48%) HF a rate of 0.3 Å/min was observed. To be assured that this etching action was not caused by the presence of dissolved molecular oxygen in aqueous HF solution, anti-oxidant hydroquinone was added to the solution. Again, the etching was observed. The independence of the etching process on dissolved oxygen was also shown by the fact that continuous bubbling of oxygen through dilute HF did not change the etch rate. It was further found that concentrated (48%) HF solution etched silicon at a lower rate than dilute HF solution. We then concluded that the etching action is most probably caused by the oxidation of silicon by the hydroxyl ions in the aqueous solution.

It is obvious, from the extreme disparity between the etch rates of SiO_2 and silicon, that the oxidation of the silicon must be the rate-controlling step in the silicon etching with SiO_2 being removed as fast as it is formed. One then expects that the silicon etching rate should be a function of the OH^- ion concentration, provided there are no other oxidants present in the solution. A number of solutions were prepared without any other oxidants except the variation of OH^- concentration by means of dilution by pure water as well as by adding hydrochloric acid, sodium fluoride, and sodium acetate. The solution compositions, the calculated OH^- ion concentrations, and the observed etch rates are given below:

Composition of solution	[OH-], moles/l	Etch rate, Å/min
H_2O 96 cc + HF (48%) 4.5 cc + HCl (40%) 8 cc	10^{-14}	0.29
HF (48%)	10^{-13}	0.30
H_2O 40 cc + HF (48%) 10 cc	2×10^{-13}	0.47
H_2O 40 cc + HF (48%) 10 cc + $NaC_2H_3O_2$ 3g	3×10^{-12}	0.59
H_2O 96 cc + HF (48%) 2.0 cc + NaF 4.3g	3.5×10^{-11}	0.78

Results are plotted in Fig. 1. As seen from the results, the dissolution rate of the silicon is far from directly proportional to the OH^- ion concentration in the aqueous solutions. It appears that the reaction between OH^- ions in the solutions and the silicon proceeds via an intermediate step of adsorption, which occurs very fast. The rate-controlling step is then the reaction between the adsorbed OH^- and the silicon surface. Let us assume that this reaction rate is proportional to the surface concentration of adsorbed [OH^-]. If the adsorption followed a Langmuir isotherm, one would expect $r = dc/(1 + gC)$ where r is the etch rate, C is the [OH^-] concentration in the solution, and d and g are constants. As seen in Fig. 1 such a function does not fit the data. Over a certain range of [OH^-] concentration, however, adsorption could follow a Temkin isotherm (1). This would give $r = a + b \log C$, which follows the data more closely.

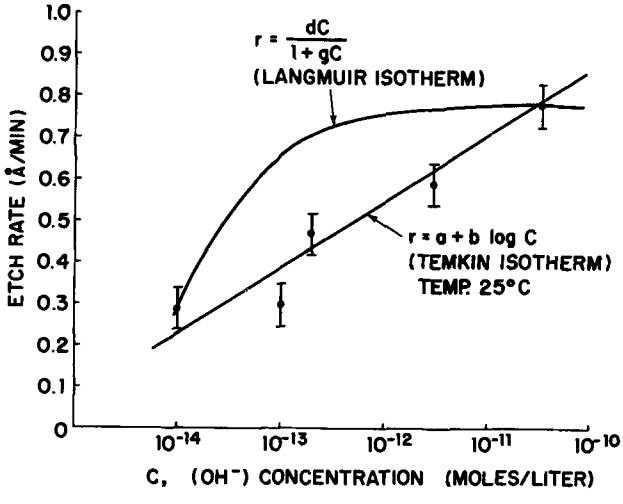

Fig. 1. Silicon etch rate vs. OH^- ion concentration in HF solutions.

Acknowledgment

The authors wish to thank Mr. J. Petrak for assistance in the experimental work.

Manuscript received Nov. 28, 1966; revised manuscript received Dec. 28, 1966.

Any discussion of this paper will appear in a Discussion Section to be published in the December 1967 JOURNAL.

REFERENCE

1. M. I. Temkin, *Z. Fiz. Khim.*, **15**, 296 (1941); Also see B. E. Conway, "Electrode Processes," pp. 81-85, Ronald Press, New York (1965).

ELECTROCHEMICAL SCIENCE

The Alkaline Manganese Dioxide Electrode

I. The Discharge Process

David Boden, C. J. Venuto, D. Wisler, and R. B. Wylie

The Electric Storage Battery Company, Carl F. Norberg Research Center, Yardley, Pennsylvania

ABSTRACT

The cathodic reduction of γ-MnO_2 in alkaline electrolyte has been studied by examination of constant current discharge curves, by x-ray diffraction and by chemical analysis. The reaction has been shown to take place by a three-step process whereby an amorphous intermediate is formed by assimilation of protons in the γ-MnO_2 lattice. As reduction proceeds the intermediate crystallizes to give Mn_3O_4 and finally $Mn(OH)_2$ depending on the electrode potential. The rapid increase in electrode resistance at approximately half of the capacity has been related to the formation of interfacial films of Mn_3O_4.

The cathodic reduction of γ-MnO_2 in alkaline electrolyte has been the subject of considerable investigation (1-6).

Cahoon and Korver (2) on the basis of x-ray crystallographic and chemical analyses concluded that the reaction proceeded by three steps. First, the manganese dioxide is reduced simultaneously to Mn_4O_7 and $Mn(OH)_2$. The second step is the reduction of Mn_4O_7 to Mn_3O_4 and $Mn(OH)_2$, and the final step is the reduction of Mn_3O_4 to $Mn(OH)_2$.

The existence of Mn_4O_7 and $Mn(OH)_2$ at the start of discharge was questioned by Bell and Huber (4) who, based on x-ray diffraction analysis, found no evidence of these compounds. It was postulated that this was perhaps attributable to the different current densities employed in the two studies. They concluded that the reaction proceeded by the homogeneous reduction of γ-MnO_2 to $MnO_{1.7}$ followed by the heterogeneous phase reduction of $MnO_{1.7}$ to $MnO_{1.47}$ and finally the heterogeneous reduction of $MnO_{1.47}$ to $Mn(OH)_2$. In this study $MnO_{1.7}$ was identified as MnO(OH) and $MnO_{1.47}$ as γ-Mn_2O_3.

It was pointed out by Kozawa and Yeager (5) that both of these studies were conducted with standard alkaline MnO_2 cells containing zinc electrodes which could possibly lead to complications in interpreting the results. In addition to this, the electrodes were subjected to a rigorous washing and drying procedure before analysis which may have caused changes in their chemical composition. Kozawa and Yeager concluded that the reaction proceeded by two steps, the first being the reduction of MnO_2 to MnO(OH) and the second the reduction of MnO(OH) to $Mn(OH)_2$.

The clear differences in the above results suggest that further work should be done to clarify the course of the discharge reaction. In the present work the cathodic reduction of γ-MnO_2 in alkaline electrolyte is interpreted on the basis of discharge curves, chemical and x-ray diffraction analysis.

Experimental

The electrodes were prepared by compacting 1g of a mixture containing 87.5% electrolytic MnO_2 and 12.5% micronized graphite around a platinum wire at 5279 kg · cm^{-2}. The electrodes were cylindrical in shape having the dimensions 0.635 cm in diameter by 0.635 cm in height. Available oxygen analyses conducted by the arsenous acid method (7) indicated that the sample of MnO_2 used had an empirical formula of $MnO_{1.92}$ giving the electrodes a nominal capacity of 0.45 amp hr based on the following discharge reaction

$$MnO_{1.92} + 1.92H_2O + 1.84e = Mn(OH)_2 + 1.84\,OH^- \quad [1]$$

The electrodes were discharged at 5 ma · cm^{-2} in 7M KOH solution at 25°C. The cell used is shown in Fig. 1. The potential of the electrodes was measured against an Hg/HgO reference electrode and converted to the hydrogen scale for plotting. Resistive polarization between the Luggin capillary tip and the electrode was measured throughout the discharge by an interruptor technique employing a Tektronix Model 535 oscilloscope. The current was interrupted for a period of 10 ms and then initiated by use of a switch. The potential transients (break and make) were recorded on the screen of the oscilloscope and photographed with a Polaroid camera. The IR drop was determined from the break in the initial part of the transient. The

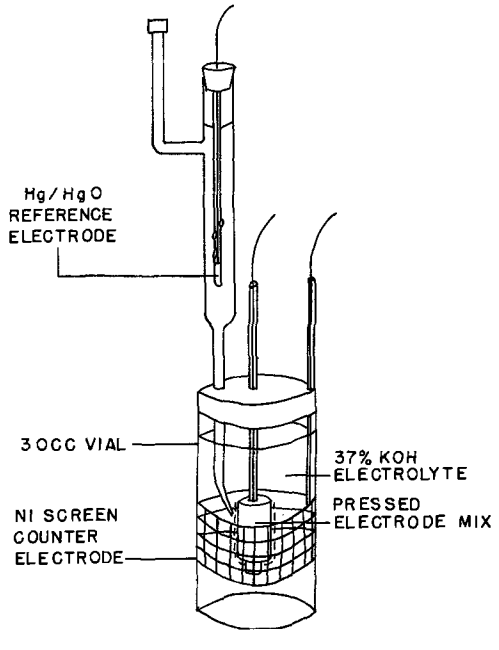

Fig. 1. Cell for discharge of MnO_2 electrodes. Hg/HgO reference electrode; 30 cc vial; 37% KOH electrolyte; pressed electrode mix; Ni screen counter electrode.

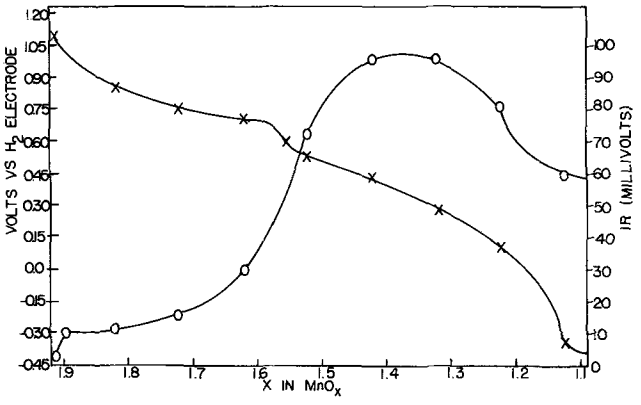

Fig. 2. Discharge curve of a manganese dioxide electrode in 7M KOH; C.D., 5 ma·cm^{-2}.

amount of oxygen diffusing to the cathode from the nickel counter electrode during discharge was neglected (5). Discharge curves recorded in this way were very reproducible, a typical curve with its corresponding IR transient being shown in Fig. 2. Two well-defined steps of approximately equal capacity are observed in the discharge curve, the first corresponding to the change $MnO_{1.92}$-$MnO_{1.52}$ and the second to the change $MnO_{1.52}$-$MnO_{1.21}$. The IR transient shows a gradual increase up to the end of the first step in the discharge curve at which point a rapid increase to a maximum is observed after which the resistance decreases to a final steady reading about six times greater than the initial value.

X-Ray Diffraction and Chemical Analyses

Electrodes prepared as described above were placed on discharge at a current of 12.5 ma (5 ma · cm^{-2}). At 0.1 increments of the nominal capacity, representative electrodes were removed from the circuit, crushed, covered with a thin film of Durco cement to prevent atmospheric oxidation, and submitted to x-ray diffraction and available oxygen analysis. No washing or drying procedures were carried out to prevent possible changes in the chemical composition due to atmospheric oxidation. The available oxygen value was compared to the theoretical value calculated from the assumption that 2**F** of electricity are required to reduce 1 mole of γ-MnO_2. Thus the coulombic efficiency of the reaction was determined together with the true empirical formula of the reduced oxide. The results of the available oxygen analyses are shown in Table I.

X-ray patterns obtained from electrodes discharged to various depths are shown in Fig. 3, and corresponding d-values calculated from the patterns are shown in Table II.

Table I. Results of chemical analysis of discharged γ-MnO_2 electrodes

Discharge to	Theoretical MnO_2, %	Actual MnO_2, %	Calculated x in MnO_x	Experimental x in MnO_x	Coulombic efficiency, mean
0.90C	68.33	67.23 67.22	1.83	1.82	113.17
0.80C	60.73	60.35 59.57	1.74	1.73	114.99
0.70C	53.14	52.36 51.75	1.64	1.63	98.67
0.60C	45.55	46.04 45.15	1.55	1.55	101.02
0.50C	37.96	38.96 39.05	1.46	1.47	97.83
0.40C	30.37	28.47 28.00	1.37	1.34	96.09
0.30C	22.78	23.81 24.63	1.28	1.29	93.50
0.20C	15.19	16.42 16.95	1.18	1.20	97.74
0.10C	7.60	15.09 15.32	1.09	1.18	89.19
0.00	0.00	13.81 13.98	1.00	1.16	81.65

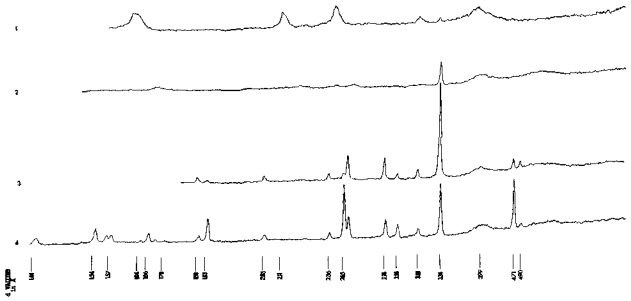

Fig. 3. X-ray diffraction patterns of γ-MnO_2: 1, starting material; 2, discharged to $MnO_{1.72}$; 3, discharged to $MnO_{1.52}$; 4, discharged to $MnO_{1.22}$.

Examination of the x-ray analyses reveals that the initial starting material is composed of γ-MnO_2 together with a small amount of β-MnO_2 and quartz as an impurity. In the initial stages of the discharge the lattice dilation observed by Bell and Huber and Brenet (8) is clearly seen. However, no d-values characteristic of the formation of new compounds are apparent. As discharge proceeds peaks having d-values characteristic of Mn_3O_4 begin to become apparent in the x-ray pattern and at levels below $MnO_{1.34}$ manganous hydroxide is detected. The chemical analyses indicate that the coulombic efficiency is 100% in the early stages of the discharge. Below $MnO_{1.5}$ the coulombic efficiency drops, presumably due to reduction of water at the cathode.

Discussion

The cathodic reduction of γ-MnO_2 in alkaline electrolyte is seen to proceed by two well-defined steps. The first step occurs between $MnO_{1.92}$ and $MnO_{1.52}$. In this region, x-ray analysis fails to detect any new crystalline phases as has been observed by other workers in $(NH_4)_2SO_4$ electrolyte (9). This is in contrast to the results of Bell and Huber who concluded that MnO(OH) is formed at the start of discharge. These authors based their conclusion on the existence of a line of d-value 1.07Å which was observed in one of their cells. The relative intensity of this line to the most intense line of MnO(OH) at d = 4.17Å is 30%. The 4.17Å line was not observed in their electrodes, therefore it seems unlikely that the 1.07Å line should be seen. It is probable that this line is in fact that observed in the starting material at 1.06Å, the slight difference being attributable to lattice dilation. If the line corresponding to 1.07Å is interpreted as above, the results of Bell and Huber and the present work are in fairly good agreement. No evidence of $Mn(OH)_2$ or Mn_4O_7 is seen in the initial stages of discharge, contrary to the findings of Cahoon and Korver.

The available oxygen analysis shows that the γ-MnO_2 is being reduced with 100% coulombic efficiency in this region; therefore changes must be occurring in the composition of the electrode. A possible explanation is that protons are being assimilated into the lattice thus causing dilation accompanied by some strain (8) according to

$$MnO_2 + nH^+ + ne = MnO_{(2-n)}(OH)_n \quad [2]$$

or

$$MnO_2 + nH_2O + ne = MnO_{(2-n)}OH_n + nOH^- \quad [3]$$

This process continues until the lattice is strained to the point at which it becomes unstable and crystallizes to a more stable phase. The intermediate formed is amorphous to x-rays and would not be detected by conventional techniques. Examination of the x-ray patterns of Fig. 3 clearly shows the increasingly amorphous nature of the reaction product in the early part of the discharge. At a composition approaching $MnO_{1.44}$ rapid recrystallization to a new phase is observed with

Table II. X-ray diffraction analyses (d value in Å) and chemical analyses of partially discharged γ-MnO_2

Calculated empirical formula based on coulombs passed

$MnO_{1.92}$	$MnO_{1.83}$	$MnO_{1.74}$	$MnO_{1.64}$	$MnO_{1.55}$	$MnO_{1.46}$	$MnO_{1.37}$	$MnO_{1.28}$	$MnO_{1.18}$	$MnO_{1.09}$	$MnO_{1.00}$
						4.90 M	4.91 M	4.92 M	4.90 M	4.90 M
						4.71 H	4.72 H	4.71 H	4.71	4.71
3.35 G, Q	3.35 G, Q	3.35 G, Q	3.35 G, Q	3.35 G, Q	3.35 G, Q	3.35 G, Q	3.35 G, Q	3.35 G, Q	3.35 G, Q	3.35 G, Q
3.11 B	3.11 B	3.11 B								
						3.07 M	3.08 M	3.08	3.08	3.08
						2.87 M, H	2.87 M, H	2.87	2.87	2.87
					2.75 M	2.76 M	2.76 M	2.76 M	2.76 M	2.76 M
				2.53						
			2.51							
		2.47			2.48 M	2.48	2.48	2.48	2.48	2.47
	2.43						2.45 H	2.45	2.45	2.45
					2.41	2.41				
2.40 γ	2.40	2.40	2.40	2.40						
						2.36 M, H	2.36	2.36	2.36	2.36
		2.19	2.19							
		2.17								
	2.14									
		2.13								
2.11 γ										
						2.03 M	2.03	2.03	2.03	2.03
						1.825 H	1.827	1.825	1.825	1.825
						1.794 M	1.797	1.796	1.798	1.796
							1.700	1.699	1.699	1.698
				1.693						
			1.685		16.89					
	1.676 G	1.675	1.675	1.677			1.677	1.677	1.675	1.673
							1.658 H		1.657	1.657
	1.657									
1.629 γ		1.624					1.640 M	1.637	1.637	1.637
							1.575 M	1.574	1.573	1.574
				1.540			1.566 M	1.566	1.565	1.564
				1.534						
				1.432						

B = βMnO_2; γ = γMnO_2; G = graphite; Q = quartz; M = Mn_3O_4; H = $Mn(OH)_2$.

many new peaks appearing in the x-ray pattern. These peaks give d-values characteristic of Mn_3O_4 which is probably formed by a reaction of the type

$$3MnO_{(2-n)}(OH)_n + (4-3n)H^+ + (4-3n)e = Mn_3O_4 + 2H_2O \quad [4]$$

This result is essentially in agreement with that found by Cahoon and Korver. At this point in the discharge curve a rapid drop in potential is observed together with a sharp increase in the electrode resistance. This is similar to observations made on the Leclanché cell (10) and is consistent with the rapid recrystallization of a highly resistive oxide at the electrode/electrolyte interface or at the electrode/contact interface. The distinction between Mn_3O_4 and γ-Mn_2O_3 is difficult on the basis of x-ray values because the compounds have very similar x-ray patterns. A number of peaks are present however in the Mn_3O_4 pattern (d = 1.57, 1.534, 1.43) which are absent in γ-Mn_2O_3, and these were observed in our results. The weight of evidence thus lies with Mn_3O_4 although the existence of γ-Mn_2O_3 cannot be completely ruled out.

At a composition approaching $MnO_{1.34}$ manganous hydroxide is starting to crystallize, and this process continues until the end of discharge. To determine whether $Mn(OH)_2$ is formed from Mn_3O_4 or the amorphous phase an experiment was conducted whereby an electrode composed of Mn_3O_4 and graphite was subjected to electrochemical reduction under the same conditions as the γ-MnO_2 electrodes. A number of coulombs were passed equivalent to the complete reduction of Mn_3O_4 to $Mn(OH)_2$ based on the reaction

$$Mn_3O_4 + 4H_2O + 2e = 3Mn(OH)_2 + 2OH^- \quad [5]$$

The electrodes were then analyzed by x-ray diffraction and chemical analysis. No evidence of reduction could be detected by either method. It thus appears clear that $Mn(OH)_2$ is a reduction product of the amorphous phase according to

$$MnO_{(2-n)}OH_{(n)} + (2-n)H^+ + (2-n)e = Mn(OH)_2 \quad [6]$$

Conclusion

The cathodic reduction of γ-MnO_2 in strongly alkaline solutions proceeds by the following steps.

1. Protons are assimilated into the γ-MnO_2 lattice causing dilation and the formation of an amorphous phase according to

$$MnO_2 + nH^+ + ne = MnO_{(2-n)}OH_{(n)}$$

2. Protons are taken up by the intermediate until saturation is reached whereupon it recrystallizes to form Mn_3O_4.

$$3MnO_{(2-n)}OH_{(n)} + (4-3n)H^+ + (4-3n)e = Mn_3O_4 + 2H_2O$$

3. At potentials below 0.40v *vs.* hydrogen the amorphous phase crystallizes directly to $Mn(OH)_2$

$$MnO_{(2-n)}OH_{(n)} + (2-n)H^+ + (2-n)e = Mn(OH)_2$$

The final product of discharge is $Mn(OH)_2$ although any Mn_3O_4 formed is not subsequently reduced and remains in the electrode.

Manuscript received Nov. 10, 1966; revised manuscript received Jan. 30, 1967.

Any discussion of this paper will appear in a Discussion Section to be published in the December 1967 JOURNAL.

REFERENCES

1. W. S. Herbert, *This Journal*, **99**, 190C (1952).
2. N. C. Cahoon and M. P. Korver, *ibid.*, **106**, 745 (1959).
3. G. S. Bell and R. Huber, *Electrochim. Acta*, **10**, 509 (1965).
4. G. S. Bell and R. Huber, *This Journal*, **111**, 1 (1964).
5. A. Kozawa and J. F. Yeager, *ibid.*, **112**, 959 (1965).
6. A. Kozawa and R. A. Powers, *ibid.*, **113**, 870 (1966).
7. I. M. Kolthoff and E. B. Sandell, "Textbook of Quantitative Inorganic Analysis," Macmillan Company, New York (1946).
8. J. P. Brenet and S. Ghosh, *Electrochim. Acta*, **7**, 449 (1962).
9. W. C. Vosburgh and Lou Pao-Soong, *This Journal*, **108**, 485 (1961).
10. C. Drotschmann, *Batterien*, **18**, 721 (1965).

Structure and Stoichiometry of Nickel Hydroxides in Sintered Nickel Positive Electrodes

Michael A. Aia

General Telephone & Electronics Laboratories Incorporated, Bayside, New York

ABSTRACT

Differential thermal analysis (DTA) is shown to be a powerful tool in the study of the structure of electrochemically active materials. DTA was combined with chemical and x-ray diffraction analysis to follow both the electrolytic development in KOH solutions and the thermal decomposition of the charged state of sintered nickel electrodes impregnated with nickel hydroxide. The charged state contains active oxygen, insoluble potassium, water of constitution, and water of hydration. The electrochemical capacity is close to the electrochemical equivalent of the active oxygen formed on charging. The layer lattice is distorted and decomposes exothermically to NiO when heated above 100°C.

The formation and state-of-charge of Ni positive electrodes have been studied extensively by chemical analysis (1-3), magnetochemical analysis (3), x-ray diffraction (1-4), and recently by infrared absorption analysis (5). To date, no definitive information has been obtained by differential thermal analysis (DTA) although considerable effort has been expended (6).

The present work shows that valuable insight into structural changes occurring in Ni positive electrodes can be obtained by DTA, provided that the instrumental parameters are recognized and controlled. Compositional analyses are made at various states-of-charge to show how the electrolyte interacts with the electrochemically active material.

Experimental Methods

The DTA apparatus was a standard unit manufactured by the Robert L. Stone Company of Austin, Texas. The sample holders contained a Platinel II, ring-type differential thermocouple, which is especially suited for precise work with small samples because of the high sensitivity of Platinel II (comparable to chromel-alumel) and the readily reproducible sample geometry. Samples were prepared by grinding the sintered electrode with a mortar and pestle, after thorough washing and drying at 60°C. Analysis for active oxygen in the ground electrodes gave results in good agreement with those found by Labat (3) for electrodes analyzed immediately after charging (see Fig. 6). The sample (1-10 mg) was weighed into a small, disposable Al pan which then was placed on one side of the thermocouple ring. A pan containing an inert reference material was placed on the other side. A 10 mg pellet of Al, made from Al foil, was a good reference material for the conditions used. The results were more reproducible and trends were much better defined when the samples were pelletized. The samples were not diluted with inert material, although this is common practice in DTA work. All the thermograms shown were traced directly from the experimental curves.

A flow of about 60 cm^3/min of helium was passed through the sample chamber to inhibit oxidation reactions. Oxidation of the sintered nickel in the electrodes was shown to have a negligible effect below 350°C by making blank runs with carbonyl nickel powder and also by analyzing for hydrogen in the gases liberated from the samples using a mass spectrometer; a maximum of 0.5 cc H_2 (STP) per gram of sample was evolved. The furnace was programmed to give a linear temperature rise of 10°C/min. The effect of heating rate was investigated and is reported below. Heating was terminated at 500°C because the reactions of interest occurred at lower temperatures.

Samples of $Ni(OH)_2$ were precipitated at 100°C from nickel salts with various anions using methods given by Cairns and Ott (7). Samples of electrode materials were prepared after thorough washing and drying of 80% porous sintered Ni plaques (0.5 x 2.25 x 0.045 in.) impregnated with 96% nickel hydroxide-4% cobalt hydroxide (1.1g) by a procedure similar to that described by Fleischer (8). All eletrochemical cycling was done in 7*N* KOH solution with a typical carbonate content of 0.5 g/l. Electrodes were washed overnight with running cold water and, in some cases, with boiling water in a continuous extractor. For electrodes dried in vacuum, a pressure of 5×10^{-2} Torr was maintained by a mechanical pump.

A simple magnetic susceptibility technique was developed to determine the weight per cent of active material in the impregnated plates both before and after cycling. This determination eliminated the need for mechanical separation of metallic nickel before analysis. The amount of metallic Ni (ferromagnetic) was determined directly, while the active material (paramagnetic) was obtained by difference. The magnetic method makes use of the fact that the magnetic susceptibility of the active material is very low compared with that of metallic nickel. Details of the procedures are as follows. A 5-15 mg sample (weighed to 0.1 mg) of the powdered electrode material was added to a previously weighed glass sample tube, and the total weight was recorded. The apparent weight increase per milligram of the sample in a magnetic field of about 500 oe was determined by suspending the tube from one arm of a balance at a fixed distance between the poles of a large permanent magnet. The balance was capable of weighing reproducibly to 0.01g. An apparent weight gain of 50 mg/mg sample was typical, indicating that the force of magnetization was high compared with the sample weight. These results would be expected for a sample containing a high percentage of a ferromagnetic material such as metallic nickel. The weight increase for a 10 mg sample of carbonyl nickel powder was then determined in the same manner and was, typically, 100 mg/mg. To calculate the percentage of metallic nickel in the electrode material the weight increase per milligram of sample was divided by that of the nickel powder and then multiplied by 100%. Synthetic standards containing 50:50 of carbonyl nickel powder and chemically precipitated (7) $Ni(OH)_2$ or $Ni_2O_3 \cdot H_2O$ were analyzed by this method; the resulting values of metallic nickel were accurate to within 1.5%. Unformed plates were found to contain 50 ±2% green nickel-cobalt hydroxide; after 1 to 100 cycles in 30% KOH, 47-52% of active material was found. These and other results gave direct evidence that the sintered Ni matrix of

electrodes of this type was not appreciably oxidized during electrochemical cycling, even with extensive overcharging, and further established that the samples used for DTA could be considered to consist of 50% Ni-50% active material.

Nickel was analyzed by precipitation with dimethylglyoxime and also by atomic absorption. Potassium and cobalt were determined by atomic absorption. Active oxygen was determined by dissolving 0.1g of the powdered electrode material in sodium acetate-buffered acetic acid solution containing potassium iodide and starch indicator solution; the iodine liberated was titrated with 0.1*N* sodium thiosulfate solution. The active oxygen [O] was then calculated using the following equation

$$(\text{Volume of } Na_2S_2O_3, \text{ml})\ (\text{Normality})\ \frac{16}{2000} = \text{g [O]}$$

Water was determined by heating at 400°-600°C in a stream of argon and collecting the effluent in a preweighed drying tube containing magnesium perchlorate. Correction for the metallic nickel in the samples was made before calculating the results given in Table II.

Results and Discussion

To detect reproducible differences in thermal behavior, the important experimental parameters must be carefully controlled. These parameters include sample weight, sample particle size, crystallinity, and shape, sample geometry, and heating rate. For example, the effect of heating rate on the decomposition of $Ni(OH)_2$ is demonstrated in Fig. 1. There is a gradual loss of loosely bound H_2O up to about 200°C where the lattice begins to decompose by dehydroxylation. It can be seen that the dehydroxylation reaction appears to occur more discretely as the heating rate is increased. The temperature at the reaction peak (T_{max}) increases considerably over the range 5-16°C/min but changes only slightly from 16-20°C/min. The fact that the same amount of dehydroxylation occurs within each DTA peak was determined by graphical integration of the area under each peak. The results are summarized in Table I. A heating rate of 10°C/min was selected for all subsequent work because it was convenient and gave reproducible thermograms.

Effect of anions during precipitation of $Ni(OH)_2$.—In the impregnation of sintered Ni plaques for use in batteries Ni nitrate, perhaps because of higher solubility, is usually preferred over Ni sulfate. However the sulfate is used to make the active material for tubular Ni electrodes. It is of interest to know what effects the Ni salt has on the precipitated $Ni(OH)_2$. Figure 2 gives a comparison of the DTA thermograms

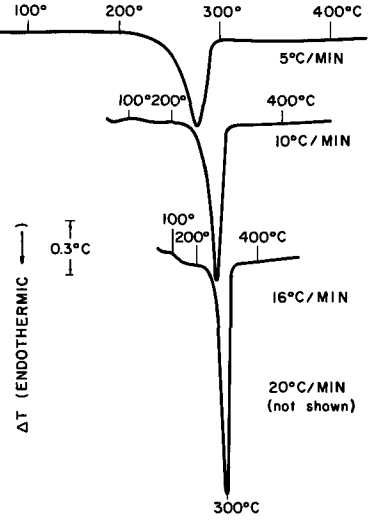

Fig. 1. Effect of heating rate on decomposition of $Ni(OH)_2$

Table I. Effect of heating rate on the dehydroxylation of $Ni(OH)_2$ precipitated from nitrate solution

Rate of heating, °C/min	Threshold decomposition temp, °C	T_{max}, °C	Relative area under peak
5	210	275	100
10	220	294	97
16	222	304	98
20	222	306	97

of $Ni(OH)_2$ precipitated from four different Ni salt solutions. The $Ni(OH)_2$ from the nitrate exhibits the sharpest decomposition peak. Dehydroxylation of $Ni(OH)_2$ prepared from the formate and acetate starts and peaks over the same region of temperatures (225°-296°C) as the nitrate. The behavior is different for the sulfate-derived $Ni(OH)_2$ which does not start to decompose until 262° and does not peak until 324°C (confirmed by duplicate runs). The difference in thermal behavior has been attributed by Duval (9) to the absorption of $SO_4^=$ ions which are eliminated only beyond 700°C. Similar sorption problems are known to occur when nickel chloride is the starting material. DTA thus readily shows the effects of changing the anion in the precipitation process.

Changes in structure with electrochemical cycling.—Tuomi (10) has discussed the process known as forming in nickel electrode technology. Forming occurs during initial electrochemical cycling in alkaline solution and induces complex chemical and crystallographic changes, and, especially, a stable electrochemical capacity. Cycling is manifested by the development of so-called higher oxides of Ni during the oxidation part of the cycle (charging) and by subsequent reduction to a material having the over-all structure of $Ni(OH)_2$ during discharge. The changes in $Ni(OH)_2$ due to cycling are still not well char-

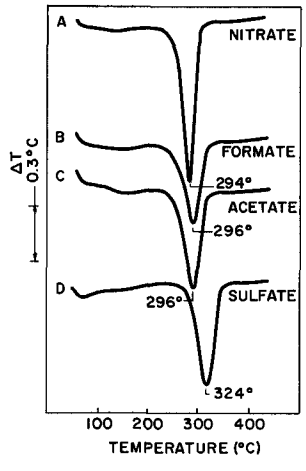

Fig. 2. Effect of nickel salt used to prepare $Ni(OH)_2$

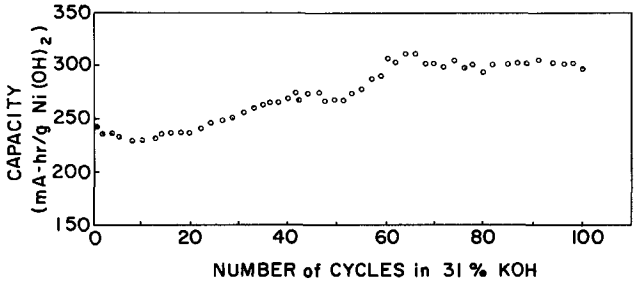

Fig. 3. Changes in positive capacity with cycling for the electrodes used in this work. Each electrode contained 1.1g $Ni(OH)_2$. For a transfer of one electron the theoretical capacity is 289 ma·h/g $Ni(OH)_2$. Electrodes were charged 3 hr at the 2-hr rate, and discharged at the 2-hr rate to 0.0v vs. Hg/HgO reference.

acterized. For example, the infrared spectra of pure $Ni(OH)_2$, unformed $Ni(OH)_2$, and formed $Ni(OH)_2$ are practically indistinguishable from each other (5), and yet considerable changes in the DTA thermograms, as well as in the storage capacity and composition, occur as a function of cycling. It is shown in Fig. 3 that for the sintered Ni electrodes used in this work, the capacity initially drops slightly, then builds up to a plateau after 60 cycles, for the conditions indicated. The results are typical of several electrodes studied. At a later point (Table II) we will see that appreciable amounts of tightly bound potassium and active oxygen are always found in electrodes after formation.

Additional effects of forming $Ni(OH)_2$ are shown in the DTA curves of Fig. 4. Considerable structural reordering occurs during the forming process. For example, the $Ni(OH)_2$ in an unformed plate (curve A) is well crystallized and decomposes much like pure $Ni(OH)_2$ precipitated from Ni nitrate at 100°C (Fig. 2, curve A), except that its dehydroxylation starts at lower temperatures and peaks at 268° instead of 294°. This difference could not be traced to the presence of Ni metal from the matrix of the electrode and seemed to be due to the smaller particle sizes of the electroformed $Ni(OH)_2$. The same amount of active material (5 mg) is represented in both Fig. 2 and 4 (curves A). A drastic lowering of the over-all crystallinity of the $Ni(OH)_2$ occurs when the plate is charged and discharged for the first time in 31% KOH (Fig. 4, curve B). Subsequent cycling at the 2.5-hr rates of charge and discharge only partially restores the crystallinity lost during the first cycle, even after 100 cycles (curves C and D). These findings offer indirect evidence that the $Ni(OH)_2$ in sintered Ni electrodes undergoes a pronounced decrease in particle size or ordering during the electrochemical formation processes. Because the capacity (and presumably the available surface area) decreases during formation cycling (Fig. 3), it seems more probable that the DTA curves reflect more a decrease in ordering than in particle size. Garn (11) has shown how the mode of thermal decomposition of minerals, observed by DTA, is closely related to the crystal size and the structural ordering (*i.e.*, the crystallinity) of the samples.

Evolution of the charged state.—Thermal dehydroxylation of $Ni(OH)_2$ forms NiO and H_2O. The reaction is endothermic and causes a well-defined DTA peak above 200°C, as shown in Fig. 1, 2, and 4. A broader endotherm that appears at lower temperatures is caused by the evolution of loosely bound H_2O from the lattice. These DTA peaks are also observed in discharged electrodes (Fig. 4), in which the active material is known to have the over-all structure of $Ni(OH)_2$. A good picture of some of the changes that occur in $Ni(OH)_2$ during the charging process is given by DTA. For example, Fig. 5 shows the thermograms for electrodes in progressively increasing states-of-charge ranging from the green, unformed state (curve A) to the extensively overcharged state (curve J).

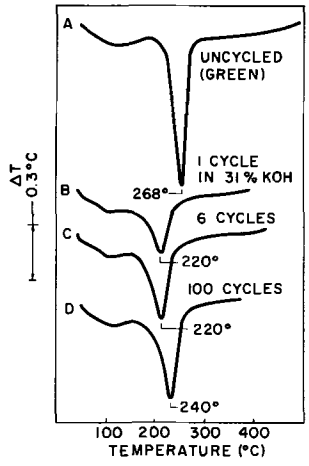

Fig. 4. Effect of formation and cycling on thermal behavior of $Ni(OH)_2$ in impregnated positive electrodes. Cycled plates were discharged to 0.0v vs. Hg/HgO reference.

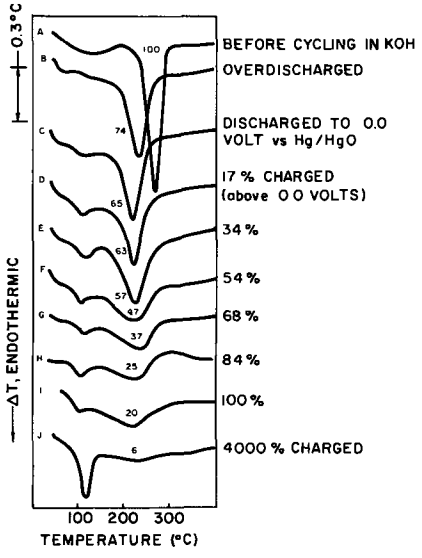

Fig. 5. Development of the charged state of $Ni(OH)_2$ impregnated positive electrodes.

The gradual decrease of dehydroxylation of $Ni(OH)_2$ as a well-defined reaction is seen by the decrease in the relative areas under the characteristic $Ni(OH)_2$ peak; the relative areas are indicated by the numbers given in Fig. 5. Dehydroxylation occurs, however, even in material that has been greatly overcharged, indicating that this structural feature of $Ni(OH)_2$ is retained in the highest states-of-charge. We shall see later (Fig. 8) that part of the endotherm caused by decomposition of the charged state is obscured by a concurrent exo-

Table II. Chemical analyses for dried sintered Ni electrodes in states-of-charge varying from uncharged to overcharged (based on active material in the electrodes)

State-of-charge	% Ni	% K***	% Act. oxygen [O]	% H_2O***	Mole ratios**		
					K/(Ni + Co)	[O]/(Ni + Co)	H_2O/(Ni + Co)
Green, uncycled	—	<0.04	<0.06	20.0	—	—	—
Overdischarged	56.3	0.2	1.6	21.6	<0.01	0.10	1.20
Discharged to 0v	55.5	0.2	3.0	20.3	<0.01	0.19	1.14
17% charged*	57.7	0.5	4.1	13.8	0.01	0.25	0.75
34% charged	57.3	1.0	4.7	14.2	0.02	0.29	0.77
54% charged	60.7	1.8	6.3	14.9	0.04	0.37	0.77
68% charged	58.6	3.1	6.8	15.7	0.08	0.41	0.84
84% charged	55.5	4.5	7.8	11.8	0.12	0.50	0.66
100% charged	56.4	5.4	8.8	12.6	0.14	0.55	0.70
660% charged	63.4	7.0	13.0	10.0	0.16	0.81	0.50

* Electrodes were discharged to 0v then charged with the indicated per cent of 1 F/g-atom (Ni + Co).
** The active material also contained 2.1-2.5% cobalt, *i.e.* the electrodes were impregnated with a coprecipitated mixture of 96% $Ni(OH)_2$-4% $Co(OH)_2$.
*** Potassium and water were determined on samples which were washed extensively with boiling water in a continuous extractor.

thermic reaction, believed to be caused by extensive lattice reordering and loss of surface area during the conversion of the charged state of NiO.

When $Ni(OH)_2$ is charged, the broad peak near 120°C (Fig. 5, curve A) becomes sharply defined indicating the presence of a discretely bound species. This sharp peak is characteristic of the charged state and is found in materials containing as little as 15-20% of charge, which was the amount remaining in electrodes discharged to 0.0v *vs.* Hg/HgO (*e.g.*, Fig. 5, curve C). Simultaneous DTA-effluent gas detection (12) confirmed that the peak at 120°C was accompanied by the evolution of gas, which proved to be water of hydration. Drying experiments showed that 8.9% H_2O was lost from overcharged active material which partially decomposed to NiO when dried to constant weight at 140°C, after it had been previously dried under vacuum at 25°C for 18 hr. Under the same drying conditions, over-discharged material lost only 4.0% H_2O and showed only the x-ray diffraction pattern of $Ni(OH)_2$. It is obvious that dehydroxylation occurs at a lower temperature in the charged state than in the discharged state.

Using DTA, it was established that the sharp DTA peak characteristic of water of hydration in the charged state reflects the zeolitic properties of the lattice, *i.e.*, H_2O was quickly taken up from the ambient atmosphere after the electrode was heated (in helium) to temperatures as high as 520°C. From this it appears that the H_2O lost at 120°C can function as a means of mass transport during electrochemical cycling and may be associated with K^+ ions. Because vibrations characteristic of free hydroxyl groups are not found in the infrared spectrum of the charged state (5), the potassium cannot be present as KOH.

Analysis of composition.—To establish a chemical basis for understanding the charging process the Ni, Co, K, H_2O, and active oxygen content of electrodes was determined as a function of the state-of-charge. Analytical results are summarized in Table II. Total oxygen (not shown) was determined by neutron activation analysis and found to be essentially the same in both the overdischarged and overcharged states, 33.6 and 33.8%, respectively. This agrees with the result that the sum of active oxygen and water is 1.3 g · mole/g · atom Ni + Co.

From Table II it can be seen that potassium and active oxygen,[1] [O], are not detected in uncharged, green plates but are always found in plates that have been cycled. As the electrodes are brought to 100% charge (1**F**/g atom Ni) and then overcharged in 31% KOH solution, both K and [O] increase to large values. The potassium was insoluble and could not be removed by extended washing with boiling water; however, 80% of the active oxygen or the bonding that gives rise to active oxygen was lost after just 1 hr in a continuous extractor. Migration of potassium ion proceeds in a direction which is contrary to the flow of current, as suggested earlier by Tuomi (10). The distribution of insoluble potassium in nickel-oxide electrodes has recently been studied qualitatively by electron probe analysis with similar results (13).

Table II shows that after overcharging, K comprises about 14 mole % of the cations in the active material. The nature and bonding of the K^+ ions and their effect on the structure requires further study; it is possible that the K^+ ions occupy cation defect sites (*i.e.*, Ni^{2+} sites) or are bound between layers of oxygen octahedra (as in micas) or are substituted for protons on hydroxyl sites. If the alkali metal cations go into Ni^{2+} sites, then it would be expected that Li^+ ions would more favorably replace Ni^{2+} ions than would K^+ ions, on the basis of ionic radii. Electrodes

[1] The active oxygen is expressed as [O] to indicate that after dissolving in acid it has the strong oxidizing properties of atomic or nascent oxygen and is capable of oxidizing iodide to iodine in acid solution; this reaction is commonly used to determine [O] in H_2O_2. There is, however, no physical evidence that O-O linkages exist in the active material.

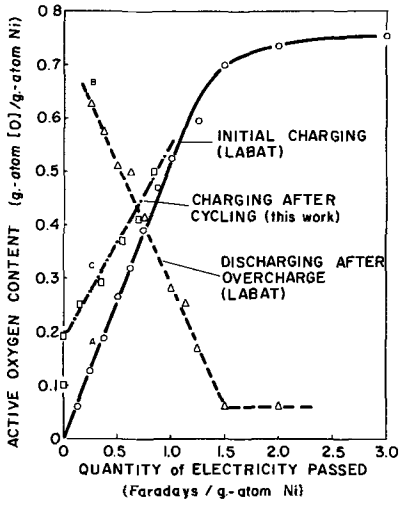

Fig. 6. Active oxygen content as a function of charge passed during polarization in concentrated KOH solutions. The polarization times were 4 hr/F for curves A and B, and 2.7 hr/F for curve C.

charged in saturated LiOH solution showed a maximum Li content of only 0.004% after washing. This result is in apparent disagreement with the evidence for the formation of $LiNiO_2$ species during charging in LiOH found by Tuomi. However, the washing may have caused hydrolysis of the lithium nickelate to yield LiOH and NiOOH.

The electrochemical activity of $Ni(OH)_2$ arises from complex electronic and crystallographic interactions between the nickel ions and hydroxyl groups in the structure. However, it appears realistic to discuss the general mechanism of the electrochemical activity as if the oxidation were originating at the OH sites in the lattice. One is interested in knowing how the electrochemical equivalent of active oxygen in the compositions suggested by Table II is related to the Faradaic capacity of the electrodes. The electrochemical equivalents of active oxygen were calculated from the present results (Table II) and also from data given by Labat (3). These results are summarized in Fig. 6. Curve A shows that on the initial charging, the active oxygen, determined without washing or drying the electrode, increases linearly with the amount of current passed and attains the theoretical value of 0.5 [O] after 1**F** has passed (*i.e.*, 100% efficiency); overcharging is less efficient. When the electrode is discharged after overcharging (curve B), the loss of active oxygen is 0.45 [O]/**F**, which represents an efficiency of 90%. It is obvious that there is hysteresis; both curve B and Table II show that an appreciable amount of [O] is retained after overdischarging. Curve C indicates that although [O] is not produced as efficiently during recharging (lower slope than curve A), after 1**F** of recharging current the mole ratio is about 0.55 [O]/Ni because the line does not start at zero [O]. It seems reasonable to conclude that the active oxygen content gives an adequate indication of the extent of change in Ni-O bonding which gives rise to energy storage by nickel hydroxide.

Labat has shown that the magnetic susceptibility (which reflects the number of unpaired electron spins) decreases almost linearly with the increase of active oxygen content over the range 0-1 g · atom [O] per g · atom Ni during charging of $Ni(OH)_2$ (3). He interpreted this behavior as proof of the formation of Ni(III) and Ni(IV) valence states during charging of $Ni(OH)_2$. The rigorous establishment of the valence of the nickel atoms requires spectroscopic information concerning the electronic states of the system and has not been investigated in the present work. One problem encountered in the present study should, however, be mentioned. Although not shown in Table II, electrodes were prepared with an active oxygen content

of 1.4 g · atom [O]/g · atom Ni after extensive overcharging in saturated LiOH (Li content of the electrode was <0.005%). This ratio indicates that nearly 3 F/g atom Ni were chemically stored. To explain this ratio in terms of valence changes, one would have to postulate a Ni(V) state, which is not reasonable. The point made is that, while Labat was able to correlate magnetic susceptibility and active oxygen content of nickel hydroxides, one is not always able to correlate active oxygen content with the valence state of nickel.

An over-all, oversimplified electrochemical reaction for the generation of active oxygen could be

$$2\,OH^- \rightarrow [O] + H_2O + 2e^- \qquad [1]$$

The source of OH^- groups could be either the electrolyte or the $Ni(OH)_2$ itself. In the first case, mass transport of [O] from the electrolyte to the active material is implied. In the second case, only intramolecular rearrangement of adjacent OH groups of $Ni(OH)_2$ is implied. Mass transport of [O] from the electrolyte should not decrease the amount of water of constitution (*i.e.*, the number of OH groups) in the $Ni(OH)_2$, whereas intramolecular rearrangement should cause the conversion of more than half of the OH groups to [O]. The last column of Table II shows that the total H_2O content of the dried, charged state is much less than that of the discharged state. The lower hydroxyl content is confirmed by thermal analysis. The DTA curves of Fig. 5 clearly show the decrease of water of constitution (hydroxyl groups) as a function of increasing state-of-charge. Other thermal methods of analysis also show that decomposition of the lattice of the charged state is accompanied by the evolution of O_2 as well as H_2O and that the amount of H_2O of constitution is much lower than that for $Ni(OH)_2$; the results of thermogravimetric and mass spectrometric analysis will be presented in detail in a later report. The present results suggest that the increase in active oxygen in the charged state is accompanied by the loss of total H_2O and of OH groups of the $Ni(OH)_2$. Infrared analysis (5) has shown that the OH and H_2O groups of the charged state are hydrogen bonded.

Drying of charged electrodes.—Static thermal analysis of the charged state was performed to determine the effects of drying temperature on the structure, weight loss, and charge retention of overcharged plates dried in vacuum (5 x 10^{-2} Torr) at temperatures of 25°-300°C, after thorough washing. Figure 7 summarizes the results of drying experiments. X-ray diffraction analysis showed only diffuse bands for the dried, active material and a gradual transition from the layer structure of γ-NiOOH (1) to that of NiO as indicated on Fig. 7. The lines that have been attributed to β-NiOOH were not detected in any of the samples. In this paper γ-NiOOH is used to refer to a set of diffuse x-ray diffraction lines (and particularly a line around d = 6.8-7.0Å) which have been reported in the literature. It should be made clear that the actual composition of the charged state is considerably more complex than NiOOH and that the crystal structure is still unknown.

The capacity curves in Fig. 7 show that the charged electrode must be dried above 100°C before an appreciable loss in capacity is observed on the initial discharge. Capacity is lost rapidly at 150°-250°C where lattice decomposition occurs, as would be predicted from DTA (Fig. 5). The amount of lost capacity that can be regained on subsequent recycling decreases as the drying temperature increases, as seen by the convergence of the capacity curves. There is still a measurable amount of capacity in the electrode after drying at 300°C. The correlation between structure and retention of capacity can be further deduced directly from Fig. 7.

The weight loss from the charged electrodes was determined up to 400°C by thermogravimetric analysis at reduced pressure (15 Torr, air) of a powder sample previously dried at 25°C *in vacuo* (Fig. 7, curve C). The values of weight loss obtained from the static experiments were slightly different and were uncertain because the electrodes almost certainly regained some weight by sorption processes during cooling. For example, nickel oxide produced by thermal treatment of $Ni(OH)_2$ below 400°C is known to be a very active "getter" of gases (14). The capacity lost by the charged state during drying is an increasing function of the amount of weight lost by the active material only above 100°C. Weight loss above 100°C reflects the extent of loss of active oxygen and of decomposition of the layer lattice to form NiO with the rocksalt structure.

The dried samples were also examined by DTA, and some of the results are shown in Fig. 8. The curves reveal three main features, a sharp endothermic peak near 100°C, a broad endothermic peak near 230°C, and a very broad exothermic peak near 300°C. The origin of the first two peaks has been discussed previously; it is only necessary to add that the reappearance of the

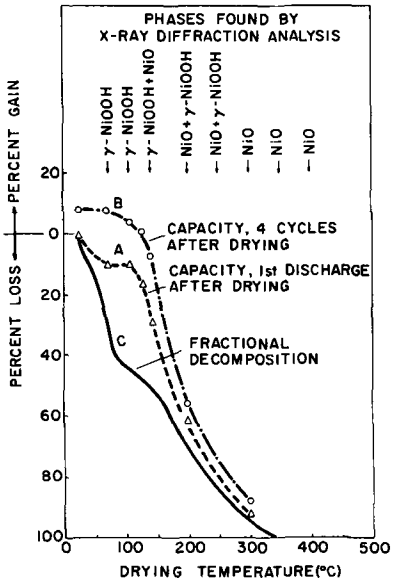

Fig. 7. Capacity loss, weight loss, and structure, as a function of drying temperature. Curves A and B show positive electrode capacity after drying and cycling in 31% KOH as per cent of capacity before drying. Curve C shows weight loss as per cent of the total weight loss (17.7% of the active material) by thermogravimetric analysis in air at a heating rate of 125°C/hr.

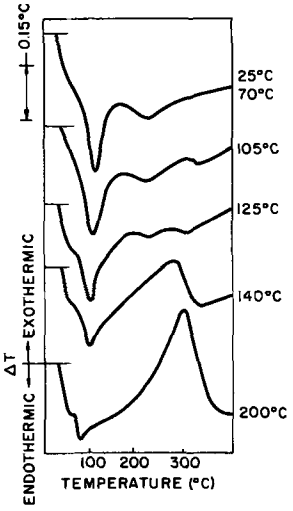

Fig. 8. DTA of charged nickel positive electrodes after thermal treatment at indicated temperatures.

first peak in samples that had been dried above 105°C indicates rehydration and confirms the zeolitic nature of the lattice. The broad exothermic reaction observed in the charged electrodes dried at 140° and 200° is of a type frequently encountered in solids undergoing extensive reordering or recrystallization, as discussed by Garn (11). The peak can be explained by postulating that extensive reordering and loss of surface area accompany the transformation of the distorted layer lattice of the charged material to the rocksalt lattice of NiO. It is also possible that exothermic recombination of oxygen atoms to form O_2 occurs; pyrolysis in a mass spectrometer showed that the evolution of O_2 peaked near 300°C. However, the loss of O_2 from MnO_2 and Mn_2O_3, two other compounds containing active oxygen, has been shown to be an endothermic process (15). The exothermic peak seems to provide additional evidence that the layer lattice is highly disordered and thermodynamically unstable in the charged state. A sample dried at 300°C (not shown) did not exhibit the exotherm; this confirmed x-ray diffraction results which indicated that the charged material had almost entirely converted to NiO during drying above 250°.

Summary

Differential thermal analysis (DTA) has been demonstrated to be a powerful tool in the study of the electrochemically active materials and to provide structural information not easily obtained by other methods of analysis. The main results are as follows:

1. The initial cycling of a green (unformed) $Ni(OH)_2$-impregnated electrode causes a drastic change in the atomic ordering and chemical composition of the active material, which is only partly restored after 100 cycles in KOH solution.

2. The development of a distorted layer lattice during the charging of well-crystallized $Ni(OH)_2$ is readily followed by DTA.

3. Thermal analysis of the charged state of the nickel hydroxide electrode is characterized by (*a*) a well-defined endothermic reaction near 120°C due to evolution of zeolitic H_2O which may be associated with K^+ ions, (*b*) a broad endothermic reaction peaking near 225°C, caused by decomposition of the layer lattice to form O_2, H_2O, and poorly crystallized NiO, and (*c*) a broad exothermic reaction peaking near 300°C, which suggests reordering of the distorted lattice during formation of well-crystallized NiO and additional O_2 and H_2O.

4. Chemical analyses of the active material demonstrate that at least some of the active oxygen is produced at the expense of hydroxyl groups of $Ni(OH)_2$ during charging and that active oxygen accounts for the electrochemical capacity of the electrode. Potassium ions are taken up from the electrolyte and bound to the lattice during charging in concentrated KOH solution; on the contrary, lithium ions are not taken up during charging in saturated LiOH solution at 25°C.

5. After thorough washing to remove electrolyte, charged electrodes may be vacuum dried at temperatures up to 100°C with little loss in initial or permanent capacity.

Acknowledgment

The electrodes and powder samples were prepared by M. S. Pak. The chemical analyses were performed under the supervision of R. Weberling, J. Cosgrove, and D. Oblas of the Materials Analysis Section. The x-ray diffraction patterns were supplied by A. Calvano. The author benefited from frequent discussions with F. P. Kober and from the encouragement given to the work by P. Goldberg. He is grateful also to J. P. Harivel, of the research laboratories of Societe d'Accumulateurs Fixes et de Tractions, (SAFT), Paris, for providing details on the analytical procedure for active oxygen.

Manuscript received Sept. 21, 1966; revised manuscript received Jan. 17, 1967. This paper was presented at the Philadelphia Meeting, Oct. 9-14, 1966.

Any discussion of this paper will appear in a Discussion Section to be published in the December 1967 JOURNAL.

REFERENCES

1. O. Glemser and J. Einerhand, *Z. anorg. u. allgem. Chem.*, **261**, 43 (1950).
2. W. Feitknecht, H. R. Christen, and H. Studer, *ibid.*, **283**, 88 (1956).
3. J. Labat, Thesis, *Univ. Bordeaux, Ann. Chim. (Paris)*, **9**, 399 (1964); A. Pacault and J. Labat, *Compt. rend.*, **258**, 5421 (1964).
4. A. J. Salkind and P. F. Bruins, *This Journal*, **109**, 356 (1962).
5. F. P. Kober, *ibid.*, **112**, 1064 (1965).
6. P. Ritterman and H. N. Seiger, "Investigation of Battery-Active Nickel Oxides," NASA Reports No. CR-54196, CR-54295, CR-54402, CR-54654, and CR-54832 (1964-65), NASA Lewis Res. Ctr., Cleveland, Ohio.
7. R. W. Cairns and E. Ott, *J. Am. Chem. Soc.*, **55**, 527 (1933).
8. A. Fleischer, *This Journal*, **94**, 289 (1948).
9. C. Duval, "Inorganic Thermogravimetric Analysis," 2nd ed., p. 356, Elsevier Publishing Co., New York (1963).
10. D. Tuomi, *This Journal*, **112**, 1 (1965).
11. P. D. Garn, "Thermoanalytical Methods of Investigation," pp. 34-48, 95-106, Academic Press, New York (1965).
12. W. W. Wendlandt, "Thermal Methods of Analysis," pp. 297, 307, Interscience Publishers, New York (1964).
13. F. P. Kober and P. Lublin, *This Journal*, **113**, 396 (1966).
14. S. J. Teichner and J. A. Morrison, *Trans. Faraday Soc.*, **51**, 961 (1955).
15. T. Matsushima and W. J. Thoburn, *Can. J. Chem.*, **43**, 1723 (1965).

The Anodic Dissolution of Cadmium

J. W. Johnson, E. Deng, S. C. Lai, and W. J. James

Departments of Chemical Engineering and Chemistry, The University of Missouri at Rolla, Rolla, Missouri

ABSTRACT

The anodic dissolution of cadmium has been studied in aqueous solutions containing Cl^-, Br^-, I^-, Ac^-, $SO_4^=$, and NO_3^- ions. The normal valence (+2) was found in all solutions with the exception of NO_3^-. The apparent valence (calculated) of cadmium ions in nitrate solutions varied from 1.2 to 2.0 and was found to be a function of NO_3^- concentration, current density, and temperature. An anodic dissolution mechanism has been proposed involving local corrosion and disintegration of the anode which is consistent with the experimental results.

Since early in this century, various investigators have noted and reported discrepancies in the actual and theoretical quantities of Cd dissolving anodically in certain oxidizing electrolytes (primarily nitrates) (1-3). This phenomenon has also been reported for Mg (4,5), Be (6,7), Zn (8,9), Al (10,11), and Sn (12,13), to name a few.

Several theories have been proposed to explain the behavior. They are: (*a*) complex ion ($Cd \cdot Cd^{+2}$) formation, (*b*) uncommon valence ion (Cd^+) formation, (*c*) film control, (*d*) local corrosion, and (*e*) disintegration. The uncommon valence ion theory has been widely accepted, but recent papers have somewhat discounted its validity, especially as pertains to Be (7), Mg (4,14,15), and Zn (9,16). Experiments carried out in this laboratory with amalgamated anodes also make it doubtful that the theory applies to Cd (17).

This investigation concerns the anodic dissolution of Cd in electrolytes (*ca.* neutral) containing various anions both with and without Cd ions present. The anions selected show some variation in the solubilities of their Cd salts and a considerable variation in their ability to complex with Cd ions. Also, they have been associated with studies of the anodic disintegration of other metals (18-23). It was hoped that some insight might be gained on the processes responsible for the low faradaic efficiency.

Experimental

The Cd anodes were prepared from ASARCO special high-purity (99.999+%) rod. All solutions employed analytical grade chemicals and distilled water. The anodes were fabricated by press-fitting small machined Cd specimens into Teflon holders. A platinized-platinum cathode was used. The electrolyses were carried out in the usual H-cell (300 ml electrolyte capacity) under an inert atmosphere (prepurified nitrogen). When no Cd ions were initially present in the electrolyte, the Cd dissolved was determined by EDTA titration. When Cd ions were present, a direct weight loss method was used. A calomel (1*N*) reference electrode in conjunction with a salt bridge was used for the potential measurements. The apparatus and procedure have been described (7,9).

Apparent valence of Cd *in nitrate electrolytes in the absence of* Cd^{+2}.—The anodic dissolution of Cd was studied in KNO_3-K_2SO_4 solutions at temperatures of 25°, 45°, and 65°C. The NO_3^- concentration was varied from 0 to 1*N*, while the total electrolyte concentration was held constant at 1*N* to insure good conductance. Apparent valences were calculated using the equation

$$V_i = \frac{VW}{W_i} \qquad [1]$$

where V_i is the apparent valence of the dissolving Cd, V normal valence = 2, W is the calculated weight of Cd lost from the anode (determined from coulombic data), and W_i is the actual weight of Cd lost from the anode (determined by titration or weight loss).[1] The apparent valence of the Cd ions as a function of current density is shown in Fig. 1a, b, and c for the various temperatures. It may be noted that the apparent valence is affected by current density, NO_3^- concentration, and temperature. In these solutions (with the exception of 1*N* K_2SO_4), a gray film, later shown to be a mixture of $Cd(OH)_2$ and minute Cd particles, was formed very rapidly on the anode surface on be-

[1] Note also that the apparent valence is the product of the current efficiency of the anode and the normal valence.

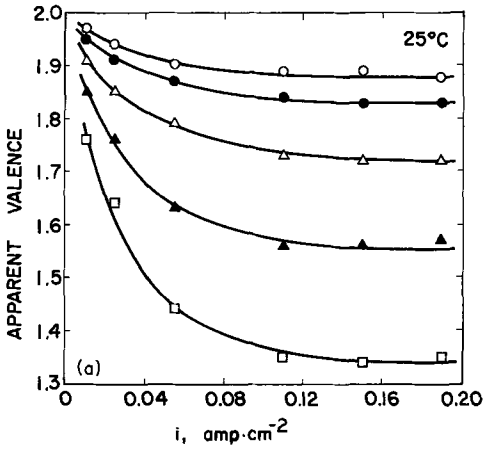

Fig. 1a. Apparent valence of cadmium dissolving anodically in KNO_3-K_2SO_4 solutions at 25°C. ○, 0.01*N* KNO_3-0.99*N* K_2SO_4; ●, 0.03*N* KNO_3-0.97*N* K_2SO_4; △, 0.1*N* KNO_3-0.9*N* K_2SO_4; ▲, 0.3*N* KNO_3-0.7*N* K_2SO_4; □, 1*N* KNO_3.

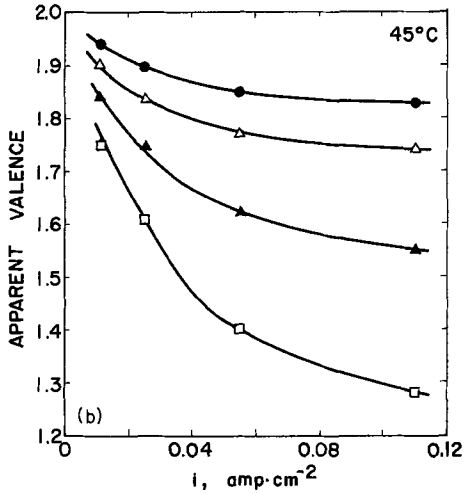

Fig. 1b. At 45°C. Symbols are the same as in Fig. 1a.

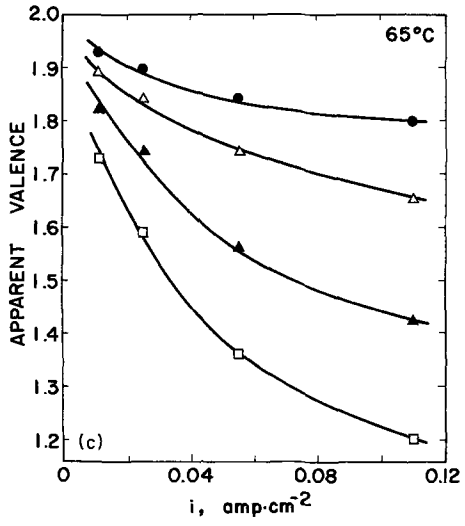

Fig. 1c. At 65°C. Symbols are the same as in Fig. 1a.

ginning the electrolysis. The film appeared to thicken with some darkening as the current density was increased. At higher current densities, > 0.010 amp · cm^{-2}, small portions of the film spalled off the surface. These portions turned completely white [Cd → $Cd(OH)_2$] within a few minutes if allowed to remain in contact with the electrolyte or moist air. The extreme reactiveness is believed to be due to the small size of the metallic particles. Numerous attempts to determine quantitatively the amount of particles formed as a function of current density were unsuccessful. However, a small amount of the spalled gray film was collected by rapidly removing the anolyte from the cell during electrolysis, filtering with a vacuum filter, and rinsing the film thoroughly with dry acetone. Although much of the gray color faded during this operation, the remainder was stabilized by the acetone rinse. An x-ray analysis showed the film to be a mixture of Cd and $Cd(OH)_2$. Microscopic studies showed a $Cd(OH)_2$ matrix with metallic particles dispersed throughout.

Apparent valence of Cd *in various electrolytes in the presence of* Cd^{+2}.—Apparent valence measurements were made in $CdCl_2$-KCl, $CdBr_2$-KBr, CdI_2-KI, $CdSO_4$-K_2SO_4, $Cd(Ac)_2$-KAc, and $Cd(NO_3)_2$-KNO_3 solutions at 25°C. The ionic strength was held constant at 1.5. The Cd^{+2} concentration was varied from 10^{-3} to 1*N* and the current density from 10^{-3} to 10^{-1} amp·cm^{-2}.

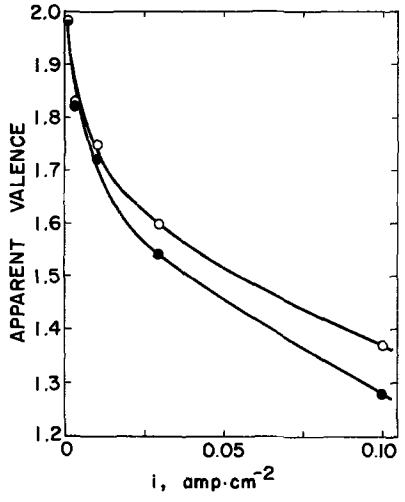

Fig. 2. Apparent valence of cadmium dissolving anodically in $Cd(NO_3)_2$-KNO_3 solutions (ionic strength = 1.5) at 25°C. ○, 1N Cd $(NO_3)_2$; •, 0.001, 0.01, and 0.1N $Cd(NO_3)_2$.

The normal valence of two was obtained for Cd in all solutions except those containing NO_3^-. Figure 2 shows a plot of the apparent valence *vs.* current density for these latter solutions. In all the electrolytes, except those containing NO_3^-, a very thin, tightly adherent, brownish-black film was noted. This was believed to be CdO as reported by Huber (24). In NO_3^- solutions, a gray film similar to that mentioned previously was present.

Polarization studies.—Potentials of the Cd electrode were measured at 25°C in solutions of $CdCl_2$-KCl, $CdBr_2$-KBr, CdI_2-KI, $Cd(NO_3)_2$-KNO_3, $CdSO_4$-K_2SO_4, and $Cd(Ac)_2$-KAc. The current density was varied from 10^{-3} to 10^{-1} amp · cm^{-2}. The overpotentials were calculated as the difference between the electrode potential at a given current density and the rest potential (potential at zero current density) in the same solution. Very stable potentials were obtained within a few minutes in all solutions except those containing NO_3^-. In NO_3^- solutions, the potentials fluctuated widely at current densities greater than 10^{-2} amp · cm^{-2}. The fluctuations seemed to be associated with a rapid passivation and activation of the electrode, possibly caused by spalling of the gray film from the electrode. Rest potentials and Tafel slopes for the Cd electrode in the various electrolytes are shown in Table I. The linear portions of the curves existed over a current range of approximately one order of magnitude (10^{-3} to 10^{-2} amp · cm^{-2}). Above current densities of 10^{-2} amp · cm^{-2}, the potential rose rapidly, probably due to IR drop in the reference and/or passivation of the metal. The potentials were not noticeably affected by stirring.

Discussion

The deviation from Faraday's law of the anodic dissolution of Cd is evidently associated with the nitrate ion. Its oxidizing capability must be important as the production of nitrite ion in an amount nearly equivalent to the deviation has been reported (8, 17). In this study, it alone of the anions present possessed this capability.

Nitrate ions are most likely reduced at local cathodic sites on the Cd surface. That such sites are active during anodic dissolution is shown by the evolution of hydrogen that occurs simultaneously with such processes on certain metals. The conspicuous absence of evolved hydrogen during the anodic dissolution is probably due to the high hydrogen overpotential of Cd. The apparent valence in the various electrolytes

Table I. Rest potentials and Tafels slopes for the cadmium electrode in various electrolytes (ionic strength = 1.5) at 25°C.

Electrolyte	Rest potential, v (NHS)	Tafel slope, v
0.001*N* $CdCl_2$-1.499*N* KCl	−0.599	0.036
0.01*N* $CdCl_2$-1.485*N* KCl	−0.560	0.023
0.1*N* $CdCl_2$-1.35*N* KCl	−0.520	0.014
1*N* $CdCl_2$	−0.453	0.038
0.001*N* $CdBr_2$-1.499*N* KBr	−0.609	0.036
0.01*N* $CdBr_2$-1.485*N* KBr	−0.589	0.036
0.1*N* $CdBr_2$-1.35*N* KBr	−0.557	0.020
1.0*N* $CdBr_2$	−0.459	0.031
0.001*N* CdI_2-1.499*N* KI	−0.687	0.032
0.01*N* CdI_2-1.485*N* KI	−0.669	0.027
0.1*N* CdI_2-1.35*N* KI	−0.631	0.021
1*N* CdI_2	−0.450	0.024
0.001*N* $CdSO_4$-0.999*N* K_2SO_4	−0.539	0.028
0.01*N* $CdSO_4$-0.987*N* K_2SO_4	−0.519	0.028
0.1*N* $CdSO_4$-0.867*N* K_2SO_4	−0.484	0.024
0.001*N* $Cd(Ac)_2$-1.499*N* KAc	−0.551	0.026
0.01*N* $Cd(Ac)_2$-1.485*N* KAc	−0.521	0.019
0.1*N* $Cd(Ac)_2$-1.35*N* KAc	−0.529	0.018
1*N* $Cd(Ac)_2$	−0.450	0.026
0.001*N* $Cd(NO_3)_2$-1.499*N* KNO_3	−0.418	0.065
0.01*N* $Cd(NO_3)_2$-1.485*N* KNO_3	−0.399	0.076
0.1*N* $Cd(NO_3)_2$-1.35*N* KNO_3	−0.349	0.079
1*N* $Cd(NO_3)_2$	−0.264	0.060

can be readily explained if NO_3^- acts as a depolarizer. In solutions containing no NO_3^-, local corrosion cannot occur and the normal valence is observed. When NO_3^- is present, it removes hydrogen from the local cathodes, corrosion proceeds along with anodic dissolution, and a valence lower than normal is observed. The metallic particles appearing in the gray surface film probably result from a disintegration of the electrode caused by a combination of local corrosion and anodic dissolution. These two processes would undermine and dislodge particles whose formation is initiated by the protection of an area by the local cathodic (depolarization) reaction. Also, uneven current densities on the electrode surface caused by nonuniform or disrupted surface films would lead to a similar situation.

With this concept of the anodic dissolution, a model can be described mathematically to give the apparent valence of Cd as follows.

Consider the total rate that Cd is being removed from the electrode surface as the summation of separate rates in a manner similar to that proposed by Hoey and Cohen (15). For this case, anodic dissolution, local corrosion, and disintegration will be considered. Thus

$$r_t = r_e + r_c + r_d \qquad [2]$$

but,

$$W/W_i = r_e/r_t = r_e/(r_e + r_c + r_d) \qquad [3]$$

and from Eq. [1]

$$V_i = 2r_e/(r_e + r_c + r_d) \qquad [4]$$

The rate of anodic dissolution is proportional to the current density in the external circuit as related by Faraday's law

$$r_e = k_e i \qquad [5]$$

The local corrosion rate would be a function of several variables, among which are the electronegativity of the metal, the number of local cathodes (purity and metallic structure), hydrogen ion concentration, depolarizer (NO_3^-) concentration, corrosion potential, and the rate at which local cathodes are uncovered. Undoubtedly, the expulsion of Cd ions from the electrode during the anodic dissolution (passage of current) ruptures the protective film and exposes the metal underneath. A greater rate of rupturing the film (increasing current) will expose more metal with its associated local cathodes and allow local corrosion to occur faster, *i.e.*, the rate at which local cathodes are uncovered is a function of current density. This is essentially the concept proposed by Robinson and King (25) in which the corrosion rate of a metal increases with increasing current. Thus, for a given metal specimen

$$r_c = k_c' i^a C^b_{NO3-} C^f_{H+} C^g_{Cd+2} \qquad [6]$$

If the local corrosion rate is controlled by the depolarization reaction rather than by the deposition of H^o on the local cathodes, then C_{H+} and C_{Cd+2} should have little influence, and

$$r_c = k_c\, i^a\, C^b_{NO3-} \qquad [7]$$

Disintegration was proposed as occurring as a consequence of local corrosion, so as a first approximation

$$r_d = k_d' r_C = k_d\, i^a\, C^b_{NO3-} \qquad [8]$$

therefore

$$\begin{aligned} V_i &= 2k_e i/(k_e i + k_c i^a C^b_{NO3-} + k_d i^a C^b_{NO3-}) \\ &= 2/(1 + k' i^m C^n_{NO3-}) \\ &= 2 - 2k' i^m C^n_{NO3-} + 2(k' i^m C^n_{NO3-})^2 - \ldots \end{aligned} \qquad [9]$$

Neglecting terms with orders of two or higher gives

$$V_i = 2 - k\, i^m\, C^n_{NO3-} \qquad [10]$$

which can be conveniently tested with data from Fig. 1 and 2. Log-log plots of $2 - V_i$ *vs.* i and C_{NO3-} are shown in Fig. 3 and 4. Average values for m and n evaluated from the slopes of these plots are 0.49 and 0.41, respectively. The lines through the data points in the figures have been drawn using these slopes. This is seen to correlate the data very well.

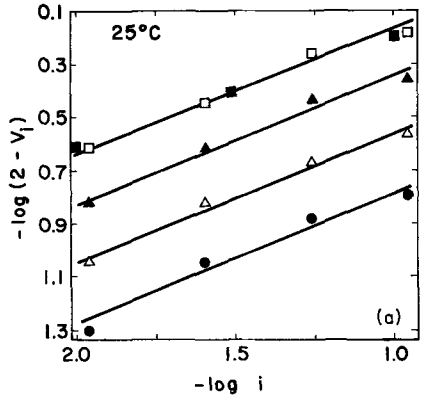

Fig. 3a. Effect of current density on the apparent valence of cadmium at 25°C. ●, 0.03N KNO_3-0.97N K_2SO_4; △, 0.1N KNO_3-0.9N K_2SO_4; ▲, 0.3N KNO_3-0.7N K_2SO_4; □, 1N KNO_3; ■, 1N $Cd(NO_3)_2$.

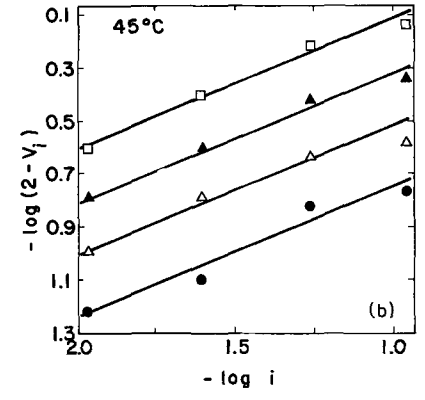

Fig. 3b. At 45°C. Symbols are the same as in Fig. 3a

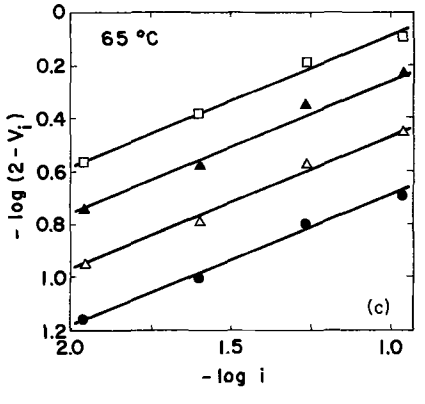

Fig. 3c. At 65°C. Symbols are the same as in Fig. 3a

The effect of C_{Cd+2} can be seen by leaving this term in Eq. [6] and reducing it in the previously described manner to

$$V_i = 2 - k\, i^m\, C^n_{NO3-}\, C^p_{Cd+2} \qquad [11]$$

Figure 5 shows a log-log plot of $(2 - V_i)\ C^{-0.41}_{NO3-}$ *vs.* C_{Cd+2} for various constant current densities. These plots are approximately linear, with a slope p equal to 0.005, thus showing that the effect of Cd^{+2} is slight.

The constancy of the exponents in Eq. [10] and [11] with temperature compels the proportionality constant k to account for the temperature variation of V_i. An

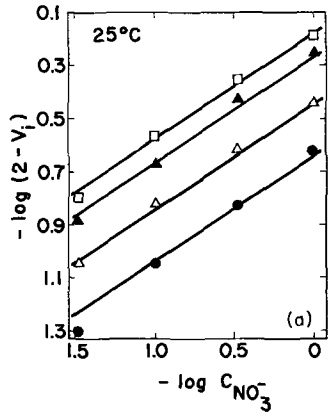

Fig. 4a. Effect of NO_3^- concentration on the apparent valence of cadmium at 25°C. •, 0.011 amp·cm^{-2}; △, 0.025 amp·cm^{-2}; ▲, 0.055 amp·cm^{-2}; □, 0.110 amp·cm^{-2}.

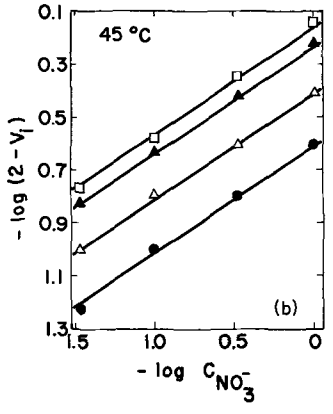

Fig. 4b. At 45°C. Symbols are the same as in Fig. 4a

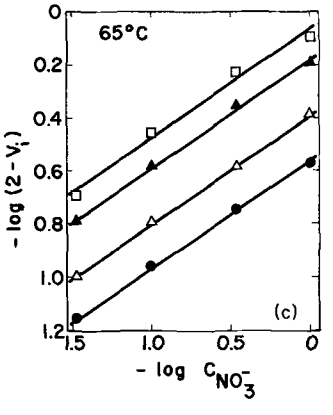

Fig. 4c. At 65°C. Symbols are the same as in Fig. 4a

Arrhenius plot was prepared as shown in Fig. 6 which gave an activation energy of 810 cal and k equal to 8.72 exp (—810/RT). Inasmuch as the k-value is a ratio of rate constants (see Eq. [9]), this activation energy should be regarded more as a method of expressing a temperature variation rather than as having any mechanistic significance. Substituting numerical values in Eq. [10] gives

$$V_i = 2.00 - 8.72\ i^{0.49} C^{0.41}{}_{NO_3^-} \exp(-406/T) \quad [12]$$

which can be used to calculate the apparent valence of Cd ions (or the current efficiency of the Cd anode).

Linear regions were observed in the overpotential *vs.* log i plots at current densities less than 0.01 amp · cm^{-2}. Since the current efficiencies were approximately 100% in all the solutions except NO_3^-, the slopes can probably be associated with the electrochemical dissolution mechanism. Lake and Casey (26)

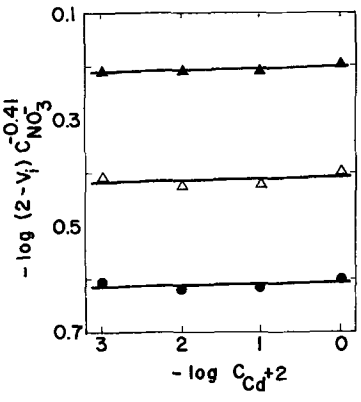

Fig. 5. Effect of Cd^{+2} concentration on the apparent valence of cadmium at 25°C. •, 0.01 amp·cm^{-2}; △, 0.03 amp·cm^{-2}; ▲, 0.10 amp·cm^{-2}.

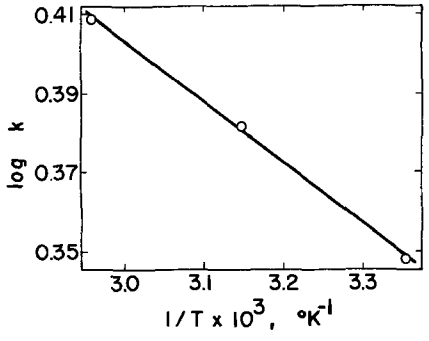

Fig. 6. Effect of temperature on the apparent valence of cadmimum (k from Eq. [10]).

have suggested that Cd dissolves either as the oxide or as a complex and that $Cd(OH)_2$ precipitates when solubility limits are reached. This, together with observations from these studies, suggests a mechanism as follows

$$Cd(s) + H_2O\ (aq) \rightarrow Cd(OH)(s) + H^+\ (aq) + e \quad [13]$$

$$Cd(OH)\ (s) \rightarrow CdO\ (s) + H^+\ (aq) + e \quad [14]$$

$$CdO\ (s) + 4\,X^-\ (aq) + H_2O \rightarrow CdX_4^=\ (aq) + 2\,OH^-\ (aq) \quad [15a]$$

or

$$CdO\ (s) + H_2O\ (aq) \rightarrow Cd^{+2}\ (aq) + 2\,OH^-\ (aq) \quad [15b]$$

where X^- represents halide ions which are known to complex readily with Cd^{+2}. For either [15a] or [15b] controlling, the theoretical Tafel slope would be 30 mv, approximately equal to that observed. In nitrate solutions, the anodic dissolution is accompanied by local corrosion and disintegration whose rates are varying with current density. Therefore, the measured potentials are probably mixed potentials and do not have mechanistic significance.

Conclusions

The anodic dissolution of Cd has been studied in aqueous solutions containing various cations (K^+, Cd^{+2}) and anions (Cl^-, Br^-, I^-, Ac^-, $SO^=$, NO_3^-). The calculated valence of the Cd ions was the normal value (+2) in all solutions except those containing NO_3^-. In the latter solutions, the calculated (apparent) valence was less than two (anodic efficiency less than 100%) and was a function of NO_3^- concentration, current density, and temperature.

The low efficiency of the Cd anode in nitrate solutions is explained in terms of a mechanism in which the anodic dissolution is accompanied by local corrosion and disintegration. The role of NO_3^- is that of

a depolarizer which removes H° from local cathodic sites on the anode surface. (Cd has a relatively high hydrogen overvoltage and hence hydrogen is not evolved.) Momentary protection of portions of the anode surface (local cathodic sites, uneven film formation, or film disruption) allows anodic dissolution to undermine and ultimately detach metal particles from the surface. These particles are noted in surface films on the anode and the phenomenon by which they are formed has been termed "anodic disintegration." This mechanism leads to a mathematical model which is consistent with the experimental results.

Acknowledgment

The authors are grateful for support of this work by the Office of Naval Research.

Manuscript received Nov. 14, 1966; revised manuscript received Jan. 18, 1967. This paper was presented at the Philadelphia Meeting, Oct. 9-14, 1966. This is Paper No. 15 from the Graduate Center for Materials Research, Space Sciences Research Center at Rolla.

Any discussion of this paper will appear in a Discussion Section to be published in the December 1967 JOURNAL.

REFERENCES

1. G. Bredig, *Z. Phys. Chem.*, **32**, 127 (1900).
2. E. F. Burton, *Phil. Mag.*, **11**, 425 (1906).
3. M. C. Del Boca, *Helv. Chim. Acta*, **16**, 565 (1933).
4. M. E. Straumanis and B. K. Bhatia, *This Journal*, **110**, 357 (1963).
5. R. L. Petty, A. W. Davidson, and J. Kleinberg, *J. Am. Chem. Soc.*, **76**, 363 (1954).
6. B. D. Laughlin, J. Kleinberg, and A. W. Davidson, *ibid.*, **78**, 559 (1956).
7. M. E. Straumanis and D. L. Mathis, *J. Less-Common Metals*, **4**, 213 (1962).
8. D. T. Sorensen, A. W. Davidson, and J. Kleinberg, *J. Inorg. Nucl. Chem.*, **13**, 64 (1960).
9. W. J. James and G. E. Stoner, *J. Am. Chem. Soc.*, **85**, 1354 (1963).
10. E. Raijola and A. W. Davidson, *ibid.*, **78**, 556 (1956).
11. M. E. Straumanis and K. Poush, *This Journal*, **112**, 1185 (1965).
12. M. L. Rumpel, A. W. Davidson, and J. Kleinberg, *J. Inorg. Chem.*, **3**, 935 (1964).
13. M. E. Straumanis and M. Dutta, *ibid.*, **5**, 992 (1966).
14. J. H. Greenblatt, *Corrosion*, **18**, 125t (1962).
15. G. R. Hoey and M. Cohen, *This Journal*, **105**, 245 (1958).
16. M. E. Straumanis and Y. Wang, *Corrosion*, **22**, 132 (1966).
17. Y. C. Sun, M. S. Thesis, University of Missouri at Rolla, 1964.
18. J. W. Johnson, C. K. Chi, and W. J. James, *Corrosion*, in press.
19. J. S. Sanghvi, M. S. Thesis, University of Missouri at Rolla, 1965.
20. B. W. Jong, M. S. Thesis, University of Missouri at Rolla, 1966.
21. C. I. Lu, M. S. Thesis, University of Missouri at Rolla, 1966.
22. Y. C. Sun, Ph.D. Thesis, University of Missouri at Rolla, 1966.
23. C. K. Wu, M. S. Thesis, University of Missouri at Rolla, 1967.
24. K. Huber, *This Journal*, **100**, 376 (1953).
25. J. L. Robinson and P. F. King, *ibid.*, **108**, 36 (1961).
26. P. E. Lake and E. J. Casey, *ibid.*, **105**, 52 (1958).

Rate-Controlling Processes in the High-Temperature Oxidation of Tantalum

John Stringer[1]

Metal Science Group, Battelle Memorial Institute, Columbus Laboratories, Columbus, Ohio

ABSTRACT

The oxidation of tantalum in the temperature range 500°-950°C is approximately linear. At atmospheric pressure, the rate constant increases with temperature in the temperature range 500°-650° and 800°-950°C, but decreases slightly as the temperature increases from 650° to 800°C. The reaction rate depends on the square root of the oxygen pressure at low pressures and high temperatures, but at lower temperatures the pressure dependence decreases as the pressure increases. On the basis of experimental evidence in the literature, it is concluded that in the temperature range 500°-800°C the rate-controlling process is a reaction at the interface between the atmosphere and a layer of tantalum pentoxide growing adherently on the metal surface. This interface reaction is preceded by an equilibrium adsorption of oxygen on the interface, the adsorption taking place with dissociation. In the temperature range 800°-950°C, the over-all linear rate is a consequence of the diffusion-controlled growth of adherent pentoxide to a critical thickness, at which the scale fails from the metal. The corollary to this conclusion is that the rate of the diffusion process must be strongly dependent on the oxygen pressure.

The oxidation of tantalum, and the not-dissimilar oxidation of niobium, has been studied extensively for both practical and theoretical reasons. The reaction kinetics are of considerable interest, since the dependence of the reaction rate on both temperature and oxygen pressure is unusual.

After an initial period (a few minutes at 950°C and a few hours at 500°C) the reaction rate becomes approximately constant (linear rate law). The linear rate constant increases with temperature from 500° to 650°C and from 800° to 950°C, but decreases slightly in the temperature range 650°-800°C. The rate constant increases with pressure, the effect decreasing as the pressure increases. Increasing the temperature increases the pressure at which the pressure-dependence starts to diminish.

The principal reaction product is tantalum pentoxide, Ta_2O_5. The oxide grows adhering to the metal surface and is formed under compressive growth stresses. Eventually these cause the scale to fail from the metal surface. Growth of adherent oxide recommences immediately on the freshly exposed metal surface, and repetition of this process produces a laminated detached scale. In addition to the pentoxide, platelets of a suboxide are formed penetrating into the metal from the scale/metal interface. Finally, oxygen also dissolves in the metal.

While the oxidation of niobium has a number of points of similarity to that of tantalum, notably in the temperature- and pressure-dependence of the rate

[1] Present address: Department of Metallurgy, University of Liverpool, Liverpool, England

constant, there are also a number of important differences. In addition to the pentoxide, stable lower oxides are formed. The platelets of a metastable suboxide are much less evident, particularly at higher temperatures. Finally, the pentoxide exhibits a phase change at approximately 800°C, and there is a clear change in the reaction kinetics associated with the change.

In this paper, the effect of a number of variables on the kinetics and reaction-product morphology are reviewed in an attempt to identify the rate-controlling processes in the oxidation of tantalum in the linear oxidation region for temperatures of 500°-950°C and oxygen pressures of 1-60,000 Torr.

Effect of Experimental Variables on Experimental Results

Impurities in the metal.—No systematic study has been made of the effect of impurities on the rate of oxidation of tantalum, but the rate constants reported by a number of investigators (1-5) over a period of 10 years using tantalum from a number of sources agree closely, suggesting that the effect of impurities is small.

Insufficient observations of the other features such as scale structure and morphology were reported in most of the earlier investigations to permit evaluation of the effect of impurities on these.

Grain size.—Only one systematic study of grain-size effects has been made and that was relatively limited in scope (6). No effect of grain size on reaction rate was observed. There do appear to be differences in the scale morphology and in the suboxide platelet distribution as a function of grain size. In coarse-grained samples, long, straight suboxide plates are formed, and these produce pores in the outer detached pentoxide (7). In fine-grained samples, in contrast, the size of the platelets is limited by the grain size, and thus the voids in the pentoxide are difficult to discern. While the grosser features of the scale on coupon specimens are not obviously affected by the tantalum grain size, it has been demonstrated that, over convex surfaces, the pore lines can act as paths for tensile fractures in the detached scale (6, 7). Therefore, it is possible that the scale morphology over convex surfaces may show a grain-size dependence.

Cold work.—Cold work apparently has no effect on the linear oxidation rate in this temperature range (6). The suboxide plates appear curved in cold-worked specimens, but apart from this there is no apparent effect on oxide morphology.

Surface preparation.—Since the linear oxidation is a thick-film, steady-state process, no effect of initial surface preparation would be expected, and, in fact, none is observed (6).

Specimen shape.—It has been demonstrated that, at 820° and 925°C, ¼-in. diameter spheres oxidize more rapidly than ½-in.-diameter spheres which in turn oxidize more rapidly than coupon specimens (6). This is consistent with the tendency of coupon specimens to oxidize more rapidly at the edges and corners than at the centers of the flat faces. The scale formed over convex surfaces contains fissures normal to the metal surface penetrating inward from the outside, and it appears that these fissures are produced by tensile stresses in the outer layers of the oxide, generated by the pressure of the newly forming oxide layers beneath. There is no obvious difference at steady state in the structure of the oxide plates as a function of specimen shape.

Specimen texture.—There is a clear orientation dependence of the oxidation rate at the higher temperatures. At 925° and 820°C {110} faces oxidize more rapidly than any others; {100} faces oxidize more slowly (8). At 600° and 500°C there is no obvious effect of orientation. As a consequence, one might expect the oxidation rate to be a function of texture at high temperatures. No study of this has been made yet.

The oxide structure is clearly a function of orientation. Under steady-state reaction conditions, the suboxide platelets are always formed parallel to $\{100\}_{Ta}$ throughout this temperature range. At higher temperatures the lines of pores above the platelets act as crack paths, and, if the plates lie at 45° to the surface, scale fracture under the compressive growth stresses is facilitated. As a result, the laminations in the detached scale are much thinner above {110} faces than above {100} faces (8).

Gaseous impurities.—Small amounts of gaseous impurities in the oxidizing atmosphere have not been studied in any detail, but they appear to have a negligible effect on the oxidation rate and the scale structure.

Temperature and Pressure Dependence of the Oxidation Rate

The first experiments on the pressure dependence of the oxidation rate were performed by Peterson *et al.* (1), who described their results by the empirical equation

$$\text{rate} = K_1 \frac{K_2 P_{O_2}}{1 + K_2 P_{O_2}} \qquad [1]$$

Later, Cowgill and Stringer (9) pointed out that at low pressures this reduces to

$$\text{rate} \propto K_1 K_2 P_{O_2} \qquad [2]$$

whereas experiment showed that

$$\text{rate} \propto k\, P_{O_2}^{1/2} \qquad [3]$$

Accordingly, these investigators (9, 3) suggested replacing Eq. [1] by

$$\text{rate} = K_1 \frac{K_2 P_{O_2}^{1/2}}{1 + K_2 P_{O_2}^{1/2}} \qquad [4]$$

This point was confirmed by Kofstad (4), who suggested a modified form of Eq. [4].

On a direct plot of rate *vs.* pressure, there is not a great deal of difference between the fit obtainable with Eq. [1] and [4]; but a plot of log rate *vs.* log pressure, by expanding the low pressure region, emphasizes the difference between the two forms.

Figure 1 shows a set of results for the oxidation of a tantalum coupon at 600°C. The full line is the best fit using Eq. [4]; with the rate in g/cm²/sec and the pressure in Torr, $K_1 = 6.53 \times 10^{-6}$, and $K_2 = 0.031$. In Fig. 2 the same equation is plotted over five orders of pressure and compared with constant pressure data from the literature. Plainly, the agreement between the various investigators is excellent: it is not possible to fit these data using Eq. [1].

The empirical Eq. [1] and [4] can be interpreted in terms of a reaction mechanism in which the rate-controlling process is linearly dependent on the ad-

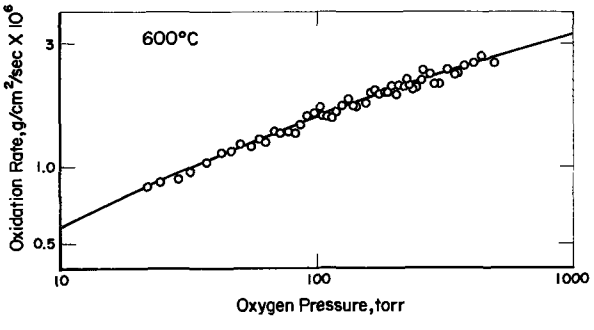

Fig. 1. Pressure dependence of the oxidation of tantalum at 600°C; data from a varying pressure experiment.

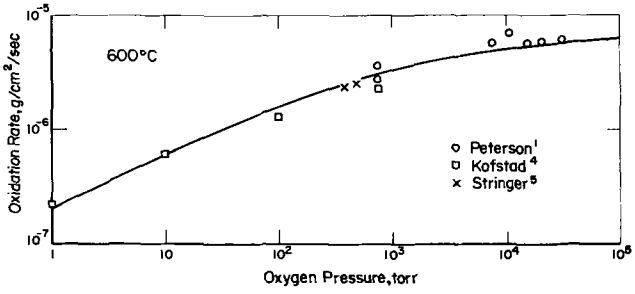

Fig. 2. Pressure dependence of the oxidation of tantalum at 600°C; constant pressure data from the literature. The curve is the same as for Fig. 1.

sorbed oxygen concentration at some interface. In the case of Eq. [1] the oxygen is adsorbed as molecules; in the case of Eq. [4] the adsorption takes place with dissociation, and the oxygen is adsorbed as atoms.

If this is the situation, one may expect that the temperature dependence of K_1, which is related to the rate of the rate-controlling process, will be given by a conventional Arrhenius equation

$$K_1 = K^{\circ}_1 \exp\left(\frac{-Q_1}{RT}\right) \qquad [5]$$

and the temperature dependence of K_2, which is related to the adsorption process, will be given by a Langmuir expression

$$K_2 P_{O_2}^{1/2} = K^{\circ}_2 T^{-5/2} \exp\left(\frac{Q_2}{RT}\right) \qquad [6]$$

In this expression, the $T^{-5/2}$ term arises from the temperature dependence of the concentration of the gas phase at constant pressure T^{-1} and the temperature dependence of the reciprocal of the partition function of the gas for unit volume, $T^{-3/2}$. In these expressions R is the gas constant, T is the absolute temperature, and Q_1 and Q_2 are positive energies. Conventionally, K°_2 is regarded as being independent of temperature, but the temperature dependence of K°_1 is more uncertain: it is assumed to be small in comparison with that of the exponential term. Substituting [5] and [6] into [4]

$$\text{rate} = \frac{K^{\circ}_1 K^{\circ}_2 T^{-5/2} \exp\left(\frac{Q_2 - Q_1}{RT}\right)}{1 + K^{\circ}_2 T^{-5/2} \exp\left(\frac{Q_2}{RT}\right)} \qquad [7]$$

In this work, both K°_1 and K°_2 are regarded as being independent of temperature.

Figure 3 shows the rate constants reported in the literature by a number of investigators, corrected to a pressure of 760 Torr where necessary using the experimentally determined pressure dependence. The full line is drawn according to Eq. [7] with Q_1 = 67,700 cal/mole and Q_2 = 70,000 cal/mole. The fit is quite good over the range 500°-820°C. The $T^{-5/2}$ terms cannot be neglected, since the variation of the exponential terms is small at elevated temperatures, but the shape of the curve does not depend significantly on their inclusion: the value of Q_2 is merely altered slightly.

One would expect this mechanism to cease to operate at high temperatures and low pressures because the adsorbed surface concentration would fall so low that the adsorption step would become the rate-determining process. At 760 Torr and 800°C the volume per molecule in the gas phase is approximately 10^{-19} cm^3. Assuming the sites on the adsorption interface are roughly 4 x 10^{-8} cm apart, the surface concentration will equal the mean concentration in the atmosphere adjacent to the surface when the fractional surface coverage θ falls to approximately 10^{-2}. One would not

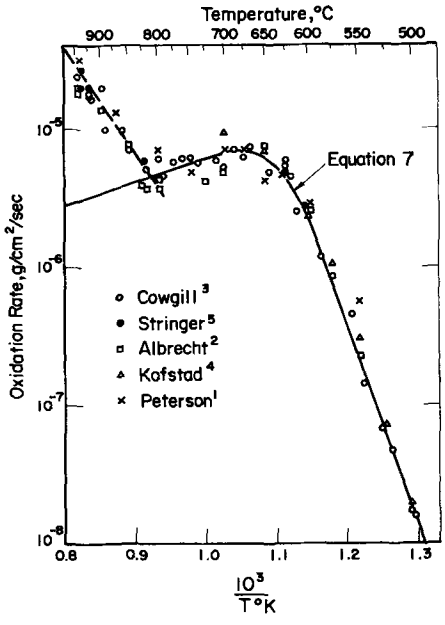

Fig. 3. Oxidation rate of tantalum as a function of temperature at an oxygen pressure of 760 Torr showing the fit of the adsorption model.

expect therefore that the mechanism would continue to describe the reaction when θ is appreciably less than this.

The fractional coverage of the adsorption interface θ is given by

$$\theta = \frac{K_2 P_{O_2}^{1/2}}{1 + K_2 P_{O_2}^{1/2}} \qquad [8]$$

and Fig. 4 shows θ calculated for the curve shown in Fig. 3. At the temperature at which Eq. [7] ceases to describe the experimental results, θ is approximately 10^{-3}, close to the estimate above. However, it must be stressed that this merely indicates that the mechanism does not continue to give a fit to the data in regions where this is physically unlikely: it does not predict or help in understanding the high-temperature process.

For the empirical fit of the data shown in Fig. 2 one calculates $\theta_{760} = 0.46$, which is the value at 628°C according to Fig. 4. The experimental data at 650°C are shown in Fig. 5, and good fit is obtained with K_1 = 8.0 x 10^{-5} and K_2 = 0.004. These two values correspond to $\theta_{760} = 0.099$, equivalent to a temperature of 679°C according to Fig. 4. While these agreements

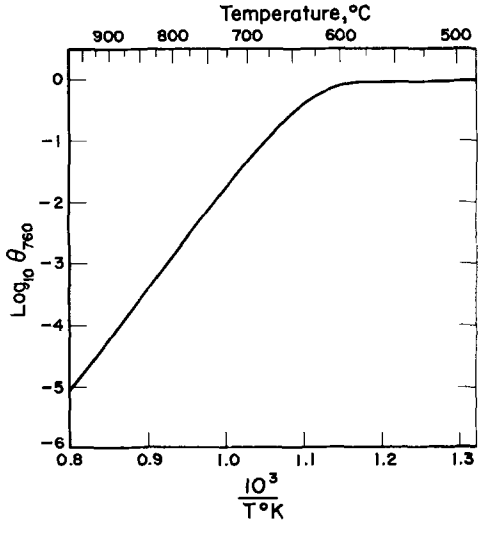

Fig. 4. Fractional surface coverage at an oxygen pressure of 760 Torr, θ_{760}, as a function of temperature.

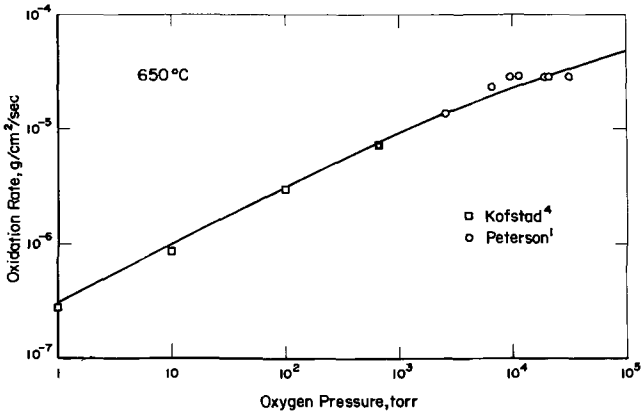

Fig. 5. Pressure dependence of the oxidation of tantalum at 650°C.

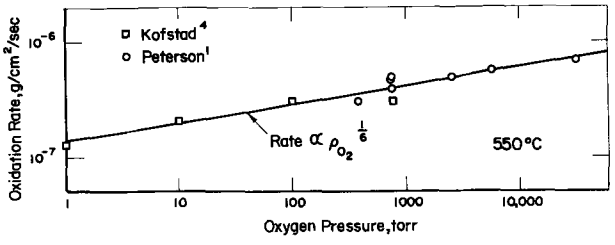

Fig. 6. Pressure dependence of the oxidation of tantalum at 550°C.

are not exact, they are sufficiently close to be satisfactory.

There are some important defects in the theory, however. Equations [4] and [7] imply that, as the pressure changes, the general form of the temperature dependence remains the same, and, in particular, that the negative slope of the higher temperature range remains the same. Kofstad's data (10) suggest that this is not so; at 10 Torr and below the rate increases slightly with temperature in the range 650°-800°C. No other investigation in this temperature and pressure range has been reported.

At 550°C one would expect θ_{760} to be in the range 0.92-0.98, but the published data of Kofstad (4) and Peterson (1) shown in Fig. 6 are better fitted by an equation of the form

$$\text{rate} \propto P_{O_2}^{1/6} \qquad [9]$$

However, this may be fortuitous. Kofstad's data alone are not inconsistent with Eq. [4] and correspond to a high value of θ.

Scale Morphology

It is clear that the properties of the tantalum pentoxide scale vary as a function of temperature. At the low temperatures the scale is soft and weak, and the layers in the laminar detached scale are thin. At high temperatures the scale is hard and strong, and the layers are much thicker. Actually, the scale is most fragmentary at about 600°C; the scale formed at 500°C appears to be far more coherent with a greater layer thickness, and the scale at 820°C is clearly much more continuous. Typical scales are shown in Fig. 7. Because of this, it is tempting to suggest that the origin of the maximum in the rate of 650°C and the anomalous temperature dependence between 650° and 800°C is related to the changing properties of the scale. In fact, this suggestion has been made by Aylmore, Gregg, and Jepson (11) in the case of niobium.

If the oxidation is assumed to take place by the repeated (parabolic) diffusion-controlled growth of adherent scale layers to a critical thickness at which they fail, an average linear rate constant K_l will result

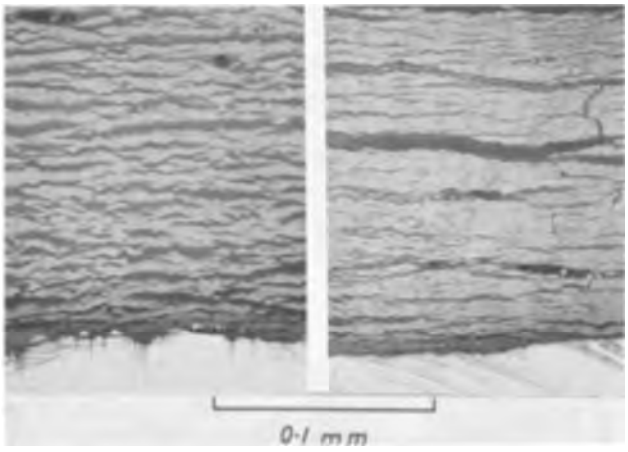

Fig. 7a. Cross sections of oxidized samples showing the lamina thickness in the detached pentoxide. Sample oxidized at 500°C, 450 Torr.

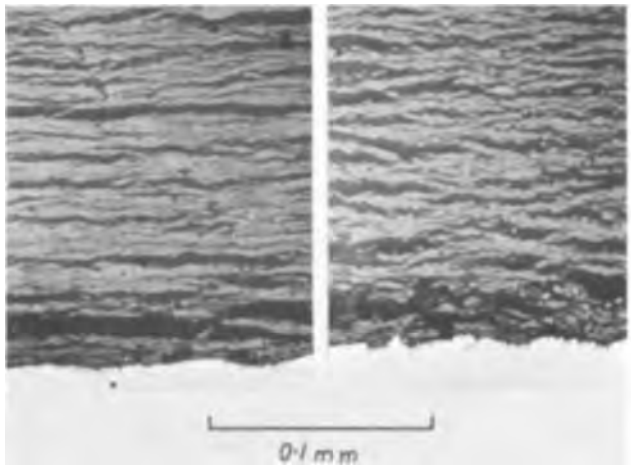

Fig. 7b. Oxidized at 600°C, 450 Torr

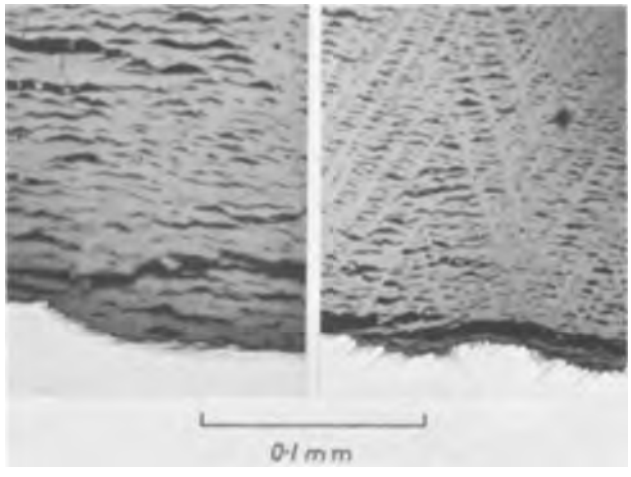

Fig. 7c. Oxidized at 820°C, 450 Torr

which is related to the parabolic rate constant K_p and the critical scale thickness w_c

$$K_l = \frac{K_p}{w_c} \qquad [10]$$

If the anomalous temperature dependence is solely a result of the change in the scale properties, one can easily calculate, using Eq. [9] and Fig. 3, the sort of change one would need to see in the critical scale thickness. Between 600° and 800°C the scale should

increase in thickness by approximately 100 times. It is extremely difficult to obtain a quantitative measure of the layer thickness because of the wide variation from point to point, the loss of resolution due to multiple reflection in the oxide, and the indeterminate effects of cooling; but it is difficult to obtain a value of greater than 10 times for the change in the layer thickness in this temperature range.

However, the qualitative parallel between the temperature dependence of the rate and that of the scale layer thickness is interesting and may well be significant.

Suboxide Structure and Morphology

Since the suboxide or suboxides are metastable at all temperatures, one cannot prepare them in bulk to examine their properties. The metal + suboxide/pentoxide interface is irregular, and one must polish some way back from the interface to obtain good x-ray results, but the volume fraction of the suboxide is too small even at very short distances from the interface and the structures appear to be too close to that of tantalum itself to obtain reasonable results. Further, all one's observations of necessity must be made on specimens cooled from reaction temperature. Studies have been made on the structure of the suboxides formed in the very early stages of the oxidation, prior to the complete coverage of the surface by the pentoxide, using high-temperature x-ray diffraction and hot-stage metallography (12). It is dangerous to assume, however, that these suboxides are the same as those present in the steady-stage process (8) since, for example, the growth stresses associated with the adherent Ta_2O_5 are absent.

Recently, Stringer (7) pointed out that, above suboxide platelets lying more or less normal to the metal/oxide interface, lines of pores are formed in the pentoxide and argued that the existence of these pore lines in the scale is evidence for the presence of the platelets at reaction temperature. Using this as an indication, it appears very likely that all the platelets observed in cross sections of specimens cooled from steady-state reaction in this temperature range were present at temperature and have not precipitated on cooling. Pore lines are evident in scales formed at 600°-950°C, although as the temperature decreases they become more difficult to see.

All the platelets formed during the steady-state (linear) reaction in the temperature range 500°-925°C are parallel to $\{100\}_{Ta}$ (8).

Finally, Fig. 8a shows, in polarized light, a section through the broad part of a platelet in a specimen oxidized at 925°C, 450 Torr. There is evidence of an internal structure, which might suggest a transformation in the platelet on cooling. However, the same type of internal structure is observed in platelets formed throughout the whole temperature range, (Fig. 8b shows the internal structure in plates formed at 500°C) so that any transformation must take place below 500°C. It is also possible that this is a domain structure formed at temperature, but so far it has not been possible to determine this.

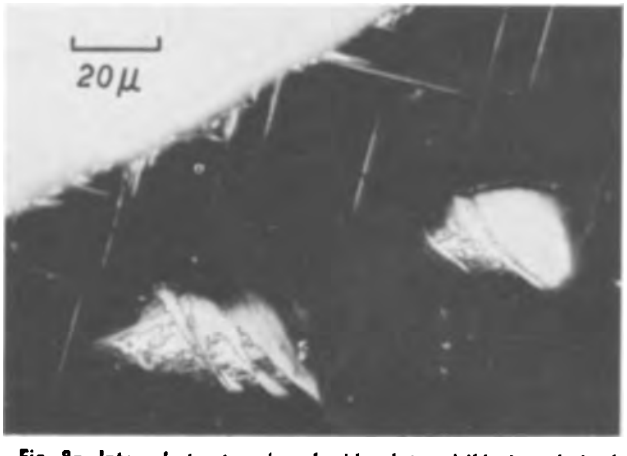

Fig. 8a. Internal structure in suboxide plates visible in polarized light; oxidized at 925°C, 450 Torr.

Fig. 8b. Oxidized at 500°C, 450 Torr.

It appears, therefore, that one cannot interpret the observed temperature dependence of the rate constant in terms of a change in structure or habit of the suboxide. Every indication is that they are the same throughout the whole temperature range. While the number of platelets seems a little less at 950°C than at lower temperatures, there appear to be at least as many at 800° as at 600°C, so that again one cannot explain the anomalous temperature dependence in terms of varying volume fraction of suboxide at the interface.

Scale Failure Modes

The scale grows adhering to the metal surface, and in cross section it appears that both Ta_2O_5/Ta and Ta_2O_5/suboxide interfaces may exist. However, it may be that a very thin layer of suboxide is present between the pentoxide and the metal, and in fact in polarized light a bright line is often visible between the metal and the adherent oxide, both of which appear dark. The dark coloration of the adherent pentoxide in polarized light is of interest. It also appears dark in oblique (dark-field) illumination but white in normal illumination, whereas the detached oxide appears white in all illumination. The color is darkest at the oxide/metal interface and becomes lighter away from the interface (5). The effect may be due to a stoichiometry gradient across the scale, but the striking similarity between polarized light and dark-field illumination suggests that the effect may be due to the absence of internal reflection from flaws in the oxide.

An adherent scale growing under compression on a metal surface may fail either by shear or by blistering from the metal surface. Clearly, shear is a much easier process and is probably much more common; blister-type fractures are sometimes observed, however. For tantalum oxidized at 925°C, 450 Torr, it has been observed that above $\{110\}_{Ta}$ faces the oxide lamellae are much thinner than those above the $\{100\}_{Ta}$ faces, and that this occurs because the pore lines which result from the oxidation of the suboxide plates act as crack paths (8). At 820°C this feature is still evident, but at lower temperatures there is no obvious dependence of laminar thickness on orientation. This may be because a new mode of scale failure operates at low temperatures, or may suggest that a single crack, once nucleated, propagates over a large distance. The oxidation rate is also a function of surface orientation, and in general the faces with the thinnest layer thickness oxidize most rapidly.

The oxidation rate is also a function of surface curvature at higher temperatures, and there is some evidence to suggest that the layer thickness also varies with surface curvature. Stringer (6) reported that at 820° and 925°C ¼-in.-diameter spheres oxidized more rapidly than ½-in.-diameter spheres which in turn

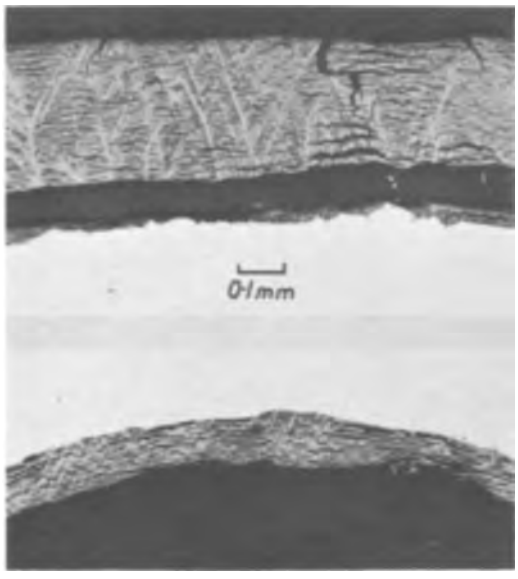

Fig. 9. Scale formed on the outer (upper photograph) and inner (lower photograph) surfaces of a tantalum tube oxidized 100 min at 820°C, 420 Torr; outer radius 6.35 mm, inner radius 1.45 mm, length 9.5 mm.

oxidized more rapidly than coupons. There was no detectable effect of surface curvature on the rate at 600°C. The scales on the spheres contained large radial fissures, apparently due to the tensile stresses produced in the outer layers of the scale by the outward pressure of the newly forming oxide.

Figure 9 shows the scale formed on the outer and inner surfaces of a cylinder oxidized at 820°C. The outer radius of the tube was 6.35 mm, the inner radius was 1.45 mm, total length was 9.5 mm. The cylinder was machined from bar stock and recrystallized, using the same preparation techniques that were used for the spheres (6) to eliminate any possibility of texture effects. The total oxide thickness was approximately three times greater on the convex outer surface than on the concave inner surface. The difference in rate diminishes as the inner radius increases; Figure 10 shows the scale formed on the outer and inner surfaces of a cylinder of internal radius 5.87 mm and external radius 6.35 mm, oxidized at 820°C. The difference in rate is negligible, although the scale formed on the outer surface contains the radial fissures and that on the inside does not. Clearly, the radial fissures do not affect the oxidation rate, and thus the difference in rate for the smaller radius must lie in the scale-fracture process at the interface. The scale layers on the concave surface are thicker in the case of the smaller diameter cylinder, but apparently not as much as three times greater. However, this cannot be determined quantitatively with any great precision. The general effect is much the same at 925°C

Although it is difficult to make categoric statements on the basis of cooled and sectioned samples, it seems likely that the interfaces present in the system are

atmosphere/Ta_2O_5

Ta_2O_5/suboxide

suboxide/Ta

and, possibly,

Ta_2O_5/Ta

One cannot dismiss the possibility of very thin layers of other suboxides, but no evidence for these has been produced. Interfaces between the atmosphere and the metal and between the atmosphere and the suboxides either do not exist or are transitory.

Rate-Controlling Processes

Plainly, the "repeated-parabolic" scaling model described before accords well with the anisotropy of

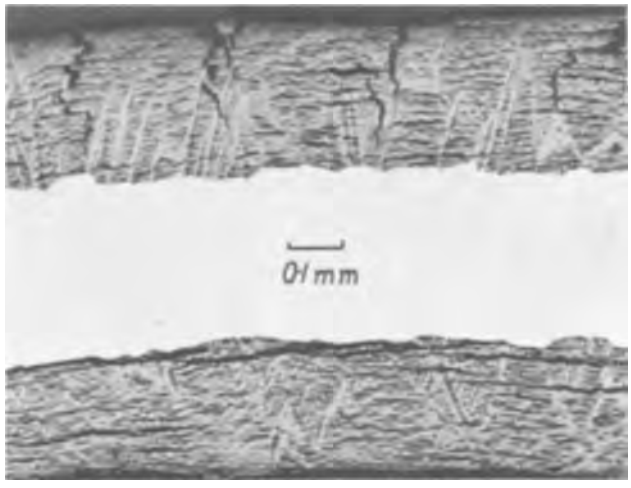

Fig. 10. Scale formed on the outer (upper part) and inner (lower part) surfaces of a tantalum tube oxidized 90 min at 820°C, 420 Torr; outer radius 6.37 mm, inner radius 5.86 mm, length 6.34 mm.

oxidation at elevated temperatures, and numerically the agreement is fair: at 925°C the {110} faces oxidize 5 to 10 times as fast as the {100} faces, and the scale laminations over the {100} faces are 5 to 10 times thicker than those over the {110} faces. If one accepts that failure of the scale is easier on a convex than on a concave surface, it also accords with the curvature-dependence of the oxidation rate at high temperatures, although here the quantitative fit is less easy to evaluate.

However, while qualitatively the variation in laminar thickness parallels the temperature dependence of the rate constant, the quantitative agreement is poor. In addition, it is difficult to reconcile the high pressure dependence of the linear rate constant with this model.

The defect structure of Ta_2O_5 is apparently complicated. Hartmann (13) reported that it was an n-type semiconductor, and, since marker experiments indicate a mobile anion, it was generally assumed that oxygen vacancies were mobile. However, Kofstad (14) has shown that the oxide is p-type at higher oxygen pressures and n-type at lower oxygen pressures, the transition pressure increasing as the temperature increases. An n-type oxide would not be expected to show a significant dependence of diffusion-controlled growth on the oxygen pressure, but a p-type scale should exhibit pressure-dependent growth. The magnitude of the pressure dependence depends on the detailed defect structure, but Kofstad (10) has shown that at pressures in the range 1-760 Torr at 900°C there is an initial parabolic growth of Ta_2O_5 for which

$$K_p \propto P_{O_2}^{1/5.5} \qquad [11]$$

While the critical scale thickness would not be expected to show any direct dependence on the oxygen pressure, it might depend on the rate of the diffusion-controlled growth, thus enhancing the apparent pressure dependence of K_l. However, it would be very surprising if w_c varied as $(K_p)^{-2}$, which would be required to give the observed pressure dependence of K_l.

A linear reaction rate may also result from an interface controlled process. In this event, the reaction rate is linear on a microscopic scale; the adherent growth of the scale to the critical thickness is also linear. There is, of course, nothing in the scale morphology incompatible with this concept.

If the adherent Ta_2O_5 layer is very thin, so that transport through it is very rapid in comparison with the reactions at the pentoxide/metal + suboxide interface, the oxygen activity at this interface would equal that at the atmosphere/pentoxide interface, and so a rate-controlling process at the inner interface would not be incompatible with the observed pressure de-

pendence of the reaction. However, in general, some oxygen-activity gradient must exist across the adherent layer to provide the driving force for the oxygen flux required by the reactions at the inner interface, and so one would expect the oxygen activity at the inner interface to be rather less than that at the outer scale/atmosphere interface. This would have the effect of reducing the apparent pressure dependence of the reaction.

It would appear more likely, therefore, that the rate-controlling process is a reaction at an interface in direct contact with the atmosphere, although one cannot at this stage reject the alternative possibility. The observed temperature dependence may then be explained in one of two ways:

(*A*) The reaction interface or the interface process changes abruptly at 800°C. Below this temperature, oxygen is adsorbed on an interface, dissociating as it is adsorbed. The agreements with the adsorption model in the range 500°-800°C are regarded as real; the apparent disagreements, in the low temperature-pressure dependence, for example, are due to experimental variations between the different investigators. Above 800°C the rate-controlling process is situated at a different interface, again between the atmosphere and one of the solid phases; or, alternatively, there is a change in the rate-controlling process at the original interface. There is insufficient evidence to indicate whether or not an adsorption process precedes this high-temperature reaction.

(*B*) Again there are two reaction interfaces involved, but in general both are present simultaneously. As the temperature is raised the relative area of one increases. The low-temperature temperature dependence is then typical of one of these processes, and the high-temperature temperature dependence of the other. The anomalous temperature range is where both contribute to a significant extent, and is thus a transition region. The low-temperature process is independent of the oxygen pressure, and the high-temperature process depends on the square root of the oxygen pressure. Increasing the pressure at any temperature increases the relative contribution of the low-temperature process, so the adsorption-type pressure-dependence curves again represent transition processes. All the numerical fits with the adsorption model are regarded as fortuitous. This model is much more qualitative than the first.

It is possible to combine the features of these models: one can regard the temperature dependence as being due to a gradual transition in rate-controlling mechanism, but accept that one or both of these processes involve an adsorption step.

However, as discussed earlier, there is every indication that the oxide and suboxide structure and morphology is essentially the same throughout the whole temperature range, and that, in particular, the only interface between the atmosphere and a solid phase is between the gas and the adherent pentoxide layer. For the high-temperature process, furthermore, it is extremely difficult to see how an interface process can show such a clear dependence on the surface curvature or on the scale failure process.

Conclusions

On the basis of the arguments presented above, it appears that the only tenable model for the oxidation involves two distinct processes.

In the range 500°-800°C the fit with the adsorption model seems far too good to be accidental. Not only can the temperature dependence in this range be explained, but the values of θ calculated from the temperature dependence at constant pressure agree quite well with those calculated from the pressure-dependence data at constant temperature. In addition, the process ceases to operate at about the temperature one would expect from a rough calculation.

Since the only interface with the atmosphere is at the outer surface of the adherent Ta_2O_5 layer, the adsorption must take place there. If one accepts that no internal interface process can show a linear dependence on the oxygen concentration at that interface, it follows that the rate-controlling process must also be at the Ta_2O_5/atmosphere interface. The reactions at this interface may be written

$$O_2/gas \rightarrow 2\,O_{ads} \quad [12]$$

$$O_{ads} + O\square/x \rightarrow O/Ta_2O_5 \quad [13]$$

or,

$$O_{ads} \rightarrow O\,\triangle/x \quad [13a]$$

Here the subscript x indicates the outer surface of the adherent scale layer. The ionicity of the species has not been considered, The oxygen vacancies are produced (or oxygen interstitials are consumed) in the scale-forming process at the metal/scale interface

$$2Ta/_{metal} \rightarrow Ta_2O_5 + 5\,O\square/o \quad [14]$$

or

$$2Ta/_{metal} + 5\,O\,\triangle/o \rightarrow Ta_2O_5 \quad [14a]$$

$$O\square/o \xrightarrow{\text{diffusion}} O\square/x \quad [15]$$

$$O\,\triangle/x \xleftarrow{\text{diffusion}} O\,\triangle/o \quad [15a]$$

Similar equations involving possible suboxides may be written, but they do not affect the over-all mechanism. Equation [13] is regarded as the slow step in this sequence.

However, while it is less likely, the reactions at the outer interface may be rapid and the diffusion through the adherent oxide very rapid, and, provided the adherent layer is thin enough, the oxygen activity may be effectively the same at the inner interface as at the outer.

The reaction mechanism clearly alters above 800°C, and, because of the dependence of the rate on surface curvature and because of the apparent correlation between laminar thickness and the linear rate, one must conclude that above 800°C the linear rate is a result of a repeated parabolic process, with the diffusion step (Eq. [15]) being the slow process.

In fact, Kofstad (10) has shown that the initial nonlinear reaction at 900°C is parabolic and that at higher temperatures and lower pressures the rate curves do have the appearance of repeated parabolas. This is probably due to the fact that w_c increases as the temperature is increased so that the "smoothing out" of the repeated parabolae to an over-all linear rate is not possible. The activation energy of the high-temperature process contains the temperature dependence of the parabolic growth rate and the temperature dependence of the scale layer thickness. Since the latter clearly increases with temperature, the real temperature dependence of the parabolic rate constant must be greater than that of the linear rate. The activation energy for the linear rate is approximately 35,000 cal/mole, while Kofstad (10) gives an activation energy of 45,000 cal/mole for the initial parabolic rate in the range 900°-1050°C.

However, in this range the linear rate constant depends on the square root of the oxygen pressure (approximately). According to Kofstad (10) the parabolic rate constant varies as $P_{O_2}^{1/5.5}$ at pressures above the n → p transition and is independent of pressure at pressures well below the transition. Therefore, for the linear rate to exhibit the observed pressure dependence, the critical scale thickness w_c (which cannot depend directly on oxygen pressure) must depend on the rate, and in fact

$$w_c \propto (K_p)^{-2} \propto P^{-1/3} \quad [16]$$

It is extremely difficult to measure w_c with any accuracy, but at 1000°C Kofstad's data (10) show no obvious pressure dependence of the scale thickness at the break-away from the initial parabola. At 1200°C w_c is approximately 1.5 times as great at 1 Torr as at

10 Torr; Equation [16] gives a value of 2.15. While the data are clearly insufficient to confirm or deny the model, they are equally clearly not inconsistent with it.

Acknowledgment

The experimental work was performed by R. O. Dodds and the metallography by C. H. Brady. The research was supported by the Columbus Laboratories of Battelle Memorial Institute. Thanks are due to Per Kofstad, 1966 Institute Fellow at the Columbus Laboratories, who made a number of helpful criticisms and suggestions.

Manuscript received Nov. 10, 1966. This paper was presented at the Philadelphia Meeting, Oct. 9-14, 1966.

Any discussion of this paper will appear in a Discussion Section to be published in the December 1967 JOURNAL.

REFERENCES

1. H. C. Peterson, W. M. Fassell, and M. E. Wadsworth, *J. Metals*, **6**, 1038 (1954).
2. W. M. Albrecht, W. D. Klopp, B. G. Koehl, and R. I. Jaffee, *Trans. AIME*, **221**, 110 (1961).
3. M. G. Cowgill, Ph.D. Thesis, Liverpool, 1963.
4. Per Kofstad, *J. Inst. Metals*, **90**, 253 (1961-1962).
5. J. Stringer, *This Journal*, **112**, 1083 (1965).
6. J. Stringer, Proc. Journees Int. Sur l'Ox. des Metaux, Brussels, 1965, To be published.
7. J. Stringer, *J. Less Common Metals*, **11**, 111 (1966).
8. J. Stringer, *ibid.*, to be published.
9. M. G. Cowgill and J. Stringer, *ibid.*, **2**, 233 (1960).
10. Per Kofstad, *Tidskrift for Kjemi, Bergvesen, og Metallurgi*, **6**, 127 (1963).
11. D. W. Aylmore, S. J. Gregg, and W. B. Jepson, *This Journal*, **107**, 495 (1960).
12. Per Kofstad and O. J. Krudtaa, *J. Less Common Metals*, **5**, 477 (1963).
13. W. Hartmann, *Z. Physik*, **102**, 709 (1936).
14. Per Kofstad, *This Journal*, **109**, 776 (1962).

Carburization of Fe-Cr Alloys During Oxidation in Dry Carbon Dioxide

C. T. Fujii and R. A. Meussner

Naval Research Laboratory, Washington, D. C.

ABSTRACT

Iron-chromium alloys (1-15 w/o [weight per cent] Cr) oxidized in dry carbon dioxide at 700°, 900°, and 1100°C form duplex scales which are similar in structure to those generated in H_2O-Ar atmospheres, *i.e.*, a detached but continuous outer layer of iron oxides (predominantly FeO) and a porous inner layer of FeO and Fe-Cr spinel particles. Carburization accompanies this oxidation at all temperatures, and the resulting microstructural changes, the carbides formed, the hardness increases and the carbon content of homogeneous specimens are related to the equilibria of the Fe-Cr-C system. The carburization and the continued high oxidation rates, in spite of the detached duplex structure of the scale, require that a gaseous transfer of oxygen and carbon occur within the voids separating the outer and inner oxide layers. This requirement suggests a carbon permeation of the dense outer scale and the generation of a CO_2-CO atmosphere in these voids which is carburizing as well as oxidizing to the alloy.

The high-temperature oxidation of iron-chromium alloys in carbon dioxide produces two-layered scales which are very similar in structure to those generated on these alloys in atmospheres of H_2O-Ar (1). An example of this scale structure is illustrated by the micrograph of Fig. 1. The outer layer of iron oxides is dense and crack-free while the inner layer of wustite and an Fe-Cr spinel is relatively porous. The oxidation process generates large voids between the outer and inner scale layers, but the extension of these voids does not appear to alter the high oxidation rates of these alloys. In fact, these rates are comparable to that of pure iron where the scale remains rather adherent and the diffusion of iron is unhindered by voids.

Within the proper experimental limits of time and temperature linear rates are observed for the oxidation of iron in CO_2-CO mixtures, and there is general agreement that the reaction at the gas:oxide interface is the rate determining process (2-4). Thus, the diffusion of iron through the oxide is sufficiently rapid to preclude the observation of parabolic oxidation rates. Similarly, the oxidation rates of Fe-Cr alloys indicate that an adequate flux of iron to the gas:oxide interface is maintained in spite of the extensive voids separating the outer from the inner scale layer. Although this detachment is never complete, the remaining columns of oxide connecting the two layers appear to be adequate as diffusion paths for the iron required by the oxidation reaction at the outer-oxide:gas interface. Since the integrity of the outer detached scale layer is preserved, an alternative source of iron must be provided to augment the "normal" diffusion process through the connecting oxide columns if the high oxidation rates are to be sustained.

The experimental evidence in the previous study of the oxidation of Fe-Cr alloys in water vapor indicated a substantial contribution to the iron flux in the

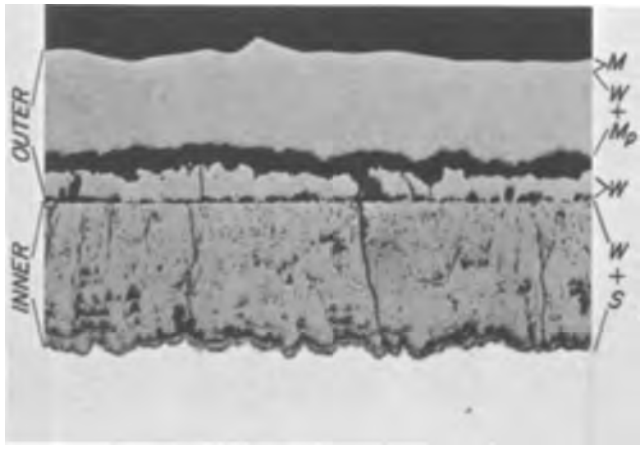

Fig. 1. Unetched microstructure of a typical two-layered scale, from Fe-15Cr alloy oxidized for 24 hr at 900°C in 1 atm of dry CO_2. Magnification approximately 60X.

outer scale layer by the decomposition of wustite at the inner surface of this oxide layer (1, 5). The iron released by this process diffuses through the scale and reforms FeO at the gas: oxide interface, and the oxygen released provides the atmosphere for the growth of the inner scale. The transport of oxygen across the voids is necessarily gaseous, and in this case a H_2O-H_2 mixture was suggested as the vehicle for the transport of oxygen within the voids. A similar mechanism for the oxidation of iron and Fe-Si alloys in oxygen-water vapor mixtures has been subsequently and independently suggested by Rahmel and Tobolski (6, 7).

The present detailed metallographic study of the scales formed on the Fe-Cr alloys oxidized in carbon dioxide suggests that a gaseous transport of oxygen from the outer to inner scale layer also occurs in this system and that carbon is an active participant as a carrier. Thus, a CO_2-CO atmosphere is generated in the voids, and the mechanism by which the two-layer scale structures are formed in carbon dioxide is analogous to that in H_2O-Ar atmospheres. This analogy requires that the scale is permeable to carbon. However, in contrast to oxidation in water vapor where the solution of hydrogen in the alloy produces no structural changes, the accumulation of carbon in the alloy is easily discerned through microstructural evidence (carbide precipitation in many instances) and hardness increases. Evidence for the carburization of the alloy is provided in the detailed description of the specimen structures in the present paper. A subsequent paper will describe the effects of temperature, carbon dioxide partial pressure, and alloy content on the oxidation rates.

Because these results show carburization in a highly oxidizing atmosphere (CO_2 at atmospheric pressure) they suggest that similar effects may occur during the oxidation of many complex high-temperature alloys in carbon bearing atmospheres. Thus accelerated oxidation rates as well as significant changes in the chemistry and properties of these alloys may stem from this vapor transport process. These effects have been largely ignored in evaluations of alloy oxidation, and only a few recent publications give any attention to contamination of the alloy by carbon during oxidation (8-11). Even in basic studies of the oxidation mechanisms of iron and binary iron alloys in which CO_2-CO atmospheres are often employed, carburization accompanying oxidation appears to have escaped the notice of most previous investigators.

Experimental

The apparatus used in continuously recording the weight-gain of the specimen during each experiment and the essentials of the gas purification and metering systems, have been previously described (5). Commercial "bone-dry" grade carbon dioxide, passed through two traps cooled by dry ice-acetone, provided the oxidizing atmosphere at a flow rate of 200 ml/min (approximately 16 cm/min linear flow rate in the oxidation chamber) and 1 atm pressure. The specimens were of the same alloys used in the previous study, and the same annealing and chemical cleaning procedures were used in preparing these specimens (5).

Table I. Composition of Fe-Cr alloys

Element	Weight per cent of element in the alloy				
	Fe-1Cr	Fe-5Cr	Fe-10Cr	Fe-15Cr	Fe-20Cr
Cr	0.99	5.0	9.9	14.8	19.5
C	0.001	0.007	0.005	0.005	0.007
S	0.007	0.010	0.010	0.008	0.008
P	0.004	0.004	0.006	0.007	0.003
Si	0.02	0.04	0.05	0.04	0.05
Mn	0.01	0.04	0.06	0.08	0.07
O*	—	0.027	0.024	0.031	0.035
N*	—	0.0010	0.0019	0.0028	0.0037

* The oxygen and nitrogen contents were determined by vacuum fusion, not determined in Fe-1Cr alloy.

The compositions of the alloys are shown in Table I. All of the experiments were terminated by lowering the furnace from around the oxidation chamber, thus causing the specimen to cool rapidly in the flowing carbon dioxide atmosphere. The results reported here are from oxidation experiments at 700°, 900°, and 1100°C. At each temperature, the oxidation times were approximately constant for all alloys and the total weight gain per unit area of all specimens were approximately equivalent, *i.e.*, 50 hr at 700°C yielding a weight gain of 25 mg/cm^2; 24 hr at 900°C, 70 mg/cm^2; and 3 hr at 1100°C, 70 mg/cm^2.

Examinations of the oxidized specimens included studies of the surface character of the outer scale layer, powder x-ray diffraction analysis of the outer and inner scales, identification of carbides, carbon analyses, detailed metallographic studies, and microhardness measurements. The oxide samples for the x-ray diffraction analyses were carefully removed from one side of each specimen leaving the oxide layers on the reverse side intact. The specimen was then vacuum impregnated and mounted in an epoxy resin for metallography and hardness measurements.

Oxidation Results

While the oxidation experiment is kinetic in nature and thermodynamic equilibrium is not attained in all parts of the system, the oxide structures and the carbides precipitated in the alloys at temperature are, nevertheless, in agreement with the Fe-Cr-O equilibrium diagram from Seybolt's work (12) and the equilibrium data of the Fe-Cr-C system reported by Bungardt, Kunze, and Horn (13). There must be a finite oxygen solubility in the alloy and a carbon solubility in the oxides, but these are assumed to be very limited, and thus the constructions of the respective ternary diagrams are not significantly altered. The fact that the oxides and carbides observed experimentally conform to the equilibrium diagrams indicates that these assumptions are reasonable.

For the description of the oxidation products and the carburization data, the scale structures may be conveniently divided into (*i*) outer scale, (*ii*) inner scale, and (*iii*) subscale and alloy. Since the oxide structures are similar to those produced in H_2O-Ar atmospheres, and these have been described in detail previously (1), the present emphasis will be on the differences in the structures of these specimens oxidized in carbon dioxide and those oxidized in water vapor, and on evidence of carburization of the alloys.

The constitution and microstructural characteristics of the scales formed on Fe-Cr alloys in carbon dioxide are summarized in Table II. These are general observations and apply to all alloy compositions investigated, *i.e.*, the 1, 5, 10, and 15 w/o Cr alloys. The differences in the structures and composition of the oxides which may be ascribed to chromium content will be described in the text in the appropriate sections.

Outer scale.—The composition of the outer scale is dependent on the temperature and the oxidation time. Lower temperatures and longer times favor increasing amounts of the higher oxides of iron because of the decreased rate of iron delivery to the gas: oxide interface. This tendency toward the progressive generation of layers of the higher iron oxides is indicated by the summary of the outer scale structure in Table II where it can be seen that a magnetite surface layer and a hematite surface layer formed on the 900° and 700°C, respectively.

Figure 2a shows the scale structure produced on an Fe-5Cr specimen oxidized for 50 hr at 700°C. This outer scale structure, typical for all of the alloys oxidized at this temperature and for this length of time, is composed of three oxide layers, wustite, magnetite, and hematite. Covering the surface of the thin hematite layer is a dense growth of fine hematite needles. The moderate thickness of the middle layer of magne-

Table II. Summary of constitution and microstructural characteristics of scales and alloys

Feature	Temperature (oxidation time)		
	700°C (50 hr)	900°C (24 hr)	1100°C (3 hr)
1. Surface topography	Fine hematite needles	Faceted, M (no oxide needles)	Faceted, W (no oxide needles)
2. Outer scale	H – M – W Small voids in M layer, otherwise dense	M – (W + M_p) Dense	(W + M_p) Dense
3. Voids between outer and inner scale	Small Considerable area of oxide bridges between outer and inner layer	Moderate	Extensive
4. Inner scale	(W + S_p) Porous	(W + S_p) Porous	(W + S_p) Porous
5. Subscale	Few oxide particles; either S_p or R	Few oxide particles; either S_p or R	Few oxide particles; either S_p or R
6. Alloy	All compositions have carbides ppt'd at temp. Increase in hardness	Fe-15Cr has carbide ppt'd at temp. Increase in hardness	No carbides at temp. Increase in hardness.

Legend of abbreviations: H, hematite, αFe_2O_3; M, magnetite, Fe_3O_4; M_p, *magnetite ppt'd on cooling*; W, wustite, FeO; S_p, FeCr spinel, $(Fe,Cr)_3O_4$; R, rhombohedral Cr_2O_3 or $(Cr,Fe)_2O_3$.

tite indicates that the initial formation of this layer occurs relatively early since this is a comparatively slow growing layer. The source of the voids which are visible within this layer has not been established.

The scales formed at 900° and 1100°C are structurally similar except that as a consequence of the shorter oxidation time and the higher temperature, the surface magnetite is not generated on the specimens in the 1100°C group. With this exception the microstructure of an Fe-15Cr specimen oxidized at 900°C (Fig. 1) is typical of specimens from the 900° and 1100°C experiments. The outermost wustite layer at both temperatures is oxygen-rich, and evidence for this is the proeutectoid precipitation of magnetite in this outer layer in all of these specimens. With extended oxidation times a second wustite layer is usually generated on the inner scale surface as shown in Fig. 1. This layer is free of precipitated magnetite, an indication of the difference in the oxygen content of these two wustite layers which comprise the outer scale.

The external topography of these specimens were characteristic of the oxide phase at that surface, *i.e.*, short red needles of hematite at 700°C, dull, rough, magnetite crystals at 900°C, and large, lustrous, highly faceted wustite crystals at 1100°C. The wustite surfaces formed in carbon dioxide produced no needles or whiskers, which had been characteristic of these surfaces formed in $0.1H_2O$-0.9Ar atmosphere. This

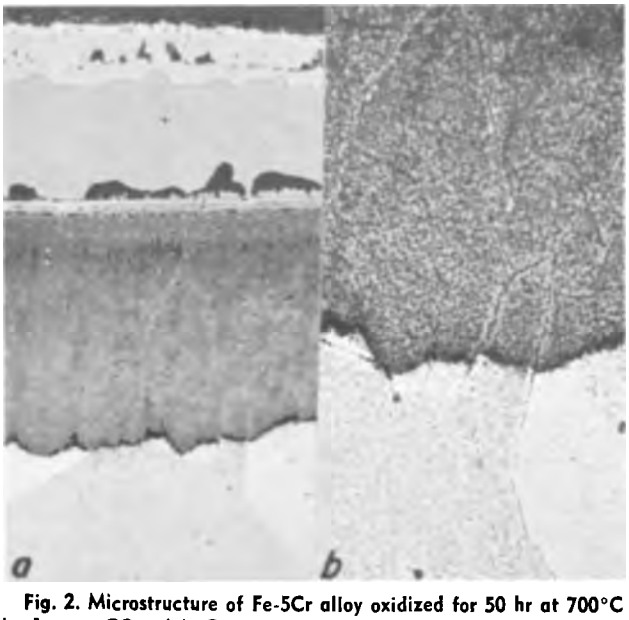

Fig. 2. Microstructure of Fe-5Cr alloy oxidized for 50 hr at 700°C in 1 atm CO_2. (a) General structure of scale and alloy etch: picral + HCl; magnification approximately 225X; (b) inner scale and alloy showing fine carbide distribution; etch: picral + HCl; magnification approximately 375X.

change in the wustite topography, as well as the greater proportion of the higher oxides of iron at 700° and 900°C, is probably related to the higher oxidation rates obtained in pure carbon dioxide at 1 atm pressure.

Chemical analysis of bulk outer scales from specimens oxidized at 900° and 1100°C showed 0.1-0.3 w/o Cr present in these detached outer oxides. (None of the more adherent outer scales from the 700°C specimens could be removed without gross inner scale contamination.) However, further analysis by fluorescence methods of the outer and inner surfaces of these outer scales revealed that the chromium was not uniformly distributed in this oxide layer. The chromium was concentrated on the inner side of the wustite layer (as high as 2-3 w/o Cr) and none was detected at the external surface. This suggests that the presence of chromium in these scales is due to the adherence of Fe-Cr spinel particles to this wustite layer during its detachment from the inner scale, and that there is no appreciable chromium mobility in wustite. The solubility of chromium in this phase has been generally regarded as being low, but recently Levin and Wagner showed by electrical conductivity measurements that above 860°C as much as 0.67 w/o Cr is soluble in wustite (14). In the present experiments, Fe-Cr spinel particles were not obvious in the metallographic sections of these scales. A substantial chromium solubility in wustite would explain the absence of a chromium-rich second phase; however, it is possible that much of the chromium detected in these wustite layers is present as small spinel particles adhering to the inner surface.

The extent of the voids which separate the outer and inner scale layers is related to the oxidation temperature. As shown in Fig. 2a, at 700°C the voids are small, and thus substantial areas of adherence between the scales remain. At 900°C the detachment is much more extensive and frequently, as in Fig. 1, the outer scale appears to be completely detached. However, other sections of the structure show wustite bridges connecting the layers, but the total cross-sectional area of these connecting oxide bridges is small. A similar detached outer scale develops at 1100°C, except that the increased oxidation rate at this higher temperature generates an even larger void volume. These voids between the outer and inner scales are a result of the growth processes responsible for the formation of the two-layer structure and are not due to cooling at the termination of an experiment. Any mechanism proposed for the oxidation of these alloys must necessarily provide a means for maintaining an iron flux to the outer-scale: gas interface in spite of these voids.

Inner scale.—The inner scale at all three temperatures is porous and composed of two phases, wustite and an Fe-Cr spinel. The ratio of spinel to wustite in this layer increases with increasing chromium concentration in the alloy, but remains relatively independent of the oxidation time. Accompanying the in-

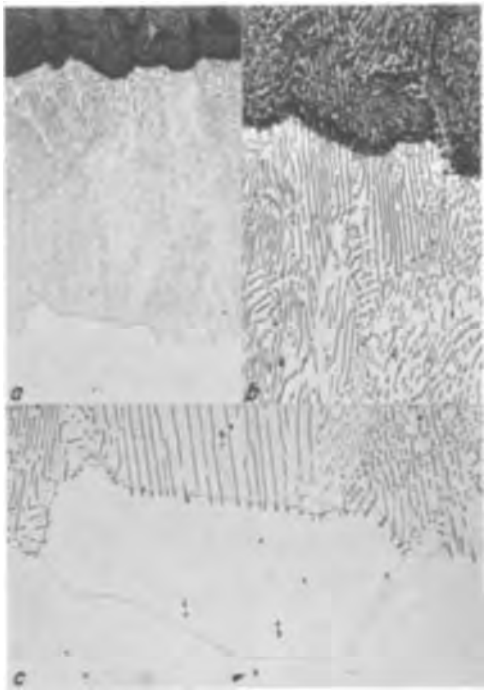

Fig. 3. Carbide formation in Fe-15Cr alloy oxidized for 24 hr at 900°C in CO_2 (Fig. 1 shows general scale structure). (a) Inner scale and alloy showing lamellar carbides, magnification 110X; (b) inner-scale:alloy interface, magnification 250X; (c) lamellar carbide zone:ferrite interface, magnification 250X. All etched with picral + HCl.

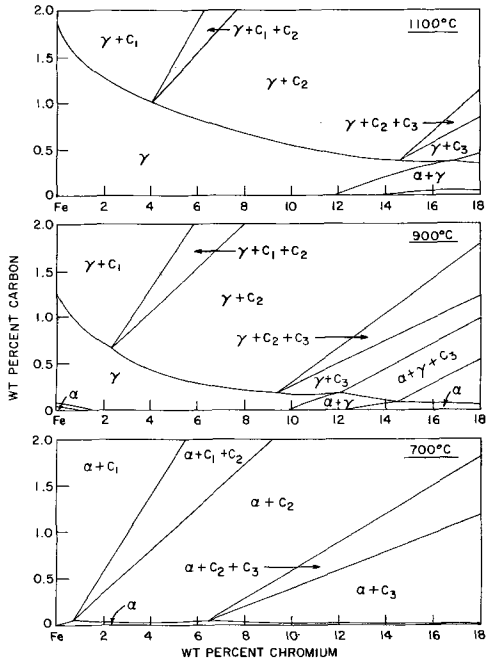

Fig. 4. Isothermal sections of the Fe-Cr-C system at 700°, 900°, and 1100°C [after Bungardt, Kunze, and Horn (13)] in which C_1 = $(Fe,Cr)_3C$, C_2 = $(Fe,Cr)_7C_3$, and C_3 = $(Fe,Cr)_4C$.

crease in spinel formation is an increase in the porosity of the inner scale. In the ferritic alloys, in which carbides are formed during the oxidation experiment, spinel replicas of the carbides are produced in the inner scale as these carbide particles become accessible to the oxidant at the inner-scale:alloy boundary. The spinel replicas are clearly shown in the microstructures of Fig. 2b and 3b for two ferritic alloys oxidized at 700° and 900°C, respectively. It can be seen that the carbide distribution pattern in the alloy is maintained in the spinel replicas of the inner scale. All specimens in which carbides were precipitated at temperature show this in the inner oxide structure. These include the Fe-5Cr, Fe-10Cr, and Fe-15Cr specimens oxidized at 700°C and the Fe-15Cr specimen oxidized at 900°C.

Subscale and alloy.—Internal oxidation and carburization occurring in the alloy in the region of the inner-scale:alloy interface produce metallographically observable changes as well as a hardening of the alloy. These reactions occur concurrently, and both must significantly alter the chromium activity in this zone. In contrast to the relatively high population of Fe-Cr spinel or rhombohedral oxide particles formed by internal oxidation in H_2O-Ar atmospheres, the competitive carburization reaction markedly reduces the depth of this zone and the size and population of the oxide particles precipitated. The metallographic and optical characteristics of the internal oxide particles formed in carbon dioxide are similar to those formed in water vapor, and it is assumed that these oxides formed in carbon dioxide are of similar compositions, *i.e.*, an Fe-Cr spinel or rhombohedral oxide [$(Fe,Cr)_3O_4$ or $(Fe,Cr)_2O_3$].

Electron microprobe scans of several of these specimens revealed a relatively uniform chromium distribution throughout the alloy and no indication of the pronounced chromium depletion in the region of the alloy adjacent to the subscale noted in the water vapor-oxidized specimens (1). The lack of a chromium gradient and the relatively limited number and size of subscale particles in the zone of internal oxidation are undoubtedly related to and affected by the presence of carbon in these alloys. The uniformity of the hardness profiles suggests that the mobility of carbon in these alloys is high and much greater than that of oxygen or chromium. Under these conditions, the lack of a zone of chromium depletion and the diminution in internal oxidation may not be entirely unexpected if the presence of carbon reduces the mobility of chromium or significantly reduces the solubility or diffusivity of oxygen in the alloy.

Carburization Results

The carburization accompanying the oxidation of these Fe-Cr alloys is clearly indicated by the changes in the microstructure and hardness of the remaining alloy. The resulting microstructures appear to conform to those predicted by the Fe-Cr-C ternary diagrams of Fig. 4 which were constructed from the equilibrium data of Bungardt, Kunze, and Horn (13). For the ferritic specimens (those that remain ferritic at the oxidation temperature) the interpretation is rather straightforward. However, for the austenitic specimens the interpretation is complicated by the nature and kinetics of the decomposition of the chromium-carbon austenite during the rapid cooling of the specimen at the termination of the oxidation experiment. Within the broad range of alloy compositions and oxidation temperatures employed in these studies, a multitude of variations in microstructures were observed. All of these provide evidence of an active carburization accompanying the oxidation reactions in pure carbon dioxide. A number of the more significant aspects of these specimens will be discussed in the following sections.

The histogram of Fig. 5 is a convenient means of ordering the hardness data from this series of experiments. These hardness values are average microhardness measurements (5-10 measurements averaged) taken at midthickness of the specimen (stippled) and taken near the inner-scale:alloy interface (horizontal hatched). The difference in these two average hardness values reflects the compositional variation from edge to center. Since electron microprobe studies of other specimens oxidized under similar conditions have revealed no significant variation of the chromium content of the alloy across the thickness of the specimens, this hardness variation is ascribed to a carbon gradient. The constitution of the alloy at the oxidation temperature is indicated above each of the bars of the histogram. In this designation "C" indicates

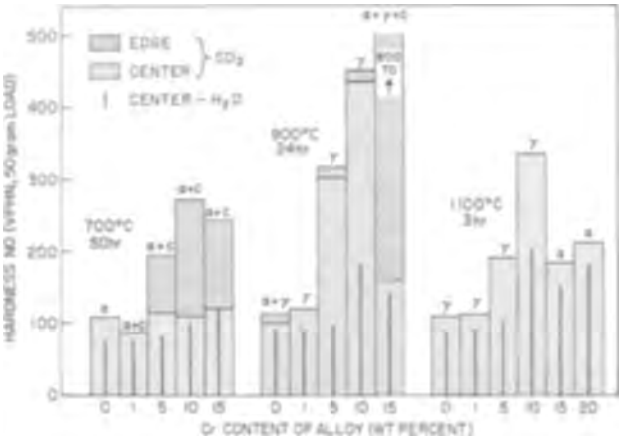

Fig. 5. Histogram of the changes in hardness of the alloy resulting from oxidation in 1atm CO_2. Solid bars indicate hardness of these alloys oxidized in a carbon free atmosphere, *i.e.*, H_2O + Ar.

a carbide present at temperature. The solid bars superimposed on this plot represent the hardnesses of identical specimens oxidized in water vapor and, thus, the hardness of the carbon-free alloys when cooled under very similar conditions. The increases in the hardness of the alloys oxidized in carbon dioxide immediately suggest that the specimens have been carburized during the oxidation.

700°C specimens.—Iron and all of the Fe-Cr alloys are ferritic at 700°C and, as shown in Fig. 4, none can take up much carbon without exceeding the solubility limit of the α-field. With the exception of the iron specimen, all were carburized to such an extent that carbides formed in the alloys at temperature. The iron specimen revealed no evidence that carbides formed, but sufficient carbon had dissolved to delineate the sub-grain structure on etching. Contrastingly, the Fe-1Cr specimen contained fragmentary grain boundary films of carbides and little, if any, carbide within the grains. With increased chromium content the activity of carbon is reduced. The resultant increased activity gradient accelerates carbon solution and leads to a rapid saturation of the ferrite and carbide precipitation. Hence the higher carbide concentration and edge hardness in the higher chromium alloys. The spinel replicas of the carbides in the inner scale, shown for a Fe-5Cr alloy in Fig. 2b, are ample evidence that the carbides were generated during the oxidation. This figure shows a continuous grain boundary film of carbide and a dense distribution of carbide particles within the grains. The grain boundary carbide frequently permeated the entire thickness of the specimen, while the grain body carbides were concentrated near the inner-scale: alloy interface and generally absent at the mid-thickness of the specimen.

For the identification of the carbides formed in these alloys during the oxidation-carburization, the carbides were chemically extracted and examined by x-ray diffraction. The specimens employed, and the results obtained, are listed in Table III. Two specimens from the 900°C oxidation series are included: the Fe-15Cr specimen of Fig. 3 which formed a lamellar carbide layer during oxidation, and the Fe-5Cr specimen which metallograpically showed no evidence of carbide. The latter specimen thus served as a check on the metallography and a "blank" on the extraction method. Polished specimens of each of these samples were coated with a thin evaporated carbon film and then deeply etched in a 2 v/o (volume per cent) bromine-methanol solution. By virtue of the surface carbon film and the network of grain boundary carbides, the extracted carbides retained their relative positions within the specimen and permitted sampling from selected areas for x-ray diffraction studies. The central portion of the 700°C specimens contained predominantly grain

Table III. Phases extracted from Fe-Cr specimens oxidized in carbon dioxide

Specimen		Extracted phases		
Alloy, w/o	Oxidation temp, °C	Grain body	Grain boundary	Alloy: innerscale
1	700	(no specimen)	$\underline{C_1}+C_2$	$C_1+C_2+S_p$
5	700	C_2	C_2	C_2+S_p
15	700	$\underline{C_2}+C_2$	$C_2+\underline{C_2}$	$C_2+C_2+S_p$
15	900	C_3		$W+S_p$
5	900	"C"		$W+S_p$

Note: the underscored carbide phase is the *major* constituent in the extracted mixture.
Phase designations: C_1, $(Fe,Cr)_3C$ [orthorhombic]; C_2, $(Fe,Cr)_7C_3$ [rhombohedral]; C_3, $(Fe,Cr)_4C$ [cubic]; "C", very fine carbides or carbon; S_p, $(Fe,Cr)_3O_4$ [spinel]; W, FeO [cubic].

boundary carbides; the region near the inner-scale: alloy interface contained both grain boundary and grain body carbides. Samples from these areas were unavoidably contaminated with the complementary carbide, but significantly enriched in one type so that the grain boundary and grain body carbides could be identified by their relative intensities in the two diffraction patterns. The predominant phase in the x-ray sample is underlined in the table.

The carbides identified in the 700°C specimens are in substantial agreement with the equilibrium carbides to be expected from the Fe-Cr-C system of Fig. 4. The only exception is the rhombohedral $(Fe,Cr)_7C_3$ carbide (C_2) found present in the grain boundaries of the Fe-15Cr specimen. The lamellar carbide formed in the Fe-15Cr specimen at 900°C was identified as the cubic $(Fe,Cr)_4C$ carbide (C_3). A more complete analysis of the microstructure of this specimen will be offered in a succeeding section. The Fe-5Cr "blank" specimen supported the metallographic observation, *i.e.*, no carbide particles were recovered. The extracted material was extremely fine and yielded only weak, broad, diffraction bands. Thus the carbon was retained in solution in the acicular (martensitic) matrix, or precipitated during cooling as extremely fine carbides —either too fine to diffract, or too fine to survive the chemical extraction.

The last column of Table III identifies the phases in samples scraped from the alloy interface of the inner scale. In addition, x-ray diffraction patterns were obtained from samples from various positions within the inner scale. These results indicate that at 700°C, oxidation of the carbides to spinel replicas is completed within the inner scale, while at 900°C this oxidation is rapid and virtually complete at the inner-scale: alloy interface.

900°C specimens.—As indicated by the hardness data of Fig. 5, the series of specimens oxidized for 24 hr at 900°C shows the greatest variation in hardness changes produced by the carburization. The expansion of the γ-loop by carbon, shown in Fig. 4, permits the austenite phase to form in the normally ferritic end members of the alloy series, *i.e.*, Fe-1Cr and Fe-15Cr. Sufficient carbon was also introduced into the iron specimen to cause the surface adjacent to the inner scale to transform to austenite, *i.e.*, a carbon concentration in excess of 0.015 w/o. On cooling, carbon was rejected as discontinuous carbides at the new ferrite boundaries. The Fe-5Cr and Fe-10Cr alloys are, of course, fully austenitic at this temperature when carbon-free.

The carbon concentration in the Fe-1Cr specimen was sufficient to convert the entire specimen to austenite. During cooling the growth of primary ferrite (low C and low Cr) concentrated the carbon in the remaining austenite. The enriched austenite subsequently transformed at a relatively high temperature to colonies of fine pearlite. Since the matrix is low C, low Cr ferrite, the hardness of the specimen remains virtually unaltered. The microstructures of Fig. 6

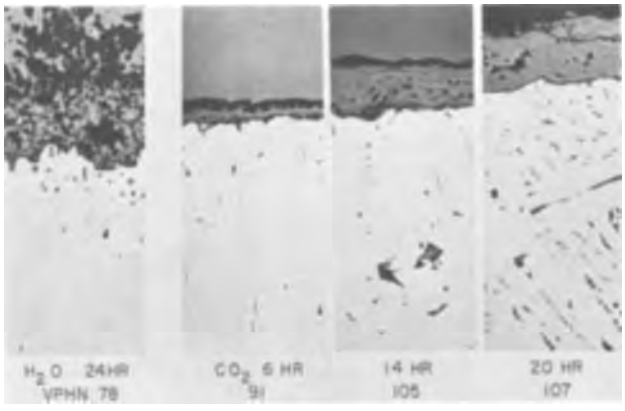

Fig. 6. Progressive pearlite formation in Fe-1Cr alloy oxidized at 900°C in CO_2. Comparative microstructure of alloy oxidized in H_2O + Ar at left; etch: Nital + picral. Magnification approximately 200X.

illustrate the progressive increase of pearlite in the structure (progressive increase of carbon in the alloy) with increasing oxidation time in carbon dioxide. The left microstructure is of a specimen oxidized in water vapor at 900°C. Under these conditions the alloy remained completely ferritic and the internal oxidation zone penetrated deeply into the alloy. These differences in the microstructure of the specimens oxidized in water vapor and carbon dioxide give clear evidence of carburization in the carbon dioxide atmosphere and, equally significant, show that the carbon concentration increases as the oxidation period is lengthened.

The Fe-5Cr and Fe-10Cr alloys, both fully austenitic at 900°C, can dissolve rather large amounts of carbon. In the Fe-5Cr specimen the carbon containing austenite rejects some ferrite on cooling and the remainder of the enriched austenite transforms to a martensite of moderate hardness. The Fe-10Cr specimen should reject a low C, high Cr ferrite as a primary phase; however, even this reaction is suppressed by the rapid cooling and a martensitic structure of relatively high hardness results.

The microstructure of the Fe-15Cr alloy oxidized at 900°C has been illustrated in Fig. 3 and the identity of the lamellar carbides established as $(Fe,Cr)_4C$ through x-ray diffraction (Table III). X-ray fluorescence analysis of the same sample used for the diffraction study indicated an Fe:Cr ratio near one, *i.e.*, 52-54% Fe, 48-56% Cr. These results are in accord with the 900°C isotherm of the Fe-Cr-C system (Fig. 4). The core of the sample remains ferritic, but may dissolve up to 0.05 w/o C, thus the slight increase in hardness of this phase shown in Fig. 5. The boundary between the ferrite core and the lamellar carbide zone corresponds to the $\alpha + \gamma + C_3$ three-phase field. Faintly visible at this interface is a second narrow zone. This might well correspond to the $\alpha + C_3$ field required by the phase diagram, for it contains only these two phases. However, it may represent the regrowth of ferrite around the carbides during cooling. To accommodate either interpretation requires only a minor adjustment in the ferrite composition or the phase boundaries, but neither is known with sufficient accuracy to permit this distinction. The matrix of the zone containing the lamellar carbides was austenite during the carburization at 900°C and from Fig. 4 would contain approximately 0.12 w/o C. This high-carbon austenite, transformed to martensite on cooling, together with the high concentration of lamellar carbides produce the very high hardness of this layer.

1100°C specimens.—The microstructure and hardness changes of the 1100°C series of specimens require little comment because those containing up to 10 w/o Cr are rather similar to the 900°C austenitic specimens. However, it should be noted that although these specimens were exposed to the oxidation-carburization reactions for only 3 hr (the oxidation rates were very high at this temperature), the hardness increases, and hence the total carbon solution, are considerable and not much lower than those produced at 900°C in 24 hr. Thus, both reactions, oxidation and carburization, occur at greatly increased rates at 1100°C.

The Fe-15Cr and Fe-20Cr specimens remain ferritic at this temperature and, unlike any of the other specimens, these alloys produce an initial rhombohedral (Cr_2O_3) scale that is protective. The protectiveness of this scale is short-lived for the 15 w/o Cr alloy but moderately durable for the 20 w/o Cr alloy. As a consequence, the scale formed on the Fe-20Cr specimen varied in thickness and the attack on the underlying metal was correspondingly varied. The Fe-15Cr specimen which ultimately achieved an oxidation rate only slightly lower than that of the lower chromium alloys, showed only a minor increase in hardness at this temperature and did not generate the lamellar carbide layer observed in this alloy at 900°C. The phase equilibria of Fig. 4 suggest the reason for this great change in the observed carburization. At 1100°C it is unlikely that the carbon potential is adequate to stabilize a carbide, for this would require the production of austenite containing more than 0.45 w/o C. The lack of a stable carbide means that there is no way to deplete the alloy of chromium to permit austenite to form at lower carbon potentials. Thus the alloy remains ferritic, becomes saturated with carbon at a low concentration, and shows only a minor increase in hardness. Near the inner-scale:alloy interface small regions were observed which may have been austenite at 1100°C as a result of chromium depletion through oxide formation. However, these were always small isolated areas and this interpretation is rather speculative. The observed microstructure and hardness changes, however, are compatible with a carburizing process occurring during oxidation. In this case, just as with iron at 700°C, the saturation level for carbon in the ferrite is very low.

Correlation of hardness and carbon content.—In the preceding sections the microstructures and hardness changes were shown to be compatible with the phase equilibria of the Fe-Cr-C system, the new phases generated within the specimens were identified as carbides, the progressive formation of pearlite in the Fe-1Cr specimens oxidized at 900°C was illustrated, and a few estimates of the carbon concentrations achieved have been deduced from the observed phase transformations. In order to develop a correlation between the carbon content and hardness for one alloy composition, specimens were systematically carburized, the hardness measured, and the specimens then analyzed for total carbon content. The Fe-10Cr alloy was selected for this study because at 900°C it is austenitic, capable of dissolving significant amounts of carbon without the complication of carbide formation, and had shown a dramatic hardness increase when oxidized in carbon dioxide at this temperature. Accordingly, specimens of this alloy were carburized in an atmosphere in which the CO_2-CO ratio was controlled at 0.3. At this low oxygen potential wustite is not stable, and little oxidation accompanied the carburization. Four specimens were carburized in this atmosphere for periods of 1-20 hr at 900°C. Following the carburization of each specimen, the CO_2-CO atmosphere was replaced with purified argon and a 15-hr diffusion period at 900°C provided to remove the edge-to-center carbon gradient. After sectioning and measuring the hardness of each specimen, the surface oxide was removed by grinding and the specimens analyzed for carbon by combustion.

The data from these carburized specimens are shown in Fig. 7 (open circles), together with the zero carbon datum point (H_2O-Ar oxidation at 900°C) and three points (triangles) from subsequent experiments in which large specimens of the Fe-10Cr alloy were oxidized in CO_2-CO atmospheres (1 to 4 CO_2-CO ratios) at 1000°C and analyzed for carbon. An extrapolation of these data to the hardness measured for the Fe-10Cr specimen oxidized in pure carbon dioxide

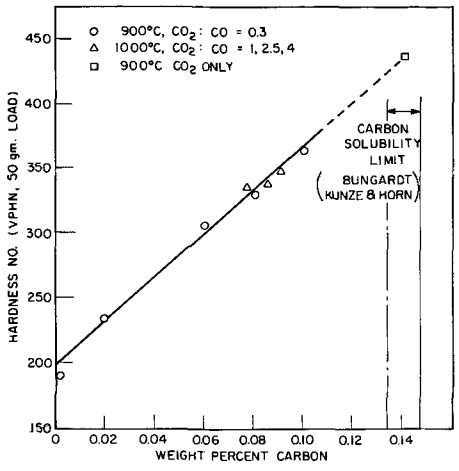

Fig. 7. Correlation between hardness and carbon content of Fe-10Cr alloy oxidized in CO_2 and CO_2-CO atmospheres.

(square) indicates a carbon content of 0.14 w/o. This carbon concentration nearly coincides with the solubility limit of carbon in austenite containing 10 w/o Cr as determined by Bungardt *et al.* (13), Fig. 4. The higher hardness at the edge of this oxidized specimen may indicate a very limited amount of carbide present in this area, thus suggesting that the carburizing potential of the gas phase within the scale structure is high even though the oxidizing atmosphere employed is pure carbon dioxide. Similarly the 330 VPHN hardness of the Fe-10Cr alloy oxidized at 1100°C (Fig. 5) suggests that a carbon content of approximately 0.08 w/o was achieved during the 3 hr of exposure to carbon dioxide.

Discussion

The recent literature provides other evidence for the accumulation of carbon in Fe-Cr alloys, in stainless steels, and in certain special steels used in fabrication of atomic reactor components. These carbon accumulations occurred during oxidation experiments in carbon dioxide or CO_2-CO mixtures which are normally considered non-carburizing (8-11). The rationale for the carburization of the alloys and steels under these conditions appears to be that the accumulation of carbon monoxide, a reaction product, eventually renders the oxidizing atmosphere, carburizing as well. To account for the carburization of a variety of Cr-bearing steels in a flowing carbon dioxide atmosphere, McCoy suggested that the presence of pores in the outer oxide layer provided gaseous pathways and pockets for accumulation of carbon monoxide. On the other hand, Jepson, Antill, and Warburton, in an extensive study of the reaction of a 20Cr-25Ni Nb-stabilized steel in carbon dioxide and carbon monoxide, suggest that carbon has considerable mobility in the oxide. Thus it was proposed that the carburization of the steel in these studies was caused by carbon which was deposited on the oxide surface and then transferred through the oxide by a diffusion mechanism. These, then, represent two divergent views on the mechanism for the observed carburization of the steels. There is probably merit in both views because the scales differ in composition and structure in these two studies and this could lead to different means by which carbon accumulates in the steels. Clearly, it is necessary that the scales be carefully examined and characterized before any coherent and logical scheme for the oxidation and carburization of these alloys and steels can be offered.

The present experiments show that the outer layer of the duplex scale structure is continuous and free of any cracks, fissures, or pores which are observable by optical microscopic methods. The kinetic results suggest that this sound scale condition is maintained throughout the experiment and, thus in order to carburize the alloy, carbon must permeate the growing outer wustite layer. The carbon solubility and mobility in wustite have not been established, but the experimental indications are that the presence of a dense scale *per se* does not deter the carburization of the alloy. On the contrary, outer scale integrity is necessary to prevent direct access of carbon dioxide, which is decarburizing, to the porous inner scale and the alloy. Carbon accumulation in the alloy implies that there is a solubility and a mobility of carbon in wustite which are sufficient to sustain the diffusional transport of carbon through the outer scale.

While the experimental evidence suggests a carbon permeation of the outer scale (no evidence of direct admission of gaseous carbon dioxide), there is doubt as to the reaction which is responsible for the initial carbon deposition on the external oxide surface. Carbon dioxide is generally considered noncarburizing under these experimental conditions, and, therefore, the generation and local accumulation of carbon monoxide is clearly a necessary prerequisite for carburization to occur. The experiments show that the rate of carbon accumulation in the alloy closely parallels the oxidation rate, but this is not unexpected since the generation of carbon monoxide is directly related to the oxidation rate. What remains obscure is the nature of the surface reaction of the adsorbed carbon monoxide which yields carbon. Reactions such as [1] a disproportionation of carbon monoxide or [2] the reduction of carbon monoxide are often suggested as carburizing processes. These reactions are represented by the partial equations

$$2CO_{(ads)} \rightarrow CO_{2(g)} + C \qquad [1]$$

$$CO_{(ads)} \rightarrow [O] + C \qquad [2]$$

where subscripts (ads) and (g) are abbreviations for "adsorbed" and "gas", [O] is an oxygen incorporated into an oxide lattice site at the surface, and C is free carbon on the oxide surface. However, neither is entirely satisfactory in the present instance, since reaction [1] is hindered by the high proportion of carbon dioxide in the atmosphere and the high temperature, and reaction [2] is precluded by the fact that carbon monoxide is reducing to all three iron oxides. It is conceivable that the feasibility of reaction [1] is enhanced by a sufficient local accumulation of carbon monoxide so that, kinetically, the reaction can occur. However, there is no direct evidence for this, and further speculation about the surface carbon monoxide reaction appears unwarranted at this time.

While the processes responsible for the production and transport of carbon through the outer scale remain unresolved, the continued high oxidation rates in spite of extensive voids and the carburization of the alloy in a normally decarburizing atmosphere suggest the generation of a CO_2-CO atmosphere within the voids. Thus the mechanism for the oxidation of the Fe-Cr alloys in carbon dioxide is similar to that proposed for H_2O-Ar atmospheres (5) with the CO_2-CO replacing the H_2O-H_2 as the oxygen carrier between the outer and inner scale layers. In this situation, however, the carburizing reaction has significant consequences in that considerable structural changes occur within the alloy, a point obviously worthy of consideration in the structural use of similar materials at high temperature in normally noncarburizing CO_2-CO mixtures. The generation of an oxidizing-carburizing atmosphere within the voids and the prevention of direct access of carbon dioxide by a dense, continuous outer oxide layer, are both necessary to explain the observations in the present experiments.

Acknowledgment

The contributions of Mr. Ove Mylting in the carbon analysis and Mr. Edward J. Brooks in the electron microprobe and x-ray fluorescence analyses are gratefully acknowledged.

Manuscript received Nov. 17, 1966; revised manuscript received Feb. 4, 1967. This paper was presented in part at the Philadelphia Meeting, Oct. 9-14, 1966.

Any discussion of this paper will appear in a Discussion Section to be published in the December 1967 JOURNAL.

REFERENCES

1. C. T. Fujii and R. A. Meussner, *This Journal*, **110**, 1195 (1963).
2. K. Hauffe and H. Pfeiffer, *Z. Metalkunde*, **44**, 27 (1953).
3. W. W. Smeltzer, *Acta Met.*, **8**, 377 (1960).
4. F. S. Pettit and J. B. Wagner, Jr., *ibid.*, **12**, 35 (1964).
5. C. T. Fujii and R. A. Meussner, *This Journal*, **111**, 1215 (1964).
6. A. Rahmel and J. Tobolski, *Corrosion Sci.*, **5**, 333 (1965).
7. A. Rahmel and J. Tobolski, *Werkstoffe u. Korrosion*, **16**, 662 (1965).
8. H. Inouye, "High Temperature Reactions of Type 304 Stainless Steels in Low Concentrations of CO_2 and CO," pp. 317-342 in Proceedings Vol. I, Conference on Corrosion of Reactor Materials, June 4-8, 1962, International Atomic Energy Agency, Vienna (1962).
9. H. E. McCoy, *Corrosion*, **21**, 84 (1965).
10. W. B. Jepson, J. E. Antill, and J. B. Warburton, *Brit. Corrosion J.*, **1**, 15 (1965).
11. H. T. Daniel, J. E. Antill, and K. A. Peakall, *J. Iron Steel Inst.*, **201**, 154 (1963).
12. A. U. Seybolt, *This Journal*, **107**, 147 (1960).
13. K. Bungardt, E. Kunze, and E. Horn, *Arch. Eisenhuttenw.*, **29**, 193 (1958).
14. R. L. Levin and J. B. Wagner, Jr., *Trans. Met. Soc. AIME*, **233**, 159 (1965).

DTA and X-ray Studies of Electroless Nickel

J.-P. Randin, P. A. Maire,[1] E. Saurer,[2] and H. E. Hintermann

Laboratoire Suisse de Recherches Horlogères, Neuchâtel, Switzerland

ABSTRACT

Electroless nickel and mixtures of nickel and phosphorus powders were studied by differential thermal analysis. The evolution of heat during the rise of temperature of the electroless nickel specimens is either 17 or 11% of the heat of formation of Ni_3P, which is the final reaction product. The value of 17% corresponds to electroless nickel with phosphorus contents $\leq$ 8 w/o, that of 11% to contents $>$ 10 w/o. X-ray analysis has shown that the reaction product is Ni_3P and that no other phosphide is present. Thus one may assume, that electroless nickel in the as-plated state is a supersaturated solid solution of phosphorus in nickel as a metastable intermediate state between that of a mixture of nickel plus phosphorus and the equilibrium system of nickel plus Ni_3P.

Electroless nickel is a binary alloy of nickel and phosphorus. According to Gutzeit (1), the phosphorus content varies between 3 and 15 w/o depending on the bath composition and the deposition parameters.

Several authors (2, 3) expect the phosphorus to be present as nickel phosphide Ni_3P in the as-plated electroless nickel. Fléchon (4) indicates that the chemical reactivity of the alloy presents some analogy with elementary phosphorus. Further, Graham, Lindsay, and Read (5) show that electroless nickel is not amorphous as several authors believed (2, 4, 6), but is rather a supersaturated solid solution of phosphorus in crystalline nickel. Goldenstein, Rostoker, Schossberger, and Gutzeit (2) present some qualitative thermodynamic data on this matter.

In an attempt to establish the nature of the chemical state of phosphorus in as-plated electroless nickel, x-ray and differential thermal analysis (DTA) were carried out on this system.

Experimental Procedure

Preparation of deposits.—An acid bath of the following composition was used: $NiCl_2 \cdot 6H_2O$: 30 g/l; $CH_2(OH)COOH$: 30 g/l; $COOH(CH_2)_2COOH$: 10 g/l; NaF : 3 g/l; NaOH to adjust the desired *p*H. The reducing agent was sodium hypophosphite, added to the bath in a concentrated solution of 500 g/l at constant rate. If the *p*H and the nickel concentration are kept constant during the entire deposition time, coatings of uniform phosphorus distribution can be obtained (7). By adjusting the *p*H of the bath between 5.0 and 4.0; deposits with phosphorus contents between 3.5 and 11.4 w/o are produced for an introduction rate of hypophosphite of 0.05 mole/h. Powdery samples were prepared by seeding the bath with palladium chloride. Electroless nickel was also deposited on pure nickel[3] wire and the coatings stripped off thereafter mechanically. The differential thermal analysis carried out on both types of samples did not show any noticeable difference. The deposits on nickel wire, however, showed a strong preferred orientation.

Differential thermal analysis.—The measurements were made with a Netzsch[4] microcalorimeter under argon atmosphere either in a nickel sample holder or in Pyrex phials sealed under vacuum. The heating rate was 2°/min, the weight of the samples 500-600 mg. The accuracy of the measurements depends largely on the reaction rate and is assumed to be ±5% for samples containing 12 w/o phosphorus and ±20% for alloys with phosphorus contents of about 4 w/o. The high phosphorus alloys have sharper reaction peaks.

X-ray.—The x-ray investigation was carried out on cylindrically agglomerated powder samples of 1 cm^2 cross section, pressed at 25 t/cm^2. Particles smaller than 400 mesh (37 mμ) were used. Under these conditions of pressure and particle size distribution, the intensity of the diffraction lines was insensitive to further changes of these two parameters towards higher pressures and smaller particle sizes. The samples did not exert any preferred orientation.

The diffraction peak intensities and the angular position of its maxima were determined on a Philips x-ray diffraction unit equipped with a scintillation counter and a pulse height analyzer. Filtered CoK_α radiation (voltage 30 kv, current 10 ma, Fe filter) was used. The scanning speed was 1/8° 2θ per minute. The width of the divergence slit was 1°, that of the receiving slit 0.2 mm.

Results and Discussion

Differential thermal analysis.—All the reactions are

[1] Present address: Compagnie des Montres Longines, Saint-Imier, Switzerland.

[2] Present address: Institut de Physique de l'Université, Neuchâtel, Switzerland.

[3] AT Nickel, Ni 99% min.; H. Wiggin and Company, Ltd., England.

[4] Netzsch, Selb (Bayern), West-Germany.

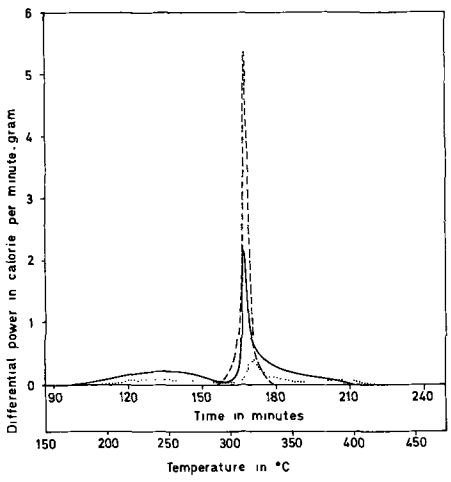

Fig. 1. DTA curves of electroless nickel: ------, 4.5 w/o phosphorus; ———, 7.8 w/o phosphorus; — — —, 11.7 w/o phosphorus.

exothermic. The shape of the DTA curves, *i.e.*, ΔT *vs.* temperature, depends on the phosphorus content of the electroless nickel (Fig. 1).

At phosphorus contents larger than 10 w/o one single sharp peak appears at a temperature of 310°C. At lower percentages of phosphorus two reactions are observed. Between 6 and 8 w/o phosphorus a diffuse line of low intensity shows up covering the entire temperature interval from 200° to 300°C. The second peak appears at the same temperature of 310°C as before, yet less intensive and markedly broadened toward the high-temperature side of the scale. At low phosphorus concentrations of some 4 w/o, broadening of this latter peak is even more pronounced, and the reaction fades away only toward 420°C.

Thus, two reaction areas can be distinguished : one below 300°C, the other above 300°C. The reaction heat of the former will be called Q_1 that of the latter Q_2. The measured Q_1 and Q_2 are plotted on Fig. 2 as a function of the phosphorus content. The heat Q_2 is proportional to the phosphorus content of the electroless nickel while Q_1 passes through a maximum at about 8 w/o phosphorus and vanishes thereafter at a concentration higher than 10 w/o. It appears that the total heat released is proportional to phosphorus content only up to 8 w/o.

Two reactions occur at concentrations below 10 w/o while only one is observed above this concentration.

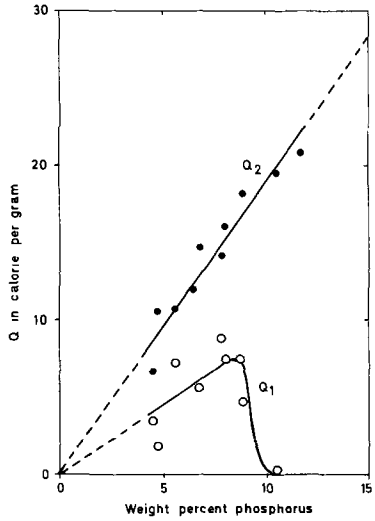

Fig. 2. Energy evolved during heating of electroless nickel as a function of its phosphorus content: ○ Q_1, reaction heat for T <300°C; • Q_2, reaction heat for T >300°C.

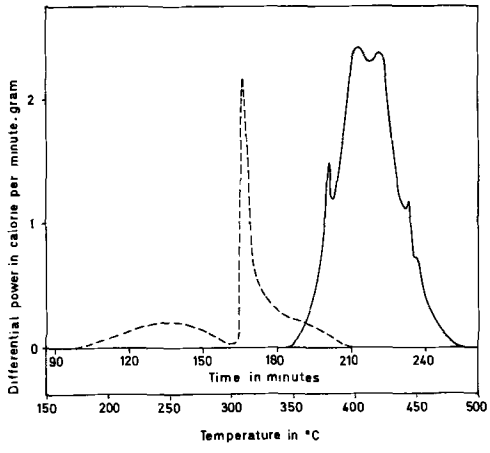

Fig. 3. DTA curves of electroless nickel and Ni + red phosphorus at intermediate phosphorus contents: — — — electroless nickel 7.8 w/o phosphorus; ——— Ni + 7.8 w/o red phosphorus.

An x-ray study on two samples containing 8 w/o phosphorus, one heated to completion of the reaction, the other to partial completion only, namely to 550° and 285°C, respectively, revealed two distinct phases. For heat-treated samples at 285°C the x-ray diagrams compare well to those obtained by Graham *et al.* (5) for as-plated electroless nickel, while those heat-treated to completion of the reaction show sharp diffraction peaks of a phosphide and a nickel phase.

Comparison between heats of reaction of a nickel-phosphorus mixture and of electroless nickel.—Mixtures of nickel[5] with red[6] or white[7] phosphorus produce heats of reaction of the same order of magnitude (Fig. 3). They compare well with the results found by Weibke and Schrag (8) who indicate a value of 48.4 kcal/mole for the formation of Ni_3P at 630°C. As mentioned before, the heat of reaction of the electroless nickel is a function of its phosphorus content. The heat Q_2 of the single reaction which occurs at phosphorus contents above 10 w/o is 5.9 kcal/mole Ni_3P. The total heat of reaction $Q_1 + Q_2$ for alloys with less than 8 w/o phosphorus is 8.9 kcal/mole Ni_3P.

These results are in accordance with those of Goldenstein *et al.* (2) who state that the thermal evolution of specimens with phosphorus contents of 7-10 w/o is considerably higher than 1 kcal/mole.

Ni_3P is the last product of a series of reactions in the solid state for both electroless nickel and a mixture nickel + red phosphorus, as will be shown in the next section. However, the heat evolved on heating of electroless nickel is only some 11-17% of the heat of formation of Ni_3P.

X-ray.—Nickel and nickel phosphide, Ni_3Po, samples were studied by x-ray diffraction methods. Fléchon (4) indicates for Ni_3P a tetragonal structure (a = 8.91Å, c = 4.39Å) and states the extinction condition to be h + k + l = 2n. Unfortunately almost all the Ni_5P_2 and Ni_2P lines coincide with those of nickel or Ni_3P, so that it is impossible to assert the existence of a Ni and a Ni_3P phase only.

To prove that all phosphorus of the samples is transformed during heating to Ni_3P with the exclusion of any other phosphide, it had to be shown that by allowing the stoichiometric amounts of Ni and P to form Ni_3P to react, *i.e.*, 14.96 w/o phosphorus, no pure phase of Ni was allowed to remain at completion of the reaction. The procedure to prepare and investigate the samples is given in some details hereafter: samples of between 0 and 15 w/o phosphorus content were pre-

[5] Carbonyl-nickel powder Type 122, The International Nickel Company (Mond) Ltd.

[6] E. Merck A.G. Darmstadt, West-Germany.

[7] Siegfried A.G. Zofingen, Switzerland.

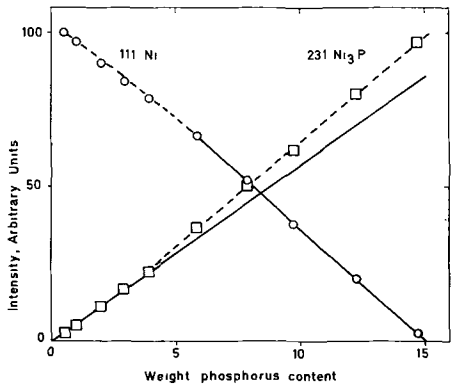

Fig. 4. Intensity of the 111 and 231 reflections of Ni and Ni_3P, respectively, as a function of the phosphorus content on agglomerated powder samples of a mixture of Ni + Ni_3P at different concentrations in phosphorus. ○ 111 Ni; ---- □ 231 Ni_3P; ——— calibration curve.

pared by mixing and pressing powders of Ni and Ni_3P. The reflections 111 of nickel and the 231 of Ni_3P were recorded and measured as they show strong intensities and are well separated from other lines. Figure 4 shows that from a value of 5 w/o phosphorus onward the intensity of the 111 reflection of nickel decreases linearly with increasing phosphorus content and intercepts the abscissa at 15 w/o. The intensity of the 231 reflection of Ni_3P does not rise linearly with increasing phosphorus content. Rather, due to weaker absorption of the diffracted beam and stronger secondary radiation, a deviation of the intensity toward higher values becomes progressively important as the phosphorus concentration of the samples continues to increase. As a consequence, the measured diffraction intensities from electroless nickel have been corrected by the amount of this effect. This is for each phosphorus concentration the ordinate difference between the experimentally determined curve and its tangent through 0 w/o phosphorus.

Three series of electroless nickel samples were analyzed after a heat treatment at 400°, 500°, and 800°C, respectively. X-ray intensity measurements were also performed on a mixture of carbonyl-nickel + red phosphorus heated at 800°C. For all samples a linear decrease of intensity of the 111 reflection of nickel and its disappearance at the stoichiometric composition was observed. The relation of the corrected intensities of the 231 line of Ni_3P *vs.* phosphorus content is linear too, and shows an intercept at the abscissa at 0 w/o phosphorus (Fig. 5). These results demonstrate that heat-treated electroless nickel consists solely of the two phases: Ni and Ni_3P, with the exclusion of any other phosphide.

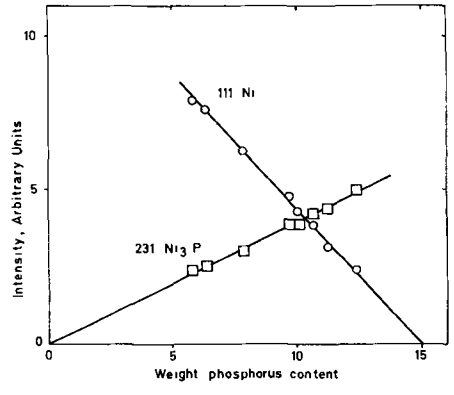

Fig. 5. Intensity of the 111 reflection of Ni and corrected intensity of the 231 reflection of Ni_3P from electroless nickel heat treated at 800°C for 2 hr as a function of its phosphorus content: ○ 111 Ni; □ 231 Ni_3P.

The lattice parameter of electroless nickel samples annealed at 800°C after agglomeration was determined using Nelson-Riley extrapolation techniques. Values between 3.5237 and 3.5242 ± 0.0003Å were obtained. The average of these values compare well with the ASTM value of 3.5238Å. The atomic radii of phosphorus and nickel are 1.28 and 1.24Å, respectively (9), *i.e.*, they differ by somewhat more than 3%. From the copper-phosphorus system for which the atomic radii of both elements are the same, *i.e.*, 1.28Å (9), it has been shown (10) that the addition of 0.58 w/o phosphorus to copper changes its lattice parameter from 3.6078 kX at 0 w/o phosphorus to 3.6092 kX at 0.58 w/o phosphorus. By analogy it can be concluded that the same amount of phosphorus in nickel would change its lattice parameter even more drastically. Hence, from the very excellent concordance of the measured lattice parameter for electroless nickel with the ASTM value, it must be concluded that the phosphorus content in the heat-treated nickel phase is very low and that therefore only a little if any phosphorus occupies substitutional or interstitial positions in the lattice of the heat-treated electroless nickel.

Conclusions

Differential thermal analysis shows that the heat evolution during heating of electroless nickel corresponds to about 17% of that of the heat of formation of Ni_3P for phosphorus contents smaller than 8 w/o, and about 11% of this heat of formation for samples containing more than 10 w/o phosphorus. Further it could be shown by x-ray analysis that the reaction product is Ni_3P at the exclusion of the presence of any other phosphides. The nickel phase in heat-treated alloys contains very little or no phosphorus in interstitial or substitutional positions.

Therefore the as-plated electroless nickel may be, as proposed by Graham *et al.* (5), a supersaturated solid solution of phosphorus in nickel as a metastable intermediate state between that of a mixture of nickel plus phosphorus and the equilibrium system of nickel plus Ni_3P. It can be considered that this intermediate state includes phosphorus atoms chemically bonded to nickel atoms as a phosphide since 83-89% of the heat of formation of the stable state of nickel plus Ni_3P is released. This latter supposition is not confirmed by previous work of other authors (2, 5) as they do not find any diffraction lines from a phosphide phase in their electron diffraction studies. However, as the diffraction lines of nickel and phosphides often coincide wholly or in part and as the grain size of the as-plated electroless nickel is extremely small and therefore causes a strong line broadening, the diffraction lines from a phosphide phase would be hardly discernible. Moreover, the phosphide phase is expected to precipitate in extremely small grain size, too.

Acknowledgment

The authors wish to thank Professor P. Dinichert, Director of the L.S.R.H. for his advice and interest in this work and for permission to publish this paper. They also wish to acknowledge the valuable assistance of Dr. E. Hofer in the x-ray studies, particularly the lattice parameter determination.

Manuscript received Oct. 24, 1966; revised manuscript received Feb. 1, 1967.

Any discussion of this paper will appear in a Discussion Section to be published in the December 1967 JOURNAL.

REFERENCES

1. G. Gutzeit, *Plating*, **46**, 1158 (1959).
2. A. W. Goldenstein, W. Rostoker, W. Schossberger, and G. Gutzeit, *This Journal*, **104**, 104 (1957).
3. Van Royen, *Electroplating Metal Finishing*, April, 114 (1957).
4. J. Fléchon, Thesis, Nancy, 1960.
5. A. H. Graham, R. W. Lindsay, and H. J. Read, *This Journal*, **109**, 1200 (1962); **112**, 401 (1965).

6. K. T. Ziehlke, W. S. Dritt, and C. H. Mahoney, *Metal Prog.*, **77**, 84 (1960).
7. J.-P. Randin and H. E. Hintermann, *Plating*, to be published.
8. F. Weibke and G. Schrag, *Z. Elektrochem.*, **47**, 222 (1941).
9. R. P. Elliott, "Constitution of Binary Alloys," 1st ed., p. 874, McGraw-Hill Book Co., New York (1965).
10. W. B. Pearson, "A Handbook of Lattice Spacings and Structure of Metals and Alloys," p. 594, Pergamon Press, New York (1958).

Penetration of Electrophoretic Deposits into Cylindrical Tubes

Douglas A. Olsen and Peter J. Boardman

Archer Daniels Midland Company, Minneapolis, Minnesota

and Stephen Prager

Department of Chemistry, University of Minnesota, Minneapolis, Minnesota

ABSTRACT

The process of electrophoretic deposition of organic coatings has the inherent advantage of superior penetration of the electrodeposited film into the interior of hollow metal objects. In the work reported here a mathematical treatment of the extent of penetration of electrodeposited film into a tube is developed, based on a model that assumes electrophoretic deposition ceases when either (*i*) the film is sufficiently thick to block the passage of current or (*ii*) the supply of polymer particles to the substrate is inadequate. Experimental data relating the length of film penetration to polymer concentration, applied voltage, tube radius, and time are also reported. Good agreement between theory and experiment is obtained.

The electrophoretic deposition of organic materials was first reported by Sheppard and Eberlin (1) in 1925. In the intervening years there has been a wealth of information published on the use of classical electrophoresis for separations and for studying double layer phenomena. Investigations of electrophoretic deposition and of the electrode reactions involved in the process have been few and fragmentary, however. One of the more complete studies was that of Fink and Feinleib (2) in 1948, which also includes a rather complete bibliography of earlier work.

Recently the phenomenon of electrophoretic deposition has been successfully applied to an industrial painting process (3), and additional reports, mostly of a practical nature, have begun to appear (4). From several studies (2, 5, 6) of the electrophoretic deposition of synthetic resins the following facts have been obtained. Of the two steps in the process, that of movement of the particles toward the electrode and that of reaction at the electrode, the latter is the controlling step. Deposition of the resin at the anode occurs as a result of coagulation by metal ions and/or hydrogen ions, with the metal ions being formed by anodic dissolution of the metal and the hydrogen ions resulting from the anodic discharge of hydroxyl ions. The deposition obeyed Faraday's law at least approximately. Unlike the deposition of metals, the electrical equivalent weight of a resin is variable depending on the degree of neutralization.

From a practical point of view the electrophoretic deposition process has several inherent advantages. One of them is its so-called "throwing power" which is the subject of this investigation and is defined as the ability of an electrophoretically deposited resin film to penetrate into the interior of a hollow metal object (6). In practical terms this ability permits the formation of resin films in difficult to reach corners, nooks, and pockets of an irregular work piece (7). The deposition of films on interior surfaces, however, is a considerably slower process than on exterior surfaces. Previous work in this laboratory (6) has shown that the actual deposition mechanism on the metal surface remains the same, but that the potential gradient controlling the migration of emulsion particles to the interior anode surface changes as deposition occurs. In the present study a mathematical formulation of throwing power has been developed and the validity of the resulting equations has been tested.

Mathematical Formulation

Before proceeding to the mathematical formulation of this section it is instructive to consider a qualitative view of throwing power (6). Figure 1 shows two views of an idealized throwing power apparatus, *viz.*, a hollow cylindrical anode immersed in a resin dispersion and perpendicular to a flat cathode. The electric field is represented by the equipotential surfaces shown as solid lines. At the onset of electrodeposition the field would be as shown at the left of Fig. 1. The emulsion particles being drawn to the anode follow the lines of force which are everywhere perpendicular to the equipotential surfaces. As shown, at $t = 0$ an emulsion particle in the bulk of the dispersion would migrate to the outside of the metal tube. The emulsion particles inside the tube are not subjected to an electric field and are not attracted to the inner wall of the tube. At the entrance to the tube one component of the field is perpendicular to the inner wall thus providing lines of force for the emulsion particles to follow. Thus, the outside of the tube is completely coated within a few seconds from the onset of the electrodeposition. On the inside of the tube, the mouth is coated immediately while the interior regions of the tube are not coated at all. Turning now to the right of Fig. 1, the process of electrodeposition is shown

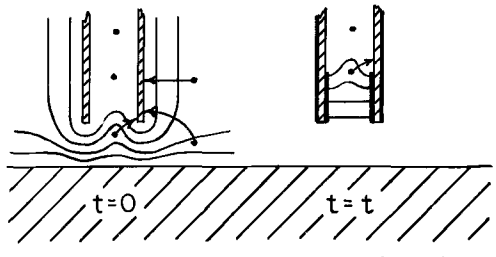

Fig. 1. Lines of force and emulsion particle pathways during electrophoretic deposition.

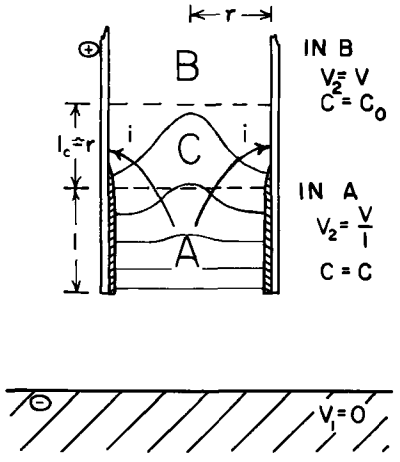

Fig. 2. Expanded view of the tube interior near the transition region.

after a period of time. The equipotential surfaces are shown only for the inside of the tube since the outside of the tube has long since been coated. Toward the mouth of the tube there is an electrodeposited layer which is essentially a nonconductor. The equipotential surfaces are now perpendicular to the nonconducting deposit except in the transition region. As at $t = 0$ deposition occurs only in the transition region. As the coated region is enlarged the transition region penetrates into the tube.

In order to develop a mathematical formulation from the qualitative point of view of Fig. 1 it is necessary to consider the transition region in greater detail. At any instant the tube can be divided into three regions as shown in Fig. 2. In region A the walls have been covered by an insulating film of resin; in this region the potential is essentially constant over a given cross section of the tube, the potential does vary linearly with distance along the axis, *i.e.*, there is an axial potential gradient V/l. In region B the potential is constant at V. Region C is the transition region, and, as discussed above, it is here that deposition of resin occurs on the walls of the tubes. It is to be expected that the length of C will be proportional to r with a proportionality constant of order unity. No current flows from C into B, since there is no potential gradient in B. Since one component of the field in C is perpendicular to the wall there is also a component of the current density perpendicular to the wall. Hence all the current flowing from region A into region C by virtue of the potential gradient in region A must pass out through the wall of the tube in region C. Thus the current density, i, on this portion of the tube wall is given by

$$2\pi r^2 i = \pi r^2 \kappa \frac{V}{l} \qquad [1]$$

where κ is the conductivity of the suspension. Equation [1] may be simplified to give

$$i = \frac{\kappa}{2}\frac{V}{l} \qquad [2]$$

From this point on, two possible models may be considered. It is assumed that the deposition in region C ceases (or is at least considerably slowed down) due to: (*a*) the insulating properties of the deposited film, *i.e.*, the deposition ceases after the passage of a given quantity of coulombs, or (*b*) the depletion of resin particles from the dispersion in the immediate vicinity of the tube wall. It is expected that the former would be dominant at long times, when the current density i has become low because of the large value of l, whereas the latter would tend to be more important during the initial stages of the experiment, when i is still relatively high.

Proceeding to the mathematical formulation of model (*a*) it has been shown elsewhere (6) that the deposition of resin obeys Faraday's laws. Thus the mass m deposited per unit area per unit time is given by

$$\frac{1}{A}\frac{dm}{dt} = \frac{R}{\mathbf{F}} i \qquad [3]$$

where i is the current density, R is the equivalent weight, and $\mathbf{F}$ is Faraday's constant. From Eq. [3] it is obvious that the rate of deposition of resin per unit area in region C is proportional to the current density. It is also apparent that after a time t_c the rate of deposition in region C is markedly reduced, due to the insulating properties of the deposited film of some limiting surface density ρ

$$t_c = \frac{\rho}{\frac{1}{A}\frac{dm}{dt}} \qquad [4]$$

Since t_c is the time taken for resin of surface density ρ to deposit over the width r of region C, the film is advancing at a velocity dl/dt given by

$$\frac{dl}{dt} = \frac{r}{t_c} \qquad [5]$$

Substitution from Eq. [2], [3], and [4] into Eq. [5] gives

$$\frac{dl}{dt} = k\frac{rC_0V}{l} \qquad [6]$$

where $k = \alpha R/2\rho\mathbf{F}$, and where it has also been assumed that the conductivity κ is proportional to the resin concentration C_0 with a proportionality constant α. This, of course, does not imply that the resin dispersion carries the current, but rather that current transporting ions are introduced into the dispersion in proportion to the resin concentration.

The regime described by model (a) is dominant at long times, *i.e.*, when the time t and the length of penetration l exceed certain critical values t^* and l^*. Thus Eq. [6] may be integrated with these values as lower limits to give

$$l^2 - l^{*2} = 2krC_0V(t - t^*) \qquad [7]$$

In order to evaluate t^* and l^* it is first necessary to deal with the regime described by model (b) which is dominant at times less than the critical value t^*.

To treat model (b) we must calculate the time t_c required for the resin concentration of the dispersion at the tube wall to drop from $C = C_0$ to $C = 0$ under the application of a constant current density i. This decay is controlled by the diffusion equation

$$\frac{\partial C}{\partial t} = D\frac{\partial^2 C}{\partial x^2} \qquad [8]$$

where D is the diffusion constant of the resin and x is the distance from the tube wall. Equation [8] is subject to the initial condition

$$C(x,0) = C_0 \qquad [9]$$

and the boundary condition

$$i = \epsilon D\frac{\partial C}{\partial x} \qquad \text{at } x = 0 \qquad [10]$$

ϵ being a constant of proportionality. The solution of Eq. [8] subject to Eq. [9] and [10] is given by Carslaw and Jaeger (8)

$$C(0,t) = C_0 - \frac{2i}{\epsilon}\left(\frac{t}{\pi D}\right)^{1/2} \qquad [11]$$

The time t_c when the resin concentration drops to zero is therefore

$$t_c = \frac{\pi\epsilon^2 D C_o^2}{4i^2} \quad [12]$$

Just as for model (a), after time t_c the rate of deposition in region C is reduced. In this instance, however, the rate is reduced because of the exhaustion of resin from the vicinity of the interface and not because of the insulating properties of the built-up film. Once again we can argue that it takes a time t_c to cover a strip of width r, and that the velocity of the advancing film is given by

$$\frac{dl}{dt} = \frac{r}{t_c} \quad [13]$$

Substitution of Eq. [2] and [12] into Eq. [13] then gives

$$\frac{dl}{dt} = k' \frac{rV^2}{Dl^2} \quad [14]$$

where $k' = \alpha^2/\pi\epsilon^2$. Since Eq. [14] is expected to apply at short times it may be integrated, ignoring effects near the entrance of the tube, subject to the conditions that $l = 0$ at $t = 0$ and that $t < t^*$, *viz.*

$$l = \left(\frac{3k'}{D}\right)^{1/3} r^{1/3} V^{2/3} t^{1/3} \quad [15]$$

The transition from regime (b) to regime (a) will occur when the values of dl/dt calculated from Eq. [6] and [14] are of a comparable magnitude; to obtain l^* we therefore equate the right-hand sides of Eq. [6] and [14]

$$l^* = \frac{k'}{k} \frac{V}{C_o D} \quad [16]$$

and substitution of Eq. [16] into Eq. [15] then gives

$$t^* = \frac{k'^2}{3k^3} \frac{V}{C_o^3 D^2 r} \quad [17]$$

so that Eq. [7] becomes

$$l = \sqrt{2krC_oVt + K\frac{V^2}{C_o^2 D^2}} \qquad K \equiv \frac{k'^2}{3k^2} \quad [18]$$

At $t = t^*$ the first term of Eq. [18] is twice the second term, and it also becomes more dominant with increasing time.

As will be seen below the experimental results show that $t > t^*$ applies most of the time. Thus the discussion is concerned chiefly with the verification of Eq. [18]. For $t < t^*$ Eq. [15] would apply.

Experimental Procedure

The determination of throwing power of an electrophoretically deposited film is an extension of a procedure reported previously for films deposited on exterior surfaces (6). Essentially the procedure consists of submerging a clean bare steel tube (0.9 cm ID by 25 cm in length) in an emulsion contained in a circular one gallon tank (6.5 in. ID by 7.5 in. high). The tank acts as the cathode and the steel tube as the anode. The rectifier (Dresser Electric Company, Detroit, Michigan) used in this work operates within 0-1000v d.c. and 0-5 amp with a capacity of 10,000w.

The throwing power was measured as the length of penetration of the electrodeposited film into the interior of the steel tube. Initially the tubes were sawed open and the length of penetration measured. In later tests a thin metal strip was inserted into the tube. After the test was completed the strip was removed and the length of penetration was easily measured. The steel tube could not be reused without thorough cleaning. The length of penetration into the hollow tubes was measured as a function of voltage, resin concentration, tube radius, and time.

The resins used in this work were proprietary polycarboxylic acid resins of an experimental nature. Of necessity resins from several batches were used; however, they were all similar in nature to AROLON® EP7992-15-104 resin (Archer Daniels Midland Company) which has an acid value of 50 to 60. The resins were first neutralized to about 40% of the acid value with diethyl amine with sufficient water added to make a paste. The emulsions were prepared by inverting the water-amine-resin paste in about equal parts of water and then adding slowly with rapid agitation sufficient water to make an emulsion of the desired per cent solids; 6% in most instances.

Results and Discussion

As will be discussed in this section model (a) is the dominant model, and consequently Eq. [18] provides the best understanding of the relationship between the length of penetration and the other variables. The various dependencies necessary to test the validity of Eq. [18] are obtained by rearrangement and are of the form $y = mx + b$.

The first such equation is

$$\frac{l^2}{V} = 2krC_o t + K\frac{V}{C_o^2 D^2} \quad [19]$$

which predicts a linear graph of l^2/V plotted *vs.* V for the region $t > t^*$. As can be seen from Fig. 3 a graph of l^2/V *vs.* V is almost independent of V thus establishing that the slope K is small and is effectively zero between 200 and 600v. From a consideration of Eq. [17] it is also apparent that a small value of K dictates a small critical value t^*. Therefore it is to be expected that most of the effects observed in this study will be due to regime (a) where $t > t^*$.

Since K is effectively zero Eq. [18] predicts a linear graph of l plotted *vs.* $\sqrt{V}$ passing through the origin. This is shown to be true experimentally in Fig. 4.

The other variables to be considered are resin concentration C_o, tube radius r, and time t. Rearrangement of Eq. [18] gives

$$l^2 C_o^2 = 2krC_o^3 Vt + K\frac{V^2}{D^2} \quad [20]$$

which predicts a linear $l^2C_o^2$ *vs.* C_o^3 dependence pass-

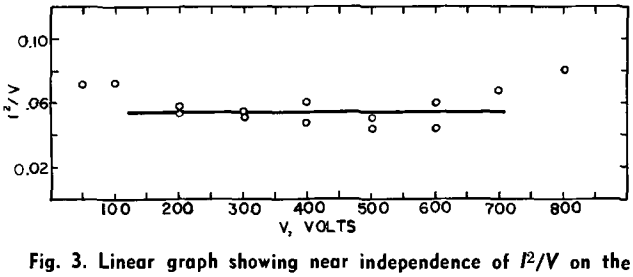

Fig. 3. Linear graph showing near independence of l^2/V on the applied voltage V.

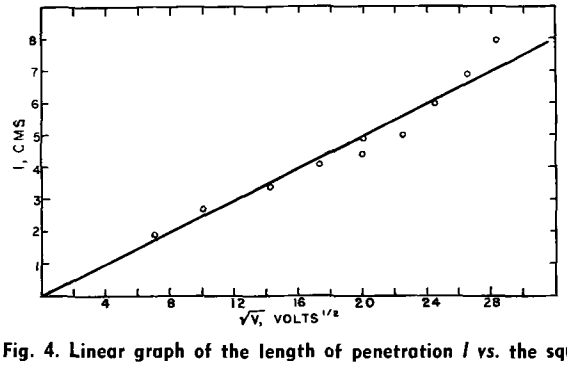

Fig. 4. Linear graph of the length of penetration l *vs.* the square root of the applied voltage $\sqrt{V}$.

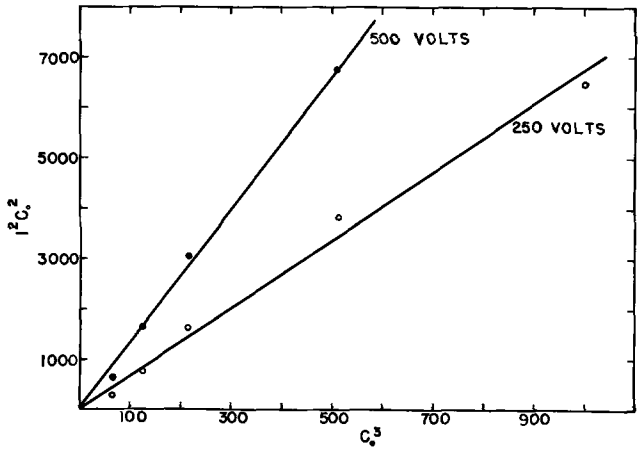

Fig. 5. Linear graph of $l^2C_o^2$ vs. C_o^3 predicted by Eq. [18] for negligible K.

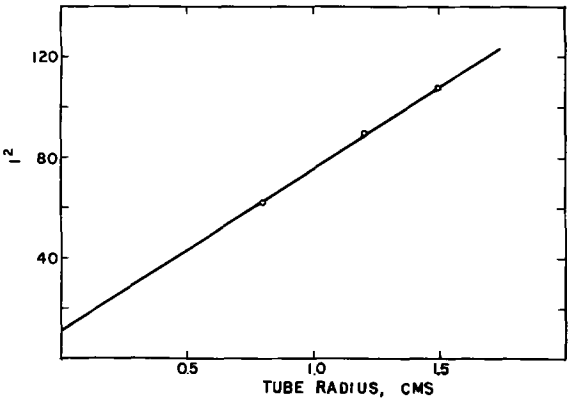

Fig. 6. Linear graph of l^2 vs. tube radius r

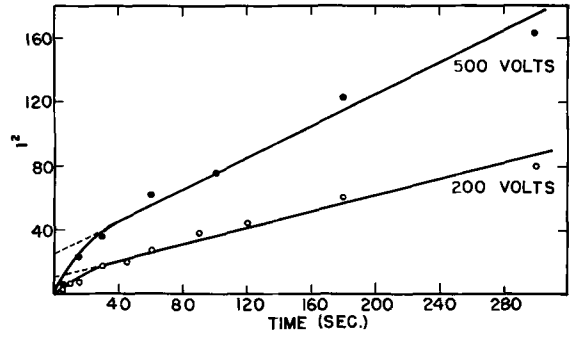

Fig. 7. Linear graph of l^2 vs. time t

ing through the origin provided K is negligible. In a similar manner

$$l^2 = 2krC_oVt + K\frac{V^2}{C_o^2D^2} \qquad [21]$$

where a linear graph of l^2 vs. r is predicted and which will pass through the origin if K is negligible. The experimental verification of a negligible K for each dependence is shown in Fig. 5 and 6, respectively. Close inspection of Fig. 6 shows that a straight line intercepting the ordinate near the origin is also a possibility thus indicating K may be small rather than zero. For the time dependence Eq. [22]

$$l^2 = 2krC_oVt + K\frac{V^2}{C_o^2D^2} \qquad [22]$$

predicts a linear l^2 vs. t passing through the origin if K is negligible. If the graph of the experimental results shown in Fig. 7 is extended it intercepts the ordinate near the origin. Thus K is, at best, small in this instance. Some variation in K between dependencies is expected since slightly differing experimental resins were used for each. From Eq. [17] for a finite K there is a finite critical value of the time t^*. Prior to time t^* Eq. [15] shows that l^2 vs. $t^{2/3}$ dependence would be expected. Such a dependence when replotted on l^2 vs. t coordinates is not inconsistent with the short time period data of Fig. 7.

Table I. Tube penetration with inserts
V = 500v, r = 1.20 cm

t, sec	l^*, cm	l, cm	$l^2 - l^{*2}$, cm
15	0[a]	6.8	46
15	6.8	9.3	42
15	9.3	11.9	55
15	11.9	14.3	60
15	14.3	16.3	64
30	1.0[b]	9.7	94
30	3.0	10.6	104
30	5.0	11.8	114
30	7.0	12.5	107

[a] In this series the electrophoretically deposited resin was baked between runs thus providing a cured film insert.
[b] In this series the inserts were thin lengths of tygon tubing.

A consideration of Eq. [7] presents the interesting possibility of placing insulating inserts in the tubes prior to deposition. If the length of the insert exceeds l^* then t^* coincides with the onset of deposition (*i.e.*, $t^* = 0$). Thus Eq. [7] becomes

$$l^2 - l^{*2} = 2krC_oVt \qquad [23]$$

where l is considered to be the length of penetration of film plus the length of the insert. Thus if uniform deposition times are used the quantity $l^2 - l^{*2}$ should be constant for all values of l and l^*. This is shown to be true experimentally in Table I where values of $l^2 - l^{*2}$ are displayed and are seen to essentially constant.

In view of the good agreement between the theory developed above and experimental results shown here it is very probable that the model on which the theory is based is indeed realistic.

In regard to possible applications of this study Eq. [18] shows that, of the factors considered, the most practical means of increasing the length of penetration into a tube is to increase the applied voltage or the resin concentration. If the constant K is sizeable an increase in the applied voltage would be especially effective.

Finally, the equations developed here should also describe penetration of aerosols into electrically charged tubes such as encountered in electrostatic spraying. It is also possible that the present work, with suitable modifications, might describe the anodizing of interior surfaces of cylindrical tubes.

Manuscript received Oct. 31, 1966; revised manuscript received Jan. 3, 1967.

Any discussion of this paper will appear in a Discussion Section to be published in the December 1967 JOURNAL.

REFERENCES

1. S. E. Sheppard and L. W. Eberlin, *Ind. Eng. Chem.*, **17**, 711 (1925).
2. C. G. Fink and M. Feinleib, *Trans. Electrochem. Soc.*, **94**, 309 (1948).
3. See, for example: (*a*) H. N. Bogart, G. L. Burnside, and G. E. F. Brewer, Society of Automotive Engineers. Paper No. 650270(988A), Detroit, Mich. Jan. 1965; (*b*) G. L. Burnside and G. E. F. Brewer, Official Digest/*J. Paint Tech.*, **38**, 96 (1966).
4. For reviews see: (*a*) L. A. O'Neill, *Review*, **37**, 217 (1964); (*b*) "Electrophoretic Paint Deposition," Translation and Technical Information Services, Braintree (Essex), England, Oct., 1965.
5. S. R. Finn and C. C. Mell, *J. Oil Colour Chem. Assoc.*, **47**, 219 (1964).

6. D. A. Olsen, Official Digest/*J. Paint Tech.*, **38**, 429 (1966).
7. G. E. F. Brewer, M. E. Horsch, and M. F. Madarasz, (*a*) American Chemical Society, Div. of Organic Coatings, Vol. 25, No. 2, p. 158, Atlantic City, Sept., 1965; (*b*) Official Digest/*J. Paint Tech.*, **38**, 452 (1966).
8. H. S. Carslaw and J. C. Jaeger, "Conduction of Heat in Solids," 2nd ed., p. 75, Oxford University Press, London (1959).

Annealing Behavior of Fine-Grained Nickel Electrodeposits

R. Weil, H. J. Sumka,[1] and G. W. Greene[2]

Department of Metallurgy, Stevens Institute of Technology, Hoboken, New Jersey

ABSTRACT

The effect of thickness on the annealing behavior of fine-grained nickel electrodeposits was studied. The first structural change on heating occurred at 310°C in the thinnest sample (0.13μ) and at 255°C when the thickness exceeded 1.2μ. Heating slightly above these respective temperatures resulted in the same structure regardless of the original thickness. The mechanism by which the first structural change occurred and which therefore was independent of thickness appeared to consist of crystallite rotation rather than uniform boundary movement. The structural changes in the samples were recorded by cinematography during annealing in the electron microscope.

In an earlier study (1), of the annealing of several types of nickel electrodeposits, it was found that microstructural changes in the bulk portion occurred at lower temperatures than those near the surface. This observation corresponded to the findings of Bailey (2) and Hu (3) that the recrystallization temperatures of cold-worked, thin films were higher than those of bulk. However, a quantitative study of the effect of the sample thickness on the annealing temperature at which structural changes occur has not yet been conducted. Electrodeposits are especially suited for such an investigation because by the proper choices of substrate and plating conditions it is possible to produce specimens with the same structure over a wide range of thicknesses. A study of the effect of thickness on the annealing behavior of electrodeposits was therefore undertaken. In addition, thin electrodeposits were heated in the electron microscope and the structural changes directly observed and recorded by cinematography in order to investigate the mechanisms of recrystallization.

Experimental Procedure

Nickel deposits ranging in thickness from 0.13 to 40μ were plated in a Watt's bath also containing 1 g/l 1-5 naphthalene disulfonic acid (Na salt). The substrate, an electroformed, fine-grained and randomly oriented copper sheet, and the plating conditions were the same as in the earlier (1) experiments. A special holder was constructed which exposed an area of 6.00 x 6.00 cm of the substrate to the plating solution. The average thicknesses of the specimen were then calculated from the weight of metal deposited. It was assumed that the density of the electrodeposits was the same as that of wrought nickel.

Small specimens were cut out of the center region of each deposit. The copper substrate was stripped from the deposit in an aqueous solution containing 500 g/l CrO_3 and 50 g/l H_2SO_4. The pieces were annealed in vacuum at various temperatures for 1 hr and then examined by transmission-electron microscopy. The thicker deposits were thinned by the Bollmann (4) method from both sides after annealing. Thinning from both sides insured that the foil which was examined came from the center part of the deposit. The first annealing temperature was selected on the basis of the earlier study (1). If no structural change was observed, the temperature was raised. If a change was observed, the temperature was lowered. This procedure was followed until a temperature range not exceeding 10°C was determined, at the lower end of which no structural change had occurred and at the upper end of which an alteration had taken place.

A 700Å-thick deposit was produced in the same manner as the thicker ones. Specimens from this deposit supported on nickel grids were placed in the heating stage of a Hitachi HU-11 electron microscope. The temperature was raised to 320°C and the structural changes were recorded on motion picture film using a Bolex camera with a f 1.4 Switar lens focussed on the fluorescent screen of the electron microscope.

Results

A typical structure of the deposits in the as-plated condition is shown in Fig. 1. It consists of fine crystallites with poorly defined boundaries and some contrast variation within each. The change in the structure upon annealing is shown in Fig. 2. Larger grains have formed. However, these grains still exhibit substructure as well as twin markings. The boundaries between the small crystallites of the remaining matrix have become more clearly defined.

As already indicated, it was possible to determine the range of less than 10°C between the highest temperature at which a structure like Fig. 1 was still observed and the lowest at which a morphology like that shown in Fig. 2 was seen. These temperature ranges, called

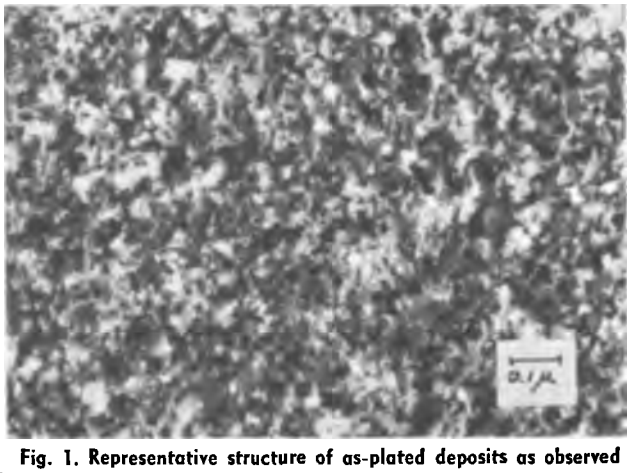

Fig. 1. Representative structure of as-plated deposits as observed by transmission-electron microscopy.

[1] Present address: Department of Material Science, Northwestern University, Evanston, Illinois.

[2] Present address: Department of Industrial Metallurgy, The University, Birmingham, England.

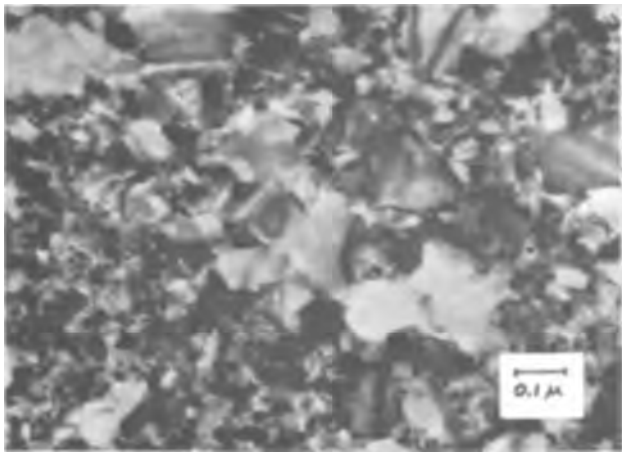

Fig. 2. First structural changes on annealing

T_{sc}, for the samples of various thicknesses are listed in Table I and graphically represented in Fig. 3.

An attempt was made to find the cause of the somewhat anomalous behavior of specimen 104. The discrepancy was reproducible and thought to be due to variation in the purity of the deposit. In view of the bath additive used, the sulfur content was indicative of the amount of codeposited foreign material. The sulfur contents are therefore listed in Table I. It is seen that samples 103 and 104 have lower sulfur contents than the rest. However, the T_{sc} of sample 103 falls on the curve with the other sample. Therefore no definite reason for the anomalous behavior of sample 104 can be given at this time.

Samples annealed at the upper temperature of the T_{sc} range exhibited essentially the same structure regardless of thickness. It therefore appears that the mechanisms in the early stage of recrystallization were not thickness dependent.

When the thicker samples were annealed at temperatures considerably above T_{sc}, relatively large, fully recrystallized grains were formed. In the thin foils, however, heating to corresponding temperatures resulted in certain areas becoming thicker at the expense of others as shown in Fig. 4. The areas devoid of metal, which have the light contrast, consisted of nickel oxide, as identified by electron diffraction. Figure 4 shows that the metal regions had recrystallized. The grains are smaller however than those obtained in thicker samples after annealing at corresponding temperatures. In many instances, the oxide regions were observed to be continuous, surrounding the metallic ones.

By examining the motion picture film of the annealing of thin foils in the heating stage of the electron microscope it was possible to make some deductions about the mechanism responsible for the first structural changes. A series of enlargements of every sixth frame of the motion picture is shown in Fig. 5. The time interval between the frames in Fig. 5 was ½ sec. It can be seen that the larger grains of the kind shown in Fig. 2 form by the coalescence of small crystallites. This phenomenon can be observed in several areas in Fig. 5. In the region designated in the eighth picture by the letter A there is initially a small crystallite showing light contrast. Immediately to the left of this crystallite is another which is gray in the first frame and becomes progressively lighter. When the two crystallites have the same contrast, there is still a small darker stripe separating them. In the last frame this

Table I. T_{sc} and sulfur contents of samples of varying thicknesses

Sample No.	Thickness, μ	T_{sc}, °C	Sulfur content, % by weight
101	36.2	250-255	0.12
102	29.7	250-255	0.16
103	2.88	258-264	0.083
104	1.22	255-259	0.097
105	0.77	272-279	0.15
106	0.39	279-285	0.18
107	0.30	283-287	0.21
108	0.25	298-303	0.17
109	0.17	296-301	0.23
110	0.13	306-310	Not determined

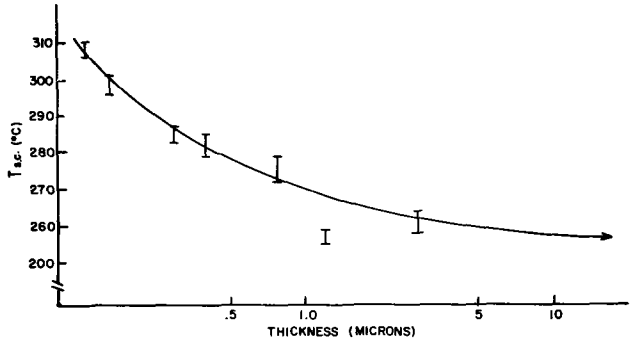

Fig. 3. Variation of T_{sc} (temperature range in which first structural change occurred) with sample thickness.

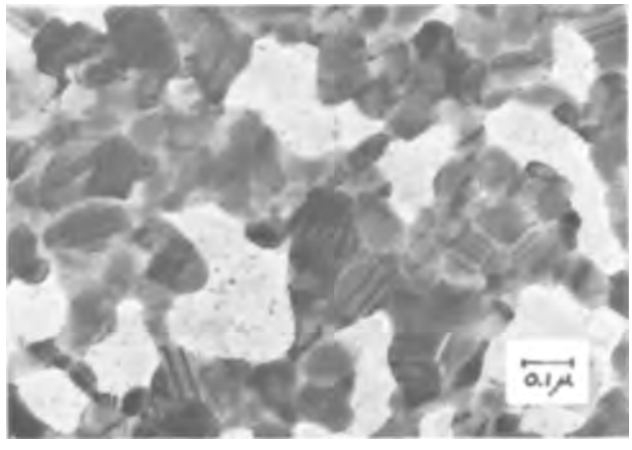

Fig. 4. Structure after annealing 700Å-thick samples at a temperature considerably above T_{sc}.

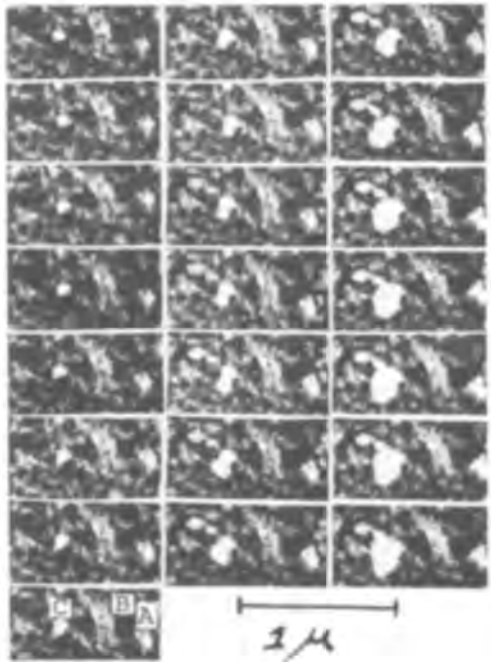

Fig. 5. Series of frames from motion picture showing sequence of first structural changes in 700Å-thick sample on annealing in the electron microscope.

stripe has almost disappeared. A similar process in which crystallites of varying dark shades assume the same black contrast can be seen in region B. In the area under C an initially small, light-contrast crystallite grows not by uniform boundary motion, but rather by a process which results in neighboring regions slowly changing contrast. Two other crystallites which become light with increasing time can also be seen to join the light one, marked C at its upper left corner. The contrast was not usually uniform throughout such a growing region and its substructure could be observed readily by tilting the specimen. Unfortunately the crystallites were too small to permit the determination of their individual orientation.

Discussion

There are several possible reasons for the effect of thickness on T_{sc}. All the samples were found by electron diffraction to be covered with an oxide film. Such a film is probably an impediment to the motion of defects. In addition to the oxide, adsorbed material as well as surface tension can impede the processes which are believed to be responsible for producing the first structural changes on annealing. Internal microstresses of the type which broaden diffraction lines are believed (1) to be associated with the excess stored energy of electrodeposits of the fine-grained, randomly oriented type used in this study. These stresses thus provide the driving force for the processes which occurred on annealing. Such stresses can be relieved partially near the surface which would result in a weaker driving force and a correspondingly higher temperature at which the processes can start in the thin samples. A study of the relationship between microstress and the annealing process is currently in progress, and an additional one on the effects of surface contamination is planned.

As the type of structure shown in Fig. 2 was observed in all samples regardless of thickness, it is probable that the mechanism observed in the motion picture is common to all the deposits which were studied. The regions of uniform contrast become the recrystallized grains.

The size of these grains appears to depend on the thickness of the deposits. The effect of thickness on the grain size after recrystallization in cold-worked material was studied by Furubayashi, Fujita, and Taoka (5). These investigators found an increase in grain size with increasing sample thickness with a very sharp rise when the sample thickness exceeded 1μ. The same relationship appears to apply to electrodeposits. As Fig. 4 illustrates, the thin films can actually increase their thickness locally so as to be able to form larger grains.

The formation of the larger grains from the small crystallites shown in Fig. 5 can only be explained by a crystallite-rotation mechanism. As the contrast is determined primarily by the deviation of crystal planes from a diffracting position, the observed matching of the shading implies a lattice rotation. Thus it appears that neighboring crystallites rotate to match the lattice orientation of the growing grains. The matching of the lattice planes at the stage shown in Fig. 2 is, however, not complete in all directions as tilting into different diffraction conditions revealed a misorientation. Twins were also frequently observed. Votava (6) observed similar contrast variation within growing recrystallized grains in copper, which had been cold-worked. Hu (7) suggested that recrystallized grains form by coalescence of subgrains in cold-worked metals. It would be desirable to have further proof of the rotation mechanism. Therefore some experiments with initially larger-grained deposits which would permit an accurate determination of the crystal orientations by electron diffraction are planned.

Acknowledgments

Part of the work reported here was supported by the Undergraduate Science Education Program of the National Science Foundation. The sulfur analyses were performed by the Paul D. Merica Research Laboratory, International Nickel Company. This article is based on project papers submitted by H. J. Sumka and G. W. Greene to the faculty of Stevens Institute of Technology in partial fulfillment of the requirements for the degree of Bachelor of Engineering with High Honor.

Manuscript received Dec. 16, 1966; revised manuscript received Jan. 27, 1967. This paper was presented at the Philadelphia Meeting, Oct. 9-14, 1966.

Any discussion of this paper will appear in a Discussion Section to be published in the December 1967 JOURNAL.

REFERENCES

1. R. Weil, W. N. Jacobus, Jr., and S. J. DeMay, *This Journal*, **111**, 1046 (1964).
2. J. E. Bailey, *Phil. Mag.*, **5**, 833 (1960).
3. H. Hu, *Trans. Metallurgical Soc., AIME*, **224**, 75 (1962).
4. W. Bollmann, "Electron Microscopy, Proc. Stockholm Conference, 1956," p. 316, Almquist and Wiksell, Stockholm (1957).
5. E. Furubayashi, H. Fujita, and T. Taoka, "Electron Microscopy 1966," Sixth International Congress for Electron Microscopy, Kyoto, **1**, 415 (1966).
6. E. Votava, *Acta Met.*, **9**, 870 (1961).
7. H. Hu, "Electron Microscopy and Strength of Crystals," G. Thomas and J. Washburn, Editors, p. 564, Interscience, New York (1963).

Adsorption, Absorption, and Degassing in the Oxygen-Niobium System at Very Low Pressure

R. A. Pasternak[1] and B. Evans[2]

Stanford Research Institute, Menlo Park, California

ABSTRACT

The interaction of low-pressure oxygen with niobium has been investigated at temperatures between 300° to 2100°K. Four main kinetic patterns can be distinguished. At temperatures close to 300°K adsorption proceeds to the formation of a saturated surface layer. At intermediate temperatures (about 500°-800°K) a thin oxide layer is formed; simultaneously oxygen dissolves and diffuses into the metal. At higher temperatures (800°-1700°K) oxygen dissolves rapidly and irreversibly; the observed kinetics can be explained by a surface mechanism involving two adsorption states. Finally, at very high temperatures (1700°K and higher) niobium oxides evaporate from an oxygen-niobium solution. The kinetics of evaporation indicates that a mixture of NbO_2 and NbO evolves, the composition of which shifts from the former to the latter with decreasing oxygen concentration.

The mechanism of sorption of active gases by refractory metals is of considerable interest in the context of corrosion and embrittlement. Nitrogen sorption by niobium at high temperature and low pressure has been described recently (1-3). This paper presents the results of a similar investigation of the oxygen-niobium system.

Experimental

The sorption kinetics of the oxygen-niobium system was investigated by the constant pressure technique [described in detail elsewhere (1-3)]. In this approach the sorption rates are measured directly, and the amounts sorbed are found by integration.

The sample, a ribbon, is heated by means of a simple d-c bridge circuit which supplies virtually constant power. The temperature of the sample remains constant during sorption since its emissivity is not significantly affected by dissolved gas (4, 5). The observed change in resistance is thus a measure for the concentration of solute. It has been shown previously that for the oxygen-niobium system (6) [and also for the nitrogen-niobium system (7)] the resistance at constant temperature is proportional to concentration and that this proportionality is independent of temperature, *i.e.*, Mathieson's rule is obeyed. Gebhardt and Rothenbacher (6) report a resistivity $\rho_0 = 13.96$ μohm cm at 273°K for clean niobium and a resistivity coefficient of solution $\gamma = \Delta\rho/\rho_0 \cdot 1/c = 0.30$ $(a/o)^{-1}$ for the temperature range 273°-1273°K. The resistivity ρ_0 of the one sample to which all the data given here refer, was 14.5 μohm cm, and in the sorption runs at high temperatures a linear relationship was observed also between resistance and amount of gas dissolved.

[1] Present address: Sardar Patel University, Vallabh Vidyanagar, State of Gujarat, India.

[2] Present address: Field Emission Corporation, McMinnville, Oregon.

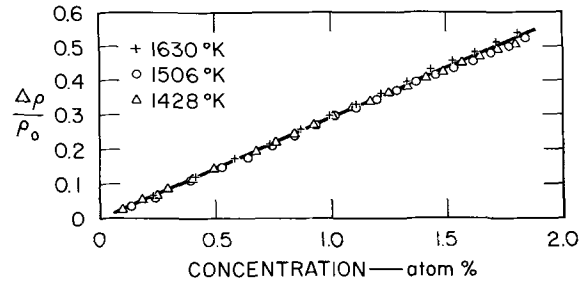

Fig. 1. Increase in the resistivity due to dissolved oxygen, expressed as fraction of the resistivity of pure Nb at 273°K.

This is shown in Fig. 1 for three runs at 1428°, 1506°, and 1630°K. The curves coincide; the average resistivity coefficient of solution is 0.3 ± 0.02 $(a/o)^{-1}$ and was assumed to apply over the entire temperature range studied. The agreement with the previous value (6) is undoubtedly fortuitous in view of the uncertainties in the measurement. The amount of oxygen dissolved in the sample could now be obtained independently by integrating the sorption rate curves based on pressure measurements, and by resistance measurements. Any discrepancy would indicate formation of an oxide phase (which would have a different resistivity from the metal) either in the bulk or on the surface.

Moreover, resistance measurements permitted a quantitative evaluation of the kinetics of the degassing reaction, which is not associated with pressure changes (see section on results); they were also the basis for defining the sample purity. A sample was assumed to be free of oxygen, if after repeated heating to about 2100°K its room temperature resistance did not decrease further.

The sample temperature was measured above 1300°K with an optical pyrometer, or was derived from resistance measurements after correcting for the effect of dissolved gas. Lower sample temperatures were defined in terms of a linear interpolation of resistance between 300° and 1300°K.

A magnetic deflection-type mass spectrometer served to monitor CO contamination (generally encountered in ultrahigh vacuum systems) as well as the pressure dependence of the ion gauge sensitivity. CO partial pressures consistently below 1% were found, even at high sample temperatures. The gas source was analytical grade oxygen from a glass bottle, connected to the system by a bakeable ultrahigh vacuum valve. Between 10^{-7} and 10^{-5} Torr, the ion gauge and mass spectrometer readings were proportional; at lower pressures the ion gauge readings were consistently higher. This discrepancy has been explained by oxygen ion emission from the grid of the ion gauge (8); the pressures given here are therefore based on the mass spectrometer readings.

The samples for this and the nitrogen study were thin ribbons rolled from high-purity, zone-refined stock. They all were originally microcrystalline with a (110) texture. At the end of the experiments they exhibited large crystals of 1 mm magnitude, and high preferred orientation; however, (110), (111), (100), and (311) textures were observed for different samples. The reason for this variation is obscure. The effects of surface orientation on the sorption kinetics were not explored quantitatively, but the over-all

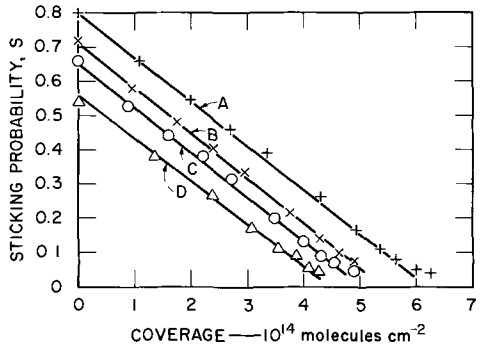

Fig. 2. Sticking probability of oxygen at 3 x 10^{-8} Torr on niobium at 300°K, as function of coverage. Curves A to D are for oxygen concentrations in the sample of 0, 0.01, 0.02, and 1 a/o.

kinetic pattern did not differ significantly for the four samples studied. Data are reported for only one of them; its dimensions were 24 x 0.112 x 0.0025 cm.

Results and Discussion

This low-pressure study is concerned primarily with the mechanisms of adsorption, solution in the homogeneous metal phase, and degassing. Four patterns of interaction can be distinguished; they are determined by temperature, and to a lesser extent by pressure.

Adsorption at room temperature.—In Fig. 2 linear plots of sticking probabilities *vs.* amount adsorbed are shown. The sample was flash heated for a few seconds to about 1800°K in ultrahigh vacuum, and after it had cooled to ambient temperature (which required about 2 min) it was exposed to oxygen at a pressure of 3 x 10^{-8} Torr. Curves A, B, and C represent adsorption runs for oxygen concentrations in the sample of about 0, 0.01, and 0.02 a/o. The concentrations were established by flash heating the sample after repeatedly adsorbing oxygen on it; the adsorbed oxygen is not released but dissolves. Curves identical to D are found at larger oxygen concentrations in the sample (here 1 a/o). The four sticking probability curves are approximately parallel, straight lines. The deviations at very low sticking probabilities are likely to be an ion gauge artifact.

The linearity of the curves suggests that adsorption of molecular oxygen on unoccupied sites is the rate-determining step at room temperature. Their parallel displacement indicates that the oxygen coverage on a flash-heated sample increases significantly with the oxygen concentration in the bulk. This appears to be a true bulk effect since long-time annealing at temperatures between 1300° and 1800°K does not reproduce the sticking probability curve of a clean sample. The sample can be reactivated only by removal of oxygen from the bulk of the sample (see below). The relationship between bulk concentration and surface properties will be discussed in more detail later.

Sorption at intermediate temperatures.—At temperatures above approximately 500°K sorption proceeds beyond an amount equivalent to a monolayer. In Fig. 3 the sticking probability and the resistance observed in a typical run are plotted *vs.* time. Constant power input equivalent to an initial temperature of 745°K was established; then, at t_1, oxygen was admitted at a pressure of 3 x 10^{-6} Torr. The initially high sticking probability drops gradually to a low constant value; the resistance decreases also and goes through a minimum at t_2. When at t_3 the gas flow is stopped, the resistance increases more rapidly and approaches a constant value. We explain these observations as follows. Since the sample is heated at constant power, the decrease in resistance (*i.e.*, in temperature) between t_1 and t_2 indicates an increase in its emissivity; this is ascribed to the build-up of a surface oxide[3] which is also expected to have a smaller sticking probability for oxygen, than the metal. Either a uniform oxide skin is formed which grows in thickness or initially separate oxide patches gradually coalesce over the entire surface. At t_2 a quasi-steady state is reached; the rate of adsorption becomes equal to both the rate of diffusion of oxygen through the oxide layer and into the metal; the emissivity (and the temperature) is now constant, and the sample resistance increases because of gas solution (which undoubtedly takes place also in the time interval between t_1 and t_2). After t_3, the resistance increases more rapidly because the oxide layer dissolves gradually, and consequently the emissivity decreases, until the original temperature is finally re-established. The oxygen concentrations derived by integration of the rate curve, and from the increase in resistance, 0.23 and 0.24 a/o, agree closely.

At 3 x 10^{-6} Torr, the described kinetic pattern was observed to about 800°K. The upper temperature limit increases with pressure.

The study of the sorption mechanism in the intermediate temperature range was not pursued systematically despite its potential value for diffusion measurements and its significance in respect to corrosion, since the present investigation is focused on the mechanism of homogeneous solution and degassing.

Sorption at high temperatures.—In sorption experiments at high temperatures the resistance increases proportionally with the amount sorbed (Fig. 1); no oxide phase is formed and the gas dissolves uniformly in the metal. In Fig. 4 three sorption curves at a pressure of 3 x 10^{-6} Torr are shown; they are expressed as sticking probability *vs.* bulk concentration. The initial sticking probabilities are approximately the same, 0.7, and the same constant value of 0.2 is ap-

[3] The electron diffraction pattern of a surface film which was stripped from a similar sample indicates that NbO is formed.

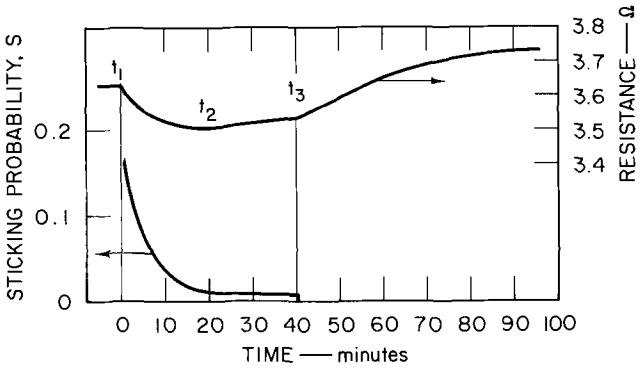

Fig. 3. Resistance and sticking probability as function of time during oxygen sorption at 3 x 10^{-6} Torr. Constant power input is maintained into the sample, equivalent to an initial temperature of 745°K.

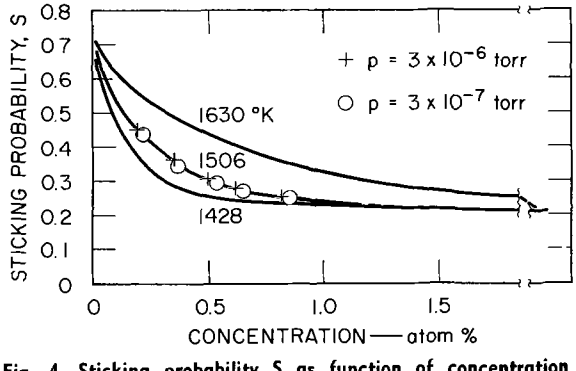

Fig. 4. Sticking probability S as function of concentration at constant, high temperatures. Control pressure 3 x 10^{-6} Torr, except when marked differently.

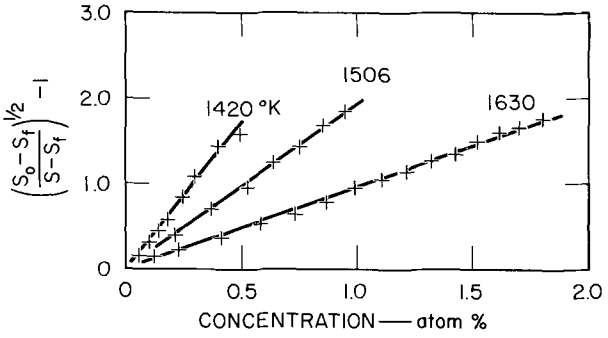

Fig. 5. Data of Fig. 4 plotted in the form of $[(S_o - S_f/S - S_f)^{1/2} - 1]$ vs. concentration (see text).

proached at high concentration.[4] However, the initial part of the curve is steeper at lower temperatures. (The theoretical interpretation, Fig. 5, will be discussed later.)

The sticking probabilities are functions of concentration and temperature only and are established virtually instantaneously after any change in conditions. The pressure independence is illustrated by the curve for 1506°K in Fig. 4. In this run the pressure was alternated between 3 x 10^{-7} and 3 x 10^{-6} Torr. The sticking probabilities at the two pressures lie on the same smooth curve. No pressure effects on the sticking probability were observed in other high-temperature experiments, *i.e.*, the sorption rates are proportional to pressure.

The temperature dependence of the sticking probability was studied also at approximately constant concentrations. Oxygen at a pressure of 3 x 10^{-7} Torr was sorbed in well-defined increments, and the sticking probabilities were rapidly measured for a series of temperatures. In order to minimize the exposure to oxygen and the concentration change during such a temperature series, the temperatures were derived from the resistances (which were corrected for the effect of dissolved oxygen). Constant sticking probabilities were established virtually instantaneously from whichever direction the new temperature was approached. The data, in a presentation which will be discussed below, are given in Fig. 6. The closely

[4] The sticking probability remains constant even when eventually a new phase precipitates (indicated by a change in the slope of the resistance curve). Since formation of a surface oxide, which has a low activity for oxygen adsorption, would be accompanied by a drop in sticking probability, the oxide phase apparently precipitates internally.

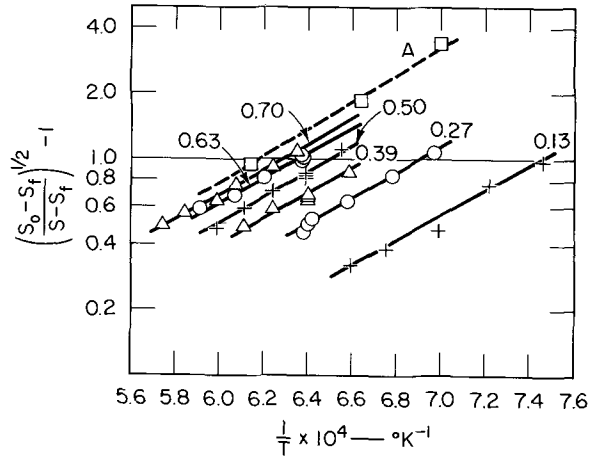

Fig. 6. Plots of log $[(S_o - S_f/S - S_f)^{1/2} - 1]$ vs. reciprocal temperatures at constant concentrations (marked in atom per cent). Curve A is derived from the slopes of the straight lines in Fig. 5, and is equivalent to the plot for unit concentration.

bunched points represent measurements at both increasing and decreasing temperature. (Sticking probabilities larger than one half the maximum value tended to drift downward probably because of an increase in concentration, and are not included.)

A model for explaining the high-temperature kinetics must take into account the following observations and postulates in addition to the detailed kinetics: (*A*) Diffusion is so fast relative to the rate of sorption that dissolved oxygen is at all times virtually uniformly distributed in the metal. This deduction from experiments is supported by an estimate, analogous to that for nitrogen in niobium (2), based on the known diffusion coefficient of oxygen in niobium (9). (*B*) No oxide is formed on the surface or in the bulk. This is indicated by the linearity between resistance and total concentration. Also, the concentrations in this study are far below the saturation limit of oxygen, and no high concentration can be built up at the surface because of the high diffusion rate. (*C*) Removal of oxygen from the sample in any form is insignificant at the temperatures of the experiments (see next section). (*D*) The sample surface exhibits quite uniform crystallographic orientation. Since samples of different orientation show the same kinetic pattern, crystallographic surface heterogeneity cannot be an essential factor in the sorption kinetics. (*E*) The dependence of the observed sticking probability on only bulk concentration and temperature indicates that an equilibrium between oxygen in the bulk and on the surface exists.

We postulate that oxygen adsorbs irreversibly in two independent atomic states differing in binding energy, and that the adsorption process in either state is described by $O_2 + 2$ sites $\rightarrow 2\,O$. Then, the rate law (referred to unit area) assumes the form

$$\frac{dM}{dt} = \nu p S = \nu p[k_1(n_1 - \sigma_1)^2 + k_2(n_2 - \sigma_2)^2] \quad [1a]$$

and

$$S = k_1(n_1 - \sigma_1)^2 + k_2(n_2 - \sigma_2)^2 \quad [1b]$$

where S is the observed sticking probability, k_i are the rate constants of adsorption, n_i the total numbers of sites, and σ_i the coverages in the two states. We further assume that the two adsorption states are at all times in quasi equilibrium with the solution, *i.e.*, transfer between bulk and surface is rapid. These equilibria are given by

$$\frac{\sigma_i}{n_i - \sigma_i} = K_i^o \frac{C}{1 - C} \approx K_i^o C = K_i c \quad [2]$$

where the solute density C is expressed as a fraction of all the interstitial positions in the metal structure and K_i^o is the distribution coefficient. Since in our experiments the bulk concentration, c, is always small, of the magnitude of 1 a/o, $(1 - C)$ is approximately unity and Eq. [2] can be simplified as shown. By rearrangement of Eq. [2] one obtains

$$(n_i - \sigma_i) = \frac{n_i}{1 + K_i c} \quad [3]$$

We finally assume that K_1 is small (thus, $(n_1 - \sigma_1) \approx n_1$) and that K_2 is large. These two assumptions are equivalent to the statement that the free energy change for transfer of oxygen atoms from the surface to the bulk is small for state 1 and large for state 2. By substitution in Eq. [1b] the rate law, in terms of bulk concentration, is

$$S = k_1 n_1^2 + k_2 n_2^2 (1 + k_2 c)^{-2} \quad [4]$$

The experimental sticking probability is for an oxygen-free sample, *i.e.*, at the beginning of the run,

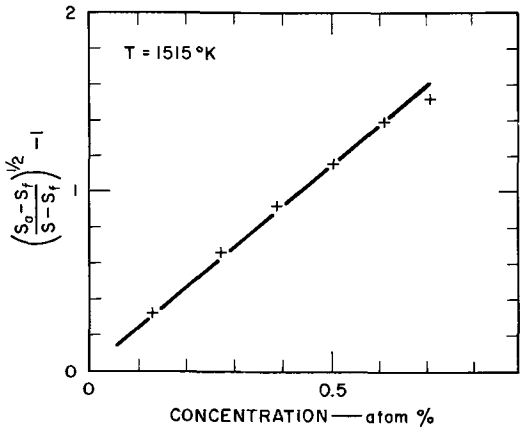

Fig. 7. Plot of $[(S_0 - S_f/S - S_f)^{1/2} - 1]$ at 1515°K vs. concentration, derived from Fig. 6.

$S_0 = k_1 n_1^2 + k_2 n_2^2$; and at higher concentrations it approaches the value $S_f = k_1 n_1^2$. Both limiting values are found to be temperature independent; thus, adsorption in either state is not activated. By introducing the limiting conditions in Eq. [4] and rearranging we obtain

$$f(S) \equiv \left(\frac{S_0 - S_f}{S - S_f}\right)^{1/2} - 1 = K_2 c \qquad [5]$$

This general function of S is dependent on both the oxygen concentration in the bulk and on temperature, since the distribution constant K_2 is temperature dependent also ($K_2 = K_0 \exp[\Delta H/RT]$).

As a test of the postulated model, $f(S)$ was derived from the three experimental sticking probability curves given in Fig. 4 and plotted *vs.* c (Fig. 5); a good fit to straight lines is obtained. The logarithms of the three slopes plotted *vs.* $1/T$ (Fig. 6, curve A) lie approximately on a straight line also. Moreover, the function $f(S)$ was evaluated from the sticking probabilities at constant concentrations, measured as function of temperature in the sorption run at 3 x 10^{-7} Torr (see above), and its logarithm was plotted *vs.* $1/T$ (Fig. 6). The points for each concentration define parallel straight lines; they are also parallel to line A which formally represents the data points for unit concentration. As a final test, the function $f(S)$ at 1515°K was read from Fig. 6, plotted *vs.* concentration (Fig. 7). The points lie on a straight line which passes through the origin, as required by [5].

A heat of 27 kcal/g atom is derived from Fig. 6 for the transfer of adsorbed oxygen in state 2 into the bulk; i.e., the oxygen atoms have an appreciably higher binding energy on the surface than when dissolved. An energy barrier for solution of gases exists also for other metals, such as molybdenum or tungsten; they adsorb active gases, but do not dissolve them to any significant extent.

Our model also explains at least qualitatively the effect of oxygen concentration on the room temperature adsorption kinetics. On flash heating an oxygen-covered sample, the adsorbates in both states dissolve. However, during cooling, the surface state of high binding energy is partly repopulated, and at higher bulk concentration, it approaches saturation. However, the state of low binding energy remains unoccupied. Thus, the observed sticking probabilities will decrease with bulk concentration to approach a constant value. (Low energy electron diffraction or field emission microscopy studies of surface coverage and its dependence on bulk concentration would be valuable for confirming our model for sorption and solution.)

The mechanism of oxidation of niobium has been studied previously, however mostly at moderate or higher pressures (10-14). Even in three recent investigations (15-17) which are closest in experimental conditions to the present study, the pressures employed were still higher by a factor of about one hundred or more. Large cross sections of the samples, compared to that used here, in combination with the higher pressure may have caused concentration gradients which would affect the sorption kinetics (16). Moreover, integral amounts, sorbed during rather large time intervals, were measured by gravimetric methods or derived from resistances; the concentration increments in each step were usually of the magnitude of 1 a/o. Thus, no data on the detailed kinetics of sorption at very low concentrations could be obtained. However, these studies agree in gross features with the present one. Proportionality between sorption rate and pressure, and a linear rate (here found at concentrations above approximately 1 a/o) were observed. Gebhardt and Rothenbacher (16) also report high initial sticking probabilities of about 0.5. The slight decrease of the initial sticking probability with temperature, which contrasts with the constancy found here, may be an artifact arising from the linear extrapolation of the integrated rate curves from higher to zero concentration.

High-temperature degassing.—When a sample containing oxygen is heated in ultrahigh vacuum, the pressure in the system does not increase significantly even at 2100°K, *i.e.*, no molecular oxygen is evolved. This is in agreement with the thermodynamics of the Nb-O system. The vapor pressure of oxygen over its solution in niobium, as derived from the dissociation pressure of NbO and its solubility in niobium (18), is very low ($p_{O_2} \approx 10^6 c^2 \exp[-18000/RT]$ Torr); at 1 a/o and 2100°K, it is about 10^{-13} Torr. However, on prolonged heating, the sample resistance decreases to approach a constant value. Simultaneously, and dark deposit forms on the wall, which very actively sorbs oxygen when it is subsequently admitted. Since the vapor pressure of the metal is insignificant except at the highest temperatures employed, an unsaturated oxide must evaporate.

The kinetics of the evaporation process was measured quantitatively, by maintaining the sample, which previously had been loaded with a known amount of oxygen, at constant temperature and recording continuously its resistance. At the end of each run which, especially at lower temperatures, extended only over a limited resistance interval, the sample was thoroughly degassed at 2100°K. The final resistance at room temperature was higher than prior to the particular sorption-degassing cycle, by about 1-2% for every atom per cent of oxygen dissolved. This suggested evaporation of a mixture of NbO and NbO_2. The resistances measured during the runs were corrected for the removal of metal (assuming a constant O/Nb ratio of the vapor) and were converted to oxygen concentrations by the relationship given in the experimental section.

First or second order kinetics can be expected depending on which species evaporates predominantly

$$\ln c_0/c = k_1 t$$

or

$$\frac{1}{c} = \frac{1}{c_0} + k_2 t$$

The experimental data fit well the second order kinetics at higher concentrations (Fig. 8). Thus, it appears that primarily NbO_2 evaporates, according to $Nb_{(s)} + 2\,O_{(s)} \rightarrow (NbO_2)_{gas}$. The Arrhenius plot (Fig. 9) of the rate constants k_2 derived from the linear part of the rate curves results in an activation energy of 120 kcal/g mole of oxygen (or NbO_2), and in a preexponential factor of 10^{11} (a/o min)$^{-1}$. Since for our sample the volume-to-surface ratio was about 10^{-3} cm, the preexponential factor for a ratio of unity would be about 10^8 cm (a/o min)$^{-1}$.

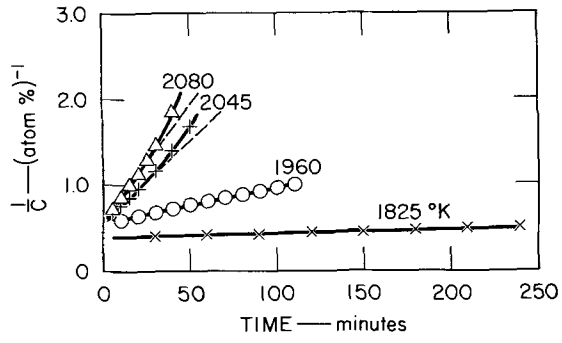

Fig. 8. Second order rate curves for oxygen removal from the sample.

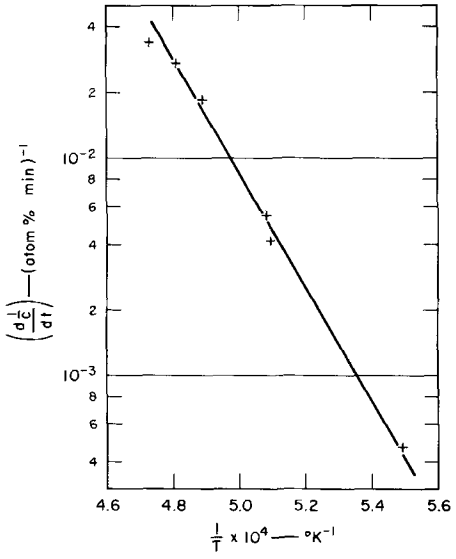

Fig. 9. Arrhenius plot of the second order rate constants for oxygen removal from the sample.

Deviations from the second order plot are found at lower concentrations, in a direction which may represent the approach to a first order rate law (Fig. 8). However, the low concentrations are rather unreliable because of the uncertainty in the definition of the final resistance, and their quantitative interpretation in terms of a first order rate law did not lead to consistent results.

The oxygen removal from niobium, (and from tantalum) has been thoroughly investigated by Gebhardt *et al.* (19). At 1900°-2300°K, oxygen and niobium evaporated from a 1.6 a/o solution in the atomic ratio of about 1.4-1.2. The kinetics of degassing obeyed a first order law at low concentrations, *i.e.*, NbO was apparently the principal evaporating species. The activation energy of evaporation was 130 kcal/g atom of oxygen (or NbO). Deviations in the direction of a second order law were noticeable at concentrations approaching 1 a/o. Thus, the kinetic patterns observed by Gebhardt *et al.* and by us are at least qualitatively similar. Moreover, for identical temperatures the absolute oxygen evaporation rates per unit area, at an oxygen concentration of 1 a/o, differ by less than a factor of 10. This agreement is rather close in view of the experimental uncertainties, particularly in temperature.

Finally, the observed similar activation energies of evaporation of the two species from solution is in agreement with the small temperature dependence of the Nb/O ratio, observed by Gebhardt *et al.* They are also close to the heats of sublimation estimated from the literature; they are 134 and 131 ± 15 kcal for NbO and NbO_2, respectively.

Comparison between Sorption Mechanisms of Oxygen and of Nitrogen

The low-pressure interaction of nitrogen with niobium has been described previously (1, 2) and has also been compared with preliminary data for oxygen (21).

The kinetics of high-temperature sorption both of nitrogen and of oxygen by niobium can be explained to a large extent by the thermodynamics of the two systems. The heat of solution of nitrogen is rather low, about 50 kcal/g atom; therefore the solution, which is atomic, decomposes at higher temperatures into nitrogen and the metal, and no volatile nitride exists. Consequently, high-temperature sorption of nitrogen is reversible and obeys an approximately parabolic rate law in respect to concentration. Moreover, the heat of adsorption is of the same magnitude as the heat of solution; thus, the surface coverage is found to be always low at the low nitrogen concentrations studied. For oxygen, the heat of solution is high, 90 kcal/g atom; thus, molecular oxygen is not released; however, at very high temperatures oxygen is removed in the form of volatile niobium oxides. Moreover, two adsorption states apparently exist. The heat of adsorption in one of them is appreciably higher than the heat of solution, and therefore significant surface coverages are encountered even at low bulk concentration. The resulting irreversible kinetics of oxygen has been discussed in detail in the preceding sections.

The high-temperature sticking probabilities on the clean metal are about 0.8 for oxygen and 0.05 for nitrogen; this large difference may be indicative of the higher affinity of niobium for oxygen. These sticking probabilities are temperature independent for either gas; thus adsorption is nonactivated.

Finally, the room temperature kinetics for the two gases is significantly different also. The sticking probability curve for nitrogen, which is approximately horizontal to quite high coverages [found also for nitrogen and molybdenum (21) and on tungsten (22) filaments], is not affected by the nitrogen concentration in the bulk. The linear curve for oxygen, however, shifts with bulk concentration, thus indicating an increase in initial surface coverage. The saturation coverage for nitrogen is about half that of oxygen on the clean sample; moreover, it was found in exploratory experiments that nitrogen was not adsorbed when the oxygen concentration in the sample was significant. Thus, it appears that at room (or high) temperature nitrogen adsorbs on niobium only in the surface state of high binding energy, but we suspect that at lower temperatures it would occupy the low energy state also. A similar two-step adsorption is found in the nitrogen-molybdenum (23, 24) and nitrogen-tungsten systems (22).

Acknowledgment

The authors are indebted to Dr. D. Cubicciotti for critical review of the manuscript.

This research was supported by the United States Atomic Energy Commission.

Manuscript received Aug. 1, 1966; revised manuscript received Dec. 22, 1966.

Any discussion of this paper will appear in a Discussion Section to be published in the December 1967 JOURNAL.

REFERENCES

1. R. Gibson, B. Bergsnov-Hansen, N. Endow, and R. A. Pasternak, "Transactions, The Tenth National Vacuum Symposium," American Vacuum Society, p. 88 (1963).
2. R. A. Pasternak, B. Evans, and B. Bergsnov-Hansen, *This Journal*, **113**, 731 (1966).
3. R. A. Pasternak and R. Gibson, *Acta Met.*, **13**, 1031 (1965).
4. B. Evans and R. A. Pasternak, *Trans. Met. Soc. AIME*, **236**, 942 (1966).
5. J. R. Cost and C. A. Wert, *Acta Met.*, **11**, 231 (1963).
6. E. Gebhardt and R. Rothenbacher, *Z. Metallk.*, **54**, 443 (1963).

7. R. A. Pasternak and B. Evans, *Trans. Met. Soc. AIME*, 233, 1196 (1965).
8. P. A. Redhead, *Vacuum*, **13**, 253 (1963).
9. R. W. Powers and M. V. Doyle, *J. Appl. Phys.*, **30**, 514 (1959).
10. D. W. Aylmore, S. T. Gregg, and W. B. Jepson, *This Journal*, **107**, 495 (1960).
11. T. Hurlen, *J. Inst. Met.*, **89**, 273 (1960).
12. D. W. Bridges and W. M. Fassel, Jr., *This Journal*, **103**, 326 (1956).
13. J. V. Cathcart, J. J. Campbell, and F. P. Smith, *ibid.*, **105**, 442 (1958).
14. W. D. Klopp, C. T. Sims, and R. I. Jaffee, *Trans. Am. Soc. Metals*, **51**, 282 (1959).
15. H. Inouye, in "Columbium Metallurgy," p. 649 Interscience Publishers, Inc., New York (1960).
16. E. Gebhardt and R. Rothenbacher, *Z. Metallk.*, **54**, 689 (1963).
17. P. Kofstad and S. Espevik, *This Journal*, **112**, 153 (1965).
18. R. T. Bryant, *J. Less-Common Metals*, **4**, 62 (1962).
19. E. Gebhardt, E. Fromm, and D. Takob, "Metals for the Space Age," Proceedings, 5. Plansee Seminar, p. 421, Springer-Verlag (1965).
20. R. A. Pasternak, Transactions, Vacuum Metallurgy Conference (1965), p. 1, American Vacuum Society (1966).
21. R. A. Pasternak and H. Wiesendanger, *J. Chem. Phys.*, **34**, 2062 (1961).
22. G. Ehrlich, *J. Chem. Phys.*, **34**, 29 (1961).
23. R. A. Pasternak, N. Endow, and B. Bergsnov-Hansen, *J. Phys. Chem.*, **70**, 1304 (1966).
24. M. W. Roberts, *Trans. Faraday Soc.*, **59**, 698 (1963).

Electrochemical Studies in Molten Li_2CO_3-Na_2CO_3

H. E. Bartlett[1] and K. E. Johnson[2]

Chemistry Department, Sir John Cass College, London, England

ABSTRACT

It has been confirmed that C and O^{2-} are the cathode products and CO_2 and O_2 the anode products of electrolyzing Li_2CO_3-Na_2CO_3 at 550°C. In the presence of oxide, CO_3^{2-} is oxidized at platinum to $CO_2 + \frac{1}{2}O_2$ by a 6-electron process involving the substrate metal. Ag^+/Ag is a satisfactory reference electrode for the concentration range 4×10^{-3} to $4 \times 10^{-2}M$ Ag^+. Formal potentials of other systems on a molal scale are: Co^{2+}/Co — 0.946v, Ni^{2+}/Ni — 0.862v, CO_2, O_2/CO_3^{2-} — 0.270v, Ag^+ in SO_4^{2-}/Ag + 0.253v. Several other metals corrode or are noble. Ag is corroded by $CO_2 + O_2$ mixtures to a saturation concentration of $1.3 \times 10^{-1}M$ Ag^+ to 550°C. On cooling solutions of Ag^+ in Li_2CO_3-Na_2CO_3, a black precipitate of metal is obtained. The bearing of these observations on the corrosion of carbonate fuel cell cathodes is discussed.

Molten carbonates are well known as fuel cell media, but the basic electrochemistry of these solvents has received attention only recently.

The electrolytic reduction product of molten carbonates at temperatures below 600°C has been identified qualitatively as carbon (1-4), and the reduction product at 700°C is thought to be carbon monoxide (2).

The products of oxidation of the melts were shown to be carbon dioxide and oxygen in ratios strongly dependent on conditions (5): at high current densities the CO_2:O_2 ratio approaches 2:1 while at low current densities it is about 1:6 and in the presence of Na_2O_2 about 1:3. Plots of the discharge potential at low current densities *vs.* pO^{2-} and $\log_{10} p_{CO_2}$ were both shown to have slopes of 80 mv at 560° (1) from which it was concluded that O^{2-} was the species discharged under these conditions. Other experiments indicated that oxide was discharged at a more negative potential than carbonate ion itself.

EMF measurements have established the reversibility of the CO_2, O_2/CO_3^{2-} electrode in Li_2CO_3-Na_2CO_3 at 700°C (6) and of the O_2/O^{2-} electrode (at fixed CO_2 pressure) in carbonate (7) and carbonate-sulfate (8) melts.

A theoretical emf series for molten carbonates has been obtained (9) and an experimental order of reactivity of certain metals deduced from potentiostatic polarization curves (10). The reactions of silver in molten carbonates have been observed variously: the transfer of silver from a working fuel cell cathode to the anode (11), the loss in weight of silver upon anodizing (12, 13), the dependence of O^{2-} discharge potential at Ag on pO^{2-} in only basic melts (14), and a reduction wave for a 5×10^{-2}M Ag_2O solution in $(LiNaK)_2CO_3$ (14) have been reported. The limited corrosion of Pt to Li_2PtO_3 was also noted (12).

The present study was designed to establish a practical emf series for Li_2CO_3-Na_2CO_3 at 550°, to investigate the limiting electrode reactions at this temperature and to attempt to throw light on the working of a silver cathode in a carbonate fuel cell.

The success of the work was governed by the ability to use alumina for containing the solvent, a fact which is determined by reaction kinetics and not thermodynamics. The only other material which could be used in current-carrying as opposed to equilibrium studies, magnesia, suffers from two disadvantages: its acid solubility and its iron impurity content.

Experimental

AnalaR Na_2CO_3 and reagent grade Li_2CO_3 were oven dried at 120°C and mixed in equimolar proportions. [The eutectic mixture contains 53.3% Li_2CO_3 and melts at 500° (15)]. A large Purox alumina crucible (250 ml capacity), containing smaller aluminous porcelain or alumina crucibles, was then filled with the mixture and placed in a glass envelope which was stoppered by an aluminum foil-lined silicone bung.

The system was heated under vacuum in an air or potassium nitrate thermostat for 12 hr at 350°C, the temperature was raised to 450°C and dry CO_2 (dried by silica gel and molecular sieve, grade 4A) was admitted to the envelope. The temperature was then raised to 550°C and maintained at 550°C for 12 hr after which the silicone bung was replaced by one bearing the electrodes. The process of melting reduced the bulky powder to a liquid with surfaces 0.5 cm below the tops of the smaller crucibles which thus became wetted. The compartmenting crucibles could also be wetted by upsetting and righting them. The films of molten carbonate served later as salt bridges between compartments.

The electrodes consisted of (*a*) rods or coiled wire supported by thin alumina tubes (Co, Ni, Rh, Fe, Ag,

[1] Present address: Atomic Energy Board, Private Bag 256, Pretoria, South Africa.

[2] Present address: Department of Chemistry, University of Saskatchewan, Regina, Saskatchewan, Canada.

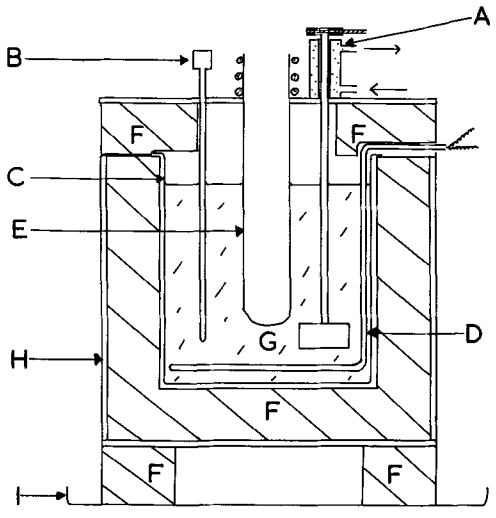

Fig. 1. Molten salt thermostat: A, water-cooled bearing for stirrer; B, thermometer probe; C, stainless steel container; D, stainless steel sheathed electrical heating element; E, glass envelope; F, alumina firebrick insulation; G, molten KNO_3; H, asbestolite box; I, aluminum safety tray.

Cu) and (b) thin Pt wire sheathed in glass well above the melt level, with and without Pt foil at the end. For the CO_2, O_2/CO_3^{2-} electrode, mixtures of the gases were bubbled over Pt foil electrodes, after having been mixed in two, 1*m* drying tubes; their proportions were measured by means of capillary flow meters, in turn calibrated with a bubble flow meter. Silver sulfate reference electrode solutions (16) were prepared from dry Ag_2SO_4 and oven-dried $(Li,Na,K)_2SO_4$ (mole ratio 78:8.5:13.5) and placed in closed aluminous porcelain tubes (Thermal Syndicate type 525 or Andermann's Pythagoras porcelain).

A 50 ml capacity outer alumina crucible and one compartment were used in the gas analysis experiments. In these, any oxygen was displaced by nitrogen before the electrolysis and the evolved gases were collected in a gas buret. The actual analyses were performed with a Haldanes' apparatus (17) using 25% KOH and alkaline pyrogallol as absorbents. Successive samples of gas were analyzed until the CO_2 content reached a constant small value.

Either an air thermostat or a molten salt bath was employed for the measurements. The air thermostat had two disadvantages: the heating elements burnt out fairly frequently and the mild steel fans had a working life of only six months. The molten nitrate bath (Fig. 1) could not be used safely above 570°C because of slow distillation of KNO_3. Both thermostats were controlled by a Fielden type TCB7 temperature controller which switched 10% of the heating current through a bank of resistors when the temperature, as determined by the thermometer probe, became too great. The temperature at any point remained constant to ±1°, and the temperature gradient in the region of the cell compartments was 0.5° cm^{-1}. The temperature within the cell was measured by a chromel-alumel thermocouple.

Current-voltage curves were obtained with a Cambridge photographic polarograph (rate of polarization 300 mv min^{-1}, full scale deflection 350 μa). A Wadsworth potentiostat was used for controlled potential work. Large currents were derived from a bank of accumulators or an Eliminac d-c power supply and the charge measured with a hydrazine sulfate coulometer (18). A Metrohm coulometer type ME211 was the source of small constant currents (up to 20 ma with an accuracy of ±0.2%) for coulometric generation of metal ions in solution; it contains a built-in stop-clock. Potentials were measured with a Pye portable or a Cropico type P3 potentiometer.

At the completion of a set of measurements the compartments were removed with gold-tipped tongs and, after cooling, washed on the outside, dried, and weighed. The carbonate on the inside was then dissolved out in dilute HCl and the crucibles dried and reweighed. If oxide was present, it was determined by difference, the CO_2 evolved with HCl being weighed. Silver was dissolved in nitric acid and determined gravimetrically as chloride. Cobalt was determined colorimetrically as the Nitroso-R complex (19). Nickel in solution was determined by cathode ray polarography using a K1000 model polarograph (Southern Instruments Ltd.): the peak height at —0.97v *vs.* a mercury pool was compared for the unknown and several standards at *p*H ~ 8.

Results

Electrolytic reduction.—A bulky black mass of carbon was obtained at a platinum cathode at 550°C upon electrolysis of a compartmented melt. The weight of material insoluble in HCl produced by passing 230 coulombs was 7.1 mg compared with 7.0 mg to be expected for a 4-electron process. Greater charge yielded less carbon than expected, and it was found in these cases to have spread along the salt bridge and reached the anode compartment. Microchemical analysis of an acid-insoluble sample gave 90% C, 1% S, and 9% residual alkali metal salts. X-ray analysis showed this material to be amorphous. Tests for CO, carbide, and free alkali metal as reduction products proved negative.

Electrolysis with a potential difference exceeding 3v yielded some sulfide in addition to carbon (presumably from sulfate impurity).

The quantity of oxide produced at the cathode was not reproducible but was always in excess of that predicted for CO_3^{2-} reduction to C because of some thermal decomposition.

Electrolytic oxidation.—The results of oxidation at 1 cm^2 Pt electrodes are presented in Table I. With uncompartmented cells, a brown film formed on the anode and the CO_2 : O_2 ratio departed from 2 : 1 when a small volume of melt was used.

Current-voltage curve.—The current-voltage curve obtained with a dipping Pt micro-electrode is depicted in Fig. 2; it was not reproducible in detail from —0.5 to —1.45v *vs.* the Ag^+/Ag reference electrode.

Metal ion/metal systems.—Silver.—Silver was anodized under CO_2 at 1 atm pressure, and the current efficiency found to be close to 100% (coulombs passed 9.76, Ag^+ expected 10.9 mg, Ag^+ found 10.7 mg). With melts prepared merely by melting oven-dried salts under CO_2 (3) the current efficiency was poor. Solutions of Ag^+ in the melt were colorless, but decomposed to form black silver metal on cooling. Con-

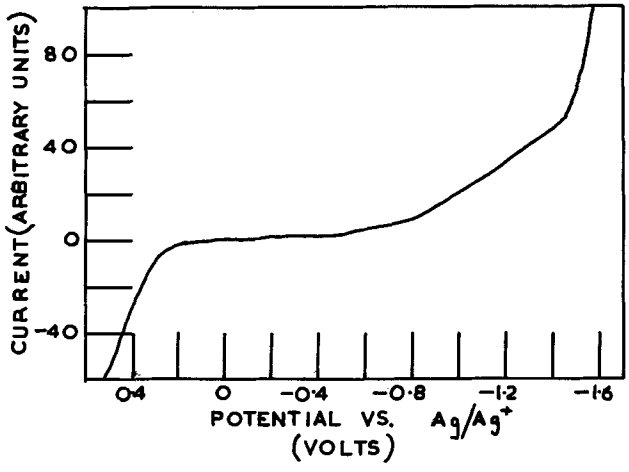

Fig. 2. Current-voltage curve for $LiNaCO_3$ under CO_2 at 550°

Table I. Anodic oxidation of Li_2CO_3-Na_2CO_3 at 550°C

Current density, ma cm^{-2}	Vol. of CO_2 at STP ml (±0.02)	Vol. of O_2 at STP ml (±0.02)	Ratio CO_2:O_2	Coulombs passed	No. of electrons to give 1 molecule of CO_2
1.90	8.9	4.2	2.1:1	70.7	1.8
2.90	16.1	8.4	1.9:1	141.5	2.0
3.90	3.11	1.54	2.0:1	80.3	6.0
4.70	3.56	3.14	1.1:1	94.6	6.2

1 and 2 refer to compartmented, 3 and 4 to uncompartmented cells.

centration cells were generated coulometrically, and the measured emf's are presented in the Nernst plot in Fig. 3 where the gradient in the concentration range 4 x 10^{-3} to 4 x $10^{-2}M$ is 0.163v. The reversibility of the Ag^+/Ag electrode was further confirmed by the micropolarization response of one electrode with respect to one unpolarized and its stability as a function of time, *e.g.*, the emf between a Ag/Ag^+ in carbonate electrode and a Ag/Ag^+ in sulfate electrode (see below) was constant to ±3 mv for 8 hr.

A significant impurity in the carbonates is chloride so the effect of added chloride (KCl) on the Ag^+/Ag potential was studied: at low concentrations of Cl^- there was no effect (cf. Fig. 3) but at higher concentrations (~2*M*) the potential became unstable and a white not a black precipitate separated on cooling.

Simple weight loss experiments showed that silver immersed in the carbonate was not corroded by CO_2 alone, but was corroded by O_2 (together with the minimal amount of CO_2 formed thermally) and even more by a 2:1 mixture of CO_2 and O_2.

Cobalt and nickel.—Only with melts prepared as outlined under Experimental could cobalt and nickel be coulometrically oxidized under 1 atm CO_2 to solutions of the bivalent ions, which were blue and red-brown, respectively. On cooling the nickel solutions a green color formed and CO_2 was evolved. The current efficiencies determined were 100 and 98% (Co^{2+} expected for 22.5 coulombs = 6.88 mg; Co^{2+} found = 6.85 mg; Ni^{2+} expected for 12.5 coulombs = 5.33 mg; Ni^{2+} found = 5.2 mg). The results of concentration cell studies appear in Fig. 4 where the line of theoretical slope is drawn through each set of points.

With wet melts (where the samples were not vacuum treated before melting) a black precipitate was obtained on anodizing cobalt and either a green or a black film formed on a nickel anode. When bearing the green film, a nickel electrode had a rest potential of —0.6v and when bearing the black film a rest potential of —0.1v (*vs.* 0.01m Ag^+/Ag reference electrode). The black film only formed at high current densities.

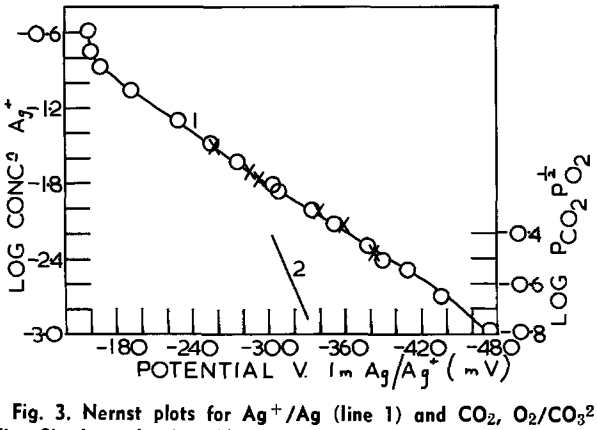

Fig. 3. Nernst plots for Ag^+/Ag (line 1) and CO_2, O_2/CO_3^{2-} (line 2) electrodes in $LiNaCO_3$ at 550°. O measurements without added chloride; X measurements with 0.354M chloride.

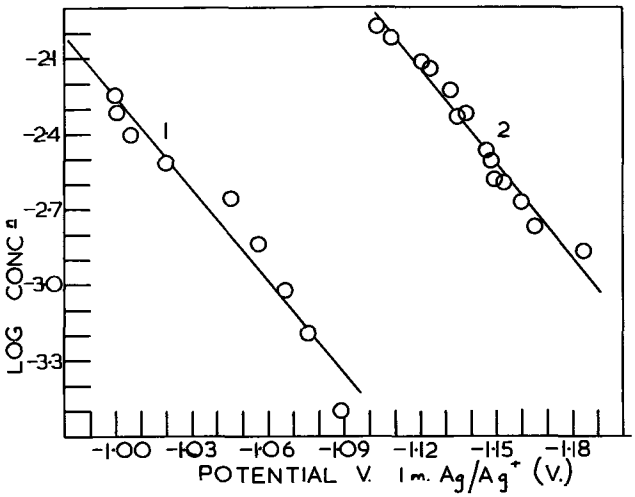

Fig. 4. Nernst plots for Ni^{2+}/Ni electrode at 570° (line 1) and Co^{2+}/Co electrode at 540° (line 2) in $LiNaCO_3$.

Other metals.—Iron reduced the solvent and rhodium and platinum proved to be noble. Copper became covered with oxide and colored the melt green on anodization; it had a rest potential of ~ —0.45v (*vs.* 0.01*M* Ag^+/Ag) after this treatment.

Silver sulfate electrode.—Concentration cell measurements on the system Ag/Ag^+ in Li_2CO_3-Na_2CO_3// Ag^+ in $(Li,Na,K)_2SO_4/Ag$ are plotted in Fig. 5 where the line has the theoretical Nernst slope. All the points are within 15 mv of the line, but the stability of each individual sulfate electrode was ±1 mv. The silver sulfate electrode, unlike the silver carbonate electrode, behaved ideally under nitrogen or air.

CO_2, O_2/CO_3^{2-} *electrode.*—A silver sulfate electrode was calibrated *vs.* an Ag^+ in Li_2CO_3-Na_2CO_3 electrode and then used to study the potential of the CO_2, O_2/CO_3^{2-} electrode as a function of gas composition. The Nernst equation for the system at 550° is

$$E = E^{0\prime} + 0.0815 \log_{10} p_{CO_2} p_{O_2}^{1/2}$$

and Fig. 6 shows a plot of E *vs.* $\log_{10} p_{CO_2} p_{O_2}^{1/2}$ where the line has the theoretical slope. The range of oxygen partial pressure, p_{O_2}, studied was 0.056 to 0.775, above which the electrode response was sluggish and a

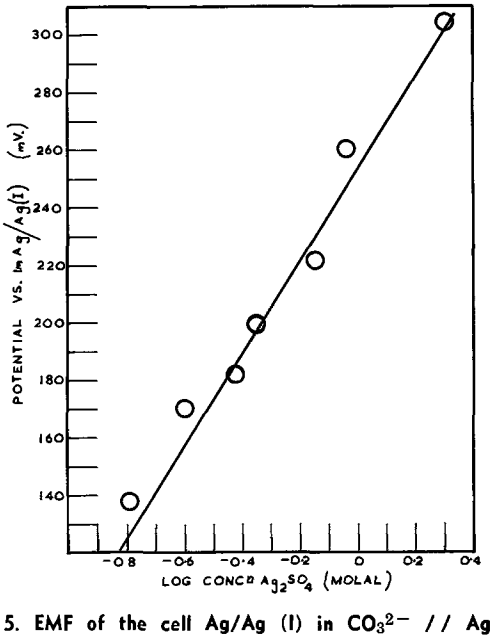

Fig. 5. EMF of the cell Ag/Ag (I) in CO_3^{2-} // Ag (I) in SO_4^{2-}/Ag as a function of Ag_2SO_4 concentration; temperature, 540°C.

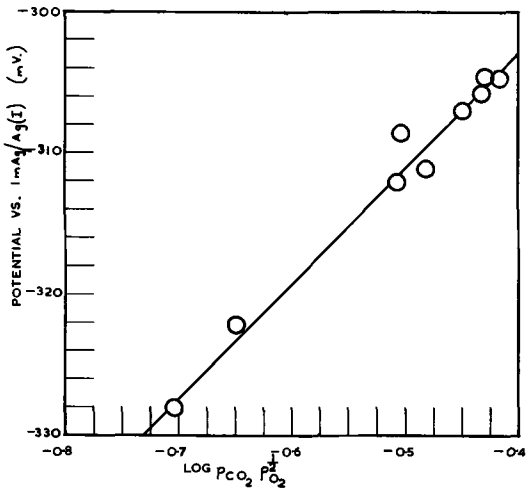

Fig. 6. Nernst plot for CO_2, O_2/CO_3^{2-} electrode in $LiNaCO_3$ at 550°.

brown film formed on the Pt indicator electrode. The emf passed through a maximum at $p_{O_2} \simeq 1/3$, as the Nernst equation predicts.

Discussion

Solvent electrode processes.—Electrolytic reduction of the melt at 550°C undoubtedly yields carbon and oxide but the experimental observations do not distinguish between the processes

$$(a)\quad CO_3^{2-} + 4e^- \rightarrow C + 3\,O^{2-}$$

$$(b)\quad CO_3^{2-} \rightleftharpoons CO_2 + O^{2-}$$
$$CO_2 + 4e^- \rightarrow C + 2\,O^{2-}$$

$$(c)\quad CO_3^{2-} + 2e^- \rightarrow CO + 2\,O^{2-}$$
$$2CO \rightarrow C + CO_2$$
$$CO_2 + 4e^- \rightarrow C + 2\,O^{2-}$$

or

$$(d)\quad CO_3^{2-} \rightleftharpoons CO_2 + O^{2-}$$
$$CO_2 + 2e^- \rightarrow CO + O^{2-}$$
$$2CO \rightarrow C + CO_2$$
$$CO_2 + 4e^- \rightarrow C + 2\,O^{2-}$$

although the yield of carbon rules out processes (*c*) and (*d*) without the final 4-electron step. Thermodynamic calculations (20) for pure Li_2CO_3, the more readily reduced component of the mixture, indicate that at 550°C the reduction of CO_2 to C should occur at —1.01v (*vs.* $CO_2,O_2/CO_3^{2-}$) and the reduction of CO_3^{2-} to C should occur at —1.65v. The formation of CO is not favored, by either route, below 700°. The current-voltage curve could be ascribed to the reduction of dissolved CO_2 followed by direct reduction of carbonate, but it is not possible to exclude residual moisture and heavy metals as the source(s) of the residual current up to —1.45v. Sulfate impurity is clearly not reduced at these potentials.

Electrolytic oxidation of the pure melt yielded CO_2 and O_2 according to the process

$$CO_3^{2-} - 2e^- \rightarrow CO_2 + \tfrac{1}{2}\,O_2$$

The oxide concentration at the anode of a small uncompartmented cell would be expected to be high so that significant contributions from the process

$$O^{2-} - 2e^- \rightarrow \tfrac{1}{2}\,O_2$$

are not then unexpected. The brown film formation and the yield of 1 mole of CO_2 per 6**F** in the uncompartmented cell electrolyses may be reconciled with the oxidation of Pt to Li_2PtO_3 (12), *e.g.*

$$Pt + CO_3^{2-} - 6e^- \rightarrow Pt^{4+} + CO_2 + \tfrac{1}{2}\,O_2$$

$$Pt^{4+} + 2Li^+ + 3\,O^{2-} \rightarrow Li_2PtO_3$$

These findings are supported by the work of Arkhipov, Trunov, and Stepanov (5).

Table II. Formal potentials in Li_2CO_3-Na_2CO_3

Couple	Temperature, °C	$E^{0\prime}$ *M*, v	E^0 M, v	$E^{0\prime}$ mole fraction, v	E (9)
Co^{2+}/Co	540	−0.946(±0.008)	−0.921	−1.036	−0.94
Ni^{2+}/Ni	570	−0.862(±0.009)	−0.835	−0.955	−0.89
$CO_2,O_2/CO_3^{2-}$	550	−0.270(±0.002)	−0.220	−0.451	−0.55
Ag^+/Ag	540-570	0	0	0	0
Ag^+ in SO_4^{2-}/Ag	540	+0.253	+0.250	+0.274	

EMF series.—This is very limited. Table II shows the formal potentials of the various electrodes on three concentration scales. The densities of carbonate and sulfate solvents were taken as 2.029 (21) and 2.13 ml^{-1} (22) respectively. The column E (9) refers to the calculated potentials of the pure salts at 600°C (9) and shows reasonable agreement with $E^{0\prime}$ mole fraction in Li_2CO_3-Na_2CO_3. The corrosion of Ag, Ni, and Co reported by Janz and co-workers (9, 23) using a ternary alkali carbonate mixture above 600°C, was not apparent in this solvent at 550°C. This corrosion may be the result of insufficient drying of melts since films, and a precipitate were formed by Co and Ni in wet Li_2CO_3-Na_2CO_3 or it may merely reflect the instability of Ag_2CO_3 solutions at 600° (see later). Ag_2CO_3 itself and Ag_2O both decompose to the metal below 500°C. The details of film and precipitate formation constitute a separate study: it suffices to suggest that CoO,NiO, and "Ni_2O_3" are probably the entities concerned.

The Nernst plot for Ag^+ in carbonate shows curvature at both high and low concentrations. At high concentrations we would expect CO_3^{2-} discharge and at low concentrations, corrosion to Ag^+ by impurities.

Indeed, the formal potential of the $CO_2,O_2/CO_3^{2-}$ electrode is negative with respect to that of Ag^+ in carbonate, and this implies that the reaction

$$2Ag^+ + CO_3^{2-} \rightarrow 2Ag + CO_2 + \tfrac{1}{2}\,O_2$$

would be spontaneous when all the components were at unit activity and the reverse process would proceed at 550°C until an activity of Ag^+ equal to $1.4 \times 10^{-2} M$ was reached. This corresponds to the point at which lines 1 and 2 of Fig. 3 cross. In fact a maximum concentration of Ag^+ of $1.3 \times 10^{-1} M$ can be generated, from which we deduce an activity coefficient of 0.11 for this particular solution. Further passage of current through a silver anode in a melt $1.3 \times 10^{-1} M$ in Ag^+ only led to evolution of CO_2 and O_2. Concentrations corresponding to the upper curved portion of Fig. 3 would include Ag metal corroded from the electrode.

The experiments with added chloride were not definitive beyond indicating a reaction at high Cl^- concentrations.

Corrosion of Ag in fuel cells.—When silver metal is made the working cathode of a fuel cell, CO_2 and O_2 are passed over it and will naturally corrode it until the saturation concentration of Ag^+ is obtained. If the Ag^+ is removed from the cathode by diffusion or cooling, in which case Ag is precipitated, further metal will be corroded from the cathode. The greater corrosive nature of mixtures of CO_2 and O_2 over O_2 alone is consistent with the order of electrode potentials (5) and is particularly important in this context.

The mixture of spent fuel gases containing H_2O with the cathode oxidant is also liable to accelerate the corrosion.

Acknowledgment

It is a pleasure to thank Texas Instruments Inc. for their support of this work and particularly for a maintenance grant (to H.E.B.).

Manuscript received Sept. 6, 1966; revised manuscript received Nov. 14, 1966. This paper was presented at the Cleveland Meeting, May 1-6, 1966.

Any discussion of this paper will appear in a Discussion Section to be published in the December 1967 JOURNAL.

REFERENCES

1. J. Dubois and R. Buvet, *Bull. Soc. Chim. France*, **1963**, 2522.
2. G. J. Janz and A. Conte, *Electrochim. Acta*, **9**, 1269 (1964).
3. M. D. Ingram, B. Baron, and G. J. Janz, *Electrochim. Acta*, in press.
4. Yu. K. Delimarskii, O. V. Gorodis'kii, and V. F. Grishchenko, *Doklady Akad. Nauk SSSR*, **156**, 650 (1964).
5. G. G. Arkhipov, A. M. Trunov, and G. K. Stepanov, *Tr. Inst. Elektrochim., Akad. Nauk. SSSR, Ural'sk. Filial*, **4**, 41 (1963); *C.A.*, **60**, 14124g (1964).
6. A. M. Trunov and C. K. Stepanov, *Tr. Inst. Elektrochim, Akad. Nauk SSSR, Ural'sk. Filial*, **2**, 97 (1961); *C.A.*, **59**, 9589c (1963).
7. G. J. Janz and F. Saecusa, *Electrochim. Acta*, **7**, 393 (1962).
8. H. Flood, T. Frland, and K. Motzfeld, *Acta. Chem. Scand.*, **6**, 257 (1952).
9. M. D. Ingram and G. J. Janz, *Electrochim. Acta*, **10**, 783 (1965).
10. P. Decobert and O. Bloch, *Bull. Soc. Chim. France*, **1962**, 1887.
11. D. L. Douglas, "Fuel Cells," G. J. Young, Editor, Reinhold Publishing Co., New York (1960).
12. G. J. Janz, A. Conte, and E. Neuenschwander, *Corrosion*, **19**, 292t (1963).
13. G. J. Janz, E. Neuenschwander, and A. Conte, *Corrosion Science*, **3**, 177 (1963).
14. J. Dubois, *Ann. Chem. (Paris)*, **10**, 145 (1965).
15. E. J. Cairns and D. I. McDonald, *Nature*, **194**, 441 (1962).
16. K. E. Johnson and H. A. Laitinen, *This Journal*, **110**, *314 (1963)*.
17. A. E. Heron and H. N. Wilson in "Comprehensive Analytical Chemistry," C. L. Wilson and D. W. Wilson, Editors, vol. 1A, p. 271, Elsevier, London (1959).
18. J. J. Lingane, "Electroanalytical Chemistry," Interscience, New York (1958).
19. A. I. Vogel, "Quantitative Inorganic Analysis," p. 795, Longmans, London, (1960).
20. H. E. Bartlett and K. E. Johnson, *Can. J. Chem.*, **44**, 2119 (1966).
21. A. T. Ward and G. J. Janz, *Electrochim. Acta.*, **10**, 849 (1965).
22. F. M. Jaeger and J. Kahn, *Proc. Acad. Sci. Amsterdam*, **19**, 381 (1916).
23. G. J. Janz and A. Conte, *Electrochim. Acta*, **9**, 1279 (1964).

Galvanostalametry: A Technique for Chemical Analysis

John L. Sligh and Abner Brenner

National Bureau of Standards, Washington, D. C.

ABSTRACT

A method utilizing a novel technique to designate the end-point of a diffusion controlled electro-reducible or -oxidizable reaction has shown promising analytical capability. The apparatus consists of a J-shaped, evacuated glass tube in which a column of electrolyte is suspended under tensile stress in the longer limb. One electrode is sealed into the top of the J and the other into the short limb. The formation of a minute amount of gas at the upper electrode by electrolytic discharge of hydrogen or oxygen causes the column of electrolyte to suddenly drop. It has been found that, in the constant-current electrolysis of a suitable supporting electrolyte containing an electroreactive ion, the transition time required for the column to drop is a function of the concentration of the ion. The use of this method as an analytical tool and its relationship to chronopotentiometry are discussed.

A survey of the principles and applications of galvanostalametry was the subject of a previously published paper by the present authors (1). Briefly, the method involves the dropping of a vertical column of electrolyte which is metastably suspended in an evacuated glass tube under the tensile stress of its own weight. Electrolytic production of a gas (usually hydrogen or oxygen) at an indicator electrode which is sealed into the top of the column causes the column of electrolyte to suddenly collapse. The fall of the column indicates the final stage in an electrolytic reaction, similar to the point of inflection in a plot of electrode potential *vs.* time in chronopotentiometry.

The suspension of the electrolyte in the evacuated tube results from the adhesion of the liquid to the top of the glass tube and the cohesion of the liquid. It is well known that liquids possess considerable tensile strength. Briggs (2) showed that only a monomolecular layer of hydrogen or oxygen on the indicator electrode sufficed to disturb the metastable equilibrium and cause the column to drop. This characteristic makes the method a very sensitive means for the detection of the initial generation of gas at an electrode. The fall of the column immediately breaks the electrical circuit, and this feature can be used to record the period of current passage automatically.

The analytical application of galvanostalametry depends on the relation that the transition time or the period before the column drops (with passage of a constant current) varies with the concentration of an electrochemically active substance (except for the constituents of water). The fall of the column indicates that the concentration of the oxidizable or reducible ion at the electrode solution-interface has been depleted and a new reaction, the discharge of hydrogen or oxygen, has begun. The measured time must be corrected by a blank, which is the period before the column drops in the presence of a supporting electrolyte, that is one which involves only the decomposition of water on electrolysis. For most of the experiments, the blank amounted to about 0.3 sec. This subject is discussed in more detail in the text.

Apparatus

The apparatus described in the previous publication (1) has been simplified and made smaller for the analytical applications. An attractive feature of the galvanostalametric procedure is the relative economy of the experimental equipment compared to that of other automatic electroanalytical methods.

The analytical cell, shown in Fig. 1, was constructed in two pieces. The main part consisted of a vertical glass tube, the lower end of which terminated in an elbow which enlarged into a spherical reservoir of about 30 ml capacity. The latter was equipped with a tubular opening which was used for introducing the electrolyte and the secondary electrode, as well as for evacuating the vessel. The upper end of the vertical tube carried an "O" ring, connector for connecting to the top part of the cell. This part was a small vertical

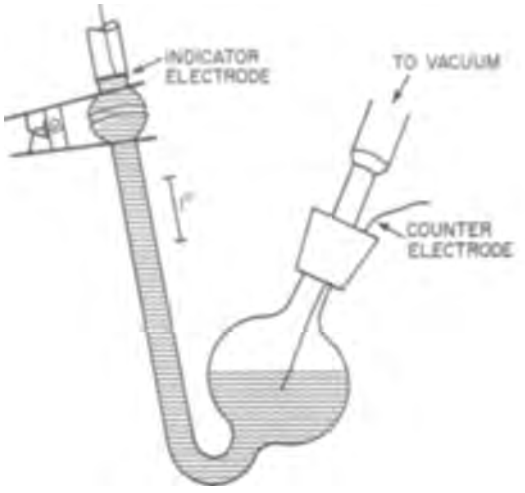

Fig. 1. Diagram of vessel used for analytical applications of galvanostalametry. Length of column of liquid, 25 cm; diameter of column, 7mm; volume of bulb, 30 ml.

extension in which was sealed a platinum disk, 0.5 cm in diameter, serving as indicator electrode. The extension was readily attached to the main section with a clamp to make a vacuum-tight vessel. The demountable feature of the extension, holding the indicator electrode, was a considerable improvement over the earlier apparatus, as it permitted easy removal for cleaning and inspection. The vessel was evacuated by an ordinary vacuum pump after introducing the electrolyte. The degree of evacuation was not critical as it was limited by the vapor pressure of the liquid. A good aspirator can be used.

The period of electrolysis, which was terminated by the dropping of the columns, could be timed with an ordinary stop watch. Since most of the determinations were of the order of only several seconds, timing was done more accurately with an electric stop clock with the smallest division 0.01 sec, thus permitting estimation to a few milliseconds. The dropping of the column caused almost a complete cessation of current flow and at the same time a large voltage build-up across the electrolytic cell. The timer could be stopped automatically by a relay which was triggered either by the increase of voltage across the cell or by the decrease of voltage across a resistor.

An investigation with an oscillograph showed that the time interval between the incipient drop of the column and the cessation of current flow was about 0.3 sec. The stoppage of current was not instantaneous because a diminishing current continued to flow between the falling liquid and the electrodes via the film of liquid draining down the walls of the tube. This period of time could constitute a serious loss of precision in experiments which involved a transition time of only a few seconds. The precision of determining the end-point was considerably improved by using an electronic relay that operated on a change of about 100 mv, which is about 1% of the voltage change that occurred across the cell at the end-point. This increased the precision in detecting the initiation of the dropping of the column to a few hundredths of a second.

Details of Experimental Manipulation

About 20 ml of the electrolyte to be examined was introduced into the cell through the tubular opening in the reservoir by a means of a 20 ml graduated syringe. A length of vacuum rubber tubing fitted with a screw clamp was attached to the tubulation, and the cell was evacuated. The screw clamp was adjusted continuously to avoid violent boiling of the solution. On completion of the evacuation, the screw clamp was tightened. At this point the levels of electrolyte in the column and the reservoir were equal. The cell was next inverted slowly, permitting the solution to flow from the reservoir into the evacuated tube. This must be done carefully as a sudden impact of the liquid would produce minute bubbles which would rise very slowly. After residual gas bubbles had floated upward and were trapped in the reservoir, the vessel was righted; the column of liquid then remained suspended in the vertical tube. Electrical connections were made to the electrodes, a constant current was passed, and the period of its duration measured before the fall of the column. A delay of 2 min was interposed between successive measurements, to allow the electrode to return to a reproducible condition. Consecutive measurements generally checked within 1 or 2%.

In most of the experiments a constant current of 2.5 ma was used with the platinum electrode (area 0.2 cm^2). The current from a 135v battery passed through a resistance in series with the cell. The resistance served to keep the current approximately constant despite the development of polarization in the cell.

Transition Time Involved in the Decomposition of Water

The analytical application of galvanostalametry depends on the time (transition time) required to deplete the concentration of an electrochemically active ion (with a constant current) at the electrode solution-interface. The dropping of the column indicates this time. As already noted, the collapse of the column results from the discharge of hydrogen or oxygen, which form a monomolecular film of gas on the electrode. Thus the analytical determination also involves a transition time for the electrolysis of water and the relation of this transition time to that required for the discharge of the other ions must be made clear.

The first experiments with the dropping of the column were done by Briggs (2) who discharged a condenser through electrodes. His results indicated that the dropping of the column, in the absence of reactive ions other than hydrogen and oxygen, was dependent on the passage of a certain minimum number of coulombs through the system, which we shall refer to as the critical charge. He did not determine the time of current flow, but since the discharge of a condenser was used the time was short.

The present experiments were made to determine if the blank transition time in water (0.5M H_2SO_4) for the formation of a monolayer of hydrogen, followed a relationship similar to that of other electroactive ions. Since the current from a condenser is not constant, the current was obtained from a square wave generator in pulses ranging from a millisecond to about 1 sec. Because the charges obtainable were small, an indicator electrode of small area was chosen so that the current density on it would be of sufficient intensity to cause the column to drop. The indicator electrode was made by sealing a platinum wire 0.4 mm in diameter in glass tubing and then exposing the cross section of the wire.

In these experiments, the procedure for determining the transition time consisted in making a series of determinations using square wave pulses. In each successive experiment the amplitude of the pulse, having a fixed pulse width, was increased until one was found that caused the column to fall.

The results of the measurements, which are given in Table I, confirm Briggs' view that, to a first approxi-

Table I. Cathodic pulse current data showing the approximate constancy of the critical charge in 0.5M sulfuric acid.

Pulse duration, msec	Current, ma	Critical charge, coulombs × 10^{-6}
0.03	132	4
0.1	46	4.6
0.5	12.5	6.25
1.0	7.25	7.25
5.0	2.1	10.5
10.0	1.1	11

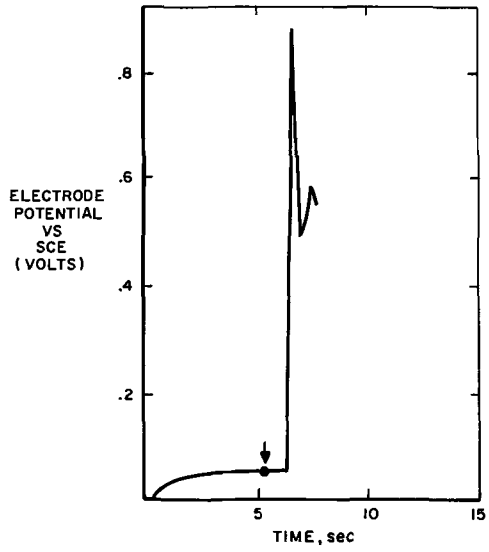

Fig. 2. Relation between voltage and time in the dropping of a column by anodic oxidation of 0.05M iodide ion in 0.5M sulfuric acid solution. The trace was made with an oscillograph. The arrow indicates the position of the point of inflection of the curve that would be used for chronopotentiometry.

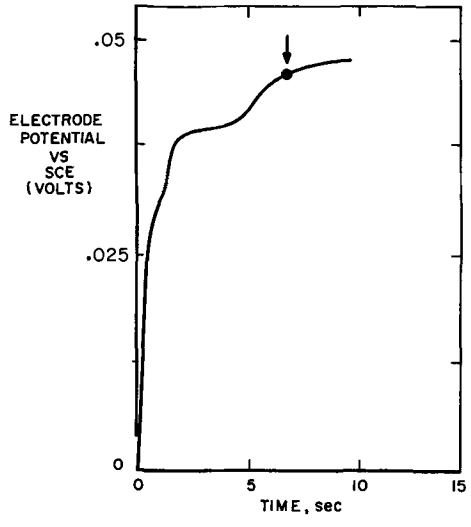

Fig. 3. Amplified portion of the curve of Fig. 2 in the region of the point of inflection. Trace obtained with an oscillograph.

mation, a constant amount of charge is required to drop the column. The variation in the critical charge was only about threefold for a more than a 300-fold variation in the duration of the pulse. Thus, to a first approximation, $Q_c = It_a$ = constant, where Q_c is the critical charge, I is the current, and t_a is the transition time for water. The transition time t_a is, thus, inversely proportional to the current

$$t_a = \frac{Q_c}{I}$$

This point of inflection was found to precede the dropping of the column in galvanostalametry. It was observed with a recording oscillograph that has a full-scale response of less than 1 msec. A reproduction of an oscillograph trace is shown in Fig. 2. The point of inflection indicated by the arrow was too small to be clearly seen on the same trace as that including the galvanostalametry end-point. To make the inflection point clear, an amplification of the lower part of Fig. 2 is shown in Fig. 3.

This observation shows that the galvanostalametry transition time includes a small additional time (for the critical charging of electrodes) beyond the point of inflection. However, this does not cause a difficulty in analytical determinations, since a calibration can be made with solutions of known concentration.

Galvanostalametry Determinations of Concentration

For determination of the concentration of an ion by galvanostalametry, a calibration curve was made using a few solutions of known concentration. The plot of the square root of transition time *vs.* concentration was linear. The reproducibility of determinations was usually of the order of 1.5% under the best conditions. With some ions, difficulties were occasionally encountered owing to the failure of the electrode to function. This will be discussed in the relevant places in the following treatment of analytical applications. Both homogeneous and heterogeneous electrode reactions were investigated.

The transition time for the discharge of hydrogen or oxygen, therefore, differs from the transition time t_b for the discharge of ions which are under diffusion control as given by the Sand (3) equation

$$t_b = K\left(\frac{C}{I}\right)^2$$

where K is a constant, C is concentration (mole/cm^3), and I is the constant electrolysis current (amp).

This latter relation limits the applicability of galvanostalametry for short transition periods, such as milliseconds. This is because as the current I increases, the transition time t_b for the discharge of an ion decreases rapidly (inversely as the square of the current), whereas the transition time, t_a, for the decomposition of water decreases more slowly. Thus, in the range of milliseconds, the value of t_b becomes of the same order as t_a and there is a loss of accuracy in determining t_b.

The effect of a short transition time on a determination is shown by the data in Table II. In these experiments the current used in each experiment was increased as the iodide concentration was increased, so as to keep the transition time in each experiment about 1 msec. The critical charge (blank correction in the absence of iodide ion) was relatively large, 7.5 x 10^{-6} coulombs. The quantity of charge used for discharging iodide ion is considered to be the difference between the blank and the value given in column 2. It ranged from about 1 x 10^{-6} coulombs for the 0.01M iodide solution to about 5 x 10^{-6} coulombs for the 0.10M solution, which values are smaller than the blank correction. These data show that galvanostalametry would not be very accurate for small transition times because of the large blank correction.

Relation of the End-Points of Galvanostalametry and Chronopotentiometry

The end-point in chronopotentiometry is the point of inflection of a curve of electrode potential *vs.* time. The change in voltage at the end-point varies with the system, but it is not large, ordinarily of the order of several tenths of a volt. The end-point of the reaction is best obtained from a graph.

Table II. Effect of sodium iodide concentration on the critical charge for a fixed transition time of 1 msec in 0.5M sulfuric acid

Molar concentration	Critical charge, coulombs × 10^{-6}	Coulombs* for oxidation of iodide ion
0.00	7.5	—
0.01	8.6	1.1
0.04	10.4	2.9
0.1	12.0	4.5

* Critical charge with iodide present minus critical charge at zero concentration.

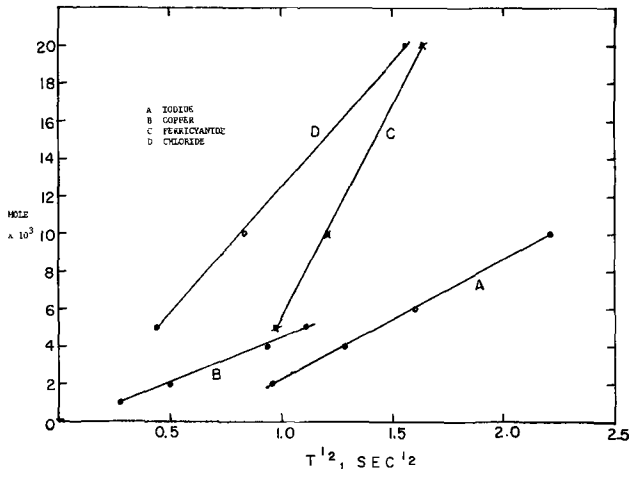

Fig. 4. Relation between concentration and time in the dropping of a column in galvanostalametry experiments.

Copper ion in copper sulfate solution.—A copper plated platinum indicator electrode was used for determining the copper ion concentration in copper sulfate solutions acidified with sulfuric acid. A platinum indicator electrode was not satisfactory, because the copper had to be dissolved anodically before each determination, and this procedure altered the surface of the platinum sufficiently to influence the transition times for subsequent copper determinations. The data obtained with several different concentrations of cupric ion are plotted in Fig. 4. The reproducibility was about 1.5%.

Cadmium.—Transition times for the reduction of cadmium ion were well defined at a platinum indicator electrode employing cadmium chloride in a supporting electrolyte of 1.0M sodium sulfate at pH 5. Measurements made at a constant current of 2.5 ma (current density of 12 ma/cm^2) are shown in Table III. The cadmium deposit was anodically removed from the platinum electrode between each determination, as subsequent determinations on the cadmium coated electrode yielded larger transition times than those obtained on platinum. Presumably, this difference was caused by an oxide film on the cadmium deposit. A transition time was not obtained in a solution 0.5M in sulfuric acid because of the greater ease of hydrogen discharge.

Oxidation of iodide ion.—The oxidation of iodide ion in a supporting electrolyte of 0.5M sulfuric acid yielded the most reproducible results of any of the determinations. A reproducibility greater than 1.5% was obtained with a platinum electrode and the results were not influenced by the care of the electrode. Typical results are given in Fig. 4.

Chloride.—The chloride determination was studied in a solution of cadmium chloride which was 0.5M in sulfuric acid. A platinum indicator electrode was used as anode. The dependency of the transition time on the chloride ion concentration is shown by data in Fig. 4.

Table III. Transition times for various ions as a function of concentration at a constant current of 2.5 ma

Conc, M	Cd^{++}	Br^-	$Cr_2O_7^{--}$*	MnO_4^-*	$C_2O_4^{--}$
0.02	2.05	2.82	36.5	32.13	2.40
0.01	0.66	1.20	9.6		1.13
0.005		0.66			0.84
0.004	0.12			4.57	
0.002			1.75	3.2	
0.001			1.27		

* High values observed for dichromate and permanganate ions indicate the dependence of galvanostalametry on equivalent concentration.

The ability to determine chloride ion by galvanostalametry was unexpected, because on the one hand the discharge of oxygen should occur before that of chloride, and on the other, discharge of chlorine in the gaseous state should drop the column.

Bromide.—The galvanostalametry determination of bromide ion was made with sodium bromide in a supporting electrolyte of 0.5M sulfuric acid. The transition time for the oxidation of the bromide ion was well defined, but successive measurements yielded shorter transition times than the initial value. Reproducible values of the transition time having the same value as the initial one were obtained by allowing the platinum electrode to stand idle for at least 2 hr between successive determinations. A more convenient method of normalizing the electrode was to apply an alternating current of 200 Hz at a current density of 5 amp/dm^2 for about 30 sec to the electrode after a determination. This permitted successive determination to be made without delay. Data obtained for a few bromide solutions of various concentrations are shown in Table III. A plot of these results show a marked deviation from linearity, probably due to the expedient employed to normalize the electrode.

Permanganate.—The experiments with permanganate ion were conducted with a solution of potassium permanganate in a supporting electrolyte of 0.5M sulfuric acid with a platinum electrode used as cathode. The transition times were about the same as those for solutions of other ions of the same normality.

The data in Table III show that the transition time varied with concentration in a regular manner. The use of this technique may be of interest in filling a gap in electrochemical methods, inasmuch as polarography is not suitable for determining permanganate ion (4).

Dichromate.—Dichromate was determined by cathodic reduction in a supporting electrolyte of 0.5 sulfuric acid. The determination of the transition time was attended with some difficulty because the result was dependent on the condition of the platinum electrode. For example, no indication of a transition time was observed if the electrode was cleaned in concentrated nitric acid. However, if it was treated anodically in the test solution prior to the determination, cathodic transition times were obtained similar to those observed with permanganate ion. Furthermore, the electrode continued to be serviceable for an entire series of determinations without additional anodic treatment. Similar to the results for the permanganate ion, the transition time was of the same order of magnitude as that obtained with simpler ions of the same normality.

Ferricyanide ion.—The determination of this ion also depended on the condition of the platinum indicator cathode, and the phenomena were similar to that observed with the dichromate ion. No transition time was observable with ferricyanide in a supporting electrolyte of 0.5M sulfuric acid until the electrode had once been made anodic.

Oxalate.—The determination of oxalate ion was also complicated by the necessity for specially treating the platinum anode. In contrast to the two preceding cases, no transition time was observed if the electrode was first made anodic. Satisfactory results were obtained after treating the anode with nitric acid. The data showing the variation of transition time with concentration are given in Table III. The absence of a transition time with an oxidized platinum electrode was previously reported by Lingane (5).

Discussion

The range of concentrations covered in our investigation was 10^{-3} to 10^{-2} equivalents per liter for the most part, since the prime objective was the applicability of the technique to the determination of a

variety of ions in moderately dilute solution. However, concentrations up to 1*N* were easily measured with reproducible transition times. For the best precision, the transition times should be held to less than 10 sec. Concentrations smaller than $10^{-4}N$ were difficult to measure with any precision.

The graphs in Fig. 4 show that generally the square root of the transition time is a linear function of concentration. However, the straight lines appear to be directed toward the origin in only two cases, namely, copper and cadmium. Therefore, the relation between the transition time, t, and the concentration, C, does not, in general, follow Sand's equation for linear diffusion

$$t_b = K\left(\frac{C}{I}\right)^2$$

Chronopotentiometry has been shown to follow this law closely (6, 7).

The following explanation is offered for the failure of all of the plots of C *vs.* $t^{1/2}$ to pass through the origin in the galvanostalametry experiments (see Table III and Fig. 4). In all these experiments it is necessary to subtract from the experimentally determined time for dropping of the column a blank or correction term. The latter represents the time required for the column to fall with a solution which contains the supporting electrolyte (for example, sulfuric acid) in the absence of the electrochemically active ion (which is to be determined). This correction or blank is valid in the experiments in which a metal is deposited at the cathode, because the solution at the electrode interface is almost completely depleted of the depositing ions and contains only the supporting electrolyte. This is the probable reason that the plots of C *vs.* $t^{1/2}$ pass through the origin for the determination of cadmium and copper ions. However, in the determination of anions, the solution at the interface at the moment the column is dropped contains a high concentration of the soluble oxidation product, for example, bromine or ferrocyanide ion. The correction or blank for an electrode in these media may be considerably larger than that for a solution in their absence containing only the supporting electrolyte. This discrepancy appears in the plots for the anions (except chloride ion) as an apparent transition time for zero concentration (where the extension of the straight line plot crosses the x-axis).

The slopes of the plots of C *vs.* $t^{1/2}$ approximately agree with Sand's equation

$$\text{Slope} = \frac{C}{t^{1/2}} = \frac{2i}{\pi^{1/2}n\mathbf{F}AD^{1/2}}$$

In the experiment for cadmium in Table III, the experimental value of the slope is 0.0125. The value calculated from the above equation with $n = 2$; $\mathbf{F} = 10^5$ coulombs; $A = 0.2$ cm^2, and $D = 10^{-5}$ is 0.024 which is of the right order of magnitude. The slopes of the plots for permanganate and dichromate ion (Fig. 4) are both approximately 0.0045. These are also of the right order of magnitude, since the slopes should be about 1/3 that of the line for cadmium, since $n = 5$ and 6 for these ions.

The difficulty encountered with reproducibly conditioning the indicator electrode requires more study. This difficulty applies also to chronopotentiometry. The sensitivity of the transition time to the surface condition of the electrode indicates that the galvanostalametry technique might be used to study and evaluate the catalytic nature of metal surfaces.

The galvanostalametric technique has several practicable advantages for the determination of a single ion. First of all, simple equipment is required, and no reference electrode or expensive recording instrument for measurement of electrode potential are needed. The end-point of the determination is both visual and dramatic and the determination itself can be made very rapidly. As a demonstration, an electric timer, actuated by the electronic cutoff mentioned earlier, was used to determine the concentration of copper ion in a copper sulfate solution. By using a large current, the transition time was reduced to less than a second. The dial of the timer was directly marked in units of concentration. On pushing an electrical switch, the dial of the timer spun and stopped almost in the twinkling of an eye, giving the concentration. We have dubbed this technique "Push-button analysis" and believe that it should find application in routine work.

The main drawback to galvanostalametry is the restriction on the composition of the solution to be analyzed. For example, if several electroreducible ions were present, such as cadmium, copper, and silver cations, a composite result for all three would be obtained at the cathode. In such a situation, chronopotentiometry would permit the determination of the most readily discharged metal (silver) by virtue of the point of inflection of the voltage-time curve. However, the following points of inflection would represent simultaneous discharge of two or more cations and the computation of each is sufficiently complicated to be difficult if not infeasible.

Acknowledgment

The authors wish to express their thanks to the Air Force Materials Laboratory, Research and Technology Division, Air Force Systems Command, whose financial support made this investigation possible.

Manuscript received Sept. 29, 1966; revised manuscript received Jan. 16, 1967.

Any discussion of this paper will appear in a Discussion Section to be published in the December 1967 JOURNAL.

REFERENCES

1. J. L. Sligh and A. Brenner, *This Journal*, **110**, 1136 (1963).
2. L. J. Briggs, *J. Chem. Phys.*, **21**, 779 (1953).
3. H. J. Sands, *Phil. Mag., London*, **6**, 45 (1901).
4. M. v. Stackelberg, P. Klinger, W. Kock, and E. Krath, *Forschungsberichte Tech. Mitt Krupp*, Essen, **2**, 59 (1959).
5. J. J. Lingane, "Electroanalytical Chemistry," 2nd ed., p. 635 (1958).
6. L. Gierst and A. Juliard, *J. Phys. Chem.*, **57**, 701 (1953).
7. P. Delahay, "New Instrumental Methods in Electrochemistry," chap. 8, Interscience Publishers, Inc., New York (1954).

The Role of Hydrogen Peroxide in Oxygen Reduction at Platinum in H_2SO_4 Solution

A. Damjanovic, M. A. Genshaw, and J. O'M. Bockris

The Electrochemistry Laboratory, The University of Pennsylvania, Philadelphia, Pennsylvania

ABSTRACT

The rotating disk electrode with a concentric ring is used to analyze the role of H_2O_2 in the reduction of O_2 to H_2O in acid solutions. No H_2O_2 is formed as an intermediate in the reaction path of oxygen reduction to water. Only when the residual impurities from the not sufficiently purified solutions are adsorbed at the electrode does a parallel reaction path appear in which H_2O_2 is formed as an intermediate that does not reduce further to H_2O with any significant rate. The mechanism of O_2 reduction to H_2O involves a first charge transfer step as rate-controlling under Temkin conditions of adsorption.

In the study of the mechanism of oxygen reduction to water, it is desirable to establish what part hydrogen peroxide is playing in the over-all reaction. In electroreduction of O_2 at Pt electrodes the rotating disk electrode with a concentric ring (1-4) was successfully used to examine whether H_2O_2 is formed or not (5-11). However, it was not possible to distinguish if H_2O_2 is formed as an intermediate in an over-all reaction path or if it is produced in a parallel reaction.

The method of the rotating disk electrode with a ring has recently been extended to enable a diagnostic plot to be made which permits a clear distinction between reaction intermediates and the products in a parallel reaction path (12). This diagnostic plot is obtained from the equation

$$\frac{I_d}{I_r} = \frac{x+1}{N} + \frac{x+2}{N} \cdot \frac{1.61\, k_3 \nu^{1/6}}{D^{2/3}\omega^{1/2}} \qquad [1]$$

In this equation, I_d is the current at the disk electrode, I_r is the current at the ring electrode, and x is the ratio of the current at the disk electrode due to the reaction which does not result in the formation of intermediates to the current at the same electrode due to the formation of intermediates, N is the geometric factor for the electrode assembly which can readily be obtained (2-4), k_3 is the rate constant for the further reaction of intermediate at the disk electrode, ν is the kinematic viscosity, D is the diffusion coefficient of intermediates, and ω is the angular velocity. The plot of I_d/I_r *vs.* $\omega^{-1/2}$ enables the quantities, x and k_3, to be obtained, and hence, to distinguish between reaction intermediates and products of a parallel reaction.

This method, using the rotating disk electrode with a ring, together with the usual kinetic measurements, is used here to analyze the mechanism of oxygen reduction at platinum electrodes in acid solutions with a particular emphasis on establishing what part H_2O_2 is playing in the over-all electrode reaction.

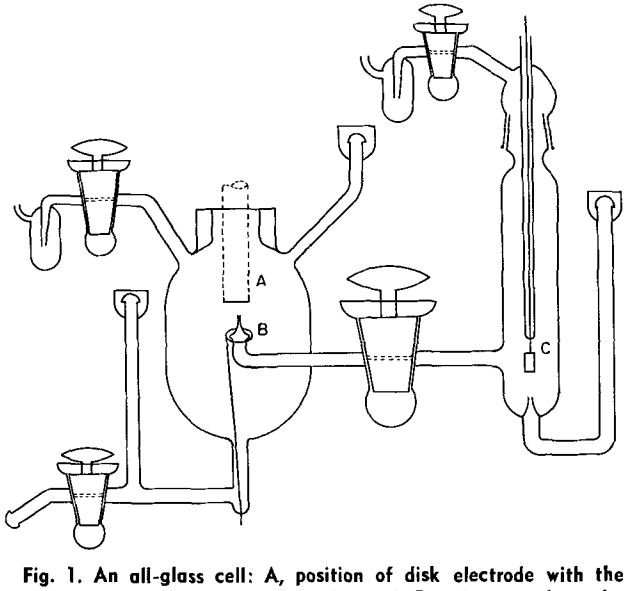

Fig. 1. An all-glass cell: A, position of disk electrode with the concentric ring; B, counter electrode; and C, reference electrode.

Experimental

The rotating disk apparatus is a modified version of the design used by Yeager at Western Reserve University. The electrode consists of a platinum cylinder which is press fit into Teflon. In the present experiments, the area of the disk electrode is 0.178 cm^2. The factor N is 0.38, as calculated from the dimensions of disk and ring electrodes (13) and confirmed by an experiment with a redox reaction ($Fe^{+++} \rightarrow Fe^{++}$).

The rate of rotation of the electrode assembly was determined by comparing a signal produced by a coil placed near a magnet attached to the shaft of the disk electrode with that of a standard frequency produced by an audio oscillator.

The all-glass cell is shown in Fig. 1. It consists of a spherical main compartment which has a water seal at the top to match the mating part on the shaft bearings assembly. Gas inlets are provided above and below the solution level. The inlet above the solution level permits the maintaining of a slight overpressure of oxygen without stirring the solution using a gas bubbler as an outlet. The reference electrode is a hydrogen electrode located in a compartment isolated by a closed stopcock from the main compartment.

A thin capillary from the reference electrode extends upward toward the center of the disk electrode. The counter electrode is a platinum disk which surrounds the Luggin capillary and is placed parallel to the rotating disk electrode. This shape and the position of the counter electrode were chosen to give as uniform a current density as possible.

For the electrochemical purification of the solution a separate vessel, illustrated in Fig. 2, was attached to the cell. It consisted of a tube packed with a platinized platinum gauze as one electrode and a small platinum wire as a counter electrode. An additional small compartment was attached to this tube to hold a calomel reference electrode. A nitrogen gas pump was used to circulate the solution through the purification vessel and the main cell.

The cell, purification vessel, and gas trains were cleaned thoroughly before use. Between experiments the cell was soaked in a mixture of HNO_3 and H_2SO_4. The purification trains for oxygen and nitrogen were often regenerated.

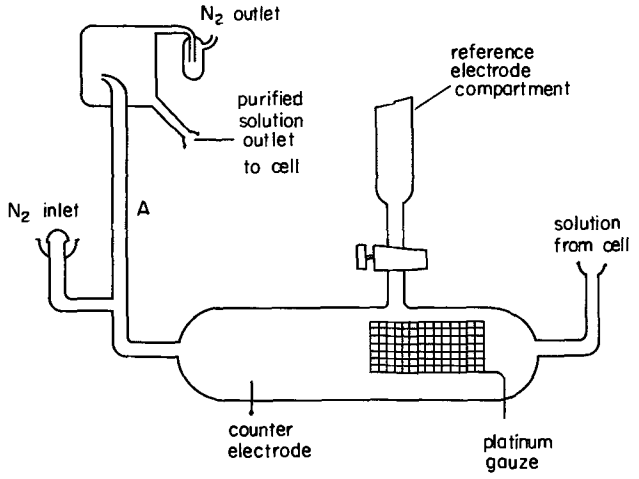

Fig. 2. Cell for the electrochemical purification of solution. This is an attachment to the main cell.

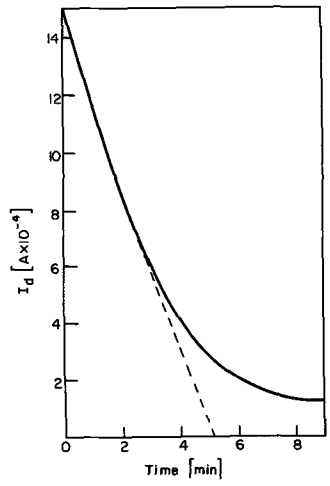

Fig. 3. Time dependence of current at the disk electrode in "insufficiently" purified solutions. Potential of the disk is 0.40v. $\omega = 120\ \pi\ \text{sec}^{-1}$.

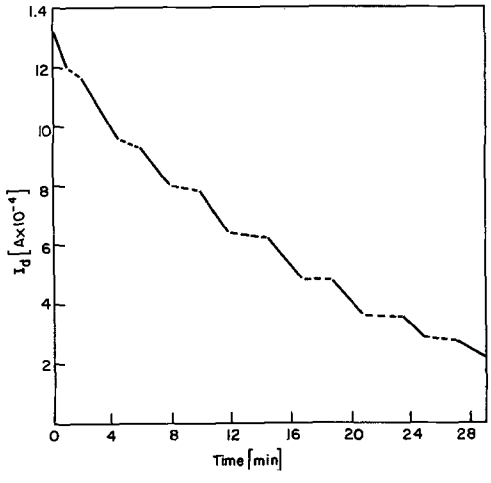

Fig. 4. Time dependence of current at the disk electrode with interrupted rotation. Solid line, $\omega = 120\ \pi\ \text{sec}^{-1}$; dotted line, $\omega = 0\ \text{sec}^{-1}$. Potential of the disk electrode is 0.60v.

The disk electrode with the ring was mechanically polished using 0.3 μ Gamel as a final polishing medium. The ring electrode was then lightly platinized. Both electrodes were thoroughly washed before experiments with sulfuric acid and conductivity water. The electrode pretreatment consists of potentiostating the disk electrode first at 1.4v for about 1 min and then at 0.0v for another minute.

Sulfuric acid solutions (0.1*N*) were prepared from Baker Analyzed reagent H_2SO_4 and conductivity water. Two procedures were used to purify the solution. In one, sulfuric acid was treated (14) by H_2O_2. For the present experiments, this purification procedure was found insufficient, and in the following it is referred to the solution purified by this procedure as "insufficiently purified." In the second procedure, the electrochemical purification was carried out by potentiostating the platinized gauze in the purification vessel at about 300 mv anodic to a hydrogen electrode in the same solution[1] while the solution was circulated through the purification vessel. This circulation was achieved when bubbles of N_2 forced the solution to rise in a tube (A, Fig. 2). Prepurified nitrogen, which was used for this purpose, was further purified by passing through two charcoal traps at the temperature of solid CO_2. After the purification by potentiostating (for 5 to 10 hr), the vessel was separated from the main cell by stopcocks. The solutions purified in this way are referred to here as "pure."

During the electrochemical purification, the solution was saturated by N_2. After the purification, the N_2 is replaced by O_2 at 1 atm.

A Wenking 61R potentiostat was used to control the potential of the disk electrode. The potential of the disk electrode was usually changed in steps of 50 mv in the potential range of 1.0-0.0v. If H_2O_2 is formed at the disk electrode it diffuses to the ring electrode. The ring electrode is kept at 1.4v so that all H_2O_2 diffusing to it is oxidized. At this potential the contribution to the ring current from the O_2 evolution is small. The ring electrode potential was controlled with a low impedance potential divider using the disk electrode as a reference. Keithley 600 A electrometers were used for current measurements.

Results

Electrode behavior in "insufficiently purified" solutions.—At all potentials below about 0.8v, the current at the disk electrode was time dependent and usually reaches a steady value in time of the order of minutes. The fastest change in the current occurs between 0.4 and 0.2v at electrodes which were brought to these potentials after they had been potentiostated anodic to 1v (for a few seconds) and then reduced at 0.0v for about 10 sec. This is illustrated in Fig. 3 for an electrode at 0.4v. The rate of change of current, and the time for an electrode at a given potential to come to a steady state is strongly dependent on the rate of electrode rotation. If the rotation is interrupted, a far smaller decrease in disk current is observed during the time the electrode is stationary, as shown by the dashed line in Fig. 4. The ring current also changes with the potential of the disk electrode and time.

The dependence of the disk current upon potential and time for a given rate of disk rotation is shown in Fig. 5. A maximum in the disk current is observed at about 0.6v, and a minimum at about 0.3v. This maximum may be obtained either by increasing or decreasing disk potential as indicated by arrows in the figure. The maximum, however, tends to decrease with time. The initial "activity" of an electrode can, however, be restored if the electrode were brought to a potential anodic to 1.0v for a short (order of seconds) time, followed by the reduction at 0.0v.

The plots I_d/I_r, where I_d and I_r are the steady-state currents at the disk and ring electrodes, respectively, *vs.* $\omega^{-1/2}$ are given in Fig. 6. A series of lines, one for each electrode potential, are parallel to the $\omega^{-1/2}$ axis.

At low current densities, Tafel behavior is observed with $\partial V/\partial \log i = -0.07$v, and the exchange current density $\log i_o = \overline{10.7} \pm 0.3$.

[1] In the following, all potentials refer to hydrogen electrode potential in the same solution.

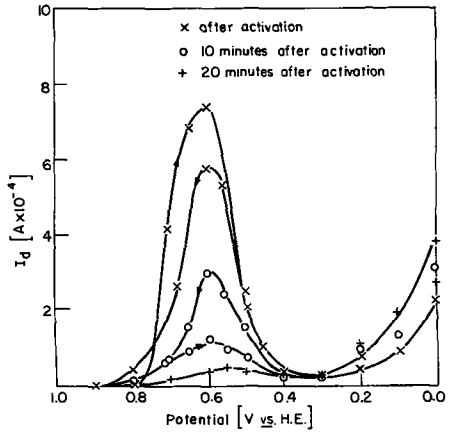

Fig. 5. Current at the disk electrode *vs.* potential in "insufficiently purified" solution. Effect of time on the current is shown. Arrows indicate the direction of measurements.

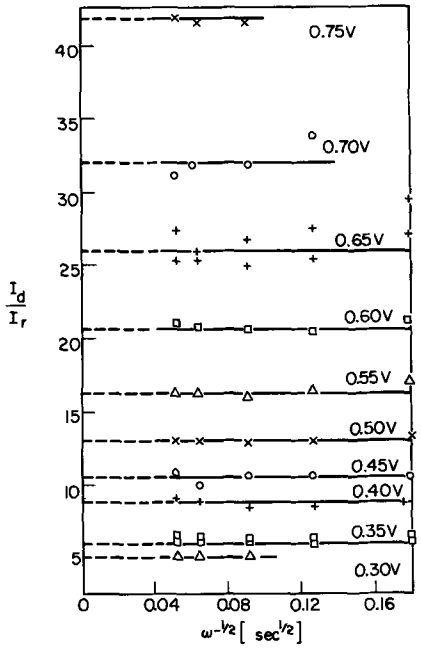

Fig. 6. Dependence of I_d/I_r on $\omega^{-1/2}$. Potentials of the disk electrode are given in the figure.

Electrode behavior in "pure" solutions.—The electrochemical purification by potentiostating at 0.3v proved to have a profound effect on the electrode behavior. The rate of decrease of the disk current with time is one to two orders of magnitude less than that in the "insufficiently purified" solutions. No significant current over the residual one was observed at the ring electrode for any potential of the disk electrode except those cathodic to about 0.15v. In Fig. 7, currents at the disk and ring electrodes are plotted *vs.* disk potential for a given rate of rotation. After the limiting current at the disk electrode was reached, the current changes little with potential until below about 0.15v when it starts decreasing. Just at that point, current at the ring electrode increases.

At low currents, Tafel behavior is observed with $\partial V/\partial \ln i$ and log i_o having about the same values as in "insufficiently purified" solution. A plot of log $(1-I)/I_{lim}$ *vs.* log I has a slope of 1. This shows that the reaction is first order in respect to oxygen (15). Here, I is the disk current for a given potential in the range close to the limiting current, I_{lim}.

When toluene was added to a "pure" solution, the rate of decrease of the disk current became similar to that in "insufficiently purified" solutions (Fig. 8).

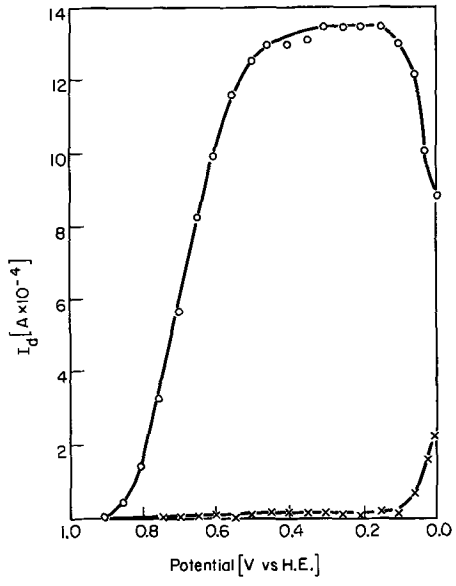

Fig. 7. Disk and ring currents for oxygen reduction at platinum in "pure" H_2SO_4. ○: disk current; X: ring current. $\omega = 120\ \pi$ sec^{-1}.

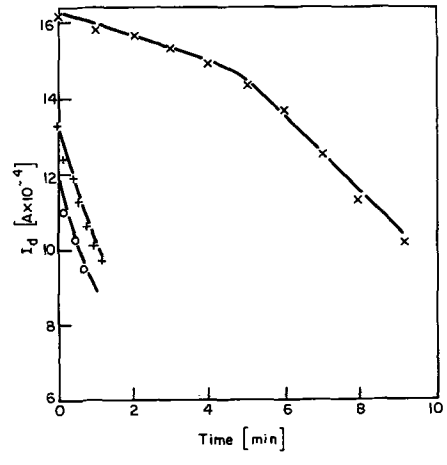

Fig. 8. Effect of toluene on time dependence of disk current. X, before addition of toluene; ○ and +, after the addition of toluene.

Discussion

The following experimental observations made in this work and elsewhere need discussion:

1. Hydrogen peroxide is formed in oxygen reduction on Pt in acid solutions (5, 6, 7, 16-30).
2. The yield of hydrogen peroxide is a function of potential and time (17, 18).
3. The oxygen reduction currents (to H_2O) at a constant potential are higher and the yield of hydrogen peroxide lower following an activation process of oxidation and reduction (16, 18, 21, 23).
4. In "insufficiently purified" solutions, the rate of the decrease of oxygen reduction current increases with the increasing rate of disk rotation. and
5. Much less hydrogen peroxide is produced in "pure" solutions.

These observations may be discussed in terms of the following models:

1. An electrode surface changes with time of contact with the solution. For instance, each individual grain of the polycrystalline electrode exposes initially one crystal plane to the solution. With time, via surface diffusion of adions, new crystal planes form at which catalytic activity changes (decreases).
2. A small amount of oxides on the electrode surface acts catalytically for oxygen reduction (23). It

is possible that, during oxygen reduction, these oxides are gradually being reduced and the over-all catalytic activity decreases.

3. It was suggested (5, 6) that the adsorption of anions or cations changes with potential and time and induces changes in the rate of oxygen reduction to H_2O and H_2O_2. and

4. Adsorption of impurities blocks the surface of the electrode and causes a change in the activity and also in the reaction path.

Change of the disk current with time.—Since the time dependence of disk current is strongly dependent on the rate of electrode rotation,[2] diffusion from the solution must be playing a major role in the changes which are occurring at the electrode surface. If the observed time dependence is due entirely to diffusion of some species to the electrode surface, a concentration of these species may be estimated in the following way.

For the diffusion to a rotating disk, Levich (31) gives the formula

$$j = 0.62\, D^{2/3}\, \nu^{-1/6}\, \omega^{1/2}\, c \qquad [2]$$

where c is the concentration of residual species in the solution, and other symbols are the same as in Eq. [1]. The steady-state disk current corresponds to the reaction rate at the surface at equilibrium coverage by adsorbed species. If the change in the current is attributed to a complete cessation of the reaction at those sites which are covered by adsorbed species, then the reaction rate for a given potential is related to the coverage by these species.

By extrapolating the initial line in Fig. 3 to zero current, it is calculated that about 300 sec would be required to reach a monolayer coverage. If it is now assumed that each molecule diffusing to the surface covers only one site at the surface (a low assumption if the species are organic), the monolayer coverage is about 2.5×10^{-9} mole/cm^2. The diffusional flux is then about 10^{-11} mole/sec cm^2. Using 10^{-5} cm^2/sec for D, 10^{-2} cm^2/sec for ν, and 378 sec^{-1} for ω, c is calculated to be 1×10^{-7} mole/l. This low concentration of species in the solution can already account for the observed change in disk current if initially all species reaching the electrode surface become adsorbed at it. After the electrochemical purification of the solutions the concentration of the species must be much lower than this as the change with time in disk current is much less.

If the electrode surface was undergoing some structural change (surface recrystallization or oxide reduction), there is no obvious reason for the dependence of the change in the disk current on the rate of rotation. There is also no reason why purification of the solution would affect the rate of this change. Hence, the observed change with time of disk current cannot be caused by changes in the properties of the electrode surface, which do not involve interaction of the surface with species diffusing from the solution.

It is unlikely that the adsorption of ions from the sulfuric acid can be causing the time dependent effects. The concentration of the sulfuric acid ($0.1N$) is so high that the adsorption cannot be diffusion controlled. If a slow activated adsorption process was occurring, no dependence on the rate of rotation should be observed. Ion adsorption has been observed on mercury to be a rapid process which is probably complete within 1 sec (32). Furthermore, the electrochemical purification should not affect the observed rate by which disk current changes with time.

Adsorption of residual impurities.—The adsorption of residual impurities from the solution may account for the observed time effect. The calculated concentration of 1×10^{-7} mole/l of species which are causing the effect is consistent with usually estimated (33, 34) concentration of residual impurities in insufficiently purified H_2SO_4 solutions. Slower changes with time of the disk current which are brought about by the electrochemical purification supports the model involving the presence of trace impurities in the solution. These impurities can be removed by the electrochemical purification used in this work.

Nature of the residual impurities.—Residual impurities appear to be oxidizable at the platinum electrode at higher potentials ($\geqq \sim 1$v). Thus, the depolarization of an electrode observed in the oxygen evolution at low current densities when sulfuric acid is not sufficiently purified is apparently due to the oxidation of the impurities. If such solution is anodically pre-electrolyzed, depolarization occurs at lower current densities (35, 36).

A fact which supports the identification of the impurities as organic compounds is the apparent partial reversibility of the adsorption. The maximum in the disk current as a function of potential is obtained starting from either the cathodic or the anodic direction. The increase in the cathodic current when the potential is made more anodic must be due to a decrease in the extent of "inhibition" of the reaction. The decrease in "inhibition" is likely due to the desorption of the "inhibiting" species, which are not easily oxidized at these low potentials.

The experiment in which toluene was added to "pure" solution shows that toluene causes the same type of effect as the residual impurity in "insufficiently purified" or impure solutions (Fig. 8). This also supports the view that the residual species in the solution are of organic nature.

With the passage of time, however, the apparent desorption with the change in potential occurs less and less readily until it is no longer noticed (see Fig. 5). This behavior requires a change in the nature of the adsorbed species. With organic molecules such changes may occur if they are partially oxidized at the surface. After a slow partial oxidation has occurred, the desorption of the "carbon skeleton" (37) would be much more difficult than the desorption of the original molecules. Alternately, if a spectrum of organic compounds is present as residual impurities, the most strongly adsorbed will displace the ones which are less strongly adsorbed, resulting in a decrease in the ease of desorption.

It appears, therefore, that organic, rather than inorganic, species are likely residual impurities that adsorb on the electrode surface.

Mechanism of O_2 reduction in the presence of residual impurities.—Adsorbed impurities greatly effect the mechanism and the kinetics of O_2 reduction, particularly in the potential range cathodic to about 0.7v.

If O_2 reduction proceeds along two paths so that

$$O_2 + 4H^+ + 4e^- \xrightarrow{k_1} 2H_2O \qquad [3]$$

$$O_2 + 2H^+ + 2e^- \xrightarrow{k_2} H_2O_2 \qquad [4]$$

$$H_2O_2 + 2H^+ + 2e^- \xrightarrow{k_3} 2H_2O \qquad [5]$$

reaction [3] represents one over-all path, and [4] and [5] the other in which H_2O_2 is formed as an intermediate which may reduce further to H_2O with the rate proportional to k_3, then the diagnostic plot given by Eq. [1] can be applied here.

The lines parallel to the $\omega^{-1/2}$ axis in the I_d/I_r *vs.* $\omega^{-1/2}$ plot (Fig. 6), show that k_3 is zero for the potentials at which the measurements were made. The intercepts at ordinate are greater than $1/N$ and change with potential. This means, according to Eq. [1], that x is not zero and that it changes with disk potential. With the definition of x as the ratio of the current due to reaction [3] to that due to reaction [4], it follows that O_2 reduction proceeds in two parallel reaction paths. Since $k_3 \approx 0$, the H_2O_2 formed in a parallel reaction

[2] In "insufficiently purified" or not purified solutions.

path (Eq. [4]) does not reduce further to H_2O with any appreciable rate.

The question still remains, whether in the path of oxygen reduction which leads to water (Eq. [3]), H_2O_2 is also formed as an intermediate but has a high rate constant for the further reduction of the hydrogen peroxide to water. If this were the case, then H_2O_2 which is produced in the other path (Eq. [4]) presumably on sites of different activity would be expected to diffuse to the sites which are active for H_2O_2 reduction in the hypothetical path

$$O_2 \rightarrow H_2O_2 \xrightarrow{\text{fast}} H_2O \qquad [6]$$

Since H_2O_2 would be produced at all sites on the surface and only be reduced at some sites, the rate constant for reduction of H_2O_2 would be averaged over the surface so that the diagnostic plot would resemble that for a single path ($x = 0$) with H_2O_2 as an intermediate which has a dependence on the rate of rotation. This is clearly not the case, as I_d/I_r is not dependent on the rate of rotation. Hence, the path of oxygen reduction which leads to water does not have a hydrogen peroxide intermediate.

In "pure" solutions, I_r approaches zero. Hence, at low coverage with residual impurities, all the oxygen is reduced to water (and no diagnostic plot is possible).

Now, the adsorption of impurities causes a decrease in the over-all rate of oxygen reduction (decrease in I_d with time) and this is concurrent with an increase in the amount of hydrogen peroxide formed (increase in I_r). Thus, the adsorption results in the appearance of the additional path in which H_2O_2 is produced.

Since, in the absence of the effect of impurities, no H_2O_2 is produced, and in the presence of impurities, H_2O_2 is produced in a path parallel to the path which does not involve the formation of intermediate, it is rationalized that hydrogen peroxide is produced at sites which are affected by impurities, and the water producing path occurs at sites not affected by impurities. Furthermore, since Tafel slopes and i_o's are approximately the same both in pure and in insufficiently purified solutions and the Tafel region corresponds to a region of minimum hydrogen peroxide formation (I_d/I_r in Fig. 6 is sharply increasing at potentials more anodic than 0.65v and Tafel region is anodic to 0.70v) the mechanism of oxygen reduction to H_2O in both solutions are expected to be the same. This supports the deduction that the sites at which H_2O is formed in insufficiently purified solution are not affected by adsorbed impurities (adsorption free sites).

Mechanism of O_2 reduction to water.—It has recently been discussed (38, 39) that on Pt electrodes O_2 reduction may occur either on oxide covered or on oxide free surfaces. The mechanism of the reaction on these two types of surfaces are not the same. The electrode pretreatment in the present work ensures that the disk electrode is oxide free.

The experimental facts relevant to determine the mechanism are the following: (*i*) H_2O_2 is not an intermediate in the reaction path; (*ii*) the reaction is the first order in respect to oxygen; and (*iii*) $\partial V/\partial \ln i \approx -RT/\mathbf{F}$. Parameters under (*ii*) and (*iii*) are the same as previously reported (38). The pH dependence as reported by other workers (38) is given by $\partial V/\partial \text{ pH} \approx -100$ mv.

The stoichiometric number can be obtained from (40)

$$p' - p'' = p/\nu \qquad [7]$$

where p' is the reaction order of the rate-controlling step for the forward reaction, and p'' for the backward reaction. p is the over-all forward reaction order for the reaction given by Eq. [3], and ν is the stoichiometric number.

Experimentally, it is found that $p' = 1$. Since, in general (40) $p'' \leq 0$, and $\nu \geq 1$, p'' must be equal to zero, and the stoichiometric number is one.

The formation of intermediates such as $O_2^=$, HO_2^-, and H_2O_2 are excluded, as hydrogen peroxide is not detected. If positively charged intermediates are excluded, the possible intermediates which can form before the rate-controlling step are hence O_2^- and HO_2.

Reaction path under Langmuirian condition of adsorption.—The equation (41)

$$b_c = -\frac{\nu RT}{(n_c + \beta n^*)\mathbf{F}} \qquad [8]$$

restricts the number of permissible paths. In this equation b_c is the cathodic Tafel slope, n_c the number of electrons transferred before the rate-determining step, n^* the number of electrons transferred in the rate-controlling step, and β the symmetry factor ($=\frac{1}{2}$). Since $\nu = 1$, and $b_c = -RT/\mathbf{F}$, and since n_c and n^* must be integral numbers, two possibilities arise

$$n_c = 1,\ n^* = 0 \qquad [9]$$

and

$$n_c = 0,\ n^* = 2 \qquad [10]$$

The second possibility requires a simultaneous two electron transfer which is highly improbable. Thus, only the first possibility is tenable. The path must then have a single electron transfer followed by a rate-controlling step which does not have an electron transfer. The following paths satisfy this requirement

Path (A) $O_2 + e^- \rightleftharpoons O_2^-$ [11]

$O_2^- \rightarrow$ products [12]

Path (B) $O_2 + H^+ + e^- \rightleftharpoons HO_2$ [13]

$HO_2 \rightarrow$ products [14]

The path A is not pH dependent, and path B has a pH dependence of $-RT/\mathbf{F}$, and neither is in agreement with the reported dependence (38) for $(\partial V/\partial \text{pH})$ of -100 mv. Hence, under Langmuir conditions, neither of the permissable paths are tenable.

Reaction path under Temkin conditions of adsorption.—Since the coverage with adsorbed oxygen species is approximately linear with potential in the Tafel region of oxygen dissolution and the intermediate values of coverages are reported (38, 42), the kinetics under Temkin adsorption conditions should be considered. If the rate-controlling step is according to

$$M + O_2 + H^+ + e^- \rightarrow MHO_2 \qquad [15]$$

where M stands for a site at the metal surface, then all reaction steps after this step must be considered as being in quasi-equilibrium. Such a step is

$$MOH + H^+ + e^- \rightleftharpoons M + H_2O \qquad [16]$$

The rate expression for [15] under Temkin conditions is (38, 43, 44)

$$i = k[H^+][O_2] \exp(-\beta\mathbf{F}V/RT) \exp[-\beta f(\theta)] \qquad [17]$$

Now, $f(\theta)$ can be obtained from [16] if the rate expressions for forward and backward reaction are equated and $\ln \theta$ term is neglected in respect to θ. It is

$$f(\theta) \approx V\mathbf{F}/RT - \ln[H^+] \qquad [18]$$

Substituting [18] into [17]

$$i = k[H^+]^{3/2}[O_2] \exp(-V\mathbf{F}/RT) \qquad [19]$$

This rate expression gives a pH dependence of $-3RT/2\mathbf{F}$, which is close to that reported (38). Thus, under Temkin conditions the first charge transfer is rate-controlling. This analysis confirms the previous one (38) concerning the mechanism of O_2 reduction on oxide free Pt electrodes in acid solution.

Formation of H_2O_2 below 0.15v.—In pure solutions, H_2O_2 is formed only in the region cathodic to about

0.15v (Fig. 7). In this potential region (0.2-0.0v) hydrogen is adsorbed at the electrode (45-50). At 0.1v hydrogen adsorption already amounts (46) to ~180 μcoul/cm^2. The sites which become occupied by hydrogen may not any longer be suited for oxygen adsorption which is required for the reduction to water. Then, a chemical reaction between the oxygen and adsorbed hydrogen may occur

$$O_2 + 2H \rightarrow H_2O_2 \quad [20]$$

If it is assumed that this reaction occurs on the sites covered by adsorbed hydrogen, its rate expression[3] is

$$i_{H_2O_2} = k_2[O_2]\theta_H^2 \quad [21]$$

The rate expression for the reaction of direct reduction of O_2 to H_2O then becomes

$$i = k[O_2](1 - \theta_H) \exp(-VF/RT) \quad [22]$$

when allowance is made for the decrease in area for the reaction due to the coverage with adsorbed hydrogen.

As θ_H approaches unity, the reaction product changes from H_2O to H_2O_2. Thus the change in the products observed can be accounted for qualitatively by this model.

However, the model has one drawback. A rhodium electrode also becomes covered with a monolayer of adsorbed hydrogen (51) at 0.00v. Hence, a similar behavior would be expected. However, no increase in the yield of hydrogen peroxide was observed (52), even at 0.00v. This is an evidence that geometric factors alone are not causing the changes of product observed at platinum. An alternative explanation is suggested below.

It is now established (53) that O_2 reduction to H_2O on bare Pd electrodes follow the same path and has the same rate-controlling step as on bare Pt electrodes. On gold electrodes, the mechanism is different and the product of the reduction is H_2O_2. In a series of palladium-gold alloys, the mechanism changes at the alloy composition where the d-band is expected to become filled. If unpaired d-electrons are a requirement for reduction of O_2 to water, then the hydrogen peroxide may be produced when all of the d-electrons are paired. The unpaired d-electrons of the surface atoms may be paired by interaction with the adsorbed H, and as a consequence of this, O_2 may no longer dissociate on adsorption, and O_2 reduces to H_2O_2 rather than H_2O. This model would predict a smooth change-over from no H_2O_2 to a quantitative yield of H_2O_2 when all of the d-electrons are paired, and the change in product from H_2O to H_2O_2 should occur in the initial region of hydrogen adsorption, *e.g.*, from 0.30 to 0.15v. However, this need not be the case since even a very small number of unpaired d-electrons which may remain at 0.15v can maintain the reduction to water. This is seen from the behavior of gold-palladium alloys which show a slow change in kinetics for oxygen reduction as the number of unpaired d-electrons decreases. The fact that on Rh electrode H_2O_2 is not a product even at 0.0v does not exclude above the model. Rhodium is expected to have about 1.7 unpaired d-electrons per atom. Thus, the adsorption of one hydrogen atom per one rhodium atom cannot result in a complete pairing of d-electrons and cause a change in the reaction product.

Summary of the Conclusions

In the case of oxygen reduction on Pt electrodes, the method of the rotating disk electrode with a concentric ring is shown to be useful in distinguishing between the reaction intermediates and the products in a parallel reaction path.

Oxygen reduction at oxide free Pt electrodes in pure acid solutions is a four electron process leading to H_2O. The rate-controlling step is consistent with the first charge transfer under Temkin conditions of adsorption. Hydrogen peroxide is not an intermediate in the path leading to water. In these pure solutions, H_2O_2 is formed only at potentials cathodic to 0.15v. This is interpreted as being due to the presence of adsorbed hydrogen at the electrode.

At potentials anodic to about 0.15v hydrogen peroxide forms only if the solution contains residual impurities, mostly organic ones, which adsorb at the surface. In this case, H_2O_2 forms in a reaction path parallel to that in which O_2 is reduced to H_2O. The rate of further reduction of H_2O_2 to H_2O is small in comparison to the rate at which H_2O_2 is formed.

[3] If reaction [20] occurs in two stages then θ_H should replace θ_H^2 in Eq. [21].

Acknowledgments

The authors wish to thank their sponsor, the U. S. Army Electronics Material Laboratory, Fort Monmouth, New Jersey (Contract No. DA-36-039-Sc88921) for financial support of this work. They also wish to thank Professor E. Yeager for making available the drawings of the rotating disk electrode apparatus, and Dr. L. N. Nekrasov, for discussion of the technique.

Manuscript received Aug. 24, 1966; revised manuscript received Jan. 23, 1967.

Any discussion of this paper will appear in a Discussion Section to be published in the December 1967 JOURNAL.

REFERENCES

1. A. N. Frumkin and L. N. Nekrasov, *Doklady Akad. Nauk SSSR*, **126**, 115 (1959).
2. Yu. B. Ivanov and V. G. Levich, *ibid.*, **126**, 1029 (1959).
3. V. G. Levich, "Physicochemical Hydrodynamics," p. 327, Prentice-Hall, Inc., Englewood Cliffs, N. J. (1962).
4. J. Albery and S. Bruckenstein, *Trans. Faraday Soc.*, **62**, 1920 (1966).
5. L. Müller and L. N. Nekrasov, *Electrochim. Acta*, **9**, 1015 (1964).
6. L. Müller and L. N. Nekrasov, *Doklady Akad. Nauk SSSR*, **154**, 437 (1964).
7. A. N. Frumkin, L. N. Nekrasov, V. G. Levich, and Yu. B. Ivanov, *J. Electroanal. Chem.*, **1**, 84 (1959).
8. L. N. Nekrasov and L. Müller, *Doklady Akad. Nauk SSSR*, **149**, 1107 (1963).
9. L. Müller and L. N. Nekrasov, *ibid.*, **157**, 416 (1964).
10. L. Müller and L. N. Nekrasov, *J. Electroanal. Chem.*, **9**, 282 (1965).
11. L. Müller and V. V. Sobol, *Elektrokhimiya*, **1**, 111 (1965).
12. A. Damjanovic, M. Genshaw, and J. O'M. Bockris, *J. Chem. Phys.*, **45**, 4057 (1966).
13. S. Bruckenstein, Private communication.
14. W. Visscher and M. A. V. Devanathan, *J. Electroanal. Chem.*, **8**, 127 (1964).
15. A. C. Riddiford, in the Rotating Disc System, to be published.
16. A. N. Frumkin, E. I. Khrusheva, M. R. Tarasevich, and N. A. Shumilova, *Elektrokhimiya*, **1**, 17 (1965).
17. A. Kozawa, *J. Electroanal. Chem.*, **8**, 20 (1964).
18. G. Bianchi and T. Mussini, *Electrochim. Acta*, **10**, 445 (1965).
19. T. N. Belina and A. I. Krasil'schikov, *Zhur. Fiz. Khim.*, **28**, 1286 (1954).
20. D. T. Sawyer and R. J. Day, *Electrochim. Acta*, **8**, 589 (1963).
21. D. T. Sawyer and L. V. Interrante, *J. Electroanal. Chem.*, **2**, 310 (1961).
22. M. W. Breiter, *Electrochim. Acta*, **9**, 441 (1964).
23. J. J. Lingane, *J. Electroanal. Chem.*, **2**, 296 (1961).
24. C. M. Quinn and M. W. Roberts, *Trans. Faraday Soc.*, **60**, 899 (1964).
25. D. Winkelmann, *Z. Elektrochem.*, **60**, 731 (1956).
26. H. A. Laitinen and I. M. Kolthoff, *J. Phys. Chem.*, **45**, 1061 (1941).
27. I. M. Kolthoff and J. Jordan, *J. Am. Chem. Soc.*, **74**, 4801 (1952).
28. W. C. Schumb, C. N. Satterfield, and C. N. Wentworth, "Hydrogen Peroxide," Reinhold Publishing Corp., New York (1955).
29. A. I. Krasilshchikov, Soviet Electrochem., Proc. Conf. Electrochem. (English Transl.), 4th, Moscow, 1956 (Pub. 1959) (1961).

30. J. Giner, *Z. Elektrochem.*, **64**, 491 (1960).
31. V. G. Levich, "Physicochemical Hydrodynamics," p. 69, Prentice-Hall, Inc., Englewood Cliffs, N. J. (1962).
32. K. Müller, Private communication.
33. A. M. Azzam *et al.*, *Trans. Faraday Soc.*, **46**, 918 (1950).
34. S. Gilman, *Electrochim. Acta*, **9**, 1025 (1964).
35. A. Damjanovic, A. Dey, and J. O'M. Bockris, *ibid.*, **11**, 791 (1966).
36. J. O'M. Bockris and A. K. M. S. Huq, *Proc. Roy. Soc.*, **A237**, 271 (1956).
37. B. J. Piersma, Thesis, University of Pennsylvania (1965).
38. A. Damjanovic and V. Brusic, Paper submitted for publication.
39. A. Damjanovic and J. O'M. Bockris, *Electrochim. Acta*, **11**, 376 (1966).
40. J. O'M. Bockris, "Modern Aspects of Electrochemistry," pp. 185, 186, J. O'M. Bockris and B. E. Conway, Editors, Butterworths, London (1954).
41. T. P. Hoar, Proc. Meeting Intern. Conn. Electrochem. Thermodyn. Kinet., 8th, (1956), Butterworths, London, p. 439.
42. H. Wroblowa, M. L. B. Rao, A. Damjanovic, and J. O'M. Bockris, To be published.
43. J. G. N. Thomas, *Trans. Faraday Soc.*, **57**, 1603 (1961).
44. B. E. Conway and E. Gileadi, *ibid.*, **58**, 2493 (1962).
45. F. P. Bowden, *Proc. Roy. Soc. (London)*, **A125**, 446 (1929).
46. F. G. Will and C. A. Knorr, *Z. Elektrochem.*, **64**, 258 (1960).
47. H. Dietz and H. Goehr, *Electrochim. Acta*, **8**, 343 (1963).
48. H. Dietz and H. Goehr, *Z. Physik. Chem. (Leipzig)*, **223**, 113 (1963).
49. S. Schuldiner and R. M. Roe, *This Journal*, **110**, 332 (1963).
50. P. K. Migal and V. A. Tsiplyakova, *Zhur. Fiz. Khim.*, **34**, 1153 (1960).
51. F. G. Will and C. A. Knorr, *Z. Elektrochem.*, **64**, 270 (1960).
52. M. Genshaw, A. Damjanovic, and J. O'M. Bockris, To be published.
53. A. Damjanovic and V. Brusic, To be published.
54. P. Dolin, B. Ershler, and A. Frumkin, *Acta Physicochim. URSS*, **13**, 779 (1940).
55. A. Damjanovic, R. Jahan, and J. O'M. Bockris, To be published.

Gallium Arsenide Electrode Behavior

W. W. Harvey

Ledgemont Laboratory, Kennecott Copper Corporation, Lexington, Massachusetts

ABSTRACT

The anodic dissolution reaction of GaAs was found to proceed quantitatively in well-stirred solutions of KOH and $HClO_4$ with the formation of soluble, tripositive Ga and As compounds. Disintegration of the anode was noted under natural convection. Passivity ensued at high anodic currents in $HClO_4$ electrolyte, with an abrupt active-passive transition and a gradual passive-transpassive transition. In H_2SO_4 electrolyte, the passive region extended to the highest attainable anodic potentials. No substantial differences in electrochemical behavior were found between Ga(111) and As($\bar{1}\bar{1}\bar{1}$) surface orientations. The influence of the semiconductor properties of p-type GaAs on the cathodic polarization was confined to low current densities. Galvanostatic anodic-cathodic cycling revealed significant details of the photopotentials and eliminated the hysteresis in the cathodic polarization curves.

It was anticipated that, following the diversion of much research emphasis in semiconductor physics from germanium and silicon to compound semiconductors, workers in the field of semiconductor electrochemistry would also turn to the latter materials. It happens, however, that germanium and, to a lesser extent, silicon possess physical and chemical properties which are peculiarly favorable for revealing effects of bulk semiconductor properties on electrode behavior. For this and other reasons, the literature, at the beginning of the present investigation, contained a bare handful of papers on gallium arsenide electrochemistry—so fundamental a characteristic as the stoichiometry of the anodic dissolution reaction had not been established.

Williams (1) had concluded from his study of photovoltaic effects at binary-semiconductor/electrolyte interfaces that GaAs behaves as an inert electrode capable of exchanging electrons with a redox couple in the solution. This conclusion was based on observations that the electrode potential of n-type GaAs *vs.* saturated calomel varied in the same direction as the oxidation potential of the redox couple, and became strongly more negative on illumination. Subsequently, Haisty (2) experimented with photoetching and gold chemiplating of GaAs. Plating was observed at the nonilluminated and etching at the illuminated region on n-type material. The reverse occurred for p-type material when the photovoltage had the opposite sign. The results obtained by the two investigators are consistent except for the matter of inertness. Haisty noted that in fairly concentrated acid or base the anodic oxidation products were soluble, but in other electrolytes a film was formed.

A study of electrolytic polarization and photopotentials for both n- and p-type GaAs was carried out by Pleskov (3), who reported that the limiting anodic current for n-type is proportional to the incident light intensity at low values of the latter. Breakdown was observed to occur at a critical potential which varied in an inverse manner with the bulk electron concentration. The occurrence of avalanche breakdown and the low magnitude of calculated hole diffusion currents as compared to observed anodic currents, together with imperfect saturation of the latter led the author to conclude that holes are supplied mainly by space charge generation. Influences of semiconductor properties on cathodic polarization behavior were not as pronounced as the chemical effects responsible for hysteresis in the recorded curves.

In a meeting presentation, Greenberg and Sanders (4) reported measurements of current multiplication at n-type GaAs electrodes. They obtained sharp saturation of the anodic current and, for the ratio of limiting anodic current to absorbed light intensity, the values 2.1 and 1.5 in 1.0*N* HCl and 1.0*N* KOH, respectively. Anodic current resulted in dissolution of the crystals, whose surfaces acquired "unstable brown films."

Such was the state of knowledge of the GaAs/electrolyte interface. The observed similarities and differences with respect to germanium and silicon electrodes

were generally in accord with what was known or anticipated concerning the electronic and chemical properties of GaAs. Recently, three rather more extensive studies of GaAs electrochemistry have been published. Included are the measurements of differential capacitance and cathodic reduction of surface oxides by Birintseva and Pleskov (5), the determination of the hole participation factor and the current efficiency of anodic dissolution by Efimov and Erusalimchik (6), and the investigation of the anodic dissolution mechanism for (111)- and $(\bar{1}\bar{1}\bar{1})$-oriented surfaces by Gerischer (7). Certain findings of the present research are in disagreement with earlier reported results; these and some previously unexplored electrochemical features will be elaborated on.

Stoichiometry of the Electrode Reactions

One bit of information presently unavailable, yet essential for the calculation of standard potentials of possible electrode reactions, is the standard free enthalpy of formation $\Delta G°_{298}$ of gallium arsenide. Thermochemical data (8) for several related compounds are presented in Table I, which also lists electronegativities from Pauling (9) and from a more recent compilation (10) [two and three significant figures, respectively]. No correlation is evident between the standard enthalpies of formation of the compounds GaSb, InAs, and InSb and differences in electronegativities of the constituent elements. As a rough approximation, the unknown $\Delta H°_{298}$ for GaAs was taken to be the same as that of InSb (—3.5 kcal/mole).

When this assumed value is combined with the standard entropy of formation from Table I, the quantity —3.1 kcal/mole is obtained for $\Delta G°_{298}$ of GaAs. The absolute error cannot be so great as to alter the conclusions to be drawn from Table II; namely, that the 6-electron anodic reactions are favored over the corresponding 8-electron reactions in both acid and alkaline solution and that cathodic hydrogen evolution is much more probable than arsine formation.

Experimental

Gallium arsenide electrodes were fashioned in the form of (111)-oriented disks, 4-mm or 8-mm diameter, and of the order of 1-mm thick. The (111), "A" or gallium faces were distinguished from the $(\bar{1}\bar{1}\bar{1})$, "B" or arsenic faces by etching the initially abraded surfaces in $1HF:1H_2O_2:1H_2O$. The identification of polarity according to the chemical etch patterns was confirmed for one pair of surfaces by means of anomalous x-ray dispersion. The crystals from which electrodes were cut had the following characteristics

n-type (undoped)	0.85 ohm-cm, 2.0 x 10^{15} carriers/cm^3, mobility 3700 cm^2/v-sec
p-type (Zn-doped)	0.012 ohm-cm, 4.2 x 10^{18} carriers/cm^3, mobility 125 cm^2/v-sec

Table I. Electronegativities and thermochemical data

	IIIA	VA	III-V	$-\Delta H°_{298}$
	Ga	As	GaSb	5.0 ± 0.2 kcal
Pauling	1.6	2.0	InAs	7.4 ± 0.6 kcal
Gray	1.81	2.18	InSb	3.5 ± 0.1 kcal
	In	Sb		
Pauling	1.7	1.9		
Gray	1.78	2.05	GaAs: $\Delta S°_{298}$ = −1.4 cal/deg	

Table II. Standard potentials for some GaAs electrode reactions

	$\Delta G°$, kcal	$E°$, v
$GaAs + 2H_2O = Ga^{+3} + HAsO_2(aq) + 3H^+ + 6e^-$	−16.5	+0.11
$GaAs + 4H_2O = Ga^{+3} + H_3AsO_4(aq) + 5H^+ + 8e^-$	+9.3	−0.05
$GaAs + 8OH^- = H_2GaO_3^- + AsO_3^- + 3H_2O + 6e^-$	−128.0	+0.92
$GaAs + 12OH^- = H_2GaO_3^- + AsO_4^{-3} + 5H_2O + 8e^-$	−159.3	+0.86
$GaAs + 3H^+ + 3e^- = Ga + AsH_3(g)$	+47.0	−0.69
$GaAs + 3H_2O + 3e^- = Ga + AsH_3(g) + 3OH^-$	+102.3	−1.47

The provision of suitably low resistance electrical contacts proved an important consideration, particularly for n-type electrodes. A satisfactory procedure consisted of sputtering gold onto a clean, freshly abraded surface and then effecting some penetration of the gold into the GaAs surface layer by heating in a reducing atmosphere (H_2/N_2 mixture) for ½ hr at 300°C. For the majority of experiments a bead of indium was alloyed to the gold layer, thus permitting a reliable pressure contact to be made. Where accurate electrode weight changes were required, "precipitated silver metal" was compacted between the sputtered gold layer and a metal rod.

Current-voltage characteristics of pairs of contacts affixed to opposite faces of the same specimen were measured. Electrical contacts were considered satisfactory when the combined resistance of contacts plus electrode was constant and not significantly greater than the resistance of electrode alone (as calculated from the bulk resistivity) over the current range of interest. Thereupon the superfluous contact was removed. Of the previously cited publications dealing with aspects of GaAs electrode behavior, only that of Pleskov (3) makes specific note of concern with and the means employed for circumventing rectification and high resistance at the metal-GaAs contacts.

Electrodes were cemented with Apiezon W black wax into a circular recess at the end of a glass capillary tube. The wax and projecting edge of the GaAs disk were then coated with commercial purified paraffin, excluding all but the desired face from contact with the electrolyte. It was thus possible to make advantageous use both of the adhesiveness of the black wax and the chemical inertness of the paraffin. The surface was most often wet-abraded (3000-mesh garnet) before mounting as indicated and subsequently was generally chemically polished (10 v/o Br_2 in methanol) before insertion in the electrochemical cell.

A Pyrex cell was employed which could accommodate up to three working electrodes, symmetrically situated with respect to a pivotal Luggin capillary. The counter electrode compartment was separated from the main body of the cell by a glass frit. A stream of purified, deoxygenated nitrogen served to purge both the cell volume and the electrolyte in a connected solution reservoir. Reagent grade salts and perchloric acid were used without purification; sulfuric acid and alkaline solutions were made up from Acculute volumetric standards. The distilled water used had room temperature resistivity in excess of 10^{-6} ohm-cm and was obtained from an all-Pyrex still fed with demineralized and Millipore-filtered water. The cell temperature was 25°C throughout and, unless otherwise noted, experiments were carried out in room light and with magnetic stirring of the electrolyte.

Results and Discussion

Over-all electrode reactions.—In agreement with the observations of other investigators, n-type GaAs electrodes were found to exhibit a large, negative photovoltage on open circuit; p-type electrodes showed a smaller, positive photovoltage in the solutions studied. Furthermore, the limiting anodic current for n-type was both very small in the dark and extremely sensitive to light. Gas was evolved at appreciable current densities during cathodic but not anodic polarization; the steady-state anodic reaction was always GaAs dissolution. In a number of cases a loosely adherent brown coating formed on the anode; this substance was isolated and found by x-ray diffraction to be gallium arsenide rather than some oxidation product. [Greenberg and Sanders (4) and Gerischer (7) reported a dark coating, whose identity was correctly established by the latter.]

The indicated disintegration or undermining of the anode could be eliminated by effecting vigorous mass-transport conditions at the interface. Table III summarizes coulometric measurements carried out on ini-

Table III. Coulometry of the anodic dissolution reaction for p-GaAs, 20 ma/cm²

Expt. No.	Surface	Disk diameter, mm	Electrolyte	Electron number
1	A(111)	4	0.5*N* KOH	5.88_0
2	A(111)	8	0.5*N* KOH	5.92_6
3	B($\bar{1}\bar{1}\bar{1}$)	8	0.5*N* KOH	5.99_2
4	B($\bar{1}\bar{1}\bar{1}$)	8	1.0*N* $HClO_4$	5.99_8
5	A(111)	8	1.0*N* $HClO_4$	6.10_0

tially abraded p-type anodes at 20 ma/cm² and 25°C, with magnetic stirring of the electrolyte. Anode weight losses were determined directly. In general, as techniques were refined the electron number more closely approached the value 6; the single instance of an apparent electron number in excess of 6 appeared to be due to severe attack of the rim of the GaAs disk, leading to possible exposure of the edge of the gold film to the electrolyte.

Following anodic dissolution, a positive test was obtained for arsenite in the electrolyte. It appears certain that gallium arsenide normally undergoes anodic dissolution with the formation of trivalent gallium and trivalent arsenic, a conclusion in agreement with that expressed in ref. (6) and (7). Moreover, the stoichiometry is the same for both surface polarities. In experiments 2-5 of Table III, the cathode was a GaAs disk of surface polarity opposite to that of the anode. There were no weight changes of the cathodes, within weighing errors, attending prolonged cathodic hydrogen evolution at current densities of 20 and 80 ma/cm². Evidently, arsine formation is not a significant part of the cathodic process at the current densities indicated.

Electrode polarization characteristics.—Preliminary anodic etching experiments with an n-type GaAs hemisphere in 0.5*N* KOH, carried out perforce under strong illumination, gave some indication of a reduced rate of attack along the [110] zone, including the (111) plane, as compared to the ($\bar{1}\bar{1}\bar{1}$) plane. However, the anodic etch patterns were not nearly so well defined as those obtainable with germanium hemispheres—one infers a lower degree of crystalline perfection for the GaAs—and the polarization experiments to be described allow little distinction to be made between the electrode kinetics of nominally A and B surfaces. On the other hand, anodic dissolution of both surfaces is definitely retarded relative to other orientations. Only one example is given by the photographs of Fig. 1, which depict the surface of an n-type electrode of B($\bar{1}\bar{1}\bar{1}$) surface polarity following anodic etching in 2*N* NaOH under illumination. There is clear evidence of higher-than-average current density at the rim of the disk; there also appears to be little remaining of the original surface orientation. The major reflecting planes in this particular etch pattern were identified as ($\bar{2}\bar{2}3$) by means of a two-circle goniometer.

Figures 2 and 3 illustrate the similarity in polarization behavior of the nominally A and B surfaces. The data points were obtained potentiostatically and represent quasistationary current densities measured at roughly 30-sec intervals. It is apparent that little quantitative significance can be attached to rest potentials in this system. On the other hand, the anodic polarization behavior was nicely reproducible, obeying a Tafel relation over at least four decades of current density. Within experimental error, Tafel slopes were the same (82 mv) for both electrodes.

The upward swing of the anodic curves at the highest current densities is an indication of a resistive component of the electrode potential measured *vs.* the saturated calomel half-cell. Thus, the data at high

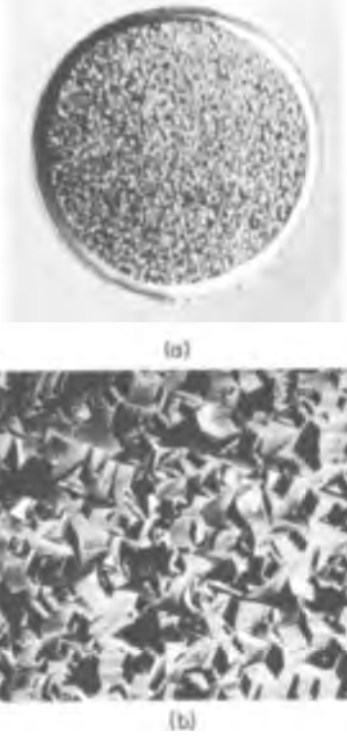

Fig. 1. Etch pattern resulting from anodic dissolution in 2N NaOH of an n-GaAs disk, 4-mm diameter, with B($\bar{1}\bar{1}\bar{1}$) surface orientation. Magnification before reproduction: (a) 20X, (b) 160X.

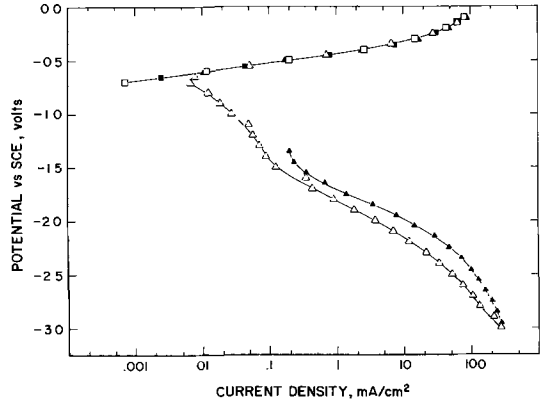

Fig. 2. Anodic and cathodic polarization curves for a p-GaAs, A(111) electrode in 0.5N KOH, 25°C: △, incr. $|\eta|$; ▲, decr. $|\eta|$; □, incr. $|\eta|$ (repeat); ■, decr. $|\eta|$ (repeat). The symbol η in this and subsequent figure captions stands for "overpotential."

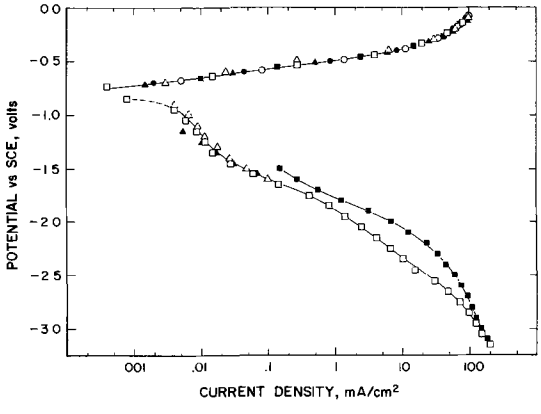

Fig. 3. Anodic and cathodic polarization curves for a p-GaAs, B($\bar{1}\bar{1}\bar{1}$) electrode in 0.5N KOH, 25°C. Sequence of measurements: △, ▲, □, ■, ○, ● (see Fig. 2 caption).

anodic overpotentials, when replotted as potential, U, *vs.* (linear) current density, j, yield straight lines with slopes, $R = dU/dj$, equal to 2.8_3 and 3.0_5 ohm-cm^2 for the A and B electrodes, respectively. The indicated magnitude of R is too large to be accounted for by the corresponding quantity for semiconductor bulk plus electrical contact to the back surface and is probably determined by the effective resistance (11) between electrode and Luggin capillary tip. Actually, for these and other cases it was found that the subtraction of jR from the measured electrode potentials apparently overcompensates for ohmic resistance; the corrected Tafel plots invariably leveled off at high current densities.

The cathodic behavior was more strongly influenced by chemical factors than by bulk semiconductor properties. Note in this regard the absence of an electron-limited current, together with an insensitivity to illumination at all but the lowest cathodic currents. These findings are in general agreement with those of Pleskov (3). The curves reported here were obtained subsequent to anodic polarization, and it is clear from examination of Fig. 2 and 3 that beyond a certain region of cathodic overpotential the nature of the GaAs surface becomes altered so that the polarization curve is not retraced on decreasing the overpotential. By way of comparison, Birintseva and Pleskov (5) obtained evidence for the anodic formation of a surface oxide phase in acid solution, but only of the order of one monolayer of cathodically reducible oxidation product in alkaline solution.

In addition to a shift of approximately 0.8v to more positive potentials, as compared to the 0.5*N* KOH electrolyte, the anodic polarization curves for p-type GaAs in 1.0*N* $HClO_4$ exhibit a passive region. Results for one surface orientation only are shown (Fig. 4), since the data for the second are virtually superposable, even to the extent of reproducing all details of the complicated cathodic behavior. The effect of prior anodic polarization on the cathodic behavior was more pronounced in the acid electrolyte, consistent with more extensive oxidation of the electrode surface. As in the alkaline electrolyte, the cathodic behavior of the p-type electrodes employed was much more a function of their chemical than of their semiconducting nature.

In 1.0*N* $HClO_4$ the anodic Tafel slope was 68 mv. The resistive contributions to measured overpotentials in the prepassive region were 1.5_4 and 1.8_8 ohm-cm^2 for an A and a B electrode, respectively, multiplied by

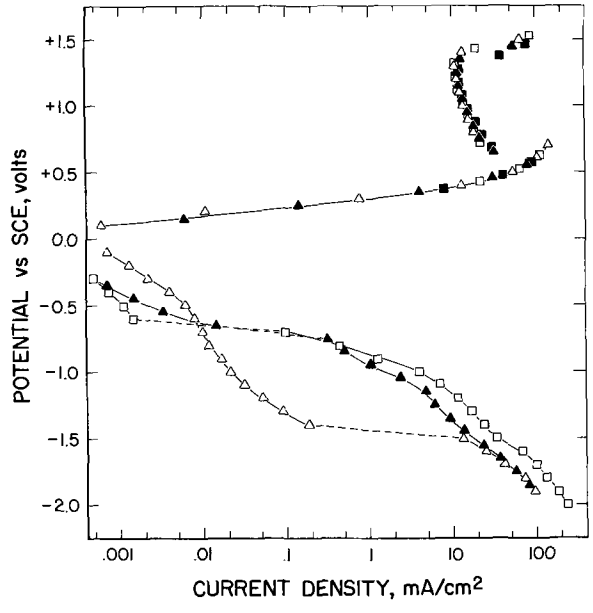

Fig. 4. Anodic and cathodic polarization curves for a p-GaAs, B($\bar{1}\bar{1}\bar{1}$) electrode in 1.0N $HClO_4$, 25°C. Sequence of measurements: same as Fig. 2.

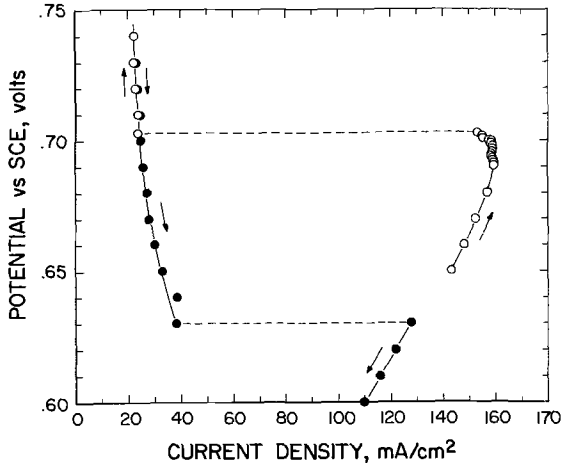

Fig. 5. Details of the active-passive transition for a p-GaAs, B($\bar{1}\bar{1}\bar{1}$) electrode in 1.0N $HClO_4$, 25°C.

current density. The transition from active to passive condition was abrupt; the critical potential could be located potentiostatically to within 1 mv (Fig. 5). Reestablishment of the active condition was attended by pronounced hysteresis, although the passive-to-active transition was equally abrupt. In the absence of stirring, current densities were lower in the prepassive and throughout the passive regions, but intense light had no perceptible effect on the kinetics.

By contrast to the active-passive transitions, that between passive and transpassive regions was gradual with, moreover, a drifting of the current at a fixed electrode potential. It is possible that the former is, in reality, continuous in keeping with the suggestion of Osterwald (11) relative to the effect of an included jR component.

Anodic polarization in $HClO_4$ to the extent indicated by Fig. 4 (about 30 sec/point) resulted in deep pitting of the GaAs surface and heavy attack of the rim. Although, as shown in Fig. 6, the pits formed on an A and a B surface are readily distinguishable (as in chemical etching), the microtextures of the rest of the surface and, indeed, of the pits themselves proved to be rather similar. The passive film is not thought to be the dark coating which appeared at high anodic current densities, since the latter could be dislodged mechanically, but was not reduced electrochemically.

The most pronounced effect of changing the anion from perchlorate to sulfate was the extension of the passive region to the most positive attainable potentials. The anodic polarization data given in Fig. 7 are for an A(111) surface orientation; results were virtually identical for a B($\bar{1}\bar{1}\bar{1}$) electrode as well as for

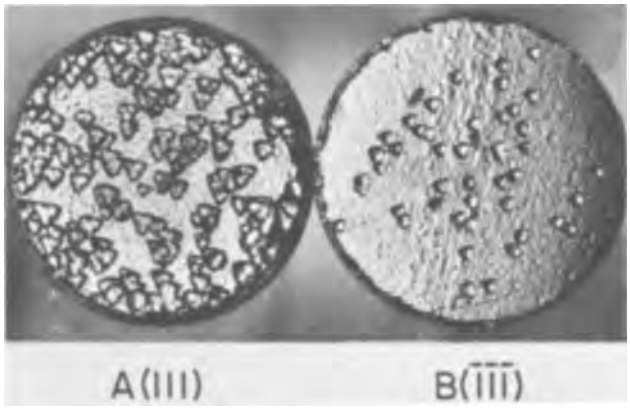

Fig. 6. Gross appearance of differently oriented p-GaAs electrodes, 8-mm diameter, following anodic passivation experiments in $HClO_4$.

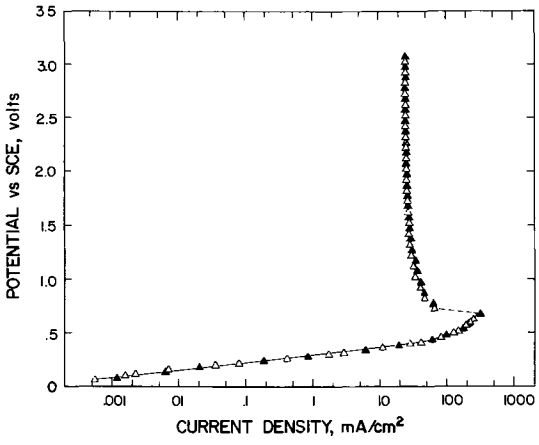

Fig. 7. Anodic polarization behavior of a p-GaAs, A(111) electrode in 1.0N H_2SO_4, 25°C: △, incr. η; ▲, decr. η.

a second A(111) electrode. The value of b derived from Fig. 7 is 62 mv. The active-passive transition was abrupt in both directions, but without appreciable hysteresis.

Additional comparisons of passivation characteristics in the two solutions are interesting. Thus, the Flade potential in 1.0*N* H_2SO_4 and that for the direction of increasing overpotential in 1.0*N* $HClO_4$ have sensibly the same value, namely about +0.70v *vs.* SCE; however, the maximum current density is greater in the former (~325 as compared to ~150 ma/cm²), as is the passive current density (~25 as compared to ~15 ma/cm²). The difference in *p*H between normal solutions of sulfuric and perchloric acid is thought to be insufficient to account for differences in passivation behavior, especially since hydrogen ion is a product of the anode reaction. One is led to a consideration of the probable composition of the passive film.

Both the sulfate and perchlorate of trivalent gallium have appreciable solubilities, as confirmed in separate experiments. It was also found that a gallium arsenite could not be isolated, although gallium arsenate was precipitated in the *p*H range 2-8. Arsenic trioxide is known to be only moderately soluble in acid solution, as noted by Straumanis and Kim in their report (12) on the growth of As_2O_3 crystals on GaAs etched with dilute and concentrated HNO_3 and also with aqua regia. (It would be difficult to reconcile their identification of the product as As_2O_3 with the known reducing properties of this substance were it not readily demonstrable in the laboratory that the oxidation of solid As_2O_3 by the reagents employed proceeds very slowly at room temperature.) Haisty (2) identified a dark blue film formed on p-type GaAs in dilute KCl by photogalvanic etching as β-Ga_2O_3, which is also the product of thermal oxidation (13). However, as noted previously, oxide films were formed only at intermediate *p*H's.

The published observations most pertinent to the passivation behavior of GaAs are possibly those of Revesz and Zaininger (14), who obtained a Ga_2O_3-As_2O_5 film by anodic oxidation of p-type GaAs in acetic anhydride saturated with KNO_3. They concluded that the film was essentially amorphous with a Ga/As atom ratio of 1.3, possibly a glass modification of the silica-like composite oxide $GaAsO_4$. It is conceivable that an anodic film of this nature is formed at sufficiently high current densities in aqueous acid electrolytes, leading to retardation of the anodic dissolution reaction. The rate of the implied further oxidation of arsenic to the +5 state would likely be enhanced by perchlorate and so result in diminished passive and maximum prepassive currents relative to H_2SO_4 electrolyte.

The narrowness of the range of passive potentials observed in $HClO_4$ is probably a consequence of the

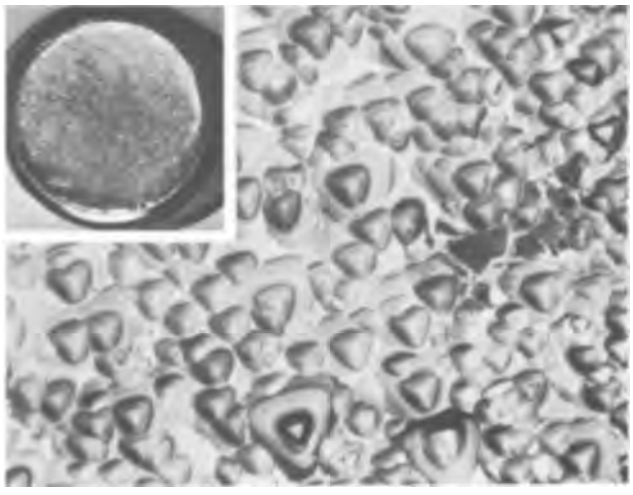

Fig. 8. Gross appearance (inset) and surface features of a p-GaAs, A(111) electrode, 4-mm diameter, following anodic passivation experiments in H_2SO_4. Magnification before reproduction: 200X.

severe pitting which occurs (Fig. 6). The absence of pits on GaAs electrodes having undergone similar anodic treatment in H_2SO_4 provides a marked contrast (Fig. 8). Visible in the latter figure are vestiges of a loosely adherent, dark film of GaAs. The strongly nonuniform distribution of electrode current density associated with pitting and transpassivity is probably also responsible for the hysteresis in the active-passive transition observed in $HClO_4$ electrolyte. There follows a consideration of some experiments performed with the aim of understanding better the cathodic behavior.

Cathodic photopotentials.—It was of interest to explore further the photoresponse of p-type GaAs cathodes. The absence of an electron-limited current has been noted here as well as by others, although Pleskov (3) found the overpotential for hydrogen evolution to be greater for p-type GaAs ($p = 2 \times 10^{18}$ cm^{-3}) than for n-type ($n = 10^{18}$ cm^{-3}). It seems clear that at the higher current densities the electrons required for the cathodic process are either generated at a sufficient rate within the electrode or at its surface or are derived from the valence band. The abrasion of the back surface prior to applying the gold contact is not thought to be a factor because of the very short lifetime and consequent short diffusion length of minority carriers in GaAs (15).

Initially, the positive photopotential was enhanced by application of a small cathodic current. The clear indication is that the negative space charge was increased in the way expected for consumption of minority carriers by the cathodic reaction. Continuous illumination at very low cathodic current densities

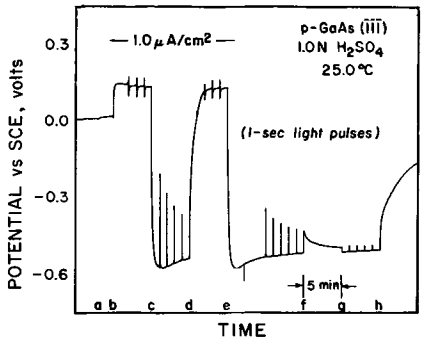

Fig. 9. Charging curves and photopotentials at a low current density. Events: a, begin magnetic stirring; b and d, begin anodic charging; c and e, begin cathodic charging; f to g, continuous illumination; h, current off.

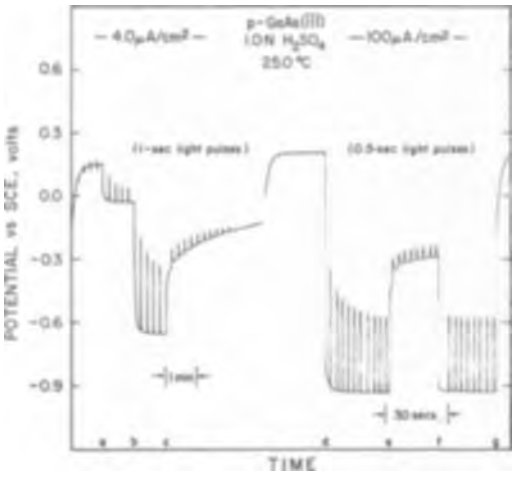

Fig. 10. Charging curves and photopotentials at intermediate current densities. Events: a, anodic current off; b, d, and f, begin cathodic charging; c and e, cathodic current off; g, begin anodic charging.

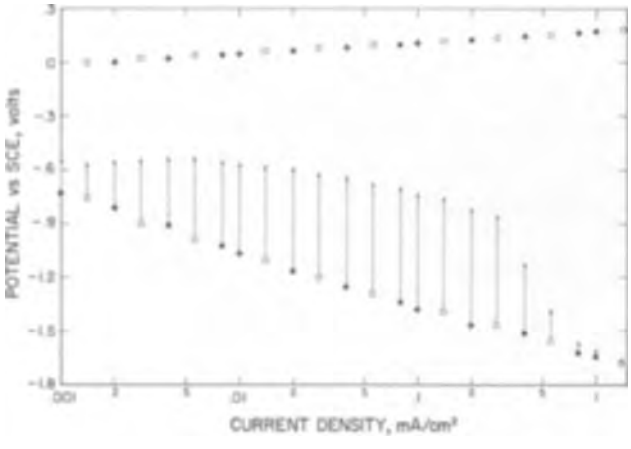

Fig. 11. Galvanostatic anodic-cathodic polarization of a p-GaAs, A(111) electrode in 0.99N Na_2SO_4/0.01N H_2SO_4; pH 2.85, 25°C. Arrows indicate the change of cathodic potential under illumination. ○, incr. $|\eta|$; ●, decr. $|\eta|$.

caused the magnitude of the photopotential to decrease more rapidly than in the dark (Fig. 9). The contribution of continued cathodic current to the observed relaxation of the photopotential may result from the change in the chemical state of the surface, with an attendant adjustment of the potential difference across the interface. Superposed on this effect is that of continued illumination (Fig. 9), which appears to be associated with a trapping phenomenon; possibly the light is absorbed by trapping centers and effects the release of minority carriers.

At somewhat higher cathodic current densities (Fig. 10), the cathodic photopotential becomes both larger and less time dependent. At still higher current densities, the cathodic charging curve is characterized by overshoot and, eventually, by greatly diminished photoresponse.

It was found that the quasistationary potentials obtained from cyclical charging yield polarization curves in which much of the previously encountered complicated cathode behavior is absent (Fig. 11). Evidently, the chemical state of the GaAs surface is altered in a more reproducible way as a consequence of anodic-cathodic cycling. From Fig. 11 it is seen that not only do the curves for increasing and decreasing overpotential coincide, but the cathodic branch has now a well-defined Tafel region. The values of the coefficient b in the given electrolyte are 62 mv for the anodic branch and 300 mv for the cathodic. The anodic photopotentials (not shown) were small throughout.

The following interpretation of the cathodic photopotentials is offered. Up to about 10 μa/cm^2 the cathode potential under illumination is sensibly constant, indicating that the light was sufficiently intense to bring the surface region to the flat-band condition (not that for the unpolarized electrode, which occurs at a potential slightly more anodic than the rest potential, but that corresponding to the new surface configuration brought about by cathodic current). Thereafter the light potential begins to fall off and for a decade or so of current density does so in parallel with the dark potential. In this range, increments of overpotential fall largely across the space-charge region. At still higher current densities an increasing fraction of the applied overpotential falls across the interface, with the consequence that the chemical state of the surface becomes more drastically altered—conceivably, surface As atoms are removed as arsine, leaving a Ga surface—and the light potential approaches the dark. Eventually, the semiconductor nature of the p-type GaAs is no longer manifest in its cathodic behavior.

Remarks

Certain difficulties experienced in studies of gallium arsenide electrochemistry stem from the compound nature of the electrode material; in most instances it probably does not make sense to think in terms of the composition GaAs in the immediate vicinity of the interface with the electrolyte. That is, one must consider that the existence of a surface layer with Ga/As atom ratio different from unity is the probable state of affairs. Thus, the usual picture of the Helmholtz layer may not be adequate for the electrode side of the interface.

The indistinguishability in polarization behavior of the (111) and $(\bar{1}\bar{1}\bar{1})$ surface orientations may be related to the factor just mentioned. There is also the likelihood, as mentioned earlier, that as a consequence of preferential etching, little of the real surface retains the (111) or $(\bar{1}\bar{1}\bar{1})$ orientation. Finally, as suggested by Gerischer (7) to explain similarities in anodic behavior, dismantling of the crystal by anodic reaction probably proceeds by removal of Ga and As atoms in pairs rather than singly.

There are serious discrepancies in the literature regarding the participation of holes in GaAs electrode processes. A photoinjection method indicated that 2.8-4.0 holes (4) are required per GaAs unit entering the electrolyte at the limiting anodic current. On the other hand, studies based on the redox method developed by Gerischer and Beck (16) for germanium give variously 1-6 (6) and 6 (7) for the same quantity.

A great deal more knowledge has to be gained before the contributions of different possible sources to the supply of minority carriers can be sorted out. Probably generation-recombination in the field of the space charge region is more important than in the volume, but the relative importance of thermal generation-recombination at the surface is not known. Some results presented here point to trapping as a factor in the charge distribution, whereas other authors have invoked field-induced ionization of deep lying impurities. In short, it may not be profitable to attempt to fit the electrochemical behavior of compound semiconductors wholly within the simple model which works well for germanium.

Acknowledgments

The author is indebted to M. J. Redman for solubility measurements of gallium compounds, to A. N. Mariano for x-ray work and optical goniometry, to E. J. Moreau for metallography, and to M. R. Randlett for gold sputtering. The assistance of A. E. Clark with the experimentation is gratefully acknowledged.

Note added in proof: Since this paper was written, two items of especial pertinence have appeared in the literature. It has been reported that $-\Delta G^\circ_{298}$ for GaAs is of the order of 9 kcal/mole [A. S. Abbasov *et al.*, *Doklady Akad. Nauk S.S.S.R.*, **170**, 1110 (1966)]. Hence, the standard oxidation potentials of Table II are too positive by $0.26/n$ v, where n is 3, 6, or 8. Recently, Gerischer and Mattes [*Z. physik. Chem. Neue Folge*, **49**, 112 (1966)] have demonstrated convincingly the attainability of electron-limited currents with p-GaAs cathodes. Observations of others to the contrary are probably not ascribable to cathodically produced electron-hole generation centers, as may form on Ge cathodes. Very likely, it will be found that certain techniques of producing contacts to the back surface result in obliteration of the inherent limiting current.

Manuscript received Nov. 23, 1966. This paper was presented at the Cleveland Meeting, May 1-6, 1966.

Any discussion of this paper will appear in a Discussion Section to be published in the December 1967 JOURNAL.

REFERENCES

1. R. Williams, *J. Chem. Phys.*, **32**, 1505 (1960).
2. R. W. Haisty, *This Journal*, **108**, 790 (1961).
3. Yu. V. Pleskov, *Doklady Akad. Nauk S.S.S.R.*, **143**, 1399 (1962).
4. S. A. Greenberg and R. N. Sanders, Extended Abstracts of Electronics Division, ECS Fall Meeting, New York (1963), Abstract No. 157, p. 117.
5. T. P. Birintseva and Yu. V. Pleskov, *Izvest. Akad. Nauk S.S.S.R., Ser. Khim.*, **2**, 251 (1965).
6. E. A. Efimov and I. G. Erusalimchik, *Elektrokhimiya*, **1**, 818 (1965).
7. H. Gerischer, *Ber. Bunsengesellschaft physik. Chem.*, **69**, 578 (1965).
8. P. M. Robinson and M. B. Bever, "Intermetallic Compounds," Chap. 3, J. H. Westbrook, Editor, John Wiley and Sons, to be published.
9. L. Pauling, "The Nature of the Chemical Bond," 3rd ed., p. 93, Cornell University Press, Ithaca, N. Y. (1960).
10. H. B. Gray, "Electrons and Chemical Bonding," p. 72, W. A. Benjamin, Inc., New York (1964).
11. J. Osterwald, *Z. Elektrochem.*, **66**, 401 (1962).
12. M. E. Straumanis and C. D. Kim, *This Journal*, **111**, 1186 (1964).
13. H. T. Minden, *ibid.*, **109**, 733 (1962).
14. A. G. Revesz and K. H. Zaininger, *J. Am. Ceram. Soc.*, **46**, 606 (1963).
15. C. Hilsum and B. Holeman, "Carrier Lifetime in GaAs," Proceedings of the International Conference on Semiconductor Physics, Prague 1960, p. 962, Academic Press, New York (1961).
16. H. Gerischer and F. Beck, *Z. physik. Chem.*, **13**, 389 (1957).

Transient Response of Chemically Interacting Solid-Gas Systems

I. Theoretical Considerations

Seong T. Hwang and G. Parravano

Department of Chemical and Metallurgical Engineering, University of Michigan, Ann Arbor, Michigan

ABSTRACT

The transient response of the rate of a surface reaction between gas and solid phases is discussed mathematically. The over-all reaction is assumed to be the results of two elementary steps: adsorption of reactants and desorption of products. Expressions for the nonsteady rates of the two steps are derived and applied to the case of simultaneous occurrence of both steps. This results in a surface catalyzed reaction. It is shown how the analysis of the transient response permits the determination of some of the fundamental parameters of the elementary steps including the values of the step rate constant, the nature and concentration of the adsorbed intermediates. The contribution of nonsteady state kinetics to the elucidation of basic problems on the reactivity of solid surfaces is outlined.

The elementary steps of solid-gas reactions involve physical and chemical phenomena taking place at different rates. This is particularly valid for chemical changes occurring at a phase boundary, since the peculiar environment and structure of a phase boundary provides a wider spectrum of possibilities and conditions. Thus, a range of reaction relaxation times is to be expected in heterogeneous kinetics: from rapid electronic transitions, to slow transfer of atoms or ions among surface positions, and between surface and bulk phases. A detailed study of these various processes is a formidable, but necessary task for reaching a comprehensive understanding of heterogeneous and surface processes.

In the past, studies have been performed on the nonsteady rate of reaction of FeO in CO_2-CO and H_2O-H_2 mixtures (1) and of decomposition of HCOOH on Pd (2). In general, relatively high temperatures are preferred for these investigations, since the identification of the physical process corresponding to the measured relaxation times may be carried out with more confidence.

In view, however, of the fact that many surface reactions, mostly catalytic, take place at lower temperatures with fast rates, it is pertinent to inquire how far the pattern of physicochemical behavior emerging from high-temperature studies can be extrapolated to the lower temperatures of interest. To investigate this problem and to find out the extent to which low-temperature results may be utilized to extract meaningful information about surface-gas interactions, we have analyzed theoretically the transient response of chemically interacting solid-gas systems and performed experimental investigations to test the theoretical analysis.

Two considerations guided the present effort: first, the scattered but extensive literature reports of initial drifts of surface activity of many solids used as catalysts; in some cases, the direction of the activity change with time was qualitatively related to and found consistent with the reaction scheme derived from steady state velocity information (3); second, a close scrutiny of the nonsteady state behavior should be of great interest for mechanistic studies in hetero-

geneous and surface reactions since the reactivity of the phase boundary is greatly influenced by chemical interactions with the surrounding phase occurring during the establishment of the reaction steady state.

The nonsteady state discussed in this work is characterized by the time dependence of the reaction conversion, resulting from a forced perturbation of one of the reaction parameters under conditions of negligible kinetic influence of mass and heat transfer effects. The present communication summarizes the theoretical derivations and their use to obtain information on the value of the rate constants of some of the elementary reaction steps and upon the nature of the reaction intermediates. In the following communication (4) the application of the analysis to experimental results is outlined.

Description of the Model

Consider an ionic solid, MX, whose nonmetallic component is assumed to be in the form of X^{-2} ions, interacting with gas phase molecules AX and B, according to the equations

$$AX(g) + MX\ \text{surface} \underset{\overleftarrow{k_1}}{\overset{\vec{k_1}}{\rightleftharpoons}} A(g) + X_a \qquad [1]$$

$$B(g) + X_a \underset{\overleftarrow{k_2}}{\overset{\vec{k_2}}{\rightleftharpoons}} BX(g) + MX\ \text{surface} \qquad [2]$$

where X_a represents species adsorbed on the MX surface. Simultaneous occurrence of reactions steps [1] and [2] yields the over-all catalytic reaction

$$AX(g) + B(g) \rightleftarrows A(g) + BX(g) \qquad [1a]$$

Two points are noteworthy in connection with this model: (*a*) the individual reaction steps [1] and [2] modify the stoichiometry and, thus, the metal/nonmetal ratio of MX; and (*b*) this ratio is influenced by X_a only and not by the adsorption of any other species (reactants and/or products).

As was shown previously (5), the rates of reactions [1] and [2] may be plotted as a function of the nonmetal/metal ratio of the catalyst (Fig. 1). This ratio, expressing the influence of the surface on the reactivity of the system, constitutes a reaction variable, together with the partial pressure of the gas phase components. If it is assumed that the total surface concentration of X, $[X_{aT}]$, remains unchanged during the reaction steady state, $\dot{X}_{aT} = 0$, it is possible to state that the numerical difference between the rates of reactions [1], $\dot{X}_a(1)$, and [2], $\dot{X}_a(2)$, gives the net rate of change of the surface concentration of X, $\dot{X}_{aT} = \dot{X}_a[1] - \dot{X}_a[2]$. If reaction [1a] is carried out with constant partial pressures $(p^o_{AX})_1$ and $(p^o_B)_1$ in a flow system, the steady state condition is represented by point A (Fig. 1). Modification of the reactant partial pressures to $(p^o_{AX})_2$ and $(p^o_B)_2$ produces a new steady state (point E, Fig. 1), corresponding to a different value of the nonmetal/metal ratio of the solid.

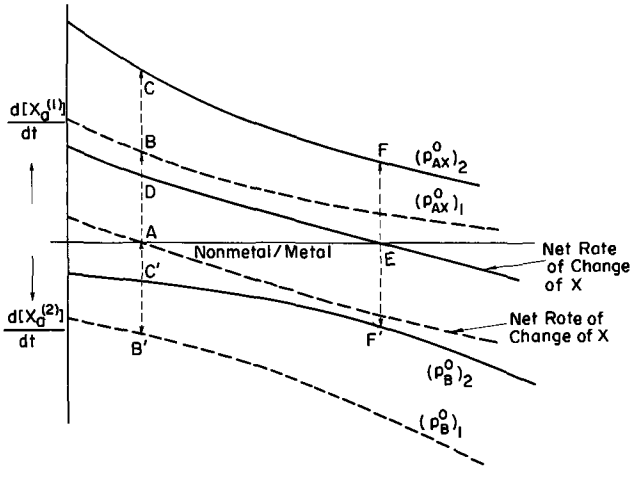

Fig. 1. Adsorption and desorption rates of X_2 *vs.* nonmetal-to-metal ratio in MX, $p^o_{AX_2} > p^o_{AX_1}$, $p^o_{AX_1} + p^o_{B_1} = p^o_{AX_2} + p^o_{B_2}$

Nonsteady-State Reaction Kinetics

The total amount of reaction intermediate which at any time is adsorbed on the MX surface is given by the algebraic sum of the amounts initially present, $X_a(i)$, and those resulting from reaction [1], $X_a[1]$ and reaction [2], $X_a[2]$

$$X_{aT} = X_a(i) + X_a[1] + X_a[2] \qquad [3]$$

The reaction conversions for step [1] α_1, and step [2], α_2, are defined as

$$\alpha_1 = \frac{p_A}{p^o_{AX}} = \frac{X_a[1]}{hp^o_{AX}} = \frac{p^o_{AX} - p_{AX}}{p^o_{AX}} \qquad [4]$$

$$\alpha_2 = \frac{p_{BX}}{p^o_B} = -\frac{X_a[2]}{hp^o_B} = \frac{p^o_B - p_B}{p^o_B} \qquad [5]$$

where the superscript ^{o} refers to values at time $t = 0$ and h is a suitable constant. Expressing the influence of the surface on the reaction rate by means of the surface coverage, θ, the latter becomes for the reaction step [1] θ_1 and [2] θ_2

$$\theta_1 = \frac{X_a(i) + X_a[1]}{S} = \frac{X_a(i) + hp^o_{AX}\alpha_1}{S} \qquad [6]$$

$$\theta_2 = \frac{X_a(i) + X_a[2]}{S} = \frac{X_a(i) - hp^o_B\alpha_2}{S} \qquad [7]$$

where S is the surface area of MX. The rates of steps [1] and [2] may, then, be simply formulated

$$-\frac{dp_{AX}}{dt} = \vec{k}_1\, p_{AX}(1-\theta_1) - \overleftarrow{k}_1\, p_A\, \theta_1 \qquad [8]$$

$$-\frac{dp_B}{dt} = \vec{k}_2\, p_B\, \theta_2 - \overleftarrow{k}_2\, p_{BX}(1-\theta_2) \qquad [9]$$

where $\vec{k}_1$, $\vec{k}_2$, $\overleftarrow{k}_1$, and $\overleftarrow{k}_2$ are the forward and backward rate constants for step [1] and [2], respectively.

Substituting expressions [4], [5], [6], and [7] in Eq. [8] and [9], integrating from $t = 0$ to $t = t$ to obtain the relationships $\alpha_1 = f(t)$ and $\alpha_2 = f(t)$ and substituting the latter in Eq. [8] and [9], the rates of conversion change as a function of time are found to be

$$\frac{d\alpha_1}{dt} = \left[\vec{k}_1\left(1 - \frac{X_a(i)}{S}\right) - \alpha_1{}^o\left(\vec{k}_1\frac{h}{s}p^o_{AX} + \vec{k}_1 - \vec{k}_1\frac{X_a(i)}{S} + \overleftarrow{k}_1\frac{X_a(i)}{S}\right)\right] \exp\left[-\left(\vec{k}_1\frac{h}{S}p^o_{AX} + \vec{k}_1 - \vec{k}_1\frac{X_a(i)}{S} + \overleftarrow{k}_1\frac{X_a(i)}{S}\right)t\right] \qquad [10]$$

$$\frac{d\alpha_2}{dt} = \left[\vec{k}_2\frac{X_a(i)}{S} - \alpha^o{}_2\left(\vec{k}_2\frac{h}{S}p^o_B + \vec{k}_2\frac{X_a(i)}{S} + \overleftarrow{k}_2 - \overleftarrow{k}_2\frac{X_a(i)}{S}\right)\right] \exp\left[-\left(\vec{k}_2\frac{h}{S}p^o_B + \vec{k}_2\frac{X_a(i)}{S} + \overleftarrow{k}_2 - \overleftarrow{k}_2\frac{X_a(i)}{S}\right)t\right] \qquad [11]$$

In the derivation of Eq. [10] and [11], the terms containing α^2 have been neglected, since reaction [1a] proceeds from left to right and the absolute magnitude of the coefficients of the α^2 terms is always smaller than that of the linear terms in α. Furthermore for small values of the reaction conversion $\alpha^2 << \alpha$. Equations [10] and [11] represent the time variation of the rate of reaction conversion during the nonsteady rate period and may, therefore, be used to characterize the nonsteady state rate of reaction steps [1] and [2].

The linear plot of the logarithms of the rate of change of reaction conversion *vs.* time gives (for step [1])

$$\text{slope} = \vec{k}_1 \frac{h}{S} p^{o}_{AX} + \vec{k}_1 - \vec{k}_1 \frac{X_a(i)}{S} + \overleftarrow{k}_1 \frac{X_a(i)}{S} \quad [12]$$

$$\text{intercept} = \alpha^{o}_1 \left(\vec{k}_1 \frac{h}{S} p^{o}_{AX} + \vec{k}_1 - \vec{k}_1 \frac{X_a(i)}{S} + \overleftarrow{k}_1 \frac{X_a(i)}{S} \right) - \vec{k}_1 \left(1 - \frac{X_a(i)}{S} \right) \quad [13]$$

A similar, two equation system is obtained for reaction step [2]. Under the experimental conditions generally employed in surface studies (see following paper) (4) $\overleftarrow{k}_1 \frac{X_a(i)}{S} << \vec{k}_1 \frac{h}{S} p^{o}_{AX}$, and the terms in $\overleftarrow{k}_1$ and $\overleftarrow{k}_2$ in the slopes and intercepts of the linear plots of Eq. [10] and [11] may be neglected. Consequently, from systems of equations of the type of [12] and [13] it is possible to evaluate $\vec{k}_1$, $\vec{k}_2$, $X_a(i)$, S and h.

Reaction Intermediates

The problem of deriving information on the chemical nature of the surface intermediate X_a is dependent on the model of the reactive surface used. If the catalytic solid is an ionic (or partly ionic) compound, a logical choice for the surface centers responsible for surface reactivity are point defects, ionic and/or electronic. This assumption permits the formal discussion of surface defect reactions in a manner similar to that employed for the crystal interior. It is, however, necessary to distinguish between two sets of conditions under which the surface chemical equilibrium between adsorbed species and the solid is: (*a*) rapidly established in relation to the time constant of the rate experiments; (*b*) not rapidly established. In the first instance, it is possible to apply the mass action expression to surface defect reactions, while this will not be possible in the second instance. The latter case corresponds to the formation of a surface space charge layer of thickness considerably larger than ionic radii.

The chemical nature of the reaction intermediate is directly related to the type of surface bonding between adsorbent and adsorbate during reaction [1a]. We shall discuss the instance in which adsorbed X species are considered to occupy surface positions equivalent to normal lattice sites, even though some of the neighboring atoms may be missing. To express this in a simple fashion one may consider three limiting cases: neutral X_a, singly charged ion X_a^{-1}, and doubly charged ion X_a^{-2}. Whenever equilibria between adatoms and surface sites are established, the following reactions should be considered

$$X_{aT} + 2e^- = X^{-2} \quad \text{(n-type)} \quad [14]$$

$$X_{aT} = X^{-2} + 2e^+ \quad \text{(p-type)} \quad [15]$$

$$X^{-}{}_{aT} + e^- = X^{-2} \quad \text{(n-type)} \quad [16]$$

$$X^{-}{}_{aT} = X^{-2} + e^+ \quad \text{(p-type)} \quad [17]$$

Since X^{-2} ions are the constituents of the MX lattice, in large excess and randomly distributed, it is justifiable to set $[X^{-2}] \cong$ constant. From reaction equilibria [14] to [17], one obtains

$$[X_{aT}] = K_{14} \frac{1}{n^2_{e-}} \quad \text{(n-type)} \quad [18]$$

$$[X_{aT}] = K_{15}\, n^2_{e+} \quad \text{(p-type)} \quad [19]$$

$$[X_{aT}^{-1}] = K_{16} \frac{1}{n_{e-}} \quad \text{(n-type)} \quad [20]$$

$$[X_{aT}^{-1}] = K_{17}\, n_{e+} \quad \text{(p-type)} \quad [21]$$

where K_{14} to K_{17} are the equilibrium constants of reactions [14] to [17] and n_{e-}, n_{e+} are the concentrations of excess electrons and electron holes, respectively. Equations [18] to [21] relate the concentration of the adsorbed intermediate, as X_a or X_a^{-1}, to the electron or hole concentration. If the adsorbed intermediate is present as X_a^{-2} ions, it is clear that the concentration of the latter will not be dependent on the electron or hole concentrations.

If reaction equilibria [14] to [17] do not occur rapidly, it is possible to obtain the relations between the concentrations of the intermediate and excess electrons or electron holes by means of the condition of electrical neutrality for any volume element of the solid, including the surface

$$[X_{aT}^{-1}] = C\,(n_e^{o} - n_{e-}) \quad \text{(n-type)} \quad [22]$$

$$[X_{aT}^{-1}] = C'\,(n_{e+} - n^{o}_{e+}) \quad \text{(p-type)} \quad [23]$$

$$[X_{aT}^{-1}] = \frac{C}{2}\,(n^{o}_{e-} - n_{e-}) \quad \text{(n-type)} \quad [24]$$

$$[X_{aT}^{-2}] = \frac{C'}{2}\,(n_{e+} - n^{o}_{e+} \quad \text{(p-type)} \quad [25]$$

where C, C' are appropriate constants. In this instance if X_a is present as a neutral species, $[X_a]$ becomes independent of n_{e-} and n_{e+}.

By means of Eq. [3], [10], and [11], it is possible to derive an expression between the total amount adsorbed, X_{aT}, and the sum of the rates of conversion change: $(d\alpha_1/dt) + (d\alpha_2/dt)$. Substitution in this latter expression of the appropriate Eq. [18] to [25] permit the development of a series of relationships between reaction conversion and electron or hole concentration. These expressions are unique for each of the various cases discussed and may be used as a criterium for evaluating the role of the three intermediates considered. The detailed derivations are presented elsewhere (6), while the results are schematically plotted in Fig. 2 and 3. The graphs show that the various possibilities arising from: (*a*) electronic nature of surface (p- or n-type), (*b*) presence or absence of surface space charge, and (*c*) chemical nature of the adsorbed intermediate, may be uniquely distinguished. In addition to the cases reported in Fig. 2 and 3, it should be recalled that whenever the intermediate is the neutral species X_a and surface-bulk equilibria are not readily set up, $[X_a]$ is independent on the activity of electrons or holes, while a similar situation arises for the reaction intermediate X_a^{-2} whenever surface-bulk equilibria are readily established. Cases intermediate among those considered are characterized between the appropriate limiting possibilities. Thus, nonsteady-state kinetic results may be used to arrive at definite information on the nature of the reaction intermediates, its concentration, and its bonding characteristics.

Physical Quantities Required for the Application of the Derived Expressions

The graphical representation of the rate equations for the various conditions considered (Fig. 2 and 3) permits the interpretation of nonsteady rates in terms

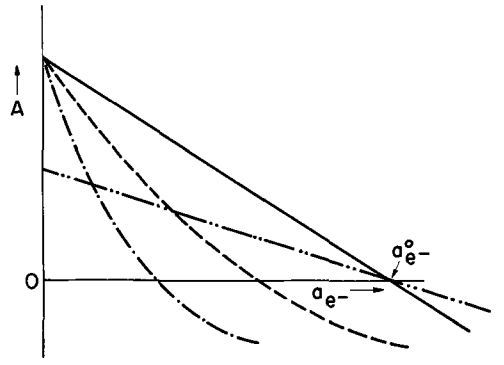

Figure 2. Nonsteady-state rates vs. activity of excess electrons for n-type catalyst. Surface equilibria established: - - - - X_a^{-1} intermediate, -.-.-; X_a^{-2} intermediate; surface equilibria not established: ——— X_a^{-1} intermediate; -..-..- X_2^{-2} intermediate.

$$A = \frac{p^{\circ}_{AX}\frac{s}{h}\left[\vec{k}_1\left(1-\frac{X_i}{S}\right)-\frac{d\alpha_1}{dt}\right]}{\frac{\vec{k}_1 h}{S}p^{\circ}_{AX}+\vec{k}_1-\vec{k}_1\frac{X_i}{S}+\overleftarrow{k}_1\frac{X_i}{S}} + \frac{p^{\circ}_{B}\frac{h}{S}\left(\frac{d\alpha_2}{dt}-\vec{k}_2\frac{X_i}{S}\right)}{\frac{\vec{k}_2 h}{S}p^{\circ}_{B}+\vec{k}_2\frac{X_i}{S}+\overleftarrow{k}_2-\overleftarrow{k}_2\frac{X_i}{S}}$$

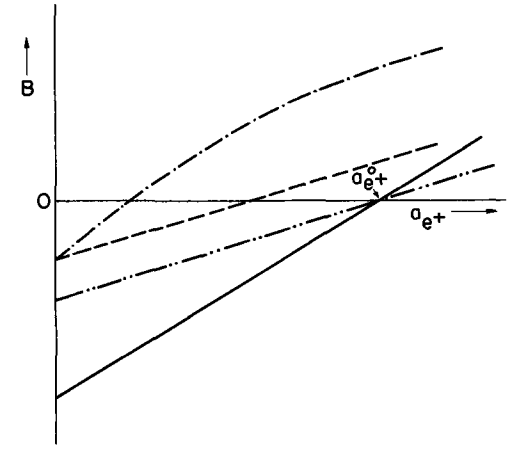

Figure 3. Nonsteady-state rate vs. activity of electron holes for p-type catalyst. Surface equilibria established: - - - - X_a^{-1} intermediate -.-.-. X_a^{-2} intermediate. Surface equilibria not established: ——— X_a^{-1} intermediate, -..-..- X_a^{-2} intermediate.

$$B = \frac{p^{\circ}_{AX}\frac{h}{S}\left[\vec{k}_1\left(1-\frac{X_i}{S}\right)-\frac{d\alpha_1}{dt}\right]}{\frac{\vec{k}_1 h}{S}p^{\circ}_{AX}+\vec{k}_1-\vec{k}_1\frac{X_i}{S}+\overleftarrow{k}_1-\frac{X_i}{S}} + \frac{p^{\circ}_{B}\frac{h}{S}\left(\frac{d\alpha_2}{dt}-\vec{k}_2\frac{X_i}{S}\right)}{\frac{\vec{k}_2 h}{S}p^{\circ}_{B}+\vec{k}_2\frac{X_i}{S}+\overleftarrow{k}_2-\overleftarrow{k}_2\frac{X_i}{S}}$$

of the reaction models discussed. It is, therefore, of interest to point out the experimental measurements needed for the application of the theoretical analysis.

At the outset it is necessary to set up a reaction steady state to define the initial surface coverage of the solid phase [$X_a(i)$]. This is done in a flow reactor by establishing well-defined experimental conditions of partial pressures, flow rate, and temperature. The set of conditions defines an arbitrary, but reproducible steady state, reaction conversion, and surface concentration of intermediate species. Subsequently, a condition of nonsteady-state rate of reaction is obtained by perturbing through a step change one of the reaction variables, the most suitable being the partial pressures of one or both of the reagents without modifying the total pressures. During the nonsteady period, the conversion of AX and B is followed by chemical or equivalent analytical method. Simultaneously, the variation of the concentration of electrons (or electron holes) in the solid is determined by means of a convenient technique (electrical conductivity, thermoelectric power). Thus, the experimental values of α_1, α_2, n_{e^-}, n_{e^+} as a function of time can be introduced into Eq. [10] and [11], and plots similar to Fig. 2 and 3 may be drawn. Comparison between the theoretical and experimental slopes of the linearized plots permits the determination of the correct model of the reaction and reaction intermediates. The time range used in performing the perturbation and in following the response of the system determines the kind of phenomena which are recorded. Thus, if one confines the perturbation time in the milli or microsecond range and records the system response within a similar space of time, elementary steps of electron transfer, rearrangement, and excitation are likely to be observed and studied. On the other end, longer transient and response times are related to slow activated transfer of matter across, along and beyond the phase boundary.

Conclusions

The study of the conversion of a surface reaction during nonsteady-state conditions together with the simultaneous determination of the electron or hole concentration of the catalyst may be used to obtain information on the nature of the reaction intermediates, of the surface bonding and reactivity. This knowledge is the basis for a rational approach to the understanding of surface reaction, and of phenomena related to surface reactivity, namely, surface heterogeneity, promotion, poisoning, and doping effects.

Acknowledgment

This work was supported by a research grant from the National Science Foundation. The authors gratefully acknowledge this support.

Manuscript received July 20, 1966; revised manuscript received Feb. 23, 1967.

Any discussion of this paper will appear in a Discussion Section to be published in the December 1967 JOURNAL.

REFERENCES

1. S. Stotz, *Ber. Bunsenges. Physik. Chemie*, **70**, 37 (1966).
2. H. J. Schonnagel and C. Wagner, *ibid.*, **69**, 699 (1965).
3. A. Amano and G. Parravano, "Advances in Catalysis," vol. IX, p. 716, Academic Press, Inc., New York (1957).
4. S. T. Hwang and G. Parravano, *This Journal*, **114**, 482 (1967).
5. H. Kobayashi and C. Wagner, *J. Chem. Phys.*, **26**, 1609 (1957).
6. S. T. Hwang, Ph.D. Thesis, University of Michigan, 1965.

Transient Response of Chemically Interacting Solid-Gas Systems

II. Reduction Oxidation Reactions on Cobalt Ferrite

Seong T. Hwang and G. Parravano

Department of Chemical and Metallurgical Engineering, University of Michigan, Ann Arbor, Michigan

ABSTRACT

The transient behavior of the reacting system: $N_2O + CO \rightarrow N_2 + CO_2$ on cobalt ferrite, $CoFe_2O_4$, was studied experimentally by perturbing the reaction steady state with a rapid variation in the N_2O and CO partial pressures, at 190° and 300°C. To follow the nonsteady behavior, measurements were carried out on the time dependence of the reaction conversion and of the thermoelectric power of the sample. The latter quantity was used to calculate the variation of excess or defect electron concentration of the sample during the transient state. Two ferrite samples were used: $Co_{0.994}Fe_{2.006}O_4$ (n-type) and $Co_{1.097}Fe_{1.903}O_4$ (p-type). The experimental results have been analyzed according to the treatment of nonsteady reaction rates presented in the previous communication. The analysis showed that at 300°C the oxygen, adsorbed on the cobalt ferrite surface during reaction, is in the form of neutral oxygen atoms, O, for n-type cobalt ferrite, and intermediate between neutral oxygen and singly ionized oxygen ions, O^-, for p-type samples. At 190°C, adsorbed oxygen is wholly in the form of O^- ions. The results are discussed in the light of previous studies on the structure and surface reactivity of $CoFe_2O_4$.

In the previous communication (1) expressions for the nonsteady state of solid-gas reactions have been derived and the treatment has been aimed at obtaining information on the nature of the intermediate species formed at the surface as a result of the heterogeneous reaction. In order to apply the theoretical considerations to a practical situation, we have studied the nonsteady rate of oxidation of $CoFe_2O_4$ with N_2O and reduction with CO. It is assumed that the reduction and oxidation steps may be represented by

$$N_2O_{(g)} + \text{Surface} \rightarrow N_{2(g)} + O_{(ads)} \quad [1]$$

$$CO_{(g)} + O_{(ads)} \rightarrow CO_{2(g)} + \text{Surface} \quad [2]$$

The measurements were carried out with reaction steps [1] and [2] occurring simultaneously by using a gas mixture of N_2O + CO. The nonsteady rates of reaction steps [1] and [2] were followed by measuring the conversions to N_2 and CO_2. The kinetic analysis (1) of the transient behavior permitted the independent determination of the forward rate constants of steps [1] and [2].

Under steady-state conditions, the rates of steps [1] and [2] are equal, and the surface acts as a true catalytic agent.

The choice of $CoFe_2O_4$ was dictated by the possibility of producing ferrite phases with excess or defect electrons without the need to introduce doping agents or drastic variations in the chemical composition of the catalyst. The preparation of cobalt ferrite phases with excess or defect of electrons is simply obtained by modifications of the Co/Fe ratio (2). The electronic structure of $CoFe_2O_4$ has been investigated in detail, and as a result measurements of thermoelectric power may be used to follow the concentration of excess or defect electrons during reaction conditions. It is then possible to throw light on the interesting question of the relation between the nature of the reaction intermediate, surface reactivity and electronic structure of the solid.

Experimental

Materials.—$CoFe_2O_4$ was prepared by means of standard ceramic techniques, involving three successive firings and ball millings. Two samples with final compositions of $Co_{0.994}Fe_{2.006}O_4$ (n-type) and $Co_{1.097}Fe_{1.903}O_4$ (p-type) were prepared. Compositions were determined by chemical and x-ray fluorescence analysis.

The finished spinel powder was pressed at 24,000 psig into cylindrical samples and sintered at 1130°C for 12 hr in air. The sintered samples (particle size $\approx 10\mu$) were air cooled and ground with disk emery paper to obtain slabs having dimensions of 7/16 x 1/32 x 13/16 in. Electrical contacts to the samples were made by coating both ends with "liquid bright gold," and subsequent heating to about 600°C to decompose the solvent. N_2O, CO, and O_2, from commercial cylinders, (prepurified grade) were dried before use. CO was passed through Ascarite and He through CuO (350°C) and a charcoal trap cooled with dry ice.

Apparatus.—The ferrite slab was supported in the reaction vessel by two pieces of 2 mm bore capillary tubings, grooved at each end to hold the sample tightly in place. Au foils were mounted at each end between the capillary tubing and the slab, and the ends were pressed firmly by Au plated springs, hung between the support and the capillary tubing. The temperature gradient across the sample, generally between 2°-3°C, was controlled by a secondary Au heating coil wound on the outside of the capillary tubing. The thermoelectric emf was measured by Au wire leads, spot welded on each Au electrode. Temperatures at both ends of the sample were measured by chromel-alumel thermocouples, spot welded to each Au foil. The thermoelectric emf for temperature indication was measured with a potentiometer and a d-c null detector, while the thermoelectric power of the sample was obtained with a d-c microvoltammeter.

Procedure.—A sketch of the apparatus is shown in Fig. 1. Gases from the purification train passed through flowmeters and into the reactor-thermoelectric power cell. CO_2 was collected in two wash bottles in series, containing a known amount of a 0.1*N* $Ba(OH)_2$ solution. N_2 was analyzed by gas chromotography. A solenoid valve was used to obtain a stepwise change in the partial pressures of the reactants during the nonsteady-state experiments. The total pressure of the system was always maintained at 1 atm.

In the adsorption and desorption experiments, He was passed through the reaction vessel until the sam-

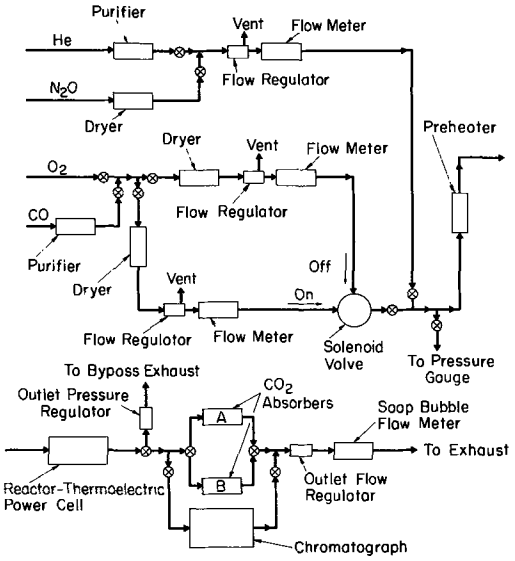

Fig. 1. Apparatus used for nonsteady-state rate experiments

ple thermoelectric power reached a constant value. O_2 was then introduced into the stream and the variation in the thermoelectric power as a function of time was noted. For reaction rate experiments the conversions of N_2O and CO, the thermoelectric emf and temperatures at both ends of the catalyst were measured as a function of time. The total pressure and flow rate were kept constant before and after the stepwise change in the partial pressures of the reactants. Thermoelectric power and conversion changes could be returned to the initial values whenever the original ratio of reactant gas partial pressures was restored around the sample.

Additional details on the materials and procedures used are recorded elsewhere (3).

Experimental Results

Preliminary investigations showed that the thermal emf was a linear function of the temperature gradient, ΔT, with ΔT values up to 24°C, and that for $\Delta T = 0$, a small emf was present (Fig. 2). This error does not directly influence the thermoelectric power measurements, and no effort was made to eliminate it. The values of the thermoelectric power during O_2 adsorption and desorption is shown in Fig. 3 and 4. The results indicated a decrease in thermoelectric power of both samples on O_2 adsorption, suggesting that the concentration of excess electrons decreased in the n-type sample (Fig. 3), while that of electron holes increased in the p-type sample (Fig. 4). From previous work (2a), it was claimed that $CoFe_2O_4$ be-

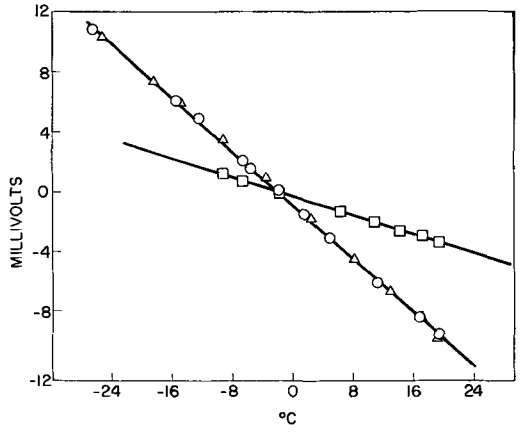

Fig. 2. Thermoelectric emf vs. temperature differences in various gases for $Co_{0.994}Fe_{2.006}O_4$; T (average), 300°C; total pressure, 1 atm; □, He; △, O_2; ⊙, air.

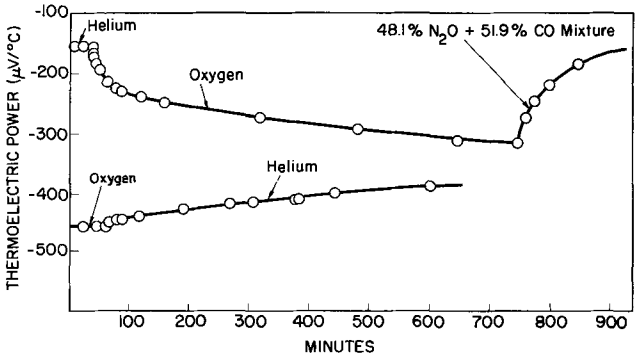

Fig. 3. Thermoelectric power of $Co_{0.994}Fe_{2.006}O_4$ vs. time in He, O_2, and N_2O + CO mixture; T, 300°C; total pressure, 1 atm.

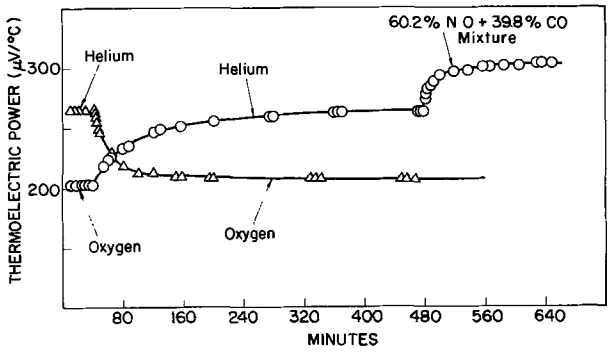

Fig. 4. Thermoelectric power of $Co_{1.097}Fe_{1.903}O_4$ vs. time in He, O_2, and N_2O + CO mixture; T, 300°C; total pressure, 1 atm.

comes a two carrier semiconductor in air at > 160°C. This fact was confirmed in subsequent observations on the variation of thermoelectric power of $CoFe_2O_4$. On n-type samples it was found that O_2 adsorption at 250°C decreased at first the negative thermoelectric power. Upon further adsorption, the samples became p-type and the positive thermoelectric power increased with O_2 adsorption. The results reported on Fig. 3 show that at 300°C, O_2 adsorption increased the negative thermoelectric power of an n-type sample in apparent contrast with the previous observations. Similar considerations apply to the results reported in Fig. 4. Apparently, the temperature of the transition between single to double carrier behavior depends critically on sample composition, particularly near the minimum and maximum values of the thermoelectric power. Introduction of a mixture of 48.1% N_2O + CO into the reactor during the chemisorption experiments produced changes in the thermoelectric power of the sample in the direction of increasing the concentration of electrons for n-type (Fig. 3), or in the direction of decreasing the concentration of electron holes for p-type (Fig. 4).

The rates of reactions [1] and [2] were not influenced by the gas flow rate within the range used in the nonsteady-state experiments, 18 to 40 cc/min (Fig. 5).

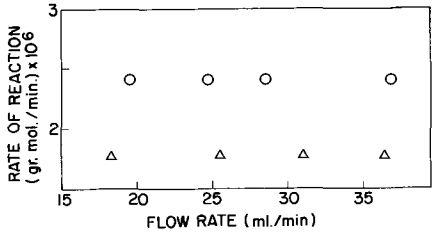

Fig. 5. Rate of reaction vs. flow rate, T, 300°C; p_{N_2O}, 0.398 atm; p_{CO}, 0.602 atm; ⊙, $Co_{0.994}Fe_{2.006}O_4$; △, $Co_{1.097}Fe_{1.903}O_4$.

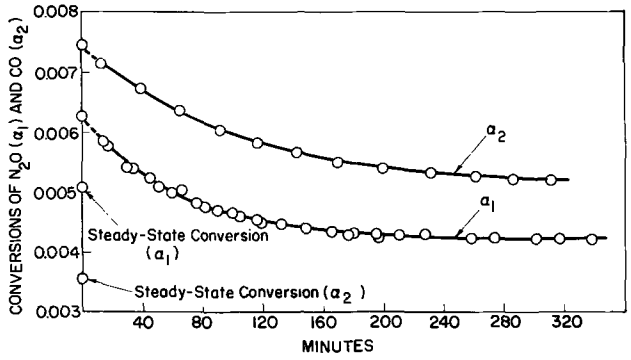

Fig. 6. Conversions of N_2O and CO vs. time after a stepwise change in partial pressures, for $Co_{0.994}Fe_{2.006}O_4$; initial steady state $p°_{N_2O}$ = 0.410 atm; $p°_{CO}$ = 0.590 atm; final values p_{N_2O} = 0.605 atm; p_{CO} = 0.395 atm; T, 300°C.

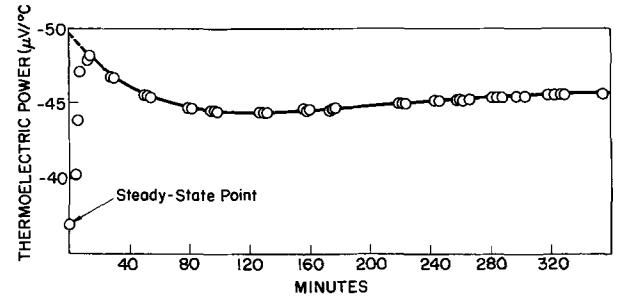

Fig. 7. Change of thermoelectric power as a function of time after a stepwise change in partial pressures for $Co_{0.994}Fe_{2.006}O_4$; initial steady state: $p°_{N_2O}$ = 0.590 atm; $p°_{CO}$ = 0.590 atm; final values: p_{N_2O} = 0.605 atm; p_{CO} = 0.395 atm; T, 300°C.

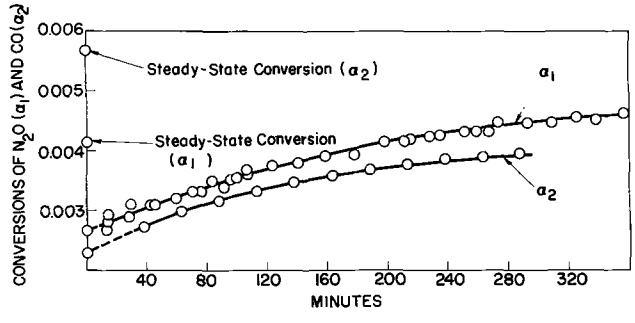

Fig. 8. Conversions of N_2O and CO vs. time after a stepwise change in partial pressures for $Co_{0.994}Fe_{2.006}O_4$; initial steady state: $p°_{N_2O}$ = 0.578 atm, $p°_{CO}$ = 0.422 atm; final values: p_{N_2O} = 0.402 atm; p_{CO} = 0.598 atm; T, 300°C.

After the establishment of a reaction steady state, nonsteady-state conditions were obtained by a stepwise perturbation of partial pressures of both reactants at the same total pressure, temperature, and flow rate which prevailed at the steady-state conditions. Figure 6 shows the conversions of N_2O and CO, defined as

$$\alpha_{N_2O} = (p°_{N_2O} - p_{N_2O})/p°_{N_2O} = p_{CO_2}/p°_{N_2O},$$

$$\alpha_{CO} = p_{CO_2}/p°_{CO}$$

where the superscript o refers to initial steady-state conditions, and Fig. 7 gives the values of the thermoelectric power as a function of time for the n-type ferrite at a temperature of 300°C, when p_{N_2O} and p_{CO} were changed from 0.410 and 0.590 atm (steady-state conditions) to 0.605 and 0.395 atm.

Figures 8 and 9 show the results for the same ferrite samples subjected to changes in p_{N_2O} from 0.578 to 0.402 atm, and in p_{CO} from 0.422 to 0.598 atm.

Figures 10 and 11 present reaction conversions and thermoelectric power as functions of time for the

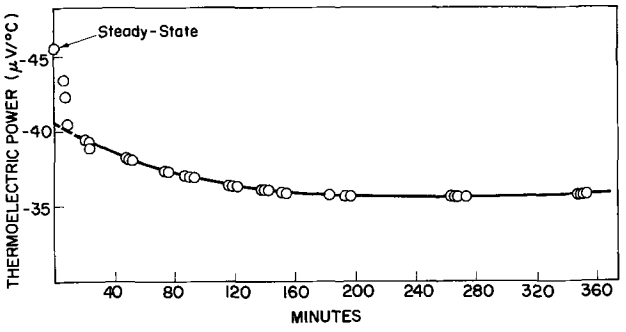

Fig. 9. Change of thermoelectric power as a function of time after a stepwise change in partial pressures for $Co_{0.994}Fe_{2.006}O_4$; initial steady state: $p°_{N_2O}$ = 0.578 atm; $p°_{CO}$ = 0.422 atm; final values; p_{N_2O} = 0.402 atm; p_{CO} = 0.598 atm; T, 300°C.

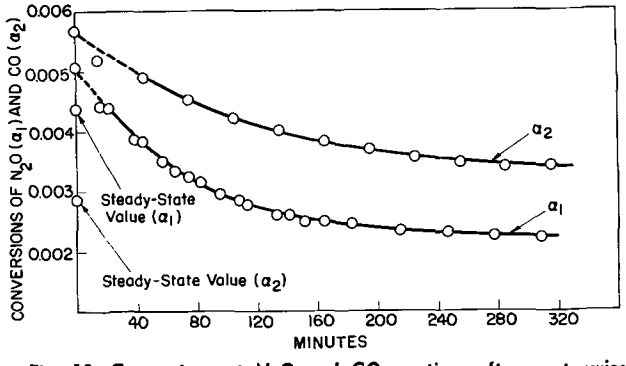

Fig. 10. Conversions of N_2O and CO vs. time after a stepwise change in partial pressures for $Co_{1.097}Fe_{1.903}O_4$; initial steady state: $p°_{N_2O}$ = 0.397 atm, $p°_{CO}$ = 0.603 atm; final values: $p°_{H_2O}$ = 0.599 atm; $p°_{CO}$ = 0.401 atm; T, 300°C.

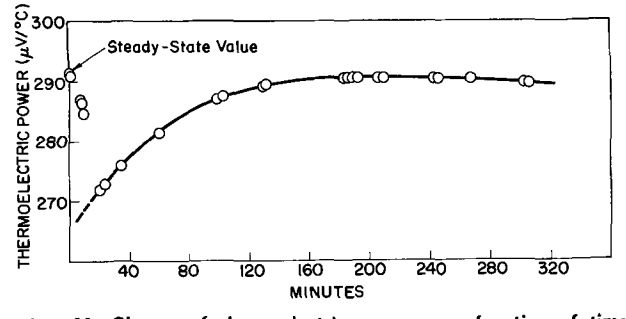

Fig. 11. Change of thermoelectric power as a function of time after a stepwise change in partial pressures for $Co_{1.097}Fe_{1.903}O_4$; initial steady state: $p°_{N_2O}$ = 0.397 atm, $p°_{CO}$ = 0.603 atm; final values: p_{N_2O} = 0.599 atm, p_{CO} = 0.40 atm; T, 300°C.

p-type ferrite sample at a temperature of 300°C, when p_{N_2O} and p_{CO} were changed from 0.397 and 0.603 atm (steady-state values) to 0.599 and 0.401 atm, respectively.

Figures 12 and 13 present similar results for the p-type sample at a temperature of 190°C.

Discussion

By graphical differentiation of the experimental results, the values of $\ln(d\alpha_1/dt)$ and $\ln(d\alpha_2/dt)$ were calculated as a function of time, and are plotted in Fig. 14, 15, 16, and 17. The plots show that the straight-line relation, required by Eq. [10] and [11] in the preceding paper, is well obeyed. The analytical treatment of these equations requires that the condition $\overleftarrow{k}_1 \frac{X_a(i)}{S} << \vec{k}_1 \frac{h}{S} p°_{N_2O}$ be obeyed. In this expression $\overleftarrow{k}_1 X_a(i)$, S, and h are the step rate constant, the amount of adsorbed intermediate initially present, the surface area, and a constant, respectively. Typical re-

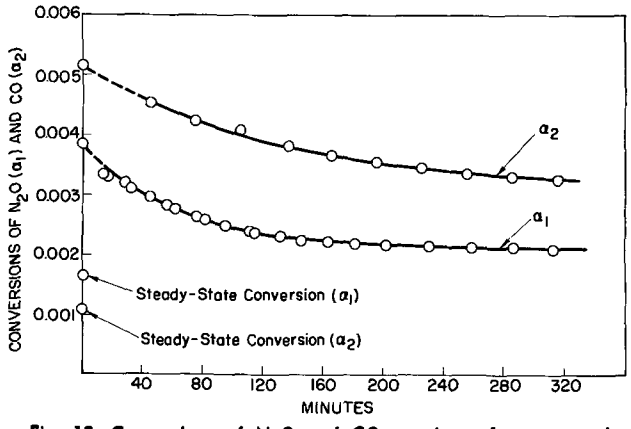

Fig. 12. Conversions of N_2O and CO vs. time after a stepwise change in partial pressures for $Co_{1.097}Fe_{1.903}O_4$; initial steady state: $p°_{N_2O}$ = 0.396 atm; $p°_{CO}$ = 0.604 atm; final values: p_{N_2O} = 0.603 atm, p_{CO} = 0.397 atm; T, 190°C.

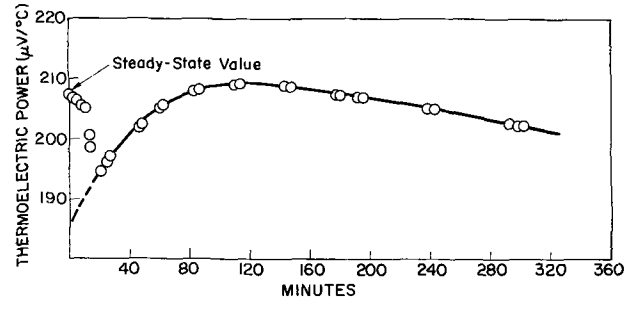

Fig. 13. Change of thermoelectric power as a function of time after a stepwise change in partial pressures for $Co_{1.097}Fe_{1.903}O_4$; initial steady state: $p°_{N_2O}$ = 0.396 atm, $p°_{CO}$ = 0.604 atm; final values: p_{N_2O} = 0.603 atm, p_{CO} = 0.397 atm; T, 190°C.

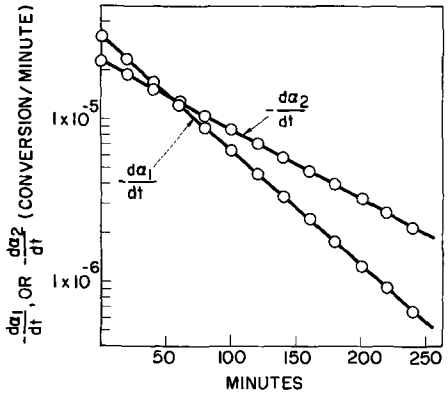

Fig. 14. Rate of change of conversion of N_2O or CO as a function of time for $Co_{0.994}Fe_{2.006}O_4$; initial steady state: $p°_{N_2O}$ = 0.410 atm, $p°_{CO}$ = 0.590 atm; final values: p_{N_2O} = 0.605 atm, p_{CO} = 0.395 atm; T, 300°C.

sults (3) at 300°C show that $\vec{k}_1 \frac{h}{S} p°_{N_2O} + \overleftarrow{k}_1 \frac{X_a(i)}{S}$ = 0.01618 and $\vec{k}_1 \left(1 - \frac{Xa(i)}{S}\right) = 6.85 \times 10^{-5} > \frac{X_a(i)}{S} \overleftarrow{k}_1$. Thus, the above condition is satisfied. Although no generalization about the validity of this condition is possible and each case must be verified, it is clear that the condition will always be satisfied provided that h is made large enough (large reactor volume). By means of the values of the calculated slopes and intercepts of the plots in Fig. 14 to 17, it is possible to obtain the numerical values of $\vec{k}_1$ and $\vec{k}_2$, the forward rate constants for steps [1] and [2], and of

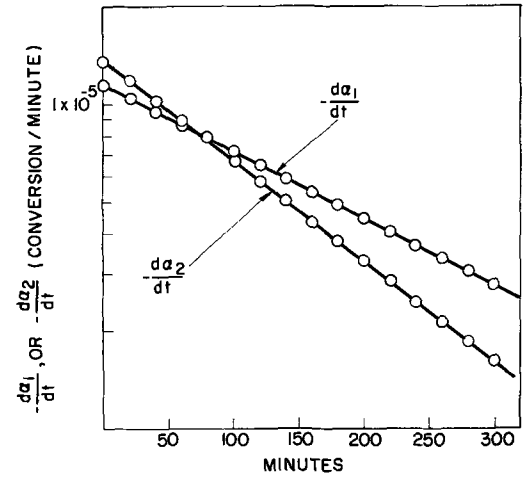

Fig. 15. Rate of change of conversion of N_2O or CO as a function of time for $Co_{0.994}Fe_{2.006}O_4$; initial steady state: $p°_{N_2O}$ = 0.578 atm, $p°_{CO}$ = 0.422 atm; final values: p_{N_2O} = 0.402 atm; p_{CO} = 0.598 atm; T, 300°C.

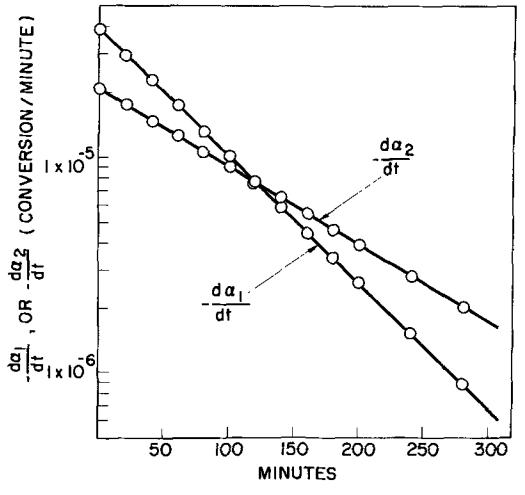

Fig. 16. Rate of change of conversion of N_2O or CO as a function of time for $Co_{1.097}Fe_{1.903}O_4$; initial steady state: $p°_{N_2O}$ = 0.397 atm, $p°_{CO}$ = 0.603 atm; final values: p_{N_2O} = 0.599 atm, p_{CO} = 0.401 atm; T, 300°C.

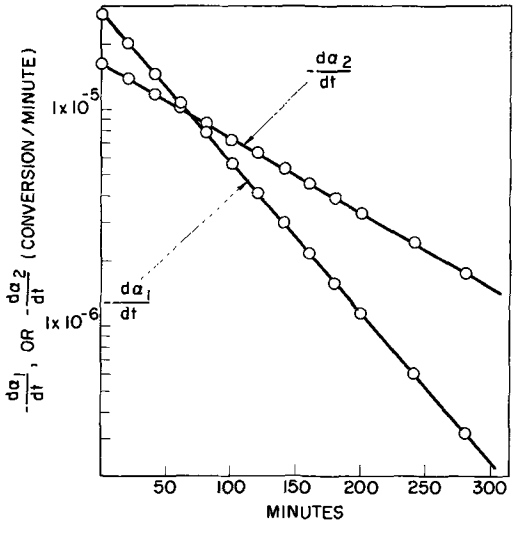

Fig. 17. Rate of change of conversion of N_2O or CO as a function of time for $Co_{1.097}Fe_{1.903}O_4$; initial steady state: $p°_{N_2O}$ = 0.396 atm, $p°_{CO}$ = 0.604 atm; final values: p_{N_2O} = 0.603 atm, p_{CO} = 0.397 atm; T, 190°C.

Table I. Results of the analysis of nonsteady rates of reaction steps [1] and [2] on cobalt ferrite

Ferrite type	Temp, °C	$\frac{p_{N_2O}}{p_{CO}}$	θ	$\vec{k}_1$, min^{-1}	$\vec{k}_2$, min^{-1}	$\frac{\vec{k}_1}{\vec{k}_2}$
n	300	0.700	0.44	1.22×10^{-4}	1.12×10^{-4}	1.08
n	300	1.36	0.55	5.3×10^{-6}	5.4×10^{-5}	0.98
p	300	0.665	0.49	5.8×10^{-6}	5.36×10^{-5}	1.08
p	190	0.665	0.49	6.5×10^{-5}	4.96×10^{-5}	1.31

Table II. Specific surface areas of catalysts from rate experiments, A_K, and liquid nitrogen adsorption, A_N

Catalyst type	Temp, °C	A_K, m^2/g	A_N, m^2/g
n	300	0.833	0.850
p	300	0.605	0.650
p	190	0.716	0.650

the initial surface coverage with adsorbed oxygen, θ, for the various experimental conditions. The results of the calculations are collected in Table I.

The calculation of the initial surface coverage $\theta = \frac{X_a(i)}{S}$, reported in Table I, is based on information on S, the total catalytic surface available, as determined directly from the rate measurements. It is instructive to compare the value of S obtained from the rate experiments with that directly determined by BET measurements. From the present results, the following values of h/S (atm^{-1}) were calculated: 218.7 (n-type, 300°C), 384.9 (p-type, 300°C), 401.0 (p-type, 190°C). Since $h = \frac{V}{RT} = \frac{201.5}{82.06 \times 573} = 4.28 \times 10^{-3}$ (g atoms/atm), where 201.5 is the reactor volume in cc, then, $S = h/218.7 = 1.958 \times 10^{-5}$ g atom. Taking the cross-sectional area of an adsorbed oxygen atom equal to 13.5Å (2), we obtain $S = 6.02 \times 10^{23} \times 1.98 \times 10^{-5} \times 13.5 \times 10^{-20} = 1.62$ m^2 which corresponds to a specific surface area of (1.62/1.94) = 0.833 m^2/g, to be compared to a value of 0.850 m^2/g from BET measurements. Similar calculations for the other catalysts are collected in Table II.

The comparison between the two sets of values is satisfactory, and it may be taken as supporting evidence for the reaction scheme and kinetic derivation presented. It should be noted that the value A_K is temperature dependent. This is a result of the method of derivation used.

By means of the plots presented in Fig. 2 and 3 of the preceding paper (1), it is possible to obtain information on the chemical nature of the oxygen intermediate. To this end, the following expressions relating electron concentration to thermoelectric power were used (2a)

$$eQT = -\alpha - \bar{k}T \ln \frac{N}{n_{e-}}, \quad (n_{e-} >> n_{e+}) \qquad [3]$$

$$eQT = \beta + \bar{k}T \ln \frac{N}{n_{e+}}, \quad (n_{e-} << n_{e+}) \qquad [4]$$

where e, Q, N, n_{e-}, n_{e+}, $\bar{k}$, α, and β are the electron charge, the thermoelectric power, the number of ions per cc in $CoFe_2O_4$, the excess electron, and the defect electron (hole) concentrations, the Boltzmann constant, and two constants (2a), respectively. To employ Eq. [3] and [4], the following assumptions must be made: (a) the numerical values of n_{e-} and n_{e+} are small enough to permit the use of Boltzmann statistics; (b) the value of N is constant in the composition range employed; (c) the significant energy levels in $CoFe_2O_4$ include only localized levels for Co^{II} and Fe^{II}, and no normal bands (from oxygen or metal ions) are introduced. Equations [3] and [4] show that the thermoelectric power in $CoFe_2O_4$ is dependent on the concentration of electrons or electron holes, the temperature, and bulk composition. At constant temperature and composition, electron (de)localization accompanying adsorption or desorption of O_2 induces a change in the thermoelectric power of the solid. Since reaction step [1] corresponds to O_2 adsorption, while reaction step [2] corresponds to O_2 desorption, it is conceivable to attribute to these steps the observed variations in thermoelectric power in the course of our experiments with N_2O and CO.

Quantitatively, it was found (7) that the changes in thermoelectric power on adsorption can be described by

$$\frac{(n_e-)_c}{(n_e-)_o} = \exp\left\{\frac{\omega}{\delta}\frac{Q^c - Q^o}{\kappa}\right\} \text{ for } \delta < \omega$$

and

$$\frac{(n_e-)_c}{(n_e-)_o} = \exp\left\{\frac{Q^c - Q^o}{\kappa}\right\} \text{for } \delta \geqq \omega$$

where $(n_e-)_c$, $(n_e-)_o$, Q^c, and Q^o are the electron concentration and thermoelectric power after and before adsorption, respectively, and δ and ω are the thickness of the surface space charge layer and of the thermal gradient, respectively. The value of δ is small (appendix B), but the value of ω is not known. Thus, the application of Eq. [3] and [4] is valid only if $\delta \leq \omega$. If $\delta > \omega$, the application of Eq. [3] and [4] will give an upper limiting value for n_{e-}. It should be recalled that in previous work on the adsorption of O_2 and H_2 on $CoFe_2O_4$ (4) in the same temperature range employed in the present investigation, the condition $\delta \leq \omega$ was found to be valid.

Solving Eq. [3] and [4] for n_{e-}, n_{e+} and substituting the values into Eq. [18] to [25] and [10] and [11] of the preceding paper (1), it is possible to obtain expressions relating the sum of the conversion changes $(d\alpha_1/dt) + (d\alpha_2/dt)$ to the corresponding Q values.

As explained in the previous communication (1), linear plots of the reaction conversion *vs.* Q yield different slopes according to the equation used to characterize surface equilibrium (Eq. [14] to [17] of the preceding communication). Thus, the expected slopes differ for each of the assumed types of surface oxygen.

If surface equilibria are not established during reaction conditions, the analysis will not yield linear plots of the function $\ln (d\alpha/dt) = f(Q)$. In this instance, Eq. [22] to [25] of the preceding communication (1) should be used.

The details of the analysis are reported elsewhere (3), and only a summary of the results is given here. It was found that the experimental results could be easily fitted when the assumption of the establishment of surface equilibria is made. The corresponding mathematical equations relating chemical conversion to thermoelectric power for the two possibilities of neutral surface intermediate O, and singly ionized O^- are:

(a) Neutral surface intermediate, O:

$$\ln \left\{ \frac{p^o_{N_2O}\frac{h}{S}\left[\vec{k}_1\left(1 - \frac{[O]_1}{S}\right) - \frac{d\alpha_1}{dt}\right]}{\vec{k}_1\frac{h}{S}p^o_{N_2O} + \vec{k}_1 - \vec{k}_1\frac{X}{S} + \overleftarrow{k}_1\frac{[O]_1}{S}} + \frac{p^o_{CO}\frac{h}{S}\left(\frac{d\alpha_2}{dt} - \vec{k}_2\frac{[O]_i}{S}\right)}{\vec{k}_2\frac{h}{S}p^o_{CO} + \vec{k}_2\frac{[O]_i}{S} + \overleftarrow{k}_2 - \overleftarrow{k}_2\frac{[O]_i}{S}} + \frac{[O]_i}{S} \right\} = -\frac{2}{3}10^{-8}\frac{e}{Q} + C'_1 \qquad [5]$$

where C'_1 is a constant, and the equation is valid for n- or p-type samples.

(b) Singly charged surface intermediate, O^-:

$$\ln \left[\frac{p^\circ_{N_2O} \frac{h}{S} \left[\vec{k}_1 \left(1 - \frac{[O]_i}{S} \right) - \frac{d\alpha_1}{dt} \right]}{\vec{k}_1 \frac{h}{S} p^\circ_{N_2O} + \vec{k}_1 - \vec{k}_1 \frac{[O]_i}{S} + \overleftarrow{k}_1 \frac{[O]_i}{S}} + \frac{p^\circ_{CO} \frac{h}{S} \frac{d\alpha_2}{dt} - \vec{k}_2 \frac{[O]_i}{S}}{\vec{k}_2 \frac{h}{S} p^\circ_{CO} + \vec{k}_2 \frac{[O]_i}{S} + \overleftarrow{k}_2 - \overleftarrow{k}_2 \frac{[O]_i}{S}} + \frac{[O]_i}{S} \right] = \frac{1}{3} 10^{-8} \frac{e}{k} Q + C'_2 \quad [6]$$

where C'_2 is a constant and the equation is valid for n- or p-type samples. A typical plot of Eq. [5], constructed by means of the experimental results, is presented in Fig. 18. All experimental results could be fitted with either Eq. [5] or [6].

A calculation of the order of magnitude of the thickness of the surface space charge layer (Debye length), expected on the surface of $CoFe_2O_4$ during adsorption, corroborates the conclusion on the ready establishment of surface-bulk equilibria. In fact, the electron concentration for the n-type sample, computed with Eq. [3] from the minimum observed value of the thermoelectric power, $-50(\mu v/°C)$, and $T = 300(°C)$, $\alpha = 1kT$ (erg), $N = 1 \times 35 \times 10^{22}$ (cc^{-1}), is found to be $n_{e^-} = 2.005 \times 10^{22}$ (cc^{-1}) at 300°C. Similarly, from Eq. [4] and the maximum observed value of the thermoelectric power, 290 ($\mu v/°C$) for the p-type sample and $\beta = 6kT$ (erg), it is found that $n_{e^+} = 1.89 \times 10^{23}$ (cc^{-1}).[1] With these limiting values and $\epsilon = 12$, the Debye length is of the order of a few angstroms for both samples (3). The possibility of doubly ionized oxygen as a surface intermediate, O^{-2}, requires, as previously explained, that no influence of the reacting mixture upon the thermoelectric power be found (1). Since this was not observed, O^{-2} ions are eliminated as kinetically significant. The comparison between the expected and observed reaction between conversion and thermoelectric power for the two cases, O^- and O,

[1] This value is about one order of magnitude larger than the number of metal ions per cubic centimeter of the spinel (1.35×10^{22}). It should be noted that, for the energy level scheme of $CoFe_2O_4$ here employed (2a), equating N in Eq. [3] and [4] to the number of metal ions per cc in the solid is permissible with very narrow energy levels only. This condition determines the numerical value of the transport coefficient β. Taking $\beta \approx 4kT$, then $n_{e^+} \approx N$.

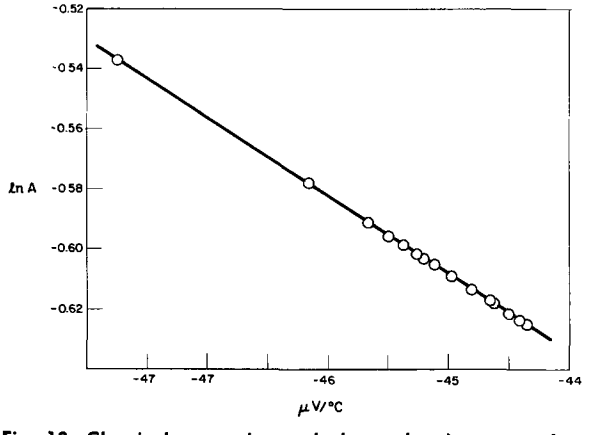

Fig. 18. Chemical conversion and thermoelectric power plotted according to Eq. [5]. A, left hand side of Eq. [5] steady state: $p^\circ_{N_2O} = 0.410$ atm, $p^\circ_{CO} = 0.590$ atm; nonsteady state: $p^\circ_{N_2O} = 0.605$ atm, $p^\circ_{CO} = 0.395$ atm; $Co_{0.994}Fe_{2.006}O_4$, 300°C, total pressure = 1 atm.

Table III. Nature of surface oxygen intermediate during the oxidation and reduction of surface cobalt ferrite

Temp, °C	Ferrite type	Calculated slopes,* °K/μv		Experimental slope, °K/μv	Catalytic intermediate
		Catalytic O	Intermediate O^{-1}		
300	n	−0.0232	−0.0116	−0.0260	O
300	n	−0.0232	−0.0116	−0.0263	O
300	p	−0.0232	−0.0116	−0.0191	O and O^{-1}
190	p	−0.0232	−0.0116	−0.0123	O^{-1}

* From Eq. [3] and [4] of this paper and [18] to [25] of preceding paper.

is presented in Table III. The results show that for the n-type ferrite, good agreement is obtained by assuming that neutral oxygen species cover the surface during reaction steps [1] and [2], while for the p-type sample the assumption of monocharged ions is in better agreement at low temperature. With increasing temperature there is more contribution from neutral species.

From these conclusions, it is possible to single out three important observations. The first refers to the time constant of the adsorption and desorption effects. As shown, the former is in the range of minutes or more, and the question arises as to the physical nature of this phenomenon. It is clearly a case of "slow" adsorption. Many adsorption systems previously investigated exhibit an initial rapid adsorption (seconds or less) followed by a slow adsorption (hours). While it is not too difficult to relate the rapid process with electronic transitions and transfers, it has been generally more difficult to establish the nature of the slow process. It has been variously attributed to adsorption, surface diffusion, or reaction with the solid (5). In the present case it is not easy to see how the latter can take place with a formal surface coverage of less than a monolayer. Diffusional exchanges with the interior of the solid can be ruled out as kinetically significant. In fact, a simple calculation shows that at 300°C the time required for diffusion of a few per cent of adsorbed species in the crystal interior is of the order of seconds for a layer of thickness comparable to the size of the ferrite particles used (Appendix A). Thus, the most likely possibility is that the observed relaxation effects are resulting from slow, activated surface diffusional transport. Although we have not determined whether a slow decrease of surface area of the samples took place during the experiments, we suggest that the nature of the surface transport is similar to that controlling sintering of small solid particles at low temperatures. A large amount of ill-defined surfaces are generally present in powdered solids at grain boundaries and other macroscopic crystal imperfections. The rearrangement of matter along and into the imperfections is kinetically significant during sintering. At low temperatures this process is controlled by surface diffusion, and the rate of the latter is influenced by adsorption from the surrounding gas atmosphere (8). Therefore, it is suggested that the long relaxation times for adsorption and desorption found in this study are related to surface mass transport effects of the solid. Pore contribution to these effects was probably quite small since it can be shown that most of the active surface was external. In fact, assuming cubic particles with a density of 5.2 (4) (g/cc) and 10μ size, the theoretical surface area is 0.115 (m^2/g). This value is within an order of magnitude of the value obtained from the rate experiments (Table II).

The second important observation refers to the different electronic localization which is experienced by the adsorbed oxygen on the two spinel samples. The results show that (a) there is more electron localization in the p-type sample; the presence of electron holes in the semiconducting solid produces a more

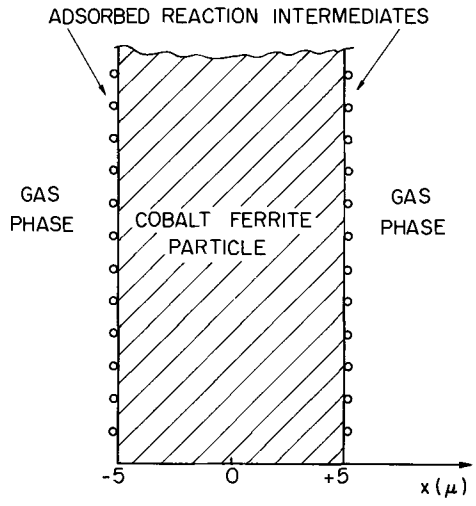

Fig. 19. Model used for bulk-surface diffusion calculations

polarized surface bond; (*b*) electron localization increases with decreasing temperature. Since Co^{+3} and Fe^{+2} ions are responsible for the difference in physicochemical properties of the two samples, it is conceivable that the variations in electron localization of the surface bond may also be ascribed to these ions, a more ionic bond being established between Co^{+3} and O_2 in respect to Fe^{+2} and O_2. At present there is no independent support for such a conclusion.

The final observation refers to the actual rate of the catalytic reaction. In fact, it has been found that the rate of the reaction was faster on the n-type ferrite as compared to the p-type. Since gas phase oxidation conditions prevailed, this result is at variance with correlations on the catalytic activity indicating that for oxidation reactions (N_2O decomposition), p-type oxides induce a faster catalytic rate (6).

It should be emphasized that this result has been obtained without the use of solid state doping, and it is, therefore, free of the criticism often expressed on the influence of doping and its concentration on the solid surface.

Conclusions

The applications of the theoretical analysis of the transient behavior of solid-gas systems to the reduction and oxidation of the surface of various samples of $CoFe_2O_4$ have shown that: (*a*) electron localization of the bond linking the adsorbed oxygen intermediate to the ferrite surface is larger for p-type than for n-type samples and, as a result, the intermediates for reactions [1] and [2] are O (n-type), O and O^- (p-type) at 300°C and O^- (p-type) at 190°C; and (*b*) the kinetic reactivity of the adsorbed oxygen is larger for O than O^-; thus, n-type ferrite is more reactive than p-type ferrite.

Acknowledgment

This research was supported by a grant from the National Science Foundation. This support is gratefully acknowledged.

Manuscript received July 29, 1966; revised manuscript received Feb. 3, 1967.

Any discussion of this paper will appear in a Discussion Section to be published in the December 1967 JOURNAL.

APPENDIX A

The possible contribution to the observed effects of ionic diffusion between the interior and the surface of the crystal may be easily evaluated. Consider the idealized model of a slab of ferrite of uniform thickness of 10μ, and let us calculate the unidimensional diffusion of oxygen ions through the slab. To simplify matters, let us assume the following boundary conditions, $C = C_0$ and $-5 \times 10^{-4} \leq x \leq 5 \times 10^{-4}$ (cm) for $t = 0$, and $C = C_s$ and $x = \pm 5 \times 10^{-4}$ (cm) for $t \geq 0$, where x is the distance between the two surfaces of the slab, starting from the slab median (Fig. 19). These conditions mean that the concentration of oxygen ions is C_0 throughout the solid during steady-state conditions. At the time of the stepwise pressure change ($t = 0$), the concentration of oxygen at the surface becomes C_s. The solution of the one dimensional Fick's second equation gives

$$C_s - \overline{C} = \frac{8(C_s - C_0)}{\pi^2} \sum_1^\infty \frac{1}{(2n-1)^2} \exp[-(2n-1)^2 \pi^2 Dt/a^2] \quad [A\text{-}1]$$

where D, $\overline{C}$, and a are the diffusion coefficient, the average concentration of oxygen in the solid, and ½ the slab thickness, respectively. Using the values $D = 3 \times 10^{-12}$ cm²/sec (2b), $a = 5\mu$, the times required for 0.5 and 1% of the adsorbed oxygen to diffuse into the bulk of the solid are found to be 6 and 22 sec, respectively. This time is much smaller than that corresponding to the response studied in this investigation (5-6 hr).

APPENDIX B

The use of the Debye expression, $\delta = \left(\frac{\epsilon kT}{8\pi ne^2}\right)^{1/2}$, for the calculation of the thickness of the surface space charge layer, δ, is based on the validity of the application of the Boltzmann distribution under our experimental conditions. This is a permissible procedure whenever the following conditions are satisfied: $E - E_F > kT$ for n-type and $E_F - E > kT$ for p-type samples, where E_F is the Fermi level. Using the values $E - E_F = 0.275 - \nu$ and $E_F - E = 0.275 + \nu$ (2a) where $\nu = -kT/2 \ln \mu_2/\mu_1 = -(0.0295/2) \ln 10^4 = -0.136$ ev (190°C) and $\nu = -0.0025$ (300°C), it is found: $E - E_F = 0.500$ ev > 0.0489 ev ($= kT$ at 300°C); $E_F - E = 0.051$ ev (300°C); $E_F - E = 0.139$ ev > 0.0295 ev ($= kT$ at 190°C). In these equations μ_1 and μ_2 represent the electron and the electron hole mobilities. Therefore, the Boltzmann expressions are applicable and the use of the Debye expression for the calculation of the space charge layer is valid.

REFERENCES

1. S. T. Hwang and G. Parravano, *This Journal*, **114**, 478 (1967).
2. (a) G. H. Jonker, *J. Phys. Chem. Solids*, **9**, 165 (1959); (b) W. Muller and H. Schmalzreid, *Ber. Bunsengesell. Physik Chemie*, **68**, 270 (1964).
3. S. T. Hwang, Ph.D. Thesis, University of Michigan, 1965.
4. R. G. Squires and G. Parravano, *J. Catalysis*, **2**, 324 (1963).
5. A. J. Allawand and R. Chaplin, *Trans. Faraday Soc.*, **28**, 22d, 1932; G. C. A. Schmit and N. H. deBoer, *Nature*, **168**, 1040 (1951).
6. R. M. Dell, F. S. Stone, and P. F. Tiley, *Trans. Faraday Soc.*, **49**, 201 (1953).
7. G. Parravano and C. A. Domenicali, *J. Chem. Phys.*, **26**, 359 (1957).
8. H. M. O'Bryan and G. Parravano, *Materials Science and Engineering*, **1**, 177 (1966).

Technical Note

Instrumentation for Potentiostatic Corrosion Studies in Distilled Water

C. A. Youngdahl and R. E. Loess

Metallurgy Division, Argonne National Laboratory, Argonne, Illinois

Aspects of polarization measurements in high-resistance media, such as distilled water, have been discussed in previous articles (1, 2). The advantages of measuring the sample metal potential when no current is flowing (the interrupter technique) have been noted, and apparatus has been described. An important part of the instrumentation employed is a specialized pulse voltmeter in the measurement circuit, as indicated in Fig. 1(a). Potentiostatic corrosion studies, as distinct from polarization curve measurements, may be made in distilled water corrosion environment by a similar technique, as shown in Fig. 1(b). A simple potentiostat circuit is connected to the pulse voltmeter through an adjustable bias voltage supply. Incorporated in the potentiostat are automatic means of adjusting the polarization current, as shown, to maintain the selected polarization potential between the sample and reference electrode. Unidirectional polarizing current is employed to simplify the system: if current reversal is needed during a given test, manual adjustments are required.

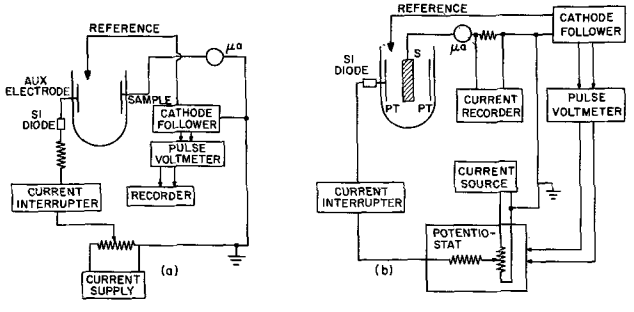

Fig. 1(a). Apparatus for measurement of polarization curves. Fig. 1(b). Apparatus for potentiostatic corrosion studies.

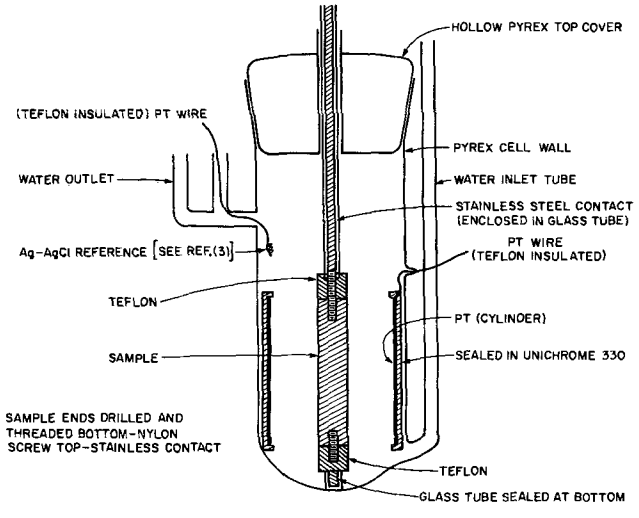

Fig. 2. Sectional view of polarization cell

What follows will deal primarily with pulse voltmeter circuitry similar to that in ref. (1), appropriately modified for connection into a potentiostat loop and for the benefits deriving from semiconductor components. A circuit for an electromechanical potentiostat built prior to the general advent of transistors (and now in use) is included. Behavior of the control loop system in corrosion studies of aluminum samples in 70°C distilled water is described.

Polarization Cell: Physical and Electrical Characteristics

The geometry and materials of construction of the sample-cell system, shown in Fig. 2, determine its electrical behavior and thus will be described briefly. The Pyrex cell is held in a 70°C water bath to maintain constant temperature. The corrosion medium is degassed, distilled water of R_s = 1.0-1.6 megohm cm (25°C) prior to entry into the cell. The water is heated to 70°C and added to the cell at the rate of 6 ml/min to refresh the cell solution, the excess overflowing to the drain. A constant solution resistivity is not attained because of the influence of sample corrosion, the rate of which changes with time. A hollow platinum cylinder of 5.75 cm ID fits closely inside the closed, cylindrical cell and serves as a current-carrying electrode. The outer surface and edges of the platinum are insulated with an inert wax (Unichrome 330) to prevent error due to uneven current density, an effect discussed in (2).

The sample is a solid cylinder of 1100 aluminum, 0.89 cm in diameter and 9.72 cm long (27.18 cm^2 surface area). Sample ends are blanked off with Teflon insulators to maintain equal current density at all exposed areas. The platinum and aluminum pieces are positioned coaxially, and the heights of the exposed surfaces are equal, again to produce uniform (though unequal) current density over both electrodes. The reference contact is a silver/silver chloride electrode (3) in the solution at the point where water leaves the cell. This arrangement minimizes addition of unwanted chloride ion to the test solution in the cell. The solution resistance between sample and platinum resulting from this construction changes typically from a relatively low and variable value at the beginning of test to about 18 kohms after several hours due to changes in resistivity noted above.

The open-circuit solution potential difference between sample and reference electrode (after an initial equilibration period and without externally applied current) is near 800 mv. The controlled potential selected for a given run may be within a few hundred millivolts above or below this value, and a maximum deviation of 10 mv from the voltage selected has been deemed acceptable. Sufficient circuit resistance is employed to nullify the effect of the sam-

ple-platinum voltage as an unwanted source of polarizing current.

It is of importance to note that during polarizing current interruptions the potential of a polarized specimen tends to decay slowly toward the open-circuit value. This property of the cell-sample system makes it unnecessary generally to provide external means of driving the sample potential in the direction of natural decay, *i.e.*, the externally applied polarizing current may be unidirectional. The advantage of this will become evident in a subsequent discussion of pulse voltmeter circuit operation. Another pleasant consequence of the relatively slow rate of decay of sample potential is to reduce the potentiostat rise time requirement to a range easily accommodated by electromechanical techniques. Further discussion of sample potential decay is included in subsequent sections.

Current Supply and Current Interrupter

The current supply indicated in Fig. 1(b) is not a critical component of the system. Voltage supplied to the 20 kohms potentiometer shown has typically been 75-90v. A 20 kohms slider resistor (shown) limits the cell current to a maximum of 4.5 ma (@ 90v), a value somewhat higher than the maximum needed for control of the sample.

The interrupter of Fig. 1(b) is the vacuum tube circuit described in ref. (1). The circuit interrupts the polarizing current for 6 msec once every 100 msec. Precise timing is not necessary nor is synchronization with external circuitry. Leakage resistance across the (vacuum tube) switch must be greater than 10 megohms during current interruptions to prevent a potential error greater than 1 mv (due to solution IR drop) in the cell herein described, given the solution resistances and polarization current levels encountered in the present work. Noise presented by the interrupter to the cell during current interruptions must likewise be sufficiently small or reproducible to satisfy the accuracy requirements. The aforementioned circuit fulfills these needs. A transistorized interrupter is currently being evaluated and appears satisfactory although relatively limited with respect to maximum polarizing source voltage at an acceptable leakage current value.

Character of the Voltage Measurement Problem

Pulsating polarization current flowing through the cell produces a pulsating voltage pattern at the measurement terminals, *i.e.*, the sample and reference electrode contacts, as shown in Fig. 3. Note that the figure represents the reference electrode voltage as varying

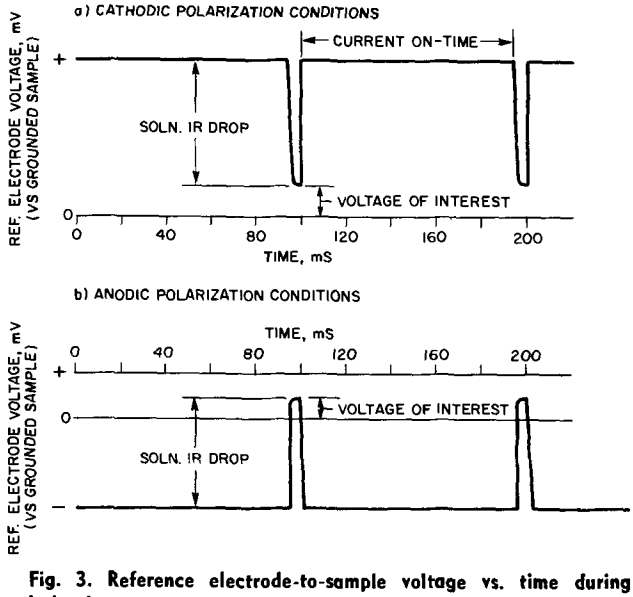

Fig. 3. Reference electrode-to-sample voltage vs. time during polarization.

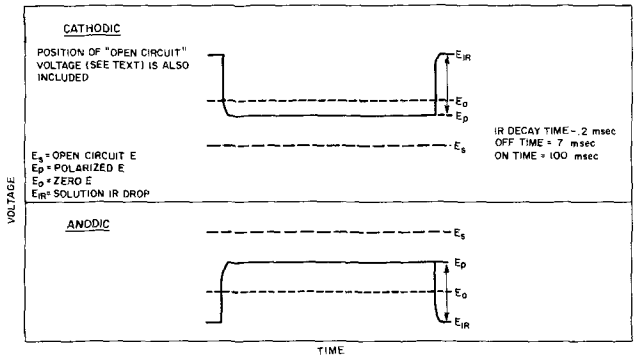

Fig. 4. Input signal during current interruption; biased suitably for presentation to PVTM.

with respect to a fixed metal sample potential; since the sample, having a relatively large surface area, is in practice grounded, and the instrumentation is constructed accordingly. As the figure indicates, the voltage of interest, *i.e.*, the sample-to-reference electrode voltage, is present by itself only about 6 msec of every 100 msec period. During the remainder of each period the polarization current flows through the solution, producing a variable voltage (IR drop) across the solution, which acts in series with the voltage of interest to produce the results shown in Fig. 3. The measurement scheme requires that the decay of the solution IR drop be complete (to within the acceptable error limit) before the voltage of interest has decayed significantly, as suggested in Fig. 4. Under these conditions, the voltage of interest may be monitored accurately during the 6 msec interruption period. No difficulty with respect to voltage decay has been encountered with the cell arrangement described. The relatively rapid IR voltage decay is achieved by maintaining sufficiently low cell-to-ground capacitance (except at sample surface), which includes the capacitance in wiring connected directly to the cell (except that of the grounded sample). The apparatus can accommodate somewhat greater IR decay times, which have been encountered in higher resistance cells.

Pulse Voltmeter: Design Considerations and Functional Description

The pulse voltmeter receives a fluctuating voltage such as those of Fig. 3. Its function is to determine the value of the voltage of interest regardless of the value of the solution IR drop voltage and to provide a nonpulsating output voltage which varies in accord with the former. The fluctuating voltage is biased as shown in Fig. 4 and presented to the voltmeter circuit, given in Fig. 5(b) and (c).

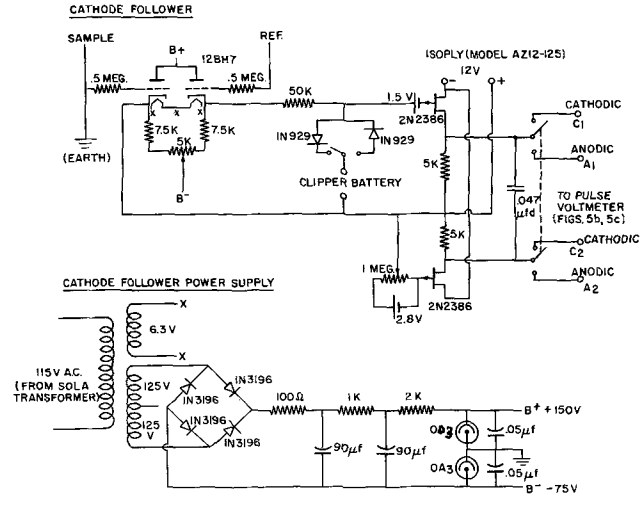

Fig. 5(a). Voltmeter circuit

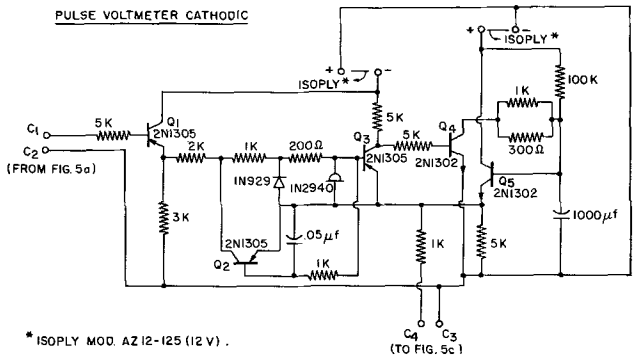

Fig. 5(b). Voltmeter circuit

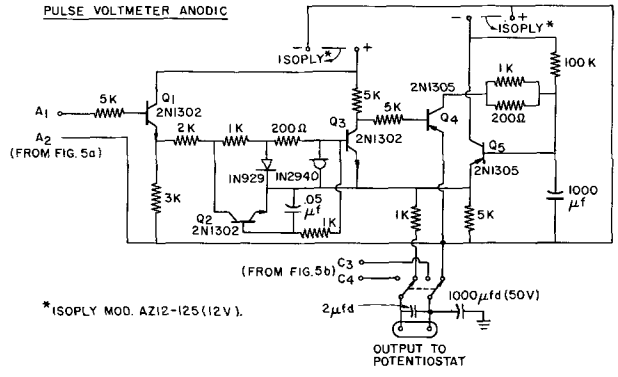

Fig. 5(c). Voltmeter circuit

Isolation and signal conditioning stages.—A vacuum tube cathode follower input stage [Fig. 5(a)] is employed to provide a high input resistance and minimum input capacitance, thus minimizing the amount of cell loading through the reference electrode. A balanced circuit design is used to avoid error due to changes in ambient temperature. Voltage excursions greater than 2v occur only when the irrelevant solution IR pulses are present and would impose design difficulties in succeeding circuitry. These excursions are therefore limited in the clipping circuit following the cathode follower. The amplitude-limited pulses are then transferred by a source follower impedance transformer to the pulse voltmeter proper.

Pulse voltmeter proper.—It has been found feasible to evaluate voltages such as those of Fig. 3 directly, without need of d-c amplification. Such a technique has been described in (1), in which a thyratron detector was employed. The present application differs from that of (1) in that voltmeter output leads which do not pulsate with respect to ground are desired for connection to succeeding potentiostat circuitry. The use of a readily inverted tunnel diode detector and choice of either npn or pnp transistors as needed permit design freedom not available in (1) and facilitate realization of the behavior desired.

Functionally, the voltmeter proper consists of (*i*) a voltage-triggered oscillator having a sharp threshold (stable within a 10 mv band), and (*ii*) a storage capacitor connected to a slow charging path and to a keyable, rapid discharge path controlled by the oscillator. These elements are shown functionally in Fig. 6. Individual cycles of the oscillator cause small decrements of charge in the capacitor. A stable loop is formed by connecting the capacitor back to an input terminal of the oscillator. With no voltage applied to input A, the capacitor will charge to the voltage threshold value of the oscillator, which will then produce pulses as needed to hold the capacitor voltage at that value. Since the circuit is so arranged that voltage inputs at A and B are additive, a small voltage applied to A reduces that needed at B to maintain the threshold voltage level. Thus the small voltage applied at A results in an equivalent decrease in voltage at the output terminal. Appropriate selection of charging rate (relatively slow) in relation to discharge rate (determined by oscillator frequency and discharge resistance) permits short pulses at A to function similarly to a steady voltage applied at that point. While the rates employed have been selected appropriately for the polarization system described, these rates are not critical values within the appropriate range. In Fig. 5 the voltage triggered oscillator circuit includes the components connected between the emitter of Q1 and the base of Q3. The discharge circuit consists of Q3 and Q4. Q1 and Q5 serve as impedance transformer emitter followers, and the storage capacitor and charging source components are evident. Two pulse voltmeter circuits are provided, one for cathodic and the other for anodic polarization conditions.

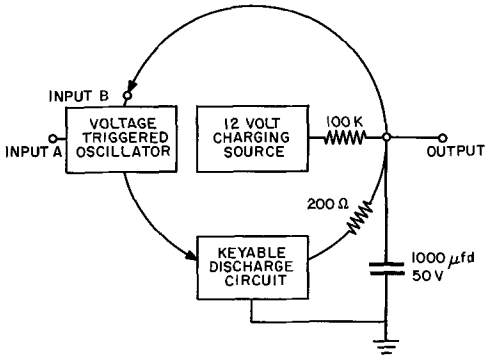

Fig. 6. Functional sketch of pulse voltmeter

Sensitivity and stability such as that of the tunnel diode discriminator make possible the foregoing method of polarization voltage measurement. The voltage sensitivity of this circuit is in the range of 1 mv, permitting realization of low over-all error in the range of 10 mv as specified above. Temperature stability of the IN2940A diode specified should be superior to that of the IN2940 actually used by the authors. Drift of voltmeter output voltage with the input shorted was observed to be less than 10 mv for periods of 10 days with laboratory air temperature variations of ±0.5°C.

Potentiostat

The potentiostat, indicated in Fig. 1(b), employs thyratron voltage discriminators which monitor the output voltage of the voltmeter. These tubes switch motor control circuits to adjust a potentiometer in the

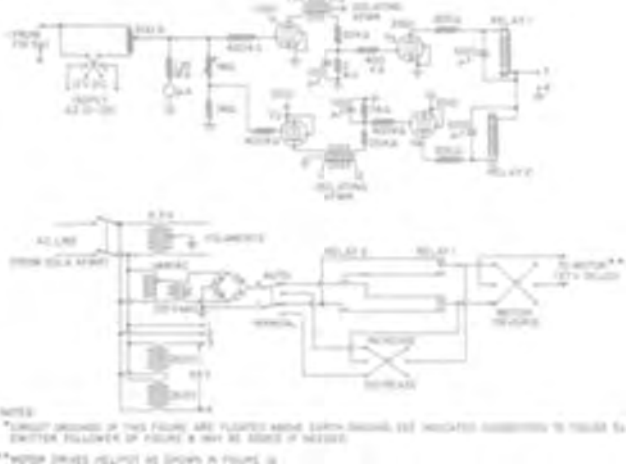

Fig. 7. Potentiostat

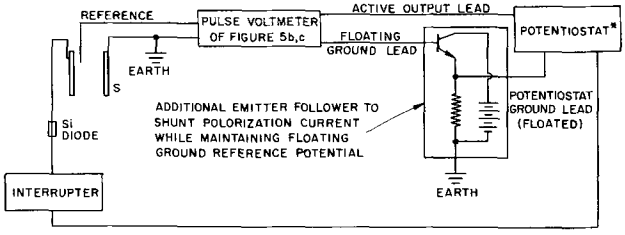

*FEEDBACK AMPLIFIER CONTROLLED POTENTIOSTAT AND FLOATING POWER SUPPLY

Fig. 8. Arrangement of feedback amplifier controlled potentiostat employed with interrupted polarizing current, illustrating grounding modifications.

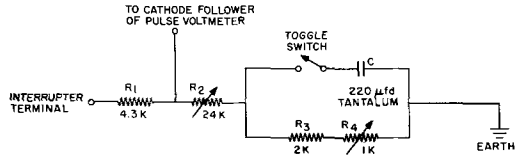

R_1 AND 2 REPRESENT CELL SOLUTION RESISTANCES: VALUES WERE DERIVED FROM OBSERVED IR DROPS IN CELL (R_2) AND GEOMETRICAL CONSIDERATIONS.

R_3 AND 4 REPRESENT CORROSION FILM RESISTANCE: VALUE RANGE WAS DERIVED FROM SLOPE OF SAMPLE POLARIZATION CURVE (REFS.1 AND 2).

C REPRESENTS THE CAPACITANCE BETWEEN SAMPLE METAL AND SOLUTION, WHERE THE INDUCED SAMPLE POLARIZATION IS INCLUDED AS A CAPACITIVE CHARGE EFFECT: VALUE WAS CHOSEN TO YIELD VOLTAGE DECAY RATE (DURING CURRENT INTERRUPTION) SIMILAR TO THAT OBSERVED IN CELL.

Fig. 9. Mock cell for apparatus tests

current supply as shown. The amount of current is thus changed to restore the desired electrode potential difference. A circuit diagram of the potentiostat presently used is given in Fig. 7. The apparatus may be made from components commonly found in the laboratory.

If an additional potentiostat unit of this type were to be constructed by the authors, tunnel diode sensing circuit and transistors might be substituted for the thyratrons and relays of the rather out-dated circuit given. Alternatively a feedback amplifier controlled potentiostat scheme appears applicable. An arrangement being evaluated is sketched in Fig. 8. As another alternative, commercially produced potentiostats are available and may be employed, since requirements to be met in this section are not unusual. (However, the known commercial units are comprised largely of circuits and components superfluous in this application.) Interested readers may contact the authors for current results of a continuing evaluation of alternative potentiostat schemes.

Operational Procedure

Initial adjustments.—Initial adjustments are made with the cathode follower disconnected from the cell and the measuring input shorted. Cathode follower balance and source follower bias controls are adjusted for zero voltage difference between the signal leads at the output of each of these stages. The input short is then removed and replaced by a d-c voltage source equal to the desired polarization potential. The source follower bias control is again adjusted to restore the stage output voltage to near zero: a value of 0.3v is preferred, negative for cathodic and positive for anodic polarizing conditions. The output voltage of the pulse voltmeter then assumes a steady value which is taken as the setpoint for potentiostatic control: the potentiostat bias is adjusted to stop the correcting motor under these conditions. (See below for minor correction to accommodate offset error during operation.) The cathode follower input is then disconnected from the known voltage source and connected to the cell. The control loop is closed by connection of the polarizing current lead to the cell, and the system is allowed to control the potential of interest. Manipulation of the motor speed and override controls of the potentiostat in initial minutes of the test facilitates prompt assumption of control at the desired potential by the automatic system. The manual adjustment period is minimized by presetting the current source, given some foreknowledge of the current value required.

Apparatus tests and maintenance.—An advantage of the control mode employed over the feedback amplifier mode arises from the infrequent need for automatic corrective action after a relatively steady polarization condition is reached. The control loop described may be opened for the purpose of brief apparatus checks merely by switching off the motor power: polarizing current remains at a steady value, and apparatus tests and adjustments may be accomplished without disturbing the cell conditions, with the measuring apparatus disconnected from the cell.

The bias values described above are checked periodically, since bias changes affect the control setpoint directly. Tests are made at intervals of several days and adjustments made if needed. Interrupter power supply batteries have been changed weekly: replacement schedules for bias cells have not been determined.

When a potentiostatic corrosion test is not in progress, operational tests are made conveniently with the mock cell shown in Fig. 9. Derivation of component values is explained in the figure. With the mock cell connected in place of the polarization cell and capacitor C in the circuit, the voltage across C should be maintained automatically at a setpoint established in the manner described above, regardless of gradual changes in R_2 and R_4 (Fig. 9). An offset error of the order of 10 mv is normally observed, which is rather independent of polarization current in the range of 10 μa to 1 ma, and thus may be allowed for in setpoint adjustment. Capacitor C may be switched out (and the system readjusted) to observe the offset error directly or to test operationally for interrupter leakage.

Acknowledgment

The equipment described is in use in a study of the aqueous corrosion of aluminum under potentiostatic conditions, being conducted by J. E. Draley and R. E. Loess of the Metallurgy Division.

This work was done under the auspices of the U. S. Atomic Energy Commission.

Manuscript received Dec. 12, 1966.

Any discussion of this paper will appear in a Discussion Section to be published in the December 1967 JOURNAL.

REFERENCES

1. J. E. Draley, W. E. Ruther, F. E. DeBoer, and C. A. Youngdahl, *This Journal*, **106**, 490 (1959).
2. J. E. Draley, F. E. DeBoer, and C. A. Youngdahl, *ibid.*, **108**, 622 (1961).
3. Ives and Janz, "Reference Electrodes, Theory and Practice," Academic Press, New York (1961).

Brief Communication

A Rapid Solid-Electrochemical Method for Studying High-Temperature Diffusion in Metals

Douglas O. Raleigh

North American Aviation Science Center, Thousand Oaks, California

A method involving the measurement of diffusion-limited currents in the solid-electrolyte cell Ag| AgBr| Au was used to determine the diffusion coefficient of silver in silver-gold alloys at 400°C. D values of order 10^{-14} cm^2/sec were measured at five points in the alloy composition range 10-60 a/o Ag in a single day's experiment with one metal sample. D values from duplicate runs on a gold single crystal agreed to an average of 3% and matched results on a polycrystalline gold foil to an average of 12%. By contrast, standard metallurgical techniques involving radiotracers and sectioning generally cannot be extended below $D \sim 10^{-11}$ cm^2/sec and require several weeks of annealing as well as precise sectioning techniques.

In a previous publication (1), results were reported on measurements of the double layer capacitance of the solid electrolyte AgBr against Pt and Au electrodes. The method involved the use of so-called solid state polarization cells, which have the general configuration

reversible electrode| solid electrolyte| inert electrode

and of which the cell Ag| AgBr| Au is an example. These cells have the property that if a potential of suitable polarity (negative at the Ag electrode in the present case) and small compared to the electrolyte decomposition potential is applied, there can be no steady-state ionic cell current. Under these conditions, the inert electrode interface functions to first order as a capacitative interface and, for the present cell, a steady-state silver activity $a_{Ag} = \exp(-\epsilon\mathbf{F}/RT)$ is electrochemically defined at this interface. Here, ϵ is the applied cell voltage, and $\mathbf{F}$ is Faraday's constant. In the previous work, potential steps were applied to similar cells and the transient cell current used to determine the double layer capacitance. In the case of Pt inert electrodes, the transient cell current could be unambiguously assigned to double-layer recharging (1, 2), but effects were reported for Au electrodes that involved the diffusion of metallic silver into the electrode at surface activity a_{Ag}. The purpose of the present study was to ascertain whether such effects could be used to determine the diffusion coefficient of Ag in Au and whether a general method for studying diffusion in metal systems might be involved.

Solid-electrolyte cells have been used previously for the study of rate processes at elevated temperatures (3), most recently by Rickert (4) in measuring the diffusion of oxygen in silver at 760°-900°. General application of these methods to metal diffusion, however, (in particular to small D values) requires knowledge of the relative roles of double layer charging and low-level electronic currents in the electrolyte. In the present cell, applying a voltage E establishes activity a_{Ag} on the time scale of the AgBr| Au double layer charging. For the Au electrode, it is believed that this activity is manifested as a partial monolayer of electrodeposited silver (1, 2). If Ag diffuses from the electrode surface to the interior, activity a_{Ag} is maintained by the electrodeposition of more Ag on the surface, a process involving the migration of Ag^+ ions in the electrolyte and the electrons in the external circuit. Since each Ag atom diffusing into the electrode is thus replaced, the diffusion flux is measured exactly by the cell current. This "diffusion current" persists until the kinetics of the diffusion process become negligible. At this point, the Au electrode has the characteristics of an Au-Ag alloy of activity a_{Ag}.

If the applied voltage is now changed to E', a new silver activity a'_{Ag} is established at the Au surface, and diffusion occurs until the Au electrode is re-equilibrated at a'_{Ag}. The situation is analogous to placing an infinite reservoir of silver at activity a'_{Ag} on the surface of an Ag alloy of silver activity a_{Ag}. If C_0 and C_1 are the atomic silver concentrations corresponding to a_{Ag} and a'_{Ag}, the diffusion current will be given by the well-known Cottrell equation

$$i = \mathbf{F}A(C_1 - C_0)(D/\pi t)^{1/2}$$

where A is the electrode area. Use of the current-time data and known activity-composition data (5, 6) for the Ag-Au system to determine D values depends on whether the diffusion current (which decays as $t^{-1/2}$) is still large enough to be seen against the low-level electronic cell current (7) when the double-layer charging process is completed.

In the experimental arrangement, a single-crystal pellet of AgBr, prepared as previously described (8), was springloaded between a square of Ag foil and a planar gold electrode. The latter was a polycrystalline foil in run 1 and a gold single crystal pellet in runs 2 and 3. In runs 1 and 2, a silver wire was embedded in the periphery of the AgBr pellet, about midway between the main electrodes, to serve as a reference electrode. Because of the short diffusion lengths involved ($\sqrt{Dt}$), it was important to have a smooth gold surface for A in the Cottrell equation to correspond to the geometric electrode area. Electropolishing in fused 1:1 NaCl-KCl at 750° gave a specular surface on which electron micrographs showed no significant roughness down to 500Å. The assembled cell was outgassed and heated under vacuum to the neighborhood of the AgBr melting point (425°) with an applied potential (231 mv) corresponding to 10 a/o Ag at the Au interface at 400°. Interface contact was achieved either by flash-melting the electrolyte in the neighborhood of the electrodes (runs 1, 3) or prolonged annealing under pressure just below the melting point (run 2). The cell was then cooled to 400°, placed under an argon flow, and about an hour allowed for equilibration.

Five successive voltage steps were applied at about 75-min intervals, each corresponding to a 10 a/o increase in the Ag concentration at the Au electrode surface. In runs 1 and 2, the cell voltage and voltage steps were applied with an electronic potentiostat (1,2), using a voltage follower in the feedback from the reference electrode. This arrangement, however,

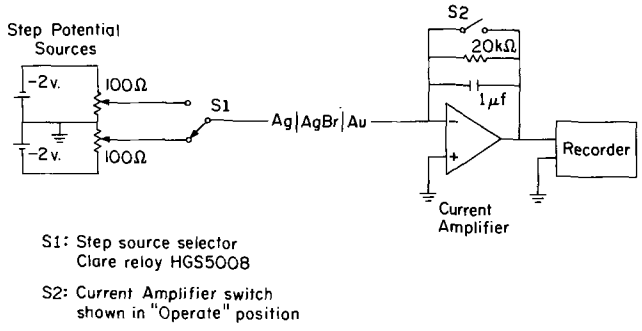

Fig. 1. Circuitry diagram for run 3

was found unnecessary because of negligible polarization at the Ag electrode and negligible iR drop in the electrolyte during the diffusion measurements. In consequence, the voltages in run 3 were applied directly via two battery-voltage divider setups and the use of a mercury relay to switch the cell between them. A low-impedance current-recording device was afforded by the use of a Philbrick SP656 operational amplifier in conjunction with a Moseley X-Y recorder. Figure 1 shows the arrangement for run 3.

Current-time data were recorded continuously for about 300 sec after voltage step application and intermittently till the application of the following step. Initial peak currents $\sim$ 100 μa were obtained which fell gradually to the approximate level of the steady-state electronic current (several μa). Following data acquisition from the last voltage step in run 1, the cell was cooled to room temperature at the existing voltage (55 mv, corresponding to 60 a/o Ag at 400°) and dismantled. The Au electrode had a uniform silvery appearance where it had contacted the electrolyte. In run 2, the cell voltage was returned to 231 mv after the last voltage step, the cell allowed to equilibrate, and then cooled under bias and dismantled. In this case, the electrode interface had a gold appearance. In all runs, the electrolyte was found to be bonded tenaciously to both electrodes. For run 3, the Au single crystal from run 2 was cleaned of any adherent AgBr in hot concentrated HBr, rinsed, dried, and reassembled into a new cell.

In all cases, plots of cell current *vs.* $t^{-1/2}$ were extremely linear in the range 10-100 sec after step application and showed only minor variations from linearity (0.1-0.3 μa) at times out to 4500 sec (75 min). The Y-intercept ($t = \infty$) gave values of the constant electronic current whose magnitude and cell voltage dependence were in excellent agreement with theory (9) and previous experiment (7). At times below 10 sec, the current showed an upturn from linearity attributable to residual double layer recharging, in accord with previous studies (1, 2). The slopes of the plots in the 10-100 sec range were used, together with the activity-composition data of Wachter (5) and Kubaschewski (6) for the Ag-Au system at 400°, to calculate D values. Results are shown in Fig. 2. Since the voltage steps represent jumps from one composition to another, the D values are arbitrarily plotted at the median compositions.

A further experimental point should be mentioned. The use of successive voltage steps to determine D values across the composition range assumes that, in the time between successive steps, diffusion has proceeded sufficiently to result in an essentially uniform composition over the diffusion distance represented by the 10-100 sec data range (~30-100Å). This assumption was tested in one instance by repeating a voltage step after an overnight wait at the initial potential. The resultant current slope agreed to several per cent.

Slifkin *et al.* (10) have measured the self-diffusion coefficient of Ag in a number of Ag-Au alloy compositions at 635°-1010° by standard metallurgical techniques and derived empirical expressions for its temperature dependence. For comparison with our results, self-diffusion coefficients at 400° were calculated from these expressions, plotted as a function of composition, and interpolated values at our compositions taken from a best smooth curve through the points. The Darken equation (11) was then used with available thermodynamic data (5, 6) to calculate the corresponding chemical diffusion coefficients for comparison with our D values. The results are plotted on Fig. 2. Agreement ranges from good to remarkable, considering the inherent uncertainties in such a comparison and in D values in general.

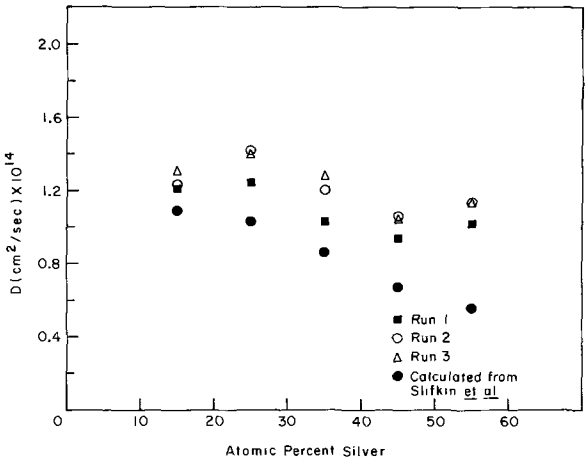

Fig. 2. Diffusion coefficient of Ag in Au-Ag alloys of various compositions at 400°.

It is felt that the present method may have wide applicability. A solid electrolyte cell Me| MeX| M′ may be used as a source of fixed and controllable activity of metal Me at the M′ surface to study diffusion over a wide range of alloy composition. It is required that metal M′ be more noble than Me to avoid side reaction with the electrolyte. Application to other solid-electrolyte systems (*e.g.*, Cu| CuI, Pb| $PbCl_2$) will require investigation of their electrochemical properties, which it is hoped this work will stimulate. Further results on the present system will be reported shortly (12) and in a future publication.

Acknowledgment

The author is greatly indebted to Mr. Harry Crowe for considerable assistance in all phases of the experimental work.

Manuscript received Jan. 23, 1967. This paper was presented at the Dallas Meeting, May 7-12, 1967.

Any discussion of this paper will appear in a Discussion Section to be published in the December 1967 JOURNAL.

REFERENCES

1. D. O. Raleigh, *J. Phys. Chem.*, **70**, 689 (1966).
2. D. O. Raleigh, *J. Phys. Chem.*, May 1967.
3. D. O. Raleigh, "Progress in Solid State Chemistry," Vol. 3, Ch. 3, H. Reiss, Editor, Pergamon Press, Oxford (1967).
4. H. Rickert and R. Steiner, *Z. Physik. Chem. N.F.*, **49**, 127 (1966).
5. A. Wachter, *J. Am. Chem. Soc.*, **54**, 4609 (1932).
6. O. Kubaschewski and O. Huchler, *Z. Elektrochem.*, **52**, 170 (1948).
7. B. Ilschner, *J. Chem. Phys.*, **28**, 1109 (1958).
8. D. O. Raleigh, *J. Phys. Chem. Solids*, **26**, 329 (1965).
9. C. Wagner, *Proc. Int. Comm. Electrochem. Thermo. Kinetics (CITCE)*, **7**, 361 (1957); *Z. Elektrochem.*, **60**, 4 (1956).
10. W. C. Mallard, A. B. Gardner, R. F. Bass, and L. M. Slifkin, *Phys. Rev.*, **129**, 617 (1963).
11. See, for instance, P. G. Shewmon, "Diffusion in Solids," pp. 125-127, McGraw-Hill Book Co., New York (1963).
12. D. O. Raleigh, Paper presented at the Dallas Meeting, May 7-12, 1967.

SOLID STATE SCIENCE

Kinetics of Tantalum Corrosion in Aqueous Electrolytes, II

K. Lehovec and John D'Amico[1]

Research and Development Laboratories, Sprague Electric Company, North Adams, Massachusetts

ABSTRACT

Transients of the voltage between a tantalum foil and an aqueous electrolyte have been induced by application of d-c current or else a-c voltage steps during the growth of a thin protective oxide film. These transients were analyzed in terms of the dependences on voltage and oxide thickness of (*a*) the ionic current causing the oxide growth and (b) the current required for charge neutralization. Certain discrepancies between the theoretical model used to analyze the transients and the experimental data indicate a more complex behavior of the oxide than that of an ideal capacitor shunted by a voltage dependent resistor responding instantaneously to changes in the voltage.

In a previous paper (1) the spontaneous corrosion of tantalum in aqueous electrolytes was investigated by measuring capacitance and voltage changes *in situ*. This paper attempts to clarify the mechanism of oxide growth.

The growth of a protective oxide film involves two processes; (*i*) a transport through the oxide film of the ions which participate in film growth, and (*ii*) a current flow which neutralizes the charge transported by these ions. Usually this neutralizing current is carried by electrons and/or holes, although it is conceivable that other carriers such as protons can be involved in special cases. However, for the sake of brevity, we shall refer to the two currents mentioned under (*i*) and (*ii*) as the ionic and the electronic currents, I_I and I_E. A more precise description would be "the ionic current leading to film growth" for I_I and "the current through the oxide causing charge neutralization, but not oxide growth" for I_E.

The rate of oxide film growth can be derived assuming a simple mechanism for one of the two currents, I_I or I_E, as the rate-determining factor for corrosion resulting in a continuous film of the reaction product. For instance, diffusion of ions involved in film growth leads to parabolic corrosion kinetics (2). In the case of the protective oxide films formed on Al and Ta in air, tunneling of electrons through the film providing charge neutralization (3), or else injection of ions from the metal interface by a high field mechanism (4), have been postulated as the rate-determining processes. The latter mechanism (4) (Mott-Cabrera theory) has found wide acceptance in the literature. However, in the case of air oxidation of tantalum at or near room temperature, discrepancies with the Mott-Cabrera theory (4) have been observed (5).

In the case of anodic oxidation of tantalum and aluminum both anions and cations contribute simultaneously to the ionic current I_I (6-8). Moreover, the ionic transport may conceivably proceed in several charged states, such as OH^- and O^{--}. There are possible contributions to I_E by electron transport, hole transport, and even by transport of H^+ ions (9-11). For a given species such as electrons, there may be several competing transport mechanisms, *e.g.*, diffusion and field driven current flow in the bulk of the oxide, tunneling through the entire oxide, and thermionic emission across barriers at the boundaries of the oxide, or even across the entire oxide. Interaction of various charge carrying species may occur. Space charges may lead to a significantly nonlinear voltage distribution. The structure and dielectric properties of the oxide in close proximity to the metal substrate may conceivably differ from those of the bulk of macroscopically thick anodic oxide films. Image force potentials extend through most, if not all, of the oxide films encountered in spontaneous corrosion of Al and Ta in air, and the discrete nature of charges at the outer oxide surface leads to large field variations in the oxide along the metal-oxide interface. Last, but not least, the oxide growth may be governed by charge transport at certain structural faults (12-16), particularly, when means for lateral charge transport along the outer oxide surface exist, as in the case of corrosion in an electrolyte.

In view of all these actual or potential complications, it would be rather remarkable if a single mechanism based on a simple concept should be able to account for the formation of protective oxide films on tantalum and aluminum.

The corrosion of tantalum in aqueous electrolytes appears to be particularly well suited to investigate the mechanism of the formation of a protective film, since (*i*) no tantalum is dissolved in the electrolyte and (*ii*) the presence of a conducting outer phase (the electrolyte) enables continuous measurements of the potential across the oxide and of the oxide thickness by means of the oxide capacitance. The transformation of the measured capacitance into the oxide thickness utilizes the plate capacitance formula and thus involves surface area and dielectric constant of the oxide. Significant contributions to the capacitance from electrolyte space charge layers can be avoided by using highly conducting electrolytes and measuring at sufficiently low frequencies. Potential errors in determining oxide thickness, *d*, from capacitance measurements have been discussed in ref. (1).

[1] Present address: Rensselaer Polytechnic Institute, Troy, New York.

The growth rate of the oxide film is determined by the requirement of quasi-charge neutrality[2] (Kirchhoff's law)

$$I_E = I_I + I \quad [1]$$

in conjunction with Faraday's law

$$\partial d/\partial t = \lambda I_I \quad [2]$$

In Eq. [1] we have included the more general case that an external d-c current, I, is permitted to flow. The numerical value for the coefficient λ in Eq. [2] is the same as used in ref. (1).

From the measured capacitance as a function of time, t, the oxide thickness, d, has been derived by the plate-capacitor equation and the ionic current was obtained from Faraday's law [2]. Using Kirchhoff's law [1] the electronic current was then derived. However, since both oxide thickness and voltage change with time simultaneously, experimental methods must be devised to determine the relation between I_I and I_E and V and d. Over a small range of oxide thickness, d, and oxide voltage, V, the dependencies of the ionic and electronic current on d and V can be characterized by the four coefficients

$$\alpha_E = \partial \ln I_E/\partial V]_d \quad [3]$$

$$\alpha_I = \partial \ln I_I/\partial V]_d \quad [4]$$

$$\beta_E = \partial \ln I_E/\partial d]_V \quad [5]$$

and

$$\beta_I = \partial \ln I_I/\partial d]_V \quad [6]$$

of a Taylor series of ln I_E and ln I_I. These coefficients have been defined in terms of the logarithms of currents rather than currents proper in view of the nearly exponential dependencies of these currents on voltage [constant Tafel slope]. Thus α_E and α_I are the Tafel slopes of the ionic and electronic currents.

This paper deals with experimental methods to derive these coefficients and a comparison of the results with theoretical values expected for various simple charge transfer mechanisms through the oxide.

Experimental Methods

Sample preparation, test cell and measurement circuit were the same as described in (1) and shown in its Fig. 1 and 2. In order to determine the voltage and thickness relations for the currents I_I and I_E, an external electrical signal was applied to the oxide and its effect on the d-c voltage, and on the growth rate was measured. Two techniques have been used, the "d-c method" and "transient method."

D-C method.—After spontaneous corrosion had proceeded for a certain time, a series of cathodic d-c current pulses was passed through the sample as shown in the lower curve of Fig. 1. The d-c voltage and equivalent series capacitance of the cell responded as shown in the upper and middle portions of the figure. The following effects can be noted: Following the stepwise change of the cathodic current, there is a transition to a new quasi-stationary level of voltage and capacitance. This transition will be analyzed in more detail in Fig. 2. At present we are interested in the shift of d-c potential marked ΔV in Fig. 1 and in the quasi-stationary rates of capacitance change before and after the change of cathodic current. The ionic current can be derived from the quasi-stationary rate of capacitance change with time by combining the plate capacitance equation with Faraday's law leading to the relation given in Fig. 1. In this manner the relation $I_I(V)$ is obtained. The relation $I_E(V)$ is then obtained by Kirchhoff's law (1). During the sequence of small cathodic currents the oxide thickness continues to increase. In order to obtain the relations $I_I(V)$ and $I_E(V)$ at a constant oxide thickness, a correction for the change in oxide thickness is required. This correction will be discussed in Appendix D, using the relations developed in the Appendices A and B.

A drawback of the d-c method is the fact that the corrections to constant thickness (Appendix D) require certain parameters, which have to be taken from the open-circuit corrosion data of the preceding period. In some cases these parameters vary fairly rapidly with oxide thickness so that the values used for the correction may become ill-defined.

For large cathodic currents one has $I >> I_I$, and, therefore, $I \simeq I_E$, so that the cathodic current voltage relation $I(V)$ provides directly the electronic current relation $I_E(V)$. Thus, in order to derive $I_E(V)$, no significant time interval of the quasi-stationary state is required since I_I is not needed. Thickness corrections become unimportant. However, at these large cathodic current densities, hysteresis phenomena may be encountered. It is impractical to wait until the "hysteresis" has fully decayed after a current switch since this would necessitate a significant correction to constant thickness.

The difficulties arising from "hysteresis" and from the correction for constant oxide thickness led us to favor the a-c method to be described in the next section, which rapidly alternates small cathodic and anodic bias voltage so that no d-c current results.

Transient method.—This method utilizes the voltage transient following a stepwise change in an external signal, such as d-c current I (Fig. 1) or else a small applied a-c voltage in the audio-frequency range (Fig. 2). A transient is characterized by its time constant, τ, and the voltage increment ΔV, which were determined as follows (Fig. 2): The linear voltage-time relationship following the transient was extrapolated through the transition period and formed the

[2] It will be shown in Appendix E that charge neutrality, while not exactly satisfied, is a very good approximation.

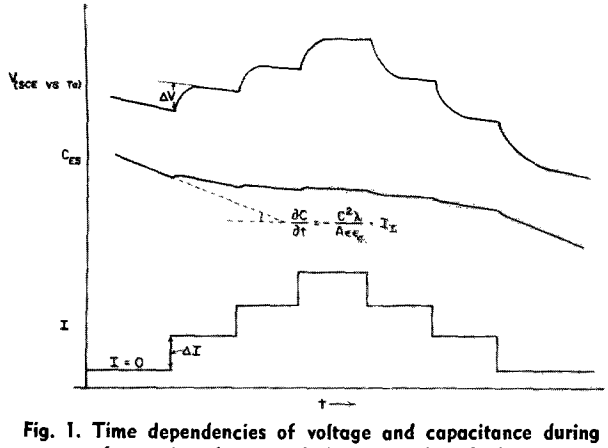

Fig. 1. Time dependencies of voltage and capacitance during a sequence of stepwise changes of the external cathodic current, I.

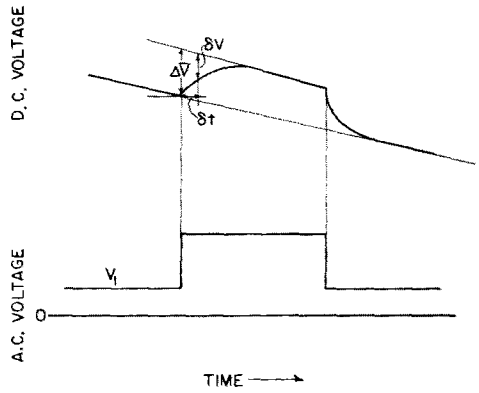

Fig. 2. Transients of d-c voltage ΔV following a stepwise change in the a-c voltage amplitude V_1.

base line for determination of voltage increments δV. A semilogarithmic representation of voltage increment *vs.* time increment δt since the switch of the external signal gave a straight line, provided that the changes of a-c voltage amplitude (in the case of Fig. 2) or else of external current ΔI (Fig. 1) were sufficiently small. From the slope of these plots τ was obtained and extrapolation to $\delta t = 0$ gave ΔV.

From the time constant τ and the oxide capacitance[3] an equivalent parallel resistance can be calculated by means of

$$R_\tau = \frac{\tau}{2\,C_{ES}} \qquad [7]$$

The factor 2 is added because the cell capacitance lies parallel to the capacitance C_{ES} of the symmetric branch of the bridge circuit.

In the case of the voltage transient induced by the change in the electrical current, ΔI, a "d-c incremental resistance" can be defined by

$$\overline{R} = \Delta V/\Delta I \qquad [8]$$

The experimental data used for the theoretical analysis of the growth mechanism in terms of ionic and electronic currents, I_I and I_E, were: (*i*) the change of quasi-stationary d-c potential, ΔV, before and after the transient, respectively; (*ii*) the time constant, τ, of the transient; (*iii*) the incremental field during quasi-stationary growth periods

$$F_i = -\partial V/\partial d \qquad [9]$$

and (*iv*) the "attenuation length" l, of the growth rate, defined by

$$l = -\frac{\partial d}{\partial \ln[\partial d/\partial t]} \qquad [10]$$

The "oxide thickness" d is determined by the plate capacitance equation from the equivalent series capacitance of the cell which was monitored continuously by means of an a-c signal of about $V_1 = 9$ mv amplitude and 100 Hz frequency. During the transient studies the amplitude was raised temporarily to about 30 mv as shown on bottom of Fig. 2.

In order to obtain a unique correlation between α_E, α_I, β_E, and β_I and the four experimental parameters ΔV, τ, F_i and l, we assumed that I_E and I_I are instantaneous functions of voltage V and oxide thickness, d. As will be shown in the Appendices A and B, this assumption leads to the relations given in Table I for the case of sufficiently small amplitudes of the a-c voltage V_1. Actually the value V_1^2 listed in Table I should be replaced by ΔV_1^2 *i.e.*, the value of V_1^2 during the increased a-c amplitude minus the value of V_1^2 which was continuously applied at the oxide film. In order to simplify notation, the analysis of Appendix A and B assumes that no a-c signal is applied except when inducing a transient.

[3] It is shown in ref. (1) that the oxide capacitance can be approximated by the equivalent series capacitance of the cell, C_{ES}, at 100 Hz in high-conductivity electrolytes.

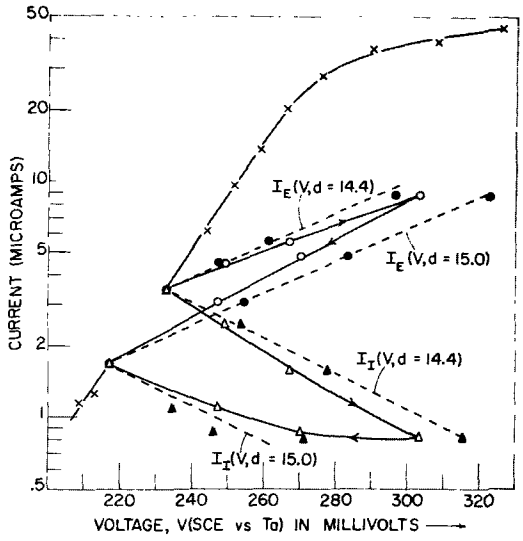

Fig. 3. Ionic and electronic currents as functions of the voltage, SCE vs. Ta, (a) during spontaneous corrosion, $I°_I = I°_E$, points marked by x; and (b) during a sequence of cathodic currents I = 2, 4, 8, 4 and 2 microamps; ionic currents uncorrected (△) and corrected (▲) to constant thickness; electronic currents uncorrected (O) and corrected (●) to constant thickness.

Appendix C contains the analysis of the d-c voltage transient induced by a large change in a-c amplitude V_1.

Experimental Results

D-C analysis.—Figure 3 shows an example of the voltage dependences of the ionic and electronic currents as obtained by the d-c analysis. The points marked by x are the open-circuit growth rates, converted into ionic currents by Eq. [2] and plotted *vs.* the open-circuit voltage. When the oxide thickness reached the value $d = 14.4$Å, a series of cathodic currents, $I = 2$, 4, 8, 4 and 2, μa, was passed through the sample. The voltages at the end of each constant current period, and the corresponding growth rates transferred into I_I, are marked by open triangles. The electronic currents marked by circles were obtained by Kirchhoff's law [1] from these I_I-values and the external currents. The curve connecting the ionic currents and that connecting the electronic currents do not retrace for ascending and descending external currents due to the change of oxide thickness during the sequences of cathodic currents. Corrections to "constant oxide thickness" have been made by shifting the voltage for each current point in accordance with Eq. [2] of Appendix D. The points for ascending cathodic currents have been corrected to the initial thickness, $d = 14.4$Å, and those for descending cathodic currents to the final thickness, $d = 15.0$Å. The points at the largest applied current, $I = 8.0$ μa; for which $V = 305$ mv, $I_I \simeq 0.8$ μa, and $I_E = 8.8$ μa, thus appear twice

Table I. Expressions for α_I, α_E, β_I, and β_E in the special cases: $I = 0$ (spontaneous corrosion); $I \simeq -I_I°$ (large anodic currents) and $I_I° \simeq 0$ (large cathodic currents)

Coefficient	$I = 0$	$I \simeq -I°_I$	$I°_I \sim 0$
α_I	$-\frac{C_{ES}}{I_I°\tau} - 2\frac{\Delta V}{V_1^2}$	$\frac{2\,C_{ES}}{I\tau} = -\frac{4\,\Delta V}{V_1^2}$	—
α_E	$\frac{C_{ES}}{I_I°\tau} - 2\frac{\Delta V}{V_1^2}$	—	$\frac{2\,C_{ES}}{I\tau} = -\frac{4\,\Delta V}{V_1^2}$
β_I	$-\left(\frac{C_{ES}}{I_I°\tau} + 2\frac{\Delta V}{V_1^2}\right) F_i - l^{-1}$	$\frac{2\,C_{ES}}{I\tau} F_i = -\frac{4\,\Delta V}{V_1^2} F_i$	—
β_E	$\left(\frac{C_{ES}}{I_I°\tau} - 2\frac{\Delta V}{V_1^2}\right) F_i - l^{-1}$	—	—

each after the correction, once on the curve for $d = 14.4$Å and once on the curve for $d = 15.0$Å.

The correction to constant thickness requires the slopes α_I and α_E of the corrected curves, as well as F_i, l, and d for each measured point. It is easy to find self-consistent values of α_I and α_E since the slopes of the corrected curves do not differ greatly from those of the uncorrected curves. Values for F_i and l were obtained by extrapolation of graphs using the open-circuit corrosion data prior to $d = 14.4$Å.

The corrected points $I_E(V, d = 14.4\text{Å})$, $I_E(V, d = 15.0\text{Å})$ and $I_I(V, d = 14.4\text{Å})$ fall on straight lines. However, the corrected points $I_I(V, d = 15.0\text{Å})$ deviate considerably from the straight line drawn with a slope equal to that of $I_I(V, d = 14.4\text{Å})$. This deviation which will be termed here "hysteresis" is an after effect of the passage of large d-c currents and relaxes substantially slower than the time constants τ usually observed for a voltage change following a stepwise change of current.

The slopes of the dotted lines in Fig. 2 provide $\alpha_I = -17.4$ v^{-1} and $\alpha_E = 16.4$ v^{-1}; and the vertical displacements of the dotted lines in combination with the thickness increment $\Delta d = 0.6$Å provide $\beta_I = 2.6$Å^{-1} and $\beta_E = -0.73$Å^{-1}. By drawing the two dotted lines for I_I parallel to each other, and also those for I_E, we have ignored a possible dependence of α_I and α_E on d. The accuracy of the d-c analysis is affected adversely by hysteresis phenomena and assumptions on F_i and l which enter the correction to constant thickness and this prevents us from obtaining the dependences of α_I and α_E on d for small increments of d.

Coinciding curves I_E (V) for different d-values were found for some samples. Furthermore, in these cases these curves coincided also with spontaneous corrosion data, $I^o_E \simeq I^o_I$ *vs.* V. This indicates that in these samples the electronic current depends only on voltage, but not on thickness; *i.e.*, that $\beta_E \simeq 0$. Such behavior is expected if charge neutralization occurs at a fault which is not blocked by the oxide growth.

Figure 3 shows that I_I and I_E depend exponentially on the voltage, V. This suggests to define α_I and α_E as derivatives of the logarithm of currents. The coefficients α_I and α_E are thus related to the anodic and cathodic transfer coefficients.

The exponential dependences of I_I and I_E on voltage are used in the analysis of the voltage transient in Appendix A.

Transient analysis—spontaneous corrosion.—Table II lists values of $\overline{R}$ and R_τ for the cathodic current steps mentioned in the caption of Fig. 3. Note that R_τ is slightly, but consistently larger than $\overline{R}$. Values of $\overline{R}$ calculated by Eq. [5] of Appendix A with α_I, α_E, I_I, and I_E from Fig. 3 are given in the last column of the table. The increase of $\overline{R}$ for descending current steps relative to that for ascending current steps arises not only from the increase in oxide thickness which has taken place, but is affected also by the hysteresis phenomenon mentioned previously.

Figure 4 shows a typical dependence of the d-c voltage change $\overline{V} - V_O = \Delta\overline{V}$ on the a-c voltage amplitude V_1. The relation between $\overline{V} - V$ and V_1 is

Table II. D-C and a-c resistances, $\overline{R}$ and $R\tau$, as function of the cathodic currents for the data of Fig. 2. Also listed is $\overline{R} = (\alpha_E I_E - \alpha_I I_I)^{-1}$ according to Eq. [A-5] with I_E, I_I, and α_I, and α_E from Fig. 2

I, μa from	to	$\overline{R}$, kilohms	$\overline{R}_\tau$, kilohms	$(\alpha_E I_E - \alpha_I I_I)^{-1}$, kilohms
0	2	9.4	10.7	8.5
2	4	10.6	11.4	8.5
4	8	10.3	10.5	7.3
8	4	10.3	11.9	8.4
4	2	15.0	16.5	12.4
2	0	16.8	18.2	15.8

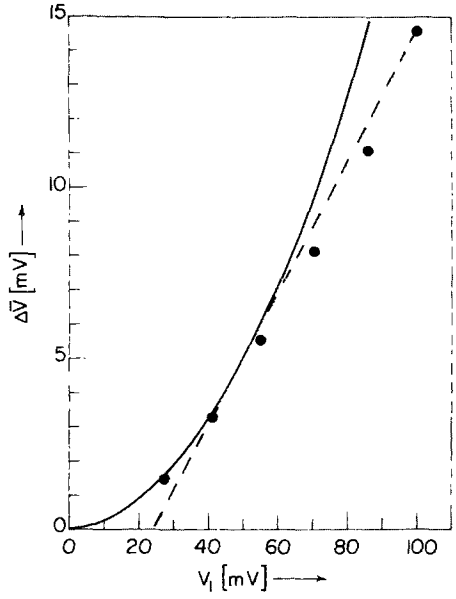

Fig. 4. D-C voltage change as function of a-c voltage amplitude. Full line Eq. (15) of Appendix A and dotted line Eq. (5) of Appendix C, using $\alpha_I = -25$ V^{-1} and $\alpha_E = 17$V^{-1}.

quadratic for sufficiently small a-c voltages and becomes linear for large a-c voltages. The quadratic range and the linear range have been fitted by the theoretical expressions Eq. [15] of Appendix A and Eq. [5] of Appendix C with $\alpha_I = -25$ v^{-1} and $\alpha_E = +17$ v^{-1}, and I = 0. Since α_I and α_E depend on oxide thickness, these values cannot be compared immediately with those of Fig. 3.

It may seem that a better fitting linear approximation could be achieved by a different selection of α_I and α_E. However, Eq. [5] of Appendix C defines not only the slope of the linear relation, but also the point of intersection. In addition, the coefficient of the quadratic approximation of Eq. [15] Appendix A must match the experimental data. Thus, we have three experimental data to be fitted by the choice of two constants α_E and α_I.

Figure 5 shows the ratio $(\overline{V} - V_o)/V_1^2$ of the quadratic range (small V_1) as function of the oxide thickness during open-circuit corrosion for three aqueous electrolytes of widely varying pH-values, namely, sulfuric acid of pH $\simeq$ 1, a highly concentrated (3.44 w/o) NaCl-solution of pH $\simeq$ 7 and a NaOH-electrolyte of pH $\simeq$ 13.5. Figure 5 shows a minimum at 13.5Å in sulfuric acid electrolyte and at 16Å in sodium chloride electrolyte. Figure 6 shows time constants, τ, as function of the oxide thickness, d, for the same runs as used in the previous figures: τ increases with oxide thickness except at thicknesses $d \lesssim 9$Å in sulfuric acid.

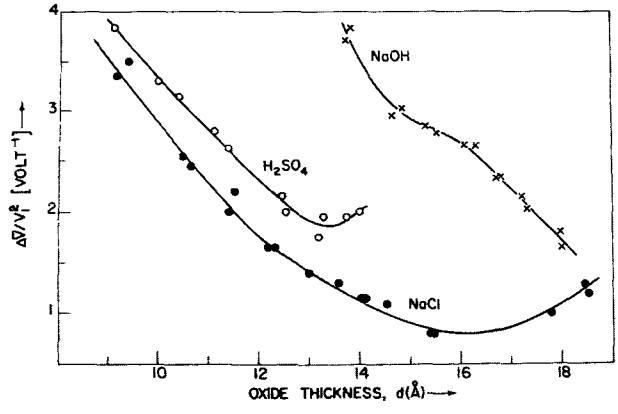

Fig. 5. $\Delta\overline{V}/V^2_1$ vs. d during spontaneous corrosion

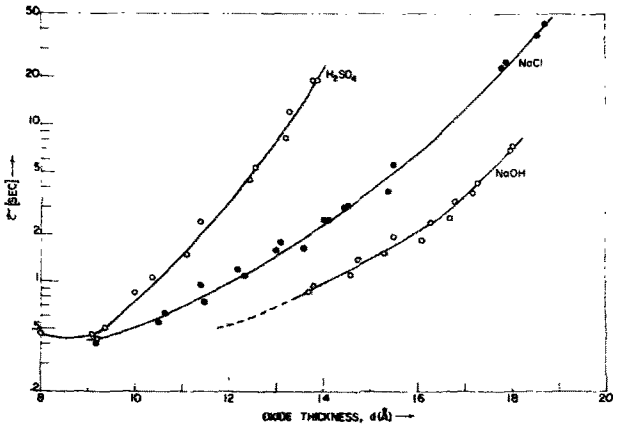

Fig. 6. τ vs. d during spontaneous corrosion

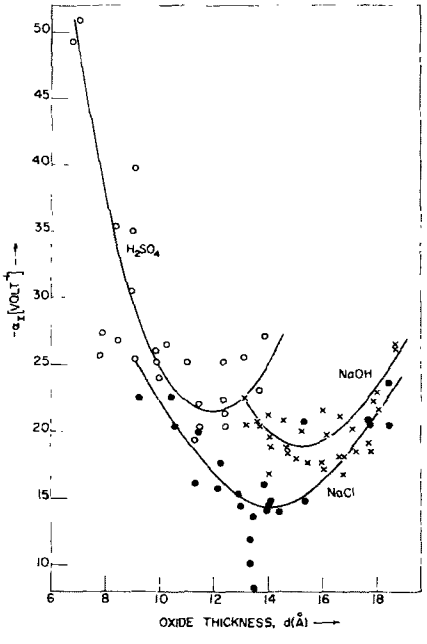

Fig. 7. α_I vs. d during spontaneous corrosion

The lateral displacement of the curves for the three electrolytes in Fig. 5 and 6 is in agreement with the changes in apparent thickness as measured in different electrolytes for the same oxide film (1). Values of F_i and l can be derived from the figures given in ref. (1) and, therefore, will not be presented here.

The values of $(\overline{V}-V_o)/V_1^2$ and $C_{ES}/(I_1^o\tau)$ can be combined with data of F_i and l to obtain the α's and β's by the equations listed in Table I. I_1^o was derived by Faraday's law, Eq. [2], from the growth rate. The steep dependence of τ on d shown in Fig. 6 is partly compensated by that of I_1^o on d in the product $I_1^o\tau$.

The coefficients α_I (Fig. 7) and β_I (Fig. 8) are obtained by addition of terms of equal sign (Table I); on the other hand, α_E (Fig. 9) and β_E (Fig. 10) are obtained by subtraction so that the resulting value can be quite inaccurate if each term is much larger than their difference. This applies particularly to β_E. Points in the Fig. 7-10 for the same electrolyte include results from several different samples and runs, which in part, accounts for the wide scatter of the points. Reproducibility of the α's and β's of a sample in the same electrolyte (NaOH) was good in four identical runs performed.

The dominant term for α_I, α_E and β_I is $C_{ES}/\tau I_1^o$ which accounts for the similar trend of these coefficients with d. The coefficient β_E (Fig. 10) is generally negative except at very small thicknesses in sulfuric acid where positive values appear. However, these positive values

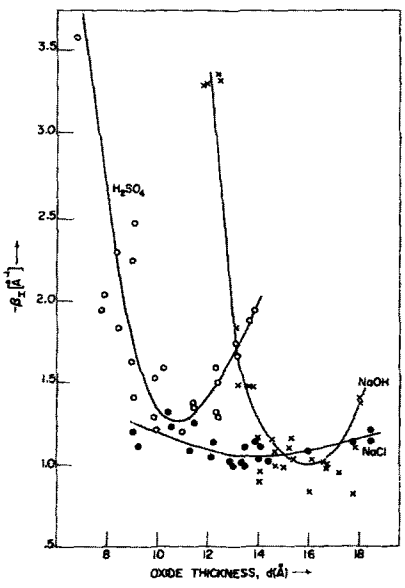

Fig. 8. α_E vs. d during spontaneous corrosion

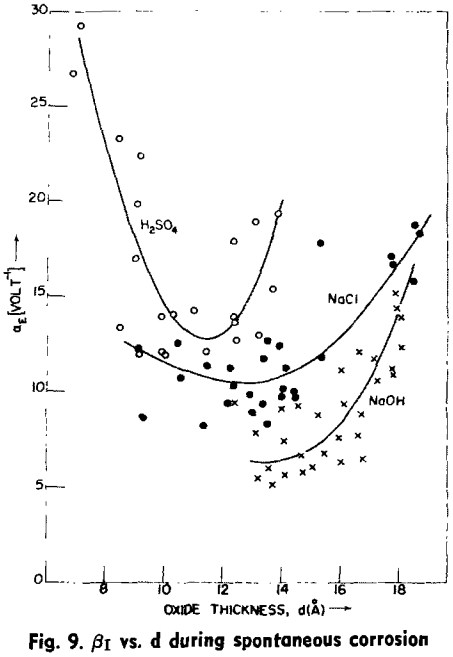

Fig. 9. β_I vs. d during spontaneous corrosion

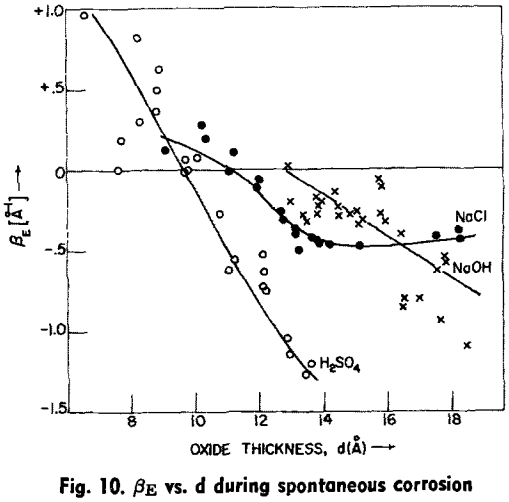

Fig. 10. β_E vs. d during spontaneous corrosion

could be the results of some small experimental error since β_E is obtained as the difference of two large values.

Transient analysis—anodic oxidation.—Values of α_I and β_I for thicknesses larger than 20Å can be obtained conveniently by using anodic oxidation. During constant current anodic oxidation the oxide thickness, d, and the voltage, V, vary linearly with time until a certain voltage, which we shall call "leakage potential" is approached. At this potential, the leakage current through the oxide (presumably electrons flowing from the electrolyte to the tantalum) becomes equal to the external current. When the leakage potential is approached, the oxide growth slows down and eventually stops. With increasing current densities, the leakage potential shifts to larger negative voltages, SCE *vs.* Ta, and the corresponding oxide thickness increases.

Figure 11 shows the incremental field F_i obtained by Eq. [9] from the electrode potential *vs.* oxide thickness for constant current anodization in H_2SO_4 and NaCl electrolytes. Above 20Å, the incremental fields are nearly constant over a wide range of thicknesses until the respective leakage potentials are approached and the incremental fields decrease. The curve for an electrolyte of NaOH is quite similar.

Comparison of thickness increment with anodization current indicated that the assumption of 100% current efficiency was satisfied through the thickness range where F_i remained constant.

Figure 12 shows the dependence of the time constants, τ, on thickness. When the leakage potential is approached, the time constants fall off rapidly. In the range where Faraday's law is satisfied, τ is found to be constant with thickness in the case of NaCl, but decreases slightly in the case of the NaOH electrolyte and by as much as a factor 1.5 in the range from 15 to 50Å in the case of the H_2SO_4-electrolyte.

At constant current anodization of 100% efficiency α_I can be calculated from τ, and, independently from $(\overline{V} - V_0)/V_1^2$ (Table I). However, it was found that the α_I-values calculated from $\Delta V/V_1^2$ are larger than those calculated from τ. An example is shown in Fig. 13 where the expression

$$B = -\alpha_I \cdot d \qquad [11]$$

has been plotted for anodic oxidation. Also plotted

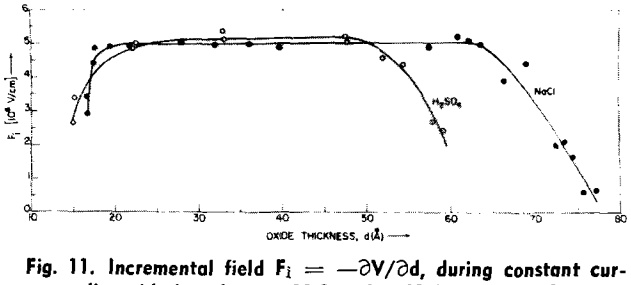

Fig. 11. Incremental field $F_i = -\partial V/\partial d$, during constant current anodic oxidation; I = —11.9 and —31.6 μA for H_2SO_4 and NaCl electrolytes, respectively.

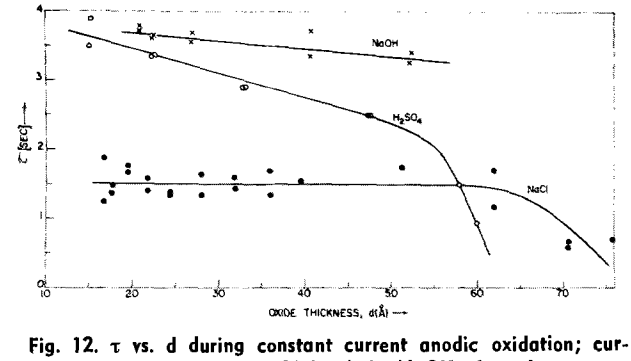

Fig. 12. τ vs. d during constant current anodic oxidation; currents as in Fig. 11; I = —11.9 μA in NaOH electrolyte.

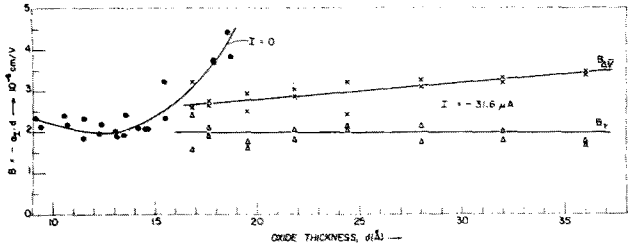

Fig. 13. B = $-\alpha_I d$ during spontaneous corrosion (•) and during constant current anodic oxidation (x, △) in NaCl electrolyte. The growth rate during spontaneous corrosion corresponded to an internal current of 24 μa at 12.3Å and 0.31 μa at 18.6Å.

are values of B for spontaneous corrosion, where measurements of τ and $\Delta\overline{V}$ must be combined in order to obtain α_I by the expressions of Table I.

In general, α_I is a function of V and of d. Comparing the values of α_I, (*a*) from anodic oxidation and (*b*) from open-circuit corrosion, at the same thickness d, we may expect differences in α_I, since the voltages in both cases are different. Only if thicknesses and voltages and thus the ionic currents were equal, we would expect equal α_I's. This was approximately the case at the minimum of the α_I– curve during open-circuit corrosion, where the ionic current by Eq. [2] is about 10 μa, which is of the same order as the current of 31 μa used during anodic oxidation. For thicknesses larger than those corresponding to the minimum of α_I, the current density at spontaneous corrosion drops off rapidly to values of the order of 1 to 0.1 μa when the spontaneous corrosion becomes so slow that experiments were stopped.

From the values of α_I and F_i, we may obtain $\beta_I = \alpha_I \cdot F_i$ in the range of anodic oxidation of 100% efficiency, *i.e.*, if $I = -I_I$. Since F_i is very nearly constant in this range, the plots of β_I reflect essentially the behavior of α_I and will not be given.

The range where the leakage potential is approached is characterized by (*i*) $I_I < -I$; (*ii*) a decrease in F_i; and (*iii*) a decrease in τ. The fact that $I_I < -I$, suggests that the electronic current I_E so far neglected, becomes noticeable and eventually dominant. An analysis of F_i, l, τ and $(\overline{V} - V_0)/V_1^2$ in this range could be used in principle to obtain α_E and β_E for the electronic current near the leakage potential. However, it was found that the behavior near the leakage potential differed so widely for different samples and even for different runs of a given sample that no such analysis was attempted.

Temperature dependence.—Preliminary measurements indicated that $\Delta V/V_1^2$ decreases with increasing temperature during spontaneous corrosion and may even change its sign. Since $\Delta V/V_1^2 = (-\alpha_I - \alpha_E)/4$ (Table I), this indicates that either α_E increases with temperature much more than $-\alpha_I$, or else $-\alpha_I$ decreases much more than α_E.

Capacitance transients.—During the transient studies, reversible changes of capacitance with external cathodic current, I (Fig. 1) and with a-c voltage, V_1, at zero external current were observed. The magnitude of these capacitance changes is shown in Table III. Note that the change of cathodic current by 0.4 μa and the change of a-c potential from 11 to 169 mv cause

Table III. Effect of a cathodic current *I*, and of an a-c potential V_1 on the d-c potential and on capacitance ($C = 270$ μf; $d \approx 17$Å); pH ~ 1, H_2SO_4 electrolyte.

I, μa	V_1, mv	ΔV, mv	τ, sec	ΔC_{DS}, μf	Δd, A
0 → 0.4	11	37	180	+0.5	−0.032
0.4 → 0	11	−40	210	−0.5	+0.032
0	11 → 160	34	46	+5.5	−0.35
0	160 → 11	−36	205	−6.4	+0.41

changes of d-c potential of similar magnitude; however, the changes in capacitance are an order of magnitude larger in the case of the a-c voltage. This shows that the capacitance changes are not merely due to the d-c voltage changes.

Discussion

We shall first discuss the values of the coefficients α_I, α_E, β_I, and β_E as expected for various charge transport mechanisms which either have been observed on "thick" anodic oxides (thick in comparison to the range covered by our investigation) or else have been proposed to occur during the air oxide formation on tantalum and aluminum.

These values will then be compared with the α_I, α_E, β_I and β_E coefficients derived from our experiments. Finally, we shall discuss observations which cast some doubt on the validity of the simple model used by us to extract the α's and β's from our experimental data.

The reaction

$$2Ta + 5H_2O \rightarrow Ta_2O_5 + 5H_2 \qquad [12]$$

generates an electric field in the oxide of a polarity which tends to move positive charges from the metal toward the electrolyte or negative charges in the opposite direction. These are the flow directions for the cations and anions participating in oxide growth. The emf of the reaction [12] is (in volts)

$$E = 1.05 + 0.059 \cdot (pH) \qquad [13]$$

since 0.81v is the free energy of the reaction under standard conditions and 0.24v is the correction for the SCE *vs.* the hydrogen electrode. Equation [13] provides 1.1, 1.4, and 1.9v for our electrolytes H_2SO_4, NaCl, and NaOH, respectively. When a voltage V is applied across the oxide, the average field in the oxide becomes

$$F = (E - V)/d \qquad [14]$$

If E is a constant, independent of oxide thickness, then

$$d\frac{\partial F}{\partial d} = -F + F_i \qquad [15]$$

During constant current anodization in the thickness range where F_i is a constant (Fig. 11), Eq. [15] is satisfied by $F = F_i = \text{const}$, so that Eq. [14] can be transformed into

$$E = V + d\,F_i \qquad [16]$$

E-values derived in this manner were $E \approx 0.9$v for the H_2SO_4 and NaCl-electrolytes, and 1.6v for the NaOH-electrolyte. The differences between E_1 by Eq. [16] and E_2 by Eq. [13] are similar to those reported by Vermilyea (17) for the HNO_3 and NaOH-electrolytes of pH = 0.6 and 13.5, respectively. The discrepancy between E_1 and E_2 may arise from contact potentials Ta *vs.* electrolyte-oxide interface.

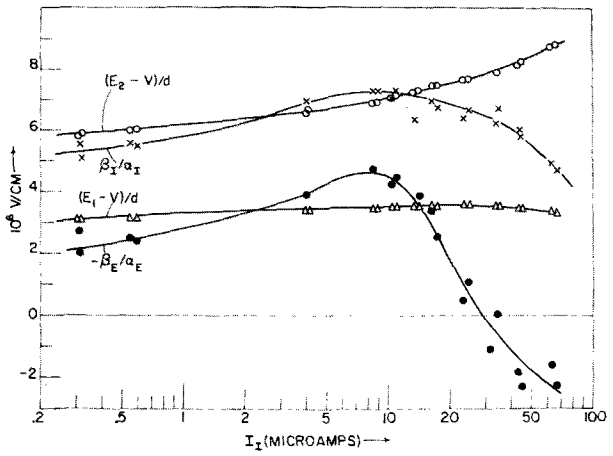

Fig. 14. β_I/α_I, $-\beta_E/\alpha_E$ and $F = (E-V)/d$ as functions of the ionic current derived from the growth rate during spontaneous corrosion in NaCl-electrolyte; $E_1 = 0.9$v and $E_2 = 1.4$v.

If the ionic current, I_I, would depend on thickness and voltage only through the average field F of Eq. [14] with E being constant the relation

$$\beta_I/\alpha_I = F \qquad [17]$$

should be valid, as seen readily from the definitions of β_I and α_I. This relation is indeed satisfied for constant current anodization, $I_I \approx -I$, where $\beta_I/\alpha_I = F_i$ (Table I), and since $F = F_i$, if $\partial I/\partial d = 0$.

In order to investigate whether the relation [17] applies in the range accessible by spontaneous corrosion, β_I/α_I and F were plotted *vs.* I_I (Fig. 14). Two curves for F are shown, one based on $E_1 = 0.9$v and the other on $E_2 = 1.4$v. The experimental values β_I/α_I show a pronounced downtrend toward the right. The curve $(E_2 - V)/d$, while fitting β_I/α_I at lower ionic currents exhibits a pronounced uptrend at higher currents. The curve $(E_1 - V)/d$ exhibits a slight downtrend at higher ionic currents, but lies much lower than β_I/α_I at the lower ionic currents. Thus we conclude that either the ionic current cannot depend on voltage and oxide thickness through the field F, or else the parameter E in Eq. [14] for F is not a constant (18), but changes from low values $E \simeq E_1$ to higher value $E \simeq E_2$, as the oxide thickness increases and the ionic current decreases. The Mott-Cabrera theory (4) is based on an exponential dependence of the ionic current on the field (14). Such a relation is not in agreement with the coefficients β_I and α_I as determined by us. Studies of air oxidation (5) of tantalum at or near room temperature also do not support the Mott-Cabrera theory.

Since the dependence of the ionic current through the oxide on voltage and thickness changes significantly at the small oxide thicknesses encountered in spontaneous corrosion, it appears doubtful that the corrosion currents can be derived by comparing the voltage-time dependence during spontaneous corrosion to values extrapolated from the voltage-current dependence for thicker anodic films (19, 20).

Studies of anodic oxidation of tantalum and other valve metals lead to the relation (21)

$$I_I = A \exp BF \qquad [18]$$

for oxide films which were generally much thicker than those encountered in spontaneous corrosion for oxide films. If this relation applies, our coefficient α_I is related to B by Eq. [11]. The B-values thus obtained for constant current anodization (Fig. 13) are indeed of the order of the transient B-values given in the literature (22, 23, 24).

In the range $d \gtrsim 13$Å, *i.e.*, for the thicknesses larger than that at the minimum of α_I at spontaneous corrosion, the values of $B = -\alpha_I \cdot d$ from spontaneous corrosion differ from those derived during constant current anodization (Fig. 13). This suggests that B for these thin oxides depends on the ionic current density, I_I, or on the voltage, V, and is not a constant as observed for thick anodic oxides where Eq. [18] and [14] appear to apply fairly well.

Recently the relation

$$I_I \simeq A' \exp B'\sqrt{F} \qquad [19]$$

has been proposed (25) instead of Eq. [18]. This relation leads to a dependence of α_I on V, which is much too small, however, to account for the differences of $B = -\alpha_I d$ for spontaneous corrosion and anodic oxidation shown in Fig. 13.

The expression [14] for the average field in the oxide implies that the changes in the measured voltage, ΔV, extend entirely across the oxide, and not partially across a solution double layer. If part of ΔV

would extend across such a double layer, $\overline{R}$ should be larger than R_T, while, in fact, R_T appears to be slightly larger than $\overline{R}$ (Table II).

The carriers causing charge neutralization move opposite to the flow which is induced by the average electric field [14]. Carrier flow against the electric field can occur by: (*a*) thermionic emission; (*b*) tunneling, and (c) diffusion. Furthermore, the possibility of localized flow at faults in the oxide, even pinholes, must be considered.

With respect to the last mentioned possibility, there is a large amount of evidence for leakage paths localized at faults or defects in the oxide (12-16). Vermilyea described techniques to make these spots visible by plating out metals (16). The spreading resistance into the electrolyte at these leakage points provides an upper limit for the current flow. If the entire potential V extends across this spreading resistance, the coefficient α_E should be the reciprocal of the voltage, V, which is of a reasonable order of magnitude.

If the number of flaws remains unchanged as the oxide grows, we would expect that $\beta_E = 0$. On the other hand, if the number of flaws or their effective area decreased due to blocking by lateral oxide growth from adjacent regions, negative values of β_E should arise.

Regarding the charge transfer mechanisms through the bulk oxide, evidence suggests electron rather than hole flow (16). Mott (3) has discussed thermionic emission and tunneling of electrons through a thin oxide barrier of height W. Theoretical expressions for α_E, β_E and $-\beta_E/\alpha_E$ for these cases are listed in Table IV.

The electron current due to thermionic emission is governed by the Boltzmann factor $e^{-W/kT}$, which lead to $\beta_E = 0$ and $\alpha_E = 40$ v^{-1} at room temperature, in disagreement with the experimental data. The observed values, $\alpha_E \simeq 10$ v^{-1}, could arise by a dual barrier model of symmetric potential barriers, as discussed for oxygen reduction on passivated Zr (26). Such dual barriers might exist at the faults where oxide growth is prevented and most of the current I_E is concentrated.

The tunnel current is governed by the factor[4] $\exp\left[-2d\left(\frac{2m^*W}{h/2\pi^2}\right)^{1/2}\right]$ provided that the tunneling is not limited by the lack of acceptors at the oxide electrolyte interface. Numerically $2\left(\frac{2m^*W}{h/2\pi^2}\right)^{1/2} \simeq 1$Å, for m^* equal to the free electron mass and $W \simeq 1$ ev. Table IV indicates that the ratio $-\beta_E/\alpha_E$ is independent of m^* and should be larger than $2F$. The data of Fig. 14 shows that $-\beta_E/\alpha_E$ is smaller than $2F$. Therefore, the tunnel model does not seem to account for the observed values of β_E and α_E.

Since none of the existing theories on the growth of protective films agrees with the experimental data for α_I, β_I, α_E and β_E, we have speculated on novel mechanisms which may explain these data. The existence of a minimum for α_I, α_E and β_I suggests that there is a transition from one dominant mechanism to another, or else that there is a fairly drastic change in the behavior of the dominant mechanism. As a possible cause for such a drastic change, we like to mention the following: From the average charge density at the oxide-electrolyte interface, $\epsilon\epsilon_0 F$, one may derive the average spacing of these charges. For sufficiently thin oxide films, the field at the tantalum opposite to these charges will be much larger than the average field of Eq. [14]. Moreover, the actual field at the metal oxide interface at positions opposite to a positive tantalum ion just arrived at the oxide electrolyte interface may even have a polarity opposite to that of the average field. This would, of course, facilitate the flow of electrons to preserve charge neutrality.

As a possible explanation for positive values of β_E, it is suggested that the net electron current arises as the difference of a forward current Ta to electrolyte and a back flow, electrolyte toward metal. The decrease of the back flow with increasing oxide thickness may cause positive values of β_E for the net current.

However, before theorizing in detail on the mechanisms of current transport, it would be well to have available measurements on the temperature dependences of α_I, α_E, β_I and β_E; and to clarify the following inadequacies of the model on which the derivation of α_I, α_E, β_I and β_E was based: (*i*) the dependence of "oxide thickness" on the electrolyte in which it is measured (1, 27); (*ii*) the unusually large temperature dependence of the oxide capacitance (1); (*iii*) the dependence of oxide capacitance on current, I, and on the amplitude of a-c voltage signal (Table III) [see also (27)]; (*iv*) the discrepancy between $\overline{R}$ and R_T (Table II); (*v*) the discrepancy between α_I as determined (*a*) from the time constant τ and (*b*) from the voltage change ΔV of a transient during anodic oxidation.

The evaluation of α_I from ΔV requires an assumption on the coefficient γ_I of the quadratic term in the dependence of current on voltage (Appendix A). The assumption made was based on the exponential voltage dependence shown in Fig. 3, in which case $\gamma_I/\alpha_I = \alpha_I/2$. In the case that Eq. [19] with [14] applies, one has $\gamma_I/\alpha_I = (\alpha_I/2)\left(1 - \frac{1}{B'\sqrt{F}}\right)$ which approaches the relation (A-13) for $B'\sqrt{F} >> 1$. It thus appears that the assumption made on γ_I does not account for the discrepancy between α_I (ΔV) and $\alpha_I(\tau)$.

In a formal manner one might use the identity $\alpha_I(\Delta V) = \alpha_I(\tau)$ of Table I to derive a value of $C_o \neq C_{ES}$ by means of the Eq. [4] of Appendix A. This value of C_o should be characteristic for the time constants of the transient, $\tau \simeq 1$ sec, rather than for 100 Hz at which C_{ES} is measured. However, such a formal treatment would not be sufficient to describe the results of slow changes in the space charge distribution in the oxide which may occur following the switch to a new, constant potential across the oxide.

The observations listed under (*i*) — (*v*) above indicate that the oxide does not behave as an ideal capacitor shunted by a resistor which is an instantaneous function of voltage. Further evidence for this statement are: The observations of Van Winkel *et al.* (22) regarding the frequency dependence of the equivalent parallel resistance of the oxide (changes as large as a factor of 3 between 100 and 1 Hz measured with anodic d-c current flowing) and the well-known discrepancy between the B-values of the relation [18] as derived by d-c (21) and transient methods (22-24).

Conclusions

1. The coefficients, $\alpha_I = \partial \ln I_I/\partial V)_d$, $\alpha_E = \partial \ln I_E/\partial V)_d$, $\beta_I = \partial \ln I_I/\partial d)_V$, and $\beta_E = \partial \ln I_E/\partial d)_V$, have been derived as functions of oxide thickness by combining measurements of the time dependences of V and d with those of time constant τ and voltage change $\Delta\overline{V} = \overline{V} - V_o$ of certain transients. The model used pre-

[4] The shape of the barrier may change the numerical coefficient of the exponent slightly, but that should not affect the following discussion.

Table IV. The coefficients α_E and β_E for thermionic emission and tunnel emission as suggested by Mott (3)

	α_E	β_E	$-\beta_E/\alpha_E$
Thermionic emission	q/kT	0	0
Tunnel emission[+]	$\left(\frac{2m^*}{h/2\pi^2}\right)^{1/2} qd$	$-2\left(\frac{2m^*W}{h/2\pi^2}\right)^{1/2}$	$2(F + \phi/d)$

[+] Using $W = \phi + q(E - V)$.

dicts a relation between $\Delta\overline{V}$ and τ at constant current anodization of 100% efficiency. However, this relation is only approximately satisfied, which sheds some doubt on the validity of the values obtained for α_I, α_E, β_I and β_E beyond a first order estimate.

2. The coefficients α_I and β_I during anodic oxidation at constant thickness in the thickness range 20-50Å are generally consistent with an anodic current depending on voltage and oxide thickness only through the average field $F = (E - V)/d$. The Tafel slope, $B = \partial \ln I_I/\partial F = -\alpha_I d$ agrees with published values derived by transient methods.

3. A plot of the growth rate during spontaneous corrosion *vs.* β_I/α_I shows that the ionic current is not merely a function of the electric field, F, particularly during the initial part of spontaneous corrosion.

4. The experimental evidence indicates that the growth of a protective oxide film on tantalum is more complex than assumed earlier (3, 4). Likely complicating factors include structural defects, and strong space charge polarization in the film, several species participating in the charge transfer mechanism and the fields due to discrete charges in thin oxides being quite different from those of quasicontinuous charge densities.

5. Clarification of the growth mechanism requires experimental methods to determine α_I, α_E, β_I and β_E as functions of oxide thickness and temperature. An improved model for evaluation of transients is required which removes the discrepancy between $\alpha_I(\tau)$ and $\alpha_I(\Delta V)$ at constant current anodization.

Manuscript received Nov. 7, 1966; revised manuscript received Feb. 3, 1967. This paper was presented at the Cleveland Meeting, May 1-6, 1966.

Any discussion of this paper will appear in a Discussion Section to be published in the December 1967 JOURNAL.

APPENDIX A

Transients of Small Magnitude

The following mathematical analysis is based on the assumption that the currents I_I and I_E at a constant temperature are well-defined functions of oxide thickness and of voltage V. By development for small increments from the point d_o, V_o I_I^o, one obtains

$$I_I/I_I^o - 1 = \alpha_I(V - V_o) + \beta_I(d - d_o) + \ldots \quad [A\text{-}1]$$

and

$$I_E/(I_I^o + I) - 1 = \alpha_E(V - V_o) + \beta_E(d - d_o) + \ldots \quad [A\text{-}2]$$

where the relation [1] has been used for the quasistationary currents I_I^o and I_E^o before the transient. During the transient the conservation of charge requires that

$$(C_{ES} + C_o)\ \partial V/\partial t = I_I + I - I_E \quad [A\text{-}3]$$

which reduces to Kirchhoff's law [1] in the quasistationary state $\partial/\partial t = 0$. In Eq. [A-3] C_o denotes the oxide capacitance, and C_{ES} is the capacitance in the symmetric branch of the bridge circuit. Inserting [A-1] and [A-2] into [A-3] and letting $I \to I + \Delta I$ and $d - d_o \simeq 0$, one obtains an exponential voltage relaxation of time constant

$$\tau = \frac{C_{ES} + C_o}{\alpha_E(I_I^o + 1) - \alpha_I I_I^o} \quad [A\text{-}4]$$

and of amplitude

$$\Delta V = \Delta I[\alpha_E(I_I^o + I) - \alpha_I I_I^o]^{-1} \quad [A\text{-}5]$$

According to these relations the resistances defined by Eq. [3] and [4] ought to be equal provided that $C_o \simeq C_{ES}$. Because of $\overline{R} = R_\tau$, measurement of ΔV and of τ for the same current pulse do not provide two independent relations for calculating α_E and α_I. In the special case that $I = 0$, Eq. [A-5] provides a well-known expression (28) for the "corrosion resistance" in terms of the anodic and cathodic transfer coefficients which are related to α_I and α_E, respectively.

Next we shall analyze the transient generated by an a-c voltage applied at the oxide. Let

$$V = \overline{V} + V_1 \sin \omega t \quad [A\text{-}6]$$

where $\overline{V}$ is the time average over an a-c cycle. Let us consider first the case of quasistationary corrosion at $I = 0$. In this case, Kirchhoff's law $\overline{I_E} = \overline{I_I}$ applies to the time averages of the electronic and ionic currents. However, Kirchhoff's law does not apply to the instantaneous currents. During the cathodic half of the cycle the electronic current prevails, and during the anodic half of the cycle the ionic current prevails. If the dependence of I_E and I_I on $\overline{V}$ is nonlinear, the d-c potential $\overline{V}$, has to adjust in order that $\overline{I_I} = \overline{I_E}$. The time dependence of this adjustment is described by Eq. [A-3] with I_I, I_E, and V replaced by $\overline{I_I}$, $\overline{I_E}$, and $\overline{V}$. In order to analyze the change $\Delta\overline{V}$ which arises from the step increase of V_1, developments of I_E and I_I to higher than first order terms are required.

Let

$$I_I = I_I^o[1 + \alpha_I(V - V^o) + \gamma_I(V - V^o)^2 + \ldots] \quad [A\text{-}7]$$

Insert Eq. [A-6] and average over a cycle to obtain

$$\overline{I_I} = I_I^o[1 + \alpha_I(\overline{V} - V^o) + \gamma_I(\overline{V} - V^o)^2 + \gamma_I V_1^2/2 + \ldots] \quad [A\text{-}8]$$

The corresponding expression for $\overline{I_E}$ is obtained by replacing I_I^o by $I + I_I^o$ and α_I, γ_I by α_E, γ_E. Inserting these expressions into the relation $\overline{I_E} = \overline{I_I} + I$ provides

$$\Delta\overline{V} = \overline{V} - V^o = \left[\frac{V_1^2}{2}\right] \cdot \frac{I_I^o\gamma_I - (I_I^o + I)\gamma_E}{-I_I^o\alpha_I + (I_I^o + I)\alpha_E} \quad [A\text{-}9]$$

if we neglect $\gamma_I(\overline{V} - V^o)$ *vs.* α_I, and $\gamma_E(\overline{V} - V^o)$ *vs.* α_E as small order terms. Inserting Eq. [A-9] into [A-8] and neglecting the term $\gamma_I(\overline{V} - V^o)^2$ we obtain

$$\frac{\overline{I_I} - I_I^o}{I_I^o} = \frac{V_1^2}{2} \cdot \frac{(I_I^o + I)(\alpha_E\gamma_I - \alpha_I\gamma_E)}{-I_I^o\alpha_I + (I_I^o + I)\alpha_E} \quad [A\text{-}10]$$

Experimental data (Fig. 2) suggest voltage-dependences for I_E and I_I of the forms

$$I_I = I_I^o\, e^{\alpha_I(V - V_o)} \quad [A\text{-}11]$$

and

$$I_E = (I_I^o + I)\, e^{\alpha_E(V - V_o)} \quad [A\text{-}12]$$

so that

$$\gamma_I = \alpha_I^2/2 \quad [A\text{-}13]$$

and

$$\gamma_E = \alpha_E^2/2 \quad [A\text{-}14]$$

Inserting these values into Eq. [A-9] and [A-10], one obtains

$$\Delta V = \overline{V} - V^o = -(V_1^2/4) \cdot \frac{I_I^o\alpha_I^2 - (I_I^o + I)\alpha_E^2}{I_I^o\alpha_I - (I_I^o + I)\alpha_E} \quad [A\text{-}15]$$

and

$$\frac{\overline{I_I} - I_I^o}{I_I^o} = \alpha_E\alpha_I\frac{V_1^2}{4} \cdot \frac{(I_I^o + I)(\alpha_I - \alpha_E)}{-I_I^o\alpha_I + (I_I^o + I)\alpha_E} \quad [A\text{-}16]$$

The expression [A-4] for the time constant τ applies regardless of whether the transient is caused by a change in the external current or in the a-c voltage. Elimination of α_E from the Eq. [A-15] and [A-4] leads to a quadratic equation for α_I with the roots

$$\alpha_I = \frac{2C_{ES}}{\tau I}\left\{1 \pm \left[\left(\frac{I + I_I^o}{I_I^o}\right)\left(1 + \frac{\tau I}{2C_{ES}}\frac{4\Delta V}{V_1^2}\right)\right]^{1/2}\right\} \quad [A\text{-}17]$$

Expressions for the special cases: $I = 0$ (spontaneous corrosion), $I \simeq -I_I^o$ (large anodic current) and $I_I^o \simeq 0$ (large cathodic current) are listed in Table I.

APPENDIX B

Determination of the Coefficients β_E and β_I

Having determined α_I and α_E, we may obtain β_I and β_E from the changes of d-c voltage $\overline{V}$ with thickness d, and of thickness with time as follows: Insert Eq. [A-1] and [A-2] into Eq. [1] and differentiate with respect to d, to obtain

$$-\frac{\delta V}{\delta d} = F_i = \frac{\beta_I I_I^o - \beta_E (I + I_I^o)}{\alpha_I I_I^o - \alpha_E (I + I_I^o)} \quad [B\text{-}1]$$

The second relation required to calculate the β's is provided by the time dependence of the oxide thickness. Since $\partial d/\partial t$ is related to I_I by Faraday's law [2], one obtains for the expression [10] by means of [A-1] and [9]

$$l = -I_I^o \cdot \{[\partial I_I/\partial d]_V + [\partial I_I/\partial V]_d \cdot \partial V/\partial d\}^{-1}$$
$$= (\alpha_I F_i - \beta_I)^{-1} \quad [B\text{-}2]$$

By solving the Eq. [C-1] and [C-2] for β_I and β_E, one obtains

$$\beta_I = \alpha_I F_i - l^{-1} \quad [B\text{-}3]$$

and

$$\beta_E = \alpha_E F_i - l^{-1} \cdot I_I^o/(I + I_I^o) \quad [B\text{-}4]$$

Thus measurements of $V(d)$ and $d(t)$ permit the determination of F_i and l, which, combined with α_I and α_E, yield β_I and β_E. Expressions for special cases are listed in Table I.

APPENDIX C

Transients of Large Magnitude

According to Eq. [A-9], the voltage change ΔV depends quadratically on the a-c amplitude in the limit of the small signal approximation, where terms of higher than the second order in Eq. [A-7] can be neglected. In the case of larger a-c signals, and if Eq. [A-11] is valid, we have

$$\bar{I}_I = I_I^o \cdot e^{\alpha_I(\bar{V} - V_o)} \cdot f(\alpha_I V_1) \quad [C\text{-}1]$$

where

$$f(y) = 1/(2\pi) \int_0^{2\pi} e^{y \sin x}\, dx \quad [C\text{-}2]$$

is the modified Bessel-function of order zero, which can be approximated for $y >> 1$ by

$$f(y) \approx e^y/\sqrt{2\pi y} \quad [C\text{-}3]$$

Inserting Eq. [B-1] with [B-3] and the corresponding equation for $\bar{I}_E$ into Kirchhoff's law, one obtains the dependence of ΔV on V_1 for $|\alpha_I| V_1 >> 1$, and $\alpha_E V_1 >> 1$, which becomes for the special case that $I = 0$:

$$\bar{V} - V_o = \frac{|\alpha_E| - |\alpha_I|}{\alpha_I - \alpha_E} V_1 + \frac{\ln|\alpha_I/\alpha_E|}{2(\alpha_I - \alpha_E)} \quad [C\text{-}5]$$

APPENDIX D

Corrections to Constant Thickness for the D-C Analysis

One has from Eq. [A-1]

$$\delta I_I = I_o[\alpha_I \delta V + \beta_I \delta d] = I_o \alpha_I \delta V^* \quad [D\text{-}1]$$

where

$$\delta V^* - \delta V = \frac{\beta_I}{\alpha_I} \delta d = \left(F_i - \frac{1}{\alpha_I l}\right) \delta d \quad [D\text{-}2]$$

In transforming the last equation, we used Eq. [B-3] to eliminate β_I. Since $\alpha_I < 0$ and $F_i > 0$, both terms in parenthesis are positive. A similar correction applies to I_E *vs.* V. However, since $\alpha_E > 0$, F_i and $-1/\alpha_E l$ have opposite signs. It turns out that $F_i - 1/\alpha_E l$ is negative, so that the correction of the voltage scale for the $I_E - V$ plot has the opposite sign to that of the $I_I - V$ plot.

APPENDIX E

Validity of Kirchhoff's Law for Quasi-Stationary Condition

The average field in the oxide layer is given by [14] assuming that changes of the measured potential electrolyte *vs.* tantalum during oxide growth arise entirely from potential changes across the oxide, *i.e.*, that potential changes across the double layer in the electrolyte adjacent to the oxide can be neglected.

Since the oxide growth rate during spontaneous corrosion decreases with time, the ionic current through the oxide decreases accordingly, and this requires some change of the field F with time. This in turn requires that

$$S\epsilon\epsilon_0\, \partial F/\partial t = I_I - I_E \neq 0 \quad [E\text{-}1]$$

which appears to contradict our assumption $I_I = I_E$ in the quasi-stationary case. However, the left hand side can be transformed by means of [12], [2], and [9] into $C_{ES}\lambda I_I(F_i - F)$ where we used $C_o = S\epsilon\epsilon_0/d \simeq C_{ES}$. Thus Eq. [E-1] becomes

$$\frac{I_I - I_E}{I_I} = C_{ES}\lambda(F_i - F) \quad [E\text{-}2]$$

Insertion of numerical values on the right-hand side gives values smaller than, or of the order of 10^{-3}, so that $I_I \simeq I_E$ appears to be a valid approximation.

The same argument can be applied to the case of a finite external current.

REFERENCES

1. K. Lehovec and J. D'Amico, *This Journal*, **114**, 363 (1967).
2. C. Wagner, *Z. Physik Chem.*, **21B**, 25 (1933); *ibid.*, **32B**, 447 (1936).
3. N. F. Mott, *Trans. Faraday Soc.*, **35**, 1175 (1939).
4. N. Cabrera and N. F. Mott, *Rep. Progr. Phys.*, **12**, 163 (1949).
5. D. A. Vermilyea, *Acta Met.*, **6**, 166 (1958).
6. J. A. Davies, J. P. S. Pringle, R. L. Graham, and F. Brown, *This Journal*, **109**, 999 (1962).
7. J. A. Davies and D. Domeij, *ibid.*, **110**, 849 (1963).
8. J. J. Randall, Jr., W. J. Bernard, and R. R. Wilkinson, *Electrochim. Acta*, **10**, 183 (1965).
9. P. F. Schmidt, F. Huber, and R. F. Schwartz, *J. Phys. Chem. Solids*, **15**, 270 (1960).
10. A. Middelhoek, *This Journal*, **111**, 379 (1964).
11. G. M. Krembs, *ibid.*, **110**, 938 (1963).
12. D. A. Vermilyea, *J. Appl. Phys.*, **27**, 963 (1956).
13. D. A. Vermilyea, *This Journal*, **110**, 250 (1963).
14. N. Schwartz and M. Gresh, *ibid.*, **112**, 295 (1965).
15. R. Dreiner and J. Schimmel, *ibid.*, **111**, 453 (1964).
16. D. A. Vermilyea, *J. Appl. Phys.*, **36**, 3663 (1965).
17. D. A. Vermilyea, *This Journal*, **101**, 389 (1954).
18. R. Dreiner, K. Lehovec, and J. Schimmel, *ibid.*, **112**, 395 (1965).
19. M. Maraghini, G. V. Adams, Jr., and P. van Ryssel-berghe, *ibid.*, **101**, 400 (1954).
20. H. A. Johansen, G. B. Adams, Jr., and P. van Rysselberghe, *ibid.*, **104**, 339 (1957).
21. L. Young, "Anodic Oxide Films," Academic Press, London and New York (1961).
22. P. Winkel, C. A. Pistorius, and W. Ch. van Geel, *Philips Research Rpts.*, **13**, 277 (1958).
23. J. F. Dewald, *J. Phys. Chem. Solids*, **2**, 55 (1957).
24. D. A. Vermilyea, *This Journal*, **104**, 427 (1957).
25. L. Young and F. G. R. Zobel, *ibid.*, **113**, 277 (1966).
26. R. E. Meyer, *ibid.*, **107**, 847 (1960).
27. D. A. Vermilyea, *J. Phys. Chem. Solids*, **26**, 133 (1965).
28. R. E. Meyer, *This Journal*, **106**, 930 (1959).

Deposition of Tantalum and Tantalum Oxide by Superimposed RF and D-C Sputtering

F. Vratny

Bell Telephone Laboratories, Incorporated, Murray Hill, New Jersey

ABSTRACT

The advantages and flexibility of glow discharge diode sputtering for the deposition of thin films can be greatly extended by the simultaneous application of a d-c and rf field at the cathode. The combined field increases the plasma density and prevents the formation of a dielectric film on the cathode during reactive sputtering. This technique allows: (*i*) operation at sputtering pressures of 0.5-2.0 millitorr with a tantalum deposition rate of ~80 Å/min, or a two-fold increase in tantalum deposition rate for pressures in the 10 to 20 millitorr range; (*ii*) high deposition rates (50 to 100 Å/min) for the deposition of Ta_2O_5 and MnO_x by reactive sputtering in pure oxygen.

Cathodic sputtering has proven to be an important process in the field of microelectronics for the deposition of many thin film materials (1). This technique is particularly important for tantalum based films which have a wide use for fabrication of reliable resistors and capacitors (2). However, the technique of cathodic sputtering is limited in its capacity for thin film formation since the deposition rate is largely determined and limited by the sputtering pressure and cathode voltage. Typically at a cathode voltage of 4 kv and a current density of 0.25 ma/cm^2, a sputtering pressure of 20 millitorr, and a 13 to 16 cm diameter cathode, the deposition rate of tantalum is about 80Å/min. This rate can be increased by a factor of about three by variation of the sputtering pressure, voltage, and interelectrode spacing. For this range of deposition rates, the depositing tantalum film incorporates substantial quantities of inert sputtering gas as well as many reactive residuals that are present in the vacuum system during deposition. At a pressure of 20 millitorr of inert gas and an initial pressure of 2×10^{-6} Torr, there is as much as 10 a/o (atomic per cent) impurity, of which about 2% is argon (3). This amount of rare gas may affect the electrical properties and stability of these films. Enhancement of the deposition rate should reduce the impurity content of these films. Alternatively, reduction of the sputtering gas pressure, without loss of deposition rate, should reduce the amount of inert gas in the film.

Tantalum oxide is particularly difficult to deposit as the deposition rate in pure oxygen is in the range of 0.5 to 5.0 Å/min (4). Several techniques are available to enhance the deposition rate as the microwave oxygen plasma techniques of Ligenza (5), the Hot Cathode Discharge (6) techniques, which is not generally applicable to reactive sputtering, the magnetic confinement Penning Discharge (7) technique which may be inconvenient for magnetic film deposition and physically difficult to realize in many vacuum systems.

Alternately, Moore (8) and Gawehn (9) employed rf techniques to generate ion beams for sputtering, while Wehner (10) employed an rf technique to sputter dielectrics directly. The technique of rf dielectric sputtering has been explored in depth by Jorgenson and Wehner (11) and Davidse and Maissel (12) for the preparation of thin films.

The method described in this paper represents a more flexible technique as it combines a number of separate functions by applying both d-c and rf power directly to the sputtering cathode. It is possible to employ metallic cathodes for both the deposition of metallic and dielectric films.

When an rf field is applied to a discharge, the charged particles decribe oscillatory paths in response to the alternating field. Electrons traveling under the influence of a superimposed rf and d-c field have a larger total path than with a d-c field alone. The larger path increases the probability of electron-gas atom collisions leading to an increase in positive ion current density at the cathode for a given pressure. This results in an increase in the rate of sputtering and film deposition. The manner in which electrons interact in a gas is dependent on the gas pressure or electron mean free path, the frequency of the rf field and the interelectrode spacing. At low pressures where the mean free path is greater than the interelectrode separation, the electrons are excited and traverse the electrode space with almost no gas collisions. As an example in argon, electrons (13) with an energy of 0.4 ev at a pressure of 10 millitorr have a mean free path of 10 cm or roughly the dimension of conventional interelectrode spacing. At pressures where the mean free path of the electron is less than the interelectrode spacing yet the frequency of the field is less than the collision frequency of the gas the electrons make many collisions for each oscillation of the field and the electrons tend to drift in phase with the field. An example of this method of ion generation is found in low frequency (60 ~) a-c and a-c + d-c sputtering (14) where the electrons alternately bombard the cathode and substrate.

At higher frequency, the electrons can make many oscillations of smaller amplitude between gas collisions. In this case, the electron cloud would appear to be stationary and would result in an intense plasma which can be extracted by a superimposed d-c field. This is the range of frequency of interest to this particular paper for it is by the "standing" cloud that we hope to produce an intense ion cloud that can be extracted by a d-c field. At still higher frequencies (microwave), the electrons are under the influence of a standing wave with oscillatory electric and magnetic components and as a result the electrons are distributed in space in response to cavity parameters, *i.e.*, cell or electrode dimensions and the frequency that is producing the standing wave.

The presence of the rf field serves further to prevent the formation of a dielectric layer at the cathode during reactive sputtering with electronegative gases. As the ion density can be maintained by the rf field, the resultant bombardment at the cathode decreases the chance of significant insulator formation. Should an insulator surface be produced, the rf induced charge at the surface (10) would maintain the sputtering process and further decrease the insulator formation process. Due to the higher ionization probability and the reduction in the breakdown strength of the gas (19), the rf field permits operation at lower sputtering pressures than are normally encountered in d-c diode sputtering. Finally, these processes can be

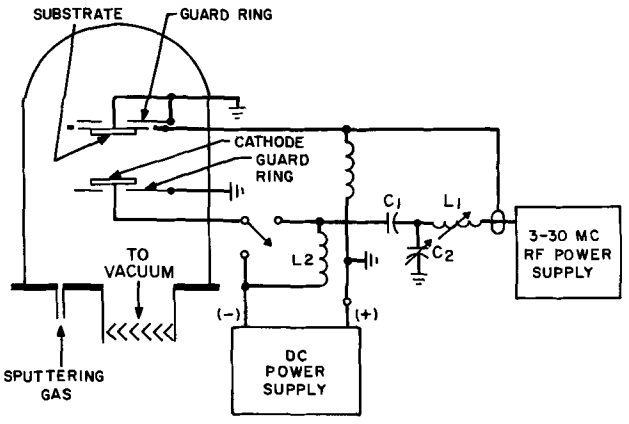

Fig. 1. Schematic of thin film deposition system

utilized with the usual large diameter (10-40 cm) cathodes encountered in d-c diode sputtering configurations, therefore not sacrificing the uniformity and film producing capability found in such systems.

Experimental

The vacuum chamber used in this work was a stainless steel bell 46 cm in diameter by 92 cm high and had a view port in line with the cathode. It was pumped by a 10.2 cm oil system that was liquid nitrogen trapped, see Fig. 1. This system had an ultimate pressure of 1 x 10^{-6} Torr and a leak rate of 0.05 millitorr liter/sec. Sputtering gas was admitted at a constant flow rate and the desired pressure was maintained by throttling the pump with a high vacuum valve. The cathode was 13 cm in diameter and 7.6 cm from the substrate. Normally, the bell jar, the fixtures, and the substrate were held at ground potential and either d-c or d-c and rf power was transmitted to the cathode through a coaxial line. The simultaneous application of power required a filtering network to protect personnel and equipment. A capacitor (C_1) was used on the rf line and an inductor (L_2) was used on the d-c line. Coupling or impedance matching to the sputtering machine was accomplished by link or transformer couple as well as T,L- and pi-networks (15). An L-network (C_2 and L_1) is indicated in Fig. 1. Alumino borosilicate glass slides to be coated were cleaned in Alconox and Igepal followed by a sequential rinse in water, hydrogen peroxide, and distilled deionized water.

Results

In a rare gas (argon) used for direct metal deposition, the application of rf power to a normal d-c diode sputtering arrangement produces an increase in the plasma density, as indicated by the larger plasma conductance (see Fig. 2). Using only d-c plasma excitation at 50 millitorr of argon, the current at a given voltage is smaller [curve (I)] than with combined plasma excitation by d-c and 100w of rf power [curve (II)]. In this example, the plasma conductance is improved by a factor of three at 500v, a factor of two at 1000v, and a factor of ½ at 2500v. At lower pressures (5 millitorr), the d-c excited plasma has a very small conductance at 3000v and a zero conductance at 2000v [curve (III)]. Yet, with superimposed d-c and rf plasma excitation there is a significant conductance for voltages as low as of 500v. The significance of the large plasma conductance is that it makes feasible a much lower pressure range for sputtering.

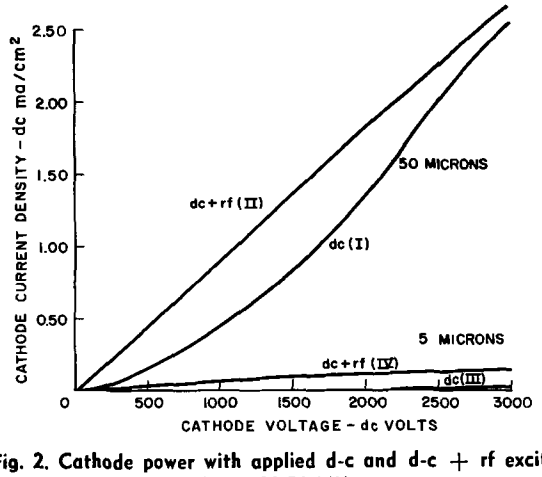

Fig. 2. Cathode power with applied d-c and d-c + rf excitation in argon; rf power ≈ 100w at 13.56 MHz.

Table I. Comparison of the deposition rate of tantalum with and without rf enhancement

Method	Argon pressure, millitorr	Deposition rate, Å/min	d-c Current density, ma/cm²
d-c	20	80	0.35
d-c + rf	20	176	0.50
d-c	1.5	0*	0
d-c + rf	1.5	76	0.23

* Discharge could not be maintained: cathode diameter 13 cm, cathode spacing 7.6 cm, cathode voltage 4 kv.
rf Power ≈ 200w, V = 280 Vpp, 13.56 mc.

These improvements in the plasma density, the plasma conductance, are reflected in the deposition rate of the cathode material. As an example (Table I) in the sputtering of tantalum, at a pressure of 20 millitorr of argon and a d-c cathode potential of a 4 kv, we have a deposition rate of ~80 Å/min of tantalum. With the application of d-c and rf plasma excitation, the rf at 200w, there is a deposition rate of 176 Å/min.

Further, by reducing the sputtering pressure to ~1.5 millitorr, a glow discharge could not be obtained with a d-c potential alone on the cathode. With the d-c + rf plasma excitation, not only could a discharge be obtained but the sputtering rate was ~76 Å/min, nearly that obtained at 20 millitorr, and the process was more efficient in terms of current density. A significant feature in this phase of the work is the ability to use lower sputtering voltages for a given pressure, *i.e.*, the 80 Å/min sputtering rate might easily have been obtained with rf + d-c plasma excitation at 20 millitorr and a 3 kv cathode potential.

In a reactive gas, the d-c discharge deposition rate is inversely proportional to the reactive gas partial pressure. As an example (Fig. 3) for the reactive

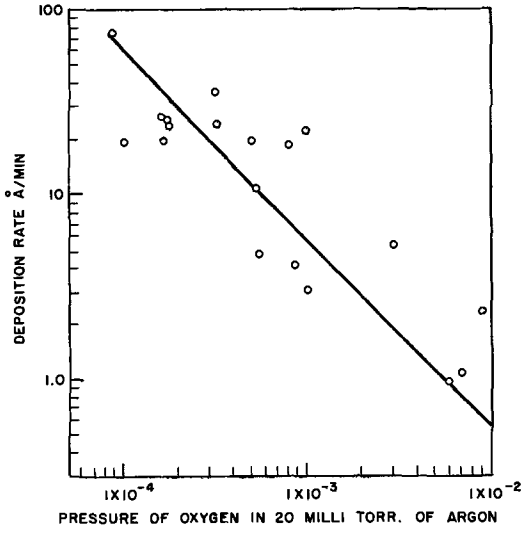

Fig. 3. Deposition rate of tantalum oxide as a function of oxygen partial pressure in argon (Å/min = 6 x $10^{-3}/P_{O_2}$); cathode voltage 4 kv, total pressure 20 millitorr.

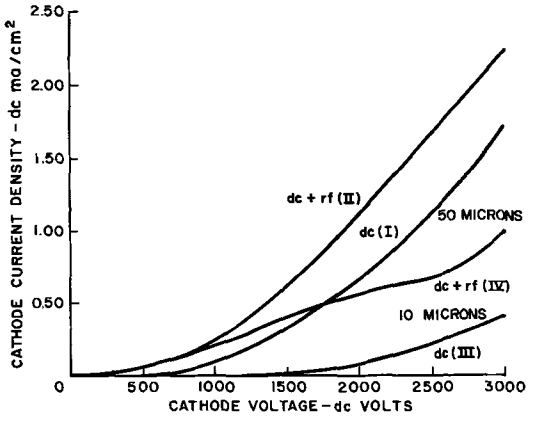

Fig. 4. Cathode power with applied d-c and d-c + rf excitation in oxygen; rf power ≈ 100 w at 13.56 MHz.

sputtering of tantalum oxide by the d-c diode sputtering technique, the deposition rate has been found to be relatively constant over the range corresponding to oxygen solution in tantalum. The deposition rate begins to drop however, in the range in which tantalum oxide begins to precipitate (at about 1 x 10^{-4} Torr). Higher pressures are normally used to assure stoichiometry, but at a loss in the deposition rate. At a pressure of 1 x 10^{-3} Torr the deposition rate is 5 Å/min.

The rf + d-c plasma excitation method appears to offer a solution to this problem for the plasma conductance in pure oxygen is improved by dual excitation (Fig. 4). At a high pressure (50 millitorr) a 100% improvement occurs in the plasma conductance at voltages above 1000v (curve I for d-c plasma excitation, curve II for d-c + rf excitation) while at low pressure (10 millitorr), the improvement is more pronounced with as much as a factor of two improvement in the plasma conductance at 1500-2000v (curve III for d-c plasma excitation, curve IV for d-c + rf excitation).

The improvement in the plasma density, the plasma conductivity, is directly correlated with an improvement in the deposition rate of the tantalum oxide insulating film. As an example (Table II), the deposition of tantalum oxide from a tantalum cathode is 0.1 Å/min by d-c diode reactive sputtering at a cathode potential of 4 kv and an oxygen pressure of 20 millitorr. With 200w of rf power added, the deposition rate is 58 Å/min. Manganese oxide is sputtered from a manganese cathode at a deposition rate of 1 Å/min by the d-c diode sputtering technique while the addition of 200w of rf power increases the deposition rate of ~100 Å/min. Aluminum oxide is sputtered from an aluminum cathode at 8 Å/min by the d-c diode sputtering technique. Addition of 200w of rf power increases the deposition rate to ~80 Å/min.

Component Results

The data for single samples, at one thickness and set of conditions, is found in Table III. For tantalum

Table II. Oxide film comparison of the deposition rate of oxide film materials with and without rf enhancement of the rate in oxygen

Method	Cathode material	Deposited material	Deposition rate, Å/min
d-c	Tantalum	Ta_2O_5	0.1
d-c + rf	Tantalum	Ta_2O_5	58
d-c	Manganese	MnO_x	1.0
d-c + rf	Manganese	MnO_x	100
d-c	Aluminum	Al_2O_3	8
d-c + rf	Aluminum	Al_2O_3	80

Cathode diameter 13 cm, cathode spacing 7.6 cm, cathode voltage 3-4 kv.
rf Power ≈ 200w, V = 280 Vpp, 13.56 mc, oxygen pressure ≈ 20 millitorr.

Table III. Comparison of oxide film materials prepared by d-c + rf sputtering technique

	Ta-Ta_2O_5 gold	Ta-Ta_2O_5* MnO_x-gold	Ta-Al_2O_3 gold
Thickness (Å) of oxide	1000	2000 Ta_2O_5 300 MnO_x	400
Capacitance per unit area ($\mu f/cm^2$)	0.26	0.096	0.25
Tan δ(1kc)	0.02	0.007	0.01
ϵ	26	22	10
Area = 0.1 cm^2			

* Anodic tantalum oxide of ~ 2000Å.

oxide deposited on tantalum, at a thickness of 1000Å, the capacitance per unit area (0.1 cm^2) is 0.26 $\mu f/cm^2$, with a calculated dielectric constant of ~26 and a dissipation factor of 0.02. The dissipation factor is at least ten times better than film prepared by other vacuum techniques and is nearly as low as tantalum oxide films prepared by aqueous anodization (16) which typically exhibit a dissipation factor of less than 0.01.

For manganese oxide deposited on anodic tantalum oxide we find that at a thickness of 300Å of manganese oxide a capacitance per unit area of 0.096 $\mu f/cm^2$ results and a dissipation factor of 0.007. This is comparable in quality to anodically prepared tantalum oxide (17) with metal counter electrodes, which has a capacitance density of 0.1 $\mu f/cm^2$ and dissipation factor less than 0.01, while the dissipation factor is considerably improved compared to thermally formed manganese oxide. For aluminum oxide deposited on tantalum at a thickness of 400Å a capacitance per unit area of 0.025 $\mu f/cm^2$ and a dielectric constant of ~10 with a dissipation factor of 0.01 results. This result is better than previously reported information on alumina films as these films exhibit a nominal dielectric strength measured at a voltage ramp of ~30 v/min of roughly 1 x 10^6 v/cm for 0.1 cm^2 samples compared with previously reported results of 6 x 10^5 v/cm for 0.0625 cm diameter spot samples (18).

The general method of rf + d-c plasma excitation demonstrates advantages for the deposition of metal films. First it can be used without alteration of presently existing d-c diode sputtering equipment. The technique is particularly useful at lower pressure and lower cathode voltages for studies of sputtering gas impurity effects and growth and orientation effects that are determined by the deposition rate. It also allows for the direct deposition of dielectrics from metal cathodes which are generally more readily available in higher purity than many dielectric materials. Therefore many dielectric materials can be directly deposited by this technique.

Manuscript received Oct. 27, 1966; revised manuscript received Dec. 22, 1966. This paper was presented at the Cleveland Meeting, May 1-6, 1966.

Any discussion of this paper will appear in a Discussion Section to be published in the December 1967 JOURNAL.

REFERENCES

1. N. Schwartz and R. W. Berry, "Thin Film Components and Circuits in Physics of Thin Films," Vol. 2, 363-419, G. Hass and R. E. Thun, Editors, Academic Press (1964).
2. D. A. McLean, N. Schwartz, and E. D. Tidd, *Proc. IEEE*, **52**, 1450 (1964).
3. W. Guldner, *Anal. Chem.*, **35**, 1744 (1963); *Proc.* Elect. Comp. Conf. 1964, p. 9.
4. L. Lloyd, *Solid State Electronics*, **3**, 74 (1961); R. Scot Clark and C. D. Orr, *Proc.* Elect. Comp. Conf. 1965, p. 31.
5. J. R. Ligenza, *J. App. Phys.*, **36**, 2703 (1965).
6. N. Laegreid, G. K. Wehner and B. Meckel, *ibid.*, **30**, 374 (1959).
7. E. Kay, *ibid.*, **34**, 760 (1963).
8. W. J. Moore and C. D. O'Brian, "Chemical Reac-

tions of Ionic Beams," NSF-G986, June 1, 1956; *N. Y. Acad. Sci.*, **67**, 600 (1957); *J. Chem. Phys.*, **1957**, 90.
9. H. Gawehn, *Z. Angew. Phys.*, **14**, 458 (1962).
10. G. S. Anderson, W. N. Mayer, and G. K. Wehner, *J. App. Phys.*, **33**, 2991 (1962).
11. G. V. Jorgenson and G. K. Wehner, ibid., **36**, 2672 (1965).
12. P. D. Davidse and L. I. Maissel, *ibid.*, **37**, 574 (1966).
13. J. Townsend, "Electrons in Gases," p. 54, D. Von Nostrand Co., Inc. New York (1947).
14. F. Vratny and D. J. Harrington, *This Journal*, **112**, 484 (1965).
15. B. Goodman, "The Radio Amateur's Handbook," American Radio Relay League, Newington, Conn. (1966).
16. F. Vratny, *Amer. Ceramic Bull.*, **45**, 401 (1966).
17. J. H. Cash and R. S. Clark, Paper presented at the Cleveland Meeting, May 1966.
18. R. G. Freiser, *This Journal*, **113**, 357 (1965).
19. E. W. B. Gill and A. von Engel, *Proc. Roy. Soc., London*, 1947, p. 446.

Incorporation of Ions in Anodic Oxide Films on Zirconium and Their Effect on Film Behavior

J. C. Banter

Metals and Ceramics Division, Oak Ridge National Laboratory, Oak Ridge, Tennessee

ABSTRACT

Transmission spectra of anodically formed ZrO_2 films show that certain anions such as phosphate, sulfate, and several carboxylates are incorporated in these films when they are formed in solutions containing these ions. Furthermore, hydrous ZrO_2 films result from anodizing in strongly oxidizing electrolytes. Films formed in many other solutions contain no incorporated ions. Film conductivity and thickness measurements indicate that incorporated ions increase the electrical resistance of the films, as well as limit their growth. It is suggested that these effects arise from lowered rates of diffusion of electrons and oxygen ions through the films and that the lowered diffusion rates result from the space charge created by the incorporated ions.

In prior work on anodic oxide films on zirconium (1, 2) we formed our films in a complex organic solution containing water, glycerin, ethyl alcohol, and lactic, citric, and phosphoric acids. This solution was developed for the specific purpose of minimizing the variations in film thickness across the surface of anodized polycrystalline specimens. The solution met this purpose admirably. However, we had noticed for some time that anodic films formed in this solution were always thinner than those formed at comparable voltages in the more commonly used 1% KOH solution. We also noted that films formed in this solution dissolved into the zirconium-base metal at a much slower rate during vacuum annealing than did those formed in 1% KOH (3).

These observations suggested that the films formed in these two solutions differed in some manner. Therefore, we initiated an experimental program to see if we could determine the nature of this difference and what effects it might have on the film behavior. This paper reports the results of this investigation and those of additional work which was suggested by preliminary results.

Experimental

Rectangular specimens of 0.020-in. thick zirconium foil were prepared by a previously described procedure (2). Oxide films were formed on specimens by anodizing for 30 sec at constant voltages in the organic solution as well as in each of the following solutions: 0.5M H_3PO_4, 0.5M H_2SO_4, 0.5M citric acid, 0.5M oxalic acid, 0.5M lactic acid, 1% KOH, 0.5M $(NH_4)_3BO_3$, saturated H_3BO_3, 0.25M Na_2MoO_4, 0.5M $K_2Cr_2O_7$, 0.5M K_2CrO_4, and 0.5M KNO_3. Clear windows of the oxide film were made on each specimen by dissolving the base metal away from a rectangular area with a 20% solution of bromine in ethyl acetate. The infrared transmission spectrum of each of these films was then recorded on a Perkin-Elmer Model 21 spectrophotometer.

Other duplicate specimens were anodized for 30 sec at a constant voltage of 100v in all of the above solutions except lactic acid, H_3BO_3, $K_2Cr_2O_7$, K_2CrO_4, and KNO_3. The reflectance of each of these specimens was recorded throughout the ultraviolet-visible region of the spectrum with a Perkin-Elmer Model 4000 A spectrophotometer equipped with a spectral reflectance attachment. The film thicknesses were calculated from the observed interference patterns using refractive index and phase shift data reported elsewhere (1, 4).

The d-c conductivity of each film was then measured. The specimens were masked with electrical tape so that only a known flat area of about 0.75 cm^2 was exposed. The specimen was connected in series with a Model 610 B Keithley electrometer and an external power supply. One electrical contact was made directly to the substrate and the other contact was made to the exposed oxide by immersing it beneath the surface of a pool of mercury. A known voltage (1-2v) was applied across the film, and the current flow was read from the electrometer. The applied voltage was always greater than 100 times the full-scale input drop of the electrometer so the film resistance was given simply by dividing the applied voltage by the measured current. Conductivities were calculated from the exposed film areas, film thicknesses, and the measured resistances.

To check for suspected differences in their chemical reactivities, films were formed on two specimens to approximately the same thickness (1700Å) in two different electrolytes. One film was formed at 100v in the organic solution, and the other was formed at 63v in 1% KOH. Each specimen was dipped into a 5% solution of HF for successive 10-sec periods with the specimen being washed free of HF between each dip. The film thickness was estimated after each dip by comparing its interference color with those on a set of standard specimens whose thicknesses had previously been determined spectrophotometrically, and varied from 0 to 3500Å. The infrared transmission spectrum of a film formed in the organic solution and chemically thinned in this fashion was also recorded.

Results

The spectrum of the anodic film formed in the 1% KOH solution is shown in Fig. 1. The ZrO_2 absorption band at 14.3μ seen in this spectrum recurs in the

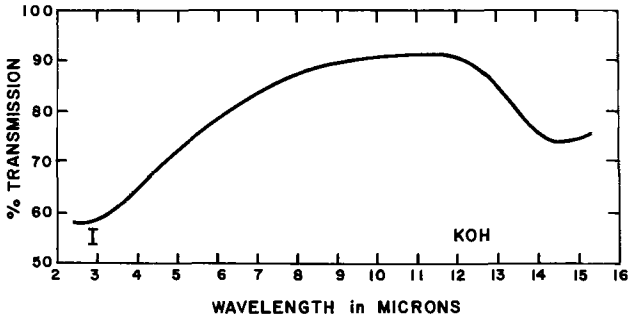

Fig. 1. Infrared transmission spectrum of an anodic ZrO_2 film formed at 125v in 1% KOH solution.

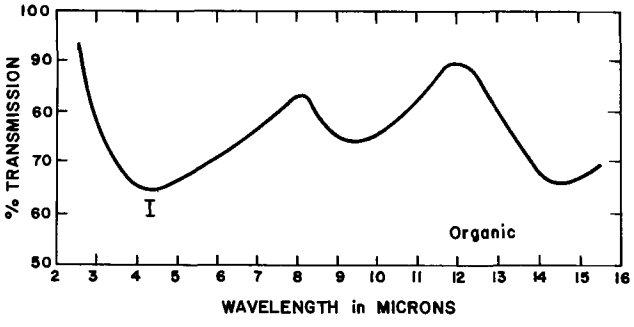

Fig. 2. Infrared transmission spectrum of an anodic ZrO_2 film formed at 400v in the organic solution.

spectra of all the films measured. The band just below 3μ is not a true absorption band but a minimum in the transmitted intensity resulting from first-order interference effects in the film. Similar interference minima occur in most of the spectra to follow, and their position is noted by the letter I on each spectrum.

The spectrum of the film formed in the complex organic solution shown in Fig. 2 exhibits an absorption band at about 9.3μ which was not seen with the KOH film. Miller and Wilkins (5) have shown that the absorption band for the phosphate ion in inorganic compounds falls between 9 and 10μ. Therefore, the 9.3μ band observed here is attributed to phosphate ions incorporated in the film during anodization. A similar band occurs in the spectra of films formed in H_3PO_4 solutions.

An absorption band appears at 9.0μ in the spectrum of the film formed in H_2SO_4 as shown in Fig. 3. This band is characteristic of the sulfate ion suggesting that it is also incorporated into anodically formed films.

Figure 4 presents the spectrum typical of films formed in solutions of the organic acids. The double absorption bands with peaks at about 6.5 and 7.2μ in this spectrum are typical of absorption arising from the resonance between the two possible C-O bonds in the carboxylate ion structure. This indicates the presence of oxalate, lactate, and citrate ions in these films, again presumably incorporated during anodization.

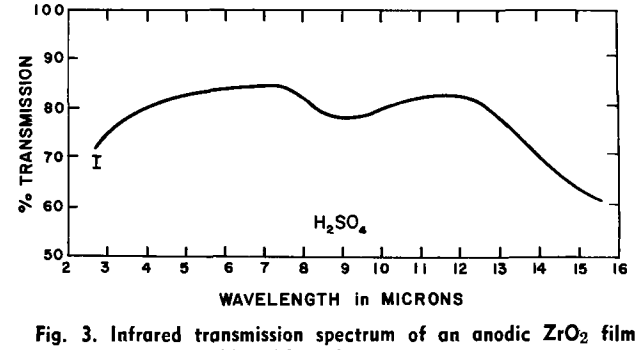

Fig. 3. Infrared transmission spectrum of an anodic ZrO_2 film formed at 100v in 0.5M H_2SO_4 solution.

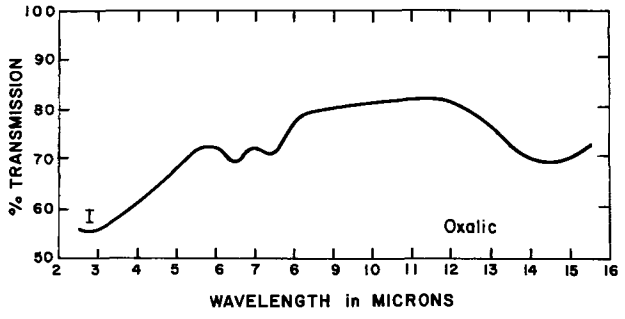

Fig. 4. Infrared transmission spectrum of an anodic ZrO_2 film formed at 150v in 0.5M oxalic acid.

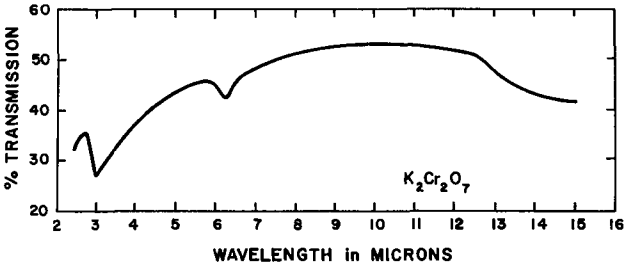

Fig. 5. Infrared transmission spectra of anodic ZrO_2 films formed at 100v in 0.5M $K_2Cr_2O_7$.

Neither the spectra of the films formed in the borate solutions nor the spectrum of the film formed in Na_2MoO_4 exhibit absorption bands other than those attributable to the film itself or interference effects. Thus, these films are similar to the one formed in KOH in that they apparently contain no impurity ions.

The spectrum of the film formed in $K_2Cr_2O_7$ is shown in Fig. 5. The two absorption bands at 3.1 and 6.2μ in this spectrum are at positions corresponding to the stretching and bending modes of the O-H bond in bound water. These two bands, as well as the broadening of the 14.3μ ZrO_2 band, are characteristic of the hydrated oxide indicating that such an oxide is formed on anodization in these solutions. There is no indication of other ions in these films. The spectra of the films formed in both K_2CrO_4 and KNO_3 also indicate a hydrated film.

The results of the thickness and conductivity measurements are summarized in Table I. The films formed in solutions which produced incorporated ions were much thinner, on the average, than those formed in solutions producing ion-free films. The conductivities of the two types of film also differ, with the average value for ion-free films being about 35% higher than the average value for the films containing ions.

The dissolution by HF of the two films formed to approximately the same thickness in KOH and the complex organic solution is represented in Fig. 6. The KOH film did not appear to dissolve at all after 2 min exposure to the HF. The organic film dissolved rapidly at first; but on reaching a thickness of about 950Å after 90-sec exposure, the dissolution ceased. The 9.3μ ab-

Table I. Thickness and conductivities of anodic oxide films formed on zirconium at 100v in various anodizing solutions

Anodizing solution	Film thickness, A		Film conductivity (ohm^{-1} cm^{-1}) × 10^{14}	
	Specimen 1	Specimen 2	Specimen 1	Specimen 2
Organic	1780	1736	1.50	1.68
0.5M H_3PO_4	1801	1775	1.89	1.69
0.5M H_2SO_4	1646	1653	1.64	1.72
1% KOH	2675	2675	2.50	2.40
0.5M $(NH_4)_3BO_3$	2360	2360	2.19	2.24
0.5M oxalic acid	1603	1580	1.50	1.59
0.5M citric acid	1806	1819	2.05	1.92
0.25M Na_2MoO_4	2588	2588	2.39	2.26

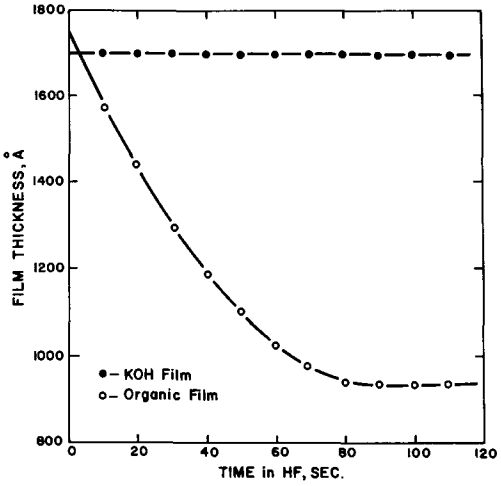

Fig. 6. Comparison of the dissolution in 5% HF of the films formed in 1% KOH and the organic solution.

sorption band attributed to phosphate ion was not evident in the spectrum of the chemically thinned film.

Discussion

The detection of incorporated ions in anodic films was not completely unexpected. Plumb (6) and Bernard (7) both found phosphorus in anodic films formed on aluminum in phosphate solutions, and Bogoyavlenskii and Dobrotvorskii (8) found both carbon and cobalt occluded in such films formed in carbonate solutions containing cobalt in a complex anion. Bernard and Randall (9) found boron in anodic Al_2O_3 films formed in borate-glycol solutions. Others (10-12) have variously reported the occlusion of phosphorus and sulfur in anodic tantalum and niobium oxide films formed in phosphate or sulfate solutions.

Many of these workers have suggested that the incorporated materials are present in the films as anions. However, the spectrographic and radiochemical methods they used to detect their presence could not truly define the chemical species. The present work shows quite clearly that the impurities found in the anodic films on zirconium are present as phosphate, sulfate, and carboxylate ions, and lends credence to the speculations of these prior workers.

It was surprising that the KOH film was not attacked by the HF solution. However, this fact gives an indication of the distribution of the phosphate in the film. Smyth, Tripp, and Shirn (10) and Randall, Bernard, and Wilkinson (11) have shown that in anodic films formed on tantalum in phosphate solution, there is a phosphorus-free layer of oxide adjacent to the metal surface. Above this they found a second layer, of thickness equal to 50-65% of the total film thickness, through which the incorporated phosphorus was evenly distributed. The portion of the film formed in the complex organic solution remaining after the initial dissolution of about 750Å of its thickness was not attacked further on exposure to the HF solution. This remaining layer was shown to be ion-free, as was the KOH film which was not attacked by the HF. This indicates that the phosphate ion contained in the film was held in the outer 750Å layer that was dissolved. This layer represented about 44% of the total film thickness. Thus, it appears that the phosphate-ion impurities are incorporated in thinner layers in anodic films on zirconium than in anodic films on tantalum. Whether the phosphate impurities are evenly distributed in this layer, as they are in films on tantalum, cannot be definitely determined from these results. However, the dissolution rate of this outer layer appears to be reasonably constant as the thickness decreases suggesting such a distribution. Although no attempt was made to determine the distributions of the sulfate or carboxylate ions occluded in the films, they would presumably be similar to that of the phosphate ion. Draper (12) feels that sulfur found in films formed on tantalum and niobium in sulfate solutions is distributed throughout the thickness of the films, but presents no real evidence in support of his position.

Because of their ease of preparation, anodic oxide films on zirconium are often used in experimental studies with the assumption that results may be equated with the behavior of corrosion films under the same conditions. The detection of impurity ions in anodic films formed in phosphate, sulfate, and carboxylate solutions, and the detection of a hydrated oxide product when anodizing in electrolytes containing strongly oxidizing ions suggests that films formed in these particular solutions should not be used for this purpose. These films are not strictly equivalent to corrosion films, which are presumably pure oxide. In fact, solutions other than those investigated here may also produce films with ion impurities; and great care should be exercised in choosing electrolytes in which to form films for such use. Present results indicate that films formed in solutions of $(NH_4)_3BO_3$, H_3BO_3, Na_2MoO_4, and especially those formed in dilute KOH should be suitable to use in this capacity since they appear to be free of occluded ions.

Indeed, the ions occluded in films lead to other types of film behavior quite different from that observed with ion-free films. For example, the ions seem to impart greater electrical insulating character to the films as indicated by the higher conductivity of the ion-free films. Results of the thickness measurements further suggest that these ions very effectively limit the film growth during anodization. This growth is generally pictured as proceeding via the diffusion of oxygen in the form of oxide ions through the film toward the metal with a counter diffusion of oxide-ion vacancies and electrons. It was shown (11) that the phosphorus in anodic films on tantalum was immobile in the layer of oxide in which it was contained. If the ions detected here are similarly immobile, they could create a stationary negative space charge which would oppose the diffusion of both oxide ions and electrons through the films. This would lower both the ionic and electronic conductivity of the film during its growth, thereby producing thinner films for a given voltage than would be obtained were the space charge not present. A similar limiting of the mobility of oxygen was suggested for phosphorus-containing films on tantalum (10). This model for the growth-limiting effect suggests that pre-anodizing zirconium to cover it with one of these ion-containing films may prove beneficial in increasing its corrosion resistance. It has been reported (10) that tantalum covered with an anodic film containing occluded phosphorus gained 25% less weight when heated at 400°C in oxygen than did tantalum with a film containing no phosphorus.

The drastic reduction of the rate of dissolution of anodic films on zirconium into the underlying metal is apparently a further consequence of the presence of ion impurities in these films. For example (3), the thicknesses of films formed on zirconium in the complex organic solution and 1% KOH decreased by 50 and 710Å, respectively, when the specimens were heated in vacuum at 450°C for 16 hr. This dissolution process is also considered operative in the over-all corrosion mechanism of the metal, and any decrease in the rate of dissolution should improve its corrosion behavior. Since the ions are confined to an outer layer of the film, it is not immediately clear just how they affect a process occurring some distance away at the metal-oxide interface. One possible explanation is that the kinetics of the dissolution are such that the rate-controlling step is the filling of anion vacancies which result from the dissolution with oxygen ions from the outer portion of the films. The rate of filling these vacancies would then be equivalent to the rate of diffusion of oxygen ions through the outer oxide layer containing the ions. This model agrees well with the experimental observations.

Conclusions

Polyatomic ions such as phosphate, sulfate, and various carboxylates are incorporated in anodic oxide films formed on zirconium in solutions containing these ions. These ions are occluded in an outer layer of the film with ion-free oxide between this layer and the substrate metal. The presence of these ions greatly affects the chemical reactivity of the films. The ions also appear to enhance the electrical resistivity of the films and limit their growth rate as well as their rate of dissolution into the underlying metal. These effects are attributed to the ions creating an immobile space charge in the outer layer which opposes the diffusion of both oxygen ions and electrons through this portion of the film.

Acknowledgments

The author expresses his appreciation to M. L. Picklesimer for valuable discussions relative to this work. Further thanks are due G. C. Nelson for aid in preparation of data presentations. Research was sponsored by the U. S. Atomic Energy Commission under contract with the Union Carbide Corporation.

Manuscript received Aug. 24, 1966; revised manuscript received Dec. 23, 1966.

Any discussion of this paper will appear in a Discussion Section to be published in the December 1967 JOURNAL.

REFERENCES

1. J. C. Banter, *This Journal*, **112**, 388 (1965).
2. J. C. Banter, *Electrochem. Technol.*, **4**, 237 (1966).
3. J. C. Banter, Unpublished work.
4. N. J. M. Wilkins, *Corrosion Sci.*, **4**, 17 (1964).
5. F. A. Miller and C. H. Wilkins, *Anal. Chem.*, **24**, 1253 (1952).
6. R. C. Plumb, *This Journal*, **105**, 498 (1958).
7. W. J. Bernard, *ibid.*, **109**, 1082 (1962).
8. A. F. Bogoyanlenskii and G. N. Dobrotvorskii, *J. Appl. Chem. USSR* (English Transl.) **35**, 1496 (1962).
9. W. J. Bernard and J. J. Randall, Jr., *This Journal*, **108**, 822 (1961).
10. D. M. Smyth, T. B. Tripp, and G. A. Shirn, *ibid.*, **113**, 100 (1966).
11. J. J. Randall, Jr., W. J. Bernard, and R. R. Wilkinson, *Electrochim. Acta.*, **10**, 183 (1965).
12. P. H. G. Draper, *Acta Met.*, **11**, 1061 (1963).

The Effect of Various Optical Radiations and Water Vapor on the Trapping Spectrum of CdS

Paul A. Faeth

Lewis Research Center, National Aeronautics and Space Administration, Cleveland, Ohio

ABSTRACT

Trapping levels in a cadmium sulfide single crystal were studied by the thermally stimulated current method. In all, six trapping levels were detected in the crystal. A study of the shallow traps, which occurred at 0.04, 0.12, and 0.13 ev below the conduction band edge, indicated that electrons could be excited directly to the 0.13 ev level. A peak in the photoconductivity was observed at —60°C when the crystal was cooled in the presence of IR and 533 mμ light. The center with level at 0.13 ev appears to behave as a recombination center for temperatures greater than —60°C and as a trapping center which can be emptied optically at temperatures less than —60°C. Other experiments involving cooling during illumination indicated the presence of another trapping level which apparently could not be filled from the conduction band. Water vapor which was adsorbed on the crystal surface produced thermally stimulated current (TSC) peaks at 80°-100°C in the absence of any treatment of the crystal by light. The appearance and magnitude of these TSC peaks were affected by light as well as the partial pressure of water vapor. Pumping over the crystal with adsorbed water present also stimulated currents. Both of the latter observations are believed due to the dissociation of an adsorbed species such as $(H_2O)^-$ on the crystal surface.

Cadmium sulfide is a material of considerable interest because of its photoconductive properties. It has found wide use as a photoconductor and more recently has shown promise as a solar cell material (1). The photoconductive properties of cadmium sulfide are modified by the presence of electron and hole traps in the crystal (2, 3) and by adsorbed gases, which may produce electrical effects similar to traps (4-6). It is reasonable to suppose, therefore, that the operation of devices such as the cadmium sulfide solar cell will be affected by the presence of traps and adsorbed gases. Indeed, adsorbed water vapor seriously damages cadmium sulfide solar cells and photoconductors.

In an effort to obtain further insight into the effect of gases and light on the photoconductive properties of cadmium sulfide, an experimental study was made of some of the effects of water vapor and light on the trapping spectrum of cadmium sulfide. Water vapor is notorious for causing experimental difficulties in high vacuum equipment. Unless special precautions and equipment are employed which remove and eliminate water from the system one cannot be sure that the presence of water vapor is not somehow responsible for some of the experimental effects observed. In less elegant vacuum systems this is especially true. In addition, the use of light in the presence of water vapor may cause additional effects such as photosorption to occur. Several experiments were performed which seemed to indicate this may be the case.

The effect of various illuminations and water vapor on trapped carriers was studied in a single crystal of high resistivity cadmium sulfide by using the TSC technique. Various wavelengths of light were used singly and in combination with other wavelengths to populate the trapping levels. The purpose of this procedure was to make qualitative observations of the manner in which radiation filled and emptied the traps in a relatively dry system. In another series of experiments, water vapor was allowed to adsorb on the crystal surface. The effect on the thermally stimulated current was observed in order to determine qualitatively if adsorbed water vapor affected this electrical property of the crystal. The trapping levels observed in this research on cadmium sulfide occur at energies

which are in good agreement with those previously reported for electron traps, and it is assumed that only electron traps were observed.

Experimental Apparatus and Procedure

The determination of trap depths in cadmium sulfide by measuring the TSC is a most informative technique. The TSC is that additional current produced in the crystal when mobile carriers are released from trapping centers by thermal energy. The mobile carriers are usually excited into the trapping centers by illumination with optical radiation at low temperatures. Recent reviews of this subject for cadmium sulfide have been given by Nicholas and Woods (7) and Dittfeld and Voigt (8).

The measuring system that was used is similar to the one described by Bube (9). A beam splitter was provided so that the sample could be exposed to two different water-filtered radiations, either simultaneously or separately. Only estimations of intensity were made. Specific radiations or bands were obtained by using narrow band interference filters and/or Wratten (W-) filters and a quartz-iodine light source (10). The sample was exposed to light through a photographic shutter.

The sample was contained in a vacuum-jacketed Dewar and could be exposed to various gaseous atmospheres. Helium was used as the heat-transfer medium. Oxygen, nitrogen, and helium gases were introduced through a liquid-nitrogen cold trap. Oxygen and nitrogen used in the pumping experiments were distilled from the cold trap to a pressure of 1 atm into the measuring system which was at room temperature. The sample was then cooled to liquid nitrogen temperature. The crystal did not come in contact with a pool of liquid O_2 or N_2. Water vapor was carried into the system by passing helium through a bubbler at room temperature.

The specimen of cadmium sulfide was obtained from the Clevite Corporation. The crystal was sulfur compensated and had an initial dark resistivity of about 10^{10} ohm-cm. The crystal had been grown by evaporating pure cadmium sulfide in an inert atmosphere and had less than 1 ppm of electrically active centers. Ohmic indium contacts were used in conjunction with platinum leads. In most cases a potential of 180v was applied across the sample. A low order external resistor (2.9×10^4 ohms) in series with the sample was used as a current detector. The voltage change across this resistor was monitored with a nanovoltmeter and was recorded.

Only minor difficulty was encountered in obtaining reproducible dark current measurements from day to day. In general, the dark current which was measured without optical stimulation from liquid-nitrogen temperature to the highest temperature of the run was reproducible, but it was observed that the previous history (11) of the sample was important to the reproducibility of the dark current obtained. Repeated measurements of the dark current showed only slight displacements if the sample was consistently stored in the dark. It was further observed that infrared radiations at liquid-nitrogen temperatures caused the dark current to be suppressed. Subsequent experiments of white-light-excited TSC curves always resulted in peak suppression (12, 13) after an IR radiation and indicated a residual effect of the infrared radiation that was not easily dissipated between cycles.

The data for trap depth calculations were obtained by heating the crystal at various linear heating rates (β) and observing the temperature of maximum conductivity (T_m). Trap depths were determined from plots of the equation $\ln T_m^2/\beta = E/kT + \text{const.}$ (3, 7). Once having established the trap energies associated with the various peaks a constant heating rate was not used for other TSC experiments (unless specified) since a relatively fast rate appeared to improve peak resolution. The rapid heating rate was linear up to

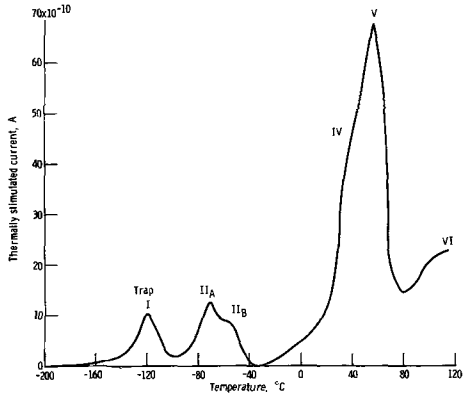

Fig. 1. Thermally stimulated current curve of as-received cadmium sulfide sample.

—70°C at which temperature deviations could be observed. The deviations were constant between runs.

Experimental Results and Discussion

The observation of a specific trap emptying and the relative concentration of trapped carriers depends on a number of variables (2) among which are: (*i*) the previous history of the sample; (*ii*) the radiation used as stimulation (including radiation combinations); (*iii*) the temperature at which the radiation took place; and (*iv*) the ambient atmosphere and its effect on (*i*), (*ii*), and (*iii*).

A typical thermally stimulated current curve is shown in Fig. 1. This curve was generated by cooling the crystal in the dark, illuminating it with white light and then warming it. Figure 1 shows the current peaks produced from the trapping levels which are designated as I, II_A, II_B, IV, V, and VI. Trap III (Fig. 3) could not be filled by the technique used to fill the other traps and will be discussed below. The two peaks, II_A and II_B, appeared as one if 533 mμ illumination time was applied for times greater than 1 min. The low-temperature traps I, II_A, and II_B, had energy depths below the conduction band edge of 0.042, 0.12_5, and 0.13_1 ev, respectively. These values are the least squares average of 12 determinations using heating rates in the range 0.04-0.3°C/sec.

Traps IV, V, and VI found at higher temperatures were not as reliably reproduced as those occurring at low temperatures. They could occasionally be induced to appear by subjecting the crystal to special treatments. However, reliable data could not be obtained which would permit significant trap depth calculations.

An attempt was made to fill electronic traps near the conduction band of cadmium sulfide by exciting electrons with optical radiation directly from the valence band (12). Kulp (14) reports that direct filling can be accomplished from a level 1.79 ev below the conduction band with wavelengths greater than 690 mμ for special cadmium sulfide "storage" crystals. The TSC of the two traps located at 0.04 and 0.13 ev mentioned above was observed after 30-sec excitation at liquid nitrogen temperatures with 501, 533, 578, and 697 mμ radiation. A transient, as well as a small sustained photoconductivity, was observed during excitation with the 500 series. Wavelengths greater than 697 mμ indicated no photoconductivity of either kind. The participation of the conduction band during excitation in these cases limits an interpretation of direct filling from the valence band. Even though the relative filling of the two traps was as expected for direct filling, one cannot be certain of the origin of all electrons that have entered the trap.

Cooling during illumination.—Another set of experiments was performed to demonstrate in a more definitive way that electrons were being excited from the valence band to shallow trapping levels near the

conduction band and involved cooling during illumination. Cooling in the presence of white light produced a curve similar to those obtained by Bube (15) and Kulp (14). As the temperature was reduced, the photocurrent increased showing a broad peak cresting at about —80°C. Bube explained this effect as a change in a defect center from a recombination center to a trapping center as the temperature was lowered. If a shallow trapping center participates in the photoconductive process and is being populated directly from the valence band, a change in the photoconductivity might be observed as the number of electrons excited to this level is changed. An attempt was made to observe such an effect with the known level at 0.13 ev. A band of light (533 mμ peak) was applied to the crystal whose energy was slightly more than enough to excite electrons from the vicinity of the valence band to this level above room temperature. At liquid nitrogen temperature the filter energies were not sufficient to promote electrons to the trap level from the valence band due to the displacement of the band edge. Cooling in the presence of 533 mμ light produced only a steady decrease in the photoconductivity; the expected change in the photoconductivity was not observed. Subsequent TSC curves showed, however, that electrons were trapped in the 0.13 ev level. The absence of the expected change may be due to this center behaving as a recombination center at higher temperatures and as a trapping center at lower temperatures in which case the conduction band may not be involved appreciably. Bube (15) has observed a maximum in the decay time at about —50°C for CdS:Cl:Cu crystals, but little corresponding change in the photoconductivity.

At low temperatures the application of IR to a filled trap system produced transient current flow indicating that electrons were being excited to the conduction band. Some of this conductivity resulted from the emptying of the shallow trap levels. A TSC determined after such treatment indicated that the shallow traps were empty. Cooling in the presence of IR · ($\lambda > 800$ mμ) to keep the shallow traps empty and 533 mμ light to fill them from the valence band produced the curve shown in Fig. 2. This curve can be explained by assuming a mechanism similar to that proposed by Bube. Although the peak temperature at —60°C may have no special significance, it is very

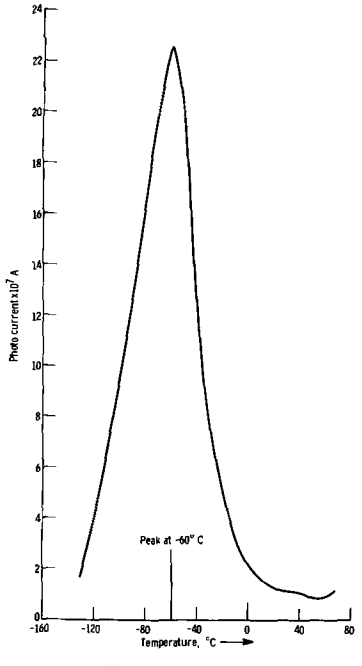

Fig. 2. Photocurrent of CdS crystal as a function of temperature using 533 mμ light and IR.

nearly the same as that found for the TSC emptying of the 0.13 ev level and suggests that the Fermi level may be in the vicinity. At temperatures above —60°C the center appears to behave as a recombination center. Below —60°C the center behaves as a trap which can be optically emptied.

The decrease in photoconductivity shown in Fig. 2 for temperatures less than —60°C can be explained if the effect of the variation of band gap with temperature is considered. The use of white light in such an experiment readily provides combinations of all the energies needed to promote a sustained high photoconductivity at all temperatures below —60°C. Consequently, the effect of the movement of the band edge is masked. If electrons are excited directly from the valence band to the level at 0.13 ev, the number excited can be reduced as the band gap increases and will be limited by the pass of the filter and the density of states in the valence band. At —60°C the energy between the valence band edge and the trap level is calculated (3) to be about 2.33 ev and corresponds with the energy peak of the 533 mμ filter from the valence band edge. If a high density of states is concentrated at the valence band edge, the energy profile of the filter may be reflected in the photoconductivity as the temperature decreases. If the density of states decreases as the edge is approached from below (16), something other than the filter profile might be expected. Some discrepancy may also arise if the thermal and optical excitation energies from the valence band to the trap level are not equivalent. The energy difference from the peak to half peak of the filter was about, ±0.03 ev. The energy difference calculated from Fig. 2 for temperatures less than —60°C due to the displacement of the band edge from peak to half peak is about 0.02 ev. The decrease in photoconductivity below —60°C appears to be due to the decreased participation of the 0.13-ev level in the photoconductive process and is probably due to the inability of any of the wavelengths applied to promote electrons to this level.

Another series of experiments was performed during which time the irradiation was applied to the sample continuously during the cooling process. Woods and Nicholas (13) using cadmium sulfide and Bube (17) using cadmium sulfide and mixed cadmium sulfide-cadmium selenide crystals have performed similar experiments and report a new trap at 0.73-0.83 ev. As mentioned above, when the white light was used, the photocurrent decreased as the temperature was reduced from 100°C, leveled near room temperature, reached a maximum near —80°C, and then decreased steadily until liquid-nitrogen temperature was reached. After cooling in the presence of white light (heat filter passing wavelengths less than 800 mμ), the resultant TSC curve (solid curve of Fig. 3) showed the presence of peak III occurring at about 0-10°C. Traps I and II were well filled and trap II showed no resolution.

A similar experiment was conducted by using only 533 mμ illumination and resulted in the long dashed curve, which shows the exclusion of the new peak. (Traps I and II were filled as shown by the solid curve, but are excluded from the drawing for clarity.) A detail of the area around 0°-10°C is shown in the inset of Fig. 3. Although photoconduction was evident during the cooling process (electrons in the conduction band), it did not appear that trap III could be filled from the conduction band. The behavior of the system indicated by the solid and long-dash curves suggested the necessary participation of at least a second wavelength present in white light to achieve the filling of trap III.

To test this hypothesis the specimen was exposed to two illuminations simultaneously as the sample was cooled. The primary illumination was 533 mμ light; the secondary illumination was a band of light formed by the heat filter and various Wratten filters.

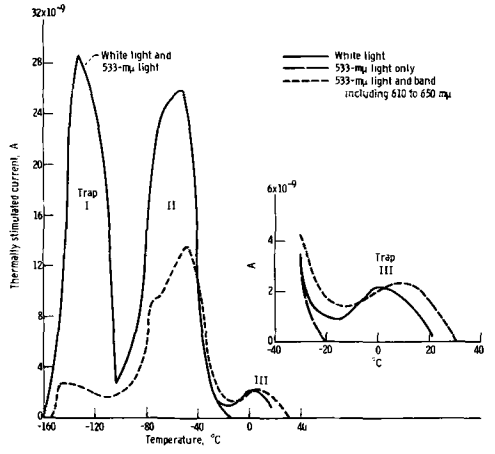

Fig. 3. Thermally stimulated current curve obtained after cooling during illumination.

The Wratten filters were changed between experiments and were such that additional increments of shorter wavelengths could be passed with each succeeding filter in the series. This procedure revealed that the secondary wavelength needed to allow trap III to fill lay in the region 610-650 mμ. The short-dash curve (Fig. 3) illustrates the results. Secondary wavelengths greater than 650 mμ did not produce a filling of trap III and indicates a threshold energy for filling of about 2.0 ev. Further support for direct filling of traps is found in these results, since the energy complement required to fill the reported trap at 0.41 ev (7) directly from the valence band would correspond to a wavelength of about 621 mμ. It is also apparent from Fig. 3 (short-dash curve) that the secondary wavelength tends to keep the shallow traps empty.

Bube (17) has shown that a similar trap appears to fill most efficiently when the Fermi level is about 0.45 ev below the conduction band. Assuming that trap III is the same as that observed by Bube (17) and Nicholas and Woods (7), the results illustrated in Fig. 3 indicate that this trap can be filled readily by direct excitation from a lower state which, on the basis of the threshold required, appears to be near the valence band.

Effect of water on thermally stimulated current.—An interesting effect on the TSC was produced by water vapor. Since Bube (18) has shown that water vapor produces a reduced photoeffect for cadmium sulfide, it was pertinent to determine whether water vapor would affect the TSC. Consequently, a series of experiments was performed in which water vapor was purposely introduced into the system. The sample was then cooled to liquid nitrogen temperature, and the TSC was measured without illumination of the sample at any time. Without exception a complex peak appeared in the vicinity of 80°-100°C. The partial pressure of water vapor in the system was subsequently decreased by reducing the total pressure to 1/6 atm. The pressure was then restored to 1 atm with dry helium. The results of a series of such manipulations are shown in Fig. 4. The results indicate that the presence of water vapor produces simulated TSC peaks, the areas of which are a function of the partial pressure of water in the system. The appearance of two peaks in curves 2 and 3 immediately suggests a heterogeneous surface, with at least two different sorption sites.

After pumping for several hours at room temperature the normal dark current curve could be obtained. However, infrared (30 sec) illumination (W-87) at room temperature followed by cooling to liquid nitrogen temperature (no illumination) and subsequent heating indicated the reappearance of the 80°-100°C peak (but to a much reduced degree). When white light was used as excitation at room

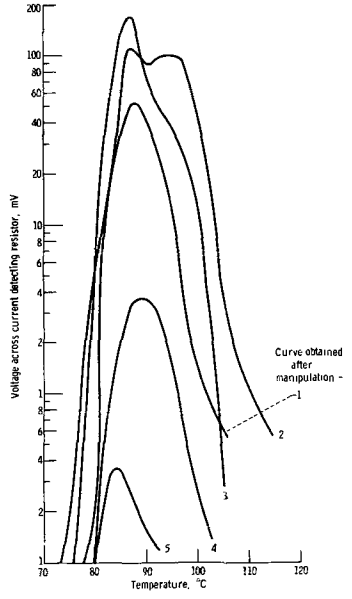

Fig. 4. Thermally stimulated current curves produced by manipulating water vapor pressures; heating rate 0.28°C/sec.

temperature, a broad TSC peak was produced which crested in the 80°-100°C region. Similar experiments in a relatively dry system did not produce this peak. The appearance of a TSC peak under these conditions might be attributed to photosorption of water vapor since small amounts of water vapor undoubtedly were still present. The work of Sebenne and Balkanski (19) has shown that water is adsorbed by cadmium sulfide surfaces, at which place these authors suggest it attaches an electron to form $(H_2O)^-$ ions. Desorption of sorbed water by heating the crystal could release electrons to the bulk of the crystal from the breakup of such a species and thereby produce a peak in the TSC.

After water vapor had been introduced and substantially removed by pumping to give the normal dark current curve. TSC curves, obtained by illumination with white light at liquid nitrogen temperatures, showed that the peaks at 60° and 100°C were separate and building (Fig. 5). After three temperature cycles without changing the charge of helium, a broad peak tending to crest near 80°C was produced. This result suggests possibly that the amount of water vapor on the surface of the crystal was increasing between cycles and was probably coming from the walls of the sys-

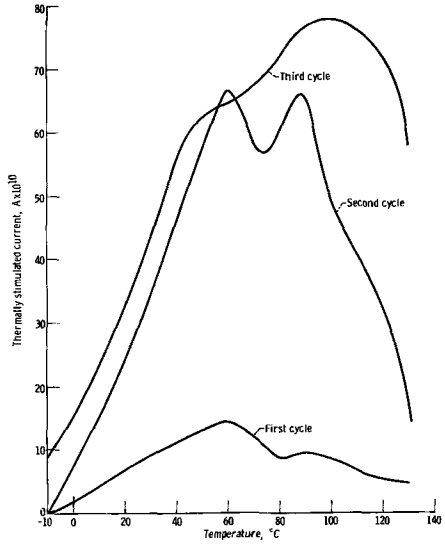

Fig. 5. TSC obtained by thermal cycling without changing He

tem at higher temperatures. Further pumping on the system again reduced the peaks in the region 60°-100°C.

The low-temperature traps (I and II) remained relatively empty during these water treatments, although their presence could be detected. This result indicates that sorbed water vapor has hindered the filling of these levels and can be explained in part by assuming some of the sorbed water acts in the capacity of recombination centers (3) and/or traps as indicated by the TSC peaks shown in Fig. 4. If the capture cross section and the escape cross section for the shallow traps are small (7, 17), then the presence of relatively large capture cross-section centers such as sorbed water vapor could hinder the filling of the shallow traps. This could be accomplished if electrons in the conduction band reacted at a faster rate with recombination centers than with empty shallow trapping centers. The IR wavelengths of white light probably were effective also in maintaining these levels empty.

After water treatment and subsequent removal by pumping only, a TSC, obtained using 533-mμ-illumination for 2 min at liquid nitrogen, showed the strong reappearance of electrons in traps I and II and the absence of the 80°-100°C peak. This result would seem to indicate that these shallow levels are preferentially filled by this excitation (in the absence of IR but in the presence of small amounts of sorbed water vapor) and that the filling process probably involves a substantial amount of direct filling from lower levels. If electrons in the shallow traps are to recombine via the conduction band, they must enter the conduction band via a relatively small escape cross section ($< 10^{-22}$ cm^2) (7) before recombination can occur, in which case electrons so trapped (directly) would be expected to be observed via a TSC. This result also suggests that the shallow traps were not destroyed, but could not be filled using the white light conditions mentioned above. The same experiment performed in the presence of larger partial pressures of water showed a water peak as in Fig. 4 and also the peaks of traps I and II.

Bryant and Cox (20) find a trap at 0.86 ev which empties at ~100°C. This trap seems to have some similarity to the 100°C trap noted above and might be attributed to adsorbed water vapor. These authors believe this trap to be the one located at 0.83 ev by Nicholas and Woods (7), in which case it could also be the trap located by Bube (17) at 0.73 ev. Nicholas and Woods describe this trap as one which empties via first-order decomposition of an unusual trap complex. This description fits that of an adsorbed species such as $(H_2O)^-$ or O_2^- in the case of oxygen and has been suggested by Bube (17), in the case of oxygen, as a possible explanation for the photochemical processes observed by these authors. The apparent cross section of this center in cadmium sulfide is reported as ~ 10^{-15} to 10^{-14} cm^2 (7, 17) and compares reasonably well with the cross-sectional area of an adsorbed gas molecule (~ 10.6Å^2 for water at 24°C) (21). If an electron becomes associated with a sorbed water molecule as $(H_2O)^-$ on the surface of cadmium sulfide, then the escape cross section of the electron on dissociation of this species and the effective area of the sorbed molecule may be similar. The fact that adsorbed water appears to produce recombination as well as trapping centers suggests that fast and slow states, respectively, are likely to be found on the surface of CdS.

Effect of pumping on the TSC.—Evacuation of the helium in the system between experiments frequently produced a current spike as the pressure decreased below approximately 1 mm. This peculiar effect was reproducible and was observed at room and liquid nitrogen temperatures (Fig. 6). After a dark current determination, if the sample was returned to liquid nitrogen temperature in the dark, was pumped and a current spike obtained, a subsequent TSC measurement would show a peak at 60°C. This result supports the idea that surface trapped electrons are associated with sorbed gases and that on desorption via pumping some electrons remain trapped. If the Fermi level extends to the surface (22), dissociation of a surface trapped species such as O_2^- (at liquid N_2) located below the Fermi level might result in the creation of a surface trapped electron associated only with the solid surface. A subsequent TSC could indicate the presence of the new surface-only trapped electron. The pumping effect was not observed in an oxygen or nitrogen atmosphere. At room temperature the pumping spikes could be obtained only after illumination (white light or 533 mμ). Infrared (W87) illumination occasionally produced the spikes but not always. The fact that pumping at room temperature would not produce a current pulse unless the crystal was first illuminated suggests that at room temperature the number of sorbed species (most likely to be residual H_2O) increases when the free electron concentration is increased by illumination.

The areas under the curves of Fig. 6(a) for room temperature and liquid nitrogen temperature pumping correspond to the participation of 6.5 x 10^{13} and 1.2 x 10^{11} electrons/cm^2, respectively. These values represent a participation of less than 10% of the surface at room temperature and less than 1% at liquid nitrogen temperature.

The curve illustrated in Fig. 6(b) is typical of the pumping curves obtained after the crystal had been stored in the dark for several weeks (a "rested" crystal). The curve was obtained by pumping over the crystal during continued illumination with 501 mμ light at 78°K. After continued application of the pumping sequences the curve illustrated in Fig. 6(a) was typical of the results obtained.

The results presented above seem to indicate that water vapor in addition to O_2 may be an active component of residual air when studies are made of the trapping properties of cadmium sulfide. Sorbed water appears not only to act as a recombination center but also as an electron trap. The adsorption of water vapor

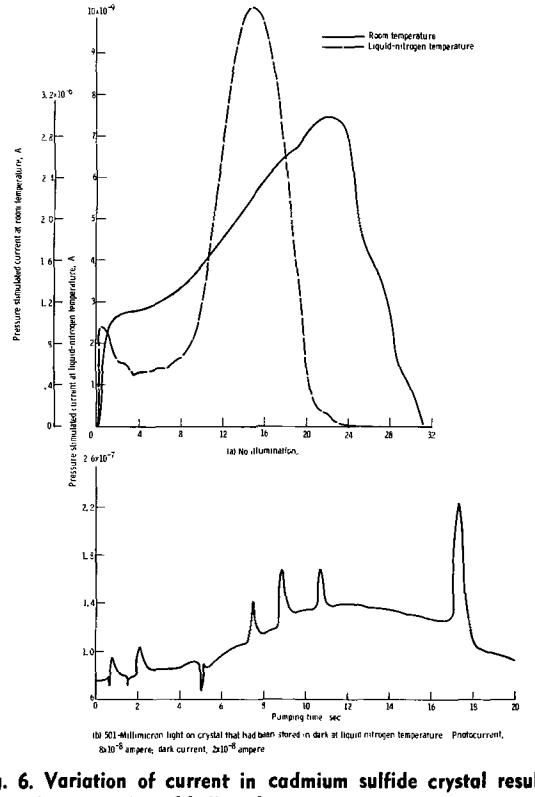

(b) 501-millimicron light on crystal that had been stored in dark at liquid nitrogen temperature. Photocurrent, 8×10^{-8} ampere; dark current, 2×10^{-8} ampere

Fig. 6. Variation of current in cadmium sulfide crystal resulting from cyclic evacuation of helium from system.

alone is sufficient to produce TSC peaks and seems to be related to some of the unusual thermal and vacuum effects noted for traps in cadmium sulfide. Illumination in the presence of adsorbed water vapor causes deep traps to appear while shallow traps remain relatively empty. Direct filling of shallow traps using appropriate monochromatic radiation less than the band edge can occur even in the presence of recombination centers. Direct filling is also evident when trap III is filled using a threshold energy of approximately 2.0 ev.

Manuscript received March 25, 1966; second revised manuscript received Jan. 23, 1967.

Any discussion of this paper will appear in a Discussion Section to be published in the December 1967 JOURNAL.

REFERENCES

1. F. A. Shirland and J. R. Hietanen, Proc. of the 19th Annual Power Sources Conf., May 18-20, 1965, pp. 177-180.
2. A. Rose, "Concepts in Photoconductivity and Allied Problems," Interscience Publishers, New York (1963).
3. R. H. Bube, "Photoconductivity of Solids," John Wiley & Sons, Inc., New York (1960).
4. Peter Mark, *J. Phys. Chem. Solids*, **25**, 911 (1964).
5. C. E. Reed and C. G. Scott, *Brit. J. Appl. Phys.*, **15**, 1045 (1964).
6. C. E. Reed and C. G. Scott, *ibid.*, **16**, 471 (1965).
7. K. H. Nicholas and J. Woods, *J. Appl. Phys.*, **15**, 783 (1964).
8. H. J. Dittfeld and J. Voigt, *Phys. Stat. Sol.*, **3**, 1941 (1963).
9. R. H. Bube, *J. Chem. Phys.*, **23**, 18 (1955).
10. R. Stair, W. E. Schneider, and J. K. Jackson, *Appl. Optics*, **2**, 1151 (1963).
11. J. S. Skarman, *Solid State Elec.*, **8**, 17 (1965).
12. S. J. Tutihasi, *J. Opt. Soc. Amer.*, **46**, 443 (1956).
13. J. Woods and K. H. Nicholas, *Brit. J. Appl. Phys.*, **15**, 1361 (1964).
14. B. A. Kulp, *J. Appl. Phys.*, **36**, 553 (1965).
15. R. H. Bube, *J. Phys. Chem. Solids*, **1**, 234 (1957).
16. N. B. Kindig and W. E. Spicer, *Phys. Rev.*, **138** A561 (1965).
17. R. H. Bube, G. A. Dussel, Ching Tao Ho, and L. D. Miller, *J. Appl. Phys.*, **37**, 21 (1966).
18. R. H. Bube, *J. Chem. Phys.*, **21**, 1409 (1953).
19. C. Sebenne and M. Balkanski, *Surface Sci.*, **1**, 22 (1964).
20. F. J. Bryant and A. F. L. Cox, *Brit. J. Appl. Phys.*, **16**, 1065 (1965).
21. H. K. Livingston, *J. Am. Chem. Soc.*, **65**, 569 (1944).
22. P. Mark, *J. Phys. Chem. Solids*, **26**, 959 (1965).

Ternary Condensed Phase Systems of Gallium and Arsenic with Group IB Elements

M. B. Panish

Bell Telephone Laboratories, Incorporated, Murray Hill, New Jersey

ABSTRACT

Data obtained from a series of differential thermal analysis studies have been used, along with x-ray and electron beam microprobe analyses, and a regular solution interpolation procedure to construct a major part of the equilibrium ternary liquidus-solidus phase diagrams of the Ga-As-Cu, Ga-As-Ag, and Ga-As-Au systems. In these systems the GaAs primary phase field occupies a major part of the phase diagram.

Studies of the Ga-As-Cu, Ga-As-Ag, and Ga-As-Au ternary systems have been undertaken because of the current interest in gallium arsenide p-n junctions made by diffusion or solution growth, in photo- and electroluminescence of variously doped gallium arsenide and in the fabrication of ohmic contacts on GaAs. The ternary phase diagrams define the conditions for the existence of GaAs in the presence of a third component, and contain part of the data necessary for the interpretation of diffusion and solubility studies which are needed to further our understanding of the incorporation of a dopant material into a binary semiconductor.

These systems are of particular interest because Cu, Ag, and Au are particularly rapid diffusers in GaAs, have rather deep lying acceptor states which are as yet not well understood, and in the case of copper, represent a major source of contamination of GaAs.

The Binary Phase Systems

Ga-As.—Gallium and arsenic form a single congruently melting compound, GaAs, with a melting point of 1238°C (1, 2). Thurmond (3) has utilized the solubility measurements of Koster and Thoma (2) and Hall (4), along with an adaptation of the regular solution treatment of Vieland (5) to construct the binary GaAs liquidus curves.

Ga-Cu.—This system has been summarized by Hansen (6). It is characterized by the existence of four major peritectically formed intermediate phases with rather extensive composition ranges. There is only one eutectic point on the liquidus curve. This point occurs on the gallium rich side of the diagram at 29.6°C.

Ga-Ag.—The Ga-Ag system has been summarized by Hansen (6). It is characterized by the existence of four major phases formed peritectically or by solid state transitions. Two of the important peritectic transformations occur at 611° and 326°C. There is only one eutectic point on the liquidus. This occurs at 29.7°C and approximately 97 a/o (atom per cent) Ga.

Ga-Au.—This system has recently been re-evaluated by Cooke and Hume-Rothery (7). The system consists essentially of a solid solution region and several peritectically formed solid solution phases in the gold rich region. The liquidus temperature drops very sharply in the gold rich region to a first eutectic at 346.7°C and about 70 a/o Au. Other eutectics occur at 339.4°C and about 65 a/o Au, 448.6°C and 45 a/o Au and 30°C near 100% Ga. The compounds AuGa and $AuGa_2$ melt congruently at 461.3° and 491.3°C, respectively.

As-Cu.—A limited amount of information is available for the As-Cu system and has been summarized by Elliot (8). The system is characterized by the existence of an extensive solid solution region of arsenic in Cu, a congruently melting compound Cu_3As (mp 827°C) and a peritectically formed transitional compound Cu_5As_2. A compound of approximate composition Cu_8As is formed via a solid state reaction at 380°C. There are eutectic points at 685° and 81.5 a/o Cu, and at 600°C and 54 a/o Cu. No information is available for compositions containing more than about 45 a/o As.

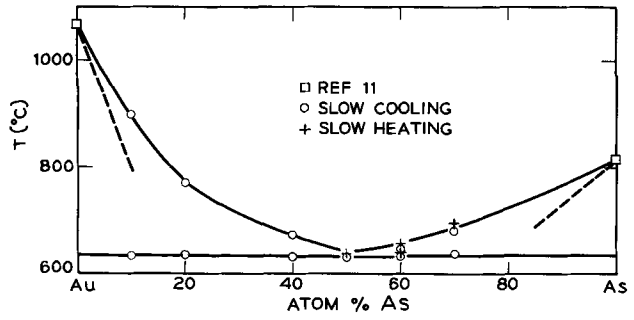

Fig. 1. Thermal effects observed on cooling and heating mixtures in the As-Au binary system.

As-Ag.—The As-Ag system is essentially simple eutectic in nature with an extensive region of solid solubility and several transitional solid solutions in the silver rich region. The eutectic point occurs at 540°C and 25.3 a/o As. The system has been summarized by Hansen (6) and Elliot. (8).

As-Au.—The liquidus curve for this system is presented here. It appears that the system is of the simple eutectic type with the eutectic composition at 51 a/o As and at 632° ± 3°C. The liquidus data and eutectic temperature reported here (Table I, Fig. 1) differ considerably from the data reported earlier by Schleicher (9). Since the latter work was done in open crucibles, there is some doubt about the composition of the samples studied and a disagreement in reported liquidus temperature is not surprising. The difference in eutectic temperature, 635°C (this work) and 665°C (ref. 2), cannot be accounted for.

The data reported here are in reasonable agreement with the limiting slopes (which represent lower limits for solid phases with no mutual solid solubility) calculated from

$$\frac{d \ln x}{d\, 1/T} = -\frac{\Delta H_m}{R}$$

on the arsenic and gold rich sides of the diagram as shown in Fig. 1.

Electron beam microprobe studies of samples with compositions on each side of the eutectic showed only phases consisting of Au or As present with only a very slight amount of mutual solid solubility.

Experimental

Semiconductor grade arsenic with purity better than 99.99% was used in this work. Reclaimed gallium with purity better than 99.99% was used, and for many of the runs GaAs was used instead of the elements. The use of GaAs was necessary when the relative amounts of Ga and As were high in order to prevent explosions resulting from the exothermic reaction of the elements. The GaAs was generally prepared from the elements by passing arsenic vapor over liquid gallium. The copper used was high conductivity grade, the silver was a reagent grade with purity better than 99.99% and the gold was obtained from Engelhard with purity better than 99.9%.

Fused-silica capsules with volumes of about 3 cm^3 which were about two-thirds filled with melt were used for the differential thermal-analysis experiments. The experimental details are similar to those which have already been described for the study of the Ga-As-Zn system (10), except that most cells, other than those used for studies in the As-Au binary system, were held at about 1250°C for a short time before cooling.

In an attempt to determine the extent to which errors resulting from supercooling occur, DTA analyses for a number of points were obtained by both heating and cooling. The rates of heating and cooling were varied from about 1°C/min to about 5°C/min.

X-ray and electron beam microprobe analyses of the DTA samples were done by standard techniques where possible. In regions of the systems where large amounts of Cu, Ag, or Au were present it was not possible to obtain powder samples, and no attempt was made to obtain x-ray data in these regions.

Results

The temperatures at which thermal effects were observed when melts of various compositions were cooled are given in Table I for the As-Au system, in Table II for the Ga-As-Cu system, in Table III for the Ga-As-Ag system, and Table IV for the Ga-As-Au system. In each case T_1 represents the temperature at which the surface of primary crystallization is reached, T_2 is the temperature at which a second solid phase precipitates, T_3 is the temperature at which a ternary eutectic or peritectic transition occurs, and T_4 is attributable either to solid state transitions or further eutectic transitions.

Table I. Thermal effects in the As-Au system*

Composition (a/o)

As	Au	T_1 °C	T_2 °C
10.0	90.0	902	633
20.0	80.0	770	636
40.0	60.0	673	631
50.0	50.0	639	630
50.0	50.0	—	630**
60.0	40.0	645	633
60.0	40.0	657**	640**
70.0	30.0	683	638
70.0	30.0	695**	—

* From cooling curves except where otherwise noted.
** Slow heating.

Table II. Thermal effects in the Ga-As-Cu system*

Composition (a/o)

Ga	As	Cu	T_1 °C	T_2 °C	T_3 °C	T_4 °C	Cut
50.0	10.0	40.0	940	640	239	—	A
50.0	25.0	25.0	1082**	†	†	—	A
50.0	25.0	25.0	1078	670	237	—	A
50.0	40.0	10.0	1176	640	‡	—	A
8.75	8.75	82.5	863	692	—	—	B
18.75	18.75	62.5	837	~682	~670	—	B
27.5	27.5	45.0	1010	686	666	—	B
35.0	35.0	30.0	1105	685	668	—	B
42.5	42.5	15.0	1174	686	665	—	B
5.0	50.0	45.0	868	606	592	322	C
20.0	50.0	30.0	1053	605	595	325	C
35.0	50.0	15.0	1163	607	595	‡	C
8.5	20.5	71.0	703	689	668	—	—
7.5	29.0	63.5	837	700	666	—	—

* From cooling curves except where otherwise noted.
** Slow heating.
† Not done.
‡ Not observed.

Table III. Thermal effects in the Ga-As-Ag system*

Composition (a/o)

Ga	As	Ag	T_1 °C	T_2 °C	T_3 °C	T_4 °C	Cut
50.0	5.0	45.0	920	446	—	285	A
50.0	15.0	35.0	1025	†	—	†	A
50.0	30.0	20.0	1130	443	—	285	A
50.0	40.0	10.0	1178	†	—	†	A
50.0	40.0	10.0	1187**	—	—	—	A
5.0	5.0	90.0	819	726	—	—	B
8.75	8.75	82.5	727	725	—	—	B
17.5	17.5	65.0	940	732	—	—	B
30.0	30.0	40.0	1073	738	—	—	B
40.0	40.0	20.0	1152	735	—	—	B
5.0	50.0	85.0	860	632	534	404	C
5.0	50.0	85.0	875**	636*	538**	—	C
15.0	50.0	35.0	990	633	530	410	C
30.0	50.0	20.0	1119	630	530	430 420	C
40.0	50.0	10.0	1192	640	535	—	C
40.0	50.0	10.0	1198**	†	†	—	C

* From cooling curves except where otherwise noted.
** Slow heating.
† Not done.

Table IV. Thermal effects in the Ga-As-Au system*

Composition (a/o) Ga	As	Ag	T_1 °C	T_2 °C	T_3 °C	T_4 °C	Cut
50.0	2.5	47.5	925	~440**	—	—	A
50.0	7.5	42.5	1010	~425**	—	—	A
50.0	20.0	30.0	1120	~442**	—	—	A
50.0	35.0	15.0	1172	~428**	—	—	A
50.0	42.5	7.5	1212	~420**	—	—	A
5.0	5.0	90.0	885	616	582	—	B
5.0	5.0	90.0	†	619‡	586	—	B
12.5	12.5	75.0	628	598	583	—	B
12.5	12.5	75.0	615	610	584	—	B
12.5	12.5	75.0	†	†	590‡	—	B
15.0	15.0	70.0	680	638	583	—	B
20.0	20.0	60.0	790	635	581	—	B
27.5	27.5	45.0	942	642	582	—	B
35.0	35.0	30.0	1075	~610	588	—	B
40.0	40.0	20.0	1120	635	588	—	B
40.0	40.0	20.0	1132‡	†	†	—	B
42.5	42.5	15.0	1164	†	†	—	B
45.0	45.0	10.0	1194	~640	588	—	B
45.0	45.0	10.0	1204‡	†	†	—	B
0.0	50.0	50.0	639	630	—	—	C
0.0	50.0	50.0	**	632	—	—	C
2.5	50.0	47.5	646	629	582	—	C
5.0	50.0	45.0	650	619	579	—	C
5.0	50.0	45.0	650‡	622‡	586‡	—	C
7.5	50.0	42.5	698	654	620	588	C
7.5	50.0	42.5	†	660	†	†	C
10.0	50.0	40.0	752	657	609	587	C
10.0	50.0	40.0	†	†	610‡	591‡	C
12.5	50.0	37.5	830	660	605	590	C
15.0	50.0	35.0	845	652	585	580	C
15.0	50.0	35.0	870‡	652‡	583‡	†	C
25.0	50.0	25.0	1120*	650	~585	580	C
25.0	50.0	25.0	1134‡	†	†	†	C
37.0	50.0	13.0	1132	645	—	576	C
40.0	50.0	10.0	1166	658	580	575	C
40.0	50.0	10.0	1175‡	†	†	†	C
27.0	8.0	65.0	828	408	372	—	D
35.0	22.5	42.5	1018	411	372	—	D
61.5	15.0	23.5	1098	492	—	—	—

* From cooling curves except where otherwise noted.
** Supercooling observed.
† Not done.
‡ Slow heating.

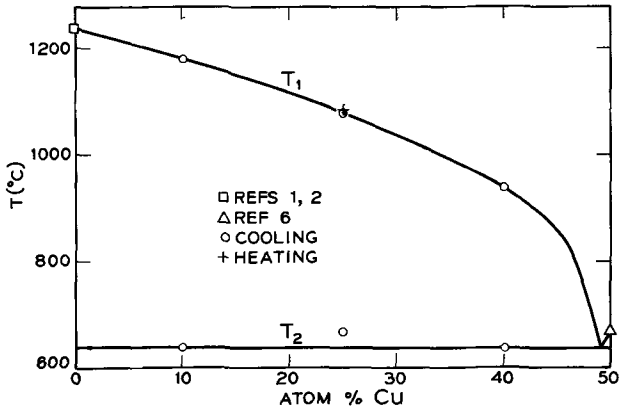

Fig. 2. Thermal effects observed on cooling and heating mixtures with compositions on cut A (Fig. 11) in the Ga-As-Cu system.

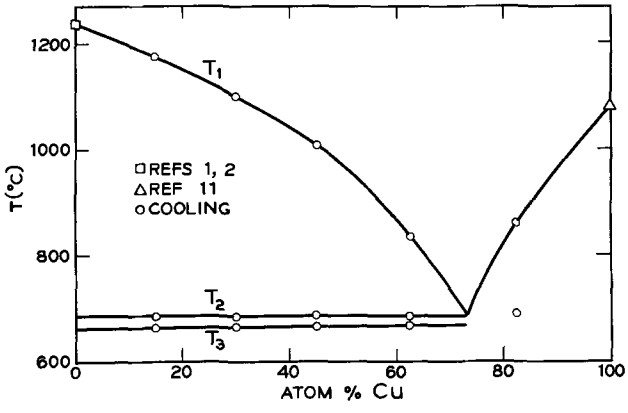

Fig. 3. Thermal effects observed on cooling mixtures with compositions on cut B (Fig. 11), the GaAs-Cu cut, in the Ga-As-Cu system.

The data given in Tables I, II, III, and IV are plotted in Fig. 1-10. The melting points of pure Cu, Ag, Au, and As were taken as 1083°, 961°, 1063°, 817°C, respectively (11). For each ternary system data were obtained along the following three cuts in the ternary system; Cut A, GaAs to 50 a/o Ga-50 a/o metal; cut B, GaAs to 100% metal; cut C, GaAs to 50 a/o As-50 a/o metal. When necessary data were obtained for other compositions in the ternary system. Since the major objective of this work is to delineate the GaAs primary phase field of each of the systems, most of the experimental data was obtained in that part of each phase system and no attempt has been made to delineate in detail the portions of the phase diagrams involving other primary phase fields.

Construction of the Ternary Phase Diagrams

The ternary diagrams were constructed primarily by the use of the binaries described above as boundaries and cuts A, B, and C as guides for the location of isotherms, eutectic boundaries, and eutectic and peritectic points. As will be discussed separately for each ternary diagram below, x-ray and electron beam microprobe data were used in the interpretation of the DTA data.

The ternary isotherms in the GaAs primary phase field were interpolated by a regular solution procedure. This procedure was recently suggested by Furukawa and Thurmond (12), and has been applied by them to the 900°C isotherm of the Ga-As-Cu system and by this author to the Ga-As-Ge and Ga-As-Sn systems (13) among others. The application of the procedure in this work is identical to that already reported for the group IV elements with Ga and As (13).

The Ga-As-Cu *system.*—For this system DTA data were obtained along cuts A, B, and C and for several other compositions in the ternary, (Fig. 2-4). The ternary diagram with isotherms in the GaAs primary phase field computed as described above is shown in Fig. 11. The regular solution estimations calculated from the data on the Ga and As sides of the diagram [as described in ref. (13)] were in good agreement for the 1100°C isotherm but were in increasingly poor agreement at lower temperatures. As described previously (13), the isotherms drawn are interpolations of the computed curves weighed to favor each computed isotherm in the region where it was most applicable. The experimental data of Furukawa and Thurmond (12) for compositions on the 900°C isotherm are shown in Fig. 11. Luzhnaya *et al.* (14) have reported liquidus data for the Cu_3As-GaAs cut which are in agreement with this work.

The DTA thermal effects noted for compositions along cut A (Fig. 2) are attributable to the primary phase precipitation of GaAs at T_1, the precipitation of an alloy based upon Cu_9Ga_4 at about 640°C (T_2), and the peritectic formation of $CuGa_2$ at 238°C (T_3). All three phases were identified by their x-ray powder patterns.

The thermal effects observed for cut B (Fig. 3) are attributable to the primary precipitation of GaAs at T_1 from 0 to 73 a/o copper, to the precipitation of the alloy based upon Cu_9Ga_4 at about 686°C (T_2) and to a ternary eutectic at 667°C where GaAs, Cu_9Ga_4, and Cu_3As precipitate simultaneously. The three phases mentioned were identified by their x-ray powder patterns. In addition a phase indexed as Cu_6As but referred to as Cu_8As by Elliot (8) was observed in the x-ray photographs. This phase forms by a solid state reaction at about 380°C according to Hansen (6). A corresponding thermal effect was not observed in this work.

The thermal effects noted for compositions along cut C (Fig. 4) are attributable to the primary precipitation of GaAs at T_1, the precipitation of As at 606°C (T_2), and to a ternary eutectic at 594°C (T_3) at which GaAs, As, and Cu_3As precipitate simultane-

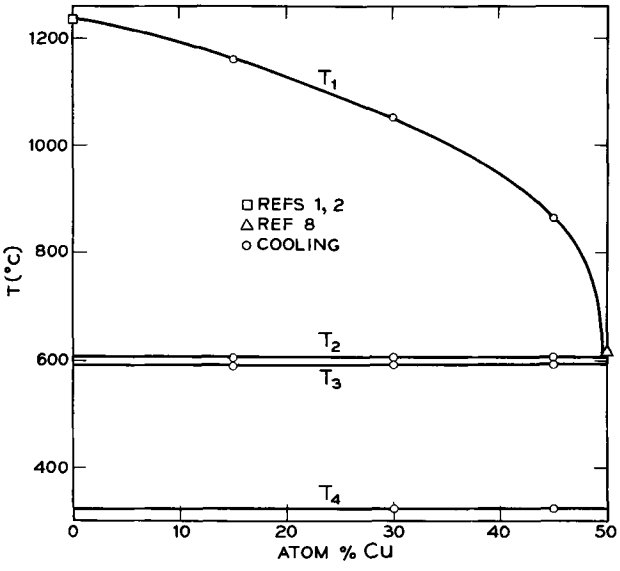

Fig. 4. Thermal effects observed on cooling mixtures with compositions on cut C (Fig. 11) in the Ga-As-Cu system.

ously. The x-ray patterns contained too many lines for unequivocal identification, but are consistent with above interpretation, as are the results of the electron beam microprobe examination of the DTA samples.

The isotherms for the copper rich regions, the positions of the boundaries between primary phase fields near the Cu-As binary and the ternary eutectic points at 667° and 594°C have not been determined precisely, but have been drawn in Fig. 11 in such a manner as to be consistent with the experimental data. The subliquidus thermal effects of Luzhnaya *et al.* are not consistent with the phase diagram of Fig. 11 in the region of Cu_3As. Further study is required to clarify this region of the system. The 1200° isotherm was obtained simply by interpolating the data on cuts A, B, C, and the Ga-As binary, and drawing the isotherm through the points thus obtained.

The Ga-As-Ag *system.*—For this system data was obtained only along cuts A, B, and C, (Fig. 5-7). The ternary diagram with isotherms computed as described above is shown in Fig. 12. The regular solution curves calculated separately for the isotherms in the GaAs primary phase field from experimental data on each

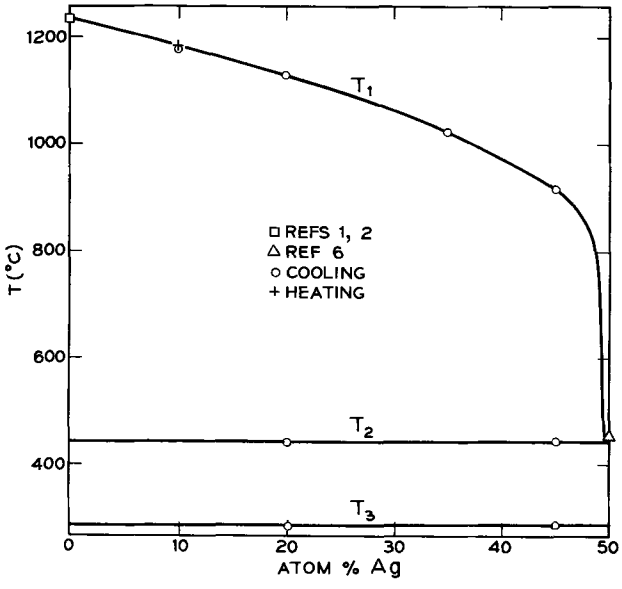

Fig. 5. Thermal effects observed on cooling and heating mixtures with compositions on Cut A (Fig. 12) in the Ga-As-Ag system.

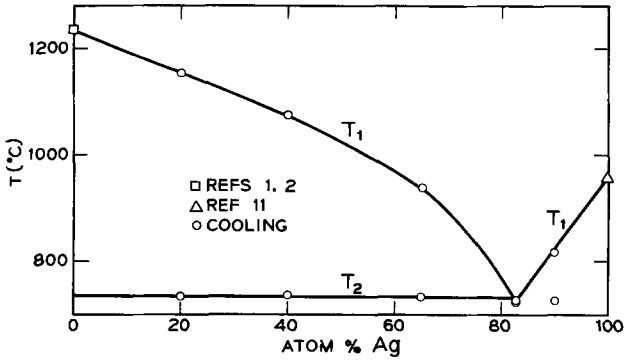

Fig. 6. Thermal effects observed on cooling mixtures with compositions on cut B (Fig. 12), the Ga-As-Au cut, in the Ga-As-Ag system.

side of the phase diagram [as described in ref. (13)] gave sets of curves which were in excellent agreement with each other. Gubskaya *et al.* (15) have reported DTA data for one point in this system at the ternary composition Ag_3GaAs_2. Their data are consistent with the data reported in this work.

The thermal effect (T_3) noted for several points in cut A at 285°C (Fig. 5) apparently results from the peritectic formation of a phase based on the phase which precipitates at 326°C in the Ga-Ag binary (6). Electron beam microprobe measurements show that in a DTA sample on cut A the phases present were GaAs, Ag (principally), and a phase containing roughly similar amounts of Ag and Ga.

Cut B (Fig. 6) resembles, but is not, a true pseudobinary. For starting compositions in the 0-82 a/o Ag region, T_1 represents the primary precipitation of GaAs. T_2 is the intersection of the GaAs crystallization path with the eutectic valley for the simultaneous precipitation of GaAs and silver alloys. The crystallization path for compositions in the Ag primary phase is not strictly on cut B and T_2 in this region is slightly different from T_2 in the GaAs primary phase field. Electron beam microprobe measurements indicate that for starting compositions on cut B in the GaAs primary phase field the only phases present in the cooled DTA samples are GaAs and Ag. The amounts of Ga and As dissolved in the Ag appear to be small.

The DTA, x-ray and microprobe data for samples on cut C (Fig. 7) are consistent with the interpretation that T_1 represents the precipitation of the GaAs primary phase, T_2 the precipitation of As along

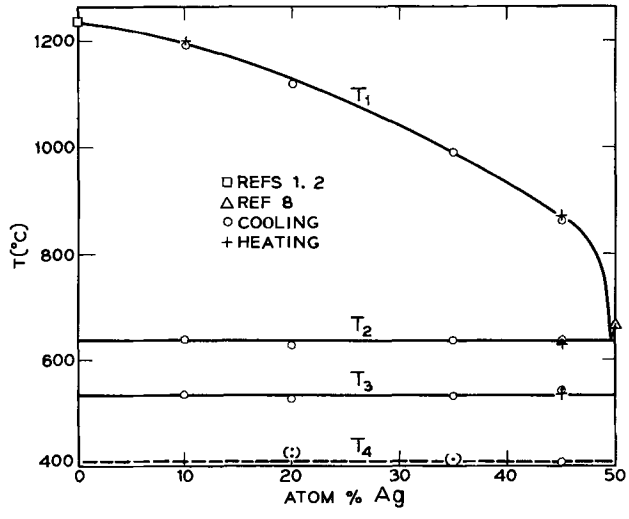

Fig. 7. Thermal effects observed on cooling and heating mixtures with compositions on cut C (Fig. 12) in the Ga-As-Ag system.

with GaAs, and that T_3 is the ternary eutectic representing the simultaneous precipitation of GaAs, As, and an intermediate phase based upon the binary phase designated Σ by Hansen (6). T_4 apparently represents the decomposition of the Σ phase to As and Ag alloys, corresponding to the transition in the As-Ag binary at 374°C (6).

In the ternary diagram (Fig. 12) the positions of the isotherms in the Ag primary phase field, the location of the eutectic boundaries between the primary phases, and the position of the ternary eutectic observed in samples with starting compositions on cut C are drawn to be consistent with the data of Fig. 5-7 but have not been determined precisely.

The Ga-As-Au *system.*—For this system DTA data was obtained along cuts A, B, and C (Fig. 8-10), at two other points along a fourth selected cut (cut D, Fig. 13) in the GaAs primary phase field and at one point on the $AuGa_2$-GaAs cut. The regular solution isotherms calculated as described in ref. (13) from the DTA data on the Ga and As rich sides of the system were in poor agreement. The data along cut D and the $AuGa_2$-GaAs cut were obtained in order to aid in the drawing of the ternary isotherms in the GaAs primary phase field. The additional data showed that even though the calculated isotherms were in poor agreement with each other when extrapolated across the phase diagram, a close approximation to the correct isotherm was obtained when the curves were drawn so as to strongly favor each computed isotherm in the region where it was most applicable.

The GaAs-GaAu system (cut A, Fig. 8) appears to be pseudobinary in nature, consisting almost entirely of the primary phase field of GaAs. The observed eutectic point at ~440°C is somewhat in doubt because of extensive supercooling in runs in which it was observed. The phases GaAs and GaAu were observed in x-ray powder photographs and confirmed with electron beam microprobe examination of the cooled DTA samples.

The liquidus curve of cut B (Fig. 9) resembles that of a simple eutectic system, T_1 representing the first formation of GaAs or Au on cooling the liquid. Au is precipitated in a solid solution which may contain as much as 25 a/o Ga. The T_2 curve in the gold rich region must vary with composition in this region as a consequence of the varying composition of the Au-Ga solid solution which is the primary phase. T_3 is probably the temperature at which a ternary eutectic comprising GaAs, As, and Au containing 1-3 a/o Ga precipitates. The T_3 thermal effect is ambiguous. The DTA curves for several samples gave evidence that two thermal effects may occur near T_3.

The cooled DTA samples from cut B were examined primarily with an electron beam microprobe. In all cases GaAs was observed. Arsenic crystals were observed in samples which contained more than 50 a/o Au in cut B. The arsenic crystals were probably not resolved by the microprobe in samples very rich in GaAs. The Au phase was observed in all samples and contained amounts of Ga varying from about 3 a/o to about 25 a/o. Varying Au-Ga concentrations are to be expected since the composition of this alloy varies while it precipitates.

The temperatures at which thermal effects were

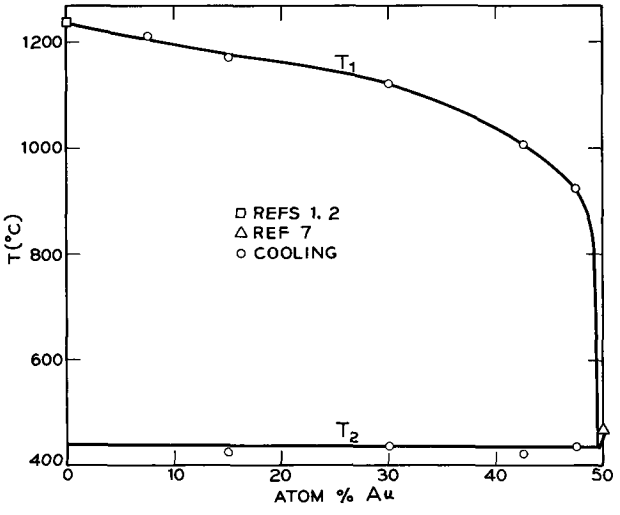

Fig. 8. Thermal effects observed on cooling mixtures with compositions on cut A (Fig. 13), the GaAs-GaAu pseudobinary.

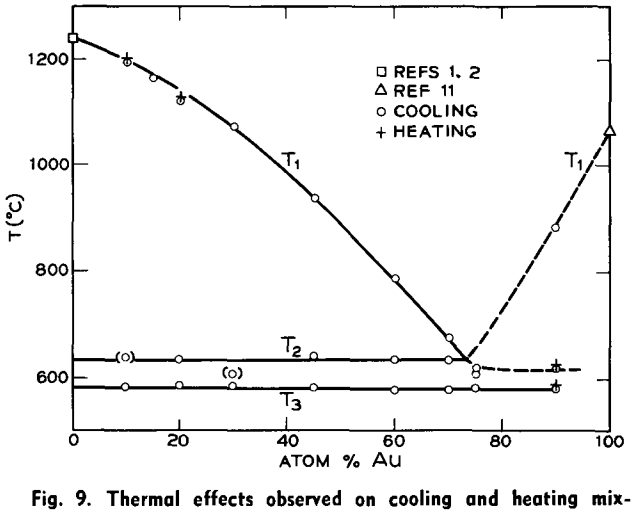

Fig. 9. Thermal effects observed on cooling and heating mixtures with compositions on cut B (Fig. 13) the GaAs-Au cut, in the Ga-As-Au system.

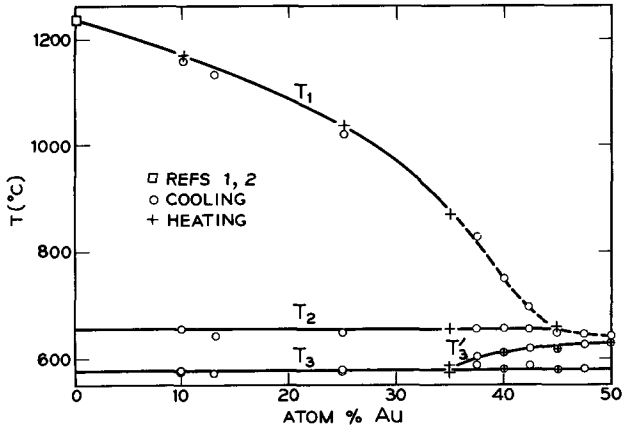

Fig. 10. Thermal effects observed on cooling and heating mixtures with compositions on cut C (Fig. 13) in the Ga-As-Au system.

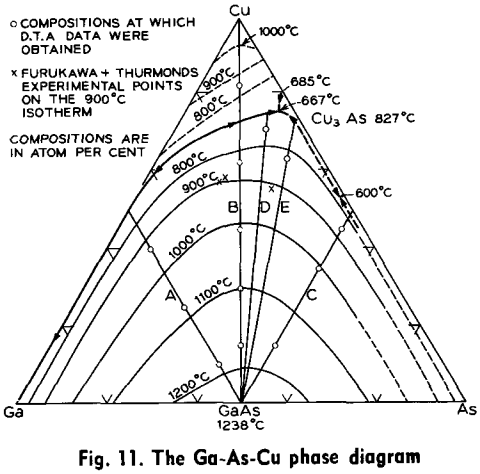

Fig. 11. The Ga-As-Cu phase diagram

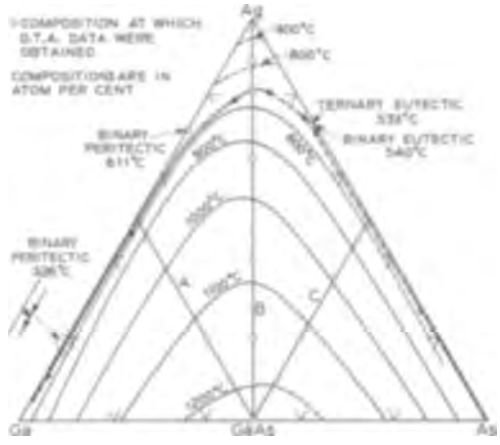

Fig. 12. The Ga-As-Ag phase diagram

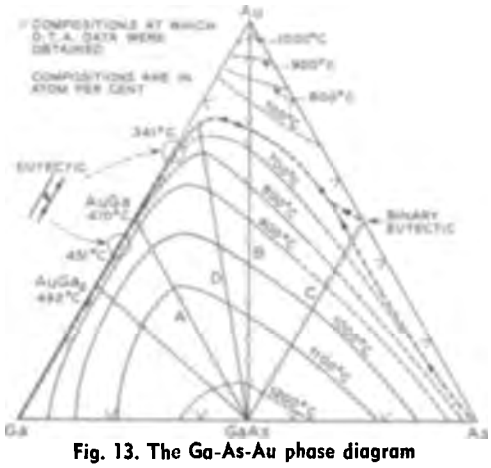

Fig. 13. The Ga-As-Au phase diagram

noted in cut C are shown in Fig. 10. Over most of the composition range T_1 clearly is the result of the primary precipitation of GaAs, and T_2 results from the first precipitation of As. T_3 seems to be the result of two thermal effects very close in temperature.

At gold concentrations at and above 35 a/o the situation is less well defined. The two thermal effects at T_3 separate and are shown in Fig. 10 as T_3 and T_3'. In all cases the only solid phases observed with the microprobe are GaAs, As, and Au containing small amounts of Ga in solid solution. In samples containing more than 35 a/o Au it is no longer possible to identify GaAs as the primary phase in electron beam microprobe photographs of polished samples. It is obvious that further study will be needed to clarify the ternary diagram in the region of the As-Au binary.

Only one experimental point was obtained on the GaAs-$AuGa_2$ cut. X-ray powder photographs and microprobe studies reveal GaAs and $GaAu_2$ as the only phases present in the sample. Only T_1 and T_2 thermal effects were noted with T_2 being identical (within experimental error) with the melting point of $GaAu_2$. It may be concluded therefore that the GaAs-$AuGa_2$ system is essentially a true pseudobinary system consisting almost entirely of the primary phase field of GaAs.

The positions of the isotherms in the Au primary phase field, the position of the ternary eutectic near the Au-As binary, and the location of the eutectic boundaries between the primary phases have not been determined precisely, but have been drawn in Fig. 13 in such a manner as to be consistent with the data of Fig. 1, 8-10 and the available data for the Ga-Au binary.

Conclusion

Extensive portions of the ternary liquid-solid phase diagrams of the Ga-As-Cu, Ga-As-Ag, and Ga-As-Au systems have been obtained. Emphasis has been placed on delineation of the position of isotherms in the GaAs primary phase field, and the determination of the extent of this phase field. Other primary phase fields and the boundaries between them have been identified and delineated in somewhat less detail.

Acknowledgments

The author is indebted to C. D. Thurmond for his helpful suggestions during the course of this work. The aid of Mr. S. Sumski with some of the experimental work, and of Mr. H. Schreiber for the electron beam microprobe studies is gratefully acknowledged.

Manuscript received Nov. 30, 1966.

Any discussion of this paper will appear in a Discussion Section to be published in the December 1967 JOURNAL.

REFERENCES

1. M. B. Panish, *This Journal*, **113**, 861 (1966).
2. W. Koster and B. Thoma, *Z. Metallk.*, **40**, 291 (1955).
3. C. D. Thurmond, *J. Phys. Chem. Solids*, **26**, 785 (1965).
4. R. N. Hall, *This Journal*, **110**, 385 (1963).
5. L. Vieland, *Acta Met.*, **11**, 137 (1963).
6. M. Hansen, "Constitution of Binary Alloys," McGraw-Hill Book Co., New York (1958).
7. C. J. Cooke and W. Hume-Rothery, *J. Less Common Metals*, **10**, 42 (1966).
8. R. P. Elliot, "Constitution of Binary Alloys, 1st Supplement," McGraw-Hill Book Co., New York (1965).
9. A. P. Schleicher, *Int. Z. Metallog.*, **6**, 18 (1914).
10. M. B. Panish, *J. Phys. Chem. Solids*, **21**, 291 (1966).
11. D. R. Stull and G. C. Sinke, "Thermodynamic Properties of the Elements," Am. Chem. Soc. (1956).
12. M. Furukawa and C. D. Thurmond, *J. Phys. Chem. Solids*, **26**, 1535 (1965).
13. M. B. Panish, *J. Less Common Metals*, **10**, 416 (1966).
14. N. P. Luzhnaya, G. F. Nikolskaya, and Wang Ping-nan, *Izv. Akad. Nauk SSSR, Neorg. Materialy*, **1**, 1328 (1965); *Inorg. Mtls.*, **1**, 1212 (1965).
15. G. F. Gubskaya, Wang Ping-nan, N. P. Luzhnaya, and D. L. Kudruatsin, *Izv. Akad. Nauk SSSR, Neorg. Materialy*, **1**, 188 (1965); *Inorg. Mtls.*, **1**, 169 (1965).

Large Area Silicon Junctions by Epitaxial Growth Technique

T. L. Chu and G. A. Gruber

Westinghouse Research Laboratories, Pittsburgh, Pennsylvania

ABSTRACT

Epitaxial growth is a promising junction formation technique for large area silicon devices because of its ability to provide: (*i*) silicon layers with chemical and structural perfection superior to conventional silicon crystals, (*ii*) flexible dopant concentration and distribution, and (*iii*) p-n junctions of better perfection than diffused junctions. Using the pyrolysis of silane in a flow system, epitaxial silicon layers of good structural perfection, as indicated by chemical etching and optical microscope examinations, have been deposited on {111} oriented substrates at 1080° at rates up to 1.5 μ/min. The resistivity of the grown layer was controlled by using diborane and phosphine as p- and n-dopants, respectively. The radial resistivity of epitaxial layers has been found to be of considerably better uniformity than that of conventional silicon crystals. Large area epitaxial p-n junctions prepared by depositing *n*- and p-layers successively on low resistivity n-type substrates have been found to be superior to diffused shallow junctions in electrical characteristics and are advantageous for the fabrication of power devices.

The epitaxial growth of silicon using the thermal reduction or decomposition of silicon compounds on surfaces of silicon substrates has been utilized extensively in the fabrication of integrated circuits and other types of small area devices during the past few years. In these epitaxial devices, the dopant concentration and distribution have been programmed and controlled to an extent not obtainable by other fabrication techniques. In addition to the flexibility of dopant control, the epitaxial growth technique is potentially capable of providing silicon layers with chemical and structural perfection superior to conventional silicon crystals. Both Czochralski and float-zone crystals used for device fabrication have been shown to possess various types of microdefects and inhomogeneous dopant distribution (1-3). The quality of silicon crystals, therefore, becomes a limitation of the performance of many types of large area devices, and the epitaxial approach appears attractive. Furthermore, the use of the epitaxial growth technique could also eliminate the defects, such as dislocation clusters, slip lines, stress, etc., introduced into the vicinity of p-n junctions by the alloying or diffusion processes.

The epitaxial growth technique is promising for the formation of large area junctions. However, the requirements of the properties of epitaxial layers, such as the crystal perfection, radial resistivity uniformity, etc., are more stringent and more difficult to achieve for large area devices than those for small area devices. For large area devices, these properties must be highly uniform over the entire area of the device to minimize localized breakdown. The crystal perfection of the epitaxial layer is particularly important since one major defect in the layer renders a large area device useless. Nevertheless, these requirements can be fulfilled by optimizing the growth conditions, and epitaxial growth will ultimately become an important technique for the fabrication of large area devices.

In this work, the advantages of the epitaxial growth technique have been utilized for the preparation of silicon p-n junctions of a few square centimeters area. Using the pyrolysis of silane and appropriate dopants, shallow junctions were prepared by depositing n- and p-layers successively on low resistivity n-type substrates. Similar junctions were also prepared by the diffusion technique. Epitaxial structures were found to have considerably better electrical characteristics than diffused junctions. They have yielded, after emitter diffusion, power transistors with good characteristics. The experimental methods and results are described in this paper.

Epitaxial Growth of Silicon by Silane Pyrolysis

The epitaxial growth of silicon can be achieved in a gas flow system by the thermal reduction of silicon halides and the pyrolysis of silane. The silane process has been reported by several workers (4); the relative merits of this process and the commonly used tetrachloride process are fairly well established. The pyrolysis of silane is thermochemically and kinetically more favorable than the thermal reduction of silicon tetrachloride. Silane is thermochemically unstable at room temperature and above and decomposes rapidly at temperatures above 600°C, thus enabling the growth of silicon at lower temperatures. The use of lower substrate temperature not only reduces the diffusion of impurities between adjacent layers of silicon, but also minimizes the liberation of impurities from the susceptor used for the support and heating of substrates. Furthermore, the pyrolysis of silane is essentially chemically irreversible; the undesirable consequences of chemical transport associated with the tetrachloride process can be eliminated, and the resistivity of the epitaxial layer can be better controlled. On the other hand, the silane process has the disadvantage that the thermal instability of silane tends to promote nucleation by pyrolysis in the gas phase. The solid silicon formed in the gas phase is in the form of large atomic clusters of random orientation, and the deposition of these clusters on the growing interface would interfere with oriented growth. The gas phase nucleation, however, can be suppressed by optimizing the experimental conditions.

The pyrolysis of silane was carried out at atmospheric pressure using hydrogen as a diluent. Semiconductor grade silane, purchased from the Gray Chemicals Company, was used without further purification. This material was found to yield n-type silicon with an electrical resistivity higher than 100 ohm-cm. Hydrogen was purified by diffusion through a palladium-silver alloy. Hydrogen-diborane, hydrogen-arsine, and hydrogen-phosphine mixtures, purchased from the Matheson Company, were used as dopants. All reactant gases were passed through a filter before entering the deposition tube to remove any solid particles. The substrates were n-type, 0.008-0.012 ohm-cm Czochralski silicon slices of 1-in. diameter, with main faces of {111} orientation.

The deposition process was carried out in a horizontal, water-cooled fused silica tube of 55 mm ID. The support, heating, and surface preparation of substrates have been described previously (5). During the growth process, hydrogen at a flow rate of 21 l/min was used as the diluent for silane, the concentration

of silane in the reactant was 0.01-0.5% and the substrate temperature was in the range of 1050°-1200°C. The structural perfection of the epitaxial layer was evaluated by chemical etching and optical microscope techniques (6), and the resistivity profile of the epitaxial layer was evaluated by the spreading resistance technique (7).

Deposition Rate and Structural Perfection

In the epitaxial growth process under study, the first important consideration is to minimize homogeneous nucleation through the pyrolysis of silane in the gas phase. This condition can be achieved by using water-cooled reaction tube, low partial pressure of silane in the reactant, and high gas-flow velocity over the substrate surface. Using deposition apparatus of a given geometry and a given flow rate of the diluent, the gas phase nucleation was found to be insignificant in a limited range of reactant composition and substrate temperature. In general, the extent of the gas phase nucleation decreased with decreasing temperature, and at a given temperature, the contribution of gas phase reactions increased with increasing concentration of silane. At 1080°C, for example, epitaxial silicon of good crystal perfection was obtained using a hydrogen-silane mixture containing 0.5% silane or less at a flow rate of 21 l/min. When the concentration of silane was increased to 0.7%, however, polycrystalline inclusions were incorporated into epitaxial silicon due to the gas phase nucleation. Also, as the substrate temperature was increased to 1200°C, the gas phase reaction became pronounced when the silane concentration was only 0.3%.

The deposition rate of silicon can be adjusted over a wide range by varying the concentration of silane in the reactant. Figure 1 shows the average deposition rate of silicon at a substrate temperature of 1080°C, using a hydrogen flow rate of 21 l/min, as a function of the concentration of silane. This rate was 1.5 and 0.19 μ/min when the reactant contained 0.5 and 0.013% silane, respectively. The lower growth rate is useful for accurate thickness control of thin layers. In the temperature range 1050°-1150°C, the average deposition rate was essentially the same within the experimental error, indicating that the deposition process in this temperature range is diffusion-controlled. At higher temperature, say 1200°C, the deposition rate decreased due presumably to the increased contribution of gas phase reactions.

Under conditions where the gas phase nucleation is negligible, epitaxial silicon deposited by the pyrolysis

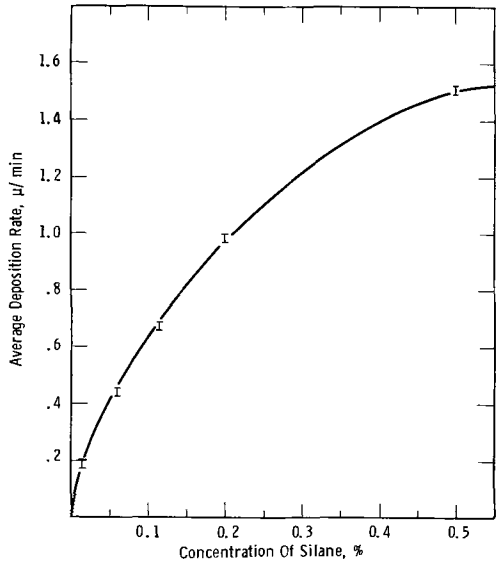

Fig. 1. Average deposition rate of silicon as a function of concentration of silane in hydrogen. Hydrogen flow rate = 21 l/min, substrate temperature = 1080°C.

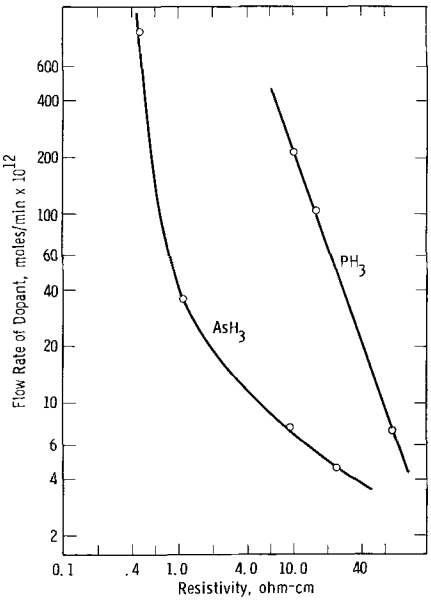

Fig. 2. Resistivity of n-type epitaxial silicon as a function of flow rate of arsine and phosphine. Silicon was deposited by the pyrolysis of silane at 1080°C using hydrogen containing 0.2% silane at a flow rate of 21 l/min.

of silane was found to be essentially free of process-induced defects, such as stacking faults, growth pyramids, polycrystalline inclusions, etc. Furthermore, the structural perfection of epitaxial silicon was independent of the deposition rate up to 1.5 μ/min.

Resistivity Control of Epitaxial Silicon

Epitaxial silicon deposited from silane at 1080°C, without intentional doping, was n-type with a resistivity higher than 100 ohm-cm. The control of resistivity of n-type epitaxial silicon by using arsine and phosphine as dopants was studied in a series of experiments using hydrogen containing 0.2% silane at a flow rate of 21 l/min. The substrates used in these experiments were p-type, and the resistivity of the epitaxial layer was determined by the four-point probe technique. The results are shown in Fig. 2, where the resistivity of epitaxial silicon, in the range of 0.4-60 ohm-cm, is plotted as a function of the flow rate or arsine and phosphine. At a given flow rate of the dopant, the doping efficiency of arsine is considerably higher than that of phosphine. For example, when the epitaxial layer was of 10 ohm-cm resistivity, the P/Si ratio in the gas phase was approximately twelve times that in the solid silicon, and the As/Si ratio in the gas phase was about one-half of that in the solid. This can be attributed to the higher thermal stability of phosphine. The thermal instability of arsine would result in more rapid depletion of arsine than silane when the reactant mixture is passed through the reaction tube, and large resistivity variations among specimens in a run have been observed. Thus, in spite of the considerably higher diffusion coefficient of phosphorus in silicon than that of arsenic in silicon, the use of phosphine as a dopant is more advantageous for minimizing resistivity variations.

The resistivity of p-type epitaxial silicon was controlled by using diborane as a dopant. At a given substrate temperature, the maximum obtainable concentration of boron in epitaxial silicon was found to be considerably lower than the solubility of boron in silicon at the same temperature. At 1080°C, for example, the highest boron concentration obtained was approximately 2×10^{17} cm^{-3}, irrespective of the B_2H_6/SiH_4 molar ratio in the reactant mixture. This is less than one-thousandth of the solubility of boron in silicon at the same temperature (8). To obtain epitaxial silicon of higher dopant concentration, it was necessary to

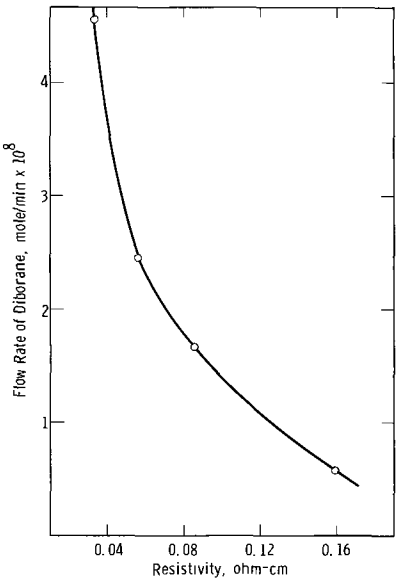

Fig. 3. Resistivity of p-type epitaxial silicon as a function of flow rate of diborane. Silicon was deposited by the pyrolysis of silane at 1140°C using hydrogen containing 0.1% silane at a flow rate of 21 l/min.

carry out the deposition at higher substrate temperatures. Figure 3 shows the resistivity of p-type epitaxial silicon, deposited at a substrate temperature of 1140°C using hydrogen containing 0.1% silane at a flow rate of 21 l/min, as a function of the flow rate of diborane. Under these conditions, epitaxial silicon with boron concentrations higher than 10^{19} cm^{-3} was obtained. The doping efficiency of diborane was approximately 25%.

To determine the radial resistivity profile of epitaxial silicon, a spreading resistance probe was applied to the as-grown surface of epitaxial silicon specimens along several diameters at various intervals. In many cases, epitaxial silicon was found to possess less radial resistivity fluctuations than float-zone or Czochralski crystals. An example is shown in Fig. 4 where the local resistivity of an n-type, phosphorus-doped epitaxial silicon layer with an average resistivity of 5 ohm-cm was measured along a diameter at 1 and 0.1 mm intervals. In all cases, the deviation of the local resistivity from the average resistivity was less than 10%.

Large Area Shallow p-n Junctions

Large area shallow p-n junctions were prepared by both diffusion and epitaxial techniques. In the former, n-type epitaxial layers of 10 ohm-cm resistivity and 25μ thickness deposited on 1-in. diameter 0.01 ohm-cm n-type substrates were subjected to boron diffusion at 1150°C, using boron tribromide as a diffusant in a flow system. The junction depth was 5μ, and the surface concentration of boron in silicon was approximately 10^{18} cm^{-3}. These junctions, approximately 4 cm^2 in area, were found to support voltages up to 200v; however, the reverse currents were often rather high, 100 ma or higher, at these voltages. To determine the cause of the softness of these functions, many specimens were made into mesas and the reverse characteristics of each mesa determined. It was found that mesas with high reverse currents invariably had many localized areas with etch figures of various shapes associated with high concentrations of dislocations, as shown in Fig. 5 and 6. Etch figures shown in Fig. 5 were due to contaminants on the specimen surface; the reaction between silicon and contaminants at the diffusion temperature yielded sufficient stress to generate dislocations. Etch figures shown in Fig. 6 were due to tweezer or probe marks introduced into the specimen by various handling processes before diffusion; the stress caused by these damages were relieved during the diffusion process by the formation of dislocations. The process-induced defects are, therefore, responsible for the high reverse currents of the mesas under consideration. Since the reverse currents of these mesas were found to be reduced considerably after a gettering process at 900°C, using phosphorus pentoxide as the gettering agent (9), one may conclude that the precipitation of heavy metals at dislocations is more harmful than the dislocations themselves. On the other hand, mesas with no or very few etch figures exhibited reasonably

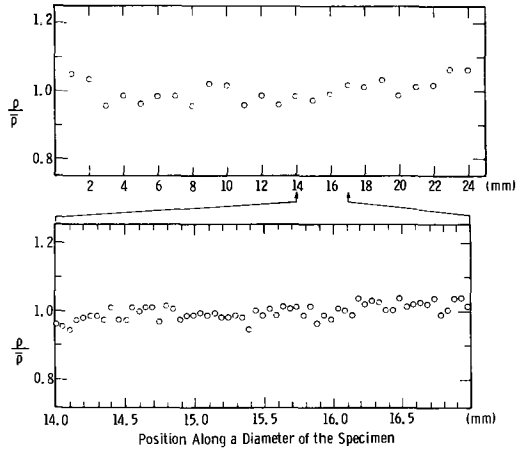

Fig. 4. Resistivity profile of an n-type epitaxial silicon layer with an average resistivity of 5 ohm-cm along a diameter of the specimen, $\bar{\rho}$ is in each case the average resistivity.

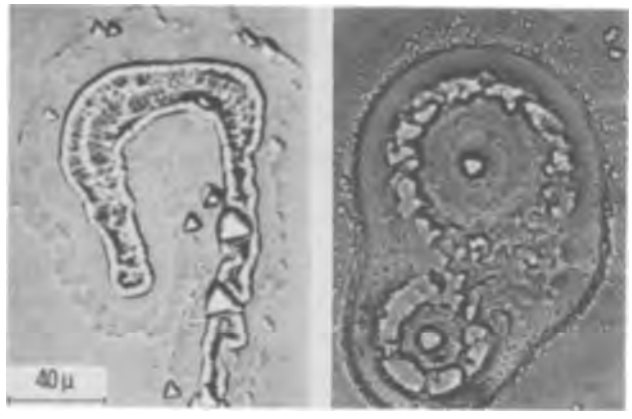

Fig. 5. Irregularly shaped etch figures and associated dislocations in epitaxial silicon after boron diffusion (Sirtl etch, 2 min).

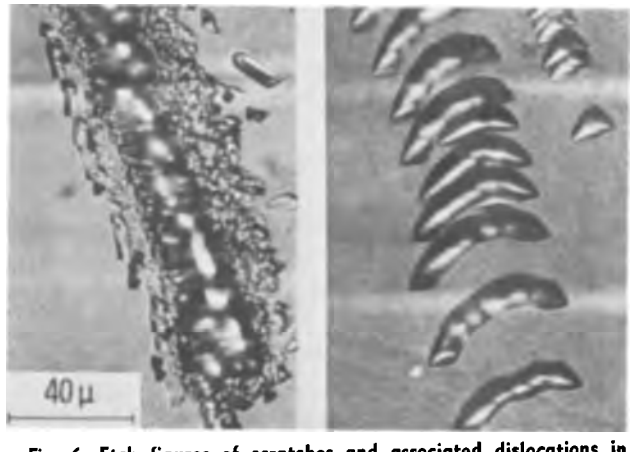

Fig. 6. Etch figures of scratches and associated dislocations in epitaxial silicon after boron diffusion (Sirtl etch, 2 min).

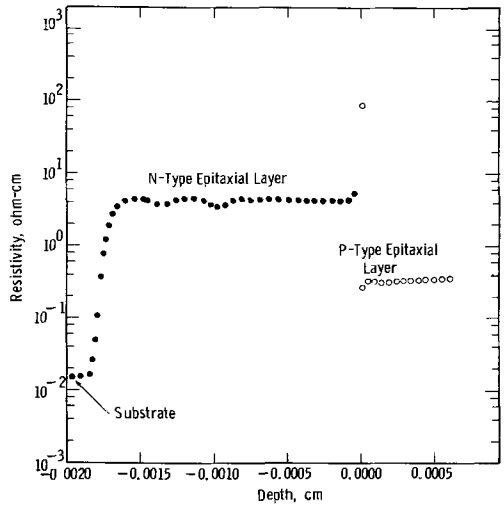

Fig. 7. Resistivity profile of n- and p-type epitaxial silicon layers deposited successfully on low resistivity n-type substrate by the pyrolysis of silane at 1080°C, ·, n-type; o, p-type.

good reverse characteristics even before the gettering process. Thus, while diffusion-induced defects only reduce the yield of small area devices, they are very serious in large area devices. Also, the fabrication of large area defect-free shallow junctions by the diffusion technique is a difficult and exacting task.

Large area epitaxial p-n junctions were prepared by depositing 15-30μ of 5-10 ohm-cm n-type layers and 5-6μ of 0.1-0.5 ohm-cm p-type layers successively on 0.01 ohm-cm n-type substrates. An example of the resistivity profile of an epitaxial structure is shown in Fig. 7 where an 18-μ, 4 ohm-cm n-layer and a 6-μ, 0.3 ohm-cm p-layer were deposited. Junctions of approximately 4 cm^2 were isolated from the epitaxial structures by a grooving technique. The reverse voltage of these junctions depends on the resistivity and thickness of the n-layer. For example, the epitaxial junctions were found to support 350 and 200v when the n-layer resistivity and thickness were 10 ohm-cm, 30μ, and 5 ohm-cm, 20μ, respectively. The reverse currents at these voltages were usually 1 ma or less. However, polycrystalline inclusions in the epitaxial layer were found to cause high reverse currents at low voltages. Epitaxial junctions with even one inclusion supported less than 50v.

The epitaxial growth technique is, therefore, superior to the diffusion technique for the fabrication of large area shallow junctions. Furthermore, the preparation of epitaxial junctions is considerably simpler in practice than epitaxial-diffused junctions used in certain types of devices such as transistors. The epitaxial junctions described above, after phosphorus emitter diffusion at 1100°C, have produced transistors with a current carrying capacity of 100 amp, V_{CE} = 170v at 1 ma, V_{CB} = 175v at 1 ma, and h_{FE} = 15 at 10 amp (10).

Summary and Conclusions

The epitaxial growth of silicon by the pyrolysis of silane in a flow system has been studied in detail with the objective of using this technique for the preparation of large-area junction structures. Large area epitaxial silicon layers of good structural perfection, uniform radial resistivity profile, and with resistivity controlled over a wide range have been deposited on silicon substrates of {111} orientation under a variety of conditions.

Shallow p-n junctions of a few square centimeters area have been prepared by both diffusion and epitaxial techniques. The diffused junctions frequently showed high reverse currents due to process-induced defects. The electrical characteristics of epitaxial junctions were considerably better, and power transistors have been prepared from these junctions after the emitter diffusion. Epitaxial growth is, thus, a promising junction formation technique for large area silicon devices.

Acknowledgments

The authors wish to thank Dr. P. J. Kannam and Mr. R. G. Mazur for their valuable contributions to this work. This work was supported in part by the George C. Marshall Space Flight Center of the National Aeronautics and Space Administration under Contract NAS8-11432, and the Air Force Cambridge Research Laboratories under Contract AF16(628)-4220.

Manuscript received Nov. 14, 1966.

Any discussion of this paper will appear in a Discussion Section to be published in the December 1967 JOURNAL.

REFERENCES

1. J. W. Faust, Jr., H. F. John, and R. Stickler, in "Physics of Failure in Electronics," vol. 4, p. 367; M. E. Goldberg and J. Vaccaro, Editors, (1966). H. F. John, J. W. Faust, Jr., and R. Stickler, "Micro-Inhomogeneity Problems in Silicon," *IEEE Transactions* on Parts, Materials, and Packaging, PMP-2, 51 (1966).
2. R. G. Mazur, *This Journal*, **114**, 255 (1967).
3. K. E. Benson, *Electrochem. Tech.*, **3**, 332 (1965).
4. See, for instance, B. A. Joyce and R. R. Bradley, *This Journal*, **110**, 1235 (1963); S. R. Bhola and A. Mayer, *RCA Rev.*, **24**, 511 (1963); S. E. Mayer and D. E. Shea, *This Journal*, **111**, 550 (1964).
5. T. L. Chu, *This Journal*, **113**, 717 (1966).
6. T. L. Chu and J. R. Gavaler, in "Metallurgy of Advanced Electronic Materials," G. E. Brock, Editor, p. 207 (Metallurgical Society Conferences, vol. 19), Interscience, New York (1963).
7. R. G. Mazur and D. H. Dickey, *This Journal*, **113**, 255 (1966).
8. F. A. Trumbore, *Bell System Tech. J.*, **39**, 205 (1960).
9. S. W. Ing, Jr., R. E. Morrison, L. L. Alt, and R. W. Aldrich, *This Journal*, **110**, 533 (1963).
10. T. L. Chu and P. J. Kannam, in "Physics of Failure in Electronics," vol. 4, p. 242, M. E. Goldberg and J. Vaccaro, Editors (1966); P. J. Kannam, D. A. Walczak, and T. L. Chu, Electrochemical Society Electronics Division Extended Abstracts, **15**, 1, 101 (1966).

Phase Relations and Thermoelectric Properties of the Alloy Systems $SnTe\text{-}Bi_2Te_3$ and $PbTe\text{-}Sb_2Te_3$

Richard A. Reynolds

Texas Instruments Incorporated, Dallas, Texas

ABSTRACT

The phase relations in the quasi-binary systems $SnTe\text{-}Bi_2Te_3$ and $PbTe\text{-}Sb_2Te_3$ have been determined using differential thermal analysis, x-ray diffraction, electron microprobe, and optical metallographic techniques. The system $SnTe\text{-}Bi_2Te_3$ forms a continuous series of solid solutions from 45 to 100% Bi_2Te_3, and the maximum solubility of Bi_2Te_3 in SnTe was found to be about 5%. The system $PbTe\text{-}Sb_2Te_3$ contains a eutectic and exhibits little solubility of either component in the other. Measurements of the thermal and electrical properties of the $SnTe\text{-}Bi_2Te_3$ alloys showed that they are either n-type or p-type depending on composition, and that the carrier concentrations are degenerate ($\geqq \pm 6 \times 10^{19}/cm^3$). At 300°K Seebeck coefficients are typically 90 $\mu v/°K$. The thermal conductivity is about 1.3×10^{-2} watts/°K-cm and nearly independent of temperature and composition. The maximum thermoelectric figure of merit obtained at 300°K for these alloys was $0.66°K^{-1}$.

The quasi-binary alloy systems $PbTe\text{-}Sb_2Te_3$ and $SnTe\text{-}Bi_2Te_3$ were investigated in order to determine their phase relations and thermoelectric properties. The possibility of the formation of ternary compounds in these systems was suggested by previous investigation (1) of the quasi-binary system $PbTe\text{-}Bi_2Te_3$, in which the compound $PbTe \cdot 2Bi_2Te_3$ was found, and the quasi-binary system $SnTe\text{-}Sb_2Te_3$, in which the compound $SnTe \cdot Sb_2Te_3$ was found. The object of the investigation was to determine whether or not there existed compositions which possess properties useful for thermoelectric power generation applications. The binary compounds and their ternary isomorphous alloys (*e.g.*, PbTe-SnTe alloys) possess useful thermoelectric properties; hence, the cross-substitutional alloys $SnTe\text{-}Bi_2Te_3$ and $PbTe\text{-}Sb_2Te_3$ may possess unique and useful properties and investigation of these alloy systems is required.

Materials and Experimental Procedure

Materials used to make specimens were of the following purities (weight per cent): Sb, 99.99%; Pb, Sn, Bi, and Te, all 99.999%.

Specimens for metallographic, x-ray, and physical property measurements were weighed as 10 or 20g samples, placed in quartz capsules with an inside diameter of 8 or 10 mm, and sealed at a pressure of 10^{-3} Torr. The samples were melted, after which the capsules were rocked vigorously for mixing and then quenched in water. Samples for annealing were cut from the as-cast ingots and encapsulated in quartz tubes at a pressure of 10^{-3} Torr.

Samples for x-ray diffraction studies were ground to powder with a mortar and pestle, sifted through a 300 mesh screen, and mounted on glass slides. Diffraction patterns were determined on a Norelco Diffractometer using Cu K_α radiation. Identical results were obtained on ground samples and ground and annealed samples.

Metallographic specimens were mounted in bakelite and mechanically polished with 0.1μ alumina. Etching was done either with a solution of 1 part HNO_3, 1 part HCl, and 2 parts saturated solution of $K_2S_2O_8$ in H_2O, or with a cathodic etching apparatus.

Resistivity measurements were made with a Keithly Milliohmmeter, which contained its own chopped d-c current supply. The use of chopped current prevented the occurrence of temperature gradients in the specimen due to the Peltier effect at the current lead-specimen contacts. Current contacts and potential measuring contacts were soldered for measurements from 77° to 300°K. Above 300°K pressure contacts were used.

Seebeck coefficients were determined using a ΔT across the specimen of 10°-20°C. Thermocouple and Seebeck voltages were measured with an L&N K-3 potentiometer. Soldered contacts were used.

Thermal conductivity was measured by the steady-state method of Stamper and Bryant (2). Samples used were 8 mm in diameter and 6 mm long.

Hall effect measurements were made using the method of Dauphinee and Mooser (3). The system used was capable of measuring Hall coefficients as small as 0.05 cm^3/coulomb, but in all cases (except pure Bi_2Te_3) the Hall coefficient was found to be smaller than this.

Differential thermal analysis (DTA) was performed using 50g samples, and employed indium as the comparison standard. The DTA capsules were cylindrical (22 mm diameter by 25 mm long) and had a thermocouple well in the bottom. The capsules were sealed at a pressure of 10^{-3} Torr. Heating and cooling rates were varied between 1.6 and 4.0°C/min. Reactions in the specimen capsule leading to temperature differences between the sample and the standard of 2°C or more could be detected. An automatic control circuit cycled each sample through the temperature range of interest, and each point of the DTA data represents the average of two or more cycles. All points were reproducible to ± 1°C, except the cooling points on the liquidus lines, which scattered a little more due to varying degrees of supercooling in each cycle.

Since the heat effects associated with reactions occurring in the solid state are usually very small, and the solid-state transformation kinetics are very slow in these alloy systems, the DTA data for these systems furnish no conclusive evidence about the phase relations at temperatures below the solidus temperature.

Results

The System $PbTe\text{-}Sb_2Te_3$.—DTA measurements revealed the existence of a quasi-binary eutectic between the two binary compounds (Fig. 1). X-ray diffraction data showed only the diffraction patterns of PbTe and Sb_2Te_3 in all the alloys. Optical metallographic examination showed that all compositions were two-phase, containing only PbTe and Sb_2Te_3. The maximum solubilities of Sb_2Te_3 in PbTe, and of PbTe in Sb_2Te_3 were both less than 5%.

The lack of appreciable terminal solid solubility and the failure to form new phases discouraged performing further work on alloys in this system.

The System $SnTe\text{-}Bi_2Te_3$.—Results of the DTA measurements are plotted in Fig. 2 (a phase diagram will be proposed after consideration of all experimental

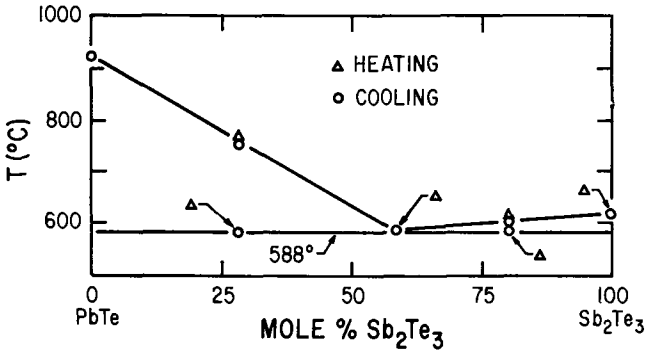

Fig. 1. DTA data and proposed phase diagram for the quasi-binary system PbTe-Sb_2Te_3. The arrows which attach several pairs of points indicate that they coincide exactly.

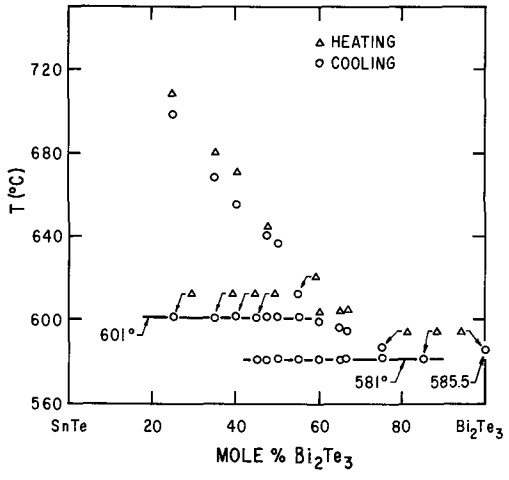

Fig. 2. DTA data for the quasi-binary system SnTe-Bi_2Te_3. The arrows which attach several pairs of points indicate that they coincide exactly.

data). In samples of less than 60% Bi_2Te_3 the heat effect on cooling associated with the isothermal arrest at 581°C was very small (less than 1% of the total heat evolved). On heating, this arrest was observed only in the 85% Bi_2Te_3 alloy. In alloys containing less than 60% Bi_2Te_3 the only isothermal arrest during heating occurred at 601°C. The appearance of the arrest at 581°C on cooling alloys containing less than 85% Bi_2Te_3 is due to peritectic incasement (4) occurring during the liquid-solid transformation. Absence of this arrest in the heating cycle is due to annealing occurring while the DTA sample was in the solid state during the cycling process. Metallographic and x-ray data described below show that alloys containing more than 45% Bi_2Te_3 are all single-phase, thus ruling out the possibility that the isothermal reaction at 581°C is due to a eutectic reaction.

Optical metallographic examination of samples annealed at 550°-580°C revealed that compositions containing 5-40% Bi_2Te_3 were two-phase, but compositions containing 45% or more Bi_2Te_3 were single-phase (Fig. 3a and 3b). Samples annealed at temperatures lower than 550°C did not yield any conclusive data because the annealing kinetics were extremely slow. Examination of as-cast alloys revealed that SnTe is the primary phase of solidification in compositions of less than 60% Bi_2Te_3.

X-ray diffraction patterns of annealed alloys containing 40% or less Bi_2Te_3 exhibited the diffraction patterns of SnTe and a second phase of hexagonal structure (see Fig. 3a). Annealed specimens containing 45% or more Bi_2Te_3 exhibited only the lines of one phase having the crystal structure of Bi_2Te_3 (hexagonal). The c/a ratio for this phase showed a monotonic increase from 6.68 at 45% Bi_2Te_3 to 6.88 at 85% Bi_2Te_3 and 6.97 at 95% Bi_2Te_3. The indexed pattern of several Bi_2Te_3 alloys are given in Table I. The change in c/a is due entirely to an increase in c as the Bi_2Te_3 content is increased from 45 to 100%. It should be noted that the DTA measurements showed the 85% Bi_2Te_3 alloy to melt isothermally, and that Fig. 3b suggests that it is single-phase.

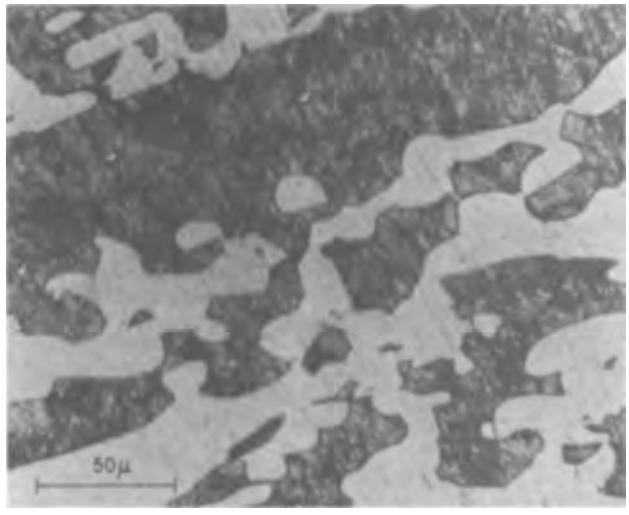

Fig. 3a. Micrograph of etched 75 mole % SnTe-25 mole % Bi_2Te_3 alloy. Dark phase is SnTe.

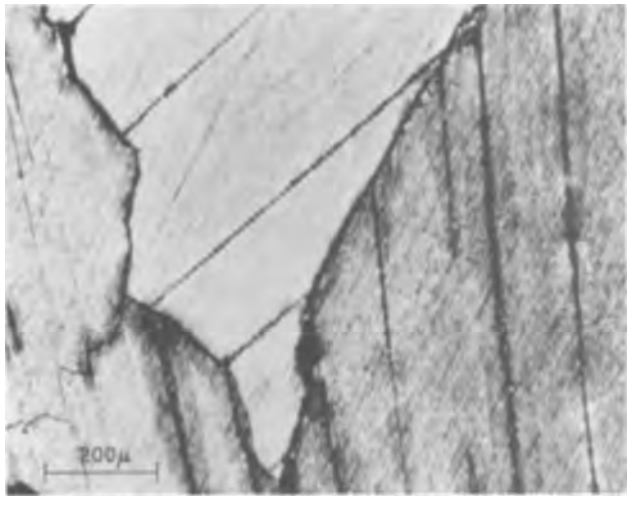

Fig. 3b. Micrograph of etched 15 mole % SnTe-85 mole % Bi_2Te_3 alloy.

In order to confirm that the 85% Bi_2Te_3 alloy is single-phase, the sample in Fig. 3b was subjected to electron microprobe analysis. Nine x-ray intensity measurements to determine local compositions were done at random positions on a polished and etched surface of 1 cm diameter using a 1.0μ diameter spot size. Within 95% confidence the Bi, Te, and Sn contents were identical at all nine sampling spots, thus confirming that the 85% Bi_2Te_3 alloy is single-phase and homogeneous.

Seebeck coefficient measurements showed that alloys up to 47.5% Bi_2Te_3 were p-type; 50% Bi_2Te_3 alloys were n-type as cast but became p-type on annealing; alloys between 52.5% and 85% Bi_2Te_3 were n-type; alloys containing 95% or more Bi_2Te_3 were p-type. Resistivity vs. temperature for several annealed samples is given in Fig. 4. The small positive temperature coefficient of resistance suggests the alloys are degenerate. The broad maximum in the curves at about 300°C may be a result of the long heating times in-

Table I. X-ray diffraction data for $SnTe$-Bi_2Te_3 alloys. Patterns have been indexed for a hexagonal crystal structure, but can also be indexed for a rhombohedral crystal structure. All observed diffraction lines are listed, but all possible reflections are not. The pattern of the 95% Bi_2Te_3 alloy is indistinguishable from that of pure Bi_2Te_3

	50% Bi_2Te_3 a = 4.40Å c = 29.63Å				85% Bi_2Te_3 a = 4.40Å c = 30.21Å				95% Bi_2Te_3 a = 4.38Å c = 30.45Å			
HK.L	d_{calc}	d_{meas}	I/I_o	HK.L	d_{calc}	d_{meas}	I/I_o	HK.L	d_{calc}	d_{meas}	I/I_o
								10.1	3.78	3.78	30
10.1	3.75	3.78	5	10.1	3.78	3.78	10	01.5	3.22	3.22	100
01.5	3.21	3.21	100	01.5	3.22	3.22	100	01.8	2.70	2.69	30
10.7	2.83	2.81	2			2.725	2	10.10	2.37	2.37	100
00.12	2.47	2.45	5	10.10	2.365	2.365	90	01.11	2.23	2.24	50
10.10	2.34	2.34	90	11.0	2.196	2.196	90	11.0	2.19	2.19	90
01.11	2.198	2.196	90	00.15	2.016	2.016	50	00.15	2.03	2.03	70
11.3	2.149	2.147	30	20.5	1.817	1.811	50	10.13	2.00	2.00	10
		2.060	5	00.18	1.683	1.680	2	20.5	1.813	1.814	60
00.15	1.975	1.982	60	02.10	1.610	1.609	50	20.8	1.699	1.703	30
20.5	1.815	1.814	50	20.11	1.570	1.560	2	02.10	1.611	1.611	50
02.7	1.738	1.734	2	11.15	1.489	1.483	50	20.11	1.568	1.565	50
11.12	1.643	1.633	5	12.5	1.400	1.398	50	11.15	1.489	1.488	60
02.10	1.603	1.603	50	12.8	1.347	1.347	2	00.21	1.453	1.450	10
11.15	1.470	1.472	50	10.22	1.298	1.295	10	01.20	1.413	1.414	50
21.5	1.401	1.398	50	00.24	1.261	1.266	10	12.5	1.397	1.396	50
10.20	1.381	1.385	50	20.20	1.184	1.184	2	12.8	1.342	1.342	30
21.7	1.367	1.362	2	10.25	1.152	1.152	2	21.10	1.300	1.299	30
11.15	1.317	1.312	2	22.0	1.100	1.098	5	00.24	1.270	1.265	30
21.10	1.296	1.295	30	30.15	1.074	1.074	10	03.3	1.249	1.253	10
10.22	1.269	1.266	30					11.21	1.209	1.211	10
20.20	1.170	1.171	10					20.20	1.188	1.189	30
10.25	1.133	1.133	5					10.25	1.159	1.162	30
22.0	1.100	1.100	2					12.17	1.120	1.120	10
20.23	1.068	1.068	5								
12.20	1.034	1.034	10								

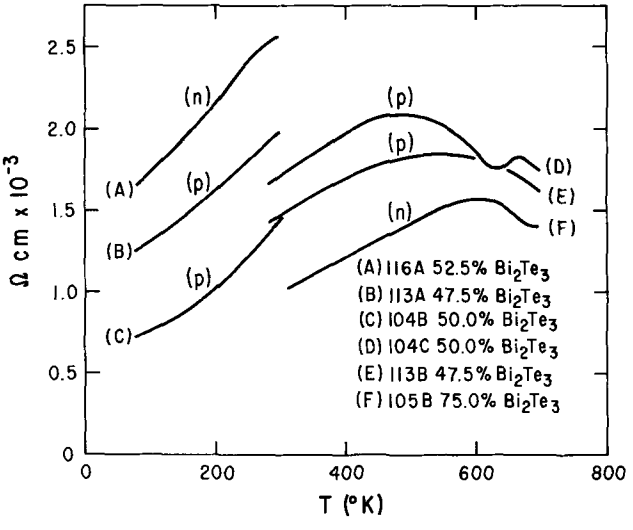

Fig. 4. Resistivity vs. temperature for several alloys having compositions near 50 mole % SnTe. Carrier type is indicated by a small "n" or "p" on each curve.

Table II. Seebeck coefficients for several $SnTe$-Bi_2Te_3 alloys.

% Bi_2Te_3	47.5		50.0		52.5	
T°K	95	301	96	284	91.6	301
α, μV/°C	+14.0	+71.5	+21.5	+91.0	−30.2	−71.0

Table III. Thermal conductivity of $SnTe$-Bi_2Te_3 alloys in w/°K-cm. The electronic contribution has been calculated using the measured resistivity and assuming the alloys to be degenerate.

% Bi_2Te_3	T°K	$K_{tot.}$	$K_{el.}$	K_L
0.00	85	55×10^{-3}	41.5×10^{-3}	13.5×10^{-3}
ref. (11)	300	66×10^{-3}	44.4×10^{-3}	21.6×10^{-3}
	85	11.6×10^{-3}	2.73×10^{-3}	8.87×10^{-3}
47.5	305	12.1×10^{-3}	5.05×10^{-3}	7.05×10^{-3}
	86	13.4×10^{-3}	2.10×10^{-3}	11.30×10^{-3}
50.0	201	12.75×10^{-3}	3.87×10^{-3}	8.88×10^{-3}
	304	15.22×10^{-3}	4.31×10^{-3}	10.91×10^{-3}
	88	13.35×10^{-3}	1.22×10^{-3}	12.13×10^{-3}
52.5	302	12.50×10^{-3}	2.85×10^{-3}	9.65×10^{-3}
100.0	85	67.0×10^{-3}	7.0×10^{-3}	60.0×10^{-3}
ref. (12)	300	29.0×10^{-3}	12.0×10^{-3}	17.0×10^{-3}

volved (1-2 hr) causing decomposition of the specimens. The Hall coefficient was too small to be detected in alloys containing 95% or less Bi_2Te_3, apparently due to a low mobility and high carrier concentration.

Table II gives the Seebeck coefficients near room and liquid nitrogen temperatures for compositions near 50% Bi_2Te_3.

Table III presents thermal conductivity data for compositions near 50% Bi_2Te_3, together with published values for SnTe and Bi_2Te_3. The measured value of K has been divided into lattice (K_l) and electronic (K_{el}) contributions by assuming the alloys to be degenerate electronic conductors and computing K_{el} from the formula

$$K_{el} = \frac{\pi^2}{3}\left(\frac{k}{e}\right)^2 \frac{T}{\rho}$$

where k is Boltzmann's constant, e is the electronic charge, T the absolute temperature, and ρ the resistivity.

Discussion of the System $SnTe$-Bi_2Te_3

The DTA data alone (Fig. 2) would suggest the existence of an intermediate phase which melts by peritectic reaction at 601°C and has a composition of about 50% Bi_2Te_3, and that a eutectic reaction occurs at 581°C and 85% Bi_2Te_3. However, x-ray, electron microprobe, and metallographic results all show a continuous series of solid solutions from 45 to 100% Bi_2Te_3. These two groups of data may be reconciled if it is assumed that there exists a single phase between 45 and 100% Bi_2Te_3, the phase being formed by peritectic reaction at about 45% Bi_2Te_3 and 601°C, and exhibiting a minimum in the liquidus at 85% Bi_2Te_3 and 581°C. The presence of the 581°C reaction in alloys containing less than 85% Bi_2Te_3 is the result of nonequilibrium freezing during the peritectic reaction as explained previously. This conclusion is supported by the observation that the heat effect at 581°C is observed on heating only in the 85% Bi_2Te_3 alloy. A phase diagram showing the course of the liquidus and solidus lines is presented in Fig. 5.

The high solubility of SnTe in Bi_2Te_3 is favored by two factors if it is presumed that the Sn atoms occupy Bi sites in the Bi_2Te_3 lattice. First, the Sn sites in SnTe are octahedrally coordinated by Te and the Bi sites in Bi_2Te_3 are nearly octahedrally coordinated by their six nearest neighbor Te atoms (10). This suggests that the nature of the chemical bonds between

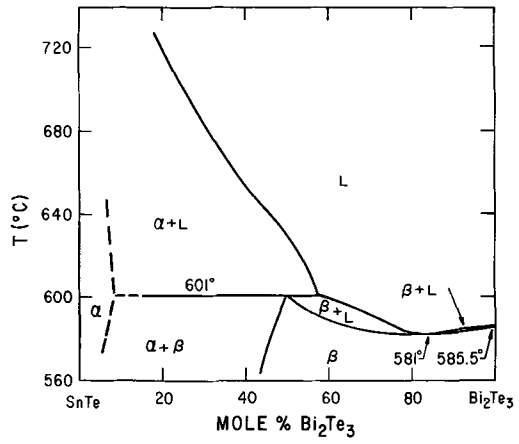

Fig. 5. Proposed phase diagram for the quasi-binary system $SnTe$-Bi_2Te_3.

Sn and Te are similar to those between Bi and Te, so that Sn can easily be incorporated into the Bi_2Te_3 crystal. Second, the Sn atom is smaller than the Bi atom, so that relative size should not prevent the substitution of Sn for Bi in Bi_2Te_2. If Sn is incorporated on Bi sites, then there would be a stoichiometric deficit of one Te atom for every two SnTe molecules dissolved in the Bi_2Te_3 crystal. This deficit may be accommodated by either the formation of Te vacancies, or by the creation of antistructure defects [the antistructure defect is a Bi atom on a Te site, or *vice versa*, and is believed to be the predominant native disorder in Bi_2Te_3 (6)].

It is not possible to determine with certainty whether the degenerate carrier concentrations and changes in carrier type are direct consequences of the incorporation of Sn into the Bi_2Te_3 lattice, or of a high concentration of lattice defects as occurs in SnTe (5) and Bi_2Te_3 (6). Since the incorporation of SnTe molecules into Bi_2Te_3 produces a Te deficit (see above) and Bi_2Te_3 which has a Te deficit is p-type (6), conduction by holes should be favored in these alloys. Furthermore, Sn has been observed to act as an acceptor in Bi_2Te_3 when added in small amounts (7, 8). Thus the expected electrical activity of Sn would also favor p-type conductivity. The fact that the SnTe-Bi_2Te alloys are n-type over most of the single-phase region suggests that the addition of large amounts of Sn to Bi_2Te_3 alters either the method of incorporation of Sn into the lattice or the bandstructure of the crystal. The former possibility might arise due to the large stoichiometric deficit of Te resulting from the incorporation of SnTe into the Bi_2Te_3 lattice. The latter possibility might arise due to the changes in the lattice parameters on alloying Bi_2Te_3 with SnTe. Soonpaa (9) has correlated carrier type with the c/a ratio of Bi_2Te_3 alloys and concluded that alloys are either n-type or p-type depending on whether c/a is greater or less than 6.98. The n-type SnTe-Bi_2Te_3 alloys, which have $c/a < 6.98$, are in conflict with Soonpaa's conclusions.

The best thermoelectric figure of merit for the SnTe-Bi_2Te_3 alloys which can be computed from the experimental data is 0.40-0.66 x 10^{-3}/°K at 300°K for compositions near 50% Bi_2Te_3. Although this best value could be improved somewhat by using higher purity materials and more precise control of the Sn:Bi:Te ratios, it still is sufficiently less than the figure of merit of other materials currently available to make these alloys of little commercial importance.

Acknowledgments

This research was carried out in the Semiconductor Exploration Laboratory of Texas Instruments Incorporated, Dallas, Texas, while the author was participating in the Summer Development Program of the company. Particular thanks go to Dr. Louis G. Bailey and Maurice Brau for their excellent guidance and advice.

Manuscript received Dec. 19, 1966; revised manuscript received Feb. 6, 1967.

Any discussion of this paper will appear in a Discussion Section to be published in the December 1967 JOURNAL.

REFERENCES

1. E. I. Elagina, N. Kh. Abrikosov, *Russian J. Inorganic Chem.*, **4**, 738 (July, 1959) (English translation).
2. J. Stamper and M. Bryant, *Bull. Am. Phys. Soc.*, **6**, 175 (1961).
3. T. M. Dauphinee and E. Mooser, *Rev. Sci. Instr.*, **26**, 660 (1955).
4. See, for example, N. F. Rhines, "Phase Diagrams in Metallurgy," p. 85-89.
5. R. F. Brebrick, *J. Phys. Chem. Solids*, **24**, 27 (1963).
6. C. Satterthwaite and R. Ure, *Phys. Rev.*, **108**, 1164 (1957).
7. A. Birkholtz, *Z. Naturforsch.*, **13a**, 780 (1958).
8. F. Rosi, B. Abeles, and R. Jensen, *J. Phys. Chem. Solids*, **10**, 191 (1959).
9. H. Soonpaa, *ibid.*, **25**, 1107 (1964).
10. J. Drabble and C. Goodman, *ibid.*, **5**, 142 (1958).
11. Westinghouse Research Laboratories, Thermoelectric Quarterly Progress Report No. 2, June 11, 1960, p. 19.
12. T. Harman, B. Paris, S. Miller, and H. Goering, *J. Phys. Chem. Solids*, **2**, 181 (1957).

ELECTROCHEMICAL SCIENCE

Fuel Cell Oxidation of Hydrogen on Movable, Partially Submerged Platinum Anodes

H. J. Davitt and L. F. Albright

School of Chemical Engineering, Purdue University, Lafayette, Indiana

ABSTRACT

The electrochemical oxidation of hydrogen was investigated potentiostatically at 30°C and atmospheric pressure using two movable flat-plate platinum anodes which were partially immersed in 1.0*N* H_2SO_4. The importance of meniscus formation, electrolyte film formed on the exposed portion of the anode, surface roughness, and hydrogen adsorption on the exposed portion of the anode is demonstrated by transient currents resulting from vertical movements of the anodes. The two anodes of different surface roughnesses, one surface altered by sandblasting and the other by platinizing, were tested at the following conditions: (*a*) stationary positions, (*b*) lowering and raising at constant rates (0.7 to 23.8 cm/min), and (*c*) sudden lowering and raising (greater than 480 cm/min). Surface roughness was a determining factor in the evaluation of the data. The roughness of both anodes was temporarily changed by an electrochemical oxidation-reduction technique. The results of the investigation lend support to the thin film model for porous gas diffusion electrodes.

The mechanism occurring on fuel cell electrodes is very complex because of surface geometry including surface roughness, equilibrium conditions, and thermodynamic and kinetic considerations (1). Several investigators (2-9) who considered some of the more theoretical aspects of the fuel cell reactions believe that mass transport of the reactant to the electrode is often if not always rate-limiting; however, they do not agree on the controlling step. Diffusion of dissociated hydrogen on the electrode has been suggested as the controlling step (5). Will (9) and Maget and Roethlein (6), however, believe that the predominant transport step is through the upper portion of the intrinsic meniscus and the adjacent film, in which case the entire surface of the electrode above the meniscus has a high ohmic resistance permitting poor ionic mobility and hence presumably allowing little current flow. Pshenishnikov *et al.* (7) reported results on smooth electrodes in which the film above the meniscus actually contributed more current than did the meniscus itself. Weber *et al.* (8) came to essentially the same conclusions as did Will; however, they believe that a 3-phase zone exists. Cobb (2), using molten carbonates as electrolyte, indicated that the meniscus as well as its shape plays a very important role in the electrochemical reaction. The meniscus is considered by most to be involved in the hydrogen transfer. Certainly the meniscus characteristics would be significantly affected by surface roughness.

Since the rate-determining step of molecular hydrogen transport is often through the meniscus, reduction of this resistance would result in much higher currents. Ennis (3) found for example that, if the anode were raised or lowered in the electrolyte at a constant rate, larger currents were obtained than those of a stationary electrode at equilibrium. In addition, transient currents resulted from fast vertical movements of the partially immersed anode. In all cases these currents were larger than steady-state values and decayed quickly to equilibrium. Will (9) reported high transient currents on lowering the anode, but he found that the currents were depressed on raising it. The apparent contradiction found by Will and Ennis concerning the nature of the transient currents has not yet been explained, but may be caused by differences in the surface roughness of the electrodes.

In the present investigation, two anodes were roughened by sandblasting and by electrochemical techniques. Surface roughness has been found important in explaining factors which affect transient currents when the anodes are raised or lowered.

Equipment and Operating Procedures

The fuel cell consisted of two compartments connected by a fritted glass disk. The anode compartment was constructed of a partially submerged glass cylinder into which the anode could be raised. The top of the cylinder was fitted with a rubber stopper containing hydrogen inlet and outlet ports. The other compartment contained the counter electrode.

The anodes used were 0.0075-cm (0.005-in.) thick platinum foil approximately 2.5 cm wide by 8.0 cm long. A No. 20 gauge platinum wire was spot welded to the top of each electrode and connected through a rubber cap on each Pyrex glass tube to a No. 18 gauge copper wire. Surface roughness of the platinum foil anodes was modified in the following manner: anode S was sandblasted and cleaned in concentrated hydrofluoric acid; anode R was platinized for 120 sec in a 10% chloroplatinic acid solution at a current density of 18.5 ma/cm^2. The anodes were cleaned before most runs in hot concentrated nitric acid (dilution 1:3) and washed with distilled water before use; this procedure will be termed the "normal" electrode conditions. In some cases, the anodes were "activated" by an oxidation-reduction technique in 2.0*N* H_2SO_4: oxygen was evolved at the anode for 12 hr at a current density of approximately 0.17 amp/cm^2, it was washed with distilled water and reduced in a similar sulfuric acid solution for 4 min at a current density of approxi-

mately 0.05 amp/cm². The platinum oxide layer was believed to be completely reduced in this latter step since a hydrogen equilibrium potential was obtained in less time than it took to set up the cell and make a measurement (less than 3 min).

The electrolyte was 1.0*N* H_2SO_4 prepared from 96.5% reagent grade sulfuric acid. The electrolyte was saturated with hydrogen gas and maintained at 30° ±0.2°C. A saturated calomel electrode (SCE) was used as a potential reference, and unless otherwise stated all potentials are referred to this standard. A Duffers Model 600 potentiostat with auxiliary equipment was used to control the potential of the anode to within ±0.005v. A Sargent Model SR automatic self-balancing potentiometer was used to record the current output of the cell.

A specially designed elevator, which could be driven by motor or turned by hand, was used to raise or lower the anodes to within ±0.02 cm. A ring stand, fitted with stops and a sliding clamp attached to the anode Pyrex glass tube, was used to raise and lower (snap-raise or snap-lower) the test electrodes by hand rapidly.

Results

Anodes at stationary positions.—The currents obtained with the platinized anode and the sandblasted anode at various stationary positions were measured as a function of the emergent height (the distance between the top edge of the anode and the surface of the electrolyte) for the following conditions: 0.15 and 0.55v applied voltage and for both a "normal" anode and for one that had been preoxidized-reduced just before the run. The relationships of current to height for the "normal" platinized anode, Fig. 1, curves 1 and 2, are similar to those explained earlier by Will (9). At emergent heights of 6-8 cm, the meniscus was ragged; the currents were also less regular and consistent.

Immediately after the preoxidation of the platinized anode, the currents obtained at 0.55v (curve 4) were generally lower by about 1 ma than curve 2; however, these currents tended to increase toward curve 2 within several hours. This gradual increase in current with time was not observed at 0.15v. The results for the sandblasted anode are shown in Fig. 2, and each curve shown is the average of several runs which also gave reasonably good reproducibility as indicated by a statistical evaluation. The current obtained with the sandblasted anode were often as low as 40% of those obtained with the platinized anode. Preoxidation of the sandblasted anode caused the current to increase by about 100% (although currents were generally less than for the other anode) for applied voltages of both 0.15 and 0.55v. Both anodes when preoxidized gave similar currents at 0.55v.

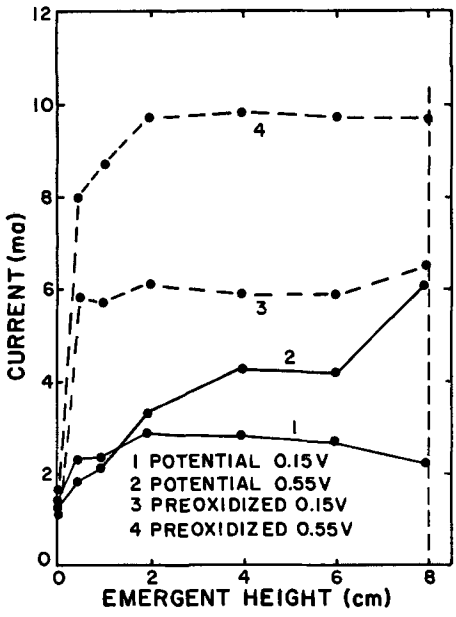

Fig. 2. Average current as a function of the sandblasted anode's emergent height under normal and preoxidized-reduced conditions at potentials of 0.15 and 0.55v.

Although the surface areas of the two anodes used in this investigation were not measured directly, the results and methods of preparing the anodes are quite similar to those of Will (9) for two of his anodes. It seems safe to conclude that relative surface roughness of the anodes are also similar, namely 10 and 88, respectively.

Anodes moved at steady rates.—Numerous runs were made in which the two anodes were raised or lowered at various constant rates. Figure 3 indicates such results for the platinized anode as a function of

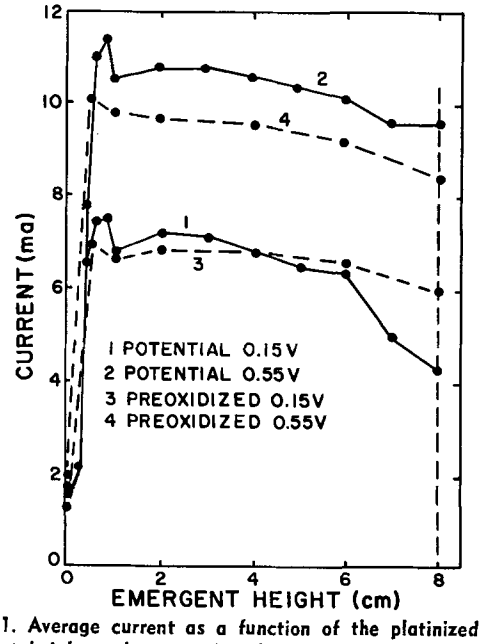

Fig. 1. Average current as a function of the platinized anode's emergent height under normal and preoxidized-reduced conditions at potentials of 0.15 and 0.55v.

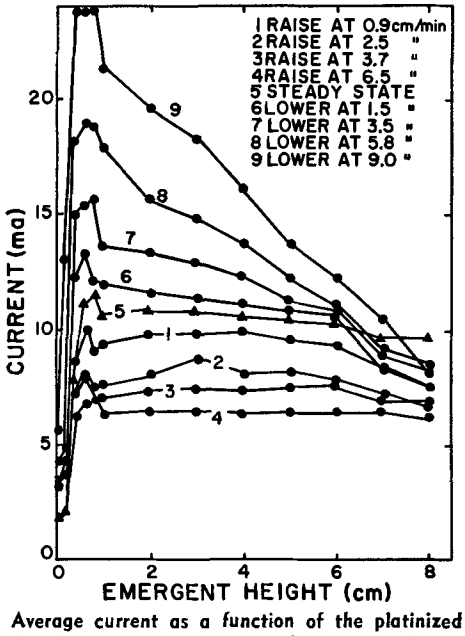

Fig. 3. Average current as a function of the platinized anode's emergent height with average rate of raising and lowering as parameters; potential 0.55v.

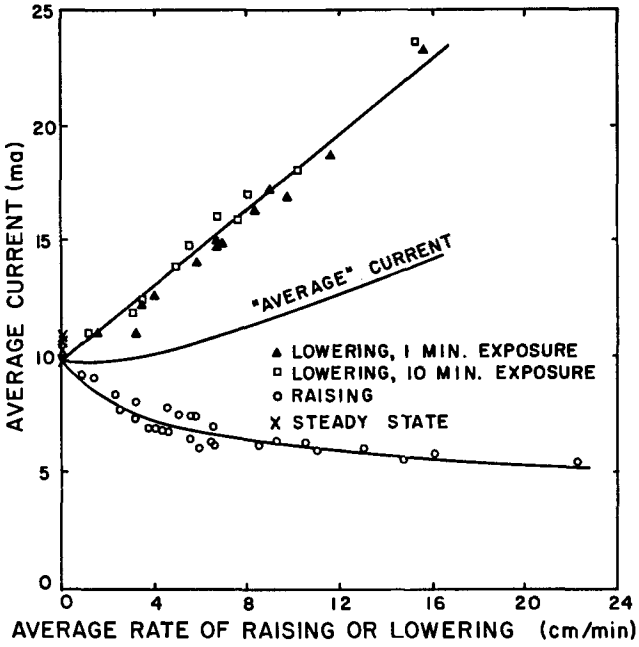

Fig. 4. Average current as a function of average rate of raising and lowering the platinized anode at a potential of 0.55v.

emergent height as the anode was moved at 0.55v. The current clearly increased as the rate of lowering increased. Curve 5 is for the stationary anode (also curve 2 of Fig. 1). Raising the anode caused the current to decrease as is indicated by curves 1-4.

The average current for each run shown in Fig. 3 was determined by graphically integrating and averaging. Figure 4 shows a plot of these average currents as a function of the average rate of raising and lowering the anode. Runs in which the anode was exposed to hydrogen for 10.0 min before lowering perhaps gave slightly higher currents by about 5% than those with 1.0-min exposure; however, more data would be required to evaluate this difference statistically. The middle curve of Fig. 4 designated as "average" current is the arithmetical average of the curves for lowering and raising. Such an average current might be expected if a cylindrical rotating anode were to be used in a fuel cell. In such a fuel cell, one portion of the anode would correspond to the raising experiments and the opposite portion to the lowering experiments.

Similar runs were made for the sandblasted anode at 0.55v, and the results are shown in Fig. 5. The currents obtained were significantly less than those obtained with the platinized anode. However raising the sandblasted anode at rates greater than about 4 cm/min increased the current. Experiments were also made at

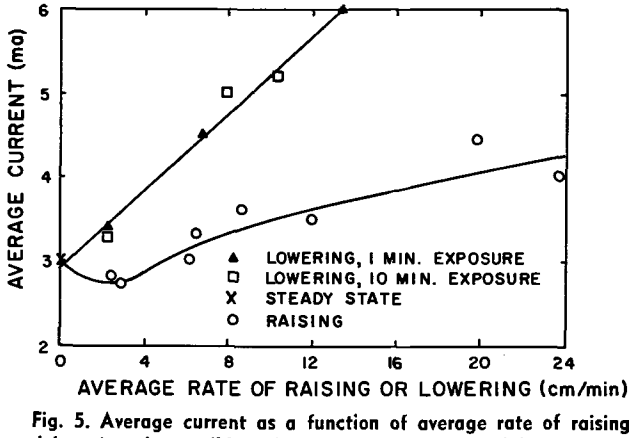

Fig. 5. Average current as a function of average rate of raising and lowering the sandblasted anode at a potential of 0.55v.

Table I. Constants for Eq. [1] and [2]

Anode	Applied voltage, v	a	b	c	d
Platinized	0.15	6.6	0.99	5.1	0.50
Platinized	0.55	9.8	0.82	9.0	1.24
Sandblasted	0.15	2.1	0.22	—	—
Sandblasted	0.55	2.9	0.23	—	—

0.15v in which both anodes were moved at steady rates. The types of curves obtained were similar to those obtained at 0.55v.

Average currents for runs in which the anode was lowered could in all cases be fitted by the following type of empirical equation

$$\text{Current} = a + b \text{ (rate of lowering in cm/min)} \quad [1]$$

Currents for the platinized anode as the anode was raised were correlated at rates from 0.9 to 22 cm/min by the following empirical equation

$$\text{Current} = c - d \ln_e \text{ (rate of raising in cm/min)} \quad [2]$$

Values of a and b and of c and d were determined by regression analyses, and Table I indicates the values obtained. The value a represents the average current for the stationary anode. The significance of these values will be discussed later.

Currents after sudden raising or lowering of anode. —Numerous experiments were made in which both anodes were suddenly raised or lowered in less than 0.5 sec from one position to another. These changes in position are designated as snap-raises and snap-lowerings. In all cases the emergent height of the anodes was never less than 2.0 cm. Figure 6 indicates the results of runs for the platinized anode as it was moved from emergent heights of 2-6 cm and back for both 0.15 and 0.55v. When this anode was raised, the current decreased in the first second, then immediately increased somewhat (to a value less than steady state), and then decreased slightly for about 0.5 min. From 0.5-10.0 min the current increased slightly and leveled off after about 10 min. When the anode was snap-lowered, the current increased to a value off the scale of the recorder (*i.e.*, greater than 12.5 ma). The current decreased to less than 12.5 ma within 6 sec, a minimum current was experienced after about 1 min, and then the current increased slightly and leveled off by the end of 10 min.

Preoxidation of the platinized anode did not have any significant effect on the transient currents obtained during snap-raises and lowerings. In all runs with

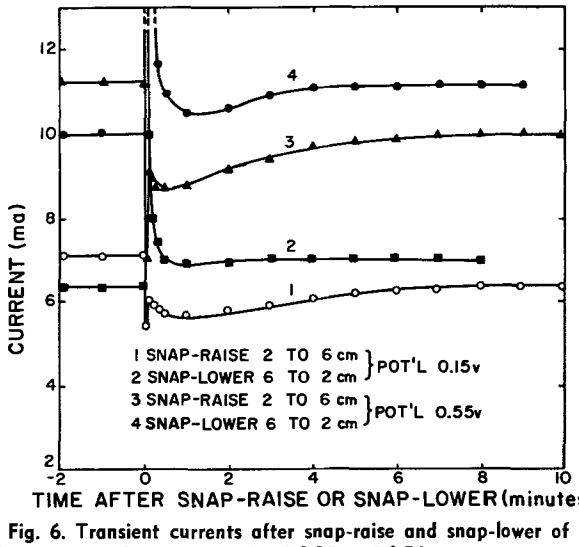

Fig. 6. Transient currents after snap-raise and snap-lower of the platinized anode at potentials of 0.15 and 0.55v.

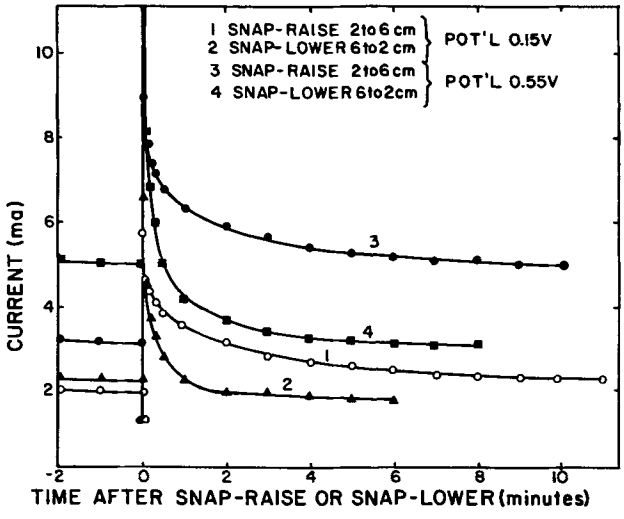

Fig. 7. Transient currents after snap-raise and snap-lower of the sandblasted anode at potentials of 0.15 and 0.55v.

this anode, the meniscuses obtained during snap-raises and lowerings looked smooth and well-formed.

The currents obtained with snap-raises and lowerings of a "normal" sandblasted anode are shown in Fig. 7. The general characteristics of the curves obtained are similar to those of the platinized anode except that the transient currents on raising were about 3 times greater than the currents at stationary conditions. When the sandblasted anode was then preoxidized and snap-raised at 0.55v, the results obtained 160 and 1730 min after preoxidation are shown as curves 2 and 3 of Fig. 8. Curve 1 is shown for purposes of comparison (also curve 3 of Fig. 7). Preoxidation drastically changed the type of curves obtained with snap raises; there was an instantaneous current reduction, quick rise of current above the steady-state value; the current then decreased to a minimum after about 0.5 min and then increased to a plateau by the end of 10 min. After 1730 min (about 29 hr), the character of the curve was similar to that of curve 1, although the currents were higher in all cases. Snap-lowering runs for the preoxidized sandblasted anode showed the same phenomena as previously described and shown in Fig. 7.

Discussion and Results

Results of this investigation support the postulate that the rate-controlling step of the over-all process is

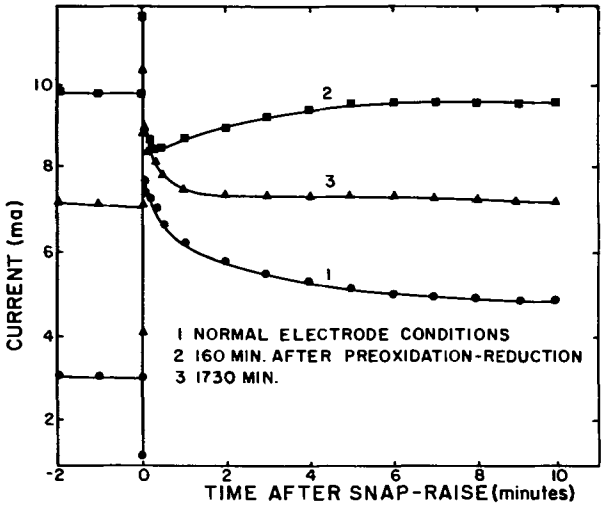

Fig. 8. Transient currents after snap-raise of the sandblasted anode under normal and preoxidized-reduced conditions at a potential of 0.55v.

mass transfer of the hydrogen to the anode through the upper edge of the meniscus and of the film just above it. As indicated in Fig. 1 and 2, the maximum current is obtained just as the meniscus first develops when the anode is raised from the electrolyte.

Surface roughness was found to be an important factor in the transient currents developed as the anode was raised or lowered. With the sandblasted anode which was macroscopically rough but microscopically smooth, good agreement was obtained with the results of Ennis (3), *i.e.*, increased currents were obtained as the anode was both lowered and raised. With the platinized anode, however, which is microscopically rough, good agreement was obtained with the results of Will (9), *i.e.*, increased currents when the anode was lowered but decreased currents as it was raised. The preoxidation-reduction of the sandblasted anode probably microscopically roughened the anode (11, 12), resulting in transient currents for raising that were intermediate between those of the two anodes under normal conditions (see Fig. 6 and 8).

Shibata (11, 12) concludes that preoxidation-reduction of platinum produces an active unstable platinum surface with an activity comparable to the platinized-platinum electrode. Comparisons of Fig. 1 and 2 and of Fig. 6 and 8 can be interpreted in terms of this model. After the preoxidation-reduction technique the current *vs.* emergent height curves (Fig. 1 and 2) of both anodes were more regular, indicating a more uniform surface. At 0.55v (curve 4, Fig. 1) the current of the peroxidized platinized anode was initially lower than under normal conditions (curve 2). Some active sites may have been "sealed off" by the production of this temporary active surface. Such a phenomenon was not apparent at 0.15v or on the sandblasted anode at either potentials.

Will and Knorr (10) found that essentially no hydrogen adsorbs on platinum electrodes at potentials greater than 0.4v relative to the normal hydrogen electrode (NHE). Will (9) states that a voltage gradient probably exists in the meniscus-film region parallel and adjacent to the anode, starting from the applied potential in the bulk solution and decreasing toward the reversible hydrogen electrode potential. This voltage gradient resulting from the slow transport of hydrogen ions from the reaction zone into the bulk electrolyte causes concentration gradients of molecular and atomic hydrogen to exist along the anode surface. Therefore, a larger portion of the exposed anode surface should be at potentials low enough for hydrogen adsorption at 0.15 than at 0.55v, relative to the saturated calomel electrode. Consequently, on lowering the anode, the slope of the curve of average current *vs.* average rate of lowering should be larger at 0.15 than at 0.55v. The platinized anode supports this postulate since the corresponding slopes were found to be 0.99 and 0.82 ma/cm/min (Table I). However, for the sandblasted anode, the two different potentials had little or no affect on the slope. Since the meniscus on the sandblasted anode was ragged on lowering, the film, if one existed, was presumably extremely thin; consequently a large voltage gradient existed and most of the exposed anode surface at both potentials was at a potential lower than 0.4v (NHE).

As mentioned previously the sandblasted anode was macroscopically rougher than the other anode, due to the sandblasting. Therefore, when the platinized anode was suddenly raised, the liquid film which was pulled up was undoubtedly smaller and drained more quickly than the corresponding film on the other anode which tended to "hang up" on the coarse structure. The preoxidation-reduction technique discussed earlier should produce a temporary surface structure on the sandblasted anode somewhat intermediate between these two extremes. This intermediate condition was shown to exist (see Fig. 8) and did slowly revert back to the normal condition.

When both anodes were quickly raised, the current

instantaneously decreased. This could be due to either or both of the following: (*i*) an increased film thickness resulting in a larger barrier to hydrogen diffusion, or (*ii*) by removal of that portion of the anode which was originally in equilibrium near the top of the meniscus and replaced by a lower portion of the electrode in equilibrium with a much smaller concentration of hydrogen. The film apparently drains very rapidly from the platinized anode as evidenced by the short peaks following the first instantaneous decrease (curves 1 and 3, Fig. 6). These same peaks for the sandblasted anode are quite large (curves 1 and 3, Fig. 7) indicating that the film drained slowly enough to permit establishment of high currents. These transient currents are not believed to be affected by the potentiostat, since it has a stated rise time of 25 μsec for a 0.01v square wave input.

Upon constant raising of the anode (Fig. 4 and 5), the effect of surface roughness is apparent at speeds much slower than those of a rapid or snap-raise. The sandblasted anode shows a modest current increase following a small depression at very slow rates of raising, whereas, the platinized anode exhibits a continuously decreasing current of an asymptotic nature.

Results of these experiments support the theory that a liquid film exists above the intrinsic meniscus and that no 3-phase zone exists. During experiments with the platinized anode when it was raised from an emergent height of 6.0-7.0 cm, the portion of the electrode directly above the apparent meniscus edge appeared to become "dry" with a very distinct upper boundary. This dry region encompassed that portion of the electrode greater than 6.0 cm which was previously discussed and regarded as nonuniform. As this portion of the electrode became dry, the current which was initially at steady state decreased approximately 0.5 ma to a new steady state. The actual shape of the meniscus itself probably changed during this film separation and accounted for the current decrease. It is important to note that a distinct visible film boundary did exist. This phenomenon was not observed on the sandblasted anode. The existence of the film may depend on surface roughness, and if the film does exist it contributes very little to the total current.

Conclusions

Surface roughness of a partially submerged platinum anode has an important effect on currents at a stationary electrode and the transient currents obtained when the anode is raised or lowered. Surface roughness affects both the meniscus and film formation, which in turn affects the currents. Preoxidation followed by reduction temporarily alters the surface roughness of platinum.

At stationary electrode conditions, a thin film covers the exposed portion of partially submerged, heavily platinized-platinum electrodes. This film may or may not cover the exposed portion of a partially submerged "smooth" anode; however, this film was not found to contribute significantly to the total current.

Acknowledgment

The financial support of The Indiana Gas Association is gratefully acknowledged.

Manuscript received Sept. 2, 1966; revised manuscript received Feb. 23, 1967.

Any discussion of this paper will appear in a Discussion Section to be published in the December 1967 JOURNAL.

REFERENCES

1. M. Eisenberg, "Fuel Cells," Chap. 2, Will Mitchell, Jr., Editor, Academic Press, New York (1963).
2. J. T. Cobb, Ph. D. Thesis, Purdue University, 1966.
3. R. Ennis, M.S. Thesis, Purdue University, 1965.
4. S. R. Faris, *Nature*, **199**, 754 (1963).
5. E. Justi, *et al.*, *Verl d. Akad. d. Wissensch*, u.d. Lit., Wiesbaden (1959).
6. H. J. R. Maget and R. Roethlein, *This Journal*, **112**, 1034 (1965).
7. A. G. Pshenishnikov, *et al.*, *Elektrokhimiya*, **1**, 418 (1965).
8. H. C. Weber, *et al.*, *This Journal*, **109**, 884 (1962).
9. F. G. Will, *ibid.*, **110**, 145 (1963).
10. F. G. Will and C. A. Knorr, *Z. Elektrochem.*, **64**, 258 (1960).
11. S. Shibata, *Bull. Chem. Soc. Japan*, **36**, 525 (1963).
12. S. Shibata, *ibid.*, **37**, 410 (1964).

Substructures in Oxide Scales on Nickel, Cobalt, and Nickel-Cobalt Alloys

G. C. Wood, J. M. Ferguson, B. Vaszko, and D. P. Whittle

Corrosion Science Division, Department of Chemical Engineering, The University of Manchester Institute of Science and Technology, Manchester, England

ABSTRACT

Scales produced on nickel, cobalt, and nickel-cobalt alloys in pure oxygen at 1000° and 1200°C have been studied, after different cooling procedures, in plan and section by optical and electron microscopy. Very large columnar grains are separated from the metal core by a thin layer of fine equiaxed grains. Subgrain boundaries are revealed on the surface of nickel-rich scales by a form of growth or by thermal etching and of cobalt-rich scales by Co_3O_4 precipitation. In section, the visibility of Co_3O_4 decorating subboundaries can be accentuated by preferential chemical etching. Growth facets and steps and thermal etch pits produced by surface processes are clearly evident on scale surfaces, certain of the etch pits probably being associated with emergent dislocations. Control of the alloy composition and cooling conditions leads to precipitation of Co_3O_4 either randomly, or along subgrain boundaries, or as very fine particles along preferred directions in the (Ni,Co)O grains.

Following the very early studies of oxidation phenomena, in which the elementary ideas of kinetic, mechanical, structural, and topographical aspects were proposed, came a long period in which the field was dominated by kinetic studies which reached, in some cases, a considerable degree of sophistication. In recent years, however, the limitations of this approach have been appreciated by many workers, and kinetic

measurements have been supplemented by carefully documented topographical, structural, and microanalytical information.

Thus, to characterize an alloy oxidation process reasonably fully it is necessary to know the kinetic rate constants for the surface oxide and any internal oxide formation, together with the interdiffusion coefficient of the alloying elements and the solubility and diffusion rate of oxygen in the alloy. Additionally, a full knowledge of morphological, epitaxial, structural, and microanalytical data is required at various stages of oxidation and often a rate-determining layer must be isolated. The lattice defect structure and semiconducting properties of this layer must be ascertained by techniques such as electrical conductivity measurements and radioactive tracer techniques.

The state of development of the oxidation field has now reached the stage where, in addition to the above information, much more must be established about phenomena affecting the mechanical properties of films and scales, factors which are highly significant in determining the oxidation behavior. By analogy with the study of metals and ceramics, there are two approaches whereby this more fully integrated picture of the oxidation process may be attempted. One involves the direct measurement of mechanical properties of oxides and oxide/metal combinations such as the stress developed, tensile properties, creep rates, fracture properties, and hardness. Preliminary measurements along these lines have already been made by other workers (1-9), although much remains to be done. The second approach, an essential one in the long run to understand processes such as slip, fracture, and creep fully, is to establish a sound understanding of the grain structure and substructural detail of films and scales. This involves a knowledge of grain nucleation, recrystallization, and grain growth phenomena during scaling and subsequently of subgrain boundary and dislocation distribution. In certain instances precipitation phenomena within the scale are also important. The present paper reports a preliminary study of such phenomena in scales.

Information on the substructure and mechanical properties is most urgently needed for oxides such as Cr_2O_3, Al_2O_3, Nb_2O_5, and ZrO_2 which commonly fail by spalling. However, although the problem is by no means as severe with nickel and cobalt, the oxides of these metals are much easier to study in this way and are therefore more suitable for preliminary studies. Thus nickel-cobalt alloys, which are homogeneous and single-phase, produce single layers of a single oxide solid solution (Ni,Co)O when oxidized above 900°-950°C, cobalt being only slightly preferentially oxidized. Such layers grow according to a parabolic relationship mainly by the outward movement of cations, and metal concentration gradients have recently been obtained through such scales at various stages of oxidation (10). The system has the additional advantage that on cooling scales below 900°-950°C, Co_3O_4 is precipitated within the scale to an extent determined by the alloy composition and the cooling rate, thus permitting study of preferential sites for precipitation. This is because (Ni,Co)O, saturated with oxygen at the oxidation temperature, becomes supersaturated on cooling, thus promoting the precipitation. Additionally, for slow cooling in oxygen or air the surface layers would tend to be converted to Co_3O_4 by continued oxidation.

Experimental Procedure

In preparing the scaled specimens which were to be studied in plan and section by optical and electron microscopy, it was recognized that as well as identification of normal growth features, recourse would probably be necessary to the established methods of observing substructure in metals, namely thermal etching, chemical etching, and defect decoration. A form of thermal etching was obtained by carrying out the oxidation at high temperatures. Decoration could be controlled to some degree by careful choice of the alloy and cooling conditions.

Annealed specimens of nickel, cobalt, and of Ni-10.9% Co and Ni-80.0% Co, of purity in excess of 99.95%, were used for most experiments, but comparable results were also obtained for the pure metals with spectrographically pure material. The surfaces were generally electropolished at 0.39 amp/cm^2 in 60% sulfuric acid (s.g. 1.6) at 30°C for 3 min or lightly mechanically polished on 1μ diamond suspension. After washing in alcohol and drying, the specimens were oxidized by immediate exposure to pure flowing oxygen for various times at 1000° or 1200°C. They were subsequently cooled by quenching in water, by furnace cooling (2°C/min) or generally at an intermediate rate of approximately 150°C/min. Unless otherwise stated in the captions the last cooling rate is applicable.

Certain scales were examined directly in plan, but others were fractured by bending the completely oxidized specimen or were prepared conventionally in section, finishing on diamond suspension. The grain structure of scales in section on pure nickel was sometimes revealed by a relatively long polishing time. With cobalt and Ni-80.0% Co it could be accentuated by etching in 30% V/V HCl in ethyl alcohol at 50°C for 15-30 sec, which functions by attacking Co_3O_4 precipitates in grain boundaries. Microhardness traverses across scale sections were made at room temperature, using a Reichardt microhardness tester with loads in the range 5-100g, but usually 50g.

The electron microscopical examination of the surfaces of the scales was made using standard replica techniques, in conjunction with an A.E.I., E.M.6 microscope. The two-stage formvar/carbon replica technique was found to be the most suitable. This produced a carbon replica, negatively shadowed with a platinum/carbon alloy, nominally normal to the surface. The alternative method, involving chemically stripping a direct carbon film as a replica, was also used with relatively flat surfaces where it could easily be removed.

Results and Interpretation

At the present stage of development of this work, the causes of all the surface features cannot be precisely stated because of general ignorance of the relative contributions of directional preferential growth through the oxide lattice, surface diffusion, and evaporation and surface-tension phenomena. For the sake of presentation, it will be assumed that the very large crystal facets, involving entire grain or subgrain surfaces, are due to preferential growth along certain directions whereas smaller steps, striations, or etch pits within the grains are due to surface diffusion and possibly evaporation. The term "thermal etching" will be employed although it is recognized that this process, as employed as a technique in revealing the surface structure of metals and ceramics, is often carried out *in vacuo*, conditions clearly favoring evaporation processes. However, thermal etching is also known to occur in gaseous atmospheres, including those which are mildly oxidizing. The oxide surface will be attempting to assume a minimum surface free energy configuration revealing close-packed planes, grain boundaries, and dislocation networks. This simple picture will require substantial modification in due course. The possibility of obtaining surface features due to mechanical deformation of the oxide or to vacancy coalescence on cooling should not be neglected.

Unfortunately it is not possible to make a quantitative appraisal of the phenomena at this stage. This would require a very detailed study of each factor discussed and would in any case be rendered difficult by existing doubts about surface tension, surface diffusion, and evaporation contributions to surface features on all materials and about 1:1 correlation between etch pits and emergent dislocations.

Table I. Scale Thicknesses

Alloy	Oxidation time and temperature	Scale thickness, μ
Nickel	12 hr, 1200°C	40
Ni-10.9% Co	4 hr, 1000°C	13
	5 min, 1000°C	10
Ni-80.0% Co	50 hr, 1000°C	270
	12 hr, 1200°C	500
Cobalt	12 hr, 1200°C	900

Scale thicknesses.—In those cases where scales have been examined in plan, it is of value to know the scale thicknesses; consequently these are given in Table I.

Oxide grain size and distribution.—Figure 1a shows a section through a thick scale produced on nickel by oxidation for 288 hr at 1200°C. The action of the diamond polishing suspension is sufficient to delineate the grain boundaries mildly and gives clearer results than etching in boiling orthophosphoric acid solution which tends to stain the specimen. The scale consists of a single major layer with large columnar grains extending from the outer interface to a thin region of fine equiaxed grains adjacent to the metal. The pores in this inner region appear to be associated with the more friable oxide there. Scales on zone-refined nickel have large grains extending nearer to the metal.

Figure 1b shows in section a remarkably uniform and pore-free single-layer scale on cobalt oxidized for 4 hr at 1000°C. During cooling at 150°C/min, Co_3O_4 precipitation has clearly occurred along the columnar grain boundaries and to some extent at preferred sites within the grains in the outer half of the scale and probably nearer the metal, although it is not visible there through being small. A similar section of a cobalt specimen, completely oxidized in 65 hr at 1200°C, cooled at 150°C/min and etched in alcoholic hydrochloric acid solution, is depicted in Fig. 1c. Again,

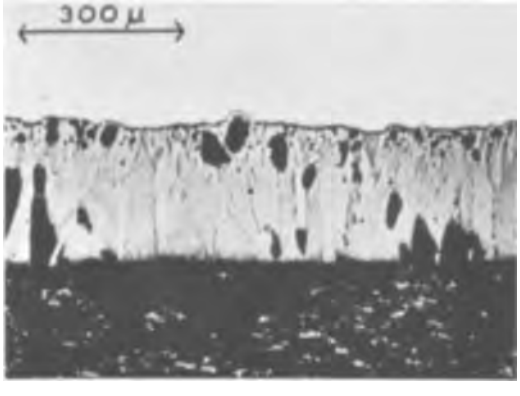

Fig. 1a. Grain size and distribution in section. Nickel oxidized for 288 hr at 1200°C.

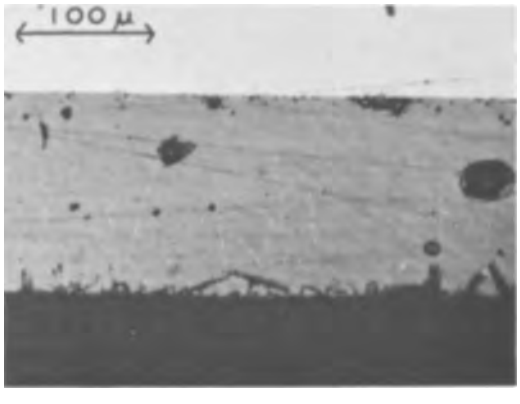

Fig. 1b. Grain size and distribution in section. Cobalt oxidized for 4 hr at 1000°C.

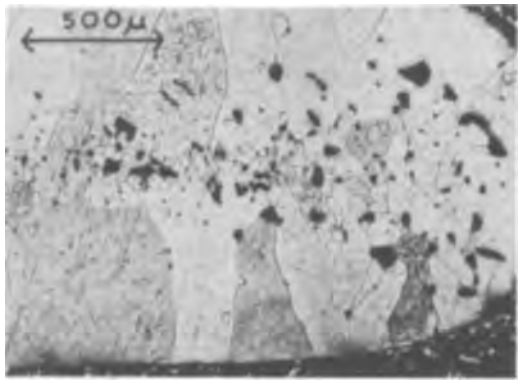

Fig. 1c. Grain size and distribution in section. Cobalt fully oxidized after 65 hr at 1200°C, etched.

massive outer columnar grains are separated by an inner layer of fine grains. The latter may be partly associated with impurities collecting there and inhibiting grain growth, or affecting mechanical constraints near the metal/oxide interface by reducing scale plasticity, as indicated by Vallée (17). It is noteworthy that the region of small equiaxed grains is thicker near the end of the specimen which could indicate that mechanical factors operative there influence the structure, although clearly the scale has been sufficiently plastic to accommodate volume changes in this vicinity. Indeed the scale has shown sufficient plasticity to accommodate virtually all volume changes because, apart from a few pores which may have been produced or enlarged during the polishing process, there is no gap in the center of the specimen as often occurs when scales grow by cation diffusion. Special experiments on spheres, cylinders, and various angular specimens with very sharp corners all showed adherent uniform scale on cooling from 1000° or 1200°C, confirming that scale plasticity at these temperatures is sufficient to eliminate effects of mechanical factors on the oxidation rates.

Etching reveals the relatively fine precipitation of Co_3O_4 within the grains because it acts by attacking the Co_3O_4. It is likely that the Co_3O_4 is decorating subgrain boundaries but it is difficult to be precise at this magnification. Additionally there is a tendency for Co_3O_4 precipitation from scales on pure cobalt to be so extensive that its location is sometimes throughout the grains in a random fashion. The general grain structures just described are somewhat similar to those previously reported for nickel (13), cobalt (15, 17), and iron (25).

Microhardness traverses across sections of the thick scales at room temperature showed that the hardness values decreased from 650-750 kg/mm^2 for NiO to 450-500 kg/mm^2 for (Ni,Co)O on Ni-80% Co and 300-350 kg/mm^2 for CoO. These ranges cover the scatter from numerous specimens examined, repeated values from individual specimens giving much closer results. The small equiaxed grains near the metal/oxide interface and at the ends of the specimens gave values 10-20% lower than in the outer columnar grains. Co_3O_4 precipitates, of the size observed here, also seemed to reduce the measured hardness of CoO-rich grains by a similar amount. There was, however, no obvious hardness gradient across any scale section. In the case of the Ni-80% Co alloy, where such a gradient would be expected on the grounds of composition changes, this is because the grain size and precipitation effects would tend to obscure the gradient. The hardness values were generally independent of the oxidation temperature within the experimental error. Hardness values of these oxides which are relatively brittle at room temperature can only be considered as relative and do not directly imply similar trends at temperature. The measurements were generally made with a 50g load, although the values were apparently un-

affected in the range 5-100g. Douglass (6), working on ZrO_2, used much higher loads and found a dependence of hardness with load under these conditions. Although hardness values obtained at temperature are obviously more valuable, it is still useful to have measurements of scale properties at or near room temperature, because spalling on cooling or thermal cycling is clearly partly determined by the latter.

Figure 2a displays the massive grains on the surface of cobalt oxidized for 12 hr at 1200°C, followed by quenching in water, the characteristic grain shape and grain boundary network showing remarkably clearly. The apparent size of these grains lies in the range 100-400μ, which agrees well with values measured in section. No Co_3O_4 is evident in this specimen because its deposition was prevented by the rapid water quench. By analogy with similar grains on cobalt (18) and nickel (13), examined by x-ray diffraction techniques, the large flat surfaces parallel to the surface may be identified as {100} planes and the sides of the few large pits in the grain boundaries in Fig. 2a and 2b (appearing black) as {111} planes. These large faceted pits seem more common on nickel surfaces, particularly at high temperatures (19). Similar surface grain patterns have been reported by other workers (14, 16). In one study of cobalt oxidation the grain surfaces are reported to be flatter at higher temperatures and on annealed surfaces (17).

Figure 2b displays the effect of cooling a similarly oxidized specimen at about 150°C/min. Co_3O_4 is precipitated in a relatively finely divided form at preferred sites in the surface, such as subgrain boundaries and other regions of dislocation emergence. The distribution is similar to that of the specimen shown in section in Fig. 1c.

The surface of the scale on Fig. 3a, which was produced on Ni-80.0% Co by oxidation for 70 hr at 1200°C and cooled at 150°C/min, shows some irregular cracks. These may well have followed subgrain boundaries decorated by Co_3O_4 during the cooling process. This emphasizes the importance of reactions occurring during the cooling process as well as at temperature and the effects of the differential cooling characteristics of the alloy and scale. For comparison, Fig. 3b shows a fracture surface of a scale on cobalt, completely oxidized for 65 hr at 1200°C and subsequently cracked in half. Fracture steps are clearly visible, and the dots indicate Co_3O_4 precipitates, comparable in size to those seen in plan, which could well act as stress raisers. Cracks were transgranular in the oxide which is not very ductile at room temperature.

Oxide subgrain size and distribution.—Electron microscopy enables the subgrain structures to be studied in much greater detail. Thus, Fig. 4a shows the surface of a scale in Ni-10.9% Co oxidized for 4 hr at 1000°C, this scale being about 13μ thick (Table I) and having a surface composition of (Ni,Co)O containing about 20% cobalt without any Co_3O_4 precipitate (10). The outer surfaces of the columnar grains viewed in plan are about 1.5-5μ wide, and the subgrains within them are typically 1.5 x 0.4μ. The fine veinlike structure revealing the subgrains is produced by the surface phenomena mentioned previously. It is worth

Fig. 3a. Fracture of scale. Ni-80.0% Co oxidized for 70 hr at 1200°C and cooled at 150°C/min.

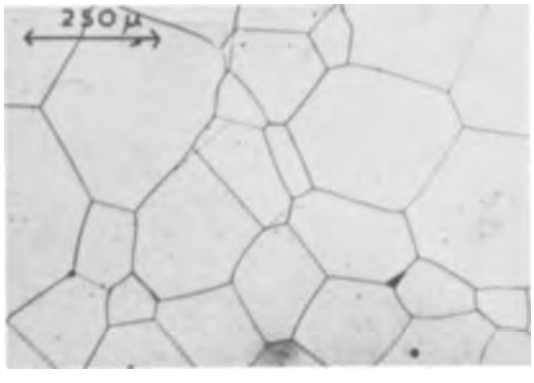

Fig. 2a. Grain size and distribution in plan, together with other topographical details. Cobalt oxidized for 12 hr at 1200°C and quenched in water.

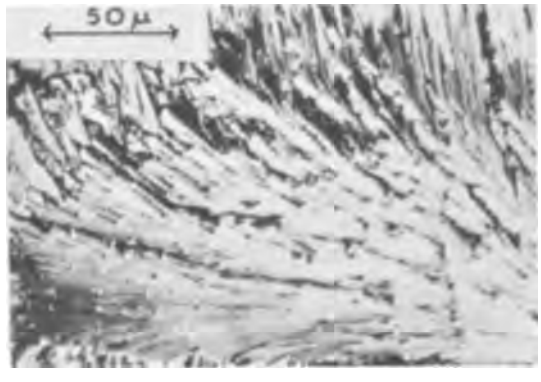

Fig. 3b. Fracture of scale. Fracture surface of cobalt specimen, completely oxidized for 65 hr at 1200°C.

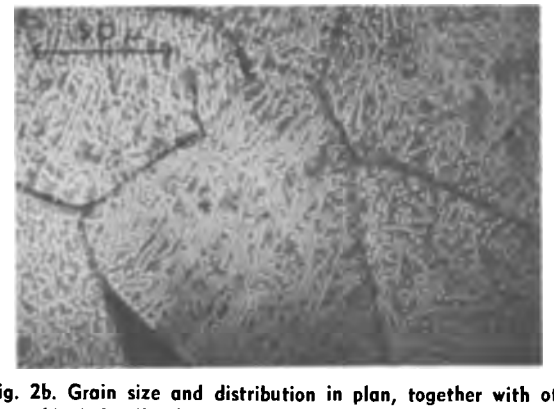

Fig. 2b. Grain size and distribution in plan, together with other topographical details. Cobalt oxidized for 12 hr at 1200°C.

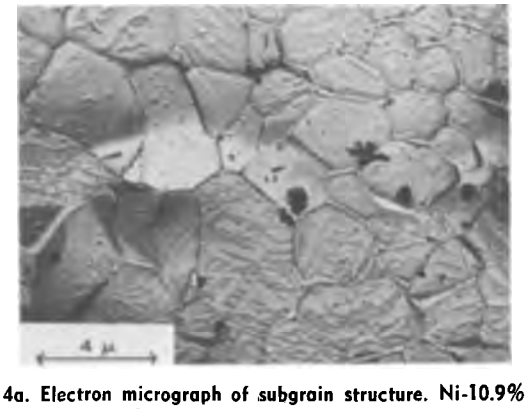

Fig. 4a. Electron micrograph of subgrain structure. Ni-10.9% Co oxidized for 4 hr at 1000°C.

Fig. 4b. Electron micrograph of subgrain structure. Ni-80.0% Co oxidized for 5 min at 1000°C.

noting that the melting points of NiO and CoO are 1960° and 1805°C, respectively.

Another method of showing up the subgrain structure, displayed for Ni-80.0% Co oxidized for 5 min at 1000°C (Fig. 4b), is to select the alloy and cooling conditions so that Co_3O_4 is precipitated preferentially along the boundaries. The subgrains are somewhat larger than for Ni-10.9% Co which is to be expected because of the faster oxidation rate. This micrograph also demonstrates that such precipitation is not always necessarily associated with surface topographical features. Thus, the Co_3O_4 is not related to the stepped surface, the origin of which is discussed in latter sections. Some of the small dots indicated may be Co_3O_4 nuclei.

Growth facets, steps and striations, and etch pits.— Figure 5a shows the surface of a nickel specimen oxidized for 12 hr at 1200°C. Apart from the large flat grains, previously identified by analogy as {100} surfaces and the large facets in grain boundaries which have {111} surfaces, numerous pits are present within the grains, aligned in two directions. It is likely that these are thermal etch pits and are not produced by vacancy coalescence on cooling or indeed by directional growth. The large faceted pits in the grain boundaries possibly originally grew from such pits although, as indicated earlier, they may have appeared by directional lattice growth. The typical pit size is 2-5μ and there are approximately 10^6 pits/cm^2 which lies within the very wide range of 10^6-10^9/cm^2 for the dislocation density in annealed materials. It cannot be stated categorically that the pits were initially associated with emergent dislocations, but this is likely. The method seems to have possibilities for revealing dislocations in thermally formed oxides, for example by the observation of etch pit location after progressive macroscopic film thinning. Chemical etching in hot nitric acid, which is said (19) to produce dislocation etch pits in NiO produced by flame fusion and subsequent annealing at 1620°C in argon, failed to increase the pit density.

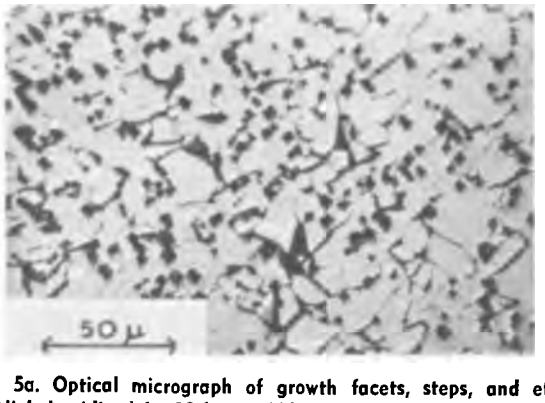

Fig. 5a. Optical micrograph of growth facets, steps, and etch pits. Nickel oxidized for 12 hr at 1200°C.

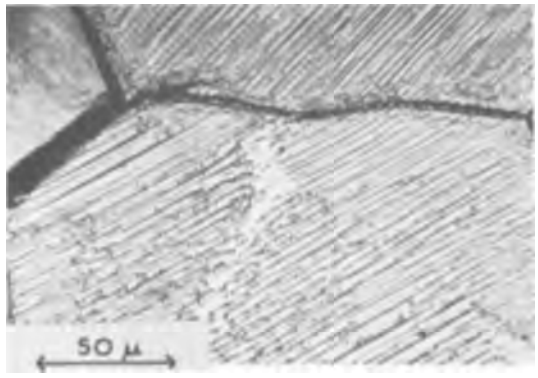

Fig. 5b. Optical micrograph of growth facets, steps, and etch pits. Ni-80.0% Co oxidized for 12 hr at 1200°C and furnace cooled.

Numerous steps, extending entirely across a grain in a direction depending on its orientation, are depicted in Fig. 5b. This specimen of Ni-80.0% Co was furnace cooled after oxidation for 12 hr at 1200°C so the surface is very rich in Co_3O_4. Although the steps are related to growth phenomena and surface diffusion they bear similarity to striations which have been observed during nucleation processes on metal surfaces.

Figure 5c shows a remarkable wealth of detail on the surface of a specimen of Ni-80.0% Co oxidized for 50 hr at 1000°C. Within each clearly visible grain are terraces of growth steps revealing cubic planes. There are also possibly a few terraced etch pits and a display of fine pimplelike particles which are the Co_3O_4 precipitate particles.

The differences from specimen to specimen and from region to region in those features of surface topography related to surface diffusion processes are determined in part by impurities as well as the oxide substructure, temperature, and cooling rate. These impurities, derived from the gas or conceivably from the metal, poison surface sites and thus control the step size and the rate of step movement across the surface.

Certain of the features visible in the optical microscope are examined at greater magnification in electron micrographs in Fig. 6. For example Fig. 6a gives considerable detail of very fine steps or striations, of different orientation from grain to grain. These are only a fraction of a micron in size, compared with the micron-size steps observed on the specimen in Fig. 5b. Figure 6b gives the detail of grains about 10μ in size. Certain regions of certain grains are covered with fine pock marks, typically 1000Å in diameter with about 10^8/cm^2. An important feature is that the grains appear truncated, supporting the idea of removal of material. In certain regions the pock marks look like fine etch pits without any special shape.

The pits on the surface of scale on nickel (Fig. 5a) are shown at much higher magnification in Fig. 6c. Some of the pits are square, confirming the surface

Fig. 5c. Optical micrograph of growth facets, steps, and etch pits. Ni-80.0% Co oxidized for 50 hr at 1000°C.

Fig. 6a. Electron micrograph of growth facets, steps and etch pits. See Fig. 6b, c, d, and e. Nickel oxidized for 12 hr at 1200°C.

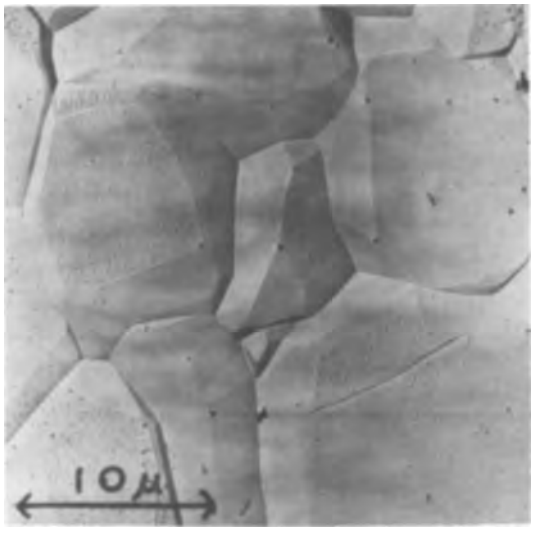

Fig. 6b. Nickel oxidized for 12 hr at 1200°C

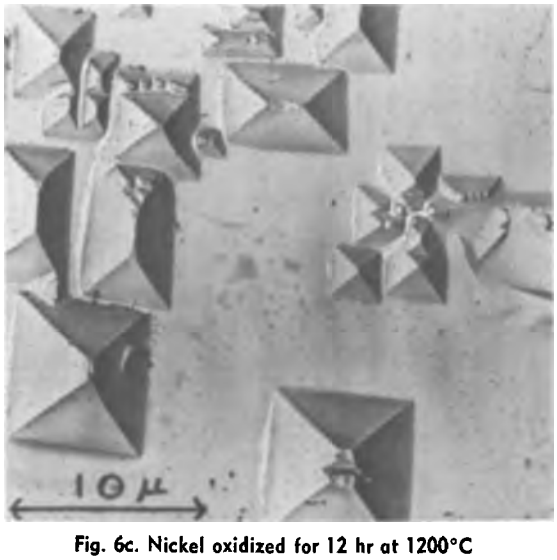

Fig. 6c. Nickel oxidized for 12 hr at 1200°C

faces of the large grains to be {100}, but some are rectangular, possibly due to the joining together of two smaller pits. There are also small features at the pit bases which have not yet been identified.

Pits of a similar type, but much smaller and less sharply defined, were found on Ni-80.0% Co oxidized for 12 hr at 1200°C and water quenched (Fig. 6d), which would therefore possess a (Ni,Co)O surface containing about 80% cobalt, without any Co_3O_4 pre-

Fig. 6d. Ni-80.0% Co oxidized for 12 hr at 1200°C and water quenched.

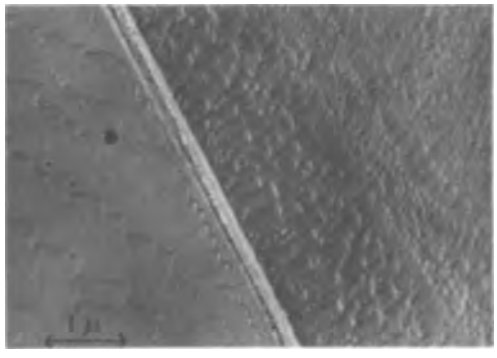

Fig. 6e. Ni-80.0% Co oxidized for 12 hr at 1200°C and furnace cooled.

cipitation. The pit density over the surface is $10^7/cm^2$ and their size is in the range 0.2-1.5μ.

The ranges of size, shape and number of pits on the surfaces of the specimens illustrated in Fig. 6c and 6d are in general agreement with comparable features observed with metals and ceramics (21-23).

Figure 6e is of interest because it shows a scale grain boundary at high magnification on furnace-cooled Ni-80.0% Co oxidized for 12 hr at 1200°C. The surface will be nearly all Co_3O_4, and the different step shapes are visible on either side of the boundary.

Figure 7 shows aligned growth features in some grains on a specimen surface, which will be almost

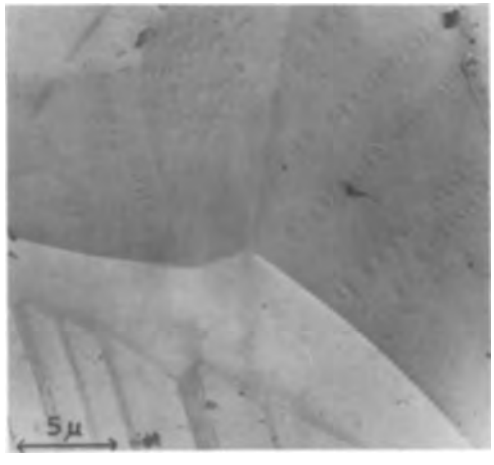

Fig. 7. Electron micrograph of terraces and lined up shallow etch pits on cobalt oxidized for 12 hr at 1200°C and furnace cooled.

entirely Co_3O_4. These are rows of what are apparently shallow etch pits, all in the same direction within a given grain, but in different directions from grain to grain. It may be proposed that these etch pits are associated with rows of emergent dislocations. The etch pits are generally 0.1-1μ apart, being closer near boundaries where they stop. These features are remarkably similar to dislocation pile-ups observed by transmission in thin foils of stainless steel (22) and also in lithium fluoride (23). The separations in stainless steel were typically 0.04μ and in lithium fluoride 2-10μ. Variations in stacking fault energy make direct comparisons impossible. The origin of the pile-ups, if such they are, is not known, but it should be pointed out that the outer Co_3O_4 layer was produced on cooling slowly and some plastic deformation must have occurred during this process. This explanation is favored by the shallowness of the pits, which would have been produced in a relatively short time at a lower temperature than others described earlier. Large widely separated steps are apparent on other parts of the micrograph.

Nature of Co_3O_4 precipitation in scales.—When the surface of Ni-80.0% Co oxidized for 5 min at 1000°C and cooled at 300°C/min was examined by electron microscopy the grains and subgrains were clearly revealed (Fig. 8a). Certain grains show a fine veined structure revealing subgrains, but the most important feature is the directional precipitation of small Co_3O_4 particles during cooling, there being two main directions of alignment. The Co_3O_4 particles are typically 1000-5000Å wide and up to a micron in length, but this depends on the grain orientation. They are rodlike in shape and there are about 10^7-10^8/cm^2, suggesting they are at dislocation sites. It is, however, conceivable that the precipitation is of a Widmanstatten-type, but this is difficult to judge purely from surface considerations. One reason for this fine separated precipitation is that the cooling rate was almost twice as fast as with previous specimens showing agglomerated precipitate.

Unfortunately this very fine precipitation, which could well be used for dislocation decoration studies, is difficult to reproduce because it is a critical function of composition, temperature, cooling rate and oxygen pressure. For example Fig. 8b, which was prepared at a slightly slower cooling rate, shows (at higher magnification) acicular Co_3O_4 particles, but these are somewhat larger and appear randomly distributed within the scale.

Conclusions and Discussion

1. For nickel, cobalt, and Ni-Co alloys, oxidized at 1000° or 1200°C, large columnar grains are separated from the metal core by a thin layer of fine equiaxed grains. Differential polishing characteristics of the regions of different grain size probably at least partly explain reports of double-layer scales in earlier work.

2. Subgrain boundaries may be revealed on the surface of nickel-rich scales by the growth form or thermal etching and of cobalt-rich oxides by Co_3O_4 precipitation. In section it is often advisable to accentuate this by chemical etching.

3. Growth facets and steps and thermal etch pits produced by surface processes are evident on scale surfaces. Certain of the etch pits are probably associated with emergent dislocations. Sometimes shallow etch pits, lined up in a direction related to the orientation of the oxide grain, may reveal rows of piled up emergent dislocations.

4. Co_3O_4 can be precipitated randomly, or along subgrain boundaries or as very fine particles along preferred directions in (Ni,Co)O grains. This technique is promising as a method of obtaining dislocation decoration in thermally formed oxides.

The immediate problem is clearly to obtain a more fully documented picture of the influence of alloy composition, temperature, oxygen pressure, cooling rate, and degree of cold work of the metal on the features observed. It should be possible to study substructure in the oxides of similar metals such as iron (9, 26) and copper (9) and subsequently in oxides of chromium, niobium, and aluminum. The feasibility of following dislocation distribution through scales, possibly by thinning, should be attempted using thermal and chemical etching and decoration techniques. Methods of examining thin films, thinned regions of thick scales, and partly oxidized foils by transmission are also clearly desirable, particularly in view of the greater wealth of comparable micrographs of this type in the allied fields of metals and ceramics. It must be recognized that the structure of oxides, and consequently their properties (4, 5), may be quite different when forming by passage of a large ionic flux in one direction from when formed by compaction of powders or other means. It is also generally held that behavior in a barrier layer of oxide next to the metal determines the stress developed, adhesion properties, etc., to a large degree. Nevertheless, the properties of bulk scales will undoubtedly have some influence on behavior because they have to attempt to maintain continuity with the metallic core during growth and subsequent cooling. Various aspects of this work are now in hand. The long-term hope is that the substructure of scales may eventually be used to explain their mechanical properties, about which much more information is likely to emerge in the next decade. When these two aspects have been fully explored, an "integrated theory" of many metal and alloy scaling processes will be much nearer completion.

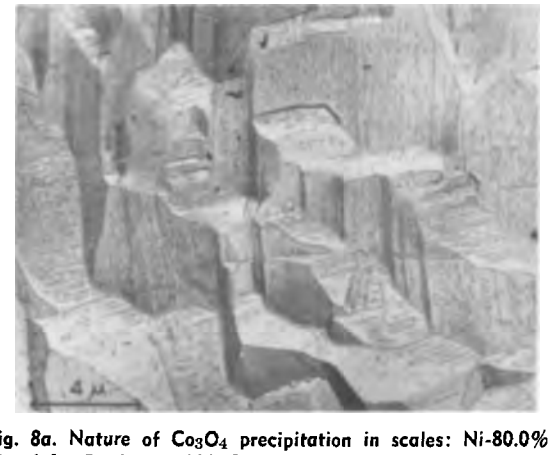

Fig. 8a. Nature of Co_3O_4 precipitation in scales: Ni-80.0% Co oxidized for 5 min at 1000°C and cooled at 300°C/min.

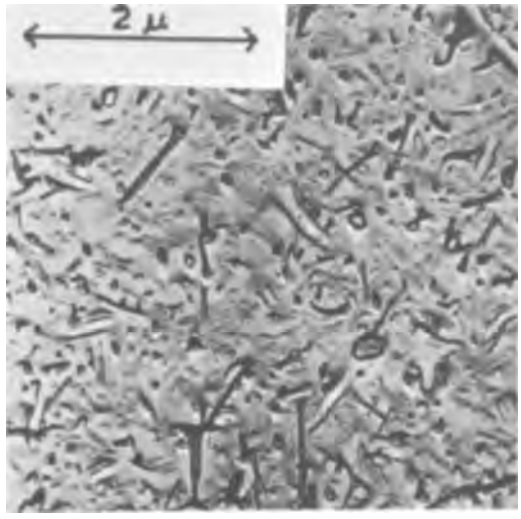

Fig. 8b. Nature of Co_3O_4 precipitation in scales: Ni-80.0% Co oxidized for 5 min at 1000°C.

Acknowledgments

The authors' thanks are due to Professor T. K. Ross for providing facilities and to the Science Research Council for a maintenance allowance to one of them (J.M.F.). International Nickel Limited kindly supplied most of the metals and alloys.

Manuscript received July 27, 1966; revised manuscript received Feb. 26, 1967.

Any discussion of this paper will appear in a Discussion Section to be published in the December 1967 JOURNAL.

REFERENCES

1. P. D. Dankov and P. V. Churaev, *Doklady Akad. Nauk. SSSR*, **73**, 1221 (1950).
2. W. Jaenicke, S. Leistikow, and A. Stadler, *This Journal*, **111**, 1031 (1964).
3. J. D. Mackenzie and C. E. Birchenall, *Corrosion*, **13**, 783t (1957).
4. D. H. Bradhurst and J. S. Ll. Leach, *Trans. Brit. Ceram. Soc.*, **62**, 793 (1963).
5. D. H. Bradhurst and J. S. Ll. Leach, *This Journal*, **113**, 1245 (1966).
6. D. L. Douglass, *Corrosion Sci.*, **5**, 255 (1965).
7. R. F. Tylecote, *J. Inst. Metals*, **78**, 301 (1950).
8. R. F. Tylecote, *Mem. Sci. Rev. Met.*, **62**, 241 (1965).
9. G. Vagnard and J. Manenc, *ibid.*, **61**, 768 (1964).
10. G. C. Wood and J. M. Ferguson, *Nature*, **208**, 369 (1965).
11. T. Takeda and H. Kondoh, *J. Phys. Soc. Japan*, **17**, 1315 (1962).
12. J. P. Baur, E. S. Bartlett, J. N. Ong, and W. M. Fassell, *This Journal*, **110**, 185 (1963).
13. J. Paidassi, *Acta Met.*, **3**, 447 (1955).
14. J. Sartell and C. H. Li, *J. Inst. Metals*, **90**, 92 (1961-1962).
15. D. Fuller and H. S. Suarez, *A.B.N. Bol. Assoc. Brasil metais, Sao Paolo*, **17**, 63, 195 (1961).
16. D. W. Bridges, J. P. Baur, and W. M. Fassell, *This Journal*, **103**, 614 (1956).
17. M. G. Vallee, Rapport CEA-R.2424, Centre d'Etudes Nucleaires de Saclay (1964).
18. C. A. Phalnikar, E. B. Evans, and W. M. Baldwin, *This Journal*, **103**, 367, 429 (1956).
19. G. C. Wood and I. G. Wright, *Corrosion Sci.*, **5**, 841 (1965).
20. A. J. Forty, *Advances in Physics*, **3**, 1-25 (1954).
21. S. Amelinckx, "The Direct Observation of Dislocations," Academic Press, New York and London (1964).
22. M. R. Louthan, *Corrosion*, **21**, 288 (1965).
23. A. R. C. Westwood, *Phil. Mag.*, **5**, 981 (1960).
24. W. G. Johnston, *Prog. Ceram. Sci.*, **2**, 1 (1962).
25. J. Paidassi and L. Berry, *Compt. rend.*, **258**, 565 (1964).
26. L. Himmel, R. F. Mehl, and C. E. Birchenall, *Trans. AIME*, **197**, 827 (1953).

On the Passivity of Iron-Chromium Alloys

I. Reversible Primary Passivation and Secondary Film Formation

Robert P. Frankenthal

Edgard C. Bain Laboratory For Fundamental Research,
United States Steel Corporation Research Center, Monroeville, Pennsylvania

ABSTRACT

Electrochemical studies, as well as microscope observations, on an Fe-24% Cr alloy in H_2SO_4 have shown that at least two distinct, potential-dependent films are formed. The primary film, which is responsible for the initial passivation, is stable only within a few millivolts of the primary activation potential. A secondary film, which forms at more positive potentials, grows to a thickness greater than 10Å and, with increasing potential and time, becomes very stable and resistant to reduction. The primary passivation process is reversible. The "thickness" of the primary film at the primary activation potential corresponds to less than the equivalent of one oxygen atom per surface metal atom. From this "thickness" and from the *p*H-dependence of the primary activation potential (81 mv/pH), it is suggested that the primary passivation process forms a film containing chromium and oxygen ions and possibly also some constituent of the electrolyte solution.

The passivation of iron-chromium alloys has been studied widely, yet our understanding of the mechanism of this process is still very limited. Two basic problems have not been resolved: (*i*) the composition and thickness of the passivating film and (*ii*) the effect of the *p*H of the electrolyte solution on the activation potential, *i.e.*, the potential corresponding to the initial rise in the anodic current upon going from the passive region into that of anodic dissolution.

Olivier (1) reported that 0.008 coulombs/cm^2 were required to passivate an 18% Cr alloy; combining this with results from B. E. T. measurements, he concluded that the thickness of the passivating film was about 20Å. The data of Heumann and Schürmann (2) indicate that 0.2 coulombs/cm^2 are required to passivate this alloy. King and Uhlig (3) interpret their anodic polarization data to indicate that the passivating film is an adsorbed film of oxygen, as does Kolotyrkin (4) from his capacitance data. However, Aronowitz and Hackerman (5) believe that the passivating film consists of an adsorbed monolayer of oxygen through which cations migrate to form an amorphous oxide on top of the adsorbed layer.

Rocha and Lennartz (6), using a potentiodynamic method (120 mv/hr), obtained a dependence of the activation potential on pH of 120 mv/*p*H for alloys with Cr content > 14%, as well as for Cr;[1] King and Uhlig (3) indicated that this dependence is a function of the rate of potential sweep and adjusted their sweep rate so that they obtained an activation potential shift of 59 mv/*p*H. Aronowitz and Hackerman (5) claim that it is not possible to remove the passivating film on alloys with Cr content > 12% without severe cathodic treatment or repolishing the surface. While the data in the above references are significant and instructive, much of the interpretation is speculative and based on incomplete knowledge and understanding of the systems.

In this paper we have combined light and electron microscope observations with electrochemical mea-

[1] Vetter (7) tries to show that the data of Rocha and Lennartz for chromium can be forced to give a slope of 58 mv/*p*H.

surements in the hope of obtaining a better understanding of this complex system. We will show that the film that is stable in the neighborhood of the activation potential, and which shall be called the primary passivating film, is different from the film that exists at more positive potentials and is called the secondary film. The primary film may be formed and reduced reversibly, that is, no hysteresis is observed in the potential-current relationship; while the secondary film is difficult to reduce. A primary activation potential is associated with the primary passivation process and its dependence on *p*H is quite different from that of the apparent activation potential (associated with the secondary film), which has been measured by other investigators.

Experimental

The alloy investigated was a high-purity, vacuum melted Fe-24% Cr alloy which had the following analysis: Cr-23.8%; C-0.0075%; N-0.0068%; O-0.050%; P-<0.005%; S-0.004%; Si-<0.01%; Al-<0.005%; Cu-<0.01%; Mg-<0.001%; no other elements were detected. The electrodes were machined as previously described (8) except that flats were ground on the cylinder so that microscope examinations could be made easily. After machining the electrodes were annealed for 150 hr at 760°C and quenched in water. The surface layer was removed by mechanical polishing on "microcloth" using 1μ alumina particles. The cell, electrolyte preparation, potentiostat, potential-drive apparatus and auxiliary equipment have been described previously (8). Potentials are reported relative to the standard hydrogen electrode (SHE). The electrolyte was 1*N* H_2SO_4, except in the experiments in which the effect of *p*H was studied. In these experiments the ionic strength was kept constant by the addition of K_2SO_4. All experiments were conducted at 24°C.

Just before insertion into the cell, the samples were electropolished by the method of Sewell *et al.* (9). On insertion into the cell, the specimen surface was cathodically reduced at —0.5v for several minutes, and then the potential was rapidly switched to the initial potential for that experiment.

Coulometric reduction of the passivating film was done by using a standard amperostatic circuit consisting of a battery and a variable resistance. The potential of the electrodes was followed with a Beckman Research *p*H-meter and recorded on a Honeywell Electronik 19 recorder. To observe the nature and the extent of the anodic attack on the surface, light microscopy and electron microscopy using germanium-shadowed carbon replicas were employed.

Results

Potential-current relationships.—The potential-current relationships are a function of the direction in which the potential is changed, the rate of potential change, the potential at which the surface is passivated in the case of the potential being varied from the passive into the active region, and the mode of surface preparation. These effects are shown partly in Fig. 1 and in Table I, and they are summarized in this section.

Figure 1 depicts the potential-current relationships for the alloy in 1*N* H_2SO_4 as measured under three different sets of experimental conditions to be described below. The cathodic loop (indicated by the breaks in the curves) is due to the evolution of hydrogen. The activation potential, E_a, corresponding to the initial rise in the anodic current upon going from the passive region into the anodic loop, is the minimum in the cathodic loop of either curve. In the system under discussion, the activation potential can easily be determined to within ±1 mv and reproducibility is better than ±2 mv for any given set of experimental conditions.

In Fig. 1 curve "a", the data indicated by the squares give the potential-current relationship for a potential sweep from negative to positive potentials. This curve may be measured either by the potentiostatic steady-state technique or by the potentiodynamic method at 100 mv/hr. If one reverses the direction of potential sweep, *i.e.*, goes from the passive region to more negative potentials, the potential-current relationship shows a hysteresis (Fig. 1, curve b) the extent of which is dependent on the rate of potential sweep and the passivating potential. Curve b was obtained by passivating at +0.5v and sweeping the potential at 100 mv/hr.

Reversibility can, however, be achieved, that is the hysteresis can be completely eliminated (Fig. 1, curve a, circles) if the surface has been carefully reduced and etched so as to remove all traces of films prior to passivation and if the passivation potential is not permitted to exceed the activation potential by more than a few millivolts (<5 mv). The following treatment is necessary to achieve this reversibility. The surface is cathodically reduced at —0.5v; the potential is then shifted to the value corresponding to the peak anodic current density and held for a sufficient time to permit between 100 and 200 atomic layers to be anodically dissolved. With the potential still maintained at this value, the electrolyte is flushed from the cell and clean electrolyte is introduced. The potential is then rapidly shifted into the passive range, within 5 mv of the activation potential. By this procedure it was possible to achieve complete reversibility of the potential-current curve,[2] independent of the length of time of passivation. The activation potential determined in this manner was reproducible to better than ±2 mv. It will be referred to as the primary activation potential to dif-

Table I. Variations in the apparent activation potential, E_a, with rate of potential sweep and passivating potential, E_p

Sweep rate, mv/hr	E_p, v	E_a, v
Steady state*	—	−0.130**
100	+0.48	−0.150
400	+0.48	−0.184
400	−0.02	−0.155
1000	−0.02	nm***

* Steady-state determination. The potential was maintained at any value until the current was constant for at least 10 min. As the activation potential was approached, the potential was varied in steps of 2 mv.
** Primary activation potential.
*** Not measurable due to the fact that at these high potential sweep rates E_a is so negative that it is masked by the high cathodic hydrogen evolution current.

[2] This cannot be associated with enrichment of one of the alloy components in the surface layer during anodic dissolution since curve b can be measured in the manner indicated in the text after anodic dissolution.

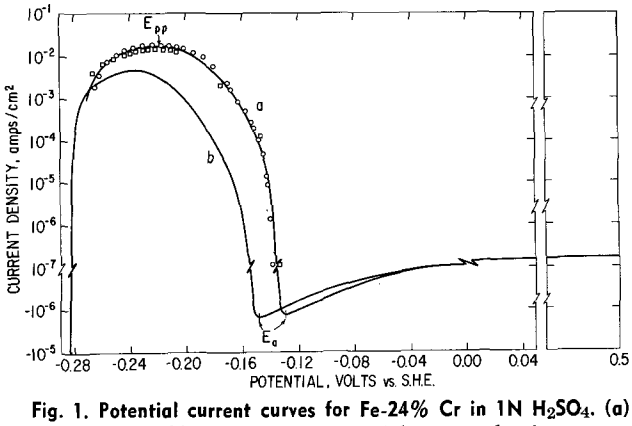

Fig. 1. Potential current curves for Fe-24% Cr in 1N H_2SO_4. (a) Illustrates reversible behavior in potential range of primary passivating film. □-(—) to (+) potential sweep; o-(+) to (—) potential sweep; (b) illustrates hysteresis due to presence of secondary film.

ferentiate it from the apparent activation potential, such as observed in curve b, Fig. 1.

The apparent activation potential for sweeps from positive to negative potentials is a function of the passivation potential and the rate of the potential sweep. Some typical results in 1*N* H_2SO_4 are summarized in Table I.

Mode of breakdown of passivating film.—Pickering and Frankenthal (8) showed that during a potential sweep at 100 or 200 mv/hr from +0.5v into the anodic loop, local breakdown of the passivating film occurs followed by crystallographic pitting of the substrate; physical or chemical inhomogeneities in the passivating film not associated with dislocation termini or grain boundaries in the alloy appear to be the most probable sites for film breakdown.

It has now been observed that local breakdown of the passivating film followed by pitting of the substrate occurs (Fig. 2) if the surface is passivated at potentials as near as 10 mv to the primary activation potential prior to a slow potential sweep, *e.g.*, 100 mv/hr, into the anodic loop. If the specimen is passivated within 5 mv of the primary activation potential and then the potential is swept into the anodic loop, pitting is never observed, but only a general attack over the surface (Fig. 3), indicating that the passivating film has been reduced uniformly. If the surface is passivated at 5 to 10 mv positive with respect to the activation potential prior to the potential sweep, a uniform attack is observed over most of the surface. However, a few grains (perhaps 10%) show pitting instead of general attack. In this case the observed pits were always triangular indicating an effect of crystallographic orientation on the structure of the passivating film. When the potential of a specimen after passivation at +0.5v is swept to within less than 5 mv of the primary activation potential, maintained there until a steady state is achieved (several hours) and then swept into the anodic loop, only a general attack over the surface, and not pitting, is observed.

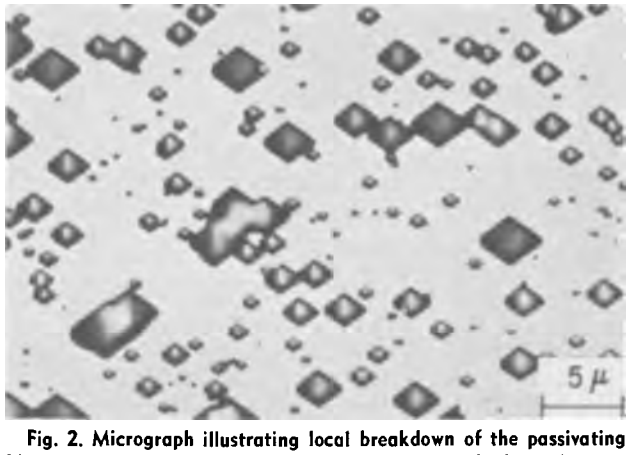

Fig. 2. Micrograph illustrating local breakdown of the passivating film as evidenced by crystallographic pitting of the substrate. Surface passivated at +0.5v prior to potential sweep.

Fig. 3. Carbon replica of surface illustrating general reduction of passivating film as evidenced by general corrosion of the surface. Surface passivated at —0.12v prior to potential sweep.

Cathodic chronopotentiometry.—To learn more about the properties of the passivating film, cathodic potential-time curves were measured at constant current. Such curves for a surface passivated at potentials near the primary activation potential are shown in Fig. 4. The potential associated with each curve is the potential of passivation. The primary activation potential is —0.130v, and the curve for the reduction of the passivating film formed at this potential is shown. At —0.140v the potential corresponds to the lower part of anodic loop, the observed current density being 5 μa/cm^2. At —0.100 the potential is well into the passive region. The observed "thickness" (expressed in millicoulombs/cm^2) of the passivating film at the primary activation potential lies between 0.40 and 0.68 mc/cm^2 and is independent of the length of time of passivation. A value of 0.7 mc/cm^2 corresponds to an oxygen to surface-metal-atom ratio of 1:1, assuming a two-electron transfer per oxygen atom and an average density of surface metal atoms of 2 x 10^{15}/cm^2, as calculated from the density of the alloy. The observed variations in "thickness" are most likely due to variations in the surface roughness factor for the different specimens used. Since the geometric area was used to calculate the coulombic density, all the values are high. Two other errors may affect the coulometric measurements: (*i*) only a partial correction[3] was made for the current due to hydrogen evolution at the film-reduction potential, again resulting in measured thicknesses that are too high; (*ii*) low thicknesses would be measured if self-activation, due to side reactions, occurred concurrently with the cathodic reduction. If self-activation were operative, the measured thickness would increase with increasing current density (decreasing time for reduction). From Fig. 5 it is concluded that appreciable self-activation that would significantly change the measured thickness does not occur at the primary activation potential. However, at more negative passivation potentials, self-activation does occur during cathodic reduction as evidenced by the apparent increase in thickness with increasing cathodic current density for a specimen passivated at —0.140v (Table II). On opening the circuit after passivation at this potential, self-activation occurred within 72 sec; at the primary activation potential and at more positive potentials self-activation does not occur on opening the circuit.

The potential-time curves for a specimen passivated

[3] The correction made was equal to the net cathodic current density measured at the reversible activation potential. Since the reduction potential is more negative, the cathodic current density would be somewhat higher, but not easily ascertainable.

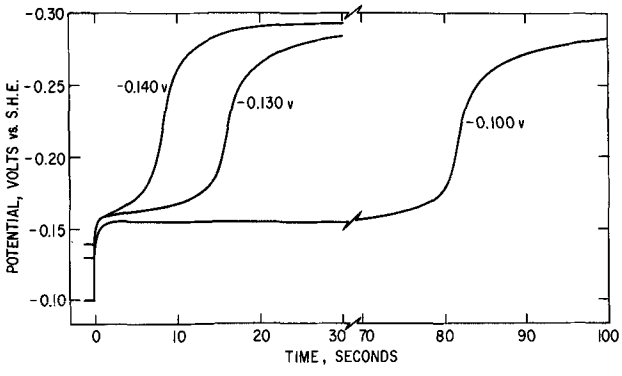

Fig. 4. Cathodic reduction after passivation at different potentials near the reversible activation potential. Current density is 25 μa/cm^2. Passivation potential indicated next to each curve.

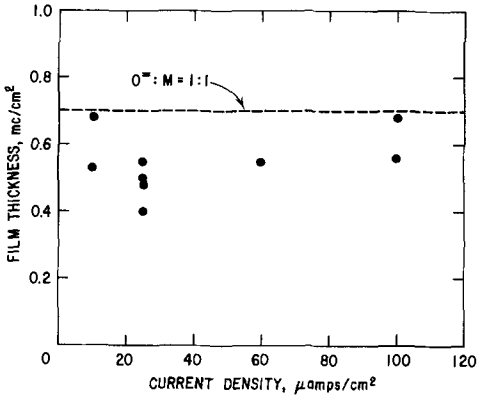

Fig. 5. Effect of cathodic current density on the coulombic thickness of the primary passivating film at the reversible activation potential.

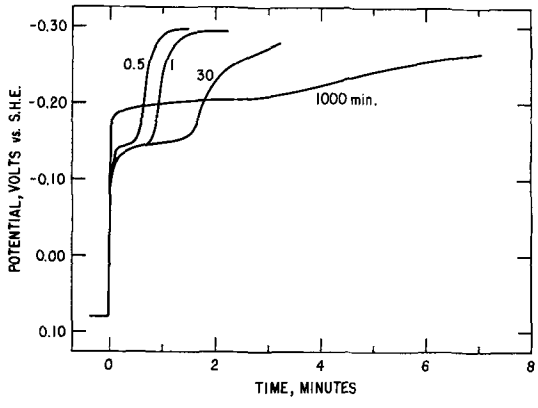

Fig. 6. Cathodic reduction after passivation at +0.08v for different length of time. Current density is 25 μa/cm². The time of passivation, in minutes, is given next to each curve.

for different times at +0.08v prior to reduction of the passivating film are shown in Fig. 6. After passivating the surface for 0.5 min the current density was still greater than it is after complete passivation; after 1 min the surface was completely passive. The reduction potential for a surface passivated up to 30 min is —0.14v. At 30 min the potential break is not as sharp as at the shorter times, while at 1000 min the potential break is almost completely washed out and the reduction potential has been shifted to about —0.20v. In Fig. 7 the potential-time relationship is given for a surface passivated at +0.48v for 2 min. The potentials of both the peak and the plateau following it are considerably more negative than those observed after passivation at +0.08v (Fig. 6). The peak has previously been observed by Caplan, Harvey, and Cohen (10); the potential of it as observed by Caplan *et al.* is the same as that shown here if a correction is made for the difference in pH of the solutions used.

Effect of solution pH.—The effect of the electrolyte solution pH in the range of 0-2 on the primary activation potential, E_a, is shown in Fig. 8, along with the effect of the pH on the primary passivation potential, E_{pp}, *i.e.*, the potential corresponding to the peak anodic current density (see Fig. 1). The relationships may be described by

$$E_a = -0.107 - 0.081\ pH$$

Table II. Apparent variations in film thickness with cathodic current density; surface passivated at —0.140v

Current density, μa/cm²	Film thickness, mc/cm²
10	0.11
25	0.20
33	0.23

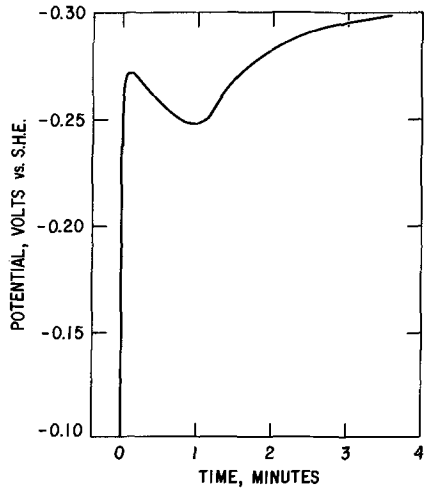

Fig. 7. Cathodic reduction after passivation at +0.48v shows high degree of irreversibility. Current density is 25 μa/cm².

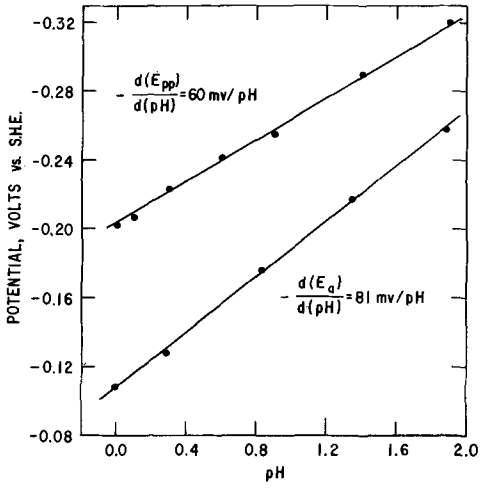

Fig. 8. Effect of solution pH on the reversible activation potential, E_a, and on the primary passivation potential, E_{pp}, potential corresponding to the peak anodic current density.

and

$$E_{pp} = -0.204 - 0.060\ pH$$

If the experiments are performed so as to measure the apparent activation potential instead of the primary one, a variety of E_a — pH relationships can be obtained depending on the passivation potential and the rate of potential sweep. For example, if the surface is passivated at +0.5v and a sweep rate of 100 mv/hr is employed, the observed relationship is

$$E_a = -0.113 - 0.100\ pH$$

over the same pH range and with the same degree of scatter as shown in Fig. 8. This is in reasonable agreement with the work of Rocha and Lennartz (6), who used a sweep rate of 120 mv/hr.

Discussion

The results show that the passivating film in the immediate potential neighborhood (within 5 mv) of the primary activation potential has quite different properties from the film that is stable at more positive potentials. The former will be referred to as the primary passivating film and the latter as the secondary film.

Primary passivating film.—It has been demonstrated that starting with a cathodically reduced and anodically etched surface, the primary passivation process is reversible, *i.e.*, no hysteresis is observed. This has not heretofore been established for either ferritic or austenitic chromium steels (Cr content >12%). On the contrary, the general belief has been that the

passivation of these alloys is an irreversible process (5, 6, 11, 12) in the sense that the anodic polarization curves show a hysteresis, such as illustrated in Fig. 1. The present work, however, clearly shows that the primary passivating process is reversible and that irreversibility results from secondary effects at potentials exceeding the primary activation potential by more than 5 to 10 mv. The proper surface pretreatment is essential to achieve reversibility. For example, cathodic reduction for several minutes at —0.5v, at which potential the current density is approximately 30 ma/cm^2, was found not to be sufficient. The anodic dissolution that is necessary apparently undercuts any remaining film on the surface.

The potential-current behavior also correlates with the microscope observations (Fig. 2 and 3). The primary passivating film is reduced uniformly over the surface, as would be expected for a film that is formed and reduced reversibly. However, as the passivation potential is made more positive and the degree of irreversibility increases, the reduction of the film becomes both localized and more difficult (Fig. 2 and Table I).

The thickness of the primary passivating film, as measured coulometrically, shows that the passivating process introduces less than the equivalent of one $O^=$ per surface metal atom into the passivating film (Fig. 5). Self-activation, the only error that could make the observed values low, was shown not to be significant. On the other hand, a correction for the two approximations made, roughness factor equal to 1, and the approximate correction for hydrogen evolution, would make the true thickness less than the measured thickness. After anodic dissolution during surface preparation, the surface is etched; a reasonable value for the roughness factor would be between 1.2 and 2. A further semiquantitative correction can be made for the hydrogen-evolution current. Assuming Tafel behavior and a slope of 60 mv/current decade, the current can be extrapolated from the primary activation potential to the film reduction potential; applying this correction reduces the calculated thickness by roughly 20%. Taking both the above corrections into consideration, a more correct ratio of $O^=$/metal atom appears to be between 0.2 and 0.5.

The slope of the plot of *p*H *vs.* the primary activation potential does not agree with any of the previously published results (3, 6, 7). This is not surprising since these workers measured the apparent activation potential instead of the primary activation potential. Under those conditions the slope is a function of the kinetics of the reduction of the secondary film and is not related to the primary passivation process.

For understanding the mechanism of passivity, it is the reaction that produces the primary passivating film at the primary activation potential that is important, because with the formation of the secondary film no further decrease in the anodic reaction rate is observed (Fig. 1). Since the primary passivating film has not previously been detected, it is not possible to apply published[4] theories of passivity directly to its formation. These [*e.g.*, see ref. (5), (13), and (14)] might better apply to the formation of the combined primary and secondary passivating films as they exist at potentials more positive than the primary activation potential. We propose two hypotheses not mutually exclusive that can explain the observed data for the primary passivating film.

The first hypothesis envisions a film of chromium and oxygen ions covering the surface. Using the upper limit of 0.5 for the ratio of oxygen ions to surface metal atoms at the primary activation potential, the concentration of oxygen in the film is 1 x 10^{15} atoms/cm^2. With an ionic radius of 1.40Å and a simple square lattice, this quantity of oxygen would cover 78% of the surface. Assuming the other 22% to be covered by chromium ions with an ionic radius of 0.7Å, the ratio of chromium to oxygen in the film would be approximately one, which is a very reasonable value.

On the other hand, if the ratio of oxygen ions to surface metal atoms is close to the lower limit of 0.2, one may suggest either a lower valence state for the chromium ion or the introduction of some constituent(s) of the electrolyte solution into the film to account for complete coverage. The latter is, perhaps, more reasonable since the variation of passive behavior of metals and alloys from electrolyte to electrolyte is well known.

The variation of the primary passivation potential, E_{pp}, with *p*H (60 mv/*p*H) is consistent with the variation of an equilibrium potential for a simple metal-oxygen interaction. The variation of the primary activation potential, E_a, with *p*H (81 mv/*p*H) is not as easily understood. It may be determined by kinetic factors, in which case its meaning is obscure. However, it may also be determined by the quasi-equilibrium reaction that established the passivating film at this potential, in which case it is diagnostic for the mechanism of passivation. That the primary activation potential may be an equilibrium potential stems from the following experimental facts: (*i*) this potential can be approached from either direction; (*ii*) the primary passivating film at this potential is stable with respect to time; (*iii*) the rate of dissolution and reformation of the film at steady state is exceedingly small, less than 10^{-7} amp/cm^2 (the current density in the passive potential region); hence it is quite possible that the exchange current density for the equilibrium reaction is larger than this kinetic rate. Thus, the potential may be an equilibrium potential for the reaction that forms a film of fixed composition from the metal and solution constituents. The dependence of 81 mv/*p*H may then be explained by assuming that the activity of the solution constituent in the film is *p*H-dependent. For example, if $SO_4^=$ were the constituent its activity would be governed by the equilibrium $HSO_4^- \rightleftarrows H^+ + SO_4^=$. At other potentials between E_{pp} and E_a, one may then expect the film to have a different composition, *i.e.*, activity of oxygen, a specific composition being associated with each potential.

The irreversible formation of the secondary film is evidenced by its localized reduction (Fig. 2). From the hysteresis (Fig. 1, curve b) and from the data in Table I it is evident that the reduction of the secondary film is also very slow with respect to the rates of potential change employed. This is shown by the shift of the apparent activation potential in the negative direction with increasing rate of potential change and by the lower anodic current densities in curve b, indicative of some residual film on the surface at these potentials. The shift of the apparent activation potential in the negative direction with increasing positive passivating potential may be due to either a thickening of the passivating film with increasing potential or to an aging effect which changes some of the properties of the film. It will be argued later that both occur.

In the case of the localized breakdown of the secondary film, the apparent activation potential corresponds to the initial breakdown of the local sites. Much, but not all, of the secondary film can be reduced given sufficient time, as demonstrated by the experiment in which the surface was allowed to reach a steady state at a potential close to the primary activation potential after having been passivated at +0.5v; the potential sweep that followed then resulted in a general attack on the surface. It was also possible to passivate a surface at +0.5v and then do a slow potential sweep into the anodic loop; upon allowing the current to remain at any potential in the anodic loop, it would eventually drift close to the appropriate value on the reversible potential-current curve (a, Fig. 1). However, complete reversibility of the curve could not be achieved under these conditions, indicating that traces of the secondary film still remained on the sur-

[4] Uhlig (15) has recently proposed that the passivating film is initially similar to the reconstructed nickel-oxygen layer proposed by investigators in the low-energy electron diffraction field.

face. This was most evident at potentials near the activation potential, at which the currents were sufficiently low so that small deviations could easily be observed.

That the growth and formation of the secondary film is a slow process can best be seen from the cathodic reduction curves in Fig. 6. Although the surface was completely passivated after 1 min, the coulombic thickness after 30 min is approximately twice that after 1 min. The film reduction potentials for 0.5, 1, and 30 min correspond closely to those for the reduction of the primary passivating film. However, after 30 min one sees the first signs of irreversibility as the potential break is no longer so sharp; after 1000 min the potential break is completely washed out and the reduction potential has been shifted 60 mv negative. Both observations show that the film has become very difficult to reduce. From this it appears that the secondary film forms by a thickening of the primary film followed by growth of a film of a different nature. It is suggested that the thickening may be due to the completion of coverage of the surface with a monolayer of oxygen. Further adsorption of oxygen is then accompanied by the diffusion of metal ions into the adsorbed array, thereby forming an amorphous oxide or hydroxide layer, which constitutes the secondary film. This process would be both time and potential dependent as has been found for the formation of this film.

The secondary film forms much faster at +0.48v than at +0.08v and is even more difficult to reduce (Fig. 7). It is thus impossible to determine the thickness of the film formed at +0.48v.

Summary and Conclusions

1. The primary passivation process is reversible and a primary activation potential is associated with it.
2. The primary passivating film, containing less than one $O^=$ per surface metal atom, exists only in the immediate potential neighborhood of the primary activation potential.
3. At more positive potentials a secondary film, which does not further decrease the anodic current density, is formed by a process that involves both a thickening of the primary passivating film and then an aging process.
4. It is suggested that the primary passivation process forms a film containing chromium and oxygen ions and possibly also some constituent of the electrolyte solution.

Acknowledgment

The author wishes to thank Dr. S. Barnartt, S. S. Brenner, R. A. Oriani, and H. W. Pickering for many helpful discussions. Thanks are also due to Mrs. G. L. Cleaveland for help with much of the experimental work and to R. C. Glenn for the electron microscopy.

Manuscript received Jan. 10, 1967; revised manuscript received March 13, 1967. This paper was presented at the Dallas Meeting, May 7-12, 1967.

Any discussion of this paper will appear in a Discussion Section to be published in the December 1967 JOURNAL.

REFERENCES

1. R. Olivier, "Passiviteit van Ijzer en Ijzer-Chroom Legeringen," Dissertation Leiden, 1955; Proc. Sixth Meeting CITCE, 1954, p. 314, Butterworths Scientific Publications, London.
2. T. Heumann and R. Shürmann, *Werkstoffe u. Korrosion*, **12**, 560 (1961).
3. P. F. King and H. H. Uhlig, *J. Phys. Chem.*, **63**, 2026 (1959).
4. Y. M. Kolotyrkin, *Z. Elektrochem.*, **62**, 664 (1958).
5. G. Aronowitz and N. Hackerman, *This Journal*, **110**, 633 (1963).
6. H. J. Rocha and G. Lennartz, *Arch. Eisenhüttenw.*, **26**, 117 (1955).
7. K. J. Vetter, "Elektrochemische Kinetik," pp. 605-606, Springer Verlag, Berlin (1961).
8. H. W. Pickering and R. P. Frankenthal, *This Journal*, **112**, 761 (1965).
9. P. B. Sewell, C. D. Stockbridge, and M. Cohen, *Can. J. Chem.*, **37**, 1813 (1959).
10. D. Caplan, A. Harvey, and M. Cohen, *This Journal*, **108**, 134 (1961).
11. R. Littlewood, *Corrosion Sci.*, **3**, 99 (1963).
12. N. D. Greene and R. B. Leonard, *Electrochim. Acta.*, **9**, 45 (1964).
13. N. Hackerman, *Z. Elektrochem.*, **62**, 632 (1958).
14. H. H. Uhlig, *ibid.*, **62**, 626 (1958).
15. H. H. Uhlig, Paper presented at the Third International Corrosion Congress, Moscow, 1966.

Platinum Oxidation Kinetics with Convective Diffusion and Surface Reaction

R. W. Bartlett

Stanford Research Institute, Menlo Park, California

ABSTRACT

The rate of oxidation of platinum is affected by the reversible surface reaction, $O_2 + Pt \leftrightarrows PtO_2(g)$, and by transport of the oxide vapor through a gaseous boundary layer. Both are considered in an analysis of the oxidation kinetics. Mass transfer coefficients for diffusion of the oxide vapor are calculated from the Nusselt numbers applicable to specific sample geometries and flow conditions. The equilibrium constant for oxidation of platinum is used to calculate the forward and backward specific rate constants for steady-state oxidation at the surface. A combined rate equation, including both convective diffusion and surface oxidation, is derived and used to calculate oxidation rate curves at a variety of pressures and temperatures. Good agreement with experimental data is obtained. Rate predictions in high velocity flow where experimental data have not been taken are presented.

At temperatures above approximately 800°C, platinum oxidizes slowly to produce a volatile species, $PtO_2(g)$, that is comparatively unstable (1). The PtO_2 molecule may diffuse away from the oxidizing platinum surface and subsequently dissociate or, because of collisions with surrounding gas molecules, return to the platinum surface for dissociation on impact. During oxidation at fixed temperature, pressure, and other parameters affecting the oxidation process, a steady-state condition will result at the platinum surface in-

volving the forward and backward rates of the reversible oxidation reaction

$$O_2(g) + Pt \underset{k_b}{\overset{k_f}{\rightleftarrows}} PtO_2(g) \qquad [1]$$

to yield a net oxidation of platinum and migration of $PtO_2(g)$ away from the surface.

Several experimental factors can influence the gaseous diffusion and alter the apparent oxidation rate. This situation was first recognized by Fryburg and Murphy (2), who pointed out that the use of furnaces for measuring the rates of oxidation of platinum has lead to widely varying results that are highly dependent on the gas flow rate. With the exception of the work by Fryburg and co-workers (3, 4) previous experimental rate studies of the oxidation of platinum (5-8) have failed to consider the role of diffusion of $PtO_2(g)$ from the platinum surface. This omission is understandable in view of the commonly held misconception that gaseous diffusion is kinetically important only when oxidation rates are very fast. As late as 1963, arguments for Langmuir-type adsorption of molecular oxygen followed by dissociation were presented (8) to explain the failure of the platinum oxidation rate to increase in direct proportion with the oxygen pressure except at very low pressures.

The purpose of this paper is to present a kinetic treatment of the oxidation of platinum, considering simultaneously (*i*) convective diffusion of $PtO_2(g)$ through the gaseous boundary layer adjacent to the sample and (*ii*) the surface oxidation reaction.

Oxidation rates are calculated independently of experimental data, using boundary layer theory and the equilibrium constant (1) for oxidation of platinum to $PtO_2(g)$ (Eq. [1]). Rates are calculated for free convection, *e.g.*, convective mixing caused by gravity forces only, and for a few cases of Newtonian forced flow convection. The approach is similar to a previous study of the oxidation of tungsten (9), which occurs by an irreversible reaction and is rate limited by the convective diffusion of oxygen to the surface.

The calculated rates are compared with Fryburg's experimental data (3, 4). Fryburg employed small (0.0287 cm wide) electrically heated platinum ribbons mounted in a cold wall chamber. At pressures above 100 mm Hg, the ribbon was extended horizontally rather than used as a vertical hairpin element. Chamber size is an important consideration since a quantitative analysis of free convective diffusion of $PtO_2(g)$ in the gaseous boundary layer adjacent to the sample depends on an absence of convective hindrance by the container. Fryburg's chamber diameter was 3.2 cm. Since the boundary layer thickness is related to the characteristic dimension of the sample, in this case the ribbon width, no difficulties from the container wall are encountered for a free convection analysis.

Theory.—The oxidation rate could be calculated from either a surface reaction rate equation or a convective diffusion equation separately if the steady-state value of the platinum oxide vapor pressure at the surface, $p_{PtO_{2(s)}}$, were known. The value of $p_{PtO_{2(s)}}$ cannot be measured conveniently since any measuring probe would disturb the boundary layer. However, $p_{PtO_{2(s)}}$ is the parameter connecting the gaseous diffusion step and the surface reaction step of the oxidation process. Because the gaseous diffusion rate, $\dot{X}_D$, and the surface reaction rate, $\dot{X}_S$, must be equal (there are no other material sources and sinks)

$$\dot{X}_D = \dot{X}_S \qquad [2]$$

p_{PtO_2} is uniquely determined for any set of conditions, temperature, pressure, sample configuration, and flow.

The boundary-layer diffusion rate is described in terms of the escape of $PtO_2(g)$ from the surface through an oxygen or air envelope by the following equation

$$\dot{X}_D = \left(\frac{M_o}{\rho}\right)_{Pt} k_m \frac{(p_{PtO_{2_s}} - p_{PtO_{2_\infty}})}{p_t} \qquad [3]$$

where $\dot{X}_D$ is a metal recession rate (cm/sec), (M_o/ρ) is the ratio of equivalent weight to density for platinum required to convert a molar oxidation rate to a surface recession rate, k_m is the mass transfer coefficient which is calculated using boundary layer theory, $p_{PtO_{2_\infty}}$ is the platinum oxide vapor pressure beyond the boundary layer ($p_{PtO_{2_\infty}} \doteq 0$), and p_t is the total pressure or the stagnation pressure in a flowing system. For oxidation in oxygen $p_t = p_{O_2}$ and for oxidation in air or mixtures of inert gas and oxygen, $p_t > p_{O_2}$.

The platinum surface oxidation rate, $\dot{X}_S$, based on the steady-state condition for the reaction given by Eq. [1], is

$$\dot{X}_S = \left(\frac{M_o}{\rho}\right)_{Pt} (k_f p_{O_2} - k_b p_{PtO_{2_S}}) \qquad [4]$$

Since the oxidation rate is slow and $p_{O_2} >> p_{PtO_{2S}}$, there is no perturbation in the oxygen pressure as the surface is approached. Fryburg and Petrus have shown that the activation energy for oxidation is equal to the free energy of reaction determined by Alcock and Hooper (1), *i.e.*, the low-pressure oxidation of platinum can be calculated from equilibrium data in a manner analogous with Langmuir's method for calculating vapor pressures from rates of evaporation. It is assumed that the unstable PtO_2 molecules are dissociated on striking the platinum surface, which is equivalent with an assumed condensation coefficient of unity. Consequently, the backward rate constant k_b in Eq. [4] is the surface collision frequency of PtO_2 molecules based on gas kinetics

$$k_b = (2\pi MRT)^{-1/2} \qquad [5]$$

where M is the molecular weight of PtO_2. The specific rate constants are related through the equilibrium constant, K_{eq}, for the oxidation reaction of Eq. [1]

$$K_{eq} = k_f/k_b \qquad [6]$$

Inserting Eq. [5] and [6] in Eq. [4] yields

$$\dot{X}_S = \left(\frac{M_o}{\rho}\right)_{Pt} (2\pi MRT)^{-1/2} (K_{eq} p_{O_2} - p_{PtO_{2S}}) \qquad [7]$$

By combining the diffusion and surface rate Eq. [2], [3], and [7], the unknown PtO_2 vapor pressure at the surface can be eliminated

$$\dot{X} = \frac{\left(\frac{M_o}{\rho}\right)_{Pt} (2\pi MRT)^{-1/2} K_{eq} p_{O_2}}{1 + \frac{(2\pi MRT)^{-1/2} p_t}{k_m}} \qquad [8]$$

Equation [8] is valid at all pressures and temperatures where a volatile platinum oxide species is produced. It covers both the convective diffusion controlled rate region (high pressures) and the surface reaction controlled rate region (low pressures). It is valid for static and flowing gases and for mixtures of oxygen and nitrogen or other inert gases, and through the dependence of the mass transfer coefficient, k_m, it includes the effect of sample size.

All of the terms in Eq. [8] are system constants. The most complex of these is the mass transfer coefficient, k_m, which is related to the dimensionless Nusselt number (10) for mass transfer Nu_m

$$k_m = \frac{Nu_m p_t D}{L R T_g} \qquad [9]$$

where D is the gaseous diffusion coefficient, L is the

characteristic sample dimension (ribbon width), R is the gas constant, and T_g is the average gas temperature. The diffusion coefficient varies with gas temperature and pressure and was calculated with the Chapman-Enskog equation

$$D_{(cm2/sec)} = \frac{1.86 \times 10^{-3} \sqrt{\frac{1}{M_{O_2}} + \frac{1}{M_{PtO_2}}} \left(\frac{T_g^{3/2}}{p_t}\right)}{\sigma^2_{O_2} \Omega_D} \quad [10]$$

using the collision cross section $\sigma = 3.433$ and parameter $\Omega = 0.74$ for oxygen (11). The Nusselt number is obtained from published semiempirical correlation curves relating the Nusselt number with the Grashoff number and Schmidt number for free convection and the Reynolds number and Schmidt numbers for forced convection (Newtonian flow). These correlations are used extensively in engineering analyses of fluid processes. In calculating free convection rate data, the correlation curve for vertical surfaces (12), in which μ_g is the gas viscosity and g is the acceleration of gravity, was used, see Fig. 1. The Chapman-Enskog theory was used to calculate the gas viscosity. Oxidation rate calculations in the laminar flow range were made for long cylinders (wires), using the Chilton-Colburn type of correlation by Sherwood and Pigford (13) shown in Fig. 2. Further details on calculating mass transfer coefficients for simple sample geometries are given by Bird, Stewart, and Lightfoot (10).

Results and Discussion

Isothermal rate curves calculated with rate Eq. [8] for oxidation of platinum in pure oxygen and air are shown in Fig. 3, for a ribbon width of 0.0287 cm and

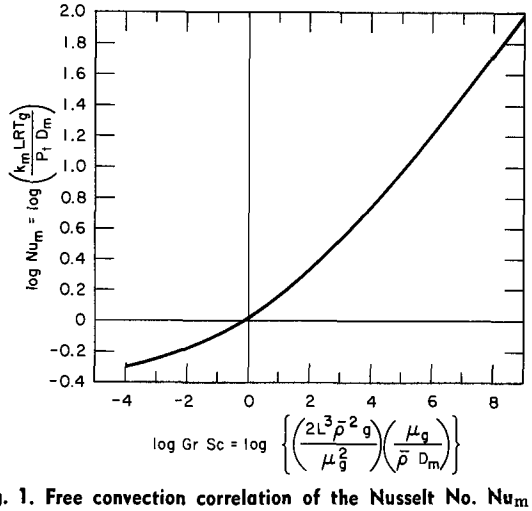

Fig. 1. Free convection correlation of the Nusselt No. Nu_m with Grashoff No. Gr and Schmidt No. Sc for vertical surfaces (12).

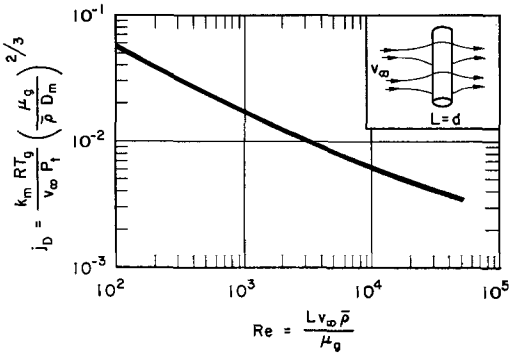

Fig. 2. Forced convection correlation (Newtonian flow) of the Chilton-Colburn dimensionless group j_D with the Reynolds No. Re for cylinders.

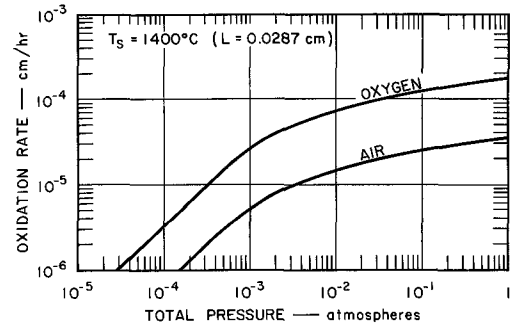

Fig. 3. Calculated static platinum oxidation curves for 0.0287 cm ribbon at 1400°C based on Eq. [8].

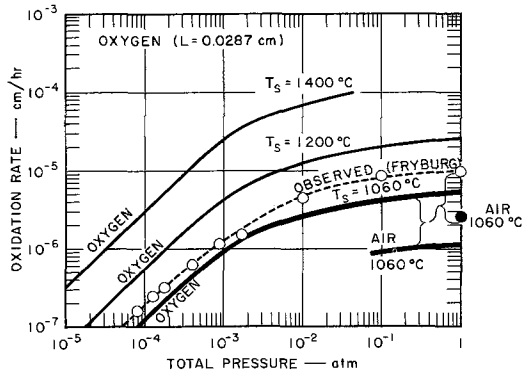

Fig. 4. Comparison of calculated rate curves with experimental oxidation data points for 0.0287 cm platinum ribbons.

temperature of 1400°C. The rate in air is lower because $p_t > p_{O_2}$. Although nitrogen is chemically inert, it impedes the transport of PtO_2 molecules through the boundary layer.

From Fig. 3 and rate equation [8], it can be seen that at low pressures the oxidation rate is directly proportional to the oxygen pressure, the rate is controlled by the surface reaction, and $1 >> (2\pi MRT)^{-1/2} p_t/k_m$. At high pressures, the oxidation rate increases very slowly with pressure, the rate is controlled by PtO_2 diffusion, and $1 < (2\pi MRT)^{-1/2} p_t/k_m$.

Calculated platinum oxidation rate isotherms are also shown as solid curves in Fig. 4. Curves of oxidation in oxygen at 1060°, 1200°, and 1400°C are presented, and a partial curve for oxidation in air at 1060°C is included. The equilibrium constants (1) used in making the rate calculations are listed in Table I. The effect of air ($p_t > p_{O_2}$) is to lower the oxidation rate to about one-fourth of the rate in the same partial pressure of oxygen. These curves are based on a free convection correlation (Fig. 1) with the characteristic dimension, $L = 0.0287$ cm, the ribbon width used by Fryburg (3, 4).

The experimental results obtained in static oxygen by Fryburg and Petrus at 1060°C are shown as open data points in Fig. 4. The solid datum point is their experimental value for oxidation in static air at 1 atm. For both air and oxygen, the theoretical rates calculated independently of the experimental data agree with the experimental data within a factor of two, or less, over the entire oxygen pressure range, and the lowered oxidation rate in air is correctly estimated. Calculated theoretical rates agreed equally well with

Table I. Equilibrium constants for oxidation of platinum[1]

$Pt + O_2 \rightleftarrows PtO_2(g)$

Temp, °C	K_{eq}
1060	5.9×10^{-7}
1200	2.5×10^{-6}
1400	1.3×10^{-5}

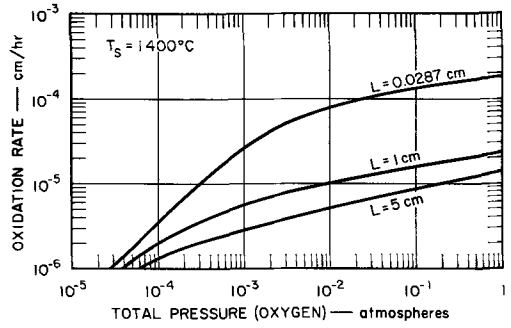

Fig. 5. Effect of sample size on the oxidation rate of platinum ribbons.

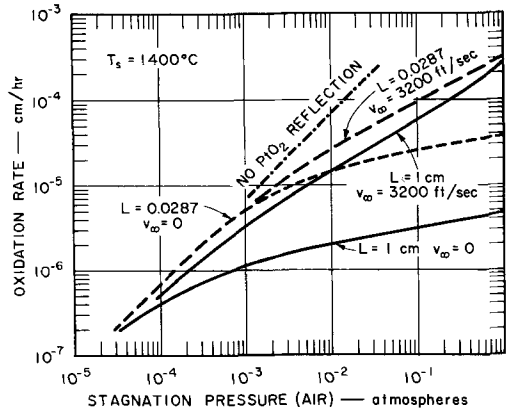

Fig. 6. Effect of forced flow on the oxidation rates of 0.0287 cm diameter platinum wire and 1 cm diameter platinum cylinders.

experimental rates at other temperatures and pressures, but since the experimental data were most extensive at 1060°C the comparison at this temperature is presented.

The effect of sample size on calculated theoretical platinum oxidation rates (free convection) are shown in Fig. 5. Calculated oxidation rates decrease with increasing ribbon width in agreement with experimental results.

Calculation of platinum oxidation rates in a high velocity air stream were made using the correlation of Fig. 2 for long cylinders. Isothermal oxidation rate curves were calculated for a free stream velocity of 3200 ft/sec (equivalent velocity behind the bow wake) for two cylinders, a 0.0287 cm diameter wire and a 1 cm diameter rod. The high flow rate curves are compared with curves for static oxidation of the same samples in Fig. 6. The curves show oxidation rate *vs.* stagnation pressure. In making a direct comparison between static air oxidation rates and forced flow oxidation rates, consideration should be given to the increase in stagnation pressure over ambient pressure in high velocity streams.

At low-pressures, high-gas flow velocities have little effect on the oxidation rate since there are too few gas molecules present to form a diffusion boundary layer. Subsequently, as pressure decreases the oxidation rate asymptotically approaches the steady-state surface oxidation rate that would occur with no reflection and dissociation of PtO_2 molecules in the surface. At high pressures, high flow velocities increase the oxidation rate because of the decreased boundary layer thickness and corresponding increase in the mass transfer coefficient, k_m.

Conclusions

In summary, oxidation rates of platinum can be calculated from the Nusselt number, using accepted dimensionless fluid correlations. The equilibrium constant, K_{eq}, for platinum oxidation is needed to establish the oxide vapor pressure at the metal surface required for a solution of the boundary layer diffusion problem. With this limited amount of information, oxidation rates can be calculated over a large temperature range and pressure range in good agreement with experimentally observed rates. The method also permits a valid calculation of oxidation rates in high gas velocities where experimental determinations of rate data are difficult, and the rate equation accounts for differences in oxidation rates caused by sample size and inert gas dilution (air *vs.* oxygen).

Acknowledgment

The author is indebted to George C. Fryburg for permission to quote his experimental data and for helpful discussions during preparation of this paper.

Manuscript received Dec. 19, 1966; revised manuscript received Feb. 27, 1967. This paper was presented in part at the Philadelphia Meeting, Oct. 9-14, 1966.

Any discussion of this paper will appear in a Discussion Section to be published in the December 1967 JOURNAL.

REFERENCES

1. C. B. Alcock and G. W. Hooper, *Proc. Roy. Soc.*, **A254**, 551 (1960).
2. G. C. Fryburg and H. M. Murphy, *Trans. Met. Soc. AIME*, **212**, 660 (1958).
3. G. C. Fryburg and H. M. Petrus, *This Journal*, **108**, 496 (1961).
4. G. C. Fryburg, *Trans. Met. Soc., AIME*, **233**, 1986 (1965).
5. O. Kubaschewski, *Elektrochem.*, **49**, 446 (1943).
6. F. E. Carter and Lincoln, cited "Corrosion Handbook," H. H. Uhlig, Editor, p. 703, John Wiley & Sons, Inc., New York (1948).
7. E. Raub and W. Plate, *Z. Metalk.*, **48**, 529 (1957).
8. C. A. Krier and R. I. Jaffee, *J. Less-Common Metals*, **5**, 411 (1963).
9. R. W. Bartlett, *Trans. Met. Soc. AIME*, **230**, 1097 (1964).
10. R. B. Bird, W. E. Stewart, and E. L. Lightfoot, "Transport Phenomena," Chap. 21, John Wiley & Sons, Inc., New York (1960).
11. R. B. Bird, W. E. Stewart, and E. L. Lightfoot, *ibid.*, Chap. 16.
12. M. Jakob, "Heat Transfer," vol. 1, p. 525, John Wiley & Sons, Inc., New York (1949).
13. T. K. Sherwood and R. L. Pigford, "Absorption and Extraction," 2nd ed., p. 70, McGraw-Hill, New York (1952).

Stress Corrosion Cracking of Titanium Alloys

I. Ti:8-1-1 Alloy in Aqueous Solutions

T. R. Beck

Boeing Scientific Research Laboratories, Seattle, Washington

ABSTRACT

Stress corrosion cracking of titanium: 8% Al-1% Mo-1% V alloy notched tensile specimens was investigated in various salt solutions under potentiostatic conditions. Stress corrosion cracking of duplex annealed Ti:8-1-1 alloy occurred in chloride, bromide, and iodide solutions, but did not occur in other solutions such as fluoride, hydroxide, sulfide, sulfate, nitrate, or perchlorate. The ultimate strength was strongly dependent on potential. The velocity of crack propagation and current flowing into the crack in chloride, bromide, and iodide solutions were linearly related to the applied potential above a potential of —900 mv to the saturated calomel electrode. An electrochemical mechanism controlling the velocity is implied.

The first known report on stress corrosion cracking (SCC) of titanium dates back to Kiefer and Harple, 1953 (1), who described cracking phenomena with commercially pure titanium in red fuming nitric acid. "Hot salt cracking" of titanium alloys was discovered in the mid 1950's in connection with creep in turbine blades. The subject became very active in the early 1960's because of the impact of SCC on the supersonic transport program. This phenomenon becomes significant above 250°C. A considerable amount of sponsored research has been conducted on this topic, some of which has been reported (2).

The first known report of stress corrosion cracking of titanium alloys in room temperature aqueous environments was that of Brown, 1965 (3). He found that precracked specimens of titanium: 8% aluminum-1% molybdenum-1% vanadium alloy (Ti:8-1-1) were susceptible to SCC in sea water. This touched off a new flurry of investigation for suitable less-susceptible alloys. Although much applied work was done and suitable, less-susceptible alloys were found, the mechanism of SCC in titanium alloys was unknown.

A basic research program to study the mechanism of titanium SCC was begun at the Boeing Research Laboratories in 1965. This paper describes results of the initial electrochemical studies with Ti:8-1-1 alloy. A discussion of electrochemical theory will follow in another paper (4).

All potentials recorded in the experiments are given in millivolts in this paper. Unless otherwise stated, the saturated calomel electrode (SCE) is the zero standard of reference.

Experimental

Titanium: 8-1-1 was chosen as the alloy for initiating the program because it had been shown by prior investigators to be one of the commercially available titanium alloys most susceptible to SCC. It was available in two heat-treatments; mill annealed and duplex annealed. The mill annealed treatment consisted of holding the sheet at 788°C for 8 hr, followed by furnace cooling. The duplex annealed treatment consisted of reheating mill annealed sheet to 788°C for 15 min followed by air cooling. The composition and tensile properties of the material used in this investigation are given in Table I.

Tensile tests were performed with notched specimens in a 10,000 kg Instron Model TT universal testing instrument. The specimens were gripped in Instron G-61-10F Type 10F wedge action jaws.

The tensile specimen geometry is shown in Fig. 1. The criteria for selection of the specimen geometry were:

1. The specimens should be such a size and shape that stress corrosion cracking could be produced.
2. The specimens should fit the jaws and capacity of the tensile machine.

Table I. Composition and Tensile properties of metal used in this investigation[a]

	Duplex annealed[b]	Duplex annealed	Mill annealed
Thickness, in.	0.050	0.060	0.060
Sheet No.	2936	2194	2026
Heat-treat No.	B9093-F-2284	3960831	D2654
Composition, %			
Al	8.0	7.6	7.55
Mo	1.00	1.05	1.05
V	1.01	0.98	0.95
Fe	0.04	0.11	0.16
C	0.03	0.04	0.045
N	0.0045	0.0008	0.001
H	0.0069	0.0042	0.005
O	0.075	0.109	0.047
Yield strength KSI	129.2	137.8	148.0
	129.5	137.5	148.7
		137.6	149.8
UTS-KSI	141.6	145.8	156.2
	141.4	144.9	156.9
		144.9	158.7
Elongation, %	10.5	11.5	13.0
	10.5	12.0	13.0
		10.5	13.0

[a] Data from Boeing Airplane Division.
[b] This sheet used for most of the tensile experiments reported herein.

3. The specimens should be inexpensive and easy to produce and use so that hundreds could be used to screen environmental effects.

It was also considered desirable that the specimens should be designed according to fracture mechanics

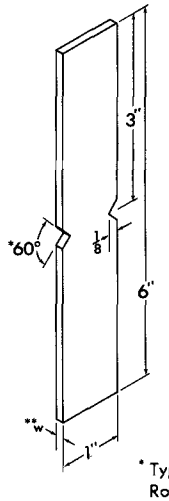

* Typical Notch Root Radius = 0.001"
**w = 0.05 to 0.06"

Fig. 1. Tensile specimen geometry

concepts, but this was not compatible with the above criteria. It is intended to follow up later with larger size specimens designed according to fracture mechanics concepts.

Specimens were prepared by shearing from sheet stock slightly oversize blanks; the two long edges were machined to finished dimensions. The first specimens were double notched, but later specimens were single notched. Tolerance on the net section width was held to ±0.002 in. The cutter was resharpened between the final passes during cutting of the notches in order to minimize cold working and to obtain a more precise notch root radius. Most specimens had a notch root radius of 0.001 in. Cutting oil was subsequently removed from the specimens by a kerosene followed by an acetone rinse. The later samples were anodized to 70-80v in a 1N sulfuric acid bath to minimize electrolytic reactions on the surface during the tensile tests. Specimens were not precracked. In the tensile tests, a crosshead velocity of 0.005 cm/min was selected as standard for most of the tests. This selection was made after a preliminary screening to determine effect of crosshead speed on specimen strength as described under results. The specimens were usually preloaded in the elastic region to about 1000 kg (2200 lb) at a crosshead velocity of 0.05-0.10 cm/min. This procedure permitted tests to be completed in a period of 10-30 min. Rapid testing was considered necessary in order to evaluate a wide range of environments. Force *vs.* time plots were recorded in each test.

Tests were made in air and in various electrolyte solutions with the specimen potentiostatically held at a preset potential. The Teflon cell configuration used in the potentiostatic tests is illustrated in Fig. 2. A Wenking Model 6379 TR potentiostat was used. Electrical connection to the specimens was made through the wedge action jaws. Current flowing to the specimen was recorded *vs.* time during the test using an x-axis speed of 1/50 in./sec on a Moseley Model 2D x-y plotter.

The first tests were made with 3½% sodium chloride (0.6M solution) corresponding to the total salt content of sea water. Other salt solutions for comparison were also made 0.6M. Concentration effects were studied later.

Results

Load-time curves.—Typical load-time curves for single-notched duplex annealed Ti:8-1-1 specimens are shown in Fig. 3. Failure in 0.6M sodium chloride is compared to that in air. The ultimate force, U_S, at failure in sodium chloride solution at a titanium potential of —500 mv is considerably less than the ultimate force, U_A, in air. The typical appearance of fracture in salt solutions under SCC susceptible conditions is shown in Fig. 4. The fracture is initially square under SCC conditions, later changing to slant shear failure. In air, the duplex annealed Ti:8-1-1 specimens failed almost entirely in slant fracture. The period of propagation of square fracture in NaCl is designated by B and the period of slant fracture by C in Fig. 3. Most specimens were preloaded to 1000 kg (2200 lb) as shown, in order to save time. The first visible evidence of a plastic zone by appearance of a dimple on the surface around the root of the notch occurred at 1300 to 1500 kg.

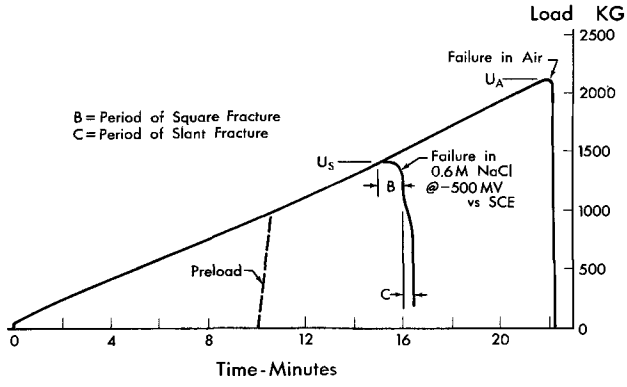

Fig. 3. Load-time curves for single-notched duplex annealed Ti:8-1-1 specimens.

Current-time curves.—A typical plot of current flowing under SCC conditions is given in Fig. 5. In the period, A, before SCC commences, the current mea-

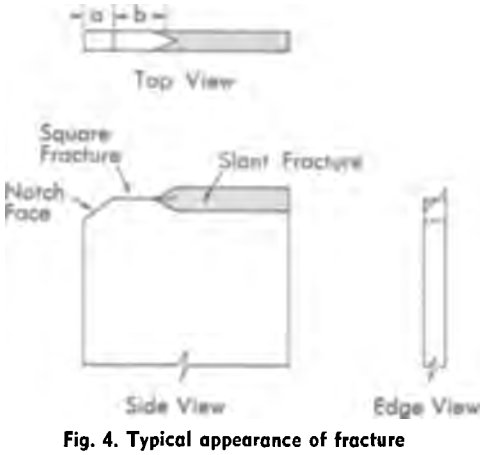

Fig. 4. Typical appearance of fracture

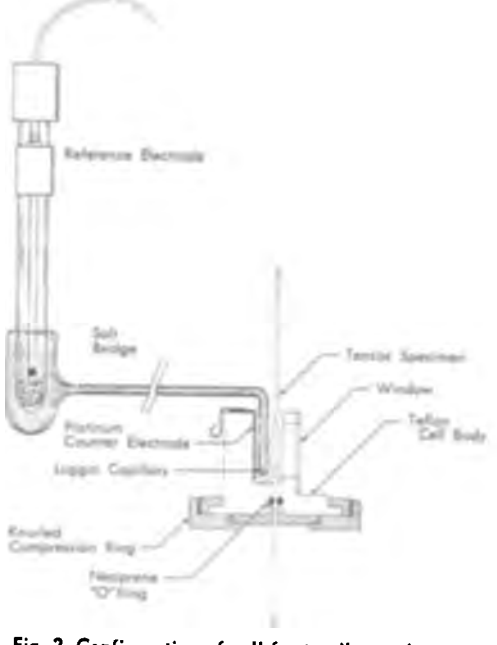

Fig. 2. Configuration of cell for tensile specimens

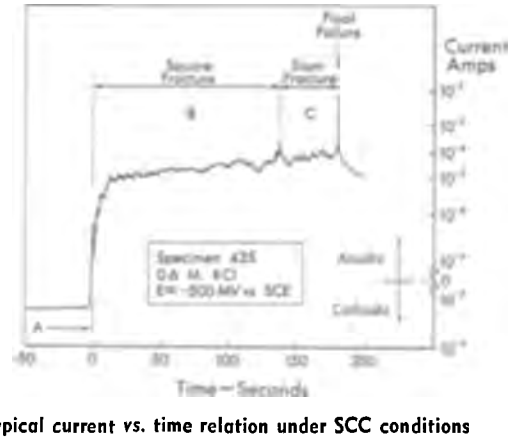

Fig. 5. Typical current *vs.* time relation under SCC conditions

sured is that flowing to the old exterior surface of the specimen. This current may be anodic or cathodic depending on the salt solution and applied potential. Later specimens were anodized to minimize this background current. Anodizing did not appear to influence the SCC behavior. When stress corrosion cracking started, the current jumped in the anodic direction designated by the region B in Fig. 5. Transition to the shear mode or slant failure, region C, was accompanied by a peak in current. The peak correlated with the observed change on the specimen surface from square to slant fracture. A high anodic current peak accompanied the final failure. Time for propagation of square fracture could be directly measured from the current time plots, which were obtained for every run. In cases where the background current in period A was large, either anodic or cathodic due to high positive or negative polarization, the crack propagation current and time were sometimes obscured.

A typical pattern of current *vs.* time for a potential giving immunity to stress corrosion cracking is shown in Fig. 6. The first evidence of anodic current pips is difficult to define, but there was generally a peak at point X followed by a long period of an irregular current of a few microamperes until slant failure occurred. Point X generally occurred at a load of about 1400 kg for the single-notched duplex-annealed Ti: 8-1-1 specimens. The irregular anodic current is presumably due to anodizing of metal in cracks in the oxide film in the plastic zone around the root of the notch. Because of its low value, this current was easily obscured by current flowing to the old surface.

Effect of crosshead velocity.—Early in the program, the effect of crosshead velocity was investigated in order to determine a suitable value to use in the tests. Results are shown in Fig. 7 for the double-notched, duplex-annealed Ti: 8-1-1 specimens in air and in 0.6M sodium chloride at a potential of —500 mv. The strengths plotted are the ultimate values, U_A and U_S, illustrated in Fig. 3. Stress corrosion cracking appeared to occur at crosshead velocities of less than 10^{-1} cm/min. A velocity of 5 x 10^{-3} cm/min was chosen as standard for all subsequent tests as this gave measurable differences in a short period of time.

The stress shown at the right of Fig. 7 was based on the notch section area. The unnotched specimens with slightly higher strength had the same net cross section

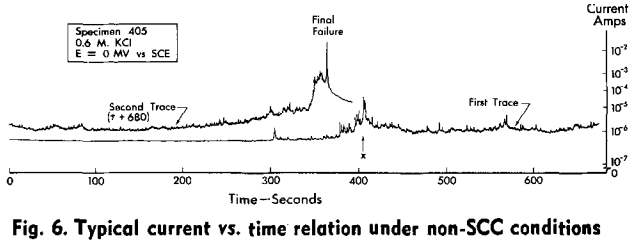

Fig. 6. Typical current *vs.* time relation under non-SCC conditions

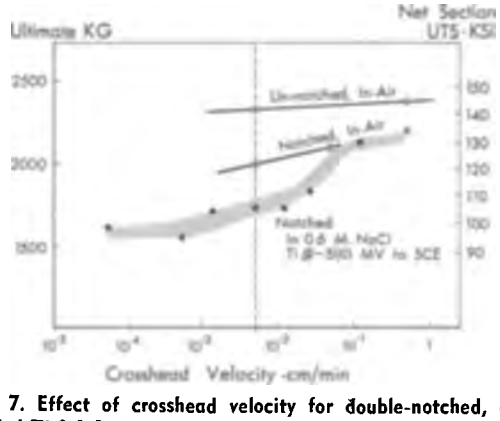

Fig. 7. Effect of crosshead velocity for double-notched, duplex-annealed Ti:8-1-1.

as the notched specimens at the notched section indicating that duplex annealed Ti: 8-1-1 is notch sensitive. There appears to be reasonable agreement of tensile strength of the unnotched specimens to the data in Table I for duplex-annealed Ti: 8-1-1.

Effect of notch radius.—The effect of notch radius was investigated in order to specify the tolerance on the machining of the notches and to determine variability in results due to this factor. Double-notched specimens of duplex-annealed Ti: 8-1-1 alloy were machined with notch root radii of 1, 2, 5, and 20 mils (0.0025, 0.005, 0.012, and 0.05 cm) for these tests. Two specimens had a notch root radius of about 0.5 mils (0.0012 cm), produced by pressing a knife blade into a 1 mil radius notch.

Results in air and 0.6M lithium chloride, potassium bromide, and potassium iodide solutions are shown in Fig. 8. The results in air and in LiCl at a potential +1000 mv were within the same scatterband and indicated some notch sensitivity. Specimens in LiCl at —500 mv showed SCC susceptibility for notch radii of 5 mils and less, but SCC immunity for 20 mil radius. All specimens with notch radii in the range of 1 to 20 mils were susceptible in KBr and KI at a potential of +1000 mv. Two specimens with 20 mil notch radius were electropolished in the notches and tested at +1000 mv in KI solution; little or no sensitivity was indicated.

It was decided, based on these tests, to use 1 mil radius machined notches as standard.

Effect of halide ions.—Stress corrosion cracking of Ti: 8-1-1 alloy in aqueous environments at room temperature has been found to be very specific to three ions; chloride, bromide, and iodide, and to date no others. Other anions investigated were fluoride, hydroxide, sulfide, sulfate, nitrite, and perchlorate. There also appeared to be no cation effect within the limits of accuracy of the experiments for the alkali and alkaline earth cations used. The ultimate load *vs.* potential for neutral fluoride, chloride, bromide, and iodide is given in Fig. 9. The experimental points are not shown for the purpose of clarity, but the scatterband width is indicated in the lower left of Fig. 9.

At potentials more negative than about —1000 mv, the specimens appeared to be cathodically protected in all solutions. At all potentials, the NaF solution gave results in the same scatterband as the air values. At potentials more positive than —1000 mv, SCC susceptibility in varying degrees occurs in chloride, bromide, and iodide solutions. A region of anodic protection

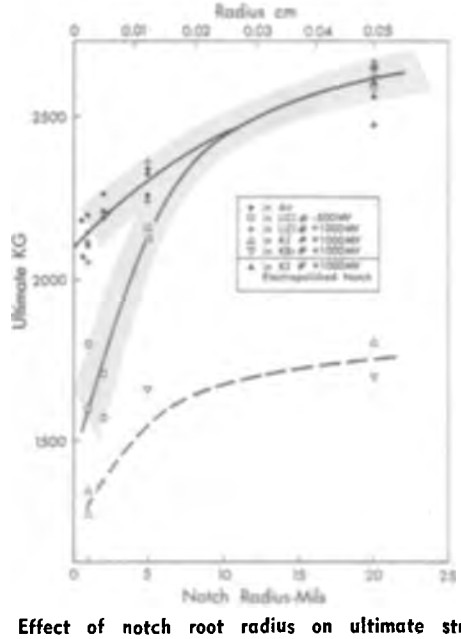

Fig. 8. Effect of notch root radius on ultimate strength

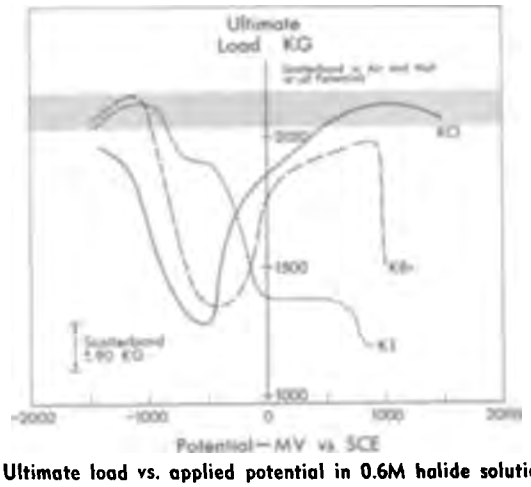

Fig. 9. Ultimate load vs. applied potential in 0.6M halide solutions

occurs in chloride and bromide solutions. Pitting corrosion and flocculent white precipitate were observed at +1000 mv in KBr solution and +2000 mv in LiCl solution. A photograph of a specimen failed in 0.6M KBr solution, Fig. 10, shows the pits and short radial lines on the surface that appeared to be normal to the stress direction around the notches. Although there was a decrease in strength in KI solution at about +700 mv, no pitting or white precipitate were observed.

The ultimate strength shown in Fig. 9 is actually a measure of the stress for initiation of stress corrosion cracking, but there is a close correlation to propagation. It was found, for example, that SCC could be initiated at —500 mv in chloride solution and stopped by switching the potential to either the anodic or cathodic protection zone. It was also found that SCC could be initiated at higher loads than normal at —500 mv by first loading in the anodic or cathodic protection zone to a point approaching failure at that potential and then switching to —500 mv.

The power of the potentiostatic technique is demonstrated in Fig. 9. Specimens on open circuit have a rest potential that is variable depending on metal composition, history of the surface, trace impurities in solution, etc. A range of at least +500 to —500 mv was observed on titanium. In this range many changes occur, accounting in part for the large variability in strength observed by others under open-circuit conditions.

Crack propagation velocity and associated current.— Crack propagation velocity was measured by two means: (*i*) by visually observing the progress of the crack past scribed pencil lines on a specimen surface, and (*ii*) by dividing the square-fracture length (b in Fig. 4) by the square-fracture time (B in Fig. 5). A comparison of the two methods is shown in Fig. 11. There appeared to be reasonable good agreement for this specimen at —500 mv in 0.6M LiCl.

It would have been desirable to make all velocity correlations using initial crack velocity from visual observation of crack length. This was a tedious measurement and only a few were made. Data were available, however, from the experiments already made to calculate average crack velocity. If the ratio of average velocity to initial velocity is relatively constant, correlation using average velocity appears justified at this time.

Average crack propagation velocity was found to be linear with applied potential in 0.6M chloride, bromide, and iodide solutions for those specimens that failed below about 1500 kg load. These data, based on square fracture length and time, are plotted in Fig. 12. This is probably one of the more significant findings in this work thus far, as it demonstrates that, once initiated, the crack propagation velocity is determined by electrochemistry.

The current during square-fracture crack propagation as measured from current *vs.* time plots such as shown in Fig. 5 is plotted in Fig. 13. The average initial current and the average final current just before initiation of shear fracture appear to be linear with applied potential. The average current was estimated by drawing by eye a horizontal line through about 30

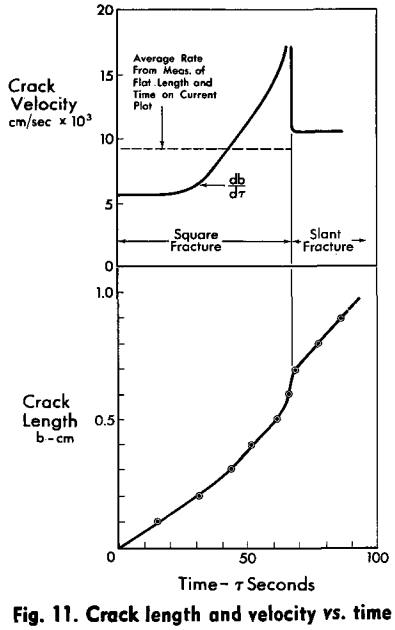

Fig. 11. Crack length and velocity vs. time

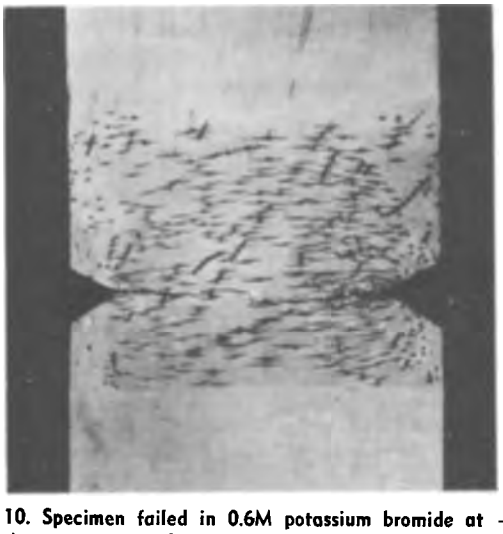

Fig. 10. Specimen failed in 0.6M potassium bromide at +1000 mv (pitting corrosion condition).

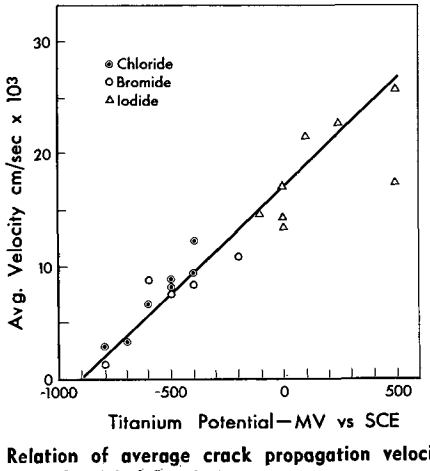

Fig. 12. Relation of average crack propagation velocity to applied potential in 0.6M halide solutions.

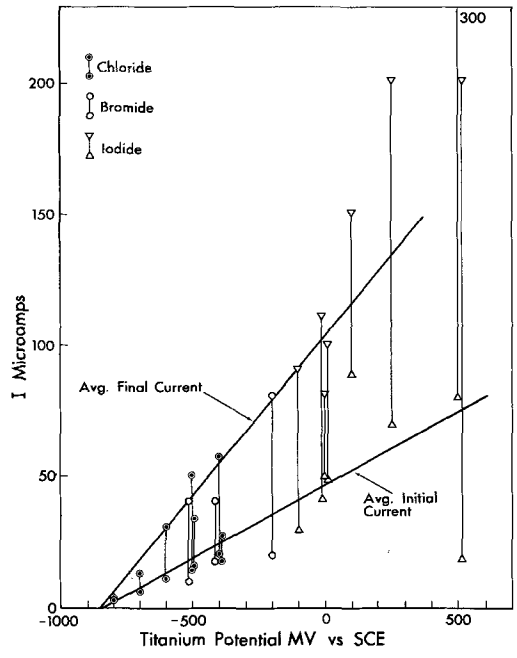

Fig. 13. Relation of crack propagation current to applied potential in 0.6M halide solutions.

sec of the irregular current plot. That the ratio of final current to initial current appears to be constant up to at least zero mv to SCE lends some assurance that the correlation using average velocity was justified.

The values of the intercepts on the potential axes in Fig. 12 and 13 play an important role in the analysis presented in the following paper (4). The intercepts in Fig. 12 and 13 are —900 and —850 mv, respectively.

Effect of concentration.—The effect of concentration was studied using hydrochloric acid solutions. The pattern of strength *vs.* potential was similar to that shown in Fig. 9 at concentrations from 6M to 0.006M. At 0.0006M anodic protection did not occur until about +1000 mv. The resistivity of the solution was apparently too high for the potentiostat to maintain effective control.

It was found that stress corrosion cracking in chloride solution could be suppressed by addition of hydroxide or fluoride. SCC was suppressed in iodide solution by addition of hydroxide or perchlorate. The molar ratio of inhibitor to SCC agent to suppress SCC completely was on the order of 10-100 to 1.

Effect of temperature.—Temperature of the specimen and electrolyte from 0° to 74°C had little effect on ultimate load within the limits of experimental error in chloride electrolytes with specimen at —500 mv as shown in Table II. Further, the relatively small change in velocity with temperature suggests control by mass transport rather than kinetics.[1] The temperature of 0°C was obtained by pouring liquid nitrogen into the cell until the surface of the electrolyte froze to ice around the specimen. The 74°C temperature was obtained by shining heat lamps on the specimen and cell and controlling temperature with an epoxy insulated thermocouple in the electrolyte.

Effect of heat-treatment.—Experiments were conducted to investigate the effect of heat treatment of Ti:8-1-1 and the preliminary results are summarized in Fig. 14. The results on duplex-annealed material have already been described. In contrast it can be seen that notched specimens of the alloy in the mill-annealed condition are relatively brittle under all conditions of test and are relatively insensitive to the environment.

Fractographic analysis.—Numerous electron photomicrographs of square-fracture surfaces have shown that specimens fractured in aqueous salt solutions exhibited transcrystalline cleavage of the α-phase in Ti:8-1-1 alloy. Ductile rupture occurs in the β-phase.

[1] Note added in proof: Subsequent experiments indicate an activation energy on the order of 2 kcal.

Table II. Effect of temperature on ultimate load and crack propagation velocity at potential of —500 mv in chloride solutions

Specimen No.	Electrolyte	Temp, °C	Ultimate load = kg	Crack velocity, cm/sec × 10^3
473	0.6M KCl	0	1500	4.6
Avg. of several specimens	0.6M KCl	21	1300 ± 90	8
145	0.6M LiCl	74	1340	5.0[a]

[a] Velocity could be larger than this value because time of transition to shear could not be determined.

Conclusions

The following conclusions are based on experiments with duplex annealed Ti:8-1-1 alloy specimens in aqueous solutions:

1. Notched specimens are susceptible to stress corrosion cracking in chloride, bromide, and iodide solutions.
2. Notched specimens are not susceptible in fluoride, hydroxide, sulfide, sulfate, nitrite, or perchlorate solutions. Fluoride, hydroxide and perchlorate were found to inhibit SCC in chloride, bromide, and iodide solutions for molar concentration ratios in excess of 10-100 to 1.
3. No significant cation effect was observed for hydrogen ion and alkali and alkaline earth metal ions.
4. SCC is accompanied by an anodic current.
5. There is a maximum rate of elongation of notched tensile specimen above which shear failure occurs rather than SCC.
6. Precracking is not necessary, but there is a minimum notch root radius above which SCC does not occur in chloride solutions. SCC was found to occur in bromide and iodide solutions with a larger root radius, at potentials above the pitting potential. Electropolishing the notch inhibited SCC in iodide solution.
7. The load for initiation of SCC appeared to be related to the first visible indication of plastic deformation around the root of the notch.
8. Cathodic protection occurred at potentials more negative than —1000 mv to SCE in chloride, bromide, and iodide solutions. An anodic protection zone of potential occurred in chloride and bromide but not in iodide solution.
9. Susceptibility occurs in hydrochloric acid solutions to concentration at least as small as 0.0006M (20 ppm).
10. Average velocity of crack propagation during SCC is linearly related to potential in chloride, bromide, and iodide solutions. Data for the three ions were correlated by the same line which had an extrapolated intercept of —900 mv to SCE at zero velocity. There is

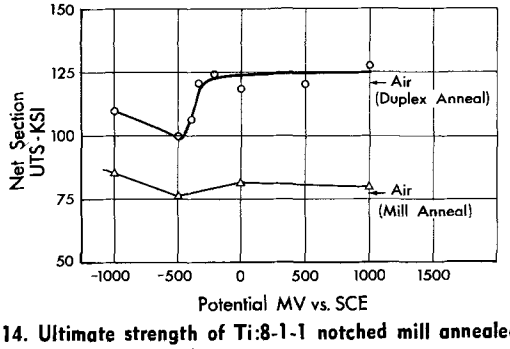

Fig. 14. Ultimate strength of Ti:8-1-1 notched mill annealed and duplex annealed in 0.6M LiCl.

a relatively small temperature effect on velocity from 0° to 74°C.

11. The anodic current during SCC was also related linearly to potential in chloride, bromide, and iodide solutions. An electrochemical mechanism controlling velocity is implied.

12. Electron photomicrography indicates transcrystalline cleavage of alpha phase on SCC fracture faces.

Acknowledgment

The author is indebted to Dr. M. J. Blackburn for considerable help in designing and conducting the experiments, Mr. Paul Olson who contributed his skill to designing and building the cells and fixtures used in this program, and Mrs. H. Wallner who conscientiously conducted most of the tensile tests and kept the records in order.

Manuscript received Nov. 17, 1966. This paper was presented in part at the Philadelphia Meeting, Oct. 9-14, 1966.

Any discussion of this paper will appear in a Discussion Section to be published in the December 1967 JOURNAL.

REFERENCES

1. G. C. Kiefer and W. W. Harple, *Metal Progress*, p. 74 (February 1953).
2. ASTM Pacific Area National Meeting, Seattle, Wash., Oct. 31, 1965; R. V. Turley and C. H. Avery; R. F. Simenz, J. M. Van Orden, and G. G. Wald; D. E. Piper and D. N. Fager; etc.
3. B. F. Brown, ASTM Annual Meeting, Lafayette, Ind., June 13-18, 1965.
4. T. R. Beck, To be published.

Electrodeposition of Coherent Deposits of Refractory Metals

V. Mechanism for the Deposition of Molybdenum from a Chloride Melt

S. Senderoff and G. W. Mellors

Research Laboratory, Consumer Products Division, Union Carbide Corporation, Cleveland, Ohio

ABSTRACT

After observing an irreversible step in the electrode process in all cases of coherent deposition of metals from molten fluorides, a chronopotentiometric study of the KCl-LiCl-K_3MoCl_6 system which produces coherent molybdenum deposits was undertaken. It was found that in this case also, the electrode process was irreversible at 600°C, a temperature at which coherent deposits are produced, and became more reversible as the temperature increased. The irreversible behavior of the electrode and the decrease of bath stability with decrease in concentration of molybdenum could be explained on the basis of the following mechanism

$$[Mo_2Cl_9]^{-3}(l) + 3Cl^-(l) \underset{\text{slow}}{\rightleftharpoons} 2[MoCl_6]^{-3}(l) \qquad (A)$$

$$[MoCl_6]^{-3}(l) + 3(e) \rightarrow Mo^0(s) + 6Cl^-(l) \qquad (B)$$

$$\left|\begin{array}{l}\\ \Delta \rightarrow\end{array}\right. \frac{2}{5}Mo(s) + \frac{3}{5}MoCl_5(g) + 3Cl^-(l) \qquad (C)$$

The failure of the electrode to behave in a Nernstian manner at 600°C is ascribed to the slowness of the dissociation in step (*A*). Its more nearly Nernstian behavior at 700° and 800°C probably results from the increased rate of this dissociation and is associated with decreased coherency of deposits at these temperatures.

In a recent series of papers (1-4) it was shown that in each case in which a coherent deposit of a refractory metal was obtained from fused salt systems, the metal production step in the electrode process was irreversible. In niobium and tantalum deposition, the irreversibility was apparently the result of a slightly soluble intermediate, while in the case of zirconium, it may have resulted from corrosion of the the deposit by the solvent. In all of these studies the system under investigation was a fluoride electrolyte which had been demonstrated to be a general medium for the coherent deposition of refractory metals (5). It had been shown earlier that a chloride electrolyte may be used to deposit molybdenum (6) coherently under certain conditions, and a study of static potentials in this system indicated that the Mo/Mo^{3+} electrode behaved reversibly in accordance with Nernst's Law (7). The study of the kinetics of the electrode process by chronopotentiometry was undertaken to determine whether reversibility of the electrode was maintained under the dynamic conditions during deposition or whether it was a property of the static electrode system only.

Experimental

The general procedures and equipment used in previous investigations (2-4) were used with the following modifications:

1. The reference half-cell consisted of a silver rod immersed in solution of 1 mol % AgCl in the KCl-LiCl eutectic mixture (41.2 mol % KCl-58.8 mol % LiCl) contained in a recrystallized alumina crucible (Morganite ΔRR). This crucible was held in the cup designated C in Fig. 2 of ref. (4).

2. The test solutions were prepared by making an electroplating solution with K_3MoCl_6 in KCl-LiCl as described earlier (6) and electrolyzing until satisfactory plates were produced. This solution was quickly frozen, analyzed, and portions were then added to purified KCl-LiCl to make the diluted solutions required for chronopotentiometry. The K_3MoCl_6 was prepared as previously described (8).

3. The crucible containing the test solutions [designated I in Fig. 2, ref. (4)] was molybdenum.

Chronopotentiometric runs were made with a platinum disk 1 cm^2 in area as indicator electrode and a molybdenum strip as counter electrode. As will be dis-

cussed below, the solutions were unstable at low concentrations and high temperatures so each concentration was run as rapidly as possible at various current densities at the lowest temperature (600°C), then at higher temperatures, and finally cooled and a few current densities repeated at the initial temperature of 600°C. Only those runs in which the transition time constant of the initial chronopotentiograms was reproduced at the end of the run were used in interpreting the results. Samples for analysis were taken at the conclusion of each set of runs at a fixed temperature.

Results

The electroplating bath which formed the stock solution for the chronopotentiometric runs contained 4.8 w/o (weight per cent) Mo (8.8×10^{-4} moles/cc at 600°C)[1] at a mean valence of 2.9 as determined by chemical analysis.[2] This solution could not be used for chronopotentiometric studies since at this high concentration a microelectrode 0.01 cm^2 in area was required in order that reasonable current densities and transition times could be employed. Such electrodes were made by sealing platinum or tungsten wires in a quartz tube, but did not yield satisfactory chronopotentiograms. Satisfactory runs were made on diluted solutions containing initially 1.7×10^{-4}, 1.0×10^{-4}, and 5.8×10^{-5} moles/cc Mo, but the last of these lost 36% of its molybdenum content within the short time required to complete nine chronopotentiograms at 600°C. A solution starting with 3.5×10^{-5} moles/cc lost 97% of its molybdenum content after only five runs at 600°C and could not be used to obtain significant data. The two more concentrated solutions showed negligible molybdenum losses at 600°C but lost concentration slowly at 700° and 800°C. Because of the progressive instability of the solutions with decreasing concentration and increasing temperature, only a limited range of concentrations could be studied.

Figures 1A and 1B are typical cathodic chronopotentiograms at 600° and 700°C. They show a single plateau at —0.18 and 0.0v, respectively. The small irregularity near —0.7v is caused by a trace impurity and may be ignored. The static potential observed on a molybdenum electrode in this solution is +0.05v at 600° and 700°C *vs.* the Ag/AgCl (0.3M), KCl, LiCl electrode, and is nearly independent of temperature except when the electrolyte decomposes, thereby decreasing the concentration and raising the mean valence. At 800°C, values varying between +0.17 and +0.23v are observed for the static potential, the variability being related to the instability of these dilute solutions at this temperature.

[1] Density data taken from ref. (9).

[2] The sample is dissolved in excess ferric sulfate and back titrated with dichromate. The mean valence is calculated from the titer and the total Mo content. The latter is determined colorimetrically on the thiocyanate complex of molybdenum after dissolving the sample and fuming it in H_2SO_4 containing a few drops of HNO_3.

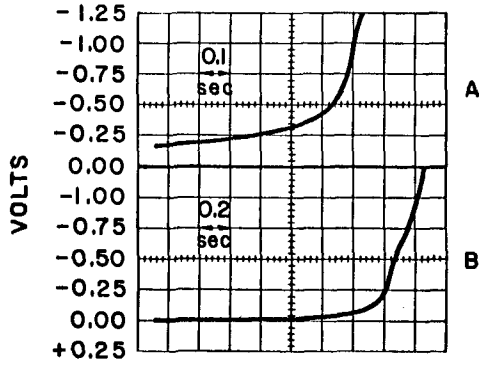

Fig. 1. Chronopotentiograms for the reduction of K_3MoCl_6 in KCl-LiCl.

	a	b
Temp, °C	600	700
Concentration, moles/cm^3	17×10^{-5}	13×10^{-5}
Current density, ma/cm^2	200	150

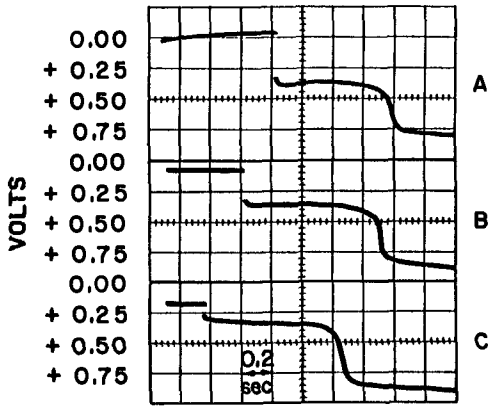

Fig. 2. Cathodic-anodic chronopotentiometry of K_3MoCl_6 in KCl-LiCl, cathodic portion on the left.

	a	b	c
Temp, °C	600	700	800
Concentration, moles/cm^3	17×10^{-5}	13×10^{-5}	12×10^{-5}
Current density, ma/cm^2	100	150	175

Figures 2A, B, C are cathodic-anodic chronopotentiograms at 600°, 700°, and 800°C, respectively. While at 600°C the ratio of backward-to-forward transition times is 1.0, this ratio is anomalously large at 700°C (1.7) and 800°C (3.3). Table I shows the chronopotentiometric data for the results at 600°, 700°, and 800°C.

Discussion

Stability of the solution.—Although the plating solution at a concentration of 4.8 w/o Mo is stable up to at least 800°C, the approximate fivefold and tenfold dilutions represented by solutions I and II in Table I showed slight concentration losses at 700°C and additional losses at 800°C. The dilution of approximately 15-fold represented by solution III fell from a concentration of 5.8×10^{-5} to 3.7×10^{-5} moles/cc even at 600°C and was too dilute at 800°C for satisfactory study. On diluting the plating solution to 1/25 of its original concentration, it decomposed at 600°C before even a few runs could be made. Upon decomposition, a volatile material is evolved from the solution and a dark powder is precipitated. When this approximately 25-fold dilution was quenched after a 2-hr hold at 600°C, two layers developed. The white upper layer contained less than 10^{-6} moles/cc Mo, and the lower black one contained 3.4×10^{-4} moles/cc Mo. The initial nominal concentration based on the dilution of the plating bath was 3.5×10^{-5} moles/cc, and the x-ray spectrum of the black material showed lines characteristic of Mo metal and MoO_2 (the latter undoubtedly a product of the aqueous separation procedure). One may conclude that the decomposition is a disproportionation yielding a volatile higher chloride of molybdenum and molybdenum metal. However, while a disproportionation may be furthered by higher temperature, it is extremely unusual for it to be enhanced by dilution. In fact, if the process is of the nature of

$$5MoCl_3(l) \leftrightarrows 2Mo(s) + 3MoCl_5(g) \qquad [1]$$

then decrease in concentration of $MoCl_3$ in solution (as K_3MoCl_6) should drive the reaction to the left rather than toward additional disproportionation. To account for the observed effect of temperature and concentration, another process must be postulated in addition to the observed disproportionation. While in aqueous systems dilution frequently results in decomposition of complexes and disproportionation, this would not be expected in this case since the concentration of the ligand, chloride ion, is essentially unaffected by varying the concentration of $MoCl_3$ in a large excess of KCl-LiCl. One process which would be

Table I. Chronopotentiometric data for reduction of K_3MoCl_6 in KCl-LiCl eutectic mixture

	Conc. K_3MoCl_6, moles $cm^{-3} \times 10^{-5}$	CD, amp/cm^2 Min.	Max.	$E_{1/4}$, v, average[a]	$i\tau^{1/2}$, amp $sec^{1/2}$ cm^{-2}, average[a]	$i\tau^{1/2}/C$, amp $sec^{1/2}$ cm, $mol^{-1} \times 10^{-2}$
				A. 600°C		
I	17.0[b]	0.100	0.300	-0.17 ± 0.03	0.161 ± 0.002	9.5
II	10.0[b]	0.075	0.150	-0.18 ± 0.02	0.088 ± 0.002	8.8
III	3.7[c]	0.025	0.100	-0.18 ± 0.02	0.029 ± 0.002	7.8
				B. 700°C		
I	13.0[c]	0.150	0.300	-0.01 ± 0.01	0.178 ± 0.005	13.7
II	7.0[c]	0.050	0.150	-0.04 ± 0.01	0.095 ± 0.005	13.5
III	3.0[c]	0.030	0.100	-0.04 ± 0.01	0.027 ± 0.002	9.0
				C. 800°C		
I	12.0[c]	0.175	0.350	$+0.11 \pm 0.02$	0.182 ± 0.009	15.1
II	5.8[c]	0.100	0.200	$+0.10 \pm 0.01$	0.104 ± 0.003	18.0

[a] Based on 6 or 7 runs at each concentration.
[b] Final and initial values not significantly different.
[c] Final value at end of series.

favored by decreasing concentration is dissociation of a polymer to form a monomer in solution. The equilibrium

$$M_n \leftrightarrows nM \qquad [2]$$

is driven to the right on decreasing the concentration in accordance with the equilibrium expression

$$\frac{[M]^n}{[M_n]} = K \qquad [3]$$

Polynuclear ions such as $[W_2Cl_9]^{-3}$, $[Mo_2F_9]^{-3}$, $[Mo_3Cl_7]^{-1}$, and others are known and, if one may postulate that an ion such as $[Mo_2Cl_9]^{-3}$ exists, the concentration dependence of the decomposition can be explained by a process such as

$$[Mo_2Cl_9]^{-3}(l) + 3Cl^-(l) \leftrightarrows 2[MoCl_6]^{-3}(l)$$
$$\rightarrow \frac{6}{5}MoCl_5(g) + \frac{4}{5}Mo(s) + 6Cl^-(l) \qquad [4]$$

That is, if the molybdenum is present in a stable binuclear ion in equilibrium with a less stable mononuclear one, decreasing the concentration favors dissociation of the binuclear to the mononuclear ion, which then disproportionates. Increasing the temperature can be expected to increase the tendency toward disproportionation of the mononuclear ion. A spectroscopic study could probably settle definitely the question of whether such a binuclear (or polynuclear) ion of molybdenum exists, and the behavior with dilution described above can only be considered as very indirect evidence for it. However, as will be seen below, the concept will prove useful again in correlating the kinetics of the electrode reaction.

The electrode process.—Examination of Table I reveals that the transition time constant, $i\tau^{1/2}/C$, is reasonably invariant at 600°C at all concentrations and also at 700°C at the higher concentrations. In Fig. 3 are plotted the values of $i\tau^{1/2}$ *vs.* C from Table I. Because of the restricted range of concentrations accessible for study and the unreliability of the data at low concentration and high temperature, too much significance cannot be ascribed to the straight lines drawn. Therefore, it cannot be unambiguously demonstrated from these data that the reaction is subject to diffusion control, although it may be.

However, it can be shown conclusively in a number of ways that the reaction is not reversible at 600°C, and that it becomes more nearly reversible and approaches Nernst behavior at higher temperatures. First, examination of Fig. 2A reveals a 0.4v difference of potential between the anodic and cathodic processes at 600°C. In a reversible process this should be twice the IR drop. If it is assumed that the 17 x 10^{-5} moles/cc K_3MoCl_6 does not materially change the conductivity of the KCl-LiCl mixture [2.34 Ω^{-1} cm^{-1} at 600°C (9)], it is calculated that the IR drop at 100 ma/cm^2 on 1 cm^2 electrodes 1.5 cm apart is a maximum of 0.064v. The observed difference is therefore more than six times the IR drop, and can only represent irreversibility of the electrode process. This difference in potential between the anodic and cathodic processes decreases to 0.3v at 700°C and to 0.18v at 800°C. At 800°C the conductivity of the KCl-LiCl mixture is 3.14 Ω^{-1} cm^{-1} so that the IR drop at 175 ma/cm^2 with the same electrode configuration is 0.084v. Here the total difference is almost exactly twice the IR drop, indicating that at 800°C the anodic and cathodic processes are nearly reversible. Table II indicates the approach to reversibility of the electrode process with increasing temperature.

Table II. Comparison of IR drop in electrolyte with observed polarization of anodic and cathodic processes

Temp, °C	KCl-LiCl Eutectic, κ, ohm^{-1} cm^{-1}	C.D., amp/cm^2	2 x IR, v (1.5 cm electrode separation)	Observed potential difference, v (from Fig. 2)
600	2.34	0.100	0.128	0.4
700	2.81	0.150	0.162	0.3
800	3.14	0.175	0.168	0.18

An identical conclusion can be reached by comparing the $E_{1/4}$ values of the cathodic reduction with the observed static potential values. In Table I it is seen that the average $E_{1/4}$ values at 600°, 700°, and 800°C are, respectively, —0.18v, —0.03v, and +0.11v. The static potential, which is almost temperature independent, is +0.05v. Because measurements become difficult at 800°C, the $E_{1/4}$ value observed is probably not significantly different from the static potential; at 700°C it is polarized cathodically by only 80 mv, and

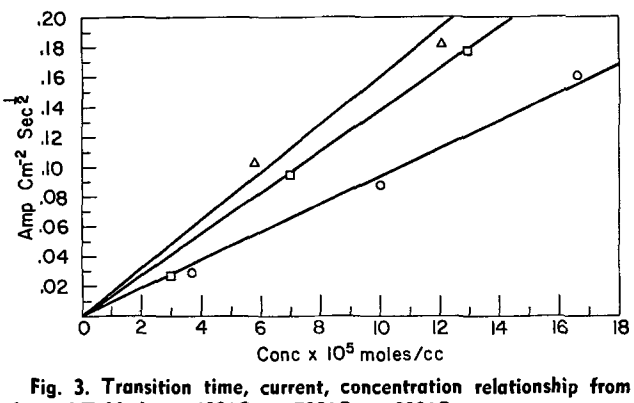

Fig. 3. Transition time, current, concentration relationship from data of Table I. ⊙ 600°C; ⊡ 700°C; △ 800°C.

at 600°C by 230 mv, again showing a considerable departure from reversibility at 600°C with nearly reversible behavior at 800°C. The variation of $E_{1/4}$ with the concentration expected when a metal is the product of the reaction is not detectable in these experiments, because at 600°C the variation of one decade in concentration for a three-electron reaction will produce a change in $E_{1/4}$ of only 58 mv. Since the variation of concentration was less than fivefold, the expected change in potential over the whole concentration range is about 35 mv, which is at the borderline of the precision of these measurements.

Selis (7) gives the static standard potential of Mo/Mo^{3+} with respect to Pt/Pt^{++} on the molar scale of Laitinen (10) as —0.603v at 450°C. In the present work a static potential value of +0.05v at 600°C was observed between Mo/Mo^{3+} (0.1M) and Ag/Ag^{+} (0.3M). Since the temperature coefficients of these cells are very small, the difference of 150°C in temperatures of measurement may be ignored and on converting the observed static potential to the standard value on the same scale, a standard potential of —0.72v is obtained. This may be considered reasonable agreement in view of the different methods, conditions, and solutions used.

A final and probably conclusive demonstration of the lack of reversibility at 600°C with approach to reversibility at the higher temperatures is the plot of E *vs.* $\log f(t)$ as a test for Nernstian behavior. Visual comparison of the shapes of the plateaus in Fig. 1A and 1B is sufficient to demonstrate that they are very different from each other. A plot of E *vs.* $\log (\tau^{1/2} - t^{1/2})/t^{1/2}$ and *vs.* $\log (\tau^{1/2} - t^{1/2})$ for the cases of the soluble and insoluble products, respectively, did not produce straight lines for any chronopotentiograms taken at 600°C. Where the best straight line was drawn through as many points as possible, ridiculous n values, some as low as 1.0, others as high as 8.5, were obtained, depending on how the line was drawn through the curve of points. However, an example of these plots for one of the chronopotentiograms taken at 700°C is shown in Fig 4. The excellent straight line obtained with the plot for the insoluble product case [*i.e.*, $f(t) = \log (\tau^{1/2} - t^{1/2})$] gives from its slope an n number of 2.8. An average of 11 such plots gives an n number for the reaction of 2.66 ± 0.28 in good agreement with the three-electron reduction expected from these trivalent molybdenum solutions. It is significant that this is the first case observed in this study of refractory metal deposition in which linear behavior was found with the plot for an insoluble product. Previous cases where insoluble intermediate compounds were observed still showed linear behavior with the plot of soluble products. This may be explained by pointing out that a slightly soluble compound must first saturate the liquid at the interface and by that time most of τ has been completed. However, it is clear that when an extremely insoluble material such as a refractory metal is deposited at the electrode, the case for an insoluble product holds strictly. It is also interesting that at 600°C the ratio $t_{anode}/t_{cathode}$ is equal to 1.0, as shown in Fig. 2A. This confirms that an insoluble product is produced, and since the electron number (at 700°C) has been shown to be three, this insoluble product must be molybdenum metal. The higher $t_{anode}/t_{cathode}$ ratios obtained at higher temperatures are anomalies and are believed to be due to molybdenum which entered the platinum before the chronopotentiometric run began. It was observed that mere immersion of the platinum in the electrolyte at 700° and 800°C produced a thin diffusion coating of molybdenum in the platinum which must be removed by vigorous treatment with 1:1 HNO_3 or by anodizing in the molten electrolyte.

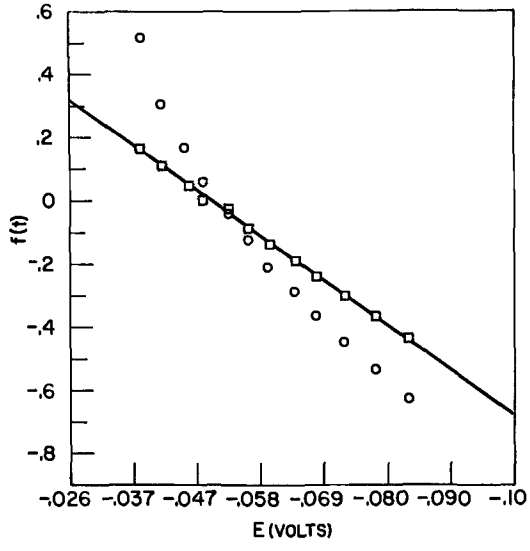

Fig. 4. Nernst plot of chronopotentiogram for reduction of K_3MoCl_6 in KCl-LiCl. ⊙ f(t) = log $(\tau^{1/2} - t^{1/2})/t^{1/2}$; ⊡ f(t) = log $(\tau^{1/2} - t^{1/2})$. Temp, 700°C; current density, 100 ma/cm²; concentration, moles/cm³ = 7 x 10^{-5}.

From the foregoing it is evident that the molybdenum is reduced from the trivalent state to metal at 600°C in a single irreversible step which progressively becomes more reversible as the temperature is raised, so that at 800°C all criteria for reversibility are satisfied. The criteria for reversibility, which in this investigation proved most significant, were cathodic-anodic potential difference, polarization of $E_{1/4}$, and the Nernst plot of E *vs.* $\log (\tau^{1/2} - t^{1/2})$. This observation of the irreversibility at 600°C must be correlated with the observation over ten years ago that the molten chloride-molybdenum plating solution gave good coherent deposits only at 600°C and that at 900°C powders were obtained (6). Steady-state polarization tests performed at that time also indicated notably higher polarization at 600°C than at higher temperature (11). This observation of coherent plates associated with irreversibility at low temperature, and decreasing coherency at higher temperatures coupled with increasing reversibility of the system is another example of the close connection between coherent plating and irreversible electrode behavior.

Reactions of the reducible species.—One apparent anomaly still requires explanation as does the source of the irreversibility of the system. Selis (7) found by static potential measurements exact Nernst dependence on concentration of the observed equilibrium potential at temperatures between 460° and 540°C. Under the dynamic conditions of chronopotentiometry, however, Nernstian behavior is not observed at 600°C. This may be explained if a slowly established equilibrium is displaced by the electrode process so that in static measurement an equilibrium always exists such that the concentration of the potential determining species is proportional to the total molybdenum concentration, while in the cathodic process at a finite rate the equilibrium state is not maintained. A polynuclear ⇆ mononuclear ion equilibrium of the type of reaction [4] can be such a process. If the mononuclear ion is reduced electrolytically to metal as fast as it is produced, it would not be able to disproportionate; and if its concentration is kept low by a slow rate of dissociation of polynuclear ion, the electrode would not behave in a Nernstian manner. Finally, the value of $n = 3$ calculated from the static potential data by Selis and from the chronopotentiometry of the present work indicates that the six-electron reduction of the binuclear complex is totally irreversible under these conditions and thus does not affect the potential measurements. It is interesting, therefore, that the same postulate which is consistent with the concentration dependence of the stability of the solution can also explain the observations regarding the static and dynamic electrode potentials in the system.

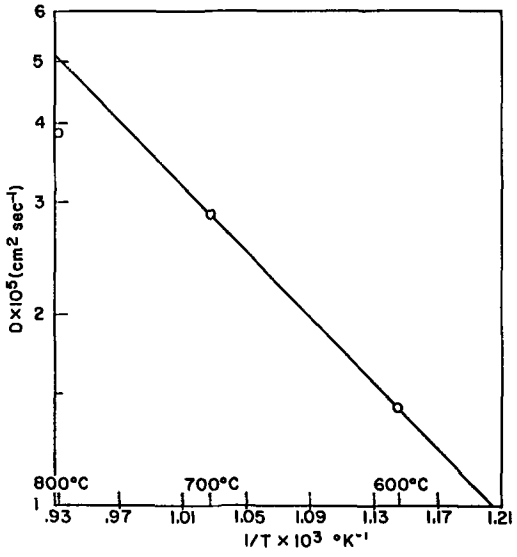

Fig. 5. Activation energy for diffusion of chloromolybdate (III) ion in KCl-LiCl.

Transport properties.—By taking $n = 3$ one can calculate the diffusion coefficient, D, of the reducible species, $[MoCl_6]^{-3}$, from the lines of Fig. 3, the slopes of which equal $\frac{1}{2}\pi^{1/2}n\mathbf{F}D^{1/2}$. At 600°, 700°, and 800°C, respectively, these equal 1.43×10^{-5}, 2.89×10^{-5}, and 3.87×10^{-5} cm^2 sec^{-1}. A plot of log D *vs.* $1/T$ is shown in Fig. 5 in which only the two lower temperatures are used to draw the line because of the poor reproducibility of the measurements at 800°C. The slope of the line corresponds to an activation energy of 11.9 kcal mol^{-1}, and may be compared with the value of 9.8 kcal mol^{-1} for the trivalent bismuth ion obtained by Thalmayer *et al.* (12) in the KCl-LiCl solvent. The value of the diffusion coefficient at 750°C taken from the line of Fig. 5 is 3.8×10^{-5} cm^2 sec^{-1}, which is one-half that found for Ag^+ in the same solvent at that temperature (13) and is a reasonable difference which one would expect for a trivalent as compared to a monovalent ion (12).

Summary

The electrodeposition of molybdenum from the chloride electrolyte occurs as a single three-electron irreversible step at 600°C. It becomes more reversible with increasing temperature, while at the same time the plate becomes less coherent. The source of the irreversibility has not been unambiguously established, but the peculiar decomposition of the electrolyte with decreasing concentration suggests that a slow[3] dissociation of a binuclear (or polynuclear) ion to a mononuclear one may be involved both in the irreversible electrode reaction and in the chemical decomposition. The postulated process may be written:

$$[Mo_2Cl_9]^{-3}(l) + 3Cl^-(l) \xrightarrow{\text{slow}^3} 2[MoCl_6]^{-3} \quad (1)$$

$$[MoCl_6]^{-3}(l) + 3e \rightarrow Mo^0(s) + 6Cl^-(l)$$

$$\xrightarrow{\Delta} \frac{2}{5}Mo(s) + \frac{3}{5}MoCl_5(g) + 3Cl^-(l)$$

[5]

Acknowledgment

The authors are indebted to Professor H. A. Laitinen for his advice and criticism throughout the course of the work and to R. L. Zupancic and G. W. Sheffield who carried out the experiments.

Manuscript received Dec. 5, 1966.

Any discussion of this paper will appear in a Discussion Section to be published in the December 1967 JOURNAL.

REFERENCES

1. G. W. Mellors and S. Senderoff, *This Journal*, **112**, 266 (1965).
2. S. Senderoff, G. W. Mellors, and W. J. Reinhart, *ibid.*, **112**, 840 (1965).
3. G. W. Mellors and S. Senderoff, *ibid.*, **113**, 60 (1966).
4. S. Senderoff and G. W. Mellors, *ibid.*, **113**, 66 (1966).
5. G. W. Melors and S. Senderoff, Canadian Pat. No. 688,546 (1964).
6. S. Senderoff and A. Brenner, *This Journal*, **101**, 16 (1954).
7. S. M. Selis, *ibid.*, **113**, 37 (1966).
8. S. Senderoff and A. Brenner, *ibid.*, **101**, 28 (1954).
9. E. R. VanArtsdalen and I. S. Yaffe, *J. Phys. Chem.*, **59**, 118 (1955).
10. H. A. Laitinen and C. H. Liu, *J. Am. Chem. Soc.*, **80**, 1015 (1958).
11. S. Senderoff and A. Brenner, *This Journal*, **101**, 31 (1954).
12. C. E. Thalmayer, S. Bruckenstein, and D. M. Gruen, *J. Inorg. Nucl. Chem.*, **26**, 347 (1964).
13. S. Senderoff, E. M. Klopp, and M. L. Kronenberg, Final Report, Contract NOrd 18240, Part II, Sept. 15, 1962.

[3] The actual rate of the dissociation has not been determined but it is undoubtedly of an order corresponding to the operating current density range of the plating process (~50 ma/cm^2).

Vapor Deposition of Tungsten by Hydrogen Reduction of Tungsten Hexafluoride

Process Variables and Properties of the Deposit

Jean F. Berkeley, Abner Brenner, and Walter E. Reid, Jr.

National Bureau of Standards, Washington, D. C.

ABSTRACT

An investigation of the variables involved in the deposition of tungsten from a mixture of tungsten hexafluoride and hydrogen has shown that the fastest rate of deposition (about 5 mils thickness in 2 min) was obtained at atmospheric pressure with a hydrogen/tungsten hexafluoride ratio of 1.5 (by volume) at a temperature of 800°-850°C. The presence of hydrogen fluoride or chloride in the reacting gases diminished the rate of deposition. The deposits had about the same hardness, electrical conductivity, and density as commercial wrought tungsten. The tensile strength of the deposits was about 30,000 lb/in.^{2}. The internal stress within the deposits was also about 30,000 lb/in.^{2}. Codeposition of carbon, from carbon monoxide, greatly increased the hardness of the deposits.

About 1958, the Metal Deposition Section of the National Bureau of Standards undertook an investigation of the deposition of tungsten, which project was supported by the Special Projects Section of the Department of the Navy. This organization was interested in producing either tungsten nozzles or graphite nozzles coated with tungsten for use on rocket engines. Since tungsten has not been electrodeposited from aqueous solutions in the uncombined state (although it has been codeposited with other metals as alloys), the only processes considered were electrodeposition from fused salt baths and deposition from the vapor phase.

We were not successful in obtaining smooth tungsten deposits 1 or 2 mm thick from fused salt baths. We tried the borate-tungstate bath of Davis and Gentry (1) and various baths prepared (in the absence of air) by dissolving tungsten dichloride or tetrachloride in melts of alkali chloride or fluorides. Subsequently, McCawley, Kenahan, and Schlain (2) and Mellors and Senderoff (3) obtained improved results from fused salt baths.

We found deposition of tungsten from the vapor phase by published methods also unsatisfactory. Deposition of tungsten from the vapor of the carbonyl (4) was too slow, and sufficiently thick, smooth deposits could not be obtained from either this system or the tungsten hexachloride-hydrogen system (5).

We modified the latter process by substituting tungsten hexafluoride for tungsten hexachloride and obtained very superior results (6). At about the same time that we were engaged on this phase of the investigation we learned that the Bureau of Mines (7) was also working on this process for the purpose of producing highly pure tungsten. The hexachloride is a solid (mp 270°C) which requires a temperature above 200°C to produce an adequate vapor, whereas the hexafluoride is a gas at room temperature (bp 19°C) and was easily passed into the reaction chamber from a commercial cylinder. No lower valent halides were formed and deposition of tungsten occurred over a wider range of temperature and vapor composition.

The hexafluoride process found some special applications (8-13) for preparing objects of tungsten, but has yet no large use. In particular, it is now in operation for the production of tungsten spherules (12) which are used in powder metallurgy. The conditions of deposition which have been used for these various items were essentially those which were disclosed in the initial brief publications on the subject (6) and may not have been the optimum.

Since the process appears to have potential engineering and commercial applications, more information on the operation of the process and on the properties of the deposit was warranted. The objective of this investigation was to determine the effects of the operating variables on the rate of deposition and on some of the properties of the deposits and to investigate other phenomena associated with the reaction.

Experimental Apparatus and Procedure

Although the vapor plating process allows a wide latitude of choice of equipment, for this research we required an experimental setup that enabled specimens of uniform thickness to be prepared at a controlled temperature from a reaction mixture of known composition. The commonly used flowing system was not satisfactory because the gases could not be proportioned with sufficient accuracy, and a deposit of uniform thickness was not obtained because of the more rapid deposition on the windward side of the substrate. Temperature control of the specimen was also more difficult in a flowing system.

In this investigation we deposited tungsten from a static volume of gas. The substrate was a nickel tube about 4 in. (10 cm) long, 0.125 in. (3.0 mm) in diameter with a wall thickness of 0.01 in. (0.25 mm). The end of the tube was plugged so that deposition did not take place on the inside. We believe that the results obtained with the static system are qualitatively applicable to the flowing system, that is, a change in the value of a process variable produces changes of the same type and direction in both static and flow systems.

The tube was inductively heated by being suspended in a work coil about 1.5 in. (4 cm) in diameter and 6 in. (15 cm) long. Five to 15 sec were required to reach a temperature of 1000°C. The temperature of the tube during deposition was measured with a thermocouple, which was placed in the interior of the tube. Temperature was controlled within about 10° by manually operating the cores of three auxiliary coils (all water cooled) which were in series with the main work coil. The temperature was constant within this limit over the central 2-in. length of the tube.

The reaction chamber (see Fig. 1) was a cylinder of stainless steel about 10 in. (25 cm) in diameter and 24 in. (60 cm) long. It had a volume of approximately 1 ft^3 (30 liters). This large volume was necessary to prevent the concentrations of the reacting gases from changing from their initial values by more than 5 or 10%.

In preparing the chamber for an experiment it was first evacuated to about 0.05 Torr. Hydrogen was introduced to the desired pressure, as read on a mercury

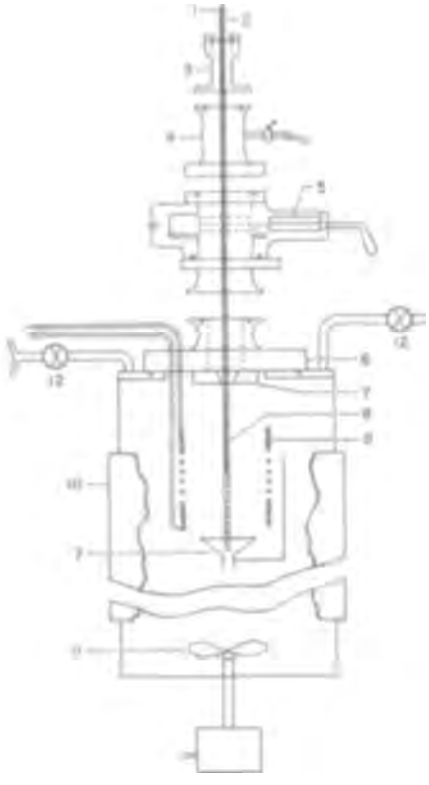

Fig. 1. Schematic view of vapor-plating chamber: 1, specimen holder, 3/16 in. nickel tube; 2, thermocouple inside (1); 3, lid; 4, antechamber; 5, cut-off valve, dotted lines representing closed position; 6, lid to plating chamber; 7, specimen guide; 8, specimen; 9, r.f. induction work coil; 10, heater band; 11, motor-driven gas stirrer; 12, gas ports.

manometer, and next the tungsten hexafluoride. The two gases were then mixed by a motor driven propeller in the bottom of the reaction vessel. This was necessary because of the large difference in the density of hydrogen and tungsten hexafluoride (the latter being about 150 times more dense than hydrogen).

The induction unit was next turned on and maintained at the required temperature long enough to provide a thickness of deposit which usually ranged between 3 and 10 mils (75 and 250μ). The rate of deposition varied from about 1 to 3 mils/min, hence, a plating period of 2-3 min was adequate.

To permit the plating of more than one specimen from a single filling of the reaction chamber, the latter was provided with an air lock, as shown in Fig. 1. The main part of the air lock was a vacuum-tight sliding gate valve, which had an opening about 2 in. (5 cm) in diameter. Several specimens could be obtained from a single filling of the chamber before the composition of the gases changed more than 10%. The reactive gas mixture could be allowed to remain in the chamber for a few weeks without detriment to the plating process.

At the conclusion of a set of runs the gases in the reaction chamber were removed by drawing dried air through the equipment with a water aspirator, which also served to absorb WF_6 and HF.

The plated specimens were treated with nitric acid to dissolve the nickel substrate. Thus, the tungsten specimen was obtained in the form of a thin-walled tube. The tubular shape of the specimen made possible the handling of the fragile deposits without mechanical damage.

The special items of equipment and the procedures involved in the measurement of the properties of the deposits are described under each property.

Effect of Plating Variables on the Rate of Deposition and Appearance of Deposit

Ratio of reactants.—The reaction involved in the deposition of tungsten from the hexafluoride is

$$WF_6 + 3H_2 \rightarrow W + 6HF$$

Although the stoichiometric ratio of the reactants is three volumes of hydrogen to one of tungsten hexafluoride, this ratio did not give the optimum results at all temperatures. To a first approximation, at a given temperature, the rate of deposition appeared to depend upon the concentration of tungsten hexafluoride in the gas. For example, at 800°C a faster rate of deposition was obtained with a ratio of hydrogen to tungsten hexafluoride of 1.5 than with 3.0, as shown in Fig. 2. Over the lower part of the temperature range, there was little difference in rate between the ratios, as the curves for the latter seem to branch from a common trunk. Figure 3 gives the data of Fig. 2 in a different form. It shows that at 500°C the rate is not affected by the ratio of reactants. The rates of deposi-

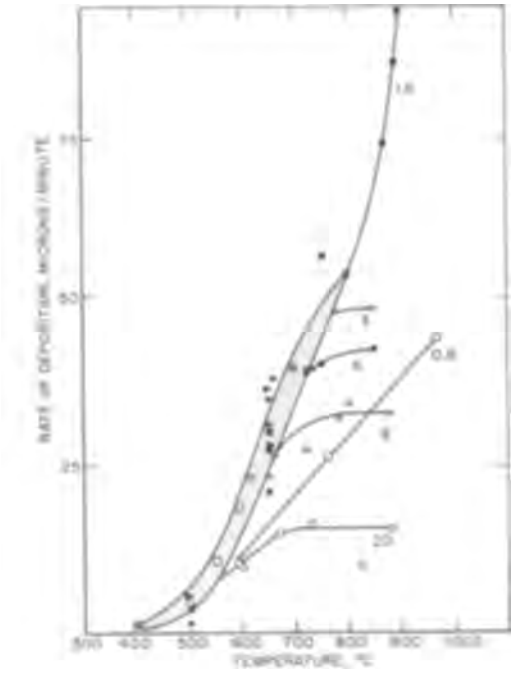

Fig. 2. Rate of deposition of tungsten from various gas compositions at 1 atm. The number on a curve represents: (Partial pressure of H_2)/(Partial pressure of WF_6). The shaded area indicates (a) that the curves run together at lower temperatures and (b) that the relation between thickness and temperature is not reproducible enough to be represented by a line.

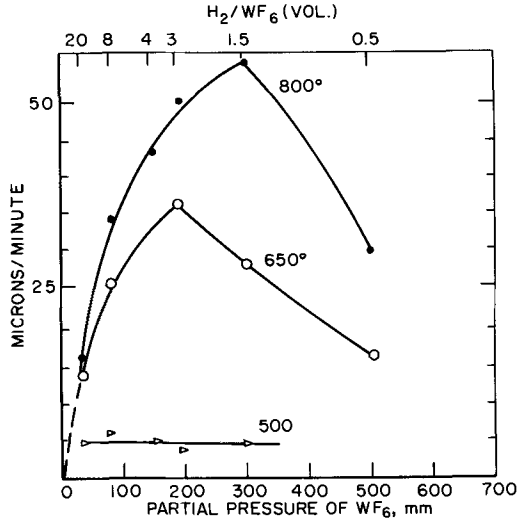

Fig. 3. Rate of deposition of tungsten as a function of the concentration of WF_6.

tion shown in Fig. 2 are to be considered as illustrative only, inasmuch as the rate varies with the size and shape of a specimen and on the period of time that the deposition is allowed to proceed.

Pressure of gas.—Figure 4 shows that the rate of deposition increases with the total pressure of the mixed reactants. There appeared to be no advantage in operating the process at a pressure lower than atmospheric. In this respect the process differs from most other vapor deposition processes, which usually operate at less than atmospheric pressure, often with the addition of a diluent gas.

Miller and Barnett (14-16) deposited tungsten at a pressure of only about 10^{-3} Torr for the purpose of obtaining thin deposits in the range of 1000Å in thickness. Deposition was very slow, about 300Å/hr. This result is in accord with the trend in Fig. 4.

We made a few experiments in a bomb at pressures up to 170 atm to determine if this made possible the deposition of tungsten at a lower temperature. The lowest temperature at which deposition occurred was 300°C. At 400°C the reduction of tungsten hexafluoride to metal was about 90% complete. In some of these experiments a higher than stoichiometric ratio of hydrogen to tungsten hexafluoride was used in the expectation of obtaining tungsten fluorides in which the metal had a lower valence than 6, but no such compounds were observed. However, Golovanov and coworkers (17) obtained brightly colored di-, tetra-, and pentafluorides of tungsten at a temperature of 275°C.

Temperature.—As already mentioned, deposition of tungsten can take place at a temperature of 300°C, but the rate is too low for the process to be practicable. This confirms the observations of Golovanov *et al.*, who reported metal deposition at 300°C but not at 275°C.

Figure 2 shows that the rate of deposition increases rapidly with temperature. The lowest temperature at which deposition proceeded at a practicable rate was 500°C.

Heestand *et al.* (17A) also reported a considerable increase in rate of deposition with temperature. They operated the process at a lower concentration of WF_6 ($H_2/WF_6 = 70$ or 140 at 10 or 20 Torr) than we did and, consequently, their rates of deposition ranged from 1/10 to 1/100 of those which we give in Fig. 2. Another reason for the difference is that they deposited the tungsten in a heated tube, under which conditions the composition of the gaseous mixture varied along the tube.

The appearance of the deposits varied considerably with plating conditions, especially with temperature. Also, the deposits grew rougher with increasing thickness. Figure 5 shows representative surfaces obtained on the substrate of nickel tubing mentioned earlier. For ratios of Vol. H_2/Vol. WF_6 greater than 3 the deposits became increasingly dendritic as the temperature rose above 650°C. At a temperature above 1000°C the deposits were masses of crystals or dendrites, not a coherent coating. However, at a ratio of 0.5 the deposits were as smooth at 950°C as the deposits obtained at a ratio of 3 at 650°C. We cannot indorse Hoertel's view (17B) that the rate of deposition must be less than 2 mils (50μ) per hour (at an $H_2/WF_6 = 4$ and a temperature of 550°C to 600°C) to obtain a smooth deposit.

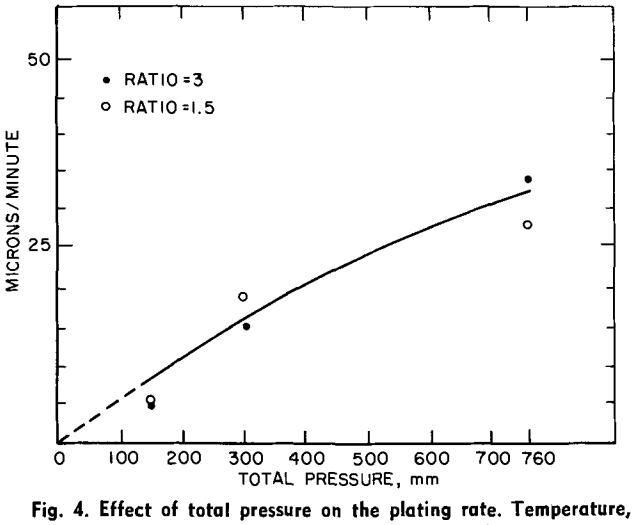

Fig. 4. Effect of total pressure on the plating rate. Temperature, constant at 650°C. Ratio = Partial pressure of H_2/Partial pressure of WF_6.

The possibility of finding gaseous compounds which added to the reacting gases will prevent the formation of dendrites and yet permit rapid deposition of thick coatings at the elevated temperatures is touched on below.

Agitation.—Qualitatively, we noted that a rapid flow of the reacting gases over a specimen increased the rate of deposition. A few experiments were made in our static system with the nickel tube rotating a few hundred revolutions per minute. The results were not very reproducible, but indicated an increase in the rate of deposition of 20-50%. Also, it resulted in smoother coatings at elevated temperatures.

Effect of oxygen, hydrogen fluoride, and hydrogen chloride on the rate of deposition.—In depositing tungsten from the static reacting gases, we noted that the rate of deposition decreased gradually, until about half or more of the available tungsten had been deposited. At this point sometimes the deposition ceased to occur on a fresh nickel tube. A low rate could be obtained at a higher temperature, or by depositing on a tungsten instead of a nickel substrate.

This decrease in the rate of deposition indicated that hydrogen fluoride was probably responsible, since there was still a substantial concentration of tungsten hexafluoride in the gas. This idea was confirmed by adding hydrogen fluoride directly to a chamber of unreacted hydrogen and tungsten hexafluoride. A concentration of hydrogen fluoride equal to about 25% of the volume of the reacting gases was sufficient to inhibit deposition of tungsten. The concentration at which the cut-off of deposition occurred was not ascertained. The effect of hydrogen fluoride on the deposition is important, because its inhibiting effect must be taken into consideration in any explanation of the mechanism of deposition. It is likely that the increased rate of deposition resulting from an increase in the rate of flow of gas or from agitation of the substrate may result as much from the removal of hydrogen fluoride as to the replenishment of the reacting gases at the surface of the substrate.

Concentrations of oxygen up to about 0.5% of the volume of reacting gases did not seem to have an appreciable effect on the rate of deposition or on the appearance, including microstructure, of the deposit. This was fortunate as it indicated that the reaction chamber did not have to be subjected to a high vacuum before admitting the reacting gases.

The effect of hydrogen chloride on the plating process was qualitatively determined. A concentration of one percent by volume reduced the rate of deposition by more than 50% and caused a finer microstructure (see Fig. 5 and 8).

Mechanical Properties of Deposits

Hardness.—The hardness measurements were made with a Knoop indenter on polished cross section of the deposits. The hardnesses of smooth deposits ranged between 600 and 1100 Knoop (see Table I). The latter hardness was that of a deposit produced at 500°C. The hardness of a dendrite of tungsten deposited at 900°C was 410 VHN.

Mills and co-workers (18) measured the Diamond Pyramid Hardness of tungsten tubes with a 100g load and obtained values ranging between 350 and 450 VHN.

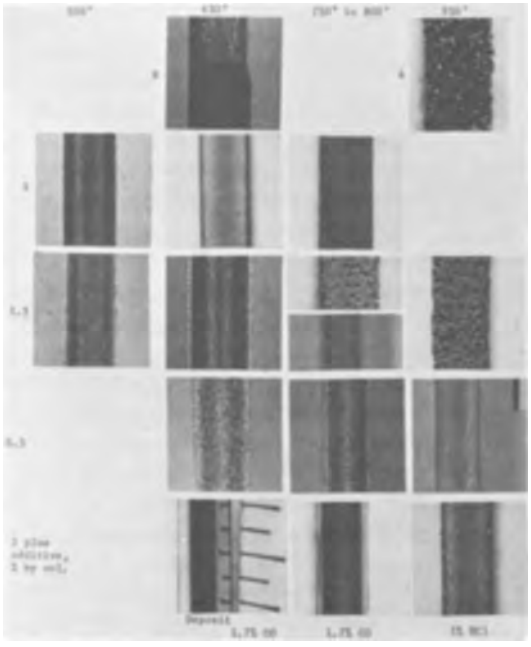

Fig. 5. Surface view of vapor deposited tungsten. Number refers to ratio vol. H_2/vol. WF_6. Magnification ca. 1½X.

They found no difference in the hardness of tubes obtained by vapor deposition and those prepared by extrusion at temperatures of 1200° and 1800°C. Basche (13) gave data on the hardness of various kinds of tungsten after annealing to temperatures between 800° and 2800°C. The range of hardnesses was about the same as reported by Mills and co-workers, but their vapor deposited tungsten was a little softer than sintered and wrought tungsten. Hoertel (17B) obtained Knoop hardness numbers between 400 and 500 (with a 100g load) on tungsten deposited between 500° and 600°C.

Tensile strength.—The specimens used for the measurement of tensile strength were similar to those employed in a study of the properties of chromium deposits (19). Tungsten tubes, formed as described above, about 1 in. long, of uniform wall thickness, were cemented by epoxy resin into two cylindrical metal fittings, one at each end. A 4 or 5 mm band of tungsten was left exposed. In some tests a 2 mm wide band of this exposed tungsten was anodically etched to form a necked-down section (about 20%) to induce breaking in this area. However, not all of the samples broke precisely within the etched zone. A few broke on a diagonal crossing both etched and unetched portions. Two samples broke in the unetched zone. The measurements in Table I are based on the cross-sectional area measured at the break. The strength of samples that were unetched, even though the break occurred near the fitting, agreed very well with that of the etched samples, indicating that the etching was not necessary.

The tensile strengths averaged about 30,000 lb/in.^{2} with no clear trend with conditions of deposition. The tungsten specimens heat treated at various temperatures showed a small increase in tensile strength.

Stress.—The magnitude of the stress in tungsten deposits is important since, if too high, it could prevent the fabrication of tungsten articles by plating on a master. We had determined that heat-treatment of vapor-deposited tungsten at temperatures above 900°C relieved stress, and, therefore, it would not be expected to occur in deposits produced at or above that temperature.

The measurement of the stress was done by the well-known method of depositing a metal on one side of a thin metallic substrate and measuring the resulting change of curvature. The tungsten was deposited at an elevated temperature, but the measurement of the change in curvature was done at room temperature. Hence, the use of a substrate of any other metal than tungsten would have introduced a curvature resulting from differential thermal expansion. The substrates for the test specimens were, therefore, prepared from tungsten itself.

The first step in preparing the specimen was the production of a tube of tungsten by vapor deposition. Tungsten up to a thickness of 5-10 mils (125-250μ) was deposited upon a nickel tube about 0.75 in. (2.0 cm) in

Table I. Properties of vapor-deposited tungsten

Ratio Vol H_2 / Vol WF_6	Temperature of deposition, °C	Hardness, Knoop, 100-g load	Density, g/cc	Resistivity, microhm-cm, 25°C	Internal tensile stress, psi	Tensile strength, psi	X-ray orientation
20	650	550	—	—	—	—	—
8	650	620	19.09*	5.5	24,400	34,800	—
3	500	650	19.22	5.3	—	35,000	—
	650	610	—	5.3	33,400	31,700	—
	700	—	—	5.3	—	26,500	—
	780	600	—	—	—	34,800	—
1.5	500	850 to 1100	19.02	5.3	26,700	26,000	[100]
	600	—			—	28,500	
	650	580		5.1	25,300	30,000	
	800	600		5.6	—	31,500	[100]
0.5	500	525	—	—	—	—	
	650	525	19.22	5.2	—	39,000	[100]
	760	570	19.23	5.3	—	38,300	[100]
	900	670		5.3	—	41,000	

Carbides	% (Vol.) of CO			% Carbon content		
	660	1.7	1,800	—	—	36.2**
	750	1.7	1,600	0.2	—	
	700	1.4	—	—	18.65	
	700	1.4	—	2.4		—
	750	5.2	3,300	1.1	—	—
	700	5.6	2,800	2.4	—	—
	700	11.6	2,500	2.5	17.25	—

Annealed samples*** Temp. of anneal, °C	Time, hr	
800	4.5	66,000
1100	1.0	35,300
1300	1.0	35,000
1450	1.0	40,100

* Low due to rough surface.
** At 31°C.
*** Prepared at 650°C, ratio = 3.

diameter and a few inches long. The tube was cut into rings about 0.5 in. (1.0 cm) wide and the wall was slit at one place in a direction parallel to the axis of the tube. The nickel substrate was then dissolved. The bands were annealed at 800°C or above in an inert atmosphere to relieve stress. In making a determination of stress, the tungsten band was placed on a graphite fixture [for figure, see (20)], so as to allow tungsten to deposit only on the outside surface of the band. A tensile stress in the tungsten deposit caused the slit to become wider. The change in the curvature of the band that resulted from the plating operation was determined by measuring the change in the width of the slit wtih a microscope before and after tungsten deposition. Since the changes were small the change in the width of the slit could be considered as equal to the change in the circumference, ΔC, of the band.

The temperature at which the deposits for stress measurement were produced was not definite, because the band and the graphite fixture required from 10 to 30 sec to come up to temperature or to cool down. Since the period of deposition at the desired temperature was only a minute or two, a fair proportion of the deposit was produced at intermediate temperatures. Thus, the stress must be considered as relating to a range of temperature rather than to a single temperature.

Physical Properties

Density.—The density of tungsten tubes, prepared as noted above was determined by the method of loss of weight on immersion in water. The densities (see Table I) varied from 19.02 to 19.23 g/cm^3 at 25°C. The value for tungsten is given in the literature as 19.3 g/cm^3 (21) (from x-ray data).

Electrical resistivity.—The electrical resistivity of tungsten was determined using tubes of uniform cross section, prepared as described above. The uniformity was checked by examining the contour of the tubes in a shadow-graph. The specimens were suspended in an oil bath maintained at room temperature.

The measurements were made by passing a current of known strength through the tube and measuring the voltage across a 1-cm length. The resistance, R, was then calculated. The resistivity, ρ, in ohm-cm is given by the equation

$$\rho = \frac{Rg}{19.2\,LD}$$

where R is the resistance of sample, ohms, g the weight of sample, g, L the length of sample, cm, and D the distance between voltage contacts, cm.

The average value of the electrical resistivity (see Table I) was 5.3 microhm-cm. This value is approximately the same as that given in the literature for commercial tungsten, which is 5.6 microhm-cm (21).

Structure of Deposits

All of the deposits obtained by vapor deposition from the simple gas mixture were columnar, and the cross section looked very much like that of electrodeposits from an acid copper bath or a Watt's nickel bath (20). Some of the deposits were fine-grained like the deposit from a nickel chloride bath (see Fig. 6).

The presence of carbon monoxide in the reacting gases produced a hard deposit containing tungsten carbide which was laminated (to be discussed later). Some exploratory experiments with several other additives to the reacting gases, for example, $TiCl_4$, MoF_6, BF_3, $GeCl_4$, $ReCl_5$ yielded deposits with slightly smaller grain structure. The addition of MoF_6 caused a laminated structure. The addition of $SiCl_4$ reduced the efficiency of the process and caused larger crystals. No analyses on the deposit were performed. NH_3 and H_2S, possible reducing agents, reacted with the WF_6.

There is a good possibility that suitable additives can be found which will reduce the tendency of the deposit to become nodular or dendritic at high temperature (see Fig. 8.) If this can be achieved, then deposits of tungsten 2 mm thick could be built up in an hour. There is some indication of this in experiments conducted with jets of reacting gases, for example, WF_6, impinging on a substrate in an atmosphere of hydrogen. In this circumstance a button of tungsten can be quickly built up in the region where the jet of WF_6 strikes.

Fig. 6. Microstructure of vapor deposited tungsten. The ratio = vol. H_2/vol. WF_6.

X-ray examinations of a few deposits indicated growth essentially only in the [100] direction, radially from the center of the rods. The temperature of deposition was from 500° to 800°C (see Table I). The geometry of the tungsten tubing limited our results to qualitative interpretation. McMurray and co-workers (22) had already reported that a preferred orientation of the deposits occurred with the (100) or the (111) planes parallel to the substrate. They found indications that the vapor-deposited tungsten would yield a surface of more uniform electron emission than a randomly oriented tungsten surface.

Supplemental Observations

Yield of tungsten from WF_6.—Since tungsten in the form of hexafluoride is expensive, a high yield of metal from the compound is important. In experiments in which the mixed gases with an adequate ratio of hydrogen were passed through a long, hot tube, almost all of the compound was reduced to metal. In the experiments (at 650°C) in which the reacting gases passed through a short heated section, for example, in deposition on a rocket nozzle, or over objects suspended in the gas stream, the deposition was only about 50% efficient. In the experiments with the static reactants, the rate of deposition on the tubular nickel substrates became very low when about one-half of the tungsten had been deposited out of the gas.

Reversibility of the reaction.—We made an experiment to determine if the tungsten deposit was attacked by HF. The effect of HF on tungsten in the absence of WF_6 was noted by heating vapor-deposited tungsten in commercial anhydrous HF (purity 99.9% min.) at 1 atm pressure. A slight weight-loss occurred amounting to 1 mg/cm^2 (0.5μ thickness) at 750°C and 4 mg/cm^2 (2μ thickness) at 1000°C in 10 min. Since the concentration of HF in the reacting gases during

tungsten deposition is much less than 1 atm it is not likely that the reaction reverses during the plating operation.

Uniformity of thickness of tungsten deposits.—In deposition from the vapor phase, the problem of metal distribution is smilar to that which occurs in electrodeposition. A thicker deposit occurs on edges and corners of a substrate and also on the windward side of a specimen placed in a flowing stream of reacting gases (20). More uniform distribution of the coating over an irregularly shaped object can be obtained by suspending the latter in an atmosphere of hydrogen and leading the WF_6 to the vicinity of concave or internal surfaces by means of small tubes.

The distribution of tungsten that occurs when the mixed gases flow through a heated tube has some special features that have not been explained. This matter is important because it will have a bearing on the elucidation of the mechanism of the reaction. In our experiment a copper-plated steel tube about 2.5 cm in diameter and 40 cm long was heated in a tube furnace. The hydrogen and tungsten hexafluoride were passed through individual injectors (about 0.5 cm diameter) which were placed inside the steel tube and extended to its center. The gases were thus heated up to temperature before they mingled at the center of the steel tube. The latter also contained a partition at the center to prevent the gases from flowing to the front end of the tube. In this experiment the maximum thickness of deposit (see Fig. 7) was obtained about 6 cm from the point where the gases mixed. Spacil and Wulff (23) first noticed this peculiar type of distribution in the deposition of molybdenum by the passage of molybdenum pentachloride vapor and hydrogen through a heated tube.

Heestand *et al.* (17A) also observed the maximum thickness of tungsten in a tube for deposition between 500° and 700°C. They explained this as owing to the time required for the mixture of gases to come up to temperature after entering the heated tube. However, this explanation is not valid in the light of our experiment in which the gases were preheated before mixing in the center of the hot zone.

Another peculiarity of the metal distribution was that the deposit was of nonuniform thickness circumferentially at the center of the steel tube where the gases mingled. The deposit in the 6 o'clock position was considerably thicker than in the 12 o'clock position. This result suggests that in our experiment the odd distribution might have been caused by a lack of mixing of the gases at the point where they issued from their individual tubes. To settle this point, it would be necessary to perform another experiment in which a rotating propeller is placed at the point where the gases emerged.

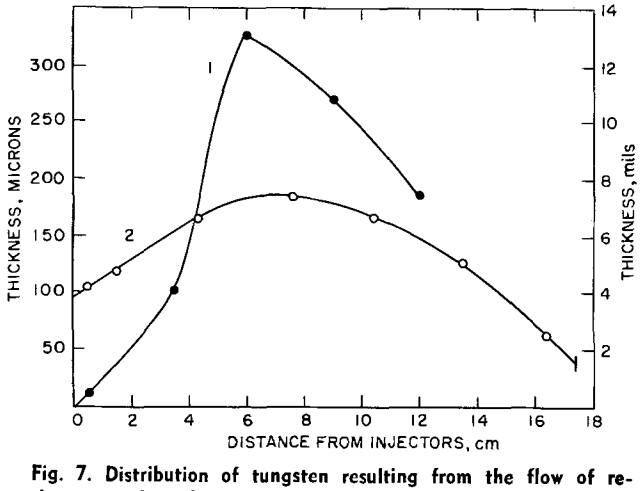

Fig. 7. Distribution of tungsten resulting from the flow of reacting gases through a heated tube. Curve 1, 640° to 670°C; curve 2, 670° ± 5°C.

The addition of HF to the reacting gases (in the proportions by volume, $HF/H_2/WF_6$ = 1.7/1.5/0.5) caused the maximum to be less pronounced, as shown in Fig. 7, curve 2, and also made the circumferential metal distribution more uniform. However, the yield of tungsten (based on amount of WF_6) was only about 40% in the presence of HF as compared with almost 100% in its absence.

Adhesion.—The adhesion of the coating was satisfactory to nickel, copper, molybdenum, graphite, and to some ceramics. Adhesion to steel was not adequate, probably because the surface of the latter was attacked before deposition began. This explanation is similar to that given by Wlodek and Wulff (24) to explain the problem with adhesion encountered in the vapor phase deposition of molybdenum from the pentachloride.

Codeposition of carbon.—Addition of carbon monoxide to the reacting gases resulted in the codeposition of carbon with tungsten. In these experiments the ratio of hydrogen to tungsten hexafluoride was 3.0. From a reaction mixture containing 1.7% CO by volume, at 650° and 750°C, smooth bright deposits were obtained (see Fig. 5). The deposit obtained at 850°C was rough. The rate of deposition in the presence of carbon monoxide was less than half that in the simple gas mixture, as shown in Fig. 9. Tungsten deposited from a gas mixture containing 5.2% CO by volume was smooth but not bright.

Table I shows the hardness and carbon content of the deposits. The high hardness of the deposit is of technologic interest. It scratches glass with ease. The carbon contents of about 2.4% indicate that this deposit must consist of more than 75% tungsten carbide, W_2C. The microstructure of representative deposits, as shown in Fig. 8, had distinct laminations.

Some of the thin carbide deposits seemed very weak, because they broke into fragments when the nickel substrate was dissolved, although deposits about 1 mm thick remained intact. The friability of the thin deposits may be enhanced by the differential thermal expansion between the nickel substrate and the deposit on cooling.

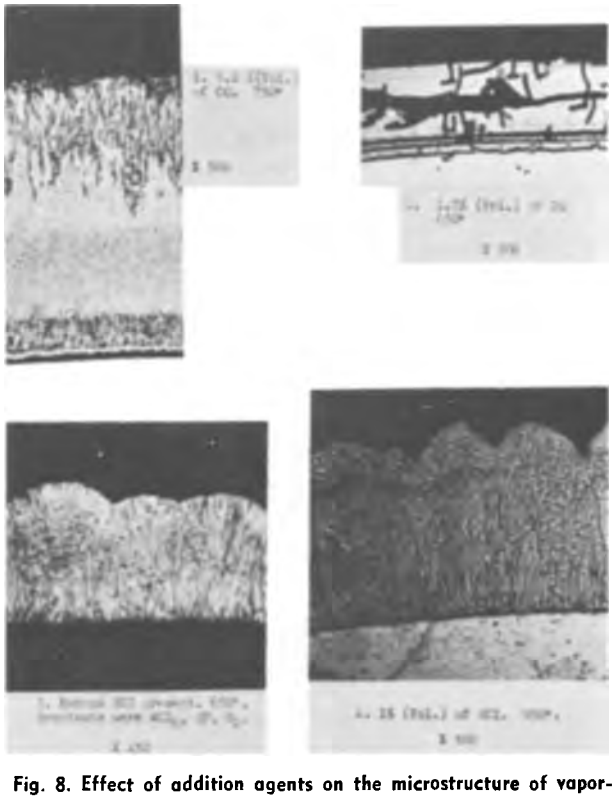

Fig. 8. Effect of addition agents on the microstructure of vapor-deposited tungsten.

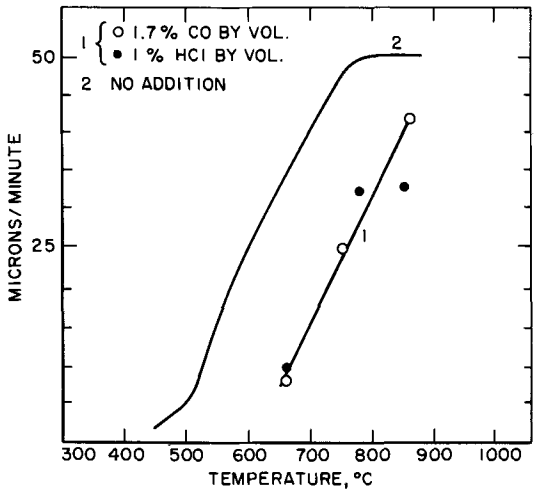

Fig. 9. Effect of separate additions of carbon monoxide and hydrogen chloride on the rate of deposition of tungsten from a mixture of 3 volumes of hydrogen and one of WF_6. Curve 2 was taken from Fig. 2.

Hoertel (17B) found that the grain size of tungsten was reduced by introducing butane, propane, or carbon dioxide into the reacting gases. The deposit obtained with butane (2% by volume) contained about 0.05% carbon; that obtained with propane (4% by volume) contained 0.04% carbon; and that obtained with carbon dioxide (24% by volume) contained 0.02% carbon. The Knoop hardness numbers of these deposits were, respectively; 1315, 1050, and 1220.

Summary of New Phenomena Observed

Any explanation of the mechanism of the reaction must take into consideration the following new phenomena which we observed in this investigation:

1. Inhibiting effect of the product HF and of HCl on the reaction.
2. Nonreversibility of the reaction (tungsten with HF).
3. Maximum in the distribution of tungsten in a heated tube.
4. Occurrence of the maximum rate of reaction of 800°C at a nonstoichiometric composition of the gas ($H_2/WF_6 = 1.5$), and at 500°C the lack of dependence of rate on composition.

Acknowledgment

The authors wish to acknowledge the support of the Special Project Office of the Department of the Navy, under whose sponsorship the initial work was done between 1958 and 1962 that led to our development of the tungsten hexafluoride process for depositing tungsten. They wish to thank the Materials Laboratory of the Wright-Patterson Air Force Base for continuing to support the project from 1963 to 1965, during which time they further investigated the process and measured some of the properties of the deposits, as reported in this publication.

Manuscript received July 29, 1966; revised manuscript received Feb. 1, 1967.

Any discussion of this paper will appear in a Discussion Section to be published in the December 1967 JOURNAL.

APPENDIX I

Purity

A study of the purity of vapor-deposited tungsten was not included in our program, as this phase of the subject had been extensively investigated by Nieberlein and Kenworthy (7) and Hoertel (25), all of the Bureau of Mines. Data have also been published by Mills and co-workers (18) and Taylor and Boon (26). The data from these various sources showed that vapor-deposited tungsten was purer than commercial tungsten used for powder metallurgy, having less than 0.01% total impurities, although some of the specimens had only about 60 ppm of impurities. Table II gives some typical analyses of vapor-deposited tungsten in comparison with other kinds. The large amounts of nickel or iron found in some samples probably came from the substrate upon which the tungsten was deposited. The analysis of a sample of tungsten which we had deposited was included in the report of Mills *et al.* (18). The purity fell within the limits shown for vapor-deposited tungsten in the table.

Table II. Purity of vapor-deposited tungsten

	Parts per million						
	Vapor deposited			Powder metallurgy	Extruded	Electrodeposited	Plasma sprayed
Element	**	***	*	**	*	*	**
Al	10	8	1	20-40	3	4	10-30
Ca	—	2	—	—	—	—	—
Cu	—	3	<0.5	—	<0.5	600	—
Fe	10	4	1-100	10-40	40	2	—
Mg	—	10	<0.5	—	<0.5	<0.5	—
Mn	—	3	<0.5	—	<0.5	<0.5	—
Ni	—	5	1-200	—	50	200	—
Si	10	28	<6	10-20	<6	2	20-40
Ti	—	—	<6	—	<6	<6	—
Mo	N.D.	1	<100	30-50	50	800	—
C	17	15	8	2-4	6	—	66-98
O_2	12	10	9	1-5	12	110	5-9
H_2	2	2	4	—	3	6	—
N_2	10	0	5	5-16	15	7	3-7
F_2	10	10	4-45	—	3	13	—

* Data of Mills *et al.* (18).
** Data of Taylor and Boone (26).
*** Data of Nieberlein and Kenworthy (7).
N.D. Not detected.

APPENDIX II

Process of Deposition Utilizing Tungsten Hexachloride as Intermediate

The deposition of tungsten from the hexafluoride is expensive because of the cost of the compound.

Since tungsten hexachloride is less expensive than the hexafluoride, a process utilizing the former would be economically advantageous. The direct use of the hexachloride in the deposition process, however, has some drawbacks, as noted earlier.

The reaction of tungsten hexachloride with hydrogen fluoride

$$WCl_6 + 6HF \rightarrow WF_6 + 6HCl$$

to produce the hexafluoride was first investigated by Ruff *et al.* (27). They mixed about a three-fold excess of liquid HF with WCl_6 and after the reaction, had some difficulty in separating the last traces of HF, which boils at about the same temperatures as WF_6. We found that passage of the gaseous HF through a tube or vessel filled with a large excess of WCl_6 resulted in the reaction of most of the HF, and the gases emanating from the reaction vessel could be directly lead into the reaction chamber and used for the deposition of tungsten. However, because of the presence of much HCl, the reaction was much slower than with the uncontaminated reactants.

The method of operating the reaction was as follows: The hexachloride was placed in a polyethylene bottle or tube which was warmed to about 50° to 70°C and the HF passed through. An endothermic reaction took place, and the vessel became perceptibly cooler. Although tungsten deposition was accomplished directly from the effluent gases, which contain WF_6 and HCl, the deposition would have proceeded faster if the HCl had been removed. Plans for this were made but not carried out. The separation of WF_6 and HCl could easily be made by passing the gases through a cool chamber in which the WF_6 would liquify and be drawn off while the gaseous HCl was allowed to escape.

In one experiment we utilized the above reaction for removing HF from the gases of our static reaction chamber. During a plating run the gases were continually circulated through a bottle of WCl_6 and back into the reaction vessel. No particular benefit accrued since the HCl was not removed from the system.

REFERENCES

1. G. L. Davis and C. H. R. Gentry, *Metallurgia*, **53**, 3 (1956).
2. F. X. McCawley, C. B. Kenahan, and David Schlain, *This Journal*, **110**, 180C (1963).
3. G. W. Mellors and S. Senderoff, *Plating*, **51**, 972 (1964); Canadian Pat. 688,546, 1964.
4. J. J. Lander and L. H. Germer, *Trans. AIME*, **175**, 648 (1948); also, *Metals Technol.*, **14**, No. 6, Tech. Pub. No. 2259 (1947).
5. C. F. Powell, I. E. Campbell, and B. W. Gonser, "Vapor Plating," John Wiley & Sons, Inc., New York (1955); C. F. Powell, J. H. Oxley, and J. M. Blocher, Jr., "Vapor Deposition," John Wiley & Sons, Inc., New York (1966).

6a. Tungsten for High-Temperature Coatings, National Bureau of Standards Technical News Bulletin, Feb. 1960.

6b. Abner Brenner and W. E. Reid, Jr., U. S. Pat. 3,072,983, Jan. 15, 1963.

6c. Abner Brenner, W. E. Reid, Jr. and J. H. Connor, U. S. Pat. 3,139,658, July 7, 1964.

7. V. A. Nieberlein and H. Kenworthy, Report of Investigations 5539, Bureau of Mines, 1959.
8. H. W. Shultze, *Metal Progr.* **76**, 74 (1959).
9. William Beller, *Missiles and Rockets*, **7**, 23 (1960).
10. E. A. Beidler and J. M. Blocher, Jr., Defense Metals Information Center, Columbus, Ohio. Final Report (on Contract NOrd-18794), Jan. 1961. PB 163227.
11. E. Mark Gold, AIAA Journal, 695-96 (March 1963). Also, ASD Tech. Report No. 61-665, Jan. 1962.
12. *Chem. & Eng. News*, **41**, Oct. 14, 31 (1963).
13. M. Basche, *Materials in Design Engineering*, **60**, 82 (1964).
14. A. Miller and G. D. Barnett, *This Journal*, **109**, 973 (1962).
15. G. D. Barnett, Arnold Miller, and J. I. Medoff, *Metal Progr.*, **81**, 75 (1962).
16. G. D. Barnett, Arnold Miller, G. R. Pulliam, and R. G. Warren, *Met. Soc. Conf.*, **19**, 263 (1962).
17. Yu. N. Golovanov, A. I. Krasovskii, V. L. Zotov, and V. P. Kuzmin, *Zh. Neorgan. Khim*, **10**, 1948 (1965).

17a. R. L. Heestand, J. I. Federer, and C. F. Leitten, Jr., (Oak Ridge National Laboratory) ORNL-3662, August, 1964.

17b. F. W. Hoertel, Bureau of Mines report of Investigations, No. 6731, 1966.

18. R. G. Mills, J. R. Lindgren, and A. F. Weinberg, NASA, CR-54277, GA-5721. Sponsored by Lewis Research Center. Issued Oct. 19, 1964.
19. A. Brenner, P. Burkhead, and C. W. Jennings, *J. Research NBS*, **40**, 31 (1948); *Ann. Proc. Am. Electroplaters' Soc.*, 32 (1947).
20. Abner Brenner, *Trans. Inst. Metal Finishing*, **38**, 123 (1961).
21. Metals Handbook, 8th ed., Vol. 1, American Soc. for Metals (1961).
22. N. D. McMuray, R. H. Singleton, K. E. Muszar, Jr., and D. R. Zimmerman, *J. Metals*, **17**, 600 (1965).
23. H. S. Spacil and J. Wulff, Final Report (on Contract DA 19-020-ORD-3760), 31 Jan. 1958. AD 156,957. PB 162,611.
24. S. T. Wlodek and J. Wulff, *This Journal*, **107**, 565 (1960).
25. F. W. Hoertel, Progress Report No. 5, Contract No. NASA N62-11027; PB 163,582. Rolla Metallurgy Research Center, Bureau of Mines, Mo. Mar. 1962. F. W. Hoertel, Progress Report No. 6, Contract No. NASA N62-1171, *ibid.*, Apr. 1962. PB 163,583. F. W. Hoertel, Progress Report No. 7, Contract No. NASA N62-12667; PB 163,584, *ibid.*, May 1962.
26. J. L. Taylor and D. H. Boone, *J. Less-Common Metals*, **6**, 157 (1964).
27. O. Ruff, F. Eisner, and W. Heller, *Z. Anorg. Chem.*, **52**, 256 (1907).

Absorption of Electrolytic Hydrogen by Nickel and Iron-Nickel Alloys

Thomas C. Franklin and P. E. Hudson[1]

Chemistry Department, Baylor University, Waco, Texas

ABSTRACT

A study was made of the absorption of electrolytically generated hydrogen by nickel and iron-nickel alloys. It was shown that the experimental rate law for the absorption of hydrogen is

$$\text{Rate of Absorption} = k[H_{ads}] + I$$

By controlling the current density it was possible to obtain experimental conditions such that the rate law agreed with the following mechanism

$$H_{ads} \rightarrow H_{abs}$$

It was shown that the primary cause for changes in the rate of absorption of hydrogen on alloying iron with nickel is changes in the amount of adsorbed hydrogen.

In conjunction with a series of correlation studies on the effect of hydrogen on different processes at solid metal electrodes and the effect of additives on these processes (1-4), a study was made of the effect of additives in solution on the rate of absorption of hydrogen into nickel wire, electrodeposited nickel, and electrodeposited iron-nickel alloy electrodes.

In earlier studies, Schuldiner and Hoare (5) found no penetration of hydrogen through palladized nickel plates or foils. In a later study, Szklarska-Smialowska and Smialowski (6) reported the formation of nickel hydride phase ($NiH_{0.7}$) when nickel was cathodically charged under appropriate conditions. In a study involving the oxidation processes at nickel electrodes, Weininger and Breiter (7) postulated that there were two forms of hydrogen sorbed at the nickel electrode. Devanathan and Selvaratnam (8) quantitatively determined the fractional coverage of the nickel electrode by hydrogen atoms. They assumed that only one hydrogen species was present and that this was the electrochemically active one.

In the present investigation emphasis was placed on the effect of solution additives, changes of hydrogen generating current density, and alloying on the rate of absorption of hydrogen.

[1] Present address: TRACOR, Inc., Austin, Texas.

Experimental

The electrodes were prepared by sealing varying lengths (2-30 cm) of the sample in Teflon spaghetti. The nickel wire electrodes were mechanically polished with emery cloth, degreased in acetone, washed with distilled water, then redistilled water, and placed in the cell for study.

The nickel plated electrodes were prepared by plating nickel wires prepared as above for a definite length of time at a known current density. The plating station was a constant current coulometer (9, 10) with a milliammeter and timer placed in the circuit. After plating, the samples were rinsed with redistilled water and placed in the cell for study.

The plating bath was of the Watts type and contained 240g of hydrated nickel sulfate ($NiSO_4 \cdot 6H_2O$), 45g of hydrated nickel chloride ($NiCl_2 \cdot 6H_2O$), and 30g of boric acid in one liter of solution. After dissolving the components, nickel carbonate was added to raise the pH. The solution was filtered and the pH lowered to 4.0 by adding dilute sulfuric acid (11).

The electrodes to be plated with iron-nickel alloys were nickel wires pretreated as previously described. The iron-nickel alloys were plated using a mixture containing different amounts of the Watts-type bath previously described and an iron sulfate bath (12). The relative composition of the alloys was determined by use of a General Electric Model XRD-5 X-ray Spectrometer.

The coulometric techniques previously used (1-4) in studies of hydrogen at solid electrodes were used in this study. Hydrogen was generated on the electrodes for varying lengths of time at at constant current density and for varying current densities at constant times by connecting the cell to a power supply. The cell was then connected to the polarograph, and the hydrogen was electrolytically oxidized. The nonpolarizable electrode was a large platinum gauze electrode. The solution was 2N sodium hydroxide.

In the experiments on the effect of additives, measured amounts of a solution of the additive in 2*N* sodium hydroxide were added to the bath. Hydrogen was then generated on the electrode electrolytically, and the hydrogen on the surface was analyzed coulometrically.

In all cases the reagents were the purest available commercially. The temperature of the cell was maintained at 25° ± 0.1°C.

A diagram of the apparatus is shown in Fig. 1.

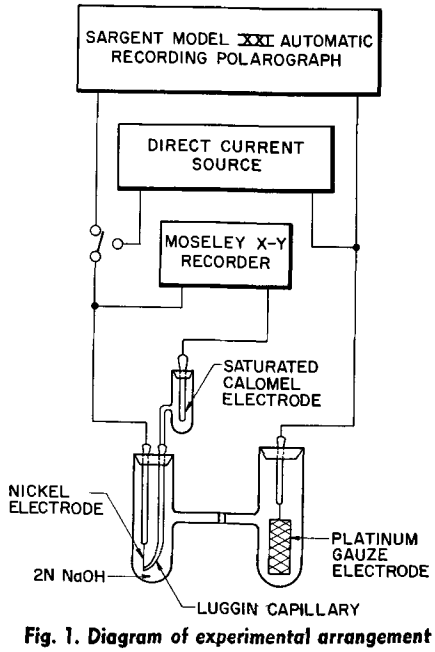

Fig. 1. Diagram of experimental arrangement

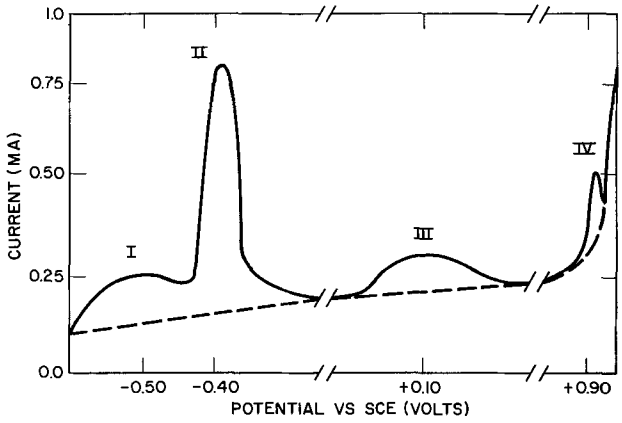

Fig. 2. Current-voltage curve for the oxidation processes at the nickel wire or electrodeposited nickel electrode.

Data and Discussion of Results

Effect of additives on the rate of penetration of hydrogen.—The general appearance of the current voltage curves for the oxidation processes at the nickel or plated nickel electrodes in 2*N* sodium hydroxide solution is shown in Fig. 2. As can be seen, four maxima appear in the curve, indicating that there are four oxidation processes, differing in potential, occurring at the electrode.

In 2*N* NaOH average values for the potentials at maxima I, II, III, and IV were —0.50, —0.40, +0.10, and about +0.91v, respectively, measured against a saturated calomel electrode (SCE).

Weininger and Breiter (7) proposed that the oxides of nickel are formed by the following mechanisms:

$$(a)\ Ni + OH^- = NiOH + e^-$$

$$(b)\ NiOH + OH^- = Ni(OH)_2 + e^-$$

$$(c)\ Ni(OH)_2 + OH^- = NiO(OH) + H_2O + e^-$$

Electrodes of varying length were prepared and the number of coulombs required for the formation of maxima III and IV determined. The results in Table I show that maxima III and IV required essentially the same number of coulombs for formation. From the comparison of the potentials and the number of coulombs involved with the data of Weininger and Breiter, it can be concluded that maxima III and IV can be identified as being caused by the formation of $Ni(OH)_2$ (III) and NiO(OH) (IV). Since, in the scheme of Weininger and Breiter, there should be a third peak due to the formation of NiOH, this maximum must coincide with maximum II of Fig. 2. It is evident that maximum II is much larger than either maximum III or IV, and thus it is apparent that the formation of NiOH is accompanied by another anodic process. This accompanying process is probably the oxidation of one form of hydrogen, since this is the accepted region of hydrogen oxidation. Maximum I in Fig. 2, which is at the most negative potential, is caused by the oxidation of another form of hydrogen.

In summary, the maxima in Fig. 2 may be described as being caused by: (*a*) the oxidation of one form of hydrogen; (*b*) the oxidation of a second form of hydrogen and the formation of NiOH; (c) the formation of $Ni(OH)_2$; and (*d*) the formation of NiO(OH).

Since the main concern of this work was the in-

Table I. Comparative area of maxima III and IV

Electrode length, cm	Peak III, mcoul	Peak IV, mcoul
5.0	0.47	0.47
8.2	0.59	0.58
10.0	0.58	0.59
20.0	1.25	1.29

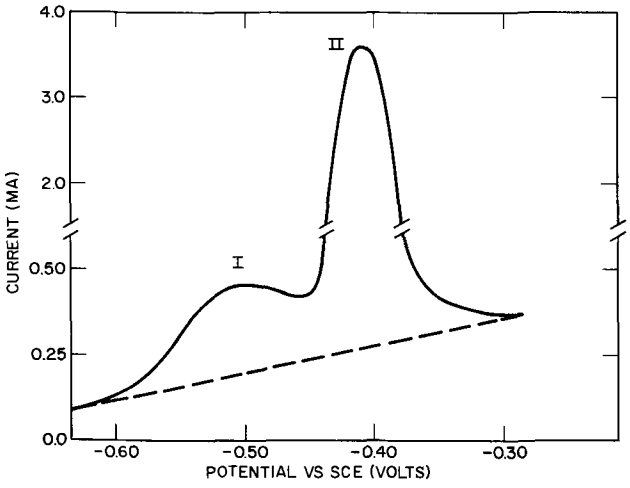

Fig. 3. Current-voltage curve for the oxidation of hydrogen on a nickel wire or electrodeposited nickel electrode.

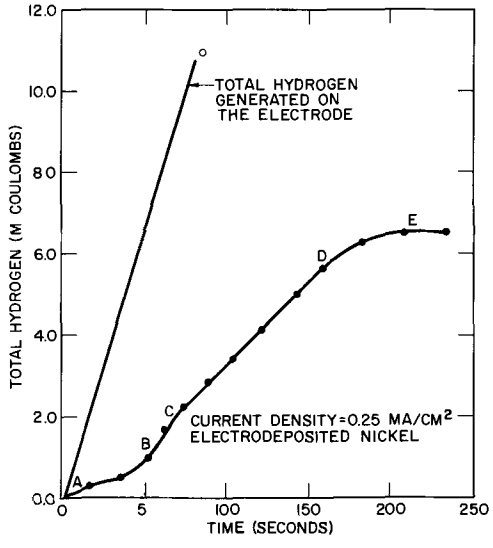

Fig. 4. Effect of time of generation on total hydrogen at the electrode.

vestigation of the hydrogen maxima, a correction due to the overlap of hydrogen oxidation and formation of NiOH was applied to all calculations and determinations involving the second form of hydrogen.

Figure 3 is a typical current-voltage curve in the hydrogen region for the oxidation of a nickel wire or electrodeposited nickel electrode on which hydrogen has been electrolytically generated. The existence of various forms of hydrogen on platinum has been shown by a number of workers (2, 13-17) and on iron by Matsuda and Franklin (4). The potentials of the two maxima were compared with the potentials observed by Matsuda in experiments run under identical conditions. The potentials of both the first and second peaks on nickel agreed within experimental error with potentials obtained by Matsuda for the oxidation of hydrogen sorbed on iron. In agreement with Matsuda, peak I has been attributed to the oxidation of adsorbed hydrogen and peak II to the oxidation of absorbed hydrogen.

The area under I can then be taken as the number of coulombs needed to oxidize adsorbed hydrogen while the area under II minus the area under peak IV can be taken as the number of coulombs needed to oxidize hydrogen in the interior of the metal. This is possible since the area under peak IV corresponds to the coulombs needed to convert $Ni(OH)_2$ to NiOOH. This corresponds to one electron for each surface nickel atom. This is the same number of coulombs that was needed to convert the nickel to NiOH. Since peak II is caused by both the oxidation of absorbed hydrogen and the formation of NiOH, this many coulombs must be subtracted.

Figure 4 shows the variations of the total area under the maxima with charging time. A similar curve was obtained with variations in current density holding the generating time constant. Examination was made of these curves along with an examination of the original current-voltage curves and a visual examination of the electrode during the charging process. These indicated that up to the region of point B, no hydrogen was visibly desorbed and in the preponderance of cases studied, only the first maximum was found on the current-voltage curves. Therefore, it was concluded that in this region the charging current was being used to reduce oxides and form adsorbed hydrogen. In the next region, BC, hydrogen begins to absorb in the nickel as shown by the formation of the second peak and in the straight line portion, CD, a steady state is reached in which hydrogen is desorbing and absorbing as fast as it is generated. This steady state was shown in that the first peak stopped growing and only the second peak increased in this region. Therefore, the major process occurring in the straight line portion, CD, other than desorption of hydrogen from the surface of the electrode, was the absorption of hydrogen by the nickel.

From these observations it was concluded that the slope of CD was a measure of the rate of absorption of hydrogen by nickel from a surface with a constant steady-state amount of adsorbed hydrogen on the surface.

The curves described above were observed for both electrodeposited nickel and nickel wire electrodes.

Figures 5 and 6 show typical families of curves obtained when 2,7-naphthalenedisulfonate ion was used as an additive and when the length was varied. Similar curves were obtained with different current densities and different additives. At low charging current densities, there was a decrease in the rate of absorption (the slope of CD) at low concentrations of the disulfonate ion, but at higher concentrations the slope increased.

At high charging current densities, there was a regular decrease in the slope with increasing concentration of the disulfonate ion. Figure 7 shows plots of the rate of absorption (the slope of CD) compared to the amount of adsorbed hydrogen. Curve A in Fig. 7 shows results obtained with different nickel electrodes. The area was varied by varying the length of wire and plating time. Some of these points are from unplated nickel and others from plated nickel.

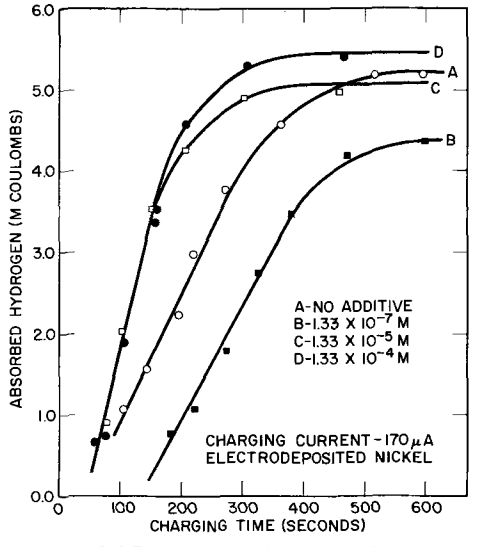

Fig. 5. Effect of 2,7-naphthalenedisulfonate ion on amount absorbed hydrogen.

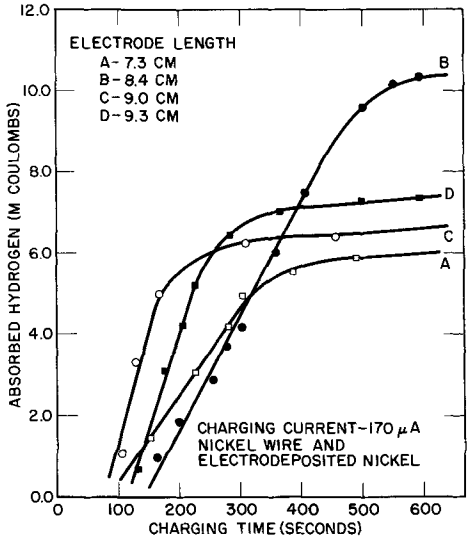

Fig. 6. Effect of surface area on amount of absorbed hydrogen.

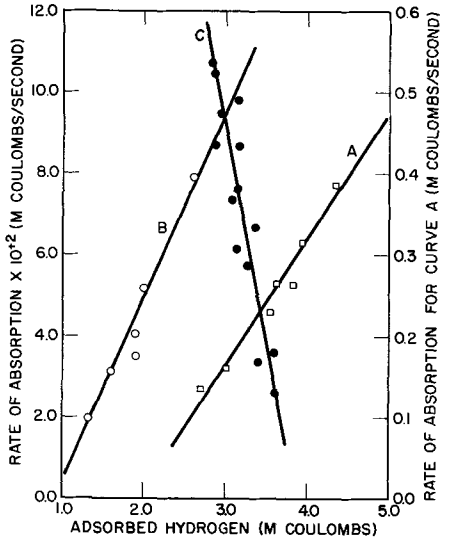

Fig. 7. Variation of rate of absorption with area under first maximum: curve A, no additive and charging current of 170μa; curve B, disodium 2,7-naphthalenedisulfonate and charging current of 1.6 ma; curve C, disodium 2,7-naphthalenedisulfonate and charging current of 170 μa.

It is apparent from these curves that the rate of absorption of hydrogen is directly proportional to the amount of adsorbed hydrogen. In the experiments performed at different charging current densities, both with and without additives, the following equation is followed

$$\text{Rate of Absorption} = k[H_{ads}] + I$$

Both the intercept I and k are influenced by changes in current density and by the presence of an additive. With any one current density and additive, k and I were constants.

This kinetic equation is indicative of a complex mechanism. The first term, however, is the expected rate law for the usually expected mechanism of absorption:

Mechanism: $H_{ads} \rightarrow H_{abs}$ (A)

Rate law: $\text{Rate of Absorption} = k[H_{ads}]$ (I)

Effect of Alloying on the Rate of Penetration of Hydrogen

In order to study the alloy systems, a generation current (1.6 ma) was selected that gave an intercept close to zero. It was assumed that since the rate law under these conditions was identical to the rate law in Eq. (I), the secondary effects were negligible and the primary mechanism of absorption was given in Eq. (A).

Table II. Composition of the iron-nickel alloys

Alloy #B	% Iron	% Nickel
1	78.0	22.0
2	73.0	27.0
3	66.0	34.0
4	51.0	49.0
5	30.0	70.0

The composition of the iron-nickel alloys prepared is shown in Table II. By using data similar to that in Fig. 5 and 6, one obtains Fig. 8 and 9, which show the rate of penetration for the various alloys. As before a straight-line relationship exists. Correcting the slopes of these lines by compensating for their varying lengths and radii, one can obtain the plot shown in Fig. 10, which shows the rate constant as a function of al-

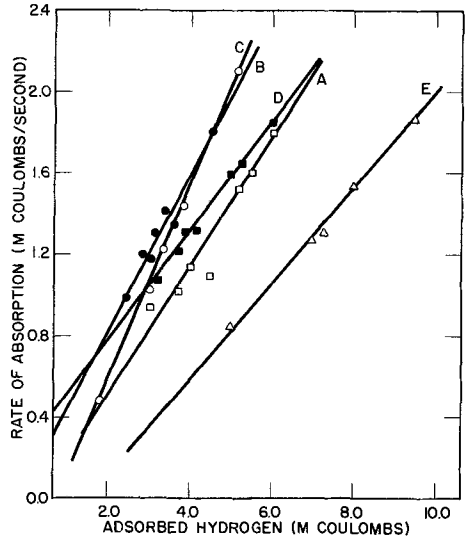

Fig. 8. Variation of rate of absorption with area under first maximum: disodium 2,7-naphthalenedisulfonate and charging current of 1.6 ma. Curve A, alloy No. 1; curve B, alloy No. 2; curve C, alloy No. 3; curve D, alloy No. 4; curve E, electrodeposited iron.

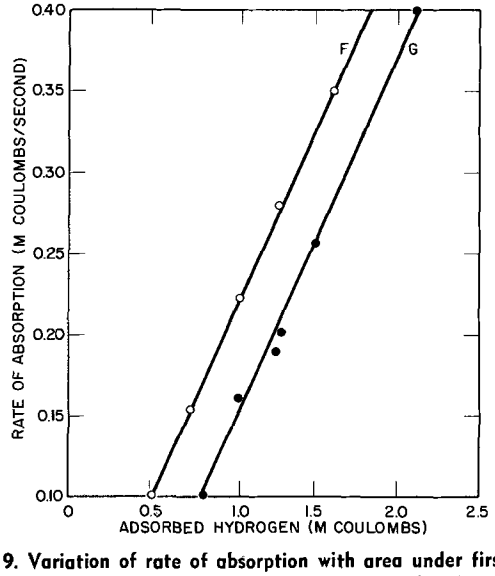

Fig. 9. Variation of rate of absorption with area under first maximum: disodium 2,7-naphthalenedisulfonate and charging current of 1.6 ma. Curve F, alloy No. 5; curve G, electrodeposited nickel.

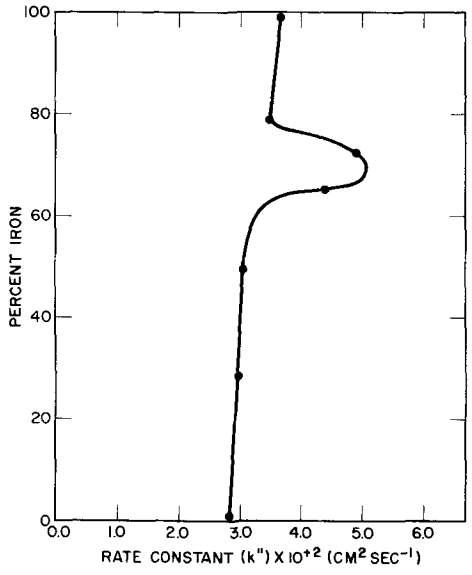

Fig. 10. Variation of rate constant with alloy composition

loy composition. There is a general decrease in the rate constant as the amount of iron in the alloy decreases except in the region between 65 to 75% iron. In this region, McKeehan (20) observed a change in crystal structure and noted a possible coexistence of the two structures and that either arrangement was on the verge on instability. It is of interest to note that on a plot of electrical resistance (of iron-nickel alloys) *vs.* percentage alloying element, there is a maximum in the curve at 30% nickel. This and several other anomalies in this region are ascribed to the fact that the iron-nickel alloys may be either ferrite, austenite, or both (21). An explanation for this increase in rate of penetration is that there are more grain boundaries in this region, and this presents an ease of penetration along these boundaries.

Summary

It has been shown that the experimental rate law for the absorption of hydrogen is

$$\text{Rate of absorption} = k[H_{ads}] + I$$

By controlling the current density it has been possible to obtain experimental conditions such that the rate law agreed with the following mechanism

$$H_{ads} \rightarrow H_{abs}$$

Studies of the effect of alloying iron with nickel show that the primary cause for changes in the rate of absorption of hydrogen is changes in the amount of adsorbed hydrogen.

Manuscript received Oct. 20, 1966; revised manuscript received March 13, 1967. This paper was presented at the Philadelphia Meeting, Oct. 9-14, 1966.

Any discussion of this paper will appear in a Discussion Section to be published in the December 1967 JOURNAL.

REFERENCES

1. T. C. Franklin and R. D. Sothern, *J. Phys. Chem.*, **58**, 951 (1954).
2. T. C. Franklin and S. L. Cooke, Jr., *This Journal*, **107**, 556 (1960).
3. T. C. Franklin and J. R. Goodwyn, *ibid.*, **109**, 288 (1962).
4. F. Matsuda and T. C. Franklin, *ibid.*, **112**, 767 (1965).
5. S. Schuldiner and T. P. Hoare, *Can. J. Chem.*, **37**, 228 (1959).
6. Z. Szklarska-Smialowska and M. Smialowski, *This Journal*, **110**, 444 (1963).
7. J. L. Weininger and M. Breiter, *ibid.*, **111**, 707 (1964).
8. M. A. V. Devanathan and M. Selvaratnam, *Trans. Faraday Soc.*, **56**, 1820 (1960).
9. C. N. Reilley, W. C. Cooke, and N. H. Furman, *Anal. Chem.*, **23**, 1031 (1951).
10. C. N. Reilley, W. C. Cooke, and N. H. Furman, *ibid.*, **24**, 1044 (1952).
11. C. C. Roth and H. Leidheiser, *This Journal*, **100**, 553 (1953).
12. W. D. Freitag, J. C. Mathias, and G. DiGuilio, *ibid.*, **111**, 35 (1964).
13. A. Eucken and B. Weblus, *Z. Elektrochem.*, **55**, 114 (1951).
14. M. Breiter, C. C. Knorr, and V. Volkl, *ibid.*, **59**, 681 (1955).
15. M. Breiter, H. Kammermaier, and C. A. Knorr, *ibid.*, **60**, 37 (1956).
16. M. Breiter, H. Kammermaier, and C. A. Knorr, *ibid.*, **60**, 119 (1956).
17. S. Schuldiner and R. M. Roe, *This Journal*, **110**, 332 (1963).
18. J. S. Ll. Leach and S. R. J. Saunders, **113**, 681 (1966).
19. T. C. Franklin, Unpublished work.
20. L. W. McKeehan, *Phys. Rev.*, **20**, 402 (1923).
21. J. W. Sands, "Metals Handbook," pp. 399-601, American Society for Metals, Novelty, Ohio (1948).

The Mechanism of the Electrooxidation of Acetylene on Gold

J. W. Johnson, J. L. Reed, and W. J. James

Departments of Chemical Engineering and Chemistry, The University of Missouri at Rolla, Missouri

ABSTRACT

Acetylene has been oxidized anodically in aqueous solutions at 80°C on gold electrodes. It was found that the partial oxidation to CO_2 was accompanied by a polymer formation. Effects of potential, acetylene partial pressure, *p*H, and temperature on the rate (current) were measured. A discontinuity in the Tafel curves was noted that indicated a change in the reaction mechanism with potential. The discontinuity was also *p*H dependent. A mechanism involving the discharge of H_2O and/or OH^- has been proposed that is consistent with the experimental results.

The electrooxidation of acetylene has been studied previously on platinized platinum electrodes (1). A reaction mechanism of the following sequence was proposed

$$C_2H_2\ (sol) \rightleftarrows C_2H_2\ (ads)$$
$$H_2O \rightleftarrows OH\ (ads) + H^+ + e$$
$$C_2H_2\ (ads) + OH\ (ads) \xrightarrow{\text{r.d.s.}} \ldots$$

The nature of the electrode is important in this mechanism as it is the source of oxygen-containing species (originating from water) for the oxidation reaction. The coverage of this species on platinum in the potential region where acetylene is oxidized is given by Dahms and Bockris as *ca.* 0.1. They also show the coverage on gold which is much smaller. This offers an indirect test of the mechanism in that it is an opportunity to observe the effect of decreasing the surface concentration of the oxygen containing species. In addition, the absence of electrons in gold for forming covalent bonds with adsorbed reactants and intermediates gives it important characteristics that deserve further study.

Experimental

Cell and apparatus.—The electrolytic cell was similar to that described previously (2, 3) unless otherwise stated. The working electrode (anode) was a rectangular piece of fine gold foil (0.005 in. thick) with a geometric area of 30.2 cm^2. The auxiliary electrode (cathode) was constructed of platinized platinum gauze. The procedure for activating the electrodes has been reported (2, 3). The reference electrodes were mercury-mercurous sulfate (1*N* H_2SO_4) for acid solutions and calomel (1*N* KCl) for basic solutions and were at 25°C during the experiments. All potentials of the gold anode are referred to the SHE as zero at the temperature of the experiment by means of the procedure described quantitatively below. All studies were made potentiostatically (except as noted) and at 80°C except for the activation energy determinations which ranged from 50° to 80°C.

Potential calculations.—The potentials listed in Table I were used in calculating the potentials of the gold anode. All, with the exception of those indicated with asterisks, were experimentally measured values. The measured potential differences between the gold anode and the reference electrodes were

$$\Delta V_{meas} = V - E_{ref,25}$$

In order that V might be referred to the SHE at the temperature of the experiment, the following relations were used

1. For the calomel (1*N* KCl) reference electrode

$$\begin{aligned} V &\equiv V - E_{H,t} \\ &= V - E_{C,25} - (E_{C,t} - E_{C,25}) + (E_{C,t} - E_{H,t}) \\ &= \Delta V_{meas} - (E_{C,t} - E_{C,25}) + (E_{C,t} - E_{H,t}) \end{aligned}$$

2. For the mercurous sulfate (1*N* H_2SO_4) reference electrode

$$\begin{aligned} V &\equiv V - E_{H,t} \\ &= V - E_{S,25} - (E_{S,t} - E_{S,25}) + (E_{S,t} - E_{C,t}) + (E_{C,t} - E_{H,t}) \\ &= \Delta V_{meas} - (E_{S,t} - E_{S,25}) + (E_{S,t} - E_{C,t}) + (E_{C,t} - E_{H,t}) \end{aligned}$$

Numerical values for terms shown in the parentheses were taken from Table I.

Reagents.—Sulfuric acid, sodium sulfate, sodium carbonate, and sodium hydroxide, "Fisher Certified" reagents; acetylene, Matheson purified (>99.6% purity); nitrogen, Matheson prepurified (>99.997% purity); and distilled water. Acetylene-nitrogen mixtures were made with the use of a dual-flow proportioner.

Coulombic efficiency.—The apparatus and procedure used to determine the coulombic efficiency in acidic solutions have been described previously (1). The cell was operated galvanostatically. In basic solutions, a gravimetric procedure was used in which the CO_2 absorbed in the 1*N* NaOH anolyte was precipitated as $BaCO_3$ by addition of barium acetate solution. The precipitate was collected, dried, weighed, and the CO_2 equivalent calculated. The exit gases from the cell were passed through a barium hydroxide absorber to insure that no CO_2 was escaping.

Table I. Data used for potential calculations

Electrodes	ΔE, v	Electrodes	ΔE, v
$E_{C,50} - E_{H,50}$	+0.2716*	$E_{C,50} - E_{C,25}$	+0.0125
$E_{C,60} - E_{H,60}$	+0.2672*	$E_{C,60} - E_{C,25}$	+0.0178
$E_{C,70} - E_{H,70}$	+0.2623*	$E_{C,70} - E_{C,25}$	+0.0230
$E_{C,80} - E_{H,80}$	+0.2567*	$E_{C,80} - E_{C,25}$	+0.0278
$E_{S,50} - E_{C,50}$	+0.362	$E_{S,50} - E_{S,25}$	+0.0063
$E_{S,60} - E_{C,60}$	+0.359	$E_{S,60} - E_{S,25}$	+0.0091
$E_{S,70} - E_{C,70}$	+0.357	$E_{S,70} - E_{S,25}$	+0.0117
$E_{S,80} - E_{C,80}$	+0.355	$E_{S,80} - E_{S,25}$	+0.0143

* Calculated from an expression given in Ives and Janz (9).
Subscripts. H, SHE; C, calomel (1*N* KCl) reference electrode; S, mercurous sulfate (1*N* H_2SO_4) reference electrode; numbers, t°C.

Results

Rest potentials.—Nitrogen was passed through the anodic and cathodic compartments for about 1 hr to remove oxygen from the cell. The flow through the anolyte was then replaced with acetylene or acetylene-nitrogen mixtures at a rate of 90 cm^3 (STP)/min. The values shown in Table II were obtained immediately on the admittance of acetylene and behaved similarly to those on platinum (1). The rest potentials varied very slightly in acidic solution, but the variation approached $\simeq$ —140 mv/pH unit in basic solutions. The rest potentials were independent of acetylene partial pressure.

Coulombic efficiency.—The results of the coulombic efficiency studies are shown in Table III.

After each test in acidic and neutral solutions, the anolyte was orange-brown in color, and the electrode had a thin, dark brown resinous film on it. The presence of the film had no noticeable effect on the current-potential relationships. At a constant potential, the current remained relatively constant (less than 10% change) for periods in excess of 24 hr, even though the film was forming. In 1*N* NaOH, the coloring of the electrolyte was present, but no film was formed on the electrode. Later experiments showed the film formed in the acidic electrolyte to be soluble in hot NaOH solutions, thus explaining its absence in the basic electrolyte.

By-product analysis.—Various tests and analyses were performed on the anolyte (both acidic and basic) and the resinous film from the acidic solutions in order to characterize the by-products.

1. The anolyte was extracted with ethyl ether, benzene, carbon tetrachloride, and n-hexane. Upon concentration of the extract, only the ether showed visible signs of any extracted material. An infrared spectrum of the extract indicated the presence of C=C and O—H bonds. A trace of the IR spectrum is shown in Fig. 1.

2. Negative results were obtained when the electrolyte was subjected to aldehyde and ketone tests,

Table II. Rest potentials for acetylene at 80°C

pH	V_{rest}, v (*vs.* SHE = 0 at 80°C)
0.35	+0.28
1.45	+0.28
6.0	+0.14
8.6	+0.03
11.6	−0.20
12.5	−0.34

Table III. Coulombic efficiency for CO_2 production for acetylene oxidation

Electrolyte	Acetylene pressure, atm	Efficiency, %
1*N* H_2SO_4	1.0	60 ± 5
	0.1	24
	0.01	3
1*N* NaOH	1.0	80 ± 10

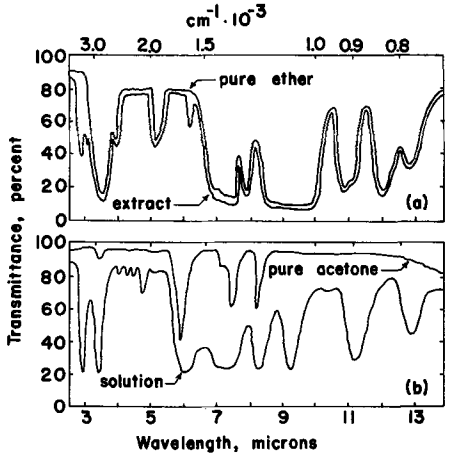

Fig. 1. Sketch of infrared spectra of (a) ether extract of acidic anolyte and (b) concentrated solution of resin dissolved in acetone.

indicating an absence of CHO and C=O groups in the by-products.

3. The resinous material was subjected to solvation tests in the solvents mentioned above plus acetone, methanol, 2*N* H_2SO_4, and 2*N* NaOH. Only in hot NaOH did the resin dissolve readily. Concentration of the acetone and methanol solvents showed visible signs of dissolved material. An infrared spectrum of the acetone solution confirmed the O—H bond and indicated a C—O bond, possibly a C—OH bond (see Fig. 1). An emulsion of the resin was also prepared with fluorlube, but IR analysis was unsuccessful.

4. A carbon-hydrogen-oxygen analysis[1] of the resinous film gave a C:H:O atomic ratio of approximately 2:2:1.

The most likely structures of the by-product that are consistent with the analyses are an unsaturated polyhydroxyl compound and a mixed hydroxyl structure with ether linkages. Any structure of the latter type with the proper C:H:O ratio contains an unconjugated enol form which has doubtful stability with respect to a keto shift. Thus, it seems that the most probable structure is of the type, —C(H)=C(OH)—C(H)=C(OH)—. A poly-hydroxyl structure of this type would be stable due to the conjugated bonding. It would also behave chemically similar to a phenol which accounts for its solubility in strong base.

Analysis of the exit gases from the electrolysis cell showed that no volatile, partially oxidized hydrocarbons were present. Hence, it was assumed that the only by-product was the polyhydroxyl compound at various degrees of polymerization.

Current-potential relation.—Tafel curves are shown in Fig. 2. The current values at a constant potential could be reproduced within 5%. There seems to be a transition region (discontinuity) in the plots for *p*H values of six and greater. This region is shifted upward along the Tafel curve as the *p*H is increased. The slope of the Tafel curve, both above and below the transition region, is approximately 140 mv. The increasing slope at the upper end of the curves is assumed to be due to either passivation phenomena or ohmic drop in the reference circuit. The time effects were essentially the same as those for the oxidation of acetylene on platinum (1). However, unlike platinum, no potential region of complete passivation was found for the gold electrode below oxygen evolution.

*p*H *effect.*—The effect of *p*H at constant ionic strength is also shown in Fig. 2. Qualitatively, in strong acids, $\partial \log i/\partial pH \simeq 0$. This value increased with *p*H, reaching unity in basic solutions.

[1] Analysis performed by Galbraith Laboratories, Knoxville, Tennessee.

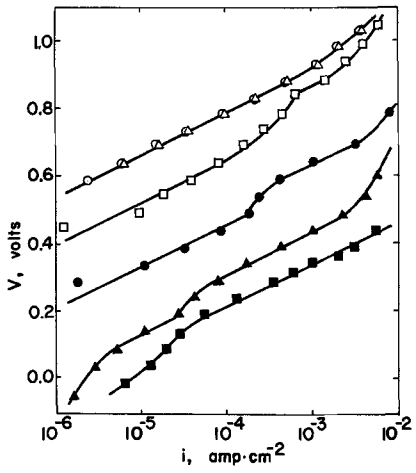

Fig. 2. Current-potential relation (P_A = 1 atm) as a function of *p*H at 80°C. (○, *p*H = 0.35; △, 1.45; □, 6.0; ●, 8.6; ▲, 11.6; ■, 12.5) (Potentials *vs.* SHE = 0 at 80°C).

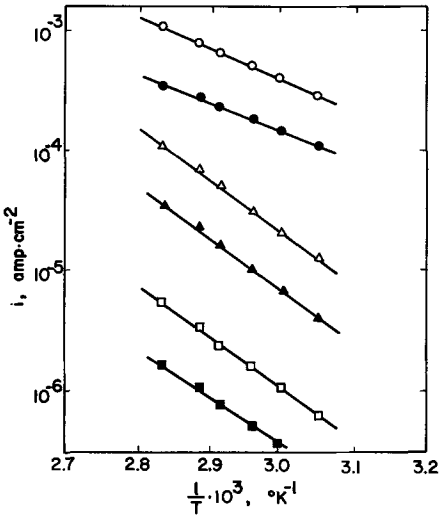

Fig. 3. Current-temperature relation (P_A = 1 atm) as a function of potential. (○, 0.368*v*, 1N NaOH; ●, 0.318*v*, 1N NaOH; △, 0.832*v*, 1N H_2SO_4; ▲, 0.732*v*, 1N H_2SO_4; □, 0.018*v*, 1N NaOH; ■, —0.032*v*, 1N NaOH; ○, ●, □, ■, below transition region; △, ▲, above transition region) (Potentials *vs.* SHE = 0 at temperature of experiment).

Temperature effect.—The effect of temperature on current in 1*N* H_2SO_4 and 1*N* NaOH (above and below the transition region) is shown in Fig. 3. Activation energies were calculated and are shown in Table IV.

Values of $\partial(E_a)/\partial V$ are approximately equal to αF = —11.5 kcal/v for α = 0.5. In 1*N* NaOH, it should be noted that the potential change does not account for the entire difference between activation energies above and below the transition region. This suggests that some change or alteration may have been made in

Table IV. Activation energies for the anodic oxidation of acetylene on gold electrodes

Electrolyte	Potential, v (*vs.*SHE = 0 at temperature of experiment)	Activation energy, kcal at SHE potential	$\partial(E_a)/\partial V$, kcal/v
1*N* H_2SO_4	0.732	19.9	—11.9
	0.832	18.8	
1*N* NaOH	0.368*	12.6	—12.0
	0.318*	13.2	
	0.018**	18.7	—12.0
	—0.032**	19.3	

* Above the transition region.
** Below the transition region.

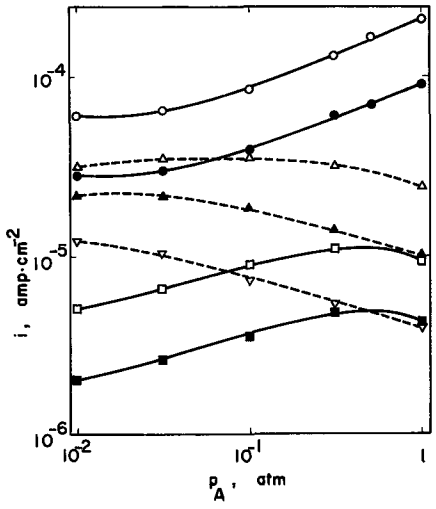

Fig. 4. Current-acetylene partial pressure relation as a function of potential at 80°C. (○, 0.268v, 1N NaOH; ●, 0.218v, 1N NaOH; □, 0.068v, 1N NaOH; ■, 0.018v, 1N NaOH; △, 0.732v, 1N H_2SO_4; ▲, 0.682v, 1N H_2SO_4; ▽, 0.632v, 1N H_2SO_4, △, ▲, ▽, □, ■, below transition region; ○, ●, above transition region.) (Potentials vs. SHE = 0 at 80°C).

the reaction mechanism. Due to mixed reactions, the reversible potential could not be evaluated in order to calculate the true (chemical) activation energy.

Pressure effect.—Partial pressure studies were made in 1*N* H_2SO_4 and 1*N* NaOH. The results are shown in Fig. 4. In 1*N* H_2SO_4, the pressure effect ($\partial i/\partial p$) was negative. In 1*N* NaOH below the transition region, the pressure effect started out negative, then became positive at pressures <0.1 atm. In 1*N* NaOH above the transition region, the effect was positive at pressures >0.1 atm and approached a constant value at pressures <0.1 atm. Under the latter conditions (1*N* NaOH, above transition region), appreciable residual currents were noted when the acetylene flow was stopped after several minutes of electrolysis. Other measurements made in fresh electrolyte showed the pressure effect to be positive over the entire range, 0.01 to 1 atm. However, due both to the residual currents and the smallness of the values, it was felt that only measurements above 0.1 atm were of sufficient accuracy to be considered valid for pressure-current correlations.

Discussion

Adsorption of Acetylene

The adsorption of acetylene on Pt has been discussed in the previously mentioned paper (1). The isotherm (Langmuir) was formulated as

$$\frac{\theta_A}{(1-\theta_A)^4} = K_p P_A$$

where θ_A is the fractional coverage by acetylene, p_A is the acetylene partial pressure, and K_p is the adsorption constant for the isotherm relating coverage to partial pressure. The order of magnitude of K_p, estimated both by an indirect method and correlation of experimental data, was 10^4-10^6 atm^{-1}. No data are available which would allow an independent evaluation of K_p for acetylene adsorption on Au from solution.

The most probable attachment of acetylene to a metal surface is (4)

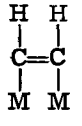

There is evidence that acetylene forms covalent bonds with the metal surface in the case of Pt and Au by rearrangement to dsp hybrids (4, 5). Platinum has 0.5 vacant d-orbitals per atom available for covalent bonding, thus acetylene was assumed to have a 4 site attachment (1). Gold has no statistically calculated d-orbitals available for covalent bonding (6), therefore the number of sites occupied (covered) will be ascertained from a scaled diagram of an acetylene molecule adsorbed on a gold surface (Fig. 5). The acetylene covers only two sites, but possibly blocks two others due to its size. Therefore, the isotherm for the adsorption of acetylene on Au is taken as

$$\frac{\theta_A}{(1-\theta_A)^n} = K_p P_A \qquad [1]$$

where n can be equal to 2 or more.

Reaction Mechanism

The rate-determining step below the transition region must exhibit the following characteristics: (*i*) Be the first electron transfer since the Tafel slope is $2(2.3\ RT/F)$, (*ii*) involve a species other than adsorbed acetylene, (or derived therefrom) since $\partial i/\partial p < 0$, and (*iii*) exhibit essentially no *p*H dependence in strong acid solutions but show a dependency, ∂ log $i/\partial p$H $\simeq 1$ in strong base solutions.

Above the transition region, the rate-determining step must: (*i*) again be the first electron transfer since the Tafel slope remains $2(2.3\ RT/F)$, (*ii*) involve adsorbed acetylene (or a species derived therefrom) since $\partial i/\partial p > 0$, and (iii) exhibit a *p*H dependence ∂ log i/∂ *p*H $\simeq 1$ in going from weak acid to strong base solutions.

There is apparently competition (branching reactions) between intermediates species in regard to the formation of the resin material and total oxidation products, CO_2 and H^+ (or H_2O). As the faradaic efficiency was not greatly affected by potential or *p*H, this competition probably occurs after the r.d.s. in the different regions. The effect of acetylene partial pressure on the efficiency will be discussed later.

Below the transition region (b.t.r.), the substances involved in the r.d.s. must be OH^- or H_2O. This is as proposed previously as a source of OH radicals involved in the oxidation of acetylene and ethylene on Pt (1-3). Currents depending on the discharge of OH^- would be diffusion limited up to *p*H's of 6 to 8 at the current densities used in this study. Thus, the reaction sequence can be represented as

$$C_2H_2 \rightleftarrows C_2H_2\ (ads) \qquad [2]$$

$$\left.\begin{aligned} H_2O &\rightarrow OH\ (ads) + H^+ + e \\ OH^- &\rightarrow OH\ (ads) + e \end{aligned}\right\}\ \text{r.d.s.} \qquad [3a],\ [3b]$$

$$C_2H_2\ (ads) + OH\ (ads) \rightarrow \ldots$$

$$\rightarrow CO_2 + H^+ + \text{electrons} + \text{resin} \qquad [4]$$

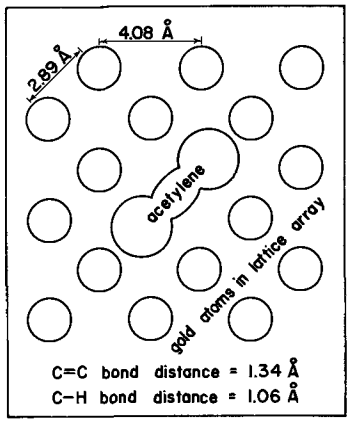

Fig. 5. Schematic diagram of an acetylene molecule adsorbed on a gold surface.

The anodic oxidation of acetylene can be expressed as

$$i_{b.t.r.} = n\mathbf{F}(k_{3a}a_{H_2O} + k_{3b}a_{OH^-})(i - \theta_T)\exp(\alpha\mathbf{F}V/RT) \quad [5]$$

where k_{3a} is the rate constant for water discharge and k_{3b} is the rate constant for OH^- discharge. The coverage of OH radicals is very low (6), and the coverage of all other intermediates can be neglected in comparison with θ_A since they occur in the reaction sequence after the r.d.s. Thus, $\theta_T \simeq \theta_A$, and

$$i_{b.t.r.} = n\mathbf{F}(k_{3a}a_{H_2O} + k_{3b}a_{OH^-})(1 - \theta_A)\exp(\alpha\mathbf{F}V/RT) \quad [6]$$

Above the transition region (a.t.r.), the r.d.s. involves either adsorbed acetylene or a radical derived therefrom. The dissociative adsorption of acetylene can be disregarded due to previous considerations of the energy involved (1) and to the pH effect observed in this study. The studies on Pt (1) also indicated there was no hydrolysis of acetylene in solution. A reaction sequence that meets all the requirements is

$$C_2H_2 \rightleftarrows C_2H_2\ (ads) \quad [7]$$

$$C_2H_2(ads) + H_2O \rightarrow C_2H_2OH(ads) + H^+ + e \quad [8a]$$

$$C_2H_2(ads) + OH^- \rightarrow C_2H_2OH(ads) + e \quad [8b]$$

(r.d.s.)

This gives the anodic oxidation rate as

$$i_{a.t.r.} = n\mathbf{F}(k_{8a}a_{H_2O} + k_{3b}a_{OH^-})\theta_A\exp(\alpha\mathbf{F}V/RT) \quad [9]$$

pH dependence.—Current-pH values were calculated from Eq. [6], representing rates below the transition region, considering the term $[n\mathbf{F}(1 - \theta_A)\exp(\alpha\mathbf{F}V/RT)]$ constant at a given potential over the entire pH range. The contribution of $k_{3a}a_{H_2O}$ was calculated from an experimental value of the current in 1*N* H_2SO_4. Here the contribution from OH^- discharge would be negligible due to its low concentration. The contribution of $k_{3b}a_{OH^-}$ was calculated in 1*N* NaOH assuming $k_{3a}a_{H_2O}$ to be insignificant. Experimentally this is justified as the $\partial \log i/\partial$ pH $\simeq 1$ in strong base. It was necessary to make a correction for the electrolyte pH at the electrode-solution interface due to the diffusion, away from the electrode, of H^+ produced by the reaction. This correction was significant only for bulk electrolyte pH's in the range 5 to 9. Using these constants, the pH dependence from Eq. [6] over the entire pH range is shown in Fig. 6. The experimental data are also included for comparison. Above the transition region, where Eq. [9] applies, it was not possible to consider the contribution of $k_{8a}a_{H_2O}$ as experimental data were available only for pH's > 6. Evaluating $k_{8a}a_{OH^-}$ in a similar manner as described above gives the pH-current relationship also shown in Fig. 6. It can be seen that Eq. [6] and [9] correlate these experimental data in their respective regions.

Partial pressure dependence.—Qualitatively, the rate dependence on acetylene partial pressure can be summarized as follows. (*A*) acid solution (below transition region), $\partial i/\partial p < 0$, Eq. [6] applies. (*B*) Base solutions (above transition region), $\partial i/\partial p > 0$, Eq. [9] applies. (*C*) Base solution (below transition region), for $p > 0.5$ atm, $\partial i/\partial p < 0$, and for $p < 0.5$ atm, $\partial i/\partial p > 0$, *i.e.*, Eq. [6] applies at higher pressures while Eq. [9] applies at the lower ones.

The data from acid solutions (b.t.r.) were correlated using Eq. [6] for which the acetylene coverage was calculated from Eq. [1] with assumed values of n and K_p as 4 and 10^4, respectively. The procedure for these calculations has been described (1). The predicted values as well as experimental data are shown in Fig. 7.

A similar treatment of data from base solution (a.t.r.) using Eq. [1] and [9] is also shown in Fig. 7. Here, values of n and K_p were 8 and 2.5, respectively. It should also be pointed out that $n = 4$ and $K_p = 3.5$ correlated the data within experimental errors, although not as well as the first-mentioned values. These pressure effects can be related to a reaction mechanism if it is assumed that the amount of acetylene adsorbed onto gold decreases as the pH of the solution increases, and H_2O (or OH^-) will undergo discharge only when adsorbed adjacent to an adsorbed acetylene molecule. The first assumption is consistent with trends noted for the adsorption of some other organic compounds from solution (7). Since the oxide (hydroxide) coverage on gold is very low at these potentials in the absence of adsorbed acetylene (6), then H_2O (or OH^-) discharge does not occur readily. Thus, the second assumption could be considered feasible. With these assumptions, the coverages of acetylene on gold can be pictured as shown in Fig. 8a and 8b. In the first case (Fig. 8a) for high coverage, it can be seen that most any adsorption site available for H_2O (or OH^-) will be adjacent to an adsorbed acetylene molecule; thus H_2O (or OH^-) will be discharged and the rate will be proportional to $(1 - \theta_A)$. If due to geometric considerations, four adjacent vacant sites were necessary

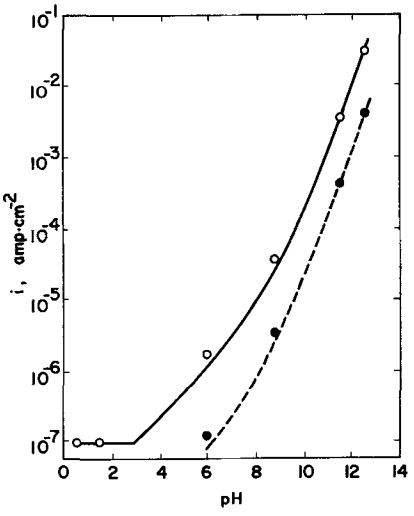

Fig. 6. Theoretical current pH relation at constant potential = 0.40v. (—, Eq. [6]; ○, experimental data below transition region; - -, Eq. [9]; ●, experimental data above transition region).

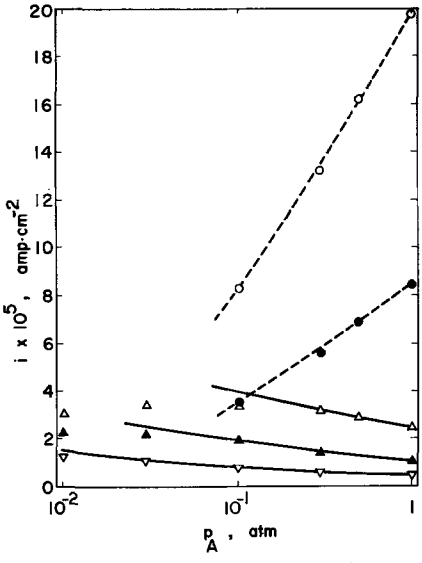

Fig. 7. Theoretical current-acetylene partial pressure relation as a function of potential at 80°C. (○, 0.268v, 1N NaOH; ●, 0.218v, 1N NaOH; - -, Eq. [9], data above transition region; △, 0.732v, 1N H_2SO_4; ▲, 0.682v, 1N H_2SO_4; ▽, 0.632v, 1N H_2SO_4; —, Eq. [6], data below transition region) (Potentials vs. SHE = 0 at 80°C).

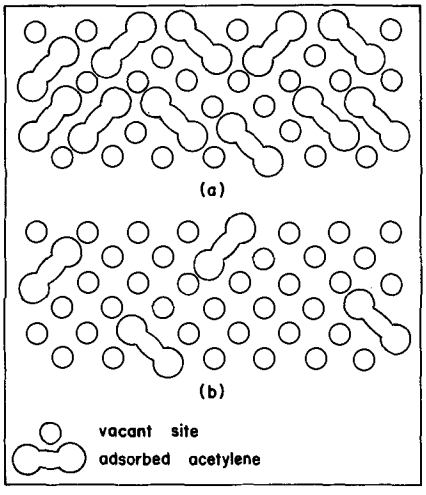

Fig. 8. Schematic diagram of acetylene molecules adsorbed on a gold surface at (a) high and (b) low coverage.

for the acetylene to adsorb, then this model would be consistent with the values of $n = 4$ and $K_p = 10^4$. In the second case (Fig. 8b) for low coverage, there are considerable available sites for water (or OH^-) to adsorb that are not adjacent to adsorbed acetylene molecules. Discharge does not occur on these sites, therefore, the rate is proportional to θ_A rather than $(1 - \theta_A)$. This case is consistent with the lower value of K_p (equal to 2.5). The higher value of n can also be rationalized to some extent if one considers that, for reaction to take place, acetylene must adsorb on a spot that has more than four adjacent vacant sites so that the discharge of water can be accommodated.

Acetylene coverages have been calculated for Eq. [6] and [9] and are shown in Table V. These coverages are also such that Langmuir-type adsorption is approximated.

In base solutions (b.t.r.) where the pressure dependence changes from negative to positive, *i.e.*, the expression for the current changes from Eq. [6] to Eq. [9], there would necessarily have to be a higher acetylene coverage than in base solutions above the transition region. This would suggest the acetylene coverage may have some potential as well as pH dependence.

Reaction products.—The most probable explanation for the incomplete oxidation of acetylene on a gold electrode is similar to that suggested by Dahms and Bockris pertaining to the anodic oxidation of ethylene on various rare metals (6). Using Pauling's equation (8) for the strength of a covalent bond between a metal and a carbon atom, it can be shown that the Au-C bond is about 45 kcal less than the Pt-C bond. Thus, a partially oxidized intermediate could break away from an Au surface before being completely oxidized much easier than from a Pt surface. Due to the reactiveness of the partially oxidized compounds (possibly radicals) and acetylene, polymerization products would be expected.

Summary

The anodic oxidation of acetylene has been studied at 80°C in solutions of H_2SO_4, Na_2SO_4, and NaOH of constant ionic strength. The reaction rate was determined as a function of potential, pH, acetylene partial pressure, and temperature. Coulombic efficiencies were determined for CO_2 production in both acidic and basic solutions. Two regions of linear Tafel behavior separated by a transition region were found.

The following kinetic parameters were noted:

Below the transition region

$$\frac{\partial V}{\partial \log i} = 140 \text{ mv}, \frac{\partial i}{\partial p} < 0$$

$$\frac{\partial \log i}{\partial \text{ pH}} = 1 \text{ (weakly acidic and basic solutions)}$$

Above the transition region

$$\frac{\partial V}{\partial \log i} = 140 \text{ mv}, \frac{\partial i}{\partial p} > 0$$

$$\frac{\partial \log i}{\partial \text{ pH}} = 0 \text{ (moderate to strong acid solutions)}$$

$$\frac{\partial \log i}{\partial \text{ pH}} = 1 \text{ (weakly acidic and basic solutions)}$$

The acetylene was partially oxidized to CO_2 with some polymer formation. The coulombic efficiency for CO_2 production was 60 ± 5% in acidic and 80 ± 10% in basic solutions and decreased with decreasing acetylene partial pressure. The most probable structure of the polymer was $-\overset{H}{\underset{|}{C}}=\overset{OH}{\underset{|}{C}}-\overset{H}{\underset{|}{C}}=\overset{OH}{\underset{|}{C}}-$. Activation energies in the linear Tafel regions varied from 12-20 kcal. The potential dependence of the activation energy, $\partial E_a/\partial V$, was −12 kcal/v.

The reaction mechanisms in the linear Tafel regions were interpreted in terms of the following sequences.

Below the transition region

$$C_2H_2 \rightleftarrows C_2H_2 \text{ (ads)}$$

$$\left.\begin{aligned} &H_2O \rightarrow OH \text{ (ads)} + H^+ + e \\ &OH^- \rightarrow OH \text{ (ads)} + e \end{aligned}\right\} \text{r.d.s.}$$

$$C_2H_2 \text{ (ads)} + OH \text{ (ads)} \rightarrow \ldots$$

Above the transition region

$$C_2H_2 \rightleftarrows C_2H_2 \text{ (ads)}$$

$$\left.\begin{aligned} &C_2H_2 \text{ (ads)} + H_2O \rightarrow C_2H_2OH \text{ (ads)} + H^+ + e \\ &C_2H_2 \text{ (ads)} + OH^- \rightarrow C_2H_2OH \text{ (ads)} + e \end{aligned}\right\} \text{r.d.s.}$$

The discharge of H_2O and/or OH^- was necessary to explain the observed pH effect.

Table V. Calculated pressure-coverage relationships for the adsorption of acetylene on gold electrodes at 80°C

Eq. [6] ($K_p = 10^4, n = 4$) P_A (atm)	θ_A	Eq. [9] ($K_p = 2.5, n = 8$) P_A (atm)	θ_A
1.0	0.90	1.0	0.25
0.3	0.87	0.5	0.20
0.1	0.83	0.3	0.17
0.03	0.78	0.2	0.14
0.01	0.72	0.1	0.10

Acknowledgments

The authors wish to thank the National Aeronautics and Space Administration for a traineeship which one of the authors (J.L.R.) held during the course of this investigation. Thanks are also due to Dr. S. B. Hanna of the Chemistry Department for helpful discussions. This paper is based on a dissertation presented by one of the authors (J.R.L.) in partial fulfillment of the degree, Doctor of Philosophy, at the University of Missouri at Rolla.

Manuscript received Aug. 12, 1966; revised manuscript received March 3, 1967. This is paper No. 16 from the Graduate Center for Materials Research of the Space Sciences Research Center at Rolla.

Any discussion of this paper will appear in a Discussion Section to be published in the December 1967 JOURNAL.

REFERENCES

1. J. W. Johnson, H. Wroblowa, and J. O'M. Bockris, *This Journal*, **111**, 863 (1964).
2. M. Green, J. Weber, and V. Drazic, *ibid.*, **111**, 721 (1964).
3. B. Piersma, H. Wroblowa, and J. O'M. Bockris, *J. Electroanalyt. Chem.*, **6**, 401 (1963).
4. B. M. V. Trapnell, "Chemisorption," Butterworths, London (1955).
5. G. C. Bond, "Catalysis by Metals," Academic Press, London, New York (1962).
6. H. Dahms and J. O'M. Bockris, *This Journal*, **111**, 728 (1964).
7. J. O'M. Bockris, D. Swinkels, and M. Green, *Rev. Sci. Instr.*, **33**, 18 (1962).
8. L. Pauling, "The Nature of the Chemical Bond," Cornell University Press, Ithaca, N. Y. (1960).
9. D. J. G. Ives and G. J. Janz, "Reference Electrodes," Academic Press, London, New York (1961).

The Thermal Temperature Coefficient of the Calomel Electrode Potential between 0° and 70°C

I. Experimental Results in Aqueous Potassium, Sodium, Lithium, Calcium Chlorides and in Hydrochloric Acid

Andre J. de Bethune, Henry O. Daley, Jr., Nancy A. Swendeman Loud, and G. Robert Salvi

Laboratory of Physical and Nuclear Chemistry, Boston College, Chestnut Hill, Massachusetts

ABSTRACT

The initial thermal temperature coefficient of the calomel electrode potential has been measured between 0° and 70°C for aqueous 1.0, 0.1, and 0.01*m* potassium chloride, sodium chloride, lithium chloride, hydrochloric acid and 0.5, 0.05, and 0.01*m* calcium chloride. Thermal diffusion of the electrolyte was impeded by the use of Vycor intermediate (thirsty glass) glass plugs in the salt bridges between the two banks of electrodes, one of which was kept at 35° while the other was varied from 0° to 70°. The thermal emfs of the fifteen cells investigated exhibited a slight curvature concave to the temperature axis. The hot electrode had the (+) polarity (cathodic in a battery sense) in all cases. Experimental data can be fairly represented by quadratic equations, and least squares values of the quadratic constants are given. The initial thermal temperature coefficients are compared with prior thermal emf data on the calomel electrode. The relative thermal emfs of the same electrode in different salts at constant chloride ion concentration are compared with values deduced from prior thermal emf observations on calomel and silver chloride electrodes or calculated from the transport entropies of chlorides obtained in thermal diffusion studies.

The thermal temperature coefficient $(dV/dT)_{th}$ of the potential of an electrode is the temperature derivative of dE/dT_2 of the initial emf (*i.e.*, before thermal diffusion sets in) $E = V'' - V'$ of the thermal cell

$$\mathrm{Cu}(T_1,V')/\mathrm{Electrode}(T_1)/\mathrm{Electrolyte}(T_1)/\mathrm{Electrolyte}(T_2)/\mathrm{Electrode}(T_2)/\mathrm{Cu}(T_2)/\mathrm{Cu}(T_1,V'') \quad [1]$$

in which the temperature T_1 is fixed and T_2 varies. The thermal temperature coefficient is given a positive value when the hot electrode is the (+) or cathodic terminal of the thermal cell, as is the case experimentally with all calomel electrodes studied.

The thermal temperature coefficient of the calomel electrode potential was originally studied by Gockel (1) and later in more detail by Richards (2). Subsequent investigations were conducted by Fales and Mudge (3), Ewing (4), Sorensen and Linderstrom-Lang (5), Kolthoff and Tekelenburg (6), Bjerrum and Unmack (7), Burian (8), Young (9), Wingfield and Acree (10), Cary and Baxter (11), and Ikeda and Kimura (12) (who investigated only differences between temperature coefficients in various aqueous chlorides). In most thermal emf studies, the temperature differential has been kept between 5° and 10°C, and the thermal temperature coefficient assumed to be valid at the median temperature, which was usually between 15° and 25°C.

Thermal emf data (13, 14) can be used to determine relative values of the entropies of diffusion transport S^D (Soret transport entropies), and of the conjugate heats of transfer Q^*, of electrolytes. They can also throw light on the several ionic transport entropies, *viz.*, the ionic entropy of electrochemical transport S^{E}_i (the so-called "absolute" partial molal entropy of an ion), and the ionic entropy of migration transport S^{M}_i [the entropy of transfer, Eastman's entropy, in Agar's (15) terminology], with its conjugate ionic heat of transfer Q^*_i, as well as the sum of the two ionic transport entropies $\bar{\bar{S}}$ $(= S^{E}_i + S^{M}_i)$ introduced by Temkin and Khoroshin (16) as the entropy of the moving ion, and referred to by Agar (15) as the transported entropy of the ion. Because of the intrinsic interest of thermal emfs as an experimental source of information for these transport entropies of electrolytes and ions, the thermal temperature coefficient of the calomel electrode was reexamined in the present investigation by measuring the thermal emf between banks of half-cells at 35°C, and at a variable temperature t ranging from 0° to 70°C, for three levels of concentration of five different aqueous chloride electrolytes.

Experimental

The thermal emf of the calomel electrode was determined for the following electrolytes: potassium chloride, sodium chloride, lithium chloride, and hydrochloric acid at 25°C concentrations of 1.0, 0.10, and 0.01 moles per liter, and calcium chloride at 25°C concentrations of 0.50, 0.05, and 0.01 moles per liter. The salts and acid used were of reagent grade. The sodium, potassium, and lithium salts were dried at 110°C and the solutions prepared by dilution of the weighed dried salt in a volumetric flask. Hydrochloric acid solutions were prepared directly by dilution of stock concen-

Table I. Parabolic least-squares constants for the thermal emf of the calomel electrode between 0° and 70°C
A's in mv/deg, *B* in mv/deg^2

Salt	Concentration, 25°C, moles/liter	Molality, moles/kg H_2O	A_{35}	A_{25}	B
KCl	0.0100	0.0100_3	0.8913_{93}	0.9212_{83}	-0.00149_2
KCl	0.1000	0.1005_7	0.7577_{80}	0.7764_{40}	-0.00093_3
KCl	1.000	1.032_7	0.5661_{38}	0.5814_{38}	-0.00076_5
NaCl	0.0100	0.0100_3	0.8917_{02}	0.9159_{82}	-0.00121_1
NaCl	0.1000	0.1004_6	0.7505_{29}	0.7672_{69}	-0.00083_7
NaCl	1.00	1.021_8	0.5392_{40}	0.5490_{40}	-0.00049_6
LiCl	0.0100	0.0100_3	0.9854_{93}	1.0236_{93}	-0.00191_0
LiCl	0.100	0.1004_5	0.8038_{31}	0.8154_{71}	-0.00058_2
LiCl	1.00	1.021_6	0.6339_{30}	0.6392_{16}	-0.00026_4
$CaCl_2$	0.0102	0.0103_0	0.8857_{04}	0.9233_{64}	-0.00188_3
$CaCl_2$	0.0493	0.0494_9	0.7588_{31}	0.7752_{11}	-0.00081_9
$CaCl_2$	0.4999	0.5071	0.5440_{09}	0.5461_{49}	-0.00010_4
HCl	0.00970	0.0097_3	0.6409_{39}	0.6782_{39}	-0.00186_5
HCl	0.1004	0.1009	0.4346_{45}	0.4646_{05}	-0.00149_8
HCl	0.9927	1.014_8	0.2765_{25}	0.2942_{25}	-0.00088_5

trated acid, and checked by titration with standard base. Calcium chloride dihydrate was weighed directly from the stock bottle, the resulting solution checked by titration with standard silver nitrate. The concentrations of the solutions used in the preparation of the calomel electrodes are listed in Table I. For each solution, the molality was computed from the 25°C molarity via International Critical Tables densities (17) since it is temperature invariant.

The apparatus consisted of 8-in. 25-mm diameter test tubes which were made into calomel half-cells with platinum in soft-glass connectors. The salt bridges were made of ¼ in. Tygon tubing with Vycor intermediate (thirsty glass) plugs (18) in each end to prevent thermal diffusion of the electrolyte. In most determinations five half-cells were connected together through a common graduated cylinder and thermostated at a given temperature until they agreed within ±0.2 mv. An identical arrangement was made in the other temperature bath. A single salt bridge provided the electrolytic connection between the graduated cylinder in the fixed temperature bath and that in the variable temperature bath.

Emf values were obtained by thermostating one bath at 35.0° ± 0.1°C and by heating the variable bath to 75° and letting it cool slowly to 35°, or alternatively by cooling the variable bath to 0° and allowing the bath to warm up slowly to 35°C. The emf of the cell was measured at intervals of one to two degrees as the variable temperature bath slowly drifted in temperature. A check for hysteresis was made by also taking emf values as the variable temperature bath was slowly heated to 75° from 35° or slowly cooled to 0° from 35°, and also by taking steady-state readings with the variable bath held at a constant temperature. No hysteresis was found in excess of the experimental scatter which generally amounted to about ±0.1 to 0.5 mv in emfs that ranged up to 33 mv between the hot and cold electrodes at the extrema of temperatures. The polarity of the calomel thermal cells was observed to be (+), *i.e.*, cathodic in a battery sense, at the hot electrode in every single instance studied.

The bias between the two banks of half-cells was measured at the beginning and at the end of each "hot" and "cold" run, by the following technique: in a "hot" run, the thermal emfs observed in the heating and cooling portions of the run between 35° and 42°-45°C were plotted on an expanded scale and extrapolated linearly to 35°, since the data are linear in this range. In a "cold" run, the same was done between 35° and 28°-25°C. The observed emfs at higher or lower temperatures were then corrected for the 35° bias obtained in this manner, so that the thermal potential of a bank of calomel electrodes was, in each instance, referred to the potential of the same bank of electrodes at 35°C.

Table II. Standard deviations of mean observations from least-squares quadratic emf at four preselected temperatures

(millivolts)

Electrolyte	5°	20°	50°	65°
0.01*m* KCl	0.42	0.20	0.23	0.23
0.1*m* KCl	0.19	0.13	0.05	0.15
1.0*m* KCl	0.10	0.06	0.07	0.10
0.01*m* NaCl	0.19	0.41	0.20	0.23
0.1*m* NaCl	0.13	0.08	0.08	0.15
1.0*m* NaCl	0.11	0.06	0.06	0.08
0.01*m* LiCl	0.59	0.33	0.83	0.60
0.1*m* LiCl	0.23	0.13	0.14	0.25
1.0*m* LiCl	0.13	0.24	0.16	0.15
0.01*m* $CaCl_2$	0.30	0.06	0.22	0.36
0.05*m* $CaCl_2$	0.29	0.05	0.08	0.46
0.5*m* $CaCl_2$	0.23	0.10	0.16	0.03
0.01*m* HCl	0.33	0.14	0.10	0.14
0.1*m* HCl	0.05	0.13	0.14	0.17
1.0*m* HCl	0.22	0.11	0.05	0.08

Results

For each of the fifteen calomel half-cell systems studied experimentally (Table I), several hundred thermal emf values were recorded between 0° and 70°-75°C. Plots of these thermal emf values *vs.* temperature were not quite linear. In each instance, there was a slight curvature concave to the temperature axis. This corresponds to a negative value of the second thermal temperature coefficient $(d^2V/dT^2)_{th.}$ The experimental data have been fitted by computer to the parabolic equation

$$V_t - V_{35} = A_{35}(t-35) + B(t-35)^2 \qquad [2]$$

The least-squares values of the constants A_{35} and B, in millivolts, are given in Table I and are valid over the temperature range investigated 0°-70°C. The deviations of the several parallel runs generally amounted to a few tenths of a millivolt from the least-squares quadratic curve. The standard deviations of the mean observed values are given, at the selected temperatures of 5°, 20°, 50°, and 65°C, in Table II. Cubic equations were also computed by the method of least-squares. Since the cubical constants amounted to only a few thousandths of a microvolt, positive or negative, in each case, it was decided to retain the simpler quadratic form as a more convenient and adequately precise vehicle for the summarizing of the several thousand thermal emf points observed in this study.

The original least-squares quadratic equation [2] was converted to the equivalent 25°C quadratic equation

$$V_t - V_{25} = A_{25}(t-25) + B(t-25)^2 \qquad [3]$$

by noting that the 25°-value of the A constant is equal to the first-derivative of [2] at 25°, *i.e.*

$$A_{25} = [d(V_t - V_{35})/dt]_{25} = A_{35} - 20\,B \qquad [4]$$

Values of A_{25} are also given in Table II and give directly, in millivolts per degree, the thermal temperature coefficient of the corresponding calomel electrode at 25°C.

Discussion

In Fig. 1 to 5, the initial thermal temperature coefficients of the fifteen calomel electrode systems investigated in this study have been plotted, *vs.* temperature in the range 0°-70°C, as the straight lines computed from the first derivatives of the quadratic thermal emf equations [2] or [3]. The experimental scatter corresponding to the standard deviations of Table II is indicated by the vertical lines. The points plotted give the thermal temperature coefficients as determined in the work of previous observers beginning with Richards (2). Generally the agreement between the straight lines deduced from our experimental thermal emfs and the independent experimental data is good. Particularly noteworthy is Richards' fragmentary data on the 0.5*m* KCl-calomel

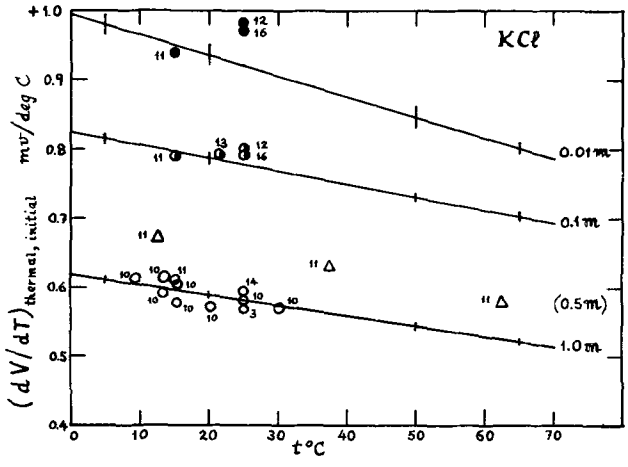

Fig. 1. Potassium chloride

Fig. 1-5. Initial thermal temperature coefficient of calomel electrodes from 0° to 70°C in KCl, NaCl, LiCl, $CaCl_2$, HCl. The lines give the first derivatives of the least squares quadratic thermal emfs as observed in this study. Comparative prior experimental data as follows: • 0.01M chloride ion; ◑ 0.1M chloride ion; △ 0.5M chloride ion. ○ 1.0M chloride ion. References for the prior experimental data. 1. Agar (15); 2. Bernhardt and Crockford (21); 3. Burian (8); 4. Butler and Turner (26); 5. Chanu (24); 6. Crockford and Hall (22); 7. Goodrich (20); Goyan (19); 8. Haase and Schönert (23); 9. Ikeda and Kimura (12); 10. Kolthoff and Tekelenburg (6); 11. Richards (2); 12. Salvi (27); 13. Sorensen and Linderstrom-Lang (5); 14. Swendeman (28); 15. Tanner (25); 16. Young (9).

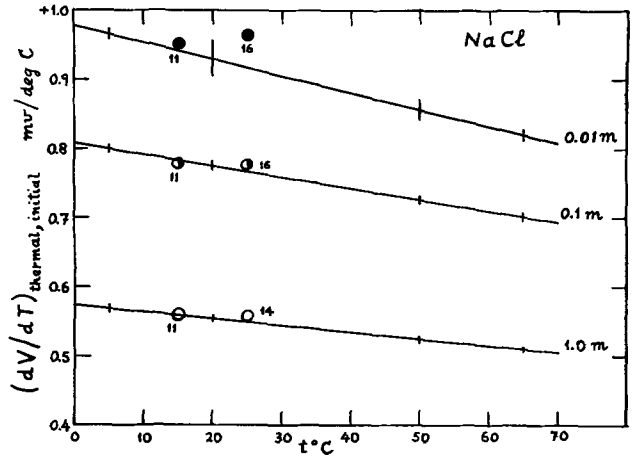

Fig. 2. Sodium chloride

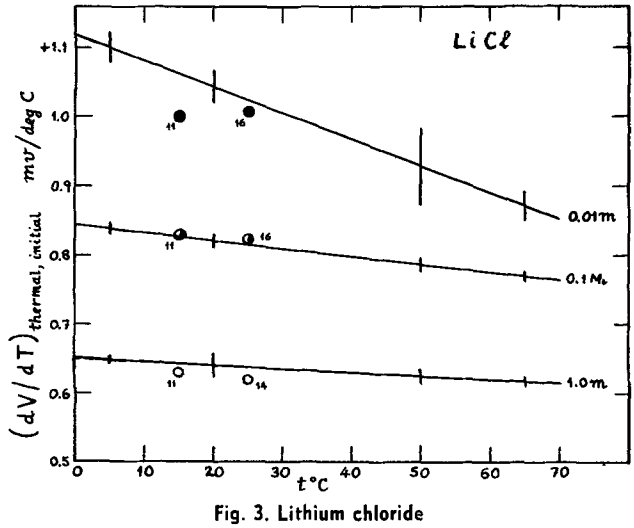

Fig. 3. Lithium chloride

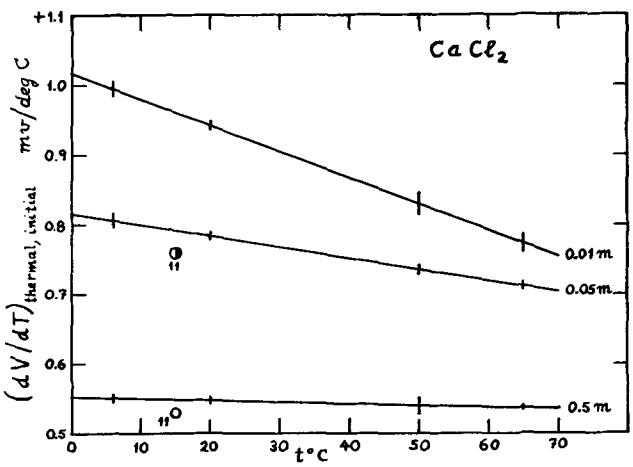

Fig. 4. Calcium chloride

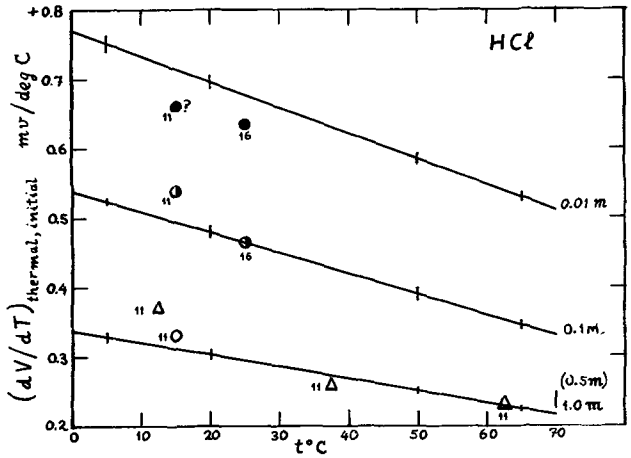

Fig. 5. Hydrochloric acid

electrode (triangles in Fig. 1) which are found to lie at the correct logarithmic spacing between our 0.1m and 1.0m KCl lines.

The comparison of the rather sparse prior data on calomel thermal temperature coefficients with our own observations shows excellent agreement for potassium, sodium, and calcium chlorides, for the 0.1m and 1.0m lithium chloride, and for the 0.1m hydrochloric acid. For the 0.01m lithium chloride (Fig. 3) and 0.01m hydrochloric acid (Fig. 5), our own temperature coefficient is a bit higher than the prior data.

Another comparison of the present data with prior experimental work is provided from the relative thermal emf of the same electrode in different chloride salts, *i.e.*, from the differences between the initial thermal temperature coefficients observed in two different electrolytes of the same chloride ion concentration. If the assumption is made, to a first approximation at least, that the electrode temperature effect is the same in both electrolytes at the same chloride ion concentration, the difference between the two initial thermal temperature coefficients measures the difference between the thermal liquid junction potentials, the Δtljp, of the two salts. At the same chloride ion concentration, these Δtljp's should be the same between the same two salts, regardless of the particular chloride-ion electrode system used. Thus the calculation of Δtljp's permits a direct comparison of the present data, and of other calomel thermal cell data, with the silver-silver chloride thermal emf studies initiated by Eastman and Goyan (19) and pursued by Goodrich (20), Bernhardt and Crockford (21), Crockford and Hall (22), and Haase and Schönert (23).

In the irreversible thermodynamic theory of thermal cells (13), it is shown that the difference between ini-

tial thermal temperature coefficients for different salts, when the electrode temperature effect can be considered eliminated, takes the following form for chloride-ion electrodes

$$(dV/dT)_{th,\,init}(\mathrm{MCl}) - (dV/dT)_{th,\,init}(\mathrm{KCl}) = \Delta \mathrm{tljp}\ (\mathrm{MCl}-\mathrm{KCl}) = (1/\mathbf{F})\,[t_K S^D(\mathrm{KCl}) - t_M S^D(\mathrm{eq.\ MCl})] \quad [5]$$

where S^D is the entropy of diffusion transport (per gram equivalent) of the salt and the t's are transference numbers. The entropy of diffusion transport (per mol) is related to the Soret coefficient, $d \ln a_\pm/dT$, *i.e.*, to the fractional change in mean ion salt activity resulting from thermal diffusion across a temperature gradient, by the expression

$$S^D(\mathrm{MCl}) = -\nu RT(d \ln a_\pm/dT) \quad [6]$$

where ν is the number of ions per molecule of the salt. Thus the measurement of Δtljp's provides a relative method for the determination of entropies of diffusion transport of salts if the value for one salt is known from an independent thermal diffusion experiment. The method, however, is sensitive to small errors in the measured thermal emfs. Conversely, Eq. [5] permits a calculation of Δtljp's from the entropies (or heats) of diffusion transport of salts as determined in thermal diffusion experiments such as those of Agar (15), Chanu (24), Tanner (25), and Butler and Turner (26).

The Δtljp's of sodium, lithium, and calcium chlorides and of hydrochloric acid, referred to potassium chloride of the same chloride ion concentration, are plotted for 1.0, 0.1, and 0.01*m* chloride ion, in Fig. 6, 7, and 8, *vs.* temperature between 0° and 70°C. The lines are based on the present series of experiments and represent the differences between the lines of Fig. 2, 3, 4, and 5 and the corresponding line in Fig. 1 (KCl). The numbers refer to the legends of the figures and identify the observers of the prior experimental data. Points labelled 9, 11, and 16 are based on relative thermal emfs of calomel electrodes; points labelled 2, 6, 7, and 8, on relative thermal emfs of silver-silver chloride electrodes; points labelled 1, 4, 5, and 15, on the results of thermal diffusion studies. In Fig. 6 (0.1*M* chloride ion), the points labelled 2 and 6 have been computed by interpolation between 0.05 and 0.25*M* chloride ion solutions.

The comparisons provided by Fig. 6-8 show generally good agreement, *i.e.*, within about ±20-50 μv/degree, between the present work and prior investigations for most of the salt pairs studied. The present results are about 40 to 60 μv/degree higher in 0.01*M* lithium chloride, and about 60 to 100 μv/degree higher in 0.01*m* hydrochloric acid. These comparisons and those of Fig. 1, 3, and 5 suggest that the thermal emfs here reported in 0.01*m* lithium chloride and hydrochloric acid may perhaps be systematically high, while those of 0.01*m* potassium chloride are perhaps systematically low. Thermal emf work has proved more troublesome in the dilute solutions, as already observed by Richards (2), especially at higher temperatures.

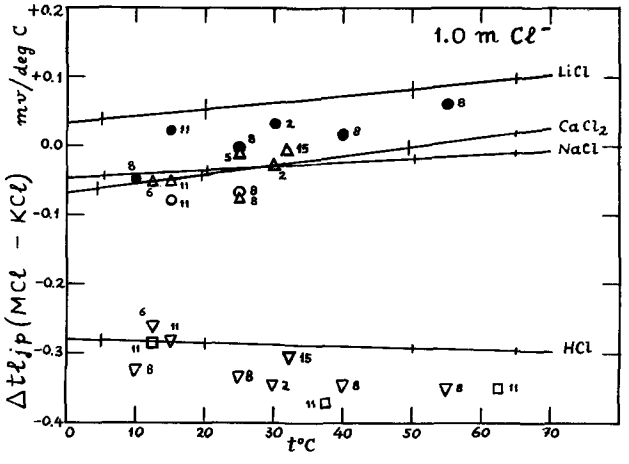

Fig. 6-8. Differences of thermal liquid junction potentials, Δtljp, referred to KCl as zero, in 1.0, 0.1, and 0.01M chloride ion. • LiCl; △ NaCl; ○ $CaCl_2$; ▽ HCl; □ HCl (0.5M, in Fig. 6). References for the points are the same as for Fig. 1 to 5.

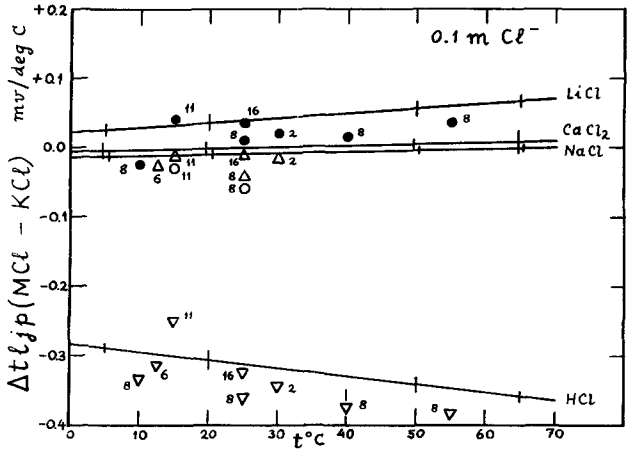

Fig. 7. 0.1*m* chloride

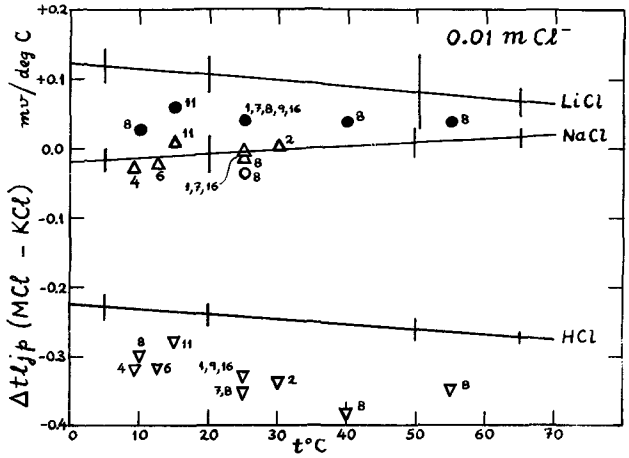

Fig. 8. 0.01*m* chloride

The thermodynamic consequences of this present experimental investigation, particularly the determination of the entropies of diffusion transport S^D of the electrolytes involved (relative to potassium chloride), and of the moving entropy $\bar{\bar{S}}$ of the chloride ion, and the estimation of the entropies of electrochemical transport S^E and of migration transport S^M of chloride and hydrogen ion, will be developed in Part II of this study.

Acknowledgment

The authors wish to express their thanks to The Electrochemical Society and the National Science Foundation for Research Fellowships (HOD), to the International Nickel Company of New York, and the Office of Saline Water of the U. S. Department of the Interior, for financial support extended to various phases of this project. They also wish to thank James A. Ahearn, Jr., George Allendorf, Salvatore A. Carrano, and Thomas P. O'Connor, for their assistance with some of the measurements, and Mary Ellen Farrey for assistance with the computer work.

Manuscript received Sept. 29, 1966; revised manuscript received Feb. 15, 1967. This paper is based on the Ph.D. dissertation of H. O. Daley, Jr., and the M.S.

Thesis of N. A. Swendeman (Mrs. Loud), and G. R. Salvi. Portions of this work were presented at the Toronto Meeting, May 3-7, 1964.

Any discussion of this paper will appear in a Discussion Section to be published in the December 1967 JOURNAL.

REFERENCES

1. A. Gockel, *Wiedemann's Ann. Physik*, **24**, 618 (1885); **40**, 453 (1890); **50**, 696 (1893).
2. T. W. Richards, *Z. Physik. Chem.*, **24**, 39 (1897).
3. H. A. Fales and W. A. Mudge, *J. Am. Chem. Soc.*, **42**, 2434 (1920).
4. W. W. Ewing, *ibid.*, **47**, 301 (1925).
5. S. P. L. Sorensen and K. Linderstrom-Lang, *Compt. rend. trav. lab. Carlsberg*, **15**, 1 (1925).
6. I. M. Kolthoff, *Chem. Weekblad*, **22**, 332 (1925); I. M. Kolthoff and F. Tekelenburg, *Rec. trav. chem.*, **46**, 18 (1927).
7. N. Bjerrum and A. Unmack, *Kgl. Danske Videnskab. Selskab, Math.-fys. Medd.*, **9**, No. 1 (1929).
8. R. Burian, *Z. Elektrochem.*, **37**, 238 (1931).
9. M. B. Young, Ph.D. Thesis, U. California (Berkeley) (1935).
10. B. Wingfield and S. F. Acree, *J. Research Nat. Bur. Standards*, **19**, 163 (1937).
11. H. Cary and W. P. Baxter, in M. Dole, "Glass Electrode," p. 166, John Wiley & Sons, Inc., New York (1941).
12. T. Ikeda and H. Kimura, *J. Phys. Chem.*, **69**, 41 (1965).
13. A. J. de Bethune, *This Journal*, **107**, 829 (1960).
14. A. J. de Bethune, T. S. Licht, and N. Swendeman, *ibid.*, **106**, 616 (1959).
15. J. N. Agar, in P. Delahay, "Advances in Electrochemistry and Electrochemical Engineering," Vol. 3, pp. 31-121, Interscience, New York (1963).
16. M. I. Temkin and A. V. Khoroshin, *Zh. fiz. Khim.*, **26**, 500, 773 (1952).
17. International Critical Tables, **3**, 54-87.
18. W. M. Carson, Jr., C. E. Michelson, and K. Koyama, *Anal. Chem.*, **27**, 472 (1955). Corning Glass Works Product Information Brochure IC-21, 5 August 1960. R. A. Durst, *J. Chem. Education*, **43**, 437 (1966).
19. F. M. Goyan, Ph.D. Thesis, University of California, Berkeley (1937).
20. J. C. Goodrich, Ph.D. Thesis, University of California, Berkeley (1941).
21. H. A. Bernhardt and H. D. Crockford, *J. Phys. Chem.*, **46**, 473 (1942).
22. H. D. Crockford and J. L. Hall, *ibid.*, **54**, 731 (1950).
23. R. Haase and H. Schönert, *Z. Physik. Chem., N.F.*, **25**, 193 (1960).
24. J. Chanu, *J. Chim. physique*, **55**, 743 (1958).
25. C. C. Tanner, *Trans. Faraday Soc.*, **23**, 75 (1927), cf. H. J. V. Tyrrell, "Diffusion and Heat Flow in Liquids," p. 287, Butterworths, London (1961).
26. B. D. Butler and J. C. R. Turner, *J. Phys. Chem.*, **69**, 3598 (1965).
27. G. R. Salvi, M. S. Thesis, Boston College (1960).
28. N. A. Swendeman, M. S. Thesis, Boston College (1959).
29. H. O. Daley, Jr., Ph.D. Thesis, Boston College (1963).

Technical Notes

Porous Carbon Fuel Cell Electrodes from Polymer Precursors

M. W. Reed and W. C. Schwemer

LTV Research Center, Dallas, Texas

The problem in obtaining an active fuel cell electrode can be considered twofold: (*i*) preparation of a corrosion resistant, conductive substrate of narrow pore spectrum to serve as a support for a catalyst specific for the desired electrode reaction, and (*ii*) deposition of an adherent, active catalyst at some step of the electrode processing. An ideal diffusion-type electrode, besides being an electronic type conductor, should be inert to the electrolyte, reactants, and products of the fuel cell. The electrode should have mechanical strength, a narrow pore size spectrum, and a disordered surface in order to furnish a large number of sites for catalyst deposition. The electrode should have specificity for the electrode reaction and a long operating life without change in electrochemical performance, physical properties, and corrosion resistance. In addition the fabrication process should produce homogeneous electrodes with reproducible properties. The fuel cell electrodes considered here are of the diffusion type with free electrolyte and gaseous reactant on opposite sides. The electrolyte is held in the pores by capillary pressure and tends to form a meniscus concave to the electrolyte; in wetted electrodes diffusion through the electrolyte film above the meniscus has been shown to be limiting in certain fuel cell electrode reactions (1).

The preparation of porous fuel cell electrodes using polyvinylidene chloride, Saran A*, as a carbon precursor by the pyrolysis reaction, $(CH_2C\,Cl_2)_x \rightarrow 2xC + 2xHCl$, shows promise. The controlled thermal decomposition of Saran A gives a stoichiometric yield of carbon free from the impurities usually found in carbons from natural sources. Saran carbon is characterized by toughness and strength not present in other carbons of equivalent density. The corrosion resistance of Saran carbons appears superior to those carbons from natural sources. Two reasons possibly contribute to this: (*a*) the lower impurity level and (*b*) the homogeneous, isotropic structure of Saran carbon which consists of only one phase. Conventional carbons have a heterogeneous, two-phase structure of conventional carbons arising from the use of a carbon source such as petroleum coke and an easily carbonized binder such as sugar.

It is known from x-ray data that poly (vinylidene chloride) consists of vinylidene chloride monomer units joined in a head-to-toe arrangement. The first step in the pyrolysis results in the liberation of hydrogen chloride and the formation of a linear polyene

[1] Saran A, courtesy Dow Chemical Company.

with alternating hydrogen and chlorine. The second step is a cyclization to a six-membered ring presumably through a Diels-Alder mechanism (2):

$$(C_2H_2Cl_2)x \xrightarrow{\Delta} (CH = CCl)x + xHCl \xrightarrow{\Delta}$$

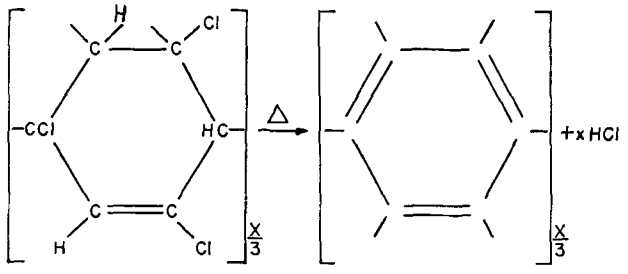

Further evolution of hydrogen chloride then occurs leading to a completely aromatic structure. Data from Jackson indicate that graphite crystallites of approximately unit cell dimensions are present in fully pyrolyzed Saran carbons (3). Saran carbon is not graphitized on a macro scale during heating to 3000°C.

Porous Saran carbon is prepared by using polyvinylidene chloride, Saran A, $(CH_2CCl_2)_x$ as the precursor; a simplified flow sheet for the Saran carbon is shown in Fig. 1. Step 1 involves compacting the powder at between 780-3500 psi by either conventional die or hydrostatic compaction of the powder in a bag. The compacts have enough green strength without a binder at this stage to be weighed and placed in a vacuum oven.

The compacts are heated to 125°C (step 2) in 30 in. Hg vacuum. The pump should be protected from the evolved HCl, boiling point —84°C, by liquid nitrogen traps. The temperature is increased to 175°C (step 3) at 10°C/hr and held for 16 hr under the 30 in Hg vacuum (step 4). The Saran pyrolysis reaction, $(CH_2C\,Cl_2)_x \rightarrow 2xC + 2xHCl$, becomes extremely rapid in the 165°-170°C range. The compacts change from white to black in color during the 175°C pyrolysis. The compacts are placed in a furnace and heated under inert gas atmosphere or vacuum to 1000°C (step 5) which completes the Saran pyrolysis to carbon.

The pore spectra and density of the carbon may be varied in a controlled manner by changing the particle size and compacting pressure of the precursor Saran powder. In this respect, the process is similar to conventional ceramic or powder metallurgical techniques.

Typical physical properties of porous uncatalyzed Saran carbon are given in Table I.

The relationship between final pyrolysis temperature and surface area of Saran carbon is shown in Fig. 2. These data indicate that pyrolysis temperatures above 1100°C should be avoided for maximum area.

Pore spectra curves are plotted in Fig. 3. The carbon pressed at 1300 psi has most of the pores between 3 and 8μ average diameter while the 930 psi specimen

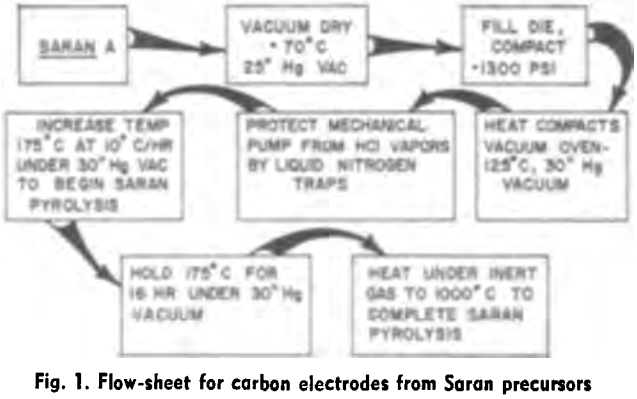

Fig. 1. Flow-sheet for carbon electrodes from Saran precursors

Table I. Physical properties of Saran carbon

Compacting pressure, psi	930	1300	2000
Apparent density, g/cm³	0.686	0.731	0.745
Available porosity, %	61.9	59.4	58.6
Available porosity, cm³/g	0.902	0.814	0.786
Surface area (4), meters²/g	1300	1300	1300
Permeability, N_2, millidarcies	53.6	46.9	30.3

has a wider pore spectra between 3 and 15μ. The carbon pressed at 2000 psi has a narrow spectrum between 1 and 4μ. A narrow pore spectrum allows a gas-liquid interface to be established in a thin electrode, the thin electrode being necessary from mass transport considerations. Gas pressures greater than about 1 psig are required to prevent electrode flooding. The electrodes, being of the gas diffusion type, must be operated near the gas break-through pressures for maximum performance.

Photomicrographs, of porous Saran carbon show the 930, 1300, and 2000 psi material in Fig. 4. Notice the

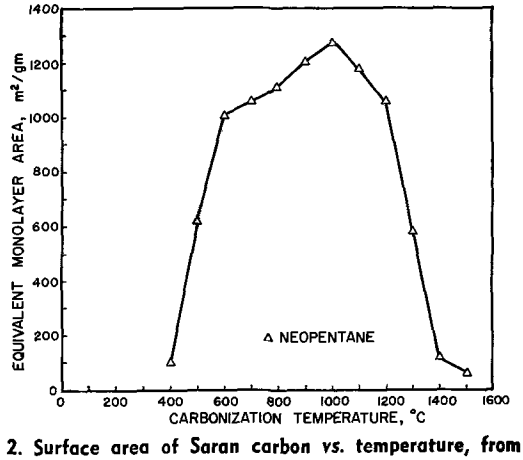

Fig. 2. Surface area of Saran carbon *vs.* temperature, from Lamond *et al.*

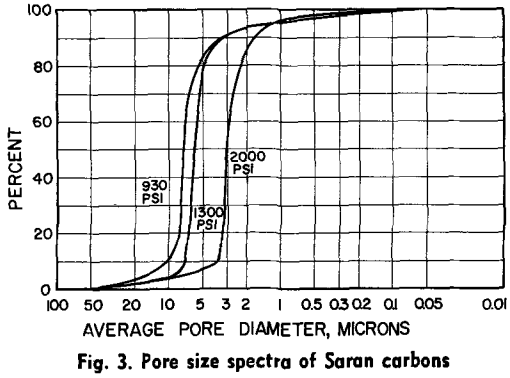

Fig. 3. Pore size spectra of Saran carbons

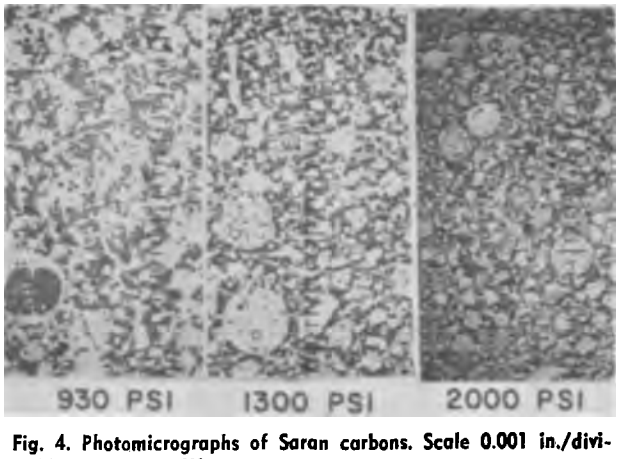

Fig. 4. Photomicrographs of Saran carbons. Scale 0.001 in./division. Magnification 50X.

small porosity apparent within the large, *ca.*, 0.004 in., carbon particles, as well as the more dense appearance of the 2000 psi material.

Electrochemical evaluation of the electrode was by the single electrode technique as given by Reed and Brodd (6). Constant direct current was impressed between the test electrode and a counter electrode. Potential was measured between the test electrode and a reference electrode through the electrolyte path in the Luggin capillary. Mercury-mercuric oxide was the reference used with potassium hydroxide electrolyte; mercury-mercurous sulfate was the reference used with sulfuric acid electrolyte. Testing was limited to fuel cell cathode materials with either air or oxygen as the oxidant. An interrupter technique was used to determine the resistance of the operating electrode (7); the data are plotted from reversible oxygen potential after correction for ohmic drop. The ohmic drop correction is 0.174v at 100 ma/cm^2 for the data on Fig. 6, for example. The open-circuit potential of these electrodes has been found to be about 0.2v below the reversible oxygen potential, indicating a peroxide mechanism at open circuit and low current densities (8). The cell exposes 5 cm^2 of electrode area to the electrolyte. The oxygen used was 99.5% minimum purity O_2. The air used was passed through an anhydrous calcium sulfate drying tower. The potassium hydroxide electrolyte was prepared by dissolving Baker reagent grade pellets (86.2 w/o KOH) in distilled water. The sulfuric acid electrolyte was prepared by diluting Baker reagent grade (97.3% H_2SO_4) with distilled water.

Polarization data in sulfuric acid electrolyte for oxygen and air electrodes with Saran carbon substrates are plotted in Fig. 5. The effect at 25°C of using air rather than oxygen is seen as a decrease in current density from 95 to 40 ma/cm^2 at a polarization of 0.465v. Moderate heating of the cell produces significant decreases in the polarization of air electrode; at 100 ma/cm^2 polarization decreases by 0.09v to 0.495v. Further, performance at 59°C on air is almost as good as that using oxygen at 25°C, 0.495v *vs.* 0.475v at 100 ma/cm^2. The polarization of the oxygen electrode at 59°C is 0.47v at a current density of 200 ma/cm^2. The increase in cell temperature from 25° to 59°C reduced the polarization by 0.1v. Note that the curves become markedly nonlinear at current densities above 70 ma/cm^2. The relatively thick, *ca.* 0.070 in., electrodes become diffusion limited at this point. The platinum catalyst used in these tests was deposited by impregnating the porous Saran carbon substrate with chloroplatinic acid at a vacuum of about 25 in. Hg. After infrared drying the platinum was reduced *in situ* by hydrogen at 400°C. Other catalyst techniques were evaluated; none were as reliable for making active cathodes.

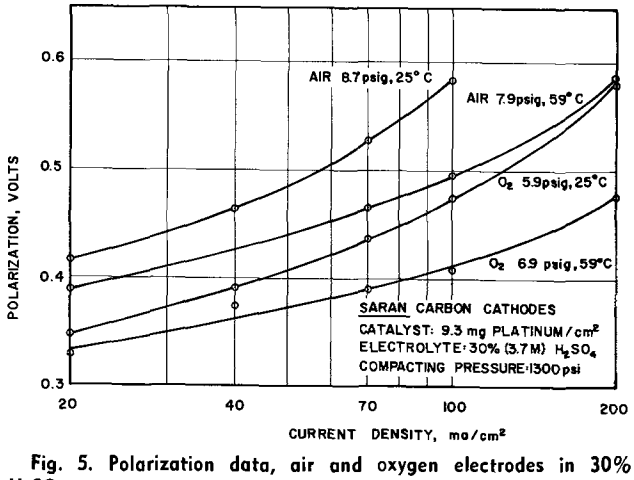

Fig. 5. Polarization data, air and oxygen electrodes in 30% H_2SO_4.

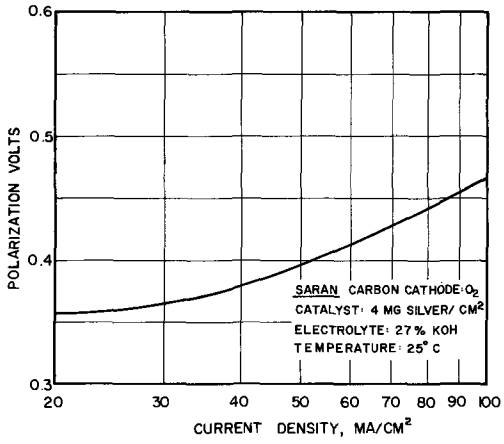

Fig. 6. Polarization data, oxygen electrode in 27% KOH

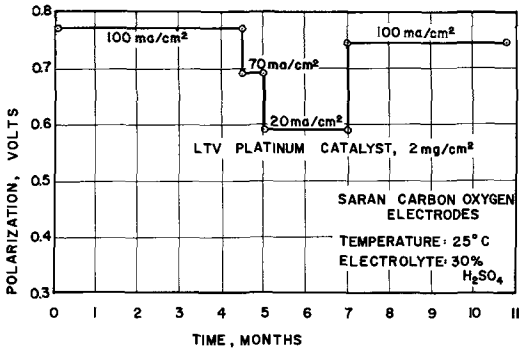

Fig. 7. Life test data, oxygen electrode in 30% H_2SO_4

Figure 6 is a polarization *vs.* current density plot of Saran carbon as an oxygen electrode material in potassium hydroxide at an oxygen pressure of 7.6 psig. The silver catalyst, 4 mg/cm^2, was deposited from a silver amine solution by reduction with formaldehyde. The polarization is 0.47v at a current density of 100 ma/cm^2. The Saran was pressed initially at 1300 psi.

The life tests in sulfuric acid of the Saran carbon cathodes compacted initially at 1300 psi have reached over ten months as shown in Fig. 7. The initial 4.5 months were at a constant current density of 100 ma/cm^2. This was changed to 70, then 20 ma/cm^2 for the next 2.5 months. The current density was changed again back to 100 ma/cm^2 for an additional four months and are still in progress. The polarization is the same or lower than when the tests were started.

Conclusions

Electrodes made of carbon from Saran polymer precursors can be made having controlled pore size spectra in the range useful for diffusion-type fuel cells.

Life tests have established that the chemical stability of the Saran carbon in acid electrolyte will allow its use in fuel cells designed for long life.

Catalysts of high activity and specificity may be deposited on the porous carbon to make fuel cell cathodes with low polarization characteristics.

Manuscript received Dec. 19, 1966; revised manuscript received March 9, 1967. This paper was presented at the Cleveland Meeting. May 1-6, 1966.

Any discussion of this paper will appear in a Discussion Section to be published in the December 1967 JOURNAL.

REFERENCES

1. F. G. Will, *This Journal*, **110**, 152 (1963).
2. F. H. Winslow, W. D. Baker, and W. A. Yager *Proc. Second Conference on Carbon*, p. 96, 1956.
3. C. Jackson, Ph.D. Thesis, University of Durham, England, 1961.

4. T. G. Lamond, J. E. Metcalf, III, and P. L. Walker, Jr., *Carbon*, **3**, 61 (1965).
5. J. R. Dacey, G. J. C. Frohnsdorff, and J. T. Gallagher, *ibid.*, **2**, 50 (1964).
6. M. W. Reed and R. J. Brodd, *ibid.*, **3**, 244 (1965).
7. M. W. Reed, LTV Research Report No. 0-71000/3R-13, 1963.
8. W. Berl, *Trans. Electrochem. Soc.*, **83**, 253 (1943).

Measurement of the Anodic Oxide Film Growth on Iron for Hours

Norio Sato and Takenori Notoya

Physical Chemistry Laboratory, Faculty of Engineering, Hokkaido University, Sapporo, Japan

In a previous study (1) of the kinetics of anodic oxide film growth on iron in a neutral solution, it was found that in the steady growth region the rate of thickening of the oxide varies with both film thickness and electrode potential in accordance with the equation

$$i = k' \exp(\beta E - Q_T/B) \quad [1]$$

where E is the potential, Q_T the film thickness, and k', β, and B are constants. Accordingly, under galvanostatic condition the potential is a linear function of the film thickness

$$E = E' + KQ_T \quad [2]$$

and at constant potential

$$i = A \exp(-Q_T/B) \quad [3]$$

which can be integrated to the equation of logarithmic law

$$Q_T = a + b \ln(t - t_0) \quad [4]$$

Increase of the film thickness, Q_T, during potentiostatic oxidation can be measured electrochemically by integrating the current-time curve obtained. However, since after a certain period of time the anodic current falls to less than the limit of experimental error, it becomes difficult for extended periods of time to obtain an accurate measure of the amount of charge passed during potentiostatic oxidation. The present note reports another convenient method for estimating the thickness of the oxide film formed by prolonged oxidation.

The experimental procedure was almost the same as that described in previous papers (1-3); the specimen was an electropolished carbonyl iron sheet of 5 x 1 cm, and the solution was a deaerated aqueous mixture of 0.15N boric acid and 0.15N sodium borate (pH = 8.42). Before the measurement, the air-formed or passive oxide film on the specimen was completely removed by cathodic reduction, and the solution was renewed at least three times.

The specimen was anodically oxidized at a constant potential of 0.0v (SCE scale) at 25° ± 0.1°C for eight different periods of time ranging from 0.5 to 50 hr, which was immediately followed by the galvanostatic oxidation at a current density of 10 μa/cm^2. Results of the galvanostatic oxidation subsequent to the potentiostatic oxidation for the various periods of time are shown in Fig. 1. It can be seen in agreement with Eq. [2] that the potential rises linearly with increase of ΔQ_T in the steady growth region, and that the $E - \Delta Q_T$ curve in the straight line range shifts in a parallel fashion toward the more noble potential region with increased time of the preceding potentiostatic oxidation and hence with increasing the initial thickness of the oxide film ${}_sQ_T$

$$E = E' + K(\Delta Q_T + {}_sQ_T) \quad [5]$$

Accordingly, ${}_sQ_T$, the thickness of the oxide film grown during the preceding potentiostatic oxidation, can be estimated from Eq. [5], where K and E' are constants at constant current density.

From Eq. [5]

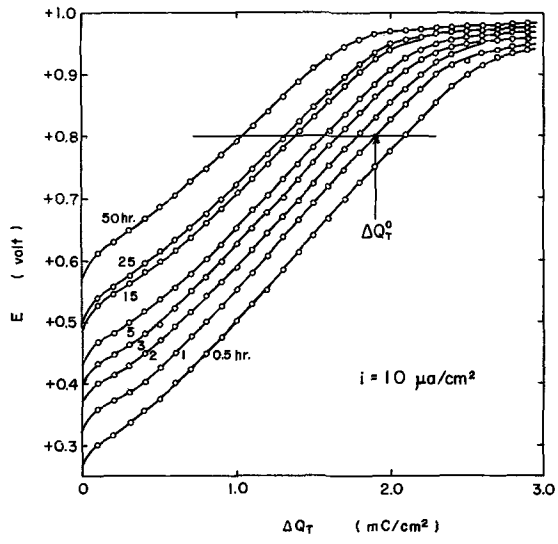

Fig. 1. Change of potential with coulomb passed during galvanostatic oxidation at 10 μa/cm^2 subsequent to potentiostatic oxidation at 0.0v for eight different hours.

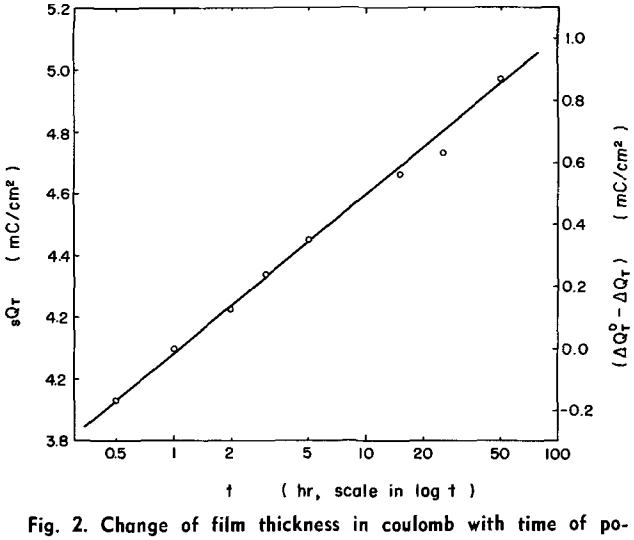

Fig. 2. Change of film thickness in coulomb with time of potentiostatic oxidation at 0.0v.

$$ {}_sQ_T = \frac{E - E'}{K} - \Delta Q_T $$

and at a given potential

$$ {}_sQ_T = {}_sQ_T^{\circ} + (\Delta Q_T^{\circ} - \Delta Q_T) \quad [6] $$

where ${}_sQ_T^{\circ}$ is a known value of ${}_sQ_T$ which can easily be measured with sufficient degree of accuracy by integration of the current-time curve obtained, for example, a value of ${}_sQ_T^{\circ}$ (1 hr, 0.0v) = 4.10 mC/cm^2 being obtained for 1 hr potentiostatic oxidation at 0.0v. The difference $(\Delta Q_T^{\circ} - \Delta Q_T)$ in coulombs at a given

potential, for example, of +0.8v can be calculated from the galvanostatic oxidation curves shown in Fig. 1.

The oxide film thickness, ${}_sQ_T$, thus calculated is plotted against the logarithm of time of the potentiostatic oxidation at 0.0v in Fig. 2. A straight line can be drawn to fit the data, indicating that at constant potential the anodic oxide film thickens according to the same kinetics represented by Eq. [3] and [4] for extended periods of time to 50 hr.

Manuscript received Jan. 30, 1967.

Any discussion of this paper will appear in a Discussion Section to be published in the December 1967 JOURNAL.

REFERENCES

1. N. Sato and M. Cohen, *This Journal*, **111**, 512 (1964).
2. N. Sato and M. Cohen, *ibid.*, **111**, 519, 624 (1964).
3. N. Sato, *Electrochim. Acta*, in press.

Electrodeposition of Coherent Deposits of Refractory Metals

VI. Mechanism of Deposition of Molybdenum and Tungsten from Fluoride Melts

S. Senderoff and G. W. Mellors

Research Laboratory, Consumer Products Division, Union Carbide Corporation, Cleveland, Ohio

In a recent report (1) it was shown that the deposition of molybdenum from a chloride melt occurs by an irreversible single step reduction, but that the usual treatment of the chronopotentiometric data was not definitive because of instability of the electrolyte in the dilute range of composition required for chronopotentiometry. In a similar study of molybdenum and tungsten deposition from a fluoride melt (2) the instability on approximately tenfold dilution of the plating solution was even greater and the concentration and temperature range amenable for study was even smaller than in the case of the chloride-molybdenum system. Nevertheless it was possible to demonstrate by techniques equivalent to those used in the chloride system that the deposition of coherent metal also involved an irreversible reduction as in all previous cases (3), and that the irreversibility was greater in the fluoride system, and extended to higher temperatures, than the molybdenum-chloride system (1).

Molybdenum deposition.—A plating solution was prepared by reacting MoF_6 with molybdenum metal in a molten eutectic mixture of KF (0.42), LiF (0.47), NaF (0.11) as described previously (2). After sufficient electrolysis to produce satisfactory plates, the solution contained 6.6 w/o (weight per cent) Mo at a mean valence of 3.3. This was diluted to yield three samples containing 0.55, 0.51, and 0.40 w/o Mo and chronopotentiograms were run on these samples as described previously (1), using a Ni/NiF_2, alkali fluoride// reference electrode (3).

During the 1-2 hr that it took to run the chronopotentiograms at 600°, 700°, and 800°C, the solutions lost 15 to 19% of their molybdenum content and the mean valences of molybdenum had risen to 4.0 or higher. The scatter of points in the $it^{1/2}$ *vs.* C plots was too great for any conclusions to be drawn from them. Plots of E *vs.* log $(\tau^{1/2} - t^{1/2})/t^{1/2}$ were nonlinear as were those of E *vs.* log $(\tau^{1/2} - t^{1/2})$. The linearity of the plots of the latter function improved with increasing temperature so that for the chronopotentiograms run at 800°C the plots were nearly linear, but the average electron number, n, calculated from the slopes was 2.0 ± 0.2. Since the total reaction was known to be reduction of trivalent molybdenum to metal, and since only a single plateau[1] was observed (see Fig. 1) this can be interpreted only as either a two-electron slow step in the reaction, or an inapplicability of the Nernst plot. In either case it implies irreversibility of the reaction.

The irreversibility is confirmed by examining the cathodic-anodic chronopotentiograms of Fig. 2 and the data in Table I, in which ΔE is the difference in E value between the initial portions of the cathodic and anodic plateaus and κ is the calculated specific conductance of the ternary alkali fluoride solvent. This was obtained from the conductivity data of Yim and Feinleib (4) for the individual components by assuming ideal additivity, *i.e*, $\kappa_{mix} = \sum_i N_i\kappa_i$ where N_i is the mole fraction of component i. In the 800°C case the

[1] When the mean valence exceeded 4.0, a second plateau at approximately 1v appeared. Under these conditions unsatisfactory deposits are obtained.

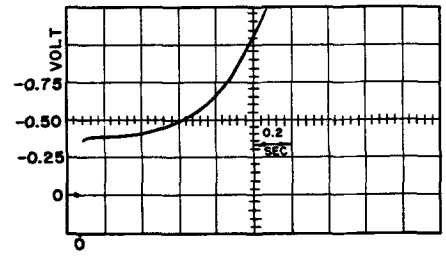

Fig. 1. Chronopotentiogram for reduction of trivalent molybdenum to metal from the alkali fluoride electrolyte. Temperature, 600°C; concentration, 11.3 x 10^{-5} moles/cc (0.55 w/o Mo); current density, 100 ma/cm^2.

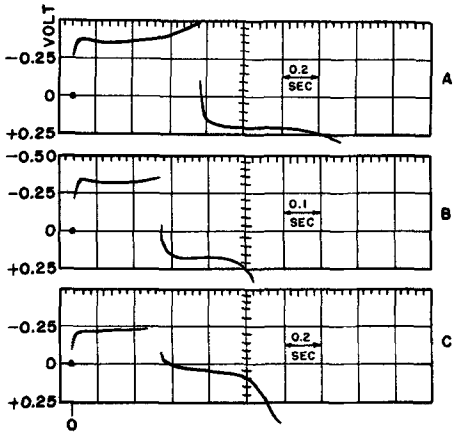

Fig. 2. Cathodic-anodic chronopotentiogram for deposition and dissolution of molybdenum metal; cathodic portion on left.

	a	b	c
Temperature, C°	600	700	800
Concentration, moles/cc	11.3 x 10^{-5}	10.5 x 10^{-5}	9.2 x 10^{-5}
Current density, ma/cm^2	100	250	200
$t_{anode}/t_{cathode}$	1.05	0.96	1.00

Table I. Comparison of IR drop in electrolyte with observed polarization of anodic and cathodic processes

Temp, °C	KF-NaF-LiF Eutectic κ, ohm^{-1}, cm^{-1}[a]	C. D., amp/cm^2	2 × IR, v, 1.5 cm electrode separation	ΔE, observed potential difference, v (from Fig. 2)
600	4.6	0.100	0.065	0.58
700	5.1	0.250	0.15	0.47
800	5.6	0.200	0.11	0.27

[a] Calculated assuming ideal solution.

conductivity data from (4) is extrapolated only about 100°C and, even if the nonideality might cause the resistivity to be as much as 30% greater than calculated as it is in the KCl-LiCl eutectic mixture (5), the observed value of ΔE would still be considerably in excess of twice the IR drop, the value expected for reversible systems. At the lower temperatures the difference between ΔE and 2(IR) is even larger. Comparison of ΔE in the fluoride system with that in the chloride melt (1), reveals that in spite of the higher conductivity of the fluoride melt, ΔE remains greater in the fluoride than in the chloride solution. Finally the average $E_{1/4}$ values for the chronopotentiograms such as those of Fig. 1 are —0.48 ± 0.06v at 600°C, —0.34 ± 0.04v at 700°C, and —0.24 ± 0.02v at 800°C. The static potential is —0.1v with little change with temperature. $E_{1/4}$ thus shows considerable polarization even at the highest temperature.

It can be concluded, therefore, that on the basis of the same criteria used in the case of the chloride melt, reduction of trivalent molybdenum to metal in fluorides is irreversible. That considerable irreversibility extends to 800°C in the fluorides, but not in the chlorides, is significant in view of the excellent plates obtained at this elevated temperature from the fluoride melt, while in the chloride, lower temperatures (*ca.* 600°C) are best for plating.

Tungsten deposition.—A plating solution containing 3.53 w/o W in the ternary alkali fluoride eutectic mixture was prepared by reacting WF_6 with tungsten metal in the molten fluoride mixture (2). The mean valence of the tungsten was 4.48. This was diluted to 0.32 w/o W by addition of alkali fluoride, and chronopotentiograms were run in tungsten crucibles at 600°C. A typical result is illustrated in Fig. 3. An average of six such runs gave an $E_{1/4}$ value of —0.34 ± 0.04v compared to a static potential of —0.05v. At higher temperatures results obtained were irreproducible due to rapid change in solution composition. Reduction in concentration of tungsten was small but its mean valence rapidly increased to 5 or above. When the valence reached 5, another plateau at —0.8v appeared and probably corresponded to the reduction of a higher valence state from which poor deposits are produced.

Another set of chronopotentiograms at 600°C on a solution containing 1.69 w/o W gave an average $E_{1/4}$ value of —0.28v and a static potential of +0.08v. The poor reproducibility even at 600°C is probably the result of composition variations during the course of the run, especially in the more dilute solution. Measurements at the higher concentration, however, required very high currents and were difficult to make.

In Fig. 4 is shown a cathodic-anodic chronopotentiogram for the deposition and dissolution of tungsten metal at 600°C. The difference in potential between the

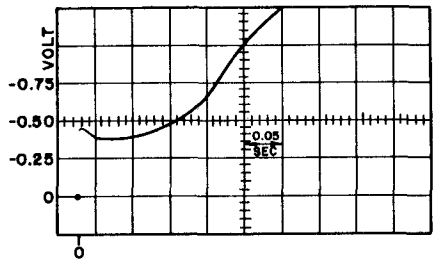

Fig. 3. Chronopotentiogram for deposition of tungsten metal from fluoride electrolyte. Temperature, 600°C; concentration, 3.6 x 10^{-5} moles/cc (0.32 w/o W); current density, 100 ma/cm^2.

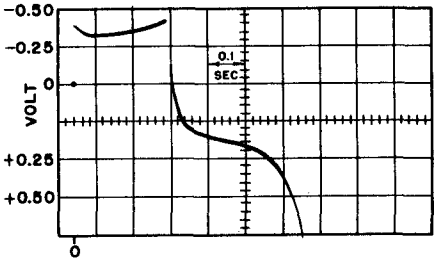

Fig. 4. Cathodic-anodic chronopotentiogram for deposition and dissolution of tungsten metal; cathodic portion on left. Temperature, 600°C; concentration, 3.6 x 10^{-5} moles/cc; current density, 75 ma/cm^2; $t_{anode}/t_{cathode}$, 1.08.

cathodic and anodic processes of 0.65v compared with 0.05v corresponding to twice the IR drop is even greater than in the molybdenum case and this indicates even greater irreversibility.

Another probable indication of irreversibility is the initial maximum in the chronopotentiogram of Fig. 3 which may result from crystallization or nucleation overvoltage.

From these results it is clear that the reduction of molybdenum and tungsten to produce coherent metal deposits from the fluoride melt involves an irreversible process as is true in all other cases of coherent deposition thus far investigated. The instability of the dilute baths makes it difficult to determine the cause of the irreversibility, but since the behavior is qualitatively similar to that of the Mo-chloride system (1), it is likely that the irreversibility arises from the same cause, *i.e.*, slow dissociation of a polynuclear complex anion of molybdenum and tungsten with fluoride to a mononuclear ion.

Manuscript received Dec. 5, 1966.

Any discussion of this paper will appear in a Discussion Section to be published in the December 1967 JOURNAL.

REFERENCES

1. S. Senderoff and G. W. Mellors, *This Journal*, **114**, 556 (1967).
2. G. W. Mellors and S. Senderoff, Canadian Pat. No. 688, 546 (June 1964).
3. S. Senderoff and G. W. Mellors, *This Journal*, **112**, 840 (1965); **113**, 66 (1966); G. W. Mellors and S. Senderoff, *ibid.*, **113**, 60 (1966).
4. E. W. Yim and M. Feinleib, *ibid.*, **104**, 626 (1957).
5. E. R. VanArtsdalen and I. S. Yaffe, *J. Phys. Chem.*, **59**, 118 (1955).

The Electrochemical Reduction of N-*p*-Nitrobenzylaniline

S. Wawzonek, T. Plaisance,[1] and T. McIntyre

Department of Chemistry, University of Iowa, Iowa City, Iowa

The report of Elbs and Gaumer (1) that the electrolytic reduction of N-*p*-nitrobenzylaniline in weakly alkaline ethanolic solution gave *p*-dianilinoazoxystilbene (I) could not be duplicated. The reduction under all

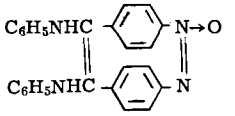

I

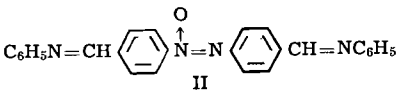

II

conditions tried gave *p*-azoxybenzylideneaniline (II). This structure was indicated by its infrared and nmr spectra, conversion to *p*-azoxybenzaldehyde melting at 193° with hydrogen chloride in ethanol, and comparison with an authentic sample (2). Elbs, Nacken, and Hofmann (3) reported that their compound was converted by hydrogen chloride in ethanol to a dihydrochloride melting at 191°C. No elemental analysis was given, however, to confirm the structure.

p-Azoxybenzylidenaniline can be formed from N-*p*-nitrobenzylaniline by simple treatment of the latter in ethanol with sodium hydroxide or sodium carbonate; no electrolytic reduction is necessary. In the electrolysis, hydroxide ion, formed since sodium acetate was used as an electrolyte, could cause the reaction. A similar type of reaction is reported when *p*-nitrobenzylpyridinium chloride or bromide is treated with aqueous alkali; *p*-azoxybenzaldehyde is formed (4). The following mechanism is suggested for this reaction;

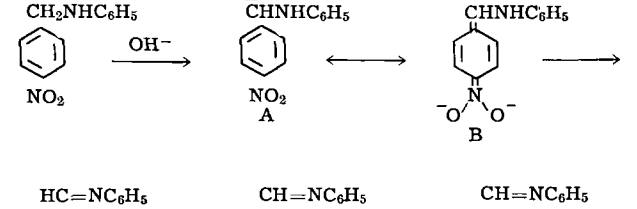

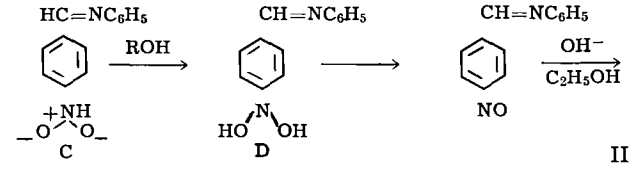

II

The formation of the anion A parallels the formation of the anion from *p*-nitrotoluene in t-butyl alcohol containing potassium *t*-butoxide (5). Eneamines containing a hydrogen on the nitrogen (B) are not stable but rearrange to the Schiff's base. The product in this case would be an intermediate (D) which is often postulated for the reduction of a nitro compound to a nitroso compound. The latter compounds in basic ethanol produce azoxycompounds (6). The conversion of *p*-nitrobenzylpyridinium chloride to 4, 4'-azoxybenzaldehyde would differ in the second step; hydroxide ion would displace the pyridine and form E which would lead to the formation of the product by similar steps.

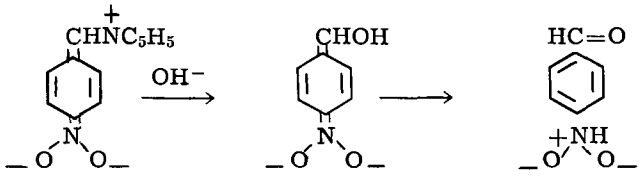

E

Attempts to prepare the cyclic compound (I) by other methods were not successful and led to high melting products. 4, 4'-Dinitrobenzil (7) on electrolysis gave a solid which melted above 360°C. The azoxy and carbonyl absorptions in the infrared were normal and not shifted to a higher frequency as would be expected if a strained ring were formed. The compound was insoluble in dimethylformamide and dimethylsulfoxide and could not be examined further.

The benzoin condensation of *p*-azoxybenzaldehyde was also attempted even though this compound probably has the transconfiguration. As expected a polymeric material was obtained melting above 345°C. A high melting compound was also obtained from the electrolytic reduction of this compound.

Electrolytic oxidation of *p*-nitrobenzylaniline at a platinum anode in acetonitrile containing sodium perchlorate gave the hydrazine (III) rather than the desired stilbene (IV). The structure (III) was indicated by the ir and nmr spectra.

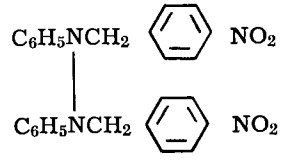

III

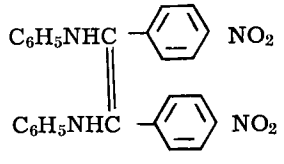

IV

The latter compound (IV) would be a critical intermediate in the formation of the cyclic compound (I). It could exist in the cis configuration necessary for further cyclization because of the size of groups involved. If the dimerization proceeded first through the azoxy group, the trans isomer would result and lead, on further reaction, to linear structures. The products actually isolated from Elbs (1) procedure melted from 180° to 270°C. The formation of the hydrazine (III) instead of the stilbene (IV) definitely eliminates the possibility of forming a cyclic product (I) in the electrochemical reduction of N-*p*-nitrobenzylaniline.

Experimental

p-Azoxybenzylidenianiline (II).—The procedure of Elbs (3) was employed. *p*-Nitrobenzylaniline (10.4g) in ethanol (120 ml) was treated with a solution of sodium acetate (2.4g) in water (6 ml) and placed in a 250-ml beaker which served as the cathode compartment. The anode compartment consists of a Coors porous cup (10.8 by 2.0 cm) and was filled with a similar solution of sodium acetate in water and alcohol. The cathode was nickel sheet metal, 3.8 cm wide and 10.8 cm long formed into a cylinder. The anode was a carbon rod 0.6 cm in diameter and 10 cm long. A power supply capable of producing 4.0 amp/dm^2 was used to carry out the electrolysis.

The electrolysis was carried out at the boiling point of the solvent and gave after 2 min a quantitative precipitation of the product. Prolonged electrolysis reduced the yield to 6.2g. If the electrolysis was carried out until 4700 coulombs (10% excess) were used the yield dropped to 3.1g. The resulting yellow solid sintered in the range from 180° to 270°C, and on repeated crystallizations from dioxane and from benzene gave a product which sintered at 185° and melted at 223°-228°C. The use of a saturated solution of sodium carbonate and a lead anode (10 cm long, 5 cm wide, and 0.3 cm thick) in the anode compartment did not change the nature of the product and only caused a faster precipitation in the cathode compartment.

The same product was obtained by using zinc and

[1] NASA Trainee, 1963-1966.

alkali in methanol, sodium hydroxide and ethanol and sodium carbonate and ethanol as reducing agents and by treating p-azoxybenzaldehyde with aniline in the presence of acetic acid. Alway (2) reported a melting point of 185°-192°C for this compound. The infrared spectrum did not show any absorption above 3200 cm^{-1} and therefore eliminated structure I for the product. Frequencies were obtained at 1637 and 1590 cm^{-1} for C = N and phenyl and 1310 cm^{-1} for the azoxy group.

The NMR spectrum in hexamethylphosphoramide at 110°C gave singlets at δ = 8.20 and δ = 8.30 ppm for the =CH hydrogen, a singlet at δ = 6.72 for the 10 phenyl hydrogens, and a complex peak centering at δ = 7.56 ppm for the other 8 aromatic protons.

p-Azoxybenzaldehyde.—This compound was formed when the reduction product (II) was treated with either gaseous hydrogen chloride in ethanol, concentrated hydrochloric acid, and ethanol and aqueous boiling acetic acid. The compound melted at 193°C [(2) 194°-195.5°C.]

Electrolytic reduction of 4,4'-dinitrobenzil.—4,4'-Dinitrobenzil (7) (1.0g) dissolved in a mixture of dioxane (50 ml) and water (18 ml) containing sodium acetate (1g) was reduced electrolytically in the cell described earlier. The anode compartment contained a lead anode and a saturated solution of sodium carbonate. At a potential of 6v a current of 1.2 amp was obtained, and the electrolysis was allowed to proceed for 3 hr. The product was a yellow solid which deposited on the cathode and melted above 360°C. It was insoluble in alcohol, dioxane, nitrobenzene, dimethylsulfoxide, dimethylformamide, and hexamethylphosphoramide. The infrared spectra gave a peak at 1310 cm^{-1} for the azoxy group and a broad peak in the 2510 to 3000 cm^{-1} region for an hydroxyl group.

Benzoin condensation of p-azoxybenzaldehyde.—p-Azoxybenzaldehyde (0.5g) was refluxed with sodium cyanide (0.1g) in ethanol (100 ml) and dioxane (5 ml) for 1 hr. The resulting yellow precipitate (0.38g) melted above 345°C and was difficult to purify. The infrared spectra gave bands at 3700 cm^{-1} for the hydroxyl and 1715 cm^{-1} for the carbonyl groups.

Electrolytic reduction of p-azoxybenzaldehyde.—The reduction of this compound was carried out using a modification of the procedure of Elbs (3). The electrolytic solution consisted of ethanol (100 ml), water (6 ml), dioxane (25 ml), and sodium acetate (4g). A yellow solid (60% yield) formed during the first 10 min of the electrolysis and melted above 320°C.

1,2-Diphenyl-1,2-bis,(p-nitrobenzyl)hydrazine (III).—A mixture of a solution (60 ml) of 0.5*M* sodium perchlorate in acetonitrile, pyridine (5 ml), and p-nitrobenzylaniline (1.0g) was electrolyzed at a platinum gauze anode. The cathode compartment consisted of a Coors porous cup and contained 0.5*M* sodium perchlorate in acetonitrile and a coil of 16 gauze copper wire as a cathode. The electrolysis was carried out using 8v, which gave a current of 0.5 amp; after 2 hr the current dropped to 0.05 amp. The resulting anolyte was concentrated to 20 ml and treated with ether (200 ml). The sodium perchlorate which precipitated was removed by filtration, and the ether was washed with water and dried over sodium sulfate. Chromatography on alumina gave 1,2-diphenyl-1,2-bis (p-nitrophenyl) + hydrazine (III) (0.3g). Recrystallization from carbon tetrachloride gave a solid melting at 161°-162°C which showed no NH bands in the infrared. Peaks were obtained at 690 and 755 cm for the five adjacent free hydrogen atoms in the phenyl groups, at 850 cm^{-1} for the two adjacent hydrogens in the p-nitrobenzyl group, and at 1475 and 1365 cm^{-1} for the nitro group. The nmr spectrum gave a singlet at δ = 4.83 ppm for the methylene protons and several peaks in the region δ = 6.7-8.1 ppm for the aromatic protons.

Anal. Calcd for $C_{26}H_{22}O_4N_4$; C, 68.70; H, 4.88; N, 12.32. Found: C, 68.42; H, 4.85; N, 12.40.

Manuscript received Jan. 3, 1967; revised manuscript received Feb. 27, 1967. This paper was abstracted from the Ph.D. thesis of one of the authors (T.P.).

Any discussion of this paper will appear in a Discussion Section to be published in the December 1967 JOURNAL.

REFERENCES

1. K. Elbs and M. Gaumer, *J. Prakt. Chem.*, **108**, 236 (1924).
2. F. J. Alway, *Am. Chem. J.*, **28**, 34 (1902).
3. K. Elbs, H. Nacken, and H. Hofmann, *J. Prakt. Chem.*, **108**, 240 (1924).
4. S. B. Hanna, *Chem. Commun.*, **1965**, 487.
5. G. A. Russell and E. G. Janzen, *J. Am. Chem. Soc.*, **84**, 4153 (1962)
6. E. Bamberger, *Ber.*, **35**, 732 (1902).
7. T. Van Es and O. G. Backebury, *J. Chem. Soc.*, **1963**, 1371.

Air Depolarized Electrolytic Oxygen Generator

R. A. Wynveen and K. M. Montgomery

TRW Equipment Laboratories, TRW Inc., Cleveland, Ohio

An electrochemical technique has been tested for obtaining pure oxygen from ambient air. The oxygen is separated from the nitrogen and other inerts by reacting the oxygen at a cell cathode and simultaneously electrolytically evolving oxygen at the cell anode.

A schematic drawing illustrating the basic assembly of a single cell and the electrode reactions are shown in Fig. 1. The process continues as long as air and power are supplied to the cell. In the event of loss in the air supply, the cathode reaction would revert to evolution of hydrogen and the over-all process becomes a conventional water electrolysis cell.

Experimental Technique

The cell used to evaluate the operating parameters is shown in Fig. 2. The electrodes consisted of a porous layer of platinum black and Teflon spread uniformly on and supported by a fine mesh nickel screen.[1] Each electrode had an area of 6¼in.^{2}. The electrolyte was a 32% solution of KOH. The end plates were nickel and then gold-plated stainless steel.

Air entered the top of the cathode compartment, passed through a baffling system, and exited through the bottom of the cell. The gas passage was designed to prevent nitrogen stagnation pockets from forming.

In the anode compartment the baffling was not necessary. Oxygen is evolved regardless of gas compartment geometry. The baffles were put into the oxygen side so that the gas compartments could be interchanged.

A schematic diagram of the test rig used in the single-cell tests is shown in Fig. 3. A compressed air

[1] American Cyanamid type AB-1.

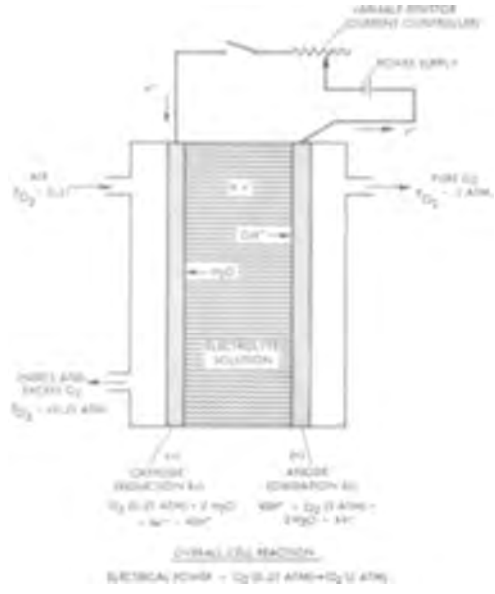

Fig. 1. Cell reactions and schematic of the TRW oxygen generator.

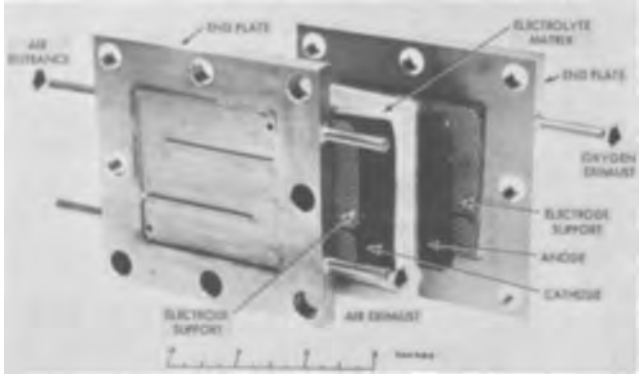

Fig. 2. Single-cell oxygen concentrator

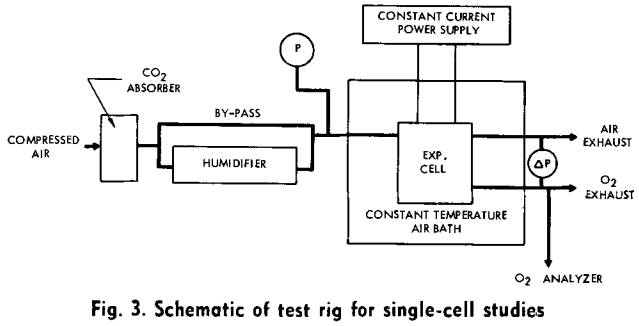

Fig. 3. Schematic of test rig for single-cell studies

source was used when cell tests were conducted at ambient pressure. A vacuum pump, simultaneously connected to the air and oxygen exhausts, was used when inlet pressures less than ambient were being tested.

The air was passed through a CO_2 absorber to remove the traces of carbon dioxide found in air to prevent it from neutralizing the KOH electrolyte. To prevent the cell from desiccating it was necessary for the net transfer of water into and out of the concentrator to be zero. This was accomplished by bubbling the air through a humidifier located in a constant temperature water bath. The vapor pressure of the water in the air entering the concentrator was thus made equal to the vapor pressure of the electrolyte, at the cell operating temperature, by controlling the water bath temperature. The moisture content of the incoming air was varied depending on the temperature and concentration of the electrolyte.

A pressure gauge was used to monitor the air inlet pressure, and a differential pressure gauge was used to measure the difference in pressure between the exit air stream and exit oxygen stream.

Results and Discussion of Results

A coulomb balance was made to demonstrate that the reactions occurring were the four electron reactions given in Fig. 1. The current put through the concentrator correlated with the oxygen consumed and the oxygen evolved as experimentally measured. The calculated and experimentally measured values of the oxygen output agreed with each other within 0.1% when four was used as the number of electrons transferred in the process.

The theoretical reversible voltage for this reaction is 0.01v. Because of activation polarization and to a small extent concentration polarization and ohmic losses, the voltages required during the electrochemical concentrating process ranged from 60 to 100 times greater than the theoretical value. The exact value was found to depend on air flow rate, air inlet pressure, cell operating temperature, number of accumulated operating hours on the cell, and cell moisture balance.

The data presented in Fig. 4 show a typical performance curve obtained with the cell. The top curve shows the voltage required to separate the oxygen and includes the IR drop. The bottom curve represents the IR free voltage. All IR free data were taken with a transistorized version of the Kordsch-Marko bridge (1).

A typical resistance value for the cell, evaluated at 100 ASF, was 0.0008 ohm-ft^2 or 0.74 ohm-cm^2.

The air flow rate into the cell was four times the stoichiometric (theoretical) air flow rate, T, for the oxygen being generated.

The air flow rate may also be expressed in terms of the percentage of the oxygen removed from the incoming air stream and transported to the anode compartment. Thus a flow rate of $4T$ means 25% of the oxygen found in the incoming air is consumed at the cathode and generated at the anode. Two T would mean 50% of the O_2 is removed, while 3 and $5T$ mean 33 and 20% are removed, respectively.

The data presented in Fig. 5 are the IR free performance contributed by the individual half-cells. The reference electrode was a platinum black-Teflon composite (the same as used for the cell electrodes), electrically isolated from the anode, but located against the porous matrix material in the same plane as the anode. The reference electrode was fed with pure oxygen from an external source through an isolated manifold system but at the same pressure as the anode compartment.

The limiting current density for the cell in the range of 120 to 130 ASF results from a gas phase polarization at the cathode. Proper geometrical design of the cathode compartment can extend the current density

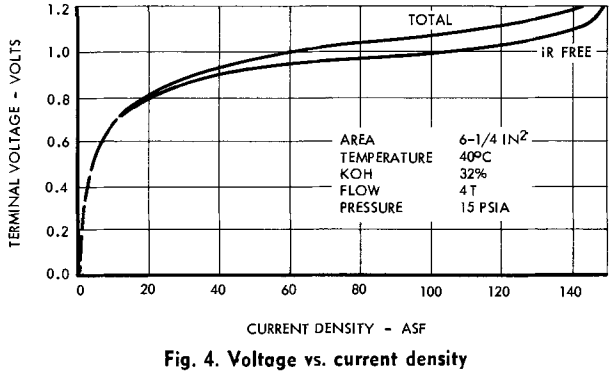

Fig. 4. Voltage vs. current density

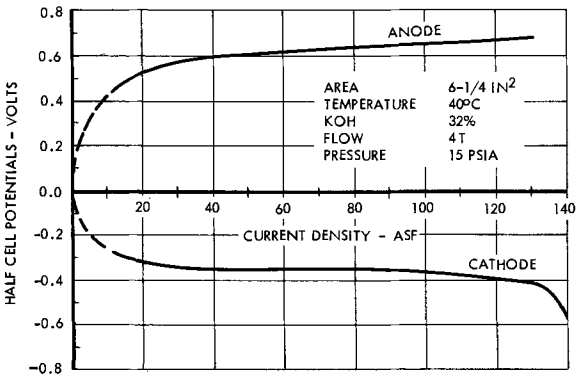

Fig. 5. Half-cell performances

over which one can operate before reaching the limiting value.

The performance of the cell is dependent on the flow rate of the incoming air. This dependency is illustrated in Fig. 6 for flow rates corresponding to 2*T*, 3*T*, 4*T*, and 5*T*. The power required to generate a given quantity of oxygen decreases as the flow rate increases although increasing the flow rate to above 5*T* had little effect on lowering the power required.

As may be observed from the curves, there is a decided difference in onset of the limiting current density between flow rates of 2*T* and 3*T*. At 4*T* and 5*T* the performance still improves (power required decreases), but at a slower rate. For this cell geometry it was found that flow rates greater than 5 had little effect on improving the concentrator's performance.

Cell performance is dependent on inlet air pressure as well as inlet air flow rates. This is illustrated in Fig. 7. Here experiments were performed at inlet pressures of 4, 6, 8, 11, and 15 psia. A constant air mass flow rate was used for all the tests. As the inlet air pressure increased the performance increased.

Both air flow rates and inlet air pressures are important in regard to cell performance. However, the cell's moisture balance is also critical. In Fig. 8 are

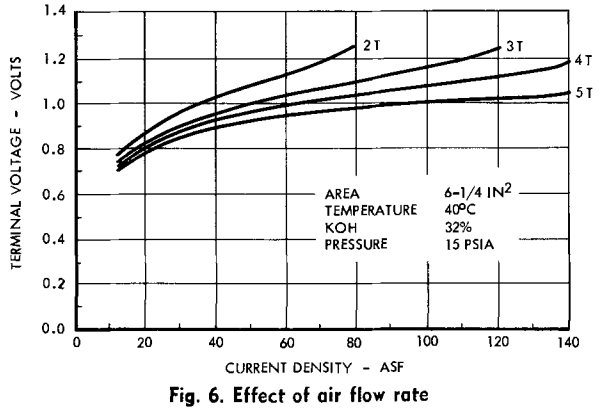

Fig. 6. Effect of air flow rate

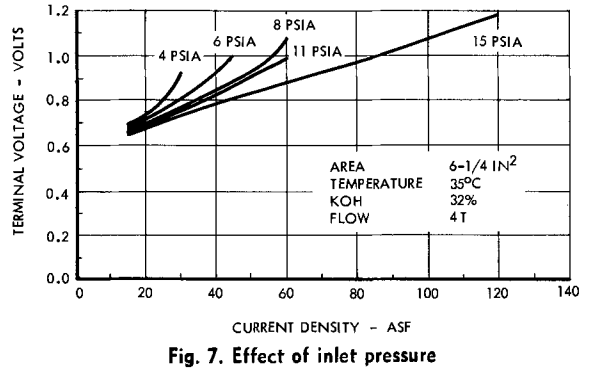

Fig. 7. Effect of inlet pressure

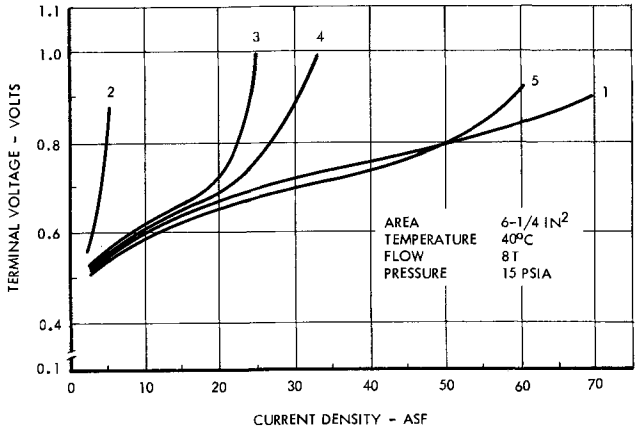

Fig 8. Effect of cell moisture balance

presented data taken during the time the cell's moisture content was varied.

Curves 1 through 5 were all obtained with the same cell. Curve 1 was the initial performance obtained while the cell had a proper moisture balance between that required by the cell and the air feed stream. Curve 2 was obtained after the cell had been desiccated, *i.e.*, that the water content of the incoming air was less than that required to match the vapor pressure of the electrolyte. Curves 3, 4, and 5 illustrate the improvement in cell performance, as the cell was brought back to its initial moisture conditions. The results presented in this figure emphasized the importance of moisture balance on cell operation and the importance of knowing that such a balance exists when performance (parametric) data are taken.

At any one moisture balance a typical family of parametric (flow rate, pressure, etc.) curves can be obtained. All experimental data presented previously were obtained under balanced moisture conditions. When the previously presented data are collected under the conditions represented in curves 2, 3, or 4 of Fig. 8, an entirely different group of relationships is found. The trends are the same, but the magnitude of values, such as the limiting current density, is markedly different. In addition, if the effect of variables, such as flow rate, is determined while the cell is either going into or out of moisture balance, the true effect of this variable is not observed. In fact, the general trends can be reversed merely by noting the change in cell performance. Therefore, moisture balance is truly important in evaluating a cell's performance characteristics.

Electrode activity is also influential. Initial performance curves taken on a cell assembled with new electrodes were always better. However, in all of these experiments the electrodes had been tested for a sufficient number of hours (typically 100-200 hr) so that changing of electrode activity was not likely to obscure the results of these tests.

These data indicate that it is essential to know the condition of the cell's moisture balance in determining the effect of parameters on cell performance when the electrolyte is held in a porous matrix.

For a cell to be reliable in producing oxygen its performance over a long period of time must be demonstrated. Data illustrating concentrator performance for over 600 hr are shown as Fig. 9. Here the current density was held constant at 40 ASF and the voltage was followed as a function of time. The variation in voltage from 0.7 to 0.9v may be observed. The tests were concluded at the end of 600 hr for sake of convenience in the laboratory.

Conclusions

The four-electron transfer process for concentrating oxygen from ambient air was experimentally demonstrated by observing that a coulomb balance predicting

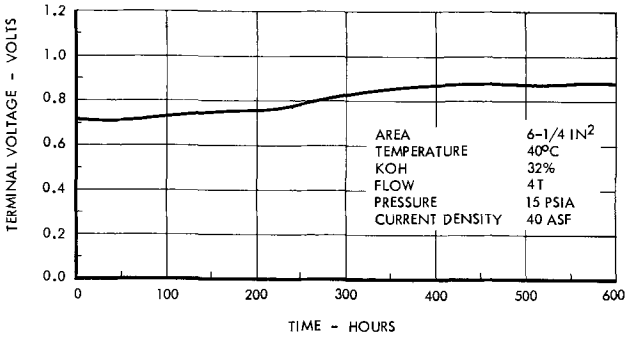

Fig. 9. Oxygen concentration performance over extended time period.

the quantity of gas generated in a given time period was within 0.1% of the experimental quantity of gas collected over this same time period.

The performance of the concentrator cell was found to vary with inlet air flow rates, inlet air pressures, and moisture balance between the water content in the inlet air stream and the vapor pressure of the electrolyte.

The limiting current density of the cell greatly increased between inlet flow rates of $2T$ and $3T$. The performance was still better at $4T$ and $5T$ but the rate of gain was slower. The higher the inlet pressure of the air stream, the better was the performance of the cell. At a 4 psia inlet this limiting value was 30 ASF. At 15 psia this limiting value was beyond 120 ASF.

In a single test the limiting current density of the cell could be varied anywhere from 5 ASF to beyond 120 ASF, depending on what the moisture balance relationship was between cell electrolyte and the vapor pressure of the water in the incoming air stream.

Acknowledgment

The authors wish to acknowledge the support received from the Equipment Laboratories of TRW, Inc. during the development of this oxygen generating concept.

Manuscript received Sept. 19, 1966; revised manuscript received Feb. 23, 1967. This paper was presented at the Cleveland Meeting, May 1-6, 1966.

Any discussion of this paper will appear in a Discussion Section to be published in the December 1967 JOURNAL.

REFERENCE

1. K. V. Kordesch and A. J. Marko, *This Journal*, **107**, 480 (1960).

On the Mechanism of Oxygen Evolution at Iridium Electrodes

A. Damjanovic and M. K. Y. Wong

The Electrochemistry Laboratory, The University of Pennsylvania, Philadelphia, Pennsylvania

Recently, the mechanisms of oxygen reaction at iridium electrodes were analyzed both for acid (1*N* $HClO_4$) and for alkaline (1*N* KOH) solutions (1). Then available kinetic parameters were found consistent with the reaction paths listed in Table I. On the basis of indirect evidence it was suggested that the likely reaction path is the "electrochemical oxide" path (2) with the second reaction step in the anodic direction as the rate-controlling at low cathodic and anodic, and the first reaction step as the rate-controlling at high anodic overpotentials. Here, additional evidence is presented supporting the electrochemical oxide path for oxygen evolution at iridium electrodes.

The pH dependence of overpotential in oxygen evolution in acid solution can discriminate between electrochemical oxide path and the other two paths of Table I. In acid solution both at low and high η's, $d\eta/dp$H is positive for the second, rate-controlling, step of the electrochemical oxide path, and negative for the third steps of the latter two paths, where the $d\eta/dp$H dependence is the same. In alkaline solution, the $d\eta/dp$H is negative both at low and high anodic overpotentials but with different values. Observed dependences are also given in Table I.

Table I. Calculated and observed pH dependence of overpotential in oxygen evolution

	Acid		Alkaline	
	Low η	High η	Low η	High η
Electrochemical oxide path (2)				
$S + H_2O \rightarrow SOH + H^+ + e^-$	RT/F	RT/F	$-RT/F$	$-RT/F$
$SOH \rightarrow SO + H^+ + e^-$	$RT/3F$	RT/F	$-RT/3F$	$-RT/F$
$2SO \rightarrow 2S + O_2$				
$S + H_2O \rightarrow SOH + H^+ + e^-$	RT/F	RT/F	$-RT/F$	$-RT/F$
$SOH + H_2O \rightarrow SOHOH + H^+$	0		$-RT/F$	$-RT/F$
$SOHOH^- \rightarrow SOHOH + e^-$	$-RT/3F$	$-RT/F$	$-RT/3F$	$-RT/F$
$SOHOH \rightarrow SO + H_2O$				
$2SO \rightarrow 2S + O_2$				
"Krasilshchikov" path (3)				
$S + H_2O \rightarrow SOH + H^+ + e^-$	RT/F	RT/F	$-RT/F$	$-RT/F$
$SOH \rightarrow SO^- + H^+$	0		$-RT/F$	$-RT/F$
$SO^- \rightarrow SO + e^-$	$-RT/3F$	$-RT/F$	$-RT/3F$	$-RT/F$
$2SO \rightarrow 2S + O_2$				
Observed dependence at Ir	+18	+48	−15	−55

Potential-anodic current density relationships are determined both in $HClO_4$ and KOH solutions of different concentrations. The experimental procedure, including the purification of the solutions, was the same as in a previous work (1). In Fig. 1 and 2, results are given for acid and alkaline solutions, respectively. These results confirmed the reported characteristics of two distinct linear V-log i regions in evolution both in

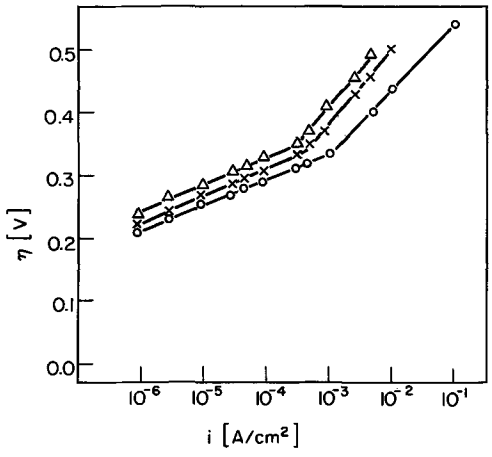

Fig. 1. V-log i at Ir in acid solutions. Open circles, pH 0.9; crosses, pH 1.9; triangles, pH 2.9.

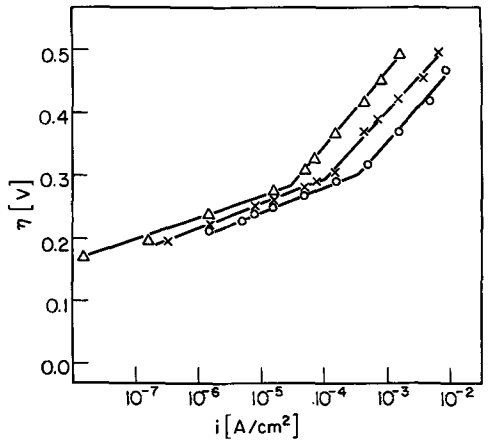

Fig 2. V-log i at Ir in alkaline solutions. Open circles, pH 14; crosses, pH 13; triangles, pH 12.

acid and in alkaline solutions with the Tafel slopes at low η's corresponding to $2RT/3F$ and at high η's to $2RT/F$. The pH dependence of overpotential in acid solutions are close to +18 and +48 mv/pH at low and high overpotentials, respectively. In alkaline solution these are −15 and −55 mv/pH. These dependences are in agreement only with the calculated dependences for the electrochemical oxide path. Present experimental evidence, hence, supports the electrochemical oxide path for oxygen evolution at Ir electrodes.

Acknowledgments

Financial support of the U. S. Army Electronics Material Laboratory, Fort Monmouth, New Jersey (Contract No. DA-36-039-Sc88921) is gratefully acknowledged. The authors thank Professor J. O'M. Bockris for discussions and encouragements during the course of this work.

Manuscript received Jan. 30, 1967; revised manuscript received Feb. 28, 1967.

Any discussion of this paper will appear in a Discussion Section to be published in the December 1967 JOURNAL.

REFERENCES

1. A. Damjanovic, A. Dey, and J. O'M. Bockris, *This Journal*, **113**, 739 (1966).
2. J. O'M. Bockris, *J. Chem. Phys.*, **24**, 817 (1956).
3. A. I. Krasilshchikov, *Zhur. Fiz. Khim.*, **37**, 531 (1963).

Improvement of a Square-Wave Technique for Capacitance Measurements

R. G. Barradas and E. M. L. Valeriote

Lash Miller Chemical Laboratories, Department of Chemistry, University of Toronto, Toronto, Ontario, Canada

The development of a square-wave charging technique for the measurement of differential capacities of the electrical double layer has been described by Hackerman and co-workers (1, 2). This method is based on analysis of the repetitive charging and discharging of the electrical double layer through a series resistance R_s. An evaluation of the technique was carried out by the authors (3) who observed a substantial dependence of the measured capacitance-potential curves, and their reproducibility, on the value of R_s. Agreement with electrocapillary data and with capacity-potential curves obtained by the impedance bridge method appeared to be better for larger values of R_s. Because of the interdependence of the experimentally variable quantities (3), values of R_s large enough to give good agreement could not be used without a change in other parameters. The simplest resolution of this problem proved to be a reduction of the area of the mercury electrode.

Experimental Results

Experiments were carried out as previously reported (3). However, in place of the 5 cm² mercury pool, a hanging mercury drop electrode of about 7 mm² area was used (Fig. 1) for which the size of the mercury drop could be controlled by an Agla micrometer syringe (Burroughs Wellcome and Company, London) similar to that reported by Narayan (4). The area of the drop could not be absolutely calculated, possibly because creepage of the solution up the glass capillary may have caused some effective increase of the amount of mercury surface exposed to the solution, and drop areas had to be calculated by relative methods. For the data displayed in Fig. 2, showing the variation of capacity with potential for a 1*N* KCl solution, the area was calculated by comparison of the differential capacity (per unit area) reported by Grahame and Parsons (5) at one potential with the total capacity determined by the charging technique at that poten-

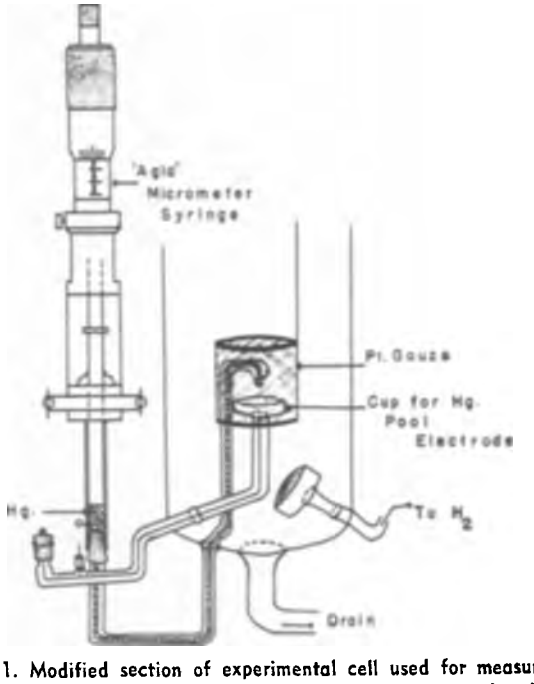

Fig. 1. Modified section of experimental cell used for measurement of double layer capacities by the square-wave charging technique.

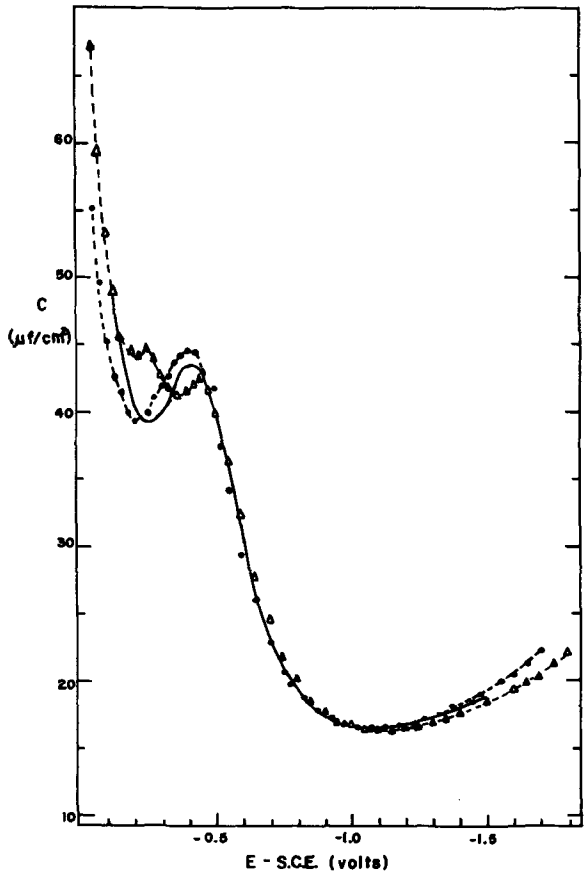

Fig. 2. Dependence of capacity on potential: Grahame and Parsons (5)-solid curve; 1N KCl measured with cathodic polarization, - - - △; 1N KCl measured without cathodic polarization, - - - •.

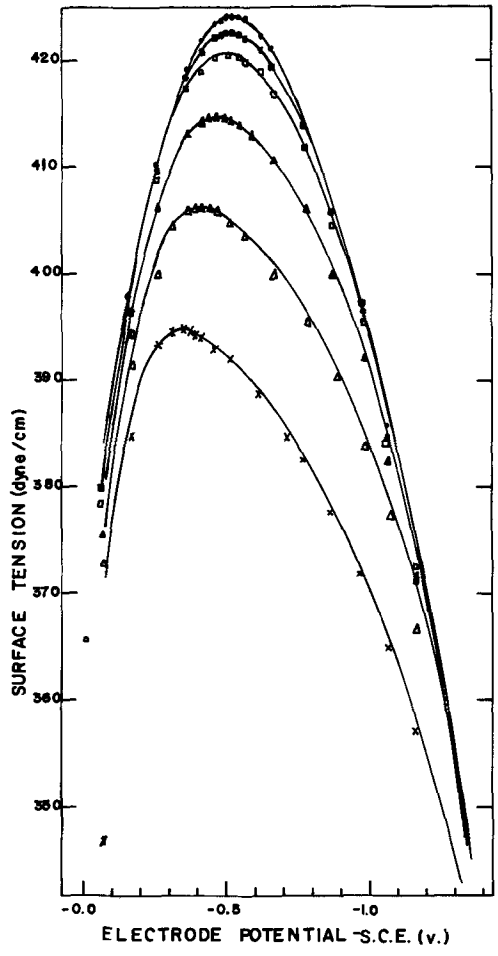

Fig. 3. Comparison of electrocapillary data (points) and doubly integrated capacity data (solid curves) for 1N KCl and 1N KCl with various concentrations of added furfurylamine. 1N KCl •; concentration of furfurylamine in 1N KCl; 0.003M ■, 0.01M □, 0.03M ▲, 0.10M △, 0.30M X.

tial. The solid curve in Fig. 2 is the data of Grahame and Parsons (5); the points were obtained for R_s = 77 K "with" and "without cathodic polarization." In the case of the curves obtained with cathodic polarization the potential was rapidly switched from —2.0v (SCE) to the potential at which the capacity was to be measured immediately before the determination.

Figure 3 displays a comparison of directly determined electrocapillary data (7) with doubly integrated capacity curves for various concentrations of furfurylamine in 1*N* KCl. The calculated surface tension data were obtained by numerical integration (6) on an IBM-7094 Computer using integration constants determined in this laboratory (7). No cathodic polarization was used when organic additives were present since it would have interfered with the attainment of adsorption equilibrium.

Discussion

For 1*N* KCl, the region of the hump at anodic rational potentials was distorted somewhat when cathodic polarization was employed, but good agreement was obtained over all of the remainder of the curve [cf. ref. (1) and (3) in which poor agreement with the literature was reported over substantial potential ranges for various inorganic electrolytes]. Without cathodic polarization there is excellent agreement at all cathodic rational potentials and only small differences at anodic rational potentials; the shape of the hump was reproduced more satisfactorily. This appears to indicate that the solution was sufficiently pure and that no advantage is gained by cathodic prepolarization. Upon additions of furfurylamine a good comparison with directly determined electrocapillary data (7) was observed (Fig. 3), and correspondingly good results were also obtained for other related organic systems.

The improved agreement would appear to support in part the suggestions of Brodd and Hackerman (2) concerning the use of the technique in determining electrode areas. Areas might be measured by comparison of capacities between small enough samples of the same metal provided that the area of at least one sample is determined by an independent method such as a gas adsorption technique.

In summary, we conclude that as expected the square-wave method is less accurate and dependable than the impedance bridge technique for fundamental double layer studies. A preferable choice would be the automatic method (8, 9[1]) of recording capacity-potential curves by the use of a phase-sensitive device supplementary to a polarograph, which gives better agreement with the results of Grahame and Parsons (5). Further evidence using the automatic recording method for mercury Teflon capillary and platinum electrodes will be later presented elsewhere (10).

Acknowledgments

Grateful acknowledgment is made to the National Research Council of Canada for financial support of this work and for the award of a studentship (to E.M.L.V.) for 1965-1966.

Manuscript received Dec. 27, 1966; revised manuscript received March 7, 1967. This paper was presented at the Buffalo Meeting, Oct. 10-14, 1965.

[1] Note typographical errata in ref. (8). There should be a connection between the junction of the 0.04 μf and 200 μf condensers and the junction of the 1.2 K resistor and the emitter of the OC71 transistor. In addition the mercury drop electrode area should read 0.02 cm².

Any discussion of this paper will appear in a Discussion Section to be published in the December 1967 JOURNAL.

REFERENCES

1. J. J. McMullen and N. Hackerman, *This Journal*, **106**, 341 (1959).
2. R. J. Brodd and N. Hackerman, *ibid.*, **104**, 704 (1957).
3. R. G. Barradas and E. M. L. Valeriote, *ibid.*, **112**, 1043 (1965).
4. R. Narayan, *J. Electroanal. Chem.*, **4**, 123 (1962).
5. D. C. Grahame and R. Parsons, *J. Am. Chem. Soc.*, **83**, 1291 (1961).
6. R. G. Barradas, F. M. Kimmerle, and E. M. L. Valeriote, *J. Polarograph. Soc.*, In press.
7. R. G. Barradas and P. G. Hamilton, Unpublished data.
8. E. M. L. Valeriote and R. G. Barradas, *J. Electroanal. Chem.*, **12**, 67 (1966).
9. Z. Kowalski and J. Srzednicki, *ibid.*, **8**, 399 (1964).
10. E. M. L. Valeriote and R. G. Barradas, In course of preparation.

Metal Membrane Electrodes

E. B. Buchanan, Jr., and J. L. Seago

Department of Chemistry, University of Iowa, Iowa City, Iowa

The specificity and simplicity of the measurement of pH with the glass electrode has induced many chemists to search for other ion-specific electrodes. A number of such electrodes have been suggested. In general, they involve the measurement of the potential developed by a concentration cell. The difference in concentration within the cell is maintained by an appropriate membrane. Thus, the ion-specific electrode is not a simple electrode but rather one-half of a concentration cell. The important element in a successful electrode of this type is the membrane. The membrane should respond to a single ionic species. For this purpose electrodes have been developed which utilize membranes fabricated from ion exchange resins (1-7), clays (8, 9), and either collodion, or paraffin, or silicon rubber which is imbedded with the crystals of a salt of the desired ion (10-15).

There are many theories and much diversity of opinion on the mechanism by which these electrodes operate. Some explanations propound a transport of ionic material through the membrane while others involve a Donnan potential developed at the surface (11, 13-15).

This study encompasses a series of membranes which involve an oxidation-reduction reaction at the surface and electron transfer through a bipolar membrane. For this purpose cells of the form

$$\text{SCE/Sample Soln.//Membrane//Ref. Soln./SCE}_{\text{(Metal)}}$$

were constructed. The metals and their respective ions selected for study were copper, cadmium, silver, and thallium. By maintaining the concentration of the solution on one side of the membrane constant and varying the concentration of the opposing side, the concentration dependence of each cell was studied.

Experimental

Apparatus.—The electrode was constructed by sealing the metal foil or billet to the end of an 18 mm glass tube. The seal was made with Hot Melt Glue obtained from Montgomery Ward. Figure 1 shows the experimental apparatus.

Potential measurements were made with a Cary Model 31 vibrating reed electrometer equipped with a Cary/Honeywell Multi-range Recorder. A recorder response of 1 mv/in. was used where possible. Otherwise, a response of 3 mv/in. was employed.

Procedure.—The concentration dependence of the membrane electrode was evaluated by measuring the potential that was developed between a pair of matched reference electrodes when the metal membrane separated the two halves of a concentration cell.

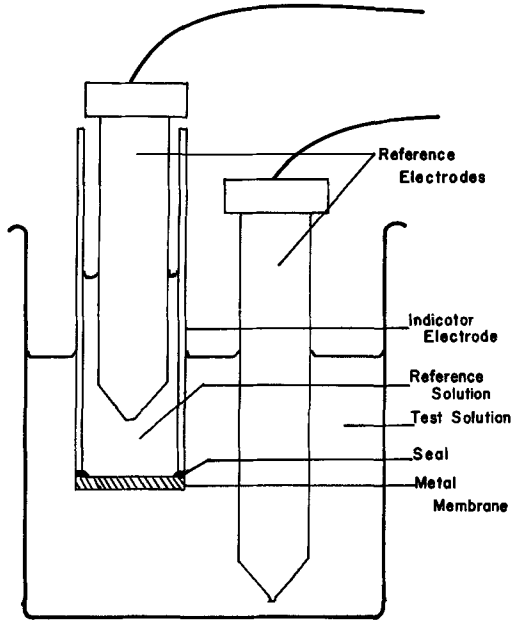

Fig. 1. Metal membrane electrode cell assembly

The solution on one side of the membrane, reference side, was maintained at a constant metal ion concentration of 0.01M. The solution on the other side, sample side, was varied between the limits specified below.

The effects of atmospheric oxygen, acidity of the solutions, and amalgamation of the membrane surfaces were examined in an attempt to achieve a theoretical response from the cells. Atmospheric oxygen was excluded from the solutions by deaerating the solutions with a rapid stream of nitrogen and storing the deaerated solutions in a nitrogen-filled glove bag. The bag is available from I²R, 108 Franklin Street, Cheltenham, Pennsylvania. The effects of acidity on the measured potential were examined by preparing two sets of solutions, one set containing only the salt of the desired ion, the other set containing, in addition to the salt, 1M sulfuric acid. The surface condition of the membrane was considered as a factor which could also influence the potential of the cell. Both the polished free metal and lightly amalgamated metal surfaces were employed. The billet or foil was amalgamated by rubbing the metal surface with mercury while the surface was submerged in 6M sulfuric acid. A limited amount of mercury was used to ensure that the mercury did not dissolve the entire membrane. It was necessary to amalgamate the membrane after it

was sealed to the glass tube since the amalgamated surface would not adhere to the glue. All experiments were performed at room temperature which was maintained at 22°-27°C. All chemicals employed were of analytical grade.

Silver membrane electrode.—A membrane of silver foil was used. Solutions of silver nitrate in the concentration range of 1 to 1 x 10^{-7}M were placed on the sample side of the membrane. All experiments were conducted in the presence of atmospheric oxygen. The reference electrodes were

$$Ag/AgCl, KCl_{sat.}/3\% \text{ Agar}, NaNO_{3sat.}//$$

Copper membrane electrode.—Both a polished copper foil and a surface amalgamated copper foil membrane were employed. Acidified copper sulfate solutions in the concentration range of 1 to 1 x 10^{-6}M were used on the sample side of the membrane. The effect of oxygen was determined by working in both the presence and absence of air. The reference electrodes were

$$Ag/AgCl, KCl_{sat.}/3\% \text{ Agar}, Na_2SO_{4sat.}//$$

Cadmium membrane electrode.—Polished cadmium metal billets and surface amalgamated cadmium billets were employed as membranes. Cadmium sulfate solutions in the range of 1 to 1 x 10^{-6}M were used on the sample side of the membrane. The effect of acidity was determined by preparing the solutions in the presence and absence of sulfuric acid. The effect of oxygen was studied by making measurements in both the presence and absence of air. Matched Beckman SCE were the reference electrodes employed.

Thallium membrane electrode.—The membranes used in this cell were made of a polished thallium billet and a surface amalgamated billet. The polished thallium billet was stored in 0.1M thallium nitrate solution. The oxide coating is removed by this storage since both thallium oxide and hydroxide are water soluble. Both acidified and neutral solutions of thallium nitrate were utilized. The experiments were conducted in the presence and absence of air. The concentration range of 0.1 to 1 x 10^{-6}M thallium nitrate was put into use on the sample side of the membrane. The reference electrodes used were matched Beckman SCE with an exterior fiber sleeve filled with saturated sodium nitrate.

Results and Conclusions

The silver membrane electrode is characterized by a rapid response. In 1 min the cell is within 0.1 mv of steady-state values. The theoretical concentration dependence is obtained over the concentration range of 1 to 3 x 10^{-6}M. Figure 2 illustrates the Nernst equation type of dependence shown by this electrode.

Cadmium metal is more readily oxidized than silver, and, therefore, greater care must be taken to secure reproducible results from the membrane surface. In the absence of air there is no significant difference between the response of the amalgamated and the pure cadmium metal membranes. In air-saturated solutions the use of the amalgamated electrode is essential if reproducible data are to be obtained. The presence of sulfuric acid in the air-saturated solutions seems to improve the response slightly. However, the main effect is a decrease in the time required to reach steady-state values. The potential was within 1 mv of the steady-state potential in 5 min. Figure 3 shows the range of concentration over which this electrode is applicable.

The requisite conditions for the theoretical response of the copper electrode are even more stringent. Only when the membrane surfaces were amalgamated, oxygen carefully excluded, and 1M sulfuric acid was present in the solution did the cell become capable of providing a theoretical response. Even under these conditions the response of the electrode was sluggish.

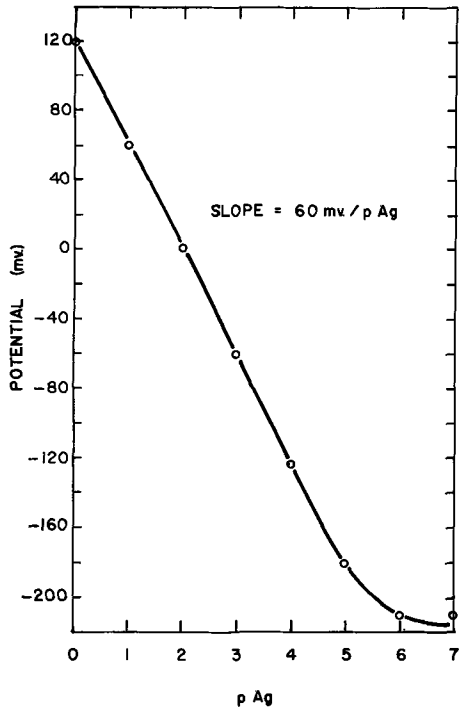

Fig. 2. Silver membrane electrode response

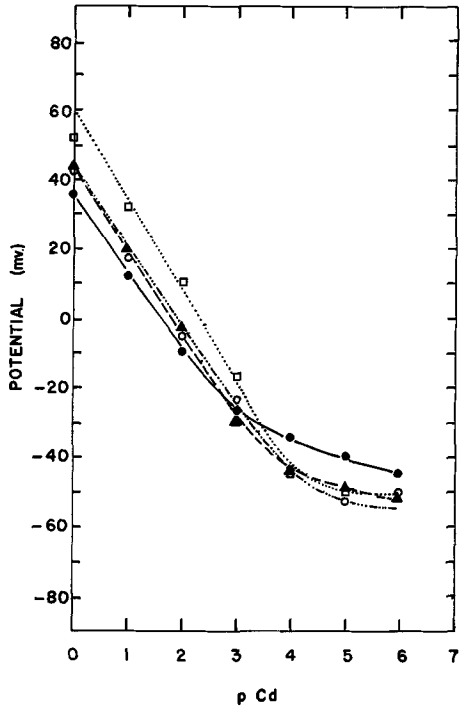

Fig. 3. Cadmium membrane electrode response: ○, cadmium metal membrane, nitrogen atmosphere; □, amalgamated cadmium membrane, nitrogen atmosphere; ●, amalgamated cadmium membrane, air; ▲, amalgamated cadmium membrane, air, 1M H_2SO_4.

Five minutes were necessary for the cell to achieve a potential that was within 1 mv of a steady-state potential. Figure 4 indicates the concentration range over which the cell is capable of producing a theoretical response.

Apparently trace amounts of oxygen catalyze the production of the Cu(I) through the formation of the insoluble Cu_2O. The production of the red oxide is minimized by the conditions which give a theoretical response. This hypothesis is supported by the observation that the copper electrode under no known conditions gives satisfactory results in the presence of

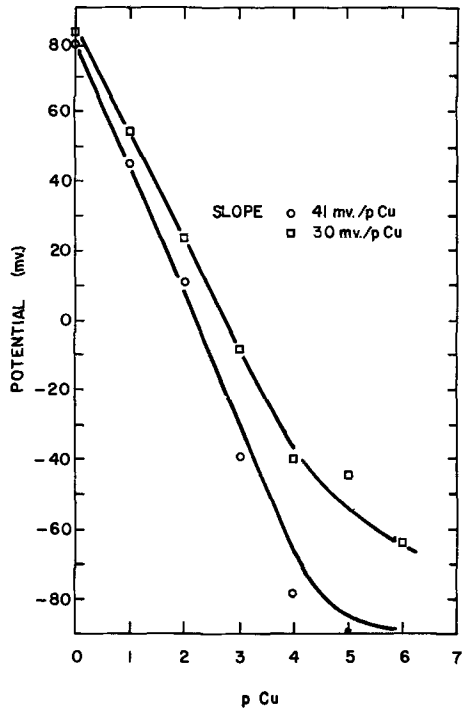

Fig. 4. Copper membrane electrode: ○, copper metal membrane, nitrogen atmosphere, 1M H_2SO_4; □, amalgamated copper membrane, nitrogen atmosphere 1M H_2SO_4.

atmospheric oxygen. Earlier attempts at the use of the copper electrode have involved a pre-equilibration of the Cu(II) solutions with metallic copper before immersion of the copper electrode under experimental conditions which assured the complete exclusion of oxygen (16).

Figure 5 shows the response of the cell utilizing a thallium billet membrane. The theoretical response is only obtained in an oxygen-free atmosphere. This is not surprising as the thallium metal reacts readily with the oxygen of the air forming a yellow oxide coating. Once the coating is removed, and its further formation is prevented, the electrode displays the desired potential. Potential values within 1 mv of steady-state values were obtained in 5 min. Amalgamation of the surface or the presence of 1M sulfuric acid had no effect on the final potential of the cell. However, in the presence of either one or both of these conditions, the response time (±1 mv from steady state) was reduced to 3 min.

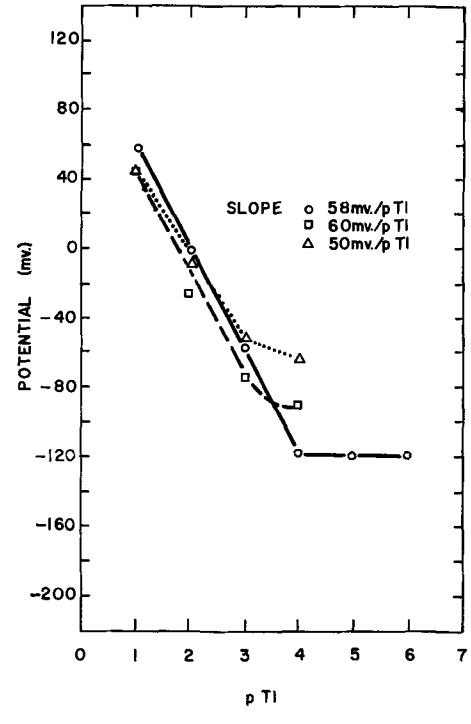

Fig. 5. Thallium membrane electrode response: ○, thallium metal membrane, nitrogen atmosphere, in the absence and the presence of 1M H_2SO_4; □, amalgamated thallium membrane in a nitrogen atmosphere; △, amalgamated thallium membrane, 1M H_2SO_4 in air.

In air, using the surface amalgamated thallium billet and neutral thallium nitrate solutions, no response was obtained. If the thallium solutions were made 1M in sulfuric acid, the amalgamated thallium billet displayed a rapid linear response to a thallium ion concentration of 1×10^{-3}. The slope of the curve was 50 mv/pTl. The authors believe the presence of the sulfuric acid prevents the air oxidation of the thallous ion to the thallic ion. In an alkaline solution the insolubility of thallic hydroxide enhances the ease of this oxidation.

The entire cell may be considered as two cells in series, bridged by an appropriate metal junction. While the membrane is a decided convenience and ensures that the metal has been subjected to the same stresses and distortions, a wire bridging the two cells would give essentially the same results. Each side of the membrane can be thought of as a single electrode which, in conjunction with a reference electrode, produces a potential corresponding to the concentration (activity) of the metal ion in solution. The value of this potential can be obtained from the Nernst equation.

$$E = E^\circ + E_{ref} + \frac{RT}{n\mathbf{F}} \ln C$$

The potential obtained for the entire cell should be the difference in potential calculated for each side of the membrane.

$$E_{cell} = E_{samp} - E_{ref}$$

Substituting the values obtained for each side from the Nernst equation and simplifying gives

$$E_{cell} = \frac{RT}{n\mathbf{F}} \ln \frac{C_{samp}}{C_{ref}}$$

which is the equation for a concentration cell without transference.

From a consideration of the cell, it is apparent that one side of the membrane is acting as an anode while the other acts as a cathode; hence, the term bipolar membrane as used above. In spite of its bipolar character, there can be no potential difference within the membrane itself since a metal cannot show an internal potential difference without a flow of current.

Within the cell there are six sites at which potentials can be considered to arise. Four of these are phase boundaries and two are liquid-liquid junctions. The two connections to the external circuit and the two solution-membrane interfaces constitute the four phase boundaries while the liquid-liquid junctions are found between the reference electrodes and the solution in each side of the cell. The liquid-liquid junction potentials are normally small, and the difference between them results in a still smaller potential. The connection to the external circuit is made through a reference electrode and, therefore, provides a constant potential. The cancellation of the potential due to the external connection and the absence of a potential difference within the membrane causes the measured potential to be a direct measure of the potential difference between the two solutions provided the liquid-liquid junction potentials are neglected. The presence of these liquid-liquid junction potentials even though they are small precludes the use of the cell for the thermodynamic measurement of activities.

The metal membranes are unique in that they involve neither an ionic transport nor the process of diffusion within the membrane. The potential at the metal membrane involves an oxidation-reduction reaction as contrasted to an adsorption or ionic transport mechanism found in other types of ion-responsive membranes. In order to function properly any metal membrane requires reversibility of the oxidation-reduction process. This imposes a serious limitation on the selection of metals as not all will exhibit the degree of reversibility required. Our data indicate that under proper experimental conditions steady-state potentials are achieved very rapidly and are reproducible.

Manuscript received July 25, 1966; revised manuscript received Feb. 14, 1967.

Any discussion of this paper will appear in a Discussion Section to be published in the December 1967 JOURNAL.

REFERENCES

1. J. S. Parsons, *Anal. Chem.*, **30**, 1262 (1958).
2. R. Nieholf, *J. Phys. Chem.*, **58**, 916 (1954).
3. S. K. Sinha, *J. Indian Chem. Soc.*, **32**, 35 (1955).
4. V. Schinderwolf and K. F. Bonhoeffer, *Z. Elektrochem.*, **57**, 216 (1953).
5. D. Woerman, K. F. Bonhoeffer, and F. Helfferich, *Discussions Faraday Soc.*, **21**, 217 (1956).
6. M. R. J. Wyllie, *J. Phys. Chem.*, **58**, 67 (1954).
7. M. R. J. Wyllie and H. W. Patnode, *ibid.*, **54**, 204 (1950).
8. C. E. Marshall, *J. Phys. Chem.*, **48**, 67 (1944).
9. C. E. Marshall and W. E. Bergman, *ibid.*, **46**, 52 (1942).
10. H. P. Gregor and K. Sollner, *J. Phys. Chem.*, **58**, 409 (1954); K. Sollner, *This Journal*, **97**, 139C (1950); *Ann. N.Y. Acad. Sci.*, **57**, 177 (1953).
11. E. Pungor, J. Havas, and K. Toth, *Acta Chim. Acad. Sci. Hung.*, **41**, 239 (1964).
12. E. Pungor, J. Havas, and K. Toth, *Z. Chem.*, **5**, 9 (1965).
13. G. A. Rechnitz, M. R. Dresz, and S. B. Zamochnick, *Anal. Chem.*, **38**, 973 (1966).
14. S. Morgazzani-Pelletier and M. A. Baffier, *J. Chim. Phys.*, **62**, 429 (1965).
15. R. B. Fischer and R. F. Babcock, *Anal. Chem.*, **30**, 1732 (1958).
16. L. H. Jenkins and V. Bertocci, *This Journal*, **112**, 517 (1965).

SOLID STATE SCIENCE

The Permeation of Isolated Anodic Zirconium Oxide Films by Potassium Nitrate

A. H. Mitchell

Pitman-Dunn Research Laboratories, Frankford Arsenal, Philadelphia, Pennsylvania

and R. E. Salomon

Department of Chemistry, Temple University, Philadelphia, Pennsylvania

ABSTRACT

The permeation of anodic zirconium oxide films by KNO_3 has been investigated. Dependence of the permeation rate on film thickness, permeant concentration, film area, and temperature was studied. Film thicknesses ranged from approximately 700 to 7000Å. Permeation rates on the order of 10^{-8} moles cm^{-2} sec^{-1} were observed. Rates were found to be directly proportional to KNO_3 concentration and film area and inversely proportional to film thickness. Apparent activation energies calculated from rate constant-temperature data varied with the film thickness. A simple model proposing permeation through a system of cylindrical charged pores is consistent with the data for thin films. The permeation of thicker films may be complicated by additional factors.

Since the advent of the use of zirconium and its alloys in nuclear reactors, the study of oxide films on zirconium has been of considerable interest. A number of investigators have studied both anodic and corrosion formed oxide films on zirconium obtaining information on their formation, structure, and electrical properties (1-8). Evidence has been found to suggest that so-called barrier-type anodic oxide films in contact with electrolyte solutions are penetrated by them (9-12). However, the nature of the flaws allowing penetration and the mechanism by which it might be accomplished remain largely speculative. In this paper, quantitative studies of the penetration of anodic zirconium oxide films by electrolyte are described, and a possible model for the permeation is proposed.

Experimental

The materials, experimental techniques, and equipment used in this investigation have been briefly described in an earlier publication (12). Specimens of chemically polished foil about 50 cm^2 in area were anodized on one side at constant voltage for 18 hr in a boric acid-sodium borate electrolyte buffered at pH 9. The anodization parameters were kept similar to those of earlier investigations (12, 13) so that the growth factor of 27 Å/v over comparable potential ranges could be reasonably assumed. Leakage current densities ranged from 1 μa cm^{-2} for the thinnest films to 4.5 μa cm^{-2} for the thickest. After anodization, the films were washed and stored in a moist atmosphere. Several specimens were anodized at the appropriate voltages to insure a range of oxide thickness for permeation measurements.

Preliminary experiments were made to determine that electrolytes and other species in solution did penetrate the oxide film. In preparation for these experiments, samples of about 1 cm^2 were cut from the anodized specimens and clamped in a simple cell prepared from two Lucite blocks and glass tubing. The isolation of an approximately 3.0 mm^2 area of film was effected with a 0.5% HF solution. The cell was then clamped in a controlled temperature bath, and solutions were carefully added to each side of the cell so that the exposed film area separated them. The cell was then left to stand for periods of from 20 to 72 hr. There was no stirring. Mechanical vibration in the cell supports was relied on to agitate the solutions sufficiently.

Quantitative permeation measurements were made in a Lucite permeation cell described in Fig. 1. Its dimensions are approximately 3.5 x 3.5 x 2 cm. The thickness of the oxide and foil was exaggerated for the sake of clarity.

The anodized foil was clamped between the two blocks, and a small area of oxide film was isolated with a 0.5% HF solution. The area was well washed. The cell was then clamped in a constant temperature bath, and conductance water was slowly added to the

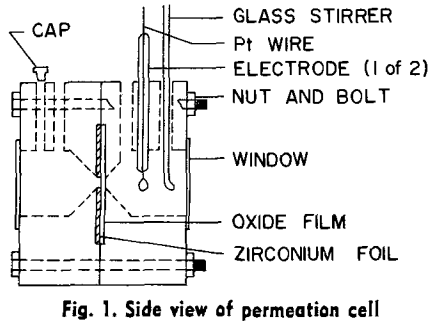

Fig. 1. Side view of permeation cell

Table I. Results of preliminary experiments

Chamber 1		Chamber 2		Time, hr	Permeation
KNO_3	0.5M	NaCl	0.5M	72	Yes
$AgNO_3$	5%	LiCl	5%	64	Yes
KNO_3	2.5M	LiCl	5.0M	50	Yes
LiCl	1.0M	KNO_3	2.5M	24	Yes
LiCl	1.0M	KSCN	1.0M	24	Yes
NaCl	1.0M	KSCN	1.0M	71	Yes
NaBr	1.0M	KNO_3	1.0M	72	Yes
KSCN	1.0M	$NaNO_3$	1.0M	17	Yes
$NaNO_3$	1.0M	KSCN	1.0M	65	Yes
H_2O		KNO_3	1.0M	20	Yes
H_2O		$Cu(NO_3)_2$	1.0M	20	Yes
H_2O		$Fe(NO_3)_3$	0.5M	20	Yes
$NaNO_3$	1.0M	H_2O		65	Yes
		Methyl orange		24	No
		Sucrose 2g/100 cc		24	No

chamber containing the electrodes while electrolyte was simultaneously added to the other chamber. KNO_3 was used in all of the measurements. Stirring was accomplished on the low concentration side with a bent glass rod. Studies were made on 27, 50, 100, 150, 200, and 250v films at temperatures of 15°, 25°, and 35°C. The permeation was monitored by measuring the increase in conductance of the water in the conductance chamber as KNO_3 permeated the exposed film.

Results

The results of the preliminary experiments are presented in Table I. The presence of permeated species on either side of the cell was detected by standard methods of qualitative analysis or by spot tests (14). Flame spectrophotometric checks were made for the presence of the alkali metal ions. All salts permeated the film in either direction. Organic molecules such as methyl orange and sucrose apparently did not penetrate the film at all.

The data resulting from the quantitative permeations consisted of the measured conductance of the water in the conductance cell at several time intervals. The conductances were converted to concentration of KNO_3 and plotted against the time. These curves, after about the first 3 min, proved to be linear. Typical curves for each film thickness are presented in Fig. 2. The rate of permeation was given by the slope and is expressed in moles sec^{-1} cm^{-2}. The permeation rates (average of three or more determinations) for all the films determined at three different temperatures are given in Table II. The rate was found to be proportional to the KNO_3 concentration, to the reciprocal film thickness for thin films, and to the area of film exposed for permeation (Fig. 3-5).

It was previously reported (12) that the permeation rate could be expressed by the empirical equation

$$r = cP = cP_o \exp(-E/RT) \quad [1]$$

where r is the rate, c is the concentration of permeating KNO_3, and P, P_o, and E are constants. With the inclusion of the film thickness and isolated area dependence, the rate for films up to 150v thick can be empirically expressed by

$$r = cP'A/L \quad [2]$$

where A is the area, L is the film thickness, and the other terms retain their identities. The constant P' was calculated. It can be seen, however, (Table III) that P' was not constant, apparently varying with the film thickness. The fact that P' is some function of the thickness was further demonstrated by the constancy of P' when the film thickness remained the same and the concentration was varied (Fig. 3). When the log of P' for films of each thickness was plotted against the reciprocal absolute temperature, straight lines were obtained.[1] The slope gave the apparent ac-

Table II. Average permeation rates for 27 through 250v films at three temperatures using 1M KNO_3

Film thickness, v	Temp	Rate (moles cm^{-2} sec^{-1} x 10^8) 15°C	25°C	35°C
27	$\bar{x}$	2.0	3.7	5.4
	s	0.03	0.26	0.08
50	$\bar{x}$	0.91	2.0	4.5
	s	0.08	0.11	0.51
100	$\bar{x}$	0.40	1.1	3.1
	s	0.03	0.18	0.25
150	$\bar{x}$	0.16	0.64	2.3
	s	0.03	0.07	0.17
200	$\bar{x}$	0.15	0.45	1.2
	s	0.06	0.09	0.03
250	$\bar{x}$	0.14	0.30	0.51
	s	0.04	0.10	0.09

$\bar{x}$ Average rate.
s Standard deviation.

[1] At constant c, A and L, $r = P''$. Plots of P'' rather than P' *vs.* $1/T$ have been shown in Fig. 6 to allow better presentation of the data for all films on a single graph.

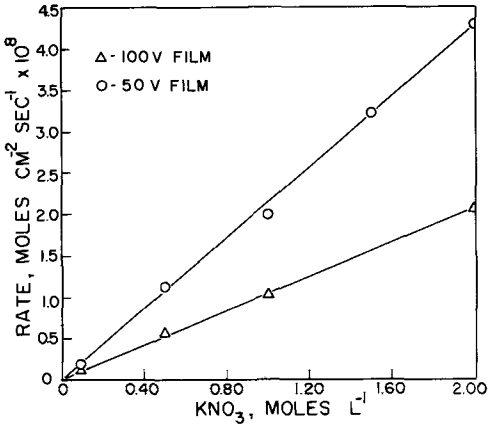

Fig. 3. Variation of the rate of permeation with concentration of permeating KNO_3 at 25°C.

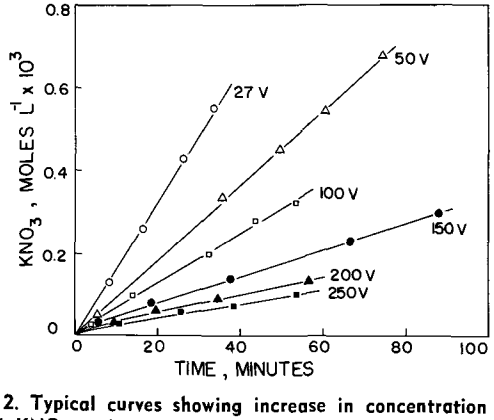

Fig. 2. Typical curves showing increase in concentration of permeated KNO_3 with time for films of several thicknesses at 25°C.

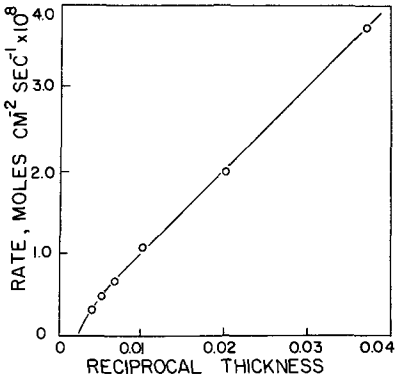

Fig. 4. Variation of permeation rate with film thickness at 25°C. The abscissa is the reciprocal of the formation voltage (volts^{-1}).

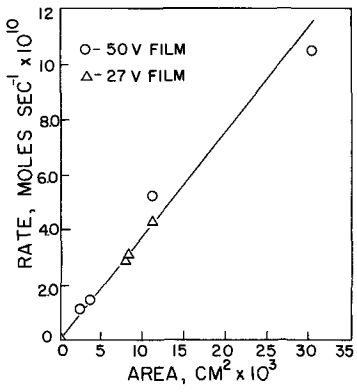

Fig. 5. Variation of permeation rate with isolated film area at 25°C for 27v films and 35°C for 50v films.

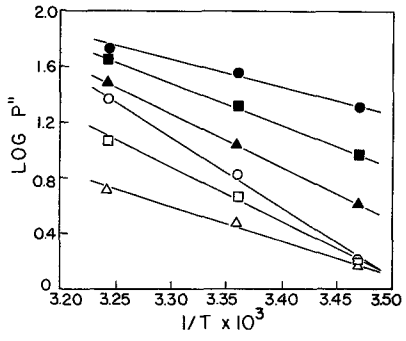

Fig. 6. Plots of log P" vs. 1/T for films of different thickness: ● 27v; ■ 50v; ▲ 100v; ○ 150v; □ 200v; △ 250v.

tivation energy, E, listed in Table IV. Although expected, no osmotic phenomena were observed. Permeation rates were affected by the pH of permeating KNO_3, increasing slightly as the pH was lowered.

Discussion

The ease of permeation at low temperatures is an indication that the membrane is broken at intervals by channels or holes. This is not a new concept for many investigators have discussed the origins of flaws that can exist in anodic films (15-17). The rectifying action and the leakage currents exhibited by anodic films have also been variously attributed to the existence of flaws, pores or weak spots (17, 18). Replica electron micrographs at magnifications of 12 to 15 x 10^3 X, however, showed film surfaces to be free of gross flaws.

A simple idea of the size of the holes may be obtained from selectivity observations. For instance (Table I) the sucrose molecule apparently did not penetrate the film. Therefore, the holes must be on the order of the dimensions of the sucrose molecule or smaller. The minimum cross sections of the sucrose molecule have been given as about 8 x 10Å.

Another indication of the pore size is the type of process occurring through the hole. Very large pores would probably be filled with electrolyte, and free diffusion of the salt in the solvent would be a likely penetrating mechanism. The activation energy for free diffusion of KNO_3 has not been reported. However, it should be near the value reported for the free diffusion of KCl which is 4.4 kcal mole^{-1} (19). The apparent activation energy for permeation of the thinnest ZrO_2 films (Table IV) is 9 kcal mole^{-1}, or twice as great. Furthermore, the apparent activation energy for permeation of porous chromic ferro- and ferricyanide membranes by KNO_3 was found to be only 5.3 kcal mole^{-1} (20). Thus, the passage of KNO_3 through ZrO_2 films is greatly restricted, and the holes must be relatively small.

Table III. Thickness dependency of the rate constant P' at 35°C for permeation of films by 1M KNO_3

Thickness, v	P', cm² sec⁻¹ × 10¹⁰
27	3.9
50	6.1
100	8.2
150	9.4
200	6.3
250	3.4

Table IV. Apparent activation energies for permeation of films by 1M KNO_3

Thickness, v	E, kcal mole⁻¹
27	1
50	14
100	18*
150	24
200	19
250	12

* A corresponding value of 17.1 was found earlier for 100v films (12).

The observed rates for permeation of ZrO_2 films are similar to the rates of diffusion of KNO_3 across porous aluminum oxide films measured by Burwell and May (21). The rates for diffusion of KNO_3 through two portions of a 42μ thick film were 4.1 and 0.49 x 10^{-9} moles cm^{-2} sec^{-1} per molar concentration drop across the membrane. These aluminum oxide films had pores estimated to be 110Å in diameter. The investigators felt that the slow rates indicated a greater resistance than could be exhibited by a simple pore system and suggested that a less porous barrier layer about 0.02μ thick exists at the base of the pores. Considering that the ZrO_2 films are 10^2 to 10^3 times thinner than the aluminum oxide films, their pores must be smaller and less numerous to exhibit similar rates.

Early in this investigation, it was noted that the process under study exhibited certain of the characteristics of steady-state permeation described by Barrer (22). (*A*) The Fick diffusion law appeared to be obeyed in the steady state. (*B*) Steady-state flow was established in a period of minutes. (*C*) The rates were proportional to the concentration and inversely proportional to the film thickness. (*D*) The permeation was temperature dependent. However, the behavior of the rate constant, which appears to be a function of film thickness, implies that the permeation cannot be completely described by a steady-state mechanism.

Another factor which may be considered to determine the permeability of membranes to ions when pores approach molecular dimensions is charges on the membrane pores due either to adsorption or ionization which act as barriers to diffusing ions as postulated by Meyer and Sievers (23). In such a case, the potential barrier may be mainly electrostatic in origin. The criteria for charged pores are the existence of a permselectivity of the membrane and of a membrane potential, the measurable membrane potential being the over-all resultant of the individual pore potentials. In the absence of membrane potential measurements, then, the permselectivity should give an indication of the presence of charged pores. Depending on the membrane potential sign an excess of either cations or anions should be transported. Such a situation would be manifested in a pH change in solution on permeation or in a discrepancy between concentrations of permeated salt as determined by methods depending on measurement of but one ion or of both ions in solution. Based on the data in Table V, there appears to be evidence for permselectivity. At low concentrations of permeant, the agreement between methods is poor while at high concentrations the agreement between the two methods of determining KNO_3 is good. These data match the observation that

Table V. Agreement of methods for determining permeated KNO_3

Sample	Permeant, moles liter^{-1}	Concentration of KNO_3 in cell By flame (moles liter^{-1} × 10^3)	By conductance (moles liter^{-1} × 10^3)
2	1.000	1.20	1.04
3	1.000	1.00	0.98
4	1.000	0.70	0.70
5	0.100	0.18	0.57
6	0.100	0.13	0.30

the permselectivity of membranes is greatest in very dilute solution diminishing and disappearing at higher concentrations (24, 25). Indications are that anion transport is favored. Supporting evidence for the existence of permselectivity is the absence of osmotic effects and the observed pH dependence of the permeation rate.

It is possible to formulate a model for the permeation based on transfer through charged pores with a length much greater than the radius. The membrane may be considered to be completely pierced by an array of cylindrical pores of radii a normal to the surface. The fixed charges, probably adsorbed protons, are confined to a surface layer of density on the inner surface of the pores. Compensating negative charges are assumed to be free. The potential on the pore axis due to the field imposed by the fixed charges can be shown to be

$$v = 2\pi a\sigma \int_{x=0}^{x=L} dx/\sqrt{a^2 + (x - P)^2} \qquad [3]$$

where σ is the surface charge density and the radius a of the cylinder is assumed to be much less than the cylinder length L. P is the distance on the axis from the near end of the cylinder to the point at which the potential is to be found. The cylinder is regarded as a series of hollow disks of thickness dx. Upon performing the integration, expressing P in terms of L and simplifying the ensuing relation by a series expansion, we arrive at the following expression for the maximum potential which from symmetry arguments is at the center of the pore.

$$v = 4\pi a\sigma \ln (L/a) \qquad [4]$$

The apparent activation energy for permeation may not be as readily equated with an activation energy for the process as can the temperature coefficient for diffusion. It may include, in addition to the activation energy for diffusion, the temperature dependence of the number of ions available to enter a hole, heats of sorption or solution of the permeant on or in the membrane, and heats of any phase changes occurring in or at the membrane surface. The rate-determining step is usually considered to be diffusion through the membrane. The observed thickness dependence of the rate constant for the ZrO_2 films may indicate, however, that interface reactions are also important (26). Assuming diffusion through the membrane pores to be the rate-determining step in the case of these ZrO_2 films, the apparent activation energy may be related to the electrostatic potential barrier which must be surmounted by a permeating ion. In this sense, the apparent activation energy may be considered as a true activation barrier.

By Eq. [4], it is evident that the model requires the potential to vary directly as the log of the pore length. A plot of the apparent activation energy for permeation *vs.* log of the film thickness shows (Fig. 7) that for the thinner films there is substantial agreement with the proposed model. Thicker films behave differently since the apparent activation energy begins to decrease. This observation is in accord with the premise that thicker films are under stress during formation and may be more susceptible to formation of microfissures in addition to an established pattern of flaws.

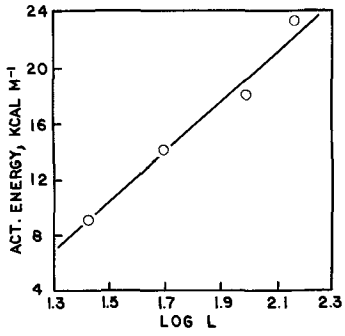

Fig. 7. Plot showing relation between the apparent activation energy, E, and film thickness.

Acknowledgment

The authors wish to thank the Pitman-Dunn Research Laboratories, Frankford Arsenal, Philadelphia, Pennsylvania, for supporting this work.

This paper is based on a dissertation presented to the Graduate School, Temple University, in partial fulfillment of the requirements for the Ph.D. degree by one of the authors (A. H. M.).

Manuscript received Nov. 3, 1966; revised manuscript received Feb. 10, 1967.

Any discussion of this paper will appear in a Discussion Section to be published in the December 1967 JOURNAL.

REFERENCES

1. A. Guntherschulze and H. Betz, *Z. Physik.*, **92**, 367 (1934).
2. R. D. Misch and W. E. Ruther, *This Journal*, **100**, 531 (1953).
3. A. Charlesby, *Acta Met.*, **1**, 340 (1953).
4. A. Charlesby and J. J. Polling, *ibid.*, **2**, 667 (1954).
5. R. W. Franklin, *Nature*, **180**, 1470 (1957).
6. R. D. Misch and F. H. Gunzel, Jr., *This Journal*, **106**, 15 (1959).
7. L. Young, *Trans. Faraday Soc.*, **55**, 632 (1959).
8. B. Cox, *Corrosion*, **16**, 86 (1960).
9. M. Maraghini, G. B. Adams, Jr., and P. Van Ryssel-berghe, *This Journal*, **101**, 400 (1954).
10. J. N. Wanklyn and D. R. Silvester, *ibid.*, **105**, 647 (1958).
11. R. D. Misch, ANL-6149, May (1960).
12. A. H. Mitchell and R. E. Salomon, *This Journal*, **112**, 361 (1965).
13. R. E. Salomon, M. W. Graven, and G. B. Adams, Jr., *J. Chem. Phys.*, **32**, 310 (1960).
14. F. Feigl, "Spot Tests," Vol. 1, Elsevier Publishing Co., New York (1954).
15. U. R. Evans, *This Journal*, **91**, 547 (1947).
16. D. A. Vermilyea, *ibid.*, **110**, 250 (1963).
17. L. Young, *Trans. Faraday Soc.*, **55**, 842 (1959).
18. D. A. Vermilyea, *J. Appl. Phys.*, **27**, 963 (1956).
19. Chem. Abstracts, **45**, 4530i (1951).
20. W. V. Malik and F. A. Siddiqi, *J. Colloid Sci.*, **18**, 161 (1963).
21. R. L. Burwell and T. P. May, *This Journal*, **94**, 195 (1948).
22. R. M. Barrer, "Diffusion In and Through Solids," Chap. 3, The Macmillan Co., New York (1941).
23. K. H. Meyer and J. F. Sievers, *Helv. Chim. Acta*, **19**, 649 (1936).
24. L. Michaelis, *Kolloid Z.*, **10**, 575 (1933).
25. R. Kunin, "Ion Exchange Resins," 2d, ed., p. 216, John Wiley & Sons, Inc., New York (1958).
26. B. J. Zwolinski, H. Eyring, and C. E. Reese, *J. Phys. and Colloid Chem.*, **53**, 1426 (1949).

Conversion of Silicon Nitride Films to Anodic SiO_2

P. F. Schmidt and D. R. Wonsidler

Bell Telephone Laboratories, Incorporated, Allentown, Pennsylvania

ABSTRACT

An introduction is given to the principles underlying the anodization of pre-existing dielectric films. In the case of amorphous silicon nitride films on a silicon substrate it is shown that conversion of the nitride film to anodic SiO_2 occurs by oxygen ions reacting with the nitrogen, the latter being evolved from the film as N_2 or as a nitrogen oxygen compound. The process has been applied to the opening of windows in $Si/SiO_2/Si_3N_4$ structures. Nitride films up to 1000Å thick can be rendered soluble by a single anodization step to 350v; thicker films require a repeated anodization. The electric field applied during anodization causes a shift in surface potential of the silicon substrate. The original surface potential can be restored by a bake in forming gas at 500°C. High-resistivity silicon tends to passivate under anodic bias; growth of an oxide film occurs only at very large current densities.

Silicon dioxide films are commonly used for the surface passivation of silicon. Diffusion or field drift of sodium ions through the SiO_2 coating of oxide passivated silicon devices can lead to failure of sodium contaminated devices. Silicon nitride is practically impermeable to sodium ions. Consequently, considerable effort has been devoted to the adaptation of deposited silicon nitride films for surface passivation of silicon devices. The art of depositing silicon nitride films has reached a high level (1).

Once the nitride film has been deposited, it is necessary to open windows in the film for diffusion or contact purposes. Since silicon nitride is soluble in hot phosphoric acid, whereas SiO_2 is very little soluble in this solvent (2), the opening of windows can be achieved by deposition of an SiO_2 film, followed by pattern generation in the SiO_2 layer by photoresist techniques and subsequent etching in hot phosphoric acid.

The present communication describes an alternative approach, in which the insoluble nitride film is converted to easily soluble anodic SiO_2 by anodization in a suitable solvent electrolyte combination. Pattern generation is achieved by the use of an SiO_2 pattern as a dielectric anodization mask; this SiO_2 pattern can be located either above or underneath the nitride film to be anodized.

Principle of the Method

When applying a sufficiently high anodic bias to the system: conductive substrate/dielectric film/electrolyte, either electrons or ions, or both, may be injected into the dielectric film. The substrate forms the cation source and the electrolyte the anion or electron source. Injection of ions can change the chemical composition of a pre-existing dielectric film, and can thus render it more soluble.[1] Injection of electrons is undesirable since it lowers the current efficiency and can damage the dielectric by avalanche formation. Electron injection can be minimized by the choice of a suitable electrolyte. In this study a 7.5 v/o solution of pyrophosphoric acid in tetrahydrofurfuryl alcohol has been used.

In the anodization of pre-existing dielectric films, the interesting feature arises that a change in the chemical composition of the film may depend on whether cations or anions are the mobile species. Thus migration of silicon ions through a pre-existing nitride film would not change its composition, but migration of oxygen ions would. The reverse situation applies, for instance, to the anodization of a pre-existing Al_2O_3 film, where migration of silicon ions changes the chemical composition of the film, whereas migration of oxygen ions does not. The nature of the substrate may thus determine whether a pre-existing dielectric film becomes soluble during anodization.

The degree of crystallinity of a pre-existing dielectric film appears to have a decisive effect on the mobility of the ionic species. The existence of grain boundaries in polycrystalline silicon nitride films favors the mobility of silicon ions and in polycrystalline alumina the mobility of oxygen ions. Thus in the anodization of polycrystalline alpha or beta Si_3N_4 films on silicon substrate, growth of new oxide occurred at the nitride/electrolyte interface, leaving the nitride film unchanged in thickness or solubility. In the anodization of polycrystalline alpha-alumina films on silicon substrate in aqueous borate solution, growth of new oxide occurred at the oxide/silicon interface, increasing the total film thickness but without changing the solubility of the pre-existing outer layer of alpha-alumina.

Amorphous silicon nitride films anodize by migration of oxygen ions, are converted to SiO_2, and become easily soluble in dilute HF. The degree to which oxygen ions migrate in polycrystalline nitride films can be enhanced to some extent by increasing the current density, *i.e.*, the applied field strength, but it is obvious that for purposes of anodization fully amorphous nitride films are preferable. This fact does not constitute an additional requirement in device processing because polycrystalline nitride films are also undesirable for other reasons; for instance, they are not effective barriers to sodium migration (4).

Mechanism of Anodization of Amorphous Nitride Films

Figure 1 shows the changes that occur in the infrared transmission spectrum of a nitride film undergoing anodization. The spectrum of the original nitride film disappears if the film is anodized to completion, *i.e.*, to the point where all of it becomes easily soluble in HF. At incomplete conversion, the spectra of both nitride and of anodic oxide are present, but the oxide spectrum disappears if the soluble outer part of the anodized film is etched in buffered HF.[2] This behavior establishes that oxygen ions penetrate into the nitride film during anodization and replace the nitrogen, but does not rule out simultaneous migration of silicon ions. Absence of silicon ion migration was proven by conversion in the SiO_2 window areas of a nitride film deposited on top of a SiO_2 pattern on a silicon substrate. After anodization and stripping of both nitride and oxide films in concentrated HF, no indication of a step in the silicon

[1] A pre-existing dielectric film may also become more soluble as a function of change in structure or hydroxyl content. This effect was observed in the anodization of thermally grown SiO_2 films (3). The structural effect is very small or absent in the anodization of silicon nitride films.

[2] The transition SiO_2/Si_3N_4 is sharp; thus the method can be used for the controlled thinning down of Si_3N_4 films.

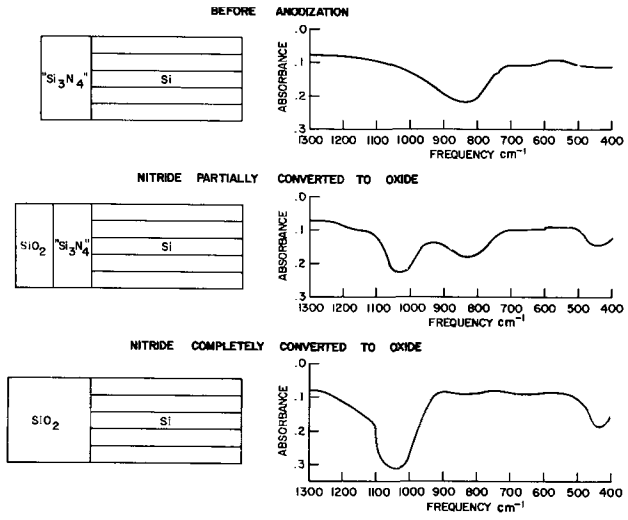

Fig. 1. Shift in infrared spectrum during anodization of silicon nitride film on high resistivity p-type silicon substrate.

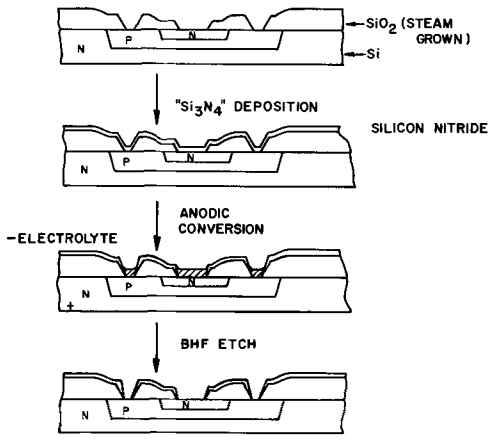

Fig. 2. Sequence of steps used for opening of windows in nitride films.

surface at the position of the former window areas could be detected by interferometry; this proves that no silicon or only very little had been consumed during the anodization.

This observation also clarifies the mechanism of the anodic conversion of the nitride film. Oxygen ions penetrate into the nitride film, yet the electric current through the rest of the nitride film is entirely electronic. Continuity of charge transport and over-all electrical neutrality of the nitride film are possible only if the oxygen ion loses its electrons, which flow off through the nitride film, and replaces the nitrogen which leaves as an electroneutral species, either elemental nitrogen or an oxygen-nitrogen compound. For the case of a Si_3N_4 film, the over-all reaction can be written as

$$6\,O^{2-} + Si_3N_4 \rightarrow 3SiO_2 + 2N_2 + 12\,l$$

The postulated evolution of a gas (nitrogen or an oxygen-nitrogen compound) during anodization also explains the observation that there is no fixed oxide to nitride thickness ratio for a given initial thickness of the nitride film; rather, the ratio appears to depend on the current density during anodization, *i.e.*, the rate of gas evolution. The faster the rate, the more porous and therefore thicker the resulting oxide film.

At a constant current density of 7 ma/cm^2 in the pyrophosphoric acid/tetrahydrofurfuryl alcohol solution it takes about 350v (and about 10 min of anodization) to convert a 1000Å nitride film completely. Complete conversion can also be achieved by anodization at a constant voltage of 215v for 18 hr, and the oxide film formed in this latter case is appreciably thinner than the constant current oxide.

The over-all anodization behavior of nitride films on silicon is not too different from the anodization of a bare Si surface. The electrolytes are the same as can be used for the anodization of silicon, and the current efficiency is similarly low, *i.e.*, a larger percentage of the current is due to oxygen discharge. Silicon nitride is more easily damaged by avalanche formation than is SiO_2, and this fact limits the anodization voltage to about 350v. Nitride films thicker than 1000Å can be rendered soluble by repeating the anodization after stripping the converted surface layer by etching in HF. The etch rate of the conversion oxide is very high, about 100 Å/sec in buffered HF (40g NH_4F + 15 cc conc. HF in 60 cc H_2O).

The process has been applied to the opening of windows in the nitride film of $Si/SiO_2/Si_3N_4$ device structures. Windows are first opened in the oxide film by photoresist techniques, and the nitride film is then deposited over the whole front surface of the wafer, as shown in Fig. 2. During anodization the SiO_2 pattern underneath the nitride film serves as a dielectric anodization mask by reducing the field strength at the location of the SiO_2; anodization thus is confined to the window areas of the pattern.

While the nitride film on top of the SiO_2 is not rendered soluble, the applied field strength at the position of the SiO_2 is usually high enough to cause a shift in surface potential of the silicon substrate, as is also observed in the Si/SiO_2/metal system in the absence of alkali ions (5). A bake in forming gas at 500°C restores the original surface potential of the silicon and the transistor gain (6).

Anodization Behavior of High-Resistivity p-Type Silicon

The spectroscopic work reported above was done on high resistivity (25 ohm-cm) p-type silicon in order to minimize free carrier absorption in the substrate. During anodization of these wafers, an unexpected difficulty was encountered: the bare back surface, instead of forming on oxide film, simply passivated *i.e.*, passed large electronic currents by discharge of oxygen. Strong illumination had no effect in preventing passivation. It was possible to force oxide growth by going to unusually high initial current densities (50-80 ma/cm^2). Once oxide growth had commenced, it was possible to reduce the current density, although it still remained appreciably larger than on lower resistivity wafers for the same rate of oxide growth.

It was of interest to determine whether the electrons were injected into the valence or the conduction band of the silicon. The first case would constitute majority carrier extraction, the second, minority carrier injection. Since the electronic levels of anions in solution are located about 4-5 or more ev below vacuum level, either situation could be realized for the particular system: high resistivity p-type silicon/pyrophosphoric acid in THF.

A distinction between hole extraction or electron injection was possible by means of a transistor configuration, utilizing a n^+p diode, the p-side of which was biased anodically, *i.e.*, in the forward direction *vs.* a platinum wire in the pyro/THF solution, while a reverse bias was applied to the n^+p junction. The resistivity of the p-base was 50 ohm-cm, its thickness 5 mils; the resistivity of the epitaxial n^+ layer was about 1 ohm-cm. Only the p-base made contact to the electrolyte.

It was found that the forward current passed in the p-base/electrolyte circuit appeared almost quantitatively in the base/collector circuit of the "liquid emitter" transistor, thus proving the occurrence of minority carrier injection. After oxide growth had been forced to occur by passage of very large currents in the emitter/base circuit, the transfer ratio was

found to have deteriorated, indicating that now fewer electrons were able to enter the conduction band of of the p-Si.

Manuscript received Nov. 29, 1966; revised manuscript received Jan. 26, 1967.

Any discussion of this paper will appear in a Discussion Section to be published in the December 1967 JOURNAL.

REFERENCES

1. Joint Symposium of the Electronics-Dielectrics and Insulation Divisions of the Electrochemical Society on Preparation and Properties of Silicon Nitride Films, Philadelphia Meeting, October, 1966.
2. W. van Gelder and V. E. Hauser, Recent news paper presented at the above symposium, Abstract No. 5.
3. P. F. Schmidt and M. J. Rand, *Solid State Communications*, **4**, 169 (1966).
4. J. Drobek and J. V. Dalton, Recent news paper, ref. (1), Abstract No. 4.
5. A. Goetzberger and H. Nigh, *Proc. IEEE*, **54**, 1454 (1966); B. E. Deal, A. S. Grove, and E. H. Snow, Recent news paper, Abstract No. 15, Philadelphia Meeting October, 1966.
6. G. H. Schneer, W. van Gelder, V. E. Hauser, and P. F. Schmidt, 1966 International Electron Device Meeting, Washington, D. C., Abstract No. 5.3.

Determination of the Thickness of Aluminum on Silicon by X-Ray Fluorescence

J. E. Cline and S. Schwartz

Electronics Research Center, National Aeronautics and Space Administration, Cambridge, Massachusetts

ABSTRACT

The thickness of deposited aluminum layers on silicon, in the range from 0 to 4μ, was shown to be determined easily by an x-ray spectrometric technique with much better sensitivity than by the usual optical interferometric measurements. Theoretical curves were calculated for two methods: (*i*) emission of characteristic aluminum fluorescence and (*ii*) absorption of characteristic silicon fluorescence. The first method gave the best results with ultimate thickness sensitivity in very thin layers of $\pm$6Å of aluminum.

In the fabrication of silicon planar transistors, diodes and integrated circuits, vacuum-deposited thin aluminum films are generally used for ohmic contacts to the active devices and for interconnections (1-3). The thickness of this aluminum layer, usually in the range 1000-10,000Å, must be carefully controlled, since too thin a layer will not have sufficient current-carrying capability and too thick a layer can lead to unreliable contacts and excess intermetallic formations. It is possible that future integrated circuit technology will call for even thinner, and more precisely controlled, deposited aluminum as part of multimetal interconnections.

This work was undertaken as a phase of a general research program to improve techniques for failure analysis and process control of microcircuits. Reliability of silicon monolithic circuits depends to a large extent on the thickness of the thin film interconnections and on their uniformity. The strength of the lead-bonding, the reliability for long-term operation, and the ability to carry high currents all depend on the control of the thickness of the aluminum used for the microcircuit interconnections.

The technique described in this paper for determining aluminum thickness has the advantages of being nondestructive, more sensitive, and more reproducible than the commonly used optical interferometric measurements, and of furnishing data in a digital form readily adaptable to automation. The x-ray fluorescence technique is conveniently applied to the entire silicon microcircuit wafer after the evaporation of aluminum and before the interconnection pattern is formed by the photoengraving process.

Experimental

The samples used in this work were polished silicon wafers on which various thicknesses of aluminum were deposited by vacuum evaporation, partly masked to form steps for determination of thickness by a Zeiss interference microscope. Thallium light was used to produce 0.27μ half-wave fringes. On each silicon slice the area of the aluminum film was greater than that of a $\frac{5}{8}$-in. circle for comparison of the thickness of the aluminum by the x-ray fluorescence method.

Two basic techniques were involved in the utilization of x-ray fluorescence for determination of the thickness of the aluminum films. In one technique, emission of the characteristic aluminum K-alpha radiation by the aluminum film, increasing with its thickness, was measured. In the other, measurements were made of the silicon K-alpha radiation emitted by the substrate, decreasing with aluminum thickness due to absorption. In both cases the aluminum and silicon fluorescence lines were activated by x-radiation from a tungsten-target tube in a Norelco vacuum x-ray fluorescence spectrometer. Tube voltages from 15 to 50 kv were used with currents up to 50 ma. The wavelengths of the x-rays (8.320 and 7.111Å for aluminum and silicon, respectively) were analyzed by a flat EDDT (ethylenediamine d-tartrate) crystal with a 2d-spacing of 8.76Å. A flow proportional detector was used with pulse amplitude discrimination to improve the signal-to-background ratio. The spectrometer was operated at a vacuum of less than 0.02 Torr pressure to eliminate absorption of the soft x-rays by the air path.

The four sample holders in the spectrometer could be readily rotated into position in the x-ray beam without breaking the vacuum. In this way several samples or standards could be quickly compared. Each sample holder could accept a wafer up to a diameter of $1\frac{1}{4}$ in. As shown in Fig. 1, a stainless steel mask with opening of 0.625-in. diameter was used in each sample holder to define the area of the aluminum film under examination. Areas of smaller size can be measured with decrease in sensitivity.

In Fig. 2, an enlarged cross section of the aluminum-coated silicon wafer is shown diagrammatically with ϕ

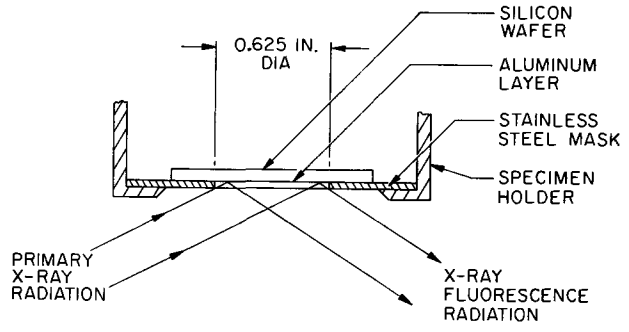

Fig. 1. Position of silicon wafer and stainless-steel mask in specimen holder.

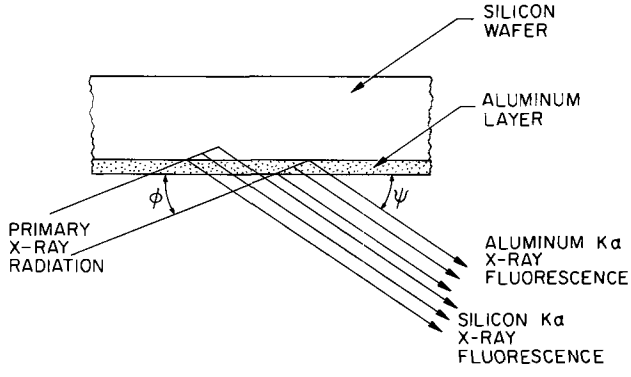

Fig. 2. Angles of incidence of primary and fluorescence radiation, showing paths of x-rays in aluminum film and silicon substrate.

representing the angle of incidence of the primary radiation with the specimen surface and ψ the angle of emission of the fluorescence radiation. These angles are determined by the position of the specimen in relation to the target of the x-ray tube and to the collimator of the spectrometer.

Results and Discussion

Aluminum K-alpha fluorescence.—The dependence of the intensity of the characteristic aluminum K-alpha radiation, I_t, on the thickness of aluminum can be expressed by

$$\frac{I_t}{I_o} = 1 - e^{-At} \qquad [1]$$

where I_o is the intensity limit of fluorescence radiation from thick (over 40μ) aluminum, t is the thickness of aluminum in microns, and A is a constant. The constant A can be calculated (4, 5) from the equation

$$10^4 A = \frac{\mu_p}{\sin\phi} + \frac{\mu_s}{\sin\psi} \qquad [2]$$

where μ_p and μ_s are the linear absorption coefficients of aluminum for the primary and fluorescence radiation, respectively. The second term was calculated from the data of Cooke and Stewardson (6), using the values $\mu_s = 1065$ and $\psi = 35°$. The first term in Eq. [2] cannot be calculated directly since μ_p is uncertain, depending on the average effective wavelength of the primary radiation. In our work the constant A was determined from the experimental data.

Using Eq. [1], a linear relationship between a function of the intensity, $f(I_t)$, and the thickness, t, can be obtained by

$$f(I_t) = -\log_{10}\left(1 - \frac{I_t}{I_o}\right) = \frac{At}{2.3026} \qquad [3]$$

The computation of values of I_t/I_o and $f(I_t)$ for a series of aluminum-coated silicon wafers measured at an x-ray tube voltage of 50 kv and current of 25 ma is shown in Table I. Similar sets of data were also

Table I. Computation of data from measurements of aluminum K-alpha fluorescence at tube voltage of 50 kv

1	2	3	4	5	6	7
t, μ	Al-std-bkgd counts/sec	Sample bkgd counts/sec	Blank counts/sec	Sample corr. for blank counts/sec	$\frac{I_t}{I_o}$	$f(I_t)$
0.00	4375.0	34.0	34.0	0	0.0000	0.0000
0.18	4314.5	325.0	33.5	291.5	0.0676	0.0304
0.35	4347.0	475.0	33.8	441.2	0.1015	0.0465
0.54	4374.0	849.5	34.0	815.5	0.1864	0.0896
0.76	4392.0	1026.0	34.1	991.9	0.2258	0.1112
1.31	4177.0	1474.0	32.5	1441.5	0.3451	0.1838
2.70	4157.5	2570.5	32.3	2538.2	0.6105	0.4095
3.58	4321.5	3126.0	33.6	3092.4	0.7156	0.5461
4.18	4344.5	3352.5	33.8	3318.7	0.7639	0.6269

obtained at 25 and 40 kv. At least five separate counts of 10 sec each were taken on the standard and five on the sample, alternating to minimize error in the ratio due to instrument drift. Since the maximum count rate used was 6400 counts/sec, it was not considered necessary to make any correction in the intensity measurements for the resolving time of the pulse counting circuit.

In columns 2 and 3 of Table I, the relative intensities of the aluminum standard and the sample, respectively, are indicated after correcting for the background measured with the spectrometer setting near the aluminum K-alpha line. In column 4, the blank intensity of an uncoated silicon wafer is shown corrected for variations in count rate from the aluminum standard. Almost all of this blank intensity was shown to be due to aluminum impurities in the stainless-steel mask in the sample holder.

The linearity of $f(I_t)$ relative to t is demonstrated by Fig. 3, plotted for the data in Table I. The slope of the line, 0.151, was computed by the method of best least squares fit. From this slope the constant A in Eq. [3] is calculated to be 0.348. In Table II a comparison is shown between the experimental values of $f(I_t)$ and the best fit values, 0.151 t. The values of t_{calc} (the thickness calculated from x-ray fluorescence data) are also compared in Table II with values of t (measured with the interference microscope). It is believed that most of the difference between experimental and best fit values can be accounted for by experimental error in the interference measurements.

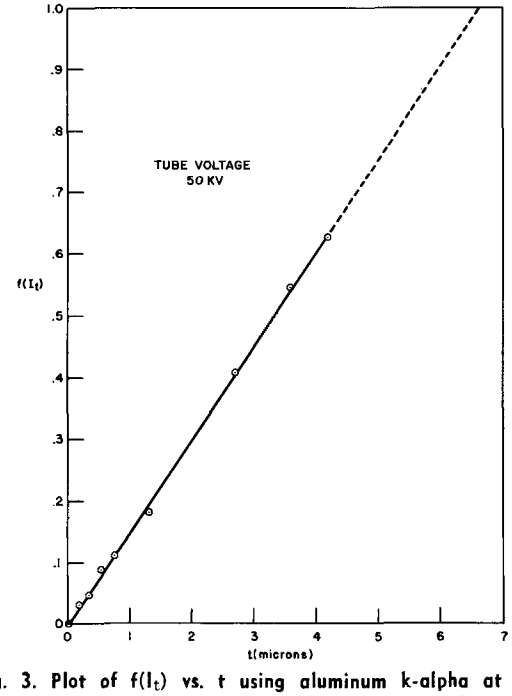

Fig. 3. Plot of $f(I_t)$ vs. t using aluminum k-alpha at 50 kv. Slope of line = 0.151, calculated from least squares fit.

Table II. Comparison of aluminum thickness measurements by interferometry and x-ray fluorescence, Al K-alpha at 50 kv, and comparison of experimental $f(I_t)$ with best fit values 0.151 t

t, μ	0.151 t	$f(I_t)$	$f(I_t)/0.151$ t_{calc}, μ	$t_{calc} - t, \mu$
0.00	0.000	0.0000	0.00	0.00
0.18	0.027	0.0304	0.20	0.02
0.35	0.053	0.0465	0.31	−0.04
0.54	0.082	0.0896	0.59	0.05
0.76	0.115	0.1112	0.74	−0.02
1.31	0.198	0.1838	1.22	−0.09
2.70	0.408	0.4095	2.71	0.01
3.58	0.541	0.5461	3.62	0.04
4.18	0.630	0.6269	4.15	−0.03

There was no indication in this set of experiments, or in other sets run at different tube voltages, that a curve other than a straight line would give a better fit of the plot of $f(I_t)$ *vs.* t.

In Fig. 4 a pair of calibration curves are shown for conversion of x-ray fluorescence data at 50 kv to aluminum thickness. It is estimated that the precision of thickness measurement for very thin aluminum films is ± 6Å, limited by the background noise in the x-ray spectrometer. For thicker films the slope of the curve, I_t/I_o *vs.* t, decreases and the precision of the x-ray measurement becomes limited by the stability of the instruments. At 50 kv the best reproducibility of counting rate of the x-ray fluorescence from the same sample was found experimentally to be ± 0.15%. Thus, it was determined from the calibration curves of I_t/I_o in Fig. 4 that the ultimate precision is ± 0.003μ at $t = 1\mu$, and ± 0.2μ at $t = 10\mu$.

The effect of variations in x-ray tube voltage on the intensity ratio, I_t/I_o, was found to be very small. When the voltage was changed from 50 to 25 kv, the slope of the line, $f(I_t)$ *vs.* t, was found to increase only by 3%.

In order to reduce background noise in the x-ray spectrometer, pulse amplitude discrimination was used with peak sensitivity at the energy of the aluminum K-alpha x-ray photons. With a relatively narrow window (energy range) of 5.0v, it was found that I_t/I_o varied significantly when the voltage of the level (bottom of the energy range) was changed. In Fig. 5 the effect of level variations on I_t/I_o measurements taken on a single sample is shown. At the optimum setting

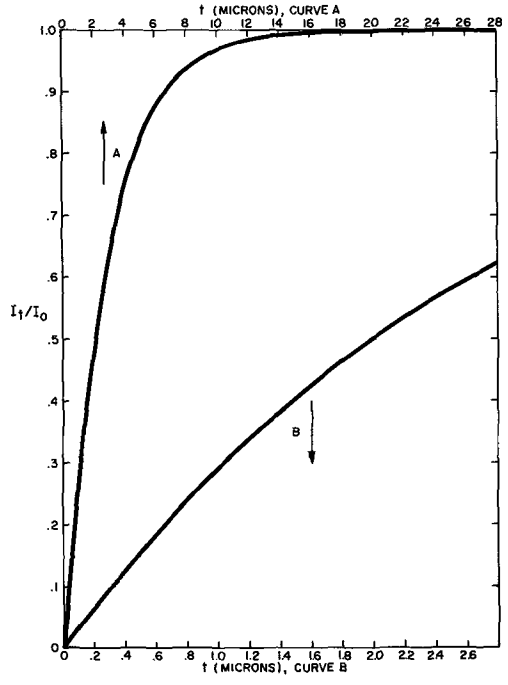

Fig. 4. Calibration curves of I_t/I_o vs. t (Al K-alpha at 50 kv). Top scale is for curve A, bottom scale for curve B.

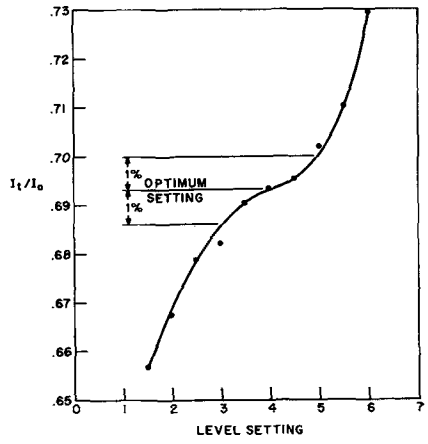

Fig. 5. Effect of level variations on I_t/I_o (Al K-alpha at 50 kv, window setting at 5.0v).

of the level at 4.0v (depending on detector voltage), a change of 0.1v in level results in a 0.07% change in I_t/I_o. For best reproducibility it is advisable to warm up the electronics for stabilization, occasionally check the level for optimum setting, and operate with as large a window that is feasible for the amount of background noise that can be tolerated in order to reduce the effect of level fluctuations.

Silicon K-alpha fluorescence.—Instead of using the aluminum K-alpha fluorescence, the thickness of the aluminum layer on silicon can also be determined by measurement of x-ray fluorescence from the substrate. In this case the maximum silicon K-alpha fluorescence intensity is obtained at zero thickness of the aluminum, and the intensity decreases exponentially as the aluminum thickness increases as shown by the relationship

$$\frac{I'_t}{I'_o} = e^{-Bt} \qquad [4]$$

where I'_t and I^0_o are the intensities of silicon K-alpha fluorescence at aluminum thickness of t (μ) and zero, respectively. The constant B can be expressed by

$$10^4 B = \frac{\mu'_p}{\sin\phi} + \frac{\mu'_s}{\sin\psi} \qquad [5]$$

where μ'_p and μ'_s are the linear absorption coefficients of aluminum for the primary radiation and silicon K-alpha fluorescence, respectively.

From Eq. [4] a linear relationship between a function of the intensity $F(I'_t)$ and t can be obtained by

$$F(I'_t) = -\log_{10}\frac{I'_t}{I'_o} = \frac{Bt}{2.3026} \qquad [6]$$

The values of I'_t/I'_o and $F(I'_t)$ were calculated from measurements at 50 kv for a series of silicon wafers coated with aluminum ranging in thickness from zero to 4.18μ.

In Fig. 6, $F(I'_t)$ *vs.* t is plotted with the slope of the line, 0.769, computed by least squares fit. From this slope the constant B in Eq. [6] is calculated to be 1.771. B is greater than A of Eq. [3] because the linear absorption coefficient of aluminum for silicon K-alpha radiation is much greater than for aluminum K-alpha (9033 and 1065). From experimentally determined constants A and B and published values of absorption coefficients the first terms on the right side of Eq. [3] and [5] are calculated to be 1620 and 2060, respectively. It is possible that this difference can be due to a variation of absorption by aluminum of the primary radiation, which has different effective wavelengths for activating fluorescence in silicon and aluminum.

In Fig. 7 a calibration cone is shown for conversion of the silicon x-ray data to aluminum thickness.

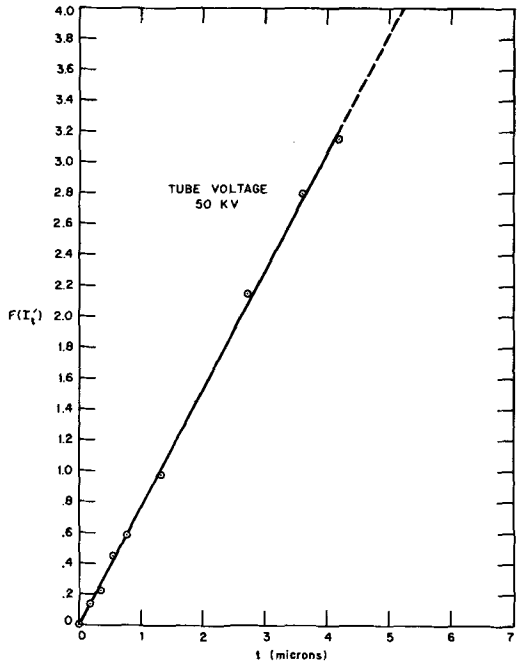

Fig. 6. Plot of $F(I'_t)$ vs. t using silicon K-alpha at 50 kv. Slope of line = 0.769, calculated from least squares fit.

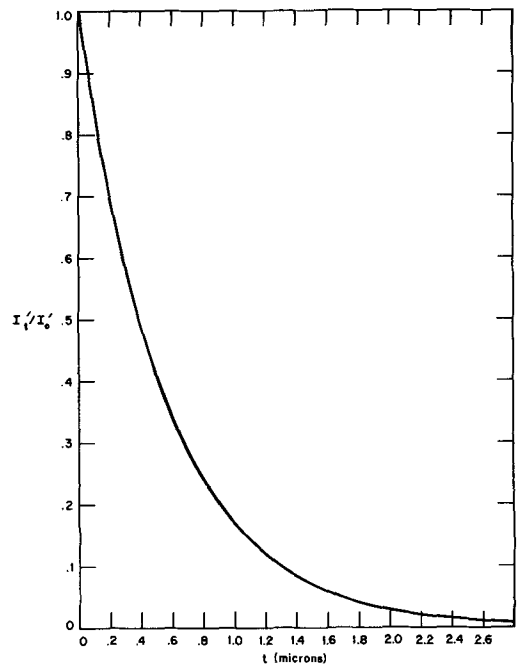

Fig. 7. Calibration curve of I'_t/I'_0 vs. t (Si K-alpha at 50 kv)

For very thin aluminum films a ± 0.3% precision in counting rate would give a precision of ± 24Å in aluminum thickness. At a thickness of 1 micron the ultimate precision is ± 0.003μ. Surface variation and presence of variable silicon dioxide under the evaporated aluminum would decrease the obtainable precision.

Conclusions

The measurement of the thickness of aluminum on silicon by calculation from x-ray fluorescence data is a convenient, nondestructive technique. For very thin films the sensitivity is ± 6Å, obtained with aluminum K-alpha fluorescence. The silicon K-alpha fluorescence can also be used, but is not recommended for measuring aluminum on integrated circuit wafers due to absorption of x-rays by the variable amount of silicon dioxide under the aluminum.

Acknowledgments

The authors wish to express their thanks to Mr. J. Gerhard for his assistance in the experimental work and to Mr. R. L. Trent for encouraging this investigation.

Manuscript received Feb. 2, 1967; revised manuscript received Feb. 21, 1967. This paper was presented at the Philadelphia Meeting, Oct. 9-14, 1966.

Any discussion of this paper will appear in a Discussion Section to be published in the December 1967 JOURNAL.

REFERENCES

1. "Integrated Circuits," R. M. Warner, Jr., Editor, p. 307, McGraw-Hill Book Co., New York (1965).
2. G. E. Moore in "Microelectronics," E. Keonjian, Editor, p. 310, McGraw-Hill Book Co., New York (1963).
3. "Integrated Circuit Technology," S. Schwartz, Editor, p. 81, McGraw-Hill Book Co., New York (to be published in 1967).
4. H. A. Liebhafsky *et al.*, in "X-Ray Absorption and Emission in Analytical Chemistry," p. 167, John Wiley & Sons, New York (1960).
5. N. Spielberg and G. Abowitz, *Anal. Chem.*, **38**, 200 (1966).
6. B. A. Cooke and E. A. Stewardson, *Brit. J. Appl. Phys.*, **15**, 1315 (1964).

Optical Spectra of Ytterbium in CdF_2

Paul F. Weller

Department of Chemistry, State University College, Fredonia, New York

ABSTRACT

Optical absorption and fluorescence studies were conducted on Bridgman-grown CdF_2 single crystals doped with YbF_3 and with YbF_3 plus codopants such as CdS, NaF, EuF_3, and CaF_2. Generally, the ytterbium absorption spectrum consisted of two lines, a weak line at 9620Å and a strong line at 9760Å. The peak height of the strong line was quite dependent on temperature and codopant. Ytterbium fluorescence lines usually occurred between 9620 and 9700Å and between 9750 and 9800Å and were very dependent on codopant. A possible fit to the experimentally observed absorption and fluorescence data is obtained if the cubic crystal field symmetry at the Yb^{+3} lattice site gives rise to a total splitting of about 475 cm^{-1} for the $^2F_{5/2}$ excited state and about 590 cm^{-1} for the $^2F_{7/2}$ ground state.

Recent EPR studies (1-4) on trivalent rare earth dopants in CdF_2 have indicated that the crystal field symmetry at the rare earth site is largely cubic. This is not the case in CaF_2 where charge compensating ions such as F^- interstitials and substitutional divalent anions such as O^{-2} and S^{-2} and monovalent cations such as Na^+ generally distort the local cubic symmetry around the RE^{+3} ion (5).

Another significant difference between RE doped CaF_2 and CdF_2 is found for Yb^{+3} doping. The cubic crystal field splitting in CaF_2 appears to be about 630 cm^{-1} for the $^2F_{5/2}$ excited state and about 800 cm^{-1} for the $^2F_{7/2}$ ground state as obtained from EPR data (5). The EPR and optical spectra estimates for the Yb^{+3} ground state splitting in CdF_2 range from 12 cm^{-1} (6) to about 110 cm^{-1} (2).

The following optical studies were made on Bridgman-grown CdF_2:Yb^{+3} single crystals in order to obtain more information on the crystal field symmetry and crystal field strength at the Yb^{+3} site in CdF_2. Various codopants such as Na^+, S^{-2}, Eu^{+3}, and Ca^{+2} were added, along with Yb^{+3}, to the CdF_2 and the effects on the Yb^{+3} absorption and fluorescence spectra observed.

Experimental

All of the single crystals reported on in this study were grown via a Bridgman-Stockbarger technique using graphite crucibles, as reported previously (7). The doping concentrations given (mole per cent) are those that were added to the sample charge. In the case of Yb^{+3} and Eu^{+3} these concentrations are reasonably accurate (segregation coefficients near unity). However, for Ca^{+2}, Na^+, and S^{-2} there is considerable segregation in CdF_2. The concentrations listed, therefore, are not the true ones but give the maximum possible values attainable (segregation coefficients less than unity).

CdF_2:Yb^{+3} *Crystals.—Absorption.*—The optical absorption spectra for the "as grown" Yb^{+3} doped CdF_2 crystal shown in Fig. 1, as well as all of the other crystals reported on below, were run on a Cary Model 14 spectrophotometer at 300°, 77°, and 6°K. Several features are of interest. There is only one strong absorption line, 9760Å, which splits into a triplet at 6°K with splittings of 6Å and 8Å from the central line. There are two other weak lines, at 9620 and 9200Å, that are essentially temperature independent. All of these lines are superposed on a broad band absorption, about 9000 to 9700Å. (The reason for this one strong absorption line is not clear. In a cubic crystal field, two absorption lines of approximately equal intensity would be expected. Crystal fields of lower symmetry would give rise to three absorption lines.)

All of the absorption lines detected at 77°K between 0.4 and 2.5μ are listed in Table I, for this

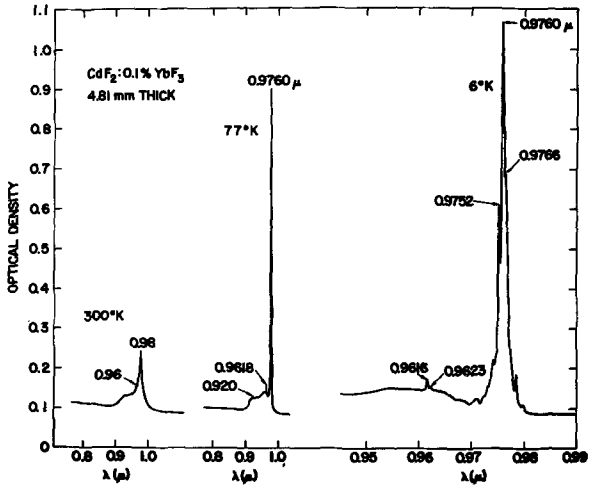

Fig. 1. The optical absorption spectrum of a CdF_2:0.1%YbF_3 crystal at 300°, 77°, and 6°K.

CdF_2:Yb^{+3} sample as well as all others described below. The absorption spectrum of Yb^{+3} in CdF_2 at low temperatures has also been reported by Weakliem (8) and by Banks and Wagner (9). Weakliem found two lines around 9500Å and one around 9200Å. All three lines appeared to be of about equal intensity and were quite weak. The spectrum of Banks and Wagner is very similar to that reported in this study. Konyukhov, Pashinin, and Prokhorov (1) report two absorption lines at 0.961 and 0.972μ for Yb^{+3} in CdF_2 at room temperature.

Fluorescence.—The fluorescence spectra in the region of 1μ were recorded at 77° and 2°K using high pressure mercury lamp excitation with a copper sulfate filter, a Perkin Elmer Model 210 monochromator and a cooled photomultiplier with type S-1 response. Figure 2 shows the emission spectrum at 77°K of the "as grown" CdF_2:0.1% YbF_3 crystal reported on above. Strong lines were observed at 9632 and 9760Å with weaker lines at 9617 and 9755Å. On cooling to 2°K the stronger lines shifted to 9625 and 9767Å and the weaker lines to 9613 and 9750Å. The two lines occurring at 9632 and 9755Å at 77° decreased significantly in intensity on cooling to 2°K. Table II gives the fluorescence lines for this sample as well as all others described below. It should be noted that the fluorescence lines are designated weak and strong in Table II, and throughout the paper, without correction for detector response.

Weakliem (8) has found fluorescence lines for CdF_2:Yb^{+3} samples at 77°K at 9600, 9640, 9705, 10,225, and 10,260Å.

Table I. The observed optical absorption lines and transition assignments at 77°K for Yb^{+3} and for Yb^{+3} plus various codopants in CdF_2 single crystals

Sample	λ(A)	Energy, cm^{-1}	Intensity	Assigned transition Strong	Weak
0.1% YbF_3	9124	10,960	vvw	7-8′b	
	9185	10,887	vw	7-8′ cubic	
	9618	10,397	w	7-7′ cubic	7-8′b
	9623	10,392	vw	7-7′ cubic	7-8′a
	9752	10,254	s	7-7′	7-7′ cubic
	9760	10,246	vs	7-7′	7-7′
0.1% YbF_3 + HF	9137	10,945	vw	7-8′b	
	9169	10,906	vw	7-8′b	
	9200	10,870	vvw	7-8′ cubic	
	9620	10,395	w	7-7′ cubic	7-8′b
	9683	10,327	m	7-7′	7-8′a
	9755	10,251	s		7-7′ cubic
	9764	10,242	vs		7-7′
1% YbF_3 + 1% NaF	9138	10,943	vvw	7-8′b	
	9194	10,877	w	7-8′ cubic	
	9213	10,854	w	7-8′ cubic	
	9260	10,799	vvw		
	9330	10,718	vw	7-8′a	
	9338	10,709	vw	7-8′a	
	9438	10,595	vvw		
	9617	10,398	m	7-7′ cubic	7-8′b
	9623	10,392	s	7-7′ cubic	7-8′a
	9750	10,256	m	7-7′	7-7′ cubic
	9759	10,247	m	7-7′	7-7′
1% YbF_3 + 1% CdS	9140	10,941	vvw	7-8′b	
	9200	10,870	vw	7-8′ cubic	
	9360	10,684	vw	7-8′a	
	9470	10,560	vvw		
	9570	10,449	vw		
	9617	10,398	w	7-7′ cubic	7-8′b
	9630	10,384	w	7-7′ cubic	7-8′a
	9754	10,252	s	7-7′	7-7′ cubic
	9760	10,246	vs	7-7′	7-7′
1% YbF_3 + 1% EuF_3	9200	10,870	vw	7-8′ cubic	
	9620	10,395	w	7-7′ cubic	7-8′b
	9625	10,390	w	7-7′ cubic	7-8′a
	9754	10,252	s	7-7′	7-7′ cubic
	9760	10,246	s	7-7′	7-7′
0.1% YbF_3 + 7% CaF_2	9200	10,870	vvw	7-8′ cubic	
	9620	10,395	w	7-7′ cubic	7-8′
	9760	10,246	vw	7-7′	7-7′

The intensities listed as very weak (vw), weak (w), medium (m), strong (s), shoulder (sh) and broad (br) cannot be compared between the various samples. Assigned transitions are given for both strong and weak crystal field splittings and are designated by the Γ level numbers involved.

Crystal treatment and codopants.—Treatment of CdF_2:0.1% YbF_3 crystals in HF gas.—The effects on the absorption and fluorescence spectra were quite pronounced when the "as grown" crystal reported on above was submitted to HF firing. A section of the crystal about 1.2 mm thick, contained in a platinum boat, was fired in flowing HF gas at about 850°C for two days. The resulting absorption spectrum is shown in Fig. 3a and the fluorescence spectrum in Fig. 2, both at 77°K. The broad absorption, between 9000 and 9700Å, of the untreated crystal was noticeably decreased, and a new absorption peak at 9683Å was present in the HF fired crystal. The fluorescence also changed. The two strong lines at 9632 and 9770Å in the untreated crystal disappeared upon HF firing, and new lines appeared around 9671 and 9679Å.

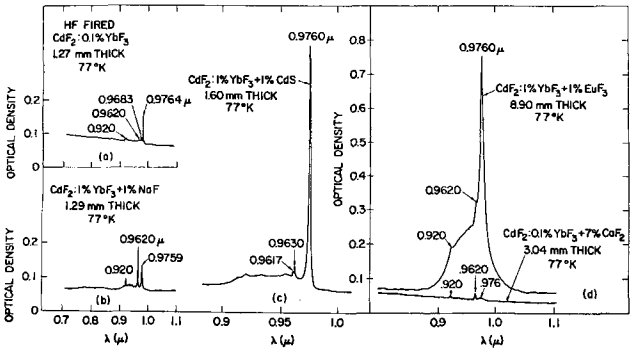

Fig. 3. Optical absorption spectra at 77°K of crystals of CdF_2:YbF_3 + various codopants: *(a)* HF fired CdF_2:0.1%YbF_3, *(b)* CdF_2:1%YbF_3 + 1%NaF, *(c)* CdF_2:1%YbF_3 + 1%CdS, *(d)* CdF_2:1%YbF_3 + 1%EuF_3 and CdF_2:0.1%YbF_3 + 7%CaF_2 (lower curve).

CdF_2:*1% YbF_3 + 1% codopant.*— The effects of Na^+, added as NaF, on the absorption and fluorescence spectrum of Yb^{+3} in CdF_2 at 77°K are shown in Fig. 3b and 4. Of particular note is the drastic reduction in intensity of the 9760Å absorption line, and the loss of the broad, 9000 to 9700Å, absorption. Banks and Wagner (9) discuss the effects of Na^+ on the Yb^{+3} absorption spectrum in more detail.

The 77°K absorption spectrum of CdF_2:Yb^{+3} codoped with CdS shown in Fig. 3c was very similar to the spectrum with no S^{-2} added. The only difference was in the splitting of the 9620Å line. The fluorescence spectrum in Fig. 4 appeared to be similar to that of a composite of the "as grown" and HF fired CdF_2:Yb^{+3} spectra. On cooling from 77° to 2°K the emission peaks shifted slightly in wavelength and became sharper. The 9763Å peak split into two lines of nearly equal intensity at 9771 and 9780Å.

The addition of Eu^{+3} as a codopant appeared to increase the intensity of the Yb^{+3} absorption peak at 9754Å in relation to the 9760Å peak. The general character of the 77°K absorption spectrum, however, did not change as is shown in Fig. 3d. Figure 5 shows the

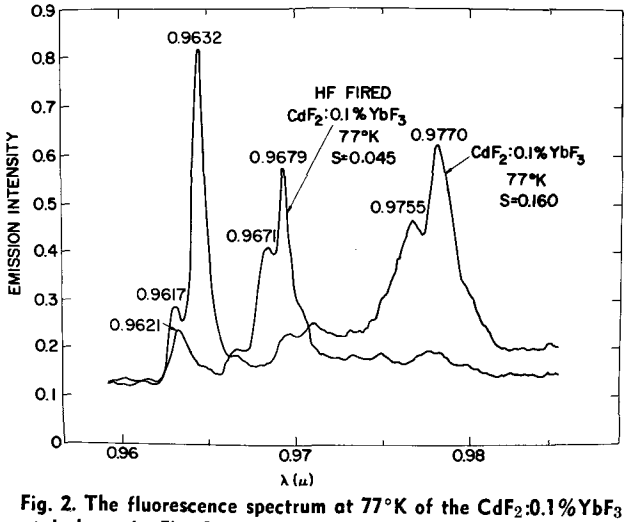

Fig. 2. The fluorescence spectrum at 77°K of the CdF_2:0.1%YbF_3 crystal shown in Fig. 1 and of the same crystal after firing in an HF atmosphere. The slit width, S, is given in mm.

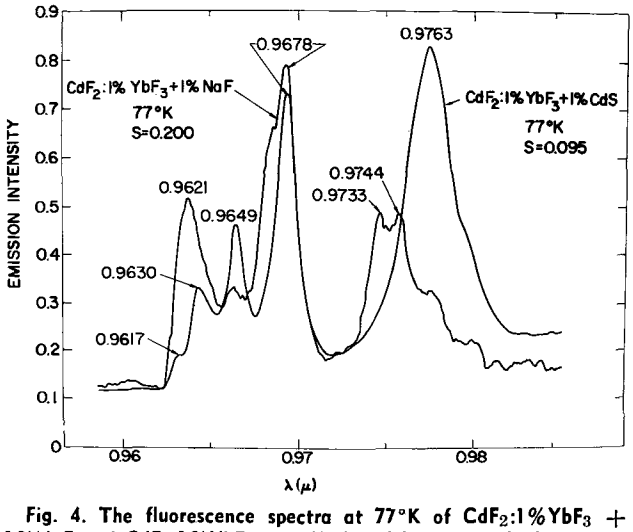

Fig. 4. The fluorescence spectra at 77°K of CdF_2:1%YbF_3 + 1%NaF and CdF_2:1%YbF_3 + 1% CdS. The slit width, S, is given in mm.

Table II. The observed optical fluorescence lines and transition assignments for Yb^{+3} and for Yb^{+3} plus various codopants in CdF_2 single crystals

Sample	λ (A)	Energy, cm^{-1}	Intensity 77°K	Intensity 2°K	Assigned transition Strong	Assigned transition Weak
0.1% YbF_3	9617	10,398	w	vw	7'-7 cubic	8'b-7
	9632	10,382	s	w	8'a-8a	8'-7 cubic or 8'a-7
	9649	10,364	vvw	vvw		
	9679	10,331	vw	vvw	8'-8 cubic	8'a-8a or 8'b-8a
	9695	10,315	vw	vvw	8'-8 cubic	8'a-8a or 8'b-8a
	9755	10,251	m	vw	8'b-8b	8'-8 cubic
	9770	10,235	s	s	7'-7	7'-7
	9887	10,114	m(br)	m(br)	phonon asstd.	7'-6, 8, 8a, 8b
0.1% YbF_3 + HF	9621	10,394	w		7'-7 cubic	8'b-7
	9653	10,359	vw		8'a-8a	
	9671	10,340	m		8'-8 cubic	8'b-8a
	9679	10,331	s		7'-7	8'a-7
	9691	10,319	w(sh)		8'b-8b	
	9733	10,274	vw		8'-6 cubic	8'-8 cubic
	9764	10,242	vw			7'-7
1% YbF_3 + 1% NaF	9621	10,394	m		7'-7	8'b-7
	9651	10,362	vw		8'a-8a	
	9673	10,338	s(sh)		8'-8 cubic	8'b-8a
	9678	10,333	s		8'-8 cubic	8'a-8a
	9733	10,274	m		8'-6 cubic	8'b-8b
	9744	10,263	m		8'b-8b	8'-8 cubic
	9762	10,244	w(sh)		7'-7	7'-7
1% YbF_3 + 1% CdS	9617	10,398	vw	vw	7'-7 cubic	
	9630	10,384	w	w		
	9649	10,364	m	m		
	9678	10,333	s	s		
	9763	10,243	s	s	7'-7	7'-7 and 7'-7 cubic
	9944	10,057	m(br)	m(br)	phonon asstd.	7'-6, 8, 8a, 8b
	10,283	9,725	w	w		phonon asstd.
1% YbF_3 + 1% EuF_3	9614	10,401	vw		7'-7 cubic	8'b-7
	9748	10,259	s		7'-7	7'-7 cubic
	9758	10,248	s		7'-7	7'-7
	9872	10,130	w(br)		phonon asstd.	7'-6, 8, 8a, 8b
0.1% YbF_3 + 7% CaF_2	9609	10,407	m	s	7'-7 cubic	
	9617	10,398	s	s	7'-7 cubic	
	9627	10,387	w	w	7'-7 cubic	
	9639	10,374	w		8'a-8a	
	9643	10,370	m	w	8'a-8a	
	9650	10,363	s	m	8'a-8a	
	10,195	9,809	vw	vw	7'-6 cubic	phonon asstd.
	10,233	9,772	vw	vw	7'-6, 8	phonon asstd.
	10,273	9,734	w	w	7'-6, 8	phonon asstd.

Intensities at 77° and 2°K listed as very weak (vw), weak (w), medium (m), strong (s), shoulder (sh) and broad (br) cannot be compared between the various samples and are uncorrected for detector response. Assigned transitions are given for both strong and weak crystal field splittings and are designated by the Γ level numbers involved.

fluorescence spectrum at 77°K. No emission was present between 9200 and 9610Å.

CdF_2:1% YbF_3 + 7% CaF_2.—The effects on the Yb^{+3} absorption and emission spectra of adding CaF_2 to CdF_2:Yb^{+3} were large, unexpected, and curious. As shown in Fig. 3d the 77°K absorption changed markedly. The intense line at 9760Å was almost gone. The reason for the drastic decrease in intensity of this absorption peak is not obvious. It is difficult to imagine a large change in crystal field strength or symmetry upon substituting a Ca^{+2} ion for a Cd^{+2} ion at these concentrations.

The fluorescence spectrum at 77°K shown in Fig. 5 revealed intense emission lines, relative to the CdF_2:Yb^{+3} crystals, between 9610 and 9660Å. Other weak lines were observed around 10,220Å but no lines were found in the 9760Å region. On cooling to 2°K only the relative intensities of the emission peaks were changed. The general character of the spectrum was preserved.

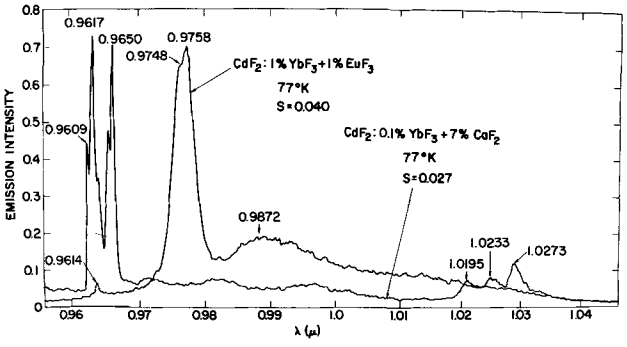

Fig. 5. The fluorescence spectra at 77°K of CdF_2:1%YbF_3 + 1%EuF_3 and CdF_2:0.1%YbF_3 + 7%CaF_2. The slit width, S, is given in mm.

Another interesting observation was the existence of Yb^{+2} as indicated by u.v. absorption bands and yellow fluorescence (10, 11). Divalent ytterbium and its u.v. absorption band might be the reason for the enhanced Yb^{+3} fluorescence at 9610 to 9650Å in the CdF_2-CaF_2 mixed crystals. This would, of course, require energy transfer between the Yb^{+2} and Yb^{+3} ions.

Discussion

Crystal field strength.—As noted above, EPR studies (5) on Yb^{+3} in CaF_2 give a cubic crystal field splitting of about 630 cm^{-1} for the $^2F_{5/2}$ excited state and approximately 800 cm^{-1} total splitting for the $^2F_{7/2}$ ground state. Kiss (12) has studied the optical spectrum of Tm^{+2} (isoelectronic with Yb^{+3}) in CaF_2. He finds a cubic crystal field splitting of 410 cm^{-1} for the excited state and 555.8 cm^{-1} between the Γ_7 and Γ_8 levels of the ground state. Calculations (13) using crystal field parameters derived from these observed optical data yield a total ground state splitting, Γ_7 to Γ_6, of about 588 cm^{-1} (as yet unobserved experimentally).

To a first approximation the crystal fields experienced by Yb^{+3} in CdF_2 and CaF_2 should not be too different. Consequently, a total crystal field splitting of several hundred wave numbers would be expected for the energy levels of Yb^{+3} in CdF_2. However, the estimates for the cubic field ground state splitting, derived from optical and EPR data, have been very much lower, ranging from 12 (6) to 110 cm^{-1} (2).

Two alternatives were selected, therefore, in trying

to fit the above absorption and fluorescence data for Yb^{+3} in CdF_2 to specific transitions on an energy level diagram. In the first case (strong crystal field) a total crystal field splitting of about 600 and 500 cm^{-1} was used for the ground and excited states, respectively. In the second case (weak crystal field) smaller crystal field splittings of about 150 and 140 cm^{-1} were tried.

Strong crystal field.—All of the absorption and fluorescent transition assignments are given in Tables I and II and a summary of the energy level splittings in Fig. 6(a).

The $^2F_{5/2}$ excited state cubic crystal field splitting ($\Gamma'_7 - \Gamma'_8$) of 475 cm^{-1} was given by the weak absorption lines near 9620 and 9200Å (10,395 and 10,870 cm^{-1}, respectively) in all of the samples. In the $^2F_{7/2}$ ground state, the cubic crystal field splittings were found to be $\Gamma_7 - \Gamma_8 = 560$ cm^{-1} using the fluorescent transitions near 9679Å in the CdF_2:YbF_3, HF fired and NaF codoped samples and $\Gamma_8 - \Gamma_6 = 30$-40 cm^{-1} using the emission lines near 9733Å in the HF fired and NaF codoped samples and near 10,195Å in the CaF_2 codoped sample. This gave a total $^2F_{7/2}$ ground state splitting of, $\Gamma_7 - \Gamma_6 = 600$ cm^{-1}.

The absorption data indicated at least two noncubic crystal field splittings for the $^2F_{5/2}$ excited state. In most of the samples the Γ'_7 energy level occurred near 10,250 cm^{-1} and the $\Gamma'_{8(b)}$ level between 10,940 and 10,960 cm^{-1}, giving a total excited state splitting, $\Gamma'_7 - \Gamma'_{8(b)} = 700$ cm^{-1}. The $\Gamma'_{8(a)}$ level was located between 10,680 and 10,718 cm^{-1} in the NaF and CdS codoped samples giving a $\Gamma'_{8(a)} - \Gamma'_{8(b)}$ splitting of about 250 cm^{-1}. In the HF fired sample, however, the Γ'_7 level and $\Gamma'_{8(b)}$ levels were placed at 10,327 and 10,945 cm^{-1}, respectively, giving a $\Gamma'_7 - \Gamma'_{8(b)}$ splitting of about 620 cm^{-1}.

The $^2F_{7/2}$ ground state splittings resulting from crystal fields of noncubic symmetry were more difficult to obtain. In most of the samples, the fluorescence data indicated that the $\Gamma_{8(a)}$ level (probably the first excited level in the $^2F_{7/2}$ ground state) occurred 340-370 cm^{-1} above the Γ_7 ground state level. The relative order of the $\Gamma_{8(a)}$ and Γ_6 energy levels is not known; the assignment in Fig. 6 was chosen arbitrarily. The second excited ground state level ($\Gamma_{8(b)}$?) seemed to lie between 625 and 709 cm^{-1} above the Γ_7 level in the CdF_2:YbF_3, HF fired and CdS codoped samples. No specific transitions were associated with the Γ_6 level, assuming that it lies more than 710 cm^{-1} above the Γ_7 ground state.

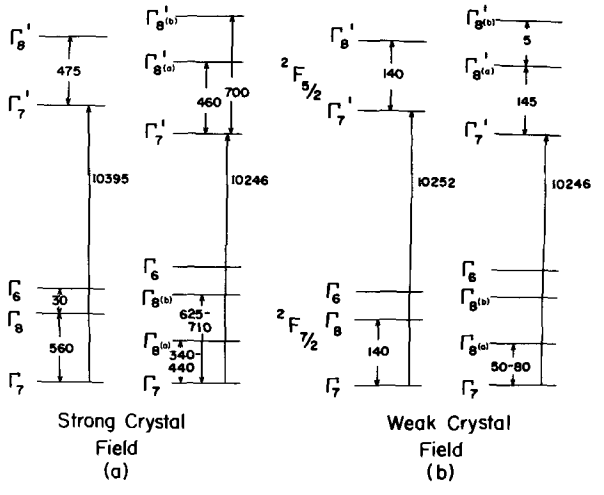

Fig. 6. Crystal field splittings for Yb^{+3} in CdF_2 according to *(a)* strong crystal field and *(b)* weak crystal field. Splittings between energy levels are given in cm^{-1}. Absorption lines between the Γ_7 and Γ'_7 levels are given in cm^{-1}. The ordering of the $\Gamma_{8(a)}$ $\Gamma_{8(b)}$ and Γ_6 ground state levels was selected arbitrarily. In both *(a)* and *(b)* cubic crystal field splittings are given on the left and noncubic crystal field splittings on the right.

There are several difficulties with this strong crystal field scheme. To explain the absorption doublets occurring near 9620 and 9760Å in most of the samples, recourse must be made to a very slight distortion of the crystal fields present at the Yb^{+3} lattice site. These might be caused, for example, by next-nearest-neighbor effects.

The fluorescence lines occurring at 9887, 9944, 10,283, 9872, 10,233, and 10,273Å seem to require a phonon assisted explanation. The fluorescence lines at 9630, 9649, and 9678Å in the CdF_2:YbF_3 + CdS sample cannot be assigned because of their temperature dependence (see Table II).

Weak crystal field.—The assigned transition are given in Tables I and II and a summary of the energy level splittings in Fig. 6(b).

The $^2F_{5/2}$ excited state energy level splitting for Yb^{+3} in a cubic crystal field was estimated to be 140 cm^{-1} for all of the samples. The absorption line near 9752Å (10,251 cm^{-1}) was used along with a line estimated to be at 9620Å (10,395 cm^{-1}) but obscured in the absorption data by the doublet arising from noncubic crystal field symmetry (see below).

The cubic crystal field splitting between the Γ_7 and Γ_8 levels of the $^2F_{7/2}$ ground state was estimated to be 130-140 cm^{-1} from the fluorescence data (the lines at 9887 and 9755Å in the CdF_2:YbF_3 sample, for example). The $\Gamma_8 - \Gamma_6$ splitting was not obtained from the data.

For the case of Yb^{+3} in noncubic crystal fields, the $^2F_{5/2}$ excited state splittings were essentially identical for all of the samples except the HF fired sample. The absorption lines at 9760, 9625, and 9620Å positioned the Γ'_7, $\Gamma'_{8(a)}$, and $\Gamma'_{8(b)}$ levels near 10,246, 10,390, and 10,395 cm^{-1}, respectively, giving the splittings $\Gamma'_7 - \Gamma'_{8(a)} = 144$ cm^{-1} and $\Gamma'_{8(a)} - \Gamma'_{8(b)} = 5$ cm^{-1}. For the HF fired sample the $\Gamma'_{8(a)}$ level was placed at 10,327 cm^{-1} giving a $\Gamma'_{8(a)} - \Gamma'_{8(b)}$ splitting of 68 cm^{-1}.

The splittings of the $^2F_{7/2}$ ground state energy levels, resulting from Yb^{+3} at a site of noncubic crystal field symmetry, were difficult to determine. The fluorescence data on most of the samples indicated that the first excited level, probably the $\Gamma_{8(a)}$, was 50-80 cm^{-1} above the Γ_7 ground state. The positions of the $\Gamma_{8(b)}$ and Γ_6 energy levels were not obtained.

Many difficulties were encountered with the weak crystal field scheme. There was no absorption detected from the Γ_7 to the Γ'_8 level or from the $\Gamma_{8(a)}$ level located only 50-80 cm^{-1} above the Γ_7. No absorption lines with energies greater than 10,400 cm^{-1} could be assigned. In the case of the HF fired sample, the $\Gamma'_{8(a)} - \Gamma'_{8(b)}$ splitting from the Γ'_8 level was quite unsymmetrical.

Several of the fluorescence lines could not be assigned with the 9617, 9630, 9649, and 9678Å lines in the CdS codoped sample and the 9639, 9643, and 9650Å lines with the CaF_2 codopant being most troublesome.

A comparison.—Neither the strong or the weak crystal field spliting model is completely satisfactory for Yb^{+3} in CdF_2. However, when the known data for Yb^{+3} in CaF_2 (6) and Tm^{+2} in CaF_2 (12) are considered along with the apparent "better fit" of the above absorption and fluorescence data to the strong field scheme, it appears that the strong crystal field splitting is favored. With either model many of the strong optical transitions observed for Yb^{+3} in CdF_2 arise from ions at sites of noncubic crystal field symmetry whereas EPR data (1-4) have indicated predominantly cubic crystal field symmetry for Yb^{+3} in CdF_2.

Crystal field symmetry.—One reason for the addition of various codopants to the CdF_2:YbF_3 crystals was to identify specific optical transitions of Yb^{+3} with certain types of local crystal field symmetry. As indicated in the previous section, this was not possible with the data obtained. There were, however, several characteristic Yb^{+3} absorption or emission lines for samples containing various codopants (presumably

Table III. The prominent absorption and fluorescence lines at 77°K for Yb^{+3} and for Yb^{+3} plus various codopants in CdF_2 single crystals

Absorption line λ (A)	Energy (cm^{-1})	Codopant in CdF_2:YbF_3 Crystal None	HF	NaF	CdS	EuF_3	CaF_2
9137-40	10,945-1		vw	vvw	vvw		
9169	10,906		vw				
9185-200	10,877-70	vw	vvw	w	vw	vw	vvw
9213	10,854			w			
9617-20	10,398-5	w	w	m	w	w	w
9623-30	10,392-84	vw		s	w	w	
9683	10,327		m				
9750-5	10,256-1	s	s	m	s	s	
9759-64	10,247-2	vs	vs	m	vs	s	vw
Fluorescence line							
9609	10,407						m
9617	10,398	w	w	m	vw	vw	s
9627-32	10,387-2	s			w		w
9639	10,374						w
9643	10,370						m
9649-53	10,3640-59	vvw	vw	vw	m		s
9671	10,340		m	s(sh)			
9679	10,331	vw	s	s	s		
9733	10,274		vw	m			
9744-48	10,263-59			m		s	
9755	10,251	m					
9760	10,246		vw	w(sh)	s	s	
9770	10,235	s					

The intensities listed as very weak (vw), weak (w), medium (m), strong (s) and shoulder (sh) cannot be compared between the various samples and are uncorrected for detector response.

corresponding to at least slightly different crystal field symmetries at the Yb^{+3} lattice site). In Table III the relative intensities of the strongest absorption and emission lines are listed for all of the samples. It can be seen from Table III that the following lines indicate the presence of particular codopants (or impurities) in CdF_2:YbF_3 crystals: (*i*) The emission lines at 9632, 9655, and 9770Å are indicative of "as grown" CdF_2:YbF_3. (*ii*) The absorption line at 9683Å and the emission line at 9671Å correspond to the symmetry in the HF fired crystals (possibly a near neighbor F^- interstitial). (*iii*) The Na^+ codopant is indicated by a, relatively, strong absorption line at 9623Å and fluorescence at 9733Å. (*iv*) The presence of S^{-2} is characterized by the position and relative intensities of the 9617-9630Å absorption doublet and the emission lines at 9649 and 9679Å along with their apparent lack of temperature dependence. (*v*) Two strong fluorescence lines at 9744 and 9760Å indicate Eu^{+3}. (*vi*) Relatively strong emission at 9609, 9617, 9643, and 9650Å is characteristic of CaF_2 codoping.

Acknowledgments

The author would like to thank the following people at the IBM T. J. Watson Research Laboratory: Mr. J. E. Scardefield for help in growing the crystals, Mr. G. D. Pettit for the optical measurements, and Drs. J. D. Axe and P. R. Wagner for interesting and helpful discussions.

Manuscript received Aug. 30, 1966; revised manuscript received Feb. 1, 1967.

Any discussion of this paper will appear in a Discussion Section to be published in the December 1967 JOURNAL.

REFERENCES

1. V. K. Konyukhov, P. P. Pashinin, and A. M. Prokhorov, *Soviet Phys. Solid State*, **4** (1), 175 (1962).
2. P. P. Pashinin and A. M. Prokhorov, "Paramagnetic Resonance," p. 197, Academic Press, Inc., New York (1963).
3. G. M. Zverev and A. I. Smirnov, *Soviet Phys. Solid State*, **6** (1), 76 (1964).
4. R. S. Title, IBM Research Center, unpublished data, 1964.
5. See, for example, M. J. Weber and R. W. Bierig, *Phys. Rev.*, **134** (6A), A1492 (1964).
6. W. Low, *Phys. Rev.*, **118** (6), 1608 (1960).
7. Paul F. Weller, *Inorg. Chem.*, **4** (11), 1545 (1965).
8. H. A. Weakliem, Project DEFENDER Report, Contract No. NONR 4133(00) ARPA Order No. 306-62, August 20, 1964.
9. E. Banks and P. Wagner, *J. Chem. Phys.*, **44** (2), 713 (1966).
10. Paul F. Weller, *Inorg. Chem.*, **5**, (5), 736 (1966).
11. P. P. Feofilov, *Optika i Spectroskopia*, **5**, 216 (1958).
12. Z. J. Kiss, *Phys. Rev.*, **127**, 718 (1962).
13. B. Bleaney, *Proc. Roy. Soc.*, **277A**, 289 (1964).

Rare Earth Cathodoluminescence in $InBO_3$ and Related Orthoborates

F. J. Avella, O. J. Sovers, and C. S. Wiggins

General Telephone & Electronics Laboratories, Inc., Bayside, New York

ABSTRACT

The cathodoluminescence from Eu^{3+} and Tb^{3+} in the orthoborates of In, Sc, Y, La, Gd, and Lu is examined. The host $InBO_3$ is shown to be particularly effective for both activators. Observed spectral details of the luminescence are related to effects of crystal symmetry on electronic transitions.

Reports of photoluminescence from rare earth activated orthoborates of the type $M^{III}BO_3$ have appeared in the literature (1-3); however, little information is available on the cathodoluminescence of those systems. Recently, Avella (4) compared the performance of Tb^{3+} in several orthoborate matrices under cathode-ray excitation and found $InBO_3$ to be an effective host for that activator. In this paper our purpose is (*i*) to report highly efficient cathodoluminescence from Eu^{3+} in $InBO_3$, and (*ii*) to examine the effects of crystal symmetry on the emission processes of Eu^{3+} and Tb^{3+} activated orthoborates of In and the rare earths.

The orthoborates of trivalent In and the trivalent rare earths Sc, Y, La, Gd, and Lu constitute a family of polymorphous compounds with crystal structures at ambient conditions which are related to three crystalline forms of $CaCO_3$: aragonite, vaterite, and calcite (5). The structure which $M^{III}BO_3$ assumes is governed by the size of the cation. Thus La^{3+}, the largest rare earth ion, forms an orthoborate with the orthorhombic aragonite structure having space group V_h^{16}-Pbnm (6), where the La ion is situated in an asymmetric lattice site with point group C_s-m. The orthoborate structures of the smaller Y^{3+} and Gd^{3+} ions are often equated with vaterite; however, Bradley *et al.* (7) have shown that these are not true vaterite isomorphs and have assigned them a probable space group of D_{3h}^2-$P\bar{6}c2$. This pseudovaterite lattice has one cation with twelvefold oxygen coordination for every two

with sixfold coordination. The two sites differ in cation to oxygen distance, but have D_3-32 point symmetry in common. Sc^{+3} and In^{+3} are the smallest ions considered here. They occupy centrosymmetric C_{3i}-$\bar{3}$ lattice sites in orthoborates having the rhombohedral calcite structure with space group D_{3d}^6-$R\bar{3}c$ (6). $LuBO_3$ is a special case having two relatively stable allotropes which crystallize either with the calcite or, if heated above 1310°C, with the pseudovaterite structure. As a group, these orthoborates offer cation environments increasing in symmetry from aragonite to pseudovaterite to calcite.

The orthoborates under consideration are optically inert. Activation occurs when rare earth luminogens are substituted for some of the host cations. Although some emission is obtained from Sm and Dy, the most efficient visible emitters in $M^{III}BO_3$ are trivalent Eu and Tb, both of which form orthoborates of the pseudovaterite type. Therefore, activator incorporation is truly isomorphous only when M^{III} = Y, Gd, or Lu. Nevertheless, with the low activator concentrations considered here, neither the aragonite nor the calcite structured compounds give evidence of lattice distortion after activation when examined by routine x-ray powder diffraction methods. Consequently, the orthoborates offer an opportunity to examine host-activator interaction as a function of cationic species and of lattice symmetry.

Experimental

The orthoborate phosphors were prepared in powder form from stoichiometric mixtures of reagent grade boric acid with the oxides of the host and activator cations having 99.9% purity or better. Optimum Eu and Tb concentrations for maximum cathodoluminescence yield were found to be 0.02 to 0.03 gram atoms/mole of phosphor. The mixtures were fired in air using platinum or fused silica crucibles at two or three intermediate temperatures, and the materials were mortared between firings. The maximum temperatures optimized for cathodoluminescence performance were 1400°C for the In, Lu (pseudovaterite), Y and Gd compounds, 1200°C for the Sc and La compounds, and 1000°C for the Lu calcite polymorph. Compound formation was verified by x-ray powder diffraction analysis.

For measurement of cathodoluminescence the phosphors were settled on 1-in.^{2} sheets of conductive glass. These sheets were positioned in a demountable cathode-ray tube and excited at 15 kv using a 7-in. raster. The luminous output was measured with an RCA 1P21 photomultiplier fitted with a Kodak Wratten 106 filter. The emission spectra were recorded using a ¾-meter Czerny-Turner spectrometer (1200 line/mm grating and 50μ slit width) and an ITT F4013 photomultiplier (S-20 response). A correction function derived from the output of an NBS 1000W quartz-iodine standard lamp served as as internal reference so that spectra were recorded directly in terms of relative energy. The C.I.E. color coordinates and values of lumen equivalent were calculated from these spectra.

Results and Discussion

Eu^{3+} *cathodoluminescence spectra.*—Figures 1a-g present spectral energy distributions for cathodoluminescence emission from Eu in the orthoborates. No provision has been made in these figures for comparison of intensities between phosphors; however, luminosity data will be discussed in a later section. From the spectra it can be seen that the fine structure of the Eu^{3+} emission differs considerably among the three polymorphs but is closely similar among the isomorphs. In the three calcite structures of Fig. 1a-c the two dominant emission lines near 590 and 596 nm can be assigned to magnetic dipole allowed $^5D_0 \rightarrow {}^7F_1$ transitions. The $^7F_1$ level is split into two components as predicted from group theoretical considerations (8). The energy difference between the two Stark levels

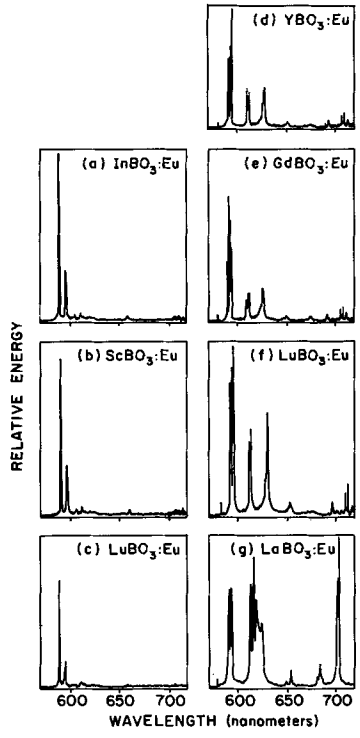

Fig. 1. Cathodoluminescence spectra from Eu activated orthoborates: (a-c) calcite structure; (d-f) pseudovaterite structure; (g) aragonite structure. (Spectra recorded at different instrumental gains.)

of approximately 190 cm^{-1} is larger than that normally observed for this Eu^{3+} multiplet. This splitting decreases slightly from In to Sc to Lu orthoborate. With Eu in the centrosymmetric C_{3i} site, electric dipole transitions are forbidden. Consequently, transitions from $^5D_0$ to the J = 2, 3, and 4 sublevels of ^7F are weak as indicated by the emission groups near 610, 660, and 710 nm, respectively; no emission is observed corresponding to the $^5D_0 \rightarrow {}^7F_0$ transition. It is possible that some of the weak emissions result from transitions which originate in a higher excited level, *e.g.*, $^5D_1$, but such assignments would require detailed studies outside the scope of this paper.

The spectra of Fig. 1d-f were obtained from Eu^{3+} in the pseudovaterite structures. Again emission lines near 590 nm constitute the dominant feature and can be assigned to $^5D_0 \rightarrow {}^7F_1$ transitions. For the D_3 site symmetry a twofold splitting of $^7F_1$ is predicted; however, two distinct types of D_3 sites are involved which make possible a total of four Stark levels and, therefore, as many as four $^5D_0 \rightarrow {}^7F_1$ emission lines. Although not clearly defined in these figures, four such emission lines are indeed observed for each of the three pseudovaterites. In each case the width of the $^7F_1$ multiplet does not exceed 100 cm^{-1}, but there is variation in the energy differences between the four sublevels as well as in the probabilities of transitions to them. As a result of lower site symmetry there is a relaxation of parity forbiddenness, and electric dipole transitions are also possible. At 581 nm a weak line appears that may be attributable to the $^5D_0 \rightarrow {}^7F_0$ transition. The emission groups between 609 and 618 nm probably result from $^5D_0 \rightarrow {}^7F_2$ transitions. These are more intense for the pseudovaterite than for the calcite polymorphs both in relation to other transitions and also on an absolute basis. Of the six lines possible, four distinct ones are observed, with one sublevel (626-628 nm emission) being considerably broadened. Intensity variations among the three pseudovaterites are also evident for these transitions. In these compounds the $^5D_0 \rightarrow {}^7F_3$ transitions give rise to weak emission at about 650 nm *vs.* 660 nm for the calcites. The transitions are about equal in intensity for the

two polymorphs. The $^5D_0 \rightarrow {}^7F_4$ emission lines near 710 nm, however, are more intense for the pseudovaterites.

The spectrum from Eu in the C_s site of the $LaBO_3$ aragonite polymorph is presented in Fig. 1g. It differs from the spectra of Fig. 1a-f mainly in that the magnetic dipole transitions are subordinate to the electric dipole transitions. The dominant group is $^5D_0 \rightarrow {}^7F_2$ with a broad emission band between 610 and 630 nm. Also of relatively high intensity is the emission near 700 nm arising from $^5D_0 \rightarrow {}^7F_4$. However, because the total emitted flux from $LaBO_3$:Eu is considerably smaller than that from the other borates, these transitions are actually no more intense than their counterparts in the pseudovaterites. The magnetic dipole allowed $^5D_0 \rightarrow {}^7F_1$ group is relatively weak here and produces three emission lines between 590 and 594 nm. The $^5D_0 \rightarrow {}^7F_0$ transition is very weakly indicated by the line at 597 nm.

Considered as a group, the spectra from the orthoborates demonstrate that a lowering of site symmetry increases the probability ratio of electric dipole to magnetic dipole transitions. This effect was recently described by Blasse *et al.* (9) using host compounds of several different compositions. On the other hand, the identical site symmetries and closely related lattice parameters of the orthoborate isomorphs combine to produce nearly identical details in the Eu^{3+} radiative transitions.

Tb^{3+} *cathodoluminescence spectra.*—Since in Tb^{3+} all the radiative transitions from the lowest excited state ($^5D_4$) to the J = 3-5 sublevels of the ^7F ground state are allowed by magnetic dipole considerations, the $M^{III}BO_3$:Tb spectra will not bear a similar analysis to that made of the Eu spectra. Also, the multiplicity of Stark levels possible in the pertinent ground and excited levels makes comparison of actual and calculated numbers of components impractical, at least for room temperature spectra. However, some correlations can be made.

Reference to the emission spectra of the Tb activated calcite isomorphs in Fig. 2a-c shows five groups of emission lines which may be assigned to transitions terminating at the following ground levels: for 475-510 nm emissions, $^7F_6$; 535-565 nm, $^7F_5$; 578-600 nm, $^7F_4$; 615-635 nm, $^7F_3$; 650-665 nm, $^7F_2$. Considering their complexity, the spectra are strikingly similar for these three isomorphs, and only small differences appear in the intensities and positions of the lines. The major portion of the emitted energy results from transitions in the $^5D_4 \rightarrow {}^7F_5$ group with the lines at about 542 and 550 nm the most intense. Such a total domination of the Tb^{3+} spectrum by this group of transitions is unusual and has not been reported for other hosts.

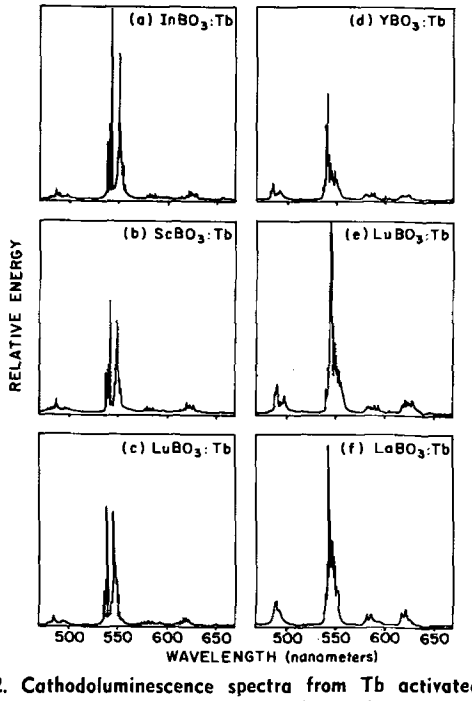

Fig. 2. Cathodoluminescence spectra from Tb activated orthoborates: (a-c) calcite structure; (d & e) pseudovaterite structure; (f) aragonite structure. (Spectra recorded at different instrumental gains.)

Emission spectra of Tb^{3+} in the pseudovaterite structures are given in Fig. 2d and e. $GdBO_3$:Tb has been excluded because of strong interference from Eu^{3+} emission which results from Eu impurity in the Gd_2O_3 starting material. The two pseudovaterite spectra are similar but not identical. The most obvious variation from the calcite spectra occurs in the absence of a strong emission line at 550 nm in the $^5D_4 \rightarrow {}^7F_5$ group. There is an intense emission at about 542 nm, but this is split into two lines in YBO_3 and into three lines in $LuBO_3$. Some of the other lines within this group do have analogues in the calcite spectra. Another variation from the calcites appears in the greater intensity of emission at 478-510 nm (from $^5D_4 \rightarrow {}^7F_6$ transitions) relative to the dominant emission.

The Tb^{3+} spectrum from the aragonite structure in Fig. 2f bears a strong resemblance to the pseudovaterite spectra. The major difference is the absence of splitting in the dominant 542 nm emission line. Other small variations in detail are also seen.

From the above observations it is evident that, just as in the case of Eu^{3+}, the Tb^{3+} emission shows closely similar spectral detail among the orthoborate isomorphs. Among the polymorphs there are spectral differences, but in comparison with the Eu^{3+} ion, it is clear that the radiative transitions in Tb^{3+} are less sensitive to changes in the crystal field.

Cathodoluminescence performance.—Performance data for the cathodoluminescence of Eu^{3+} in the orthoborate hosts are presented in Table I. Also included for comparison are data for Y_2O_3:Eu, YVO_4:Eu and $Zn_{0.21}Cd_{0.79}S$:Ag, all three of which are efficient red-emitting cathode-ray phosphors. In terms of relative luminosity, $InBO_3$:Eu is superior to all the red-emitting phosphors listed. The C.I.E. color coordinates indicate that the emission shifts from red to orange proceeding from the aragonite to the pseudovaterite to the calcite structures. From the values of lumen equivalent it can be seen that this color shift is in the direction of greater eye sensitivity. In order to determine the relative efficiencies with which these phosphors convert the excitation energy into radiant energy, it is necessary to take the emission colors into consideration. Thus, values of relative conversion efficiency were obtained from a ratio of relative luminosity to lumen equivalent, and a value of 1.00 was assigned arbitrarily to the sulfide phosphor. On this basis $InBO_3$ is a more efficient host for Eu^{3+} than any of the other borates and is comparable in efficiency to YVO_4.

The performance of the Tb-activated orthoborates under cathode-ray excitation has been reported elsewhere (4). The superiority of $InBO_3$ over the other orthoborates as a host is even more evident when Tb is the activator, since $InBO_3$:Tb has approximately 300% the conversion efficiency of YBO_3:Tb, the next most efficient $M^{III}BO_3$:Tb. In terms of relative luminosity and conversion efficiency $InBO_3$:Tb is comparable with Zn_2SiO_4:Mn phosphor.

Summary

Orthoborates of type $M^{III}BO_3$, where M^{III} = In, Sc, Y, La, Gd, and Lu, were activated with trivalent Eu and Tb, and their response to cathode-ray excitation was studied. $InBO_3$ proved to be the most effective orthoborate host for Eu^{3+} as well as for Tb^{3+}, and the conversion efficiency of $InBO_3$:Eu was found to be comparable with that of YVO_4:Eu. De-

Table I. Cathodoluminescence data for Eu activated orthoborates

Phosphor	Crystal structure	Relative luminosity	C.I.E. color coordinates x	y	Lumen equivalent, lumen/rad. watt	Relative conversion efficiency
$InBO_3$:Eu	Calcite	190	0.59	0.41	470	0.34
$ScBO_3$:Eu	Calcite	45	0.60	0.40	460	0.08
$LuBO_3$:Eu	Calcite	50	0.59	0.41	480	0.09
$LuBO_3$:Eu	Pseudovaterite	95	0.61	0.39	370	0.22
YBO_3:Eu	Pseudovaterite	100	0.62	0.38	370	0.23
$GdBO_3$:Eu	Pseudovaterite	80	0.62	0.38	360	0.19
$LaBO_3$:Eu	Aragonite	10	0.64	0.36	260	0.03
Y_2O_3:Eu	—	170	0.64	0.36	310	0.46
YVO_4:Eu	—	100	0.67	0.33	250	0.34
$Zn_{0.71}Cd_{0.79}S$:Ag	—	95	0.65	0.35	80	1.00

viation from a centrosymmetric site was shown to increase the probability of electric dipole transitions in Eu^{3+}, and closely similar spectral details were observed among the borate isomorphs for each activator.

Acknowledgments

The authors are indebted to V. Qvistorff for assistance in sample preparation and evaluation, to S. Mosca for recording the spectra, and to A. K. Levine and F. C. Palilla for helpful discussions and suggestions.

Manuscript received Dec. 5, 1966; revised manuscript received Feb. 8, 1967.

Any discussion of this paper will appear in a Discussion Section to be published in the December 1967 JOURNAL.

REFERENCES

1. H. J. Borchardt, *J. Chem. Phys.*, **42**, 3743 (1965).
2. A. Bril and W. L. Wanmaker, *This Journal*, **111**, 1363 (1964).
3. Netherlands Pat. 303,020 (1965).
4. F. J. Avella, *This Journal*, **113**, 1225 (1966).
5. E. M. Levin, R. S. Roth, and J. B. Martin, *Am. Mineralog.*, **46**, 1030 (1961).
6. R. W. G. Wyckoff, "Crystal Structures," 2nd ed., Vol. II, Chap. VIII A, Interscience Publishers, New York (1964).
7. W. F. Bradley, D. L. Graf, and R. S. Roth, *Acta Cryst.*, **20**, 283 (1966).
8. J. L. Prather, Atomic Energy Levels in Crystals, NBS Monograph No. 19, Washington, D. C. (1961).
9. G. Blasse, A. Bril, and W. C. Nieuwpoort, *J. Phys. Chem. Solids*, **27**, 1587 (1966).

$Cd_xHg_{1-x}Te$ Films by Cathodic Sputtering

Herbert Kraus, Sidney G. Parker, and James P. Smith

Texas Instruments Incorporated, Dallas, Texas

ABSTRACT

Films of $Cd_xHg_{1-x}Te$ ranging from $x = 0.05$ to $x = 0.15$ were deposited by cathodic sputtering on single crystal substrates of NaCl, Ge, and sapphire. The resulting films were amorphous, but became crystalline on annealing. Optical transmission and electron probe analysis showed a slightly lower Hg concentration in the film than was present in the source material. Although CdTe can be sputtered to give a polycrystalline film, it was not possible to obtain a film by sputtering HgTe.

Reports by several investigators indicate that HgTe and CdTe form solid solutions over the entire compositional range of the alloy (1-4). The location of the absorption edge in this system is determined by the composition of the alloy and is at 0.8μ for pure CdTe and at some value greater than 20μ for HgTe. Compositions ranging from $Hg_{0.80}Cd_{0.20}Te$ to $Hg_{0.95}Cd_{0.05}Te$ are of interest since they exhibit absorption edges beyond 8μ in the electromagnetic spectrum and can possibly be used for fabrication of intrinsic photon detectors.

The phase relationship in this alloy system suggests an equilibrium segregation coefficient greater than three for Cd in the compositional range of interest. This condition makes preparation of highly homogeneous material by conventional melt-growth methods rather difficult. Since the ultimate form of a detector made from this material is to be a layer of the alloy about 10 to 50μ thick attached to an insulating substrate and thin layers of this particular material are usually prepared by cumbersome lapping, polishing, and etching procedures, cathodic sputtering was deemed to be a desirable approach.

This paper describes some of the advantages and disadvantages of cathodically sputtered (HgCd)Te films.

Experimental

Amorphous (HgCd)Te films were prepared by cathodic sputtering from polycrystalline (HgCd)Te sources of several different compositions. Source materials of the desired nominal compositions were made from the purified elements. Appropriate quantities of ultrapure Hg (Hg-9, E. H. Sargent Comany) six-nines Cd (Cominco), and five-nines Te (ASARCO), which was further zone-refined until no impurities were detected by emission spectrography, were placed in a clean quartz ampoule. The ampoule was then evacuated and sealed. The elements were carefully heated in a rocking furnace to 30°-50°C above the liquidus of the alloy for 30-40 hr. Finally, the melt was solidified by air-quenching within 40-50 sec. Electron probe analysis showed the ingots were homogeneous. Emission spectrographic analyses revealed no impurities in samples taken from the compounded ingot. Mass spectrographic analyses were of no use, since the

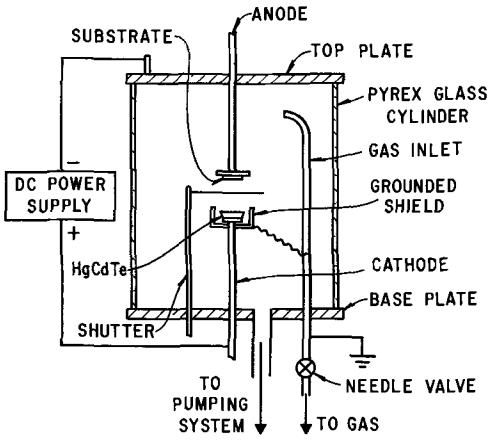

Fig. 1. Sketch of sputtering apparatus

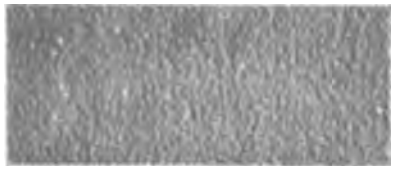

Fig. 2a. Photomicrograph of sputtered unannealed film of $Hg_{0.85}Cd_{0.15}Te$. Magnification 120X.

Fig. 2b. Photomicrograph of sputtered annealed film of $Hg_{0.85}Cd_{0.15}Te$. Magnification 400X.

multiple-charge ions of the major components produced mass interference, masking any possible impurities.

Sputtering was accomplished in a simple apparatus of conventional design, as shown in Fig. 1. All metal surfaces inside the vacuum chamber were cadmium plated to minimize contamination. The anode was a 1½-in. diameter brass disk welded to a stainless steel tube to permit cooling or heating of the substrate. The substrates and growth planes were {1,1,0} NaCl, {1,1,1} Ge, and randomly oriented sapphire, all with a 1μ in. surface finish and a 25 mm^2 surface area.

With the substrate and source material in place, the system was evacuated to approximately 10^{-3} Torr and backfilled with dry, oxygen-free argon. This cycle was repeated several times. The system was then evacuated to 1 x 10^{-5} Torr. The pressure of the system was then adjusted by increasing the argon pressure in the bell jar by use of a micrometer valve. Throughout this study dry, oxygen-free argon was used as the discharge gas to enhance the disintegration rate of the source material and prevent undesirable reactions between the sputtered deposit and the residual gas (5).

It is well known that in the sputtering process the parameters of voltage, current density, pressure, and anode-cathode distance are highly interdependent. Success in obtaining films and the resulting properties of these films differed widely with sputtering conditions. Films of the compositions of interest ranging from $Hg_{0.85}Cd_{0.15}Te$ to $Hg_{0.95}Cd_{0.05}Te$ being relatively free of pinholes and visual defects, sputtered on NaCl, Ge, and sapphire were obtained using the following conditions: voltage, 1500v; current, 470 μa; cathode current density, 0.36 ma/cm^2; anode-cathode distance, 1.0 cm; Ar pressure, 45μ; sputtering period, 4.0 hr; substrate temperature, 25°C.

Results and Discussion

Film characteristics.—Typical film thicknesses were between 30 and 50μ. The films consisted of an amorphous layer interspersed with crystallites. The amorphous and crystalline character of the unannealed films was determined by reflection electron diffraction. Heating the substrates while sputtering, to encourage crystal growth, resulted in poor film adhesion and severe losses of Hg. Cooling the substrate below room temperature during sputtering increased the amorphous character of the deposit. Substrates cooled to near 0°C were invariably 100% amorphous. Figure 2A shows a photomicrograph of the surface of a typical unannealed film of $Hg_{0.85}Cd_{0.15}Te$ sputtered on a randomly oriented sapphire substrate.

Annealing.—Films were annealed under partial Hg-vapor pressures of 3 and 150 Torr, respectively, to obtain crystal growth and to attempt to improve crystalline perfection. The sample was heated to 300°C during annealing. The best crystal growth was obtained when films sputtered on sapphire substrates were annealed for 24 hr under a partial pressure of Hg vapor of 150 Torr with the sample heated to 300°C. Figure 2B shows a photomicrograph of a formerly amorphous $Hg_{0.85}Cd_{0.15}Te$ film exhibiting [1,1,1] oriented crystallites after annealing. Similar results were also obtained with compositions of higher Hg content. Films deposited on NaCl and Ge substrates peeled off when they were annealed or on subsequent handling.

Although CdTe films were readily laid down by sputtering, no HgTe deposit was obtained by cathodic sputtering under any of the conditions attempted. Failure to obtain a HgTe film is probably caused by decomposition of the HgTe by the high energy Ar ions as they bombard the surface and/or by a low accommodation coefficient of the substrates employed. It is apparent that addition of CdTe to HgTe modifies the sputtering properties of HgTe.

Optical measurements.—Transmission measurements were carried out at room temperature with a Perkin-Elmer 337 dual-beam grating spectrometer on unannealed films sputtered on single crystal NaCl. Attempts to measure annealed films were hampered by pinholes in the film which were introduced during annealing. Figure 3 shows the curves of Log I_o/I *vs.* wavelength in microns, where I_o is the incident energy and I the transmitted energy. The absorption curves were de-

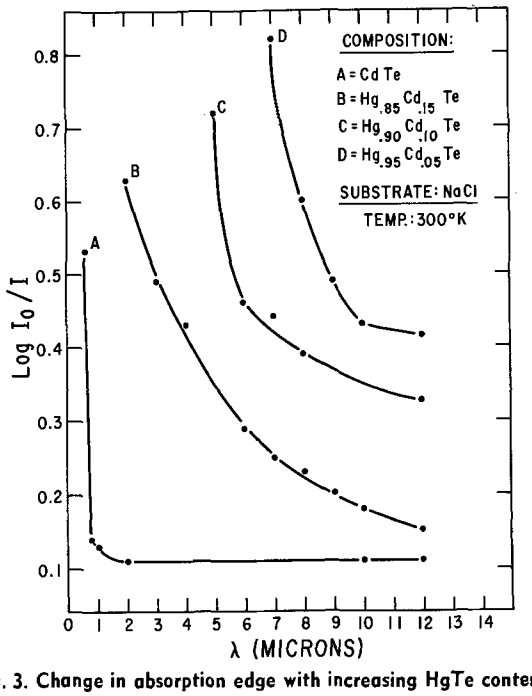

Fig. 3. Change in absorption edge with increasing HgTe content

rived from randomly chosen films whose compositions were established by electron probe analysis. It can be seen that the absorption edge shifts from 0.8μ for pure CdTe to longer wavelengths as the Hg content increases. The exact position of the energy-band edge becomes more difficult to determine from the absorptions curves as the Hg concentration is increased because of free carrier absorption beyond the band edge. However, reasonable estimates of the band gaps can be made by extrapolation.

As mentioned previously, the best films obtained were sputtered on sapphire substrates. These films were less susceptible to peeling and pinhole formation during annealing. Such a film was sputtered from a $Hg_{0.85}Cd_{0.15}Te$ source, annealed for 24 hr at 300°C under a partial Hg vapor pressure of 150 Torr, then measured for photoconductive response at 77°K. Electrical contacts were made with thin-gauge gold wire soldered with pure indium to opposite sides of the film. The final assembly was placed in a Dewar-type flask, cooled to 77°K, and measured for relative spectral response. Figure 4 shows results of the measurements. The peak response was at 3.5μ, which corresponds to an energy gap of about 0.35 ev. This value does not compare favorably with optical transmission data for bulk material of the same composition. Experimental measurements on bulk (HgCd)Te by Blue (6) show the energy gap value for $Hg_{0.85}Cd_{0.15}Te$ to be about 0.14. Because electron probe analysis shows only a small loss of Hg during sputtering, the wider band gap must be attributed to other factors. Chemical analysis data indicate variations in composition in the film, *i.e.*, the value of x in $Hg_{1-x}Cd_xTe$ varies throughout the film, despite the fact that the over-all elemental composition is very near that of the source. Therefore, material of wider band gap is most likely produced along with materials having a wide range of band gaps. It is difficult to determine accurately the band gap in the films from optical data because of scattering (7) and adsorption in the amorphous film. Further, it has been suggested that the adsorption edge position becomes more difficult to determine with increasing HgTe content because of the low values of the energy gap and of the effective electron mass (8).

Chemical composition analysis.—Bulk composition and degree of microscopic homogeneity should be known to correlate the chemical and optical properties of the alloy system. Bulk analysis of the starting material was obtained for cadmium and tellurium with the Jarrell-Ash Model 82-546 Atomic Absorption Flame Spectrometer. The degree of microscopic homogeneity was studied with the Material Analysis Company Model 400 Electron Probe Microanalyzer equipped with three analyzing channels.

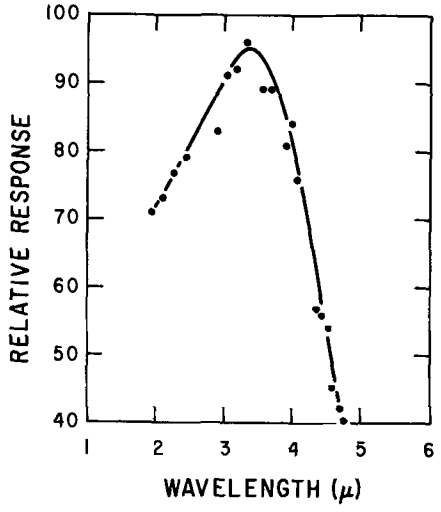

Fig. 4. Relative spectral response curve vs. wavelength of a sputtered film after annealing.

It is not too meaningful to relate analytical results to molar relationships of pseudobinary systems, but we can easily discuss the $Hg_{1-x}Cd_xTe$ compositions in terms of the x value. Of course, the x value assumes a stoichiometric composition, and the fit of the analysis to the stoichiometric composition must be stated. When x is in the range from 0.05 to 0.20, its value in $Hg_{1-x}Cd_xTe$ is very sensitive to the cadmium concentration. Cadmium varies from 1.74 to 7.27 w/o (weight per cent) in this range, whereas mercury varies from 58.86 to 51.61 and tellurium from 39.4 to 41.12 w/o. It appears useful to calculate the x value using the cadmium analysis and to compare the mercury and tellurium concentrations to the theoretical concentrations of a stoichiometric compound. Thus, a cadmium concentration of 1.74% would indicate that x was 0.05. However, if the mercury concentration were only 55.2 w/o, rendering the compound more than 3% deficient in mercury, the end result would hinge again on the assumption that no losses of tellurium occurred during compounding. The electron-probe microanalyzer was used to analyze the three components simultaneously at random 10μ diameter spots over the surface of the sample.

A list of experimental constants is given in Table I. The average of the various electron counts was used for the analysis. The data were computed with the computer program written by Brown (9). This program normalized the three components of the composition to a 100% sum. Before this normalizing step, errors in the sum ranged between —3% and +1% using HgTe and CdTe standards. The use of elemental standards and HgS resulted in errors as large as 10%; these errors were probably the result of absorption uncertainties, atomic number effects, and the creation of Cd L α fluorescence by Te L α radiation. These effects, which are not corrected in the computer program, are minimized by using HgTe and CdTe standards. The cadmium concentrations in the (HgCd)Te compounds under investigation were quite low, and the signal-to-noise ratio was high; therefore, long counting times were required for cadmium. To further eliminate errors, cadmium background counts were taken on the HgTe standard. Table II shows the comparison between theoretical values, given in parentheses, and experimental values found by microprobe analysis.

A significant change in the composition homogeneity was detected by the microprobe analysis. About 100 counts were taken randomly on the starting materials

Table I. Accelerating voltage 20 kv

Element	X-ray line	Target current 0.0500 μa Standards
Hg	M α_1	HgTe, HgS
Cd	L α_1	CdTe, Cd
Te	L α_1	HgTe, Te

Table II. Analytical results $Hg_{1-x}Cd_xTe$ Electron probe microanalyzer

	X	w/o Composition Cd	Hg	Te
Starting material	0.05	1.78 (1.74)	57.1 (58.8)	41.1 (39.4)
	0.10	3.10 (3.51)	55.2 (56.5)	41.8 (39.9)
	0.17	6.49 (6.10)	52.2 (53.1)	41.4 (40.7)
Sputtered film	0.05	1.75 (1.75)	57.5 (58.8)	40.8 (39.4)
	0.10	3.55 (3.51)	55.0 (56.5)	41.7 (39.9)
	0.17	5.96 (6.10)	51.7 (53.1)	42.7 (40.7)

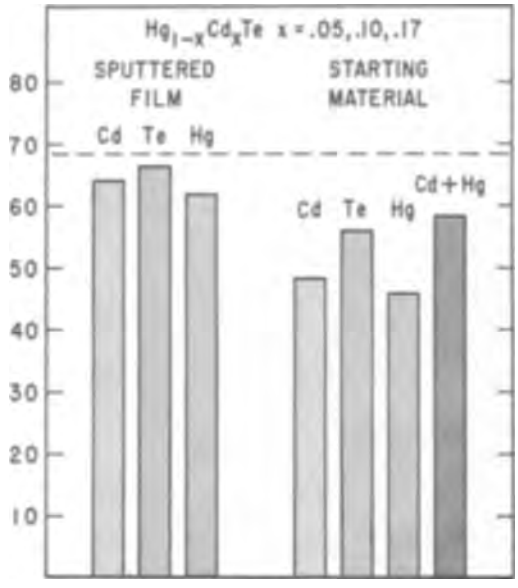

Fig. 5. Per cent of the relative x-ray intensity measurements which were within one standard deviation.

and on the sputtered film. The average count for each element was calculated, and the count deviation ($\sqrt{n}$) was determined. Since experience has indicated that the standard deviation of the x-ray readout of the electron probe microanalyzer is about twice the statistical count deviation, the average count was normalized to 100, and each individual count and the standard deviation were adjusted to fit this new value. The difference between each count and the average was obtained. If the materials analyzed were perfectly homogeneous, 68.3% of the differences would be less than one standard deviation. This statistical analysis is tabulated in Fig. 5 for the three elements in the starting material and for the sputtered films. It is seen that the sputtered films are more homogeneous than the starting material. In the starting material the cadmium and mercury sum[1] places more points in the standard deviation. This indicates that the inhomogeneity consists mainly of $Hg_{1-x}Cd_xTe$ phases rather than elemental phases.

[1] The standard deviation of a sum of two numbers N_1 and N_2 having deviations D_1 and D_2 is $\sqrt{D_1^2 + D_2^2}$.

Conclusion

Nearly homogeneous films of (HgCd)Te can be obtained by sputtering from less homogeneous sources. The slight residual inhomogeneity of the film results mainly from (HgCd)Te phases rather than elemental phases.

The films were predominantly amorphous, but crystal growth was obtained by annealing the films under partial pressures of Hg vapor.

Determining the band edge in the films from optical data becomes progressively more difficult with increasing HgTe content because of the low value of the energy gap and the effective electron mass.

Simultaneous analysis of all the components in this alloy system is essential to avoid errors in interpreting the analytical results. For this purpose, the electron microprobe and computerized computation for compositional analysis of this ternary have been found most useful.

Acknowledgment

The authors wish to thank Harry Elledge for his assistance in constructing the sputtering apparatus and preparing the films, and B. H. Breazeale for the photoconductivity measurements.

Manuscript received Nov. 3, 1966; revised manuscript received Feb. 20, 1967. This paper was presented at the Philadelphia Meeting, Oct. 9-14, 1966.

Any discussion of this paper will appear in a Discussion Section to be published in the December 1967 JOURNAL.

REFERENCES

1. W. D. Lawson, S. Nielson, E. N. Putley, and A. S. Young, *J. Phys. Chem. Solids*, **9**, 325 (1959).
2. J. Blair and R. Neunham, *Proc. Met. Soc. AIME* (1961).
3. C. M. Chapman and J. W. Moody, Battelle Memorial Institute, Columbus, Ohio. Contracts DA-44-009-ENG-4461 and DA-44-009-ENG-3951, U. S. Army Engineer R&D Lab., Ft. Belvoir, Virginia.
4. M. D. Blue, *Phys. Rev.*, **134**, A226 (1965).
5. L. Holland, "Vacuum Deposition of Thin Films," p. 415, John Wiley & Sons, Inc., New York (1961).
6. M. D. Blue, *Phys. Rec.*, **134**, A226 (1964).
7. B. T. Kolomiets and A. A. Malkova, *Fiz. Tverdogo Tela*, **5**, 4 (1963).
8. *Ibid.*
9. J. D. Brown, "A Computer Program for Electron Probe Microanalysis," College Park Research Center, Bureau of Mines, College Park, Maryland, Report of Investigations RI 6648.

Fused Glass Penetration into Thermally Grown Silicon Dioxide Films

W. A. Pliskin

IBM Components Division, East Fishkill Facility, Hopewell Junction, New York

ABSTRACT

In the manufacture of fused glass protected planar silicon devices having an underlying barrier layer of silicon dioxide, it is desirable to know the degree of penetration of the glass into the underlying layer as a results of fusing the sedimented glass powder. Penetration depths were determined from etch rate plots using P etch which etches most glasses much more rapidly than silicon dioxide. The penetration of low temperature firing lead borosilicate glasses (<600°C for 5 min) can be limited to less than 100Å. For high firing temperature silicate glasses (>1100°C for 5 min), a penetration of a few hundred angstroms is more common. Glasses fired at temperatures significantly higher than their softening points (or minimum firing temperatures) show much greater penetrations. The results are explained on a model based on the fact that the softening point of silicate glasses increases sharply with silica composition. As the glass softens, the lower layer of glass fuses with the upper SiO_2 surface to form a thin boundary glass layer with greater silica composition. As the penetration increases, the silica content of this intermediate layer increases sharply and consequently the effective softening point for the region becomes so high that further penetration is severely limited.

In the manufacture of fused glass protected planar silicon devices which have an underlying silicon dioxide layer, it is desirable to know the amount of penetration of the glass into the SiO_2. This is especially true since in many cases the glass may contain components which should not come in contact with the silicon.

By means of etch rate plots, in which the oxide plus glass film thickness is plotted against the total etch time, glass penetration depths can be determined. For high accuracy with this technique, it is necessary to have (*i*) an etch which will attack the glass much more rapidly than the silicon dioxide, and (*ii*) very accurate techniques for measuring the film thickness. The etch selected for these purposes is "P etch" which consists of 15 parts HF, 10 parts concentrated HNO_3, and 300 parts water (1). This etch is very selective in that its etch rate for thermally grown SiO_2 is only 2 Å/sec, whereas, for Pyrex (Corning 7740) it is 8 Å/sec, and for some lead borosilicate glasses, it can run as high as 500 Å/sec. Film thicknesses were determined very accurately with VAMFO (2), which is a special interferometric microscope, with which thicknesses can be determined to a precision better than 0.1% (3). This microscope is equipped with a monochromatic filter and a stage capable of rotating on an axis normal to the optical axis of the microscope so as to observe the reflected light at various angles. It should be noted that the technique does not require optically flat substrates. The film thicknesses can be determined by equations [7] given in ref. (2) or (3) or by

$$d_T = \frac{N\lambda}{2\mu_g \cos r_g} - \frac{\mu_o \cos r_o}{\mu_g \cos r_g} d_o + d_o \qquad [1]$$

where N is the fringe order for an observed interference minimum at incident angle i; λ, the wavelength of filtered light; μ_g, the glass refractive index at wavelength λ; μ_o, the SiO_2 refractive index at wavelength λ; r_g, the angle of refraction for incident angle i and refractive index μ_g; r_o, the angle of refraction for incident angle i and refractive index μ_o; and d_o, the thermal oxide thickness prior to glassing.

In some cases the thicknesses can be determined most conveniently by (3)

$$d_T = \frac{N\lambda_j}{2\mu_j \cos r} \qquad [2]$$

where μ_j is the average refractive index at λ_j for the composite film of glass and oxide. If the thickness is sufficient for the observation of more than one minimum, then both the average refractive index and d_T can be determined by finding the refractive index for which d_T is the same from sets of tabulated values. If the glass refractive index is not known beforehand, it can be determined by use of the relation

$$\mu_g = \frac{\mu_j d_T - \mu_o d_o}{d_T - d_o} \qquad [3]$$

With thinner films, different filters are used and the sets of tables used in making the interpolation are based on a dispersion system corresponding to the type of dispersion expected for the mixed glass-oxide system (3). If the total film consists of two fairly distinct components of significantly different refractive indices and comparable film thicknesses (and d_o is known) then Eq. [1] is more accurate than Eq. [2]. For example, if the two components had refractive indices of 1.5 and 1.7 and were of comparable thicknesses, then it can be shown that the thickness determined by Eq. [2] is 0.27% greater than that determined by the more accurate Eq. [1]. If the two components are significantly different in thickness or if their refractive indices are not significantly different then the thicknesses determined by the two equations are not significantly different. In those cases where significant interpenetration between the oxide and a high refractive index glass has occurred, thickness measurements in the vicinity of the boundary are more accurately determined by Eq. [2], although Eq. [1] is still sufficiently accurate for all practical purposes.

Experimental

In practice the thicknesses of thermally oxidized wafers were measured prior to glassing. The wafers were then glassed with various glasses by sedimentation techniques (4, 5). The thicknesses were measured after glassing and after various periods of etching. From the etch rate plots, the depth of penetration of the glass was determined.

Results and Discussion

With glasses having a fast etch rate and fired at temperatures close to their softening points, the demarcation is quite sharp. If the glass is fired at a temperature much above its softening point, the demarcation becomes less sharp due to penetration of the glass

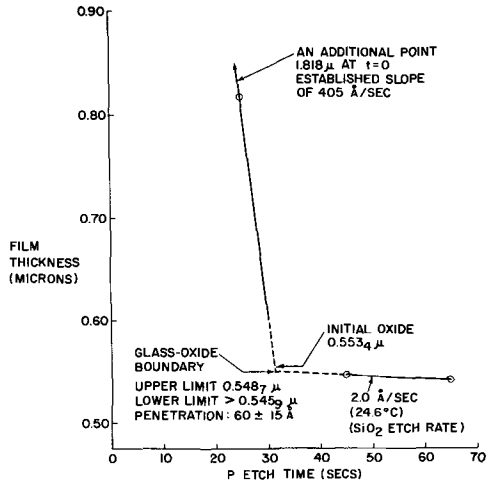

Fig. 1. Etch rate plot of 190B glass fired at 585°C for 5 min in O_2 on SiO_2 film.

into the SiO_2 and consequent formation of an SiO_2 enriched glass layer above and below the initial oxide boundary. If the glass film is formed by firing at the minimum temperature necessary to produce a good glaze, the penetration can be limited to a depth of less than 100Å for glasses whose firing temperatures are less than 600°C. For high temperature glasses (minimum glazing temperature >1100°C), a penetration of a few hundred angstroms is more common. In some cases where glasses are fired a few hundred degrees above the minimum glazing temperature, the overall penetration can be greater than 2000Å in addition to microscopically visible areas where the penetration is much greater. We define the minimum glazing temperature as the minimum furnace temperature necessary for forming a good glazed film of the sedimented powder by 5 min exposure in the furnace. It is usually close to the softening point of the glass.

To show the importance of firing temperature on the degree of glass penetration into the silicon dioxide, results will be given for glasses representing three softening point categories, low (<600°C), intermediate (~800°C), and high (>1100°C). Because of the importance of phosphosilicate glass for device passivation some results are given on the penetration of fused glass into the protective phosphosilicate layer covering the silicon dioxide.

Lead borosilicate glass 190B (low softening point).—In Fig. 1, we have shown an etch rate plot of glass 190B which is a lead borosilicate glass having a softening point of 588°C. The compositions of various glasses is given in Table I. This is a very fast etching glass. The steep slope representing the glass etching was determined by an additional point not shown on the amplified graph of Fig. 1. Because of the very fast etch rate of this glass, the etch times between film thickness measurements must be kept small. The last two points in the figure correspond to silicon dioxide since the P etch rate established by the two points is the same (2.0 Å/sec) as that of thermally grown SiO_2.

If we assume both the glass and oxide continue etching at their respective rates, then the intersection at $0.548_7\mu$ would correspond to the glass-oxide boundary, and we could conclude that the glass penetrated to a depth of about 50Å (47) into the oxide. Actually if we have interpenetration, then the etch rate near the boundary should be intermediate between that of the silicon dioxide and the glass and consequently the actual boundary should be less than $0.548_7\mu$. On the other hand, the point at $0.545_9\mu$ is in the SiO_2 since the etch rate here corresponds to that of SiO_2 and therefore the lower limit is greater than 0.545_9. It is therefore concluded that the glass penetrated 60 ± 15Å of the SiO_2. The penetration determined from these plots is the amount of over-all bulk penetration of the glass and does not show the possible penetration of a small amount of fast diffusing species into the oxide.

An etch rate plot of this same glass when fired at the same temperature (585°C) but for 20 instead of 5 min, showed a bulk penetration of 150 ±15Å. The reason for the small penetration can be explained in terms of the variation of softening point with SiO_2 composition. With most silicate glasses, the softening point increases sharply with silica composition. As the glass softens, the lower layer of glass fuses with the upper SiO_2 surface to form a thin boundary glass layer with greater silica composition. As the penetration increases, the silica content of this intermediate layer increases sharply and consequently the effective softening point for the region becomes so high that further penetration is severely limited.

Lead alumina borosilicate glass Corning X760LZ (intermediate softening point).—With higher temperature glasses, the degree of penetration is increased. This can also be explained in terms of the silica composition. Because of higher silica composition, the softening point is greater and consequently such a glass must be fired at a higher temperature to obtain a good glazed film. Furthermore, since the silica composition is significantly more than that for low temperature glasses, a greater depth of silicon dioxide must be penetrated to make a significant relative difference in the silica composition of the boundary layer and consequently in the difference between the effective softening point of the boundary layer region and the actual firing temperature.

For representation of glasses with an intermediate softening point, we have chosen Corning X760LZ. Although the softening point of this glass is about 785°C, its minimum glazing temperature is approximately 760°-770°C depending on the particle size of the sedimented glass powder (5). In this series of experiments after each etch period, photomicrographs at 400X were taken using monochromatic illumination in addition to measuring the over-all film thicknesses with VAMFO. This process was repeated several times until the oxide etch rate corresponded to that for thermally grown SiO_2. Plots of the film thickness as a function of the etch time show the amount of over-all bulk penetration of the glass into the oxide. Two examples are shown in Fig. 2 and 3 which are for firing temperatures of 770°C for 5 min (Fig. 2) and 760°C for 5 min followed by 1 min at 1100°C (Fig. 3).

Using the same procedure with Fig. 2 as in Fig. 1,

Table I. Approximate glass compositions of principle components (in weight per cent)

Glass	SiO_2	PbO	B_2O_3	Al_2O_3
190B	29	51	9	3
Corning X760LZ	51	29	13	7
General Electric GSC-1	83	0	12	5

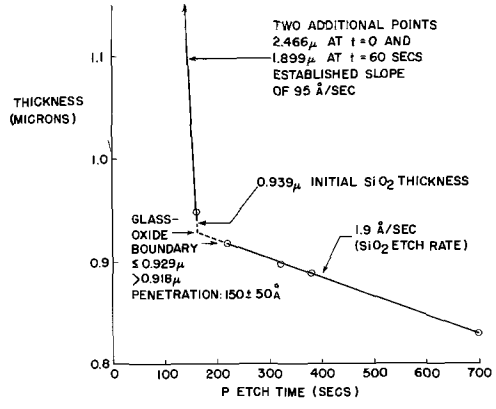

Fig. 2. Etch rate plot of X760LZ glass fired at 770°C for 5 min on SiO_2 film.

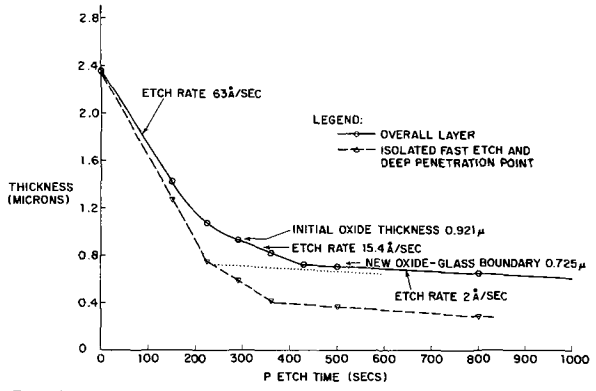

Fig. 3. Penetration of X760LZ glass into SiO_2 (F.T. 760°C—5 min, 1100°C—1 min) penetration: 1960Å (bulk), 5200Å (isolated points).

it is concluded that the penetration is 150 ±50Å. Furthermore, high-power microscopic examination showed the etching to be uniform across the wafer.

From Fig. 3, it is obvious that there has been an over-all bulk penetration into the oxide of about 2000Å. This large penetration also manifests itself in the etch rate reduction for the glass film above the initial SiO_2 film thickness at 0.921μ. In addition to this over-all bulk penetration, as shown by Fig. 3, the monochromatic photographs at high magnification show additional deep penetration into the oxide at isolated spots on the surface. It was observed that the glass over these spots etched much more rapidly than the surrounding glass. The points of deeper penetration into the oxide, observed after the removal of the glass, was not just due to the earlier arrival of the etch solution to the oxide layer at these fast etch points. This can be seen from an examination of Fig. 3 in which the thickness of the underlying film under one of these "pipes" is plotted against the etch time. From the dotted line, it is obvious that for "earlier arrival" to be the explanation, the additional penetration into the oxide must be only a few hundred angstroms rather than the 3600Å observed.

The results of this investigation together with the results obtained from other experiments involving X760LZ glass are summarized in Table II. The main point of these results is that the penetration of the glass into the oxide is minimal when the glass is fired at its minimum glazing temperature, but the penetration becomes significant at higher temperatures and longer firing times.

Table II. Penetration of X760LZ into SiO_2

Wafer	Firing conditions	Over-all bulk penetration	Isolated spot penetration below over-all layer
A	770°C—5 min	~150Å	~300Å (due to penetration through bubbles in glass)
B	760°C—5 min 1100°C—1 min	2000Å	Several 2500-4000Å penetrations and many more 1000-2500Å penetrations
C	1100°C	2000Å	Same as above. See Table III for details.
D	950°C—5 min 1100°C—1 min	2400Å	About same as for B.

Table III. Isolated penetration points in SiO_2 for X760LZ fired at 1100°C

Penetration depth below general penetration	No. in photo	Approx. population (No. per cm²)	Approximate width, μ
3700Å	2	~5 × 10³	~6
2300-3100Å	10	~25 × 10³	~5
1500-2300Å	~90	~200 × 10³	~2-4
500-1500Å	≧500	≧1200 × 10³	~½-2

The extent of the isolated point penetrations can be obtained from Table III in which the number of "pipes" and depth of penetration into the oxide is listed for Wafer C (1100°C fired for 1 min). It is thus concluded that a 1 min firing of X760LZ at 1100°C would require a silicon dioxide film thickness of several thousand angstroms to protect the surface from visible type penetrations, let alone additional penetration due to small amounts of possible fast diffusing deleterious ionic species not detectable microscopically.

High temperature silicate glass (GSC-1).— On high softening point silicate glasses, the penetration into the silicon dioxide can be as high as a few hundred angstroms even when fired at the minimum glazing temperature. With these higher temperature glasses, the glass-oxide boundary is more difficult to determine because the etch rate differential between the glass and oxide is not as great as with the lower temperature glasses. Although in one particular sample (General Electric GSC-1 glass) the firing cycle consisted of 5 min in a furnace maintained at 1190°C, the sample was within a few degrees of temperature for only 3 min. The etch rate plot for this sample showed a penetration of 320 ±100Å. If the firing cycle were altered such as to maintain the same glaze quality, the penetration would be comparable. The glaze quality is determined by the degree of smoothness of the film under microscopic observation. In another case where the wafer was fired for 15 min at 1150°C to obtain the same glaze quality, the penetration was ~400Å. In a third case where the glass was fired for 3 min in a furnace maintained at 1215°C, the penetration was also only 400Å. In this last firing, the wafer was at 1215°C for less than 1 min. It should be noted that thermal oxides which have been heated at temperatures near 1200°C have slightly faster P etch rates.

The penetration of a high temperature borosilicate through silicon dioxide can also be determined from the doping of a silicon wafer by the boron from the glass penetrating through the oxide. The simplest technique is to oxidize a high resistivity N type wafer, step etch the oxide on the wafer so as to have a range of oxide thicknesses, fire the glass, remove the glass and oxide, and then determine the silicon conductivity type with a thermal probe. By such techniques, we found that 4μ of GSC-1 glass fired at 1205°C for 1¾ hr did not penetrate 2500Å of SiO_2, but did penetrate 2400Å of SiO_2. This type experiment can only be used when the glass contains a component which will dope the semiconductor at the firing temperature. The results show only the extent of penetration of the doping material.

Reaction of fused GSC-1 glass with phosphosilicate.—We have also examined the reaction between GSC-1 glass and a phosphosilicate layer on the SiO_2. Figure 4 shows the etch rate plot obtained for a sample in which 1.8μ of GSC-1 glass was fired at 1199°C for 5 min. Prior to the glass deposition, a portion of the wafer was examined with P etch to determine the thickness of the phosphosilicate layer. The over-all film thickness was 0.870μ with 0.175μ of phosphosilicate.

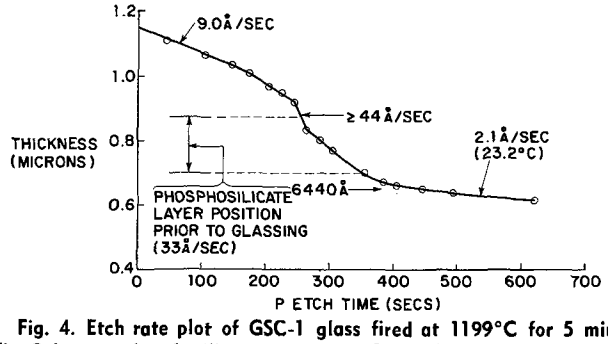

Fig. 4. Etch rate plot of GSC-1 glass fired at 1199°C for 5 min (in O_2) on a phosphosilicate containing SiO_2 film. (The removal of the top 1.5μ of GSC-1 is not shown).

The P etch rate of the phosphosilicate was 33 Å/sec. In a pure phosphosilicate the P etch rate is indicative of the phosphorus concentration.

The P etch rate plot of the sample containing the fired glass showed an unusually fast etch rate (≧44 Å/sec) corresponding to the top region of the phosphosilicate layer and the bottom region of the GSC-1 glass. This etch rate is significantly faster than that of GSC-1 or of the original phosphosilicate. It can be explained as being due to components from the glass combining with the phosphosilicate to form a fast etching glass at the glass-phosphosilicate boundary. This fast etching region is not an experimental artifact. On firing a similar sample at 1219°C for 10 min, as shown in Fig. 5, an even faster (≧65 Å/sec) intermediate etch rate region was obtained.

While the glass is being fired the phosphorus penetrates deeper into the underlying SiO_2 but due to the presence of the GSC-1 glass, the penetration is deeper on a glassed sample than on a nonglassed sample. A nonglassed piece of the same wafer which has been glassed with GSC-1 at 1219°C as shown in Fig. 5 was heated in oxygen for 10 min at 1219°C. P etch rate plots of this portion of the wafer before and after heating are shown in Fig. 6. From the decrease of the maximum etch rate from 33 to 15 Å/sec, it is concluded that the phosphorus concentration has decreased. On the other hand, where GSC-1 glass was applied, glass components combined with the phosphosilicate to give a much faster etch rate region (Fig. 4 and 5). From the "tail" at the lower end of the phosphosilicate region (Fig. 6), it is concluded that the phosphorus has penetrated 350Å of SiO_2 to the 6600Å level. In Fig. 5, with GSC-1 present, the SiO_2 boundary was down to 6300Å. The decreased etch rate at the top few hundred angstroms for the unglassed case is indicative of phosphorus outdiffusion (1). With GSC-1 glass present, the phosphorus tending to outdiffuse would combine with the lower portions of the GSC-1 to help form the very fast etch layer.

We had previously used the etch rate technique for the determination of the presence of phosphosilicate glass beneath other glasses in the failure analysis of devices (6). With faster etch rate glasses, as is the usual case with glasses of lower softening point, no significant reaction or penetration into the phosphosilicate layer was observed.

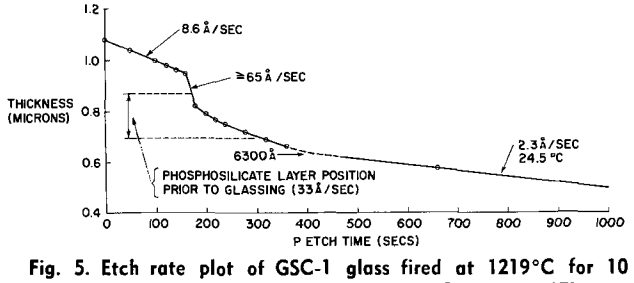

Fig. 5. Etch rate plot of GSC-1 glass fired at 1219°C for 10 min (in O_2) on a phosphosilicate containing SiO_2 film. (The removal of the top 1.6μ of GSC-1 is not shown).

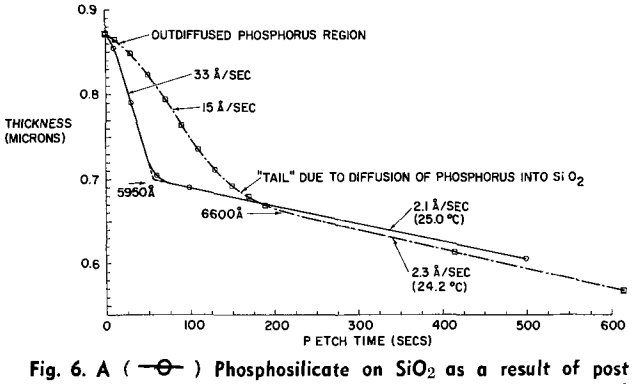

Fig. 6. A (—⊖—) Phosphosilicate on SiO_2 as a result of post oxidation of a P_2O_5 diffused silicon dioxide layer. B (— -□— —) Same wafer after oxygen exposure at 1219°C for 10 min.

Conclusions

1. Glass fused from sedimented powder penetrates into an underlying SiO_2 layer to form an intermediate glass which seals the fused outer glass to the underlying SiO_2.

2. The depth of penetration is dependent on the softening point of the glass and the temperature differential between the minimum glazing temperature (approximated by the softening point) and the actual firing temperature. For silicate glasses with softening points near 600°C, the minimum penetration from a good glazed film is approximately 50Å and for 1200°C softening point silicate glasses, it is about 400Å.

3. High temperature fused glasses penetrate more deeply into phosphosilicate than into silicon dioxide.

Acknowledgments

The author appreciates the interest and discussions of Dr. J. A. Perri and Dr. J. Riseman, would like to thank R. P. Esch for help with the experimental work and Mr. A. A. Valachovic for help in preparing the manuscript.

Manuscript received July 1, 1966; revised manuscript received Feb. 20, 1967. This paper was presented at the Buffalo Meeting Oct. 10-14, 1965.

Any discussion of this paper will appear in a Discussion Section to be published in the December 1967 JOURNAL.

REFERENCES

1. W. A. Pliskin and R. P. Gnall, *This Journal*, **111**, 872 (1964).
2. W. A. Pliskin and E. E. Conrad, *J. de Physique*, **25**, 17 (1964) and *IBM J. Res. and Dev.*, **8**, 43 (1964).
3. W. A. Pliskin and R. P. Esch, *J. Appl. Phys.*, **36**, 2011 (1965).
4. J. A. Perri, H. S. Lehman, W. A. Pliskin, and J. Riseman. Fall Meeting, E.C.S., Detroit, Michigan (1961).
5. W. A. Pliskin and E. E. Conrad, *J. Electrochem. Tech.*, **2**, 196 (1964).
6. D. R. Kerr, J. S. Logan, P. J. Burkhardt, and W. A. Pliskin, *IBM J. Res. & Dev.*, **8**, 376 (1964).

Cationic Migration in Silicon Dioxide Films on Silicon

F. C. Collins and M. Schrager

Department of Chemistry, Polytechnic Institute of Brooklyn, Brooklyn, New York

ABSTRACT

Earlier calculations of the electrostatic potential and cationic concentration profiles in metal-oxide semiconductor structures on the basis of the Poisson-Boltzmann equation are extended to the case where a maximum in potential exists in the oxide film. The presence of immobile anions terminating the cationic charges does not significantly affect the behavior of the cations if the anions are located in a thin region at the oxide-metal interface. According to this model the currents due to cationic drift in temperature-bias experiments are symmetrical about the contact potential difference between the metal and the semiconductor corrected for the space charge of the immobile anions. For a model involving cationic drift only, the flat band potential of the semiconductor from temperature bias measurements does not display this symmetry about the contact potential difference. Transient nonequilibrium distributions of the cations at low values of the applied potential which may occur because of the existence of the potential maximum in the film are discussed.

The variation of the flat band potential of oxidized silicon surfaces in metal-oxide-semiconductor (MOS) devices following temperature-bias treatments have been interpreted in terms of a drift of mobile cations (1-2). This interpretation is supported by the fact that the charge storage calculated from the ionic current-time integrals in the temperature-bias experiments is in general agreement with the observed shifts of the flat band potential as determined by C-V measurements at room temperature of temperature biased samples (3).

In an earlier paper (2), the electrostatic potential and cationic concentration profiles in a silicon dioxide film under specified values of applied bias at elevated temperatures were developed in terms of a Poisson-Boltzmann distribution of a cationic species. The previous calculations (2) were confined to the case of large values of the applied potential relative to the potential difference arising from the space charge of the cations. The alternative case is treated in the present paper. The solution exhibits a potential maximum at low values of the applied potential compared to the space charge potential.

One of the interesting and well-known characteristics of the silicon dioxide-silicon MOS devices is that while a positive potential applied to the metal electrode in a temperature-bias treatment produces large negative shifts of the silicon surface potential, the application of negative potentials to the metal electrode does not produce a negative shift. This has been shown to be consistent with the presence of mobile cations only (1, 2). In the previous paper the location of the anionic charges terminating those of the mobile cations was not specified. In the present paper, the behavior of a model in which the cations are electrically compensated by immobile anions near the oxide metal interface is investigated. Where the thickness of the sheet of anions is a small fraction of the thickness of the oxide film, it is found that the potential difference arising from the presence of the anions has little effect on the drift of the cations under applied bias.

The currents arising from the drift of the cations under externally applied bias at elevated temperature should be antisymmetrical around zero bias, according to the model. However Tarui (4) has pointed out that the contact potential difference between silicon and the given electrode metal must be added to the applied potential in order to obtain the potential difference across the oxide film. The contribution of the space charge due to the immobile anions must also be included to compute the effective potential difference across the film.

Polarization of the Film by Cationic Migration

It will simplify the presentation to present first the behavior of the model in which no account is taken of the presence of anions. The effect of immobile anions in the region at the oxide-metal interface is later considered. Only a relatively crude treatment of the effect of the anions is justified in any event because of the lack of any detailed information concerning their distribution. To this degree of approximation, the effect of the presence of anions is additive only and its contribution to the behavior of the cations rather simply handled at a later point.

As in the earlier paper (2), the present calculations are confined to the case of thermodynamic equilibrium. The concentrations $c(x)$ of cations in the oxide film is then given by

$$c(x) = c_0 \exp[-qV(x)/kT] \qquad 0 \leq x \leq X' \quad [1]$$

where the silicon-silicon dioxide interface has been selected as the origin of the coordinate x, $c_0 = c(0)$, $V(x)$ is the potential (with $V(0) = 0$) and the other symbols have their usual significance. For simplicity all cations in the system are taken to be univalent. The anions terminating the charges of the cations are assumed to be permanently located in the surface region $X - X'$ of the oxide where $x = X$ at the metal-oxide interface. As the anions are immobile, their distribution will not be governed by the Boltzmann law.

We shall assume that the concentrations of electrons and holes in the oxide are small compared to the concentrations of the ions and may consequently be neglected. Poisson's equation is then given by

$$\frac{d^2V}{dx^2} = -\frac{q}{\epsilon}c(x) \qquad 0 \leq x \leq X' \quad [2]$$

which leads to the usual expression for the Poisson-Boltzmann equation

$$\frac{d^2V}{dx^2} = -\frac{q}{\epsilon}c_0 \exp[-qV(x)/kT] \quad [3]$$

The usual device of multiplying both sides of Eq. [3] by $2(dV/dx)$ enables it to be integrated as follows

$$\left(\frac{dV}{dx}\right)^2 = \mathcal{E}_0^2 - \frac{2c_0kT}{\epsilon}(1 - e^{-qV/kT}) \quad 0 < x < X' \quad [4]$$

where the boundary condition $(dV/dx)_0 = -\mathcal{E}_0$ has been used. The solution to Eq. [4] which was previously obtained for the case that no maximum exists in the potential $V(x)$ within the oxide film is

$$x = \frac{V}{a^{1/2}} + \frac{2}{ma^{1/2}} \ln \frac{a^{1/2} + (a + b\,e^{-mV})^{1/2}}{a^{1/2} + (a + b)^{1/2}} \quad [5]$$

where

$$a = \mathcal{E}_o^2 - \frac{2\,kT}{\epsilon} c_o$$

$$b = \frac{2kT}{\epsilon} c_o \quad [6]$$

and

$$m = q/kT \quad [7]$$

the parameters a and b may be evaluated from the boundary conditions as described in the previous paper. For mathematical simplicity, we shall assume that the cations are confined to the region $0 \leq x \leq X'$. Then the total cationic surface density in the oxide film is given by

$$\sigma = \int_o^{X'} c(x)\,dx = \int_o^{X'} c(V) \frac{dx}{dV} dV \quad [8]$$

Substituting Eq. [1] and [4] into the above yields

$$\sigma = \frac{\epsilon}{q}(a + b)^{1/2} - \left(a + b\,e^{-mV_{X'}}\right)^{1/2} = \frac{\epsilon}{q}(\mathcal{E}_{X'} = \mathcal{E}_o) \quad [9]$$

where the definitions [6] and [7] have been used $V_{X'} = V(X')$ and the relation $\left(a + b\,e^{-mV_{X'}}\right)^{1/2} = \mathcal{E}_{X'}$ has been used.

For practical purposes, the parameters a and b are best evaluated in terms of the potential $V_{X'}$ and the boundary field $\mathcal{E}_o$. The latter is found from the flat band potential of the semiconductor which is experimentally determined from the bias dependence of the capacitance of the MOS structures. The method is described in Appendix (A) of ref. (2) and typical values of a and $c_o = b\epsilon/2kT$ are given in Table I of that paper.

The average distance of the cations from the silicon interface is of some interest. It is given by

$$\langle x \rangle = \frac{\int_o^{X'} x\,c_o\,e^{-mV}\,dx}{\int_o^{X'} c_o\,e^{-mV}\,dx} = \frac{V_{X'} + \mathcal{E}_{X'}X'}{\mathcal{E}_{X'} - \mathcal{E}_o} \quad [9']$$

It will be seen from the previous paper (2) that $-\mathcal{E}_{X'} \approx a^{1/2}$ to an excellent approximation. A few numerical values of the average distance $\langle x \rangle$ are given in Table I corresponding to some typical values of the observable variables. It will be seen that the distance $\langle x \rangle$ is only of the order of one lattice distance.

The solution to the Poisson-Boltzmann equation for the case that a maximum in $V(x)$ exists will now be derived. Let x_m be the point at which the potential maximum $V_{(x_m)} = V_m$ exists. The potential gradient of Eq. [5] is then given by

Table I.

$V_{X'}$, v	$-\mathcal{E}_o \times 10^{-6}$, v/cm	$-\mathcal{E}_{X'} \times 10^{-6}$, v/cm	$\langle x \rangle$, Å
10	1.00	0.3314	8.67
	2.00	0.3299	6.17
	5.00	0.3277	3.62
20	1.00	0.6661	5.01
	2.00	0.6648	4.14
	5.00	0.6627	2.75
30	2.00	0.9989	3.28
	3.00	0.9981	2.85
	5.00	0.9970	2.25

$$\frac{dV}{dx} = (a + b\,e^{-mV})^{1/2} \qquad 0 \leq x \leq x_m \quad [10]$$

$$= 0 \qquad x = x_m \quad [11]$$

$$= -(a + b\,e^{-mV})^{1/2} \qquad x_m < x \leq X' \quad [12]$$

The existence of the maximum V_m with

$$(a + b\,e^{-mV_m})^{1/2} = 0 \quad [11']$$

requires that $a < 0$ because $b \geq 0$ under all conditions as may be seen by reference to Eq. [6]. Under this requirement, the integrals of Eq. [10] to [12] take the forms [5]

$$x = \frac{2}{m(-a)^{1/2}} \left\{ \sin^{-1}\left[\left(\frac{-a}{b}\right)^{1/2} e^{mV(x)/2}\right] - \sin^{-1}\left(\frac{-a}{b}\right)^{1/2} \right\} \qquad 0 \leq x < x_m \quad [13]$$

$$x - x_m = \frac{-2}{m(-a)^{1/2}} \left\{ \sin^{-1}\left[\left(\frac{-a}{b}\right)^{1/2} e^{mV(x)/2}\right] - \pi/2 \right\} \qquad x_m < x \leq X' \quad [14]$$

The position of the potential maximum may be found from Eq. [13] and is

$$x_m = \frac{2}{m(-a)^{1/2}} \left[\frac{\pi}{2} - \sin^{-1}\left(\frac{-a}{b}\right)^{1/2}\right] \quad [15]$$

The total cationic density is again obtained by the use of Eq. [8], but is now given by

$$\sigma = \frac{\epsilon}{q}\left[(a + b)^{1/2} + \left(a + b\,e^{-mV_{X'}}\right)^{1/2}\right] \quad [16]$$

instead of by Eq. [9].

Figures 1 and 2 are plots of the potential profiles $V(x)$ and of the cationic concentration $c(x)$ for two different values of the ratio $(-a/b)^{1/2}$ for the particular case that $V_{X'} = 0$. The methods for evaluating the parameters a and b from experiment for this case is given in a later section of this paper.

Paralleling Eq. [9'], we may define an average distance from the interface for those cations which are on the left hand side of the potential maximum x_m as

$$\langle x \rangle = \frac{\int_o^{x_m} x\,c_o\,e^{-mV}\,dx}{\int_o^{x_m} c_o\,e^{-mV}\,dx}$$

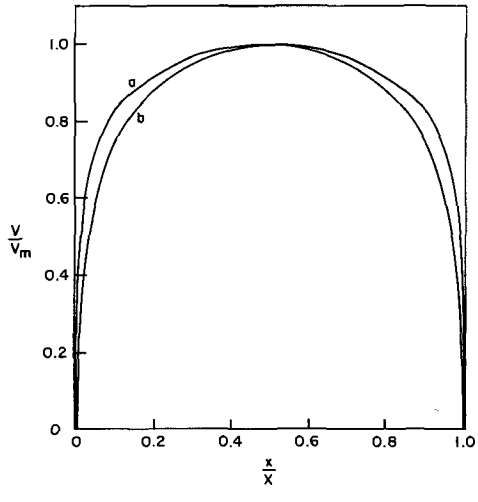

Fig. 1. Normalized potential vs. fractional distance for the symmetrical case of $V_{X'} = 0$ with a film thickness of 5000Å. Two typical values of $(-a/b)^{1/2}$ are plotted: Curve a, $(-a/b)^{1/2} = 10^{-3}$; Curve b, $(-a/b)^{1/2} = 10^{-2}$.

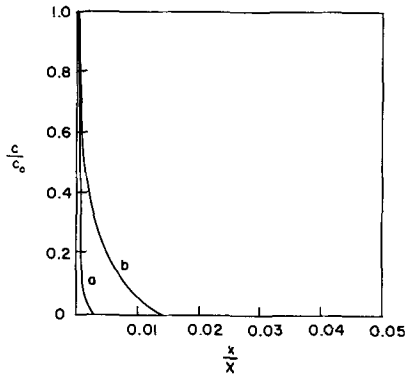

Fig. 2. Normalized cationic concentration vs. fractional distance for the two cases depicted in Fig. 1.

$$= -V_m/\mathcal{E}_0 \qquad [16']$$

Some numerical values of this average distance are given in Table II.

Effect of the Presence of Anions

For the purposes of the present possibly oversimplified analysis, we shall assume that the cations are excluded from the region $X' \leq x \leq X$ and that the anionic concentration is given by

$$C = \text{constant}, \qquad X' \leq x \leq X \qquad [17]$$

Poisson's equation

$$\frac{d^2V}{dx^2} = \frac{q}{\epsilon} C \qquad [18]$$

may now be easily integrated and yields

$$V_X - V_{X'} = \frac{qC}{2\epsilon}(X - X')^2 - \gamma_{X'}(X - X')$$

where $\mathcal{E}_{X'}$ is the field at the point X'.

It is of interest to note that if a constant total density σ_a of anions

$$\sigma_a = C(X - X') \qquad [19]$$

is introduced and the distance $X - X'$ is allowed to approach zero, the potential difference $V_X - V_{X'}$ will approach zero at the same rate. Hofstein (6) has interpreted one aspect of the time dependence of his cationic drift measurements in silicon-silicon dioxide MOS devices in terms of an initial trapping of the cations in a region of 7.5 to 8.0Å thickness at the metal oxide interface. If the trapping in the Hofstein experiments is actually caused by a layer of immobile anions as in the above model, the potential difference $V_X - V_{X'}$ must be very small at typically observed values of the total ionic density σ in accordance with Eq. [18] and [19]. A thickness of the order of 8Å would be consistent with the possible condition that the immobile anions are oxide ions terminating the amorphous silicon dioxide structure.

Table II. Some values of the average distance of the cations on the left hand side of the potential maximum from the silicon-silicon dioxide interface, in the symmetrical case where $V_{X'} = 0$. The film has been taken to be 5000Å in thickness and has been assumed to be equilibrated at a temperature of 250°C

V^0_m, v	$-\mathcal{E}_0 \times 10^{-6}$, v/cm	<x>, A	V^0_m, v	$-\mathcal{E}_0 \times 10^{-6}$, v/cm	<x>, A
0.600	0.105	570	0.400	0.105	380
	0.21	285		0.21	190
	1.05	57.0		1.05	38.0
	2.1	28.5		2.1	19.0
0.480	0.105	458	0.280	0.105	267
	0.21	229		0.21	133
	1.05	45.8		1.05	26.7
	2.1	22.9		2.1	13.3

The effective potential under which the cations distribute themselves is

$$V_{X'} = V_a + \Delta\phi - (V_X - V_{X'}) \qquad [20]$$

where V_a is the potential externally applied to the metal electrode and $\Delta\phi$ is the contact potential or the difference between the work functions of the metal and the semiconductor.

Currents Arising from Cationic Migration

It is implicit in the foregoing analysis that the shift in the flat band potential of the semiconductor under temperature bias treatment is related to the apparent charge storage. Further, the cationic currents will be antisymmetrical about the point $V_{X'} = 0$. The determination of the applied potential corresponding to the point of symmetry $V_{X'} = 0$ affords a method for obtaining the quantity $\Delta\phi - (V_X - V_{X'})$. Thus a theoretical treatment of the cationic current is of interest.

Calculation of the time-dependent currents arising from cationic migration in the film following changes in the applied bias is extremely difficult and will not be attempted here. Instead we shall compute the time integrals of the current corresponding to the transition of the system from one state of equilibrium to another following a discontinuous change of the applied bias. This requires only the calculations of the mobile electronic charges in the silicon required to terminate the equilibrium distribution of charges in the oxide film. Changes in the electronic charge in the silicon correspond to time integrals of current in the external circuit. We shall assume that the doping is sufficiently high so that the silicon is effectively degenerate at the temperature under which the cationic migration occurs. As the potential increment $\Delta\phi - (V_X - V_{X'})$ in Eq. [20] is effectively a constant, the analysis of the current integrals will be given in terms of $V_{X'}$ for the sake of simplicity.

The surface charge Q_0 in the silicon required to terminate the ionic charges in the oxide film is given by

$$Q_0 = q\int_0^{X'} c(x)\frac{X' - x}{X'}dx \qquad [21]$$

The form of the integration of Eq. [21] depends on whether a potential maximum V_m exists in the region of the integration. Where the potential maximum is absent, Eq. [21] takes the form

$$Q_0 = q\,c_0\int_0^{V_{X'}} e^{-mV}\left[\frac{X' - x(V)}{X'}\right](a + b\,e^{-mV})^{-1/2}\,dV \qquad [22]$$

In the presence of the potential maximum Eq. [21] assumes the form

$$Q_0 = q\,c_0\int_0^{V_m} e^{-mV}\left[\frac{X' - x(V)}{X'}\right](a + b\,e^{-mV})^{-1/2}\,dV - q\,c_0\int_{V_m}^{V_{X'}} e^{-mV}\left[\frac{X' - x(V)}{X'}\right](a + b\,e^{-mV})^{-1/2}\,dV \qquad [23]$$

The last two equations may be integrated by parts and yield respectively in the cases of the absence and the presence of a potential maximum

$$Q_0 = \mathcal{E}_0 - \frac{V_{X'}}{X'} \qquad \text{(maximum absent)} \qquad [24]$$

$$Q_0 = \mathcal{E}_0 - \left(\frac{2V_m - V_{X'}}{X'}\right) \qquad \text{(maximum present)} \qquad [25]$$

The integral of the current $I(t)$ following a discontinuous change of the applied potential V_a is given by

$$\int_0^\infty I(t)\,dt = A[Q_o(V'_{X'}) - Q_o(V^o_{X'})] \qquad [26]$$

where A is the area of the MOS device and $V^o_{X'}$ and $V'_{X'}$ are the potentials before and after the discontinuous change.

Evaluation of System Parameters

The foregoing equations enable the principal variables of the Poisson-Boltzmann distribution model of the cation drift to be quantitatively determined by the separate measurements of the flat band potential and of the current integral. If self consistent, these independent data would lend support to the hypothesis of the Poisson-Boltzmann distribution and to the other assumptions introduced into the model.

The model predicts that the current integrals should be antisymmetrical about the point $V_{X'} = 0$ corresponding to an applied potential

$$V^o_a = \Delta\phi - (V_X - V_{X'}) \qquad [27]$$

Thus we should have

$$Q_o(V_{X'})\ Q_o(0) = -[Q_o(-V_{X'}) - Q_o(0)] \qquad [28]$$

Preliminary measurements indicate that a point of approximate antisymmetry with respect to the current integrals does indeed exist. The applied potential V_a corresponding to the point of antisymmetry is found to be of the order of 1 V.

Where $V_{X'} >> m^{-1}$, Eq. [9] simplifies to that which is customarily used for the experimental determination of the cationic density

$$\sigma = \frac{\epsilon}{q}\mathcal{E}_o \qquad (V_{X'} >> m^{-1}) \qquad [29]$$

At low values of the potential, however, Eq. [29] is no longer valid. In particular, at the point $V_{X'} = 0$, Eq. [16] reduces to

$$= \frac{2\epsilon}{q}\mathcal{E}_o \qquad (V_{X'} = 0) \qquad [30]$$

If the density σ is constant we may conclude that

$$\mathcal{E}_o(V_{X'} = 0) = \tfrac{1}{2}\mathcal{E}_o\,(V_{X'} >> m^{-1}) \qquad [31]$$

Eq. [27] and [31] provide independent methods for determining V^o_a.

The transition between the logarithmic and inverse sine solutions to the Poisson-Boltzmann equation corresponding to the absence and the presence of a potential maximum occurs at the point at which the parameter a passes through zero. In the Appendix the range of values $V_{X'}$ corresponding to the parameter $a = 0$ for various typical values of the density σ and the other variables is evaluated and shown in Fig. 3. It appears that the transition value of $V_{X'}$ is less than 1 V in all cases.

Equation [24] and [25] may be used to determine values of the potential maximum V_m. This is done by measuring the current time integral following a change of the potential $V_{X'}$ from a value above the transition to a value below this transition. The potential maximum V^o_m which exists when $V_{X'} = 0$ is of particular interest. It is given by

$$V^o_m = \frac{V_{X'}}{2} + \frac{X'}{2\epsilon}\left\{\frac{1}{A}\int_0^\infty I\,dt - [\gamma_o(V_{X'}) - \gamma_o(0)]\right\}$$

$$= \frac{X'}{2}\left\{\frac{1}{A}\int_0^\infty I\,dt + 2\mathcal{E}_o(0)\right\} \qquad [32]$$

where here $V_{X'} >> 1$ V. The ratio $(-a/b)$ may now be immediately determined by means of Eq. [11']. From symmetry considerations, the potential maximum V^o_m is located at the point $x_m = X'/2$. The parameter a can now be obtained by the use of Eq. [15], which after the substitution of Eq. [11'], takes the form

$$(-a)^{1/2} = \frac{4}{mX'}\left[\frac{\pi}{2} - \sin^{-1} e^{-mV^o_m}\right] \qquad [33]$$

The parameter b is then determined by Eq. [6].

The determination of the parameters a and b and the point x_m of maximum potential V_m for values of the potential $V_{X'}$ other than $V_{X'} = 0$ in the domain of $a < 0$ requires rather extended numerical analysis. For the purpose of illustrating the quantitative relationships among the parameters for the case where a potential maximum exists, a short tabulation of their numerical values corresponding to typical values of the external variables are presented in Table III. In the calculations, values of the applied potential V_a have been used just balancing the work function difference $\Delta\phi$ so that the effective potential at X is zero. As elsewhere in this paper, the temperature is taken as 250°C.

Transient Nonequilibrium Cationic Distributions

When the applied potential on the MOS structure is abruptly changed the cationic distribution is slow to readjust itself. Immediately after the potential change, the distribution is in a nonequilibrium state with respect to the new applied potential on the MOS structure. It is the drift of the cations toward the thermodynamic equilibrium distribution which produces a current in the external circuit. If a potential maximum exists in the oxide film, it may impede the drift of the cations toward equilibrium.

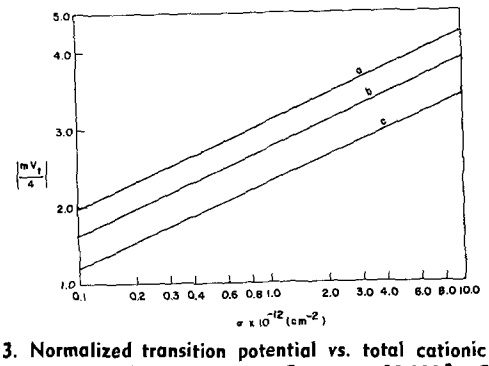

Fig. 3. Normalized transition potential vs. total cationic charge density for three film thicknesses: Curve a, 10,000Å; Curve b, 5000Å; Curve c, 2000Å.

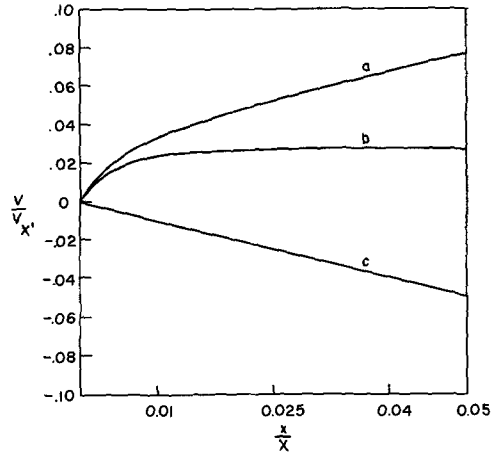

Fig. 4. Potential profile for a transient, nonequilibrium cationic distribution. Curve a represents an equilibrium potential profile corresponding to an applied potential of + 5 V at $t < t_o$. Curve b represents the instantaneous, nonequilibrium, potential profile, after a potential of — 5 V has been applied at $t = t_o$. Note the potential maximum at a fractional distance of about 0.035. Curve c represents the equilibrium potential profile for an applied potential of — 5 V.

Table III. Numeral values of system parameters corresponding to typical values of the observable variables for the case that a potential maximum exists in the film. The applied potential V_a is set opposite and numerically equal to the work function difference $\Delta\phi$. The temperature is constant at $T = 250°C$

X, A	$\sigma \times 10^{-12}$, cm^{-2}	$-\mathcal{E}_0 \times 10^{-6}$, v/cm	$V(X')$, v	$(-a)^{1/2} \times 10^{-4}$, v/cm	$b^{1/2} \times 10^{-6}$, v/cm	V_m, v	x_m/x	$(X - X')$, A	$\mathcal{E}_{x'} \times 10^{-6}$
2000	5.00	1.00	−0.0083	1.350	1.00	0.374	0.500	8.0	0.947
	5.00	2.00	0.259	1.300	2.00	0.437	0.522	8.0	4.41
	5.00	2.00	0.259	1.300	2.00	0.437	0.522	10.0	3.64
	10.00	1.00	−0.101	1.359	1.00	0.373	0.504	8.0	0.84
	10.00	2.00	−0.0083	1.359	2.00	0.434	0.500	8.0	2.00
	10.00	4.00	−0.259	1.332	4.00	0.494	0.511	8.0	5.46
5000	5.00	1.00	−0.0083	0.543	1.00	0.453	0.500	8.0	0.947
	5.00	2.00	0.259	0.536	2.00	0.511	0.508	8.0	4.41
	10.00	1.00	−0.101	0.544	1.00	0.453	0.499	8.0	0.84
	10.00	2.00	−0.0083	0.544	2.00	0.513	0.500	8.0	2.00
	10.00	4.00	0.259	0.533	4.00	0.573	0.504	8.0	5.46

Figure 4 shows the equilibrium potential distribution $V(x)$ corresponding to an applied potential of $+ 5V$ at $t = t_0-$ and the potential profile at $t = t_0+$ when the applied potential has been changed to $-5V$ at $t = t_0$. The cationic distribution remains unchanged between t_0- and t_0+. The potential profile $V(x)$ corresponding to the final equilibrium distribution of the cations at $t = \infty$ is also shown.

It is apparent that the cations initially to the left of the potential maximum must pass over the maximum in order to establish the equilibrium distribution. This, however, is a self accelerating process. The cations near the potential maximum and having energies within kT of it will drift over the maximum. In so doing, the transport of the space charge of these cations will lower the potential maximum. Additional cations are now within kT of the lowered potential maximum and will drift over it. The process becomes catastrophic when the potential maximum decreases to within kT of zero.

The net result of the above is that the observed current may not decay monotonically in time but may show a maximum after an initial induction period. The phenomenon of a current maximum has occasionally been observed in this laboratory at high total cationic densities σ. It is not as firm as might be wished for, but the observation is not an artifact.

Manuscript received Aug. 25, 1966; revised manuscript received Feb. 8, 1967.

Any discussion of this paper will appear in a Discussion Section to be published in the December 1967 JOURNAL.

APPENDIX

Calculation of Transition Potentials for the Case where $a = 0$

The transition between the logarithmic and inverse sine solutions to the Poisson-Boltzmann equation occurs at point $a = 0$. For this case, it can be shown that

$$\mathcal{E} = b^{1/2} = \frac{2}{mX'} [e^{mV_t(x')} - 1] \qquad [34]$$

and

$$\frac{q\sigma mX'}{8\epsilon} = \sinh^2 \left[\frac{mV_t(X')}{4} \right] \qquad [35]$$

where $V_t(X')$ is the transition potential between the two regions.

Figure 3 presents a plot of Eq. [35] for selected values of the experimental variables. It may be concluded from the figure that the transition potential $V_t(X')$ lies between 0.05 and 0.30v over the commonly encountered range of experimental variables where the film is equilibrated at 250°C.

REFERENCES

1. E. Yon, W. H. Ko, and A. B. Kuper, *IEEE Trans. Electron Devices ED-13*, 276 (1966).
2. F. C. Collins, *This Journal*, **112**, 786 (1965).
3. E. H. Snow, A. S. Grove, B. E. Deal, and C. T. Sah, *J. Appl. Phys.*, **36**, 1664 (1965).
4. Y. Tarui, Electrochemical Society Spring 1966 Meeting (Cleveland) (Recent News Paper).
5. B. P. Pierce, "Short Table of Integrals," p. 54, No. 412, Ginn and Co. (1929).
6. S. R. Hofstein, *IEEE Trans. Electron Devices ED-13*, 222 (1966).

Anodic Oxidation of Silicon in KNO_3-N-Methylacetamide Solution: Interface Properties

Akos G. Revesz

RCA Laboratories, Princeton, New Jersey

ABSTRACT

Silicon was oxidized anodically using constant current and/or constant voltage methods. The Si-SiO_2 interface was investigated with the MOS capacitance method. Constant current anodization results in a high density of surface states. Constant voltage anodization leads to surface state densities that roughly decrease with the final oxidation rate. Short time annealing in He at elevated temperatures removes the states from the Si forbidden band and reduces the density at zero Si surface potential to 2 x 10^{11} cm^{-2}. Positive and negative bias tests at 300°C showed a small positive ion migration effect but no interface instability.

Thermal oxidation of silicon is the most commonly used technique for the passivation of semiconductor devices and for the fabrication of the insulating film in MOS (Metal-Oxide-Semiconductor) devices. Consequently, there are many publications dealing with the properties of the Si-SiO_2 interface obtained by that method. Anodic oxidation of silicon, on the other hand, has been much less explored from this point of view. Only the following has been reported. Dubrowskii *et al.* (1) mentioned in a cursory manner that oxide films produced by anodization in very pure water protected the silicon surface from ambient effects. Boroffka (2) reported recently that anodic oxidation results in a high density of surface states ($\sim 10^{13}$ cm^{-2}) that can be reduced to $\sim$ 3 x 10^{11} cm^{-2} by post-oxidation heat treatment in hydrogen. Jahn (3) reported that the reverse bias characteristics of silicon p-n junctions passivated by thermal oxidation could be improved to a great extent by anodization at constant voltage in a KNO_3-glycol electrolyte.

The primary purpose of this investigation was to compare anodic oxidation with the thermal one on the basis of MOS interface behavior. It is shown here that constant voltage oxidation under clean conditions in a nonaqueous electrolyte followed by a short time annealing in helium at high temperature results in an interface that is comparable with that obtained by thermal oxidation. Especially noteworthy is the fact that no interface instability effects were observed at 300°C and that ion migration under bias at elevated temperature is small and of the voltage-symmetric type.

Experimental

Processing technique.—Chemically polished 10 ohm-cm p-type silicon of (111) and (100) orientations was used (except where otherwise noted). The silicon wafers were cut to a 1 by 1 cm square with a 1 cm long stem that was to be attached to a holder in the anodizing apparatus. The specimens were carefully cleaned, and just before anodization they were submerged in hydrofluoric acid and rinsed with distilled water.

Following the work of Schmidt and Michel (4) the electrolyte chosen was 0.04M solution of KNO_3 in N-methylacetamide (NMA). Since it is known that this electrolyte is hygroscopic and the oxidation process is influenced by its water content (4, 5), fresh electrolyte was used for each oxidation. No attempt was made, however, to avoid water absorption during oxidation. It is not likely that this absorption could cause any serious problem since the observed values of anodization efficiency were below 1.4%. This value is the same as the minimum in the efficiency *vs.* electrolyte water content graph of Duffek *et al.* (5), and according to their observation the most perfect oxides were produced at this water content. Since the electrolyte has a strong tendency for creeping, the upper part of the stem of the silicon specimen together with the holder was masked. The temperature during anodization was about 50°C unless otherwise noted. The cathode was a platinum sheet. The anodization was performed by constant current or constant voltage method, or by a combination of these, that is, constant current oxidation up to a given voltage followed by the constant voltage mode. The constant current density was varied from 5 to 10 ma/cm^2, the highest voltage was 300v, and the lowest current density obtained during the constant voltage mode was 0.04 ma/cm^2 in about 300 min. The range of oxide thickness extended from 160 to 1400Å.

After oxidation the specimens were rinsed in water. Some specimens were then treated in hydrogen at 500°C for 15 min, or in helium at 800°-1000°C. The hydrogen treatment was done in a conventional vitreous silica tube furnace, whereas the helium annealing was performed in an air cooled silica tube with radio frequency (rf) heating. For MOS capacitance measurements with a mercury probe the specimens were provided with nickel back contacts. For stability tests aluminum electrodes were used on the oxide.

Measurement methods.—The interface properties were evaluated on the basis of the MOS capacitance method (6). This gives the density of charges in the states at the Si-SiO_2 interface and within the oxide (lumped together as surface states) as a function of energy in the Si forbidden band. The differential capacitance of the MOS diode as function of bias was measured at 1 MHz with an automatic measuring apparatus, and the data were evaluated with a computer method (7). The results are given as density of surface states at flat band condition, N_o cm^{-2}, and as density of states within the Si forbidden band, dN/dE cm^{-2} $(ev)^{-1}$ (E being the energy, say, above the valence band). Since the distribution of states (energy-wise) was found to be approximately uniform, the value of dN/dE is independent of E. In selected cases the equivalent parallel a-c conductance as a function of bias was also measured (8).

Results

Influence of oxidation and post-oxidation treatments.—*Oxidation.*—The influence of oxidation conditions and post-oxidation treatments on the surface state density is summarized in Table I. It is clear from this table that constant current anodization resulted

Table I. Density of surface states at zero Si surface potential, N_0, 10^{11} cm^{-2} and in the Si forbidden band, dN/dE, 10^{11} cm^{-2} (ev)$^{-1}$

Anodization	Type of Si	As grown N_0	As grown dN/dE	H_2-treatment N_0	H_2-treatment dN/dE	He-annealing N_0	He-annealing dN/dE
Const. current	p	26-71	3-70	9-23	3-14	Not performed	
Const. current	p	2-60	2-55	Not performed		Not performed	
and const. voltage	p	Not measured		2-25	0-6	Not performed	
	p	Not measured		Not performed		2-4	0
	n	−17−−25	27-35	6-9	5-7	Not performed	

* The data represents the extreme values encountered in a group of 4-7 specimens, except for n-type silicon; in the latter case 2 specimens were measured. About 5 spots were measured on each specimen. The negative sign indicates the presence of acceptor rather than donor states (i.e. negative charge is associated with the interface and/or oxide).

in higher value for both N_0 and dN/dE than the combination of constant current and constant voltage modes. In the latter case the lowest values were usually obtained with relatively long anodization, corresponding to low final current densities and low final oxidation rates. If the contamination level was minimized then both N_0 and dN/dE showed a definite trend to decrease with decreasing final oxidation rate, *i.e.*, with the time of constant voltage anodization. A similar effect of the final oxidation rate for thermal oxidation was previously reported (9, 10); it was attributed to a higher degree of perfection in the interface region of the oxide grown with a lower final oxidation rate. Jahn has also observed that the reverse current of a passivated p-n junction decreased with the time of constant voltage anodization. He has attributed this effect to the removal of positive space charges from the vicinity of the Si-SiO_2 interface in the oxide.

If contamination occurred during anodization, *e.g.*, due to accidental dissolution of the copper holder, then even long time anodization with constant voltage gave rise to high value of N_0 and dN/dE, even though the field across the oxide and electrolyte opposed the entry of positive ions into the oxide.

The behavior of the two n-type specimens was unusual. In the as grown condition negative rather than positive charges were associated with the interface, *i.e.*, acceptor states were present. This situation was unstable, after H_2-treatment the usual positive charges, characteristic of donor states, appeared. This phenomenon should be investigated in greater detail.

Post-oxidation treatments.—In order to decrease the surface state density characteristic of the as grown condition two processes are generally used: H_2-treatment at around 500°C (11) and annealing in helium at 1000°-1200°C (9. 10). Both post-oxidation treatments have been investigated. As we can see from Table I, the annealing in helium is superior to the H_2-treatment from the standpoint of decreasing both N_0 and dN/dE. It is interesting to note that Jahn has found an opposite effect of heat treatment (in unspecified ambient, probably air) after constant voltage anodization of thermally oxidized silicon: the pre-anodization value of the reverse current of the p-n junction was restored. If the magnitude of the reverse current is related to the extent of an inversion layer on the surface of p-type silicon then apparently the nature of the Si-SiO_2 interface in Jahn's case is different from that in the present work.

The effects of H_2-treatment (11) and He-annealing (10) were attributed to a saturation of dangling bonds at the silicon surface and to a decrease of disorder in the oxide at the interface, respectively. Since during anodic oxidation various trapping phenomena can occur, and electrons (holes) can be released from these traps by heat treatment, it is possible that electron (hole) transfer between silicon and traps in the oxide takes place during He-annealing. A mechanism consistent with our observation could be, for instance, release of holes from the traps in the oxide and transfer to silicon. This would reduce the negative space charge there. However, the current decay during constant voltage anodization is usually accompanied by a decrease instead of an increase of the surface state density as would be expected if hole trapping were the predominant process during anodization. If one assumes, on the other hand, that electron trapping occurs during anodization then charge transfer across the interface during annealing (*i.e.*, neutralization of separated charges) would result in more negative charges in the silicon after annealing than before. Just the opposite happens in our case. Evidently, the correlation between current decay during anodization, density of states in the "as grown" conditions, and annealing behavior is not quite clear yet.

The influence of crystallographic orientation of silicon in these experiments was by far not as marked as for thermal oxidation (10). Nevertheless, the lowest values of N_0 and dN/dE after He-annealing were obtained with (100) orientation.

Stability studies.—One of the important aspects of MOS structures is their behavior at elevated temperature under the application of positive and negative bias to the metal electrode (the so-called gate). Only He-annealed specimens were tested for stability. These investigations were performed by S. R. Hofstein. The positive bias was usually 10v, the negative bias varied up to 30v. The tests were carried out in helium ambient at 300°C.

Constant voltage anodization.—A typical result for a specimen oxidized with a constant voltage mode is shown in Fig. 1. Note that the outer surface of the oxide film was not etched before the electrode deposition. It can be seen from this figure that the C-V curves after the bias-heat treatment (2 and 3) are roughly parallel with the original one (curve 1) and that the extent of this shift is comparable with that observed for thermally oxidized and annealed specimens that were prepared by an *in situ* process (12). There the voltage-symmetric nature of the instability was attributed to the migration of sodium or similar ionic impurities in the oxide that are bound to the oxide in a manner that resembles sodium in glass. The sodium was incorporated into the oxide during thermal oxidation in a more or less tightly bound form rather than in the loosely bound one characteristic of sodium associated with the surface region of the oxide (13). It is quite possible that some potassium from the electrolyte was incorporated into the anodic oxide in a similar manner. Indeed, Schmidt *et al.* observed that such an incorporation occurs and that this potas-

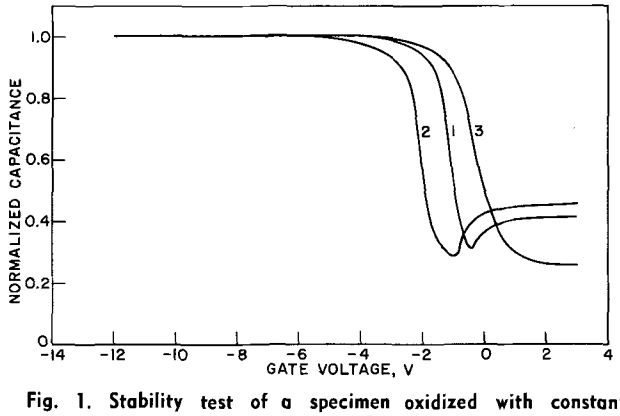

Fig. 1. Stability test of a specimen oxidized with constant voltage mode. Oxide thickness is 1000Å. Curve 1 was taken after the deposition of the aluminum electrode (gate). Curve 2 indicates saturation after applying +10v for 1 hr. Curve 3 was taken after the application of −30v for 3 min corresponding to saturation. (The higher field in the negative direction speeds up the process but does not change the saturation value.)

sium is rather immobile, in contrast to that adsorbed at the surface (14). Since in our studies etching the oxide prior to electrode deposition did not affect the instability behavior, this adsorbed potassium was apparently completely removed by post-oxidation cleaning. Furthermore, it is known that sodium or similar impurities that are associated with the oxide surface lead to a voltage-asymmetric instability behavior (15, 16) that we have not observed. The lack of interface instability (*i.e.*, the C-V curve did not shift to the left under negative bias) in these specimens is an indication of the relatively high perfection of the interface region. As with thermally grown oxides this is due to the elimination of traps in the vicinity of the $Si-SiO_2$ interface by He-annealing. Otherwise these traps could interact electronically with silicon and so cause the so-called interface instability effect (17).

Constant current anodization.—Specimens that were anodized with the constant current mode only showed a different behavior. This is demonstrated in Fig. 2. The shift caused by positive bias is about the same as in Fig. 1 (note, however, that whereas in case of Fig. 1 the time of the test was 1 hr, here it was only ½ min) but the shape of the C-V curve and the minimum capacitance differ considerably from the original ones. Evidently, interface states were introduced during the bias treatment and some of these states could even follow the a-c signal. A similar behavior, but in varying degree, was observed with specimens that were anodized with constant voltage, but became contaminated. Accidental anodic dissolution of the copper holder resulted in very large shifts and distortion of the C-V curves, even though one would think that the high field across the oxide could have prevented the incorporation of Cu-ions into the oxide.

Other properties.—Electronic conduction.—Impedance measurement on MOS capacitors occasionally showed large and asymmetric electronic conduction. Due to the very nature of the growth process anodic oxide films contain less pinholes than thermally grown ones. This has also been demonstrated experimentally (18). Thus, it is not very likely that the observed conduction is caused by simple metal to silicon contacts through pinholes in the oxide. Similar conduction phenomena were also observed with thermally grown SiO_2 films, especially with those processed by an *in situ* method (12). Both the extent of this conductance and the probability of its occurrence was found to be less for thermally grown oxides than for anodic ones even though the opposite behavior is expected. There are indications that both oxides have less conducting spots if some contamination occurred during the processing. The problem of electronic conduction in these films requires more study.

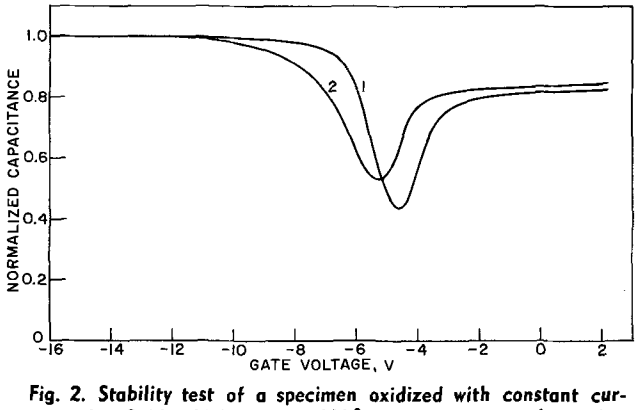

Fig. 2. Stability test of a specimen oxidized with constant current mode. Oxide thickness is 1000Å. Curve 1 was taken after electrode deposition, curve 2 after the application of +10v for ½ min.

Electron bombardment—Preliminary experiments, as performed by K. H. Zaininger, indicated that bombardment by 1 Mev electrons of MOS structures made from anodic oxide films resulted in a parallel shift of the C-V curves. This shift is equivalent to the induction of (0.8 to 4.5) x 10^{11} positive electronic charges/cm^2. This is probably due to ionization of the oxide and predominant hole trapping in the oxide (19). This value is one of the lowest ones obtained in the course of electron bombardment studies.

Interface doping.—Since it was found by Schmidt and Michel (4) that the presence of fluoride ions in the electrolyte drastically modifies the anodization behavior, an experiment was done with $NMA-KNO_3$ electrolyte saturated with NaF. The properties of the $Si-SiO_2$ interface were quite different from those obtained without fluoride. The value of N_o was very high (of the order of 10^{13} cm^{-2}) and, contrary to the usually observed behavior, it remained very high even after He-annealing. Moreover, the value of dN/dE was very high, too, and remained unaffected by the annealing. Although this particular doping is obviously not useful from a practical point of view the experiment nevertheless shows the feasibility of changing the interface properties by doping the anodization electrolyte.

Summary

The density of surface states is determined by the anodization conditions. High values were obtained by constant current anodization. In the case of constant voltage anodization the surface state density generally decreases with the anodization time, *i.e.*, with the final oxidation rate. This is attributed to greater order at the interface, but trapping phenomena can be involved, too. Constant voltage anodization to low final current densities followed by annealing in helium at elevated temperature can result in 2 x 10^{11} cm^{-2} surface state density with no states within the Si forbidden band. The relatively high perfection of this interface is shown by the lack of interface instability effects at 300°C under high field. Under these conditions the shift of the C-V curves is quite small and voltage-symmetric. This may be due to potassium ions incorporated from the electrolyte into the oxide in a relatively strongly bound form. Ions that migrate during positive bias treatment can interact with the $Si-SiO_2$ interface, leading to the appearance of interface states (*i.e.*, $dN/dE \neq 0$). If, however, the interface is relatively perfect then this interaction does not take place. This is in agreement with the concept that cooperative processes play an important role in interface phenomena (10).

Acknowledgments

R. J. Evans assisted in all phases of the work, S. R. Hofstein made the instability investigations, J. Shewchun cooperated in the impedance measurements, and K. H. Zaininger provided the apparatus to measure as well as the computer program to evaluate the MOS capacitance. S. R. Hofstein and K. H. Zaininger of this Laboratory as well as H. Boroffka and M. Zerbst of the Siemens Laboratories in Munich participated in stimulating discussions. P. F. Schmidt made valuable comments on the manuscript. A. M. Goodman and K. H. Zaininger critically read the manuscript. The author wishes to express his gratitude to all.

Manuscript received Nov. 1, 1966; revised manuscript received Feb. 8, 1967. Part of this paper was presented at the Philadelphia Meeting, Oct. 9-14, 1966.

Any discussion of this paper will appear in a Discussion Section to be published in the December 1967 JOURNAL.

REFERENCES

1. L. A. Dubrovskii, V. G. Mel'nik, and L. L. Odynets, *Russian J. Phys. Chem.*, **36**, 1183 (1962).

2. H. Boroffka, Spring Meeting of the German Physical Society, Bad Pyrmont, 1966.
3. D. Jahn, Meeting of the German Chemical Society, Bonn, 1965.
4. P. F. Schmidt and W. Michel, *This Journal*, **104**, 230 (1957).
5. E. F. Duffek, C. Mylroie, and E. A. Benjamini, *ibid.*, **111**, 1042 (1964).
6. A. Slobodskoy, K. Lehovec, and J. L. Sprague, *Phys. Stat. Sol.*, **3**, 447 (1963).
7. K. H. Zaininger, *RCA Rev.*, **27**, 341 (1966).
8. J. Shewchum and A. Waxman, *Rev. Sci. Instr.*, **37**, 1195 (1966).
9. A. G. Revesz and K. H. Zaininger, *IEEE Trans. Electron Dev., ED-13*, 246 (1966).
10. A. G. Revesz, K. H. Zaininger, and R. J. Evans, *J. Phys. Chem. Solids*, **28**, 197 (1967).
11. (a) P. Balk, Spring Meeting of Electrochemical Society, San Francisco, 1965; (b) E. Kooi, *Philips Res. Repts.*, **20**, 578 (1965).
12. A. G. Revesz, *Phys. Stat. Sol.*, **19**, 193 (1967).
13. E. Yon, W. H. Ko, and A. B. Kuper, *IEEE Trans. Electron Dev., Ed-13*, 276 (1966).
14. P. F. Schmidt, T. W. O'Keeffee, J. Oroshnik, and A. E. Owen, Electrochemical Society Meeting, Washington, 1964.
15. E. Snow, A. S. Grove, B. E. Deal, and C. T. Sah, *J. Appl. Phys.*, **36**, 1664 (1965).
16. S. R. Hofstein, *IEEE Trans. Electron Dev., ED-13*, 222 (1966).
17. S. R. Hofstein, To be published.
18. A. Polyticki and E. Fuchs, *Z. Naturforsch*, **142**, 271 (1959).
19. K. H. Zaininger, *IEEE Trans. Nucl. Sci.*, In press.

Technical Notes

A Chemical Polish That Reveals Compositional Variations in $PbSe_{(1-x)}Te_x$

Marriner K. Norr, John V. Gilfrich, and Bland Houston

U. S. Naval Ordnance Laboratory, White Oak, Silver Spring, Maryland

$PbSe_{(1-x)}Te_x$ is single phase with the NaCl structure over the range $0 \leq x \leq 1$ (1). The chemical polish described in this note was used on a single sample in which x was approximately ½. It produced a fairly flat surface except for a network of valleys which covered the surface rather uniformly. Successive applications of the polish resulted in only minor displacements of the valleys, even when the surface was ground between polishings. A dislocation etch, which is also described in this note, revealed that the dislocation density was higher in the valleys than on the plateaus. Electron probe microanalysis revealed a significant drop in the Se concentration in the valleys.

The sample was ground flat on No. 600 grit SiC paper lubricated with water. Next it was finely ground with Carborundum No. 50 Optical Finishing Powder and then polished with Linde A. Both of the latter operations were carried out on a paraffin lap lubricated with an aqueous soap solution.

The chemical polishing solution was prepared by dissolving 0.5g disodium ethylenediamine tetraacetate in 25 ml distilled H_2O and then adding 50 ml 30% H_2O_2 and 25 ml glacial acetic acid. The sample was stuck to a polycarbonate jig with paraffin. It was polished for 5 min with a figure "8" motion on a piece of twill jean cloth[1] which was stretched over a smooth Teflon plate and saturated with the solution. It was then rinsed with distilled water and dried on lens paper. The surface was shiny and free of any films or stains. An "orange peel" structure on the surface which was visible to the naked eye is shown in the slightly defocused photomacrograph (Fig. 1). The chemical polishing procedure was continued for an additional 5 min and the pattern was unchanged. The valleys were removed by repeating the fine grinding operation. When the chemical polishing was repeated, the valleys reappeared in essentially the same positions as were observed after the initial chemical polish.

[1] K. S. 2423 twill jean cloth, Exeter Manufacturing Company, Inc., Exeter, New Hampshire.

Fig. 1. Photomacrograph of a chemically polished surface of the $PbSe_{(1-x)}Te_x$ sample.

Detailed information about the topography of the chemically polished surface was obtained from photomacrographs of the interference fringes formed between the surface and an optical flat (2). The flat was coated with a thin layer of metal so that its reflectivity was about 75%. The 4360Å Hg line was used for illumination. White light illumination was used to follow the order of the fringes. The valleys were about ½ μm deep and from 25 to 75 μm across. Most of the plateaus were between 100 and 700 μm across. The tops

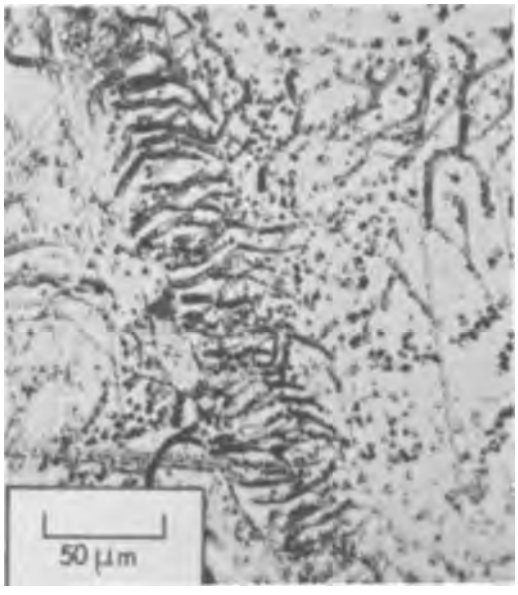

Fig. 2. Photomicrograph of the etched surface of the sample shown in Fig. 1. The distribution of the pits in one of the valleys is shown. The valley runs almost vertically across the photomicrograph. The partially developed pits are due to those dislocations introduced in the mechanical part of the preparation which were not entirely removed by the chemical polish.

of the plateaus were slightly rounded. The changes in height from the high points near the centers of the plateaus to the edges of the valleys were less than 1 μm.

The dislocation distribution in the sample was determined by etching. The etch was prepared by adding 3 ml glycerol to 13 ml 50% KOH, cooling to 25°C, and then adding 1.0 ml 30% H_2O_2. The etching was carried out by immersing the freshly polished sample in the solution for 3 min at 25°C. The etching showed the sample to be polycrystalline. Dislocation etch pits formed only on certain grains. Since the pits looked like pyramids with square bases, the grains on which they appeared probably had {100} planes nearly parallel to the surface of the specimen. The pit density in the valleys was high compared to the pit density on the plateaus. Frequently rows of pits ran across the valleys (Fig. 2).

There are several reasons to believe that these results can be explained by a spatial variation in x. The location of the valleys appears to be associated with variations in the properties of the sample. The pattern formed by the valleys is typical of the cellular structure associated with segregation due to constitutional supercooling (3). The arrangement of the dislocations would reduce the strain energy due to the lattice parameter mismatch which would be associated with variations in x (1). If constitutional supercooling is involved, one would expect the valleys to be rich in the component which lowers the melting point, Te.

Electron probe microanalysis was used to find out whether or not variations in x could be associated with the valleys. First, the sample was chemically polished and mounted in Quickmount together with a piece of PbSe which was used as a selenium standard. The conditions for the electron probe microanalysis were as follows: acceleration potential, 30 kv; specimen current, 3 x 10^{-8} amp; and x-ray wavelength, 1.106Å (Se K_α). A 60 sec point counting technique was used

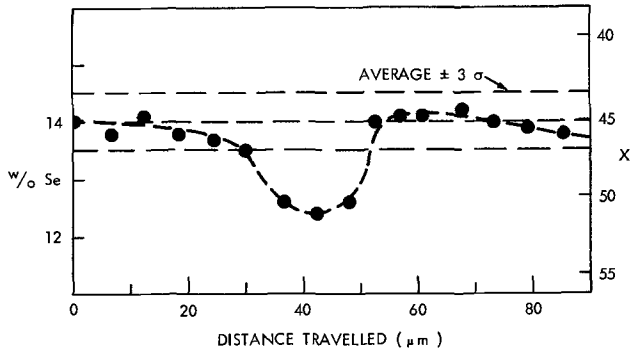

Fig. 3. The Se concentration across one of the valleys in the $PbSe_{(1-x)}Te_x$ sample shown in Fig. 1 from electron probe microanalysis (Se K_α).

in steps of 6-12 μm across two of the valleys. The relative x-ray intensity data were converted into weight per cent (w/o) Se with corrections only for absorption by the method of Birks (4).

Figure 3 is a plot of Se concentration across one of the valleys. The other valley traversed showed the same variation in Se concentration but the lower Se concentration extended over about 50 μm. The analyses indicate that the composition on the plateaus is constant (3σ = 0.5 w/o), but that there is a decrease of about 1.5 w/o in the valleys. On the plateaus the average Se concentration is about 14.0 w/o with a 3σ value of 0.5 w/o, while in the valleys it decreases to a minimum of 12.4 w/o. There is the possibility of some systematic error in these absolute values because of the uncertainties in the conversion from relative x-ray intensities to concentrations, but the relative concentrations are significant, and the lower Se concentration in the valleys is undoubtedly real. The surface topography studies indicate that the steepest slopes on the sides of the valleys are about 2°. A slope of this magnitude would not introduce an appreciable error due to the change in the x-ray "take-off" angle which is nominally 37½°.

The spatial variation in x is consistent with the model for segregation by constitutional supercooling. The preferential attack by the chemical polish could result from the variation in composition or from the strain or the higher dislocation densities associated with the rapid change in lattice parameter associated with a variation in x. Careful metallographic examination revealed no evidence of a second phase. The etch and polish described could probably be adapted to work successfully on samples with x different from ½. Also there is reason to believe that the polish would produce flat, work-free surfaces in homogeneous samples.

Manuscript received Oct. 3, 1966; revised manuscript received Feb. 23, 1967.

Any discussion of this paper will appear in a Discussion Section to be published in the December 1967 JOURNAL.

REFERENCES

1. S. Yamamoto, *Science Repts. Tohoku Univ.*, **40**, 11 (1956.)
2. S. Tolansky, "Surface Microtopography," Interscience Publishers, New York (1960).
3. B. Chalmers, "Principles of Solidification," p. 154, John Wiley & Sons, Inc., New York (1964).
4. L. S. Birks, "Electron Probe Microanalysis," chap. 9, Interscience Publishers, New York (1963).

Extraction of III-V Intermetallic Compounds from Metallic Matrices

Sylvan Z. Beer

Westinghouse Electric Corporation, Research and Development Center, Pittsburgh, Pennsylvania

Crystals of III-V and other intermetallic compounds are often grown from metallic solutions. The extraction of the desired product from the metallic matrix may prove quite troublesome. While the metal can frequently be dissolved away from the product with aqueous solutions of acids or bases, this is not always possible because of the reactivity of the nonmetallic substance with water. Frequently, the reactivity of the nonmetallics depends, to some extent, on their purity and grain size. This is known to occur in the case of aluminum nitride (1, 2) which, on synthesis, is readily attacked by acids, but which becomes less labile on prolonged heating at high temperature to the extent that it can be extracted with aqueous solutions. This communication describes a nonaqueous method for extracting many water-sensitive compounds from metallic matrices.

Experience with Established Techniques

In the course of aluminum phosphide synthesis in this laboratory, the product was obtained as fine crystals embedded in an aluminum matrix, a highly reactive form which rapidly produces α-alumina and phosphine on contact with moisture in the air. Extraction with inorganic acids or other acids in aqueous solutions was, therefore, impractical. A reagent recommended (3) for this extraction is 1,2-dibromoethane. The aluminum reacts with the reagent to form a brownish tarlike mass from which the phosphide must be extracted. While the procedure is relatively safe, the difficulties in handling and treating the resultant viscous mixture was cause for seeking a simpler process.

Few of the established procedures (4) used for stripping surface films and in the study of nonmetallic inclusions (5) were directly useful or were adaptable for use in nonaqueuos media. For instance, the electrochemical oxidation of the matrix (6), which is used with great success in aqueous solutions, is difficult to adapt to nonaqueous media. Other frequently used extraction procedures are the reactions with halogens in solution or in the gaseous state (2, 4). Chlorine at about 600°C has been used, but it presents problems because of its excessive reactivity which could lead to the destruction of the desired product. Bromine in ethanol or methanol was tried, but was found to react violently with both the aluminum and the phosphide. Similar solutions of iodine also reacted with the phosphide although more slowly. Therefore, these solutions could not be considered suitable extracting agents. Dissolution of the aluminum as an amalgam with mercury as done to extract III-V compounds from indium (7) is impractical here because of the high liquidus temperatures.

Solutions of mercuric salts in N,N-dimethyl formamide (DMF) were found to be excellent extraction reagents. The reaction is the displacement of mercury by the aluminum to form mercury and the corresponding aluminum salt. Mercuric chloride, bromide, iodide, and cyanide were found to be about equally effective. Aluminum bromide, iodide, and cyanide are soluble in hot DMF and are retained in solution, leaving the nonmetallic as the only solid phase, while the less soluble aluminum chloride precipitates out with the nonmetallic phase as a fine powder. Of the mercuric salts listed, the chloride is the least expensive and most easily obtained in pure form; it was used in most of the work reported here.

Recommended Extraction Method

The reagent is prepared by dissolving 85-100g of the mercuric salts in 100 ml of dry DMF at 80°-120°C. The conglomerate mass containing the III-V compound and the metal to be dissolved is then added to the hot solution, or, when using mercuric chloride, can be suspended in a platinum fine-mesh screen which retains the aluminum phosphide and the mercury globules but permits the escape of the aluminum chloride). The product of this reaction is then filtered through a Millipore (8) noncellulosic filter (cellulosic filters dissolve in hot DMF) and washed with additional hot DMF followed by a dry solvent such as carbon tetrachloride. Tapping the filter funnel gently makes the mercury coalesce, which simplifies the mechanical separation of the mercury from the desired product. The mercury can also be removed by distillation under reduced pressure. Finally, the solid is vacuum dried.

Discussion

Solvents other than DMF can be employed in the preparation of this reagent. However, DMF has the advantage of a high boiling point (153°C). By virtue of this property, the solvent can be adequately dried for use in the reagent by heating it at close to 140°C for a short period of time. (Alternately, the solvent can be dried over calcium hydride.) In addition, the reaction can be run at a relatively high temperature if desired, which also permits the preparation of a more concentrated reagent solution.

The relative reactivity of the reagent toward other metals or alloys as a dissolving reagent or etchant can be estimated by their standard aqueous electrode potentials (9). The dielectric constant of DMF is high (36.7), and to some extent one can assume that the relative potentials are independent of the medium. This property also contributes to the high solubility of the mercuric salts as seen in Table I. The nature of the DMF solutions is not fully understood (10), but the rather high solubilities, in the order of decreasing ionic bond, which are closer in value to each other than in the case for the aqueous solutions, indicates that DMF is a highly coordinating solvent, and that anionic solvation plays a smaller role in the dissolution process in DMF than it does in water.

The thermodynamic argument on the reactivity does not always apply as other factors often interfere. For instance, it is found that while the initial reaction of $HgCl_2$ in DMF on aluminum is fairly slow, the re-

Table I. Solubility of mercuric salts in DMF and water

Salt	Solubility (g/10 g solvent) DMF*		Water*
$HgCl_2$	17.4, 83°C	4.8, 100°C	0.69, 20°C
$HgBr_2$	18.1, 83°C	0.4, 100°C	0.061, 25°C
HgI_2	20.2, 83°C	—	0.001, 25°C

* Solubilities were determined in this laboratory to within 3% at 83.0° ± 0.5°C.
** Data taken from Handbook of Chemistry and Physics, 45th ed., Chemical Rubber Co., Cleveland, Ohio (1964-1965).

action with gallium and indium is extremely rapid. Yet, the standard potentials for the reactions are —1.66, —0.56, and —0.53v, respectively. The slow reaction of aluminum is no doubt due to the protective oxide coating. In the case of copper, the initial rapid reaction quickly ceases because of the formation of an amalgam coating. Removing the metal from the solution and heating lightly under vacuum removes the mercury film and exposes a vigorously active surface.

A different situation occurs in the reaction with silicon. Although the calculated potential for the reaction is high, the reaction does not take place due, very likely, to a SiO_2 protective film. The reaction can be made to proceed at a reasonable rate, however, by the addition of ammonium fluoride which drives the reaction forward through the formation of a stable fluoride. Mercuric cyanide is the most suitable of the salts for this purpose as it does not form the insoluble mercuric fluoride as readily as the others. Selenium too is attacked in this solution while it does not react with the ordinary reagent.

In general, however, the potential will be a good indicator of the probable reactivity as shown by the listing in Table II of the reactivity of the reagent toward various metals and nonmetals. Thus, mercuric salt solutions in DMF appear to be effective and safe reagents for the extraction of labile nonmetallics from many metallic fluxes, solutions, and parent metals. The highly concentrated form of the reagent which can be prepared in DMF as compared with water and the higher temperature at which the reaction can be run, makes this reagent attractive even in situations (5) where the presence of water is not deleterious.

Acknowledgment

The author wishes to acknowledge the extremely useful discussion on this subject with Dr. L. Mandelcorn of this laboratory, and to thank Mr. R. A. Jox for his assistance in the experimental work.

Table II. Reactivity of selected metals and nonmetals toward DMF-mercuric salt reagent

Attacked:
Indium, gallium, aluminum, iron, nickel, tin, lead, bismuth, antimony, copper, silicon,* selenium*
Not attacked:
Germanium, tellurium, aluminum phosphide, gallium arsenide, gallium phosphide.

* DMF solution of mercuric cyanide and ammonium fluoride.

Manuscript received Oct. 12, 1965; revised manuscript received Dec. 7, 1966.

Any discussion of this paper will appear in a Discussion Section to be published in the December 1967 JOURNAL.

REFERENCES

1. G. Long and L. M. Foster, *Am. Ceram. Soc.*, **42**, 53 (1959).
2. A. Rabenau, "Compound Semiconductors," Vol. 1, R. K. Willardson and Goering, Editors, p. 174 (1962).
3. A. Rabenau, *ibid.*, p. 181.
4. L. Young, "Anodic Oxide Films," Academic Press, New York (1961).
5. McKaveney *et al.*, Determination of Non-Metallic Compounds in Steel, ASTM STP 393, p. 47-74 (1966).
6. P. Klinger and W. Koch, *Stahl und Eisen*, **68**, 321 (1948).
7. R. N. Hall, *This Journal*, **110**, 385 (1963).
8. Millipore Filter Corp., Bedford, Mass.
9. "Encyclopedia of Electrochemistry," p. 414, C. A. Hampel, Editor, Reinhold Publishing Co., New York (1964).
10. A. J. Parker, *Quart. Revs.*, **16**, 163 (1962); R. S. Drago and K. F. Purcell, *Prog. Inorg. Chem.*, **6**, 271 (1964).

The Metallic Etching of Indium Antimonide and Germanium

H. D. Barber

Research and Development Laboratories, Canadian Westinghouse Company Limited, Hamilton, Ontario, Canada

and E. L. Heasell

Electrical Engineering Department, University of Waterloo, Waterloo, Ontario, Canada

When the temperature of a semiconductor in contact with a molten metal is raised in such a way that the solid and liquid phases are at all times approximately in equilibrium, the shape of the solid-liquid interface is determined by the ease with which atoms can be removed from the solid. Thus, a concave solid-liquid interface tends to become defined by the most slowly dissolving crystallographic planes during metallic (1) or chemical (2) etching. These planes are also the slowest growing planes (1) and thus define the shape of the growth face when the solid-liquid interface is convex. In the semiconductors silicon and germanium, the {111} planes have long been known (3-7) to be boundary planes or facets in such circumstances.

In the III-V compounds, {111} surfaces display similar behavior (8). However, the lower symmetry of the lattice in III-V compounds leads to two types of {111} surface (9): the A{111} surface terminating in triply bonded group III atoms and the B{111} surface terminating in triply bonded group V atoms. In general the rate of crystal growth on A{111} surfaces is greater than that on B{111} surfaces (10). A polar effect also exists in the reverse case of dissolution or metallic etching (8, 11).

Experiments in both crystal growth (12-15) and metallic etching (16) have given evidence of facet formation on {100} surfaces in III-V compounds. A similar faceting effect does not appear to have been observed in either of the elemental semiconductors, silicon, or germanium. If this is the case, it suggests that the mechanism resulting in polarity dependent effects in III-V compounds in <111> directions has an observable influence in the nonpolar <100> directions.

It is the purpose of this publication to present the results of micro-alloying experiments which demonstrate clearly the development of facet-forming planes in polar indium antimonide and nonpolar germanium under similar conditions of metallic etching; and to consider reasons for the difference in facet development on A{111} and B{111} surfaces, and for the existence of {100} facets in polar compounds.

Experimental Techniques

Crystals of indium antimonide and germanium were cut and polished to give die approximately 2 x 2 x 0.5 mm having their surfaces oriented to within one degree of the {100}, {110}, or {111}. A radiation wetting technique (17) was used to uniformly wet pellets of indium-1% cadmium to these wafers. The pellets were spherical with diameters ranging from 0.2 to 0.5 mm. Following the wetting procedure the wafer and pellet were placed on an enclosed heat sink, to ensure temperature uniformity and stability, and the entire assembly was placed in a temperature programmed furnace. For indium antimonide, the alloying was carried out in an air atmosphere with temperature rates of rise and fall during the cycle kept to about 5°C/min. Previous experiments (8) had shown that temperature rates of change less than 50°C/min were low enough to ensure that the dissolution process was controlled by crystallographic effects and not by diffusion into the solvent. The maximum temperature used was in the region of 400°C. For germanium, alloying was carried out in purified hydrogen and the rate of temperature rise above 500°C was controlled at about 2°C/min. The maximum temperature was 700°C.

After alloying, the shape of the alloyed region in the wafer surface was examined and photographed. The wafers were then encapsulated, sectioned, and etched to determine the shape of the alloyed region in planes perpendicular to the wafer surface. From these observations it was possible to determine the shape of the dissolved volume.

The advantages of the technique described above arise from the limited amount of solvent used (normally less than 400 μg) and the method of examination. When the mass of solvent is small, the mass of solute required to re-establish equilibrium after an incremental change in temperature is also small. Hence, for a given rate of temperature change the dissolution or growth rate in such a "micro-system" is always much less than that in the corresponding large system. (Typical growth rates of 10^{-4} cm/min were involved compared to 10^{-1} cm/min in a typical crystal puller.) As a result, there is no need when microalloying to resort to lengthy temperature cycles to ensure low dissolution or growth rates. Since chemical methods are employed to delineate the dissolution interface, this technique is not effected by the regrowth or residual solvent accumulations which often obscure the results of decanting or rapid quenching experiments. The usefulness of the micro-alloying technique in metallurgical observations has already been demonstrated in studies of polar effects (8) and in liquidus measurements (18).

Observations

{111} Surfaces.—The shape of the alloyed regions observed on A and B{111} surfaces of indium antimonide were with few exceptions almost perfectly hexagonal as shown in Fig. 1(a). Sections taken perpendicular to the surface and to two opposite faces of the hexagon indicated, as shown in Fig. 1(b), a flat {111} bottom, a {111} plane at one side making an angle of ~70.5° with the surface, and a {100} plane at the other side making an angle of ~55° with the surface. It was concluded that the dissolved volume was completely defined by {111} and {100} planes resulting in the shape illustrated in Fig. 1(c).

In the case of germanium, the observations confirmed the reports of other workers (3, 4, 7, 19). The shape of the alloyed region in the {111} surface tended to be hexagonal with three sides rounded and three sides well defined. The rounded sides appeared in the place of the {100} planes in Fig. 1(c) and also appeared rounded in the cross-sections which were in every other respect similar to Fig. 1(b).

{100} Surfaces.—The shape of the alloyed region in {100} surfaces of indium antimonide was invariably

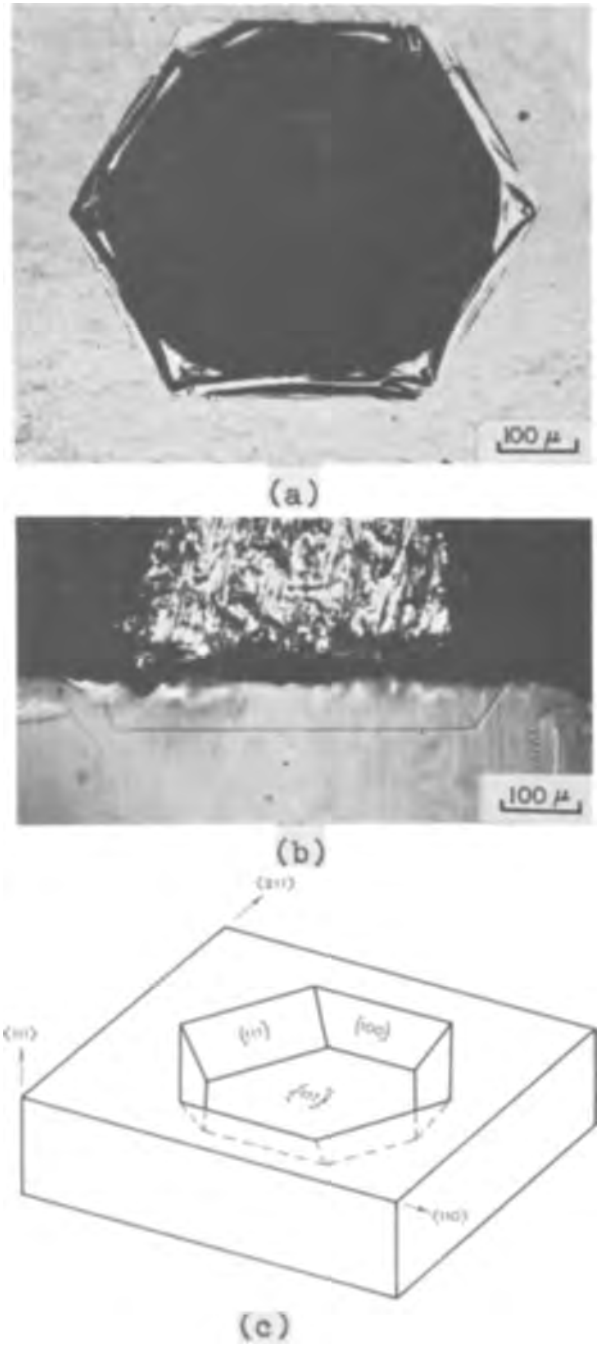

Fig. 1. Metallic etching on the {111} surface of InSb: (a) the shape of the alloyed region in the {111} surface; (b) the shape of the alloyed region in a section perpendicular to the {111} surface and to two sides of the hexagon in (a); (c) the deduced shape of the dissolved volume.

rectangular as shown in Fig. 2(a). Sections perpendicular to the surface and to two sides of the rectangle, such as that shown in Fig. 2(b), have indicated the presence of a crystallographically flat {100} bottom and of sides formed by {111} planes. From evidence presented earlier (8) it was concluded that the long sides of the rectangle were formed by the slower dissolving B{111} planes and thus that the dissolved volume assumed the shape illustrated in Fig. 2(c). It is of interest to note that as early as 1956 Millea and Tomizuka (20) reported the same rectangular morphology appearing in the {100} surfaces of indium antimonide during slow melting experiments, and tentatively attributed this to thermal gradients.

In view of a recent paper (11) giving evidence for greater dissolution rates on B{111} surfaces than on A{111} surfaces of gallium arsenide, a further experi-

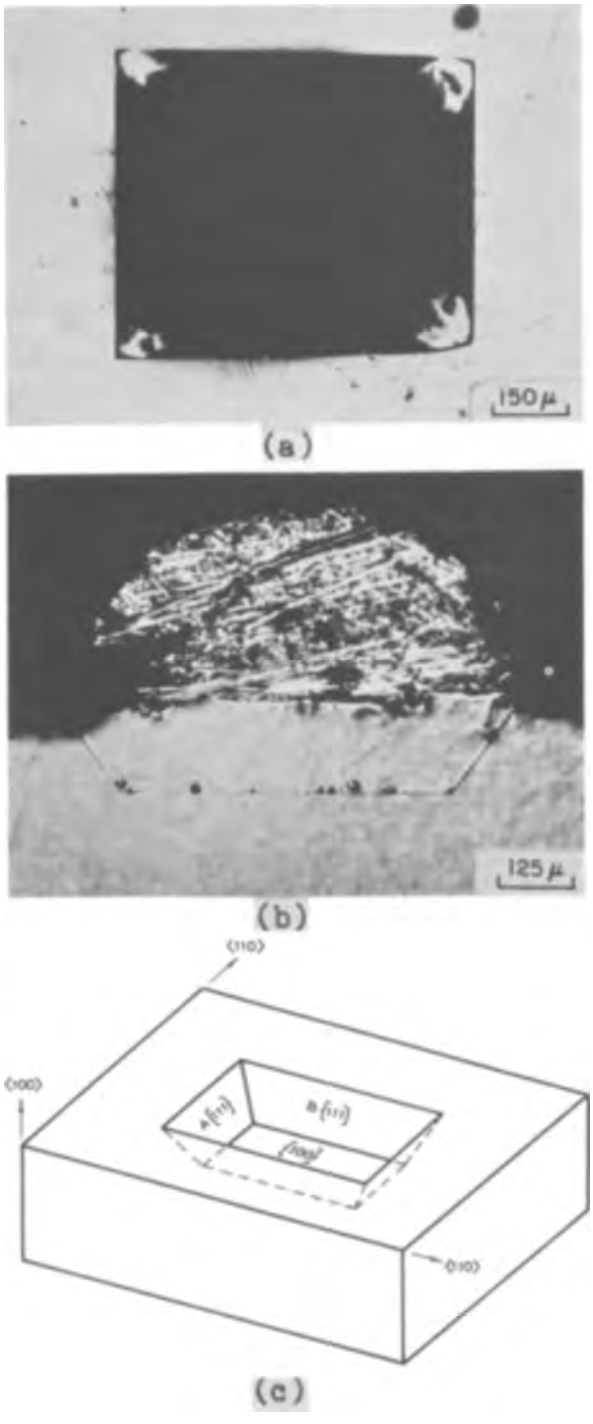

Fig. 2. Metallic etching on the {100} surface of InSb: (a) the shape of the alloyed region in the {100} surface; (b) the shape of the alloyed region in a section perpendicular to the {100} surface and to two sides of the rectangle in (a); (c) the deduced shape of the dissolved volume.

ment was undertaken. Die of {100} oriented indium antimonide were cut to permit identification of the A{111} directions by the presence of etch pits (21) after etching in 5:5:3, $CH_3COOH:HNO_3:HF$. Pellets were alloyed on both top and bottom {100} surfaces. It was observed that the long dimension of the rectangle was always rotated through 90° on one side in comparison to the other, thereby establishing that the difference could not arise from temperature gradients. It was further observed that in ten samples the sides formed by B{111} surfaces were on average 14% longer than those formed by A{111} surfaces and were never less than 5% longer. This would indicate that in indium antimonide the A{111} surface dissolves

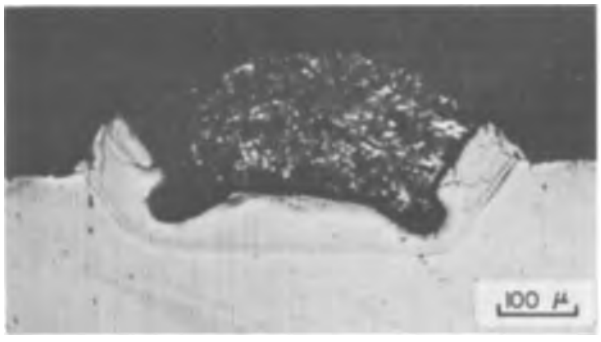

Fig. 3. The shape of an alloyed region in a section perpendicular to the {100} surface in germanium. The sides are formed by crystallographically flat {111} planes but such planarity is not present on the {100} bottom.

more rapidly than does the B{111} and that the configuration illustrated in Fig. 2(c) is accurate.

Alloyed regions on germanium {100} surfaces tended to assume a square shape on the surface and sections such as that in Fig. 3 showed the development of the {111} side planes. Although the alloying cycle was designed so that the dissolution rate was actually smaller than that for indium antimonide, the bottoms of the alloyed regions were in no case crystallographically flat. This observation is supported by those of Eer Nisse and Thompson (22) on both germanium and silicon.

The square, truncated pyramidal shape of the dissolved volume on {100} surfaces was clearly illustrated in an experiment in which indium was sputtered onto a hot germanium surface and the small indium pellets were subsequently removed by chemical etching. Some of the resulting etch pits are shown in Fig. 4.

{110} Surfaces.—For the sake of completeness, alloying on {110} surfaces was also examined. In the case of indium antimonide the shape of the alloyed region on the {110} surface generally tended to assume the form of an irregular octagon as shown in Fig. 4(a). Sections such as that in Fig. 5(b) gave no evidence for faceting on {110} planes. However, the sections did indicate the tendency for the dissolved volume to become bounded by {100} and {111} planes in the configuration illustrated in Fig. 5(c).

In the case of germanium the alloyed regions tended to assume an elongated hexagonal shape with the {100} sides of Fig. 5(a) and (c) absent. This has also been observed by Eer Nisse (19) in silicon and by Faust *et al.* (16) in both silicon and germanium. Sections across the sloping {111} sides were almost identical to that in Fig. 5(b) indicating no tendency for {110} faceting. Other sections confirmed the absence of {100} facets.

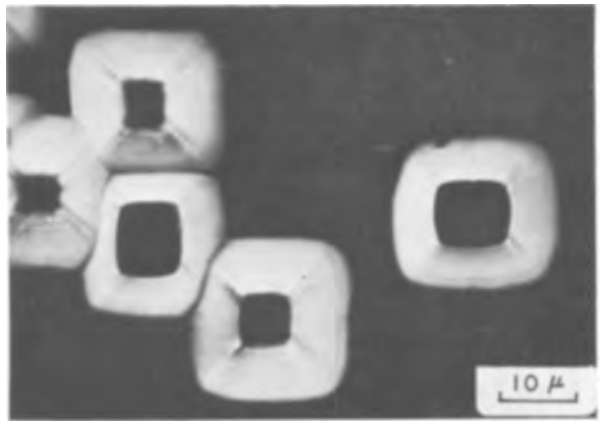

Fig. 4. Etch pits formed by sputtering indium onto a hot germanium surface indicate clearly the truncated pyramidal form of the dissolved volume on {100} surfaces.

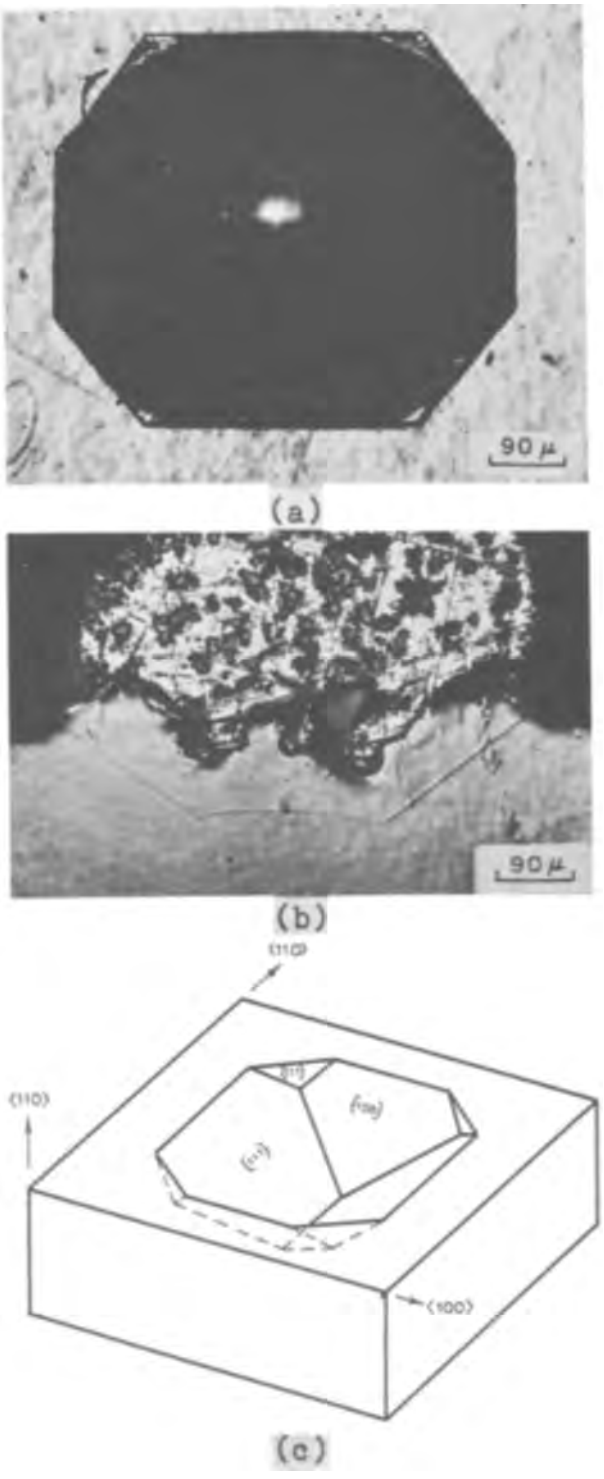

Fig. 5. Metallic etching on the {110} surface of InSb: (a) the shape of the alloyed region in the {110} surface; (b) the shape of the alloyed region perpendicular to the {110} surface and to the well developed sides in (a); (c) the deduced shape of the dissolved volume.

The above describes the results most generally observed. However, it should be added that in the germanium samples examined there were two cases in which the shape of the alloyed region on the surface indicated the possible presence of {100} boundaries: once on a {111} surface, and once on a {100} surface. No detectible {100} faceting was observed in any of the cross-sections.

Discussion

The above observations complement those of Faust *et al.* (16) and indicate that in metallic etching where diffusion effects are negligible the {100} and {111} are dissolution-limiting planes in III-V compounds while the {111} appears as the only dissolution-limiting plane in elemental semiconductors. The experiments also indicate that the A{111} surface dissolves at a greater rate than the B{111}. Since these observations cannot be explained by macroscopic considerations it is necessary to examine the statistics and energy states involved in atomic addition to or subtraction from any atomic configuration on these surfaces before some understanding of the possible forces and mechanisms in these phenomena can be achieved. For this purpose the following highly idealized models for the initial configuration of {111} and {100} surfaces were chosen and it is shown that qualitative agreement with experiment can be obtained.

{111} Surfaces.—In an earlier publication (10) the nature of {111} surfaces in polar III-V compounds was considered and it was concluded that a model for {111} surfaces, similar to that proposed by Gatos and Lavine (21), could be used to explain the differences in growth rates observed between A and B surfaces. This model assumes that A atoms attempt to bond into the A{111} surface in an sp^2 configuration. The A surface becomes more highly strained, therefore, than the B surface where the p^3 bonding tendency is closer to the equilibrium sp^3 configuration. Such a strain difference has been demonstrated experimentally by the spontaneous bending of thin slabs (23). The strain energy in a surface can be shown (10) to assist nucleation and growth and therefore, under identical circumstances, growth on an A surface would be expected to proceed more rapidly than that on a B surface. If dissolution is considered the reverse process to growth it must also proceed more rapidly on the strained A-surface. This conclusion is supported by alloying experiments (4) which have shown that the strain in heavily dislocated materials enhances the etching rate.

Although these conclusions would appear to contradict the observations of Millea and Wilcox (11), it can be shown that there is essential agreement between the experiments. Broadly speaking, crystallographic dissolution is a two-stage process. A difficult stage of atomic removal, analogous to nucleation during growth, is followed by rapid removal of an entire surface layer. It is not difficult to show that the removal of an atom in the first stage may require more than 1.5 times the energy needed for removal of an atom in the second stage. In our experiments the effects of surface strain energy on the first stage are observed. In the experiments of Millea and Wilcox the edge of the crystal provides the starting point for layer removal. Differences in dissolution observed in such experiments reflect differences in propagating a negative step and not in its nucleation. Since propagation on a B-face is typically by an A-faced step (10), layer removal on a B-face could be expected to proceed more rapidly than that on an A-face where B-faced steps develop.

{100} Surfaces.—It would seem reasonable on the basis of the electronic configuration of A atoms to assume that they tend to form sp^2 bonds on any surface in a III-V compound. As a result A atoms could bond stably into the {100} surface in the manner illustrated in Fig. 6. This A{100} surface resembles the {111} surface where the first atoms bonding to the surface can form only one bond. This should be compared to the B{100} surface or the {100} surface of nonpolar semiconductors where all atoms bonding to the surface can form two bonds and no nucleation difficulties would be expected.

If it is assumed the A atoms bond into the {100} surface as shown in Fig. 6, nucleation on such a surface requires that at least two atoms singly bond as close neighbors before growth involving double bonds can occur. Since single bonding is energetically unfavorable and the probability of two atoms single

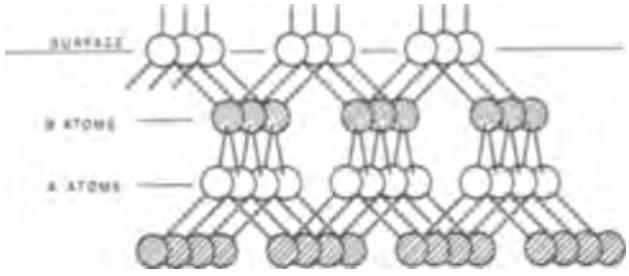

Fig. 6. The bonding configuration of a {100} surface composed of A atoms forming sp^2 bonds with the lower B layer. Only one dangling bond is associated with each A surface atom.

bonding on related sites is low, the formation of a nucleus is difficult. This difficulty in nucleating new layers on {100} surfaces in III-V compounds results in {100} faceting during crystal growth and indicates that a difficult step also exists in dissolution which results again in {100} faceting. The absence of nucleation difficulty on the {100} surfaces in nonpolar semiconductors does not necessarily imply rapid dissolution or growth but it does suggest that crystallographic faceting would be improbable. These conclusions are in agreement with the experimental observations reported here.

A more detailed discussion of possible processes for nucleation and growth on {111}, {100}, and {110} surfaces has been given elsewhere (24).

Acknowledgments

The authors wish to thank Dr. J. B. Mullin of the Royal Radar Establishment for supplying the InSb crystals used in this work.

Manuscript received July 20, 1966; revised manuscript received March 3, 1967.

Any discussion of this paper will appear in a Discussion Section to be published in the December 1967 JOURNAL.

REFERENCES

1. H. E. Buckley, "Crystal Growth," John Wiley & Sons, Inc., New York (1951).
2. B. W. Batterman, *J. Appl. Phys.*, **28**, 1236 (1957).
3. C. W. Mueller and H. N. Ditrick, *RCA Review*, **17**, 46 (1956).
4. J. I. Pankove, *J. Appl. Phys.*, **28**, 1054 (1957).
5. J. H. Wernick, *J. Metals*, **205**, 1169 (1957).
6. W. D. Edwards, *Can. J. Phys.*, **38**, 439 (1960).
7. A. Hoffmann, *Solid State Electron.*, **1**, 101 (1964).
8. H. D. Barber and E. L. Heasell, *J. Appl. Phys.*, **36**, 176 (1965).
9. C. Hilsum and A. C. Rose-Innes, "Semiconducting III-V Compounds," Pergamon Press, New York (1961).
10. H. D. Barber and E. L. Heasell, *J. Phys. Chem. Solids*, **26**, 1561 (1965).
11. M. F. Millea and W. R. Wilcox, *This Journal*, **112**, 872 (1965).
12. J. B. Mullin, "Compound Semiconductors," Vol. 1, p. 365, Reinhold Publishing Co., New York (1962).
13. A. J. Strauss, *Solid State Electron.*, **5**, 97 (1962).
14. J. W. Faust, Jr., and H. F. John, *J. Phys. Chem. Solids*, **23**, 1119-1122 (1962).
15. C. M. Wolfe, C. J. Neuse, and N. Holonyak, *J. Appl. Phys.*, **36**, 3790 (1965).
16. J. W. Faust, A Sagar, and H. F. John, *This Journal*, **109**, 824 (1962).
17. H. D. Barber and E. L. Heasell, *Solid State Electron.*, **8**, 113 (1965).
18. A. C. Papadakis, E. L. Heasell, and H. D. Barber, *Solid State Electron.*, **8**, 825 (1965).
19. E. P. Eer Nise, Ph.D. dissertation, Purdue University (1965).
20. M. F. Millea and C. T. Tomizuka, *J. Appl. Phys.*, **27**, 96 (1956).
21. H. C. Gatos and M. C. Lavine, *This Journal*, **107**, 427 (1960).
22. E. P. Eer Nisse and H. W. Thompson, *J. Appl. Phys.*, **36**, 2652 (1965); and private communication.
23. M. C. Finn and H. C. Gatos, *Surface Science*, **1**, 361 (1964).
24. H. D. Barber, Ph.D. Thesis, University of London (1965).

A Source of Elemental Iodine for Vapor Transport Studies

Samuel E. Blum

IBM Watson Research Center, Yorktown Heights, New York

The use of elemental iodine in vapor transport of semiconductors and other materials is well known. It is, however, difficult to obtain a desired amount of dry iodine in an evacuated sealed system, especially if the system requires a lengthy pumping and outgassing procedure. Generally an elaborate encapsulation technique incorporating break seals is necessary. In his book, Schaefer (1) refers briefly to the production of iodine by heating silver iodide and vanadium pentoxide. Unfortunately, no experimental details are given and the reaction itself could not be found in the literature. The feasibility of using this reaction was investigated.

Experimental

Fisher reagent grade AgI and V_2O_5 were dried at 130°C and used without purification. Mixtures of various mole fractions of the two reagents were prepared and each was intimately mixed. A weighed quantity of each mixture was placed into a tared quartz container and sealed in-vacuo into a quartz tube. The tube was of sufficient length to permit isolation of the liberated iodine from the reactants. The boat end of the tube was heated to about 510°C and held for 1 hr; the other end of the tube was kept in liquid nitrogen to facilitate the condensation of the liberated iodine. After completion of the reaction, the tube end containing the iodine was sealed off from the rest of the system. This iodine ampoule was immersed in aqueous KI and broken. The iodine content of the resulting solution was determined by titration with standardized sodium thiosulfate solution.

Results and Discussion

The yield of liberated iodine was calculated as a percentage of the total iodine in the reaction mixture. A plot of this yield as a function of the V_2O_5/AgI mole ratio is shown in Fig. 1. This curve shows that most of the iodide is oxidized and liberated as free iodine when the mole ratio V_2O_5/AgI is four. At ratios less than four the liberation of I_2 is incomplete.

This would indicate that the following reaction occurs

$$AgI + 4V_2O_5 \xrightarrow{\Delta} \frac{1}{2} I_2 + \text{Residue}$$

An identification of the residue was attempted by conventional Debye-Scherrer x-ray analysis. However, no known compounds of silver and/or vanadium or their oxides could be identified.

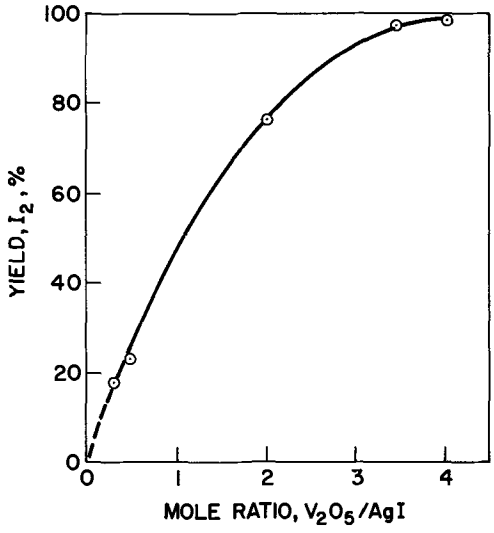

Fig. 1. Iodine yield as a function of V_2O_5/AgI mole ratio

In actual use a stock mixture of V_2O_5 and AgI is prepared and the required aliquot sealed into the vapor transport system. After liberation of the iodine the residue is isolated from the system by a second seal and removed by cutting. Assays of the reacted stock mixture showed that between 95 and 99% of the iodide is liberated as iodine; the major loss of iodine is attributed to some slight volatilization of AgI from the stock during reaction.

Acknowledgments

The author wishes to thank B. Gilbert for the iodine analyses and N. Stemple and J. Angilello for the x-ray analyses.

Manuscript received Feb. 17, 1967.

Any discussion of this paper will appear in a Discussion Section to be published in the December 1967 JOURNAL.

REFERENCE

1. H. Schaefer, "Chemical Transport Reactions," Academic Press, New York (1964).

Thermal Expansion Coefficients and Lattice Parameters between 10° and 65°C in the System GaP-GaAs

M. E. Straumanis and J.-P. Krumme

Graduate Center for Materials Research at the University of Missouri at Rolla, Missouri

and M. Rubenstein

Research Laboratories, Westinghouse Electric Corporation, Pittsburgh, Pennsylvania

The preparation of very homogeneous GaP-GaAs solid solutions was recently described and lattice parameter measurements were made (1). These solid solutions seemed to be very appropriate for the determination of their thermal expansion coefficients and the variation of the coefficient with composition of the solutions. Since the determination of the coefficients, especially within a small temperature range (between 10° and 65°C) requires a high precision in lattice constant determination (2), the measurements were repeated with an x-radiation that produced sharp interference lines at high Bragg angles.

Such an advantageous radiation was produced by a Cr target of the x-ray tube: Cr Kβ, having a wavelength of 2.08059 kX (converted into angstroms by multiplication with factor 1.00202) was used. Lattice constants were calculated from one single back reflection line 511β which appeared at Bragg angles from 83.6° to 75° depending on the GaAs content. Since this line was not very strong, (exact readings were difficult) (2, 3), more patterns were taken at each temperature. The Bragg angles were computed from the obtained asymmetric powder patterns (2-4), after measuring the positions of the lines on them with a comparator by a method described earlier in detail (5, 6). The patterns were made at certain constant temperatures (±0.1°C) in about 10° to 25° increments in a precision camera 64 mm in diameter (2, 4). The powder mounts had a thickness of 0.2 mm so that the absorption correction could be disregarded. The refraction correction was added to the final results (2, 7-9).

The linear thermal expansion coefficients α of the cubic substances were calculated from the a constants obtained at the mentioned temperatures using the relation

$$\alpha = \Delta a/a_{25}\Delta t \text{ in } °C^{-1} \qquad [1]$$

where Δa is the difference in a constants at a temperature difference Δt; a_{25} is the constant at 25°C. The expansivity αa_{25} was obtained from Eq. [1]

$$\alpha a_{25} = \Delta a/\Delta t \text{ in Å } °C^{-1} \qquad [2]$$

The samples were crushed to a fine powder, sieved through 400 mesh screen and, without annealing, were stuck to a Lindemann glass fiber, using vaseline as an adhesive. The fiber was fastened to the adjustable sample holder of the camera.

Figure 1 shows the expansivity of pure GaP. From the inclination of the straight line, using Eq. [1], the thermal expansion coefficient of GaAs was calculated to $\alpha = (4.70 \pm 0.01) \times 10^{-6}$ °C^{-1}. With this coefficient all the lattice constants measured at various temperatures of the sample were reduced to a constant at 25°C (see Table I). The value of the uncorrected constant is

Table I. Reduction of GaP lattice constants to 25°C. Final value of the constant at 25°C.

t	a_t	a_{25}
11.05	5.45043	5.45081
11.07	041	079
26.08	5.45085	082
25.95	081	079
33.25	5.45105	084
42.39	5.45117	073
42.98	118	072
51.49	5.45148	080
51.62	147	079
60.02	5.45167	078
60.07	165	076
	Average:	5.45078
	Refr. corr.:	0.00013
		a_{25} = 5.45091Å ± 0.00003*

* Standard deviation at 50% confidence limits $S_{50\%}$ (2).

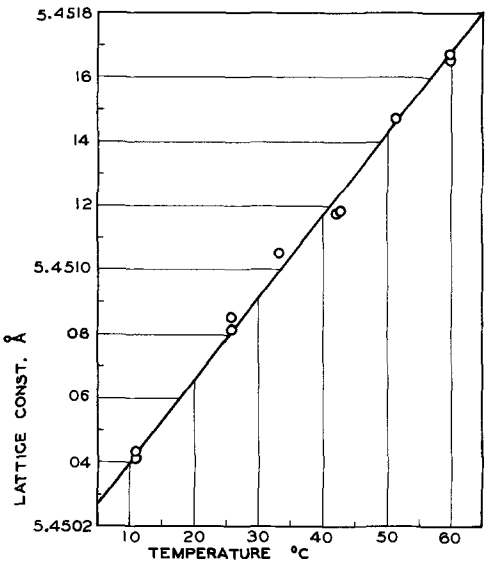

Fig. 1. Lattice parameter in Å of GaP vs. temperature. The standard deviation of ±0.00003Å is represented by the radius of the circles.

in excellent agreement with the previous determination of 5.4508Å (1). If it is desired to have the error (as given in the tables) with confidence limits of 95%, the error $S_{50\%}$ has to be multiplied by 3, or more correctly

$$S_{95\%} = 2.96\, S_{50\%} \qquad [3]$$

The lattice parameters of all other samples were measured in the same way and are listed together with the respective thermal expansion coefficients and refraction corrections added to the constants in Table II. The agreement with previous measurements (1) is good.

In order to see how the measured lattice parameters agree with the Vegard's rule, the constants are plotted against the composition in Fig. 2, which shows that the agreement is perfect within the limits of error. There might be a slight deviation close to the pure components, also observed in some other cases (11). The lattice parameters within the solid solutions a_{ss} in the range from about $x = 0.1$ to 0.9 mole fractions of As can be calculated from

$$a_{ss} = 5.4479 + 0.2023x \text{ Å} \qquad [4]$$

with an average precision of ±0.0004Å, while the outer, pure compounds, fit with a precision of only 0.003Å.

The obtained thermal expansion coefficients are plotted against the mole fraction of As in Fig. 3. There is a slight scatter and the true thermal expansion coefficients can be read from the solid curve of Fig. 3. Taking these coefficients and the constants from Fig. 2, the expansivity of the solid solutions of any composition can be calculated from Eq. [2]. The products obtained are all on a smooth curve similar to that of Fig. 3.

There is no relationship between the energy band gap of the solid solutions (1), and their thermal expansivity.

Table II. Lattice parameters (with the refraction correction added) and expansion coefficients of GaP-GaAs solid solutions.

Composition	+ Refr. corr., Å	a_{25}, Å	$\pm S_{50\%}$, Å	α, °C^{-1} × 10^6	No. of films
GaP	0.00013	5.4509$_1$	0.00003	4.70	11
$GaP_{0.8}As_{0.2}$	0.00015	5.4889$_0$	0.00030	4.92	4
$GaP_{0.6}As_{0.4}$	0.00016	5.5286$_8$	0.00008	4.70	16
$GaP_{0.5}As_{0.5}$	0.00017	5.5478$_3$	0.00010	4.97$_5$	23
$GaP_{0.4}As_{0.6}$	0.00018	5.5689$_4$	0.00010	5.24	8
$GaP_{0.2}As_{0.8}$	0.00019	5.6100$_6$	0.00018	5.35	16
GaAs (10)	0.00021	5.65321	0.00003	6.4	12

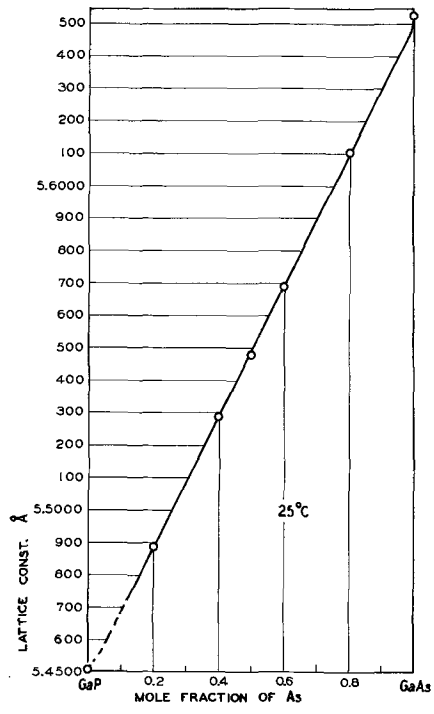

Fig. 2. Lattice constants in the system GaP-GaAs vs. composition. The radius of the circles covers even the largest standard deviation of ±0.0003Å (see Table II) completely.

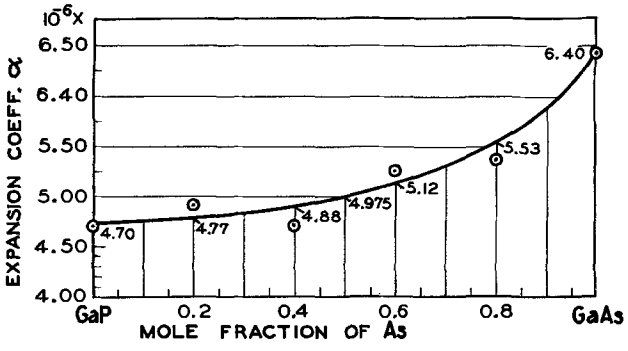

Fig. 3. Thermal expansion coefficients within the system GaP-GaAs

Acknowledgment

The present measurements were obtained as a side result of a project sponsored by the Office of Naval Research. This paper is Contribution No. 20 from the Graduate Center for Materials Research at UMR.

Manuscript received Feb. 10, 1967; revised manuscript received March 6, 1967.

Any discussion of this paper will appear in a Discussion Section to be published in the December 1967 JOURNAL.

REFERENCES

1. M. Rubenstein, *This Journal*, **112**, 426 (1965).
2. M. E. Straumanis in G. L. Clark's "Encyclopedia of X-rays and Gamma Rays," p. 700, Reinhold Publishing Corp., New York (1963).
3. K. E. Beu, *ibid.*, p. 709.
4. M. E. Straumanis, *J. Appl. Phys.*, **20**, 726 (1949).
5. H. P. Klug and L. E. Alexander, "X-ray Diffraction Procedures," p. 454, John Wiley & Sons, Inc., New York (1954).
6. L. V. Azaroff and M. J. Buerger, "The Powder Method," p. 25, 231, McGraw-Hill Publishing Co., New York (1958).
7. M. E. Straumanis, *Acta Cryst.*, **8**, 654 (1955).
8. M. E. Straumanis, *J. Appl. Phys.*, **30**, 1965 (1959).
9. M. E. Straumanis, *Acta Cryst.*, **13**, 818 (1960).
10. Taken with Crα_1 radiation ($K\alpha_1$ = 2.28503 kX x 1.00202) using the 422 line; see M. E. Straumanis and C. D. Kim, *Acta Cryst.*, **19**, 256 (1965).
11. M. E. Straumanis, L. C. Woodard, and K. S. Chopra, *Z. physik. Chem.*, **42**, 82 (1964).

Closed Tube Apparatus for the Deposition of Silicon Oxide

G. W. Heunisch

Electronic Components Laboratory, U. S. Army Electronic Command, Fort Monmouth, New Jersey

A simple, closed tube method for the deposition of thin, silicon oxide films is presented. The apparatus is primarily designed to deposit silicon oxide by thermal decomposition of tetraethoxysilane. Tetraethoxysilane has received special interest because of its high oxygen content, making possible clear, thick films (1-3) and the low temperature needed for decomposition (4). Carrier gases have been eliminated, bulky furnace apparatus has been reduced, and the unit is safe and inexpensive.

Uses of the method are restricted to those not involving highly accurate film thickness requirements. Film thickness control is within ±200Å.

Apparatus

A top view diagram of the closed tube apparatus is shown in Fig. 1. Pyrex brand glass is used throughout. The pedestal heater, Heater B, consists of a stainless steel core wrapped with nichrome heating wire and insulated from outside ambients. A 1/16 in. hole was drilled through the length of the steel core in order to apply a vacuum for mounting substrates when the heater is inverted. A platinum wire secures the substrate to the heater face when the vacuum is released. Heater A is an oil bath controlled to ±2°C.

To eliminate undesirable convection and "frosting" different heater positions were evaluated. The optimum angle was found when the pedestal heater face and substrate were vertical. This angle is critical for uniformity and is used in all subsequent experiments.

Discussion

The deposition rate of silicon oxide on silicon is linear with time. Figure 2 is a plot of film thickness *vs.* time. The pedestal heater is maintained at 400°C while the liquid tetraethoxysilane is held constant at 105°C. A temperature variation of 3°C exists across the pedestal heater. It should be noted that a pedestal temperature of 350°C results in a waxy film. The length of the tube is approximately 4 in. Longer tubes result in poor reproducibility and nonlinearity because of condensation and reaction within the tube.

At very long deposition times (>8 hr) a decrease in rate occurs, and decomposition at the liquid source becomes important. Increasing the pedestal heater temperature to 500°C does not increase the rate of decomposition appreciably as shown in Fig. 2.

Film thickness measurements are made by lapping a two degree angle across the substrate and oxide coating. The fringes produced by the application of monochromatic light are counted. The refractive index is estimated at 1.4. The low value of refractive index is chosen because of the fast solution rate of the deposited oxide in 4% buffered HF solution. At 25°C the solution rate of thermally grown oxide is 682Å/min while that of the deposited oxide is 1440 Å/min indicating a less dense film.

Films up to 20,000Å have been prepared and show no indication of cracking or other severe stress. Pinholes, however, have been found by high-temperature (1150°C) HCl vapor etch. These number 2 to 3 times those found in thermally grown oxides treated in the same manner.

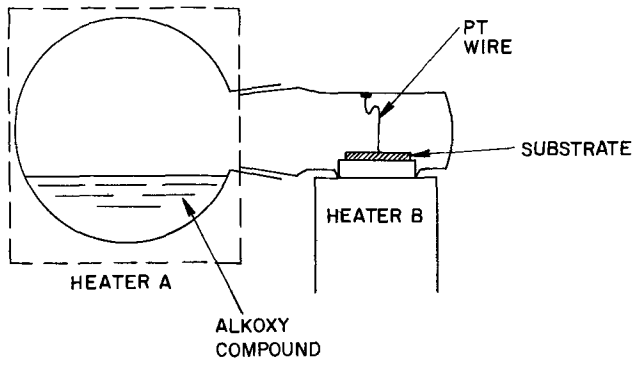

Fig. 1. Top view diagram of pedestal heated closed tube apparatus

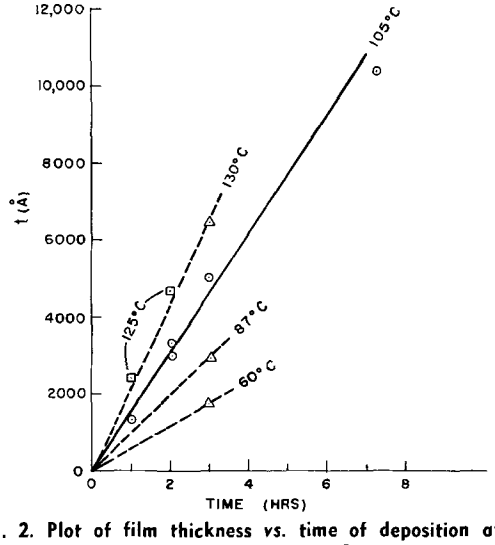

Fig. 2. Plot of film thickness *vs.* time of deposition at several liquid tetraethoxysilane temperatures: ○, △, pedestal heater 400°C; □, pedestal heater 500°C.

Manuscript received Dec. 30, 1966; revised manuscript received March 13, 1967.

Any discussion of this paper will appear in a Discussion Section to be published in the December 1967 JOURNAL.

REFERENCES

1. E. L. Jordan, *ibid.*, **108**, 478 (1961).
2. J. Klerer, *ibid.*, 1070.
3. J. E. Sandor, U. S. Pat. 3,158,505, Nov. 24, 1964.
4. Belgian Pat. 610, 246, May 14, 1962 or *C.A.*, P 8460a 1963.

Electrograph Method for Locating Pinholes in Thin Silicon Dioxide Films

J. P. McCloskey

Autonetics Division, North American Aviation, Inc., Anaheim, California

The electrochemical procedure (1) described in this paper enables simple nondestructive determinations of the precise location of pinholes or other oxide anomalies in thin dielectric material that has been superimposed on and is in contact with a conductive substrate base. The basic principles of the method were first disclosed in a presentation by Besser and Meinhard (2). The particular application presently described relates specifically to a technique used for locating oxide anomalies in thermally grown silicon dioxide passivation layers formed on both phosphorus and boron doped silicon wafers. A need exists in the industry for locating the surface defects at an early stage in production, since electrical failures subsequently occur when vacuum deposited interconnects placed over the holes are short circuited to the conductive substrate beneath. If the faulty areas could be located in the early processing stages, great cost savings and improved reliability would be realized.

An apparatus and technique for carrying out the electrograph method is given in detail in Scott (3). This apparatus could very well be used to advantage for the present application if a sensitive pressure gauge were included to permit accurate control of contact pressure and thereby prevent possible damage to the wafers. The objective of the method, as described in (3), is to obtain qualitative identification of surface components by anodic dissolution in order to chemically transfer small amounts of the surface elements to a suitable medium, usually paper. Distinctive color reactions then occur at specific areas reflecting the compositional differences in the surface. The present electrograph method, however, utilizes a different principle in that a colorless organic reagent, namely benzidine, is anodically oxidized to a colored product only at conductive sites, and does not form a colored compound with any reacting species dissolved from the surface. Since conductive sites represent areas of exposed substrate, the method is conveniently applied to the location of holes in passivation layers.

Experimental

Apparatus.—The apparatus used (see Fig. 1) consists of an electrochemical cell using an aqueous acidified solution of benzidine hydrochloride as an electrolyte. The cell is provided with a supporting stainless steel cathode, 1.5 in. in diameter by 1.5 in. high or slightly wider than the 1.25 in. silicon wafers electrographed,

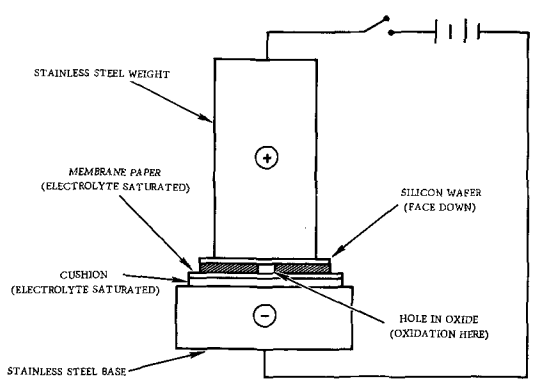

Fig. 1. Electrograph assembly diagram

and an anode of the same material, 1.0 in. in diameter by 6 in. in length, or slightly smaller in diameter than the wafers. As a support pad, a soft cloth such as felt, velvet, certain broadcloths and the like, proved satisfactory. Plain white "Millipore" membrane filter papers were used for recording the electrographs. The 47 mm diameter papers with a 0.45μ pore size furnished excellent results for the 1.25 in. silicon wafers.

Procedure.—Cover the top of the cathode base of the electrograph assembly with a soft cloth pad. Add the benzidine-hydrochloride electrolyte dropwise to the pad until it is completely saturated with the reagent. Immediately place a suitable size membrane filter paper saturated with the electrolyte on top of the pad. The membrane paper may be conveniently saturated by immersing it in a small petri dish containing the electrolyte. Add a few drops of electrolyte to the paper after placing it on the pad to ensure complete saturation. Immediately place the silicon wafer, oxide surface down, on top of the membrane paper. The oxide layer of the wafer should have previously been degassed by immersing, oxide surface up, in a petri dish containing sufficient electrolyte to cover the wafer, and evacuating for 5 min or longer under a vacuum of at least 20 mm of mercury. The evacuation step removes entrapped air from pinholes in the oxide and fills them with electrolyte. Place the anode rod on top of the conductive side of the wafer. Remove all excess electrolyte from around the anode base using an absorbent paper, such as a "Millipore" pad. If the excess electrolyte is not removed, it will tend to cause external short circuits around the wafer. Apply sufficient potential to produce a current of about 1 ma (usually about 5 to 10v) at the start, and maintain at this voltage for 5 to 10 min. Turn off the power supply, disassemble the apparatus, then remove the membrane paper for microscopic examination. Open areas in the oxide will be replicated on the paper with black markings or patterns corresponding exactly in size and shape to a mirror image of the conductive areas present in the wafer.

If repetitive electrographs are to be made of the same wafer, place the previously electrographed wafer in a large plastic beaker cover, preferably Teflon. Cover the wafer with a few ml of 6N HCl and allow 2 to 3 min for reaction. Rinse well with pure water to remove most of the benzidine hydrochloride. Repeat this operation once more. Cover the wafer with a few ml of 0.5% HF etchant and allow to react for exactly 1 min. This treatment removes about 25Å of silicon dioxide in this time period and should be sufficient to remove all of the oxide formed during the electrographing process. Rinse well with pure water to remove the etchant and reaction products. The wafer is now ready for producing another electrograph. If, however, the wafer is now to be returned to the production line, the final pure water rinse must be of 18 megohm or better quality.

Preparation of Reagents

Benzidine-hydrochloride electrolyte.—To a small beaker add 50 ml of pure water, 10 ml of concentrated hydrochloric acid, and 10g of ACS grade benzidine. Warm on a hot plate until completely dissolved. In another beaker prepare a 5% solution by adding 5g of

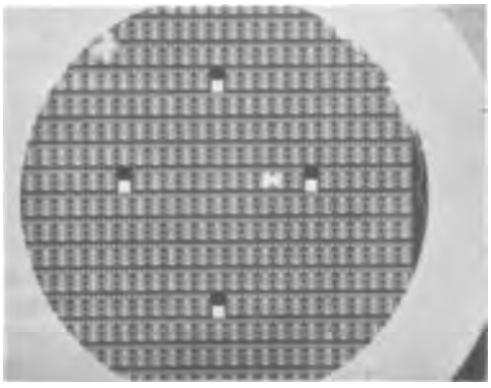

Fig. 2. Electrograph of silicon wafer containing etched microcircuitry patterns.

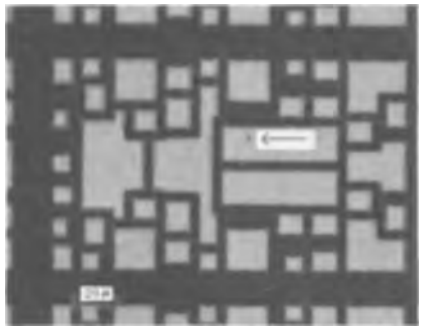

Fig. 3. One of individual integrated circuits of the electrograph of Fig. 2 showing pinhole location.

Fig. 4. Replica electron micrograph of oxide anomaly located by means of the electrograph method.

gelatin to 100 ml of boiling water. Boil for 3-5 min. Combine and mix the contents of the two beakers. Filter through a Whatman No. 40 filter paper into a one liter dark glass bottle. Dilute the filtrate to approximately one liter. Stopper bottle then invert to mix well. The reagent may be used for long periods of time if filtered each time before use.

Hydrofluoric acid etchant.—Prepare an approximately 0.5% hydrofluoric acid etchant solution by diluting 10 ml of 48% hydrofluoric acid to about one liter with pure water in a plastic bottle.

Discussion

Benzidine in acid solution can be oxidized electrochemically to a blue oxidation product (4), in accordance with the following chemical reaction

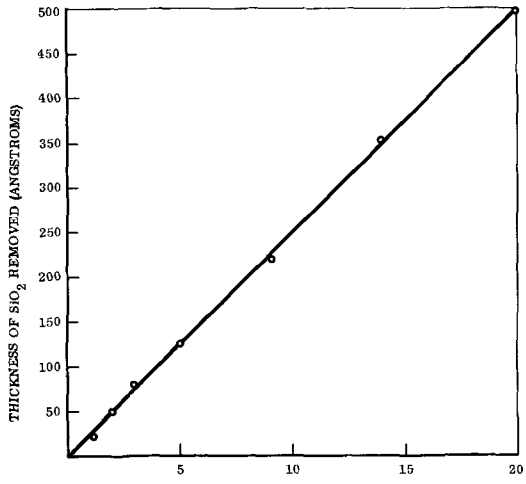

Fig. 5. Etching of silicon dioxide with 0.5% hydrofluoric acid

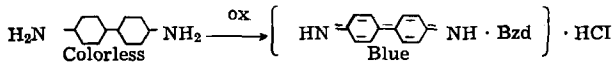

The above sensitive reaction is the basis of the electrochemical method described in this paper.

The simplified drawing of Fig. 1 illustrates the principle of the technique as applied to the determination of the location of conductive areas or holes through the silicon dioxide dielectric of silicon wafers. When a suitable anodic potential is applied to the silicon wafer, oxidation of the colorless benzidine occurs only at conducting areas such as at unwanted pinholes, etched microcircuitry and the like. The dark blue to black oxidation product formed at the conductive sites produces markings or patterns on the paper having the same size, shape, and location as a mirror image of the conductive areas of the wafer electrographed.

Figure 2 is a photograph of an electrograph prepared on a "Millipore" type membrane paper. The silicon wafer electrographed contained 280 complete integrated circuits etched into the silicon dioxide passivation layer. It will be noted that the uniformity of the pattern is broken in two areas, one to the right of center and the other in the upper left hand area. Successive electrographs duplicated the same incomplete pattern in the identical areas. The broken pattern areas represent faulty etching of the microcircuitry patterns in the oxide produced during processing of the wafer. A faulty circuitry pattern, pinhole or other oxide anomaly recorded on an electrographed membrane is not considered as such until it has been duplicated at least once.

Figure 3 is a photomicrograph (50X) of one of the individual integrated circuits selected from the electrograph shown in Fig. 2. The pinhole designated by an arrow illustrates the appearance of an oxide anomaly of this type when observed by microscopic examination of an electrograph.

Figure 4 is an electron micrograph replica of an oxide anomaly on an actual wafer magnified 5000 diameters. The anomaly on the wafer was located by means of the electrograph shown in Fig. 3.

During the course of the development of the electrolyte for the process, the benzidine was first dissolved in a slight excess of acetic acid. It was later discovered that when hydrochloric acid was substituted for the dissolution of the benzidine, a dark blue to black pattern was achieved instead of the light blue color resulting with the former acid. To further improve on the quality of the electrograph produced, a protective colloid such as gelatin was incorporated into the electrolyte to inhibit crystallization of the benzidine and thereby enhance the definition obtained.

Successive Electrographs

When a silicon wafer is electrographed, it is made the anode of an electrochemical cell and therefore some anodic oxidation of the exposed silicon occurs. If a second electrograph of the same wafer is attempted, no dark areas will form on the membrane paper since the formerly conductive sites are now covered with a thin oxide film. Chemical tests indicate that this developed oxide has an approximate thickness of about 25Å. In order that successive electrographs may be processed on the same wafer, a mild etchant was developed which would remove this ultra-thin oxide without serious attack of the main passivation layer. The etchant found suitable was an aqueous 0.5% hydrofluoric acid solution. Figure 5 shows the relationship between the thickness of silicon dioxide removed by the acid per unit contact time. It will be noted that the etching rate was linear in the time interval studied. The data for preparing the graph were obtained by treating a wafer having a silicon dioxide passivation layer of approximately 8500Å thickness, with sufficient etchant to just cover the oxide layer side for successive 1 min intervals. The amount of dissolved silicon in the etchant was then determined by a spectrophotometric chemical procedure developed for this purpose. The thickness of the oxide removed was then calculated from the micrograms of silicon dissolved in the etchant, the measured surface area in square centimeters and an assumed density of 2.15 for the silicon dioxide.

Summary

A simple nondestructive electrograph procedure has been developed for locating pinholes or other oxide anomalies in silicon dioxide passivation layers of silicon wafers. The method is most suitable for the determination of oxide anomalies in silicon wafers that contain etched patterns, such as for microcircuitry, which serve as reference guide lines in establishing the precise coordinates of the defects in the passivation layer. It is estimated that pinholes as small as 1000Å in diameter can be located by the method.

The electrograph procedure described should find applicability in the determination of surface defects in any thin dielectric material that is superimposed on and is in contact with a conductive substrate base. For example, it should be possible to determine surface defects in silicon nitride dielectric over silicon, germanium oxide over germanium, aluminum oxide over aluminum, and many others.

Acknowledgments

The author wishes to acknowledge the help derived from useful discussions with Drs. J. E. Meinhard and P. J. Besser, during development of the process. He also wishes to thank Dr. R. Nolder for the replica electron micrograph shown in Fig. 4. Also, Mr. J. Kersey is thanked for preparing the photomicrographs of the electrographed membrane papers.

Manuscript received Dec. 8, 1966; revised manuscript received Feb. 24, 1967.

Any discussion of this paper will appear in a Discussion Section to be published in the December 1967 JOURNAL.

REFERENCES

1. Autonetics patent file for J. P. McCloskey, Patent Pending.
2. P. J. Besser and J. E. Meinhard, Proceedings of the Symposium on *manufacturing in process control* and measuring techniques for semiconductors. Presentation entitled, "Investigation of Methods for the Detection of Structural Defects in Silicon Dioxide Layers," Phoenix, Arizona, March 9, 10, 11, 1966.
3. W. W. Scott, "Standard Methods of Chemical Analysis," F. J. Welcher, Editor, Vol. 3, Part A, p. 502, D. VanNostrand, New York (1966).
4. F. Feigl, "Spot Tests in Organic Analysis," p. 365, Elsevier Publishing Co., New York (1960).

DISCUSSION SECTION

This Discussion Section includes discussion of papers appearing in the *Journal of The Electrochemical Society*, Vol. 113, No. 2, 3, 6, 7, 9, 11, and 12 (February, March, June, July, September, November, and December 1966).

Electrical and Structural Properties of Langmuir Films

Robert M. Handy and Luciano C. Scala (pp. 109-116, Vol. 113, No. 2)

J. A. Spink[1]: The inability of the authors to transfer continuous Langmuir-Blodgett monolayers of calcium and barium stearates to gold surfaces raises some important issues regarding the use of the so-called noble metals as substrates for such films. Using ellipsometry to determine film thickness, other workers have also reported difficulties with the transfer of fatty acid and soap monolayers to gold surfaces. Mertens and Plumb[2] found irregularities in the transfer of 30 dynes/cm monolayers to gold films condensed on glass but not to copper and aluminum films. In a more detailed study, Hall[3] observed irregularities due to breakdown and folding of the monolayers at pressures around 40 dynes/cm and incomplete transfer only when the surface pressure was reduced to about 10 dynes/cm.

Already in his early studies in this field, Langmuir recognized the importance of the chemical nature of the solid substrate with regard to the ease with which fatty acid monolayers could be transferred and to the subsequent strength of attachment. In later work, however, Bikerman[4] emphasized the role played by the contact angle that the water made with the solid during the passage of the latter through the air-water interface and concluded: "it is clear that a monolayer on a water surface can only touch and attach itself to the solid surface if the direction of the movement of the slide and that of the water surface near the slide form an obtuse angle so that the monolayer on the water and the . . . metal can approach one another." Subsequent work, discussed below, indicates that both of these factors are important since the chemical nature and even the detailed atomic structure of the solid surface can influence the contact angle in question. Thus, the transfer ratios of unity obtained by Bikerman for chromium and brass surfaces can be explained in terms of the reactivity as well as the wettability of the solids. The concept that under a wide variety of conditions fatty acid and soap monolayers are transferred as a carpet to the solid (*i.e.*, the transfer ratio, ρ, is unity) was maintained for some time until Gaines[5] working with stearic acid, found that at low pressures ($\sim$10 dynes/cm)ρ (compared with an assumed $\rho = 1$ at 30 dynes/cm pressure) never reached unity even for reactive metals such as copper and aluminum. On the other hand, for films transferred at a pressure of 17.5 dynes/cm ρ was found to be unity for glass, mica, Pt, Cr, Cu, and Al.

A more detailed study[6] has shown that with stearic acid ρ depends on a number of factors and for very smooth silver does not reach unity even at a pressure of 30 dynes/cm. At this point it is necessary to make a distinction between solids for which $\rho = 1$ and solids for which subsequent attachment of the transferred monolayer is strong. For example, it has been shown[6] that $\rho = 1$ for mica, glass, and silica although the transferred films are relatively unstable and desorb readily. On the other hand, $\rho < 1$ for silver films condensed on mica, but the monolayer so transferred is more stable and desorbs less readily. This apparent contradiction would appear to arise from several factors. First, the wettability of certain solids during transfer seems to influence the drainage of the water film underneath the transferred monolayer in such a way that some of the molecules are returned to the Langmuir trough. This must occur at the air-water-solid line interface and has been discussed in some detail for smooth silver surfaces.[6] The wettability (or contact angle) can, of course, be influenced by the rate of withdrawal of the solid through the monolayer-covered water surface[4] so that for the silver surfaces mentioned above, ρ depends also on the rate of transfer. Second, the stability of the transferred monolayer must depend not only on the maintenance of the strong lateral Van der Waals interactions between the long hydrocarbon chains but also on the strength of the bonds formed between the polar head groups and the surface of the solid. The latter bonds will, in turn, depend on the outcome of the competition for the solid surface between the polar groups and the film of water transferred together with the monolayer.

Recent unpublished work by this author has shown that gold films ($\sim$1000Å thick) condensed on glass behave similarly to silver films in that $\rho = 0.85$ at 30 dynes/cm and only 0.65 at 10 dynes/cm. On the other hand, the transfer ratio for tin films condensed on glass was found to be equal to unity at both 30 and 10 dynes/cm, which is in agreement with the findings of Handy and Scala. This difference in behavior between metals such as silver and gold on the one hand, and copper, tin, and iron on the other[6] may be explained in terms of the chemical nature of the exposed surfaces. Thus, the principal difference must reside in the fact that, in contact with air, bulk oxide films are readily formed on the latter metals but not on the former. The relative weakness of dipole-metal image forces proposed by Fowkes[7] supports the recent experimental findings[8,9] that oxide-free metal surfaces are not wetted by water. This restricted wettability could then affect the efficiency (at least from the purely geometrical point of view advanced by Bikerman) with which monolayers can be transferred to solid surfaces of the noble metals.

In their discussion Handy and Scala draw no firm conclusions on the true nature of the discontinuities (voids) in their monolayers on gold, *i.e.*, they do not decide whether such discontinuities already exist in the monolayer at the time of transfer or whether they form after transfer because of the low stability of the monolayer on gold substrates.[10] Results obtained by the present author and discussed above suggest strongly that the films transferred to gold surfaces are less closely packed than they were on the water surface and are therefore initially incomplete.

From these considerations it remains to be said that results obtained in various physicochemical studies of Langmuir-Blodgett films transferred to solid surfaces must be treated with extreme caution. It is es-

[1] Commonwealth Scientific and Industrial Research Organization, Division of Tribophysics, University of Melbourne, Victoria, Australia.

[2] F. P. Mertens and R. C. Plumb, *J. Phys. Chem.*, **67**, 908 (1963).

[3] A. C. Hall, *J. Phys. Chem.*, **69**, 1654 (1965).

[4] J. J. Bikerman, *Proc. Roy. Soc.*, **170A**, 130 (1939).

[5] G. L. Gaines, Jr., *J. Colloid Sci.*, **15**, 321 (1960).

[6] J. A. Spink, *J. Colloid and Interface Sci.*, **23**, 9 (1967).

[7] F. M. Fowkes, *Ind. Eng. Chem.*, **56**, 40 (1964).

[8] M. L. White, *J. Phys. Chem.*, **68**, 3083 (1964).

[9] R. A. Erb, *J. Phys. Chem.*, **69**, 1306 (1965).

[10] R. W. Roberts and G. L. Gaines, Jr., Trans. 9th National Vacuum Symposium, p. 515, Los Angeles, Calif. (1962).

sential that such films are initially complete and continuous and remain stable under a variety of conditions. To see whether this has been accomplished we have employed techniques using radiolabelled molecules and electron microscopy. The latter technique is useful not only for checking the uniformity and stability of the deposited monolayers but also for revealing the atomic flatness of the metal surfaces.

R. M. Handy and L. C. Scala: The authors are in complete agreement with Dr. Spink's comments, which add to the understanding of the results presented in the paper, and wish to thank him for this contribution.

Red-Emitting Al_2O_3 Based Phosphors

V. D. Mochel (pp. 398-399, Vol. 113, No. 4)

Shannon Jones[11]: The two alumina phosphors, described as new by Mochel, appear to be rediscoveries of phosphors previously described in the literature.

The lithia-iron oxide-alumina phosphor was described by me in 1949.[12] Mochel's blue band in this phosphor is almost surely reflected radiation from the exciting source, and the color coordinates obtained by McAllister allow for no blue emission.

Mochel's calcium aluminate:Mn appears to be of the species described by Kröger in "Some Aspects of the Luminescence of Solids," p. 92 *et. seq.* Kröger studied the ratio $1CaO:6Al_2O_3$, which is within the range covered by Mochel. While Mochel used $MnCl_2$ and Kröger used $Mn(NO_3)_2$, this probably makes little difference after firing at 1450°C in air. The excitation and emission characteristics described by Mochel and Kröger are similar.

V. D. Mochel: I agree with Mr. Jones that the lithia-alumina-iron oxide phosphor I reported is undoubtedly the same as he described.[13] The major contribution of my paper to the description of this phosphor is that I was able to identify the crystalline phase giving rise to the luminescence as lithium zeta alumina ($Li_2O \cdot 5Al_2O_3$) with iron oxide as the activator. This was not done by Mr. Jones.

I am quite sure the blue band at 390 mμ is not due to reflected radiation from the exciting source as Mr. Jones asserts. As explained in my paper the emission spectra were obtained with the Aminco-Bowman Spectrophotofluorometer. With the source grating and the slit systems used, I don't see how a blue band peaking at 390 mμ could arise from the source which is set at 254 mμ. First-order scattering from the grating would center a peak at about 508 mμ, but this is not observed. In addition, blank samples of Al_2O_3 and other types of phosphors did not yield this band. It should be remembered that since there was no calibration between the two photomultiplier tubes used, the intensities of the blue band and the red band in Fig. 1 cannot be compared directly. The curves are normalized. Qualitatively, the blue band was much less intense than the red.

In regard to the calcium aluminate: Mn, Cl phosphors, I did observe luminescence in phosphors with the crystalline phase $CaO \cdot 6Al_2O_3$ as Kröger reported, but in the phosphors I described $CaO \cdot 2Al_2O_3$ was identified as the phase which exhibited the luminescence. I would not rule out the possibility of more than one phase contributing to the luminescence, however. I tried $Mn(NO_3)_2$ and MnO_2 as activators, but neither compound approached the enhancement of luminescence as produced by $MnCl_2$. Apparently the chlorine does make a difference, at least in the intensity of the emission.

[11] General Electric Co., Lamp Metal and Components Department, 1099 Ivanhoe Road, Cleveland, Ohio.

[12] Shannon Jones, *J. (and Trans.) Electrochem. Soc.*, 95, 295, (1949).

[13] Shannon Jones, *J. (and Trans.) Electrochem. Soc.*, 95, 295 (1949).

Equilibrium Pressures of Oxygen over Oxides of Lead at Various Temperatures

Earl M. Otto (pp. 525-527, Vol. 113, No. 6)

William B. White[14]: Dr. Otto, when searching for previous literature on the system lead-oxygen, apparently overlooked the recent (1964) paper by White and Roy[15] on the high oxygen pressure portion of the system. The oversight was unfortunate in that a comparison of the two sets of results provides some additional insight into the thermodynamics of the system and its phase diagram.

The two experimental techniques are quite different. Otto measured the oxygen pressure over a single phase lead oxide solid under steady-state conditions and obtained his univariant curves directly. White and Roy reacted quite small (50-100 mg) samples of oxide in equilibrium with an externally imposed high oxygen pressure in an open system then determined end product solid phase. Equilibrium univariant curves were obtained by interpolation between the data points which mapped out the bivariant fields.

A comparison of the two sets of data is shown in Fig. 1. Together these compile the most complete phase diagram of the Pb-O system yet presented. Since the vapor phase at these pressures and temperatures is essentially pure oxygen, Fig. 1 is a valid P-T projection for the Pb-O system. Not shown on the diagram are the melting relations, at which temperatures the PbO pressure becomes sufficiently high that oxygen isobars no longer coincide with the univariant curves and the polymorphic relations between the low and the high pressure form of PbO_2[16] which lie above 10,000 atmospheres.

White and Roy, unfortunately, presented their data as linear plots of pressure vs. temperature. The points on the log pressure-inverse temperature plot do not fit a straight line as well as they should. The two curves for the $2Pb_3O_4 \rightarrow 6PbO + O_2$ reaction agree fairly well and have nearly the same slope. The intermediate curve is most interesting. White and Roy could find no evidence for the lower $Pb_{12}O_{17}$ oxide although the x-ray data of Byström[17] and Anderson and Sterns[18] leave little doubt that it exists. Otto finds both phases at low pressures. Otto's $Pb_{12}O_{17} \rightarrow Pb_3O_4$ + oxygen curve agrees fairly well with the extrapolation of the high pressure curve but the low pressure $Pb_{12}O_{19} \rightarrow Pb_{12}O_{17}$ + oxygen curve lies at distinctly lower temperatures than the extrapolated curve. This situation can be resolved by assuming an invariant point of 416°C and 6 atmospheres as indicated in Fig. 1. The exact location of the invariant point is not well-defined but must lie somewhere in this region. A similar situation exists at high pressures where an invariant point at 600°C and 1156 atmospheres marks the lowest P and T at which Pb_2O_3 is a stable phase in the system. Greatest disagreement occurs in the curves describing the decomposition of PbO_2. Each set of data gives good straight lines but the lines have quite different slopes. The calculated heats of reaction are drastically different: 26.8 kcal/mole O_2 from high pressure curve compared with 66.4 kcal/mole O_2 from the low pressure curve. No attempt is made here to prove the correctness of one or the other of these curves. The temperatures are low, reaction kinetics sluggish, and some criticism could be made of either technique. It is necessary to point out, however, that thermodynamic calculations based on this reaction should be suspect.

[14] Materials Research Laboratory, Pennsylvania State University, University Park, Pennsylvania 16802.

[15] W. B. White and R. Roy, *J. Am. Ceram. Soc.*, 47, 242 (1964).

[16] W. B. White, F. Dachille, and R. Roy, *J. Am. Ceram. Soc.*, 44, 170 (1961).

[17] A. Byström, *Arkiv. Kemi, Mineral, Geol.*, A 20, No. 11 (1945).

[18] J. S. Anderson and M. Sterns, *J. Inorg. Nucl. Chem.*, 11, 272 (1959).

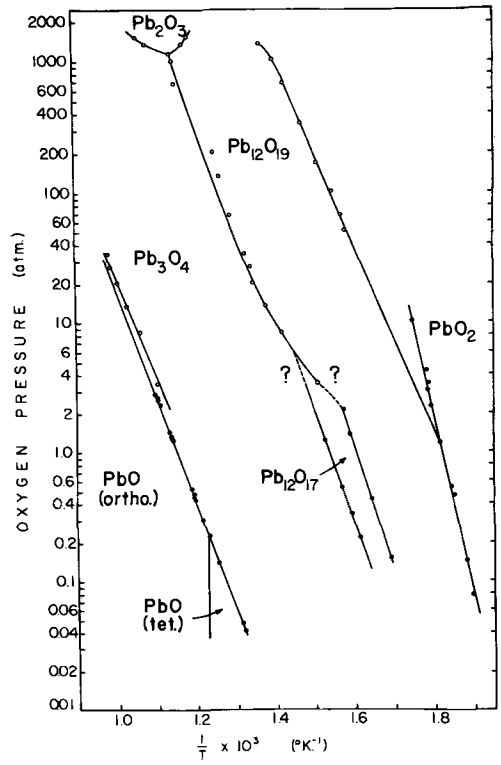

Fig. 1. Combined P-T phase diagram for the system Pb-O. Open circles are data of White and Roy[15]; solid circles are data of Otto.

E. M. Otto: My literature search was made in 1963, the experimental work was completed in the summer of 1964 and the manuscript was written shortly after I presented the paper at the October 1965 Meeting of the Society. Unfortunately, no follow-up literature search was made just before submitting the manuscript for publication.

In the second paragraph of Dr. White's comments it is stated that I measured the oxygen pressure over a single phase lead oxide solid. In dissociation experiments, I invariably produced at least part of the oxygen by partial decomposition of a lead oxide and was careful to satisfy myself that some of the oxide being dissociated remained even after equilibrium had been established; therefore, I always had a two component lead oxide system at equilibrium.

Some Aspects of the Mechanism of Hydrogen Evolution at a Mild Steel Electrode

J. S. Ll. Leach and S. R. J. Saunders (pp. 681-687, Vol. 113, No. 7)

T. C. Franklin[19]: In the article by Matsuda and Franklin[20] the data were treated from the viewpoint that absorption of electrolytically generated hydrogen by iron from sodium hydroxide solutions involved only one mechanism, the migration of adsorbed hydrogen atoms into the interior. This is in apparent contradiction to the conclusions reached in this article. It should, however, be pointed out that several experiments led us to the conclusion, in agreement with Leach and Saunders, that there are two mechanisms of absorption. The most obvious piece of data indicating this in our previous article[20] is shown in plots of rate of absorption *vs.* the amount of adsorbed hydrogen. If hydrogen is absorbed only by the migration of adsorbed hydrogen into the interior, the rate law should be

$$\text{Rate of Absorption} = k(\text{Adsorbed Hydrogen})$$

The experimentally observed rate law for any run was

$$\text{Rate of Absorption} = k(\text{Adsorbed Hydrogen}) + \text{constant}$$

This added constant shows that there is another method of producing absorbed hydrogen.

It was felt that the second mechanism involved the direct electrolytic generation, from water, of hydrogen into the skin of the metal to produce the so called "dermasorbed" hydrogen.[21] It is still felt that this mechanism would explain the data as well as the mechanism proposed by Leach and Saunders. At the time our work was done, it was not felt that enough data were available to reach any definite conclusion as to the process involved in this second mechanism and, since the intercept was relatively small, it was concluded that the primary mode of absorption was through adsorbed hydrogen.

The major point of contradiction between the two articles is our conclusion that the primary source of absorbed hydrogen is adsorbed hydrogen while this piece of work indicates that the primary source of hydrogen comes from a second mechanism. We have concluded that this contradiction arises because of the low current densities (0.83 ma/cm^2) used in our experiments compared with the current densities reported in this article. In recent work sponsored by the Welch Foundation, a study was made of the absorption of hydrogen by nickel in 2*N* sodium hydroxide solutions. These data can be interpreted also in terms of two mechanisms for producing absorbed hydrogen, one of which is potential dependent and one potential independent, in agreement with the present article. The potential independent term would correspond to the absorption of hydrogen from adsorbed hydrogen atoms while the potential dependent term could correspond to the mechanism proposed in this article or to the direct generation of hydrogen into the skin. Using this interpretation, it was determined that the relative contribution of the two mechanisms at the current densities studied was very sensitive to the current density.

Charge-Discharge Mechanisms in Electrolytic Capacitors

W. J. Bernard (pp. 749-751. Vol. 113, No. 7)

A. Dekker, M. G. J. Heijenbrok, and A. Middelhoek[22]: In his paper Bernard gives a new interpretation of the mechanism of oxide formation on the cathode of an electrolytic capacitor during its discharge.

However, it seems somewhat unlikely that prevention of oxidation of the cathode only takes place in a certain limited range of concentration of hydrogen adsorbed at the metal. We believe that the results of Bernard's experiments can be better explained in terms of anodization of the aluminum cathode by a charge larger than its product C_cV_c, where C_c is the cathode capacity and V_c the maximum voltage that can be built up across the natural oxide layer on the cathode just before forming starts. Moreover, Bernard's interpretation disagrees with our experimental results.

Three experimental arrangements are drawn schematically in Fig. 1. Figures 1a and 1b show the same circuits as given in Bernard's Fig. 1 and 2. In Fig. 1b oxidation of the cathode occurs, whereas in Fig. 1a it does not. When the capacitor in Fig. 1a is discharged, the cathode acquires part of the charge located on the anode and when the cathode capacity is large enough, the cathode potential reached is too low to change the cathode capacity by further anodization of the natural oxide layer. When the capacitor is charged again, all the positive charge on the cathode is transported to the anode by means of the battery emf, and the cathode is discharged completely at the same time. The electric

[19] Chemistry Department, Baylor University, Waco, Texas.

[20] F. Matsuda and T. C. Franklin, *This Journal*, 112, 767 (1965).

[21] T. B. Warner and S. Schuldiner, *This Journal*, 112, 853 (1965).

[22] N. V. Philips' Gloeilampenfabrieken Zwolle, The Netherlands.

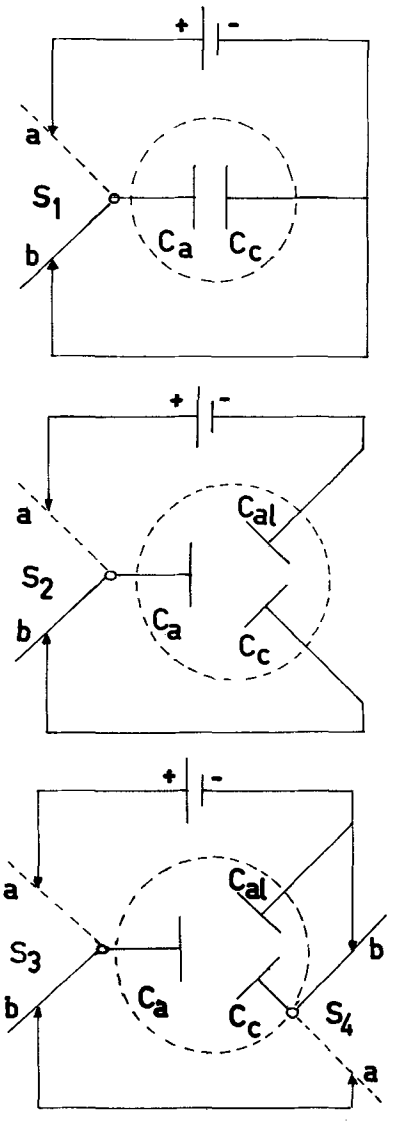

Fig. 1. Three experimental circuits for the charging and discharging of electrolytic capacitors: Fig. 1a top; 1b center; 1c bottom.

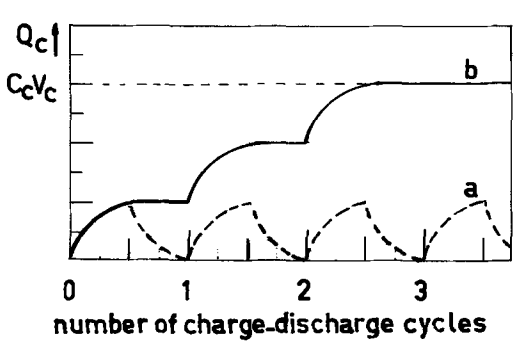

Fig. 2. Charge curve of the cathode C_c vs. number of capacitor discharges. — — — — Q_c from circuit Fig. 1a; ——— Q_c from circuit Fig. 1b.

charge on the cathode *vs.* the number of charge-discharge cycles is shown on Fig. 2, dotted line.

It can be seen from Fig. 2, that when the dimensions of the cathode in circuit in Fig. 1a are sufficiently large, *i.e.*,

$$C_c V_c \geqq \frac{C_a \cdot C_c}{C_a + C_c} \cdot V_{\text{battery}}$$

no oxidation takes place at all. In Fig. 1b however, the cathode capacity cannot discharge during the charging cycle of the anode (assuming that the leakage current is small). Subsequent discharges of the anode will increase the cathodic potential, and formation of Al_2O_3 occurs, until the battery voltage is reached. This formation starts when the cathode charge has attained the value C_cV_c (Fig. 2, curve b). In this case, a large aluminum cathode will anodize, whatever its dimensions are.

In order to discriminate between this interpretation and the hydrogen adsorption theory of Bernard, we performed a third experiment, the principle of which is given in Fig. 1c. This circuit is nearly the same as Fig. 1b, but it has the possibility of discharging the cathode before it is reconnected with the anode for recharging. For the same reason as in Fig. 1b there will be no hydrogen development or adsorption at the aluminum cathode. The counter electrode was not platinum in this case, but an etched Al-foil, having an effective surface area of about 1200 cm^2, in order to avoid the influence of the polarization capacity on the discharge of the cathode. The switching cycle is as follows: S_3 and S_4 go simultaneously to position a for 2 sec, so that the anode is charged *via* the counter electrode; then S_3 goes to position b (discharge of the anode *via* cathode), after 2 sec. S_4 goes to b (discharge of the cathode *via* the counter electrode) and 2 sec afterwards both S_3 and S_4 go to a, etc. The experiments were performed with smooth 99.99 w/o aluminum foil, cleaned by immersion in successively 2% NaOH solution (20°C-9 min), 48% H_2SO_4 (90°C-3 min), and in a mixture of 2.5% CrO_3 and 5% H_3PO_4 in water (85°C-2 min). Both the anode and the cathode surface areas were 40 cm^2. The battery emf was 10v. The anode was anodized to 15v.

The formation of oxide on the cathode was determined from the voltage achieved when the cathode is charged with a small constant current of 1.25 $\mu a/cm^2$; this "control voltage" is plotted *vs.* the number of charge-discharge cycles in Fig. 3. From Fig. 3 one may conclude that the increase of the control voltage with the number of cycles, due to oxide formation on the cathode, occurs only when the charge brought on the cathode is not allowed to leak away.

In our case, where anode and cathode have exactly the same dimensions, there is little difference in cathodic behavior between circuit of Fig. 1a and 1c, whereas adsorption of evolved hydrogen occurs only in 1a. No evidence has been shown that hydrogen evolution has any influence on the oxide formation on the cathode during discharge of the electrolytic capacitor. In fact, in both 1a and 1c the control voltage of the cathode is not zero, but about 2v, independent of

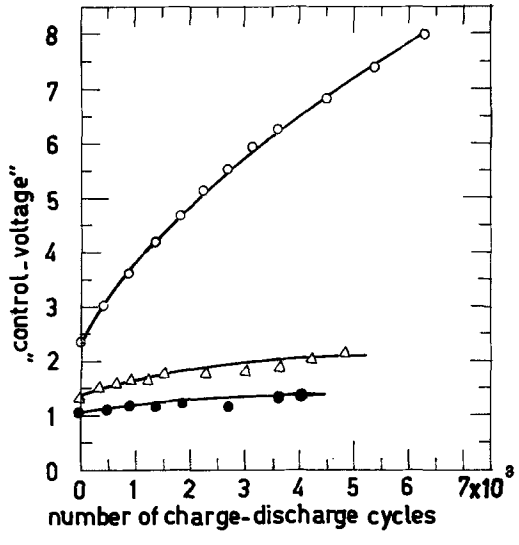

Fig. 3. Cathodic control-voltage *vs.* number of charge-discharge cycles. • result from circuit 1a; ○ result from circuit 1b; △ result from circuit 1c.

the battery emf. This effect can be accounted for quantitatively by the polarization capacity, which reduces the cathode capacity much more than the anode capacity, so that C_aV_a is not equal to C_cV_c.

The Performance of Flooded Porous Fuel Cell Electrodes

R. Brown and J. A. Rockett (pp. 865-870, Vol. 113, No. 9)

H. H. Horowitz[23]: Brown and Rockett have mathematically analyzed flooded porous fuel cell electrodes assuming model cylindrical pores and including activation, ohmic, fuel concentration, and electrolyte concentration polarization. Their calculations fit data obtained on sintered biporous nickel electrodes very well with one exception: the diffusion constants required "were 10^4-10^5 greater than the measured values indicating that a means of diffusive transport other than diffusion through the liquid is a necessary assumption." In connection with the latter point, we wish to offer our experience with another type of porous fuel cell electrode system. We were forced to conclude that the cylindrical pore model needs to be modified somewhat and that the "other means of diffusive transport" was simply gas phase diffusion.

The porous electrodes we were using consisted of platinum black or carbon impregnated with platinum, which was mixed with 15 w/o Teflon in the form of an emulsion and compressed in a 50 mesh screen of platinum or tantalum. Butane was the fuel and 3.7M sulfuric acid was the electrolyte at 95°C. The degree of flooding of the electrodes was controlled, not by the differential pressure, but by the quantity of Teflon used and by the compression step. Under the conditions used, it was found by weighing the electrodes before and after they had been contacted with electrolyte that their pores were over 80% flooded. Decreasing the degree of flooding decreased the electrode activity roughly proportionately. There was little doubt that a high degree of flooding was necessary for activity and that most of the electrode surface was under liquid.

Nevertheless, experimental evidence indicated that most of the surface area was available for reaction and that a solubility-diffusion mode of fuel transport obtained: It was possible to reach the same limiting current per milligram of platinum used by saturating the electrolyte with butane and passing it through a layer of platinum black mounted on a porous tantalum frit. These data have been published.[24]

Using reasonable estimates of the solubility and diffusion constant of butane and the ideal current densities taken from the above experiment, in an equation similar to the present authors' Eq [17] it was calculated that the active area extended only 5×10^{-4} cm from the gas liquid surface. Since the electrodes used were 0.2 mm thick, an apparent enigma arose similar to that presented in the present paper.

This enigma could be resolved by including lateral pores in the model, perpendicular to the "main" pores, and by assuming fingers of gas extending into the depths of the electrode perpendicular to its surface. If these gas filled fingers are small enough and numerous enough they can feed the entire electrode with fuel while occupying less than 20% of its volume. For example, cylindrical holes 2μ in radius in a square array spaced at 8μ on centers, occupy 20% of the total volume. Yet the entire volume of liquid within the remaining pores is within 5μ of one or more gas filled pockets. Thus, the surfaces of granules not directly exposed to gas receive fuel by diffusion through liquid filled pores more or less parallel to the electrode surface, whereas the current lines continue to flow more or less perpendicular to the surface.

We believe the new model offers a greater degree of sophistication than a simple parallel cylindrical pore model, because it makes use of the lateral pores known to be present in the sinter and permits the use of conventional diffusion constants and gas solubilities. A question remains as to the source of the gas filled pores. In Teflon bonded structures it is easy to rationalize pores in the statistical distribution, whose surfaces are so hydrophobic and whose radii are so small that they would not fill with liquid even under a partial vacuum equal to the electrolyte vapor pressure.[25] As to the source of gas filled pores in sintered nickel electrodes, perhaps the authors of the present paper could also rationalize their existence on the basis of inequalities of pore radii in manufacture and inequalities in surface wetting properties due to hydride or other film formation.

The Permeation of Electrolytic Hydrogen through Platinum

E. Gileadi, M. A. Fullenwider, and J. O'M. Bockris (pp. 926-930, Vol. 113, No. 9)

G. Dubpernell[26]: Previous criticisms of the method seem to be largely ignored. The title seems incomplete and not properly indicative, and could include a phrase such as ". . . in Sulfuric Acid Solution Poisoned With Arsenic Additions." Apparently no permeation was observed in pure $0.1N$ H_2SO_4 with platinum membranes as thin as 2×10^{-3} cm (0.0008 in.) unless As_2O_3 was added to the solution. Some explanation should be given for the impermeability, and it would be better to call the effect of arsenic additions an "activation" rather than a poisoning. In previous work membranes which refused to diffuse any hydrogen have generally been called poisoned or passive, and have been discarded rather than accepting them as the norm.

It is good to note that cracks in membranes were easily detected by the immediate effect on the anodic side as soon as the cathodic current was turned on. However, it is not clear that all such membranes were rejected. In Fig. 1, does not the vertical increase in the permeation rate when the current density is increased, indicate such a cracked membrane, and should not this membrane have been rejected instead of using the first transient as acceptable to calculate a diffusion coefficient? Is not this the same membrane with which hydrogen charging is said on page 927 to have caused further cracking?

While the writer believes that all diffusion observed is due to mechanical defects in the metal or pores of one kind or another, the assumption of hydrogen embrittlement in platinum at temperatures of 50°-80°C based on Richardson's observations in the gas phase at 700°-1000°C, does not seem proper. The assumption of a critical low current density between 70° and 80°C on page 928 seems even less in order. It does not seem logical to assume that the permeation process is diffusion controlled at extremely low current densities, and then at a critical current density that ". . . a critical change in the internal structure of the metal takes place."

Aside from taking only first transients at extremely low current densities for the calculations, apparently irregardless of whether or not the membrane was cracked, the authors state that "only transients which have the theoretically expected shape were accepted for the calculation of D." How many transients were rejected for each one accepted?

It would seem that the diffusion of electrolytic hydrogen through carefully handled thin platinum membranes has not been demonstrated, and that the as-

[23] Esso Research and Engineering Co., Central Basic Research Laboratory, P.O. Box 45, Linden, New Jersey 07036.

[24] J. A. Shropshire and H. H. Horowitz, *This Journal*, 113, 490 (1966).

[25] J. A. Shropshire, E. H. Okrent, and H. H. Horowitz, "Hydrocarbon Fuel Cell Technology," p. 539, B. S. Baker, Editor, Academic Press, New York (1965).

[26] M&T Chemicals, Inc., Ferndale, Michigan 48220.

sumption that such a diffusion can occur should be subjected to further scrutiny.

E. Gileadi, M. Fullenwider, and J. O'M. Bockris: Dr. Dubpernell has consistently opposed the notion of hydrogen diffusion through some metals (Fe, Pd, Pt) at or near room temperature, despite clear and unambiguous evidence accumulated at the Electrochemistry Laboratory of the University of Pennsylvania and several other places.

The major point is that the permeation rate J_t is found to follow the equation

$$J_t/J_\infty = \left(\frac{2}{\pi^{1/2}}\right)\left(\frac{1}{\tau^{1/2}}\right) \exp(-1/4\tau) \qquad [1]$$

where

$$\tau = Dt/L^2$$

derived for a diffusion-controlled process with the specified boundary conditions. More conveniently, this gives rise to a half rise time $t_{1/2}$ which is proportional to L^2 (L is the membrane thickness) and a steady state permeation rate J_∞ proportional to $1/L$; both of which have been verified experimentally.

One has yet to devise a pore and crack model that would fortuitously give rise to the same type of transient; give reproducible results for many membranes of the same metal, but widely different diffusion coefficients for membranes of different metals; and, in the case of Pt, yield an apparent energy of activation for diffusion of 9.6 kcal/mole.

One of the advantages of the present method of measurement of hydrogen diffusion is that any pinhole or crack in the metallic membrane is easily detected by an immediate change of current on the anodic side following any change of polarization on the cathodic side. All membranes showing such behavior were discarded. Figure 1 in our paper shows clearly that there was no crack or pinhole in the membrane originally and the diffusion coefficient was accordingly determined from the first transients. A close look will show that subsequent transients in this figure do not rise vertically.

Hydrogen embrittlement of Pt was suggested tentatively and by no means considered proven. The basis for this suggestion is the similarity of permeation transients at high current density to those observed for iron under conditions where embrittlement was shown to occur, combined with the evidence from high temperature work, that hydrogen embrittlement of Pt can indeed occur under certain conditions.

The cathodic current density determines the concentration of adsorbed hydrogen on the surface and hence the concentration c_0 of absorbed hydrogen just under the surface, in equilibrium with it. It was pointed out in the paper that when i increases beyond a particular value, c_0 exceeds the solubility of hydrogen in the metal. Molecular hydrogen can then be formed in crevices or voids inside the metal and the diffusion of atomic hydrogen through the membrane is disturbed. That the critical value of i depends on temperature is hardly surprising. In the case of Pt, it decreases with increasing temperature, indicating that the solubility of hydrogen in Pt decreases with increasing temperature.

Optical Studies of Electrolyte Films on Gas Electrodes

Rolf H. Muller (pp. 943-947, Vol. 113, No. 9)

J. J. Bikerman[27]: The optical measurements of the thickness d of liquid films draining down a vertical electrode, as described in the paper, are in a reasonable agreement with the earlier results[28,29] obtained by weighing the film and with the author's Eq. [5] which is of an older vintage[28] than believed by the author.

The main difference between the older and the new treatment is that the author pays no attention to surface roughness. The thickness d as a function of $\sqrt{t}$, t being the duration of drainage, deviated from the straight line relation (Fig. 5 of the original) when the apparent d was 0.31μ or less presumably because the hills on the electrode surface were approximately 0.31μ tall. It is shown in the earlier papers that a stagnant liquid layer exists next to the solid-liquid interface and that its thickness is nearly equal to the average height of surface hills, as measured by an independent method.

R. H. Muller: I wish to thank Dr. Bikerman for drawing my attention to his interesting work on the effect of surface roughness on gravitational drainage of oil films.

Although it is realized that the quantitative characterization of the smoothness of optically polished surfaces is difficult, indications are that the rugosity of the surfaces employed was considerably lower than the thickness (0.3-0.6μ) of the electrolyte films observed. Examination of the electrode surfaces by double beam and multiple beam interference microscopy showed the largest polishing marks present to be 0.05μ dep and about 0.02μ wide. They were oriented at random and spaced at a mean distance of 20μ with the intervening area filled with progressively finer and more closely spaced grooves. Measurements with a stylus surface tester were found to be below the resolution limit of the instrument of 0.05μ rms.

The regression analysis conducted by Bornong[30] for the dependence of the stagnant oil layer thickness on surface roughness extrapolates to 0.78μ and 0.28μ for zero roughness and, respectively, silver-copper and stainless steel alloys. These figures are surprisingly close to those given in the present work for KOH solution on silver and nickel.

It is felt, therefore, that in the experiments reported, the electrode surface roughness has not been the controlling factor for the formation of stable electrolyte films, although this parameter may be important in an analysis of technical gas electrodes.

The Pressure Coefficients of the Hydrogen Electrode Reaction

G. J. Hills and D. R. Kinnibrugh (pp. 1111-1120, Vol. 113, No. 11)

T. Pyle and C. Roberts[31]: Recent measurements of the pressure coefficient for hydrogen evolution at a mercury surface by Hills and Kinnibrugh have shown that the process has a negative volume of activation. This evidence led them to suggest that the rate-determining step in the reaction is the formation of solvated electrons in the solution adjacent to the metal surface. This proposal has been criticized by Matthews[32] on the grounds that it would lead to negligible rates of hydrogen evolution because of the high heat of activation, ΔH, for the formation of the hydrated electron. Matthews suggested that ΔH would be given by the difference between the work function of the metal ϕ, and the solvation energy of the electron, W_e; for mercury $\phi \sim 4.5$ ev and in aqueous solutions $W_e \sim 1.7$ ev this gives an apparent activation energy >60 kcal/mole which is much greater than that found experimentally, reported values range from 9 to 24 kcal/mole. If ΔH were given by $\phi - W_e$, this would present a powerful argument against the proposed mechanism. However ϕ is the energy required to remove an electron from the metal to infinity; consequently if

[27] Horizons, Inc., Cleveland, Ohio 44104.

[28] J. J. Bikerman, *J. Colloid Sci.*, 11, 299 (1956).

[29] B. J. Bornong, *Trans. Am. Soc. Lubricat. Engs.*, 7, 383 (1964).

[30] B. J. Bornong, *Trans. Am. Soc. Lubricat. Engs.*, 7, 383 (1964).

[31] Department of Chemistry and Metallurgy, Lanchester College of Technology, Priory St., Coventry, England.

[32] D. B. Matthews, Discussion of paper by Hill and Kinnibrugh, *This Journal*, 113, 1111 (1966).

Table I. Heats of activation (kcal/mole)

Metal	Cu	Hg	Ni	Pt	Co
Hydrogen evolution	10	9-24	5-16	5	3-5
Solvated electron	7.2	8.3	8.5	27	2.5

$\phi - W_e$ has any meaning at all, it is the activation energy to form solvated electrons at an infinite distance from the metal. Electrons can be solvated rather closer to the metal than this; the activation energy can be expected, therefore, to be rather smaller than that suggested by Matthews.

We believe that the closest point to the metal at which an electron may be considered to be solvated lies in the plane through the center of the first layer of water molecules which are in contact with the metal surface. In this position the electron will lie approximately in the inner Helmholtz plane and the work required to separate an electron from a metal by a distance a, the radius of a water molecule, may be estimated on the basis of a model for the work function of a metal discussed by Loeb.[33] The work required to remove an electron is considered in two parts. (a) at points closer to the metal than a critical distance x_0 the electron moves in a constant field $e/4x_0^2$. The work done in taking an electron from the metal to x_0 is $e^2/4x_0$; (b) at distances larger than x_0 the electron moves against a mirror image force. The work required to take an electron from x_0 to ∞ is $e^2/4x_0$. The work function is the sum of these two parts and equals $e^2/2x_0$. For metals, with $\phi < 5$ ev, $x_0 > a$ and the work required to separate the electron from the metal by a distance a becomes $ae^2/4x_0^2$. The activation energy for the solvation of an electron in this position becomes $ae^2/4x_0^2 - W_e$. Metals with $\phi > 5$ ev have $x_0 < a$ and the activation energy is given by $\phi - e^2/4a - W_e$.

Experimental values of the heats of activation for the deposition of hydrogen at copper,[34] mercury,[34] nickel,[34] platinum,[34] and cobalt[35] surfaces in aqueous electrolytes are compared, in Table I, with values of ΔH calculated on the basis of the model we suggest above.

The agreement between the experimental heats of activation for hydrogen evolution and the calculated heats for the formation of solvated electrons is encouraging. Experimental verification of the role played by the solvated electron in the evolution of hydrogen is only available for mercury, however the calculated values of ΔH do suggest that it may also play a dominant role in the evolution of hydrogen at copper, nickel, and cobalt surfaces. Platinum has a large work function and the activation energy for the formation of solvated electrons at the platinum-electrolyte interface is therefore large. Consequently it appears improbable that hydrogen evolution *via* the formation of solvated electrons will be significant at a platinum surface. However, in general ΔH for the formation of a solvated electron at the inner Helmholtz plane is not large and the formation of a solvated electron as a step in the evolution of hydrogen should not be discounted on the grounds that it will lead to negligible rates of hydrogen evolution.

The Cathodoluminescence of Terbium-Activated Indium Orthoborate

F. J. Avella (pp. 1225-1226, Vol. 113, No. 11)

W. L. Wanmaker and A. Bril[36]: In the paper under discussion it was stated that in one of our papers we described the photoluminescence of Tb^{3+} in alkaline earth borates[37] but did not report on the cathodoluminescence. We should like to point out that in section 5 of the paper cited by the authors we did in fact give cathode-ray efficiencies (p. 491), namely a radiant efficiency (energy conversion efficiency) of about 2%. Moreover in another paper[38] we gave a radiant efficiency of 2.2% for $2CaO \cdot Na_2O \cdot B_2O_3$-0.15 Tb. This means that these phosphors have an efficiency of about 25-30% of that of willemite (Zn_2SiO_4-Mn).[39] They are, therefore, comparable with those described in the paper under consideration.

In a third paper[40] we have given data on more efficient Tb-activated phosphors under cathode-ray excitation, namely on $LnPO_4$-Tb (where Ln = Y, La, Gd). For $GdPO_4$-Tb we found an efficiency of 5%, *i.e.*, about 65% of that of willemite.

F. J. Avella: The author is grateful to Dr. Wanmaker and Dr. Bril for supplying the information on the cathodoluminescence efficiency of their borate as well as their phosphate phosphors. References to the former[37,38] were inadvertently omitted, while the latter reference[40] was not available during preparation of the paper under discussion.

It should be noted, however, that their statement of comparable performance applies only to the Tb-activated borates containing the alkaline earths. The data given in Table I of the paper under discussion show that $InBO_3$:Tb is nearly equal to willemite in cathodoluminescence conversion efficiency and is, therefore, significantly more efficient than the alkaline earth borates as well as $GdPO_4$:Tb.

The Repeatability of the Anode Effect in Cryolite-Alumina Melts

B. J. Welch and R. J. Snow (pp. 1338-1340, Vol. 113, No. 12)

R. Piontelli, B. Mazza, and P. Pedeferri[41]: The recent systematic research work carried out in this Laboratory[42] has thrown much more light on both the overvoltage phenomena and the anode effect conditions at the cryolite-alumina melts.

The influence of the shape, orientation, and size of the anodes has been confirmed for both by investigating the behavior of the anodes represented in Fig. 1.

The apparent overvoltage on these, also before the intervention of the anode effect, includes a large ohmic contribution due to the presence of the gaseous phase in the anodic layer and on the anode surface. This contribution depends (besides on the alumina content of the baths) on the circumstances controlling the gas evacuation and thus on the shape of the anodes (being obviously greater on the anodes of the types: B, C, F, on which the permanence of the gases is favored). This statement is confirmed by the influence of mechanical vibrations impressed on the anode assembly which, by enhancing the gas evolution, reduces the ohmic contribution to the apparent overvoltage. The ohmic character of this contribution is also confirmed by the oscillographic recordings of the electrode voltage at the current inlet and outlet. Thus the amount and configuration of the gaseous phase in the anodic

[33] L. B. Loeb, "Static Electrification," Springer Verlag, Berlin (1958).

[34] R. Parsons, "Handbook of Electrochemical Constants," Butterworths, London (1959).

[35] R. Piontelli, L. P. Bicelli, M. Graziano, and A. L. Vecchia, *Atti. Accad. Nazl Lincei. Rend. Classe, Sci. Fis. Mat. Nat.*, 32, 445 (1962); *Chem. Abstract*, 58, No. 5263fg (1963).

[36] N. V. Philips' Gloeilampenfabrieken, Eindhoven, The Netherlands.

[37] W. L. Wanmaker and A. Bril, *Philips Res. Repts.*, 19, 479 (1964).

[38] W. L. Wanmaker, A. Bril, and J. W. ter Vrugt, *This Journal*, 112, 1149 (1965).

[39] A. Bril and H. A. Klasens, *Philips Res. Repts.*, 7, 401 (1952); A. Bril, in Kallmann-Spruch, "Luminescence of Organic and Inorganic Materials," p. 479, John Wiley & Sons, Inc., New York (1962).

[40] A. Bril, W. L. Wanmaker, and R. E. Schuil, in "Riehl-Kallmann-Vogel," International Symposium on Luminescence, Verlag Karl Thiemig, K. G., Munich, Germany, p. 314 (1965).

[41] Institute of Electrochemistry, Physical Chemistry and Metallurgy, Milan Polytechnic, Milan, Italy.

[42] R. Piontelli, B. Mazza, and P. Pedeferri, *R. C. Accad. Lincei.*, 36, 759 (1964); *ibid.*, 37, 3 (1964); *Metallurgia Ital.*, 57, 51 (1965); *Electrochimica Acta*, 10, 1117 (1965); *Alluminio*, 34, 623 (1965); R. Piontelli, *Electrochimica Metallorum*, 1, 191 (1966).

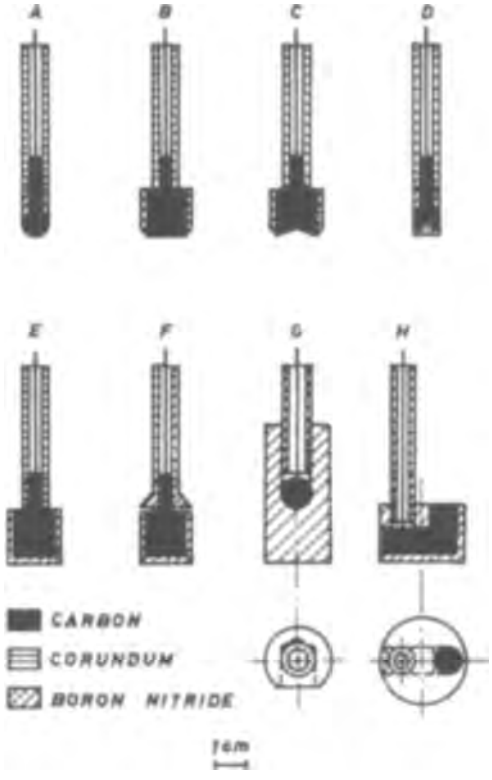

Fig. 1. Types of anodes investigated (sectional views)

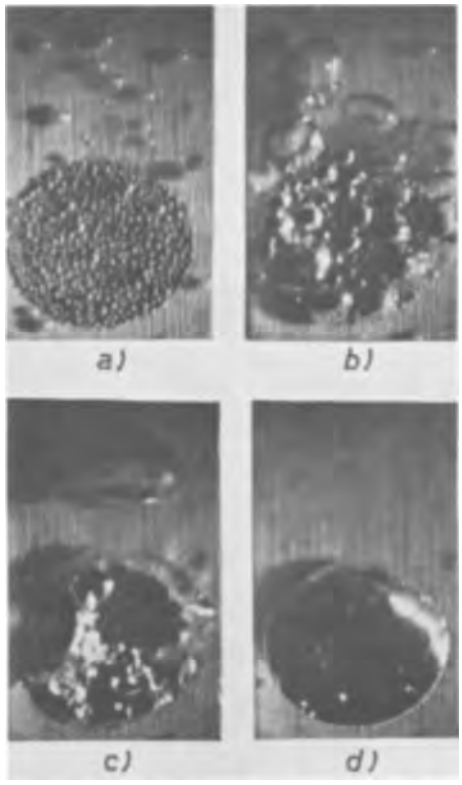

Fig. 2. Chlorine development on carbon anodes from chloride melts. Type G anode, A = 0.5 cm². Bath composition: NaCl + KCl (50 w/o). T = 850°C. G_c = 4.5 amps. (a) nucleate bubbles (G = 0.6 amps); (b) coalescence of bubbles (G = 1.85 amps); (c) transition period; (d) anode effect. Maximum framing rate: 4800 frames/sec.

region appear to be decisive also for the appearance of the anode effect occurring when the gaseous phase prevents any efficient wetting of the electrode surface.

Since this condition is obtained by the coalescence of the bubbles evolved at the electrode surface, a close analogy subsists with the phenomena encountered in the boiling of liquids in contact with a heated solid surface.

Films (up to 5000 frames/sec) on the anode effect phenomena, on carbon anodes in chloride melts, give direct evidence of this point.[43] By increasing the current density one can distinguish three typical regimes in the gas development. In the lowest current density range the gas development takes place in a nucleate form (Fig. 2a). Then coalescence of bubbles occurs (Fig. 2b) and after a transition period, in which the anode surface is covered by irregular gas blankets in violent motion (Fig. 2c), a condition is reached in which the anode is practically insulated from the bath by a permanent continuous gaseous film (Fig. 2d).

As far as the carbon-cryolite alumina melts are concerned, the quoted experiments (see footnote 42) prove that it is more appropriate to define a critical current intensity of appearance of the anode effect (G_c) rather than a critical current density, in so far as the size factor influence does not follow any simple proportionality law. The relationships established (in the laboratory experiments) may be summarized by the formula

$$G_c \simeq \psi \cdot (a + bT) \cdot A^n \cdot \{c + [Al_2O_3]^m\} \qquad [1]$$

where T is the bath temperature, A the apparent anode area, $[Al_2O_3]$ the alumina content of the bath, ψ a factor which depends only on the shape of the anode, and a, b, c, n, m are constants ($n < 1$; $m \simeq 0.5$).

For T in °C, A in cm², $[Al_2O_3]$ in w/o (referred to cryolite), and G_c in amperes, the following expression is obtained in the $[Al_2O_3]$ range 1-10 w/o and in the temperature range 1000°-1150°C

$$G_c = \psi x\{5.5 + 1.8 \cdot 10^{-2} (T - 1050)\} \; x A^{0.9} x\{-0.4 + [Al_2O_3]^{0.5}\} \qquad [2]$$

[43] R. Piontelli, A. Berbenni, B. Mazza, and P. Pedeferri, *Electrochimica Metallorum*, 1, 279 (1966).

ψ being equal to: 1 for type B, 1.4 for type A, about 1.3 for type D, G, E, H, and about 0.5 for type C anodes.

Mechanical vibrations impressed on the anode assembly increase the critical current intensity to a greater extent for type B and C anodes.

Always with reference to the cryolite-alumina melts, the importance in view of the appearance of the anode effect of the change in chemical configuration of the bath in the anodic region, due to current circulation, must be recalled.

As a consequence of the transference processes and of the electrode reaction, the relative content of the aluminum fluoride, as a component of the anodic bath layer, tends to increase.

This phenomenon occurs, magnified, in cells having a soluble anode of metallic aluminum.

In spite of the obvious differences in respect to the usual condition considered above, the study with the soluble anode cells is easier and instructive in showing (magnified again) the possible effects of the accumulation of aluminum fluoride in the anodic region.[44]

With soluble anode one may encounter anomalous voltage increments corresponding to a passivity condition which appears to be chargeable to a separation of aluminum fluoride as a solid phase. Also in this case, as in the one of the anode effect with insoluble anodes, the addition of alumina or also temperature increments[45] displaces the onset of the anomalous anode conditions toward a higher range of current intensity.

The increment of the aluminum fluoride relative content involves strong change in the chemical physical properties of the bath, by lowering conductivity and increasing vapor pressure.

[44] R. Piontelli, B. Mazza, and P. Pedeferri, *Electrochimica Metallorum*, 1, 217 (1966).

[45] It is remarkable that, in chloride melts, the temperature influence is exactly opposite.

In the case of the insoluble anode electrolysis[46], this last effect aggravates the consequences (especially the increase of power dissipation) of the presence of the gaseous products of the electrolysis.

B. J. Welch and R. J. Snow: In the work presented in our paper, we were not concerned with the phenomena associated with the anode effect, but our work was directed toward elucidation of the most reproducible parameter for applications such as *in situ* alumina analysis. We fully acknowledge the great contribution made by Professor Piontelli and his co-workers in shedding light on the phenomena causing the anode effect.

[46] In which also overvoltage phenomena before the onset of the anode effect appear to be influenced by inhibition phenomena at the electrode surface chargeable to fluorine or to some fluorine surface compounds.

It is interesting to note that they have substantiated[47] our observed lack of reproducibility of the critical current density (or intensity). In an extension of our work[48] we have also confirmed the temperature dependence presented above and elsewhere.[49, 50]

In our more detailed study we observed that the point of anode effect, as defined by either cell voltage or critical current density (or intensity), is also dependent on the carbon type used as the anode. Marked differences are observed for carbons that only have small differences in graphitic structure.

[47] R. Piontelli, B. Mazza, and P. Pedeferri, *Metallurgia Ital.*, 57, 51 (1965).

[48] R. J. Snow and B. J. Welch, *Proc. Aus. I.M.&M.*, No. 221, 43 (1967).

[49] R. Piontelli, B. Mazza, and P. Pedeferri, *Electrochimica Acta*, 10, 1117 (1965).

[50] R. Piontelli, *Electrochimica Metallorum*, 1, 191 (1966).

ELECTROCHEMICAL SCIENCE

Low-Temperature Battery System Study Using a Mixture of HF and N_2O_4

R. Keller and S. Evans

Research Division, Rocketdyne, A Division of North American Aviation, Inc., Canoga Park, California

ABSTRACT

A battery system using a mixture of anhydrous hydrogen fluoride and dinitrogen tetroxide was evaluated. Dinitrogen tetroxide was the cathodic reactant; the anodes studied were cadmium, manganese, molybdenum, and zirconium. Cadmium exhibited the best anode behavior of the candidates that were evaluated. Typical open-circuit cell voltages were: 1.14v at —40°C and 1.66v at 60°C. Cell polarization at —40°C was moderate and at 60°C was very low. It is predicted that cell voltages of 0.9v at a discharge rate of 100 ma/in.^{2} at —40°C are attainable.

Analysis of basic electrochemical data obtained during a synthesis-oriented program (1) resulted in the proposal for a battery system with a hydrogen fluoride-dinitrogen tetroxide electrolyte. Such electrolyte solutions had shown high conductivities at low temperatures; the electrochemical reduction of N_2O_4 occurred readily.

The objective of this study was to determine the feasibility of a metal anode/HF, N_2O_4/inert cathode system for possible low-temperature, primary battery application.

The discharge of this battery system is based on the anode reaction

$$M \rightarrow M^{n+} + ne^- \quad [1]$$

or

$$M + nHF \rightarrow MF_n + nH^+ + ne^-$$

and the cathodic reaction

$$4H^+ + N_2O_4 + 4e^- \rightarrow 2NO + 2H_2O \quad [2]$$

The over-all cell reaction for a cell with cadmium anode as example is

$$2Cd + N_2O_4 + 4H^+ \rightarrow 2Cd^{2+} + 2NO + 2H_2O \quad [3]$$

or

$$2Cd + N_2O_4 + 4HF \rightarrow 2CdF_2 + 2NO + 2H_2O$$

The anode in contact with the HF-N_2O_4 electrolyte is thermodynamically unstable. A suitable anode should have a low direct corrosion rate, but should undergo reasonable electrochemical dissolution. Tantalum, niobium, and tin react immediately with the solution; zinc, iron, nickel, chromium, cobalt, silver, and copper are stable in HF-N_2O_4, but are passivated by the application of anodic currents. However, zirconium, manganese, cadmium, and molybdenum have been found to be relatively insoluble in HF-N_2O_4, but dissolve electrochemically when anodic currents are applied. These metals were evaluated.

Platinized platinum was selected as the cathode material, since N_2O_4 was reduced with very little overpotential. Nickel was used as the cathode in several experiments.

A special feature of this system is that no cell divider (separator) is necessary, thus allowing for simplified design of a reserve-type cell.

Experimental

The test cell fabricated from Teflon is shown in Fig. 1. The compartment measures 1 by 1 in. with wall thicknesses of ¼ in. Grooves held 1-in.^{2} electrodes in place at opposite walls. The electrolyte covered the electrodes completely, but left a vapor space (approximately 1 in.^{3}) above the liquid. The silver-silver fluoride reference electrode (2) was contained in a sealed Kel-F tube which had an opening approximately ½ in. above the cell bottom. The Teflon cell cover was pressed against the cell body by steel bolts, and the seal was accomplished with a Teflon O-ring. The leads to the electrodes were introduced between the cell body and the O-ring. A perfect seal was not established, but the sealing was found adequate even for high-temperature experiments. Two Monel fittings on stainless-steel tubing allowed for filling and venting of the cell.

The Ag/AgF electrodes were prepared by anodizing silver wire in solutions of 0.5M NaF in anhydrous HF at current densities of approximately 12 ma/cm^2 for 5 min. Electrodes prepared by such a procedure were found (2) to have potentials within 5 mv of each other and to return to their original open-circuit potentials after momentary cathodic or anodic polarization at 0.1 ma/cm^2.

The lower part of the cell was immersed in a constant-temperature bath. A fluorocarbon slush bath was

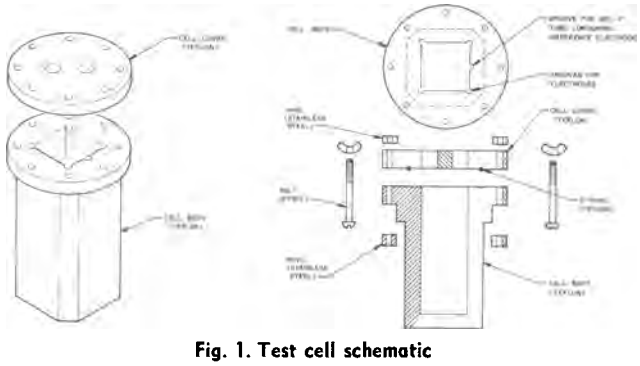

Fig. 1. Test cell schematic

used to maintain —40°C. Freon-113 with a melting point of —35°C was mixed with Freon-11 to achieve a melting point of —40°C. The temperature was normally maintained with an accuracy of ±2°C. A Kel-F oil bath was used for temperatures of 60° ± 1°C. The oil was contained in a 3-liter beaker. An immersion heater was controlled by a relay in conjunction with a contact thermometer.

Liquid anhydrous hydrogen fluoride (3) was quantitatively transferred through Monel tubing and Teflon valves into a Kel-F finger. The hydrogen fluoride was frozen by means of liquid nitrogen, and N_2O_4 was added from a burette. The mixture was allowed to thaw and was then transferred to the cell. During all these procedures, closed systems were used, except for some venting tubes.

Galvanostatic polarization curves were determined by applying a constant current and measuring the resulting potential. The current was usually raised in the sequence 1, 2.2, 5, 10, 22, 50 ma, etc., and each value was maintained for 1 min.

In galvanic studies, constant ohmic loads were applied to the cell, and the potential was recorded as a function of time. The cell currents can be readily determined from the cell voltages.

Vapor pressures were determined by placing a sample of the electrolyte in a stainless-steel bomb and measuring the pressure with a Matheson Monel gauge. The apparatus was kept in a thermostated oven.

Results

Low-temperature galvanostatic anode studies.—Anodic polarization curves of cadmium, manganese, molybdenum, and zirconium, determined at —40°C, are shown in Fig. 2. A cathodic curve for the reduction of N_2O_4 at platinized platinum is also indicated (dashed curve).

Cadmium displayed the most suitable behavior of the anodes tested. The open-circuit potential was —0.48v *vs.* Ag/AgF. The anode polarization was moderate, and the corrosion rate was negligible.

Zirconium exhibited very negative open-circuit potentials; —1.12v in one case, —0.72v in another case. The polarization characteristics were favorable. However, zirconium reacted with the electrolyte and corroded (primarily near the electrolyte surface) at a rate which was fast to moderate. Nevertheless, it may be feasible to use it for short-duration discharge.

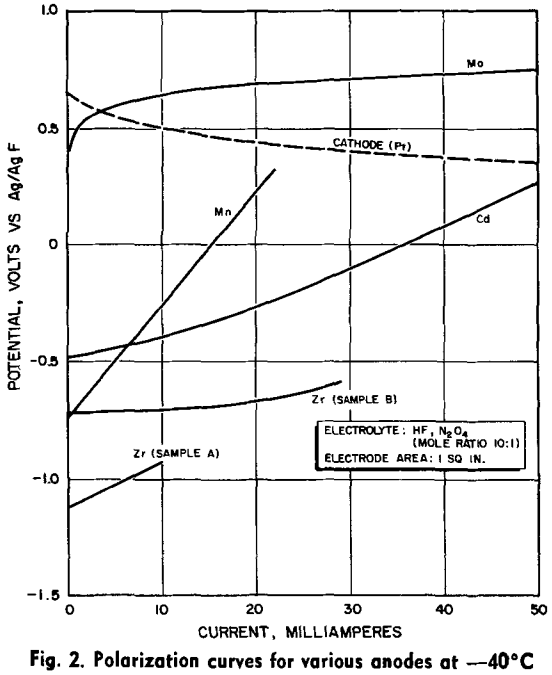

Fig. 2. Polarization curves for various anodes at —40°C

Table I. Specific electrolyte conductance at —40° and 60°C

Electrolyte	Temperature, °C	Cell resistance, ohms	Specific conductance, ohm^{-1} cm^{-1}
0.1*N* KCl	25	24	0.013
HF, N_2O_4	−40	7.6	0.041
HF, N_2O_4	60	1.06	0.18

Table II. Vapor pressure of electrolyte

Temperature		Vapor pressure	
°C	°F	psia	atm
41	106	<15	<1
50	122	20	1.4
60	140	27	1.8
71	160	37	2.5

Manganese polarized fairly severely. The open-circuit potential was somewhat more negative than the value obtained with cadmium.

Molybdenum showed good polarization characteristics but unfavorable potentials.

Cathode studies.—Based on previous experience, nickel had been suggested as electrode material for the reduction of N_2O_4. It was soon noticed, however, that the polarization at smooth nickel was too great for a battery electrode. Although the discharge characteristics were fairly flat, an initial voltage drop of approximately 0.5v was observed at low currents. Platinized platinum electrodes were found to behave very well as cathodes (Fig. 2).

Electrolyte characteristics.—A mixture of HF and N_2O_4 in the mole ratio of 10:1 was used as the electrolyte. Approximate electrolyte conductivities (Table I) were calculated from the measured values of the a-c cell resistance determined in the process of the regular experiments together with a measurement of the a-c resistance of the cell filled with an aqueous 0.1*N* KCl solution.

The results of the vapor pressure measurements are presented in Table II.

Galvanostatic cell discharge.—Galvanostatic polarization curves for the Cd/HF, N_2O_4/Pt and the Cd/HF, N_2O_4/Ni systems at —40° and 60°C are presented in Fig. 3. The potential values were not corrected for iR drops; this correction would total 300-400 mv at the low temperature for 50 ma, and approximately 50 mv at 60°C for the same current.

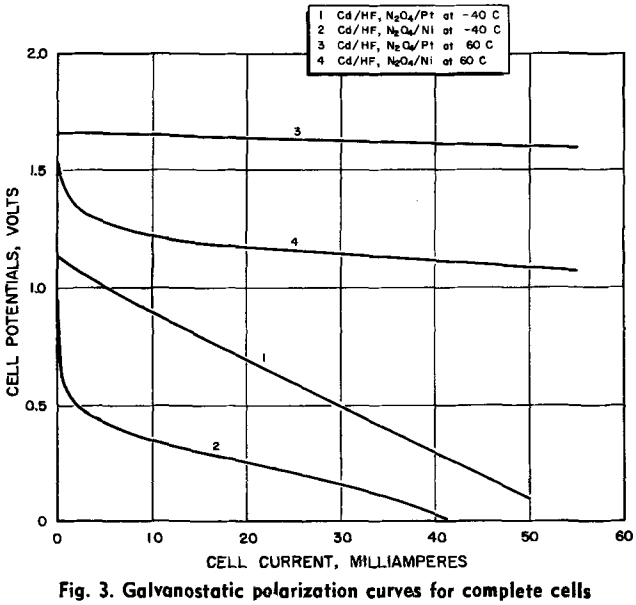

Fig. 3. Galvanostatic polarization curves for complete cells

The potential/current relationship of the cell with a platinized platinum cathode at —40°C (curve 1) was approximately linear; the bulk of the polarization originated at the cadmium anode. With a nickel cathode (curve 2), the contribution from cathode polarization was more substantial.

At 60°C the polarization characteristics of the Cd/HF, N_2O_4/Pt cell were very flat (curve 3). The correction for iR loss in curve 3 would result in practically no polarization up to 1000 ma. If an initial overpotential appearing at low currents is disregarded, the polarization curve for the cell with a nickel cathode at 60°C is flat up to 500 ma (curve 4).

A marked difference of open-circuit potentials was shown at the two different temperatures: 1.66v at 60°C and 1.12v at —40°C (for cells with platinized platinum cathodes).

Galvanic cell discharge curves.—Galvanic discharge curves of the Cd/HF, N_2O_4/Pt cell determined with various ohmic loads are presented in Fig. 4; the temperatures were —40°C (solid lines) and 60°C (dashed lines). Normally, the cell was filled with electrolyte and left on open circuit for 5 to 10 min before discharge was started. For two curves, *i.e.*, for 60 and 10 ohms, the procedure deviated slightly; the load was connected before introduction of the electrolyte or shortly thereafter. Irregularities in such cases occurred because of an adjustment in electrolyte temperature and because of a different behavior of a cell which is only partially filled (the filling procedure covered approximately 1 min). The experiments were not designed to study activation characteristics.

During the course of the experiments, the following two effects can give rise to irregular fluctuations: (*i*) electrode corrosion during the discharge, which increases the surface area and (*ii*) temperature fluctuations of the temperature bath. The main contribution of the cell polarization (disregarding iR drop) resulted from anode polarization. This is evident from galvanostatic data (Fig. 2). The anode and cathode potentials were periodically determined in addition to the continuously recorded cell potential.

At the conclusion of the discharge experiments, grayish, voluminous deposits were observed on the cadmium anodes. These layers, possibly CdF_2, were readily washed away with water.

Direct corrosion of the electrode materials was negligible at low temperature, and the galvanic discharges were all extended over periods of at least 3½ hr. Tests at 60°C were limited to periods of 1 hr because of a uniform attack of the cadmium (0.02-in.-thick sheet) by the electrolyte.

Discussion

The Cd/HF, N_2O_4/Pt system has been established as feasible for a reserve-type primary battery. Experimental discharge rates were moderate at low temperatures (—40°C) and fast at high temperatures (60°C). The use of porous anodes promises substantial improvement of cell characteristics at low temperature because the limitations originated mainly in the anode process. An increase in the active anode surface area by a factor of at least 100 should be readily attainable. Polarization of such an electrode is expected to be less than 100 mv for current densities exceeding 20 ma/cm². A reasonable estimate of the performance which can be achieved with the Cd/HF, N_2O_4/Pt system is summarized in Table III. The observed data (example) have been obtained in the present cell with 1-in.² electrodes. The predicted values are for an improved cell with reduced spacing of the same sized electrodes and with a porous cadmium anode.

The list of possible anode metals has not been exhausted during the present investigation. A more detailed study of anodic characteristics of metals could reveal even better anodes than cadmium. It should be possible to substitute a cheaper electrode material for platinized platinum. Porous nickel, silver, or other metals; carbon, or carbon impregnated with catalysts may allow for a fast electrochemical reaction of the N_2O_4.

The conductivity of the electrolyte at low temperature is sufficient. It should be even higher upon optimization of the HF-N_2O_4 mixture ratio; according to Seel (4) colorless mixtures containing a maximum of 25% N_2O_4 can be prepared. Also, the addition of a salt such as NaF may be beneficial.

No prohibitive corrosion phenomena were observed. Even at high temperatures (60°C), the anode material, which was 0.02-in.-thick cadmium sheet, stood up for at least 1 hr. The vapor pressure of the electrolyte was modest in comparison to some other electrolytes considered for use in low-temperature batteries. Nevertheless, improvements resulting from variation of the electrolyte composition are anticipated (4).

Somewhat less ideal is the temperature dependence of the open-circuit potential; representative measured values for the Cd/HF, N_2O_4/Pt system are 1.14v at —40°C and 1.66v at 60°C. Reversible open-circuit potentials were not measured in all cases, certainly not at nickel cathodes. If the temperature dependence of the cell voltage should prove crucial for certain applications, an improvement should be sought by investigating other anode materials.

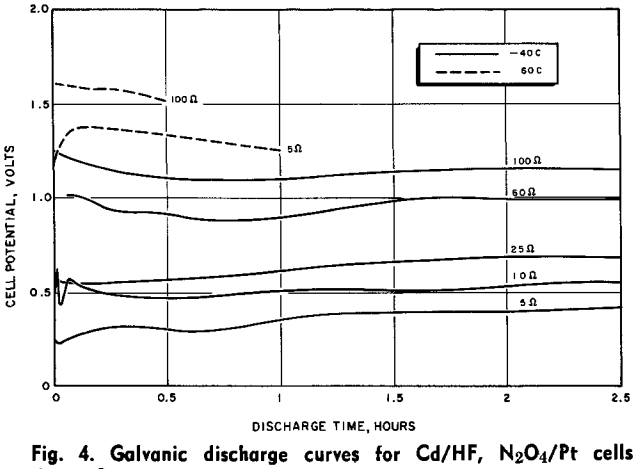

Fig. 4. Galvanic discharge curves for Cd/HF, N_2O_4/Pt cells with 1 in.² electrodes.

Acknowledgments

The authors are grateful to Dr. H. H. Rogers and Mr. J. H. Johnson for their assistance in this study. This program was supported by the Harry Diamond Laboratories, Washington, D.C., under Contract DA-49-186-AMC-289(D).

Manuscript received Oct. 14, 1966; revised manuscript received March 20, 1967. This paper was presented at the Philadelphia Meeting, Oct. 9-14, 1966.

Table III. Observed and estimated improved cell performance for the Cd/HF, N_2O_4/Pt system at —40°C

Observed at 40 ma (example)	
	mv
Cell voltage	290
Anode polarization	400
Cathode polarization	90
iR loss	360
Open-circuit cell voltage	1140

Optimized Cell at 100 ma	
(estimated by extrapolation of observed data)	
Cell voltage	920
Anode polarization (porous anode)	80
Cathode polarization	120
iR loss (reduced spacing)	20
Open-circuit cell voltage	1140

Any discussion of this paper will appear in a Discussion Section to be published in the June 1968 JOURNAL.

REFERENCES

1. R-5077, Summary Report, Research in Fluorine Chemistry, Contract Nonr 1818(00), H. H. Rogers, S. Evans, and J. H. Johnson, Rocketdyne, a Division of North American Aviation, Inc., Canoga Park, Calif., April 30, 1963.
2. Final Report, Study of Fuel Cells Using Storable Rocket Propellants, Contract NAS3-2791, Monsanto Research Corporation, May 1964.
3. H. H. Rogers, S. Evans, and J. H. Johnson, *This Journal*, **111**, 701 (1964).
4. F. Seel, *Angew. Chemie, Internat. Ed.*, **4**, 635 (1965).

Structural Studies of Porous Electrodes

E. Y. Weissman

Research and Development Laboratory, Direct Energy Conversion Operation, General Electric Company, Lynn, Massachusetts

ABSTRACT

Nondestructive techniques are described for the measurement of total electrode surface area, microporosity and pore size distribution, total porosity, and fraction of total porosity consisting of open pores. These measurements have been applied to a class of composite porous electrode structures based on platinum black, Teflon, and a metal screen current collector. They have been shown to correlate with electrochemical performance on the basis of exponential relationships of the type

$$i = a \exp (bS \text{ or } b\Sigma V)$$

where i is the current or limiting current density based on the geometric electrode area, S is the total (BET) surface area, ΣV is the cumulative micropore volume, and a and b are constants depending on the type of electrode and experimental conditions. The electrochemical performance of the electrodes was shown to increase with an increase in the percentage of total open (*i.e.*, accessible) porosity consisting of micropores. It is not clear, at present, whether the relative importance of the micro- and macro-pore structures is actually conducive to maximum or asymptote-type of optimum structure, since no macropore size distribution data are now available. Within the micropore range of 25-350Å pore radius it was shown that the range 25-200 is performance-determining for the class of composite electrode that was studied.

Porous electrode processes, in general, and many aspects of fuel cell investigations, in particular, depend heavily on continued progress in the area of electrode structure optimization. The gradual coming of age of the fuel cell technology has been accompanied by a great variety of theoretical studies attempting to model and to explain quantitatively the operation of porous, catalytic, electrodes.

Since, at least for the time being, porous electrodes are the main workhorse for a variety of fuel cell designs, such studies are entirely justified. Therefore, further clarification as to what constitutes such a structure in any given system becomes of paramount interest; any quantitative geometry measurements could then eventually be applied to existing mechanistic models or to newly derived ones in order to define the electrochemical processes occurring at a typical fuel cell electrode. Design improvements, scale-up data, and adequate quality control would be a natural outcome of such results.

The literature of experimental studies of the geometry of various porous materials, including catalysts, is very extensive. This ceases to be the case, however, when treating the problem of whole, porous, electrodes. Salkind *et al.* (1) reported on a nondestructive method [based on BET (14) gas adsorption measurements] for the determination of surface areas and pore size distributions of porous electrodes; a similar approach was used to study the preparation of platinized-platinum electrodes (2) and to check electrode surface area data obtained also by an electrochemical method (3). Others tried radiographic (4-6), electron microscopic (7), and polarized light microscopy (8) techniques for determination of porous electrode structure and operational parameters.

The importance of the "active porosity spectrum" for the preparation and statistical description of sintered plaque electrodes was described by Feuillade and coworkers (9-10), although the measurements were based on a destructive, mercury intrusion method.

Finally, Paxton *et al.* (11) reported a dependency of the concentration polarization on the micropore structure (again, determined destructively by mercury intrusion porosimetry), while Schwabe (12) indicated the range of pore radii of 100-300Å as determining the current-carrying capability of a certain type of activated carbon electrodes.

In the present paper the technique is described and results are given for a series of nondestructive measurements of surface area, porosity, and micropore size distribution. These tests were conducted on porous platinum black-Teflon-metal screen electrodes of a type previously described (13), and then related to their electrochemical performance.

Experimental

Electrodes were prepared from Teflon and various types of platinum black. The composite structure achieved also included a current collector made of 45 mesh tantalum screen. All electrodes contained 90 w/o (weight per cent) Pt (approx. 34.5 mg/cm^2), were 8.90 x 11.40 x 0.025 cm in over-all size and had an active geometric area of 46 cm^2.

Structural geometry measurements were performed on the finished electrodes at various stages in their preparation (before and after a wetproofing treatment) and evaluation (before and after electrochemical performance testing as anodes). Measurements of the "raw materials" at their various stages of preparation were also made.

Surface areas.—These data were obtained by the BET method (14), using nitrogen adsorption.

The method is based on a generalization of Langmuir's monomolecular adsorption theory, to allow for more than one layer of adsorbed molecules on the surface to be measured. An expression is obtained linking the volume of gas, V, adsorbed at pressure, p, with the saturation pressure of the gas, p_s, the volume of adsorbed gas corresponding to a monomolecular layer, V_m, and a constant, C, which is an exponential function of the heat of adsorption of the first adsorbed layer, E_a, and the heat of liquefaction of the adsorbing gas, E_l, at a given temperature T. This expression can be linearized in the form

$$\frac{p/p_s}{V(1-p/p_s)} = \frac{1}{V_mC} + \left(\frac{C-1}{V_mC}\right)\left(\frac{p}{p_s}\right) \qquad [1]$$

where:

$$C = \exp\left(\frac{E_a - E_l}{RT}\right)$$

The slope, $\frac{C-1}{V_mC}$, and intercept, $\frac{1}{V_mC}$, are obtained from a linear regression of $\frac{p/p_s}{V(1-p/p_s)}$ as a function of the relative pressure of the adsorbate, p/p_s, and the surface area follows from their values plus a knowledge of the molecular area of the adsorbate. For nitrogen, the molecular area, $M.A.$, was calculated as a function of the measured temperature of adsorption (liquid nitrogen temperature), T_s, from existing data (15)

$$M.A. = 3.749\ T_s - 273.850,\ T_s < 77.38°K$$
$$M.A. = 0.0629\ T_s + 11.4020,\ T_s \geq 77.38°K \qquad [2]$$

In general, the molecular area of nitrogen approached the value of 16.2Å².

The equipment used for the BET measurements was a slight modification of the commercially available NUMINCO-ORR Surface Area-Pore Volume Analyzer, Model No. MIC-101.

Figure 1 is a schematic representation of the experimental set-up for gas adsorption measurements. Briefly, the method consists of equilibrating various amounts of adsorbate with the previously cleaned sample (by degassing under heat), at liquid nitrogen temperatures. The necessary material balance data are derived from pressure measurements and from a knowledge of volumes that are either available from calibration values, or from helium displacement measurements. The adsorbate was nitrogen, prepurified grade, filtered through a molecular sieve trap. The helium was filtered through a molecular sieve trap in series with a liquid nitrogen-cooled activated charcoal trap. The saturation pressure of the adsorbate was determined directly, and used also for the calculation of the corresponding temperature of adsorption, according to the relationship (16)

$$T_s = \frac{6.6\ (\log_{10}p_s - 6.49594 - 255.821}{\log_{10}p_s - 6.49594} \qquad [3]$$

The electrodes were contained in specially built stainless steel sample holders. Constructional details for these holders have been given elsewhere (17).

By a judicious choice of the range of relative pressures of the adsorbate, excellent correlatability of the experimental data with the BET equation was obtained. The correlation coefficients for the regression were of the order of 100% and the average deviation (absolute value) less than 1%. Based on standard calibration samples the results were accurate to ± 3% or better, and precise to ± 1.5%.

Pore size distributions.—These data were obtained by a nitrogen capillary condensation method, using the surface area equipment (Fig. 1). The method is based on the assumption of cylindrical, noninteracting, pores and Wheeler's (18) derivation of the pore size distribution expression

$$V_p - V_a = \int_{R_c}^{\infty} \pi\,(r_w - t)^2\,L\,dr_w \qquad [4]$$

where: V_p is the total pore volume, V_a the volume adsorbed, r_w the pore radius, t thickness of the adsorbed layer, function of the relative pressure of the adsorbate, p/p_s, L the pore size distribution function, defined as the total length of all pores of radius r_w per unit weight of adsorbent, and R_c is the critical pore radius, below which all pores are completely filled by adsorbed or condensed gas, function of the relative pressure of the adsorbate p/p_s

The adsorption and desorption isotherms supplying the needed data for this method exhibit a hysteresis. The desorption points are considered to be closer to the true, thermodynamic, equilibrium; they were the only ones taken into account in the present measurements (see Fig. 2 for an example of such a desorption isotherm). Pierce's method (19) has been chosen for the numerical integration of Eq. [4].

By a careful choice of technique, pore radii could be measured covering the range 20-600Å. This covers the entire micropore region[1] and the transition micropore-macropore. A suitable nondestructive method for

[1] Defined as the region where the pore diameters are equal to or smaller than the mean free path of the gas molecule of interest; this is the situation where Knudsen diffusion prevails.

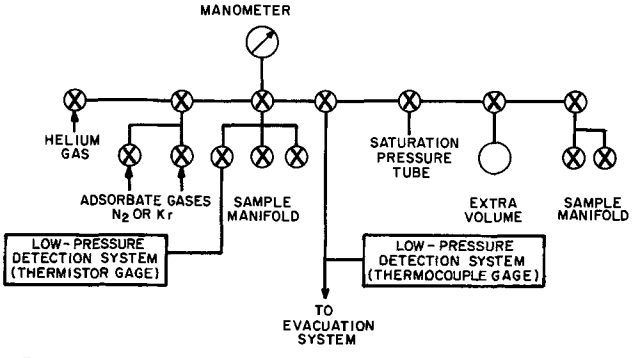

Fig. 1. Diagram of gas adsorption set-up used for surface area and pore size distribution measurements.

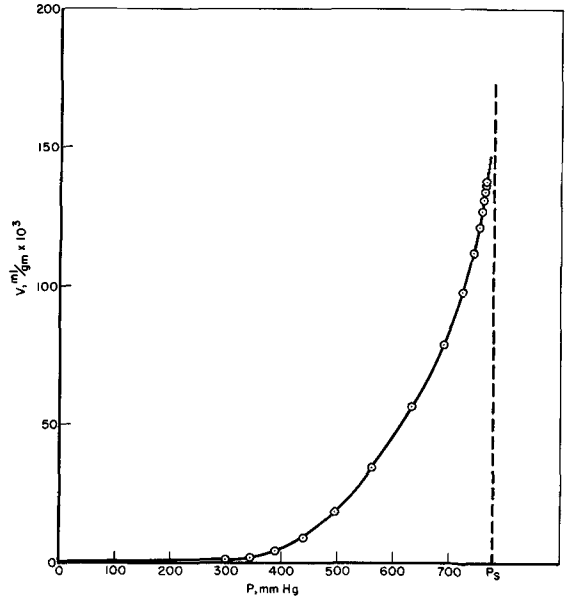

Fig. 2. Nitrogen desorption isotherm for a porous platinum-Teflon electrode.

the balance of the pores of interest, in the macropore region, has yet to be developed.

The processed data were then plotted as cumulative pore volumes *vs.* pore radius, and as pore size distribution curves (derivatives of volume in terms of radius *vs.* the average radius, *e.g.*, Fig. 3) of characteristic multi-modal shape. This afforded a "fingerprinting" of the electrodes or catalytic raw materials of interest.

Porosities.—The total porosity was calculated from measured weights of the various solid ingredients (of known densities) constituting an electrode, and electrode dimensions.

The microporosity, ϵ_μ, for any given range of pore sizes, followed from a knowledge of the cumulative pore volume (as obtained from the pore size distribution measurements) for given weights and dimensions of the catalytic structure.

The fraction of total porosity consisting of open-ended pores, accessible to a fluid phase, was determined by a buoyancy method based on weight data for the electrode in air and in water (after careful and repeated vacuum-impregnation with water).

Calculations.—All the surface area, pore size distribution, and porosity calculations were processed by means of an IBM 7044 digital computer based on FORTRAN IV programs. A CALCOMP subroutine yielded the automatically plotted cumulative pore volume and pore size distribution graphs.

Electrochemical measurements.—Polarization curves were obtained for the oxidation of propane at 150°C with 90% phosphoric acid as an electrolyte. The counter electrodes were structurally similar to the anodes and operated on pure oxygen.

The anode potentials were determined IR-included and IR-free [by means of a Kordesch-Marko bridge (20)] and referred to a reversible hydrogen electrode in the same solution.

Results and Discussion

Two aspects of interest will be covered in this section: (*a*) the structural geometry measurements *per se* and their significance, and (*b*) the relationship between structural geometry and electrochemical data.

While the results have been obtained from a study of specific electrode structures it is felt that the findings and conclusions derived therefrom are sufficiently general to apply, at least qualitatively, to the entire family of porous gas diffusion electrodes based on composite Teflon-metal screen-metal black structures.

Structural geometry measurements.—Figure 2 is a typical representation of a nitrogen desorption isotherm obtained with the type of porous platinum-Teflon composite electrodes under discussion. It clearly exhibits a type 3 shape, characteristic of multi-molecular adsorption. The corresponding pore size distribution is exhibited in Fig. 3.

The first peak, always observed at radii of 20-50Å, is present also in the "raw material" (platinum black) from which the electrode is made; as such, it should mostly be representative of the intra-particle geometry characteristic of the material.

The peaks at higher pore radius values, such as 250 and 575Å in this case, are generally different to a degree from those exhibited by the powdered platinum black; consequently, they are mostly a result of the interparticle configuration obtained as a function of the electrode preparation technique and the ingredients used. The presence of characteristic peaks close to the threshold value of 600Å (radius), beyond which the capillary condensation method breaks down, makes the development of a nondestructive technique for macropore measurements of considerable interest. The need for such additional information is also suggested by the available data on the extent of total, open, porosity consisting of macropores (see Fig. 5).

Pore size distribution calculations are based on the assumption that the pores are cylindrical in shape. This is obviously not the case, and a surface area calculated on this basis (where: surface area = 2 x volume of pores/average pore radius) would be expected to be too low because of irregularities on the walls of the pores, and too high because of pore interactions. In many instances these two separate effects offset each other with a resulting agreement between the BET-calculated area and the area obtained from pore size distribution data.

Such happens to be the case with the platinum and platinum-Teflon samples; however, complete electrodes exhibit a disagreement by a factor of roughly 2, with the BET results being the lower ones. This is represented in Fig. 4 and has also been reported in the

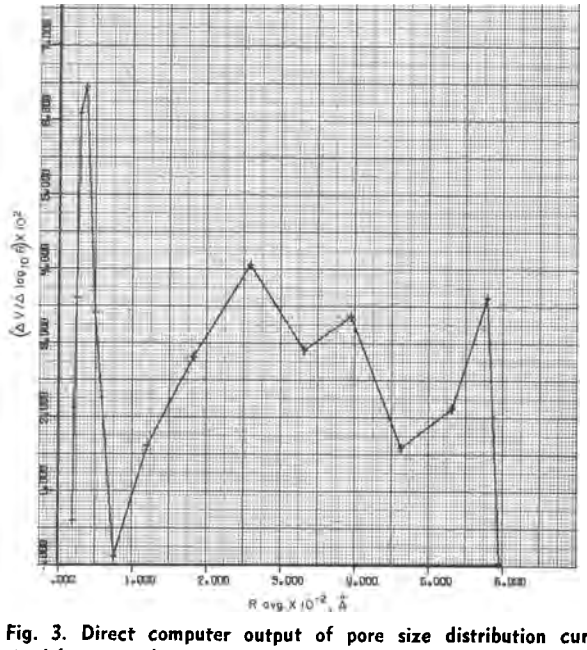

Fig. 3. Direct computer output of pore size distribution curve derived from cumulative nitrogen desorption data (Fig. 2).

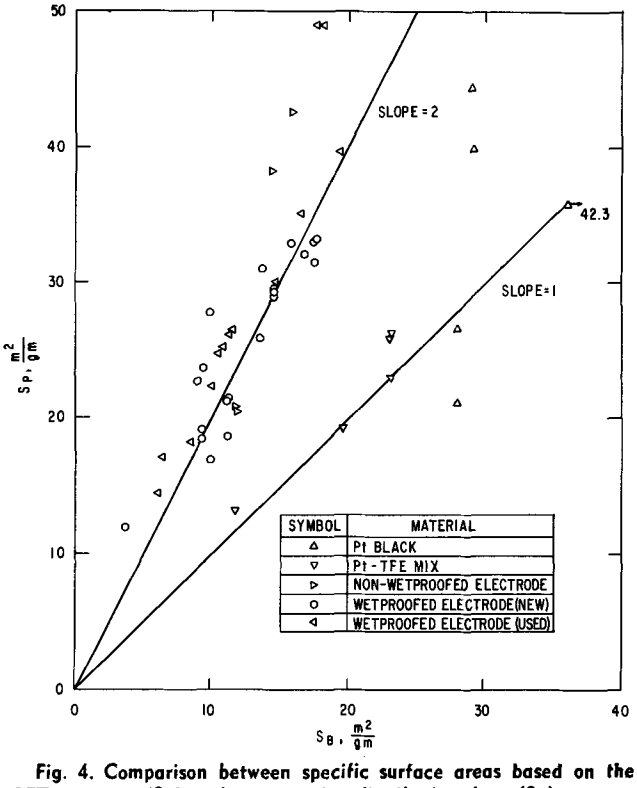

Fig. 4. Comparison between specific surface areas based on the BET equation (S_B) and on pore size distribution data (S_P).

Table I. Effect of electrode manufacturing steps on the measured BET surface areas and cumulative micropore volume for the pore radius range 25-350Å
Data in % of the original platinum black value; in brackets: the cumulative micropore volume

Platinum black type*	Measured surface area, m^2/g	Electrode pressing temperature, °F	Data (%) for: Platinum black powder	Powdered Pt-TFE mix	Finished electrode	No. of electrodes used in study
A	29.11	550	100 (100)	80 (46)	60 (46)	4
		606			52 (40)	2
		650			48 (38)	2
B_1	27.97	550	100 (100)	42 (69)	33 (72)	2
B_2	42.30	550	100 (100)	46 (74)	24 (60)	2

* Type A = Engelhard 25 (*i.e.*, Manufacturer: Engelhard Co.; Nominal specific surface area, as reported by manufacturer: 25 m^2/g); type B_1 = Bishop 24 (same general meaning); type B_2 = Bishop 35 (same general meaning).

literature, for instance for silica-alumina catalyst pellets (21). Thus, the significant geometry changes, interparticle geometry, in this case, coming into play once the electrode is prepared from certain raw materials become evident. In the discussion that follows, the results will be interpreted in terms of the more correct, BET, surface area data.

Another aspect of this geometry change, when passing from a powdered or granular material to a finished electrode structure, follows from an examination of the data in Table I. The sintering process, as evidenced by reductions in the surface area and cumulative micropore volume, is shown to depend on a variety of factors: (*a*) the electrode pressing temperatures, with more pronounced sintering at higher pressing temperatures; (*b*) the catalyst type or manufacturer; and (c) the original platinum black area; the higher the area the more extensive the extent of sintering, everything else being equal.

Further evidence regarding the dependence of electrode structure on the three above-mentioned factors as well as on a fourth one: the history of the electrode (new or used, *i.e.*, before or after electrochemical evaluation), is offered by the graphical representation in Fig. 5.

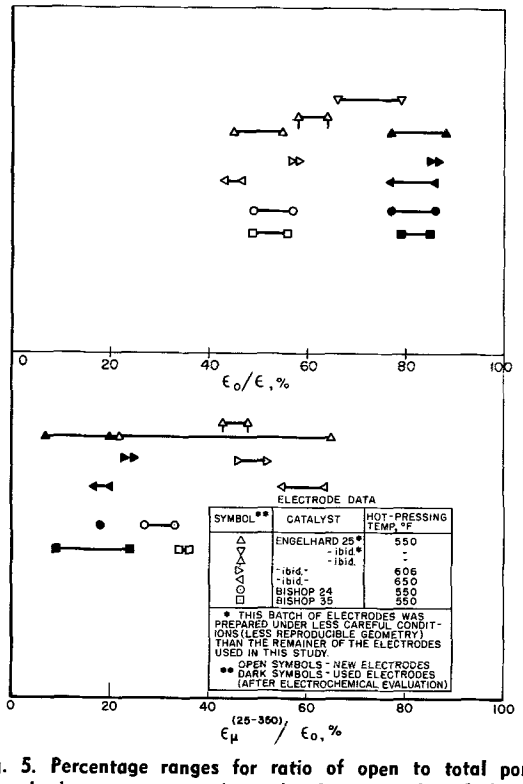

Fig. 5. Percentage ranges for ratio of open to total porosity, ϵ_o/ϵ, and micro-to open-porosity, ϵ_μ/ϵ_o, for new and used electrodes.

One immediately notes that all the electrodes, independent of their history, possess appreciable porosity fractions consisting of macropores; this is indicated by values of the ratio $\epsilon_\mu^{(25-350)}/\epsilon_o$ that are significantly lower than unity. Here, $\epsilon_\mu^{(25-350)}$ represents the microporosity based on cumulative micropore volumes for the pore radius range: 25-350Å, and ϵ_o is the total porosity of the electrode consisting of open pores.

In new electrode structures, this contribution of the macroporosity appears to be not only a function of the type of catalyst used but also of the manufacturing conditions. Thus, it increases with an increase in the hot-pressing temperature, indicating that the probably higher Teflon flow and catalyst pore masking resulting from higher pressing temperatures affect smaller pores to a larger extent.

Another finding that can be derived from Fig. 5 pertains to the fraction open porosity: ϵ_o/ϵ (where ϵ is the total porosity). This appears to become significantly larger for electrodes that have been put on load even for only a few hours. Furthermore, this added open porosity is mainly due to macropores.

The fraction open porosity also appears to change as a function of the type of catalyst used, and it increases when the hot-pressing temperature used in the manufacture of the electrode is decreased. This latter effect can be explained by the correspondingly smaller extent of sintering and of pore masking due to Teflon flow.

Figure 4 indicated a relatively constant correspondence between BET—and capillary condensation—derived values of surface area. On that basis, a correlatability between cumulative micropore volume and BET areas would be expected to follow directly. This is exhibited in Fig. 6 for a great variety of platinum black-Teflon electrodes; the "stray points" are predictably accounted for by the powdered raw material samples which, as was also shown in Fig. 4, obey a different type of relationship between the two kinds of surface area values mentioned above.[2]

The possibility of expressing cumulative micropore

[2] In this and the following figures some of the experimental points have values certain only within a range of several per cent; this is indicated by arrows pointing in the direction corresponding to the range of possible data variation.

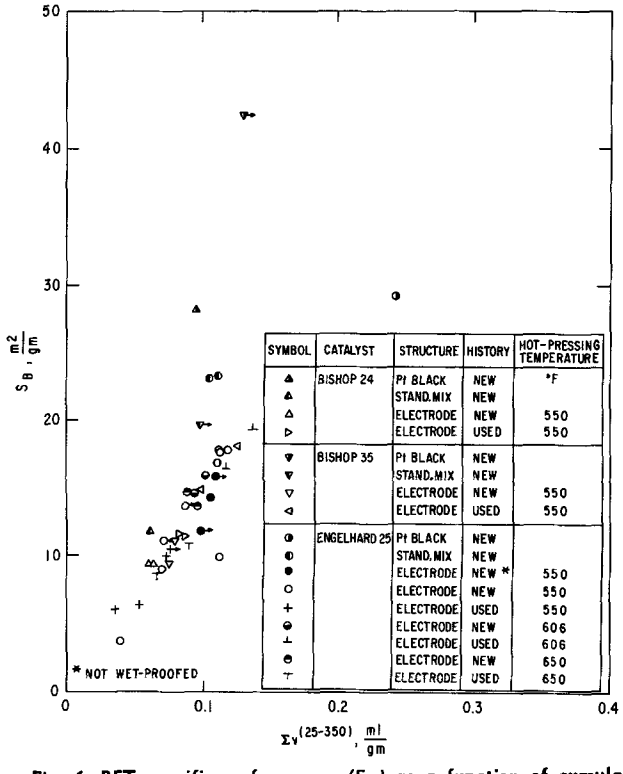

Fig. 6. BET specific surface area (S_B) as a function of cumulative micropore volume for range of pore radii 25-350Å ($\Sigma V^{(25-350)}$).

volumes in terms of BET surface areas, or vice-versa, will have a very pertinent significance in the discussion of performance *vs.* structure results that follows below.

Relationship between structural geometry and electrochemical performance.—A complete picture of the performance dependence on structure for an operating porous electrode has to await pertinent data on the true, electrochemically active area, in addition to the total area described here, as well as some quantitative information on the macropore structure. This would be essential in interpreting existing theoretical models or in deriving modified or new versions. On the other hand, from measurements currently in progress (22) it would appear that total BET areas for porous electrodes of the type considered here are quite representative of true areas as well. The results discussed in this section, while not directly applicable to a rigorous consideration of operating electrode models, are nevertheless adequate to represent characteristic trends in the dependence of electrochemical performance on porous structure.

An examination of how the current density at a chosen anode overvoltage varies as a function of the measured BET surface area suggests either a linear or an exponential type relationship. At this stage, the justification for such relationships is purely empirical; a linear regression analysis of these data, and others to be discussed in what follows, indicates somewhat better correlation coefficients (by about 5%) in the case of the exponential relationship. Accordingly, Fig. 7 is a representation of the logarithm of current density for propane oxidation, measured at an IR-free anode potential of 600 mv *vs.* H_2/H^+, *vs.* the BET surface area of the new electrodes prior to performance evaluation. This corresponds to a relationship of the type

$$i = a \exp(bS) \qquad [5]$$

where i is the current density based on the geometric electrode area, S is the surface area, and a and b are constants depending on the type of electrode and experimental conditions.

If one considers a rate limitation in terms of both activation and concentration polarizations, η_{ac}, with the value of the activation polarization: $|\eta_a| >> (RT/n\mathbf{F})$, which happens to be our case, one obtains

$$\eta_{ac} = A + B \ln i + \frac{RT}{n\mathbf{F}} \ln\left(\frac{i_L}{i_L - i}\right) \qquad [6]$$

where the various symbols have the usual significance; one notes that for an anodic process

$$A = -\frac{RT}{(1-\alpha)\, n\mathbf{F}} \ln i_o \qquad [7]$$

$$B = \frac{RT}{(1-\alpha)\, n\mathbf{F}}$$

One also notes that, for any given current density i referred to the geometric area of the electrode, the over-all polarization η_{ac} is a function of the total available area consisting of active sites and approximated in this case by the BET surface area

$$\eta_{ac} = f(S) \qquad [8]$$

While Eq. [6] is not necessarily valid in each case, particularly for porous electrodes, one observes that by combining [6], [7], and [8] and rearranging on an antilogarithm basis the following relationship is obtained.

$$i\left(\frac{i_L}{i_L - i}\right)^{(1-\alpha)} = i_o \exp[f(S)/B] \qquad [9]$$

It is interesting to note that this implicit expression of i in terms of S is also suggested, admittedly with a certain degree of scatter, by the simple form of empirical Eq. [5].

A similar form is obtained when considering only the limiting current density (again, with respect to the geometric area of the electrode) *vs.* the BET surface area; this is represented in Fig. 8.

Since cumulative micropore volumes were available for all the electrodes investigated over the pore radius range 25-350Å, their values were also considered as an independent variable instead of the surface area. Figures 9 and 10 again demonstrate an exponential dependence of geometric current density and limiting current density, respectively, on the cumulative micropore volume; this is also another way of representing the correspondence between BET surface area and micropore volume (Fig. 6).

Up to this point the treatment and representation of the experimental data would seem to suggest that

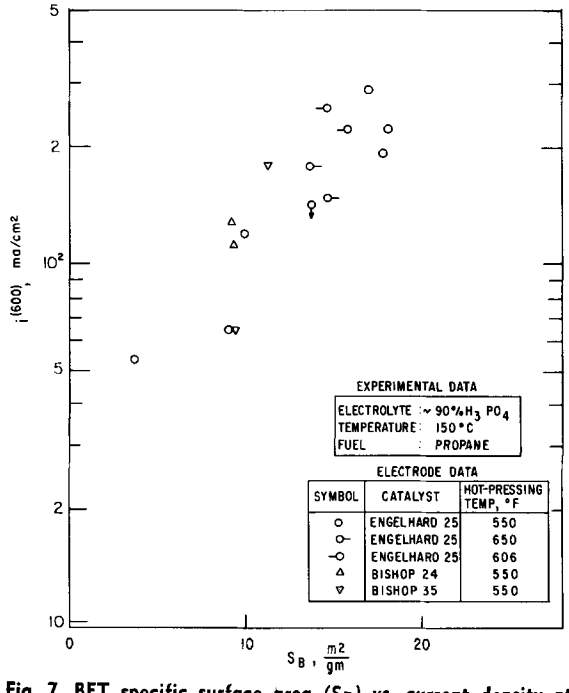

Fig. 7. BET specific surface area (S_B) *vs.* current density at an IR-free anode potential of 600 mv *vs.* H_2/H^+ ($i^{(600)}$).

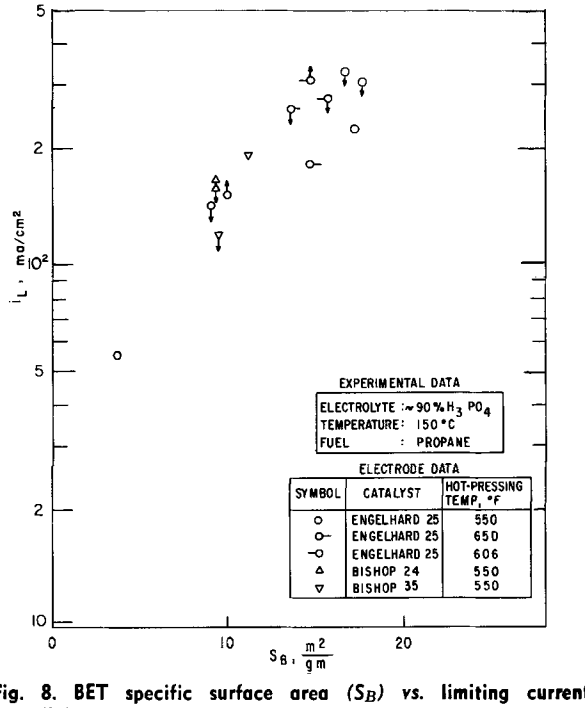

Fig. 8. BET specific surface area (S_B) *vs.* limiting current density (i_L).

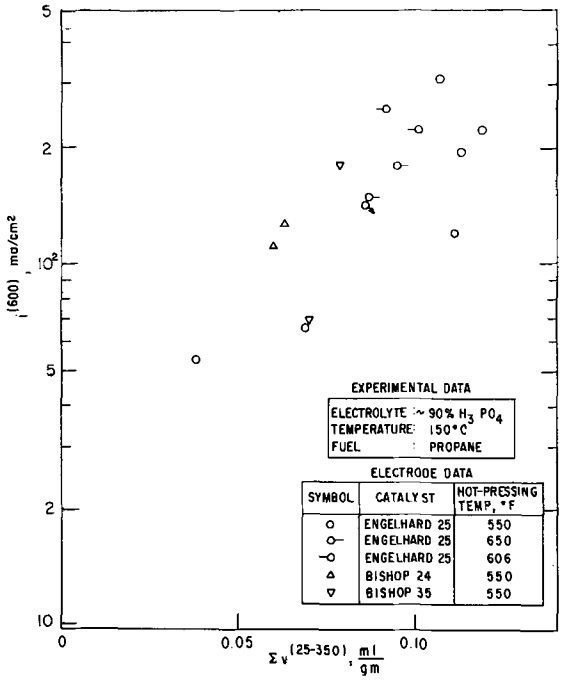

Fig. 9. Cumulative micropore volume for the pore radius range: 25-350Å ($\Sigma V^{(25-350)}$) vs. current density at an IR-free anode potential of 600 mv vs. H_2/H^+ ($i^{(600)}$).

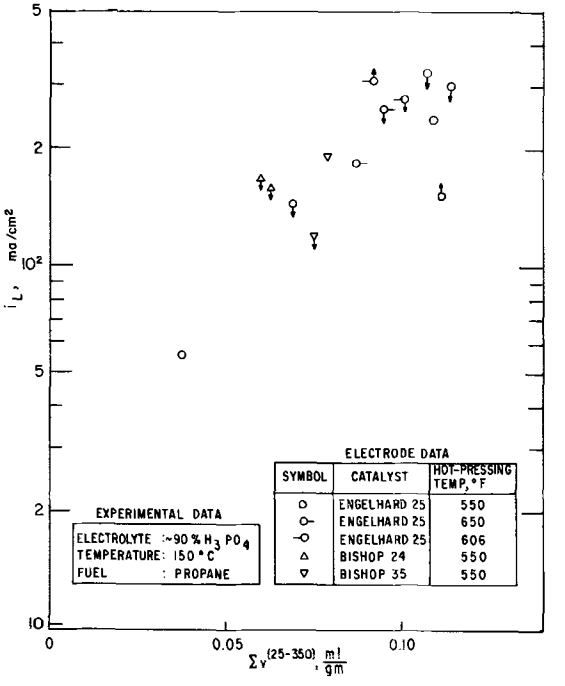

Fig. 10. Cumulative micropore volume for the pore radius range: 25-350Å ($\Sigma V^{(25-350)}$) vs. limiting current density (i_L).

macropore structure effects may not be of great consequence to the electrochemical performance of porous composite electrodes of the type examined here. Indeed, we observe a fair correspondence between the measured micropore volume and the BET surface area, indicating that most of the area is due to the micropores. This in turn is expressed as performance-determining, on an exponential basis.

On the other hand, the bearing that the macropore structure would have in this type of "mixed-pore electrode" on the dynamic capillary equilibria between the electrolyte phase and the reactant phases cannot be ignored. Certainly, on a long-term sustained-operation basis, the degree of utilization of active sites and, as a result, the electrochemical performance and rate of performance decay must be dependent on this macropore-micropore interrelationship. A number of theoretical models derived for porous electrodes are based on a variety of hypotheses on precisely these kinds of pore structure considerations.

On a short-term operation basis, as used in this work for electrochemical measurements, the importance of macroporosity may indeed be unjustifiably subtle. In order to gain some understanding on this point, one can attempt to utilize the only types of pertinent information available at present, namely, nondestructive porosity measurements.

Another aspect of interest, regarding the influence that micropore structure has on electrode performance (11, 12, 23) can be considered in a special sense. This is the question of what portion of the actually measured micropore structure appears to be of greater consequence to performance.

Both of these aspects will now be examined in some detail.

Figure 11 illustrates what happens when current density is referred to specific portions of the micropore structure. In this case, it appears that mostly the pore radius range 25-200Å is performance-determining, out of the total range under consideration, 25-350Å. This examination could conceivably be refined still further, if warranted by additional data, by considering smaller increments of cumulative pore volume. The findings are qualitatively corroborated by similar studies reported for activated carbon electrodes (12).

Figure 12 suggests this dependence on pore radius, in the micropore size range, by examining graphically the relationship between current density or limiting current density and the fraction of the total pore volume (range 25-350Å) consisting of pores in the range 25-200Å. The trend is more obvious for the case where the current density is the dependent variable but, in any case, the data scatter is such as to justify only qualitative conclusions at this point.

The relative importance of micro- and macro-pore structure is graphically represented in Fig. 13 and 14, in terms of measured porosities. A log-log dependence is exhibited between current and limiting current, respectively, and the fraction of the total open porosity consisting of micropores in the range 25-350Å. One

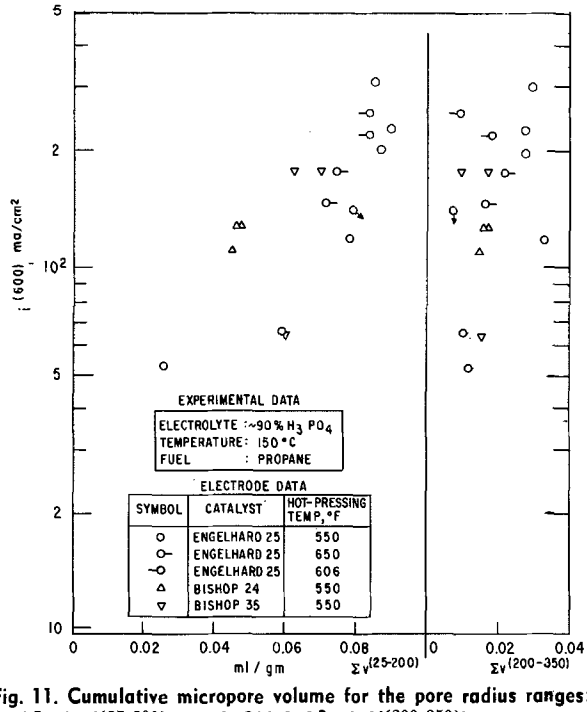

Fig. 11. Cumulative micropore volume for the pore radius ranges: 25-200Å ($\Sigma V^{(25-200)}$) and 200-350Å ($\Sigma V^{(200-350)}$) vs. current density at an IR-free anode potential of 600 mv vs. H_2/H^+ ($i^{(600)}$).

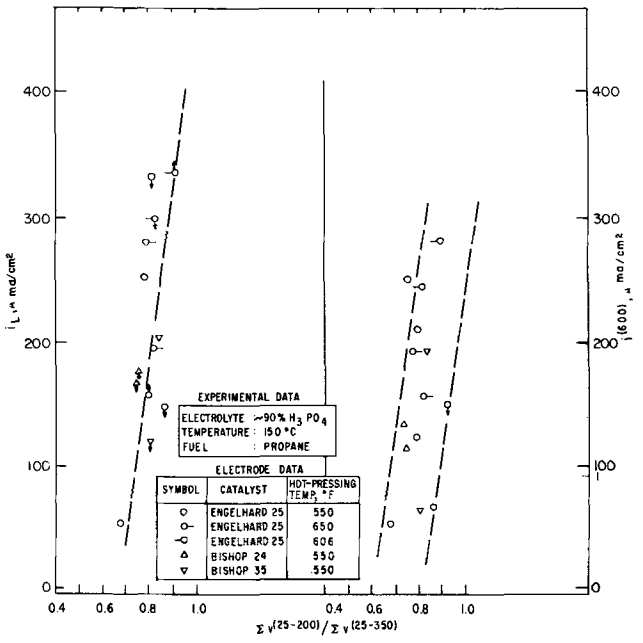

Fig. 12. Limiting current density (i_L) and current density at an IR-free anode potential of 600 mv vs. H_2/H^+ ($i^{(600)}$), as a function of the fraction of the total measured micropore volume composed of pores in the radius range: 25-200Å ($\Sigma V^{(25-200)}/\Sigma V^{(25-350)}$).

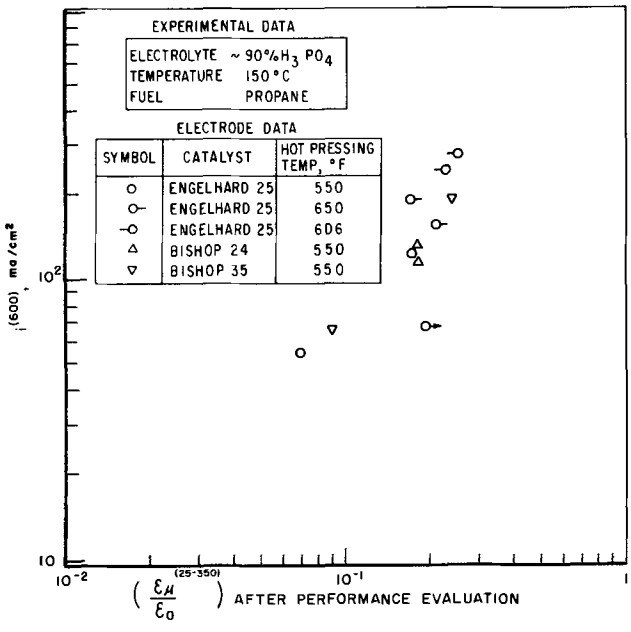

Fig. 13. Current density at an IR-free anode potential of 600 mv vs. H_2/H^+ ($i^{(600)}$) as a function of the fraction of the total open porosity consisting of micropores in the radius range: 25-350Å ($\epsilon_\mu^{(25-350)}/\epsilon_0$).

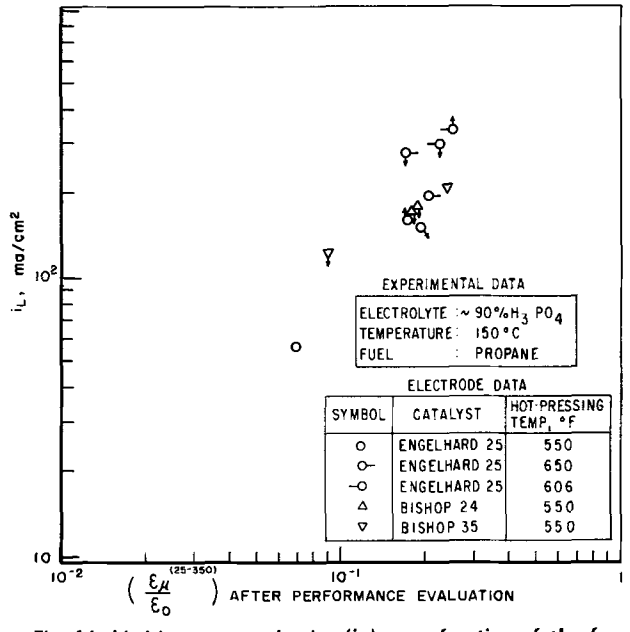

Fig. 14. Limiting current density (i_L) as a function of the fraction of total open porosity consisting of micropores in the radius range: 25-350Å ($\epsilon_\mu^{(25-350)}/\epsilon_0$).

observes the rather interesting fact that, as this porosity ratio increases in favor of more micropores, the performance improves. It is not clear at present whether this relative importance of the micro- and macro-pore structures is actually conducive to a maximum or asymptote type of optimum structure. This type of information would depend on the development of adequate nondestructive methods for the measurement of pore size distributions over a wider range than is presently possible. It is interesting to speculate, however, that in the case of apparent micropore structure control as suggested here the film mechanism used in a variety of electrode models is not necessarily dominating; instead, bulk diffusion into the smaller, flooded, pores may be controlling. Another possibility might be a capillary-type control of the diffusional process in the pores, in terms of film-activated macropores "fed" with fresh liquid surfaces from flooded micropores (23).

Thus, the existing data do seem to demonstrate the importance of extending our present knowledge of performance-structure dependence, while, at the same time, suggesting the possibility of ultimately tailoring optimum configurations from the information at hand. For the time being, any theoretical model describing the operation of the class of porous electrodes covered in the present work will have to take into account the apparent role of the micropore structure, in general, and of certain portions of this micropore structure, in particular. Whether this role will be strictly one of establishing the right electrolyte-reactant phase equilibrium or not, remains to be seen.

Conclusions

1. Nondestructive measurements of structural parameters for porous electrodes of any size are possible, and they offer the advantage of direct correlatability with electrochemical performance. Surface area and porosity can be determined for the whole electrode, the former with a great degree of precision and accuracy. The nondestructive pore size distribution measurements are presently limited to pores 600Å or less in radius, *i.e.*, to that portion of the electrode structure that is mostly in the micropore range where gas molecules would be transported by Knudsen rather than bulk diffusion.

2. Variables such as catalyst type and manufacturer, original catalyst area, electrode manufacturing conditions such as the hot-pressing temperature, and electrode history, all determine to a significant degree the values that the various structure parameters will have.

3. There is a good correspondence between BET-derived electrode surface areas and cumulative micropore volumes. Conversely, the use of electrode surface areas derived from pore size distribution data can lead to values that are higher than the BET results by a factor of roughly 2; these higher figures are believed to be in error due to the assumptions inherent in the integration of the pore size distribution equations.

4. All electrodes possess appreciable fractions of macroporosity; this fraction also appears to be the main contributor to the increase in open porosity characteristic of electrodes that have been put on load.

5. Electrochemical anode performance appears to

increase exponentially or linearly (with slightly more experimental data scatter) with electrode surface area or micropore volume. The micropores themselves play a rather important role when their contribution is compared to that of the entire electrode (in terms of porosities). Furthermore, within the micropore spectrum there are ranges of pore sizes that appear to have more bearing on the electrochemical performance than others. For a porous composite structure of the platinum black-Teflon-metal screen type the more active portion of micropores, consisting of radii in the range 25-350Å, is limited to the range 25-200Å.

Considerably more work is necessary, in terms of more data of total as well as true (electrochemically active) surface areas, and nondestructive pore size measurements encompassing the macropore as well as the micropore spectrum. This should eventually lead to a finalization and generalization of these conclusions and additional ones, as well as to working theoretical models and tailor-made optimum porous electrode geometries.

Acknowledgments

This work is a part of the program under Contract Nos. DA 44009-ENG-4909, -AMC 479(T), and -ENG 4853, with the U. S. Army Engineer Research and Development Laboratories, Fort Belvoir, Virginia, to develop a technology which will facilitate the design and fabrication of practical military fuel cell power plants for operation on ambient air and hydrocarbon fuels.

The author wishes to acknowledge the assistance of J. Lennon and co-workers for the running of the electrochemical performance tests, J. Stinson and co-workers for the computer data processing, G. McGray for the running of electrode structure measurements, and J. Foley for the manufacturing of most of the electrodes and preparation of the catalytic mixes used in the present study.

Manuscript received Nov. 9, 1966; revised manuscript received April 4, 1967. This paper was presented at the Philadelphia Meeting, Oct. 9-14, 1966.

Any discussion of this paper will appear in a Discussion Section to be published in the June 1968 JOURNAL.

REFERENCES

1. A. J. Salkind, H. J. Canning, and M. L. Block, *Electrochem. Technol.*, **2**, 254 (1964).
2. M. J. Joncich and N. Hackerman, *This Journal*, **111**, 1286 (1964).
3. D. Berndt, *Electrochim. Acta*, **10**, 1067 (1965).
4. M. Bonnemay *et al.*, *This Journal*, **111**, 265 (1964).
5. M. Bonnemay *et al.*, *Electrochim. Acta*, **9**, 727 (1964).
6. K. Appelt and A. Nowacki, *ibid.*, **11**, 137 (1966).
7. W. R. Lasko and G. P. McCarthy, *Analyt. Chem.*, **38**, 894 (1966).
8. P. Drossbach and J. Schulz, *Electrochim. Acta*, **9**, 1391 (1964).
9. G. Feuillade, *J. Chim. Phys.*, **60**, 613 (1963).
10. R. Coffre *et al.*, *J. Chim. Phys.*, **61**, 1043 (1964).
11. R. R. Paxton *et al.*, *This Journal*, **110**, 932 (1963).
12. K. Schwabe *et al.*, *Electrochem. Technol.*, **3**, 189 (1965).
13. L. W. Niedrach and H. R. Alford, *This Journal*, **112**, 117 (1965).
14. S. Brunauer *et al.*, *J. Am. Chem. Soc.*, **60**, 309 (1938).
15. Perkin Elmer—Shell Corporation: Sorptometer Manual.
16. G. E. Armstrong, *J. Research Nat. Bur. Stand.*, **53**, 263 (1954).
17. E. Y. Weissman, *Rev. Sci. Instr.*, **38**, 565 (1967).
18. A. Wheeler, "Reaction Rates and Selectivity in Catalyst Pores," Catalysis, Vol. II, P. H. Emmet, Editor, Reinhold Publishing Corp., New York (1955).
19. C. Pierce, *J. Phys. Chem.*, **57**, 149 (1953).
20. K. Kordesch and A. Marko, *This Journal*, **107**, 480 (1960).
21. J. H. Ramser and P. B. Hill, *Ind. & Eng. Chem.*, **50**, 117 (1958).
22. A. B. LaConti, Private communication.
23. R. C. Burshtein *et al.*, *Electrochim. Acta*, **9**, 773 (1964).

Electrochemical Studies on Lead in Organic Electrolytes

M. L. Bhaskara Rao

Laboratory for Physical Science, P. R. Mallory & Company, Inc., Burlington, Massachusetts

ABSTRACT

Galvanostatic anodic charge and cathodic discharge curves have been obtained for lead and lead alloys in two organic electrolytes: propylene carbonate, 1M in $LiAlCl_4$, and γ-butyrolactone, 0.5M in LiCl. Charging curves exhibited periodic (oscillatory) voltage phenomena followed by passivation. Discharge curves of pre-anodized electrodes showed a single plateau corresponding to the reduction of $PbCl_2$ to Pb. Utilization efficiencies obtained from charge and discharge coulombs ranged from 10 to 100% depending on the current density, alloy composition, and electrolyte. Differences in observed behavior have been explained, and the suitability of $Pb/PbCl_2$ electrodes for rechargeable organic electrolyte cells is discussed.

During the past few years there has been an increased interest in electrochemical investigations in organic electrolyte media. Most of these efforts have been directed toward the development of high energy density batteries. Analysis of the state of the art reveals that for a success in this endeavor it is necessary to understand more about the chemical and electrochemical behavior of the cathode salts. In the course of developmental work in this field we have earlier reported some observations on the formation and discharge of copper chloride (1). The present paper deals with electrochemical studies on lead leading to the possibility of operation of lead chloride electrodes in an organic electrolyte.

Experimental

The cell.—Electrochemical experiments were carried out in a Pyrex glass H-cell of 50-ml capacity with a sintered glass frit separating the two compartments. The cell had a suitable polytetrafluoroethylene lid with provision for mounting the electrodes and for

admitting dry argon to maintain a moisture-free inert atmosphere over the electrolyte.

Electrolytes.—The electrolytes were 1M $LiAlCl_4$ in propylene carbonate and 0.5M LiCl in γ-butyrolactone. These were prepared by dissolving calculated amounts of the salts in known volumes of pre-purified solvents. The procedures for the purification of the solvents have been described earlier (1).

Electrodes.—Solid lead foil electrodes, amalgamated lead, lead silver (5-15 w/o Ag) and lead-tin (33 w/o tin) were employed in the studies.

The lead foil samples were Fisher test grade, 5-15 mils thick. The foils were degreased in trichloroethylene and treated with 600Å polishing paper or chemically cleaned by immersing the degreased samples in 5*N* aqueous HNO_3 for 2 min at room temperature. The samples were then rinsed with water followed by acetone, and dried. The chemically cleaned electrodes had been etched in the process. Working electrodes of 2-5 cm^2 superficial area were cut from the treated samples.

Lead alloys of silver were prepared in the laboratory. The tin alloy of lead was commercial plumber's solder.

Pasted plate lead chloride electrodes were of the weight composition 9:1:0.5::$PbCl_2$: graphite: ethycellulose. These were made by spreading the mixture of the components as a paste in xylene over graphite cloth and drying the samples in air. The coulombic capacity of the electrodes was between 2.5 and 10 ma-hr/cm^2.

Measuring setup.—The electrochemical measurements were galvanostatic. The constant current was provided from an electronically controlled power supply of Electronic Measurement Inc., Model 620. The counter electrode was a strip of lithium placed in the counter electrode compartment of the H-cell. The potential of the working electrode was measured against a silver reference electrode situated in the same solution at 2 mm from the former. An E-H Labs Electrometer, Model 230, was used for potential measurement. The output from the electrometer was fed to a Mosley Autograph 680 recorder to register the data.

Anodic and cathodic measurements were made at currents between 2.5 and 10 ma cm^{-2} based on superficial area of the electrodes.

The solubility of the lead salt formed during anodization of the lead metal in the organic electrolytes was measured by polarography. Aqueous 1M HCl solutions containing 1-2 v/o (volume per cent) aliquots of the working solution were employed for the purpose. A Metrohm Polarecord Model E-261 unit was used to obtain the polarograms.

A Phillips type 422730 x-ray diffraction unit was employed to identify the electroformed salt. The measurements employed copper radiation with a nickel filter.

Results

Anodic behavior of chemically treated lead in 1M $LiAlCl_4$-P.C.—The galvanostatic anodic behavior of chemically cleaned lead in 1M $LiAlCl_4$-P.C. is shown in Fig. 1. The data in curves 1 to 4 are for apparent current densities of 2.5 to 10 ma cm^{-2}, respectively. It is seen that on anodization the lead electrodes exhibit periodic oscillation in voltage, followed by passivation. In the passive region the electrode potential increased linearly with time and indicated erratic fluctuations above 40v. Analysis revealed that the rate of change of potential with time was directly proportional to the current density in the linear region as is shown in Fig. 2. Current interruption at all stages of anodization resulted in an open-circuit voltage of approximately —0.25v *vs.* Ag. If anodization were continued to passivation, the electrodes exhibited a memory effect in that, following current interruption, the potential after the resumption of anodization rose to the value observed at the point of current interruption. This

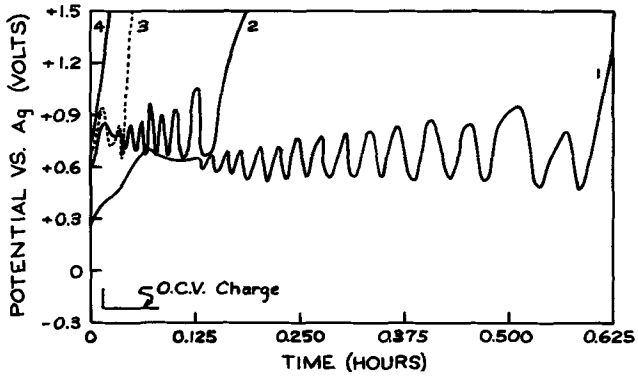

Fig. 1. Anodic charging of chemically etched lead in 1M $LiAlCl_4$-P.C. Curves 1, 2, 3, and 4 are for 2.5, 5, 7.5, and 10 ma cm^{-2}, respectively.

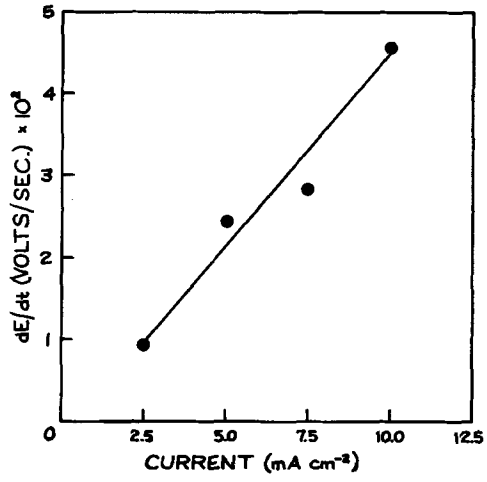

Fig. 2. Plot of (dE/dt) vs. current density

memory effect persisted even when the electrodes were left on open circuit in stirred solution as long as 5 min.

Cathodic discharge curves of electrodes pre-anodized to 40v *vs.* Ag are shown in Fig. 3. In these experiments the cathodic current densities were the same as used for anodization. It is seen from curves 1 to 3 that the electrodes exhibited overshoots in the initial stages of cathodization. However, the overshoot was far less than the potential of 40v reached at the end of the preceding anodization, and the utilization efficiencies were less than 100% at all current densities.

Anodic behavior of polished lead electrodes in 1M $LiAlCl_4$-P.C.—Figure 4 shows the successive anodic

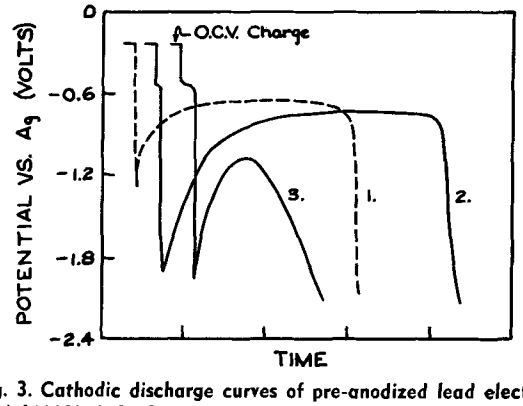

Fig. 3. Cathodic discharge curves of pre-anodized lead electrodes in 1M $LiAlCl_4$-P.C. Curves 1, 2, and 3 are for 2.5, 5, and 10 ma cm^{-2} with time scale 7.5 min, 2 min, and 1 min per division, respectively.

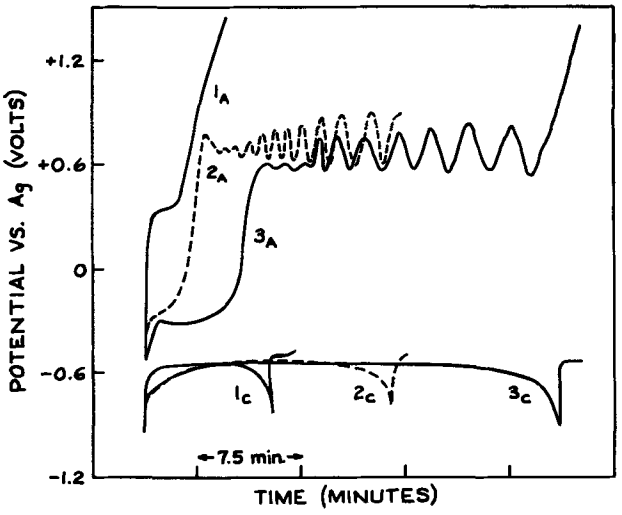

Fig. 4. Anodic charge and cathodic discharge behavior of lead in 1M $LiAlCl_4$-P.C. at current density 2.5 ma cm^{-2}. Curves 1_a and 1_c are charge discharge curves for 0.5 ma-hr cm^{-2} on 1st cycle; curves 2_a and 2_c are charge discharge curves for 1 ma-hr cm^2 on 2nd cycle; curves 3_a and 3_c are charge discharge curves for 2.5 ma-hr cm^{-2} on 3rd cycle.

and cathodic behavior of a polished lead electrode in 1M $LiAlCl_4$-P.C. at 2.5 ma cm^{-2}. Successive cycling of the same electrode increased the anodic charge before passivation from 0.5 to 2.5 ma-hr cm^{-2}. Although potential oscillation occurred during the anodization, the faradaic efficiency of subsequent cathodization was 100%.

Cathodic discharge of pasted plate lead chloride electrodes in 1M $LiAlCl_4$-P.C.—The discharges of typical pasted plate lead chloride electrodes of capacity 7.5 ma-hr cm^{-2} were similar to curves 1_c to 3_c in Fig. 4 in that the open-circuit voltage of the system was close to —0.25v *vs.* Ag. The cathodic discharge efficiency based on the known weight of $PbCl_2$ was greater than 90% at 5 ma cm^{-2}.

X-ray diffraction of the deposit formed on lead electrodes anodized in 1M $LiAlCl_4$-P.C. indicated mostly $PbCl_2$. In case of heavily anodized (>30v) electrodes some PbO_2 was observed in the $PbCl_2$ deposits.

Behavior of lead alloy electrodes.—In the anodization of lead-silver alloys (5-15 w/o Ag) in 1M $LiAlCl_4$-P.C. the oscillatory voltage behavior still persisted very nearly the same as on pure lead. The open-circuit voltages of anodized electrodes were more positive than that of the $Pb/PbCl_2/Cl^-$ system and were unsteady. The lead-tin alloy (33 w/o tin) was capable of supporting 5 ma-hr cm^{-2} anodic charge density (at 5 ma cm^{-2}) before oscillatory voltage behavior ensued. It is interesting to note that under the conditions of experimentation passivation occurred on lead even below 0.5 ma-hr cm^{-2} of anodic charge density. However, from the cathodization experiments, the calculated utilization efficiencies were found to be lower than 80%.

Anodization of the amalgamated electrodes in 1M $LiAlCl_4$-P.C. exhibited neither oscillatory phenomena nor passivation even up to 20 ma-hr cm^{-2} of anodic capacity. X-ray diffraction did not indicate any mercury halide inclusions in the $PbCl_2$ films of the anodized samples. The utilization efficiencies of these electrodes were greater than 90%.

Behavior of lead electrodes in 0.5M LiCl *in γ-butyrolactone.*—Experiments carried out to study the electrochemical behavior of lead electrodes in 0.5M LiCl in γ-butyrolactone showed neither passivation on anodic polarization nor the prepassivation oscillatory voltage behavior in the current density range of 2.5-10 ma cm^{-2}. The faradaic efficiency obtained on subsequent cathodization was less than 10% for 2.5 ma-hr cm^{-2} anodic charge. The working solution was examined to estimate the concentration of dissolved Pb^{++} ions. The analysis indicated a material balance equivalent to 100% anodic efficiency and suggested the dissolution of the electroformed Pb^{++} as the cause of low cathodic efficiency.

Lead chloride solubility.—The solubility of $PbCl_2$ in propylene carbonate, 1M $LiAlCl_4$-P.C. and γ-butyrolactone was low (<0.0005 m/l) at 25°C. However, $PbCl_2$ was soluble in 0.5M LiCl in γ-butyrolactone.

To examine this solubility behavior of $PbCl_2$ in the LiCl in γ-butyrolactone, 0.1 mole equivalent of $PbCl_2$ was added to 100 ml of γ-butyrolactone solutions containing different molarities of LiCl, and the solutions were equilibrated at room temperature by stirring the mixture over a period of a day. A complete dissolution of the lead salt was observed in solutions containing 0.2M LiCl. This indicated the formation of a soluble $PbCl_4^=$ complex.

Discussion

A comparison of the anodic behavior of chemically treated (etched), mechanically polished, and cycled electrodes shown in Fig. 1 and 4 suggests that the differences in the oscillatory voltage behavior for measurements performed at equal apparent current densities may be ascribed to the differences in the true surface area of the three types of electrodes.

Oscillatory phenomena attending electrocrystallization in aqueous media have been described (2-12) earlier. Various mechanisms involving mechanical breakdown and rehealing of anodic films or dissolution and reformation of films due to valence changes of the anodic species have been proposed to account for the oscillatory behavior. By x-ray diffraction we find that $PbCl_2$ is the major product of anodization in the experiments shown in Fig. 1 and 4. Therefore it is presumed that the oscillatory behavior observed in these experiments reflects the particular mechanism by which $PbCl_2$ is anodically formed from the lead metal.

Analysis of the passive region of the heavily anodized (>30v) lead electrodes is shown in Fig. 2. The variation of electrode potential with time follows Eq. [1]

$$\frac{(dE)}{(dt)} = k\, i_a \qquad [1]$$

where E is the electrode potential *vs.* Ag at time t during anodization under the influence of a current density of i_a; k is a proportionality constant. The formulation in Eq. [1], although approximate, is widely discussed (13) in the anodic growth of ionically conducting films. Based on the behavior in Fig. 2, the variation of the electrode potential with time is ascribed to an increase in resistance of the $PbCl_2$ film with increasing thickness. The presence of some PbO_2 in the heavily anodized electrodes is probably connected with parasitic reactions involving the solvent or impurities such as water in the electrolyte.

The cathodic discharge curves of the pre-anodized electrodes as in Fig. 3, curves 1, 2, and 3, do not reflect the IR drop in the electrode observed during anodization except for the overshoot in the initial part of the discharge curves. This is probably due to the generation of a porous conducting matrix of lead from the reduction of lead chloride and the associated large change in the density of the film. The production of large surface area electrodes observed during the cycling experiments substantiates this hypothesis. It is interesting to note from the curves in Fig. 4, 1, 2, and 3, that, provided the electrodes are not heavily pre-anodized, the utilization efficiency of $PbCl_2$ electrodes is nearly 100%. The discharge efficiency of pasted plate lead chloride electrodes was similarly high.

The absence of periodic phenomena and poor utilization efficiencies in the electrochemical behavior ob-

served for lead in 0.5M LiCl in γ-butyrolactone is explained by postulating a soluble lead species formation during anodization as in Eq. [2] and [3]

$$Pb = Pb^{++} + 2e \text{ (electrochemical)} \quad [2]$$

followed by

$$Pb^{++} + 4Cl^{-} = PbCl_2^{=} \text{ (chemical)} \quad [3]$$

The formation of the soluble tetrachloroplumbate complex during anodization and its diffusion away from the electrode accounts for the lack of periodic phenomena, passivation, and low utilization efficiency. The explanation is based on the facts that (*a*) the anodic efficiency is 100% and (*b*) $PbCl_2$, the anodic salt which is inherently sparingly soluble in γ-butyrolactone (0.0005 m/l), dissolves in lithium chloride solutions in $PbCl_2$:2LiCl mole ratio.

It is clear from the above results that of the two organic electrolytes tested, 1M $LiAlCl_4$-P.C. is better suited for the operation of lead chloride cathodes. Pasted plate lead chloride electrodes have shown 90% utilization efficiency in this electrolyte, and hence the suitability of the active material for primary cells has been attested.

The oscillatory voltage behavior and the subsequent passivation reactions of lead during anodization in 1M $LiAlCl_4$-P.C. are rather undesirable characteristics for the application of the $Pb/PbCl_2/Cl^-$ half-cell for rechargeable cells. Hence attempts were made to eliminate or minimize these effects. In one such investigation the electrochemical behavior of lead-silver, lead-tin, and amalgamated lead were studied. Of the lead-silver and lead-tin alloys tested none proved superior to pure lead, but on the other hand, anodization of amalgamated lead electrodes exhibited neither voltage oscillations nor passivation and discharged with utilization efficiency >90%. The formation of a discontinuous $PbCl_2$ film due to the presence of mercury on the surface of lead electrodes is suggested for the observed behavior. Thus the amalgamation technique seems to render the lead chloride electrodes suitable for operation in organic electrolyte secondary cells.

It is interesting to point out that the amalgamation technique has been used to overcome the undesirable characteristics of anodes in aqueous media; herein the process has served to eliminate the problems of a cathode.

Acknowledgments

The author wishes to thank Dr. Per Bro and Dr. Robert Selim for useful discussions, Mr. Leonard Griffiths for x-ray analysis, and Mr. Clintford R. Jones for preparing the alloys.

Manuscript received Dec. 29, 1966; revised manuscript received March 13, 1967. This paper was presented at the Dallas Meeting, May 7-12, 1967.

Any discussion of this paper will appear in a Discussion Section to be published in the June 1968 JOURNAL.

REFERENCES

1. M. L. Bhaskara Rao, *This Journal*, **114**, 13 (1967).
2. J. H. Bartlett, *ibid.*, **87**, 521 (1945).
3. J. H. Bartlett and L. Stephenson, *ibid.*, **99**, 504 (1952).
4. L. Meunier, CITCE Report 3 (1952).
5. E. S. Hedges, *J. Chem. Soc.*, **1926**, 2878.
6. H. Lal and H. R. Thirsk, *ibid.*, **1953**, 2638.
7. D. A. Vermilyea in "Advances in Electrochemistry and Electrochemical Engineering," P. Delahay and C. Tobias, Editors, vol. 3, p. 127, Interscience, New York (1963).
8. K. F. Bonhoeffer, *Z. Elektrochem.*, **52**, 24 (1948).
9. K. F. Bonhoeffer and H. Gerischer, *ibid.*, **52**, 149 (1948).
10. R. S. Cooper and J. H. Bartlett, *This Journal*, **105**, 109 (1958).
11. H. Lal, H. R. Thirsk, and W. F. K. Wynne-Jones, *Trans. Faraday Soc.*, **47**, 999 (1951).
12. U. F. Fanck and R. Fitzhugh, *Z. Elektrochem.*, **65**, 156 (1951).
13. L. Young, "Anodic Oxide Films," p. 6, Academic Press, New York (1961).

Effect of Heating Single Crystal Copper in H_2 and N_2 on Thin-Film Oxidation Kinetics

W. W. Bradley[1] and H. H. Uhlig

Department of Metallurgy, Massachusetts Institute of Technology, Cambridge, Massachusetts

ABSTRACT

The oxidation rate of spectroscopically pure polycrystalline and single crystal copper at 200°C in 1 atm O_2 was measured by coulometric reduction of the oxide. Growth of Cu_2O films up to 4000Å thick follows two-stage logarithmic kinetics. Pretreatment of filed polycrystalline Cu surfaces in H_2 at 450°C for 30 min decreases by 50% the thickness of oxide forming subsequently in O_2 at 200°C. Similar pretreatment in N_2, on the other hand, has little or no effect. Hydrogen pretreatment of electropolished single crystal Cu decreases oxidation of (100), has no effect on oxidation of (111), and increases oxidation of the (110) face. Pretreatment in N_2 at 450°C has no appreciable effect on subsequent oxidation of (100), contrary to H_2 pretreatment, and it increases oxidation of both (111) and (110) faces.

The oxidation rates of untreated Cu faces decrease in the order (100) > (111) > (110) in agreement with data of Gwathmey and his collaborators. Hydrogen pretreatment leads to oxidation rates, whatever the original orientation, approaching that of the (111) face; N_2 pretreatment leads to rates approaching that of the (100) face. The results appear to be best explained by a rearranged surface or submicroscopic faceting resulting from hydrogen adsorption, the preferred orientation of which approximates the (111) face. Pretreatment in N_2, on the other hand, probably because of adsorbed traces of oxygen in gas or metal, favors rearrangement having the approximate (100) orientation. Observed two-stage logarithmic kinetics for oxidation of rearranged surfaces, and the results by others of low energy electron diffraction, suggest that the first-formed adsorbed oxygen-metal film is extremely stable, maintaining its characteristic structure and orientation throughout the oxidation process. It thereby establishes oxidation rates in the thin film region independent of original crystal face. It is concluded that gaseous or vacuum pretreatment of Cu surfaces can exert a large effect on subsequent oxidation behavior.

Hydrogen annealing of Cu specimens or H_2 reduction of an air-formed oxide film on Cu is often employed as a preliminary step in studying oxidation or measuring oxidation rates (1-6). In the presently described experiments, this procedure was also followed, but it was observed that H_2-pretreated specimens that were oxidized subsequently in 1 atm O_2 at elevated temperatures within the thin film range ($<10^4$Å) reacted to a lesser extent than did the same specimens without pretreatment, or when heated initially in N_2. The obvious immediate explanation was that some hydrogen was dissolved in the metal during the pretreatment procedure becoming available during oxidation to react either with O_2, thereby limiting availability of O_2 for oxidation of copper, or to reduce some of the metal oxide which had already formed. However, calculations showed that the amount of dissolved hydrogen, assuming complete saturation, was appreciably below that required by reduction to explain the observed thinner oxide. For example, the solubility of H in Cu at 450°C, a typical pretreatment temperature, is 6.4×10^{-3} mg/100g Cu (7). Our Cu specimens were 0.6 cm thick, hence assuming saturation at 1 atm H_2, each 1 cm² of the Cu specimen contained

$$\frac{6.4 \times 10^{-3} \times 0.6 \times 8.9}{100} = 3.42 \times 10^{-4} \text{ mg H}$$

where 8.9 is the density of copper. This amount of hydrogen is able to reduce Cu_2O (mol. wt. = 143.1, density = 6.0) equal in thickness to

$$\frac{3.42 \times 10^{-4} \times 143.1 \times 10^8}{10^3 \times 2 \times 6.0} = 408\text{Å}$$

Since dissolved hydrogen is available to reduce oxide on two sides of the Cu specimen, the oxide, therefore, for H_2-pretreated Cu should be thinner to a maximum extent of 204Å. In several experiments using a filed surface of OFHC Cu, 20-min exposure to O_2 at 200°C produced an oxide film averaging 2029Å, whereas after H_2 pretreatment at 450C for ½ hr, the film thickness for the same oxidation conditions averaged 1035Å, the difference being 994Å. Hence the amount of available dissolved hydrogen to account for the thinner oxide was too small by a factor of 994/204 = 4.9, which is well outside present experimental errors.

On the assumption that hydrogen may have dissolved abnormally in our particular copper sample, the solubility was checked by Bohnenkamp at 350°C using standard methods, resulting in a value close to that reported in the literature. Change of roughness factor did not enter the explanation because parallel pretreatment in N_2 at 450°C for ½ hr did not affect subsequent oxide thickness in O_2 at 200°C, contrary to marked reduction caused by H_2 pretreatment.

Further investigation showed that dissolved hydrogen could not be the explanation in any case because, if the copper surface were electropolished after either H_2, N_2, or no pretreatment, the oxide film formed subsequently in O_2 at 200°C was now the same thickness.[2] This experiment, therefore, pointed to an effect occurring at the metal surface. For example, an impurity might diffuse to the copper surface in presence of H_2 but not in presence of N_2. Williams and Hayfield (8), in fact, who observed a lower oxidation rate after vacuum treating copper specimens, suggested that an impurity was involved, such as Fe, which diffused to the surface through grain boundaries. However, our further experiments on spectroscopically pure copper

[1] Present address: Institute of Surface and Colloid Science and Department of Civil Engineering, Clarkson College of Technology, Potsdam, New York.

[2] This was true only when oxidation was carried out at 200°C. At 250°C, the oxide film formed on H_2-pretreated Cu was somewhat thinner than on N_2-pretreated Cu, indicating some reduction of oxide by dissolved H at the higher temperature.

showed the same quantitative effect as for OFHC copper, eliminating impurities as a likely explanation. Attempts were also made to determine any supposed impurities at the surface occurring through pretreatment by machining off a thin portion of the copper surface after both H_2 and N_2 pretreatments and submitting this material for analysis employing a sensitive mass spectrometer. However, the results led to no certain conclusions regarding any one suspected impurity.

Subsequently it was found that the effects of H_2 and N_2 pretreatment were sensitive to crystal face, some faces of copper showing small or no differences in oxidation rate, depending on the gas, whereas others showed a large effect. The details of these experiments are outlined herewith.

Experimental

Specimens of commercial OFHC or spectroscopically pure copper (purchased from American Smelting and Refining Company) measured 2.5 x 2.5 cm (1 x 1 in.) and were 0.6 cm (¼ in.) thick. Single crystals (purchased from Virginia Institute of Scientific Research) cut from a 2.5 cm diameter boule were circular or elliptical in surface dimensions, but otherwise similar. A spiral Nichrome wire heater element made contact with one face of the specimen employing mica sheet insulation and a thin 18-8 stainless steel backing plate. A hole was drilled in the side of the specimen into which a chromel-alumel thermocouple was cemented. The side opposite to that in contact with the heater element was prepared for oxidation studies. Proper surface preparation, as in all thin film studies, was extremely important but was never ideal. Some measurements were made using a filed surface because this preparation was found previously to provide reproducible Volta potentials (9) which are very sensitive to surface preparation. Ten-inch Swiss cut No. 4 steel files were used for this purpose; they were cleaned each time before use by light pickling in nitric acid followed by brushing and washing in water, then immersion in distilled acetone and distilled benzene. Electropolishing, when carried out, was performed on a previously metallographically polished surface. The electrolyte consisted of 70 v/o (volume per cent) orthophosphoric acid to which 100 g/l cupric orthophosphate were added. Initial and final current density approximated 0.04 and 0.02 amp/cm^2 at a temperature of 0°C. More than 10μ of metal were removed totally. The specimen was taken out of the electrolyte without interrupting the current, immediately immersed in 10 v/o orthophosphoric acid (without current) and washed in deaerated distilled water. The acid-water rinse was repeated 4 times, the specimen then being washed in 5 consecutive bottles of deaerated distilled water through which CO_2 passed continuously. The specimens were finally dried in a stream of nitrogen gas. Total rinse time exceeding 20 min was necessary to insure complete removal of copper reaction products remaining on the surface from the electropolishing operation.

For comparison, several specimens were abraded using No. 1 followed by No. 0 grit emery paper. Such specimens were oxidized without further surface treatment.

The assembly for carrying out the oxidation runs is shown in Fig. 1. A spherical Pyrex vessel, which contained the specimen, measured 9 cm diameter; this fitted by means of a ground glass joint (omitting grease) to a glass holder through which thermocouple and heating current wires were connected to tungsten glass seals.

The procedure was to heat the specimen to temperature rapidly (2 min to reach 200°C) in nitrogen previously purified by passing over Cu at 400°C followed by a liquid N_2 cold trap. The heating current was then adjusted to the value required to maintain the specified temperature. Oxygen at 1800 ml/min (dried

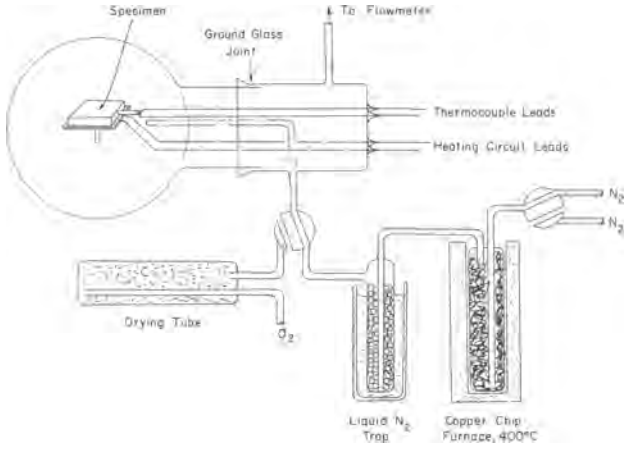

Fig. 1. Schematic diagram of oxidation cell

over $CaCl_2$) was used to flush out the nitrogen rapidly. Its entrance into the cell marked the beginning of oxidation. At the end of the oxidation period the heating current was turned off, the reaction vessel was rapidly flushed with purified N_2 at an initial flow rate of 4000 ml/min, and the specimen allowed to cool in N_2 to room temperature. Hydrogen pretreatment, when carried out, employed purified gas passed over Cu at 400°C followed by a liquid N_2 cold trap. The specimen was first heated to the required temperature in N_2 as outlined previously; the reaction vessel was then flushed out with H_2 and the temperature maintained for a specified time. The specimen temperature was then reduced to the temperature of oxidation, whereupon the vessel was flushed with N_2 for a period of 1 min at 1000 ml/min followed by flushing with O_2 as described previously. Throughout the sequence of operations, based on considerable experience, the temperature of the specimen was maintained by adjusting the heating current manually to within ±1°C of the desired temperature.

Oxide thickness was determined by coulometric reduction in accord with the technique described by Campbell and Thomas (10). The oxidized specimen was attached to a small inverted glass cell by means of a rubber gasket lightly covered with stopcock grease. A silver-silver chloride electrode located near the specimen surface followed potential change of the oxidized Cu surface during electrolytic reduction employing a d-c amplifier and a chart recorder. The cell was filled with deaerated 0.1*N* KCl, and a constant known current of approximately 0.1 ma/cm^2 was maintained with the specimen as cathode, and an auxiliary Ag wire as anode located outside the cell. From the time required to completely reduce Cu_2O of density 6.0 g/cm^3 on the surface of the specimen, the thickness of oxide was calculated to within at least ±10Å.

Results

Figure 2 shows the effect of H_2 pretreatment on oxidation of filed OFHC copper as a function of time in O_2 at 200°C. Oxidation occurs to an appreciably lesser extent after pretreatment of Cu in H_2 at 350°C for 1 hr compared to Cu not pretreated. Two-stage logarithmic kinetics applies in either case, the origin of which is discussed by Nwoko and Uhlig (11). An electropolished Cu single crystal, with exposed (100) face also oxidizes in accord with two-stage logarithmic kinetics as shown in Fig. 3. Since most subsequent comparative oxidation runs were carried out at 200°C for a fixed time of 20 min, it is seen from Fig. 2 and 3 that oxide films formed during this time correspond to second-stage oxidation. The effect of H_2 pretreatment, however, is observed in either first- or second-stage oxidation.

Although H_2 pretreatment lowers by an appreciable factor the oxide thickness formed subsequently on

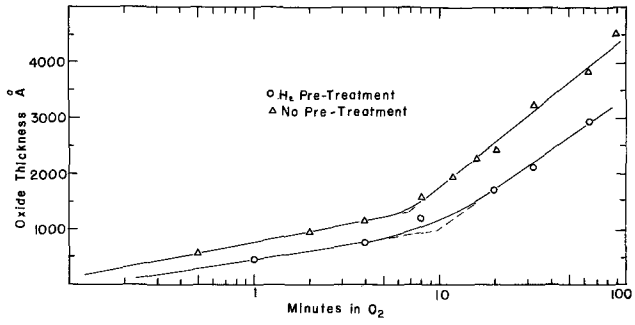

Fig. 2. Oxidation of OFHC polycrystalline copper, filed surface, in oxygen at 200°C. Pretreatment in hydrogen at 350°C, 60 min.

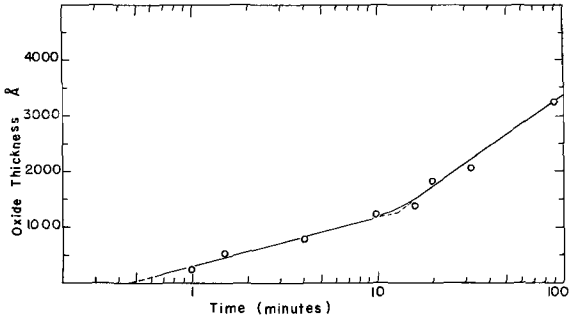

Fig. 3. Oxidation of (100) face of copper, electropolished surface, in oxygen at 200°C.

filed polycrystalline surfaces, a similar large effect is not observed for electropolished polycrystalline specimens nor for abraded specimens. The relevant data are listed in Table I presenting averaged values for the number of given specimens together with averaged deviations from the mean. Pretreatment in H_2 at 450°C lowers oxide thickness formed on filed surfaces by a factor of 0.5. On the other hand, N_2 pretreatment has little or no effect on filed surfaces, but it does increase the oxide thickness formed on electropolished and abraded surfaces by a factor of 3.7 and 1.7, respectively.

The effects of H_2 and N_2 pretreatment are sensitive to crystal face as shown by data of Table II. Further data are needed for adequate quantitative evaluation, but the preliminary results as presented indicate conclusively that the oxide formed on the (100) face is reduced in thickness by H_2 pretreatment (by a factor of 1/3.5), the (111) face is not affected, and the oxide formed on (110) is increased in thickness. Nitrogen pretreatment, on the other hand, has no effect on oxide thickness forming subsequently on the (100) face, but it increases oxide thickness on the (111) and (110) faces (by a factor of 5.4 and 11, respectively).

Specimens not pretreated follow a decreasing oxidation rate in the sequence (100) > (111) > (110) which agrees with previously reported results of Gwathmey and his collaborators (2, 5, 6). It is observed that this sequence and the differences among different faces tend to be obliterated by either H_2 or N_2 pretreatment of the Cu, but with the final oxidation rate for H_2 pretreated faces falling appreciably below that for N_2 pretreated faces. The observation of Rhodin (12) that the (110) face at or below 50°C oxidized more rapidly than did the (111) face, opposite to our results at 200°C, may relate in part to his measuring in some of his experiments a maximum oxide thickness of only 10-15Å which lies in the range of oxide nuclei dimensions. It seems reasonably certain that the mechanism of oxide growth as nuclei differs from that of its growth as a continuous film (13), the latter forming at 200° and 1 atm O_2 pressure from intergrowth of nuclei within fractions of a minute (14).

The effect of temperature and time of H_2 pretreatment of (100) Cu on subsequent oxidation in O_2 for 20 min at 200°C is shown in Fig. 4 and 5. Pretreatment for 30 min is effective above 350°C but not below. On the other hand, pretreatment for 30 min at 450°C achieved almost optimum effect on subsequent reduction of oxidation; longer times had only a slight additional effect.

Discussion

Data of Table II indicate that pretreatment of the three closest-packed faces of copper in H_2 results in an oxidation rate approaching that of the (111) face, whereas pretreatment in N_2 tends toward an oxidation rate approximating the (100) face. These effects are reversible; in other words, an H_2-treated surface subsequently treated in N_2 shows an effect characteristic of N_2 pretreatment and *vice versa*. Comparison of oxidation rates of Table II with those of Table I show that a filed surface appears to exhibit preferred orientation favoring the (100) face whereas an abraded surface favors the approximate (110) face. These orientations are in accord with an effect of H_2 pretreatment to decrease oxidation of filed surfaces but to increase instead oxidation of abraded surfaces. The exposed faces of electropolished polycrystalline OFHC surfaces consist of random orientations of which only those few near (100) are expected to oxidize rapidly. The average behavior corresponds to other orientations which oxidize slowly approximating (111) and (110) for which N_2 but not H_2 pretreatment has a

Table I. Effect of surface preparation and pretreatment on oxidation of polycrystalline OFHC copper in O_2 (1 atm) at 200°C for 20 min

Surface preparation	Oxide thickness, Å: No pretreatment	No. of spec.	Pretreated in H_2, 450°C, ½ hr	No. of spec.	Pretreated in N_2, 450°C, ½ hr	No. of spec.
Filed	2029 ± 79	5	1035 ± 15	2	2145 ± 115	2
Abraded	1213 ± 58	3	1520 ± 60	3	2013 ± 64	3
Electropolished	447 ± 96	3	405 ± 78	4	1670 ± 30	2

Table II. Effect of pretreatment on oxidation of single crystal copper in O_2 (1 atm) at 200°C for 20 min

Electropolished crystal face	*Oxide thickness*, Å: No pretreatment	No. of spec.	Pretreated in H_2, 450°C, ½ hr	No. of spec.	Pretreated in N_2, 450°C, ½ hr	No. of spec.
(100)	1812 ± 142	12	513 ± 83	6	1890**	1
(111)	370 ± 0	2	400 ± 80*	2	1995 ± 205	2
(110)	180 ± 20	2	325 ± 65*	2	2020***	1

* Temperature of pretreatment was 400°C. One specimen of (100) pretreated at 400°C instead of 450°C gave an oxide thickness of 670Å indicating only a small effect of temperature.
** Specimens pretreated at 400°C instead of 450°C gave an average oxide thickness of 1775Å.
*** One specimen pretreated at 400°C instead of 450°C gave an oxide thickness of 2260Å.

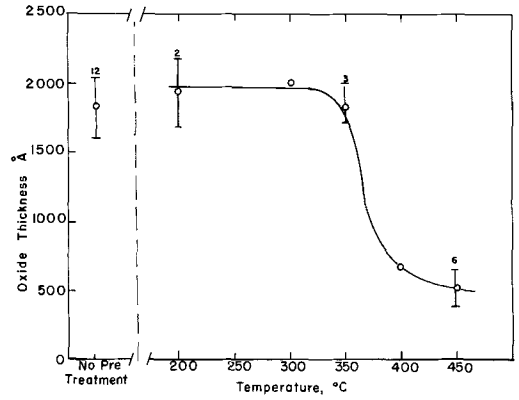

Fig. 4. Effect of temperature of hydrogen pretreatment for 30 min on oxidation of electropolished (100) face of copper in oxygen at 200°C for 20 min.

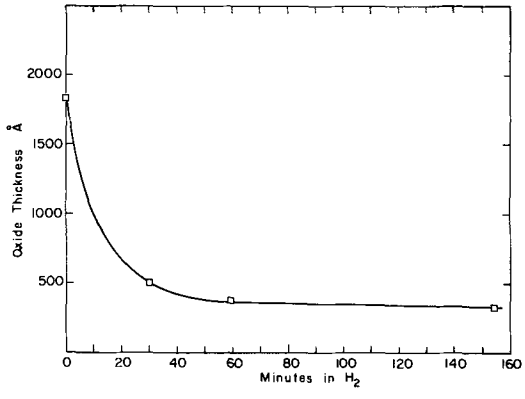

Fig. 5. Effect of time of hydrogen pretreatment at 450°C on oxidation of electropolished (100) face of copper in oxygen at 200°C for 20 min.

large effect on subsequent oxidation.

The present results can be explained in at least two ways: (*i*) effect of surface impurities, (*ii*) rearrangement of the copper surface (which may be regarded as submicroscopic faceting). The possibility that the present specimens were surface contaminated by unknown elements, the amount of which varied with N_2 or H_2 pretreatment and with crystal face, cannot be ruled out. This is especially true since only a partial monolayer of contaminant is apparently needed to appreciably change the oxidation rate, as was pointed out by Young *et al.* (5). Such a layer, for example, may change the metal work function, which on one viewpoint of thin film oxidation kinetics, could have a large effect on rate (15). Nevertheless an explanation based on surface rearrangement is also possible and perhaps more probable. For one thing, observed reproducibility of the pretreatment observations from one source of Cu to another is not characteristic of an impurity effect. Furthermore, the effect of pretreatment in N_2 or H_2 is independent of the presence or absence of grain boundaries along which diffusion of any suspected impurity would be enhanced, and also of gas flow rate which would introduce varying quantities of impurities to an exposed metal surface. In addition, the electropolished (100) Cu surface was observed under the electron microscope (60,000X) to roughen after N_2 or H_2 pretreatment corresponding to faceting of the metal surface. A systematic similar observation of other Cu faces (which remains to be done) is undoubtedly desirable for reaching a final conclusion, nevertheless the occurrence of submicroscopic faceting is made plausible on the basis alone of evidence now available.

The effect of gaseous environments at elevated temperatures to produce faceted surfaces of Cu and of other metals has been described previously by several investigators (16-21). Some explanations of the cause are based on preferential evaporation or reactivity of metal atoms, but more recently they have relied instead on variable surface energy of crystal planes. Accordingly, it is suggested that the environment (or gas dissolved in the metal) adsorbs on the metal surface reducing surface energy of some crystal faces more than others. At a sufficiently high temperature, the surface metal atoms bonded to adsorbate are able to rearrange themselves so as to favor the face or faces of lowest surface energy, resulting in microscopic facets or striations. The favored crystal faces vary with environment because adsorption on any given face also varies with environment.

If this explanation is correct, data of Tables I and II can be explained by the ability of H_2 during pretreatment to adsorb on Cu,[3] producing facets which, according to observed oxidation rates, favor the approximate (111) face. Surface diffusion of Cu plus adsorbate atoms probably occurs at an appreciable rate only above 350°C, suggesting this as the reason for an observed effect of H_2 pretreatment for 30 min also beginning at this temperature (Fig. 4). Gwathmey and Benton (16), for example, reported that single crystal Cu exposed at increasing temperatures to H_2-O_2 mixtures began to show facets at or above 360°C. On Ag, appreciable surface migration of atoms is reported to occur beginning at 230°-280°C, and on Au at somewhat higher temperatures (23). Cold working, such as is introduced by filing, would be expected to lower the temperature at which surface rearrangement is first measurable.

Nitrogen, on the other hand, does not chemisorb on copper (24) contrary to oxygen which chemisorbs even at very low partial pressures. A few experiments in the present series in which helium was used instead of N_2 as the pretreatment atmosphere showed the same effect. The influence of N_2, therefore, is probably equivalent to vacuum treatment in low-pressure O_2, the partial pressure of which is established by the dissociation pressure of Cu_2O at 400°C in the copper purification furnace (approximately 10^{-18} Torr O_2). The actual partial pressure of O_2 in our experiments, because of probable nonequilibrium flow rates, was undoubtedly higher. It was never high enough, however, to produce an oxide film showing interference colors on a copper surface maintained in flowing N_2 for 2 hr at 450°C. It is also possible, in fact, that any oxygen required for faceting may have originated not from the N_2 gas but instead from prior lattice dissolution of oxygen or from a previously air-formed oxide film. In this connection Elam (16) showed that faceting of copper in vacuum at 900°-950°C does not occur in absence of oxygen dissolved in the metal. Addition of Cu_2O to the melt or brief previous oxidation of the solid metal was required. In the complete absence of oxygen, therefore, N_2 pretreatment of Cu at 450°C might not produce faceting and, if so, would not affect subsequent oxidation rates. Experiments along these lines are still to be done. On the other hand, pretreatment of specific Cu faces at 450°C in pure H_2 would be expected to result in reproducible faceting although perhaps of submicroscopic dimensions (not visible at 1000X).

Orientation studies also support the occurrence of faceting during gaseous pretreatment. Although faceting is expected to vary with temperature because adsorption is temperature dependent, observed orientation of facets on Cu appearing at about 1000°C are not unrelated to those presumably produced at 450°C the orientation of which is inferred from presently reported oxidation behavior. Robertson (21) found that heating Cu at 1000°C in H_2-H_2O mixtures produces

[3] Although there is difference of opinion as to whether hydrogen chemisorbs on Cu (22), its adsorption in some degree at 450°C is indicated by a measurable interstitial solubility in Cu at this temperature. Alternatively, pretreatment in hydrogen thoroughly removes surface oxygen and may be equivalent in its effect to pretreatment of oxygen-free copper in ultrahigh vacuum.

facets that are thermodynamically stable near the (111) orientation. This is a face of low oxidation rate, and is also the approximate face which we conclude is formed by H_2 pretreatment at 450°C. For Cu heated at about 900°-1050°C in low pressure O_2 (*e.g.*, 10^{-4} Torr) several investigators have reported that resulting facets exhibit (111) and (100) orientation (25-28). The (100) face is rapidly oxidizing, and facets of this predominant orientation are also indicated by the present oxidation rates of Cu pretreated in N_2 (low-pressure O_2) at 450°C.

An important conclusion from the present observations is that gas or vacuum treatment of polycrystalline or single-crystal surfaces prepared in the usual manner can have large effect on subsequent thin film oxidation behavior. Since many previous investigators employed H_2-annealed specimens, the results they reported would be expected to differ from those employing vacuum-annealed specimens, accounting perhaps for initial oxidation rates that are often not in good agreement.

The fact that Gwathmey and co-workers (2, 5, 6) found low-temperature oxidation rates of Cu to vary with crystal face in the same order as for our untreated specimens, despite their use of a previous high-temperature H_2 anneal, suggests that their specimens faceted only incompletely, if at all, during pretreatment. Perhaps exposure of their Cu specimens to low-pressure O_2 during subsequent moderate vacuum outgassing and previous to oxidation counteracted earlier exposure to H_2. Lustman and Mehl's data showing a complicated effect of temperature on low-temperature oxidation rates of single crystal copper (1) may well have been the result of irreproducible faceting during incidental H_2 pretreatment.

Also of interest is the present observation that, assuming a faceted surface, Cu oxidizes continuously in accord with the newly created face or faces and not in accord with that of the original face. This is seen from Fig. 2 for which the oxide reaches a maximum thickness of about 3000Å equivalent to consumption of metal equal to 1800Å. If continuing oxidation gradually caused reversion to the oxidation rate of the original crystal face, the logarithmic equation would not be expected to hold. The speculative explanation that it does hold may reside in the extreme stability of the first-formed adsorbed oxygen-metal atom film on any specific crystal face. Observations of MacRae (29), Farnsworth (30), and others making use of low energy electron diffraction indicate that the first-formed chemisorbed oxygen film on nickel, for example, is thermally stable to a degree that it survives heating in ultra vacuum up to the melting point of Ni (1450°C).[4] Being apparently thermodynamically more stable than the oxide (13), the chemisorbed structure persists at temperatures and pressures that cause NiO to disappear. This unusually stable structure suggests that the adsorbed layer is able to persist or reproduce itself during the oxidation process, maintaining the orientation of the rearranged surface and establishing subsequent thin film oxidation rates. Were it not for this stability, the effect of faceting on thin film oxidation should be temporary and should persist only until most of the metal constituting the facets is consumed by oxidation.

[4] A similar stable chemisorbed oxygen film on Cu can be interpreted as forming on the (100) face in preference to Cu_2O after heating at 800°C in 1×10^{-3} Torr-min O_2 as reported by Mitchell *et al.* (31). The authors assume that absence of oxide is caused by solubility of oxygen in solid Cu.

Acknowledgment

Support by the Ford Foundation and by the International Nickel Company is gratefully acknowledged. The authors also thank F. L. LaQue of the International Nickel Company for arranging the mass spectroscopic analyses and H. C. Gatos of the Lincoln Laboratory (M.I.T.) for arranging the aligning and cutting of single crystal material.

Manuscript received Nov. 1, 1966; revised manuscript received March 17, 1967. This paper was presented at the Philadelphia Meeting, Oct. 9-14, 1967.

Any discussion of this paper will appear in a Discussion Section to be published in the June 1968 JOURNAL.

REFERENCES

1. B. Lustman and R. Mehl, *Trans. AIME*, **143**, 246 (1941).
2. A. Gwathmey and A. Benton, *J. Phys. Chem.*, **46**, 969 (1942).
3. T. Rhodin, *J. Am. Chem. Soc.*, **72**, 5102 (1950).
4. T. Mills and U. Evans, *J. Chem. Soc.*, **1956**, 2182.
5. F. Young, J. Cathcart, and A. Gwathmey, *Acta Met.*, **4**, 145 (1956).
6. W. Harris, F. Ball, and A. Gwathmey, *ibid.*, **5**, 574 (1957).
7. W. Eichenauer and A. Pebler, *Z. Metallkunde*, **48**, 373 (1957).
8. E. Williams and P. Hayfield in "Vacancies and Other Point Defects in Metals and Alloys," p. 131, Institute of Metals, London (1958).
9. H. H. Uhlig, *J. Appl. Phys.*, **22**, 1399 (1951).
10. W. Campbell and U. Thomas, *Trans. Electrochem. Soc.*, **76**, 303 (1939).
11. V. Nwoko and H. Uhlig, *This Journal*, **112**, 1181 (1965).
12. T. Rhodin, *J. Am. Chem. Soc.*, **73**, 3143 (1951).
13. H. H. Uhlig, Plenary Lecture, Third Int. Congress on Metallic Corrosion, Moscow, May 1966, to be published in *Corrosion Science*.
14. F. Gronlund, *J. Chim. Phys.*, **53**, 660 (1956).
15. H. Uhlig, *Acta Met.*, **4**, 541 (1956).
16. C. Elam, *Trans. Faraday Soc.*, **32**, 1604 (1936).
17. A. Gwathmey and A. Benton, *J. Chem. Phys.*, **8**, 569 (1940).
18. R. Shuttleworth, *Metallurgia*, **38**, 125 (1948).
19. B. Chalmers, R. King, and R. Shuttleworth, *Proc. Royal Soc. (London)*, **193A**, 465 (1948).
20. J. Benard, J. Moreau, and F. Gronlund, *Compt. Rend. Acad. Sci. Fr.*, **246**, 756 (1958).
21. W. M. Robertson, *Acta Met.*, **12**, 241 (1964).
22. D. Hayward and B. Trapnell, "Chemisorption," p. 75, 181, 233, Butterworth's, Washington (1964).
23. E. Andrade and J. Martindale, *Phil. Trans. Royal Soc.*, **235A**, 69 (1935).
24. Ref. 22, p. 75
25. B. Sundquist, *Acta Met.*, **12**, 67 (1964).
26. J. Moreau and J. Bénard, *Compt. Rend. Acad. Sci. Fr.*, **248**, 1658 (1959).
27. W. Stössel, *Z. Naturforsch.*, **17a**, 165 (1962).
28. F. Young and A. Gwathmey, *J. Appl. Phys.*, **31**, 225 (1960).
29. A. MacRae, *Science*, **139**, 379 (1963); *Surface Science*, **1**, 319 (1964).
30. H. Farnsworth, *Appl. Phys. Letters*, **2**, 199 (1963).
31. D. Mitchell, G. Simmons, and K. Lawless, *ibid.*, **7**, 173 (1965).

The Anodic Deposition of Iron Oxide Films on Iron

V. Markovac[1] and M. Cohen

Division of Applied Chemistry, National Research Council, Ottawa, Ontario, Canada

ABSTRACT

The anodic deposition of iron oxide films on passive iron polarized at +300 mv in boric acid/sodium borate solutions, at *p*H 7.52, containing ferrous ions has been investigated. The deposition takes place with a current efficiency of 100% based on the reaction $Fe^{++}_{(l)} - e^{-}_{o} \rightarrow Fe^{+++}_{(s)}$. The kinetics of the anodic deposition could be divided into two consecutive regions, an initial stage characterized by the formation of a film with the thickness of a unit cell, followed by a steady growth region where the rate of deposition is dependent on the ferrous ion concentration in the solution and the oxide layer thickness. Both the anodic current densities and the cathodic reduction behavior indicate that the deposited iron oxide film is different from the film formed by anodic oxidation of metallic iron in terms of both electronic conductivity and chemical composition.

In a previous study (1) it was found that iron could be anodically passivated in a neutral borate solution and that the thickness of the film varied from 8 to 30Å. It was also observed (2) that thicker films could be formed if the iron was treated anodically in the neutral borate solution containing ferrous ion.

In this paper a more complete investigation of this process of anodic oxidation of ferrous ion to form a solid film has been made. Similar processes are known for the anodic formation of lead dioxide (3) and manganese dioxide (4) from their respective ions in solution. Our investigations indicate that the kinetics of anodic deposition of iron oxide could be divided into two regions; an initial stage, and the steady growth region, where the rate of deposition depends only on the ferrous ion concentration in solution and the oxide layer thickness. Cathodic reduction experiments indicate that there is a difference in compositions between the deposited oxide and that formed by direct anodic oxidation of metallic iron.

Experimental

Apparatus.—The apparatus (Fig. 1) consisted of an electrolytic cell with storage vessels, nitrogen purification unit, and electrical equipment.

The electrolytic cell was of a cylindrical shape and had a working volume of *ca.* 40 ml. At the bottom of the cell an outlet was provided with two three-way solution lubricated stopcocks for solution transfer from two storage vessels to the cell and for removal from the cell for analysis. The storage vessels had a capacity of 2 liters each, one for standard solution and the other for solution containing ferrous ions. In the side of the cell were two tubes for the inlet of nitrogen. One tube, close to the bottom of the cell, had a sintered glass-disk sealed in its top, providing a fine and uniform bubbling of nitrogen through the solution in order to avoid concentration changes of ferrous ion at the electrode during the electrolysis. The other tube, entering the cell above the surface of solution, enabled the introduction of nitrogen into the cell and electrolysis without stirring. The outlet for nitrogen was built into the ball-joint cap on the top of the cell. The specimen (working electrode) was suspended on a tungsten wire sealed into the middle of a ball-joint cap. A set of four platinum wires 1.5 mm in diameter (counter electrode) with a total area of about 12 cm^2 was placed vertically into the cell surrounding the specimen uniformly. A saturated calomel electrode was used as the reference electrode and was connected with the cell by an electrolytic bridge, filled with the standard solution. The cell was surrounded by a water-jacket through which water at 25° ± 0.2°C was circulated.

[1] N.R.C. Postdoctorate Research Fellow. Present address: Scientific Research Laboratories, Ford Motor Company, Dearborn, Michigan.

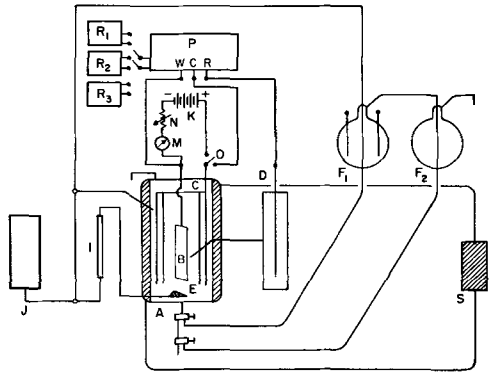

Fig. 1. Schematic diagram of apparatus: A, electrolytic cell; B, specimen; C, counter electrode; D, reference electrode; E, bubbler; F_1, F_2, storage vessels; I, flowmeter; J, nitrogen purification unit; K, battery; M, microammeter; N, variable resistance; O, switch galvanostatic-potentiostatic polarization; P, potentiostat by Wenking; w,c,r, terminals for working, counter, and reference electrode; R_1, R_2, R_3, chart recorders; S, system for water circulation at constant temperature.

The solutions in the cell and in the storage vessels were kept under a stream of purified nitrogen. High-purity tank nitrogen with an oxygen content of less than 20 ppm was further purified by passing through two washing bottles filled with Feiser's solution and a column filled with active copper spread on infusorial earth (5) maintained at 205°C. To obtain reproducibility of stirring by the bubbling of nitrogen through the solution in the cell a flowmeter was inserted in the nitrogen line in front of the cell. The volume of nitrogen passed through the particular sintered glass bubbler was a relative measure of stirring.

A potentiostat, a galvanostat, and recorders were used. Anodic polarization was carried out with a Fast Rise Potentiostat 61 R by Wenking. The voltage amplification factor is 10^4, and internal resistance less than 0.01 ohm (range 0-50 kc), rise time 10^{-6} sec. Limits for output voltage and output current are ±20v and ±300 ma, respectively. For cathodic reduction experiments a galvanostat consisting of a 12v battery and a variable large resistance was used.

The change of current with time during potentiostatic oxidation was recorded as voltage ohmic drop across a resistance of 100 ohms inserted in the current circuit. A Brush Recorder Mark II Model RD 2521 00 with 0.01-sec rise time and chart speed of 125 mm/sec was used for the initial rapid change of current and then recording was switched over to an L&N Speedomax type G recorder (range 0-1.0 mv, rise time

1 sec, chart speed 1.5 mm/sec) with a four-step voltage attenuator (ranges 100-50-10-1), following the change of current very precisely. The potential change with time during galvanostatic cathodic reduction was also recorded by an L&N Speedomax type G recorder (range 0-50 mv, chart speed 0.38 mm/sec) using a corresponding voltage attenuator covering a measuring range 0-1000 mv.

Materials.—Specimens 1x5 cm and 0.0375 cm thick with small handles were cut from Ferrovac E[2] iron sheet and mechanically polished with emery papers through to 4/0. The specimens were then electropolished in an electrolyte containing glacial acetic acid and 70% perchloric acid (20:1) at 0.4-0.5 amp/cm^2, 105 ± 5v d.c. and starting temperature of 15°C (6). To avoid overheating, electropolishing was carried out by 10-sec bursts, and a very smooth surface was obtained usually after 5-6 bursts. Then the specimen was annealed at 700°C in hydrogen and electropolished again by 2-3 10-sec bursts. For the preliminary oxidation and for cathodic reduction of the oxide layer, a standard solution containing 0.15*N* boric acid and 0.15*N* sodium borate (1:1), *p*H = 8.41 was used. Oxygen dissolved in the solution was removed by prolonged bubbling with purified nitrogen in the storage vessel. The solutions containing ferrous ion were prepared in the other storage vessel by potentiostatic dissolution of high-purity iron sheet at −650 to −700 mv in a 5:1 mixture of 0.15*N* boric acid and 0.15*N* sodium borate, *p*H = 7.52. As a counter electrode for iron dissolution, a platinum sheet of the same area was used. To prevent the precipitation of ferric hydroxide even in the presence of traces of oxygen, purified nitrogen was forced through the solution before, during, and after dissolution of iron. The concentration of ferrous ions in solution was estimated approximately from total current passed during electrolysis.

Procedure.—Specimens were prepared for deposition by first cathodically reducing the oxide on the electropolished specimen and then anodically oxidizing at +300 mv for 30 min in the standard solution (7). This forms a film of oxide approximately 25Å thick and provides a uniform reproducible surface for deposition (1). The standard solution was then replaced by the solution containing ferrous ions, and anodic oxidation was continued at +300 mv for 60 min. In order to maintain a constant ferrous ion concentration difference between the bulk of the solution and the metal oxide-solution interface during the oxidation, the solution was stirred by bubbling with a nitrogen flow of 43.0 ml/min, at 1 atm and 21°C. Immediately before and after anodic oxidation a sample of the solution from the cell was taken for analysis. Afterwards the cell and the specimen were washed out at least three times with the standard solution in order to remove any ferrous ion which remained. Cathodic reduction of the iron oxide layer from the specimen was then carried out in the standard solution with a constant c.d. of 10 μa/cm^2, until the second wave of the cathodic reduction curve was completed (2). After any desired period of time of the cathodic reduction, solution could be taken from the cell and analyzed for content of ferrous ion.

All potential data reported in this paper are referred to the saturated calomel electrode. Both change of current with time during anodic oxidation and change of potential with time during cathodic reduction were followed by chart recorders. Iron was analyzed by an orthophenanthroline method (1), the accuracy of which is about ±1%.

[2]Ferrovac E is the trade name of high-purity iron produced by Vacuum Metals Corporation, Division of Crucible Steel Company of America (C—0.007, O—0.015, N—0.0003, Mn—0.005, Si—0.008, P—0.003, S—0.006, Ni—0.005, Pb—0.001, Sn<0.001, Cr<0.003, Va <0.004, Al<0.005, Mo<0.006, Co<0.005, Cu<0.003% by weight).

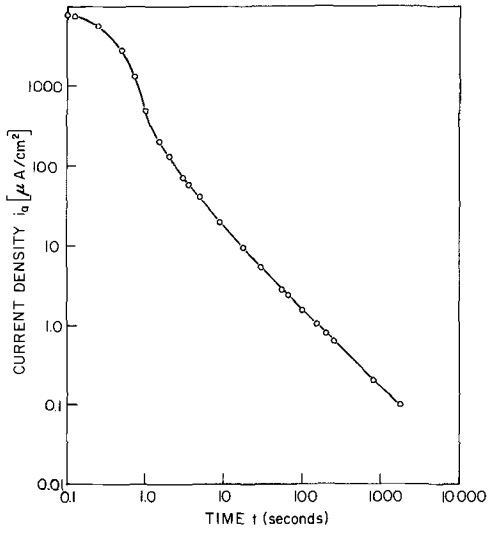

Fig. 2. Change of c.d. with time during preliminary oxidation at + 300 mv.

Results

Preliminary oxidation.—The reduced specimen was oxidized in the standard solution at a constant potential of +300 mv, for 30 min. The change of c.d. with time was recorded (Fig. 2). The total charge passed during oxidation was calculated by graphic integration of the curve and found to be 4.993 mC/cm^2. This value is in a very good agreement with the previous results (7). In order to check the nature of the oxide film, the specimen was reduced with a constant cathodic c.d. of 10 μa/cm^2. A typical cathodic reduction curve obtained (Fig. 4, curve 3a) also indicated that the surface oxide film developed by preliminary oxidation was essentially of the same type as described previously (1, 2, 7). These anodically oxidized specimens, with a film of about 25Å of oxide were used as "standard specimens" for all further anodic deposition work.

Anodic oxidation in solutions containing ferrous ions.—The standard specimens were then anodically oxidized in solutions with various concentrations of ferrous ions, at constant potential of +300 mv.[3] This passive region potential was chosen so that it was high enough to avoid dissolution of oxide or iron, and low enough to avoid oxygen evolution (1). The changes in the anodic current densities with time for eight solutions with various concentrations of ferrous ions are shown in Fig. 3 as log i_a-log t_a curves. It can be seen that a rapid current decrease is immediately followed by an arrest or plateau whose length decreases with increased ferrous ion concentration in the solution. At the end of this period the current then decreases slowly and is dependent on both the total oxide thickness and the ferrous ion concentration in the solution.

The total charge passed during anodic oxidation in solutions containing ferrous ions was obtained by graphic integration of the corresponding curves. Assuming that during anodic polarization the oxidation of Fe^{++} to Fe^{+++} occurs, it is possible, from the decrease in the concentration of ferrous ion in solution, to calculate the amount of charge which should pass during the oxidation. The calculated and the observed amount of charge are in very good agreement (Table I) and thus show that during anodic oxidation in the presence of ferrous ions, the reaction

$$Fe^{++}{}_{(l)} - e^-{}_o \rightarrow Fe^{+++}{}_{(s)} \qquad [1]$$

[3]To check the rise time to the applied constant potential, a Tektronix Model 545 oscilloscope was inserted in the measuring circuit in some experiments, and the rise of the potential was followed using a time sweep of 0.01 sec/cm. A rectangular transient was observed on the screen of the oscilloscope, i.e., a constant potential of +300 mv is reached in a shorter time than the rise time of the recorder.

Table I. Amount of charge passed in comparison to the amount of charge calculated from the decrease in the concentration of ferrous ions during anodic oxidation at +300 mv, 60 min, pH = 7.52

Exp. No.	Concentration [Fe++] mole/lit Starting	Final	Amount of charge passed $_DQ_a^{obs}$ [mC]	Amount of ferrous ions [μg] Starting	Final	Amount of ferrous ions used during oxidation [μg]	Amount of charge calculated Q_a^{cal} [mC]	$Q_a^{cal}/{}_DQ_a^{obs}$
1	0.555 × 10⁻⁴	0.265 × 10⁻⁴	110.16	115.1	54.9	60.2	104.0	0.942
2	0.835 × 10⁻⁴	0.431 × 10⁻⁴	144.02	171.4	88.3	83.1	143.7	0.998
3	0.994 × 10⁻⁴	0.575 × 10⁻⁴	160.90	208.0	120.5	87.5	151.2	0.941
4	1.620 × 10⁻⁴	1.080 × 10⁻⁴	201.69	339.2	226.7	112.5	194.5	0.965
5	2.490 × 10⁻⁴	1.760 × 10⁻⁴	271.94	521.5	369.0	152.5	263.5	0.970
6	3.210 × 10⁻⁴	2.404 × 10⁻⁴	293.81	671.5	504.0	167.5	289.5	0.986
7	3.780 × 10⁻⁴	2.880 × 10⁻⁴	334.18	800.0	610.5	189.5	327.5	0.980
8	6.030 × 10⁻⁴	4.850 × 10⁻⁴	417.00	1266.0	1016.0	250.0	432.0	1.036

Table II. Change of color with thickness of the iron oxide layer on iron

Total thickness $_TQ_a$, mC/cm²	Total thickness A	Color
11.5	133.5	goldish -gray
13.5	167.0	light -gray
15.5	200.0	gray
16.5	216.5	dark -gray
18.4	248.0	blueish -gray
19.4	264.5	grayish -blue
23.6	334.0	grayish -green
28.4	413.0	green
31.4	462.5	yellowish-green
38.2	575.5	pinkish -violet

takes place with an efficiency very close to 100%. During anodic oxidation no precipitation either in the solution or elsewhere was observed, and the oxide thickness on the iron specimen increased as noted by changes in interference colors. Hence it was concluded that all of the ferrous ion was oxidized to form a solid ferric oxide (not necessarily anhydrous) on the specimen. This process can be described as the electrochemical deposition of iron oxide. The charges passed during anodic oxidation in both the preliminary oxidation and the anodic deposition are proportional to the thicknesses of films formed. The thickness of oxide formed during anodic oxidation of iron ($_PQ_a$) was calculated from the equation

$$2Fe + 3H_2O \rightarrow Fe_2O_3 + 6H^+ + 6e^-_o \qquad [2]$$

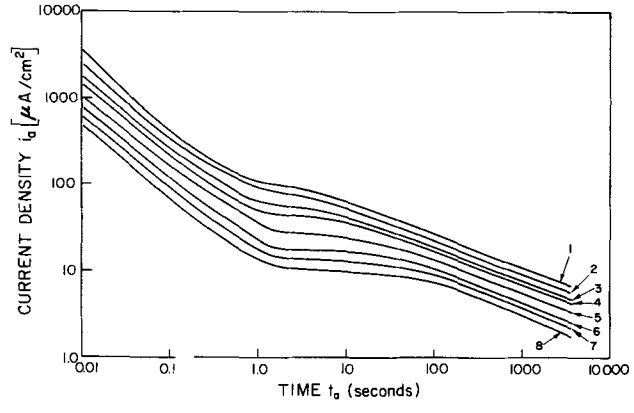

Fig. 3. Changes of the anodic c.d. with time for solutions with various concentration of ferrous ion, E_a = +300 mv.

Experiment No.	Starting [Fe++] mole/l
1	6.030 × 10⁻⁴
2	5.410 × 10⁻⁴
3	3.210 × 10⁻⁴
4	2.490 × 10⁻⁴
5	1.620 × 10⁻⁴
6	0.994 × 10⁻⁴
7	0.835 × 10⁻⁴
8	0.555 × 10⁻⁴

The thickness of oxide formed during anodic deposition ($_DQ_a$) was calculated from Eq. [1] assuming a solid product of Fe_2O_3 with a density of 5. The total oxide thickness ($_TQ_a$) is the sum of these two. The variation of color with thickness is given in Table II.

Cathodic reduction of iron oxide layer.—The iron oxide layers formed on the specimens during anodic oxidation in solutions containing ferrous ions were cathodically reduced in the standard solution at a constant c.d. of 10 μa/cm² The cathodic reduction curves for three specimens with various thicknesses of iron oxide layers are shown in Fig. 4. All curves have two typical arrests, one corresponding to reduction of ferric oxide and the other to reduction of magnetite as was shown earlier (1). The first arrests are very long, depending on the thickness of the oxide layer, *i.e.*, on the amount of ferric oxide in the oxide layer. The cathodic current efficiency for reduction of ferric oxide to ferrous ion (first arrest) for all three experiments is lower than 100% (Table III).

The second arrests show some prolongation in comparison with second arrests obtained by cathodic reduction of the surface oxide film developed by preliminary oxidation on the same specimens (Fig. 4). Assuming that the current efficiency for the reduction of magnetite to ferrous ion is 42% (1), it is possible to calculate the additional amount of magnetite formed during the deposition from the additional charge required to reduce the magnetite. Measured and calculated data are given in Table III.

Discussion

The experimental results show that the anodic deposition of iron oxide at constant potential (Fig. 3) can be divided into two parts. First, an initial region characterized by a rapid current decrease immediately followed by a plateau (arrest), and second, a steady growth region where the logarithm of the current density changes approximately linearly with logarithm of time.

Initial region.—The first step in the initial region (Fig. 5) is the charging of the double layer. With an

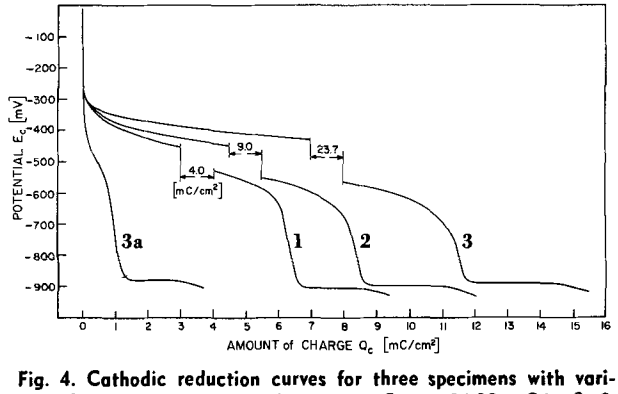

Fig. 4. Cathodic reduction curves for three specimens with various thicknesses of iron oxide layers. 1, $_TQ_a$ = 16.02 mC/cm²; 2, $_TQ_a$ = 25.17 mC/cm²; 3, $_TQ_a$ = 38.24 mC/cm²; 3a, cathodic reduction curve for specimen No. 3 after preliminary oxidation.

Table III. Relationship between thickness of deposited layer and its cathodic reduction behavior

No.	Starting concentration of Fe^{++}, mols/l	Oxidation: Amount of charge passed (a) total $_TQ_a$, mC/cm²	Oxidation: Amount of charge passed (b) during deposition of iron oxide $_DQ_a$, mC/cm²	Reduction: Cathodic current efficiency for reduction of Fe_2O_3, %	Reduction: Additional amount of charge calculated from prolonged part of 2nd arrest $_{Ad}Q_c$, mC/cm²
1	0	5.00	0	100	0
2	0.555×10^{-4}	16.02	11.02	91	0.264
3	1.62×10^{-4}	25.17	20.17	82	0.352
4	4.08×10^{-4}	38.24	33.24	76	0.475

Experiment No. 1 is typical of a specimen oxidized by the preliminary oxidation.

efficient potentiostat this process should take place in a short time at high current density (8, 9) and should follow the equation

$$i = C_D \cdot \frac{\Delta E}{\Delta t} \quad [3]$$

$$i \cdot \Delta t = C_D \cdot \Delta E \quad [4]$$

$$\Delta Q = C_D \cdot \Delta E \quad [5]$$

where C_D is the double layer capacity and ΔE the potential change. If we assume a double layer capacity of 20 μF/cm² the corresponding charge is 6 μC/cm². If one takes the maximum current density from Fig. 5, the time required to charge the double layer is 10^{-2} to 10^{-3} sec. This shows that the charging of the double layer takes place at the very beginning of the measuring region and that the number of coulombs required is small in comparison to the total amount of charge used in the initial region.

In the initial deposition region there is a rapid decrease of current density followed by a plateau (Fig. 5). The total charge passed in this period[4] is essentially the same for all concentrations of ferrous ions. However both the current density and the time to pass this constant charge are dependent on the initial concentration of ferrous ion in the solutions. The total charge corresponds to the formation of 4.55 μg Fe_2O_3 and assuming a density of 5 a thickness of 9Å. This corresponds to about 1 unit cell of Fe_2O_3. This amount of deposited iron is insufficient to cause any real change in the concentration of ferrous ion in the solution in the initial region. Hence the rapid decrease in current density must be due to the fact that the resistance of the deposited film is considerably larger (by orders of magnitude) than that of the film formed by anodic oxidation of the metal. The current plateau region which is then followed by a steady growth region, is probably due to the fact that pores in the oxide are not closed until a full unit cell thickness is formed. It should be noted that during anodic deposition the conduction process in the film is electronic, *i.e.*, electrons are transferred across the oxide to the metal. Both the initial and final current densities in the initial growth region are orders of magnitude greater than the final current density during preliminary oxidation (Fig. 2) and hence electronic conductivity of the anodically formed film is much greater than the ionic conductivity.

Steady growth region.—As can be seen in Fig. 3 in the steady growth region the logarithm of the current density varies inversely with the logarithm of time. In Fig. 6 is shown the rate of growth of the film at various starting concentrations of ferrous ion. Although there is a general decrease in the rate of growth of the film with time the curves do not fit any general law. This is probably due to the fact that the current density decreases due to more than one factor. The major decrease in current density is due to an increase in the resistance as the film grows. This increase in resistance leads to a change in potential at the oxide film-solution interface and hence a decrease in current density. A second complicating factor is the decrease in solution concentration during deposition. This decreases the overpotential for the deposition reaction and hence the rate of deposition. The major effect is probably that of resistance of the film and the distribution of potential drops between the metal substrate and the solution.

Cathodic reduction.—The cathodic reduction curves (Fig. 4) show two arrests. The first arrest corresponds to the reduction of "ferric oxide" to ferrous ion in solution following the reaction

$$Fe^{+++}{}_{(s)} + e^-{}_o \rightarrow Fe^{++}{}_{(l)} \quad [6]$$

The current efficiency for the reduction (Table III) of the deposited oxide is less than for the oxide formed by the anodic oxidation of the iron. The current effi-

[4] The intersections of the extrapolated lines from the steady growth region and the prolonged arrest lines are used for the calculation of the amount of charge in the initial region.

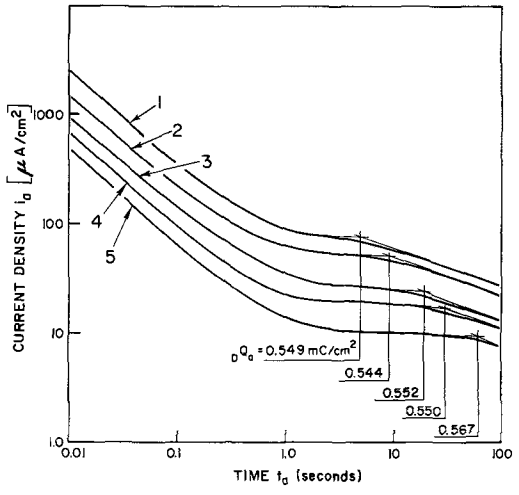

Fig. 5. Change of c.d. with time in initial region. Starting concentration of ferrous ion: 1, $5.410 \times 10^-$ mole/l; 2, $3.470 \times 10^-$ mole/l; 3, $1.620 \times 10^-$ mole/l; 4, $1.000 \times 10^-$ mole/l; 5, $0.555 \times 10^-$ mole/l.

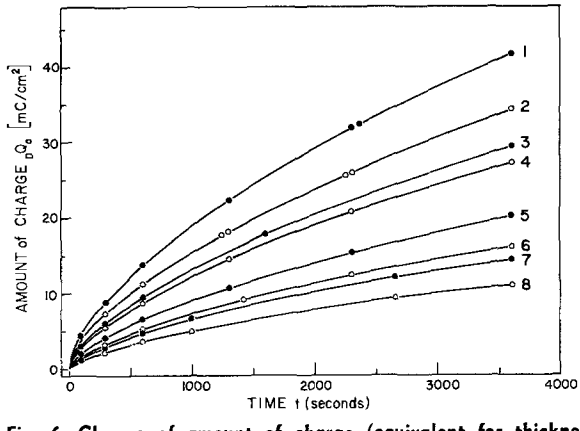

Fig. 6. Change of amount of charge (equivalent for thickness) with time for the same experiments presented in Fig. 3.

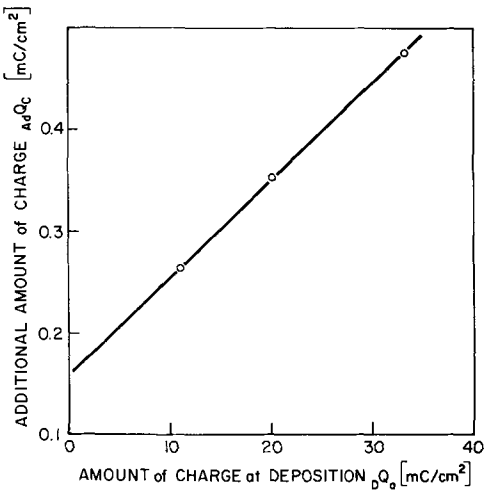

Fig. 7. Relation between the additional amount of charge used for reduction of magnetite and the amount of charge passed during anodic deposition of iron oxide for 60 min.

ciency decreases as the thickness of the film increases. This indicates that the deposited film is different from the preliminary film obtained by the oxidation of iron. This conclusion is also supported by the rapid change in film resistance which is observed during the deposition experiments. A more detailed discussion of the composition of the deposited film will be presented in a subsequent paper (10).

The second arrests of the cathodic reduction curves (Fig. 4) show some prolongation in comparison with the cathodic reduction curves obtained after preliminary oxidation for the same specimens. This means that during anodic oxidation in solutions containing ferrous ion (deposition of iron oxide) an additional amount of magnetite is also formed.

The additional amount of magnetite formed during anodic deposition of iron oxide increases with the amount of charge passed during deposition (Table III). If the additional amount of charge $_{Ad}Q_c$ (corresponding to additional amount of magnetite) is plotted *vs.* the amount of charge passed during deposition $_DQ_a$, a straight line is obtained (Fig. 7). The relation between $_{Ad}Q_c$ and $_DQ_a$ could be expressed

$$_{Ad}Q_c = A \cdot {}_DQ_a + B \qquad [7]$$

where $A = 0.956 \times 10^{-2}$ and $B = 0.159$ mC/cm² are constants obtained experimentally.

The formation of the additional magnetite during the anodic deposition of iron oxide can be explained by a flow of iron from the substrate to the oxide layer where the probable reaction

$$Fe + 4Fe_2O_3 \rightarrow 3Fe_3O_4 \qquad [8]$$

occurs.

Manuscript received July 25, 1966.

Any discussion of this paper will appear in a Discussion Section to be published in the June 1968 JOURNAL.

REFERENCES

1. M. Nagayama and M. Cohen, *This Journal*, **109**, 781 (1962).
2. M. Nagayama and M. Cohen, *ibid.*, **110**, 670 (1963).
3. A. I. Zaslavskii, Yu.D. Kondrashov, and S. S. Taklachev, *Doklady Akad. Nauk, SSSR*, **75**, 559 (1950).
4. D. T. Ferrell, Jr., and W. C. Vosburgh, *This Journal*, **98**, 334 (1951).
5. R. Fricke and J. Kubach, *Z. Elektrochem.*, **53**, 76 (1949).
6. P. B. Sewell, C. D. Stockbridge, and M. Cohen, *Can. J. Chem.*, **37**, 1813 (1959).
7. N. Sato and M. Cohen, *This Journal*, **111**, 512 (1964).
8. H. Gerischer, *Z. Elektrochem.*, **59**, 604 (1955).
9. K. J. Vetter, "Elecktrochemische Kinetik," p. 287, Springer-Verlag, Berlin, Göttingen, Heidelberg (1961).
10. V. Markovac and M. Cohen, *This Journal*, **114**, 678 (1967).

The Anodic Deposition of Iron Oxide Films on Platinum

V. Markovac[1] and M. Cohen

Division of Applied Chemistry, National Research Council, Ottawa, Ontario, Canada

ABSTRACT

The anodic deposition of iron oxide films on platinum from borate solutions containing various concentrations of ferrous ion was studied. The kinetics of deposition was essentially identical with the kinetics found using passive iron as a substrate. The film is not simple anhydrous or hydrated iron oxide but also contains some borate ion. On heating the film in vacuo hydrated boron complexes are driven off. The residue, after heating to 800°C is α-Fe_2O_3. These facts indicate that the film is formed by the oxidation of a ferrous borate type complex to an insoluble ferric hydroxy borate at the film-solution interface. The anodically deposited film is different both electrically and chemically from the film formed by the anodic oxidation of metallic iron.

It was shown in the previous paper (1) that the anodic oxidation of passive iron in solutions containing ferrous ions leads to the formation of "iron oxide" in which all iron is in the ferric state and originates from the solution. Such an anodic process is the electrochemical deposition of iron oxide, and it should be expected that a similar deposition will also take place on metals or conductors other than iron. The anodic deposition of metallic oxides on metals other than the metallic component in the oxide, has also been reported in the cases of lead dioxide (2, 3) and manganese dioxide (4, 5).

In the present work the anodic deposition of iron oxide on a platinum specimen from solutions containing various concentrations of ferrous ion was studied. These investigations show that the deposition of iron oxide on a platinum specimen takes place in a manner similar to that which was observed on the passive iron (1). The composition of the deposited film was studied using weight increase, mass spectrometry, x-ray diffraction, and chemical analysis.

[1] N.R.C. Postdoctorate Research Fellow. Present address: Scientific Research Laboratories, Ford Motor Company, Dearborn, Michigan.

Experimental

The apparatus consisting of an electrolytic cell with storage vessels, nitrogen purification unit, and electrical devices was the same as that presented in the preceding paper (1).

Smooth platinum sheets of 1 x 5 cm and 0.0127 cm (0.005 in.) thick, with small handles, were used as specimens. After degreasing in methanol and heating for a few seconds, in an ordinary oxidizing flame, the specimens were annealed in a hydrogen atmosphere at 2 Torr, at 900°C, for 24 hr. Before and after annealing there was no change in the weight of the platinum. The electron diffraction pattern after annealing was characteristic of a clean platinum surface.

The specimens were anodically oxidized at a constant potential of +300 mv in a solution of 0.15*N* boric acid and 0.15*N* sodium borate (5:1), pH = 7.52, with various concentrations of ferrous ion. Before and after anodic oxidation, the solutions from the cell were analyzed for ferrous ion. The change in the weight of the specimens resulting from anodic deposition of iron oxide was determined by weighing on a micro balance with an accuracy of $\pm 2 \times 10^{-6}$g. After anodic deposition the specimens were either cathodically reduced or chemically dissolved, or heated in an ultra high vacuum furnace. The cathodic reduction of the deposited iron oxide on the platinum specimen was carried out galvanostatically in the standard solution (equivolume mixture of 0.15*N* boric acid and 0.15*N* sodium borate, pH = 8.41) (1). With some specimens, the iron oxide layer was dissolved in about 60 ml of a mixture of hydrochloric acid and water (1:4). This solution was analyzed for ferrous ion by the o-phenanthroline spectrophotometric method. The heating of the specimen with the iron oxide layer was carried out in an ultra high vacuum furnace by increasing the temperature gradually up to 800°C. The pressure was of the order of 10^{-7} Torr. During the heating, the evolution of some gases was followed by an AEI Mass Spectrometer Type MS 10.

Results and Discussion

Anodic deposition of iron oxide.—The platinum specimens were anodically polarized at a constant potential of +300 mv in solutions containing various concentrations of ferrous ion. The change in the anodic current density with time is shown in Fig. 1. The curves are very similar to those obtained by deposition on passive iron (1) and are characterized by an initial region in which the rapid current decrease is immediately followed by an arrest, and after a transition period, a steady growth region. The total amount of charge passed during anodic oxidation was determined by graphic integration of the experimental curves of current density *vs.* time. The ratio between the calculated amount of charge[2] and that obtained experimentally, is very close to one (Table I). This confirms the fact that the anodic process on platinum at +300 mv in a solution containing ferrous ion is the deposition of an iron oxide in which all the iron

[2] Calculated from the decrease in the ferrous ion concentration during oxidation, assuming the reaction $Fe^{++} - e^-_0 \rightarrow Fe^{+++}$ (1).

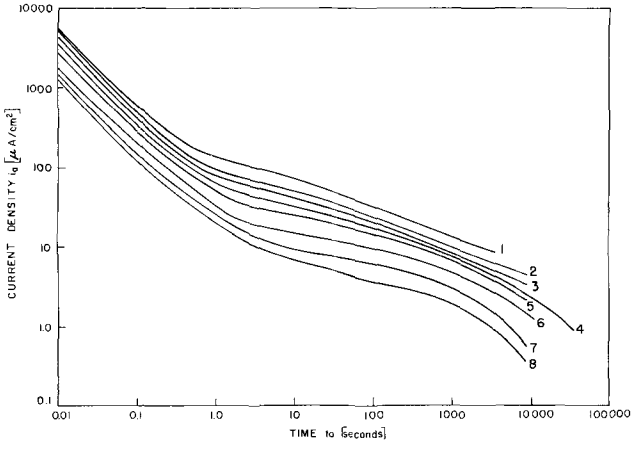

Fig. 1. Changes in the anodic c.d.'s with time during the deposition of iron oxide on the platinum from solutions with various ferrous ion concentration, E_a = +300 mv.

Experiment No.	Starting [Fe^{++}] mole/l
1	6.090×10^{-4}
2	4.980×10^{-4}
3	3.270×10^{-4}
4	2.607×10^{-4}
5	1.630×10^{-4}
6	1.164×10^{-4}
7	0.528×10^{-4}
8	0.304×10^{-4}

is in the ferric state (1). Thus the thickness of the deposited layer should be proportional to the total amount of charge passed during the oxidation. The amount of charge ${}_DQ_a$ is

$$ {}_DQ_a = \int_0^t i_D \cdot dt \qquad [1] $$

where i_D is the anodic current density and t the time of deposition.

As pointed out above, the shape of the current *vs.* time curves (Fig. 1) for platinum is almost identical with those obtained with a passive iron substrate (1). In addition there is also a very marked similarity in the current densities observed with various ferrous iron concentrations. As with the iron, it may be concluded that the initial stage comprises the completion of an 8-10Å thick film of oxide. This is followed by a steady-state deposition of oxide where the rate of deposition is dependent on the ferrous ion concentration in the solution and the oxide layer thickness. A more complete discussion of the anodic deposition process is presented in the previous paper (1).

The fact that there is good correspondence between the current densities observed with the platinum and passive iron shows that the resistance of the passive film on iron is low, that is, its electronic conductivity is similar to that of platinum. This would indicate that this anodic deposition process can take place on any conducting surface.

Table I. Ratio between the calculated amount of charge and the amount of charge observed during the anodic deposition of iron oxide on the specimens at +300 mv, pH = 7.52

Experiment No.	Concentration [Fe^{++}] mole/lit: Starting	Concentration [Fe^{++}] mole/lit: Final	Amount of charge passed ${}_DQ_a^{obs}$, mC	Time of deposition, min	Amount of ferrous ions in solution, μg: Starting	Amount of ferrous ions in solution, μg: Final	Amount of ferrous ions used during deposition, μg	Amount of charge calculated, Q_a^{cal}, mC	Q_a^{cal} / ${}_DQ_a^{obs}$
1	0.528×10^{-4}	0.114×10^{-4}	149.3	150	110.3	22.0	88.3	152.4	1.021
2	1.140×10^{-4}	0.714×10^{-4}	153.6	60	239.3	150.1	89.2	154.5	1.006
3	1.250×10^{-4}	0.509×10^{-4}	271.0	150	264.0	103.0	161.0	278.1	1.026
4	1.630×10^{-4}	0.590×10^{-4}	374.7	150	340.0	122.2	217.8	376.0	1.003
5	2.250×10^{-4}	1.092×10^{-4}	412.0	151	46.32	227.7	235.5	408.0	0.991
6	2.607×10^{-4}	0.158×10^{-4}	862.7	600	525.0	35.3	489.7	847.2	0.982
7	3.270×10^{-4}	1.898×10^{-4}	491.0	150	677.5	367.4	310.1	536.5	1.092
8	4.980×10^{-4}	3.237×10^{-4}	625.1	150	1017.5	664.2	353.3	608.0	0.973
9	5.440×10^{-4}	4.124×10^{-4}	471.4	60	1126.0	860.8	265.2	458.5	0.973
10	6.090×10^{-4}	4.711×10^{-4}	491.4	60	1259.0	969.0	290.0	501.5	1.020

Table II. Change of color with the thickness of the deposited iron oxide on platinum

Thickness* $_DQ_a$, mC/cm²	A	Color
3.2	52.9	light gray
8.5	141.0	gold
11.9	197.0	goldish gray
14.0	231.6	light gray
16.7	276.2	gray
19.0	314.0	grayish green
24.0	396.7	light green
27.2	450.0	green
29.0	479.5	greenish gold
31.0	512.2	gold
34.0	562.5	pinkish gold
37.5	620.5	pinkish violet
41.0	678.0	pink
44.0	727.6	pinkish green
52.0	860.0	green
61.0	1008.0	pinkish gold
67.0	1108.0	goldish pink
72.4	1198.0	pinkish green
79.5	1313.0	green
85.2	1410.0	dark green

* The mean values derived from 9 experiments, calculated by Eq. [1], and assuming that the specific gravity of iron oxide is 5.

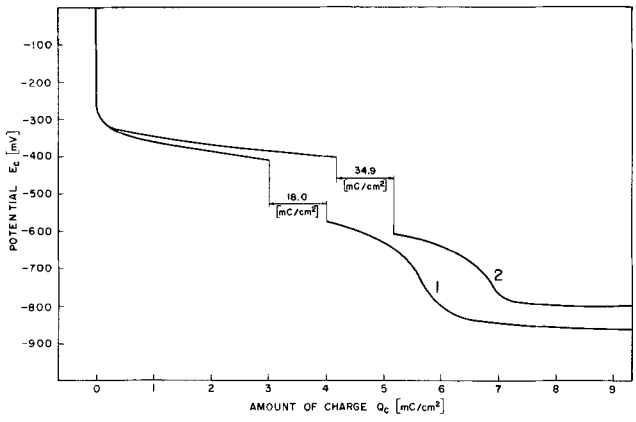

Fig. 2. Curves of cathodic reduction of iron oxide on the platinum specimen. Thickness of iron oxide: 1, $_DQ_a$ = 22.27 mC/cm²; 2, $_DQ_a$ = 47.14 mC/cm².

The growth of the iron oxide layer during the deposition is very easy to observe by the change of interference colors on the surface of the specimen. The relation between the thickness of the deposited iron oxide on the platinum specimen and its color is shown in Table II. It is clearly seen from Table II that the colors of the iron oxide on the platinum specimen are very similar to those observed by deposition of iron oxide on passive iron (1). Moreover, some colors appear several times with increasing thickness of the oxide layer and hence are repeating interference colors.

Cathodic reduction of films.—Some of the specimens were cathodically reduced in the standard solution at 10 μa/cm². Typical cathodic reduction curves are shown in Fig. 2. As can be seen from the curves there are two arrests. The first arrest corresponds to the reduction of the film at a current efficiency of about 65% during which time, from ferrous ion analysis, only about 70% of the total iron in the film is reduced to soluble ferrous iron. The reduction of the film continues during the second arrest, but with a decreasing cathodic current efficiency. The predominant reaction during this latter period is hydrogen evolution. No arrest potential due to magnetite was observed. The low current efficiency of reduction during the first arrest again indicates that the deposited film is different from the film obtained by the anodic oxidation of metallic-iron which cathodically reduces with a current efficiency of about 100% (6, 7). It may be that the low current efficiency during the first arrest is due to a simultaneous reduction of Fe^{+++} to Fe^{++} and protons in the film (present in hydroxyl groups) to hydrogen. The lower current efficiency during the second arrest is probably due to uneven reduction of the film which leads to the exposure of "bare" platinum areas to the solution before all of the film is reduced.

Composition of anodically deposited film.—Both the anodic deposition and cathodic reduction data show that the deposited film is not simply γ-Fe_2O_3. In order to obtain more information about the composition of the film a series of experiments involving material balance, chemical analysis, and heating *in vacuo* were performed.

Material balance and chemical analysis.—Some of the films were dissolved completely in dilute hydrochloric acid (1:4) and the resulting solutions analyzed for iron (Table III). It was found that within the experimental error the iron in the film corresponded almost exactly with that removed from the solution. Also, as noted above (Table I), the current efficiency for the anodic oxidation of the Fe^{++} in solution is 100%. This indicated that all the oxidized ferrous ion is in the film in the ferric state. However, the weight of the film (Table III) as determined by weighing the bare platinum and the coated platinum is substantially greater than the calculated weight of Fe_2O_3 which could be formed from the oxidized Fe^{++}. There appeared to be no simple relationship between excess weight and total amount of film formed, although the excess weight varied mainly between 60-90%.

A few experiments were performed in which the specimens with the deposited film were treated anodically (at the same potential of +300 mv) for extended periods of time in a boric acid/sodium borate standard solution containing no Fe^{++} ion. No change in weight of the specimen was observed. This shows that deposition only takes place in the presence of Fe^{++} ion.

An excess weight of 60-90% cannot be accounted for by any of the simple hydrated oxides of iron. However, it is possible that the iron is deposited, in part at least, as a borohydrate (8). To check this possibility, three specimens were prepared by anodic deposition and the film dissolved and analyzed for boron (9). The results are shown in Table IV. The boron is probably present in the film in the same valence state as in the solution and is co-deposited wtih the iron. The iron in the solution is present in part at least as a complex with the borate ion (8) and some possible

Table III. Results of weighing and dissolution of the anodically deposited iron oxide on the platinum specimens at +300 mv, pH = 7.52

Experiment No.*	Amount of Fe^{++} used in deposition, W_{dep}, μg	Corresponding amount of Fe_2O_3, μg	Weight of deposited iron oxide, μg	Excess weight over stoichiometric Fe_2O_3, %	Amount of Fe^{++} dissolved, W_{diss}, μg	$W_{diss.}/W_{dep.}$
2	89.24	127.8	212.0	65.9	93.6	1.047
3	161.0	230.2	389.0	69.0	164.0	1.018
5	236.0	337.0	623.0	84.8	—	—
6	490.0	701.0	1231.0	75.6	—	—
7	310.1	444.0	753.0	69.6	308.0	0.992
8	353.3	503.0	1020.0	103.0	372.0	1.056
10	290.0	414.0	—	—	296.0	1.021

* Additional data for these experiments are presented in Table I.

Table IV. Content of boron in the anodically deposited iron oxide

Experiment No.	Concentration [Fe++] mole/l Starting	Final	Time, min	Area, cm²	Amount of Fe++ used in deposition, μg	Corresponding amount of Fe_2O_3, μg	Total weight of oxide layer, μg	Amount of boron in oxide layer, μg	Deviation,* %
11	2.06×10^{-4}	0.591×10^{-4}	240	10	249.5	356.5	656.0	29.4	−1.4
12	2.79×10^{-4}	1.210×10^{-4}	360	5	237.5	339.5	609.0	32.8	+4.6
13	2.72×10^{-4}	0.737×10^{-4}	300	10	354.0	506.0	926.0	31.0	−8.7

* Deviation from the experimentally found total amount of oxide layer, assuming Eq. [2], [3], [3a], and [4].

Table V. Weight of the deposited iron oxide before and after the heating at 800°C in comparison with the corresponding stoichiometric ferric oxide

Experiment No.	Amount of Fe++ used in deposition, μg	Corresponding amount of Fe_2O_3, $W_{Fe_2O_3}$, μg	Real weight of iron oxide before heating, μg	Excess weight over stoichiometric Fe_2O_3, %	Weight of iron oxide after heating, W_h, μg	$\frac{W_h}{W_{Fe_2O_3}}$
5	236.0	337.0	623.0	84.8	361.0	1.070
6	490.0	701.0	1231.0	75.6	711.0	1.013
14	260.3	372.4	642.0	72.3	368.0	0.988
15	323.0	462.4	830.0	79.5	500.0	1.081

reactions for the combined deposition of iron and boron are as follows:

$$Fe[B(OH)_4]_2 \xrightarrow{+B(OH)_3 + H_2O} Fe[B(OH)_4]_3 + H^+ + e^-_o \quad [2]$$

$$Fe[B(OH)_4]_2 \xrightarrow{+H_2O} \quad [3], [3a]$$

$$FeOH[B(OH)_4] \xrightarrow{+B(OH)_3 + H_2O} FeOH[B(OH)_4]_2 + H^+ + e^-_o$$

$$FeOH[B(OH)_4] \xrightarrow{+H_2O} Fe(OH)_2[B(OH)_4] + H^+ + e^-_o \quad [4]$$

$$Fe(OH)_2 \xrightarrow{+H_2O} FeO(OH) \cdot H_2O + H^+ + e^-_o \quad [5]$$

If the assumption is made that all of the boron in the film is present as one or more of the above compounds and that the remainder of the iron is present as $FeOOH \cdot H_2O$, then it is possible to account for the total weight of the film. A material balance of this type is given in Table IV.

Effect of heating in vacuo.—Some of the specimens were put into a vacuum chamber and heated at 10^{-7} Torr up to 800°C for as long as 20 hr. During heating the water evolved was monitored with a mass spectrometer. Only minor amounts of water were observed. After cooling the specimens were reweighed. The weight of film now corresponded to Fe_2O_3 (Table V). An x-ray diffraction pattern was obtained and was typical of α-Fe_2O_3. The film was then dissolved in hot hydrochloric acid and analyzed for boron and iron. Only a minor portion of the boron remained. The solution contained 85-95% of the originally deposited iron. This was probably due to the difficulty of completely dissolving the film after heating at high temperature. The boron can sublime from the film at high temperature in the form of various boron hydrates or oxides (10, 11).

Conclusions

1. An iron oxide type film is anodically deposited on either passive iron or platinum by anodic treatment in a neutral boric acid/sodium borate solution containing ferrous ions.

2. All iron in the deposited oxide layer is in the ferric state and originates from the solution.

3. The kinetics of the anodic deposition of iron oxide can be divided into two consecutive regions, an initial state characterized by the formation of "unit cell" thickness, followed by a steady growth region where the rate of deposition is dependent on the ferrous ion concentration in the solution and the oxide layer thickness.

4. The anodically deposited film differs from films formed by the anodic oxidation of metallic iron both electrically and electrochemically. The film is largely composed of a mixture of hydrated ferric oxides and ferric boron hydroxo complexes.

5. The film is deposited by the direct oxidation of the complexed ferrous ion.

6. Since the anodic deposition of the film was obtained on both passive iron and platinum, anodic deposition of this type of film will also take place on any other suitable metal or conductive substrate.

Manuscript received July 25, 1966.

Any discussion of this paper will appear in a Discussion Section to be published in the June 1968 JOURNAL.

REFERENCES

1. V. Markovac and M. Cohen, *This Journal*, **114**, 674 (1967).
2. J. C. Schumacher, D. R. Stern, and P. R. Graham, *ibid.*, **105**, 151 (1958).
3. T. Osuga and K. Sugino, *ibid.*, **104**, 448 (1957).
4. T. Ishimo, H. Tanura, and M. Yanokava, *Osaka Univ. Tech. Report*, **6**, 359 (1956).
5. K. J. Vetter and N. Jaeger, *Electrochim. Acta*, **11**, 401 (1966).
6. M. Nagayama and M. Cohen, *This Journal*, **109**, 781 (1962).
7. M. Nagayama and M. Cohen, *ibid.*, **110**, 670 (1963).
8. R. M. Adams, "Boron, Metallo-Boron Compounds and Boranes," p. 94, Interscience Publishers, a division of John Wiley & Sons, New York, London, Sydney (1964).
9. L. Pasztor, J. D. Bode, and Q. Fernando, *Anal. Chem.*, **32**, 277 (1960).
10. L. Brewer, *Chem. Rev.*, **52**, 51 (1953).
11. S. K. Gupta and R. F. Porter, *J. Phys. Chem.*, **70**, 871 (1966).

Consecutive Electrode Reactions in the Dissolution Kinetics of Iron

Francis M. Donahue[1] **and Ken Nobe**

Department of Engineering, University of California, Los Angeles, California

ABSTRACT

The qualitative and quantitative behavior of an electrochemical system capable of exhibiting adsorption pseudocapacitance has been examined on a theoretical basis. The analysis was compared with experimental results for the anodic polarization of iron and found to be satisfactory. In addition, a method which allows the estimation of the rate constants for the equilibration step preceding the rate-controlling step for two-step, two-electron transfer processes, was suggested and verified experimentally.

The existence of adsorption pseudocapacitance due to absorbed hydrogen atoms was predicted and demonstrated by Eucken and Weblus in 1951 (1). Subsequently, Bockris and Kita (2) extended the analysis and showed that adsorption pseudocapacitance should be present, although not always measurable, for a consecutive electrode process with the rate-determining step following an electron transfer step in quasiequilibrium. Conway and Gileadi (3) extended the analysis still further by considering non-Langmuir adsorption.

Consider the following generalized reaction scheme

$$A + B \rightleftarrows C \pm e^- \quad [1]$$

$$C \rightarrow D \pm e^- \quad [2]$$

where A and B are reactants, C is an adsorbed species, D is the product, and step [2] is rate limiting. The potential dependent surface coverage of species C, θ_c, may be derived from the analysis of Bockris and Kita for Langmuir adsorption (2). In conformity with the generalized equations given above, it is

$$\theta_c = \frac{1}{1 + \frac{k^o_{-1}}{k^o_1 [A] [B]} \exp\left[\mp \frac{F}{RT}\eta\right]} \quad [3]$$

where k^o_{-1} and k^o_1 are the rate constants for the reverse and forward partial reactions at the equilibrium potential, respectively. All other terms have their usual significance. Likewise, the adsorption pseudocapacitance due to adsorbed C is given by

$$C_{ads} = \frac{F^2 Z}{RT} \frac{\frac{k^o_{-1}}{k^o_1 [A] [B]} \exp\left[\mp \frac{F}{RT}\eta\right]}{\left\{1 + \frac{k^o_{-1}}{k^o_1 [A] [B]} \exp\left[\mp \frac{F}{RT}\eta\right]\right\}^2} \quad [4]$$

where Z is the monolayer coverage feasible for the species (moles cm^{-2}).

Inspection of Eq. [3] shows that for an increasing positive overpotential (*i.e.*, anodic polarization) the surface coverage of anodically generated adsorbed species (plus sign in Eq. [1]) will increase and the surface coverage of cathodically generated species will decrease. Inspection of Eq. [4] on the other hand, reveals that adsorption pseudocapacitance goes through a maximum at the value of η corresponding to $\theta = 0.5$. Working curves of $\theta - \eta$, $C_{ads} - \eta$, and $C_{ads} - \theta$ have been published elsewhere (2-4).

A mathematical analysis or inspection of the working curves (2-4) shows that the adsorption pseudocapacitance and surface coverage are linearly related at very low and very high surface coverages. The linearity extends to values of adsorption pseudocapacitance of about 600 $\mu f\ cm^{-2}$ (3). Therefore, for values of the total measured capacitance of less than 300 $\mu f\ cm^{-2}$, *i.e.*, double layer plus adsorption pseudocapacitance, a linearity between surface coverage and adsorption pseudocapacitance may be assumed.

Previous studies relative to measurements of adsorption pseudocapacitance have been predicated upon quasi-equilibrium or steady-state analyses. However, it should be possible to treat transient phenomena in a similar fashion. It is the authors' intent to investigate theoretically the implications of the steady-state results when applied to transient phenomena and to demonstrate experimentally that the analysis can yield information which may be used independently or to corroborate and complement other experimental techniques.

Theory

Although the subsequent analysis could be presented in a general form, it will facilitate the discussion of the experimental results if the theoretical analysis is tempered by the information available concerning the behavior of iron in acidic solutions. Since measured values of the total electrode capacitance for iron electrodes have been found to be $<300\ \mu f\ cm^{-2}$ (4-7) and have increased on increasing anodic polarization (4, 6), it may be assumed that (*a*) the adsorption pseudocapacitance is a linear function of the surface coverage, and (*b*) the surface coverage is small.

Therefore, the application of an anodic galvanostatic step-function to an iron electrode would cause, after all transients have dissipated, an increased electrode potential and an increased total measured capacitance. However, the transient effects are of greater interest here and will be considered further. Figure 1 schematically represents the transient and steady-state responses. It may be assumed that the surface coverage and capacitance approach steady-state asymptotically as shown in Fig. 1b and 1c. One may then deduce the transient potential response for the assumed variation of θ under the constant current step.

At the steady state, the rate of the reaction step of interest, in terms of current density, has the following form

$$i = k\,\theta \exp[\eta/\beta] \quad [5]$$

where k is a potential independent rate constant (or combination of rate constants), θ is the steady-state coverage of intermediate, and β is the Tafel parameter. If we assume, as suggested above, that the surface coverage during a galvanostatic step approaches the new steady-state value asymptotically, we may deduce the transient potential response of the electrode from Eq. [5]. This requires that Eq. [5] must adequately describe the current, coverage, and overvoltage inter-

[1] Present address: Department of Chemical and Metallurgical Engineering, The University of Michigan, Ann Arbor, Michigan.

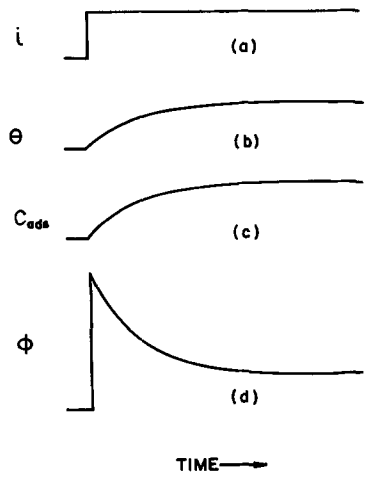

Fig. 1. Transient responses to a current pulse at an electrode exhibiting adsorption pseudocapacitance.

relationships for the transient conditions considered here within experimental error. Therefore, this analysis is precluded for times following the imposition of the step function which are of the same order of magnitude as the relaxation time for double layer charging. As a consequence of these considerations, it is seen that the potential will tend to approach steady state with a negative time derivative as shown in Fig. 1d. Transient phenomena during anodic polarization similar to that shown in Fig. 1d have been observed by many other investigators (5-11). It has been termed "superpolarization" (5). Various explanations have been suggested. Some of the experimental results to be presented below may be utilized to evaluate some of these suggestions.

In the foregoing analysis, it was assumed that the surface coverage and adsorption pseudocapacitance increase monotonically to the steady-state condition as a consequence of an anodic current step function. By a rather simple extension of the steady-state analysis, this can be demonstrated theoretically, and the experimental requirements for verification may be ascertained. The rate of buildup of the intermediate during anodic polarization at any instant is (from the mechanism given by [1] and [2])

$$\left(\frac{d\theta}{dt}\right)_t = k_{1t}[A][B] - (k_{1t}[A][B] + k_{-1t})\theta_t \quad [6]$$

In the present analysis, k_2, the rate constant for the rate-determining step, has been ignored. At the steady state

$$\left(\frac{d\theta}{dt}\right)_{ss} = 0 = k_{1ss}[A][B] - (k_{1ss}[A][B] + k_{-1ss})\theta_{ss} \quad [7]$$

It should be noted that the rate constants here are potential dependent. Hence, if one chooses values of time (t) such that $|\eta_t - \eta_{ss}| < 2RT/\mathbf{F}$, then $k_{jt} \approx k_{jss}$. In this way, [7] may be subtracted from [6] to yield

$$\left(\frac{d\theta}{dt}\right)_t = (k'_1[A][B] + k'_{-1})(\theta_{ss} - \theta_t) \quad [8]$$

where the primed rate constants are now defined as the rate constants at the resulting steady-state potential. Consequently, due to their unique specification, they are potential "independent." They should not be confused with the rate constants used in Eq. [3], which are associated with the reversible potential.

From the discussion above concerning the linear relationship between surface coverage and adsorption pseudocapacitance, one may replace θ with C_{ads} in Eq. [8]. Integration of the resulting equation between the limits of $t = 0$ and $t = t$, yields

$$\ln\left[\frac{(C_{ss} - C_t)}{(C_{ss} - C_o)}\right] = -(k'_1[A][B] + k'_{-1})t \quad [9]$$

From the analysis immediately above, it is seen that the surface coverage does increase monotonically during the anodic step function and further that the pseudo-first order rate constants for the quasi-equilibrium step, *i.e.*, Eq. [1], may be evaluated from measurements of the adsorption pseudocapacitance during the transient potential excursion.

Decay phenomena following anodic polarization may be treated similarly, but the experimental data exhibited considerably more scatter than the charging case (4) and will not be discussed further here.

Experimental

The test cell and the electronic circuitry will be discussed elsewhere (12). The electrode materials used in the present study were zone-refined iron[2] and Armco iron in the form of cylindrical electrodes as before (7). The electrolyte was 1*N* H_2SO_4, and the experiments were performed at room temperature.

Capacitance measurements were made by applying short (~8 msec) galvanostatic pulses to the electrode at open circuit while photographically recording the potential-time trace from an oscilloscope screen as before (7).

Capacitance measurements during anodic polarization were performed as noted above. The one important difference was that the electrode was already undergoing polarization. Consequently, the pulse current was superimposed on the already existing polarizing current. As had been noted previously (13), the measured capacitance during polarization was dependent on the ratio of the pulse to polarizing current (5). However, beyond a certain limiting ratio, the measured capacitance varied little with pulse current. All results listed here were in the latter region.

Results and Discussion

Bockris and coworkers (5) have suggested a mechanism for the active iron electrode which has subsequently been verified experimentally (5, 6, 10). Since the suggested mechanism is similar in form to that of the generalized Eq. [1] and [2] given here, it should be possible to analyze experimental work on the active iron electrode in terms of the treatment given above.

The potential-time behavior of zone-refined iron and Armco iron as a consequence of an anodic current step function is shown in Fig. 2 and 3, respectively. A comparison of the extent and duration of the transient maxima for the two samples indicates that the phenomenon of "superpolarization" is not an unique property of the electrolyte, but is dependent on the electrode material under study. Consequently, analyses predicated on a diffusional process, *e.g.*, hydrogen ion transport (2), fail to explain the discrepancy noted between the two electrodes in the same electrolyte. Suggestions that electrode impurities (8) or electrolyte impurities (10) cause the slow potential transients cannot be evaluated unequivocally. Kelly (10) found that replacement of the electrolyte removed the slow transients for zone-refined iron and concluded that electrolyte impurities were the source of these difficulties. Since slow transients were not noted here for the zone-refined iron, the present work cannot effectively differentiate between electrode and electrolyte impurity as the cause of the transient phenomenon observed for iron. However, it should be noted that none of the solutions tested here were pretreated as stringently as those of Kelly (10). Consequently, the results reported here may be construed as having been taken under "impure" conditions and seem to refute the contention that electrolyte impurities are the source of slow transients in the case of zone-refined iron.

[2] Donated by the Iron and Steel Institute. Prepared in rod form by Battelle Memorial Institute and designated as Bar 65A.

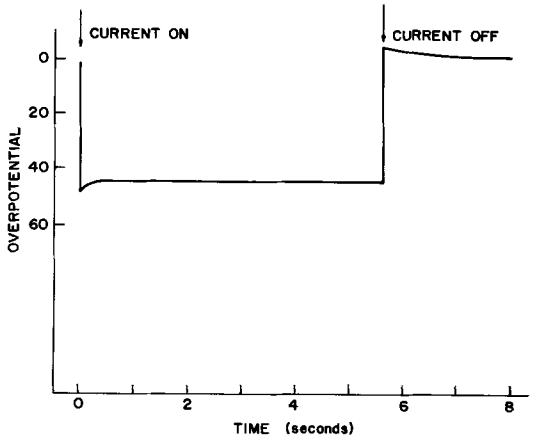

Fig. 2. Typical potential-time behavior of zone-refined iron; current density = 1 ma/cm^2.

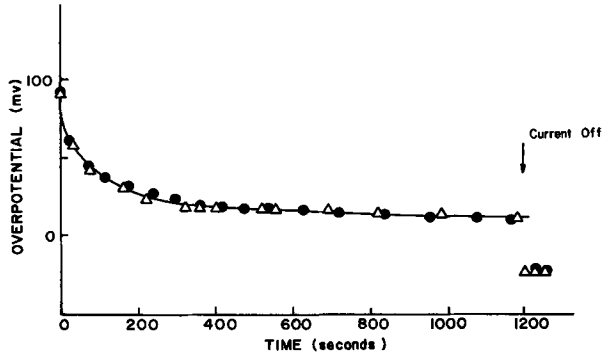

Fig. 3. Typical anodic polarization behavior of Armco iron samples; current density = 1 ma/cm^2.

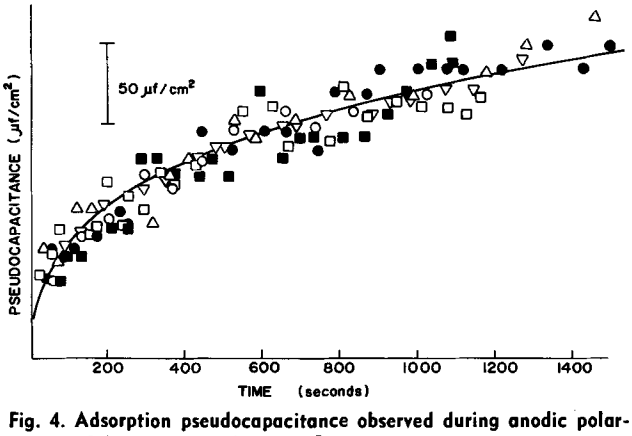

Fig. 4. Adsorption pseudocapacitance observed during anodic polarization of Armco iron at 1 ma/cm^2.

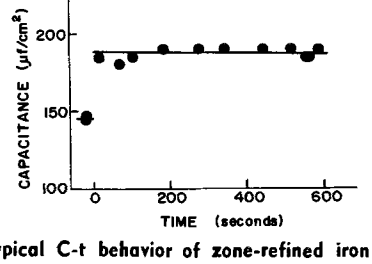

Fig. 5. Typical C-t behavior of zone-refined iron during anodic polarization; current density = 1.0 ma/cm^2.

A comparison of the potential and pseudocapacitance transients for zone-refined iron (Fig. 2 and 5) and Armco iron (Fig. 3 and 4) along with the discussion of these transients earlier in this paper suggest that the rate of equilibration of the first step in the iron dissolution reaction is a function of the bulk purity of the substrate.

Table I. Electrochemical data of Armco Iron shown in Fig. 4

Symbols (see Fig. 4)	○	□	△	▽	●	■
Corrosion potential, mv *vs.* SCE	−487	−499	−479	−480	−480	−479
Polarization potential at 1 ma/cm^2, mv *vs.* SCE	−465	−464	−469	−469	−466	−468
Capacitance prior to polarization, μf/cm^2	179	160	228	211	211	222
Immersion time, hr	31	27	56	57	59	55
Corrosion current density,* μa/cm^2	60	88	66	64	64	60
Cathodic Tafel slope, mv	76	71	78	78	78	74

* Obtained by extrapolating the cathodic pulse polarization curve back to the corrosion potential.

For the consistency of the kinetic analysis given above, a continuous variation of the measured total capacitance should be noted during anodic polarization until the steady state is reached. However, due to physical limitations of the experimental procedures, capacitance measurements could not be made at times shorter than about 15 sec after the initiation of polarization. Noting the potential-time responses of the two iron samples studied (Fig. 2 and 3), it can be seen that capacitance measurements during the transient are experimentally possible only for Armco iron. Capacitance data are shown for six different Armco iron electrodes in Fig. 4. The pertinent electrochemical data for these electrodes are given in Table I. In order to show the generality of the equations derived above, *i.e.*, that the kinetic analysis is essentially independent of the corrosion potential, corrosion rate, *etc.*, all the data have been normalized: the plotted capacitance values are the measured capacitances at time t minus the measured capacitance prior to polarization. Therefore, the plot shows the variation of the capacitance during anodic polarization and is in agreement with the analysis derived above.

That the increase in value of the capacitance during anodic polarization is not due to surface roughening may be seen from an inspection of Fig. 5 which shows the C-*t* behavior of a zone-refined iron electrode under conditions identical to those for the Armco iron electrodes in Fig. 4. The C-*t* plot is seen to be horizontal. This should not be construed as assuming that the surface does not roughen. It does mean, however, that, if roughening is present, it does not contribute a measurable effect on the C-*t* behavior.

In order to test the validity of Eq. [9], plots of log $(C_{ss} - C_t)$ *vs.* t were made for a number of Armco iron electrodes at current densities of 0.5, 1, and 2 ma/cm^2. A typical example of these plots is given in Fig. 6. The slope of the line shown in Fig. 6 is 1.8 x 10^{-3} sec^{-1}. Data for all three current densities average to a mean slope of 2.0 x 10^{-3} sec^{-1} with a deviation about the mean of about 20%. From the analysis given

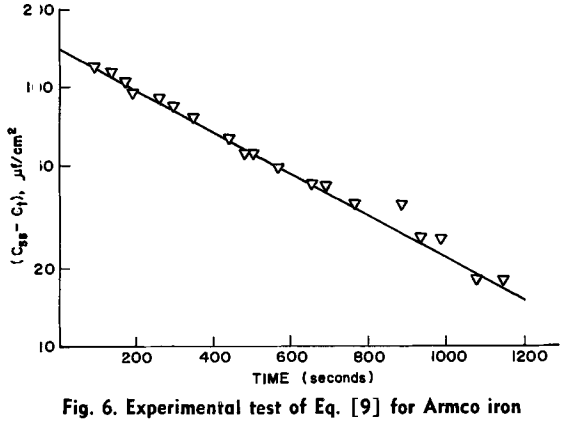

Fig. 6. Experimental test of Eq. [9] for Armco iron

above, this slope is the sum of the respective rate constants at the steady-state polarization potential.[3]

An estimate of the respective rate constants may be obtained from the sum of the rate constants (2×10^{-3} sec^{-1}), C_{ads} (measured), $C_{ads} - \theta$ curves (2-4), and Eq. [3]. Since the reversible potential for a corroding system is quite difficult to specify, one might conveniently refer the data in Eq. [3] to the corrosion potential.

The technique which has been developed here should be useful in future studies of reaction mechanisms and in understanding the role of surface properties on the adsorption of electroactive intermediates. It has already been useful in ascertaining the role of organic corrosion inhibitors (14). A similar analysis, although neglecting the possible application of capacitance measurements has been developed by Conway and Gilroy and applied to the inhibition of surface reactions by oxide formation (15).

Acknowledgment

This work was supported by funds from the University of California sea water desalinization program. Partial support was received from NASA NsG 237-62 and the Corrosion Research Council project 14. A. Akiyama assisted in the experimental work.

[3] Armco iron has been shown to exhibit an anodic Tafel slope of 30 mv under the conditions studied here (7). Consequently, if one assumes that the calculated slopes for all three current densities are referred to the polarization potential for 1 ma/cm² (and thereby, potential "independent"), the expected deviations due to the actual potential dependence would be on the order of ± 20%.

Manuscript received Feb. 1, 1966; revised manuscript received Jan. 23, 1967. This paper was presented at the Buffalo Meeting, Oct. 10-14, 1965.

Any discussion of this paper will appear in a Discussion Section to be published in the June 1968 JOURNAL.

REFERENCES

1. A. Eucken and Weblus, *Z. Elektrochem.*, **55**, 114 (1951).
2. J. O'M. Bockris and H. Kita, *This Journal*, **108**, 676 (1961).
3. B. E. Conway and E. Gileadi, *Trans. Faraday Soc.*, **58**, 2493 (1962).
4. F. M. Donahue, Ph.D. Thesis, University of California, Los Angeles, 1965.
5. J. O'M. Bockris, D. Drazic, and A. R. Despic, *Electrochim. Acta*, **4**, 325 (1961).
6. J. O'M. Bockris and D. Drazic, *ibid.*, **7**, 293 (1962).
7. F. M. Donahue and K. Nobe, "Second International Congress on Metallic Corrosion," NACE, Houston, 1966, pp. 916-924.
8. A. C. Makrides, *This Journal*, **107**, 869 (1960).
9. N. D. Greene and G. A. Saltzman, *Corrosion*, **20**, 293t (1964).
10. E. J. Kelly, *This Journal*, **112**, 124 (1965).
11. K. E. Heusler, *Z. Elektrochem.*, **62**, 582 (1958).
12. F. M. Donahue and K. Nobe, To be published.
13. F. M. Donahue and K. Nobe, Paper presented at the Washington Meeting of the Society, Oct. 11-15, 1964, Abstract No. 69.
14. F. M. Donahue, A. Akiyama, and K. Nobe, Submitted to *This Journal*.
15. B. E. Conway and D. Gilroy, *J. Phys. Chem.*, **69**, 1259 (1965).

Oxidation of Copper and Copper-Gold Alloys in CO_2 at 1000°C

I. Linear Kinetics

B. Swaroop and J. Bruce Wagner, Jr.

Department of Materials Science and Materials Research Center, Northwestern University, Evanston, Illinois

ABSTRACT

The oxidation rates of copper (99.999 w/o) and copper-gold alloys (Cu-5.32 a/o Au and Cu-10 a/o Au) have been studied as a function of partial pressure of carbon dioxide at 1000°C. The oxidation rates are initially linear. When a certain oxide thickness is attained, there is a decrease in the rate after which the kinetics again become linear. For all the samples the linear rate constant decreases nonlinearly with decreasing partial pressure of CO_2. In addition, the effect of various flow rates of carbon dioxide on the oxidation rate of pure copper has been studied.

The rate of oxidation of a metal may be controlled by one or more of the following processes: (*i*) transport of the gas to the reaction site; (*ii*) dissociation of the gas on the surface (a phase boundary reaction); (*iii*) transport of ions and electrons across an oxide layer; (*iv*) a phase boundary reaction at the oxide-metal interface.

The purpose of the present investigation was to determine the mechanism of oxidation of copper and copper-gold alloys in very low oxygen pressures provided by an atmosphere of carbon dioxide at 1000°C. In the case of the oxidation of copper in carbon dioxide, the oxygen pressure due to the dissociation of CO_2 is very nearly equal to the value of the oxygen pressure for the coexistence of copper and cuprous oxide (see Table I). Consequently, great care must be exercised in interpreting the kinetics, as will be discussed.

Linear oxidation kinetics have been reported for copper in oxygen by Wagner and Grunewald (1) and by Baur, Bridges, and Fassel (2), and in carbon dioxide by Margulescu and Cismark (3).

The oxidation of iron (4) and cobalt (5) in CO_2-CO mixtures has been shown to obey linear kinetics initially and to transform to parabolic kinetics (diffusion controlled kinetics) after a certain initial film thickness was attained. The linear kinetics were inferred to be due to the dissociation of CO_2 into CO and adsorbed oxygen atoms or ions.

Pettit and his co-workers (4) have shown that the linear oxidation of iron in CO_2-CO mixtures obeys an equation of the form

$$K_L \alpha [k' P_{CO_2} - k'' P_{CO}] \qquad [1]$$

Table I. Partial pressures of oxygen in equilibrium with copper and its oxides at 1000°C

Reaction	P_{O_2}, atm
1. $CO_2 = CO + \frac{1}{2}O_2$	1.2×10^{-5}
2. $Cu_2O = 2Cu + \frac{1}{2}O_2$	5.6×10^{-7}
3. $2CuO = Cu_2O + \frac{1}{2}O_2$	1.4×10^{-1}

where K_L is the experimental linear rate constant (g oxygen/cm^2-sec), P_{CO_2} and P_{CO} are the partial pressures of CO_2 and CO, respectively, and k' and k'' are two constants. These constants are functions of the crystal plane exposed to the gas and of the oxide composition, in particular the concentration of excess electrons or excess electron holes. For thin oxide films, Pettit and Wagner (4) inferred that the concentration of excess electrons or holes is virtually constant and does not appear explicitly in the rate equation. The present study involves thin oxide layers (thickness $\leq 5 \times 10^{-4}$ cm) of Cu_2O on copper and on copper-gold alloys.

Experimental

Rectangular coupons, 0.5 x 0.5 in., were prepared from copper and from copper-gold alloys (5.32 and 10 a/o). Both the copper and gold were 99.999+% pure. The alloys were melted in a graphite mold under a vacuum of 10^{-6} mm Hg. In addition, a single crystal of copper in the form of a right cylinder, 3.1 mm thick and 12.6 mm in diameter with the end faces parallel to (100) planes was obtained from Research Crystals, Inc., Richmond, Virginia. The purity of this crystal was listed as 99.999%

The samples were prepared as follows: (*A*) Pure copper rod, 0.360 in. diameter, was cold rolled into sheets about 0.040 and 0.020 in. thick, respectively, in equal reduction passes. (*B*) Samples from these sheets were annealed 24 hr at 1000°C in a sealed quartz tube under a vacuum of 10^{-6} mm Hg. The grain diameter was about 1 mm or larger. (*C*) The copper-gold alloys were cold-rolled to 0.020 in. thickness and annealed as in (*B*). All specimens were polished mechanically on emery paper followed by a polish using Linde "A" alumina powder. In the case of the single crystal and for some of the polycrystalline samples, the specimens were subsequently electropolished and then washed successively in water, acetone, and in ethyl alcohol.

The oxidation rates were measured gravimetrically by methods described previously (5). "Bone dry"[1] CO_2 and CO_2 diluted with argon were used as oxidizing gases. Both the carbon dioxide and the argon were passed through separate columns of copper turnings at 300°-350°C and then through magnesium perchlorate to remove oxygen and water vapor. In order to test whether any residual impurities, especially traces of oxygen, were affecting the observed kinetics, the following experiments were performed. Research grade CO_2 ($O_2 < 10$ ppm, $N_2 < 100$ ppm and $H_2 < 10$ ppm) was used in several runs. No difference in kinetics was observed from those obtained using bone dry CO_2. In addition, pure copper samples were suspended in the purified argon (initial purity >99.998%). No weight change was observed in 24-48 hr. A few runs were carried out in oxygen-argon mixtures. A linear flow rate of 0.9 cm/sec was used for most runs except when the effect of gas flow rate on oxidation kinetics was studied.

Results and Discussion

Figures 1, 2, 3, and 4 show typical oxidation rate curves for the pure copper and the alloys. For all samples, there was an initial linear oxidation rate which was followed by a second linear oxidation rate after a certain critical oxide thickness was attained. This thickness ranged from 0.40 to 0.60 x 10^{-4} cm, assuming a dense layer of Cu_2O. The oxygen partial pressure for the equilibrium dissociation of CO_2 at 1000°C is less than that for the formation of cupric oxide as is shown in Table I. In addition, no CuO was found by x-ray analyses of the oxides. The rate constants for the second linear rate are smaller than those for the first linear kinetics. Pettit and co-workers (4, 5) have shown that the oxidation of iron and cobalt in CO_2-CO mixtures involved two successive stages of linear kinetics.

[1] Bone dry is a trade name of the Matheson Company, Inc. It is 99.8% pure with moisture as the major impurity.

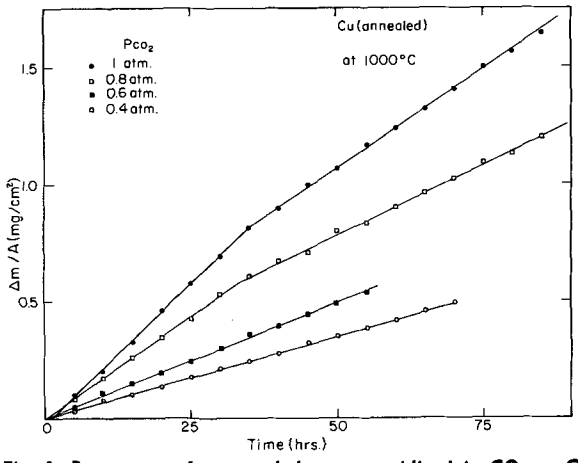

Fig. 1. Rate curves for annealed copper oxidized in CO_2 or CO_2 diluted with argon at a total pressure of one atmosphere. The linear gas flow rate was 0.9 cm/sec.

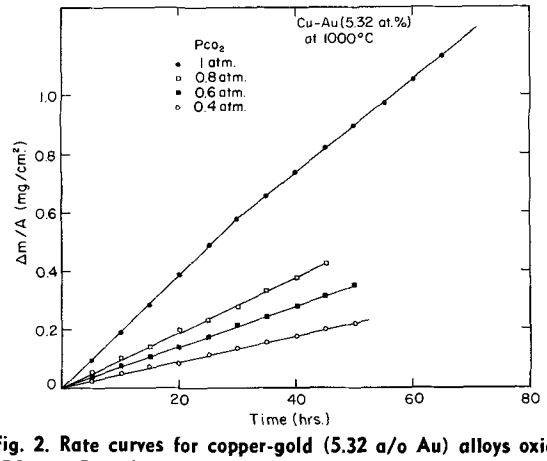

Fig. 2. Rate curves for copper-gold (5.32 a/o Au) alloys oxidized in CO_2 or CO_2 diluted with argon. The linear gas flow rate was 0.9 cm/sec.

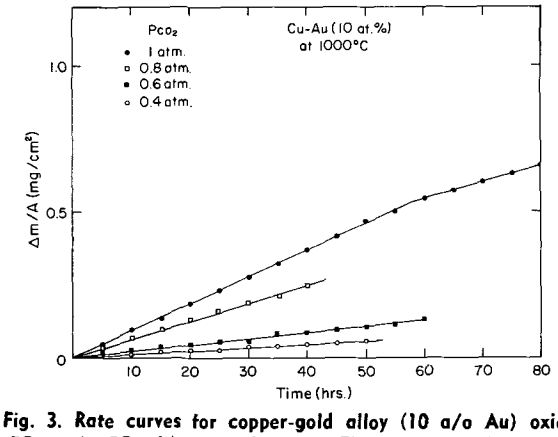

Fig. 3. Rate curves for copper-gold alloy (10 a/o Au) oxidized in CO_2 or in CO_2 diluted with argon. The linear gas flow rate was 0.9 cm/sec.

The linear rates were a function of the oxide planes exposed at the oxide-gas interface. Initially the oxide crystals were epitaxially related to the substrate. As the film thickened, the orientation of the oxide planes exposed to the gas changed. This change was correlated with the change in linear kinetics.

For the present study, the first linear kinetics are discussed. In order to show that gas transport to the samples was not rate determining the following calculation was made for 1000°C. According to Kiukkola and Wagner (6)

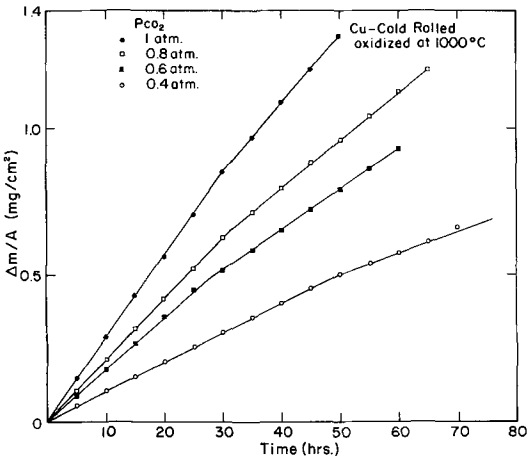

Fig. 4. Rate curves for cold rolled copper oxidized in CO_2 or in CO_2 diluted with argon. The linear gas flow rate was 0.9 cm/sec.

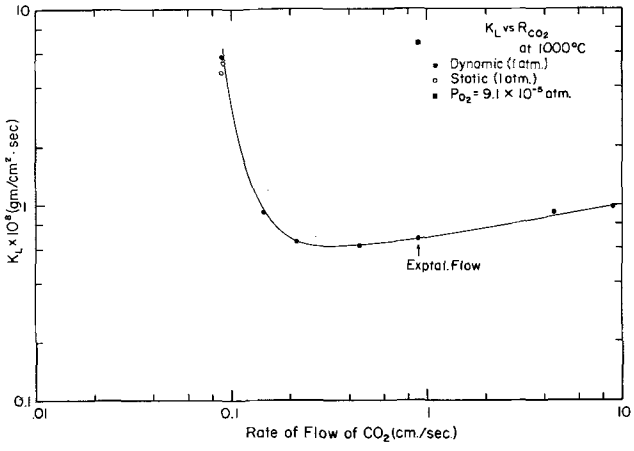

Fig. 5. Effect of linear gas flow rate of CO_2 on the first linear rate constant. The open circles represent data taken in a closed system of static CO_2. The square denotes an experimental result for an argon-oxygen mixture of $P_{O_2} = 9.1 \times 10^{-5}$ atm at a linear flow rate of 0.9 cm/sec.

$$2Cu(s) + \tfrac{1}{2}O_2(g) = Cu_2O(s);\ \Delta G^\circ_1 = -18.2 \text{ kcal} \quad [2]$$

The dissociation of carbon dioxide is given by

$$CO(g) + \tfrac{1}{2}O_2(g) = CO_2(g);\ \Delta G^\circ_2 = -41.0 \text{ kcal} \quad [3]$$

so that

$$2Cu(s) + CO_2(g) = Cu_2O(s) + CO(g);\quad \Delta G^\circ_3 = +22.8 \text{ kcal} \quad [4]$$

from which it follows that

$$\left[\frac{P_{CO}}{P_{CO_2}}\right]_{Cu,\,Cu_2O} = K_3 = \exp\left[\frac{-\Delta G^\circ_3}{RT}\right] = 1.2 \times 10^{-4} \quad [5]$$

If all the carbon dioxide reaching the sample reacted completely to oxidize the copper to Cu_2O then the weight increase per unit time, Δm°, is

$$\Delta m^\circ = M_o\, 1.2 \times 10^{-4}\, n^\circ_{CO_2} \quad [6]$$

where $M_o = 16$ is the atomic weight of oxygen and $n^\circ_{CO_2}$ denotes the number of moles CO_2 passed over the sample per unit time. The usual flow rate was 0.9 cm/sec through a reaction tube of 2.85 cm^2 cross section. During a run lasting 10 hr, the weight change should have amounted to 8 mg if transport of CO_2 to the surface were rate determining. The experimental weight change was 0.25 mg for a run on annealed copper lasting 10 hr in CO_2 at a pressure of 1 atm. The calculation shows that gas transport to the surface was not rate determining. Because the experimental weight change was much less than that calculated for gas transport and because the kinetics were linear, it is concluded that a phase boundary reaction is rate determining. Likewise the total uptake of dissolved oxygen for the size of copper samples used would amount to only 0.015 to 0.025 mg. This weight change is much less than those obtained from the experimental runs so that most of the weight gain resulted from Cu_2O. Furthermore, the change in linear kinetics with time (Fig. 1-4) would tend to rule out gas transport as being rate determining.

Finally, an empirical study of the oxidation rate as a function of the flow velocity of CO_2 was made (see Fig. 5). Between 0.2 cm/sec and 0.9 cm/sec, the oxidation rates were virtually the same. At lower flow rates (<0.2 cm/sec) the oxidation rate increased. An experiment was run at zero gas flow, *i.e.*, in a static system of about 5 liters total volume. This experiment yielded a linear rate constant (K_{L1}) as equal to 4.8 x 10^{-8} g·cm²·sec^{-1}, very nearly that observed for a gas flow rate of 0.09 cm/sec (K_{L_1} = 5.2 x 10^{-8} g·cm^{-2}·sec^{-1}). Probably for the static run and in the runs at low flow rates, the carbon dioxide has time to dissociate in the gas phase according to Eq. [3], whereby the oxygen partial pressure is calculated to be about 1.2 x 10^{-5} atm. To test this assumption, an experiment was run in an oxygen-argon mixture where P_{O_2} = 9.1 x 10^{-5} atm with the mixture flowing over the sample at 0.9 cm/sec. The linear rate constant amounted to 6.84 x 10^{-8} g·cm^{-2}·sec^{-1}. It would be expected that the run in static CO_2 would yield a slightly lower oxidation rate because of the presence of CO in the gas phase, in addition to the lower oxygen partial pressure.

Table II summarizes the data for the initial rates on pure copper as a function of pretreatment of the samples. The relative oxidation rates decrease in the order: cold-worked polycrystalline; mechanically polished and annealed polycrystalline; electrochemically polished and annealed polycrystalline; single crystal which was electrochemically polished and annealed. The relative rates are probably due to the different crystal planes of the oxide exposed to the gas. This explanation is consistent with the results of Pettit and co-workers (4) for the oxidation of iron to wüstite.

The copper-gold alloys exhibited a lower rate of oxidation than did the annealed copper samples. In these cases, gold was inert. The activity of copper coexisting with the Cu_2O was less than that on the pure copper samples. The ratio of the values of the rate constants for the two alloys is almost a constant, approximately 10/5.32 (see Table III). This suggests that the relative amount of copper at the metal-oxide interface

Table II. Linear rate constants (K_{L1}) for copper at 1000°C in 1 atm of CO_2

Pretreatment	K_{L_1} (g/cm²·sec)
1. Cold worked (Mech. polished)	8.9 × 10⁻⁹
2. Mech. polished, annealed	6.8 × 10⁻⁹
3. Electrochem. polished, annealed	6.1 × 10⁻⁹
4. Electrochem. polished, annealed single crystal (100)	3.7 × 10⁻⁹

Table III. Linear rate constants (K_{L1} g/cm²-sec) for copper and Cu-Au alloys at 1000°C in various partial pressures of CO_2 for a linear flow rate of 0.9 cm/sec

P_{CO_2}	Cu, annealed	Cu, cold worked	Cu-Au (5.32 a/o)	Cu-Au (10 a/o)
	$K_{L_1} \times 10^9$	$K_{L_1} \times 10^9$	$K_{L_1} \times 10^9$	$K_{L_1} \times 10^9$
1	6.87-7.10	8.93	5.25-5.0	2.5-2.3
0.8	4.75-4.90	6.49	2.75-2.55	1.28
0.6	2.8-3.1	4.6-5.0	2.0-1.90	0.71
0.4	2.0	2.72	0.90	0.35

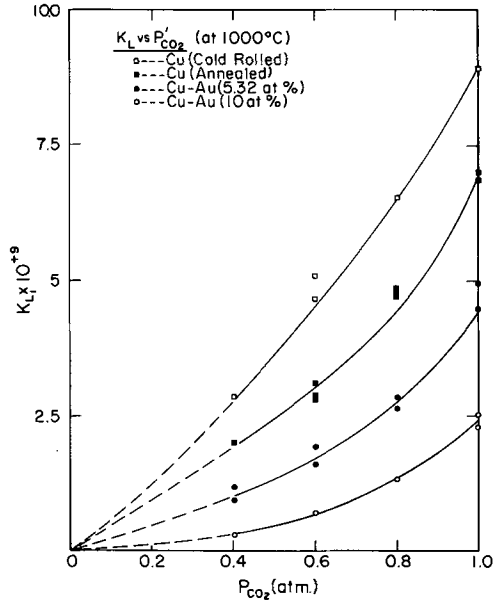

Fig. 6. Dependence of the first linear rate constant, K_{L1}, on the partial pressure of CO_2 in a CO_2-argon mixture. All data were from runs at a linear gas flow rate of 0.9 cm/sec.

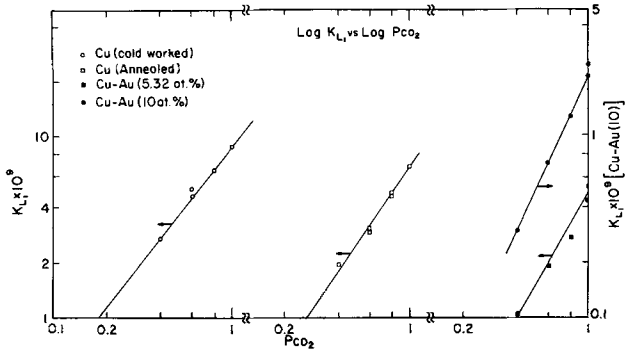

Fig. 7. Graph of log K_{L1} vs. log P_{CO_2}. The slopes of the lines are: (a), cold-rolled copper, 1.3; (b), annealed copper, 1.5; (c), Cu-Au (5.32 a/o), 1.75; (d), Cu-Au (10.0 a/o), 2.06.

and therefore the relative amounts of cuprous oxide are responsible for the difference in rates because the gas presumably dissociates on the cuprous oxide.

Equation [1] could not be tested because of the difficulty in maintaining a CO/CO_2 ratio of the order of one part in 10^4. The dependence of the rate constants on partial pressure of CO_2, using argon as a diluent gas, is shown in Fig. 6 for all the metals studied. The constants obeyed an empirical equation of the form

$$K_{L1} = C P^n_{CO_2} \qquad [7]$$

where C is a constant and n is a number dependent on the metal used. Figure 7 shows a plot of log K_L *vs.* log P_{CO_2}. The values of n for the various metals vary between 1.3 and 2.08. A value of n greater than unity is unusual for oxidation of metals in CO_2. When nickel and a nickel-chromium alloy were oxidized in CO_2, Fueki (7) found that the linear rates were proportional to the partial pressure of CO_2, *i.e.*, $n = 1$ in Eq. [7]. These results were shown to be consistent with the mechanism described in Eq. [1]. Hauffe and Pfeiffer (8) found that the oxidation of iron to wüstite in CO_2-CO mixtures obeyed a pressure dependence of $(P_{CO_2}/P_{CO})^{2/3} \propto P_{O_2}{}^{1/3}$. Pfeiffer and Laubmeyer (9) found the linear oxidation rate of iron to wüstite in low pressures of oxygen obeyed a pressure dependence of $P_{O_2}{}^{0.7}$. The pressure dependences have been inferred to be due to a chemisorption mechanism (10). The pressure dependence observed in the present studies cannot be due to this mechanism since the observed values of n are greater than one. Furthermore, the value of n decreases from those obtained on the copper samples to those of the alloys. The data only show that the reaction occurs at the gas-oxide interface.

It should be mentioned that the present kinetic data do not obey a logarithmic law as has been discussed for thin film oxidation studies on copper and for other metals (10, 11).

Conclusions

The initial growth of an oxide on copper and on copper-gold alloys (5.32 a/o and 10 a/o) in CO_2 at 1000°C is governed by linear kinetics when the linear gas flow is 0.9 cm/sec. Two linear rates are observed. The first linear stage changes to a second linear stage at an oxide thickness of 0.4 to 0.6 x 10^{-4} cm. The linear rates were not proportional to the first power of the partial pressure of CO_2. The rate determining step under these conditions is at the gas-oxide interface. At low flow rates, the oxidation rates are more rapid, presumably due to the CO_2 having time to dissociate in the gas phase prior to a reaction with the sample.

Acknowledgment

Work on this paper was supported by the United States Atomic Energy Commission.

Manuscript received Jan. 6, 1967; revised manuscript received March 17, 1967. This paper was presented at the Philadelphia Meeting, Oct. 9-14, 1966.

Any discussion of this paper will appear in a Discussion Section to be published in the June 1968 JOURNAL.

REFERENCES

1. C. Wagner and K. Grünewald, *Z. Physik Chem.*, **B40**, 197 (1938).
2. J. P. Baur, D. W. Bridges, and W. M. Fassell, Jr., *This Journal*, **103**, 274 (1956).
3. I. G. Murgulescu and D. Cismaru, *Acad. rep. populare Romine Studii. cercetari chim.*, **7**, 197 (1959).
4. F. S. Pettit, R. Yinger, and J. B. Wagner, Jr., *Acta Met.*, **8**, 617 (1960); F. S. Pettit and J. B. Wagner, Jr., *ibid.*, **12**, 35 (1964).
5. F. S. Pettit and J. B. Wagner, Jr., *ibid.*, **12**, 41 (1964).
6. K. Kiukkola and C. Wagner, *This Journal*, **104**, 379 (1957).
7. K. Fueki and J. B. Wagner, Jr., *ibid.*, **112**, 1079 (1965).
8. K. Hauffe and H. Pfeiffer, *Z. Metallk.*, **44**, 27 (1953).
9. H. Pfeiffer and C. Laubmeyer, *Z. Elektrochem.*, **59**, 579 (1955).
10. K. Hauffe, "Oxidation of Metals," Plenum Press, New York, English Ed. (1965).
11. U. Evans, "Metallic Corrosion, Passivity and Protection," pp. 137-141; Edward Arnold and Co., London (1948); H. H. Uhlig, "Corrosion and Corrosion Control," p. 166, John Wiley & Sons, Inc., New York (1962).

Rate of Solution of Rotating Tantalum Disks in Liquid Tin

T. F. Kassner

Metallurgy Division, Argonne National Laboratory, Argonne, Illinois

ABSTRACT

The dissolution kinetics of tantalum in liquid tin have been investigated under the well-defined hydrodynamic conditions produced by the rotating-disk sample geometry. Dissolution data were obtained under laminar flow conditions (Reynolds No. 1 x 10^3 to 1 x 10^5) for the temperature range 800°-1200°C. Much of the experimental data was found to be in a region of mixed transport control; however, for specific conditions of temperature and velocity, both limiting cases for reaction and diffusion control were also observed. The solubility of tantalum in liquid tin was determined over the temperature range 600°-1200°C. The diffusion coefficient of Ta-182 in liquid tin was also measured at temperatures between 500° and 1100°C by the capillary-reservoir method. These data were used in the convective-diffusion model set forth by Levich to calculate values for the diffusion-controlled dissolution flux. The model was extended to include the range of Schmidt numbers between 4 and 1000. A Schmidt number of ~25 in the tantalum-tin system at 1200°C resulted in a 12% reduction in the calculated dissolution flux. Within the limits of error of the experimental diffusion data, the dissolution flux from the model was in agreement with the experimental values in the region of diffusion control.

The convective-diffusion model for mass transport to or away from a rotating disk first formulated by Levich (1, 2) has been extended (3) to include the range of Schmidt numbers commonly encountered in liquid-metal systems at high temperatures. The purpose of this paper is: (*a*) to give the flux equation for rotating disks applicable to systems in which the Schmidt number, ν/D, ranges between 4 and 1000, and (b) to present kinetic, diffusion, and solubility data that can be used to demonstrate the applicability of the model to a high-temperature liquid-metal system.

When it is assumed that the solute concentration of the liquid is independent of radial and angular position but is solely dependent on the axial distance from the disk surface, and also that steady-state transport across the diffusion layer is achieved rapidly; the convective-diffusion equation in cylindrical coordinates can be written as

$$V_Z(Z)\frac{dC}{dZ} = D\frac{d^2C}{dZ^2} \qquad [1]$$

where V_Z is the axial component of the velocity, D is the solute diffusion coefficient, and C is the solute concentration.

Cochran's (4) exact solution to the Navier-Stokes and continuity equations for fluid motion near a rotating disk yielded a series relationship between V_Z and Z. The first three terms of the series for small values of Z were used with the boundary conditions for a disk undergoing dissolution in a large volume of liquid to obtain a solution to Eq. [1] for the concentration distribution of solute near the disk surface. The maximum (initial) flux of solute from Fick's first law can then be written as

$$J_m = \frac{D(C_{sat} - C_B)}{1.805\,\omega^{-1/2}\nu^{1/6}D^{1/3}I_{(D/\nu)} + 1.124\,D(\nu\omega)^{-1/2}\exp\left[-3.11\,(\nu/D)\right]} \qquad [2]$$

where ν is the kinematic viscosity of the liquid, cm²/sec; ω the angular velocity of the disk, radians/sec; C_{sat} the solubility of the solute in the liquid, g/cm³; and C_B the initial solute concentration in the liquid, g/cm³. $I_{(D/\nu)}$ is the value of an integral in the solution to Eq. [1] and is a function of the reciprocal Schmidt number.

Table I. Value of the integral $I_{(D/\nu)}$ for a range of Schmidt numbers between 4 and 1000

(Schmidt No.)$^{-1}$ (D/ν)	Integration limit 1.9944 $(\nu/D)^{1/3}$	Value of the integral $I_{(D/\nu)}$
0	∞	0.8934
0.001	19.944	0.9209
0.002	15.830	0.9286
0.003	13.828	0.9341
0.004	12.564	0.9385
0.005	11.663	0.9424
0.006	10.967	0.9457
0.007	10.426	0.9487
0.008	9.972	0.9515
0.009	9.588	0.9541
0.010	9.257	0.9564
0.020	7.347	0.9747
0.030	6.419	0.9877
0.040	5.832	0.9981
0.050	5.414	1.0068
0.060	5.094	1.0143
0.070	4.839	1.0209
0.080	4.629	1.0268
0.090	4.450	1.0321
0.100	4.297	1.0368
0.110	4.162	1.0412
0.120	4.043	1.0451
0.130	3.937	1.0488
0.140	3.841	1.0521
0.150	3.754	1.0552
0.160	3.674	1.0580
0.180	3.532	1.0631
0.200	3.410	1.0675
0.250	3.166	1.0762

From ref. (3)

$$I_{(D/\nu)} = \int_0^{1.9944(\nu/D)^{1/3}} \exp\left[-X^3 + 0.885\left(\frac{D}{\nu}\right)^{1/3}X^4 - 0.394\left(\frac{D}{\nu}\right)^{2/3}X^5\right]dX$$

The values of $I_{(D/\nu)}$ listed in Table I were determined by a computer integration for the 28 D/ν values between 0.001 and 0.250. Gregory and Riddiford (5) solved the same problem for several D/ν values between 0.001 and 0.004 by a graphical integration method in which the first two terms of the series expansion defining V_Z were used. They showed that when $D/\nu = 0.001$, $I(0.001)$ was 3% greater than the $I(O)$ approximation employed by Levich (1). The

values in Table I result in a 4% correction to the $I(O)$ approximation for $D/\nu = 0.001$ and a 17% correction for $D/\nu = 0.250$.

The convective-diffusion boundary layer, δ_D, is defined by denominator of Eq. [2]. For D/ν values pertinent to this study, the second term in the denominator of Eq. [2] is negligibly small compared to the first so that Eq. [2] can be rewritten as

$$J_m = 0.554\, I_{(D/\nu)}{}^{-1}\, D^{2/3}\, \nu^{-1/6}\, \omega^{1/2}\, (C_{sat} - C_B) \quad [3]$$

Equation [3] is applicable to laminar flow which, for a polished and dynamically balanced disk, extends to Reynolds numbers of the order of 10^5. The Reynolds number for a disk of radius R is defined as $Re = \omega R^2/\nu$. For the 5.08 cm diameter disks used in this work, the upper limit for ω was $\sim$ 20 radians/sec at the higher temperatures.

The temperature dependence of the diffusion-controlled dissolution flux was obtained by inserting the following Arrhenius expressions for the temperature dependence of D, ν, and C_{sat} into Eq. [3].

$$D = D_o \exp\left(\frac{-Q_D}{RT}\right) \quad [4]$$

$$\nu = \nu_o \exp\left(\frac{+Q_\nu}{RT}\right) \quad [5]$$

$$C_{sat} = C_o \exp\left(\frac{-\Delta H_{soln}}{RT}\right) \quad [6]$$

The result is given below for the case where the initial concentration of the liquid, C_B, is zero

$$J_m = 0.554\, I_{(D/\nu)}{}^{-1}\, D_o{}^{2/3}\, \nu_o{}^{-1/6}\, \omega^{1/2} \exp\left(-\frac{4Q_D + Q_\nu + 6\Delta H_{soln}}{6RT}\right) \quad [7]$$

For the temperature interval and Schmidt numbers applicable to this work, the temperature dependence of $I_{(D/\nu)}$ becomes negligibly small. From Eq. [7], the temperature dependence of the maximum dissolution flux, Q_{Jm}, is related to the activation energies for solute diffusion, Q_D, and viscosity, Q_ν, and the overall heat of solution of the solute in the liquid, ΔH_{soln} by the relation

$$Q_{Jm} = \frac{1}{6}\,(4Q_D + Q_\nu + 6\Delta H_{soln}) \quad [8]$$

Sufficient experimental data have been obtained to predict the magnitude of the dissolution flux from Eq. [3] and the temperature dependence of the flux from Eq. [8]. These values can then be compared with the experimental dissolution data.

Experimental

The tantalum disks were machined from 0.11 cm thick annealed polycrystalline sheet. The analysis of the material is given in Table II. The disks were ground flat on metallographic paper and then given a light chemical polish in a 50:20:20 sulfuric-hydrofluoric-nitric acid solution. A thin tantalum support rod was electron-beam welded to the disk and the rod was fitted with a quartz protection tube. The support rod was attached to another rod which passed through a rotary push-pull vacuum seal, and the system was dynamically balanced before inserting it into the furnace tube.

Table II. Analysis of the tantalum sheet

	Ppm by weight
C	11
O	33
N	44
Fe	9
Cu	1
Ni	2
Si	7
Nb	25
Cr	<1
Ti	<5
Al	<10
Mo	<10
W	<40
Ta	Bal.

The "four-nines plus" purity tin melts were contained in 66 mm ID quartz crucibles. Each melt of about 3200g was deoxidized by bubbling dry hydrogen through it at 500°C in another furnace.

A run was started by lowering the disk into the liquid tin and setting the desired rotational speed. The temperature of the liquid was held to ±2°C and the angular velocity of the disk was maintained to ±1% of the set value. Samples of the tin reservoir were obtained at desired time intervals with quartz sampling tubes.

The following thermal neutron activation method was used to analyze the samples for tantalum. The 0.40 cm diameter by 3.5 cm long cylindrical samples were removed from the quartz sampling tubes and then weighed and capsulated in polyethylene tubes. Samples of pure tin of similar size were also weighed and sealed in polyethylene tubes for use as tin standards. Tantalum standards were prepared by dissolving an accurately tared tantalum wire in a measured volume of a 50:50 HF-HNO_3 solution. One ml quantities of the standard solution were quantitatively transferred to polyethylene tubes and the capsules were sealed. The samples and standards were irradiated for 4 hr in a neutron flux of 1.6 x 10^{11} n/cm^2-sec. A counting system incorporating a large well-type scintillation detector and a pulse height analyzer was used to determine the sample and standard activities in the region of the 1.121, 1.188, and 1.223 mev Ta-182 peaks. Major interference by the 9.4 day half-life Sn-125 peak at 1.07 mev was eliminated by the pulse height analyzer. However, the activity of the Ta-Sn samples was corrected for tin activity with the information from the tin standards. There was essentially no self-absorption within the samples for the sample geometry and gamma-ray energies involved (6). Tantalum concentrations as low as 0.5 ppm could be determined routinely by the method.

Results

Representative concentration *vs.* time plots for two of the runs are shown in Fig. 1. The initial slope of each curve was used along with the area of the disk and the weight of the tin reservoir to obtain the values for the maximum dissolution flux of tantalum. Figure 2 is representative of the type of curve that resulted when trace amounts of air or water vapor were ac-

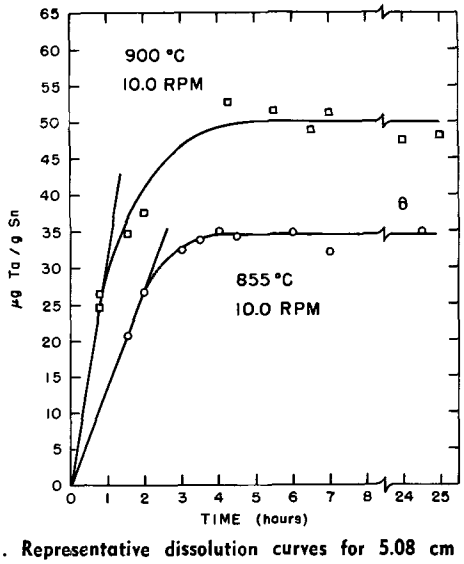

Fig. 1. Representative dissolution curves for 5.08 cm diameter disks in liquid tin.

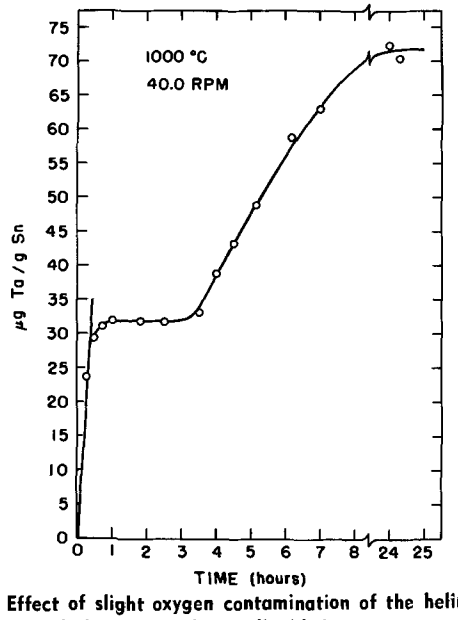

Fig. 2. Effect of slight oxygen contamination of the helium cover gas on the dissolution of tantalum in liquid tin.

cidently introduced into the helium cover gas during the sampling procedure. If the sampling problem was corrected and no additional contaminants were admitted to the system, the system attained saturation.

Dissolution curves similar to the first 3 hr in Fig. 2 were obtained for several runs in which a small air leak developed in the system. The concentration of tantalum in the tin remained at a constant low fraction of the saturation concentration. For the runs where contamination was present, tantalum was selectively oxidized out of solution at the liquid-gas interface. The dissolution process at the tantalum disk-liquid interface proceeded at a rate that could be related to the difference between the saturation concentration and the steady-state concentration of tantalum in the liquid. The latter quantity was determined by the rate of solution of the disk and the rate of removal of tantalum from solution by oxidation.

Figure 3 shows a disk sample at the conclusion of an 1100°C run in which a slight leak had developed. An x-ray powder pattern from a sample of the melt at the conclusion of the run revealed that a large amount of Ta_2O_5 was present along with tantalum. The uniform thinning of the disk substantiates the assumption that the solute concentration in the liquid was independent of radial and angular position and illustrates that the reaction surface was uniformly

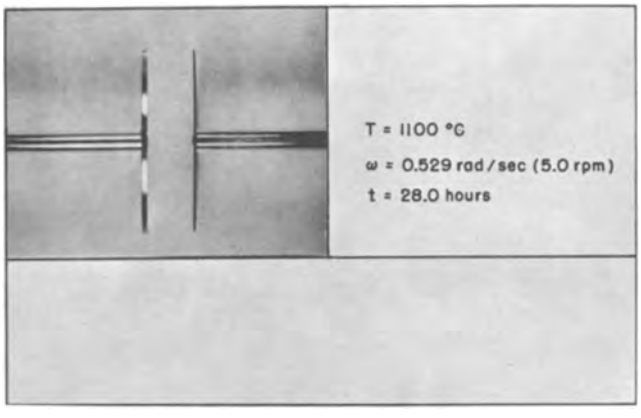

Fig. 3. Disk sample at the conclusion of a run in which the dissolution rate remained near the maximum value because of removal of tantalum from solution by selective oxidation. Uniform thinning of the disk illustrates that the reaction surface was uniformly accessible from the standpoint of diffusion.

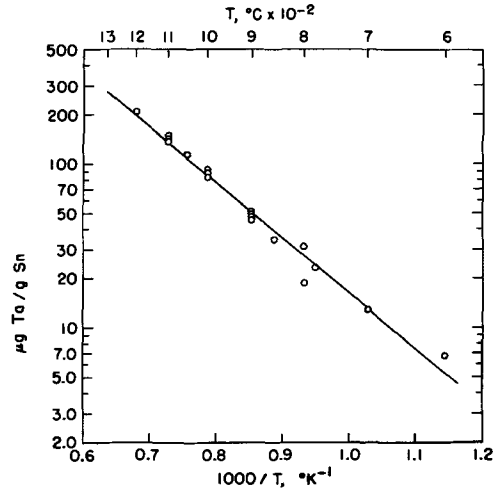

Fig. 4. Temperature dependence of the solubility of tantalum in liquid tin.

accessible from the standpoint of diffusion. Latter data will also show that, for the temperature and velocity of this run, the dissolution process was in a region of diffusion control.

The temperature dependence of the solubility of tantalum in liquid tin is given in Fig. 4. These values were obtained from dissolution curves in which saturation was readily achieved and also from a solubility run in which equilibration times from 48 to 100 hr at each temperature were used. Each point represents the average of a number of analyses. The data can be represented by the relation

$$C_{Sn}^{Ta} = (3.737 \pm 0.254)\ 10^4 \exp\left[\frac{-15{,}390 \pm 1{,}210}{RT}\right] \mu g\ Ta/g\ Sn \quad [9]$$

The over-all heat of solution of tantalum in liquid tin is 15,390 ± 1210 cal/mole at the 95% confidence level.

The results of measurements of the self-diffusion coefficient of liquid tin and tantalum in tin by the capillary-reservoir method are shown in Fig. 5. The diffusivity of Sn-113 in liquid tin was determined to check out the diffusion cell, and these data are in agreement with data of Careri *et al.* (7) and Ma and Swalin (8) for temperatures below 800°C. All of the data below 800°C were used to obtain the following Arrhenius relation for tin self-diffusion

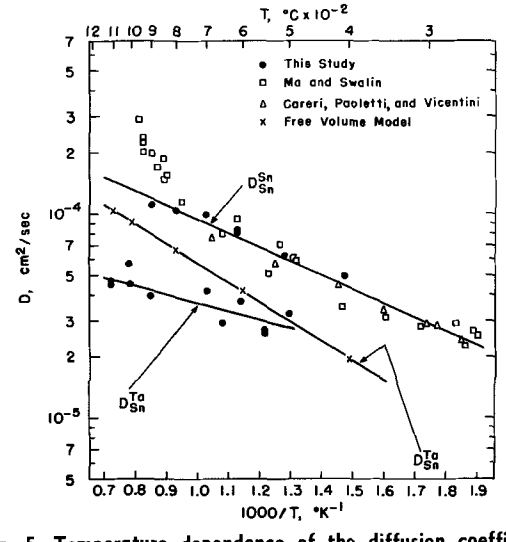

Fig. 5. Temperature dependence of the diffusion coefficient of Sn-113 and Ta-182 in liquid tin; •, x, this study; □, Ma and Swalin (8); △, Careri et *al.* (7).

$$D_{Sn^{Sn}} = (4.59 \pm 0.19)\ 10^{-4} \exp\left[\frac{-3{,}160 \pm 250}{RT}\right] \quad [10]$$

The experimental tantalum diffusion data in Fig. 5 are expressed by the relation

$$D_{Sn^{Ta}} = (9.72 \pm 0.93)\ 10^{-5} \exp\left[\frac{-1{,}930 \pm 900}{RT}\right] \quad [11]$$

at the 95% confidence level. The modified Cohen-Turnbull free-volume model (9) for solute self-diffusion in liquids yielded the following result for tantalum self-diffusion.

$$D_{Sn^{Ta}} = (4.98 \times 10^{-4}) \exp\left[\frac{-4{,}270}{RT}\right] \quad [12]$$

The data for the diffusion coefficient of Ta-182 in liquid tin fall below the tin self-diffusion data. This result is in agreement with the free volume model; however, the experimental activation energy of 1,930 cal/mole is less than half of that predicted by the model in Eq. [12].

The viscosity data for liquid tin in Fig. 6 were taken from the literature (10-13). Gebhardt's (10) data, which were measured over the largest temperature interval, result in the following expression for the kinematic viscosity

$$\nu = (7.83 \pm 0.07)\ 10^{-4} \exp\left[\frac{1190 \pm 40}{RT}\right] \quad [13]$$

Figure 7 illustrates the temperature dependence of the dissolution flux at a rotational speed of 10 rpm (Re ~5 x 10^3). The dashed line gives the temperature dependence of the dissolution flux predicted by Eq. [8]. The experimental activation energy for tantalum diffusion was inserted into Eq. [8] with the over-all heat of solution of tantalum in liquid tin and the activation for viscosity to obtain the value of Q_{Jm} of 16,870 cal/mole.

The velocity dependence of the dissolution flux at four temperatures is shown in Fig. 8. The half-power velocity dependence of the dissolution flux at constant temperature predicted by Eq. [3] is observed at the higher temperatures over an appreciable velocity range.

All of the experimental dissolution data obtained in this study are plotted in Fig. 9. By application of the half-power velocity relationship to the dashed line in Fig. 8 for the 10 rpm data, the high-temperature portion of the curves were generated for the additional velocities. The experimental data points at 1100° and 1200°C are in reasonable agreement with the temperature dependence predicted by the curves.

Discussion

The dissolution data can be examined in terms of the temperature and velocity dependence and the mag-

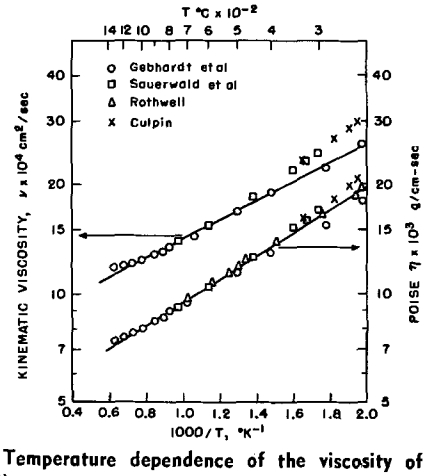

Fig. 6. Temperature dependence of the viscosity of liquid tin, ref. (10-13).

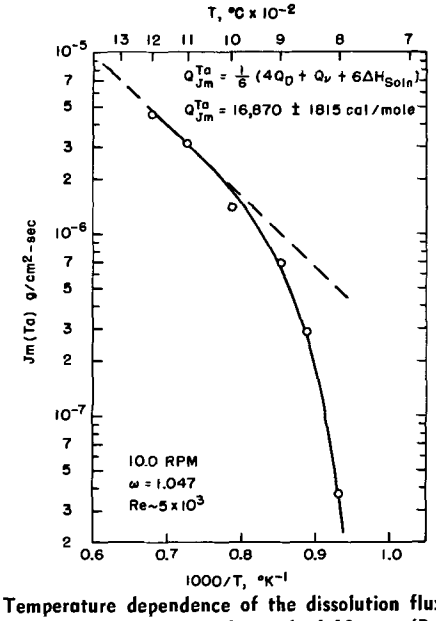

Fig. 7. Temperature dependence of the dissolution flux of tantalum into liquid tin at a rotational speed of 10 rpm (Reynolds No. ~ 5 x 10^3).

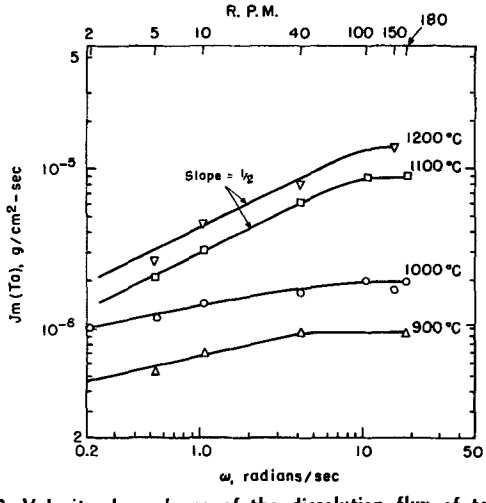

Fig. 8. Velocity dependence of the dissolution flux of tantalum into liquid tin at four temperatures between 900° and 1200°C.

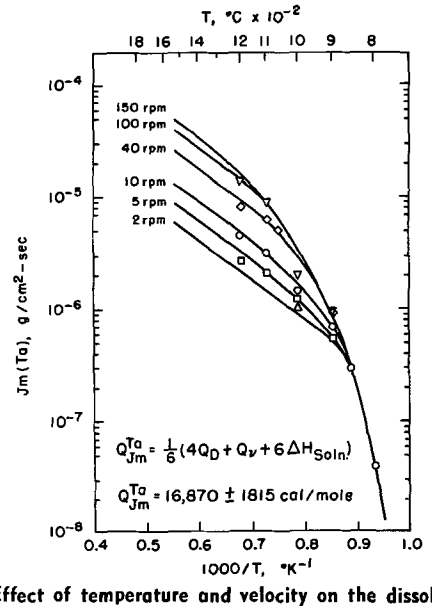

Fig. 9. Effect of temperature and velocity on the dissolution flux of tantalum into liquid tin under laminar flow conditions (Reynolds No. 1 x 10^3 to 1 x 10^5).

Table III. Comparison of experimental and calculated values of the dissolution flux and the diffusion coefficient of tantalum in liquid tin

At 1100°C: ρ_{Sn}* = 6.398 g/cm³, $D_{Exptl.}$ = 4.8 × 10⁻⁵ cm²/sec,			C_{sat} = 134 μg Ta/g Sn, D/ν = 0.040,		ν = 12.1 × 10⁻⁴ cm²/sec $I_{(D/\nu)}$ = 0.9981	
RPM	Re	ω	$\omega^{1/2}$	J_m**(Exptl.)	J_m(Calc.)	D(Calc) cm²/sec
100	5.59 × 10⁴	10.5	3.24	8.71 × 10⁻⁶	6.99 × 10⁻⁶	6.0 × 10⁻⁵
40	2.23 × 10⁴	4.19	2.05	6.00 × 10⁻⁶	4.41 × 10⁻⁶	7.9 × 10⁻⁵
10	5.59 × 10³	1.05	1.02	3.11 × 10⁻⁶	2.21 × 10⁻⁶	8.2 × 10⁻⁵
5	2.82 × 10³	0.53	0.73	2.05 × 10⁻⁶	1.57 × 10⁻⁶	7.6 × 10⁻⁵
At 1200°C: ρ*Sn = 6.337 g/cm³, $D_{Exptl.}$ = 5.0 × 10⁻⁵ cm²/sec,			C_{sat} = 194 μg Ta/g Sn, D/ν = 0.043,		ν = 11.8 × 10⁻⁴ cm²/sec $I_{(D/\nu)}$ = 1.0007	
RPM	Re	ω	$\omega^{1/2}$	J_m**(Exptl.)	J_m(Calc.)	D(Calc) cm²/sec
40	2.30 × 10⁴	4.19	2.05	7.90 × 10⁻⁶	6.77 × 10⁻⁶	6.3 × 10⁻⁵
10	5.75 × 10³	1.05	1.02	4.48 × 10⁻⁶	3.39 × 10⁻⁶	7.7 × 10⁻⁵
5	2.90 × 10³	0.53	0.73	2.63 × 10⁻⁶	2.40 × 10⁻⁶	5.7 × 10⁻⁵

* Density values are from ref (10).
** The dissolution flux, J_m, is in units of g Ta/cm²-sec.

nitude of the dissolution flux. When the activation energies for competing rate processes in a reaction differ in magnitude by a significant amount, a change in slope in the Arrhenius plot of the rate can occur depending upon the temperature interval that is investigated. Arrhenius plots of this type have been observed for the oxidation of graphite (14, 15), the oxidation of metals which form volatile oxides such as molybdenum (16), and also for the dissolution of metals in acids (17). The decrease in the activation energy with increasing temperature was indicative of a transition from surface or reaction control to transport control. The data in Fig. 7 indicate a similar transition in this system. As the temperature increases, the temperature dependence of the dissolution flux approaches the value of 16.9 kcal predicted by the model for diffusion control. Temperature limitations imposed by the apparatus would not permit a quantitative check of the activation energy over a wider temperature interval. The large activation energy of ~90 kcal at the low temperatures can be associated with the surface reaction for the rate of transport of tantalum across the solid-liquid interface.

Much of the experimental data in Fig. 9 was obtained in a region of mixed transport control. When the dissolution rate is a function of both the rate of the surface reaction and the rate of diffusional transport through the boundary layer, a change in experimental conditions can result in a shift of reaction control toward one of the limiting cases. For example, a decrease in velocity from 150 to 5 rpm at 1100°C shifts the dissolution process from mixed transport control to diffusion control. The effect of temperature on the dissolution process noted earlier for the 10 rpm data in Fig. 7 is also applicable to the other velocities; however, as the velocity increases, the transition from mixed to diffusion control moves to higher temperatures.

A quantitative comparison of the dissolution flux from Eq. [3] and the experimental values in a region of diffusion control is made in Table III. The calculated flux values based on experimental diffusion data are, on the average, about 20% lower than the experimental values. It should be pointed out that this difference would be reduced considerably if the 12% reduction in the calculated dissolution flux due to the $I_{(D/\nu)}$ correction were not applied. The D values for each of the runs in Table III were obtained by inserting the experimental flux values into Eq. [3]. While these D values are approximately 30% higher than the least squares values from the capillary-reservoir method, they fall within the plus two sigma limit of the experimental diffusion data.

The relatively small difference in the diffusion coefficients by the two methods cannot be attributed to the thermodynamic factor in the relationship between the chemical and tracer diffusion coefficients, *i.e.*, $D_{Ta} = D_{Ta}^*\ (1 + d \ln \gamma_{Ta}/d \ln N_{Ta})$. In the event that the tantalum-tin solution deviates from ideal or dilute solution behavior, the diffusion coefficients from the capillary-reservior method become chemical diffusivities since the solute concentrations in the capillaries were near saturation while the solute concentration in the reservoir remained near zero. Thus, the thermodynamic driving force in the diffusion measurements was analogous to that during dissolution in a region of diffusion control.

An experimental problem inherent in the measurement of the diffusion coefficient in this system could easily lead to the low D values. The quartz capillaries were filled from a tin reservoir saturated with high specific activity tantalum at temperatures between 500° and 1100°C. Autoradiographs of the filled capillaries indicated that the activity was distributed homogeneously. The capillaries were subsequently diffused at temperatures from 10° to 20°C above the filling temperature to insure that all of the activity returned to solution. However, in view of the low solute concentrations involved in this study, there is the possibility that the above condition was not completely attained. This factor may be the primary reason for the low diffusion results since the same experimental methods that were employed in the tin self-diffusion measurements were applied to these measurements.

Conclusions

The data presented in this paper provide a critical test of the convective-diffusion model in a high-temperature liquid metal system. The velocity and temperature dependence of the dissolution flux under conditions of diffusion control are in good agreement with the model. The flux values also agree within the limits of error of the experimental diffusion data. The validity of the assumption that the solute concentration is independent of radial position, which leads to the important property that the magnitude of the convective-diffusion boundary layer is constant over the surface of the disk, was evidenced by the uniform thinning of the disk under the laminar flow conditions.

The modified flux relation now applicable to a wide range of Schmidt numbers resulted in a 12% reduction in the calculated dissolution flux in the tantalum-tin system. The correction factors would be significant when diffusion coefficients are calculated from the flux relation in systems with Schmidt numbers below 1000.

A shift in reaction control for the dissolution process

resulting from changes in experimental conditions has been amply demonstrated in a liquid metal system.

Acknowledgment

The author wishes to acknowledge the assistance of D. L. Rink who set up and operated the experiments. This work was performed under the auspices of the United States Atomic Energy Commission.

Manuscript received Feb. 20, 1967.

Any discussion of this paper will appear in a Discussion Section to be published in the June 1968 JOURNAL.

REFERENCES

1. V. G. Levich, *Discussions Faraday Soc.*, **1**, 37 (1947).
2. V. G. Levich, "Physicochemical Hydrodynamics," 2nd ed., Prentice Hall, Inc., Englewood Cliffs, N. J. (1962).
3. T. F. Kassner, ANL-6985, November 1965.
4. W. G. Cochran, *Proc. Cambridge Phil. Soc.*, **30**, 365 (1934).
5. D. P. Gregory and A. C. Riddiford, *J. Chem. Soc.*, **731**, 3756 (1956).
6. E. L. Field, *Nucleonics*, **11**, 66 (1953).
7. G. Careri, A. Paloetti, and M. Vicentine, *Nuovo Cimento*, **10**, 1088 (1958).
8. C. H. Ma and R. A. Swalin, *J. Chem. Phys.*, **36**, 3014 (1962).
9. T. F. Kassner, R. J. Russell, and R. E. Grace, *Trans. Am. Soc. Metals*, **55**, 858 (1962).
10. E. Gebhardt, M. Becker, and H. Sebastian, *Z. Metallk.*, **46**, 669 (1955).
11. F. Sauerwald and K. Töpler, *Z. anorg. u. allgem. Chem.*, **157**, 117 (1926).
12. E. Rothwell, *J. Inst. Metals*, **90**, 389 (1961-1962).
13. M. F. Culpin, *Proc. Phys. Soc. (London)*, **B70**, 1069 (1957).
14. E. A. Gulbransen, K. F. Andrew, and F. A. Brassart, *This Journal*, **110**, 476 (1963).
15. M. Levy and P. Wong, *ibid.*, **111**, 1088 (1964).
16. E. A. Gulbransen, K. F. Andrew, F. A. Brassart, *ibid.*, **110**, 952 (1963).
17. M. B. Abramson and C. V. King, *J. Am. Chem. Soc.*, **61**, 2290 (1939).

Potential of Aluminum in Aqueous Chloride Solutions

T. Hagyard and W. B. Earl[1]

Department of Chemical Engineering, University of Canterbury, Christchurch, New Zealand

ABSTRACT

By using a high-speed technique described in ref. (1), anodic (aluminum dissolution) polarization data have been obtained for aluminum surfaces free from oxide films and from the normal concurrent hydrogen evolution. Similarly cathodic (hydrogen evolution) polarization data have been produced for oxide-free aluminum surfaces on which the usual simultaneous anodic process has been suppressed. These results have been applied to the interpretation of the static "mixed" potential reported in ref. (1). It has been deduced that at the mixed potential the anodic area most probably comprises less than 0.5% and the cathodic area 99.5% of the total surface.

Measurements of anodic and cathodic polarization on highly reactive metals such as aluminum, magnesium, and titanium are commonly made on specimens covered with the usual spontaneously formed oxide film, and it is likely that the effective area for such measurements is that of pores in the film so that conclusions from such measurements are subject to considerable doubt.

These difficulties may be avoided and considerable new insight obtained as to the electrode process if, instead, observations are made on surfaces newly formed in contact with the solution, provided that the experimental method is suited to the very fast processes which then become apparent.

For aluminum it was found (1) that a new aluminum surface, formed sufficiently rapidly under aqueous potassium chloride, underwent first a very rapid fall in potential reaching a minimum value in a few microseconds and that this represented the reversible potential of aluminum uncomplicated by concurrent hydrogen evolution. During the following millisecond, it was found that the potential then increased due to the onset of hydrogen evolution and became stabilized after about 1 msec at a mixed potential which then remained substantially constant in the absence of oxygen. In the presence of dissolved air, the potential rose further, due to oxide film formation, becoming constant after some 5-10 sec at a much more positive value.

The present work was directed at using the large differences in time constants between the first two processes to provide a means of obtaining polarization curves for the anodic dissolution of aluminum and for the cathodic evolution of hydrogen on aluminum. These curves cannot be obtained by normal means for the following reasons. For both processes oxide films must be absent, and so far as the authors are aware no data for such a condition have been published. In the present work, oxide films were certainly absent first because an atmosphere of purified hydrogen (see experimental section) was maintained from the initial cutting of the new aluminum surface, and second because observations were limited to the first millisecond after cutting and contamination of the surface by oxygen or any other trace impurities takes place with time constants that are very long in comparison [see ref. (1), p. 2293]. (Experimentally observed time for effect of oxygen is *ca.* 3 sec, and a simple calculation shows that the time for the arrival of a monolayer of oxygen atoms by diffusion alone in air saturated solutions is *ca.* 5 sec.)

For the anodic dissolution of aluminum, a major difficulty in measurements of the overvoltage by normal techniques is that concurrent hydrogen evolution cannot be prevented. Consequently the total anodic current is greater than the external current. Also since two processes are proceeding simultaneously the area which is actually acting as anode is in considerable doubt. In the present work these difficulties were avoided by observing the potential of a polarized newly cut aluminum surface during the first few microseconds, this procedure being justified in a later section and in ref. (4). For this short time it seemed (1) that the whole of the exposed surface must be anodic and that hydrogen evolution, time constant 1 msec, would contribute negligibly to the current. Consequently it is claimed that the polarization data produced by these means were the first observations in

[1] Present address: Shawinigan Chemicals Limited, Montreal East, Quebec, Canada.

which substantially all the surface was anodic and in which no appreciable hydrogen evolution was taking place.

For the measurements of the polarization of hydrogen discharge, another property of the system had to be used. If an electrode at the mixed potential is cathodically polarized from an external source, then the potential will move in a more negative direction and, if the polarizing current density is continually increased, the "mixed" potential will eventually equal and then become more negative than the reversible potential of aluminum in that solution, and at this point the anodic reaction must cease. By polarizing the newly cut surface at current densities high enough to produce potentials more negative than the normal peak potential, this condition was fulfilled, and the data so obtained therefore referred to an aluminum surface none of which was anodic, *i.e.*, to a wholly cathodic surface on which the only process occurring was the discharge of hydrogen ions.

Experimental

The experimental cell of polyethylene is shown diagramatically in Fig. 1 in which, during use, the electrode, 4, was driven at 1000 cm/sec past a ruby cutter, 8, by the impact of a spring-driven hammer on the anvil, 1, thereby cutting a notch, area some 10^{-3} cm^2, in the flange of the electrode and coming to rest clear of the electrode and embedded in the polyethylene insulation, 9. The electrode, before cutting, was entirely covered by a coating of polyethylene, 9, some 0.5 mm thick providing an insulation resistance around 50 Mohm. By reducing the thickness of the flange which was to be cut to a limit of 0.05 mm, it was possible to reduce the time of cutting to 5 μsec [cutting time in the range 5-100 μsec (5-15 μsec) did not affect the cathodic (anodic) results; although cutting velocity was altered however, the maximum obtainable was always used for obvious reasons]. An antisplash guard of PTFE, 3, was provided. The electrode moved in a duralium bush, 2, which was electrically connected to the electrode so as to avoid electrostatic effects.

Polarizing current was supplied via a platinum wire electrode, 7, purified hydrogen (from "Milton Roy" palladium diffuser, impurity content less than 0.01 ppm), was supplied via 6. The solution was thus saturated with H_2 at a pressure essentially atmospheric. Connection to the *N* calomel electrode was made through a cellophane membrane via 5, it being necessary for high-speed circuitry to provide a salt bridge of large cross section shown so as to keep the resistance of the measuring circuit down to about 1000 ohms. The potential was fed to a cathode follower of impedance 10^9 ohms and thence to the oscilloscope, the total circuit rise time being 6 μsec. [Subsequent experiments performed first using a high-speed cathode follower (rise time 0.1 μsec) and later again without a cathode follower with the cell directly coupled to a high speed oscilloscope (rise time 0.023 μsec) gave the same results.]

The polarizing current was supplied by the transistor circuit, Fig. 2. The latter was necessary because the cathode follower between the test electrode and the oscillograph became deranged if more than 4.5v was applied to it. Nevertheless, it was essential that the chosen polarizing current (0.1 — 1000 μa) must remain constant, starting immediately the cut closed the electrolytic circuit but not imposing more than 4.5v on the cathode follower during the completely insulated period before cutting the specimen. The circuit in Fig. 2 permitted this and had a time constant of <1 μsec.

The above cell differed from that used in ref. (1) because in the latter the electrode was stationary and the cutter moved past it. In doing so it left a cavity, the collapse of which delayed the wetting of the electrode surface. The present design overcame this difficulty and, as will be mentioned, also eliminated possible concentration polarization due to the very high rate of shear produced in the surface film of electrolyte.

Results

Anodic polarization.—A solution 1M KCl + 0.00033M $AlCl_3$ of *p*H 3.2 was used throughout, the aluminum ion being present so that the reversible potential of the aluminum electrode would be defined.

Typical oscillograph traces are shown in Fig. 3. In all traces herein potentials are on the hydrogen scale. In these traces the 1000 Hz sinusoidal trace was used as time base and as the potential calibration. Before the cut, the potential of the still insulated electrode was + 4.5v and on making the cut the trace became more negative due to the ionization of the aluminum. The rate of fall was probably limited initially by the speed of the cathode follower-oscilloscope circuit. The minimum potential was that recorded for the polarization curves. The subsequent rise to the mixed po-

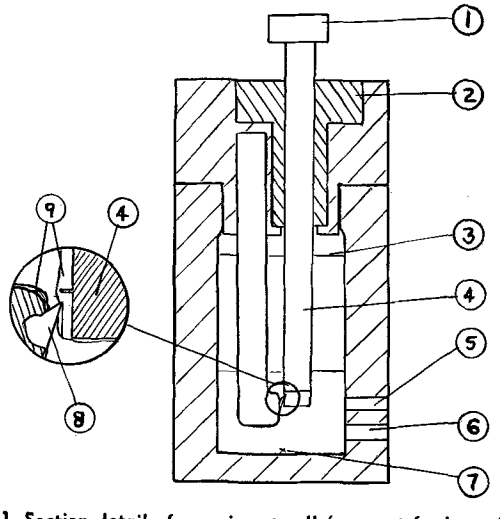

Fig. 1. Section detail of experiment cell (see text for legend)

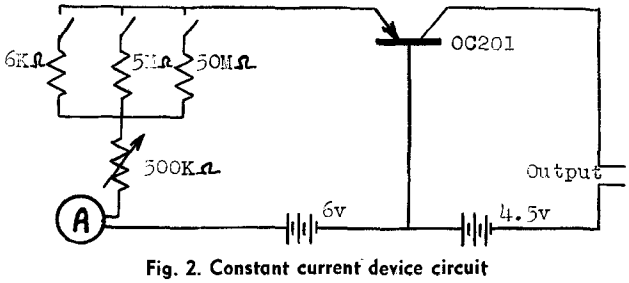

Fig. 2. Constant current device circuit

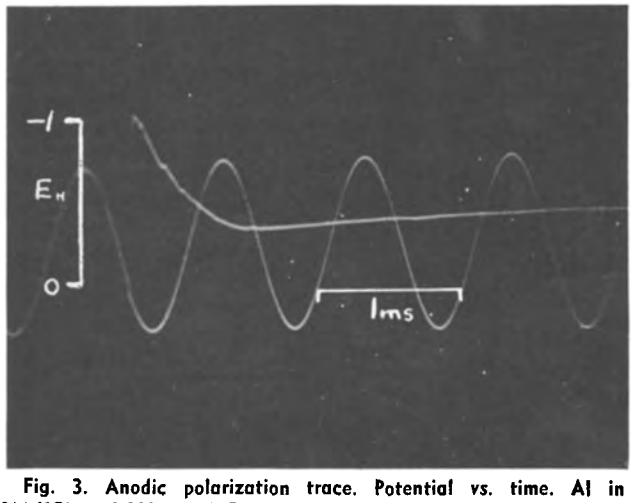

Fig. 3. Anodic polarization trace. Potential vs. time. Al in 1M KCl + 0.00033M $AlCl_3$, *p*H 3.2.

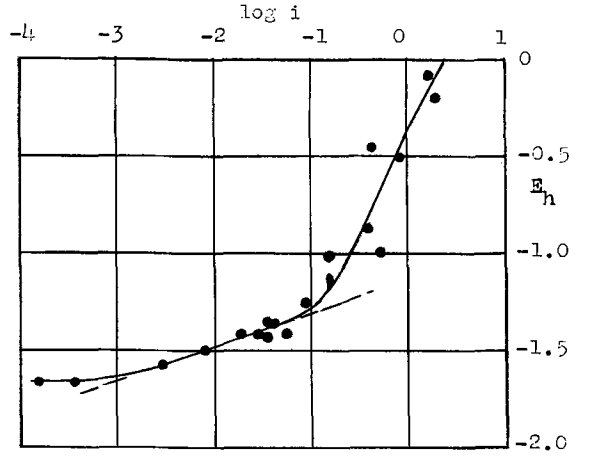

Fig. 4. Anodic polarization curve Al in 1M KCl + 0.00033M $AlCl_3$, pH 3.2.

tential is evident from Fig. 3, but is irrelevant to the measurements of anodic polarization. Using various impressed currents and measuring the apparent area of the cut surface gave the polarization plot of Fig. 4.

The justification for using minimum potentials attained during the first 10-30 μsec after cutting the electrode is based on two grounds. When cutting is fast enough (complete in <15 μsec) then the minima occur most often about 20 μsec and independently of cutting time. Observations in the absence of polarizing current gave minimum potentials in this solution ($AlCl_3$ = 0.00033M) of —1.65v, and this may be compared with the calculated E_o = — 1.66v quoted by Latimer (2). If the activity were equal to the concentration, then the measured potential here should in fact have been —1.71. Latimer's value refers naturally to unit aluminum ion activity, but has not been confirmed experimentally nor is the aluminum ion activity known in these solutions. The agreement seems satisfactory for present purposes especially in view of the wide confidence limits at present obtainable. Additional justification for these high-speed potential measurements is provided by similar measurements on cadmium by Chapman (4). In this work 10-30 μsec values of the potential of cadmium in cadmium chloride were compared with the values obtained by standard static potentiometric methods. Cadmium was chosen as being substantially free from concurrent hydrogen evolution. Agreement within some 10 mv was found thus confirming that equilibrium potentials of metals may be measured in the short times used in the present work.

The results in Fig. 4 are more scattered than could be wished, but this is not surprising in view of the experimental difficulties including inevitable scatter due to the roughness of the cut surface not being under control. The plot of potential *vs.* log i is here interpreted, as a first approximation, in terms of a charge-transfer-controlled single step process of the type represented by

$$i = i_o\left[\exp\left(\frac{-\beta n\mathbf{F}\eta}{RT}\right) - \exp\left(\frac{(1-\beta)n\mathbf{F}\eta}{RT}\right)\right]$$

Bockris (5). Where η, as in this work, exceeds + 100 mv, the first term is negligible and a linear Tafel plot of the form $\eta = \frac{RT}{(1-\beta)n\mathbf{F}} \ln \frac{i}{i_o}$ should be obtained. Here $1-\beta$ is the fraction of the interface potential difference effective in the anodic charge transfer process. When the current density is increased to the point where other reaction steps become rate controlling, the linearity is expected to fail, as is normal experience, and these results tend to confirm this.

In Fig. 4 the best straight line has been computed for all points at anodic current densities less than 0.1 amp/cm², above which current density marked deviation is likely. The slope $\frac{RT}{(1-\beta)n\mathbf{F}}$ is found to be 0.18 v/log i with 90% confidence limits 0.12 to 0.24. Hence $\alpha = (1-\beta)n$ = 0.34 with 90% confidence limits 0.53 to 0.25.

The intercept (i_o) of the polarization curve with the reversible potential (our minimum potential —1.65v) is found to be 9 x 10^{-4} amp/cm² with 90% confidence limits 2 x 10^{-4} to 5 x 10^{-3} amp/cm².

Cathodic polarization (hydrogen overvoltage on aluminum).—A solution of 1M KCl pH 3.2 was used throughout, aluminum ion being excluded so that only hydrogen could be discharged.

A typical trace is shown in Fig. 5b. In this trace the electrode potential before cutting is —4.5v, and after cutting becomes more positive very quickly, reaching its most positive value in about 30 μsec at a value appreciably more negative than the reversible potential of aluminum. There follows a slow fall of some 100 mv with a time constant rather less than 1 msec. The potential after 1 msec was that used in obtaining the cathodic polarization curve, Fig. 6, since all observations showed that equilibrium was substantially reached after this time. Concentration polarization, which might have been expected with these unbuffered solutions, was in no case detectable during this short period immediately following the cut even at the highest current densities used. This was apparently due to the extremely effective suppression of the diffusion layer at the electrode surface because of the

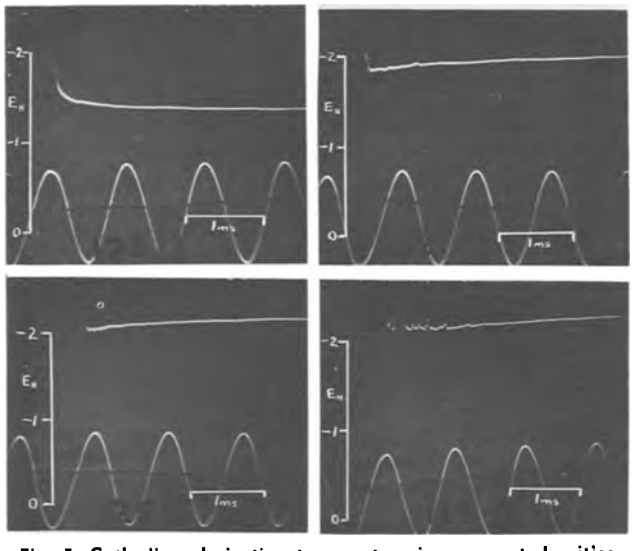

Fig. 5. Cathodic polarization traces at various current densities. Al in 1M KCl, pH 3.2 (a) (top left) $i<10^{-2.2}$ amp/cm² (b) (top right) and (c) (bottom left) $10^{-2.0}<i<10^{-0.2}$ amp/cm² (d) (bottom right) $i>10^{-0.2}$ amp/cm².

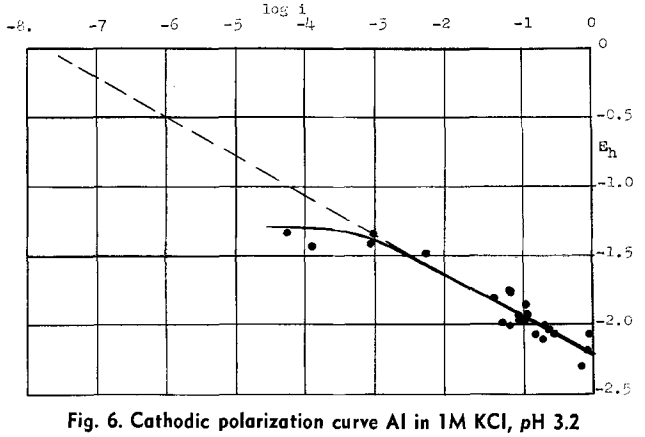

Fig. 6. Cathodic polarization curve Al in 1M KCl, pH 3.2

large velocity difference of 1000 cm/sec between electrode and solution.

Figure 5a shows by contrast that at current densities sufficiently low for the potential to be more positive than the aluminum potential in this solution [see ref. (1), Fig. 5g], then the oscillograph trace is different in form, now rising smoothly to a constant value which is in reality a mixed potential, part of the current being supplied internally from aluminum dissolution at local anodes. The potentials after 1 msec were nevertheless still used for the data of Fig. 6, although it is understood that the points so obtained cannot lie on the correct Tafel line since the measured external current is, in fact, less than the total current in these cases. This accounts for the break in the curve, Fig. 6, at around —1.5v.

The different forms to be observed in the early stages of the traces in Fig. 5 are discussed in a later section. For the present, Fig. 6, derived from the steady potentials after 1 msec, should represent in the lower portion, below —1.6v, the polarization of hydrogen evolution at a wholly cathodic aluminum surface, free from oxide films and at such high overvoltage (more than —1.4v) that the Tafel equation might be expected to be obeyed. Consequently, the best straight line has been computed from those experimental points below —1.67v and is shown in the figure. The straight portion has a gradient of 0.29 v/log i resulting in $\alpha = 0.21$ with 90% confidence limits 0.16 and 0.30 where α is defined by

$$\eta = \frac{RT}{\alpha \mathbf{F}} \ln \frac{i_o}{i}$$

The dotted extrapolation of the straight line to $\eta = 0$ gives $i_o = 7 \times 10^{-8}$ amp/cm^2 with 90% confidence limits 1×10^{-9} and 6×10^{-6}.

Discussion of Results

The mixed potential, in the absence of external current, was observed in these measurements to be —1.30v in substantial agreement with —1.28v recorded in ref. (1). If now the current densities at which the anodic and cathodic Tafel lines reach —1.30v be taken from Fig. 4 and 6, respectively, 1.15×10^{-1} and 5.5×10^{-4} amp/cm^2, then the anodic and cathodic areas operative at the mixed potential are in the inverse ratio, *viz.*, 1:210. Thus, based on the most probable results, represented by the lines in Fig. 4 and 6, only 0.5% of the surface was anodic. Taking into account the standard error on each intercept, the 90% confidence limits for the anodic area are found to be 5% and 0.05% of the total surface. It is quite evident that the anodic is much smaller than the cathodic area at equilibrium.

Obtaining this information was the main object of this work, but the oscillograph traces produced under cathodic polarization, in addition give some hints as to probable electrode mechanisms.

When a new aluminum surface is exposed in the absence of external current, it would be expected that the initial potential would approximate to the (unknown) zero charge potential of aluminum in the solution. All observations made on unpolarized electrodes have indicated that the newly cut surface was initially at a potential lying between +1 and —1v, and it seems likely that the zero charge potential is in this region assuming the equilibrium establishing this occurs in less than a few microseconds. Very quickly thereafter, ionization of aluminum provides the electrons for charging the double layer capacitance to the minimum potential. This process has been shown to be very rapid.

Similar reasoning applies to the anodically polarized surface and explains the shape of the oscillograms.

If the electrode were polarized cathodically, it would still be expected that the double layer on the new surface would act as a capacity initially between +1 to —1v and would draw electrons from the stray capacitance, already at a high negative potential (4.5v), moving the potential in microseconds in a positive direction to a value near the zero charge potential. Since the stray capacitance was in fact only 1% of the usual double layer capacitance of around 20 μF/cm^2, then the potential should first have been driven quite close to that of zero charge before again becoming negative due to the constant impressed cathodic current balanced by hydrogen evolution. This behavior was never observed, and there has never been any sign of a break in the smooth descent of the oscillograph traces. Hence it may be concluded, tentatively, that whereas on open circuit or during anodic treatment a double layer can be formed very rapidly by ionization of the abundant surface atoms of aluminum, this type of double layer cannot be formed when the potential is held initially far above the reversible potential of aluminum. It is presumed that in this case a double layer of quite different properties is formed and that its capacity initially must be very small compared with that of aluminum in equilibrium with its ions, or alternatively that its rate of formation is much slower, otherwise there would be a marked break in the descending trace.

Another property of the cathodic traces is seen clearly in Fig. 5b and c where the trace descends to a minimum and then rises over about 1 msec to an equilibrium value some 100 mv more negative. The minimum in the trace could well represent the formation of adsorbed hydrogen atoms on the aluminum surface, accumulating over about 1 msec to the point where the rate of combination to molecules equals the current. This would imply that combination to molecules is the rate determining process. That the situation is more complicated than this is shown by traces such as Fig. 5d which were repeatedly obtained at current densities exceeding 0.7 amp/cm^2. The initial period of unstable potentials shown in the figure and always lasting approximately 1 msec is intriguing and seems to represent a process of molecular hydrogen formation of an explosive or chain reaction type. Obviously such speculations are premature in view of the paucity of the data, but there seems to be a possibility that oscillograph traces such as these could well be an unusually direct means of investigating the mechanism of hydrogen discharge.

Conclusions

By observations up to 30 μsec after the formation of a new aluminum surface in 1M KCl + 0.00033M $AlCl_3$ an anodic polarization curve for aluminum dissolution, free from simultaneous hydrogen evolution, has been obtained. For that portion to which the Tafel equation could be expected to apply it has been found that the most probable values for α and i_o are

$$\alpha = 0.34$$

and

$$i_o = 9 \times 10^{-4} \text{ amp/cm}^2$$

By observations after 1 msec during cathodic polarization in 1M KCl at such negative potentials that aluminum ion production was not possible, similar data for hydrogen evolution on aluminum have been found. The most probable values are

$$\alpha = 0.21$$
$$i_o = 7 \times 10^{-8} \text{ amp/cm}^2$$

The technique eliminates the possibility of interference by oxide films or trace impurities.

At the open circuit mixed potential on clean aluminum in 1M KCl it follows that, using mean values, 0.5% of the surface is anodic and 99.5% is cathodic.

Transient phenomena were observed which indicate increased complexity in the hydrogen discharge process at high current densities.

Manuscript received May 4, 1966; revised manuscript received April 13, 1967.

Any discussion of this paper will appear in a Discussion Section to be published in the June 1968 JOURNAL.

REFERENCES

1. T. Hagyard and J. R. Williams, *Trans. Faraday Soc.*, **57**, 2288 (1961).
2. W. M. Latimer, "The Oxidation of the Elements and their Potentials in Aqueous Solutions," Prentice-Hall, New York (1938).
3. K. M. Chapman, "The Potential of the Cadmium Electrode," B. E. Project Report, University of Canterbury, 1961.
4. T. Hagyard and K. M. Chapman, *This Journal*, **113**, 961 (1966).
5. J. O'M. Bockris, U.S. Dept. of Commerce, National Bureau of Standards, Circ. 524, p. 248.

Electrolytic Dissolution of Binary Alloys Containing a Noble Metal

H. W. Pickering

Edgar C. Bain Laboratory for Fundamental Research, United States Steel Corporation Research Center, Monroeville, Pennsylvania

and C. Wagner

Max-Planck-Institut für Physikalische Chemie, Göttingen, Germany

ABSTRACT

In the electrolytic dissolution of binary alloys the concepts of ionization and redeposition of a metal, coupling of the anodic reactions in accordance with the concepts of irreversible thermodynamics, and volume diffusion in the presence of given supersaturations of single and double vacancies are analyzed theoretically. The ionization-redeposition mechanism is in principle possible but only if coupling of the anodic reactions occurs. Volume diffusion may be operative *via* divacancies. Results from x-ray investigations and from measurements with a rotating disk-ring electrode for copper-gold alloy indicate that interdiffusion of the constituent metals in the alloy occurs to a significant extent and dissolution of Au does not take place. Electrochemical measurements with a Cu-Zn alloy involving 30 a/o (atomic per cent) Zn give no indication of occurrence of the ionization-redeposition mechanism.

When a single-phase binary alloy A-B is anodically dissolved in an aqueous solution, the mode of dissolution may be (*a*) simultaneous dissolution of the two constituent metals of the alloy, or (*b*) preferential dissolution of the less noble metal of the alloy with the more noble metal accumulating on the alloy surface. For the latter mode it is necessary that the difference between the single electrode potentials of the two constituent metals in the electrolyte involving possibly complexing agents is sufficiently large, *i.e.*, several times greater than $RT/\mathbf{F}$, and that the potential of the dissolving alloy is higher than that of the less noble metal A and significantly lower than that of the more noble metal B. A spongy layer of the remaining more noble metal has been reported especially for Cu-Zn and Au-Cu alloys (1-11). Obviously, there must be a transport mechanism by virtue of which the atoms of the less noble metal A reach the surface and atoms of the more noble metal B aggregate. It is the objective of this paper to discuss pertinent transport mechanisms and to obtain experimental evidence for the occurrence of one or the other of these mechanisms.

Theoretical

When one metal is preferentially dissolved it may be assumed that one or more of three mechanisms operate: (*i*) both metals ionize followed by redeposition of the more noble metal; (*ii*) only the less noble metal ionizes and enters the solution while the atoms of the more noble metal aggregate by surface diffusion; and (*iii*) only the less noble metal ionizes and enters the solution and atoms of both metals move in the solid phase by volume diffusion.

Ionization-redeposition mechanism.—The ionization-redeposition mechanism may be examined by considering, for example, the dissolution of a Cu-Zn alloy. Assume first that the anodic reactions

$$\mathrm{Zn(Cu\text{-}Zn)} = \mathrm{Zn^{2+}\ (aq)} + 2e^- \qquad [1]$$

$$\mathrm{Cu(Cu\text{-}Zn)} = \mathrm{Cu^{2+}\ (aq)} + 2e^- \qquad [2]$$

are independent of each other and also independent of the cathodic redeposition reaction

$$\mathrm{Cu^{2+}\ (aq)} + 2e^- = \mathrm{Cu\ (nearly\ pure)} \qquad [3]$$

Since the activity of Cu in Cu-Zn is less than unity with respect to pure copper, the single electrode potential for equilibrium of reaction [2] in a solution of given Cu^{2+} ion concentration is more noble than that of reaction [3] involving pure copper. Thus, dissolution of copper from Cu-Zn according to reaction [2] can take place only if the electrode potential is more noble than the equilibrium electrode potential for reaction [2] and thereby even somewhat more noble than the equilibrium electrode potential for reaction [3]. Consequently, if a short-circuited couple of Cu-Zn and pure copper is made the anode with a predetermined current, one has to expect that copper ions enter the solution from the Cu-Zn surface and from the pure copper surface as well, provided that there is no coupling between reactions [1] and [2]. However, if in accordance with the principles of irreversible thermodynamics, coupling between reactions [1] and [2] occurs, *i.e.*, the coefficients for cross terms in the general rate equations are finite, the anodic dissolution of copper from Cu-Zn alloy according to reaction [2] may take place at a potential less noble than the equilibrium potential for reaction [3]. The copper ions that enter the solution from the Cu-Zn surface may then be redeposited at the copper surface according to reaction [3]. The occurrence of ionization and redeposition of copper during dissolution of a Cu-Zn alloy may be readily checked with the help of the rotating assembly of a disk of Cu-Zn alloy surrounded by a ring of pure copper described below.

The concept of coupling between reactions [1] and [2] is only a formal description of rate relations which may eventually be found. If the hypothesis of coupling of reactions [1] and [2] is supported by the aforementioned experiment, one may ask for a model in atomistic terms. The following model is suggested. If a Cu-Zn electrode is subjected to anodic dissolution there is the tendency for zinc atoms to enter the solution as ions preferentially and for copper atoms to remain at the surface in the form of adsorbed atoms which migrate at random and may aggregate in order to form grains of virtually pure copper. Since diffusion of adsorbed Cu atoms to grains of virtually pure copper requires an activity gradient, the average activity of copper on the surface may be higher than unity, and thus the steady-state potential for partial equilibrium between adsorbed copper atoms and the solution may be less noble than the equilibrium potential between bulk copper and the solution. If this situation prevails, zinc and copper ions may be dissolved from a Cu-Zn electrode, and copper may be plated out at the same electrode potential on the surface of copper grains where the concentration of adsorbed copper atoms is close to the equilibrium value with the bulk crystal.

Surface diffusion mechanism.—Aggregation of adsorbed atoms of the more noble metal by virtue of surface diffusion leads primarily to the formation of patches of monolayers. In addition, atoms of the more noble metal may pile up on the initial patches of monolayers, and thus small three-dimensional crystals of the more noble metal may be formed. If these crystals grow in all three dimensions, there is the tendency to form finally a dense layer of the more noble metal which prevents further anodic dissolution of the less noble metal. This is to be expected especially if the mole fraction of the more noble metal is high as, *e.g.*, in alpha brass. The significance of surface diffusion has been emphasized most recently by Feller (11), but it has still to be shown that this mechanism accounts for all observations.

Volume diffusion mechanism.—Mechanism [3] involving ionization of the less noble metal and movement of both metals in the atomic state by volume diffusion would normally be considered inoperable on the basis of diffusivities extrapolated from high-temperature measurements. Use of this extrapolation implies that (*a*) equilibrium concentrations of vacancies (and interstitials) are established at room temperature as at elevated temperatures, and (*b*) the contribution of diffusion along small-angle grain boundaries and along dislocations is negligible at room temperature. Many authors have already pointed out that the second condition may not be satisfied and, therefore, the effective (average) diffusion coefficient at room temperature may be considerably greater than the value of the volume diffusion coefficient obtained by extrapolation of high-temperature data. In addition, it is possible that also the first condition is not satisfied as is discussed next.

Anodic dissolution of metal may be considered as an analogue (12) of vaporization of a metal; the latter is assumed to take place in the kink-step-terrace model of a surface after Kossel (13) and Stranski (14) first, by detachment of an atom from a kink corresponding to the formation of an adsorbed atom along the step and then along the terrace, and followed by desorption of an adsorbed atom into the gas phase. Direct vaporization of an atom from a kink or step position is also a possible but rare event. Further, vaporization of an atom from a complete lattice layer (terrace site) acompanied by formation of a surface vacancy may occur, but this would require a high activation energy. These events are, therefore, assumed to be rare events. Likewise, anodic dissolution of a pure metal is assumed to occur with the formation of an adsorbed atom as an intermediate.

A new situation arises when an alloy A-B is subjected to anodic polarization and only atoms of the less noble component A enter the solution as ions. As an example consider a Cu-Au alloy involving 10 a/o Au in H_2SO_4(aq), as investigated by Gerischer and Rickert (6). In this case virtually only copper enters the solution as Cu^{2+} ions. A partial step on the surface with a sequence of Cu and Au atoms is shown in Fig. 1. When a current is passed in the anodic direction, first a copper atom from position 1 may move from its kink position in order to become an adsorbed atom and subsequently to enter the solution as an ion. Then, the gold atom initially at position 2 may also move to become an adsorbed atom. Thus, the Cu atom initially at position 3 becomes the last atom in the step and may be ionized by the same mechanism which has been assumed for the copper atom initially at position 1, as is also true for the copper atom initially at position 4. The gold atom now at the end of the step may also move to become an adsorbed gold atom. In view of the continuous increase of the concentration of adsorbed gold atoms, there is, however, an increased tendency of gold atoms to move back to the kink positions at the end of a step. Thus, after removal of a sizeable fraction of copper atoms from the step, it happens only very rarely that a copper atom occupies the last position in a step and is free to move from its kink position and to be desorbed as an ion. This leads to electrochemical polarization, *i.e.*, the electrode assumes a potential considerably above the equilibrium potential. The increase in the driving force necessary to maintain a constant current may now make it possible that an atom not at the end of a step, *e.g.*, the copper atom at position 8 may enter the solution as a divalent ion. As the driving force is further increased, Cu atoms from complete lattice layers may enter directly the solution as Cu^{2+} ions. In this way, surface vacancies are formed continuously. Surface vacancies in a partially complete step may be filled by lone adsorbed atoms or by a sequence of movements of atoms in a step. Surface vacancies in a complete lattice layer may also be filled by adsorbed lone atoms. In addition, atoms from the lattice layer underneath the surface may fill surface vacancies whereby excess monovacancies and also divacancies in the interior of the alloy may be created. In view of the random walk of these vacancies, excess vacancies will appear not only directly next to the surface, but also in a certain volume of the crystal underneath the surface. Diffusion of monovacancies and divacancies into the interior of the alloy is limited because of the presence of dis-

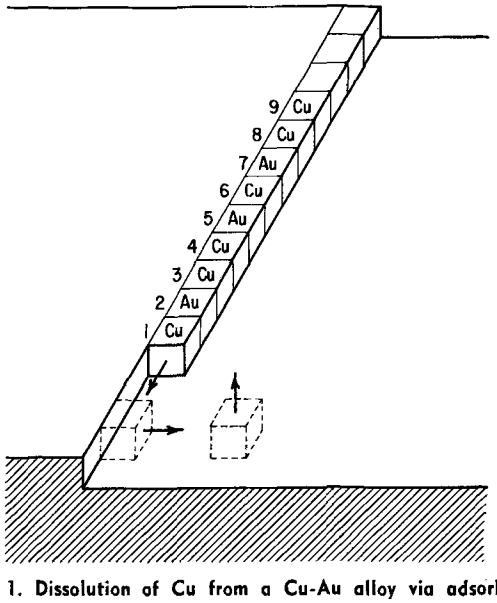

Fig. 1. Dissolution of Cu from a Cu-Au alloy via adsorbed Cu atoms as intermediates.

locations which are sinks for vacancies. In view of the continuous production of vacancies at the surface, the number of available sinks for vacancies in the vicinity of the surface is reduced and subsequently excess vacancies may diffuse to greater distances from the surface while anodic dissolution is continued. The build-up of an excess vacancy concentration in the vicinity of the surface, which has already been considered by Schottky (15) in conjunction with the oxidation of metals at elevated temperatures and suggested by Forty (16) in conjunction with dezincification at room temperature, would also enhance chemical diffusion, *i.e.*, movement of copper atoms from the bulk alloy to the surface and backward diffusion of gold atoms according to the gradient of the Cu/Au ratio. In this way, more and more copper atoms may enter the solution as Cu^{2+} ions, and the alloy next to the surface would become enriched with respect to gold. The removal of copper may be facilitated by roughening of the surface.

Harrison and Wagner (9) have theoretically analyzed diffusion processes during the preferential dissolution of Cu from solid Cu-Ni alloys in liquid Ag at 1000°C and have shown that a plane solid-liquid interface is not stable. In accord herewith they have observed that a highly rugged interface is formed while preferential dissolution of Cu proceeds. In particular, they have observed wedges filled with liquid metal protruding into the interior of the alloys. Similarly, preferential anodic dissolution of Cu from Cu-Au alloys at room temperature may proceed. Primary wedges filled with electrolyte may originate especially at sites where grain boundaries or dislocations reach the surface. Branching of the wedges may occur to form networks. In the case of copper which contains a small fraction of gold, small volume elements can become undermined and eventually lose contact with the sample as is known to occur during electrolytic refining of copper. In copper-gold alloys containing larger fractions of gold, *i.e.*, over 5 a/o, as well as in Cu 30 w/o (weight per cent) Zn, an adherent porous layer results as has been reported by various authors (1-11). One may ask, however, whether diffusion via excess vacancies is sufficiently rapid so that the above mechanism can be operative.

Monovacancies cannot account for diffusion of copper at room temperature because the diffusivity $D_{\square}$ of monovacancies is too low. According to Ramstetter, Lampert, Seeger, and Schüle (17) $D_{\square}$ in pure copper at 25°C equals $3 \cdot 10^{-19}$ cm²/sec. Thus, according to Einstein, the mean square displacement of a monovacancy $\overline{\Delta x^2}$ for $t = 1000$ sec is only $\overline{\Delta x^2} = 2D_{\square}t = 6 \cdot 10^{-16}$ cm² which is of the order of the square of the distance between neighboring Cu atoms. Instead, diffusion of copper atoms via divacancies may be operative because their diffusivity (17), $D_{\square\square} = 1.3 \cdot 10^{-12}$ cm²/sec in copper at 25°C, is much higher, as is shown by the following calculation.

Consider anodic dissolution of copper from a Cu-Au alloy with a plane surface and one-dimensional diffusion normal to the surface. The initial condition is

$$c = c_o \text{ at } x > 0,\ t = o \qquad [4]$$

where c is the local and c_o is the bulk concentration of Cu (mol/cm³) in the Cu-Au specimen and x is the distance from the initial metal surface. Assume that during anodic dissolution the concentration of copper atoms at the surface is virtually equal to zero

$$c = 0 \text{ at } x = x_s \qquad [5]$$

where x_s is the instantaneous distance of the liquid-solid interface from the position of the surface at $t = 0$.

The amount of Cu arriving at the surface of the alloy in mol per unit area per unit time is $D(\partial c/\partial x)_{x=x_s}$. Thus, the rate of recession of the liquid-solid interface equals

$$\frac{dx_s}{dt} = V_m D \left(\frac{\partial c}{\partial x}\right)_{x=x_s} \qquad [6]$$

where V_m is the molar volume whose dependence on composition is disregarded for the sake of an approximation, and D is the interdiffusion coefficient for movement of Cu *vs.* Au atoms. The value of D with due regard to the contribution of excess vacancies is calculated below.

If the interdiffusion coefficient D is independent of composition and location, Fick's second law reads

$$\frac{\partial c}{\partial t} = D \frac{\partial^2 c}{\partial x^2} \qquad [7]$$

Equations [4] to [7] are satisfied by

$$x_s = 2\gamma (Dt)^{1/2} \qquad [8]$$

and

$$c = c_o \left(1 - \frac{\operatorname{erfc} \dfrac{x}{2(Dt)^{1/2}}}{\operatorname{erfc} \gamma}\right) \qquad [9]$$

where γ is a constant which is calculated below. Substitution of Eq. [8] and [9] in Eq. [6] yields

$$\pi^{1/2} \gamma \cdot \operatorname{erfc} \gamma \cdot e^{\gamma^2} = c_o V_m = N^o_{Cu} \qquad [10]$$

where $c_o V_m = N^o_{Cu}$ is the bulk mole fraction of copper in the Cu-Au alloy. If N^o_{Cu} is close to unity, γ is large. Therefore, one may use the approximation

$$\operatorname{erfc} \gamma \cong \frac{e^{-\gamma^2}}{\pi^{1/2}\gamma} \left(1 - \frac{1}{2\gamma^2} + \dots\right) \text{ if } \gamma >> 1 \qquad [11]$$

Substituting Eq. [11] in Eq. [10] one obtains

$$\gamma \cong \left[\frac{1}{2(1 - N^o_{Cu})}\right]^{1/2} \text{ if } N^o_{Cu} \cong 1 \qquad [12]$$

If $1 - N^o_{Cu} = 0.10$ corresponding to an alloy containing 10 a/o Au, γ equals 2.23.

With the help of Eq. [8] and [9] the flux j_{Cu} of Cu atoms toward the surface is found to be

$$j_{Cu} = D \left(\frac{\partial c}{\partial x}\right)_{x=x_s} = \frac{c_o e^{-\gamma^2}}{\operatorname{erfc} \gamma} \left(\frac{D}{\pi t}\right)^{1/2} \qquad [13]$$

Substituting Eq. [11] and [12] and $c_o = N^o_{Cu}/V_m$ in Eq. [13] one has

$$j_{Cu} \cong c_o \gamma \left(\frac{D}{t}\right)^{1/2} \cong \frac{N^o_{Cu}}{V_m} \left[\frac{D}{2(1 - N^o_{Cu})t}\right]^{1/2} \text{ if } N^o_{Cu} \cong 1 \qquad [14]$$

The corresponding current density i for the formation of divalent copper ions equals

$$i = 2j_{Cu}\mathbf{F} = N^o_{Cu} \frac{2\mathbf{F}}{V_m} \left[\frac{D}{2(1 - N^o_{Cu})t}\right]^{1/2} \qquad [15]$$

where $\mathbf{F}$ is the Faraday constant.

The "effective thickness" δ of the interdiffusion zone may be defined as usual by the relation

$$\delta = \frac{c_o - c(x = x_s)}{(\partial c/\partial x)_{x=x_s}} \cong \frac{c_o}{(\partial c/\partial x)_{x=x_s}} \qquad [16]$$

Substituting Eq. [13] in Eq. [16] and using Eq. [11] and [12] one obtains

$$\delta = [2(1 - N^o_{Cu})Dt]^{1/2} \qquad [17]$$

If interdiffusion takes place essentially *via* divacancies and correlation effects are disregarded, D in the vicinity of the surface may be expressed approximately as

$$D = D_{\square\square} N^s_{\square\square} \quad [18]$$

where $D_{\square\square}$ is the diffusivity of a divacancy and $N^s_{\square\square}$ is the mole fraction of divacancies in the vicinity of the surface. $N^s_{\square\square}$ is supposed to be much higher than the equilibrium mole fraction $N^{Eq}_{\square\square}$ prevailing in the alloy at the beginning of electrolysis.

If annihilation of vacancies during their diffusion into the interior of the alloy can be disregarded and the diffusivity $D_{\square\square}$ is independent of the alloy composition, diffusion of excess divacancies from the surface into the bulk alloy is governed by Fick's second law

$$\frac{\partial N_{\square\square}}{\partial t} = D_{\square\square} \frac{\partial^2 N_{\square\square}}{\partial x^2} \quad [19]$$

with the initial condition

$$N_{\square\square} = N^{eq}_{\square\square} \text{ at } x > 0,\ t = 0 \quad [20]$$

and the boundary condition

$$N_{\square\square} = N^s_{\square\square} \text{ at } x = x_s = 2\gamma (Dt)^{1/2} = 2\gamma (D_{\square\square} N^s_{\square\square} t)^{1/2} \quad [21]$$

where γ is given by Eq. [10] or [12].

Equations [19] to [21] are satisfied by

$$N_{\square\square} = N^{eq}_{\square\square} + (N^s_{\square\square} - N^{eq}_{\square\square}) \times \frac{\operatorname{erfc}[x/2(D_{\square\square} t)^{1/2}]}{\operatorname{erfc}[\gamma (N^s_{\square\square})^{1/2}]} \cong N^s_{\square\square} \operatorname{erfc}\,[x/2(D_{\square\square} t)^{1/2}]$$

$$\text{if } N_{\square\square} >> N^{eq}_{\square\square};\ \gamma (N^s_{\square\square})^{1/2} << 1 \quad [22]$$

From Eq. [22] we calculate the distance at which $N_{\square\square} = \tfrac{1}{2} N^s_{\square\square}$,

$$x(N_{\square\square} = \tfrac{1}{2} N^s_{\square\square}) = 2(D_{\square\square} t)^{1/2} \operatorname{erfc}^{-1} (\tfrac{1}{2}) \quad [23]$$

From Eq. [21] and [23] it follows that the distance between the position at which $N_{\square\square} = \tfrac{1}{2} N^s_{\square\square}$ and the position of the instantaneous surface is

$$x(N_{\square\square} = \tfrac{1}{2} N^s_{\square\square}) - x_s = 2(D_{\square\square} t)^{1/2} [\operatorname{erfc}^{-1} (\tfrac{1}{2}) - \gamma (N^s_{\square\square})^{1/2}] \quad [24]$$

$= 2 \cdot 10^{-5}$ cm for $N^o_{Cu} = 0.90$; $\gamma = 2.23$; $N^s_{\square\square} = 10^{-2}$; $t = 1000$ sec at 25°C. This distance may be used as a measure of the penetration of excess vacancies into the interior of the alloy. Dividing through corresponding sides of Eq. [24] and Eq. [17] and substituting $D = D_{\square\square} N^s_{\square\square}$ according to Eq. [18], one obtains

$$\frac{x(N_{\square\square} = \tfrac{1}{2} N^s_{\square\square}) - x_s}{\delta} = \frac{2^{1/2}}{(1 - N^o_{Cu})^{1/2}} \left[\frac{\operatorname{erfc}^{-1}(\tfrac{1}{2})}{(N^s_{\square\square})^{1/2}} - \gamma \right] \quad [25]$$

If the mole fraction of vacancies near the surface is much less than unity, *e.g.*, $N^s_{\square\square} \leqq 10^{-2}$, and further $N^o_{Cu} \cong 1$, the expression on the left side of Eq. [25] is much greater than unity, *i.e.*, the depth of penetration of the excess divacancies is much greater than the effective thickness of the interdiffusion zone, *i.e.*, the divacancy concentration in the interdiffusion zone does not vary exceedingly and thus, if $D_{\square\square}$ were independent of the alloy composition, the assumption of a constant diffusion coefficient in Eq. [7] would be a reasonable approximation. Actually, $D_{\square\square}$ in Au is higher than in Cu (18). Therefore, interdiffusion may be even faster than estimated in the foregoing calculation.

For these conditions the current density i calculated from Eq. [15] is rather high, *viz.*,

$$i \sim 2 \cdot 10^{-4} \text{ amp/cm}^2 \quad [26]$$

The "effective thickness" of the interdiffusion zone calculated from Eq. [17] is

$$\delta \sim 10^{-6} \text{ cm} \quad [27]$$

The assumption of a mole fraction of vacancies as high as 10^{-2} at and in the vicinity of the surface may be questioned. In particular, divacancies diffusing into the interior may be annihilated at dislocations, or they may aggregate and form quadruple vacancies and further multiple vacancies, *i.e.*, voids. Thus the current density calculated in Eq. [26] represents an upper limit.

The value calculated in Eq. [26] is a true current density. The apparent current density, defined as the quotient of current divided by the geometrical surface area, may be higher if the actual surface area is greater than the geometrical surface area because of roughening of the surface. Thus the apparent current density may be even higher than the value calculated in Eq. [26]. By the same token, an apparent current density of $2 \cdot 10^{-4}$ amp/cm^2 may be obtained with a divacancy mole fraction which is considerably lower than 10^{-2} as assumed for the evaluation in Eq. [26].

The foregoing considerations show that volume diffusion may be instrumental for preferential dissolution of Cu from Cu-Au alloys at room temperature. For acceptance of this mechanism, further experimental evidence is needed. This may be obtained with the help of x-ray investigations of the surface of samples subjected to anodic dissolution.

If gold is redeposited or if adsorbed gold atoms aggregate by virtue of surface diffusion, the lattice constant of these particles or of the sponge would be that of pure gold. In this case an x-ray diffraction pattern would contain rings at the gold positions (which may be broad). If, however, volume diffusion in a region next to the surface takes place as is suggested by the above considerations, a gradual variation in lattice parameter as a function of distance from the electrolyte-alloy interface would exist because of the sharp gradient of the mole fraction of gold between unity and that of the original alloy in a region next to the interface of the order of 10^2 lattice constants. Thus one would obtain a pattern of broad diffraction rings resulting from x-ray scattering of alloy regions of variable composition with a maximum of the intensity at a certain angle.

Investigations of this kind have been conducted already by Graf (19) in 1932. Cu-Au alloys involving 25 a/o Au etched by nitric acid at 25°C showed the x-ray diffraction rings of pure gold. Cu alloys involving 10 a/o Au etched in various solutions with less pronounced oxidizing solutions at 70°C (alcoholic solution of picric acid with or without dissolved oxygen; alkaline solution of sodium tartrate with dissolved oxygen) yielded x-ray patterns with very broad diffraction rings which indicated the presence of alloy crystals with copper contents ranging continuously from 20 to 40 a/o (*i.e.*, 60 to 80 a/o Au). The same is true for Cu-Au alloys involving 15 or 20 a/o Au attacked by sodium polysulfide solution at room temperature. These findings are in accordance with the concept of enhanced volume diffusion. Graf obtained these indicative results by using chemical attack in solutions whose oxidizing power was not well-defined with the help of a photographic technique. More conclusive results were obtained from experiments to be described where alloy samples were treated anodically at well-

defined potentials and were examined by modern x-ray intensity recording methods.

Electrochemical Measurements

General procedure.—Electrochemical measurements were conducted at 23° ± 2°C in order to check whether (*a*) gold is ionized from a Cu 10 Au alloy, or (*b*) copper is redeposited when a Cu 30 Zn alloy is dissolved anodically and both components are ionized.

For these measurements, there was used a rotating disk-ring electrode, which has been introduced by Frumkin and Nekrasov (20) for the detection of intermediates in electrode reactions (see Fig. 2). The theory for the interplay of diffusion and convection has been worked out by Ivanov and Levich (21). The disk electrode was the alloy subject to anodic dissolution at a predetermined current I_d and the resulting potential E_d was measured. The ring electrode was kept at a predetermined potential E_r appropriate for the deposition of the more noble metal with the help of a Wenking potentiostat and the resulting current I_r was measured. The circuit is shown in Fig. 3.

The cell, approximately 5 cm in diameter and 15 cm high, is shown in Fig. 4. A stream of prepurified

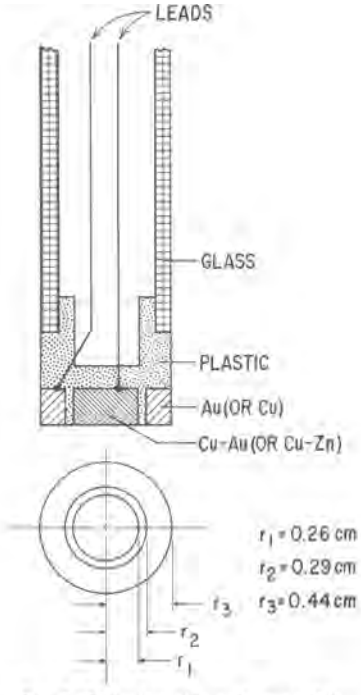

Fig. 2. Disk-ring electrode assembly

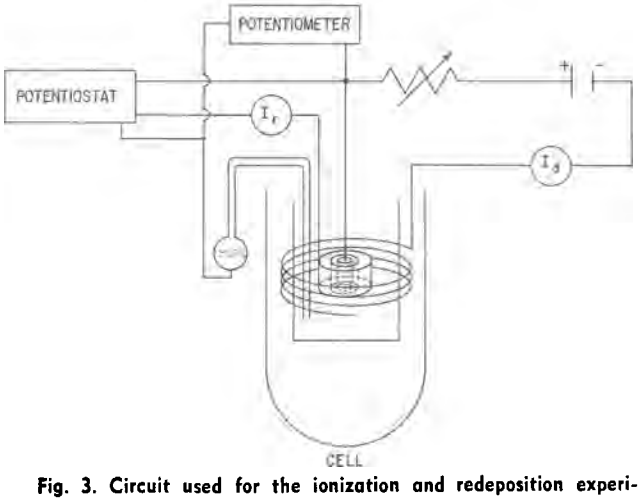

Fig. 3. Circuit used for the ionization and redeposition experiments.

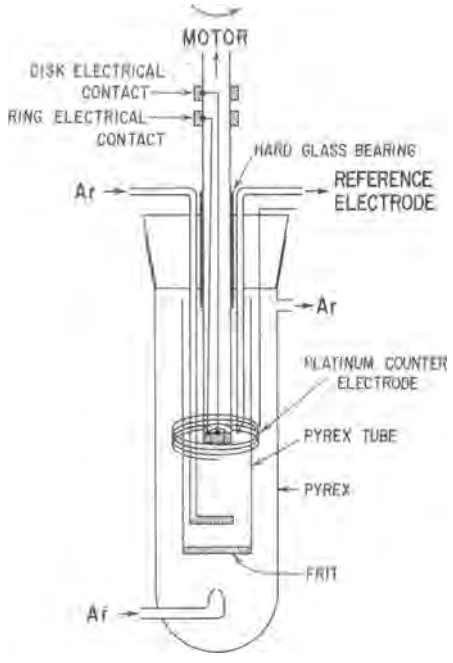

argon was passed through the cell in order to remove oxygen. The reference cell was a mercury-mercurous sulfate electrode in contact with 0.1 or 1.0*N* H_2SO_4 when sulfate electrolytes were used and a 1*N* KCl calomel electrode when a chloride electrolyte was used. The potentials are all reported relative to the standard hydrogen electrode (SHE). To minimize potential differences in the solution, an excess of supporting electrolyte was present in the bulk solution.

Consider conditions where both components of the alloy are ionized to a certain extent. Let j_o be the rate of dissolution of the more noble metal in mol/cm²-sec at the disk electrode. By virtue of rotation of the assembly, the solution in the hydrodynamic boundary layer is swept outward and thus ions of the more noble metal approach the ring electrode and are discharged. If at the potential E_r all ions of the more noble metal approaching the surface of the ring electrode are discharged, the local flux for redeposition of the more noble metal in mol/cm²-sec at distance r from the center is (21)

$$j(r) = \frac{0.4\, j_o}{1 + \frac{k\delta_e}{D}} \frac{r_1^2 r_2}{r^3} \frac{\left[1 - \frac{3}{4}\left(\frac{r_1}{r_2}\right)^3\right]^{1/3}}{\left[1 - \left(\frac{r_2}{r}\right)^3\right]^{1/3}\left[1 - \frac{3}{4}\left(\frac{r_1}{r}\right)^3\right]} \quad [28]$$

$$\text{if } r_2 \leqq r \leqq r_3$$

where r_1, r_2, and r_3 are the radii of the three zones shown in Fig. 2, D is the diffusion coefficient of the ions of the more noble metal, δ_e is the effective thickness of the diffusion boundary layer, and k is the rate constant for electrochemical redeposition of the more noble metal at the disk electrode, the rate being assumed to be proportional to the ion concentration C_s at the surface of the disk electrode, *i.e.*, equal to kC_s.

If only ions of the more noble metal are discharged at the ring electrode, the total current at the ring electrode is obtained by calculating from Eq. [28] the integral over the surface of the ring electrode. This gives for the dimensions reported in Fig. 2

$$I_r = \frac{0.53\, I_o}{1 + \frac{k\delta_e}{D}} \quad [29]$$

where I_r is the current at the ring electrode and $I_o = \pi r_1^2\, n\, j_o$ (with n as the valence of the ions) is the

partial current for the dissolution of the more noble metal at the disk electrode. Thus, I_r/I_o has its highest value, *i.e.*, 0.53, when no redeposition of the more noble metal at the disk electrode occurs, corresponding to $k \to 0$. If redeposition does occur, $k > 0$ and $I_r/I_o < 0.53$. It must be noticed that I_r is always lower than I_o since a certain fraction of the metal ions produced at the disk electrode remains in the boundary layer at the rim of the ring ($r = r_3$) and is swept into the bulk solution. In view of considerations recently published by Riddiford (22), a rigorous validity of Eq. [29] cannot be expected since details of the design in Fig. 2 are not in accord with requirements for ideal hydrodynamic flow. The experiments reported in what follows were made mainly in order to obtain qualitative rather than quantitative information. Minor deviations from Eq. [29] are, therefore, not significant for the evaluation of the experimental data.

Investigations on Cu-Au *alloys.*—The disk electrode was a Cu 10 Au alloy (10 a/o Au) prepared from 99.999% Cu and 99.99% Au, and the ring electrode was pure gold. Immediately prior to a run, the electrodes were polished on fine emery, rinsed in distilled water and dried. The electrolyte was 1*N* $CuSO_4$ + 0.1*N* H_2SO_4, and the rotation speed was 2900 rpm. Oxygen and hydrogen were excluded from the system. Thus at pH $\cong$ 1 only the reaction

$$Au^{3+}(aq) + 3e^- \rightarrow Au(s) \qquad E^o = 1.50 \qquad [30]$$

may occur at the ring electrode if its potential is between 0.5 and 1.2v. Accordingly a potential E_r = 1.1v was selected.

The relation between the observed potential E_d of the disk electrode and the applied current I_d is shown in Fig. 5 for two different runs. At all applied currents I_d, the current at the ring electrode was practically nil, *i.e.*, less than 2 μa. This is an indication that practically no gold is ionized from the Cu 10 Au alloy in accordance with the fact that the potential of the alloy according to Fig. 5 was much lower than the standard electrode potential of gold for reaction [30]. Consequently, aggregation of the remaining gold atoms during the anodic dissolution of copper must occur by surface diffusion, or volume diffusion must be operative as has been discussed already.

Investigations on Cu-Zn *alloys.*—If the Cu 30 Zn alloy (30 a/o Zn) is subjected to anodic dissolution, both components are dissolved according to previous investigations and results reported below. The main purpose of the following experiments was to obtain data for the recovery ratio in conjunction with Eq. [29]. The disk electrode was a Cu 30 Zn alloy prepared from 99.98% Cu and 99.995% Zn, the ring electrode was pure copper, the electrolyte was 1*N* $ZnSO_4$ + 0.05*N* $HC_2H_3O_2$ + 0.05*N* $NaC_2H_3O_2$ of pH $\sim$ 5 and the rotational speed either 290 or 2900 rpm. Preliminary experiments indicated that a potential E_r as low as —0.30v was required in order to discharge all copper ions approaching the surface of the Cu ring electrode. At E_r = — 0.30v and I_d = 0 there was observed a significant residual current at the ring electrode denoted by I_r^o presumably due to hydrogen evolution. Thus the current $I_{r(Cu)}$ for copper deposition at the ring electrode was taken to equal the measured current at the ring electrode I_r less the residual current I_r^o. The latter was necessarily an interpolated value from data obtained intermittently when I_d = 0. The current for dissolution of copper from the Cu 30 Zn disk electrode I_o was taken to equal the impressed current I_d times the mole fraction of Cu in the alloy. Data listed in Table I for a typical run with a rotational speed of 2900 rpm show that the recovery ratios for different impressed currents I_d agree approximately with the value of 0.53 according to Eq. [29] for k = 0, *i.e.*, for vanishing redeposition of copper at the disk electrode. Essentially the same results were obtained for a rotational speed of 290 rpm instead of 2900 rpm. This agreement would be expected only in the absence of redeposition at the disk since δ_e in Eq. [29] is inversely proportional to the square root of the rotational speed (23). These results agree in essence with results most recently obtained by Feller (11).

Table I. Typical potentials of the disk (E_d), measured currents (I_r) and interpolated residual currents (I_r^o) at the ring and recovery ratios $I_{r(Cu)}/I_o$ as a function of the dissolution current (I_d) applied to a Cu 30 Zn disk electrode. The electrolyte was 1*N* $ZnSO_4$ + 0.05*N* $HC_2H_3O_2$ + 0.05*N* $NaC_2H_3O_2$ and the potential of the ring electrode was —0.30v (SHE)

I_d (μa)	50	100	500	1000	3000
E_d (volt)	0.252	0.264	0.301	0.320	0.387
I_r (μa)	62	78	233	435	1239
I_r^o (μa)	43	44	55	80	190
$I_{r(Cu)}/I_o$	0.54	0.49	0.51	0.51	0.50

Data were also obtained for pure copper as the disk electrode with all other conditions the same. The recovery ratio was found in approximate agreement with the theoretical value of 0.53. This is an indication that the setup was functioning properly.

In view of the limited accuracy of the measurements reported in Table I, redeposition of a minor fraction of copper of the order of 10% or less cannot be ruled out. A more definite information was yielded by a second series of experiments where the disk and the ring electrode were practically short-circuited (see Fig. 6). The currents I_d and I_r were obtained by measuring the IR drop across resistors R_1 and R_2 with the help of a galvanometer calibrated before the run. The

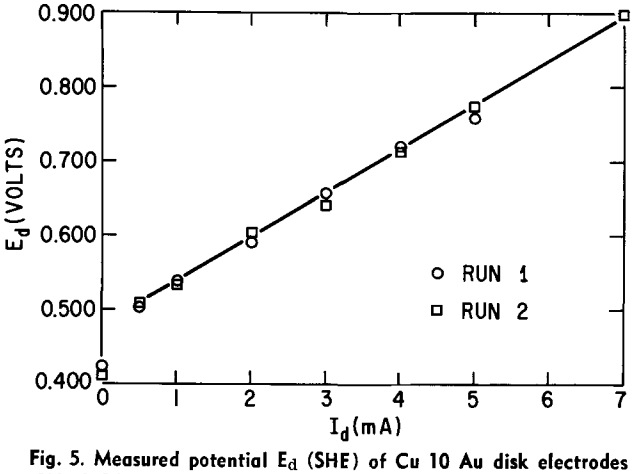

Fig. 5. Measured potential E_d (SHE) of Cu 10 Au disk electrodes in 1N $CuSO_4$ + 0.1N H_2SO_4 vs. the applied current I_d.

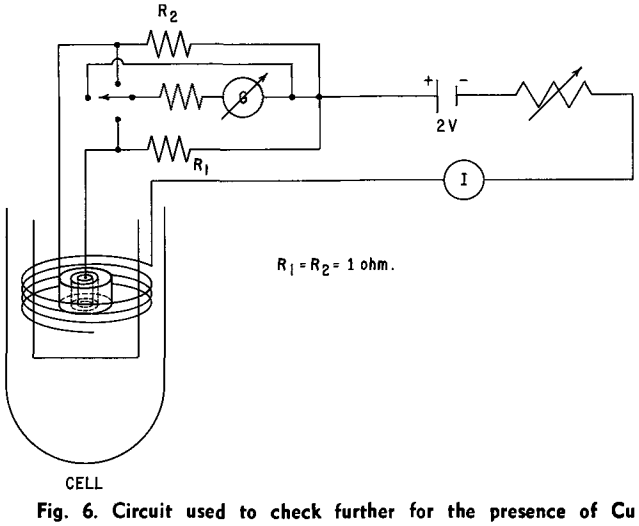

Fig. 6. Circuit used to check further for the presence of Cu redeposition during anodic dissolution of Cu 30 Zn alloy.

Table II. Dissolution currents at the disk (I_d) and at the ring (I_r) electrodes for currents ($I_d + I_r$) applied in the anodic direction on the Cu 30 Zn disk-Cu ring couple in 1N $ZnSO_4$ + 0.05N $HC_2H_3O_2$ + 0.05N $NaC_2H_3O_2$

I_d, μa	I_r, μa
48.3	1.7
96.2	1.7
293	6.9
473	31.6

highest IR drop across the 1 ohm resistors was 0.47 mv. Thus the potential difference between the disk and the ring electrode was always negligible. The electrolyte was the same as for the first series of experiments and the rotation speed was 2900 rpm. In order to eliminate accumulation of copper ions in the bulk solution, fresh electrolyte was used for each run and measurements were begun with the lowest value of the impressed current I_d. Thus the concentration of copper ions at the ring electrode was determined essentially by that prevailing at the disk electrode due to dissolution of the alloy. Results are shown in Table II. The current at the ring electrode was always anodic. Thus no redeposition of copper was found. On the contrary, copper was dissolved at the potential prevailing during dissolution of the alloy.

Discussion.—It is noteworthy that virtually no gold is dissolved from a Cu 10 Au alloy, whereas Cu and Zn are dissolved simultaneously from a Cu 30 Zn alloy. This divergence is understandable since the Cu 10 Au alloy the less noble metal prevails, whereas in the Cu 30 Zn alloy the more noble metal prevails. Preferential dissolution of zinc from the Cu 30 Zn alloy, however, may occur at much lower current densities than used in this investigation in accord with reports that dezincification of brass is observed especially when the supply of oxygen is low (1-3). According to Feller (11), preferential dissolution of zinc does occur when the alloy contains more than 75 a/o zinc.

X-ray Investigations

To test for the occurrence of volume diffusion during the anodic dissolution of Cu-Au alloys, foils of the Cu 10 Au alloy were prepared by rolling, followed by annealing in evacuated quartz capsules at 700°C for 1 hr. For anodic treatment a foil was partially lacquered to expose an area of 3 cm^2 and inserted vertically in place of the disk-ring electrode in the vessel shown in Fig. 3. A platinum wire counter electrode was centered around it in the inner tube. The electrolyte was either 1.0*N* H_2SO_4, or buffered 1*N* NaCl. Current densities of 1, 5, and 20 ma/cm^2 were applied. X-ray diffraction examination of the foils mounted in a diffractometer stage was made with CuK_α radiation.

After dissolution in both solutions broad regions of diffracted intensity occurred over a range of angles θ, extending approximately from the θ value characteristic of pure gold to that of the original alloy. For example in (b) of Fig. 7 and 8, a broad region of diffracted intensity is observable between the {111} diffraction lines of Cu 10 Au and pure gold. At a later stage of dissolution a maximum characteristic of gold-rich alloy is observable (see c of both figures), which as more coulombs are passed shift toward θ values characteristic of alloys richer in gold. For dissolution in 1*N* H_2SO_4 the maximum is seen after 19.2 coulombs/cm^2 have passed to correspond to virtually pure gold (see d of Fig. 7). For dissolution in buffered

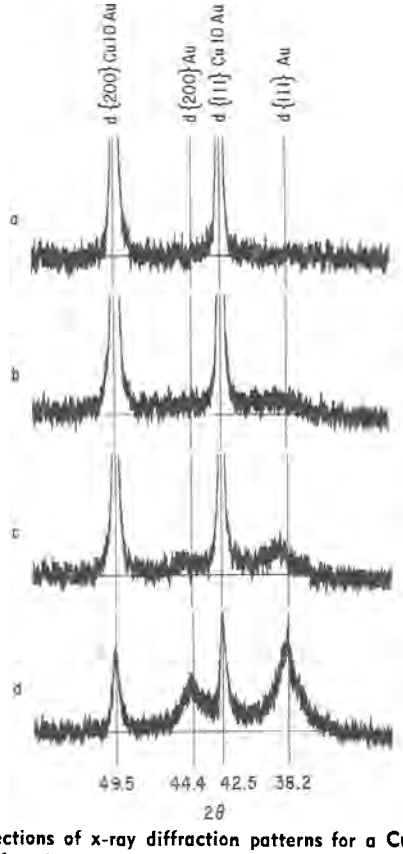

Fig. 7. Sections of x-ray diffraction patterns for a Cu 10 Au foil specimen after increasing amounts of dissolution at 20 ma/cm^2 in 1N H_2SO_4 illustrating increased diffracted intensity over broad ranges of angle θ, e.g., $42.5 > 2\theta > 38.2°$, as would be expected if alloy regions of variable composition were present. a, Prior to anodic dissolution; b, 1.2 coulombs/cm^2 passed; c, 2.4 coulombs/cm^2 passed; d, 19.2 coulombs/cm^2 passed.

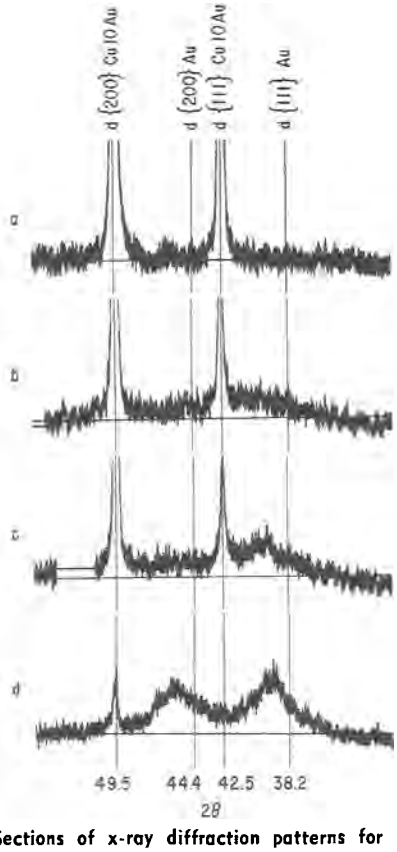

Fig. 8. Sections of x-ray diffraction patterns for a Cu 10 Au foil specimen after increasing amounts of dissolution at 20 ma/cm^2 in buffered 1N NaCl, illustrating increased diffracted intensity over broad ranges of angle θ, e.g., $42.5 > 2\theta > 38.2°$, as would be expected if alloy regions of various composition were present. a, Prior to anodic dissolution; b, 1.2 coulombs/cm^2 passed; c, 2.4 coulombs/cm^2 passed; d, 19.2 coulombs/cm^2 passed.

1*N* NaCl the maximum after the same number of coulombs/cm² have passed is seen to correspond to a gold-rich alloy (see d of Fig. 8). The intensity of the original alloy peak decreases accordingly. Broad regions of diffracted intensity were also observed for the lower current densities, and for all of the first four diffraction lines investigated, although their development occurred to a lesser and lesser extent the higher was the index of the diffracting plane. The latter is in part a result of the fact that the Bragg angle increases as the index of the plane increases, and therefore deeper portions of the specimen contribute more heavily to the diffracted intensity. A calculation of the depth x to which 50% of the diffracted intensity corresponds in the case of pure gold, gives the following values for the first four lines of gold:

Diffraction plane	{111}	{200}	{220}	{311}
x in microns	0.27	0.32	0.45	0.52

This shows that the effective depth of penetration of the incident beam is of the order of 3000Å for the {111} planes, and shows further that it increases sharply as the index of the plane increases. Thus, actual comparisons may be best made for the profile sections corresponding to the {111} planes.

According to Eq. [27] zones of variable composition are fairly thin and, therefore, make a very minor contribution to the x-ray diffraction pattern initially when the alloy has a plane surface. At a later stage of anodic dissolution, however, roughening occurs, *i.e.*, primary, secondary, and tertiary wedges protruding in various directions are formed. Thus the volume of alloy having a variable composition now can make a significant contribution to the x-ray diffraction pattern. Accordingly, the x-ray diffraction pattern shows broad lines characteristic of gold-rich alloy, lines of the bulk alloy and also a significant intensity between the lines.

When more copper is leached out, the depth of the zone of nearly pure gold grows. Thus the intensity of the gold lines increases, whereas the intensity between the lines of gold and the original alloy may decrease because of adsorption. Even under these conditions, however, the lines of the bulk alloy may still be rather strong when there are regions next to the surface of the alloy where protruding wedges filled with electrolyte are not formed.

Metallographic examination of the cross section of the x-ray specimens after the final dissolution corresponding to 19.2 coulombs/cm² shows a "reacted," dark layer extending from the surface to an average depth of about 8 microns for anodic dissolution of the Cu 10 Au foils in both solutions as shown in Fig. 9 and 10. For the sodium chloride solution many large local penetrations were observed within the reacted region as seen in Fig. 10. A few of these penetrations also extended into the alloy both trans- and intergranularly. The presence of a reacted layer is also in accord with results of experimental investigations (1-11). In particular, Pickering and Swann (10) with the help of transmission electron microscopy resolved individual pores (which measured only a few hundred Å in diameter in Cu-Au alloys which had been dissolved

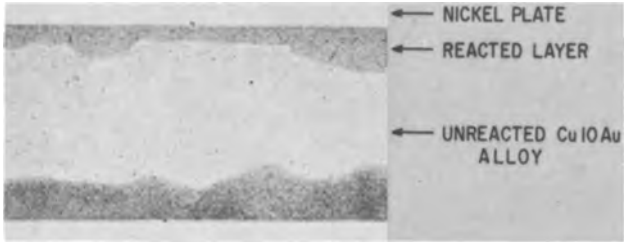

Fig. 9. Cross section of a Cu 10 Au sheet specimen after anodic dissolution of 1 ma/cm² in 1N H_2SO_4 for 320 min (19.2 coulombs/cm² passed). Magnification approximately 340X.

Fig. 10. Cross section of a Cu 10 Au sheet specimen after anodic dissolution at 1 ma/cm² in buffered 1N NaCl solution for 320 min (19.2 coulombs/cm² passed). Magnification approximately 340X.

in certain chloride media containing oxygen). In the present work the number of moles of Cu dissolved per unit area is $it/2\mathbf{F}$. The copper content of a layer of depth δ_p per unit area is $\delta_p N^{o}_{Cu}/V_m$. Assuming complete removal of copper up to depth δ_p as a limiting case, one has

$$\delta_p = \frac{it}{2\mathbf{F}} \cdot \frac{V_m}{N^{o}_{Cu}} \qquad [31]$$

For it = 19.2 coul/cm² one obtains a calculated value $\delta_p = 7\mu$ in approximate agreement with the average measured depth of 8μ.

Concluding Remarks

Further research is needed in order to test whether other alloys exhibiting preferential anodic dissolution of the less noble component behave similarly to Cu-Au alloys. Further, additional research is needed in order to investigate under which conditions Zn may be preferentially dissolved from copper-rich Cu-Zn alloys with formation of a copper sponge.

Acknowledgment

The authors are indebted to Dr. H. Schmalzried of the Max Planck Institut für Physikalische Chemie for many helpful discussions. Appreciation is also expressed to W. F. Kindle of the Edgar C. Bain Laboratory for Fundamental Research for his help in preparing the micrographs. The Cu 30 Zn alloy and Zn metal was kindly provided by Professor P. Haasen of the University of Göttingen. One of us (H.W.P.) gratefully acknowledges the United States Steel Corporation for having sent him to the Max-Planck Institut für Physikalische Chemie, Göttingen Germany for the 1964-1965 year.

Manuscript received Nov. 18, 1966; revised manuscript received March 29, 1967. This paper is based on work performed at the Max-Planck Institut für Physikalische Chemie in 1964-1965 while one of the authors (H.W.P.) was on leave from the Edgar C. Bain Laboratory for Fundamental Research.

Any discussion of this paper will appear in a Discussion Section to be published in the June 1968 JOURNAL.

REFERENCES

1. R. B. Abrams, *Trans. Am. Electrochem. Soc.*, **42**, 39 (1922).
2. G. D. Bengough, R. M. Jones, and R. Pirret, *J. Inst. Metals (London)* **23**, 65 (1920).
3. G. D. Bengough and R. May, *ibid.*, **32**, 81 (1924).
4. L. Graf, *Metallforschung*, **2**, 193, 207 (1947).
5. L. Graf, *Z. Metallkunde*, **40**, 275 (1949).
6. H. Gerischer and H. Rickert, *ibid.*, **46**, 681 (1955).
7. F. W. Nothing, *Metall*, **10**, 520, 1033 (1956).
8. R. Bakish and W. D. Robertson, *Trans. AIME*, **206**, 1278 (1956).
9. J. D. Harrison and C. Wagner, *Acta Met.*, **7**, 722 (1959).
10. H. W. Pickering and P. R. Swann, *Corrosion*, **19**, 369t (1963).
11. H. G. Feller, Habilitationsschrift, Technische Universität Berlin (1965).
12. W. K. Burton, N. Cabrera, and F. C. Frank, *Phil. Trans. Roy. Soc.*, **A243**, 299 (1951).

13. W. Kossel, *Nachr. Ges. Wiss. Göttingen, Math. Physik. Kl.*, **1927**, 135.
14. I. N. Stranski, *Z. physik. Chem.*, **136**, 259 (1928).
15. W. Schottky, *Z. Elektrochem.*, **63**, 784 (1959).
16. A. J. Forty, "Physical Metallurgy of Stress Corrosion Fracture," T. N. Rhodin, Editor, p. 111-113; Interscience Publishers, New York, (1959); A. J. Forty and P. H. Humble, Proceedings 2nd International Congress on Metallic Corrosion, 80 (1963).
17. R. Ramstetter, G. Lampert, A. Seeger, and W. Schüle, phys. stat. sol., **8**, 863 (1965).
18. W. Schüle, A. Seeger, D. Schumacher, and K. King, *ibid.*, **2**, 1199 (1962).
19. L. Graf, *Metallwirtschaft*, **11**, 77 (1932).
20. A. N. Frumkin and L. I. Nekrasov, *Dokl. Akad. Nauk. S.S.S.R.*, **126**, 115 (1959); *Proc. Acad. Sci. U.S.S.R. Phys. Chem. Sect.*, **126**, 385 (1959).
21. Yu. B. Ivanov and V. G. Levich, *Dokl. Akad. Nauk. S.S.S.R.*, **126**, 1029 (1959); *Proc. Acad. Sci. U.S.S.R. Phys. Chem. Sect.*, **126**, 505 (1959); V. G. Levich, "Physiochemical Hydrodynamics," p. 329ff, Prentice-Hall, Inc., Englewood Cliffs, N. J. (1962).
22. A. C. Riddiford, "Advances in Electrochemistry and Electrochemical Engineering," Vol. 4, pp. 47-116, P. Delahay, Editor, Interscience, New York (1966); pp. 67ff.
23. V. G. Levich, *Acta Physicochim. U.R.S.S.*, **17**, 257 (1942).

Technical Notes

Corrosion Resistance of Platinum, Copper Nickel, and Tantalum in Liquid Oxygen Difluoride

S. M. Toy

Missile & Space Division/Astropower Laboratory, Douglas Aircraft Company, Inc., Newport Beach, California

The corrosion rates of metals and alloys in fluorine-containing oxidizers at cryogenic temperatures are small due to the formation of passive fluoride films (1-3). Low corrosion rates are difficult to measure with conventional methods since the total weight change is very small. In the present study, the corrosion resistance of platinum, copper, nickel, and tantalum in liquid oxygen difluoride is estimated from changes in solution capacitance and conductance between two plates of these materials.

Experimental

Nickel (99.55%; 0.0635 cm thick) specimens, 4.18 x 2.22 cm, were separated at a distance of 1½ mm by glass spacers. Platinum (99.9%; 0.051 cm thick), copper (99.46%; 0.094 cm thick), and tantalum, (99.89%; 0.0254 cm thick) specimens, 2.54 x 5.18 cm, were also separated by 1½ mm glass spacers. Ni was pickled in a nitric acid etch (1 HNO_3/1 H_2O). Ta plates were pickled in a chromic acid solution (saturated chromic acid in sulfuric acid). No etch was used to clean Pt. Cu plates were cleaned with nitric acid etch. The specimens were connected by nickel wires to a four terminal test probe except for Cu specimens where Cu leads were used.

Either a pair of platinum and copper plates or nickel and tantalum plates were inserted into an all-metal test bomb (type 316 stainless steel) which served as a container for OF_2. The two sets were 0.635 cm apart. All parts were in a LOX clean condition (4). The test bomb was checked for leaks at 4 atm with helium at room temperature and overnight at liquid nitrogen temperatures. After the helium was evacuated, OF_2 was introduced and condensed to a liquid at a low temperature (see Fig. 1). The cell constant of each pair of plates was determined by measuring the cell resistance in 0.1*N* KCl. The cell

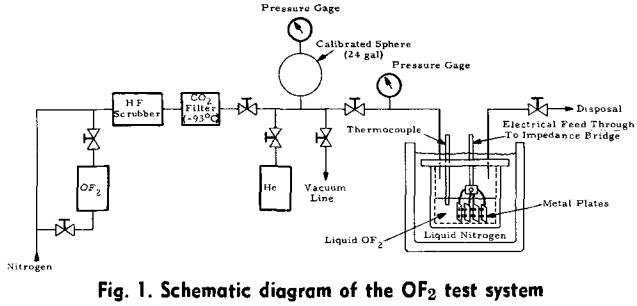

Fig. 1. Schematic diagram of the OF_2 test system

constant for Pt was the same when measured in a glass container or in the metal test bomb.

The capacitance and equivalent circuit parallel resistance were measured by a General Radio Impedance Bridge (1650-A) at 1000 Hz. The specific conductance, k_c was calculated from the resistance and the cell conductance, and the parallel resistance, R_p was calculated from the usual expression, $R_p = (2\pi f C_p D)^{-1}$, where C_p is parallel capacitance, D is dissipation factor, and f is frequency.

Oxygen difluoride (99.5+% purity) was purchased from Allied Chemical Company and was purified by passing the vapor through a column of NaF pellets to remove traces of HF down to 0.02 v/o HF as an acid fluoride. NaF-HF (5). CO_2 (max. 0.5%) was removed by filtering at —93°C. No CO_2 solids were observed in the OF_2 after filtering.

Results and Discussion

Platinum and copper corrosion test.—The capacitances of platinum and copper cells in vacuum were 2.5 pf/cm² and 2.6 pf/cm², respectively. The relative dielectric constant (ϵ) was found to be 2.3 ± 0.1 for

liquid OF_2 at —197° from $\epsilon = C_{pc} + C_t/C_t$ where C_p is the measured capacitance and C_t the theoretical capacitance in vacuum or air.[1]

This value agreed well with the dielectric constant calculated from the corrected capacitance, $C_{pc} = C_p - C_o$, and C_t and the dimensions of the cells. The dielectric constant of liquid oxygen difluoride is calculated to be 2.2 ± 0.1. The dielectric constant of liquid fluorine has been reported as 1.5 (3).

C_{pc} for OF_2 was less than 0.8 pf/cm². The dielectric constant did not markedly change within the investigated temperature range. The C_{pc} of OF_2 *vs.* time measured between the platinum and the copper plates indicates that these metals are passive and do not corrode under these conditions (Table I). Visual examination of the platinum and copper plates supported this conclusion.

The conductance of OF_2 is less than 1.7×10^{-9} ohm^{-1} cm^{-1}, the limit of the present instrumentation.

Nickel and tantalum corrosion test.—The capacitance (C_o) of nickel and tantalum plates in air was 3.3 pf/cm² and 6.3 pf/cm², respectively. In contrast to the platinum and copper test, the specific solution conductance, k_c, was measurable, *i.e.*, 10^{-8} $ohm^{-1}cm$. Table II illustrates the increase of conductance due to

$$^1\epsilon = \frac{C_{pc} + C_t}{C_t} \quad \text{where } C_t \simeq 0.6 \text{ pf/cm}^2 \text{ (theoretical)}.$$

Table I. Capacitance measurements by Pt and Cu plates in liquid OF_2

Time, hr	Temp, °C	Pt Cp, pf/cm²	Cu Cp, pf/cm²
0	−182	3.0	2.9
½	−193	3.3	3.5
1	−195	3.3	3.4
1½	−197	3.3	3.3
2	−198	3.3	3.4
2½	−200	3.2	3.3
3	−191	3.2	3.3
3½	−196	3.2	3.2
4	−175	3.0	3.0
4½	−172	3.0	3.0

Note:
R_p
k_c 10^{-9} ohm^{-1} cm
R 11 Meg
$D = 0$
Pressure = 0 (atms)
A = 12.47 cm², apparent area for Pt and Cu.

Table II. Capacitance measurements by Ta and Ni plates in liquid OF_2

Time, hr	Temp, °C	Ta C_{pc}, pf/cm²	Ta $k_c \times 10^8$, ohm^{-1} cm^{-1}	Ni C_{pc}, pf/cm²	Ni $k_c \times 10^8$, ohm^{-1} cm^{-1}
0	−148	2.0	1.0483	2.2	0.6228
½	−166	2.6	1.2037	2.3	0.5450
1	−151	3.2	1.4444	2.3	0.4844
17	−89	6.2	2.7083	6.7	1.0381
18	−95	7.0	2.7083	6.5	1.0381
18½	−93	5.9	2.3214	6.3	0.9909

Apparent area, A_{Ta} = 12.47 cm²
Apparent area, A_{Ni} = 8.62 cm².

Table III. Corrosion rate of metals in liquid OF_2 at —110°F in mils per yr (MPY)

Material	Test duration 1 Day	21 Days	4 Months	1 Year
Copper	0.0	0.01	0.005	0.0007
Nickel	0.9	0.02	0.002	0.0007
Tantalum	—	0.02	—	—

solvation of tantalum and nickel ions. The solution resistance for Ta was found to be half that for Ni electrodes. The lower solution resistance for Ta than for Ni indicates tantalum is less corrosion resistant. The fact that the solution conductance for Ni and Ta remains in their own range with time indicates cross contamination is not a problem.

Table II gives capacitance data for Ta and Ni plates in liquid OF_2. C_{pc} measured for Ta was higher than for Ni at both —156° and —92°C.

From the $C_{pc} + C_t$ values, a metal fluoride film capacitance, C_1, can be calculated and differentiated from the solution capacitance, C_2 (6). C_2 for Ta was larger and C_1 smaller than for Ni. A larger C_2 indicates thicker surface film for tantalum. Both comparisons indicate Ta is more susceptible to corrosion than Ni.

A nickel fluoride (NiF_2) film was identified by electron diffraction techniques on corroded Ni specimens.

A marked increase in capacitance and a decrease in solution resistance between Ta electrodes occurred when the temperature of OF_2 was increased from —156° to —92°C. Therefore, an appreciable increase in corrosion attack of tantalum by OF_2 is expected at the higher temperatures.

Corrosion rates of copper, nickel, and tantalum by weight change method are given in Table III for comparison (7). Only the 21-day test indicates copper is more passive in OF_2 than nickel and tantalum.

Manuscript received May 17, 1966; revised manuscript received Feb. 21, 1967.

Any discussion of this paper will appear in a Discussion Section to be published in the June 1968 JOURNAL.

REFERENCES

1. W. D. English, S. W. Pohl, and N. A. Tiner, Paper presented at 6th National Symposium, Materials for Space Vehicle Use, Vol. 3, Soc. Aero-Space Materials and Process Engrs. Meeting, Seattle, Wash., Nov. 1963.
2. S. Kleinberg and J. F. Tompkins, Tech. Report No. ASD-TDR-62-250, WADC, March 1960.
3. R. N. Doescher, Memorandum No. 9-16 Jet Propulsion Lab., Calif. (Sept. 6, 1949).
4. Cleanliness of Components for Use in Oxygen Fuel and Pneumatic Systems, George C. Marshall Space Flight Center, NASA Specification MSFC-SPEC-164, July 27, 1964.
5. S. G. Turnbull, A. F. Benning, G. W. Feldmann, A. L. Linch, R. C. McHarness, and M. K. Richards, *Ind. Engr. Chem.*, **39**, 3P286-288 (1947).
6. P. Delahay, "Instrumental Analysis," pp. 149-160, The MacMillan Co., New York (1957).
7. N. A. Tiner, W. D. English, and S. M. Toy, AF33(657)-0162, AFML-TR-65-414 (1965).

Vacuum-Deposited Thin Films of the Type PbS_xSe_{1-x}

B. A. Riggs[1]

Physics and Infrared Section, General Dynamics, Pomona, California

Individually, both the lead salt compounds PbS and PbSe have been widely used as radiation detectors sensitive to near-infrared wavelengths. Mixed compounds of the form PbS_xSe_{1-x}, however, offer potentially useful detectors of intermediate wavelength, broad band, and perhaps unique response. As Scanlon (1) has shown, the isomorphism and common cation of the constituent compounds makes possible a complete series of solid solutions. Such synthesis in bulk reactions is difficult however, and most detector applications require thin-film configurations.

Potter and Kretschmar (2) have previously demonstrated the utility of vacuum-deposition in producing thin films of the type $InAs_ySb_{1-y}$. They utilized a so-called, four-temperature evaporation method in achieving the otherwise difficult synthesis of these III-V compounds. The foregoing considerations led to the present efforts relative to formation of mixed-compound lead salt films. In the present case, however, the grain-by-grain, or "flash" evaporation technique (3) was employed.

Depositions were made in a commercial vacuum-evaporation unit (Mikros VE-20) fitted with a rotating-table powder feed device similar to that described by Beam and Takahashi (4). The feed mechanism, unique to the "flash" method, is required to supply a continuous stream of the granulated evaporant to a preheated evaporation source. The latter was a well-type Ta box source with a quartz insert set into the well. The insert was employed to avoid evaporating from the Ta surface (5). Carefully cleaned glass microscope slides were used as substrates and positioned 4 in. above the source heater.

The starting material for each evaporation consisted of mechanical mixtures of accurately weighed portions of sized (100-200 mesh) PbS and PbSe powders. The latter were obtained from Research Inorganic Chemical Company and were of five-nines stipulated purity. Target mixtures consisting of 2:1, 1:1, and, 1:2 PbS:PbSe (mol) were chosen. Individual powder fractions were weighed to the nearest 0.1 mg on a Sartorious balance. The weighed fractions of PbS and PbSe were then mixed mechanically in glass vials.

A typical evaporation utilized about 0.2g of a given mixed-powder sample which was placed in the feed hopper of the evaporation unit. The system was evacuated to about 8×10^{-7} mm Hg and allowed to outgas while heating the glass substrate to 280°-300°C. Depositions were made at a rate of 10-20 Å/sec giving thin-film deposits 1-2μ thick and 1 in. in diameter.

Subsequent to deposition, a diffractometer-profile was obtained by x-ray irradiation of each film on its substrate. Filtered Cu radiation from a Siemens instrument was used to scan 2θ values between 15° and 90°. In addition to the film deposits, a diffraction profile was also made for the individual PbS and PbSe starting materials. This was done by dusting the powder (—200 mesh fraction) over petroleum jelly applied to a microscope slide.

Figure 1 is a schematic reproduction of a portion of the diffraction profiles obtained for the starting PbSe powder and the mixed-film deposit of 16.5 mol % PbS. The latter is representative of the other mixed-compound films. As Figure 1 shows, the starting PbSe powder was not exclusively single phase and this was also true of the PbS starting material. Both the PbS and PbSe diffraction traces showed the (111)

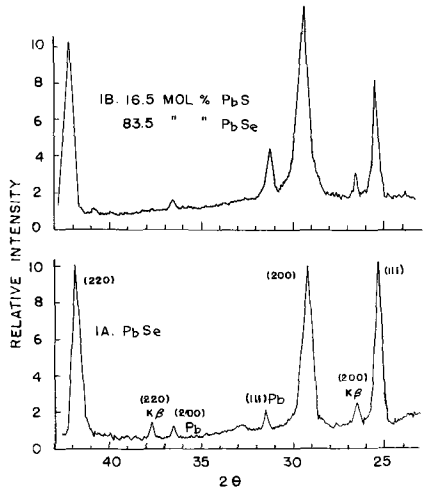

Fig. 1. A portion of the x-ray diffraction profiles for the 16.5:83.5 (mol %) PbS:PbSe thin film (top) and for 99.999% PbSe powder (bottom).

and (200) reflections for Pb superposed on the compound patterns. These "extraneous" lines show that both of the starting materials were Pb-rich non-stoichiometric compounds, and this imbalance was reproduced in the mixed-compound film deposits as illustrated by the 16.5 mol % film of Fig. 1. The diffracted intensity of the (111) Pb peak appears greater in the above film than in the PbSe pattern. This apparent enhancement is believed to be the consequence of the additive effects of the Pb-rich nature of both starting compounds. Some anion loss also may have occurred in the deposition. In addition, some preferred orientation in the film deposits is indicated by the stronger diffracted intensities of (200) and (220).

It was also apparent that the PbS_xSe_{1-x} films were compositionally varying reproductions of the basic PbS-type pattern. As a consequence, it was possible to calculate the lattice parameter for each case as a function of composition. For this purpose (hkl) in the back-reflection region giving the best $K\alpha_1/K\alpha_2$ resolution was used. These data are given in Table I and plotted in Fig. 2.

As Fig. 2 illustrates, the PbS-PbSe system conforms closely to Vegard's law and even the indicated deviation may be more apparent than real. That is, the thin films likely contain stresses and faulting not present in the powder samples used to obtain the terminal a_o values of Fig. 1. The close agreement between the latter and the published (ASTM) values is noteworthy. In view of the demonstrated a_o composition relationship, it is reasonable to expect that other

Table I. Lattice parameters for PbS_xSe_{1-x} thin films

Composition, mol % PbS	Form	(hkl)	a_{hkl}, A
16.5	Thin Film	(420)	6.081
44.6	Thin Film	(600)	6.030
76.8	Thin Film	(511)	5.970
PbS	Powder	(420)	5.932 (5.936)*
PbSe	Powder	(600)	6.119 (6.124)*

* ASTM values.

[1] Present address: Department of Metallurgical Research, Kaiser Aluminum & Chemical Corporation, Spokane, Washington.

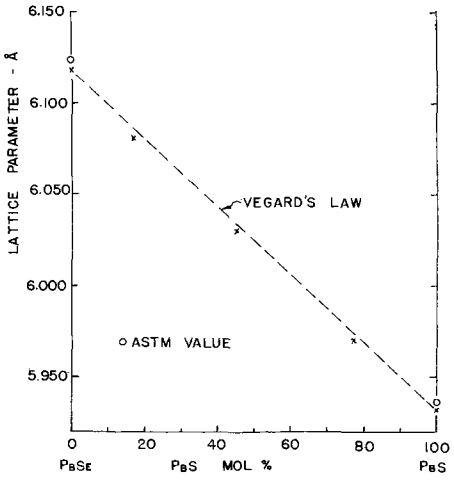

Fig. 2. Lattice parameter (a_o) vs. molar composition for the PbS-PbSe system.

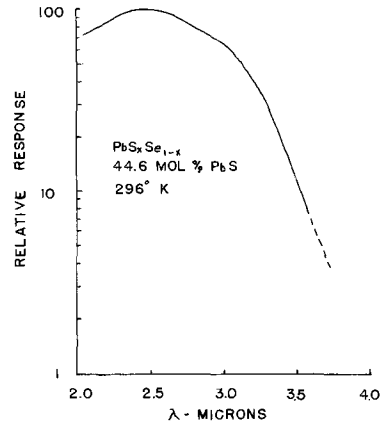

Fig. 3. Spectral response vs. wavelength for a sensitized PbS_xSe_{1-x} (44.6 mol % PbS) detector at room temperature.

physical properties dependent on bonding, such as thermal expansion coefficients, would vary in a similar fashion. This provides the opportunity to match more closely such parameters between film and substrate and thereby attain epitaxial deposits of relatively low defect densities.

In spite of the indicated nonstoichiometry one other deposition was made for purposes of electro-optical evaluation using the 44.6 mol % PbS composition. Several individual films were obtained from this deposition by appropriate masking. These films were rendered photosensitive by heating them in air for a short period subsequent to deposition. Gold electrodes were then deposited so as to define a sensitive area 0.16 cm on a side. Such films exhibited resistances of about 150 kohm.

Signal-to-noise ratios for three such cells were obtained by irradiation with a 600°C black body simulator located 15 cm from the cell and chopped at 1200 Hz. A Hewlett-Packard wave analyzer (5 Hz bandwidth), Perry amplifier, IRI voltage integrator, and Tektronix wave-form monitoring oscilloscope were utilized in the measuring circuit together with a load resistor matching the cell resistance. With this arrangement best- and worst-case signal-to-noise ratios of 770 and 120 were measured at room temperature.

It was also possible to derive a spectral response curve from the best of the above cells by using a Perkin-Elmer Model 13-U spectrophotometer. The relative response as a function of wavelength is shown in Fig. 3. This spectral response suggests the detector is responding as a homogeneous unit rather than as a sum of two separable components. This result then would tend to confirm the x-ray diffraction results presented previously.

The present results indicate that sensitive photodetectors of the PbS_xSe_{1-x} type can be produced by vacuum-deposition techniques. It is believed that improved detectors of this type can be realized by use of selected quality PbS and PbSe starting materials and by optimizing the desposition parameters and sensitization procedure.

Acknowledgment

The assistance provided by Mr. D. E. Wilson in obtaining the x-ray data is most gratefully acknowledged. The writer is also indebted to Mr. G. C. Knight and Mr. J. R. Nelson for their valued contributions relative to the electro-optical evaluation.

Manuscript received Feb. 1, 1967; revised manuscript received March 13, 1967.

Any discussion of this paper will appear in a Discussion Section to be published in the June 1968 JOURNAL.

REFERENCES

1. W. W. Scanlon, "Sol .State Phys.," Vol. 9, Academic Press, New York (1959).
2. R. F. Potter and G. G. Kretschmar, *Infrared Phys.*, **4**, 57 (1964).
3. E. K. Müller and J. L. Richards, *J. Appl. Phys.*, **35**, 1233 (1964).
4. W. R. Beam and T. Takahashi, *Rev. Sci. Instr.*, **35**, 1623 (1964).
5. R. B. Schoolar and J. N. Zemal, *J. Appl. Phys.*, **35**, 1848 (1964).

Polarization at Impervious and Porous Bromine Redox Electrodes

E. I. Onstott

Los Alamos Scientific Laboratory, Los Alamos, New Mexico

In the original work on desalination by bromine redox (1) a porous carbon anode was used in conjunction with a porous carbon cathode as a method of separating the depleted portion of electrolyte (anolyte) from the enriched portion (catholyte). In principle a single porous electrode in conjunction with an impervious electrode can serve the same useful function of separating the electrolysis products if recombination by convective transfer can be avoided.

Impervious electrodes have some advantages in multistage design, and it was therefore of interest to test the properties of an impervious electrode when used as an anode and also when used as a cathode.

Since dissolved bromine is used as a depolarizer in

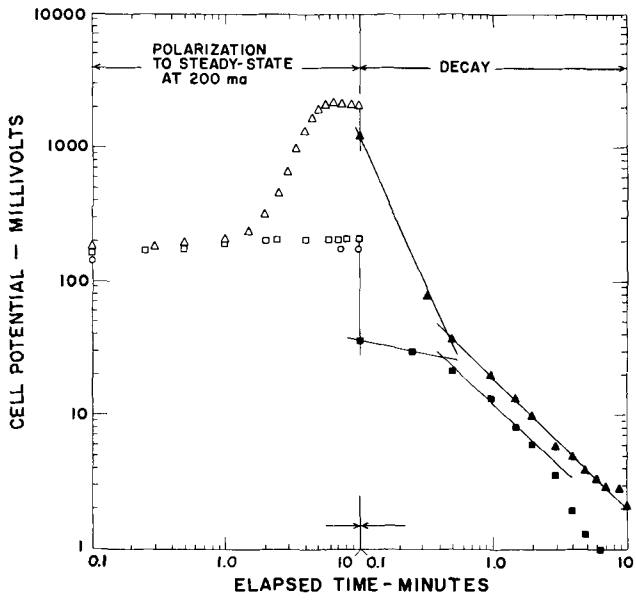

Fig. 1. Electrolysis followed by open-circuit decay of 0.05M NaBr containing about 0.03M Br_2.

the bromine redox method, the most obvious method of testing seemed to be that of measuring electrode polarization at constant current as a function of time, than to observe the decay of the cell potential with time with the driving source removed.

Experimental

Experimental procedures were much the same as reported previously (1). The electrolysis cell was modified by replacing one porous electrode with a high-purity graphite plate about 6 mm thick and having the same geometric surface area. A single exit consisting of a hole about 6 mm in diameter was drilled in the plate in the same position as the exit shown previously for each porous electrode (1). Electrolyte feed flow (countercurrent to the force of gravity) was controlled with a Beckman Model 746 metering pump operated at an input flow rate of 20 ml/min. The anolyte and catholyte flows were approximately equal at 10 ml/min each.

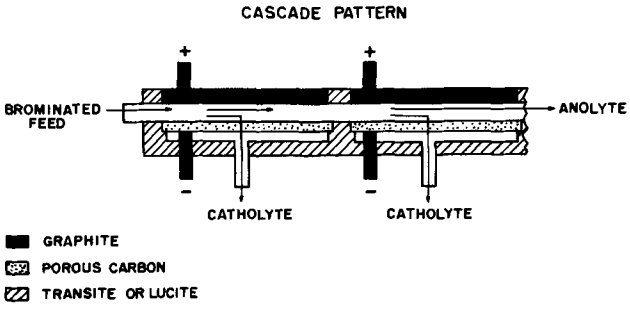

Fig. 2. Practical geometry for cascading cells

Results

The data in Fig. 1 show that an impervious graphite anode behaves very much like a porous carbon anode, but the potential required at steady-state is about 10% higher. With an impervious cathode, however, the potential required at steady state is an order of magnitude higher. These data show clearly that high cathode polarization results from depletion of bromine at the impervious cathode. Use of a porous carbon cathode, however, minimizes polarization by allowing bromine replacement by electrolyte flow through the porous cathode, and the energy requirements for electrochemical desalination are much lower than when an impervious cathode is used.

The data for potential decay indicate also that there are much larger differences in bromine concentration between the anode and cathode when the cathode is made the impervious electrode compared to the converse geometry.

Figure 2 shows a practical geometry for cascading cells. The cathode is placed on the bottom to take advantage of the stabilizing effect of gravity on the electrolyte density gradient. A small pilot plant has been constructed and operated with forty cells in series utilizing this design. Results of this investigation will be reported elsewhere.

Manuscript received March 17, 1967. This work was performed at Los Alamos Scientific Laboratory under the auspices of the Atomic Energy Commission.

Any discussion of this paper will appear in a Discussion Section to be published in the June 1968 JOURNAL.

REFERENCE

1. E. I. Onstott, *This Journal*, **111**, 966 (1964).

Brief Communication

The Rotating Disk Electrode, Hydrodynamic Boundary and Diffusion Layers by Laser Interferometry

R. N. O'Brien

Chemistry Department, University of Victoria, Victoria, B. C., Canada

It has recently become possible to build long path interferometers to study concentration contours in electrochemical cells where the path difference between interfering beams in a wedge-type interference cell is 2 cm or greater. Such a cell has been described recently (1) and the theory presented (2). The present cell has been modified from those previously described only in that a disk electrode of the parabolic shape recommended by Riddiford (3) to give stable flow patterns is admitted from the top and a counter electrode from the bottom. The cell as before consists of a Teflon cylinder whose axis is at 90° to the axis of

the electrode, with partially reflecting glass flats in the end and a cylinder insert whose axis coincides with the axis of rotation of the electrode, with its sides sliced off to allow the laser beam to pass through.

The expression for the location of wedge fringes on the interferometer wedge is: $2\mu t \cos\phi = n\lambda$ (μ is the refractive index; t is the thickness of the cell; $\cos\phi$ is about one when ϕ, the angle of incidence, is close enough to zero to give good fringes; n is the order of interference; and λ is the wavelength of the light used). If λ is 6328Å, the common gas laser frequency, the liquid has a refractive index of 1.3540 and t is 1 cm, n is calculated to be 42,810. This means that one fringe shift, that is when the displacement of the fringe brings it to the position where the next fringe would have been if it had remained straight, represents a change of one part in 42,810 in refractive index. If, however, a solution is used, only the part of the refractive index due to the solute will vary and in the case below, one fringe shift is one part in 240. For the present experimental set-up this means one part in 240 change from the bulk concentration of all solutes present.

When a disk is rotated in a liquid the application of the shearing force to the layers of liquid near the disk should result in a change in density; the thermodynamic $P\Delta V$ term that describes the dilation should be proportional to the shearing force applied and hence useful in evaluating liquid viscosities (4). The change in density is related to the change in refractive index by the Lorentz-Lorenz expression $R_M = \frac{M}{p}\left(\frac{\mu^2-1}{\mu^2+2}\right)$, where R_M is the molar refraction, M the molecular weight, p the density, and μ the refractive index. Since it is difficult to see how, in the solution considered, the dilation can occur in anything but the solvent, we will consider only the change in density of water. The molar refraction of H_2O is 1.64624 and detection of one fringe shift due to change in density represents a change in refractive index from 1.33315 at 24°C to 1.33312; consequently, a dilation of one part in 14,875. Since 1/10 of a fringe shift can be detected, the limits of measurement are one part in 148,750 or this is a very sensitive dilatometer.

Figure 1 contains four frames taken from a 16 mm motion picture film taken at 12 fps of a 3.50 mm diameter Ni disk in a 2N NaOH solution which is also 0.1M in $K_4Fe(CN)_6$ and 0.1M in $K_3Fe(CN)_6$ at 24°C. In the first frame a current of 20 μa or 2.5 ma/cm^2 is passing. The disk is not rotating and the apex of the wedge is to the left. The nickel disk is coated with catalyzed polyurethane so that no current passes except on the bottom of the disk. The disk is the cathode and the $K_4Fe(CN)_6$ being generated is more dense than the bulk solution, so natural convection is causing a reversal of the concentration gradient outside the simple diffusion layer, analogous to effects noted in other systems (5). Since the current density is far from the limiting current density in this system, it is assumed [as found to be essentially true in acidified $CuSO_4$ solution (6)] that only the electroactive species change concentration.

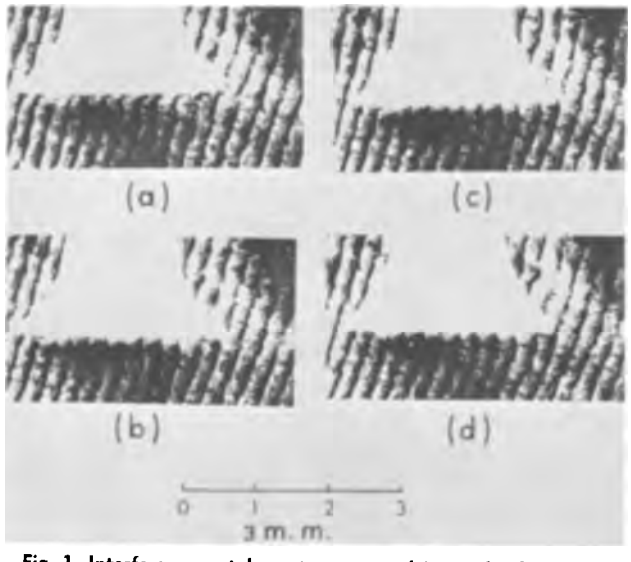

Fig. 1. Interferograms taken at one second intervals of a rotating disk electrode. The current density is 2.5 ma/cm^2 in a 2 NaOH solution which is also 0.1M in each of $K_3Fe(CN)_6$ and $K_4Fe(CN)_6$ at 24°C. In frame (a) the disk is not rotating and is the cathode, and a diffusion layer affected by natural convection is evident. Immediately following frame (a), rotation was started and reached 250 rpm in (b) and a stable pattern was established by (d). In frame (d) a hydrodynamic shear layer is the only visible feature.

In the second frame, taken one second later, the disk is rotating at about 250 rpm or the rim speed is about 5 cm/sec. Most of the concentration gradient $\left(\frac{\partial[K_4Fe(CN)_6]}{\partial x} - \frac{\partial[K_3Fe(CN)_6]}{\partial x}\right)$ previously established has already been swept away as a much thinner diffusional layer is set up, undetectable by this apparatus. Some convective effects are still evident at the same location in this frame as in the previous one, indicating that the effect of rotation progresses, as expected, through the layers at a finite rate. That is, the previously set up processes relax at a measurable rate. The direction of rotation is such that the rim of the disk nearest the camera is moving from right to left.

The third frame shows a deflection of the fringes in the opposite direction (to the left), except for the solution very close to the electrode. In the last frame, one second later, a hydrodynamic shear zone has been established to the exclusion of any recognizable diffusion layer. The total fringe shift at the center of the disk is again about ¾ of a fringe as in the diffusion layer, but the layer is about twice as thick so the refractive index gradient is only half as steep. A diffusion layer must still exist, but it can be confidently stated that since it cannot be detected by this apparatus (and hence its extent and the concentration gradient in it cannot be determined), its thickness must be less than 0.02 mm since measurements have been made in other systems at this distance (7).

Figure 2 was produced by tracing the center of fringes in a system in which the disk is the anode

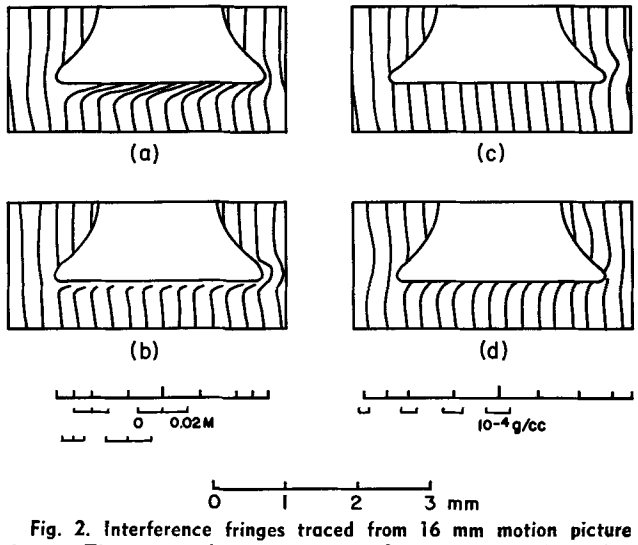

Fig. 2. Interference fringes traced from 16 mm motion picture frames. The current density is 5 ma/cm^2 in the same solution but the disk is now the anode, no convection is occurring, there is only ¼ sec between frames and the dilation in the hydrodynamic shear zone gives a fringe shift in the same direction as the oxidation of $K_4Fe(CN)_6$ in the diffusion layer.

and no natural convection occurs, all other conditions the same except as noted. The frames were taken at ¼ sec intervals. Frame (a) shows a well developed diffusion gradient at twice the current density as in Fig. 1 (5 ma/cm^2), and the apex of the wedge is to the right. Frame (b) shows the diffusion layer set up under nonrotating conditions being swept tangentially outward in accord with Riddiford's theory (3). Frame (c) shows an intermediate regime. In frame (d) the diffusion layer has been established at a thickness undetectable by this apparatus. The hydrodynamic dilation shear gradient is, as expected, in the same direction as the concentration gradient previously established.

Since the effects being viewed in this work are independent of the thickness of the cell (as attested by unperturbed fringes appearing in the edges of the frames), and are the result of viewing a disk of perturbation, the usual formula $2\mu t = n\lambda$ must have a variable t. Now $t = 2d \sin \frac{d}{r}\frac{\pi}{2}$, where d is the distance from the center of the perturbed disk of fluid and r is the radius of this disk. Scales in concentration and density units have been calculated for specific marked points, and are, of course, only applicable to those points. They can only be used as a rough guide to judge as to whether the fringe shift follows the indicated sine function.

Experiments were also performed in which a nickel rod was encased in a Teflon tube. The outside diameter of the Teflon was twice that of the nickel rod, and the Teflon tube outside diameter was 3.5 mm. The surface of the Teflon and nickel were gently polished flat while assembled together and just prior to mounting in the interferometer. The nickel could be rotated while the Teflon remained stationary, or both could be rotated at the same speed. When current was passed in the same electrolyte as above without rotation, then rotation begun after an appreciable diffusion layer was present, the patterns of perturbation to the fringes were similar in both cases to the bell-shaped disk recommended by Riddiford. The configuration in which only the electrode moved showed a slightly better flow pattern (*i.e.*, more closely horizontal, or tangential, motion of the electrolyte away from the electrode). It is thought that both the flow patterns and the dilation in the shear zone will have an effect on current distribution which has recently been the subject of theoretical calculations (8).

Further experiments are planned to firmly establish flow patterns around the rotating disk and to explore the system's usefulness as a dilatometer.

Acknowledgment

The work reported was performed in association with the Inorganic Materials Research Division of the Lawrence Radiation Laboratory while the author was a Visiting Scholar in the College of Chemistry, the University of California, Berkeley. The author is grateful for their support and for valuable conversations with C. W. Tobias.

Manuscript received Jan. 16, 1967; revised manuscript received March 21, 1967.

Any discussion of this paper will appear in a Discussion Section to be published in the June 1968 JOURNAL.

REFERENCES

1. J. Leja and R. N. O'Brien, *Nature*, **210**, 1217 (1966).
2. R. N. O'Brien, *Rev. Sci. Instruments*, **35**, 803 (1964).
3. S. Azim and A. C. Riddiford, *Anal. Chem.*, **34**, 1023 (1962).
4. E. A. Flood, Personal communication, theory to be published.
5. R. N. O'Brien, W. F. Yakymyshyn, and J. Leja, *This Journal*, **110**, 820 (1963).
6. R. N. O'Brien and H. J. Axon, *Trans. Inst. Metal Finishing*, **34**, 41 (1957).
7. R. N. O'Brien, *This Journal*, **113**, 389 (1966).
8. J. Newman, *ibid.*, **113**, 501, 1235 (1966).

SOLID STATE SCIENCE

The Preparation and Properties of Thin Film Silicon-Nitrogen Compounds Produced by a Radio Frequency Glow Discharge Reaction

R. C. G. Swann, R. R. Mehta, and T. P. Cauge

ITT Semiconductor Research Department, Palo Alto, California

ABSTRACT

Silicon nitride was deposited by a radio frequency glow discharge reaction of silane and ammonia. Films were deposited at a fixed substrate temperature of 300°C but the silane/ammonia concentration was varied between 3 and 50%. The effect of changing gas concentrations has been correlated with the change in physical and electrical properties of the deposited material. In particular, measurements of dielectric constant, loss factor, and voltage breakdown strength have been made as well as surface studies by the MOS technique. Material properties have also been qualitatively studied by monitoring IR absorption, chemical etch rate, and film growth rate.

The advent of MOST's and high field devices has revealed some limitations in the use of silicon dioxide as a gate insulator or passivating medium. In particular, attention has been drawn to the inability of the oxide to stop fast diffusing alkali metals, *e.g.*, sodium, potassium, or lithium. The relatively low dielectric constant of SiO_2 also imposes design problems where very high frequency operation is desired. Silicon nitride is one of several materials that has been selected to overcome these problems, and its physicochemical properties were studied to compare it to the oxide.

The silicon nitride was deposited by reacting ammonia and silane in a radio frequency glow discharge which was reported earlier by Sterling and Swann (1). This is now one of several processes under investigation both here and in other laboratories. The merits of the rf glow discharge method with respect to deposition temperature, film purity, stoichiometry, and instrumentation are considered below.

Depositions can be carried out at any desired substrate temperature, even below room temperature with the necessary refrigeration facilities. However, structural modifications of the film have been observed to take place at deposition temperatures higher than room temperature, as exemplified by densification of the film structure resulting in lower etch rates. A similar effect has been reported after the annealing of sputtered oxides (2). This factor coupled with a thermal limitation imposed by the substrate, (*e.g.*, melting point or movement of diffusion front) may in turn determine the deposition temperature. In this report, a substrate temperature of 300°C has been studied, to achieve acceptable etch rates and yet maintain a good film structure without resorting to temperatures used in the pyrolytic process.

The rf discharge process can utilize gaseous sources which in general are available in an extremely pure form and so offers a purer source than, for example, sintered target materials used in some sputtering processes. It should be noted, however, that this process is not restricted to hydrides or even silicon compounds, *e.g.*, boron nitride from boron trichloride and ammonia. Electrode contamination is also eliminated by the use of an external energy source to produce an electrodeless discharge. Films produced in a d-c or low frequency discharge often suffer from electrode impurities as well as changes in chemistry (*e.g.*, polymer formation has been observed in a low frequency glow discharge reaction) (3).

In most sputtering systems, stoichiometry is limited by the target material whereas this process will enable a choice of film stoichiometry by simply controlling the proportions of the reactants. For example, compounds of silicon and oxygen have been produced by varying the ratio of nitrous oxide to silane, and SiO, Si_2O_3, and SiO_2 have been identified by the authors in an earlier study.

The apparatus is very simple (Fig. 1), requiring no internal electrodes, targets, biasing, or water cooling facilities as employed in sputtering systems. The apparatus simplicity is in contrast to the complexity

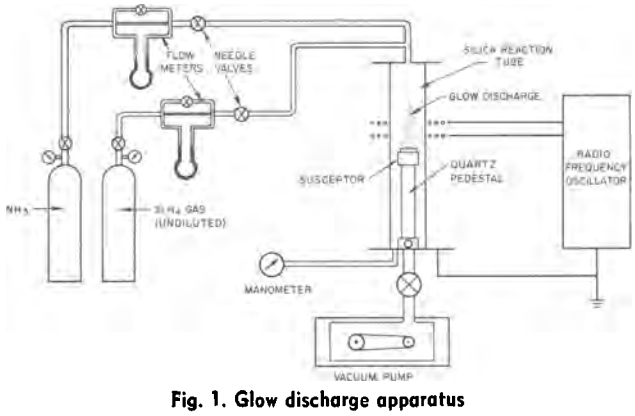

Fig. 1. Glow discharge apparatus

of the chemical reactions which take place in a glow discharge environment.

Glow Discharge Reactions—General

The glow or "cold" discharge referred to in this text occurs between the Townsend and the arc discharge which are only part of the family of electrical breakdown phenomena. Discharges can be further classified into two different types which have been detailed by Babat (4). The capacitive or "E" type discharge is excited by an electric field and the inductive or "H" type discharge is excited by a magnetic field. The latter is probably of greater significance in the system used for this work, as evidenced by incomplete chemical reactions in the case of high frequency capacitive discharges in the absence of internal electrodes.

The physical processes involved in a glow discharge are not simple, since they involve the interaction of positive ions, electrons, and excited molecules as well as the presence of neutral atoms and molecules. From a chemical standpoint, reaction products can be formed by the breaking of existing bonds, or the formation of new bonds, free radicals, and metastable ions. In the latter case, ions can even behave as catalysts by giving up their latent energy to associated molecules at the recombination sites. These sites can be the reaction tube walls or any object placed in the discharge which absorbs energy released by the recombination. All these possible events indicate the complexity of plasma chemistry.

A complete understanding of discharge reactions requires detailed study which has not been attempted in this present work. Here, a semi-empirical approach has been taken to optimize growth conditions. Future studies will include measurements of electron temperature and its relationship to chemical bonding and reaction yield.

Apparatus

Figure 1 shows the general arrangement of the apparatus. The chemical components of the silicon nitride are supplied from gaseous sources of undiluted silane and anhydrous ammonia. (The gases were supplied by Matheson Company, Newark, California, having the following purities—silane 99% + 1% H_2 and anhydrous ammonia 99.99%.) Small flow rates of the gases are monitored through calibrated capillary-type flow meters in conjunction with regulating valves. The gases are mixed and fed into a reaction tube which is continuously evacuated to pressures in the 10^{-1} Torr range. System pressure was monitored by a McLeod vacuum gauge to eliminate any gaseous decomposition.

A 1 MHz, 500w, high impedance radio frequency generator, Model 500M (special) Stanelco, Boreham Wood, England, was used to supply energy to the low pressure gas stream by means of a radio frequency coil which surrounds the fused silica reaction tube. The generator can supply energy for both chemical reaction and substrate heating when desired. The substrate temperature was measured by an infrared pyrometer; Thermodot Model TD 6A (Radiation Electronics Company).

Experimental

It has been reported (5) that the above system will enable changes in film stoichiometry by varying the ratios of the gaseous constituents. A study of the silicon nitride system was therefore made by changing the silane to ammonia concentration from 3 to 50% by volume. The total gas flow rate and substrate temperatures were maintained constant at 11 cc/min and 300°C, respectively.

Films were deposited on mechanically polished n-type silicon wafers, cut in the 111 plane and of resistivity (2-3) ohm-cm. Slices were precleaned in HF and hot HNO_3 m with intermediate washes in deionized water. Samples for electrical evaluation were evaporated with chrome and gold contact areas (1.25 x 10^{-3} cm^2) on the nitride and an ohmic gold film on the reverse side. Capacitance and loss factor measurements were made on a G. R. (1 kc) digital bridge and a Boonton (100 kc) bridge with applied d-c bias of + 10v to the Cr-Au gate electrode to ensure maximum capacitance values. MIS C-V plots were obtained for several devices on each wafer to evaluate surface state charge Q_{ss}. Automatic plotting on an X-Y recorder, at a measurement frequency of 100 kHz, showed less than 10% variation in Q_{ss} over the wafer.

Growth and etch rates.—Figure 2 shows the rate of film deposition *vs.* silane concentration under conditions of constant radio frequency power, gas flow rate, and substrate temperature. Thicknesses were monitored approximately by observation of the interference fringes.

For accurate determination of film thickness, a step was etched with pure HF, over which a thin coating of aluminum was evaporated, and the step height measured using a Hilger Watts multiple beam interferometer. For film thicknesses less than 2000Å the error in measurement is ± 20Å. Above this thickness the probable error is greater (up to 40Å).

The growth rate is substantially linear, having a rate of 180Å/min at 50% silane concentration and 35 Å/min at 10% concentration.

Etch rates were determined for a 1:8 HF/NH_4F solution since this gave a controlled rate. Samples were prepared by selective protection with KPR and then etched to approximately half their total thickness. The KPR was removed and a reflecting surface was evaporated over the step for measurement as described above. Etch rates were of the order of 50 Å/min with a decrease to 20 Å/min at higher silane concentrations. It has been noted that at much higher substrate temperatures the etch rate is significantly decreased.

Infrared spectroscopy.—Figure 3 shows the spectra for identical silicon nitride depositions but with different KBr preparations. The top graph shows the I-R grade KBr powder with its characteristic absorption bands. The heavy graph is the result of a silicon nitride deposition onto a preformed KBr pellet. This shows the broad silicon-nitrogen absorption peak for a silane gas concentration of 25%. The main band ranges from 9-14μ and peaks at approximately 12.1μ.

The dotted absorption peak at ~ 9.4μ is found to occur when the same deposition is made on powdered KBr which is subsequently pressed into pellet form. This Si-O shoulder has also been seen on the Si_3N_4 spectra published in the literature (6). We postulate the presence of free silicon in the nitride which becomes oxidized on exposure to the atmosphere. (A similar effect has been noted by other workers (7, 8) when powdering crystalline silicon.) Samples prepared by the KBr powder technique show a shift in

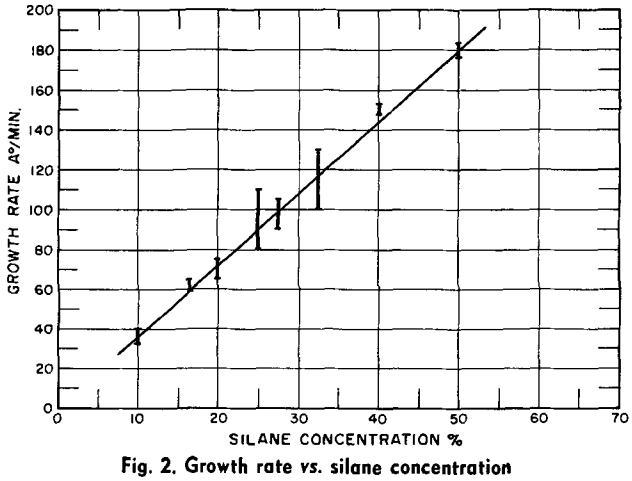

Fig. 2. Growth rate *vs.* silane concentration

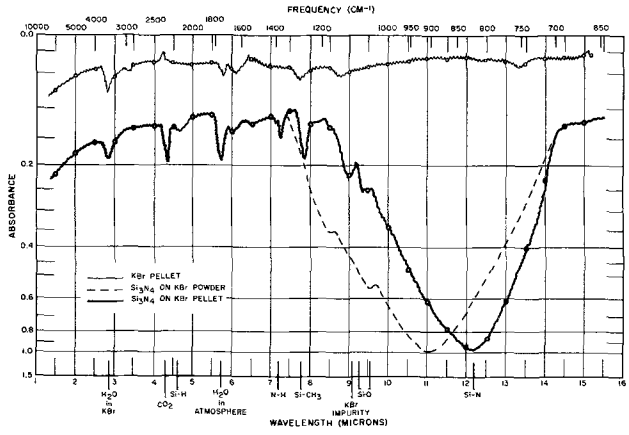

Fig. 3. Infrared spectra

the Si-O peak from 9.85 → 9.55μ for a 6 → 50% change in silane concentration. The Si-N peak is correspondingly influenced by the amount of Si-O bonds present.

We have observed a peak at 4.6-4.7μ as reported in the literature (9). We would rather attribute this to Si-H bonds, which occur at lower energies, than to Si ≡ N triple bonds.

More recent work has been to study the infrared absorption by transmission through silicon nitride which was deposited onto a single crystal silicon wafer (600μ thick, 40 ohm-cm, N-type) mechanically polished on both surfaces. A gradual change in the absorption peak from 11.6 to 12.2μ was observed for a change from 1 to 50% silane, respectively. The shift to a higher wavelength supports our earlier hypothesis that the layers become silicon rich at high silane concentrations. When using the more recent technique, as opposed to the KBr method, there is virtually absence of the Si-O band which suggests that, in the case of high silane concentrations, the free silicon is bound within the film and not available for oxidation.

Dielectric constant and loss factor.—Figure 4 shows the dielectric constant *vs.* silane concentration for film thicknesses of approximately 1000Å. Its value is seen to change from 7 to 11 for a corresponding change in silane concentration from 3 to 50%. The value of dielectric constant for bulk silicon nitride is quoted (10, 11) between 9 and 10. In thin film form many workers (6, 12-16) have reported various values in the range 6-8 and some as high as 12. In this present work the variation is attributed to changes in stoichiometry, especially the amount of silicon, free or chemically bonded, in the deposited layer. Additional evidence to support such a hypothesis is seen at high silane concentrations where the value of dielectric constant approaches that of bulk silicon. Also at these high concentrations the resistivity and breakdown field strength are tending toward the values typical of bulk silicon.

Measurement of loss factor *vs.* silane concentration revealed a trend to become more lossy as amorphous silicon is approached. A typical tan δ value at 1 kc/s is 0.0007 increasing to 0.002 at 50% concentration.

In drawing up the data for dielectric constant *vs.* silane concentration an anomalous effect was noted for film thickness slightly greater or less than 1000Å. In particular values greater than expected were observed for thicknesses less than 1000Å for a given silane concentration. Therefore a detailed study of this effect was undertaken at a given SiH_4/NH_3 (1:3) concentration over the thickness range 800 → 5000Å. Figure 5 shows the change which occurs in the dielectric constant plotted as a function of film thickness. We are tentatively attributing this phenomenon to stress, which is known to exist in films deposited by this technique. A more detailed analysis of this effect will be reported (17).

Resistivity and dielectric breakdown.—Both resistivity and dielectric strength have been measured as a function of silane concentration. Resistivities were obtained from steady-state values of current for a field of 4 x 10^5 v/cm. A change from 8 x 10^{16} ohm-cm to 5 x 10^{12} ohm-cm has been observed for concentrations in the range 9 to 50% silane, respectively.

Breakdown field strength has similarly decreased from approximately 6 x 10^6 v/cm at 9% silane to 1 x 10^6 v/cm at 50%.

Figure 6 shows the change in resistivity when plotted as a function of breakdown strength. Extrapolation of the lower portion of this graph gives the resistivity of glow discharge prepared amorphous silicon (10^{11} ohm-cm) at a breakdown voltage of 3 x 10^5 v/cm, which is a typical avalanche breakdown field for crystalline silicon. Dielectric strengths of 1.5 x 10^7 v/cm have been obtained for thicker films.

C-V measurements.—C-V measurements were made on the samples in order to evaluate their interfacial properties (18). Figure 7 shows a typical plot where the broken line represents the theoretical curve in the absence of surface charges, N_{SS}, and metal semiconductor work function difference, ΔW. The voltage offset ΔV, at flat band condition, is a direct measurement of N_{SS} for the static curve 1.

Figure 8 shows the change in surface charge density with silane concentration. At concentrations >20% there is a general tendency to lower the surface charge density from 5 x 10^{12} charges/cm^2 to 10^{11}/cm^2. At concentrations lower than 10% the density is around 8 x 10^{12}/cm^2.

Sample preheat conditions, *i.e.*, gaseous ambient and the presence of the rf glow discharge, have an effect on the surface state densities. Elimination of the discharge during the heating cycle results in lower

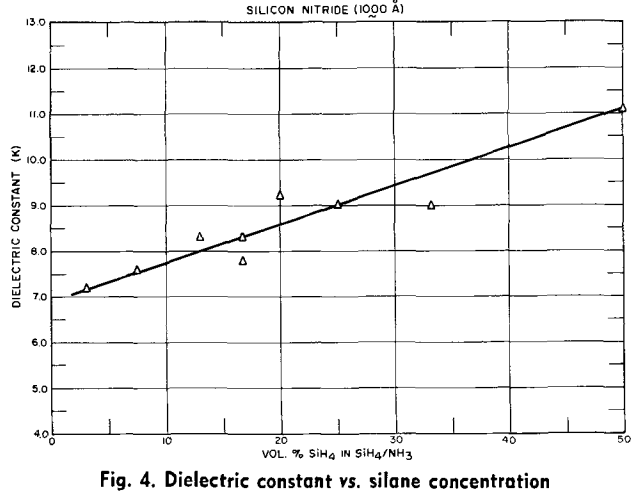

Fig. 4. Dielectric constant *vs.* silane concentration

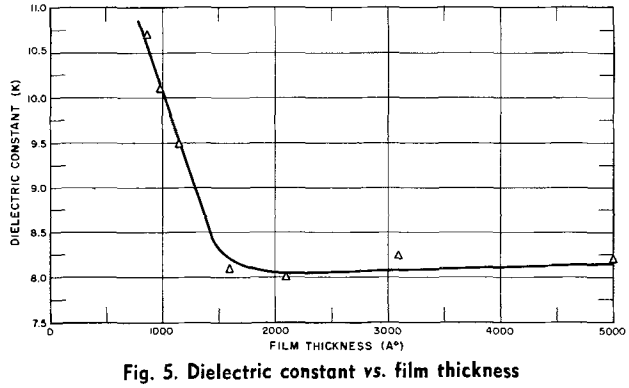

Fig. 5. Dielectric constant *vs.* film thickness

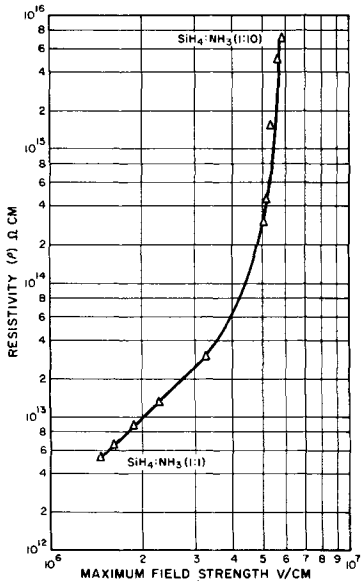

Fig. 6. Resistivity vs. dielectric field strength

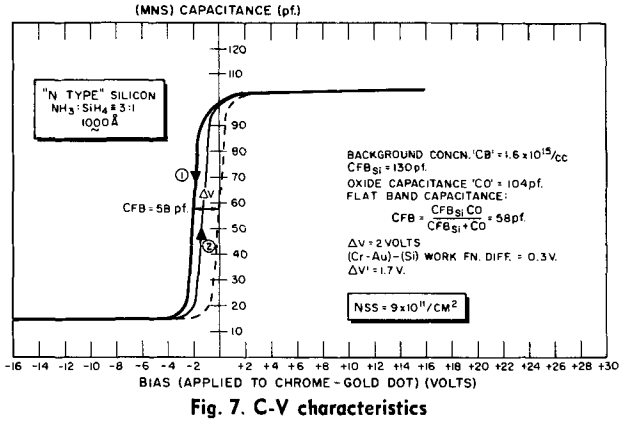

Fig. 7. C-V characteristics

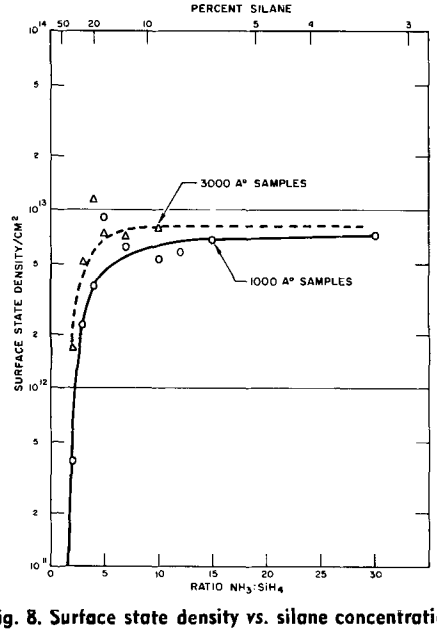

Fig. 8. Surface state density vs. silane concentration

surface charges. The hysteresis, *i.e.*, the difference in N_{SS} values as calculated from curves 1 and 2 in Fig. 7, depends on the amplitude of the scanning bias and can be as large as $\sim 10^{12}$ charges/cm^2. All factors controlling surface charge density and hysteresis have not been determined, and work is continuing.

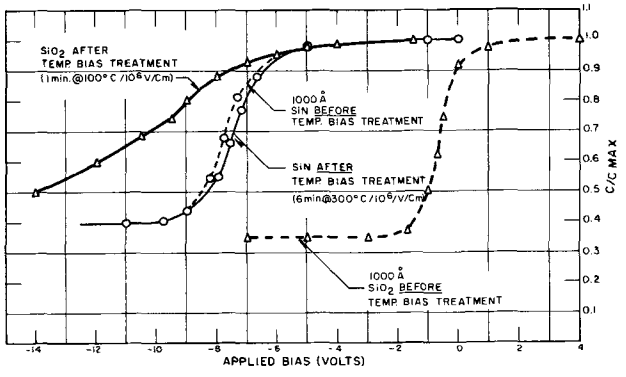

Fig. 9. C-V plots for comparison of SiO_2 and SiN after sodium contamination followed by a bake-bias treatment.

Barrier to sodium migration.—These low temperature nitrides form a barrier against the migration of sodium ions. This was tested in the following experiment with two silicon wafers. One wafer was deposited with nitride (1000Å, 30% silane concentration) and the other contained a thermally grown oxide (1000Å). Both were rinsed in NaOH solution (0.1% normal) and then evaporated with Cr-Au contacts. Their instability due to sodium drift was measured by plotting C-V curves before and after temperature-bias treatment. Figure 9 shows that for SiO_2 the drift in the C-V curves was about 9v for a temperature of 100°C and field of 10^6 v/cm applied for 1 min. For silicon nitride, no perceptible drift (<0.3v) was observed at the same applied field for 6 min at an elevated temperature of 300°C.

Silicon device passivation characteristics.—MIS transistors were fabricated from a 1000Å layer of silicon nitride (deposited using 3:1 NH_3/SiH_4, onto 2 ohm-cm N-type silicon). The threshold voltage for the subsequent P channel devices was −4.5v, G_m (at 1 ma I_D) = 500 μmhos and mobility $\overline{\mu}_p$ = 110 cm^2/v sec. The V-I characteristics of the source and drain junctions indicated diodes comparable in performance to those passivated with thermal SiO_2. The results, coupled with the absence of sodium migration, indicate that the low temperature nitride is suitable for passivating silicon planar devices.

Further measurements on surface studies and device passivation will be reported in the future.

Conclusions

Both growth and etch rates have demonstrated the compatibility of this material with existing semiconductor technology. Infrared and electrical data have shown the ability of this process to provide reproducible layers as well as controlled behavior.

The low substrate temperature offers an attractive feature for passivating P-N junctions where movement of the diffusion front is not desired.

Acknowledgments

The authors wish to thank David Bunzow for his assistance in experimental work and contributions during discussions, Dorman Pitzer for his help in physical measurements, and Roy Woodruff and Toni Downs who provided assistance with device preparation and evaluation.

Manuscript received Jan. 4, 1967; revised manuscript received March 24, 1967. This paper was presented at the Philadelphia Meeting, Oct. 9-14, 1966.

Any discussion of this paper will appear in a Discussion Section to be published in the June 1968 JOURNAL.

REFERENCES

1. H. F. Sterling and R. C. G. Swann, *Solid State Electronics*, 8, 653 (1965).
2. W. A. Pliskin, AVS 13th National Vacuum Symposium, San Francisco, 1966.

3 H. F. Sterling and J. H. Alexander, Standard Telecommunications Laboratories, Ltd., Harlow, England, Private communication.
4. G. I. Babat, *J. Inst. Elect. Eng.*, Pt. III, 94, Jan. 1947.
5. "The Preparation and Properties of Silicon Dioxide Layers," Annual Report on Research Project RP7-30 (1965), Standard Telecommunications Laboratories, Ltd., Harlow, England.
6. A. R. Janus and G. A. Shirn, "Preparation and Properties of Reactively Sputtered Silicon Nitride," Addendum to Handbook of "Proceedings of Symposium on the Deposition of Thin Films by Sputtering," June 9, 1966, University of Rochester, New York.
7. A. Many, Y. Goldstein, N. B. Grover, "Semiconductor Surfaces," p. 114, North Holland Publishing Company, Amsterdam, 1965.
8. H. F. Sterling, Private communication, 1966.
9. S. M. Hu, *This Journal*, **113**, 695 (1966).
10. O. Glemser, K. Beltz, and P. Naumann, *Z. anorg. allgem. chem.*, **291**, 51 (1957).
11. N. L. Parr, *The Engineer*, **222**, No. 5762, 18 (July 1966).
12. V. Y. Doo, D. R. Nichols, and G. A. Silvey, *This Journal*, **113**, 1279 (1966).
13. M. J. Grieco, F. L. Worthing, and B. Schwartz, Electrochemical Society Abstracts, Philadelphia Meeting, 1966, Abstract No. 148.
14. S. M. Hu and L. V. Gregor, *ibid.*, Abstract No. 150.
15. A. R. Janus and G. A. Shirn, *ibid.*, Abstract No. 149.
16. G. A. Brown, W. C. Robinette, and H. G. Carlson, *ibid.*, Recent News Paper No. 1.
17. R. C. G. Swann, T. P. Cauge, and R. R. Mehta, To be published
18. A. S. Grove, B. E. Deal, E. H. Snow, and C. T. Sah, *Solid State Electronics*, **8**, 145 (1965).

The Preparation and Properties of Amorphous Silicon Nitride Films

T. L. Chu, C. H. Lee, and G. A. Gruber

Westinghouse Research Laboratories, Pittsburgh, Pennsylvania

ABSTRACT

Amorphous silicon nitride films have been deposited in a gas flow system by the ammonolysis of silicon tetrachloride and the nitridation of silane with ammonia on heated substrate surfaces. The dependence of the deposition rate on the substrate temperature and the reactant composition and flow rate are discussed. The deposited films have been shown by the chemical analysis and electron beam induced crystallization to have the composition Si_3N_4. The density, refractive index, infrared absorption, and dissolution rate of deposited silicon nitride films have been determined. The substrate temperature during the deposition process appears to have the most significant influence on these properties, particularly density and dissolution rate. Silicon nitride films can be used as masks against the diffusion of aluminum, boron, and phosphorus into silicon. However, these dopants have been found to react with silicon nitride in varying degrees at high temperatures, and these reactions must be considered in determining the thickness of silicon nitride film required for masking purposes.

Silicon nitride has been known as a refractory for over a century. Crystalline silicon nitride ceramics, obtained by the reaction-sintering or hot-pressing technique, are noted for their chemical inertness, high temperature strength, high electrical resistivity, good thermal shock resistance, and extreme hardness (1). They have been used for many high temperature applications, such as container for molten metals and glasses, radiation heat shields, rocket-nozzle inserts, stator blades for gas turbines, etc. Very recently, silicon nitride has been used as a dielectric in electronic devices, utilizing its imperviousness to supplement the more commonly used silicon dioxide (2). The disadvantages of silicon dioxide, such as the high permeability toward moisture and other impurities, associated with its inherent structural porosity are well known. To be useful in devices, however, silicon nitride must be prepared in the form of amorphous and adherent films on semiconductor surfaces; the amorphous films possess more uniform properties than polycrystalline films.

In this work, the thermochemistry of the formation of silicon nitride from silicon and silicon compounds has been considered. The ammonolysis of silicon tetrachloride and the nitridation of silane with ammonia in a flow system were used to deposit silicon nitride films on silicon substrates. The properties of these films, such as structure, composition, density, refractive index, infrared absorption, dissolution rate, and masking ability, were studied. The experimental approaches and results are discussed in this paper. Wherever appropriate, comparisons with results of other workers are also made.

Preparation of Silicon Nitride Films

Thermochemistry of formation of silicon nitride.— Silicon dioxide has been produced by a number of chemical reactions, such as the oxidation of silicon or silane, and the hydrolysis of silicon halides. Analogous reactions can be used for the formation of silicon nitride (1). The standard free energy changes of (*a*) the nitridation of silicon and silane with nitrogen or ammonia and (*b*) the reaction of silicon tetrachloride with ammonia or nitrogen-hydrogen mixtures in the temperature range 1000° to 1500°K, calculated from the JANAF thermochemical data (3), are shown in Fig. 1. All these reactions are thermochemically feasible. It should be noted that the reactions using ammonia are more favorable than similar reactions using nitrogen because of the higher free energy of formation of ammonia. The use of ammonia is also advantageous kinetically; nitrogen is chemically inert due to the large bond energy in the molecule.

Not all reactions shown in Fig. 1 are suitable for the deposition of amorphous silicon nitride films. The nitridation of silicon is a slow process at 1300°C and above because of the diffusion-controlled mechanism (4). Furthermore, the heating of single crystal silicon

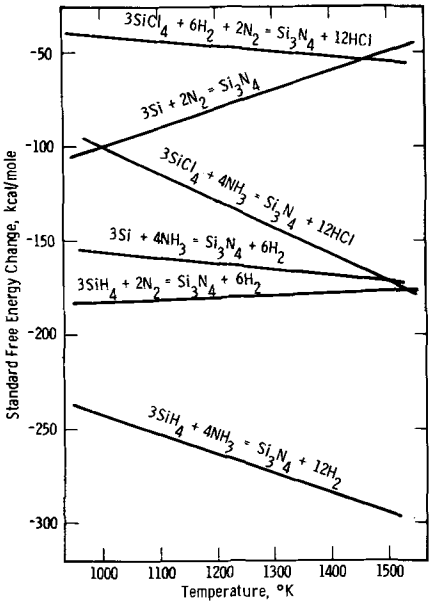

Fig. 1. Free energy changes of the formation of silicon nitride from silicon, silicon tetrachloride, and silane.

wafers of {111} orientation in nitrogen or an argon-nitrogen mixture has been found to produce discontinuous films of crystalline α-silicon nitride (5). Similar results have been obtained when single crystal silicon wafers were heated in ammonia at one atmosphere pressure (6). These films are not suitable for many device purposes because of grain boundaries.

The ammonolysis of silicon tetrachloride is a complicated reaction. When ammonia is present in excess, silicon diimide is the principal product at room temperature (7). $SiCl_4 + 6\ NH_3 \rightarrow Si(NH)_2 + 4NH_4Cl$. The silicon diimide formed polymerizes readily, and its pyrolysis yields α-silicon nitride according to the following equation (8)

$$6[Si(NH)_2]_x \xrightarrow[-2\ NH_3]{400°C} 2[Si_3(NH)_3N_2]_x \xrightarrow[-NH_3]{650°C}$$

$$3[Si_2(NH)N_2]_x \xrightarrow[-NH_3]{1250°C} 2\alpha\text{—}Si_3N_4$$

The deposition of silicon nitride films on silicon substrates by the reaction between silicon tetrachloride and ammonia in the temperature range 550°-1250°C has been reported recently (9). Earlier attempts to prepare silicon nitride films by the reaction of silicon tetrabromide, nitrogen, and hydrogen at 960°C were not successful (10).

The reaction between silane and ammonia is less complex, involving presumably the formation of silicon-hydrogen radicals or silicon and its subsequent reaction with ammonia. The deposition of amorphous silicon nitride films has been accomplished by this reaction using an rf discharge technique (11) or high temperatures (6, 12, 13).

Experimental.—The deposition of silicon nitride was carried out in a flow system using the ammonolysis of silicon tetrachloride and the nitridation of silane with ammonia on heated substrate surfaces. In the ammonolysis process, hydrogen was used to carry silicon tetrachloride into the reaction tube. No diluent was used in the nitridation process to eliminate any nitrogen deficiency in the deposit, in contrast with the large excess of hydrogen used in other reported work (12, 13). Ammonia used in this work was of better than 99.995% purity.

The deposition process was carried out in a horizontal fused silica tube of 55 mm I.D. In the ammonolysis technique, ammonia and silicon tetrachloride were introduced separately into the reaction tube since they react instantaneously at room temperature. Furthermore, the reaction tube was maintained at 375°C to eliminate the condensation of ammonium chloride, a by-product of the reaction. In the nitridation process, on the other hand, the reaction tube was water-cooled to minimize homogeneous nucleation in the gas phase. Single crystal silicon wafers of {111} orientation, chemically polished with a nitric acid-hydrofluoric acid mixture, were used as substrates in all experiments. They were supported on a silicon-coated susceptor in the reaction tube, and the susceptor heated externally by an rf generator.

The thickness of silicon nitride films was determined in the following manner. For films of a few microns thickness, direct measurement of the fractured cross section of the specimen with an optical microscope was used. The thickness of thin films was determined by using sodium light interference fringes in an etched wedge. The wedge was produced by dissolving a portion of the film in 49% hydrofluoric acid while the remainder was masked with Apiezon W wax. The refractive index of silicon nitride is taken as 2.0 in these determinations, and one interference fringe of sodium light corresponds to a thickness of 1470Å.

Results and discussion.—The most important criterion of obtaining adherent films by the chemical deposition technique is that the reaction should take place predominately on the substrate surface. In the ammonolysis technique, the wall of the reaction tube was maintained at 375°C, and the reactant mixture produced no deposit on the wall before reaching the substrates. Furthermore, by using a low partial pressure of silicon tetrachloride in the reactant mixture and a high gas velocity over the substrate surface, the deposited films were transparent and adherent to the substrate. Thus, no solid intermediates of the ammonolysis of silicon tetrachloride were produced in the volume of the reaction tube. The polymerization of silicon diimide and other intermediates is presumably a slow process.

Silicon nitride films were deposited on silicon substrates at 1000°-1200°C using ammonia at flow rates of 6-16 l/min and silicon tetrachloride at flow rates of 3×10^{-4} to 3×10^{-3} moles/min. Under these conditions, adherent and transparent films were obtained, and the deposition rate was found to be essentially independent of temperature in the temperature range studied. Some examples showing the dependence of the deposition rate on the composition and flow rate of the reactant mixture are summarized in Table I.

The deposition of silicon nitride films by the nitridation of silane with ammonia was studied in more detail; this technique is simpler and more flexible in operation than the ammonolysis of silicon tetrachloride. A large excess of ammonia was also used to minimize any nitrogen deficiency in deposited films. The effect of substrate temperature on the deposition rate was studied in the temperature range 800°-1200°C. The flow rate of silane was 2 ml/min, and that of ammonia was 20 or 40 l/min, corresponding to SiH_4/NH_3 molar ratios of 10^{-4} or 5×10^{-5}. The results are shown in Fig. 2. The deposition process is comprised of several consecutive steps: diffusion of reactants to the substrate surface, their absorption and subsequent reaction on the surface, the desorption of by-products, and their diffusion away from the surface. At substrate temperatures below about 1000°C,

Table I. Deposition rate of silicon nitride as a function of reactant composition and flow rate

Flow rate of NH_3, l/min	$SiCl_4/NH_3$ molar ratio	Average deposition rate, μ/min
16	6×10^{-3}	0.8
12	6×10^{-3}	0.95
6	6×10^{-3}	1
6	3×10^{-3}	0.65
6	1.2×10^{-3}	0.5

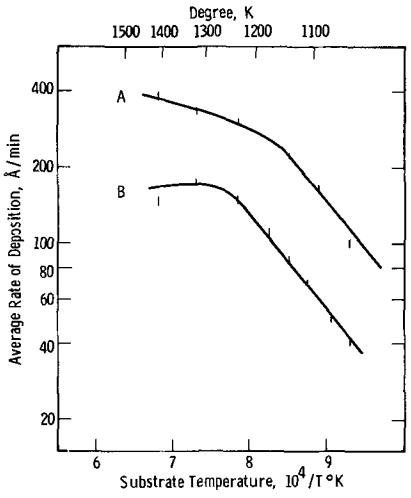

Fig. 2. Temperature dependence of deposition of silicon nitride films. A: Flow rate of NH_3 = 20 l/min, flow rate of SiH_4 = 2 ml/min. B: Flow rate of NH_3 = 40 l/min, flow rate of SiH_4 = 2 ml/min.

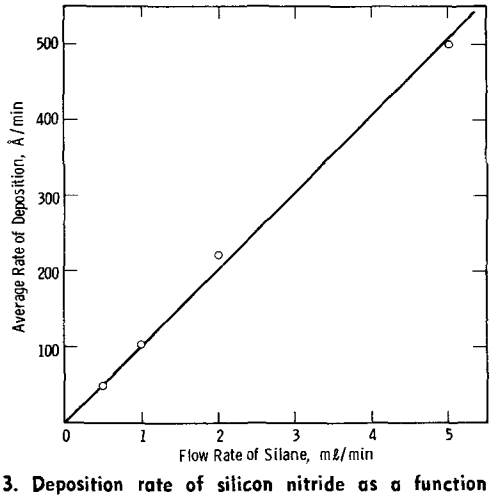

Fig. 3. Deposition rate of silicon nitride as a function of the silane flow rate. Flow rate of NH_3 = 20 l/min, substrate temperature = 900°C.

the deposition rate varied exponentially with temperature, with an apparent activation energy of 17 kcal/mole, indicating that chemical processes on the substrate surface are presumably the rate-determining step. At higher temperatures, the deposition rate leveled off with increasing temperature, indicating that the diffusion processes become more important.

The effects of reactant composition on the deposition rate of silicon nitride films were studied using ammonia flow rate of 20 l/min at a substrate temperature of 900°C. The flow rate of silane was varied from 0.5 to 5 ml/min; the results are shown in Fig. 3. In this concentration range, the deposition rate appeared to be a linear function of the silane concentration.

Properties of Silicon Nitride Films

Structure and composition.—Silicon nitride films deposited on silicon substrates by the ammonolysis of silicon tetrachloride or the nitridation of silane with ammonia were uniform, transparent, and highly adherent to the substrate. [The cracking of the film and the warping of the substrate at large film thickness were observed, as reported by others (12).] They exhibited no structural features when examined with an optical microscope. Several films were examined by both reflection and transmission electron microscopy; in the latter case, the substrate was removed by jet etching using a hydrofluoric-nitric acid mixture. Very diffused ring patterns were observed in all cases

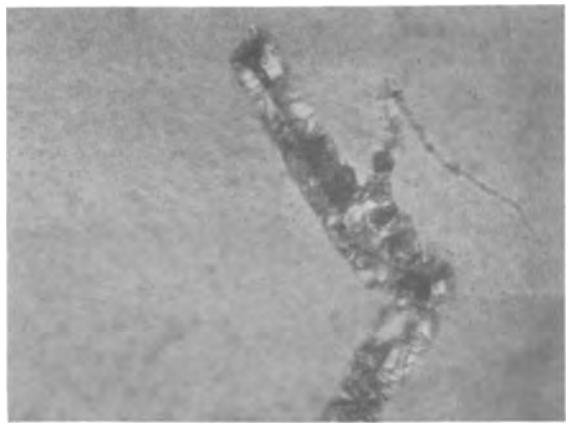

Fig. 4. Alpha-silicon nitride crystallite in an amorphous silicon nitride film deposited at 1200°C. Magnification 30,000X.

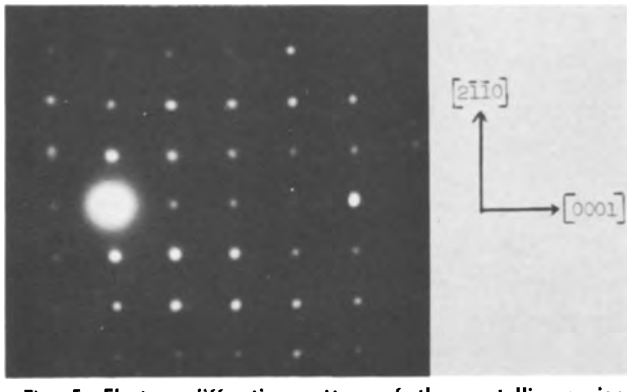

Fig. 5. Electron diffraction pattern of the crystalline region shown in Fig. 4.

indicating the amorphous nature of the film. In films deposited at 1200°C, however, localized regions of single crystalline α-silicon nitride have been observed. An example is shown in Fig. 4; this crystallinity was presumably induced by foreign impurities or defects on the substrate surface before deposition. Figure 5 shows the electron diffraction pattern of the crystalline region shown in Fig. 4, the surface of the nitride crystal being of $\{11\bar{2}0\}$ orientation, perpendicular to the basal plane. These results are different from those obtained when a large excess of hydrogen is used in the nitridation process. In the latter case, small crystallites appeared on the substrate surface at 900°-1000°C, and their concentration increased with increasing temperature of deposition (13).

Silicon nitride films deposited at 800°-1000°C were annealed at 1200°C in a nitrogen atmosphere for 4 hr or longer. The resulting films remained amorphous as indicated by the diffuse electron diffraction patterns.

Amorphous silicon nitride films were found to crystallize after being subjected to an intense electron beam in the electron microscope. Figure 6 shows the crystallized region of an amorphous film; the diffraction pattern of this region, shown in Fig. 7, was identified as that of single crystalline α-silicon nitride with its surface parallel to the basal plane. Thus, the composition of the amorphous film is Si_3N_4. Bombardment of silicon nitride films with a very intense electron beam resulted in the decomposition of the film to yield diffraction patterns characteristic of polycrystalline silicon.

The composition of amorphous silicon nitride films deposited by the nitridation of silane was also determined by chemical analysis. Silicon nitride layers were separated from the substrates by dissolving the substrate in a 10 : 1 HNO_3-HF mixture. The nitrogen content of the specimens was determined by an al-

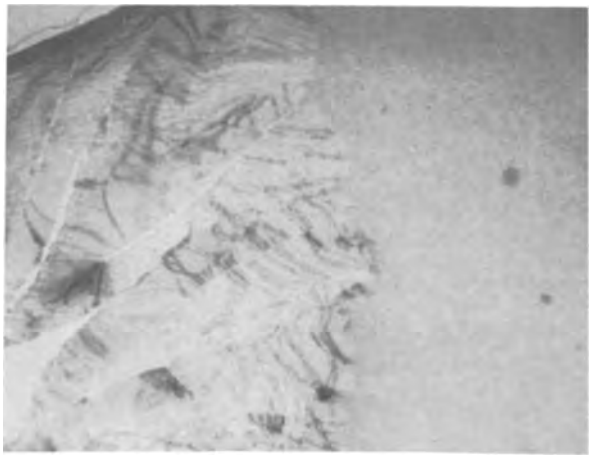

Fig. 6. Portion of an amorphous silicon nitride film crystallized by electron beam heating in an electron microscope. Magnification 30,000X.

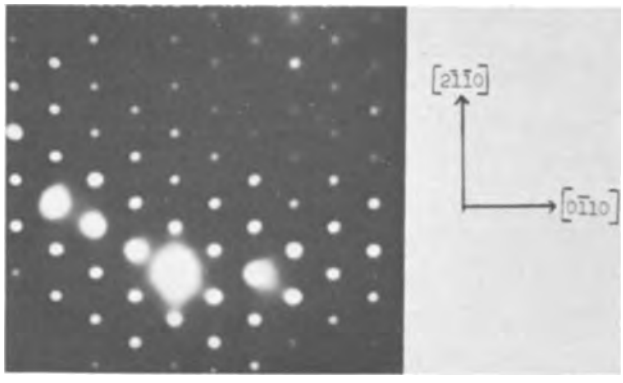

Fig. 7. Electron diffraction pattern of the crystallized region shown in Fig. 6.

kali fusion technique. A weighed amount of the specimen, about 0.1g, was mixed with 5g of sodium hydroxide in a platinum crucible, and the mixture was heated in a tube furnace to about 700°C for about 2 hr. The liberated ammonia, from the reaction between silicon nitride and sodium hydroxide, was carried by a nitrogen flow, absorbed in a saturated solution of boric acid, and titrated with 0.1*N* hydrochloric acid. The silicon analysis was also carried out by alkali fusion; a similar quantity of specimen was heated with a mixture of $NaNO_3$ and Na_2CO_3 in a platinum crucible. The resulting mass was treated with perchloric acid, and the precipitated silica was washed, and ignited at 1000°C for 1 hr. The weight of silica is used to determine the silicon content of the specimen. The results of the chemical analysis of deposited films and silicon nitride powder supplied by the Union Carbide Metals Company are shown in Table II; the composition of the deposited films is seen to correspond to Si_3N_4.

Density, refractive index, and infrared absorption.—The density of silicon nitride films, deposited by the ammonolysis and nitridation techniques, was determined by the floating equilibrium technique using a mixture of methylene iodide and bromoform. The results are summarized in Table III; the nitride films deposited at higher temperatures possess higher density as expected. It is also noted that the density of amorphous silicon nitride approaches that of the crystalline modification as the deposition temperature increases, while the density of amorphous silica (2.2g cm^{-3}) is considerably lower than that of quartz (2.65g cm^{-3}).

Table II. Chemical composition of silicon nitride films

Specimen	% Si	% N
Film deposited at 900°C	60.5	39.9
Film deposited at 930°C	59.1	40
Union Carbide Si_3N_4 powder	58.4	37
Si_3N_4, theoretical	60.08	39.92

Table III. Density of silicon nitride films

Reaction	Deposition temp, °C	Density, g cm^{-3}
$SiH_4 + NH_3$	850	2.78
	950	2.82
	1100	2.92
$SiCl_4 + NH_3$	1200	3.01
α-Si_3N_4, theoretical (1)		3.18

The refractive index of silicon nitride film was determined by an optical interference technique. The nitride film was removed from a portion of the specimen by masking and etching techniques to produce a smooth wedge. A portion of the specimen surface was metallized across the wedge with an aluminum film of about 500Å thickness. The displacement of thallium light (λ = 5350Å) interference fringes on crossing the wedge in the metallized and nonmetallized portions was measured using a Zeiss double beam interferometer. The fringe displacement on the metallized portion, p, is related to the absolute thickness of the film, and that on the nonmetallized portion, q, is related to the optical thickness of the film. The refractive index of the silicon nitride film, 1 + q/p, was determined to be 2.00 ± 0.04, irrespective of the chemical reaction used for the deposition process and the substrate temperature. However, ellipsometric measurements indicate that the refractive index of silicon nitride films, deposited by the nitridation process, at 5460Å increases slightly with increasing temperature of deposition. Typical values are 1.975 ± 0.005, 1.980 ± 0.005, and 2.020 ± 0.005 for films deposited at 800°, 950°, and 1200°C, respectively.

The infrared absorption spectra of silicon nitride films deposited by ammonolysis and nitridation techniques were taken on a Model 531 Perkin-Elmer Spectrophotometer. They all showed a broad absorption band with maxima at 830-860 cm^{-1} depending on the deposition temperature; this absorption is associated with one of the Si-N bond stretching frequencies. A typical example is shown in Fig. 8. In this case, a nitride film of 0.85μ thickness was deposited on an n-type 40 ohm-cm silicon substrate at 950°C, and the absorption peak is at about 850 cm^{-1}. Qualitatively, the absorption peak is shifted toward higher frequencies at higher deposition temperatures. For example, films deposited at 1000° and 1100°C showed absorption peak at 860 cm^{-1}.

Dissolution rate in hydrofluoric acid.—In contrast to crystalline silicon nitride, amorphous silicon nitride is soluble in concentrated hydrofluoric acid. The dissolution rate of amorphous silicon nitride is affected by porosity, impurities, etc., in the film, and provides a

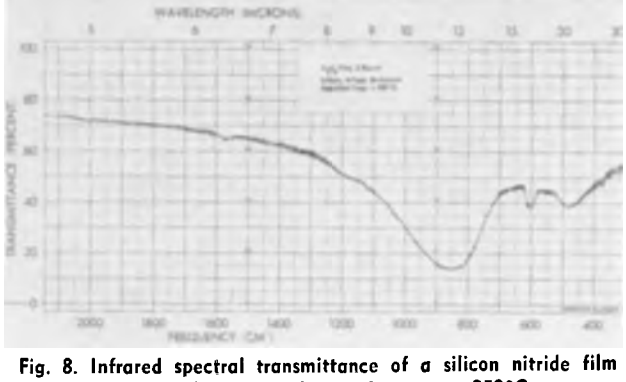

Fig. 8. Infrared spectral transmittance of a silicon nitride film deposited on n-type 40 ohm-cm silicon substrates at 950°C.

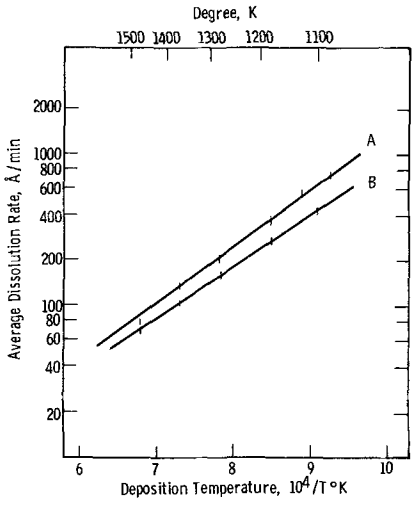

Fig. 9. Dissolution rate of silicon nitride in 49% HF at 24°C as a function of deposition temperature. A: Flow rate of ammonia = 20 l/min, flow rate of SiH_4 = 2 ml/min. B: Flow rate of ammonia = 40 l/min, flow rate of SiH_4 = 2 ml/min.

qualitative comparison of nitride films prepared under different conditions. Whenever localized areas of crystalline silicon nitride are present, these areas are essentially unaffected by hydrofluoric acid.

The dissolution rate of silicon nitride films deposited by the nitridation technique under conditions shown in Fig. 2 was determined at 24°C, using 49% hydrofluoric acid as the etchant. The temperature of deposition appears to have the most pronounced influence on the dissolution rate of silicon nitride films, as shown in Fig. 9. The linear relations shown here probably have no theoretical significance. The dissolution rate increases rapidly with decreasing deposition temperature. This is due presumably to the higher density of the films deposited at higher temperatures. Figure 9 also indicates that at a given substrate temperature, the dissolution rate also increases with increasing rate of deposition. Silicon nitride films deposited by the ammonolysis technique showed similar dependence of dissolution rate on the deposition temperature and deposition rate. Furthermore, the dissolution rate of silicon nitride films deposited at low temperatures was found to decrease after annealing at higher temperatures due to densification.

Masking ability.—Amorphous silicon nitride, because of its higher density, is expected to be more impervious than amorphous silica. The activation energy of dopant diffusion in silicon nitride should also be very high due to its refractory nature. Silicon nitride films have been shown to be more effective than silica films for masking against the diffusion of dopants into silicon (14). The capabilities and limitations of silicon nitride films as masks against the diffusion of aluminum, boron, and phosphorus into silicon were studied in this work.

Silicon nitride films deposited on silicon substrates at 800° to 1100°C by the ammonolysis or nitridation technique were used in the diffusion experiments. The silicon substrates were n-type, 20-50 ohm-cm resistivity for the diffusion of aluminum and boron, and were p-type, 10-20 ohm-cm resistivity for the diffusion of phosphorus. The silicon nitride film was removed completely from selected areas of the specimen by masking and etching techniques. The aluminum diffusion was carried out at 1150°C in a sealed fused silica tube using aluminum-silicon eutectic as the source material. A silicon nitride film of 0.18μ thickness deposited by the ammonolysis technique was found to show negligible deterioration after 44 hr of diffusion. The resistivity of silicon under the nitride film remained the same, while in unmasked regions, the surface concentration of aluminum in silicon and junction depth were estimated to be 10^{16} cm^{-3} and

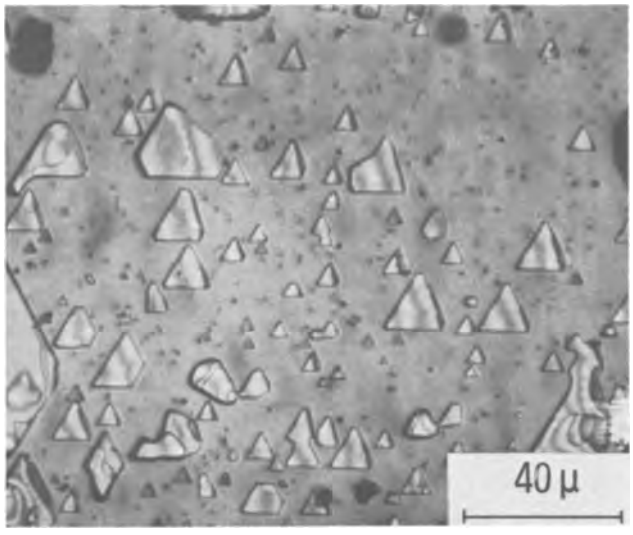

Fig. 10. Surface of a silicon nitride film after subjected to aluminum diffusion in a closed tube at 1150°C for 98 hr.

23μ, respectively. As the duration of diffusion increased, however, the silicon nitride film gradually deteriorated. Figure 10 shows the surface of a silicon nitride film after having been subjected to aluminum diffusion in a closed tube at 1150°C for 98 hr.

The boron diffusion was carried out using a two-step process. In the first step, boron oxide glass was deposited on the specimen surface at 1100°C for an hour using boron tribromide as the source. A diffused layer of about 3μ deep with a surface concentration of 10^{20} cm^{-3} was formed in the unmasked regions of the specimen. The boron oxide glass was then removed by using aqueous hydrofluoric acid before the second step of diffusion, or "drive-in." The masking ability of silicon nitride is independent of the "drive-in" step if the boron oxide glass is completely removed. A silicon nitride film of 500Å thickness deposited by the nitridation technique was found to be successful for masking the diffusion of boron under the conditions used here. Figure 11 shows the angle-lapped and stained surface of a specimen, where a nitride film of 500Å was used in the masked region and the "drive-in" step was carried out at 1200°C for 16 hr. The junction depth in the unmasked region was about 20μ, and silicon under the nitride film was found to remain n-type with essentially no change in resistivity.

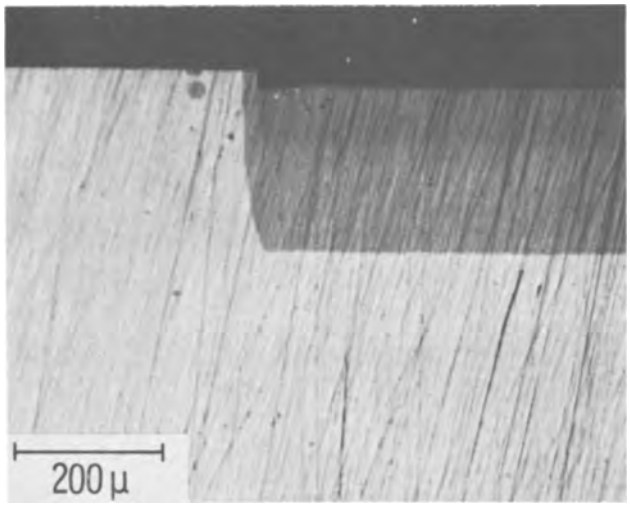

Fig. 11. Angle-lapped and HF stained surface of a specimen showing the effectiveness of a 500Å thick silicon nitride film as a mask against the diffusion of boron into silicon. Boron oxide glass was deposited at 1100°C for 1 hr followed by heating at 1200°C for 16 hr.

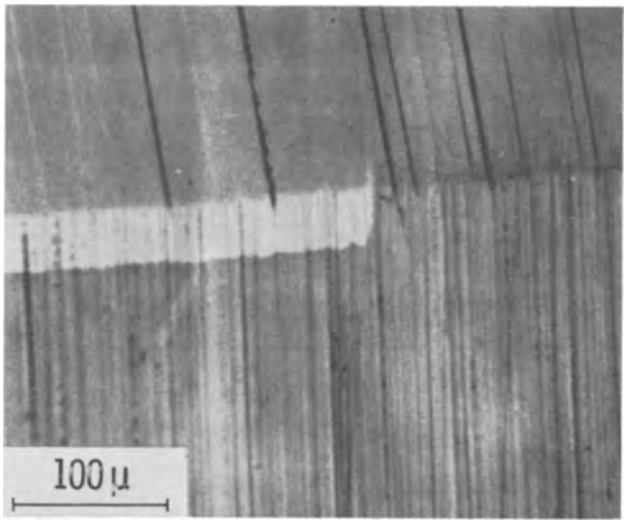

Fig. 12. Angle-lapped and HF stained surface of a specimen showing the effectiveness of a 1300Å thick silicon nitride film as a mask against the diffusion of phosphorus into silicon. Phosphorus oxide glass was deposited at 1100°C to yield a junction depth of 3μ and a surface concentration of 10^{21} cm^{-3}.

It should be pointed out, however, that silicon nitride reacts slowly with boron oxide at high temperatures. Thicker films used by others (14) are perhaps more desirable.

In the phosphorus diffusion process, phosphorus oxide glass was deposited on the specimen surface at 1100°C for 1 hr using phosphorus oxytrichloride as the source. A diffused layer of 3μ thickness with a surface concentration of about 10^{21} cm^{-3} was formed in unmasked regions. Phosphorus pentoxide was found to be more reactive toward silicon nitride than boron oxide. A silicon nitride film of 1000Å thickness deposited by the nitridation technique was found to be completely reacted under the conditions used here. In contrast to silicon nitride, the reaction product between silicon nitride and phosphorus pentoxide dissolves readily in diluted hydrofluoric acid. A nitride film of 1300Å was sufficient to mask the diffusion of phosphorus as shown in Fig. 12; however, thicker films are necessary for many device purposes.

Summary and Conclusions

Amorphous silicon nitride films have been deposited on silicon substrates in a gas flow system by the ammonolysis of silicon tetrachloride or the nitridation of silane with ammonia on heated substrate surfaces. The ammonolysis reaction is complicated by the formation of ammonium chloride and polymeric intermediate products. The nitridation reaction is more flexible for the deposition of silicon nitride films. In this deposition process, the chemical processes on the substrate surface are the rate-determining step at temperatures below 1000°C, and the diffusion processes become more important at higher temperatures.

All silicon nitride films, including those annealed at 1200°C for several hours, have been shown to be amorphous by electron diffraction examinations. However, foreign impurities or defects on the substrate surface could catalyze the formation of crystalline silicon nitride, particularly at high substrate temperatures. Amorphous silicon nitride films can be crystallized into α-silicon nitride by using electron bombardment in an electron microscope. This crystallization phenomenon and the use of chemical analysis have shown that the composition of silicon nitride films deposited in this work is Si_3N_4.

The density, refractive index, infrared absorption, and dissolution rate of deposited silicon nitride films are dependent on the substrate temperature during the deposition process. Films deposited at high temperatures are characterized by higher density and lower dissolution rate than those deposited at lower temperatures.

Amorphous silicon nitride is more dense and more impervious than amorphous silica. Silicon nitride films are, therefore, expected to be more effective than silica films for masking against the diffusion of dopants into semiconductors. However, silicon nitride has been found to react in varying degrees with the commonly used dopants for silicon at high temperatures, particularly phosphorus pentoxide. These reactions must be considered when deep junctions are required.

Acknowledgments

The authors wish to thank Y. C. Kao for discussions on diffusion problems, A. J. Noreika for electron diffraction studies, T. W. O'Keeffe for ellipsometric measurements, and Mrs. M. Theodore for assistance in chemical analysis.

Manuscript received Dec. 27, 1966; revised manuscript received March 6, 1967. This paper was presented at the Philadelphia Meeting, Oct. 9-14, 1966.

Any discussion of this paper will appear in a Discussion Section to be published in the June 1968 JOURNAL.

REFERENCES

1. P. Popper and S. N. Ruddlesden, *Trans. Brit. Ceram. Soc.*, **60**, 603 (1961).
2. See, for instance, N. C. Tombs, H. A. R. Wegener, R. Newman, B. T. Kenney, and A. J. Coppola, *Proc. IEEE*, **54**, 87 (1966).
3. JANAF Interim Thermochemical Tables, The Dow Chemical Co., Midland, Michigan.
4. G. G. Deeley, J. M. Herbert, and N. C. Moore, *Powder Metallurgy*, **8**, 145 (1961).
5. A. N. Knopp and R. Stickler, *Electrochem. Tech.*, **3**, 84 (1965).
6. T. L. Chu, M. H. Francombe, G. A. Gruber, J. J. Oberly, and R. L. Tallman, "Deposition of Silicon on Insulating Substrates," Final Report, Contract AF 19(628)-4220, AFCRL 65-574, AD 619992, Westinghouse Research Laboratories, July 1965
7. M. Billy, *Compt. rend.*, **242**, 137 (1956).
8. O. Glemser and P. Naumann, *Z. anorg. allgem. Chem.*, **298**, 134 (1958).
9. M. J. Grieco, F. L. Worthing, and B. Schwartz, Electrochemical Society Extended Abstracts of Dielectric and Insulation Division, **3**, No. 2, 47 (1966).
10. C. R. Barnes and C. R. Geesner, *This Journal*, **107**, 98 (1960); **110**, 361 (1963).
11. H. F. Sterling and R. C G. Swann. *Solid State Electronics*, **8**, 653 (1965).
12. V. Y. Doo, D. R. Nichols, and G. A. Silvey, *This Journal*, **113**, 1279 (1966).
13. K. E. Bean, P. S. Gleim, and W. R. Runyan, Ref. 9, p. 41.
14. V. Y. Doo, *IEEE Transactions on Electron Devices*, ED-13, 561 (1966).

The Heat-Treatment of Anodic Oxide Films on Tantalum

VI. The Effect of Chemical Thinning

Donald M. Smyth

Research and Development Laboratories, Sprague Electric Company, North Adams, Massachusetts

ABSTRACT

The dielectric properties of anodized tantalum, which has been heat-treated in air, have been studied as a function of subsequent chemical reduction of the oxide thickness. The results are in quantitative agreement with an exponential distribution of dielectric losses decreasing monotonically from the Ta-Ta_2O_5 interface.

It has been found that the dielectric properties of anodic oxide films on tantalum, which have been heated to 300°-500° in air or oxygen, are explainable on the basis of an exponential conductivity gradient across the oxide (1). This conductivity was assumed to be related to oxygen deficiency in the Ta_2O_5 which results from extraction of oxygen from the oxide by the underlying tantalum metal. Thus the equilibration of the oxide between the reducing character of the metal and the oxidizing ability of the ambient air leads to a gradient of stoichiometry, and hence of conductivity, across the oxide. This explanation would require that the conductivity in the oxide decrease monotonically from the Ta-Ta_2O_5 interface (unless there is an oxygen-excess, p-type conducting region at the other interface). Qualitative evidence has been presented which shows that the major portion of the conductivity lies near the metal (2). The purpose of this report is to show that the spatial distribution of losses in the heat-treated oxide is in quantitative agreement with the proposed model.

A-C bridge measurements give no information about the spatial distribution of dielectric losses in a given piece of dielectric. In effect, such measurements yield a collection of incremental thicknesses, each with a known equivalent parallel conductivity, but cannot distinguish between the possible sequential arrangements of these increments. The only technique now available for obtaining the spatial distribution of losses is to make consecutive measurements as the dielectric is chemically thinned. This technique can lead to serious misinterpretation if the dissolution is so nonuniform as to open paths through the oxide to the underlying metal, but, with suitable precautions, meaningful results can be obtained (3-6).

The conductivity across the heat-treated film is expressed as

$$\sigma = \sigma_1 e^{ax} \qquad [1]$$

where x is the distance from the Ta_2O_5-electrolyte (or electrode) interface, and σ_1 is the conductivity at $x = 0$, the point of lowest conductivity. (σ_1 has no physical reality; it is merely the value obtained by extrapolation of the conductivity gradient measured near the Ta-Ta_2O_5 interface as shown in Fig. 1). It has previously been shown that the equivalent series capacitance, C_s, can be expressed as

$$\frac{1}{C_s} = \frac{1}{aA\epsilon\epsilon_0} \ln \frac{\omega\epsilon\epsilon_0}{\sigma_1} \qquad [2]$$

where ϵ is the dielectric constant of the oxide, ϵ_0 is the permittivity of free space, ω is the angular frequency of the bridge signal, and A is the sample area [1]. $\omega\epsilon\epsilon_0$ is frequently abbreviated as

$$\sigma_0 = \omega\epsilon\epsilon_0 \qquad [3]$$

[2] and [3] are approximations which are valid in the region

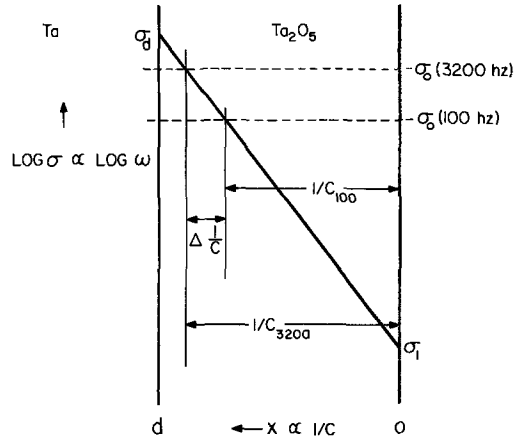

Fig. 1. Schematic representation of the relationship between the frequency dependence of capacitance and the distribution of conductivity.

$$\left(\frac{\omega\epsilon\epsilon_0}{\sigma_1}\right)^2 >> 1 >> \left(\frac{\omega\epsilon\epsilon_0}{\sigma_d}\right)^2 \qquad [4]$$

where σ_d is the conductivity at the Ta-Ta_2O_5 interface. σ_0 is further defined as the conductivity level such that the thickness between $x = 0$ and its intersection with the conductivity profile gives C_s when substituted into the parallel plate formula. In other words the intersection of σ_0 and $\sigma(x)$ defines an effective dielectric thickness, x, as in Fig. 1. From [1] and [2] it can be seen that the frequency dependence of capacitance is related to the position dependence of conductivity

$$\left[A\epsilon\epsilon_0 \frac{d\frac{1}{C_s}}{d\ln\omega}\right]^{-1} = a = \frac{d\ln\sigma}{dx} \qquad [5]$$

Since the slope, a, which can be measured only near the Ta-Ta_2O_5 interface, is independent of oxide thickness once the gradient has been established by heat-treatment, $d\frac{1}{C_s}/d\ln\omega$ should similarly be independent of subsequent thinning. This is the basis of the experimental test.

An 18.4 cm^2 sample of 0.010 in. tantalum sheet was anodically oxidized to 150v and then heated in air at 400° for 30 min. After cooling, the frequency dependence of capacitance was measured in an electrolyte of 40% H_2SO_4 and the measurement repeated after successive thinnings in 48% HF. The sample preparation and other experimental details have been described previously (1, 2, 7). It is sufficient to compare the change in $1/C$ between the same two frequencies in each case; the values at 100 and 3200 Hz were used. (See the schematic representation in Fig. 1.) The

Table I. Frequency dependence of capacitance ($\Delta 1/C = 1/C_{3200} - 1/C_{100}$) for anodized tantalum

	Preceding operation	Equivalent voltage thickness, v	$\Delta \frac{1}{C}$, μf^{-1}
1.	First heat	160	0.0409
2.	First thin	130	0.0408
3.	Second thin	105	0.0402
4.	Reheat		0.0236
5.	Third thin	85	0.0259
6.	Reanodize	160	0.0067
7.	Third heat		0.0416
8.	Fourth thin	130	0.0430
9.	Fifth thin	105	0.0421
10.	Fourth heat		0.0240
11.	Sixth thin	80	0.0264

Table II. Calculations from thinning data based on exponential conductivity gradient

Step	log σ_d/σ_1	Thickness observed, v	Thickness calculated, v	tan δ observed	tan δ calculated
1.	23.96	160	—	0.0322	—
2.	19.13	130	127.7	0.0413	0.0417
3.	15.66	105	104.5	0.0531	0.0529
4.	27.95	105	—	0.0271	—
5.	22.89	85	85.6	0.0371	0.0337
6.	—	—	—	—	—
7.	23.77	160	—	0.0325	—
8.	19.29	130	129.8	0.0411	0.0413
9.	15.23	105	102.5	0.0578	0.0547
10.	27.06	105	—	0.0281	—
11.	24.31	80	81.5	0.0440	0.0381

equivalent anodization voltage thickness was determined by visual comparison with the interference colors of a set of standards made by anodic oxidation at 5v intervals. The initial color corresponded to a 160v film on the standard which was not prepared under identical conditions.

The results are presented in Table I in the form of two complete, experimental cycles separated by step 6, reanodization of the sample to 150v. The validity of the proposed model is indicated by a comparison of Δ 1/C for steps 1, 2, and 3; 7, 8, and 9; 4 and 5; and 10 and 11. The constancy of Δ 1/C is quite good for the first two sets. For the latter two, the thinning was becoming noticeably nonuniform as indicated by some variation in the interference colors, but the agreement is still reasonable.

These results actually confirm only that no significant dielectric losses were present in the portion of oxide removed by thinning, and thus indicate only that the property-determining losses are located closer to the Ta-Ta_2O_5 interface. In order to confirm the exponential distribution by this type of analysis it would be necessary to remove 80-90% of the oxide to determine how the properties change as the lossy oxide is removed. It is very unlikely that thinning of Ta_2O_5 to this extent by dissolution in HF could be accomplished without opening physical flaws in the oxide.

From the data obtained during this experiment it is possible to make a detailed check of the applicability of the exponential gradient theory. Calculated and observed values are shown in Table II where the data refer to measurements made at 34° and 100 Hz. The step numbers refer to the sequence listed in Table I. The calculations were based on $\sigma_d = 9 \times 10^{-7}$ ohm^{-1} cm^{-1} [estimated from Fig. 4 of ref. (1)], and $\sigma_0 = \omega\epsilon\epsilon_0 = 1.6 \times 10^{-9}$ [ϵ was taken as 1.05 x 27.6 where the factor of 1.05 is a correction for the irreversible increase in ϵ caused by heat-treatment (2, 7)]. The analysis can be better understood by reference to Fig. 2 which depicts the conductivity gradient across the heat-treated oxide (the solid diagonal from σ_d to σ_1). The capacitance after heat-treatment measures x_1, the effective dielectric thickness. The value of σ_1 can be calculated from the relation

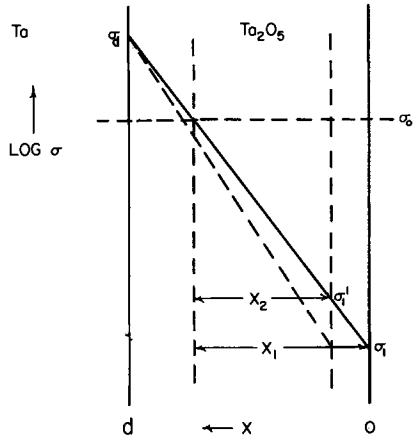

Fig. 2. Schematic representation of the analysis of dielectric losses of heat-treated, anodized tantalum after thinning.

$$\tan \delta = \frac{\pi}{2 \ln (\sigma_0/\sigma_1)} \qquad [6]$$

which was derived in ref. (1) and is accurate within the limitations of [4]. After thinning the oxide to the right-hand, vertical, dashed line, the new capacitance measures x_2, and σ'_1 can be obtained by the principle of similar triangles

$$\frac{\ln \frac{\sigma_0}{\sigma_1}}{x_1} = \frac{\ln \frac{\sigma_0}{\sigma'_1}}{x_2} \qquad [7]$$

Then a new tan δ can be calculated from σ'_1 and [6] and compared with the experimental value. [All experimental values of tan δ were corrected for the electrolyte resistance by subtraction of the extrapolated value of R_s at $1/f = 0$ (8)]. The agreement with observed values is particularly good for steps 2, 3, 8, and 9.

Another important point comes out of these data. When the sample was initially heated the capacitance and tan δ increased as usual, reflecting the effect of the losses due to increased conductivity. When the sample was reheated after thinning, however, the capacitance and losses both decreased. This behavior is anticipated by the proposed model. During the initial heating, the equilibrium conductivity gradient is established between σ_d and σ_1, which are determined solely by the equilibrium conditions at the two interfaces. As a result of the thinning process σ_1 is increased above this equilibrium, heat-treatment value (see Fig. 2). On reheating, a new gradient is set up across the reduced thickness between the original, equilibrium values of σ_d and σ_1 (the diagonal, dashed line in Fig. 2). This results in a steeper gradient which is observed as a decrease in both capacitance and tan δ. This new gradient is the same as that which would have been obtained by heat-treatment of a sample originally anodized to this thickness. (The steeper gradient means that less thickness is effectively shorted out and that there is a sharper boundary between conducting and insulating oxide.) This is perhaps the most direct evidence that physical damage to the oxide during heat-treatment does not play a significant role in the determination of the dielectric properties. Further heating could only result in further damage which would cause another increase in capacitance and losses.

The calculated conductivity gradients for the heat-treated samples (steps 1, 4, 7, and 10) are slightly steeper than previously reported. It should be particularly noted that the gradients for the reheated films after thinning are steeper than those of the original heated films (4 and 10 *vs.* 1 and 7). This is in line with a second-order effect which has been noted consistently throughout this work. The equilibrium value

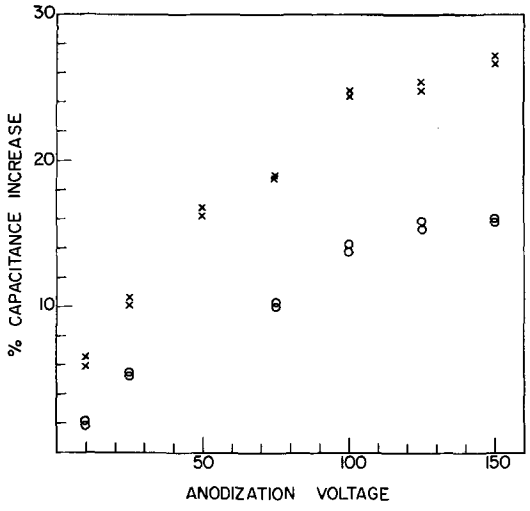

Fig. 3. Equilibrium capacitance increase due to heat-treatment at 400° in air as a function of oxide thickness (50 Hz data): x relative to unheated capacitance; o relative to reanodized capacitance after heat-treatment.

of log σ_d/σ_1 is larger the thinner the film. It has previously been stated that the percentage capacitance change due to heat-treatment is independent of film thickness for anodization voltages above 50v, but that the change is less for thinner films. This behavior is shown in detail in Fig. 3 which shows the equilibrium percentage capacitance change after heating at 400° in air relative to both the unheated capacitance and also to the capacitance after 4 hr of reanodization at the formation voltage subsequent to heat-treatment. The former thus includes the effects of both the conductivity gradient and the permanent increase in dielectric constant, whereas the latter includes only the effect of the conductivity gradient. The reanodization time is approximately that necessary to remove the effects of the conductivity gradient; no attempt was made to test each sample for the precisely appropriate time. The capacitance increase is a smooth function of film thickness, with a tendency to flatten out toward the greater thicknesses. As a first order approximation it appears that a certain portion of the thickness does not participate in the establishment of the equilibrium gradient, and that this inert portion assumes a relatively greater importance with decreasing film thickness. The reason for this behavior is obscure at present.

In summary, the results of these experiments are in good agreement with the theory of an exponential conductivity gradient. The constancy of $d(1/C)/\ln \omega$ with thinning indicates that there are no significant dielectric losses in the outer third of the heat-treated oxide. The agreement between the calculated and observed values of tan δ for the thinned oxide depends entirely on the validity of [6] which was derived specifically from the proposed model. When thinned, heat-treated samples are reheated, the reproducible decrease in series capacitance and tan δ is a necessary consequence of the theory and indicates that the heat-treatment results in no significant physical damage to the oxide. These factors, together with those discussed in the earlier papers in this series, represent practically irrefutable evidence that there is a monotonic, exponential distribution of dielectric losses in the heat-treated oxide. Previously discussed results lead to the conclusion that these losses are most likely due to electronic conduction related to the stoichiometry of the oxide.

Acknowledgment

The technique of following the dielectric properties as a function of oxide thinning was suggested by Dr. Charles A. Steidel of the Bell Telephone Laboratories.

Manuscript received Jan. 11, 1967; revised manuscript received Feb. 23, 1967.

Any discussion of this paper will appear in a Discussion Section to be published in the June 1968 JOURNAL.

REFERENCES

1. D. M. Smyth, G. A. Shirn, and T. B. Tripp, *This Journal*, **111**, 1331 (1964).
2. D. M. Smyth and T. B. Tripp, *ibid.*, **110**, 1277 (1963).
3. M. A. Heine and M. J Pryor, *ibid*, **110**, 1205 (1963).
4. G. C. Wood and A. J. Brock, *Nature*, **209**, 773 (1966).
5. J. J. Randall, Jr., W. J. Bernard, and R. R. Wilkinson, *Electrochim. Acta*, **10**, 183 (1965).
6. R. Dreiner and J. Schimmel, *This Journal*, **111**, 453 (1964).
7. D. M. Smyth, G. A. Shirn, and T. B. Tripp, *ibid.*, **110**, 1271 (1963).
8. W. J. Bernard, *ibid.*, **108**, 446 (1961).

Electroluminescence of Lead-Containing Zinc Sulfide Films

Hitoshi Sakamoto

Research Department, Dai Nippon Toryo Company, Ltd., Chigasaki, Kanagawa, Japan

ABSTRACT

Electroluminescent thin films of ZnS:Cu,Pb,Cl are prepared by means of vacuum evaporation followed by post-firing. Lead incorporation is found to have a great effect on luminosity and emission spectrum. Brightness wave form is usually asymmetric with respect to each half cycle of applied a-c voltage, and as negative d-c bias is superposed on it, a new emission peak appears. It might be concluded from several experimental results that the asymmetry is due to inhomogeneities in copper distribution and quenching centers, and the new peak is caused by a d-c mechanism, perhaps by tunneling. An activation energy for copper diffusion in the films is obtained as 0.61 ev using a luminescence method.

Up to now, several papers (1-5) have been presented on the electroluminescence (EL) of thin films, where mechanisms of EL are discussed. Vlasenko and others (1) concluded that the excitation of EL in ZnS:Mn film is due to an impact mechanism. Thornton (3) proposed a mechanism of excitation by the injection of minority carriers in p-n junctions, which are randomly distributed in the volume of phosphors. According to Goldberg and Nickerson (4), heterojunctions are considered to be responsible for excitation mechanisms. However, the experimental data from which they reached their conclusions might

cover only part of the truth. Since experimental data depend on the preparation of luminescent films, inconsistencies in the above-mentioned works may be due to the different samples investigated. Most of them were Mn-activated phosphors, presumably because they are easier to prepare than phosphors containing no manganese. Since, even in powder cases, Mn-activated phosphors behave differently in electroluminescence and photoelectroluminescence from phosphors otherwise activated, it is doubtful that mechanisms in Mn-activated phosphor apply to the general phenomena of EL in fluorescent thin films of the ZnS:Cu,Cl series. To probe these ambiguous points, the author first tried to improve the luminescence properties and preparative reproducibilities of luminescent films of the ZnS:Cu, Cl series and found that lead incorporation in the films had remarkable effects on brightness, emission color, and reproducibility of the films.

This paper deals with experimental results and discussions on the preparation and EL properties of the ZnS:Cu,Pb,Cl films mentioned above.

Preparation

Thin luminescent films of ZnS:Cu,Pb,Cl were made by a two-step process of evaporation and postfiring similar to that described previously (6, 7). In evaporation, for the first 10 min a substrate was kept at 200°C by a nichrome heater attached near the rear surface of the substrate; after turning off the current of the heater, the substrate was heated slightly by radiation from the evaporation source-heater. The equilibrium temperature of the substrate was about 80°C. This method of heating substrates was most adequate to obtain tightly adherent and transparent films of good performance in this work. The evaporation was done in 60 min at an average of about 300 Å/min. The postfiring was done at a fixed temperature between 500° and 700°C for 10 to 20 min in an argon atmosphere. Cells with about 1 cm^2 area were used in the following investigation. Specimens were composed of tin-oxide coated Pyrex or quartz, a luminescent film about 2μ thick, and an aluminum film evaporated directly on the film. The original phosphor powders used as starting material were prepared in the usual way so that necessary contents of copper, lead, and chlorine were included in the host crystals of ZnS. X-ray and electron diffraction patterns with these films revealed that they have cubic structure with some traces of hexagonality, and the degree of crystallization is increased with postfiring.

Results

Luminescent properties.—In Fig. 1 effects of lead incorporation are shown on films postfired at 600°C for 20 min. Figure 1(a) is a comparison of emission spectra between ZnS:Cu,Cl and ZnS:Cu,Pb,Cl films made from powder phosphors initially activated with 2 x 10^{-3} g/g ZnS of Cu and with the same amount of Pb, and Fig. 1(b) shows the effect of Pb contents added to the phosphor on brightness and on the ratio of the blue to yellow component of luminescence of the film, where excitation is with an a-c field of 5 kc, 30v. The color components were measured through the "blue" and "visual brightness" filters of a Spectra brightness spot meter. It is obvious that in the ZnS:Cu,Pb,Cl films the blue component is more remarkable than that of the ZnS:Cu, Cl film, and both the brightness and the blue component increase with increasing Pb concentration of the original powder phosphors. The luminous intensity of the film with the concentration of 10^{-3} g/g ZnS of lead is approximately four times as high as when no lead was added. The following investigations were made with the films prepared in the same way as those used in Fig. 1 except where otherwise noted.

From the thermoluminescence shown, together with the temperature dependence of EL in Fig. 2, the film

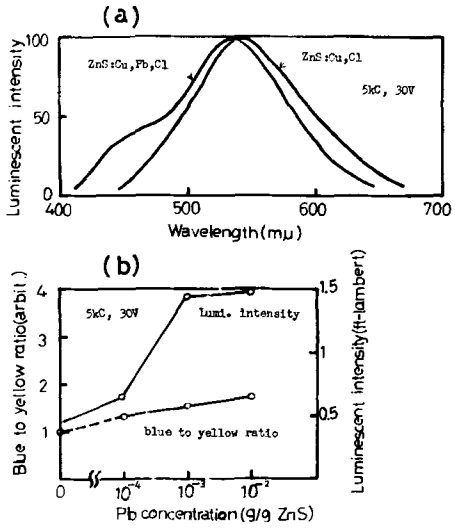

Fig. 1. Effects of lead-incorporation (a) on emission spectrum, and (b) on brightness and on the ratio of blue to yellow components of EL.

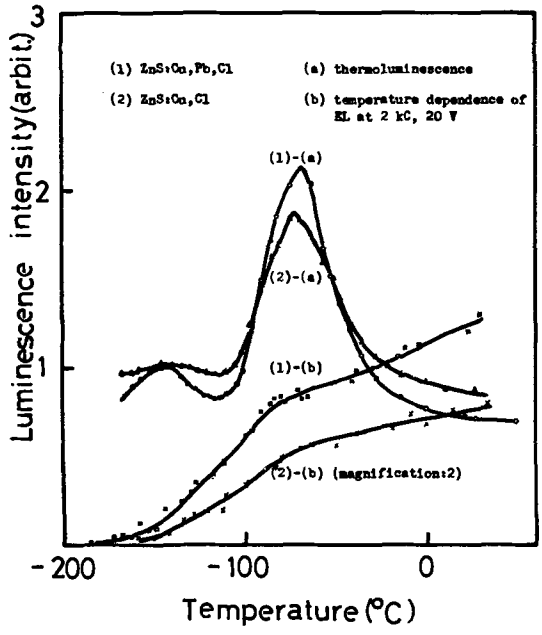

Fig. 2. Thermoluminescence and temperature-dependence of EL in a ZnS:Cu,Pb,Cl film compared with those of a ZnS:Cu,Cl film.

is found to have two peaks corresponding to 0.28 and 0.43 ev, respectively, if a frequency factor is assumed as 10^{10} sec, which is similar to those of the original powder phosphor. Although no signs showing the existence of deeper traps are perceptible from the thermoluminescence, the film shows luminescence with rather longer persistence under uv excitation, compared with the powder; this becomes more appreciable with lower lead content. In the absence of lead, the glow curve is not changed substantially except that in most cases the peak corresponding to the shallower trap becomes lower. The voltage-dependence of the luminescence of the film fits the well-known relationship (8) $B = Bo \exp(-C\sqrt{V})$ which is very familiar with conventional EL, within three orders of magnitude or more of the variation of luminescence intensity. The film has only weak d-c response, except when d.c. is superposed on an a-c field as seen later.

D-C current-voltage characteristics.—Evaporated films without any posttreatment have peculiar d-c

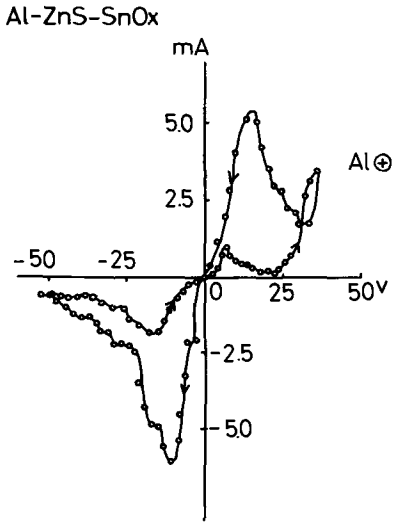

Fig. 3. Current-voltage characteristics of an evaporated film

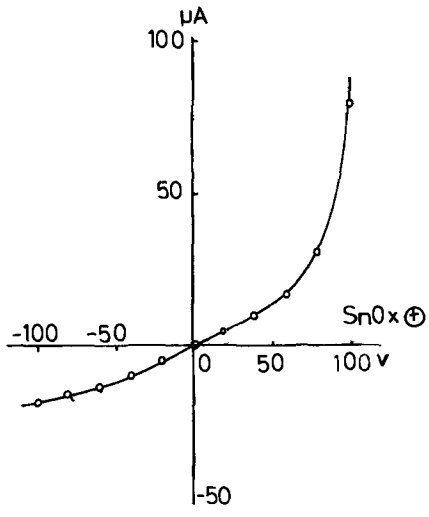

Fig. 4. Typical current-voltage relationship of a postfired luminescent film.

current-voltage characteristics. Figure 3 shows such a relationship. As voltage applied across a film which has a fairly high resistivity at first is gradually increased, at a critical voltage of some tens of volts a rapid increase occurs in current through the film. In the film thus made conductive, a negative resistance region appears on tracing the curve of current-voltage characteristics, both for increasing and decreasing voltage. This is rather noisy and varies in extent from film to film or in repeated measurement on the same sample, but is a pronounced and reproducible phenomenon, independent of the polarities of the applied voltage. However, the negative resistance characteristics should not be considered as related directly to luminescence phenomena of the film nor to any specific activator, since the phenomenon was observed regardless of the kind of activators and it disappears after postfiring. There are some cases where, at the initial application of voltage, heat-treated films show rather low resistivity of the order of hundreds of ohms between the metal and tin oxide electrodes; after such structural defects as pin holes and cracks, which cause leakage current, have been burnt out by short-circuit current through them, they become luminescent and highly resistive (several megohms). This does not mean such an essential "forming" as reported by Goldberg (4). Evidence for this view is given by the fact that, as an insulating layer made up of various materials, *e.g.*, SiO, pure ZnS, or organic materials, are put in between the film and the aluminum electrode, luminescence sets in at the first application of voltage without any forming procedures in all cases. The postfired luminescent films show more or less rectifying properties in their current-voltage relationship as seen from Fig. 4 where the direction of greater current or the forward direction is usually such that the glass side is positive. The extent of the current rectification and the behavior of the over-all current flow vary appreciably in different specimens because of slight variations by unknown factors during preparation.

Brightness wave form.—Figure 5(a) depicts a typical waveform of luminescence when a specimen is excited with a sinusoidal a-c field. It can easily be seen that at the positive polarity of voltage on the aluminum electrode, emission occurs strongly, having two peaks, P_1 and P_1', and at the reverse polarity it becomes negligible. In some other cases the emission at the negative polarity is also detectable but rather weak. Asymmetric brightness waveforms were observed also by Thornton (9) in a ZnS:Cu,Cl film, which, together with clipping or d-c bias of the applied voltage, was used to confirm separability of ex-

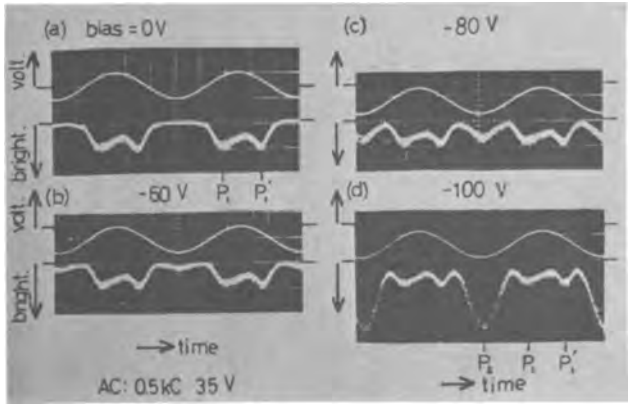

Fig. 5. Typical brightness wave forms under excitation with sinusoidal a-c field with and without a d-c bias on it. Positive voltage on the aluminum electrode is to the top of the pictures and zero levels of the voltage and brightness are marked by short-lines drawn beside them.

citation and recombination steps in EL. In this work, a small pulse superposed on the sinusoidal voltage was used to confirm this separation, which technique is familiar to workers in this field (10). The experiment leads to a conclusion similar to Thornton's, that excitation and recombination take place separately, the former occurring as the metal electrode is negative prior to the latter, that is, such a delayed emission occurs as proposed by Waymouth and Bitter (11) and others (12).

A negative d-c bias on the Al electrode superposed on sinusoidal voltage makes no change in the brightness waveform in the region of rather low bias, but, as seen from Fig. 5(b) to (d), at higher bias voltage, a new peak P_2 becomes pronounced, whereas the other peaks P_1 and P_1' remain almost unchanged. Figure 6 features the bias-voltage dependencies of P_1, P_2, and d-c current I_{dc} through the film at 0.5 kc a-c field. This behavior does not change in essence with other frequencies and voltages in the a-c field. It can be seen that both the peak P_2 and the d-c current I_{dc} vary nearly exponentially with the bias voltage. The dependencies of P_2 and I_{dc} on temperature are rather small as shown in Fig. 7, in great contrast to those of P_1 and P_1'. On the other hand, a positive d-c bias also causes a new peak in phase with the a-c voltage although it is so small that it is hardly distinguished from peaks P_1 and P_1' even at a much higher bias-voltage than in the case of the negative bias. Neither positive nor negative bias gives any

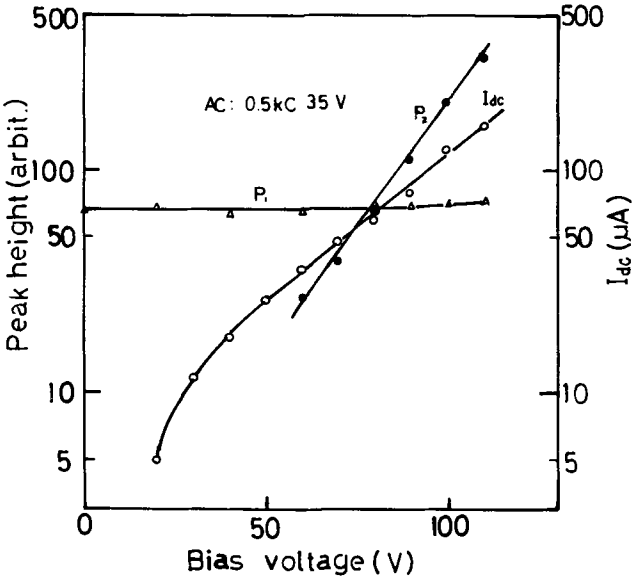

Fig. 6. Bias-voltage dependence of P_1, P_2, and I_{dc}

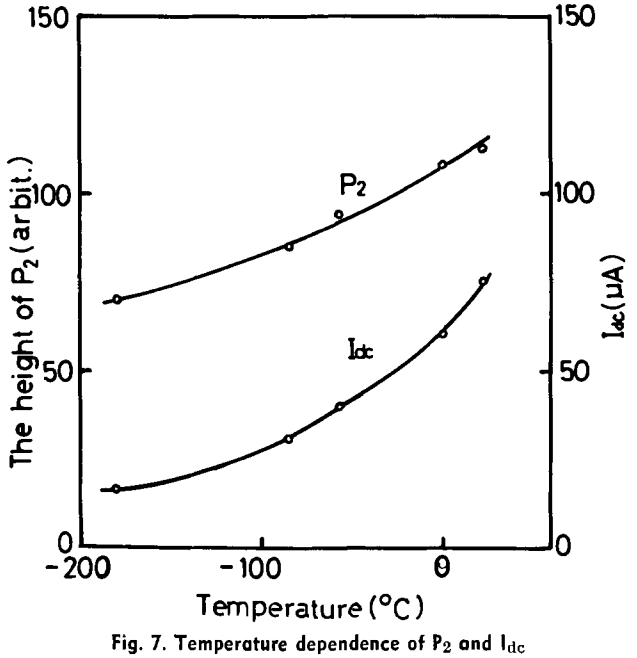

Fig. 7. Temperature dependence of P_2 and I_{dc}

drastic influence on the height and on the phase of P_1 and P_1', contrary to the result in the above reference (9). A small pulse superposed on a-c voltage also gives a pronounced influence on the peak P_2. The behavior, however, is quite opposite to those of P_1 and P_1', that is, there cannot be observed any sign to show the separability of excitation and recombination. In the build up of EL there is also present a contrast between P_1 and P_2. Peak P_2 does start without any build up, whereas peak P_1 needs several cycles to get its steady-state magnitude, as is well known in usual intrinsic EL (13).

Cathodoelectroluminescence or electrocathodoluminescence.—Some measurements were carried out to examine the effects of electric field on cathodoluminescence. Figure 8 illustrates the brightness waveforms of cathodoluminescence modified by a sinusoidal field. The field quenching of cathodoluminescence with positive polarity on the glass side is quite marked, so that the total effect of the modification results in quenching of cathodoluminescence. On varying the intensity of the electron beam, the brightness waveform changes from the modified form to that of

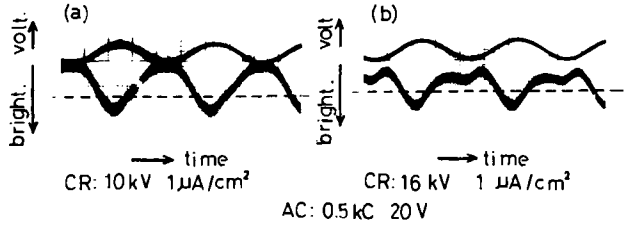

Fig. 8. Brightness waveforms of cathodoluminescence modified by a-c field. Dashed lines display the zero field cathodoluminescence level.

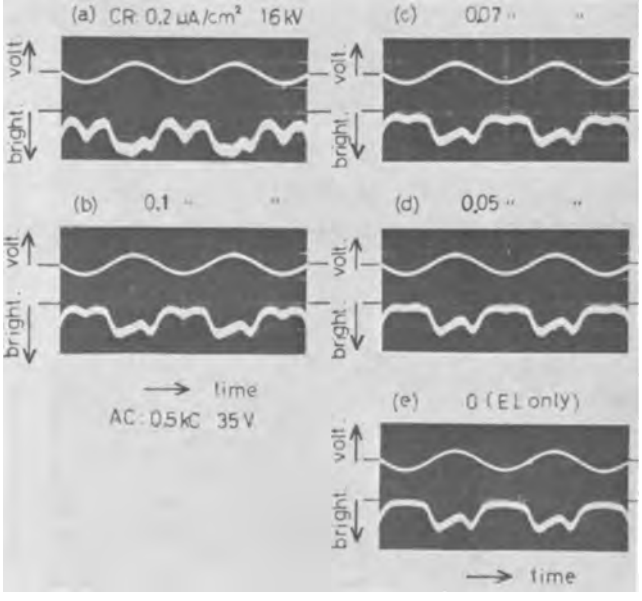

Fig. 9. Brightness waveform of cathodoluminescence superposed with EL, as both luminescences have comparable intensities. Positive voltage on the aluminum electrode is to the top of the pictures and zero levels of the voltage and brightness are marked by short lines drawn beside them.

electroluminescence. In Fig. 9 there are shown from (a) to (e) brightness waveforms with different beam intensities. As EL is competitive to cathodoluminescence, both field modified and EL waveforms can be observed to exist together, and with increasing cathodoluminescence, the modified pattern comes to dominate the over-all wave form. It is obvious that no sign of cathodoelectroluminescence appears, that is, EL is not stimulated to any degree by the electron beam, since the height of the EL peak does not vary to a noticeable degree, as seen from Fig. 9.

Copper distribution.—As is described in the Discussion, the copper added as an activator is expected to be distributed unhomogeneously throughout the films and to cause some asymmetric behavior in luminescence. The expectation gives the author a motivation to investigate the problem of copper diffusion into the film. Experiments were performed by means of a simplified technique as stated below.

Assuming that the number of luminescence centers, N, is proportional to copper-concentration $C(x)$, which is expressed as a function of the distance x from the top surface of the film, the total luminescence output B is approximately given as

$$B = \int_0^l A\eta\, C(x) \frac{dE}{dx} dx = A\eta \int_0^l C(x) \frac{dE}{dx} dx \simeq A\eta Em \int_0^l C(x)\, dx \quad [1]$$

where l is the film thickness, η is the efficiency of the center, dE/dx is the absorbed energy per unit length,

Em is the mean value of dE/dx in the film, and A is a constant. On the other hand, Fick's second law concerning diffusion yields the following equation by the assumption of the boundary conditions that $C = 0$ at $t = 0$, $C = C_1$ at $x = 0$, and $\partial c/\partial x = 0$ at $x = l$,

$$1 - \frac{\overline{C}}{C_1} = \frac{8}{\pi^2} \sum_{m=0}^{\infty} \frac{1}{(2m+1)^2} e^{-D\left(\frac{2m+1}{2l}\pi\right)^2 t} \quad [2]$$

where $\overline{C}$ is the mean value of the copper concentration at time t, which is equal to $\frac{1}{l}\int_0^l C(x,t)\,dx$, and C_1 is the saturated copper concentration in the equilibrium state. Using Eq. [1], $\overline{C}/C_1$ can be substituted by $B(t)/B(\infty)$ which is determinable experimentally.

In order to eliminate the effects of promoted crystallization by heat-treatment for diffusion, which results in increasing η, specimens prepared as follows were used. First, films 2μ thick were made up on quartz substrates by evaporation of a manganese-activated powder phosphor, followed by post-heating; then metallic copper was evaporated on the films to be diffused into them by different heat-treatment. For these specimens, $B_{Cu}(t)/B_{Mn}(t)/B_{Cu}(\infty)/B_{Mn}(\infty)$ can be decided instead of $B(t)/B(\infty)$, where the subscripts of Cu and Mn mean luminescence intensities due to copper and manganese, respectively. As an excitation source, cathode rays of 30 kev were used, where the variation in dE/dx is calculated as 20% in the films according to a previous work (14); this may be ignored as compared with other gross assumptions. The brightnesses of the specimens heated for 30 min and 2 hr were taken as $B(t)$ and $B(\infty)$, respectively. For the Cu-emission an interference filter with a transmission peak at 480 mμ was used, while the Mn emission was measured at 584 mμ through another interference filter. The result is shown in Fig. 10, in which the straight line expresses the relation

$$D = 2.5^{-7} \exp\left(-\frac{0.61}{kT}\right) \quad [\mathrm{cm^2/sec}] \quad [3]$$

where the activation energy for copper diffusion is obtained as 0.61 ev, that is, 14 kcal/mole. From this result, by heat-treatment for 30 min at 700°C, copper concentration at the rear, is calculated to reach 68% of that of the front. Since the films examined for luminescence properties were made from finished

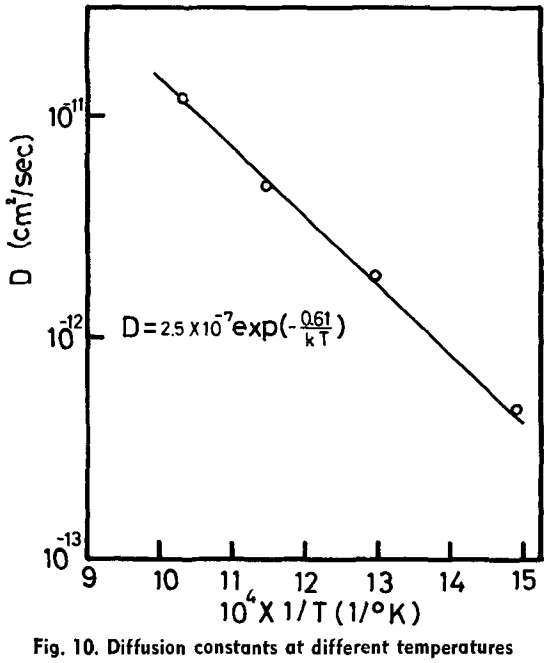

Fig. 10. Diffusion constants at different temperatures

Table I. Variations of copper concentration in a film during evaporation

Sampling	Copper concentration, g/g ZnS	
	ZnS:Cu,Pb,Cl	ZnS:Cu,Cl
In the film evaporated		
From the beginning to 10 min	1.17×10^{-4} (17%)	2.10×10^{-4} (27%)
Between 10 and 20 min	1.70×10^{-4} (25)	—
Between 20 and 30 min	3.00×10^{-4} (44)	2.92×10^{-4} (37)
In the residual in the source		
After evaporation for 30 min	9.75×10^{-4} (143)	—
Found in the original powder phosphor	6.82×10^{-4} (100)	7.80×10^{-4} (100)
Added in the original powder phosphor	20×10^{-4}	20×10^{-4}

powder phosphors, copper is supposed to be more homogeneously distributed than expected from the above result, so far as the luminescence center is concerned. Barriers due to copper, however, still seem to have some distributions.

Discussion

The evaporated films in this experiment are somewhat colored, which coloring becomes more pronounced as the lead content increases and gradually diminishes by postfiring. The coloring is attributed either to metallic copper, lead, or zinc, produced during evaporation by decomposition of the components of the powder phosphor. Table I shows how copper concentration in a film varies during evaporation. It is of note that the content of evaporated copper in a ZnS:Cu,Pb,Cl film varies markedly during evaporation and a decrease occurs in the copper concentration from the top to the rear surface of the film. Together with this, in view of the fact that an absorption appears in the vicinity of 450 mμ (15), which is characteristic of copper and becomes stronger with lead incorporation in the phosphor, the layer might be considered to be composed largely of metallic copper. It is also seen that the variation in the copper concentration also occurs in the absence of lead, but it is appreciably moderated The increase in the brightness of EL in the film containing lead would be considered to have some connection with the existence of this copper-rich layer, which might favor the formation of a potential barrier necessary for the excitation of EL. The behavior of lead which promotes the blue component of luminescence was reported also by Homer *et al.* (16) with powder phosphors doped highly with copper. Since any sample does not show remarkable emission by excitation either with electric field or with ultraviolet if only lead is incorporated, lead may act only as an auxiliary element to promote the blue emission of copper at the expense of the green, instead of contributing as its characteristic emission center. The blue center of copper was proposed by Blicks *et al.* (17) to be related to the association of the interstitial and substitutional copper. A situation like this might arise in this case by the displacement of the substitutional copper atoms which are forced out of their normal positions by the lead incorporation.

The experimental results on voltage-dependence, pulse-superposition, and build-up lead to the following conclusion. The same mechanisms as in the conventional a-c EL are available to interpret the behaviors of peaks P_1 and P_1'. The impact mechanism by accelerated electrons in potential barriers, commonly believed for excitation, seems to be most relevant. Since any cases without rather high copper concentration failed to yield good EL films, it does not seem unreasonable that a Cu_2S-phosphor contact is responsible for the potential barrier for excitation (18). The asymmetric brightness waveform might be considered to be caused by the following situations. In the region near the tin oxide electrode, the barrier is hardly formed owing to rather low copper concen-

tration as described before; moreover, as revealed in the results of electrocathodoluminescence, this region is rich in quenching centers, which might be produced due to some contaminations of the film by a reaction with the tin oxide or with other contaminants during evaporation and postfiring. The asymmetry was not remarkable in a film well made by alternately repeating evaporation and postfiring several times to get a desirable total thickness. This supports the above consideration because in such a film the barriers and the luminescence centers seem to be more uniformly distributed. On the other hand, from the facts that peak P_2 is not a delayed emission, that its temperature dependence is so little compared with those of the peaks P_1 and P_1', and its occurrence does not give any significant effects on the other peaks, the emission of the P_2 is thought to be due to a different excitation mechanism from those of the others. Tunneling of electrons with high energy through a barrier from the metal could be a part of a possible mechanism. The polarity dependence of peak P_2 may be thought to be related to the rectifying properties in the I-V curve, which is caused by asymmetric contacts between the film and the electrodes. As for the contacts, some dead layer is supposed to be built up in the vicinity of the tin oxide since the resistivity of the conductive glass was usually raised by some orders of magnitude by forming the luminescent film on it, while, on the aluminum side, the deposited copper and some oxide layer are expected to exist. It is, however, still obscure how these factors act on the rectifying properties in the I-V relationship. The experiments on electrocathodoluminescence indicate that the EL is not enhanced to any degree by cathode rays. This behavior is similar to that of powder phosphors except for Mn-activation (19). Although clear elucidation of the mechanisms responsible for the negative resistance is difficult unless further experiments are explored, it has now been found that adsorbed moisture gives a remarkable effect on the negative resistance.

Acknowledgment

The author expresses his sincere thanks to Mr. H. Shigemura for industrious assistance throughout this work. He is also indebted to Dr. T. Toryu for useful discussions.

Manuscript received Aug. 11, 1966; revised manuscript received Nov. 8, 1966. This paper was presented in part at the San Francisco Meeting, May 9-13, 1965.

Any discussion of this paper will appear in a Discussion Section to be published in the June 1968 JOURNAL.

REFERENCES

1. N. A. Vlasenko and A. M. Yarem, *Optika i Spektroskopiya*, **18**, 467 (1965).
2. S. Namba and M. Takeda, *Oyo Buturi*, **32**, 609 (1963).
3. W. A. Thornton, *Phys. Rev.*, **116**, 893 (1959); **122**, 58 (1961), *This Journal*, **108**, 636 (1961).
4. P. Goldberg and J. W. Nickerson, *J. Appl. Phys.*, **34**, 1601 (1963).
5. W. J. Harper, *This Journal*, **109**, 103 (1962).
6. C. Feldman and M. O'Hara, *J. Opt. Soc. Am.*, **47**, 300 (1957).
7. W. A. Thornton, *J. Appl. Phys.*, **30**, 123 (1959).
8. P. Zalm, G. Diemer, and H. A. Klasens, *Philips Research Rept.*, **10**, 205 (1955); *This Journal*, **104**, 130*C* (1957).
9. W. A. Thornton, *Phys. Rev.*, **123**, 1583 (1961).
10. P. Zalm, *Philips Research Rept.*, **11**, 353 (1956).
11. J. F. Waymouth and F. Bitter, *Phys. Rev.*, **95**, 941 (1954).
12. W. R. Watson, J. J. Dropkin, and A. T. Halpin, Abstract No. 38, Paper presented at the Chicago Meeting, May 1954.
13. C. H. Haake, *J. Appl. Phys.*, **28**, 245 (1957).
14. H. Sakamoto and S. Tanaka, *Oyo Buturi*, **29**, 412 (1960).
15. M. P. Givens, "Solid State Physics," Vol. 6, p. 313, Academic Press Inc., New York, London (1958).
16. H. H. Homer, R. M. Rulon, and K. H. Butler, *This Journal*, **100**, 566 (1953).
17. H. Blicks, N. Riehl, and R. Sizmann, *Z. Physik*, **163**, 594 (1961).
18. W. W. Piper and F. E. Wiliams, *Brit. J. Appl. Phys. Suppl.*, **4**, S39 (1955).
19. D. A. Cusano, "Luminescence of Organic and Inorganic Materials," p. 494, John Wiley & Sons, Inc., New York (1962).

A New Masking Technique for Semiconductor Processing

D. M. Brown, W. E. Engeler, M. Garfinkel, and F. K. Heumann

General Physics Laboratory, General Electric Research and Development Center, Schenectady, New York

ABSTRACT

A new masking method utilizing an intermediate integral Mo film is described. The Mo mask is a practical method for etching very high resolution patterns in passivating dielectric films including films of silicon nitride which heretofore have been unmanageable. The Mo film has much better masking properties than the photoresists now used.

For a number of years the semiconductor industry has been dominated by a single material, Si, and by its oxide, SiO_2. The diffusion masking and passivating properties of thermally grown SiO_2 and the ability to produce an etched design pattern in this oxide by photoengraving using photoresist (KPR) techniques has been central to the semiconductor process technology. Recently, however, a new material, silicon nitride (Si_3N_4), has been introduced which promises to perform not only many of the functions previously reserved exclusively for the oxide, but which may also be useful for other tasks as well (1). It is, for example, a more effective diffusion mask since it is less permeable than SiO_2 to standard semiconductor dopants (2). In addition, it is more impervious to alkali metals than SiO_2 (3). Because alkali ion drift in SiO_2 is one of the main causes of semiconductor device instability, silicon nitride passivation should, therefore, improve device stability. Since Si_3N_4 has a higher degree of chemical stability than SiO_2 and is not as easily penetrated by water (4) and other atmospheric gases, it should generally have better passivation properties.

A problem exists, however; Si_3N_4 has a very, very low reactivity to known solvents, being only very slowly dissolved by concentrated (48%) HF. Several

minutes are required to remove a few hundred angstroms. Chemical etching of this type lifts the photoresist masking films in current use from the nitride before the unmasked nitride regions can be removed by the etch. Nitride patterns are thus difficult to form.[1]

This adherence problem was also originally observed in SiO_2 processing. It was solved for SiO_2 by using a less reactive etch. This etch commonly referred to as "buffered HF"[2] increases the durability of the photoresist sufficiently to enable the etch to dissolve the SiO_2 before the resolution of the mask pattern is destroyed. For thick layers of SiO_2, however, a single layer of KPR in buffered HF is marginal. These solutions are practicable for SiO_2 because of its rapid dissolution rate in HF. These solutions are not practical for Si_3N_4. The problems of dissolution rate and photoresist life are brought into sharper focus by the data given in Table I which compares dissolution rates of SiO_2 and nitride coatings in HF and buffered HF and photoresist lifetimes on SiO_2 and Si_3N_4 when in these acid solutions. For example, the time required to etch 1000Å of Si_3N_4 is clearly beyond the endurance of a KPR mask. Figure 1 shows how concentrated HF destroys a KPR film on a nitrided wafer. The KPR pattern is severely cracked after only 5 sec in concentrated HF which destroys its masking ability. Because of these problems, an improved masking technique would be desirable. This report discusses results achieved by a new technique for masking, which utilizes an integral layer of Mo. This intermediate layer of Mo, which is not soluble in concentrated HF adheres to the nitride film, serves as a mask during the nitride etching, and provides an excellent base for the adhesion of the photoresist film.

Experimental Techniques and Results

A silicon wafer was prepared and a layer of pyrolytic Si_3N_4 deposited on its surface at 1000°C. A layer of Mo was then evaporated onto the wafer by electron beam heating, in a high vacuum oil-free vacuum system. A layer of KPR was then applied, and a pattern developed in this material. The photoresist was baked at 200°C for 2 hr in dry nitrogen. The wafer was etched using a Ferricyanide etch (3). This etch quickly removed the molybdenum that remained unprotected by the photoresist. The KPR pattern was thus transferred to the Mo layer. The wafer was then etched in concentrated HF until the Si_3N_4 not covered by the photoresist and Mo was removed. Seven minutes of etching were required. The Mo and photoresist were removed by etching in hot cleaning solution.

Figures 2 and 3 show some of the results achieved by this technique. Figure 2 shows an over-all view of a pattern formed in a 1000Å (blue) Si_3N_4 film. The pattern dimensions are 0.028 x 0.008 in. The smallest hole in the pattern is 0.00029 in. A comparison be-

[1] Silicon nitride etching by hot phosphoric acid using silicon dioxide as a mask has recently been shown to be a useful technique (5).

[2] 10 parts NH_4F (40%) to one part conc. HF.

[3] 92g $K_3Fe(CN)_6$, 20g KOH, 300g H_2O; other etches may also be suitable.

Table I. Film etch rates

	In concentrated HF, Å/min	In buffered HF, Å/min
Silicon dioxide	50,000	1000
Silicon nitride*	150	15
Silicon oxy-nitride**	3,000	125

Diffusion mask	Time to etch through mask In: Buffered HF, min	Conc. HF	KPR Photoresist Life† In: Buffered HF, min	Conc. HF, min
5000Å SiO_2	5	6 sec	10	—
1000Å Si_3N_4	66	7 min	—	<½

* Si_3N_4 films referred to here have been grown by the pyrolytic decomposition of silane (SiH_4) and ammonia (NH_3) gases at 1000°C. The etching properties of silicon nitride depend on the conditions for its formation and on subsequent heat-treatments.

** The silicon-oxy-nitride compound is prepared in the same manner as the silicon nitride except in this instance small amounts of O_2 are added to the ammonia and silane gas mixture (6).

† Photoresist life in the etching solution is defined as the approximate time it takes to lift the edges of the photoresist mask or crack the photoresist mask or for the etch to permeate the photoresist to an extent that destroys the resolution of the pattern.

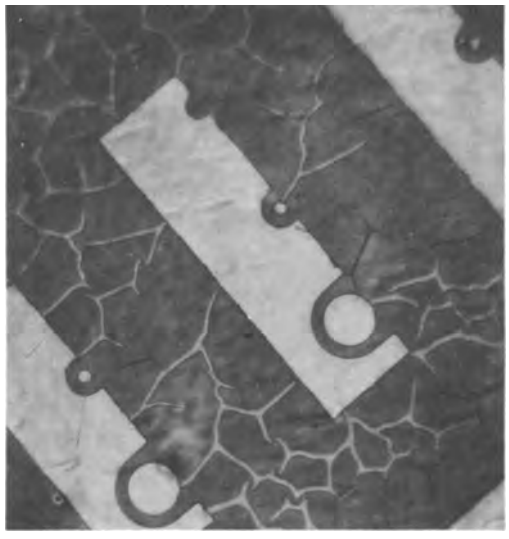

Fig. 1. Cracked KPR pattern on a silicon nitride film resulting from 5-sec immersion is concentrated HF. Dark regions are KPR and light regions are nitride.

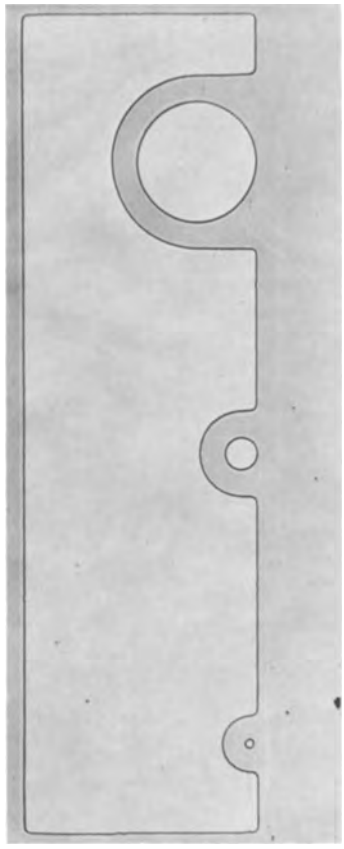

Fig. 2. Over-all pattern. Light regions are bare silicon. Dark region is nitrided silicon. The over-all pattern dimensions are 28 mils long by 8 mils wide; the holes are, respectively, 4 mils, 1.1 mils, and 0.29 mil in diameter.

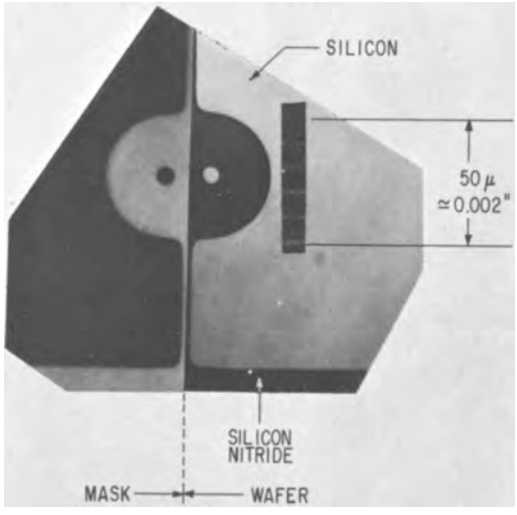

Fig. 3. Composite photograph showing a detailed view of the ¼ mil hole in Fig. 2; the mask is shown at the left and the resulting nitride pattern on the right. The scale divisions are 10μ (≃0.0004 in.) each.

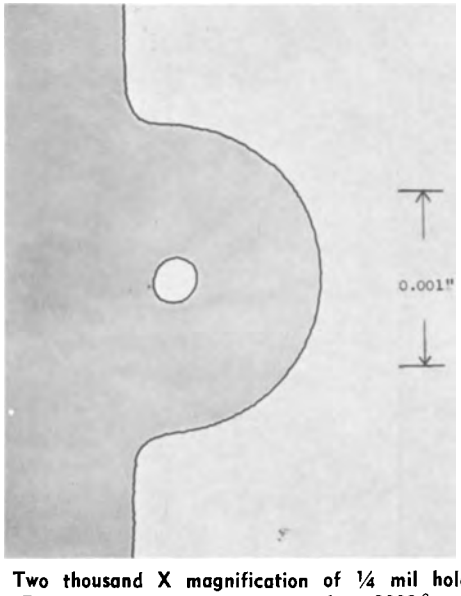

Fig. 4. Two thousand X magnification of ¼ mil hole shown in Fig. 3. Estimated resolution is better than 3000Å as determined by measuring the amount of "wiggle" in the straight line portions of the pattern.

tween the original mask and the smallest hole produced in the nitride is shown in Fig. 3. The mask is shown to the left of the nitride pattern. The resolution was estimated using Fig. 4 which is a a picture of the region shown in Fig. 3 using 2000X magnification. The edge of the pattern is straight to better than 3000Å. The size of the large half circle is faithfully reproduced. However, the small hole is elliptical in shape, being correct in length, but half a micron narrower than the mask. This is most probably due to incomplete etching of the Mo at the bottom of the photoresist hole during the Mo etching step.

In the above tests, the Mo layer was evaporated onto a hot substrate in high vacuum. Other tests were carried out using sputtered Mo films. The thickness of the Mo films ranged from 700 to 8000Å. The thicker films resulted in poorer edge definition due to the required increase in Mo etching time, but resolution comparable to the thickness of the films was achieved. For good definition, the thinner film is sufficient and results in the excellent resolution described above. None of the problems encountered during any of the process steps could be attributed to the Mo mask.

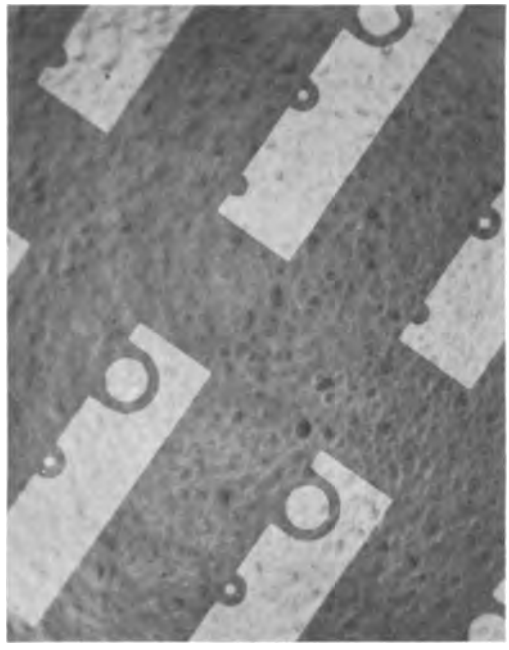

Fig. 5. Pattern etched in silicon nitride using Mo mask and 28 min of immersion in concentrated HF. There are no holes visible in silicon nitride regions which have been protected by the Mo mask. Silicon nitride is 3000Å thick (dark regions). Light regions are bare silicon.

Standard KPR problems associated with linked monomer residue, exposure control, and humidity were the most troublesome.

During our investigations it became apparent that, although KPR is not soluble in HF, the KPR film can be permeated and penetrated by this strong acid. This permeation may be the cause of many of the difficulties connected with KPR masking of SiO_2. If HF penetrates the mask, it will etch a pinhole in the oxide. Figure 5 shows the pattern formed in 3000Å of Si_3N_4 by using a Mo mask and etching in concentrated HF for 28 min. What is noteworthy here is the absence of pinholes in the Si_3N_4 even after the long immersion in concentrated HF. This indicates that the Mo film is continuous, pinhole-free, and insoluble in HF.

Conclusion

This investigation has shown that Mo masking techniques can reproduce high resolution patterns in Si_3N_4 films ranging in thickness from 500 to 3000Å. Furthermore, the nitride regions covered by the Mo film appear to be free of holes even after long immersions in concentrated HF.

It is important to emphasize that KPR sticks extremely well to Mo, and the Mo etching step, which only takes a few seconds, does not damage the KPR mask. This means that there is a very high probability that the pattern and resolution of the original photo-

Table II. Mo mask process steps

1.	Silicon nitride coating	Any thickness without cracks and pinholes is workable.
2.	Mo deposit	Evaporated or sputtered* Mo films. About 1000Å or thicker is suitable, depending on the desired resolution.
3.	Photoresist	Standard KPR techniques.
4.	Mo etching	A few seconds in ferricyanide etch, depending on thickness. The etch rate of the Mo film in this etch is about 150Å/sec.
5.	Silicon nitride etching	Concentrated (48%) HF.
6.	KPR and Mo removal	Hot cleaning solution, or other methods.

* Electron beam evaporation in an ion pumped oil free vacuum system and "Triode" sputtering in Ar gas was used in this investigation.

mask is transferred to the Mo film which is insoluble and not permeable to HF. These combined properties of KPR on Mo and the durability of the Mo mask in HF eliminate the need for prolonging the lifetime of the photoresist in HF.

In summary, the molybdenum masking technique as outlined in Table II has been shown to be highly successful for etching patterns in pyrolytically formed silicon nitrides. The technique should be applicable for etching silicon dioxide patterns whenever the standard KPR or KMER techniques are marginal and particularly when prolonged etching can produce pinholes which are caused by the permeation of the photoresist by HF.

Acknowledgments

The authors wish to thank Gerry Gidley for coating many of the silicon wafers with Si_3N_4, Lloyd Keifer for building the triode sputtering apparatus, and George Charney for operating the sputtering and evaporation systems.

Manuscript received Feb. 8, 1967; revised manuscript received March 17, 1967.

Any discussion of this paper will appear in a Discussion Section to be published in the June 1968 JOURNAL.

REFERENCES

1. T. Maguire, *Electronics*, p. 156, Jan. 10, 1966.
2. V. Y. Doo, D. R. Nichols, and G. A. Silvey, Recent News Paper presented at the Buffalo Meeting of the Society, Oct. 10-14, 1965; Electronics Division Abstract 9.
3. J. V. Dalton, Paper presented at the Cleveland Meeting, May 1-6, 1966; Electronics Division Abstract 23.
4. F. M. Fowkes, T. E. Burgess, and G. Hutching, *ibid.*, Philadelphia, 1966; Electronics Division Abstract 175.
5. W. Van Gelder and V. E. Hauser, Recent News Paper presented at the Philadelphia Meeting October 9-14, 1966; Electronics Division Abstract 5.
6. F. Heumann, P. V. Gray, and D. M. Brown, To be published.

Some Properties of Vapor Deposited Silicon Nitride Films Using the SiH_4-NH_3-H_2 System

Kenneth E. Bean, Paul S. Gleim, and R. L. Yeakley

Texas Instruments Incorporated, Dallas, Texas

and W. R. Runyan

Texas Instruments Incorporated and Southern Methodist University, Dallas, Texas

ABSTRACT

The effects of process variables on the growth rate and properties of insulating films grown from a hydrogen-silane-ammonia mixture have been studied. Growth rate *vs.* $1/T$ is observed to have a break at 900°C, coincident with an observed amorphous-polycrystalline transition. Hardness, growth rate, and refractive index are found to move toward values appropriate for silicon as the per cent ammonia is reduced. The thermal expansion coefficient can be varied from approximately that of silicon to appreciably more by increasing the per cent ammonia. A variety of other properties, such as breaking strength and Youngs' modulus were also measured and are discussed.

Several methods for the synthesis of silicon nitride have been reported (1-8). While most of these are particularly applicable to large ceramic objects, some of them, for example the silane-ammonia-hydrogen reaction described here have proven satisfactory for thin film deposition.

The flow system employed for this work was quite conventional and the reactor was a resistance heated horizontal cold wall unit. The substrates used for film deposition were single crystal silicon of various orientations. Vapor phase etching (9-11) (for example, HCl in H_2 at 1200°C) was used for substrate clean-up prior to these depositions. Omission of this step usually gave films with many visible defects, but it has been reported that, if the film is to be used as the insulator in an MIS transistor, etching is deleterious (12).

Morphology and Film Composition

Films deposited at temperatures below 900°C[1] appear amorphous and show no x-ray diffraction lines. Between 900° and 1000°C some small crystallites grow over the surface, and above 1100°C they are almost continuous. Figure 1 shows representative areas from each of these temperature ranges. Others (1) have not reported the high crystallite concentrations at temperatures as low as 1100°. Emissivity correction of the temperature combined with higher deposition and flow rates used here could explain the difference. An enlarged view of the crystallites deposited at approxi-

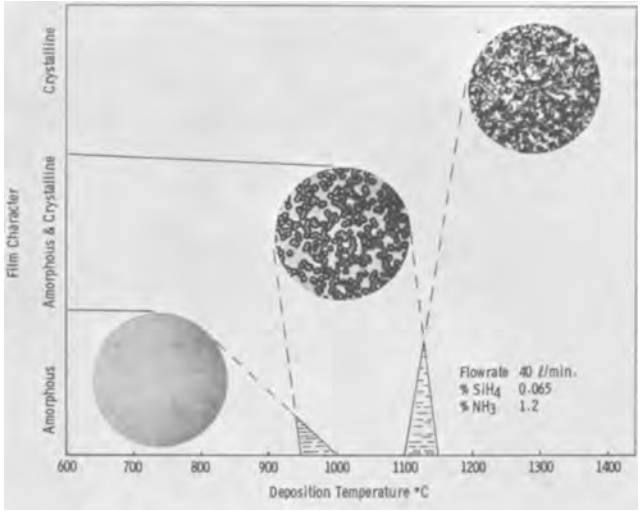

Fig. 1. Film character *vs.* deposition temperature

[1] Optical pyrometer-uncorrected.

Fig. 2. High temperature crystallites. Magnification 105X

mately 1200°C for an extended period of time is shown in Fig. 2. X-ray diffraction data indicate that these crystallites are α Si_3N_4.

The composition of the amorphous films has not yet been determined. There are some data based on neutron activation analysis which indicate a possible formula of $Si(NH_2)_4$ (13) (See, for example, ref. 4, p. 88). Direct chemical analysis of films prepared in a similar fashion indicated a composition of Si_3N_4 (14). Because of the varying physical properties that are observed as deposition conditions are changed, it seems probable that the actual amorphous film composition can be varied over rather wide limits from silicon rich to nitrogen rich. Additionally, those films deposited at lower temperatures may contain hydrogen as well as silicon and nitrogen.

Deposition Behavior

The effect of temperature on deposition rate is shown in Fig. 3. Log rate *vs.* 1/*T* plots are given for silane concentrations of 0.095 and 0.065% (all percentages are volume %) with a fixed concentration of 1.2% ammonia. The film growth rate increases rapidly with temperature up to about 900°C. Above this temperature the growth rate becomes less temperature dependent. The apparent activation energy below 900°C is approximately 52 kcal/mole, and above 900°C 6 kcal/mole.

There are three possible explanations for the apparent change in deposition rate.

1. The decomposition of the silane before it reaches the substrate as postulated by Doo *et al.* (1).
2. The difficulty of measuring film thickness by ellipsometer when crystallites start to cover the surface. The energy striking the surface is scattered, and

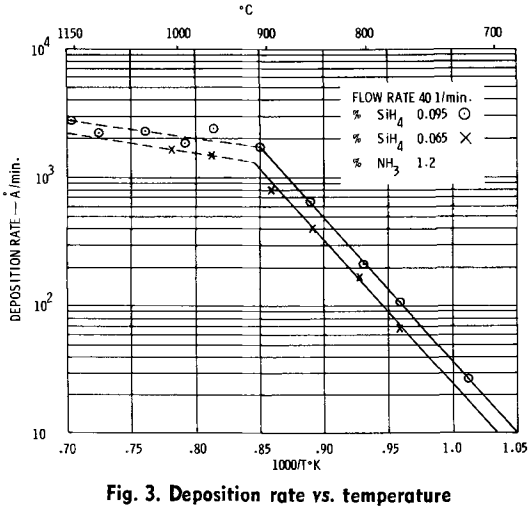

Fig. 3. Deposition rate vs. temperature

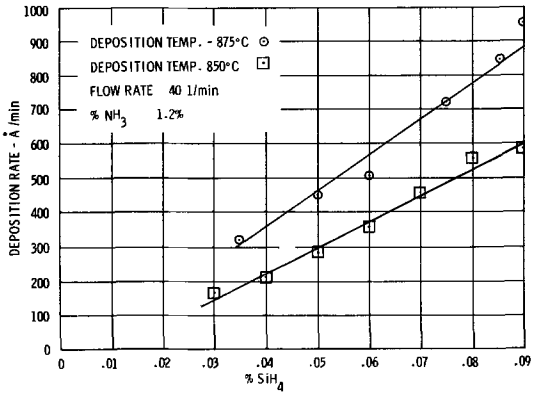

Fig. 4. Deposition rate vs. per cent SiH_4

only a portion is returned to the ellipsometer detector.

3. The decrease may mark the entrance into a diffusion controlled reaction which would be expected to be nearly temperature insensitive.

A plot of deposition rate as a function of per cent silane at deposition temperatures of 850° and 875°C is shown in Fig. 4. These data indicate a linear relationship of deposition rate with respect to silane concentration. Extrapolation of the curves indicate a deposition rate approaching zero at 0% silane as would be expected.

A plot of deposition rate as a function of ammonia concentration of 0.03, 0.065, and 0.095% silane is shown in Fig. 5. Note the 0.065% silane curve. Below an ammonia concentration of about 0.3% there is an increase in deposition rate due apparently to a change in the stoichiometry of the film. It is postulated that films deposited with an ammonia concentration below 0.3% and with a 0.065% silane concentration are silicon rich (see Index of Refraction discussion under optical properties). This corresponds to a silane-ammonia ratio of approximately 1:5. For the other two silane percentages shown, the increase in deposition rate occurs at nearly the same silane-ammonia ratio. It is also interesting to note that the deposition rate at very low ammonia concentration approaches the silicon deposition rate from pure silane in this reactor.

Films approximately 5000Å thick were deposited on silicon substrates for a study of the effect of thermal cycling. Film thicknesses were measured on the ellipsometer (15), the slices were subjected to 2- and 10-min hydrogen cycles at 1000° and 1200°C, and the films were remeasured. These results are collected in Table I. The top two slices were heated for 2 min at 1200°C. The next two slices were heated 2 min at 1000°C followed by a 10-min treatment at 1200°C. Note that the loss in thickness for the two different treatments was roughly the same (~150Å). Six slices were cycled for 2 min at 1000°C with a negligible loss

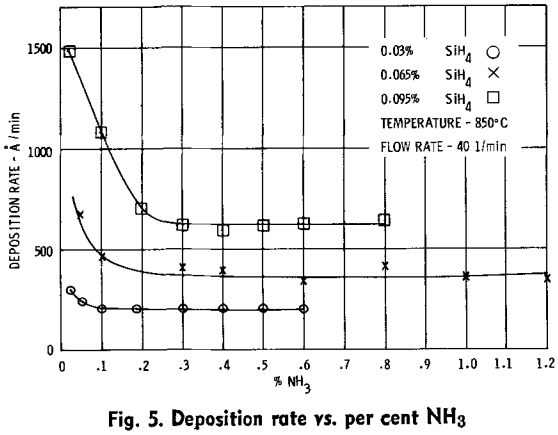

Fig. 5. Deposition rate vs. per cent NH_3

Table I. Stability of Silicon nitride films to thermal cycling in hydrogen

Sample	Index of † refraction	Original thickness, Å	Thickness after 2 min in H_2 at 1200°C	Thickness after 2 min in H_2 at 1000°C	Δt in Å
1	2.0	5065	4950		−115
2	2.0	4870	4700		−170
3	2.0	5140	4995‡		−145
4	2.0	5340	5115‡		−225
5	2.0	5660		5620	−40
6	2.0	4835		4845	+10
7	2.0	5140		5135	−5
8	2.0	4095		4095	−0
9	2.0	5380		5340	−40
10	2.0	5310		5315	+5

† No change after heat cycling.
‡ 2 min at 1000°C and 10 min at 1200°C.

in thickness. These experiments indicate that the films are quite stable at 1200°C in H_2. As further evidence of stability there was no change observed in the index of refraction after thermal cycling.

Etch Studies

A series of etch rate studies was made using Bell No. 2[2] etch contained in a constant temperature bath which was controlled to within ±0.1°C of the desired temperature. Slices with a known silicon nitride film thickness were etched for a specified length of time with constant stirring and then remeasured on the ellipsometer to determine the change in film thickness.

The effect of etch temperature on etch rate is shown in Fig. 6. The films were deposited at the usual deposition conditions. Calculation of apparent activation energy from these data gave a value of 15 kcal/mole.

A plot of etch rate *vs.* changing ammonia concentration at an etch temperature of 25°C is shown in Fig. 7. Above approximately 0.4% ammonia the etch rate is uniform (~6.25 Å/min), but below this concentration the etch rate decreases rapidly and approaches zero. This is taken as additional evidence that the films become silicon rich in this region and with Bell No. 2 as an etchant one would expect this decrease in etch rate. The effects of varying the percentage silane on the etch rate can be seen in Fig. 8. Again, as the films become silicon rich the etch rate decreases.

The etch resistance of 2000Å silicon nitride and 2000Å silicon dioxide films to a mixture of 5% HCl in hydrogen at 1200°C for 2 min was compared. The silicon dioxide film was grown thermally. The results are shown in Fig. 9. The silicon nitride film is almost impervious to HCl and H_2. The triangular pit

[2] Bell No. 2 = 300 cc H_2O—200g NH_4F—45 cc HF.

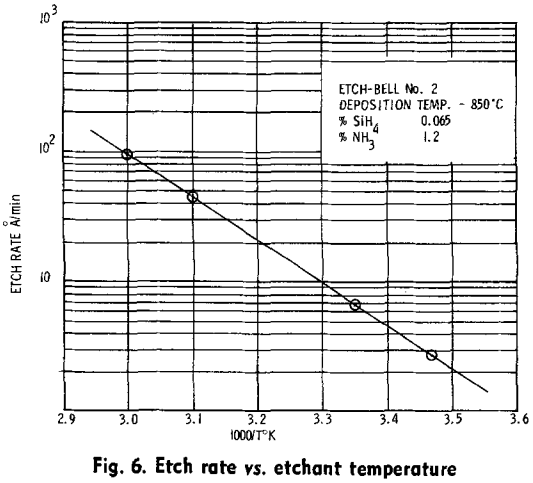

Fig. 6. Etch rate *vs.* etchant temperature

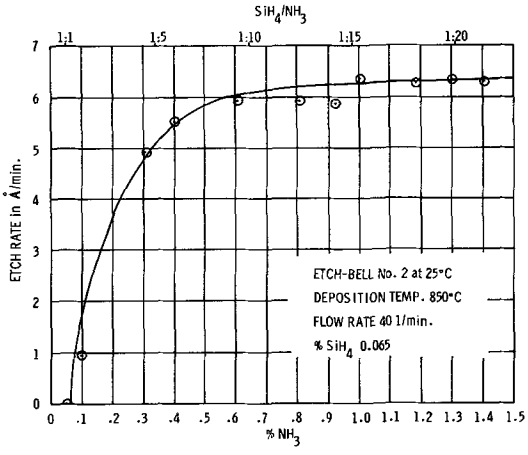

Fig. 7. Etch rate *vs.* per cent NH_3

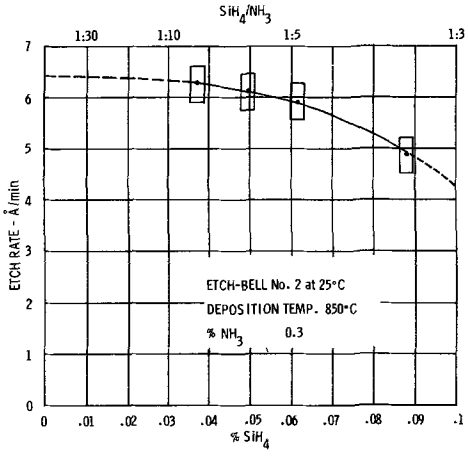

Fig. 8. Etch rate *vs.* per cent SiH_4

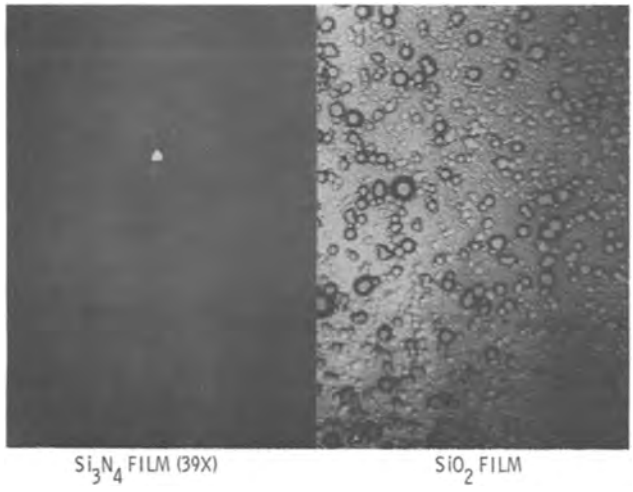

Fig. 9. Etch resistance of silicon nitride *vs.* silicon dioxide

probably resulted from HCl attacking the silicon through a pinhole in the silicon nitride film. The silicon dioxide film has been completely removed, and etching of the silicon surface has occurred.

Optical Properties

Optical transmittance data were obtained over the range from 0.2 to 24μ. Between 0.2 and 0.4μ, films deposited on fused silica blanks were used. Figure 10 gives a typical curve and indicates an absorption edge at about 0.28μ (4.4 ev). Between 0.4 and 8μ there appears to be no absorption bands. Above 8μ the most prominent absorption is that due to the Si-N

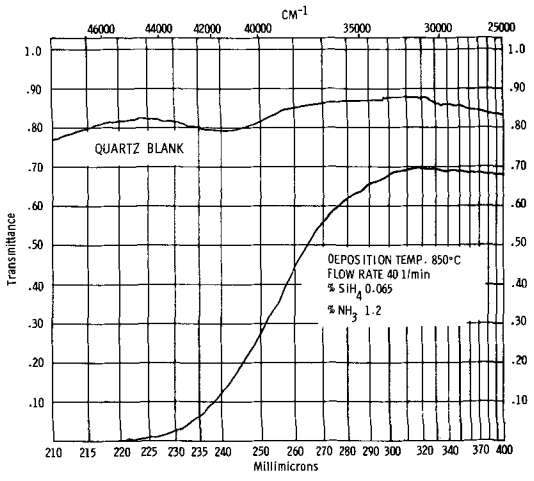

Fig. 10. Optical transmission (0.2-0.4μ) of silicon nitride

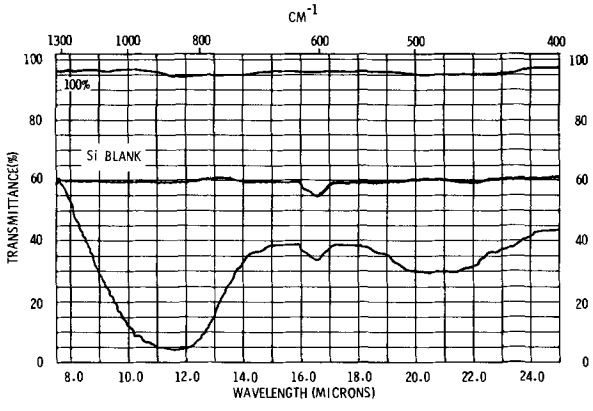

Fig. 11. Infrared transmission (8.0-24.0μ) of silicon nitride

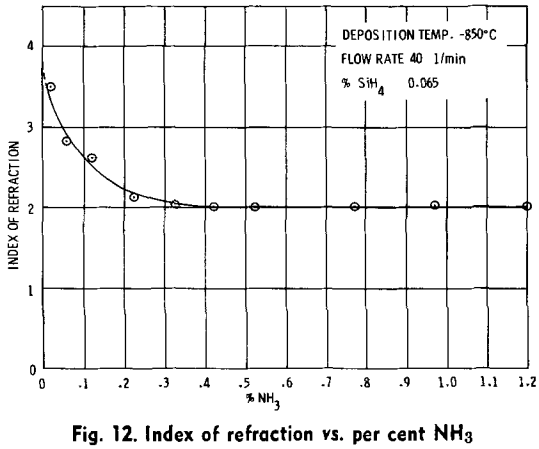

Fig. 12. Index of refraction vs. per cent NH_3

bond which occurs in the 10-12μ range as shown in Fig. 11.

The index of refraction of several films was determined from ellipsometer measurements at 5461Å. In Fig. 12 the refractive index *vs.* ammonia percentage is shown for 0.065% silane. Over most of the compositional range studied, it varied from 2.0 to 2.05, but as the gas stream percentage of ammonia decreased below 0.3% an increase in the index of refraction was noted. It is presumed that the index increases uniformly to that of silicon (about 4.02) as the ammonia concentration is decreased to zero. This is taken as confirming evidence of the silicon rich nature of such films.

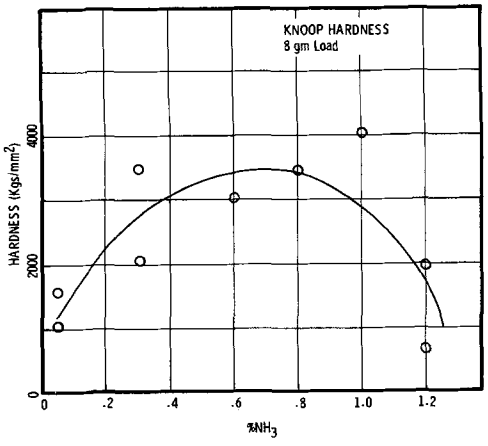

Fig. 13. Knoop hardness vs. per cent NH_3

Mechanical Properties

Microhardness measurements were made on a series of 10,000Å thick films deposited on a silicon substrate. The silane concentration was held constant at 0.065% with NH_3 percentage from 0.05 to 1.2. The results are shown in Fig. 13 and indicate appreciably softer films at each end of the composition range. The variation at the low ammonia end coincides with the observed change of index of refraction (Fig. 12), but the decrease at the other end was unexpected and is not yet explained. A Knoop indentor was used to minimize penetration, and a very light load (~8g) was required to prevent film cracking. Indentations were made using a weight sliding in a modified Reichert microscope objective housing. Measurements were then made using a Reichert microscope with Namorski contrast. Because of the light load used and the correspondingly small indentations, reproducibility was poor even for hardness measurements. The points indicated in the graph are actually averages of several readings which sometimes differed by as much as 100%. Despite the scatter, however, the films are definitely softer at each end of the composition range.

Moh's hardness measurements were made on a series of films deposited at various temperatures from 800° to 1200°C. These data are shown in Fig. 14 and indicate a change in behavior at about 900°C, which is in agreement with the deposition rate *vs.* $1/T$ and the morphology data.

Young's modulus and breaking strength were determined from one film 0.34 mil thick deposited from a gas composition of 0.1% NH_3, 0.065% SiH_4, and 99.84% hydrogen. Holes were etched through the silicon substrate in diameters of 55, 75, and 180 mils. Young's modulus was then computed from deflection *vs.* pressure as measured on the 180 mil diameter film (Fig. 15). This value, coupled with maximum pressure required for failure, was used to compute breaking stress. This stress increased as the size of the

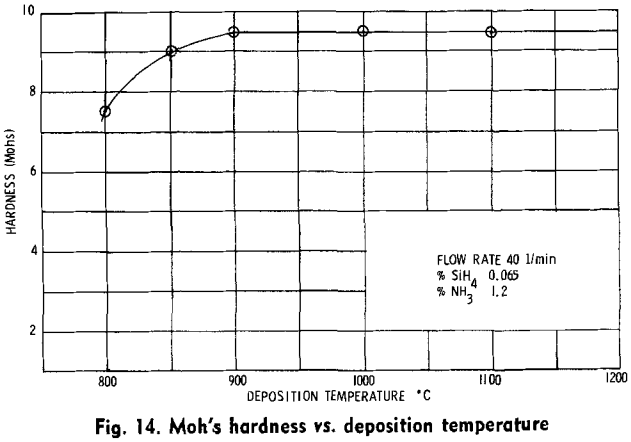

Fig. 14. Moh's hardness vs. deposition temperature

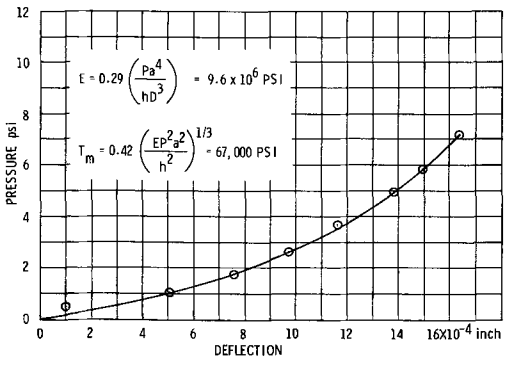

Fig. 15. Pressure vs. deflection for silicon nitride film

hole decreased and would be expected since the edges become progressively smoother as the hole became smaller. Values ranged from 67,000 psi for the largest diameter to 135,000 psi for the 55 mil diameter. It should be noted that these data are from a silicon rich film. The equations used for computation are

$$E = 0.29 \left(\frac{Pa^4}{hD^3} \right)$$

and

$$T_m = 0.42 \left(\frac{E P^2 a^2}{h^2} \right)^{1/3}$$

where E is Young's modulus in psi, T_m the maximum breaking stress in psi, P is pressure differential applied to the film, in psi, a the diameter of the hole, in inches, h film thickness, in inches, and D deflection of film at center of hole, in inches. These are approximations cited in Timoshenko and Woinowsky- Krieger (16) and are appropriate for deflections greater than film thickness.

The thermal expansion coefficient was not measured directly, but it is reasonably close to and somewhat greater than that of silicon (4.2×10^{-6}, 0°-1000°C) and can be changed by compositional variation of the reactant stream. Figure 16 shows this change by a plot of slice curvature (1 in. diameter) *vs.* per cent ammonia. Note that this value is appreciably larger than that reported for sintered samples, which is 2.5×10^{-6}/°C (5).

Conclusions

The physical, optical, and mechanical properties of the films can be varied by changing the deposition conditions. When compared to silicon dioxide films, the silicon nitride films are more stable in H_2 and H_2-HCl mixtures at the temperatures studied. The latitude of parameters observed and their increased stability over normally used insulators should add to the usefulness of such films.

Acknowledgments

The authors would like to thank A. Ray Hilton and Charlie E. Jones, Jr., for ellipsometer data, R. D. Dobrott and J. A. Arnold for the x-ray data, Stacy B. Watelski for photomicrographs, and Marion Johnson and Marvin Morris for assistance in depositing the films.

Manuscript received Nov. 30, 1966; revised manuscript received March 27, 1967. This paper was presented at the Philadelphia Meeting, Oct. 9-14, 1966.

Any discussion of this paper will appear in a Discussion Section to be published in the June 1968 JOURNAL.

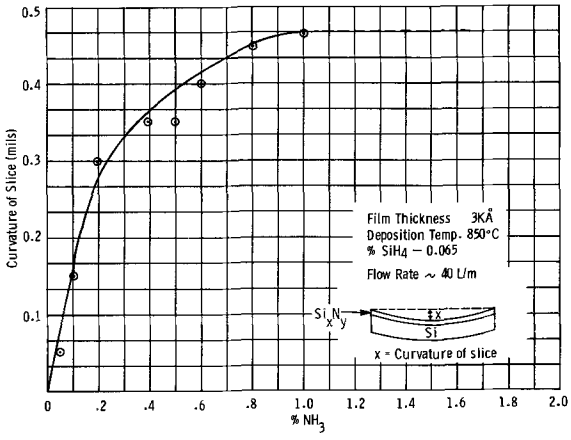

Fig. 16. Slice curvature vs. per cent NH_3

REFERENCES

1. V. Y. Doo, D. R. Nichols, and C. A. Silvey, *This Journal*, **113**, 1279 (1966).
2. S. M. Hu, Recent News Paper presented at the Buffalo Meeting October 1965.
3. H. F. Sterling and R. C. G. Swann, *Solid State Electronics*, **8**, 653 (1965).
4. A. S. Berezhnoi, "Silicon and Its Binary System," Translated from Russian, Consultants Bureau, New York, 1960.
5. P. Popper and S. N. Ruddlesden, *Trans. Brit. Ceramic Soc.*, **60**, 603 (1961).
6. A. M. Sage and J. H. Histed, *Powder Met.*, **8**, 196 (1961).
7. C. R. Barnes and C. R. Geesner, *This Journal*, **110**, 361 (1963) (see also *ibid.*, **107**, 98 (1960).
8. J. W. Mellor, "A Comprehensive Treatise on Inorganic and Theoretical Chemistry," Vol. VIII, p. 115.
9. K. E. Bean and P. S. Gleim, *This Journal*, **110**, 265C (1963).
10. G. A. Lang and T. Stavish, *RCA Rev*, **XXIV**, 488 (1963).
11. T. L. Chu, G. A. Gruber, and R. Stickler, *This Journal*, **113**, 156 (1966).
12. V. Y. Doo and D. R. Nichols, Paper presented at the Philadelphia Meeting, October 1966.
13. George A. Brown, William C. Robinette, and H. G. Carlson, "Electrical Characteristics of Silicon Nitride Films," *This Journal*, To be published.
14. C. H. Lee, T. L. Chu, and G. A. Gruber, Paper presented at the Philadelphia Meeting, October 1966.
15. R. J. Archer, *J. Opt. Soc. Am.*, **52**, 970 (1962).
16. S. Timoshenko and S. Woinowsky-Krieger, "Theory of Plates and Shells," p. 405, McGraw-Hill Book Co., New York (1959).

Impurity Distribution in Single Crystals

III. Impurity Heterogeneities in Single Crystals Rotated during Pulling from the Melt

K. Morizane, A. Witt, and H. C. Gatos

Department of Metallurgy and Center for Materials Science and Engineering, Massachusetts Institute of Technology, Cambridge, Massachusetts

ABSTRACT

The characteristics of crystal growth from the melt by a Czochralski-type technique under rotation were investigated with experimental arrangements in which the thermal and rotational axes did not coincide. A pronounced type of impurity heterogeneity was studied in particular. It was attributed to a periodic remelt process associated with rotation and was shown to be a limiting case of the normally observed rotational striations. A theoretical analysis is presented which accounts for the observed experimental results. According to this analysis the microscopic growth rate of the "core" region in crystals pulled in the <111> direction is constant, whereas the microscopic growth rate of the "off core" region undergoes pronounced periodic fluctuations as a result of the thermal asymmetry of the experimental arrangement.

Previous studies concerning the distribution of impurities in single crystals pulled from the melt have shown that periodic impurity heterogeneities in the form of striations are quite common (1-3). Depending on their origin these heterogeneities are usually referred to as rotational and nonrotational striations. Nonrotational striations are characterized by a random appearance, widely varying intensity, and are continuous throughout the crystal. Rotational striations, on the other hand, exhibit a high degree of periodicity and increased intensity in going from the crystal interior to the periphery.

The formation of both types of striations is commonly attributed to a dependence of the distribution coefficient on the growth rate (4). Accordingly, nonrotational striations reflect irregular temperature fluctuations of the melt which may originate in thermal convective currents and power input variations. Rotational striations are believed to be caused by a lack of thermal symmetry in the melt, *i.e.*, by a spatial separation of the thermal and rotational axes (5). In studies concerned with a formation of impurity striations it is usually assumed that the temperature fluctuations which lead to growth rate variations are small and generally exclude the possible occurrence of remelt phenomena (1, 6). Remelting has been imposed on pulled crystals by deliberate power input changes (7). This procedure has served to develop a rate growth technique for the production of rectifying junctions (8). We believe that such remelt phenomena are quite common in most crystals pulled from the melt.

Experimental Procedure

Single crystals of InSb containing Te as intentionally added impurity (2-50 mg Te in 50g melt) were grown in the <111> direction using a Czochralski-type puller and proportional temperature control. The crystals were subsequently cut along a (211) plane parallel to the growth axis and mechanically polished. The impurity distribution was revealed by a recently developed permanganate etchant (1HF, 1CH_3COOH, and 1$KMnO_4$ 0.05M) (9). In a typical etching operation the etchant was applied with a cotton applicator to the semiconductor surface immediately after polishing and rinsing. Etching proceeded steadily without a noticeable incubation period and was interrupted by rinsing after about 3 min. Etching times in excess of 5 min resulted in a slight reduction of resolution and were therefore avoided. Pitting, which usually accompanies etching with CP4 was never observed with the present etchant.

A Reichert microscope (Zetopan-F) equipped with a Nomarski interference contrast attachment was employed in this study. Individual striations could thus be resolved with a spacing of less than 0.2μ. This spacing corresponds to the limit of resolution of the optical system. It is quite likely that the resolution of the etching process exceeds this limit. Details of the surface preparation were previously reported (3).

Experimental Results

Single crystals grown without rotation revealed periodic heterogeneities in impurity distribution (Fig. 1) which vary in sharpness and intensity. Of particular interest for the present investigation are the intense striations which appear as deep depressions on the etched surface.

Crystals pulled in the same system but with rotation exhibited the so-called rotational striations (Fig. 2) of increased intensity and high periodicity. In all rotated crystals examined, the intensity of these striations decreased in going from the crystal periphery to the axis of rotation (Fig. 2).

In view of the reported dependence of the formation of rotational striations on a lack of thermal symmetry (5) we investigated the lateral temperature distribution in the melt. These measurements were performed with rotating thermocouples which were attached to the seed holder. They showed that along a circumference 6 mm in radius (from the center of rotation) there was a temperature variation of 2.4°C during a full rotation. By adjusting the location of the furnace thermal asymmetry could be reduced but not eliminated. The decreased thermal asymmetry resulted in rotational striations of decreased intensity in the pulled crystals.

Figure 3 depicts a crystal in which nonrotational striations as well as rotational striations of high intensity are simultaneously present. The interaction of the two types of striations leads to the abrupt termination and partial disappearance of some nonrotational striations. It is believed that this disappearance is due to the occurrence of local remelting. It is seen that the resulting remelt lines have a significantly different appearance when compared with the usual nonremelt striations (see also Fig. 2). Their primary characteristics is an increased intensity and sharpness which reflects abrupt and extensive impurity concentration changes. Such remelt striations

Fig. 1. Nonrotational impurity striations in the off core region of an InSb single crystal grown in the <111> direction. In addition to the ordinary striations there are three lines indicated by the arrows of high intensity and sharpness. They are attributed to a remelting process. (For plane shown and etchant in all figures see text). Magnification 325X.

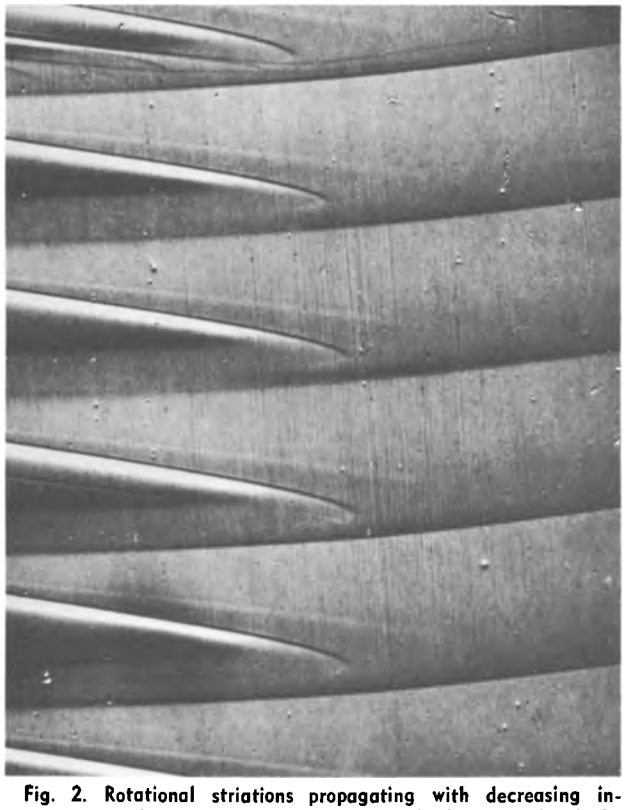

Fig. 2. Rotational striations propagating with decreasing intensity from the periphery to the center (right to left) of the crystal. Note the protruding part of the "core" region. (Compare with schematic representation of Fig. 8). Magnification 325X.

may appear also in the form of nonrotational striations (Fig. 1).

Remelt striations frequently interfere with the normal formation of the (111) impurity "core" which is a result of an (111) facet formation at the growth interface (Fig. 4). The observed abrupt changes of the core boundary are due to regrowth, following remelting, at a curved crystal melt interface at which the supercooling required for nucleation on the (111) facet is no longer necessary. Thus, rotational striations of the remelt type essentially control the lateral expansion of the impurity core which always increases with increasing spacing of consecutive remelt striations and recedes as their spacing decreases. This phenomenon is seen in Fig. 5 where closely spaced striations (resulting from reduction in the pulling rate) led to the actual disappearance of the impurity core. The core reappears after the spacing of the

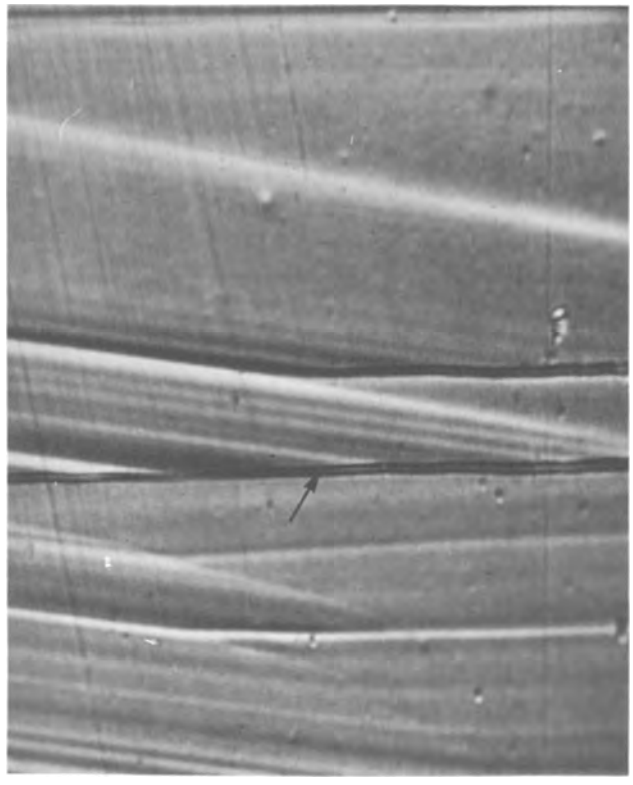

Fig. 3. Interaction of rotational remelt striations with regular nonrotational striations. The abrupt termination of nonrotational striations is caused by partial remelting associated with the formation of rotational striations. Magnification 315X.

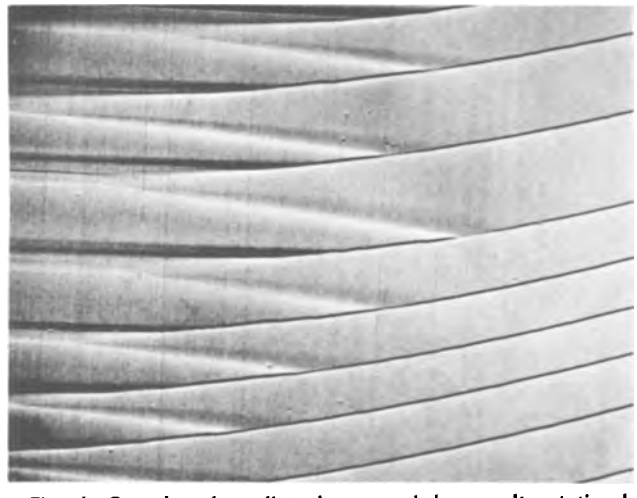

Fig. 4. Core boundary distortion caused by remelt rotational striations. The interaction of rotational striations with the impurity core has resulted in the partial elimination of the core region. (Compare with Fig. 2 and 8). Magnification 210X.

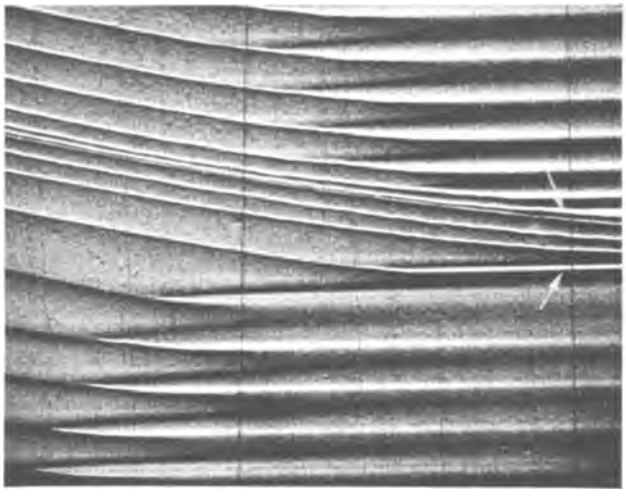

Fig. 5. Elimination of the impurity core in part of the crystal (between arrows) as a result of close spaced rotational striations of the remelt type. Magnification 165X.

Fig. 6. Irregular remelt striations in the off core region. Magnification 150X.

striations was brought to its original value. It is apparent that the interaction of the remelt striations with the impurity "core" becomes more pronounced as the curvature of the crystal-melt interface increases.

Rotational striations appear always as rather smooth curved lines of somewhat varying intensity provided that they are not associated with remelting. Remelt striations, on the other hand, frequently exhibit certain irregularities. In several crystals remelt striations were observed with rather irregular shapes, indicating the presence of significant disturbances at the growth interface (Fig. 6). These disturbances are very likely associated with localized "faceting" in the remelt area. A similar phenomenon can also be observed in Fig. 7 which depicts a crystal in which a small twin was formed. Highly irregular remelting can be observed on the left side of the twin while the right side exhibits remelt striations which are very smooth. The origin of this phenomenon is not understood at present.

Analysis of the Effect of Thermal Asymmetry on Rotational Crystal Growth

Rotational striations due to localized remelting are similar in appearance to remelt striations caused by intentional power input variations. The mechanisms of formation, however, are basically different. Remelting caused by crystal rotation occurs only on a small section of the crystal-melt interface, while remelting due to power input variations takes place

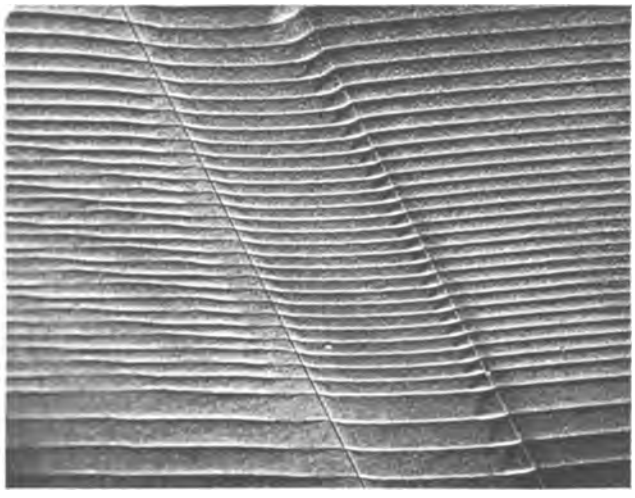

Fig. 7. Remelt striations in a crystal which was twinned. The striations are smooth and regular on the right side of the twin and highly irregular on the left side. Magnification 70X.

more or less instantaneously across the whole interface.

The formation of rotational striations will be considered in a crsytal pulled in the <111> direction (Fig. 8) with a pulling rate V_o and a rotational rate R. The distance of separation of the parallel rotational and thermal axes is d. The crystal grows with the rotational axis as its center and assumes a convex growth interface with a circular (111) facet of radius r ($r > d$) centered about the thermal axis. A fixed temperature distribution in the melt is assumed unperturbed by convection or rotation. This assumption appears valid whenever V_o and R are small. In the crystals investigated V_o was varied between ½ and 2 in./hr and R from 2 to 10 rpm. Since the temperature distribution in the melt determines the location as well as the shape of the crystal-melt interface the position of the growth facet during rotation will be stationary about the fixed thermal axis. Thus, the impurity core (which is the result of an increased impurity incorporation on the (111) growth facet) assumes the form of a "screw" during rotational pulling. Consequently, any cut along a plane which contains the axis of rotation will exhibit a sinusoidally fluctuating core boundary with an amplitude d and a "wave length" V_o/R (Fig. 8).

Under the above conditions the growth facet rotates on its own plane and growth proceeds in the <111> direction with a constant rate V_o. The curved "off core" interface, however, cannot advance at a constant

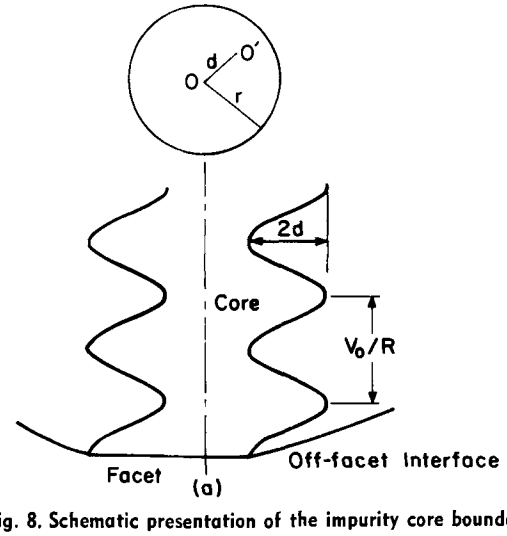

Fig. 8. Schematic presentation of the impurity core boundary

rate since its shape and location is determined by the fixed temperature distribution in the melt and the location of the thermal axis which does not coincide with the rotational axis. The resulting asymmetry of the interface with regard to the axis of rotation leads to a condition whereby each point on the "off core" interface is subjected to a different but constant growth rate during rotation. It can be shown (see Appendix) that for a temperature variation of ΔT for a full rotation the instantaneous growth rate at any point is given by

$$V = V_o - \frac{2\pi\Delta TR}{G}\cos 2\pi Rt = V_o(1 - \alpha\cos 2\pi Rt);$$

$$\alpha = \frac{2\pi\Delta TR}{V_oG} \quad [1]$$

where G is the temperature gradient in the melt adjacent to the growth interface. The minimum growth rate during each rotation is accordingly

$$V_{min} = V_o(1 - \alpha) \quad [2]$$

From Eq. [2] it is apparent that when $\alpha > 1$ then $V_{min} < 0$, *i.e.*, local remelting takes place. The extent of remelting increases with increasing rotational rates R and decreasing pulling rates V_o. At the same time any decrease in the temperature gradient in the melt will result in a decrease of V_{min} and, thus, will increase the probability of remelting.

Discussion

Whenever the solid-melt interface of a growing crystal is subject to temperature fluctuations the instantaneous (microscopic) growth rate is bound to vary. In the presence of a sinusoidal temperature change the time interval during which increased growth rate takes place is the same as the time interval during which a decreased growth rate occurs. Thus, the portion of the crystal grown under increased rate is larger than the corresponding portion grown under a decreased rate within a given cycle. A greater impurity concentration (for a distribution coefficient smaller than one) is expected in the portion grown under an increased rate than in the portion grown under a decreased rate (4). In the presence of thermal asymmetry the off core region of a crystal is subjected to such sinusoidal temperature fluctuations during rotation. Accordingly a crystal grown under rotation should exhibit impurity heterogeneities consisting of alternating helical broad and narrow bands of an increased and decreased impurity concentration, respectively. The narrow bands (whose width may amount to a line depending on the extent of thermal asymmetry) constitute the so-called rotational impurity striations.

The extent of the growth rate variation during rotation increases with increasing thermal asymmetry (Eq. [1]). Since the rotational temperature variation is zero at the center of rotation and increases toward the crystal periphery, it is expected that the rotational striations will reflect a radially decreasing growth rate (V). The observed intensity change of the rotational striations in the outward direction (Fig. 2) is consistent with this model. It is further apparent from the model that, even in the regions between the rotational striations, the growth rate and thus the impurity concentration, is not constant but varies continuously. Obviously, the experimentally determined impurity distribution coefficients are subject to error whenever thermal asymmetry is present, as manifested by rotational striations. In such a case reliable values of effective distribution coefficients can be obtained only in the "core" region of crystals grown exactly in the <111> directions.

The sharpness of the rotational striations reflects the magnitude of V_{min} during each rotation. Thus, remelt striations ($V_{min} < 0$) are a limiting case of regular impurity striations which result from excessive temperature variations. Thus a local remelt process is responsible for the observed partial disappearance of nonrotational striations (Fig. 3) and the pronounced changes of the crystal core boundaries (Fig. 4).

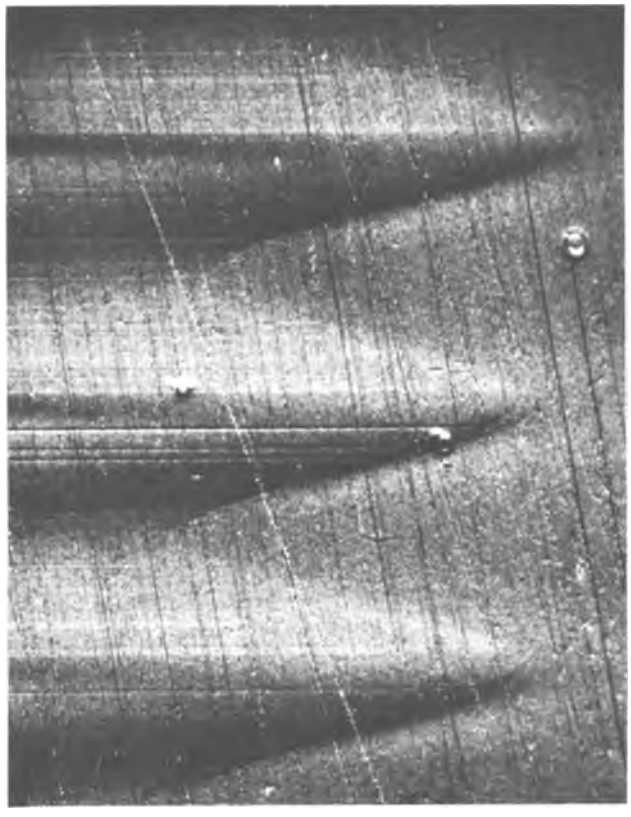

Fig. 9. Sinusoidally shaped core boundary along a single crystal on a (211) plane which contains the rotational axis. Magnification 385X.

Impurity core boundaries of sinusoidal shape as indicated by the present model are very infrequently observed in single crystals (Fig. 9) since their appearance depends on rather ideal growth conditions (no localized remelt phenomena) and a very precise (211) cut. Thus, deviations of the growth axis from the <111> direction lead to a vertically inclined growth facet and result in rather complex core boundaries (Fig. 10). A rather common deviation of the core boundary from that predicted is due to the effect of local remelting discussed earlier.

The present model is qualitatively consistent with the experimental results. A quantitative confirma-

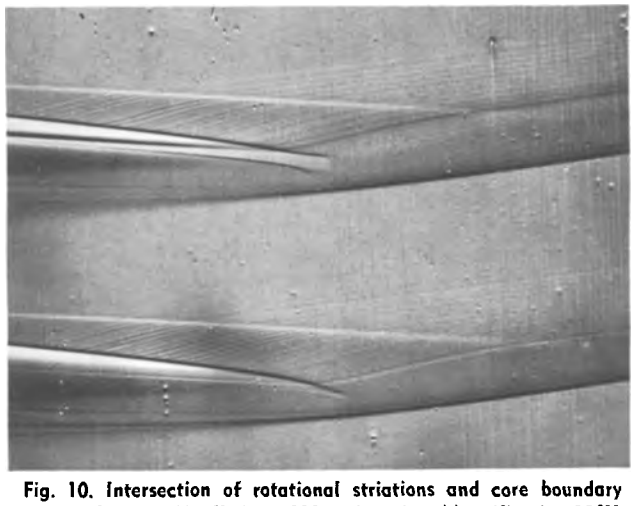

Fig. 10. Intersection of rotational striations and core boundary in a crystal grown 6° off the <111> direction. Magnification 310X.

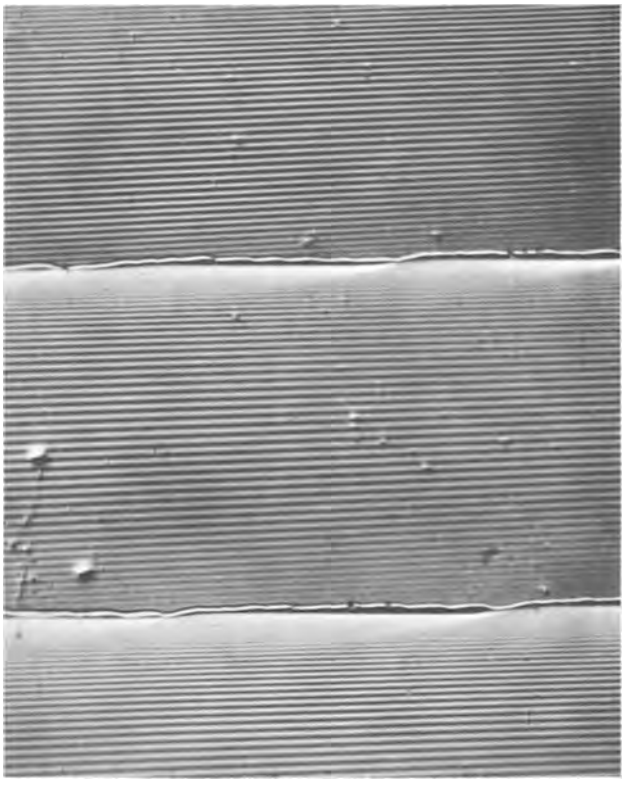

Fig. 11. Vibrational striations (18 per sec) superimposed on remelt type rotational striations in the "off core" region (see text). Magnification 430X.

tion would require knowledge of the instantaneous local growth rates or alternately the determination of concentration profiles across individual impurity striations. Because of the limited resolution of autoradiography and microresistivity measurements, microvariations in impurity distribution associated with rotational striations can only be deduced from etching experiments.

While this paper was being prepared we succeeded in introducing into single crystals high-frequency striations which are superimposed on the regular striations. Such high-frequency striations were introduced by subjecting the melt to controlled vibrations. Since these vibrations do not affect the normal growth process it becomes possible from their known frequency and their local separation to determine quantitatively the instantaneous microscopic growth rates in the various parts of the grown crystal (Fig. 11). The asymmetry in spacing of vibrational strictions above and below the "remelt" line shows directly the occurrence of remelting. Detailed results obtained with this technique will be discussed in a future report.

Acknowledgment

This work was supported by the United States Atomic Energy Commission under Contract AT (30-1)-3208. The authors wish to express their appreciation to Mr. C. J. Herman and Mr. W. J. Fitzgerald for their skillful laboratory assistance.

Manuscript received Feb. 27, 1967; revised manuscript received April 6, 1967.

Any discussion of this paper will appear in a Discussion Section to be published in the June 1968 JOURNAL.

APPENDIX

Equation [1] in the text can readily be arrived at with the aid of Fig. 12. A is an arbitrary point on the

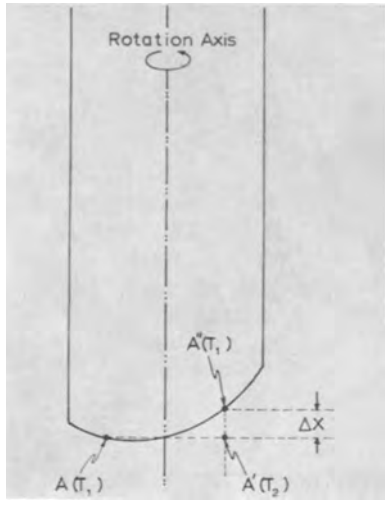

Fig. 12. Schematic presentation of rotational crystal growth in the presence of thermal asymmetry.

crystal-melt interface at a temperature T_1. During a complete revolution about the axis of rotation (without pulling) a maximum temperature T_2 is encountered at A'. Taking $T_2 - T_1 = \Delta T$, the temperature gradient, G, in the melt between A' and A'' on the solidification isotherm is then given by

$$G = \frac{\Delta T}{\Delta x} \qquad [1A]$$

Assuming steady-state conditions and that the solidification isotherm is stationary during rotational pulling at V_o (does not change position during crystal growth) then the vertical translation x of any point on the solidification isotherm is sinusoidally fluctuating with time as follows

$$x = V_o t - \Delta x \sin 2\pi R t \qquad [2A]$$

by combining [1A] and [2A] one obtains

$$x = V_o t - \frac{\Delta T}{G} \sin 2\pi R t$$

and the instantaneous rate of growth is given by

$$V = \frac{dx}{dt} = V_o - \frac{2\pi \Delta T R}{G} \cos 2\pi R t \qquad [3A]$$

taking $\alpha = 2\pi \Delta T R / G V_o$ one obtains

$$V = V_o(1 - \alpha \cos 2\pi R t) \qquad [4A]$$

REFERENCES

1. P. R. Camp, *J. Appl. Phys.*, **25**, 459 (1954).
2. A. Mueller and M. Wilhelm, *Z. Naturforsch.*, **19a**, 254 (1964).
3. K. Morizane, A. F. Witt, and H. C. Gatos, *This Journal*, **113**, 51 (1966); A. F. Witt and H. C. Gatos, *ibid.*, **113**, 808 (1966).
4. J. A. Burton, R. C. Prim, and W. P. Slichter, *J. Chem. Phys.*, **21**, 1987 (1953).
5. R. G. Rhodes, "Imperfections and Active Centers in Semiconductors," p. 186, Pergamon Press, New York (1964).
6. J. R. Carruthers, *Can. Met. Quart.*, **5**, 55 (1966).
7. R. N. Hall, *J. Phys. Chem.*, **57**, 836 (1953).
8. M. Tanenbaum, L. B. Valdes, E. Buehler, and N. B. Hannay, *J. Appl. Phys.*, **26**, 686 (1955).
9. A. F. Witt, *This Journal*, **114**, 298 (1967).
10. A. Trainor and B. E. Bartlett, *Solid State Electronics*, **2**, 106 (1961).

Control of the Surface Potential of Germanium by Means of a Variable *p*H Electrolyte Containing Hydrogen Peroxide and Potassium Chloride

G. Brouwer

Philips Research Laboratories, N. V. Philips' Gloeilampenfabrieken, Eindhoven, Netherlands

ABSTRACT

A new form of surface stabilization of germanium is discussed. When the germanium is in contact with an electrolyte containing hydrogen peroxide and potassium chloride the surface potential is a linear function of the pH. To within a constant difference its value is equal to the voltage measured between the germanium and a calomel electrode. No current flows through the interface. A new stationary state is obtained in a few minutes after the *p*H has been changed. The range of surface potentials covered is 360 mv.

Many transistor properties depend on the state of charge of the semiconductor surface, characterized by the surface potential, Ψ_s. When it is desired to vary Ψ_s, the electrons, or holes, must be induced to leave the semiconductor bulk to occupy states which have been made accessible in the exterior, by chemistry, for example. An illustrative case is found in the junction between intrinsic and doped germanium, which explains the principles of the new method.

Figure 1a shows an electron energy level diagram of both parts of the junction before contact is made. No excess charge is present, and the hatched conduction band and the cross-hatched valance band are completely straight. There is a difference of Fermi potentials $\phi_i - \phi_n$ between the intrinsic and n-type material (1) given by

$$\phi_i - \phi_n = \beta \log (n/n_i) \qquad [1]$$

$$\beta = 2.30\, kT/q \qquad [2]$$

in which $\beta = 60$ mv at room temperature, k is the Boltzmann constant, T the absolute temperature, and q the absolute electronic charge. The common logarithm is employed throughout this paper. The value n, which is given by the doping level, is the free electron concentration in the conduction band and n_i is the specific value for pure germanium: $n_i \approx 10^{13}$/cm^3. When the dopant concentration, n_D, equals 10^{17}/cm^3 the difference of Fermi potential amounts to 240 mv. After contact is made the electrons of the n-type material will cross the boundary into the region with the lower Fermi level.[1] As the electrons carry a charge, a double layer is built up at the interface which discourages further crossings. Equilibrium is established when the driving force of the electrons and holes, $F(e^-) = -q \operatorname{grad} \phi$, becomes zero. The width of the space charge is greater in the material with the lower concentration of mobile charge-carriers, that is in the intrinsic germanium. Accordingly, most of the drop in the electrostatic potential, Ψ, is found on this side of the junction, as is shown in Fig. 1b. To a good approximation the interface potential Ψ_s equals the original difference of Fermi potentials

$$\Psi_s = \beta \log (n/n_i) \qquad [3]$$

When the doping is varied from 10^{17}/cm^3 of shallow acceptors to the same density of shallow donors, Ψ_s can be varied from -240 to $+240$ mv.[2]

This principle is applicable not only to homojunctions but also to heterojunctions. From the point of view of a research tool it is interesting to have a junction between a solid and a liquid, because the latter can be doped at room temperature. In this case a continuous variation of Ψ_s can be achieved, provided the Fermi level of the liquid can be controlled. In this paper the germanium/water junction is studied, and the position of the Fermi level in the latter is discussed next.

It is interesting to study water from the point of view of compound semiconductors (2) with a possible deviation from stoichiometry and allowing for mobile centers. At room temperature no free electrons and holes are present in water. It is a wide-gap semiconductor in which the bands can be disregarded. As is the case in all wide-gap compounds, the position of the Fermi level must be stabilized by partially filled electron states. Pure, stoichiometric water already contains charged defects, hydroxyl ions, OH^-, and hydrogen ions, H^+ or OH_3^+. These defect pairs are created by proton exchange between two neighboring

[1] When a tenfold increase of the concentration of the electrons in the conduction band is introduced the Fermi level is raised by 60 mev and the Fermi potential is lowered by 60 mv according to the definition given in Fig. 1.

[2] Two different definitions of the surface or interface potential are commonly employed. First, Ψ_s is defined as the difference of the electrostatic potential at the surface or interface and the neutral bulk. Second, Ψ_s can be defined as the distance between the mid-gap position Ψ_i and the Fermi potential, as shown in Fig. 1. In the case of intrinsic germanium both definitions are identical.

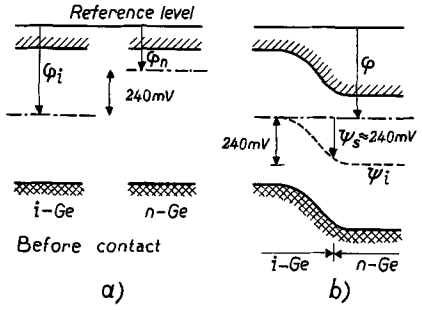

Fig. 1. Energy band diagram of the junction between intrinsic and n-type germanium, illustrating the principle of the surface stabilization method.

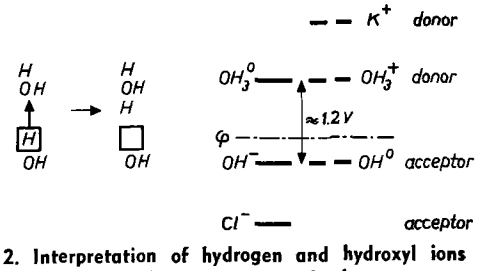

Fig. 2. Interpretation of hydrogen and hydroxyl ions in water in terms of defect electron-donor and electron-acceptor levels.

water molecules. In Fig. 2, a somewhat artificial approach is given. Suppose that this time more energy is spent and a neutral hydrogen atom is transferred from one water molecule to an adjacent one (3). Two free radicals are formed, OH and OH_3, of which the former defect shows a hydrogen deficiency with associated electron-acceptor character, whereas the latter has an excess of hydrogen with a resulting electron-donor character. As the donor level is situated above the acceptor level, both defects become charged by a simple electron transfer.

If the Fermi level is to be stabilized in the vicinity of the OH^- level, both OH and OH^- groups must be present. The free radicals can be introduced in associated form as hydrogen peroxide. When the preference for association is marked, few free radicals will exist even when the peroxide concentration is considerable. Yet the OH concentration is quite stable as a result of buffering by the peroxide. Suppose two electrons from the germanium were transferred to two OH groups, giving two OH^- groups, then dissociation of the peroxide will replenish the lost free radicals. When ϕ_{OH^-} is the particular potential at which the Fermi level coincides with the OH^- level, the Fermi potential is given by

$$\phi_{OH^-} - \phi = \beta \log [OH^-]/[OH] \qquad [4]$$

At a constant $[H_2O_2]$ or [OH], the Fermi potential can be varied by means of the pH.

Assuming, for the moment, that no chemical reaction occurs between the germanium and the electrolyte, the situation at the interface is given in Fig. 3. On the left-hand side of Fig. 3a the semiconductor is represented by the conduction and valence band, which are the allowed states for free electrons and holes. The bands are curved as a result of a space charge. In the solution the electron levels have been limited to the defect donors and acceptors. Some space charge is also present on this side of the junction, but it is assumed that the variation of Ψ in the solution can be neglected. Thus all OH^- states are at the same level. The Fermi potentials are equal on both sides, as only electron exchange was supposed to occur. The value of Ψ_s is completely determined by $[H_2O_2]$ and pH. What happens when the pH is increased by one unit is shown in Fig. 3b. According to [4] the Fermi level in the electrolyte is raised by 60 mev, or the Fermi potential lowered by 60 mv. Then Ψ_s is bound to increase by 60 mv as well. Thus the surface potential will vary by 60 mv per pH unit.

In Fig. 3 it is assumed that a calomel electrode with a saturated salt bridge is also present in the solution. This electrode exchanges Cl^- ions with the electrolyte and as $[Cl^-]$ is kept constant by the salt bridge, the position of the Fermi potential in the metallic lead, denoted by ϕ (cal), is invariant to the pH. The cell voltage is equal to the difference of the Fermi potential of the germanium and of the lead to the calomel electrode. Therefore it varies by 60 mv per pH unit, whatever the type of the germanium. Provided the variations of Ψ are restricted to the germanium, the surface potential and the cell voltage obey the same Nernst law theoretically and the measured

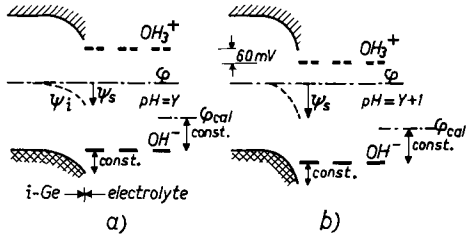

Fig. 3. Energy level diagram of the junction between germanium and water; (a) and (b) are distinguished by a difference in pH values of one unit.

voltage should be a direct measure of Ψ_s. The limitations of this relation will be discussed later. The variation of Ψ_s with the pH is the result of an exchange of electrons

$$e^-\ (Ge) + OH \rightleftharpoons OH^-, \text{ or } 2e^-\ (Ge) + H_2O_2 \rightleftharpoons 2\ OH^- \qquad [5]$$

The introduction of the peroxide leads to a deviation from stoichiometry in the water, resulting in an excess of acceptors over donors. The pH can be varied by addition of acids, such as HCl, and bases, such as KOH. In the presentation, given in this paper, HCl can be considered to be an associate of a very energetic electron-acceptor, Cl^-, and a defect donor, OH_3^+, which have exchanged an electron. In a similar way KOH is an associate of an energetic donor, K^+ and a defect acceptor, OH^-. Neither HCl nor KOH is able to disturb the balance of donors and acceptors.

Experimental

In order to check the theory given so far, the relation between the surface potential Ψ_s and the germanium/calomel voltage has to be investigated as a function of the pH. A convenient way to determine Ψ_s is to measure the conductivity of the germanium parallel to the interface with the electrolyte. This conductivity can be varied when charge is transferred from the semiconductor to the solution. This can be done by varying the pH of the solution, containing H_2O_2 and KCl or by the field effect (20), in which an external voltage is applied between the germanium and an electrolyte, serving as a polarized field electrode. In order to evaluate Ψ_s, a germanium electrode, which also serves as a conductivity cell[3], is put into a solution together with a saturated calomel electrode with salt bridge and a glass-membrane electrode. The voltage between the last-mentioned electrodes is a direct measure of the pH. The germanium conductivity cell is adapted to the van der Pauw measuring technique (5). It consists of a slice 0.4 mm in thickness with (100) planes cut ultrasonically into the shape of a Swiss cross with a central area of 1 mm^2. After polishing and etching, four tin contacts are alloyed to the bars on one side. The nonalloyed side and a Plexiglas mould are cemented to a Teflon plate. Plastic insulated wires are pulled through holes in the mould and soldered to the contact. Then the mould is filled with a mixture of Araldite and a hardener. Overnight the cell is ready for removal from the greasy Teflon plate. The now exposed side of the slice is slightly ground, polished, and subsequently etched for 20 min in slow etch consisting of two equal volumes of 0.5M KOH and 10M H_2O_2. The liquid is gently stirred and in the end about 0.05 mm of germanium is removed. After rinsing in deionized water the cell is ready to enter the electrolyte. As the conductivity of intrinsic germanium is very sensitive to temperature, the latter is kept constant to within 0.02°C. A two-stage thermostat is employed in which the temperature is measured with intrinsic germanium thermometers. The actual measuring vessel consists of polythene and the solution is stirred by a magnetically driven centrifugal pump made of Teflon.

The circuit in Fig. 4 is used for measuring the conductivity of the van der Pauw cell. The latter has four contacts: I_1 and I_2 are used as current contacts and V_1 and V_2 as voltage probes. Via the galvanometer G of a Kipp micrograph this voltage is compared with a constant voltage of 10 mv. A control system regulates the current through the sample in such a way that the galvanometer carries no current. Any deviation from zero is amplified opto-electrically and the resulting signal is used to drive a servo motor which is coupled to two potentiometers, one of which is normally employed for internal feedback. This circuit is disconnected, but the spare potentiometer P is connected to a battery. As the sliding contact moves from posi-

[3] This conductivity cell exclusively serves the purpose of measuring the conductivity of the germanium.

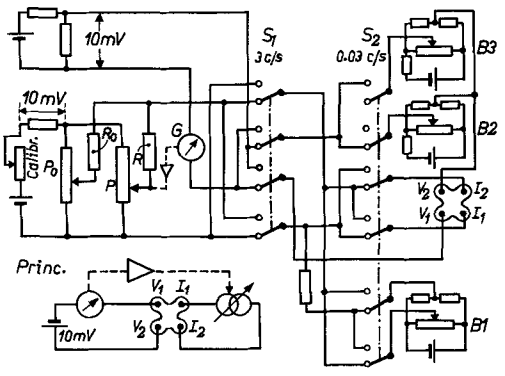

Fig. 4. Circuit employed for the measurement of the surface conductivity of germanium. The insert explains the principle.

tion 0 to 100 the voltage over one part of the potentiometer increases linearly and from it a linear current source is derived by means of a large resistance R. The source feeds the current contacts of the conductivity cell. Full-scale deflection of the recorder corresponds to 100 μohm^{-1}, including the van der Pauw geometry factor 0.221 for samples with fourfold symmetry. A calibrated auxiliary circuit P_o, R_o extends the range of the instrument in discrete steps of 100 μohm^{-1}. To avoid the customary d-c errors, a multiple vibrating-reed switch S_1 serves as a commutator operating at a frequency of 3 c/sec. The van der Pauw technique requires two independent measurements and a relay S_2 interchanges I_1 and V_2 every 30 sec. Three manually operated auxiliary circuits are employed: B_1 compensates the small difference of two consecutive readings which should be zero if the symmetry of the sample is complete; B_2 eliminates the influence of parasitic emf during the first 30-sec period, B_3 during the second one to prevent a 3 c/sec nuisance-signal. The conductivity as a function of time appears as a trace of dots on the recorder. The pH and the germanium-calomel voltage are recorded simultaneously.

It is important to keep the measuring voltage as small as 10 mv, because this is much smaller than kT/q, so that there are no rectification difficulties. In order to reduce a possible by-pass current through the electrolyte, the contact area must be limited (6).

Results

The experimental relation between the germanium/calomel voltage and the glass/calomel voltage which measures the pH, is given in Fig. 5. The electrolyte contains 0.01M H_2O_2 and 0.1M KCl and, in order to facilitate the pH control, 0.002M acetic, phosphoric, and boric acid as buffers (4). The germanium is intrinsic 50 ohm-cm material. In the range of pH values between 2 and 10 a straight line at an angle of 45° is found and the germanium/calomel cell can be employed as a pH meter (7). Within experimental error, 2 ohm-cm n-type and p-type germanium give the same voltage against calomel. When the pH is cycled, in the absence of H_2O_2, a scattering of up to 200 mv is found in the germanium/calomel voltage. Addition of H_2O_2 then invariably makes the germanium electrode more negative. When the concentration of H_2O_2 exceeds 0.001M no further increase of the cell voltage is observed. Without a high concentration of KCl the germanium electrode becomes slow. A few minutes after the pH has been varied a new stationary voltage is measured, provided both H_2O_2 and KCl are present in sufficient amounts. Stirring the liquid has no appreciable effect on the measurements. At pH > 10 the germanium/calomel voltage becomes unstable.

Simultaneously with the emf measurements, the conductivity of the 50 ohm-cm germanium cell has been determined and the result is plotted in Fig. 6. The temperature has been kept at 25° ± 0.02°C. Four series of measurements were made in a single day, alternately in the direction of increasing and of diminishing pH values. In order to check the influence of parallel conductivity through the electrolyte, two conductivity cells of the type described in the Experimental section were employed, one current and one voltage probe of each being connected to the measuring equipment, so that the current had to pass through the electrolyte. The by-pass conductivity was found to be negligible in the acid and neutral ranges, but not entirely so in the alkaline region. Uncertainty of geometrical factors did not allow for a correction of the conductivities presented in Fig. 6. Generally it is found that reproducibility is best in the acid and neutral regions. The liquid was always stirred during all experiments.

Finally the following experiment was performed: in addition to the germanium and the calomel electrode, a gold and a platinum electrode, both sandblasted, were inserted into the same solution, and the voltage against calomel as a function of the pH is also given in Fig. 5. The measuring points of both noncorroding electrodes almost coincide, but a nearly constant difference of some 800 mv is observed with respect to germanium. The same insensitivity to the peroxide concentration is present both in the germanium/calomel and gold/calomel cell (8).

A very slow etching of the germanium occurs when it is in contact with the solution employed, which is greatest at alkaline pH values. The etching rate can

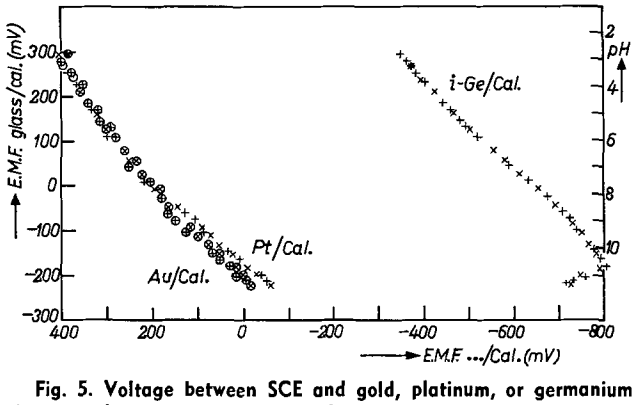

Fig. 5. Voltage between SCE and gold, platinum, or germanium (horizontal axis) as a function of pH vs. a glass/calomel system (vertical axis). The electrolyte contains 0.01M H_2O_2 and 0.1M KCl.

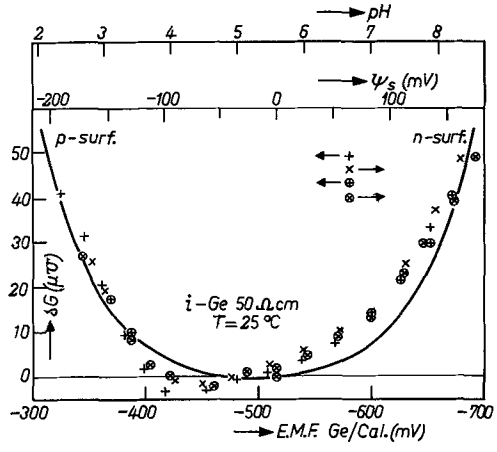

Fig. 6. Experimental relation between the germanium/calomel voltage (horizontal axis) and the surface conductivity of the germanium (vertical axis). Theoretically, the horizontal axis is also a direct measure of the surface potential, Ψ_s, and of the pH. The theoretical relation between surface conductance and surface potential is shown by the solid curve.

be judged from the variation of the conductivity of the cell with time. In the range of pH values between 2 and 8 no conductivity variations can be detected in an 8-hr period when intrinsic germanium is employed, but the sensitivity is increased by a factor 25, when 2 ohm-cm n- or p-type material is used.

Discussion

The simple theory of a passive germanium/electrolyte junction seems to explain the main experimental results. When both H_2O_2 and KCl are present, the germanium/calomel voltage varies by 60 mv per pH unit as predicted. When H_2O_2 is not present, the system is so poorly defined that no reproducible voltages can be measured unless extreme precautions have been taken (9). Even then the situation at the electrode is confused.

According to the model presented in this paper, the surface potential Ψ_s should show the same variations with pH as the cell voltage. The theoretical conductivity contribution along the interface from the surface layer of the germanium, δG, is determined by the bulk doping and the surface potential Ψ_s. This relation between δG and Ψ_s is plotted in Fig. 6, assuming that the bulk mobilities, $\mu_n = 3740$ cm^2/vsec and $\mu_p = 1870$ cm^2/vsec, are still valid at the surface (10). The fit of theoretical and experimental δG *vs.* cell voltage curves is quite satisfactory.

The assumption of a passive germanium/electrolyte junction is in contradiction, however, with other observations. When the germanium is in contact with oxygen-free water, no reaction occurs but, as soon as oxygen gas is admitted, the etch rate is finite (11). Such a slow etching rate is also found when H_2O_2 is present in the solution. When H_2O_2 is added to a H_2O_2-free solution, theory predicts a lowering of the Fermi level in the electrolyte and a decrease of the germanium/calomel voltage. In the experiment the germanium becomes more negative. If germanium behaved as a passive electrode with respect to the H_2O_2/2 OH^- redox-couple, it should be possible to replace the germanium by the noncorrosive gold or platinum electrodes without change in the cell voltage. Experimentally the germanium is roughly 800 mv negative with respect to either gold or platinum. Ellipsometric measurements performed by Bootsma and Meyer (12) provide evidence of the existence of a transparent layer of a width of 30Å at most, when the composition of the electrolyte is the same as in the previous experiments.

Theory and experiment can be reconciled completely when it is assumed that the germanium and the water, containing H_2O_2, react to give some form of oxide, say GeO_2, in which the oxygen transport is carried effectively by singly charged defects. In that case it can be shown that the resulting emf across the intermediate layer is independent of the pH. Thus the Fermi potentials on the germanium side and in the electrolyte are maintained at different levels. Provided some limiting conditions are satisfied, the intermediate layer does not interfere with the dependence of the germanium/calomel voltage and Ψ_s on the pH. The new situation at the interface is illustrated in Fig. 7a. The width of the oxide layer is exaggerated with respect to the width of the space charge region in the germanium. Theoretical treatment of the oxide is discussed in the next section.

So far, no mention has been made of interface states. From the work of Mead and Spitzer (13) it is known that at the germanium/metal interface the position of the Fermi level is completely determined by such states. If these states were also present at the germanium/solution junction, it would be impossible to change Ψ_s. Oxidation of the germanium generally reduces the number of surface states (14). An interface state density of 10^{12}/cm^2, when charged, gives a drop of about 30 mv across a layer 30Å in width. Thus the surface stabilization is insensitive to interface states, provided their concentration is low enough.

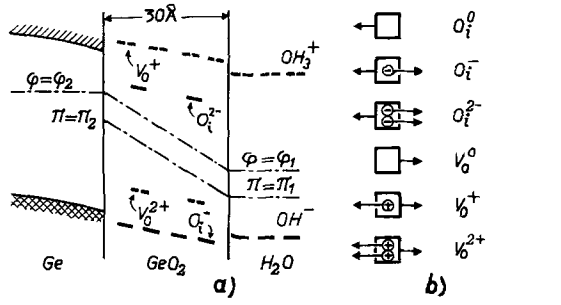

Fig. 7(a). Germanium/oxide/water: as a result of reaction between H_2O_2 and germanium, a difference in Fermi potentials is maintained across the oxide. Fig. 7(b). Force acting on various possible defects; all force vectors are equal.

Often Cu^{2+} ions in the solution are troublesome, but when H_2O_2 is present and pH < 8, the Fermi level is very low and the copper ions remain in the doubly charged state (15).

When H^+ or OH^- groups can be desorbed a pH dependent variation of Ψ is to be expected in the electrolyte, contrary to what was assumed. The experiments give no evidence of such a desorbtion in the range 3 < pH < 8.

Intermediate Layer

In the previous section, arguments were put forward for the existence of an intermediate layer. Little is known about its composition, but first the composition GeO_2 will be assumed, though the conclusions to be drawn are not restricted to this compound.

Wagner, Schottky, and Hauffe have given a theory of oxidation (16), which can also be applied to the germanium/oxide/electrolyte system and can explain the emf across the oxide. A very simplified version of the reaction

$$Ge + 2H_2O_2 \rightleftharpoons GeO_2 + 2H_2O \qquad [6]$$

is given in Fig. 8. In this diagram the following phases are represented from left to right: Ge, GeO_2, and H_2O, containing H_2O_2 as an additive. The difference between the upper and middle row of the diagram is a simultaneous displacement to the left of all oxygen atoms in the oxide plus two borrowed from the peroxide. Thus an additional layer of oxide is created. At the same time chemical energy is consumed. As such a simultaneously motion of atoms is unrealistic, defects that will do the job more efficiently must be found such as, for instance, interstitial oxygens O_i and oxygen vacancies V_O. When two O_i particles traverse the oxide completely an additional layer is formed. A continuous creation of O_i particles occurs according to the reaction

$$2H_2O_2 \rightleftharpoons 4\,OH \rightleftharpoons 2H_2O + 2\,O_i \qquad [7]$$

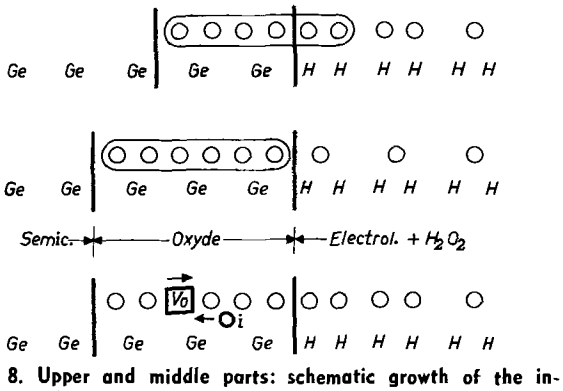

Fig. 8. Upper and middle parts: schematic growth of the intermediate layer; simultaneous motion of oxygen is involved; lower part: growth of the oxide is the result of defect transport.

and annihilation in accordance with

$$2\,O_i + Ge \rightleftharpoons GeO_2 \qquad [8]$$

Although no equilibrium exists between both extremes of the oxide, a local equilibrium can be expected if the diffusion of defects through the layer is the rate-limiting process. Then the concentration of interstitials is constant at the germanium/oxide interface (2) and proportional to the peroxide concentration at the oxide/electrolyte interface (1). Because the density of interstitials is greater at side (1) than at the opposite side, a diffusion of these particles toward the germanium occurs. The driving force is given by

$$F(O_i) = -q \text{ grad } \beta \log [O_i]/N_O \equiv -q \text{ grad } \pi \qquad [9]$$

in which N_O is a temperature-dependent constant, and the identity gives a definition of π. The loss of chemical energy resulting from the motion of the O_i particles in the force field $F(O_i)$ could be eliminated if an O_i were forced to take up an electron at (1), which could be yielded at a higher Fermi potential at interface (2). The electron, temporarily trapped at the interstitial, has to be conveyed against the gradient of the Fermi potential. This means that a complete balance of forces can be obtained, as is illustrated in Fig. 7b. The mean force, acting upon O_i^-, is given by

$$F(O_i^-) = -q \text{ grad } (\pi - \phi) = 0 \qquad [10]$$

because the majority of the mobile charge-carriers is of the type O_i^- and no current is allowed to flow in the stationary state. Integration of [10] yields

$$\phi(1) - \phi(2) = \pi(1) - \pi(2) \qquad [11]$$

As the values of $\pi(1)$ and $\pi(2)$ are given by the local equilibria [7] and [8], the emf across the oxide depends on the hydrogen-peroxide concentration only, and not on the pH. As required, the emf is the result of a finite force, acting over a finite distance. A stable voltage across the oxide can only be expected when one kind of charged defect is present, such as O_i^- and its associated particle V_O^+. The latter need not be treated separately as it gives the same result as O_i^- and also obeys the same electrochemical potential as O_i^-.

So far, special assumptions have been made as to the composition of the intermediate layer and the dominating type of charged defect, but the conclusions can be generalized. As long as the Fermi level in the electrolyte is stabilized by the H_2O_2 and the pH, the emf across the layer will be constant and the germanium/calomel voltage will always vary by 60 mv per pH unit. In the most general case the layer consists of GeO_mH_n and the dominating defects are given by $(O_pH_q)^{r-}$ and $(GeO_{m-p}H_{n-q})^{r+}$. At the interface with the germanium the negative defects are discharged and they should form a new layer according to

$$2p/m\,Ge + 2\,(O_pH_q)^{r-} \rightleftharpoons 2p/m\,GeO_mH_n + 2r\,e^-(Ge) \qquad [12]$$

provided $p/q = m/n$. The generation of negative defects proceeds by the reaction

$$2r\,OH^- 2 + (2p\text{-}q\text{-}r)\,H_2O_2 \rightleftharpoons 2\,(O_pH_q)^{r-} + 2(p\text{-}q)\,H_2O \qquad [13]$$

and the total reaction of the germanium/calomel cell reads

$$2r\,e^-(Ge) + 2p/m\,GeO_mH_{mq/p} + 2r\,Cl^- + 2r\,Hg + 2(p\text{-}q)\,H_2O \rightleftharpoons 2r\,e^-(Hg) + r\,Hg_2Cl_2 + 2p/m\,Ge + 2r\,OH^- + (2p\text{-}q\text{-}r)\,H_2O_2 \qquad [14]$$

Because the coefficient of the electron terms and of the OH^- is the same, the cell voltage varies by 60 mv per pH unit, as long as only one type of charged defect dominates the layer. More complicated relations are found when several consecutive regions are present in the layer, each of which is dominated by a different type of charged defect.

Another interesting point is the coefficient in front of the H_2O_2, which can be positive, negative, or zero, according to whether H_2O_2 is consumed, produced, or not necessary at all.

When the concentration of electrons in the germanium conduction band is kept constant at the surface by artificial means and Ψ can vary in the intermediate layer only, the variation of this drop of Ψ across it will always be 60 mv per pH unit. This is the case when the germanium bands are kept flat by means of a voltage applied between the germanium and the calomel electrode.

The insensitivity to the high-level concentrations of hydrogen-peroxide can be explained in two ways. It is possible that the oxide/solution interface is covered completely by OH groups. Then, according to [7] and [11] the emf is independent of $[H_2O_2]$, as [4] is required at the solution interface only. In the solution, K^+ and Cl^- keep Ψ constant, and ϕ is no longer of any interest. An alternative is excess of the deviation from the stoichiometry ultimately possible in water, which would lead to the formation of a second phase, oxygen gas.

Relation to Other Work

No surface stabilization work on germanium similar to that described in this paper has so far come to the notice of the author. A letter has been published on silicon, however (18). Three objections can be raised to the work referred to in this letter. (*a*) The electrolyte was doped by Ce^{4+} at pH = 0, but a well-defined Fermi level requires both Ce^{4+} and Ce^{3+} in fixed concentrations. The Ce^{4+} state, however, is essentially unstable and decays into Ce^{3+} such that a sufficient constant $[Ce^{3+}]$ will no doubt have been obtained to suggest greater stability than the results turned out to have. (*b*) Then the silicon/calomel voltage and Ψ_s must be expected to vary by 60 mv for every tenfold increase of $[Ce^{4+}]$. This is certainly not in accord with the experimental results presented in the letter. (*c*) Finally, the measured emf was given as depending on the doping of the silicon, in contradiction to theory in general (19).

A number of studies have been made of the germanium/electrolyte interface (20) in which an external voltage is applied between the germanium and the calomel electrodes. The position of the Fermi level in the electrolyte is never stabilized in these experiments, although anodic polarization prior to the measurements might lead to short-lived stability at the interface. The surface potential is either derived from capacity measurements or from conductivity experiments. It is possible to determine the applied germanium/calomel voltage at which the bands are flat. When this voltage is plotted as a function of the pH of the solution, a variation of 60 mv per pH unit is found. As the semiconductor is kept space-charge free, some sort of double layer must be present at the germanium/solution interface, and the drop of Ψ across it is pH-dependent. As the total variation of the applied voltage necessary for flat bands is 480 mv, a drop in Ψ of at least 240 mv has to be explained. None the less, electrokinetic measurements reveal but small fields in the electrolyte (21). It is known that anodic oxidation forms quite substantial layers, exceeding 100Å in a strongly alkaline solution (22). This can be understood, for the compensation current can flow through the external circuit and the charged defects can be transported without opposing fields. The experimental results can be explained by an intermediate layer as the carrier of the double layer. As the efficiency of the oxide growth at higher voltages is only a few per cent, the greater part of the conduction through the oxide must be of electronic nature. Then the discharge of OH^- groups could result in the local formation of H_2O_2 temporarily. Im-

mediately after cessation of the anodic polarization the reaction

$$H_2O_2 + 2\,OH^- \rightleftharpoons 2\,O_i^- + 2\,H_2O \qquad [15]$$

results in $[O_i^-] \sim [OH^-]$. It is clear that such a proportionality will also be obtained after a mild cathodic treatment but the ratio $[O_i^-]/[OH^-]$ will be much smaller. At the germanium/oxide interface a local equilibrium is established by the reaction

$$Ge + 2\,O_i^- \rightleftharpoons GeO_2 + 2\,e^-\ (Ge) \qquad [16]$$

and when the bands are kept flat or the value $[e^-(Ge)]$ is constant $[O_i^-]$ is also constant. Both diffusion and an electric field act on O_i^- and the mean force $F(O_i^-)$ equals[4]

$$F(O_i^-) = -q\ \text{grad}\ (\beta \log [O_i^-]/N_i - \Psi) \qquad [17]$$

where N_i is a temperature-dependent constant. When the current flow in the flat-band condition can be neglected $F(O_i^-) = 0$ and the drop of Ψ across the oxide varies by 60 mv per *p*H unit according to [17]. This voltage also depends on the type of pretreatment, cathodic or anodic. Again the case can be generalized to an arbitrary type of layer and defect. It is not sufficient that [17] is obeyed for, if the drop of Ψ is 240 mv, a certain space-charge carrying capacity is required. Excluding interface states, for the moment, it is possible to calculate the density of singly charged defects necessary at the interface with the electrolyte as a function of the width of the layer. In the case of accumulation of O_i^- the Poisson-Boltzmann equation gives the following approximate result (23)

$$[O_i^-(o)]/[O_i(x)] = (L+x)^2/L^2 \qquad [18]$$

where x is the distance from the electrolyte/oxide interface and L is the Debije-Hückel screening distance for a flat geometry. This L is inversely proportional to the square root of $[O_i^-(o)]$ and when the latter is $10^{19}/cm^3$, $L \approx 10$Å. The product of these quantities gives the number of electronic charges per square centimeter present in the space charge layer, $10^{12}/cm^2$ in this case. At a distance $x = 100\ L = 1000$Å, $[O_i^-(x)]$ has decreased by a factor 10^4 and a drop of about 240 mv is present across the oxide.

The 240 mv drop can also be explained by a density of surface states of $10^{12}/cm^2$ at the germanium/oxide interface but such states, if fast enough, would cause anomalous capacitance *vs.* Ψ_s curves and generally these anomalies are absent in the experiments.

If no intermediate layer were present, interface-state densities of $10^{13}/cm^2$ would be needed and very high fields would be the result. There seems to be a general rule in nature that intermediate compounds are formed whenever the field strength at a junction becomes too high, because the mismatch of both Fermi levels is excessive. A number of examples can be found. When two metals with a large difference of work functions are brought together an intermediate intermetallic compound is formed which initiates alloying. A p-n junction in germanium, in which Li is employed as a donor, tends to build up an intermediate phase of intrinsic germanium (24). The intermediate layer of the germanium/electrolyte system is another example.

When a comparison is made between the work described in ref. (20) and this paper, the conclusion must be drawn that only in the presence of H_2O_2 and KCl, the charge exchange between the germanium and the solution is intense enough to give a well-determined electrode potential and only in this case a chemical stabilization of Ψ_s can be obtained.

Conclusions

A chemical control of the surface potential of germanium can be obtained with a germanium/water junction, when the latter contains sufficient H_2O_2 and KCl and the *p*H is stabilized. When the *p*H is varied both the surface potential and the voltage of the cell germanium/calomel change by 60 mv per *p*H unit. No current flows through the interface. The range of surface potentials covered is 360 mv. The germanium/calomel voltage is a direct measure of the surface potential. Extreme cleaning procedures are eliminated by buffering all essential concentrations.

[4] Equation [17] is compatible with [10].

Acknowledgment

The author is indebted to Mr. J.A.M. Dikhoff for a valuable discussion on oxidizing agents.

Manuscript received Dec. 27, 1966; revised manuscript received March 28, 1967.

Any discussion of this paper will appear in a Discussion Section to be published in the June 1968 JOURNAL.

REFERENCES

1. W. Shockley, "Electrons and Holes in Semiconductors," D. van Nostrand Co., New York (1950).
2. F. A. Kröger and H. J. Vink, "Solid State Physics," vol. 3, F. Seitz and D. Turnbull, Editors, Academic Press Inc., New York (1956).
3. R. Braams, *Nederlands Tijdschr. Natuurk.*, **32**, 138 (1966); F. Haber and J. Weiss, *Proc. Roy. Soc. London*, **A147**, 332 (1934).
4. S. Glasstone, "An Introduction to Electrochemistry," D. van Nostrand Co., New York (1962).
5. L. J. van der Pauw, *Philips Research Repts.*, **13**, 1 (1958).
6. W. W. Harvey, *This Journal*, **109**, 638 (1962).
7. G. Brouwer, *Physics Letters*, **21**, 339 (1966).
8. J. P. Hoare, *This Journal*, **112**, 608 (1965).
9. B. Lovrecek and J. O'M. Bockris, *J. Phys. Chem.*, **63**, 1368 (1959).
10. C. B. G. Garrett and W. H. Brattain, *Phys. Rev.*, **99**, 376 (1956); R. H. Kingston, and S. F. Neustadter, *J. Appl. Phys.*, **26**, 718 (1955).
11. W. W. Harvey and H. C. Gatos, *This Journal*, **105**, 654 (1958).
12. G. A. Bootsma and F. Meyer, *Surface Sci.*, **7**, 250 (1967); R. J. Archer, *J. Optical Soc. Am.*, **52**, 970 (1962).
13. C. A. Mead and W. G. Spitzer, *Phys. Rev.*, **134A**, 713 (1964).
14. A. H. Boonstra, J. van Ruler and M. J. Sparnaay, *Proc. Koninkl. Nederland. Akad. Wetenschap.*, **B66**, 70 (1963).
15. M. Pourbaix, "Atlas d'Équilibres Électrochimiques," Gauthier-Villars, Paris (1963).
16. K. Hauffe and W. Schottky, "Halbleiter Probleme V," F. Sauter, Editor, Friedr. Vieweg & Sohn, Braunschweig (1960).
18. H. U. Harten, *Z. Naturforsch.*, **16a**, 1401 (1961).
19. P. J. Holmes, "The Electrochemistry of Semiconductors," Academic Press, New York, London (1962).
20. K. Bohnenkamp and H. J. Engell, *Z. Electrochem.*, **61**, 1184 (1957); M. Hoffmann-Perez and H. Gerischer, *ibid.*, **65**, 771 (1961); H. U. Harten and R. Memming, *Physics Letters*, **3**, 95 (1962); P. J. Boddy and W. H. Brattain, *This Journal*, **110**, 570 (1963). Reviews of the semiconductor/electrolyte interface are given by: J. F. Dewald in "Semiconductors," N. B. Hannay, Editor, Reinhold Publishing Co., New York (1959); H. Gerischer in "Advances in Electrochemistry and Electrochemical Engineering," Interscience Publishers, New York, London (1961); V. A. Myamlin and Yu. V. Pleskov, *Russ. Chem. Revs.*, **32**, 207 (1963).
21. W. Eriksen and R. Caines, *J. Phys. Chem. Solids*, **14**, 87 (1960).
22. K. H. Beckmann, *Ber. Bunsen Gesells*, **70**, 842 (1966).
23. G. Brouwer, *Philips Research Repts.* **18**, 432 (1963).
24. E. M. Pell, *J. Appl. Phys.*, **31**, 291 (1960).

Epitaxial Growth of Germanium on Single Crystal Spinel

D. J. Dumin

RCA Laboratories, Radio Corporation of America, Princeton, New Jersey

ABSTRACT

Films of germanium have been grown on single crystal spinel, $MgAl_2O_4$ grown with excess Al_2O_3, *via* the pyrolysis of germane, GeH_4. The films were single crystal when the growth temperature exceeded 500°C, but contained a high degree of twinning, strain, and grain boundaries. Film thicknesses have ranged from 0.2 to 49 μm. The electrical properties of films grown on (100) and (111) spinel have been measured as a function of growth temperature. The Hall mobility increased with increasing growth temperature, up to growth temperatures of about 750°C, where island growth began. Mobilities of the order of 300 cm^2/vsec have been obtained in 7μ thick films. The acceptor concentration increased as the growth temperature decreased, and this increase in acceptor concentration has been attributed to increased defect density, the defects acting as acceptors. The growth rate of the films was found to increase with increasing growth temperature with an activation energy of 47.5 kcal/mole. The films and substrate were deformed after growth due to the different coefficients of thermal expansion between germanium and spinel and this deformation has been used to estimate that the films were under a compressive stress of about 10^9 dynes/cm^2. The deformation of Ge on spinel is not as great as Si on spinel or sapphire reflecting both the closer match in coefficients of thermal expansion and the decreased temperature change from growth temperature to room temperature.

Prompted by the usefulness of epitaxial silicon-on-sapphire films in the fabrication of MOS transistors (1), the deposition of germanium films on sapphire substrates by chemical vapor transport has been studied (2). Germanium has been epitaxially grown on germanium substrates via the pyrolysis of germane, GeH_4 (3). The growth of germanium from germane has the advantage of being compatible with the use of gaseous hydrides such as arsine, phosphine or diborane as controlled doping agents. In this paper the growth of single crystal layers of germanium on spinel, $MgAl_2O_4$ + excess Al_2O_3, is reported using the pyrolysis of germane. Electrical and mechanical properties of the germanium layers were measured and are reported. The germanium-on-spinel system was chosen to take advantage of the closer match of coefficients of thermal expansion as compared with the match between silicon and sapphire or spinel. Furthermore, because the growth temperature is lower, the strain produced on cooling from growth temperatures to room temperatures should be less. Instead of sapphire, spinel was chosen as the substrate since it is a cubic material and less lattice mismatch can be expected than for sapphire. The use of spinel as a substrate for the epitaxial growth of silicon has been reported (4), and the high quality of these silicon films prompted the use of spinel as a substrate for the germanium growth.

Experimental Techniques

The germanium films were grown in a vertical reaction chamber similar to the horizontal chamber previously described (3). The substrate, on a susceptor of silicon-carbide coated graphite, was heated by R-F induction. The walls of the growth chamber were kept cool to prevent deposition of germanium on the walls. The germane was diluted with hydrogen from a palladium diffuser to about 0.03% by volume of germane in hydrogen. The flow of the hydrogen was sufficient to assure turbulence in the reaction chamber. Provisions were made to supply diborane, arsine, and phosphine to the gas stream for doping of the germanium.

The spinel was flame fusion magnesium aluminate grown with excess Al_2O_3 to produce boules with $MgO:Al_2O_3$ ratios between 1:2 1/2 and 1:3 1/2. The boules were oriented, cut, and mechanically polished to a scratch-free surface. Both (111) and (100) orientations have been used. Prior to growth the spinel wafer was prefired in hydrogen for 10 min at 1100°C. This treatment removed a major portion of the work damage resulting from the mechanical polishing operation without leading to exsolution of the excess Al_2O_3 in the spinel (5). Growth rates were varied from 0.1 to 3 μm/min by either varying the ratio of GeH_4 to H_2 or by varying the growth temperature. The electrical properties of the films appeared to be relatively insensitive to growth rate for growth rates between 0.3 and 1 μm/min.

The films were grown at temperatures between 400° and 900°C. The temperature was measured by either optical or infrared pyrometer focused on the substrate and suitably corrected for emissivity and absorption (6, 7). The films grown at temperatures below 500°C were polycrystalline as determined by the presence of rings in Laue back reflection patterns. Above 500°C the ring pattern gave way to a spot pattern with the presence of stress, twinning, and grain boundaries becoming evident. Subgrain boundaries in the substrates were replicated in the germanium films and were visible optically as regions differing slightly in reflectivity. Above 750°C the formation of unconnected islands of germanium was observed and, while those islands observed microscopically appeared to be good single crystals, the films were often electrically discontinuous. The surface tension of the films apparently increased with increasing growth temperature and increasing film thickness resulting in the observed island formation. (111) germanium was grown on (111) spinel and (100) germanium was grown on (100) spinel. A photograph of a 20 μm thick film grown on (100) spinel is shown in Fig. 1a along with the etch pattern of this film after polishing and chemical etching as shown in Fig. 1b. The Laue back reflection photograph taken on this film is shown in Fig. 1c, where strain and misorientation are evident. Diffractometer measurements have confirmed the single crystal nature of the germanium films.

After growth, the deformation of the film and the substrate was measured using a light section microscope (8). A Hall sample was delineated in the film by masking and etching. The resistivity, Hall mobility, and film thickness were then measured. The film thickness was also measured *in situ* by infrared interference techniques. The carrier concentration was derived from the Hall data using $N = 1/\rho e \mu$ where N is the number of free carriers, ρ is the resistivity, e is

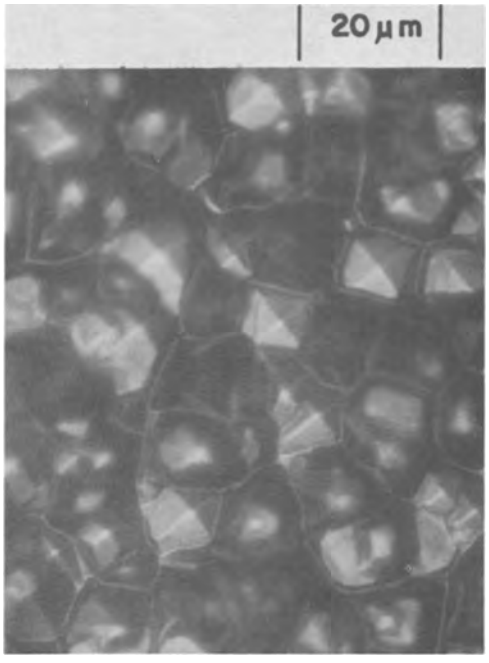

Fig. 1. A 20 μm film of germanium grown on (100) spinel: Fig. 1a, photograph of the surface of the film.

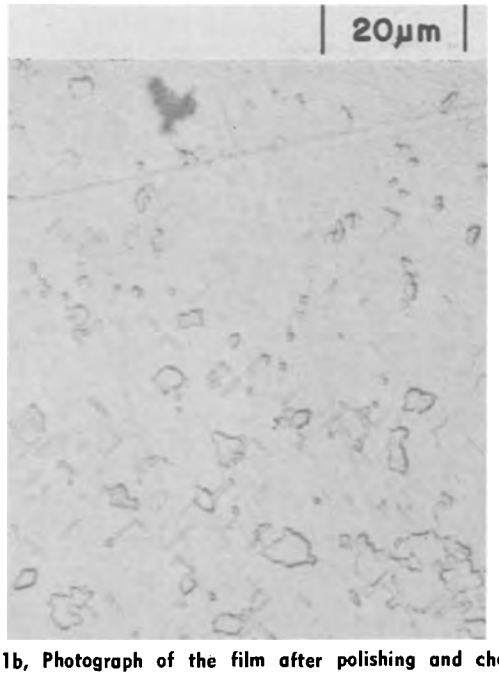

Fig. 1b, Photograph of the film after polishing and chemical etching.

the electron charge, and μ is the Hall mobility. The sign of the Hall voltage was used to determine the film conductivity type.

Experimental Results

The growth rate *vs.* growth temperature was measured using a constant ratio of germane to hydrogen of 0.03% by volume. The films were grown at a constant flow rate of GeH_4-H_2 for a fixed time, and the thickness of the films was measured after growth. The growth rate was found to increase from 0.1 μm/min at 575°C to 0.375 μm/min at 750°C as shown in Fig. 2. The activation energy associated with the growth has been calculated from the data of Fig. 2 as 47.5 kcal/mole, which lies between the zero order and first order reaction activation energies for the thermal decomposition of GeH_4 (9).

The electrical properties of p-type films grown on

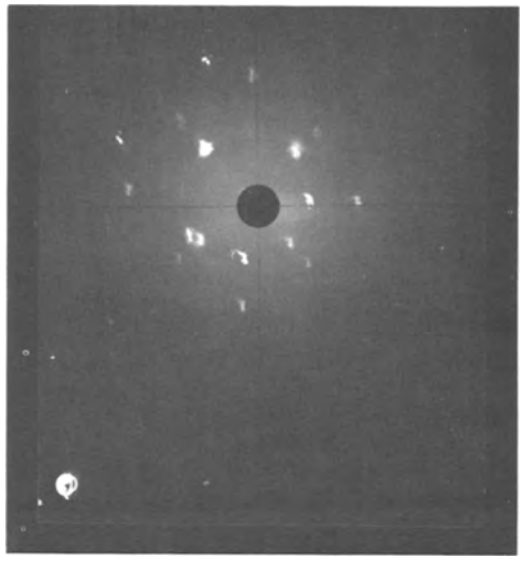

Fig. 1c, Laue back reflection photograph

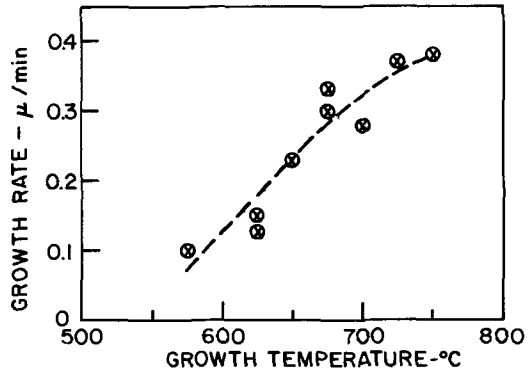

Fig. 2. Growth rate *vs.* growth temperature using 0.03% GeH_4 in H_2 mixture.

(100) and (111) spinel are shown in Fig. 3. The measured values of resistivity and mobility are shown in Fig. 3a and Fig. 3b, respectively, and values of acceptor concentration calculated from these data are shown in Fig. 3c. The Hall mobility increased as the growth temperature increased, indicative of improving crystal structure with higher growth temperatures. This was confirmed by chemically etching films grown at 500° and 700°C and noting that the edge dislocation density decreased for films grown at the higher temperature. Island growth was observed at growth temperatures above 750°C, and while the islands were relatively free of dislocations the films were often discontinuous electrically and very thick layers had to be grown to connect the individual islands.

The resistivities of the films were nearly independent of growth temperature at about 0.1 ohm-cm p-type as deposited from the GeH_4-H_2 mixture. The carrier concentration as derived from the Hall data

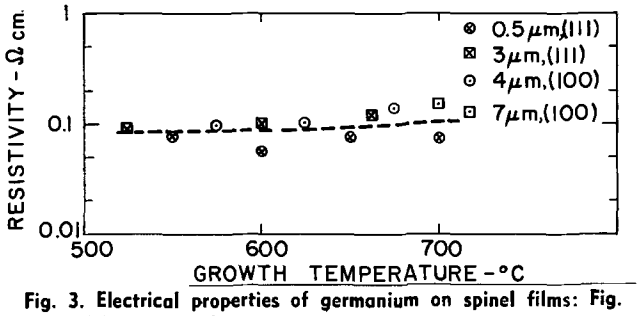

Fig. 3. Electrical properties of germanium on spinel films: Fig. 3a, Resistivity *vs.* growth temperature.

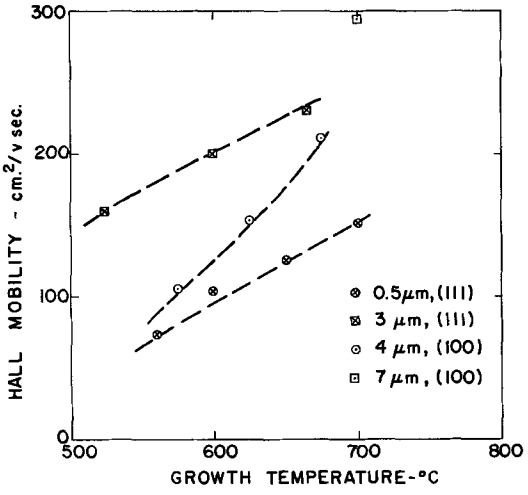

Fig. 3b, Hall mobility vs. growth temperature

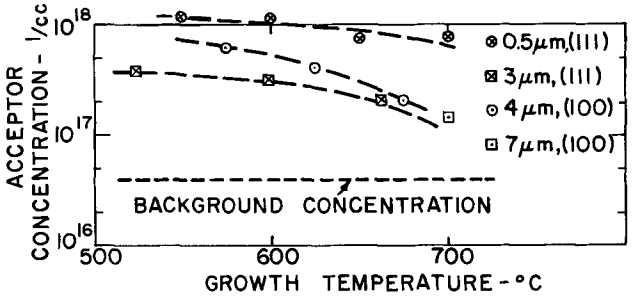

Fig. 3c, Acceptor concentration vs. growth temperature

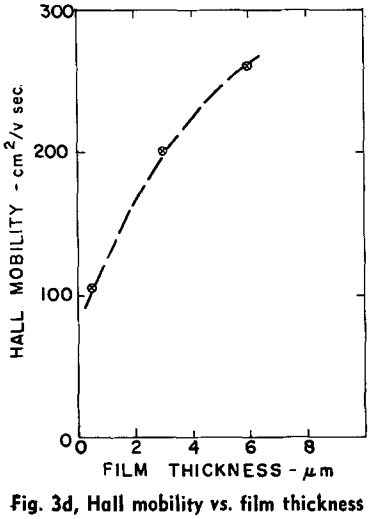

Fig. 3d, Hall mobility vs. film thickness

decreased as the growth temperature increased, but was always greater than the concentration of acceptors obtained in germanium films grown epitaxially on bulk germanium under similar conditions to those used for growth of Ge on spinel. When the source of germane used to grow these films was used to grow germanium films epitaxially on bulk germanium, the measured carrier concentration varied between $3 \cdot 10^{16}$/cc and $6 \cdot 10^{16}$/cc presumably due to small quantities of diborane in the GeH_4. This concentration is shown in Fig. 3c as the background acceptor concentration. The acceptor concentrations found in the films grown on spinel, however, were much larger, of the order of 10^{17}/cc to 10^{18}/cc. This increase in acceptor concentration is attributed to crystalline defects in the germanium films acting as acceptors. That crystalline defects can act as acceptors in bulk germanium has already been shown (10). Similar conclusions concerning the action of defects in germanium films vacuum deposited on CaF_2 (11) and silicon films grown on sapphire (12) have been reported. The increase in acceptor concentration observed in the films grown at about 500°C correlated with the increase in defect density observed by dislocation etching of these films. No autodoping of the germanium by aluminum from the spinel substrates has been observed in these films as has been the case in silicon films grown epitaxially on sapphire (13). This lack of aluminum autodoping results from the lower growth temperature used here.

As the films became thicker, the Hall mobility increased as shown in Fig. 3d for films grown on (111) spinel. The increase in mobility was attributed to improvement in the crystal structure and to a lessening of the effects of surface scattering in the thicker films. The films grown on (111) spinel had a somewhat higher hole mobility than the films grown on (100) spinel as shown in Fig. 3b.

The deformation of the germanium-on-spinel films was found to be less than for films of silicon grown on spinel, indicative of the closer match in coefficients of thermal expansion of the germanium and spinel and the lower growth temperature used in the germanium growth. The deformation of the germanium on spinel films as shown in Fig. 4a was also found to be isotropic, something not observed in silicon-on-spinel films. The displacement of the center of 0.95 cm disks of spinel after deposition is plotted in Fig. 4b as a function of germanium film thickness. Two thicknesses of substrate were used, 0.25 and 0.38 cm. Since the deformation should vary as the reciprocal of the substrate thickness squared (8), the deformation on the 0.26 cm substrate should be about twice that on the 0.38 cm substrate. This is approximately the ratio of the deformations described in Fig. 4b. No differences in deformations on the (100) or (111) spinel were observed.

The stresses in the germanium films have been estimated from the deformation using the following constants: Young's modulus for spinel = $3.3 \cdot 10^{12}$ dyne/cm², Poisson's ratio for spinel = 0.25 (14-16). Stresses of the order of 10^9 dynes/cm² have been calculated. This is approximately the stress that would be calculated using $\sigma = E\Delta\alpha\Delta T$ where σ is the stress, E is Young's modulus of the spinel, $\Delta\alpha$ is the difference in expansion coefficients and ΔT is the difference between growth temperature and room temperature. The films were under compressive stress as expected. The expansion coefficient of the spinel is reported to be greater than that of the germanium, and we ob-

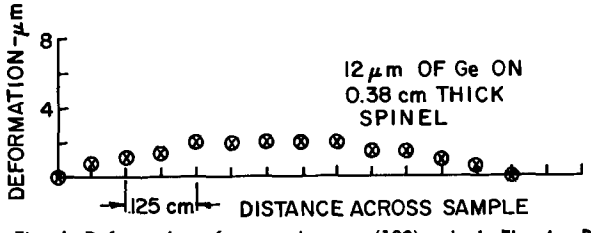

Fig. 4. Deformation of germanium on (100) spinel: Fig. 4a, Deformation across a 0.95 cm disk of spinel.

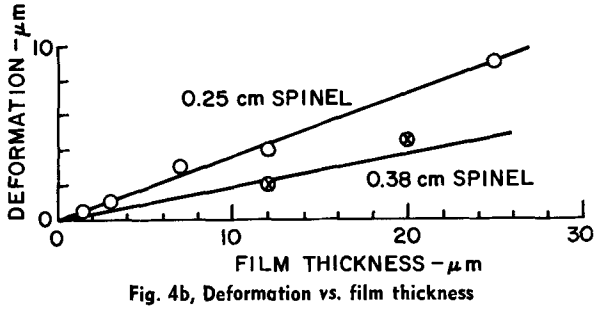

Fig. 4b, Deformation vs. film thickness

served that the films were deformed with the germanium surface convex.

Conclusions

Germanium thin films have been grown epitaxially on single crystal spinel substrates of (111) and (100) orientation. The Hall mobility increases with increasing growth temperature until island growth sets in at growth temperatures above 750°C. The incidence of island growth at temperatures above 750°C is probably indicative of a high surface mobility of the nucleating atoms. For a constant GeH_4-H_2 ratio the growth rate increased with growth temperature with an activation energy of 47.5 kcal/mole. The films were under compressive stresses of the order of 10^9 dynes/cm^2 as determined from the deformation of the films.

Acknowledgments

The author wishes to thank C. W. Mueller, P. H. Robinson, and J. A. Amick for their many useful technical comments during the course of this work and during preparation of the manuscript and R. F. Adams and R. O. Wance for assistance in the electrical measurements. The Laue back reflecting measurements and the diffractometry work were performed by R. T. Smith and E. Krieger.

Manuscript received Feb. 8, 1967; revised manuscript received March 25, 1967.

Any discussion of this paper will appear in a Discussion Section to be published in the June 1968 JOURNAL.

REFERENCES

1. C. W. Mueller and P. H. Robinson, *Proc. IEEE*, **52**, 1487 (1964).
2. R. F. Tramposch, *Appl. Phys. Letters*, **9**, 83 (1966).
3. E. A. Roth, H. Gossenberger, and J. A. Amick, *RCA Rev.*, **24**, 499 (1963).
4. H. Seiter and C. Zaminer, *Z. angew, Phys.*, **20**, 158 (1965); H. M. Manasevit and D. H. Forbes, *J. Appl. Phys.*, **37**, 734 (1966).
5. A. Kokkas and P. H. Robinson, Private communication.
6. F. G. Allen, *J. Appl. Phys.*, **28**, 1510 (1957).
7. F. Joña and H. R. Wendt, *ibid.*, **37**, 3637 (1966).
8. D. J. Dumin, *ibid.*, **36**, 2700 (1965).
9. Kenzi Tamaru, Michel Boudart, and Hugh Taylor, *J. Phys. Chem.*, **59**, 801 (1955).
10. G. L. Pearson, W. T. Read, Jr., and F. J. Morin, *Phys. Rev.*, **93**, 666 (1954).
11. B. W. Sloope and C. O. Tiller, *J. Appl. Phys.*, **38**, 140 (1967).
12. D. J. Dumin, *ibid.*, **38**, 1909 (1967).
13. D. J. Dumin and P. H. Robinson, *This Journal*, **113**, 469 (1966).
14. O. J. Whittemore, Jr., and N. N. Ault, *J. Am. Ceram. Soc.*, **39**, 443 (1956).
15. C. J. Engberg and E. H. Zehms, *ibid.*, **42**, 300 (1959).
16. T. H. Ramsey, Jr., *ibid.*, **42**, 645 (1959).

Mixed Conduction in $Zr_{0.85}Ca_{0.15}O_{1.85}$ and $Th_{0.85}Y_{0.15}O_{1.925}$ Solid Electrolytes

John W. Patterson,[1] E. C. Bogren, and Robert A. Rapp

Department of Metallurgical Engineering, The Ohio State University, Columbus, Ohio

ABSTRACT

The d-c polarization technique according to Wagner was applied for the first time at elevated temperatures for the determination of $\sigma_\ominus$ and $\sigma_\oplus$ in the $Zr_{0.85}Ca_{0.15}O_{1.85}$ and $Th_{0.85}Y_{0.15}O_{1.925}$ electrolytes over a range of oxygen activity and temperature. The applicability of the technique and an improved method for data analysis are demonstrated. Experimental difficulties and limitations are discussed. The total conductivity of $Zr_{0.85}Ca_{0.15}O_{1.85}$ was determined over a range of oxygen activity and temperature.

Stabilized zirconia with the $Zr_{0.85}Ca_{0.15}O_{1.85}$ composition exhibits a high ionic conductivity because of its CaF_2-type structure with a high ionic defect concentration. Since the introduction of the $Zr_{0.85}Ca_{0.15}O_{1.85}$ electrolyte by Kiukkola and Wagner (1), it has been used in about fifty high-temperature galvanic cell, fuel cell, and oxygen pressure gauge investigations. Lattice parameter, density (2-4), and x-ray diffraction peak intensity (4, 5) measurements indicate that Ca^{+2} ions substitute directly on Zr^{+4} sites and give rise to a significant fraction (7.5%) of vacant oxygen ion sites. The P_{O_2}-independence of the total conductivity (1, 6), the corresponding value for the oxygen self-diffusion coefficient (6, 7) and the numerous excellent correlations of galvanic cell voltages to known free energy data have served as evidence that electrical conduction in $Zr_{0.85}Ca_{0.15}O_{1.85}$ at elevated temperatures is primarily due to the migration of doubly charged anion vacancies. The P_{O_2} range of predominant ionic conductivity ($t_{ion} > 0.99$) extends at least from 1 atm oxygen pressure down to a moderately low P_{O_2} which has been estimated from several indirect measurements (5, 8-10).

[1] Present address: Department of Metallurgy, Iowa State University, Ames, Iowa.

Doping the CaF_2-type structure of pure ThO_2 with Y_2O_3 results in an analogous cation substitution with the creation of oxygen vacancies (11-13). For the $Th_{0.85}Y_{0.15}O_{1.925}$ composition at 1000°C, predominant ionic conductivity with a P_{O_2} independent total conductivity covers a wide P_{O_2} range between $P_{O_2} \approx 10^{-6}$ atm and a very low P_{O_2} which has not yet been established (9, 14, 15). The predictions from the dilute solution theory of Lasker and Rapp (14) indicate that a relatively highly doped electrolyte composition like $Th_{0.85}Y_{0.15}O_{1.925}$ should exhibit a wider P_{O_2} range of predominant ionic conduction than a composition containing less Y_2O_3 dopant.

The total conductivity σ_T (ohm^{-1}-cm^{-1}) of a material containing s independently migrating carrier species is given by

$$\sigma_T = \sum_{i=1}^{s} q_i^2 c_i B_i = \sum_{i=1}^{s} \sigma_i \qquad [1]$$

where q_i is the charge (coulombs/particle), c_i the concentration (particles/cm^3), B_i the absolute mobility (particles-cm^2/sec-volt-coulomb) and σ_i the partial conductivity of the i species. The important carrier candidates for the doped oxides $Zr_{0.85}Ca_{0.15}O_{1.85}$

and $Th_{0.85}Y_{0.15}O_{1.925}$ are presumed to be $V_{\ddot{O}}$, $\oplus$, and $\ominus$, where $V_{\ddot{O}}$ is a vacant oxygen ion site and where $\oplus$ and $\ominus$ denote positive holes and excess electrons, respectively. Conductance due to the migration of cation defects is negligible (16-18). Thus, addition of 15 mole % CaO to ZrO_2 and of 15 mole % $YO_{1.5}$ to ThO_2 greatly increases the partial anion vacancy conductivity, *i.e.*, $\sigma_{V_{\ddot{O}}} = q^2 v_{\ddot{O}}\, c_{V_{\ddot{O}}}\, B_{V_O}$. For sufficiently high dopant levels, $c_{V_{\ddot{O}}}$ is so large relative to electronic defect concentrations that the $\sigma_{V_{\ddot{O}}}$ term dominates σ_T of Eq. [1] over wide ranges of P_{O_2} at elevated temperatures.

Presumably the P_{O_2} dependences of the partial excess electron conductivity $\sigma_\ominus$ and the partial positive hole conductivity $\sigma_\oplus$ are dictated by the local equilibria

$$\tfrac{1}{2}\, O_2(g) + V_{\ddot{O}} + 2\ominus = O_O^x \qquad [2]$$

and

$$\tfrac{1}{2}\, O_2(g) + V_{\ddot{O}} = 2\oplus + O_O^x \qquad [3]$$

where O_O^x is an oxygen ion on its lattice site. If the abundant dopant cations and the compensating oppositely charged anion vacancies are sufficiently dissociated, these species should dominate the neutrality condition, $\sum_{i=1}^{s} c_i q_i = 0$, with

$$[V_{\ddot{O}}] = [Ca_{Zr}^{11}] \text{ for } Zr_{0.85}Ca_{0.15}O_{1.85} \qquad [4]$$

and

$$[V_{\ddot{O}}] = \tfrac{1}{2}[Y_{Th}^{1}] \text{ for } Th_{0.85}Y_{0.15}O_{1.925} \qquad [5]$$

where $[V_{\ddot{O}}]$, $[Ca_{Zr}^{11}]$, and $[Y_{Th}^{1}]$ represent the concentrations of the fully ionized, dissociated species. At a given temperature, $[V_{\ddot{O}}]$ should be established by the dopant content and therefore change only slightly with P_{O_2}, so that the equilibrium constants for Eq. [2] and [3] give $c_\ominus \propto P_{O_2}^{-1/4}$ and $c_\oplus \propto P_{O_2}^{+1/4}$ if a dilute solution of electronic defects is assumed. These same dependences extend immediately to $\sigma_\ominus$ and $\sigma_\oplus$, respectively, if, as is frequently presumed (1, 14, 19), the quantities $B_\ominus$ and $B_\oplus$ are independent of $c_\ominus$ and $c_\oplus$.

On the other hand, excessive association of the dopant cations and anion vacancy defects to form neutral aggregates should cause departure from the $P_{O_2}^{-1/4}$ and $P_{O_2}^{1/4}$ dependences of $\sigma_\ominus$ and $\sigma_\oplus$ if the concentrations of dissociated and charged vacancy defects and dopant cations were insufficient to dominate the neutrality condition. Such a proposal has been advanced by Kröger (20) for $Zr_{0.85}Ca_{0.15}O_{1.85}$ to explain the effect of small aliovalent-cation additions on the electronic conduction in $Zr_{0.85}Ca_{0.15}O_{1.85}$. However, the agreement between the dilute solution theory (dissociated defects) and the experimentally determined values for $\sigma_\oplus$ in $ThO_2 - Y_2O_3$ solutions (14, 15) indicates the validity of Eq. [5] even if a significant fraction of these species were associated in neutral aggregates. Further experimental determinations of the variation of $\sigma_\ominus$ and $\sigma_\oplus$ with P_{O_2} at elevated temperatures would assist in establishing the degree of dopant-vacancy association.

The primary objectives of the present work were to measure directly $\sigma_\ominus$ and $\sigma_\oplus$ in $Zr_{0.85}Ca_{0.15}O_{1.85}$ and $Th_{0.85}Y_{0.15}O_{1.925}$ and σ_T in $Zr_{0.85}Ca_{0.15}O_{1.85}$ over a wide range of P_{O_2} in the temperature range 800°-1000°C. The corresponding measurements of σ_T for $Th_{0.85}Y_{0.15}O_{1.925}$ have been reported by Lasker and Rapp (14). The present study represents the first attempt to measure electronic conductivities in oxide electrolytes at high temperatures using the polarization technique as described by Hebb (21) and Wagner (19, 22). The high-temperature polarization studies of oxides by Danforth and Bodine (23) and by Vest and Tallan (24) have not involved the use of a reversible electrode.

Partial Electronic Conductivities from Polarization Measurements

The d-c polarization techniques employed in this investigation have been described elsewhere (19, 22, 25) and have been used previously to study electronic conduction in the halides of Ag (26, 27), Cu (28), and Tl (29). Application of the technique to the oxide specimens of this investigation follows the same principles. Briefly, the cell (I)

Reversible Electrode | Oxide Specimen | Nonreversible Electrode (I)
$x = 0$ $x = L$

is subjected to a d-c emf below the decomposition voltage of the specimen. The electrode at the right ($x = L$) is made negative so that anions within the specimen are repelled from the nonreversible (Au, Pt) electrode at $x = L$ and hence migrate initially to the reversible electrode where they are consumed. The reversible electrode must therefore function simultaneously as an electronic lead and an oxygen sink and at the same time maintain a known oxygen chemical potential μ_{O_2} at $x = 0$. To perform these functions, the chosen reversible electrodes consisted of a metal-metal oxide or metal oxide (1)-metal oxide (2) equilibrium two-phase mixtures. Because the noble metal nonreversible electrode cannot provide oxygen, the local oxygen activity at $x = L$ is reduced during the transient through oxygen ion depletion. Finally, steady-state is reached in which the oxygen concentration gradient at each position in the oxide represents a force on the anions which is equal and opposite to the electrostatic force, so that net charge transport by ionic species vanishes. Because the transport of anion species and the consideration of nonmetal chemical potentials are involved in this study, it is worthwhile to review Wagner's theoretical treatment (19, 22) in terms of mobile anionic defects as follows.

Local equilibrium at any location within the oxide specimen of cell (I) is presumably dictated by the reactions [2] and [3]. In the presence of an electrostatic field, the equilibria [2] and [3] are described by the equilibrium relationships

$$\tfrac{1}{2}\mu_{O_2} + \eta_{V_{\ddot{O}}} + 2\eta_\ominus = \mu_{O_O^x} \qquad [6]$$

and

$$\tfrac{1}{2}\mu_{O_2} + \eta_{V_{\ddot{O}}} = 2\eta_\oplus + \mu_{O_O^x} \qquad [7]$$

where η_i is the electrochemical potential of the appropriate species, and is defined as

$$\eta_i = \mu_i + z_i \mathbf{F} \phi \qquad [8]$$

where $\mathbf{F}$ is the Faraday constant, ϕ the electrostatic potential, and μ_i and z_i the chemical potential and valence, respectively, of the species i. Subtracting Eq. [7] from Eq. [6]

$$\eta_\ominus + \eta_\oplus = \mu_\ominus + \mu_\oplus = 0 \qquad [9]$$

Because the dopant content virtually fixes the concentration of oxygen ions and oxygen vacancies in a homogeneously doped oxide electrolyte with immobile cations, this material behaves like a virtually stoichiometric compound and hence exhibits only a very small fractional change in oxygen content for large changes in μ_{O_2}. This condition insures that

$$\mu_{O_O^x} = \text{constant} \qquad [10]$$

and

$$\mu_{V_{\ddot{O}}} = \text{constant} \qquad [11]$$

within the oxide specimen in cell (I), regardless of the local oxygen activity or the state of polarization. Using Eq. [8], [10], and [11] in Eq. [6] and [7]

$$\tfrac{1}{4}\mu_{O_2} + \mu_{\ominus} = \text{constant} \quad [12]$$

and

$$\tfrac{1}{4}\mu_{O_2} - \mu_{\oplus} = \text{constant} \quad [13]$$

The low concentrations of excess electrons and positive holes which obtain at any location within a doped oxide electrolyte may be described by the laws of dilute solutions, *viz.*,

$$c_{\ominus} = c^{o}_{\ominus} \exp\left[(\mu_{\ominus} - \mu^{o}_{\ominus})/RT\right] \quad [14]$$

and

$$c_{\oplus} = c^{o}_{\oplus} \exp\left[(\mu_{\oplus} - \mu^{o}_{\oplus})/RT\right] \quad [15]$$

For such low concentrations, the excess electron and positive hole mobilities may be regarded as concentration independent. Thus, combining Eq. [1] and [12] through [15],

$$\sigma_{\ominus} = \sigma^{o}_{\ominus} \exp\left[-(\mu_{O_2} - \mu^{o}_{O_2})/4RT\right] \quad [16]$$

and

$$\sigma_{\oplus} = \sigma^{o}_{\oplus} \exp\left[(\mu_{O_2} - \mu^{o}_{O_2})/4RT\right] \quad [17]$$

where the reference state for each polarization experiment is chosen as the electrolyte at the oxygen activity of the reference electrode at $x = 0$. It should be noted that all of the above relations result from the chemical nature of the electrolyte, and not from any consequences of the polarization experiment.

The partial current density I_i for species i within the oxide specimen of cell (I) is given by (22)

$$I_i = -(\sigma_i/z_i\mathbf{F})(\partial\eta_i/\partial x) \quad [18]$$

At steady state in the polarization experiment $I_{ion} = 0$ so that

$$(\partial\eta_{V_O^{\cdot\cdot}}/\partial x) = 0 \quad [19]$$

Then the steady-state current density I_∞ is due only to the migration of excess electrons and positive holes so that

$$I_\infty = I_{\ominus} + I_{\oplus} = (1/\mathbf{F})\left[\sigma_{\ominus}(\partial\eta_{\ominus}/\partial x) - \sigma_{\oplus}(\partial\eta_{\oplus}/\partial x)\right] \quad [20]$$

where $I_{\ominus}$ and $I_{\oplus}$ are the partial excess electron and partial positive hole current densities. From Eq. [6], [7], [10], and [19], it follows that

$$-(\partial\eta_{\ominus}/\partial x) = (\partial\eta_{\oplus}/\partial x) = \tfrac{1}{4}(\partial\mu_{O_2}/\partial x) \quad [21]$$

Substituting Eq. [16], [17], and [21] into [20] gives

$$I_\infty = -(\tfrac{1}{4}\mathbf{F})\{\sigma^{o}_{\ominus}\exp\left[-(\mu_{O_2} - \mu^{o}_{O_2})/4RT\right] + \sigma^{o}_{\oplus}\exp\left[(\mu_{O_2} - \mu^{o}_{O_2})/4RT\right]\}(\partial\mu_{O_2}/\partial x) \quad [22]$$

for the steady-state current density at any location within the oxide specimen. However for a specimen of uniform cross sectional area, I_∞ is independent of location x so that Eq. [22] may be integrated over the specimen length L to give

$$I_\infty L = -\frac{RT}{\mathbf{F}}\left[\sigma^{o}_{\ominus}(1 - \exp\left[-(\mu^{L}_{O_2} - \mu^{o}_{O_2})/4RT\right]) + \sigma^{o}_{\oplus}(\exp\left[(\mu^{L}_{O_2} - \mu^{o}_{O_2})/4RT\right] - 1)\right] \quad [23]$$

where $\mu^{L}_{O_2}$ is the effective oxygen chemical potential at the nonreversible electrode ($x = L$) in cell (I).

In view of Eq. [6], [10], and [19]

$$\eta^{L}_{\ominus} - \eta^{o}_{\ominus} = -\tfrac{1}{4}(\mu^{L}_{O_2} - \mu^{o}_{O_2}) \quad [24]$$

where $\eta^{L}_{\ominus}$ is the electrochemical potential of excess electrons at $x = L$ in the oxide specimen. Assuming that $\eta_{\ominus}$ is essentially constant across the current lead/electrode and specimen/electrode interfaces, Eq. [24] reduces to

$$E = -(\tfrac{1}{4}\mathbf{F})(\mu^{L}_{O_2} - \mu^{o}_{O_2}) \quad [25]$$

Substituting Eq. [25] into [23] gives

$$I_\infty = RT/\mathbf{F}L\{\sigma^{o}_{\oplus}[1 - \exp(-u)] + \sigma^{o}_{\ominus}[\exp(u) - 1]\} \quad [26]$$

where $\sigma^{o}_{\oplus}$ and $\sigma^{o}_{\ominus}$ are the partial positive hole and partial excess electron conductivities (ohm^{-1}-cm^{-1}), respectively, for the oxide electrolyte at the μ_{O_2} of the reversible electrode, and the dimensionless quantity u is given by

$$u = E\,\mathbf{F}/RT \quad [27]$$

The current I_∞ in Eq. [26] is positive if positive holes migrate from left to right in cell (I), and the emf E is positive if the left-hand (reversible) electrode in cell (I) is positive. As seen, the derivation of Eq. [26] assumes independent migration of all species, local equilibrium throughout the specimen, independence of $B_{\oplus}$ and $B_{\ominus}$ on concentrations and concentration gradients of ionic and electronic defects, zero ionic current at steady state, and negligible specimen decomposition.

All previous investigations (22, 25, 26-28) involving this d-c polarization technique have been restricted to experimental conditions in which either $\sigma^{o}_{\oplus}$ or $\sigma^{o}_{\ominus}$ dominated in an expression analogous to Eq. [26]. In these cases, evaluation of the predominant term was obtained from either a current plateau of an I_∞ *vs.* E plot or from the intercept of a log I_∞ *vs.* E plot. Consideration of these limiting cases for interpreting quantitatively I_{oo} *vs.* E d-c polarization data is unsuccessful, however, under experimental conditions in which $\sigma^{o}_{\oplus}$ and $\sigma^{o}_{\ominus}$ are of comparable magnitudes. The method used in the present investigation is valid in the limiting cases mentioned above as well as in cases where $\sigma^{o}_{\oplus}$ and $\sigma^{o}_{\ominus}$ are comparable. Dividing both sides of Eq. [26] by $[1 - \exp(-u)]$ gives

$$I_\infty/[1 - \exp(-u)] = \frac{RT}{\mathbf{F}L}[\sigma^{o}_{\oplus} + \sigma^{o}_{\ominus}\exp(u)] \quad [28]$$

A "converted" plot of $I_\infty/[1 - \exp(-u)]$ *vs.* $\exp(u)$ according to Eq. [28] should give a straight line of slope $(RT/\mathbf{F}L)\sigma^{o}_{\ominus}$ and intercept $(RT/\mathbf{F}L)\sigma^{o}_{\oplus}$.

All previous investigations have been restricted to cation-conducting electrolytes and negative emfs. For this case, the present method then consists of plotting $I_\infty/[\exp(u) - 1]$ *vs.* $\exp(-u)$ which gives a straight line of slope $= (RT/\mathbf{F}L)\,\sigma^{o}_{\oplus}$ and intercept $= (RT/\mathbf{F}L)\sigma^{o}_{\ominus}$. Application of this method to the polarization curve of Ilschner (26) for AgBr in equilibrium with Ag at 372° and 353°C is shown in Fig. 1. This converted data plot demonstrates the linearity predicted and has been used to evaluate $\sigma^{o}_{\oplus}$ as well as $\sigma^{o}_{\ominus}$ under conditions where AgBr decomposition is

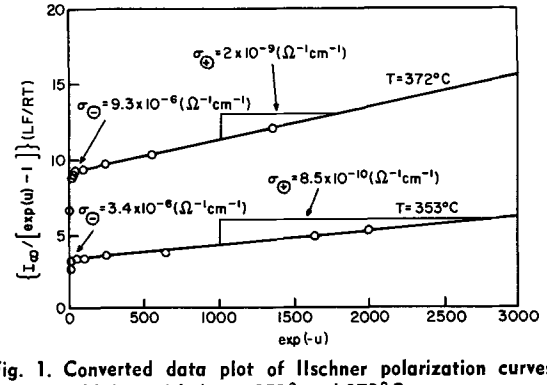

Fig. 1. Converted data plot of Ilschner polarization curves for AgBr in equilibrium with Ag at 353° and 372°C.

negligible. Proper extrapolation of these $\sigma_{\oplus}^{\circ}$ values over more than five orders of magnitude to $P_{Br_2} = 1$ atm gives order of magnitude agreement with data from Raleigh (27). This method for the simultaneous determination of $\sigma_{\oplus}^{\circ}$ and $\sigma_{\ominus}^{\circ}$ has been used to interpret the polarization data of the present investigation.

Experimental Materials and Apparatus

The $Zr_{0.85}Ca_{0.15}O_{1.85}$ polarization specimens were prepared from a mechanical mixture of —325 mesh 99.9% pure Wah Chang ZrO_2 and 99.86% pure Baker Reagent $CaCO_3$. The cold-pressed ½ in. diameter by 1/10 in. thick specimens were calcined in air at 1100°C for 4 hr and further sintered in air at 1600° and 1800°C for 4 and 2 hr, respectively. The $Th_{0.85}Y_{0.15}O_{1.925}$ polarization specimens consisted of ThO_2 powder prepared by converting 99.9% pure $Th(NO_3)_4$ and 99.9% pure Y_2O_3 powder; the specimens were sintered at 2300°C for 2 hr in vacuum ($P < 10^{-4}$ Torr). After firing, all the specimen surfaces were abraded and dusted carefully. Each specimen was then coated on one side with an electrically continuous layer of Au applied by vapor deposition in vacuum.

The reversible electrodes used for cell (I) were prepared from reagent quality materials to yield two-phase equilibrium mixtures of Cu_2O-CuO, Cu-Cu_2O, Co-CoO, Fe-FeO, Cr-Cr_2O_3, Nb-NbO, and V-VO. With the exceptions of the Cu_2O-CuO and V-VO electrodes, the reversible electrode mixtures contained about a 20:1 weight ratio of metal to metal oxide. The Cu_2O-CuO and V-VO electrodes were prepared to ensure the existence of both phases in the temperature range 800°-1000°C. In Table I are listed the equilibrium oxygen activities for the various reversible electrodes, as calculated from reliable thermodynamic data. The nonreversible electrode consisted of a Pt cylinder ½ in. in diameter and about 1/10 in. thick pressed against the vapor deposited Au layer on the oxide specimen.

In the polarization experiments, the emf was provided from a d-c constant voltage supply. Current was measured with a Kiethley 153 microvolt-ammeter. The current was recorded on a chart recorder to facilitate the prompt detection of steady-state conditions. An L&N K-2 potentiometer was used to measure the applied voltage. Voltages up to about 600 mv were applied, while the steady-state currents ranged from about 0.1 to 100 μa depending on the temperature and the electrolyte material.

The a-c conductivity study was performed on similarly prepared CaO-doped ZrO_2 "H" cells (30) of 12, 15, 18, and 21 mole % CaO. The prototype cell

Reversible electrode	CaO-doped ZrO_2 specimen	Reversible electrode

(II)

(where both electrodes for a given experiment are of identical composition) was used for all the a-c measurements. The a-c experiments involved the use of Cu-Cu_2O, Ni-NiO, Cr-Cr_2O_3, Nb-NbO, V-VO, and Ti-TiO electrodes, and measurements were made at 50°C intervals in the temperature range 800°- 1000°C with the use of a 1592 Hz Wayne-Kerr Universal Bridge.

For both d-c and a-c measurements, the cells were held suspended horizontally in a spring-loaded cell holder similar to that previously described (30, 31). Temperatures were indicated by a calibrated Pt/Pt-Rh thermocouple contacting an electrode. The cell temperature was held constant to ± 0.5°C during measurements by the manual supply of the current to the tube furnace surrounding the cell. To minimize interactions with the surrounding gas, purified He of ambient pressure was set at a P_{O_2} approximating that of the cell by passing the gas over a combustion boat filled with the two-phase electrode mixture of the cell placed immediately upstream from the cell.

Table I. Equilibrium oxygen activities for reversible electrodes

Electrode	$-\log P_{O_2}$ (1000°C)	$-\log P_{O_2}$ (900°C)	$-\log P_{O_2}$ (800°C)
Cu_2O, CuO	0.89	1.82	2.89
Cu, Cu_2O	6.29	7.43	8.83
Ni, NiO	10.35	11.99	13.94
Co, CoO	11.98	13.52	15.10
Fe, FeO	14.89	16.71	18.90
Cr, Cr_2O_3	21.79	24.39	27.48
Nb, NbO	25.10	28.03	31.52
V, VO	26.40	29.36	32.87
Ti, TiO	34.76	38.44	42.81

Results and Discussion

Polarization study.—An extensive series of preliminary experiments was required to discover and minimize the experimental difficulties introduced in this initial application of the Wagner polarization technique to oxides at high temperatures. In particular, the Ni-NiO mixture was found to be unsuitable for use as a reversible electrode in these experiments. Apparently, the diffusion of nickel ions in NiO is too slow to enable the electrode to function simultaneously as an oxygen sink and yet maintain Ni-NiO equilibrium at the mixed conductor/electrode interface. Further, relatively large open-circuit emf's (30-300 mv) persisted for long periods of time for cells involving the Ni-NiO electrode.

The "instability" of the steady-state current was studied under changing experimental conditions. In these preliminary experiments, the steady-state current was established for a given emf and temperature while the He flow rate, total gas pressure, Pyrex wall temperature, and cold trap levels were varied. Because all of these changes affected the steady-state current, the system was redesigned so that all greased joints were positioned on the upstream side of the liquid nitrogen cold trap. Further, all Pyrex and mullite tubing between the cold trap and the furnace chamber was thereafter maintained at 200°-300°C. With these precautions and with evacuations between subsequent runs, polarization currents showed very little instability over long periods of time. Evacuation of the furnace chamber during steady state seemed to increase the conductance of extraneous leakage paths in parallel with the polarized specimen. High-purity He was found to provide less instability than technical-grade He. From these experiments, the use of an extremely pure inert gas atmosphere of ambient pressure was found to be essential for d-c polarization experiments at high temperatures.

For each type of reversible electrode, *I vs. E* polarization traverses were conducted at 1000°, 900°, and 800°C using specimens of $Zr_{0.85}Ca_{0.15}O_{1.85}$ in one series of experiments and $Th_{0.85}Y_{0.15}O_{1.925}$ in a second series. The resulting data were converted to $I_\infty/[1 - \exp(-u)]$ and $\exp(u)$ values and plotted to determine the values of both $\sigma_{\oplus}^{\circ}$ and $\sigma_{\ominus}^{\circ}$ corresponding to equilibration of the specimen with the μ_{O_2} fixed by the reversible electrode. Despite experimental precautions, *I vs. E* transverses for the three electrodes of lowest μ_{O_2} did not correspond to Eq. [28], but exhibited ohmic behavior; these data were not considered significant. Apart from apparent linearity of the $I_\infty/[1 - \exp(-u)]$ *vs.* $\exp(u)$ (converted data) plots for most runs, an independent check on the validity of Eq. [26] is available for any traverse in which $\sigma_{\oplus}^{\circ}$ is much smaller than $\sigma_{\ominus}^{\circ}$ (*i.e.*, the converted data plot extrapolates through the origin). The log I_∞ *vs. E* plot for sufficiently large *E* from such a traverse should show a straight line with the predicted slope

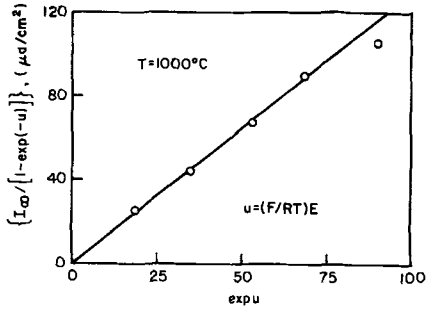

Fig. 2. Converted data plot for d-c polarization measurements with the cell Fe, FeO/$Zr_{0.85}Ca_{0.15}O_{1.85}$/Au,Pt at 1000°C.

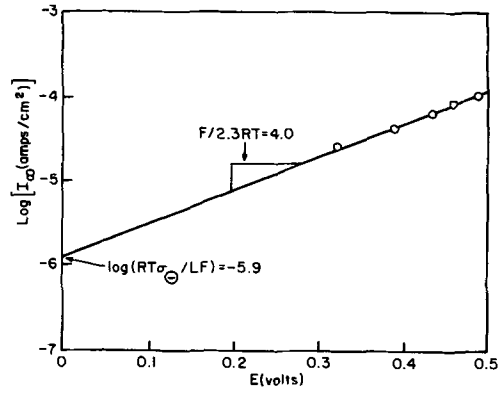

Fig. 3. Plot of log I_∞ vs. E for the cell Fe-FeO/$Zr_{0.85}Ca_{0.15}O_{1.85}$/Au,Pt at 1000°C.

$\mathbf{F}/2.30\,RT$ and with an intercept log $(RT/FL)\,\sigma_\ominus^\circ$. Such a traverse was provided by the 1000°C traverse of the cell

$$\text{Fe, FeO} \mid Zr_{0.85}Ca_{0.15}O_{1.85} \mid \text{Au, Pt} \qquad \text{(III)}$$

The data from this traverse are plotted as $I_\infty/[1-\exp(-u)]$ *vs.* exp (u) in Fig. 2 and as log I_∞ *vs.* E in Fig. 3. The line in Fig. 3 has a slope of 4.0 v^{-1}, which is the value of $\mathbf{F}/2.303\,RT$ at $T = 1273$°K. This agreement between theory and experiment serves to confirm the validity of applying Eq. [26] to describe data derived from polarization traverses for an ionically conducting oxide at elevated temperatures. The values of $\sigma_\ominus^\circ$ deduced from the slope of Fig. 2 and the intercept of Fig. 3 are identical. It may be noted also that since the derivation of Eq. [26] presumes $P_{O_2}^{-1/4}$ and $P_{O_2}^{1/4}$ dependences of $\sigma_\ominus$ and $\sigma_\oplus$, the check provided by cell (III) at 1000°C affords additional strength to the presumption of significant dissociation between dopant cations Ca_{Zr}'' and vacancies $V_O^{\cdot\cdot}$.

The values of log $\sigma_\ominus$ and log $\sigma_\oplus$ derived from data conforming to Eq. [28] were plotted *vs.* the value of log P_{O_2} corresponding to equilibrium coexistence of the reversible electrode constituents. These results for $Zr_{0.85}Ca_{0.15}O_{1.85}$ are shown in Fig. 4, and those for $Th_{0.85}Y_{0.15}O_{1.925}$ are given in Fig. 5. The values of log $\sigma_\oplus$ shown on these plots are those derived from high P_{O_2} conditions where minor side effects are expected to have little effect on the intercept values used to calculate log $\sigma_\oplus$. On the other hand, values of log $\sigma_\ominus$ under these high P_{O_2} conditions have not proved to be significant due to background currents. The data for the very low P_{O_2} reversible electrodes exhibited ohmic behavior as well as other inconsistencies and were therefore deleted for the most part. Accordingly, only 1000°C data appear on the low P_{O_2} region of Fig. 4, and these data are not thought to be significant. These observations of ohmic behavior for the low P_{O_2} electrodes in conjunction with $Zr_{0.85}Ca_{0.15}O_{1.85}$ have led to the exclusive use of cell (III) and the following cell (IV) for determining

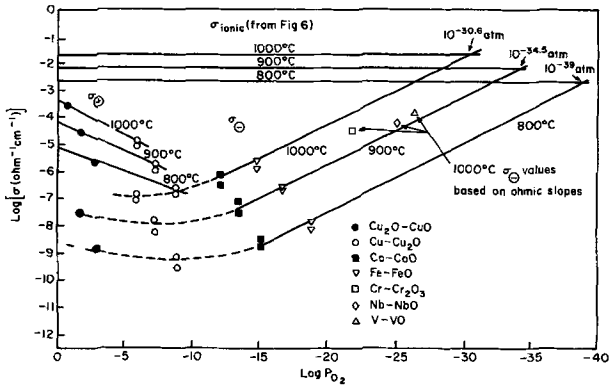

Fig. 4. Plot of log $\sigma_\ominus$, log $\sigma_\oplus$ and log σ_{ionic} vs. log P_{O_2} for polarization study of $Zr_{0.85}Ca_{0.15}O_{1.85}$ at 1000°, 900°, 800°C.

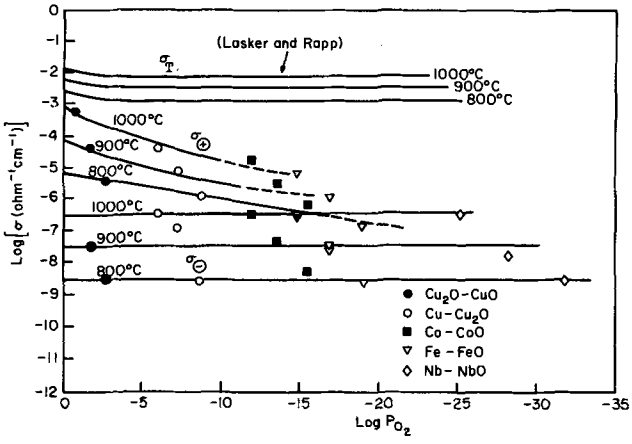

Fig. 5. Plot of log $\sigma_\ominus$, log $\sigma_\oplus$, log σ_T vs. log P_{O_2} for polarization study of $Th_{0.85}Y_{0.15}O_{1.925}$ at 1000°, 900°, 800°C.

$\sigma_\ominus$ in $Zr_{0.85}Ca_{0.15}O_{1.85}$

$$\text{Co} - \text{CoO} \mid Zr_{0.85}Ca_{0.15}O_{1.85} \mid \text{Au, Pt} \qquad \text{(IV)}$$

The lines for $\sigma_\ominus$ for $Zr_{0.85}Ca_{0.15}O_{1.85}$ of Fig. 4 have been drawn with the assumption of a $P_{O_2}^{-1/4}$ dependence. Comparing these polarization values of $\sigma_\ominus$ for $Zr_{0.85}Ca_{0.15}O_{1.85}$ with ionic conductivities determined from the results of the a-c measurements given below, Schmalzried's (5, 8) $P_\ominus$, for which $\sigma_{ion} = \sigma_\ominus$, was calculated. For the temperatures 800°, 900°, and 1000°C, these values are about 4 orders of magnitude below those deduced solely from the a-c conductivity results described below. From open-circuit emf measurements with $Zr_{0.85}Ca_{0.15}O_{1.85}$ at 1000°C, Schmalzried (5) estimated $P_\ominus$ at 10^{-24} atm whereas Steele and Alcock (9) reported $P_\ominus$ equal to 10^{-23} atm. The work of Lasker and Rapp (14), however, indicated a poor correlation between t_{ion} and $E_{meas.}/E_{thermod.}$ for cells involving metal/metal-oxide electrodes in a region of mixed conduction. The more recent work of Tretjakov and Schmalzried (10) indicates that $P_\ominus$ for $Zr_{0.85}Ca_{0.15}O_{1.85}$ at 1000°C is lower than 10^{-26} atm.

A comparison of the present polarization measurements with those of Vest and Tallan (24) on $Zr_{0.85}Ca_{0.15}O_{1.85}$ would not be meaningful. In addition to the fact that Vest and Tallan did not employ a well-defined reversible electrode in their polarization cell, they did not report any polarization results for $Zr_{0.85}Ca_{0.15}O_{1.85}$ above about 750°C nor did they report the effect of oxygen potential on the steady-state current for this material.

The values of log $\sigma_\oplus$ for $Th_{0.85}Y_{0.15}O_{1.925}$ shown in Fig. 5 were derived from the appropriate converted

data plots for high P_{O_2} cells. Interestingly, these values are not sufficiently large to rationalize the rise in total conductivity (14) observed in $Th_{0.85}Y_{0.15}O_{1.925}$ near $P_{O_2} = 1$ atm at 800°-1000°C. The values of log $\sigma_\ominus$ derived from the converted data plots are also shown in Fig. 5 and appear to exhibit P_{O_2} independence, which indicates that the actual values of $\sigma_\ominus$ in $Th_{0.85}Y_{0.15}O_{1.925}$ are below the limits of resolution for the apparatus used in this investigation. In other words, leakage conductances around the specimen exceeded the electronic conduction through the bulk of the specimen under these conditions. Preliminary experiments in which a void space (He gas) replaced the specimen yielded the same magnitude for this leakage conductance. Because the leakage conductance showed a positive temperature dependence and increased on evacuation of the system, electron transport via the gas phase is suspected as the principal leakage. Despite the precautions which were taken, another possible source of leakage current at steady state is a small ionic contribution maintained by the reduction of O_2 molecules of the gas phase at the nonreversible electrode, passage of oxygen ions through the electrolyte, and oxidation of metal at the reversible electrode. This attempt to resolve $\sigma_\ominus$ in $Th_{0.85}Y_{0.15}O_{1.925}$ indicates that $\sigma_\ominus$ is at least between 3 to 4.5 orders of magnitude less than σ_{ionic} in $Th_{0.85}Y_{0.15}O_{1.925}$ down to P_{O_2} values corresponding to Nb-NbO equilibrium between 800° and 1000°C. These upper limits on $\sigma_\ominus$ together with total a-c measurements by Lasker and Rapp (14) allow an estimation of the maximum low P_{O_2} such that $t_{ion} > 0.99$. These values are $P_{O_2} = 10^{-34.3}$ atm at 1000°C, $10^{-39.5}$ atm at 900°C, and $10^{-44.7}$ atm at 800°C.

Although the improved method of data analysis should in principle yield values for both $\sigma_\oplus$ and $\sigma_\ominus$ for all experimental conditions, it was found for these polarization measurements at high temperatures that leakage conductances which shunt the cell generally precluded a meaningful determination of the conductivity for the minority carrier. Likewise, experimental distinction between ±1/4 and ±1/6 slopes of log σ *vs.* log P_{O_2} plots of polarization data was not possible due to cell-to-cell experimental variations introduced by the assembly procedure in combination with a high level of ohmic leakage conductances. Consequently, correlation of log $\sigma_\oplus$ and log $\sigma_\ominus$ results obtained from different electrodes cannot be used to infer defect structure models. However, the values of $\sigma_\oplus$ in $Th_{0.85}Y_{0.15}O_{1.925}$, and values of $\sigma_\oplus$ and $\sigma_\ominus$ in $Zr_{0.85}Ca_{0.15}O_{1.85}$ obtained by the d-c polarization technique in this investigation are thought to be significant, despite the difficulties encountered in the determination of the conductivity of the minority carrier in a given run.

The determination of a significant shunting electronic conductance in the polarization study of $Th_{0.85}Y_{0.15}O_{1.925}$ suggests an improvement in the experimental setup not only for future polarization studies but also for galvanic cell investigations. Presuming that the principal electronic leakage is a result of thermionic emission, this leakage should be considerably reduced for polarization studies by the placement around the cell of a metallic cylinder which would be maintained at some considerable positive potential relative to the cell. Such an electron collector might also prove important to galvanic cell studies. It is well recognized that electronic conduction through the electrolyte will result in a transport of mass through the electrolyte under open-circuit conditions. Especially when metal-metal oxide electrodes are involved, polarization of the electrodes could result in electrode potentials below the reversible potentials, so that again low cell voltages would result. Thus, minimization of open-circuit electronic leakages through the use of a surrounding electron collector may also prove important in galvanic cell studies. Guard-ring techniques have been used previously by Mitoff (32) and Vest *et al.* (33).

Total conductivity studies of CaO-*doped* ZrO_2.—The results of the total conductivity studies of CaO-doped ZrO_2 are shown in Fig. 6, 7, and 8. Figure 6 shows the variation of σ_T for $Zr_{0.85}Ca_{0.15}O_{1.85}$ as a function of log P_{O_2} at the temperatures 800°, 850°, 900°, 950°, and 1000°C. The plateaus indicate predominate ionic conductivity while the branches at the right may be

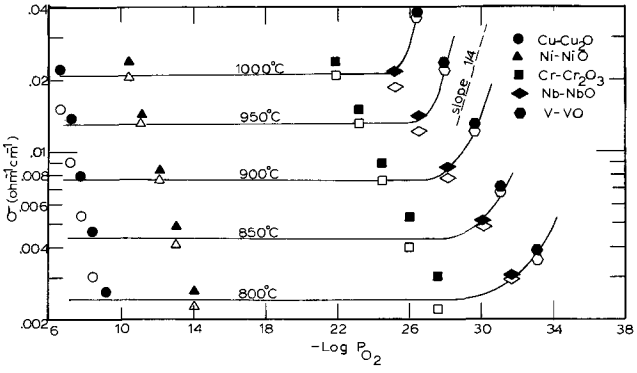

Fig. 6. Oxygen pressure dependence of total conductivity for $Zr_{0.85}Ca_{0.15}O_{1.85}$ at 800°-1000°C; ● and O denote separate experiments.

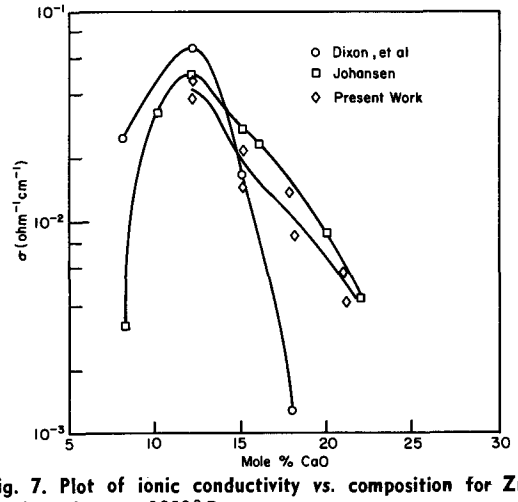

Fig. 7. Plot of ionic conductivity *vs.* composition for ZrO_2 + CaO electrolytes at 1000°C.

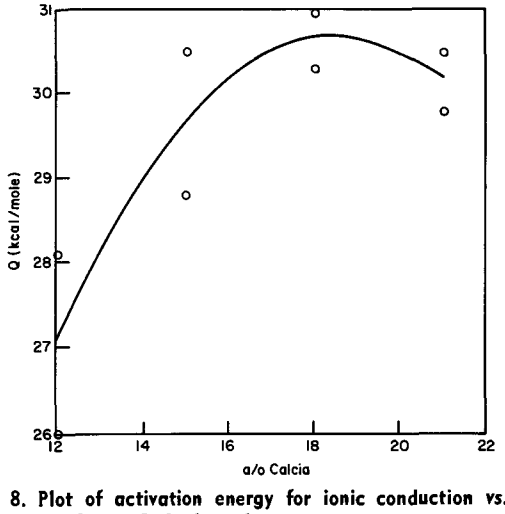

Fig. 8. Plot of activation energy for ionic conduction *vs.* composition for ZrO_2 + CaO electrolytes.

attributed to the onset of electronic conduction. These branches are expected to approach a ¼ slope in accordance with the $P_{O_2}^{-1/4}$ dependence anticipated for $\sigma_\ominus$. The anticipated ¼ slope was not verified from the a-c measurements of this study because the Ti-TiO electrodes (at very low P_{O_2}) failed to yield reliable or reproducible results despite extended experimental attempts. Although the $Zr_{0.85}Ca_{0.15}O_{1.85}$ specimens used for this a-c study were prepared independently of those used in the polarization study, the results of both studies were combined in order to compare the relative magnitudes of ionic and electronic conduction in $Zr_{0.85}Ca_{0.15}O_{1.85}$. Attributing the rise in log σ_T for the V — VO electrodes to the onset of $\sigma_\ominus$ leads to $P_\ominus$ values of $10^{-34.7}$ atm at 800°C, $10^{-30.2}$ atm at 900°C, $10^{-26.5}$ atm at 1000°C.

Other values of $P_\ominus$ from the literature and from the polarization measurements have been discussed. The difference in $P_\ominus$ between the a-c and d-c methods may be attributed either to differences in trace impurity contents in the specimens, or else to contamination of $Zr_{0.85}Ca_{0.15}O_{1.85}$ by the V — VO electrode in the a-c study. In the latter case, $P_\ominus$ should be lower than that obtained from the a-c measurements.

The effect of CaO dopant concentration on σ_{ion} for doped-ZrO_2 at 1000°C is given in Fig. 7. In Fig. 8 is given the empirical activation energy Q for ionic conduction in CaO-doped ZrO_2. The decrease in σ_{ion} and increase in Q with dopant content above 12 mole % CaO is in agreement with other investigations (24, 34-38).

Conclusions

From this initial use of the Wagner d-c polarization technique for the investigation of electronic conductivity in oxide electrolytes at elevated temperatures, the following results were forthcoming:

1. An improved method for plotting polarization data was demonstrated which allows the simultaneous determination of both $\sigma_\oplus$ and $\sigma_\ominus$ from a single experimental run;
2. Values for $\sigma_\oplus$ and $\sigma_\ominus$ in $Zr_{0.85}Ca_{0.15}O_{1.85}$ and $\sigma_\oplus$ in $Th_{0.85}Y_{0.15}O_{1.925}$ were determined for several oxygen chemical potentials at temperatures of 1000°, 900°, and 800°C;
3. Experimental difficulties were encountered in the application of the polarization technique at very low oxygen activities and in the determination of the conductivity of the minority electronic carrier;
4. The P_{O_2} ranges for predominant ionic conductivity were estimated for the oxide electrolytes.

The total conductivity for a series of ZrO_2 + CaO electrolyte compositions was determined over a range of P_{O_2} and temperature.

Acknowledgment

Helpful discussions by C. Wagner and the cooperation of the Aerospace Research Laboratory at Wright-Patterson Air Force Base are appreciated. This research was supported under Contract No. AT (11-1)-1440 by the United States Atomic Energy Commission. This paper is based on portions of the theses by E. C. Bogren in partial fulfillment of the requirements for the degree Master of Science and by J. W. Patterson for the degree Ph.D. in Metallurgical Engineering, The Ohio State University.

Manuscript received Jan. 18, 1967.

Any discussion of this paper will appear in a Discussion Section to be published in the June 1968 JOURNAL.

REFERENCES

1. K. Kiukkola and C. Wagner, *This Journal*, **104**, 373 (1957).
2. F. Hund, *Z. phys. Chem.*, **199**, 142 (1952).
3. A. Hoffman and W. Fischer, *Z. phys. Chem. (N.F.)*, **17**, 30 (1958).
4. A. Diness and R. Roy, *Solid State Communications*, **3**, 123 (1965).
5. H. Schmalzried, *Ber. Bunsenges. physik. Chem.*, **66**, 572 (1962).
6. W. Kingery, J. Pappis, M. Doty, and D. Hill, *J. Am. Ceram. Soc.*, **42**, 393 (1959).
7. L. Simpson and R. Carter, *ibid.*, **49**, 199 (1966).
8. H. Schmalzried, *Z. Phys. Chem. (Frankfurt)*, **38**, 87 (1963).
9. B. Steele and C. Alcock, *Trans. Met. Soc. AIME*, **233**, 1359 (1965).
10. J. Tretjakov and H. Schmalzried, *Ber. Bunsenges. physik. Chem.*, **69**, 396 (1965).
11. F. Hund and R. Mezger, *Z. physik. Chem.*, **201**, 268 (1952).
12. F. Hund, *Z. anorg. u allgem. Chem.*, **274**, 105 (1953).
13. E. Subbarao, P. Sutter, and J. Hrizo, *J. Am. Ceram. Soc.*, **48**, 443 (1965).
14. M. Lasker and R. Rapp, *Z. phys. Chem. (N.F.)*, **49**, 198 (1966).
15. J. E. Bauerle, *J. Chem. Phys.*, **45**, 4162 (1966).
16. D. Bray and U. Merten, *This Journal*, **111**, 447 (1964).
17. W. Rhodes and R. Carter, abstracted in *Bull. Am. Ceram. Soc.*, **41**, 283 (1962).
18. Z. Volchenkova and S. Pallguev, *Trudy Inst. Elektrokhim, Akad. Nauk S.S.S.R., Ural Filial 1*, **119** (1960).
19. C. Wagner, *Proc. Int. Comm. Electrochem. Thermo. and Kinetics* (CITCE), 7th meeting, London 1955, Butterworth Scientific Publications, London (1957).
20. F. Kröger, *J. Am. Ceram. Soc.*, **49**, 215 (1966).
21. M. Hebb, *J. Chem. Phys.*, **20**, 185 (1952).
22. C. Wagner, *Z. Elektrochem.*, **60**, 4 (1956); **63**, 1027 (1959).
23. W. Danforth and J. Bodine, *J. Franklin Inst.*, **260**, 467 (1955).
24. R. Vest and N. Tallan, *J. Appl. Phys.*, **36**, 543 (1965).
25. D. Raleigh, "Progress in Solid State Chemistry," Chap. 3, Pergamon Press, Oxford (1967).
26. B. Ilschner, *J. Chem. Phys.*, **28**, 1109 (1958).
27. D. Raleigh, *J. Phys. and Chem. Solids*, **26**, 329 (1965).
28. J. Wagner and C. Wagner, *J. Chem. Phys.*, **26**, 1597 (1957).
29. A. Morkel and H. Schmalzried, *ibid.*, **36**, 3101 (1962).
30. R. A. Rapp, *Trans. Met. Soc. AIME*, **227**, 371 (1963).
31. R. A. Rapp and F. Maak, *Acta Met.*, **10**, 63 (1962).
32. S. P. Mitoff, *J. Chem. Phys.*, **41**, 2561 (1964).
33. R. W. Vest, N. M. Tallan, and W. C. Tripp, *J. Am. Ceram. Soc.*, **47**, 635 (1964).
34. H. Johansen and J. Cleary, *This Journal*, **111**, 100 (1964).
35. J. Dixon, L. Lagrange, V. Merten, C. Miller, and J. Porter, *ibid.*, **110**, 276 (1963).
36. D. Strickler and W. Carlson, *J. Am. Ceram. Soc.*, **47**, 122 (1964).
37. F. Trombe and M. Foex, *Compt. rend.*, **236**, 1783 (1953).
38. E. C. Subbarao and T. C. Tien, *J. Chem. Phys.*, **39**, 1041 (1963).

Technical Notes

Phase Diagram of the Pseudo-Binary System Ag_2Te-In_2Te_3 and Semiconducting Properties of $AgIn_9Te_{14}$

Ping-Wang Chiang,[1] D. F. O'Kane,[2] and Donald R. Mason[3]

Department of Chemical and Metallurgical Engineering, The University of Michigan, Ann Arbor, Michigan

Hahn *et al.* (1) have made x-ray analyses at six compositions within the Ag_2Te-In_2Te_3 pseudo-binary system and reported that all the materials crystallized in chalcopyrite structures. Austin *et al.* (2) and Zhuze *et al.* (3) studied the optical and electrical properties of $AgInTe_2$ and reported that its energy gap is 0.9 ev. O'Kane (4) investigated the electrical properties of $AgIn_3Te_5$. No work has been done on the compound $AgIn_9Te_{14}$ which is at the composition 10 mole % Ag_2Te in In_2Te_3.

Experimental Results

DTA measurements have been made on samples within the Ag_2Te-In_2Te_3 pseudo-binary system using either the equipment described by Barnes *et al.* (5) or an Aminco Thermoanalyzer, or both. The transition temperatures obtained in either apparatus on samples of the same composition agreed within 2°C. The study of the phase diagram indicates that $AgIn_9Te_{14}$ exists as a peritectic compound. Electrical conductivity and Hall effect measurements using the circuit described by LaBotz *et al.* (6) have been made on the single-phase portion of a zone-refined ingot of this material.

Phase diagram of the Ag_2Te-In_2Te_3 *pseudo-binary system.*—DTA measurements have been made on quenched samples at 0, 2.5, 5, 8, 10 (two samples), 12.5, 20, 35, 40, 55, 60, 80, and 90 mole % Ag_2Te; on annealed samples (450°-600°C for 4 to 23 days) at 17 and 50 mole % Ag_2Te; on both quenched and annealed samples at 25, 43, 52, 55, 58, 65, 70, 82, 85, and 95 mole % Ag_2Te; and on zone-refined samples at 10 and 30 mole % Ag_2Te. The thermograms of the annealed samples did not differ from those of the quenched samples. The composition distribution of a zone-refined sample should be different from that of an as-cast one and is not interpreted here. However, it was observed that the thermogram of the single-phase portion of the 10 mole % Ag_2Te alloy was identical to the thermogram of the quenched sample, thus indicating the existence of the compound $AgIn_9Te_{14}$.

Based on these DTA measurements, the tentative phase diagram shown in Fig. 1 has been constructed. In the low Ag_2Te region, the solid solution of Ag_2Te in In_2Te_3 (which melts peritectically at 674°C in this system) may extend to 3 mole % Ag_2Te. However, this tentative conclusion reguires confirmation by x-ray diffraction studies. In addition, two more peritectic compounds exist. One at 7.5 mole % Ag_2Te melts at 686°C, and the other at 10 mole % Ag_2Te melts at 694°C. The congruent compound at 25 mole % Ag_2Te which melts at 699° ± 1°C has a very wide homogeneity range. The compound at 50 mole % Ag_2Te

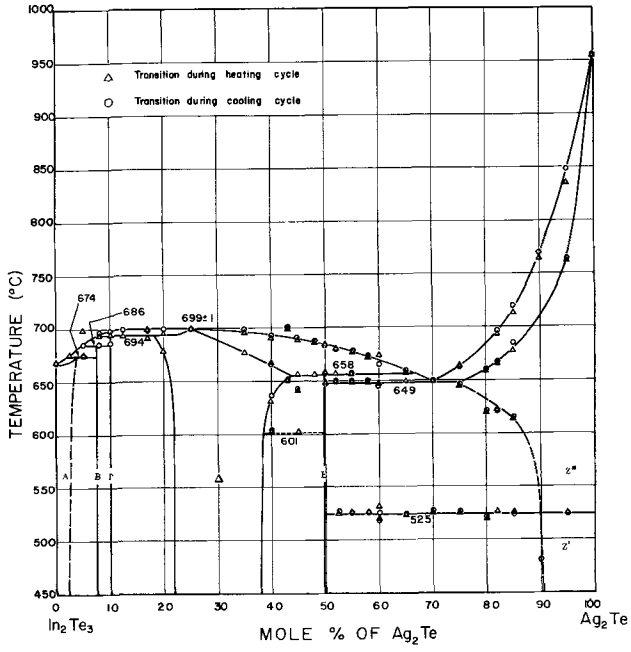

Fig. 1. Tentative phase diagram for the Ag_2Te-In_2Te_3 pseudo-binary system.

($AgInTe_2$) melts peritectically at 658° ± 5°C. The phase diagram of the high Ag_2Te region is relatively simple. At 70 mole % Ag_2Te, there is a eutectic point at 649° ± 2°C. It appears that the solubility of In_2Te_3 in Ag_2Te may be high. However, this should be confirmed by x-ray diffraction. In addition to the solid-solid transition at 525° ± 2°C, the Ag_2Te phase has a solid-solid transition at 150° ± 3°C which is not shown in the figure.

Electrical properties of $AgIn_9Te_{14}$.—Electrical conductivity and Hall coefficient measurements have been made on specimen No. 186(2), a single phase polycrystalline portion of an ingot with the nominal composition $(Ag_2Te)(In_2Te_3)_9$, which had ten zone-refining passes. Figure 2 shows a plot of the logarithm of the electrical conductivity *vs.* the reciprocal absolute temperature, and Fig. 3 shows a plot of the logarithm of $|R_H T^{3/2}|$ *vs.* the reciprocal absolute temperature. The material was n-type. The composition was verified by a DTA measurement which showed a transition temperature of 694°C. At room temperature, the material has an electrical conductivity of 2.5 x 10^{-6} mho/cm, which increases as the temperature increases. The intrinsic energy gap of $AgIn_9Te_{14}$ estimated from the slopes of the plots above 330°C is 1.50 ev from the electrical conductivity data and 1.5 ev from the Hall coefficient data. A donor energy level

[1] Present address: Research Laboratory, Tecumseh Products Inc., Ann Arbor, Michigan.

[2] Present address: Thomas J. Watson Research Center, IBM Corporation, Yorktown Heights, New York.

[3] Present address: Physical Electronics, Radiation Incorporated, Melbourne, Florida.

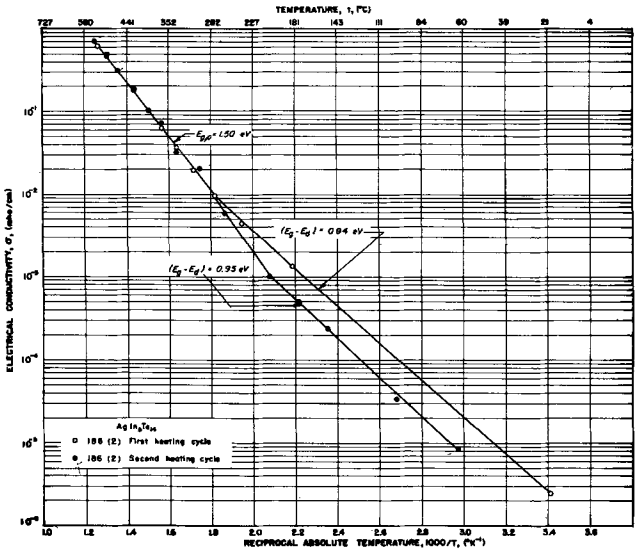

Fig. 2. Logarithm of electrical conductivity vs. reciprocal absolute temperature for $AgIn_9Te_{14}$.

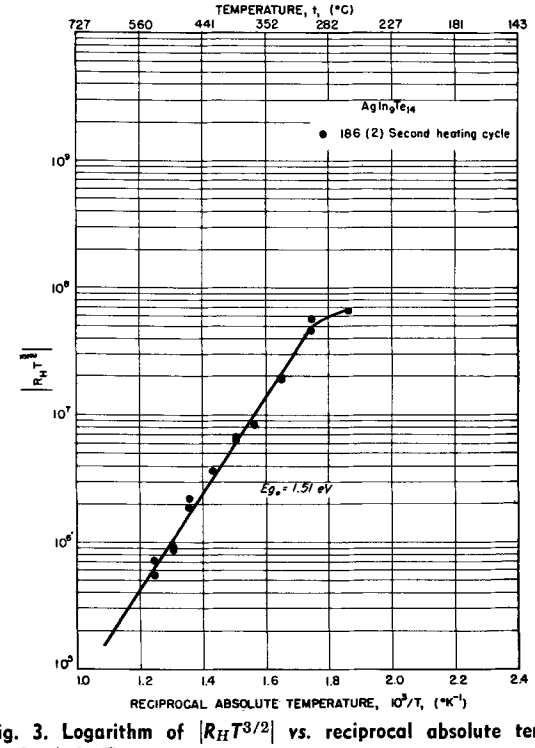

Fig. 3. Logarithm of $|R_H T^{3/2}|$ vs. reciprocal absolute temperature for $AgIn_9Te_{14}$.

0.95 ev below the bottom of the conduction band is observed at temperatures below 200°C. Log $|R_H\sigma|$ is plotted against log T as shown in Fig. 4. The data were scattered. A slope of —1.0 is obtained by a least square correlation for temperatures above 600°K, indicating that lattice scattering is probably the dominant scattering mechanism. The Hall mobility of $AgIn_9Te_{14}$ is 40 cm²/v-sec at 600°K.

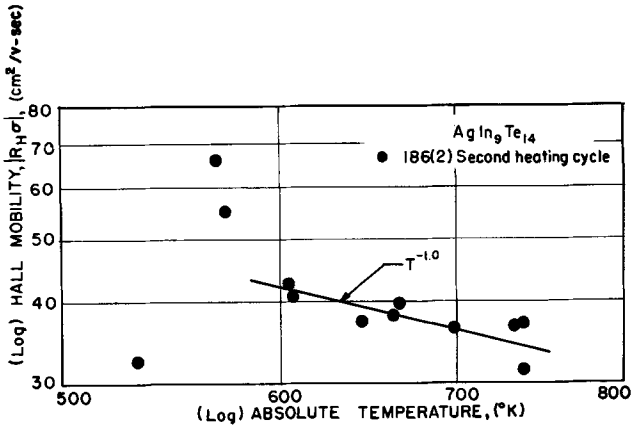

Fig. 4. Logarithm of $|R_H\sigma|$ vs. logarithm of absolute temperature for $AgIn_9Te_{14}$.

Discussion

No x-ray, density, or Seebeck measurements were made on the compound $AgIn_9Te_4$. Hahn (1) reported lattice parameters at 9 mole % and 20 mole % Ag_2Te as a = 6.19 kX, c = 12.38 kX, and c/a ratio of 2.0. According to our phase diagram, these values should be characteristic of $AgIn_9Te_{14}$.

The decrease in conductivity and the decrease in the temperature at which the activation energy changes from 0.95 to 1.50 ev on the second heating cycle are probably due to the loss of the most volatile component, Te.

The 1.50 ev energy gap of this material is greater than that of 1.1 ± 0.1 for $AgIn_3Te_5$ reported by O'Kane (4) and that of 1.20 ± 0.05 observed for In_2Te_3 (7).

Manuscript received Nov. 22, 1966; revised manuscript received March 17, 1967. Contribution No. 30 from the Semiconductor Materials Research Laboratory, The College of Engineering, The University of Michigan, Ann Arbor, Michigan. This work has been supported by Texas Instruments Incorporated, Dallas, Texas and the National Science Foundation. Some of DTA analyses were carried out at Tecumseh Products Research Laboratory, Ann Arbor, Michigan.

Any discussion of this paper will appear in a Discussion Section to be published in the June 1968 JOURNAL.

REFERENCES

1. H. Hahn, G. Frank, W. Klinger, A. D. Meyer, and G. Storger. *Z. anorg. u. allgem. chem.*, **271**, 153 (1953).
2. I. G. Austin, C. H. L. Goodman, and A. E. Pengelley, *This Journal*, **103**, 609 (1956).
3. V. P. Zhuze, V. M. Sergeeva, and E. L. Shtrum, *Soviet Physics, Technical Physics*, **3**, 1925 (1958).
4. D. F. O'Kane and D. R. Mason, *This Journal*, **111**, 546 (1964).
5. C. E. Barnes, B. M. Kulwicki, G. D. Rose, and D. R. Mason, *Electrochem. Tech.*, **2**, 142 (1964).
6. R. J. LaBotz, D. R. Mason, and D. F. O'Kane, *This Journal*, **110**, 127 (1963).
7. P. W. Chiang, Ph.D. Thesis, University of Michigan, Ann Arbor (1965).

Vapor Grown SiAs Crystals

S. W. Ing, Jr., Y. S. Chiang, and W. Haas

Research Laboratories, Xerox Corporation, Webster, New York

Single crystals of SiAs in the form of tiny needles have been grown by Wadsten (1) from the melt, and the crystal structure has been determined. However, other properties of the material have not been reported in the literature. We have grown SiAs crystals of sufficient size, using a vapor transport technique, to enable us to study some of the SiAs crystal physical properties.

The crystal growth was carried out in an evacuated quartz tube. Elementary Si (99.9999% purity) and As (99.999% purity) were placed at opposite ends of the tube. I_2 or AsI_3 was used as the transport agent and was introduced into the tube along with the As in an I_2-to-As ratio of 0.5 to 1%. The tube was then placed in a two-zone furnace with the Si located at the hot zone between 1000° and 1100°C and the As at the cooler zone around 450°C. The temperature gradient between the zones was approximately linear. In 24 hr, a mass of SiAs crystals appeared in a region where the temperature was measured to be around 900°C. The crystals grew in a flat ribbon fashion with the larger ones measuring over 1 cm long as shown in Fig. 1. Frequently, an individual ribbon would be made up of two or three crystals with grain boundaries running along the length of the ribbon.

X-ray measurements were made on the vapor-grown single crystals. The results showed that these crystals are monoclinic and have the symmetry of the space group C2/m which is in agreement with the findings of Wadsten (1). The growth direction of the ribbons was found to parallel the c-axis. The crystals were analyzed chemically,[1] and the results showed a one-to-one ratio of Si-to-As with an accuracy of determination of 1 a/o (atomic per cent).

In some batches, Te was added to the As source in the reaction tube; the atomic ratio of Te-to-As was 1:2. The resulting crystals has the same appearance as without the addition of Te. Chemical analyses showed that these crystals contained about 5 a/o of Te. X-ray measurements showed no alteration in the crystal structure when Te was incorporated.

The SiAs crystals have metallic, highly reflecting surfaces and are completely transparent in the yellow-red region of the spectrum but not in the blue region. Observation in polarized light shows that the crystals are strongly pleochroic. Between crossed nicols, the crystals exhibit straight extinction and in convergent light a biaxial interference figure. Figure 2 shows two faces of a single-crystal SiAs between crossed nicols in the 45° position. A and B are different faces of the crystal, and a growth line can be seen running across the crystal.

[1] Chemical analyses were performed by the Schwarzkopf Microanalytical Laboratory, Woodside, New York.

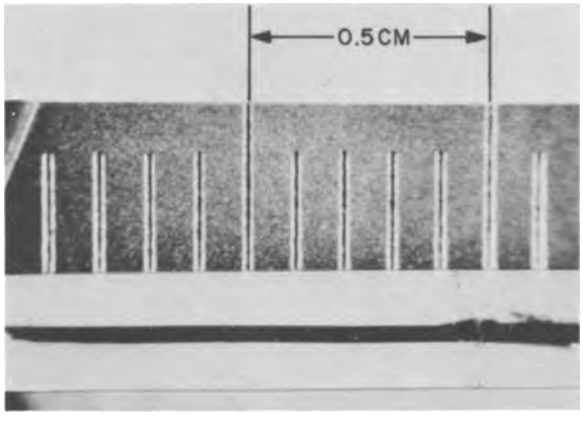

Fig. 1. Vapor grown SiAs crystal

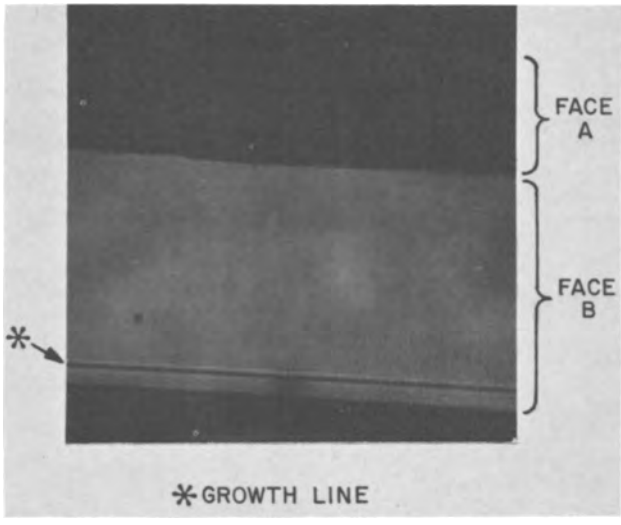

Fig. 2. Light transmission of a SiAs crystal between cross nicols; magnification 100X.

Optical transmission measurements of the Te-doped SiAs crystals have also been made using polarized light. The measurements were made with a Perking Elmer Model 16U monochromator which has resolutions of 25 and 79Å at light wavelengths of 4200 and 7400Å, respectively. The relative optical density spectra with the light polarized perpendicular and parallel to the c-axis of the crystal are presented in Fig. 3. No reflection measurements were made. The optical density spectra indicate that the material has an optical bandgap of around 2.2 ev. This value certainly represents a lower limit of the optical bandgap energy. The spectra also reveal a few small peaks in the long wavelength region. A significant amount of shift in the absorption spectrum was observed between the light polarized perpendicular and the light

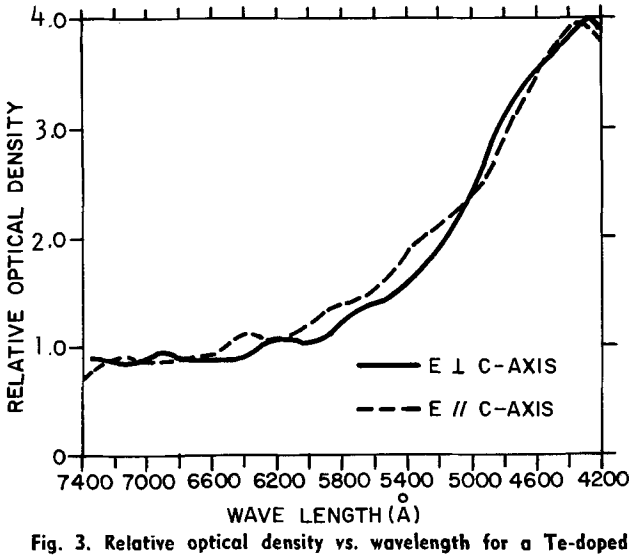

Fig. 3. Relative optical density vs. wavelength for a Te-doped SiAs crystal.

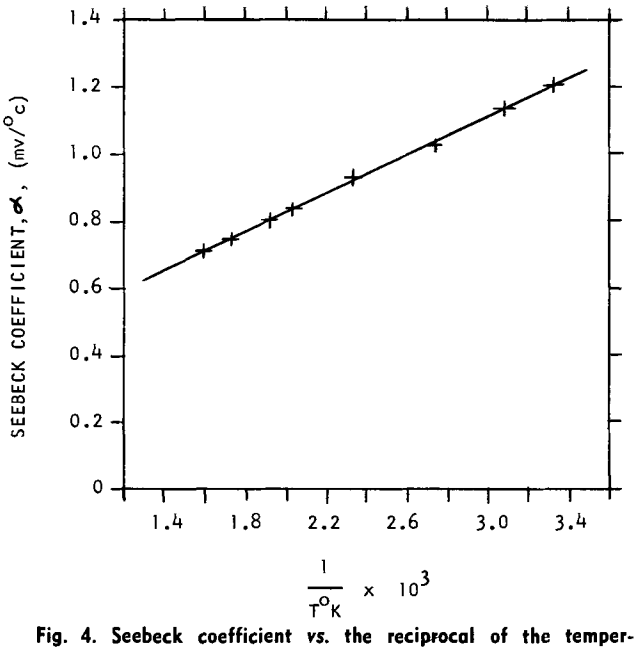

Fig. 4. Seebeck coefficient *vs.* the reciprocal of the temperature of a SiAs crystal doped with 5 a/o Te.

polarized parallel to the crystal c-axis. Several crossings of the spectra were observed in the short wavelength region: we cannot, at present, advance an explanation for these crossings.

Thermoelectric measurement indicated that the SiAs crystals were n-type. A Seebeck coefficient of 1.9 mv/°C was obtained near room temperature. The bulk resistivities of the undoped crystals at 22°C were 10^7 ohm-cm as measured by using the familiar 4-contact technique. The resistivity increased exponentially with increasing reciprocal temperature in the temperature range measured (295°-500°K). An activation energy of 0.43 ev was obtained. The Te-doped crystals were also n-type, but exhibited lower resistivities of around 1.4 x 10^3 ohm-cm. A lower activation energy, about 0.28 ev, was observed in the doped material. The Seebeck coefficient of the doped crystal has been measured as a function of temperature in the range 300°-620°K. The results are plotted *vs.* the reciprocal of the temperature in Fig. 4. A linear relationship is observed. By using the simplified expression (2), $\alpha = -(k/e)(\delta - E_f/kT)$, where α is the Seebeck coefficient, k the Boltzmann constant, e the electronic charge, δ a constant depending on the carrier scattering mechanism, E_f the Fermi energy, and T the absolute temperature, the δ and the E_f have been calculated based on the data obtained, to be 3.0 and 0.29 ev, respectively. The value of 3.0 for δ indicates that lattice scattering is the controlling mechanism for electron transport. The calculated Fermi energy agrees closely with the activation energy (0.28 ev). The Fermi level appears fixed either by a set of deep lying donor states or by the negatively charged centers located approximately 0.28 ev below the conduction band if the material is highly compensated. A Ga-In eutectic was used as the contacts in making the electrical measurements. These contacts are ohmic as indicated by the linear current-voltage relationship obtained with applied fields increasing up to 100 v/cm.

The electrical and the optical properties of SiAs clearly characterize the material as a semiconductor. Since it is a group IV-V compound, the atomic bonding within the crystal must satisfy the valence saturation rule (3), *i.e.*, $m(\mu-1) = xX$, where m is the number of cations and x the number of anions in the chemical formula, μ the valence of the cation, and X the valence of the anion. The term $(\mu-1)$ indicates the formation of a cation-cation bond for each cation present. These requirements are indeed satisfied based on the crystal structure of SiAs as proposed by Wadsten (1).

Acknowledgment

The authors wish to thank Mrs. P. S. Unger for the x-ray measurement, Dr. R. H. Zallen for the optical transmission measurement, and Dr. C. Wood for helpful discussions.

Manuscript received Feb. 20, 1967; revised manuscript received March 8, 1967.

Any discussion of this paper will appear in a Discussion Section to be published in the June 1968 JOURNAL.

REFERENCES

1. T. Wadsten, *Acta Chem. Scand.*, **19**, 1232 (1965).
2. R. R. Heikes and R. W. Ure, Jr., "Thermoelectricity: Science and Engineering," Chap. 11. Interscience Publishers, New York (1961).
3. F. Hulliger and E. Mooser, *J. Phys. Chem. Solids*, **24**, 283 (1963).

The Kinetics of Propane Adsorption on Platinum in Hydrofluoric Acid

Elton J. Cairns[1] and Adrian M. Breitenstein[2]

General Electric Company, Research & Development Center, Schenectady, New York

ABSTRACT

As a first stage in the investigation of the electrochemical oxidation of saturated hydrocarbons on platinum in acid electrolytes, the rate of adsorption of propane on a smooth platinum electrode was studied at 90°C in 37 mole % HF. Using an all-PTFE apparatus and single linear voltage sweep techniques, the surface coverage by hydrocarbon species was measured as a function of adsorption time and potential. The steady-state coverage resulting from propane adsorption shows a sharp maximum at 0.2v (*vs.* rhe). The amount of the most electrochemically active species is highest at 0.3v. The adsorption rate follows Langmuir kinetics with a third-order dependence on free surface. The rate constant has been measured for 0.2 and 0.3v at 90°C.

During the last few years there has been an active interest in the direct anodic oxidation of saturated hydrocarbons in fuel cells (1-10). Exploratory fuel cell investigations pointed out the usefulness of strong acid electrolytes in this connection. The acidic electrolytes which have received the most attention in hydrocarbon fuel cells are sulfuric acid (1), phosphoric acid (2-4), hydrofluoric acid (5-8), and cesium fluoride-hydrofluoric acid mixtures (5, 6, 9, 10). In order to understand better the kinetics and mechanisms involved in the over-all process of anodic oxidation of hydrocarbons, it is desirable to study the various individual steps in the process, starting with the adsorption of the hydrocarbon on a suitable electrode material in the presence of electrolyte.

Some work on the adsorption of methane (11) and ethane (12, 13) on platinum in perchloric acid has been done at temperatures below those where significant reactivity is shown in fuel cells. The results of Gilman (12) on ethane adsorption on platinum in perchloric acid were interpreted in terms of the kinetics of the adsorption process, the adsorption being second order in free surface and first order in ethane concentration. Propane adsorption on platinum in phosphoric acid has been studied (14, 15), but since the adsorption process was diffusion-controlled, no rate expressions could be derived from those results. Butane adsorption on platinum in sulfuric acid has been measured at steady state by tracer methods (16), and under unsteady-state conditions by the use of flow-through porous electrodes (17); neither investigation yielded quantitative kinetic information.

In order to study the kinetics of the adsorption process, it is necessary to perform the adsorption experiments under conditions where diffusion is not controlling. This requires that the product of the concentration of dissolved hydrocarbon and its diffusion coefficient be large enough (and therefore, diffusion fast enough) that the adsorption step is the slower process. It is known that hydrofluoric acid enhances the solubility of saturated hydrocarbons in water (18), and it is expected that the fluoride anion is not adsorbed on platinum electrodes (19, 20). For these reasons and because of the fact that fuel cells using hydrofluoric acid electrolyte oxidize saturated hydrocarbons at high current densities, it was decided that a study would be made of the adsorption of a saturated hydrocarbon on platinum in hydrofluoric acid. Propane was selected as the simplest typical saturated hydrocarbon because it is the smallest molecule containing both CH_2 and CH_3 groups, and it exhibits good reactivity on platinum in hydrofluoric acid (5, 6).

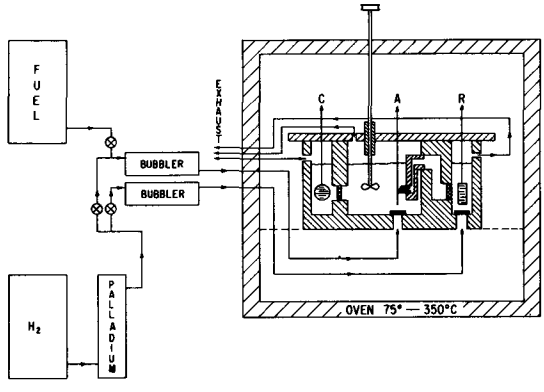

Fig. 1. Schematic diagram of PTFE cell, air thermostat and gas supplies.

Experimental

A schematic diagram of the PTFE three-compartment electrochemical cell, the air thermostat, and gas supplies is shown in Fig. 1. The working electrode compartment (~ 100 cm^3) had provision for bubbling argon or propane over the platinum wire working electrode, and provision for stirring by means of a two-bladed paddle stirrer which could be operated at any speed over the range 0-5000 rpm. A platinum thermocouple well allowed accurate temperature measurement of the electrolyte. Porous PTFE separators were used between the compartments. A PTFE Luggin capillary connected the working electrode compartment to the reference electrode compartment. The reference electrode compartment contained two platinized platinum flags (2 cm^2) which served as reversible hydrogen reference electrodes. Their potentials were observed to remain within 0.2 mv of each other at all times. The counter electrode was a platinized platinum flag of 2 cm^2 area. A forced-convection air thermostat controlled the air stream temperature to within ±0.1°C; control of the electrolyte temperature was better.

The working electrode consisted of a smooth platinum wire 0.146 cm in diameter with an exposed portion 1.034 cm long having a hemispherical end. The surface of the electrode was polished as follows: The Pt wire was mounted in a chuck on the shaft of a high-speed (20,000 rpm) motor with speed controller, and its end was made hemispherical by the application of fine emery paper as the electrode was rotated (~ 2000 rpm). Next, No. 600A emery paper was used to remove the pitted and mechanically damaged (from

[1] Present address: Argonne National Laboratory, Argonne, Illinois 60439.

[2] Present address: Materials & Processes Laboratory, General Electric Company, Schenectady, New York 12309.

the wire-drawing process) surface. When no more pits were visible at 50X, the electrode was washed in hot chromic acid, rinsed in distilled water, and annealed carefully in a hydrogen-air flame. The electrode was given a final series of polishing steps using spherical-grained Al_2O_3 powder in wet velvet. This wet-polishing proceeded in 3 stages using 20, 1, and 0.05μ particle sizes in succession, with microscopic examination at 50 and 100X between stages. When the surface appeared smooth at 100X after polishing with 0.05μ powder, the electrode was rinsed in distilled water, annealed, and cleaned by application of alternate anodic and cathodic currents ($\sim$ 10 ma/cm^2) in purified 37 m/o HF. The "true" surface area of the polished electrode was determined by cathodic hydrogen deposition using a linear voltage sweep. The true area was found to be 0.5467 cm^2, assuming 220 μcoul/true cm^2 for hydrogen deposition. This area corresponds to a roughness factor of 1.15.

The electrolyte solution was prepared from quartz redistilled water and Mallinckrodt analytical reagent grade hydrofluoric acid (48 w/o HF) containing a maximum of 5 ppm of heavy metals impurities and a maximum of 100 ppm H_2SiF_6. The HF and water were mixed to produce the 37 m/o HF azeotrope (boiling point, 112°C) which was then purified by distillation in an all-PTFE apparatus. The first and last portions of the distillate were discarded. The center-cut (about 60% of the starting material) was further purified in an all-PTFE cell by an electrochemical treatment consisting of alternate potentiostatic adsorption of impurities on a large ($\sim$ 50 cm^2, r.f. $\simeq$ 1000) platinum electrode and subsequent electrochemical oxidation at intervals of 15-20 min for 24 hr at 90°C. The electrolyte was then transferred to the all-PTFE cell of Fig. 1 where final electrochemical purification took place at 90°C for 48 hr, using a 4 cm^2 platinized platinum electrode (r.f. $\simeq$ 100). All electrochemical purification procedures were carried out under an argon atmosphere using Matheson 99.998% minimum purity argon with oxygen removed (Cu turnings at 800°C).

All gases fed to the electrochemical cell were first saturated with electrolyte solution vapor at the cell temperature using Pt and PTFE bubblers. All tubing and fittings downstream from the bubblers were made of PTFE. The propane used was of two grades: Phillips Research Grade, 99.99+ % pure, and Matheson Instrument Grade, 99.5% minimum purity. Both yielded identical results. The hydrogen was prepurified grade, 99.95% minimum, further purified by diffusion through a silver-palladium tube.

The electrochemical measurements were carried out with the aid of the instruments shown schematically in Fig. 2. The potentiostat was a Wenking fast-rise, model 6301RS, the function generator was a Hewlett-Packard Model 202A, modified for single pulse operation, the potentiometer was an L&N Model K-3, and the oscilloscope was a Tektronix type 555 dual-beam, X-Y, with type D preamplifiers. A make-before-break wafer switch allowed convenient switching from one signal source to another. It was necessary to adopt very careful shielding, guarding, and grounding practices in order to obtain the very low noise levels desired ($\pm$ 5 μa for 1 cm^2 electrodes).

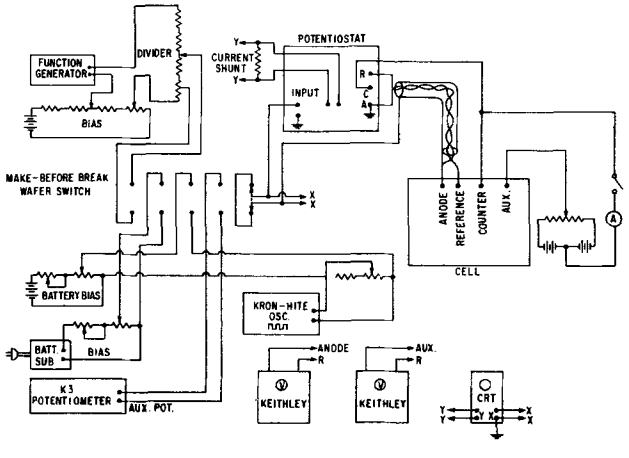

Fig. 2. Block diagram of electronics used for measurement of propane adsorption.

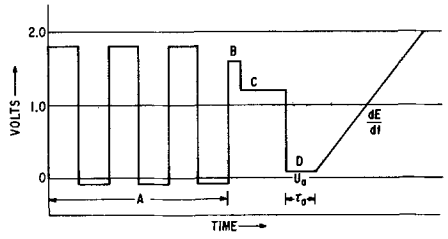

Fig. 3. Voltage sequence for propane adsorption measurement

The electrochemical studies centered around the determination of the amount of electrical charge required either for the anodic oxidation of adsorbed species on the electrode, or for the cathodic deposition of hydrogen on the electrode, usually in the presence of adsorbed hydrocarbon species. In these studies, it was necessary to prepare a reproducibly clean electrode surface. This was done by use of the well-known method of alternately passing anodic and cathodic currents. In this case, the alternate anodic-cathodic treatment was applied potentiostatically using a Kron-Hite square wave generator (Fig. 2) as a signal source for the potentiostat. This cleanup cycle is portion A of the voltage sequence shown in Fig. 3. Each anodic and cathodic potentiostatic pulse was 15 sec in duration, and the voltages were set at values such that equal anodic and cathodic charges were passed. Usually, 10 pulses were more than sufficient to prepare a clean, reproducible electrode surface. This cleanup was performed immediately prior to every experiment, and served to remove all species from the electrode surface which could be oxidized, reduced, and repelled from the surface by high and low potentials (about 1.8 and —0.04v *vs.* rhe). The rate of transition between 1.8 and — 0.04v was made slow enough that surface roughening of the electrode could not take place (21). After the cleanup was completed, the electrode and surrounding electrolyte were prepared for the adsorption step: a protective oxide layer was rapidly formed by stepping the potential up to 1.6v for 6 sec (step B, Fig. 3), and the potential was then dropped to 1.2v (step C) to maintain the oxide layer without passing any additional current. During step C, the propane (or argon) was bubbled (10 cc/min) and stirring was continued at 400 rpm for 60 sec, after which bubbling was stopped and stirring continued for an additional 60 sec to sweep any gas bubbles away from the electrode; the desired mass transport situation was established: usually, quiescent, propane-saturated electrolyte (120 sec of no bubbling or stirring). The working electrode was then stepped to a potential U_a at which reduction of the protective oxide layer took place (within a couple of milliseconds) and propane was allowed to adsorb on the electrode surface for a time τ_a, after which an anodic (or cathodic) linear voltage sweep of speed dE/dt v/sec was applied. The current-voltage trace during application of the voltage sweep was photographed from the screen of the oscilloscope, giving a permanent record of the oxidation of the species on the electrode surface (or a record of hydrogen deposition in the presence of the adsorbed species). Experiments performed as just described, but in the presence of argon rather than propane, gave results characteristic of the behavior of the electrode-electrolyte system alone, which were used as "blanks" in data reduction. The use of this type of voltage sequence in connection with adsorption studies has been reported by Gilman (22).

The details of the various voltage sequences used and their application will be clear from the discussions below. The areas under the current-voltage traces were measured with a compensating polar planimeter and were used for determining the amount of adsorbed material on the electrode surface, as described below.

Results

The objective of this work, as indicated above, was to determine the kinetics of the adsorption process for propane on platinum in hydrofluoric acid. In order to obtain results of sufficient accuracy for a kinetic analysis, it is necessary that the current-voltage trace in the presence of adsorbed propane be reproducible and significantly different from the "blank" trace in the presence of argon and that this difference be a measure of the amount of material adsorbed on the electrode surface. A sample trace, together with its corresponding blank is shown in Fig. 4 for 180 sec of propane adsorption at 0.3v (*vs.* rhe) and 90°C, the anodic sweep speed being 10 v/sec. The area between the two traces (Q) has the units of charge (coulombs), and this charge may be made up of several contributions:

$$Q = Q_{HC} + \Delta Q_{dl} + \Delta Q_O + Q_{diff} \qquad [1]$$

The term Q_{HC} is the charge required to oxidize the hydrocarbon species which were adsorbed on the electrode at the end of time τ_a (the start of the sweep), the numerical value of which is desired. The term ΔQ_{dl} is the change in the charge stored by the double layer as the voltage sweep is applied. This is a very small term (about 1-2%, usually), and can be corrected for (approximately) by noting the difference in current between the argon blank trace and the propane trace (see Fig. 4) in the potential range 0.4-0.6v. The term most difficult to correct for quantitatively is ΔQ_O, which is the change in the charge requiring to oxidize the platinum surface to the potential where the two traces merge (about 1.7v). This change exists because a very small amount of hydrocarbon species stays on the electrode surface until higher potentials (say, 2v) are reached (see below), since the rate of oxidation of this small amount of residue was not high enough to keep up with the voltage sweep. The value of ΔQ_O was always very small compared to Q_{HC} (less than 4%), and was readily determined with sufficient accuracy for use in Eq. [1]. Any additional propane which diffuses to the electrode surface and is adsorbed and oxidized during the anodic sweep is accounted for as Q_{diff} and causes an increase in the charge Q. This effect can easily be avoided by proper choice of sweep speed (see below). Since all of the terms on the right-hand side of Eq. [1] are small compared to Q_{HC} under appropriate experimental conditions, it is possible to obtain Q_{HC} to a high degree of accuracy, using small correction terms of only moderate (percentage) accuracy.

Two peaks are present in the propane trace of Fig. 4: a sharp one near 0.8v and a broad one near 1.2v. It is of interest to follow the behavior of these peaks separately, because it is likely that they represent different classes of materials on the electrode surface. The peak at 0.8v will be called type I, and represents material which is rapidly oxidized (high currents) at relatively low potentials. The broad peak at 1.2v will be called type II and represents material which is oxidized more slowly (lower currents) and over a broader potential range. The separation of the total area Q ($\approx Q_{HC}$) into the two component areas is indicated by the shading in Fig. 4. The exact shape of the shaded area in the overlap region does not have much influence on the results, but was drawn corresponding to the boundary expected from two overlapping probability distribution curves having the shapes of the type I and type II peaks. It was observed that the presence of adsorbed hydrocarbon tended to modify the shape of the rising portion of the trace representing the oxidation of the platinum surface, but this effect was small. It is possible, however, that this slight change in shape of the current-voltage curve for oxidation of the platinum surface could cause an error in the Q_I values, amounting to a few per cent of the values quoted. This effect probably does not influence the Q_{HC} values.

Steady-state surface coverage as a function of potential.—Since it was expected that the rate and extent of propane adsorption would vary with adsorption potential (U_a), a set of survey experiments was performed to determine the adsorption potentials to be used in the detailed kinetics studies. A fixed adsorption time (τ_a) of 300 sec was chosen, since this was sufficient for reaching essentially steady-state surface coverages (see later). The value of ${}^{1.7}_{0.5}Q_{HC}$, the charge required for oxidation of adsorbed hydrocarbon species in the potential range 0.5-1.7v, was determined as a function of potential, as shown in Fig. 5. Note that the results are expressed on the basis of "true" surface area of the electrode. The charge under the type I peak, with suitable corrections for double layer effects, is also presented in Fig. 5. Note that the largest total amount of material (in terms of charge) was present at 0.2v, where only a very little type I was present, while the largest amount of type I was found at 0.3v.

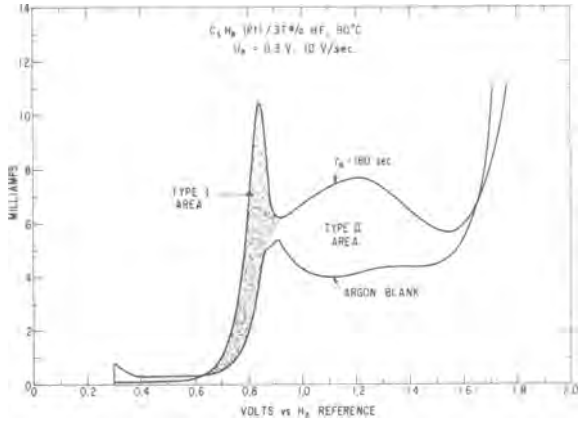

Fig. 4. Sample current-voltage traces for 180 sec of propane adsorption on Pt in 37 m/o HF at 90°C and for argon under the same conditions. Shaded portion indicates area of type I peak.

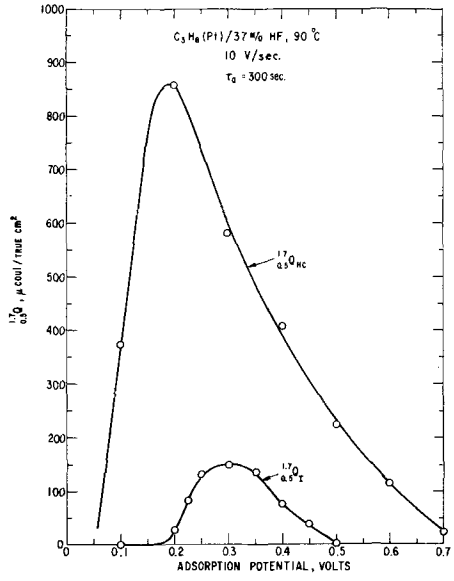

Fig. 5. Charge required for the oxidation of surface species resulting from the adsorption of propane for 300 sec, as a function of adsorption potential.

There are several major processes responsible for the establishment of the maximum in the $^{1.7}{}_{0.5}Q_{HC}$ curve of Fig. 5, the shape of which is in good agreement with the results of Brummer *et al.* in H_3PO_4 (14). At low potentials, the steady-state coverage decreases rapidly with decreasing potential because of hydrogenation-desorption of the hydrocarbon species (12) [largely as propane (23, 24)] and because of a competition between propane and (electrochemically produced) hydrogen for surface sites, the hydrogen tending to prevent propane adsorption. The result is a low coverage with "propane" at low potentials. At the higher potentials, the steady-state value of $^{1.7}{}_{0.5}Q_{HC}$ decreases with increasing potential because of the fact that the adsorbed hydrocarbon species are being electrochemically oxidized and are leaving as CO_2 and H_2O (24). In addition, the stoichiometry of the material on the surface is that of partially oxidized and dehydrogenated species, requiring less charge for oxidation to CO_2 and H_2O than the material which was present at 0.2v (see below).

The potentials 0.2 and 0.3v were selected for the more detailed adsorption rate studies because a comparison could be made between the results obtained with a maximum amount of type I present, and those with the maximum total adsorption (in terms of charge), but only a small amount of type I.

For the adsorption rate studies, the value of Q_{HC} was determined as a function of adsorption time τ_a for several sweep speeds between 1 and 100 v/sec. By plotting the value of Q_{HC} as a function of sweep speed for each τ_a, a plateau value of Q_{HC} could be found, assuring the elimination of any ΔQ or Q_{diff} contribution, since these contributions are dependent on sweep speed. The plots of $^{1.7}{}_{0.5}Q_{HC}$ *vs.* sweep speed for U_a = 0.3v are shown in Fig. 6, where $^{1.7}{}_{0.5}Q_{HC}$ is the charge measured for the 0.5467 cm² true area electrode. Note that the values of Q_{HC} were constant over the sweep-speed range of 2.5-25 v/sec. The plateau values of Q_{HC} for both U_a = 0.2 and 0.3v found in this way were used in all subsequent analyses of results.

Propane adsorption at 0.3v.—Because of the experiences of other investigators in finding that the adsorption of hydrocarbons was diffusion-limited, it was in order to establish the conditions under which the diffusion limitation could be avoided in this work to permit the determination of the adsorption rate law in the absence of diffusion limitations. The fact that a significant amount of material was adsorbed in only 50 msec at 0.3v (cf. Fig. 6) indicated that these results should be tested for diffusion control. If the adsorption process was diffusion controlled, and if $^{1.7}{}_{0.5}Q_{HC}$ is proportional to the number of moles of propane diffusing to the electrode surface, then $^{1.7}{}_{0.5}Q_{HC}$ as a function of time should follow the semi-infinite cylindrical diffusion equation, in the absence of convection.

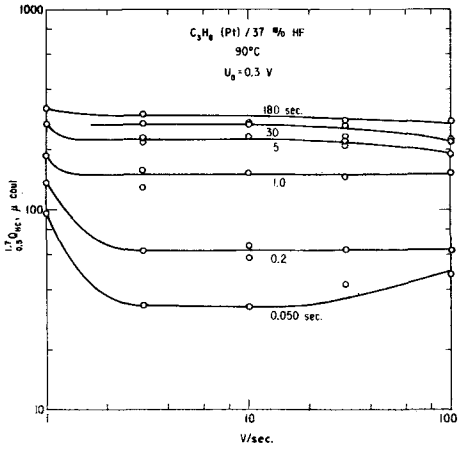

Fig. 6. Charge required for the oxidation of adsorbed species between 0.5 and 1.7v, as a function of anodic sweep speed, for several adsorption times. Propane was adsorbed at 0.3v and 90°C.

The differential equation for semi-infinite cylindrical diffusion to an electrode of constant potential in the absence of convection has been solved by Rius, Polo, and Llopis (25). The solution is

$$i = \frac{4\,n\mathbf{F}D_{AB}C_\infty}{\pi^2 r_o}\int_0^\infty \frac{\exp\left(-\frac{D_{AB}t}{r_o^2}Z\right)}{J_o^2(Z) + Y_o^2(Z)}\frac{dZ}{Z} \qquad [2]$$

Tables of the integral have been published by Jaeger and Clarke (26). An approximate solution for short times, integrated with respect to time to yield coulombs of material transferred to the surface after time t, is given by

$$Q = \frac{n\mathbf{F}D_{AB}C_\infty}{r_o}\left[\frac{t^{1/2}r_o}{\pi^{1/2}D_{AB}{}^{1/2}} + \frac{t}{2} - \frac{D_{AB}{}^{1/2}t^{3/2}}{4\,\pi^{1/2}r_o} + \frac{D_{AB}t^2}{8\,r_o^2} - \ldots\right] \qquad [3]$$

or,

$$Q = \frac{n\mathbf{F}D_{AB}C_\infty}{r_o}f(t) \qquad [4]$$

where Q = coul/cm² sec of propane diffusing to the electrode; D_{AB} = diffusion coefficient of propane in 37 m/o HF at 90°C, cm²/sec; n = number of equivalents per propane molecule; C_∞ = solubility of propane in 37 m/o HF at 90°C, moles/cm³; r_o = radius of electrode, cm; and t = time, sec.

In order to use Eq. [3] to test for diffusion-limited adsorption, it is necessary to know the value of the diffusion coefficient of propane in 37 m/o HF at 90°C. Since the physicochemical properties of 37 m/o HF are very similar to those of water, the value for the diffusion coefficient of propane in water was used as a starting point. The value of the group $(T/D_{AB}\mu)$ used by Wilke and Chang (27) in their correlation of liquid-phase diffusion coefficients was calculated, using the properties of the propane-water system. The measured value of the diffusion coefficient of propane in water at 29.9°C is 1.28 x 10^{-5} cm²/sec ± 2%, as reported by Saraf and Witherspoon (28). This value, and the viscosity of water were used to calculate the value of the group $(T/D_{AB}\mu)$, giving 3.05 x 10^7 °K — sec/cp — cm², in excellent agreement with an estimate of this group using Wilke and Chang's correlation. Since this group is not a function of temperature (27), it is only necessary to have the value of the viscosity of 37 m/o HF at 90°C in order to calculate the diffusion coefficient of propane in this electrolyte at 90°C. The viscosity of the electrolyte was measured at 24° and 96°C, using an all-PTFE Ostwald-type viscometer calibrated with water at each temperature. The values obtained, and that calculated for 37 m/o HF at 90°C are given in Table I, along with the calculated diffusion coefficients, using the value of $(T/D_{AB}\mu)$ given above. The value of the diffusion coefficient for C_3H_8 in 37 m/o HF, 3.516 x 10^{-5} cm²/sec at 90°C was then used in Eq. [3] to calculate the values of the bracketed expression, designated $f(t)$ in Eq. [4].

Using the calculated values of $f(t)$ for each adsorption time τ_a up to 1 sec, the plateau values of $^{1.7}{}_{0.5}Q_{HC}$ from Fig. 6 and some additional data for 10 v/sec

Table I. Properties of 37 m/o HF

Property	Temperature		
	24°C	90°C	96°C
Viscosity, centipoise	0.9492	—	0.3175
Density, g/cm³	1.148	—	1.076
$D_{C_3H_8\text{-}HF}$, cm²/sec	1.026 x 10^{-5}	3.516 x 10^{-5}	—

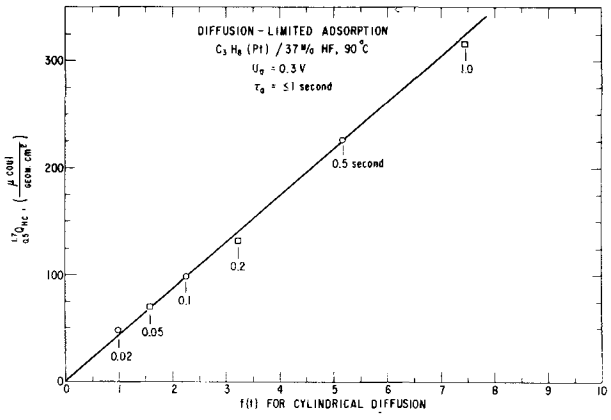

Fig. 7. Plot of $^{1.7}{}_{0.5}Q_{HC}$ vs. $f(t)$ for cylindrical diffusion, indicating that the adsorption of propane at 0.3v from 37 m/o HF at 90°C is diffusion controlled for about the first second of the adsorption period.

were plotted against $f(t)$ as shown in Fig. 7. The linearity of this plot indicates that the adsorption process is diffusion-limited for times shorter than 1 sec, and that $^{1.7}{}_{0.5}Q_{HC}$ must be proportional to the total amount of propane adsorbed on the electrode. For values of τ_a greater than 1 sec, $^{1.7}{}_{0.5}Q_{HC}$ falls below the expected curve, indicating that some other process is limiting for $\tau_a > 1$ sec. The proportionality between $^{1.7}{}_{0.5}Q_{HC}$ and $f(t)$ for small τ_a gives support to the use of Q_{HC} as a direct measure of surface coverage, even under conditions where diffusion does not happen to be rate limiting. The value of the slope of the line in Fig. 7 is directly related to the solubility of propane in the electrolyte as indicated by Eq. [3]. The calculation of the solubility from the slope requires a knowledge of the ratio of $^{1.7}{}_{0.5}Q_{HC}$ to the total amount of charge required to oxidize all of the propane which arrives at the electrode surface. This ratio was found to be 0.685 (see later), and was used together with the value 17 for n (see later) to give a solubility of 8.13 x 10^{-8} moles C_3H_8/cm^3. This solubility corresponds to 0.145 m-mol/l-atm as the Henry's law constant, and is in the same range as the values experimentally determined for C_3H_8 in water and aqueous H_3PO_4 at 90°C (30).

The plateau values of $^{1.7}{}_{0.5}Q_{HC}$ for all adsorption times at $U_a = 0.3$v are shown in Fig. 8, together with the component values $^{1.7}{}_{0.5}Q_I$ and $^{1.7}{}_{0.5}Q_{II}$. The rate of adsorption at 0.3v was diffusion-limited for less than 1 sec, the rate decreasing to a kinetically determined one as adsorption proceeded. In less than 100 sec, the electrode adsorbed about 90% of the amount that it adsorbed in 10^4 sec, which value it seemed to approach asymptotically. The values of $^{1.7}{}_{0.5}Q_I$ and $^{1.7}{}_{0.5}Q_{II}$ were obtained by integrating the type I and type II peaks separately, as indicated in Fig. 4, and the plateau values were determined from plots of Q_I and Q_{II} against sweep speed. These plateau values are the ones plotted in Fig. 8. It was found that the type I species was formed (and oxidized) rapidly, hence the higher sweep speeds (20-100 v/sec) were required to establish its plateau values. Note that the type I material starts appearing only after the surface is largely covered with type II.

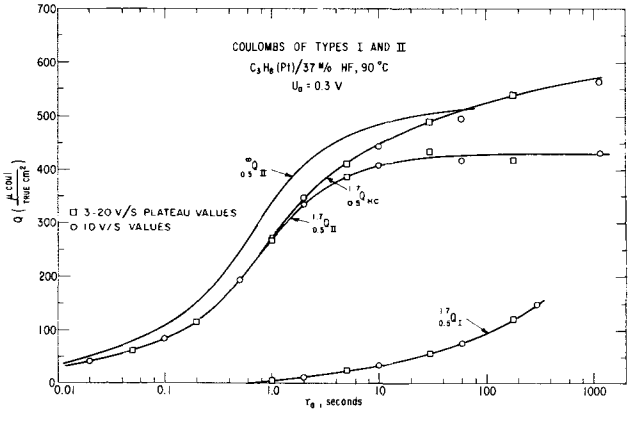

Fig. 8. Plateau values of $^{\infty}{}_{0.5}Q_{HC}$, $^{1.7}{}_{0.5}Q_{HC}$, $^{1.7}{}_{0.5}Q_I$, and $^{\infty}{}_{0.5}Q_{II}$ as a function of adsorption time for propane on Pt in 37 m/o HF at 0.3v, 90°C.

In order to learn more about the species on the electrode surface, it is necessary to have not only a measure of the number of coulombs required to oxidize the material on the surface, but also a measure of the fractional coverage, or its equivalent. This information would then allow the calculation of the number of electrons per monolayer, or per surface site, required to oxidize the carbonaceous species; hence, some information about stoichiometry and oxidation state of the surface species would be obtained.

The fractional surface coverage by carbonaceous species was measured by the blockage of the surface for hydrogen deposition and for oxygen evolution. In the case of hydrogen deposition, a linear cathodic sweep was used to measure the amount of hydrogen which could be deposited on that portion of the surface not blocked by adsorbed hydrocarbon species. The usual pretreatment and adsorption steps A through D of Fig. 3 were used, followed by a linear cathodic sweep. The number of coulombs required to saturate the remaining free surface with hydrogen was measured by integration of the area under the cathodic curves in the range 0.3-0.0v, except at the highest sweep speeds where integration to somewhat lower potentials was required in order to include all of the hydrogen deposited before rapid hydrogen evolution set in (29).

The relationship for the fraction of the surface covered by hydrocarbon species (and therefore not available to hydrogen) is expressed by

$$^{0.0}{}_{0.3}\theta_{HC} = \frac{^{0.0}{}_{0.3}Q_{SH} - ^{0.0}{}_{0.3}Q_H}{^{0.0}{}_{0.3}Q_{SH}} \qquad [5]$$

where $^{0.0}{}_{0.3}Q_{SH}$ is the number of coulombs required for cathodic hydrogen deposition starting at 0.3 *vs.* rhe, in the presence of argon (or for $\tau_a = 0$), corrected for double layer charging. $^{0.0}{}_{0.3}Q_H$ is the number of coulombs required for cathodic hydrogen deposition starting at 0.3v in the presence of adsorbed hydrocarbon, corrected for double layer charging.

As with the Q_{HC} experiments, complete sets of $^{0.0}{}_{0.3}\theta_{HC}$ values were determined for the full range of sweep speeds for each value of τ_a. The values of $^{0.0}{}_{0.3}\theta_{HC}$ were plotted against sweep speed, and the results showed two plateaus for each value of τ_a. At low sweep speeds ($\leq$ 3 v/sec) the plateau value of $^{0.0}{}_{0.3}\theta_{HC}$ indicated the coverage by material which was not readily hydrogenation-desorbed. This material can be identified as type I from the propane adsorption work of Grubb and Lazarus (24) and from the ethane work of Gilman and co-workers (12, 13), in which it was found that type I material is very difficult to hydrogenate-desorb, while type II does so very readily, even at only 60°C. In addition, the time of appearance and rate of increase of $^{0.0}{}_{0.3}\theta_{HC}$ at low sweep speeds ($\leq$ 0.3 v/sec) corresponded very well to $^{1.7}{}_{0.5}Q_I$ in Fig. 8. For these reasons, the plateau values of $^{0.0}{}_{0.3}\theta_{HC}$ at low sweep speeds were assigned to the type I species.

The plateaus of $^{0.0}{}_{0.3}\theta_{HC}$ at high sweep speeds ($>$ 30 v/sec) were taken to correspond to the total amount of adsorbed material, because the cathodic sweep depositing hydrogen was so fast that no detectable hydrogenation-desorption took place. The plateau values of $^{0.0}{}_{0.3}\theta_I$ (low sweep speeds) and $^{0.0}{}_{0.3}\theta_{HC}$ (high sweep speeds) are plotted in Fig. 9. The data points for $^{0.0}{}_{0.3}\theta_{HC}$ for times less than 5 sec were not mea-

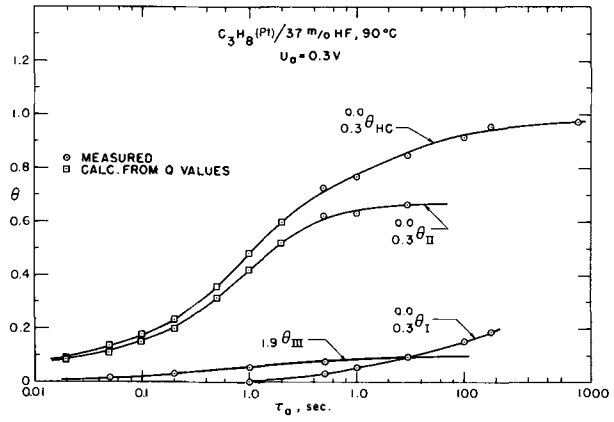

Fig. 9. Fractional surface coverage of all species as a function of adsorption time for an adsorption potential of 0.3v.

sured directly by means of the cathodic sweeps because the plateau values of θ for short adsorption times had not been reached at the fastest sweep speeds used in this study (100 v/sec). The curve of $^{0.0}_{0.3}\theta_{HC}$ for short times was calculated from the corresponding Q_{HC} values, using the number of electrons per surface site determined below.

The fractional surface coverage of the small amount of carbonaceous residue present at 1.9v during the anodic sweep was measured by its blockage of oxygen evolution in a manner similar to the blockage of hydrogen deposition during a cathodic sweep. This diminution of oxygen evolution current by adsorbed species was taken as a direct measure of the fractional surface coverage

$$_{1.9}\theta_{HC} = \frac{_{1.9}i_{Ar} - _{1.9}i_{HC}}{_{1.9}i_{Ar}} \qquad [6]$$

where $_{1.9}i_{Ar}$ is the current at 1.9v with argon present instead of propane (this is the same as $_{1.9}i_{HC}$ at $\tau_a = 0$) and $_{1.9}i_{HC}$ is, the current at 1.9v in the presence of adsorbed propane, as read from the voltage-sweep oscillogram. The value 1.9v was chosen because it was located in the linear region of the Tafel plots for oxygen evolution. The diminution of oxygen evolution was accepted as a quantitative measure of the fractional surface coverage by hydrocarbon species because plots of the plateau values of $_{1.9}\theta_{HC}$ *vs.* $f(t)$ from Eq. [3] gave good straight lines for adsorption times of up to 1 sec. This, coupled with the information of Fig. 7, is evidence for the validity of Eq. [6].

The values of $_{1.9}\theta_{HC}$ for various adsorption times, calculated using Eq. [6], plotted against sweep speed show two plateaus for each τ_a. At the low sweep speeds, essentially all of the type II material was oxidized before the potential reached 1.9v, and only a small amount of a very refractory residue, called type III, remained. This type III material was much more difficult to oxidize than either type I or type II, but it was completely removed by the cleanup procedure employed between experiments. At the high sweep speeds, a small amount of type II material was left on the surface, in addition to the type III. The small amounts of type II material left on the surface at high sweep speeds correspond to the slight decreases of $^{1.7}_{0.5}Q_{HC}$ which were found at the high sweep speeds. The maximum accumulation of type III, which was found at long times, was less than 0.1 monolayer, as shown in Fig. 9.

The values of $^{0.0}_{0.3}\theta_{II}$ in Fig. 9 were obtained from the expression

$$^{0.0}_{0.3}\theta_{II} = {}^{0.0}_{0.3}\theta_{HC} - {}^{0.0}_{0.3}\theta_{I} - {}_{1.9}\theta_{III} \qquad [7]$$

Now that values of Q and θ as a function of time for types I and II are known, it is possible to calculate the number of electrons per H site obscured required for the oxidation of these species. This will give some information about the state of oxidation of these materials. The stoichiometry of type I can be established from a plot of $^{1.7}_{0.5}Q_I$ *vs.* $^{0.0}_{0.3}\theta_I$, the slope of which is the number of electrons required for the oxidation of type I to CO_2 and H_2O, per H site obscured

$$n_I = \frac{^{1.7}_{0.5}Q_I}{^{0.0}_{0.3}\theta_I Q_{SH}} \qquad [8]$$

Figure 10 shows the plot, which indicates that the stoichiometry is constant with surface coverage over the full range of time and coverage. The slope corresponds to 2.95 electrons per H site, indicating a partially oxidized species. This is consistent with other kinds of studies which also led to the conclusion that type I was partially oxidized (13, 24). Such a species, consistent with $3e^-$/H site, could be

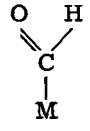

A plot similar to Figure 10 was prepared for the type II species, with the result that $n_{II} = 3.47$, which could correspond to a partially dehydrogenated propane molecule, which obscures 5 H sites after dehydrogenation. If 3 hydrogen atoms are lost by the dehydrogenation, then there are 17 e^-/adsorbed "propane," yielding $n_{II} = 3.40$ in good agreement with the experimental result. Such an arrangement could be

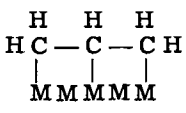

The value $n_{II} = 3.47$ is also in good agreement with a value of 3.71 found by Grubb and Lazarus (24) at a lower temperature and a lower potential; the difference is in the expected direction. Now that n_{II} is known, it is possible to make a small correction for the type II material not completely oxidized at the intermediate sweep speeds used to obtain $^{1.7}_{0.5}Q_{II}$. This correction was calculated from

$$_{1.9}Q_{II} = {}_{1.9}\theta_{II} n_{II} Q_{SH} \qquad [9]$$

and was added to $^{1.7}_{0.5}Q_{II}$ to give $^{\infty}_{0.5}Q_{II}$, as shown in Fig. 8. The ratio of $\left(\frac{^{\infty}_{0.5}Q_{HC}}{^{1.7}_{0.5}Q_{HC}}\right)$ used earlier for the calculation of the propane solubility was obtained from the $^{\infty}_{0.5}Q_{II}$ values, with an additive correction for the type III species on the surface, using the estimated value of 3.9 for n_{III}.

In addition to the calculation of the oxidation stoichiometry of the surface species, Fig. 9 can be used

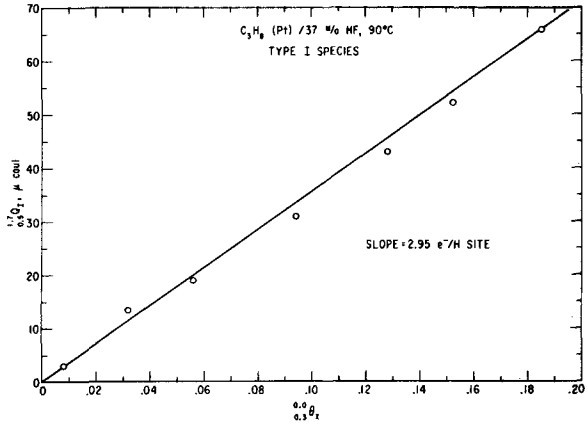

Fig. 10. Determination of the charge required for oxidation of type I material, per hydrogen site obscured.

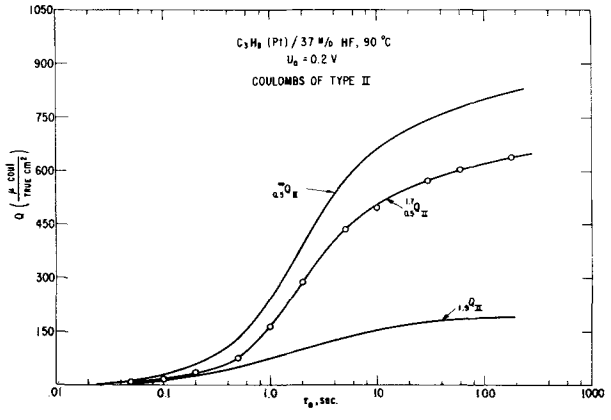

Fig. 11. Charge required for the oxidation of type II species resulting from propane adsorption at 90°C and 0.2v.

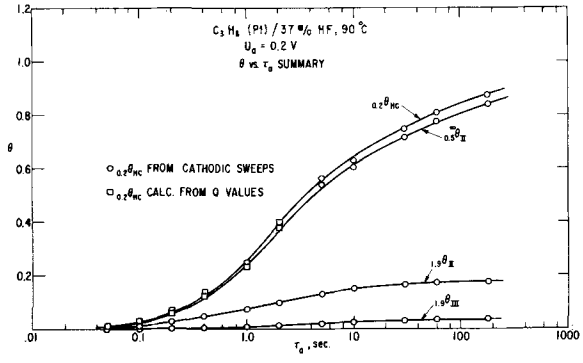

Fig. 12. Fractional surface coverages of the species resulting from propane adsorption at 90°C and 0.2v.

for the determination of the kinetic law followed by the adsorption of propane. This will be done later, after the results for U_a = 0.2v have been presented.

Propane adsorption at 0.2v.—Propane adsorption was studied at 0.2v, because very little type I material was formed at this potential, and because the largest total amount of propane was adsorbed (in terms of coulombs for its oxidation) at this potential. The experimental procedures were the same as those used for U_a = 0.3v, with the exception that the potential was held at 0.2v *vs.* rhe during the adsorption time τ_a. The sweep speed was varied from 1 to 100 v/sec, and the adsorption time covered the range 0.01 to 180 sec.

As above, all ${}^{1.7}{}_{0.5}Q_{HC}$ results were plotted against sweep speed, and the plateau values were used for the preparation of Fig. 11. Note that in the earlier stages of adsorption, ${}^{1.7}{}_{0.5}Q_{HC}$ is smaller for U_a = 0.2v than for U_a = 0.3v, indicating that adsorption is slower at 0.2v, and probably not diffusion limited, even at the shortest time studied; thus all of the data for U_a = 0.2v can be used in the kinetic analysis to be performed below.

Cathodic sweep experiments yielded information about ${}^{0.0}{}_{0.2}\theta_{HC}$ in the same manner as described above, but with a slight modification. Because some hydrogen is present on the electrode surface at 0.2v, it is necessary to include this in the calculations corresponding to Eq. [5]. The modified equation is

$$ {}^{0.0}{}_{0.2}\theta_{HC} = \frac{\Sigma Q_{H,\,\tau=0} - \Sigma Q_H}{\Sigma Q_{H,\,\tau=0}} \qquad [10] $$

where $\Sigma Q_H = {}^{0.0}{}_{0.2}Q_H + {}^{0.5}{}_{0.2}Q_H$. It is necessary to sum all of the charge required for saturating the free surface with hydrogen, not just that which is deposited below 0.2v, in order to obtain the fractional total surface available to hydrogen deposition. The value of $\Sigma Q_{H,\,\tau=0}$ is the same (within a few per cent) as ${}^{0.0}{}_{0.4}Q_{SH}$, measured for purposes of surface area determination.

The results for ${}^{0.0}{}_{0.2}\theta_{HC}$ were plotted against sweep speed for each τ_a, and the high sweep-speed plateau values (absence of hydrogenation-desorption) were then used to prepare the curve for ${}^{0.0}{}_{0.2}\theta_{HC}$ shown in Fig. 12. Note that a complete monolayer is not formed for times approaching 10^3 sec, even though ${}^{0.0}{}_{0.2}\theta_{HC}$ = 0.5 is achieved in less than 4 sec. Clearly, the rate of adsorption depends strongly on surface coverage.

The surface coverage of type III material was determined in the same manner as described above for U_a = 0.3v, using the low sweep-speed plateau values from the ${}_{1.9}\theta_{HC}$ *vs.* sweep speed plots. The ${}_{1.9}\theta_{III}$ curve thus obtained is shown in Fig. 12. As for U_a = 0.3v, ${}_{1.9}\theta_{III}$ stays very low, even at long adsorption times. The value of ${}_{1.9}\theta_{II}$ reaches somewhat higher values at U_a = 0.2v than it did for U_a = 0.3v, as might be expected from the fact that the total number of coulombs of material on the surface is greater at 0.2v, and essentially all of this material is type II, which oxidizes less readily than the type I present at 0.3v.

A correction for the type II material left on the surface above 1.7v was made according to Eq. [9], using the n_{II} value obtained from a plot of ${}^{1.7}{}_{0.5}Q_{II}$ *vs.* ${}^{1.7}{}_{0.5}\theta_{II}$ as was done for U_a = 0.3v. This corrected curve ${}^{\infty}{}_{0.5}Q_I$, is shown in Fig. 11. The value of n_{II} was 4.50 e^-/H site, higher than that for 0.3v, as would be expected for a surface species less oxidized and less dehydrogenated, because of the lower value of U_a.

The curve for ${}^{0.0}{}_{0.2}\theta_{HC}$ for short times was completed using the relationship

$$ {}_{0.2}\theta_{HC} = \frac{{}^{1.7}{}_{0.5}Q_{II}}{n_{II}Q_{SH}} + {}_{1.9}\theta_{II} + {}_{1.9}\theta_{III} \qquad [11] $$

as was done for 0.3v. Now, with the curves of θ_{HC} available for both 0.2 and 0.3v, over the full range of adsorption times, it is possible to perform an analysis of the kinetics of adsorption.

Adsorption kinetics at 0.2v and 0.3v.—Because the θ_{HC} curves of Fig. 9 and 12 are smooth, well-behaved functions of time, it seemed likely that the data were amenable to a straightforward kinetic analysis. The general character of the θ_{HC} *vs.* log τ_a curves is suggestive of Langmuir kinetics, because of the very distinct decrease in adsorption rate as the fraction of free surface ($\theta_F = 1 - \theta_{HC}$) decreases. The Langmuir rate law may be written as

$$ \frac{d\theta_{HC}}{dt} = k_{ads}C_{HC}(1 - \theta_{HC})^m \qquad [12] $$

where m is the order of reaction with respect to free surface, and represents the number of surface sites involved in the rate-determining step of the adsorption process. The problem is to determine if Eq. [12] fits the observed rates, and if so, to evaluate m and k_{ads}. Taking the log of both sides of Eq. [12] yields

$$ \log\left(\frac{d\theta_{HC}}{dt}\right) = \log k_{ads}\,C_{HC} + m \log(1 - \theta_{HC}) \qquad [13] $$

By plotting log $(d\theta_{HC}/dt)$ against log $(1-\theta_{HC})$, the value of m can be found from the slope, and the value of k_{ads} C_{HC} can be determined from the intercept on the log $(d\theta_{HC}/dt)$ axis. These plots were made, using graphically determined values of $d\theta_{HC}/dt$ from the data of Fig. 9 and 12. Both sets of data gave straight lines with m = 3.0. The values of $k_{ads}C_{HC}$ were 1.3 for U_a = 0.3v and 0.35 for U_a = 0.2v.

Knowing the value of m, Eq. [12] was integrated, yielding

$$ \left(\frac{1}{\theta_F{}^2} - \frac{1}{\theta_{F,\,t_o}{}^2}\right) = 2k_{ads}C_{HC}(t - t_o) \qquad [14] $$

where $\theta_{F,\,t_o}$ is the free surface at some reference time t_o. Equation [14] was used for a final consistency

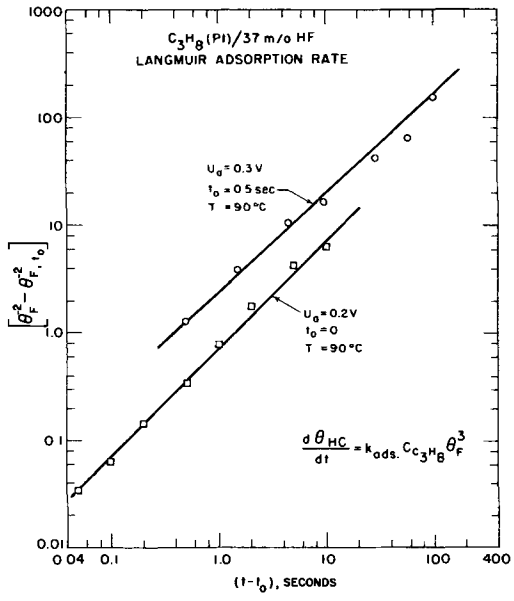

Fig. 13. Langmuir adsorption kinetic plot for the adsorption of propane on Pt in HF at 90°C. The adsorption potentials were 0.2v and 0.3v vs. rhe.

check on the fit of the data to the third-order rate law. A plot of log $(1/\theta_F^2 - 1/\theta_{F,t_o}^2)$ *vs.* log $(t - t_o)$ should yield a straight line of unit slope, the intercept of which is $2k_{ads}C_{HC}$. This plot is shown in Fig. 13, from which it can be seen that a very good fit was obtained for both sets of data, over the full ranges of time and surface coverage. The value of t_o for $U_a = 0.3$v was set at 0.5 sec because for shorter times, the absorption process was diffusion-controlled, as indicated by the results of Fig. 7.

Discussion

The rate of adsorption for propane on platinum in 37 m/o HF for $U_a = 0.2$ and 0.3v *vs.* rhe at 90°C has been found to be proportional to the third power of the fraction of free surface available for adsorption. This suggests that three platinum surface sites are involved in the rate-determining step of the adsorption of propane. It is possible that not all of these three sites are involved in a direct bonding to the adsorbate; one or two may be sterically obscured from involvement in the adsorption of other propane molecules. Since the Langmuir expression for adsorption kinetics is followed over a wide range of surface coverages, it is likely that the heat of adsorption changes little with surface coverage. An example of the type of adsorption which may take place initially is given by

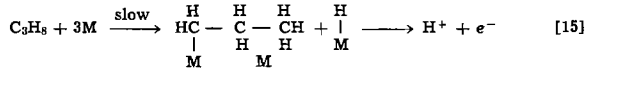

The adsorption process has an activation energy in the range of 15-20 kcal/mole (31) indicating a dissociative chemisorption, producing hydrogen atoms, which are quickly oxidized at $U_a = 0.2$ and 0.3v. The M which is not bonded to the propane in Eq. [15] indicates the possibility of steric hindrance. The rate of adsorption is affected by potential, being a factor of 3.7 higher at 0.3v than at 0.2v, which effect is expected on the basis that more rapid removal of the product H_{ads} increases the rate of adsorption. The values of k_{ads} are 1.6 x 10^7 cm^3/mole-sec for $U_a = 0.3$v and 4.3 x 10^6 cm^3/mole-sec for $U_a = 0.2$v at 90°C, using a value of 8.13 x 10^{-8} moles/cm^3 for the concentration of propane in the electrolyte.

After the initial rate-determining adsorption step (*e.g.*, Eq. [15]), the adsorbate is probably easily (and rapidly) dehydrogenated further, resulting in the bonding of the propane to more platinum sites, yielding hydrogen, which is consumed. The additional bonding causes straining of the carbon-carbon bonds, leading to fracture of the molecule. This may be indicated schematically, as follows

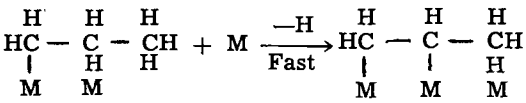

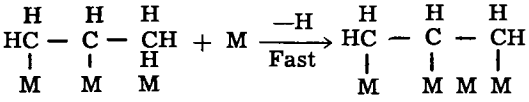

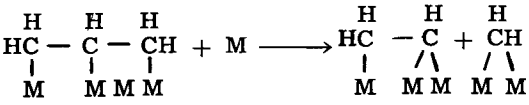

All of the products of the progressive dehydrogenation indicated above should yield saturated hydrocarbons on hydrogenation-desorption. All of the above fragments are considered to comprise the type II material on the electrode surface, which is oxidized over a broad range of potentials centered around 1.2v.

The product of reaction [15b] obscures 4 surface sites and yields 17 electrons on oxidation to CO_2 and H_2O, or about 4.25 e^-/H site, in reasonable agreement with the experimental result of 4.5 e^-/H site for $U_a = 0.2$v. The products of reaction [15c] yield 3.40 e^-/H site, compared to the value of 3.47 observed for type II at $U_a = 0.3$v. These comparisons are not intended as an identification of species, but merely serve to show that the suggested reactions are not incompatible with the experimental results.

In addition to dehydrogenation and carbon-carbon bond cleavage, partial oxidation takes place at potentials above about 0.15v (24, 13), yielding a product which is not hydrogenation-desorbed, and requires less than 4 e^-/CO_2 for its oxidation to CO_2 and H_2O (24). The oxidation of the type I species was found to require 2.95 e^-/H site, suggesting the following reactions

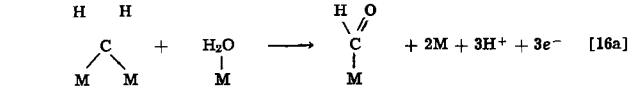

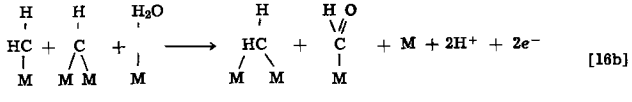

where the HCO species requires $3e^-$/H site for its oxidation, in agreement with the value found for the type I species. The type I species is the most easily oxidized, yielding high current densities at relatively low potentials. It is probably the type I species which is responsible for the high current densities obtainable at low overvoltages from hydrocarbon fuel cells.

In parallel with reactions [16a] and [16b], a further dehydrogenation of the products of reactions [15a], [b], and [c] can take place, yielding a carbon-rich residue which is not rapidly oxidized, and remains on the surface at potentials as high as 1.9v under anodic voltage sweep conditions. This material is expected to behave like what has been called type III above.

Conclusions

Propane adsorbs on platinum from a 37 m/o HF solution at 90°C at a rate which is third-order in free surface, at potentials of 0.2 and 0.3v *vs.* rhe. The kinetic expression is

$$\frac{d\theta_{HC}}{dt} = k_{ads}C_{HC}(1 - \theta_{HC})^3$$

The adsorption rate constant is a function of potential, having the values 4.3 x 10^6 cm^3/mole-sec at 0.2v and 1.6 x 10^7 cm^3/mole-sec at 0.3v *vs.* rhe, both at 90°C. This adsorbed propane, called type II requires 3.5 — 4.5 e^-/H site for its oxidation, depending on adsorption potential.

The adsorbed propane yields a partially oxidized surface species (type I) which is much more electrochemically active (oxidized more rapidly at lower potentials) than the initially adsorbed propane and requires 3 e^-/H site for its oxidation to CO_2 and H_2O. In a process concurrent with (and presumably parallel to) the formation of type I, a relatively unreactive residue (probably carbon-rich material) is formed, which is oxidizable at reasonable rates only at potentials significantly above 1.7v *vs.* rhe. This material, called type III, is present in only small amounts (< 0.1 monolayer accumulates in hundreds of seconds) at 90°C.

Acknowledgments

The authors are grateful to Dr. S. Gilman for the loan of a design for the all-PTFE electrochemical cell, and for helpful discussions. Dr. F. G. Will kindly provided the circuit for modifications in the function generator. Dr. A. D. Tevebaugh collaborated in the design, construction and testing of the apparatus.

This work is a part of the program under contracts DA 44-009-AMC-479(T) and DA 44-009-ENG-4909, ARPA Order No. 247 with the U. S. Army Engineer Research and Development Laboratories, Fort Belvoir, Virginia, to develop a technology which will facilitate the design and fabrication of practical military fuel cell power plans for operation on ambient air and hydrocarbon fuels.

Manuscript received Feb. 18, 1967; revised manuscript received May 3, 1967. This paper was presented at the Cleveland Meeting, May 1-6, 1966.

Any discussion of this paper will appear in a Discussion Section to be published in the June 1968 JOURNAL.

REFERENCES

1. H. Binder, A. Köhling, H. Krupp, K. Richter, and G. Sandstede, *This Journal*, **112**, 355 (1965).
2. W. T. Grubb and L. W. Niedrach, *ibid.*, **110**, 1086 (1963).
3. R. Jasinski, J. Huff, S. Tomter, and L. Swette, *Ber.*, **68**, 400 (1964).
4. H. G. Oswin, A. J. Hartner, and F. Malaspina, *Nature*, **200**, 256 (1963).
5. E. J. Cairns, *This Journal*, **113**, 1200 (1966).
6. E. J. Cairns, in "Hydrocarbon Fuel Cell Technology," B. S. Baker, Editor, Academic Press, New York (1965).
7. E. J. Cairns and E. J. McInerney, Paper presented at the Cleveland Meeting of the Society, May, 1966, Abstract No. 84; see also Extended Abstracts of the Industrial Electrolytics Div., **2**, 1 (1966).
8. E. J. Cairns and E. J. McInerney, Paper presented at the Philadelphia Meeting of the Society, Oct. 1966, Abstract No. 8; see also Extended Abstracts of the Battery Div. **11**, 19 (1966).
9. E. J. Cairns, *Nature*, **210**, 161 (1966).
10. E. J. Cairns and G. J. Holm, Paper presented at the Washington, D. C. Meeting of the Society, Oct. 1964, Abstract No. 30; see also Extended Abstracts of the Battery Div., **9**, 75 (1964).
11. L. W. Niedrach, *This Journal*, **113**, 645 (1966).
12. S. Gilman, *Trans. Faraday Soc.*, **61**, 2546, 2561 (1965).
13. L. W. Niedrach, S. Gilman, and I. Weinstock, *This Journal*, **112**, 1161 (1965).
14. S. B. Brummer, J. I. Ford, and M. J. Turner, *J. Phys. Chem.*, **69**, 3424 (1965).
15. S. B. Brummer and M. J. Turner, in "Hydrocarbon Fuel Cell Technology," B. S. Baker, Editor, Academic Press, New York (1965).
16. R. J. Flannery and D. C. Walker, *ibid.*
17. J. A. Shropshire and H. H. Horowitz, *This Journal*, **113**, 490 (1966).
18. E. B. Butler, C. B. Miles, and C. S. Kuhn, Jr., *Ind. Eng. Chem.*, **38**, 147 (1946).
19. D. C. Grahame, *Chem. Rev.*, **41**, 441 (1947).
20. A. N. Frumkin in "Advances in Electrochemistry and Electrochemical Engineering, Vol. 5, p. 3, John Wiley & Sons, Inc., New York (1963).
21. S. Gilman, *J. Electroanal. Chem.*, **9**, 276 (1965).
22. S. Gilman, *J. Phys. Chem.*, **67**, 1898 (1963).
23. L. W. Niedrach, *This Journal*, **111**, 1309 (1964).
24. W. T. Grubb and M. E. Lazarus, Paper presented at the Philadelphia Meeting of the Society, Oct. 9-14, 1966, Abstract No. 6.
25. A. Rius, S. Polo, and J. Llopis, *Anal. Fis. Quimica (Madrid)*, **45B**, 1029 (1949).
26. J. C. Yeager and M. Clarke, *Proc. Roy. Soc., Edinburgh*, **A61**, 229 (1942).
27. C. R. Wilke and P. Chang, *AIChE J.*, **1**, 264 (1955).
28. D. N. Saraf and P. A. Witherspoon, *Science*, **142**, 956 (1963).
29. S. Gilman, *J. Electroanal. Chem.*, **7**, 382 (1964).
30. J. Paynter and D. I. Macdonald in Hydrocarbon-Air Fuel Cells, Semi-Annual Technical Summary Report No. 7, ARPA Order No. 247, Contract Nos. DA 44-009-ENG-4909; AMC-479T; ENG-4853, Gen. Elec. Co. to USAERDL, Ft. Belvoir, Va. (January 1-June 30, 1965).
31. E. J. Cairns and A. M. Breitenstein in Hydrocarbon-Air Fuel Cells, Semi-Annual Technical Summary Report No. 6, ARPA Order No. 247, Contract Nos. DA 44-009-ENG-4909; AMC-479 (T); Gen Elec. Co. to USAERDL, Ft. Belvoir, Va. (July 1-Dec. 31, 1964).

Correction

In the paper "Permeation of Isolated Anodic Zirconium Oxide Films by Potasium Nitrate" by A. H. Mitchell and R. E. Salomon which appeared on pages 599 to 602 of the June 1967 issue of the *Journal*, the apparent activation energy for 27v films listed in Table IV, page 601 should be 9 kcal $mole^{-1}$ instead of 1 kcal $mole^{-1}$.

Catalysis of the Electrochemical Oxidation of Formaldehyde and Methanol by Perrhenate

Joseph A. Shropshire

Government Research Laboratory, Esso Research and Engineering Company, Linden, New Jersey

ABSTRACT

The electrooxidation of formaldehyde and methanol on platinum in sulfuric acid solution is catalyzed by rhenium heptoxide. The process requires that the rhenium species remain adsorbed at the platinum surface throughout the cycle. Studies have been carried out to define the mechanism and comparisons made with the previous results with molybdates.

As a result of recent widespread interest in the development of hydrocarbon fuel cells, a substantial effort has been devoted to studies of the mechanisms of adsorption and electrooxidation of low molecular weight fuels such as methanol, formaldehyde, and formic acid (1-6). These studies, many of which have been directed at platinum surfaces in strong acid media, have contributed substantially to a general understanding of the electrooxidation of carbonaceous fuels and the concommitant improvement of practical fuel cell systems. In a previous paper (7) the usefulness of soluble molybdates in improving the electrochemical oxidation of methanol and formaldehyde on platinum has been reported. In that study it was shown that the observed improvements were a result of catalytic enhancement through chemical reduction of adsorbed molybdate by the fuel and subsequent electrochemical reoxidation. This "surface redox" (as it was termed in the previous paper) substantially improved the electrical efficiency of methanol and formaldehyde oxidation provided that overpolarization and loss of adsorbed molybdate were avoided.

In the present study, it has been observed that small quantities of heptavalent rhenium display similar effects on the electrooxidation of formaldehyde and methanol on platinum in H_2SO_4. A series of investigations has been carried out to define the advantages and limitations of this system and to determine if in fact a catalytic mechanism similar to that observed with molybdate is operative.

Experimental Techniques and Equipment

Electrodes used in this study were of two types. For performance studies (polarization-log current) of CH_3OH and HCHO in rhenium-containing electrolytes, the electrodes were prepared by pressing powdered platinum black into platinum screens. The platinum, prepared by the reduction of H_2PtCl_6 by $NaBH_4$ in aqueous solution, was found to have high surface area and to provide high activity for this purpose. In the chronopotentiometric studies on this system, small platinized platinum electrodes of about 0.25 cm^2 apparent area were used. All electrochemical measurements in these systems were carried out in conventional glass "H" cells with anode and cathode compartments separated by glass frits. Voltage measurements were made against commercial saturated calomel reference electrodes through Luggin capillaries containing H_2SO_4 of concentration equal to that in the cell proper.

Due to the practical necessity of high conductivity for fuel cell electrolytes, studies were carried out in 3.7M H_2SO_4, a solution exhibiting near-optimum conductivity. High-purity rhenium heptoxide was obtained from the University of Tennessee (8) and used without further purification. Other pertinent experimental details will be found in the previous publication (7). All polarizations in this study are referred to the saturated calomel electrode (SCE), measured difference in this reference *vs.* NHE being 0.194v at 25°C in the systems involved.

Oxidation of Formaldehyde and Methanol in the Presence of Perrhenate

The electrochemical oxidation of formaldehyde and methanol in acid media is a highly irreversible process. Despite a computed difference of about 0.14v in theoretical potential, both fuels react on platinum electrodes at about the same potential level. This similarity has led to the belief that oxidation of both fuels involves a common slow step, possibly the "reduced CO_2" intermediate described by Giner (9). The product of the electrooxidation of either fuel in acid is essentially 100% CO_2 at steady state (4-6). Tafel slopes of about 0.06 v/decade are commonly observed on platinum catalysts (Fig. 1).

As in the case of molybdate, the addition of low concentrations of rhenium heptoxide to the acid electrolyte prior to fuel addition was found to result in substantial changes in the electrochemical performance curves (Fig. 1). In the range of 1-100 ma/cm^2 polarization for HCHO oxidation decreased by nearly 0.3v. Methanol showed substantial differences from HCHO with polarization decreases of 0.15-0.20v. Tafel slopes were generally somewhat curved, with b values of the order of 0.10-0.14 v/decade. In contrast to the observations previously made with molybdate, the polarization curves were continuous and unbroken to current levels beyond several hundred ma/cm^2. As in the case of direct electrooxidation on platinum, the observed product was carbon dioxide (evolved). The polarization curves showed no hysteresis during repeated cycling up to the highest current levels. Occasionally, after severe overpolarization, transient responses typifying oscillation between two stable states would be observed on slowly decreasing the current load. While addition of perrhenate to the electrolyte prior to fuel addition gave guaranteed improvements

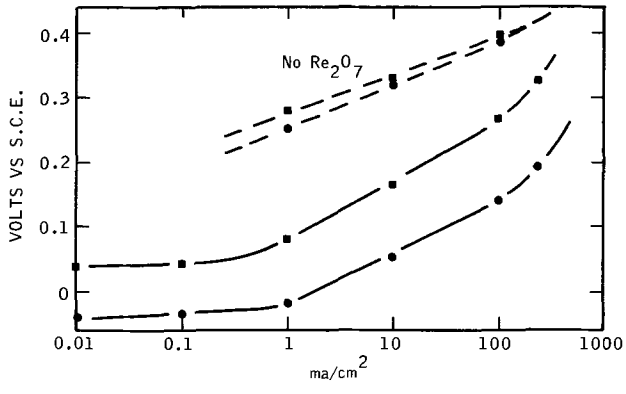

Fig. 1. Best observed performance on $NaBH_4$-reduced platinum in 0.002M Re_2O_7 — 3.7M H_2SO_4, 82°C; ● HCHO; ■ CH_3OH.

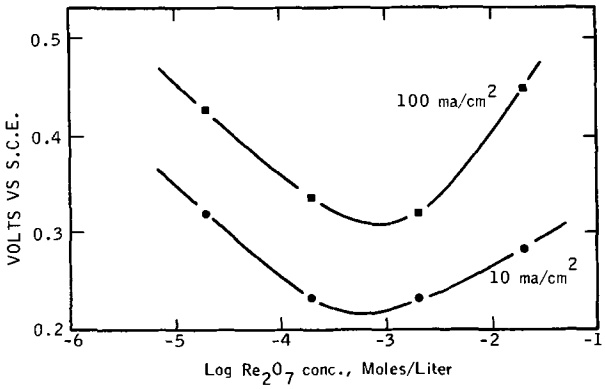

Fig. 2. Effect of Re_2O_7 concentration on CH_3OH performance on $NaBH_4$-reduced platinum, 3.7M H_2SO_4, 82°C.

it was generally observed, in contrast to molybdate, that the system would attain the low polarization level of performance under load cycling regardless of the order of addition of fuel and perrhenate.

A series of experiments designed to test the concentration dependence on perrhenate indicated optimum performance for CH_3OH at a perrhenate concentration of about 10^{-3}M. This concentration dependence was somewhat less critical at low current densities as shown in Fig. 2. There is reason to believe that this perrhenate concentration corresponds roughly to the value necessary to produce maximum coverage of the platinum surface (Appendix I). It is not known, however, to what extent, *i.e.*, in terms of monolayer coverage, the adsorption exists.

The effect of temperature on the electrochemical reaction of CH_3OH in the presence of perrhenate was investigated in the range 25°-90°C on an electrode potentiostatted at 0.4v polarization (from $E°_{25}$ CH_3OH). The Arhennius plot showed a straight line relationship over the range with a slope indicative of an activation energy of about 10.2 kcal/mole. This value is substantially less than that normally found for the direct electrooxidation of CH_3OH on platinum black (15-18 kcal/mole) while at the same time much too high to indicate any diffusion effects involving a reduced rhenium species.

Nature of the Perrhenate Reduction

With these indications of catalytic currents, steps were taken to determine the nature and extent of perrhenate reduction in the 3.7M H_2SO_4 system. It was observed that no visible reaction took place between CH_3OH or HCHO and perrhenate in H_2SO_4 solution in the absence of platinum. If a platinum black electrode was immersed in 0.002M Re_2O_7 — 3.7M H_2SO_4 and fuel added, a small quantity of gas evolution from the electrode was observed. This was taken to represent that quantity of fuel oxidized to CO_2 in reducing the perrhenate adsorbed on the platinum surface. Since this CO_2 evolution was simply a transient phenomenon it is assumed that the reduced rhenium species remains adsorbed and undergoes no further interactions under open-circuit conditions in the presence of fuel.

Using the platinum black microelectrode, a system was assembled to study the reactions of perrhenate in the voltage range of interest for fuel oxidation. Chronopotentiograms obtained on the platinum black microelectrode in 0.002M Re_2O_7 — 3.7M H_2SO_4 (25°C) showed the presence of a well-defined anodic wave after polarization to 0.0v SCE (Fig. 3). This oxidation wave showed a half wave potential of about +0.4v (S.C.E.) under the high current conditions used, and the reduction potentials ($E_{1/2} \simeq +$ 0.2v SCE) necessary to produce the species oxidized during this wave are still substantially positive to the computed theoretical potentials for HCHO and CH_3OH. Thus, on thermodynamic considerations alone, both these fuels

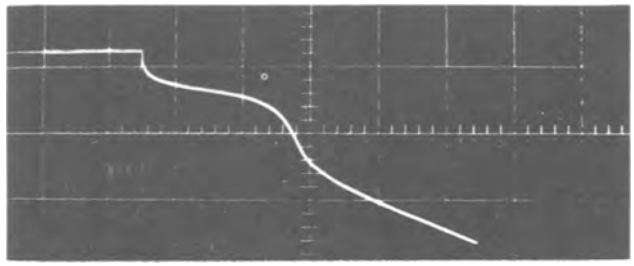

Fig. 3. Anodic chronopotentiogram on platinized platinum microelectrode in 0.002M Re_2O_7 — 3.7M H_2SO_4, following cathodization to 0.0v SCE. Top 0.0v SCE, 300 mv/div (positive downward), 1 sec/div left to right, 40 ma/cm², 25°C.

would be expected to chemically reduce the adsorbed perrhenate, producing an Re(VI)/Re(VII) ratio in accord with the standard free energy change for the respective reactions.

While for the purposes of the fuel cell study presented here, the exact valence change in the initial perrhenate reduction need not be known, a series of coulometric and chronopotentiometric studies was carried out to determine this parameter. These investigations have been reported elsewhere (10, 11). The results indicate that the initial reduction involves a univalent change to the Re(VI) state. Under long-term coulometric analysis on platinum, however, it was found that this state was capable of disproportionating to Re(IV) and Re(VII) states. The reader is referred to the original publications for details of these studies.

Chronopotentiometry on Platinized Platinum

Since it was apparent that the over-all reaction of fuel and perrhenate did not involve the rhenium species in solution, a study of the factors involved in perrhenate adsorption and interaction with fuel was made using the anodic stripping technique of Pavela (12). In this method, the preconditioned electrode was placed in the solution of adsorbate for a desired interval, removed rapidly to a rinse solution to remove excess bulk solution, then placed in a cell containing 3.7M H_2SO_4 and the anodic stripping transient recorded. While this technique suffers the drawback of permitting the determination of strongly adsorbed material only, it nevertheless allows the separation of the independent factors in perrhenate and fuel adsorption.

The 0.25 cm² platinized electrode used for this study was preconditioned by evolving H_2 and O_2 successively a few times in H_2SO_4 solution with final equilibration (potentiostatted) at 0.0v (SCE) before removal to the adsorbate solutions. Anodic transients, with the exception of Fig. 8, were recorded in pure 3.7M H_2SO_4. While the general behavior of HCHO and CH_3OH is equivalent, the stronger adsorption of HCHO makes the effects with that fuel somewhat more pronounced, and transients obtained with HCHO have been used to illustrate the behavior.

It was found that a few seconds immersion of the platinum electrode in 3.7M H_2SO_4 — 0.025M Re_2O_7 was sufficient to produce a tenaciously held layer of perrhenate which oxidized (after potentiostatting at 0.0v SCE) at about the same potential levels observed previously in perrhenate solution (Fig. 4). The blank transient, shown in Fig. 4a, clearly shows the initial regions of pseudocapacitance from oxidation of chemisorbed hydrogen atoms, the steep so-called double layer region, followed by platinum oxide formation at more positive voltages. By comparison, the electrode with adsorbed perrhenate shows loss of about one-half the hydrogen pseudocapacitance, indicating that the rhenium species is blocking hydrogen chemisorption sites. The tenacity of the perrhenate adsorption is indicated in Fig. 5, which shows the transient obtained after four cycles from 0.0-1.2v SCE on the adsorbed layer of Fig. 4b. The approx-

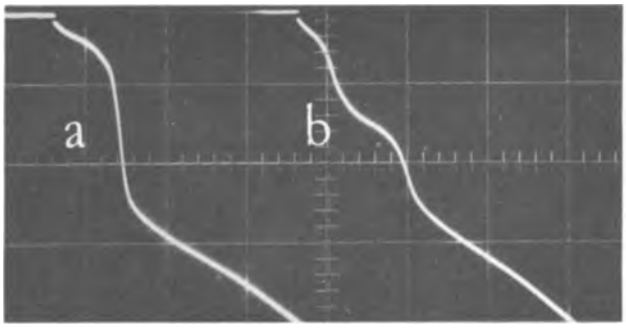

Fig. 4. Chronopotentiograms on platinized platinum in 3.7M H_2SO_4: (a) blank, (b) following 2-min dip in 0.025M Re_2O_7 — 3.7M H_2SO_4 and rinse. Conditions as in Fig. 3 except 160 ma/cm^2.

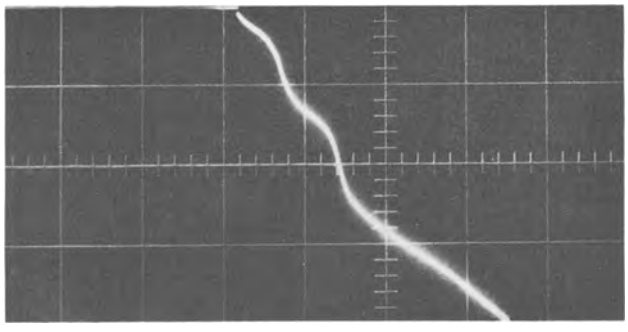

Fg. 5. Transient obtained after four cycles from 0.0 to 1.2v SCE on electrode of Fig. 4b; conditions as in Fig. 4.

imate equivalence of these transients indicates that the rhenium species remains strongly adsorbed in both valence states over a wide potential range. It was found that this single chemisorbed layer of perrhenate was capable of producing markedly improved steady-state electrooxidation of HCHO in a subsequent test in 1M HCHO — 3.7M H_2SO_4 up to current levels of several hundred ma/cm^2.

Immersion of the platinized electrode in 3.7M H_2SO_4 — 1M HCHO with no perrhenate resulted in the rapid formation of a tightly bound layer of HCHO with an oxidation transient as shown in Fig. 6. The absence of pseudocapacitance in the range 0.0-0.25v SCE is indicative that formaldehyde occupies the majority of the surface, including these sites normally held by adsorbed hydrogen atoms. Oxidation of this strongly held HCHO appears to occur only at or near voltages at which platinum oxidation occurs.

If the electrode is immersed in perrhenate solution, rinsed, then immersed in HCHO solution, both species occupy parts of the surface simultaneously as shown by the presence of both characteristic waves in the transient of Fig. 7a. The quantity of perrhenate appears comparable to that observed in the absence of formaldehyde, and absence of hydrogen pseudocapacitance suggests that the HCHO is present on these hydrogen-type sites not occupied by the perrhenate. As was reported earlier for molybdate, it was again recognized that the strongly adsorbed HCHO apparently does not interact with the adsorbed perrhenate. Thus, no significant catalytic enhancement of the rhenium oxidation wave by strongly held HCHO is observed, as evidenced by the fact that HCHO remains on the surface until electrooxidized (Fig. 7a). As indicated in Fig. 7b, however, the direct electrooxidation of HCHO near platinum oxide levels does have a substantial effect on the adsorption of the rhenium species. The single transient (of Fig. 7a) serves to remove a substantial part of the adsorbed perrhenate. This effect is less severe in the case of coadsorbed methanol with a major fraction of the perrhenate surviving after methanol is oxidized from the surface.

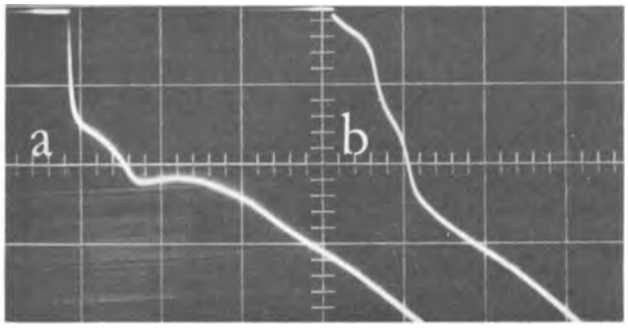

Fig. 7. Chronopotentiograms on platinized platinum in 3.7M H_2SO_4: (a) after 2-min dip in acid-perrhenate solution, rinse, 2-min dip in acid—formaldehyde solution and rinse; (b) first subsequent transient on same electrode; conditions same as in Fig. 4.

In accord with the suspected catalytic mechanism, anodic stripping of a preadsorbed layer of perrhenate in a solution containing 1M HCHO — 3.7M H_2SO_4, showed a sustained interaction. As shown in Fig. 8, the catalytic enhancement of the rhenium oxidation wave by HCHO solution is to all appearances sustained indefinitely at the normal rhenium oxidation potential. Noting that these transients were obtained at 160 ma/cm^2, the high current capability of the catalytic interaction is confirmed.

Discussion

Based on the foregoing observations, the Pt-perrhenate-fuel interaction appears to closely resemble that observed previously for molybdate in H_2SO_4 solutions. Thus, in brief

Adsorption

$$\text{Re (VII) (soln)} \rightleftarrows \text{Re (VII) (Strongly Adsorbed)}$$

Chemical Reaction

$$n[\text{Re (VII)}_{ads}] + \begin{pmatrix} \text{HCHO} \\ \text{CH}_3\text{OH} \end{pmatrix} \rightarrow n\,[\text{Re (VI)}_{ads}] + \text{CO}_2 + (n-1)\,\text{H}_2\text{O (fast)}$$

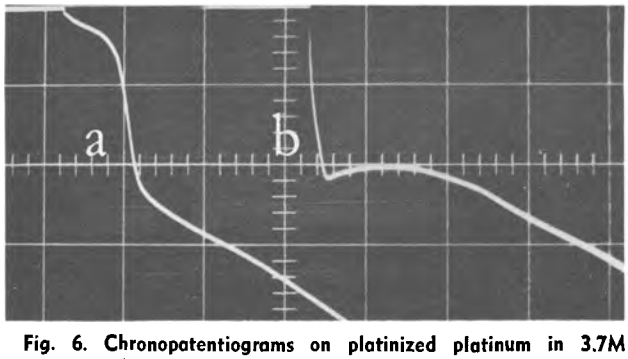

Fig. 6. Chronopatentiograms on platinized platinum in 3.7M H_2SO_4: (a) blank, (b) after 2-min dip in 1M HCHO — 3.7M H_2SO_4 and rinse; conditions as in Fig. 4.

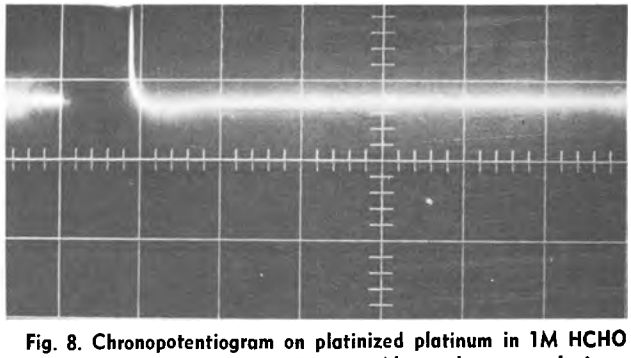

Fig. 8. Chronopotentiogram on platinized platinum in 1M HCHO — 3.7M H_2SO_4 after 2-min dip in acid—perrhenate and rinse; conditions as in Fig. 4 except 2 sec/div.

Electrochemical Reaction

$Re\ (VI)_{ads} \rightarrow Re\ (VII)_{ads} + e^-$ (potential determining)

Since the complete chemical and electrochemical reactions occur only for the strongly adsorbed rhenium species it would appear that the term "surface redox" is applicable to this case as well as molybdate.

Based on the observations to date, the slow step in this mechanism differs from that observed for molybdate. It would appear, based on the high current capability of HCHO and CH_3OH on high area platinum electrodes in perrhenate solution (Fig. 1), that the chemical reaction rates of both fuels with perrhenate adsorbed in platinum are substantially high. At the same time, however, the difference in reducing power of the two fuels is evident in the observed polarization differences during operation. In addition, the Tafel slopes of 0.10-0.14 v/decade tend to indicate that we are actually observing the one-electron charge-transfer limited reoxidation of Re(VI). The observed temperature dependence does little to clarify the issue since it lies in a range possibly applicable to either a chemical or electrochemical limitation. Since the observed polarization differences in HCHO and CH_3OH operation correspond reasonably well with the computed theoretical potential difference it is perhaps best to accept the view that the charge-transfer limitation is observed, with the surface Re(VI) concentration fixed by the relative reducing power of the fuel. This condition simply requires that the perrhenate reaction with HCHO exhibit the expected free energy advantage over CH_3OH reaction, but that the rate of approach to chemical equilibrium be rapid for both fuels. This differs from the molybdate case in that a slow chemical reaction step is observed relatively clearly in that instance.

In this scheme no pretense of knowledge is made as to the exact nature of the adsorbed rhenium species. It seems clear, however, based on the residual hydrogen pseudocapacitance and transients with coadsorbed fuel that strongly adsorbed perrhenate occupies no more than half the surface. As in the molybdate case, it seems highly significant that catalytic enhancement of the Re(VI) oxidation does not occur with strongly adsorbed fuel. Thus, catalytic interaction is observed only when the perrhenate-containing electrode is anodized in the presence of dissolved fuel. It is not meant to imply, however, that interaction with a weaker, perhaps physically adsorbed, fuel state is precluded. In a recent paper (13), the suggestion has been advanced that efficient direct electrooxidation of fuels such as HCHO and CH_3OH is precluded near the expected potentials due to an excessively strong adsorption and blockage of low polarization water-discharge processes. The failure of strongly adsorbed HCHO and CH_3OH to react catalytically with adsorbed molybdate and rhenate species, while less strongly adsorbed fuel does react, would seem to provide some implications along those same lines.

Summary

The use of perrhenate as a cocatalyst in the complete oxidation of HCHO and CH_3OH on platinum in acid electrolyte results in a substantially higher efficiency for the reaction. The improvement results from the catalytic chemical reaction of the fuel with an adsorbed perrhenate species with subsequent electrooxidation of its reduced form. This surface redox reaction is quite similar in many respects to that previously reported for molybdate, but differs in that the adsorption of perrhenate is apparently much stronger and rates of HCHO and (particularly) CH_3OH chemical reaction with perrhenate are substantially higher. Since loss of perrhenate from the electrode under normal operating conditions appears to be minimal, this redox system shows a substantial advantage over platinum alone for the operation of practical methanol-air cells.

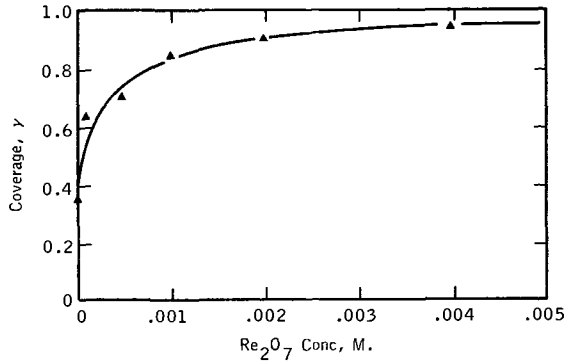

Fig. 9. Adsorption isotherm for Re_2O_7 on platinized platinum, derived from capacitance data, 25°C.

Acknowledgments

The work reported in this paper was made possible by the support of the Advanced Research Projects Agency under Order No. 247 through the U.S. Army Electronics Laboratories (Contract No. DA 36-039 SC-89156). Permission to publish is gratefully acknowledged. The author wishes to thank H. E. Frew for carrying out much of the experimental work.

Manuscript received March 8, 1967; revised manuscript received April 27, 1967.

Any discussion of this paper will appear in a Discussion Section to be published in the June 1968 JOURNAL.

APPENDIX

It is stated above that the apparent optimum in Re_2O_7 concentration corresponds closely to that which produces maximum surface coverage. This conclusion was derived from a study of the effect of Re_2O_7 on the capacitance of a platinum black electrode. Studies were carried out in which the initial (linear) voltage-time response to a square wave current pulse was recorded from a platinized platinum electrode potentiostatted at voltage levels in the range 0.0-1.2v SCE. The square wave current was derived from mercury relay switching between parallel potentiostatic and constant current circuits. The switch was actuated by a Tektronix pulse generator at 40 Hz. Voltage deviations from the potentiostatted level were not allowed to exceed 20 mv. Under those conditions the potentiostat was easily able to return the potential to its prearranged value prior to the next current pulse. Transients were recorded and photographed from the oscilloscope display.

It was found that the addition of Re_2O_7 to the acid solution had a substantial effect (decrease) on the capacitance of the platinum electrode in the range 0.2-0.6v SCE. This capacitance decrease at 0.5v was treated in terms of the familiar parallel plate capacitor model (14) to derive a surface coverage parameter. Thus,

$$C_{meas} = \gamma C^o_{Pt-Re} + (1 - \gamma)\ C^o_{Pt}$$

where C^o_{Pt-Re} is taken as that capacitance level which is not changed by further additions of Re_2O_7.

The isotherm (25°C) derived from this treatment is shown in Fig. 9. It is clear that the adsorbed Re_2O_7 layer is substantially complete in the concentration range 1-3 x 10^{-3}M Re_2O_7. This level corresponds very well with that observed to produce optimum performance. As pointed out previously, however, it should be kept in mind that this is an approach to maximum "functional" coverage, and gives no quantitative measurement of the extent of coverage in terms of the true surface area. The apparent decrease in performance at higher Re_2O_7 concentration may reflect the further blocking by Re_2O_7 of surface sites normally occupied by fuel in the optimum case.

REFERENCES

1. S. B. Brummer and A. C. Makrides, *J. Phys. Chem.*, **68**, 1448 (1964).
2. M. W. Breiter, *Electrochim. Acta*, **7**, 533 (1962).
3. S. Gilman, *J. Phys. Chem.*, **67**, 1898 (1963); *ibid.*, **68**, 70 (1964).

4. B. L. Tarmy *et al.*, Rept. No. 1, Contract DA 36-039-SC 89156, Esso Research and Engineering Co., 1 Jan. 1962-30 June 1962.
5. H. Krupp *et al.*, *This Journal*, **109**, 553 (1962).
6. M. J. Schlatter, Preprint of the Div. of Petroleum Chem., ACS 6B-149 (1961).
7. J. A. Shropshire, *This Journal*, **112**, 465 (1965).
8. Professor Melaven, University of Tennessee, Knoxville 16, Tenn.
9. J. Giner, *Electrochim. Acta*, **8**, 857 (1963); *ibid.*, **9**, 63 (1964).
10. J. Shropshire, *J. Electroanal. Chem.*, **9**, 90 (1965).
11. J. Shropshire, submitted to *J. Electroanal. Chem.*
12. T. O. Pavela, *Ann. Acad. Sci. Fennicae, Ser. A*, **2**, 59 (1954).
13. J. Shropshire, *Electrochim. Acta*, **12**, 253 (1967).
14. R. J. Flannery *et al.*, American Oil Co., Contract DA 11-022-ORD-4023, Rept. No. 6, April 1963.

Galvanic Corrosion Characteristics of Aluminum Alloyed with Group IV Metals

D. S. Keir, M. J. Pryor, and P. R. Sperry

Metals Research Laboratories, Olin Mathieson Chemical Corporation, New Haven, Connecticut

ABSTRACT

The electrochemical behavior of aluminum alloyed with selected Group IV elements has been investigated in 0.1*N* sodium chloride solution. Of the group IV elements studied only tin had a major effect on aluminum; Al-Sn alloys carried surface oxide films of very low ionic resistance, exhibited potentials more active than —1.0v on the hydrogen scale and gave very large galvanic currents when coupled to mild steel cathodes. The conditions permitting entry of a group IV alloying addition from the metal into the surface oxide film have been partly clarified.

Considerable effort has been directed by the writers' laboratory to clarifying the manner in which various aqueous electrolytes modify the electron and ion conductivities of the thin film of γ-Al_2O_3 that is always present on essentially pure aluminum in nearly neutral solutions. The frequency dispersion of the loss tangent of the film has been one of the main experimental values measured. Electrolytes that have been studied include the corrosive sodium halides (1-5) and sodium sulfate (5) together with passivating sodium chromate solutions (6). Halide ions from solution appear to be able to enter the structure of the surface γ-Al_2O_3 film and to create additional cation vacancies in the film without necessarily changing its thickness, crystallographic structure, or topography. The additional cation vacancies, so produced, lower the ionic resistance of the γ-Al_2O_3 film but do not change its electronic resistance. The relative effectiveness of the halide ions in entering the alumina lattice and lowering ionic resistance is in the order $F' > Cl' > Br' > I'$ (1). Simple immersion of oxide-covered aluminum in aqueous sodium sulfate solutions does not appear to result in any defect structural modification of the film, and so the ion and electron resistances remain unchanged (5). The defect structural aspects of passive films formed in chromate solutions are more complicated and include an increase in electronic resistance (compared with thermal γ-Al_2O_3) combined with a decrease in ionic resistance (6). The former has been ascribed to the inclusion of a small concentration of protons in the film replacing aluminum ions and the latter to the presence of low ionic resistance crystalline γ-Al_2O_3 located in the outer portion of the passive film.

With the exception of some limited study of aluminum purity at levels above 99.997% (1) none of the foregoing studies were concerned with modification of surface film defect structure resulting from alloying the base aluminum. The work described in this paper is accordingly concerned with this latter variable. Group IV elements appeared to be of particular interest when alloyed with aluminum. If they were able to enter the cation lattice of the natural oxide film in the quadrivalent condition and replace trivalent aluminum ions, they should result in the creation of additional cation vacancies and lowered ionic resistance much in the fashion of halide ions previously studied. Such alloys could well have interesting electrochemical properties.

Accordingly, in the present work, the electrochemical properties of aluminum alloyed with silicon, germanium, titanium, zirconium, and tin were studied. Because a significantly lowered ionic resistance of the surface film will result in a displacement of corrosion potential in the active direction, these alloys are potentially interesting in the field of sacrificial protection. Accordingly, the electrochemical method used to study these alloys primarily involved investigation of their galvanic behavior when coupled to mild steel in sodium chloride solution. The electrochemical studies were augmented by impedance studies of the surface oxide films in sodium chloride solution only when significant improvement in current output was observed in the galvanic experiments. Of the above alloys of aluminum with group IV elements, only the Al-Sn system, in certain structural conditions, deviated markedly from the galvanic behavior of pure aluminum. The investigation has thrown new light on the metallurgical and associated defect structural requirements in the surface oxide film that must be met before significant changes can be made to the electrochemical behavior of an aluminum alloy carrying a stable surface oxide film.

Experimental and Results

Materials.—All alloys were prepared with high-purity (99.992%) aluminum as a base. The high-purity aluminum was induction melted, in air, in alumina crucibles. All binary and ternary alloying additions were added to the melt at a temperature of 730°C and thoroughly stirred to ensure homogeneity. The melts were degassed with gaseous chlorine for 10 min, the melt temperature lowered to 670°C, and the alloys poured into massive copper chill molds having internal dimensions of 2.5 x 2.5 x 15.0 cm. Group IV alloying additions were evaluated at a level of around 0.1 to 0.2% by weight (Table I). Aluminum-tin alloys of a wider compositional range from 0.02-0.3% by weight were prepared for more extensive investigation of this system. All aluminum-tin alloys had

Table I. Chemical composition and number of coulombs flowing in 48 hr in galvanic cells of aluminum alloys with mild steel in 0.1*N* NaCl solutions

% Group IV alloying addition*	% Fe	% Si	Coulombs flowing in 48 hr
0.12 Sn	0.004	0.003	726, 868, 983
0.10 Ge	0.004	0.003	7, 7
0.20 Si	0.004	—	9, 44
0.10 Ti	0.004	0.003	25, 11
0.17 Zr	0.008	0.003	4, 6
—†	0.001	0.001	20, 21

* By weight.
† 99.997% pure aluminum.

Table II. Chemical composition of mild steel cathodes

C	P	Mn	Cr	Ni	Mo	Si	Cu
0.016	0.002	0.019	0.021	0.021	<0.03	<0.01	0.09

0.004% iron and 0.003% silicon as the major impurities.

The mild steel cathodes were cut from commercial mild steel sheet 0.11 cm thick having the chemical composition shown in Table II. All solutions were made up from A.R. reagent grade chemicals and distilled deionized water.

Material preparation.—Mild steel cathodes were cut as specimens 1 cm wide having 5 cm in length (10 cm^2) exposed to the sodium chloride electrolyte. Prior to the galvanic experiments the cathodes were degreased in benzene, etched in 50% by volume hydrochloric acid, washed, dried in acetone, exposed to dry air over phosphorus pentoxide for 24 hr, and weighed.

Aluminum alloy specimens were machined from the castings in the form of square rods having dimension of 0.5 x 0.5 x 8.0 cm. In the galvanic experiments only 5 cm of the rod (10 cm^2) were immersed in the electrolyte. The machined specimens were degreased in benzene, etched in 1.0*N* NaOH for 5 min, washed, dried in acetone, exposed to dry air over phosphorus pentoxide for 24 hr, and weighed.

Selected Al-Sn alloy castings were given a thermal treatment. This treatment involved heating in air at 620° ± 3°C for 16 hr and immediately quenching in still water. Thereafter samples were machined and prepared for the galvanic experiments in the standard manner described above. Alloys treated in this fashion will be referred to as "homogenized" alloys in the text.

Certain of the homogenized Al-Sn alloys were given a subsequent thermal treatment designed to ensure precipitation of tin from solid solution. This thermal treatment comprised reheating for 24 hr at 400°C and quenching in still water. Aluminum-tin alloys receiving this precipitation treatment will be described as "heterogenized" alloys in the subsequent text.

Experimental methods.—Galvanic experiments.—Galvanic couples of 10 cm^2 of the appropriate aluminum alloy coupled to 10 cm^2 of mild steel were investigated using the cell and the experimental method described earlier by two of the authors (7). Experiments were conducted at least in duplicate and usually in triplicate. Briefly the cell is a glass unit with an electrolyte capacity of 100 ml. In the present work 0.1*N* NaCl solution was used throughout at a temperature of 25° ± 0.05°C. The cell, which is closed, provides electrical connections for the dissimilar electrodes, mounted rigidly 2.0 cm apart, together with one for a saturated calomel reference electrode. The two metals were connected together through a 1-ohm external resistor across which the potential drop and accordingly the galvanic current could be measured continuously. Connection of the reference electrode with the anode through a high impedance recorder permitted the closed circuit cell potential[1] to be monitored.

The galvanic currents and cell potentials were recorded continuously for 48 hr, the standard duration of all galvanic experiments in this paper. After any experiment had been terminated the aluminum anode was freed from corrosion product by treatment in 2% chromic-5% phosphoric acid at 85°C, rinsed, dried, and reweighed. The steel cathode was similarly cleared in 1:1 HCl inhibited with Rhodine 41, rinsed, dried, and reweighed. From the above measurements the following important electrochemical information could be obtained: (*i*) whether the aluminum alloy completely protected the steel cathode; (*ii*) the number of coulombs flowing; (*iii*) the weight loss of the anode and; (*iv*) from a combination of 2 and 3 the anodic efficiency of galvanic corrosion of the aluminum alloy anode. Correlation of these variables with alloy composition and structure could then be carried out.

Capacitance-dielectric loss studies.—The specific resistance of the surface oxide film was measured by a minor modification of the a-c technique described earlier by two of the authors (3). Measurements were confined to a frequency of 1 kc only because ionic resistivity was of primary importance in this study (4, 5). Unlike previous studies the measurements were made in 0.1*N* NaCl instead of in a chromate solution because the interaction of defects produced by tin in the alloy and chloride in the environment was of primary interest. Specimens having an exposed area of 0.8 cm^2 with tin contents from 0.02-0.08%, were immersed in 0.1*N* NaCl at 25°C for 30 min. At this time series capacitance and dielectric loss were measured directly by a General Radio 716-C capacitance bridge by application of a 50 mv p-p signal across the oxide covered specimen and a large concentric platinum grid counter electrode. Parallel resistivity was calculated from the two measurements using an analog for the film of a capacitor with a simple parallel resistance as had been utilized in previous studies (2-6). Measurements were conducted in the homogenized and heterogenized conditions.

Results.—The number of coulombs flowing in 48 hr in galvanic couples of steel coupled to aluminum alloyed with the five group IV elements are shown in Table I. Also included are results for unalloyed high-purity aluminum coupled to mild steel. Table I shows that only tin produces any major effect in increasing the current flow in these couples. However, the difference between the Al-Sn alloy and the other alloys, including pure aluminum, is very large. The steel was completely protected by pure aluminum and Al-Sn alloys but not by the other alloys.

Accordingly, attention was focused mainly on the Al-Sn system. A series of binary alloys containing from 0.02-0.3% Sn was subjected to the same electrochemical investigation in the "as-cast" condition. The effect of Sn content on anodic weight loss, number of coulombs flowing, anodic efficiency, and closed circuit cell potential is shown for triplicate specimens in Fig. 1, 2, 3, and 4. It may be seen from these figures that, in the as-cast condition, tin raises the number of coulombs flowing significantly as well as the anodic weight loss. The effect of tin becomes readily apparent at a concentration of around 0.1% by weight and above. Furthermore, tin reduces anodic efficiency and lowers the closed circuit cell potential from around —0.5v to around —1.0v on the hydrogen scale at tin levels of 0.1% or more.

However, the results for as-cast specimens are highly erratic, and no clear trend exists, at least in anodic weight loss and number of coulombs flowing, at tin contents between 0.1-0.3%. This behavior is related to the constitution of the Al-Sn binary system (13). The solid solubility of tin in aluminum at the

[1] All potentials in this paper are expressed on the standard hydrogen scale.

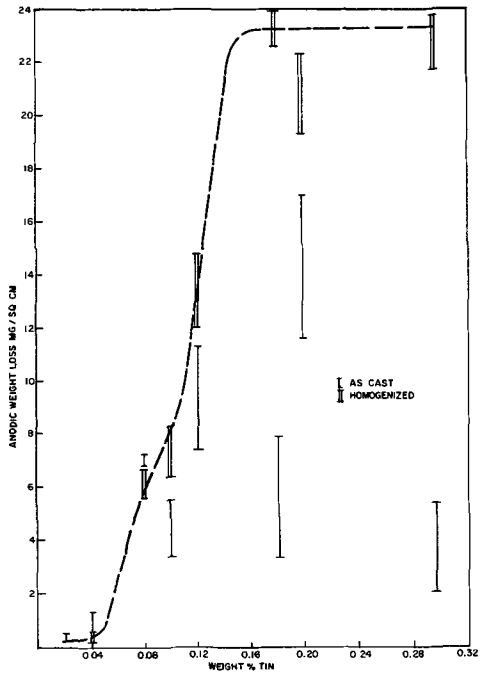

Fig. 1. Effect of tin content of aluminum on anodic weight loss when coupled to steel in 0.1*N* NaCl for 48 hr.

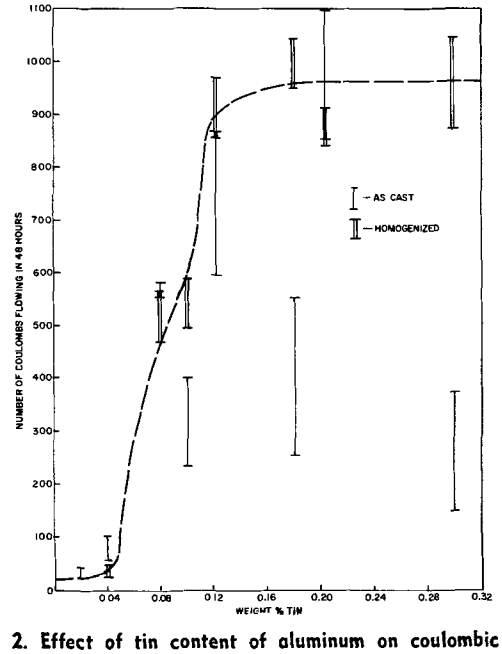

Fig. 2. Effect of tin content of aluminum on coulombic output when coupled to steel in 0.1*N* NaCl for 48 hr.

eutectic temperature (228.3°C) is very low being only around 0.02%. However, a small solubility loop exists around 620°C where the tin solubility is greater. The maximum solubility of tin in aluminum at this temperature is still somewhat doubtful. Hardy *et al.* (8) has found a value of 0.10% by weight, but Samuels (9), using some identical samples, reported a higher value of 0.11%. Irrespective of the actual maximum value of solid solubility at this temperature, it is clear that nonequilibrium solidification in this type of phase diagram will tend to leave somewhat variable amounts of tin in solid solution in the as-cast condition. This contention is supported by the photomicrograph of an as-cast Al-0.08% Sn alloy in Fig. 5(a). Here it is evident that the microstructure is very heterogeneous. The small discrete black spherical particles are metallic tin whereas the deeply etched bands

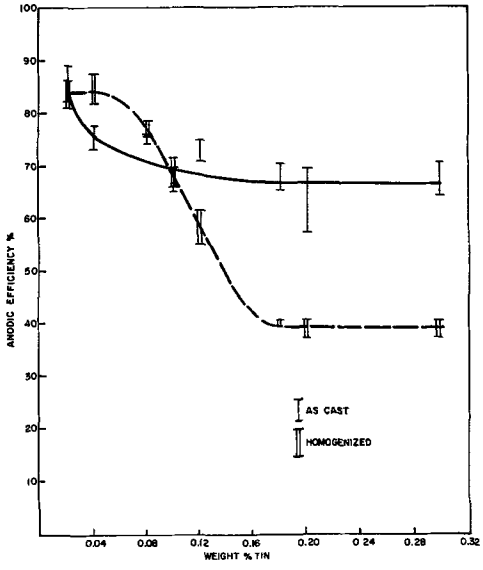

Fig. 3. Effect of tin content of aluminum on anodic efficiency when coupled to steel in 0.1*N* NaCl for 48 hr.

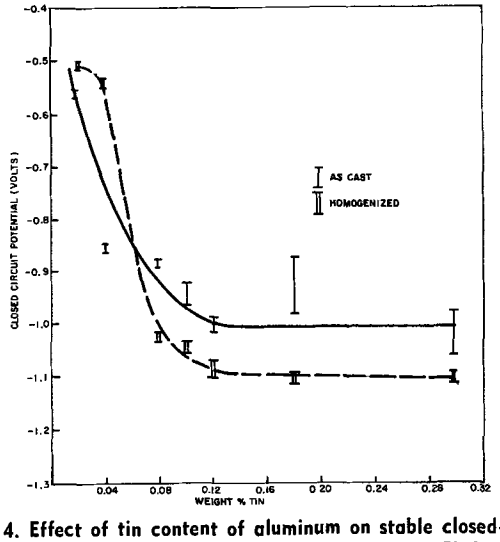

Fig. 4. Effect of tin content of aluminum on stable closed-circuit potential (*vs.* H_2) when coupled to steel in 0.1*N* NaCl for 48 hr.

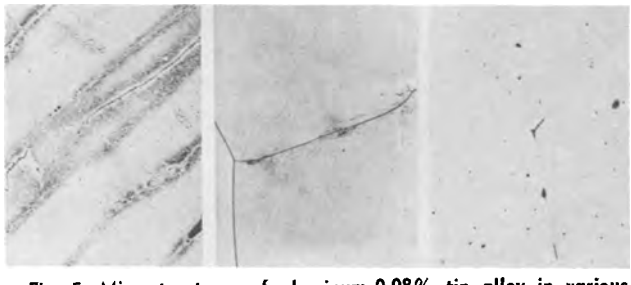

Fig. 5. Microstructures of aluminum-0.08% tin alloy in various metallurgical conditions. Magnification approximately 340X. (a) (left) As-cast, showing cored solid solution (tin-rich areas are darkened) and tin particles in grain boundaries; (b) (center) homogenized (620°C for 16 hr) and quenched, showing uniform solid solution; (c) (right) heterogenized (400°C for 24 hr following homogenization), showing precipitated tin particles.

may either represent concentrations of tin in solution or very fine tin particles. The difficulty of distinguishing between these conditions accounts for much of the disagreement in locating the phase boundary in the aluminum-rich end of the Al-Sn equilibrium diagram.

With the obvious heterogeneity of the Al-0.08% Sn alloy in the as-cast condition, and with the observa-

tion from ref. (13) that this amount of tin could be taken into solid solution at 620°C, a series of Al-Sn alloys was homogenized at 620°C as described earlier. The homogenized castings were quenched to retain the tin in solid solution. The microstructure of the Al-0.08% Sn alloy after homogenizing is shown in Fig. 5(b), which is a typical solid solution microstructure showing none of the gross heterogeneity found in the as-cast condition. The galvanic experiments conducted earlier in the as-cast condition were repeated in the homogenized condition. Results are also shown in Fig. 1-4. Reproducibility of results, in triplicate specimens, was markedly improved, and well-defined trends in electrochemical behavior became apparent. Anodic weight loss and coulombic output now rose sharply at about 0.05% Sn and reached a plateau at around 0.1% Sn or slightly above (Fig. 1 and 2). Anodic efficiency was lessened in the homogenized condition (Fig. 3) and closed circuit cell potential was around 0.1v more active above 0.1% Sn than in the as-cast condition (Fig. 4).

The results of impedance studies of the oxide film stable on Al-Sn alloys in 0.1*N* NaCl are shown in Fig. 6. γ-Al_2O_3 films on pure aluminum have an a-c resistivity of around 10^{10} ohm cm at 1 kc (3). Tin dissolved in solid solution markedly lowers this value to around 7×10^7 ohm cm at 0.08% Sn. This experiment represents the combined effects of tin and chloride ions in reducing resistivity at a frequency of 1 kc. Previous work (3) has shown that chloride ions alone reduce 1 kc resistivity to around 2×10^9 ohm cm only. It is clear, therefore, that the majority of the much larger decrease in resistivity seen in Fig. 6 is due to tin in the alloy although the possibility of a synergistic interaction between the tin and chloride ions cannot be ruled out. Aluminum-tin alloys containing from 0.02-0.08% tin were also heterogenized at 400°C as described earlier to precipitate most of the tin from solid solution. A typical photomicrograph of a heterogenized Al-Sn alloy is shown in Fig. 5(c) and it is evident that the precipitation treatment was quite effective. Despite the numerous leakage paths that must exist in the surface oxide film from this amount of elemental second phase carrying, at best, a very poorly protective and low resistance film, Fig. 6 shows that average film resistivity in the heterogenized condition is significantly higher than in the homogenized single phase condition. Furthermore, precipitation of tin from solid solution destroys completely the beneficial effect that tin in solid solution will exhibit in greatly raising the level of current output in a galvanic couple with iron in sodium chloride solution (Fig. 7).

Discussion

The effect of tin on the galvanic behavior of Al-Sn alloys coupled to mild steel in sodium chloride solution is quite remarkable as shown in Fig. 1-4. Tin in aluminum can debase the closed couple circuit potential by as much as 0.6v and can increase galvanic output by over 30 times that of pure aluminum in the same couple. The results in Fig. 6 show that 1 kc a-c resistivity of the surface oxide film is lowered by over two orders of magnitude compared with that figure obtained previously for γ-Al_2O_3 films on pure aluminum (3). Here it does appear that Sn^{4+} ions have been able to enter the surface oxide film on aluminum, replacing aluminum ions and thus creating additional cation vacancies. Were tin to be present in the oxide film as Sn^{++}, the marked drop in resistivity at 1 kc (Fig. 6) would not be observed; neither would the marked changes in electrochemical behavior be expected. It is possible that some very small concentrations of Sn^{++} may exist in the oxide film immediately adjacent to the metal interface, because of thermodynamic considerations. However, from Fig. 6 their importance, if present, is quite minor and the bulk of the tin surface oxide film is clearly doped with Sn^{4+} ions and controls the behavior of the aluminum alloy as an anode.

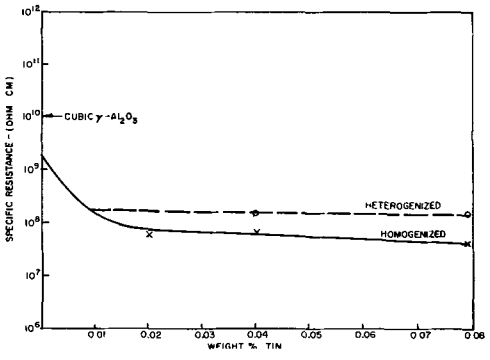

Fig. 6. Specific a-c resistance of surface oxide film formed on Al-Sn alloys in 0.1*N* NaCl, calculated from capacitance and loss at 1 kc.

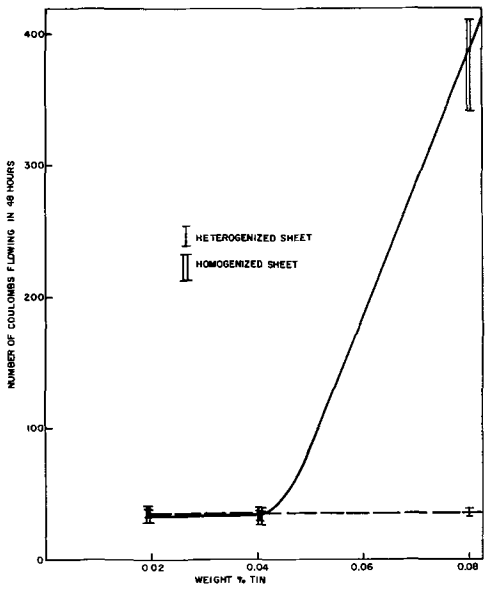

Fig. 7. Effect of tin remaining in solid solution in aluminum on coulombic output when coupled to steel in 0.1*N* NaCl for 48 hr.

The form in which tin is present in the metal is quite critical in enabling the alloying addition to enter the surface oxide. Figure 7 shows clearly that tin, as a series of elemental particles, will produce virtually no enhancement of galvanic current output. Likewise, despite the obvious presence of many low resistance leakage paths in the surface oxide film on heterogenized Al-Sn alloys [Fig. 5(c)] the average film resistivity is higher on heterogenized Al-Sn alloys than on similar single phase homogenized alloys. Evidently tin will only reduce the resistivity of the aluminum oxide film if it is dispersed relatively uniformly in the aluminum solid solution substrate. Despite the fact, that only around 0.1% tin can only be retained in a metastable solid solution, at room temperature it still appears to be distributed sufficiently uniformly so as to permit relatively reproducible doping of the surface oxide film with the attendant decrease in ionic resistivity.

The form of the weight loss and coulomb flow curves in Fig. 1 and 2 as a function of tin content further emphasizes the importance of the amount of tin retained in metastable solid solution at room temperature. Quantities of tin up to around 0.04% have little effect on the electrochemical properties of Al-Sn alloys despite the fact that they lower the oxide film resistivity (Fig. 6). The effect of these small quantities of tin is not sufficient from Fig. 4 to debase the potential of the couple (or the aluminum alloy) suffi-

ciently to permit evolution of hydrogen from a steel cathode. Accordingly, galvanic corrosion of these alloys with thin surface films only moderately doped with Sn^{4+}, is cathodically controlled by dissolved oxygen reduction at the steel cathode in the same fashion as with pure aluminum as an anode (10). Quite similar current outputs must be anticipated with a similar cathode, electrolyte, and cell geometry, under these conditions. As the tin content is further increased, the anode potentials and the cell potentials are debased into the potential region where hydrogen may be freely evolved from the steel cathodes (11). Brisk hydrogen evolution from the steel cathode (and from the Al-Sn anodes) characterizes all galvanic experiments conducted on homogenized alloys containing 0.08% Sn and more. The current output is no longer limited by diffusion of dissolved oxygen and now increases sharply with increasing tin content as long as tin can be added and retained in metastable solid solution. Galvanic corrosion is still however, likely under cathodic control. From Fig. 1, 2, and 4 it appears that the maximum solid solubility of tin in aluminum is between 0.10 and 0.12% with the form of the curves suggesting that the maximum solubility is slightly in excess of 0.1% at 620°C as had been found by Samuels (9). Indeed, in the Al-Sn system galvanic experiments or potential measurements are probably a more effective method of locating the phase boundary than conventional optical metallography. Further increases in tin content above 0.12% result only in the presence of more elemental tin out of solid solution. It follows from the above that this extra elemental tin produces no increase in galvanic current output (Fig. 2), but does result in some further decrease in anodic efficiency (Fig. 3) presumably due to the provision of low resistance local cathodes.

As-cast Al-Sn alloys exhibit variable galvanic behavior intermediate between that of homogenized and heterogenized Al-Sn alloys. Because the tin retained in solid solution is highly dependent on uncontrolled variables during solidification, maximum solid solubility is seldom obtained and the tin distribution is nonuniform [Fig. 5(a)]. Variable galvanic results are therefore not surprising.

The curves of anodic efficiency *vs.* tin content in the homogenized condition (Fig. 3) do not match completely the weight loss, current flow, and cell potential curves. The latter all become relatively insensitive to tin content above 0.10-0.12% Sn whereas the former does not show a plateau till around 0.2% Sn. Pure aluminum generally shows a very high efficiency of anodic dissolution of around 85% or more in sodium chloride solution (7, 10). This is due to its single valency and due to the fact that, in chloride solutions at a potential of around —0.5v, aluminum itself is a poor cathode due to the high electronic resistance of its natural oxide film (11). In the above potential range only 1-5% of an oxide covered aluminum cathode is active at any given time at current densities below 10 $\mu a/cm^2$. In galvanic corrosion under similar conditions an aluminum anode should also be reluctant to act as an effective local cathode, this fact resulting in high anodic efficiencies. When sufficiently small amounts of tin in solid solution have been added (up to 0.04%) so that galvanic corrosion is still controlled by oxygen diffusion to the steel cathode, no change in anodic efficiency is seen. This argues that these small amounts of tin do not reduce the electronic resistance of the oxide film despite the fact that they lower ionic resistivity (Fig. 6). This is in accord with the previously expressed views on the form in which tin is present in the oxide. Such is clearly not the case in the as-cast condition (Fig. 3) where the elemental tin that is present out of solution [Fig. 5(a)] reduces average electronic resistance of the film by providing low resistance local cathodes. In this case even small quantities of tin reduce anodic efficiency. As more tin is added in solid solution and the potential of the couple moves into the range where hydrogen can be evolved both from the cathode and the anode, anodic efficiency decreases. Presumably the additional driving force for the local cell reaction overcomes to some degree the effect of the high electronic resistance oxide film permitting it to function as a more effective local cathode. As the solid solution becomes saturated with tin and now contains second phase particles of elemental tin, anodic efficiency continues to drop presumably due to the second phase tin particles acting as low resistance local cathodes. The lower values of anodic efficiency in the homogenized condition are attributed to the fact that the tin particles are smaller than in the as-cast condition and so exhibit a greater ratio of spherical surface area to volume as the corrosion advances into the metal.

The fashion in which the Al-Sn anodes corrode is of some interest. As-cast alloys with their heterogeneous distribution of tin corrode nonuniformly and often intergranularly. Typically corrosion follows the dark etching bands shown in Fig. 5(a). Homogenized Al-Sn alloys containing 0.1% Sn or less also corrode somewhat nonuniformly and by shallow pitting. Presumably completely uniform distribution of tin was not achieved despite the homogenizing treatment. Since tin is known to be strongly clustered in aluminum-tin solid solutions (12) this result is in accord with the anticipated metallurgical structure of the metastable solid solution. Homogenized Al-Sn alloys containing 0.12% Sn or more corroded quite uniformly when coupled to steel. Presumably the numerous small local cathodes are beneficial in ensuring uniformity of anodic corrosion despite the fact that their presence results in the loss of some anodic efficiency.

There is finally the question remaining as to why tin is so effective in reducing the ionic resistance of oxide films on Al-Sn alloys while other group IV elements are virtually without effect. Ti, Zr, Si, and Ge have solid solubilities at least as high as that of tin and in most cases higher. Yet they do not significantly increase current output. It is believed that these dissimilar effects can be rationalized by more detailed considerations of the γ-Al_2O_3 crystal lattice. γ-Al_2O_3 is a pseudospinel and has a close packed fcc oxygen lattice. The structure of the cation lattice is poorly understood, but it doubtless contains a number of cation vacancies at stoichiometry. Accordingly, a foreign cation can likely assume one of two types of positions in the γ-Al_2O_3 cation lattice: (*A*) it may replace an aluminum ion in a filled cation position in the lattice or (*B*) it may enter an already vacant position in the cation lattice.[2]

Alternative (*A*) will tend to create additional cation vacancies and (*B*) will tend to annihilate preexisting cation vacancies (and increase electronic conductivity). It is evident from the present work that tin enters the aluminum lattice in the quadrivalent condition in replacement for aluminum ions, *i.e.*, Sn^{4+} ions substitute by alternative (*A*). However, the oxides of Si, Ti, Zr, and Ge all have very strong tendencies to form highly stable, high melting point compounds with alumina. A natural precursor to the formation of such components would be for the foreign cations to enter vacant sites in the γ-Al_2O_3 cation lattice. In this case ionic resistivity would not be lowered neither would high galvanic outputs be observed. Accordingly, it is considered that with defect spinels such as γ-Al_2O_3 classic substitution and doping effects will only be obtained when the oxide of the doping element is free from strong chemical interaction with the defect spinel itself.

Acknowledgments

The authors wish to thank the Aluminum Division of the Olin Mathieson Chemical Corporation for their support of this work and for their permission to pub-

[2] The same argument is pertinent to the existence of a foreign ion in an interstitial position, an eventuality which is considered to be quite unlikely in a lattice containing a significant number of vacant cation sites.

lish the results. The authors are also indebted to Dr. T. J. Gray for his many helpful discussions.

Manuscript received March 16, 1967; revised manuscript received April 28, 1967.

Any discussion of this paper will appear in a Discussion Section to be published in the June 1968 JOURNAL.

REFERENCES

1. M. J. Pryor, *Z. Elektrochem.*, **62**, 782 (1958).
2. J. J. McMullen and M. J. Pryor, "First International Congress on Metallic Corrosion," p. 52, Butterworths, London (1961).
3. A. F. Beck, M. A. Heine, D. S. Keir, D. vanRooyen, and M. J. Pryor, *Corrosion Sci.*, **2**, 133 (1962).
4. M. A. Heine and M. J. Pryor, *This Journal*, **110**, 1205 (1963).
5. M. A. Heine, D. S. Keir, and M. J. Pryor, *ibid.*, **112**, 24 (1965).
6. M. A. Heine and M. J. Pryor, *ibid.*, In the press.
7. M. J. Pryor and D. S. Keir, *ibid.*, **105**, 629 (1958).
8. H. K. Hardy, *J. Inst. Metals*, **80**, 431 (1951-2).
9. L. E. Samuels, *ibid.*, **84**, 333 (1955-6).
10. M. J. Pryor and D. S. Keir, *This Journal*, **104**, 269 (1957).
11. M. J. Pryor, *ibid.*, **102**, 605 (1955).
12. S. Ceresara and T. Federghi, *Phil. Mag.*, 10, 893 (1964).
13. Annotated Equilibrium Diagram No. 14, Institute of Metals, London, 1955.

Calculation of Currents of Local Galvanic Cells

John A. Simmons, Sam R. Coriell, and Fielding Ogburn

Institute for Materials Research, National Bureau of Standards, Washington, D. C.

ABSTRACT

The current flow for a local electrolytic cell with rectangular anode and cathode is calculated as a function of a polarization parameter, electrolyte thickness and conductivity, anode and cathode size, and zero current potential difference. The total current is obtained from the numerical computation (with error analysis) of a series solution of Laplace's equation assuming a linear polarization relation at the electrode-electrolyte interface. For high values of the polarization parameter and sufficiently thick electrolytes an asymptotic formula obtains for the current approximately proportional to the anodic fraction, as was found by Waber *et al.* However, in general the cell geometry greatly influences the amount of current flow, especially for anode shapes near to linear rather than near to square. This effect can be greater than an order of magnitude. The calculated results are compared with experimental data obtained by Ogburn and Schlissel and are shown to be in good agreement. Corrosion currents in randomly pitted surfaces may be estimated from the above results.

Local electrolytic cells occur frequently in corrosion—wherever pitting occurs. Whether they are due to local breakdowns of passivity, imbedded impurities, or imperfections of metal coatings they lead to pits and corrosion damage and have been the subject of many investigations. By making appropriate approximations, a theoretical analysis of such local cells can be carried out.

Using a model of an alternating array of infinitely long coplanar electrodes, Waber *et al.* (5) calculated the galvanic cell current in terms of the thickness of the electrolyte layer, the sizes of the electrodes, the conductivity of the electrolyte, σ, and the polarization parameter, $k (k = \sigma|de/dj|$, where de/dj is the slope of the potential-current density curve). In this paper we carry out a similar calculation for the current due to a rectangular lattice of cells assuming that the cathodes and smaller anodes are rectangular and lie in one plane. This model comprises a generalization of the one dimensional geometry employed by Waber *et al.* (1-7). Although in some cases the total corrosion current is independent of cell geometry, being a function only of the anodic fraction (the ratio of anodic area to total area), it is shown that in general the cell geometry may influence the corrosion current by more than one order of magnitude. This effect is especially pronounced for thin electrolytes and low polarization. In addition to permitting calculation of the current due to a lattice of cells, the rectangular model may also be used to determine the current in an isolated rectangular corrosion cell. Currents calculated for such cells are shown to be in good agreement with the experimental results of Ogburn and Schlissel (8).

There are certain assumptions which are implicit in this treatment. The cell geometry, electrolyte composition, surface conditions of the electrodes, and so forth, are assumed to be unvarying and uniform. (For example, we do not consider the effects of local cells within the cathodic or anodic areas.) Furthermore we assume, as did Waber *et al.*, that the polarization parameter, k, is the same for both electrodes of a cell and is independent of current density. For many cells, this requirement of a single polarization parameter is not too severe. For instance, in the case of pitting corrosion where the current densities of the small anode are generally much higher than those of the cathode, the polarization behavior of the cathode is of little consequence and only that of the anode is of significance. Further, although a logarithmic polarization law or more accurate empirically determined law is certainly better, a judiciously chosen approximating linear law still can be expected to represent many of the salient features of corrosion behavior.

The ensuing derivation and discussion will be in terms of an anode embedded in a cathode. The mathematics is equally applicable to the reverse situation, a cathode embedded in an anode, if one recognizes that the direction of the current will change, but not its magnitude.

The corrosion current due to a random array of pits is of considerable practical interest. Our results apply directly to a regular rectangular array of pits, but such an array can be used to approximate a random array.

Derivation of Corrosion Current

In this section we derive an equation for the total electric current I for the corrosion cell whose geometry is illustrated in Fig. 1. The cell is a rectangular parallelepiped with sides of length 2a, 2b, and c. We choose our coordinate system so that the x, y, and z axes are parallel to those cell edges of length 2a, 2b, and c, respectively. The origin of the coordinate system is taken so that the eight corners of the cell

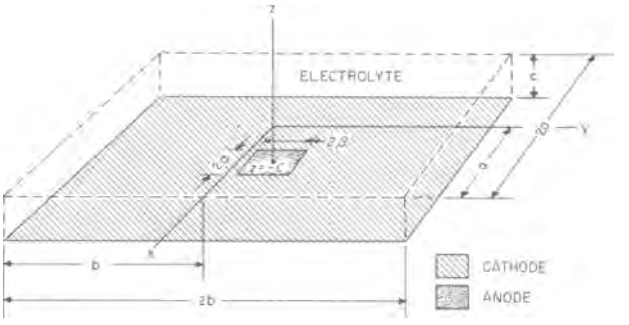

Fig. 1. Cell geometry with coplanar electrodes on the plane $z = -c$ and origin located on the top surface of the electrolyte.

are located at (±a, ±b, 0) and (±a, ±b, —c) as indicated in Fig. 1. For mathematical convenience, the surface containing both the anodic and cathodic areas is placed in the plane $z = -c$. The corrosion pit which acts as the anode is assumed to be a rectangle centered at $x = 0$, $y = 0$, with sides of length 2α and 2β parallel to the x and y axes, respectively. The cathode surrounds the anode and constitutes the rest of the cell surface lying in the plane $z = -c$. The remaining 5 sides of the corrosion cell are taken to be perfect insulators.

To find the total current which governs the rate of corrosion we shall solve first for that potential distribution, $P(x, y, z)$, in the whole cell induced by the emf difference of the two electrodes as modified by a linear polarization at the metal-electrolyte interface. The local current flow at the interface is obtained from the potential distribution by Ohm's law

$$I(x, y, -c) = -\sigma \left.\frac{\partial P}{\partial z}\right|_{(x,y,-c)} \qquad [1]$$

where σ is the conductivity. Since all cell faces are insulators except the anode and cathode surfaces, the total current flowing in the system can be obtained by integrating the local current distribution over either of the electrodes. Thus we shall obtain the total current in the corrosion cell by integrating over the anode surface the local current distribution deduced from the cell potential distribution.

The potential distribution P in the cell is given by the solution of Laplace's equation

$$\nabla^2 P = 0 \qquad [2]$$

subject to the boundary conditions (9)

$$\left.\frac{\partial P}{\partial x}\right|_{x=\pm a} = \left.\frac{\partial P}{\partial y}\right|_{y=\pm b} = \left.\frac{\partial P}{\partial z}\right|_{z=0} = 0 \qquad [3a]$$

$$P(x, y, -c) = E + k \left.\frac{\partial P}{\partial z}\right|_{z=-c}$$

for $|x| < \alpha$ and $|y| < \beta$ [3b]

and

$$P(x, y, -c) = k \left.\frac{\partial P}{\partial z}\right|_{z=-c} \quad \text{for } |x| > \alpha \text{ or } |y| > \beta \qquad [3c]$$

Equation [3a] describes the fact that there are insulating walls at $x = \pm a$, $y = \pm b$, and $z = 0$. In Eq. [3b], E is the potential for zero current flow, and k is the linear polarization constant arising from the assumed linear polarization law at the metal-electrolyte interface.[1] We have also taken both electrodes to have the same linear polarization constant, k, as previously discussed.

We solve Laplace's equation by using the method of separation of variables, *i.e.*, we let $Q(x, y, z)$ be a particular solution of Laplace's equation of the form

$$Q(x, y, z) \equiv X(x)\, Y(y)\, Z(z) \qquad [4]$$

From Eq. [2], X, Y, and Z, satisfy the following equations

$$\frac{d^2X}{dx^2} + \lambda^2 X = 0 \qquad [5a]$$

$$\frac{d^2Y}{dy^2} + \mu^2 Y = 0 \qquad [5b]$$

and

$$\frac{d^2Z}{dz^2} - \kappa^2 Z = 0 \qquad [5c]$$

where λ, μ, and κ are in general complex numbers and $\kappa^2 = \lambda^2 + \mu^2$. The solutions to Eq. [5] are

$$X = c_1 \sin(\lambda x) + c_2 \cos(\lambda x) \qquad [6a]$$

$$Y = c_3 \sin(\mu y) + c_4 \cos(\mu y) \qquad [6b]$$

and

$$Z = c_5 \exp(\kappa z) + c_6 \exp(-\kappa z) \qquad [6c]$$

where $c_1 \ldots, c_6$ are constants. We may assume without loss of generality that each of the functions, X, Y, Z satisfies the boundary conditions given in Eq. [3a] and that $X(x)$ and $Y(y)$ are symmetric about $x = 0$ and $y = 0$, respectively, so that

$$Q(x,y,z) = C_{lm} \cos(\pi lx/a) \cos(\pi my/b) \cosh(rz/a) \qquad [7]$$

and try an expansion for

$$P(x,y,z) = \sum_{l=0}^{\infty} \sum_{m=0}^{\infty} C_{lm} \cos(\pi lx/a) \cos(\pi my/b) \cosh(rz/a) \qquad [8]$$

where $l \equiv a\lambda/\pi$ and $m \equiv b\mu/\pi$ are positive integers or zero, $r^2 = a^2\pi^2[\lambda^2/a^2 + m^2/b^2]$ and C_{lm} are the expansion coefficients to be determined from Eq. [3b] and [3c].

It is convenient to define a step function $S_{\alpha\beta}$ such that

$$S_{\alpha\beta} = \begin{cases} 1 & |x| < \alpha \text{ and } |y| < \beta \\ 0 & |x| > \alpha \text{ or } |y| > \beta \end{cases} \qquad [9]$$

The boundary conditions given in Eq. [3b] and [3c] may then be written as

$$P(x,y,-c) = ES_{\alpha\beta} + k \left.\frac{\partial P}{\partial z}\right|_{z=-c} \qquad [10]$$

Combining Eq. [8] and [10] we obtain

$$\sum_{l=0}^{\infty} \sum_{m=0}^{\infty} C_{lm} \cos(\pi lx/a) \cos(\pi my/b) [\cosh(rc/a) + (kr/a) \sinh(rc/a)] = ES_{\alpha\beta} \qquad [11]$$

Multiplying both sides of Eq. [11] by $\cos(\pi l'x/a)$ $\cos(\pi m'y/b)$ and integrating over x and y from $-a$ to a and $-b$ to b, respectively, we find that

$$C_{lm} = 4Eg_{\alpha l}g_{\beta m} \{(1 + \delta_{ol})(1 + \delta_{om}) [\cosh(rc/a) + (kr/a) \sinh(rc/a)]\}^{-1} \qquad [12a]$$

where

$$g_{\alpha l} = (1 - \delta_{ol})(\pi l)^{-1} \sin(\pi l\alpha/a) + \delta_{ol}(\alpha/a)$$

$$g_{\beta m} = (1 - \delta_{om})(\pi m)^{-1} \sin(\pi m\beta/b) + \delta_{om}(\beta/b) \qquad [12b]$$

and

$$\delta_{ij} = \begin{cases} 1 ; i = j \\ 0 ; i \neq j \end{cases}$$

[1] As indicated, for example, by Wagner (9) or Waber (7) few electrolytic cells are truly linearly polarized. In general the graph of current density, j, *vs.* surface potential, e is curved rather than straight and intersects the $j = 0$ axis at E_c, the open circuit single electrode potential. However when a linear approximation of slope M is used for the polarization curve of an electrode, the value of e corresponding to $j = 0$ is not E_c but some other constant E_c'. It is the value of σ.M that is used as the constant k for both electrodes, where M is the slope at the operating current densities of the polarization curve for the controlling electrode (or the best approximation thereto), and the value of [E_c' (anode) $-E_c'$ (cathode) that is used as the constant E].

In order to demonstrate that the series expansion given in Eq. [8] for $P(x, y, z)$ is sufficiently general to satisfy the mixed boundary condition given by Eq. [10], it suffices to show that the series for $P(x, y, z)$ converges and that the series for $\partial P/\partial z$ obtained by differentiation of Eq. [8] converges uniformly in the region $|x| \leq a$, $|y| \leq b$, $-c \leq z \geqq 0$ (10). The series given for P may easily be seen to converge uniformly and absolutely throughout this region. Using a simple generalization of Dirichlet's convergence criterion (10) it is possible to show that $\partial P/\partial z$ converges uniformly on all closed sets of the region which do not intersect the line $z = -c$ and $|x| = \alpha$ or $z = -c$ and $|y| = \beta$. On these anomalous lines the series for $\partial P/\partial z$ converges, but, due to the nature of the step function occurring in Eq. [10] nonuniform convergence appears at the anode boundaries. Furthermore, due to the separation of variables technique the region of nonuniform convergence is projected along the lines bounding the anode but extending beyond the anode in the x and y directions. However, since $\partial P/\partial z$ converges everywhere, it is evident that changing the polarization behavior on a system of lines produces no effect in the current flow density and hence the series given by Eq. [8] and [12] correctly represents the solution to Eq. [2] and [3].

The local current distribution at the metal electrolyte interface, $I\ (x, y, -c)$, may now be obtained from Eq. [1] by

$$I\ (x, y, -c) = \sigma \sum_{l=0}^{\infty} \sum_{m=0}^{\infty} (r/a)\ C_{lm} \cos\ (\pi l x/a) \cos\ (\pi m y/b) \sinh\ (rc/a) \quad [13]$$

where C_{lm} are given in Eq. [12]. The total current flowing in the corrosion cell is obtained by integrating $I\ (x, y, -c)$ over the anode surface, so that

$$I = \int_{-\alpha}^{\alpha} \int_{-\beta}^{\beta} I\ (x, y, -c)\ dx dy \quad [14]$$

Substituting Eq. [13] into Eq. [14], interchanging the order of summation and integration,[2] and carrying out the explicit integration gives

$$I = (16\ \sigma E a b) \sum_{\substack{l=0 \\ l^2+m^2>0}}^{\infty} \sum_{m=0}^{\infty} [g_{\alpha l}^2\ g_{\beta m}^2/\ (1 + \delta_{ol})\ (1 + \delta_{om})]\ [k + (a/r) \coth\ (rc/a)]^{-1} \quad [15]$$

To evaluate I explicitly we first make use of an upper bound for I which is, in fact, an asymptotic approximation for I when

$$\begin{aligned} k/a &>> 1 \\ k/b &>> 1 \\ c/a &\gtrsim 1 \\ c/b &\gtrsim 1 \end{aligned} \quad [16]$$

such as the case of a thick electrolyte layer and very high values of k. In this case the hyperbolic terms in the denominator may be ignored and we have

$$I \simeq I_A \equiv (16\ \sigma E a b/k) \sum_{\substack{l=0 \\ l^2+m^2>0}}^{\infty} \sum_{m=0}^{\infty} [g_{\alpha l}^2\ g_{\beta m}^2/ (1 + \delta_{ol})\ (1 + \delta_{om})] \quad [17]$$

In general, even when the conditions [16] are not satisfied one sees that

$$I \leq I_A \quad [18]$$

The expression for I_A may be evaluated explicitly using the identity

$$\sum_{j=1}^{\infty} \{[\sin^2\ (j\theta)]/j^2\} = \tfrac{1}{2}\ \theta\ (\pi - \theta) \quad [19]$$

to yield

$$I_A = (4\sigma E \alpha\beta/k)\ [1 - \alpha\beta/ab] \quad [20]$$

It does not seem possible to obtain an analytic expression for the general current I, but I may be computed numerically as discussed below.

Numerical Evaluation

To facilitate the calculation of I numerically, we make use of the asymptotic expression I_A as given by Eq. [17] and write

$$\begin{aligned} I &= I_A - (I_A - I) = I_A - (16\ \sigma E a b/k) S \\ &= (4\ \sigma E \alpha\beta/k)\ [1 - (\alpha\beta/ab) - 4(ab/\alpha\beta) S] \end{aligned} \quad [21]$$

where the sum

$$S \equiv \sum_{\substack{l=0 \\ l^2+m^2>0}}^{\infty} \sum_{m=0}^{\infty} g_{\alpha l}^2 g_{\beta m}^2\ [(1 + \delta_{ol})\ (1 + \delta_{om})\ \{1 + (kr/a) \tanh\ (cr/a)\}]^{-1} \quad [22]$$

on the right hand side of Eq. [21] becomes vanishingly small for conditions approaching those given in Eq. [16]. Since I_A is given in closed form by Eq. [20] we need only evaluate the sum, S. This has been done numerically on a 7094 computer by summing over a finite region in the l, m plane. To further simplify the calculations and economize on computer time we have restricted the physical constants a, b, α, β in such a way that the parameters

$$\begin{aligned} A^{-1} &\equiv (a/\alpha) \\ B^{-1} &\equiv (b/\beta) \\ s^{-1} &\equiv (b/a) \end{aligned} \quad [23]$$

are integers. This restriction imposes some limitation on the problem geometry, but may be removed if desired. On insertion of Eq. [23] into Eq. [21], we have

$$I = (4\sigma E \alpha\beta/k)\ [1 - AB - (4S/AB)] \quad [24]$$

where, since $r = \pi(l^2 + s^2 m^2)^{1/2}$ and since both $g_{\alpha l}$ and $g_{\beta m}$ depend only on A and B, respectively, the computed sum, S, and the normalized current

$$I^* \equiv (kI/4\sigma E \alpha\beta) \quad [25]$$

depend only on the parameters A, B, c/a, k/a, s.

In order to make the numerical results meaningful, we must derive an error bound for the remaining terms which are not included in the numerical sum. Such a bound is derived in the Appendix.

Results and Discussion

In this section we give the results for numerical calculation of the corrosion current emphasizing the case when $a = b$ and $\alpha = \beta$ and present a comparison of the theory with experimental results of Ogburn and Schlissel.

Case 1: $\alpha = \beta$ and $a = b$.—In Tables I-IV, the corrosion currents are summarized for a series of values α/a between 10^{-5} and 0.5 and k/a between 10^{-4} and

Table I. Computation of I^* for various values of α/a, and k/a (when $\alpha = \beta$ and $a = b$); $c/a = 1.0$

I^* k/a \ α/a	0.5	10^{-1}	10^{-2}	10^{-3}	10^{-4}	10^{-5}
10^2	0.75	0.99	1.00	1.00	1.00	1.00
10^1	0.73	0.98	1.00	1.00	1.00	1.00
10^0	0.61	0.92	1.00	1.00	1.00	1.00
10^{-1}	0.26	0.60	0.92	1.00	1.00	1.00
10^{-2}	0.054	0.18	0.61	0.92	1.00	1.00
10^{-3}	0.0084	0.033	0.18	0.61	0.92	1.00
10^{-4}			0.033	0.18	0.61	0.92

[2] Interchange of summation and integration may easily be seen to be valid when the limits of integration lie inside the anode. Continuity of the sum of the integrals as the limits tend to α, β on the anode surface guarantee a consistent definition for the total current over the entire anode.

Table II. Computation of I^* for various values of α/a, and k/a (when $\alpha = \beta$ and $a = b$); $c/a = 10^{-1}$

I^* k/a \ α/a	0.5	10^{-1}	10^{-2}	10^{-3}	10^{-4}	10^{-5}
10^2	0.74	0.99	1.00	1.00	1.00	1.00
10^1	0.70	0.98	0.99	1.00	1.00	1.00
10^0	0.47	0.89	0.98	1.00	1.00	1.00
10^{-1}	0.17	0.56	0.92	1.00	1.00	1.00
10^{-2}	0.040	0.17	0.61	0.92	1.00	1.00
10^{-3}	0.0068	0.031	0.18	0.61	1.00	1.00
10^{-4}			0.033	0.18	0.61	1.00

Table III. Computation of I^* for various values of α/a, and k/a (when $\alpha = \beta$ and $a = b$); $c/a = 10^{-2}$

I^* k/a \ α/a	0.5	10^{-1}	10^{-2}	10^{-3}	10^{-4}	10^{-5}
10^2	0.70	0.99	0.99	1.00	1.00	1.00
10^1	0.48	0.91	0.99	1.00	1.00	1.00
10^0	0.19	0.65	0.98	0.99	1.00	1.00
10^{-1}	0.061	0.28	0.89	0.98	1.00	1.00
10^{-2}	0.018	0.088	0.56	0.92	1.00	1.00
10^{-3}	0.0041	0.020	0.17	0.61	0.92	1.00
10^{-4}			0.031	0.18	0.61	0.92

Table IV. Computation of I^* for various values of α/a, and k/a (when $\alpha = \beta$ and $a = b$); $c/a = 10^{-3}$

I^* k/a \ α/a	0.5	10^{-1}	10^{-2}	10^{-3}	10^{-4}	10^{-5}
10^2	0.48	0.91	0.99	0.99	1.00	1.00
10^1	0.19	0.65	0.99	0.99	1.00	1.00
10^0	0.062	0.28	0.91	0.99	1.00	1.00
10^{-1}	0.020	0.097	0.65	0.98	0.99	1.00
10^{-2}	0.0062	0.031	0.28	0.89	0.98	1.00
10^{-3}	0.0018	0.0092	0.088	0.56	0.92	1.00
10^{-4}			0.020	0.17	0.61	0.92

10^2 for four orders of magnitude of c/a. Most of the results are accurate to within 2% although a few may have inaccuracies of as much as 5%.

The results of Tables I and IV are illustrated in Fig. 3 and 4. Additional extrapolated points have been added to fill out the calculated surface. As may be seen for $\alpha/a << c/a$ and $\alpha/a << k/a$, $I^* \cong I_A^*$, where $I_A^* = 1 - (\alpha/a)^2$ is the normalized asymptotic current, and $I_A^* \cong 1$ except when $\alpha/a > 0.1$; in fact the graph of I_A^* is the same as the front contour curve of the I^* surface in Fig. 3 on which $k/a = 100$ and $c/a = 1$. Thus the extrapolation for small values of α/a in these figures is clearly justified. The two points for which $k/a = 10^{-4}$ and $\alpha/a = 0.1$ or 0.5 on each of the two surfaces require excessive machine time to calculate and have been interpolated graphically using the additional fact that $I^* = I^*_A \equiv 0$ when $\alpha/a = 1$. Calculations using $c/a > 1$ appear to be unnecessary, at least when $\alpha/a \leq 0.5$, since the use of larger c's gives negligible effect on I^*.

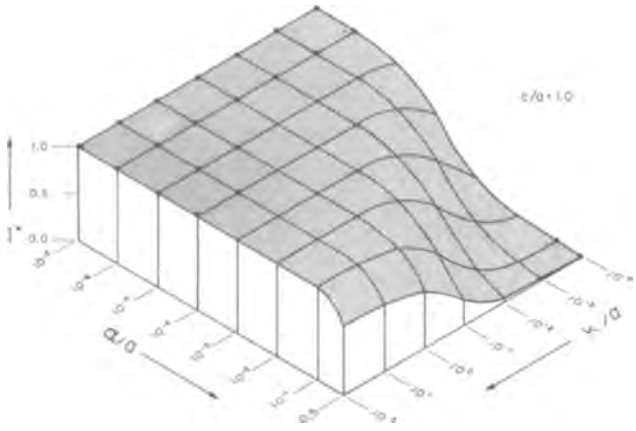

Fig. 3. Normalized current as a function of polarization parameter and cathode size with $c/a = 1$. Extrapolated points are indicated by large dots.

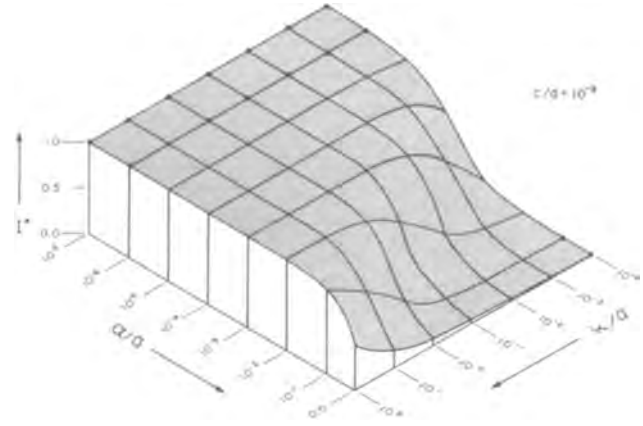

Fig. 4. Normalized current as a function of polarization parameter and cathode size with $c/a = 10^{-3}$. Extrapolated points are indicated by large dots.

As seen from Eq. [25], I^* depends only on the ratios α/a, c/a, and k/a; Tables I-IV have been made up accordingly. To render these tables more useful, the separate dependence of I^* on a, when α, c, k are held fixed, is given in Table V for a series of values of c and k where α has been fixed at 10^{-2} cm. Due to the dependence of I^* on the ratios α/a, c/a, k/a, fixing α imposes no real limitation on the range of applicability of the results. It is clear from Table V that α/a has the greatest effect on I^* when c/a and k/a are large, *i.e.*, when $I^* \simeq I^*_A$. Thus we may conclude that when $\alpha/a \leq 0.1$ the error introduced by assuming $a = \infty$ is less than 1%. This fact has been used to simplify the calculations of Table I-IV; *e.g.*, I^* for $c = 10^{-2}$ cm, $\alpha = 10^{-2}$ cm, $a = 1.0$ cm, $k = 10^{-2}$ cm is the same as I^* for $c = 10^{-1}$ cm, $\alpha = 10^{-1}$ cm, $a = 1.0$ cm, $k =$

Table V. Dependence of I (in amperes) on cathode size for various values of c and k. In all cases $\alpha = 10^{-2}$ cm, $E = 0.31$v and $\sigma = 0.25 \times 10^{-4}$ ohm^{-1} cm^{-1}. Values are accurate to 0.1% except where indicated, and when $k = 10^2$ all computed values of I coincide with those of I_A to within 0.1%

c \ k		10^{-4} cm	10^{-1} cm	10^{2} cm
10^{-4} cm	$a/\alpha =$ 2	0.28×10^{-6}	0.879×10^{-8}	0.232×10^{-10}
	3	0.28×10^{-6} 4% Error	0.881×10^{-8}	0.274×10^{-10}
	6	0.28×10^{-6}	0.881×10^{-8}	0.299×10^{-10}
	10	0.28×10^{-6}	0.881×10^{-8}	0.303×10^{-10}
	100		0.881×10^{-8}	0.305×10^{-10}
10^{-1} cm	$a/\alpha =$ 2	0.977×10^{-6}	0.222×10^{-7}	0.232×10^{-10}
	3	0.100×10^{-5}	0.260×10^{-7}	0.276×10^{-10}
	6	0.101×10^{-5} (0.5% Error)	0.281×10^{-7}	0.301×10^{-10}
	10	0.101×10^{-5} (1.5% Error)	0.284×10^{-7}	0.307×10^{-10}
	100		0.286×10^{-7}	0.310×10^{-10}
10^{2} cm	$a/\alpha =$ 2	0.977×10^{-6}	0.222×10^{-7}	0.232×10^{-10}
	3	0.100×10^{-5}	0.260×10^{-7}	0.276×10^{-10}
	6	0.101×10^{-5} (1% Error)	0.281×10^{-7}	0.301×10^{-10}
	10	0.102×10^{-5} (2% Error)	0.284×10^{-7}	0.307×10^{-10}
	100		0.286×10^{-7}	0.310×10^{-10}

10^{-1} cm since replacement of $a = 10$ cm by $a = 1$ cm in the second case produces no effect.

As pointed out by various authors (2, 9, 11, 12) the size of the polarization constant k affects the nature of the current distribution as well as the magnitude of the corrosion current. As indicated in Fig. 3 and 4 and as expressed in Eq. [24], for large k/a and small α/a the effect of k is essentially that of a resistance when σ is held constant. However, when $k/\alpha \gtrsim 1$ the influence of k becomes less pronounced until (for example, when $c/a = 1$ and $\alpha/a = 0.5$) change of k/a by a factor of 10 from 10^{-2} to 10^{-3} produces an increase in I of only about 1.5. This latter effect is a consequence of the behavior of the series representation given by Eq. [15] for I. Here it may be seen that as $k \to 0$, the qualitative behavior of the series is of the type $I \simeq O(\ln k)$ as $1/k \to \infty$. Thus $I^* \simeq O(k \ln k)$ which tends to zero as k tends to zero.

Case 2: $\alpha \neq \beta$ and/or $a \neq b$.—Currents produced by configurations where $\alpha \neq \beta$ or $a \neq b$ involve too many parameters to permit a general compilation of results. However, certain trends are relatively clear. Thus, as observed above when $\alpha = \beta$, $a = b$, the dependence of I^* on a and b for α/a, β/a, α/b, and β/b all <0.1 may be expected to be negligible; this has been verified in a number of special cases. The effect of changing the ratio a/α while maintaining the anode area, $\alpha\beta$, constant produces significant effects on the corrosion current as indicated in Fig. 5 where I^* *vs.* β/α is graphed for the six possible combinations of $c/a = 10^{-3}$ or 1.0 and $k/a = 10^{-3}$, 10^{-2}, or 100. Here $a = b$ and the anodic fraction $\alpha \cdot \beta / a \cdot b = 1/1296$. It should be noted that when one of the anode dimensions, say β, is taken equal to the correspondent cathode dimension, *i.e.*, b, the model employed here reduces to that employed by Waber *et al.* and Eq. [21] becomes equivalent to their expression for the corrosion current. For ratios of β/α between 1 and 2 the amount of corrosion current is seen to vary by less than about 10%. This result is relatively independent of the anodic fraction for anodic fractions $\lesssim 0.5\%$ and holds for all configurations where α/a, α/b, β/a, and β/b, are all less than 0.1. Thus, in treating problems involving random corrosion pits where the pits are approximately circular in shape, *i.e.*, the ratio of the maximum diameter to minimum diameter is less than 2, errors of $\leq 10\%$ may be expected. Further, the more oblong pits, which produce the greatest corrosion current and thus the greatest rate of corrosion, should have the fastest growth rate among various anode shapes.

In Fig. 5 when $\beta/\alpha = 1296$, *i.e.*, when $\beta = b = 1$, the geometry is that of the one dimensional strip model. As may be seen for small values of k and small electrolyte thickness, variation in the anode shape from a square to a one-dimensional strip produces as much as a factor of 13.5 in the corrosion current while for large values of k and thick electrolytes the anode geometry produces no significant effect. The effects due to anode geometry shown in Fig. 5 are expected to be magnified for smaller anodic fractions, (provided that $k/\alpha \lesssim 1$) and thinner electrolytes. On the other hand, when k and c are sufficient large $I \cong I_A$ (the asymptotic corrosion current value) which is independent of anode geometry.

Experimental comparison.—Using the computer program developed for determining the corrosion current, calculations have been made for comparison with experimental data of Ogburn and Schlissel (8). Figures 6 and 7 taken from ref. (8) show the experimental and calculated results for the case of Ni-Fe electrolytic cells with synthetic rain water electrolyte in which the (*i*) anode diameter and (*ii*) electrolyte thickness, respectively, have been varied. In both experiments $a = 2.5$ cm, $b = 0.5$ cm, and the open circuit potential of 0.3v was used as an estimate of E. For Fig. 6, $c = 100$ cm, $\sigma = 53 \times 10^{-6}$ ohm^{-1}, and k was estimated to be 95.4×10^{-4} cm. The anodes, which were circular in shape, have been approximated by squares of equal area: $\alpha = \beta = 0.00225$, 0.00675, and 0.01 cm. For Fig. 7, $\sigma = 105 \times 10^{-6}$ ohm^{-1} cm^{-1}, k was estimated to be 189×10^{-4} cm, and $\alpha = \beta = 0.01$ cm for a square of area equal to that of the circular anode. The electrolyte thickness ranged from 0.004 to 0.015 cm. Although these data show extensive scatter due

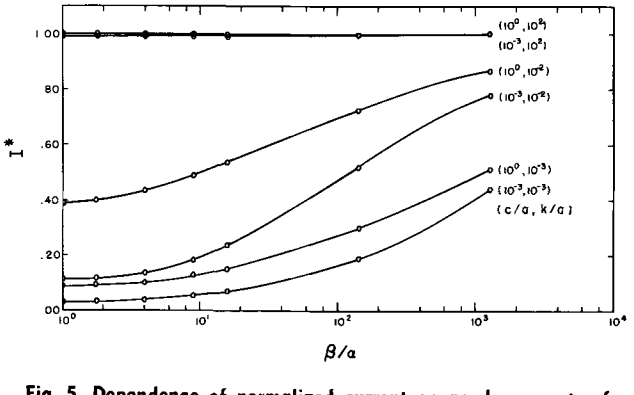

Fig. 5. Dependence of normalized current on anode geometry for various values of c/a and k/a. In all cases $a = b$ and the anodic fraction $\frac{\alpha \cdot \beta}{a \cdot b} = 1/1296$.

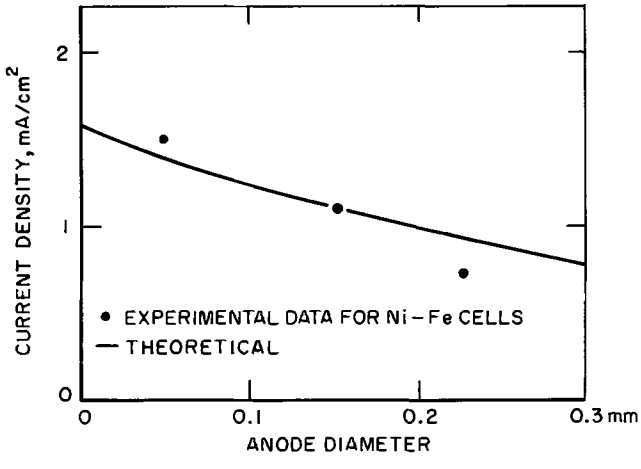

Fig. 6. Comparison of experimental and theoretical results for the effect of anode size on cell current.

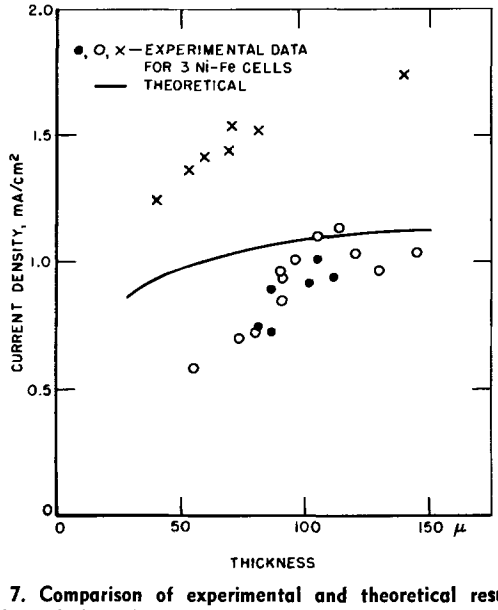

Fig. 7. Comparison of experimental and theoretical results for the effect of electrolyte thickness on cell current.

to experimental difficulties (8) and comprise a very limited check on the theory presented in this paper, they are in reasonable agreement with the theoretical calculations.

Acknowledgment

The authors wish to thank ARPA for partial support of this work.

Manuscript received Nov. 16, 1966; revised manuscript received May 5, 1967.

Any discussion of this paper will appear in a Discussion Section to be published in the June 1968 JOURNAL.

REFERENCES

1. J. T. Waber, *This Journal*, **101**, 271 (1954).
2. J. T. Waber and M. Rosenbluth, *ibid.*, **102**, 344 (1955).
3. J. T. Waber, *ibid.*, **102**, 420 (1955).
4. J. T. Waber and B. Fagan, *ibid.*, **103**, 64 (1956).
5. J. T. Waber, J. Morrissey, and J. Ruth, *ibid.*, **103**, 138 (1956).
6. J. T. Waber, *ibid.*, **103**, 567 (1956).
7. J. T. Waber, *Corrosion*, **13**, 95t (1957).
8. F. Ogburn and M. S. Schlissel, *Plating*, **54**, 54 (1967).
9. C. Wagner, *This Journal*, **98**, 116 (1951).
10. E. T. Whittaker and G. N. Watson, "A Course of Modern Analysis," 4th ed., p. 17, Cambridge (1963).
11. C. Kasper, *Trans. Electrochem. Soc.*, **77**, 353, 365 (1940); **78**, 131, 147 (1940); **82**, 153 (1942).
12. T. P. Hoar and J. N. Agar, *Discussion Faraday Soc.*, **1**, 162 (1947).

APPENDIX

Analysis of Numerical Error Bound

We consider a rectangular region in the l, m plane, $0 \leq l \leq l^*$, $0 \leq m \leq m^*$, where $l^*/m^* = s$ as illustrated in Fig. 2. The magnitude of l^* is ultimately dependent on either available computer time or the degree of accuracy desired. The expression for the error, which consists of the sum over those mesh points lying outside the summing rectangle, may be calculated by breaking up the error sum into two regions, $l \leq ms$, $l \geq ms$ separated by the diagonal line $l = ms$. The methods for computing the error bound for these two regions are the same, so we shall discuss only the region $ms \leq l$.

We shall further subdivide the region $ms \leq l$ by defining the blocks

$$S_n : \begin{cases} n \leq mB < n+1\ , \quad n = 0, 1, 2 \ldots \\ l^* \leq l \end{cases} \qquad [26]$$

We shall bound the error in each of the blocks S_n.

The set of points included in the union of the blocks S_n includes the entire region $sm \leq l$ lying outside the summing rectangle and a considerable portion of the region $l \leq ms$ as seen in Fig. 2. However, the contribution of the overlap portion to the error has been shown to be unimportant and is only included for simplicity of the final error expressions.

In each of the blocks S_n, we use the following approximations

$$\sin(\pi y) \leq 4y(1-y) \qquad 0 \leq y \leq 1$$
$$g_{\alpha x} \leq 1/\pi x$$
$$(\pi b/a)\tanh(cr/a) \geq v \equiv (\pi k/a)\tanh(\pi cl^*/a)$$
$$1 + (rv/\pi) \geq 1 + lv \qquad [27]$$

The bound for S_o, which contributes the major error, may be separately calculated by showing

$$\sum_{l>l^*}^{\infty} \sum_{m \leq B^{-1}} g^2_{\alpha l}\, g^2_{\beta m} \{(1+\delta_{ol})(1+\delta_{om})\,[1 + (kr/a)\tanh(cr/a)]\}^{-1} \leq \int_0^{B^{-1}} (4By)^2 (1-By)^2 (\pi y)^{-2}\, dy \int_{l^*}^{\infty} (\pi x)^{-2} (1+xv)^{-1}\, dx \qquad [28]$$

so that

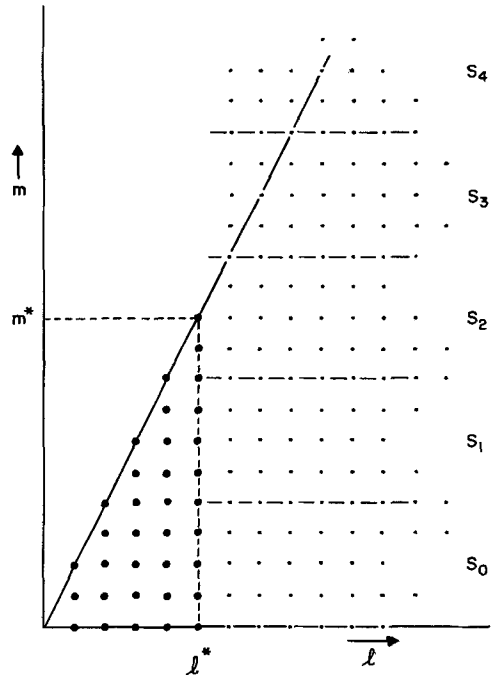

Fig. 2. Schematic representation of summing regions for error analysis.

$$\text{Err } S_o \leq (16B/3\pi^4)\,[(l^*)^{-1} - v \ln\{1 + (vl^*)^{-1}\}] \qquad [29]$$

To bound the error sum for the remaining blocks, we observe

$$\text{Err } S_n \leq (16/\pi^4)\left[\sum_{l=l^*+1}^{\infty} l^{-2}(1+vl)^{-1}\right] \times \left[(B^2/n^2)\sum_{m=(n/B)}^{[(n+1)/B]-1} (Bm-n)^2\,[1-(Bm-n)]^2\right]$$
$$\leq (16B^2/\pi^4 n^2)\{[(1/30B) + (1/16)] \times [(l^*)^{-1} - v\ln\{1 + (vl^*)^{-1}\}]\} \qquad [30]$$

so that

$$\sum_{n=1}^{\infty} \text{Err } S_n \leq (16B^2\, s_2/\pi^4)\,\{[(1/30B) + (1/16)] \times [(l^*)^{-1} - v\ln\{1 + (vl^*)^{-1}\}]\} \qquad [31]$$

where

$$s_2 \equiv \sum_{n=1}^{\infty} n^{-2} \simeq 1.645$$

Thus the error for $ms \leq l$ is bounded by

$$(16B/\pi^4)\{(l^*)^{-1} - v\ln[1 + (vl^*)^{-1}]\} \times \{(1/3) + (s_2/30) + (Bs_2/16)\} \qquad [32]$$

and the total error in the approximation to S is bounded by the inequality

$$\text{Error } (l^*) \leq (16/\pi^4)\left\{\left(\frac{1}{3} + \frac{s_2}{30}\right)(As+B) + \frac{s_2}{16}(A^2 s + B^2)\right\} \times \{(l^*)^{-1} - v\ln[1 + (vl^*)^{-1}]\} \qquad [33]$$

The values of m^* utilized ranged from 5 to 1400 and Error (l^*) was generally taken at 2%.

The High-Temperature Oxidation of Fe-Cr Alloys in the Composition Range of 25-95% Cr

C. S. Tedmon, Jr.

Research and Development Center, General Electric Company, Schenectady, New York

ABSTRACT

The oxidation behavior of Fe-Cr alloys containing 25-95% Cr has been studied over the temperature range of 1000°-1300°C. Near-parabolic kinetics were observed, but detailed structural analysis indicated that the scaling kinetics cannot be interpreted solely in terms of diffusion transport mechanisms. Structural characteristics of the scale and the scale-alloy interface must be considered. The tendency to spall increased with increasing Cr content; spalling behavior is analyzed in terms of the mechanical properties of both the oxide and the alloy. The Wagner analysis relating interdiffusion in the alloy to oxidation rates was applied to the Fe-Cr system, and qualitative agreement with experimental results was found. The observation that parabolic rate constants decreased with decreasing Cr content is discussed.

The extensive literature concerning the oxidation behavior of iron-chromium binary alloys is primarily oriented toward alloys containing up to about 26% Cr. (All compositions are reported in weight per cent.) Very little work has been directed to compositions richer in Cr.

The oxidation behavior of alloys containing less than 13% Cr is very complicated; scales form consisting of spinels and various other Fe and Cr oxides. Seybolt has shown, however, that when the Cr concentration at the metal-oxide interface exceeds 13% Cr_2O_3 is the stable oxide (1). Many of the Fe-Cr binary alloys which form Cr_2O_3 scales have oxidation kinetics controlled principally by cation diffusion through the oxide, although other factors such as surface preparation, scale adherence and blistering (2, 3), and oxide volatilization (4-6) may cause the kinetics to exhibit departure from parabolic behavior. Differences in the thermal expansion coefficients of metal and its oxide may also give rise to spalling tendencies. Tylecote has reviewed and summarized some of the factors which influence the adherence of oxides on metals (7, 8).

Another factor which must be considered when analyzing the oxidation behavior of Fe-Cr alloys is the gradual depletion in the Cr content of the alloy which occurs during oxidation. The interdependence of diffusion processes in the metallic and the oxide phase has been treated theoretically by Wagner (9). Wood and Whittle have experimentally demonstrated that, in the range of Cr contents of 28-68%, replenishment of Cr to the alloy oxide interface increases with decreasing bulk Cr content (10). This effect was attributed to the observation that the self-diffusion coefficients for Cr in Fe-Cr alpha-phase alloys increase with decreasing Cr content (11, 12).

There is a widespread technological need for new high-temperature, oxidation-resistant alloys. For certain applications at elevated temperatures where sigma-phase embrittlement is not a problem, binary Fe-Cr alloys rich in Cr are of interest. It was the purpose of this investigation to survey the high-temperature oxidation behavior of Fe-Cr binary alloys in the composition range of 25-95% Cr, and to attempt to elucidate the effects of such parameters as bulk alloy composition, temperature of oxidation, thermal expansion of alloys and oxides, and diffusive processes in the alloy and the oxide.

Experimental

Sample preparation.—Alloys in the range of 25-70% Cr were made from Ferrovac iron (vacuum-melted electrolytic iron). Fifty and 100g buttons were arc-melted under purified argon; the buttons were remelted 5 times to insure homogeneity. They were then hot-rolled at about 600°C to a final thickness of about 0.08 cm. For compositions containing more than 70% Cr, the procedure was the same except that samples were cut from the as-cast buttons.

Oxidation experiments.—Rectangular samples were obtained having a surface area of about 5 cm^2. All samples were surface ground and polished through No. 400-grit SiC paper and degreased and cleaned in toluene and acetone immediately before insertion into the spring balance furnace. With the exception of one set of experiments, all weight-gain data reported were obtained from samples having abraded surfaces. Since surface preparation has been demonstrated to have an effect on the scaling rates of certain Fe-Cr alloys (13, 14), a set of experiments was carried out on the Fe-45% Cr alloy in which various polishing and etching procedures were used to prepare the sample surface.

Isothermal weight-gain data were obtained using a helical quartz spring; the sample was hung on a sapphire rod that was suspended from the spring. The system was evacuated and the furnace brought to temperature. The desired atmosphere (dry O_2 at 100 Torr) was introduced into the furnace and the run was commenced. Sample temperature was measured with a Pt/Pt-10Rh thermocouple located in an Alundum tube, with its junction about ¼ in. from the center of the sample. Temperature control was about ± 5°C. Sample weight-change was determined by following a fiducial mark on the sapphire rod with a cathetometer. The sensitivity was about ± 30 $\mu g/cm^2$. When a run was completed, the furnace was turned off and the system was evacuated.

Thermal expansion measurements.—The coefficients of thermal expansion for alloys in the composition range of 13-100% Cr were measured using a Chevenard mechanical dilatometer. Differential measurements were made against a fused SiO_2 standard. Both heating and cooling cycles were recorded. All tests were carried out in an argon atmosphere.

Electron microbeam probe measurements.—Samples of Fe-45% Cr and Fe-80% Cr alloys were oxidized for 51 hr at 1100°C in pure O_2. The oxidized samples were then mounted in an electrically conducting base of copper-filled diallyl phthalate for examination in the microprobe. Scans for both elements were carried out in a Cambridge Mark II unit, which had been modified (15) so that the sample could be translated under a static beam in 4μ increments. The data at each point were collected on a scalar for a 10-sec counting period. The operating conditions were 30 kv with a specimen current of 0.1 μa, which resulted in 2000-9000 counts being recorded in the 10-sec interval, depending on the alloy and the component being scanned. Standard

data were taken at the beginning and the end of the run to correct for instrumental drift. Corrections were also made for background radiation and counter-tube dead time. The corrected relative intensities were converted to compositions using the Poole and Thomas atomic number correction (16), Philibert's absorption correction (17), and Castaing's fluorescence correction as modified by Green to correct for overvoltage (18). Using these procedures, the accuracy of the data is believed to be ± 5% of the total amount present.

Auxiliary measurements.—Metallographic and x-ray data were obtained using standard procedures. Debye-Scherrer patterns of oxide scale were made for various alloy compositions and oxidation temperatures; lattice parameters were also calculated. On several samples, the extent of metal recession and the thickness of the oxide scale were determined metallographically as a check on the weight-gain data.

Results

Kinetic measurements.—Gravimetric runs on samples of various compositions were run over the temperature range of 1000°-1300°C. Typical weight-gain *vs.* time data, plotted on logarithmic coordinates, are presented in Fig. 1a through 1e. A slope of ½ would indicate parabolic kinetics. It is apparent that most of the alloys exhibited rates which were approximately parabolic, although the 1100°C data for the lower Cr compositions are less consistent. Some of the runs were repeated to check the reproducibility of the data; generally fair agreement was found. For example, the 1100°C data plotted in Fig. 1e show about the best reproducibility obtained in these experiments at that temperature. Consequently, there resulted considerable scatter in rate constant data, which will be discussed later.

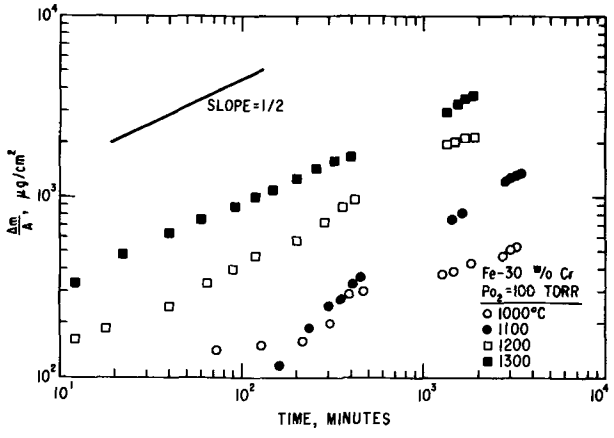

Fig. 1a. Typical gravimetric data for Fe-30% Cr alloys for the temperatures indicated.

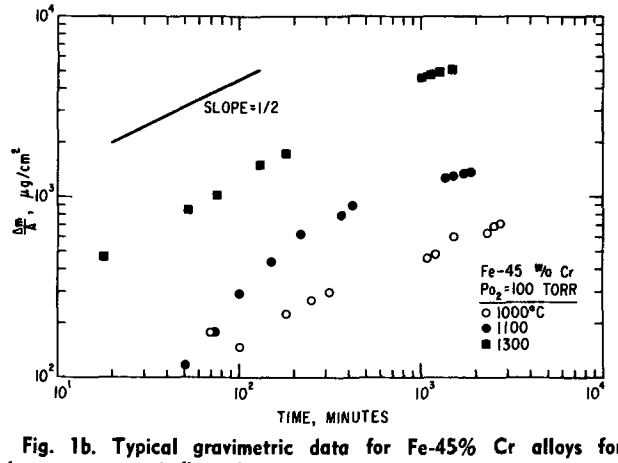

Fig. 1b. Typical gravimetric data for Fe-45% Cr alloys for the temperatures indicated.

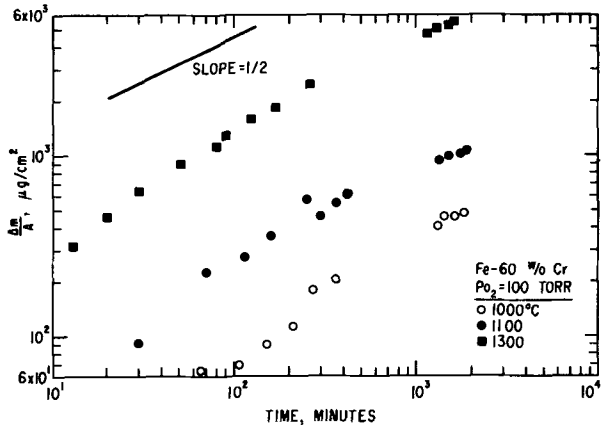

Fig. 1c. Typical gravimetric data for Fe-60% Cr alloys for the temperatures indicated.

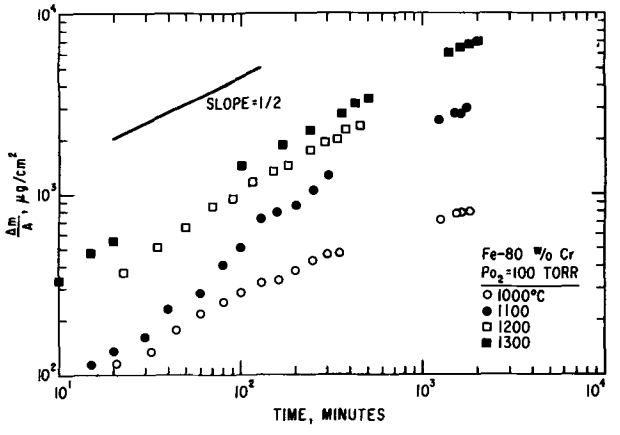

Fig. 1d. Typical gravimetric data for Fe-80% Cr alloys for the temperatures indicated.

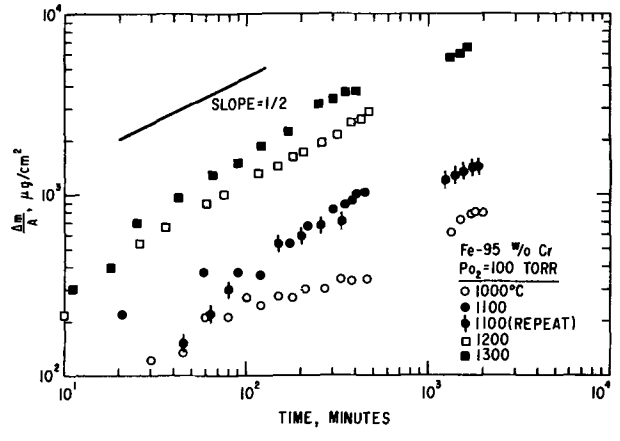

Fig. 1e. Typical gravimetric data for Fe-95% Cr alloys for the temperatures indicated.

It has been established that oxide volatilization, probably occurring by the reaction

$$Cr_2O_3(s) + \frac{3}{2}O_2(g) \rightarrow 2CrO_3(g) \qquad [1]$$

can influence the oxidation kinetics of Cr and Fe-Cr alloys (4-6). However, volatilization losses are usually negligible for short-time oxidation runs such as reported here (6), and indeed the amount of metal-recession measured on several samples was found to be consistent with the corresponding gravimetric data.

For data that fit the relation

$$\frac{\Delta m}{A} = (k_p t)^{1/2} \qquad [2]$$

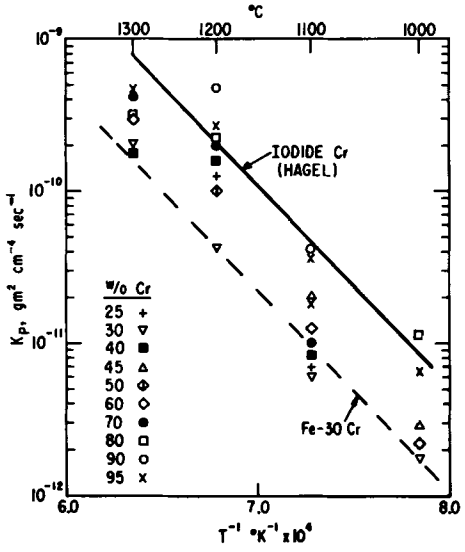

Fig. 2. Temperature dependence of the parabolic rate constant for the oxidation of various Fe-Cr binary alloys.

the parabolic rate constant, k_p, was determined. In Eq. [2], $\Delta m/A$ is the weight-gain per unit area, g-cm^{-2}, and t is the oxidation time in seconds. The temperature dependence of these data is shown in Fig. 2. The solid line indicates the temperature dependence of high-purity (iodide-grade) Cr, as given by the expression (4)

$$k_p \text{ (g}^2\text{ cm}^{-4}\text{ sec}^{-1}) = 0.111 \exp(-59{,}000 \pm 1800/RT) \quad [3]$$

It is obvious that there is considerable scatter in the variation of the rate constant data for a given composition at various temperatures, which obviates the possibility of determining the dependence of an activation energy for oxidation on alloy composition. A possible exception to this is the Fe-30% Cr alloy data, which plot on a straight line approximately parallel to the line for the iodide Cr. It is evident, however, and important to note, that most of the rate constant data for almost all alloys lie below the curve for pure Cr.

The compositional dependence of k_p is shown in Fig. 3. There is a clear trend of decreasing parabolic rate constant with decreasing Cr content of the alloy. The 1100°C data show the most scatter, which is not unexpected in view of the corresponding gravimetric data shown in Fig. 1 for this temperature. The values for pure Cr were obtained from ref. (4).

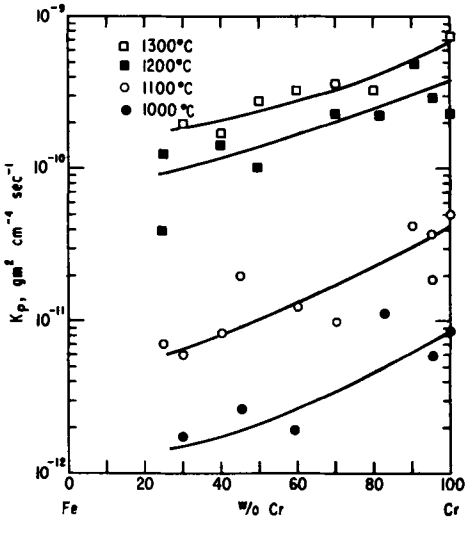

Fig. 3. Composition dependence of the parabolic rate constant of Fe-Cr binary alloys.

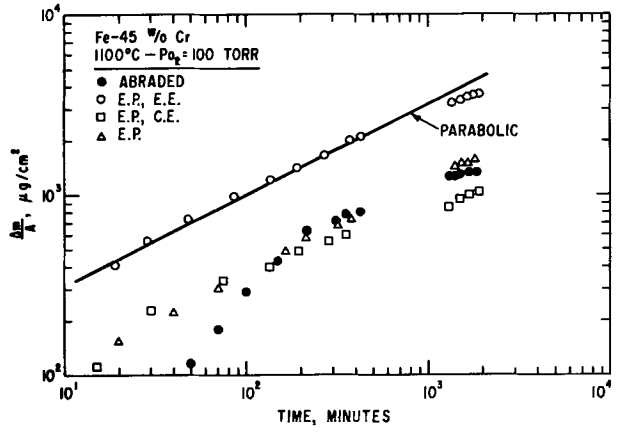

Fig. 4. Effect of surface preparation on the oxidation rate of Fe-45 w/o Cr alloy at 1100°C. Symbols: E.P., Electropolished in a 1:20 solution of 70% perchloric acid in ethyl alcohol for 60 sec. at 40v; E.E., electrolytically etched in a 1:20 solution of 48% HF in water for 50 sec at 3.2v; C.E., chemically etched in a 1:20 solution of 48% HF in water for 15 sec.

Figure 4 presents gravimetric data for samples of Fe-45% Cr that had various different surface preparations prior to oxidation. All the data exhibited essentially parabolic kinetics, and there was a negligible difference in the kinetics for samples that had been abraded, electropolished followed by chemical etching, or just electropolished. The sample which had been electropolished and then electro-etched oxidized considerably faster, however. Possible reasons for this effect will be discussed later.

Thermal expansion coefficients.—The compositional dependence of the coefficient of thermal expansion, at 1100°C, for the range of 13-100% Cr is shown in Fig. 5. The data for Fe-26% Cr include values obtained for several lots of commercial Type 446 stainless steel (Fe + 25-27 Cr). There is a fairly well-defined maximum in the curve in the vicinity of 23% Cr. At 1100°C, the thermal expansion coefficient for Cr_2O_3, obtained by extrapolation of data presented by Tylecote (7), is about 7.5 x 10^{-6}/°C. The mismatch in thermal expansion between the oxide and metal, which may be as much as a factor of 2, will certainly give rise to stresses in the oxide and local shear stresses in the metal adjacent to the metal-oxide interface when the sample temperature is changed, for instance, during cooling to room temperature after a run.

Metallographic observations.—Two general kinds of metallographic observations were made. First, the external surfaces of "as-oxidized" samples were examined at both low and high magnification. Thus topological features of the oxide scale could be observed, along with other structural characteristics such as oxide grain size and texture. Transverse cross-sections were then made, in order to examine other

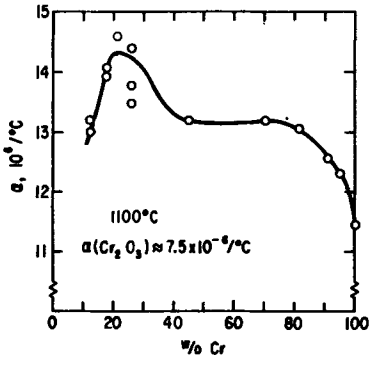

Fig. 5. Thermal expansion coefficient vs composition for the Fe-Cr system at 1100°C.

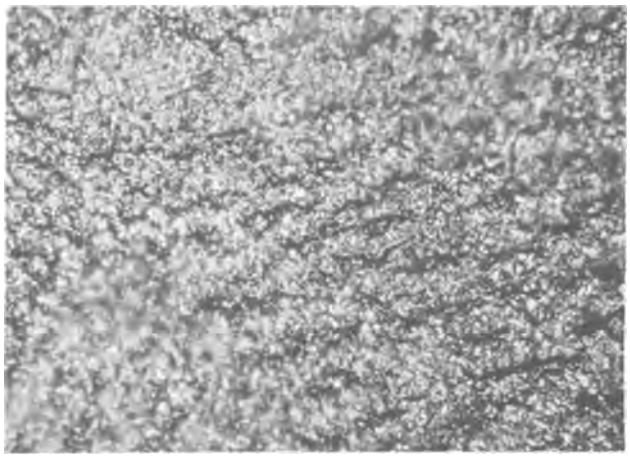

Fig. 6. Micrograph of the external surface of an Fe-30 Cr alloy sample oxidized at 1000°C for 53 hr. Magnification approximately 500X.

properties such as scale density, adherence to the metal, and the nature of the metal/oxide interface.

As is often the case with thermally grown oxides, the grain size was quite small, with the largest grains being about 50μ in diameter. There was no apparent dependence of oxide grain size on either oxidation temperature or bulk composition of the alloy.

The surface topology of the oxidized samples was quite interesting, in that the scales were usually quite wrinkled and irregular. Figure 6, for example, is a photomicrograph of the surface of a sample of Fe-30% Cr alloy oxidized for 53 hr at 1000°C. The oxide scales formed on alloys of this composition were usually quite adherent. At this rather high magnification (approximately 500X) it is readily apparent that the scale is quite wrinkled. The surface appearance of the oxide scales did not depend on oxidation temperature, but was sensitive to bulk alloy composition. An example of this is presented in Fig. 7, which is a low magnification (14X) photomicrograph of a sample of the Fe-70% Cr alloy. Blistering, ridges, and other surface irregularities are obvious and spalled regions are also present. In fact, alloys of this composition or richer in Cr spalled very badly; this particular sample was mostly spalled, and the region shown is one of the few places where the scale was at least partially intact and adherent. Note the difference in magnification betwen Fig. 6 and 7; at 14X, the surface of the sample shown in Fig. 6 would appear smooth and uniform.

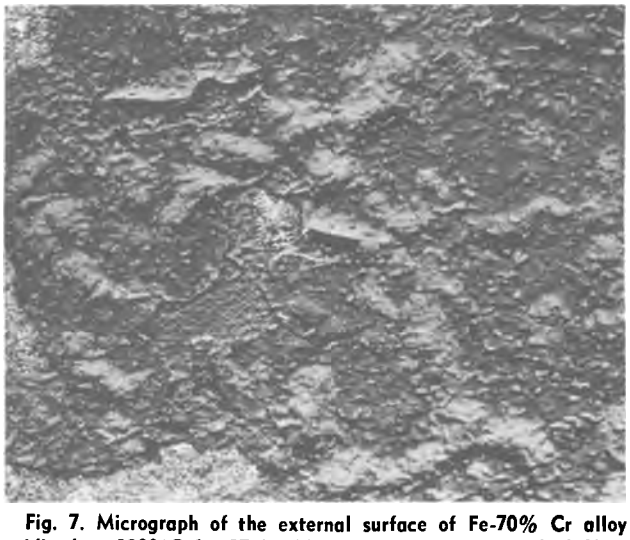

Fig. 7. Micrograph of the external surface of Fe-70% Cr alloy oxidized at 1300°C for 27 hr. Magnification approximately 14X.

In addition to the nonuniformity of the scales, there was oxidation attack at grain boundaries. This was most evident when examining the surface topology of spalled samples, as is shown for an Fe-70% Cr sample in Fig. 8. This sample was oxidized for 50 hr at 1000°C. An additional example of this grain boundary attack is shown in Fig. 9, which is a transverse cross section of a sample of Fe-30% Cr alloy oxidized for 30 hr at 1300°C. Note that where each grain boundary in the metal terminates at the oxide, there is excessive attack. There is also an area of accelerated attack where there is no metal grain boundary termination. Possibly the grain boundary responsible for this effect does not intersect the plane of the photomicrograph.

No obvious correlation could be found between grain boundary attack and spalling or between composition and grain boundary attack. The presence of voids in the scale near metal grain boundary junctures was common.

A general observation was that spalling during cooling became more severe as the Cr content of the alloy increased. As a first approximation, alloys containing less than 50-60% Cr showed considerably more spalling resistance than those alloys richer in Cr. This is opposite of what would have been anticipated from the consideration of the thermal expansion mismatches of the oxide and the alloys. From Fig. 5, it might be expected that spalling would be most severe in the range of 25-40% Cr, where the thermal expansion coefficients of the alloys are nearly a factor of two greater than that of the scale. Since spalling was most severe for alloy compositions where thermal expan-

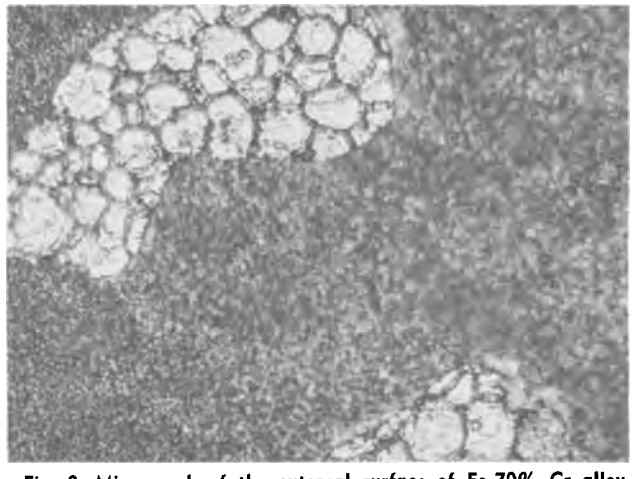

Fig. 8. Micrograph of the external surface of Fe-70% Cr alloy oxidized for 50 hr at 1000°C. Note grain boundary attack in spalled area. Magnification approximately 250X.

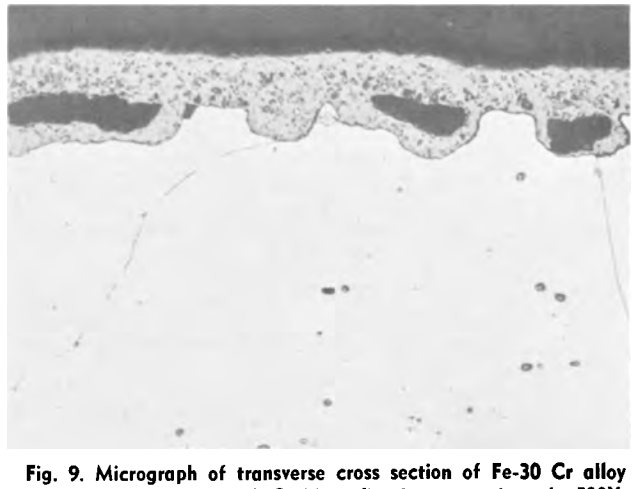

Fig. 9. Micrograph of transverse cross section of Fe-30 Cr alloy oxidized for 30 hr at 1300°C. Magnification approximately 500X.

sion mismatch was the least, it is apparent that some other explanation for the spalling tendencies is necessary. This point will be discussed later.

X-ray investigations.—Debye-Scherrer patterns were taken from the scales found on all alloy compositions. Room temperature lattice parameters were calculated, and values of $a_o = 4.960 \pm 0.001$Å and $c_o = 13.590 \pm 0.003$Å were obtained, regardless of the bulk composition of the alloy on which the scale formed, which implies that the amount of Fe dissolved in the Cr_2O_3 was very small. DiCerbo and Seybolt have reported lattice parameter data for the Fe_2O_3-Cr_2O_3 system (19). At the Cr_2O_3-rich end, the compositional dependence of the a_o parameter may be approximated by the relation

$$a_o \text{ (Å)} = 4.959 + 0.001 \text{ (\% } Fe_2O_3\text{)} \quad [4]$$

This relation is valid to Fe_2O_3 concentrations of about 30%. The lattice parameter data attained in this study therefore indicate that the Fe_2O_3 content in the Cr_2O_3 scales is less than 1%. This is in agreement with Seybolt's results (1).

Chromium-depletion at the metal oxide interface.—As was shown by the above results and by the work of Seybolt (1), the oxidation product of Fe-Cr binary alloys containing more than about 13% Cr is Cr_2O_3 which contains little or no Fe. Therefore, as the alloy oxidizes, the metal matrix becomes depleted in Cr. If depletion reaches the point that the Cr composition at the metal/oxide interface becomes less than 13%, then formation of a nonprotective oxide will ensue (1). Consequently, it is of considerable practical interest to have knowledge of the rate and extent to which Cr-depletion occurs in an alloy as oxidation proceeds and, in particular, to know the alloy composition at the metal/oxide interface.

A theoretical analysis of the problem has been presented by Wagner (9). He considered the case of a binary alloy of components A and B, in which only A oxidizes, and derived expressions which gave the composition of A as a function of distance from the metal/oxide interface and time. Of particular interest is his expression for the alloy composition at the interface. Using Wagner's notation, the mole fraction of A at the metal/oxide interface is given by

$$N_{A(i)} = \frac{F(u) - N_{A(b)}}{F(u) - 1} \quad [5]$$

where $N_{A(b)}$ is the mole fraction of A in the bulk, *i.e.*, the initial concentration of *A*. The term $F(u)$ is given by

$$F(u) = \pi^{1/2} u[1 - \text{erf}(u)] \exp(u^2) \quad [6]$$

where the general argument u is defined by the equation

$$u = \left(\frac{k_c}{2D}\right)^{1/2} \quad [7]$$

In Eq. [7], k_c is the Wagner "corrosion rate constant" ($cm^2\ sec^{-1}$), defined by the relation

$$\Delta x_{\text{metal}} = (2k_c t)^{1/2} \quad [8]$$

where Δx_{metal} is the amount of metal consumed during oxidation. The term D in Eq. [7] is the interdiffusion coefficient of the alloy (assumed by Wagner to be composition independent). Note that as defined by Eq. [5]-[8]

$$N_{A(i)} = f(k_c, D, N_{A(b)}) \quad [9]$$

Thus, in order to calculate the interface composition, only the oxidation rate constant, the interdiffusion coefficient, and the bulk, or initial composition of the alloy are required. Unfortunately, the interdiffusion coefficient D for the Fe-Cr system is composition-dependent (12, 20), so there is ambiguity as to which value of D should be used in the calculation of the interface composition. A conservative estimate of the

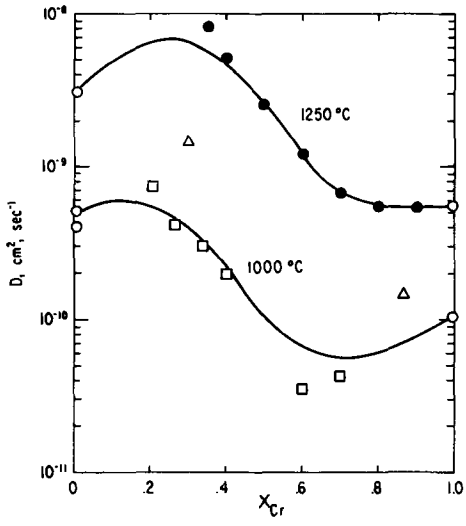

Fig. 10. Interdiffusion data for Fe-Cr system at temperatures indicated. • Ref. (12); □ ref. (16); △ Gorbunov *et al.* [taken from ref. (16)]; O calculated from ref. (17) and (18).

interface composition may be made in the following manner. By substituting Eq. [6] and [7] into Eq. [5], it can be seen that the minimum value of $N_{A(i)}$ possible for a given bulk concentration $N_{A(b)}$ will be determined by the minimum value of D for the composition range of interest. This is intuitively reasonable, since as it becomes more difficult for Cr atoms to move to the interface from the interior of the alloy, it would be expected that $N_{A(i)}$ would decrease. The substitution of Eq. [6] into [5] can be greatly simplified by the approximation

$$F(u) \cong \pi^{1/2} u, u << 1 \quad [10]$$

As an example of how the calculation of a minimum value of $N_{A(i)}$ is carried out, consider an Fe-30% Cr alloy. The minimum value of $N_{A(i)}$ possible for this alloy will be determined by the minimum value of D that exists in the composition range of 0-30% Cr. Obviously, values of D for Cr contents greater than 30% are of no interest in this case. Therefore, by choosing the minimum value of D that exists in the composition range of interest, *i.e*, the range 0% Cr to $N_{A(b)}$, it is possible to calculate the minimum value of $N_{A(i)}$ for the alloy that could occur at a given temperature.

Figure 10 presents all of the interdiffusion data for the Fe-Cr system that the author was able to find. It is surprising that for a system of such practical interest as Fe-Cr there are so few data.

Values of k_p for 1250°C were estimated by interpolation from the data shown in Fig. 1. The relationship between the "corrosion rate constant," k_c, and the "parabolic rate constant," k_p, as used in this study is given by

$$k_c = \frac{1}{2}\left[\frac{M_{Cr_2O_3}{}^{Cr}}{M_{Cr_2O_3}{}^{O}} \cdot \bar{V}_{Cr}\right]^2 \cdot k_p \quad [11]$$

where $M_{Cr_2O_3}{}^{Cr}$ and $M_{Cr_2O_3}{}^{O}$ are the grams of Cr and O per mole of Cr_2O_3, respectively, and $\bar{V}_{Cr}$ is the specific volume of Cr.

Using data as outlined above, the minimum value of $N_{A(i)}$ as a function of $N_{A(b)}$ was calculated for 1000° and 1250°C oxidation. The values used in the computations are given in Table I.

It should be remembered that the values of D presented in Table I are the minimum values that occur in the composition range of 0% Cr to $N_{A(b)}$. The results of the calculation are shown in Fig. 11.

Because of the uncertainties in the values used in the calculation, especially in D, the curves shown in Fig. 11 can be interpreted in semiquantitative terms only. They do, however, bring out several salient fea-

Table I. Values used in calculation of $N_{A(i)}$

$N_{A(b)}$ (Cr)	D_{min} (cm^2 sec^{-1})	k_c (cm^2 sec^{-1})	$F(u)$	$N_{A(i)}$ (Cr)
		T = 1000°C		
0.30	4.0×10^{-10}	1.5×10^{-13}	2.4×10^{-2}	0.28
0.45	1.5×10^{-10}	2.6×10^{-13}	5.2×10^{-2}	0.42
0.60	6.6×10^{-11}	1.9×10^{-13}	6.7×10^{-2}	0.57
0.80	5.6×10^{-11}	8.7×10^{-13}	1.3×10^{-1}	0.77
0.95	5.6×10^{-11}	5.7×10^{-13}	1.0×10^{-1}	0.94
		T = 1250°C		
0.30	3.0×10^{-9}	6.8×10^{-12}	6.0×10^{-2}	0.25
0.45	3.0×10^{-9}	9.4×10^{-12}	7.0×10^{-2}	0.41
0.60	1.2×10^{-9}	7.1×10^{-12}	9.6×10^{-2}	0.57
0.80	5.5×10^{-10}	2.0×10^{-11}	2.0×10^{-1}	0.75
0.95	5.5×10^{-10}	3.4×10^{-11}	2.5×10^{-1}	0.93

tures. The calculations predict that the amount of Cr depletion at the metal-oxide interface will be quite small, on the order of a few per cent. This means that the replenishment of Cr to the metal-oxide interface should take place at rates that are fast compared to the rate of Cr loss in oxidation. Because the amount of depletion is expected to be small, Cr_2O_3 should always be the stable oxide in these alloys, regardless of the extent of oxidation, as long as the Cr content in the center of the sample is maintained at $N_{A(b)}$.

It is of interest to compare the predicted values of Cr depletion with experimental observations. The results of the probe scans are presented in Fig. 12. Traces for both elements are presented. Within experimental error, the compositions sum to 100%. No gradient could be observed in the Fe-45% Cr alloy, although scans were made at several points along the specimen, and consequently the composition near the interface is essentially the same as the bulk composition. A depleted zone was observed in the Fe-80% Cr alloy, with the interface composition being about 68%. Since the accuracy of the probe data is believed to be about ± 5% of the total amount present, the error in determining the Cr content at the interface would be about ± 3.5%.

It should be mentioned that considerable difficulty was experienced in measuring alloy compositions accurately and reproducibly at distances within about 10μ from the metal/oxide interface. The most probable reason for this is that the difference in hardness between the oxide scale and the alloy inevitably leads to some rounding-off of the metal near the interface, even when using the best metallographic procedures, such as vibratory polishing. This rounding-off of the metal can lead to an attenuation of the emitted x-rays. Furthermore, with the best focussing conditions, the incident electron-beam intersects a sample area of about 1μ^2. The amount of excited material in the alloy will therefore be several cubic microns, representing a volume that can be a few microns in diameter. Hence,

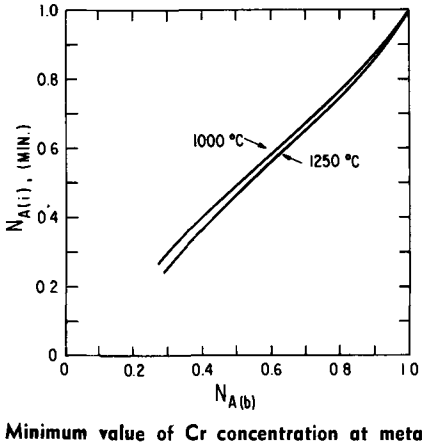

Fig. 11. Minimum value of Cr concentration at metal/oxide interface ($N_{A(i)}$) vs. bulk Cr concentration ($N_{A(b)}$), at temperatures indicated.

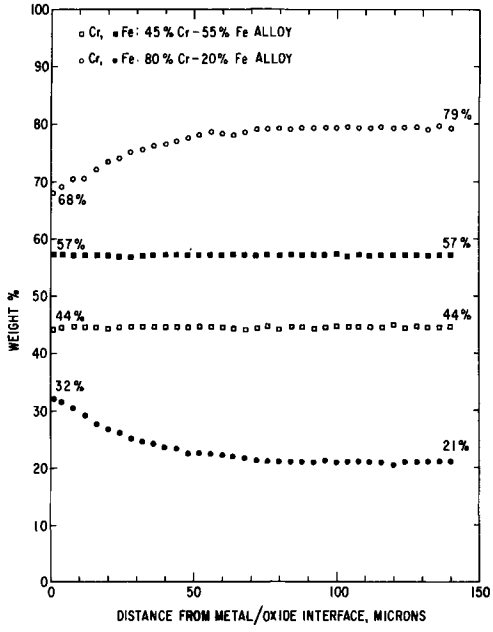

Fig. 12. Alloy compositions as a function of distance from the metal/oxide interface, for alloys oxidized 51 hr at 1100°C.

as the metal/oxide interface is approached to within 2 or 3μ, the excited volume emitting x-rays could include part of the scale, which in general has a different composition than the alloy. Using very great care, reliable composition data might be obtained as close as 5μ from the interface; a more reasonable distance would be about 10μ. Of course, if the metal/oxide interface is irregular, the situation becomes all the more complicated.

Discussion

Although parabolic kinetics were generally observed for all compositions and temperatures, it is apparent from the structural features of the scales and the variations in rate constant data that other factors besides diffusive transport mechanisms must be considered in attempting to understand the oxidation of Fe-Cr alloys. The fact that the gravimetric data plot in a smooth, continuous manner, with essentially parabolic kinetics, suggests that, at the temperature of oxidation, the scales which form are structurally integral and grow primarily by ionic diffusion. It is reasonably well established that in Cr_2O_3, cation diffusion (with appropriate concurrent electronic diffusion) proceeds much faster than anion diffusion (1, 4, 10, 23) and, therefore, will be rate-controlling. It is not known at this point whether the blistering and other structural irregularities in the scales formed during isothermal oxidation, during cooling, or both. The smooth appearance of the data suggests that scale deformation occurred during cooling. Scale porosity of the type shown in Fig. 9, however, could have formed at temperature. If the porosity in the scale of this alloy (Fe-30% Cr) did form under conditions of isothermal oxidation, then the true area for oxidation would be less than the apparent geometric area of the sample (assuming mass transport across the voids is negligible), and seemingly slower kinetics would result. However, if blister volume is small and the blisters form at random times, then parabolic kinetics would still obtain. The cause of the accelerated attack at grain boundaries is not known, although it could be induced by impurities which segregated there.

It is reasonably certain that spalling occurred during cooling. In support of this is the observation that spalled surfaces were fairly bright and untarnished. Since the samples cool slowly in the furnace, this implies that spalling probably occurs below 600°C. Presumably there is some minimum stress required to

cause spalling. The value of this stress will depend on many factors, such as the amount of porosity in the scale, the nature of the metal/oxide interface, relative strengths of the scale and the alloy, and the thickness of the scale. Specimen geometry will also be important. In any case, however, the stress required for spalling will be equal to the sum of the stresses generated during isothermal oxidation (σ_I) plus stresses arising during athermal conditions (σ_A), *i.e.*,

$$\sigma_s = \Sigma\sigma_I + \Sigma\sigma_A \qquad [12]$$

Cohen and his co-workers have observed the formation of highly irregular scales on both pure Cr and Fe-Cr alloys (2, 14, 24, 25), and concluded that the defects in the scales formed during the isothermal oxidation. The origin of the defects was believed to be associated with compressive stresses generated in the scale during growth (14). If that were the case, then the isothermal contribution to σ_s in Eq. [12] would be small, since stress relief is occurring at temperature. Other evidence that the isothermal stress contributions will be small are the observations by Westbrook (26), who has shown that the hardness of most common oxides decreases rapidly at temperatures above about one-half the absolute melting point. For Cr_2O_3, 0.5 T_m = 860°C, so it is reasonable on that basis to expect Cr_2O_3 to be capable of plastic deformation at temperatures of 1000°C or higher.

The strong dependence of spalling behavior on composition in these alloys cannot be accounted for by the mechanical properties of the oxide, however. Since Cr_2O_3 scales have essentially stoichiometric compositions, independent of the bulk composition of the alloy, it would be expected that the mechanical properties of the oxide ought to be independent of the bulk alloy composition. Of course, it is possible that the defect concentration of the scale could vary with alloy composition, in which case the mechanical properties would vary in a related manner. However, there is no evidence to support this.

Some insight into this problem may be gained by considering the compositional dependence of the high-temperature strength of Fe-Cr binary alloys, which is presented in Fig. 13 (27). The high-temperature strength of the alloys increases rapidly with increasing Cr content; for example, at 1000°C, the hardness increases by more than a factor of 4 as the Cr content is increased from 50 to 100%. It is suggested, therefore, that the Fe-rich alloys have more resistance to spalling because their relative lack of high-temperature strength permits them to accommodate by plastic flow the stresses arising during cooling from mismatch in thermal expansion coefficients. These data provide support for the hypothesis that stress relief by plastic deformation of the metal adjacent to the scale is an important factor in preventing or reducing spalling. In summary, then, the principal contribution to the spalling stress arises during athermal conditions. Stresses generated under isothermal conditions, during scale growth, are relieved by plastic deformation of both the scale and the metal. During cooling, however, the yield stress of the oxide increases and the scale is no longer capable of relieving stress by flow. Consequently, stress relief will depend on the capability of the metal adjacent to the scale to flow. Alloys rich in Cr have higher strengths at a given temperature than alloys rich in Fe; consequently they cannot deform as easily and therefore spall more readily.

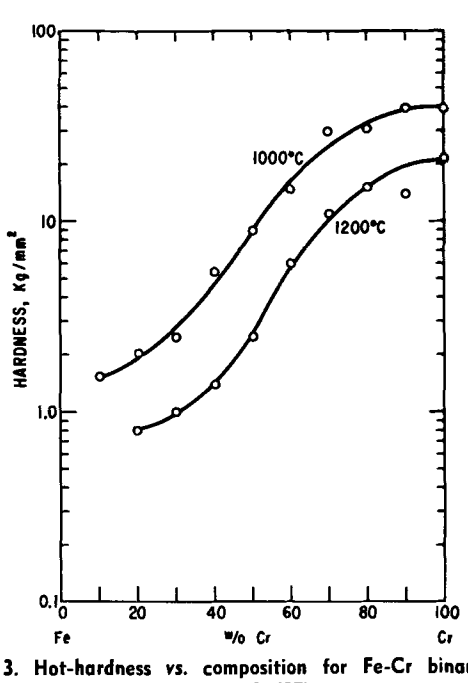

Fig. 13. Hot-hardness *vs.* composition for Fe-Cr binary alloys at temperatures indicated, after ref. (27).

The results from the interface-depletion experiments and calculations may be considered to be in fairly good agreement. The results of the microprobe scans are in excellent agreement with the data of Wood and Whipple (10). It is evident, at least from the data obtained from the Fe-80% Cr alloy, that somewhat greater Cr depletion occurs in the alloy during oxidation than was predicted from the calculation. The Cr concentration near the interface was observed to be 68 ± 3.5%, indicating a depletion of about 12%, whereas the predicted depletion would be about 4% (obtained by interpolation of the data in Table I). A more refined method of calculating interface compositions from Wagner's equation may be possible, but is probably not warranted at this time because of the lack of good data, particularly interdiffusion coefficients.

The decrease in rate constant, k_p, with decreasing Cr content (Fig. 3) is of interest. If Fe^{+2} ions were present in solid solution in the scale, a decrease in Cr^{+3} diffusion would be expected, according to the model of Hauffe (28). However, only amounts on the order of the Cr_2O_3 cation-vacancy concentration are required, so it is not obvious why an extended dependence on Fe concentration is observed. An alternative explanation is that, as the over-all Cr content of the alloy is decreased, the Cr content at the metal/oxide interface is decreased. In the temperature range of 1200°C, the Fe-Cr system is nearly thermodynamically ideal (29, 30), hence the Cr activity at the interface is essentially numerically equivalent to the mole fraction of Cr at the interface. As the Cr content of the alloy is decreased, the Cr content and therefore the Cr activity at the metal/oxide interface decreases. For oxidizing conditions where the partial pressure at the gas/oxide interface remains invariant, a decrease in Cr activity at the metal/oxide interface will decrease the chromium activity gradient across the oxide, resulting in slower oxidation kinetics. This argument is very similar to that used by Phalnikar *et al.* (31) to explain their results for the Co-Cr system.

Finally, it is of interest to speculate on the sensitivity of oxidation kinetics to surface preparation. Caplan *et al.* (13) have demonstrated a pronounced dependence of surface preparation on the oxidation of pure Cr and Fe-Cr alloys in the range of 0-26% Cr. In particular, they found that Fe-Cr alloys with electropolished surfaces had a markedly higher initial reaction rate during high-temperature oxidation than samples with other surface preparations. It has been suggested by Wood (3) that such an effect could be caused by the presence of a thin film which contained Cr^{+6} ions. The presence of these ions in the scale during the initial stages of oxidation would lead to an increased cation vacancy concentration and hence increased oxidation rates. In this study, the sample prepared by electropolishing did not exhibit kinetic behavior markedly different from the sample that had an abraded surface or an electropolished-chemically

etched surface. It is possible that the sample which had been given an electro-etch prior to oxidation did have on it a thin film containing Cr^{+6} ions, in which case Wood's argument would apply.

Conclusions

The oxidation behavior of Fe-Cr alloys in the composition range of 25-95% in dry O_2 has been studied and found to be composition-dependent. Essentially parabolic kinetics were observed over the entire range of Cr concentrations; parabolic rate constants decreased with decreasing Cr content. Alloys containing less than about 50-60% Cr had superior resistance to spalling than did alloys richer in Cr. Although severe mismatch exists in the coefficients of thermal expansion of the alloys and Cr_2O_3, it is suggested that stress relief by plastic flow of the metal near the scale/alloy interface plays a dominant role in reducing spalling tendency. The Wagner analysis relating metal interdiffusion in alloys to oxidation rates of the alloys was applied to the Fe-Cr system. It was concluded that Cr depletion at the metal/oxide interface will not be a significant problem.

Acknowledgments

Appreciation is extended to D. E. Broecker, who made the kinetic measurements, and to R. E. Carter, P. J. Jorgensen, A. U. Seybolt, and D. W. White, who critically reviewed the manuscript.

Manuscript received Feb. 28, 1967; revised manuscript received April 26, 1967.

Any discussion of this paper will appear in a Discussion Section to be published in the June 1968 JOURNAL.

REFERENCES

1. A. U. Seybolt, *This Journal*, **107**, 147 (1960).
2. D. Caplan and M. Cohen, *ibid.*, **112**, 471 (1965).
3. G. C. Wood, *Corr. Sci.*, **2**, 173 (1962).
4. W. C. Hagel, *ASM Trans. Quart.*, **56**, 583 (1963).
5. D. Caplan and M. Cohen, *This Journal*, **108**, 438 (1961).
6. C. S. Tedmon, Jr., *ibid.*, **113**, 766 (1966).
7. R. F. Tylecote, *J. Iron and Steel Inst.*, **195**, 380 (1960).
8. R. F. Tylecote, *J. Iron and Steel Inst.*, **196**, 135 (1960).
9. C. Wagner, *J. Electrochem. Soc.*, **99**, 369 (1952).
10. G. C. Wood and D. P. Whittle, *J. Iron Steel Inst.*, **202**, 979 (1964).
11. H. W. Paxton and T. Kunitake, *Trans. AIME*, **218**, 1002 (1960).
12. H. W. Paxton and E. J. Pasierb, *ibid.*, **218**, 794 (1960).
13. D. Caplan, A. Harvey, and M. Cohen, *This Journal*, **108**, 134 (1961).
14. D. Caplan, A. Harvey, and M. Cohen, *Corr. Sci.*, **3**, 161 (1963).
15. E. Lifshin and R. Hanneman, General Electric Research and Development Center Report 65-RL 3944M, April, 1965.
16. D. M. Poole and P. M. Thomas, *J. Inst. Metals*, **90**, 228 (1962).
17. J. Philibert, in "Third International Symposium on X-Ray Optics and X-Ray Microanalysis," H. H. Pattee, V. E. Cosslett, and A. Engstrom, Editors, p. 379, Academic Press, New York (1962).
18. M. Green, *op. cit.*, p. 319.
19. R. K. DiCerbo and A. U. Seybolt, *J. Am. Ceram. Soc.*, **42**, 430 (1959).
20. G. A. Davies, A. B. Ponter, G. C. Wood, and D. Whittle, *This Journal*, **113**, 959 (1966).
21. R. Borg, D. Lai, and O. Krikorian, UCRL Report No. 6885, March 1962.
22. H. W. Paxton and R. A. Wolfe, *Trans. Met. Soc. AIME*, **230**, 1426 (1964).
23. W. C. Hagel and A. U. Seybolt, *This Journal*, **108**, 1146 (1961).
24. D. Caplan and M. Cohen, *Trans. AIME*, **194**, 1057 (1952).
25. D. Caplan, P. E. Beaubrien, and M. Cohen, *Trans. Met. Soc. AIME*, **233**, 766 (1965).
26. J. H. Westbrook, *Rev. Hautes Temper. et Refract.*, **3**, 45 (1966).
27. C. S. Tedmon, Jr. and J. H. Westbrook, To be published.
28. K. Hauffe, "Progress in Metal Physics" 4, p. 89, Pergamon Press, London (1953).
29. C. L. McCabe, R. G. Hudson, and H. W. Paxton, *Trans. Met. Soc. AIME*, **112**, 102 (1958).
30. O. Kubaschweski and G. Heymer, *Acta Met.*, **8**, 416 (1960).
31. C. A. Phalnikar, E. B. Evans, and W. M. Baldwin, Jr., *This Journal*, **103**, 429 (1956).

Thermal Regeneration of Oxide Covered Iron {100} and {110} Surfaces

H. Thomas Yolken and Jerome Kruger

Institute for Materials Research, National Bureau of Standards, Washington, D. C.

ABSTRACT

The effects of ultrahigh vacuum annealing on thin oxide films grown to a limiting thickness at room temperature on {100} and {110} iron surfaces were studied using an ellipsometer. After vacuum annealing at 400°C or above these films, which showed essentially no change in optical properties, grew when reexposed to 1 x 10^{-5} Torr of oxygen at 25°C. This process could be repeated several times, with the film each time exhibiting a greater limiting thickness until a thickness was reached which could not be appreciably increased by further annealing. The thermal regeneration of oxide covered iron can be explained by a phase change of the oxide film from Fe_3O_4 to FeO on annealing at about 400°C or above. Cooling to room temperature causes the reappearance of Fe_3O_4. Thin areas in the oxide film and some enrichment of iron in the film are the results of the phase changes. Concurrently, the adsorbed monolayer of oxygen anions is incorporated in the oxide during annealing.

When some metal surfaces are exposed to oxygen at room temperature, an oxide film grows until a limiting thickness is reached. If this oxide covered metal surface is then annealed in vacuum, the oxide film which had previously ceased growing will start to grow again when reexposed to oxygen at room temperature. This effect was called "thermal regeneration" by Dell (1) who studied the oxidation of cobalt, nickel, and copper. Thermal regeneration, or a process resembling it, has also been studied by Zettlemoyer and co-workers (2) (copper, nickel, and cobalt); Dell and Stone (3) (nickel); Anderson and Klemperer (4) (nickel); and Burshtein and co-workers (5) (iron).

Several possible mechanisms have been proposed by these authors to explain thermal regeneration: (*i*) the incorporation of the monolayer of oxygen anions into the oxide during heating in vacuum, and then the subsequent adsorption of a new monolayer of oxygen anions on readmission of oxygen at room temperature (1, 2, 4); (*ii*) the dissolution of the oxide into the bulk of the metal in some systems [*i.e.*, Cu] (1); (*iii*) the recrystallization of the oxide film into thicker crystallites which cover part of the surface leaving bare metal exposed in between (1, 4); and (*iv*) the diffusion of metal to the oxide-gas interface (5).

This study is a continuation of previous work done in our laboratory on the early stages of oxidation of polycrystalline iron (6). In the present study, the oxidation of {100} and {110} iron surfaces is investigated, and the effects of thermal regeneration on oxide films formed on these surfaces are studied.

The present work differs from that of previous workers in several respects. The changes produced by annealing were followed by observing variations in film thickness and properties with an ellipsometer capable of detecting changes as small as 0.5Å in film thickness (7). Annealing temperatures from 25° to 700°C were investigated. This was an extension of the temperature range studied by Burstein and co-workers (5) for iron (25°-300°C) and its importance will be discussed later. The emphasis in this study was on direct surface measurements of well-defined single crystal surfaces prepared in ultrahigh vacuum. This was not the case for previous work in the literature except for the photoelectric measurements on evaporated, polycrystalline nickel films by Anderson and Klemperer (4). Our work also included the use of a mass spectrometer to detect possible evaporation or desorption of oxygen from the oxide film during annealing.

Experimental Procedure

Vacuum system.—The ultrahigh vacuum system was an ion pumped, bakeable, stainless steel system. Pure hydrogen or oxygen could be introduced by diffusion through nickel or silver thimbles (8), respectively. Precise control (± 5%) of the oxygen pressure was obtained by allowing the oxygen from the silver diffusion leak to build up behind a precision mechanical leak valve before admission to the system. The ambient pressure after a 325°C bake for 8 hr was 5 x 10^{-10} Torr[1] as measured by a triggered cold cathode discharge gauge. The gauge produced no detectable contamination. Gases in the system were analyzed by a bakeable 90° magnetic deflection mass spectrometer capable of detecting partial pressures of 10^{-13} Torr. The specimen chamber contained strain-free quartz windows positioned perpendicular to the ellipsometer light beam, which was at a 66° angle of incidence with the iron surface.

Specimen preparation.—Smooth, flat, strain-free (as determined by x-ray diffraction), and clean (monolayer or less of adsorbed gas) {100} and {110} surfaces (about 1 cm^2 surface area) were prepared from floating-zone refined iron[2] obtained from the Battelle Memorial Institute. The preparation of these oxide free specimens is described elsewhere (9).

The temperature of the specimen was determined by an infrared pyrometer which had been calibrated previously using a thermocouple attached to a dummy specimen. The infrared pyrometer removed the possibility of contamination to the specimen by a thermocouple.

Oxidation and thermal regeneration.—All oxidation was done at an oxygen pressure of 1 x 10^{-5} Torr and 25°C. The kinetics of oxidation of clean iron {100} and {110} surfaces were studied by admitting oxygen to the system after the specimen had been cleaned by using the procedure mentioned earlier. Ellipsometric measurements were made during the film growth to determine film thickness. The method used to evaluate these results is described elsewhere (10).

After a limiting oxide thickness[3] was reached, the oxygen was pumped out of the system and a pressure of 5 x 10^{-10} Torr was obtained. The specimen was

[1] 1 Torr = 133.32 newton/$meter^2$.

[2] As received—gaseous impurities (ppm by weight): O_2 (vacuum fusion), 2.1; S (colorimetric), 4 ± 3; C (combustion-conductometric), 3 ± 3; N_2 (vacuum fusion), 0.5; H_2 (vacuum fusion), 0.3. Major metallic impurities (ppm): Al, 15; Cr, 5; Co, 5; Cu, 7; Ni, 20; P, 9; Si, 10.

[3] Growth rate less than 10^{-12} cm/s.

thermally regenerated by heating to a given temperature using R.F. induction heating and then cooling to room temperature. During annealing the mass spectrometer was used to analyze the gases being evolved. Thermal regeneration was studied using annealing temperatures from room temperature to 700°C and various annealing times. Ellipsometric measurements were repeated to detect any changes in the film that resulted from heating in vacuum. Oxygen was readmitted to the system at a pressure of 1×10^{-5} Torr, and ellipsometric readings were taken during oxidation of the thermally regenerated surface at 25°C.

After a new limiting thickness was reached the system was evacuated to 5×10^{-10} Torr. The specimen was thermally regenerated a second time by annealing at a given temperature and then cooling to room temperature. Oxygen was readmitted, and the regenerated surface oxide grew again. This cycle was repeated several times.

Results

Initial oxidation of {100} and {110} iron surfaces.—Figure 1 shows the growth kinetics of the early stages of oxidation of the unregenerated {100} and {110} surfaces of iron. The data for the later stage of the oxidation of the {100} and {110} surfaces of iron follows either a direct logarithmic growth rate (Fig. 2) or an inverse logarithmic growth rate. These results are given here to show that growth kinetics of the film that is to be thermally regenerated. They are in agreement with our earlier work (9) where a detailed discussion of the results for polycrystalline iron is given. There have been several proposed mechanisms for oxidation such as this at room temperature in the thin film region (<100Å) (12-16).

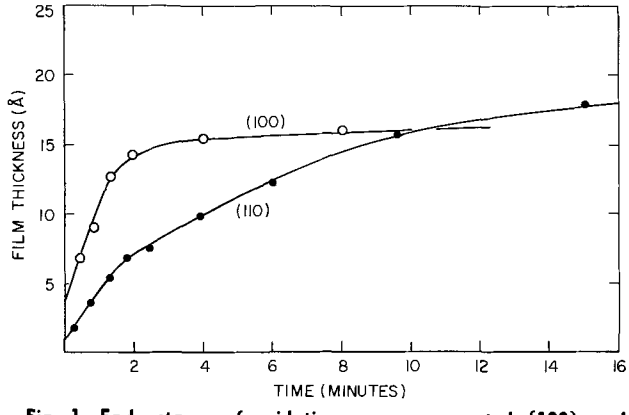

Fig. 1. Early stages of oxidation on unregenerated {100} and {110} surfaces of iron at 25°C and 1×15^{-5} Torr of oxygen.

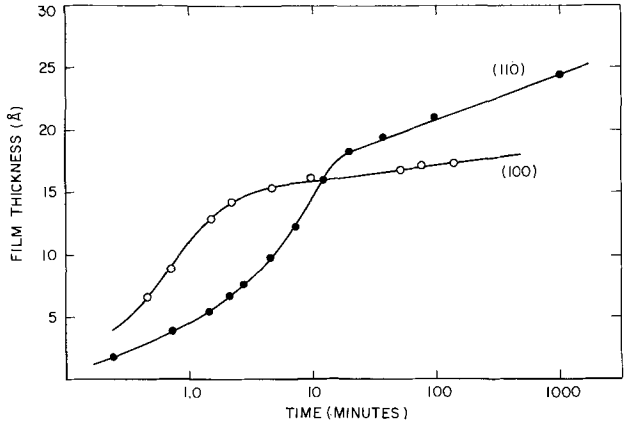

Fig. 2. Direct logarithmic plot of the oxidation of unregenerated {100} and {110} iron surfaces at 25°C and 1×10^{-5} Torr of oxygen.

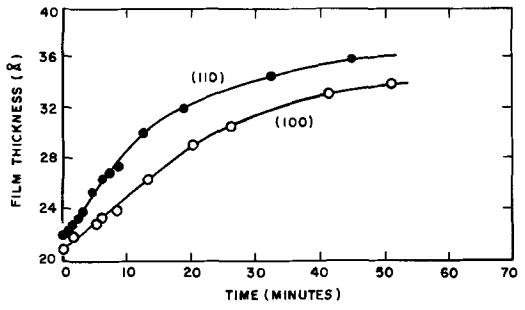

Fig. 3. Early stages of the oxidation of an iron surface once regenerated at 500°C; the {100} and {110} regenerated surfaces were oxidized at 25°C and 1×10^{-5} Torr of oxygen.

Thermal regeneration of oxide covered {100} and {110} iron surfaces.—After the initial oxidation, the film was annealed at various temperatures in a vacuum. This annealing, which altered the film so that further film growth could occur on the readmitting of oxygen at room temperature, caused very little change in the ellipsometer readings, no more than 0.1° in the polarizer or analyzer values. In Fig. 3 the kinetics of the early stages of oxidation of an oxide film so regenerated one time at 500°C for 1 min on both {100} and {110} iron surfaces are shown. The rates are less than those for the oxidation of the unregenerated surfaces. Also, the initial (nonlogarithmic) portion of the curves involves less film growth for the regenerated case. The data for the regenerated surfaces also followed a logarithmic growth in the latter stages of oxidation as can be seen from Fig. 4.

The increases in oxide thickness on each thermal regeneration and oxidation (ΔX) decreases with successive thermal regenerations until ΔX reaches a constant low value of about 2-3Å at an over-all oxide thickness of approximately 100Å. Figure 5 shows ΔX for successive regenerations at 600°C.

Figure 6 shows the effect of annealing temperature (all anneals shown are 30 sec at temperature); ΔX does not decrease as shown in Fig. 5, but tends to increase, when the temperature is raised in the 400°-700°C range. This is in spite of the fact that the ΔX values shown here for successive temperature changes are smaller than they would be if each regeneration at higher temperature were made on a new unregenerated film. Thus, the increase is damped due to the decreasing effect of successive regeneration.

Annealing in the 200°-400°C range produced ΔX's of only 2-3Å, while ΔX's greater than this could only be produced by annealing at temperatures greater than roughly 400°C. It should also be noted in Fig. 6 that ΔX decreases as expected from Fig. 5 when the temperature is held at 485°C for two successive regenerations. Room temperature annealing for periods as

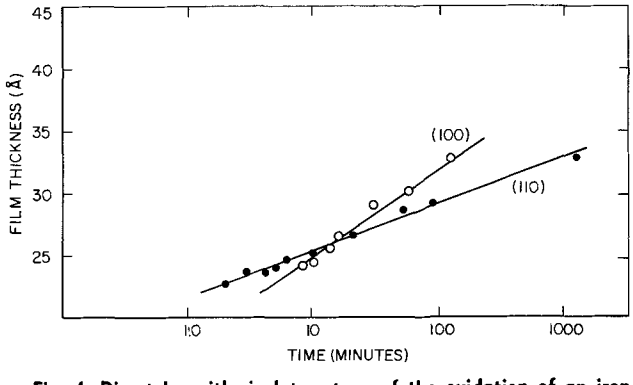

Fig. 4. Direct logarithmic later stage of the oxidation of an iron surface twice regenerated at 500°C. The {100} and {110} regenerated surfaces were oxidized at 25°C and 1×10^{-5} Torr of oxygen.

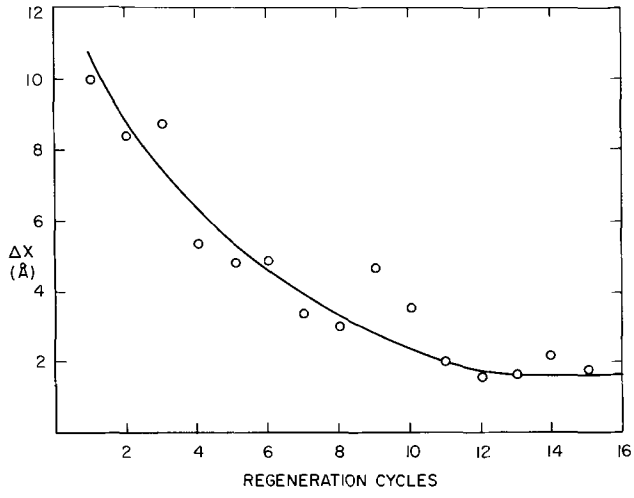

Fig. 5. Variation of the increase in oxide thickness on each thermal regeneration and oxidation (ΔX) with successive thermal regenerations at 600°C and oxidation cycles at 25°C and 1 × 10^{-5} Torr of oxygen.

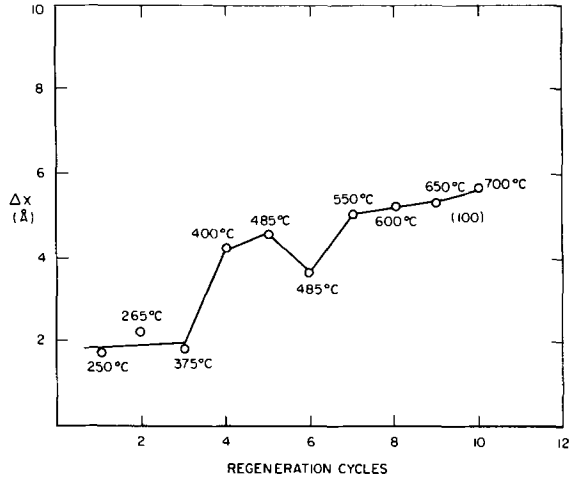

Fig. 6. Effect of annealing temperature in the 250°-700°C range on ΔX for a {100} surface.

long as two weeks in ultrahigh vacuum produced no detectable regeneration. ΔX also appeared to be independent of annealing time for times greater than about 30 sec (shortest time studied) to the longest time studied (15 min at 375°C).

Figure 7 shows electron micrographs of the {100} surface with about 25Å of oxide before thermal regeneration and with about 100Å of oxide after 12 cycles of oxidation and thermal regeneration. The regenerated surface is noticeably roughened compared to the unregenerated surface.

During annealing from room temperature to 700°C no detectable amounts of oxygen were evolved. However, annealing specimens contaminated with carbon did produce CO, along with a noticeable reduction in the film thickness as determined ellipsometrically. This problem did not occur for specimens with low carbon content (10 ppm). After annealing "carbon free" specimens the film thickness appeared to remain constant or to decrease very slightly (< 3Å); an increase in film thickness never occurred during annealing.

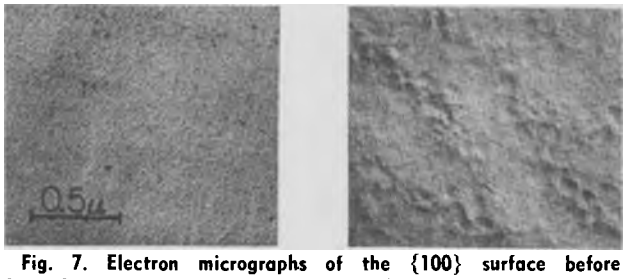

Fig. 7. Electron micrographs of the {100} surface before thermal regeneration and after 12 thermal regeneration and oxidation cycles. C-Pt replica. (a) (left) Before regeneration, 25Å oxide; (b) (right) after regeneration, 100Å oxide.

Discussion

These data can be used to construct a plausible explanation of thermal regeneration which depends on the phase transformation that occurs in Fe_3O_4 on heating above about 400°C. The importance of this phase transformation on the thermal regeneration of iron was not detected by Burstein and co-workers (5) in their iron powder studies, because they worked below 300°C. The transformation temperature usually quoted is 570°C, but this is in equilibrium with 1 atm of air. Transformation of Fe_3O_4 to FeO in vacuum below 570°C was reported by Haase (18). Also, recent (low angle-high energy electron diffraction) work on iron in the same type of system by Mitchell and Sewell (19) shows this transformation to occur at about 450°C in ultrahigh vacuum. They state that this transformation appears to be time, temperature, and oxide thickness dependent. Finally, low energy electron diffraction studies of a {100} iron surface by Pignocco and Pellissier (20) have also shown that for coverages of oxygen in the monolayer or less range, an FeO type structure is stable in ultrahigh vacuum at 25°C.

These transformations will produce two changes in the film: (*i*) an increase in its iron content and (*ii*) thin areas. The first change occurs because iron from the bulk will diffuse into the oxide to supply the iron needed for the following reaction:

$$Fe_3O_4 + Fe\ (\text{bulk}) \xrightarrow{\text{heat in vacuum}} 4Fe_{x<1}O \quad (\text{cation deficient})$$

On cooling, the FeO will transfer back to Fe_3O_4 resulting in an iron rich film

$$4FeO \xrightarrow{\text{cooling in vacuum}} Fe_3O_4 + Fe\ (\text{precipitated})$$

As Fig. 7 shows, the second change due to recrystallization initiated by the transformation produces a film that is much less uniform in thickness (thin areas and roughening). Since large values of ΔX occur only above about 400°C (the average of several experiments), the phase change which occurs at about the same temperature is indicated as being responsible for the roughening.

Since the ellipsometer readings were almost constant both before and after annealing, this roughening can be attributed to a rearrangement of oxide and not a removal of oxide from the surface. On readmission of oxygen at room temperature these thin areas should grow back to a limiting thickness first following linear and then logarithmic kinetics.

Besides the possible production of thin areas by the phase transformation as described above, iron enrichment in the Fe_3O_4 lattice by diffusion, or the presence of precipitated iron produced after the transformations may be the main reasons for the ability of the film to grow after cooling. The fact that the optical measurements after annealing change very little indicates, however, that drastic changes in the film composition have probably not taken place.

The decrease in ΔX with successive regeneration cycles is consistent with the explanation described because as the film roughens and thickens with each cycle, ΔX decreases. This occurs because the possibility for producing areas by recrystallization thin enough to be below the limiting thickness decreases as the over-all film thickness increases. Thus, ΔX should finally become zero when the thin areas in the film are

no longer regenerated to less than the limiting thickness. The fact that ΔX is never reduced to zero, but always remains about 2-3Å is probably due to two causes: readsorption of a monolayer or less of oxygen on the surface, and a slight film growth due to the Fe_3O_4 being richer in iron after the transformation from FeO.

The small amount of growth observed when oxygen is admitted at room temperature after annealing at temperatures below 400°C can be attributed to the above-mentioned readsorption of a monolayer or less of oxygen and its subsequent incorporation upon annealing. This is probably the first step in every instance of growth after annealing and cooling.

The effect of increasing temperature, which increases ΔX in the 400°-700°C range, is consistent with the explanation given for thermal regeneration in one or both of the following ways: (*i*) FeO (wüstite) has a variable composition with the oxide becoming richer in iron as the temperature is increased. This will result in an iron rich Fe_3O_4 whose composition is dependent on the annealing temperature of the FeO; (*ii*) higher temperatures could produce rougher surfaces due to enhanced grain growth of FeO during annealing.

In summary, these data thus suggest that the following two steps, either together or separately, are involved in the thermal regeneration of iron: (*a*) incorporation of the adsorbed monolayer of oxygen into the oxide from 250°C to the highest temperature studied, 700°C; (*b*) a phase change from Fe_3O_4 to FeO on annealing from 400° to 700°C and a phase change back to Fe_3O_4 on cooling. Thin areas in the oxide films and enrichment of iron in the oxide are a result of these phase changes.

Acknowledgment

The authors wish to thank Mrs. Mary Ann Giles for providing them with the electron micrograph.

Manuscript received Feb. 2, 1967. This paper was presented at the Buffalo Meeting, October 10-14, 1965.

Any discussion of this paper will appear in a Discussion Section to be published in the June 1968 JOURNAL.

REFERENCES

1. R. M. Dell, *J. Phys. Chem.*, **62**, 1139 (1958).
2. A. C. Zettlemoyer, Yung Fang Yu, J. J. Chessick, and F. H. Healey, *ibid.*, **61**, 1319 (1957).
3. R. M. Dell and F. S. Stone, *Trans. Faraday Soc.*, **50**, 501 (1954).
4. J. S. Anderson and D. F. Klemperer, *Proc. Roy. Soc. London*, **258A**, 350 (1960).
5. R. Kh. Burshtein, G. M. Kornacheva, and N. A. Shurmovskaya, *Doklady Akad. Nauk SSSR*, **146**, 631 (1962).
6. J. Kruger and H. T. Yolken, *Corrosion*, **20**, 29t (1964).
7. A. B. Winterbottom, Kgl. Norske Vindenskab Selskabs Skrifter 1955, No. 1.
8. N. R. Whetten and J. R. Young, *Rev. Sci. Instr.*, **30**, 472 (1959).
9. H. T. Yolken and J. Kruger, *J. Opt. Soc. Am.*, **55**, 842 (1965).
10. J. Kruger and W. J. Ambs, *ibid.*, **49**, 1195 (1959).
11. N. Cabrera, *Phil. Mag.*, **40**, 175 (1949).
12. N. F. Mott, *Trans. Faraday Soc.*, **35**, 1175 (1939).
13. N. F. Mott, *ibid.*, **43**, 429 (1947).
14. K. Hauffe and B. Ilschner, *Z. Elektrochem.*, **58**, 382 (1954).
15. T. B. Grimley and B. M. W. Trapnell, *Proc. Roy. Soc.*, **234**, 405 (1956).
16. A. T. Fromhold, Jr. and E. L. Cook, *J. Chem. Phys.*, **44**, 4564 (1966).
17. O. Kubaschewski and B. E. Hopkins, "Oxidation of Metals and Alloys," 2nd ed., p. 101, Butterworth, London (1962).
18. O. Haase, *Z. Naturforschg.*, **11a**, 46 (1956).
19. D. Mitchell and P. B. Sewell, *This Journal*, **113**, 206C (1966).
20. A. J. Pignocco and G. E. Pellissier, *ibid.*, **112**, 1188 (1965).

Thermodynamic Interaction between Zinc and the Dilute Solutes Antimony, Bismuth, and Cadmium in Solution In Liquid Lead

R. D. Pehlke, K. Okajima,[1] and T. L. Moore[2]

Department of Chemical and Metallurgical Engineering, The University of Michigan, Ann Arbor, Michigan

ABSTRACT

The activity of zinc has been measured in dilute liquid lead alloys containing small additions of a third element. The study which was conducted in the temperature range 450°-650°C employed a galvanic cell with a liquid chloride electrolyte. The concentration cell was

Zn (Pure Liquid)	Zn^{++} (In Fused KCl + LiCl Electrolyte)	Zn + Third Element in Pb (liquid alloy)

The activity of zinc in the dilute lead-zinc binary shows Henry's law behavior at concentrations up to 0.0375 mole fraction zinc. The activity of zinc in lead exhibits a strong positive deviation from Raoult's law, the activity coefficient at infinite dilution being 11.4 at 550°C. Measurements have been made of the influence of antimony, bismuth, and cadmium on the activity coefficient of zinc in liquid lead. Antimony markedly decreases the activity coefficient, while cadmium and bismuth slightly decrease the activity coefficient of zinc in liquid lead. These results have been summarized in terms of first-order interaction parameters which can be expressed as a function of temperature by the relations

$$\epsilon_{Zn}^{Sb} = -\frac{8840}{T°K} + 2.84$$

$$\epsilon_{Zn}^{Bi} = -\frac{2950}{T°K} + 2.81$$

$$\epsilon_{Zn}^{Cd} = -\frac{1000}{T°K} + 0.68$$

The thermodynamic interaction between elements dissolved in liquid metallic solutions is of both scientific and engineering interest. An adequate representation of the equilibria encountered in systems involving liquid metallic solutions is only possible if the effects of one solute on the activity coefficients of other solutes are taken into account. The determination of these mutual thermodynamic influences, or interaction parameters, has been attempted on both theoretical and experimental grounds.

The theoretical, or more often empirical, considerations employed in an effort to determine a general approach to predicting interaction parameters have been the subject of several contributions to the scientific literature. Several approaches have been attempted including correlation with the electron to atom ratio (1), or relative electronegativity (2-4). A systematic variation of interaction parameters on the basis of periodicity with atomic number has been noted by several investigators including Ohtani and Gokcen (5). Alcock and Richardson (6) have used a chemical approach in considering solvent-solute and intersolute binding energies to derive a semiquantitative expression for predicting interaction parameters. Similar concepts have been employed in other investigations (7, 8).

The primary goal of these investigations has been to develop a method for predicting intersolute effects based on information relating to the physical structure and general thermodynamic properties of liquid metallic solutions. The theoretical progress has been limited, largely because of the lack of experimental results on which theoretical models could be based. Although a number of investigations have treated interactions between solutes, much of the research has been limited to interstitial elements in liquid iron (9), and to certain nonferrous alloys in more concentrated solutions (10). Some recent work (4, 11-15) has been directed toward a systematic investigation of intersolute effects in dilute metallic solutions.

An estimation of the activity coefficient of a solute in a liquid metallic solution can be made based on the activity coefficient in a dilute binary, if additional terms are added which relate to interactions with any additional dilute solute elements. Wagner (16) has suggested an expression for calculating the activity coefficient of a dilute solute based on the Taylor series expression for the logarithm of the activity coefficient

$$\ln\gamma_i = \ln\gamma_i^{o} + \left[x_i \left(\frac{\partial \ln\gamma_i}{\partial x_i}\right)_{x_i=x_j=0} + x_j \left(\frac{\partial \ln\gamma_i}{\partial x_j}\right)_{x_i=x_j=0} + \dots \right] + \left[\frac{1}{2} x_i^2 \left(\frac{\partial^2 \ln\gamma_i}{\partial x_i^2}\right)_{x_i=x_j=0} + x_i x_j \left(\frac{\partial^2 \ln\gamma_i}{\partial x_i \partial x_j}\right)_{x_i=x_j=0} + \frac{1}{2} x_j^2 \left(\frac{\partial^2 \ln\gamma_i}{\partial x_j^2}\right)_{x_i=x_j=0} + \dots \right] + \dots \quad [1]$$

where i = primary solute, j = added solute(s), k = solvent, and x_i, etc = concentration in mole fraction. The higher order terms of the expansion take into account the effects of the interaction of every dilute solute and their combined effect on the activity coefficient of the primary solute. The small contribution of these terms in dilute solutions can be accounted for by extrapolation to zero concentration. The partial derivatives in the resulting first-order expression are of the form

[1] Present address: Department of Metallurgy, Nagoya University, Nagoya, Japan.
[2] Present address: Inland Steel Company, East Chicago, Indiana.

$$\epsilon_i^i = \left(\frac{\partial \ln \gamma_i}{\partial x_i}\right)_{x_i=0}, \text{ self-interaction parameter} \quad [2]$$

$$\epsilon_i^j = \left(\frac{\partial \ln \gamma_i}{\partial x_j}\right)_{x_i=x_j=0}, \text{ ternary interaction parameter} \quad [3]$$

and are customarily given the shorthand notations ϵ_i^i, the self-interaction for solute i, and ϵ_i^j, the individual interaction parameter relating the influence of various solutes, j, on the logarithm of the activity coefficient of solute i. Since these expressions form a convenient means for handling data on solute interactions, the available literature was surveyed (17, 18) for the purpose of presenting experimental data in this form. This survey of the literature revealed limitations of the available data. The purpose of the present investigation was, therefore, to evaluate experimentally the interaction between several alloying elements and zinc dissolved in liquid lead. It is hoped that this investigation will extend present data and expand the possibilities for additional theoretical work in this area.

The interactions studied in this investigation were those between antimony and zinc, bismuth and zinc, and cadmium and zinc in dilute solution in liquid lead. Other related studies (19, 20) have been discussed elsewhere.

Experimental Technique

The galvanic cells employed in this investigation can be represented by

Pure Zn (reference standard)	KCl + LiCl + $ZnCl_2$ (electrolyte)	Zn + Third Element in Pb (liquid alloy)

The reversible cell potential was determined over the range 450°-650°C, and the activity coefficient of zinc in the alloy was calculated relative to the standard of pure zinc by employing the relationship

$$\gamma_{Zn} = \frac{1}{x_{Zn}} e^{-n\tilde{F}E/RT} \quad [4]$$

where $\tilde{F}$ = Faraday's constant, E = measured emf, n = valence of zinc, taken as 2. The interaction parameters were then determined from the limiting slopes of plots of $\ln\gamma_{Zn}$ *vs.* concentration of the solutes.

The experimental apparatus and procedures have been described previously in detail (4, 11, 12). Recrystallized alumina crucibles, 1 in. high by ⅝ in. in diameter, were used as containers for the zinc reference electrode or lead-base alloy electrodes. Either four or five electrode crucibles were held in a larger recrystallized alumina crucible which contained the fused chloride electrolyte. In the runs with the cadmium and bismuth additions one of the five alloys in each cell was a binary zinc-lead alloy, while the remaining four electrodes were ternary alloys containing the same mole fraction zinc plus various amounts of a given third element. In these experiments the electrode potentials could be measured relative to the pure zinc standard, or relative to the binary alloy of the same zinc content. In the course of this and related studies (19, 20), data were accumulated on a large number of binary electrodes, thus permitting an accurate determination of the activity of zinc in dilute binary solution with lead.

The galvanic cell assembly was enclosed in a gastight Vycor tube which was provided with a Pyrex head through which the electrode leads and thermocouple were passed. The electrode leads were 18 gauge tantalum wire. An L&N Type K-3 potentiometer was used to measure the emf of the galvanic cells and of a chromel-alumel thermocouple.

The electrolyte was the eutectic mixture of potassium chloride and lithium chloride plus approximately 5 w/o zinc chloride. These electrolyte salts were J. T. Baker reagent grade chemicals. The eutectic potassium lithium chloride salt was vacuum refined in the liquid state, and the zinc chloride was dried at 200°C prior to use. The metals were supplied by The American Smelting and Refining Company and were of 99.999% minimum purity.

After assembly the cell was held at 500°C for 36 hr to permit homogenization of the liquid phase. After 24 hr, 4 or 5 readings were taken at 15-min intervals to insure that the system had reached steady state. For the ternary alloys, the emf measurements were made over the temperature range 450°-650°C at roughly 50° intervals. After each change in temperature, approximately 3 hr were allowed for thermal equilibrium to be established in the cell before readings were taken again. All runs lasted a minimum of 72 hr.

A temperature variation of less than ±1°C was maintained during the period lasting from 45 to 60 min, in which 4 or 5 separate cell potential measurements were made. Data were compiled for each case by taking averages of these separate measurements.

Experimental Results

Binary lead-zinc system.—The activity coefficient of zinc in liquid lead has been measured in the temperature range 450°-800°C and at zinc concentrations ranging up to 0.05 mole fraction zinc (20). The activity coefficient shows a strong positive deviation from Raoult's law, having a value of 11.4 at 550°C. The results of 28 independent experiments involving 140 individual measurements of the zinc activity in this composition and temperature range were analyzed statistically. The results of this analysis showed that ϵ_i^i is of such magnitude that substantial deviations from Henry's law are apparent at zinc concentrations around 0.05 mole fraction, but deviations from Henry's law are small enough to be neglected at concentrations up to and including 0.0375 mole fraction zinc. In the Henry's law region, the activity coefficient of zinc in dilute solution in liquid lead is given by the expression

$$\log \gamma^\circ_{Zn} = \frac{1215}{T_{°K}} - 0.418 \quad [5]$$

This correlation is in good agreement with the results of Kleppa (21) and Kozuka *et al.* (22).

Lead-zinc-antimony system.—Sixteen dilute ternary alloys in the lead-rich corner of the system were studied. These alloys represented a 4 by 4 matrix of 4 levels of zinc and antimony: 0.015, 0.0250, 0.0375, and 0.050 mole fraction. In addition, previous measurements (20) on the lead-zinc binary system were used in evaluating the interaction parameters.

The emf-temperature relationships were linear and nearly parallel for all compositions studied in the temperature range 450°-650°C. The experimental results are summarized in Table I.

The thermodynamic interaction parameter defined as (16)

$$\epsilon_i^j = \left(\frac{\partial \ln \gamma_i}{\partial x_j}\right)_{x_i=x_j=0} \quad [6]$$

was determined by plotting the natural logarithm of the zinc activity coefficient *vs.* the mole fraction of antimony at each constant composition of zinc. The limiting slope of each plot gave the value

$$\left(\frac{\partial \ln \gamma_{Zn}}{\partial x_{Sb}}\right)_{x_{Sb}=0;\ x_{Zn}=\text{ const.}}$$

This graphical technique is illustrated in Fig. 1 at a zinc mole fraction of 0.015. Plotting these slopes against the zinc concentration and extrapolating to $x_{Zn} = 0$ yielded the ternary interaction parameter

$$\left(\frac{\partial \ln \gamma_{Zn}}{\partial x_{Sb}}\right)_{x_{Sb}=x_{Zn}=0}$$

Table I. Experimental results for ternary lead-zinc-antimony system

x_{Zn}	x_{Sb}* = 0.0 Emf at 550°C	x_{Sb}* = 0.0 $\left(\frac{\partial E}{\partial T}\right)$	x_{Sb} = 0.015 Emf at 550°C	x_{Sb} = 0.015 $\left(\frac{\partial E}{\partial T}\right)$	x_{Sb} = 0.025 Emf at 550°C	x_{Sb} = 0.025 $\left(\frac{\partial E}{\partial T}\right)$	x_{Sb} = 0.0375 Emf at 550°C	x_{Sb} = 0.0375 $\left(\frac{\partial E}{\partial T}\right)$	x_{Sb} = 0.050 Emf at 550°C	x_{Sb} = 0.050 $\left(\frac{\partial E}{\partial T}\right)$
0.015	62.5_7	0.22_9	67.0_3	0.23_1	69.9_6	0.21_9	72.6_0	0.21_6	76.3_9	0.21_5
0.025	44.4_1	0.20_0	48.9_6	0.19_8	53.1_9	0.19_7	55.0_5	0.19_2	57.7_6	0.19_1
0.375	29.9_4	0.18_3	34.6_5	0.17_8	36.4_0	0.17_4	40.1_6	0.17_4	43.0_7	0.17_2
0.050	21.2_4	0.15_7	24.9_6	0.16_1	27.4_3	0.15_9	30.8_4	0.15_8	33.3_5	0.15_6

* Values from correlation of 28 electrodes.
Emf in mv; $(\partial E/\partial T)$ in mv/°C.

Table II. Experimental results for ternary lead-zinc-bismuth system

x_{Zn}	x_{Bi} = 0.0 Emf at 550°C	x_{Bi} = 0.0 $\left(\frac{\partial E}{\partial T}\right)$	x_{Bi} = 0.015 Emf at 550°C	x_{Bi} = 0.015 $\left(\frac{\partial E}{\partial T}\right)$	x_{Bi} = 0.025 Emf at 550°C	x_{Bi} = 0.025 $\left(\frac{\partial E}{\partial T}\right)$	x_{Bi} = 0.0375 Emf at 550°C	x_{Bi} = 0.0375 $\left(\frac{\partial E}{\partial T}\right)$	x_{Bi} = 0.050 Emf at 550°C	x_{Bi} = 0.050 $\left(\frac{\partial E}{\partial T}\right)$
0.015	61.9_7	0.24_4	—	—	62.0_0	0.24_2	63.4_0	0.24_5	64.4_9	0.24_7
	—	—	61.4_7	0.22_9	62.2_6	0.21_8	63.7_8	0.22_4	62.9_0	0.22_1
0.025	43.7_6	0.19_6	—	—	44.2_5	0.19_5	45.5_4	0.19_6	46.1_2	0.19_8
	—	—	44.1_0	0.19_5	44.5_8	0.19_6	45.6_4	0.19_7	45.7_6	0.19_7
0.0375	29.9_4*	0.18_3*	30.9_4	0.17_7	31.7_7	0.17_8	32.6_4	0.17_8	32.0_3	0.17_6
0.050	22.2_4	0.15_3	—	—	22.9_4	0.15_2	23.3_8	0.15_2	24.2_0	0.15_3
	—	—	23.0_9	0.16_7	23.6_7	0.15_6	24.3_9	0.16_7	24.3_1	0.16_5

* Value from correlation of 28 electrodes.
Emf in mv; $(\partial E/\partial T)$ in mv/°C.

as shown in Fig. 2.

An alternate method also can be used to determine the interaction parameter. This consists of plotting $\ln\gamma_{Zn}$ *vs.* x_{Zn} for constant mole fractions of antimony and then plotting the intercept $(\ln\gamma_{Zn})_{x_{Zn}=0}$ *vs.* x_{Sb}. The interaction parameter $(\epsilon_{Zn}^{Sb})_{x_{Sb}=0}$ obtained by the first method is mathematically equivalent with the interaction parameter $(\epsilon_{Zn}^{Sb})_{x_{Zn}=0}$ determined by

$$x_{Zn}=0 \qquad x_{Sb}=0$$

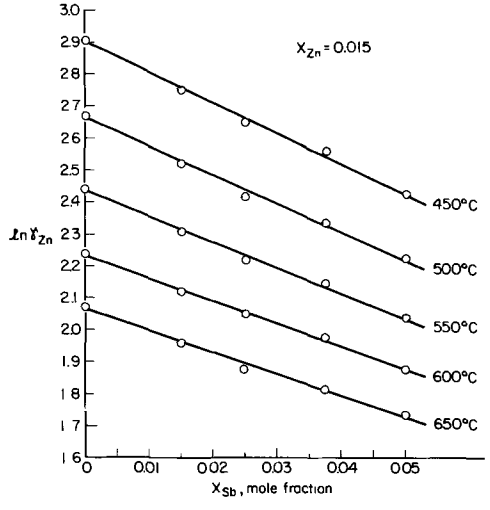

Fig. 1. Logarithm of zinc activity coefficient vs. mole fraction antimony at 0.015 mole fraction zinc.

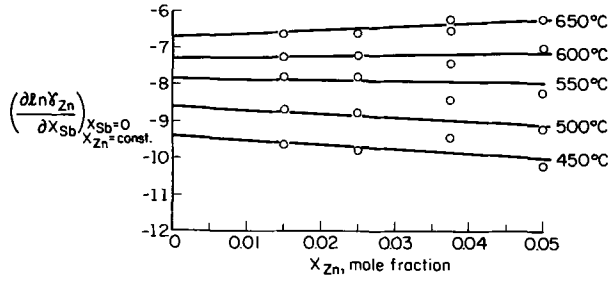

Fig. 2. Slope of zinc activity coefficient-antimony relation at infinite antimony dilution vs. mole fraction zinc.

the second method.

The interaction parameter can be shown over reasonably small temperature ranges to vary linearly with reciprocal temperature in the form (17)

$$\frac{\partial \epsilon_i^j}{\partial(1/T)} = \frac{1}{R}\left(\frac{\partial^2 H}{\partial x_i \partial x_j}\right)_{x_i=x_j=0} \qquad [7]$$

This relationship was applied to the present results and the interaction parameters were plotted against the reciprocal absolute temperatures as shown in Fig. 7. A strict linearity was observed, implying a constant value of the second derivation of molar enthalpy. The equation representing this relationship is

$$\epsilon_{Zn}^{Sb} = -\frac{8840}{T_{°K}} + 2.84 \qquad [8]$$

Lead-zinc-bismuth system.—In this system, measurements were carried out on single-phase liquid solutions in a temperature range from 450°-650°C. The emf was measured both with increasing temperature and with decreasing temperature. A 4 by 4 composition matrix at bismuth and zinc solute concentrations of 0.015, 0.025, 0.0375, and 0.05 mole fraction was studied. In addition, replicate experiments were carried out at bismuth and zinc mole fractions of 0.015, 0.025, and 0.05 mole fraction. Furthermore, in evaluating the interaction parameters, data on the lead-zinc binary system were used to define the intercepts at 0% bismuth.

The emf-temperature relationships were linear and nearly parallel for all compositions studied. Experimental results are summarized in Table II. Employing the same method outlined above for the lead-zinc-antimony system, $\ln\gamma_{Zn}$ *vs.* x_{Bi} relations were plotted as shown for example in Fig. 3 at a zinc mole fraction of 0.025. The limiting slopes of plots of the type shown in Fig. 3, taken at $x_{Bi} = 0$, were plotted against x_{Zn}. The values at $x_{Zn} = 0$ define the interaction parameters, ϵ_{Zn}^{Bi}, as shown in Fig. 4. The interaction parameters, ϵ_{Zn}^{Bi}, thus obtained are plotted against reciprocal absolute temperature in Fig. 7. A strict linearity was found which may be represented by the relationship

$$\epsilon_{Zn}^{Bi} = -\frac{2950}{T_{°K}} + 2.81 \qquad [9]$$

The zinc-bismuth interaction parameter is slightly negative and shows a moderate dependence on temperature over the range studied in this investigation.

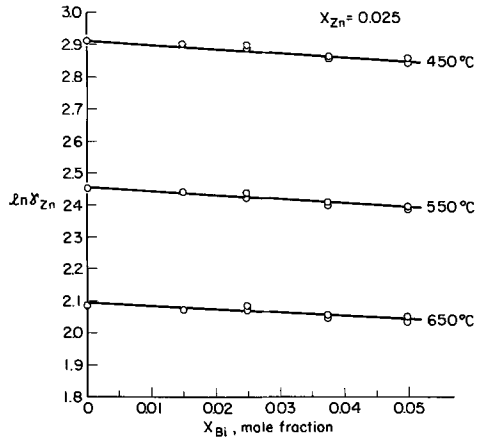

Fig. 3. Logarithm of zinc activity coefficient vs. mole fraction bismuth at 0.025 mole fraction zinc.

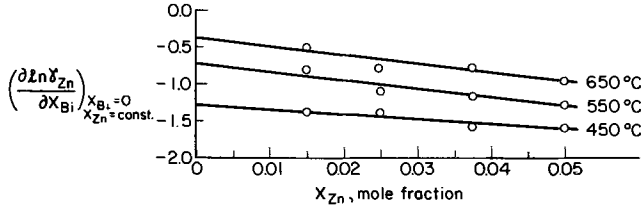

Fig. 4. Slope of zinc activity coefficient-bismuth relation at infinite bismuth dilution vs. mole fraction zinc.

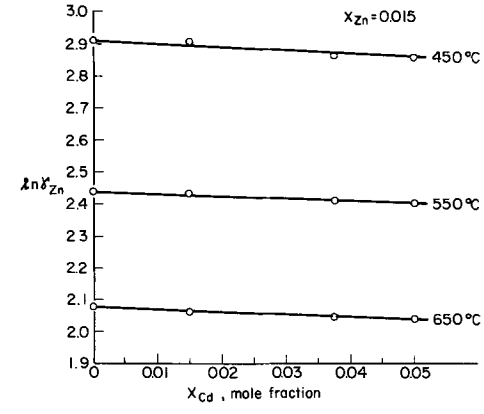

Fig. 5. Logarithm of zinc activity coefficient vs. mole fraction cadmium at 0.015 mole fraction zinc.

Lead-zinc-cadmium system.—The alloy compositions studied and the experimental results are summarized in Table III. The emf-temperature relationships for these alloys were linear. Using the same procedure outlined above for lead-zinc-antimony and lead-zinc-bismuth systems, the interaction parameter, ϵ_{Zn}^{Cd}, was evaluated over the temperature range 450°-650°C. The variation of the natural logarithm of the activity coefficient of zinc with cadmium concentration is shown in Fig. 5 at a zinc mole fraction of 0.015. The limiting slopes of plots of this type, taken at $x_{Cd} = 0$, were plotted against mole fraction zinc. The values at

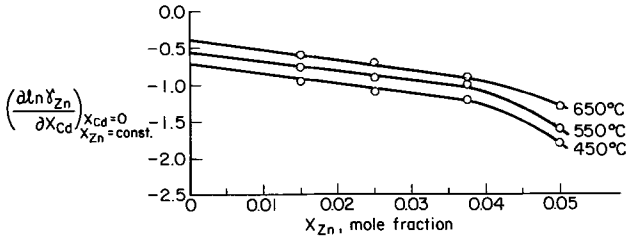

Fig. 6. Slope of zinc activity coefficient-cadmium relation at infinite cadmium dilution vs. mole fraction zinc.

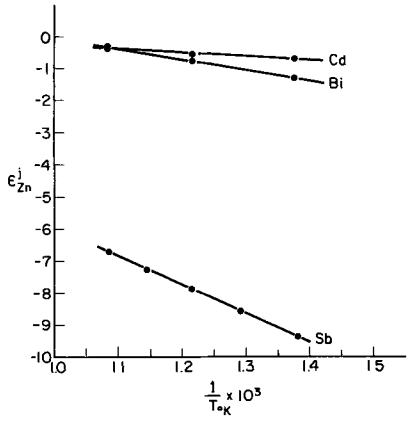

Fig. 7. Interaction parameters vs. reciprocal temperature

$x_{Zn} = 0$ define the interaction parameters, ϵ_{Zn}^{Cd}, as shown in Fig. 6.

The interaction parameters, ϵ_{Zn}^{Cd}, thus obtained are plotted against reciprocal absolute temperature in Fig. 7. The variation of the interaction parameter with reciprocal temperature is given by the relationship

$$\epsilon_{Zn}^{Cd} = -\frac{1000}{T_{°K}} + 0.68 \qquad [10]$$

A comparison between the interaction parameters of the lead-zinc-antimony, lead-zinc-bismuth, and lead-zinc-cadmium systems is shown in Fig. 7. The zinc-antimony interaction parameter is negative and shows a strong temperature dependence over the range of temperatures studied for this investigation. The zinc-bismuth and zinc-cadmium interaction parameters are much less negative and not as dependent on temperature.

Discussion

In the study of dilute solutions by the galvanic cell technique, the cell should be reversible, conduction in the electrolyte should be purely ionic, the valence of the active element in the electrolyte must be known, and there should be no significant displacement reactions taking place.

The reversibility of these cells was inferred by the consistent behavior of the cell emf which was stable during the experimental observations and drifted very little over prolonged periods of operation. The emf-temperature relations were linear, and the binary data were consistent with the galvanic cell results of other investigators at higher concentrations of zinc

Table III. Experimental results for ternary lead-zinc-cadmium system

	$x_{Cd} = 0.0$		$x_{Cd} = 0.015$		$x_{Cd} = 0.025$		$x_{Cd} = 0.0375$		$x_{Cd} = 0.050$	
x_{Zn}	Emf at 550°C	$\left(\frac{\partial E}{\partial T}\right)$	Emf at 550°C	$\left(\frac{\partial E}{\partial T}\right)$	Emf at 550°C	$\left(\frac{\partial E}{\partial T}\right)$	Emf at 550°C	$\left(\frac{\partial E}{\partial T}\right)$	Emf at 550°C	$\left(\frac{\partial E}{\partial T}\right)$
0.015	62.3$_8$	0.22$_0$	62.5$_6$	0.22$_3$	—	—	63.7$_3$	0.22$_2$	63.8$_3$	0.22$_1$
0.025	44.6$_0$	0.18$_8$	45.1$_0$	0.18$_9$	45.3$_1$	0.18$_8$	46.1$_7$	0.18$_7$	—	—
0.0375	31.9$_7$	0.17$_7$	32.5$_0$	0.17$_7$	—	—	33.1$_1$	0.17$_4$	33.4$_8$	0.17$_5$
0.050	17.6$_7$	0.15$_9$	18.6$_9$	0.15$_7$	19.4$_8$	0.15$_8$	—	—	20.3$_9$	0.15$_6$

Emf in mv; $(\partial E/\partial T)$ in mv/°C.

(21, 22). Consideration was given to the possible error caused by displacement reactions. Emf measurements in the lead-zinc system are possible at low zinc concentrations because of the relatively large difference in the standard free energy of formation of the respective metal-chlorides. A consideration of displacement reactions was made based on the analysis of Wagner and Werner (23, 24) and an estimation made of the extent of error to be expected in the experimental systems examined in this investigation. The order of magnitude of such displacement errors on the measured cell potential at 500°C was estimated for the lead-zinc system to be well below 1% for a zinc concentration of 0.01 mole fraction. The errors caused by displacement reactions involving the added third elements, antimony, bismuth, and cadmium, in the dilute ternary alloys were shown to be of the same order of magnitude.

Summary

The galvanic cell method has been used to determine the interaction parameter of zinc in ternary lead-zinc-j alloys containing the added third elements antimony, bismuth, or cadmium. The interaction parameters were shown to vary linearly with reciprocal absolute temperature, the effect of antimony being to markedly decrease, whereas bismuth and cadmium slightly decrease, the activity coefficient of zinc. The variations of these interaction parameters with temperature are given by the following relations

$$\epsilon_{Zn}^{Sb} = -\frac{8840}{T_{°K}} + 2.84$$

$$\epsilon_{Zn}^{Bi} = -\frac{2950}{T_{°K}} + 2.81$$

$$\epsilon_{Zn}^{Cd} = -\frac{1000}{T_{°K}} + 0.68$$

Acknowledgment

The authors gratefully acknowledge the contribution of Dr. J. V. Gluck in discussions and in critical assessment of the experimental data. This work was supported in part by the Atomic Energy Commission under Contract Number AT(11-1)-1352. This work is based in part on a research program carried out by one of the authors (T.L.M.) in partial fulfillment of the requirements for the M.Sc. degree in Engineering (metallurgical) at the University of Michigan.

Manuscript received March 10, 1967; revised manuscript received April 18, 1967.

Any discussion of this paper will appear in a Discussion Section to be published in the June 1968 JOURNAL.

REFERENCES

1. W. Himmler, *Z. Physik. Chem*, **195**, 244 (1950).
2. D. L. Sponsellor, Ph.D. Thesis, University of Michigan, 1962.
3. C. F. Obenchain, Ph.D. Thesis, University of Michigan, 1964.
4. J. V. Gluck, Ph.D. Thesis, University of Michigan, 1965.
5. M. Ohtani and N. A. Gokcen, *Trans. Met. Soc. AIME*, **218**, 533 (1960).
6. C. B. Alcock and F. D. Richardson, *Acta Met.*, **5**, 385 (1958).
7. H. Wada, *Trans. Nat'l. Res. Inst. for Metals (Japan)*, **6**, 1 (1964).
8. H. Wada and T. Saito, *Trans. Japan Inst. of Metals*, **2**, 15 (1961).
9. J. Chipman, *J. Iron Steel Inst.*, **180**, 97 (1955).
10. O. Kubaschewski and J. A. Catterall, "Thermochemical Data of Alloys," Pergamon Press, London (1956).
11. W. M. Boorstein and R. D. Pehlke, *This Journal*, **111**, 1269 (1964).
12. S. T. Cleveland, K. Okajima, and R. D. Pehlke, *J. Phys. Chem.*, **69**, 4085 (1965).
13. K. Okajima and R. D. Pehlke, *Trans. Met. Soc. AIME*, **230**, 1731 (1964).
14. J. V. Gluck and R. D. Pehlke, *ibid.*, **239**, 36 (1967).
15. J. V. Gluck and R. D. Pehlke, *ibid.*, **239**, 562 (1967).
16. C. Wagner, "Thermodynamics of Alloys," pp. 51-3, Addison-Wesley, Cambridge, Mass. (1952).
17. J. M. Dealy and R. D. Pehlke, *Trans. Met. Soc. AIME*, **227**, 1030 (1963).
18. J. M. Dealy and R. D. Pehlke, *ibid.*, **227**, 88 (1963).
19. K. Okajima and R. D. Pehlke, *J. Japan Inst. Metals*, **29**, 961 (1965).
20. K. Okajima and R. D. Pehlke, "Thermodynamic Interactions and Liquidus Phase Boundaries in the Lead Corner of the Pb-Zn-Ag and Pb-Zn-Au Systems," *Trans. Met. Soc. AIME*, August 1967.
21. O. J. Kleppa, *J. Am. Chem. Soc.*, **74**, 6052 (1955).
22. Z. Kozuka, Y. Nakai, and J. Moriyama, *J. Japan Inst. Metals*, **28**, 407 (1964).
23. C. Wagner and A. Werner, *This Journal*, **110**, 326 (1963).
24. J. M. Dealy and R. D. Pehlke, Private communication.

Pressure Effects on the Electrical Properties of Polycrystalline Boron

Terrell N. Andersen, Onnig H. Bezirjian, and Henry Eyring

Institute for the Study of Rate Processes, University of Utah, Salt Lake City, Utah

ABSTRACT

The electrical resistances of β-rhombohedral and tetragonal polycrystalline boron were measured at temperatures from 25° to 300°C and pressures from 1 atm to 60 kb (kilobars); the thermoelectric power was measured to 13 kb. Pressures were applied with an anvil press. With increasing temperature the resistance, R, continually decreased and the thermoelectric power, Q, at first increased and then levelled off. The shapes of the log R *vs.* $1/T$ and Q *vs.* T curves are explained by intrinsic conduction at high temperatures going to extrinsic conduction at the lowest temperatures studied. In the intrinsic region an increase in pressure causes a reduction in the resistance, energy gap, and thermoelectric power of boron. For the low-temperature extrinsic region pressure lowers the resistance and hardly affects the thermoelectric power. These effects are discussed.

The effects of pressure on the band gap have been studied for several elements such as the group IV semimetals, phosphorus, selenium, and iodine (1-3). Although quite a number of electrical measurements have been made on boron at atmospheric pressure, work at elevated pressures is sparse. Hamann (4) has reported the electrical resistance of a boron sample at room temperature and pressures up to 40 kb, and Vereshchagin *et al.* (5) have measured the resistance of boron at room temperature from 25 to 250 kb. The crystal form of the boron in both of the above studies was unspecified, but both studies revealed a decrease in resistance with increasing pressure, as well as an absence of any phase transitions. Studies of boron are made difficult by the fact that it has several crystal modifications, the structures of which are all quite complex (6), and only one of which appears to be commercially available. Furthermore, the melting point of boron is very high (2300°C) which makes purification of it difficult (especially since the forms other than β-rhombohedral crystallize to β-rhombohedral upon being melted and recrystallized) (6).

In the present work the effects of pressure and temperature on the electrical resistance and thermoelectric power of three polycrystalline boron samples have been studied. The three materials studied were β-rhombohedral and a tetragonal modification of boron, both prepared in this laboratory, and a commercially available β-rhombohedral boron. Since the two types of crystals prepared here appeared to have similar impurity content, which was at least an order of magnitude lower than that of the commercial β-rhombohedral boron, the study was intended to serve also as a comparison of the importance of structural *vs.* purity differences on electrical properties of boron.

Preparation and Identification of Boron

Being unable to purchase tetragonal boron, we prepared it, as well as some β-rhombohedral boron, using the hot filament technique (7) in which BBr_3 was reduced by H_2 on a glowing Ta filament. The conditions of preparation (8) were identical for the two modifications except for the filament temperature which measured 1250°C in the case of the tetragonal boron and 1575°C for the β-rhombohedral. The actual filament temperatures may have been a little higher than those measured since the temperatures were measured with an optical pyrometer of the disappearing filament type without correction for the cell not being a black body. The flow rate of H_2 was 200 cm^3 min^{-1}, the total pressure was 1 atm, and the temperature of the BBr_3 (through which H_2 was bubbled) was −20°C. Reaction times were up to 30 hr during the early stages of which β-tantalum diboride was formed on the filament surface with boron growth later (after a few hours) continuing on the tantalum diboride. The only control of purity was through selection of the starting materials. The Ta wire (0.05 mm diameter) was 99.9+% pure, the BBr_3 was 99+% pure, and 99.99% H_2 was passed through activated alumina for further purification. Emission spectrographic qualitative analysis of the deposited boron (with carbon electrodes) showed only traces (up to a few hundredths per cent total) of Si, Cu, Mg, Ag, and Ta. The commercial β-rhombohedral sample was obtained from U. S. Borax Research and was of 99.+% purity.

Identification of the deposited boron was made by means of x-ray diffraction using a Guinier focusing camera (9). Details of our identification and x-ray results (as well as the details of the preparation of our tetragonal boron) are listed here because (*i*) several tetragonal modifications of boron have been prepared, all from somewhat similar experimental conditions (6), (*ii*) the tetragonal boron we prepared was deposited on tantalum, which is a different substrate than this modification has previously been deposited on, and (*iii*) the use of the focusing camera gives better line positions than would seem to have been obtained using previous methods. The crystalline samples showed crystal faces, but these were too small and imperfect to use in making microscopic identifications (8). Diffraction d-values and visually estimated intensities for the tetragonal boron are shown in Table I along with the determined cell constants and hkl values. The x-ray patterns were indexed using a computer program (8) which utilizes a modified version of Ito's method (10). The powder pattern of our tetragonal samples matched closely to the tetragonal pattern of Talley *et al.* (11), ASTM Card No. 11-617. Their sample was prepared by the reduction of BBr_3 with H_2 using W and Re filaments at 1267°C. Their d-spacings were computed from patterns recorded with a diffractometer using filtered Co and Cu radiations.

The x-ray powder pattern of our β-rhombohedral sample (the d-spacings of which were also obtained with the Guinier focusing camera) was in close agreement with that of Hughes *et al.* (12), ASTM Card No. 11-618.

The densities of the prepared tetragonal and β-rhombohedral samples, as determined by the flotation method, were 2.345 ± 0.020 and 2.356 g/cm^3, respectively.

Experimental Procedure

The boron to be studied was finely powdered and formed into cylindrical pellets. Each pellet was then pressed into an annular pyrophyllite retaining ring of approximately the same thickness as the pellet and approximately 1/32 in. in wall thickness. The sample-containing pellet was pressed between two opposed

Table I. Powder diffraction data for deposited tetragonal boron

d(Å)	hkl	Relative intensity
7.9215	101	10
7.155	110,002	10
6.416	111	10
5.816	102	10
5.038	200,112	100
4.679	201	30
4.3265	211,103	30
4.133	202	40
3.957	113	30
3.829	212	30
3.489	221,203	20
3.2875	301,203	10
2.856	223,005	10
2.760	321,303	30
2.658	313,115	30
2.5245	400,224	10
2.449	410,304	10
2.424	411,323	20
2.386	330,314	40
2.2445	420,332	10
2.317	421,403	10
1.763	441,425	10
1.549	337	10
1.513	623	15
1.481	535	10
1.4545	624	10
1.442	700	10
1.393	641	10
1.375	642	40
1.330	723	10

$a_o = 10.12$Å; $c_o = 14.14$Å

anvils which derived their thrust from a hydraulic ram. The retaining ring acted to prevent the extrusion of the boron from the pressurized region. The over-all pellet diameter was ¼ or ½ in. with a final thickness of about 1/25th the pellet diameter.

During the resistance measurements the sample was heated by means of a split furnace, and a thermocouple against the sample served to measure the temperature. For thermoelectric power masurements, heating tapes were used to control the temperature of each anvil individually, such that the desired temperature differences between the two boron-copper contacts could be obtained. Thermocouples, which were in contact with each junction, served to detect the required temperatures which differed by about 25°C. The mean of the two temperatures was taken as that of the sample. Sufficient insulation was placed around the anvils and sample that gradients did not exist between the thermocouples and sample, and the heating rate of about 1 deg/min was adequate to assure temperature equilibrium as shown by the agreement of resistance readings during heating and cooling cycles. Since boron oxidizes in air at several hundred degrees, some runs were made in an N_2 atmosphere, by encasing the entire press in an N_2-inflated polyethylene sack. Since the results in N_2 were in agreement with those in air, it appeared that the pyrophyllite rings, alone, prevented oxidation.

Direct-current resistance measurements were made by passing current through the anvil faces and measuring the potential drop across them with a Keithley electrometer (the resistance of the pyrophyllite was several orders of magnitude greater than that of the boron and could hence be neglected). The Seebeck voltages were measured with a Keithley electrometer or with a potentiometer coupled with a very sensitive galvanometer. These voltages were due only to the boron as shown by the lack of potentials of the observed order of magnitude for pyrophyllite alone. Resistance measurements were made both at constant pressure with varying temperature and at constant temperature with increasing pressures. The recorded pressures were computed directly from the gauge pressure and the anvil area. Although pressure gradients exist across flat anvil faces, the expected errors from these would not affect the present discussion. Samples were first subjected to the maximum experimental pressure, and then the pressure was slowly released. Pressure was increased again slowly to the desired pressure and held constant while measurements were made. This compaction of the sample minimized extrusion during the experiments. Also, the resistance at the low pressure end of the first pressure cycle was higher and that at the high pressure end usually slightly lower than for subsequent cycles.

Experimental Results

Evidences that the measured resistance changes were due to the boron, itself, and not to boron-metal contacts, boron-boron contacts, or space charge are (*i*) the measured resistance was ohmic for potentials across the sample of from 1 to 90v, (*ii*) electrical resistance readings rapidly came to equilibrium upon application of current, (*iii*) various metal contacts (Cu, Pt, etc.) gave identical resistance readings, and (*iv*) powdered samples of various particle size (—100 to —300 mesh) gave the same results. Furthermore the resistances, energy gaps, and thermoelectric power values from this work at low pressures (as well as from other work on polycrystalline boron) are in agreement with the values found in single crystal work for material of comparable purity.

Figure 1 shows that the resistance for all the samples continually decreases with increased pressure, which supports the earlier findings (4, 5). The curves for boron at higher temperatures (up to 300°C) are similar in shape to those of Fig. 1 and are shifted successively to lower R values (they are not necessarily parallel). Equation [1] was used to obtain the experimental activation energy, E_{act}, for conduction.

$$\rho = \frac{1}{\sigma} = A' \exp(E_{act}/kT) \qquad [1]$$

Here ρ is the resistivity, σ is the conductivity, A' is a term which varies much more slowly with T than does the exponential, and k and T are Boltmann's constant and the temperature. Details of the terms in [1] will be given later. Since $R = \rho L/A$ where L and A are the length and area of the sample, then

$$E_{act} = k\ \partial\ \ln R/\ (1/T) \qquad [1]$$

Plots of log R *vs.* $1/T$ are shown in Fig. 2 from which it is seen that the slope (*i.e.*, the activation energy) increases with increasing temperature, and appears to reach a limiting value.

The thermoelectric power is defined as

$$Q = -\Delta V/\Delta T \qquad [3]$$

where ΔV is the potential difference (Seebeck voltage) and ΔT the temperature difference between the two boron-metal junctions. The thermoelectric power, for the various boron samples studied, is shown in Fig. 3

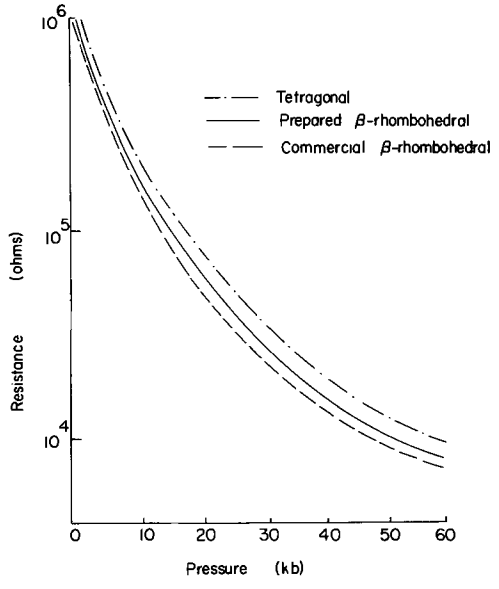

Fig. 1. Resistance *vs.* pressure at 25°C for polycrystalline boron

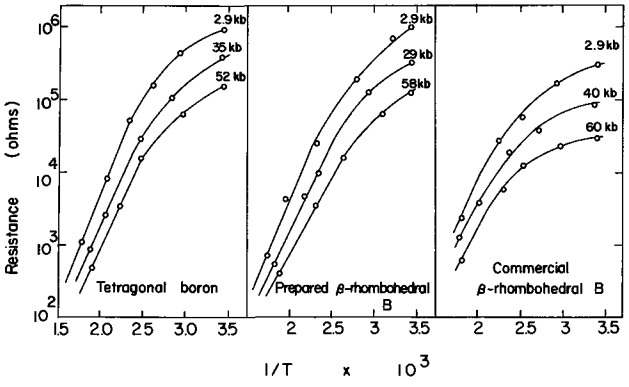

Fig. 2. Resistance (log scale) *vs.* $1/T$ at various pressures for boron samples.

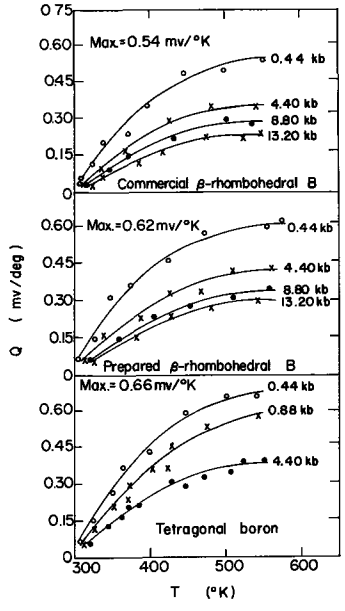

Fig. 3. Thermoelectric power, Q, *vs.* T at various pressures for boron samples.

as a function of the average sample temperature and at various pressures. The pressures employed were lower than in the case of the resistance studies, since larger sample thicknesses and hence anvil diameters (½ in. instead of ¼ in.) were required in order to separate the junctions sufficiently for accurate temperature measurements. Since the thermoelectric power, as well as the relative potential of the cold junction, has the same sign as the majority carrier (for extrinsic semiconductors) or the carrier of highest mobility (for intrinsic semiconductors), it is seen that the samples studied are all p-type.

Discussion

The shapes of the resistance and Seebeck curves as functions of temperature are consistent with the idea that the boron conducts extrinsically in the low-temperature region going smoothly to intrinsic conduction at the highest temperatures attained (300°C). Purely extrinsic conduction was seemingly not attained at our lowest temperatures as shown by the rapidly changing curvature of the log R *vs.* $1/T$ curves. Higher impurity contents or lower temperatures would have been required for this limit. On the other hand these curves are linear (or nearly linear in the case of the less pure commercial β-rhombohedral boron) in the experimental high-temperature limit, and the samples thus appear to behave intrinsically. Other resistance studies of polycrystalline boron, made only at atmospheric pressure but with wider temperature variation or impurity variation, have shown the intrinsic region to be reached near 200°C for samples with purity comparable to that in the present study (13, 14). Likewise, the thermoelectric power curves show leveling at the highest temperatures which indicates the onset of intrinsic properties with the accompanying decrease in thermoelectric power (cf. Eq. [6]). Thermoelectric power measurements on single crystal boron (of purity comparable to ours) at 1 atm have shown Q to rise, then level out and finally decrease with increasing temperature (15-17). In the above studies the temperature at which Q reached a plateau was 125°-300°C, and the maximum Q values were 550-750 μv deg^{-1}, in satisfactory agreement with the present work. The polycrystalline boron in the work of Uno (21) did not yield a maximum in the Q *vs.* T curve. This is perhaps due to the presence of impurities as evidenced by lower resistivities obtained compared to other workers. In ref. (15) the thermoelectric power *vs.* T curves for n- and p-type boron join at $T \simeq 500$°C, but the n- boron was very impure. The "typical" p-type boron gave a maximum thermoelectric power value at approximately 250°C.

Intrinsic Region

We assume in this discussion that at the highest temperatures studied the boron is intrinsic and that its properties may be formulated accordingly. The energy gap is large enough that Fermi-Dirac statistics may be replaced by Boltzmann statistics (assuming the Fermi level to lie half way between the conduction and valence bands). In this region the density of holes in the valence band, n_h, is equal to the density of electrons in the conduction band, n_e. We then have for the conductivity, σ, (19)

$$\sigma = |e|(n_e\mu_e + n_h\mu_h)$$
$$= |e|(\mu_h + \mu_e)2\left(\frac{2\pi kT}{h_2}\right)^{3/2}$$
$$(m^*_e m^*_h)^{3/4} \exp(-E_g/2kT) \quad [4]$$

Here e is the electronic charge, μ_h and μ_e are the mobilities of holes and electrons, m^*_h and m^*_e are the effective masses of the holes near the top of the valence band and the electrons near the bottom of the conduction band; E_g is the energy gap between the bottom of the conduction band, E_c, and the top of the valence band, E_v; k, T, and h have their usual significance. Since $E_g = 2E_{act}$ from Eq. [1] and [4], E_g is readily obtained from Fig. 2 (assuming the mobility, μ, varies more slowly with T than does $\exp(-E_g/2kT)$), and is shown in Fig. 4 for the highest temperatures studied, 300°C. If $\mu \propto T^{-7/4}$ as was found by Hagenlocher (20) for polycrystalline β-rhombohedral boron, then $|d(-E_g/2kT)/d(1/T)|$ is more than ten times larger then $|d \ln \mu/d(1/T)|$.

From Fig. 2 it is noted that the log R *vs.* $1/T$ curves for the commercial β-rhombohedral boron (especially for 2.9 kb) have not reached a limiting slope as evi-

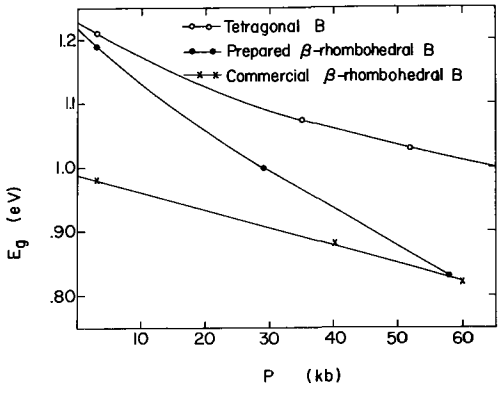

Fig. 4. Energy gap, E_g, *vs.* P for boron samples at 300°C

denced by the fact that the three highest temperature points do not lie on a straight line. This is due to the high concentration of impurities giving appreciable extrinsic conduction, even at the highest temperature. Thus it may be assumed that the energy gap *vs.* pressure curve for intrinsic β-rhombohedral boron more closely follows that for the prepared material than that for the commercial boron. The E_g values extrapolated to 1 atm in Figure 4 (*i.e.* 1.2-1.3 eV), are in fair agreement with other workers in the field for tetragonal (14, 16, 18, 21, 22) and β-rhombohedral boron (13, 17, 20, 23-30). The energy gap values of the above workers range from 1.1 to 1.6 eV, which is a considerable spread of values for the energy gap of one material. Although the present work cannot solve the problem of this variation, it is noted from the above literature that no obvious energy gap differences exist between β-rhombohedral and tetragonal boron, or between single crystal and polycrystalline material. The present results show that E_g for β-rhombohedral and tetragonal boron are about the same at low pressures while E_g for the latter is greater at high pressures. The explanation of this result must await x-ray data for boron at elevated pressures. Impurities, which in the present study are seen to lower the activation energy for conduction at $T \leq 300°C$, are probably responsible for a sizeable portion of the variation of E_g observed in the literature. Since intrinsic and extrinsic conduction are parallel mechanisms, the production of proportionately many intrinsic carriers is required in order to observe bulk intrinsic properties. This is usually accomplished by elevating the temperature. Figure 4 shows that the same result apparently can also be obtained by increasing the pressure as shown by the convergence of E_g for the β-rhombohedral boron samples of different purity. It is seen that dE_g/dP for tetragonal boron decreases from -6×10^{-3} ev/kb at 3 kb to -2.5×10^{-3} ev/kb at 60 kb; the corresponding values for β-rhombohedral boron are -9×10^{-3} ev/kb at 3 kb and -6×10^{-3} kb at 60 kb. This order of band gap deformation with pressure is often found for semiconducting elements and compounds which have been studied (1), though dE_g/dP has been found to be either positive or negative depending on the material.

The thermoelectric power, Q is obtained from integrating the Thomson relation

$$\sigma_T = T\, dQ/dT \qquad [5]$$

where σ_T, the Thomson coefficient, is obtained from the thermal and electrical current density expressions (31). A direct expression for the thermoelectric power of an intrinsic semiconductor has been derived by Johnson and Lark-Horowitz (32) under the assumptions that (*a*) Fermi statistics may be replaced by classical statistics, (*b*) the conduction electron and hole densities are equal, and (c) the only important scattering of carriers is due to the covalent lattice. Assumptions (*a*) and (*b*) were already used in writing expression [4] and appear justified from the size of E_g and the evidence that the intrinsic region had been reached. Q is given by (32)

$$Q = -\frac{k(c-1)}{|e|(c+1)}\left(\frac{E_g}{2kT} + 2\right) \qquad [6]$$

where

$$c = \mu_e/\mu_h \qquad [7]$$

From energy gap values interpolated from Fig. 4 and the maximum Q values of Fig. 3, c was calculated from Eq. [6], the results of which are shown in Fig. 5. From the results it can be seen that the hole mobility is greater than the electron mobility, and that the difference decreases with an increase in pressure. The decreases in the resistance and thermoelectric power with increasing pressure may both be explained by the energy bands broadening with a decrease in lattice parameter, such that the upper edge of the valence band and lower edge of the conduction band approach each other. If carrier scattering were due to some

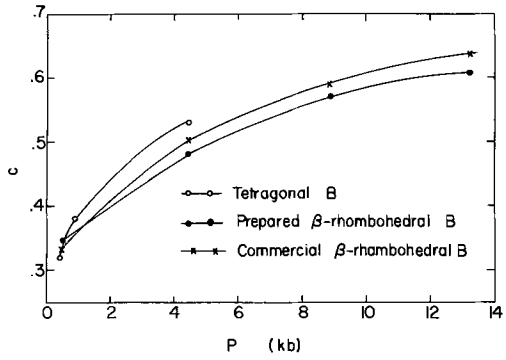

Fig. 5. Ratio of electron mobility to hole mobility, c, as a function of pressure for boron samples at 275°C.

cause other than the covalent lattice (*e.g.*, an ionic impurity), the 2 in Eq. [6] would be replaced by some other small integer. However such an effect would hardly affect c since $E_g/2kT \geqq 10$.

From Fig. 5 one observes that the mobility ratio and its variance with pressure are the same for all the boron samples independent of crystal structure or purity. From Fig. 4 we see that impurities significantly affected the energy gap. This would indicate that the mobility (the scattering mechanism) is due to the lattice vibrations and not to the impurities which produce extrinsic carriers. Differences in E_g with structure increased with pressure, being comparatively small at 13 kb, the highest pressure at which thermoelectric power measurements were made.

Extrinsic Region

In the low-temperature region (25°C) of the present study the intrinsic conductivities extrapolate to resistance values more than twenty times larger than the measured resistance (except for prepared β-rhombohedral boron at 58 kb, for which $R_{\text{intrin}} > 6R_{\text{meas}}$); the activation energies are also only a small fraction of those for the intrinsic region. Thus the room temperature electrical properties would seem to be dominated by extrinsic carriers from one or several sources, the latter being likely as evidenced by the changing slopes of the log R *vs.* $1/T$ plots. Because these slopes are changing with T it is not possible to isolate activation energies for a given process. However the following observations can be made for the extrinsic region: (*a*) the resistance decreases with increasing temperature, (*b*) as the temperature is decreased the thermoelectric power becomes less positive, extrapolating to negative values at temperatures a little below room temperature, (c) the resistance decreases with increasing pressure, and (*d*) increasing pressure decreases the thermoelectric power when the latter is positive, the effect of pressure diminishing as Q and T decrease.

The low-temperature thermoelectric power results indicate that donor and acceptor levels are both operative below and near room temperature with the p-type conduction predominating as T increases. Such an effect has been observed previously at atmospheric pressure (16, 17). The thermoelectric power under these conditions is given by

$$Q = \frac{Q_h n_h \mu_h + Q_e n_e \mu_e}{n_h \mu_h + n_e \mu_e} \qquad [8]$$

and accordingly $Q \lesseqgtr 0$ for $Q_h n_h \mu_h \lesseqgtr Q_e n_e \mu_e$. As the temperature is increased from some value less than 275°K, excitation of electrons from the valence band to an acceptor level causes an increase n_h, and this increase is the dominating factor in causing σ and Q to increase.

The continued increase in Q with T up to 500°K

may be explained as the result of a further increase in n_h with respect to n_e, with Q_h being greater than the maximum Q value recorded in Fig. 3. In this case holes and electrons both insignificantly contribute to Q at all temperatures studied, Q again decreasing at $T > 600°K$ because of n_e (cf. Eq. [8]) catching up with n_h as intrinsic conduction occurs. Any decrease in ionization energy for carrier production, caused by increasing pressure, would result in large increases in the numbers of carriers. Thus P would affect both Q and σ through n_+ and n_-.

An alternative interpretation for the data can be given which involves the production of so many positive carriers, with increasing temperature, that above about 350°K $Q_h\mu_h n_h >> Q_e\mu_e n_e$. Based on this model Eq. [8] reduces to

$$eQT \simeq eQ_hT = E_F - E_v + AkT \qquad [9]$$

Here E_F is the Fermi energy and A is a constant which depends on the transfer of kinetic energy by the carriers from the hot to the cold junction. For reasonable values of A (4 or less), $d(eQT)/dT$ as obtained from the present data is an order of magnitude larger than $d(AkT)/dT$, so the Fermi level increases with respect to the valence band as T increases. This model, with the present data, leads to the conclusion that n_h varies slowly with temperature while μ_h increases by about the same factor as σ. It then follows from Eq. [9] and Fig. 3 that pressure causes a decrease in $E_F - E_v$, and hence increases the number of carriers, n_h, and also the conductivity. The latter is given by

$$\sigma = |e|n_h\mu_h = |e|\mu_h 2\left(\frac{2\pi m^* kT}{h^2}\right)^{3/2} \exp(-(E_F - E_v)/kT)$$
$$= |e|\mu_h N \exp(-(E_a - E_v)/kT) \qquad [10]$$

Here E_F is the Fermi energy, E_a is the energy of the acceptor level, and N is a function of the effective mass of the carriers and the impurity density-of-states. The major effect of pressure on σ, from the above model, is to decrease the ionization energy, $E_a - E_v$. The effect of pressure in decreasing the ionization energy for carrier production has previously been observed for silicon (33) and thallous halides (34).

If the second model is correct, boron may then be thought of as a hopping semiconductor similar to NiO doped with lithium (35). In the latter case the increase of conductivity with temperature is due to an increase in mobility. Uno *et al.* (13) have interpreted their thermoelectric power data on various impure boron samples in terms of a single trapping level, and deduced that μ increased exponentially with temperature while n was about constant. On the other hand, Hagenlocher (20) found μ to be proportional to $T^{-7/4}$, which is more nearly classical semiconductor behavior; μ decreases with temperature due to lattice scattering. Such discrepancies are difficult to reconcile since impurities and their effects on the electrical properties are very difficult to control in boron, and hence problems such as opposite, compensating carriers are not under control. Thus the energy level scheme for the present extrinsic samples could be much more complicated than the discussion depicts, with an interplay of several donors and acceptors (and perhaps more than one charge-carrying band) yielding the observed results.

Acknowledgment

The authors acknowledge the financial support of this work through the U. S. Army Research Office-Durham. They also thank Messrs. W. B. Jensen and M. Bingham for assistance with the x-ray computer programming and analysis. To Professor F. W. Cagle is extended appreciation for the use of and suggestions concerning the Guinier focusing camera.

Manuscript received March 6, 1967; revised manuscript received May 5, 1967.

Any discussion of this paper will appear in a Discussion Section to be published in the June 1968 JOURNAL.

REFERENCES

1. W. Paul and D. M. Warschauer, "Solids Under Pressure," McGraw-Hill Book Co., Inc., New York (1963).
2. W. Paul, "High Pressure Physics and Chemistry," Vol. 1, R. S. Bradley, Editor, Academic Press, New York (1963).
3. A. S. Balchan and H. G. Drickamer, *J. Chem. Phys.*, **34**, 1948 (1961); B. M. Riggleman and H. G. Drickamer, *ibid.*, **37**, 446 (1962).
4. S. D. Hamann, *Austral. J. Chem.*, **11**, 391 (1958).
5. L. F. Vereshchagin, A. A. Semerchan, S. V. Popova, and N. N. Kuzin, *Doklady Akad. Nauk SSSR*, **145**, 757 (1962).
6. A. E. Newkirk in "Boron, Metallo-Boron and Boranes," R. M. Adams, Editor, Interscience Publishers, New York (1964).
7. A. W. Laubengayer, D. T. Hurd, A. E. Newkirk, and J. L. Hoard, *J. Am. Chem. Soc.*, **65**, 1924 (1943).
8. O. H. Bezirjian, Ph.D. thesis, University of Utah, 1967.
9. A. Guinier, "Théorie et Téchnique de la Radiocrystallographie," Dunod, Paris (1956).
10. L. V. Azaroff and M. J. Buerger, "The Powder Method in X-Ray Crystallography," McGraw-Hill Book Co., Inc., New York (1958).
11. C. P. Talley, S. LaPlaca, and B. Post, *Acta Cryst.*, **13**, 271 (1960).
12. R. E. Hughes, C. H. L. Kennard, D. B. Sullengen, H. A. Weakliem, D. E. Sands, and J. L. Hoard, *J. Am. Chem. Soc.*, **85**, 361 (1963).
13. G. K. Gaule, J. T. Breslin, J. R. Pastore, and R. A. Shuttleworth in "Boron Synthesis, Structure, and Properties," J. A. Kohn, W. F. Nye, and G. K. Gaulé, Editors, p. 159, Plenum Press, New York (1960).
14. E. S. Greiner and J. A. Gutowski, *J. Appl. Phys.*, **28**, 1364 (1957).
15. W. C. Shaw, D. E. Hudson, and G. C. Danielson, U.S.A.E.C Report ISC 380, August, 1953
16. W. C. Shaw, D. E. Husdon, and G. C. Danielson, *Phys. Rev.*, **107**, 419 (1957).
17. Texaco Experiment, Inc., I. R. King, G. R. Taylor, Jr., F. E. Wawner, Jr. and C. P. Talley, Technical Documentary Report No. ASD-TDR-62-427, Jan., 1963, Contract AF 33(616)-7884.
18. R. Uno, T. Irie, S. Yoshida, and K. Shinohara, *J. Sci. Res. Inst. (Tokyo)*, **47**, 216 (1953).
19. A. J. Dekker, "Solid State Physics," Chap. 12, Prentice-Hall, Inc., Englewood Cliffs, N. J. (1963).
20. A. K. Hagenlocher in "Boron, Synthesis, Structure, and Properties," p. 128, J. A. Kohn, W. F. Nye, and G. K. Gaulé, Editors, Plenum Press, New York (1960).
21. R. Uno, *J. Phys. Soc. Japan*, **13**, 667 (1958).
22. J. Lagrenaudie, *J. Phys. Radium*, **13**, 554 (1952); **14**, 14 (1953).
23. J. Jaumann and J. Schnell, *Z. Naturforsch.*, **20a**, 1639 (1965).
24. W. Neft and K. Seiler, "Boron," Vol. 2, "Preparation, Properties and Applications," p. 143, G. K. Gaulé, Editor, Plenum Press (1965).
25. E. I. Adirovich and L. M. Goldshtein, *Soviet Phys. Solid State*, **8**, 1968 (1967).
26. W. Dietz and H. Herrmann in "Boron," Vol. 2, "Preparation, Properties and Applications," p. 107, G. K. Gaulé, Editor, Plenum Press (1965).
27. W. R. Eubank, L. E. Pruit, and H. Thurnauer in "Boron, Synthesis, Structure, and Properties," *op. cit.*, p. 116.
28. C. B. Hood and M. O. Thurston, *This Journal*, **109**, 66 (1962).
29. R. A. Brungs and V. P. Jacobsmeyer, *J. Phys. Chem. Solids*, **25**, 701 (1964).
30. T. Niemyski and W. Zawadzki, *Phys. Letters*, **2**, 30 (1962).
31. F. Seitz, "Modern Theory of Solids," Chap. 4, McGraw-Hill Book Co., Inc., New York (1940).
32. V. A. Johnson and K. Lark-Horovitz, *Phys. Rev.*, **92**, 226 (1953).
33. M. I. Nathan and W. Paul, *ibid.*, **128**, 38 (1962).
34. G. A. Samara and H. G. Drickamer, *J. Chem. Phys.*, **37**, 408 (1962).
35. F. J. Morin, *Phys. Rev.*, **93**, 1199 (1954).

Overpotential-Time Variation for Galvanostatic Charging with Potential Dependent Capacitance

Leonard Nanis
School of Chemical Engineering, University of Pennsylvania, Philadelphia, Pennsylvania
and Philippe Javet
Institute for Direct Energy Conversion, University of Pennsylvania, Philadelphia, Pennsylvania

ABSTRACT

The nonlinear differential equation for the time variation of overpotential during galvanostatic charging is solved by introducing a close approximation for the second term of the rate equation. The results obtained are in close agreement with known solutions, covering all values of transfer coefficient, and are simple in form. Further, potential dependent capacitance is readily treated and is shown to have a considerable effect on the overpotential transient.

A simple and useful relation describing the time variation of overpotential, η, following the switching on of a constant current density, J_T, has been determined. In the absence of mass transport effects (activation overpotential only), two separate reactions take place simultaneously at the electrode-electrolyte interface:

1. the normal Faradaic relation, involving current density J_F;

2. charging of the double layer capacity, C, using current density J_C.

It is well-known that (for a cathodic reaction)

$$\frac{J_F}{J_o} = \exp\left(-\frac{\alpha ZF\eta}{RT}\right) - \exp\left(+\frac{(1-\alpha)ZF\eta}{RT}\right) \quad [1]$$

$$J_C = C\frac{d\eta}{dt} \quad [2]$$

$$J_T = J_F + J_C \quad [3]$$

The differential equation obtained from the above relations is nonlinear, because of the terms arising in Eq. [1], and cannot be integrated. In the most general case, C is a function of η, and the relation between t and η is thus further complicated. Two types of simplification can be made for the solution of Eq. [1], [2], [3].

1. The capacitance may be considered to be independent of potential. This has been done by some authors (1-3) who can ultimately obtain the relation between time and overpotential, but only for particular values of the transfer coefficient, α, *i.e.*, $\alpha = 0$; 0.5; 1.

2. The Faradaic component of the current, J_F, may be approximated, *i.e.*, Eq. [1] is modified by (*a*) linearization of the exponentials by series expansion, which gives the well-known result

$$\frac{\eta}{\eta_\infty} = 1 - \exp\left(\frac{-ZFJ_o}{RTC}t\right) \quad [4]$$

limited, however, to small values of η_∞. (*b*) Tafel approximation obtained at high overpotentials when the second exponential term of Eq. [1] is negligible in comparison with the first term. The Tafel approximation has been used for the decay transient by Frumkin (4), but the application of the Tafel relation for the charging transient has never been used, owing to the fact that this approximation does not pass through the origin of $\eta - J$ coordinates, which leads to very important errors at small times.

Modification of Rate Equation

The present approach consists of modifying the rate expression (Eq. [1]) to a form which is reasonable as an approximation of the $\eta - J$ relation and which is simple enough to be integrated. The procedure consists of setting the second exponential term of Eq. [1] equal to unity. The effect of this step is best seen in Fig. 1 as a vertical shift of the Tafel approximation so as to begin at the $\eta - J$ origin as does the full rate equation (Eq. [1]). In a graphical sense, the new approximation appears to be only a fair representation of Eq. [1]; however, fitting at the origin of $\eta - J$ proves to be advantageous for transient $\eta - t$ computation. Using the modified Eq. [1] together with Eq. [2] and [3], there is obtained

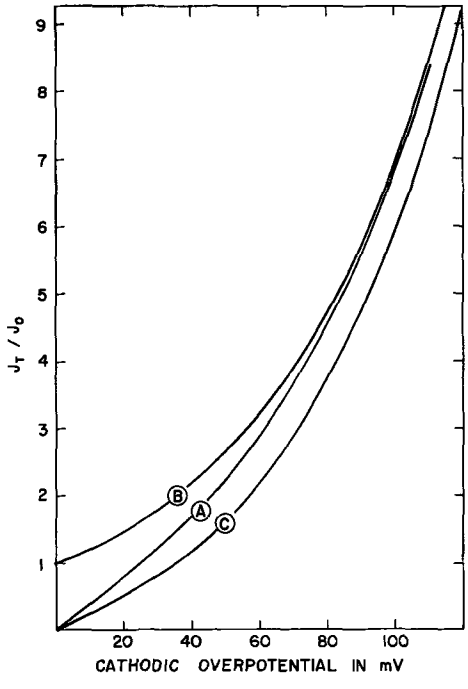

Fig. 1. Comparison of exact and approximate $\eta - J$ relations

A **Full rate equation:**

$$J_T/J_o = \exp\left[-\frac{\alpha ZF}{RT}\eta\right] - \exp\left[+\frac{(1-\alpha)ZF}{RT}\eta\right]$$

B **Tafel approximation:** $J_T/J_o = \exp\left[-\frac{\alpha ZF}{RT}\eta\right]$

C **Tafel modified to go through the origin ($\eta = 0$, $J = 0$):**

$$J_T/J_o = \exp\left[-\frac{\alpha ZF}{RT}\eta\right] - 1$$

For all curves: $\alpha = 0.5$; $Z = 1$; $T = 300°K$.

$$J_T = J_o \left\{ \exp\left(\frac{-\alpha Z\mathbf{F}\eta}{RT}\right) - 1 \right\} + C\frac{d\eta}{dt} \quad [5]$$

Equation [5] may readily be integrated to yield a relation between time and overpotential (for constant C) as

$$t = -\frac{C}{J_o + J_T}\eta - \frac{RTC}{\alpha Z\mathbf{F}(J_o + J_T)} \ln\left[1 + \frac{J_o}{J_T}\left(1 - \exp\left(\frac{-\alpha Z\mathbf{F}\eta}{RT}\right)\right)\right] \quad [6]$$

The form of Eq. [6] for small time, *i.e.*, η small, is such that the logarithmic term becomes negligible; the remaining first term is identical with the small time result for Eq. [4] if $J_T >> J_o$. It is to be expected that Eq. [6] will be an increasingly accurate description of the $\eta - t$ transient as the approximated region of low overpotential is more rapidly traversed, *i.e.*, when the total current density is very much greater than the exchange current density, $J_T >> J_o$.

It is useful to compare previously obtained analytic results with the present solution given in Eq. [6]. For the special case of $\alpha = 1.0$, Karasyk (3) obtained the expression

$$\eta = \frac{RT}{Z\mathbf{F}} \ln\left[\frac{\exp\left[\frac{-Z\mathbf{F}(J_o + J_T)t}{RTC}\right] + \frac{J_o}{J_T}}{1 + J_o/J_T}\right] \quad [7]$$

In the present study, the form of the approximation used in Eq. [5] may also be considered as a special case of $\alpha = 1$. It may be shown by rearrangement of Eq. [6] that the exact form of the special result of Karasyk (3) (Eq. [7]) for $\alpha = 1$ is obtained.

A graphical check of Eq. [6] has been made in Fig. 2 using an analytic solution due to Rojter *et al.* (1) and also Karasyk (3) for the special case of $\alpha = 0.5$. This special result is valid if $J_o/J_T \leq 0.15$ and is

$$\eta = \frac{RT}{\alpha Z\mathbf{F}} \ln\left[\frac{J_o}{J_T} + \left(1 - \frac{J_o}{J_T}\right) \exp\left[\frac{-\alpha Z\mathbf{F}J_T t}{RTC}\right]\right] \quad [8]$$

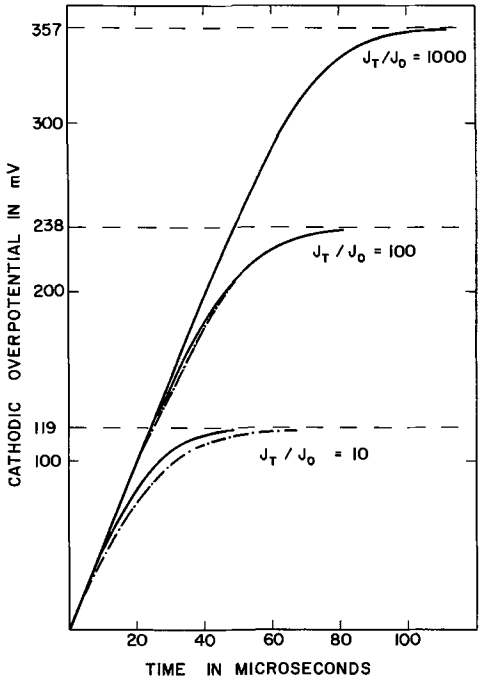

Fig. 2. Comparison of present integrated solution (Eq. [6], full line) with the analytic result of Karasyk (Eq. [8], dotted line). For both curves: $\alpha = 0.5$; $Z = 1$; $C = 20\ \mu\text{F cm}^{-2}$; $T = 300°\text{K}$; $J_T = 10^{-1}$ amp cm^{-2}.

As shown in Fig. 2, Eq. [8] is closely matched by Eq. [6] with improving accuracy as the steady state overpotential increases. As pointed out above, exact agreement between Eq. [6] and completely correct analytic results exists at $\alpha = 1.0$ and graphical correlations indicate excellent agreement for $\alpha = 0.5$, even though Eq. [6] is based on an assumption equivalent to setting $\alpha = 1$. Mattsen (2), using analog computer solutions to Eq. [1], [2], [3] has concluded that the $\eta - t$ transient does not depend strongly on the value of α. Thus, Eq. [6] and the well-known Eq. [4] can be used to bracket all practical cases of activation overpotential transient since, although the accuracy of Eq. [6] as α approaches zero may become poor, most real cases of electrode reactions are associated with a transfer coefficient close to 0.5.

Potential Dependent Capacity

The interesting feature of Eq. [5] is that it can be integrated even in the most general case of an interfacial capacitance which is itself a function of potential. For practicality, a polynomial series representation of $C = f(\eta)$ is suitable. For a simple linear dependence of capacitance with overpotential given as

$$C(\eta) = C_o + 2C_1\eta \quad [9]$$

equation [5] may be integrated using a series summation based on the binomial expansion for the denominator of the overpotential integral. The result is

$$t = \frac{1}{(J_T + J_o)}\left[-C_o\eta + C_1\eta^2 + \sum_{m=1}^{\infty}(-1)^m C_o \frac{I^m}{mb}\exp(-mb\eta) + \sum_{m=1}^{\infty}(-1)^m \frac{2C_1 I^m}{m^2b^2}(-mb\eta - 1)\exp(-mb\eta) - \sum_{m=1}^{\infty}(-1)^m I^m\left(\frac{C_o}{mb} - \frac{2C_1}{m^2b^2}\right)\right] \quad [10]$$

where $I = \dfrac{J_o}{J_o + J_T}$ and $b = \dfrac{\alpha Z\mathbf{F}}{RT}$

and the boundary condition $\eta = 0$, $t = 0$ has been used. The form of Eq. [10] is apparently complicated, but the series terms are rapidly convergent because of the alternating sign. The first two terms in the brackets of Eq. [10] are already the $m = 0$ terms of the summation. Thus, for polynomial representation of $C = f(\eta)$ involving higher order terms than shown in Eq. [9], it should be expected that the corresponding zero order summation terms which will arise, analogous with Eq. [10], will consist of the polynomial coefficients of the equivalent of Eq. [9] in association with the next higher order of overpotential.

Application

Two hypothetical cases of capacitance variation with potential have been treated:

Case 1: Capacitance increasing with cathodic overpotential $C(\eta) = 4.0 - 53.4\eta$, $\mu\text{F cm}^{-2}$
Case 2: Capacitance decreasing with cathodic overpotential $C(\eta) = 20.0 + 53.4\eta$, $\mu\text{F cm}^{-2}$
Case 3: $C = 12\ \mu\text{F cm}^{-2}$

For the numerical coefficients chosen for Case 1 and 2, a typical set of conditions has been chosen in which the steady-state overpotential is attained within the physically meaningful domain indicated by the capacitance-overpotential functions. In particular, substitution of the appropriate $C = f(\eta)$ coefficients in Eq. [10] for $J_o = 10^{-3}$ amp cm^{-2}, $J_T = 0.1$ amp cm^{-2}, $\alpha = 0.5$, $Z = 1$, $T = 300°\text{K}$, leads to a steady-state overpotential of 238 mv in all cases, but the

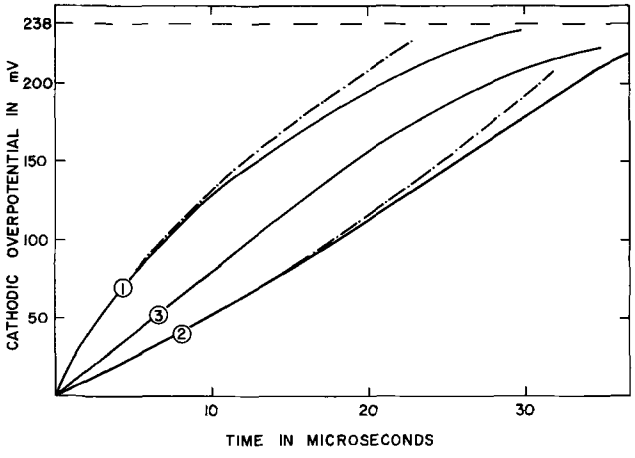

Fig. 3. Galvanostatic transient as described by Eq. [10] for three different capacitance-overpotential relations:

1. $C(\eta) = 4.0 - 53.4\ \eta$, $\mu F\ cm^{-2}$
2. $C(\eta) = 20.0 + 53.4\ \eta$, $\mu F\ cm^{-2}$
3. $C = \text{const.} = 12\ \mu F\ cm^{-2}$

In cases 1 and 2, the dotted lines represent the contribution of the zero order terms only from Eq. [10].
For all curves: $\alpha = 0.5$; $Z = 1$; $T = 300°K$.

$$J_T = 0.1\ \text{amp cm}^{-2};\ J_o = 10^{-3}\ \text{amp cm}^{-2}.$$

transients are considerably different. The results for the three cases are shown in Fig. 3 both for the application of Eq. [10] in its entirety and also for the zero-order terms of Eq. [10]. It may be seen that zero-order terms alone are a good approximation allowing a rapid estimation of the transient. Practically, in the case chosen, the time error made by using only the zero-order terms amounts to 10% only for potentials greater than 75% of the steady-state potential in Case 1 and greater than 93% of the steady-state potential in Case 2. Thus, in most cases, the summation terms in Eq. [10] may be omitted since they are associated with the final convergence to a steady value and the initial behavior of the $t - \eta$ transient may be readily estimated from $C - \eta$ curves of the type shown in the present examples. Furthermore, it is evident in Fig. 3 that the curves for Cases 1 and 2 have a nonnegligible curvature in the vicinity of $t = 0$ (due to the occurrence of quadratic overpotential in the zero-order summation terms). It is clear that caution should be exercised in the procedure of extrapolating $\eta - t$ transient curves to obtain the capacitance from the slope at zero time. In particular, good resolution of potential and time is needed near to the beginning of the transient. In principle, it should be possible to analyze overpotential transients to determine the nature of the capacitance-potential variation. The present results may readily be shown to conform, at least at small times, with the general criterion for nonconstant capacitive systems devised by Budewski and Stoinoff (5).

Acknowledgment

The financial support of NASA (Grant NSG-316) is gratefully acknowledged.

Manuscript received April 18, 1967. This paper was presented at the Dallas Meeting, May 7-12, 1967.

Any discussion of this paper will appear in a Discussion Section to be published in the June 1968 JOURNAL.

REFERENCES

1. W. A. Rojter, W. A. Juza, and E. S. Polujan, *Acta Physicochim. URSS*, **10**, 389 (1939).
2. J. M. Matsen, *This Journal*, **110**, 222 (1963).
3. L. Karasyk, R. W. Law, and H. B. Linford, *ibid.*, **111**, 237 (1964).
4. A. Frumkin, *Acta Physicochim. URSS*, **18**, 23 (1943).
5. E. Budewski and Z. Stoinoff, *Electrochim. Acta*, **12**, 101 (1967).

LIST OF SYMBOLS

J_F	Faradaic current density, amp cm^{-2}
J_o	exchange current density, amp cm^{-2}
J_T	total current density, amp cm^{-2}
J_C	capacitive current density, amp cm^{-2}
C	double layer capacity per unit area, $\mu F\ cm^{-2}$
η	overpotential (sign according to IUPAC recommendations), mv
Z	number of electrons involved in the electrochemical reaction, eqt · mol^{-1}
F	Faraday constant, 96,500, amp · sec · eqt^{-1}
R	gas constant, 8.314, Joule $°K^{-1}$ · mol^{-1}
T	absolute temperature, °K
t	time, sec
b	$\alpha \frac{ZF}{RT}$, $\frac{\text{amp} \cdot \text{sec}}{\text{erg}}$
α	transfer coefficient
I	$J_o/(J_o + J_T)$
m	summation subscript

Impurity Effects in High Current Density Cl_2 Electrodes

D. A. J. Swinkels

Electrochemical Laboratory, General Motors Corporation, Indianapolis, Indiana

ABSTRACT

The development of high current density porous electrodes (>1 amp/cm^2) places increasing demands on the purity of the gas fed to the electrode. The concentration polarization associated with inert impurities in the electroactive gas is treated for the Cl_2 electrode in fused LiCl. The Cl_2 electrode consists of porous carbon or graphite which is not wetted by fused LiCl.

The presence of electro-inactive impurities in the gas feed to a porous gas electrode can result in the rapid build-up of considerable polarization due to the accumulation of these inactive impurities in the pores (1). This is particularly true for high current density systems such as the Cl_2 electrode in fused alkali halides. Commercial grades of Cl_2 typically contain 0.5% of inert impurities such as N_2 and CO_2. When the rate at which Cl_2 is supplied to the electrode is exactly sufficient to maintain the electrode reaction (*i.e.*, the electrode is dead ended) these inert impurities rapidly accumulate at the electrode-electrolyte interface. The impurities can leave the interface by dissolution in the electrolyte and diffusion into the bulk or by back diffusion against the flowing Cl_2 stream.

The first of these is negligible because of the low solubility and low diffusion coefficients involved. If we assume that the impurity has the same solubility and diffusion coefficient as Cl_2 (2) then the maximum rate of diffusion through the electrolyte at 1 atm (j) is typically

$$j = -D\frac{\Delta C}{\Delta x} \quad [1]$$

$$= -4 \times 10^{-5} \times \frac{0-10^{-6}}{1} N_i = 4 \times 10^{-11} N_i \quad [2]$$

where N_i = mole fraction of impurities at the interface.

This assumes that the impurity concentration is zero at a distance of 1 cm from the Cl_2 electrode (due to reaction with Li for example) and has a solubility of 10^{-6} moles/cm^3 at 1 atm.

At current density of 3 amp/cm^2 the flux of Cl_2 is $i/2\mathbf{F} \approx 1.5 \times 10^{-5}$ moles/sec. Hence, the maximum concentration of impurities in the Cl_2 feed which can be removed by this process is $4 \times 10^{-11} N_i/1.5 \times 10^{-5} = 2.67 \times 10^{-6} N_i$. Since N_i must be less than unity the impurity level must be less than 2.67 ppm.

However, as current is drawn from a Li-Cl_2 cell more electrolyte is generated at the electrodes which can dissolve $10^{-6} N_i P_T$ moles of impurity per cubic centimeter of electrolyte, where P_T is the total pressure. Since the transport number of Li^+ in LiCl is 0.75 (3) then 0.75 of the new electrolyte is generated at the Cl_2 electrode. One mole of Cl_2 will then produce 1.5 moles of LiCl at the Cl_2 electrode which can dissolve $43 \times 10^{-6} N_i P_T$ moles of impurity. For typical values of $P_T = 5$ atm and $N_i = 0.05$ an impurity level of ≈ 11 ppm can be tolerated.

Much larger quantities of impurities can be removed from the electrode by flowing excess Cl_2 either through the porous electrode or behind the porous electrode. A study of the latter type of electrode (a "flow-by" electrode) is reported here.

Theory

Back diffusion of impurities in the pores against the flowing Cl_2 gas can be treated as a linear diffusion problem and is described by Eq. [3].

$$\frac{\partial C}{\partial t} = D\frac{\partial^2 C}{\partial x^2} - \frac{\partial (Cv)}{\partial x} \quad [3]$$

where C = concentration of impurity gas, v = velocity of gas flow, and x = linear dimension in the direction of net flow.

The transient problem described by Eq. [3] has recently been treated (4). Since under most conditions steady state is reached in a few seconds all experiments were done under steady-state conditions, *i.e.*,

$$\frac{\partial C}{\partial t} = 0$$

Equation [3] after integrating once with respect to x becomes

$$D\frac{dC}{dx} - Cv = j \quad [4]$$

where j is the net flux of impurity through the pore under steady-state conditions.

We now assume that the impurity does not react or dissolve at the gas-liquid interface in which case $j = 0$.

Hence

$$D\frac{dC}{dx} - Cv = 0 \quad [5]$$

The solution of Eq. [5] is

$$\ln C(x) = \frac{vx}{D} + \text{constant} \quad [6]$$

If at $x = 0$ the impurity content is kept at a constant value C_o by flowing gas past the electrode Eq. [6] becomes

$$C(x) = C_o \exp\frac{vx}{D} \quad [7]$$

Since fused LiCl does not wet porous graphite, the total length (L) of the diffusion path is equal to the thickness (t) of the porous electrode times the tortuosity (τ) of the pores within the porous material.

The concentration of impurity at the gas-liquid interface is then

$$C_s = C_o \exp\frac{vL}{D} \quad [8]$$

The velocity of gas flow within the pores in the x direction is given by

$$v = \frac{iRT}{n\mathbf{F}P_T\phi} \quad [9]$$

where i = current density per geometrical cm^2, ϕ = porosity, and P_T = total pressure.

Hence

$$C_s(i) = C_o \exp\left(\frac{iRT\tau t}{n\mathbf{F}P_T\phi D}\right) \quad [10]$$

or in terms of the impurity pressure

$$P_s(i) = P_o \exp\left(\frac{iRT\tau t}{n\mathbf{F}P_T\phi D}\right) \quad [11]$$

where P_o = impurity pressure in the incoming gas, and $P_s(i)$ = impurity pressure in the gas at the gas-liquid interface at current density i amp/cm^2. The concentration polarization of such an electrode during discharge compared to the potential of the same electrode at open circuit consists of two parts: the polarization in the gas-phase (η_g) and the polarization in the electrolyte (η_e)

$$\eta_g(i) = \frac{RT}{n\mathbf{F}} \ln \frac{P_{Cl_2}(\text{Bulk})}{P_{Cl_2}(\text{Electrolyte interface})} = \frac{RT}{n\mathbf{F}} \ln \frac{P_T - P_o}{P_T - P_s(i)} \quad [12]$$

$$\eta_e(i) = \frac{RT}{n\mathbf{F}} \ln \frac{P_{Cl_2}(\text{Electrolyte interface})}{P_{Cl_2}(\text{Electrode surface})} = \frac{RT}{n\mathbf{F}} \ln \frac{i_L}{i_L - i} \quad [13]$$

where i_L = limiting current density for the given Cl_2 pressure at the gas-liquid interface

$$i_L = K[P_T - P_s(i)] \quad [14]$$

The maximum current which can be drawn for a given value of P_T and P_o is given by

$$i_L = K[P_T - P_s(i_L)] \quad [15]$$

In Eq. [14] and [15] K is a constant for a given porous graphite equal to the limiting current density which could be obtained from the given material with absolutely pure Cl_2 at 1 atm.

It is assumed here that the pressure drop across the electrode is negligible under the test conditions. The total concentration polarization at a given current density is then the sum of $\eta_g(i) + \eta_e(i) = \eta_t(i)$. It should be noted that this polarization is the difference between the electrode at a current density i compared to that same electrode at open circuit not compared to that same electrode in pure Cl_2. To refer the electrode potential back to a pure Cl_2 electrode Eq. [12] should be

$$\eta_g(i) = \frac{RT}{n\mathbf{F}} \ln \frac{P_T}{P_T - P_s(i)} \quad [12A]$$

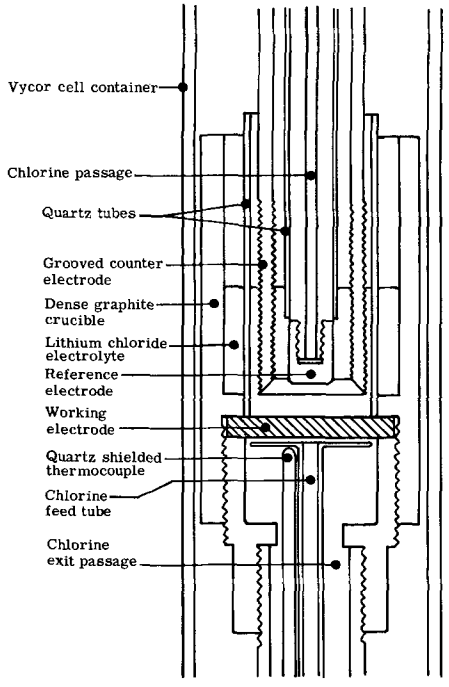

Fig. 1. Cell used in impurity effect studies

All polarizations used in this paper are referred to the OCV with impure Cl_2 gas.

Experimental

The cell and accessories.—A schematic diagram of the cell used in these studies is shown in Fig. 1. Lithium chloride electrolyte is contained in a graphite crucible, the bottom of which consists of a piece of porous graphite (Pure Carbon Company Grade FC-11). This porous graphite was the working electrode to which Cl_2 or mixtures of Cl_2 and Ar could be fed. The quartz feed tube below the electrode was flanged in order to insure uniform chlorine flow past the entire inner electrode surface. A thermocouple placed in the gas stream was used to control the temperature of the system. A quartz insert inside the graphite crucible exactly defined the useful area of the working electrode.

The reference and counter electrodes were mounted concentrically. The reference electrode electrically isolated by a quartz tube was slipped inside a hollow counter electrode which was grooved to give maximum surface area.

To prevent the development of a pressure difference between the inside and the outside of the counter electrode vertical slots were cut to above the electrolyte level. The entire assembly was placed inside a Vycor tube and was heated by means of clamshell heaters outside the Vycor container. The reference electrode was fed with commercial chlorine which was passed through a sulfuric acid drying bubbler. The chlorine and argon which were fed to the test electrode were also obtained from commercial cylinders. They were passed through concentrated sulfuric acid drying bubblers and introduced into a mixing chamber which consisted of a 500 ml flask filled with ceramic beads. The gases effectively mixed in this manner then flowed into the cell.

Gas analysis.—After flowing past the electrode, the gas mixture passed through an exit tube which was adapted for taking syringe samples for analysis by means of gas chromatography. A Barber-Coleman, Series 5000 gas chromatography was used to determine the amount of argon in the sample. A soda-lime absorption column was used to remove the Cl_2 from the sample so that only the impurity entered the detector. The impurity level of the gas sample was determined by comparing the amount of argon detected in a sample of known volume to an equal volume of pure argon.

Procedure.—Cells were assembled in air and heated in an argon or helium atmosphere to 650°C overnight to make sure the graphite parts were clean and dry. LiCl was previously purified by melting under vacuum and bubbling HCl through the melt which was contained in a graphite crucible. The melt was then allowed to solidify and was stored in a He drybox until needed. LiCl was crushed in the drybox and introduced into the cell by momentarily removing the reference electrode and pouring the salt down the counter electrode tube.

After the salt melted the reference electrode was introduced and connected to its Cl_2 supply. A mixture of Ar and Cl_2 was then supplied to the working electrode, and samples of the exit gas were analyzed until a constant composition was reached.

A current sweep was then applied to the working and counter electrodes. Voltage *vs.* current plots were recorded on a Varian F-80 x-y recorder. The current sweep rate was such that the current density changed by about 0.1 amp/cm^2/min. The sweep rate was determined by sweeping in both directions (increasing and decreasing currents) at various rates until the hysteresis in the I-V plot was less than 5%. Several plots at varying degrees of recorder sensitivity were obtained for each impurity level.

Electrode thickness varied from 1/16 to 3/4 in., but all electrodes were cut from a single block of FC-11 to give maximum uniformity of electrodes.

Results and Discussion

Each set of plots, obtained in the manner described above, was used in conjunction with IR measurements obtained from pulse transients to determine the polarization of the electrode under study. A set of curves was obtained for each thickness and impurity level at different recorder sensitivities. Thus, an average value of the polarization at each current density was obtained. Reproducibility of the polarization for a given set of conditions was better than ±10% except at very low polarizations (< 10 mv).

These average polarizations plotted *vs.* current density for various thicknesses and impurity concentrations are shown in Fig. 2 to 6 (solid lines).

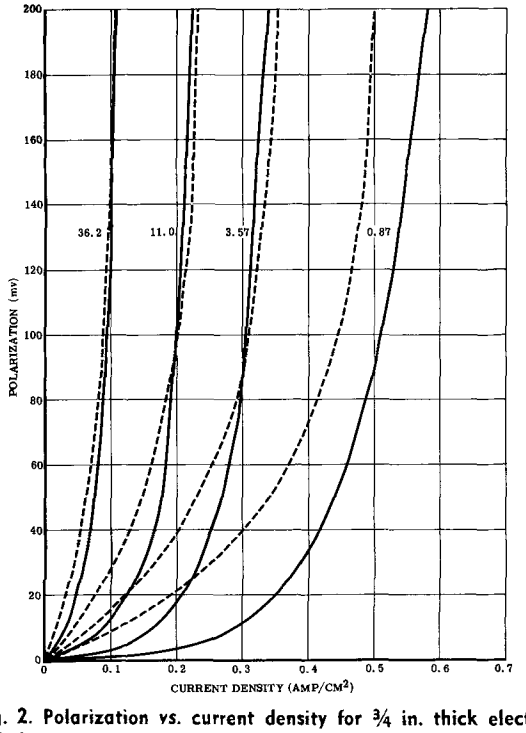

Fig. 2. Polarization *vs.* current density for ¾ in. thick electrode. (Solid line, experimental; dashed line, theoretical; % impurity indicated on curves.)

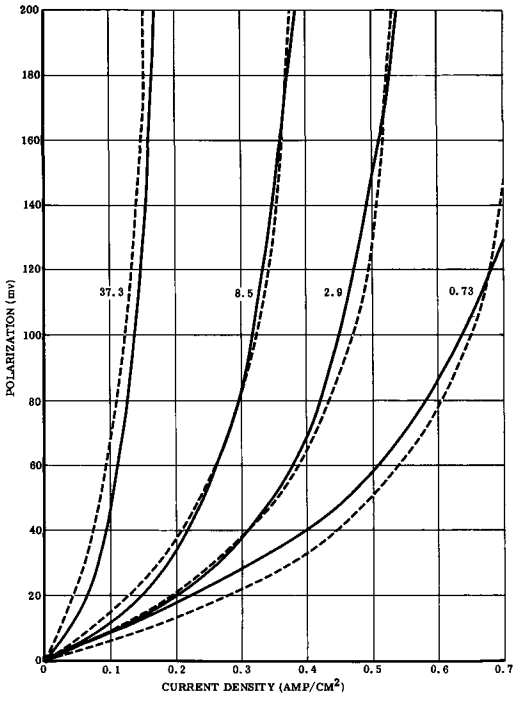

Fig. 3. Polarization *vs.* current density for ½ in. thick electrode. (Solid line, experimental; dashed line, theoretical; % impurity indicated on curves.)

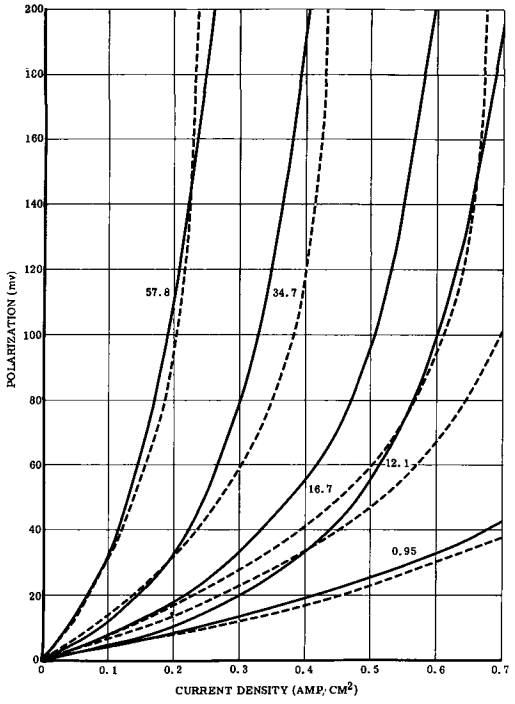

Fig. 5. Polarization *vs.* current density for ⅛ in. thick electrode. (Solid line, experimental; dashed line, theoretical; % impurity indicated on curves.)

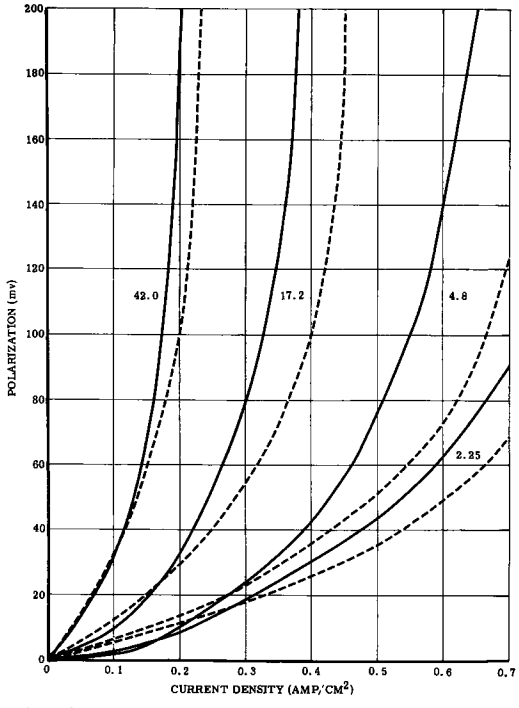

Fig. 4. Polarization *vs.* current density for ¼ in. thick electrode. (Solid line experimental; dashed line, theoretical; % impurity indicated on curves.)

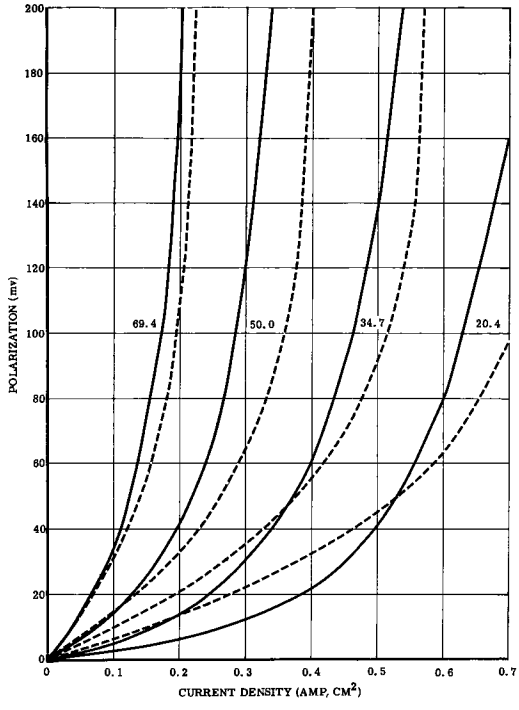

Fig. 6. Polarization *vs.* current density for 1/16 in. thick electrode. (Solid line, experimental; dashed line, theoretical; % impurity indicated on curves.)

Using Eq. [12] and [13] theoretical polarization *vs.* current density curves were calculated for the experimental conditions used. These are shown as dashed lines on Fig. 2 to 6. In these calculations the following constants were used: K = limiting current density which could be obtained on FC-11 with pure Cl_2 at 1 atm; K = 1.2 amp/cm². This value is within the range of values previously reported for FC-11 (1), but is significantly higher than the average value previously obtained. This is due to variations in the FC-11 material as well as the fact that the previous data were for impure Cl_2. The value of K = 1.2 amp/cm² has not been observed experimentally since sufficiently pure Cl_2 was not available. It is rather the present best estimate of what could be obtained.

The diffusion coefficient D for a binary gas mixture may be calculated (5) from

$$D = \frac{0.00185\, T^{3/2} \left[\dfrac{M_1 + M_2}{M_1 M_2} \right]^{1/2}}{P\sigma^2_{12}\Omega_D}$$

where T = temperature (°K); M_1,M_2 = molecular

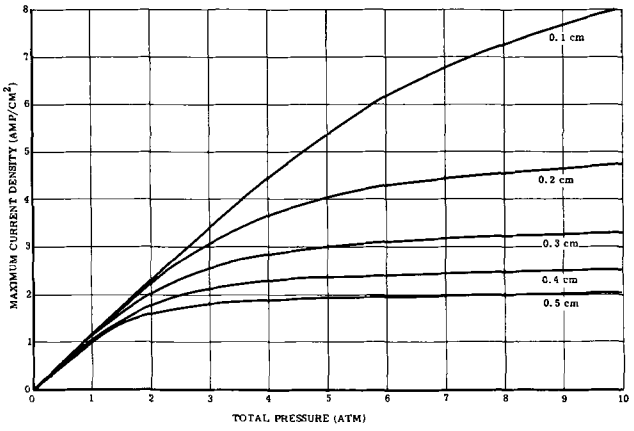

Fig. 7. Maximum current density (i_L) calculated for FC-11 porous graphite as a function of electrode thickness and total pressure at a 1% impurity level.

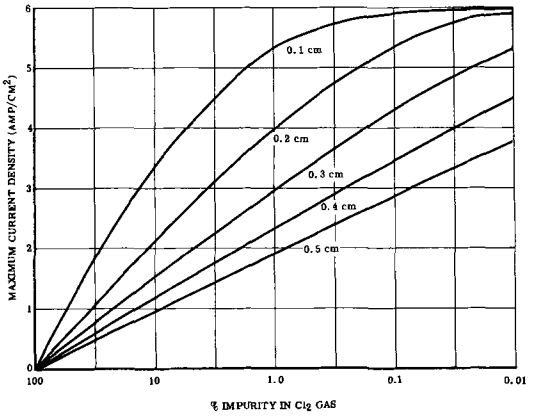

Fig. 8. Maximum current density (i_L) at a total pressure of 5 atm as a function of electrode thickness and impurity level.

weights of the two gases; $\sigma_{12} = \frac{1}{2}(\sigma_1 + \sigma_2)$; $\sigma_1, \sigma_2 =$ collision diameters; and $\Omega_D =$ collision integral available from tables (5).

For argon and chlorine we have: $M_1 = 39.95$, $M_2 = 70.91$, $\sigma_1 = 3.418$Å, $\sigma_2 = 4.115$Å, $\Omega_D = 0.8652$ and hence, $D = 0.842/P$ cm^2 sec^{-1} where P is total pressure in atmospheres.

Another constant used is the porosity $\phi = 0.22$. This value of the porosity only takes into account the larger pores in FC-11, *i.e.*, the pores between particles. It does not include the much smaller pores within the particles since these pores do not contribute appreciably to the flow of gases through the porous body.

The tortuosity τ is calculated as before (1) from

$$\tau = 0.765\ \phi^{-0.65} \qquad [14]$$

It is clear from Fig. 2 to 6 that the agreement between theory and experiment is excellent at the low polarizations shown. One shortcoming of the present treatment is that the theoretical treatment predicts very little increase in current density beyond $\eta = 0.2$v, whereas experimentally a 10-20% increase is observed in going from $\eta = 0.2$v to $\eta = 1.0$v. This will be treated in more detail in a future publication. Figure 7 shows what is predicted for various pressures and electrode thicknesses at a fixed impurity level of 1%. Increasing the total pressure has beneficial effects only for thin electrodes.

Figure 8 shows the maximum current density which can be obtained at 5 atm as a function of impurity level for various thicknesses. For a 0.5 cm thick electrode an impurity level of less than 1000 ppm is necessary to reach a current density of 3 amp/cm^2. The same current density can be reached with a 0.1 cm thick electrode with over 10% impurities in the Cl_2. Thus, electrode thickness has a large effect on the performance of this type of electrode.

Finally it is clear from Eq. [14] that the performance at a given impurity level is related to the porosity and pore size distribution of the graphite since these determine the value of K.

Conclusion

The effect of inert impurities in Cl_2 on the performance of flow-by electrodes has been demonstrated experimentally at 1 atm. The data have been compared with a theoretical treatment of the diffusion processes involved and good agreement was obtained.

The results indicate that at high current densities inert impurities can quickly poison porous electrodes unless some means of removing the inert gas is provided.

Acknowledgments

The author wishes to thank R. N. Seefurth for his assistance in the experimental portion of this work and D. W. Austermiller for supplying the purified LiCl. The author is grateful to General Motors Corporation for permission to publish this work.

Manuscript received Nov. 14, 1966; revised manuscript received April 7, 1967.

Any discussion of this paper will appear in a Discussion Section to be published in the June 1968 JOURNAL.

REFERENCES

1. A. Winsel, *Advanced Energy Conversion*, **3**, 427 (1963).
2. D. A. J. Swinkels, *This Journal*, **113**, 6 (1966).
3. F. R. Duke and A. L. Bowman, *ibid.*, **106**, 622 (1959).
4. R. E. Niggemann, Private communication.
5. R. C. Reid and T. K. Sherwood, "The Properties of Gases and Liquids," p. 268-9, McGraw-Hill Book Co., New York (1958).

Technical Notes

The Double Layer Capacitance in Aqueous Solution

1. Polycrystalline Silver

N. A. Hampson, D. Larkin, and J. R. Morley

Chemistry Department, Loughborough University of Technology, Leicestershire, England

A number of studies of the double layer capacitance of polycrystalline silver in aqueous solution have been reported (1-9). Agreement among observed values is poor, and the values of the parameters which are required by the Stern theory (10) to adjust for changes in electrolyte type and concentration are improbable. There has been considerable disagreement regarding the position of the point of zero change (pzc), values have ranged from 0.51v (NHE) to the more probable value, —0.7v.

There is however general agreement that during the early stages of electrode/electrolyte contact, pronounced capacity changes occur. Wagner (4) observed a rapid reduction of double layer capacity on a freshly formed silver surface in contact with KCl solution. Gerischer and Fischer (11) found that the double layer capacity on silver fell to one half of its initial value in about 5 min at room temperature. Although certain results might be explained by the adsorption of impurities from solution on to the electrode in general impurity levels have been satisfactorily controlled. Moreover initial changes in electrode activity have been reported for other metals, *e.g.*, zinc (12), lead (13), and copper (14), and it is likely that pronounced changes in double layer structure occur on all metals during the early stages of electrode/electrolyte contact.

The purpose of this note is to present recent experimental findings of the double layer capacity of silver in sodium perchlorate solution.

Experimental

The Schering bridge, electrolytic cell, and purification procedure have been described elsewhere (12). For the present experiments the bridge was polarized using a potentiometer symmetrically applied across the bridge in series with a 40 henry choke. Potentials were measured with an electrometer (Wayne-Kerr precision-type M141) against an HgO/Hg reference electrode. The silver electrode was prepared from silver wire (2.553×10^{-2} cm^2 superficial area; 99.9999% supplied by Johnson-Matthey and Company) sheathed with polyethylene (this material was shown to be suitable for electrode construction by adding it to electrolyte in which the capacity of a sitting mercury drop electrode conformed to established data-addition produced no capacity change). Water was twice distilled from deionized stock, all chemicals were of A. R. quality.

The flat X-section of the silver wire formed the working electrode. Electrodes were polished mechanically on roughened glass lubricated with water. Etching (10% HNO_3 or 10% $HClO_4$) was carried out either chemically (30 sec) or electrochemically (10 ma/cm^{-2}). Electrodes were thoroughly washed with water before introduction (wet) into the cell.

Results

Electrometric measurements indicated that the electrode was readily polarizable in the region 0.5v to —1.1v (NHE). Outside this region faradaic current flowed particularly at the more positive potentials.

Some initial change in double layer capacity measurement were observed, but provided that the polarizable region was swept from potentials more negative than 0.4v (NHE) capacity readings quickly stabilized and differential capacity curves reproducible over many hours were taken as indicative of a clean silver surface. For example a mechanically polished and chemically etched electrode in 1M $NaClO_4$ at 23°C held at —0.1v NHE gave a double layer capacity (212 c/sec) after 1 min of 108 μF/cm^{-2} and a stable value of 84 μF/cm^{-2} after 30 min. Changes of double layer capacity were generally more pronounced with electrodes which had only been mechanically polished.

Figure 1 shows differential capacity curves typical

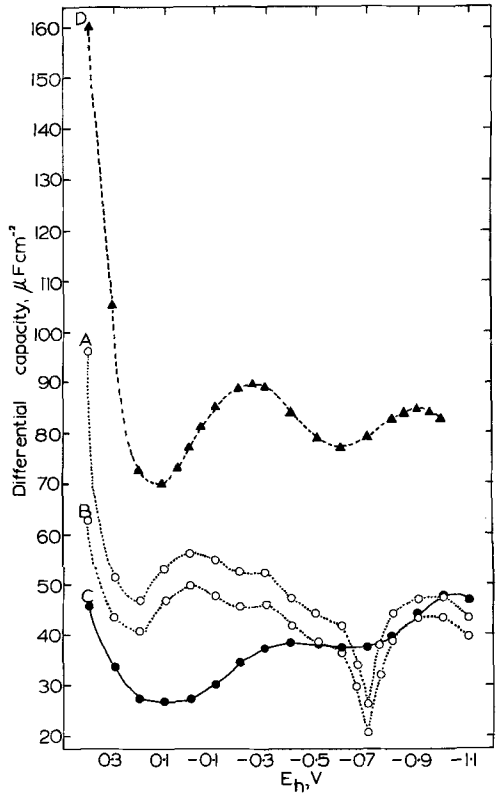

Fig. 1. Differential capacity curves for polycrystalline silver in $NaClO_4$ solutions at 23°C; pH, 6.5-7. Curve A, 0.01M $NaClO_4$; held at —0.3v (NHE) for 1 hr; swept from negative potentials; 212 c/sec. Curve B, 0.01M $NaClO_4$; held at —0.3v (NHE) for 1 hr; swept from negative potentials; 1000 c/sec. Curve C, 0.01M $NaClO_4$; held at —0.4v (NHE) for 1 hr; swept from 0.4v (NHE); 212 c/sec. Curve D, 1M $NaClO_4$; held at —0.3v (NHE) for 1 hr, swept from negative potentials; 212 c/sec.

of a clean surface determined at 212 and 1000 Hz. Generally capacity values were within ± 20% of the values shown. Figure 1 also shows a capacity curve swept from potentials more positive than 0.4v. The sharp minimum at —0.7v, indicating the position of the pzc, is absent (in all cases), and curves were not reproducible; attempts to reestablish differential capacity curves typical of a clean silver surface by cathodic polarization were not successful. Capacity curves in which the minimum at —0.7v was absent were often obtained with electrolytically etched electrodes.

For comparison a typical differential capacity curve obtained with a clean silver surface in relatively concentrated (IM) electrolyte is also included in Fig. 1.

Discussion

The position of the capacitance minimum in the differential capacity curves obtained with dilute solutions, —0.7v (NHE), indicates the pzc, and confirms Russian work (5, 9). A capacitance minimum is not a satisfactory criterion for the position of the pzc if potential dependent adsorption, *e.g.*, of H or O on Pt or Pd. In the case of Ag (also Sn, Cd, Pb) in the polarizable region the adsorption of these species is not a complication (relatively small frequency dispersion-pseudocapacitance, high hydrogen overpotential similar to Hg, absence of hysteresis effects in the range 0.38 to —1.1v [NHE]).

The ease with which electrodes became irreversibly affected at potentials positive to 0.4v (NHE) suggests that this might be the reason for conflicting double layer capacitance data particularly with electrolytically etched surfaces where the potential is much more positive than 0.4v. The disappearance of the capacity minimum under these conditions indicates the influence of adsorbed reaction products.

The form of the differential capacity curve in molar electrolyte is very similar to that of mercury confirming the work of Ramaley and Enke (8). Since impurity levels were satisfactorily controlled the relatively high value of the differential capacity in the more concentrated electrolyte indicates that the surface of the silver electrode is relatively rough. Time dependence is very pronounced and appears to be a simple equilibration process. That a simple mechanical polished (surface layers structurally disturbed) should show more initial capacity change than a chemically etched (partially equilibrated) surface is in agreement with this suggestion.

A small dispersion of frequency is shown clearly in Fig. 1. Since the possibility of crevices between the electrode and sheath was absent in this work, dispersion must be ascribed to surface roughness as discussed by De Levie (15).

Summary

Differential capacity curves for clean silver surfaces in dilute and 1M sodium perchlorate solution are recorded. The differential capacitance is dependent on electrode/electrolyte contact time.

Manuscript received March 20, 1967; revised manuscript received April 4, 1967.

Any discussion of this paper will appear in a Discussion Section to be published in the June 1968 JOURNAL.

REFERENCES

1. P. Ruetschi, *This Journal*, **110**, 835 (1963).
2. V. I. Veselavsky, *Acta Physicochim. U.R.S.S.*, **11**, 815 (1939).
3. A. Hickling and D. Taylor, *Discussions Faraday Soc.*, **1**, 227 (1947).
4. C. Wagner, *This Journal*, **97**, 71 (1950).
5. D. I. Leikis, *Doklady Akad. Nauk S.S.S.R.*, **135**, 1429 (1960).
6. F. P. Bowden and E K. Rideal, *Proc. Roy. Soc.*, **A120**, 59 (1928).
7. J. J. McMullen and N. Hackerman, *This Journal*, **106**, 341 (1959).
8. Louis Ramaley and C. G. Enke, *ibid.*, **112**, 947 (1965).
9. D. I. Leikis, E. S. Sevastianov, and I. G. Dagaeva, *ibid.*, **113**, 134 (1966).
10. P. Delahay, "Double Layer and Electrode Kinetics," p. 35 *et seq.*, Interscience Publishers Inc., New York (1965).
11. H. Gerischer and R. P. Fischer, *Z. Elektrochem.*, **58**, 819 (1954).
12. J. P. G. Farr and N. A. Hampson, *Trans. Faraday Soc.*, **62**, 3494 (1966).
13. J. P. G. Farr and N. A. Hampson, *ibid.*, **62**, 3502 (1966).
14. E. Mattsson and J. O'M. Bockris, *ibid.*, **55**, 1586 (1959).
15. R. De Levie, *Electrochim. Acta*, **10**, 113 (1965).

A Specimen Holder for Precise Electrochemical Polarization Measurements on Metal Sheets and Foils

W. D. France, Jr.

Chemistry Department, Research Laboratories, General Motors Corporation, Warren, Michigan

Experimental difficulties often arise when sheet-metal electrodes are exposed for precise electrochemical polarization measurements. Both solution contamination and crevice effects, which cause marked data distortion (1), must be avoided, and a solderless electrical contact that is insulated from the electrolyte must be provided. Our laboratory evaluations of sheet specimens that were masked by tape, paint, or resin encapsulation have caused us to lose confidence in these procedures. Therefore, we have designed the rapidly assembled sheet specimen holder illustrated in Fig. 1 for use in conventional polarization cells. The polycarbonate and Teflon combination provides the strength, compressibility, and solution resistance necessary for this application (2, 3). Circular specimens, cut with a die and punch, are positioned on the replaceable Teflon gasket within the holder, followed by a copper disk contact whose electrical lead wire passes through a Teflon insulator. The threaded Teflon bolt is tightened with sufficient torque to compress the sheet against the gasket. The exposed specimen pictured in Fig. 2 exhibits a typical, distinct demarcation between the corroded and the protected areas that demonstrates the effectiveness of the seal. Accumulation of corrosion products and evolved gas at the specimen face is avoided by an oblique entrance angle.

Figure 3 shows two potentiodynamic anodic polarization curves for an annealed stainless steel (Fe-18Cr-12Ni-0.08C) in hydrogen-saturated, 1.0*N* H_2SO_4 at 25 °C. Following a standard procedure, we polished specimens on 600-grit SiC, degreased them in boiling benzene, rinsed them in distilled water, and immersed them in the test solution 1 hr before automatically plotting the experimental semilogarithmic curves at

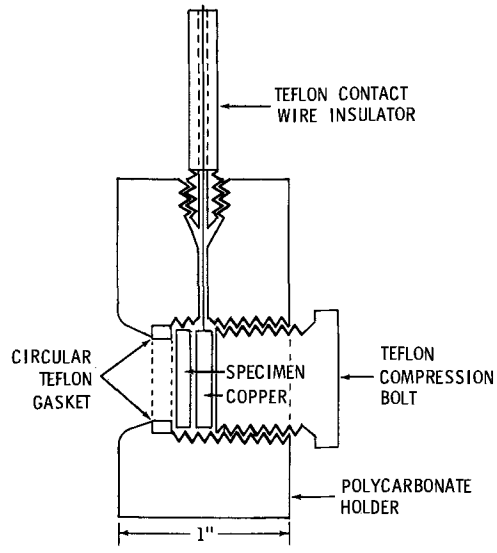

Fig. 1. Specimen holder for metal sheets and foils (side view)

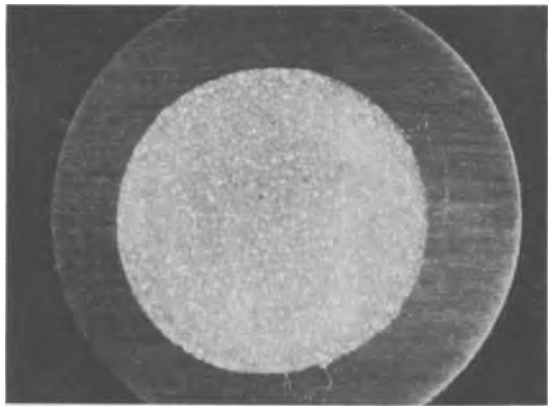

Fig. 2. Photomicrograph of exposed sheet-metal specimen. Magnification 3.5X.

1.2 v/hr, using apparatus similar to that described earlier (4, 5).

Curve A represents the results for a sheet specimen exposed in the described holder, and curve B represents the results for a bulk specimen of the same alloy mounted on a Stern-Makrides assembly (6). The sheet specimen curve effectively duplicates the standard curve, showing no evidence of crevice effects or shielding of the specimen electrode.

This sheet specimen holder is easily fabricated and has the advantage of rapid and effective assembly. Besides providing a known and reproducible exposed

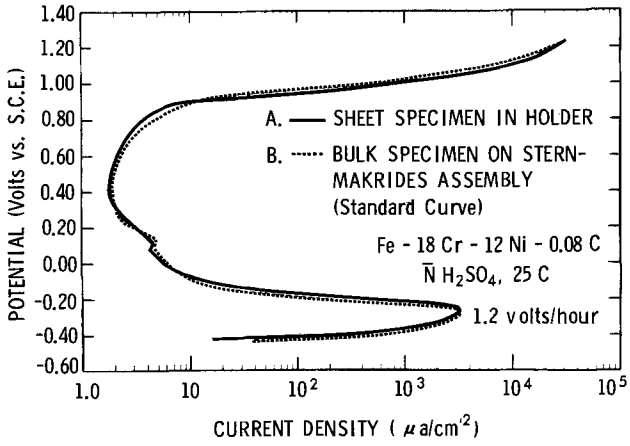

Fig. 3. Potentiodynamic anodic polarization curves for Fe-18Cr-12Ni-0.08C Alloy in *N* H_2SO_4 at 25°C. Curve A, sheet specimen mounted in holder; curve B, bulk specimen mounted on Stern-Makrides assembly.

area for each experiment,[1] edge effects are completely avoided, and a geometrically equivalent surface is exposed, as recommended elsewhere (7). Laboratory experiments have demonstrated that this mounting technique provides an efficient means for exposing any sheet specimen, including polished, coated, or plated surfaces as well as thin foils.

Acknowledgment

The author thanks Mr. R. L. Spencer for machining the sheet specimen holders and for suggesting several improvements incorporated into the final design.

Manuscript received March 8, 1967.

Any discussion of this paper will appear in a Discussion Section to be published in the June 1968 JOURNAL.

REFERENCES

1. N. D. Greene, W. D. France, Jr., and B. E. Wilde, *Corrosion*, **21**, 275 (1965).
2. Materials Selector Issue, Materials in Design Engineering, October 1964, p. 233.
3. M/DE Special Report No. 202, Materials in Design Engineering, January, 1963.
4. B. E. Wilde and N. D. Greene, Scientific Report No. 3, Air Force Cambridge Research Laboratories, AF CRL-64-518, June 15, 1964.
5. N. D. Greene, Experimental Electrode Kinetics, Rensselaer Polytechnic Institute, Troy, N. Y., 1965, p. 3 and 19.
6. M. Stern and A. C. Makrides, *This Journal*, **107**, 782 (1960).
7. H. G. Feller and J. Osterwald, *ibid.*, **111**, 119 (1964).

[1] A 0.445 in. (1.13 cm) diameter orifice provides a 1.0 cm^2 exposed specimen area, which is highly desirable for recording potentiodynamic polarization curves, since recorded current (μa) is then current density ($\mu a/cm^2$).

Brief Communications

Comments on the Paper "Transport Processes in the Thermal Oxidation of Silicon"

P. J. Jorgensen

General Electric Company Research and Development Center, Schenectady, New York

The paper "Transport Processes in the Thermal Oxidation of Silicon" by Raleigh (1) is actually a discussion of the paper "Effects of an Electric Field on Silicon Oxidation" (2). Raleigh concludes that at the present time it is not possible to determine whether an ionic transport process or a molecular transport process predominates. He begins by asserting "that the external application of an electric field *per se* cannot provide a steady-state driving force for a diffusion-controlled process such as the thermal oxidation of silicon" and further that the voltage at which oxidation ceases is "unrelated to the free energy of formation of SiO_2."

The first assertion has been adequately treated by Collins and Nakayama (3) in their recent paper on "Transport Processes in the Thermal Growth of Metal and Semiconductor Oxide Films." These authors point out that the application of an electric field using insulating electrodes, which do not provide an external path for electron flow, does not cause an increase in the flux, in accordance with Raleigh's assertion. However the use of electrodes which are in ohmic contact with the oxide film provides an external path for electrons and an increase in the ionic flux is to be expected. In the silica oxidation experiments discussed by Raleigh, electrodes in ohmic contact were used, and therefore an increase in ionic flux is to be expected.

The second assertion in Raleigh's paper concerning the so-called halt voltage being unrelated to the free energy of formation has recently been discussed by Kröger (4). Wagner (5) has also written an excellent treatise on the effect of an external electric field applied to a growing oxide layer. In this unpublished memo Wagner treats the situation in which corrosion is stopped by a potential difference across the growing film.

The argument briefly stated is as follows: The flux of a given species J_i, in mol/cm^2 sec, may be expressed as

$$J_i = -\frac{\sigma_i}{Z_i^2\mathbf{F}^2}\left(\frac{\partial \mu_i}{\partial X} + Z_i\mathbf{F}\frac{\partial \Phi}{\partial X}\right) \qquad [1]$$

where σ_i is the conductivity due to the ith species, Z_i is the valence, $\mathbf{F}$ is Faraday's constant, μ_i is the chemical potential, and Φ is the local electrical potential. From the principles of electrochemistry the difference in potential ($\Delta\psi$) across an oxide film is

$$\Delta\psi = -\frac{\eta_e'' - \eta_e'}{\mathbf{F}} \qquad [2]$$

where η_e'' and η_e' are the electrochemical potentials of the electrons at the oxide-gas and metal-oxide interfaces, respectively.

Since $\eta_e = \mu_e - \mathbf{F}\Phi$. Then

$$\Delta\psi = \frac{(\mu_e'' - \mu_e')}{\mathbf{F}} + \Phi'' - \Phi' \qquad [3]$$

from [1], if $J_i = 0$, then

$$\frac{\partial \Phi}{\partial X} = -\frac{1}{Z_i\mathbf{F}}\frac{\partial \mu_i}{\partial X} \qquad [4]$$

The term $(\Phi'' - \Phi')$ in Eq. [3] is equal to the integral of Eq. [4]. Now considering the case where only the anions are mobile, and using the definition for the chemical potential of oxygen atoms $\mu_0 = \mu_1 + Z_1\mu_e$ where the subscript 1 refers to anions and $Z_i = -2$, then the chemical potential of the molecular oxygen is $\mu_{0_2} = 2\mu_0 = 2\mu_1 - 4\mu_e$ and one obtains

$$\Delta\psi\ (J_1 = 0) = \frac{\mu_0' - \mu_0''}{Z_1\mathbf{F}} = \frac{\mu_{0_2}'' - \mu_{0_2}'}{4\mathbf{F}} \qquad [5]$$

which illustrates the relationship between the change in free energy, and the voltage at which a reaction can be stopped. Hence the stopping voltage is related to the change in free energy.

The conclusion that available data do not allow one to decide whether an ionic or a molecular type process predominates during the oxidation of silicon merits discussion.

The voltage necessary to stop an oxidation reaction will be E_o regardless of the magnitude of the electronic transport number, where

$$\Delta G = -n\mathbf{F}E_o \qquad [6]$$

and ΔG is the change in free energy, n is the number of equivalents involved in the reaction, $\mathbf{F}$ is Faraday's constant, and E_o is the theoretical cell voltage. If a molecular transport process occurs simultaneously, the value of E_o might be lowered in value somewhat as discussed by Schmalzried (6). However, this reduction in the value of E_o is not expected in the case of the oxidation of silicon since the transport of oxygen through the silica layer is rate determining, and equilibrium can most probably be established at the oxide interfaces.

The application of a voltage equal and opposite in sign to E_o across the growing oxide layer would stop any ionic transport, but a further increase in voltage would be necessary in order to establish a decomposition rate of the oxide which would be equal to the formation rate of oxide by a simultaneous molecular and ionic transport process.

Experiments (7) on approaching the stopping voltage from voltages greater than E_o, *i.e.*, reducing the oxide with an electric field have shown a correlation with E_o of ± 5-10 mv, indicating, within experimental error, a negligible amount of oxygen transport by a molecular process.

Some of the effects of an applied electric field on the rate of permeation of oxygen through fused silica have also been investigated (8). A schematic represen-

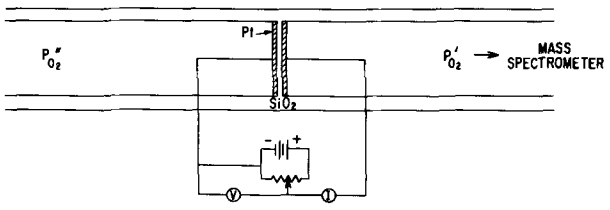

Fig. 1. Schematic drawing of the permeation cell.

tation of the permeation cell which was used is shown in Fig. 1.

Corning 7940 fused silica having a negligible alkali ion content was used for the membrane and GE 204a fused silica tubing was used for the outside walls of the cell. The system was baked at 1000°C under a vacuum for several weeks to remove the hydroxyl content in the Corning 7940 silica. Other details of the experimental apparatus have been previously described (8). The application of a pressure of 10^{-7} mm of oxygen on the mass spectrometer side of the cell and 323 mm of oxygen on the opposite side at 1000°C under open-circuit conditions yielded a permeation rate of 1.68×10^{-12} cm^3 gas (STP) per sec for a 1 mm thick membrane, per cm^2 area per cm Hg gas pressure difference. Interpolating Norton's (9) oxygen permeation data through fused SiO_2 to obtain a rate of permeation at 1000°C yielded a value of 1.85×10^{-12} with the above quoted units. These values are in excellent agreement and indicate the placing of sputtered platinum electrodes on the SiO_2 does not measurably interfere with the permeation process.

Open circuit potentials were developed when an oxygen pressure difference was applied across the silica. The calculated ionic transport numbers ranged between 0.40 and 0.53 varying with the magnitude of the pressure difference. These voltages again indicate an ionic transport.

The application of 6 Torr of oxygen to one side of the permeation cell and 10^{-7} Torr to the other side, *i.e.*, the mass spectrometer side (see Fig. 1), yielded an ionic transport number of 0.40. Using this value and Faraday's laws, the amount of oxygen due to ionic transport was calculated at zero volts. The amount calculated per second was 8.2×10^{-13} g equiv, and the amount measured using the mass spectrometer was 7.2×10^{-13} g equiv. The difference between these values is within experimental error. Again indicating a negligible molecular transport compared to the ionic transport.

Finally there are many small points in Raleigh's paper which are incorrect, but are beyond the scope of this communication. However, two of these minor points should be commented on:

1. The statement that "oxygen ions were involved in the oxidation of zinc" (10) is misleading in that it infers that diffusion of oxygen ions through ZnO is the rate-determining step in the oxidation of zinc. The effects of an electric field on the oxidation of zinc place no restrictions on which ion is rate limiting and the oxide may form either at the zinc-zinc oxide interface or the oxide-platinum electrode interface.
2. An impure SiO_2 exhibits pure ionic conductivity, as the purity increases, the fraction of the ionic conductivity decreases. The high-purity SiO_2 used in the permeation experiments and the SiO_2 formed on the silicon had ionic transport numbers near 0.40. This fact causes Raleigh's model for the stopping voltage to predict a value greater than 3v, which is unrealistic. Hence his model to account for the stopping voltage is suspect.

In conclusion, the application of an electric field across growing oxide layers can affect the rate of oxidation. The voltage at which a reaction can be stopped is directly related to the free energy of formation, and available experimental evidence indicates that an ionic process could be the predominant transport mechanism for oxygen through SiO_2. However, the linear pressure dependence on the permeation and oxidation rates argues strongly for the diffusion of oxygen molecules, and this fact must be properly accounted for in terms of ionic and electronic transport, before the conclusion can be made that the prevailing mechanism of oxidation of silicon involves only ionic and electronic transport processes.

Acknowledgments

The author wishes to express his gratitude to Dr. D. A. Vermilyea and S. P. Mitoff for many stimulating discussions, and to Professor Carl Wagner for his comments and permission to refer to his unpublished memo.

Manuscript received April 26, 1967.

Any discussion of this paper will appear in a Discussion Section to be published in the June 1968 JOURNAL.

REFERENCES

1. D. O. Raleigh, *This Journal*, **113**, 782 (1966).
2. P. J. Jorgensen, *J. Chem. Phys.*, **37**, 874 (1962).
3. F. C. Collins and T. Nakayama, *This Journal*, **114**, 167 (1967).
4. (a) F. A. Kröger, "The Chemistry of Imperfect Crystals," North Holland Publishing Co., Amsterdam (1964); (b) F. A. Kröger, *Proc. Brit. Ceram. Soc.*, **1**, 167 (1964).
5. C. Wagner, Private communication.
6. H. Schmalzried, *Z. Phys. Chem. N. F.*, **38**, 87 (1963).
7. P. J. Jorgensen, To be published.
8. P. J. Jorgensen and F. J. Norton, VII International Congress on Glass, 310, Gordon and Breach, New York (1966).

The Anodic Dissolution of Electrodeposited Nickel

P. A. Brook, D. B. Jenkins, and M. Saleem

Department of Metallurgy, The University of Nottingham, University Park, Nottingham, England

The anodic dissolution of electrodeposited metals should reveal details of their structure; this note reports some such observations. All initial deposits were made on polycrystalline copper strip from a standard Watts nickel bath as described previously (1) except that a current density of 20 amp/ft^2 for 2 hr was used. After preparation the deposits were anodically dissolved for various times at 20 amp/ft^2 in an electrolyte of 100 g/l $NiSO_47H_2O$ or 100 g/l $NiCl_26H_2O$ or N/11.9 HCl. After dissolution the surface was examined by electron microscopy of carbon replicas.

The as-plated surface showed the typical pyramidal structure previously reported (1, 2). For the sulfate electrolyte, the attack appears as a generalized pitting for times of up to 1 min (Fig. 1), but with increasing time the pits coalesce to form steps which run parallel to the basal edges of the pyramids (Fig. 2). Another feature of the dissolution is the coalescence of the pits

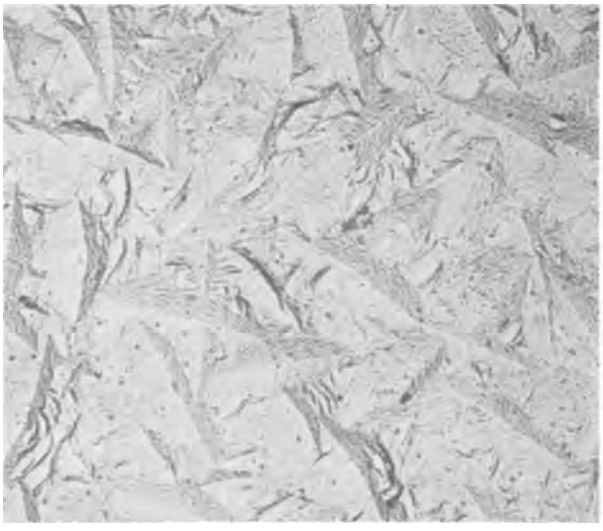

Fig. 1. Nickel surface after 1 min dissolution. Magnification 8000X.

Fig. 2. Nickel surface after 2 min dissolution. Magnification 8000X.

across one pair of opposite pyramidal edges causing the original pyramid to become more ridgelike. After 10 min the step spacing has increased to form ledges, and the breakdown of the pyramids has reached an advanced stage although in many cases ridges are still clearly visible (Fig. 3).

Dissolution in the chloride electrolytes produces similar effects, but ledge formation is less well defined.

It appears that dissolution does not take place from the emergent screw dislocation and the initial attack is, apparently, random. However, at about 2 min the process has assumed a crystallographic characteristic since the steps are parallel to the pyramid basal edges. Hulett and Young (3) have discussed step formation

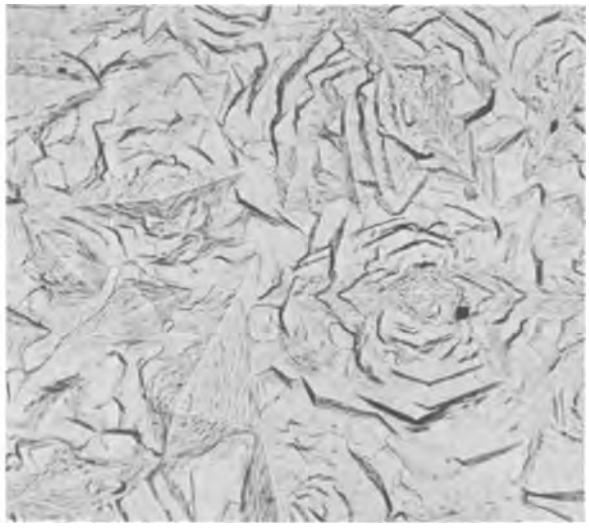

Fig. 3. Nickel surface after 10 min dissolution. Magnification 8000X.

during the dissolution of (111) copper faces, and they suggest that there is a threshold step spacing of about 500-700Å beyond which there is no interaction between steps. The earliest discernible steps on the dissolving nickel faces occur after about 2 min and their spacing is about 600Å. This takes no account of the inclination of the pyramidal faces, but for normal values the step spacing will be changed only to a small extent. Once formed the steps interact to form the ledges shown in Fig. 2.

The side faces of the pyramids are not smooth, and in some cases striations are visible as if the pyramids are formed by piling up of macrolayers.

This seems to be confirmed by the present results. The dissolution takes place from the edges of the macrolayers initially in an apparently random manner, but later there is an ordered process forming visible steps which move across the surface interacting to form ledges.

At the moment it is not possible to explain the persistence of the ridges long after the main pyramidal structure has gone.

Acknowledgment

The authors would like to thank the Scientific Research Council for a grant for the purchase of an electron microscope.

Manuscript received May 19, 1967.

Any discussion of this paper will appear in a Discussion Section to be published in the June 1968 JOURNAL.

REFERENCES

1. J. A. Crossley, P. A. Brook, and J. W. Cuthbertson, *Electrochim. Acta*, **11**, 1153 (1966).
2. B. C. Banerjee and P. L. Walker, *This Journal*, **109**, 436 (1962).
3. L. D. Hulett, Jr. and F. M. Young, Jr., *ibid.*, **113**, 410 (1966).

Electrochemical Studies on the Effect of Water in Nonaqueous Electrolytes

A. N. Dey

Laboratory for Physical Science, P. R. Mallory & Company, Inc., Burlington, Massachusetts

The role of water in nonaqueous electrochemistry is not very well understood. Although problems related to the cathodic deposition of lithium from nonaqueous media containing water have been reported (1), the questions as to whether water behaves like a solvent or a cathode active material, as to whether water interacts with the electrolyte or the solvent, etc., are still quite open. We report here some experimental results which provide answers to some of the above questions.

The effect of water on the cathodic discharge reactions in a nonaqueous medium was studied by deliberately adding known amounts of water to the electrolyte and carrying out galvanostatic and potential sweep experiments. The galvanostatic experiments consisted of imposing a constant cathodic current on the working electrode (placed in an H-type cell) and recording the potential of the electrode against a reference Ag wire electrode (placed within 0.5 cm of the electrode) as a function of time. The potential sweep experiments consisted of imposing a linearly varying potential (with respect to Ag wire reference) on the electrode at various sweep rates, and recording the current as a function of potential with an X-Y recorder.

Propylene carbonate (PC) was used as a solvent and anhydrous $LiClO_4$ and $Mg(ClO_4)_2$ as electrolyte salts. The initial concentration of water in the distilled PC was between 10^{-3} to 10^{-2} M/liter, as determined by gas chromatographic analysis.

The cathodic galvanostatic transient on a copper electrode in $LiClO_4$-PC gave rise to three distinct plateaus (in the potential-time curves) in the potential ranges of —1.0 to —1.5, —1.5 to —2.5, and —2.5 to —3.0v *vs.* the Ag wire reference before the lithium deposition potential was reached. The above transient was found to be reproducible when the electrodes were chemically etched with dilute HNO_3 before every transient. On the deliberate addition of water, it was found that the length of only the second plateau (corresponding to the potential range —1.5 to —2.5v) increased, whereas the other two remained constant. The presence of OH^- was also detected on the electrode when the transient was discontinued in the middle of the second plateau by using the following simple test. The electrode was removed from the electrolyte and immediately placed in water containing phenolphthalein. The appearance of blue color on the electrode as well as in aqueous medium showed that there was enough LiOH (sparingly soluble in the electrolyte) present on the electrode to change the *p*H of aqueous solution of phenolphthalein. The above evidence led to the conclusion that water discharged on the copper electrode from the $LiClO_4$-PC system at a potential corresponding to the second plateau in the galvanostatic transient. The reasons for the first and the third plateau were not very clear at this stage. However, the lengths of the first and the third plateaus were negligible compared to the length of the second plateau at higher concentrations of water (*e.g.*, 1.0 M/liter). It was found that $i\tau^{1/2}$ (i is the cathodic current density, and τ is the transition time corresponding to the second plateau only) was independent of i over a range of half a decade of current density. The dependence of $i\tau^{1/2}$ on the concentration of added water showed a very interesting property. Figure 1(A) shows a plot of $i\tau^{1/2}$ *vs.* the concentration of added water in 1M $LiClO_4$ in PC. There was a sharp break

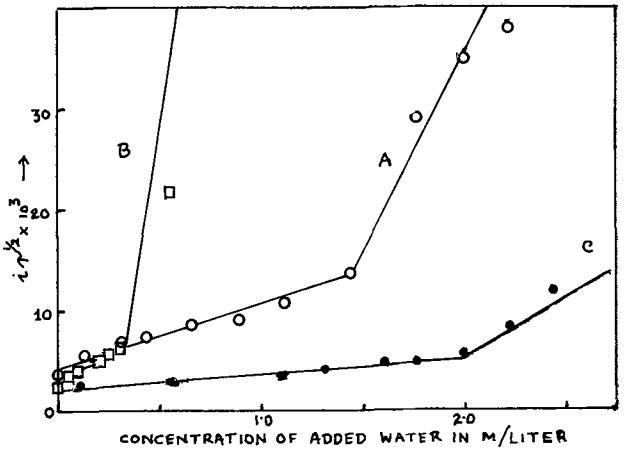

Fig. 1. Dependence of $i\tau^{1/2}$ on the concentration of added water in (A) 1.0M $LiClO_4$ in PC, (B) 0.1M $LiClO_4$ in PC, and (C) 0.5M $Mg(ClO_4)_2$ in PC.

in the curve giving rise to two linear regions having two distinctly different slopes. The slope at the lower concentrations of water was much lower than expected on the basis of linear diffusion (Sand's equation) (2). The diffusion coefficient calculated from the lower slope was of the order of 10^{-8} cm²/sec whereas it was of the order of 10^{-6} cm²/sec at the higher slope. The transition point (*i.e.*, the concentration at which the two lines intersect) was reproducible within ± 10%. The point of break appeared to depend on the concentration of $LiClO_4$. It occurred at a lower concentration of added water (0.33 M/liter) at lower concentrations (*e.g.*, 0.1M) of $LiClO_4$ [Fig. 1(B)]. The transition point also depended on the nature of the cation. In 0.5M $Mg(ClO_4)_2$, the transition point occurred at 2.0 M/liter [Fig. 1(C)].

The results of the potential sweep experiments were identical with the above results. A distinct current peak corresponding to water discharge in the potential range of —1.5 to —2.5v was observed. The peak current i_p was found to be dependent on the sweep rate, v, and $i_p/v^{1/2}$ was found to be independent of the sweep rate at constant concentration within the range examined (200 to 50 mv/sec) in conformity with the equation (2)

$$i_p = AD^{1/2}Cv^{1/2}$$

where A is a constant for the particular system, D is the diffusion coefficient, and C is the concentration of the discharging species. The plot of i_p *vs.* C, the concentration of added water, showed the transition point to occur [Fig. 2(A)] at exactly the same concentration of added water (1.45 M/liter) as was found in the galvanostatic experiment. The dependence of the transition point on the concentration of the salt and the cation was also found to be similar to that found in the galvanostatic expriments.

The effect of the substrate on the transition point was studied by using the potential sweep method. Figure 2 shows a plot of the peak currents as a function of the concentration of added water on three substrates: Cu, Ni, and Pt. As is evident from the figure, there is no substrate effect.

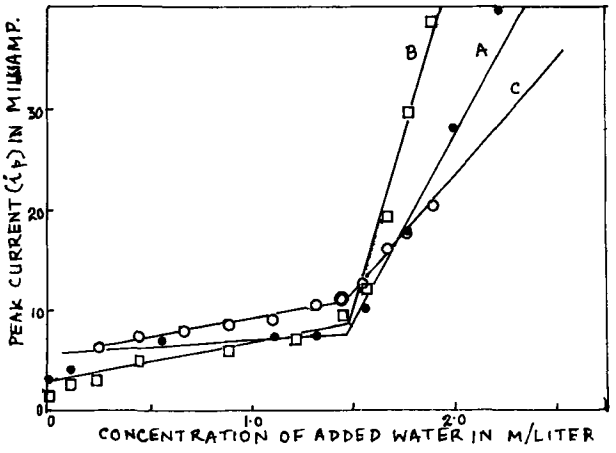

Fig. 2. Dependence of peak current (i_p) at a sweep rate of 200 mv/sec on the concentration of added water in 1M $LiClO_4$ on (A) copper, (B) nickel, and (C) platinum substrates.

An interpretation of the above experimental results in terms of a change of diffusion coefficient of the discharging species with concentration appears to be rather improbable. Considering the fact that water was the discharging species corresponding to the peaks and plateaus of the potential sweep and galvanostatic experiments, respectively, a simple interpretation of the above results can be given as follows. The affinity of water for cations is well known in aqueous solutions (3). It can be similarly postulated that water interacts with the dissolved salts in the nonaqueous medium to such an extent that it may not discharge, depending on the salt/water ratio. When sufficient water is added to satisfy the hydration requirements of the salts, the excess water can discharge normally, giving rise to a sharp break in the $i\tau^{1/2}$ *vs.* C or i_p *vs.* C curves. The bound water would behave differently from the free water both electrochemically and physically.[1] The dependence of the transition point on the concentration of the added salt can be explained by this hypothesis. The divalent Mg^{++} ion is known to be hydrated more strongly than the monovalent Li^+ ion. Therefore, a stronger interaction would be expected in 0.5M $Mg(ClO_4)_2$ than in 1M $LiClO_4$, if cations are involved in the interaction. Although the concentration of ClO_4^- was identical in both 1M $LiClO_4$ and 0.5M $Mg(ClO_4)_2$, the transition point increased from 1.45 to 2.0 M/liter in going from $LiClO_4$ to $Mg(ClO_4)_2$. This indicates that the cations rather than the anions participate in the interactions between the water and the dissolved salts in PC. However, interactions with the anions cannot be ruled out.

The above interactions constitute a bulk phenomenon, and no substrate effects would be expected, as was found to be the case. More detailed results concerning this phenomenon will be reported in a subsequent paper.

[1] The decrease in the diffusion coefficient of water due to its interaction with the cation does not appear to be very likely as the diffusion coefficients (4) of a number of salts in aqueous medium are of the order of 10^{-5} cm^2/sec.

Acknowledgment

The author is indebted to Dr. Per Bro, Dr. M. L. B. Rao, and Dr. R. G. Selim for encouragement and stimulating discussions.

Manuscript received May 19, 1967. This paper will be presented at the Chicago Meeting, Oct. 15-20, 1967.

Any discussion of this paper will appear in a Discussion Section to be published in the June 1968 JOURNAL.

REFERENCES

1. K. R. Hill and R. G. Selim, Research and Development of a High Capacity Nonaqueous Secondary Battery, Final Report, August 1965, NASA CR-54880, Contract No. NAS 3-2780, P. R. Mallory & Co. Inc.
2. P. Delahay, "New Instrumental Methods in Electrochemistry," Chap. 6, Interscience Publishers Inc., New York (1962).
3. J. O'M. Bockris and B. E. Conway, "Modern Aspects of Electrochemistry," Chap. 2, Vol. I, Butterworths Scientific Publications, London (1954).
4. G. Kortum and J. O'M. Bockris, "Textbook of Electrochemistry," Vol. II, p. 704, Elsevier Publishing Co., New York (1951).

Silicon Nitride Films by Reactive Sputtering

S. M. Hu and L. V. Gregor

IBM Components Division, East Fishkill Facility, Hopewell Junction, New York

ABSTRACT

Silicon nitride films (from 500 to 7500Å in thickness) have been deposited on silicon and silicon dioxide by reactive sputtering of a silicon cathode in a N_2 glow discharge. Both d-c and rf sputtering have been investigated. Physical and chemical properties of silicon nitride films prepared by sputtering were examined in reference to the process variables. The rate of deposition was approximately proportional to the square root of rf power density. Film density increased with power density, and decreased with gas pressure. Optimum gas pressure was in the range 3-10 x 10^{-3} Torr. Higher pressures resulted in less dense and electronically leaky films. Dielectric constant and etch rate in HF solution appeared to correlate well with film density. Residual pressure higher than 1-2 x 10^{-6} Torr was found to have a most detrimental effect. Argon and nitrogen gas mixtures resulted in excess silicon incorporation in the deposited nitride films.

Silicon dioxide has for the past several years been the most important material to serve the multiple function of insulation, passivation, and diffusion masking. Because of its chemical nature and its structural characteristics, there are a number of shortcomings inherent in silicon dioxide. The most serious of these is its low resistance to diffusion of certain impurities and to field migration of ions, which causes instability and deterioration of surface characteristics of electronic devices, and, in particular, field effect devices. From the properties of crystalline silicon nitride one may extrapolate to the generally superior properties of amorphous silicon nitride compared to silicon dioxide, except for higher electronic conductivity.

Precisely because of its desirable high resistance to the diffusion of atomic, molecular, or ionic species, silicon nitride cannot be grown on a silicon substrate by thermal nitridation, either in nitrogen or in anhydrous ammonia, in contrast to the thermal oxidation of silicon in oxygen and in steam. Experiments with thermal nitridation (1) and plasma anodization (2) failed to produce coherent silicon nitride films on silicon substrates. In addition, thermal nitridation or oxidation has a limitation on the scope of its use to silicon only. A deposition method thus seems to be a more logical approach.

Sterling and Swann (3) and Doo *et al.* (4) have succeeded in the deposition of continuous amorphous silicon nitride films by means of vapor phase reaction of silane and anhydrous ammonia. At the same time the authors and Pennebaker (5) also succeeded in obtaining continuous silicon nitride films, properly identified as silicon nitride (dielectric constant 6.0-7.0; IR absorption band at 11.5-12μ) by means of d-c and rf reactive sputtering, respectively. Recently, others have described various processes for depositing silicon nitride (6).

Sputtering deposition of insulating-passivating films over semiconductors is a process which involves more difficulties than the sputtering of metal films. Some of these are: (*i*) most insulating films are chemical compounds rather than elements, and thus there is the problem of the control of the stoichiometry of the films; (*ii*) although impurities affect the resistivity of metal films considerably, this is a relatively small effect except for superconductive films; the conductivity changes in insulators, however, caused by the presence of impurities, is generally several orders of magnitude; (*iii*) there is also a surface charge problem arising from one or a combination of the following: substrate surface damage, trapped impurities, interface mismatch, and interfacial stress. In addition, there is another fact that sets silicon nitride apart from silicate glasses: The high melting point, high hardness, and essentially covalent nature, make thermal annealing almost impossible. To understand these many complex problems and to relate them to parameters of the sputtering process, various properties of the films, such as carrier injection, electric conduction, ion migration and impurity diffusion, surface charge and trapping centers, etc., should be studied.

Reactive sputtering has been used to prepare oxide glasses (7, 8). It is a logical extension that silicon nitride may also be prepared by reactive sputtering in a nitrogen plasma. However, there is an additional factor: the possible contamination of the system by oxygen, because oxygen is much more reactive than nitrogen. This is much more critical to d-c sputtering than rf sputtering, as was found out in the course of this work. In the case of reactively sputtered silica, although Sinclair and Peters (7) found that the infrared absorption spectrum and the refractive index as well as the density of the film to be the same as ordinary fused silica, they found the dielectric strength to be less than 10^6 v-cm^{-1}, which is only 20% of the dielectric strength of the thermally grown silicon dioxide film. These they believed were caused by microscopic flaws in the thin films.

High-frequency fields were first used by Anderson *et al.* (9) and Davidse and Maissel (10) for sputtering of dielectric targets, to enable the neutralization of the ion-bombarded dielectric surface via displacement currents. In addition to its originally intended use for dielectric sputtering, tthe rf sputtering process involves a number of interesting characteristics which make it advantageous for physical and reactive sputtering of metals and semiconductors as well. These features were found from a comparison of the results of dc and rf sputtering of silicon nitride.

Experimental

Three different experimental systems were used in this investigation. The first, which was employed for dc reactive sputtering, was constructed of glass. The second system consisted of a stainless steel bell jar, and both d-c and rf sputtering were studied. The third system was constructed solely for rf sputtering, and consisted of a cylindrical glass bell jar with aluminum top and base plates. Most of the results discussed were obtained with the latter system. The system is generally similar to that described previously (10), except that the dielectric target has been replaced by a polycrystalline silicon disk, 4 in. in diameter, and ¼ in. in thickness, soldered to the cathode (see Fig. 1). The cathode was water-cooled to reduce gas evolution. Although the rf field applied to the "cathode" was with respect to ground, the cathode potential was actually formed because of the very low mobility of positive ions. The dark space is a function of pressure

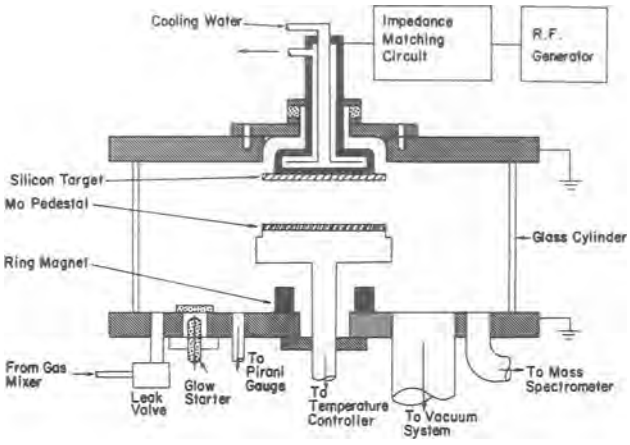

Fig. 1. Schematic diagram of rf sputtering apparatus.

and applied voltage. It was always visible in d-c sputtering, but it was not visible in rf sputtering with zero magnetic field. In a field of ~12 gauss caused by a permanent ring magnet below the cathode, however, the dark space was again very clearly visible. With or without a magnetic field, a glow discharge could be sustained at pressures as low as 2×10^{-3} Torr, although it was necessary to start the discharge by auxiliary means (usually a high frequency Tesla coil applied to a window of the sputtering chamber). In both d-c and rf operation, the chamber and the substrate pedestal were all grounded.

Nitrogen was used in all cases except where other gases are specifically mentioned. To study the effect of mixing with other gases, each of the gases used was first passed through a flowmeter, and then mixed together and branched to the exhaust and the system respectively through two needle valves. Nitrogen used contained less than 1 ppm of water and oxygen. To minimize gas contamination during sputtering, advantage was taken of purging with high throughput to maintain system pressure, *i.e.*, the pumping system was not throttled during sputtering.

Films were usually deposited on polished silicon substrates except for samples prepared for uv absorption spectroscopy, in which case the films were deposited on fused quartz plates, and some samples were deposited on various special substrates for other purposes. Typical examples of such substrates are oxidized silicon, gallium arsenide, germanium, various glasses, and metallic substrates including aluminum, copper, gold, and molybdenum. Satisfactory adherence was obtained for these substrates, although adhesive force and interfacial stress had not been measured. The silicon substrates used were of 5-10 and 0.012 ohm-cm resistivity respectively (both p- and n-type), the former being for preparation of films for surface studies and infrared spectroscopy; the latter being for investigation of electric and dielectric properties. The HCl vapor-polished surface of these substrates was cleaned by means of collodion stripping, which was found to be an excellent method for minimizing surface contamination. The cleaning of the substrates was found to be absolutely essential in producing good quality films.

The frequency of the rf field was 13.6 MHz. The rf wave was fed to the cathode through an impedance matching circuit (10). Since sputtering power density, expressed in watts per cm^2 of cathode, and peak-to-peak voltage are interrelated and dependent on gas pressure, system geometry, and rf frequency, the power density was chosen as the controlled factor while the peak-to-peak voltage was measured. The choice was only a matter of convenience. However, the choice of peak-to-peak voltage as an independent variable to be controlled may be more compatible with the d-c sputtering process and more suitable for theoretical analysis, especially following the established practice in d-c sputtering. The floating d-c voltage at the cathode during rf sputtering could not be controlled independently and is determined primarily by the rate of generation and drift velocities of the positive ions in the plasma. This d-c voltage could not be measured accurately. However, measurement with a high voltage probe showed it to be more than 90% of the half-peak voltage above ground. In the cases studied, the maximum floating potential at the substrate surface was ~ —40v.

Results and Discussion

D-c vs. rf reactive sputtering.—Although it is not certain that what is true for the reactive sputtering of silicon nitride may be applicable to the reactive sputtering of other insulator films, it is quite clear that rf reactive sputtering gives superior results to d-c reactive sputtering for the deposition of silicon nitride films. With d-c reactive sputtering, oxygen contamination was found to be a problem difficult to eliminate. The oxygen did not come from the nitrogen gas used, since analysis showed the nitrogen gas to contain <1 ppm each of oxygen and water. Further purification of the nitrogen gas by passing it through a silica tube filled with copper turnings heated to 700°C for removing oxygen followed by passing it through a cold trap for removing moisture did not show any improvement. Furthermore, the glass sputtering system seemed to show lesser tendency toward oxygen contamination, while in the all-metal sputtering system, the oxygen contamination was predominant. In rf sputtering with the all-metal system, oxygen contamination did not occur under normal conditions. Intentional incorporation of 1% of oxygen into the nitrogen stream did not give any appreciable amount of silicon-oxygen bonds detectable by infrared spectroscopy, although its effects on such properties as electronic conduction, carrier trapping and etching rate in HF solution have not yet been established.

From these observations, it appeared that the contaminating oxygen or oxygen bearer (H_2O, CO, etc.) might have come from the wall of the sputtering chamber. The evolution of these gases might have been caused by negative ion bombardment. A glass chamber wall would accumulate negative charges as a result of negative ion bombardment and become self-biased with respect to the ground, until it reached a static potential high enough that further ion bombardment became negligible. In the case of rf sputtering, the peak-to-peak voltage was usually in the range of 2 kv, and the net dc voltage across the dark space was below 1 kv. On the other hand, because of much lower sputtering rate, it was necessary to use higher voltages in the d-c sputtering, usually in the range of 2-4 kv. No quantitative data are available concerning the relative negative ion concentrations in the d-c and rf glow discharge, nor about the excited species of nitrogen in the two cases.

The difference in the net d-c voltage across the anode and the cathode between the d-c and the rf sputtering also appeared to cause a film damage problem, to the disadvantage of the d-c sputtering. The film damage was most probably caused either by negative ion bombardment, or electron bombardment, or both. This damage exhibited itself in various forms, such as high film leakage current, surface charge, and more obviously, in some extreme cases, as a grain-textured film surface observable by electron microscopy. Unfortunately, a higher d-c voltage was needed because of the low deposition rate in d-c sputtering, due to the extremely low efficiency in the d-c glow discharge. Figures 2 and 3 show the surface texture of deposited silicon nitride films by d-c and rf reactive sputtering, respectively.

Another phenomenon usually observed in high voltage d-c sputtering was the appearance of an absorption band at 4.7μ in the IR spectra. It is not clear whether this was caused by negatively charged particle bombardment. The possible chemical constituents

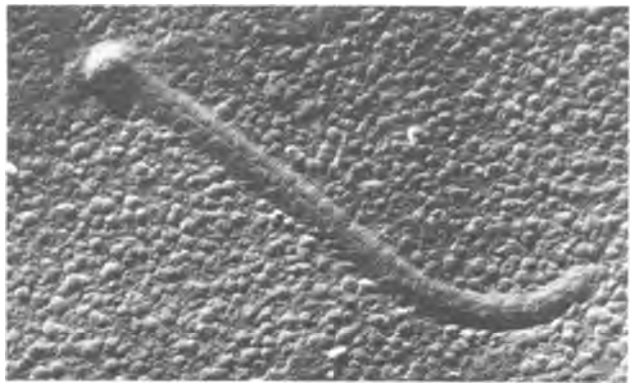

Fig. 2. Surface texture of silicon nitride film by dc sputtering

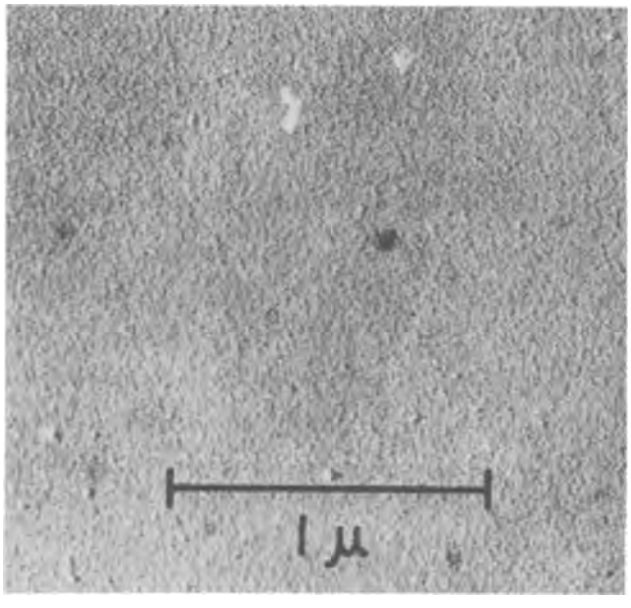

Fig. 3. Surface texture of silicon nitride film by rf sputtering

that might give rise to this absorption band include Si ≡ N, Si—H, N=Si=O, N=C=O, C=N, N=N=N, etc. One cannot rule out the presence of oxygen and oxygen bearers such as water, as well as carbon constituents mainly due to the presence of contamination hydrocarbons and their ions. The much higher rate of deposition, the absence of oxide contamination and film damage, and the improved chemical and physical properties of silicon nitride films prepared by rf reactive sputtering led to the choice of the rf process as the method to be studied in detail. The rest of the data to be presented pertain to rf reactive sputtering.

Effect of power density.—In rf reactive sputtering the power density had multiple and interrelated effects on such properties as film density, film etch rate in hydrofluoric acid solutions, film conductivity, dielectric constant, surface charge at the silicon-silicon nitride interface, C-V hysteresis of MIS devices, as well as rate of deposition.

At a fixed N_2 pressure, the rate of deposition was approximately proportional to the square root of the power density. There was also indication of a threshold power density for film deposition. At 4 x 10^{-3} Torr, the rate of deposition is shown in Fig. 4. It should be noted that the rate of deposition will depend strongly on the geometry of the sputtering system, and in particular on the diameter of the target and the spacing between the target and the substrate. Hence, the results shown in Fig. 3 can only be regarded as a typical example. In this case, the target had a diameter of 10 cm, and the spacing was 4 cm. Scaling to another system cannot be readily calculated, but in

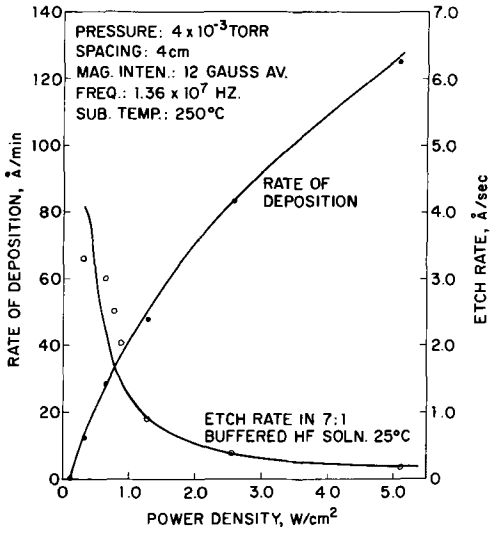

Fig. 4. Effect of power density on deposition and film etch rates in HF.

general, the efficiency of both sputtering and deposition will increase with target diameter, until it reaches a limiting value for electrodes of infinite diameter.

Etch rate is a very sensitive indicator of both chemical and structural properties of an amorphous solid. For example, the etch rate in dilute HF solution has been found to be directly related to the phosphorus concentration in a phosphosilicate glass film (2). The etch rate of an amorphous film, such as silicon nitride, in dilute HF solution varies over a very wide range. It goes up drastically when the film becomes structurally looser. It is apparently related to the film density. One sees from Fig. 3 that the etch rate at 25°C of sputtered films in 7:1 buffered HF solution (7 parts 40% NH_4F aqueous solution and 1 part 49% HF aqueous solution) goes up sharply when the power density is below 1.0 w/cm². When the etch rate is below 1 Å/sec, as is the case with typical silicon nitride films, practical problems arise in photolithography when the film is applied to device manufacturing. On the other hand, the low etch rate is an indicator of the good quality of a nitride film. It has been observed that films with etch rate (in 7:1 HF solutions at 25°C) of 10 Å/sec or higher failed to mask diffusion of steam, oxygen, and certain dopants. Such films were also electrically conductive.

The primary effect of the power density was its relationship with the kinetic energy of the depositing particles as well as negative ion bombardment. The floating d-c potential at the "cathode" with respect to the ground can be given by an empirical formula $w = kV^2$, where w is the power density and V is the space charge potential. The factor k is a complicated function of other parameters such as system geometry, gases used, pressure, etc. The increase in power density results in the deposition of denser films. This is shown in Fig. 5. The film density of reactively sputtered silicon nitride was thus approximately 2.8 g/cm³ when deposited at power density below 1.0 w/cm², and increased to about 3.0 g/cm³ at power density higher than 2.5 w/cm². The density was determined by differential weighing technique using a Cahn microbalance. The substrate was vapor polished silicon. The films were deposited to thicknesses of 3500-5000Å. The differential weighing technique gave an error of <0.5% of the net film weight. However, the over-all error was estimated to be approximately ±2%, arising mainly from thickness measurement using Tolansky interferometry. The crystallographic density of both α- and β-silicon nitride is 3.18 g/cm³ (11, 12). Thus, the deposited amorphous films of silicon nitride were somewhat structurally looser. This seems to confirm

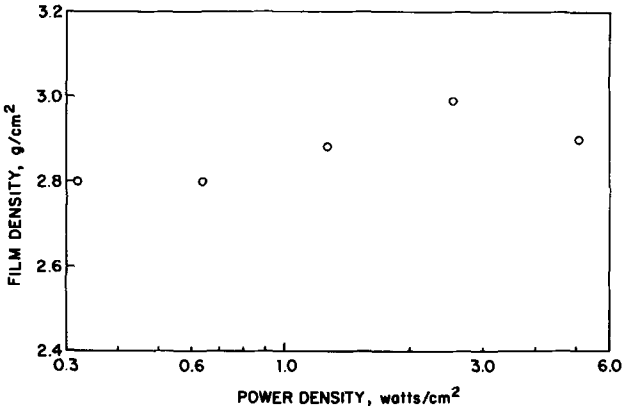

Fig. 5. Film density as a function of sputtering power density

the previous hypothesis (13) that shifting of the infrared absorption band from 10.7μ for crystalline β-silicon nitride to ~12.0μ for amorphous films of silicon nitride was the result of the structural looseness of the amorphous films. Indeed, the structural looseness of the deposited films affected not only the etch rate of the films in HF solutions and the position of the infrared absorption band, but also the barrier to impurity diffusion, injection and trapping of charge carriers, as well as dielectric constant of the films, which will be discussed in a later section.

However, there is a major detrimental effect in the use of high power density, which is the deterioration of silicon surface properties. The total surface charge, as measured from the C-V characteristics of MIS devices made of the sputtered silicon nitride films, was observed to increase with sputtering power density. When the power density was below 0.64 w/cm^2, the surface charge was about 0.5-1.0 x 10^{12} e/cm^2, which is defined as the n-shift of the silicon surface. At a power density of ~1.2 w/cm^2, the surface charge in silicon (with respect to the flat band condition) was ~3 x 10^{12} e/cm^2. When the power density was increased to 2.5 w/cm^2 and above, the surface charge was 10^{13} e/cm^2 or larger. Quite frequently, at this higher power level, a transition in the C-V curve could not be obtained due to the dielectric breakdown of the nitride films, indicating a surface charge density of greater than 3.5 x 10^{13} e/cm^2. This surface charge generally could not be significantly reduced by annealing processes. In fact, there were a few samples in which the n-shift was seen to increase somewhat after annealing. This is in certain respects similar to what has been observed in thermal silicon dioxide-silicon interfaces, where the n-shift increases after 450°-500°C heat-treatment and is generally thought to be due to the thermal decomposition of certain oxygen-bearing complexes into electrically active centers (14).

There appeared to be at least one bit of evidence in support of the hypothesis of particle bombardment-induced surface charge. A sample prepared at ¾ in. distance showed a surface charge density of $>1.5 - 2 \times 10^{13}$ cm^{-2} by means of MIS C-V measurement. The silicon nitride film was then stripped off, and the surface conductivity was measured by means of a three-point probe. An increase was found in carrier density at the surface to ~10^{18} cm^{-3}, assuming a 100Å accumulation layer. This value is an order of magnitude lower than the charge found from the MIS C-V measurement before the silicon nitride film was stripped off. Although small, the increase in conductivity was definite.

An electron photomicrograph was taken of the silicon surface after the silicon nitride film was carefully removed to just expose the bare silicon. No structural damage was observed in the micrograph.

Effect of residual pressure.—The residual background pressure of the vacuum system was found to be one of the most detrimental factors affecting various properties of the silicon nitride films. It is believed that the detrimental elements associated with high residual pressure are hydrocarbons or other molecules from the pump fluids. A residual pressure of 10^{-6} Torr was sufficiently high to be harmful. At a residual pressure of 3-5 x 10^{-6} Torr, the damaging effect on the silicon nitride films became mechanically observable. In the worst case, poor adhesion of the sputtered film to the silicon substrate resulted. The films could be scratched with stainless steel points, and occasionally even disintegrated during the HF etching process. Gradual decomposition and deposition of organic materials on the sputtering chamber walls and the back streaming of pump fluids made it imperative that the sputtering system be periodically and frequently cleaned.

At a lower degree of contamination due to the same cause mentioned above, poor adhesion might not be detectable by mechanical testing. However, when the samples were subject to heat treatment at 1050°C for a period of 30 min, "blisters" *i.e.*, film separations, developed and some blisters appeared to have exploded and left microscopic openings behind (see Fig. 6.) At a still lower background pressure, neither poor adhesion nor blisters were observed. However, more subtle effects on properties such as electric conductivity, carrier trapping and dielectric hysteresis could not be ruled out. In addition, the resistance to impurity diffusion was also affected. Samples prepared under the conditions of a contaminated sputtering system failed to mask diffusion of zinc, gallium, steam, and even phosphorus. As might be expected, the uncontrolled contamination also greatly increased the dissolution rate of the film in HF solutions. In conclusion, to obtain good films, the residual pressure should be below 10^{-6} Torr and no organic materials or vacuum grease, etc., should be present in the sputtering chamber.

Mass spectrometric analyses of the gases before and during the sputtering showed most gaseous impurities to be CH_4, CO H_2O, C and CO_2. Little, if any O_2 was observed.

Oxygen contamination.—Formerly, it was thought that very small amounts of oxygen or water in the nitrogen would be deleterious to the entire sputtering deposition process, because it was believed that oxygen and water are much more reactive than nitrogen in the glow discharge. Hence, in earlier experiments

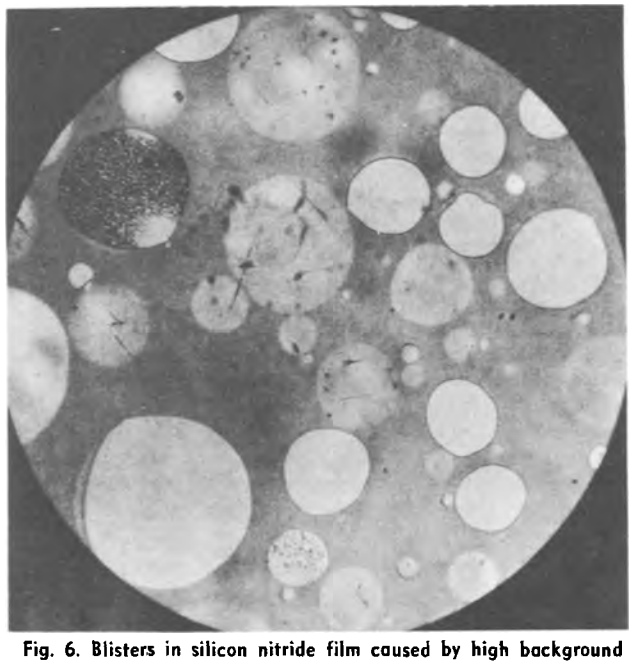

Fig. 6. Blisters in silicon nitride film caused by high background pressure.

with d-c sputtering, care was taken to purify the nitrogen gas by first passing it through copper turnings in a quartz tube at 700°C followed by freezing out residual moisture and condensable materials in a liquid nitrogen trap. Analyses of the line nitrogen before purification, however, showed oxygen and water to be present at less than 1 ppm. Hence, it was supposed that the contaminating oxygen and water must have come from the walls of the sputtering chamber (c.f. the discussion in the section of d-c *vs.* rf sputtering). To test how much more reactive oxygen is than nitrogen in an attempt to understand the reactive sputtering mechanism, oxygen was incorporated into the nitrogen stream at volume concentrations from 1 to 5%. At 1.0% oxygen concentration (total pressure 18 x 10^{-3} Torr, spacing 1½ in., power density 4 w/cm²), a film was obtained which showed the regular IR band due to Si-N bond stretching (12μ), and very little, if any, Si-O constituent. The band at 4.6-4.7μ again showed up, similar to the case of high voltage d-c reactive sputtering (2-5 kv). A mixture of Si-N and Si-O was observed with 2% O_2 in N_2 sputtering gas. When the oxygen content was increased to 5.0%, the film formed showed an IR band characteristic of Si-O stretching (9.4μ) and little, if any, Si-N band.

Effect of gas pressure.—It was found that the gas pressure was very critical to the quality of the films deposited. No good quality films have been obtained with pressure greater than 40 x 10^{-3} Torr in rf reactive sputtering. In d-c sputtering, unfortunately, the gas pressure used had to be of this magnitude or higher because of the very inefficient collision of electrons with gas molecules in a d-c field, which is essential to the sustention of the ionization process. At high gas pressure, especially in rf reactively sputtering where the floating d-c voltage is low (1.0-1.5 kv), the films deposited were generally very leaky electrically, and the etch rate was of the order of 10 Å/sec in 7:1 buffered HF solution at 25°C. The films failed to block diffusion of certain impurities, including steam and oxygen at high temperatures. The surface charge was seemingly low with the increase of gas pressure. However, larger C-V hysteresis in MIS devices was observed. From Fig. 7, it is seen that the etch rate of the deposited films increased drastically with the increase of gas pressure beyond 20 x 10^{-3} Torr. This could not be attributed to the lowering of the film density alone. There is reason to believe that more impurities were trapped in the films during the deposition. The density of the deposited films generally decreased with the increase of gas pressure, as is seen in Fig. 8. As the gas pressure decreased below 2.5 x 10^{-3} Torr, the efficiency of ionization became greatly reduced, and one started to observe the spreading of the

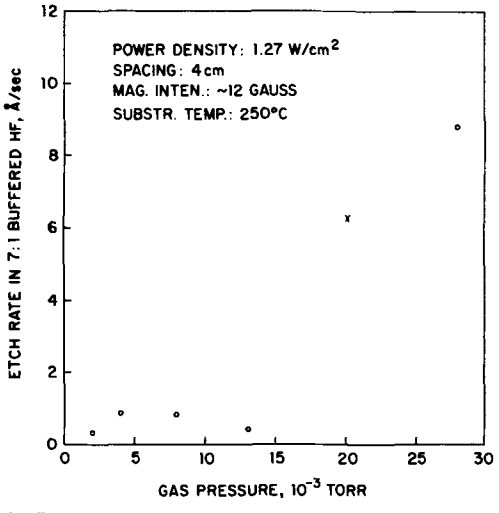

Fig. 7. Effect of gas pressure on film etch rate in a buffered HF solution.

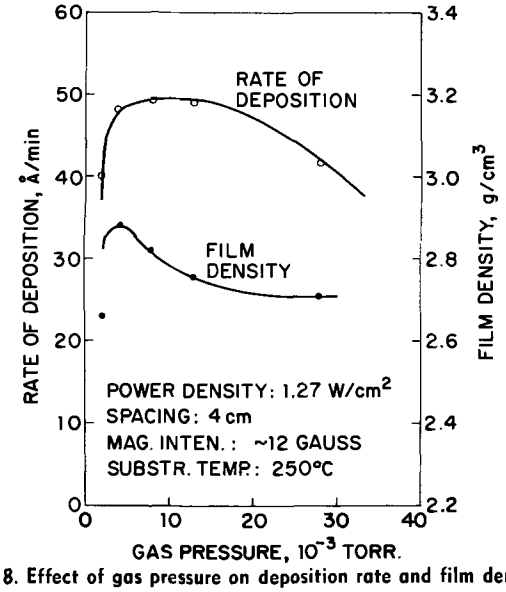

Fig. 8. Effect of gas pressure on deposition rate and film density

plasma over the entire sputtering system. The average magnetic field in this case was 12 gauss. Reasonably stable glow discharge could be maintained down to 2.0 x 10^{-3} Torr with this magnetic field intensity. However, at this low ionization efficiency, the rate of deposition decreased sharply. The density of the deposited film also decreased abruptly. It should be noted that with 1.27 w/cm² power density, the cathode d-c floating potential did not change significantly with gas pressure. The variation was from ~1.4 kv at 28 x 10^{-3} Torr to 1.6 kv at 2 x 10^{-3} Torr. From this observation, it can be argued that negative ion bombardment played an important role in densifying deposited films during sputtering at high power density, for one would expect the sputtered particles to be more energetic in the 2 x 10^{-3} Torr case, while the concentration of the negative ions might be much lower. Thus, less negative ion bombardment caused the film to be somewhat less dense at extremely low pressure,

The rate of deposition was relatively constant in the pressure range 4 to 20 x 10^{-3} Torr under described conditions, and dropped off rapidly at the low pressure end, while it dropped off more slowly with increasing pressure.

With increased magnetic field of, for example, 100 gauss, the ionization efficiency and stability of glow discharge at low pressure probably could be improved.

Reactive sputtering in argon and nitrogen mixture.—Experiments were made with reactive sputtering of a silicon cathode in mixtures of argon and nitrogen with various percentages of nitrogen concentration. It was found that two distinctive phases were obtained by reactive sputtering in a A + N_2 mixture of below 5% N_2 and above 10% N_2. Above 10% N_2, the films obtained were transparent and insulating. The infrared absorption band remained practically unchanged at 12.0μ. Below 5% N_2, the films obtained had a metallic lustre and were semiconducting. The infrared absorption band was shifted to ~13-14μ, and considerably broadened (Fig. 9). This deposit of silicon nitride is believed to be the dispersed phase of Si-N in an amorphous matrix of silicon. An MIS structure of such a phase deposited on a p-type silicon substrate showed a p-i diode characteristic, *i.e.*, $i \propto \exp q\mathbf{V}/2kt$, in the forward bias sense.

The i-V characteristics of films deposited in these gas mixtures is shown in Fig. 10. One sees that the films became progressively more conductive with the decrease of nitrogen concentration. This seemed to imply the non-stoichiometry of the films sputtered in mixtures of N_2 + A. Measurement of the dielectric constant of the deposited films also showed a trend

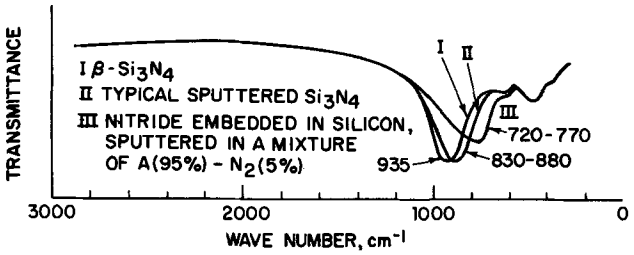

Fig. 9. Infrared spectrum of normal sputtered silicon nitride

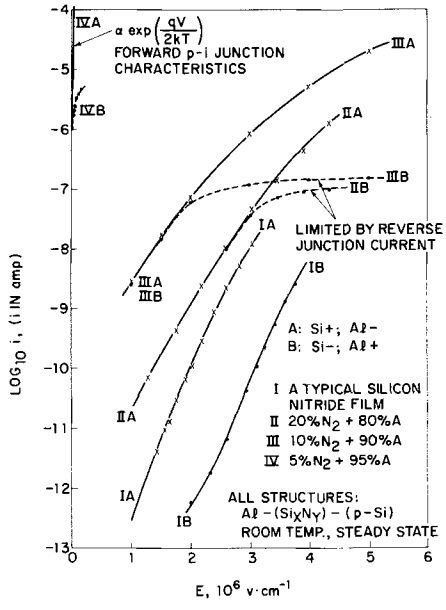

Fig. 10. Effect of gas composition on reactive sputtering formation of Si_xN_y.

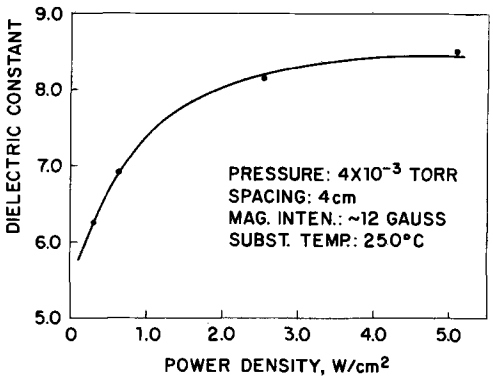

Fig. 11. Effect of power density on the dielectric constant of sputtered films.

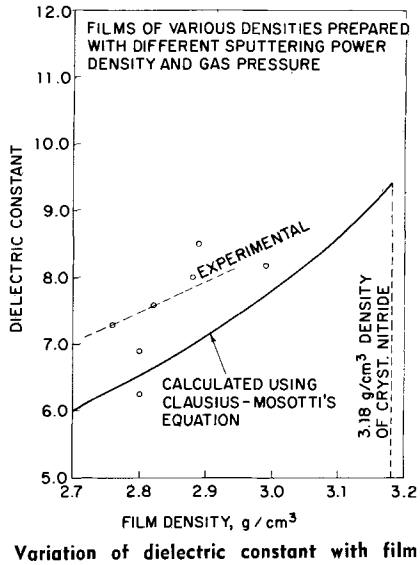

Fig. 12. Variation of dielectric constant with film density of sputtered silicon-nitride.

of increase with decreasing nitrogen concentration, indicating excess silicon incorporation at lower end of the nitrogen concentration in the N_2 + A mixture.

Dielectric constant of sputtered silicon nitride films.—The dielectric constant of silicon nitride films was given as 6.5 in an earlier work (13). Apparently, the films on which the measurement of the dielectric constant was based earlier were somewhat less dense, and there was evidence of trace contamination of silicon dioxide. More extensive evaluation of the dielectric constant of films deposited under various conditions indicated that no unique value existed for the amorphous silicon nitride films. It varied widely with conditions under which the films were formed, and may range from 6.2 to 8.5. If an average range should be given, it would probably be 7.5-8.0. For example, films deposited with various power densities, and otherwise similar conditions appeared to have their dielectric constant increased, initially rapidly, to a limiting value of 8.2-8.5 (Fig. 11). The reason is apparently the difference in the density of the various films formed. A plot of the dielectric constant of various films, prepared under conditions of various power densities and gas pressures, against the film density is shown in Fig. 12. Assuming the constancy of all types of polarizability in the nitride films involving no physical interaction nor variation of chemical constituents, a curve of dielectric constant *vs.* film density based on the Clausius-Mosotti equation is also shown in Fig. 12 for comparison. The curve was calculated using the crystallographic density of 3.18 g/cm^3 (11, 12), and a dielectric constant of 9.4 (15) for the crystalline material. It is seen from this plot that the dielectric constant seems to be consistently higher than would be predicted from a simple Clausius-Mosotti relationship. Three possible causes may be reasonable for this high dielectric constant: (*i*) the increase of molecular and dipole polarizabilities due to looser structure; (*ii*) the presence of shallow impurity levels in the amorphous films causing higher electronic polarization; and (*iii*) the possible inclusion of silicon. The first and the second causes are believed to be more likely for films deposited in pure nitrogen.

Ion and impurity migration in silicon nitride films and silicon nitride-silicon dioxide composite films.—Although little data were available in the literature concerning the migration of ions and atomic impurities in crystalline silicon nitride, it was speculated that the migration rate must be negligible compared with silicon dioxide because of its tight network and largely convalent nature (based on sp^2 planar bonding between N and Si atoms). With due allowance for the slightly less dense amorphous network yet with the absence of grain boundaries, the amorphous silicon nitride film can be expected to possess the same virtue. This speculation has been supported by experimental data obtained in this laboratory.

Ionic migration.—This work has not attempted to study mobilities of various ions in silicon nitride films quantitatively, because of the unavailability of a relatively simple method to determine minute quantities of different impurities in the nitride film. Two techniques have been used to study ionic migration in silicon nitride in this work, and have furnished some qualitative data. One method which was developed by Yamin in the study of polarization in SiO_2, is based on the observation of polarization and depolarization current by applying a slow triangular voltage across a thin film (16).

An example is shown in Fig. 13-a. From this figure, one sees that ionic polarization is essentially negligible

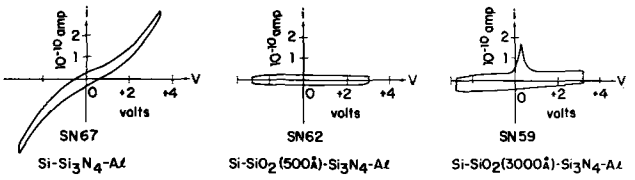

Fig. 13. Yamin-loop study of ionic polarization Si_3N_4 and SiO_2 —Si_3N_4 at 400°C.

in silicon nitride up to 400°C. However, one did see measurable electronic conductivity. In Fig. 13-b, it is shown that a thin layer (~500Å) of SiO_2 between silicon nitride and silicon is capable of blocking electronic conduction in the MIS structure. With the SiO_2 layer increased to 3000Å, ionic polarization becomes observable, presumably occurring in the SiO_2 layer, although the electronic conductivity is still blocked (Fig. 13-c).

The second method is based on the detection of the ions which under a positve d-c bias at elevated temperatures had migrated and piled up at the Si-silicon nitride interface by measuring the corresponding change in carrier density in the space charge layer at the silicon surface. The determination of the excess in the space charge layer is made by determining plate charge at flat-band situation, the so-called MOS C-V measurement. Experiments with controlled Na^+ contamination as well as contamination with isopropanol, indicated that Na^+ and H^+ did not migrate appreciably through a 600Å layer of nitride. It is interesting to note that, even though the etch rate could be increased greatly, and even more so the conductivity increased with change of sputtering conditions such as increased pressure and unidentified background contamination, the ability of the nitride film to block ion migration was still remarkable. Sample 992a is an example, which consisted of 5100Å of thermal SiO_2 and 600Å of sputtered silicon nitride (25 x 10^{-3} Torr N_2 pressure). The conductivity of the composite film was low because of the SiO_2 layer. After controlled contamination by evaporating NaOH onto the surface, the sample was subject to annealing at 300°C for 30 min and then subject to each of the following steps of temperature-bias treatment (bias at +30v; each step 30 min). The results are shown in Table I.

It is also noted that the hysteresis phenomenon usually observed in silicon nitride, which has been suggested to be caused by injection of holes from silicon into silicon nitride film and the subsequent trapping (17, 18), was not observed with the M-nitride —SiO_2 —Si structure. At a much higher field of 3-4 x 10^6 v-cm^{-1}, the normal type of hysteresis could be observed, in contrast to simple M-nitride —Si structure (18).

Diffusion of other impurities.—Experiments showed that when high quality sputtered silicon nitride films were obtained, substances such as water, oxygen, phosphorus, and gallium did not diffuse through the films at temperatures of 1050°-1200°C.

The ability of silicon nitride films to block gallium is quite remarkable. Experimental results were obtained with two different film specimens. The first was prepared by depositing silicon nitride onto silicon at a power density and pedestal temperature which would produce an etching rate of 2.5 Å/sec. From Fig. 4, this is seen to be 0.7 w/cm^2. This film was then coated with KTFR, exposed, and etched to produce the diffusion windows. The second film was deposited on a

Table I. Results

Temp, °C	$-\Delta V_{FB}$ volts
200	1
300	3-5
400	70-72
450	195-240

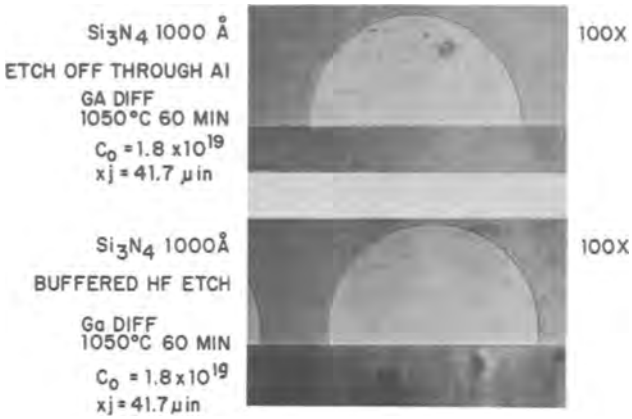

Fig. 14. Stained angle-lapped cross-section of gallium diffusion junction through window of silicon nitride diffusion mask.

silicon wafer which had a previously etched pattern of aluminum 0.5μ thick to conform to the diffusion window pattern. The film deposition was done at 2.5 w/cm^2, *i.e.*, the silicon nitride etch rate was exceedingly low. Hence, the aluminum pattern was then dissolved out, carrying away the silicon nitride and opening the diffusion windows. Both specimens were then exposed to gallium vapor at 1000°C for 60 min. The results were similar; both films were effective masks. Figure 14 shows typical stained angle-lapped cross sections of the junctions. The definition of the edge of the window is somewhat better for the etched film.

Conclusions

Good quality silicon nitride films can be prepared by reactive sputtering of a silicon cathode in nitrogen under proper conditions. The rate of deposition is in the practical range of ~ 100 Å/min. For good results, the residual pressure in the chamber should be well below 10^{-6} Torr. The gas pressure is preferably in the lower end of the range from 4-10 x 10^{-3} Torr. The density of the films is somewhat lower than that of the crystalline material, with an average of about 2.9 g/cm^3, and the dielectric constant is higher than would be predicted from the film density.

In general, high power sputtering is preferred. In this case, surface damage and total surface charge may become a problem. However, the flexibility of the combination of various sputtering factors and the use of low temperature process make it possible to produce films with varying properties for various applications.

Acknowledgments

The authors wish to thank Dr. L. Maissel for his many helpful suggestions and encouragement, and Drs. P. Davidse and D. R. Kerr for stimulating discussions. Dr. Kerr also helped with the Na^+ contamination experiment. They are also indebted to Messrs. R. Baker, Jr., R. F. Marvel, and J. A. Petrak for assistance in the experiment.

Manuscript received Jan. 25, 1967; revised manuscript received April 14, 1967. This paper was presented at the Philadelphia Meeting, Oct. 10-14, 1966. This work was supported in part by the United States Air Force Avionics Laboratory, Wright-Patterson Air Force Base, under Contract No. AF 33(615)-5386.

Any discussion of this paper will appear in a Discussion Section to be published in the June 1968 JOURNAL.

REFERENCES

1. P. J. Burkhardt, Private communication.
2. S. M. Hu, Unpublished data.
3. H. F. Sterling and R. C. G. Swann, *Solid-State Electronics*, 8, 653 (1965).
4. V. Y. Doo, *et al.*, Paper presented at the Buffalo Meeting of the Society, October, 1965.
5. W. Pennebaker, Private communication.

6. Electrochemical Society, Joint Symposium (Dielectrics and Insulation and Electronics-Semiconductor Divisions) on Silicon Nitride, Oct. 12 and 13, 1966, Philadelphia, Pa.
7. W. R. Sinclair and F. G. Peters, *J. Am. Ceram Soc.*, **46**, 20 (1963).
8. R. M. Valletta, J. A. Perri, and J. Riseman, *Electrochem. Technol.*, **4**, 402 (1966).
9. G. S. Anderson, W. N. Mayer, and G. K. Wehner, *J. Appl. Phys.*, **33**, 2991 (1962).
10. P. Davidse and L. Maissel, *ibid.*, **37**, 574 (1966).
11. E. T. Turkdogan, P. M. Bills, and V. A. Tippett, *J. Appl. Chem.*, **8**, 295 (1958).
12. D. Hardie and K. H. Jack, *Nature*, **180**, 332 (1957).
13. S. M. Hu, *This Journal*, **113**, 693 (1966).
14. R. Y. Desphande, *Solid State Electronics*, **8**, 619 (1965).
15. O. Glemser, K. Beltz, and P. Naumann, *Z. anorg. u. allgem. Chem.*, **291**, 51 (1957).
16. M. Yamin, *IEEE Trans. Electron Devices*, **ED 12**, 88 (1965).
17. S. M. Hu, Paper presented at the Electrochemical Society Meeting, Philadelphia, Oct. 10-14, 1966.
18. S. M. Hu, D. R. Kerr, and L. V. Gregor, *Appl. Phys. Letters*, **10**, 97 (1967).

APPENDIX I. A Summary of Some Physical Properties of Crystalline Silicon Nitride

For comparison with amorphous films by reactive sputtering, and for convenience of quick reference, a table of physical properties has been compiled, and provided below.

Phase	α and β — Si_3N_4	*(a)*
Transition temp.	$\alpha \rightarrow \beta$, 1400°C, sluggish	*(a)*
Crystal system	Hexagonal	*(a)*
Space group	α, P31c; β, Pb 3/m	*(a)*
Lattice parameters	α(a = 7.738Å, c = 5.617Å)	*(a)*
	β(a = 7.608Å, c = 2.991Å)	*(a)*
Crystallographic density	α, 3.184 g cm^{-3}	*(a)*
	β, 3.187 g-cm^{-3}	*(a)*
Si-N	1.72Å	*(a)*
Experimental density	3.448 g-cm^{-3}	*(b)*
Index of refraction	2.1	*(c)*
Dielectric constant	9.4	*(d)*
Energy gap	3.9-4.0 e.v.	*(e)*
Infrared absorption band	10.6μ (Si-N)	*(f)*
Electric resistivity	10^{13}-10^{14} ohm-cm	*(e, g)*
Melting point	1900°C (under pressure)	*(f)*
Heat capacity	0.1746 cal. g^{-1} $°C^{-1}$ (0-995°C)	*(h)*
	0.2145 cal. g^{-1} $°C^{-1}$ (0-585°C)	*(h)*
Thermal expansion coefficient	α 3.0 x 10^{-6} $°C^{-1}$; β 3.5 x 10^{-6} $°C^{-1}$	*(i)*
Thermal conductivity	0.067 cal cm^{-1} $°C^{-1}$ sec^{-1}	*(j)*
Solubility in silicon	$<10^{12}$ atoms cm^{-3} (room temp)	*(f)*
	$\sim 10^{19}$ atoms cm^{-3} (in melt at m.p.)	
Hardness	>9 Moh's scale	*(j)*
Heat of formation	$\Delta H_{298.1} = -179.250$ kcal mol^{-1}	*(k, l)*
Entropy	$S_{298.1} = 22.8$ cal mol^{-1} $°K^{-1}$	*(k, l)*
Free energy of formation	$\Delta G°_{298.1} = 154.740$ kcal mol^{-1}	*(k, l)*
At 1700°K	$\Delta H_{1700} = 176.300$ kcal mol^{-1}	*(m)*
	$\Delta G_{1700} = 176.300 + 0.07835$ T kcal mol^{-1}	*(m)*

(a) D. Hardie and K. H. Jack, *Nature*, **180**, 332 (1957).
(b) L. Weiss and T. Englehardt, *Z. anorg. Chem.*, **65**, 38 (1910).
(c) W. P. Forgeng and B. F. Decker, *Trans. Met. Soc. AIME*, **47**, 343 (1958).
(d) O. Glemser, K. Beltz, and P. Naumann, *Z. anorg. u allgem. chem.*, **291**, 51 (1957).
(e) G. B. Samsonov, *Proroshkovaya Met. Akad. Nauk Ukr. S.S.R.*, I, 53 (1961); CA 56, 8142c (1962).
(f) W. Kaiser and C. D. Thurmond, *J. Appl. Phys.*, **30**, 427 (1959).
(g) G. B. Samsonov and G. G. Tsekulya, *Ukr. Fiz. Zh.*, **5**, 615 (1960).
(h) E. Friedrich and L. Sittig, *Z. anorg. chem.*, **143**, 283 (1925).
(i) S. Iwai and A. Yasunaga, *Naturwiss.*, **46**, 473 (1959).
(j) P. Popper and S. N. Ruddlesden, *Trans. Brit. Ceram. Soc.*, **60**, 603 (1961).
(k) F. D. Rossini *et al.*, *Circ. Bur. Stand. No. 500*, 150 (1952).
(l) K. K. Kelley, *U.S. Bur. Mines, Bull. No. 407* (1937).
(m) W. B. Hincke and L. R. Brantley, *J. Am. Chem. Soc.*, **52**, 48 (1930).

Polycrystalline Zinc Oxide Dielectrics

R. A. Delaney and H. D. Kaiser

IBM Components Division, East Fishkill Facility, Hopewell Junction, New York

ABSTRACT

This paper describes a dielectric material with certain properties unique to prior art and offers a practical method of resolving some of the circuit problems encountered in low-impedance circuits with extremely fast switching times. The basic material is semiconducting polycrystalline zinc oxide. Modifications of this base material are obtained by thermal diffusion doping via grain boundaries. The end result is a polycationic complex material with controlled valency characteristics. Specific attention is focused on those properties which make these materials uniquely suited for microminiature high-frequency, low-impedance decoupling or filter-type capacitor devices. Utilizing screen printing technology, devices with apparent low-frequency dielectric constants on the order of 3000 and high-frequency dielectric constants of 1700 have been achieved. These devices attenuate high-frequency signals with either a damped oscillatory or critically damped response. This system of device dielectrics belongs, respectively, to either the semiconducting or semi-insulating classes of solids.

Zinc oxide is a well-known n-type semiconductor, the properties of which have been investigated by many workers (1-8). Excellent reviews of much of this work have been made recently by Thomas and by Heiland, Mollwo, and Stockmann (9, 10). Although the properties of bismuth oxide are less well characterized, some work has been done (11-13), and it is well established that under most circumstances it is a p-type semiconductor (13). Some of the dielectric, resistive, and electroluminescent properties of zinc oxide with additions of bismuth oxide have been reported recently by Kosman and Gesse (14), Kosman and Pettsold (15), and Delaney and Kaiser (16).

The present investigation supplements and extends the previous ones in a specific area, namely, that of utilizing the material in the form of a silk-screened

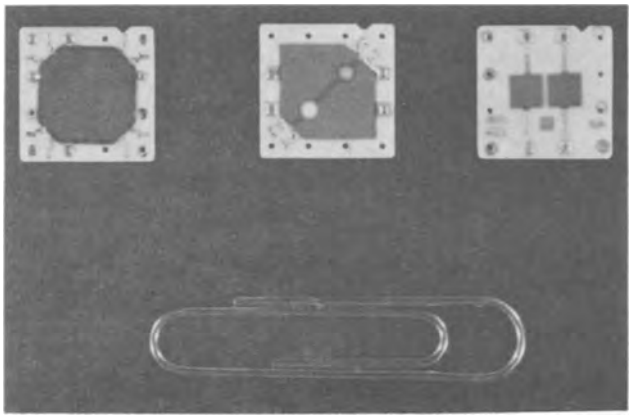

Fig. 1. Typical completed capacitor units utilizing the new nonlinear dielectric system.

parallel plate capacitor suitable for incorporation in high speed microelectronic switching circuits. Typical examples of such units appear in Fig. 1.

Zinc Oxide

Zinc oxide crystallizes in the hexagonal wurtzite lattice in which the oxygen ions are arranged in the hexagonal close packing and the zinc ions occupy half the tetrahedral interstitial positions. It is an n-type semiconductor with an excess of interstitial zinc atoms which are responsible for the conductance electrons in the crystal.

Its semiconducting properties can generally be said to be due primarily to interstitial zinc atoms. It thus can be considered as an electronic semiconductor with a large energy gap of 3.2 ev, classified somewhere between the heteropolar alkali halides and the homopolar semiconductors of the group IV elements. It is known to be a nonstoichiometric substance with an unstable oxygen content and changing semiconducting properties.

Zinc Oxide with an Admixture of Bismuth Oxide

The electric properties of zinc oxide, an n-type semiconductor, are changed considerably by the admixture of bismuth oxide, a p-type semiconductor. The most interesting property of such a mixture is the high dielectric constant. Initial experiments performed by Kosman and Gesse (14) give effective dielectric constants as high as 1500. This is very spectacular when one considers that the dielectric constant of polycrystalline zinc oxide is on the order of 30 or 40 and that of bismuth oxide on the order of 10 or 20. They found that dielectric constant is strongly dependent on the sintering temperature, the increase with increasing sintering temperature being more pronounced with a low bismuth oxide content.

This system has properties of nonlinear symmetrical and asymmetrical resistivity depending on fabrication methods. By changing the specimen fabrication, one can obtain electrical conductivities from 10^{-6} to 10^{-11} mho/cm. Recent investigations on this system with constant, alternating, and impulse voltages by Kosman and Pettsold (15) show that the conductivity is increased considerably if the excitation is accomplished by the impulse method. The I-V characteristics for both constant as well as alternating excitations within a wide voltage interval approximates

$$I \alpha V^{\eta} \qquad [1]$$

where the coefficient of nonlinearity (η) is dependent on the conductivity.

Sample preparation.—All capacitors were prepared by silk-screening techniques as shown in Fig. 2. The capacitors were fabricated on 96% alumina substrates in a simple parallel plate configuration. In most cases the area of the plates was 0.01 in.^{2}. The bottom plate and associated lead were silk-screened using a suitable conductive paste. In most cases a gold-platinum paste was used. Quenching was accomplished by removing the units from the furnace at temperature and immediately placing them on a large aluminum block. Electrical connectors were made with copper pins placed through the holes in the substrate, which were subsequently soldered to the conductive leads from the capacitor (Fig. 2).

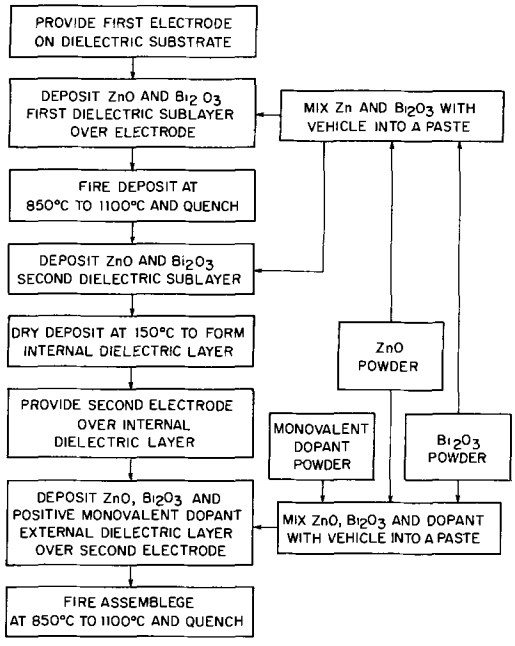

Fig. 2. Flow chart for fabrication of ZnO dielectric systems

Electrode.—The effects of various materials when used as part of the electrode system were also studied. It was found that gold, platinum, and combinations thereof give comparable results, while silver, even in combination with up to 35% platinum or 20% palladium, is extremely detrimental to the system. Apparent doping of the system by silver lowers the dielectric constant to roughly that of pure zinc oxide fired with platinum electrodes under comparable conditions. The use of various lead glasses as electrode fluxes had no adverse effects, while the incorporation of Bi_2O_3 as a flux strongly doped the ZnO and gave a capacitor whose properties were insensitive to the amount of Bi_2O_3 in the body. However, when up to 10% Bi_2O_3 was added to a silver-bearing electrode, it did not overcome the effects of the silver, indicating extremely strong diffusion of silver into the capacitor body.

Thermal effects.—An extended study was made of the variation of capacitance, conductance, and d-c resistance with temperature using capacitors made from the 5% Bi_2O_3 material. The results are summarized in Fig. 3 and 4. The change in capacitance in the region −50° to +150°C can be expressed quite accurately by the relation

$$C = C_o e^{\alpha T^3} \qquad [2]$$

where α is determined by both the temperature and soak time of firing. The d-c resistivity may be approximated by

$$R = R_o e^{-\beta T}$$

where β is also governed by the firing conditions.

It can also be seen that both the capacitance and resistance at a given temperature and the slope of the curve vary considerably with the firing conditions. Capacitance measurements at liquid nitrogen temperatures (−196°C) show that the dielectric constant of the zinc oxide −3% bismuth oxide system has dropped from ~ 1500 to ~ 40, that of the polycrystalline zinc oxide.

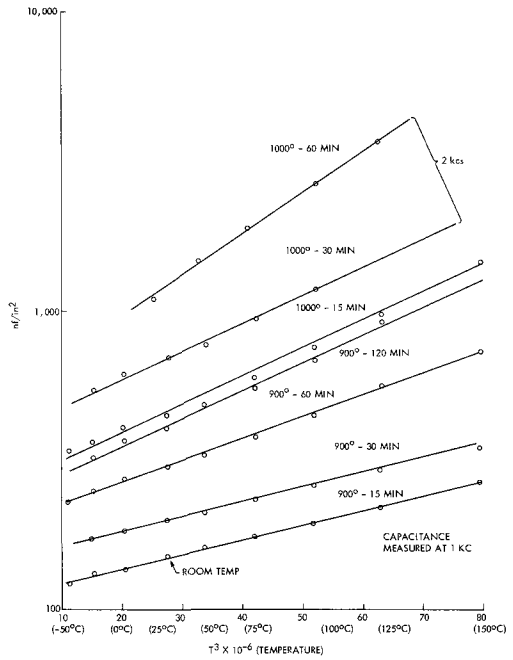

Fig. 3. Capacitance *vs.* temperature for various firing times

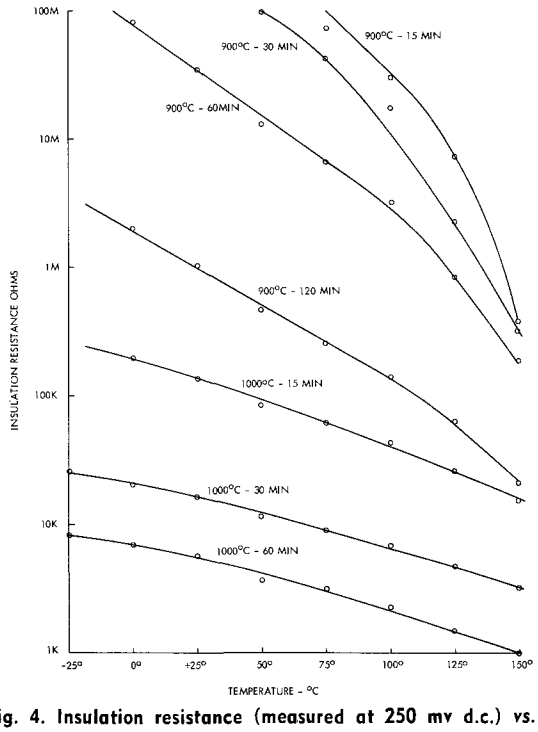

Fig. 4. Insulation resistance (measured at 250 mv d.c.) *vs.* temperature for various firing times.

Frequency response.—The frequency response was measured over the range 1 kcps to 50 Mcps (Fig. 5 and 6). The higher firing temperatures and longer times have a deleterious effect on the variation of capacitance and conductance with frequency, the capacitance falling off more rapidly and the conductance more slowly with higher temperature and longer firing times. The capacitance varies almost linearly and reasonably slowly with frequency, and the conductance varies directly as frequency, that is

$$G \alpha \omega \qquad [4]$$

thus indicating that the quality factor (Q) should be approximately invariant with frequency. The quality factor as used here is defined as the average energy stored to energy dissipated within the capacitor.

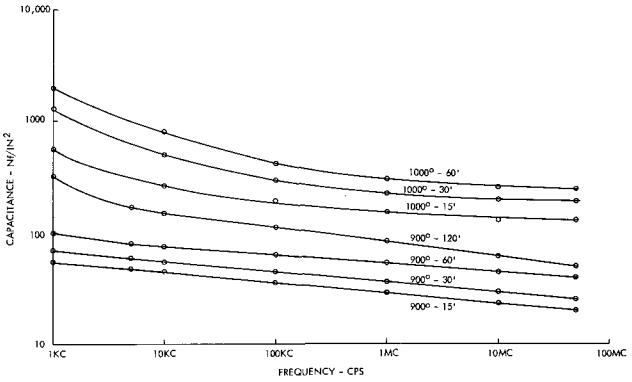

Fig. 5. Capacitance *vs.* frequency

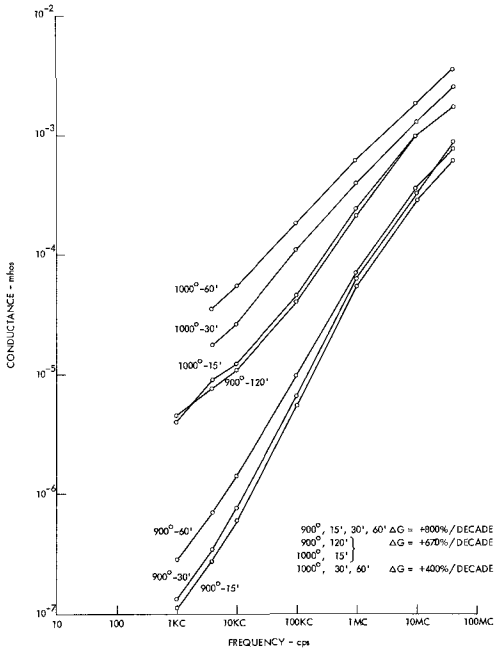

Fig. 6. Conductance *vs.* frequency for various firing parameters

Quenching.—As may be suspected from the nature of zinc oxide, the rapidity of the quench after firing has a strong influence on the final parameters. This is illustrated in Fig. 7 which shows the quench rates achieved by suspending the samples in still air, or placing them on a large alumina or aluminum block.

Drastic quenching has been achieved by deflecting the cold gas from expanding liquid CO_2 onto the device surface. The temperature was lowered from 1000° to 0°C in 60 sec. A capacitance of 100 μf/in.^{2} resulted; however, the resultant d-c resistivity was only 10 ohm-cm.

QUENCHING METHOD	t (u)	DAMP (%)	C_pA (NF IN^2)	KE (eff)	R_p (Ω) DC-1/4 V	10MC
AIR	19	72	320	1060	500	20
ALUMINA	20	72	275	910	625	20
ALUMINUM	19	82	480	1600	50	10

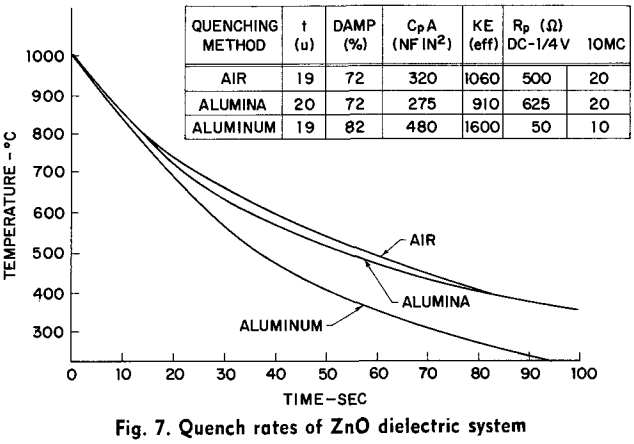

Fig. 7. Quench rates of ZnO dielectric system

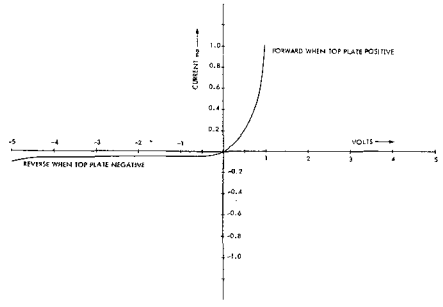

Fig. 8. D-C current-voltage relationship showing rectifying properties of the ZnO system.

Voltage response.—The investigation of the influence of a d-c bias on the electrical parameters revealed some unusual features. There is also a slight directional or rectification effect in both capacitance and conduction as "forward" and "reverse" bias curves do not superimpose at higher biases.

This directional effect becomes much more obvious when the top plate of the capacitor is solder coated and biased positive. This may be partially due to the change in work function of the top plate.

This asymmetry is also noticeable in the V-I curves of Fig. 8, especially for the soldered samples. The junction is asymmetric in nature and polarity dependent for similar electrodes.

When dissimilar electrodes are separated by a sufficiently thin insulating film, current can flow between them in an asymmetric mode by various current transfer mechanisms. If the electrodes are of the same metal, the junctions are symmetric and polarity independent. This leads to the conclusion that there may be some potential here for a rugged, low-cost power diode (17).

Since this rectification is undesirable in a capacitor, the condition can be corrected by the use of a solder stop-off, *i.e.*, an inert coating over the top plate to prevent the adhesion of solder during tinning. It was found that a layer of the dielectric material screened over the top plate and fired in the final step was most effective.

Topology.—Since there was some speculation as to whether or not the capacitance was due to a bulk effect or to a high capacitance at the electrode-dielectric interface, a determination of capacitance and d-c resistance *vs.* thickness was made. If the capacitance were due to a bulk effect, it should follow the usual relation for a parallel plate capacitor.

$$C \approx K\epsilon \frac{A}{d} \qquad [5]$$

If the capacitance were in any large degree due to an interface effect, it should be nonlinear with regard to reciprocal thickness or follow a linear law with a large additive constant.

Results are given in Fig. 9. The dielectric constant is approximately invariant with thickness, and the capacitance follows the normal law for parallel plate capacitors. This rules out the electrode-dielectric interface as being a major source of the capacitance. However, it does not rule out the possibility of the capacitance being due to some type of three-dimensional barrier layer or interface effect involving the individual grains of zinc oxide. Since this effect would be distributed throughout the whole layer, it could very easily exhibit the usual type of thickness dependence.

The resistance follows a nonohmic relationship, that is (Fig. 10).

$$R = t^m + R' \qquad [6]$$

Since differences in slopes and intercepts were obtained for different electrode-dielectric combinations,

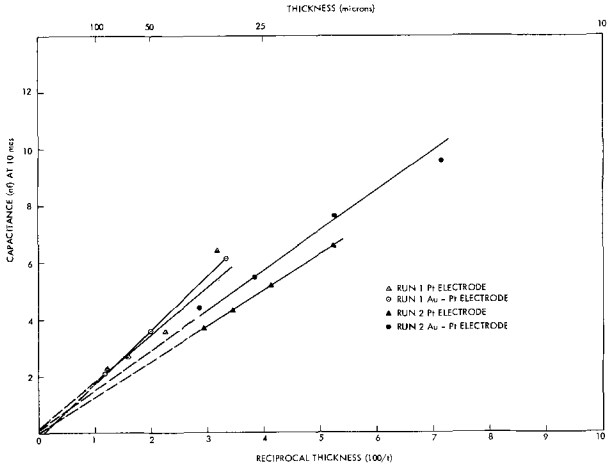

Fig. 9. Capacitance vs. thickness for ZnO + 3% Bi_2O_3

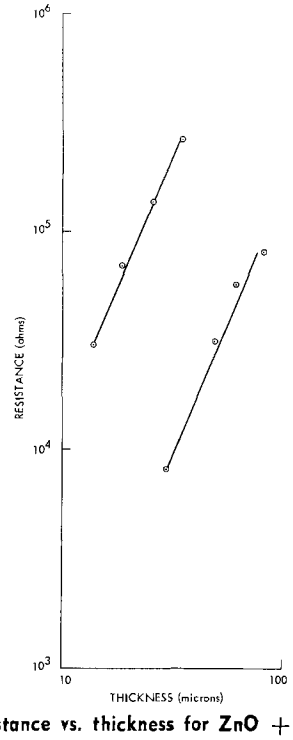

Fig. 10. Resistance vs. thickness for ZnO + 3% Bi_2O_3 and Au-Pt electrodes.

it is possible that the resistance is at least partially governed by interface effects.

Further Materials Development

General.—Zinc oxide is n-type, and bismuth oxide is basically p-type. X-ray diffraction studies show that with up to 15% bismuth oxide content the mixture retains the zinc oxide lattice. Subsequent diffraction studies show that the lattice structure remains unchanged regardless of sintering temperature, cooling conditions, or subsequent heat-treatments. Based on this evidence, it is theorized that a depletion layer of relatively high resistance is formed around the zinc oxide granules by shallow diffusion of the bismuth oxide. That this layer is not at the electrode-dielectric interface is shown by the thickness dependency experiment. The zinc oxide bismuth oxide interface interpretation leads to a situation similar to that discussed by Koops (18) for semiconducting nickel-zinc ferrites and summarized by Volger (19). In these models, a physical picture of conducting grains separated by layers of poorly conducting material is successfully equated to an electrical analog of parallel

Table I. Parametric values of the nonlinear capacitor

Dielectric system	Damping coefficient, %	D-C resistivity, ρ_{d-c} in ohm-cm @ 100 v/cm	Impedance, ohm at 100 → 700 Mc	Effective dielectric constant 1 Kc	Effective dielectric constant 5 Mc	Dielectric thickness, cm
ZnO*	80 → 85	10^5	2	160	80	0.0025
ZnO + Bi_2O_3*	80 → 85	10^3	2	2000	1000	0.0020
ZnO + Bi_2O_3**	80 → 85	2×10^5	3	3400	1700	0.0020
ZnO**	80 → 85	10^5	2.5	3800	1900	0.0025

* Glass fluxed platinum electrodes.
** Bismuth oxide fluxed platinum electrodes.

Table II. Doping effects of the zinc oxide dielectric

Example	Dopant material, 1.0 mole %	D-C resistivity, ohm-cm × 10^6	Damping, %	Capacitance, Nf/in.^{2}	Dielectric constant	Q value
11	$Cu(NO_3)_2$	10-25	98	300-350	600-700	1-1.2
12	$CuSnO_3$	50-150	98	325-375	700-800	1.3-1.5
13	$Cu(NO_3)_2$ + TiO_2	1-5	98	325-275	700-800	1-1.2
14	TiO_2	0.1-0.5	80	350-400	1000-1100	40-50
15	$BaTiO_3$	0.05-0.1	80	400-450	800-900	35-40
16	CuAcetate	5-10	98	350-400	900-1000	1.3-1.5
17	$CuTiO_3$	1-5	98	400-500	900-1000	1-1.2

RC network connected in series. By using this model, Koops was able to calculate curves which fit the experimental data fairly closely.

As a material for a capacitive device, zinc oxide with 3% bismuth oxide meets or exceeds most requirements when fabricated into a simple parallel plate configuration and fired at 1000°C for 60 min followed by rapid quenching as can be seen in Table I.

Factors which give rise to high effective capacitance values also produce high-conductance values. One would rather like to maximize the effective capacitance effect but at the same time minimize the conductance. In fact, one would like to convert this zinc-bismuth oxide mixture from a semiconducting dielectric to a semi-insulating dielectric while retaining the depletion layer mechanism for high effective capacitive values.

One logical approach would be to diffuse a monovalent dopant into the defect zinc oxide lattice to fill vacant cation sites. This would give a polycationic arrangement with a high population of electron deficient cation sites acting as electron "traps."

Success has been achieved with this approach. As a specific example, this study first considers a zinc-bismuth oxide semiconductor doped with copper. Doping was accomplished through volume diffusion by the direct addition of copper titanate. The resistivity of the dielectric increased from 10^4 to 10^8 ohm-cm. This, however, cannot be accomplished without a 50% decrease in effective dielectric constant due to a dilution effect. As expected, the dielectric dissipation also dropped. An additional effect was observed, *viz.*, a change in frequency characteristic from a damped oscillatory to a critically damped response.

The latter effect is unusual since one might expect the opposite to occur. As the dielectric approaches the insulator state, the effective shunt resistance increases and thus is capable of storing charge for longer periods of time, *viz.*, the relaxation time diminishes. Thus, the damping coefficient should approach zero, and the dielectric should respond as a pure oscillating network. However, due to the monovalent substitution doping at the cationic site, a small effective series resistance on the order of an ohm is introduced into the printed dielectric network. It is this effective series resistance that causes critical damping. The effect of the series resistance becomes apparent at high frequencies when the reactance drops below this value and the complex impedance becomes constant in value.

To eliminate the dilution effect brought about by direct addition of the doping material, it was decided to utilize a unique characteristic of screen printing technology. The dopant material was screened over the porous top electrode and then fired so that the monovalent cationic species thermally diffuses through the zinc-bismuth oxide grain boundaries.

The top electrode acts as a selective barrier to the dopant material prohibiting the undesired dilution of the internal dielectric by large amounts of the anionic species. This technique attains the same high resistivity as did volume diffusion through the crystal interior, but unlike the latter exhibits only a 20% decrease in effective dielectric constant instead of the 50% due to dilution.

Volume diffusion doping.—In the first series, the dopant was incorporated directly into the zinc-bismuth oxide dielectric. Utilizing the above method, several test samples were fabricated to evaluate the effect of various monovalent substitutions into the semiconducting zinc-bismuth oxide dielectric.

In each of the samples, the dielectric composition was composed of 97% by weight of zinc oxide, 3% by weight bismuth trioxide, and either silver, lithium, or copper dopant in concentrations as shown in Table II.

These capacitors were given a series of standard tests which included measurement of the dielectric resistance at 1v d-c., and damping and capacitance at 10 megacycles. The effective constant was calculated.

The results of these examples indicated that dielectrics having the desired characteristics of high d-c resistance and near critical damping can be made using silver, lithium, or copper dopant. The copper dopant was shown to be the superior to silver and lithium in raising the d-c resistivity.

Having established that monovalent copper substitution produced the more favorable results, it now became important to determine the optimum fabrication technique needed. This technique became quite evident during the course of subsequent investigation.

The procedure for the preparation of the dielectric composition and for the fabrication of the capacitor devices for this group of examples was identical to those above. It can be seen from Table II that the dielectric exhibiting the most pronounced affect utilized 1 mole % copper titanate as the source of copper. A dielectric constant on the order of 900-1000 was achieved, critical damping was obtained, and the d-c resistance was quite high. Other copper salts showed poorer dielectric constant characteristics. Examples 13, 14, and 15 using varying amounts of titanium dioxide or barium titanate were used to determine whether the doping was caused by the monovalent copper or the titanium dioxide. It can be seen from the results that examples 14 and 15 produced di-

electrics with small damping coefficients and Q values which were much too high. Only in example 13 which contained the copper nitrate dopant in addition to the titanium dioxide was the substitution valency effect obtained. It is therefore concluded that the titanate or titanium dioxide is not responsible for the effects noted.

Grain boundary diffusion doping.—Although the conductivity of the semiconductor zinc-bismuth oxide is lowered by monovalent copper substitution and the damping coefficient increased, it was noted that the first system (volume diffusion) shows a marked decrease in apparent dielectric constant due to the presence of the inert material. While adequate for some applications, this system would not be suitable for applications requiring a higher effective dielectric constant. The above examples infer that perhaps by grain boundary diffusion doping of the monovalent ion, one could still minimize the conductivity and yet maximize the dielectric constant due to elimination of the dopant anion from the semiconductor dielectric.

Work done with experimentally determined grain boundary self-diffusion of silver (20), the diffusion of gold into copper bicrystal grain boundaries (21), etc., shows that a theoretical diffusion-penetration relationship for grain boundary diffusion can be developed. One might picture grain boundary diffusion (and similarly for surface diffusion) as diffusion along a thin layer of high diffusivity material sandwiched between large volumes of low diffusivity material after the Fisher model (21, 22) (Fig. 11).

Assuming this diffusion model and the above boundary conditions and further assuming that the lateral diffusion concentration penetration in the vicinity of the grain boundary is greater than the uniform lattice diffusion penetration in regions well removed from the grain boundary, one can obtain a simple analytical expression for the concentration of laterally diffused material in the vicinity of the grain boundary.

Control of the cationic substitution into the lattice can be controlled through grain boundary diffusion. During the fabrication process as shown in Fig. 12, the monovalent dopant in the external dielectric layer 38 is diffused through the pores of the second electrode 34 into the grain boundaries of the dielectric body 36. Preferably, this is done by firing or sintering the assembly at a temperature of 1000°C for a period of approximately 1 hr to diffuse the monovalent dopant from dielectric layer 38 through the pores of the second electrode 34 and into the grain boundaries of the dielectric body. The capacitor is then removed from the furnace and again quenched. The result of the above technique transforms the semiconducting zinc-bismuth oxide dielectric via cationic monovalent substitution diffusion doping into a semi-insulating dielectric.

Two types of initial semiconductor dielectric materials were prepared for this series of examples. The first included 97% by weight zinc oxide, 3% by weight bismuth trioxide, and a 1 mole % of copper titanate. The second dielectric material included 97% by weight zinc oxide and 3% by weight bismuth trioxide.

The examples are distinguished by the presence or absence of a dopant in the internal or external dielectric layer as given in Table III. Examples 20 and 21 differ in that the external layer in example 20 fully covers the second electrode and touches large areas of the internal dielectric layer as illustrated in Fig. 9 while example 21 has its external dielectric layer restricted to a small dot-shaped area which contacts only the second electrode and does not touch the internal dielectric material.

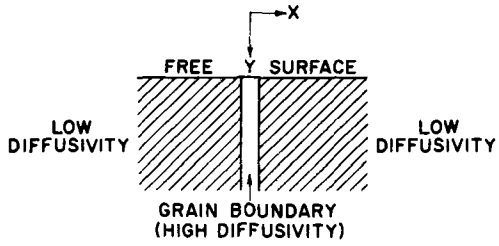

Fig. 11. Fisher model for grain boundary diffusion

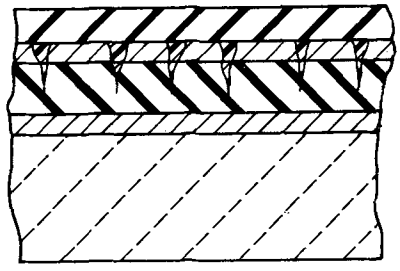

Fig. 12. Schematic model showing grain boundary diffusion of the monovalent dopant.

Example 18 shows that with no dopant in either dielectric layer the d-c resistance is low, Q is low, damping is only 80%, and the apparent dielectric constant is high. Example 19 shows the effect of having dopants in the first and second dielectric layer and has excellent properties except for its unduly low dielectric constant and higher impedance. The surprising 50% increase in dielectric constant, as compared to the example 19 capacitor, is shown in examples 20 and 21 wherein a dopant is present only in the external dielectric layer and not in the internal dielectric layer. No difference in properties was noted between examples 20 and 21, so the touching of the first and second dielectric layers is of minor importance, thus establishing the grain boundary diffusion phenomena through the top electrode. Further evidence is given by the time at formation temperature *vs.* electrical characteristics which closely follows what would be predicted by the diffusion equation.

Device Technology

Utilizing this dielectric system, printed ceramic capacitors as described earlier were manufactured and evaluated.

Frequency response.—Since the specifications of the physical dimensions and electrical parameters are dependent on actual device application, it was decided to devise a capacitor test pattern which would solely yield the dielectric response independent of its geometry. This method is feasible since it has been experimentally demonstrated that these printed dielectrics can be scaled with their respective parametric experimental values being quite accurately predictable from calculations based on actual geometrical dimensions.

Table III. Effects of Cu dopant in the zinc dielectric

Example	Dopant present in: Internal dielectric layer	Dopant present in: External dielectric layer	RC resistance, ohm-cm	Damping, %	Dielectric constant, 5 Mc	Q-value, 52 Mc	Impedance, ohms, 100 → 700 Mc
18	No	No	10^4	80	2000	0.1-0.3	1
19	Yes	Yes	10^8	98	1000	1-2	2-3
20	No	Yes	10^8	98	1500	1-2	1-2
21	No	Yes	10^8	98	1500	1-2	1-2

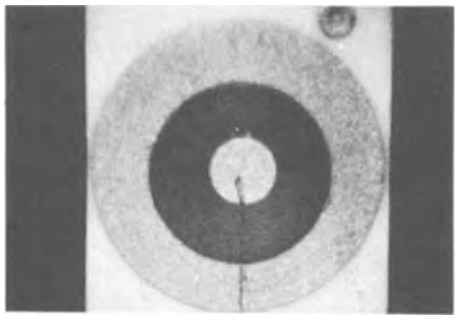

Fig. 13. Picture of concentric bullseye capacitor pattern used for all frequency evaluation testing. Innermost disk is top electrode, middle disk is dielectric body, and outer disk is lower electrode. Effective capacitor plate area is the same as the area of the top electrode.

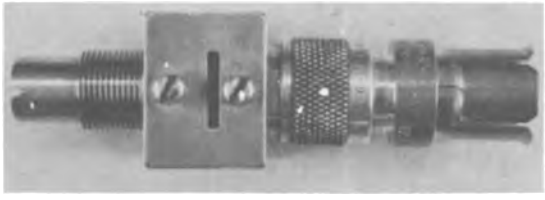

Fig. 14. Jig assembly used to measure samples shown in Fig. 13. A spring loaded copper ball connected to the inner line of the coaxial fixture makes contact to the inner electrode while the outer lip of the fixture contacts the outer electrode. The screw presses the sample onto both contacts.

The choice of a suitable pattern should be such that it does not exhibit any effective series land or plate resistance or inductance, the pattern used is shown in Fig. 13. Likewise, it is equally important to use a jig assembly which also does not exhibit either series resistance or inductance, the jig used is shown in Fig. 14. Figures 15 and 16 show the dielectric constant, dissipation, impedance, reactance, and both equivalent parallel and series resistance characteristics of this dielectric system as a function of frequency. Note the dispersion occurring at 2 x 10^8 Hz in both the dissipation and parallel reactance curves indicating a resonant frequency point. A calculation of the relaxation time, τ_o, by extrapolation of the impedance in the limit to d-c conditions at 25°C gives

$$\tau_o \equiv K_\epsilon \rho_o = (RC)\ \text{static} = 5.3 \times 10^{-9}\ \text{sec}$$
$$\nu_o \equiv \tau_o^{-1} \cong (5.3 \times 10^{-9}\ \text{sec})^{-1} \cong 1.9 \times 10^8\ \text{sec}^{-1} \quad [7]$$

which is in remarkably close agreement with the experimental dispersion point of 2 x 10^8 sec^{-1} noted in Fig. 15. This observed dispersion would correspond to a bulk resistivity of about 200 ohm-cm; a value that is in accord with reported values for single crystals such as noted in the Maxwell-Wagner dispersion as discussed by Hahn (22). Note the splitting of the equivalent parallel and series reactances from the impedance curves at 1 MHz, both asymptotically approach a constant value with the parallel combination roughly equaling the numerical value of the impedance. The dispersion of the equivalent parallel reactance at 200 MHz is identical to the frequency noted for the dissipation dispersion. Finally, note that the impedance asymptotically approaches a constant value. This latter response is modified somewhat when the dielectric is used in a parallel plate capacitor device pattern. The printed lead series inductance and resistance causes a sharper bend in the knee of the impedance curve and shifts it to the left as seen in Fig. 17. Although not shown in the figure, the impedance curve remains flat out to the low gigacycle range, with the limiting value of the impedance between 1 and 2 ohms.

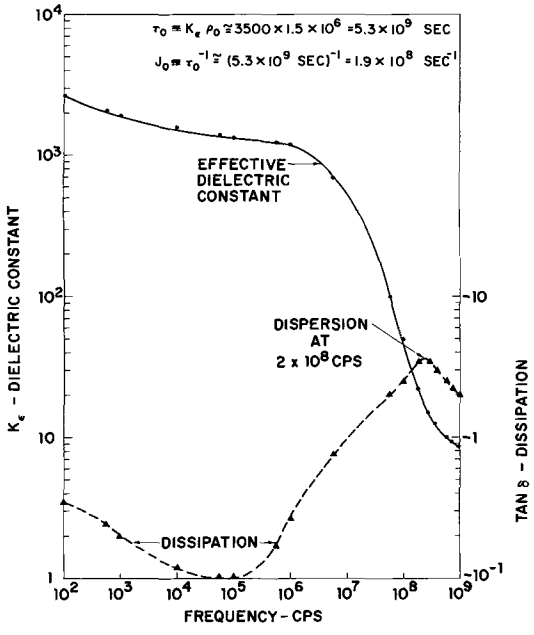

Fig. 15. Dielectric constant and dissipation response vs. frequency

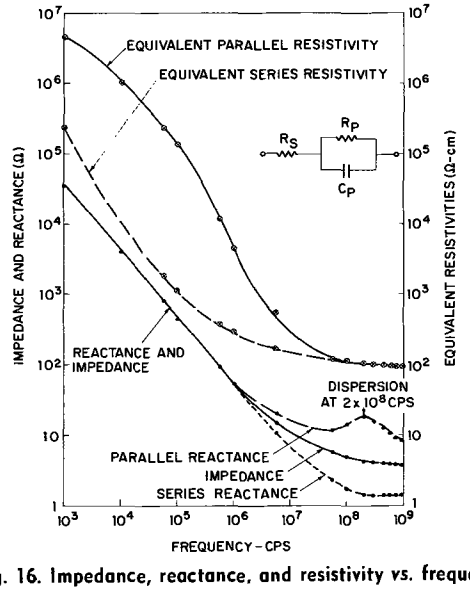

Fig. 16. Impedance, reactance, and resistivity vs. frequency

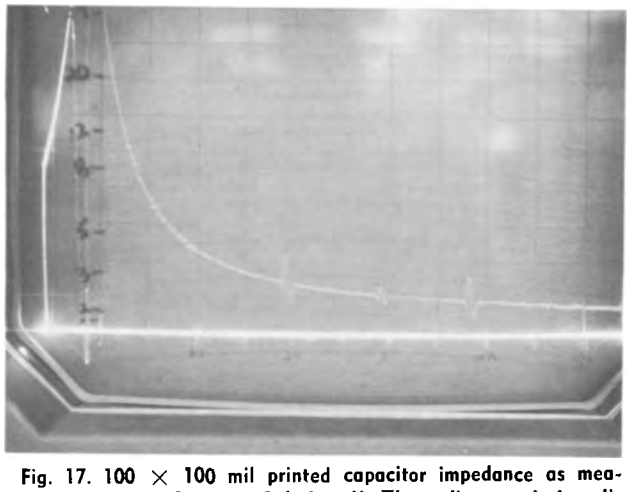

Fig. 17. 100 × 100 mil printed capacitor impedance as measured on a Rhode-Schwartz Polyskop II. The ordinate axis is calibrated in ohms. The abscissa in megacycles, the frequency marker blips are located at every 10 MHz. The curve is a visual display of complex impedance vs. frequency.

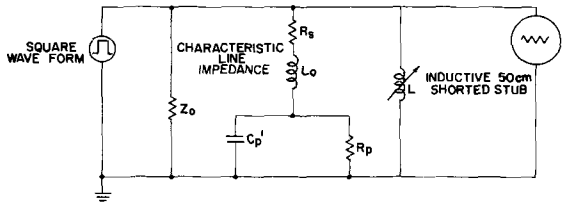

Fig. 18. Equivalent pulse-resonance complex impedance circuit

This is in close agreement to the plotted curve in Fig. 16 which asymptotically approaches 1.4 ohms.

Since computers use pulse signals for internal communication, it was decided to test this capacitor system in a pulsed network. These capacitors were incorporated into a tunnel diode circuit array and functioned very successfully. Evaluation of this system was done by subjecting it to a fast repetitive signal: it was allowed to resonate with a known inductance. A sampling oscilloscope was used to detect the response of the resonant network and display it as a resonant exponentially damped wave form. Such a measurement yielded the amount of damping, time of cycle, and resonant inductance value. With these parametric values, the capacitance and conductance of the decoupling capacitor device was calculated.

The measuring circuit described earlier is essentially an RLC circuit, as shown in Fig. 18, which is pulsed with a square wave. This circuit has a transient response. If one were to study the manner in which this circuit behaves when, following some initial stimulus, it is left to its own devices; that is to say, when it is permitted to execute its own unique natural behavior, one would find that it takes the form of a decaying oscillation as shown schematically in Fig. 19.

This solution of the characteristic response in the limit as the impedance goes to infinity has the general form of the cubic equation

$$s^3 + as^2 + bs + c = 0 \qquad [8]$$

which can be solved by Cardan's method if transferrable to a reduced form or by the trigonometric method if "irreducible." However, in the range of interest it can be shown that the s^3 term may be neglected and Eq. [8] reduces to the familiar quadric form with general solution

$$s = -\frac{b}{2a} \pm \sqrt{\left(\frac{b}{2a}\right)^2 - \frac{c}{a}} \equiv -\alpha \pm \sqrt{\alpha^2 - \omega_o^2} \qquad [9]$$

where α is referred to as the damping coefficient and the radian frequency, and ω_o is referred to as the natural frequency of the physical system described by the RLC circuit.

Four distinct possibilities can now occur, depending on the relative values of α and ω_o: (*a*) the aperiodic or overdamped case wherein $\alpha > \omega_o$; (*b*) the critically damped case where $\alpha = \omega_o$; (c) the damped oscillatory

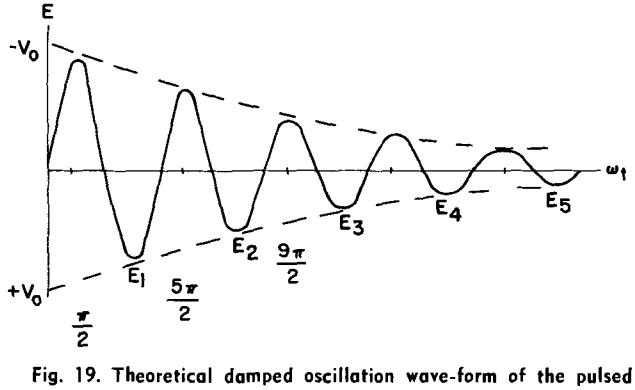

Fig. 19. Theoretical damped oscillation wave-form of the pulsed L-C resonant measuring circuit.

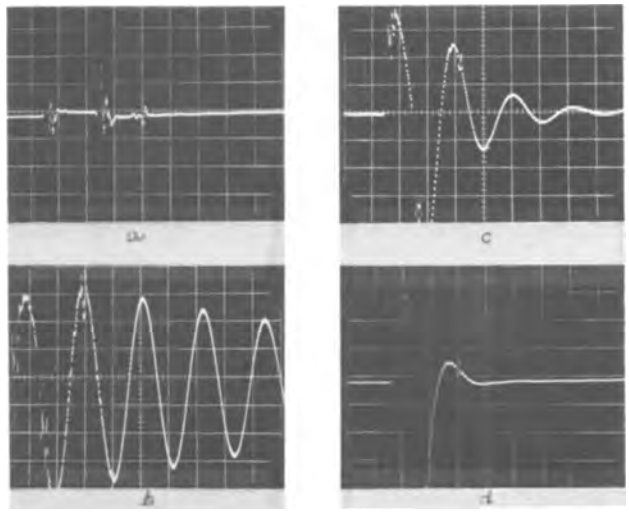

Fig. 20. Sampling scope display of (a) shorted stub impedance trace; (b) standard high impedance capacitor which resonates with the inductance of the shorted stub (oscillatory case; $\alpha = 0$); (c) low impedance decoupling capacitor which damps out 80% of the inductance of the shorted stub (damped oscillatory case; $\alpha < \omega_o$); (d) low impedance decoupling capacitor which critically damps out the inductance of the shorted stub (critically damped case; $\alpha = \omega_o$).

case wherein $\alpha < \omega_o$; and (*d*) the oscillatory case wherein $\alpha = 0$.

Each of these cases is shown pictorially (pictures of scope trace) in Fig. 20. The response of Fig. 20c is that of the zinc-bismuth oxide semiconducting dielectric as discussed previously. Figure 20d is characteristic of the present monovalent copper doped semi-insulating dielectric.

The critically damped nature is brought about by an inherent low series resistance introduced by the cationic monovalent dopant. To determine the damping coefficient, consider Fig. 19. The damped wave form may be represented by the product of a sinusoidal function and a decaying exponential,

$$E = V_o\, e^{-\alpha t} \sin \omega_o t \qquad [10]$$

One may accurately determine the amount of damping by taking the voltage ratio (vertical axis of the sampling scope) of the two wave crests in the first cycle. The damping envelope itself (represented by the dashed curve of Fig. 19) is characteristic of the damping coefficient. Thus we have

$$\frac{E_1}{E_2} = e^{\alpha(t_2 - t_1)} \frac{\sin \omega_o t_1}{\sin \omega_o t_2} = e^{\alpha(t_2 - t_1)} \qquad [11]$$

$$\alpha = \nu_o \ln \frac{E_1}{E_2} \qquad [12]$$

Using this concept and solving for Eq. [9] one obtains as a solution for the capacitance and conductance

$$C = \left[\nu_o^2 \left(4\pi^2 + \ln^2 \left(\frac{E_1}{E_2}\right)\right) (L + L_o) \right]^{-1} \qquad [13]$$

$$G = \left[2\nu_o C \ln \left(\frac{E_1}{E_2}\right) - \frac{Z_o R_s C + L}{Z_o(L + L_o) + LR_s} \right] \qquad [14]$$

Thermal response.—Thermal shock test.—Both systems were tested for mechanical reliability by testing their ability to withstand thermal shocks of 100°C differential. The samples were placed in a programmed delta chamber and cycled between 0° and 100°C with a 1-min rise time, 2-min soak time, 2-min fall time, and 2-min lapse time. The results show no apparent drifting of dielectric constant, dissipation, or resistivity values and no dielectric failures.

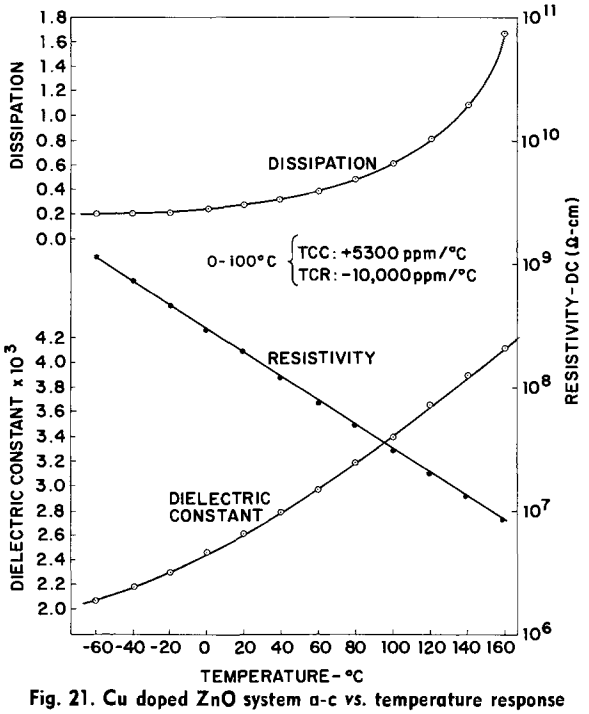

Fig. 21. Cu doped ZnO system d-c vs. temperature response

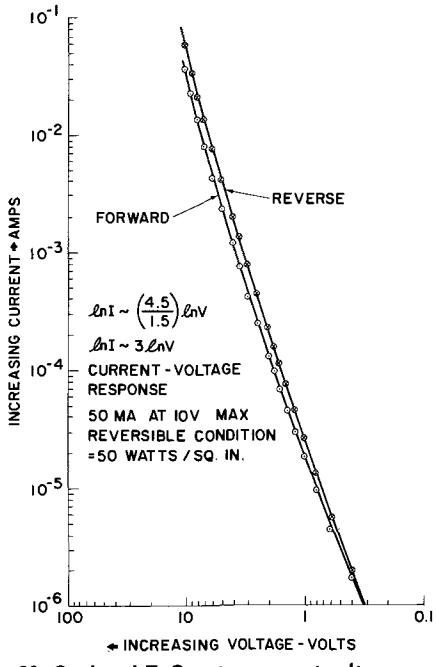

Fig. 22. Cu doped ZnO system current-voltage response

Temperature characteristics.—The dielectric constant, dissipation, and d-c resistivity were evaluated as a function of temperatures from —25° to 160°C in incremental steps of 25°C (see Fig. 21). The frequency characteristics were evaluated at 1 kHz and voltage characteristics at 1 vdc. Note that the frequency characteristics are an increasing function of temperature while the voltage is decreasing.

Room storage and thermal aging.—As a final consideration of thermal properties, this system was also tested for its room storage stability and thermal aging rate if any.

All samples, fabricated as explained earlier, were resubjected to a final processing step, *viz.*, soaking at 250°C for 5 min. They were withdrawn at temperature and allowed to cool to room temperature rapidly in a dessicator. Measurement began exactly 1 hr after withdrawal and terminated after several readouts at 1152 hr. Except for readouts, these units were continuously stored in a dessicator supplied with fresh dissicant at frequent intervals. The results of this test indicate that this system shows no apparent drift during room storage and exhibits no apparent thermal aging.

Electrical response.—A current-voltage evaluation was conducted on this system on 0.01 in.² parallel plate capacitors at 25°, 50°, and 75°C. This system exhibits a nonlinear assymetric d-c resistivity, *viz.*, it is a polar semi-insulator.

There is about a 2 to 1 ratio between reverse and forward resistivities at a given voltage and temperature. There is also a 2 to 1 ratio in resistivities between temperatures at a given voltage and polarity, the higher $\rho_{d\text{-}c}$ values are in the lower temperature-voltage ranges.

An expanded plot of the 25°C test is shown in Fig. 22. The relation between current and voltage appears in Eq. [15].

$$\ln I \sim 3 \ln V \text{ or } I \sim V^3 \qquad [15]$$

This dielectric is capable of an overload of 50 w/in.² before dielectric breakdown occurs. In fact, these samples will emit a dull glow prior to "burn out." The burn out phenomena occurs as a spark avalanche over the entire plate area.

Environmental response.—Low voltage tests.—Accelerated temperature humidity life testing was conducted on typical capacitor units fabricated from this dielectric system under the following matrix:

Dry: Voltage stresses of 0.1, 0.25, 0.50 and 1.0v d.c. each at temperatures of 100°, 125°, and 150°C for a 12 test cell matrix.

Wet: Saturated relative humidity conditions (samples placed over water in closed chamber) at 95°C and 0.25v d.c. voltage stress. All samples were evaluated at 25°C and ambient environment.

Although corrosion of electrode plates produced open-circuit failures, not one failure was attributed to dielectric short circuit degradation. Units that were not open circuits operated normally with less than ±15% deviation in capacitance from initial conditions. This is remarkable in view of the stressed condition brought to bear by the corroded electrodes.

Moisture seems to affect capacitance by shifting the high-and low-frequency drift patterns. Under ambient RH conditions capacitance drift for low frequency was generally negative and less than —15%, while high-frequency capacitance drift was generally positive (never greater than —5%) and less than + 10%. Saturated RH testing brought about a reversal of this drift pattern. In general, topography does not seem to affect the dielectric drift patterns.

Higher voltage tests.—Several units were further tested under dry conditions at 0, 2.5 and 5.0v d.c. (accelerated stress) each at 60°, 90°, 120°, and 150°C. There were no dielectric failures in any test cell except the following:

5v d.c. — 120°C

5v d.c. — 150°C

Capacitance drifting generally occurred in the high voltage-temperature cells but was confined to less than +10%. Dielectric dissipation drift was found to increase positively with an increase of temperature and voltage with a maximum drifting of about +300%. Resistance drift was found to decrease with an increase of temperature and voltage with a maximum drifting of about —300%. This tends to indicate that the drift in dielectric dissipation is caused almost entirely by the drift in resistance. Again, all sample units were evaluated at 25°C and ambient humidity.

Device types.—Figures 23a and b, Fig. 24a and b, and Fig. 25a and b show various forms of multiple

Fig. 23. Independently operable juxtaposed pair of parallel capacitors with common lower ground plane.

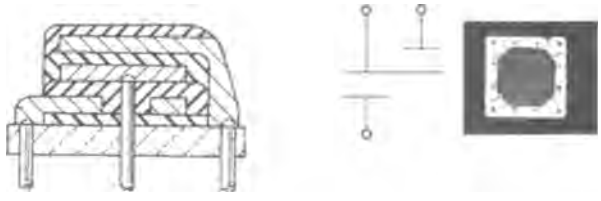

Fig. 24. Independently operable pair of stacked parallel capacitors with common interposed ground plane.

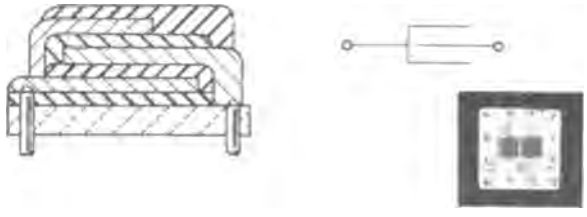

Fig. 25. A stacked parallel capacitor network with interleaved electrodes.

capacitors that may be made utilizing this semi-insulating dielectric material. Figure 23 shows an independently operable pair of juxtaposed parallel capacitors with a common ground plane and the equivalent circuit. Figure 24 shows an independently operable pair of parallel stacked capacitors with a common interposed ground plane and the equivalent circuit. Figure 25 shows a stacked parallel capacitor network with interleaved electrodes and equivalent circuit illustrated.

Discussion

In the foregoing experimental study it was pointed out that a semiconducting dielectric can be converted into a semi-insulating dielectric by monovalent substitution doping at the cationic lattice site.

The zinc-bismuth oxide semiconductor is characterized as a damped oscillatory network with about 80% effective damping due to the existence of a very low effective dielectric shunt resistance at high frequency. After monovalent substitution doping, the resulting semi-insulating dielectric becomes a critically damped network with effective damping reaching values greater than 98%. This effect is due to a small effective series resistance on the order of an ohm being introduced into the dielectric network.

This semi-insulating dielectric system is unique to dielectrics and can be used with screen printing technology to produce useful capacitor devices for applications requiring high K_e — low Q decoupling or filter capacitors capable of critical damping. The chemical-physical nature of this system of dielectrics offers a wide area of further research into yet unknown and new phenomena.

Acknowledgments

The authors would like to extend their appreciation to Dr. A. H. Mones for his advice and encouragement and Mrs. Mary M. Garner, William C. Covert, and Richard K. Spielberger for their laboratory assistance.

Manuscript received May 25, 1966; revised manuscript received April 19, 1967. This paper was presented in part at the Cleveland Meeting, May 1-6, 1966.

Any discussion of this paper will appear in a Discussion Section to be published in the June 1968 JOURNAL.

REFERENCES

1. N. H. Langton and D. Matthews, *Brit. J. Appl. Phys,*. **9**, 453 (1958).
2. P. Kasai, *Phys. Rev.*, **130**, 989 (1963).
3. H. Rupperecht, *J. Phys. Chem. Solids*, **6**, 144 (1958)
4. D. G. Thomas, *ibid.*, **15**, 86 (1960).
5. D. G. Thomas and J. Lander, *J. Chem. Phys.*, **25**, 1136 (1956).
6. D. G. Thomas, *J. Phys. Chem. Solids*, **3**, 229 (1957).
7. G. P. Mohanty and L. Azaroff, *J. Chem. Phys.*, **35**, 1268 (1966).
8. A. R. Hutson, *Phys. Rev.*, **108**, 222 (1957).
9. D. G. Thomas, "The Chemistry of Some Compound Semiconductors, in Semiconductors," N. B. Hannay, Editor, Reinhold Publishing Corp., New York.
10. G. Heiland, E. Mallwo, and F. Stockmann, *Solid State Phys.*, **8**, 191 (1959).
11. T. Zolyan and A. Regal, *Soviet Phys. Solid State*, **5**, 1762 (1964).
12. A. Fidrya, *Uch, Zap. Leningr Gos. Ped. Inst. im A. I. Gertsena*, **207**, 249 (1961).
13. R. Mansfield, *Proc. Phys. Soc., (London)*, **62B**, 476 (1949).
14. M. S. Kosman and J. A. Gesse, *Izvent. Akad. Nauk S.S.R. Ser. Fiz.* (Eng trans.) **22**, 312 (1958).
15. M. S. Kosman and E. G. Pettsold, *Leningrad Gos. Pedag. Inst.*, **207**, 191 (1961).
16. R. Delaney and H. Kaiser, *IEEE Trans.*, PMP No. 1/2, 9-24 (1966).
17. R. Delaney and H. Kaiser, IBM Technical Disclosure Bull., **6** [10], March 1964.
18. C. G. Koops, *Phys. Rev.*, **83**, July 1951.
19. J. Volger, "Dielectric Properties of Solids in Relation to Imperfections, Progress in Semiconductors," Vol. 4, John Wiley & Sons, Inc., New York (1960).
20. T. C. Fisher, *J. Appl. Phys.*, **22**, 74 (1951).
21. A. E. Austin and N. A. Richard, *ibid.*, **33**, 3569 (1962).
22. E. E. Hahn, *ibid.*, **22** (1951).

The Anodic Oxidation of Aluminum in the Presence of a Hydrated Oxide

Robert S. Alwitt

Research & Development Laboratories, Sprague Electric Company, North Adams, Massachusetts

ABSTRACT

The effect of a hydrated oxide on the kinetics of anodic oxidation of aluminum has been studied and the properties of the resulting composite oxides compared with those of purely anodic oxides. The presence of a hydrate layer reduced the amount of anodic oxide needed to support a given voltage and increased the current efficiency to as much as 100%. Water was lost from the oxide during anodization, probably as the result of transformation of boehmite to γ-Al_2O_3, which was incorporated into the barrier layer. The dielectric strength was greater for a composite oxide than for an oxide produced in the absence of a hydrate, though the dielectric constants were probably not very different. The impedance characteristics of a composite oxide indicated fewer microfissures than in a purely anodic oxide.

The formation of an oxide film on aluminum by the sequential processes of reaction in hot water followed by anodic oxidation produces a composite oxide with some unique properties. This process has been of technological importance for some time in the manufacture of electrolytic capacitors (1, 2), but has received scant attention in the scientific literature. Altenpohl (3) briefly mentioned that the anodic oxide grows underneath the hydrate and that the latter is partially consumed by the growing film. He suggested that water is eliminated from the consumed portion of the hydrate whenever this portion crystallizes into γ-Al_2O_3 under the influence of a high electric field. Unfortunately, no experimental evidence accompanied this discussion. Burger and Cheseldine (4, 5) also advanced the idea that the barrier portion of the composite oxide consists of both anodic oxide and converted hydrate, but their data were insufficient to confirm this.

The lack of information on the composite oxide prompted us to perform the investigation reported here of the effect of a hydrated oxide on the kinetics of anodic oxidation, and the properties of the resultant composite oxide. Our data support the hypothesis that some hydrate is dehydrated during anodization and becomes converted to barrier oxide. Moreover, details of this process are presented that have not been available previously.

Experimental Procedures

Commercially etched 99.97% pure aluminum foil was used throughout. The increased surface area improved the sensitivity of weight measurements and the "corrugations" increased the rigidity and strength of the isolated oxide, greatly simplifying handling procedures. Any change in surface area over the range of oxide thickness studied was sufficiently small to have no effect on the interpretation of results. Sample size was 6.4 x 7.6 cm for weight and charge measurements and smaller samples, 2.6 x 3.6 cm, were used for impedance measurements. The foil was not treated in any way prior to hydration in boiling water at atmospheric pressure.[1] Anodic oxidation was at 2 ma/cm^2 in 100 g/l boric acid at 90°C. The boric acid was electronic grade, and distilled deionized water with a resistivity *ca.* 500,000 ohm-cm was used throughout. Foils were rinsed in acetone and dried at 85°C for about 10 min prior to weighing. Weights were accurate to ± 0.1 mg.

The oxide film was isolated from base metal by slowly dissolving the metal in a warm solution of 10% bromine in methanol, followed by thorough rinsing with several changes of hot methanol. Bernard and Randall (6) found that this technique could be used to quantitatively recover hydrated oxide. To check its efficacy with anodic oxide, a sample anodized at room temperature in a solution of 30% ammonium pentaborate in glycol was immersed in bromine-methanol. The oxide recovered was equal to 98% of the amount calculated for the expected current efficiency of 100% (7).

The water content of the oxide was taken to be the weight loss that resulted on heating the isolated oxide for 2 hr at 900°C.

In some instances the oxide was dissolved from base metal by immersing samples in an aqueous solution of 2% CrO_3 + 5% H_3PO_4 at 85°C. For samples covered solely with hydrated oxide a sufficient immersion time was calculated from the data of Bernard and Randall (6). To insure complete dissolution of anodic oxide, samples were alternately immersed and weighed until the rate of weight loss dropped to that of the base metal.

Aluminum dissolved in the electrolyte was determined using a method of Sandell [procedure A in ref. (8)] based on the extraction of aluminum hydroxyquinolate by chloroform and photometry of the resultant yellow extract. In some electrolytes a white precipitate formed during anodization. This was collected and considered to be Al_2O_3 after heating for 2 hr at 600°C. The total weight of dissolved aluminum was the sum of that found in solution and in the precipitate.

Impedance measurements were made with a conventional a-c bridge that measured the equivalent series capacitance and RC product. Two measuring solutions with different resistivities were used. The first, 50 g/l H_3BO_3 adjusted to neutral *p*H with NH_4OH, had a resistivity of about 400 ohm-cm. The second solution had a resistivity of about 10 ohm-cm and was used previously by Burger and Cheseldine (4). It had a composition of 2.5% ammonium pentaborate, 12.5% ammonium formate, 10% glycol, and 75% water. The measuring cell was designed to hold a foil sample equidistant between two platinized plates spaced 1 cm apart.

Results

Properties of the hydrated oxide.—Bernard and Randall (6) found that the oxide produced in boiling water was a water enriched boehmite, with approximately two moles of water per mole of Al_2O_3. This oxide is not a good dielectric. Some of their experiments were repeated using etched foil and excellent agreement was obtained.

The growth of hydrated oxide in boiling water followed a logarithmic rate law over the interval 1-30 min (data in columns 1 and 2 of Table I). The deviation at the shorter time may have been due either to

[1] A mild alkaline cleaning resulted in a slightly greater rate of hydration, but had no affect on hydrate composition.

Table I. Effect of hydrate on anodic oxidation 200v barrier film

Boil Time, min	ΔW, mg/dm²	Wt. Al_2O_3, mg/dm² Total	Anodic	Charge, Q, meq.	Current eff, %	$W_{Al}/_{0Q} \times 100$
0	0	64.9	64.9	5.23	73.0	15.7, 24.6
0.67	7.5			3.27		
1	15.0	61.0	42.9	2.66	95.0	9.0
5	24.5	64.2	35.2 (33.6)	1.97	105.5 (100.7)	0, 0.7, 0.8
30	39.8	85.2	38.1*	2.24		

* Weight of anodic Al_2O_3 calculated from charge, assuming 100% current efficiency. Total oxide is the sum of calculated weights of anodic and hydrated oxides.

uneven hydration of the surface or the production of an oxide of lower water content. The hydrate thickness was calculated to be about 100 Å/mg of weight gain, based on the density of isolated hydrate films measured in toluene (6). Since these films are porous, the true thickness would be greater than this.

Samples of two different etched foils and an unetched foil was boiled for 1, 3, and 5 min, and then the oxide was dissolved in CrO_3-H_3PO_4 solution. The weight of hydrated oxide and the water content were calculated from the weight changes. The water content ranged from 24 to 30% with an average value of 27%. There were no significant differences among the different types of foil or the different reaction times. Burger and Cheseldine (9) found the composition of the hydrate produced in boiling water to be constant at 27% H_2O for immersion times from 5 to 60 min. In all subsequent calculations it was assumed that the hydrated oxide contained 27% water.

Effect of the hydrate on the anodization process.— Foils were anodized to 200v after immersion in boiling water for times up to 30 min. The oxide films were then isolated and heated at 900°C for 2 hr. The effect of the hydrate on weight of oxide, charge, and current efficiency is summarized in Table I. Each entry is the average for two samples.

The total weight of Al_2O_3 was that found after heating at 900°C. The calculated weight of Al_2O_3 grown during the boil (based on average hydrate composition) was subtracted from the total to obtain the weight of anodic oxide. The current efficiency is the ratio of equivalents of anodic oxide to equivalents of charge passed during anodization, expressed as a per cent. The last column in Table I gives the weight of dissolved aluminum as a per cent of the charge passed. The data in the last column were obtained in a separate set of experiments.

When the weight of hydrate is a large part of the total oxide weight, deviation from the average hydrate composition can introduce significant error in the calculated weight of anodic oxide. It was estimated for a 5-min boil that uncertainties in the hydrate composition could introduce an error of ± 6% in the weight of anodic oxide.

An alternate method can be used to calculate the weight of anodic oxide. The observed weight gain during anodic oxidation (ΔW_{an}) represents the difference between the weight of oxygen gained and the weight loss from reduction of water content (ΔW_{H_2O}) and dissolution of aluminum (W_{Al}). The weight of anodic oxide is then,

$$W_{anodic} = (102/48)\ (\Delta W_{an} + \Delta W_{H_2O} + W_{Al}) \quad [1]$$

A precipitate forms during anodization if W_{Al} is large, and the experimental error in determining W_{Al} is then probably as great as the uncertainty in hydrate composition. When W_{Al} is small, the major source of error is in the quantity ΔW_{H_2O}, the difference between the calculated weight of water in the hydrate and the weight loss at 900°C.

In the last column in Table I it is seen that W_{Al} is very small for a 5-min boil, and may be neglected in Eq. [1] without introducing serious error. For this case it was estimated that the uncertainty in ΔW_{H_2O} could result in a ± 3% error in the weight of anodic oxide calculated from Eq. [1]. This method was used to arrive at the figures in parentheses in Table I. These are believed to be more accurate than the corresponding figures arrived at by the first method.

The presence of a hydrated oxide sharply reduced the amount of anodic oxide required to produce a 200v barrier film. The total weight of oxide changed little for boil times of 5 min or less. The small decrease in total oxide weight with a 1-min boil could be due to experimental error, but under some conditions the total weight of composite oxide may be less than that of a purely anodic oxide because of a greater dielectric strength. This is discussed in a later section.

The current efficiency with no hydrate was usually about 70-75%, but sometimes dropped as low as 50%. The presence of a hydrated oxide greatly improved the current efficiency, so that after a 5-min boil the efficiency was close to 100%. (Spectrographic analysis of two composite oxides made with 5-min boils showed the presence of 0.17% and 0.37% boron. If present as B_2O_3, this would contribute 0.5-1.0% to the apparent weight of oxide.) The combination of improved current efficiency and reduced anodic oxide resulted in charge consumption with a 5-min boil less than 40% of that required in the absence of a hydrate. Such reduced charge was one of the earliest benefits attributed to the presence of a hydrate layer (1). The increase in charge for the 30-min boil is very likely a real effect, since a similar observation has been made by Randall (10).

Copious gas evolution was sometimes observed at the anode when a hydrate film was absent. This was presumably oxygen, but no attempt was made to verify this. This gas evolution would account for the fraction of the charge not consumed in oxide formation and aluminum dissolution. There was negligible gas evolution during formation of films to 200v after a boil of 1 min or longer. Both gas evolution and aluminum dissolution increased when thicker films were formed. For example, for films formed to 400v after a 5-min boil the current efficiency was only 92.6% and dissolved aluminum accounted for 2.6% of the charge.

When a foil sample was anodized in a solution of 30% ammonium pentaborate in ethylene glycol at room temperature and constant current, current efficiency was 100%, and dV/dt was constant up to at least 200v. When a sample was boiled in water for 5 min and then anodized in 100 g/l H_3BO_3 at 90°C, current efficiency was again 100%, but dV/dt was not constant. A typical recorder trace is shown in Fig. 1. The values of dV/dt initially and at 200v are indicated. There was some variation among samples, but the general pattern was that for the initial 15-25v the voltage rise was constant at a value between 7 and 9

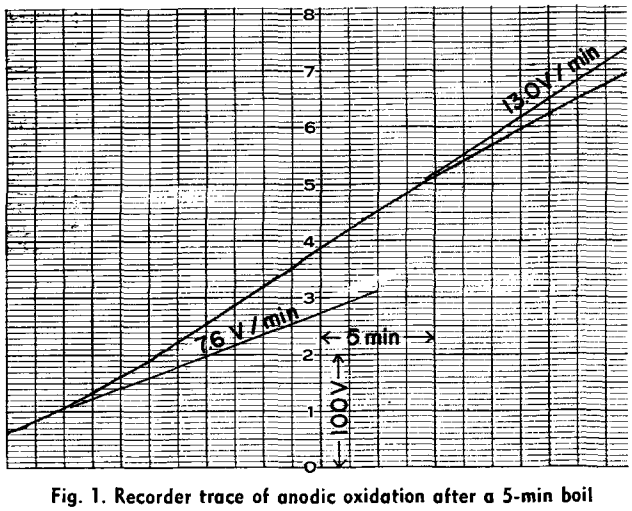

Fig. 1. Recorder trace of anodic oxidation after a 5-min boil

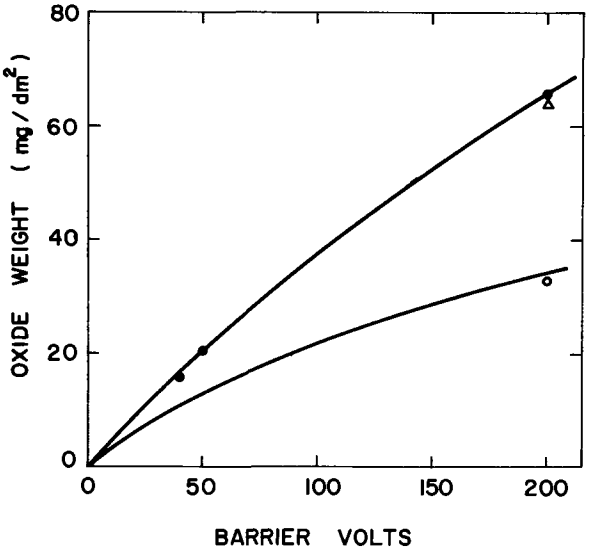

Fig. 2. Effect of hydrate (5-min boil) on oxide weight: ● = total oxide weight with no hydrate; △ = total oxide weight with hydrate; ○ = anodic oxide weight with hydrate.

v/min. The voltage then increased more rapidly into the range 50-100v until dV/dt was between 12 and 14 v/min. The rate of voltage rise was then constant to above 200v where increased aluminum dissolution and gas evolution accompanied a decrease in dV/dt. The same behavior was obtained with plain foil as with etched foil.

The change in oxide weight with increasing anodization voltage is shown in Fig. 2. The total oxide weight was measured after heating at 900°C. The open circle and triangle are data from Table I, while the lower curve represents average anodic oxide weights calculated from several recorder traces of voltage *vs.* time, assuming 100% current efficiency. The weight of total oxide in the absence of initial hydrate is shown by the top curve. It is possible that some hydrate was produced during anodization since the isolated 40 and 200v oxides formed in the absence of initial hydrate lost 0.2 and 0.8 mg/dm², respectively, at 900°C.

Composition and structure of the composite oxide.—Water content.—The oxide films contained less water after anodization than was present in the initial hydrate. In Table II the weight loss at 900°C of a 200v composite oxide is compared with the water content of the hydrate film. The difference between these two quantities represents the water depleted during anodization and is given in the last column of the table. This quantity varied little over a threefold range in hydrate weight, which implies that the reaction responsible for the loss of water did not occur uniformly throughout the hydrate.

The decrease in water content with increasing thickness of barrier oxide for foils that initially received a 5-min boil is shown in Fig. 3. The points represented by dark circles were determined from the 900°C weight loss while the open circles were calculated in the same way as the last entry in Table II. The com-

Table II. Water content of 200v composite oxides

Boil time, min	Weight of H_2O, mg/dm²		
	Hydrate	Composite oxide, ΔW at 900°C	Difference, ΔW_{H_2O}
0	0	0.8	
1	6.7	2.8	3.9
5	10.9	6.9	4.0
30	17.6	—	4.5*

* Calculated from ΔW_{an} and charge, using Eq. [1] and an assumed current efficiency of 100%.

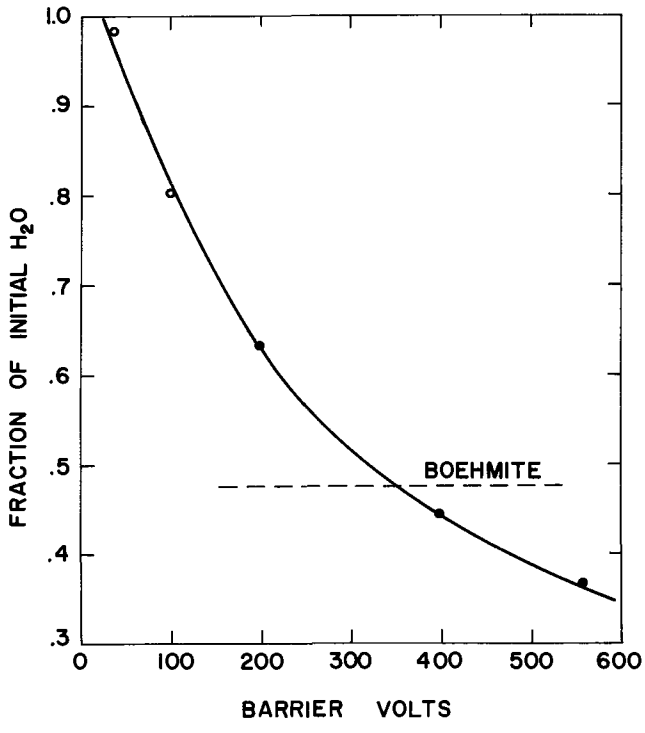

Fig. 3. Water content of composite oxide made with 5-min boil: ○ = calculated; ● = experimental.

position corresponding to boehmite for the hydrate is indicated by the horizontal dashed line. It would seem that during the formation of the first 25v of barrier film little or no water was lost. This corresponds in magnitude with the initial period of constant dV/dt.

The loss of water could occur in three ways: (*a*) expulsion of water from the oxide to the solution; (*b*) reaction of aluminum ions with water from the hydrate instead of with species from solution to form oxide (4), *viz.*, $2Al^{+3} + 3H_2O \rightarrow Al_2O_3 + 6H^+$; and (*c*) reaction of water from the hydrate with base metal to form oxide, *viz.*, $2Al^{o} + 3H_2O \rightarrow Al_2O_3 + 3H_2$.

If (*c*) is the prevailing mechanism, then the total weight of metal reacted should exceed that consumed by the initial hydration and charge passed during anodization. To examine this, two foil samples were given a 5-min boil, anodized to about 200v, and then the oxide was dissolved in CrO_3-H_3PO_4 solution. It was calculated that the average weight of aluminum consumed by hydration and anodization was 34.4 mg, compared with an observed metal weight loss of 33.0 mg. If water reacted with base metal, it was estimated that an additional weight loss of 5 mg should have been observed. Clearly, mechanism (*c*) is not consistent with the experimental results.

Mechanisms (*a*) and (*b*) cannot be distinguished on the bases of weight changes and charge passed. Indeed, we have devised no way to determine which of these mechanisms prevail.

Water distribution.—Two isolated 200v composite oxides made with a 5-min boil were heated at several temperatures between 600° and 900°C. The average weight loss at each step is given in Table III. Sixty eight per cent of the water was removed at 600°C, but not until 900°C did it appear that all the water was removed. This contrasts with the results of Bernard and Randall (6) who found that at 600°C, 97% of the water was removed from the film produced by the reaction of aluminum and boiling water. Thus, some of the water remaining in the composite oxide is bound much more strongly than is the water in the initial hydrate. This water, as hydroxyl groups, may be a part of the γ-Al_2O_3 structure in the barrier oxide (11, 12).

Table III. Removal of water from composite oxide (5-min boil, 200v)

Temp, °C	Time, hr	Wt. loss, mg/dm²
600	2	4.7
700	2	1.1
800	2	0.8
800	Overnight	0.15
850	2	0.1
900	4	0.05
		6.9

X-ray analyses.—Diffraction patterns of several oxides were made using a Debye-Scherrer powder camera. Only qualitative results were obtained. A significant amount of γ-Al_2O_3 was found in a 200v oxide formed in 100 g/l H_3BO_3 at 90°C with no hydrated oxide present. The pattern for a 200v composite oxide formed in the same way, but after a 5-min boil showed about the same amount of γ-oxide present, and also a lesser amount of boehmite. No evidence of a crystalline phase was found for a 200v oxide formed in a solution of 30% ammonium pentaborate in glycol at room temperature.

Impedance measurements.—Capacitance vs. film thickness.—For the discussion of Fig. 4 it is convenient to introduce the dielectric strength, D, defined as the ratio of barrier volts to barrier thickness. Then $1/C = (k/\epsilon D)V$, where ϵ is the dielectric constant and k is a constant. The product ϵD was constant for oxide formed in the absence of initial hydrate. Up to about 50v ϵD was the same, with or without an initial hydrate produced by reaction with boiling water for 5 min. The oxide grown in the interval 50-200v had about a 50% higher ϵD product when the hydrate was present. (Assuming no change in the initial 50v oxide, which may not be the case.)

Frequency and electrolyte dependence.—Impedance measurements were made on oxide films formed in three different ways:

Oxide H, Five minutes in boiling water, then anodized to 200v at 90°C in aqueous 100 g/l H_3BO_3.
Oxide NH, No hydration, anodized as for oxide H.
Oxide NHG, No hydration, anodized to 245v at 25°C in 30% ammonium pentaborate in ethylene glycol.

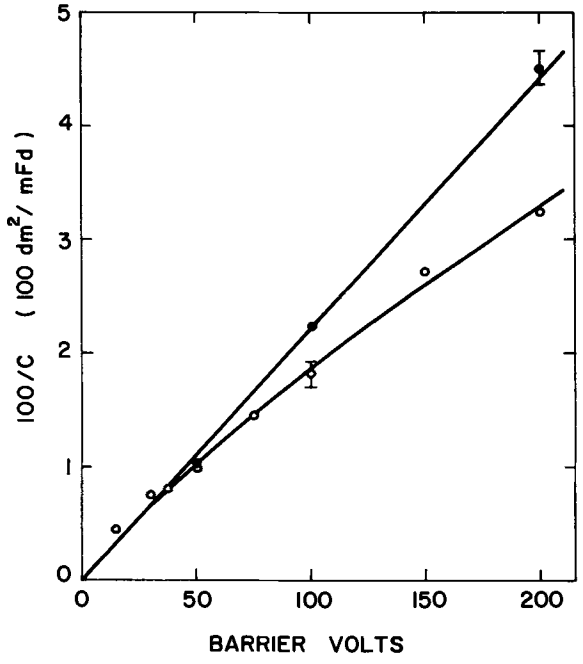

Fig. 4. Effect of hydrate (5-min boil) on capacitance at 120 Hz: ● = no hydrate; ○ = hydrate. Each point is average for at least two samples; vertical lines show range of six samples (I) and five samples (I).

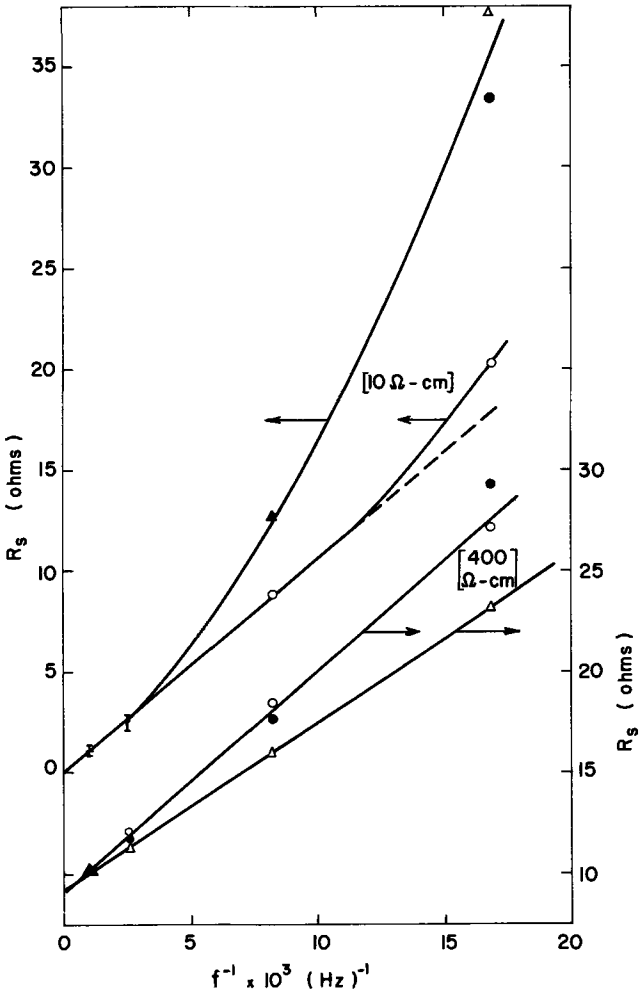

Fig. 5. Frequency dependence of series resistance in two measuring solutions: ○ = oxide H, ● = oxide NH, △ = oxide NHG.

Impedance measurements were made over the frequency range 60-1000 Hz in two solutions with resistivities of about 10 and 400 ohm-cm. The results are shown in Fig. 5 and 6.

The results in the 400 ohm-cm solution with oxides H and NHG were close to those predicted by theory (13, 14). Plots of $1/C$ *vs.* log f and R_s *vs.* $1/f$ were linear, and the ratio of the slopes of these lines was 9.7 (H) and 8.8 (NHG), which compares with a predicted ratio of 9.2. The value of R_s for oxide NH deviated slightly from linearity at the lowest measuring frequency (Fig. 5) and the ratio of the slopes for this oxide was only 6.9.

When viewed on unetched foil, oxide NH had a hazy appearance and contained random, irregularly shaped black spots with a characteristic dimension 0.03-0.1 mm. After heating isolated oxide at 900°C these spots disappeared. Electron probe microanalysis detected no impurity elements within the particles. Their exact nature is unknown, but they may be a secondary oxide phase or a localized dispersion of fine metallic aluminum particles (15). Oxide NHG and all composite oxides were always clear and free of blemishes.

In the 10 ohm-cm solution none of the oxides gave linear impedance plots. Oxides NH and NHG exhibited exceedingly high R_s at low frequencies, while the deviation for oxide H was only slight. The plots of $1/C$ *vs.* log f were slightly curved for all oxides due to high series capacitance at low frequencies. Additional anodic polarization (healing) did not remove these effects, indicating the absence of large fissures.

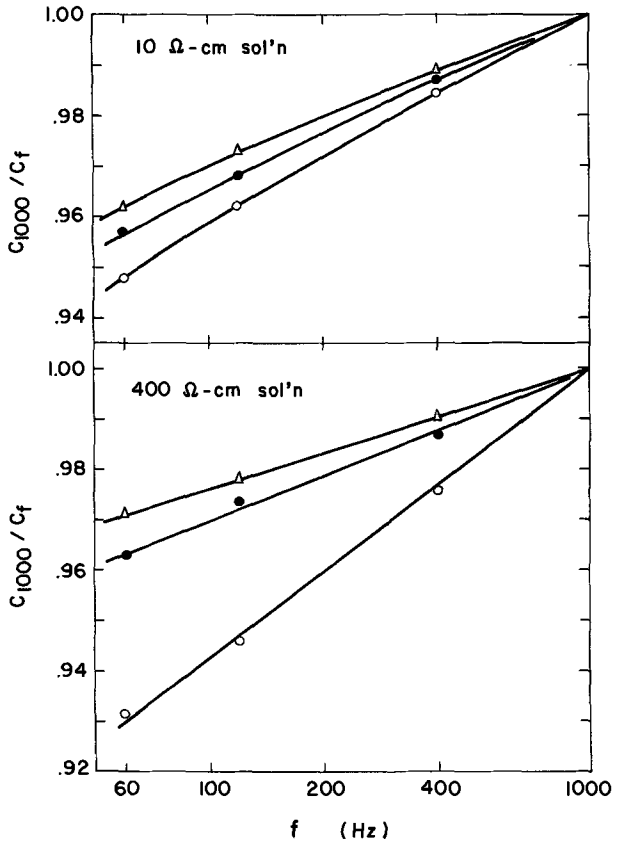

Fig. 6. Frequency dependence of series capacitance in two measuring solutions: ○ = oxide H, ● = oxide NH, △ = oxide NHG.

Young (16) has attributed this type of dependence on measuring solution conductivity to the presence of microfissures in the oxide film. From the relative values of R_s in the 10 ohm-cm solution it seems that the presence of a hydrate results in either the formation of an oxide with less microfissures, or reduces the effect of any existing microfissures. None of the known properties of these oxides can explain the improved low-frequency behavior of the composite oxide. One possibility that can be suggested is that forces could be distributed across the barrier/hydrate interface, relieving stresses within the barrier layer and thus reducing microfissures.

Surface area.—The hydrated oxide is very porous, so the only way it could become part of a barrier layer is if the anodic oxide grew into the interstices. This would result in a reduction of surface area. No change in surface area would be expected if the anodic oxide grew only under the hydrate. Thus, surface area measurements are important evidence in determining the role of the hydrate.

The surface areas of specimens that received a 5-min boil and were then anodized were determined using a dynamic BET method employing nitrogen adsorption. The following results were obtained, expressed as surface area/projected area. Each figure represents a different sample:

Barrier volts	Area ratio, m^2/dm^2
0	4.51, 5.33
200	2.11, 2.56
400	1.74

The surface area prior to hydration was too small to be determined by this method, but from capacitance measurements on samples anodized to low voltages this area was estimated to be about 0.1 m^2/dm^2.

The significant decrease in surface area during anodization supports the idea that hydrate is incorporated into the barrier layer. The larger decrease in area during the first 200v compared with the next 200v increment is qualitatively similar to the decrease in water content with film thickness (Fig. 3).

Discussion

The most satisfactory explanation of the anodization results is that some hydrate was converted to barrier oxide by dehydration during anodic oxidation, so that the total barrier oxide was the sum of anodic oxide plus converted hydrate. Boehmite is usually dehydrated to form γ-Al_2O_3 at about 450°C, but the transformation can occur as low as 350°C (17). Under the influence of an electric field, the hydrate lattice may be sufficiently distorted to permit the transformation at still lower temperatures. Precedents for field-assisted crystallization are the production of γ-Al_2O_3 during anodic oxidation at 90°C (as seen in this experiment) and the formation of anodic α-Al_2O_3 at less than 300°C (18). The high field in the barrier layer during anodization will not exist in the bulk of the hydrate layer. However, it probably does extend some small distance across the barrier/hydrate interface, and in this surface region field-assisted dehydration would occur. This would account for the observation that the weight of water lost was independent of the amount of bulk hydrate present (Table II). Since there is evidence that hydroxyl groups exist within the anodic portion of the composite oxide, complete dehydration would not be required for conversion to barrier film.

It appears that there is an inhibition period for the dehydration of hydrate, during which the ϵD product is unaffected by the presence of hydrate. However, the barrier oxide formed during this time is not identical with that produced in the absence of a hydrate as evidenced by the difference in anodic oxide weights that exists from the very start of anodization.

Although no direct determination could be made of the amount of hydrate converted to barrier oxide, it is possible to compare several estimates of this quantity. The fraction of hydrate converted was assumed to be equal to each of expressions (a)-(c), where W_{H_2O} is the weight of water in the initial hydrate and

$$1 - \Delta W_{H_2O}\ (900°C)/W_{H_2O} \quad (a)$$
$$1 - \Delta W_{H_2O}\ (600°C)/W_{H_2O} \quad (b)$$
$$1 - (\text{surface area composite oxide/surface area initial hydrate}) \quad (c)$$

ΔW_{H_2O} is the weight loss of the composite oxide at the indicated temperature. Expression (b) is an attempt to account for water that may be in the barrier oxide. The fraction converted was calculated in these ways for 200v and 400v composite oxides made with a 5-min boil. The results are shown below:

	(a)	(b)	(c)
200v	0.37	0.57	0.43-0.60
400v	0.56	—	0.65

Considering the assumptions inherent in each of these estimates, the agreement is reasonably good.

Making the further assumption that the true fraction converted lies within the range of the above estimates enables us to examine the dielectric properties of the composite oxide. The weight of barrier oxide in the 200v composite oxide was calculated using the limits of 37 and 60% hydrate conversion. The ratio of the dielectric strength of the composite oxide to that of a film with no hydrate (assuming equal density barrier oxides) and the ratio of dielectric constants could then be determined, with the following results:

	37%	60%
$D_{comp.}/D_o$	1.43	1.24
$\epsilon_{comp.}/\epsilon_o$	1.05	0.91

Thus, the major effect of the hydrate is to produce a barrier film with significantly greater dielectric strength, with little or no change in dielectric constant. A similar calculation for 400v films led to the same conclusion. This argument also holds when considering the composite oxide *vs.* amorphous films formed in glycol-borate electrolyte, since for the same weight of oxide these latter films had the same capacitance (120 Hz) as films formed in aqueous boric acid with no hydrate.

The improved current efficiency for oxide formation in the presence of a hydrate could be due to two factors. First, the reduced barrier oxide/electrolyte contact area would decrease any general oxide dissolution, although this could not account for the complete absence of dissolution. Second, no black spots were observed in the composite oxide, and these were probably sites for secondary reactions such as oxygen evolution. The more fundamental question as to the cause and elimination of these defects remains unanswered.

Conclusions

1. The presence of a hydrate layer during anodic oxidation of aluminum not only reduces the amount of anodic oxide needed to support a given voltage, but also increases the current efficiency to as much as 100%.

2. The loss of water during anodic oxidation is associated with transformation of hydrate into barrier oxide. The high temperatures needed to remove water from the isolated composite oxide suggest that some water, as hydroxyl groups, is present in the anodic oxide.

3. The dielectric strength of a composite oxide is greater than that of an oxide produced in the absence of a hydrate. The impedance characteristics of a composite oxide indicate it contains fewer microfissures than a purely anodic oxide.

Acknowledgments

Stimulating discussions with D. M. Cheseldine helped initiate this work. Further discussions with W. J. Bernard and J. J. Randall, Jr., during the course of this study were most helpful. The author is grateful to R. Heggie for the surface area determinations.

Manuscript received Feb. 17, 1967.

Any discussion of this paper will appear in a Discussion Section to be published in the June 1968 JOURNAL.

REFERENCES

1. G. F. Coggins, U. S. Pat. 2,396,685 (1946).
2. D. Altenpohl, U. S Pat. 2,859,148 (1958).
3. D. Altenpohl, *This Journal*, **108**, 628 (1961).
4. F. J. Burger and D. M. Cheseldine, 1st Semi-Annual Report, Contract DRB9596-S38/1, Defense Research Board (Canada) (1964).
5. F. J. Burger and D. M. Cheseldine, 2nd Semi-Annual Report, Contract DRB9596-S38/1, Defense Research Board (Canada) (1965).
6. W. J. Bernard and J. J. Randall, Jr., *This Journal*, **107**, 483 (1960).
7. W. J. Bernard and J. W. Cook, *ibid.*, **106**, 643 (1959).
8. E. B. Sandell, "Colorimetric Determination of Traces of Metals," 3rd ed., p. 234, Interscience Publishers, Inc., New York (1959).
9. F. J. Burger and D. M. Cheseldine, *This Journal*, **107**, 1025 (1960).
10. J. J. Randall, Jr., Private communication.
11. G. W. Brindley and M. Nakahira, *Nature*, **183**, 1620 (1959).
12. I. David and A. J. E. Welch, *Trans. Faraday Soc.*, **52**, 1642 (1956).
13. L. Young, *ibid.*, **51**, 1250 (1955).
14. P. Winkel and D. G. deGroot, *Philips Research Repts.*, **13**, 489 (1958).
15. M. E. Straumanis and K. Poush, *This Journal*, **112**, 1185 (1965).
16. L. Young, *Trans. Faraday Soc.*, **55**, 842 (1959).
17. B. C. Lippens and J. H. deBoer, *Acta Cryst.*, **17**, 1312 (1964).
18. S. Tajima, M. Soda, T. Mori, and N. Baba, *Electrochim. Acta*, **1**, 205 (1959).

Luminescence Efficiency of Silicon Carbide Doped with Boron and Nitrogen

R. M. Potter

Lighting Research Laboratory, General Electric Company, Cleveland, Ohio

and D. A. Cusano

General Electric Research and Development Center, Schenectady, New York

ABSTRACT

Luminescence quantum efficiencies of the order of 10% have been measured at 300°K for α-SiC doped with boron and nitrogen. The values obtained using cathode-ray and 3650Å excitation agree within the uncertainty of the measurements.

This paper reports some new results on the quantum efficiency[1] of luminescence in both single crystal and powdered SiC doped with boron and nitrogen. The measurements were made using cathode-ray and 3650Å uv excitation, at 77°K and at room temperature. Until recently, (1, 2) the quantum efficiency of SiC at room temperature had been reported as extremely poor. The present work has shown that room temperature quantum efficiencies of the order of 10% are possible for suitably prepared SiC:B,N powders and crystals.

[1] In this paper, quantum efficiency is defined as the ratio of luminescence photons generated to electron-hole pairs produced by excitation.

Experimental Procedures and Results

SiC:B,N powder phosphors used in the investigation were kindly supplied by Addamiano, who has described their preparation in detail (3, 4). Briefly, they were prepared by firing at around 2500°C a mixture of "semiconductor grade" silicon and "spectroscopically pure" graphite along with 10^{-4} to 5×10^{-4}

Table I. Impurity analysis of SiC:B,N samples by emission spectroscopy

Element	Powder	Crystal
B	20 ppm	6 ppm
Mg	ND < 0.5	≦0.6
Fe	ND < 5	ND < 5
Ge	ND < 3	ND < 4
Al	ND < 2	4
Be	ND < 0.1	ND < 0.1
Mo	ND < 2	ND < 4
Sn	ND < 2	ND < 7
V	ND < 6	ND < 6
Cu	ND < 1	ND < 1
Ag	ND < 0.2	ND < 0.2
Zn	ND < 15	ND < 15
Ti	ND < 3	ND < 3
Zr	ND < 2	ND < 3
Co	ND < 4	ND < 3
Ni	ND < 3	ND < 3
Ca	3	1

mole fraction boron in Ar gas containing a small percentage of N_2. As shown in Table I, the impurity levels in the product (aside from boron) were generally too low to be detected by emission spectroscopy. Samples prepared without adding boron exhibited no room temperature photoluminescence. As noted in ref. (4), these powders consist of a mixture of several α-SiC polytypes. The luminescence peaks near 6000Å (Fig. 1a).

Single crystals were prepared by a modified Lely technique (1). The charge was Carborundum "high-purity" SiC grain, acid-washed to remove surface impurities. Controlled amounts of BCl_3 and N_2 were mixed with the furnace atmosphere (flowing Ar) throughout the run in concentrations which yielded a light green (n-type) product. Bright room temperature photoluminescence was found in a minority of the crystals; the bulk appeared considerably dimmer. It should be noted however that, when BCl_3 was omitted from the atmosphere, the photoluminescence was much dimmer and no bright individuals were found.

Because of the scarcity of bright samples, it was only possible to analyze a batch of crystals of generally low brightness (see Table I). This analysis is useful in establishing the background level of impurities from the furnace and from the SiC charge. The analysis shows that the common SiC impurities, except Al and B, are below the detection limits of emission spectroscopy.

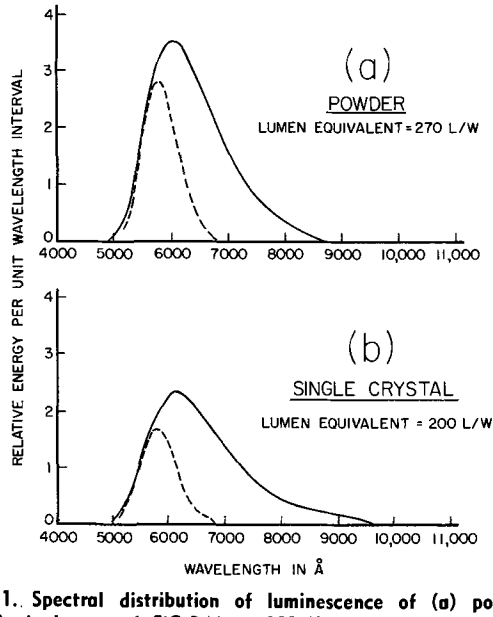

Fig. 1. Spectral distribution of luminescence of (a) powdered and (b) single crystal SiC:B,N at 300°K; excited by a 15 kv, 1 μa/cm^2 electron beam. Dashed curves are the product of the normalized photopic eye response and the spectral distribution.

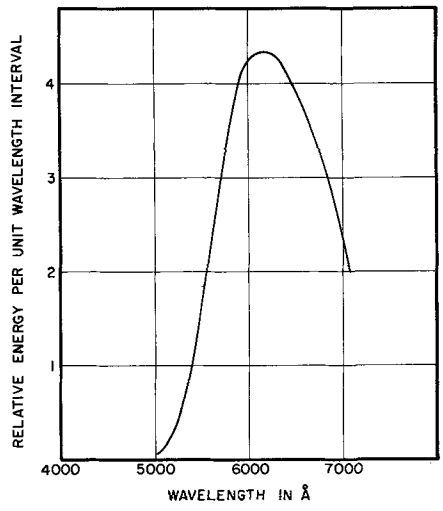

Fig. 2. Spectral distribution of luminescence of the single crystal of SiC:B,N at 300°K, excited by uv.

The structure of the crystal selected for the measurements was not determined, but the luminescence spectrum peak is close to that ascribed to the 21R polytype (3), *i.e.*, 6200Å (see Fig. 1B and Fig. 2).

Powder sample, 3650Å excitation.—The quantum efficiency of the powder under 3650Å excitation was determined by comparing the fluorescent output with that of a powdered sodium salicylate standard whose quantum efficiency is reported to be 0.45 (5). A filtered G.E. AH-6 mercury lamp was used to excite the samples with about 10^{-2} w/cm^2 of uv light peaking near 3650Å with some energy from 3300 to 3850Å. The photoluminescence measurements were carried out using a grating spectrophotometer with an external optical system which accepted a fixed small solid angle of the emitted fluorescence (see Fig. 3a). The detector was a RCA 1P22 photomultiplier. The total optical system plus detector was calibrated in terms of relative energy per unit wavelength interval. The curves in Fig. 1 and 2 were plotted in these units.

For the quantum efficiency estimates, the spectral distribution data were obtained for the SiC sample and the sodium salicylate standard under identical 3650Å intensity. These data were converted to relative photons per unit energy interval plots (not

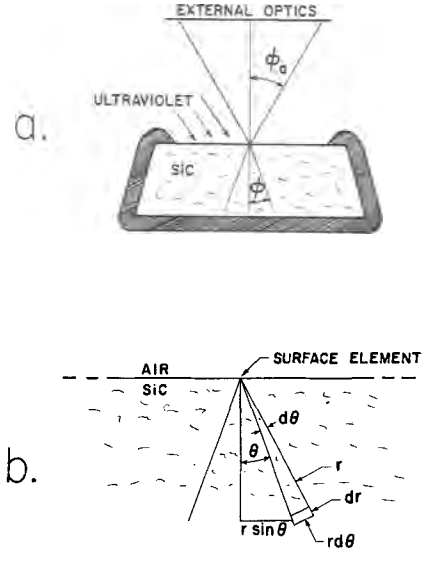

Fig. 3. (a) Experimental arrangement used for single crystal SiC:B,N, and (b) diagram illustrating the geometric approach used to establish the optical factor.

shown); the ratio of the areas under the curves in these plots are equal to the ratio of photon outputs.

The correction factor by which this ratio must be multiplied to give the quantum efficiency is

$$K_p = \frac{(1-R_{uv})_s}{(1-R_{uv})_p} \cdot \frac{2}{(1+R_e)_p} = \frac{0.53}{0.92} \cdot \frac{2}{1.50} = 0.77$$

where R is diffuse reflectance, the subscripts s and p denote the sodium salicylate standard and the powdered SiC, respectively, and R_e is the diffuse reflectance of the SiC for its own emission. (It was assumed that the fluorescence and the reflected uv were perfectly diffuse for both sample and standard.) Using 45% for the quantum efficiency of sodium salicylate, the quantum efficiency under uv excitation of a typical SiC:B,N powder was found to be about 6.4%.

Single crystal, 3650Å excitation.—The quantum efficiency of single crystal SiC:B,N was also obtained by comparison with sodium salicylate. In this case, the crystal surfaces except the central region of a smooth natural face were painted black with kerosene "dag." This procedure virtually eliminated multiple internal reflections and also simplified the corrections to be made below in deriving internal quantum efficiency.

These corrections can be understood by reference to Fig. 3b. The fluorescent light incident on an infinitesimal surface element of the crystal which originates within the solid angle corresponding to $d\theta$ is

$$dL = A(2\pi e^2 \sin\theta dr)\left(\frac{\cos\theta}{r^2}\right) e^{-kr\cos\theta}$$

where A is a constant, r is the distance of a light-producing volume element from the infinitesimal surface element, and k is the absorption constant for 3650Å light. The first term in parentheses is the volume element, the second term arises from the assumption of isotropic emission within the volume element, and the third represents the variation of relative emission intensity with vertical distance from the surface of the crystal. This expression integrates to $(2\pi A/k)(1-\cos\phi)$ for an angle ϕ in the crystal accepted in the external optical system. The fraction of the light generated in the whole hemispherical solid angle which is accepted in the solid angle corresponding to ϕ is then $(1-\cos\phi)$. The relation of the internal acceptance angle ϕ to the external (in air) acceptance angle, ϕ_a, is given by Snell's law: $\phi_a = n\sin\phi$, where n = refractive index of SiC at 6200Å.

This gives a fraction accepted (for small values of ϕ_a)

$$f_x \cong \frac{\sin^2\phi_a}{2n^2}$$

For the sodium salicylate powder, fluorescence is diffuse, and the fraction accepted is

$$f_p = \sin^2\phi_a$$

The optical correction factor when comparing crystal and standard is then

$$K_x = \frac{(1-R_{uv})_s}{(1-R_{uv})_x} \cdot \frac{1}{(1-R_e)_x} \cdot 2 \cdot \frac{f_p}{f_x} = \frac{(1-R_{uv})_s}{(1-R_{uv})_x} \cdot \frac{4n^2}{(1-R_e)_x}$$

where the $(1-R_e)_x$ term corrects for emitted light lost by specular reflection at the crystal-air interface and redirected toward the absorbing dag base, and the factor 2 accounts for the loss of the half of the light emitted initially toward the dag base. After substitution of the refractive index at 6200Å (2.63) and the reflectance values, one obtains

$$K_x = \frac{0.53}{0.775} \cdot \frac{4(2.63)^2}{0.80} = 23.7$$

The 3650Å diffuse reflectance of the sodium salicylate was measured by comparison to MgO powder (reflectance assumed 100%); the SiC specular reflectances were calculated for normal incidence from the refractive indices (6) (2.81 at 3650Å). Using this value of K_x, a quantum efficiency of 18% was deduced for the crystal selected.

Cathode-ray excitation.—The cathode-ray efficiency measurements were made at 15 kv and 22.5 kv, at current densities of 0.01 to 0.1 μa/cm^2, for 77° and 300°K. Both powders and single crystals were bombarded and viewed at 45° to the sample surface. The cathodoluminescent brightness in foot lamberts was measured with a Salford Electrical Instruments, Ltd. photometer. The external power efficiencies (watts out/watts incident) were determined directly from the photometric measurements using the lumen equivalents of the radiation (see Fig. 1) and the power in the incident beam. The best of these efficiencies for powdered and single crystal SiC were found to be 2.7 and 0.08%, respectively.

It was then assumed (conservatively) that ~6 ev of cathode-ray energy were needed to create an electron-hole pair which then resulted in an emitted photon of ~2 ev, giving a correction factor of 3. The remaining correction for powder and crystal is analogous to that for ultraviolet excitation above, since a brightness measurement also implies a diffuse source. The complete correction factor becomes

$$K_p = 3\frac{2}{(1+R_e)_p} = 4.0 \quad \text{for the powders and}$$

$$K_x = 3 \cdot \frac{4n^2}{(1-R_e)_x} = 105 \quad \text{for the crystals}$$

The quantum efficiencies of SiC:B,N deduced by correcting the above external power efficiencies are then ~ 12% for the powder and ~ 8% for the crystals.

In summary, the four determinations of quantum efficiency at 300°K are compared in Table II. At 77°K, the quantum efficiencies for both types of excitation are about two times greater than the 300°K values.

Discussion

The lower value of efficiency found under uv excitation for the SiC:B,N powder may be accounted for by (*i*) the samples used for the two measurements were from different preparations, (*ii*) the uv excitation intensity was much higher than the cathode-ray excitation intensity. (We have found that efficiency varies as the —0.1 to —0.3 power of excitation intensity), and (*iii*) the assumption of diffuse reflectance of uv may be a poor one. The higher value of efficiency found under uv excitation for the single crystal may be due to the difference in penetration of the electrons and the uv (~ 3μ compared to ~ 10μ), and suggests that the single crystal may not be uniform in properties near the surface. (The same crystal was used for the uv and cathode-ray measurements). We feel that our results indicate a quantum efficiency of between 5 and 20% for SiC:B,N at 300°K.

SiC is an indirect material and, as such, might be expected to have a low efficiency for luminescence resulting from band to band recombination or recombination by way of shallow levels. There is, however, no theoretical barrier to high efficiency radiative re-

Table II. Quantum efficiencies of SiC:B,N

	SiC:B,N powder	SiC:B,N single crystals
Ultraviolet	6%	18%
Cathode ray	11%	8%

combination involving deep levels, which is undoubtedly the case for SiC:B,N. The same is true for the 7000Å emission of GaP, for which fairly high injection electroluminescence efficiencies have been reported recently (8-10).[2]

Acknowledgments

The authors are indebted to Dr. A. Addamiano for supplying samples of powdered SiC:B,N and to Dr. R. P. Taylor for the analytical work.

Manuscript received Nov. 5, 1965; revised manuscript received March 24, 1967.

Any discussion of this paper will appear in a Discussion Section to be published in the June 1968 JOURNAL.

[2] In fact, even radiative recombination by way of shallow donor acceptor levels is efficient for GaP at low temperatures (9).

REFERENCES

1. A. Addamiano, R. M. Potter, and V. Ozarow, *This Journal*, **110**, 517 (1963).
2. E. E. Violin and G. F. Kholuyanov, *Soviet Physics—Solid State*, **6**, 465 (1964), translated from Fizika Tverdage Tela, **6**, 593 (1964).
3. A. Addamiano, *This Journal*, **111**, 1294 (1964).
4. A. Addamiano, *J. Phys. Chem. Solids*, **26**, 669 (1965).
5. F. J. Studer, Private communication.
6. J. S. Prener, Private communication.
7. R. N. Hall, *J. Appl. Phys.*, **29**, 914 (1958).
8. H. G. Grimmeiss and H. Scholz, *Phys. Letters*, **8**, 233 (1964).
9. R. A. Logan, M. Gerschenzon, F. A. Trumbore, and H. G. White, *Appl. Phys. Letters*, **6**, 113 (1965).
10. M. Gerschenzon, F. A. Trumbore, R. M. Mikulyak, and M. Kowalchik, *J. Appl. Phys.*, **36**, 1528 (1965).

Closed System Vapor Growth of Bulk CdS Crystals from the Elemental Constituents

Naim Hemmat and Martin Weinstein

Tyco Laboratories, Inc., Bear Hill, Waltham, Massachusetts

ABSTRACT

The growth of large, high-purity CdS monocrystals has been accomplished by a closed system technique. Crystals weighing up to 150g, 9 cm in length by 25 mm in diameter have been grown in a closed quartz ampoule directly from the high-purity elemental constituents. The technique lends itself to the preparation of high-purity CdS, since the possibility of extraneous impurity pick-up is minimized. Homogeneous doping during vapor growth has also been accomplished. In addition, techniques are described whereby bulk crystals containing 10^3 dislocation/cm^2 have been prepared. The mechanisms of dislocation production, propagation, and removal are discussed in the specific context of constrained growth from the vapor phase.

A number of methods have been proposed for the growth of large, high-purity, single crystals of CdS (1-3). Many procedures have also been described for the synthesis of CdS. In general, the two basic methods are precipitation from aqueous solution of Cd with H_2S (4) and precipitation from vapor phase reaction (5).

In the latter approach, commonly known as the Frerich's method (6), the metal is vaporized in one section of the furnace and carried over to the reaction zone by a carrier gas (H_2) where it reacts with H_2S to form the metal sulfide vapor. The sulfide subsequently is deposited in a cooler zone of the furnace. The Frerich's technique and all its modifications can therefore be described as a chemical vapor transport process. This type of vapor phase technique requires a composite assembly in which a relatively large surface area of the system is in contact with the constituent elements and the compound. This paper describes in detail a new closed-system synthesis and growth technique by which large, high-purity, and uniformly doped single crystals of CdS are grown from starting charges of Cd and S.

Synthesis of CdS

In order to minimize contamination and improve crystal homogeneity, an attempt was made to synthesize CdS in a closed reaction tube.

The experiments that led to the successful synthesis of CdS in a closed vessel can be summarized as follows: stoichiometric quantities of high-purity (99.9999+%) Cd in the form of shot (United Mineral and Chemical Corporation, New York) and S (99.999%) type A-58, fragmented pieces (American Smelting and Refining Company, South Plainfield, New Jersey) were sealed in a 25 mm ID, 20 cm long, clear quartz tube under vacuum (10^{-6} Torr). The sealed reaction tube was positioned in the uniform temperature zone of a horizontal resistance furnace. A number of experiments following various time-temperature cycles were conducted. The time-temperature cycle for which complete synthesis was successful consisted of holding the charge at 600°C for 12 hr, followed by 24 hr at 900°C and then gradually increasing the temperature to 1200°C. The charge was maintained at 1200°C for 8 hr or more and then cooled to room temperature. Figure 1 is a macrograph of the CdS crystallites obtained in a run following this specific time-temperature cycle. The resulting crystals have a transparent yellowish-brown color and are randomly sized single crystals in the form of hexagonal rods and platelets, some with extremely well-defined crystallographic faces. The size of the crystals ranges up to 3 x 4 x 8 mm.

In general, it was experienced that in order to avoid an explosive reaction the system had to be held at 600° and 900° for a minimum of 20 hr. On examination it was concluded that the explosive reaction was intimately associated with the initial formation of a CdS film that surrounded the liquid Cd and retarded the Cd + S → CdS reaction. Such observations have previously been noted by Reisman and Berkenblit (7). The CdS film forms in some cases below the melting point of Cd. At 600° the film became thicker and much less porous. The thick film grown at 600° was capable of sustaining the internal pressure equal to the Cd vapor pressure at this temperature. If this thick, tenacious film was not given sufficient time to grow, the

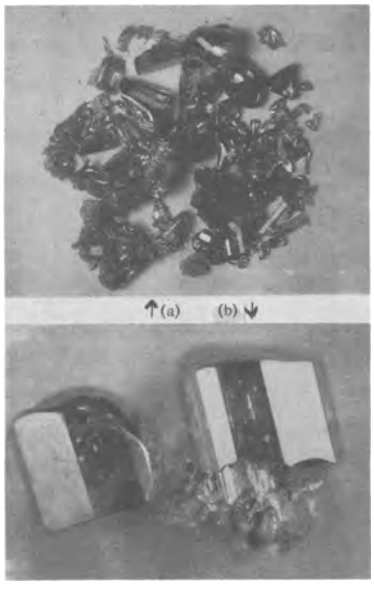

Fig. 1. CdS crystallites produced by closed tube synthesis approach, (a) 1X, (b) 8X.

film fractured at a temperature above 700° and the exothermic reaction Cd + S → CdS took place in a violent manner. At 900° Cd (or S) diffusion through the CdS film was sufficiently fast so that, after 20 hr at temperature, the reaction goes to completion. If the synthesis reaction is not carried to completion, above approximately 925°, the vapor pressure of S becomes sufficiently high ($P_S \sim 35$ atm) to cause failure of the 1.5 mm thick quartz capsule.

Based on an analysis of the results obtained from these experiments, it was concluded that the synthesis of CdS directly from the elements in a closed system is feasible; in order for the synthesis to be carried to completion successfully, the constituent elements should be separated initially by means of a proper temperature gradient in order to avoid the formation of a CdS film at low temperatures on the Cd melt. Also in order to avoid excessive pressure build-up, the S reservoir must be kept below 500° while the exothermic reaction is in progress.

The synthesis procedure finally arrived at utilized a batch-type technique. Stoichiometric quantities of S and Cd were initially placed into the growth ampoule and sealed under vacuum (10^{-6} Torr). The tube was then placed into a movable furnace which allowed observation of the ampoule during reaction. The furnace was first passed over the Cd reservoir in order to cause vaporization of Cd with subsequent deposition of a Cd film in the central portion of the tube. Next, the furnace was manually moved to the S reservoir where vaporization of the S occurred with subsequent deposition of a portion of the S charge again in the central portion of the tube. The furnace was then moved to the center of the tube where reaction of the constituent films took place. For a 100g elemental charge approximately 5-7g of CdS was formed per pass at the central portion of the reaction tube. This process was repeated until all reactants were consumed.

The CdS prepared by this technique is a yellowish powder containing fine needlelike crystallites. The above described closed system technique was also found to be applicable to the synthesis of high-purity CdSe, ZnSe, and ZnS, provided that the optimum temperature-time cycle was used for each compound.

It has been reported that deviations from stoichiometry in CdS crystals significantly affect their electrical properties (8). It is also known that an excess of one of the constituent elements can radically change the crystal growth parameters (9). For these reasons it was found advisable in certain cases to extract the excess free elements from the synthesized CdS charge prior to single crystal growth. The extraction of excess constituent elements was readily accomplished using the following procedure. The initial reaction tube was made a few inches longer than the intended growth ampoule. Following the synthesis the sealed reaction tube was positioned in a two-zone furnace (with temperature flats of approximately 1050° and 800°) for 2 to 4 hr, with a portion of the tube exposed to ambient temperature. This procedure resulted in the sublimation of the entire charge at the hotter zone and crystallization at the 800° region; during this recrystallization process the excess Cd or S condensed at the coolest region of the tube. The tube was then brought to room temperature and the ampoule resealed, isolating the region containing the volatile element from the remainder of the tube containing the recrystallized CdS charge. (This process, of course, can only be utilized in the case of undoped charge.)

Crystal Growth

After the synthesis step, the growth ampoule was positioned inside a mullite tube in a travelling horizontal furnace. Since the vapor pressure of CdS at 1200° is ~ 0.25 atm the mullite tube was maintained under dynamic vacuum so as to reduce the stress on the quartz tube, thus reducing the rate of devitrification and preventing collapse of the ampoule during the run. In practice, the pointed end of the growth ampoule is positioned relative to the temperature gradient of the furnace as shown in Fig. 2. Figure 3 is a schematic representation of the crystal growth apparatus. The optimum speed of the furnace travel is dependent on the temperature profile of the furnace; 0.25°/hr (corresponding to approximately 0.3 mm/hr) was found to be the most practical rate for growth. It should be noted that the amount of charge relative to the length of capsule and temperature gradient determines the exact temperature corresponding to the start of nucleation. The temperature of the furnace was controlled to ± 0.25° by a Honeywell precision set point system Model No. 687081. When the crystal growing run was terminated, the temperature of the furnace was decreased gradually (25°/hr to room

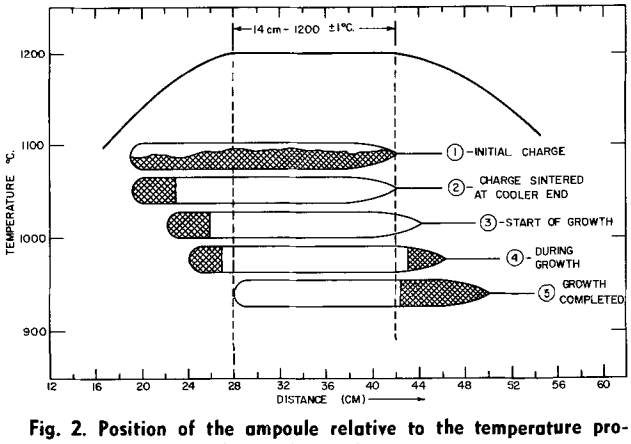

Fig. 2. Position of the ampoule relative to the temperature profile at various stages of crystal growth.

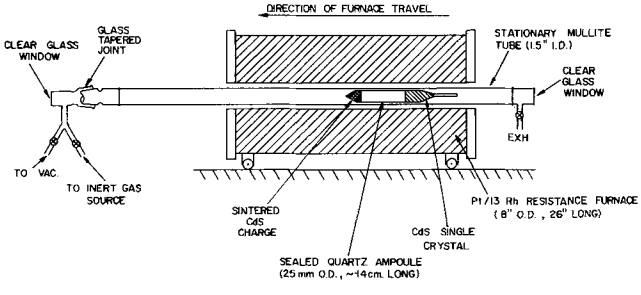

Fig. 3. Schematic drawing of crystal growth apparatus

temperature) by automatic programming, to avoid thermal strain. A thorough analysis of the growth rate as a function of distance was made to improve process reliability and yield.

CdS single crystals weighing up to 150g and 25 mm in diameter have been grown by the method described. Figure 4 is a photograph of some typical crystals grown by this approach. It was also feasible to grow single crystals of CdS with nearly the same dimensions in a vertical apparatus.

It was experienced that a Cd excess of approximately 400 ppm did not affect single crystal growth. We have found, however, that excess S inhibits the growth process by severely decreasing the dynamic vapor pressure of CdS. The excess S suppresses the sublimation rate more than Cd since it has a higher vapor pressure than Cd. Therefore, in order to maintain the relationship $K = P_{Cd} \times P_{S_2}$, P_{Cd} decreases to a point where sublimation is seriously retarded. Utilizing the previously described technique we have observed that the growth of single crystals from high-purity Cd and S necessitates more careful control of process variables (temperature, ampoule position, rate of growth, etc.) than the growth from a doped charge or from commercially available presynthesized compound.

Doping of CdS

The pure crystals grown by the closed system synthesis and growth technique exhibit a resistivity in the range 0.01-0.1 ohm-cm. This low resistivity may well be the consequence of a tendency for CdS to grow slightly off stoichiometry. The Hall mobility of these crystals varied on average from 300 cm^2/v-sec to 350 cm^2/v-sec at room temperature (25°).

The closed system technique also lends itself to the doping of crystals. For example, when 10^{18} atoms/cc of Cu (~55 ppm) were added in the form of CuS to the initial elemental charge prior to synthesis, the crystals exhibited a resistivity of approximately 10^3 ohm-cm with a variation of less than ±15% along their entire length. The Cu doped crystals exhibit a uniform transparent-reddish color. Also it was experienced that the resistivity of the pure crystals could be increased by approximately an order of magnitude by adding excess S (corresponding to a P_S of approximately 200 mm Hg at 1200°) to the initial elemental charge, prior to synthesis.

The impurity concentration of the bulk grown CdS crystal was analyzed by mass spectrometry. The overall analysis is given in Table I. Total impurities, other than carbon and sodium, were found to be approximately 2 ppm atomic. The carbon concentration was not homogeneous, varying from 0.1 to 1 ppm. Sodium varied between 0.4 and 3.8 ppm. Impurities not listed were not detected and have concentrations less than 0.3 ppm atomic, except O, Mn, Fe, and Zn which are interfered with by the background lines of S and Cd combinations.

Fig. 4. Photograph of CdS crystals grown from Cd and S by the closed system technique. The dark crystal is CdS doped with 10^{20} atom Cu/cm^3.

Table I. Impurity concentrations in the CdS crystals grown from initial charge of high-purity elements*

Element	Detection limit	CdS sample
Li	0.01	0.07
C	0.05	0.1-1.0
N	0.05	0.5
F	0.06	0.1
Na	0.01	0.4-3.8
Mg	0.05	0.2
Al	0.02	0.3
K	0.01	0.7
Ca	0.02	0.14
Cr	0.06	0.06

* Mass Spectrographic Analysis by A. J. Socha, L. S. Higbie, and R. K. Willardson, Bell and Howell Research Center, Pasadena, California.

Crystal Perfection

In order to facilitate the structural analysis of the grown crystals, an etchant composed of 35% phosphoric acid saturated with CrO_3 with 65% HCl (denoted "HPC") was developed which produced distinct and reproducible etch pits on the (0001) face of CdS. Prior to etching, the (0001) faces were mechanically polished and chemically repolished by heating in phosphoric acid at 100° for 30 min. The chemical polish removed the surface damage introduced by mechanical polishing. Etching of the chemically polished specimens was carried out for 10 to 20 sec at room temperature without agitation. For specimens with higher etch pit densities, shorter etching times were employed to prevent overlapping of pits. Also, a number of adjacent wafers (with planes perpendicular to the c-axis) were etched in a similar manner and examined microscopically. It could be demonstrated that the etch pit denoted the emergence of a line defect at the crystal surface thereby indicating a 1:1 correspondence between etch pits and emergent dislocations.

In most cases, a chemical etch should produce soluble or gaseous products. Insoluble products generally contaminate the surface inhibiting further action of the etch or mask its effect. Reaction of the (HPC) etch on CdS most probably proceeds as follows

$$3CdS + 2H_3PO_4 \rightarrow Cd_3(PO_4)_2 + 3H_2S \quad [1]$$

$$H_3PO_4 + CrO_3 + 3HCl \rightarrow CrPO_4 + 3H_2O + 1.5Cl_2 \quad [2]$$

$$H_2S + 4H_2O + 4Cl_2 \rightarrow H_2SO_4 + 8H^+ + 8Cl^- \quad [3a]$$

$$CdS + 4H_2O + 4Cl_2 \rightarrow CdSO_4 + 8HCl \quad [3b]$$

It is to be noted that the products $CdSO_4$, $Cd_3(PO_4)_2$, $CrPO_4$, and Cl_2 are either soluble in water or are gaseous. It is also to be noted that with time, depletion of Cl_2 gas will weaken the effect of the etch; for this reason a freshly made etch is necessary for best results.

Figure 5 is a photomicrograph of the (0001) plane (the "Cd-face") (10) of CdS. The effect shown was produced by heating a polished oriented sample in phosphoric acid for approximately 15 min. It is to be noted that a series of layers form a uniform background for a few highly symmetrical hexagonal terraces. In order to determine the origin of the "terracing effect," a section of the (0001) plane was bevelled 5 degrees and again was polished chemically. The direction of terracing changed, indicating that the lamellar effect produced by chemical polishing merely reveals the deviation of surface orientation from the basal plane.

Typical pits produced by the (HPC) etch are shown in Fig. 6 The hexagonal pits are produced on the (0001) face in which the uppermost layer is com-

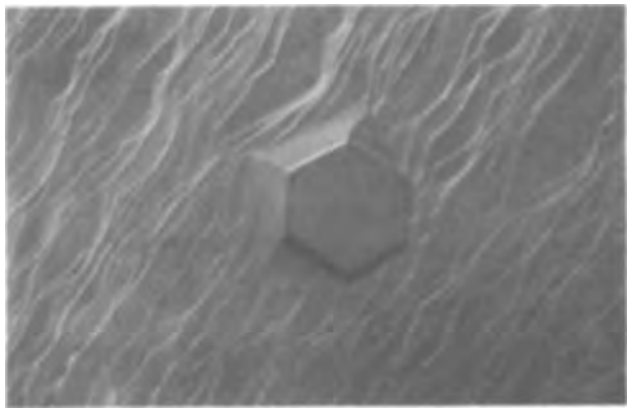

Fig. 5. Photomicrograph of a (0001) of CdS heated in phosphoric acid for 15 min (235X).

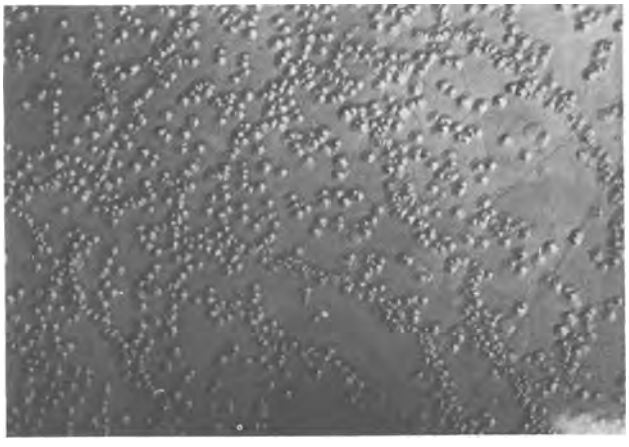

Fig. 6. Typical etch-pits produced by "HPC" etch on a (0001) plane, 30X.

posed of Cd atoms but not on the opposite $(000\bar{1})$ face which terminates with sulfur atoms. This effect arises because of the noncentrosymmetric structure of CdS. Reproducibility of these pits was confirmed by successively lapping and etching crystals with low etch-pit densities and retracing individual pits.

The distribution of dislocations in bulk single crystal CdS was studied by cutting wafers along the length of a large crystal the "c"-axis of which was perpendicular to growth direction. Figure 8 shows a composite photomicrograph of the (0001) plane of the entire surface of a slice (5X) taken from the midsection of this large single crystal. The crsytal weighed approximately 100g and was 4.2 cm long. The sawtooth pattern shown in Fig. 7 is actually an etch-pit pattern produced by the (HPC) etch.

Prior to etching, the surface was chemically polished. It is noted that the first region of the crsytal to grow contains an extremely high dislocation content. The observed dislocation aggregates act as a source for numerous low angle boundaries dispersed throughout the bulk of the crystal. Another source of dislocations appears to be present at the periphery of the crystal where the crystal is in contact with the quartz ampoule. The midsection of the crystal constitutes a third highly dense region; that is where the low-angle boundaries originating from the two mentioned sources intersect. The lowest etch-pit density is found in the last portion of the crystal to grow.

Figure 8 is a plot of the etch pit density as a function of distance along the length of a pure crystal. The c-axis was approximately 15 degrees from the growth direction in this crystal. Etch pit densities were determined on eight wafers cut perpendicular to the "c"-axis, the slices being 6 mm thick. It is noted that in the first grown section of the crystal, the dislocation density is high at the edge and center of the crystal. The density at the edge and center remains nearly constant through the midsection of the crystal but sharply decreases as it approaches the last grown region.

In the course of the imperfection study, two unique types of etch-pit patterns were distinguished. Figure 9 is a photomicrograph of the pattern of the first type in which the etch-pits originate from a mechani-

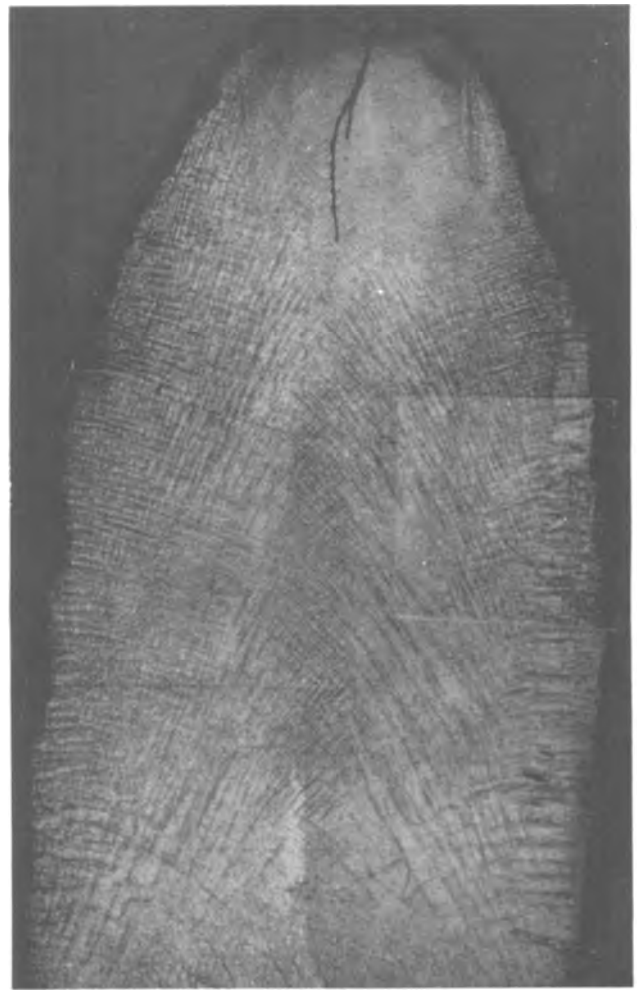

Fig. 7. A composite photograph of the etch-pit pattern on (0001) plane of a slice taken from the mid-section of a large single crystal of CdS (5X).

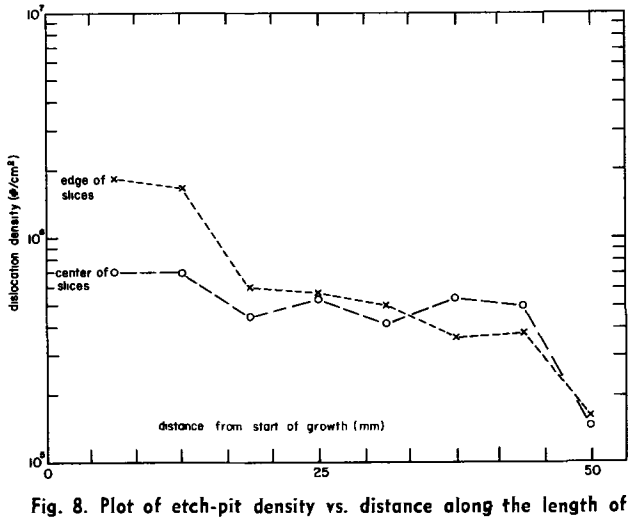

Fig. 8. Plot of etch-pit density vs. distance along the length of a pure crystal.

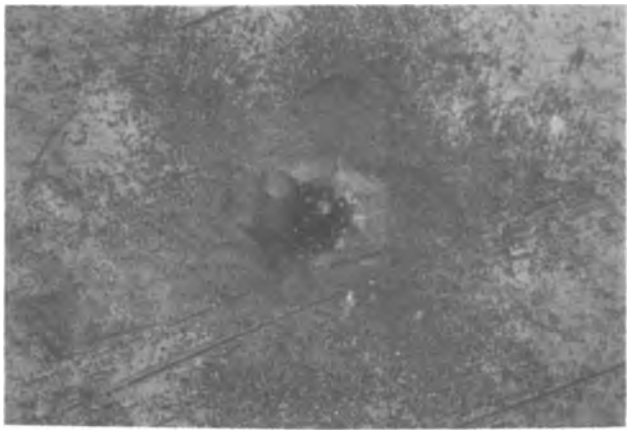

Fig. 9. Etch-pit pattern originating from a mechanically damaged point source (pure crystal) 275X.

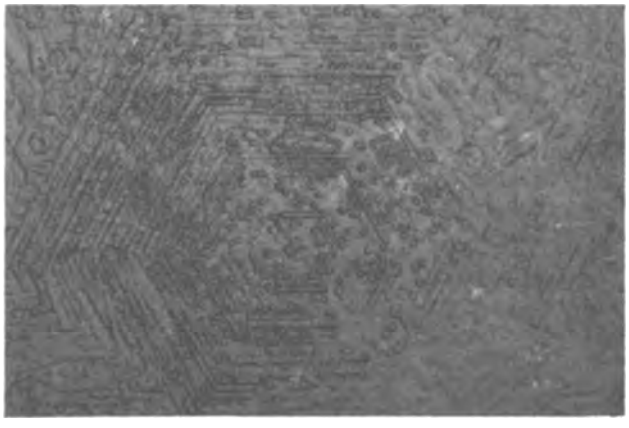

Fig. 10. Etch-pit pattern aligned in $<11\bar{2}0>$ directions associated with stress originating at the periphery of the region (pure crystal) 275X.

cally damaged point source. In this type of pattern the etch-pits disperse along the $<11\bar{2}0>$ direction, gradually disappearing some distance from the source. Figure 10 shows a pattern of a second type in which the etch pits are also aligned in $<11\bar{2}0>$ directions but collectively form an aggregate of unicentered hexagonals. In this latter type of disorder, it is suspected that slip is caused by stress originating at the periphery of the region.

The direction of etch pit alignment was established from the geometry of the hexagonal pits. By a careful study of Laue back reflection photographs and light figure patterns of etched single crystals of CdS having Wurtzite type (B_4) structure, it was confirmed that the arms of the hexagonal etch pits on (0001) surface extend in the $<11\bar{2}0>$ directions. The Burger's vector directions were established from the observation of slip traces and the movement of dislocations during crystal bending.

For the most part the pit-arays on the (0001) plane were found to align in $<10\bar{1}0>$ directions, with $\{1\bar{2}10\}$ planes as the glide system. These arrays constitute a group of edge dislocations with Burger's vector $b = a_o\sqrt{3}$ in $<10\bar{1}0>$ directions where a_o is the lattice constant. This type of edge dislocation in CdS has also been identified by Nishimura (11). In addition to the dislocations formed in $<10\bar{1}0>$ directions, we also observed a formation of dislocations in $<11\bar{2}0>$ directions, most likely having a Burger's vector of $b = a_o$ (see Fig. 11a). This type of dislocation has also been observed by Woods (12). Figure 11b shows a particular region on the (0001) plane where both types of dislocations intersect.

An attempt was also made to determine the structure of imperfections terminating at the $(000\bar{1})$ "S-face." Figure 12 shows the effect of heating a crystal in H_3PO_4 for approximately 1 hr. It is to be noted that the $(000\bar{1})$ plane in this case consists of an interlaced spiral growth pattern, indicating the influence of screw dislocations on the growth mechanism. Upon close examination, the sixfold symmetry characteristic of the basal plane is noted within the growth spirals. The region on the lower left hand side of Fig. 12 shows a different grain, which has not been affected by etching due to misorientation relative to "c"-axis.

Based on observations of the dislocation pattern, it was concluded that the dislocation density could be minimized by starting growth from a low dislocation density properly oriented seed crystal and/or by using a semiflexible container to reduce the thermal stress (and subsequent dislocation generation) produced during cooling.

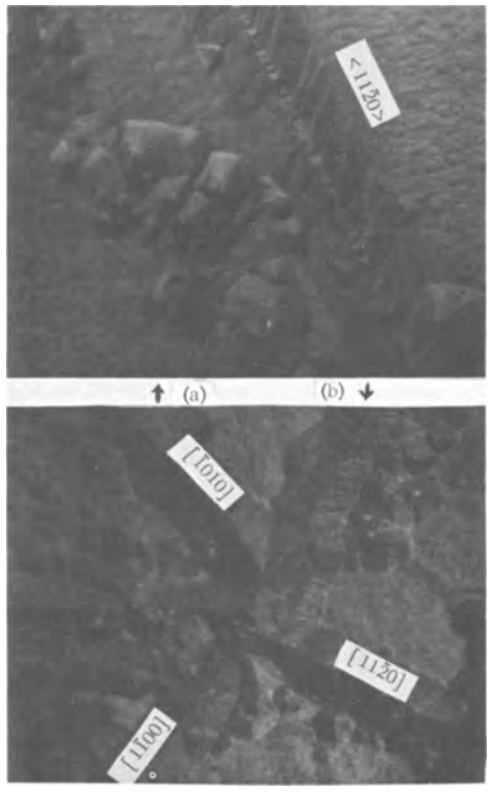

Fig. 11. Photomicrograph of (a) dislocations formed in $<11\bar{2}0>$ directions, (b) a region showing intersection of dislocations, formed in $<11\bar{2}0>$ and $<10\bar{1}0>$ directions.

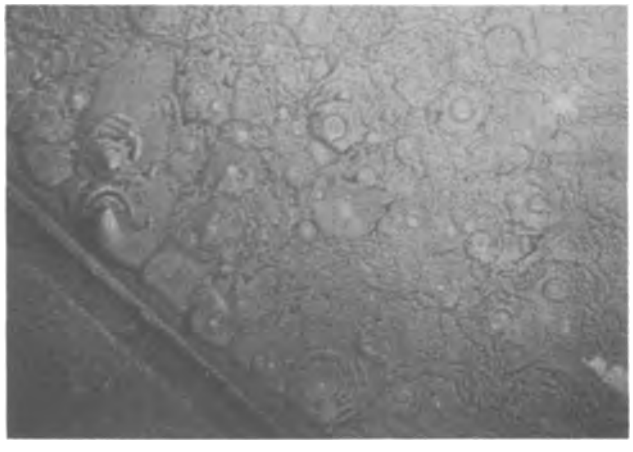

Fig. 12. Photomicrograph of (0001) "S-face" heated in H_3PO_4 at 100°C, 1 hr.

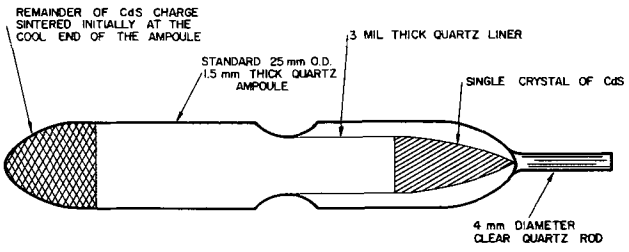

Fig. 13. Schematic drawing of ampoule assembly utilizing thin quartz liner.

Since the system was readily adaptable to the latter approach, a few experiments were carried out to determine the validity of the initial hypothesis. Figure 13 shows schematically the assembly with the 3 mil semiflexible quartz liner. The charge was positioned inside the thin ampoule. The main ampoule and the liner were sealed under high vacuum at the same time. Also a sufficient quantity of CdS powder was placed between the two ampoules to equalize the pressure inside and outside the liner. This prevented inflation of the thin liner at the growth temperature due to the vapor pressure of CdS. The single crystals obtained using this technique exhibited a dislocation density of 3 x 10^3/cm^2, two orders of magnitude lower than the crystals grown in the standard ampoule.

Conclusions

Synthesis and growth of large single crystals of CdS have been successfully accomplished by a closed system technique. This technique lends itself to growth of high purity, uniformly doped bulk crystals. In this technique contamination due to the carrier gas and/or intermediate handling of the compound is eliminated. Also the reaction (or growth) chamber surface area in contact with the elements and compound is considerably minimized. (Only 1.5 cm^3 is needed per gram of compound.) From the standpoint of the system assembly, the closed system technique is extremely economical; *i.e.*, the source-to-product conversion efficiency approach 100%, and the length of the crystal is not limited by the temperature profile of the furnace. This technique also makes possible the growth of CdS crystals under a predetermined vapor pressure of one of the constituent elements.

Acknowledgments

The authors would like to thank Mr. J. Faiola for his experimental assistance. This work was supported by the United States Army Materials Command, Harry Diamond Laboratories, under Contract DA-49-186-AMC-239(0).

Manuscript received Dec. 21, 1966; revised manuscript received April 28, 1967. This paper was presented at the Philadelphia Meeting, Oct. 9-14, 1966.

Any discussion of this paper will appear in a Discussion Section to be published in the June 1968 JOURNAL.

REFERENCES

1. L. C. Greene, D. C. Reynolds, S. J. Czyzak, and W. M. Baker, *J. Chem. Phys.*, **29**, 1375 (1958).
2. R. H. Fahrig, *Electrochem. Tech.*, **1**, 362 (1963).
3. W. W. Piper and S. J. Polich, *J. Appl. Phys.*, **32**, 1278 (1961).
4. E. T. Allen and J. L. Cranshaw, *Am. J. Sci.*, **34**, 310 (1912).
5. R. Lorenz, *Chem. Ber.*, **24**, 1509 (1891).
6. R. Frerichs, *Naturwissenschaften*, **33**, 387 (1946); *Phys. Rev.*, **72**, 594 (1947).
7. A. Reisman and M. Berkenblit, *J. Phys. Chem.*, **67**, 22 (1963).
8. F. A. Kroger, H. J. Vink, and J. Volger, *Philips Res. Rep.*, **10**, 39-76, 260 (1955).
9. B. M. Bulakh and I. B. Mizets'ka, *Ukr. Fiz. Zh.*, **7**, 1125 (1962).
10. G. A. Wolff, J. J. Frawley, and J. R. Hietanen, *This Journal*, **111**, 22 (1964).
11. Jiro Nishimura, *J. Phys. Soc. Japan*, **15**, 732 (1960).
12. J. Woods, *Brit. J. Appl. Phys.*, **11**, 296 (1960).

Electrical and Transport Properties of Cu in InAs

C. S. Fuller and K. B. Wolfstirn

Bell Telephone Laboratories, Incorporated, Murray Hill, New Jersey

ABSTRACT

The solubility and diffusion of Cu in InAs has been investigated by means of electrical and radiochemical methods. The solubility determined by equilibration with an external Cu phase follows the relation $N_{Cu} = 4.0 \times 10^{22} \exp(-1.0 \text{ ev}/kT)$. The Cu solubilities determined from diffusion measurements in air were significantly lower presumably because of a different surface composition. The diffusion follows the relation $D = 0.0036 \exp(-0.52 \text{ ev}/kT)$. Cu is present almost exclusively as a single-charged interstitial donor in InAs. Defect acceptors, $\sim 3 \times 10^{15}$ cm^{-3}, are introduced into InAs by quenching from 875°C. These react with Cu giving about double the acceptor concentration. The maximum number of acceptors (substitutional Cu) introduced is essentially equal to the original donor concentration $\sim 10^{16}$ cm^{-3}. The possibility of drifting Cu to produce space-charge layers in InAs similar to Li in Ge is discussed.

Materials problems still restrict the utility of many of the III-V semiconductors. This is true, for example, of InAs where intensive efforts at purification (1, 2) have only succeeded in reducing the residual donors present to $\sim 10^{16}$ cm^{-3}. It has been suggested (1) that these may be native defects (antistructure) rather than residual impurities, although this remains to be proven. In addition to the residual donors, the question as to whether InAs crystals contain significant concentrations of vacancy clusters, is of interest in many applications. Such clusters are believed present in Ge (3), InSb (4), and in large concentration in GaAs (5).

The purpose of the present work is to obtain information on both of the problems mentioned above, through the use of ^{64}Cu as a probe. For example, interactions between substitutional Cu, or between vacancies produced by Cu, and donor antistructure disorder, As_{In}, might be expected. Also, since Cu interacts with vacancies present in clusters or present in

associates with impurity atoms in Ge (3), Si (6) and many compound semiconductors, it is of interest to examine InAs for similar reactions.

Before the above problems can be undertaken, it is necessary to know considerably more than is known at present about the electrical and diffusion behavior of Cu. The electrical effects of Cu in InAs have already been investigated. Edmond and Hilsum (7, 8) showed that Cu is responsible for heat treatment effects (9) in InAs and that Cu diffuses rapidly producing donors. They also found that it becomes electrically inactive (precipitates) when crystals diffused with Cu are allowed to stand at room temperature. On the other hand very little quantitative information on either the detailed electrical behavior or the diffusion of Cu is available in the literature. Another object of the present work therefore is to help fill this gap in our knowledge.

Materials and Methods

The undoped single crystal InAs employed in this work was prepared by the Czochralski technique (Monsanto Chemical Company) and had the following properties: electron concentration was 1.6-2.0 $\times$ 10^{16} cm^{-3} (298°K) and 1.4-1.8 $\times$ 10^{16} cm^{-3} (77°K); electron mobility was 27,000 (298°K) and 58,000 (77°K) cm^2/v-sec; etch pit density was 100 cm^{-2}. Mass spectrographic analyses on the crystal showed the following: all metallic impurities and S, Se, and Te <0.5 atomic part per million; carbon, oxygen, and nitrogen <1.0 part per million. Specimens (~50 mils thick) were prepared by cutting perpendicular to the growth axis [111] and lapping on No. 303 grade Aloxite abrasive in water to remove the cutting damage. Etching was done by means of bromine in methyl alcohol (10).

Copper, either ordinary Cu or Cu containing the radioactive isotope ^{64}Cu, was introduced into the InAs crystals by diffusion. This was done by electroplating Cu on one or more surfaces of the specimen (one face for the diffusion determinations). In some experiments known amounts of Cu, less than enough to saturate at the temperatures in question, were applied by "chem-plating" from 0.1*N* solutions.

The ternary phase diagram, Cu:In:As, has not as yet been investigated in any detail. We determined that Cu forms a eutectic melt with InAs at 340° ± 5°C. Consequently, for temperatures above this we assume that equilibrium alloys corresponding to the pseudo-binary liquidus form on the surface at each temperature. Below the eutectic temperature it is often difficult to achieve surface equilibrium. Consequently, the practice was adopted of prealloying all specimens at ~400°C for 2-5 sec prior to diffusion. No prealloying was employed for the solubility determinations. The error introduced in the diffusion runs by the prealloy treatment was estimated by examining the penetration of Cu radiochemically. This was found to affect only the first 15μ and, since most of the diffusions penetrated 0.5 mm or more, the correction is small and has been neglected.

Diffusions were carried out by heating the specimens in air on a stainless steel block controlled to within 1°C. All saturations were done in silica ampoules (0.001 Torr) placed in furnaces controlled to within 1°C. The accuracy of the temperatures was to ±1°C and was checked by melting pure Pb (327.4°C) and Sn (231.9°C) and by boiling water. Quenching required less than 1 sec on a metal block (22°C) or, for the encapsulated specimens, about 3 sec, in water at room temperature.

Electrical measurements were made by means of point contacts in a van der Pauw (11) arrangement at 300° and 77°K. These measurements are precise to ±2%. In calculating the electron concentrations, the relation $n = 1/R_H e$ was assumed in which R_H is the Hall coefficient and e is the electronic charge. Because of the high electron-to-hole mobility ratio (~100) in InAs the simple expression above holds for n-type specimens. However, for p-type specimens the two-carrier Hall expression must be used. We found that R_H determined in this way on Cu diffused Zn-doped InAs (p-type) was very inaccurate as a measure of the hole concentrations. Consequently, almost all of the electrical measurements reported here were made on extrinsic n-type specimens. A few measurements are reported for specimens which are intrinsic at 300°K. Because of the high mobility ratio, however, the simple expression is correct to within our experimental error even for these.

Penetration curves were determined by lapping the surfaces of the diffused specimens (after removal of the edge activity) parallel to the diffusion plane and counting the gamma activities of the grindings. Diffusion was approximately on the (111) plane, but no effect of the crystallographic direction is expected. Depth measurements were made by means of a Zeiss optimeter to ±2μ. The Cu concentration, plotted at the midpoint of each layer, was calculated from the corrected activity of Cu in each layer, the layer thickness, the specimen area, and the density of InAs (5.66). The surface concentration corresponding to each diffusion may be determined by extrapolation of the penetration curve to the origin taken as the surface of the specimen. Better values, however, are obtained from extrapolation of the best theoretical curves fitting the data (see below). This method was employed here.

The diffusion coefficient, D, was calculated from the "constant surface concentration" boundary condition (12)

$$C_x = C_o \operatorname{erfc} (x/2\sqrt{Dt}) \quad [1]$$

where C_x is the concentration at distance x from the specimen surface, C_o is the concentration at $x = 0$, erfc is the so-called complementary error function (1—error integral), and t is the time of diffusion at constant temperature.

A graphical procedure described previously (13) was employed to determine D. This consists of matching the log-log plot of the penetration curve to that of the complementary error function plotted against $x/2\sqrt{Dt}$ on the same scale. This procedure has an advantage when, as here, the data points are necessarily rather far apart (the short half life of ^{64}Cu precludes as detailed an analysis as might be desired), and the determinations near the origin are likely to be uncertain. The diffusion coefficients are calculated by reading the experimental distances corresponding to unity on the complementary error function plot. This provides values of $2\sqrt{Dt}$ and, since t is known, values for D.

Although solubilities can be determined from the C_o values as described above, this procedure usually does not yield as reliable results as the direct method which involves saturation with active Cu at each temperature. The latter method, however, fails when the diffusion coefficient becomes too small (below ~200°C) since the times then become too long. Both methods have been employed here. As shown below, however, the results do not agree. This is attributed to the fact that the surface phases differed in the two procedures.

Results

Diffusion and solubility of Cu.—The diffusion results are given in Fig. 1. These show the best fits to the complementary error function curves for the five temperatures: 248°, 342°, 393°, 449°, and 506°C. Figure 2 shows a semilog plot of D, calculated from Fig. 1, *vs.* reciprocal absolute temperature. The point at 506°C is low probably because of the appreciable heat-up time. An activation energy for diffusion of 0.52 ev (12.0 kcal) is obtained. Figure 3 is a semilog plot of the solubility against reciprocal absolute temperature including results from both the diffusion measurements and the direct determinations employing ^{64}Cu. The results from the two methods are not the same. Reasons for this are discussed below. A plot of the in-

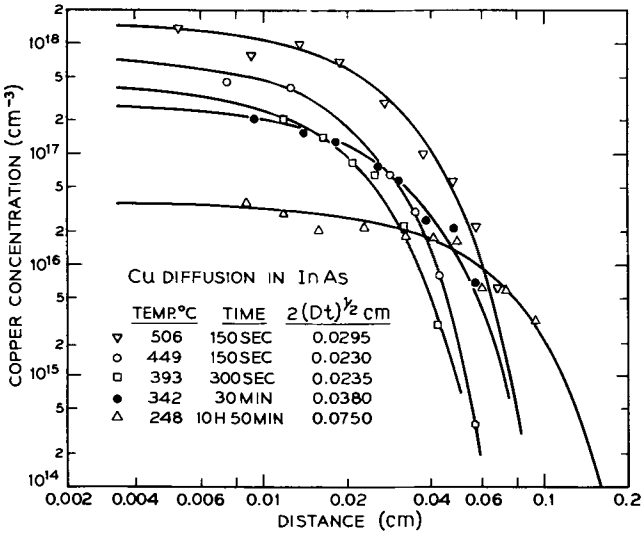

Fig. 1. Points show experimental determinations of Cu concentration as a function of distance from the surface for as-grown InAs specimens diffused at 248°, 342°, 393°, 449°, and 506°C. Solid lines show best fits of complementary error function (erfc U) curve plotted against $U = x/2\sqrt{Dt}$ to the same scale as the experimental data. Values of $x = 2\sqrt{Dt}$ which correspond to unity for the function U are given in the legend.

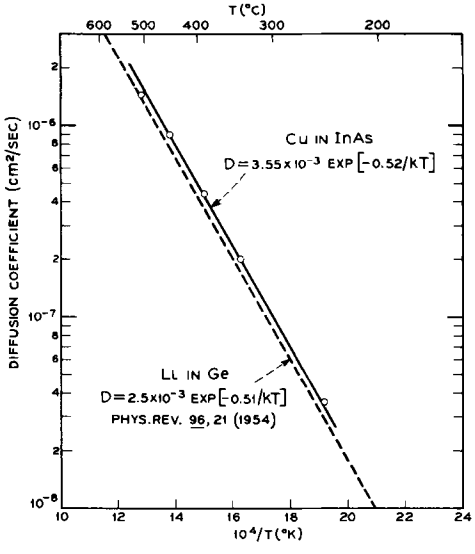

Fig. 2. Plot of diffusion coefficients derived from Fig. 1 vs. reciprocal absolute temperature. Data for Li in Ge are plotted (dashed line) for comparison.

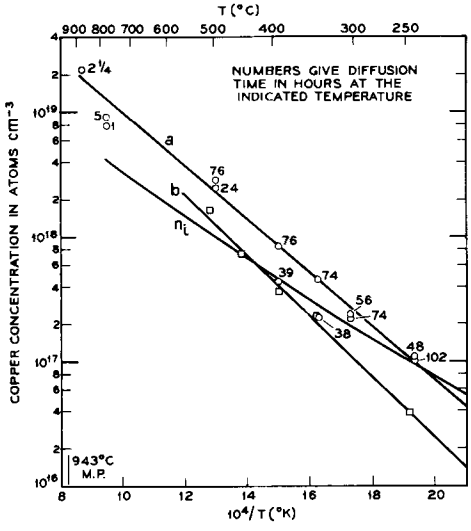

Fig. 3. Solubility of Cu in InAs. Open circles, determined radiochemically by saturation from an external Cu phase; open squares, determined from the solid curves of Fig. 1 by extrapolation, prealloyed at 440°C. A calculated curve of the intrinsic carrier concentration, n_i, for InAs is included.

trinsic carrier concentration, calculated using $m_e^* = 0.02\ m_o$, $m_h^* = 0.41\ m_o$, and $E_G = 0.47$ ev, is included in Fig. 3.

Electron-to-Cu ratio.—Table I shows a comparison of the electron and Cu concentrations for various InAs specimens. It is evident that the [e]/[Cu] ratios, except for specimen 14 are less than unity by appreciable amounts. This is because of rapid precipitation of Cu during and after cooling from the diffusion temperatures. Specimen 14 was prepared using a limited amount of Cu so that the specimen after diffusion was uniformly undersaturated. Table I shows that for this case the [e]/[Cu] ratio is essentially unity indicating that all of the Cu is interstitial, Cu_i. The ratio observed (1.08) deviates from unity by somewhat more than is expected from our estimated error. This may be caused by Cu leaving substitutional positions. Evidence for such Cu is discussed below.

Table I also shows the strong effect of the degree of supersaturation on the extent of precipitation during quenching. Thus only about 4% of the Cu remains electrically active when specimens saturated at 875°C are quenched to room temperature in about 3 sec. This is a result of the high diffusion coefficient of Cu_i (10^{-5}-10^{-7} cm²/sec) in the cooling range.

Substitutional Cu.—The result above, namely, that Cu in InAs is essentially all present as an interstitial donor is interesting, because in every case so far in-

Table I. Ratio of electron to Cu concentration in InAs

Specimen[a]	Saturation Temp, °C	Saturation Time, hr	Cu conc. ($\times 10^{17}$ cm^{-3})	Electron conc. (24°C) ($\times 10^{17}$ cm^{-3})[b]	Ratio [e]/[Cu]
1	242	48	1.08	0.83	0.77
2	243	102	1.03	0.80	0.78
3	305	55	2.35	1.89	0.80
4	305	73	2.22	1.83	0.82
5	342	38	2.26	1.73	0.76
6	343	74	4.54	3.85	0.85
7	393	39	4.34	3.81	0.88
8	393	76	8.26	7.06	0.86
9	495	24	24.7	9.20	0.37
10	496	76	27.8	5.85	0.21
11	778	1	78.2	12.60	0.16
12	778	5	90.2	4.38	0.05
13	875	2	218.0	8.28	0.04
14[c]	875	1	12.4	13.40	1.08

[a] Czochralski grown crystal, undoped, ~2 × 10^{16} cm^{-3} N-type. All specimens were ~1 mm thick.
[b] Corrected for initial electron concentration.
[c] This specimen was purposely undersaturated.

Table II. Acceptors in InAs quenched in the presence and absence of Cu

Specimen	Initial electron conc at 25°C ($\times 10^{16}$ cm^{-3})	Temp, °C	Cu conc. (cm^{-3})	Type	Final electron conc. at 25°C (cm^{-3})	Change in carrier conc. (cm^{-3})	Acceptor conc. (cm^{-3})
D-3	1.93	820[a]	4.13×10^{16}	N	5.4×10^{16}	$(+)3.47 \times 10^{16}$	6.6×10^{15}
		901[b]	3.77	N	5.1	(+)3.17	6.0
D-4	1.99	820[c]	—	N	1.74×10^{16}	$(-)2.5 \times 10^{15}$	2.5×10^{15}

[a] Limited Cu source, 3 sec quench to 300°K.
[b] Fast quench to 78°K.
[c] Control specimen, 3 sec quench to 300°K, no Cu present.

vestigated up to now Cu exists in solution in a large part as substitutional (acceptor) Cu, designated Cu_S. In order to investigate the possibility that some Cu is substitutional in InAs the following additional experiments were carried out:

(*i*) Small amounts of labeled Cu were introduced into InAs at high temperatures (800°-900°C) in order to favor substitution. The specimens were rapidly quenched and measured both for Cu and electron content.

Table II gives these results together with those on a control specimen (D4) of InAs not containing Cu but given the same heat treatments. It is clear from the control specimen that $\sim 3 \times 10^{15}$ cm^{-3} acceptors (vacancy defects) are quenched into InAs during rapid cooling from high temperatures. This is quite analogous to Ge (3). From the specimens diffused with Cu in Table II it is evident that about twice as many acceptors are introduced as are introduced in the control specimen. This suggests that Cu in these occupies the vacancies (presumably In vacancies) and thus becomes a doubly charged acceptor.

(*ii*) Several specimens of undoped InAs were saturated at 658°C with labeled Cu and then extracted at 658°C with In or Ga to remove the Cu. The extraction with In was much slower (at the same temperature) than the Ga. With Ga it was possible to remove essentially all the Cu at 658°C in about 10 hr. The electrical results on these specimens (allowing for the original donor) indicate that $< 3 \times 10^{14}$ cm^{-3} substitutional Cu remains under these conditions. Hence, if substitutional Cu forms at 658°C, it is lost on extraction. Vacancy acceptors left by the Cu are also apparently lost under these conditions.

(*iii*) Labeled Cu was introduced into InAs specimens at 342°, 495°, 778°, and 875°C. The specimens were quenched to room temperature and measured electrically. They were then annealed at 115° ± 5°C and the changes in electron concentration (25°C) measured at intervals as a function of time. The results are shown in Fig. 4. The initial electron concentration (after the Cu diffusion but before the 115°C anneal), n_o, reflects the loss of Cu because of precipitation. The concentrations of Cu introduced were the saturated amounts except for the specimen prepared at 875°C which was purposely undersaturated. It is evident from Fig. 4 that in all cases the electron concentration, n_f, finally reached on annealing at 115°C is less than the electron concentration in the original crystal (indicated by an arrow on Fig. 4). The amounts of the compensation vary among the different specimens reaching a maximum of 1.6×10^{16} cm^{-3} for the specimen prepared at 495°C. The significance of these data is discussed below.

(*iv*) About 10^8 cm^{-2} dislocations were introduced into a specimen of InAs by bending to a radius of 1.2 cm at ~825°C. Originally n was 1.94×10^{16}, the mobility was 27,400 cm^2/v-sec at 24°C. After bending n was 1.84×10^{16} cm^{-3}, and the mobility was 26,250. After saturation at 500°C for 17 hr with Cu, n was 3.75×10^{17} cm^{-3} and the mobility was 21,600. These results are entirely comparable to those observed on unbent InAs specimens and show that Cu does not substitute to any great extent in InAs. The final mobility value (21,600 cm^2/v-sec) agrees with the value expected for 3.75×10^{17} cm^{-3} scattering centers (Fig. 5). This indicates that $\lesssim 2 \times 10^{16}$ cm^{-3} substitutional Cu is present since the additional scattering, even assuming singly charged ions, would be easily detectable.

Hall mobility.—Figure 5 shows a plot of the electron mobility as determined from Hall measurements

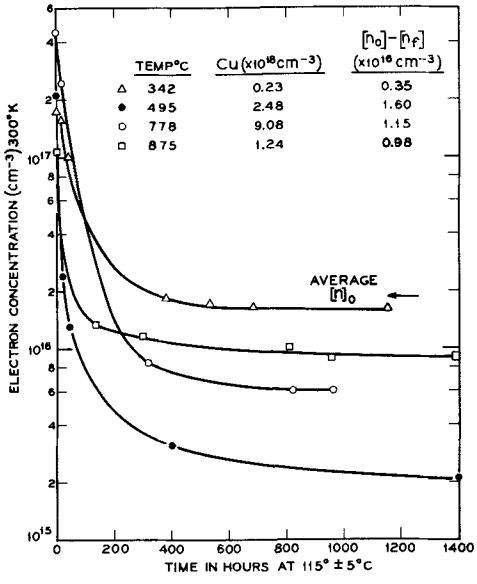

Fig. 4. Decrease in electron concentration n as a function of time at 115° ± 5°C after Cu-diffusions at 342°, 495°, 778°, and 875°C. Cu concentrations and differences between initial and final n's are given on figure. Arrow shows average n in specimens before Cu diffusion.

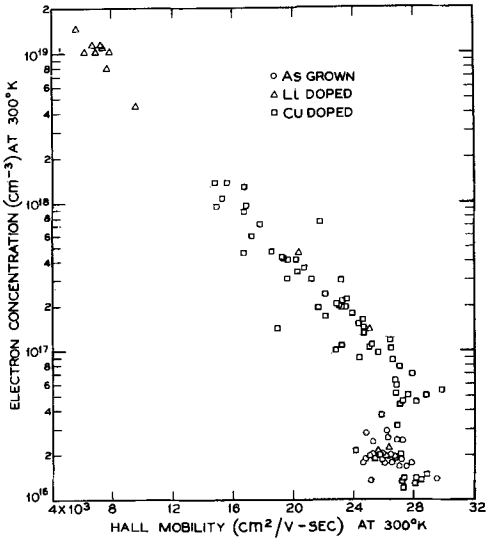

Fig. 5. Electron mobility (24°C) as a function of electron concentration for as-grown InAs and InAs diffused with Cu and Li.

at 22°-24°C as a function of n for Cu-doped InAs. Some data on Li-diffused InAs are included. The scatter in the results may be due in part to the presence of precipitates. Also shown on Fig. 5 are values for the mobilities measured on the original specimens before Cu diffusion. The scatter here is about the same. However, the mobilities for the same values of n are lower (14). We attribute this to a more nonuniform distribution of the original donors as compared to the mobile Cu_i^+ donors.

Discussion

Diffusion and solubility of Cu.—A comparison of the diffusion of Cu in InAs to that of Cu and other fast-diffusing elements in other semiconductors is interesting. The entropy and enthalpy terms for diffusion as indicated by the equation (Fig. 2)

$$D = 0.0036 \exp(-0.52/kT) \quad [2]$$

show that, in analogy with H, He, and Li in Ge and Si (15) and with Cu in Si (16), Cu in InAs is essentially a pure interstitial. The diffusion apparently proceeds with little or no participation of vacancies. In fact, as Fig. 2 shows, the diffusion of Cu in InAs is almost identical in all respects to that of Li in Ge. This is in contrast to Cu in Ge (16), GaSb (17), InSb (4) and GaAs (18) and to Li in GaSb (19) and GaAs (20) where marked substitution occurs. Substitution in GaSb, however, occurs readily only after plastic deformation (bending). Bending InAs, in contrast, does not markedly increase Cu substitution as was shown above. The fact that the diffusion of Cu in InAs follows ideal diffusion also supports the simple interstitial as opposed to a dissociative (21) mechanism.

As for the other interstitial diffusions, D_0 for Cu in InAs (corresponding to the pre-exponential in Eq. [2]) can be calculated (22) from

$$D_0 = (a_0^2\nu/8) \exp[(-\Delta H/R)\partial(\mu/\mu_0)/\partial T] \quad [3]$$

where a_0 is the lattice constant (6.06Å), ν is the lattice vibration frequency (23) ($5.15 \times 10^{13}/2\pi$), ΔH the enthalpy (12.0 kcal), R, the gas constant, (1.98 cal/deg), and μ the appropriate elastic modulus (C_{12}) with μ_0 the value at 0°K. Since these moduli for InAs are known only for room temperature (23), an estimate (1.5×10^{-4} dynes/cm^2 deg) for the quantity $\partial(\mu/\mu_0)/\partial T$ was made by interpolation between values for InSb and GaAs (24). D_0 calculated in his way is 0.0015 compared to 0.0036 found by experiment. This is about the same order of agreement found for interstitial diffusions in Ge and Si.

Although only preliminary results of the authors are available for the diffusion of Li in InAs, these indicate that Li is slower diffusing than Cu. This is in qualitative agreement with the relative interstitial diffusivities of Li and Cu in Ge and Si and with theoretical predictions (25).

So far no adequate theory of interstitial or of the closely related dissociative mechanism of diffusion exists. The Wert-Zener theory (21) provides a thermodynamic basis for treating diffusion based on lattice distortion. It does not treat the local potentials which differ for each diffusant and host crystal. An attempt to consider these has recently been made (25) in which the repulsive potentials due to overlap of nonbonding electrons and the polarization of the crystal by the ionic charge on the diffusant are taken into account. The fact (Fig. 2) that Li and Cu show almost identical behavior in spite of their large difference in ionic radii (~40%) shows the need for a theory which takes into account these additional factors. From simple distortion considerations Ge and InAs are expected to behave quite differently toward Li and Cu.

The interesting point about the solubility of Cu in InAs is that it is the highest interstitial solubility so far found for Cu in any of the elementary and III-V semiconductors. It is comparable to that of Li in Ge and Si. Cu precipitation at room temperature is slower than Cu in Si because the diffusion coefficient of Cu in InAs is markedly lower (16).

It was noted previously (Fig. 3) that the solubilities determined directly by saturation do not agree with those determined from the diffusion measurements, although the external phase was Cu alloy in both instances. The diffusion results give solubilities which are about a factor of 2 lower, although the enthalpy of solution (slope) is about the same in the two cases. The reason for the difference is not clear. However, the diffusions were done in air at atmospheric pressure whereas the solubilities were determined essentially in the absence of air. Therefore, a difference in the compositions of the surface phases could account for the different solubility results. In fact, a specimen equilibrated to the lower curve in Fig. 3 added additional Cu almost equivalent to the upper curve when heated in the same manner as the solubility specimens.

Nature of the compensation introduced by Cu.—The acceptors introduced into InAs by quenching from 850°-900°C are very similar to those found for Ge (3) and Si (6). In all cases 3-4 x 10^{15} cm^{-3} acceptor defects are introduced after quenching from temperatures near the melting points. Evidence that more acceptors are introduced in InAs when heat-quenched in the presence of 1-5 x 10^{17} cm^{-3} Cu is given in Fig. 4. This figure shows that the loss of electrons, due to Cu donor precipitation at 115° ± 5°C, leaves acceptors. At 495°C nearly all of the original donors are compensated or paired.

Measurements of electron mobility (25°C) show only small changes for the different final specimens in Fig. 4, but the specimen treated at 495°C does show a somewhat higher value (27,200 cm^2/v-sec) than the higher temperature ones (26,000 ± 200 cm^2/v-sec). This may indicate that pair formation occurs between the residual donor in InAs and substitutional Cu or vacancy defects produced by the Cu.

The fact that more acceptors, rather than less as might be expected, are formed at 495°C compared to 778° or 875°C, suggests that the trapping of both vacancies by the original donors and of Cu by the trapped vacancies may be critically dependent on diffusion temperature and quench rate. For example, it is possible that vacancies are trapped more effectively at 495°C than at 778° or 875°C because of the slower quench-rate at 495°C and that this results in the formation of more acceptors.

The specimen diffused at 342°C (Fig. 4) shows only a small concentration (~3 x 10^{15} cm^{-3}) of residual acceptors after annealing at 115°C. This suggests that fewer vacancies are dissociated from the clusters at the lower diffusion temperature.

Some observations suggest that Cu is removed from vacancies and so becomes interstitial at temperatures as low as ~200°C. For example the specimen diffused at 495°C (Fig. 4) after the final anneal at 115°C (n = 2.1 x 10^{15} cm^{-3}) was heated to 193°C for 5 min. The value of n rose to 5.3 x 10^{16} cm^{-3} which is 1.7 x 10^{16} cm^{-3} above the Cu solubility at this temperature (3.6 x 10^{16} cm^{-3}).

This increase in n can be understood if the original donors are assumed to have a shallow and a deep donor level. Formation of a Cu_{In}=D^{++} pair at 115°C could account for a 1:1 compensation by Cu_s if all the donors were paired. According to this hypothesis p-type material would not be obtained after the 115°C anneal since only those vacancies (assumed single-charged) which were trapped by the original donors are available for reaction with Cu. The observed increase in n at 193°C results from the dissociation of the Cu-donor pair into Cu_i^+ donors and a vacancy-donor pair both of which are assumed to be completely ionized at room temperature. The following reactions may be postulated:

$$V_x \rightleftarrows xV \quad [4]$$

$$e^- + V^- + D^{++} \rightleftarrows V^-D^{++} + e^- \quad [5]$$

$$V^-D^{++} + 2e^- + Cu_i^+ \rightleftarrows Cu_s{=}D^{++} \quad [6]$$

The varying degrees of compensation (Fig. 4) on this picture depend on the extents to which the reactions [5] and [6] proceed to the right. These in turn are dependent on the diffusion temperature, the quench rate, and the final temperature. The diffusion temperature determines the extent of cluster dissociation, Eq. [4]. The quench-rate and final temperature determine the fraction of vacancies and Cu trapped, Eq. [5] and [6].

The above observations indicate that Cu is capable of reacting substitutionally in InAs, presumably with In vacancies already present in the crystal. Cu does not appear to react with vacancies generated at dislocations and other loci as it does in Ge. Furthermore, as we have seen, bending InAs does not initiate Cu substitution as it does in GaSb (17).

The limit to which Cu can be present substitutionally seems to be determined by the number of vacancies present in clusters or by the concentration of donors originally present in the crystal. We assume here that the latter may be identifiable with InAs antistructure donors. This view limits the concentration of substitutional Cu to that of the donors, namely $\sim 10^{16}$ cm^{-3}.

Possibility of drifted pn junctions using Cu.—The diffusion coefficient of Cu in InAs is almost identical with that of Li in Ge. This raises the question as to whether Cu might be used to broaden the pn junction space-charge region as is now done by means of Li drift (26). Cu is expected to have some advantages over Li since it is much less reactive and hence will not be lost as readily at surfaces. Also, because of its higher average atomic number, InAs offers an advantage over Ge for particle counters. However, there are serious problems with InAs.

One of these is the presence of the residual donors, a subject which has been discussed above. Unless these can be removed almost completely so that hole conduction is predominant at a very low level, compensation cannot be achieved with donor Cu. Removal of the original donor centers has so far not been accomplished.

Another problem is presented by the fact that the intrinsic carrier concentration, n_i, for InAs is large ($\sim 10^{15}$ cm^{-3}) at temperatures where the diffusion coefficient is of the correct magnitude to allow drift ($\sim 10^{-12}$ cm^2/sec).

The question of whether InAs is worthwhile for particle detector applications, therefore, cannot be readily answered. If the residual donors can be removed it may be profitable to investigate Cu drifting in InAs below room temperature. It is doubtful, however, that a performance superior Li-drifted Ge will be easily achieved.

Acknowledgment

The authors wish to thank D. S. Malm for carrying out the mass spectrometer analyses.

Manuscript received April 19, 1967.

Any discussion of this paper will appear in a Discussion Section to be published in the June 1968 JOURNAL.

REFERENCES

1. D. Effer, *This Journal*, **108**, 257 (1961).
2. G. R. Cronin, R. W. Conrad, and S. R. Borrello, *ibid.*, **113**, 1336 (1966).
3. A. G. Tweet, *J. Appl. Phys.*, **30**, 2002 (1959).
4. J. H. Stocker, *Phys. Rev.*, **130**, 2160 (1963).
5. J. Blanc, R. H. Bube, and L. A. Weisberg, *J. Phys. Chem. Solids*, **25**, 225 (1964).
6. C. S. Fuller and K. B. Wolfstirn, *ibid.*, **26**, 1463 (1965).
7. C. Hilsum, *Proc. Phys. Soc. (London)*, **73**, 685 (1959).
8. J. T. Edmond and C. Hilsum, *J. Appl. Phys.*, **31**, 1300 (1960).
9. J. R. Dixon and D. P. Enright, *ibid.*, **30**, 753 1462 (1959), J. R. Dixon, *ibid.*, **30**, 1412 (1959).
10. C. S. Fuller and H. W. Allison, *This Journal*, **109**, 800 (1962).
11. L. J. van der Pauw, *Philips Research Repts.*, **13**, 1 (1958).
12. J. Crank, "Mathematics of Diffusion," Clarendon Press, Oxford (1956).
13. C. S. Fuller and J. A. Ditzenberger, *J. Appl. Phys.*, **27**, 544 (1956). This method was suggested by J. Bardeen.
14. C. Hilsum and A. C. Rose-Innes, "Semiconducting III-V Compounds," p. 132, Pergamon Press Inc., New York (1961).
15. A. van Wieringen and N. Warmholtz, *Physics*, **22**, 849 (1956); R. C. Frank and J. E. Thomas, Jr., *J. Phys. Chem. Solids*, **16**, 144 (1960); L. C. Luther and W. J. Moore, *J. Chem. Phys.*, **41**, 1018 (1964); C. S. Fuller and J. C. Severiens, *Phys. Rev.*, **92**, 1322 (1953), *ibid.*, **96**, 21 (1954).
16. R. N. Hall and J. H. Racette, *J. Appl. Phys.*, **35**, 379 (1964).
17. C. S. Fuller and K. B. Wolfstirn, *ibid.*, **36**, 3613 (1965).
18. C. S. Fuller and J. M. Whelan, *J. Phys. Chem. Solids*, **6**, 173 (1958).
19. R. D. Baxter, R. T. Bate and F. J. Reed, *ibid.*, **26**, 41 (1965).
20. C. S. Fuller and K. B. Wolfstirn, *J. Appl. Phys.*, **33**, 2507 (1962).
21. C. A. Wert and C. Zener, *Phys. Rev.*, **76**, 1169 (1949); C. Zener, *J. Appl. Phys.*, **22**, 372 (1951).
22. F. C. Frank and D. Turnbull, *Phys. Rev.*, **104**, 617 (1956).
23. D. Gerlich, *J. Appl. Phys.*, **34**, 2915 (1963).
24. O. Madelung, "Physics of III-V Compounds," John Wiley & Sons, New York (1964) Translated by D. Meyerhofer.
25. K. Weiser, *Phys. Rev.*, **126**, 1427 (1962).
26. E. M. Pell, Nat. Acad. of Sci. Report NAS-NSS 32, Publication 871 (1961) 136.

Studies of Sodium in SiO_2 Films by Neutron Activation and Radiotracer Techniques

T. M. Buck, F. G. Allen,[1] J. V. Dalton, and J. D. Struthers

Bell Telephone Laboratories, Incorporated, Murray Hill, New Jersey

ABSTRACT

Electrical instabilities in SiO_2 films under high fields at elevated temperatures have been widely attributed to mobile ionic impurities, with sodium suspected as the most important ion. Phosphate glass treatments on SiO_2 are known to have a stabilizing effect. This paper reports neutron activation experiments to determine sodium contamination on and in steam-grown SiO_2 films and also diffusion and drift experiments with tracer sodium. Phosphate glass-treated SiO_2 films were included in the samples. SiO_2 films grown and handled under various conditions had sodium densities of 7×10^{11} to 3×10^{14} atoms/cm^2, which could be easily removed or exchanged by washing and light etching. Densities remaining inside the 6000Å films after washing and light etching were $\gtrsim 4 \times 10^{11}$-4×10^{12}/cm^2.

Tracer diffusions into SiO_2 at 600°C produced profiles which were high near the surface and lower through the interior of the film, similar to those observed by neutron activation for unintentional sodium contamination. Phosphate glass layers on SiO_2 absorbed and stopped the sodium under similar conditions. With an applied field at elevated temperature (+4v, 1 min, 400°C) tracer sodium drifted through an SiO_2 film under gold dot electrodes, piled up at the Si-SiO_2 interface, and carried a substantial part of the charge transported. There was no detectable diffusion in uncharged areas. A layer of phosphate glass applied over an SiO_2 film absorbed sodium and prevented it from drifting into the SiO_2 film under the gold dots.

Intensive study has been made in a number of laboratories (1-8) in recent years of the electrical behavior of metal-silicon dioxide-silicon (MOS) structures because of their importance as devices and because new designs for junction devices employ structures in which high fields are applied across passivating oxide films. Certain types of electrical instability observed in MOS structures (2, 6-8), and also in junction devices (9), have been attributed to drift of oxygen vacancies (2) or, more commonly, to ionic impurities in the oxide. Sodium in particular has been suspected (7, 9) as an important impurity because of its known high mobility in quartz and vitreous silica (10, 11) and its common occurrence as a contaminant. It was found (12) that a layer of phosphate glass over an SiO_2 film could eliminate or drastically reduce the drift behavior. In some cases the electrical instabilities have been reproduced and studied by deliberate addition of sodium (nonradioactive) (7, 9, 13, 14) to the SiO_2 film.

The aims of the work reported in this paper were: (*i*) to determine sodium contamination levels on and in as-grown SiO_2 films and in silicon substrates by neutron activation analysis; (*ii*) to follow deliberately added tracer sodium in diffusion and drift experiments. Phosphate glass-treated SiO_2 films were included in the samples for both neutron activation and tracer experiments. Where the results can be compared they are in general agreement with those recently reported by Yon, Ko, and Kuper (15), and also by Carlson, Fuller, and Osborne (16). However, there are differences in experimental approach and information obtained.

Neutron Activation Experiments

Materials and experimental procedure.—Six neutron activation experiments were carried out, five at the Brookhaven National Laboratory and one at the Union Carbide reactor at Tuxedo, New York. Samples included silicon slices with steam-grown SiO_2 films, slices with phosphate glass layers over SiO_2 films, and etched slices which had never been oxidized. A weighed sample of sodium carbonate was included in each run for calibration. In the activations at Brookhaven samples were contained in polyethylene or quartz capsules which were placed in a water-cooled reaction chamber where they were exposed to a thermal neutron flux of 1 x 10^{13}/cm^2 sec for 2-3 days. Fast neutron flux was estimated to be a few per cent of this. At the Union Carbide reactor aluminum capsules were used and the chamber was not water-cooled; sample temperatures may have risen as high as 500°C. After samples were returned from irradiation they were washed and etched progressively in dilute buffered HF and the Na^{24} activity remaining on the sample after each step was counted. Oxide thickness was determined by comparing colors with oxide films of known thickness. Counting was done on either the 1.37 Mev or 2.76 Mev gamma peaks of Na^{24} ($T_{1/2}$ = 15 hr). When the 1.37 Mev peak was used, etching was delayed for about 24 hr after irradiation to permit sufficient decay of Si^{31} activity at 1.27 Mev ($T_{1/2}$ = 2.6 hr). No such delay was required for the 2.76 Mev peak, but the gain in higher activity was offset by reduced counting efficiency for the higher energy γ's. Counting was done on a single-channel RIDL pulse height analyzer with a well-type 2 × 2 in. sodium iodide scintillation crystal, or on a 100-channel TMC analyzer (Gammascope) with a flat-faced 3 × 3 in. crystal. The entire gamma spectrum up to 3 Mev was scanned frequently to verify that sodium was present, and decay times were determined when feasible.

Results of neutron activation experiments.—Figure 1 shows results of one neutron activation run which was reasonably representative of the others. Sodium concentration per square centimeter remaining on the sample is plotted against thickness of oxide remaining, as the sample was washed and then etched in toward the Si-SiO_2 interface. In this experiment there were ten slices of each type of sample. Each slice had 2 cm^2 of oxide surface area. The ten slices were etched individually to the same oxide thickness in each step. Activity was then measured on all ten together as one sample. In some other runs only one slice of each type was used; the curves were similar to those of Fig. 1, but counting rates and sensitivities (Na atoms/cm^2/count/minute) were correspondingly lower. The sensitivity in this run, using the 2.76 Mev peak, was in the range 2.4-4.4 × 10^{11} Na atoms/count/minute or 1.2-2.2 × 10^{10} Na atoms/cm^2/count/minute. The stand-

[1] Present address: Bellcom Inc., Washington, D. C.

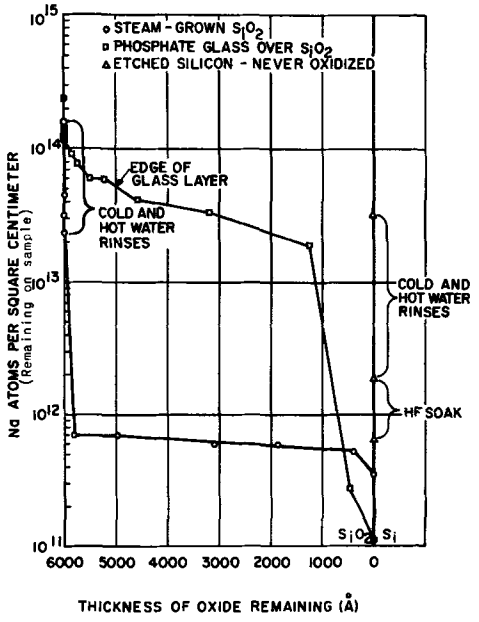

Fig. 1. Removal of sodium by washing and etching after neutron activation.

ard deviation of the points varies from 0.5% for the high initial points to about 5% for the low points. Standard deviations are indicated directly on all other distribution plots. The silicon substrate material used in the experiment was 100 ohm-cm n-type, phosphorus doped. In all other experiments to be discussed the silicon was 100 ohm-cm p-type, boron doped.

The plot for steam-grown SiO_2 in Fig. 1 shows an initial sodium density of $>10^{14}/cm^2$, most of which washed off, or perhaps exchanged for nonradioactive sodium, during washing. A light etch ($\sim$ 150Å) removed most of the remaining sodium. The curve shows a slight downward slope through the middle region and a drop at the interface, corresponding to a pile-up in this region. The total counting rate decreased from 12,000/min to 35/min in this series of etches. Background count was 9/min. Since sodium per square centimeter remaining on the specimen is plotted in Fig. 1, the downward slope is a measure of local concentration (cm^{-3}).

The concentration is high near the outer surface ($\sim 10^{19}/cm^3$), low in the middle ($3 \times 10^{15}/cm^3 \pm 1 \times 10^{15}/cm^3$) with a turn-up at the Si-SiO_2 interface ($\leq 10^{16}/cm^3$). The results are similar to those of ref. (15) and (16) although the interior concentration indicated in the present work is somewhat lower.

The etched silicon sample was treated and handled in the same manner as the oxidized sample except that it was never oxidized. Like the oxidized silicon it had considerable sodium which could be washed off. This may have come from the etching and cleaning, or subsequent handling, or both. An HF soak removed some Na which remained after hot and cold water rinses, presumably adhering tightly to the very thin oxide layer present on any etched Si surface. Neutron activation analysis of phosphate glass-treated samples has given rather unexpected results, one of which is shown by the plot in Fig. 1. In this case and in several other experiments a relatively high sodium concentration was found in the SiO_2 film beyond the edge of the phosphate glass layer which could be determined by an abrupt change in etching rate. This was surprising since phosphate glass layers are known to eliminate drift behavior believed to result from ionic impurities, and one might have expected all the sodium to be found in the 1000Å glass layer. (The phosphate glass was deposited on a steam-grown SiO_2 film by exposure to P_2O_5 vapor for 10 min at 1050°C.) As will be shown later, tracer experiments with Na^{22} do show a blocking and gettering action by phosphate glass for sodium which has been deliberately deposited on the surface. Therefore, in the neutron activation results it seems likely that the sodium deep in the SiO_2 is associated with phosphorus.

Some sodium may have been carried by phosphate glass through pinholes or other flaws in the SiO_2 layer, although in this case one might expect it to etch out of the holes readily and appear to be in the outer glass layer. Phosphorus may have penetrated into the SiO_2 layer as a result of neutron bombardment. Schmidt (17) has recently reported phosphorus penetration deep into SiO_2 and into the silicon substrate under fast neutron bombardment of $3 \times 10^{17}/cm^2$ total flux at 300°C. He has also studied a sample from one of our sodium experiments in which samples were maintained close to room temperature and found a phosphorus diffusion tail extending beyond the glass layer into the SiO_2 and Si. (During irradiation the phosphate glass-treated samples and untreated SiO_2 samples were in separate containers, so the transfer of phosphorus, and possibly sodium to the untreated samples observed by Schmidt (17) could not have occurred in our samples.) Carlson, Fuller and Osborne (16) using higher temperatures and longer times for their diffusions saw considerable phosphorus penetration beyond the oxide-glass interface. They showed some results in which the sodium was more effectively segregated in the glass layer than in our case, but also they showed one sample in which sodium at a concentration of $\sim 1 \times 10^{18}/cm^3$ had penetrated to the silicon interface. In the experiment at the Union Carbide reactor very high sodium contamination ($1\text{-}5 \times 10^{14}/cm^2$ inside the film) was detected. In this case it was evident that sodium produced by transmutation of Al (Al^{27} n, α Na^{24}) had evaporated from the capsule onto the samples and diffused into the oxide at the elevated temperature ($\sim$ 500°C) of this experiment. The phosphate glass treated sample showed considerable sodium beyond the glass layer.

Data for SiO_2 films from curves like those of Fig. 1 are summarized in Table I which gives ranges of values for sodium contamination at the surface, inside SiO_2 films, and in silicon substrates. (Results from the Union Carbide reactor are not included.) A variety of oxidation and handling conditions are represented in Table I; the work has been of an exploratory nature rather than an exhaustive study in which each process factor has been studied independently. However, certain observations can be enumerated:

(*i*) Unintentional sodium contamination on the films varied over almost three orders of magnitude, that inside the film over one order, and these levels are easily sufficient to account for the type of electrical instability which has been attributed to some mobile ion in SiO_2 films.

(*ii*) Improvements in furnace cleanliness and in handling techniques, *e.g.*, the use of a dust-free, laminar-flow hood, yielded reductions in sodium activity.

(*iii*) The lowest total sodium contamination was observed on a sample supplied by Schmidt (18) which had been oxidized by O_2 in a special furnace (quartz tube inside another quartz tube inside a high purity

Table I. Summary of data for SiO_2 films

	SiO_2 films	Etched Si (never oxidized)
Na removed by Wash and light etch (100-300A)	7×10^{11}-$3 \times 10^{11}/cm^2$	2×10^{13}-$2 \times 10^{11}/cm^2$
Na inside SiO_2 film	4×10^{11}-$4 \times 10^{12}/cm^2$ (7×10^{15}-$7 \times 10^{19}/cm^3$)	
Na in Si (Average in 5-16 mil slice)	6×10^{13}-$1.2 \times 10^{15}/cm^3$	8×10^{12}-$1.7 \times 10^{11}/cm^3$

alumina tube). The sample was encapsulated in quartz for activation.

(*iv*) The lowest value listed (7×10^{15}/cm^3) for sodium inside the SiO_2 film was obtained on a film which was steam-grown in a standard quartz tube furnace. This, however, was not necessarily the cleanest oxide tested. Other oxide samples, *e.g.*, those supplied by Schmidt or by Goetzberger (field-grown) (19) may have had less sodium inside but the sensitivity for detection was not good enough in those experiments to prove it.

(*v*) The silicon itself did not appear to be an important source of sodium since the levels in silicon samples which had never been oxidized were always somewhat lower than in oxidized samples from the same crystal.

(*vi*) The outstanding feature of the neutron activation experiments was that a large fraction of the total sodium could be removed by washing and light etching. Although the possibility of exchange for nonradioactive sodium in the water or acid cannot be ruled out, the results show that large reductions in sodium contamination could be achieved if very pure water and acid were used. These results are consistent with those of Schmidt (18) who eliminated electrical drift effects by light etching.

Other contaminants were found in the samples cleaned and oxidized by standard techniques. In several cases the gamma spectra showed the presence of copper in the silicon substrate, and phosphate glass samples prepared by the PBr_3-O_2 reaction showed bromine in the glass layer and in the oxide under the glass.

Tracer Experiments

Diffusion into SiO_2 *films.*—Tracer diffusion experiments were performed with Na^{22} ($T_{1/2} = 2\frac{1}{2}$ yr). The carrier-free isotope was received as an acid solution of NaCl of specified concentration which permitted calibration of counting rate in terms of sodium atoms. Radioactive sodium was applied to oxidized silicon slices (1 cm^2) by evaporation from a hot platinum boat on which a few drops of diluted solution had been dried in a manner similar to that reported by Logan and Kerr for nonradioactive sodium (14). This procedure yielded deposits of density 3×10^{13}-1×10^{14}/cm^2. Post-diffusion autoradiographs showed that these deposits on SiO_2 were sometimes free of spots but on other occasions had a few spots which may have been associated with flaws in the SiO_2 film. In contrast, deposition by drying a dilute solution directly on an oxidized slice always resulted in a very spotty distribution. Progressive etching showed that the nonuniformity of the dried-solution samples persisted through the film to within a few hundred Angstroms of the silicon interface. Evaporation from a hot source was therefore used in all the tracer experiments to be discussed. Deposits on phosphate glass were entirely free of spots. Sodium distribution profiles in the films were determined by progressive etching and counting of the 0.51 Mev gamma activity remaining on the slice. Sensitivity was typically 2.5×10^{10} Na atoms/count/minute.

Figure 2 shows the sodium profile (Na atoms/cm^3 *vs.* depth in the film) in a steam-grown SiO_2 film which was diffused for 22 hr at 600°C in a forming gas atmosphere (85% N_2, 15% H_2). Forming gas was suggested by A. A. Bergh who had observed enhancement of sodium effects on transistors, presumably because of a hydrogen interaction which accelerates sodium migration. The profile shows sodium concentration high near the surface and lower through the middle region with a dip and a turn-up near the Si-SiO_2 interface. The curve of Fig. 2 is similar to some reported by Yon, Ko, and Kuper (15).

The behavior of a phosphate glass-treated SiO_2 film is shown in Fig. 3. Sodium was deposited and diffused into the glass-treated film under the same conditions

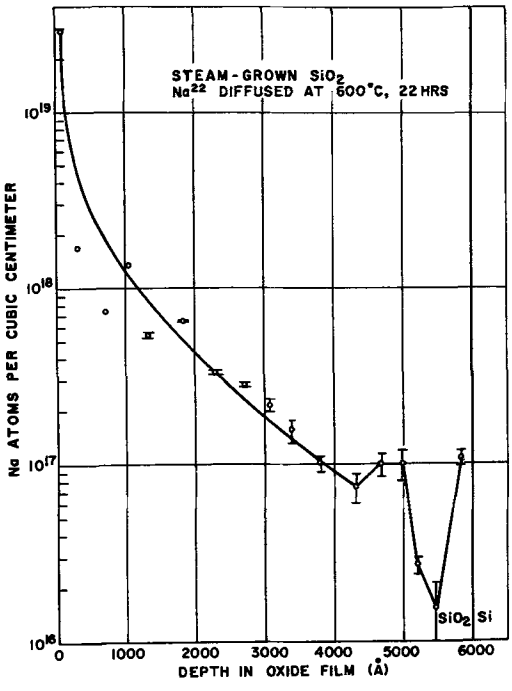

Fig. 2. Na profile in SiO_2 film after diffusion, 22 hr at 600°C. Standard deviations are indicated on all distribution profiles.

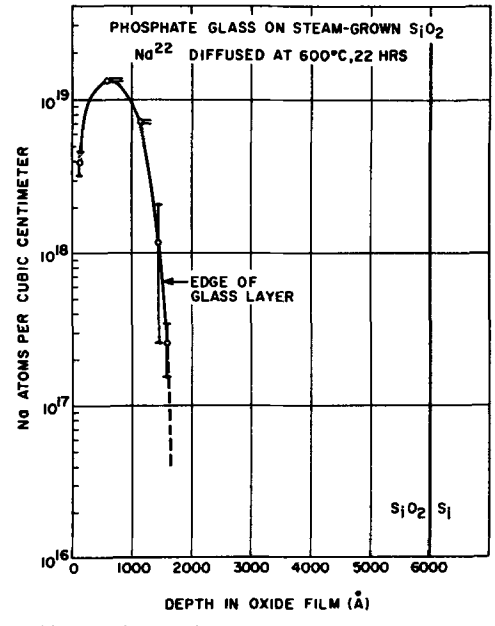

Fig. 3. Na profile in phosphate glass-treated SiO_2 film after diffusion, 22 hr at 600°C.

used for the plain SiO_2 film of Fig. 2. However, in Fig. 3 it may be seen that the sodium was stopped in or very close to the phosphate glass layer as defined by etching rate. Additional experiments under the same conditions have shown some variation in the shape of the sodium profile in the glass layer, but always a reduction of sodium activity to background level beyond the glass layer. Typically, the counting rate on a sample was reduced from an initial value of 2700 counts/min down to background (26 counts/min) just beyond the glass layer. In contrast, the counting rate on an untreated SiO_2 film (Fig. 2) was reduced from 2826 to 284 counts/min (above the background of 26) by etching to the same depth.

Another significant difference between the two types of films was that very little sodium activity could be washed off the phosphate glass after diffusion, whereas with untreated SiO_2 more than half of the

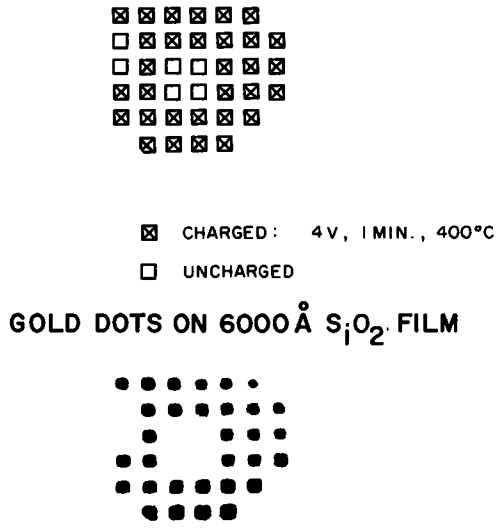

Fig. 4a (top) Diagram of gold dots on SiO_2 film for sodium drift experiment. Na^{22} was deposited on sample before gold dots were put down. Fig. 4b (bottom) Autoradiograph of Na^{22} in SiO_2 film after drifting (4v, 1 min, 400°C). Sample was washed and gold dots removed before exposure.

total activity was easily removed by washing. The greater uniformity of sodium, or freedom from spots, in the phosphate glass layer has already been mentioned. The sodium had evidently been absorbed into the glass and stopped there.

Drift experiments with tracer sodium.—The influence of an electric field on tracer sodium in SiO_2 was studied at 400°C. Figure 4a is a diagram of a specimen designed for these experiments by M. Yamin, who also performed the drifting and charge measurements by a method described previously (6). $Na^{22}Cl$ was evaporated onto an oxidized silicon slice. Square gold dots were then deposited through a mask. The dots marked X were then charged, one at a time, by applying 4v (+) for 1 min. The charge was measured by integrating the transient charging current. The silicon slice was held at 400°C for more than an hour during this operation.

After charging of the gold dots was completed, the sample was cooled and washed and the gold dots removed by aqua regia. An autoradiograph taken at this point is shown in Fig. 4b. By comparison with Fig. 4a it may be seen that sodium activity (indicated by darkening) remained only in areas which had been covered by charged gold dots. There was no detectable diffusion in uncharged areas, under gold dots or elsewhere. This was consistent with some earlier diffusion experiments (1 hr, 400°C in air) in which no sodium diffusion could be detected by counting. (Sodium activity was present before washing; the sodium was not lost by exchange during heating.)

Figure 5 shows the sodium profile in the film under the gold dots, as determined by etching and counting. Computations of sodium concentration values (cm^{-3}) were made using only the area under charged gold dots. Ninety per cent of the radioactive sodium was found to be piled up within 800Å of the SiO_2-Si interface. This result is in agreement with the charge distribution inferred by Snow *et al.* (7) from capacitance-voltage measurements on (nonradioactive) sodium-drifted SiO_2 films. All of the sodium detected in the film accounts for about 20% of the total charge introduced. The density of tracer sodium under the dots was $3 \times 10^{13}/cm^2$ and, since neutron activation results have shown that sodium contamination levels may be higher than this, it is likely that the remaining 80% of the charge was carried by sodium present as unintentional contamination.

The images of the gold dots in Fig. 4b are fairly distinct, *e.g.*, the image of the lower left-hand dot clearly

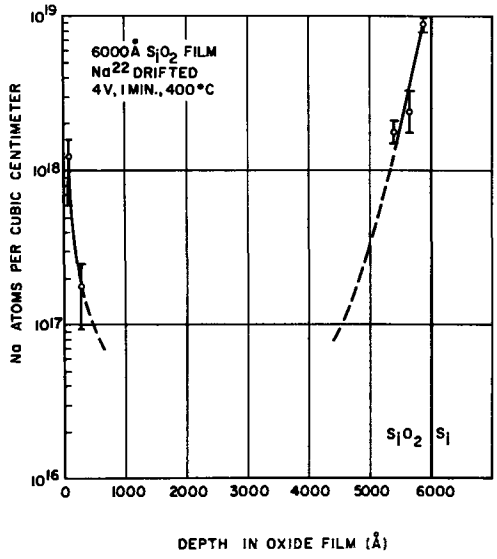

Fig. 5. Na profile in SiO_2 film under gold dots after drifting.

shows that a corner had been removed. Thus there was no appreciable thermal diffusion either directly into the film or laterally in the film or along the Si-SiO_2 interface. The sodium followed electric field lines (13).

A similar tracer drift experiment was performed on a phosphate glass-treated sample at 400°C. However, in this case, as expected (6), no charging current flowed when the 4v bias was applied to the gold dots. Figure 6a shows the gold dot pattern and Fig. 6b shows an autoradiograph taken after thorough washing and removal of the gold dots. It shows a uniform darkening over the entire area of the slice. With stepwise etching the image grew weaker but remained uniform; there was never any image of the dots which

Fig. 6a (top) Diagram of gold dots on phosphate glass-treated SiO_2 film for sodium drift experiment. Fig. 6b (bottom) Autoradiograph of Na^{22} in phosphate glass-treated sample after attempt to drift.

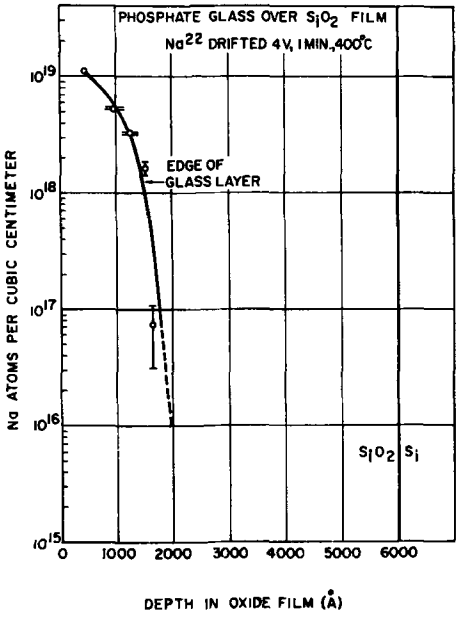

Fig. 7. Na profile in phosphate glass-treated sample after attempt to drift.

had been charged. The sodium had evidently been quickly and uniformly absorbed by the phosphate glass at 400°C, and the applied bias caused no redistribution. Figure 7 shows the sodium profile in this film, all of the sodium confined in or close to the phosphate glass layer. No sodium activity was detected in the silicon substrate after any of the drift experiments at 400°C.

Discussion and Summary

The neutron activation results on SiO_2 showed relatively high sodium concentrations on or near the surface which could be removed or exchanged by washing and light etching. Sodium concentrations at the surface could be reduced by improvements in processing. Average sodium concentration inside the films was as low as $7 \times 10^{15}/cm^3$, or $4 \times 10^{11}/cm^2$ in a 6000Å film, and improved sensitivity might have shown lower values in some films.

Tracer diffusion experiments in SiO_2 at 600°C produced profiles high at the outer surface, low through the middle region and with a dip and turn-up at the Si-SiO_2 interface. This characteristic profile suggests some barrier at the outer surface of the oxide. The difficulty of diffusing large negative ions such as Cl^- required for charge neutrality may account for it (15).

At 400°C diffusion from NaCl into SiO_2 (in air) was very slight but drift under gold dots with +4v applied was very rapid. The ease with which the sodium ions move under an applied field suggests that small potential differences in the oxide, *e.g.*, electrochemical potentials and work function differences, may influence the sodium distribution which is frozen in a film at room temperature.

Phosphate glass layers clearly showed a blocking action for tracer sodium in diffusion and drift experiments. Sodium on the surface penetrated readily into the glass layer but was held there against further diffusion into the SiO_2 region. More extreme conditions would presumably show a limit to the blocking action as found by Kerr (20) in electrical measurements. In neutron activation experiments significant sodium concentrations were found beyond the phosphate glass layer as defined by etching rate. It seems likely that this sodium is associated with phosphorus deep in the SiO_2 layer which may have gotten there during deposition of the glass layer, or by some effect of neutron bombardment.

The tracer drift results clearly illustrate the fact that even though an SiO_2 film grown by a very clean process might be free of internal sodium contamination it would still be vulnerable to subsequent contamination by sodium which could drift in to the silicon interface very readily under bias at elevated temperatures.

Acknowledgments

The authors are indebted to M. Yamin for designing the specimen for drift experiments and performing the charging operation, to P. F. Schmidt for obtaining a phosphorus profile, and to R. Kraetsch for supplying oxide film samples. The authors have had helpful discussions with several associates, in particular, C. S. Fuller, Miss K. B. Wolfstirn, W. M. Gibson, and D. W. Maurer.

Manuscript received July 20, 1966; revised manuscript received April 1, 1967. This material was presented at the IEEE Silicon Interface Specialists Conf., Las Vegas, Nevada, Nov. 15-16, 1965.

Any discussion of this paper will appear in a Discussion Section to be published in the June 1968 JOURNAL.

REFERENCES

1. L. M. Terman, *Solid State Electronics*, **5**, 285 (1962).
2. J. E. Thomas, Jr. and D. R. Young, *IBM J. Res. and Dev.*, **8**, 368 (1964).
3. A. S. Grove, B. E. Deal, E. H. Snow, and C. T. Sah, *Solid State Electronics*, **8**, 145 (1965).
4. E. H. Nicollian and A. Goetzberger, *IEEE Trans.*, **ED-12**, 108 (1965).
5. K. H. Zaininger and G. Warfield, *ibid.*, **ED-12**, 179 (1965).
6. M. Yamin, *ibid.*, **ED-12**, 88 (1965).
7. E. H. Snow, A. S. Grove, B. S. Deal, and C. T. Sah, *J. Appl. Phys.*, **36**, 1664 (1965).
8. S. R. Hofstein, *IEEE Trans.*, **ED-13**, 222 (1966).
9. J. R. Mathews, W. A. Griffin, and K. H. Olson, *This Journal*, **112**, 899 (1965).
10. H. E. Wenden, *Amer. Mineralogist*, **42**, 859 (1957).
11. A. E. Owen and R. W. Douglas, *J. Soc. Glass Tech.*, **43**, 159T (1959).
12. D. R. Kerr, J. S. Logan, P. J. Burkhardt, and W. A. Pliskin, *IBM J. Res. and Dev.*, **8**, 376 (1964).
13. A. Goetzberger, *Solid State Electronics*, **9**, 871 (1966).
14. J. S. Logan and D. R. Kerr, Solid State Device Research Conference, Princeton, N. J., June 21-23, 1965.
15. E. Yon, W. H. Ko, and A. B. Kuper, *IEEE Trans.*, **ED-13**, 276 (1966) presented at Electrochem. Soc. Meeting, Buffalo, N. Y., Oct. 10-14, 1965.
16. H. G. Carlson, C. R. Fuller, and J. Osborne, Recent News Paper, Electrochem. Soc. Meeting, Buffalo, N. Y., Oct. 10-14, 1965.
17. P. F. Schmidt, *Appl. Phys. Letters*, **8**, 264 (1966).
18. R. Schmidt, Recent News Paper, Electrochemical Society Meeting, San Francisco, May 9-13, 1965.
19. A. Goetzberger, *This Journal*, **113**, 138 (1966).
20. D. R. Kerr, paper given at IEEE Silicon Interface Specialists Conference, Las Vegas, Nevada, Nov. 15-16, 1965.

Measurement of the Retention of Fluoride by Silicon and Silicon Dioxide Surfaces

G. B. Larrabee, K. G. Heinen, and S. A. Harrell

Texas Instruments Incorporated, Dallas, Texas

ABSTRACT

Techniques are described for the production of fluorine-18 labeled HF etches and their use in the study of the retention of fluoride on silicon and silicon dioxide surfaces. Results are presented that show fluoride is retained by a chemical adsorption mechanism.

In the fabrication of planar silicon semiconductor devices it is necessary to etch the silicon dioxide films on the surface of the device. Hydrofluoric acid is used in all of these SiO_2 etches with various additives to modify the etch rate. The subsequent washing and removal of residual fluoride is important to ensure good device characteristics and long term device stability.

The chemical analysis for trace quantities of residual fluoride ion is extremely difficult, particularly if the fluoride is entrapped and/or chemically adsorbed on the silicon dioxide film. Dissolution of the film to free the fluoride for subsequent analysis is not possible because these films are only soluble in fluoride containing etches. Neutron activation analysis via $^{19}F(n, \gamma)^{20}F$ cannot be used in a silicon matrix because of the large yield of 2.3 minute aluminum-28 from the $^{28}Si(n, p)^{28}Al$ reaction. The preponderance of 1.78 Mev gamma from the aluminum-28 precludes the detection of the 1.62 Mev gamma from fluorine-20. The 10.7 second half-life of fluorine-20 prohibits waiting for other activities to decay away.

The use of radiotracer 118 minute fluorine-18 was only attractive if fluorine-18 tagged hydrofluoric acid could be produced and the etch solution formulated using this $H^{18}F$. Fluorine-18 has been produced by several workers (1, 2) by the $^{6}Li(n, t)^{4}He$; $^{16}O(t, n)^{18}F$ reaction but the final product is either in NaOH or HCl solution. However the problem in this work was to produce $H^{18}F$ in sufficient yield and with a high enough specific activity to tag an etch solution containing up to 10% fluoride ion.

Experimental

The fluorine-18 was produced by irradiating 7-9g of $^{6}Li_2CO_3$,[1] containing 10 mg/g LiF as carrier, at a flux of 2×10^{12} n/sec/cm^2 for 2 hr at the Texas A&M University reactor. The high neutron capture cross section (945 barns) of lithium-6 made it necessary to use a special irradiation container such that a thickness of not greater than 2 mm of $^{6}Li_2CO_3$ would be presented to the neutron flux.

A cylindrical quartz irradiation container was constructed with inner wall separations of 2 mm as shown in Fig. 1. The $^{6}Li_2CO_3$ was introduced through the upper tube to fill the cylinder wall cavity. The container was then sealed off at the bottom of the fill tube and a loose fitting polyethylene plug placed in the bottom to help scatter neutrons into the inner part and thus increase the yield.

At the end of the irradiation the container was inverted, allowing the powder to move down out of the inner wall cavity. It was placed in an all Teflon distillation apparatus, Fig. 2, the top was screwed on tightly, and the quartz container broken. Through a small port on the top, 40 ml of 9M H_2SO_4 was added and the Teflon distillation flask was sealed. The flask was heated with a heating mantle to distill 5 ml of solution containing the fluorine-18 into a polyethylene receiver.

[1] Lithium carbonate was purchased from Oak Ridge National Laboratory and was 95.44% lithium-6 and 4.56% lithium-4.

The etch solution to be studied was tagged with this $H^{18}F$ and a suitable aliquot was reserved for analysis for fluoride ion and fluorine-18 content. Gamma spectra were run immediately after distillation and again the next day (10 half-lives elapsed) and no extraneous activities were observed.

Fig. 1. Quartz irradiation container used in the production of fluorine-18.

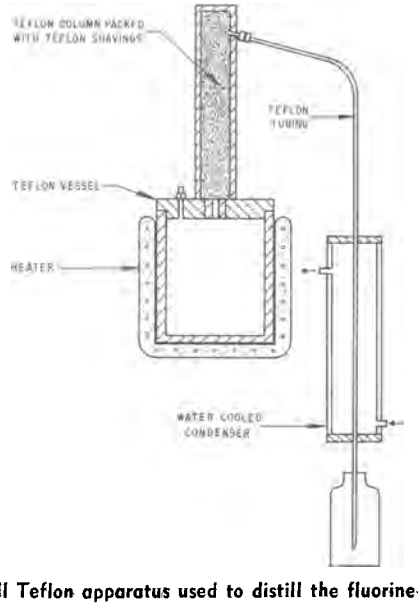

Fig. 2. All Teflon apparatus used to distill the fluorine-18 labeled HF.

The decay of fluorine-18 proceeds via 0.65 Mev positron emission. Since positrons annihilate to form two back to back 0.511 Mev gammas, it is possible to use gamma-gamma coincidence counting. The background for this counting technique, with the particular instrument settings used in this work, was one count per minute. The detection limit on the samples used in this study, was calculated to be 1.4×10^{13} atoms/cm^2 of silicon surface area with a counting error corrected for background of less than 17% with a confidence level of 90%.

The silicon slices were etched in a plexiglass etching vessel containing 3-5 ml of tagged etch solution. In each etch experiment two slices (20.3 cm^2 surface) were processed and counted.

Results

Buffered fluoride etch.—The retention of fluoride on silicon and silicon dioxide films was determined by preparing a fluorine-18 labeled etch solution (400g NH_4HF_2, 500 ml H_2O, 90 ml HF). The silicon slices were etched and washed as described in Table I. Fresh water washes were used for each slice. It can be seen that the bare or unoxidized slices retained more fluoride than the slices with 5000Å SiO_2 films.

1:10 Hydrofluoric acid.—A 1:10 hydrofluoric acid etch was labeled with fluorine-18 and the silicon slices were etched and washed as shown in Table II. In this experiment the silicon slices were washed by two different techniques. In one case only hot water washes were used while on duplicate slices a hot nitric acid wash was given as soon as the slices were removed from the etch. This was then followed by three hot water washes.

Unoxidized slices washed with hot nitric acid retained significantly more fluoride than the corresponding slices washed with hot water. The amounts of fluoride retained by hot water washed slices agree well with the values obtained for the buffered HF etch (Table I). On the other hand, the slices with 5000Å SiO_2 films retained fluoride at concentrations comparable to those observed on duplicate slices etched in buffered fluoride etch (Table I).

There are several salient points that must be considered in postulating a mechanism for the retention of fluoride ion by silicon and silicon dioxide films. Both silicon and silicon dioxide retain fluoride ion after repeated washings. Silicon surfaces retain more fluoride than SiO_2 surfaces and hot nitric acid washing causes more fluoride to be retained on silicon surfaces than hot water washing. Silicon dioxide films retain the same amount of fluoride with either hot nitric acid or water washing.

Table I. Retention of fluoride from buffered fluoride etch

Silicon sample	Etch time, min		Rinse, min			Fluoride concentration, atoms/cm^2
A. Unoxidized slices						
Chemically polished	2	25°C	2	25°C	H_2O	2.1×10^{14}
Chemically polished	2	25°C	2	95°C	H_2O	2.4×10^{14}
Chemically polished	0.4	60°C*	2	25°C	H_2O	1.9×10^{14}
B. Oxidized slices						
5000Å oxide film	2	25°C	2	25°C	H_2O	9.3×10^{13}
5000Å oxide film	2	25°C	2	95°C	H_2O	5.5×10^{13}
5000Å oxide film	0.4	60°C*	2	25°C	H_2O	4.0×10^{13}
5000Å oxide film	0.4	60°C*	2	95°C	H_2O	4.1×10^{13}

* Etch time adjusted for 60°C etch so that an amount of oxide would be removed equal to the 25°C etch.

Table II. Retention of fluoride from 1:10 HF etch

Silicon sample	Etch time, min, 25°C	Rinse	Fluoride concentration, atoms/cm^2
A. Unoxidized slices			
Chemically polished	5	3 × 95°C H_2O	1.1×10^{14}
Lapped	5	3 × 95°C H_2O	1.9×10^{14}
Chemically polished	5	1 × 105°C HNO_3, 3 × 95°C H_2O	7.5×10^{14}
Lapped	5	1 × 105°C HNO_3, 3 × 95°C H_2O	4.9×10^{15}
B. Oxidized slices			
5000Å oxide film	0.5	3 × 95°C H_2O	1.2×10^{14}
5000Å oxide film	0.5	1 × 105°C HNO_3, 3 × 95°C H_2O	5.1×10^{13}

Discussion

The tenacious behavior of the fluoride ion must be ascribed to the strength of the silicon-fluoride bond (136 kcal/mole compared to 106 kcal/mole for Si-O) on the silicon or SiO_2 surface. Iler (3) and Atalla *et al.* (4) report that HF treated silicon surfaces are strongly hydrophobic and Iler (3) suggests that this is due to the nonpolar character of the SiF surface. This would also suggest that the Si-F bond is not easily broken by hydrolysis. Attala *et al.* (4) observed that boiling in water, organic solvents or water containing detergents did not produce a hydrophillic surface. They also observed that boiling in nitric acid produced a hydrophillic surface.

The hot nitric acid treatment of etched silicon surfaces in our fluoride tracer studies indicates that the surface fluoride is not removed with this nitric acid treatment but is probably entrapped in a freshly grown SiO_2 film which itself is hydrophillic.

Kimberlin (5) feels that a fluoride surface explains the fact that silica gel treated with HF is hydrophobic. This would indicate a similar tenacious retention of fluoride by silica surfaces.

The chemical bonding of fluoride to silicon and silicon dioxide surfaces would suggest a chemical adsorption mechanism. If chemical adsorption is operative, there should be only a given number of sites available for adsorption. On <111> oriented single crystal surfaces there are 4.8×10^{14} sites/cm^2, assuming a surface roughness factor of one for a polished and chemically etched surface. In this work, for both etches, the amount of fluoride retained on these surfaces averaged 1.9×10^{14} atoms/cm^2.

The enhanced retention of fluoride ion by silicon surfaces on rinsing in hot concentrated nitric acid is probably due to a rapid growth of surface SiO_2 which physically traps the fluoride ion. Once this physical entrapment occurs, repeated washings will not remove the fluoride ion. The fact that hot nitric acid washing of a freshly etched SiO_2 film does not increase the fluoride retained, tends to support this theory. No further growth of oxide would occur to entrap fluoride ion on oxide films.

On silicon dioxide films it is more difficult to estimate the total number of available Si-OH sites available for the fluoride to replace and form stable Si-F bonds. Iler (4) has shown that a fully hydrated surface has 8×10^{14} silanol (Si-OH) groups per cm^2 of surface. Lowen and Broge (6) in a study of the effects of dehydration and chemisorbed materials on the surface properties of amorphous silica showed that the number of available silanol groups was related to the absolute dehydration temperature according to Eq. [1]

$$\text{Si} - \text{OH groups/cm}^2 = 5200 \times (1/T_A - 1/1600) \times 10^{14} \quad [1]$$

For a silica film grown on silicon at 1100°C there would be only 5.4×10^{13} Si-OH groups available. However this figure is complicated by the fact that partial rehydration can occur on prolonged exposures to high relative humidity (> 50%). The samples used in this work had been exposed to less than 50% humidity for only a few days. For these reasons one would expect less than 10^{14} atoms/cm^2 of fluoride chemisorbed assuming a surface roughness of one and this is what was observed.

Attala *et al.* (4) have pointed out that as little as 1/10,000 of a monolayer of an ionic impurity is sufficient to invert the surface of one ohm-cm silicon.

While it might be argued that chemically adsorbed fluorine is not an ionic impurity, the Si-F bond has 70% ionic character (7) and would be strongly polarized. Cunningham *et al.* (8) reported that a specimen of p-type silicon soaked in HF, rinsed and stored in a dry nitrogen ambient exhibited a strong n-type inversion layer. These data along with the demonstrated strong adsorption of fluoride point out the potential problems in device fabrication.

While the results presented here are adequately explained by chemisorption, subsequent work has shown that higher amounts of fluoride can be retained by different types of silica films. This is particularly true of heavily boron doped films where enhanced adsorption has been observed. Further work will be required to completely understand the variation in fluoride retention by the different types of oxides. The use of fluorine-18 labeled etches as described in this work appears to offer the best method of studying this phenomenon.

Acknowledgment

The authors are indebted to Donald Meyer for his comments and suggestions on part of this work. The staff of the Texas A&M Nuclear Science Center, particularly John Randall and Dave Mueller, were most cooperative in providing assistance during the irradiation and processing of the fluorine-18 activity.

Manuscript received April 7, 1967.

Any discussion of this paper will appear in a Discussion Section to be published in the June 1968 JOURNAL.

REFERENCES

1. C. D. Thomas, Jr., J. A. Sondel, and R. C. Kerns, *Int. J. Appl. Rad. Isotopes*, **16**, 71 (1965).
2. K. Beg, and F. Brown, *ibid.*, **14**, 137 (1963).
3. R. K. Iler, "The Colloid Chemistry of Silica and Silicates," Cornell University Press, Ithaca, N. Y. (1955).
4. M. M. Atalla, E. Tannenbaum, and E. J. Scheibner, *Bell System Tech. J.*, **38**, 749 (1959).
5. C. N. Kimberlin, U. S. Pat. 2,477,695 (Standard Oil Development Co., 1949).
6. W. K. Lowen and E. E. Broge, *J. Phys. Chem.*, **65**, 16 (1961).
7. L. Pauling, "The Nature of the Chemical Bond," Cornell University Press, Ithaca, N. Y. (1960).
8. J. A. Cunningham, L. E. Schariff, and S. S. Baird, *Electrochem. Technol.*, **1**, 242 (1963).

The Etching of Silicon Nitride in Phosphoric Acid with Silicon Dioxide as a Mask

W. van Gelder and V. E. Hauser

Bell Telephone Laboratories, Inc., Allentown, Pennsylvania

ABSTRACT

The water content of phosphoric acid in etching silicon nitride and silicon dioxide plays an important role. An increase in water content increases the etch rate of silicon nitride and decreases the etch rate of silicon dioxide. The highest possible temperature for a fixed water content at atmospheric pressure in the system H_2O-P_2O_5 is realized by boiling the liquid and refluxing the vapor phase. Refluxed boiling phosphoric acid at 180°C was found to be a useful etchant for silicon nitride films. The etch rate is 100 Å/min. Under the same conditions deposited silicon dioxide had an etch rate of 0-25 Å/min depending on the method of preparation, and elemental silicon 3 Å/min. Etch rates of silicon nitride, silicon dioxide, and silicon in refluxed boiling phosphoric acid were measured as a function of temperature (and concentration) in the range of 140°-200°C. All etch rates increased with temperature. The "apparent" activation energies are 12.7, 27.6, and 26.4 kcal/mole, respectively. The etch rate of silicon nitride in phosphoric acid of constant concentration (94.5% H_3PO_4) was measured as a function of temperature only. In this case the "real" activation energy was 22.8 kcal/mole. The difference in etch rate between silicon nitride, deposited silicon dioxide, and silicon offers a technique for etching contact holes in silicon nitride using deposited silicon dioxide as a mask. Such a technique was used successfully in making transistors with silicon nitride over SiO_2 as a junction seal.

A good deal of attention has recently been focussed on silicon nitride (Si_3N_4) as a semiconductor junction seal, partly or fully replacing silicon dioxide. The reason for this is that Si_3N_4 is a better mask than SiO_2 against diffusants of all kinds including water, oxygen, and sodium. The better masking properties of Si_3N_4 go hand in hand with lower etch rates in HF or buffered HF. Silicon nitride films prepared by various deposition processes ($SiCl_4$ + NH_3, SiH_4 + NH_3 and d-c plasma) were reported to exhibit "very slight" diffusion of sodium (1). These films all had low etch rates in buffered HF[1] (~10Å/min). This meant that new ways of etching contact holes had to be developed because photoresist material, now used for etching SiO_2, does not mask sufficiently against buffered HF at the excessively long etching times necessary (2 hr for a film 1200Å thick). Silicon nitride films have a reasonably fast etch rate (200-300 Å/min) in concentrated HF (48%), but it was found that the ordinary photoresist materials, as used for SiO_2, do not mask sufficiently against the concentrated HF. Even if a good etching mask for concentrated HF were available, the etching of a contact hole in Si_3N_4 which is deposited on an SiO_2 film will present the problem of undercutting because the underlying SiO_2 is etched much faster than Si_3N_4 in concentrated HF.

This paper reports etching experiments with Si_3N_4, SiO_2, and Si in phosphoric acid. It was found that Si_3N_4 has a high etch rate in refluxed boiling phosphoric acid, compared to SiO_2 and elemental Si. Accordingly, phosphoric acid can be applied as an etchant for Si_3N_4 using deposited SiO_2 as a mask.

[1] Composition: 40g NH_4F + 60 ml H_2O + 15 ml 48% HF.

Etching Conditions

The silicon nitride films for the etching experiments with phosphoric acid were deposited by use of a pyrolytic process with SiH_4 and NH_3 at 880°C. [Silicon nitrides prepared by a d-c plasma process (2) and by

a process using $SiCl_4 + NH_3$ at 1000°C had approximately the same etch rate in phosphoric acid as the silicon nitride prepared from $SiH_4 + NH_3$.]

SiO_2 films were deposited in three different ways as follows:

1. $SiCl_4 + H_2 + O_2$ at 880°C
2. $SiH_4 + N_2 + O_2$ at 350°C
3. Same as No. 2 but densified for 20 min in O_2 at 800°C.

Film thickness was measured interferometrically with a Perkin-Elmer 202 spectrophotometer in the ultraviolet and visible wavelength range. A detailed description of the technique is given by Reizman and van Gelder (3). Reference (3) also gives the refractive index of the Si_3N_4 films as a function of wavelength. At $\lambda = 5460$Å the refractive index was 1.97.

A few tests were made to determine the etch rate of silicon in phosphoric acid. Silicon slices for this purpose were 58 ohm-cm p-type and were mechanically polished on both sides. The etch rate was determined by weighing on a microbalance before and after etching. In one case (at 180°C) a silicon slice half covered with SiO_2 was etched for 2 hr. The SiO_2 was then removed, aluminum was evaporated, and the step height in the silicon was measured with a multiple beam interferometer. The two methods agreed to within ±10%.

At first the phosphoric acid was kept in an open beaker at 200°C. The acid was initially 85% H_3PO_4 by weight and was slowly heated from room temperature to 200°C. The etching process was started after the acid had reached a constant temperature of 200°C for 1 hr. At that point most of the water in the acid had evaporated (partly by boiling), but the acid was not necessarily in equilibrium with atmospheric moisture. It was, in fact, observed that the Si_3N_4 etch rate was slowly decreasing with time which was explained by assuming that the acid was still losing water. According to Brown and Whitt(4) the vapor phase in equilibrium with phosphoric acid up to 250°C is virtually pure water (0.03% P_2O_5 at 250°C). Figure 1 gives the vapor pressure of phosphoric acid solutions *vs.* temperature for various concentrations. This figure shows, for instance, that phosphoric acid containing 75.3% P_2O_5 has a vapor pressure of 37 mm Hg at 200°C. This means that even a highly concentrated phosphoric acid of 75.3% P_2O_5 will still lose water when kept in an open beaker at 200°C because the water vapor partial pressure in a normal atmospheric ambient of 25°C and 50% relative humidity is 12 mm Hg.

To overcome the problem of keeping the acid concentration at a constant and known value later etching experiments were done with boiling phosphoric acid at atmospheric pressure and at constant temperatures ranging from 140° to 200°C with emerging water vapor constantly being condensed and returned to the boiling acid. Under these refluxing conditions the acid remains at a constant temperature and concentration. The slices were held in a quartz basket. The "boiler" was a quartz 1-liter round-bottom flask provided with a thermometer well, a reflux water-cooled condenser, and a wide, ground-glass tapered connector to admit the basket with slices.

Figure 1 is basically a part of the pressure-temperature diagram of the two component system H_2O-P_2O_5. The concentration of phosphoric acid can best be expressed in terms of weight per cent P_2O_5. However, for commercially available phosphoric acid the concentration is given as weight per cent H_3PO_4. The concentrations in Fig. 1 are therefore expressed both in per cent P_2O_5 and in per cent H_3PO_4. Applying Gibbs' phase rule to the system H_2O-P_2O_5 for the two phases liquid and gas in equilibrium, we find that there are two degrees of freedom. This means that of the three variables pressure (p), temperature (T), and concentration (x) we can choose only two while the third variable is fixed when the choice is made. For instance, the highest concentration of commercially available phosphoric acid is 85% H_3PO_4. This liquid boils at 154°C (see Fig. 2) or, in other words, at 154°C its vapor pressure is 760 mm Hg (see Fig. 1). If the boiling liquid is totally refluxed we have chosen the vapor pressure to be constant at 760 mm Hg (or whatever the local barometric pressure is) and the concentration at 85% H_3PO_4. Consequently, the temperature as, the third variable, is fixed at 154°C and cannot change unless p or x is changed. The higher boiling phosphoric acids in this work were obtained by letting some water vapor escape and the lower boiling acids were obtained by adding water.

In addition to measuring the etch rates as a function of the boiling temperature (and therefore necessarily also as a function of the concentration) the etch rate of silicon nitride was measured as a function of temperature only, at a constant concentration of 94.5% H_3PO_4. Refluxed boiling phosphoric acid at 200°C has a concentration of 94.5% H_3PO_4. This acid was cooled down and held at 158° and 140°C to measure the etch rate. Care was taken to let no water vapor escape. It should be noted that in the case of refluxed boiling acid the temperature is controlled by the amount of water in the system and not by the amount of heat put into the system.

Results

Table I shows results of etching experiments with Si_3N_4 and SiO_2, comparing "open beaker" phosphoric

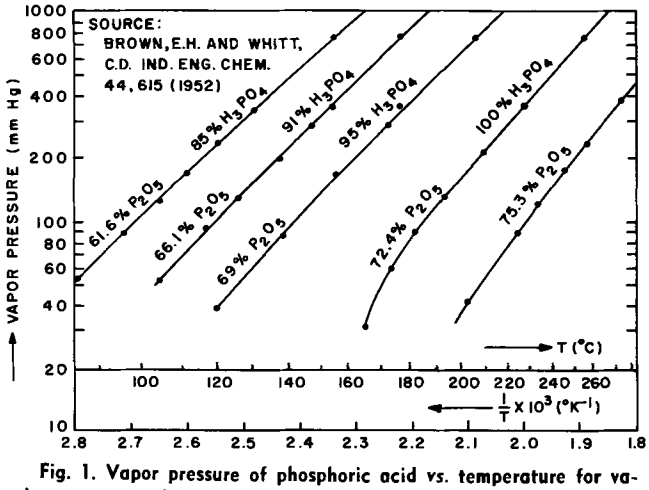

Fig. 1. Vapor pressure of phosphoric acid *vs.* temperature for various concentrations.

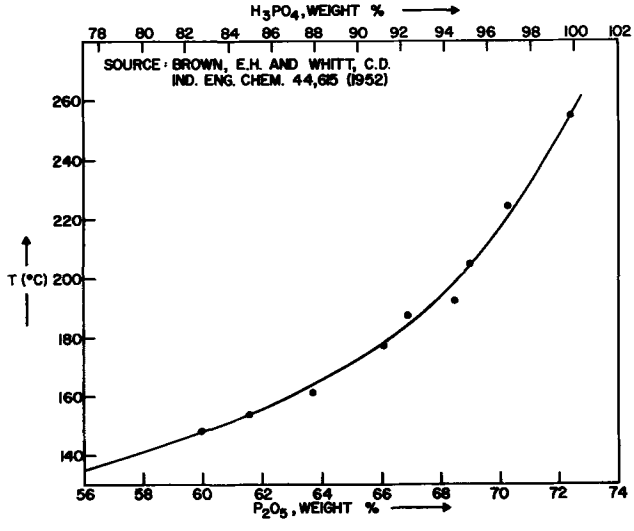

Fig. 2. Boiling point of phosphoric acid at 760 mm Hg *vs.* concentration.

Table I. Etch rates of Si_3N_4 and SiO_2 in H_3PO_4 (Å/min)

Type of film	Si_3N_4	SiO_2	SiO_2	SiO_2	
Method of film preparation	$SiH_4 + NH_3$ 880°C	$SiCl_4 + O_2 + H_2$ 880°C	$SiH_4 + O_2$ 350°C Not densified	$SiH_4 + O_2$ 350°C Densified at 800°C	Acid concentration at P_2O_5
Open beaker H_3PO_4 200°C	30	70	250	Not measured	>75.3% (>100% H_3PO_4)
Refluxed boiling H_3PO_4 200°C	178	32	Not measured	Not measured	68.5% (94.5% H_3PO_4)
Refluxed boiling H_3PO_4 180°C	105	10	25	0	66.4% (91.5% H_3PO_4)

acid at 200°C with refluxed, boiling phosphoric acid at 200° and 180°C. It is shown that the etch rate of Si_3N_4 was increased by a factor of 6 in going from open beaker acid to refluxed acid at 200°C. A factor of 2.2 was observed in the opposite direction for SiO_2 (deposited from $SiCl_4$, O_2, and H_2 at 880°C). In other words at a constant temperature of 200°C an increase in water content caused an increase in the etch rate of silicon nitride and a decrease in the etch rate of silicon dioxide.

The etch rates of Si_3N_4, SiO_2, and Si in refluxed boiling phosphoric acid were measured as a function of boiling temperature and are represented in Fig. 3 by the solid lines. Note that the acid concentration necessarily varies with the boiling temperature. An increase in boiling temperature goes together with an increase in acid concentration and *vice versa* as indicated by the abscissas of Fig. 3. The slope of the Si_3N_4 line in Fig. 3 is smaller than the slope of the SiO_2 line because the water content affects the etch rate of Si_3N_4 and SiO_2 in an opposite direction. The "apparent" activation energies derived from the straight solid lines in Fig. 3 are 12.7, 27.6, and 26.4 kcal/mole for Si_3N_4, SiO_2, and Si, respectively.

Figure 3 also shows a dashed line drawn through three points. This represents the etch rate of silicon nitride as a function of temperature only, at a constant concentration of 94.5% H_3PO_4. The "real" activation energy is 22.8 kcal/mole. The much steeper slope of the dashed line confirms that at one particular temperature a higher water content causes a higher etch rate for silicon nitride.

It is apparent that SiO_2 is quite suitable as a masking layer for Si_3N_4 films against attack by the boiling phosphoric acid. Since standard photoresist masking

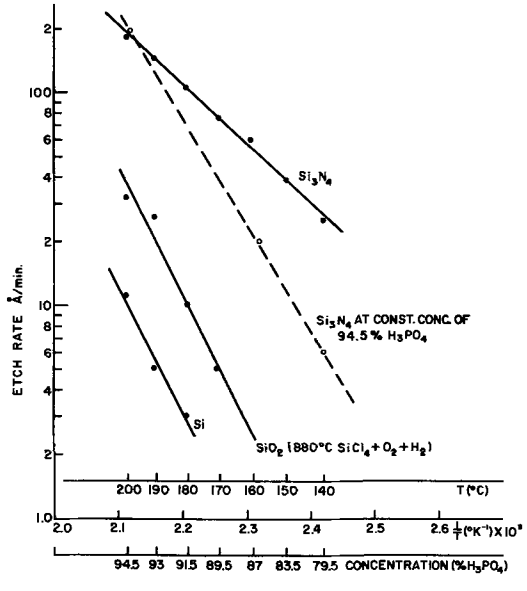

Fig. 3. Solid lines: etch rate of Si_3N_4, SiO_2, and Si in refluxed boiling phosphoric acid at atmospheric pressure as a function of boiling temperature and acid concentration. Dashed line: etch rate of Si_3N_4 at a constant concentration of 94.5% H_3PO_4 as a function of temperature only.

techniques can be used to open windows in an oxide film that has been deposited on top of a Si_3N_4 film, it is possible therefore, in turn, to dissolve out Si_3N_4 which lies exposed in the opened window areas by use of refluxed boiling phosphoric acid. If the Si_3N_4 is deposited on SiO_2, the SiO_2 can in turn be dissolved with buffered HF using the Si_3N_4 as a mask. It appeared that steam grown SiO_2 has about the same low etch rate as Si in refluxed boiling phosphoric acid. Undercutting of SiO_2 below the Si_3N_4 did occur to a certain extent, but it did not present a problem in making contacts to transistors if the SiO_2 layer is not too thick (<6000Å). As can be seen from Fig. 3 a temperature of 180°C appears to be a good choice since it combines reasonably fast dissolution of Si_3N_4 with very little attack on the masking SiO_2 layer.

Mechanism

Water has been found to play a vital role in various etching processes. For instance Finne and Klein (5) found that water is an active component in their amine-catechol etchant for silicon, generating hydroxyl ions in the amine solvent system. The hydroxyl ions supposedly ". . . oxidize the silicon to a hydrated silica (which) . . . is then brought into solution by coordination with pyrocathechol which serves as a chelating agent for the silica in the presence of the amine solvent." Hu and Kerr (7), as another example, found that dilute HF etches silicon faster than concentrated (48%) HF.

An exact mechanism for the etching process of Si_3N_4 in phosphoric acid and for the role of water is not given here. It is suggested however that the water is essential in hydrolyzing the Si_3N_4 to some form of hydrous silica and ammonia, the ammonia remaining in solution as ammonium phosphate. The low etch rate of SiO_2 in boiling H_3PO_4 at 180°C could be explained by the fact that the Si-O-Si bond is stronger than and not as easily hydrolyzed as the Si-N bond. With regard to the "open beaker" method it should be noted that concentrated phosphoric acids obtained by boiling off water from orthophosphoric acid (or by adding P_2O_5 to it) are members of a continuous series of amorphous condensed phopshoric acid mixtures, extending from orthophosphoric acid (H_3PO_4) via pyrophosphoric acid ($H_4P_2O_7$) and metaphosphoric acid (HPO_3) to pure P_2O_5 (6). Accordingly it is suggested that the high temperature, low water content acid attacked SiO_2 faster than Si_3N_4 because a soluble phosphorus-silica complex was formed between the "poly" phosphoric acid and the SiO_2 in which the Si-O bonds are largely preserved.

Remarks, Conclusions, and Recommendations

Refluxed boiling phosphoric acid at 180°C was found to be a convenient etchant for Si_3N_4 films. The etch rate is of the order of 100Å/min. Deposited SiO_2 can be used as a mask. Its etch rate under the same conditions is approximately 10 Å/min, depending on the deposition temperature. Many silicon planar transistors were made using this technique to etch contact holes in Si_3N_4 films. Delineation of contact holes is good. Holes with a width of 5μ are easily produced.

For Si_3N_4 and SiO_2 it was found that the water content of the phosphoric acid plays an important role. At constant temperature addition of water increased

the etch rate of Si_3N_4 and decreased the etch rate of SiO_2. The maximum possible temperature at atmospheric pressure for a fixed water content was realized by boiling the acid and "refluxing" the vapor phase.

For safe operation of the etching bath boiling aids such as Teflon-coated stirring bars should always be used.

Acknowledgments

The authors acknowledge the technical assistance of A. S. Szupper.

Manuscript received Feb. 2, 1967; revised manuscript received April 10, 1967. This paper was presented at the Philadelphia Meeting, Oct. 9-14, 1967.

Any discussion of this paper will appear in a Discussion Section to be published in the June 1968 JOURNAL.

REFERENCES

1. J. V. Dalton, "Sodium Drift and Diffusion in Silicon Nitride Films," Recent News Paper presented at the Cleveland Meeting of the Society, May 3, 1966.
2. W. C. Erdman and A. Androshuk, Recent News Paper presented at Philadephia Meeting of the Society, Oct. 12, 1966.
3. F. Reizman and W. van Gelder, *Solid State Electronics*, To be published in 1967.
4. E. H. Brown and C. D. Whitt, *Ind. Eng. Chem.*, **44**, 615 (1952).
5. R. M. Finne and D. L. Klein, Paper presented at the Toronto Meeting of the Society, May 6, 1964.
6. Kirk-Othmer, Encyclopedia of Chemical Technology.
7. S. M. Hu and D. R. Kerr, *This Journal*, **114**, 414 (1967).

Macroscopic Defects in Epitaxial Silicon

E. R. Shaw[1] and K. M. Busen

Research and Development Laboratories, Sprague Electric Company, North Adams, Massachusetts

ABSTRACT

A macroscopic defect in epitaxial silicon layers, known as hillock, has been studied. In addition to other causes described by several authors, the origin of the defect was found to be a microalloy which is liquid at deposition temperatures and which is positioned on the substrate surface prior to epitaxial growth. The microalloy arises from an interaction between contaminants and the substrate. A model is proposed which explains phenomena observed in conjunction with the growth of a hillock.

Among the commonly observed defects in epitaxial silicon layers are dislocations and stacking faults. Another type of defect often occurring in epitaxial layers has been the subject of many recent publications (1-3). This defect which is shown in Fig. 1 has been described by a variety of terms such as tetrahedral growth, macroscopic pip, tripyramid, or hillock. In the following discussion the defect will be referred to as a hillock. The general consensus of the literature cited above is that hillocks are caused by an impurity (as α-SiC or SiO_2) on the surface of the substrate. A similar origin has been postulated for stacking faults. This would mean that the origin of a hillock must be at the substrate surface, and apparent evidence for this is presented in the literature (4, 5). It is shown in this paper, however, that for the hillocks studied in conjunction with this work, the origin penetrates the substrate surface. In addition, evidence has been found which supports a liquid drop model for the growth of hillocks.

[1] Present address: RCA, Home Instruments Division, Indianapolis, Indiana.

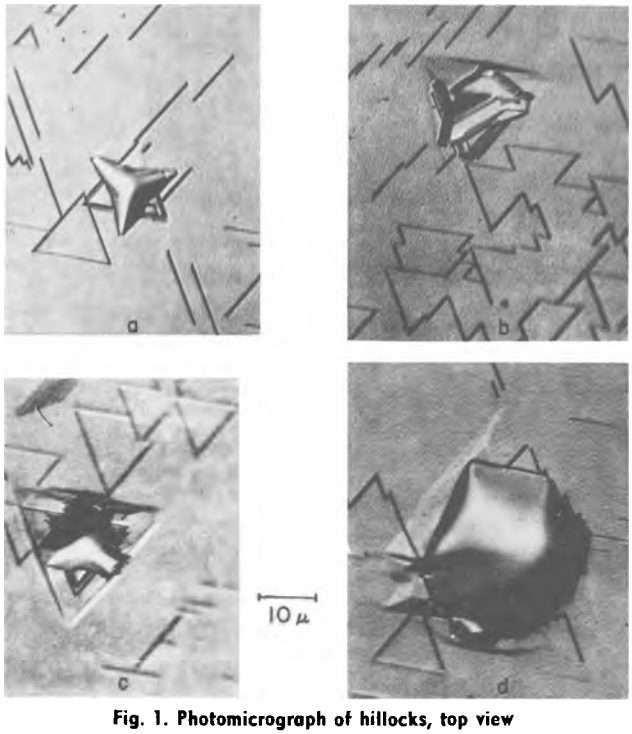

Fig. 1. Photomicrograph of hillocks, top view

Experimental and Results

Epitaxial silicon layers were prepared by the hydrogen reduction of silicon tetrachloride at 1250°-1400°C. The substrate material came from Czochralski grown crystals with a dislocation density of about 500-1000 cm^{-2}. The thickness of the epitaxial layers was between 0.1 and 1 mil. Several system designs based on those reported by Li (6) and Theuerer (7) as well as a commercial "Ecco" multiple slice unit were employed. Substrate material used included both n- and p-types in the limits of 0.001 to 50 ohm-cm. The hillocks were investigated by the following methods:

(*A*) Optical microscopy. This portion of the study was carried out using a Leitz Metallographic Microscope model MM5 with magnifications up to 1200X.

(*B*) Electron microscopy. Negative replication techniques were employed, the samples being shadowed at approximately 15°.

(*C*) Microprobe analysis. Probe spectral scans were conducted using an EdDT crystal and 20 kv at 0.1 μa.

(*D*) Cross-sectioning perpendicular to the surface and decorating with either chromium (Sirtl etch) or copper.

(*E*) Polishing parallel to the surface and decorating at various depths the growth layer with either chromium or copper.

The following observations were made via the above mentioned experimental techniques:

1. Under standardized conditions of cleanliness hillocks occur only when specific crystals are employed as a substrate material. This observation was confirmed by preparing slices from different crystals

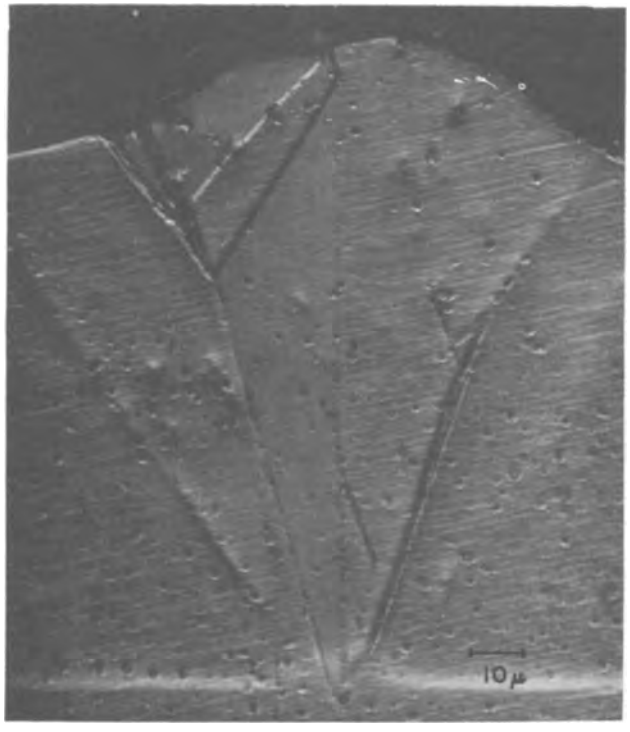

Fig. 2. Photomicrograph showing the origin of a hillock to be below the substrate surface.

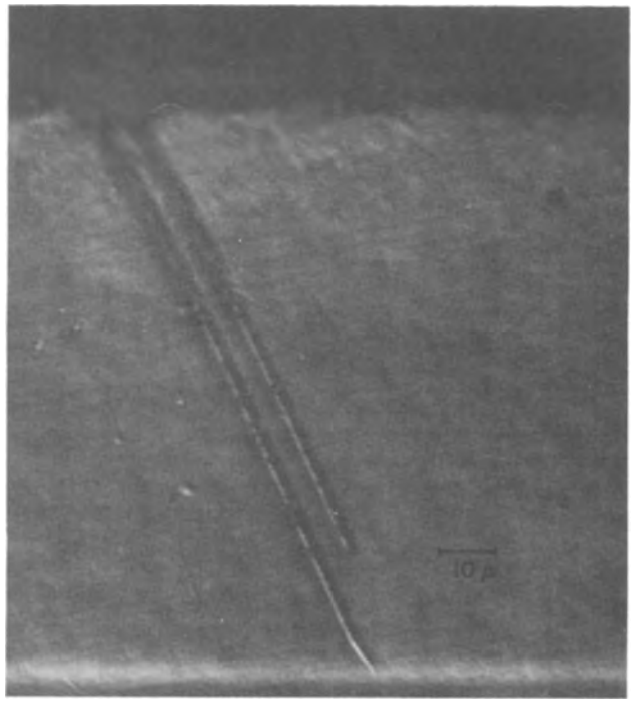

Fig. 3. Photomicrograph showing a stacking fault terminating at the interface.

in experimentally identical manners and depositing epitaxial layers on them simultaneously. Only wafers from crystals, which had previously yielded hillocks, produced hillocks in this experiment.

2. Hillocks generally do not form if the substrate is heated to 1300°-1400°C in hydrogen for 45-90 min prior to deposition.

3. Hillocks which were examined do not terminate at the substrate surface, but rather penetrate below it as shown in Fig. 2. In this figure a cross section through a hillock is shown. The white line at the bottom end of the hillock is a delineated junction between the substrate and the epitaxial layer.

4. Stacking faults, delineated by the same etch, do not penetrate the substrate surface as shown in Fig. 3, where the white line at the bottom is again a delineated junction between substrate and epitaxial layer. This observation is consistent with similar observations already reported in the literature (8).

5. Both copper and chromium (Sirtl etch) decorations of the surface show the hillocks embedded in a circular region (Fig. 4 and 5), which also contains high concentrations of what appear to be dislocations.

6. A hillock is of polycrystalline structure as shown by electron microscopy.

7. Hillocks are observed on (100) oriented substrates (Fig. 6) as well as on (111) oriented ones.

8. In an extra experiment it was observed that substrate material from a crystal, which was known to yield hillocks during epitaxy, when heated in hydrogen for approximately 1 min to temperatures equal to or greater than growth temperatures yielded small ($\sim 10\mu$ diameter) defects as shown in Fig. 7. (These defects will be referred to as "pockets.")

9. Microprobe analysis reveals high concentrations (600-10,000 ppm) of impurities to be present in the hillocks and "pockets" studied. Impurities which have been identified are aluminum, chlorine, phosphorus, sulfur, titanium, and gold.

Discussion and Conclusions

The hillocks reported in the literature have been observed to originate at the substrate surface. However, the hillocks examined in this study were found to originate below the interface (see observation 3).

During the investigations it was realized that some

Fig. 4. Photomicrograph of defects in the "ring" around the hillock.

substrate material rather consistently gave epitaxial layers with hillocks, whereas other material did not. This observation has also been made by others (3). In particular, only certain n-type and certain p-type crystals with impurity concentrations of 10^{20} cm^{-3} and 10^{20}-10^{14} cm^{-3}, respectively, gave rise to hillocks in epitaxial layers. (It is important to emphasize that not all substrates in these resistivity ranges gave hillocks.)

A closer examination of substrates from those crystals which do give hillocks revealed that, on heating to temperatures of 1250°C or greater, small pockets formed on the surface (observation 8). Similar pockets have been observed by Pearson *et al.* (9) and Goodman (10) and have been shown to be sites of local

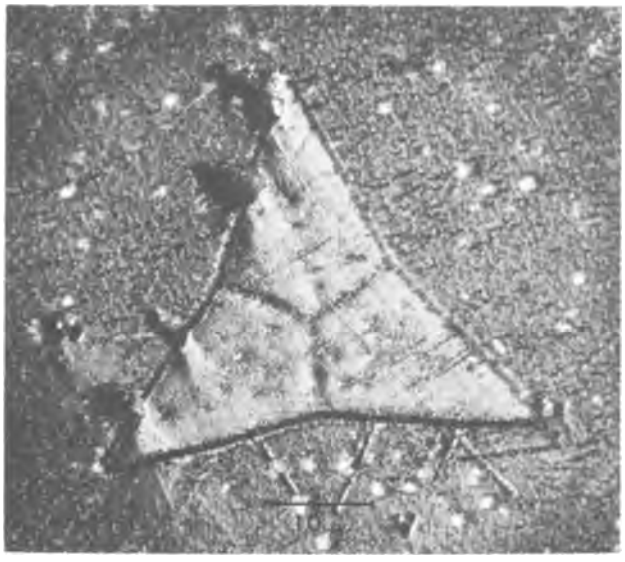

Fig. 5. Photomicrograph of hillock within epitaxial film after polishing and Sirtl etching which shows an area of a different resistivity around the hillock.

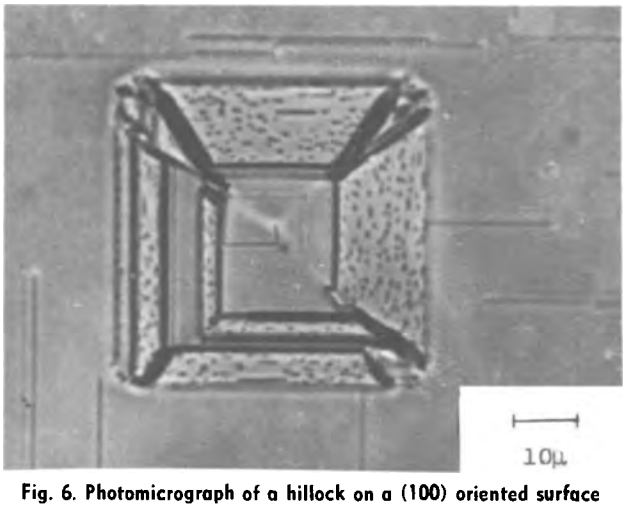

Fig. 6. Photomicrograph of a hillock on a (100) oriented surface

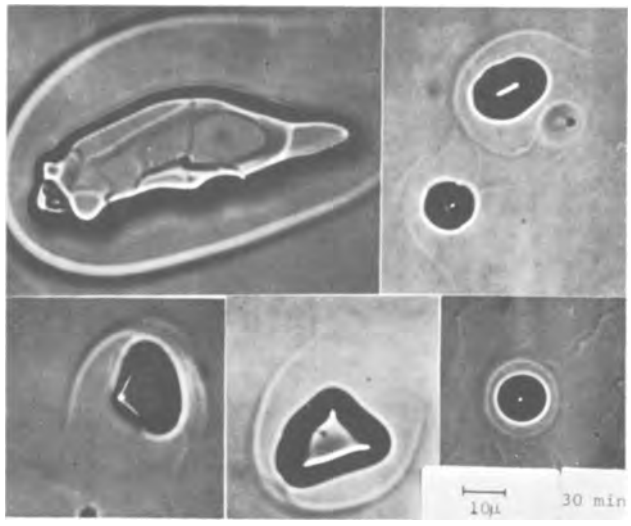

Fig. 7. Photomicrograph of defects which occur when certain substrate material is heated to epitaxial temperatures in hydrogen. These defects have been found to be the origin of hillocks.

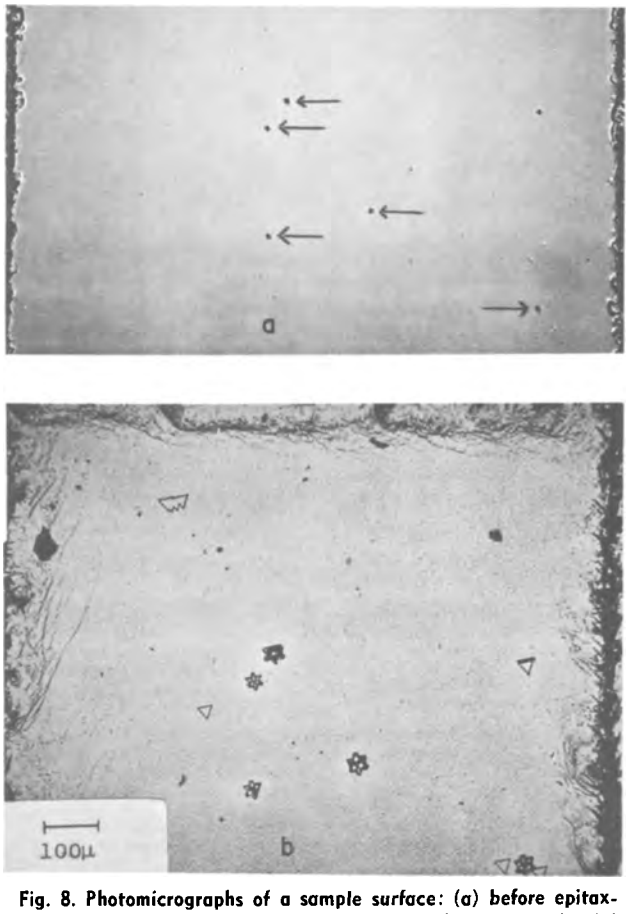

Fig. 8. Photomicrographs of a sample surface: (a) before epitaxial growth with defects as shown in Fig. 7; (b) after epitaxial growth with hillocks on sites of defects. This figure has been retouched for publication purposes.

melting due to impurity particles on the surface which depress the melting point of silicon at that particular point. Detailed examination of the effect of these pockets on epitaxial growth revealed that hillocks nucleate only at these pockets as shown in Fig. 8. Therefore, a direct link is established between a microalloyed pocket on the bare substrate surface (compare observation 8) and the occurrence of a hillock in the epitaxial layer subsequently grown on such a surface. Because pockets were observed on highly doped n-type crystals the conclusion was drawn that there is a relation between a high doping level and the appearance of pockets. The fact that p-type crystals of higher resistivities yielded pockets too may be explained by assuming that these crystals (which were purchased) had a high p-type concentration but were compensated by a suitable amount of n-type. Such unwanted material has been observed to be on the market from time to time. The link between highly doped crystals and pockets may be a precipitate of doping impurities at preferred sites as dislocations. Such a precipitate could cause a local source for an alloy pit. By the same token it can be inferred that contaminates from the ambient as well as from handling processes are potential local sources for pockets too.

Once a hillock has nucleated it must be propagated within the epitaxial layer. The mechanism of propagation is not understood, but there are observations which may give some hints for the nature of the hillock growth. One observes for example that the applied Sirtl etch (or copper etch) delineates a circular region around the star-shaped hillock (see Fig. 4 and 5). The region is of a different shade than the surrounding silicon and may indicate a different resistivity. This observation together with the formation of the pockets can be utilized to advance the following model: If one assumes that the initial pocket is an alloy between an impurity and the substrate and that this alloy migrates upward as a thin liquid layer on

top of the growing hillock,[1] then one is able to rationalize both the observed circular region and the apparent difference in resistivity: The circular region is a consequence of surface tension between liquid layer and epitaxial surface and the resistivity change arises from continuous dissolution and recrystallization of silicon within the migrating liquid layer. Also considerable internal structure is observed within the hillock pointing to some complications during the growth process. One also observes (see Fig. 1a-d) that the majority of the hillocks are associated with stacking faults. Stacking faults have been considered as a mechanism of relieving strain in growing layers (12) and very probably serve a similar function in the case of hillocks.

Polycrystalline formation very probably takes place during crystallization as evidenced by the electron microscope data. They do not give a simple silicon structure but rather a structure, which has not been resolved, and is quite complex. Since microprobe analysis has shown a high content of impurities at the hillocks and since it is known that grain boundaries act as a gettering center for impurities during crystal growth support is given to the model above.

[1] A similar model has been employed by Wagner (11) who observed that silicon whiskers grow under a gold drop, which moves up during growth.

Manuscript received Oct. 20, 1965; revised manuscript received March 24, 1967. This paper was presented at the San Francisco Meeting, May 9-13, 1965.

Any discussion of this paper will appear in a Discussion Section to be published in the June 1968 JOURNAL.

REFERENCES

1. G. R. Booker and R. Stickler, *J. Appl. Phys.*, **33**, 3281 (1962).
2. T. L. Chu and J. R. Gavaler, *Phil. Mag.*, **9**, 993 (1964).
3. E. I. Givargizov, *Sov. Phys. Solid State*, **6**, 1415 (1964).
4. D. P. Miller, S. B. Watelski, and C. R. Moore, *J. Appl. Phys.*, **34**, 2813 (1963).
5. M. Inoue, *This Journal*, **112**, 189 (1965).
6. C. H. Li, *ibid.*, **109**, 952 (1962).
7. H. C. Theuerer, *ibid.*, **108**, 649 (1961).
8. W. C. Dash, *J. Appl. Phys.*, **33**, 2395 (1962).
9. G. L. Pearson and R. G. Treuting, *Acta Cryst.*, **11**, 397 (1958).
10. C. H. L. Goodman, *Solid-State Electronics*, **3**, 72 (1961).
11. R. S. Wagner *et al.*, *J. Appl. Phys*, **35**, 2993 (1964).
12. T. L. Chu and J. R. Gavaler, *This Journal*, **110**, 388 (1963).

Technical Notes

On the Eu^{3+} Fluorescence of Mixed Metal Oxides

VI. Temperature Dependence of the Fluorescence

G. Blasse and J. de Vries

Philips Research Laboratories, N.V. Philips' Gloeilampenfabrieken, Eindhoven-Netherlands

In earlier parts of this series of papers the spectral energy distribution and the photoluminescent efficiency of well-defined Eu^{3+}-activated mixed metal oxides have been studied (1-5). It was found, among other things, that a relation exists between the position of the broad uv absorption band (charge-transfer band) of the Eu^{3+} ion and the maximum quantum efficiency for excitation in this band (4). We have now studied the temperature dependence of a number of Eu^{3+}-activated phosphors in which the Eu^{3+} center is directly excited by short-wave uv excitation. Phosphors that are excited in the host lattice were not studied because the temperature dependence of the energy transfer from host lattice to activator, as found, *e.g.*, by Botden (6), may complicate the final results in this case.

The preparation and analysis of the phosphors were described in the preceding papers. The temperature dependence of the fluorescence of the phosphors was determined by irradiating the phosphor with the radiation from a high-pressure mercury discharge lamp with a Schott UG 5 filter (2 mm) and a $NiSO_4$ filter (600 g/l, 2 cm) placed in front of it. For phosphors that have the excitation band in the 300 mm region the $NiSO_4$ filter was omitted. The phosphor was spread on a copper plate which could be either heated or cooled by liquid nitrogen. A photomultiplyer fitted with a Schott OG 5 filter (2 mm) was used for detecting the Eu^{3+} fluorescence. Figure 1 presents some of the curves obtained.

For all phosphors investigated, except $LaAlO_3$:Eu, the light output below room temperature is practically independent of temperature.

For none of the phosphors, except $LaAlO_3$:Eu, is the emission completely quenched below 700°K. We

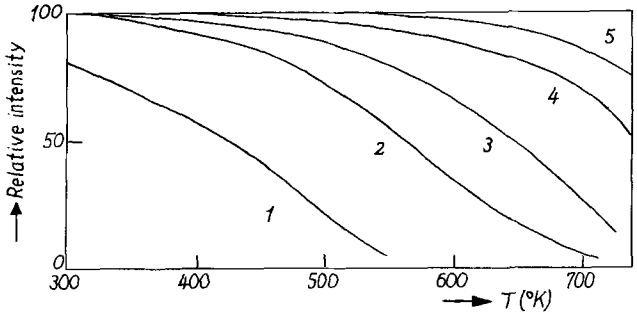

Fig. 1. Temperature dependence (above room temperature) of the fluorescent emission of $LaAlO_3$:Eu (2%) (curve 1), $LaYO_3$:Eu (curve 2), Gd_2O_3:Eu (monoclinic, curve 3), Gd_2O_3:Eu (cubic) and $LaBO_3$:Eu (both curve 4), and $YAl_3B_4O_{12}$:Eu (curve 5).

Table I. Properties of some Eu^{3+}-activated phosphors

Phosphor	Eu^{3+} concentration, a/o	Position charge-transfer band (λ_{max}, nm)	Quantum efficiency for excitation with λ_{max} (%)[e]	Quenching temperature, $T_{0.5}$, °K
$GdBO_3$	3	235[a]	80-100[a,b]	>>800[a]
Gd_2O_3 (cubic)	3	243[a]	70[a]	750[a]
Y_2GeO_5	2	247[c]	35[c]	630[d]
$YAl_3B_4O_{12}$	3	249[c]	35[c]	>750[d]
Gd_2O_3 (monoclinic)	3	255, 220[c]	30[c]	650[d]
$GdAlO_3$	2	263[c]	25[c]	600[d]
$LaBO_3$	3	270[a]	20[a]	~750[d]
$LaYO_3$	2	291, 236[c]	15[b,c]	560[d]
$LaAlO_3$	2	310[c]	10[b,c]	420[d]

[a] See ref. (17).
[b] Inaccurate data, λ_{max} being far from 250-270 nm, where q was actually measured.
[c] See ref. (4).
[d] This work.
[e] At room temperature.

therefore consider the temperature at which the emission output is half of the low temperature value as the quenching temperature ($T_{0.5}$).

Table I gives the position of the charge transfer band (λ_{max}), the quantum efficiency for excitation in this band ($q\lambda_{max}$) at room temperature and the quenching temperature ($T_{0.5}$). It must be kept in mind that the quenching temperature may depend on the preparation circumstances, as does the quantum efficiency (7), so that the values of $T_{0.5}$ in Table I cannot be considered as very accurate data. For the host lattices $LaAlO_3$ and $YAl_3B_4O_{12}$ we also studied the variation of the temperature dependence with Eu^{3+} concentration. In the case of $YAl_3B_4O_{12}$ there is no concentration dependence, not even up to 100% Eu, but in $LaAlO_3$ there is a rapid decrease of $T_{0.5}$ with increasing Eu^{3+} concentration. At 2% Eu the value of $T_{0.5}$ is 420°K, but at 5% Eu it is 300°K.

Discussion

From Table I it follows that the quenching temperature decreases if the quantum efficiency at low temperatures (practically equal to that at room temperature) is lower and if the charge-transfer band moves to lower energies. The borate host lattices, especially $YAl_3B_4O_{12}$ and $LaBO_3$, are an exception, because the quenching temperature of the Eu^{3+} fluorescence in these host lattices is much higher than expected from the correlation mentioned above. This correlation, however, is a little suspicious for the following reason. Usually charge-transfer absorption bands move to longer wavelengths with increasing temperatures. Phosphors that have this band at very short wavelengths show, therefore, an increasing absorption in this band with increasing temperatures (and a too high value of $T_{0.5}$), phosphors that have this band at wavelengths considerably longer than 254 nm show a decreasing absorption with increasing temperatures (and a too low value of $T_{0.5}$). We therefore restrict ourselves to a discussion of the relatively high values of $T_{0.5}$ of the borate phosphors (and a too low value of $T_{0.5}$). Nevertheless, the correlation probably exists, because the charge-transfer excitation bands are usually very broad (for example, the half-width value of this band in the case of $YAl_3B_4O_{12}$:Eu is about 13000 cm^{-1}), so that corrections due to the temperature dependence of the excitation band will only make the correlation less marked, but will not remove it. We restrict ourselves to a discussion of the most striking result, *viz.*, the relatively high values of $T_{0.5}$ of the borate phosphors.

The phosphors under investigation are excited in the charge-transfer band of the Eu^{3+} center. Between the corresponding energy level and that of the fluorescing $^5D_0$ level a large number of energy levels exist, from which radiationless processes can occur as shown by Bril, Blasse, and Bertens (8). Such a large number of radiationless processes complicates the problem drastically. Moreover, the decay mechanism of the radiationless processes is unknown. Within a 4f configuration multiphonon processes are a probable possibility for radiationless decay. These have been considered by Kiel (9). The rate of a multiphonon process involving n phonons with energy $h\nu$ is proportional to

$$\{(\exp h\nu/kT - 1)^{-1} + 1\}^n \qquad [2]$$

so that this rate has a constant value at low temperatures ($h\nu >> kT$) and varies with T^n in the limit $kT >> h\nu$. For host lattices that have high-energy phonons available the number of phonons in the multiphonon process, n, is relatively small and the temperature dependence of these processes relatively weak (compare Eq. [2]). This is the case for compounds containing a lighter element such as the borates. The BO_3 group in $YAl_3B_4O_{12}$ and $LaBO_3$ has a vibration frequency of 1250 cm^{-1}, the BO_4 group in YBO_3 (10) has 1000 cm^{-1} (11). This might be the reason for the relatively high quenching temperature found in borate host lattices.

It is interesting to note that the fluorescent emission of the Eu^{3+} ion in borates does not show transitions down from the $^5D_1$ levels, not even at concentrations lower than 1 a/o, whereas these transitions are usually observed in our phosphors at low Eu^{3+} concentrations (12). The $^5D_1$-$^5D_0$ transition involves an energy separation of only about 1750 cm^{-1}, so that usually three phonons must be created. In borates, however, two phonons suffice. Analogous results were reported by Bhaumik and Nugent for Eu^{3+} chelates (13), where the C = O and C = C stretching vibrations make important contributions to the relaxation process. For certain applications of Eu^{3+}-phosphors the use of host lattices that have high-energy phonons available may be profitable in view of the weak temperature dependence of the luminescence and the absence of green lines in the emission.

The temperature dependence of the Tb^{3+} fluorescence in borate host lattices is extremely weak (14). This might also be ascribed to the high-energy phonons available in these lattices.

At high Eu^{3+} concentrations the number of radiationless transitions can be increased by the concentration quenching of the Eu^{3+} fluorescence. Therefore we studied the concentration dependence of the temperature dependence of the Eu^{3+} fluorescence in $YAl_3B_4O_{12}$, for which host lattice no concentration quenching is observed, not even up to 100% Eu (15), and in $LaAlO_3$, for which lattice concentration quenching has already been found at some 4% Eu (16). The temperature dependence of the fluorescence of $EuAl_3B_4O_{12}$ is almost equal to that of $YAl_3B_4O_{12}$:Eu with low Eu^{3+} concentration, whereas the quenching temperature of the fluorescence of $LaAlO_3$:Eu decreases from 420° to 300°K, if the Eu^{3+} concentration increases from 2 to 5 a/o. These results agree with the earlier work on concentration quenching in $YAl_3B_4O_{12}$:Eu and $LaAlO_3$:Eu.

We conclude that, whatever the exact nature of the nonradiative decay mechanism may be, the energy of the phonons available plays a role in this mechanism.

For Eu^{3+} fluorescence in solutions the same conclusion holds in view of the work of deuterated compounds (18).

Manuscript received March 2, 1967.

Any discussion of this paper will appear in a Discussion Section to be published in the June 1968 JOURNAL.

REFERENCES

1. G. Blasse, A. Bril, and W. C. Nieuwpoort, *J. Phys. Chem. Solids*, **27**, 1587 (1966).
2. G. Blasse and A. Bril, *Philips Research Repts.*, **21**, 368 (1966).
3. G. Blasse and A. Bril, *J. Chem. Phys.*, **45**, 2350 (1966).
4. G. Blasse, *J. Chem. Phys.*, **45**, 2356 (1966).
5. G. Blasse and A. Bril, *J. Chem. Phys.*, **45**, 3327 (1966).
6. Th. P. J. Botden, *Philips Research Repts.*, **6**, 425 (1951).
7. F. A. Kröger, *ibid.*, **2**, 240 (1947).
8. A. Bril, G. Blasse, and J. A. A. Bertens, To be published.
9. A. Kiel in "Quantum Electronics," p. 765, P. Givet and N. Bloembergen, Editors, Columbian University Press, New York (1964).
10. W. F. Bradley, D. L. Graf, and R. S. Roth, *Acta Cryst.*, **20**, 283 (1966).
11. J. P. Laperches and P. Tarte, *Spectrochim. Acta*, **22**, 1201 (1966).
12. G. Blasse and A. Bril, Unpublished results. See also A. Bril, W. C. Nieuwpoort, W. L. Wanmaker, G. Blasse and C. D. J. C. de Laat, Int. Conf. on Luminescence, Budapest, 1966.
13. M. L. Bhaumik and L. J. Nugent, *J. Chem. Phys.*, **43**, 1680 (1965).
14. W. L. Wanmaker and A. Bril, *Philips Research Repts.*, **19**, 479 (1964); W. L. Wanmaker, A. Bril, and J. W. ter Vrugt, *This Journal*, **112**, 1147 (1965).
15. G. Blasse, *J. Chem. Phys.*, In press.
16. L. G. van Uitert, R. C. Linares, R. R. Soden, and A. A. Ballman, *ibid.*, **36**, 702 (1962).
17. A. Bril and W. L. Wanmaker, *This Journal*, **111**, 1362 (1964).
18. W. R. Dawson and J. L. Kropp, *J. Opt. Soc. Amer.*, **55**, 822 (1965); P. K. Gallagher, *J Chem. Phys.*, **43**, 1742 (1965).

Wettability Measurements on Rough, High-Energy Surfaces

Robert O. Lussow, Louis H. Wirtz, and Harold A. Levine

Components Division, International Business Machines Corporation, East Fishkill Facility, Hopewell Junction, New York

Liquid drop size measurement for determining surface characteristics of solids has been used for many years. Typical methods use the contact angle between the liquid droplet and the solid surface (1) or the measurement of the height of the sessile drop (2). These measurements are readily applied to very smooth surfaces and in particular to low-energy surfaces. However, when one wishes to examine high-energy surfaces that exhibit some degree of roughness, the interpretation of the data is complex and accurate analysis is difficult (3, 4). This note describes a method for determining the relative wettability of high-energy surfaces that exhibit some degree of surface roughness.

The method presented is based on the contact area between a droplet of liquid and a solid surface when both are in equilibrium with the vapor of the liquid. A drop of liquid will spread over a solid surface until the forces attracting the liquid to the surface balance the cohesive forces within the liquid. If the droplet and solid are in equilibrium with the vapor of the liquid, the droplet dimensions will remain constant after the foregoing condition is reached. Since the cohesive forces of the liquid do not change, the area covered by a droplet of a given volume will be determined by the forces exerted on the liquid by the solid surface. One can compare the areas covered by droplets of equal volume to obtain a relative measure of the forces exerted by different surfaces.

A simple technique for determining the area covered by such droplets is to photograph the droplets at their equilibrium spread size from an overhead position. The droplet size is obtained by measuring the image size from the photograph and correcting this value for photographic magnification. On rough, high-energy surfaces, the droplet cross sections may vary from circular to ameboform shapes. The contact areas may be estimated as accurately as desired by the application of the usual methods for irregular areas (5). However, if the droplets have smooth peripheries and approach circularity in cross section, one can measure the maximum and minimum axis to find an average representative diameter. When this method is used, one can calculate a representative circular area or use the average diameters themselves to compare wettability.

Experimental

Procedure.—To determine the wettability of a solid, the sample is placed in the environmental chamber, a rectangular glass calibration chip is placed on its surface, and the chamber is closed. The ambient atmosphere of the chamber is air saturated with vapors of the liquid from which the droplets are formed. After the solid has equilibrated with the vapor, the chamber is opened and the liquid drops are placed on the sample surface. The droplets are formed at the tip of a microsyringe needle and placed on the solid, without the syringe needle touching the solid surface. The environmental chamber is closed, and the droplet is allowed to attain its equilibrium contact size with the solid. The droplet and the chip are photographed through an optically flat, transparent cover without disturbing the equilibrated system. The apparatus used is shown in Fig. 1.

The contact area between the solid and liquid was estimated by use of the average diameter technique. The wettability of each sample was determined by the average value of the contact diameters of four water droplets, one placed in each quadrant of the surface. The correction for photographic magnification was calculated by comparing the true dimensions of the calibration chip with its dimensions in the photograph. With 95% confidence the wettability results obtained in this manner were reproducible within $\pm 2.5\%$.

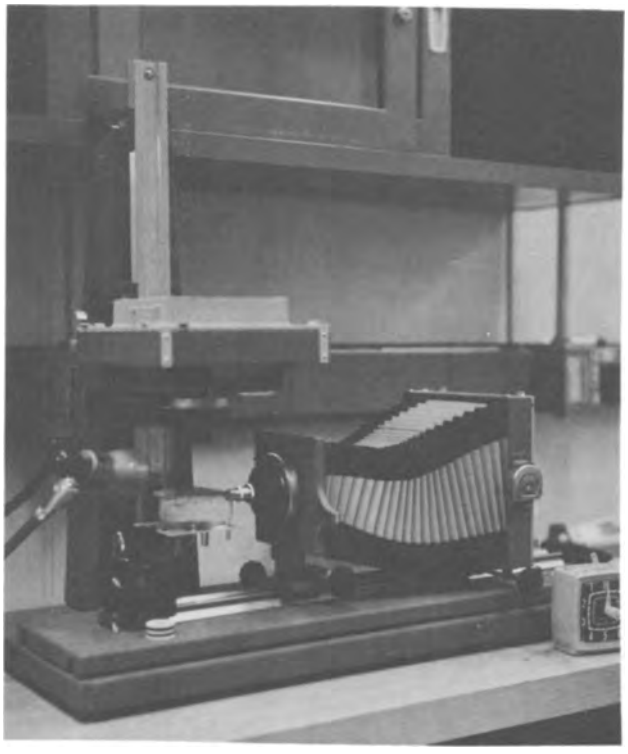

Fig. 1. Wettability apparatus

Materials.—The surfaces used for these experiments were thin layers of SiO_2 prepared by oxidation of n-type epitaxial silicon. The oxide layer was grown by thermal oxidation at 970°C in an alternating ambient atmosphere of steam and dry oxygen. The resulting oxide layers were about 6000Å thick.

The liquid used to create the atmosphere in the environmental chamber and to form the liquid droplets was boiled, 5 x 10^4 mhos, deionized water. Droplet size in all measurements was 4.0 x 10^{-6} liters. Figure 2 shows a typical set of water droplets and calibration chip on a thermal SiO_2 surface. The photographic magnification was of the order of 4X.

Results.—Table I shows the water wettability of thermal SiO_2 surfaces at three different stages: (*i*) after initial outgassing, (*ii*) after chemical treatment described in Table I, and (*iii*) after final outgassing. Both outgassing operations were at 50°C for 30 min at about 100 millitorr pressure. Wettability in all cases increased after the chemical surface treatment. The final vacuum outgassing of wafers treated with H_2O, HNO_3, and H_2SO_4 caused wettability to decrease to values close to those obtained after the initial outgassing. For surfaces treated with the HF-NH_4F mixture, final outgassing reduced wettability, but the ultimate values were greater than those obtained after initial outgassing.

Table I. Effect of chemical treatment on the water wettability of thermal SiO_2

Sample treatment	Wettability, D_T, in.		
	After initial outgassing	After treatment[a]	After final outgassing
D.I. H_2O	0.130	0.180	0.127
Boil 30 min	0.133	0.168	0.128
HNO_3 (conc)	0.128	0.140	0.126
35°C, 10 min	0.134	0.149	0.129
HF-NH_4F mixture[b]	0.129	0.286	0.142
25°C, 30 sec	0.130	0.240	0.139
H_2SO_4 (conc)	0.127	0.158	0.127
95°C, 10 min	0.122	0.155	0.125

[a] After treatment shown in first column, the samples were rinsed in flowing deionized water at room temperature for 5 min (which was blown off with N_2) and air oven dried for 10 min at 110°C.
[b] A mixture of 1 part conc HF to 7 parts 17M NH_4F.

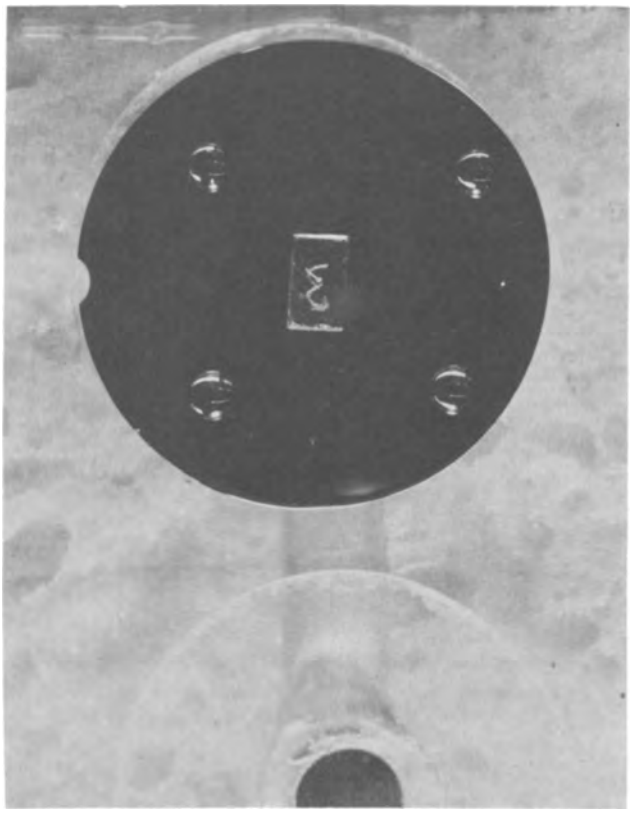

Fig. 2. Contact areas between water droplets and thermal SiO_2 surfaces.

Table II shows the water wettability changes on thermal SiO_2 brought about by exposure to various ambient conditions at elevated temperatures. Wettability measurements were made as for Table I. Exposure to steam at 350° and 500°C caused an increase in surface wettability. The 500°C samples showed the largest increase. Subsequent vacuum outgassing reduced the wettability of all samples, but not to the values after initial outgassing. Two of the final outgassed samples from the 500°C steam exposure were heated at 750°C in dry N_2. Their wettability was reduced to values below their original, initial outgassing wettability. Subsequent vacuum outgassing of the 750°C samples produced no change in their surface wettability.

These data illustrate the use of the proposed method for following water wettability changes on thermal SiO_2 surfaces. The water wettability of these surfaces has been shown to be important in the production of microelectronic devices (1); the significance of these values will be the subject of a forthcoming publication (6).

Table II. Effect of heat-treatment in various ambient atmospheres on the water wettability of thermal SiO_2

Sample treatment	Wettability, D_T, in.		
	After initial outgassing	After treatment	After final outgassing
350°C steam/N_2	0.125	0.146	0.132
1.0 hr[a]	0.124	0.148	0.133
	0.127	0.145	0.136
	0.129	0.146	0.133
500°C steam/N_2	0.126	0.150	0.146
1.0 hr[a]	0.124	0.153	0.144
	0.126	0.162	0.140
	0.124	0.157	0.139
750°C N_2	0.144	0.112	0.112
0.5 hr	0.139	0.111	0.111

[a] Nitrogen at 1.0 cfm was swept through the vapor phase of a steam generator and then over the sample. All samples were cooled in dry N_2.

Manuscript received March 7, 1967; revised manuscript received May 3, 1967.

Any discussion of this paper will appear in a Discussion Section to be published in the June 1968 JOURNAL.

REFERENCES

1. W. A. Zisman, *Advan. Chem. Ser.*, No. 43, 1-51 (1963), A. A. Berg, *This Journal*, **112**, 467 (1965). W. A. Weyl, *Glass Ind.*, **28**, 231 (1947).
2. J. F. Padday, Second International Congress on Surface Activity, III, p. 136, Academic Press Inc., New York (1957).
3. R. N. Wentzel, *Ind. Eng. Chem.*, **28**, 988 (1936).
4. R. E. Johnson, Jr., and R. H. Dettre, *Advan. Chem. Ser.*, No. 43, p. 112 (1963); R. H. Dettre and R. E. Johnson, *ibid.*, p. 136; F. M. Fowkes, *ibid.*, p. 99.
5. R. S. Burington, "Handbook of Mathematics Tables and Formulas," 4th ed., p. 17, McGraw-Hill Book Co., Inc., New York (1965).
6. R. O. Lussow, To be published.

Brief Communication

Propagation of Growth Striae in GaAs Epitaxial Films

P. Wang, F. Pink, and J. Sciola

Semiconductor Division, Sylvania Electric Products Inc., Woburn, Massachusetts

We have carried out epitaxial deposition of GaAs films on (100) GaAs substrates cut from Te-doped <111> single crystals of doping impurity concentration greater than 10^{18} atoms cm^{-3} grown by the Czochralski technique. The deposition was carried out in a three-zone furnace using Ga and AsH_3 sources in a hydrogen ambient, and HCl as the carrier for Ga, similar to the one reported by Tietjen and Amick (1). A peculiar topography on the (100) epitaxial film surface was observed which was not seen on films grown on (111) substrates cut from the same material. This surface feature becomes more pronounced after etching in a chromic acid etch developed for revealing crystallographic defects on low index planes in GaAs (2). Figure 1 illustrates one such specimen before and after a 3-min etch.

A number of GaAs (100) substrates went through a heat treatment cycle with no deposition and did not show this surface topography, *i.e.*, there was no thermal etching.

The regularly spaced, uniform band structure reminds one of the growth striations observed in single crystal GaAs (3, 4). The spacing is within the range of 10-50μ, corresponding to those previously reported for GaAs single crystals pulled by Czochralski-type techniques (3). In order to establish any relationship between the surface band structure and growth striae, a number of thick GaAs epitaxial films were grown with no intentional doping on these substrates at temperatures lower than 700°C and then cleaved from the film surface. The nn^+ interface was delineated by a 10-sec dip in a $AgNO_3$-HNO_3-HF-water solution. The cleaved surface was etched in the chromic acid etch from 2 to 10 min. Typical specimens are shown in Fig. 2.

It is clearly seen that the single crystal <111>

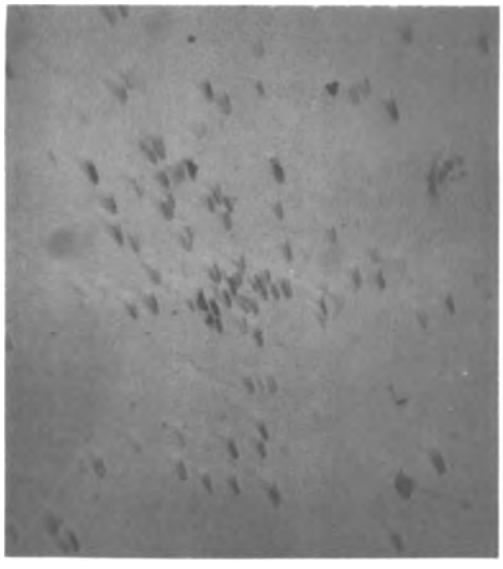

Fig. 1a. (100) GaAs epitaxial film surface topography specimen 3330-71: after deposition. Magnification approximately 120X.

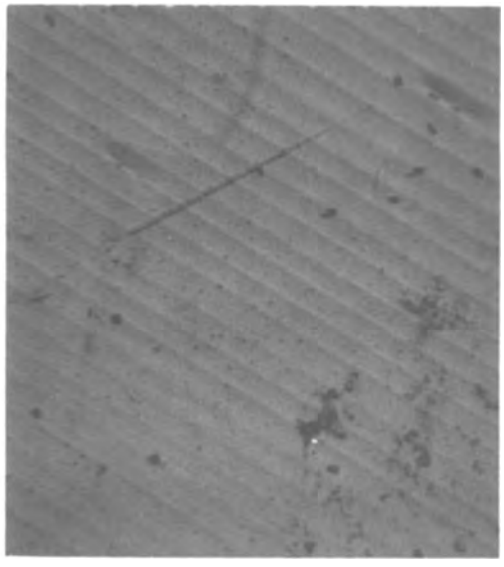

Fig. 1b. Some as Fig. 1a after 2 min in chromic acid etch. Magnification approximately 120X.

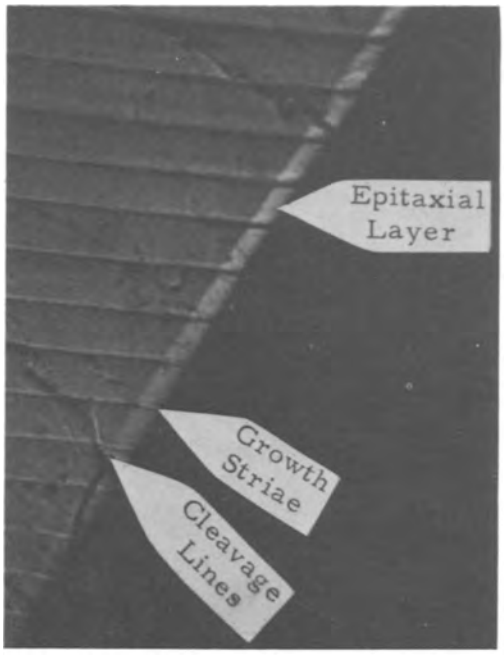

Fig. 2a. (100) GaAs epitaxial film cross-sectional view on cleaved specimen: specimen 3330-71, film thickness, 7.6μ. Magnification approximately 520X.

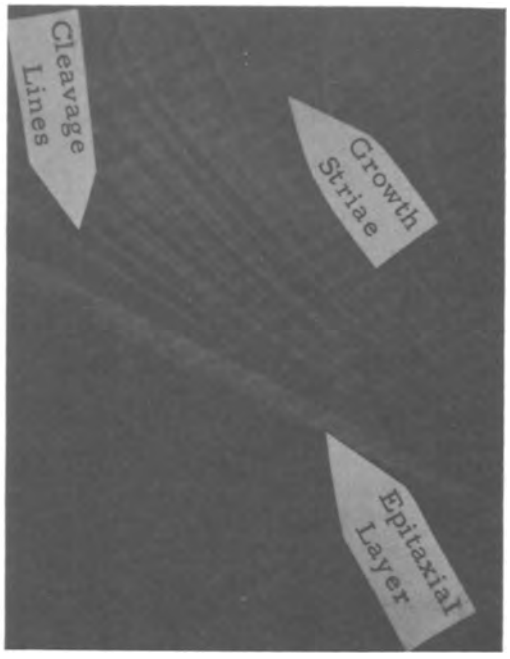

Fig. 2b. Same as Fig. 1a of specimen 3330-13, film thickness, 20μ. Magnification approximately 200X.

growth striae propagate in perfect alignment into the (100) epitaxial film, with equal spacing and revealed with almost identical contrast. The single crystal growth striae are generally attributed to periodical heterogeneous distribution of impurities along the growth axis (5). However, from our observations, we may speculate that the propagation of growth striae in the epitaxial film is at least partly associated with a defect structure. These striae reached through the entire epitaxial film thickness of 10-20μ. At the deposition temperature of less than 700°C, it is inconceivable that a tellurium diffusion front will move that far in less than 100 min. In addition, we detected only very faint contrast of striation in the film after the delineation etch; this striae propagation became well-defined only after the dislocation etch, indicating its probable association with a defect structure. Of course, this observation does not rule out that there was a preferred tellurium diffusion along dislocations. The exact nature of this defect structure is yet to be determined. The peculiar behavior of this unidirectional generation of defects or propagation of growth striation is not explained. We plan to pursue this point in the future.

Acknowledgments

The authors wish to express their appreciation to R. Yee, W. Russell, and A. Hathaway in growing the GaAs epitaxial films.

Manuscript received April 27, 1967.

Any discussion of this paper will appear in a Discussion Section to be published in the June 1968 JOURNAL.

REFERENCES

1. J. J. Tietjen and J. A. Amick, *This Journal*, **113**, 724 (1966).
2. M. S. Abrahams and C. J. Buioedri, *J. Appl. Phys.*, **36**, 2855 (1965).
3. T. S. Plaskett and A. H. Parsons, *This Journal*, **112**, 954 (1965).
4. G. R. Cronin *et al.*, *ibid.*, **113**, 292 (1966).
5. W. P. Sliehter and J. A. Burton in "Transistor Technology," Vol. 1, p. 119. Bell Telephone Laboratories, Inc. and Western Electric Co. (1952).

Deformation of Passive Films

S. F. Bubar and D. A. Vermilyea

General Electric Research and Development Center, Schenectady, New York

ABSTRACT

An estimate of the ductility of a passive film can be made by straining the metal covered by the film and observing the current required to keep the film at its normal thickness. For the metals tested, the relative ductilities of passive films as measured by this technique decrease in the order tantalum; 16 Cr, 14 Ni, bal. Fe; type 304 stainless steel; iron; aluminum; 60 Ni, 16 Cr, bal. Fe; zirconium; and 80 Ni, 20 Cr.

In a previous publication (1) we reported that anodic oxide films on tantalum were surprisingly ductile, while those on zirconium and aluminum were much more brittle. In this paper we describe experiments which show that the thin passive films formed on many metals also have appreciable ductility.

Experimental

The electrical circuit used is basically the same as that described previously (1) with a few changes. A small constant speed electric motor provided a strain rate of 28.7%/min; an Anotrol model 4100 potentiostat maintained specimen potential, and a Varian G-14A-1 recorder measured the voltage drop in a precision resistor, produced by the anodizing current. A saturated calomel electrode, connected to the cell by a salt bridge (to prevent chloride contamination) and to the potentiostat, was used as a reference electrode. All experiments were conducted at room temperature.

Consider the following. If a specimen is held at a constant anodic potential, a rapidly decreasing anodizing current is observed. This current quickly becomes negligible when the passive film thickness reaches a value characteristic of the potential. If the specimen is strained the passive film must either elongate and thin, or crack. If during straining the potential at which the film was grown is maintained, an anodizing current would be observed as either the thinning film grows to maintain thickness, or the cracked film repairs itself. It may be shown that both cases yield approximately the same current. Consider now the case of a specimen on which the passive film was grown at a higher potential than that maintained during elongation. The film thickness is greater than that which would be produced at the elongation potential. If the film is brittle, it cracks on elongation and generates an anodizing current of the same magnitude as for the specimen strained at the anodizing potential. If the film is ductile, however, it will thin and elongate, and no anodizing current will flow until the film thickness is decreased to a value characteristic of the potential being maintained during elongation.

If curves are obtained for specimens anodized at the elongation potential and at a higher potential, the difference between these curves is a measure of the ductility of the film.

All specimens were prestrained slightly to eliminate slack in the system and to insure axial stressing of the specimen and film. There is a finite time required at start-up for the motor to reach its normal operating speed, corresponding to a strain of approximately 0.5%, and therefore we do not regard these experiments as providing good evidence for any elastic deformation of the passive films. We assume the deformations noted to be plastic.

The aluminum wire used was drawn from ingots of 99.9999% purity. The zirconium was swaged and drawn from zone refined single crystals. Tantalum wire of 99.96% purity was obtained from National Research Corporation, and tantalum wire was swaged and drawn from zone refined single crystals. Some of this latter material was recrystallized at 1050°C in order to obtain greater wire elongation. The surface preparation of these materials involved chemical or electrochemical polishing (1).

Type 304 stainless steel was obtained from Techalloy Company, Inc., and Nichrome (approximately 60Ni, 16Cr, balance Fe) from Driver-Harris Company. A 16Cr, 14Ni, balance Fe, and an 80Ni, 20Cr alloy were arc melted and drawn in this laboratory. Zone refined iron was further purified to reduce oxygen content to <5 ppm and carbon content to <5 ppb (2). These materials were all electropolished in a mixture of acetic and perchloric acids and water following procedures given by Tegart (3). The unstable character of certain acetic-perchloric solutions and the hazards involved in their use are described by Tegart (3) and Bartlett and Turner (4). After electropolishing, the specimens were dipped several seconds in concentrated (48%) HF in order to remove the electropolishing residues. The HF treatment did not give results significantly different from specimens tested either without such treatment, or, when possible, from specimens held at cathodic potentials to reduce films initially present.

Results and Discussion

Current-elongation curves are shown in Fig. 1 through 9. When a specimen fractured there was either a large increase of current if fracture occurred within the cell or a rapid current decrease if the break occurred outside; such current excursions have not been included in the figures. The film thicknesses given in parentheses in the figures were calculated from the difference between the potential at which the film was formed and the standard potential for the reaction between metal and water to form metal oxide, using for Ta_2O_5-17 Å/v, for ZrO_2-20, for Al_2O_3-14, for chromium containing alloys-16 (assuming the film was Cr_2O_3), and for iron oxide-17, using data given by

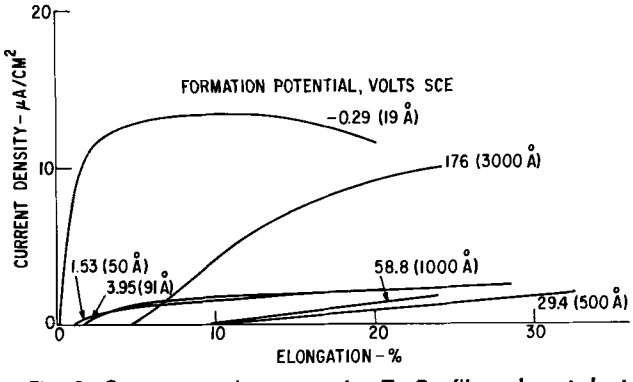

Fig. 1. Current-extension curves for Ta_2O_5 films elongated at —0.29v SCE in 1% ammonium borate.

Nagayama and Cohen (5). The approximate character of these thickness values should be obvious.

Some discussion of errors and difficulties of interpretation is in order. First, a capacitive current flow accompanies stretching because the exposed area decreases as the wire diameter decreases. Calculations and simple experiments have shown this current to be less than 10^{-8} amp/cm^2, and hence negligible compared to the observed currents. Second, the observed current at any time is the sum of currents from all increments of area on which the film is thin enough to produce current flow. Suppose the film cracks, exposing bare metal. The current on that area is initially high and decreases rapidly with time (about as t^{-1}), but is never zero and always contributes to the total current. Quantitative interpretation of current elongation curves is therefore very difficult. Third, nonuniform deformation of the metal, for instance at local slip bands or near inclusions, may cause early deformation or fracture of portions of the film and hence abnormally large currents. Inhomogeneities in the film itself, for instance at inclusions, may also cause local fracture. For these reasons these tests underestimate the true ductility of the reaction films. Finally, if a crack having a width less than the film thickness occurs and if oxygen ions move the current flow will be larger than expected for just the crack area since a hemicylinder of new film will be formed under the crack. This latter error, while probably negligible for most cracks, is also in a direction to result in an underestimation of the film ductility.

A further difficulty becomes evident from a comparison of the results shown in Fig. 1, for Ta_2O_5, with the results reported previously using the technique of measuring tunnel currents through very thin films formed in the cracks of a thicker insulating film. The previous work (1), which also underestimated the film ductility for reasons similar to those given above, indicated that there was essentially no cracking (limit of detection $\sim 10^{-3}$%) of Ta_2O_5 films less than 100Å thick upon 10% elongation. If 10^{-2}% bare surface was exposed the film reformation current would be about 10^{-9} amp/cm^2, while Fig. 1 shows that 50 and 100Å Ta_2O_5 films gave currents of the order of 10^{-6} amp/cm^2 on straining a few per cent. Since the previous method is better suited to the detection of small bare areas in insulating films, it is apparent that the current measured in the present method may be much larger than that corresponding to the bare area produced. This very serious complication severely hampers interpretation. The large currents may arise because of ion drift in the film during straining. The electric field applied during straining is smaller than the forming field of about 10^6 to 10^7 v/cm but is still large. If deformation of the film occurs, as with Ta_2O_5, so that ions are being moved parallel to the surface by mechanical forces, the electric field may be expected to cause some drift perpendicular to the surface. This phenomena is related to the reports by Bradhurst and Leach (6) and by Leach and Neufeld (7) that film deformation can be enhanced by ionic current flow.

It seems that the interpretation of the data reported here must be confined to qualitative statements of the following kind. First, the observation of smaller currents for a film strained at a potential less positive than its forming potential is evidence for film deformation rather than film fracture. Second, the method may very seriously underestimate the true film ductility. Third, it is not likely that the combination of mechanical deformation and a smaller electric field would yield a current as great as that produced by the full forming field, and hence the coincidence of current-elongation curves for thick and thin films is evidence for film fracture.

With the above considerations in mind, we now discuss the data. It is evident from Fig. 1 that the main features of ductility of Ta_2O_5 films reported previously are confirmed by the present technique. Thus

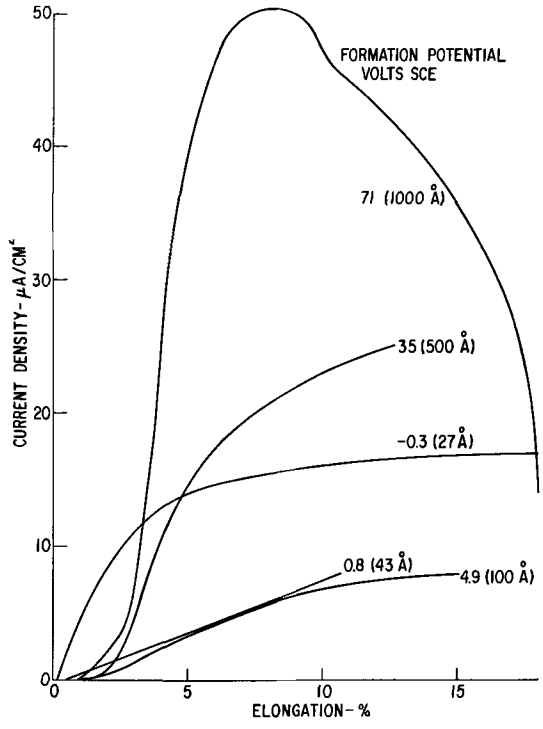

Fig. 2. Current-extension curves for Al_2O_3 films elongated at —0.3v SCE in 1% ammonium borate.

films less than 1000Å thick are very ductile, while thicker films are more brittle. We did not notice any effect of metal purity in these tests while the earlier method indicated that flaws present in films on less pure material nucleated fracture. Apparently the previously mentioned ion drift in the present method masks any effect of flaws. Films formed and tested in ammonium borate, sodium sulfate, and sodium phosphate solutions all gave very similar results.

Figure 2 shows that thin Al_2O_3 films have some ductility, while thicker films appear to be entirely brittle. Poor adhesion probably accounts for the very large currents observed for the thicker aluminum oxide films. Edeleanu and Law (8) reported evidence that the thin natural corrosion film was brittle. They reported cracking only on some grains, and lack of reproducibility. Their results are not inconsistent with our finding of limited ductility. No significant differences were observed in mechanical properties between films formed in ammonium borate and in sodium sulfate.

For ZrO_2, Fig. 3, the curves indicate that all films crack immediately on straining. Thicker films continue

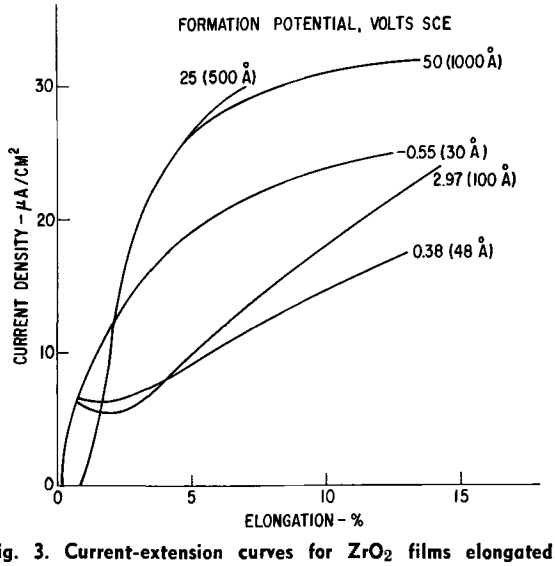

Fig. 3. Current-extension curves for ZrO_2 films elongated at —0.55v SCE in M Na_2SO_4.

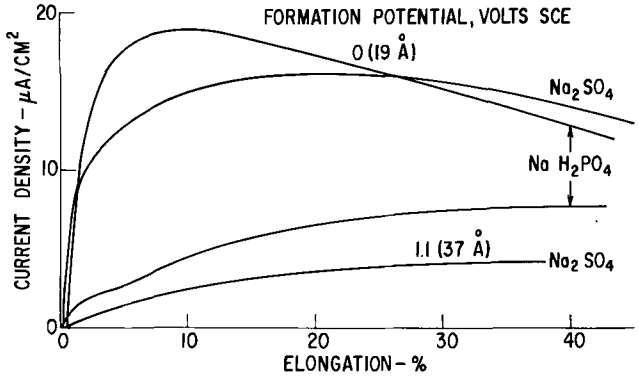

Fig. 4. Current-extension curves for type 304 stainless steel elongated at 0v SCE in M Na_2SO_4 and in M NaH_2PO_4.

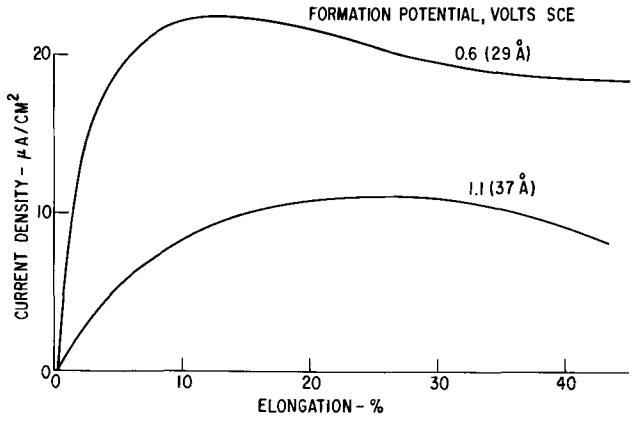

Fig. 5. Current-extension curves for type 304 stainless steel elongated at 0.6v SCE in M Na_2SO_4.

to crack, probably with loss of adhesion. The thinner films are evidently capable of some limited deformation as shown by the results at higher strains. The initial cracking may be associated with high local deformation of the metal.

Figures 4 and 5 give data for type 304 stainless steel. Results in phosphate and sulfate solutions both indicate appreciable ductility, although the current-elongation curves are somewhat different. Figure 5 shows that the current at a given elongation is greater when the difference between forming potential and straining potential is less, as might be expected from the ion drift hypothesis. We attempted to determine whether chloride ions would influence the results by anodizing in sodium sulfate solutions and testing in a solution containing M Na_2SO_4 and M NaCl. The results were essentially the same as with Na_2SO_4 alone. However, Swann and Embury (9) have given evidence for rupture of films formed on 18Cr, 8Ni stainless steel in

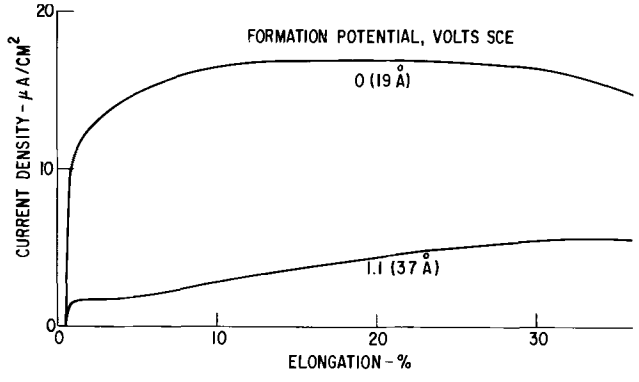

Fig. 6. Current-extension curves for 16 Cr, 14 Ni balance iron alloy elongated at 0v SCE in M Na_2SO_4.

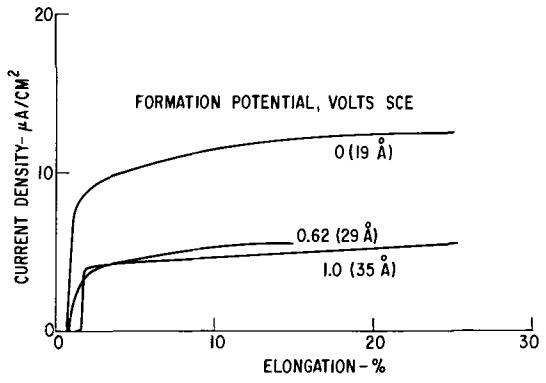

Fig. 7. Current-extension curves for commercial nichrome elongated at 0v SCE in M Na_2SO_4.

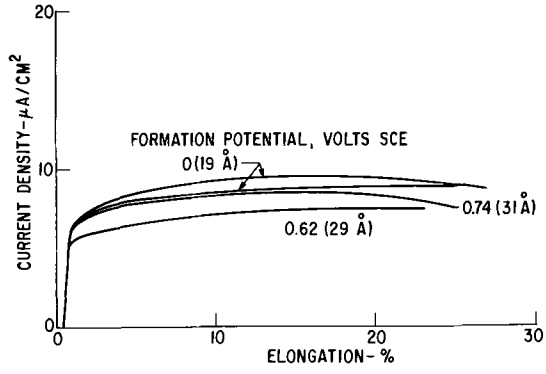

Fig. 8. Current-extension curves for 80 Ni, 20 Cr alloy elongated at 0v SCE in M Na_2SO_4.

boiling 42% $MgCl_2$. A comparison is difficult because of the very different techniques.

The laboratory produced 16Cr, 14Ni, balance iron alloy gave results similar to those for type 304 stainless steel, as shown in Fig. 6. The intent was to compare the film on a "dirty" commercial alloy (304) with the film on a high-purity alloy of similar composition and structure. This objective was frustrated by the finding that the laboratory alloy was not entirely homogeneous. Presumably it contains fewer interstitials, and the inhomogeneities arose from incomplete mixing during melting. In any case the results for the two materials are very similar.

The commercial nichrome alloy, Fig. 7, could not be anodized above about 0.5v SCE without the passage of large currents. The curve for 1.0v in Fig. 7 is almost identical to that obtained with an anodizing potential of 0.6v, and it is likely that the film thicknesses produced by the two potentials are no different. Appreciable ductility is indicated for this film.

Figure 8 gives data for the laboratory prepared 80Ni, 20Cr alloy. Anodizing voltages were limited for this

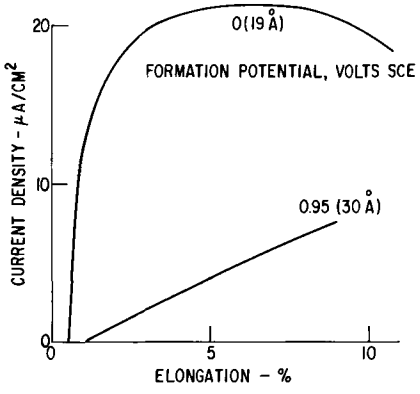

Fig. 9. Current-extension curves for iron elongated at 0v SCE in 1% ammonium borate.

Table I

Metal	%C Wire elongation 5%	%C Wire elongation 10%
Ta (50Å)	91.5	89
16Cr, 14Ni, bal. Fe	87	84
304 Stainless	86	77
Fe	81	56
Al (average of 3)	75	50
60Ni, 16Cr, bal. Fe	56	54
Zr	52	38
80Ni, 20Cr	16	18

alloy also. The films appear to be substantially less ductile than those on the Cr, Ni, Fe alloys. This alloy also proved to be inhomogeneous.

For pure iron, Fig. 9, the data again suggest appreciable ductility for the oxide film.

In order to make a semiquantitative comparison of materials we have listed in Table I the value of %C, which is defined by the equation

$$\%C = \frac{i_e - i}{i_e} \times 100 \qquad [1]$$

in which i_e and i are the currents (at the same elongation) for specimens anodized at the straining potential and at a higher potential, respectively. The value of %C gives a rough measure of the fraction of the newly generated specimen area which is covered by the original oxide film; for a completely ductile film %C should be 100, while for a brittle film it should be 0.

Conclusions

The ductility of some of these passive films may be as great as that of Ta_2O_5, which evidently can be stretched as much as 50%. Because of the difficulties of interpretation it is perhaps premature to speculate about the mechanisms of deformation and implications. Perhaps the easy deformation results from ion motion under the applied electric field, as suggested by Bradhurst and Leach (6) and by Leach and Neufeld (7). The presence of water, which is known to enhance deformation of some nonmetallic materials (10, 11), may also be important. Finally, the difference in ease of deformation of bulk oxides and passive films may be associated with differences in the structures of these two types of materials. One implication of the results may be that the explanation for the better resistance of high nickel alloys to stress corrosion cracking does not lie in the reaction film ductility.

Acknowledgment

The authors are greatly indebted to Dr. D. F. Stein of this laboratory for assistance and advice concerning the purification of the iron wire.

Manuscript received March 7, 1967.

Any discussion of this paper will appear in a Discussion Section to be published in the June 1968 JOURNAL.

REFERENCES

1. S. F. Bubar and D. A. Vermilyea, *This Journal*, **113**, 892 (1966).
2. D. F. Stein, J. R. Low, and A. U. Seybolt, *Acta. Met.*, **11**, 1253 (1963).
3. W. J. M. Tegart, "Electrolytic and Chemical Polishing of Metals," Pergamon Press, London (1956).
4. R. K. Bartlett and H. S. Turner, *Chem. and Ind. 1933*, (1965).
5. M. Nagayama and M. Cohen, *This Journal*, **109**, 781 (1962).
6. D. H. Bradhurst and J. S. Ll. Leach, *ibid.*, **113**, 1245 (1966).
7. J. S. Ll. Leach and P. Neufeld, *Proc. Brit. Ceramic Soc.*, No. 6, 49 (1966).
8. C. Edeleanu and T. J. Law, *Phil. Mag.*, **7**, 573 (1962).
9. P. R. Swann and J. D. Embury, "High Strength Materials," p. 327, John Wiley & Sons, New York (1965).
10. J. H. Westbrook and P. J. Jorgensen, *Trans. AIME*, **233**, 425 (1965).
11. D. T. Griggs and J. D. Blacic, *Science*, **147**, 292 (1965).

Anodic Dissolution of Zinc in Potassium Nitrate

M. E. Straumanis, J. L. Reed, and W. J. James

Departments of Metallurgical Engineering, Chemical Engineering, and Chemistry, University of Missouri at Rolla, Missouri

ABSTRACT

The apparent valence of pure zinc dissolving anodically in 3% KNO_3 was determined as a function of current density, temperature, and ultrasonic agitation. The apparent valence of zinc dissolving anodically at 24°C diminishes from 2.01 ± 0.01 at low current densities to 1.86 at about 50 ma and remains fairly constant up to about 80 ma cm^{-2}. This valence is affected to some extent by the preparation, *e.g.*, polishing of the electrode, but is independent of its structure (mono- or polycrystal). Ultrasonic vibrations do not influence the apparent valence at high current densities. In all cases a black film (corrosion product) spalls off the anode but to a larger extent with ultrasonics. The apparent valence decreases with increasing temperature (measurements between 25° and 68°C) and again with increasing current density, and appears to vary as a function of metal history. Fine metallic Zn particles are found in the dark corrosion product. The average size of the particles increases with increasing temperature. On the basis of the above, it is concluded that the normal valency of zinc ions, +2, does not change during anodic dissolution in nitrate solutions, but the apparent valence of less than 2 arises as a consequence of increased local corrosion and of surface disintegration of the anode. Both occur outside the electrical circuit thus accounting for the lower coulombic equivalent. A mechanism for the disintegration phenomenon is presented.

When either Zn or Cd (having a normal valence of +2) is dissolved anodically in aqueous neutral salt solutions, containing nitrate, chlorate, or bromate ions, the number of coulombs required to dissolve one gram equivalent of metal is less than the faradaic weight equivalent, especially at high current densities. Other active metals, such as Be, Mg, Al, In, Ga, Tl, Fe, Sn, and Pb also exhibit this phenomenon.

One mechanism which has received wide acceptance is the concept of the "uncommon valence ion" as pro-

posed by Epelboin (1) for zinc undergoing anodic dissolution in perchlorate solution. Later work on Zn, Cd and other metals by Davidson and co-workers (2-6) has supported this mechanism, the results having been attributed to the expulsion of univalent ions.

The purpose of this study was to obtain experimental data for the anodic dissolution of zinc in 3% aqueous KNO_3 as a function of: (*i*) current density, (*ii*) temperature, and (*iii*) ultrasonic vibrations, and to establish a mechanism consistent with the results.

Experimental

Effect of Current Density

Apparatus.—The apparatus consisted of a 400 ml cell, a zinc electrode made of either a polycrystalline bar (99.99% purity) or of a single crystal (exposed surface nearly parallel to the basal plane, 99.95% purity), an external d-c source, a sensitive milliammeter, a decade type resistance box, a knife switch, and a platinum cathode, all connected in series. A microburet of 10 ml capacity with 0.02 ml graduations was used to titrate the zinc content of the electrolyte following electrolysis.

Procedure.—The zinc electrodes were polished shortly before each run. Two hundred ml of a 3% KNO_3 solution were transferred to the thermostatted cell (24.0° ± 0.5°C). Air was not excluded because experiments in a N_2 atmosphere gave the same results within the limits of error. The Zn anode and the Pt cathode were then inserted and connected in series with the external circuit and the circuit closed. A timer and milliammeter were used to measure the number of coulombs passed (checked by a copper coulometer). After a sufficient time interval the circuit was broken and the electrodes removed from the beaker. Any loosely adhering film on the anode was removed by scrubbing with a rubber policeman in the electrolyte. Two drops of 6M HCl added dissolved the sediment. The clear solution was then diluted to 500 ml with distilled water. Aliquots of 100 ml volume were withdrawn from this solution, heated to about 90°C, buffered to pH of 10, and titrated with disodium EDTA standardized against 99.99% pure Zn, using Erichrome Black T as indicator. Thus, the weight loss w of the Zn electrode was calculated.

Results

Influence of current density.—The valence V was determined from Eq. [1]

$$V = ItA/\mathbf{F}w \qquad [1]$$

where It is the quantity of electricity in coulombs, A the atomic mass of Zn, $\mathbf{F}$ is Faraday's constant, and w the weight loss of the anode (calculated from titration data). The measurements were performed over a current density range of 0.5 to 85 ma·cm^{-2} with a possible error range of ±1%. Since the behavior of a polycrystalline and of the single crystal anode (0001 plane exposed) was the same (see Table I), the resulting

Table I. Calculated valence of Zn ions going into solution at 24.0° ± 0.1°C from M-monocrystalline or P-polycrystalline Zn anodes

Time, sec	Current density, ma·cm^{-2}	Zn anode	Valence calculated
63,000	0.38	M	2.00
25,900	0.52	P	2.01
32,800	0.75	M	2.03
86,400	0.57	P	1.99
2,500	19.85	M	2.00
2,500	22.41	P	2.00
2,500	33.30	M	1.95
2,500	34.10	P	1.94
2,500	55.10	M	1.85
2,000	57.0	P	1.84
2,500	79.4	M	1.86
2,000	74.1	P	1.85

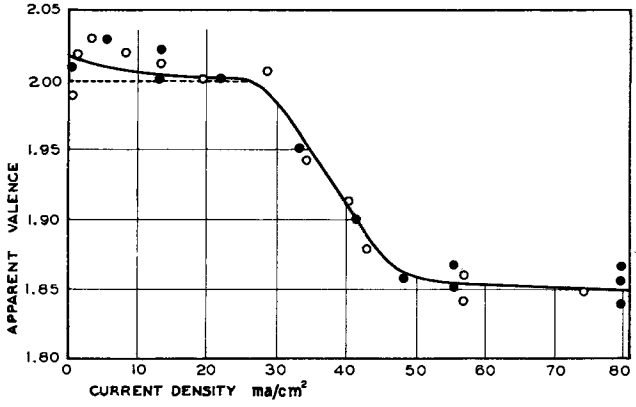

Fig. 1. Calculated valence as a function of current density for Zn dissolving anodically in 3% KNO_3. Dots, monocrystal; circles, polycrystal.

data were combined and are presented graphically in Fig. 1.

At low current densities (< 30 ma·cm^{-2}) a very thin, usually spotty, black film was observed on the face of the anode. On removal from the electrolyte the film turned grayish white after about 5 min exposure. Tests at higher current densities (> 30 ma·cm^{-2}) resulted in a thicker and continuous black film. Also a white precipitate was observed directly below the vertical electrode. An x-ray analysis of the deposit revealed it to be ZnO.

Since there was no difference between a mono- and polycrystalline anode, no attempt was made to use various crystalline planes for dissolution. Table I and Fig. 1 show that the calculated valence of Zn-ions approaches, with increasing current density, a fairly constant value of 1.86 ± 0.01, which is in agreement with the results of previous investigators (2). However, the constant value of about 2 at small current densities (up to 30 ma·cm^{-2}) is not always observed. Depending on experimental conditions, the drop can start at a much lower current (7). The calculated valence drops lower, even down to 1.65 if the consecutive tests are performed without repolishing the electrode, merely transferring it (after rinsing with distilled water) to a fresh solution to start another run.

A black film was always observed forming on the Zn anode. At low current densities the film was thin and its thickness increased with the current. On removal of the anode from the solution, the black film turned grayish white in a few minutes, as observed for Mg (8). X-ray analysis showed the grayish film to consist of ZnO and/or $Zn(OH)_2$. If the Zn anode was etched slightly with dilute H_2SO_4 before the run, the black film formed at electrolysis spalled from the anode upon application of ultrasonic agitation. A sample of the gray black sediment was collected, quickly rinsed by decantation with water, and then washed with dry acetone. Even then part of the sample turned white after filtering. The darkest flakes were examined under the microscope, using oil immersion objectives, at magnifications of 1430. In the reflected light parts of the sample revealed a multitude of shiny metallic particles embedded in the corrosion product ZnO or $Zn(OH)_2$. The diameter of the smallest particles was of the order of 10^{-5} mm. Larger chunks, as found during electrolysis of Zn in $NaBrO_3$ solutions (9), were also observed floating around in the oil. All the metallic particles were completely opaque to transmitted light. They consisted of Zn, as proved by x-ray diffraction.

It is, therefore, clear that the deviation from Faraday's law or the calculated lower valence of Zn ions (Fig. 1, Table I) is, in part, the result of surface disintegration of the Zn anode during dissolution which occurs outside the faradaic current and, hence, contributes to the calculation of ions of lower valence.

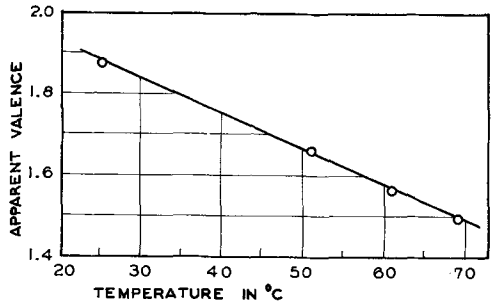

Fig. 2. Apparent valence as a function of temperature for Zn dissolving anodically in 3% KNO_3 solution. 50 to 80 ma.cm^{-2} (see Fig. 1.).

Thus, this valence is only apparent, particularly as the existence of Zn^+ has not been confirmed analytically (2). Furthermore, no lower valence was calculated when the disintegration of the anode was prevented, *e.g.*, by amalgamation (10). Amalgams as anodes produce only normal valence ions, as found for Al(11), Ga(12), In(13), Tl(14), and Sn(15). Unfortunately it is difficult to collect the particles and quantitatively determine the amount of Zn particles present due to the high activity of the fine particles. However, the presence of metallic particles in large amounts, and the absence of Zn^+, together with the absence of disintegration (in case of an amalgamated anode) and the calculated normal charge of the Zn-ions are sufficient evidence for anodic surface disintegration.

Effect of temperature on apparent valence.—The apparatus and procedure were similar to previous studies. The cell was open to the atmosphere and any evaporation which occurred during electrolysis was corrected by addition of water at the same temperature to the electrolyte. The apparent valence as a function of temperature is shown in Fig. 2.

Some current density experiments were also performed at a temperature of 87°C. At this temperature the apparent valence dropped to 1.13 and to 1.10 for a poly- and monocrystal at current densities of 57 and 79 ma·cm^{-2}, respectively. Under such conditions the apparent valence seemed to be a function of time, current density, and perhaps of crystal structure. A large amount of gray corrosion product was observed on the bottom of the reaction beaker. On treatment with HCl, the material evolved hydrogen, indicating that chunks of Zn were still present in the hydroxide, while the fine metallic particles had rapidly reacted with H_2O (hydrolysis) at the elevated temperature. The larger chunks were also detected microscopically. The electrolyte contained nitrite ions, the amount of which was proportional to the decrease in apparent valence.

The activation energy.—It was speculated that this temperature dependence could be related to the activation energy by assuming that the over-all rate constant k was proportional to the normal valence less the apparent valence. Accordingly, an Arrhenius plot of log(2 minus apparent valence) *vs.* reciprocal temperature was made as illustrated in Fig. 3. An activation energy of ~4.2 kcal was found from the slope of the straight line.

Application of ultrasonic vibrations.—The beaker used in the previous experiments was replaced by an ultrasonic cell of equivalent diameter and connected to an ultrasonic generator. Vibrations of a frequency of 32,500 cycles sec^{-1} and of maximum possible amplitude were passed through the reaction cell during the electrolysis. The results were both of quantitative as well as of qualitative nature. The average value for the apparent valence of a poly- and monocrystalline anode at current densities between 50 and 80 ma·cm^{-2} was about 1.84 ± 0.01, while without ultrasonics a valence of 1.86 ± 0.01 was obtained. Thus, the

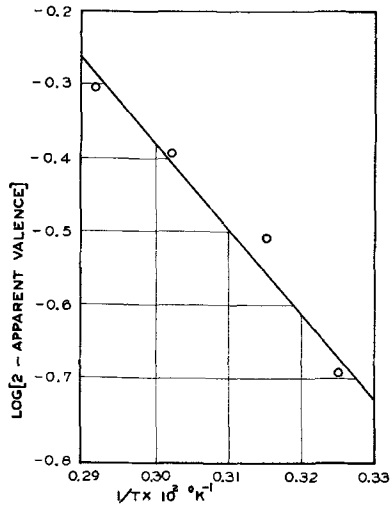

Fig. 3. The variation of log (2 minus apparent valence) with reciprocal absolute temperature.

difference was very small and within the limits of error. With ultrasonic stirring the solution turned gray black in a few minutes and the electrodes became barely visible. When the circuit was opened and ultrasonic stirring stopped, the dark flakes settled to the bottom. As previously mentioned, the sediment contained metallic Zn in the form of very fine particles or larger chunks. A few drops of concentrated HCl were added to the electrolyte to determine quantitatively the Zn which spalled from the anode. The sediment dissolved easily. Etched Zn electrodes gave the same apparent valence as nonetched ones. The gelatinous $Zn(OH)_2$ film generally formed during electrolysis was not present to any appreciable degree.

Discussion and Conclusions

At current densities of 50 to 80 ma·cm^{-2}, the apparent valence of zinc was found to be 1.86 ± 0.01. This value is in agreement with the results of previous works cited (2, 10). However, when the current density dropped below 50 ma·cm^{-2} the valence started increasing, and below 30 ma·cm^{-2} values close to the normal oxidation state of two were obtained.

These results are more in accord with the concept of anodic disintegration rather than with that of formation of lower valence ions, since the rate of mass loss due to breakout of particles from the anode must be a function of the instantaneous current density (16). On this basis one would expect a decrease in the apparent valence with increasing current density possibly to some limiting value (Fig. 1). This expectation was clearly verified for Mg and Cd anodes (17). It is noteworthy that at low current densities, <10 ma·cm^{-2}, the metal surface was in most cases completely free of the black surface film, suggesting that no disintegration of the anodic surface occurred.

Furthermore, it is difficult, on the basis of lower valence ion formation, to explain the appearance of the very small and larger metallic particles, usually embedded in the surface oxide layer, which impart the dark color to the latter. According to the older theory Zn particles should appear as a consequence of a reduction-oxidation reaction

$$2Zn^+ \rightarrow Zn^{++} + Zn \qquad [2]$$

However, the improbability of such reactions, especially as regards very active metals, has been discussed previously (8, 11, 18).

All these results can be satisfactorily explained by assuming that the only faradaic process is

$$Zn \rightarrow Zn^{++} + 2e \qquad [2a]$$

In addition to [2a] there is surface disintegration, oxidation (reactions [3] and [4]) and self dissolution,

thus resulting in more Zn dissolved than expected according to [2a].

The exact mechanism of surface disintegration is presently not known in detail, but the observations made with Zn anodes suggest a mechanism as follows: The Zn anode adsorbs onto its surface NO_3^-, similarly as is proposed for BrO_3^- (9)

$$Zn + NO_3^- \rightarrow ZnO + NO_2^- \quad [3]$$

This action increases with increasing nitrate concentration resulting in a decreased apparent valence (7). Simultaneously, hydrolysis may also occur

$$ZnO \text{ (on the Zn surface)} + H_2O \rightarrow Zn(OH)_2 \quad [4]$$

These generally thin oxide layers will vary in adherence and thickness, depending on the surface structure of the Zn anode. There will be places where the oxide layer adheres very well and where it will be thicker, causing partial passivation of the anode. On application of an anodic current the weakest spots will be attacked first and there the Zn^{++} will go into solution, partially undermining the passive spots, but no noticeable separation of these weakened metallic places from the anode will occur. With an increase of the current density, the flow of the electrons from the anode will be increased. Since the positive ions in the solid will be in excess, ions (Zn^{++}) will be driven into solution by a repulsion force corresponding to the Nernst solution tension P. It is, possibly, not always realized how large this force is. It can be calculated from Nernst's original equation

$$P = p \cdot \exp(-\epsilon n\mathbf{F}/RT) \quad [5]$$

where p is the osmotic pressure of the Zn^{++} in the electrolyte, ϵ the potential of Zn (=—0.76v, hydrogen scale), n the valence of Zn-ions, **F** Faraday's constant, R the gas constant, and T the absolute temperature. For a standard Zn electrode a value of P of about 10^{26} atm is obtained which represents the free energy expressed in pressure units. If only a part of this pressure (due to the limited current) is in action, even then the pressure which drives the ions into solution is enormous. Therefore, the moving ions may hit the oxide layer on the electrode surface with such force that this layer breaks away from the surface. However, if the layer adheres well to the metal, it can carry small particles of the electrode metal with it (19). And this is what is observed: metallic particles in an oxide network. The oxide may react further with H_2O, Eq. [4], and then the particles will appear embedded in a white oxide or hydroxide layer (11). The particles break away at places where their contact with the bulk of the electrode is somehow weakened, e.g., by undermining. The clean metallic surface is now able to react again with the electrolyte or with the NO_3^- according to Eq. [3] and after some time the process of disintegration can start again at the same site. However, at high current densities there will be less time for the oxidation reaction [3]. Hence, the degree of disintegration and the apparent valence will approach a constant value with increasing current (Fig. 1). Under such conditions the apparent valence may even increase because there will be less opportunity for the ions, going into solution, to take with them parts of the oxide layer containing fragments of the anodic metal (14).

Thus, the degree of disintegration and, hence, the apparent valence will depend on the quality of the oxide layer on the Zn anode, the formation of which depends on the nature of the electrolyte: there may be electrolytes producing porous or weakly adhering layers, or both, and as a result the apparent valence will be close to normal.

This concept explains why the apparent valence is the same for both poly- and monocrystalline anodic surfaces. Evidently oxide layers of the same quality are produced on Zn of various surface structures (in the same solutions). The grain boundaries are of little influence since disintegration occurs within these borders (the grains themselves are not falling out). However, if the anode surface is not repolished between the runs, the surface becomes rough and there will be an increased possibility for breakout of larger metallic particles together with the oxide layer: a lower apparent valence is observed (down to 1.65). Forces introduced by ultrasonic vibration are small as compared with those represented by Eq. [5]. Therefore, these vibrations will not markedly influence the degree of disintegration and the apparent valence. However, ultrasonic agitation is sufficient to disperse the oxide flakes loosely adhering to the Zn electrode, especially the white gelatinous hydroxide which is formed on the Zn particles (Eq. [4]). All this is consistent with the experimental results, and the white hydroxide is not found on the Zn anode if ultrasonic waves are applied.

It is more difficult to understand the influence of temperature on the degree of disintegration. Although the temperature coefficient of potential change $\partial\epsilon/\partial T$ for Zn is known (20), there are still some difficulties in the application of the original Nernst equation, as the osmotic pressure p (Eq. [5]) changes (increases) with temperature. However, considering the derivation of the equation, the solution pressure P will increase with temperature and, hence, the degree of disintegration. The apparent valence will decrease (Fig. 2). The increased P may not be the only reason for the increased disintegration rate, because compressional stresses between the anodic film and the bulk of the anode may increase with temperature and force the film to crumple or dilate. In addition hydrogen developed due to the very slow reaction

$$Zn + 2H_2O \rightarrow Zn(OH)_2 + 2H \quad [6]$$

may increase the spalling of the oxide layer containing larger metallic particles. The activation energy of about 4.2 kcal (Fig. 3) suggests other possible rate determining steps such as adsorption or some other physical process.

The Zn particles which spall from the electrode are very small and completely clean toward the side of the anode. They, therefore, will be vary active and react with water according to [6] and still faster with an oxidizer, if such is present in the electrolyte. In nitrate solution reaction [3] occurs. Indeed, NO_2^- ions can be proved to be in solution and their amount is proportional to the amount of departure from the apparent valency (2-6). If disintegration of the Zn anode is prevented, NO_2^- ions are not present in the electrolyte (10, 17).

In conclusion, the assumption of formation of lower valence ions, the presence of which cannot be proved, is not necessary and does not account for the experimental data. It is very improbable that the number of lower valence Zn ions formed will depend on current density, the nature of the electrolyte, the temperature, and the surface treatment of the anode. Surface disintegration of the dissolving anode can account for the observed facts, including the reducing ability of the anolyte.

Acknowledgment

The authors are grateful to the Office of Naval Research for the support of the metallic disintegration studies.

Manuscript received March 27, 1967. This paper will be presented at the Chicago Meeting, Oct. 15-19, 1967. It is Contribution No. 22 from the Graduate Center for Materials Resarch.

Any discussion of this paper will appear in a Discussion Section to be published in the June 1968 JOURNAL.

REFERENCES

1. I. Epelboin, *Z. Elektrochem.*, **59**, 689 (1955).
2. D. T. Sorensen, A. W. Davidson, and J. Kleinberg, *J. Inorg. Nucl. Chem.*, **13**, 64 (1960).

3. R. L. Petty, A. W. Davidson, and J. Kleinberg, *J. Amer. Chem. Soc.*, **76**, 363 (1954).
4. E. Raijola and A. W. Davidson, *ibid.*, **78**, 556 (1956).
5. B. D. Laughlin, J. Kleinberg, and A. W. Davidson, *ibid.*, **78**, 559 (1956).
6. A. W. Davidson and F. Jirik, *ibid.*, **72**, 1700 (1950).
7. Y. C. Sun, "Anodic Behavior of Zn in Aqueous Salt Solutions," Ph.D. Thesis, University of Missouri at Rolla (1966).
8. M. E. Straumanis and B. K. Bhatia, *This Journal*, **110**, 357 (1963).
9. M. E. Straumanis and Y. Wang, *Corrosion*, **22**, 132 (1966).
10. W. J. James and G. Stoner, *J. Amer. Chem. Soc.*, **85**, 1354 (1963).
11. M. E. Straumanis and K. Poush, *This Journal*, **112**, 1185 (1965).
12. M. E. Straumanis and K. Poush, *ibid.*, **111**, 795 (1964).
13. M. E. Straumanis and R. L. Martin, *Z. anorg. allgem. Chem.*, **334**, 321 (1965).
14. M. E. Straumanis and R. L. Martin, *Corrosion Sc.*, **5**, 765 (1965).
15. M. E. Straumanis and M. Dutta, *Inorg. Chem.*, **5**, 992 (1966).
16. G. A. Marsh and E. Schaschl. *This Journal*, **107**, 960 (1960).
17. W. J. James, M. E. Straumanis, and J. W. Johnson, *Corrosion*, **23**, 15, Fig. 6 and 8 (1967).
18. M. E. Straumanis and D. E. Mathis, *This Journal*, **109**, 434 (1962); *J. Less Common Met.*, **4**, 213 (1962).
19. M. E. Straumanis, *This Journal*, **105**, 284 (1958).
20. A. J. Bethune and N. A. S. Loud, "Standard Aqueous Electrode Potentials and Temperature Coefficients," Self edition, 1964.

Adherence and Porosity in Ion Plated Gold

C. F. Schroeder and J. E. McDonald

Sandia Corporation, Albuquerque, New Mexico

ABSTRACT

The accelerated ion deposition process is shown to provide gold films and coatings which are strongly adherent even when deposited on oxidized beryllium-copper substrates. The porosity of these coatings when deposited under conditions which provide high substrate surface temperature is undetectable at thicknesses of approximately 2μ and is the result of the formation of a gold-copper solid solution.

The ion plating process developed by Mattox (1) has been demonstrated to provide excellent adherence across a film-substrate boundary, and the observed adherence is apparently less dependent on meticulous precleaning treatment than in conventional deposition processes. Further, qualitative observation of the films deposited by the process has indicated that nonporous deposits could be obtained in thicknesses in the micron range and that the porosity resulting from substrate surface contamination can be eliminated or controlled. It is the purpose of this paper to discuss the adherence and porosity of ion plated gold films and to project a mechanism for the formation of the adherent, nonporous deposits formed.

Experimental Procedure

The apparatus used to deposit the ion plated gold is shown in Fig. 1 and is essentially that described by Mattox (1). Specimens were prepared in the configuration shown in Fig. 2a, in order that subsequent adherence tests could be performed.

The specimens used for adherence determination were firmly clamped to the substrate holder to maximize heat transfer and are indicated as the low-temperature group. In contrast, the specimens on which porosity and alloying observations were made were supported along approximately 0.8 cm^2 at the sample ends to minimize heat transfer to the substrate holder and are called the high-temperature group. Porosity data for the low-temperature group are also reported.

Sample Preparation

High-temperature group.—Specimens were 0.8 cm thick annealed beryllium copper alloy, not heat-treated. Surfaces were lightly abraded with steel wool and rinsed in acetone prior to plating.

All ion bombardment and ion plating was at 5 kv, 0.5 ma/cm^2. Specimens in the low-temperature group were ion plated for 2 min. Specimens in the high temperature were argon ion bombarded for 10 min and ion plated for times as shown in Table I.

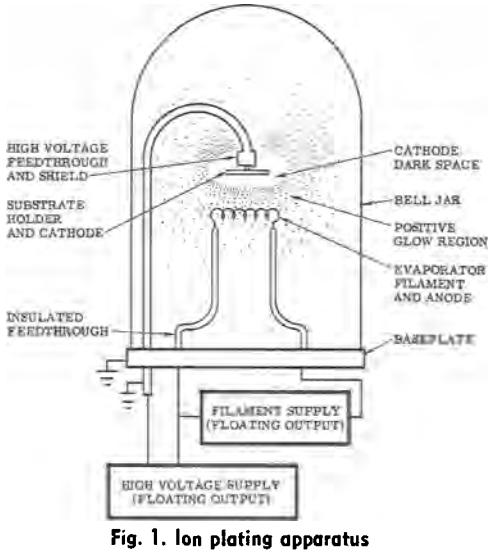

Fig. 1. Ion plating apparatus

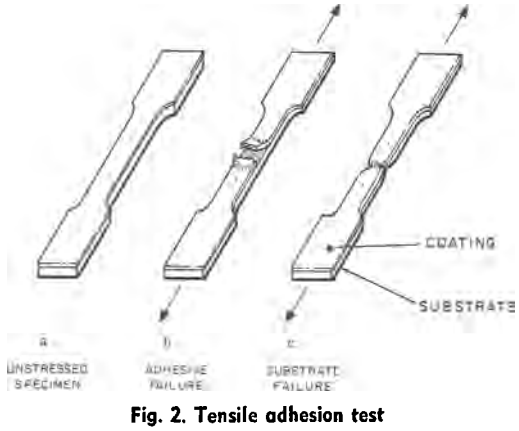

Fig. 2. Tensile adhesion test

Table I. Porosity—high temperature group

Sample	Deposition time, min	Film thickness, μ	Porosity pores cm^{-2}	Film composition, w/o Au
HT 1	1	1.8	0	94
HT 2	1.2	3.9	0	73
HT 3	1.2	3.8	0	69
HT 4	1.2	3.6	0	68
HT 5	1.2	3.7	0	74
HT 6	3	6.3	0	72
HT 7	3	7.2	0	73
HT 8	3	6.8	0	71
HT 9	3	—	<1	75
HT 10	3	5.9	0	73
HT 11	5	9.0	0	68
HT 12	5	9.7	0	71
HT 13	5	9.3	0	73
HT 14	5	8.7	0	73
HT 15	5	8.2	0	72

Low-Temperature group.—Specimens were 0.15 cm thick annealed beryllium-copper alloy (B-194) which were heat-treated to condition AT[1] by the following processes: Oxide-free substrates were produced by heat-treating at 300°C for 180 min in argon followed by acid cleaning in nitric, acetic phosphoric acid mixture (3*N*, 4*N*, 8*N*, respectively).

Approximately 0.2μ of oxide coating was produced by heating at 300°C for 175 min in argon and 5 min in air. Approximately 2μ of oxide coating was produced at 300°C for 180 min in air.

All heat-treated specimens were vapor degreased in trichloroethylene and rinsed in alcohol prior to plating.

Test Procedures

The relative adherence of the coatings was measured by means of a tensile test in which the film is deposited onto one side of a specimen (Fig. 2a). The measurement involves the observation of the strain required to produce adhesive failure between the film and substrate as in Fig. 2b. Since the maximum elongation which can be observed is associated with the rupture of the substrate, and the ductility of the beryllium-copper increases as a result of increased thermal input from the discharge, the strain to adhesive failure reported is normalized to cohesive substrate failure. Substrate failure without film failure occurs as in Fig. 2c.

Coincidentally, the effects of bombardment on the condition of the beryllium-copper substrate were also observed. These are reported as Knoop hardness of the beryllium-copper as a function of bombardment time. The values obtained are shown in Fig. 3 and are the average of five indention hardness measurements taken on transverse sections of the coated specimens.

From these hardness data, an estimate of the bulk substrate temperature obtained during plating can be made. The extent of overaging shown, *i.e.*, δ phase precipitate growth, indicates a temperature of approximately 150°-200°C (over the range of bombardment times indicated).

Film thicknesses were measured using beta backscatter techniques except where alloy coatings invalidated such measurements. In those cases, optical metallography supplemented the measurement.

For porosity estimates, films were exposed to moist hydrogen sulfide and the number of spots of copper sulfide visible in 1 cm^2 (under 75X magnification) was reported as a relative porosity measure.

[1] Solution treated, quenched, and precipitation hardened (2).

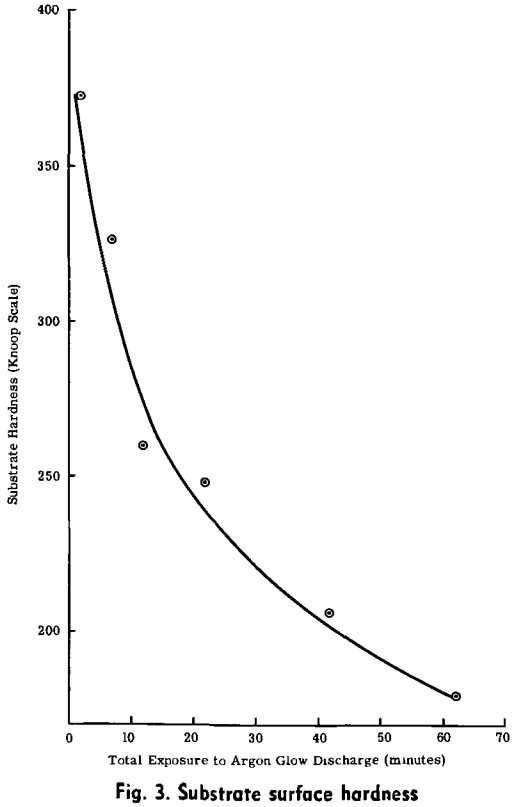

Fig. 3. Substrate surface hardness

Results

The results of the adherence investigations for ion plated samples are shown in Fig. 4 and presented as normalized strain *vs.* the energy dissipated in the glow discharge. It can be seen from Fig. 4 that only on the heavily oxidized surfaces is there any dependence of adherence on bombardment time or energy input within the ranges explored. One might expect a correlation to exist between the energy input required to produce the maximum measurable adherence and the amount of oxide present on the surface in terms of the dissociation and sputtering of copper oxide. It is true that the energy expended during a 20-min ion bombardment is the correct order of magnitude to sputter the quantity of oxide present; however, subsequent metallography on transverse sections indicates that the oxide is still present but broken up into islands in the interfacial region. The areas between these copper oxide islands are characterized by a sharp gold-copper interface.

In the low-temperature group (adhesion experiment), no alloying or diffusion was detectable across the gold copper interface even though the bulk temperature reached approximately 150°-200°C. Analysis of the gold films stripped from the substrate indicated substantially <1% Cu content. Porosity experiments were carried out on both the low- and high-temperature groups and are presented in Table I and II. The data for the ion plated samples in the low temperature group may be represented by the expression

$$PT^n = K \qquad [1]$$

where P is the pore count per unit area and T is the film thickness. The determined values of n and K are 1.3 and 1.2 x 10^{-3}, respectively, and agree well with

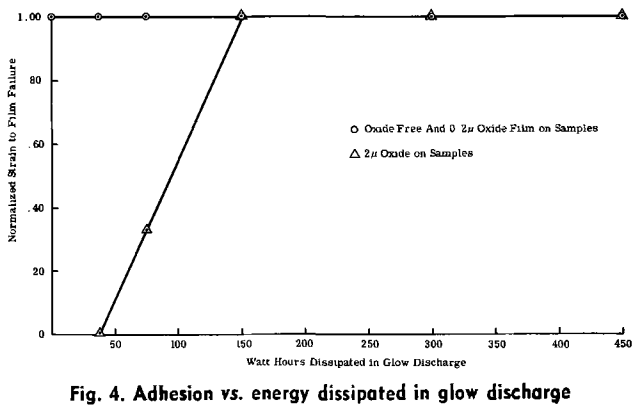

Fig. 4. Adhesion *vs.* energy dissipated in glow discharge

Table II. Porosity—low temperature group

Sample	Oxide thickness, μ	Coating method	Ion bombardment time, min	Film thickness, μ	Porosity pores/cm²
1A	0	Electroplate	—	2.1	10
B	0.2			1.6	97
C	2			1.9	241
2A	0	Vacuum evaporation	5	5.2	19
B	0.2			5.9	38
C	2			4.8	83
3A	0	Vacuum evaporation	20	1.9	15
B	0.2			2.0	26
C	2			1.8	58
4A	0	Ion plate	0	1.1	16
B	0.2			0.2	2713
C	2			0.4	849
5A	0	Ion plate	5	1.8	180
B	0.2			0.8	435
C	2			0.3	1653
6A	0	Ion plate	10	6.9	10
B	0.2			7.6	63
C	2			5.7	87
7A	0	Ion plate	20	5.1	19
B	0.2			1.7	12
C	2			6.7	17
8A	0	Ion plate	40	2.0	53
B	0.2			2.1	16
C	2			2.4	30
9A	0	Ion plate	60	1.6	8
B	0.2			1.7	30
C	2			1.6	14
10A	0	Vapor hone and ion plate	0	2.1	17
B	0.2			1.8	66
C	2			2.3	23

the earlier work of Frant (3) for electroplated gold deposition. It should be noted, however, that the electroplated and evaporated films show increased porosity with oxide film thickness, *i.e.*, while K is 6.3×10^{-4} for oxide-free specimens, K increases to 1.9×10^{-3} for 0.2μ oxide and 4.4×10^{-3} for 2μ oxide.

The striking absence of detectable porosity in the high-temperature group is attributed to the lack of a heat sink, and, therefore, temperature increases occur during ion bombardment which are significantly greater than reported for the low temperature group. Included also in Table II is the analysis of the stripped coating as obtained by x-ray absorption and gravimetric techniques. Such analysis are obviously averages over the bulk of the film and were supplemented by surface composition measurements using the electron microprobe. It is striking that these surface compositions are ~54 a/o (atomic per cent) gold. These results are consistent with the bulk analysis (~45 a/o, ~70 w/o gold) reported above and with the distribution of gold and copper in a typical specimen as shown in Fig. 5. This distribution curve was also obtained by the electron microprobe. In addition, x-ray diffraction analysis indicate that the films are a continuous series of solid solutions of gold-copper.

A set of independent experiments were conducted on these specimens (high-temperature group) to determine the effective bulk substrate temperature the beryllium-copper alloy had experienced. Beginning with the substrate in the AT condition and investigating the decrease in hardness indicated a bulk temperature of approximately 400°C. Comparable temperatures were indicated by the rate of hardness increase of annealed beryllium-copper with ion bombardment time.

Discussion

The absence of porosity can be directly attributed to the formation of the gold-copper solid solution which has been demonstrated to be unreactive to a corrosive atmosphere (4); however, the more interesting phenomena which will require interpretation is the mechanism of formation of the alloy coatings. Two principal experimental results require explanation: (*i*) the existence of a constant surface composition in the alloy film, and (*ii*) an apparent diffusion constant for copper and beryllium into the film which is orders of magnitude above the rate calculable from the indicated bulk temperature of the substrate.

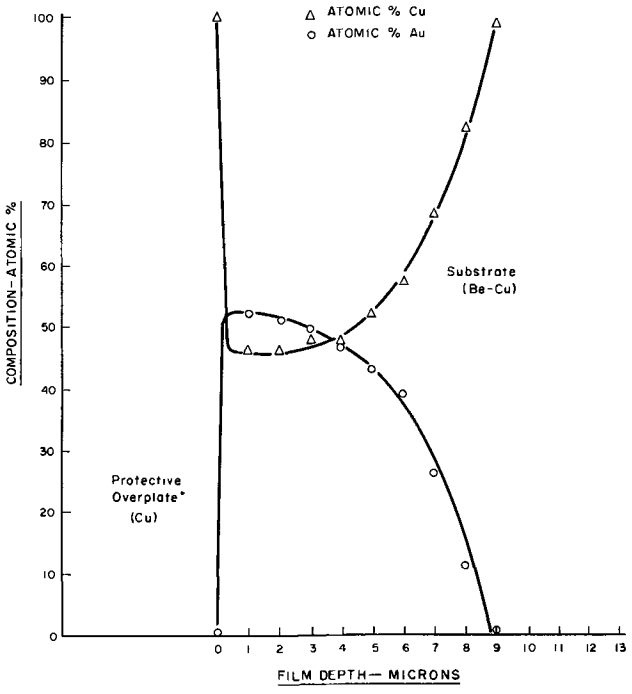

Fig. 5. Copper-gold interfacial distribution

The existence of a constant surface composition alloy film is the result of the fact that the sputtering yield of this gold-copper solid solution is 0.4 that of pure gold and the continued ion bombardment during the deposition would sputter the pure copper and gold phases at rates considerably greater than the solid solution formed by diffusion. The reduced sputtering yield of the minimum melting temperature

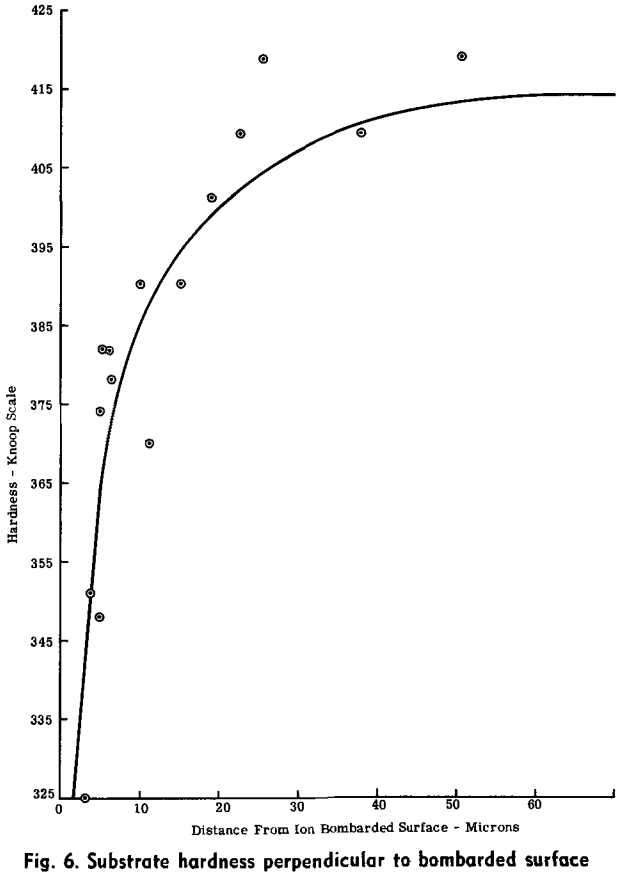

Fig. 6. Substrate hardness perpendicular to bombarded surface

solid solution is consistent with the work tabulated by Wise (5).

The formation of the minimum melting temperature solid solution requires the diffusion of copper into the gold film at rates comparable to the deposition rate of the gold onto the substrate surface. This observation allows an estimate of the diffusion rate of copper into the gold of about 2×10^{-8} cm^2/sec. This value is comparable to the equilibrium diffusion rate at temperatures of 750°C and is obviously in disagreement with a maximum bulk temperature of 400°C.

The picture is further complicated by the lesser diffusion of gold into the substrate as shown by Fig. 5 as well as etched metallographic specimens which indicate a sharp interfacial boundary between the solid solution and the substrate.

These contradictory observations can be rationalized by the existence of an extremely sharp temperature gradient near the surface undergoing bombardment. Such a gradient has been indirectly observed in the overaging of the surface layers of AT condition beryllium-copper and is illustrated in Fig. 6 as the microhardness variation with depth. Electron microscopy of these same specimens also verifies the fact that the thermal history of the surface regions ($<0.5\mu$ depth) differs drastically from that of the bulk material. The model thus generated provides that gold is deposited on a sufficiently hot surface to permit copper diffusion outward at a rate which allows the formation of a solid solution consistent with the deposition rate. The counter diffusion of gold into the substrate material also occurs, but encounters a rapidly decreasing temperature gradient and produces a sharp interface (sharp in terms of the electron microprobe resolution of 1μ). Excess gold or copper in the region of the free surface would be removed by the increased sputtering yields of these elements.

Implicit in this model is the conclusion that as the thickness of the alloy coating is increased the temperature of the interface will decrease until the copper diffusion rate can no longer support a constant film composition at the free surfaces. In these experiments this limit has not been reached at coating thicknesses of 10μ. This is apparently the result of the relatively low thermal conductivity of the beryllium-copper (0.25). Comparable experiments with a pure copper substrate (thermal conductivity 0.91) produce copper concentration gradients in the film at a thickness of $>5\mu$.

Conclusions

The adherence of gold deposited by ion plating onto beryllium-copper is relatively independent of surface contamination. Only in the case where gross oxidation exists, is adherence dependent on removal of the surface contamination layer.

Low porosity gold alloy films at coating thicknesses of less than 2μ result when the deposition parameters permit a sufficiently high interfacial temperature to allow copper to diffuse into the coating.

A model is presented to explain a constant composition alloy formed in terms of its sputtering yield and a sharp thermal gradient near the substrate surface.

Manuscript received March 6, 1967; revised manuscript received May 16, 1967. This work was supported by the United States Atomic Energy Commission.

Any discussion of this paper will appear in a Discussion Section to be published in the June 1968 JOURNAL.

REFERENCES

1. D. M. Mattox, *Electrochem. Technol.*, 2, 295 (1964).
2. "Metals Handbooks," T. Lyman, Editor, American Society of Metals, Metals Park, Novelty, Ohio (1961).
3. M. S. Frant, *This Journal*, **108**, 774 (1961).
4. W. Z. Friend and E. M. Wise, "Corrosion Resistance of Gold" in "Gold-Recovery, Properties and Applications," pp. 185-195, E. M. Wise, Editor, D. van Nostrand Co., Inc., Princeton, N. J. (1964).
5. E. M. Wise, "Gold Alloy Systems" in "Gold-Recovery, Properties and Applications," pp. 110-112, E. M. Wise, Editor, D. van Nostrand Co., Inc., Princeton, N. J. (1964).

Investigations of Electrocrystallization at Silver Electrodes

W. Michael Krebs[1] and David K. Roe

Department of Chemistry and Laboratory for Nuclear Science,

Massachusetts Institute of Technology, Cambridge, Massachusetts

ABSTRACT

Electrochemical studies have been carried out on silver single crystals using a probe technique which permitted areas from 1 to 30 x 10^{-4} cm^2 to be investigated. Electrolytes were composed of acidified silver perchlorate at constant ionic strength. Cyclic current-voltage curves, involving quantities of silver corresponding to 0.3-15 atom layers, clearly revealed the greater reactivity of freshly deposited silver compared to the substrate. Deposition did not proceed in a layer-like fashion, but rather gave rise to hemispherically shaped deposits. The phenomena associated with the anodic and cathodic processes under linear voltage scan and potentiostatic conditions were analyzed successfully in terms of changes in the total deposit (active) area.

Current measurements are sufficiently sensitive to permit detecting the deposition or dissolution of the equivalent of considerably less than a monolayer of metal. When the electrode on which deposition and dissolution occurs is more noble than the deposit, a problem arises concerning the properties of the electrode system: trace metal/metal ion. Hertzfeld (1) first considered the possibility of variations in the thermodynamic activity of a metal which only partially covers an inert electrode. He proposed that the applicability of the Nernst equation could be extended to partial monolayers by equating the activity term to the degree of coverage.

In some contrast with this model are the findings of Haissinsky (2) who employed radiographic analysis to elucidate the nature of deposition onto an inert (*e.g.*, platinum) electrode. The nonuniform distribution of metal found immediately suggested that the electrode surface was heterogeneous and a controlling factor.

Byrne and Rogers (3) have considered some of the thermodynamic aspects of fractional monolayer and trace deposition. Four ideal cases were described which considered both the distribution and population of

[1] Present address: Tyco Laboratories, Inc., Waltham, Massachusetts.

energetically favorable sites on the electrode and the relative energy differences for deposition onto the inert substrate and deposition onto existing deposits.

In three of these cases, a varying number of sites on the inert electrode is energetically more favorable for deposition than on the metal of interest. As a result, monolayer coverage can occur depending on the density of such sites. The phenomenon of "undervoltage" is associated with these three cases.

In the fourth case, however, deposition onto the metal itself is sufficiently more favorable to require nucleation as a prerequisite for deposition. Large overvoltages will be a characteristic of this process.

It must be added that situations similar to the above could exist even when the electrode and deposit are of the same metal. The number and type of growth sites would be important in determining the deposition characteristics, but at lower overvoltages than for inert electrodes. Furthermore large "undervoltages" are precluded.

Berzins and Delahay (4), in their theoretical treatment of the reversible deposition of an insoluble substance, recognized the possibility of activity changes during the early stages of deposition preceding complete coverage, but neglected this complication. Nicholson (5), using the same assumptions and approach, derived the corresponding anodic stripping equation. The sudden drop to zero predicted for the anodic current by the equation was contrary to the more gradual decrease and tailing found experimentally. In an attempt to treat the anodic stripping of monolayer quantities of deposit, Nicholson assumed monolayer deposition, with the activity proportional to the fractional coverage. Good agreement for silver on platinum was followed by much poorer agreement in the case of copper and lead.

Alternate conditions which would be in accord with the general characteristics of anodic stripping curves include (*i*) alloying of the deposited metal with the substrate, and (*ii*) changes in the total active (deposit) area.

The first condition is of limited applicability in the cases of interest for solid state diffusion is not suggested by experiment, although it could result in tailing of the type observed.

The second alternative is based, in part, on the observations of Haissinsky (2) and Vahramian (6) and is consistent with the observations of Kaischew *et al.* on the nucleation of silver (7) and mercury (8) on platinum cathodes. Vahramian explained the startling lack of agreement among the polarization curves which had been obtained for silver by noting that current densities were meaningful only if expressed in terms of the active electrode area. This latter quantity was not equal to the electrode area, and moreover increased during deposition.

Thus, in cases where deposition commences at active sites, which subsequently grow, profound changes in active area will occur even when the quantities involved lie in the monolayer range.

In the work to be described, the unusual nature of the current-potential and current time curves associated with the deposition and stripping of mono- and polylayer equivalents of silver on a silver substrate was analyzed and found to be attributable to the changes occurring in the deposit area. The greater reactivity of the freshly deposited silver permitted the separation of the deposit and substrate contribution during stripping. Previous observations (10,11) have shown that freshly deposited metals often are more "active" than the substrate and that activity changes with time (12). This topic and many others have been reviewed and discussed recently (13).

Experimental

Single crystal rods of silver 2 x 20 mm were grown from 99.99 + % pure silver wire by a modified Bridgeman method. The single crystal spheres were prepared from these rods using a modification of the fusion technique described by Roe and Gerischer (9). This involved melting one end of the mounted rod in a purified hydrogen atmosphere to form a clinging, molten droplet which, when allowed to freeze slowly, resulted in a single crystal sphere. The (111) facets which formed on the surface of the sphere were quite insensitive to induced vibration during the freezing process even when the perturbation was severe enough to cause rippling in the surrounding surface.

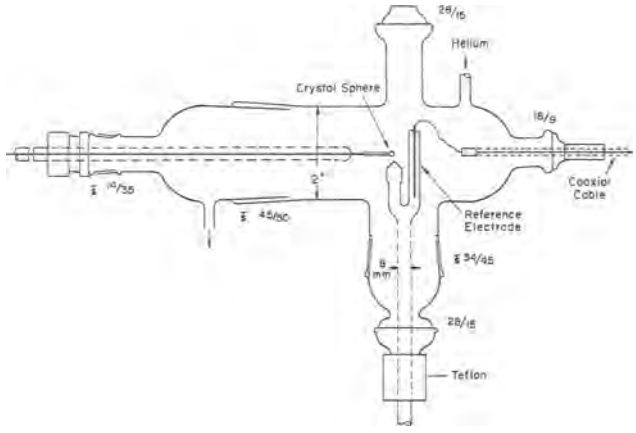

Fig. 1. Electrochemical cell

After cooling, the crystal was withdrawn into the ground glass joint and transferred to the electrochemical cell which is seen in Fig. 1. This operation was carried out with a rapid flow of gas through the joint assembly to prevent the electrode from contacting the air.

The atmosphere in the cell was helium which had been purified, deoxygenated, and humidified by passage through Anhydrone, activated charcoal, 13X Linde molecular sieves at −200°C, and finally, 0.1*N* silver perchlorate.

The probe assembly seen at the bottom of the cell contained the electrolyte and counter reference electrode. The probe tip had a small orifice to permit the formation and maintenance of a narrow column of electrolyte between the bulk electrolyte contained within the probe and the selected area on the crystal sphere. The diameter of the column was determined by that of the tip orifice. Both Teflon and silver cones were employed as tips, the latter serving also as the counter reference electrode. When utilizing Teflon cones, a length of pure polycrystalline silver wire having a geometric area of at least 1 cm^2 was used.

There are several distinct advantages to using a probe technique rather than attempting to mask off areas. Not only is the danger of contamination from the masking agent eliminated, but also the electrode area/electrolyte volume ratio is several orders of magnitude more favorable, resulting in a corresponding decrease in the danger of contamination. For the arrangement used, this ratio was at least a 2500 times that for a 1 cm^2 electrode in 50 ml of electrolyte.

The electrolyte column was formed by positioning the tip to within 0.3 mm of the crystal area and tapping the base of the probe. This operation was facilitated by the use of a binocular microscope. Electrolyte contact areas on the crystal were calculated from the diameter of the electrolyte column which was measured via a calibrated micrometer eyepiece. These areas usually ranged between 1×10^{-4} to 3×10^{-3} cm^2. An a-c bridge was used to measure the cell resistance.

The electrolyte was silver perchlorate and perchloric acid. The former was prepared from reagent grade silver nitrate, sodium hydroxide, and perchloric acid by the repeated precipitation and dissolution of silver hydroxide. The first 5-10% of the precipitate was discarded each time. After standardization of the final

solution of silver perchlorate, solutions 0.005, 0.099, and 0.05M in silver ion were made up, sufficient perchloric acid being added to bring the ionic strength to 0.1.

All water was doubly distilled from quartz. The final step in cleaning the glassware and cell parts was simmering in perchloric-nitric acids for several hours.

A system utilizing three G. A. Philbrick UPA-2 chopper stabilized operational amplifiers provided the linear voltage scans and current amplification. A Keithley Model 610A electrometer was employed to monitor the cell voltage and activate one axis of a Houston Model 100 X-Y plotter. Current-time variations were followed on a Varian Model G-11 strip chart recorder.

Following the completion of a series of measurements on an electrode, it was etched in hot dilute nitric acid, rinsed well, then remelted to form a new crystal sphere.

Results

The (111) facets which formed on the spherical crystals were roughly triangular in shape, and *ca.* 150 x 100μ. Surrounding each facet were a series of descending concentric steps as can be seen in Fig. 2a and 2b. The height and width of the steps varied over a wide range, averaging 2μ and 10μ, respectively. No microsteps or irregularities were visible on the surface of the steps at a magnification of 1000X.

The measurements to be described were all performed on these step regions. The electrochemical behavior of the (111) facets alone will be reported in a future communication.

Following cathodic and anodic polarizations, representative electrodes were examined microscopically in order to determine the mode of deposition and dissolution. Micrographs, such as in Fig. 3a, showed that deposition had commenced mainly at the edges of the steps. More extensive deposition led to the mound or hemispherically shaped deposits seen in Fig. 3b. In this case, the steps have been all but obliterated by the deposits. In a similar manner anodic attack also commenced at the step edges.

Cyclic current voltage curves were obtained on the steps utilizing scan rates between 0.05 and 1.0 mv/sec.

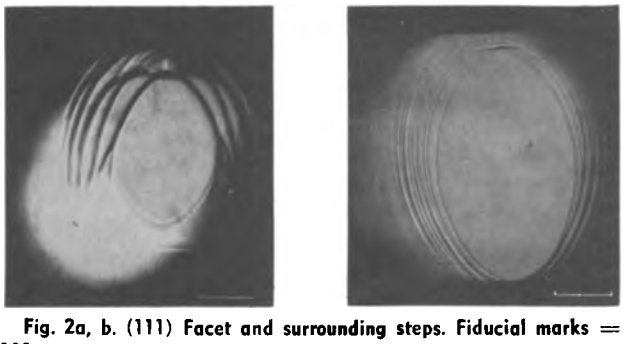

Fig. 2a, b. (111) Facet and surrounding steps. Fiducial marks = 100μ.

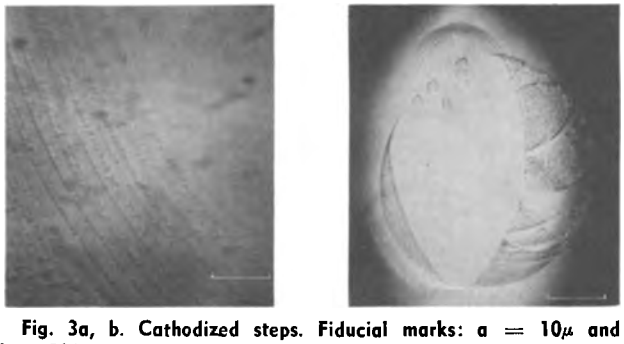

Fig. 3a, b. Cathodized steps. Fiducial marks: a = 10μ and b = 100μ.

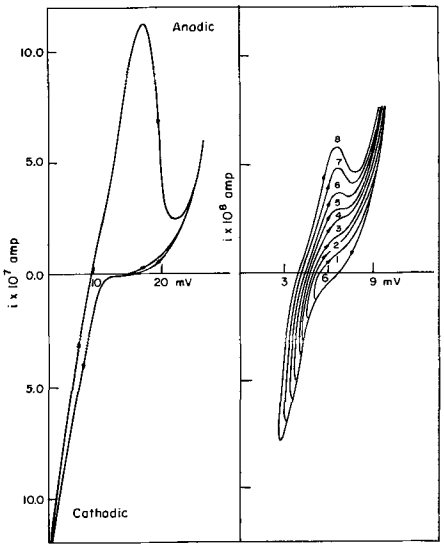

Fig. 4. Cyclic current-potential curves. [Ag^+]:0.05 m/l. Scan rate: 0.57 mv/sec (L); 0.15 mv/sec (R). Electrolyte contact area: 2.3 x 10^{-3} cm^2 (L); 2.5 x 10^{-3} cm^2 (R).

In all cases, the scans were started from the rest potential, the first usually being in the anodic direction. In order to avoid significant IR drops, and to keep the quantity of deposit to between 0.3 and 15 atom layers, the scans were usually restricted to ± 30 mv of the rest potential.

Most of the cyclic current-potential curves obtained showed some degree of hysteresis which, in extreme cases, appeared as a distinct anodic peak similar to that in Fig. 4a.

Throughout this section, the following terms will be used and are defined as follows.

The initial anodic scan is the anodic current-potential curve obtained on deposit-free steps.

The return anodic scan is the anodic current-potential curve obtained immediately following deposition.

The junction point is that point where the return anodic scan joined and followed the initial anodic scan.

The consistent lack of hysteresis in cyclic scans restricted to the anodic region clearly demonstrated that the deposited silver was responsible for the hysteresis in return anodic scans. The proportionality existing between the quantity deposited and degree of resulting hysteresis was established by running a series of cyclic scans involving progressively greater amounts of deposit. Such a series is to be seen in Fig. 4b.

The quantitative nature of this dependence was established on integrating both the cathodic scans and subsequent anodic peaks. In an attempt to correct for the simultaneous removal of substrate silver, the initial anodic scan was subtracted from the anodic peak in each case. The agreement between the two quantities, of 95%, represents the average of twenty determinations involving a variety of scan rates, silver ion concentrations, and electrodes.

It was not unexpected that the return anodic scans were strongly time dependent in the region up to the junction point. Holding the potential in this region resulted in an exponential-type decay in the current to a value close to that of the initial anodic scan at that potential. Beyond the junction point, both the initial and return anodic scans exhibited only a slight time dependence, which appeared as a very slow increase in the current when the scan was halted. An additional characteristic of the junction point was that the entire current potential curve could usually be reproduced after, but not before, it had been passed.

The anodic behavior of the cathodized steps was investigated potentiostatically by depositing a determinable quantity of silver via a linear voltage scan,

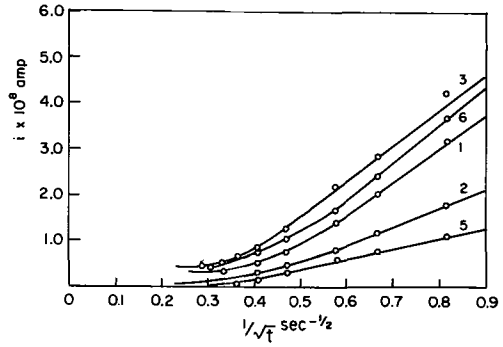

Fig. 5. Potentiostatic stripping of deposit. $[Ag^+] = 0.05$ m/l. Electrolyte contact area: 1.5×10^{-4} cm².

Curve	Anodic overvoltage, mv	Amount of deposit, μ coulomb	Quantity removed, μ coulomb
1	4.5	0.143	0.142
2	3.3	0.155	0.084
3	7.5	0.128	0.207
5	4.0	0.145	0.041
6	7.5	0.135	0.196

adjusting the applied voltage to an anodic value with the cell out of circuit, then recording the current-time variations after switching the cell into circuit. A preliminary current-potential curve was run on all electrodes as a check for satisfactory stripping behavior and to determine the initial anodic scan for purposes of correcting for the substrate contribution. The anodic overvoltage is defined as the difference between the open circuit potential immediately following deposition and the stripping potential.

In anticipation of diffusion control, the current-time data were replotted in the form i *vs.* $1/\sqrt{t}$. A typical series of plots obtained on one electrode can be seen in Fig. 5. The curves showed initial linearity which when extrapolated intersected the $1/\sqrt{t}$ axis, as is expected for the complete removal of a labile deposit. Depending on the stripping potential with respect to the preliminary initial anodic scan, the plots either intersected the time axis or levelled off to a steady state. The latter situation occurred when the stripping potential lay within the initial anodic scan, signifying the simultaneous removal of substrate silver.

The effect of decreasing the silver ion concentration was to increase the over-all linearity of the plots. All the other features remained the same. It is interesting to note that the degree of removal of the deposited silver was not normally quantitative under potentiostatic conditions, but was strongly dependent on the anodic overvoltage.

The deposition process was also investigated under potentiostatic conditions. Preliminary current-voltage curves were obtained on all electrodes in order to insure that the silver deposited during a series of cathodizations could be stripped off after each, thus minimizing history effects which would have otherwise resulted due to the accumulation of deposit.

Again, in anticipation of diffusion control, the data were plotted in the form i *vs.* $1\sqrt{t}$. Although similar to the anodic stripping plots, these differed in that the extrapolated initial linear portions intersected the current axis, and, in several instances, the current increased after having leveled off. In Fig. 6 is shown a typical series of plots obtained on one electrode.

Discussion

The near quantitative agreement between the amount of silver deposited and the amount represented by the subsequent anodic peak, in conjunction with the cathodic position of this peak relative to the initial anodic scan, was interpreted to mean that the deposited silver was more reactive than the substrate.

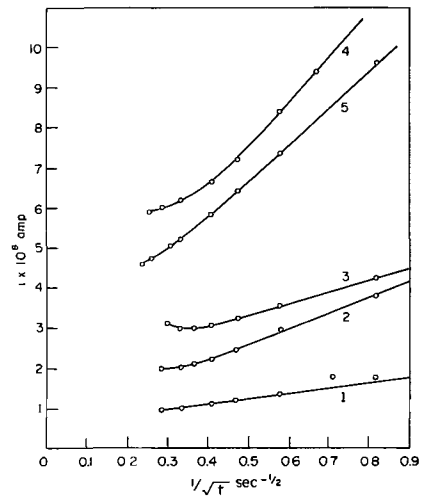

Fig. 6. Potentiostatic deposition on one electrode. $[Ag^+] = 0.05$ m/l. Electrolyte contact area $= 1.9 \times 10^{-4}$ cm².

No.	Quantity deposited, μ coulomb	Cathodic overvoltage, mv
1	0.15	2.1
2	0.40	3.9
3	0.36	5.1
4	1.65	6.6
5	1.37	5.1

It is interesting to note, in this connection, that a similar observation concerning the greater reactivity of freshly deposited silver at silver cathodes has been reported by Mamantov (10).

In spite of the over-all variability found in the current potential curves obtained on different electrodes, and even on different portions of the same electrode, the fact that the behavior of specific areas could be reproduced on returning to them strongly suggests that the source of the variability existed in the electrode surface itself, *i.e.*, type and density of growth sites, and was not due to some external factors.

Despite the fact that the system was not the optimum for stripping analysis studies, it did have the advantage that deposition occurred in a fairly regular pattern yielding deposits whose shape could be closely approximated by hemispheres.

Insofar as the quantities of silver involved ranged below a monolayer, and the substrate could be considered inert, the situation was analogous to that treated by Nicholson (5). However, since there was no question that the deposit area changed greatly during the course of deposition and stripping, it appeared more than likely that the electrochemical phenomena accompanying the above processes reflected these area changes. The model chosen was that of a polyelectrode of changing area.

In the derivations of the equations for the reversible stripping under potentiostatic and linear scan conditions which are presented in Appendix 1, it was necessary to make several assumptions either because of a lack of the necessary information or to maintain the simplicity of approach.

(*i*) All deposits were assumed hemispherical and of equal size.

(*ii*) The activity of the deposits was constant. The observed dependance of the stripping efficiency on the anodic overvoltage under potentiostatic conditions does, however, imply variations in the reactivity of the deposits. Since the source of such a variation is not know, no provision for it has been made in the derivation.

(*iii*) The electrolyte is considered to be completely homogeneous at the start of the stripping. This is not strictly true since stripping immediately followed

deposition. However, the reproducibility of multiple cyclic scans and the small quantities of silver involved relative to the amount present in the electrolyte column alone, indicated that any compositional inhomogeneities at the electrode surface were of minor importance.

(*iv*) Conditions for semi-infinite linear diffusion existed. A calculation of the integral thickness of the Nernst diffusion layer for the worst case yielded a value considerably less than the average length of the electrolyte column.

Diffusion to a single hemisphere is, of course, hemispherical rather than linear. In a situation such as the present, involving many hemispheres, the linear approximation will improve as the degree of overlap of the individual diffusion layers increases. From the quantity of deposit and number of deposits used in the calculations, the distance between deposits was calculated, assuming uniform size and distribution. This distance was of the order of one deposit radius. Thus for low scan rates, the linear approximation probably was not too bad. In any event, the complexity of the nonlinear diffusion equations associated with hemispherical diffusion also prompted the approximate treatment.

(*v*) It was assumed that true potential control exists. Although the IR drop was considerable in some cases due to the high cell resistance, only those data have been analyzed in which the maximum IR drop was under 0.5 mv.

It should be added that no provision has been made for simultaneous substrate removal during stripping. Any contribution was subtracted from the experimental curves before comparing them with those calculated.

The derived equation for the linear scan stripping of silver is

$$i = -3\mathbf{F}\gamma C^{\circ} N^{1/3} (\beta D)^{1/2} G\{\beta t\}$$

$$X \left\{ Qc^{1/3} - \frac{\mathbf{F}\gamma C^{\circ} N^{1/3} D^{1/2}}{\beta^{1/2}} \left[G\{\beta t\} - \frac{2(\beta t)^{1/2}}{\pi^{1/2}} \right] \right\}^2 \quad [1]$$

where

$$G\{\beta t\} = \exp(\beta t)\ \mathrm{erf}\ [(\beta t)^{1/2}]$$

$$\gamma = 2\pi \left(\frac{3M}{2\pi} \right)^{2/3}$$

$$M = \frac{\text{at. wt}}{\mathbf{F}\delta}$$

Qc = quantity of deposit at $t = 0$

N, the number of hemispheres, is the only adjustable parameter in the equation. The resemblance between this equation and the anodic form of Berzins and Delahay's Eq. [5] becomes apparent if one notes that the squared quantity within the major parenthesis is proportional to the total deposit or active electrode area. At low scan rates (*ca.* 1 mv/sec) the calculated plots tend to rise fast and decay more slowly whereas the reverse is true at faster scan rates (*ca.* 30 mv/sec). At the scan rates employed experimentally, increasing N for a given Qc tended to sharpen the peaks. In making the experimental-calculated comparisons, the value of N chosen was that required for the best fit. Four typical comparisons can be seen in Fig. 7.

The derivation for the potentiostatic case was similar (Appendix 1) yielding the following equation

$$i = -\frac{3\mathbf{F}D^{1/2}\gamma N^{1/3} C^{\circ}[\exp(\phi\eta) - 1]}{(\pi t)^{1/2}} \quad [2]$$

$$X \left\{ Qc^{1/3} - \frac{2\mathbf{F}D^{1/2}\gamma N^{1/3} C^{\circ}[\exp(\phi\eta) - 1] t^{1/2}}{\pi^{1/2}} \right\}^2$$

where γ and Qc are defined as before.

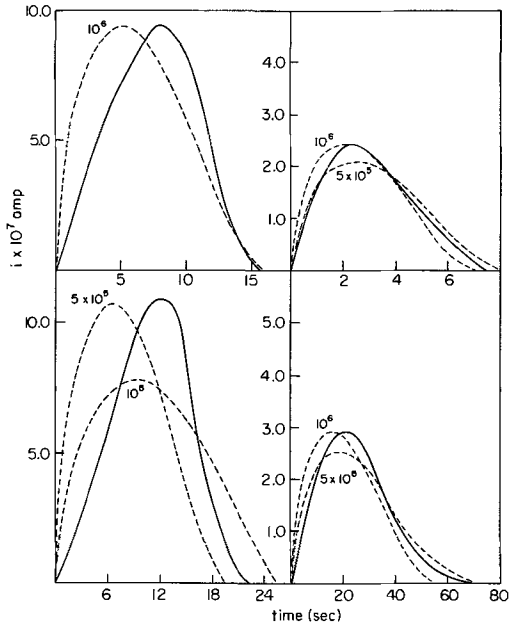

Fig. 7. Comparisons of experimental and calculated curves for the linear scan stripping of deposit. Calculated curves:— Value of N used indicated.

Plot	Amount of deposit, μ coulomb	Scan rate, mv/sec	Electrolyte contact area, cm^2	[Ag$^+$], m/l
Top L	9.0	0.57	3.0×10^{-3}	0.05
Top R	1.01	1.0	3.0×10^{-3}	0.05
Bottom L	12.9	0.57	2.2×10^{-3}	0.05
Bottom R	9.23	0.10	3.0×10^{-3}	0.05

N was again the only adjustable parameter and the squared quantity within the major parenthesis was proportional to the total deposit area. The calculated i *vs.* $1/\sqrt{t}$ plots were strikingly similar to the experimental curves showing initial linearity which gave way to curvature at longer times, followed by intersection of the time axis.

Decreasing the concentration of the electro-active species served to increase the over-all linearity of the plots, as had been observed experimentally. Before comparing the experimental and calculated curves, the substrate contribution was accounted for, when necessary, by subtracting the steady state current value from the curves. The amount of silver remaining was used for Qc. N was chosen on the basis of best fit. Three typical comparisons can be seen in Fig. 8.

The mathematical treatment of the corresponding cathodic case for either linear scan or potentiostatic conditions proved to be far more complex than for the anodic stripping case. Consequently, a finite difference method had to be adopted. The Cottrell equation and the Berzins and Delahay equation (4) were employed after first substituting for the constant area term a time dependent expression. The two modified equations are

$$i(t + \Delta t) = \frac{\mathbf{F}A(t)D^{1/2} C^{\circ}}{(\pi t)^{1/2}} [1 - \exp(-\phi\eta)] \quad [3]$$

for the potentiostatic case, and

$$i(t + \Delta t) = \frac{2}{\pi^{1/2}} \left(\frac{n\mathbf{F}}{RT} \right)^{1/2} n\mathbf{F}C^{\circ} D^{1/2} \gamma^{1/2} A(t) Y[(\beta t)^{1/2}] \quad [4]$$

for linear scan deposition.

Where

$$A(t) = 2\pi \left[\frac{3MQ(t)}{2\pi\mathbf{F}\delta} \right]^{2/3}$$

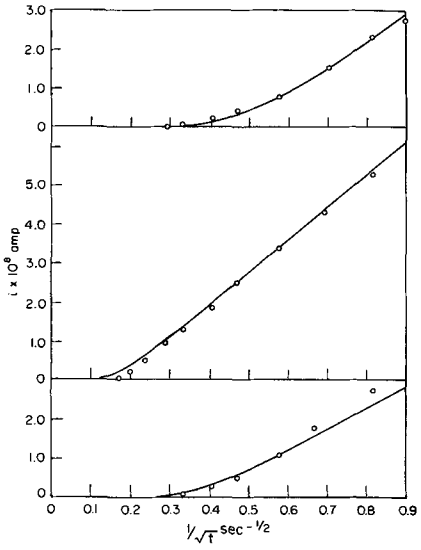

Fig. 8. Comparisons of experimental and calculated curves for the potentiostatic stripping of deposit. Experimental points: ○.

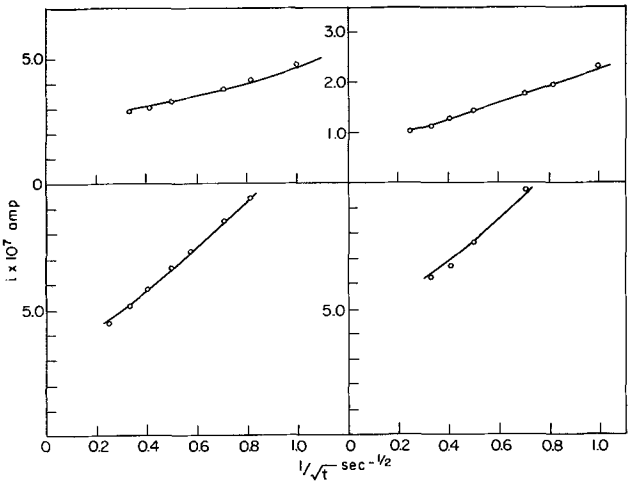

Fig. 9. Comparisons of experimental and calculated curves for a series of potentiostatic depositions. Experimental points: ○ Electrolyte contact area = 1.2 x 10^{-3} cm^2.

Plot	Amount of deposit, μ coulomb	Anodic overvoltage, mv	N	[Ag^+], m/l
Top	0.159	5.0	10^5	0.05
Middle	0.544	10.0	10^6	0.005
Bottom	0.157	5.0	5 x 10^4	0.05

$$Q(t) = Qi + \Delta t \sum_{n=0}^{n} i(0.005 + n\,\Delta t)$$

and

$$Y[(\beta t)^{1/2}] = \exp(-\beta t) \int_0^{(\beta t)^{1/2}} \frac{\exp(z)\,dz}{z^{1/2}}$$

$$t = 0.005 + n\,\Delta t \text{ sec}$$

The treatment contains all the assumptions present in the derivation of the original equation, *i.e.* semi-infinite linear diffusion, constant deposit activity, plus a hemispherical shape for the deposits. The equations were set up for a single deposit.

Because this type of calculation has to be started at some time greater than $t = 0$, this was chosen to be 0.005 sec at which time the deposit contains Qi coulomb of silver. Consequently, several values of Qi were used in each series of calculations. The time interval chosen was 0.01 sec. As can be seen from the equations, the area used in calculating the current at time t + 0.01 sec is that based on the amount of silver deposited up to time t.

Due to the lengthy, repetitive nature of the computations the procedure was programmed for an IBM 7044 computer.

In comparing the experimental curves with those calculated, the value of Qi chosen for the latter was based on the best curve shape. The value of N used was chosen to give the correct current range. Qi and N were not completely independent parameters.

In general, a larger value of Qi was required in the potentiostatic case than for linear scan deposition. This was expected since at the low sweep rates used, more silver had been deposited during the first 0.005 sec under potentiostatic conditions. Through the equation relating the area at any time with the quantity of silver, the active electrode area can be calculated and compared with the total area contacted by electrolyte. For a typical case involving an electrolyte contact area of 10^{-3} cm^2, one microcoulomb of deposit, and

Plot	Cathodic overvoltage, mv	Q_i coulomb	N
Top L	5.1	10^{-13}	9 x 10^5
Top R	3.0	10^{-13}	8 x 10^5
Bottom L	5.1	10^{-12}	5.5 x 10^5
Bottom R	7.0	10^{-12}	4.2 x 10^5

10^6 sites the deposit area would be *ca.* 8 x 10^{-5} cm^2 which is 8% of the total area.

The shape of the calculated i *vs.* $1/\sqrt{t}$ plots agreed very well with the experimental curves. Under proper conditions, the calculated current increased after having decreased as had been noted experimentally. It is interesting to note that in comparing a series of potentiostatic depositions carried out on the same electrode, the value of Qi required for best fit tended to increase, indicating that some deposited silver remained after the anodic stripping which followed each cathodization. A typical set of comparisons is presented in Fig. 9.

Similar agreement was found for the linear scan deposition of silver. A series of comparisons can be seen in Fig. 10.

It is of interest to speculate on the possible reason for the greater lability of the freshly deposited silver. In this regard it should be noted that the deposits on the steps were not well defined, as were those formed on the facets, but rather were mound-like. The degree of removal of the deposited silver, via linear voltage scan, could be reduced by 10-20% by holding the cell at open circuit for 5-10 min before stripping. Furthermore, the epitaxial deposits formed on the (111) facet (see Fig. 3b) were not preferentially removed under conditions of anodic polarization, nor did they yield the characteristic stripping behavior of the stepped regions. These observations suggest that the greater lability of the deposits on the steps is crystallographic in origin but there is no direct information as to why there is a difference. Possible reasons are differences in growth sites (dislocations) or differences in the (apparently) major deposition mechanism. The decreased stripping efficiency with time is readily interpreted as due to a recrystallization process. This process arises through the exchange current with silver ions as well as by surface migration of atoms; the former path is considered to be more probable in this case because of the high value of the exchange current, although strong evidence (12) has been collected for surface diffusion in the case of copper electrodes.

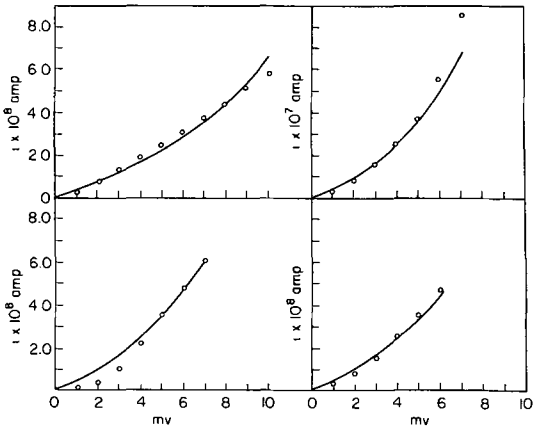

Fig. 10. Comparisons of experimental and calculated curves for linear scan deposition. Experimental points: ○ $[Ag^+] = 0.05$ m/l.

Plot	Scan rate, mv/sec	Electrolyte contact area, cm^2	Q_i coulomb	N
Top L	0.572	3×10^{-4}	10^{-13}	3.5×10^5
Top R	0.572	• 3.7×10^{-3}	10^{-14}	1.3×10^7
Bottom L	1.0	1.0×10^{-4}	10^{-14}	1.3×10^6
Bottom R	1.0	1.0×10^{-4}	10^{-14}	1.2×10^6

Conclusions

Confirmation of Mamantov's (10) observation regarding the greater reactivity of freshly deposited silver has been obtained. Of far greater importance is the fact that the phenomena associated with the deposition and stripping of the equivalent of sub- and polyatomic layers of silver on silver can be attributed to changes in the deposit area alone. The system used is particularly well suited to such a study because of the regular nature of the deposits formed. It would be of great interest to apply the model to the case of silver deposition and stripping at platinum electrodes.

Acknowledgment

One of the authors (W.M.K.) is indebted to the National Institutes of Health for a predoctoral fellowship (1962-1966). This work was supported in part by the U.S. Atomic Energy Commission through funds provided under Contract AT(30-1)-905.

Manuscript received March 15, 1967; revised manuscript received May 26, 1967.

Any discussion of this paper will appear in a Discussion Section to be published in the June 1968 JOURNAL.

REFERENCES

1. K. F. Herzfeld, *Physik. Z.*, **13**, 29 (1913).
2. M. Haissinsky and A. Coche, *J. Chem. Soc. Suppl.*, **2**, 397 (1949).
3. J. T. Byrne and L. B. Rogers, *This Journal*, **98**, 457 (1951).
4. T. Berzins and P. Delahay, *J. Amer. Chem. Soc.*, **75**, 555 (1953).
5. M. M. Nicholson, *J. Amer. Chem. Soc.*, **79**, 7 (1957).
6. A. T. Vahramian, *Compt. Rend. de l'Acad. des Sci., URSS*, **22**, 238 (1939).
7. R. Kaischew and B. Mutaftschiew, *Z. Physik. Chem.*, **204**, 334 (1955).
8. R. Kaischew and B. Mutaftschiew, *Electrochem. Acta*, **10**, 643 (1965).
9. D. K. Roe and H. Gerischer, *This Journal*, **110**, 350 (1963).
10. G. Mamantov, D. L. Manning, and J. M. Dale, *J. Electroanal. Chem.*, **9**, 253 (1965).
11. V. Kohlschütter and A. Torricelli, *Z. Elektrochem.*, **38**, 213 (1932).
12. J. O'M. Bockris and H. Kita, *This Journal*, **109**, 928 (1962).
13. J. O'M. Bockris and A. Damjanovic, "Modern Aspects of Electrochemistry," Vol. 3, Chap. 4, Bockris and Conway, Editors, Butterworth, Washington, D. C. (1964).

APPENDIX 1

A. Derivation of Equations for Linear Scan Stripping

Solving Fick's Law for linear diffusion

$$\frac{\partial C(x,t)}{\partial t} = D\frac{\partial^2 C(x,t)}{\partial x^2} \qquad [A\text{-}1]$$

using the following initial and boundary conditions

$$C(o,t) = C^\circ \exp(\beta t),\ C(x,o) = C^\circ,$$
$$\text{and } C(x,t) = C^\circ \quad x \to \infty$$

where

$$\beta = \frac{nFv}{RT}$$

results in

$$C(x,t) = \frac{C^\circ}{2}\exp(\beta t)\left\{\exp[x(\beta/D)^{1/2}]\left[\operatorname{erfc}\left[\frac{x}{2(Dt)^{1/2}} + (\beta t)^{1/2}\right]\right] + \exp[-x(\beta/D)^{1/2}]\left[\operatorname{erfc}\left[\frac{x}{2(Dt)^{1/2}} - (\beta t)^{1/2}\right]\right]\right\} + C^\circ \operatorname{erf}\left(\frac{x}{2(Dt)^{1/2}}\right) \qquad [A\text{-}2]$$

Differentiating [A-2] and setting $x = 0$ yields

$$\left(\frac{dC(x,t)}{dx}\right)_{x=0} = -\frac{C^\circ \beta^{1/2}}{D^{1/2}}\exp(\beta t)\operatorname{erf}[(\beta t)^{1/2}] \qquad [A\text{-}3]$$

The relationship between the flux at the electrode surface

$$\left(\frac{dC(x,t)}{dx}\right)_{x=0}$$

and the change in deposit area with quantity of silver as a function of time is derived as follows. All primed quantities refer to a single deposit.

For the Hemisphere Model

$$V'(t) = MQ'(t) = \frac{2\pi r'^3}{3}$$

where

$$M = \frac{\text{Atomic weight}}{F\rho}$$

$$A'(t) = 2\pi r'^2$$

Substituting and rearranging yields

$$A'(t) = 2\pi\left(\frac{3M}{2\pi}\right)^{2/3} Q'(t)^{2/3} \qquad [A\text{-}4]$$

For N deposits, [A-4] becomes

$$A(t) = NA'(t) = \gamma N^{1/3} Q(t)^{2/3} \qquad [A\text{-}5]$$

where

$$\gamma = 2\pi\left(\frac{3M}{2\pi}\right)^{2/3}$$

Since

$$D\left(\frac{dC(x,t)}{dx}\right)_{x=0} = \frac{d}{dt}\left(\frac{Q(t)}{FA(t)}\right) \qquad [A\text{-}6]$$

By substituting [A-5] into [A-6] and differentiating, one obtains

$$\left(\frac{dC(x,t)}{dx}\right)_{x=0} = \frac{Q(t)^{-2/3}}{3FD\gamma N^{1/3}}\frac{dQ}{dt} \qquad [A\text{-}7]$$

To obtain the current-voltage relationship for the hemisphere model, Eq. [A-3] is equated to [A-7] yielding

$$Q(t)^{-2/3}\,dQ = -3F D^{1/2}\gamma N^{1/3}\beta^{1/2}C^\circ \exp(\beta t)\operatorname{erf}[(\beta t)^{1/2}]dt \qquad [A\text{-}8]$$

Upon integrating both sides, from Qc at $t = 0$ to $Q(t)$ at $t = t$, the following equation is obtained

$$Q(t) = \left[Qc^{1/3} - FD^{1/2}\gamma N^{1/3} C^\circ \beta^{-1/2}\left\{\exp(\beta t)\operatorname{erf}[(\beta t)^{1/2}] - \frac{2(\beta t)^{1/2}}{\pi^{1/2}}\right\}\right]^3 \qquad [A\text{-}9]$$

where

Qc = the initial quantity of deposit present.

Noting that $i(t) = dQ(t)/dt$, Eq. [A-9] is differentiated with respect to time to give

$$i = -3\mathbf{F}\gamma C^\circ N^{1/3} (\beta D)^{1/2} \exp(\beta t) \operatorname{erf}[(\beta t)^{1/2}] \left\{ Qc^{1/3} - \mathbf{F}\gamma C^\circ N^{1/3} D^{1/2} \beta^{-1/2} \left[\exp(\beta t) \operatorname{erf}[(\beta t)^{1/2}] - \frac{2(\beta t)^{1/2}}{\pi^{1/2}} \right] \right\}^2 \quad [A\text{-}10]$$

B. Derivation of Equations for Potentiostatic Stripping

Solving Fick's law for linear diffusion [A-1] for the following boundary and initial conditions

$$C(o,t) = C^\circ \exp(\phi\eta), C(x,o) = C^\circ, \text{ and } C(x,t) = C^\circ \quad (x \to \infty)$$

one obtains

$$C(x,t) = C^\circ [\exp(\phi\eta) - 1] \operatorname{erfc}\left[\frac{x}{2(Dt)^{1/2}}\right] + C^\circ \quad [A\text{-}11]$$

Differentiating [A-11] with respect to x and setting $x = 0$

$$\left(\frac{dC(x,t)}{dx}\right)_{x=0} = \frac{C^\circ[1 - \exp(\phi\eta)]}{(\pi D t)^{1/2}} \quad [A\text{-}12]$$

The current-time relationship for the hemisphere model is obtained by equating [A-12] and [A-7] thus yielding

$$Q(t)^{-2/3}\, dQ = \frac{3\mathbf{F}\gamma D^{1/2} N^{1/3} C^\circ}{(\pi t)^{1/2}} [1 - \exp(\phi\eta)]\, dt \quad [A\text{-}13]$$

Integrating both sides of [A-13] from Qc at $t = 0$ to $Q(t)$ at $t = t$

$$Q(t) = \left[Qc^{1/3} - \frac{2\mathbf{F}D^{1/2}\gamma N^{1/3} C^\circ}{\pi^{1/2}} [\exp(\phi\eta) - 1]\, t^{1/2} \right]^3 \quad [A\text{-}14]$$

Differentiating [A-14] with respect to t yields the current

$$i = -\frac{3\mathbf{F}D^{1/2}\gamma N^{1/3} C^\circ}{(\pi t)^{1/2}} [\exp(\phi\eta) - 1] \left\{ Qc^{1/3} - \frac{2\mathbf{F}D^{1/2}\gamma N^{1/3} C^\circ}{\pi^{1/2}} [\exp(\phi\eta) - 1]\, t^{1/2} \right\}^2 \quad [A\text{-}15]$$

Appendix 2

List of Symbols Used

A	Area cm^2
C°	Bulk silver ion concentration moles/cm^3
D	Diffusion coefficient for silver ion taken as 1.6 x 10^{-5} cm^2/sec
$\mathbf{F}$	Faraday constant
M	Atomic weight of silver/$\mathbf{F}\rho = 10^{-4}$ cm^3/coulomb
N	Number of hemispheres
Qc	Quantity of silver deposit removed, coulomb
Qi	Quantity of silver in a single hemisphere at t = 0.005 sec
t	Time, sec
v	Scan rate volt/sec
β	$n\mathbf{F}v/RT$
γ	$2\pi(3M/2\pi)^{2/3}$
η	Overvoltage
ρ	Density g/cm^3
ϕ	$n\mathbf{F}/RT$

Hydrodimerization of Acrylonitrile

Y. Arad, M. Levy, I. R. Miller, and D. Vofsi

Plastics Research Laboratory, The Weizmann Institute of Science, Rehovoth, Israel

ABSTRACT

The reduction of acrylonitrile by electrolysis and by reaction with alkali metal amalgams was studied in acid and in neutral media. It was shown that the adiponitrile yield increases with the concentration of the acid. This was explained by assuming protonation of acrylonitrile by the acid, followed by interaction with the alkali metal and dimerization of the free radicals formed. In neutral media it was shown that tetraalkyl ammonium salts have a specific solvating effect on the reactants. Contrary to previous views it was proved that high adiponitrile yields can be obtained not only by electrolysis in the absence of alkali metal ions but also by reduction with alkali metal amalgams.

The hydrodimerization of acrylonitrile (AN) by direct electrolysis or by alkali metal amalgams has been the subject of many investigations, due to the importance of the hydrodimer, adiponitrile (ADN), as an intermediate in the manufacture of Nylon 66. The primary reactions of electron transfer and interaction of the anions or radical ions formed are of fundamental interest and are not yet well understood. Numerous patents have dealt with the reduction by alkali metal amalgams. Knunyants *et al.* (1) and Katchalsky *et al.* (2) have carried out the reaction in strongly acid media. They claim relatively high yields of ADN together with minor quantities of propionitrile (PN). The disadvantage of the method is that a large portion of the alkali metal is wasted on reaction with the acid to give off hydrogen, instead of reacting with the AN. More recently, Baizer (3a) developed a direct electrolytic method which has attracted a lot of attention and has achieved commercial realization. The method is based on the finding that quaternary ammonium salts can dissolve high concentrations of AN and yield on electrolysis mainly ADN without any losses on side products such as PN or hydrogen. In a series of articles published by Baizer (3) he discusses the various problems involved in the electrolytic hydrodimerization of both acrylonitrile and other vinyl derivatives. In comparing the electrolytic and amalgam reductions, he arrived at a conclusion that electrolysis in the presence of alkali metal ions is merely *in situ* amalgam reduction. On electrolysis in neutral solution in the presence of alkali metal ions he obtained a low yield of ADN and a high yield of PN while in the presence of quaternary ammonium salts his product consisted mainly of ADN. He therefore concluded that it is necessary to avoid any use of amalgams or alkali metal ions and restricted his work to electrolysis in the presence of quaternary ammonium salts.

In the course of our studies of both the amalgam and the electrolytic reactions we have shown that although Baizer's conclusions were logical when based on his experimental data, additional data prove that the presence of alkali metals is not the cause for PN

formation. High yields of ADN can be obtained even with amalgam reductions, in neutral solutions, provided a suitable reaction medium is chosen.

After this work was completed, Matsuda (11) published a note proving that AN can be dimerized by alkali amalgams provided a proper solvent is used. His findings are in full agreement with our data and in contradiction with Baizer's interpretation.

In this work we have carried out a polarographic study of AN reduction to clarify some of the problems involved in the hydrodimerization. We then studied the reduction of AN in HCl solution by alkali metal amalgam, following the work of Knunyants and others, and compared the reduction reaction by direct electrolysis and by amalgam in neutral media. From these results in conjunction with Baizer's experiments we arrived at our conclusions.

Experimental and Results

Polarography in neutral solution.—All the polarographic measurements were carried out on a Metrohm Polarecord E261R polarograph. The supporting electrolyte was tetramethylammonium bromide (TMABr).

The reduction of AN was studied in aqueous solution in the concentration range of 10^{-3}M to 1M. The experiments carried out at high concentrations did not give well-defined polarograms and were very irreproducible. We therefore limited our studies to concentrations of AN up to 2 x 10^{-1}M. The half wave potential $E_{1/2}$ is between —1.95 and —2.02v. The number of electrons involved in the reduction was calculated and found to be $n=1.84$. The value reported by Platonova (4) is 1.6, while Sevastyanova and Tomilov (5) found $n=2.32$. Lazarov *et al.* (6) calculated from polarographic and galvanometric measurements, $n=2$. It seems therefore, justified to conclude that the reduction involves a two electron transfer process.

Polarography in acid solution.—Most polarographic studies in acid pH's are carried out in buffer systems or in the presence of phenol, benzoic acid, and such proton donors which do not give hydrogen discharge waves in the range of the reduction wave of the investigated compound. As we had special interest in hydrodimerization in the presence of HCl we decided to carry out our polarographic measurements also in the presence of HCl. The acid itself gives a wave for hydrogen discharge at $E_{1/2}$ = 1.6v. When a solution of both HCl and AN is analyzed it is possible to obtain two waves provided the acid concentration is low. The first coincides exactly with the hydrogen wave and the diffusion current equals the diffusion of HCl itself and the second is the AN reduction wave. The total diffusion current is equal to the current of AN. However, when one works at a constant AN concentration and increases gradually the acid content the hydrogen wave increases until it reaches the height of the AN diffusion current and then only one wave is observed. This is demonstrated in Fig. 1. The measured drop time was $t=3$ sec, and the rate of mercury flow was $m=2.55$ mg/sec. The height of the mercury reservoir was 55 cm. In order to determine the ratio of HCl/AN where a single wave appears, we carried out a series of experiments where, for every AN concentration, the HCl concentration was gradually increased. By interpolation we found in every case the acid concentration where a single wave appears and plotted this HCl concentration against the corresponding AN concentration (Fig. 2). The slope of the line gives (HCl)/(AN) = 0.65, the average experimental value for the appearance of a single wave. The presence of KCl does not interfere with the single wave of AN/HCl and the K wave appears at more negative values of —2.2v.

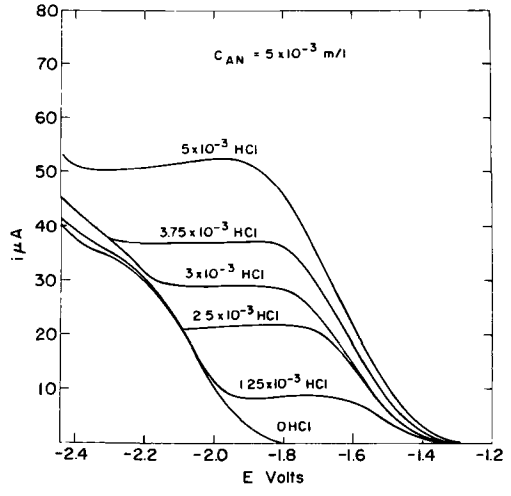

Fig. 1. Polarographic waves of AN with increasing concentrations of HCl.

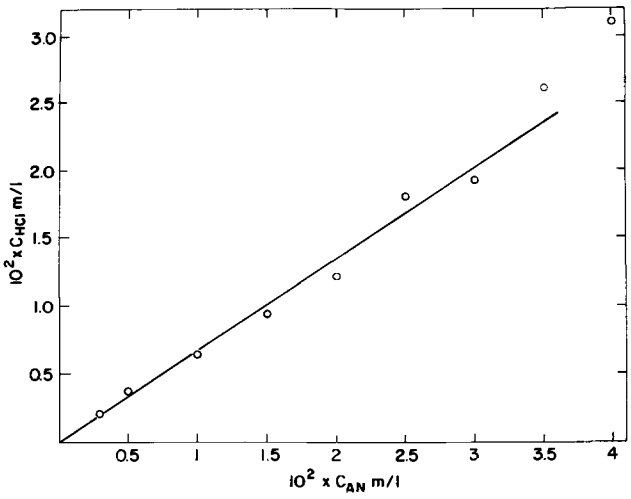

Fig. 2. Interpolated values for HCl concentration yielding a single wave with AN *vs.* the corresponding AN concentrations.

In the presence of acid the over-all cathode reaction may be written as

$$AN + nH^+ + ne \rightarrow ANH_n$$

Taking the values for diffusion constants of AN, D_{AN} = 8.2 x 10^{-6} cm²/sec (4) and of H^+, D_{H^+} = 9.3 x 10^{-5} cm²/sec, one can calculate the number of electrons involved in the reduction step. When the ratio of concentration HCl/AN=0.65 the diffusion currents for AN and HCl may be considered equal and therefore

$$n_{AN}C_{AN}D_{AN}^{1/2} = n_H + C_H + D_{H^+}{}^{1/2}$$

hence

$$n_{AN} = 2.2$$

This number depends of course, on the values of the diffusion constants used and could therefore vary slightly. It shows, however, that the reduction under these conditions involves two electrons and two protons and should lead to PN exclusively. This point will be further elaborated in the Discussion.

Amalgam reduction in acid solutions.—Knunyants *et al.* (1) and Katchalsky *et al.* (2) have carried out K-amalgam reductions of AN dissolved in 10-20% HCl. They claimed ADN yields of 60-80% and PN yields of about 10%, based on the amount of AN consumed in the reaction. We have repeated their experiments in order to get a quantitative correlation between the HCl and AN concentrations in the reacting mixture on the one hand and the yields of ADN, PN, and H_2 on the other.

The experiments were carried out in the following way: The reaction flask, described in Fig. 3, consisted of a glass tube, 20 cm long, provided with a cooling jacket, a supply of amalgam through a capil-

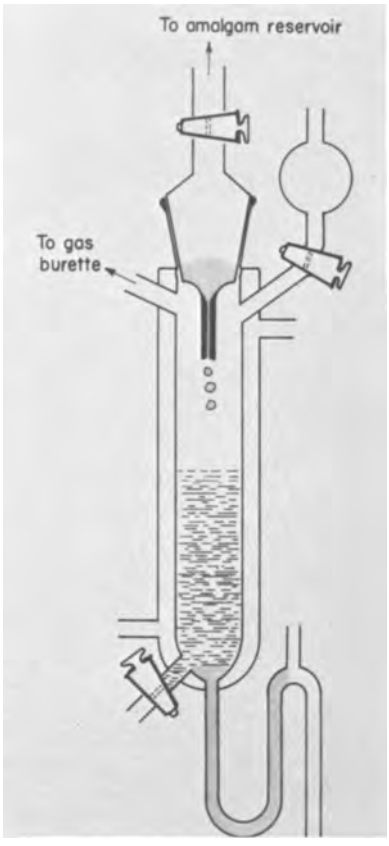

Fig. 3. Reaction flask for amalgam reduction in acid media

lary at the top of the tube, a narrow syphon at the bottom for the outflow of the depleted amalgam, two stopcocks for introduction of the solution and recovery of the products, and a gas buret for measuring the hydrogen evolved. In every experiment 15 cc of a 5% AN solution were used (experiments with 2 and 10% AN were also carried out). The amalgam was freshly prepared by electrolysis of KOH, and was kept under a layer of toluene until used. The concentration of the alkali metal was 4-9 m moles/100 g amalgam. The hydrogen evolved ensured proper mixing of the reaction mixture. The temperature was kept at 5°C. At the end of the reaction the K concentration in the depleted amalgam was determined by titration. The reaction mixture was diluted with water, made strongly alkaline with KOH, a weighed amount of butyronitrile was added as internal marker, and the organic components were extracted with methylene chloride. The products were analyzed by gas chromatography on a polyester resin as stationary phase. In every experiment the per cent conversion was kept low (under 30%) in order to avoid the interference of large quantities of alkali chloride precipitating during the reaction. The calculated yields refer to cyano group equivalents and are based on the potassium metal consumed. The results of experiments for 5% AN in HCl solution of concentrations ranging from 1 to 20%, are presented in Fig. 4. As could be expected the amount of hydrogen evolved increases with the HCl concentration while the PN decreases. The interesting fact is that ADN increases with the increase in HCl concentration, and considering the decrease in PN, it amounts to an increase in the ADN/PN ratio roughly proportional to the square of the HCl concentration. This accounts for the fact that prior to Baizer's work the hydrodimerization was carried out preferentially at high HCl concentration in spite of the large losses in alkali metal reacting with the acid. The effect of the nature of the alkali metal was studied by reacting K, Na, and Li amalgams with a 5% AN solution in 20% HCl. The results are presented in Fig. 5. The

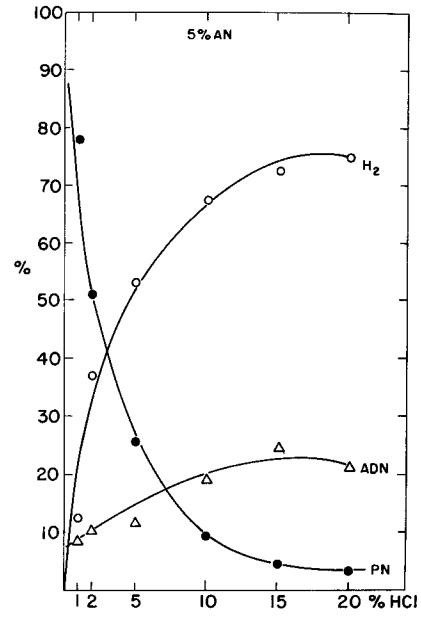

Fig. 4. Per cent yields of H_2, PN, and ADN calculated on the basis of reacted potassium metal.

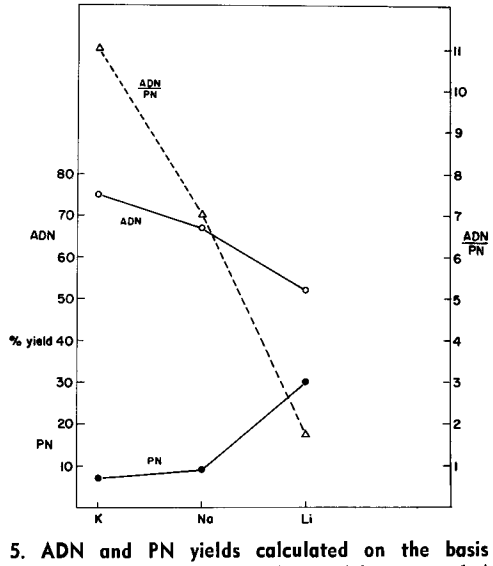

Fig. 5. ADN and PN yields calculated on the basis of reacted AN, for K, Na, and Li amalgams. The ratio of ADN/PN for the same metals.

yields of ADN and PN are calculated, in this case, in respect to the amount of reacted AN and also refer to cyano group equivalents. It can be seen that the ADN yield decreases, while the PN yield increases, thus making the ADN/PN ratio decrease sharply in the order K, Na, Li.

Amalgam and electrolytic reduction in neutral solutions.—Numerous experiments carried out in HCl solutions, or even in buffered solutions at pH 5 have shown that no ADN can be obtained by direct electrolysis. In order to compare electrolytic and amalgam reductions we had to restrict ourselves to neutral or slightly alkaline media. We have used solutions buffered with 1M phosphates (see Table I), to maintain a pH between 6.5-8. We have also designed the electrolytic and amalgam cells in such a way as to obtain comparable conditions at the mercury interface for both sets of experiments. The electrolysis cell was comprised of a cathode compartment and an anode compartment separated by a sintered glass diaphragm. The mercury cathode (3 cm^2 area), and the catholyte were stirred mechanically. The cathode voltage was

Table I. Comparison of electrolysis and amalgam reactions in neutral media

Type of experiment	Buffer	pH	QmF	Kmeq	2PN/H_2	2ADN/PN
Electrolysis	NaK phosphate	6.3-7.4	7.2	—	20	0.05
Electrolysis	NaK phosphate	6.3-7.4	7.2	—	13	0.09
Electrolysis	$(CH_3)_4N$ phosphate	7.0-7.8	7.6	—	6.4	0.04
Electrolysis	$(CH_3)_4N$ phosphate	6.5-7.4	7.2	—	4.2	0.09
K amalgam	Na, K phosphate	6.2-7.7	—	5.3	22	0.09
K amalgam	Na, K phosphate	6.2-7.7	—	5.4	26	0.05
K amalgam	Na, K phosphate	6.2-8.6	—	4.9	25	0.08

maintained at —2.0v *vs.* a calomel electrode. The currents used were approximately 100 ma, and the experiments were carried out for 1-3 hr each. The amalgam reactor was made from a 20 mm diameter glass tube (same as the cathode compartment in the electrolysis cell). The amalgam was introduced through a side capillary tube into the bottom of the reactor where a small pool of amalgam formed. The surface area of this amalgam pool was the same as the mercury cathode in the electrolysis experiments. The reacted amalgam then overflowed through a syphon system into a measuring cylinder. Here also both the amalgam and the reaction solutions were stirred mechanically. The rate of flow of the amalgam was adjusted to be equivalent to the electric current, thus approaching, as much as possible, the conditions in the electrolytic runs. The results are presented in Table I. The AN concentration was 5%, and the phosphate buffer was 1M. The *p*H was measured before and after the reaction, and the values are given in the third column. Column 4 gives the number of mili Farads used in every electrolysis run, and column 5, the number of milliequivalents of K metal reacted. 2PN/H_2 and 2ADN/PN represent molar ratios.

From Table I one can see that identical results are obtained from electrolytic or from amalgam reductions in neutral media. It is also evident that replacing the Na^+ and K^+ by $(CH_3)_4N^+$ does not affect any change on the ADN/PN ratio. This is contrary to Baizer's observations. The discrepency is due to the difference in experimental conditions and will be dealt with in the Discussion. In order to check our experimental technique, we also repeated some experiments, under the same conditions as prescribed by Baizer, namely, a high concentration of AN in concentrated aqueous solution of tetraethylammonium p-toluene sulfonate; we obtained results identical with those reported by that author.

Discussion

Acid media.—Electrolysis experiments in the presence of M^+ or $(CH_3)_4N^+$ in acid media yielded only hydrogen and PN without any trace of ADN. The polarographic runs under similar conditions also show that the AN wave disappears and only the hydrogen discharge wave remains. Thus electrolytic reduction of AN in the presence of acid is apparently carried out by the hydrogen atoms discharged at the cathode. It was shown that the single wave appears when two hydrogen atoms are discharged for every AN molecule diffusing to the cathode. This means, that the reduction should result in PN formation, in accordance with the findings of the electrolysis experiments. It was also shown that potassium ions in solution do not affect the products of the reaction. This is in accord with the polarographic analysis that shows that the potassium wave does not interfere with the HCl-AN wave.

The amalgam experiments, on the other hand, yield hydrogen, PN, and also ADN. The interpretation of this difference between the electrolytic and amalgam reactions may be due to the fact that while the bulk of the solution in both cases is acid, the reaction site, *i.e.* the mercury interface, is more alkaline in the amalgam reaction. In the latter case the metal cations are in very high concentration in the double layer and will therefore affect the outcome of the reaction. The short life intermediate formed will interact with acid to give PN. In the case of lithium amalgam, this product has a higher reduction potential and will therefore give higher yields of PN (see Fig. 5).

The mechanism of formation of ADN must take into consideration the rather interesting fact that the ADN yield increases as a function of HCl concentration. This suggests that a bonding between HCl and AN may be formed. It is well known that strong acids induce N-protonation of nitriles and form crystalline nitrilium salts, *e.g.*, acetonitrile yields with anhydrous HCl, a crystalline compound having a formula of $CH_3-\underset{\underset{Cl}{|}}{C}=N=H$ (7, 8). Interaction with the acid would probably also account for the fact that the solubility of AN increases from 5% in water to 10% in a 20% solution of hydrochloric acid. If protonation of the nitrile in aqueous acid can be assumed, an equilibrium would be established

$$CH_2=CH-C\equiv N + H^+ \rightleftarrows CH_2=CH-C\equiv \overset{+}{N}H$$

This would be followed by interaction with an alkali metal atom (Me) from the amalgam to produce an intermediate radical, which will isomerize to give

$$CH_2=CH-C\equiv \overset{+}{N}H + Me \rightarrow (CH_2=CH-\dot{C}=NH) + Me^+ \rightleftarrows \dot{C}H_2-CH_2-C\equiv N + Me^+$$

The free radicals thus obtained will yield ADN on dimerization. One should realize that when dealing with a reaction taking place on the mercury interface the concentration of free radicals at the reaction site is very high and therefore the probability of dimerization is much higher than for polymerization. The later reaction does, in fact, take place to some extent and can be diminished somewhat by free radical inhibitors. The above mechanism is in complete accord with the one recently suggested by Misono *et al.* (9) for the hydrodimerization of acrolein in p-toluenesulfonic acid solution.

Neutral media.—From our polarographic data we concluded that in neutral media a two electron transfer takes place to yield the dinegative ion $AN^=$. In the case of amalgams the double adduct MeANMe is probably formed. From the results presented in Table I it seems that in neutral media the amalgam and electrolytic reduction give the same results, and in the latter case the presence or absence of alkali cations does not affect the results. We can therefore treat the two cases similarly and consider the active species as $AN^=$. As no acid is present the $AN^=$ formed will have a longer life, and it can interact either with water or with another molecule of AN in a mechanism similar to that suggested by Baizer (3a).[1]

$$(CH_2-\underset{\underset{CN}{|}}{CH})^= + H_2O \xrightarrow{k_1} CH_3-\underset{\underset{CN}{|}}{CH}^- \xrightarrow{+H_2O} CH_3-\underset{\underset{CN}{|}}{CH_2} \qquad [1]$$

$$(CH_2-\underset{\underset{CN}{|}}{CH})^= + CH_2=\underset{\underset{CN}{|}}{CH} \xrightarrow{k_2}$$

[1] Beck (12) suggests that the intermediate anion is $-CH_2-CH_2-CN$. On energetic grounds this does not seem plausible to us.

$$\begin{array}{l} {}^{-}CH-CH_2-CH_2-\bar{C}H \\ \quad\;\; | \qquad\qquad\quad | \\ \quad CN \qquad\qquad CN \end{array}$$

$$\xrightarrow{+2H_2O} \begin{array}{l} CH_2-CH_2-CH_2-CH_2 \\ \quad | \qquad\qquad\quad | \\ \quad CN \qquad\qquad CN \end{array} \qquad [2]$$

The rate of reaction [1] will be determined by the interaction with the first molecule of water because the anion $CH_3-\bar{C}H$ formed can either give PN on
|
CN
interaction with another molecule of water or initiate the polymerization of AN. Since very little polymer is formed we can neglect this polymerization reaction and consider that every such anion formed will have to lead eventually to PN. The rate of reaction [2] will be determined by the interaction with AN to give the dimeric dianion $^{-}CH-CH_2-CH_2-CH^{-}$. Here
| |
CN CN
again we neglect the polymerization reaction, and therefore this anion will have to lead to ADN formation on protonation. We can thus consider that the ADN/PN ratio will be given by the equation

$$\frac{ADN}{PN} = \frac{k_2(AN)}{k_1(H_2O)}$$

In order to be able to estimate the rate constant from our data we have to know the concentrations of AN and H_2O in the reaction site which is the mercury interface. This will depend on the relative polarities of the two species and also on interaction factors with the solvent medium. Since we do not know, at this stage, the various factors involved we will only assume that the ratio of the concentrations AN/H_2O at the mercury interface is proportional to the ratio in the bulk of the solution. The AN concentration in our experiments was 1M, the water concentration about 50M, and the average experimental value for ADN/PN = 0.08. We therefore estimate $k_2/k_1 = 4$, leading to the rather unexpected results that AN is more reactive than water towards the di-anion species. This can be rationalized on the grounds that both reactions will need little or no activation energy and it is only the entropy factors that will determine the rate constants. In this case of interaction of two similar molecules such as $AN^{=}$ and AN the steric factors are much more favorable and therefore it is conceivable that it will be faster. Increasing the AN concentration will increase the ADN yield as is also evident from Baizer's results. The same effect can also be achieved by decreasing the water concentration, *e.g.*, by working at high salt content. This was done by Baizer when carrying out electrolysis in a solution of 13% AN in a 40% solution of Na or K p-toluene sulfonate to yield a ratio of ADN/PN = 0.65. From our data we could predict a value ADN/PN = 4 x 3/30 = 0.4, in fairly good agreement with the value obtained by Baizer. This is not the case, however, with a concentration of 40% AN in 50% tetraethylammonium p-toluene sulfonate solution. There, we would expect a value of ADN/PN = 4 x 8/20 = 1.6, and the experimental value from both our data and Baizer's is higher than 100. We conclude, therefore, that it is the presence of tetraethylammonium tosylate that is responsible for the higher yields of ADN, rather than the presence of alkali metals being responsible for the higher yields of PN, according to Baizer's claims. This point could be settled by interacting alkali amalgam with an AN solution of tetraethylammonium tosylate. If our argument is correct we should be able to obtain high ADN yields in spite of the presence of alkali metals. This was really shown to be the case for K, Na and even Li amalgams. They all yielded ADN/PN ratios higher than 100 when reacting with a 40% AN solution in 60% (Et_4N)pTS. Similar results were also reported by Matsuda (11) and in ICI patents (13).

Other quaternary ammonium ions such as trimethylbenzylammonium were also very effective while tetramethylammonium was much less effective. A full study of the effect of the cationic and the anionic parts of the salt as well as the effect of the salt concentration and the AN concentration is in progress. At this stage we can only state the well-established fact that salts like tetraethylammonium p-toluene sulfonate have a pronounced effect on the yield of ADN in both electrolytic and amalgam reactions.

Feoktistov *et al.* (14) have studied the effect of water on the electrochemical reduction of AN in dimethyl formamide in the presence of tetrabutylammonium iodide. They claim that the accumulation of large organic cations in the electric double layer leads to a decrease in the volume occupied by the water molecules, thus leading to a lower protonation to propionitrile and to a higher probability of the $AN^{=}$ reacting with a neutral AN. This may be an over simplification of the problem. In a more general way we may say that the effectiveness of these salts may be due to their large ionic size and to the peculiar characteristic of their aqueous solutions as discussed for example by Wen and Saito (10). These characteristics and their ability to solvate both water and AN enables them to change the path of the reaction of alkali metal amalgams from the normal reduction to PN to hydrodimerization into ADN.

Acknowledgment

The authors are indebted to UCB (Union Chimique —Chemische Bedrijven) S.A. Bruxelles, for financial support of this work.

Manuscript received Feb. 6, 1967; revised manuscript received May 2, 1967.

Any discussion of this paper will appear in a Discussion Section to be published in the June 1968 JOURNAL.

REFERENCES

1a. I. L. Knunyants *et al.*, U.S.S.R. Pat 105.286 (1954); 1b. I. L. Knunyants and N. P. Gambaryan. *Uspekhi Khim.*, **23**, 781 (1954).
2. A. Katchalsky, D. Vofsi, and J. Padova, Israel Pat. 13842 (1960).
3a. M. M. Baizer, *This Journal*, **111**, 215 (1964); 3b. M. M. Baizer and J. D. Anderson, *ibid.*, **111**, 223 (1964); 3c. M. M. Baizer, *J. Org. Chem.*, **29**, 1670 (1964); 3d. M. M. Baizer and J. D. Anderson, *ibid.*, **30**, 1348 (1965).
4. M. W. Platonova, *J. Anal. Chem., U.S.S.R.*, **11**, 317 (1956).
5. I. G. Sevast'yanova and A. P. Tomilov, *Zhur. Obshchei Khim.*, **33**, 2815 (1963).
6. S. Lazarov, A. Trifonov, and T. Vitanov, *Z. Phys. Chem.*, **226**, 221 (1964).
7. A. Hantzsch, *Ber.*, **64**, 667 (1931).
8. L. E. Hinkel and G. J. Traharne, *J. Chem. Soc.*, **1945**, 866.
9. A. Misono, T. Osa, and T. Yamagishi, *J. Chem. Soc. Japan, Indust. Chem. Section*, **69**, 945 (1966).
10. W. Y. Wen and S. Saito, *J. Phys. Chem.*, **68**, 2639 (1964).
11. Fujio Matsuda, *Tetrahedron Letters*, **49**, 6193 (1966).
12. Fritz Beck, *Chem. Ing. Techn.*, **37**, 607 (1965).
13. ICI Australian Pat. 662661 (1964).
14. L. G. Feoktistov, A. P. Tomilov, and I. G. Sevast'yanova, *Electrokhimiya*, **1**, 1300 (1965).

Adsorption and Oxidation of Methanol on a Platinum Electrode

T. Biegler and D. F. A. Koch

Division of Mineral Chemistry, CSIRO, P.O. Box 124 Port Melbourne, Victoria, Australia

ABSTRACT

Kinetics of adsorption of methanol from 1M H_2SO_4 onto a Pt electrode is examined. The electrode potential is stepped from 1.55v to a value in the range 0.2-0.7v, and an anodic current flows due to chemisorption of methanol. The resulting current-time curves are analyzed according to Elovich kinetics, a procedure which allows evaluation of the initial current for a clean surface. A rate equation for adsorption is obtained on the basis of the potential and concentration dependence of initial current. Steady-state equations for coverage and current are derived with the assumption of irreversibility for the adsorption and further oxidation reactions. The nature of the adsorbed intermediate is discussed by comparing the charges used in forming and oxidizing a monolayer, and the evidence suggests it has the same oxidation state as CO.

The mechanisms of oxidation of organic fuels at catalytically active electrodes, in particular platinum, have been studied intensively over the past few years (1). The electrochemical behavior of these systems is complex. Current-voltage curves can show several maxima and are strongly dependent on time and the prehistory of the electrode; a steady state is an elusive condition although conventional polarization curves have found a limited application; reaction orders are generally fractional and sometimes negative; the reactions involve adsorbed species which remain attached to the electrode during washing or exposure to air and can subsequently be detected electrochemically.

In their interpretation of current-voltage curves Bagotskii and co-workers (2-5) have concluded that (*a*) adsorption of reactants follows a logarithmic isotherm, (*b*) only adsorbed species are oxidized, and (c) the catalytic activity of the electrode is modified by the formation of various kinds of surface oxides. On this basis they have explained the presence of current minima in similar potential regions for a number of compounds and have developed kinetic equations which account for the shapes of the curves and their dependence on reactant concentration.

The present work is concerned with adsorption and oxidation of methanol in the low potential region. It is clear from recent work (5-8) that adsorption of methanol involves dehydrogenation of the molecule. If the process occurs at open circuit, the potential of the electrode falls (7), the surface becoming covered with H atoms and a chemisorbed methanol residue. At constant potential, however, ionization of the H atoms occurs and the chemisorption of methanol is accompanied by an anodic current (5, 9). We have used this fact to characterize the adsorption process by means of a simple potential-step technique.[1] In general, our results confirm the conclusions of the Russian workers concerning the kinetics of adsorption and its role in the over-all reaction, but we differ considerably in matters of detailed interpretation.

Experimental

An all-glass cell of conventional design contained the working electrode of 30 gauge Pt wire sealed into soft glass to expose 4.5 mm (geometric area 0.0454 cm^2). Determination of maximum H adsorption for this electrode from potential sweep measurements (10, 11) gave a value of 350 $\mu coul/cm^2$, indicating a roughness factor of about 1.7. A few runs using a larger Pt foil electrode (1.69 cm^2) gave comparable results. Currents are quoted on the basis of geometric electrode area.

The counter electrode (Pt) was in a compartment separated from the main body of the cell by a glass sinter, and the reference electrode (saturated calomel) was well isolated from the cell by a bridge (1M H_2SO_4) closed at one end by a fine sinter and terminating in a Luggin capillary in the cell. All potentials are quoted with respect to the standard hydrogen electrode (—0.245v *vs.* SCE).

The supporting electrolyte, 1M H_2SO_4, was prepared from AnalaR reagent and water redistilled from alkaline permanganate. Reagent grade methanol was used, and neither distillation of the methanol nor preelectrolysis of the supporting electrolyte affected results significantly. Nitrogen was purified by passage over heated copper turnings and through a cold trap, followed by scrubbing in a presaturator containing the solution under investigation.

A simple bias unit of potential dividers and switches was used to program the electrode potential which was controlled by a Wenking fast rise potentiostat; the final potential step operated through a mercury-wetted relay. By discharging a capacitor through the relay coil, rectangular pulses of duration 10-500 msec (depending on the capacitor value) could be obtained.

Current was measured as the voltage drop across a decade resistance box. Transients were observed on a Tektronix type 533 oscilloscope with type B plug-in amplifier and photographed with a type C12 camera. All measurements were made at 25°C.

Results and Discussion

Qualitative features of current-time transients.—The adsorption reaction at low potentials was studied by holding the electrode for a period t_{ox} at a fairly positive potential ϕ_{ox}, around +1.5v, where coverage by species other than oxide was negligible, and then stepping the potential to the desired value ϕ. For 0.7v $> \phi >$ 0.2v, the sequence of events is as follows (Fig. 1). The oxide layer is rapidly reduced and a large cathodic current flows. This region is not resolved with the current and time scales of Fig. 1. As the surface is reduced, sites become vacant for the adsorption of methanol, and the current soon becomes anodic. The time at which the current changes sign depends on the extent of initial oxidation of the surface and the kinetics of surface reduction and methanol adsorption; it is usually in the range 30-50 msec. The anodic current then rises steeply to a maximum and decays at a relatively slow rate. A similar decrease in anodic current with time has been observed (5, 9) in experiments where methanol is rapidly added to a supporting electrolyte in which a Pt electrode is held at a low potential. However, the pulse technique used here allows the current to be followed at shorter times

[1] After completion of this manuscript, a paper by S. S. Beskorovainaya, Yu. B. Vasil'ev, and V. S. Bagotskii [*Electrokhimiya*, 2, 167 (1966)], in which a similar potential step technique was used, came to our attention.

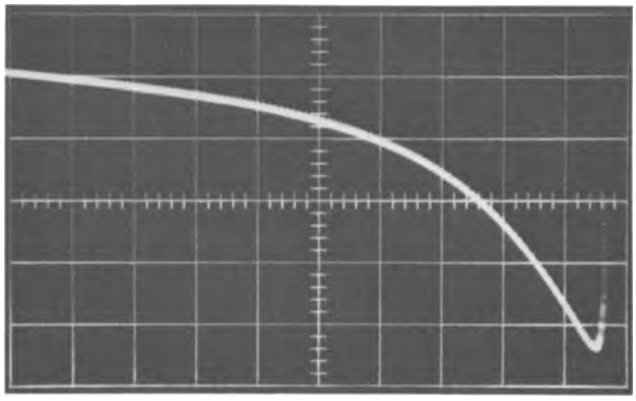

Fig. 1. Current/time curve for methanol adsorption. 0.5M methanol, ϕ_{ox} = 1.55v, t_{ox} = 20 msec, ϕ = 0.37v. Horizontal scale 200 msec/cm vertical 3.33μa/cm. Cathodic potential step occurs at 0.2 cm from left-hand edge.

(the anodic maximum is reached in as little as 50 msec), and the importance of this will become clear below.

The shape of the early portion of such a current-time curve depends largely on the kinetics of reduction of the Pt surface and hence on ϕ_{ox} and t_{ox}, as well as on ϕ. At constant ϕ, the other factors can be varied between wide limits without altering significantly the latter part of the curve. If ϕ_{ox} is less than about 1.1v, insufficient oxide is formed and, on reduction, the surface does not reach full activity. At too high potentials (>1.75v) oxygen is evolved, and its reduction after the cathodic step influences the measured current. The value of t_{ox} determines the amount of oxide formed and hence the kinetics of its reduction. With longer t_{ox} surface reduction is slower and the anodic peak is slightly lowered and shifted to longer times. However, this shift in the maximum does not influence later portions of the current-time curves.

As our aim was to observe as much of the transient as possible, the procedure finally adopted was to anodize at 1.55v for short periods (~15 msec, a time appropriate to the small electrode but too short for the larger one) and repeat with manual switching of the relay until the surface reached a maximum activity. In other words, a series of rectangular pulses of short duration separated by intervals of a few seconds was applied between the potential of interest, ϕ, and 1.55v. After a few such pulses the desired condition of maximum anodic current after the cathodic potential step was attained. This activation procedure resulted in very reproducible current-time curves. A surface cleaning program similar to that of Gilman (11), which gave a more complete and less easily reduced Pt surface oxide, was not suitable for the present purposes.

Analysis of current-time curves.—Curves of the same general shape as Fig. 1 are found in the potential range 0.2-0.7v. The current decreases with potential (see below) and 0.2v represents about the lower limit at which the transient can be measured with the present equipment. It is important to note that below about 0.55v there is no appreciable steady-state current, the curve eventually decaying to zero.

These curves can be interpreted if the oxidation of methanol is considered to occur in two stages, the first being a chemisorption process involving dehydrogenation of the molecule and the second the further oxidation of the adsorbed species to CO_2; at low potentials the first process is much the faster. Similar views have also been put forward by Petrii *et al.* (8, 9) and Bagotskii and Vasil'ev (2, 5). The first step is written as

$$CH_3OH \rightarrow A_{ads} + n_1H^+ + n_1e \qquad [1]$$

and its rate is expected to decrease as the product, chemisorbed methanol (A_{ads}), accumulates on the surface. Thus, the form of the current decay curves reflects the way in which adsorption kinetics varies with surface coverage, provided that further oxidation of A_{ads} is slow.

The Elovich equation [see *e.g.* (12)] is frequently used to describe the kinetics of adsorption onto heterogeneous surfaces and has in fact recently been applied to the methanol system (4, 5). In a form appropriate to the present case the Elovich equation for the rate of reaction [1] is

$$I_1 = I_i \exp(-m_1\theta) \qquad [2]$$

which indicates that the current I_1 decreases exponentially with θ, the fractional coverage by A_{ads}, from an initial value I_i. The constant m_1 has the significance that, in the model where the free energy of activation $\Delta G_\theta^{o\neq}$ for adsorption on a heterogeneous surface increases linearly with coverage

$$m_1 = \frac{1}{RT}\frac{d\,\Delta G_\theta^{o\neq}}{d\theta} \qquad [3]$$

At potentials less than 0.55v, the approach to zero steady-state current indicates that the rate of further oxidation of A_{ads} is negligible compared with its rate of formation, at least over most of the curve. Under these circumstances

$$\theta = Q_t/Q_{sat} \qquad [4]$$

where Q_t is the charge passed to time t *via* reaction [1] and Q_{sat} is the charge needed to give θ = 1. Also

$$I_1 = \frac{dQ_t}{dt} = Q_{sat}\frac{d\theta}{dt} \qquad [5]$$

From [2] and [5]

$$\frac{d\theta}{dt} = \frac{I_i}{Q_{sat}}\exp(-m_1\theta) \qquad [6]$$

Integrating with boundary condition t = 0, θ = 0 gives

$$\exp(m_1\theta) = \frac{I_i m_1 t}{Q_{sat}} + 1 \qquad [7]$$

Using [7] and [2] and rearranging gives

$$\frac{1}{I_1} = \frac{1}{I_i} + \frac{m_1 t}{Q_{sat}} \qquad [8]$$

A current-time relationship of this form has previously been applied to the kinetics of Pt surface re-

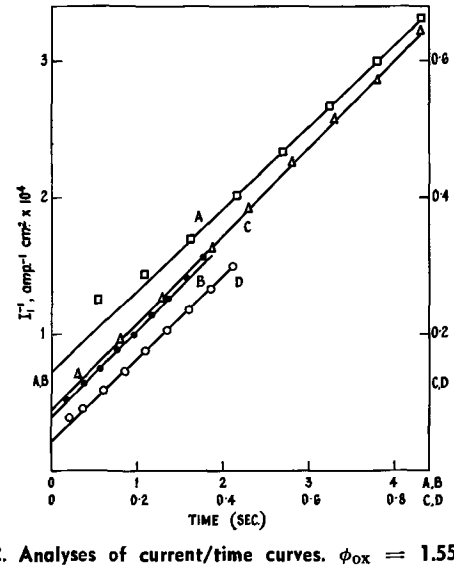

Fig. 2. Analyses of current/time curves. ϕ_{ox} = 1.55v, t_{ox} = 20 msec. A, 0.05M methanol, ϕ = 0.42v; B, 0.5M methanol, ϕ = 0.32v; C, 1.0M methanol, ϕ = 0.37v; D, 2.0M methanol, ϕ = 0.37v.

duction (13). Analyses of current-time curves for methanol adsorption according to Eq. [8] are shown in Fig. 2. Deviations occur at the very beginning of the curve, as a result of the influence of oxide reduction discussed above, and also after a time interval which corresponds to some 50% of the charge passed until the steady state is reached. The latter departures from Eq. [8] have at least two reasons: (*A*) Evaluation of the integrated current from Eq. [4] and [7] gives

$$\int_o^t I_i dt = Q_t = \frac{Q_{sat}}{m_1} \ln\left(1 + \frac{m_1 I_i t}{Q_{sat}}\right) \qquad [9]$$

which shows that the above equations cannot hold for long times since they predict an indefinite increase in Q_t. (*B*) As the current decays, any contribution from a further (slow) oxidation of A_{ads} or impurities becomes more significant.

It is found that for $\phi > 0.45$v significant deviations from Eq. [8] occur, the slopes of I_1^{-1} *vs.* t plots becoming dependent on potential. However, within the range 0.2-0.45v and over the concentration range examined, 0.05-5M methanol, the slopes of these plots are found to be constant, within experimental error, at 6.1 ± 0.6 x 10^3 cm^2 coulomb^{-1} based on the geometric area. We consider that so long as a slope of this value is obtained, extrapolation of these plots can reasonably be expected to yield the correct value of I_i^{-1} and hence give a measure of the rate of reaction [1] on a bare Pt surface. This assumption forms the basis of the study of the kinetics of this reaction.

Potential dependence of adsorption rate.—The potential dependence of I_i for 0.2M methanol is shown in Fig. 3. A Tafel slope of 125 mv is found at low potentials, but then the current passes through a flat maximum at about 0.55v. It is interesting to note that Beskorovainaya *et al.* (4) report a similar result, using an entirely different technique, for adsorption rates at constant, but not zero, coverage. The maximum in Fig. 3 occurs well before the main current peak, observed at 0.8-0.9v under sweep or steady-state conditions, which is supposed to be due to inhibition by Pt surface oxidation (14-16).

Three explanations for the departure from a Tafel relation can be suggested.

(*A*) A real decrease in the velocity of the rate-determining step of reaction [1] occurs, due to factors connected with the potential dependence of double layer structure, *e.g.*, hydrogen and oxygen adsorption.

(*B*) At higher potentials, the method of analyzing current-time curves is invalid and gives erroneously low I_i values. In support of this is the fact that the decrease in slopes of I_1^{-1} *vs.* t plots coincides with the departure from linearity in Fig. 3.

(*C*) At sufficiently high currents a different step of reaction [1], possibly involving a potential-independent surface reaction, becomes rate-determining. In this regard, there is some evidence from concentration dependence studies (see below) to suggest that rate limitation of reaction [1] is closely connected with the attainment of a certain current density.

Bagotskii and Vasil'ev (5) favor the first explanation and claim that the adsorption rate is highest when the combined coverage by hydrogen and oxygen is least. The Tafel behavior is then explained on the basis of an exponential increase in rate with decrease in H coverage which varies linearly with potential. However, the linear region in Fig. 3 extends to 0.47v, well beyond the H region [see *e.g.*, (1)], so that the above explanation for Tafel behavior seems unlikely. Furthermore, the decrease in rate observed at 0.55v occurs well below the minimum potential (~0.8v) for oxygen adsorption (10) and in view of these objections, an alternative explanation for Tafel behavior is desirable. Thus, if chemisorption is considered to be a charge transfer process as in reaction [1] an exponential dependence of rate on potential is to be expected. At present it is difficult to assess the relative importance of (*B*) and (*C*) above in explaining the observed departures from Tafel behavior.

Concentration dependence of adsorption rate.—Bagotskii and Vasil'ev (5) have shown that adsorption of methanol at constant coverage and potential follows first order kinetics. Figure 4 shows the variation of I_i with methanol concentration at three potentials. A linear dependence, in agreement with (5), is found at the lowest potential while curvature starts at 2M methanol for 0.37v and 1M for 0.42v. We feel it is significant that these deviations from linearity, together with the departure from a Tafel region mentioned above, occur when the current exceeds about 2 ma/cm^2 and the comments made in (C) above also hold here.

Rate equations for oxidation of methanol.—With the above mentioned limitations on potential and methanol concentration, the experimentally determined initial rates of reaction [1] can be described by

$$I_i = n_1 F k_1 C_m \exp\left(\frac{\beta_1 F \phi}{RT}\right) \qquad [10]$$

where the symmetry factor $\beta_1 \approx 0.5$, C_m is the methanol concentration and k_1 a rate constant. The product $n_1 k_1$ has the value 1.4 x 10^{-8} cm sec^{-1} at $\phi = 0$v, based on geometric electrode area.

Combination of Eq. [2] and [10] gives the full rate expression for reaction [1]

$$I_1 = n_1 F k_1 C_m \exp\left(\frac{\beta_1 F \phi}{RT}\right) \exp(-m_1 \theta) \qquad [11]$$

The further oxidation of chemisorbed methanol can be formulated

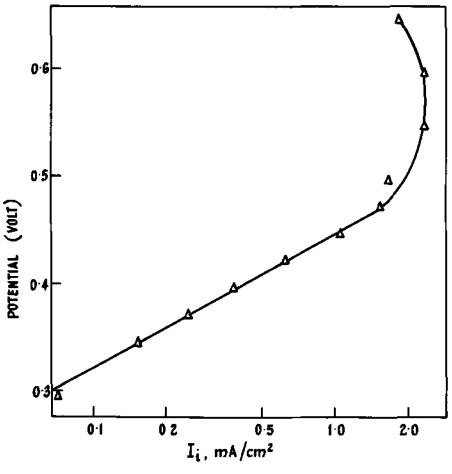

Fig. 3. Tafel plot for initial adsorption current (I_i). Methanol concentration 0.2M.

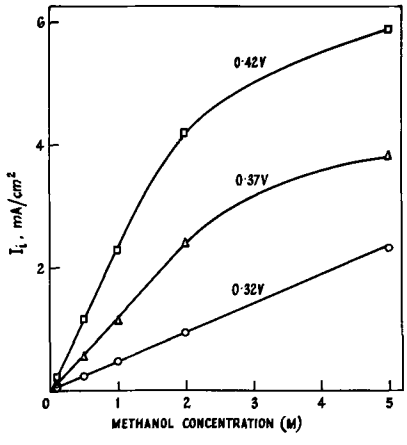

Fig. 4. Concentration dependence of initial adsorption current (I_i) at potentials indicated.

$$A_{ads} + H_2O \rightarrow CO_2 + n_2H^+ + n_2e \quad [12]$$

and, in view of the kinetics observed for reaction [1], a reasonable rate equation for this second step is

$$I_2 = n_2Fk_2 \exp\left(\frac{bF\phi}{RT}\right) \exp(m_2\theta) \quad [13]$$

where the constant b is determined by the Tafel characteristics of reaction [12].

This view of the mechanism of methanol oxidation is similar to those expressed in recent Russian work (2, 8) and Eq. [13] has the same form as Eq. [5] of ref. (2). Although combination of this type of relation with a logarithmic isotherm for adsorption of the intermediate has successfully been used to explain the observed fractional order of the over-all oxidation with respect to bulk methanol (2), we suggest an alternative interpretation of this result, as shown below.

Steady-state conditions.—There are strong grounds for considering both reactions [1] and [12] to be irreversible. The reversible methanol potential is close to $\phi = 0$v so all measurements are done at overpotentials of at least 0.2v. Experimentally it is found that desorption does not occur when an electrode bearing chemisorbed methanol is washed or transferred to a pure supporting electrolyte solution (9, 17). Furthermore, the hydrogen deposition method used to determine methanol coverages (3-5, 18) relies entirely on the irreversibility of the system.

With the assumption of irreversibility, the steady-state condition for constant θ (denoted by θ_{ss}) is that

$$\frac{I_1}{n_1} = \frac{I_2}{n_2} \quad [14]$$

From Eq. [11], [13], and [14] we obtain

$$\theta_{ss}(m_1 + m_2) = \ln\frac{k_1}{k_2}C_m + \frac{F\phi}{RT}(\beta_1 - b) \quad [15]$$

whence

$$\left(\frac{\partial\theta_{ss}}{\partial \ln C_m}\right)_\phi = \frac{1}{m_1 + m_2} \quad [16]$$

and

$$\left(\frac{\partial\theta_{ss}}{\partial\phi}\right)_{C_m} = \frac{F}{RT}\left(\frac{\beta_1 - b}{m_1 + m_2}\right) \quad [17]$$

The total current is the sum of I_1 and I_2 so that, using condition [14], the steady-state current is given by

$$I_{ss} = I_1\left(1 + \frac{n_2}{n_1}\right) \quad [18]$$

Introduction of equations for I_1 ([11]) and θ_{ss} ([15]) yields, after rearrangement,

$$\ln I_{ss} = \ln(nFk_1C_m) + \frac{\beta_1F\phi}{RT} - \frac{m_1}{m_1 + m_2}\left\{\ln\frac{k_1}{k_2}C_m + \frac{F\phi}{RT}(\beta_1 - b)\right\} \quad [19]$$

where $n = n_1 + n_2$.

Hence

$$\left(\frac{\partial \ln I_{ss}}{\partial \ln C_m}\right)_\phi = \frac{m_2}{m_1 + m_2} \quad [20]$$

and

$$\left(\frac{\partial\phi}{\partial \ln I_{ss}}\right)_{C_m} = \frac{RT}{F}\left(\frac{m_1 + m_2}{bm_1 + \beta_1m_2}\right) \quad [21]$$

The important result is that this treatment predicts variations of coverage and current with methanol concentration (Eq. [16] and [20]) which are very similar to those obtained (2, 5) when adsorption is presumed to be at equilibrium and to follow a logarithmic isotherm. Bagotskii and Vasil'ev (5) contend that the attainment of a definite concentration-dependent coverage is proof of a reversible equilibrium isotherm for the adsorption of methanol. The above evidence for irreversibility and the successful explanation of the concentration dependence of steady-state coverage and current on the basis of a strictly irreversible mechanism make this contention seem highly unlikely. We feel that similar considerations could have far-reaching implications in the interpretation of other electrocatalytic oxidations and support Brummer's recent remarks (19) concerning the relevance of adsorption "isotherms" in such studies.

It is not surprising that [16] has the characteristics of a logarithmic Temkin isotherm since the rate equation for the reverse of reaction [1] would contain an $\exp(m\theta)$ term as does [13]. In general, the rates of change of free energy and free energy of activation for adsorption with coverage are related through a symmetry factor [see *e.g.*, ref (20)], *i.e.*

$$m = \alpha f \quad [22]$$

where f appears in the Temkin isotherm

$$\theta = \frac{1}{f}\ln C_m + \text{const} \quad [23]$$

If it is assumed that $m_1 = m_2$ and that $\alpha = 0.5$ in [22], then the coefficient in [16] is the same as in the corresponding reversible isotherm. The two mechanisms are therefore experimentally indistinguishable on this point.

Experimental verification of [20] has been given (2) with values for $(\partial \ln I_{ss}/\partial \ln C_m)_\phi$ of 0.55-0.6 for methanol and similar values for other organic compounds. These results could be criticized on the grounds that they do not refer to steady-state measurements but were obtained with a sweep technique. However, we have carried out steady-state measurements, reached within several minutes, on the methanol system and find values of 0.53 increasing to 0.75 for concentrations up to 1M over the potential range 0.55-0.8v (Fig. 5). The maxima which occur at high concentrations and low potentials (Fig. 5) are probably due to the retardation of reaction [12] through a "high coverage" effect as suggested in ref. (2). It should be stressed that the above equations are only applicable within the validity of both the basic rate expressions, and

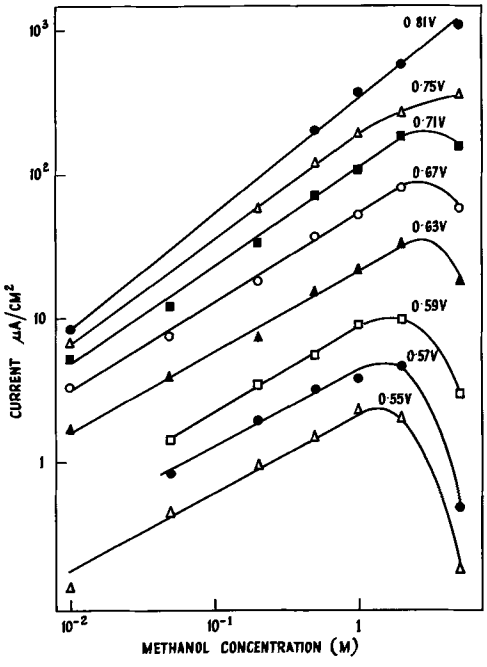

Fig. 5. Concentration dependence of steady-state current at potentials indicated.

Table I. Charges obtained by integration of current/time curves

Methanol concentration, M	Potential, v	Charge μcoul·cm^2
1	0.25	570
1	0.30	585
1	0.35	740
2	0.25	635
2	0.30	720

0.55v is probably the upper limit for this condition. The correct value of $m_2/(m_1 + m_2)$ is therefore close to 0.5 so that $m_1 \approx m_2$.

Evidence for the validity of the other coefficients, Eq. [17] and [21], is not overwhelming. With the assumption that $\beta_1 = b = \frac{1}{2}$, [17] shows that θ_{ss} should be independent of potential. Published results are somewhat encouraging on this point since Breiter and Gilman (18) and Lal *et al.* (9) find coverage independent of potential up to 0.6v while Khazova *et al.* (3) dispute this and give a bell-shaped curve with a maximum at 0.4-0.5v. There are reasons for believing that none of these experiments may have been able to produce correct results. Khazova *et al.* (3) have already pointed out that the procedures used in (9) and (18) both involve passage of the electrode through a potential region of high and, more importantly, fast adsorption prior to the coverage measurement. The irreversibility of the adsorption process then ensures that high coverages are also measured in the lower potential range. A possible objection to the measurements in ref. (3)-(5) (there are appreciable differences in the low potential data given in these references) is that insufficient time was allowed for the steady state to be reached at low potentials and concentrations. Thus, according to [7]

$$I_i t = \frac{Q_{sat}}{m_1} \{\exp(m_1\theta) - 1\} \qquad [24]$$

so that the time needed to reach a given value of θ is inversely proportional to I_i. For example, the data in ref. (5) indicate that for 0.5M methanol at 0.5v, a coverage of 0.8 is reached in about 10 sec. Assuming a Tafel slope of 120 mv for I_i the same coverage would be reached in 3000 sec at 0.2v and, if the steady-state coverage ($\sim$0.9) were indeed independent of ϕ, it would only be reached in a somewhat longer period. These experiments were apparently extended to 1200 sec, but longer term runs are needed to establish conclusively the potential dependence of θ_{ss}. For these reasons we prefer to consider the question still open.

With regard to [21], Bagotskii and Vasil'ev (2) found Tafel slopes of $\sim$120 mv for methanol oxidation in the low potential region; their measurements do not refer strictly to the steady state. Lal *et al.* (9) found a short linear region (0.45-0.6v) in steady-state Tafel plots with a slope of 60 mv. We have also obtained linear plots, over the same potential range, with slopes of around 90 mv. Taking $m_1 = m_2$ and $b = \beta_1 = 0.5$, Eq. [21] predicts a slope of 118 mv. The experimental discrepancies need to be resolved before any conclusions can be drawn.

Nature of adsorbed intermediate.—This is perhaps the central problem in elucidating the reaction mechanism. Giner (21) confirmed the existence of such an intermediate and suggested it had the composition CO or HCOOH. Podlovchenko and Gorgonova (6) used charging curves to determine the relative amounts of hydrogen and methanol adsorbed at open circuit. Finding that the two charges were about equal they concluded that three H atoms were lost upon chemisorption and therefore the intermediate was CHO. Bagotskii and Vasil'ev (5) compared the charge passed during adsorption at constant potential after adding methanol to the cell with the charge needed to oxidize the chemisorbed layer so produced. Although they gave no data, they claimed that these charges were equal and agreed with the assignment of a formula CHO to the intermediate. This conclusion would indicate that $n_1 = n_2$ in reactions [1] and [12].

The potential-step technique developed here can be used to provide information on this question. Current-time curves for reaction [1] are integrated from $t = 0$ by using the extrapolated portion of I_1^{-1} *vs.* t plots to give data for short times. The integration is extended until a steady state is reached (50-70 sec for the high methanol concentrations used). We assume that at sufficiently low potentials all of the charge is used to produce A_{ads} which remains on the surface. Double layer charging is of course complete at the times for which measurements are made. A rather arbitrary correction has to be made for the small steady-state current which, as a first approximation, is assumed to stay constant during the experiment. Results are shown in Table I. The problems involved in integrating the long and slowly decaying "tail" of the curves suggest that these values represent lower limits in each case.

Comparison with the results of ref. (5) indicates that the higher values of Table I correspond to coverages of about 0.9. We can therefore conclude that the deposition of a monolayer of A_{ads} involves at least 740 μcoul/geometric cm^2 (440 μcoul/real cm^2) and possibly some 10% more than this value. It is now possible to calculate m_1 from the experimental slopes of I_1^{-1} *vs.* t plots (Eq. [8]) and the above value for Q_{sat}. The value so found is 4.5 which is slightly less than half the f values (Eq. [22] and [23]) determined by Bagotskii *et al.* (2-5). Since a higher Q_{sat} would have given a larger m_1, this suggests that the value used here is indeed a lower limit for Q_{sat}.

From the point of view of comparison of Q_{sat} with Q_{ox}, the charge needed to oxidize a monolayer of intermediate to CO_2, it is unfortunate that much of the work on stripping of chemisorbed methanol has employed platinized electrodes of unknown or very approximately known areas (17, 21). However, Breiter and Gilman (18) report a value for Q_{ox} of 300 μcoul/geometric cm^2 which, using their value for saturation hydrogen coverage, corresponds to 185 μcoul/real cm^2. In agreement with this we obtain a value of 200 μcoul/real cm^2 by integrating the current peak given in (9) for the oxidation of adsorbed methanol on platinized platinum. Taking the mean of these two results for Q_{ox} and our value for Q_{sat} gives $Q_{sat}/Q_{ox} = 2.3$ and by reference to reactions [1] and [12] this is also equal to n_1/n_2. If these reactions represent the mechanism correctly then $n_1 + n_2 = 6$ and the ratio n_1/n_2 can only be 1, 2, or 5 (or their reciprocals). The data indicate that the experimental ratio is closest to 2, giving $n_1 = 4$, $n_2 = 2$. The oxidation state of the adsorbed intermediate would then correspond to CO.

It is possible that the different value for Q_{sat}/Q_{ox} found in (5) could be due to the difficulty in integrating the charge passed in the initial seconds of an experiment in which methanol is added to the cell with the electrode held at constant potential. We note that in Fig. 2 of ref. (5), showing the adsorption of 0.1M methanol at 0.4v, the maximum current was 45 μa/cm^2 compared with I_i of about 200 μa/cm^2 under similar conditions in the present experiments. This discrepancy supports the suggestion that values of Q_{sat} used in (5) were in error.

Manuscript received May 15, 1967.

Any discussion of this paper will appear in a Discussion Section to be published in the June 1968 JOURNAL

REFERENCES

1. P. Delahay, "Double Layer and Electrode Kinetics," Chap. 10 and references therein, Interscience Publishers, Inc., New York (1965).
2. V. S. Bagotskii and Yu. B. Vasil'ev, *Electrochim. Acta*, 9, 869 (1964).
3. O. A. Khazova, Yu. B. Vasil'ev, and V. S. Bagotskii, *Electrokhimiya*, 1, 84 (1965).

4. S. S. Beskorovainaya, Yu. B. Vasil'ev, and V. S. Bagotskii, *ibid.*, **1**, 1029 (1965).
5. V. S. Bagotskii and Yu. B. Vasil'ev, *Electrochim. Acta*, **11**, 1439 (1966).
6. B. I. Podlovchenko and E. P. Gorgonova, *Doklady Akad. Nauk SSSR*, **156**, 673 (1964).
7. B. I. Podlovchenko, O. A. Petrii, and E. P. Gorgonova, *Elektrokhimiya*, **1**, 182 (1965).
8. O. A. Petrii, B. I. Podlovchenko, A. N. Frumkin, and Khira Lal, *J. Electroanal. Chem.*, **10**, 253 (1965).
9. Khira Lal, O. A. Petrii, and B. I. Podlovchenko, *Elektrokhimiya*, **1**, 316 (1965).
10. F. G. Will and C. A. Knorr, *Z. Elektrochem.*, **64**, 258 (1960).
11. S. Gilman, *J. Phys. Chem.*, **67**, 78 (1963).
12. D. O. Hayward and B. M. W. Trapnell, "Chemisorption," Chap. III, Butterworths, London (1964).
13. D. F. A. Koch and R. G. A. R. MacLagan, Unpublished work.
14. R. P. Buck and L. R. Griffith, *This Journal*, **109**, 1005 (1962).
15. S. Gilman and M. W. Breiter, *ibid.*, **109**, 1099 (1962).
16. W. Vielstich, *Chem. Ing. Techn.*, **35**, 362 (1963).
17. T. O. Pavela, *Ann. Acad. Sci. Fennicae*, **A59**, (1954).
18. M. W. Breiter and S. Gilman, *This Journal*, **109**, 622 (1962).
19. S. B. Brummer, *ibid.*, **113**, 1041 (1966).
20. E. Gileadi and B. E. Conway in "Modern Aspects of Electrochemistry," No. 3, Chap. 5, J. O'M. Bockris and B. E. Conway, Editors, Butterworths, London (1964).
21. J. Giner, *Electrochim. Acta*, **9**, 63 (1964).

Effect of Hydrogen Absorbed by Electrode and Electrolyte on Hydrogen Coverage

David J. BenDaniel and Fritz G. Will

General Electric Research & Development Center, Schenectady, New York

ABSTRACT

An analysis is made of the effect of atomic hydrogen absorbed by the electrode and of molecular hydrogen absorbed by the electrolyte on the hydrogen coverage of the electrode as determined by nonsteady-state methods. The cases of anodic and cathodic voltage pulses and sweeps and the significant case of anodic charging curves are treated. A numerical evaluation of the results is made for the particular case of platinum electrodes in aqueous electrolytes for which reliable data on diffusion coefficients and solubilities could be obtained. The errors that are introduced in surface coverage determinations are found to be significantly larger than assumed previously. Theoretical results are compared to some experimental data obtained by other authors and agreement within 20% is found.

The coverage of an electrode surface with atomic hydrogen can be determined with nonsteady-state methods, like the methods of applying current steps (charging curves) (1) or voltage sweeps (2). Both methods have been used frequently for this purpose in the past. However, the equivalent amount of surface charge measured with these methods contains contributions from atomic hydrogen dissolved in the interior of the electrode and from molecular hydrogen dissolved in the electrolyte. Both effects have qualitatively been recognized quite early (1). However, no quantitative description of either effect on the measured amounts of charge has been given.

In fact, considerable misunderstanding exists with regard to the size of the two effects and their possible estimations. For example, some authors (3) believe that the maximum amount of hydrogen that can diffuse from the electrolyte to the surface in the hydrogen adsorption region is given by $i_o t_1$, where t_1 is the transition time for this region and i_o the limiting diffusion current. Others (4) believe that the amount of hydrogen diffusing from the interior of the electrode to the surface can be determined from measurements in helium-saturated solutions and that this amount is applicable to solutions containing various concentrations of molecular hydrogen.

This paper analyzes in a general fashion the relevant nonsteady-state diffusion problem under the assumption of diffusion control, *i.e.*, the rates of the phase boundary reactions, like discharge and recombination, are assumed to be fast compared to the rate of diffusion. The paper establishes the errors introduced in measurements of hydrogen coverage by dissolution of hydrogen in the electrode and in the electrolyte. The particular case of clean active platinum electrodes in aqueous electrolytes is considered for which the assumption of diffusion-control is known (5, 6) to apply. The calculations show that previous rough estimates can be off by as much as two orders of magnitude. The results may be applied to any metal-electrolyte system exhibiting diffusion control and true solution behavior for hydrogen. Metals showing true solution behavior absorb hydrogen endothermically and proportionally to the square root of hydrogen pressure (7, 8).

Analysis

We consider the semi-infinite slab geometry shown in Fig. 1, in which the electrode surface is at $x = 0$, the electrode interior at $0 < x < +\infty$ and the electrolyte at $-\infty < x < 0$. The errors of the mathematical

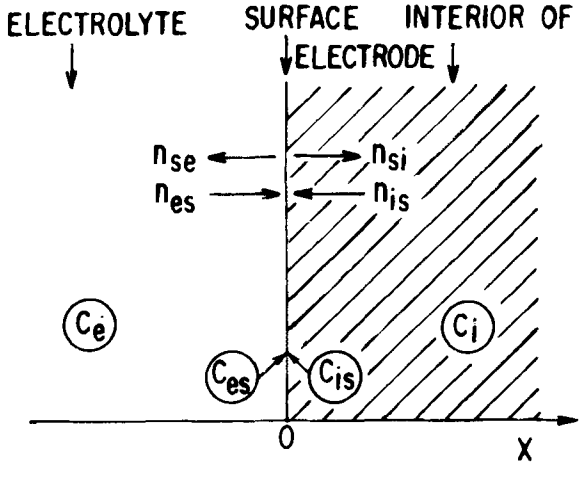

Fig. 1. Schematic diagram showing the interior of the electrode and the bulk of the electrolyte with the gas concentrations c_i and c_e, the concentrations near the surface, c_{is} and c_{es}, and the moles of gas n diffusing to and from the surface.

solutions for the semi-infinite problem due to the finite thickness of the electrode and electrolyte layer in actual practice are negligible for the experimental times of interest here.

In Fig. 1, the subscript e stands for electrolyte, s for surface, and i for interior of the electrode. Thus, c_i and c_{is} are the concentrations of atomic hydrogen in the electrode in its interior and near its surface, respectively; c_e and c_{es} are the corresponding concentrations of molecular hydrogen in the electrolyte. Also, n_{si} is the number of moles diffusing from the surface to the interior of the electrode and n_{is} is the number of moles diffusing in the opposite direction. Similarly, n_{se} and n_{es} are the number of moles diffusing from the surface into the electrolyte and in the opposite direction, respectively (see Fig. 1).

The diffusion of hydrogen both in the electrode and in the electrolyte is described by the familiar diffusion equation

$$D\partial^2 c/\partial x^2 = \partial c/\partial t \qquad [1]$$

where c is the concentration and D the diffusion coefficient of hydrogen in the electrode or in the electrolyte, respectively. The boundary conditions are determined as follows:

The concentration $c(x,t)$ vanishes for all finite times t as $x \to \infty$ in the electrode and as $x \to -\infty$ in the electrolyte. Thus, the first set of boundary conditions is

$$c_i(\infty,t) = 0 \qquad [2a]$$

$$c_e(-\infty,t) = 0 \qquad [2b]$$

In all cases of simple dissociative solution, the solubility of gases in metals is proportional to the square root of the gas pressure (8). This has been particularly shown for the absorption of hydrogen by platinum (7). Hence, for all times under equilibrium conditions

$$c_i(o,t) = c_{is}(t) = {}_oc_i\sqrt{p(t)/{}_op} \qquad [3a]$$

where ${}_oc_i$ is the standard solubility of atomic hydrogen for standard pressure ${}_op = 1$ atm.

According to Bunsen-Henry's law, the solubility of molecular hydrogen in the electrolyte is

$$c_e(o,t) = c_{es}(t) = {}_oc_e p(t)/{}_op \qquad [3b]$$

For equilibrium between molecular hydrogen and hydrogen ions, we can apply Nernst's equation for the electrode potential E

$$E(t) = -(RT/2\mathbf{F}) \ln (p(t)/{}_op) \qquad [4]$$

With [4] and the abbreviation

$$\Phi \equiv \mathbf{F}/RT \qquad [5]$$

we can obtain from [3a] and [4a] a second set of boundary conditions

$$c_{is}(t) = {}_oc_i \exp(-\Phi E(t)) \qquad [6a]$$

$$c_{es}(t) = {}_oc_e \exp(-2\Phi E(t)) \qquad [6b]$$

We consider two different initial time conditions.

1. The electrode and the electrolyte are essentially free of dissolved hydrogen, *i.e.*, a voltage $E_o >> 1/\Phi$ has been maintained for some time (several minutes) previous to $t = 0$ and is then changed in a cathodic direction.

Hence,

$$c_i(x,o) = 0 \qquad [7a]$$

$$c_e(x,o) = 0 \qquad [7b]$$

2. The electrode and the electrolyte hold equilibrium concentrations of hydrogen over finite distances $\pm x$ from the electrode surface, *i.e.*, a voltage $E_o \lesssim 1/\Phi$ has been maintained for some time and is changed in an anodic direction at time $t = 0$.

Hence,

$$c_i(x,o) = c_{is}(o) \qquad [8a]$$

$$c_e(x,o) = c_{es}(o) \qquad [8b]$$

The cases of voltage pulses and voltage sweeps will be treated below. The case of current steps (charging curves) reduces with good approximation to the case of voltage sweeps since, in the range of interest, the voltage changes to the first approximation linearly with time (1, 3, 4).

Electrode and electrolyte free of hydrogen, i.e. $E_o >> 1/\Phi$.—Cathodic voltage pulses.—At time $t = 0$, the voltage changes from its original value $E_o >> 1/\Phi$ to a value E_1 where it is maintained until at time t_1 it changes back to E_o, as shown in Fig. 2a. The analysis involves the application of standard mathematical techniques, *i.e.*, Laplace transforms.

The amount of atomic hydrogen dissolved in the electrode in moles H/cm² of electrode surface as a function of time is

$$n_{i\downarrow}(t) = 2{}_oc_i\sqrt{D_i t/\pi}\exp(-\Phi E_1)\,[1 - \sqrt{1 - t_1/t}\,u(t - t_1)] \qquad [9a]$$

The corresponding expression for the amount of molecular hydrogen dissolved in the electrolyte in moles H_2/cm² is

$$n_{e\downarrow}(t) = 2{}_oc_e\sqrt{D_e t/\pi}\exp(-2\Phi E_1)\,[1 - \sqrt{1 - t_1/t}\,u(t - t_1)] \qquad [9b]$$

The expression $\exp[-\Phi(E_o - E_1)]$ has to be added within the brackets of [9a] in cases when $E_o \approx 1/\Phi$. For [9b] the correction factor is $\exp[-2\Phi(E_o - E_1)]$. In [9a] and [9b] we define

$$u(t - t_1)\begin{cases} \equiv 0 \text{ for } t < t_1 \\ \equiv 1 \text{ for } t > t_1 \end{cases} \qquad [10]$$

If we let $t = t_1$ in [9a], we obtain the amount of hydrogen diffusing from the surface into the interior of the electrode during time t_1

$$n_{si\downarrow}(t_1) = 2{}_oc_i\sqrt{D_i t_1/\pi}\exp(-\Phi E_1) \qquad [11a]$$

For diffusion into the electrolyte we obtain from [9b]

$$n_{se\downarrow}(t_1) = 2{}_oc_e\sqrt{D_e t_1/\pi}\exp(-2\Phi E_1) \qquad [11b]$$

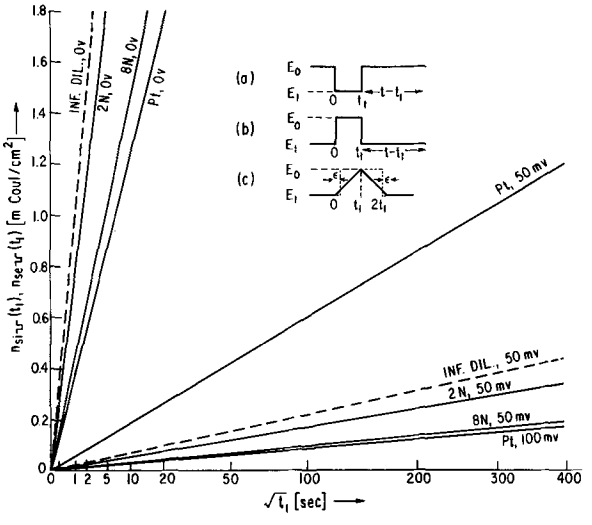

Fig. 2. Amounts of hydrogen, diffusing into Pt, *i.e.*, $n_{si}(t_1)$, and into electrolyte (8*N*, 2*N* H_2SO_4, infinite dilution), *i.e.*, $n_{se}(t_1)$, both in mcoul/cm² against $\sqrt{t_1}$. Numbers on abscissa give t_1 in sec. Voltage E_1 is parameter. Figure applies to cathodic voltage pulses (a), anodic voltage pulses (b), and anodic sweeps (c).

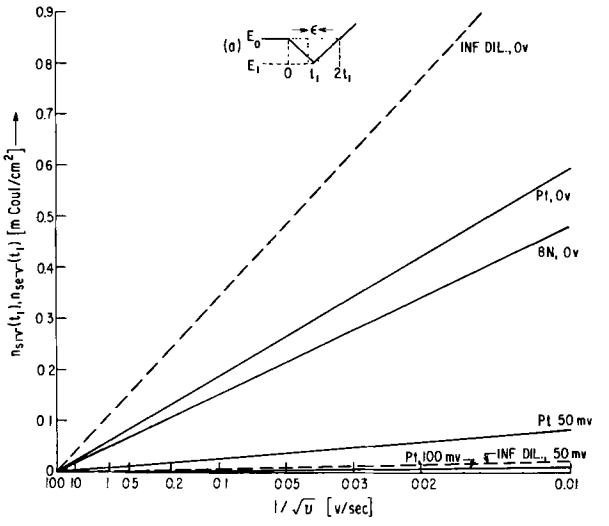

Fig. 3. Amounts of hydrogen diffusing into Pt and electrolyte during time t_1 of a cathodic voltage sweep as a function of $1/\sqrt{v}$. Electrolyte concentration and E_1 are parameters.

The fraction of hydrogen diffusing back from the interior of the electrode to its surface for times $t > t_1$ is readily obtained from [9a] and [11a] by forming

$$\nu_{iss\downarrow}(t) = [n_{i\downarrow}(t) - n_{si\downarrow}(t_1)]/\, n_{si\downarrow}(t_1) = n_{is\downarrow}(t)/n_{si\downarrow}(t_1) \quad [12a]$$

For the electrolyte $\nu_{ess\downarrow}$ is defined correspondingly. We find identical expressions for electrode and electrolyte

$$\nu_{is\downarrow}(t) = \nu_{es\downarrow}(t) = 1 + \sqrt{t/t_1 - 1} - \sqrt{t/t_1}, \quad \text{for } t \geqq t_1 \quad [12b]$$

Cathodic voltage sweeps.—At time $t = o$, the voltage starts decreasing linearly with time from its original value $E_o >> 1/\Phi$ where it had been maintained for some time prior to $t = o$, (see Fig. 3a). At time $t = t_1$, the voltage reaches its lowest value E_1 and then starts increasing linearly with time. The exact solution for this case is far more complex than for the case of voltage pulses and is given in the appendix as equation (A-2). For the times of main interest, $t = t_1$, and $t = 2t_1$, and for the usually occurring case $E_o - E_1 \geqq 0.1$v, the solutions simplify considerably.

The amount of atomic hydrogen diffusing from the surface into the interior of the electrode during time t_1 is

$$n_{sit\,v}(t_1) \approx {}_oc_i \sqrt{D_i/\Phi v}\, \exp(-\Phi E_1) \quad [13a]$$

which may also be written as

$$n_{sis\,v}(t_1) \approx \sqrt{\pi/4\Phi(E_o - E_1)}\; n_{sis\,v}(t_1) \quad [13b]$$

where

$$v = (E_o - E_1)/t_1 \quad [13c]$$

is the voltage sweep rate in v/sec. For $E_o - E_1 > 0.1$v, the error of [13a] compared to (A-2) is $< 1\%$.

The expression for the amount of molecular hydrogen diffusing from the surface into the electrolyte is simply obtained from [13a] by substituting 2Φ for Φ and ${}_oc_e$ and D_e for ${}_oc_i$ and D_i. In this case, the error for $E_o - E_1 > 0.1$v is $< 0.01\%$.

The fractions of hydrogen diffusing back to the surface from the interior and the electrolyte from t_1 to $2t_1$ are

$$\nu_{ist\,v}(2t_1) \approx 1 - [1 - 1/2\Phi(E_o - E_1)]/\sqrt{\pi\Phi(E_o - E_1)} \quad [14a]$$

$$\nu_{es\,v}(2t_1) \approx 1 - [2 - 1/4\Phi(E_o - E_1)]/\sqrt{2\pi\Phi(E_o - E_1)} \quad [14b]$$

The errors involved in these approximations for $E_o - E_1 > 0.1$v are $< 0.1\%$.

Electrode and electrolyte saturated with hydrogen, i.e. $E_1 \lesssim 1/\Phi$.—Anodic voltage pulses.—If voltages $E_1 \lesssim 1/\Phi$ have been maintained for some time prior to applying an anodic voltage pulse (see Fig. 2b), then electrode and electrolyte hold equilibrium amounts of hydrogen. At time $t = 0$, when an anodic step $E_o > E_1$ is applied, hydrogen starts diffusing from the bulk of electrode and electrolyte to the electrode surface. At the time of step reversal, t_1, hydrogen starts diffusing from surface to bulk until the original equilibrium condition is obtained again. The treatment of this case is identical to the case of cathodic voltage pulses. This is apparent if we consider that the diffusion of hydrogen from the bulk to the surface is equivalent to the diffusion of holes in the opposite direction and that the concentration of holes in the bulk as a function of time is identical to the amount of hydrogen that has diffused from the bulk to the surface. Hence, Eq. [9], [11], and [12] can be applied without changes, and we can write

$$n_{is\uparrow} = n_{si\downarrow},\; n_{es\uparrow} = n_{se\downarrow},\; \nu_{is\uparrow} = \nu_{si\downarrow},\; \nu_{es\uparrow} = \nu_{se\downarrow} \quad [15]$$

Anodic voltage sweeps.—The voltage-time function is shown in Fig. 2c. The amount of hydrogen diffusing to the surface as a function of time is a complicated function which is given in the appendix as Eq. [A-3]. For time t_1 the approximate solution for $E_o - E_1 >> 1/\Phi$

$$n_{ist\uparrow}(t_1) \approx 2\,{}_oc_i \sqrt{D_i t_1/\pi}\, \exp(-\Phi E_1)[1 - 1/2\Phi(E_o - E_1)] \quad [16]$$

is obtained from [A-3] which is in error by $<3\%$ for $E_o - E_1 > 0.4$v.

The fraction of hydrogen diffusing from time t_1 to $2t_1$ is

$$\nu_{ist\uparrow}(2t_1) \approx 1 - \sqrt{2}\,[1 - \sqrt{\pi/8\Phi(E_o - E_1)} - 1/4\Phi(E_o - E_1)]/[1 - 1/2\Phi(E_o - E_1)] \quad [17]$$

It will be shown that $\nu_{is\,A} < 0$, *i.e.*, there is a net diffusion of hydrogen from the interior to the surface from t_1 to $2t_1$.

As in the case of voltage pulses, the expressions for diffusion of molecular hydrogen from the electrolyte to the surface can simply be obtained from [16] and [17] by substituting 2Φ for Φ and ${}_oc_e$ and D_e for ${}_oc_i$ and D_i.

Numerical Evaluation and Discussion

For a numerical evaluation of the preceding analysis, we are in want of values of the solubility ${}_oc_i$ and the diffusion coefficient D_i of hydrogen in platinum near room temperature. While a number of studies has dealt with this subject from a qualitative viewpoint (9-13), there appears to be only one study (14)[1] from which ${}_oc_i$ and D_i could be determined. The values ${}_oc_i = 2.2 \cdot 10^{-5}$ mole H/cm^3 and $D_i = 3.0 \cdot 10^{-8}$ cm^2/sec were calculated for 25°C.[2]

The solubility of hydrogen in water, sulfuric acid, and potassium hydroxide near room temperature is well established (17-19). The values of three different authors agree within 5%.

For the diffusion coefficient of molecular hydrogen in water and sulfuric acid the data of different authors

[1] The loan of the relevant thesis by Professor K. J. Vetter is gratefully acknowledged.

[2] Note added during revision of manuscript: In a recent study E. Gileadi, M. A. Fullenwider, and J. O'M. Bockris [*This Journal*, 113, 926 (1966)] obtained permeation rates at 70°C which are by a factor of 8 smaller than those observed by Vetter and Knaack. These low values were obtained on platinum that had been intentionally poisoned with arsenic and will not be considered in this study. The permeation rate is generally known to decrease strongly when the surface is poisoned or inactive (15, 16).

(20-24) agree at best within ±20%. The data of Ruetschi (24), obtained at 30°C, were extrapolated to 25°C and used in this study. The following values for the solubility $_oc_e$ and the diffusivity D_e were used in the evaluation: In water $_oc_e = 7.7 \cdot 10^{-7}$ mole H_2/cm^3 and $D_e = 4.1 \cdot 10^{-5}$ cm^2/sec, in $2N$ H_2SO_4 $6.5 \cdot 10^{-7}$ mole H_2/cm^3 and $3.5 \cdot 10^{-5}$ cm^2/sec and in $8N$ H_2SO_4 $4.2 \cdot 10^{-7}$ mole H_2/cm^3 and $2.7 \cdot 10^{-5}$ cm^2/sec. All values are for 25°C. The amounts of hydrogen, n_i and n_e, will in the following be expressed in their charge equivalents (mcoul/cm^2). These are obtained by multiplying n_i with F and n_e with $2F$.

Cathodic voltage pulses.—The amounts of hydrogen diffusing into electrode and electrolyte according to Eq. [11a] and [11b] are plotted in Fig. 2 as a function of $\sqrt{t_1}$. The charges were calculated for different values of E_1 for diffusion into platinum electrodes, $8N$ H_2SO_4, $2N$ H_2SO_4, and infinitely diluted electrolytes. The formation of a monolayer of hydrogen atoms on the surface requires only 0.24 mcoul/cm^2, assuming close-packed crystal planes. Hence, the equivalent of several monolayers diffuses into electrode and electrolyte during a few seconds if E_1 is close to 0v. As E_1 increases, the hydrogen fluxes decrease exponentially. The decrease occurs far more rapidly for the electrolyte than for the electrode on account of the factor 2 in the exponential of Eq. [11b]. Thus, for $E_1 = 100$ mv the equivalent of one monolayer diffuses into the platinum during 400 sec while the amount diffusing into the electrolyte is <0.01 mcoul/cm^2.

Because of the larger values of $_oc_e$ and D_e in dilute electrolytes as compared to $8N$ H_2SO_4, 2.3 times more hydrogen diffuses into the former. The dotted lines in Fig. 2 represent an upper limit of the amount of hydrogen diffusing into any aqueous electrolyte.

The fraction of hydrogen diffusing back to the surface after step reversal at time t_1 according to Eq. [12b] is plotted in Fig. 4 as a function of $\sqrt{(t-t_1)/t_1}$. For t only slightly larger than t_1, *i.e.*, $t - t_1 \approx 0$, the fractions ν_i or ν_e approach zero. As t_1 increases, larger fractions of hydrogen diffuse from the interior to the surface. For $t = 2t_1$ the fraction $2 - \sqrt{2} \approx 0.6$ diffuses to the surface. Even if the time after step reversal is 10 times larger than the step duration t_1, only the fraction 0.84 of the hydrogen in electrode and electrolyte diffuses back to the surface. This result is explained by the fact that some hydrogen continues to diffuse into the bulk of electrode and electrolyte after step reversal.

It is interesting to note that no material constants enter into Eq. [12b]. This means that Eq. [12b] and Fig. 4 may be applied to any electrode material and electrolyte and any gas exhibiting true gas solution.

Cathodic voltage sweeps.—According to Eq. [13a] the amounts of hydrogen diffusing into electrode and electrolyte during time t_1 of a cathodic voltage sweep are inversely proportional to the square root of the sweep rate. In Fig. 3 the amounts of hydrogen are

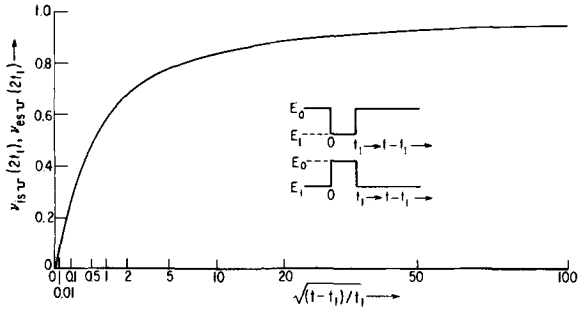

Fig. 4. Fractions of hydrogen back-diffusing to surface when applying anodic or cathodic pulses as function of $\sqrt{(t-t_1)/t_1}$. Note: numbers on abscissa give $(t-t_1)/t_1$.

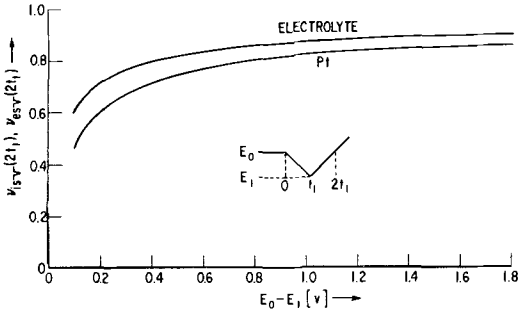

Fig. 5. Fractions of hydrogen back-diffusing to surface from t_1 to $2t_1$ as function of sweep range $E_0 - E_1$ of a cathodic sweep.

plotted against $1/\sqrt{v}$ for different values of E_1 and for diffusion into platinum, $8N$ H_2SO_4, and infinitely diluted electrolytes. We note from [13a] that the starting voltage E_o of the sweep (see Fig. 3a) does not affect the amount of hydrogen for $E_o >> 1/\Phi$. In contrast the amount decreases exponentially with increasing (more anodic) sweep reversal voltage E_1. This is understood if we consider that the concentration of hydrogen near the surface, c_{is} and c_{es} (Fig. 1), is vanishingly small for voltages $>> 1/\Phi$. It is only for voltages approaching $E_1 \lesssim 1/\Phi$ or times approaching t_1 that the diffusion of hydrogen becomes significant. In essence we can replace the cathodic sweep with a cathodic step of duration $\epsilon << t_1$ (see Fig. 3a). This assertion finds its quantitative expression in Eq. [13b] which compares the amount of hydrogen diffusing into electrode and electrolyte in the case of a cathodic sweep with that of a cathodic step applied for equal time t_1. Since [13b] was derived for $E_o - E_1 \geqq 0.1$v and since $\Phi = 38.9$ 1/v, we verify that the former is always smaller. In fact, for $E_o - E_1 = 0.4$v only about 1/4 of the amount diffuses into the electrode and 1/6 into the electrolyte.

According to [14a] and [14b] the fractions of hydrogen diffusing back to the surface between time t_1 and $2t_1$ are independent of the sweep rate and any material constants, but do depend on the sweep range $E_o - E_1$. A larger sweep range, using the analogy with a voltage step (see Fig. 3a) again, simply means more time $t - t_1$ available for the back-diffusion of hydrogen. The back-diffusing fractions are plotted in Fig. 5 as a function of sweep range. Assuming $E_1 \lesssim 1/\Phi$, we note that in the range of hydrogen coverage 0-0.4v, the fractions are approximately 0.7 for the electrode and 0.8 for the electrolyte. Considerably smaller fractions back-diffuse in the double-layer (0.4-0.8v) and oxygen adsorption regions (0.8-1.6v).

To facilitate assessing the errors involved in determining hydrogen coverages from voltage sweep experiments. Table I shows the charges due to hydrogen diffusion for some typical sweep rates and reversal voltages based on platinum in $8N$ H_2SO_4 at 25°C. The column $n_{\text{cath v}}$ gives the errors for the cathodic branch of the sweep, $n_{\text{anod v}}$ those for the anodic branch. The errors add up to the charge n_{ad} due to hydrogen coverage: $n_{meas} = n_{ad} + n_{\text{cath v}}$ (or $n_{\text{anod v}}$). Recalling that 240 μcoul/cm^2 corespond to a monolayer coverage of the electrode with atomic hydrogen, the errors are large indeed, especially if a reversal voltage of 0v is used.

The hydrogen diffusing to the electrode surface during the anodic branch of the sweep in the double layer region from 0.4 to 0.8v shows up as an equivalent capacity. The values range from 145 μF/cm^2 for 0.03 v/sec and $E_1 = 0$v to 3 μF/cm^2 for 1 v/sec and $E_1 = 0.05$v. These values have to be considered when determining double layer capacities from voltage sweep curves.

Anodic voltage pulses.—It has been mentioned before that the equations derived for the case of ca-

Table I. Charges due to hydrogen diffusion

v, v/sec	E_1, v	$E_o - E_1$, v	$n_{si\,v}$, μc/cm²	$n_{se\,v}$, μc/cm²	$n_{cath\,v}$, μc/cm²	$n_{is\,v}$, μc/cm²	$n_{es\,v}$, μc/cm²	$n_{anod\,v}$, μc/cm²
0.03	0	0.40	339	278	617	247	222	469
0.1	0	0.40	191	155	346	139	124	264
1.0	0	0.40	60	50	110	44	40	84
0.03	0.05	0.35	49	6	55	35	5	40
0.1	0.05	0.35	28	3	32	20	2	22
1.0	0.05	0.35	9	<1	9	6	<1	6
0.03	0.10	0.30	11	<1	11	7	<1	7
0.1	0.10	0.30	6	<1	6	4	<1	4
1.0	0.10	0.30	2	<1	2	1	<1	1

thodic voltage pulses are identical to those for anodic voltage pulses. Hence, Fig 2 shows the amounts of hydrogen that diffuse to the electrode surface from the bulk of electrode and electrolyte during time t_1 of applying an anodic voltage pulse. By analogy, Fig. 4 shows the fractions of hydrogen diffusing back into electrode and electrolyte after step reversal at time t_1.

Anodic voltage sweeps.—Using Eq. [11a] for cathodic pulses and noting Eq. [15], then Eq. [16] for anodic sweeps may be written as

$$n_{is\,\Lambda}(t_1) = n_{is\,\Lambda}(t_1)[1-1/2\Phi(E_o - E_1)] \qquad [18]$$

Noting that $E_o - E_1 >> 1/\Phi$ was assumed, $1/2\Phi\,(E_o - E_1)$ becomes a minor correction term. For $E_o - E_1 = 0.4$v the correction amounts to 3%. This means that the amount of hydrogen that diffuses from the interior of the electrode to the surface during time t_1 of applying an anodic voltage sweep is only slightly smaller than for the case of applying a voltage step. This is, because potentials, at which c_{is} (see Fig. 1) becomes vanishingly small, are reached for times $\epsilon << t_1$, if $E_o - E_1 >> 1/\Phi$. The effect is the same as if we would replace the sweep in Fig. 2c with a step of slightly shorter duration $t_1 - \epsilon$. The step is indicated in Fig. 2c by dashed lines. Figure 2 may be used to determine the amounts of hydrogen diffusing into the bulk of electrode and electrolyte. Equation [18] specifies the correction to be applied to the amounts thus determined.

Equation [17] represents the fraction of hydrogen diffusing from time t_1 to $2t_1$. The evaluation of [17] for $E_o - E_1 \geqq 0.1$v shows that the fraction $\nu_{i\,\Lambda}$ is always negative. This means that there is a net diffusion of hydrogen from the interior to the surface from t_1 to $2t_1$. This is in contrast to the cases discussed hitherto. Figure 6 shows how the fraction $\nu_{i\,\Lambda}$ increases with the sweep range $E_o - E_1$. From [17] we see that for very large values $E_o - E_1$ the fraction $\nu_{i\,\Lambda}$ approaches a limiting value $1 - \sqrt{2}$ which is indicated in Fig. 6 as a dashed line.

Qualitatively the net diffusion from the interior to the surface can be understood as follows. After the sweep reverses at time t_1 (see Fig. 2c), hydrogen continues to diffuse to the surface, since the concentration of hydrogen near the surface, c_{is}, is vanishingly small. For $E_o - E_1 >> 1/\Phi$ it is only at times approaching $2t_1$, that c_{is} becomes large enough to cause a diffusion of hydrogen from the surface into the interior. The amount of hydrogen that diffuses to the surface from time t_1 to $2t_1 - \epsilon$ exceeds the amount that diffuses in the opposite direction during time ϵ. Thus, we are left with a net diffusion to the surface.

For $E_o - E_1 \lesssim 1/\Phi$, ϵ is no longer small compared to t_1, and the amount of hydrogen diffusing to the surface from t_1 to $2t_1 - \epsilon$ no longer exceeds the amount diffusing in the opposite direction during time ϵ. In fact, for $E_o - E_1 << 1/\Phi$, the fraction diffusing to the surface approaches zero, while the fraction diffusing into the interior approaches the limiting value $2 - \sqrt{2}$ which one would calculate from Eq. [12b] for the application of a voltage pulse.

Equivalent arguments as above can be applied to the diffusion of hydrogen in the electrolyte. The fraction of hydrogen diffusing from the electrolyte to the surface from time t_1 to $2t_1$ is somewhat larger than for the electrode. The fraction was calculated from [17] and plotted in Fig. 6 observing that 2Φ is to be substituted for Φ.

Table II lists the amounts of hydrogen in μcoul/cm² diffusing to the surface during the anodic branch $n_{anod\,\Lambda}$ and the cathodic branch $n_{cath\,\Lambda}$ of an anodic sweep. Note that $n_{cath\,\Lambda}$ is negative, *i.e.*, the error due to diffusion makes the surface charge appear smaller: $n_{meas} = n_{ad} - |n_{cath\,\Lambda}|$. The values in Table II are calculated for Pt and $8N$ H_2SO_4 at 25°C with $E_o = 0.4$v. We note that the errors can become one order of magnitude larger than the surface charge to be determined.

Anodic charging curves.—When an anodic current step is applied to a platinum electrode, the voltage rises with time following a characteristic curve, called charging curve. In sulfuric acid and most other aqueous electrolytes, the voltage rises approximately linearly with time in certain voltage ranges (1, 3, 4). In sulfuric acid these ranges are the hydrogen adsorption region, 0-0.4v, the double layer region, 0.4-0.8v, and the oxygen adsorption region, 0.8-1.6v. Such a charging curve is schematically shown in Fig. 7.

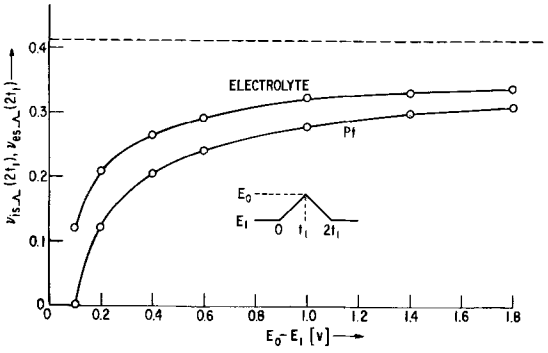

Fig. 6. Fractions of hydrogen continuing to diffuse to surface from t_1 to $2t_1$ as function of sweep range $E_o - E_1$ of an anodic sweep.

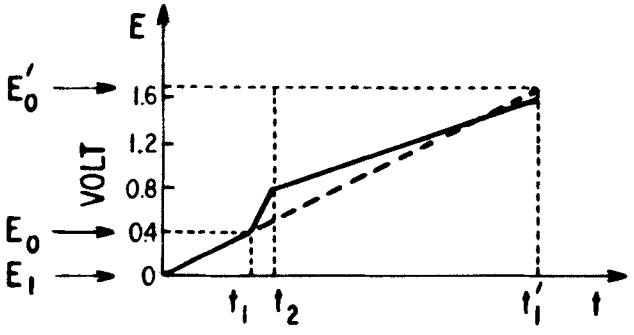

Fig. 7. Schematic diagram of anodic charging curve with hydrogen adsorption region 0 to 0.4v, double layer region 0.4 to 0.8v, and oxygen adsorption region 0.8 to 1.6v.

Table II. Amounts of hydrogen diffusing to the surface

v, v/sec	E_1, v	t_1, sec	$n_{is}\,\Lambda'$ μc/cm²	$n_{es}\,\Lambda'$ μc/cm²	$n_{anod}\,\Lambda'$ μc/cm²	$n_{si}\,\Lambda'$ μc/cm²	$n_{se}\,\Lambda'$ μc/cm²	$n_{cath}\,\Lambda'$ μc/cm²
0.03	0	13.3	1711	1720	3431	−353	−456	−809
0.1	0	4.0	799	389	1187	−164	−251	−415
1.0	0	0.4	253	297	551	−52	−79	−131
0.03	0.05	11.7	209	33	242	−40	−9	−49
0.1	0.05	3.5	114	18	132	−22	−4	−26
1.0	0.05	0.35	36	6	42	−7	−1	−8
0.03	0.10	10.0	28	<1	28	−5	<−1	−5
0.1	0.10	3.0	15	<1	15	−4	<−1	−4
1.0	0.10	0.3	5	<1	5	−1	<−1	−1

Table III. Errors $(n_{is} + n_{es})/n_{ad}$ involved in hydrogen coverage determinations

i, ma/cm²	t_1, sec	n_{is}, μc/cm²	n_{es}, μc/cm²	$n_{is} + n_{es}$, μc/cm²	$(n_{is} + n_{es})/n_{ad}$, %	$i_o t_1/n_{ad}$, %
1	2.4	650	1290	1940	810	1000
10	$6.0\cdot10^{-2}$	100	210	310	130	25
100	$3.6\cdot10^{-3}$	25	50	75	31	1.5
1000	$3.0\cdot10^{-4}$	7	15	22	9.2	0.1

It is immediately evident from a comparison of Fig. 2c and 7 that Eq. [16], derived for an anodic voltage sweep, can be used to approximately determine the amounts of hydrogen diffusing to the surface in the hydrogen adsorption region $E_o - E_1$ of an anodic charging curve. Furthermore, for all practical purposes, the concentration of hydrogen near the surface, c_{is} and c_{es}, can be considered zero for voltages >0.4v. Hence, the effect of replacing the three straight-line sections in Fig. 7 by the dotted straight line on the amounts of hydrogen calculated from Eq. [16] is negligible (<1% for $E_1 < 0.2$v). This means that Eq. [16] may be used to calculate the amounts of hydrogen diffusing to the surface during the whole time t_1' of an anodic charging curve, and Fig. 2 shows these amounts for a variety of conditions. Table III gives the errors $(n_{is} + n_{es})/n_{ad}$ involved in hydrogen coverage determinations for charging curves in $2N$ H_2SO_4 starting from $E_1 = 0$v for different charging currents i. Also given are the errors $i_o t_1/n_{ad}$ that result if one considers only steady-state diffusion (3). $i_o \approx 1$ ma/cm² is the limiting diffusion current, $n_{ad} = 0.24$ mc/cm² the surface charge due to hydrogen adsorption. It can be seen that the errors are sizeable, even at high charging currents and that the errors can be two orders of magnitude larger than those determined under the assumption of steady-state diffusion.

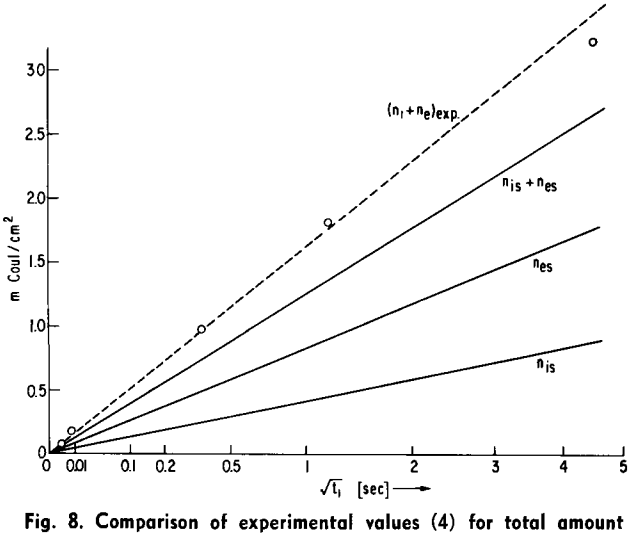

Fig. 8. Comparison of experimental values (4) for total amount of hydrogen diffusing from electrode and electrolyte (points and dotted line) with calculated curve in case of anodic charging curves.

Comparison with Experiments

Experimental results obtained by Schuldiner and Warner (4) can be used to verify the theoretical results obtained here. Conversely the present analysis enables us to interpret their relevant experiments on a quantitative basis.

Figure 8 shows experimental values for $(n_{is} + n_{es})_{exp}$ obtained by Schuldiner and Warner on a platinum bead[3] electrode in $2N$ H_2SO_4 at 23°C for 1 atm hydrogen pressure. Over the whole range af charging current densities from 0.78 to 203 ma/cm², the data points fall on a straight line when plotted against the square root of time, as required by Eq. [16]. Also shown in Fig. 8 are the calculated amounts n_{is} and n_{es} due to diffusion of hydrogen from the interior of the platinum and from the electrolyte. The first part is about half as large as the second. Their sum $(n_{is} + n_{es})$ is roughly 20% smaller than the experimental values. This is as good agreement as expected, considering that the values of D and c are not known more accurately.

The fact that the experimental data are well described by slow diffusion of hydrogen atoms from the metal interior and of hydrogen molecules from the electrolyte shows that up to current densities of at least 200 ma/cm² the assumption of fast phase boundary reactions is well justified. In particular, this means that the rates of the dissociation of hydrogen molecules and of the ionization of hydrogen atoms are fast compared to the rate of diffusion up to at least 200 ma/cm². This is in agreement with generally accepted views about the hydrogen reaction on clean active platinum electrodes (5, 6, 25).

The calculation allows a quantitative separation of the measured charge $(n_{is} + n_{es})_{exp}$ into two parts n_{is} and n_{es} which is not afforded by the experiments alone. Schuldiner and Warner believe that an experimental separation is possible by making measurements in helium saturated solutions and assuming that the value of n_{is}, thus determined holds for the whole range of hydrogen partial pressures and that only n_{es} changes. However, this is not the case. It is evident from the preceding treatment (compare Eq. [3], [6], and [16]) that both n_{is} and n_{es} increase with increasing hydrogen partial pressure. Thus, for 1 atm, n_{is} is by a factor of 4 larger than estimated by the cited authors.

Conclusions

On clean, active platinum electrodes, hydrogen absorbed by the metal and by the electrolyte contributes significantly to the total amount of charge determined with nonsteady-state methods like the current step (charging curves) and voltage sweep methods. These contributions have to be considered when deter-

[3] The diffusion distances are much smaller than the bead diameter; hence, the linear treatment can be applied.

mining surface coverages with hydrogen atoms. The magnitude of the errors increases exponentially when the starting voltage E_1 of an anodic charging curve or an anodic voltage sweep (or the reversal voltage of a cathodic sweep) is made more cathodic. With less cathodic E_1, the error due to diffusion from the electrode interior becomes proportionally much more important than diffusion from the electrolyte. Both statements are equivalent to saying that the error due to the electrolyte is proportional to the partial pressure of hydrogen while the error due to the electrode is proportional to the square root of pressure. Furthermore, the errors increase inversely proportional to the square root of the transition time of the charging curve and of the sweep rate of the voltage sweep, respectively. Typically, the total errors amount to 30% for a current density of 100 ma/cm² and 10% for 1 amp/cm² for an anodic charging curve started from 0v. For a cathodic sweep wih 1 v/sec the total errors are 45% for $E_1 = 0$v and 4% for $E_1 = 50$ mv.

Manuscript received July 20, 1966; revised manuscript received Dec. 16, 1966.

Any discussion of this paper will appear in a Discussion Section to be published in the June 1968 JOURNAL.

APPENDIX

In the following expressions, n, D, and ${}_oc$ are left without subscript and apply to both the interior of the electrode and the electrolyte. For the electrode interior $z = 1$; for the electrolyte $z = 2$. The symbol

$$a = \sqrt{(z\Phi|E_o - E_1|)/2t_1} \qquad \text{[A-1]}$$

is used for convenience.

Cathodic voltage sweeps.—The exact expression from which the approximate formulas [13a] through [14b] were derived is, for all times $t < 2t_1$,

$$n_v(t) = ({}_oc\sqrt{D/a})\Big\{\exp(-z\Phi E_o/2 + a^2t)\,\operatorname{erf}(a\sqrt{t}) - u(t-t_1)\exp[-z\Phi E_1/2 + a^2(t-t_1)]\,\operatorname{erf}(a\sqrt{t-t_1}) + u(t-t_1)\,2\pi^{-1/2}\exp[-z\Phi E_1/2 - a^2(t-t_1)]\int_o^{a\sqrt{t-t_1}}\exp(\lambda^2)\,d\lambda\Big\} \qquad \text{[A-2]}$$

Anodic voltage sweeps.—The exact expression from which the approximate formulas [16] and [17] were derived is, for all times t

$$n_v(t) = ({}_oc\sqrt{D/a})\Big\{2a\sqrt{t/\pi}\exp[-z\Phi E_1/2] - 2\pi^{-1/2}\exp[-z\Phi E_1/2 - a^2t]\int_o^{a\sqrt{t}}\exp(\lambda^2)\,d\lambda + u(t-t_1)\,2\pi^{-1/2}\exp[-z\Phi E_o/2 - a^2(t-t_1)]\int_o^{a\sqrt{t-t_1}}\exp(\lambda^2)\,d\lambda - u(t-t_1)\exp[-z\Phi E_o/2 + a^2(t-t_1)]\,\operatorname{erf}(a\sqrt{t-t_1}) + u(t-2t_1)\exp[-z\Phi E_1/2 + a^2(t-2t_1)]\,\operatorname{erf}(a\sqrt{t-2t_1}) - u(t-2t_1)\,2a\pi^{-1/2}\exp[-z\Phi E_1/2]\sqrt{t-2t_1}\Big\} \qquad \text{[A-3]}$$

These expressions were reduced to approximate forms by the use of well-known asymptotic expansions (20).

REFERENCES

1. F. P. Bowden, *Proc. Roy, Soc.*, **A125**, 446 (1929).
2. F. G. Will and C. A. Knorr, *Z. Elektrochem.*, **64**, 258, 270 (1960).
3. M. Breiter, C. A. Knorr, and W. Volkl, *ibid.*, **59**, 681 (1955).
4. S. Schuldiner and T. B. Warner, *This Journal*, **112**, 212 (1965).
5. M. Breiter, H. Kammermaier, and C. A. Knorr, *Z. Elektrochem.*, **60**, 37 (1956).
6. A. N. Frumkin and E. Aikasjan, *Izvest. Akad. Nauk*, 202 (1959).
7. A. Sieverts and E. Jurisch, *Ber.*, **45**, 221 (1912).
8. C. J. Smithells, "Gases in Metals," p. 155, Chapman & Hall, Ltd., London (1937).
9. M. Crova, *Les Mondes*, **5**, 210 (1864); *Chem. News*, **11**, 74 (1865).
10. H. V. Helmholtz, and E. Root, *Ann. Phys.*, **159**, 416 (1876).
11. G. C. Schmidt and T. Luecke, *Z. Physik.*, **8**, 152 (1922).
12. M. Bodenstein, *Z. Elektrochem.*, **28**, 517 (1922).
13. R. Koehler, *Z. Phys. Chem.*, **135**, 369 (1928).
14. M. Knaack, Ph.D. thesis, Technical University, Berlin, 1957; K. J. Vetter, "Elektrochemische Kinetik," p. 495, Springer, Berlin (1961).
15. R. M. Barrer, *Trans. Faraday Soc.*, **36**, 1235 (1940).
16. W. Seith, "Diffusion in Metallen," Springer, Berlin (1955).
17. G. Geffcken, *Z. physik. Chem.*, **49**, 268 (1904).
18. A. Christoff, *ibid.*, **55**, 627 (1906).
19. P. Ruetschi and R. F. Amlie, *J. Phys. Chem.*, **70**, 718 (1966).
20. G. Tamman and V. Jessen, *Z. anorg. Chem.*, **179**, 125 (1929).
21. V. V. Ipatieff and V. P. Teodorivich, *J. Phys. Chem. (USSR)*, **10**, 712 (1937).
22. C. R. Wilke, *Chem. Eng. Progr.*, **45**, 218 (1949).
23. M. Breiter and K. Hoffmann, *Z. Elektrochem.*, **64**, 462 (1960).
24. P. Ruetschi, Paper presented at the Cleveland Meeting of the Society, Oct. 1-6, 1966, Abstract No. 42.
25. A. N. Frumkin, "Advances In Electrochemistry," Vol. 3, pp. 287-392, P. Delahay, Editor, John Wiley & Sons, New York (1963).
26. E. Jahnke and F. Emde, "Funktionentafeln, " Teubner, Berlin (1938).

Discussion

Comments on

"Effect of Hydrogen Absorbed by Electrode and Electrolyte on Hydrogen Coverage" by David BenDaniel and Fritz G. Will

(Vol. 114, 909 (1967))

by Sigmund Schuldiner, Naval Research Laboratory, Washington, D. C.

BenDaniel and Will claim to give a general analysis of the nonsteady-state diffusion problem as applied to diffusion of H in metals and H_2 in solution to the electrode surface. Their analysis of H diffusion in the metal is based on the assumption that only diffusion of soluble H, in equilibrium with H_2 in solution, from the metal interior to the surface is the controlling factor. However, it has been known for some time that slow phase-boundary processes cannot be ignored for studies of the permeation rates of hydrogen through metals.[1] It also is known that part of the hydrogen associated with a platinum surface is strongly bonded and is not in equilibrium with H_2.[2]

Several workers[3] have shown that measurable amounts of H do not diffuse through a Pt membrane electrode when the polarization side is clean. BenDaniel and Will, however, evidently conclude that this work was not on clean surfaces and that the only acceptable work on a clean surface was that reported by Vetter and Knaack.[4] Vetter's book states that the Tafel slope found on the polarization side of their Pt membrane was 0.12. This value of Tafel slope clearly shows that the diffusion of molecular hydrogen is not rate controlling (this would give a 0.03 slope) and that the fast phase boundary (metal/solution) reactions claimed by BenDaniel and Will (which are necessary for their derivation) are not realized. The 0.12 slope found by Vetter and Knaack indeed shows that the hydrogen reaction took place on an electrode which was inactive, *i.e.*, dirty. In short, Vetter and Knaack's overvoltage and diffusion data are for a poisoned Pt electrode.

Further evidence which supports the conclusion that the Vetter and Knaack electrodes were not clean can be shown by comparing their results with those of Hoare and Schuldiner.[3] Vetter and Knaack's work at a current density of -11.5 ma/cm^2 gave an overvoltage of -340 mv, whereas Hoare and Schuldiner found at a current density of -5.3 ma/cm^2 an overvoltage of -48 mv. This, in addition to the fact that the 0.03 Tafel slope is well established for clean Pt surfaces[5] clearly shows that the diffusion of hydrogen through Pt membranes reported by Vetter and Knaack was on a Pt foil with a poisoned polarization side. This meant that a retarded phase boundary reduction to hydrogen occurred and that the atomic hydrogen formed was not in equilibrium with H_2 in solution.

BenDaniel and Will confuse the issue of electrode cleanliness and activity for hydrogen permeation. For Pt electrodes with high activity for the hydrogen formation reaction, the permeation of hydrogen through a membrane is negligible. For poisoned Pt electrodes with a low activity for the hydrogen formation reaction, the permeation of hydrogen through a membrane is appreciable. Hoare and Schuldiner[3] further showed that poisoned palladium could either lower or raise the H permeation rate. Barrer[6] did not, as claimed, show any experimental relationship between Pd electrode cleanliness and activity for hydrogen permeation. Instead, Barrer, on a purely random basis found that some Pd electrodes transmitted hydrogen faster than others. He defined the electrodes with the fastest permeation rates as the most active electrodes and postulated that they were the least poisoned. It is obvious from the work on hydrogen permeation through Pd and Pt that a little of some species which poison the hydrogen generation reaction on the polarization side of the membrane electrode can greatly increase the rate of H permeation while a substantial amount of practically any adsorbent (and perhaps even a little of some species) may retard H permeation. It is incorrect to conclude that, if hydrogen permeation is faster on one Pt electrode than another, the first is cleaner and more active for the hydrogen generation reaction than the second.

BenDaniel and Will's assumption that migration inside the metal is a function of the square root of hydrogen partial pressure is based on data obtained from the exposure of metals to hydrogen gas in either the gas or solution phase. When a potential is applied to a metal the effective hydrogen partial pressure and/or atomic hydrogen activity on the polarization side of the electrode surface is now the primary factor controlling the rate of solution and migration of H through the metal, and this will depend on the applied potential and current density up to a limiting value.[7] The partial pressure of hydrogen above the solution only would have a negligible effect. The much higher overvoltage and the associated much higher effective atomic hydrogen concentration on the polarization side of a poisoned Pt electrode explains the migration of H through such an electrode whereas on a clean electrode (low overvoltage) H migration through the metal is insignificant.

The numerical evaluation of the solubility and diffusion coefficients for hydrogen in Pt by BenDaniel and Will are much larger than would be reasonably expected. The solubility is given as 4.4×10^{-5} mole H/cm^3 and the diffusion coefficient is given as 1.5×10^{-8} cm^2/sec, both at 25°C. The solubility of H in Pt given in the literature is at least an order of magnitude lower. For example, Smith's[8] data gives 1.3×10^{-6}

[1] R. Ash and R. M. Barrer, *Phil. Mag.*, **4**, 1197 (1959).

[2] S. Schuldiner, *This Journal*, 107, 452 (1960).
C. H. Presbrey, Jr., and S. Schuldiner, *ibid.*, **108**, 985 (1961).
S. Schuldiner and R. M. Roe, *ibid.*, 110, 332 (1963).
S. Schuldiner and T. B. Warner, *ibid.*, 112, 212 (1965).
S. Schuldiner, B. J. Piersma, and T. B. Warner, *ibid.*, 113, 573 (1966).
S. Schuldiner, T. B. Warner, and B. J. Piersma, *ibid.*, 114, 343 (1967).

[3] J. P. Hoare and S. Schuldiner, *This Journal*, 103, 237 (1956).
E. Gileadi, M. A. Fullenwider, and J. O'M. Bockris, *ibid.*, 113, 926 (1966).

[4] K. J. Vetter and M. Knaack, unpublished work reported in "Elektrochemische Kinetic" by K. J. Vetter, p. 495, Springer-Verlag, Berlin (1961).

[5] L. P. Hammet, *J. Am. Chem. Soc.*, **46**, 7 (1924); *Trans. Faraday Soc.*, **29**, 770 (1933).
C. A. Knorr, *Z. Elektrochem.*, **42**, 669 (1936).
L. Kandler, C. A. Knorr, and C. Schwitzer, *Z. Physik. Chem.*, **A180**, 281 (1937).
P. Dolin, B. Ershler, and A. Frumkin, *Acta Physicochim. URSS*, **13**, 779 (1940).
S. Schuldiner, *This Journal*, **99**, 488 (1952); **101**, 426 (1954); **106**, 891 (1959).
J. O'M. Bockris and A. M. Azzam, *Trans. Faraday Soc.*, **48**, 145 (1952).
M. Breiter and R. Clamroth, *Z. Elektrochem.*, **58**, 493 (1954)

[6] R. M. Barrer, *Trans. Faraday Soc.*, **36**, 1235 (1940).

[7] S. Schuldiner and J. P. Hoare, *This Journal*, **103**, 178 (1956).

[8] D. P. Smith, "Hydrogen in Metals," p. 28, University of Chicago Press, Chicago (1948).

mole H/cm³ at 400°C. Since, Pt is an endothermic occluder of hydrogen this means that the solubility of hydrogen at room temperature will be much less.

Gileadi *et al.*[3] obtained a solubility of H in poisoned Pt at 70°C of 2.7 x 10^{-5} g atoms H/cm³. Of this it was shown that only 5-15% of the H (2 x 10^{-6} g atoms H/cm³) is free to move through the lattice. The rest of the H was relatively stable and diffused out of the metal at much slower rates than diffusion into the Pt. The solubility data at 25° would, of course, be substantially lower. The diffusion coefficient found by Gileadi *et al.* was 3.4 x 10^{-9} cm²/sec at 70° and they estimated that it would be an order of magnitude less at 25°C.

BenDaniel and Will claim that equilibrium was not obtained in the helium-saturated experiments of Schuldiner and Warner.[2] If this were so then the $P_{H_2} = O$ results of Schuldiner and Warner should be dependent on the square root of time (according to the BenDaniel and Will derivation), both owing to H in the metal interior and H_2 diffusing into the solution. In fact, Schuldiner and Warner showed that from current densities of 3.53 to 0.78 ma/cm² (0.085-0.38 sec) there was virtually no change in the amount of hydrogen oxidized. The time dependence shown in the oxygen region for this same range of current densities shows that an experimental artifact cannot explain the invariance with time in the H region.

In conclusion, BenDaniel and Will cannot assume that slow phase boundary reactions did not affect the H permeation rate found by Vetter and Knaack, or that the Vetter and Knaack Pt electrode was clean. Indeed the overvoltage data given by Vetter and Knaack definitely show that their electrode was poisoned. (It should be pointed out that even though the Vetter and Knaack data did show a 0.02-0.04 Tafel slope on the diffusion side of the electrode, the 0.12 Tafel slope on the polarization side clearly shows a poisoned Pt surface.) Work by others[3] have shown that on a clean Pt surface hydrogen diffusion through Pt is immeasurable. The assumption used by BenDaniel and Will that the rate of diffusion of hydrogen through a Pt electrode is dependent on the square root of the hydrogen partial pressure in the gas phase above the solution is not applicable to a polarized electrode.

A Lumped Parameter Electrical Model for Predicting Concentration Transients in a Reversible Transference Cell

P. G. Griffith

Solid-State Electronics Laboratory, Department of Electrical Engineering, Texas Technological College, Lubbock, Texas

and J. R. Peebles

Texas Instruments, Incorporated, Dallas, Texas

ABSTRACT

The basic phenomenological equations governing electrical conduction of ions in an electrolyte are reviewed. As an approximation, these equations are redefined in the form of differential-difference equations for an incremental region in the electrolyte. A lumped parameter model, which is analogous to an electrical network, is developed for an incremental region in the form of an iterative network. Because the model exhibits a linear relationship between concentration and current, it can be analyzed using standard circuit-theory techniques. Specific examples are considered to demonstrate the use of the model. The agreement between the transient responses, calculated from the lumped parameter models and the theoretical solution, is, in general, sufficiently close to justify the use of these models in lieu of the more complicated theoretical solution.

Recent interferometric studies (1, 2) on $Zn/ZnSO_4/Zn$ and $Cu/CuSO_4/Cu$ systems have been devoted to the investigation of only the initial portion of the concentration transient response for a constant current excitation. The purpose of this approach has been to take advantage of the first term of a series solution. Even limited to this term (a form of the complementary error function), the analysis is rather complicated.

Because of these limitations, it is desirable to develop an approximate model for such a system which is applicable to a more general current excitation and to larger values of time. The term "model" is used in the sense of a discrete approximation to the exact system under consideration. The model itself is envisioned as a lumped parameter network, similar to an electrical network, with resistors, capacitors, etc. Such a model will be developed for the electrolyte.

A lumped parameter model for the electrolyte of a reversible transference cell will be developed for some rather idealized conditions, to illustrate the modeling procedure and to demonstrate how the model can be modified for improved accuracy. As an illustration of how the lumped parameter models are employed, concentration transients will be determined for a constant current excitation. The more general transient response for different current excitations is determined by standard circuit-theory techniques.

The use of lumped parameter models to approximate distributed systems with positive and negative ions is not new (3, 4). Such models have been used with excellent results on, for example, transistors and pn junction diodes. Since these have proved to be effective tools in analyses involving many semiconductor problems, similar results can be anticipated for electrochemical systems.

Basic assumptions.—The system under consideration is assumed to be a reversible transference cell in which the electrodes are the same metal and the electrolyte is a salt of the metallic element, *e.g.*, a $Zn/ZnSO_4/Zn$ transference cell. The anode and cathode reactions are defined by the equations

$$M \rightleftarrows M^{z+} + ze \quad [1]$$

$$M^{z+} + ze \rightleftarrows M \quad [2]$$

where M = metal of which the electrode is composed, z = valence of the ion formed, e = charge on the electron. The electrolyte MA is assumed to be in equilib-

rium with its ions M^{z+} and A^{z+} according to the equation

$$MA \rightleftarrows M^{z+} + A^{z-} \quad [3]$$

We shall assume that the electrolyte consists of ions with the same valence[1] and that the electrolyte is completely dissociated; consequently, the equilibrium condition represented by Eq. [3] is tipped entirely to the right.

We shall also make the following idealized assumptions:

1. Ions are transported in the x-dimension of a planar geometry.
2. Convection currents do not exist.
3. The diffusion coefficients (D_+, D_-) for the ions are constants and related to the drift mobility coefficients (μ_+, μ_-) by the Einstein relationship $D_+/\mu_+ = D_-/\mu_- = kT/zq$, where k is Boltzmann's constant, T is the absolute temperature in degrees Kelvin, and q is the magnitude of the charge on an electron. All of these parameters are assumed to be positive constants.
4. The electrolyte is assumed to be neutral with a pH of 7 at room temperature, *i.e.*, the electrolyte represents a two-ion system.

Theory.—The basic equations[2] for the cations and anions of the electrolyte may be summarized as follows:

$$I_+ = Azq\mu_+ EC_+ - AzqD_+(\partial C_+/\partial x) \quad [4]$$

$$I_- = Azq\mu_- EC_- + AzqD_-(\partial C_-/\partial x) \quad [5]$$

$$\partial C_+/\partial t = -(1/Azq)(\partial I_+/\partial x) \quad [6]$$

$$\partial C_-/\partial t = (1/Azq)(\partial I_-/\partial x) \quad [7]$$

$$\partial E/\partial x = (zq/\epsilon)(C_+ - C_-) \quad [8]$$

where I_+, I_- = cation and anion currents, respectively, in amperes, C_+, C_- = cation and anion concentrations, respectively, in No./cm^3, A = cross-sectional area in cm^2, E = electric field intensity in volts/cm, ϵ = dielectric constant in farads/cm.

Reviewing briefly, the first two equations represent the cation and anion currents; each of these can be subdivided further into drift (*i.e.*, electromigration) and diffusion components. Equations [6] and [7] are the displacement currents, based on the conditions for continuity. Equation [8] is a form of Poisson's equation which gives the relationship between the electric field intensity and charge density, divided by the dielectric constant. All of the constants in these equations are assumed to be positive.

In order to calculate the transient response of a transference cell for a given excitation, it is necessary to solve these equations simultaneously for the appropriate boundary conditions. This is not an easy task, unfortunately, even when several approximations are made. If these equations have to be resolved for each new set of boundary conditions, it follows that little is gained from previous experience. To circumvent this problem the model concept is employed.

To illustrate the modeling procedure, consider the incremental volume of the electrolyte shown in Fig. 1.

[1] The assumption of equal valences is not necessary for the theory but is imposed only as a means for simplifying the notation for the equations to be developed.

[2] The rationalized MKS system of units will be employed in this discussion, with the exception that all units containing length will be given in centimeters rather than meters.

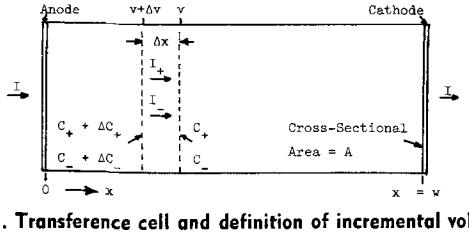

Fig. 1. Transference cell and definition of incremental volume

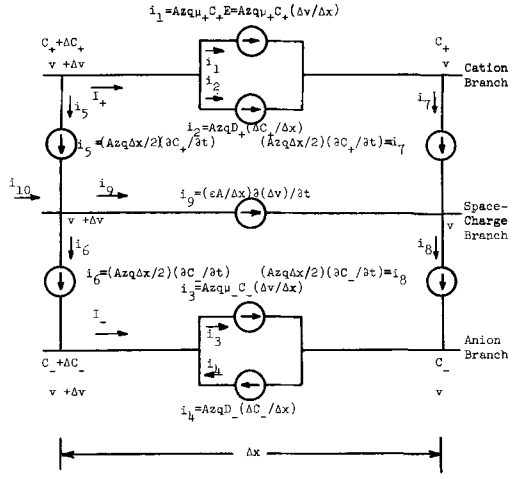

Fig. 2a. Incremental model for Eq. [4]-[8]

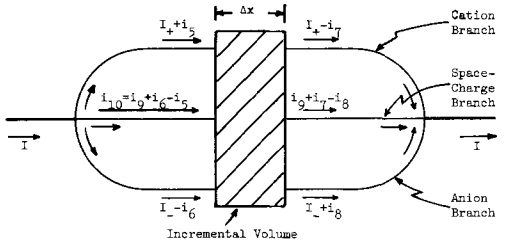

Fig. 2b. Division of the total current into its respective branch components.

As an artifice, we shall separate the cations and anions and their respective currents into two distinct regions of the electrolyte. If Eq. [4]-[8] are now synthesized for the spacial increment Δx, the incremental model shown in Fig. 2(a) results. Figure 2(b) illustrates, in a qualitative manner, the division of the total current into its respective branch components. It remains to be shown that a one-to-one correspondence exists in the limit as $\Delta x \rightarrow 0$ between the above equations and the incremental model. Referring to Fig. 2(a), the currents i_1 and i_2 are seen to be the drift and diffusion components of the cation current since $\Delta v/\Delta x \rightarrow E$ and $\Delta C_+/\Delta x \rightarrow -\partial C_+/\partial x$ in the limit as $\Delta x \rightarrow 0$. The sign conventions for the incremental parameters in Fig. 2(a) account for the mixed signs when the limits are evaluated. The anion current components i_3 and i_4 follow in exactly the same manner, except that the current i_4 is reversed in accordance with the definition of the direction for conventional current. Currents $i_5 - i_7$ and $i_6 + i_8$ are displacement currents for the cations and anions which correspond to Eq. [6] and [7] in the limit as $\Delta x \rightarrow 0$. Here we note that these currents are divided equally in the incremental region. The current i_9 is also a displacement current which tends to maintain charge neutrality in the electrolyte. (It is interesting to note that a displacement current can still flow even when charge neutrality, *i.e.*, $i_9 = 0$, applies.) The current i_9 is equal to $i_5 - i_6$, plus the summation of all displacement currents (i_{10}) from $x = 0$ to the reference point at which the incremental volume is chosen according to the equation

$$i_9 = \sum_{i=1}^{N} (\Delta I_+ - \Delta I_-)_i = Azq \frac{\partial}{\partial t}\left[\sum_{i=1}^{N} (C_+ - C_-)_i \Delta x\right] \quad [9]$$

If Eq. [9] is set equal to the defined current i_9, integrated with respect to t, and differentiated with re-

spect to x, we obtain in the limit as $\Delta x \to 0$ the following equation

$$\partial^2 v/\partial x^2 = (zq/\epsilon)(C_+ - C_-) \qquad [10]$$

It follows, thus, that Eq. [10] reduces to Eq. [8] since, $\partial^2 v/\partial x^2 = \partial E/\partial x$. Of interest is the fact that the current i_9 is equal to an electrical capacitor $C = \epsilon A/\Delta x$, multiplied by the time rate of change of voltage across the incremental volume of the electrolyte.

The next step in the modeling process is that of demonstrating that the transient associated with the displacement current i_9 decreases to zero at the relaxation time of the electrolyte. To illustrate why this is true, we shall assume that a step of current is applied to the transference cell at $t = 0$, *i.e.*, a step of positive ion current ($t_+ = 1$) at the electrode-electrolyte interfaces. If another current is already flowing in the cell when the step of current is applied, it will be assumed that this other current is changing slowly with time. The meaning of "slowly" will become clear as the argument is developed. The concentration of the electrolyte cannot change instantaneously on the onset of the step of current, ignoring regions immediately adjacent to the electrodes; thus, diffusion currents of types i_2 and i_4 throughout the electrolyte cannot change initially at the onset of the step of current but will change rather "slowly" beginning at the electrodes where the concentration initially begins to change. Currents of types i_5, i_6, i_7, and i_8 can and do change at a rate dictated by the following mechanism. Drift currents of types i_1 and i_3 change as the voltage changes across the electrolyte. It follows that the initial step of current all flows through a capacitor of $\epsilon A/w$ where w is the separation of the electrodes. This capacitor is actually shunted and distributed by incremental resistive components which carry the drift currents. The instantaneous electrical model of the electrolyte at the onset of the step of current is given by the distributed resistance-capacitance network shown in Fig. 3. The initial transient recovers at the relaxation time of the distributed R-C network according to the equation

$$\tau = \frac{\Delta C \Delta R_a \Delta R_c}{\Delta R_a + \Delta R_c} = \frac{\epsilon}{zq\mu_+ C_+ + zq\mu_- C_-} = \frac{\epsilon}{\sigma_+ + \sigma_-} \qquad [11]$$

where σ_+ and σ_- are the conductivities of the positive and negative ions of the electrolyte. Since the conductivity of the electrolyte varies with x due to current flowing prior to the application of the step input, the relaxation time is x-dependent and has a maximum value in that region of the electrolyte where the concentration is a minimum. For typical values of dielectric constants and conductivities, this relaxation time can be shown to be quite small, indeed, in comparison with the transient times that will be computed for the redistribution of ions, assuming that space-charge neutrality is present.

It should be pointed out that space-charge neutrality cannot exist unless dE/dx is zero. Since dE/dx will not be zero in the models to be developed, charge neutrality will not be met exactly. In general, this situation is not serious and can easily be tested by perturbation methods for determination of the degree of charge unbalance. It is not the intention to imply, however, that the equations can be indiscriminately manipulated.

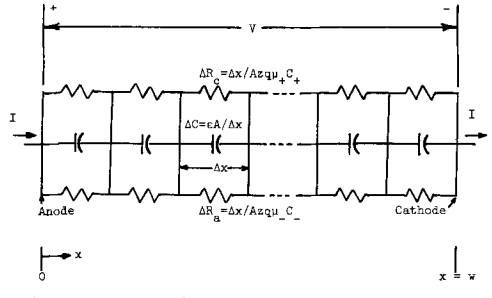

Fig. 3. Instantaneous electrical model of the electrolyte for the relaxation transient response.

Assuming the displacement current of type i_9 is zero, we shall demonstrate that the incremental model of Fig. 2 can be simplified by taking advantage of the fact that $C_+ \simeq C_-$. Solving for the electric field intensity E in Eq. [5] and substituting into Eq. [4], we obtain the equation

$$I_+ = I_-(\mu_+/\mu_-) - 2AzqD_+(\partial C_+/\partial x) \qquad [12]$$

Differentiating Eq. [12] with respect to x and substituting Eq. [6] and [7], we obtain the diffusion equation

$$\partial C_+/\partial t = \frac{2D_+\mu_-}{\mu_+ + \mu_-}(\partial^2 C_+/\partial x^2) = D_e(\partial^2 C_+/\partial x^2) \qquad [13]$$

in which the effective diffusion process is governed by the ambipolar diffusivity D_e. Referring to Fig. 2, it follows that the anion current I_- can be determined by integrating the displacement current from $x = 0$ to the reference point of the incremental model. The anion current, thus, is given by the equation

$$I_- = Azq\frac{\partial}{\partial t}\int_0^x C_+ dx \qquad [14]$$

and Eq. [12] becomes

$$I_+ = Azq(\mu_+/\mu_-)\frac{\partial}{\partial t}\int_0^x C_+ dx - 2AzqD_+(\partial C_+/\partial x) \qquad [15]$$

From these results, a modified incremental model can be synthesized as shown in Fig. 4(a). The model in its new form corresponds to Eq. [6] and [12] in the limit as $\Delta x \to 0$, for the assumed current directions in Fig. 2. The model still does not seem to be very tractable, unfortunately, in realizing the goals set forth at the outset. The basic problem stems from the fact that the anion current appears in the cation branch as a dependent current source $I_-(\mu_+/\mu_-)$. Kirchhoff's current law in conjunction with Eq. [14], will take care of this difficulty, however. Remembering that the current at the electrode-electrolyte interface is entirely positive ion, let us move the incremental volume to $x = 0$. Since the initial displacement current can be determined, it follows from Kirchhoff's current law that all currents entering the second incremental model are known. From a knowledge of the displacement current flowing in the second incremental model, all of the remaining currents can again be determined by this law. Proceeding thus from $x = 0$ to $x = w$, it is clear that a complete solution

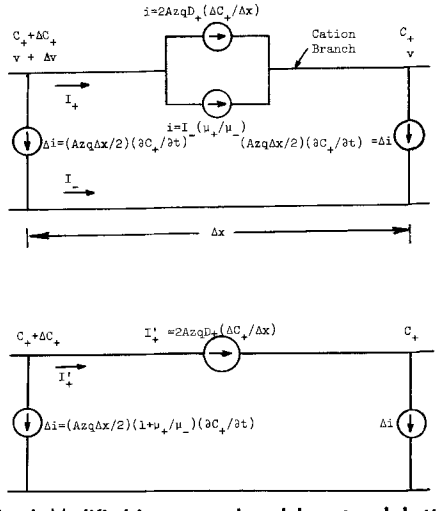

Fig. 4. Modified incremental models, a top, b bottom

can be effected, although somewhat difficult to perform in an exact analysis, assuming $i_9 = 0$.

An equivalent, but more abstract, model can be derived which avoids the dependent current source in Fig. 4(a) if we redefine the cation current in Eq. [15]. By incorporating the first term in Eq. [15] with Eq. [6], we obtain the following incremental equations

$$I_+' = -2AzqD_+(\Delta C_+/\Delta x) \quad [16]$$

$$\Delta I_+' = -(Azq\Delta x)(1 + \mu_+/\mu_-)(\partial C_+/\partial t) \quad [17]$$

where I_+' is the cation current, neglecting the contribution of the displacement component[3] (the first term in Eq. [15]). An alternative interpretation for the current I_+' is that it is the steady-state cation current that flows, after the displacement current becomes zero. The factor of two in Eq. [16] thus implies that the steady-state cation current is equally divided between drift and diffusion components. Employing this new definition for current, we can synthesize Eq. [16] and [17] as shown in Fig. 4(b), where the current in Eq. [17] is again symmetrically divided for the incremental volume.

The lumped model.—Thus far, the incremental model has been a useful tool for visualization purposes. The point of departure from a more exact analysis is to use one or more sections of the incremental model for approximation. In effect, thus, simultaneous partial differential equations are converted into simultaneous-differential-difference equations, differential in time and difference in space.

The lumped parameter model for the differential-difference approximation is obtained by letting Δx be a finite quantity in Fig. 4(b). For Δx finite and constant, the model is analogous to a lumped parameter electrical network, if we define the following analogies; concentration for voltage, current for current, $2AzqD_+/\Delta x$ for electrical conductance, $(Azq\Delta x/2)(1 + \mu_+/\mu_-)$ for electrical capacitance. Thus, the current sources in Fig. 4(b), can be replaced by lumped components analogous to electrical resistors and capacitors. In order to differentiate between the two analogies, we will follow Linvill's (3, 4) nomenclature and refer to the analog of conductance as "diffusance" and the analog of capacitance as "storance." The lumped-parameter model for an incremental region is shown

[3] Actually, the cation current in Eq. [15] consists only of drift and diffusion components. Since the first term is proportional to the displacement current as defined by Eq. [6], it is referred to, in this sense, as a displacement current.

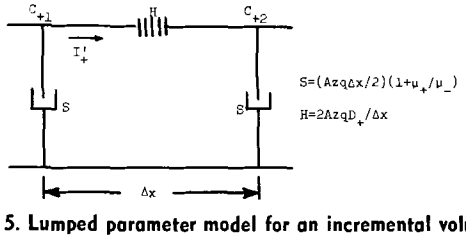

Fig. 5. Lumped parameter model for an incremental volume

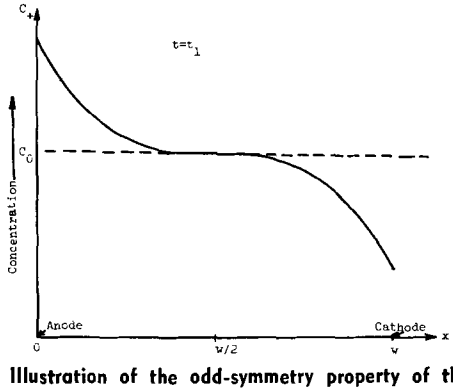

Fig. 6. Illustration of the odd-symmetry property of the excess concentration.

in Fig. 5 where the symbol H denotes diffusance and the symbol S denotes storance.

The final step in the modeling procedure is to ascertain the number of incremental regions which should be used to represent the electrolyte. This question can be answered partially by considering the odd-symmetry property of the excess concentration of the electrolyte. Let us consider the concentration profile in Fig. 6 at some instant during a transient response. For a reversible transference cell, the concentration profile will possess odd-symmetry about its equilibrium value, *i.e.*, the concentration for no excitation. Since the concentration at the center of the cell is clamped at its equilibrium value, it is seen that a model for the half-cell is sufficient to calculate the transient response. Thus, it follows that a knowledge of the excess concentration from $x = 0$ to $w/2$ can be used to determine the concentration from $x = w/2$ to w. This relationship is given by the equation

$$C_+(x,t) - C_0 = C_0 - C_+(w - x,t) = C_e(x,t) \quad [18]$$

where C_0 = equilibrium concentration and $C_e(x,t)$ = excess concentration.

It should be noted that Eq. [18] gives rise to two interesting implications. The first point to be observed is that the maximum concentration $C_+(0,t)$ at the anode cannot exceed twice the equilibrium concentration. This follows because the concentration at $x = w$, the cathode, cannot become negative. The second point to be noted is that the currents flowing in the lumped parameter model always depend on the excess concentration $C_+(x,t) - C_0$. Thus it follows that it is only necessary to consider the excess concentration in the computation of the concentration transient response. We shall take advantage of this property in the lumped parameter models.

Even though we can reduce the size of the over-all model by a factor of two by considering only a half-cell, we still have not resolved the problem of specifying the number of incremental regions to be used to approximate the region from $x = 0$ to $x = w/2$. This consideration will be deferred until the next section.

Application of the lumped parameter models.—In this section, we will use the half-cell lumped parameter models to calculate concentration transient responses for the special case of a constant current excitation. As previously indicated, the number of incremental regions necessary to approximate the region from $x = 0$ to $x = w/2$ has not been specified. Rather than take a large number of increments at the outset, we shall begin with only one incremental region ($\Delta x = w/2$), followed by two incremental regions ($\Delta x = w/4$), and, finally, three incremental regions ($\Delta x = w/6$).

Concentration transient responses will be considered for these three cases. In particular, one example will be given for the concentration response at the anode for these cases, and one example will be given, using the two-increment model, which demonstrates the spacial variation of the concentration for different normalized time increments. In order to demonstrate the accuracy of the calculations using the lumped parameter models, the theoretical response for each example will also be given in graphical form. It will be shown, that for as few as two or three increments to approximate a half-cell, that convergence to the theoretical solution is quite rapid. The theoretical solution will be given after these examples have been presented.

The first transient to be considered is that of the excess concentration at $x = 0$, the anode. The incremental models shown in Fig. 7 will be used to predict the concentration response which will be compared to the theoretical response. The models shown in Fig. 7(b) and Fig. 7(c) are obtained by letting $\Delta x = w/4$ and $\Delta x = w/6$, respectively, in Fig. 5 and cascading two or three of these sections, as required, to complete the

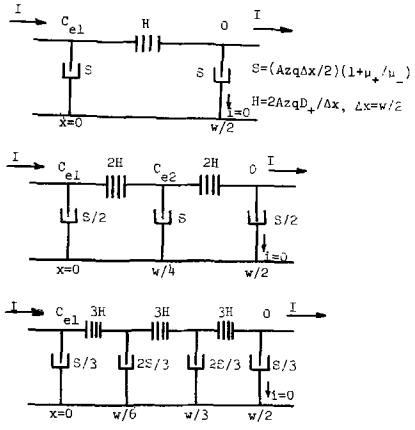

Fig. 7. Half-cell lumped parameter models for calculating excess-concentration transients: a (top) one-increment model; b (center) two-increment model; c (bottom) three-increment model.

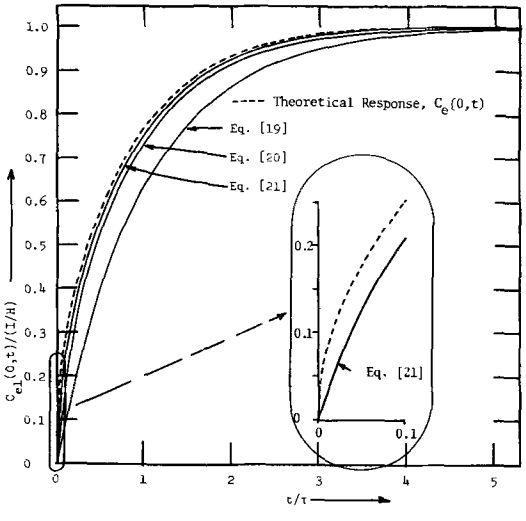

Fig. 8. Excess concentration transient responses at the anode based on the lumped parameter models and the theoretical solution.

models. For a constant current excitation I, the following equations for the excess concentration $C_{e1}(0,t)$ can be obtained by standard circuit-theory techniques (5)

$$C_{e1}(0,t) = (I/H)[1 - \exp(-t/\tau)] \quad [19]$$

$$C_{e1}(0,t) = (I/H)[1 - 0.8536\exp(-1.172t/\tau) - 0.1464\exp(-6.828t/\tau)] \quad [20]$$

$$C_{e1}(0,t) = (I/H)[1 - 0.8293\exp(-1.206t/\tau) - 0.1111\exp(-9t/\tau) - 0.0596\exp(-16.794t/\tau)] \quad [21]$$

where $\tau = S/H = w^2(1 + \mu_+/\mu_-)/16D_+$. Equations [19], [20], and [21] and the theoretical solution (Eq. [23] for $x = 0$) are plotted in Fig. 8 to illustrate the nature of the transient response and to demonstrate the rapid convergence to the theoretical response as the number of volume increments is increased. Referring to Fig. 8, it is seen that the convergence is quite good for the three-increment model, except for the initial portion of the transient response. Further, it should be noted that the principal error is represented by an almost constant time delay. If greater accuracy is desired for smaller values of time, the model is easily modified by adding more increments and readjusting parameters, as previously indicated. Although this may seem impractical, it is a relatively simple task to program digital computer to add more increments to the model since it has an iterative structure.

As a final example, an indication of the over-all concentration profile in a cell will be determined. Because of the incremental properties of the lumped parameter model, the concentration will vary linearly across each increment. In other words, if several increments are used to approximate a given cell, the concentration will vary in a piecewise-linear manner, consisting of a straight-line segment across each increment. To illustrate these ideas, let us consider the model shown in Fig. 7(b). Remembering the excess concentration at $x = w/2$ is zero and taking advantage of the odd-symmetry property of Eq. [18], the concentration profile is obtained by plotting Eq. [20] and the equation for $C_{e2}(w/4,t)$, as defined in Fig. 7(b)

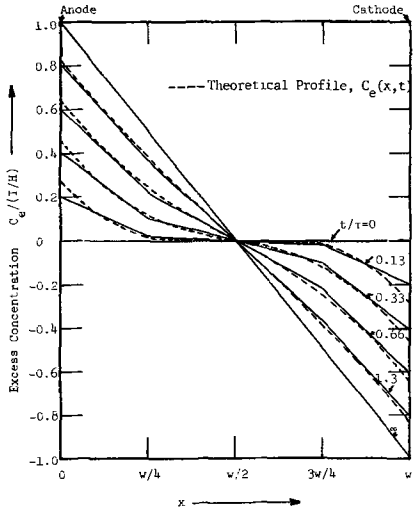

Fig. 9. Piecewise-linear excess concentration profile for the two-increment model and the theoretical profile for the cell.

$$C_{e2}(w/4,t) = (I/2H)[1 - 1.2071\exp(-1.172t/\tau) + 0.2071\exp(-6.828t/\tau)] \quad [22]$$

for different values of time. An indication of the approximate and theoretical excess concentration profiles for the entire cell is shown in Fig. 9. From Fig. 9, it follows that the concentration change initially increases more rapidly at the anode, followed by concentration build-up at $x = w/4$, until the steady-state concentration becomes truly linear on completion of the transient. Of course, the actual concentration profile exhibits curvature throughout the cell, and the piecewise-linear representation is only an approximation to the theoretical profile. Even so, the two-increment model gives a fairly accurate indication of the nature of the transient response. The three-increment model would have been even more accurate, especially at smaller values of t/τ. By considering more increments, the piecewise-linear representation can be made as accurate as desired.

The theoretical solution of the excess concentration, for the approximation set forth earlier, for the constant current excitation can be obtained by solving Eq. [13], subject to the condition at $x = 0$ that $I = -2AzqD_+(\partial C_+/\partial x)$ which is just Eq. [12] at $x = 0$ since I_- is zero and I_+ is the applied current and the condition that the excess concentration is zero at $x = w/2$. The theoretical solution is given by the equation[4] (6).

$$C_e(x,t) = (I/H)\left\{(1 - 2x/w) - (8/\pi^2)\sum_{n=0}^{\infty}\frac{1}{(2n+1)^2}\exp[-(2n+1)^2\pi^2 t/8\tau]\cdot\cos[(2n+1)\pi x/w]\right\} \quad [23]$$

[4] This equation is identical to Eq. [5], p. 113, of Carslaw and Jaeger, except for minor transformations.

This equation is plotted for $x = 0$ in Fig. 8 and is plotted as a function of x for different values of t/τ in Fig. 9.

The above examples were intended to illustrate the general procedure for employing the lumped parameter models in the computation of concentration transient responses. Even though we have restricted these examples to a constant current excitation, other types of current excitations can readily be considered in a similar manner. In particular, for other excitations the lumped parameter approach becomes even more attractive. This follows because the solution of the diffusion equation, Eq. [13], is practically intractable except for very few excitations, such as the constant current excitation.

Conclusions

The incremental model has been shown to be a convenient vehicle with which to study electrical conduction phenomena in the electrolyte of a reversible transference cell. The linear relationship between concentration and current, for the approximations set forth, suggests a tangible means for describing a distributed system with a circuit analog. This follows because the same system can be analyzed for different excitations without recourse to the exact partial differential equations which are, in general, more difficult to solve than differential-difference equations. Even though the lumped parameter model has its principal limitation in predicting rapid transients, such as the initial portion of the concentration transient for a constant current excitation, its iterative structure provides a convenient means for adding more increments to the model to improve the accuracy. For many applications, where the over-all transient is to be investigated, a two-increment model for the half-cell should be adequate.

The possibility of extending and applying the lumped parameter model to other electrolytic systems should pose some challenging and interesting problems.

Acknowledgment

The authors are most grateful for the assistance provided by the Computer Center at Texas Technological College. This work was conducted at Texas Technological College under the state-supported research grant, 191-5412.

Manuscript received Sept. 23, 1966; revised manuscript received April 10, 1967.

Any discussion of this paper will appear in a Discussion Section to be published in the June 1968 JOURNAL.

REFERENCES

1. R. N. O'Brien, W. F. Yakymyshyn, and J. Leja, *This Journal*, **110**, 820 (1963).
2. R. N. O'Brien, *ibid.*, **113**, 389 (1966).
3. J. G. Linvill, *Proc. IRE*, **46**, 1141 (1958).
4. J. G. Linvill and J. F. Gibbons, "Transistors and Active Circuits," pp. 67-106, McGraw-Hill Book Co., New York (1961).
5. H. H. Skilling, "Electrical Engineering Circuits," John Wiley & Sons, Inc., New York (1958).
6. H. S. Carslaw and J. C. Jaeger, "Conduction of Heat in Solids," pp. 112-114, Oxford Press, London (1959).

Primary and Solvent Isotope Effects in the Anodic Evolution of Oxygen

Mark Salomon[1]

School of Chemistry, Rutgers—The State University, New Brunswick, New Jersey

ABSTRACT

The use of hydrogen isotopes in studying the oxygen evolution reaction (o.e.r.) is discussed. It is shown that along with other experimental data such as pH studies, Tafel behavior, etc., the H/D-isotope effects can be used as additional criteria for the elucidation of reaction mechanisms. Normal isotope effects, *i.e.*, those corresponding to the o.e.r. being faster in H_2O than in D_2O, arise normally from considerations of the primary isotope effect. Depending on the magnitude of the solvent isotope effect, several cases involving an inverse isotope effect arise, *i.e.*, the rate of the o.e.r., is now faster in D_2O than it is in H_2O. A treatment of these isotope effects is given in this paper and experimental data for the o.e.r. at Ni anodes is discussed.

The oxygen evolution reaction (o.e.r.) has been of interest to electrochemists for many years (1-12). To mention only a few papers, the reactions occurring at the oxygen electrode have been studied by methods such as the pH effect (2,10) current-potential behavior (3-12), emf decay (6), and by oxide film formation (12). Conway and Bourgault (6, 12, 13), in their studies of the nickel-oxygen system, found that under certain conditions the rate of oxygen evolution was faster in heavy water than in light water, *i.e.*, an inverse isotope effect was experimentally observed. In 1965, Conway *et al.* (14) presented calculations and discussed the origin of this inverse isotope effect. In the present paper, a formal and more detailed analysis is presented, and the calculations briefly introduced in the original work (14) are extended to new cases as well as being developed in more detail. In general this paper deals with calculations of primary and solvent isotope effects in the o.e.r. The inverse isotope effect is attributed mainly to the solvent effect, *i.e.*, the reason why this effect appears can be traced to the evidence that the deuteroxide ion (OD^-) in D_2O is a stronger base than the OH^- ion in H_2O. Correspondingly, D_3O^+ in D_2O is a stronger acid than is H_3O^+ in H_2O (15).

[1] Present address: NASA, ERL, Cambridge, Massachusetts.

Kinetics of the O.E.R.

General considerations.—In alkaline solution, the possible kinetic sequences considered here are [cf. Bockris, ref. (2)]

$$M + OH^- \rightarrow MOH + e \quad [1]$$

$$MOH + OH^- \rightarrow MO + H_2O + e \quad [2a]$$

$$2MOH \rightarrow M + MO + H_2O \quad [2b]$$

$$2MO \rightarrow 2M + O_2 \quad [3]$$

Reactions [2a] and [2b] are considered to be alternative mechanisms therefore giving rise to two possible reaction sequences. In acid solutions, the schemes considered involve the following reactions [cf. Conway, ref. (7)]

$$M + H_2O \rightarrow MOH + H^+ + e \quad [4]$$

$$MOH + H_2O \rightarrow MO + H_3O^+ + e \quad [5a]$$

$$2MOH \rightarrow M + MO + H_2O \quad [5b]$$

$$2MO \rightarrow 2M + O_2 \quad [6]$$

where reactions [5a] and [5b] are considered to be alternative. One can of course write reactions analogous to [1]-[6] substituting deuterium for hydrogen, and these can thus serve as the basis for comparison of the H/D-isotope effect in the o.e.r.

According to MacDonald and Conway (7), the initial discharge step always occurs from a water molecule so that reactions [1] and [4], respectively, should be written as

$$M + H_2O^* + OH^- \rightarrow MO^*H + H_2O + e \quad [1a]$$

and

$$M + 2H_2O \rightarrow MOH + H_3O^+ + e \quad [4a]$$

The asterisk in Eq. [1a] indicates the original source of OH for the surface species. Hence, as in an earlier publication (16), the activated complexes corresponding to reactions [1a] and [4a], respectively, are

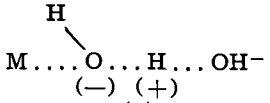

(a)

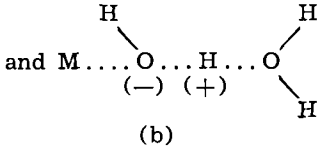

(b) [7]

and the rate-determining discharge step then involves the transfer of OH^- to the electrode surface and a proton transfer to an adjacent hydroxyl ion or water molecule in the double layer. Electron transfer to the metal then can occur when the activated complex relaxes to the final state configuration (32, 37).

To derive a rate equation for reaction [1a], the statistical method can be employed (17) as reported previously for the h.e.r. (18). The condition for equilibrium between initial and activated states for reaction [1a] is

$$\mu_M + \mu_{H_2O} + \bar{\mu}_{OH^-} = \bar{\mu}^{\ddagger} \quad [8]$$

where $\bar{\mu}$ is the electrochemical potential of the indicated species and μ is the chemical potential (19). For species i, $\bar{\mu}_i$ is defined as (19)

$$\bar{\mu}_i = \mu_i + z_i\phi_i\mathbf{F} \quad [9]$$

where ϕ_i is the inner potential of species i in the phase under consideration and z_i is the valence, including the sign, of the charged species. From statistical mechanics we have (17)

$$\mu_i = -kT \ln f_i \quad [10]$$

where f_i is the molecular partition function (p.f.) per molecule, *i.e.*

$$f_i = q_i/n_i \quad [11]$$

Hence it is clear that $\mu_i = \mu_i^\circ$ for the standard state when $n_i = 1$, and the standard state can, of course, be chosen in terms of molecules or moles. Using the latter convention, Eq. [9] and [10] can be combined to give

$$\bar{\mu}_i = -RT \ln f_i + z_i\phi_i\mathbf{F} \quad [12]$$

Taking $z = -1$ for both the OH^- and the activated complex, Eq. [8] and [12] can be combined and rearranged to give

$$f_M f_{H_2O} f_{OH^-} = f^{\ddagger} \cdot \exp[(\phi^{\ddagger} - \psi_1)\mathbf{F}/RT] \quad [13]$$

where ψ_1 is the potential at the outer Helmholz plane and $\phi^{\ddagger}$ is the inner potential of the system corresponding to the activated complex configuration. This follows from the model of the activated complex used here (Eq. [7]) and elsewhere (14, 16, 18). Since the electrode is at some potential ϕ_M and the reactants in the initial state (*i.e.*, in the outer Helmholz plane) are at some potential ψ_1, it follows that the potential $\phi^{\ddagger} - \psi_1$ is intermediate between $\phi_M - \psi_1$, *i.e.*, it corresponds to some fraction β of $\phi_M - \psi_1$. Expressed mathematically

$$\phi^{\ddagger} - \psi_1 = \beta(\phi_M - \psi_1) \quad [14]$$

From Eq. [11], [13], and [14]

$$n^{\ddagger} = n_M n_{H_2O} n_{OH^-} \frac{q^*}{q_M q_{H_2O} q_{OH^-}} \exp[\beta(\phi_M - \psi_1)\mathbf{F}/RT]$$

Removing the imaginary frequency from q^* and replacing it by $q^{\ddagger}$ (this is the frequency corresponding to the motion along the reaction coordinate), one now takes $q_M = 1$ (16, 18), multiplies by $\mathbf{F}$ and divides through by the area A (to obtain concentrations in units of moles cm^{-2}) and the above equation takes on the familiar form

$$i = \mathbf{F}\frac{kT}{h}[M][H_2O][OH^-]\frac{Q^{\ddagger}}{Q_{H_2O}Q_{OH^-}} \exp[\beta(\phi_M - \psi_1)\mathbf{F}/RT]$$

where $Q = q/A$. The terms in concentration should be replaced by ones in activities, but since we will be dealing in ratios (H_2O to D_2O), it is a good approximation to take the ratios of activity coefficients in H_2O to that in D_2O as equal to unity. Further simplification of this equation can be made by referring to the model of the activated complex in Eq. [7a]. The assumption is made (see calculations below) that the unreacting OH^- bond does not suffer any change in frequency in going from the initial to the activated state [cf. ref. (20)] so that the p.f. Q_{OH^-} cancels since it appears in both states. Taking the activity of water = 1, and considering the rate of reaction at the reversible potential, *i.e.*, ϕ_M (alk.) = $\phi r,b$ and $i = i_o$, the above equation becomes

$$i_o = \mathbf{F}\frac{kT}{h}[M][OH^-]\frac{q^{\ddagger}}{q_{H_2O}} \exp[\beta(\phi_{r,b} - \psi_1)\mathbf{F}/RT] \quad [15]$$

By an analogous procedure, the exchange current density for discharge in acid solutions is

$$i_o = \mathbf{F}\frac{kT}{h}[M]\frac{q^{\ddagger}}{q_{H_2O}} \exp[\beta(\phi_{r,a} - \psi_1)\mathbf{F}/RT] \quad [16]$$

Since similar relations can be written for the D-analogues of Eq. [15] and [16], a ratio of exchange current densities, R, can be defined as

$$R_1 = \frac{i_{o(H)}}{i_{o(D)}} = \frac{q_{D_2O}}{q_{H_2O}} \cdot \frac{q_{H^{\ddagger}}}{q_{D^{\ddagger}}} \exp[\beta\Delta\phi_b^\circ\,\mathbf{F}/RT] \quad [17]$$

and similarly

$$R_4 = \frac{q_{D_2O}}{q_{H_2O}} \cdot \frac{q^{\ddagger}{}_H}{q^{\ddagger}{}_D} \exp\beta[\Delta\phi_a^\circ\mathbf{F}/RT] \quad [18]$$

Equations [17] and [18] were obtained by assuming ψ_1 and [M] to be isotopically independent and by allowing $[OH^-] = [OD^-]$ and $[H_3O^+] = [D_3O^+]$. This latter condition permits one to write the potential difference term $\phi_{r,H^-}\ \phi_{r,D}$ in terms of the standard values, $\Delta\phi^\circ = \phi^\circ{}_H - \phi^\circ{}_D$. The remaining relations for R for reactions [2], [3], [5], and [6] shall be presented in a brief manner since they all follow from treatments similar to that described above.

Reaction scheme [1], [2a], [3].—For the case of a rate-determining step [2a], the values of R for limiting Langmuir coverages of $\theta_{MOH} \to 0$ and 1, respectively, are

$$R_{2a} = \left(\frac{q_{OD^-}}{q_{OH^-}}\right)^2 \cdot \frac{q^+_H}{q^+_D} \exp\left[(1+\beta)\Delta\phi^\circ \mathbf{F}/RT\right] \quad [19]$$

and

$$R_{2a} = \left(\frac{q_{OD^-}}{q_{OH^-}}\right)^2 \cdot \frac{q^+_H}{q^+_D} \exp\left[\beta\Delta\phi^\circ \mathbf{F}/RT\right] \quad [20]$$

If a Temkin isotherm is applicable, the rate of reaction [2] is (21, 22),

$$i_{O,2} = Z\mathbf{F}\frac{kT}{h}[MOH][OH^-]\frac{q^+}{q_{MOH}\, q_{OH^-}} \exp\left[f(\theta) + \beta\phi^\circ \mathbf{F}\right]/RT$$

where the function $f(\theta)$ has been previously defined (21, 22) as

$$f(\theta) = \phi^\circ \mathbf{F} + \text{constants}$$

By considering reaction [1] to be in quasi-equilibrium, it follows that the explicit form of the above equation is

$$f(\theta) = RT \ln [OH^-] + RT \ln\left[(1-\theta_t)/\theta_{MOH}\right] + RT \ln(q_{MOH}/q_{OH^-}) + \phi^\circ \mathbf{F} \quad [21]$$

where θ_t is the total surface coverage. Making the appropriate substitutions it is found that the theoretical expression for R_2 is identical to Eq. [19].

For a rate-determining step [3], use of the Langmuir isotherm for $\theta_{MO} \to 0$ and 1, respectively, gives

$$R_3 = \left(\frac{q_{OD^-}}{q_{HO^-}}\right)^4\left(\frac{q_{H_2O}}{q_{D_2O}}\right)^2 \frac{q^+_H}{q^+_D} \exp\left[4\Delta\phi^\circ \mathbf{F}/RT\right] \quad [22]$$

and

$$R_3 = \frac{q_{MO(D_2O)}}{q_{MO(H_2O)}} \cdot \frac{q^+_H}{q^+_D} \quad [23]$$

For the cases where the Temkin isotherm might be applicable, several cases arise for activated and nonactivated adsorption. Using Eq. [21] and employing simple equilibrium relations [cf. ref. (22)] the following R_3 values are easily obtained: (*i*) For activated adsorption we have

$$R_3 = \left(\frac{q_{OD^-}}{q_{HO^-}}\right)^4\left(\frac{q_{H_2O}}{q_{D_2O}}\right)^2 \frac{q^+_H}{q^+_D} \exp\left[\Delta\phi^\circ \mathbf{F}/RT\right] \quad [24]$$

for $\theta_{MO} \approx \theta_{MOH}$ and

$$R_3 = \left(\frac{q_{OD^-}}{q_{HO^-}}\right)^4\left(\frac{q_{H_2O}}{q_{D_2O}}\right)^2 \frac{q^+_H}{q^+_D} \exp\left[3\Delta\phi^\circ \mathbf{F}/RT\right] \quad [25]$$

for $\theta_{MO} << \theta_{MOH}$ and potential dependent.

(*ii*) For nonactivated adsorption

$$R_3 = \left(\frac{q_{OD^-}}{q_{HO^-}}\right)^4\left(\frac{q_{H_2O}}{q_{D_2O}}\right)^2 \frac{q^+_H}{q^+_D} \cdot \exp\left[2\Delta\phi^\circ \mathbf{F}/RT\right] \quad [26]$$

for $\theta_{MO} \approx \theta_{MOH}$. For the case where $\theta_{MO} << \theta_{MOH}$ (and is therefore potential dependent) R_3 is given by Eq. [22].

Reaction scheme [1], [2b], [3].—For this sequence of reactions, R_1 and R_3 values are the same as those given above. For the limiting Langmuir conditions of $\theta_{MOH} \to 0$ and 1, respectively, it can easily be shown that

$$R_{2b} = \left(\frac{q_{OD^-}}{q_{OH^-}}\right)^2 \frac{q^+_H}{q^+_D} \exp\left[2\Delta\phi^\circ \mathbf{F}/RT\right] \quad [27]$$

and

$$R_{2b} = \left(\frac{q_{OD^-}}{q_{OH^-}}\right)^2 \frac{q^+_H}{q^+_D} \quad [28]$$

For the intermediate Temkin type behavior

$$R_{2b} = \left(\frac{q_{OD^-}}{q_{OH^-}}\right)^2 \frac{q^+_H}{q^+_D} \exp\left[\Delta\phi^\circ \mathbf{F}/RT\right] \quad [29]$$

Reaction scheme [4], [5a], *and* [6].—R values for this scheme are obtained by methods very similar to that discussed above and involve mainly algebraic substitutions. Hence only the final results need be given with the exception that the $f(\theta)$ required for the Temkin cases in acid solution is defined by

$$f(\theta) = -RT \ln [H_3O^+] + RT \ln (1-\theta_t/\theta_{MOH}) + RT \ln\left[(q_{H_3O^+})(q_{MOH})/q^2_{H_2O}\right] + \phi^\circ \mathbf{F} \quad [30]$$

The relation for R_4 is given by Eq. [18]. For a rate-determining reaction [5a]

$$R_{5a} = \left(\frac{q_{D_2O}}{q_{H_2O}}\right)^3 \frac{q_{H_3O^+}}{q_{D_3O^+}} \cdot \frac{q^+_H}{q^+_D} \exp\left[(1+\beta)\Delta\phi^\circ \mathbf{F}/RT\right] \quad [31]$$

and

$$R_{5a} = \left(\frac{q_{D_2O}}{q_{H_2O}}\right)^3 \frac{q_{H_3O^+}}{q_{D_3O^+}} \frac{q^+_H}{q^+_D} \exp\left[\beta\Delta\phi^\circ \mathbf{F}/RT\right] \quad [32]$$

for the Langmuir conditions of $\theta_{MOH} \to 0$ and 1, respectively. For the Temkin case of $\theta_{MOH} \approx 0.5$, R_{5a} is given by Eq. [31].

For a rate-determining step [6], the quasi-equilibrium treatment gives

$$R_6 = \left(\frac{q_{D_2O}}{q_{H_2O}}\right)^6\left(\frac{q_{H_3O^+}}{q_{D_3O^+}}\right)^4 \frac{q^+_H}{q^+_D} \exp[4\Delta\phi^\circ \mathbf{F}/RT] \quad [33]$$

and

$$R_6 = \frac{q_{MO(D_2O)}}{R_{MO(H_2O)}} \cdot \frac{q^+_H}{q^+_D} \quad [34]$$

respectively, for $\theta_{MO} \to 0$ and $\theta_{MO} = 1$ (Langmuir conditions).

If the Temkin isotherm is applicable we again have: (*i*) Activated adsorption gives two cases, respectively, for

$$\theta_{MO} \approx \theta_{MOH} \text{ and } \theta_{MO} << \theta_{MOH}$$

$$R_6 = \left(\frac{q_{D_2O}}{q_{H_2O}}\right)^6\left(\frac{q_{H_3O^+}}{q_{D_3O^+}}\right)^4 \frac{q^+_H}{q^+_D} \exp[\Delta\phi^\circ \mathbf{F}/RT] \quad [35]$$

and

$$R_6 = \left(\frac{q_{D_2O}}{q_{H_2O}}\right)^6\left(\frac{q_{H_3O^+}}{q_{D_3O^+}}\right)^4 \frac{q^+_H}{q^+_D} \exp[3\Delta\phi^\circ \mathbf{F}/RT] \quad [36]$$

(*ii*) For nonactivated adsorption

$$R_6 = \left(\frac{q_{D_2O}}{q_{H_2O}}\right)^6\left(\frac{q_{H_3O^+}}{q_{D_3O^+}}\right)^4 \frac{q^+_H}{q^+_D} \exp[2\Delta\phi^\circ \mathbf{F}/RT] \quad [37]$$

for $\theta_{MO} \approx \theta_{MOH}$. For $\theta_{MO} << \theta_{MOH}$, R_6 is given by Eq. [33].

Reaction scheme [4], [5b], *and* [6].—The values of R_4 and R_6 will again remain unchanged. Under Langmuir adsorption conditions, it follows that

$$R_{5b} = \left(\frac{q_{D_2O}}{q_{H_2O}}\right)^3 \cdot \frac{q_{H_3O^+}}{q_{D_3O^+}} \cdot \frac{q^+_H}{q^+_D} \exp[2\Delta\phi^\circ \mathbf{F}/RT] \quad [38]$$

and

$$R_{5b} = \left(\frac{q_{D_2O}}{q_{H_2O}}\right)^3 \cdot \frac{q_{H_3O^+}}{q_{D_3O^+}} \cdot \frac{q^+_H}{q^+_D} \quad [39]$$

for $\theta_{MOH} \to 0$ and 1, respectively. For the intermediate Temkin type behavior

$$R_{5b} = \left(\frac{q_{D_2O}}{q_{H_2O}}\right)^3 \cdot \frac{q_{H_3O^+}}{q_{D_3O^+}} \cdot \frac{q^+_H}{q^+_D} \exp[\Delta\phi^\circ \mathbf{F}/RT] \quad [40]$$

Calculations

Initial state quantities.—The p.f. ratios for the various H and D species were obtained from previous calculations using spectroscopic (15, 38) and equilibrium (39, 40) data found in the literature (15). For 25°C, the appropriate p.f. ratio values are (cf. 18, 23)

$$\frac{q_{D_2O}}{q_{H_2O}} = 1437; \frac{q_{D_3O^+}}{q_{H_3O^+}} = 19{,}023; \frac{q_{OD^-}}{q_{OH^-}} = 21.15$$

The potential difference, $\Delta\phi^\circ$.—In alkaline solution, ϕ°_r for the reversible oxygen electrode can be calculated from the free energy change of the equilibrium

$$2\,OH^- \rightleftarrows \tfrac{1}{2}O_2 + H_2O + 2e_M$$

The condition for equilibrium is

$$2\bar{\mu}_{OH^-} = \tfrac{1}{2}\mu_{O_2} + \mu_{H_2O} + 2\bar{\mu}_e$$

Using Eq. [9]-[12] and taking all activities equal to unity (*i.e.*, standard states are being employed), the above equation becomes

$$(\phi^\circ_r - \phi_s)_{H_2O} = \frac{RT}{2F} \ln [Q_{OH^-}{}^2/Q_{O_2}{}^{1/2}Q_{H_2O}Q_{e(M)}]$$

Since an analogous expression exits for the reversible oxygen electrode in D_2O, it follows that

$$\phi^\circ_{r(H_2O)} - \phi^\circ_{r(D_2O)} = \Delta\phi^\circ_{alk} = \frac{RT}{2F} \ln \left\{ \left(\frac{q_{OH^-}}{q_{OD^-}} \right)^2 \frac{q_{D_2O}}{q_{H_2O}} \right\}$$

where the potential in the bulk, ϕ_s, is taken to be zero. Using the values of partition function ratios above, it is found that $\Delta\phi^\circ_{alk} = 0.0150$v at 25°C.

In acid solutions, the reversible reaction is

$$3H_2O \rightleftarrows 2H_3O^+ + \tfrac{1}{2}O_2 + 2e_{(M)}$$

and using the procedure just described,

$$\phi^\circ_{r(H_2O)} - \phi^\circ_{r(D_2O)} = \Delta\phi^\circ_{acid} = \frac{RT}{2F} \ln \left\{ \left(\frac{q_{H_2O}}{q_{D_2O}} \right)^3 \left(\frac{q_{D_3O^+}}{q_{H_3O^+}} \right)^2 \right\}$$

At 25°C, $\Delta\phi^\circ_{acid} = -0.0270$ volt.

Activated complexes.—Whereas the p.f. ratios for the initial state species were calculated from spectroscopic and equilibrium data, those for the activated complex must be estimated either from a potential energy surface, or empirically by comparison to similar stable species where force constants and vibrational frequencies are known, or can be reasonably inferred. In this paper, the latter method is used not only because of its simplicity, but because the assumptions required for analysis of the activated complex are quite similar in both cases as discussed below.

If a potential energy surface were to be constructed, the following assumptions would have to be made:

(*i*) All bonds not directly involved in the reaction do not undergo changes in vibrational frequency.

(*ii*) The activated complex can be treated as a pseudo-three or four atom system.

(*iii*) Assumption (*ii*) leads to the conclusion that a Morse function can now be used to describe the energies of the various "diatomic" species involved; *e.g.*, the O-H bond in H_2O can be treated in terms of the Morse equation.

(*iv*) Some method must be used to obtain the coulombic and exchange energies so that the London equation may be solved. Eyring's method (24) assumes the overlap integral to be zero and further assumes a constant coulombic/exchange energy ratio. A second method (25) assumes a constant value for this overlap integral (chosen to fit the experimental activation energy), and the coulombic and exchange energies can then be calculated from bonding and antibonding Morse equations. Despite some serious objections to either method (26-28), there is no doubt as to their general usefulness. In order to construct the potential energy surface for an electrochemical reaction, one would have to know the "real" activation energy so that the adjustable parameters in the theory could be properly utilized (23, 29-31).

In view of all these assumptions and difficulties, it seems perhaps more valid to use some strictly empirical method for characterization of the activated complex. In such a treatment, one has to make the following assumptions (cf. 29, 32):

(*i*) Same as (*i*) above

(*ii*) Secondary isotope effects are neglected since they are small to begin with (33) and also since the limits of reproducibility are such that it is very doubtful if such effects could be experimentally demonstrated for the o.e.r. This assumption permits us to immediately simplify the p.f. ratios involving only oxide surface species. In reactions [3] and [6], we can therefore take the p.f. ratios $q_{MO(D_2O)}/q_{MO(H_2O)}$ and $q^{\pm}_H/q^{\pm}_D$ as being equal to unity. Also differences in the ψ_1-potentials (which are very small) can be neglected on this basis (18, 29, 32), and $1 - \theta_t$ terms are assumed to be independent of isotope.

(*iii*) The symmetric stretching frequency for activated complexes of the type O . . . . . H . . . . . O are independent of isotopic substitution.

(*iv*) Assuming the activated complex in (*iii*) is linear (24), only the doubly degenerate bend need be considered. For the O-H-O bend, an average frequency of 1200 cm^{-1} will be used here as this value seems to be the most reasonable one as discussed elsewhere (18, 29, 34, 35). Hence the vibrational contribution to the activated complex p.f. ratio for this degenerate vibration is

$$\left(\frac{\sinh u^{\pm}_D}{\sinh u^{\pm}_H} \right)^2 = 0.179$$

where $u = hc\nu/2kT$ (ν being in cm^{-1}).

Using these four assumptions, the mechanics of solving $q^{\pm}_H/q^{\pm}_D$ for the above R values, reduce to simple algebraic substitution. Results of the calculations are given in Table I.

Discussion

Whereas the primary isotope effect refers to the effect by isotopic substitution on an atom undergoing transfer, the solvent isotope effect refers to the medium effect on equilibria resulting from isotopic substitution (41). In all cases where a proton or deuteron is directly involved in the activated complex, normal isotope effects arise, *i.e.*, R_1, R_2, R_4, and R_5 are greater than unity. However, for the recombination of MO species to produce molecular oxygen, an inverse isotope effect arises depending upon the solvent. This solvent isotope effect arises from the assumption of equilibria between bulk H_2O, or D_2O, and the surface species MO. Any uncertainty due to empirical assignment of frequencies to the activated complex is absent in this calculation because, as discussed above, the p.f. ratio for the activated complex is unity.

Some uncertainty undoubtedly exists in the empirical assignment of bending frequencies for activated complexes of the type O . . . . H . . . . O. A value of 1200 cm^{-1} for $\nu^{\pm}_{H,b}$ was chosen empirically because it seems to be quite reasonable by comparison to observed frequencies for stable molecules (29, 32, 35, 42).

According to Bader (35), values of $\nu^{\pm}_{H,b}$ may be expected to vary from 800 to 2000 cm^{-1} depending on asymmetry and charge distribution. Since an inverse isotope effect can also arise in the primary isotope

Table I. Kinetic parameters for O_2 evolution from H_2O and D_2O

R	Langmuir conditions $\theta \to 0$	Langmuir conditions $\theta \to 1$	Temkin conditions activ. ads.	Temkin conditions nonactiv. ads.
R_1	9.05	6.78	—	
R_{2a}	9.05	5.05	9.05	
R_{2b}	12.13	3.77	6.76	
R_3	1.50	1.00	0.19 (Eq. [24])	1.50 (Eq. [22])
			0.76 (Eq. [25])	0.38 (Eq. [26])
R_4	4.00	6.78	—	
R_{5a}	4.00	11.4	4.00	
R_{5b}	2.35	19.3	6.74	
R_6	1.00	1.00	23.2 (Eq. [35])	1.00 (Eq. [33])
			2.82 (Eq. [36])	8.12 (Eq. [37])

Table II *R*-values for various values of $\nu^{+}_{H,b}(\nu^{+}_{D,b} = \nu^{+}_{H,b}/\sqrt{2})$

$\nu^{+}_{H,b}$, cm^{-1}	R as calculated from Eq. [17]	[19]	[20]	[27]	[28]	[29]
2000	3.0	3.0	1.7	4.0	1.3	2.3
1200	9.0	9.1	5.1	12.1	3.8	6.8
800	15.0	15.0	8.3	20.0	6.2	11.2
0	25.3	25.3	14.2	34.0	10.6	19.0

effect if the zero point energy of the activated complex is greater than that for the initial state (33, 43), it is instructive to see what the minimum R values are using a value of 2000 cm^{-1} for $\nu^{+}_{H,b}$. This is shown in Table II. The isotope effects, although smaller than those in Table I, are still considerably larger than unity and within those limits, any of the primary isotope effects considered here are all "normal" ones.

Conclusion

The results of the theoretical calculations presented in this paper demonstrates that the use of hydrogen isotopes in electrochemical reactions, other than the h.e.r., can be added to the existing techniques used for the confirmation of reaction mechanisms. Although work is under progress in this laboratory extending these studies in oxygen evolution to various metals in acid and alkaline solution, other reactions such as Zn and Mg deposition and dissolution might also benefit by this treatment. In the o.e.r., the only reaction giving rise to an inverse isotope effect is the recombination step in alkaline solution. Conway and Bourgault (6, 12, 13) found a value of ~0.5 for R_3 in the o.e.r. at nickel wire anodes. The observed Tafel slopes were 60 mv for the o.e.r. in both $D_2O(OD^-)$ and $H_2O(OH^-)$ solutions, and these results are in satisfactory agreement with those predicted here for the activated adsorption scheme (see Table I). The results of these calculations show that there are some cases in which a clear cut assignment of reaction mechanism is not possible and that other criteria must be sought. However, the important thing that results from these studies is that the isotope effect, when combined with other criteria, is a useful method for evaluating these complex reactions. Recently McIntyre and Salomon (36) have found very small isotope effects in the electrochemical reduction of O_2 to peroxide and again, as in the above case, this small isotope effect can be predicted for a unique step in the overall scheme of consecutive steps.

Acknowledgments

The author would like to thank the Chemistry Department and the Research Council of Rutgers, The State University, for financial support. He would also like to thank Professor B. E. Conway in whose laboratory some of these ideas crystallized and were discussed (cf. ref. 14), and finally Dr. J. D. E. McIntyre for many critical discussions and suggestions.

Manuscript received Nov. 28, 1966; revised manuscript received March 23, 1967.

Any discussion of this paper will appear in a Discussion Section to be published in the June 1968 JOURNAL.

REFERENCES

1. M. Breiter, *Adv. Electrochem.*, **1**, 123 (1961).
2. J. O'M. Bockris, *J. Chem. Phys.*, **24**, 817 (1956); see also B. C. Conway and M. Salomon, *Electrochim. Acta.*, **9**, 1599 (1965).
3. T. P. Hoar, *Proc. Roy. Soc.*, **A142**, 628 (1933); Proc. 8th Meeting CITCE, p. 439, Butterworths, London, 1956.
4. J. O'M. Bockris and A. K. M. S. Huq, *Proc. Roy Soc.*, **A237**, 271 (1956); A. Damjanovic, A. Dey. and J. O'M. Bockris, *This Journal*, **113**, 739 (1966).
5. J. Giner, *Z. Elektrochem.*, **64**, 491 (1960).
6. B. E. Conway and P. L. Bourgault, *Can. J. Chem.* **37**, 292 (1959); **38**, 1557 (1960).
7. J. J. Mac Donald and B. E. Conway, *Proc. Roy. Soc.*, **A269**, 419 (1962).
8. N. Sato and G. Okamoto, *Electrochim. Acta*, **10**, 495 (1965).
9. J. P. Hoare, *This Journal*, **112**, 602 (1965); **112**, 1129 (1965).
10. S. Barnartt, *ibid.*, **106**, 991 (1959).
11. S. W. Feldberg, C. G. Enke, and C. E. Bricker, *ibid.*, **110**, 826 (1963).
12. B. E. Conway and P. L. Bourgault, *Trans. Faraday Soc.*, **58**, 593 (1962).
13. B. E. Conway, *Trans. Symp. Electrode Processes*, E. Yeager, Editor, John Wiley & Sons, Inc., New York (1961).
14. M. Salomon, B. E. Conway, and M. Sattar, Paper presented at the San Francisco Meeting of the Society, May 9-13, 1965. Abstract 253.
15. C. G. Swain and R. F. W. Bader, *Tetrahedron*, **10**, 182 (1960).
16. M. Salomon, *This Journal*, **113**, 940 (1966).
17. e.q. see E. A. Moelwyn-Hughes, "Physical Chemistry, "Pergamon Press, Oxford (1961).
18. M. Salomon, Ph.D. thesis, Ottawa, 1964.
19. R. Parsons, *Modern Aspects of Electrochemistry*, **1**, 103, (1954).
20. H. S. Johnston and K. S. Pitzer, *J. Assoc. Inst. Chem. Eng.*, **5**, 277 (1959).
21. G. J. N. Thomas, *Trans. Faraday Soc.*, **57**, 1603 (1961).
22. B. E. Conway and E. Gileadi, *ibid.*, **58**, 2493 (1962).
23. B. E. Conway and M. Salomon, *J. Chem. Phys.*, **41**, 3169 (1964).
24. S. Glasstone, K. J. Laidler, and H. Eyring, "Theory of Rate Processes," McGraw-Hill Book Co., New York (1941).
25. S. Sato, *J. Chem. Phys.*, **23**, 2465 (1955).
26. R. E. Weston, *ibid.*, **31**, 892 (1959).
27. K. J. Laidler and J. C. Polanyi, "Progress in Reaction Kinetics," Vol. 3, G. Porter, Editor, Pergamon Press, New York (1965).
28. H. S. Johnston, Gas Phase Reaction Rate Theory, Ronald Press, New York (1966).
29. M. Salomon and B. E. Conway, *Discussion Faraday Soc.*, **39**, 223 (1965).
30. M. Salomon, C. G. Enke, and B. E. Conway, *J. Chem. Phys.*. **43**, 3989 (1965).
31. M. Salomon, To be published.
32. B. E. Conway and M. Salomon, *Ber.*, **68**, 331 (1964).
33. L. Melander, "Isotope Effects on Reaction Rates," Ronald Press, New York (1960).
34. C. G. Swain, R. F. W. Bader, and M. Wiles, *J. Amer. Chem. Soc.*, **83**, 1945 (1961).
35. R. F. W. Bader, *Can. J. Chem.*, **42**, 1822 (1964).
36. J. D. E. McIntyre and M. Salomon, To be published. (see Abstracts for American Chemical Society Meeting, Miami, April, 1967).
37. J. O'M. Bockris and D. B. Matthews, *Proc. Roy. Soc.*, **A292**, 479 (1966).
38. C. G. Swain, R. F. W. Bader, and E. R. Thornton, *Tetrahedron*, **10**, 200 (1960).
39. E. L. Purlee, *J. Am. Chem. Soc.*, **81**, 263 (1959).
40. K. Heinzinger and R. E. Weston, *J. Phys. Chem.*, **68**, 744 (1964).
41. E. J. King, "Equilibrium Properties of Electrolyte Solutions," R. A. Robinson, Editor, Vol. 4, "Acid-Base Equilibria," Macmillan Co., New York (1965).
42. R. P. Bell, "The Proton in Chemistry," Cornell University Press, Ithaca (1959).
43. C. G. Swain, R. F. W. Bader, R. M. Esteve, and R. N. Griffin, *J. Am. Chem. Soc.*, **83**, 1951 (1961).

An Experimental Study of the Mode of Operation of Porous Gas-Diffusion Electrodes with Hydrogen Fuel

L. G. Austin[1] and Satish Almaula

Department of Fuel Science, Pennsylvania State University, University Park, Pennsylvania

ABSTRACT

Current-polarization curves from zero current to limiting current have been obtained for anodic ionization of H_2 at Teflon-bonded, platinum-black, gas-diffusion electrodes in 1*N* H_2SO_4. Limiting currents were almost linearly proportional to hydrogen pressure and varied with pressure and temperature in approximately the same way as *DC*, the product of solubility and diffusivity of dissolved H_2. Effects of mass transfer of dissolved gas appear to predominate over ohmic or kinetic effects. Based on a comparison of double-layer capacities in gas diffusion and fully flooded conditions, it is concluded that between 2 and 5% of the electrode internal area is wetted by electrolyte in the gas-diffusion condition, and the mean electrolyte penetrations are 4-7μ. It is unlikely that extended thin films of electrolyte exist on the internal surface of the electrode. It is suggested that only a thin layer near the plane electrode-electrolyte surface is wetted and takes part in reaction, and that limiting currents and polarization are due to mass transfer of dissolved hydrogen to submerged platinum-black particles. For an electrode containing 55 mg Pt-black/cm^2, the limiting current was 2.9 amp/cm^2 at 1 atm H_2 and 25°C; polarization at 1 amp/cm^2 was 30 mv.

The precise manner in which porous, gas diffusion electrodes for fuel cells operate is not known, although three distinct models have been proposed (1-3). Most treatments (4-7) have considered electrodes where the electrolyte covers a considerable fraction of the internal surface of the electrode. As discussed by Austin *et al.* (1), it is unlikely that a "thin film" of electrolyte covers the internal surface of electrodes which are strongly wet-proof, such as Teflon-bonded, platinum-black electrodes (8, 9). This type of electrode shows great promise for use in fuel cells since it is easy to make, light-weight, thin and capable of high power output without flooding.

The experiments reported here were performed in an attempt to obtain a better model for the mode of operation of wet-proofed, gas-diffusion electrodes, to form the basis for quantitative treatment of electrode design.

Experimental Techniques

Disk-shaped electrodes were placed in the Teflon electrode holder shown in Fig. 1 and the electrode surface placed horizontally in contact with 1*N* H_2SO_4, as shown in Fig. 2. The Teflon pieces of the holder were machined to give a tight press fit, and the tubes mounted in the Lucite lid in Fig. 2 were fitted with O rings to allow ready raising and lowering. The counter electrode was a clean platinum sheet, and the saturated calomel reference electrode was connected to a Luggin capillary with a KCl bridge, via a closed stopcock between the KCl and H_2SO_4 solutions. Hydrogen and nitrogen were prepurified (10) and saturated with water vapor in equilibrium with 1*N* H_2SO_4 before use; Fisher Reagent Grade sulfuric acid was fumed (11) and diluted to 1*N* strength with high-purity water (12). After assembly, it was convenient to deaerate the electrolyte with bubbled nitrogen overnight, before lowering the test electrode into the electrolyte. Any gas bubble trapped below the electrode face was readily removed by gentle flushing with the J arrangement shown in Fig. 2.

Steady-state current *vs.* voltage results were obtained with a flow of hydrogen (or hydrogen-nitrogen mixture) at 1 atm through the electrode holder, with a flow rate of at least 30 times the maximum rate of hydrogen ionization. The potential between test and reference electrode was measured with a high-impedance recorder, and current was measured by potential drop across standard resistors in series with the cell. Ohmic resistance in the electrolyte between the test electrode and the tip of the Luggin capillary was determined from the immediate change in test

[1] Present address: Department of Chemical Engineering, North Carolina State University at Raleigh, North Carolina.

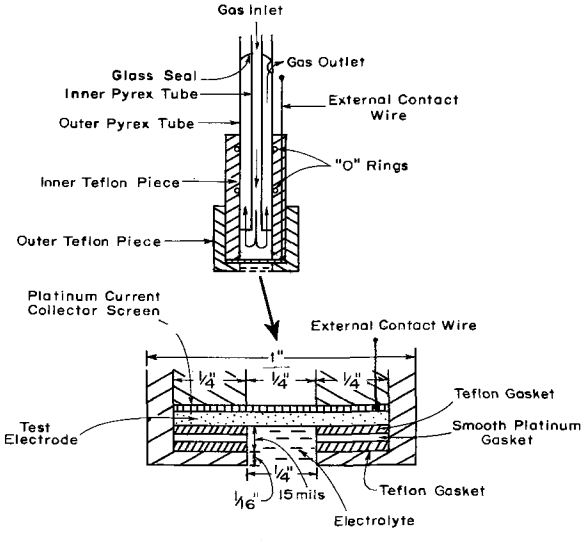

Fig. 1. Electrode holder

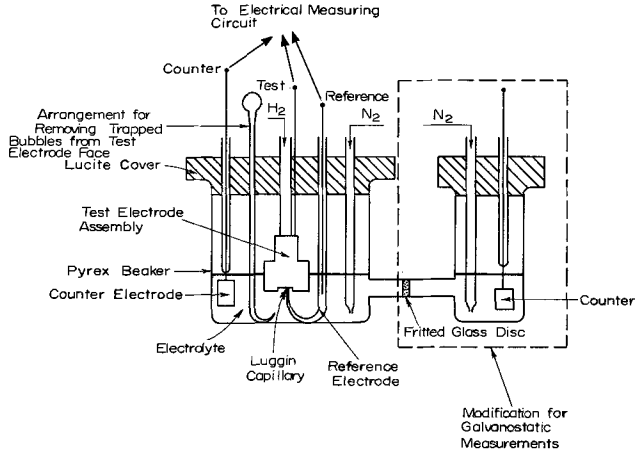

Fig. 2. Test cell

Table I. Comparison of electrode properties

Electrode	Material contents, mg/cm²		Electrode thickness, μ	Calculated porosity, %	Mean hydraulic diameter, μ	Limiting currents 1 at. H_2, 25°C, ma/cm²
CAA1	Pt Teflon screen	8-9	150	73	5.6	1,050
SM1	Pt Teflon screen	55.0 8.0 47.0	300	72	6.4	2,900
SM2	Pt Graphite Teflon Screen	13.5 13.0 3.5 35	254	60	1.3	730
FC100	Pt Carbon + wet-proofing	5-6 66-64	254	20*	0.2 [Mean pore diameter 0.5]*	300

* Pure Carbon Company catalog values.

to reference potential on passing a constant current through the test-counter electrode system. This jump was measured with an oscilloscope at fast sweep rates, using the rapid switching circuit described by Lerner (13). Results were corrected for this resistance, which was between 0.6 and 0.8 ohms. It was occasionally found that voltage cycling occurred as the limiting current was approached. A Wenking potentiostat (model 61/R) was then used to set the test electrode at 0.5v (plus the ohmic voltage loss) *vs.* standard hydrogen electrode, and the steady limiting current obtained at this potential. At the highest limiting currents obtained (3 amp/cm²), the ohmic correction was approximately 0.6v.

Double-layer capacities and surface coverage by adsorbed hydrogen were determined from galvanostatic voltage-time curves. To avoid faradaic current from gaseous or dissolved hydrogen the electrode holder was supplied with nitrogen only, and a small cathodic current passed until the electrode reached zero volts *vs.* standard hydrogen. A constant anodic current was then switched on and the voltage recorded as a function of time until it reached 1.0-1.3v; the current was reversed and voltage recorded until the potential was brought back to zero volts. This procedure was satisfactory for an immersed, flooded electrode, but a gas-diffusion electrode could not be brought to zero volts with a small cathodic current (see later) and starting potential was about 50-70 mv *vs.* standard hydrogen electrode. Since oxygen was evolved at the counter electrode during passage of cathodic current, the counter electrode was contained in a separate compartment for these tests, as shown in Fig. 2.

Mean hydraulic pore diameters were estimated from permeability measurements, using nitrogen flowing through the electrode clamped in a lucite holder with rubber seal rings.

Electrodes.—It was originally planned to test a number of electrodes covering a wide range of pore sizes, but it was found that several of the electrodes performed poorly, mainly due to flooding of the pore system. These included platinum-catalyzed electrodes of baked carbon supplied by the Pure Carbon Company (FC1, 23, 31, 36, approximately 250μ thick) and electrodes of microporous plastic material, Millipore (made by Millipore Company, Bedford, Massachusetts, types VM, RA, GS, and VF), spattered with a porous layer of platinum. Millipore type-H plated with a porous layer of platinum by the J. Bishop Company was nonwetting, but it had a high ohmic resistance and the platinum layer was so fragile that it broke when a current collector of platinum screen was pressed against it. All of these electrodes gave limiting currents of less than 100 ma/cm², performance decreased with time, and the electrodes were seen to be wet on the gas entry face. The limiting current of FC36 was approximately 20 ma/cm², and a more stable limiting current of approximately 100 ma/cm² was obtained by covering the electrolyte face with Millipore type H (nominal pore diameter of 1.5μ). The Millipore appeared to reduce flooding of the electrode. No further experiments were performed on this group of electrodes.

A second group of electrodes performed well and stable current-voltage curves were obtained. This group consisted of American Cyanamid Company CAA1, Pure Carbon Company FC100, and two electrodes, SM1, SM2, prepared in our laboratory. SM1 was made from a mix of platinum black (Fisher) with Teflon dispersion (Dupont 30, containing 59-61% solids, sp gr 0.6-0.9g Teflon/cc) diluted 10 times with distilled water, in approximate proportions of 10/1.5 of platinum-black to Teflon by weight, spread uniformly on a 45 mesh platinum screen. The mix was made to give a homogeneous paste, and the amount of Teflon stated above is not exact (see later). This was pressed at 18000 psi for 2 min, dried at 120°F for 1 hr, taken to 350°C over 5 min and sintered for 2 min at 350°C. After cooling, the electrode was rinsed with pure water and redried. SM2 was prepared in a similar manner using a mix of platinum black, SP1 graphite (National Carbon Company, New York) and Teflon in approximate proportions of 5/5/1.5 of platinum black to SP1 graphite to Teflon by weight. Later, the material contents of the electrodes were determined directly by weighing before and after burning off the Teflon (10), and these are reported in Table I.

This group of electrodes appeared from visual observation to be highly resistant to flooding at room temperature. After use as gas-diffusion electrodes, the electrodes were removed, wiped free of surface liquid with filter paper, and reweighed. FC1, 31, 36 electrodes increased in weight by approximately 10% due to penetration by electrolyte, but the second group

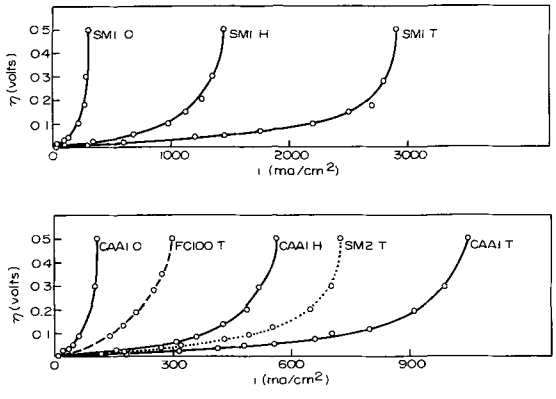

Fig. 3. Steady current polarization curves for anodic ionization of hydrogen. 1*N* H_2SO_4, 25° C; T — hydrogen ~ 1 atm; H — hydrogen ~ 0.5 atm; O — hydrogen ~ 0.1 atm.

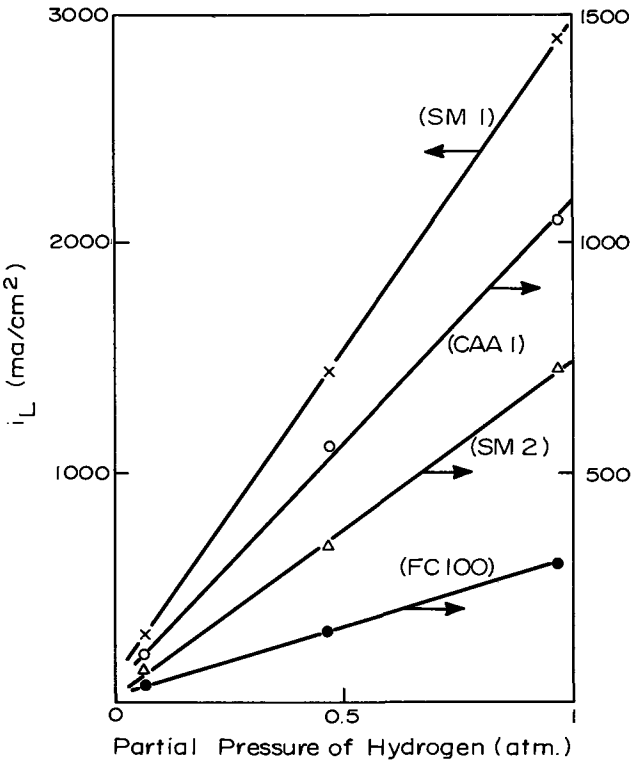

Fig. 4. Variation of limiting current densities with partial pressure of hydrogen.

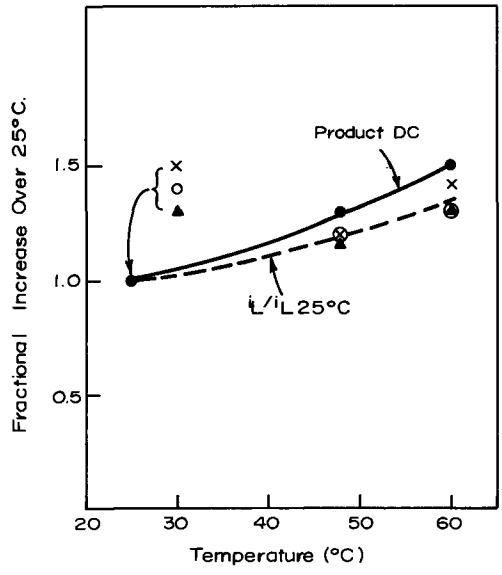

Fig. 5. Fractional increase in limiting current with temperature: X, CAA1; O, SM2; ▲, FC100.

of electrodes had weight gains of less than 0.6%. These figures do not give accurately the weight gain of electrolyte during use, since the wiping process probably removed some water from the interior, but on a comparative basis they demonstrate the resistance to electrolyte penetration of the Teflon-bonded electrodes.

Results

Some typical results of steady current-voltage measurements are shown in Fig. 3. The curves could be retraced on reducing current density, and were reproducible on a given electrode at different times. Different samples cut from a patch of electrode material gave somewhat variable results in the case of the CAA1, and very variable results for the FC100 material. The limiting currents (defined at 0.5v polarization) were almost linearly proportional to the partial pressure of hydrogen, as shown in Fig. 4. The same limiting current and current-polarization curve was obtained if several thicknesses of electrode were pressed together and used as an electrode. Limiting currents increased with temperature as shown in Fig. 5, giving an increase of 30-40% from 25° to 60°C. It should be noted that these results cannot be compared directly with results obtained using an electrolyte matrix such as porous asbestos (9), since it is probable that a matrix-electrode interface has a significant temperature rise at these high current densities.

Double layer capacities were determined from the linear slopes of the galvanostatic voltage-time traces between 0.4 and 0.6v *vs.* standard hydrogen, in the absence of hydrogen. In this region of potential there is negligible faradaic current due to ionization of adsorbed hydrogen ($[H] \rightleftarrows H^+ + e^-$) or oxygen adsorption ($H_2O \rightarrow 2H^+ + [O] + 2e^-$). The capacities were measured on electrodes in the gas-diffusion condition, and on fully immersed, flooded electrodes which had been vacuum impregnated with electrolyte. In the gas-diffusion condition the double-layer capacities

Table II. Double-layer capacities and hydrogen coverages of electrodes

Electrode	Stripping current, ma/cm^2	Double-layer capacity, fd/cm^2* Flooded	Double-layer capacity, fd/cm^2* Gas-diffusion	Hydrogen coverage, mcoul/cm^2* Flooded	Fraction of internal electrode area in contact with electrolyte (gas-diffusion condition) [Ratio of nonflooded to flooded capacities]
CAA1	6.3	2.9×10^{-1}	—	522	0.046
	18.2	2.8×10^{-1}	—	518	
	40.0	2.8×10^{-1}	—	510	
	3.8	—	1.3×10^{-2}		
	9.8	—	1.3×10^{-2}		
SM1	7.5	1.2	—	2074	0.016
	21.0	1.1	—	2100	
	49.0	1.2	—	2082	
	3.8	—	1.7×10^{-2}	—	
	9.8	—	1.8×10^{-2}	—	
SM2	7.0	3.6×10^{-1}	—	540	0.016
	23.5	3.3×10^{-1}	—	530	
	1.3	—	4.6×10^{-3}	—	
	3.8	—	4.5×10^{-3}	—	
FC100	2.0	2.8×10^{-2}	7.0×10^{-3}	17.2	(0.240)
	3.6	2.9×10^{-2}	6.7×10^{-3}	16.0	
	7.8	2.7×10^{-2}	—	16.7	
GE†		8.4×10^{-1}	—	704	

* Refers to plane area of electrode.
† General Electric electrode for comparison (17).

Table III. Effect of temperature on limiting currents

Temperature, °C	Limiting currents i_L, ma/cm² Electrodes: CAA1	SM2	FC100	(D cm²/sec) (10^5)	(C moles/cm³) (10^7)	(DC) (10^{12})	Fractional increase over 25°C of: i_L on Electrodes CAA1	SM2	FC100	DC
25	1050	728	300	3.4	7.6	25.8	1	1	1	1
48	1320	896	350	5.1	6.5	33.1	1.2	1.2	1.17	1.3
60	1500	1000	400	7.1	5.8	41.1	1.42	1.3	1.3	1.5

D = Estimated diffusion coefficient of dissolved H_2 in 1N H_2SO_4.
C = Solubility of H_2 gas in 1N H_2SO_4.
Values of D and C are approximate.
Limiting currents of SM1 were not obtained at higher temperatures because the currents exceeded the limit of the potentiostat.

were unchanged when several thicknesses of electrode were used. Table II gives the results. The coverage by adsorbed [H] at zero volts was determined from the voltage-time trace between 0 and 0.4v using

$$q_f = it - C\Delta V \qquad [1]$$

where q_f is the charge derived from surface coverage at time t and constant current i, C is the double-layer capacity and ΔV is the potential change in time t. At approximately 0.4v the current is supported entirely by double-layer charge-discharge, and q_f is the starting surface coverage in coulombs. It was not possible to measure this value for electrodes in the gas-diffusion condition because large cathodic currents were necessary to bring the electrode towards zero volts, the system was consequently contaminated with gaseous hydrogen, and a gas bubble was trapped below the electrode. Apparently the gas-diffusion condition is sufficiently reversible in the kinetic and mass transfer sense for the reaction $2H^+ + 2e^- \rightarrow 2[H] \rightarrow H_2$ diffusing out into N_2 stream to proceed at relatively high current densities, even at 50 to 70 mv positive potential. (In the flooded condition, the mass transfer of dissolved hydrogen away from the electrode has limiting currents of roughly 1 ma/cm², therefore a current density of a few ma/cm² is sufficient to bring the electrode to zero volts.)

Fig. 6 shows the permeability results, from which equivalent hydraulic pore diameters were calculated using (14)

$$J = B_o(\bar{p}/\eta)(\Delta N/L) \qquad [2]$$

where J is in moles/cm² sec, B_o is the permeability coefficient in darcies, $\bar{p}$ is the arithmetic mean pressure in atmospheres over the length, L, of the sample, η is the gas viscosity in centipoises, and ΔN is the concentration drop across the sample in moles/cm³. B_o is related to viscous area and flow path in a porous solid and is

$$B_o \simeq (\epsilon/q^2)(M^2/2)(10^8) \text{ darcies} \qquad [3]$$

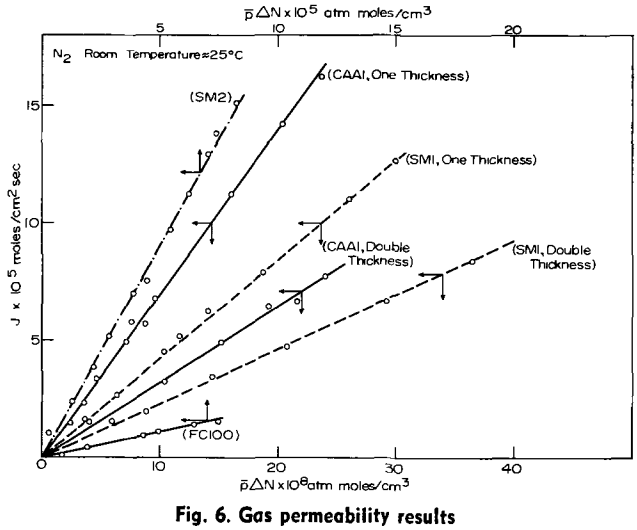

Fig. 6. Gas permeability results

ϵ is the porosity, q the tortuosity factor, and M the mean hydraulic radius of the porous solid. A plot of J *vs.* $\bar{p}\Delta N$ yields a straight line with a slope of $B_o/\eta L$, and B_o can be calculated. Knowing B_o, q, and ϵ, M can be calculated and an equivalent diameter found from $D = 4M$. Slip flow terms were found to be negligible. Table I gives the equivalent pore diameters for the four electrodes.

Discussion of Results

Figure 4 shows that limiting currents are almost linearly proportional to the partial pressure of hydrogen. This is not due to limitations of gas transfer through the nonflooded pores of the electrodes, because doubling or tripling electrode thickness had no effect on the limiting current. In addition, the maximum rate of normal hydrogen diffusion through these thin, open electrodes was calculated to be about 500 amp/cm². The magnitude of the equivalent hydraulic diameters precludes low diffusion coefficients due to Knudsen diffusion. Table III and Fig. 5 show the variation of limiting current density with temperature, compared to variation of DC with temperature, D being diffusion coefficient and C concentration of dissolved hydrogen in 1N H_2SO_4, estimated by interpolation from data quoted by Breiter (15). Making allowance for the errors in interpolation, the limiting currents increase is in close ratio to the increase in DC, indicating that simple mass transfer of dissolved gas is the rate-limiting factor. It is probable that any mechanism involving surface diffusion of hydrogen adsorbed on platinum would have a larger temperature coefficient than that found experimentally.

Figure 7 shows the values of i/i_L *vs.* polarization, η, for the different partial pressures of hydrogen. For a

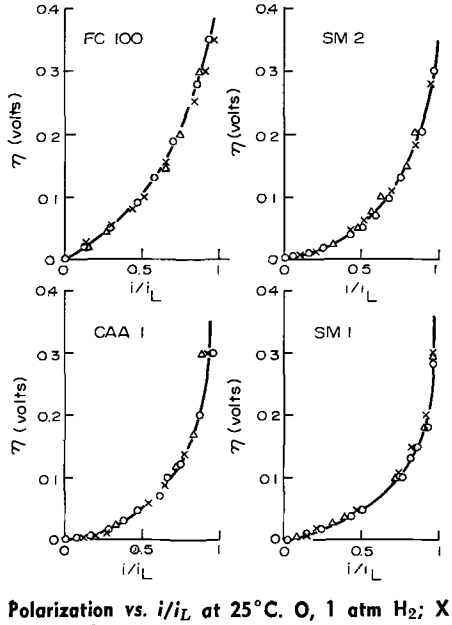

Fig. 7. Polarization *vs.* i/i_L at 25°C. O, 1 atm H_2; X 1/2 atm H_2; △, 1/10 atm H_2.

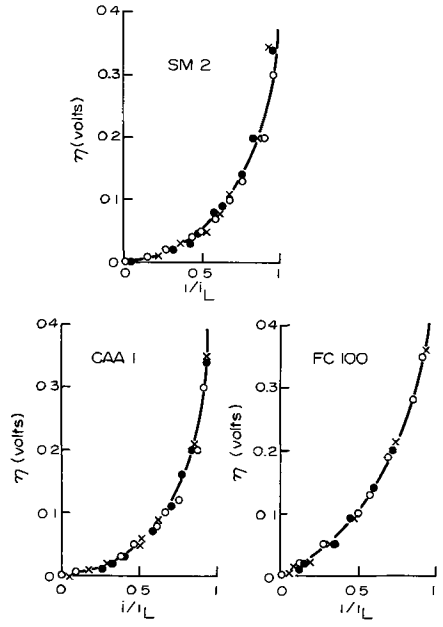

Fig. 8. Polarization vs. i/i_L at 1 atm H_2. O, 25°C; X, 48°C; •, 60°C.

given electrode, η is the same function of i/i_L for all pressures, even though i_L varies by almost a factor of 10. Similarly, Fig. 8 shows that η is a function of i/i_L for all temperatures, within experimental error. These results are strong indication that the current-polarization curves are solely dependent on mass transfer effects and have negligible contributions from kinetic or ohmic effects.

The results in Table II show that double-layer capacities and hydrogen coverage do not vary with the current densities used in the determination; therefore, there is no distributed capacity effect due to the porosity of the electrodes. The absence of distributed effects is due to the thinness of the electrodes, and the low current densities used in the determination (16). Except for FC100, the double-layer capacities in the gas-diffusion condition compared to the fully flooded condition show that only 2-5% of the internal area of the electrode is wetted by electrolyte in the gas-diffusion condition. It is highly unlikely, therefore, that any extended thin film of electrolyte covers the internal surface of the electrodes when in use as fuel cell electrodes. Mean electrolyte penetration into the electrodes was estimated as between 4 and 7μ, that is, of the same magnitude as the macropore diameter found from the permeability measurements.

Table IV gives the double-layer capacity and surface coverage by hydrogen, per cm² of platinum black area of the electrodes; a value of 30 m²/g was assumed for platinum black (17). The results are reasonably consistent and agree with those reported by the General Electric Company, although values of 70 to 100 μfd/cm² for double-layer capacity are significantly greater than the value of 56 μfd/cm² found by us for bright platinum, using the same techniques. Values of FC100 are anomalous, either due to a much lower BET area per gram of platinum catalyst, or due to incomplete flooding of the electrode even after vacuum impregnation with electrolyte.

Table V. Comparison of ratios of wetted platinum, platinum packing, and limiting currents

Electrodes	Ratio of double-layer capacities/cm² (nonflooded)	Ratio of platinum contents/cm³†	Ratio of limiting current densities
SM1 / CAA1	1.4	3.0	2.7
SM1 / SM2	3.3	3.6	4.0
CAA1 / SM2	2.4	1.2	1.4

† From weight measurements.

The comparison of the capacities per cm² of two nonflooded electrodes gives a relative measure of the total amount of wetted platinum black in the two electrodes, under actual gas-diffusion working conditions, *e.g.*

$$\frac{\text{double-layer capacity/cm}^2 \text{ of SM1}}{\text{double-layer capacity/cm}^2 \text{ of CAA1}} = \text{area of SM1 to CAA1.}$$

On the other hand, the weight of platinum black per cm³ gives the packing density of the platinum in the electrode. Comparison of the above mentioned ratio and the packing-density ratio to the ratio of limiting current densities for the two electrodes will indicate if the limiting currents are influenced (*a*) by the density of platinum-black packing or (*b*) by the total amount of wetted platinum in the diffusion condition (wetted platinum-black/cm²). Table V compares the above ratios for CAA1, SM1, and SM2 electrodes. The SM1 to CAA1 comparison indicates that the ratios for the platinum-black weights per unit volume and the limiting currents are within a reasonably close range (2.7-3.0). This is also true for the CAA1/SM2 ratios (1.2-1.4). The ratio of limiting currents does not agree with the ratio of double-layer capacities in the nonflooded condition. (In the case of SM1/SM2, all the ratios are rather close, the electrodes have nearly the

Table IV. Specific double-layer capacities and coverages of immersed electrodes

Electrode	Assumed BET area of Pt black, (cm²/g) (10⁻⁵)	Weight of platinum black in electrode, g/cm²	Weight of Teflon in electrode, g/cm²	Double-layer capacity, μfd/cm² (BET)	Hydrogen coverage [H atoms/cm² (BET)] (10⁻¹⁵)
CAA1	3	0.0158	0.0119	102	0.93
SM1	3	0.109	0.0158	73	0.6
SM2	3	0.025 +0.025 gm Graphite	0.007	88	0.65
FC100	3	0.009 +0.103 gm Carbon + wet-proof material	?	18.8	0.05
GE1†	3.67	0.100	0.018	—	0.62
GE2†	3.67	0.100	None	90	0.99

† General Electric electrodes for comparison (17).

same electrolyte penetration, and it is not possible to distinguish whether the limiting current ratio is closer to that of the packing density ratio or the wetted area ratio.) The evidence suggests that the limiting currents of the electrodes are influenced by the platinum-black packing density in the electrodes and not by the total platinum-black content.

For the platinum black-Teflon type electrodes, it is reasonable to expect that the platinum black is in small, loosely packed aggregates lying between Teflon particles and Teflon fibrils (9). The Teflon binds the platinum-black aggregates and prevents the electrolyte from penetrating the electrode material to any great degree. The flakes of graphite present in SM2 probably distributes platinum-black aggregates around the carbon flakes, while the Teflon again provides binding and hydrophobicity. The carbon tends, of course, to give less over-all porosity of the electrode material.

An approximate value of the limiting current predicted by the simple-pore model (1) can be estimated from

$$i_L = 12n\mathbf{F}D\theta C/r \qquad [4]$$

where i_L is the limiting current density per cm^2 of plane electrode area, $n = 2$ for hydrogen, $\mathbf{F}$ is Faraday's constant, θ is the area of pore mouths at the gas-electrolyte interface per cm^2 of plane electrode area, and r is the mean radius of the micropores filled with electrolyte. As before, D is the diffusion coefficient of dissolved hydrogen, C is the amount of dissolved hydrogen in equilibrium with 1 atm of hydrogen gas pressure. It is reasonable to assume that although an electrode as a whole is highly porous, the closely packed platinum-black particles will have a small porosity, say 10% of the total volume. The area of pore mouths will be proportional to this porosity, but may be several times higher if the gas-electrolyte interface within the electrode has a greater area than the plane area (see Fig. 9, for example). Further, assuming a loose packing of platinum particles in aggregates, a rough value for the pore size may be taken as 100Å, since the size of the particles is 100-200Å. At room temperature (25°C), taking $n = 2$, $\mathbf{F} = 96500$ coul/equiv, $D = (3.4)(10^{-5})$ cm^2/sec, $C = (7)(10^{-7})$ g-moles/cm^3, $\theta = 0.1$ and $r = 100$Å, the value of i_L is approximately 5 amp/cm^2. This value of i_L is, of course, strongly dependent on the values chosen for r and θ. The calculation shows only that values of 1 to 10 amp/cm^2 for i_L are feasible; this is of the same magnitude as the experimental limiting currents. Agreement has been reported (18) between the limiting current predictions of the simple-pore model and experimental results from nonwetted porous electrodes using Cl_2, in molten LiCl electrolyte.

Conclusions

Based on the experimental evidence and the discussion above, a possible physical configuration of the gas/electrode/electrolyte boundary established at the platinum-black-Teflon electrodes may be visualized as in Fig. 9. This shows electrolyte stabilized at a short distance within a platinum black-Teflon electrode. The gas side of the electrode has dry platinum aggregates and Teflon particles, while the platinum black on the electrolyte side will be wetted. The approximate size of the platinum-black particles is 100 to 200Å (8), that of Teflon particles is 0.2 to 0.5μ (8), while that of SP1 graphite flakes is roughly 0.3μ high and 20μ in diameter. There must be sufficient contact between the platinum-black particles to provide electronic conduction to the electrode screen and the current collector, but the Teflon particles appear to prevent penetration of electrolyte beyond a thin surface layer.

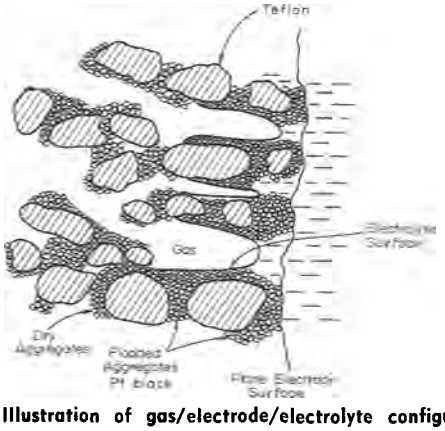

Fig. 9. Illustration of gas/electrode/electrolyte configuration

Electrodes SM1, SM2, and CAA1 are packed differently (see Table V). Compared with CAA1, SM1 has a larger part of the cross section packed with platinum-black aggregates, and since each aggregate produces current, a larger limiting current is observed for SM1. SM2 is more closely packed with material, but the platinum-black packing density is lower than SM1 or CAA1. In addition, the presence of graphite flakes tends to distribute platinum-black aggregates around the carbons, and the diffusional distance of dissolved gas to the active platinum-black may be increased, leading to lower limiting currents. Limiting currents can only be high when the mean diffusion path of dissolved gas is short, which means that small micropore diameters are necessary.

Although there is no evidence to suggest extended thin films of electrolyte within the electrode pores, there is a short, definite electrolyte penetration into the electrode. The electrolyte will tend to fill the micropores (spaces between platinum-black particles) within this penetration while some of the macropores will be free of electrolyte. Regions of flooded micropores along the walls of a macropore may lead to thin, finger-like electrolyte penetration into the electrode, as shown in Fig. 9. Thus the electrode will consist of nonflooded macropores which serve as gas feeders, plus flooded micropores, as shown. If the electrolyte penetration is considerable, long fingers of electrolyte may extend into the electrode, but in this study, since the mean electrolyte penetration is approximately 7μ or less and since the approximate macropore diameter is of the same magnitude, it is reasonable to expect that short, thumb-like penetration exists.

It is concluded that although a precise quantitative model cannot be proposed from this study, a reasonable picture of a physical model existing in nonflooded, platinum black-Teflon electrodes (operating in the gas-diffusion condition) has been obtained, and the mode of operation of such a model is reasonably close to that predicted by the simple-pore model. In these electrodes the electrolyte penetration is small, and a thin, well-packed, catalyst layer on the electrolyte side should be sufficient for efficient performance, providing other factors such as electronic conductivity are also satisfactory. A quantitative theory of current-polarization relations based on this model is under development, and recent treatments (19, 20) of models similar to that proposed here will be discussed in a future publication.

Acknowledgments

Financial support from the Harry Diamond Laboratories, Army Materiel Command, Washington, D. C., is gratefully acknowledged. Millipore material spattered with platinum was supplied by the Tyco Company; the J. Bishop Company laid platinum on millipore and carbon materials at our request, and electrode material CAA1 was supplied by the American Cyanamid Company. These organizations are sincerely thanked for supplying materials and services without charge.

Manuscript received Nov. 7, 1966; revised manuscript received April 21, 1967.

Any discussion of this paper will appear in a Discussion Section to be published in the June 1968 JOURNAL.

REFERENCES

1. L. G. Austin, M. Ariet, R. D. Walker, G. B. Wood, R. H. Comyn, *I.E.C., Fundamentals*, **4**, 321 (1965).
2. F. G. Will, *This Journal*, **110**, 145 (1963).
3. H. M. Dittman, E. W. Justi, A. W. Winsel, Symp. on Recent Advances in Fuel Cells, ACS, Div. of Fuel Chem. and Petroleum Chem., Vol. 6, No. 4-B, 139 (1961); "Fuel Cells," Vol. II, G. J. Young, Editor, Reinhold Publishing Co., New York (1962).
4. D. N. Bennion, Ph.D. thesis, University of California at Berkeley, 1964.
5. R. P. Iczkowsi, *This Journal*, **111**, 1078 (1964).
6. E. A. Grens, II, R. M. Turner, and T. Katan, Paper presented at the New York Meeting, Am. Chem. Soc., September, 1963.
7. J. A. Rockett and R. Brown, *This Journal*, **113**, 207 (1966).
8. L. W. Niedrach and H. R. Alford, *ibid.*, **112**, 117 (1965).
9. R. G. Haldeman, W. P. Colman, S. H. Langer, and W. A. Barber, "Thin Fuel Cell Electrodes," Fuel Cell Systems, R. F. Gould, Editor, Advances in Chemistry Series No. 47, American Chemical Society, 106, 1965.
10. S. C. Almaula, M.S. thesis, The Pennsylvania State University, University Park, Pa., 1966.
11. F. C. Anson, *Anal. Chem.*, **33**, 939 (1961).
12. R. W. Powers, *Electrochem. Technol.*, **2**, 163 (1964).
13. Harry Lerner, Ph.D. thesis, The Pennsylvania State University, University Park, Pa., 1964.
14. P. C. Carman, "Flow of Gases Through Porous Media," Academic Press, Inc., New York (1956).
15. M. W. Breiter and K. Hoffman, *Z. Elektrochem.*, **64**, 462 (1960).
16. L. G. Austin, "Fuel Cells," NASA, pp. 317-318 (1967).
17. General Electric Co., Air Craft Accessary Turbine Dept., Summary Report—Section I (No. 19), "Research on Low Temperature Fuel Cell Systems", Contract No. DA-44-009-ENG-3771, U.S. Army ERDL, Fort Belvoir, Va., November, 1961.
18. A. J. Swinkels, *This Journal*, **113**, 9 (1966).
19. E. A. Grens, *I.E.C. Fundamentals*, **5**, 542 (1966).
20. V. A. Chismadzev, *Elektrochim.*, **2**, 3 (1966).

Technical Notes

The Double Layer Capacitance in Aqueous Solution

II. Polycrystalline Cadmium

N. A. Hampson and D. Larkin

Chemistry Department, Loughborough University of Technology, Leicestershire, England

Exchange reactions involving cadmium are of considerable industrial and theoretical interest. The value of the rate constant at amalgam electrodes is found to be very dependent on experimental conditions; moreover it is time dependent (1, 2). Explanation of these effects has been given (1, 2) in terms of the adsorption of impurities in view of the reduction potential of Cd(II) being close to the point of zero charge (pzc). It has also been suggested (2) that all reported observations can be explained in terms of migration within the diffuse double layer.

Experiments with exchange reactions at solid cadmium electrodes have indicated interesting time dependencies (3). Discussion of these results has necessitated a knowledge of the double layer capacity-potential curves for cadmium and the position of the pzc. Although Russian workers (4, 5) had reported the results of differential capacity measurements on solid cadmium in KCl solution it was decided to redetermine the curves and to extend the results to Na ClO_4 electrolytes. In this note the results of differential capacity measurements on flat polycrystalline cadmium in aqueous KCl and $NaClO_4$ electrolytes are reported.

Experimental

Details of the electrolytic cell, electrode construction, and electrical circuit have been described previously (6,7). Electrodes (3.46×10^{-2} cm^2 superficial area) were prepared from 99.999% cadmium supplied by Société de la Vielle Montagne. Water was twice distilled from deionized stock; all chemicals were of A. R. quality.

Electrodes were polished mechanically on roughened glass, lubricated with water. Etching (10% H_2SO_4 or 10% $HClO_4$) was chemical (1 min) or electrolytic (10 ma cm^{-2}). Polished and/or etched electrodes were washed thoroughly with water and introduced directly into the cell without drying.

Results

Figure 1 shows differential capacity curves for electrolytically etched electrodes in aqueous 0.01M KCl electrolyte; chemically etched electrodes gave very similar results. Time dependence in highly purified systems was not pronounced; equilibrium was established within 30 min with both etched and mechanically polished electrodes. A feature of this work with cadmium, however, was the very high degree of electrolyte purity required to obtain time-independent values of C_L after attainment of electrode/electrolyte equilibrium. Stable values of C_L have been obtained at silver and mercury electrodes after 3-4 days (6) of electrolyte purification whereas for cadmium comparable stabilities required much longer electrolyte purification. Figure 1 shows results for an "unstable" electrode; after 24 hr the capacity curve was shifted to more positive potentials, and C_L was somewhat reduced.

Figure 2 shows the relatively small effect of frequency in sodium perchlorate electrolytes on the dif-

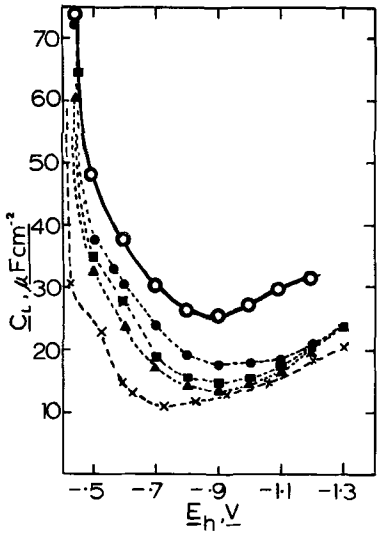

Fig. 1. Differential capacity curves for mechanically polished and for electrolytically etched electrodes, in aqueous 0.01M KCl. 25°C 2 k Hz. O Mechanical polish, 5 hr open circuit (o/c), "stable"; ● 30 min o/c electrolytic etch; ■ 2.5 hr o/c electrolytic etch; ▲ 6.5 hr o/c electrolytic etch; X 24 hr in "impure" electrolyte (3 day charcoal circulation).

ferential capacity curves. Similar results were obtained in potassium chloride electrolytes. Mechanically polished electrodes showed a greater frequency dispersion than chemically or electrochemically etched electrodes and also gave large electrode-to-electrode variations. Because of this, the majority of our experiments were made with etched electrodes.

The polarizable region is —0.5 to —1.3v (NHE); considerable faradaic current flows outside this. For all electrolytes investigated, the capacity magnitude was lowered in dilute electrolytes without any variation of the minimum potential (Fig. 3).

Figure 2 illustrates differential capacity curves in sodium perchlorate electrolytes. The minimum (—0.9 ±0.035v) is less precisely determinable than with chloride electrolytes.[1]

Discussion

Values of the pzc [—0.91 ± 0.025v (NHE)] indicated by this work compare favorably with the value re-

* It is intended to discuss the broadness of the capacity minima obtained with Cd in a later paper.

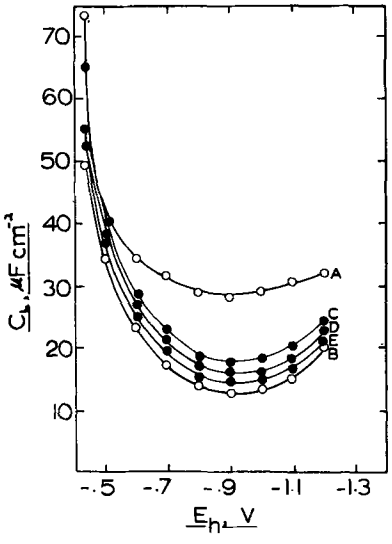

Fig. 2. Differential capacity curves and their frequency dependence in aqueous $NaClO_4$; electrolytic etch, 25°C. A, 1M $NaClO_4$ 103 c/sec; B, 0.001M $NaClO_4$ 2 kc/sec; C, 0.01M $NaClO_4$ 10 Hz; D, 0.01M $NaClO_4$ 400 Hz; E, 0.01M $NaClO_4$ 2 k Hz.

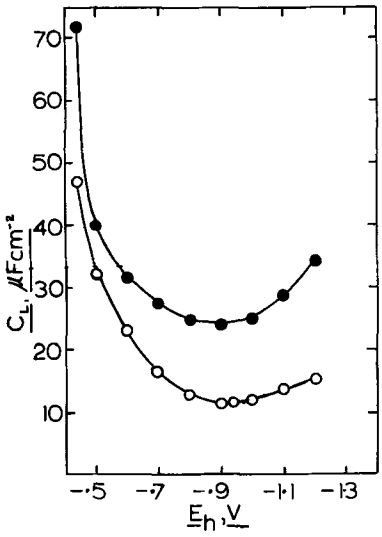

Fig. 3. Differential capacity curves in aqueous KCl; electrolytic etch 25°C, k Hz. ● 1M KCl; O 0.001M KCl.

ported by Borisova and Ershler (4) —0.9v (NHE). Differential capacity curves in perchlorate, however, were not so well defined in as much as the capacity minimum was broader. Generally, however, the shape was similar and the electrode behavior identical. The method used by these workers was essentially the same as used by us, but the Russians consider that a spherical drop of metal is the only satisfactory electrode and although a cut surface gave identical values of pzc to the spherical surface, the value of C_L and to some extent the shape of the differential capacity curve were both affected. Values of C_L reported by us for etched surfaces are reasonably close to the values of Borisova *et al.* (4).

It is of interest that the magnitude of the differential capacity of cadmium is comparable to that of a mercury electrode and indicates that the true area of cadmium is close to the superficial area.

Dispersion of capacity and time dependence due to initial surface rearrangement (8) observed with cadmium are of the same order as that observed with silver (6). The similarity between the results with chemically and with electrochemically etched surfaces may be explained in a similar manner in terms of surface atom diffusion removing relatively small differences in surface structure. However, a metal surface produced by mechanically polishing is likely to be less homogeneous (*i.e.*, shows a greater surface roughness due to fine scratches) than an etched surface. This increase in actual surface area compared to the superficial area will result in larger apparent double layer capacities on mechanically polished electrodes in relation to those at etched electrodes, as is observed. Mechanically cut (deformed surfaces) would presumably not be "normalized" with etched surfaces by this mechanism; the microscopic roughness may also explain the greater dispersion observed with mechanically polished (abraded) surfaces (9).

The need for ultrapurity in order to obtain reproducible C_L values emphasizes the role of impurities in electrode reactions involving cadmium (1). The shift of the pzc, to potentials positive with respect to its value on a clean cadmium surface, as a result of the insufficient removal of impurities from solution indicates changes in the surface charge density. Such a change would undoubtedly alter the value of the kinetic constants of any electrochemical reaction taking place at the electrode in the manner discussed by Breyer and Bauer (1).

Point of Zero Charge and Work Function

The interdependence of pzc and work function has been the subject of some considerable discussion (10).

It is interesting to note that by resiting the pzc of Cd at —0.9v and that of Ag(6) at —0.7v (NHE) the evidence for a linear relationship cited by Delahay (10) between pzc and the work function is considerably improved.

Acknowledgment

The authors wish to thank their colleague Dr. M. J. Jaycock for discussion of this work.

Manuscript received May 8, 1967; revised manuscript received June 16, 1967.

Any discussion of this paper will appear in a Discussion Section to be published in the June 1968 JOURNAL.

REFERENCES

1. B. Breyer and H. H. Bauer, "Alternating Current Polarography and Tensammetry," pp. 149-152, Interscience, New York (1963).
2. H. H. Bauer, *J. Electroanal. Chem.*, **12**, 64 (1966).
3. N. A. Hampson and D. Larkin, In preparation.
4. T. L. Borisova and B. V. Ershler, *Zhur. Fiz. Khim.*, **24**, 337 (1950).
5. T. I. Borisova, B. V. Ershler, and A. N. Frumkin, *ibid.*, **22**, 925 (1948).
6. N. A. Hampson, D. Larkin, and J. R. Morley, *This Journal*, **114**, 817 (1967).
7. J. P. G. Farr and N. A. Hampson, *Trans. Faraday Soc.*, **62**, 3493 (1966).
8. A review of many of these effects is given by R. A. Oriani and R. P. Frankenthal (Ch 11) in Metal Surfaces: Structure, Energetics and Kinetics, American Society for Metals (Seminar) Ohio (1963).
9. R. De Levie, *Electrochim. Acta*, **10**, 113 (1965).
10. P. Delahay, "Double Layer and Electrode Kinetics," p. 127, Interscience, New York (1965).

Activities of Molten Tin Alloys from EMF Measurements

Guy R. B. Elliott and Joe Fred Lemons[1]

University of California, Los Alamos Scientific Laboratory, Los Alamos, New Mexico

If the pure solvent is used as the standard state, all solvent activities must approach a value of one as the solution becomes very dilute. By definition, then, the Raoult's law value for the activity-mole fraction relationship ($a_1 = N_1 = 1$) is approached by any solution. Whether all very dilute solutions approach the unit slope also required by Raoult's law is a question which requires an experimental answer. A discussion of experiments bearing on this question has been given elsewhere [(1), and more detailed (2)].

Apparently the most clear cases of asymptotic approaches to the slope of Raoult's law are found in the work of Yanko *et al.* (3), where tin concentration cells were used with silver, gold, and antimony solutes. However, certain questions existed regarding the measurements when compared with other somewhat similar measurements (4, 5). Also certain aspects of their technique could be improved, *e.g.*, stirring, solute addition, exclusion of air, temperature uniformity, chemical purity. Finally, their temperature coefficient of emf was not consistent with Raoult's law.

If Raoult's law is obeyed (*i.e.*, the solvent activity coefficient is unity) then all cells give the same emf and temperature coefficient. This striking conclusion is independent of the materials used for solvent, solute, and electrolyte except as n depends on the ion charge. For $n = 2$ and using pure solvent at the reference electrode

$$\Delta F = -nF\epsilon = RT \ln a = RT \ln N$$

$$\epsilon/T = 9.91856 \times 10^{-5} \log N$$

Obedience to Raoult's law implies that, for the process of mixing the pure components to create the solution, $\Delta\overline{H}_{\text{solvent}}$ is zero and $\Delta\overline{S}_{\text{solvent}}$ is ideal.

Experimental

Material purification.—Commercial hydrated stannous chloride was purified in vacuum by fusion, boiling with pure tin, and triple distillation, the material being introduced into the electrochemical cell as a result of the third distillation. Molten reagent grade tin under vacuum was scrubbed by vigorously boiling $SnCl_2$, cast, remelted to bring any trapped electrolyte to the surface and finally washed with water. Silver and gold were of 99.98% purity by manufacturer's specifications. Copper was sheeting of electrolytic purity. The tungsten electrodes were cleaned electrolytically.

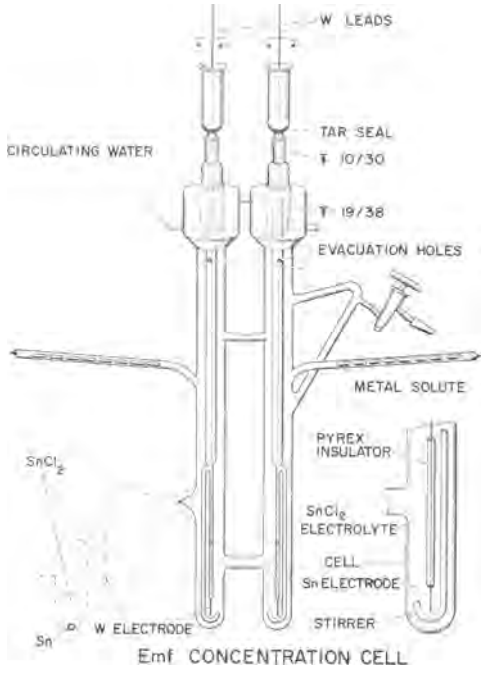

Fig. 1. H-cell design (tubes pictured slightly oversize. Evacuation through stopcock; evacuation holes are into stirrer tubes.)

The Pyrex H-cell is pictured in Fig. 1. This cell was evacuated, flamed, and loaded with argon. Weighed tin was loaded beside the stirrers and weighed solute pieces were added to one or both arms. After evacuation the tin was melted into position, the $SnCl_2$ was vaporized onto it, and the $SnCl_2$ container was melted off and removed. The closed cell was placed in the furnace and reconnected to the vacuum line to be occasionally stirred and repumped. After many hours, as the electrolyte became saturated[2] with tin (and

[1] Deceased.

[2] With considerable discrepancy the solubility of tin in $SnCl_2$ at 773°K is reported to be 3.2×10^{-5} mole fraction (6) or 2.6×10^{-2} mole fraction (7). At 573°K the value is reported to be 8.3×10^{-3} mole fraction (7).

Table I. w-$Sn_{(1)}/SnCl_{2(1)}/Sn$, $X_{(soln)}$—w concentration

Solute mole fraction[a]	EMF (measured), μv	Temperature, °K	EMF (corrected),[b] μv	Raoult's law prediction	Activity coefficient
(Gold)					
0.001098	25.9 ± 0.5	540.8		25.6	0.99990
0.003243	76.0 ± 0.5	540.9		75.7	0.99998
0.004194	98.3 ± 0.7	540.7		97.9	0.99998
0.007744	182.1 ± 1.2	540.6		181.0	0.99995
0.015517	370.2 ± 1.2	540.4		364.0	0.99973
0.024243	593.9 ± 2.0	540.3		571.2	0.99903
0.036336	924.0 ± 2.0	541.3		862.9	0.99740
0.046890	1224.0 ± 1.0	541.5		1120.1	0.99557
0.063830	1754.5 ± 1.5	542.0		1539.7	0.99087
0.093873	2784.5 ± 0.5	542.1		2301.1	0.97954
(Silver)					
0.000000	5.0 ± 0.8	531.0	(0.0)		
0.000484	5.8 ± 0.5	531.2	10.8	11.1	1.00001
0.002570	53.5 ± 0.5	534.0	58.5	59.2	1.00003
0.004314	94.3 ± 0.5	534.4	99.3	99.5	1.00001
0.010042	223.6 ± 0.2	534.7	228.6	232.4	1.00017
0.025193	557.9 ± 0.2	534.1	562.9	587.0	1.00106
0.033933	745.0 ± 0.2	534.7	750.0	795.0	1.00196
(Copper)					
0.000716	9.2 ± 0.2	534.7	(16.2)	16.5	
0.002243	44.9	534.2	51.9	51.7	0.99999
0.003866	82.2 ± 0.1	534.0	89.2	89.1	1.00000
0.008225	182.2 ± 0.1	533.9	189.2	189.9	1.00003

[a] Approximately 20g of tin in each leg.
[b] Corrections: gold, none; silver, add 5.0 μv; copper, add 7.0 μv.

possibly as traces of hydroxide were converted to oxide dissolved in the electrolyte), the cell potential for tin *vs.* tin dropped to near zero emf and became stable.

The system was now isolated at the stopcock which was not opened again during a run. By tilting the cell support slightly and tapping the cell side arm, single pieces of solute could be added while the cell remained hot. The cell then returned easily to its original position and could be stirred until the emf results were stable. Then another solute addition could be made.

The emf was measured by a Leeds and Northrup K-2 potentiometer. The furnace was isolated by partial Faraday cages attached to a ground independent of that used for working electrical equipment. A grounded stainless tube around the temperature control thermocouple (except for the exposed tip) helped prevent stray emf effects from the heater. The cell temperature was measured by a Pt/Pt 10% Rh thermocouple glass-taped to the cell just outside one metal-salt interface.

The heater was outside four large nesting nickel plated copper cylinders with air gaps between to provide a steady, uniform temperature. [The cylinders were similar to those used with the isopiestic balance (8).]

When a cell was broken open and the salt and alloy dissolved away, there was no indication of attack on either the Pyrex or the tungsten.

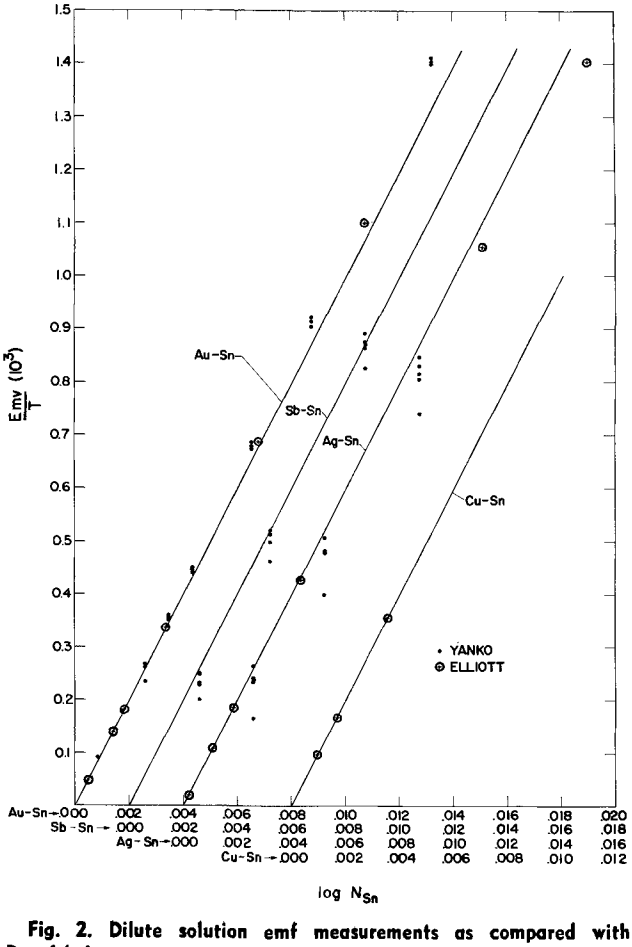

Fig. 2. Dilute solution emf measurements as compared with Raoult's law.

Results

The results are shown in Table I. Once a cell had been adequately stirred, any measurement was stable (without rapid shifts of emf) in the ± 0.1 μv range. However, there was some tendency for the cell voltage to shift over hours or days; this variation is the uncertainty given in Table I.

Figure 2 shows the data for the more dilute solutions plotted with the Raoult's law value for all temperatures shown as the solid line. The solid dots show the results of Yanko *et al.* for comparison. (Note the offset of the abscissa for the different solutes.)

Figures 3 and 4 show all the silver and gold data on Dundee type plots which examine the change of sol-

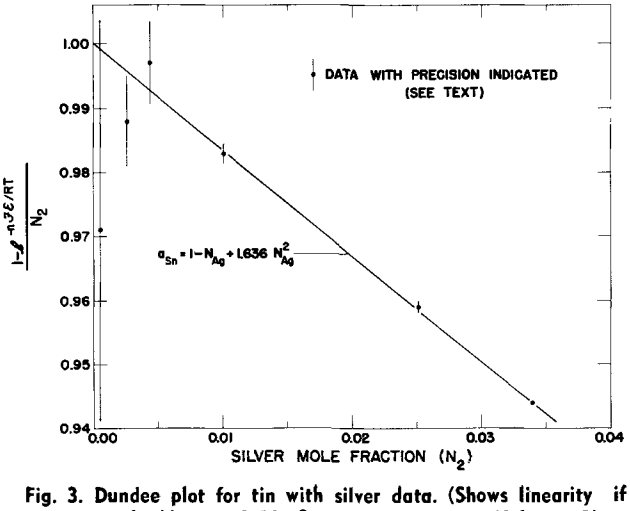

Fig. 3. Dundee plot for tin with silver data. (Shows linearity if $a_{Sn} = 1 - k_1 N_{Ag} + b N_{Ag}^2$ and unit intercept if $k_1 = 1$).

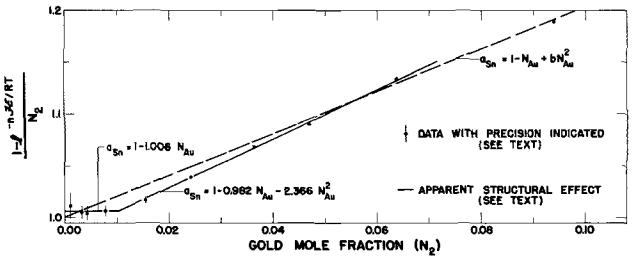

Fig. 4. Dundee plot for tin with gold data (see text)

vent activity with solute mole fraction. The bars show the experimental uncertainty.

For the corrections we have used the emf for the measurements of "pure" tin *vs.* "pure" tin except for the copper where a piece fell in too early.[3] In this case we have corrected the first emf to the Raoult's law value.

Conclusions

As can be seen in the figures, within the accuracy of the measurements, Raoult's law is approached for all three of these systems.

For the Cu-Sn system the solvent behavior is ideal over the whole range of composition measured.

For the Ag-Sn system a correction term is required which follows N_{Ag}^2. Such terms are sometimes ascribed to important solute-solute interactions.

For the AuSn system, in addition to the presence of an N_{Au}^2 term, there is an indication of a change of behavior at $N_{Au} = 0.01$. Similar abrupt changes have been observed by the authors and co-workers in continuing vapor pressure studies of cadmium alloys with gold (9), lead (10), and copper.

Since the dilute solution behavior in these systems proved to be so ideal in satisfying Raoult's law with its corollary temperature dependence, there seemed little reason to test the temperature dependence further. Instead we chose to make extensive studies of Sn-Hg and Au-Cd solutions as will be reported later.

[3] Several factors could contribute to this required correction such as small differences in impurities in the purified tin as added, trace impurities in the electrolyte scavenged more by one tin bath than by the other, or temperature differences of 0.01°K or less between the legs.

Acknowledgment

The authors wish to thank Dr. D. R. Conant for his interest and suggestions regarding this work.

Manuscript received March 9, 1967; revised manuscript received May 20, 1967.

Any discussion of this paper will appear in a Discussion Section to be published in the June 1968 JOURNAL.

REFERENCES

1. G. R. B. Elliott, J. F. Lemons, and H. S. Swofford, Jr., *J. Phys. Chem.*, **69**, 933 (1965).
2. G. R. B. Elliott, J. F. Lemons, and H. S. Swofford, Jr., "An Alternative Treatment of Solvent Activity in the Raoult's Law Region. The Gallium-Cadmium System," Los Alamos Scientific Laboratory Report, LA-2997 (July 1964).
3. J. A. Yanko, A. E. Drake, and F. Hovorka, *Trans. Electrochem. Soc.*, **89**, 357 (1946).
4. H. J. McDonald, *ibid.*, **89**, 371 (1946).
5. R. O. Frantik and H. J. McDonald, *ibid.*, **88**, 243 (1945); *ibid.*, 253.
6. J. D. Corbett and S. von Winbush, *J. Am. Chem. Soc.*, **77**, 3964 (1955).
7. A. A. Kolotnii, Sb. Tr. Tsentr. Nauchn.—Issled. Inst. Chern. Met., No. 34, 34 (1963).
8. G. R. B. Elliott and J. F. Lemons, *J. Phys. Chem.*, **64**, 137 (1960).
9. G. R. B. Elliott, C. C. Herrick, J. F. Lemons, and P. C. Nordine, "Structure in Liquid Au-Cd and Ce-Cd Solutions. Vapor Pressure and Electrical Resistivity. Liquid Compounds, Two-Liquid Regions, Premonitory Phenomena, and Freezing," Los Alamos Scientific Laboratory Report, LA-3526 (March 1966).
10. H. S. Swofford, Jr., G. R. B. Elliott, and D. R. Conant, "Further Tests of Dilute Solution Equations and Thermodynamic Relationships: The Vapor Pressure of Cadmium over Liquid Alloys containing Small Amounts of Lead," Los Alamos Scientific Laboratory Report, LA-3657 (October 1965).

Solvent Properties of Molten $NaNO_2$ Using a Freezing Point Technique

Theodore R. Kozlowski and Roger F. Bartholomew

Technical Staffs Division, Corning Glass Works, Corning, New York

The physical and chemical properties of molten alkali metal nitrates have been studied extensively because of their low melting points and ease of handling. In comparison there has been very little work reported on the properties of molten nitrites. Protsenko and co-workers (1-5) have published binary and ternary phase diagrams involving alkali and alkaline earth metal nitrites, and the electrochemical reduction of sodium nitrite has been discussed in recent papers (6-7). However, the experimental difficulties in working with molten nitrites, such as the ease of oxidation to nitrate, and the problems of drying the materials have resulted in the absence of data on these compounds. This work was undertaken as a preliminary investigation on the solvent properties of molten sodium nitrite using a freezing point technique.

Experimental conditions were constrained to permit use of the following equation for temperature change as a function of concentration

$$\Delta T = \nu K_f m \qquad [1]$$

Here ΔT is the temperature depression $T_f - T$, T_f being the melting point (°K) of the pure solvent, and T that of the solution; ν represents the number of entities dissolved in the melt that are distinguishable from the solvent; m is the molality of the solute, defined as moles of solute per 1000g solvent; and K_f is the molal cryoscopic constant in deg/mole. In deriving Eq. [1], K_f was defined as

$$K_f = \frac{RT_f^2}{\Delta H_f n_1} \qquad [2]$$

where ΔH_f is the heat of fusion of the solvent at T_f and n_1 the moles of solvent in 1000g.

Experimental

Freezing points for the melts were obtained using the cooling curve technique. The essential details of the design and operation of the cryoscopic assembly were similar to systems previously described in the literature (8, 9). One minor modification involved the

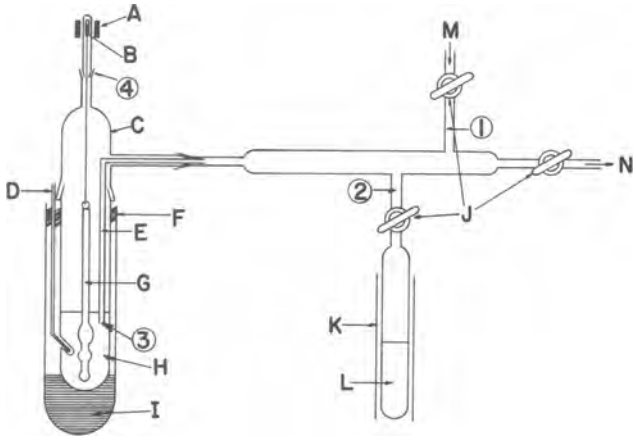

Fig. 1. Apparatus for water solubility measurements: A, solenoid; B, glass enclosed iron cylinder; C, cryoscope head; D, chromel-alumel thermocouple; E, nitrogen-water vapor delivery tube; F, small nichrome wound furnace; G, stirrer; H, melt; I, sand for support; J, vacuum stopcocks; K, water heating coils; L, water reservoir; M, nitrogen inlet; N, to vacuum pump; 1-4, numbers refer to the operation of the apparatus.

use of a motor-driven propellor-type stirrer, rather than a reciprocating magnetic stirrer, to achieve the necessary agitation for solid-liquid equilibrium at the melting point. A small gap between the cryoscope head and the stirrer shaft provided an exit port for the dry nitrogen continuously swept over the melt. A small window cut into the furnace insulation allowed continuous visual inspection and monitoring of the molten sodium nitrite. Approximately 100g of salt were used in each trial.

Diagrammed in Fig. 1 is a closed apparatus, having a capacity of 30g of molten sodium nitrite, which was constructed for water solubility measurements. With reference to Fig. 1, the initial operation consisted of evacuation, followed by immediate filling of the assembly with nitrogen at 1 atm pressure, 1. A water reservoir at known temperature, 2, was opened to the system, and the nitrogen-water vapor mixture was bubbled through the melt, 3, passing out through an opening, 4. A control run utilizing a Hygrodynamics Inc. Line operated Electric Hygrometer Indicator, No. 15-3000, established the vapor pressure of water prior to entering the melt. The simple expedient of elevating the water reservoir temperature increased the amount of water passing through the molten sodium nitrite. Cooling curves were obtained after at least an hour of bubbling nitrogen-water vapor through the melt.

Chromel-alumel thermocouples, referenced to a distilled water-ice cold junction, served as temperature sensors for all measurements. A Sargent Model MR recorder performed the function of bucking all but 2 mv of thermocouple output, amplifying and presenting the remainder as a cooling curve (8, 9) on a 10-in. time-voltage chart. Three cooling curves for given concentrations of solute were generally sufficient to attain a precision of ±0.02°C in the melting point. The melt temperature was kept below 320°C and the cooling rate was maintained at 3 deg/min. Super cooling was especially small, never exceeding 0.25°C.

The following Baker's "Analyzed" reagent grade chemicals were used: $NaNO_2$, Na_2SO_4, NaCl, $NaC_2H_3O_2$, NaSCN, Na_2CO_3, $Ba(ClO_3)_2$, and $BaSO_4$. $NaNO_2$, $Ba(ClO_3)_2$, and NaSCN were dried to constant weight in a National Appliance Company, Model 5830-4, vacuum oven at 110°C for 7 to 10 days. Similar treatment extending 1-2 days sufficed for the remaining chemicals. Concentration changes for the melt were effected by dropping pieces weighing approximately 0.1g into the melt. After each concentration change, a cooling curve was obtained only after the added solute was observed to totally dissolve.

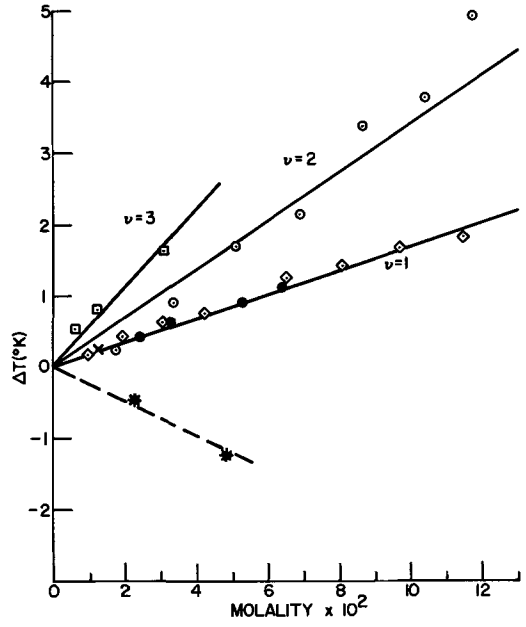

Fig. 2. Change in $NaNO_2$ freezing points (T_f—T) with added solutes: ⊙, $NaC_2H_3O_2$; ◇, Na_2SO_4; ⊡, $Ba(ClO_3)_2$; •, NaSCN; X, Na_2CO_3; *, NaCl.

Results

The average melting point for sodium nitrite was found to be 281.5°C, which is in good agreement with the value of 281°C reported by Frame *et al.* (10). Because there was no available value in the literature for the heat of fusion of sodium nitrite, it was not possible to construct the ideal freezing point curves for the solutes added. Figure 2 presents the experimental points given in Table I. The solid lines shown for $\nu = 1$, 2, and 3 were drawn using the heat of fusion obtained by least-mean-squares analyses on the data obtained for the solutes Na_2SO_4, NaSCN, and Na_2CO_3. The reasons for this are discussed later. The slope of the ΔT *vs.* m plot (*i.e.*, K_f) for the three solutes taken together gave a value of 17.0 deg/mole with a standard deviation of ±0.5 deg/mole. The heat of fusion calculated from Eq. [2], was found to be 2.48 ± 0.07 kcal/mole. The entropy of fusion, ΔS_f, was calculated as 4.47 ± 0.13 eu.

The solubility of water in molten sodium nitrite was determined by varying the vapor pressure of water above the melt and obtaining the freezing-point depression at a known vapor pressure. By assuming that water behaves in the same manner in sodium nitrite as has been found in sodium nitrate (11), *i.e.*, that water dissolves as a monomer, the following concentrations of water in the melt were obtained; 0.63 x $10^{-2}M$ at 7 mm Hg, 2.86 x $10^{-2}M$ at 19.5 mm Hg, and

Table I. Experimental data for freezing point depressions in $NaNO_2$

ΔT, °K	Molality × 10²	Solute	ΔT, °K	Molality × 10²	Solute
0.14	0.903	Na_2SO_4	0.21	1.702	$NaC_2H_3O_2$
0.40	1.991		0.89	3.301	
0.59	3.070		1.68	5.044	
0.73	4.197		2.13	6.872	
1.22	6.488		3.35	8.632	
1.40	8.046		3.75	10.381	
1.65	9.765		4.90	11.747	
1.80	11.425				
			0.52	0.596	$Ba(ClO_3)_2$
0.21	1.189	Na_2CO_3	0.77	1.192	
			1.61	3.071	
0.27	1.159	NaSCN			
0.39	2.402				
0.58	3.240				
0.89	5.223				
1.09	6.379				
−0.46	2.202	NaCl			
−1.23	4.805				

$4.54 \times 10^{-2}M$ at 37.9 mm Hg. This last value was obtained by extrapolation from the first two because, for two pressures above 37.9 mm Hg, the depression of the freezing point became independent of the vapor pressure of water. This represents the maximum solubility of water in the melt at its freezing point, which corresponds to a concentration of 31.4×10^{-4} moles water/mole sodium nitrite. An approximate value of 8×10^{-5} moles water/mole sodium nitrite-mm Hg was obtained for K, the Henry's law constant.

Discussion

Fusion of the dried material resulted in a clear yellow liquid which displayed no bubbling at atmospheric pressure under nitrogen. This condition could be maintained for weeks if the temperature of the melt was not allowed to exceed 325°C. Above this temperature, an increasing amount of fine sodium oxide precipitate (12) appeared in the melt. With continued overheating, no gas evolution was noted in or on the melt, although the flowing purge gas would have prevented the buildup of nitrogen dioxide and nitrous oxide reported to accompany the decomposition (12-14). Cooling curves obtained on pure sodium nitrite before and after decomposition displayed no change in the melting point, indicating that solubility of the Na_2O was less than $1 \times 10^{-3}M$.

The choice of solutes for freezing point measurements in sodium nitrite is limited because of double decomposition reactions which form unstable metal nitrites (15). Attempts to use cadmium and lead salts were unsuccessful because of this reason. This limits the choice of solutes to alkali or alkaline earth metal salts. Within this range of compounds, further limitations are imposed by the formation of solid solutions between sodium nitrite and salts containing potassium (16), nitrite (16), and chloride ions. In the case of $BaSO_4$ very low solubility was found, since no depression of the freezing point could be detected in a saturated solution.

The best-behaved solute was sodium sulfate, since clear solutions with no bubbling were obtained up to the highest concentration studied, $11.4 \times 10^{-2}M$. Only one point was obtained for Na_2CO_3, because attempts to go to higher concentrations resulted in bubbling and the formation of a flocculent precipitate, presumably sodium oxide. Additions of sodium thiocyanate gave well-behaved melts up to concentrations of 6.4×10^{-2} M. Above these concentrations slight evolution of gas was observed; therefore, only results in well-behaved melts are reported. These three solutes should all introduce one foreign particle in the melt, and, as can be seen in Fig. 2, they all fall on the same line. Because of this good agreement with expected behavior, these data were used to calculate ΔH_f for sodium nitrite which was then used to describe the other solute systems. The value of 2.48 ± 0.07 kcal/mole obtained is not directly comparable with published data. Estimates were made from the heat-capacity data of Voskresenskaya *et al.* (17) and from the phase diagrams reported by Protsenko and his coworkers (2, 4). In the former case the heat of fusion was estimated to be in the range 2.1 to 2.9 kcal/mole at 282°C. From the phase diagrams (Li^+, Na^+), (NO_2^-) and (Sr^{2+}, Na^+), (NO_2^-) values of 4.3 and 9.5 kcal/mole at 284°C were calculated. Our value falls toward the middle of the value obtained from the heat-capacity data, which lends good support to its accuracy. A value of 6 ± 1 kcal/mole was reported by Rapoport (18) in his work on the effect of pressure on the melting point of sodium nitrite. However, it was pointed out (19) that this method of obtaining thermodynamic data does involve considerable extrapolation, which can greatly affect the final value.

Solutions with sodium acetate gave unexpected results. Freezing-point depressions characteristic of $\nu = 2$ rather than the expected $\nu = 1$ were found. As can be seen from Fig. 2, there is considerable scatter in the points; the lowest concentration fell on the $\nu = 1$ line, but at higher concentrations the data tended to fall on the $\nu = 2$ line. Recent work by Hazlewood *et al.* (20) on the properties of molten alkali metal acetates indicated that sodium acetate was thermally stable just above its melting point of 329°C. This is 4°C higher than the highest temperature used in our work. They also pointed out that the thermal stability of molten acetates is enhanced by the absence of oxygen above the melt. Therefore, the freezing point results found for sodium acetate cannot be explained on the basis of thermal instability. The concentration of acetate was kept below $11.7 \times 10^{-2}M$ in this work, and, despite the care used in controlling the temperature, slight bubbling did occur. The behavior of alkali acetates in molten alkali metal nitrates has been examined in this laboratory using freezing point measurements, infrared, polarography, and mass spectra (21). Reactions do occur, the products being alkali nitrites, carbonates, oxides, and gases. On the basis of the results for the nitrate systems, it is suggested that the value of $\nu = 2$, found for sodium acetate in sodium nitrite, occurs because of a chemical reaction between the solute and solvent. Further study is required in order to elucidate the reaction mechanisms and products in molten nitrites. The small amount of nitrite which may be removed from the solvent because of the reaction would not significantly alter the concentration term defined in Eq. [1]. Only three concentrations are shown on Fig. 2 for the addition of $Ba(ClO_4)_2$ because, at concentrations in excess of $3.1 \times 10^{-2}M$, slight evolution of gas was noted. However, the data obtained fell on the calculated $\nu = 3$ line within experimental error. This indicates that at the lower concentrations any reaction taking place is negligible, since the expected three-particle depression was found. The addition of NaCl gave an increase in the freezing point of $NaNO_2$, indicative of solid-solution formation.

The maximum water solubility of 31.4×10^{-4} moles water/mole sodium nitrite can be compared with 14.1×10^{-4} and 3.9×10^{-4} moles water/mole melt at 20 mm Hg of water for sodium nitrate and potassium nitrate, respectively, reported by Frame *et al.* (11). All of these values are for the melts at their freezing points. A Henry's law constant of 7×10^{-5} for sodium nitrate, calculated from their data, is very near the value found for sodium nitrite. The presence of a reaction or some unusual dissolution mechanism, *e.g.*, the passage of water into the melt as $(H_2O)_2$, would have resulted in different values of K. It is suggested that the placement of water molecules in the sodium nitrite melt near its melting point proceeds with the same mechanism postulated for the nitrate, *viz.*, "interstitial dissolution." In retrospect, this conclusion could have been implied from the structural similarity of nitrite and nitrate melts, as well as the low solubilities of water found in the course of the investigation.

From the preceding discussion it is evident that sodium nitrite is not as good a solvent for cryoscopic work as sodium nitrate (22, 23). The greater chemical reactivity of the melt to added solutes and the ease with which solid solutions are formed restrict its use.

Acknowledgment

The authors wish to express their appreciation for the assistance of Mr. Dale Erdman in obtaining the cooling curves used in this work.

Manuscript received May 2, 1967; revised manuscript received June 12, 1967.

Any discussion of this paper will appear in a Discussion Section to be published in the June 1968 JOURNAL.

REFERENCES

1. P. I. Protsenko and B. S. Medvedev, *Russ. J. Inorg. Chem.*, **8**, 1434 (1963).
2. P. I. Protsenko and R. P. Shisholina, *ibid.*, **8**, 1436 (1963).

3. P. I. Protsenko and R. P. Shisholina, *ibid.*, **8**, 1438 (1963).
4. P. I. Protsenko and G. K. Shurdumov, *ibid.*, **9**, 916 (1964).
5. P. I. Protsenko and N. A. Brykova, *ibid.*, **10**, 659 (1965).
6. A. J. Calandra and A. J. Arvia, *Electrochim. Acta*, **10**, 474 (1965).
7. H. E. Bartlett and K. E. Johnson, *This Journal*, **114**, 64 (1967).
8. A. G. Keenan, *J. Phys. Chem.*, **60**, 1356 (1956).
9. C. Solomons and G. J. Janz, *Rev. Sci. Instrs.*, **29**, 302 (1958).
10. J. P. Frame, E. Rhodes, A. R. Ubbelohde, *Trans. Faraday Soc.*, **55**, 2039 (1959).
11. J. P. Frame, E. Rhodes, A. R. Ubbelohde, *ibid.*, **57**, 1075 (1961).
12. T. M. Oza, *J. Indian Chem. Soc.*, **22**, 173 (1945).
13. T. M. Oza and B. R. Walarwalkar, *ibid.*, **22**, 243 (1945).
14. A. Peneloux, *Comp. rend.*, **237**, 1082 (1953).
15. N. V. Sidgwick, "The Chemical Elements and Their Compounds," p. 695, Clarendon Press (1950).
16. "Phase Diagrams for Ceramists," E. M. Levin, C. R. Robbins, and H. F. McMurdie, Editors, pp. 339-340, American Ceramic Society (1964).
17. N. K. Voskresenskaya, G. N. Yankovskaya, and V. Ya. Anosov, *Zhur. Priklad Khim.*, **21**, 18 (1948).
18. E. Rapoport, *J. Chem. Phys.*, **45**, 2721 (1966).
19. C. W. F. T. Pistorius, *ibid.*, **45**, 3513 (1966).
20. F. J. Hazlewood, E. Rhodes, and A. R. Ubbelohde, *Trans. Faraday Soc.*, **62**, 3101 (1966).
21. T. R. Kozlowski and R. F. Bartholomew, Data being prepared for publication.
22. E. R. Van Artsdalen, *J. Tenn. Acad. Sci.*, **29**, 122 (1954).
23. G. J. Janz and T. R. Kozlowski, *J. Phys. Chem.*, **67**, 2857 (1963).

Nitrosyl Fluoride Electrolytes

Madeline S. Toy and William A. Cannon

Astropower Laboratory, Missile and Space Systems Division, Douglas Aircraft Company, Inc., Newport Beach, California

There is a growing interest in the field of low-temperature electrolytes which may be utilized in electrochemical energy conversion devices for operation at well below —60°C. As part of a study of low-temperature electrolytes, we have measured the electrical conductivities of solutions of Lewis acid fluorides in nitrosyl fluoride. The electrical conductivity of pure nitrosyl fluoride has been reported by Christe and Guertin as 5.4 x 10^{-5} ohm^{-1} cm^{-1} at —79°C (1). This value indicates a relatively high degree of self-ionization which probably occurs in the following manner

$$NOF \rightleftharpoons NO^+ + F^-$$

Toy and Cannon (2, 3) have reported the large increase of electrical conductivity of a self-ionizing solvent (bromine trifluoride) on addition of a Lewis acid fluoride (boron trifluoride). This paper describes the self-ionizing properties of nitrosyl fluoride (bp —59.9° and mp —137.5°) in the presence of fluoride ion acceptors (boron trifluoride, phosphorus pentafluoride, and arsenic pentafluoride) leading to formation of moderately conductive low-temperature electrolytic solutions below —60°C. An electrochemical energy conversion system using halogen fluoride electrolytes has been reported to be applicable at room temperature to as low as —40°C (4). This paper suggests that an electrochemical energy conversion system using nitrosyl fluoride electrolytes is capable of reaching even lower temperatures.

Experimental

Materials.—Nitrosyl fluoride and arsenic pentafluoride were obtained from Ozark-Mahoning Company. Boron trifluoride and phosphorus pentafluoride were obtained from Matheson Company. All materials were purified by low-temperature distillations. The purity of the samples was checked by infrared analysis of the vapor. The specific conductivities of boron trifluoride, phosphorous pentafluoride and arsenic pentafluoride in the liquid phase were less than 10^{-9} ohm^{-1} cm^{-1}. The specific conductivity of liquid nitrosyl fluoride reported by Christe and Guertin as 5.4 x 10^{-5} ohm^{-1} cm^{-1} at —79°C (1) falls on the specific conductivity *vs.* temperature curve of pure nitrosyl fluoride given in Fig. 1. All electrodes were high-purity commercial materials of 99.9% purity or better.

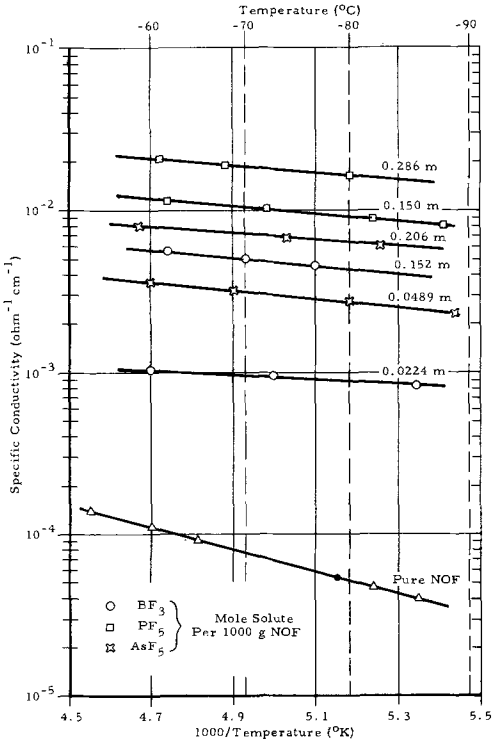

Fig. 1. Specific conductivity of NOF and NOF solutions as a function of temperature.

Apparatus.—The conductivity cell (Fig. 2) was made of stainless steel with a Teflon liner and equipped with two smooth platinum electrodes. The leads passed through Teflon plugs and were compressed between metal fittings to effect a vacuum and pressure tight seal. Temperatures were measured by a thermocouple inserted into a hole drilled in the wall of the conductivity cell. Cell constants ranging from 0.2 to 0.5 cm^{-1} were used. Cell constants were determined by measuring the resistance of standard potassium chloride solutions in the cell. In a conductivity cell of this design, the cell constant varies slightly with the volume of solution due to the variable im-

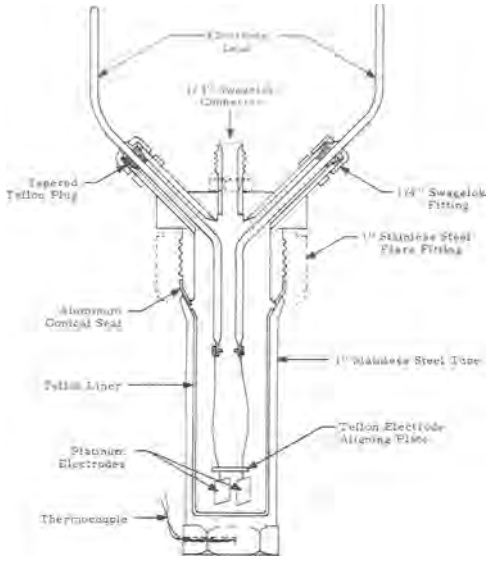

Fig. 2. Conductivity cell

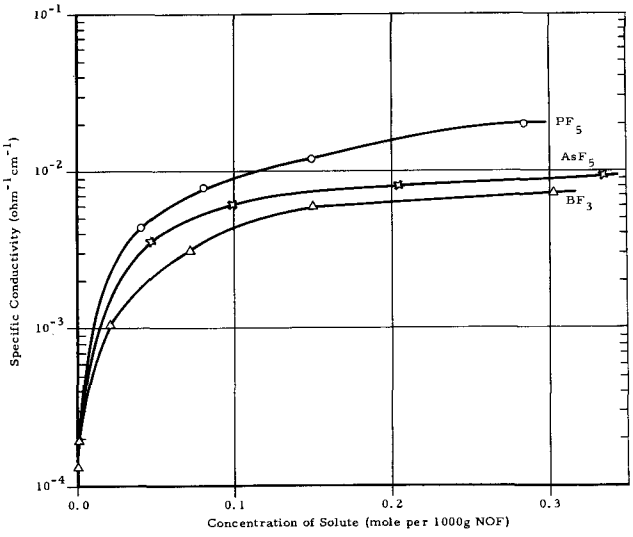

Fig. 3. Specific conductivities as a function of concentrations of BF_3, PF_5, and AsF_5 in NOF solutions at —60°C.

mersion of the platinum lead wires; therefore, calibration and measurements were made with a constant volume of solution.

Cell resistance measurements were made with a General Radio Type 1650-A impedance bridge. It was equipped with an internal, 1000-cycle signal source and tuned null detector. Measurements were also made with an external signal source ranging from 200 to 10,000 cycles to permit correction for polarization. For more sensitive balance, a Hewlett Packard 400 L vacuum tube voltmeter was used as an external null detector.

Glass systems cannot be used for handling nitrosyl fluoride; therefore, a vacuum line constructed of 304 stainless steel tubing, 316 stainless steel valves with Teflon packing, and calibrated stainless steel vapor receivers was employed for distillation and transfer of nitrosyl fluoride, boron trifluoride, and the volatile pentafluorides. Mercury manometers cannot be used. Pressure was measured with a stainless steel Bourdon gauge (30-in. vacuum to 60 psi). Careful exclusion of moisture is essential in handling these compounds as the presence of any water vapor will cause noticeable attack on stainless steel and will likewise affect conductivity measurements. The vacuum system was first degreased with trichloroethylene, rinsed with Freon, then vacuum dried. After assembly, the vacuum system was passivated by filling with gaseous fluorine to 1 atm for 1 hr. Finally the system was evacuated. Under these conditions, it is found that nitrosyl fluoride and its solutions do not attack the stainless steel appreciably during the time required to carry out the experiments, *viz*, 1-2 hr.

Open-circuit voltages of bielectrode cells were measured in a cell similar to that shown in Fig. 2 with the electrodes uniformly spaced 1 cm apart. Cell voltages were measured across the two electrodes with a vacuum tube voltmeter.

Results and Discussion

The specific conductivity of nitrosyl fluoride increases markedly on addition of boron trifluoride, phosphorous pentafluoride, and arsenic pentafluoride, and at the same time there is a decrease of the temperature coefficient of conductivity as shown in Fig. 1. The increase of specific conductivity of NOF solutions as a function of concentration of these Lewis acid fluorides is shown in Fig. 3. On evaporation of the solvent at room temperature, each solution yielded a solid residue. The infrared spectrum of each nitrosyl salt showed a strong absorption peak at about 2,350 cm^{-1} indicating $(NO)^+$ ion (5). These salts are readily soluble in liquid NOF as well as sulfur dioxide to yield moderately conductive low-temperature electrolytic solutions below 60°C (6).

The Lewis acid fluorides (BF_3, PF_5, and AsF_5) are potential electrolytes which function as acids by fluoride ion acceptance giving the cation NO^+ and the corresponding anions (BF_4^-, PF_6^-, AsF_6^-). The higher conductivity of the pentafluoride solutions compared to the boron trifluoride solution may be due to boron trifluoride being a weaker fluoride ion acceptor.

The open-circuit potentials were measured in nitrosyl fluoride solution containing 0.3*M* phosphorus pentafluoride at —70°C. Except for the tin-platinum bielectrode cell, the calculated potentials lack correlation with observed potentials. The postulated cell reactions are as follows

Anode	$M + 2F^- \rightarrow MF_2 + 2e$
Cathode	$2NOF + 2e \rightarrow 2NO + 2F^-$
Over-all cell reaction	$M + 2NOF \rightarrow 2NO + MF_2$ [1]

Standard free energy change at 25°C for lead (7-9) = —39.86 kcal; $E°$ = 0.864v (1.55v observed at —70°C).

Standard free energy change at 25°C for tin (7-10) = —38.76 kcal; $E°$ = 0.840v (1.10v observed at —70°C).

Standard free energy change at 25°C for cadmium (7-9) = —46.56 kcal; $E°$ = 1.01v (0.27v observed at —70°C).

The temperature difference may account for some of the discrepancies of calculated and observed potentials. Due to the limited data on free energy of formation of reactant NOF at —70°C, the potential of postulated cell reaction (Eq. [1]) was thus calculated at 25°C.

Acknowledgment

This work was conducted at Astropower Laboratory, Missile and Space Systems Division of Douglas Aircraft Company, Inc., under U. S. Army Advanced Research Project Agency, Contract No. DA-31-124-ARO-(D)-115. The authors are indebted to Drs. N. A. Tiner and W. D. English for helpful suggestions and to Mr. A. D. Pinkul for assistance.

Manuscript received April 24, 1967.

Any discussion of this paper will appear in a Discussion Section to be published in the June 1968 JOURNAL.

REFERENCES

1. K. O. Christe and J. P. Guertin, *Inorg. Chem.*, **4**, 905 (1965).
2. M. S. Toy and W. A. Cannon, Advances in Chemistry Series No. 54, pp. 237-244 (1966).
3. M. S. Toy and W. A. Cannon, *J. Phys. Chem.*, **40**, 2241 (1966).

4. M. S. Toy and W. A. Cannon, *Electrochem. Technol.*, **4**, 520 (1966).
5. D. W. A. Sharp and J. Thorley, *J. Chem. Soc.*, **1963**, 3557.
6. M. S. Toy and W. A. Cannon, Unpublished data.
7. R. C. Weast, S. M. Selby, and C. D. Hodgman, Editors, "Handbook of Chemistry and Physics," 46th ed., pp. D-40-44, Chemical Rubber Co., (1966).
8. H. S. Johnston and H. J. Bertin, *J. Am. Chem. Soc.*, **81**, 6402 (1959).
9. C. V. Stephenson and E. A. Jones, *J. Chem. Phys.*, **20**, 135 (1952).
10. A. Glassner, "The Thermochemical Properties of of the Oxides, Fluorides and Chlorides to 2500°K," Argonne National Lab. for U.S.A.E.C. under Contract W-31-109-eng-38 (ANL-5750).

Brief Communication

Polarographic Reductions of Benzyl Halides. A Correction

L. B. Rogers

Department of Chemistry, Purdue University, Lafayette, Indiana

and A. J. Diefenderfer

Department of Chemistry, Lehigh University, Bethlehem, Pennsylvania

An earlier report from our laboratory (1) postulated formation of the benzyl radical in electrochemical reductions of the benzyl halides primarily because mass-spectral lines derived from bibenzyl were the major ones in mass spectra of the product from controlled-potential electrolyses on the limiting-current plateau of the first reduction step. Although lines attributable to mercury in the product were also reported (1), mercury was dismissed as an impurity when products from blank electrolyses also gave mass spectra that showed mercury to be present. However, our most recent work has shown that bibenzylmercury (also benzylmercuric bromide) decomposes while its mass spectrum is being obtained and produces bibenzyl as the chief product. Mercury is also clearly present.

As a result of that finding, we have re-examined the entire process for the electrochemical reductions of the benzyl halides. The new evidence reported below supports the general mechanism suggested for allyl bromide (2).

First, a chronopotentiometric study clearly indicated that a prior (chemical) step preceded the electron transfer, in accord with the criteria of Reinmuth (3). Second, after approximately 90 min, contact with an open-circuit dropping mercury electrode (and its accumulated mercury pool), the concentration of benzyl chloride (or bromide) in a stirred 1.0*M* solution of lithium chloride in 1:1 methanol-water had decreased to half of its value. The concentration was measured by connecting the dropping electrode to a polarograph only long enough to measure the limiting current for the benzyl halide. When uv spectra of the product obtained by shaking mercury with a 5.0 mM solution of benzyl bromide in 1*M* $LiClO_4$ in 1:1 methanol-water were compared with spectra obtained using authentic samples, they indicated the formation of benzylmercuric bromide. Benzyl chloride reacted more slowly, but in a similar fashion.

When a solution of benzyl bromide was electrolyzed at −0.50v *vs.* SCE, a potential on the plateau of the first reduction step, the resulting solution had a uv spectrum with the same characteristics as those for bibenzylmercury. In addition, the isolated product did not depress the melting point of bibenzylmercury.

Finally, with regard to reduction at a potential on the second limiting-current plateau for benzyl chloride, Wawzonek *et al.* (4) have shown that, in the presence of carbon dioxide, toluene is the main product and phenylacetic acid, a minor one. That result has been interpreted as confirmation of a two-electron reduction that forms a benzyl carbanion. Although their results were obtained using solutions of the benzyl halides in dimethylformamide, a change in solvent to 1:1 methanol-water would not be expected to alter the findings.

Acknowledgment

Partial support for this study was provided by the United States Atomic Energy Commission under Contract AT(30-1)-905 at the Massachusetts Institute of Technology and Contract AT(11-1)-1222 at Purdue University.

Manuscript received May 23, 1967.

Any discussion of this paper will appear in a Discussion Section to be published in the June 1968 JOURNAL.

REFERENCES

1. L. W. Marple, L. E. I. Hummelstedt, and L. B. Rogers, *This Journal*, **107**, 437 (1960).
2. A. Kirrmann and M. Kleine-Peter, *Bull. Soc. Chem. France*, **1957**, 894.
3. W. H. Reinmuth, *Anal. Chem.*, **33**, 322 (1961).
4. S. Wawzonek, R. C. Duty, and J. H. Wagenknecht, *This Journal*, **111**, 74 (1964).

Preparation and Characterization of Manganese Oxide Thin Films

R. M. Valletta and W. A. Pliskin

IBM Components Division, East Fishkill, New York

ABSTRACT

Reactive sputtering has been found to be a desirable method for the preparation of conductive manganese dioxide films. The major parameter determining conductivity and the oxide of manganese formed by reactive sputtering is substrate temperature. At substrate temperatures in excess of approximately 350°C, low-conductivity lower oxides of manganese are formed. The infrared spectrum of films is sensitive to variations in the stoichiometry of the oxides and is a valuable tool for the characterization of manganese oxide thin films.

Manganese dioxide is a material which has aroused considerable interest because of its importance in the electrical components industry. It has been established that the physical and chemical properties of the oxides of manganese are extremely complex. The oxides MnO, Mn_3O_4, Mn_2O_3, MnO_2, and Mn_2O_7 exist (1-4). With the exception of Mn_2O_7, which has not had extensive study, these oxides exhibit at least two crystal structures and nonstoichiometry (1). In general, the lower oxides of manganese are not as good conductors as MnO_2.

Recently, interest has been generated in thin films of manganese dioxide since the introduction of these films to tantalum thin film capacitors improves both the reliability (5, 6), thermal stability (7), and yield of capacitors (6). It is believed that this results from the ability of MnO_2 to act as an oxidizing agent healing weak points in the anodic oxide by oxidizing exposed tantalum. The effect of the manganese dioxide film is especially noted in the ability of thin tantalum oxide capacitors ($\sim$ 250Å Ta_2O_5) with a film of manganese dioxide to withstand heating at temperatures in excess of 300°C without shorting (7). However, before heating, capacitors with sprayed MnO_2 layers were found to have a large dependence of capacitance on frequency. This was explained as resulting from the low conductivity of the spray deposited manganese dioxide films (7). It could be semiquantitatively explained by treating the capacitor with MnO_2 as a Maxwell-Wagner two-layer capacitor (8).

During the course of the above-mentioned investigation (7), the manganese oxide films formed by pyrolysis of a manganous nitrate solution were found to vary in composition depending on the conditions employed during the deposition. It was possible to identify the various phases prepared by the spray deposition method from the transmission infrared spectra of the oxides. Also, it was possible by use of the infrared spectrum to gain some information about the incorporation of water and NO_3^- as impurities in the films. Substrate temperature was found to be one of the most important parameters determining the phase obtained by spray deposition. However, concentration of the manganous nitrate solution and spray rate were also found to be important.

Since the resistivity of the manganese oxide is determined by composition, and the resistance of the manganese oxide layer will to a large extent determine the effect of frequency on the capacitor (7), a study was performed of the effect of various preparative parameters on the physical and chemical properties of manganese oxide thin films formed by reactive sputtering. The methods employed to prepare and characterize the films in this study were similar to those reported for reactively sputtered (9, 10) SiO_2 and SiO_2 films deposited by other techniques (10).

Cash and Clark (6) reported on the application of reactive sputtering for the preparation of manganese dioxide films. They reported that conductive MnO_2 can be prepared by reactive sputtering. They found that the percentage oxygen in the sputtering gas determined the composition of the manganese oxide. At a lower oxygen percentage, Mn_3O_4 and MnO were formed.

Experimental

The sputtering apparatus employed for deposition of the manganese oxides is shown in Fig. 1. Rods A are ½ in. diameter stainless steel support rods. B is the 8 x 8 x ⅛ in. sample support plate on which the sample wafers are fastened with clips. C is a circular grounded shield plate, the outer thin plate is 6 in. in diameter and is screwed into plate G; the inner section of C is 4¼ in. in diameter with a 2 in. diameter hole in the center. D is the 3½ in. diameter cathode on which a manganese plate is fastened by screws. E is the electrical lead which screws into the cathode and is a metal-to-glass seal with the metal part shielded by the grounded metal of the cathode support. The unshielded area of the cathode is approximately 20 cm^2. F is a ⅛ in. thick quartz plate on which the cathode rests. G an 8 in. square plate with a ½ in. diameter hole (for the electrical connection of E to the cathode) is a support for the cathode and the cathode shielding. The rods (A) are fastened to the grounded base plate so that all of the sputtering apparatus is at ground potential with the exception of the cathode (D) which is connected to the negative electrode of a high voltage d-c power supply through the connector (E). All of the metal parts of the ap-

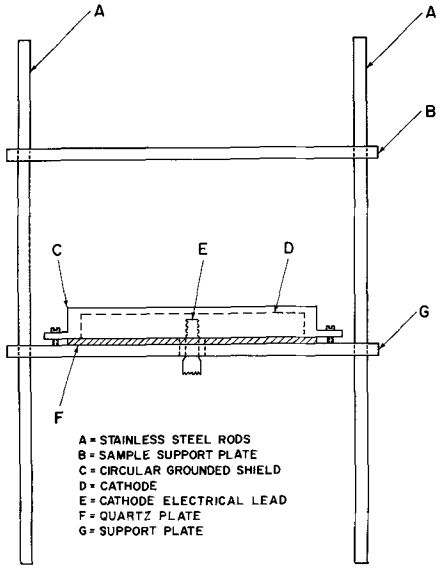

Fig. 1. Sputtering apparatus

paratus are fabricated from stainless steel. Plates B and G are supported by adjustable clamps (not shown in Fig. 1 for clarity) to allow the relative position of plates B and G to be adjusted. A horse-shoe magnet was at times placed on plate B. A nonmagnetic metallic spacer placed between plate B and the magnet adjusted the relative position of the magnet. Plates B and G had copper coils (not shown) brazed to them to allow water cooling of the plates. The sputtering apparatus was placed in a vacuum system with an 18 in. diameter bell jar.

The system was pumped to 2 x 10^{-5} mm Hg or lower prior to the deposition and a 30-min cleanup of the cathode with the wafer shielded was performed with the same gas mixture (usually pure O_2), pressure (usually 50μ) and voltage (1-4 kv) as were to be used during the deposition. The cathode-sample spacing usually was 1⅝ in. with the magnet placed 2⅝ in. from the cathode. The exact conditions described above were arrived at arbitrarily. There was no extensive investigation to determine if these conditions optimized the properties of the manganese oxide films.

The wafer temperature as a function of power was established by a thermocouple soldered to the back of a sample wafer or by temperature indicating salts deposited on the back of the wafer. The agreement between these two methods was excellent. An estimate of the difference in temperature between the front and back surface of the wafers was made. Under the assumption that all of the power used was flowing through the wafer, the maximum temperature difference between the front and the back of the silicon wafer was only 15°C. For this reason, the substrate temperatures quoted in this paper are uncorrected and are the temperatures measured at the back surface.

For infrared spectral evaluation (4000-400 cm^{-1}), the samples were deposited on thick (~ 28 mils) silicon wafers with a resistivity of 2 ohm-cm or greater. The resistivity of the films was measured by a four probe method on films deposited on ~ 5000Å of thermal SiO_2 on 7 mil thick silicon wafers. Film thicknesses were measured by using a Talysurf or Tolansky interferometric technique.

Results

In agreement with the results reported for the spray deposited films (7), the most important determinant of the phases obtained by reactive sputtering was the temperature of the substrate. The temperature of the substrate during sputtering as a function of the power input to the sample is illustrated in Fig. 2. The wafer usually attained this maximum temperature after 15-30 min of sputtering. All measurements were made at 50μ of pure O_2 with varying voltages.

The effect of varying substrate temperature on the composition of the oxides is shown in Fig. 3. All films are ~ 3000Å thick with a deposition rate of 5-10

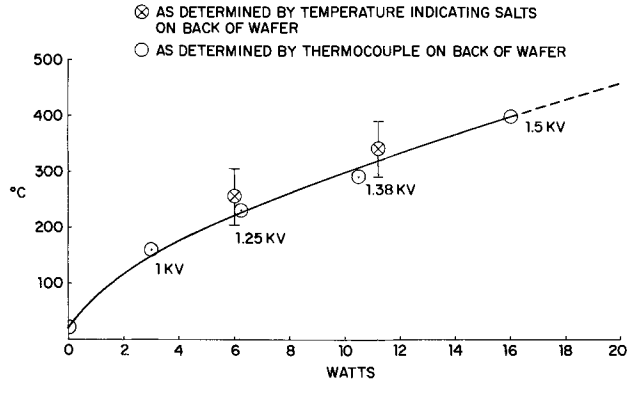

Fig. 2. Variation of temperature with power input—no magnetic field.

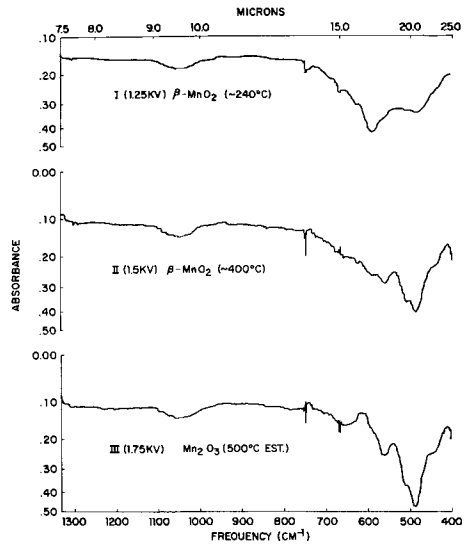

Fig. 3. Infrared spectra of films prepared with different sputtering voltages, 900-400 cm^{-1}.

Å/min. What appears to be an inverse absorption band at 610-620 cm^{-1} in some of the spectra is due to incomplete compensation of the silicon lattice absorption bands due to the use in the reference beam of a silicon wafer which is somewhat too thick. The reference silicon wafer should be somewhat thinner than the sample wafer depending on the refractive index of the sample film (11). The crystal structures of the phases were determined by electron diffraction. However, the infrared spectra has also been found to be a good method of determining the composition of the phases (7). Note in Fig. 3 that there is more similarity between spectra II and III which have different crystalline structures than I and II which are both β-MnO_2. Spectrum III is very similar to that of the spray deposited MnO_2 (7). The resistivities of these films are: I (~ 5 ohm-cm), II (~ 10^3 ohm-cm), and III (~ 10^4 ohm-cm). The spray deposited films had resistivities of ~ 10^4-10^5 ohm-cm. Thus, it can be concluded that the infrared spectra are more sensitive to the stoichiometry of the phase than the crystal structure. Since the lower oxides are poorer conductors than MnO_2, the results indicate that the sample with spectrum II was closer to Mn_2O_3 in composition than it was to MnO_2. Comparison of the results presented in Fig. 2 and 3 establish 300°-350°C as the limiting substrate temperature for the deposition of conductive MnO_2 thin films.

To increase the deposition rate, a magnetic field was introduced into the region of the glow similar to the method used for the preparation of reactively sputtered SiO_2 films (9). In addition to making it possible to increase the deposition rates to as much as 20-80 Å/min, the magnetic field performed another important function. The horseshoe magnet was placed directly above the sample. This resulted in a field primarily parallel to the wafer surface directly above the sample. The field was localized in the vicinity of the wafer with a magnitude of ~ 300-400 gauss while at the cathode the field was 50-60 gauss. It was found that not only did the magnetic field increase the plasma density, but it also made it possible to increase the power (and, therefore, deposition rate) without obtaining extreme substrate temperatures. The magnetic field parallel to the substrate surface would deflect negative ions such as O^- and also the electrons away from the sample.

The variation of substrate temperature as a function of power with the magnet 1⅝ in. from the cathode is depicted in Fig. 4.

It can be seen by comparison with Fig. 2 that with the magnetic field a power of 70w results in a sub-

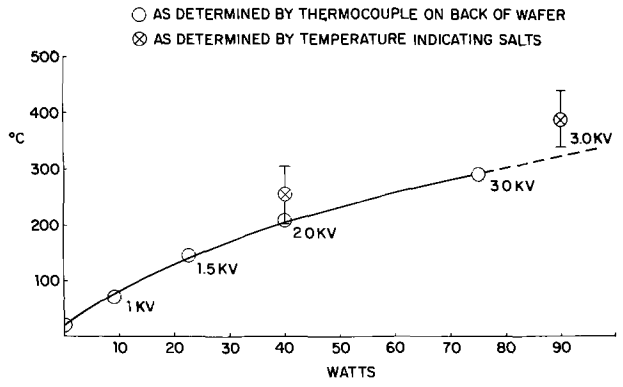

Fig. 4. Variation of temperature with power input with a magnetic field.

strate temperature of less than 350°C. However, without the magnetic field, 16w results in a substrate temperature in excess of 350°C. Clearly, the introduction of the magnetic field makes it possible to increase the power without extreme heating of the sample. It is possible to increase the power density by a factor of 4-5 and still maintain the same substrate temperatures by introduction of the magnetic field.

The uniformity of the films was not greatly affected by the inhomogeneous magnetic field. The thickness did not vary more than 5-7% over a 1¼ in. diameter wafer. Since the pressure was 50μ, the sputtered atoms suffered several collisions before deposition. This tends to decrease any nonuniformity resulting from the inhomogeneous magnetic field.

Since the temperature of the substrates was much lower with the magnetic field, it was possible to prepare conductive MnO_2 at voltages from 1-4 kv. The spectra of several samples of β-MnO_2 prepared at different voltages are presented along with the spectrum of a sample of a β-MnO_2 film prepared by sedimentation (12) in Fig. 5.

The film prepared by sedimentation was formed by centrifuging a suspension of fine particles of β-MnO_2 in a mixture of 25% isopropyl alcohol, 50% methanol, and 25% ethyl acetate. It is apparent that all of the spectra are similar except the band is shifted toward a higher wave number at higher substrate temperatures (higher voltage). There is also a band present beyond 400 cm^{-1}. This is below the limit of the Perkin-Elmer Model 337 Infracord, but it has been seen in the spectrum measured with a Perkin-Elmer Model 521 Spectrophotometer. Note also that as the substrate temperature increases (for example, spectrum II), the spectrum approaches that of the nonmagnetically prepared β-MnO_2. The band is centered close to 600 cm^{-1} with a shoulder at ~ 520 cm^{-1}. The resistivity of all of the β-MnO_2 films was between 1 and 15 ohm-cm. The variation in resistivity appeared to be random and not significantly affected by the deposition parameters. The shift in the band position is attributed to an increase in the density of the film as the substrate temperature is increased, similar to the results obtained with various deposited SiO_2 films (9, 10). The change in the shape of the spectrum at higher substrate temperatures may be reflecting some change in stoichiometry. However, it is believed that, if there is a change in stoichiometry, it is small since there is no significant change in the conductivity of the film. The resistivity of the films is in the range observed for bulk MnO_2 (13, 14).

Films were prepared at 3 kv, 50μ in the magnetic field with varying percentages of oxygen in the sputtering gas. The oxygen percentages were 100, 50, 10, and 1% O_2 in Ar. There were no significant differences in samples. All were found to be β-MnO_2 by electron diffraction with similar spectra as shown in Fig. 6. The conductivity of all the films varied between 1-15 ohm-cm. The variation again appeared to be random and was not a smooth function of oxygen percentage. It is felt that the stoichiometry of the samples is little affected by varying the oxygen percentage in the range of 100-1% O_2 in Ar. The deposition rate of the MnO_2 was 35 Å/min with 100% O_2, 60 Å/min with 50% O_2, 65 Å/min with 10% O_2 and 50 Å/min with 1% O_2. The dependence of sputtering rate on O_2 percentage did not show the large rate increase when the oxygen was reduced to 1% O_2 in Ar that had been observed for reactively sputtered SiO_2 (9).

It was established from the infrared spectra of the sputtered films that they were relatively free of water incorporation in the films. The deposition rates observed for MnO_2, however, were in the lower range of rates employed in the formation of reactively sput-

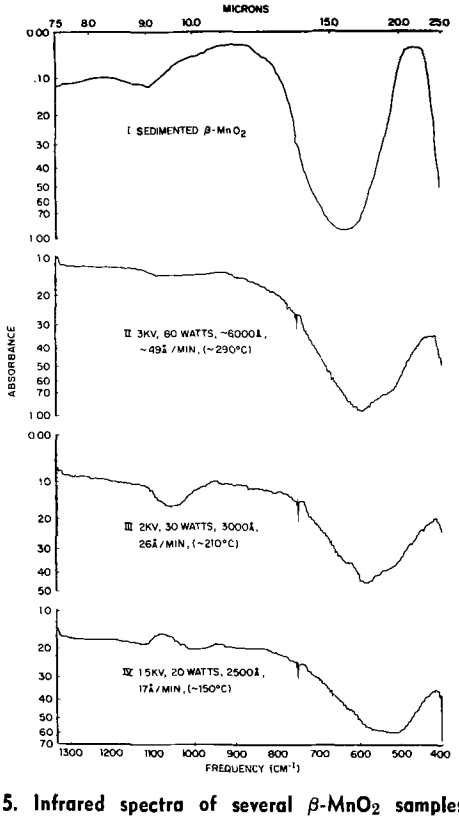

Fig. 5. Infrared spectra of several β-MnO_2 samples, 900-400 cm^{-1}.

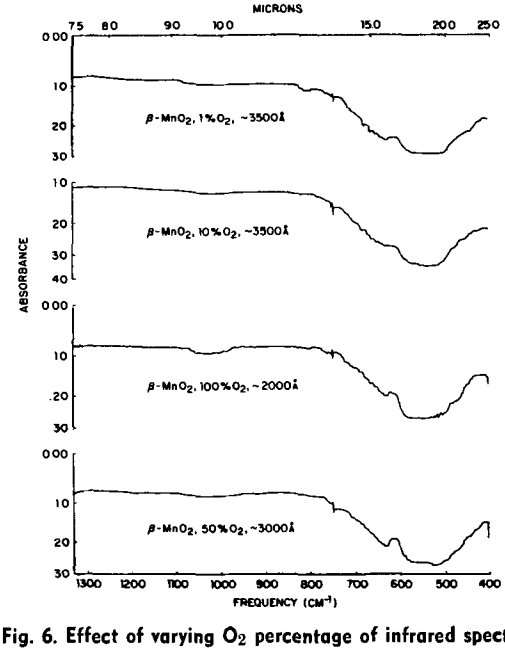

Fig. 6. Effect of varying O_2 percentage of infrared spectra

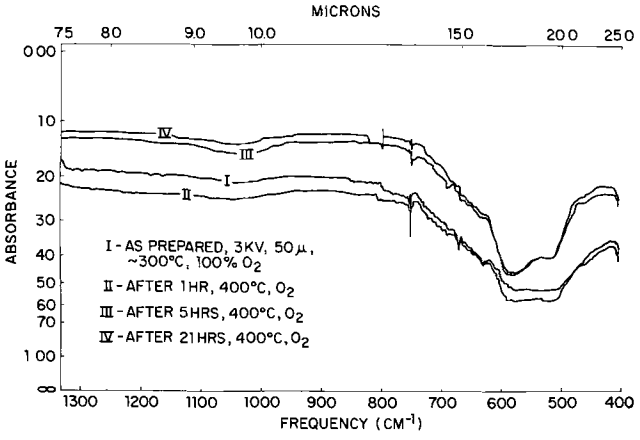

Fig. 7. Infrared spectra of a β-MnO_2 film heated in O_2 at 400°C

tered SiO_2, and at these deposition rates there was no experimentally observed incorporation of water into the SiO_2 films (9).

The reactively sputtered β-MnO_2 films were found to be susceptible to heating in various ambients. For example, a film heated for 15 min at 300°C in N_2 became much more resistive. The infrared spectrum had only one broad band centered at ~490 cm^{-1} and appeared to be intermediate to the spray deposited (7) and reactively sputtered MnO_2.

Sputtered MnO_2 films were easily reduced to Mn_3O_4 after 15 min at 300°C in forming gas. They could be reduced further by forming gas, and the behavior in reducing atmospheres was completely analogous to that observed for the spray deposited films (7). In fact, the infrared spectra can be described as almost identical.

There was some change in the spectrum of a β-MnO_2 film prepared in pure O_2 as a sputtering ambient after heating in O_2 at 400°C. The spectra are shown in Fig. 7. Note that, although there is little initial change after 1 hr at 400°C, the spectra finally look similar to those of films prepared without the magnetic field, *i.e.*, at higher substrate temperatures. The resistivity of the films is changed slightly by this treatment. It remains somewhere between 1 and 15 ohm-cm.

Once a sample has been reduced, it is not possible to reoxidize it to conductive β-MnO_2 by heating in O_2 at 400°C. The phase formed after as much as a week of oxidation (there is little change after 16 hr) is γ-Mn_2O_3. The infrared spectra is identical to that of a sprayed film after long oxidation. This phase is only formed if the film has been reduced. This suggests that a long heating of β-MnO_2 at 400°C even in oxygen would result in loss of some of the oxygen and the formation of Mn_2O_3 after long heating. This is not unreasonable when the susceptibility of bulk MnO_2 to thermal decompositon is noted. Thus, it appears that the β-MnO_2 prepared at the highest possible temperatures (Fig. 3 spectrum I) is somewhat oxygen deficient even though a good conductor.

Discussion

This study established that reactive sputtering is a desirable technique for preparing conductive MnO_2 films. Under favorable conditions, low sputtering rates ~80 Å/min and low substrate temperatures ≤~350°C, films of β-MnO_2 with a resistivity of 1-15 ohm-cm are formed. The films are relatively impurity free when prepared by this method.

In light of the complex chemistry and well-known thermal instability of the higher oxides of manganese, it is not surprising that the films show sensitivity to oxidizing and reducing ambients. This susceptibility to heating must be carefully considered in any capacitor employing these films to enhance the stability of the capacitor since it is known that the formation of a resistive manganese oxide film results in the formation of a frequency dependent capacitor (7).

It has been found that transmission infrared spectroscopy is a very sensitive technique for determining the type of manganese oxide film formed. In addition to being sensitive to stoichiometry and density changes in the same crystalline phase, it also makes it possible to determine the presence of impurities such as water.

It was not possible to make any direct correlation between the infrared spectra previously reported in the literature for manganese oxides and the thin films described herein. However, there is some similarity of the spectrum of reactively sputtered β-MnO_2 and that of finely ground MnO_2 reported by McDevitt and Baun (15). It is believed, however, that the use of infrared techniques will facilitate an understanding of the preparation and properties of manganese oxide thin films.

The study has definitely indicated that, if a conductive film of MnO_2 is required (for example, in thin film capacitors), reactive sputtering is a more desirable means of preparation than the spray deposition method.

Acknowledgment

The authors would like to express their appreciation to Mr. H. S. Lehman for helpful discussions, Dr. E. E. Gardner for making most of the four-probe resistance measurements, and Mr. R. A. Leonard for many of the experimental measurements.

Manuscript received Jan. 25, 1967; revised manuscript received May 17, 1967.

Any discussion of this paper will appear in a Discussion Section to be published in the June 1968 JOURNAL.

REFERENCES

1. G. Gattow, *Batterien*, **16**, 322 (1963).
2. G. Gattow, *ibid.*, **15**, 201 (1961).
3. G. Gattow, and O. Glemser, *Z. anorg. u. allgem. Chem.*, **309**, 20 (1961).
4. O. Glemser, G. Gattow, and H. Meisiek, *ibid.*, **309**, 1 (1961).
5. D. A. McLean and F. E. Rosztoczy, Paper presented at the San Francisco Meeting of the Society, May 1965.
6. J. H. Cash, Jr., and R. Seet Clark, Paper presented at the Cleveland Meeting of the Society, May 1966.
7. R. M. Valletta, J. S. Makris, and W. A. Pliskin, Proc. 1966 Elect. Comp. Conf., May 1966.
8. A. Von Hippel, "Dielectrics and Waves," p. 228, John Wiley & Sons, Inc., New York (1954).
9. R. M. Valletta, J. A. Perri, and J. Riseman, *Electrochem. Technol.*, **4**, 402 (1966).
10. W. A. Pliskin and H. S. Lehman, *This Journal*, **112**, 1013 (1965).
11. W. A. Pliskin, "The Effect of Moisture on R. F. Sputtered and Fused Glass Films," presented to American Ceramic Society Meeting, Washington, D. C. May 7-12, 1966; IBM Report MP 22.0078.
12. W. A. Pliskin and E. E. Conrad, *Electrochem. Technol.*, **2**, 196 (1964).
13. R. Glicksman and C. K. Morehouse, *This Journal*, **103**, 149 (1956).
14. J. S. Wiley and H. T. Knight, *ibid.*, **11**, 656 (1964).
15. N. T. McDevitt and W L. Baun, *Spectrochim. Acta*, **20**, 799 (1964).

Deposition and Properties of Aluminum Oxide Obtained by Pyrolytic Decomposition of an Aluminum Alkoxide

J. A. Aboaf

IBM Watson Research Center, Yorktown Heights, New York

ABSTRACT

Amorphous aluminum oxide films were deposited at 420°C by thermal decomposition of an aluminum alkoxide. The reducing or oxidizing atmosphere used during deposition affects the chemical and electrical properties of the oxide films. These films have shown superior characteristics when compared to SiO_2 films deposited by a similar process under the same conditions. The dielectric properties of these Al_2O_3 films compare favorably with anodized Al_2O_3 films. The resistance of these films to moisture makes them attractive as coatings for passivation of electron devices. The electrical properties of silicon and germanium surfaces covered with these Al_2O_3 films vary according to the deposition atmosphere.

In the present technology of transistor fabrication, the characteristics required of thin amorphous oxide films are numerous. These glassy films should be dense, pin-hole free, homogeneous, uniform in thickness, chemically inert but still easily etchable, of high dielectric strength, of high thermal conductivity, resistant to thermal shock, should have a coefficient of thermal expansion very near to that of the substrate on which they are deposited so that better adherence is obtained and finally should have surface passivating properties.

Vapor deposition techniques for oxide films consisting in the decomposition of metallo-organic compounds in the vapor phase, with or without oxygen, have been used extensively. The oxide mostly used is SiO_2 obtained from the pyrolysis of tetraethylorthosilicate at high temperature (650°-800°C) (1). The oxide can also be obtained at low temperature (300°-500°C), but the reaction requires the use of oxygen (2). The SiO_2 films deposited at low temperature have some shortcomings; they are not as dense as the high-temperature SiO_2; cracking occurs when films over 2000Å are heat-treated at 800°C; resistance to moisture leaves something to be desired.

Quite an extensive literature (3) exists on polycrystalline and single crystal Al_2O_3, on anodized aluminum and on films obtained by oxidation of aluminum in oxygen and water vapor. Only recently, interest was focused on Al_2O_3 obtained by vapor deposition: thermal evaporation of Al_2O_3 by electron beam bombardment (4), evaporation of aluminum and oxidation in a vacuum system in which a partial pressure of oxygen is maintained (5), and finally sputtering (6). The Al_2O_3 films obtained are considered amorphous since they do not reveal any structure to electron diffraction analysis. Al_2O_3 obtained by thermal decomposition of aluminum triethoxide in vacuo at 550°C was described by Tvorogov (7). In the present study, Al_2O_3 films were obtained by a similar process, but the aluminum alkoxide was transported to the hot zone in a carrier gas. Thick coatings of Al_2O_3 on metals and temperature resistant materials, produced by this method, were described (8) but no study of thin films for electron device applications is known to the author.

Experimental

In the process used, vapors of an aluminum alkoxide compound are transported in nitrogen, mixed with another gas (forming gas, nitrogen, or oxygen) and pyrolyzed in the hot zone of a resistance furnace.

Aluminum Tri-isopropoxide.—Various aluminum alkoxides could be used for the deposition of Al_2O_3; the results given below were obtained using aluminum triisopropoxide $Al(OC_3H_7)_3$. The latter, a crystalline, white powder was obtained from Eastman Kodak and was used without purification. Melting point of the compound is 118°C; its vapor pressure is 5 mm at 134°C (9). An emission spectroscopy analysis of the powder shows that the impurity with the highest content was silicon (100 ppm).

During vapor deposition, the aluminum alkoxide bubbler was maintained at 125°C in a constant temperature oil bath. It was noticed that, on melting the alkoxide in a nitrogen or in an oxygen atmosphere, a solid phase appeared. On cooling of the mass, the compound did not solidify, and a whitish, viscous liquid resulted. An incomplete separation of the solid phase from the liquid was made, and both portions were chemically analyzed for aluminum and isopropyl alcohol. While the composition of the viscous phase is equivalent to aluminum tri-isopropoxide, that of the solid phase could be explained only by a mixture of compounds such as $Al(OH)_3$, $Al(OR)_2OH$, $Al(OR)(OH)_2$. It appears then that the aluminum tri-isopropoxide powder used contained various products of hydrolysis.

Molecular weight determination of aluminum tri-isopropoxide (10) indicates a fourfold polymerization of this compound; this polymerization is present also in the vapor phase.

Deposition apparatus.—A schematic of the apparatus for the deposition of Al_2O_3 films on germanium, silicon, or gold substrates is shown in Fig. 1. Dry nitrogen gas is bubbled through the aluminum source at constant temperature, and vapors of the organic compound mixed with another gas (nitrogen and oxygen or forming gas) are transported to the hot zone of a resistance furnace where they pyrolyze to form Al_2O_3. The resistance furnace is 32.5 cm long and the quartz furnace tube 55 mm in diameter.

The top part of the quartz substrate holder was 20 x 2.5 cm and had a curved bottom which permitted

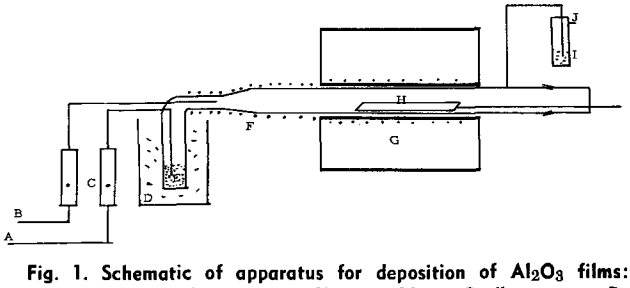

Fig. 1. Schematic of apparatus for deposition of Al_2O_3 films: A, dry N_2; B, dry N_2, O_2, or $90N_2 + 10H_2$; C, flowmeters; D, constant temperature bath; E, aluminum tri-isopropoxide; F, heating mantle; G, tube furnace; H, substrate holder; I, oil bubbler; J, exhaust.

its positioning on the bottom part of the furnace tube. All gases flowed only on the top part of the substrate holder. The temperature of the uniform hot zone on top of the substrate holder (the deposition temperature of Al_2O_3 films) was measured with a chromel-alumel thermocouple, the junction of which rested on it; this temperature was calibrated against the temperature obtained with a thermocouple situated inside the substrate holder. During deposition of Al_2O_3 films, only the temperature inside the substrate holder was recorded.

Formation of Al_2O_3 films.—The parameters involved in the deposition of Al_2O_3 films are the vapor pressure of aluminum tri-isopropoxide, deposition temperature, total flow rate of gases, and geometry of the sample holder and tube where the reaction takes place.

The aluminum tri-isopropoxide temperature was kept at 125°C. The amount of organic vapors transported by the gases was changed by varying the gas flow bubbling through the liquid. Aluminum tri-isopropoxide starts to crack at around 270°C in nitrogen, and at about 250°C in oxygen. At higher temperatures, deposition of the oxide occurs ahead of the zone of interest. The deposition at higher temperatures was made possible by using a high gas velocity so that cracking and/or deposition occur in the zone of interest. The total flow rate does have an effect on the rate of deposition of the oxide. Deposition rates of 100 Å/min could be obtained at 420°C when the total gas flow was 10 l/min. This had to be increased to 30 l/min for deposition at 600°C. The deposition rate is dependent also on the geometry of the reaction tube and substrate as these affect the flow pattern of the gases. Everything being equal, depending on the vertical positioning of the substrate holder in the furnace tube, different deposition rates were obtained. The highest deposition rate was obtained when the substrate holder was sitting on the bottom part of the furnace tube so that all gases flowed on top of it.

Film etch rates.—The etch rate of Al_2O_3 films deposited on germanium or silicon was measured by observing visually the change in interference colors on the basis of the color chart used for SiO_2 (11) adjusted for the refractive index of the Al_2O_3 film in question. The reproducibility obtained indicates that the method gives satisfactory relative values of etch rate. Two etchants were used: H_3PO_4 (85%) at 55°C and buffered HF (113g NH_4F, 22.7 cc HF 48%, and 166 cc of H_2O).

Index of refraction.—The index of refraction of Al_2O_3 films was determined by comparison with liquids of known index of refraction using the method described by Lewis (12).

Dielectric measurements.—Al_2O_3 films, 2000Å thick, were deposited on p-type germanium substrates of 0.0013-0.0015 ohm-cm resistivity. Aluminum dots, 30 mils in diameter and 5000Å thick, were evaporated through a mask over the oxide, and a film of aluminum of the same thickness was deposited on the back side of the sample. The specimen was held down by a vacuum chuck on a stage that served as one terminal of the measuring circuit (Fig. 2). The other terminal was a metal probe brought into contact with any dot by means of a manipulator. The stage was provided with a heater and an insulating cap so that the dielectric properties could be measured as a function of temperature; the temperature was measured near the aluminum dot studied by means of a chromel alumel thermocouple.

The equipment used for measurement of dielectric properties was a General Radio, Model 716-C, Schering-type bridge, generator, and detector instruments. The substitution method was used to obtain a bridge balance. The dissipation factor and capacitance of the specimen were obtained in a straightforward manner from the bridge balance conditions. The instrument allows an accuracy for the calculated capacitance of

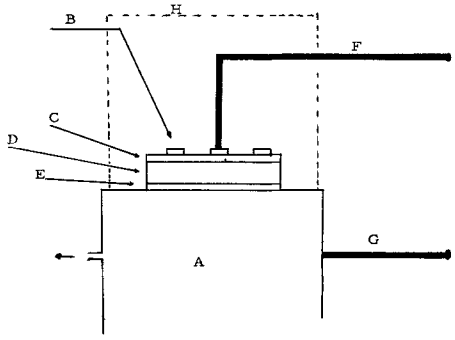

Fig. 2. Experimental set-up for measurement of dielectric properties (not to scale): A, aluminum hot stage connected to vacuum; B, aluminum dots 0.026 in. diameter 5000Å thick; C, Al_2O_3 film, approx. 2000Å thick; D, p-Ge 0.0013 ohm/cm; E, aluminum film; F, G, leads connected to measuring circuit (General Radio Bridge or to V-I circuit); H, insulating cap.

2 $\mu\mu$f or 0.2% whichever is greater and for the calculated dissipation factor 5 x 10^{-5} or 2% error whichever is larger. From the known area of the aluminum dot, and the thickness of the oxide near it as measured by double beam interferometry after etching a step, it was possible to calculate the relative dielectric constant [$k' = 3.6\ \pi t(C/A)$, t = thickness in cm, C capacitance in $\mu\mu$F, A area in cm^2], the loss factor and the a-c conductivity. Dielectric values reported are the average of at least three readings on a film and for at least three wafers.

V-I characteristics.—The same specimen geometry used for the dielectric measurements was used to obtain V-I characteristics of the oxide. A type 531 Tektronix oscilloscope with a type-0 operational amplifier plug-in unit equipped with a leakage current adapter was used. A sawtooth voltage drove the adapter, and a V-I curve was obtained on the scope.

Results and Discussion

Effect of gas ambient, temperature, and deposition rate on films.—Starting with a clean furnace tube, reproducible deposition rates of Al_2O_3 films at 420°C were obtained only after several hours of deposition. This decrease in rate of deposition in the 420° zone might be due to an increase in the decomposition rate of the incoming organic vapors because of the high surface area and/or the catalytic effect of oxide powders already deposited ahead of the hot zone. This effect was found to be more pronounced in the deposition of aluminosilicate films, obtained from the simultaneous decomposition of aluminum tri-isopropoxide and tetraethylorthosilicate, where the rate decreased to zero (13).

The rate of deposition of Al_2O_3, at equilibrium, on germanium or silicon substrates as a function of gas flow through aluminum tri-isopropoxide and for a total gas flow of 10 l/min, at 420°C is shown in Fig. 3. This rate increases with the increase of the concentration of oxygen of the gases and with the amount of aluminum tri-isopropoxide transported. The aluminum alkoxide can absorb sufficient thermal energy to cause bond rupture and formation of (Al-O) species in a nitrogen atmosphere. The oxygen content in the molecule is sufficient to form Al_2O_3. The oxygen apparently assists the process of decomposition of the organic molecule and influences the rate of deposition. While the deposition rate in nitrogen seems to become flow independent at about 2 l/min, that of oxygen is still linear at this flow.

The gaseous products evolved during the decomposition in nitrogen of aluminum tri-isopropoxide are most probably similar to those obtained for the decomposition of tetraethylorthosilicate (14). In oxygen, water vapor would also be formed. Infrared analysis of the Al_2O_3 films (Perkin Elmer Model 21 double beam spectrometer) do not show any water absorption

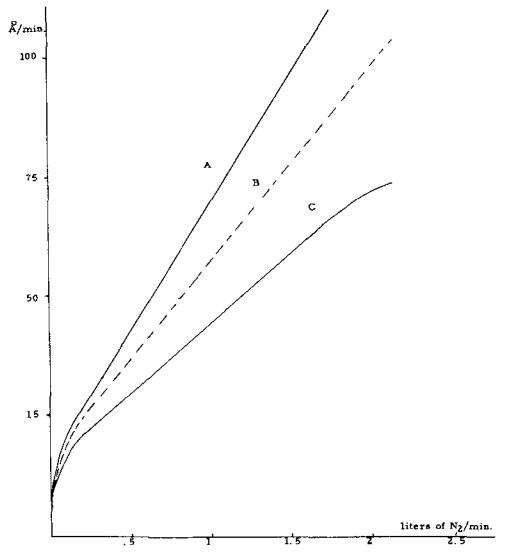

Fig. 3. Deposition rate of Al_2O_3 as a function of gas flow through $Al(OR)_3$. Temperature 420°C; total flow of gases 10 l/min: A = 83% O_2; B = 3% O_2; C = N_2 or 90N_2 + 10H_2.

band; thus, if water is formed during reaction, it is not incorporated in the oxide deposited.

Films deposited at 270°C are mechanically soft and can be easily scratched with a steel point. Their etch rate is one order of magnitude higher than those deposited at 420°C. Their dielectric properties are poor. The oxides studied below were deposited at 420°C in various ambients at a rate of 67 Å/min. It is possible to obtain deposition rates of over 100 Å/min, but the quality of the oxide deteriorates. Hazy looking oxides are deposited and a microscopic examination shows a very porous structure. These oxides have a faster rate of etching, *i.e.*, for O_2-deposited Al_2O_3, the etch rate in phosphoric acid at 55°C is 200 and 325 Å/min for deposition rates of 33 and 330 Å/min, respectively. The oxide deposition rate is linear with time and is not influenced by the amount of oxide already on the substrate.

Structure of films.—(*a*) *As-deposited.*—Oxide films deposited at 420°C, on ¾ in. diameter germanium or silicon wafers were clear, transparent, and hard. Thickness variation from one edge of the wafer to the other was less than 10%. The maximum thickness obtained without cracking of the film on a germanium substrate was approximately 1μ. A 7500Å thick film could be thermally cycled between 25° and 800°C without developing line cracks.

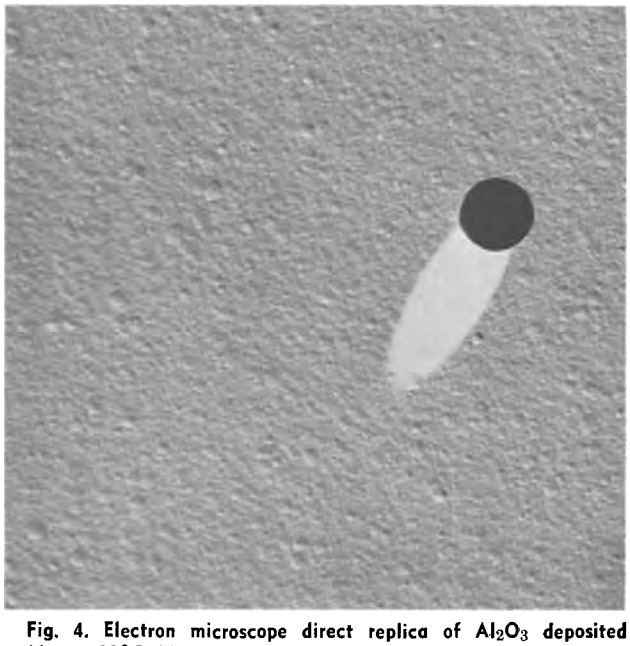

Fig. 4. Electron microscope direct replica of Al_2O_3 deposited in N_2 at 420°C. Magnification *ca.* 20,000X.

Table I. Properties of oxide films

Films deposited at 420°C, rate: 67 Å/min	Etch rate Å/min H_3PO_4 55°C	Etch rate Å/min buff. HF r. t.	Index of refraction	Dielectric constant
90 N_2-10 H_2	160	635	1.610 ± 0.006	7.7
N_2	180	820	1.600 ± 0.004	7.7
O_2	210	1000	1.594 ± 0.006	7.7
SiO_2 (low-temperature oxygen process)		1700	1.454	4.9

No structure could be detected with the optical microscope. Electron micrographs of 2000Å thick Al_2O_3 films show a uniform texture of spots, the bigger being about 1000Å in diameter (Fig. 4). These raised spots (about a few tens of Angstroms high) are seen over the entire wafer, for the N_2-deposited oxide as well as for the O_2-deposited oxide. These spots are very thin platelets and not spheres; 1000Å in diameter spots are seen when 500Å thin films are deposited. It is interesting to note that the surface of Al_2O_3 films deposited at 270°C, as seen at the electron microscope, is very smooth. It is suggested that at 420°C deposition of very fine particles occurs on top of the wafer, particles formed on cracking of the aluminum triisopropoxide prior to reaching the substrate zone in the furnace. However, the structure obtained is not porous as will be shown later.

Electron diffraction of the films deposited at 420°C shows a pattern of diffuse rings.

(*b*) *After heat-treatment.*—On heating these oxides in argon, structural and physical property changes occur. For a heat-treatment at 600°C for 1 hr, diffuse electron diffraction patterns are still obtained. After 1 hr at 800°C three phases are detected, amorphous, γ'-Al_2O_3 and γ-Al_2O_3 (respectively, fcc and spinel structure with lattice constant 3.95 and 7.9). After a 3-hr heat-treatment, only the γ and γ' phases are detected. Anodized Al_2O_3 at room temperature on heat-treatment is transformed to the γ-phase. The γ'-phase is obtained on anodization at 100°C (15).

Etching.—The Al_2O_3 films deposited at 420°C are insoluble in water, but are soluble in bases and acids. Etch rates in angstroms per minute, in phosphoric acid at 55°C, and in buffered HF at room temperature are shown in Table I. Oxides deposited on germanium etch uniformly down to the substrate as could be seen by successive electron micrographs of the resulting surface. The etch rate, in buffered HF, of the oxide deposited in forming gas is lower than that deposited in oxygen (635 and 1000 Å/min). For comparison purposes, etch rates of SiO_2 films deposited at the same rate and at the same temperature *via* thermal decomposition of tetraethylorthosilicate in oxygen are shown.

Table II. Properties of heat-treated Al_2O_3 deposited in N_2 atmosphere

	Etch rate Å/min H_3PO_4 55°C	Etch rate Å/min buff. HF r. t.	Index of refraction	Structure
As deposited at 420°C in N_2	180	820	1.600	Amorphous
Heat-treated at 600°C in argon, ½ hr	125	570	1.620	Amorphous
Heat-treated at 800°C in argon, ½ hr	85	265	1.640	Partially crystalline
in argon, 3 hr		insoluble	—	Crystalline
Heat-treated at 1000°C in argon, ½ hr		insoluble	>1.7	Crystalline

Films deposited in nitrogen at 420°C were heat-treated at various temperatures and for different lengths of time. The etch rate, in buffered HF and in H_3PO_4 at 55°C, decreases with increase temperature of heat treatment as shown in Table II. This is in agreement with the observed change in structure. After a 3-hr heat-treatment at 800°C the oxide is insoluble in both etchants. Only hot phosphoric (200°C) dissolves it.

Index of refraction.—The index of refraction, shown in Table I, is definitely higher (1.610) for films deposited in forming gas than in oxygen (1.594) and increases as a function of the temperature of heat-treatment until it reaches the index of polycrystalline Al_2O_3. The index of refraction of the as-deposited film is comparable to that of Al_2O_3 prepared by thermal evaporation using electron bombardment of polycrystalline alumina ($n = 1.60 \pm 0.01$) (4). The index of refraction reported in the literature for anodized Al_2O_3 is higher (15, 16). Dorsey (17) shows the anodized layer to be a hydrated Al_2O_3.

Masking properties.—Aluminum oxide thin films on germanium can be used for masking of n-type dopants such as antimony and arsenic at 700°C. At 800°C, a 2200Å thick film of Al_2O_3 on germanium mask gallium and indium (surface concentration of gallium 5 x 10^{19} atoms/cc; of indium 4 x 10^{18} atoms/cc) for 1 hr only. Aluminosilicate films provide somewhat better masking (13). Films with an alumina content, ranging between 70 and 90 w/o (weight per cent) act as mask against gallium for 3 hr; this range is extended to 97 w/o for indium.

Surface electrical properties.—It is known that the presence of SiO_2 on silicon tends to make the surface of silicon more n-type independent of the bulk conductivity type (18). Differences between forming gas, N_2-deposited and O_2-deposited Al_2O_3 and SiO_2 (low-temperature oxygen type, high-temperature nitrogen type) are noted when studying the surface properties of silicon and germanium covered with Al_2O_3. Metal-oxide-semiconductor measurements show that a more p-type surface occurs under forming gas or N_2-deposited Al_2O_3, while a neutral or more n-type occurs under O_2-deposited oxide (19). Enhancement mode npn field effect devices on 8 ohm-cm silicon were made using N_2-deposited Al_2O_3 while npn depletion mode devices were obtained with O_2-deposited Al_2O_3. After a heat-treatment in nitrogen, at 350°C for 2-hr, the threshold voltage was about +5v in the first case and −1v in the second (20).

Dielectric properties.—*(a) Films as-deposited and after heat-treatment.*—The dissipation factor (Fig. 5) increases as a function of the oxygen in the gas flow and is not particularly sensitive to the frequency range measured (100 cycles to 100 kc) for the oxide deposited in a neutral or reducing ambient. Some results are given in Table III. The dissipation factor for O_2-deposited Al_2O_3 is much higher (~0.75%) than that for Al_2O_3 deposited in lightly oxidizing or reducing atmospheres (*i.e.*, 0.3%). The dissipation factor of SiO_2 films deposited in oxygen at 420°C in the same conditions is shown for comparison. The dissipation factor decreases very slightly from 0.26 to 0.20% for Al_2O_3 films deposited in nitrogen when these are heat-treated to 420°C. A large decrease (from 0.75 to 0.22%) down to the dissipation factor of N_2-deposited films is observed for the same treatment for the O_2-deposited oxide. The capacitance change for the O_2-deposited oxide (3%) is higher than that for the N_2-deposited oxide (1%) (Fig. 6). After heat-treatment to 420°C, the resulting capacitance change is the same, about 1%, for all oxides. On heat-treatment of the O_2-deposited SiO_2 oxides, the dissipation factor drops from 0.16 to 0.09%. The dissipation factor of these Al_2O_3 films compares favorably with anodized aluminum capacitors (21, 22).

The dissipation factor and capacitance change as a function of temperature at 1 kc are shown in Fig. 7.

Table III. Dielectric properties of Al_2O_3 and SiO_2 films at 1 kc. Thickness: approximately 2000Å*

	N_2-Al_2O_3	O_2-Al_2O_3	O_2-SiO_2
Dissipation factor of film as deposited	0.26	0.76	0.16
Dissipation factor after heat-treatment to 420°C, ½ hr	0.22	0.25	0.09
Capacitance change of film as deposited (from 0.1 to 1 kc)	0.5	1.2	
As above + heat-treatment to 420°C, ½ hr	0.5	0.5	
Dissipation factor change from room temperature to 85°C	0.35		
Capacitance change from room temperature to 85°C	1.2		

* All figures in %.

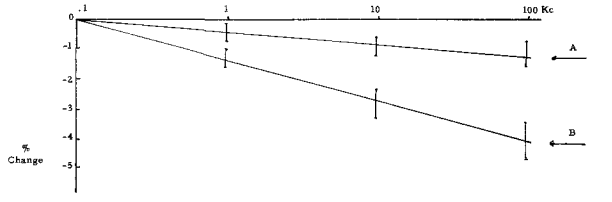

Fig. 6. Capacitance change as a function of frequency for Al_2O_3 films: A = N_2 or 90N_2-10H_2; B = 83% O_2.

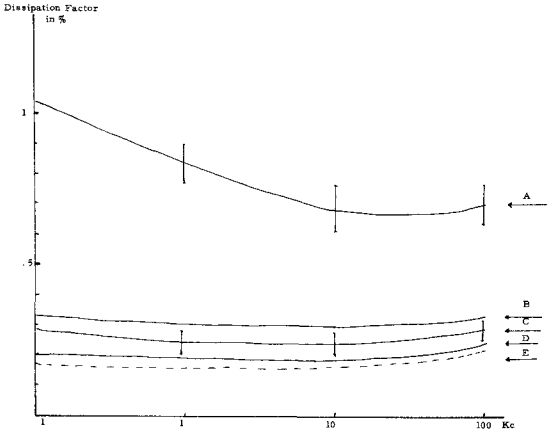

Fig. 5. Dissipation factor as a function of frequency for Al_2O_3 films (A,B,C,D) and for low-temperature SiO_2 films (E): A = 83% O_2; B = 3% O_2; C = N_2; D = 90N_2-10H_2; E = SiO_2.

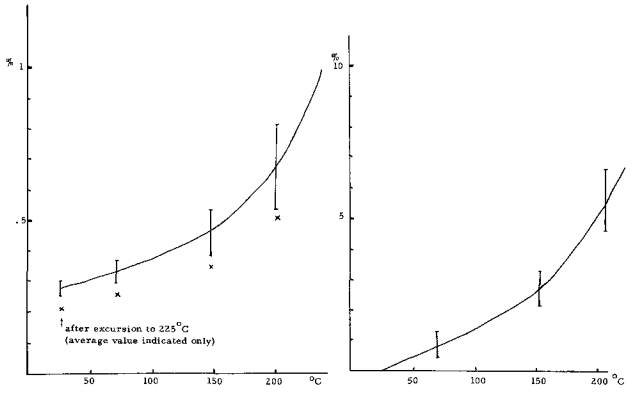

Fig. 7. *(left).* Dissipation factor (%) at 1 kc of N_2-Al_2O_3 films as a function of temperature. *(Right).* Capacitance change (%) at 1 kc of N_2-Al_2O_3 films as a function of temperature.

The retrace of the dissipation factor as a function of temperature after excursion to 220°C is also shown. The capacitance change is the same, before and after excursion to 220°C.

The dielectric constant of the as-deposited films is 7.7 ± 0.3. It was not possible to differentiate between the O_2-deposited Al_2O_3 and the N_2-deposited oxide. After heat-treating at 800°C for 1 hr, the measured dielectric constant was 8.5 very near to the value for crystalline Al_2O_3 (23).

From the dielectric constant and the dissipation factor, at 350°C, the a-c conductivity of Al_2O_3 oxide was calculated. At 350°C, the value calculated, 2×10^{-10} ohm^{-1} cm^{-1}, is in the range of values obtained by various workers for polycrystalline Al_2O_3 (24).

The dielectric breakdown of the Al_2O_3 films is better than 3×10^6 v/cm. Typical V-I characteristics gives 1 mμa at 55v for a 2000Å thick film. It was noted that sharper breakdown occurred for Al_2O_3 deposited in a reducing ambient than in an oxidizing atmosphere. A higher breakdown (6×10^6 v/cm) for N_2-deposited Al_2O_3 films is obtained after a heat-treatment at 800°C.

(b) *Effect of humidity.*—The dielectric properties of Al_2O_3 films were studied after a treatment of 22 days in a 100% relative humidity ambient at room temperature. The dielectric properties are similar to the non-treated specimen. On the contrary, O_2-deposited SiO_2 for the same treatment degrades and gave very poor dielectric characteristics.[1] Al_2O_3 films have thus the advantage of being resistant to moisture; they are superior to SiO_2 films deposited at low temperature and could be used as passivating films.

The high dissipation factor and the relatively large change in capacitance of the oxygen-deposited oxides might be due to water vapor formed during the cracking process. The reduction in the dissipation factor as well as the capacitance change on heating the specimen to high temperatures would support such a conclusion. However, infrared measurements did not show any OH absorption band after deposition. No OH band was detected after treating Al_2O_3 specimens for 22 days, at 25°C, in a 100% relative humidity ambient.

It might be possible to explain the difference in terms of an oxygen sorption mechanism. During deposition of Al_2O_3 in oxygen, incorporation of oxygen in the oxide takes place. The resulting film would be more "porous" in respect to Al_2O_3 deposited in nitrogen. This would explain the higher etching rate and the lower index of refraction of the oxide. The higher dissipation factor of the O_2-oxide and its increase with the oxygen pressure would be accounted for by the polarization of the oxygen. On heating the oxide in air, desorption of oxygen takes place with consequent reduction of the dissipation factor. A mass spectrometric study of the gas evolved on heating the oxide in high vacuum would probably shed some light on this problem.

[1] Actually cracking of SiO_2 on Ge occurred after the treatment in moist ambient. No cracking occurs when SiO_2 films are deposited on Si; the dissipation factor increases, however (25). Aluminosilicate films, of high SiO_2 content (13), also show some cracking and increase dissipation factor after the treatment in moist ambient.

Conclusion

Aluminum oxide thin films obtained by cracking of aluminum tri-isopropoxide at low temperature have shown some superior characteristics when compared to SiO_2 films obtained by a similar process in the same conditions. These films compare favorably with anodized Al_2O_3. The resistance of Al_2O_3 to moisture, its dielectric properties, and the different surface electrical properties it confers on germanium and silicon according to the deposition atmosphere make it quite attractive.

Acknowledgment

Thanks are due to Dr. T. O. Sedgwick for his many conversations, for reviewing the manuscript and for the MOS measurements, to C. F. Aliotta for the electron micrographs, to Mrs. S. Herd for the electron diffraction experiments, to P. Gansauge and H. N. Yu for the diffusion experiments. The technical assistance of W. J. Mesimer is particularly appreciated.

Manuscript received Feb. 27, 1967; revised manuscript received June 2, 1967.

Any discussion of this paper will appear in a Discussion Section to be published in the June 1968 JOURNAL.

REFERENCES

1. E. L. Jordan, *This Journal*, **108**, 478 (1961).
2. S. Krongelb and T. Sedgwick, Paper presented at the Cleveland Meeting, May 1966, Abstract No. 113.
3. Al_2O_3 data sheets, Electronic Properties Information Center, Hughes Aircraft Co., DS136, March 1964.
4. J. M. Woulbroun, Thesis, M.I.T., 1963.
5. L. H. Kaplan, *Electrochem. Technol.*, **3**, 335 (1965).
6. R. G. Frieser, *This Journal*, **113**, 357 (1966).
7. N. K. Tvorogov, *Zr. P. Kh XXXII*, **10**, 2203 (1961).
8. P. Robinson, U.S. Pat. 2,805,965, Sept. 10, 1957; F. O. Deutscher, U.S. Pat. 2,972,555, Feb. 21, 1961.
9. Beilstein Handbuch der Organischen Chemie Band 1, System 16-70, p. 1456, 1958.
10. R. A. Robinson and D. A. Peck, *J. Phys. Chem.*, **39**, 1128 (1935).
11. W. A. Pliskin and E. E. Conrad, *IBM J. Res. & Dev.*, **8**, 43 (1964).
12. A. E. Lewis, *This Journal*, **111**, 8, 1007 (1965).
13. Work in progress.
14. J. Klerer, *This Journal*, **112**, 504 (1965).
15. W. Ch.Geel and B. J. J. Schelen, *Philips Res. Rep.*, **12**, 240 (1957).
16. G. Hass, *J. Opt. Soc. Am.*, **39**, 7 (1949).
17. G. A. Dorsey, Jr., *This Journal*, **113**, 12, 169 (1966); **113**, 3, 284 (1966).
18. J. E. Thomas, Jr. and D. R. Young, *IBM Journal*, **8**, 368 (1964).
19. T. O. Sedgwick, Private communication.
20. E. C. Wurst and F. Hochberg, Private communication.
21. R. C. Merril and R. A. West, IEEE Meeting, S-224, 1965.
22. G. J. Tibol and W. M. Kaufman, *Proc. IEEE*, 1465, Dec. 1964.
23. Kingery, "Introduction to Ceramics," p. 106, John Wiley & Sons, Inc., New York (1960).
24. J. V. Florio, *J. Am. Ceram. Soc.*, **43**, 262 (1960).
25 S. Krongelb, Private communication.

Energy Transfer and Fluorescence Processes In Bi^{3+} and Eu^{3+} Activated YVO_4

S. Z. Toma, F. F. Mikus, and J. E. Mathers

Chemical and Metallurgical Division, Sylvania Electric Products Inc., Towanda, Pennsylvania

ABSTRACT

Fluorescence and excitation spectra of YVO_4:Bi and YVO_4:Eu,Bi are reported and discussed. Energy transfer from Bi^{3+} center to Eu^{3+} was observed. The absorption of Bi^{3+} in YVO_4, deduced from excitation spectra, is compared with other bismuth activated matrices.

Yttrium orthovanadate crystallizes in the tetragonal system of zircon ($ZrSiO_4$) with Y^{3+} and V^{5+} replacing Zr^{4+} and Si^{4+}, respectively. The uv properties of YVO_4:Eu phosphor have been studied extensively (1, 2), and its utility as a red emitting cathode-ray (cr) phosphor is now well known (3). In the present work we studied the luminescent properties of YVO_4 with and without various activators. In particular, we wish to report on the excitation and fluorescence spectra of YVO_4,YVO_4:Bi and YVO_4:Eu,Bi under both cr and uv excitations.

Experimental

Phosphors, as polycrystalline materials, were prepared by solid state reactions (3). UV emission and excitation spectra were measured with a Perkin-Elmer spectrofluorimeter (4). For cathodoluminescent measurements, the phosphors were settled on glass slides and irradiated with 12 kv electrons at 6 μa current. The fluorescence was recorded with a GE spectroradiometer using a 1P22 photomultiplier.

Results and Discussion

The fluorescence of various activators in YVO_4, their temperature dependence, and concentration quenching cannot be interpreted adequately without first attempting to understand the nature of the bonding among the three ions in YVO_4 itself. The broad excitation and emission spectra (Fig. 1) can be due to more than one electronic transition. Such transitions may be of the charge transfer type or among the molecular states of the VO_4^{3-} anions.

McClure (5, 6) discussed the series of isoelectronic tetrahedral ions MnO_4^{1-}, CrO_4^{2-}, VO_4^{3-}, TiO_4^{4-}, and reviewed the semiempirical calculations of the molecular orbital energies for MnO_4^{1-} and CrO_4^{2-} by Wolfsberg (7). The lowest allowed electronic transition was interpreted to be a charge transfer from a predominantly oxygen orbital to a 3d orbital. The long wavelength absorption in YVO_4 was attributed to such transitions from an experimental study of the $YV_{1-x}P_xO_4$ system (8). McGlynn and Kasha (9) studied the lowest electronic transitions of simple molecules of the type XO_y^{z-}, where O is an oxygen atom; X is a nonmetallic or a transition metal atom; y = 1, 2, 3, 4; z = 0, 1, 2, 3. The VO_4^{3-} spectrum was interpreted as $n \rightarrow \pi^*$ transition, where n is a nonbonding oxygen orbital and π^* is the antibonding molecular orbital of the whole anion.

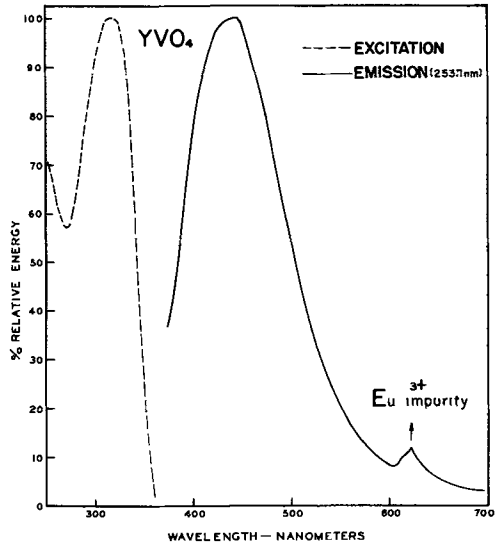

Fig. 1. Excitation and emission (253.7 nm) spectra of YVO_4

A process that can be of significance in YVO_4 is that of a charge transfer from an atomic or molecular orbital of the anion to Y^{3+}. The importance of such transitions depends on the nature and strength of the bonds in the VO_4^{3-} ion. If the latter is not a tight molecular entity, then YVO_4 woull not be appropriately considered a lattice of molecular ions but rather should be relatively more ionic in nature (6). This may enhance charge transfer processes to Y^{3+} and contribute to the formation of exciton and band processes.

A comparison of electronic spectra of MnO_4^{1-}, CrO_4^{2-}, and VO_4^{3-} suggests that the VO_4^{3-} ion is a much less tightly bound molecular unit (5, 6). IR spectra of these ions support this conclusion. The stretching force constants f_r of the M-O bond (M: transition metal) for these ions were calculated using the simple harmonic oscillator approximation (10). The results are shown in Table I which also includes the PO_4^{3-} ion. An average of the two observed stretching frequencies belonging to the A_1 and F_2 species was used. The value of f_r obtained in this manner for the PO_4^{3-} ion is in fair agreement with that calculated for YPO_4 by Wilson's GF matrix method (13). Table I indicates clearly that the V-O bond is the weakest, supporting the conclusion derived from the electronic spectra of these transition metal ions.

From a study of the molecular vibrations of tetrahedral XO_4 ions at a site symmetry D_{2d} and a consideration of the zircon structure, it was shown (13, 14) that, in YVO_4, π-bonding orbitals of a specific VO_4^{3-} ion may overlap two different Y^{3+} along the S_4 axis and, therefore, along this axis there should be a continuous overlap of π-bonding orbitals of the VO_4^{3-} group and the orbitals of Y^{3+}. This geometric and electronic coupling should contribute to a band

Table I. Fundamental frequencies (cm^{-1}) and stretching force constants (10^{-5} x dynes/cm)

Ion	$\nu_1(A_1)$	$\nu_3(F_2)$	f_r(M-O)
VO_4^{3-} (11)	824	790	4.7
CrO_4^{2-} (11)	847	884	5.4
MnO_4^{-1} (11)	845	910	5.6
PO_4^{3-} (12)	980	1082	6.6

process in YVO_4. It also may allow one to consider the S_4 axis as one large molecule and interpret some aspects of the absorption and transfer of energy as intramolecular process.

The applicability of the term "charge transfer" must decrease as the initial and final orbitals of the various ions become less localized. This delocalization can be dominant in YVO_4; hence, molecular orbitals and band processes should be more appropriate in attempting to understand the various effects in this phosphor. Addition of 0.025 m/o (mole per cent) Eu^{3+} reduces its emission peak height by about 60% under cr excitation and with 0.008% Bi^{3+}, 35% quenching was observed. Comparable effects were obtained with Tm^{3+} and Dy^{3+} additions. These results do suggest that the excited states in YVO_4 are quite mobile, and an efficient energy transfer and migration through an extended region of the crystals exists. Exciton motion, exchange effects, and nonradiative (dd) and (dq) resonance energy transfer (15) can occur and account for this efficient transport of energy. The relative importance of the various modes of transfer is difficult to ascertain from the present work.

The absorption of YVO_4 in the 360 nm region was postulated as a charge transfer transition in the V-O bond (8). This conclusion was based on the absorption spectra of the system $YV_{1-x}P_xO_4$:Eu, where the substitution of PO_4^{3-} for VO_4^{3-} ions reduced the absorption in the 3600Å region. This decrease in absorption can also be understood as a dilution effect (16). The broadness of the VO_4^{3-} (or YVO_4) band may be decreased by dilution with PO_4^{3-} (or YPO_4) ions. Similar effects were observed in $KMnO_4$, *i.e.*, band broadening in the MnO_4^- spectrum when the ion is in pure $KMnO_4$ compared to the spectrum in dilute solid solution with, for example, $KClO_4$. This effect should be even more enhanced in YVO_4 if we consider the nature of the bonding in VO_4^{3-}, as discussed earlier.

The characteristic oxidation state of bismuth is very often Bi^{3+}. The ion has $6s^2$ outer electrons, and its radius is comparable to trivalent yttrium. The effect of its utility as an activator in YVO_4 is shown in Fig. 2. This broad emission is relatively intense, and its brightness is comparable to the presently used low-pressure mercury lamp phosphors of approximate color. Its brightness decreases at elevated temperatures.

As to how Bi^{3+} addition modifies the energy levels of YVO_4, one must start with its substitution as a matrix cation for Y^{3+} and, therefore, any transitions involving Y^{3+} should also be considered for Bi^{3+}. Since the latter also possesses outer $6s^2$ electrons, we must also consider $s^2 \rightarrow sp$ transitions. The extensive theoretical and experimental work on such transitions of isoelectronic Tl^{1+} in alkali halides is well known (15, 17). The exposed nature of these outer electrons induces interactions with the neighboring anions in solids. The energies of the localized states of Tl^+ are, thus, usually treated as a function of the anion coordinates which interact differently with the ground and excited states of Tl^+. The center is, then, treated as a polyatomic molecule and configuration coordinate diagrams are used to compute the energies of the various electronic transitions. The absorption and emission of the Bi^{3+} center in YVO_4 is attributed to similar transitions, *i.e.*, $6s^2 \rightarrow 6sp$ and the interaction of the anions of the matrix with the singlet S ground and triplet, singlet P excited states of Bi^{3+}.

The excitation and fluorescence spectra of YVO_4:Eu were discussed by several investigators, as noted earlier. We studied the effects of bismuth addition to this phosphor. Since both Bi^{3+} and Eu^{3+} are primary activators, the excitation and emission spectra of YVO_4:Eu,Bi depend on the relative concentrations of the two additives. Examination of the excitation spectra of YVO_4:Eu and YVO_4:Eu,Bi for the $^5D_0 \rightarrow {}^7F_2$ transition of Eu^{3+} at 619 nm (Fig. 3) shows that the two curves cross at about 340 nm. Thus, Bi^{3+} addition to YVO_4:Eu enhances the 619 nm emission under 340 or longer wavelength excitations. This enhancement is interpreted as evidence of energy transfer from the Bi^{3+} center to Eu^{3+}. Note that at 320 nm, the excitation peak of pure YVO_4, Eu emission decreases.

Bismuth addition must increase the absorption coefficient of the phosphor with 340 nm and higher wave length excitation. Figure 4 clearly indicates this, where the peak at about 340 nm is attributed to Bi center absorption. The absorption of the latter in SrO:Bi was observed at 367.2 nm and higher energies (18). In the molten LiCl-KCl eutectic containing $BiCl_3$, Bi absorption is at 330.6 nm with a molar extinction coefficient of 7000 l/mole·cm (19). This absorption is not very different from that observed in YVO_4 and suggests that $s^2 \rightarrow sp$ transitions play a dominant role in the electronic transitions of the Bi^{3+} center in YVO_4.

The increase in the fluorescence intensity of Eu^{3+} with Bi^{3+} coactivation is due to energy transfer from the Bi^{3+} center to Eu^{3+} as mentioned earlier. Such transfer, in the absence of movement of charge carriers, can occur by radiative cascade and nonradiative resonance transfer as well as the short-range exchange mechanism. The conditions and characteristic properties of these various modes of transfer are discussed elsewhere (15, 20, 21). The broad emission of YVO_4:Bi

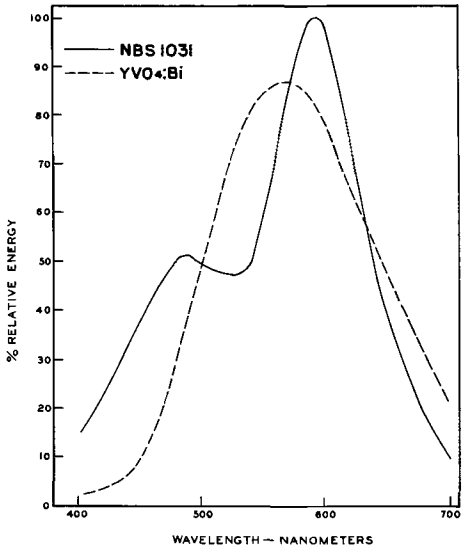

Fig. 2. Emission spectra of YVO_4:Bi (4 m/o) and calcium halophosphate NBS standard 1031 with 253.7 nm excitation.

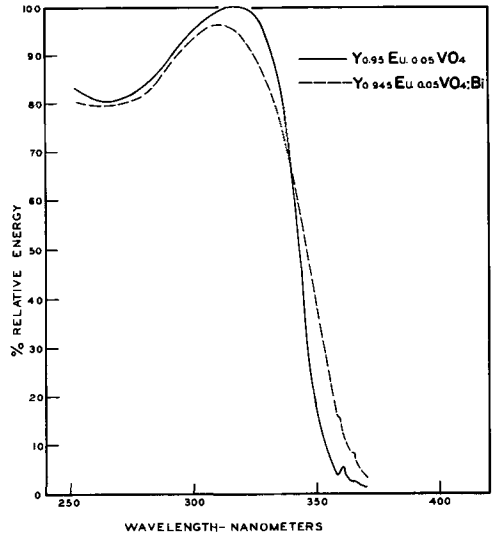

Fig. 3. Relative excitation spectra for the 619 nm Eu^{3+} emission of $Y_{0.95}Eu_{0.05}VO_4$ and $Y_{0.945}Eu_{0.05}VO_4$:Bi (0.5 m/o).

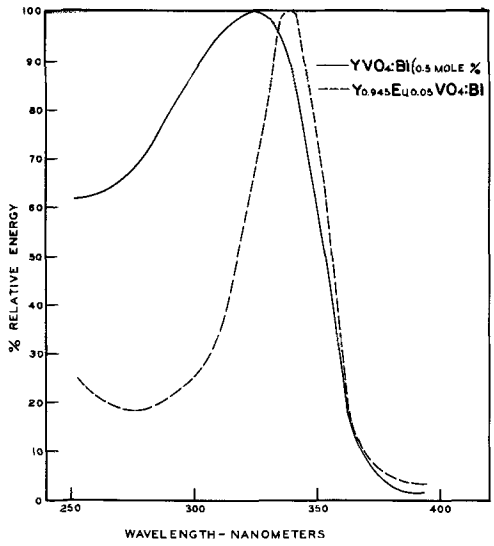

Fig. 4. Excitation spectra for the 550 nm Bi^{3+} center emission YVO_4:Bi (0.5 m/o) and $Y_{0.945}Eu_{0.05}VO_4$:Bi (0.5 m/o).

does not show any sharp depressions (missing lines corresponding to Eu^{3+} absorption) with Eu^{3+} coactivation and, since the latter absorbs weakly in this spectral range, energy transfer by the cascade process cannot be significant here and nonradiative resonance transfer should dominate.

To study the partition of excitation energy between Bi^{3+} and Eu^{3+}, the intensity of Bi^{3+} emission (peak height) with increasing content of Eu^{3+} was measured under 255, 300, and 337 nm excitations. Table II summarizes the results. On addition of Eu^{3+} to YVO_4:Bi the intensity of Bi^{3+} emission decreases under all three uv excitations. However, with 255 and 300 nm the decrease is more pronounced than under 337 nm. Hence, the ratio of the Bi^{3+} peak height with 337 nm over that for 300 or 255 nm increases with increasing concentration of Eu^{3+}. These results can be understood if we consider that 255 and 300 nm energy initially excites the matrix YVO_4 followed by competition for this energy by Eu^{3+} and Bi^{3+} centers. Under 337 nm excitation some of the energy is directly absorbed by the Bi^{3+} center (Fig. 4) and, thus, does not undergo competition with Eu^{3+}. These results should be useful in studying the nature and relative efficiencies of energy transfer from excited YVO_4 to Eu^{3+} *vs.* that for Bi^{3+} center.

The increase in Eu^{3+} emission on addition of Bi (Fig. 3) was used to indicate energy transfer between the two activators. However, even in the absence of such increase this transfer can still occur as long as one observes the characteristic Bi emission. Under cr excitation YVO_4:Eu,Bi is brighter than YVO_4:Eu (5 m/o Eu^{3+}). At very low concentrations of Bi (~500 ppm) the increase in brightness is due to a relatively slight enhancement of Eu emission as well as the appearance of the yellowish white fluorescence of Bi^{3+}, the extent of each effect being very dependent on the relative concentrations of the two activators. At high concentrations of Bi^{3+} (0.5 m/o) the Eu emission decreases with an increase in Bi emission. As in the case of uv excitation, energy transfer can occur from the Bi^{3+} center to Eu^{3+}.

Table II. Relative peak heights of YVO_4:Bi (0.5 m/o) emission under 255, 300, and 337 nm excitations with increasing Eu^{3+} concentration

Eu^{3+}, m/o	Relative peak heights	
	337/300	337/255
0	1.05	1.42
0.05	1.13	1.47
0.10	1.24	1.62
0.20	1.49	1.97
0.50	1.96	2.50

Addition of 0.5 m/o Bi^{3+} to $Y_{0.95}Eu_{0.05}VO_4$ decreases the 619 nm Eu^{3+} emission under both 320 nm and cr excitations. These effects may be related if we consider the nature of energy loss of fast electrons in matter (22). The retardation of incident electrons (primaries) occurs by detachment of electrons (secondaries) from the lattice ions. The secondary electrons, in turn, excite the matrix. The activator (Eu^{3+}) absorbs this excitation energy directly from these secondary electrons and indirectly from the excited matrix by some mode of energy transport. If we assume that with 320 nm excitation, the peak of the excitation spectrum of YVO_4 matrix, the energy is substantially absorbed by the matrix and eventually is transferred to the activator (Eu^{3+}), then, this process is similar to that discussed for cr excitation.

Bismuth addition may decrease the efficiency of energy transport from matrix to Eu, perhaps by distorting the former. Such distortion can be understood from comparing the chemical and electronic nature of Bi^{3+} and Y^{3+} ions and the fact that $BiVO_4$ does not have the zircon structure. The above decrease in Eu^{3+} emission with Bi^{3+} addition can also be due, at least partially, to simple competition for the matrix excitation energy between the two activators. Such competition is not sufficient to interpret these effects, since with smaller amounts of Bi^{3+} coactivation a slight increase in Eu^{3+} emission was observed under cr excitation, as discussed earlier.

Manuscript received June 6, 1967. This paper was presented at the Dallas Meeting, May 7-12, 1967.

Any discussion of this paper will appear in a Discussion Section to be published in the June 1968 JOURNAL.

REFERENCES

1. L. G. Van Uitert, R. C. Linares, R. R. Soden, and A. A. Ballman, *J. Chem. Phys.*, **36**, 702 (1962)
2. L. H. Brixner and E. Abramson, *This Journal*, **112**, 70 (1965).
3. A. K. Levine and F. C. Palilla, *Appl. Phys. Letters*, **5**, 118 (1964).
4. W. Slavin, R. W. Mooney, and D. T. Palumbo, *J. Opt. Soc. Am.*, **51** (1961).
5. D. S. McClure, *Solid State Phys.*, **9**, 399, 525 (1959).
6. D. S. McClure, "Electronic Spectra of Molecules and Ions in Crystals," part II, Academic Press Inc., New York (1959).
7. M. Wolfsberg and L. Helmholtz, *J. Chem. Phys.*, **20**, 837 (1952).
8. R. K. Datta, *Trans. Metal Soc. AIME*, **239**, 355 (1967).
9. S. P. McGlynn and M. Kasha, *J. Chem. Phys.*, **24**, 481 (1956).
10. K. Nakamoto, "Infrared Spectra of Inorganic and Coordination Compounds," p. 59, John Wiley & Sons, Inc., New York (1963).
11. B. Krebs and A. Muller, *J. Molecular Spectroscopy*, **22**, 290 (1967).
12. G. Herzberg, "Infrared and Raman Spectra," p. 167, D. Van Nostrand Company, Princeton, N. J. (1964).
13. R. W. Mooney and S. Z. Toma, *J. Chem. Phys.*, **46**, 3364 (1967).
14. R. W. Mooney and S. Z. Toma, *ibid.*, **46**, 4544 (1967).
15. C. C. Klick and J. E. Schulman, *Solid State Phys.*, **5**, 97 (1957).
16. Ref. (6), p. 100.
17. F. E. Williams, *J. Chem. Phys.*, **19**, 457 (1951).
18. Ref. (6), p. 170.
19. G. Pedro, D. W. James, and C. R. Boston, *J. Chem. Phys.*, **42**, 2249 (1965).
20. D. Dexter, *ibid.*, **21**, 836 (1953).
21. T. Foster, *Discussions Faraday Soc.*, **27**, 7 (1959).
22. D. Curie, "Luminescence in Crystals," chap. X, Methuen and Co., Ltd., London (1963).

Stoichiometry of Luminescent Apatites

J. G. Rabatin, G. R. Gillooly, and J. W. Hunter

Lamp Metals and Component Department, CPP, General Electric Company, Cleveland, Ohio

ABSTRACT

Total chemical analysis of luminescent apatite together with quantitative x-ray diffraction analysis for secondary phases have made it possible to delineate the maximum permissible nonstoichiometry. Based on the accuracy of the various methods and expressed as a deficiency of calcium, the extent of nonstoichiometry is less than the absence of one calcium in every 380 calcium sites. Quantitative experimental evidence is also presented to support the hypothesis for charge compensation of antimony by a corresponding oxygen substitution at halogen sites.

Stoichiometry of Luminescent Apatites

In a previous publication (1), the authors reported studies on the phase relationships of calcium halophosphate phosphor systems. Of major interest were pertinent compatibility triangles and tetrahedra. The question of the extent of nonstoichiometry of luminescent apatites was not explored. Previous publications which touch on this point have implied that the chemically measurable deficiencies or excesses of the various components of luminescent apatites were associated with gross defect structures. Ouweltjes and Wanmaker (2) suggested that halophosphates may be examples of phosphors requiring an excess of one of the components within the crystal lattice for highest efficiency. Strange (3) in considering the importance of imperfections to luminescence noted that halophosphates are improved by an excess of the acid radicals. Froelich (4) has observed from general experience that phosphor compositions are preferably nonstoichiometric. Ross (5) reported that improved halophosphates were obtained with halogen deficiencies of from 0.16 to 0.18 moles halogen per mole of apatite.

These publications would lead one to believe that fluorescence in calcium halophosphate phosphors was indeed associated with a gross defect structure, apparently one that was deficient in calcium or halogen ions. Some of the compositions mentioned by Ouweltjes and Wanmaker (2) should have one calcium empty out of every 10 calcium sites. The work of Posner and Perloff (6) would indicate that, in chemically precipitated hydroxyapatites, nonstoichiometry could exist even with calcium to phosphate ratios of 9 to 6. However, their studies do not prove conclusively the absence of secondary phases especially since they state that precipitated apatites are usually finely divided materials yielding x-ray diffraction patterns with broadened maxima. Under these conditions, the presence of a few per cent of secondary phases would be almost impossible to detect by either the optical or x-ray diffraction methods which they used.

Although calcium metaantimonate has been detected as a secondary phase (7) in most halophosphate phosphors, little attention was given to the possibility that other phases may also be present and thus contribute to the so-called "nonstoichiometry" of these phosphors. The present authors (8) have reported that under certain conditions calcium orthophosphate may be present. With the publication of phase studies (1) in this system, it becomes important to reexamine the extent of nonstoichiometry in halophosphate phosphors.

This paper deals with this general question. Experimental evidence is also presented to support the concept first proposed by Ouweltjes (9) that for trivalent antimony substitution in the apatite structure electrical neutrality is maintained by oxygen substitution for a halogen atom.

Methods

Total calcium as Ca (10, 11).—Calcium is determined volumetrically by back titration of an excess of EDTA with magnesium solution using a mixed Erichrome Black T-methyl red indicator. Manganese, which is also chelated, is determined colorimetrically, and the equivalent amount of EDTA used in complexing the Mn is subtracted from the total volume used. Results are accurate to within ±0.05 w/o (weight per cent) Ca.

Total phosphate as PO_4 (12).—After hydrolysis of any nonortho phosphate to the ortho form the phosphate is determined as the yellow molybdivanadophosphate complex by differential spectrophotometry. Results are accurate to within ±0.2 w/o PO_4.

Soluble antimony as Sb^{+3} (13, 14).—Antimony in the trivalent form is determined volumetrically by titration with potassium bromate using methyl orange indicator. The titration is based on the oxidation of trivalent antimony to the pentavalent form. Results are accurate to within ±0.01 w/o Sb.

Manganese as Mn (15).—Manganese is oxidized to permanganate using potassium periodate and determined colorimetrically with a spectrophotometer. Results are accurate to within ±0.02 w/o Mn.

Fluoride as F (16-19).—Fluorine is separated from interfering ions by steam distillation from perchloric acid solution as hydrofluo-silicic acid. The fluoride is then determined by titration with thorium nitrate using sodium alizarin sulfonate as indicator. Results are accurate to within ±0.05 w/o F.

Chloride as Cl (20-22).—Chloride is determined by a modification of the classical Volhard method. An excess of silver nitrate is added to form silver chloride and the excess back titrated with ammonium thiocyanate using ferric alum indicator. Results are accurate to within ±0.003 w/o Cl.

Calcium metantimonate as $Ca(SbO_3)_2$ (23).—Calcium antimonate or "acid insoluble" is separated by filtration from a hydrochloric acid solution and determined gravimetrically after ignition of the insoluble residue. Results are accurate to within ±0.02 w/o $Ca(SbO_3)_2$.

Calcium pyrophosphate as $Ca_2P_2O_7$ (12).—Calcium pyrophosphate as a secondary phase is determined by a modified differential spectrophotometric method as the molybdivanadophosphate complex. The phosphor is solubilized by agitating in a slurry of cation exchange resin and water. The resultant solution of halide and phosphate acids is separated from the resin by filtration. An aliquot of the filtrate is acidified and heated to hydrolyze the pyrophosphate to the ortho form. Equal size aliquots of the hydrolyzed and nonhydrolyzed solutions are treated with a mixed molybdate-vanadate solution to form the yellow molybdivanadophosphate complex. The hydrolyzed portion is compared spectrophotometrically against the nonhydrolyzed portion. Since the complex is formed with phosphate in the ortho form only, the hydrolyzed aliquot will possess a greater intensity of color that is directly proportional to the amount of Ca pyrophos-

phate that has been hydrolyzed. Results are accurate to within ±0.2 w/o $Ca_2P_2O_7$ as a secondary phase.

Calcium orthophosphate, $Ca_3(PO_4)_2$.—The method utilizes the Ge XRD-5 x-ray diffraction apparatus. Counts are made for 400 sec at 31.05° 2θ for the principal line of β $Ca_3(PO_4)_2$ and at 36.6° 2θ for background correction. The ratios of the counts are plotted against weight per cent β $Ca_3(PO_4)_2$ in mixtures containing fluorapatite and β $Ca_3(PO_4)_2$. The per cent β $Ca_3(PO_4)_2$ for the test sample is determined from this graph. Accuracy of ±0.3% β $Ca_3(PO_4)_2$ as a secondary phase can be obtained.

Results and Discussions

Total chemical analyses have been made on many commercial halophosphate phosphors. Analyses are shown in Table I for three typical phosphors. Phosphor A is a blue halophosphate, phosphor B is a white halophosphate, and phosphor C is a cool white halophosphate. It is immediately evident that, in this form, the analytical results have very limited value. The variations in PO_4 from 55.91 to 56.90% together with metal and halogen variations are real differences based on the precision of the chemical analyses as shown in the methods section. The calcium and phosphate contents as measured agree very closely with the amounts present in the formulation which were known to four significant figures. The total other cation impurities such as Sr, Ba, Na, etc., are present to less than 500 ppm. As such these are not used in the following calculations.

Before a meaningful interpretation can be made of the results shown in Table I, it is essential to determine the extent of secondary phases present in these phosphor compositions. When subjected to precision x-ray diffraction analysis for β $Ca_3(PO_4)_2$ and to chemical analysis for $Ca_2P_2O_7$, secondary phases were found in these samples. Results are presented in Table II. Phosphor A has over 9.0 w/o of secondary phases. On the other hand, phosphor C has less than 0.3 w/o of secondary phases. It is obvious that these secondary phases determine in part the differences in the constituents shown in Table I, especially in the halogen content.

With the results of Tables I and II available it is now possible to examine the stoichiometry of luminescent apatites. In considering this question, certain crystallographic principles must be observed since x-ray diffraction analyses show no unaccountable changes in unit cell parameters. The chlorofluoroapatites have the Naray-Szabo-hexagonal structure with space group $P6_3/m$. (24, 25)

The unit cell is composed of 42 sites and can be

Table I. Total chemical analysis of three calcium halophosphate phosphors

Constituent	Phosphor A, %	Phosphor B, %	Phosphor C, %
Ca	38.49	37.40	38.49
Mn	—	1.17	0.87
Sb	1.33	1.17	0.71
PO_4	56.90	56.90	55.91
F	3.18	2.76	3.33
Cl	—	0.913	0.62
Acid insol	0.22	0.27	0.06
Total	100.12	99.79	99.99

Table II. Secondary phases present in three calcium halophosphate phosphors

Secondary phase	Phosphor A, %	Phosphor B, %	Phosphor C, %
β $Ca_3(PO_4)_2$	5.1	2.7	0.0
$Ca_2P_2O_7$	4.0	4.0	0.20
$Ca(SbO_3)_2$	0.22	0.27	0.06

Table III. Luminescent apatite formulas calculated from chemical analyses

I. From total chemical analysis

Phosphor A $(Ca + Sb)_{9.71}(PO_4)_{6.00}F_{1.67}$
Phosphor B $(Ca + Mn + Sb)_{9.59}(PO_4)_{6.00}(F + Cl)_{1.77}$
Phosphor C $(Ca + Mn + Sb)_{9.97}(PO_4)_{6.00}(F + Cl)_{1.96}$

II. Formula corrected for secondary phases

Phosphor A $(Ca + Sb)_{10.00}(PO_4)_{6.00}F_{1.79}$
Phosphor B $(Ca + Mn + Sb)_{10.07}(PO_4)_{6.00}(F + Cl)_{1.92}$
Phosphor C $(Ca + Mn + Sb)_{10.00}(PO_4)_{6.00}(F + Cl)_{1.96}$

expressed as

$$M_{10}(PO_4)_6X_2 \qquad [1]$$

where M are the metal ions and X are the halogen ions. Since interstitial substitution of cations is extremely unlikely in the relatively close packed hexagonal structure of apatites only vacancies are considered (no real excess of any component exists on a unit cell basis). Finally electrical neutrality must be obeyed in any scheme of reconciling total chemical analysis with structural considerations.

Based on these factors, the total chemical analyses listed in Table I can be readily converted to moles of the cations and halogen ions per 6 moles of PO_4^{-3} ions such that the results can be compared to the theoretical stoichiometric expression, $M_{10}(PO_4)_6X_2$, previously mentioned. Further, appropriate calculations have been made to properly account for the secondary phases present in each phosphor (Table II). Calculated results are listed in Table III. These results show that, when the total chemical analyses are used to calculate the formula, the apparent nonstoichiometry of phosphors A and B are large. Phosphor A, for example, would be deficient in both Ca^{+2} and F^- ions. However, when the impurity phases are accounted for in the calculations the formulas are now much closer to stoichiometry. Deficiencies still exist in the halogen sites.

Measuring the amounts of the secondary phases present in the phosphors and using these values in calculating the formulas are major steps in determining the extent of nonstoichiometry in luminescent apatites. However, one more factor must be considered, namely the charge compensating mechanism for the substitution of Sb^{+3} for Ca^{+2} cation sites. Three possible mechanisms have been suggested. To maintain charge balance, Ouweltjes (9) proposed a simple O^{-2} substitution for X^- as Sb^{+3} substitutes for Ca^{+2}. No vacancies are necessary. The size of O^{-2} at 1.40Å is compatible with the F^- size of 1.36Å. Another mechanism proposes the creation of appropriate cation vacancies as Sb^{+3} is substituted into the apatite structure such that the vacancy concentration is expressed as equal to one-half the antimony concentration. The third mechanism as proposed by Butler and Jerome (26) involves a straightforward substitution of Sb^{+3} for Ca^{+2} ions with interstitial O^{-2} ions accounting for charge compensation. Appropriate calculations were made for each of these mechanisms and are listed in Table IV for phosphor A. The

Table IV. Calculations of phosphor A formula and charge balances for the three mechanisms of charge compensation

Calculated formula	Total cation charges	Total anion charges	Charge diff.
I *Ouweltjes mechanism* $(Ca + Sb)_{10.00}(PO_4)_{6.00}(F + O)_{2.00}$	50.11	50.11	0
II Vacancy mechanism $(Ca + Sb + vac)_{10.00}(PO_4 + vac)_{6.00}(F + vac)_{2.00}$	49.84	49.62	+0.22
III Butler and Jerome mechanism $(Ca + Sb)_{10.00}(PO_4)_{6.00}F_{(1.79+vac)}Int.\ O_{0.055}$	50.11	50.00	+0.11

Ouweltjes mechanism simply involves the addition of 0.11 moles of O^{-2} ions to the halogen sites since the Sb^{+3} concentration was 0.11 moles. The vacancy mechanism is somewhat more involved because as 0.055 vacancies are added to the cation sites to obtain electrical neutrality ([Vacancy] = ½ [Sb^{+3}] where [Sb^{+3}] = 0.11 moles), the total cation concentration becomes 10.055 relative to 6.00 PO_4. By dividing through by 1.0055 the formula is changed back to one with no excess cation sites. (This maintains a unit cell with a total of 42 sites.) The Butler and Jerome mechanism does not change the calculations since it invokes interstitial O^{-2} for charge compensation. However only 0.055 moles of interstitial O^{-2} are required for the 0.11 moles of Sb^{+3}. The results in Table IV clearly indicate the Ouweltjes mechanism most nearly fits the criteria of balanced charges and all sites being occupied by appropriate ions. The vacancy mechanism not only does not satisfy charge balance but invokes vacancies of different concentrations at all sites (Ca^{+2}, P^{+5}, O^{-2}, and X^{-}). These vacancies are relatively large for ionic crystals. The Butler and Jerome mechanism, in addition to having a slight excess of positive charges, requires a cell distortion for interstitial O^{-2} together with fluorine ion vacancies. It is unlikely that these two conditions can exist simultaneously. O^{-2} ions would tend to move from the interstitial sites into fluorine vacancies in order to relieve the stress on the unit cell. Similar calculations were made on many other luminescent apatites, and the results invariably show that the Ouweltjes mechanism fits the experimental results most closely. In every case, a significant halogen deficiency was present and, when the oxygen charge compensation mechanism as proposed by Ouweltjes was employed, the resulting formulas were much closer to stoichiometry. The deviations from stoichiometry and in charge imbalance are small and may be attributed primarily to the analytical accuracy. For instance, phosphor C showed a 0.02 excess of X^{-} ions and a 0.02 excess of negative charge.

A somewhat independent approach to the determination of stoichiometry in halophosphate phosphors involved the preferential solubility of various phosphates in ethylenediaminetetraacetic acid (EDTA) solutions. Table V lists the solubility of several phosphates in 5% EDTA at pH 10. $Ca_3(PO_4)_2$ is most rapidly soluble in EDTA. Halophosphate phosphors are incompletely soluble even after 16 hr at pH 10. The difference in solubility of apatite compared to the high rate of solubility of the impurity phases was used as a means of dissolving out the impurity phases. The results are presented in Table VI for three typical phosphors. Analyses for the $Ca_3(PO_4)_2$ and $Ca_2P_2O_7$ were made according to the procedures outlined in the methods section. Note that in all cases, the secondary phases were essentially absent after treatment with EDTA.

When phosphor A was further subjected to total chemical analysis after EDTA treatment [$Ca_3(PO_4)_2$ and $Ca_2P_2O_7$ removed] the changes in amounts of the components were significant compared to the chemical analyses before EDTA treatment. When the new data were converted to the formula based on 6(PO_4) groups the results were

$$(Ca + Sb)_{10.00}(PO_4)_6F_{1.89}$$

in agreement with those shown in Table III. When the Ouweltjes charge compensation mechanism was applied, the formula became essentially stoichiometric as shown in Table IV.

The previous results can be interpreted to mean that luminescent apatites are very close to stoichiometry. Any nonstoichiometry due to vacancies is not detectable by chemical means. Based on the accuracy of the chemical analyses, this nonstoichiometry does not exceed one phosphorous ion vacancy out of every 140 phosphorous sites. In all likelihood, the total vacancy concentrations (nonstoichiometry) are considerably less than one vacancy in 1000 sites. Schottky defects are probably present in very low concentrations. If analogy to alkali halides can be made (27), about one in every 10^5 to 10^6 anions and cations may be missing from the structure.

Table V. Per cent solubility of 1g samples of various phosphates in 250 ml of 5% EDTA at pH 10, 16 hr

Compound	% Solubility
β $Ca_3(PO_4)_2$	100
$Ca_3(PO_4)_2 \cdot CaCl_2$	100
$Ca_2P_2O_7$	100
Fluorapatite	15

Table VI. Secondary phase present in EDTA treated vs. untreated phosphors

Phosphor	% Dissolved	% β $Ca_3(PO_4)_2$	% $Ca_2P_2O_7$
A, untreated	—	5.1	4.0
A, treated	14.2	ND	<0.1
E, untreated	—	0.8	3.9
E, treated	15.7	ND	<0.1
D, untreated	—	ND	1.1
D, treated	14.2	ND	<0.1

Manuscript received Jan. 9, 1967; revised manuscript received June 4, 1967. This paper was presented at the Cleveland Meeting, May 1-6, 1966.

Any discussion of this paper will appear in a Discussion Section to be published in the June 1968 JOURNAL.

REFERENCES

1. G. Gillooly and J. Rabatin, Electronics Div., ECS, **15** [1], 25 (1966).
2. J. L. Ouweltjes and W. L. Wanmaker, *This Journal*, **103**, 160 (1956).
3. J. W. Strange, *Brit. J. Appl. Phys.*, Supp. 4, p. 4, (1954).
4. H. C. Froelich, "Preparation and Characteristics of Solid Luminescent Materials," p. 44, Cornell Symposium, John Wiley & Sons, Inc., New York (1948).
5. J. F. Ross and H. W. Sloyer, Patent No. 2,904,516 (1948).
6. A. S. Posner and A. Perloff, *J. Research Natl. Bur. Standards*, **58**, 279 (1957).
7. K. H. Butler, M. J. Bergin, V. M. B. Hannaford, *This Journal*, **97**, 117 (1950).
8. J. G. Rabatin and G. R Gillooly, *ibid.*, **111**, 542 (1964).
9. J. L. Ouweltjes, *Philips Tech. Rev.*, **13**, 346 (1951).
10. F. J. Welcher, "The Analytical Use of Ethylenediamine Tetracetic Acid," p. 105-9 D. Van Nostrand Co., New York (1958).
11. A. D. Ince and W. A. Forster, *Analyst*, **85**, 608 (1960).
12. A. Gee and V. R. Deitz, *Anal. Chem.*, **25**, 1320 (1953).
13. L. A. Wooten and C. L. Luke, *ibid.*, **13**, 771 (1941). York (1943).
14. H. H. Willard and H. Diehl, "Advanced Quantitative Analysis," p. 350, D. Van Nostrand Co., New York (1943).
15. E. B. Sandell, "Colorimetric Determination of Traces of Metals," 2nd ed., p. 430, Interscience Publishers Inc., New York (1950).
16. W. H. Willard and O. B. Winter, *Anal. Chem.*, **5**, 7 (1933).
17. W. D. Armstrong, *ibid.*, **8**, (1936).
18. R. J. Rowley and H. V. Churchill, *ibid.*, **9**, 551 (1937).
19. W. F. Huckabay, E. T. Welch, and A. V. Metler, *ibid.*, **19**, 154 (1947).
20. J. R. Caldwell and H. V. Moyer, *ibid.*, **7**, 38 (1935).

21. I. M. Kolthoff and E. B. Sandell, "Textbook of Quantitative Inorganic Analysis," p. 454, Macmillan Co., New York (1936).
22. N. H. Furman, "Scotts Standard Methods of Chemical Analysis," 5th ed., p. 271, D. Van Nostrand Co., New York (1938).
23. K. H. Butler, M. Y. Bergin, and V. M. Hannaford, *This Journal*, **97**, 117 (1950).
24. St. Naray-Szabo, *Z, Krist*, **75**, 387 (1930).
25. C. A. Beevers and D. B. McIntyre, *Mineral. Mag.*, **27**, 254 (1946).
26. K. H. Butler and C. W. Jerome, *This Journal*, **97**, 256 (1950).
27. F. C. Frank, "Chemistry of the Solid State," W. E. Garner, Editor, p. 25, Butterworth Scientific Publications (1955).

Radial Solute Segregation in Czochralski Growth

J. R. Carruthers[1]

Department of Metallurgy and Materials Science, University of Toronto, Toronto, Ontario, Canada

ABSTRACT

The radial variation of solute concentration in Czochralski-grown silicon crystals is shown to be greatly influenced by the effects of secondary liquid flows not associated with crystal rotation. These flows are caused by crucible rotation and thermal convection, and show the greatest effects in the outer regions of the growth interface.

The radial macrosegregation of solute in Czochralski-grown crystals has been quantitatively studied in germanium crystals by Dikhoff (1) and in silicon crystals by Benson (2). Dikhoff attributed his results to differences in the effective distribution coefficient on and off the (111)-type interface facet. However, as Benson points out (2), variations in the diffusion boundary layer thickness at the freezing interface will also contribute to radial macrosegregation.

In this paper, the types of liquid flow and the observed flow patterns in a simulated model are described, and the qualitative influence of these flows on the diffusion boundary layer is discussed. The data of Benson (2) on radial solute segregation in silicon crystals may be qualitatively interpreted by considering both the solute diffusion problem in the liquid at the growth interface and the flow patterns.

Fluid Flow During Czochralski Growth

Before describing the flow configurations which arise in Czochralski growth, the contributions to convection are discussed separately.

Forms of convection.—Forced convection at a rotating crystal.—The velocity boundary layer thickness has been shown (3) to be uniform across the surface of a disk rotating in an infinite isothermal medium, and is roughly equal to $(\mu/\omega)^{1/2}$ where μ is the kinematic liquid viscosity and ω the crystal rotation rate. A rigorous analysis has been performed by Cochran (3), and this has been extended for diffusion boundary layers in crystal growth by Burton, Prim, and Slichter (4). According to the model, the liquid forced outward by centrifugal acceleration is replaced by a central flow up to the disk surface. Observations confirming this mode of flow were made by Goss and Adlington (5) in a simulated transparent liquid model. Thus, if crystal rotation is the only source of convection, then no radial solute segregation would result from fluid flow effects.

Thermal convection.—It has been known for many years that thermal convection flow will be generated as steady circulation in any liquid where the temperature gradient is not aligned with the direction of gravity and no other external forces are present (6). In many geometric configurations, this flow is the steady streamline circulation generated between vertical boundaries by horizontal temperature gradients and occurs in Czochralski growth as hot liquid rising at the stationary crucible walls and falling in the center. However, when heat transfer also occurs at the horizontal surfaces, the classical Rayleigh instability may develop close to these surfaces where hot liquid is located vertically below colder liquid in an otherwise relatively stationary region of liquid (7). A detailed understanding of the cross effects of these two types of flow is now lacking, but both should result in large variations in diffusion boundary layer thickness in the absence of other forms of convection.

Forced convection in a rotating crucible.—During crucible or melt rotation around a vertical axis, the boundary layer at the upper liquid surface cannot remain uniform for the following simple reason. The rotation of an isothermal liquid in a cylindrical container results in a parabolic depression at the upper free surface, due to the velocity and pressure changes (8). Consequently, the boundary layer produced when a stationary disk is placed on the top surface should show a maximum thickness at the rotation axis where the radial velocity has its lowest value.

Combined liquid rotation and thermal convection.—When a liquid which is under thermal convection is spun about a vertical axis, a stabilizing force is provided which discourages thermal convection (9). This additional force is the Coriolis force which acts on particles having a horizontal velocity component. From an analysis by Nakagawa and Frenzen (9), it is possible to show that, in rotating liquid silicon with a free upper surface, unstable thermal convection should commence at an adverse vertical temperature gradient of 3.5°C/cm in a liquid 4 cm high which is rotating at 25 rpm. At 100 rpm, an adverse vertical gradient of 24°C/cm is required. This analysis assumes that only the vertical temperature gradient is present and that the liquid is of infinite lateral extent. Neither of these assumptions is valid for Czochralski growth, but the analysis should serve as a good basis for future work. From a similar analysis by Chandrasekhar and Elbert (10), it is possible to correlate the theoretical period of overstable oscillations, a form of instability arising from the interaction of liquid spin and thermal convection, with the observed period of growth fluctuations on the outer surface of nonrotated silicon crystals (11). Thus, the relaxation of the previous assumptions in Czochralski growth should not modify the theoretical arguments drastically.

[1] Present address: Crystal Chemistry Research Department, Bell Telephone Laboratories, Inc., Murray Hill, New Jersey.

Simulated fluid flow models.—Previous work.—Goss and Adlington (5) used a simulated transparent liquid model with dyes to observe the effects of crystal rotation on flow in an otherwise stationary liquid. They confirmed the simple picture that liquid in the immediate neighborhood of the disk is carried by friction and then forced outward by centrifugal acceleration. This fluid is replaced by an axial flow up to the center of the disk.

Turovskii and Mil'vidskii (12) attempted to view the flow occurring in a rotating, heated, transparent liquid model. Their apparatus made observations difficult, but they found that a flow was formed as an inward spiral around the upper surface which descended axially. When a disk was introduced at the upper surface, this flow was very much intensified. When the crystal was rotated, a region of localized intensive mixing was formed under the crystal because the crystal and crucible flows moved in opposite directions in this region.

Present work.—Experiments were designed to simulate fluid flow existing during Czochralski growth. A water-glycerine mixture of 42.5 w/o glycerine was selected to produce a transparent liquid with viscosity equivalent to that of most liquid metals (1-4 centipoise).

The apparatus is shown in Fig. 1 and consists of a collimated light beam imaging the quartz crucible on a ground-glass screen. A large square Lucite box was placed around the crucible and filled with glycerine to eliminate the converging effect of the cylindrical quartz crucible on the transmitted light beam. The quartz crucible was rotated independently of the Lucite box and, since interest was centered only on the flow in the crucible, baffle plates were used in the Lucite box to minimize any flow patterns in the surrounding glycerine due to crucible rotation.

The temperature gradient was established in the crucible by cooling the crystal below room temperature rather than by heating the liquid above room temperature. This procedure eliminated the necessity of heating coils around the crucible which would have obstructed the view. The crystal consisted of a copper cylinder of 1-in. diameter with a peripheral cone-shaped container around it for containing mixtures of dry ice and acetone. Both the copper cylinder and quartz crucible could be rotated independently in either direction at rates up to 98 rpm.

During operation of the model, drops of ink were injected into the bottom of the crucible by means of a capillary tube. The flow could be followed on the ground-glass screen. During all runs, an actual crystal of water-glycerine grew on the copper cylinder, and the crystal-melt interface temperature was −17.0°C. The temperature of the quartz crucible itself was held close to room temperature by the thermal inertia of the large amount of surrounding glycerine. Consequently, the maximum temperature difference which existed in the liquid was about 42°C.

Experimental results.—The flow patterns observed are shown schematically in Fig. 2 for the various situations indicated. Treating the crystal and crucible rotation rates separately, the following observations were made:

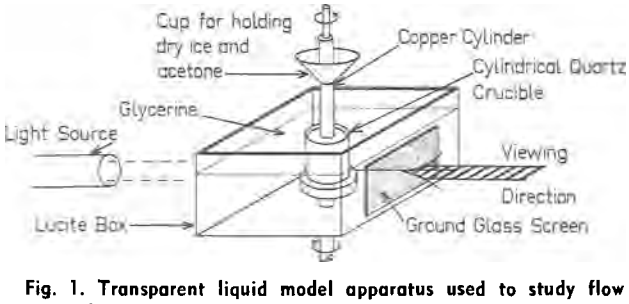

Fig. 1. Transparent liquid model apparatus used to study flow patterns during Czochralski growth.

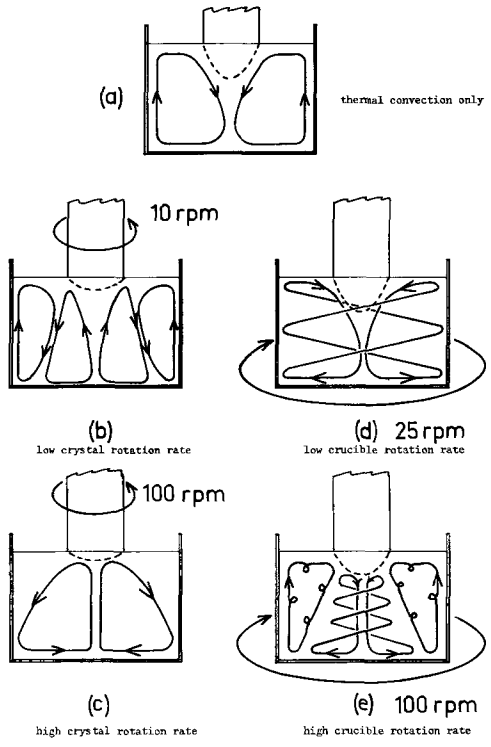

Fig. 2. Schematic flow patterns in transparent liquid model. (a) thermal convection only; (b) low crystal rotation rate; (c) high crystal rotation rate; (d) low crucible rotation rate; (e) high crucible rotation rate.

(*i*) Crystal rotation.—the liquid flow configuration for thermal convection alone, *i.e.*, no crystal rotation, is shown in Fig. 2(a). The hot liquid rose at the outer crucible wall and descended gradually near the center. At low crystal rotation rates, thermal convection flow was diminished close to the interface because the fluid flow from the rotating crystal was countercurrent to that caused by thermal convection. The deflection of streamlines is schematically illustrated in Fig. 2(b). At higher crystal rotation rates, the crystal acted like a fan, drawing liquid up at the center and spinning it out at the sides. Thermal convection is relatively unimportant in this case [Fig. 2(c)] and the assumptions made in the boundary layer analysis for the rotating disk will apply.

(*ii*) Liquid rotation.—At low crucible rotation rates, the liquid flow close to the crucible wall moved in a long closed streamline path, and the extent of thermal convection was diminished. The boundary layer at the upper surface tended to become more nonuniform, as shown in Fig. 2(d). For faster crucible rotation rates, flow separation occurred at the periphery of the crystal, and eddies developed in the outer regions of the liquid. The region close to the crystal-melt interface still possessed the same basic nonuniform flow, as shown in Fig. 2(e).

(*iii*) Combined crystal and crucible rotation.—Combinations of crystal and crucible rotation in the same directions produced only a modification of the simple crucible rotation flow. The crystal rotation did not exert its previous influence on the bulk fluid flow, except at low crucible rotation rates. For counter rotations, the central convection cell shown in Fig. 2(e) became quite stable, and ink did not move readily out of the central region. This effect is shown in Fig. 3, where the crystal and crucible were counterrotated at 60 rpm and the ink introduced into the central region continues to circulate there after several minutes.

Fig. 3. Liquid flow pattern in water-glycerine model; crucible and crystal counterrotating at 60 rpm each.

Radial Solute Segregation

The importance of fluid flow in any crystal growth technique is to influence the redistribution of solute at the growing interface. However, the relevance of convection to such transport also depends very much on other parameters, such as the equilibrium distribution coefficient, k_o, the liquid diffusion coefficient, D, and the growth rate, R. The contribution of these parameters may be determined by differentiating the Burton, Prim, Slichter expression (4) for the effective distribution coefficient, k_e, with respect to δ, the diffusion boundary layer thickness. This gives

$$\frac{\partial k_e}{\partial \delta} = \frac{\gamma(R/D)\exp(-R\delta/D)}{[1+\gamma\exp(-R\delta/D)]^2}$$

where $\gamma = (1-ko)/ko$. This relationship is valid for steady-state changes in δ and negligible lateral solute diffusion. The various solutes in silicon give the curves shown in Fig. 4 where $\partial k_e/\partial\delta$ is plotted against δ for $R/D = 100$ cm^{-1}. For a rotating crystal, the diffusion boundary layer should be about 0.01 cm for normal Czochralski growth conditions. It can be seen that in this range, only phosphorus and arsenic exhibit any large variations in solute concentration with differences in the diffusion boundary layer thickness. At faster growth rates, the other solutes (except B) will show larger radial solute variations for the same δ.

It is necessary at this point to explain why data on radial solute segregation should not be used directly to calculate the amount of preferential solute adsorption due to the facet effect, as described in previous work (1).

For the range of δ interest (0.01-0.03 cm), it is obvious from Fig. 4 that N-type solutes show an enhanced variation of concentration with boundary layer thickness. The most reliable method of separating the two effects is to grow a <100> crystal where the facet effects should be minimized. Benson (2) reports such

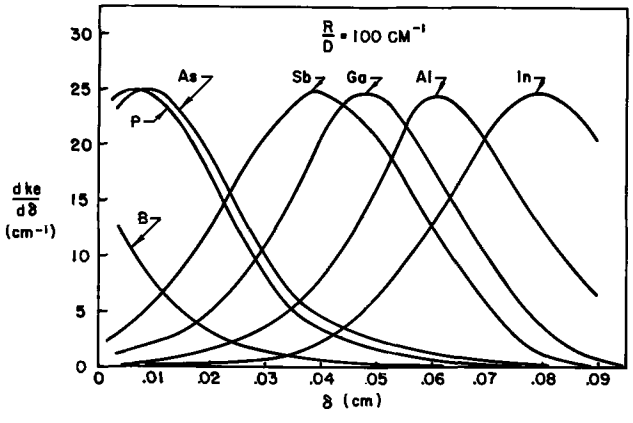

Fig. 4. Variation of solute concentration with steady-state changes in the diffusion boundary layer thickness for different solutes in silicon.

results for antimony-doped silicon crystals where a 7% radial variation was observed. From Fig. 4, using an average $\delta \approx 0.015$ cm, and assuming $R/D = 100$ cm^{-1}, it is seen that $\partial k_e/\partial\delta = 8.75$ for antimony. Thus, writing

$$\frac{\partial k_e}{\partial \delta} \approx \frac{\Delta k_e}{\Delta \delta} \approx \frac{0.07}{\Delta \delta} \rightarrow = 8.75$$

then $\Delta\delta = 0.008$ cm or $\Delta\delta/\delta = 0.53$ for the maximum variation in diffusion boundary layer shape under these growth conditions. This change in boundary layer thickness must be considered when determining the amount of solute adsorption on a facet for growth in more close packed directions.

Benson (2) has published a comprehensive study of radial solute segregation in Czochralski-grown silicon crystals, and the remainder of this paper will interpret his data using the information on fluid flow that has been presented earlier. The results of interest were obtained for phosphorus-doped crystals which, according to Fig. 4, should be quite sensitive to changes in δ for the growth rate range used by Benson. It was found that maximum variations in the radial solute distribution occurred at a crystal rotation of 10 rpm and a crucible rotation of 25 rpm, and that these effects were independent of each other. Furthermore, larger growth rates also gave larger variations, but did not displace the position of the maximum variations associated with rotation of either crystal or crucible. Lastly, larger diameters were found to give a markedly smaller degree of radial solute segregation.

The variation of radial solute distribution with crystal rotation rate will now be discussed. It is important to realize that the Cochran analysis of liquid flow around an infinite plane disk (3) must be modified in the presence of thermal convection in an otherwise stationary liquid. The linear flow velocity normal to the interface at a crystal rotation of 10 rpm is in the range, 10^{-3} to 10^{-2} cm/sec (4), whereas the thermal convection velocity is in the range 1-10 cm/sec. Furthermore, whereas the flow normal to the interface due to rotation is uniform over the radius, that flow due to thermal convection will follow more gradually curved streamlines and possess a definite stagnation point near the center of the interface. Thus, at low crystal rotation rates, the boundary layer thickness near the stagnation point remains unchanged while, at the outer regions of the interface, the thickness is reduced by the additive effects of the tangential velocity component and the thermal convection velocity. This effect will then cause an increase in the radial gradient of solute concentration as the crystal rotation increases in the low range.

The effect of crucible rotation is to inhibit thermal convection, but again not to change the position of the stagnation point, since the streamline flow at the crystal interface is quite similar to that of thermal convection, as shown in Fig. 2. Thus, the tangential flow component should again be enhanced at the outer portion of the interface and the degree of radial solute segregation increased.

Crystal rotation rates above 10 rpm were observed to be much more effective in reducing radial solute segregation than high crucible rotation rates. This effect was observed to be associated with a more rapid decrease in solute concentration and, hence, in δ near the interface center than at the outside, so that effects of secondary flow at the outer periphery are minimized.

The variation of radial solute segregation with crystal diameter will now be discussed. It is well known that an increase in diameter will decrease δ/D (13) and consequently δ alone. This decrease in δ will act in a similar way as a decrease in R to reduce radial solute segregation since, from the curve for phosphorus in Fig. 4, both effects will probably occur to left of the maximum and, hence, decrease $\partial k_e/\partial\delta$. An explanation for the decrease in δ with an increase in

crystal diameter is that for smaller crystal diameters the edge effects are of increasing importance, *i.e.*, the rotating disk analysis ceases to be valid and the boundary layer thickness becomes a function of the radius.

Summary

The radial solute segregation in Czochralski-grown silicon crystals has been shown to be greatly influenced by the effects of secondary liquid flow in the outer regions of the solid-liquid interface. The existence of interface facets will also cause large radial segregation because of the orientation dependence of the equilibrium distribution coefficient. However, the effects of liquid flow must be studied independently if unambiguous information is required on the facet effect alone. Maximum radial solute uniformity is possible only when the diffusion boundary layer at the growing interface is primarily controlled by crystal rotation, when the factor $\partial k_e/\partial\delta$ for the solute is insensitive to changes in δ at any particular growth rate and when the crystal orientation does not permit the development of an extensive close-packed interface facet on an otherwise curved interface.

Acknowledgments

The author thanks K. E. Benson and B. F. Howells of the Bell Telephone Laboratories for experimental assistance and helpful discussions. The author also thanks Professors W. C. Winegard and W. D. Baines for critical evaluations of the explanations.

Manuscript received May 29, 1967.

Any discussion of this paper will appear in a Discussion Section to be published in the June 1968 JOURNAL.

REFERENCES

1. J. A. M. Dikhoff, *Solid State Electronics*, **1**, 202 (1960).
2. K. E. Benson, *Electrochem. Technol.*, **3**, 332 (1965).
3. W. G. Cochran, *Proc. Cambridge Phil. Soc.*, **30**, 356 (1934).
4. J. A. Burton, R. C. Prim, and W. P. Slichter, *J. Chem. Phys.*, **21**, 1987 (1953).
5. A. J. Goss and R. E. Adlington, *The Marconi Rev.*, **22**, 132 (1959).
6. J. R. Carruthers, Submitted to *J. Crys. Growth*.
7. S. Ostrach, *Trans. ASME*, **79**, 489 (1959).
8. H. Rouse, "Fluid Mechanics for Hydraulic Engineers," p. 78, McGraw-Hill Book Co., New York (1935).
9. Y. Nakagawa and P. Frenzen, *Tellus*, **7**, 1 (1955).
10. S. Chandrasekhar and D. Elbert, *Proc. Roy. Soc. (London)*, **A 231**, 198 (1955).
11. J. R. Carruthers, *This Journal*, To be published.
12. B. M. Turovskii and M. G. Mil'vidskii, *Sov. Phys. Crystallog.*, **6**, 606 (1962).
13. J. A. Burton and W. P. Slichter, "Transistor Technology," Vol. I, p. 87, H. E. Bridgers, J. H. Scaff, and J. N. Shive, Editors, (1958).

Deposition of Silicon Nitride Films by the Silane-Hydrazine Process

Satoshi Yoshioka and Shigetoshi Takayanagi

Research Laboratory, Matsushita Electronics Corporation, Takatsuki, Osaka, Japan

ABSTRACT

A new pyrolytic process for depositing silicon nitride films using silane-hydrazine-hydrogen gaseous mixture is described. This system is useful at a temperature between 550° and 1150°C. The hydrazine process gives more rapid deposition rate than the ammonia process, so that the use of this process can reduce the lower limit of deposition temperature. Rate curves are presented for various temperatures and concentrations. In the lower part of the temperature range a linear dependence of log rate *vs.* $1/T$ is obtained. The rate reaches a saturation value above 750°C. The films produced are transparent, smooth, and tightly adherent. The films from this process have relatively larger etch rates in hydrofluoric acid than those from the ammonia process. Some film properties such as structure, Si-N atomic distance, Si-N IR absorption band, refractive index, density, dielectric constant, dielectric strength, and surface charge are presented.

Silicon nitride films show a high electrical resistivity, high dielectric strength, and extremely high resistance against chemicals, which properties are important for applications to microelectronic devices. Formation of silicon nitride films has been reported by reaction of silane and ammonia under a r.f. discharge (1), by pyrolytic reactions of either the silane-ammonia system (2) or the silicontetrachloride-ammonia system (3), and by reactive sputtering of silicon in nitrogen (4). This paper describes a new pyrolytic reaction between silane and hydrazine for depositing silicon nitride films and gives some properties of the films obtained by this process.

It is known that in the silane-ammonia process, for the decomposition of ammonia, the temperature of the reagent must be above 750°C to get a deposition of pure silicon nitride films (2). The use of hydrazine in place of ammonia will reduce the lower limit of the deposition temperature since the hydrazine decomposes at lower temperatures than ammonia. Indeed experimental results show that with the silane-hydrazine process adherent silicon nitride films are formed at relatively high growth rates at temperatures slightly above the decomposition temperature of silane (500°C).

Experimental

A schematic diagram of the apparatus for the film deposition is shown in Fig. 1. A mirror polished Si wafer was placed in a quartz tube of 60 mm diameter. The substrate temperature could be varied between 550° and 1150°C using r.f. heating of a graphite susceptor. The hydrazine was introduced into the reaction chamber by bubbling H_2 through liquid hydrazine kept at a constant temperature. Before entering the quartz tube this gas was mixed with a mixture

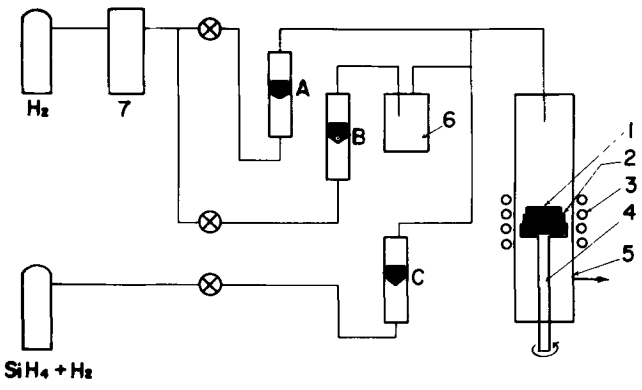

Fig. 1. Schematic diagram of the apparatus. A, B, C flowmeters; 1, silicon wafer; 2, graphite susceptor; 3, r.f. coil; 4, quartz plateau; 5, reaction chamber; 6, hydrazine saturator; 7, gas purifier.

of H_2 and SiH_4. The total gas flow rate applied was 0.6 l/min, the SiH_4 concentration was 0.03-0.4% and the SiH_4 to N_2H_4 ratio was 1 to 0.5-50. The hydrazine was purified by repeated distillation on sodium hydroxide until it showed a refractive index of 1.470 at 22°C. The sodium concentration in the purified hydrazine was about 6 ppm by flame analysis. The index of refraction of the deposited films was determined by the optical method described by Booker *et al.* (5). The density was calculated by measuring the film thickness and the weight change before and after removal of the film from the substrate. The electrical properties were measured on the MIS capacitors.

Results

Growth rates obtained are plotted as a function of the reciprocal substrate temperatures for different concentrations of the reagents for the hydrazine process and for one set of concentrations for the ammonia process in Fig. 2. In the temperature range between 550° and 650°C a straight line was obtained for the hydrazine process from which an activation energy could be calculated of about 54 kcal/mole. Above 650°C the growth rate reached a saturation value at about 750°C and then decreased slightly with a further increase of temperature. An abrupt decrease of growth rate occurred at a temperature above 1000°C, when the SiH_4 to N_2H_4 ratio was relatively small. The SiH_4-NH_3 process gave a straight line relation in the temperature range between 750° and 1000°C and showed an abrupt decrease in growth rate above 1000°C in agreement with the results obtained by Doo *et al.* (2). The growth rate of the hydrazine process changed linearly with the SiH_4 concentration in the temperature range between 550° and 1000°C (Fig. 3B). The dependence on the N_2H_4 concentration was

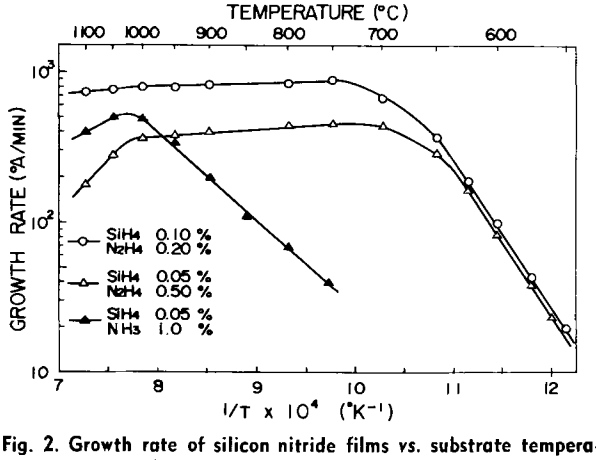

Fig. 2. Growth rate of silicon nitride films vs. substrate temperature for the SiH_4-N_2H_4 process and for the SiH_4-NH_3 process.

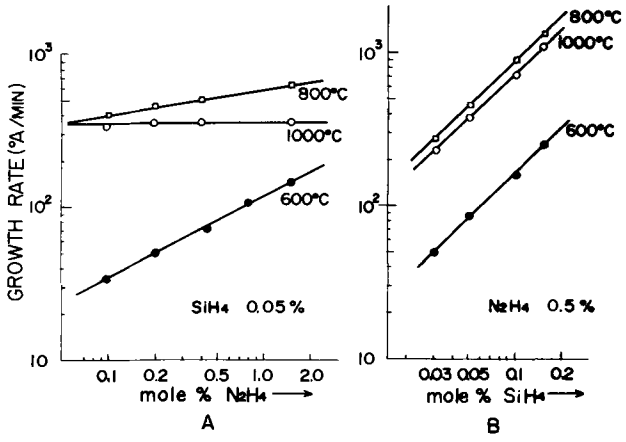

Fig. 3. Dependence of film growth rate. A, mole concentration of N_2H_4 (SiH_4 mole. conc. 0.05%); B, mole concentration of SiH_4 (N_2H_4 mole. conc. 0.5%).

more complicated; at high temperatures the growth rate became gradually independent of the N_2H_4 concentration (Fig. 3A).

Etching of films in a 20% HF solution at a room temperature showed that the etch rate of silicon nitride films prepared by the SiH_4-N_2H_4 process was strikingly dependent on the deposition temperature (Fig. 4) and higher than those grown at the same temperature by the SiH_4-NH_3 process. High etch rates of films are important in a photoengraving process for fabrications of electronic devices. A heat-treatment at a temperature higher than that of the deposition considerably reduces the etch rate as has been illustrated in Fig. 4. After such a heat-treatment some films developed cracks which probably initiated at the substrate film interface. The crack density of the films increased with the film thickness and with the growth rate. A decrease in etch rate indicates that the heat treatment resulted in a densification of the films.

Some film properties are given in Table I. The films prepared at 550°-1150°C are amorphous with extremely short range order by transmission electron diffraction (Fig. 5). From the diameter of the outer ring the spacing between neighboring atoms, probably silicon and nitrogen, was calculated as 1.3 ± 0.05Å. Electron microscopy shows no difference of surface texture between the films deposited by the SiH_4-

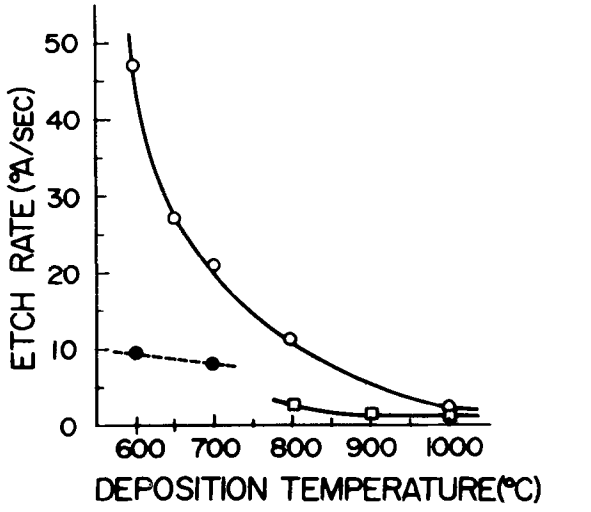

Fig. 4. Etch rate of silicon nitride films in a 20% HF vs. deposition temperature in the SiH_4-N_2H_4 process and the SiH_4-NH_3 process. ○, SiH_4 0.05%, N_2H_4 0.5%, no heat-treatment after deposition; •, SiH_4 0.05%, N_2H_4 0.5%, heat-treated for 1 hr at 900°C after deposition; □, SiH_4 0.05%, NH_3 1.0%, no heat-treatment after deposition.

Table I. Properties of silicon nitride films
Deposition temperature: 600°-1000°C, $SiH_4N_2H_4$ mole ratio: 0.1

Structure	Amorphous with extremely short range order
Si—N atomic distance	1.3 ± 0.05Å
Si—N IR band	11.3-11.1μ
Index of refraction	2.0-2.1
Density	3.0-3.1 g cm^{-3}
Dielectric constant	6.1 (Deposition temperature: 800°C)
Dielectric strength	6-10 × 10^6 v cm^{-1}
Surface charge (N_{FB})	1-3 × 10^{12} cm^{-2}
ΔN_{FB} after B. T. treatments	$\leq$ + 1 × 10^{10} cm^{-2} (− 3 × 10^6 v cm^{-1}, 150°C, 1 hr)
	$\simeq$ + 7 × 10^{10} cm^{-2} (+ 3 × 10^6 v cm^{-1}, 150°C, 1 hr

N_2H_4 and SiH_4-NH_3 process and between those deposited at 550° and 1150°C by the former process. A 1800Å film was essentially free of pinholes when heated at 800°C for 10 min in a flow of argon containing 30% chlorine.

Infrared transmission spectra of films grown by the SiH_4-N_2H_4 process showed a broad absorption band as shown in Fig. 6 due to Si-N stretching vibration. The absorption peak shifted slightly to shorter wave lengths with increasing deposition temperature. Films deposited at 600°, 800°, and 1000°C give absorption peaks at 11.3, 11.2 and 11.1μ, respectively. No shift of absorption peak was detected after heat-treatment of the films at temperatures below 1200°C for 1 hr. The absorption peak for films grown by the SiH_4-NH_3 process, however, occurred at 11.5-11.6μ.

Fig. 5. Electron diffraction pattern of a silicon nitride film deposited by the SiH_4-N_2H_4 process.

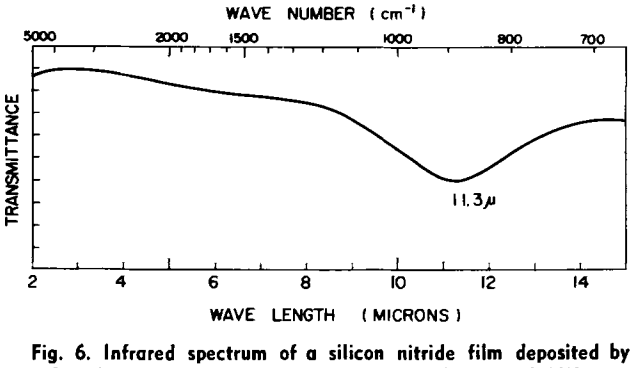

Fig. 6. Infrared spectrum of a silicon nitride film deposited by the SiH_4-N_2H_4 processs at 600°C (SiH_4 0.05%, N_2H_4 0.5%).

Discussion

The large difference between the temperatures for a certain film growth rate of the SiH_4-N_2H_4 process and the SiH_4-NH_3 process must be attributed to the fact that decomposition of N_2H_4 occurs at a lower temperature than that of NH_3. It is known that N_2H_4 is decomposed into N_2, H_2, and NH_3 by a steady-state chain mechanism (6). The initiation reaction [7] is

$$N_2H_4 \rightarrow 2NH_2 \qquad H = 60 \text{ kcal} \qquad [7]$$

In a gaseous mixture with a low concentration of N_2H_4, however, the thermal decomposition of N_2H_4 is probably a homogeneous reaction, because the propagation reactions are retarded by the collisions between the chain centers and the foreign gas molecules. The observed activation energy for the growth of silicon nitride films by the SiH_4-N_2H_4 process, about 54 kcal/mole, is close to the energy required for the N-N bond rupture of N_2H_4. So it is reasonable to assume that the N-N bond rupture is the rate-limiting step for the film growth at a temperature between 550° and 650°C. The silicon nitride films are probably formed according to

$$SiH_4 + N_2H_4 \rightleftarrows SiH_4 \cdot N_2H_4 \rightarrow Si(NH)_2 + 3H_2$$
$$2Si(NH)_2 \rightarrow (SiN)_2NH + NH_3$$
$$3(SiN)_2NH \rightarrow 2Si_3N_4 + NH_3$$

The growth rate of the films reaches a saturation value at about 750°C. This suggests that the supply of the reactants, in particular SiH_4, becomes rate determining above this temperature. The abrupt decrease in the growth rate at temperatures above 1000°C both for the SiH_4-N_2H_4 as for the SiH_4-NH_3 processes is probably caused by a decrease of the SiH_4 concentration near the substrate due to premature decomposition of SiH_4, as was suggested by Doo *et al.* (2).

The increase in etch rate with decreasing deposition temperature of silicon nitride films may be due to a decrease in the bond strength of Si-N. This is consistent with the infrared absorption data. The large decrease in etch rate after a heat-treatment at 900°C where the film does not show any shift of the absorption peak cannot be explained in the same way. No more can the effect be explained by assuming contamination of the silicon nitride films by oxygen because the reaction occurs in purified hydrogen atmosphere. The most probable cause for the large etch rates of films grown at lower temperatures will be a relatively large porosity of the films although the surface texture detected by electron microscopy does not clearly show the existence of a porous structure. The difference of etch rate between the films prepared by the SiH_4-N_2H_4 and the SiH_4-NH_3 process can also be explained by the difference of porosity.

Acknowledgment

The authors would like to thank Dr. T. Kawasaki and Dr. S. Nakajima for help with the electrical measurements and electron diffraction study respectively.

Manuscript received Feb. 6, 1967; revised manuscript received May 12, 1967.

Any discussion of this paper will appear in a Discussion Section to be published in the June 1968 JOURNAL.

REFERENCES

1. H. F. Sterling and R. C. G. Swann, *Solid-State Elec.*, **8**, 653 (1965).
2. V. Y. Doo, D. R. Nichols, and G. A. Silvey, *This Journal*, **113**, 1279 (1966).
3. M. J. Grieco, F. L. Worthing, and B. Schwartz, Paper presented at the Philadelphia Meeting of the Society, Oct. 9-14, 1966.
4. S. M. Hu, *This Journal*, **113**, 693 (1966).
5. G. R. Booker and C. E. Benjamin, *ibid.*, **109**, 1206 (1962).
6. G. K. Adams and G. W. Stocks, "Fourth Symposium on Combustion," pp. 239-248, Williams and Wilkins, Baltimore, Md. (1953).
7. M. Szwarc, *Proc. Roy. Soc.* (*London*) **A198**, 267 (1949).

A Water-Amine-Complexing Agent System for Etching Silicon

R. M. Finne[1] and D. L. Klein[2]

Bell Telephone Laboratories, Incorporated, Murray Hill, New Jersey

ABSTRACT

Ternary mixtures of water, amine, and complexing agent have been found to etch silicon. The silicon etch rate has been investigated as a function of variations in both solution and material parameters. A parallel investigation has been concerned with the etching characteristics of silicon samples coated with silicon dioxide films. Applications of this etching system to semiconductor device technology has provided a tool for the chemical shaping of silicon as well as the evaluation of protective surface films on silicon substrates.

It has been found that ternary mixtures of water, amines, and complexing agents dissolve silicon, with water being a necessary and active component of the etch. Significant among the properties of these etches are the large number of parameters on which the etch rate depends and the extremely low rate of attack on silica. It has been possible to etch silicon into unique shapes by the proper choice of etching parameters. These etches have also been used in the investigation of the etching characteristics of silica films on silicon substrates.

The etch rates in this ternary system have been found to exhibit a marked dependence on the crystallographic orientation and doping of the silicon. Due to the complex etch rate dependence and because there are also variations in etch rate related to the etch composition, a complete study of this system is extremely complicated. On the basis of data presented in this paper a reaction mechanism is proposed and some applications of the system are discussed.

An etch of this general type was first described by Crishal and Harrington (1) who reported the etch as a two-component mixture of hydrazine and pyrocatechol which etched silicon forming $(N_2H_5)_2[Si(C_6H_4O_2)_3] \cdot N_2H_4$ with accompanying evolution of nitrogen and hydrogen. The present study has shown that the silicon etch rate is a function of water content of the etch and falls to zero for anhydrous amine-pyrocatechol mixtures, and that the dissolution is accompanied by only the evolution of hydrogen.

Experimental Procedure

Equipment.—A glass refluxing system was used to prevent composition change by loss of volatile matter. A stream of nitrogen was bubbled through the etching solution to prevent air oxidation of the amine and complexing agent, and to provide agitation of the samples. Drying tubes were used to prevent moisture absorption from the air. The operating temperature was 110° ± 1°C. Reagent grade materials were used throughout.

Etch rate determinations.—The method selected for rate determination was an optical technique which utilized the extremely low etch rate on silica films (*i.e.*, ~200 Å/hr). Etch rates were determined as follows: polished silicon slices were masked with atmospheric steam-grown silica dots, etched, and the resulting step heights were measured microscopically using a focusing stage calibrated to one micron per scale division. The objective employed in the microscope had a depth of field of 1μ. The smallest step heights measured were in the order of 10μ.

Etch solutions.—For most of the etching studies described an etch composition was selected which would give close to the maximum etch rate on silicon. Although hydrazine was used for the initial experiments the majority of the work was performed with ethylenediamine. This choice was based on the higher etch rates exhibited by ethylenediamine systems, their higher stability and lower toxicity. The following composition was used for most of the work described in this paper:

Component	Formula	Amount	Mole %
Water	H_2O	8 ml	61.2
Ethylenediamine*	$NH_2(CH_2)_2NH_2$	17 ml	35.1
Pyrocatechol	$C_6H_4(OH)_2$	3g	3.7

* The abbreviation en will be used for ethylenediamine, pn for propylenediamine, hn for hexanediamine.

Etch solutions employing this molar ratio of components will be referred to as "solution 1". Solutions were freshly made for each run and stored under dry nitrogen prior to use.

Data and Discussion

Gas analysis.—The gaseous reaction products were collected from an argon flushed system and analyzed by mass spectrometry. Results of this analysis are shown below.

Major components	Concentration
Hydrogen	57%
Argon	43%
Trace components	
Nitrogen	450 ppm
Oxygen	110 ppm

The concentration ratio of nitrogen to oxygen (~4:1) suggests that their presence was due to a trace quantity of air in the system. A volumetric analysis of the hydrogen evolved for the total dissolution of weighed silicon samples in ethylenediamine-water mixtures showed the stoichiometry to be close to $2H_2$/Si both in the presence of and in the absence of pyrocatechol. For 0.0140g silicon samples (0.499 mM silicon) the following results were obtained:

Pyrocatechol content, mole %	Vol. H_2 evolved, mls at STP	Molar ratio H_2/Si
0	21.60	1.918
3.7	22.40	1.934

Product analysis.—On the basis of several known pyrocatecholato complexes of group IV elements (2) the expected empirical formula for the reaction product formed in the ethylenediamine system was $SiC_{22}N_4H_{30}O_6$. The following is a table showing the average values of three combustion analyses performed on the reaction product. This product, a white

[1] Present address: John O'Connell Associates K.K., 17-2 Akasaka 7-Chome, Minato-Ku, Tokyo, Japan.

[2] Present address: IBM, East Fishkill Facility, Hopewell Junction, New York.

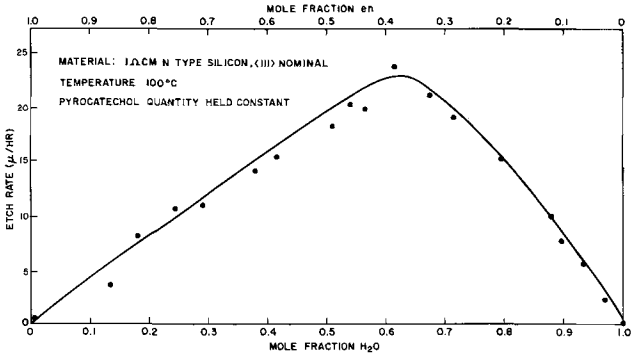

Fig. 1. Etch rate of silicon as a function of the water content of the etch with pyrocatechol content held constant.

crystalline solid, was isolated by the addition of ethanol to the reaction mixture.

Element	Found, %
C	54.31
H	6.41
N	11.05
Residue (assumed as SiO_2)	12.97

The empirical formula derived from these analyses is as follows: $Si_{1.0}C_{21.5}N_{8.7}H_{30.2}O_{5.7}$.[2]

Etching system parameters.—For the majority of the investigations in which the orientation of the crystal was not considered of fundamental significance, silicon was used which was nominally oriented; that is, within 3.5° of the major low index plane. In those cases where the orientation was considered significant, on-orientation samples within 0.5° of the plane were used.

Water content of the etch.—Figure 1 shows the etch rate of silicon as a function of the water content of the etch. The specific system considered was water-en-pyrocatechol, with 3g (0.03M) of pyrocatechol added to the water-en solutions. A maximum was observed for the etch composition corresponding to a mole ratio of water to en of approximately two. The silicon etch rates fall to zero for solutions with mole fractions of water equal to one and zero. This was found for all amines studied including hydrazine. The curve shape was found to be independent of the resistivity of the silicon in the resistivity range tested.

Pyrocatechol content of the etch.—Figure 2 shows the silicon etch rate as a function of pyrocatechol content of the etch. When the pyrocatechol was omitted the etch rate was reduced. However, the etch rate was finite in the absence of pyrocatechol. This fact, coupled with the data shown in Fig. 1, suggests that water and amine, unlike pyrocatechol, are the necessary components of the etching system.

Etchant components.—Figure 3 shows a plot of etch rate as a function of resistivity for etches using the

[2] The silicon was determined by considering the ignition residue to be SiO_2. The oxygen was determined by difference.

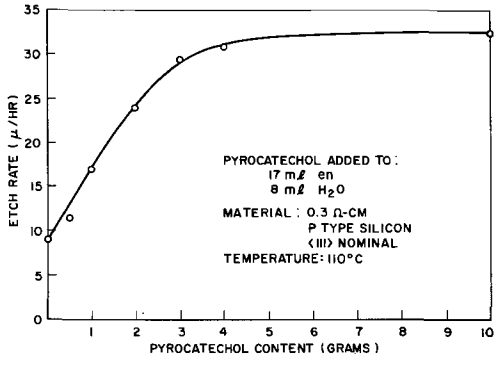

Fig. 2. Etch rate of silicon as a function of the pyrocatechol content of a constant composition en-water mixture.

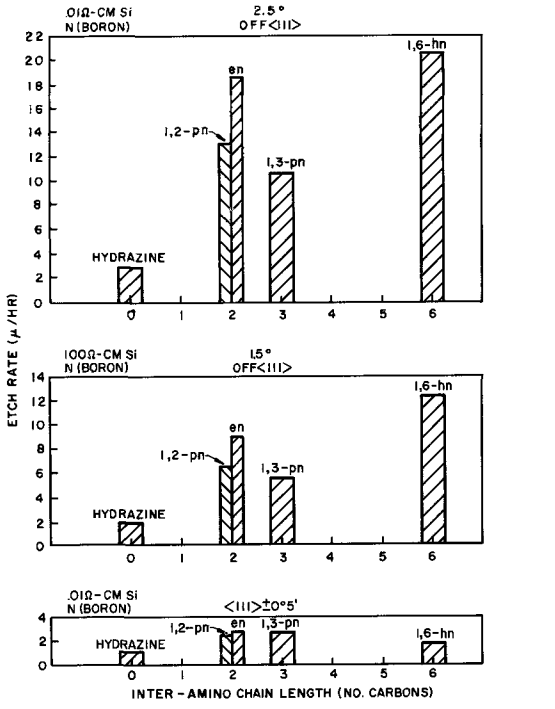

Fig. 3. Etch rate of 0.01 and 100 ohm-cm silicon as a function of the member of carbon atoms between amine groups for oriented and misoriented samples.

following amines:

Hydrazine	(NH_2-NH_2)
en	(NH_2-CH_2-CH_2-NH_2)
1,2-pn	(NH_2-CH_2-$CHCH_3$-NH_2)
1,3-pn	(NH_2-CH_2-CH_2-CH_2-NH_2)
1,6-hn	[NH_2-$(CH_2)_6$-NH_2]

The etching solutions were made using the molar composition cited in the section on etch solutions. The data shown in Fig. 3 suggest that for the amines tested the etch rate of nominally oriented silicon tends to increase with the number of carbon atoms between amine groups. For oriented silicon, no significant change in silicon etch rate was observed for the different amines tested. The behavior of 1,3-pn is discussed in the section on reaction mechanism. It is to be expected that the etch rates would be similar in the case of en and 1,2-pn since 1,2-pn can be considered a methyl-substituted en. Small differences in etch rate might be due to steric factors or electron donor properties of the substituted methyl group.

In the absence of pyrocatechol, 6 hr of etching produced a thin translucent layer on an exposed silicon surface. Figure 4 shows a photograph of such a surface layer. The dark areas are exposed regions of silicon viewed through openings in the film. The hexagonal shapes are etch pits formed in the silicon sur-

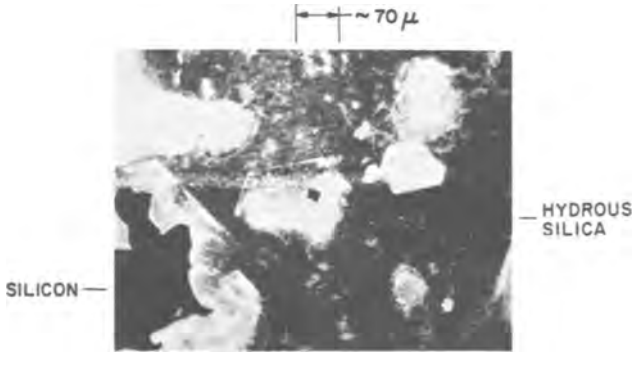

Fig. 4. Silicon surface after etching for 6 hr in an en-water mixture with no added pyrocatechol.

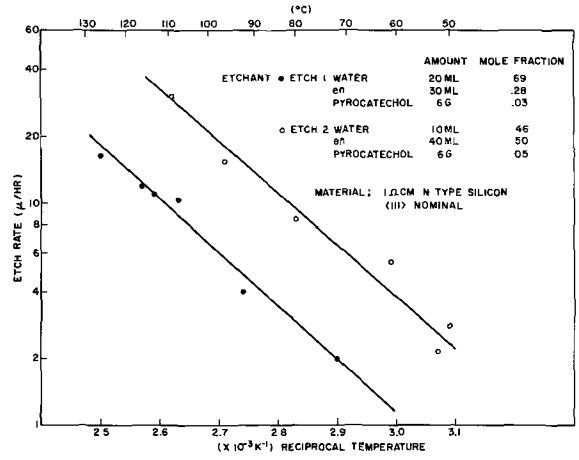

Fig. 5. Etch rate of silicon as a function of temperature for two compositions of etchant.

face. Since the crystallographic sensitivity of the etch persists in the absence of pyrocatechol it is concluded that the complexing agent does not control the sensitivity of the etch for various crystal planes.

Temperature.—A plot of etch rate as a function of temperature for two compositions of etchant is shown in Fig. 5. Etch rates were determined between approximately 50° and 127°C. From the Arrhenius equation, the apparent activation energy was determined to be approximately 11 kcal/mole (0.48 ev) for both concentrations. This indicates that the etching rate is probably not controlled by solution diffusion. The proposed etching mechanism, discussed in the following section, is based on the presence of OH^- groups. Some support for this is found in work done by Faust (3) who has determined the activation energy for the reaction between 10% NaOH solutions and silicon to be approximately 13 kcal/mole (0.56 ev). (The NaOH solution is also a preferential etch on silicon; however, it attacks silica rapidly whereas the present system does not.)

Chemical mechanism.—It has been suggested in this paper that water is a necessary etch component and plays an active part in the etching process. This is based on the observation that no silicon etching occurs for either anhydrous amine or anhydrous amine-pyrocatechol mixtures. Etching occurs only with the intentional or accidental introduction of water into the system.

The following reactions are proposed for the specific system water-en-pyrocatechol

Ionization

$$NH_2(CH_2)_2NH_2 + H_2O \rightarrow NH_2(CH_2)_2NH_3^+ + (OH)^- \quad [1]$$

Oxidation-Reduction

$$Si + 2(OH)^- + 4H_2O \rightarrow Si(OH)_6^= + 2H_2 \quad [2]$$

Chelation

$$Si(OH)_6^= + 3C_6H_4(OH)_2 \xrightarrow{\text{amine}} \left[Si(IV) \left(\begin{matrix} O \\ O \end{matrix} > C_6H_4 \right)_3 \right]^= + 6H_2O \quad [3]$$

Over-all Reaction

$$2NH_2(CH_2)_2NH_2 + Si + 3C_6H_4(OH)_2 \rightarrow 2NH_2(CH_2)_2NH_3^+ + [Si(C_6H_4O_2)_3]^= + 2H_2 \quad [4]$$

During the ionization step (Eq. [1]) hydroxyl and aminium (protonated amine) ions are formed. The hydroxyl ions, together with water, then oxidize the silicon to form hydrous silica with the evolution of hydrogen (Eq. [2]). The hydrous silica is converted to the complex pyrocatecholate which is soluble in the amine solution (Eq. [3]).

Examination of Eq. [4] shows that water does not appear in the over-all equation. This occurs because of the regeneration of water in the chelation step (Eq. [3]). Consequently, the reaction is not limited by water depletion, and the etch rate should remain constant over long periods of time in the presence of sufficient amine and complexing agent.

Several pyrocatecholato complexes of silicon were first reported by Rosenheim, Raibman, and Schendal (3). They isolated various *tris*(pyrocatecholato)silicon(IV) compounds by reacting freshly prepared silicic acid with pyrocatechol. In the present work the silicic acid was generated *in situ* at the silicon surface (Eq. [2]). The isolated ethylenediaminium compound has not been previously reported.

On the basis of the proposed mechanism we may account for the necessity for water in the system since in the absence of water no oxidation can take place. The suggested mechanism also explains the slow etch rate on silica films grown at high temperatures, since they contain few silanol (Si-OH) groups. These silica films must be converted to hydrous silica prior to their dissolution as the pyrocatecholato complex. This is apparently a slow step.

The addition of pyrocatechol to water-en solutions was found to increase the etch rate up to a limiting value (Fig. 2). At about 4 mole % pyrocatechol the rate saturates. This suggests that above this level of complexing agent the kinetics become limited by the oxidation step (Eq. [2]).

This mechanism can also account for the appearance of the silicon surface after etching in the absence of a complexing agent (Fig. 4). The limited etching of the silicon which takes place can be due to the slow dissolution of the hydrous silica by the en to form soluble *bis*(ethylenediaminium)silicate. However, the dissolution rate of the hydrous silica in this case is evidently slower than the rate of formation of the hydrous silica, resulting in a build-up of the hydrous silica layer. The dissolved areas of the surface layer may be explained as follows. Conversion of silicon to silica requires expansion of the lattice and can produce locally stressed areas which etch faster than unstressed areas. Alternatively, variations in the concentration of silanol groups on the silica surface of structural modifications of the silica may result in enhanced etching in localized areas.

This mechanism differs from that proposed by Chrishal and Harrington (1), in which an oxidation of the silicon by hydrazine was postulated, with the evolution of nitrogen and hydrogen. Analysis of the gaseous reaction products in the present system showed hydrogen to be the sole gaseous reaction product. Volumetric analysis showed the hydrogen to be present in approximately the stoichiometrically predicted amount (Eq. [2]) both in the presence and absence of pyrocatechol.

If the reaction is performed in an open system, absorption of water by the hygroscopic anhydrous amine will result in the formation of a water-amine-pyrocatechol system of uncontrolled composition. Nitrogen evolution could then occur due to the decomposition of hydrazine in the presence of absorbed water and air.

With regard to the variation of silicon etch rate with amine, the base strength of the amine cannot be taken as an index of etch rate. Gero (4) has reported on the base strengths of polymethylenediamines. He found that en was the weakest base, and that 1,3-pn was abnormally strong due to chelate ring stabilization of the monocation. The present study has shown that en has the higher etch rate. The following explanations are proposed.

An amine environment is required for the pyrocatechol to dissolve (chelate) the hydrous silica. For small chain length diamines, where the amine separa-

tion is small, the positive charge on the monocation withdraws electrons from the second amine group, reducing its protophilic activity (amine nature). For hydrazine, the cation formed is NH_2-NH_3^+. In en the charge separation is greater, and the second amine retains its protophilic activity (Eq. [1]). For 1,3-pn, the second amine is thought by Gero (4) to be hydrogen bonded in the following manner

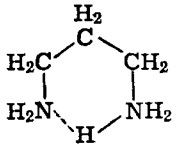

This type of cation would exhibit a lessening of amine character due to the utilization of the normally unbonded nitrogen electrons in the hydrogen bond. The succeeding cations of this diamine series should retain their amine nature and, therefore, provide a suitable environment for etching. A second possible explanation is based on the following information. Hooley (5) has observed that the dissolution rate of silica glass in aqueous solutions of alkali metal hydroxides is a function of effective cation size. The dissolution rates were found to be in the order Na > K > Li > Rb > Cs. In the present system, the protonated amine is a cation and is of an ionic size comparable to that of the alkali metal cations. Hooley (5) proposed no firm explanation of the rate variation as a function of cation size. Weiss *et al.* (6) have found that the kaolinite structure ($Al_2O_3 \cdot 2SiO_2 \cdot 2H_2O$) is expanded from an initial planar spacing of ~10Å by exposure to hydrazine. On the basis of these investigations, a relation between etch rate of Si in a cation-hydroxide system, in which dissolution involves the intermediate formation of an oxide, and oxide bond distortion due to cation intrusion seems reasonable. This may relate directly to the silicon system under study in this paper. The silica structures proposed as intermediates may undergo bond distortion as a result of the intercalation of some amine species.

Silicon parameters.—Using solution 1 the etch rates for <111>, <110>, and <100> oriented silicon were found to be approximately 3:30:50 μ/hr for the samples tested. A plot of this data is shown in Fig. 6. The data scatter for the <111> oriented samples results from the limited precision of measuring the low etch rates. Samples were randomly selected with regard to dopant, utilizing such dopants as B, P, As, Sb, Al, Ga, and In.

For samples oriented off the three major low-index planes, the etch rates of the surface were found to be a function of the dopant concentration, and the degree and direction of misorientation. As the surface was misoriented from the plane, an increase in etch rate was observed. The variation in etch rate was marked near the <111> orientation, but much more gradual near the <100> orientation. This is now being investigated.

As is the case with most solid surface reactions, a

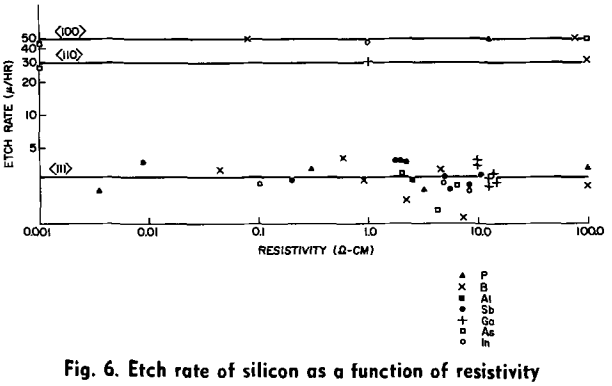

Fig. 6. Etch rate of silicon as a function of resistivity

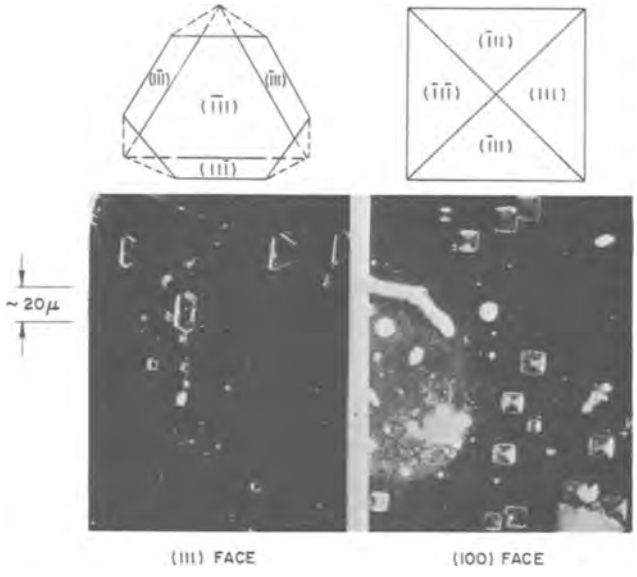

Fig. 7. Etch pit geometries in silicon for <111> and <100> oriented samples.

description of the detailed reaction mechanism is exceedingly difficult and cannot be based on kinetic studies of the gross reaction rate. Factors such as supply and movement of active surface sites on the silicon, reaction site spacing, activity of the reacting species in solution, and influence of impurities and/or absorbants on surface diffusion may all be significant. At present, evaluation of their respective roles is not possible. However, due to the diverse functional dependence of etch rate, a large amount of information can be gathered concerning this system. Because of this, it may eventually be possible to gain greater insight into the detailed reaction mechanism.

Silicon dioxide masking.—A parallel line of investigation has been concerned with etching studies on silicon substrates with a protective coating of silica. Structural inhomogeneities in the oxide may allow the etchant to penetrate to the silicon surface where localized etching takes place. Etch pits in the silicon were produced which were visible through the oxide film. These pits resulted from etching a concave surface which is bounded by slow etching planes (7). Schematic diagrams and photographs of the pits produced on two of the major low index planes of silicon are shown in Fig. 7.

Oxide porosity.—Oxide porosities were determined for various initial oxide thicknesses and various etching times. A plot summarizing this data is shown in Fig. 8. The samples used for these studies were oxidized at 1100°C in atmospheric pressure steam. The

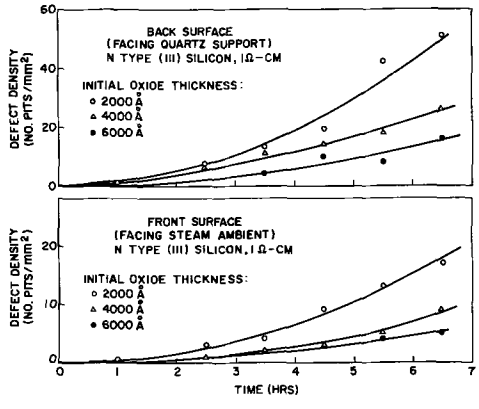

Fig. 8. Defect densities in silica films as a function of time of etching, initial oxide thickness, and surface exposure. The calibrated pinhole was formed using photolithographic techniques.

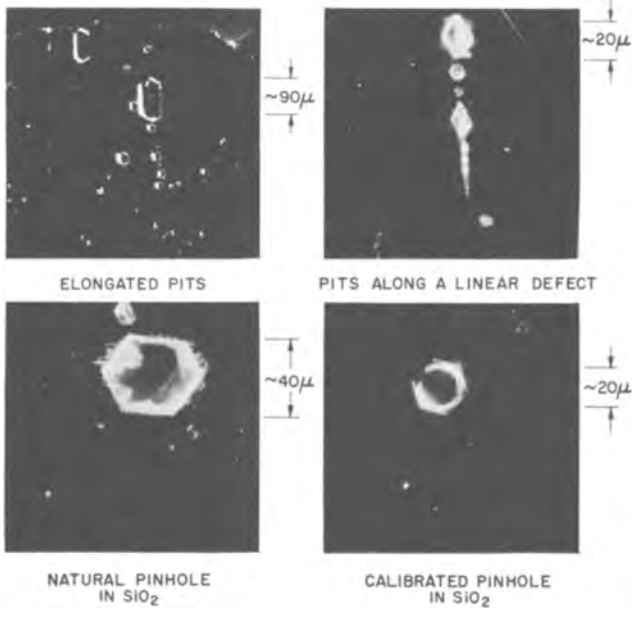

Fig. 9. Morphology of etch pits in <111> oriented silicon below silicon dioxide films.

oxide defect densities were found to be reproducible. An increase in etch pit density with time can be attributed to several causes. First, oxide defects which extend to within a few hundred angstroms of the substrate surface will etch through and initiate pits after extended etching. Second, the rate of growth of the etch pit is a function of the size of the oxide defect. Extremely small defects presumably will produce pits which are initially too small to be seen by optical microscopy. As the defect enlarges the pit size increases until the pit is visible. In addition, certain areas in the oxide may be structurally more susceptible to hydrolysis and subsequent dissolution. Of interest is the fact that while naturally occurring etch pits in <111> oriented silicon are not regular hexagons in shape, the pits formed beneath photolithographically produced round holes in the silica are. This indicates that the hexagonal shape of the pits is influenced by the geometry of the oxide defects. Examples of various etch pit shapes are shown in Fig. 9.

Oxide inclusions.—Also of interest have been the inclusions observed in silica films. These inclusions have etching characteristics grossly different from the oxide. They appear as "phantom crystals" which have unique etch pit shapes. Some of these phantom crystals manifest themselves as hexagonal shapes which disappear on further etching. Some appear as figures resembling dendritic crystals. Presumably these crystals are second phases in the silica (*e.g.*, devitrified areas) that etch at higher than the average rate of the film. Two examples of these shapes are shown in Fig. 10.

Applications

Application of the etching system described to device fabrication has shown promise in two general areas, the chemical shaping of silicon into unique shapes by utilizing the widespread control possible over the etch rate and studies of silica films. Significant in all applications is the low etch rate on silica, as well as on many metals. This allows silica or metals such as Ag, Au, Cu, or Ta to be used as etching masks, and differentiates this etch from alkali etches such as sodium hydroxide solutions which may be crystallographically sensitive but attack silica and many metals. The present etch is compatible with metals which cannot be used in HNO_3-HF systems. This may be explained by the fact that amine-soluble pyrocatecholates are formed predominantly with metals capable of attaining an oxidation state of IV (2).

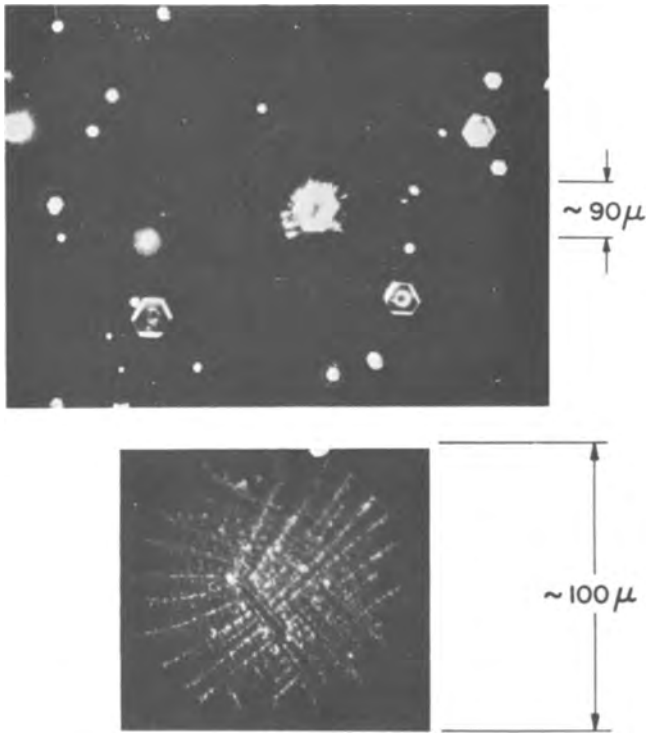

Fig. 10. Phantom crystals in silicon dioxide films

Chemical shaping with this etching system has produced silicon forms such as tapered mesas whose sides form an angle of 45° with respect to a (100) surface (Fig. 11). This is the natural shape of a mesa formed on a <100> oriented sample. Also, thin films of silicon alloys (~10μ) have been produced by etching slow or nonetching silicon alloys deposited on fast-etching silicon substrates. Germanium does not etch in this system. It has been found that silicon alloys containing as little as 5% germanium were not attacked by the etch. Therefore, when such alloys were epitaxially deposited on a silicon substrate, the substrate could be etched away leaving a nonetching film.

In the study of silica films on silicon substrates, the etch pit density in the silicon has been taken as an

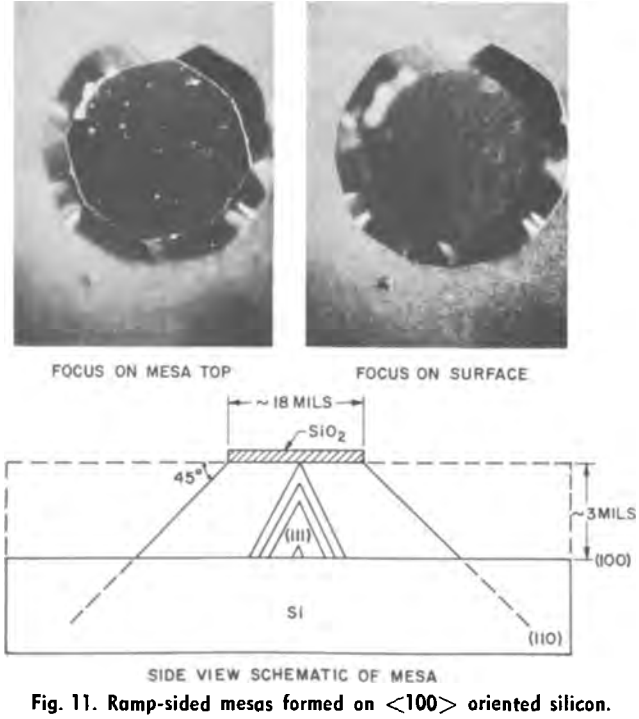

Fig. 11. Ramp-sided mesas formed on <100> oriented silicon.

index of the porosity of the silica film. This technique has been particularly applicable where low evaluation temperatures have been required. It has been shown that silica films formed by steam oxidation, plasma growth (8), and the CO_2 process (9) have approximately the same minimum porosity as determined by this technique. The chlorine gas etching system for oxide evaluation is generally used at a temperature of approximately 800°C, while the present system operates at approximately 110°C. Samples having etch pit densities of less than one and greater than 100 detectable pits per square millimeter have been observed after 2 hr of etching. In general, and in contrast to chlorine etching, individual pit growth may be observed since the etching action is slow and localized. Also, as previously mentioned, the etch pit shape is influenced by the shape of the oxide defect. Oxide inclusions or variations which have markedly different etch rates from the bulk oxide are delineated. Because of these factors, the system is a powerful tool for the study and evaluation of silica films.

Summary

It has been shown that the system water-amine-complexing agent will etch silicon and, to a much lesser extent, silica. For the specific system water-ethylenediamine-pyrocatechol, silica is etched at a rate of ~200 Å/hr while silicon etches at a rate approximately two orders of magnitude higher. The water appears to be an active component of the mixture and yields hydroxyl ions in the basic solvent system provided by the amine. Oxidation of the silicon by the water and hydroxyl ions forms hydrogen and hydrous silica at the silicon surface. The hydrous silica is removed from the silicon surface through the formation of the amine-soluble *tris*(pyrocatecholato)-silicon(IV).

For the specific etching system studied, the etch rates on <100>, <110>, and <111> oriented silicon were found to be approximately 50:30:3 μ/hr, respectively. For samples off the major low-index plane orientations the etch rates were found to be a function of resistivity and of the degree and direction of misorientation. Due to the large number of parameters which influence the etch rate, this system can be used for fundamental studies of the detailed reaction mechanism of silicon etching.

Because of the difference in etch rate on silica and silicon and the preferential nature of the etch on crystal planes, structural studies of silica films are feasible. In addition, protective oxides have been evaluated, and it has been possible to utilize the etching system for the chemical shaping of silicon to form tapered mesas and thin films of silicon.

Acknowledgments

The authors wish to thank L. A. Pompliano and D. L. Deppen for contributing some of the data used in this report.

Manuscript received Aug. 3, 1966; revised manuscript received May 1, 1967. This paper was presented at the Toronto Meeting, May 3-7, 1964.

Any discussion of this paper will appear in a Discussion Section to be published in the June 1968 JOURNAL.

REFERENCES

1. J. M. Crishal and A. L. Harrington, *This Journal*, **109**, 71C (1962). (Abstract of paper given at Los Angeles Meeting.); also, Electronic Division Abstracts, **11**, No. 1, 202 (1962).
2. A. Rosenheim, B. Raibman, and G. Schendal, *Z. anorg. u. allegem Chem.*, **196**, 169 (1931).
3. The Surface Chemistry of Metals and Semiconductors," p. 167, H. C. Gatos, Editor, John Wiley & Sons, Inc., New York (1960).
4. A. Gero, *J. Am. Chem. Soc.*, **76**, 5159 (1954).
5. J. G. Hooley, *Can. J. Chem.*, **39**, 1221 (1961).
6. V. A. Weiss, W. Thielepape, W. Ritter, H. Schafter, and G. Goring, *Z. anorg. u. allegem. Chem.*, **320**, 1 (1963).
7. B. W. Batterman, *J. Appl. Phys.*, **28**, 1236 (1957).
8. J. R. Ligenza, *This Journal*, **111**, 62C (1964). (Abstract of paper given at the Toronto Meeting.)
9. W. Steinmaier and J. Blom, *ibid.*, **111**, 206 (1964).

Activation Energies in the Chemical Etching of Semiconductors in HNO_3-HF-CH_3COOH

A. F. Bogenschütz, W. Krusemark, K.-H. Löcherer, and W. Mussinger

Research Institute of TELEFUNKEN AG, Ulm, Germany

ABSTRACT

The intent of this paper is to clarify the reaction mechanism of the etching of (111)-oriented n-silicon and n-germanium in an etching solution of fum. HNO_3, conc. HNO_3, conc. HF, and glacial acetic acid. By comparing the temperature dependence of the etching rates and the temperature dependence of the viscosities of the etching solutions it was possible to show with some reliability that the investigated etching processes are diffusion controlled reactions. The performed mathematical calculations possibly allow the forecast of the effect of organic moderators and inhibitors in diffusion controlled etching systems, if the viscosity is known.

Mixtures consisting of several components are predominantly used for the chemical etching of semiconductor single crystals. Consequently the etching process generally comprises a number of parallel and secondary reactions which can be determined analytically only with difficulty. Without accurate knowledge of the chemical reaction mechanism it is difficult to produce etching solutions having the desired effect.

The activation energy yields some of the few criteria on etching mechanisms; it may be ascertained from the curve rise when the etching rate is entered logarithmically as a function of the reciprocal absolute temperature. Some attempts were described to draw conclusions on the reaction mechanism from such values (1-5). Since low activation energies around 4.5 kcal/mol (low dependence on temperature of corrosion rate) were measured in pure diffusion

processes according to Moelwyn-Hughes (6), it seemed obvious that a diffusion process dominates in etching processes with such activation energies. This means that either the diffusion of the components effective in etching to the semiconductor surface or the removal of reaction products determines the rate. As a rule oxidation reactions feature higher activation energies.

In previous investigations no direct comparison was made between the activation energy of the etching reaction and the activation energy of the diffusion process in the etching mixture. This paper describes such investigations. Since some technical difficulties are encountered in determining the activation energy of diffusion processes, we chose as standard of comparison the viscosity of the etching solution, which is easier to measure. This seems admissible since, according to the reasoning of Eyring (7), the viscosity, plasticity, and diffusion may be considered by virtue of the kinetic theory of liquids under the uniform aspect of a monomolecular reaction, whose elementary process is the transfer, for example, of a molecule from one equilibrium state to another through a potential threshold [*cf.* (8)]. Comparisons of the activation energy of the viscosity obtained in this manner, and thus the diffusion, and the activation energy of the etching process prove that the etching process actually is governed by a diffusion process in the systems Si/HF-HNO_3-CH_3COOH and Ge/HF-HNO_3-CH_3COOH which we investigated. The activation energy of the etching process and the activation energy of the viscosity, and thus the diffusion, agree within the error limit mainly.

Consequently it will be interesting to check, by further experiments on other diffusion controlled etching systems, whether or not the effect of an added organic moderator or inhibitor, such as acetic acid, tartaric acid, oxalic acid, formic acid, citric acid, tannic acid, ethylene glycol, propylene glycol, glycerin, butylamin, amylamin and n-butyl thiobutane, may be predicted by measuring the viscosity of the solution.

Experimental Part

As etching solution for our investigations a mixture was chosen which features a corrosion characteristic linear with time over a wide range of temperatures. The solution was 50 ml HNO_3 fum., 30 ml HNO_3 (65%), 20 ml HF (40%), and 80 ml glacial acetic acid. This mixture was used for etching on polished silicon and germanium wafers, the activation energy of the etching reaction resulting from the etching. In addition the activation energy of the viscosity was ascertained in the etching solution without semiconductor. These experiments are described next.

Etching experiments.—Single-crystal (111)-oriented n-silicon having a specific resistance of 25-35 ohm-cm and single-crystal (111)-oriented n-germanium ($g = 1$ ohm-cm) were used for the etching experiments described.

Following cutting and lapping the semiconductor wafers were polished chemically and mechanically as described in ref. (9) in such manner that a flat, structureless, pure surface was produced. The arrangement used for etching the semiconductor wafers is shown in Fig. 1. In this arrangement the semiconductor wafer is placed horizontally on a sievelike Teflon mount with a recess and immersed in the etching solution. The interference with the diffusion and thus the corrosion of the under surface, caused by the Teflon sieve, is much lower than 5% and may thus be neglected. As etching bath a covered Teflon can was used so that, by means of a thermostat, the temperature of the etching solution may be kept constant during the etching process. A magnetic stirrer rotating at 180 rpm was used to stir the etching liquid. In each etching process the volume of the etching solution was 100 ml.

In order to obtain reproducible test results the etching bath was first brought up to temperature without the etching solution over a period of 15 min prior to each etching process. Subsequently the freshly prepared solution was poured in the etching bath; its temperature was controlled thermostatically for a period of 15 min. Afterward the wafers were etched for 2 min, rinsed, dried, and weighed.

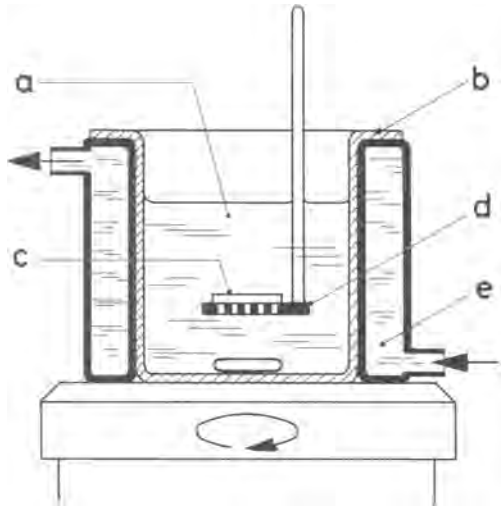

Fig. 1. Etching apparatus; (a) etching liquid, (b) Teflon container, (c) semiconductor wafer, (d) Teflon sieve, (e) thermostat.

The one-sided corrosion d followed from the equation

$$d = \frac{(G_1 - G_2)}{2F \cdot \gamma}$$

The weight $(G_1 - G_2)$ was determined by difference weighing. The surface of the wafers (F) was measured, and for the density γ the value 2.33 g/cm³ was inserted. The error caused by neglecting the narrow side surfaces of the wafer amounted to approximately 1%. The corrosion rate then corresponded to the quotient of corroded layer thickness on one side and etching time.

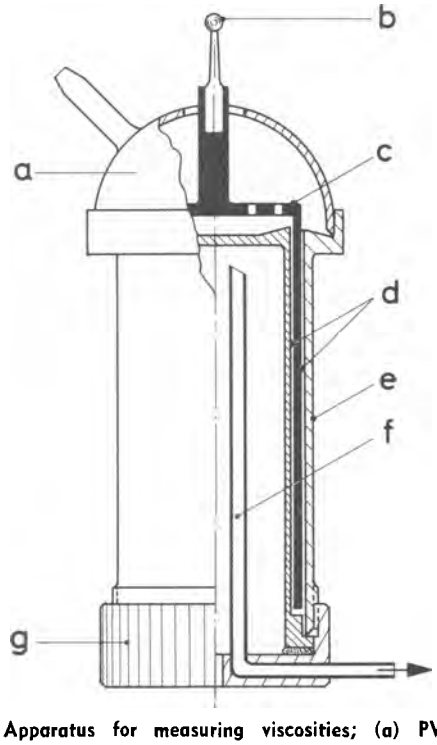

Fig. 2. Apparatus for measuring viscosities; (a) PVC-suction hood, (b) carrier ball (stainless steel), (c) measuring device (Teflon), (d) interspace for measuring solution, (e) Teflon case, (f) outlet tube to the thermostat, (g) Teflon-screw cap.

Values above 53°C were not used in the calculation of activation energy because at these temperatures the etching solution no longer features a defined composition due to the liberated nitrous gases and therefore does not yield reproducible results.

Viscosity measurements.—The viscosity measurements were performed on the same etching solution without semiconductor specimen using a Couette viscosimeter (Fig. 2). The etching solution was situated in the space between two cylinders arranged concentrically, in which a test body, likewise cylindrical, rotated. Teflon was chosen as the material for the test system. The shear force produced on the rotating test cylinder in consequence of liquid friction was measured by means of a torsion wire. In order to work at defined temperatures the test system was controlled thermostatically until the viscosity of the etching solution remained constant. Then the viscosity resulted in accordance with the equation $\eta = -\tau/D$. In this equation τ is the shear force in dyne · cm^{-2}, D is the gradient of shear force in sec^{-1}, and η is the viscosity in dyne ·-sec · cm^{-2}. This equation applies only for a Newton liquid (10), *i.e.*, for an etching solution in which the viscosity does not change under the influence of mechanical stress. Our etching solution complied with this requirement.

Evaluation of the Experimental Results

The dependence on temperature of the viscosity η is shown in Fig. 3. Accordingly ln η is a linearly rising function of $1/T$, the following thus applies

$$\eta \sim e^{\Delta E_{vis}/RT} \qquad [1]$$

For the magnitude of the activation energy ΔE_{vis} we obtained, in accordance with the Gaussian method of least squares

$$\Delta E_{vis} = 4.60 \pm 0.09 \text{ kcal/mol}$$

Equations like Eq. [1] were established empirically for liquids over fifty years ago (7). A corresponding theoretical equation

$$\eta = \frac{N \cdot h}{V} \cdot \frac{(2\pi mkT)^{1/2}}{h} \cdot \frac{6RT \cdot V^{1/3}}{\Delta E_{vap} N^{2/3}} \cdot e^{\Delta E_a/RT} \qquad [2]$$

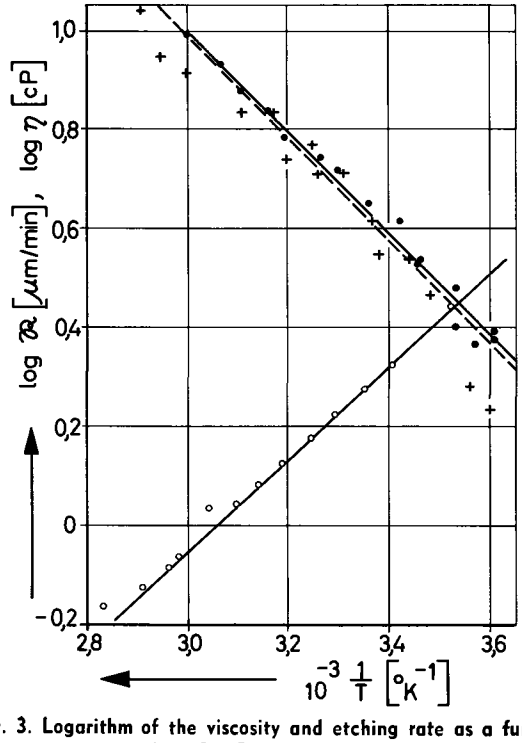

Fig. 3. Logarithm of the viscosity and etching rate as a function of temperature; • log $\mathcal{R}_1$ [µm/min] for silicon, × log $\mathcal{R}_2$ [µm/min] for germanium, ○ log η [cP].

was established by Eyring (7) [cf. (12)] by virtue of the kinetic theory of liquids. Here N is Avogadro's number, V the molar volume, h the Planck constant, k the Boltzmann constant, m the particle mass, ΔE_{vap} the molar evaporation energy, ΔE_a the activation energy per mol, R the gas constant and b the number 2 (for ordinary cube packing: for other packings the number is not very different).

If the dependence on temperature of the viscosity is determined primarily by the exponential factor in Eq. [2], then

$$\eta \sim e^{\Delta E_{vis}/RT}$$

applies in agreement with the empirical form [1] if $\Delta E_a = \Delta E_{vis}$. The dependence on temperature of the corrosion rates $\mathcal{R}_1$ and $\mathcal{R}_2$ is shown in Fig. 3 likewise. Accordingly ln $\mathcal{R}_1$ and ln $\mathcal{R}_2$ are linear falling functions of $1/T$, and it follows that

$$\mathcal{R}_{1,2} \sim e^{-\Delta E_{Etch\ 1,2}/RT} \qquad [3]$$

A connection with the form of Eq. [3] also follows from a theoretical formula by Camp (13), insofar as the etching process is characterized essentially by a single activation energy. For the magnitude of the activation energies $\Delta E_{Etch\ 1,2}$ we obtain by the Gaussian method of least squares

$$\Delta E_{Etch\ 1} = 4.72^{+0.5}_{-0.9} \text{ kcal/mol (for silicon)}$$

and

$$\Delta E_{Etch\ 2} = 4.96^{+0.1}_{-0.4} \text{ kcal/mol (for germanium)}$$

(The error was not calculated in this case but estimated only with reference to Fig. 3. It is much higher than in the findings from the viscosity measurements because the measurement of the corrosion rate is subject to a higher uncertainty.)

Within the measurement error ΔE_{vis} and ΔE_{Etch} agree for both silicon and germanium. From this fact we conclude that a diffusion determining procedure is primarily concerned in etching by the etching solution under consideration here, the type of etched semiconductor material playing only a minor part.

As regards diffusion-controlled processes it can be assumed with some justification that $\mathcal{R}$ is proportional to the diffusion coefficient D of the etching solution components effective in the corrosion process. Since according to the theory $\eta \cdot D = \text{const} \cdot T^n$ in addition, it follows that ΔE_{vis} must be equal to ΔE_{Etch} too according to [1] and [3]. The dependence on temperature of the product $\eta \cdot D$ in accordance with an exponential law, which is indicated by the theory, ought not to be significant in a small temperature range.

From the foregoing it will be seen that the condition $\eta \cdot \mathcal{R} = \text{const.}$ must be satisfied in diffusion-controlled processes. A graphic presentation of the product $\eta \cdot \mathcal{R}$ with the measured data indicates stability for both silicon and germanium over a temperature range from approximately 18° to 53°C (cf. Fig. 4 and 5). At lower temperature between 1° and 18°C possible induction periods in the corrosion may cause falsification of the test results. At temperatures above 53°C the nitrous gases start to be liberated from the

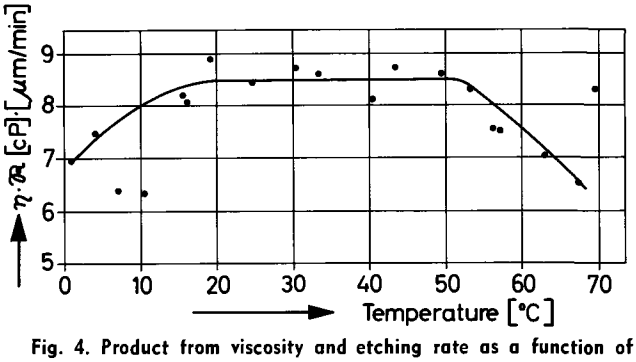

Fig. 4. Product from viscosity and etching rate as a function of temperature for the system silicon/etching solution.

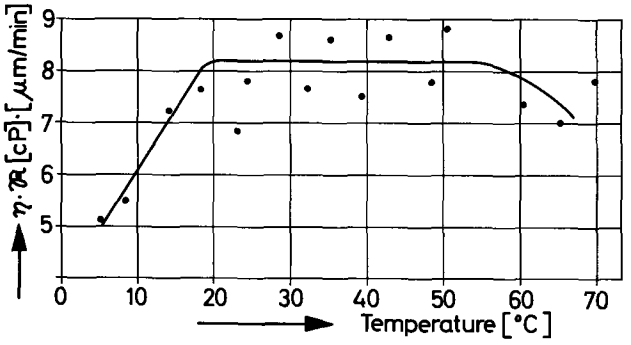

Fig. 5. Product from viscosity and etching rate as a function of temperature for the system germanium/etching solution.

etching solution thus causing a change in the composition of the etching solution.

Additional experiments, during which the glacial acetic acid moderating components were replaced by the same volumes of trichloracetic acid, o-phosphoric acid, or o-phosphoric acid saturated with P_2O_5, clearly confirm that the corrosion rate may drop by several decimal powers with increasing viscosity of the solution in diffusion-controlled etching systems. However, in such comparative cases it must be borne in mind that changes in the concentration of the moderating components may give rise to concentration shifts within the components effective in corrosion and thus alter the character of the etching system.

Manuscript received Jan. 23, 1967; revised manuscript received April 18, 1967.

Any discussion of this paper will appear in a Discussion Section to be published in the June 1968 JOURNAL.

REFERENCES

1. T. E. Burgess, *This Journal*, **109**, 341 (1962).
2. J. Bloem and J. C. van Vessem, *ibid.*, **109**, 33 (1962).
3. B. Schwartz and H. Robbins, *ibid.*, **108**, 365 (1961).
4. D. L. Klein and D. J. D'Stefan, *ibid.*, **109**, 37 (1962).
5. N. Cerniglia and P. Wang, *ibid.*, **109**, 508 (1962).
6. E. A. Moelwyn-Hughes, "Kinetics of Reactions in Solution," p. 370, Clarendon Press, Oxford (1947).
7. Eyring, *J. Chem. Phys.*, **4**, 283 (1936).
8. B. Ilschner, *Z. Metallkunde*, **57**, 194 (1966).
9. A. F. Bogenschütz, W. Langheinrich, and W. Mussinger, *Metalloberfläche*, **18**, 193 (1964).
10. K. A. Wolf, "Kunststoffe," Vol. 1, pp. 213-231, Springer-Verlag, Berlin, Göttingen, Heidelberg (1962).
11. R. H. Ewell, *J. Appl. Phys.*, **9**, 252 (1938).
12. A. Eucken, "Lehrbuch der Chemischen Physik," 3rd Ed., Vol. II, 2, p. 910, Akad. Verlagsges. Geest & Portig KG, Leipzig (1949).
13. P. R. Camp, *This Journal*, **102**, 586 (1955).

Technical Note

The Preparation and Electrical Resistance of Single Crystals of β-US_2

P. K. Smith and L. Cathey[1]

Savannah River Laboratory, E. I. du Pont de Nemours and Company, Aiken, South Carolina

Semiconducting compounds of alpha-emitting isotopes have potential applications as components of self-heating thermoelectric elements. Alpha-emitting actinide compounds with semiconductor properties are being sought, initially using uranium as a stand-in for elements with more highly radioactive isotopes.

Electrical properties of semiconductors are more meaningful when determined on single crystals. However, single crystals of pure compounds of the actinide elements with group V and VI elements are difficult to prepare because most decompose at high temperatures, have high melting points, and are incompatible with container materials. For example, orthorhombic β-US_2 transforms to tetragonal α-US_2 at 1350°C and vaporizes with a preferential loss of sulfur near 1500°C(1); thus single crystals cannot be made by melting or sublimation.

To avoid these difficulties, we have successfully used the vapor-transport technique described by Schäfer (2) to form small single crystals of orthorhombic β-US_2. Using this technique, polycrystalline US_2 was reacted with iodine at 940°C, and the gaseous uranium iodide and sulfur were transported down a temperature gradient and deposited at 700°C as single crystals of β-US_2. Resistance-temperature measurements on the β-US_2 crystals indicated that the crystals were semiconductors with a low activation energy for charge carrier generation.

Experimental

β-US_2 was prepared in two ways: (*i*) by reacting the elements, and (*ii*) by reacting H_2S with uranium. In the first method, a heavy-walled "Vycor"[2] transport tube (250 mm long x 19 mm OD and constricted to 8 mm ID in the center to minimize cross-contamination during handling) was outgassed at 1000°C under a vacuum of 10^{-4} mm. Stoichiometric quantities of electropolished, reactor-grade, natural uranium chips and reagent-grade sulfur were loaded into opposite ends of the transport tube. A thin-walled, glass ampule containing about 250 mg of spectroscopic-grade iodine (8 mg/cc to produce an iodine pressure of 2 atm at 1000°C in the tube) was placed in the transport tube. After the transport tube was sealed, the iodine was released by exploding the ampule with a torch. The sulfur was then distilled onto the uranium at 1000°C. By introducing the transport tube slowly into the fur-

[1] Present address: University of South Carolina, Columbia, South Carolina.

[2] Trademark of Corning Glass Works, Corning, New York.

nace, the rate of sulfur distillation was limited; thus the reaction rate and overheating were controlled. Thick heterogeneous layers of powdery β-US_2 and sulfur-rich phases were formed on small residual platelets of unreacted metal. This product was then transported to the other end of the tube in a controlled temperature gradient during long-term heatings.

In the second method, powdered β-US_2 was prepared by the reaction of flowing H_2S with uranium metal chips at 800°C in a tube furnace. X-ray diffraction analysis showed that the heterogeneous product was principally β-US_2, but contained small quantities of UOS. This material and iodine were loaded into the outgassed transport tube, and the β-US_2 was transported to the cool end of the tube where it deposited as single crystals.

An attempt was made to prepare US in the transport tube by the first preparative technique, using a stoichiometric ratio of the elements. The product formed on the uranium chips was predominantly β-US_2. Subsequent transport of this preparation produced β-US_2 crystals.

The crystal phases in the transported material were determined by x-ray diffraction using the Debye-Scherrer technique. The materials were analyzed chemically for uranium and sulfur and spectrographically for impurity metals. The needle crystals of β-US_2 in the product were analyzed for silicon by atomic absorption, and for iodine by spark-source mass spectrometry.

The electrical resistance of the crystals was measured from 113° to 472°K. These data were used to determine if the crystals were semiconducting and to estimate the energy gap for charge-carrier activation in the material.

The four-point mount shown in Fig. 1 was used to make resistance measurements on uniformly shaped needle crystals formed from US_2 prepared from H_2S and uranium. The back support is an epoxy-bonded, fiberglass circuit strip with copper foil on the two edges. The sample crystal spans the 1.1-mm gap between the two strips. The two potential contacts were made from No. 36 copper wire and were spaced 0.15 mm apart. All contacts with the crystal were made with gallium metal, which apparently wets the US_2 crystal and forms a nearly ohmic contact. The surface tension of the liquid gallium held the contacts in place above 300°K.

Results

In every experiment, the crystals formed at the cold end of the transport tubes were single-phase β-US_2. Two types of crystals were formed: about 80% was a fine microcrystalline powder; the remainder was needle crystals, 2-8 mm long and 0.2-0.5 mm in diameter (Fig. 2), which appeared to have grown as high-pitched spirals as if growth had proceeded along a screw dislocation.

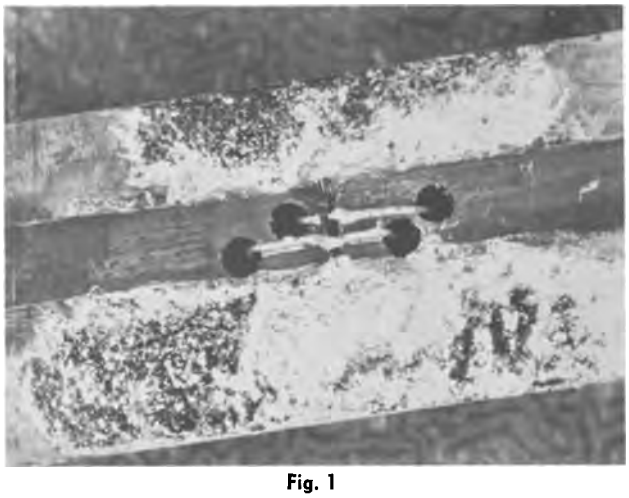

Fig. 1

Fig. 2

Transport rates were slow, about 20 mg US_2/hr for temperatures of 940°C at the hot zone and 700°C at the cold zones; only 0.3 mg/hr was transported in a 780°/600°C gradient. No transport was detected when the ΔT across the transport tube was below 140°C or when iodine was absent.

X-ray diffraction analysis of samples from both ends of the transport tubes indicated that the US_2 reacted with Vycor slowly at 700°C and more rapidly at 940°C to produce UOS. Analyses of the microcrystalline material from near the tube wall showed considerable UOS contamination in the β-US_2 after the 940°/700°C gradient heating; samples from the center of the material showed much less UOS. Much less UOS was observed in samples from the cold end of the tube relative to that in the hot end.

Chemical analyses were performed on the material transported in the 940°/700°C gradient. The composition of this acid-soluble, microcrystalline material was $US_{1.97\pm0.10}$. The total of the sulfur and uranium analyses combined with the 3.6 w/o (weight per cent) insoluble oxysulfide accounted for 100% of the sample. The principal impurities in the microcrystalline material were silicon, aluminum, and iron, as determined by emission spectroscopy (Table I). The silicon content was determined independently to be 1750 ±250 ppm.

The needle crystals by themselves were not analyzed for sulfur-to-uranium ratio. It was assumed that since the needle crystals were formed under the same pressure and temperature conditions as the microcrystalline product, the composition was the same.

The impurity concentrations in the needle crystals, particularly oxygen and silicon introduced from the reaction of US_2 with Vycor, were thought to be lower than for the microcrystalline material. The needle crystals were entirely soluble in sulfuric acid, in-

Table I. Emission spectrographic analysis of microcrystalline US_2. US_2 was formed by vapor transport in a 940°/700°C gradient

Element	Concentration, ppm	Element	Concentration, ppm
Si	>1000	Cr	15
Al	500-1000	Cu	10
Fe	500-1000	Mn	<10
Mo	500	V	1-10
Ni	50	Pb	7
B	20-50	Bi	<2
Ca	10-50	Cd	1.2
Zr	<50	Sn	<1
Mg	15	Ag	<0.1

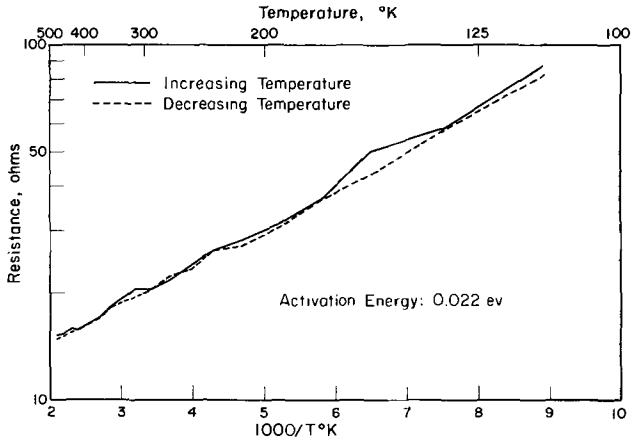

Fig. 3

dicating the absence of oxides or oxysulfides in the crystals. The iodine concentration in the needle crystals was 400 ppm.

The electrical resistance of the needle crystals decreased with increasing temperature, a behavior that is characteristic of a semiconducting material. The activation energy for charge-carrier formation was about 0.022 ev, as determined from the slope of the graph of R *vs.* $1/T$ (Fig. 3). Because of the relatively high impurity content of the crystals, it is not clear whether the conduction observed in β-US_2 is intrinsic or extrinsic. Resistance, rather than resistivity, is reported because the contacts were not uniform. Although the sample length and area could not be measured accurately, the sample areas were approximately 0.2 mm^2. The length was approximately the potential probe separation. The resistivity at 300°K is then near 25 ohm-cm. No other measurements on US_2 are reported for comparison.

Discussion

The transport of US_2 from higher to lower temperatures is consistent with either of two reactions:

$$US_2(c) + 3/2\,I_2(g) = UI_3(g) + S_2(g) \qquad [1]$$

$$US_2(c) + 2\,I_2(g) = UI_4(g) + S_2(g) \qquad [2]$$

The standard heats for the reactions in Eq. [1] and [2] at 298°K were estimated as 56 kcal and 34 kcal, respectively. Since the reactions are endothermic, transport of US_2 from high to low temperatures is expected in both cases.

Most effective transport will occur when the free energy of the reaction, $\Delta G°_T$, is near zero (2). Since the values for $\Delta H°_{298°K}$ are relatively large, transport can occur only if $\Delta S°_{298°C}$ for the reactions are positive; these values are estimated from data on analogous chemical systems to be about 38 and 17 eu, respectively. Values for $\Delta G°_T$, calculated assuming that $\Delta C°_P$ is zero, are given in Table II.

Table II. Estimated free energies *vs.* temperature for transport reactions

°C	$\Delta G°_T$, kcal	
	Reaction [1]	Reaction [2]
700	18	17
900	10	14
1200	0	9

These values are generally consistent with the observation that transport increases with an increasing average temperature and with increasing gradients. At 700°/600°C, little transport occurs by either reaction; at 940°/700°C, both reactions may contribute, with reaction [1] becoming more important as the temperatures are raised to 1200°C. Transport by a reaction involving formation of a ternary molecule such as $USI_2(g)$ may also be possible.

It should be easier to transport disulfides of transuranic elements or compounds of the actinides with the same stoichiometry combined with groups IVA, VA, and VIA elements lower in the periodic table. The heats of formation of these compounds should be lower than that of US_2. Consequently, $\Delta G°_T$ for reaction [1] stoichiometry will be closer to zero at lower temperatures than for US_2. Bro (3) has transported various rare earth ditellurides with I_2 in a 900°/700°C gradient, suggesting that ditellurides of actinide metals can be transported.

The transport of US was not observed in this work, but it should be possible. It is not immediately apparent how the transport criteria change for compounds with different stoichiometry. Generally, as the ratio of metal to nonmetal decreases, both $\Delta H°$ and $\Delta S°$ decrease. However, as $\Delta H°$ decreases, there is more amplitude to adjust the temperature to make $\Delta G°_T$ close to zero by varying the $T\Delta S°_T$ term. The transport of US_2 observed in the tube charged with equimolar amounts of uranium and sulfur (to produce US) probably is caused by the mixture of U, US_2, and higher sulfides in the US preparation.

Substituting Br_2 or Cl_2 for I_2 should increase transport rates of compounds with metal-to-nonmetal ratios of one-half, and should make possible transport of the more stable actinide compounds, *e.g.*, US. The heat of formation of $UX_3(g)$ increases from I_2 to Br_2 to Cl_2. Substitution of these halogens makes $\Delta H°_T$ smaller for reaction [1] without changing $\Delta S°_T$ significantly. Consequently, transport can be effected at a lower temperature since $\Delta G°_T$ will approach zero at a lower temperature, or transport rates should be higher for the same average gradient temperature.

Acknowledgment

The information contained in this article was developed during the course of work under Contract AT(07-2)-1 with the United States Atomic Energy Commission.

Manuscript received April 26, 1967; revised manuscript received *ca.* June 12, 1967.

Any discussion of this paper will appear in a Discussion Section to be published in the June 1968 JOURNAL.

REFERENCES

1. M. Picon and J. Flahaut, *Bull. Soc. Chem., France*, 772 (1958).
2. Harold Schäfer, "Chemical Transport Reactions," Academic Press, New York (1964).
3. P. Bro, *This Journal*, **109**, 1110 (1962).

Brief Communication

Liquid Encapsulation Zone Refining (LEZOR)

E. M. Swiggard

Naval Research Laboratory, Washington, D. C.

The use of a two-liquid zone melting system was anticipated by Pfann (1). He placed particular emphasis on the use of a liquid to support a large zone in a vertical ingot and to prevent contamination of the melt by a solid container. Metz *et al.* (2) and Mullin *et al.* (3) have applied the two-liquid system to growth of single crystals of decomposable solids in a conventional crystal puller. They used B_2O_3 as the second liquid and found that the B_2O_3, even though less dense than most semiconductor materials, wet the crucible and formed a liquid film between the crucible and the melt, hence the term "liquid encapsulation." In this work liquid encapsulation has been extended to zone refining. For the sake of brevity this author has adopted the acronym "LEZOR" to stand for liquid encapsulation zone refining. We report here a description of the vertical LEZOR technique and the results obtained with 40 ohm-cm Ge, InAs, Cd_3As_2, and Zn doped Ge.

A detailed schematic of the equipment used is shown in Fig. 1. The apparatus consisted of two resistance furnaces to keep the B_2O_3 liquid, an rf coil to maintain the molten zone, an open end capsule for the charge, a pedestal to support the capsule at the desired height, and an outer tube to contain the atmosphere. The charge was in rod form, the dimensions of which were such that it filled the capsule reasonably well but would slide readily. The capsule was heavy wall quartz (8 mm ID x 12 mm OD). One gram of previously dried B_2O_3 was placed at the bottom of the capsule and the charge on top of this. The tip of the capsule was initially positioned in the lower furnace. The system was then evacuated, and, while still pumping, the temperature of the furnace was raised to 650°C. This procedure was followed in order to remove surface moisture on the dried B_2O_3. In the case of Cd_3As_2 (mp 720°C) the furnace temperature was raised to only 550°C. The system was kept in this condition for about 1 hr before the pump was turned off and pure H_2 admitted. After a steady gas flow was established the rf generator was turned on and the tip of the capsule moved under the rf coil. During the pump out procedure the charge slowly dropped through the molten B_2O_3 until it rested on the bottom of the capsule. An inch or more of the charge was encapsulated in B_2O_3. The rf power was raised until a molten zone was established. The capsule was then lowered through the coil at 1-2 iphr. As the capsule was lowered the liquified charge, which was more dense than the B_2O_3, filled the lower part of the capsule leaving only a thin layer of B_2O_3 between the capsule and the charge. During the initial pass the furnace temperature was slowly lowered to 550°C, and minor adjustments in rf power were made. Proper shaping of the charge and careful observation during the initial pass to see that the travel did not exceed the speed with which the charge would drop through the B_2O_3 were the critical steps. If the charge was fragmented there was a tendency for the fragments to become wedged in the tube preventing them from falling into the melt. If the charge failed to fall properly, the zone separated and the B_2O_3 was left behind. Melting and refreezing of a charge not encapsulated in B_2O_3 usually resulted in a broken capsule. Sometimes the separation could be corrected by pushing with the quartz rod inserted through the top of the apparatus. Due to the high viscosity of B_2O_3 the charge was sluggish in its downward movement and occasionally had to be pushed with the rod mentioned above. If the travel exceeded the speed with which the charge would fall, the zone would separate and the same difficulties described above would occur. After the initial pass the zone refining process could be repeated without difficulty. The usual number of passes was 15-20, but in one case Cd_3As_2 was subjected to 35 zone refining passes. Figure 2 is a close-up of the liquid zone in Ge. The two solid-liquid interfaces are clearly visible. Bubbles such as the ones seen in Fig. 2 were observed, and they became more numerous on subsequent passes.

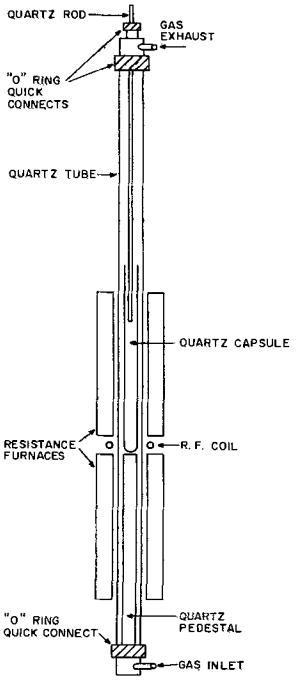

Fig. 1. Schematic of LEZOR apparatus

To complete the run the capsule was positioned so that the tip of the capsule was in the rf field, but the power was lowered so that the ingot was maintained at a temperature below its melting point but above the softening point of B_2O_3. The lower furnace was cooled to room temperature and the capsule lowered through the coil. As the tip of the capsule cooled, the B_2O_3 froze and broke the capsule and ingot. In order to evaluate the run it was necessary to dissolve the B_2O_3 in water and select unbroken pieces of the ingot for electrical measurements. Various cooling cycles were tried, but the ingot was always severely fractured.

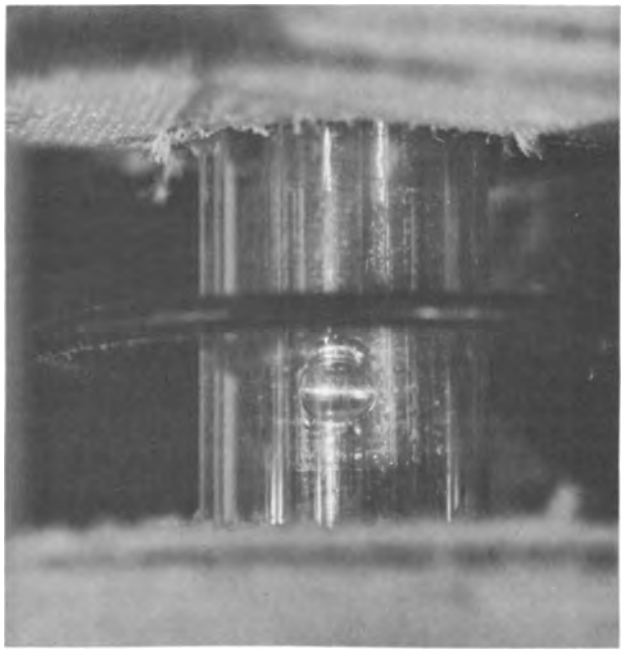

Fig. 2. Molten zone in B_2O_3 encapsulated Ge ingot

A summary of zone refining results is shown in Table I. The effectiveness of LEZOR was clearly seen in the case of Ge for which it was also observed that the low field breakdown emf at 4.2°K was 2.8 v/cm. Such a low value indicates that the concentration of compensating impurities is small. Despite the fact that high-purity InAs was zone refined 19 times it showed no change in carrier concentration. This probably indicates that the residual impurity has a segregation coefficient very close to one. The carrier concentration of Cd_3As_2 was reduced by a factor of 2. This result was achieved in both cases despite the fact that for the first ingot only a few passes were taken and the ratio of ingot length to zone length was only 6, while for the second ingot 35 passes were made and the ingot to zone length was 17. While the reduction in carrier concentration may be due to purification it is possible that improved stoichiometry or a combination of the two effects is responsible.

Table I. Impurity concentration, cm^3

Material	Starting material	After LEZOR	Zone melting phases
Ge*	8×10^{13} (p)	2.3×10^{12} (p)	18
InAs*	2×10^{16} (n)	2×10^{16} (n)	19
Cd_3As_2**	2×10^{18} (n)	1×10^{15} (n)	6
Cd_3As_2*	2×10^{18} (n)	1×10^{15} (n)	35

* Ingot length 23 cm—zone length 1.3 cm.
** Ingot length 11.5 cm—zone length 1.8 cm.

In order to study the liquid encapsulation technique with respect to volatile impurities a Zn doped Ge ingot was prepared. In this case the zinc was placed in the capsule under the B_2O_3 and the usual procedure followed. Only one zone melting pass was taken. Using the published value of the segregation coefficient of Zn in Ge (4×10^{-4}) the amount of Zn required to give an ingot containing 2×10^{17} carriers/cc was added. The resulting inogt had a uniform zinc concentration of 2.5×10^{17} carriers/cc. This result clearly shows that liquid encapsulation can prevent loss of volatile impurities and can eliminate vapor phase shunting of impurities during the zone refining process. Mullin (4) reports similar results pulling Zn doped Ge.

Severe fracture of the ingot presently limits the usefulness of LEZOR to material purification and exploratory investigations. It is possible that other encapsulating liquids and other capsule materials might be found to alleviate this problem. A possible solution would be to use a horizontal LEZOR process and remove the B_2O_3 by a gaseous reaction while it is still liquid. The reaction of B_2O_3 and methanol to form gaseous methylborate at 400°C was tried and showed considerable promise.

Acknowledgments

The author is indebted to O. Imber for technical assistance in the experimental work, E. D. Palik and B. Henvis for measurement of the carrier concentration in Cd_3As_2, and H. Shenker for valuable discussions. This work was performed under Project Defender, sponsored by the Advanced Research Projects Agency, Department of Defense, via the Office of Naval Research.

Manuscript received May 8, 1967; revised manuscript received June 2, 1967.

Any discussion of this paper will appear in a Discussion Section to be published in the June 1968 JOURNAL.

REFERENCES

1. W. G. Pfann, "Zone Melting," 2nd ed., p. 117, John Wiley & Sons, Inc., New York (1966).
2. E. P. A. Metz, R. C. Miller, and R. Mazelsky, *J. Appl. Phys.*, **33**, 2016 (1962).
3. J. B. Mullin, B. W. Straughan, and W. S. Brickell, *J. Phys. Chem. Solids*, **26**, 782 (1964).
4. J. B. Mullin, Private communication.

Corrections

In the paper "Structural Studies of Porous Electrodes" by E. Y. Weissman (July 1967 Journal, pp. 658-665), Equation [3] should read

$$T_s = \frac{6.6(\log_{10} p_s - 6.49594) - 255.821}{\log_{10} p_s - 6.49594} \qquad [3]$$

On the left hand side of Eq. [9] the exponent should read

$$(1 - \alpha)$$

High Activity Platinum Electrocatalysts for the Direct Anodic Oxidation of Saturated Hydrocarbons

E. J. Cairns[1] and E. J. McInerney[2]

General Electric Research and Development Center, Schenectady, New York

ABSTRACT

The fact that hydrocarbon fuels can be directly oxidized at reasonable current densities using fuel cells with platinum anodes and acidic electrolytes has been demonstrated previously. The next logical step was to reduce the amount of platinum electrocatalyst required for a given current density. Two approaches have been taken toward this objective: the preparation of higher activity unsupported electrocatalysts, and the use of conducting support materials to permit more effective utilization of the platinum. Results are reported for the anodic oxidation of both gaseous and liquid normal saturated hydrocarbons using a number of unsupported and carbon-supported electrocatalysts. Indications are that power densities of about 35 mw/cm^2 (resistance-free) are possible with a propane-oxygen fuel cell using 36 m/o (mole per cent) hydrofluoric acid at 105°C as the electrolyte with an anode containing 10 mg Pt/cm^2 as a carbon-supported electrocatalyst.

There has been a concerted effort during the last few years to accomplish the direct anodic oxidation of saturated hydrocarbons in fuel cells. This has been achieved by several investigators, all using platinum as the electrocatalyst. The amount of platinum used has ranged from 45 to 180 mg/cm^2 and the electrolytes used have been cesium carbonate (1, 2), sulfuric acid (3), phosphoric acid (4-6), hydrofluoric acid (7, 8), and cesium fluoride-hydrofluoric acid mixtures (7-9). The temperatures used in these investigations have ranged from 100° to 200°C. The normal saturated hydrocarbons which yielded the highest current densities were ethane, propane, and butane (2, 3, 5, 7, 10); consequently, most of the work has been done with them.

Even though acceptable performances have been obtained with the systems mentioned above, it has not been economically interesting to attempt the construction of practical power sources, largely because of the high cost of the large amounts of platinum necessary to obtain reasonable power densities. The next logical step after proving operational feasibility was to attempt to improve the economics of the system by reducing the amount of platinum required. Several approaches can be taken toward this goal:

1. Make more effective use of the platinum by preparing higher area blacks.
2. Prepare very high-area platinum on a support which can act as a current collector and perhaps also as an enhancement to the platinum activity.
3. Alloy the platinum with other metals in such a way that more activity per unit weight of platinum is obtained.
4. Replace the platinum with a less costly, but effective, electrocatalyst.

The first method listed above has not previously met with a great deal of success because platinum black with a specific surface area significantly above 15 m^2/g sinters under conditions of electrode preparation and may sinter with use at the higher fuel cell operating temperatures, resulting in a fairly rapid loss of area. The fourth method is generally considered the most difficult due to the multiple requirements placed on any successful electrocatalyst, not the least of which is excellent corrosion resistance to hot acids. The present work is concerned with approaches 1 and 2 above.

[1] Present address: Argonne National Laboratory, Argonne, Illinois.

[2] Present address: General Electric Company Major Appliances Division, Louisville, Kentucky.

Experimental

Electrolyte.—The electrolyte chosen for this work was the maximum-boiling HF-H_2O azeotrope, containing approximately 36 m/o hydrofluoric acid which boils at approximately 112°C (7, 8, 11). This electrolyte has several advantages:

1. Because it is an azeotrope, its composition can be considered essentially uniform with time and position in the system.
2. It can support high current densities at a moderate temperature, allowing a wider range of current densities to be studied, thus simplifying the analysis of results.
3. It has provided for smooth, continuous operation with no cycling of the cell potential or current with any fuel under any of the test conditions.
4. It has fluid properties similar to those of water, so pumping and flow are not a problem.

The electrolyte was prepared from Baker and Adamson reagent grade 48 w/o (weight per cent) hydrofluoric acid having less than 20 ppm impurities, and from quartz-redistilled water. The temperature of operation was 105°C. This is near the maximum operational temperature attainable with this electrolyte at atmospheric pressure, and its selection is consistent with carbon deposition considerations (12, 13) and previously observed performance-temperature relationships (8). Under these conditions, the electrolyte has a resistivity of 1.8 ohm-cm (11).

Apparatus.—All portions of the apparatus which contacted the electrolyte were fabricated of Teflon in order to prevent any contamination of the electrolyte. The cell parts are shown in Fig. 1. The gas compartments were circular, 3 mm deep, and had an area

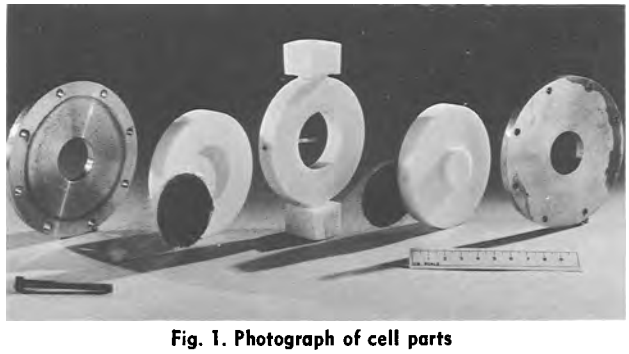

Fig. 1. Photograph of cell parts

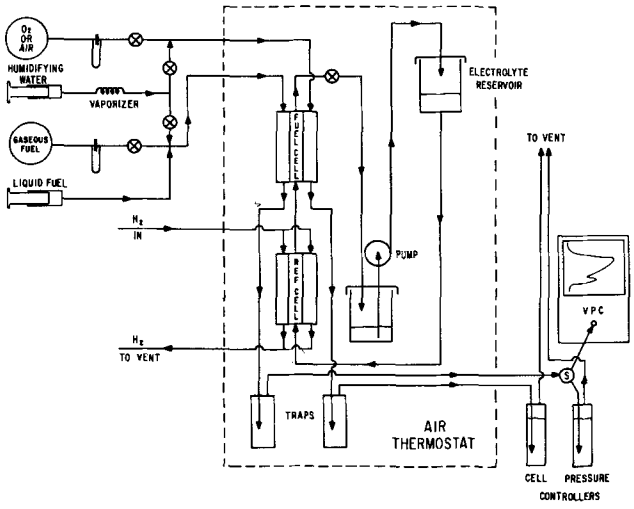

Fig. 2. Schematic diagram of fuel cell apparatus

of 11.38 cm^2. The electrolyte compartment had identical dimensions. The cell parts were assembled with electrodes as shown in Fig. 1. The assembly was held rigid by the Monel end plates and bolts.

A schematic diagram of the entire apparatus is shown in Fig. 2. This apparatus is similar to that discussed in ref. (2), (7), and (8). The fuel cell and an identical reference cell were operated in a forced-convection air thermostat maintained at 105°C. The reference cell contained two high-area reversible hydrogen reference electrodes of Teflon-bonded platinum black. Gaseous fuel and oxidant flows were controlled with needle valves and were monitored using capillary-tube flowmeters. The liquid fuel flow rate was set by use of a constant-speed (0.01%) syringe drive. The injection of humidifying water into either the fuel or oxidant stream was provided for, but this was not required with the azeotropic electrolyte. The exit gas streams from both cells passed through traps (which separated any liquid present) and then to water bubblers before venting. The exit fuel stream could be sampled and analyzed by a vapor-phase chromatograph as desired.

The electrolyte was circulated by gravity from an upper reservoir, passing upward through the reference cell and fuel cell at a flow rate of 2 or 3 cell volumes per minute. The effluent from the upper cell passed into a standpipe to eliminate any syphon action and was collected in a lower basin from which it was pumped to the upper reservoir by means of an all-Teflon microbellows pump. The electrolyte flow rate was controlled by varying the amount of head supplied by the upper reservoir.

Electrodes.—The electrodes were of the Teflon-bonded variety; 45 mesh platinum screen was used both for support and as a current collector. A porous Teflon wetproofing film was incorporated on the gas side of the electrodes. These electrodes were similar in structure to those originally reported by Niedrach and Alford (14), although the preparation techniques were sometimes different, as dictated by the physical properties and behavior of the electrocatalyst materials. When the platinum present in the electrode was in an oxidized rather than an elemental form, the removal of the aluminum foil used as a backing material during the fabrication was done electrochemically. The premature reduction of the catalyst to elemental platinum by the hydrogen generated during the chemical stripping processes was prevented by maintaining the electrode at a potential higher than that required for oxygen evolution. The hydrogen formed during the electrochemical reaction was evolved from a counter electrode sufficiently removed from the test electrode to prevent the hydrogen from diffusing back to the test electrode through the solution. The oxidized platinum present in the test electrode was subsequently reduced under carefully controlled conditions before testing in the fuel cell. This reduction was usually accomplished *in situ* by electrochemical and/or chemical methods.

Electrocatalysts.—Several electrocatalysts were tested, falling into two main categories: unsupported and supported.

The unsupported commercial electrocatalysts tested were platinum, palladium, iridium, and rhodium. The two remaining platinoid elements were not tested for the following reasons: ruthenium is corrosively attacked by the hot hydrofluoric acid electrolyte and osmium forms dangerous volatile oxides under the conditions of electrode preparation. All of the unsupported electrocatalysts were tested in the form of commercial blacks which were prepared by reduction from aqueous solution. The platinum black had a specific area of about 20 m^2/g; the palladium, iridium, and rhodium blacks had lower specific areas. Platinum was also tested by subjecting Adams catalyst ($PtO_2 \cdot H_2O$) to the previously mentioned *in situ* reduction procedures which result in a high-area platinum black. Adams catalyst from two sources was tested: commercial Adams catalyst, and some freshly prepared by the authors and denoted as PtO_2-Preparation A. The Adams catalyst was prepared by the usual procedure involving the oxidation of a platinum salt in a fused sodium nitrate bath (15-21).

Carbon is one of the few inexpensive materials which show excellent resistance to hot acidic electrolytes and is electronically conducting. Many types of carbon power are available, covering a wide range of physical properties. Not all of these powders, however, are compatible with the techniques used in the preparation of Teflon-bonded electrodes. The selection of the candidate substrates is limited to those powders which can be fabricated into useful electrode structures. The carbon powders with low specific areas (10-50 m^2/g) and particle sizes in the range 0.1-10μ have usually been employed with the most success. The one which most consistently yielded useful electrodes is a byproduct of the production of calcium cyanamid from calcium carbide. This carbon powder was obtained from the American Cyanamid Company and its properties are given in Table I (22).

Various carbon-supported electrocatalysts were prepared and evaluated. The carbon powder described in Table I was used as the substrate in every case. These electrocatalysts were prepared by various methods involving the deposition of a platinum salt from an aqueous solution onto the carbon surface. This deposition was followed either by room-temperature hydrogen reduction to elemental platinum (preparation 10) or by roasting in air to prepare an oxidized form of platinum on the carbon surface (preparations 20 and 21). When the oxidized form of platinum was present, the electrocatalyst was subjected to the previously mentioned *in situ* reduction process prior to testing.

Several commercially available carbon-supported electrocatalysts were also evaluated. Specific information concerning their preparation is proprietary and therefore was not available to the authors, but they were prepared by a variety of techniques involving the deposition of platinum black or a platinum salt on the surface of a carbon powder followed by reduction, as necessary.

Table 1. Properties of carbon powder (22)

Purity	99%
Impurities	SiO_2, CaO, Fe_2O_3, Al_2O_3
Particle diameter	0.25-2.0μ
Specific surface area	11.4 m^2/g
Resistivity @ 2000 psi	0.02 ohm-cm
Bulk density @ 2000 psi	1.28 g/cm^3
Porosity @ 2000 psi	40%
Structure	graphite

Fuels and oxidant.—Propane was chosen as the gaseous hydrocarbon fuel of primary interest and n-octane (bp = 125.7°C) was considered to be representative of the liquid hydrocarbon fuels. Matheson instrument-grade propane, 99.5 m/o minimum purity, and Philips research grade n-octane, 99.85 m/o minimum purity, were used. Other fuels tested were: Matheson ultra-high-purity methane, 99.95 m/o minimum purity; Matheson C.P. ethane, 99.0 m/o minimum purity; Matheson instrument grade n-butane, 99.5 m/o minimum purity; Phillips research grade n-pentane, 99.84 m/o minimum purity; Phillips research grade n-hexane, 99.85 m/o minimum purity; Phillips research grade n-decane, 99.49 m/o minimum purity.

The oxidant in every case reported was electrolytic grade oxygen, 99.6 m/o minimum purity.

Electrical measurements.—Electrical measurements were carried out using a 60 Hz modified Kordesch-Marko interrupter circuit (23, 24). The application of the 60 Hz interrupting frequency has been shown to have a limitation when rapid electrochemical reactions take place on electrodes containing only small amounts of active catalyst (25). The recovery of the cell potential during the period of interruption was checked using an oscilloscope to view the cell potential as a function of time during the operation of the interrupter. With an anode containing 8 mg Pt/cm^2 as a carbon-supported platinum electrocatalyst, the cell potential recovered about 5 mv at a current of 455 ma (40 ma/cm^2) when propane was used as the fuel. A high-loading (52 mg Pt/cm^2) platinum black cathode was used at all times, so this 5 mv recovery of the cell potential only reflected processes occurring at the low-loading anode used. This amounted to an error of less than 2%, within the limits of reproducibility of the results, so no correction was made.

The interrupter circuit yielded potential readings on a resistance-free basis and all results are reported on this basis unless otherwise specified. The potentials of the individual electrodes are reported with respect to a reversible hydrogen reference electrode in the same electrolyte at the same temperature. The current-potential data were taken at steady state (usually about 5 min after a change in current) and in the order of increasing current, starting at open circuit. No hysteresis effect was observed with decreasing current, except at low currents (less than 25 ma).

Resistance-included cell voltages (E_{cell}) can be estimated from the reported resistance-free ($E_{a\text{-}c}$) values using the expression

$$E_{cell} = E_{a\text{-}c} - i\rho l \qquad [1]$$

where i is the current density; ρ is the specific resistance of the electrolyte, 1.8 ohm-cm; and l is the interelectrode distance, 0.3 cm. This is only an estimate since it does not consider the (small) resistance of the electrodes.

Results and Discussion

Unsupported electrocatalysts.—The evaluation of commercially available platinoid element blacks was undertaken as a preliminary electrocatalyst survey. Emphasis was directed toward improving the specific activity of platinum when it became apparent that it was at least an order of magnitude better than the other three platinoid element blacks tested. This observation was not unexpected and is consistent with the results of other investigators (26, 27).

The sintering of high-area platinum black to a lower surface area under the conditions of electrode fabrication is one of the major problems obstructing the preparation of high-activity platinum electrodes. It was hoped that this problem could be avoided by starting with a more stable, highly oxidized form of platinum and reducing it to its elemental form after the electrode was prepared. Adams catalyst ($PtO_2 \cdot H_2O$) was selected as the starting material. An *in situ* reduction technique was then developed to accomplish the desired purpose. Initial successes prompted attempts to prepare a more optimal starting material and PtO_2-Preparation A was synthesized. A direct comparison of the propane performance in hydrofluoric acid at 105°C using the three most active unsupported electrocatalysts (Pt black, PtO_2-Commercial, and PtO_2-Preparation A) is shown in Fig. 3, where a loading of 25 mg Pt/cm^2 was used in each anode. It is evident that reduced PtO_2 is a much more active material than platinum black and the PtO_2-Preparation A electrode gave a cell performance (resistance-free) of about 150 ma/cm^2 at an anode *vs.* cathode potential of 0.4v. This was in contrast to 104 ma/cm^2 for commercial PtO_2 and 40 ma/cm^2 for platinum black. These anode *vs.* cathode potentials were calculated by determining the difference between the observed anode *vs.* reference potential and the cathode *vs.* reference potential obtained with a "standard" oxygen cathode (52 mg Pt black/cm^2) at the same current density. This standard oxygen cathode performance was determined by averaging about 15 representative cathode current density-voltage curves; this allowed cell-performance comparisons on the basis of anode performance only. The anode *vs.* cathode potentials for all the cells reported here were determined in a similar manner.

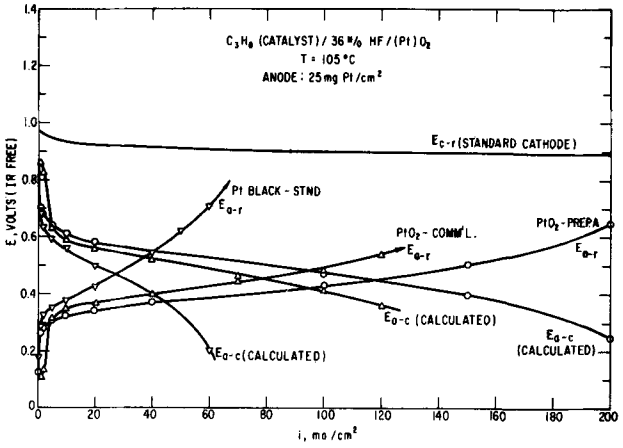

Fig. 3. Comparison of propane performance on the three most active unsupported electrocatalysts.

The propane performances with platinum black and reduced commercial Adams catalyst were determined at several levels of catalyst loading to evaluate the effect of catalyst loading on the specific performance (expressed as ma/mg Pt at an anode *vs.* reference potential of 0.5v). Figure 4 shows the results using

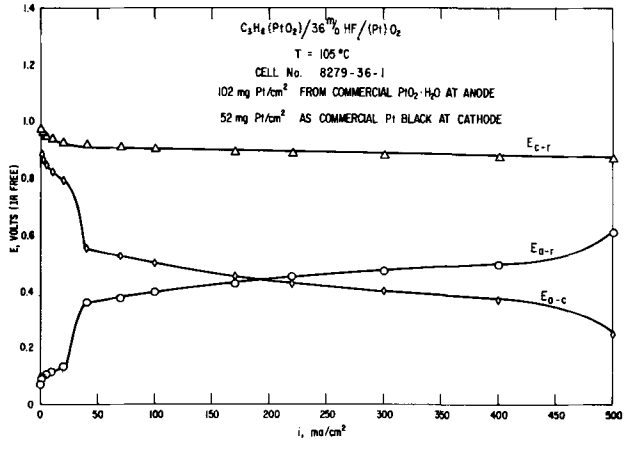

Fig. 4. Propane anode performance on reduced commercial PtO_2

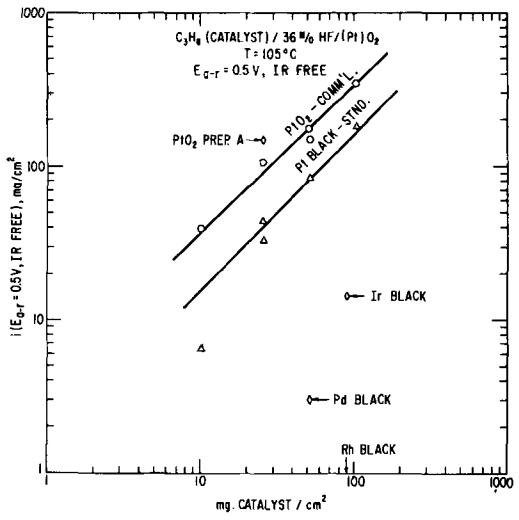

Fig. 5. Summary of the performance of propane on various unsupported electrocatalysts as a function of catalyst loading.

a high-loading anode containing 102 mg Pt/cm² reduced from commercial Adams catalyst. This cell had a limiting current density greater than 500 ma/cm², and a peak power point of about 140 mw/cm². The high platinum loading in this electrode is economically uninteresting, but the data do prove that very high levels of performance are possible with direct hydrocarbon fuel cells at 105°C using propane as the fuel.

All the results for the investigation of the unsupported electrocatalysts are presented in Fig. 5 in terms of the current density obtained with propane at an anode *vs.* reference potential of 0.5v as a function of platinoid element catalyst loading. Note that the data for commercial Adams catalyst and PtO_2-Preparation A fall above the data for commercial platinum black, indicating that these materials have higher specific activities than commercial platinum black, while the data for the other platinoid element blacks fall more than an order of magnitude below the platinum black data. It is also of interest that the data for commercial Adams catalyst and platinum black can be correlated with straight lines having a slope of nearly unity. Straight lines having a unit slope indicate that there is a direct proportionality between catalyst loading and current density. In other words, the specific activity of each of these electrocatalysts remained constant at loadings differing by an order of magnitude (10-100 mg Pt/cm²).

This invariance of the specific performance of an electrocatalyst allows all data to be related to a datum level of performance for ease of comparison. Commercial platinum black was chosen to represent this datum. A so-called "Effectiveness Ratio" was defined as the ratio of the specific performance observed with a given electrocatalyst to the specific performance observed with platinum black, both measured at the same anode *vs.* reference potential, that is

$$\text{Effectiveness Ratio} = \frac{\text{ma/mg catalyst}}{\text{ma/mg Pt black}}, \quad (E_{a\text{-}r} = \text{constant}) \qquad [2]$$

Table II presents this effectiveness ratio along with the data presented in Fig. 5, showing the comparison of propane performance using unsupported electrocatalysts at 105°C in hydrofluoric acid at an anode *vs.* reference potential of 0.5v (resistance-free). The value of the effectiveness ratio in Table II is an indication of the position (relative to platinum black) of a datum point on the current density scale of Fig. 5. As an example, a platinum electrode prepared by reducing PtO_2-Preparation A gave 3.5 times the current observed with a commercial platinum black electrode

Table II. Comparison of unsupported electrocatalysts

C_3H_8 (catalyst)/36 m/o HF/(Pt)O_2
T = 105°C
E_{a-r} = 0.5v (IR free)

Catalyst	Catalyst* loading, mg catalyst/cm²	Current density, ma/cm²	Specific current, ma/mg catalyst	Effectiveness ratio
Pt black	52	83.0	1.602	1.00
Pd black	52	3.0	0.0579	0.036
Ir black	90	14.2	0.158	0.098
Rh black	90	0.34	0.00378	0.0024
PtO_2	52	175.0	3.38	2.1
PtO_2-Prep. A	26	149.0	5.60	3.5

* This represents the catalyst content after reduction.

at the same loading. This is verified by Fig. 3, where performance data are presented for this particular case.

The effectiveness ratio allows the direct comparison of data obtained with considerably different catalyst loadings and becomes considerably more useful when the supported electrocatalysts are considered.

Carbon-supported electrocatalysts.—Supported electrocatalysts are of interest because the small crystallites which can be obtained by use of supports should make a higher percentage of the platinum available at the surface and thus allow a higher specific area electrocatalyst to be prepared. Supported electrocatalysts also should be less susceptible to sintering because the active crystallites can be widely dispersed on the support surface.

The success of the high-activity platinum black prepared from PtO_2 prompted attempts to combine the expected enhancement produced by supporting the platinum on a substrate with the avoidance of sintering during electrode fabrication by starting with a highly oxidized platinum compound. This thought led to the development of Pt/C-Preparations 20 and 21. The propane performances with Pt/C-Preparation 20 and two commercially prepared carbon-supported electrocatalysts are shown in Fig. 6. The catalyst loadings are comparable, but not equal (4.7-7.1 mg Pt/cm²). The improvement of performance obtained with Pt/C-Preparation 20 is appreciable.

The results from all the electrocatalysts tested are presented in Fig. 7 in terms of the current density obtained with propane at an anode *vs.* reference potential of 0.5v, as a function of the platinoid element catalyst loading. The data for unsupported electrocatalysts previously presented in Fig. 5 are included as closed points for purposes of comparison, while the carbon-supported platinum electrocatalysts are shown as open points. Electrocatalyst Preparations 20 and 21 and Commercial Catalyst 4 show consider-

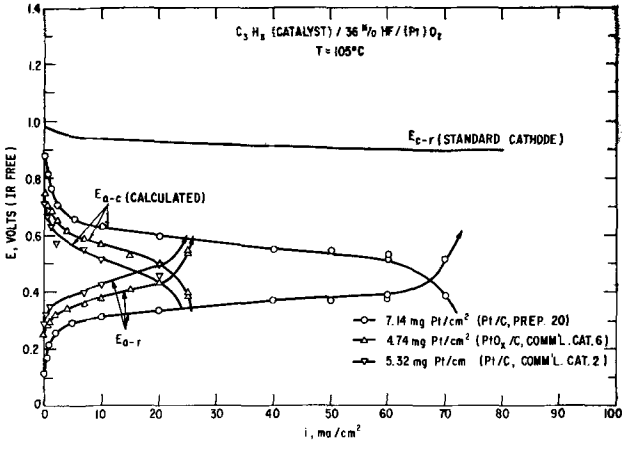

Fig. 6. Comparison of propane performance on three representative carbon-supported electrocatalysts.

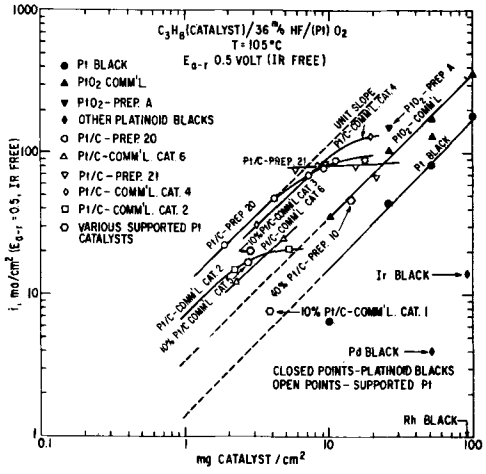

Fig. 7. Summary of the performance of propane on all the electrocatalysts tested as a function of catalyst loading.

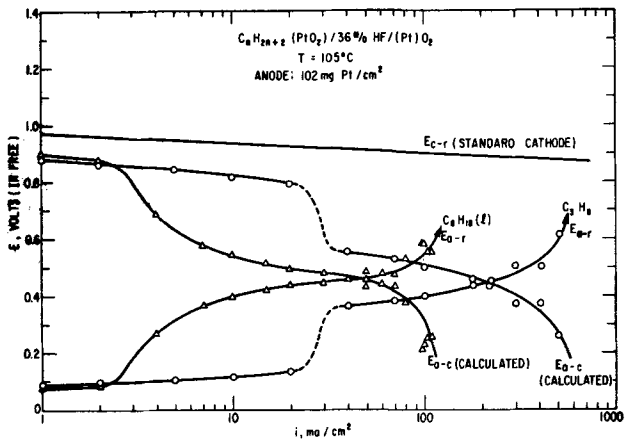

Fig. 8. Propane and n-octane anode performance on reduced commercial PtO_2.

ably higher specific activities than all the other electrocatalysts tested, but tend to deviate from a line of unit slope at the higher catalyst loadings, indicating a decrease in their specific activities. This loss of specific activity is also reflected by the reduction of the effectiveness ratios for propane performance with the carbon-supported platinum electrocatalysts at an anode *vs.* reference potential of 0.4v presented in Table III. This lower anode *vs.* reference potential is useful when comparing the carbon-supported platinum electrocatalysts because they operate at a higher voltage efficiency (28), and are approaching a maximum current condition at an anode *vs.* reference potential of 0.5v, as evidenced by the current density-voltage data presented in Fig. 6. The decrease in the specific activity of the carbon-supported electrocatalysts at high loadings should be alleviated by using substrates having higher specific surface areas. What should be noted is that effectiveness ratios near 10 have been obtained, indicating that a full order of magnitude improvement over the performance observed with commercial platinum black can be attained with these new carbon-supported platinum electrocatalysts. This means that a propane-oxygen fuel cell using 10 mg Pt/cm² at the anode as a carbon-supported electrocatalyst can deliver about 35 mw/cm²

Table III. Comparison of supported electrocatalysts

C_3H_8 (catalyst)/36 m/o HF/(Pt)O_2
T = 105°C
E_{a-r} = 0.4v (IR free)

Catalyst	Catalyst Pt content, w/o	Catalyst loading, mg Pt/cm²	Current density, ma/cm²	Specific current, ma/mg Pt	Effectiveness* ratio
Pt/C—Prep. 10	40	14.0	18.6	1.31	1.6
Pt/C—Prep. 20	7	1.9	9.70	5.14	6.3
	14	4.1	33.0	8.03	9.9
	21	7.1	65.5	8.26	10.0
	28	9.2	48.5	5.27	6.5
	35	11.0	60.5	5.48	6.7
	42	18.0	64.0	3.62	4.4
Pt/C—Prep. 21	20	5.8	41.0	7.11	8.8
	30	9.4	43.0	4.58	5.6
	40	15.0	56.5	3.72	4.6
	50	22.0	38.5	1.96	2.4
Pt/C—Comm'l Cat. 1	10	3.9	1.22	0.313	0.38
Pt/C—Comm'l Cat. 2	5	1.1	4.20	3.79	4.7
	10	2.2	7.17	3.29	4.0
	20	5.3	7.05	1.33	1.6
Pt/C—Comm'l Cat. 3	10	2.8	15.0	5.30	6.5
Pt/C—Comm'l Cat 4	10	3.2	15.0	4.76	5.8
	25	8.4	55.0	6.56	8.1
	50	19.0	70.0	3.60	4.4
Pt/C—Comm'l Cat. 5	10	2.8	6.25	2.24	2.8
Pt/C—Comm'l Cat. 6	8	2.3	6.20	2.74	3.4
	16	4.7	14.7	3.10	3.8
*Pt black	100	52.0	42.0	0.814	1.00

(resistance-free) at 105°C using hydrofluoric acid as the electrolyte.

Other fuels.—A comparison of the performance of gaseous propane and liquid n-octane on reduced commercial PtO_2 is shown in Fig. 8. The propane data presented in this figure are the same as those presented in Fig. 4, and the anode catalyst loading is the same 102 mg Pt/cm². The maximum current density obtained with n-octane was about 120 ma/cm². The ratio of the performances for propane and n-octane shown in this figure is about the same as that reported earlier for platinum black (7). These data again demonstrate, as did Fig. 4, that high levels of performance can be obtained with direct hydrocarbon fuel cells at moderate temperatures, even when liquid hydrocarbons are used as the fuel.

The specific performances of several gaseous and liquid normal saturated hydrocarbon fuels (expressed as ma/mg Pt at an anode *vs.* reference potential of 0.5v, resistance-free) on commercial platinum black, reduced commercial PtO_2 and a commercial carbon-supported platinum are summarized in Fig. 9. The data presented for commercial platinum black in this

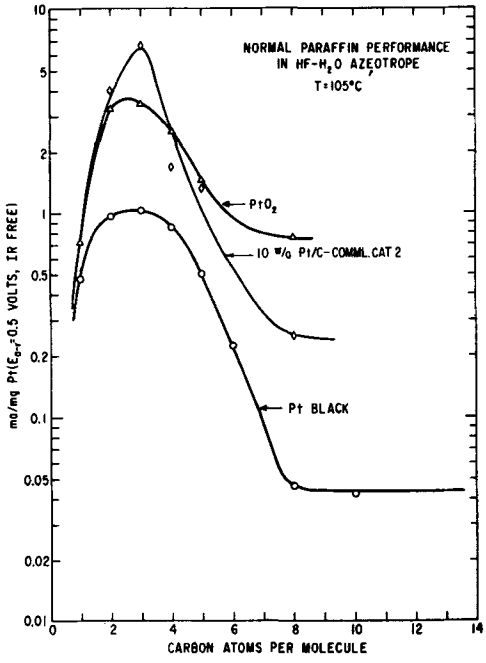

Fig. 9. Effect of molecular weight of normal saturated hydrocarbon fuels on specific performance at the anode. Platinum loadings were 52 mg commercial platinum black/cm²; 102 mg platinum (reduced from commercial $PtO_2 \cdot H_2O$)/cm²; 2.2 mg platinum/cm² as 10 w/o Pt/C, commercial catalyst 2.

figure are not the best performances observed at this catalyst loading (improvements in the electrode structure have allowed better performances to be achieved), but this was the only single electrode for which all the desired data were available. Ethane and propane give slightly higher current densities than butane, which gives higher current densities than the other hydrocarbons. Comparing the standard platinum black with the other two catalysts shows than an improved utilization of the platinum catalyst has been achieved with PtO_2 and Pt/C for all the hydrocarbon fuels tested.

In contrast to other strong-acid electrolytes (3, 29, 30) no cycling of the cell potential or current has been observed when using the hydrofluoric acid electrolyte with any fuel under any of the test conditions. This observation has previously been reported in connection with high-loading platinum black electrodes (7). The present work extends this observation to include other electrocatalysts, including low-loading carbon-supported platinum.

Conclusions

1. Both the use of higher activity forms of unsupported platinum, particularly the one reduced from Adams catalyst, and the use of carbon-supported platinum electrocatalysts are effective in reducing the amount of platinum required for a given amount of power from a direct hydrocarbon fuel cell.

2. Carbon-supported platinum electrocatalysts are effective in reducing the amount of platinum required for a given propane performance by about a factor of 10. Further improvements are likely.

3. A propane-oxygen fuel cell using 10 mg Pt/cm^2 as carbon-supported platinum at the anode can deliver about 35 mw/cm^2 (resistance-free) using a 36 m/o hydrofluoric acid electrolyte at 105°C.

4. No cycling of the cell current or potential has been observed with any saturated hydrocarbon fuel under any conditions when using the hydrofluoric acid electrolyte.

Acknowledgments

The authors wish to thank Dr. W. T. Grubb for information concerning deposition of platinum salts and Messrs. D. J. Surd and G. J. Holm for assistance in performing some of the experiments. Helpful discussions were provided by Dr. E. L. Simons and Dr. J. L. Holman. Mr. L. D. Sangermano, of the General Electric Company, Direct Energy Conversion Operation, supplied some of the Teflon binder used in these experiments.

This work is a part of the program under contracts DA-44-009-AMC-479(T) and DA-44-009-ENG-4909, ARPA Order No. 247 with the U. S. Army Engineer Research and Development Laboratories, Ft. Belvoir, Virginia, to develop a technology which will facilitate the design and fabrication of practical military fuel cell power plants for operation on ambient air and hydrocarbon fuels.

Manuscript received May 23, 1967.

Any discussion of this paper will appear in a Discussion Section to be published in the June 1968 JOURNAL.

REFERENCES

1. E. D. Cairns and D. I. Macdonald, *Electrochem. Tech.*, **2**, 65 (1964).
2. E. J. Cairns and G. J. Holm, Paper presented at the Washington, D. C., Meeting of the Society, Oct. 1964, Abstract No. 30; see also Extended Abstracts, Battery Div., **9**, 75 (1964).
3. H. Binder, A. Köhling, H. Krupp, K. Richter, and G. Sandstede, *This Journal*, **112**, 355 (1965).
4. W. T. Grubb and L. W. Niedrach, *ibid.*, **110**, 1086 (1963).
5. R. Jasinski, J. Huff, S. Tomter, and L. Swette, *Ber.*, **68**, 400 (1964).
6. H. G. Oswin, A. J. Hartner, and F. Malaspina, *Nature*, **200**, 256 (1963).
7. E. J. Cairns, *This Journal*, **113**, 1200 (1966).
8. E. J. Cairns, Paper presented at the Atlantic City Meeting of the American Chemical Soc., Sept., 1965, Abstract No. 31L; see also "Hydrocarbon Fuel Cell Technology," B. S. Baker, Editor, Academic Press, New York (1965).
9. E. J. Cairns, *Nature*, **210**, 161 (1966).
10. W. T. Grubb and C. J. Michalske, Proc. 18th Ann. Power Sources Conf., Atlantic City (May 1964).
11. E. J. Cairns, *Electrochem. Tech.*, **5**, 4 (1967).
12. E. J. Cairns, A. D. Tevebaugh, and G. J. Holm, *This Journal*, **110**, 1025 (1963).
13. E. J. Cairns and A. D. Tevebaugh, *J. Chem. Eng. Data*, **9**, 453 (1964).
14. L. W. Niedrach and H. R. Alford, *This Journal*, **112**, 117 (165).
15. R. Adams, V. Voorhees, and R. L. Shriner, "Organic Synthesis," Col. Vol. I, John Wiley & Sons, Inc., New York (1932).
16. V. Voorhees and R. Adams, *J. Am. Chem. Soc.*, **44**, 1397 (1922).
17. R. Adams and R. S. Shriner, *ibid.*, **45**, 2171 (1923).
18. A. H. Cook and R. P. Linstead, *J. Chem. Soc.*, **1934**, 946
19. W. F. Bruce, *J. Am. Chem. Soc.*, **58**, 687 (1936).
20. V. L. Frampton, J. D. Edwards, and H. R. Henze, *ibid.*, **73** 4432 (1950).
21. C. W. Keenan, B. W. Gisemann, and H. A. Smith, *ibid.*, **76**, 229 (1953).
22. R. G. Haldeman, W. P. Colman, S. H. Langer, and W. A. Barber, in "Fuel Cell Systems," p.113, R. F. Gould, Editor, Adv. in Chem. Series No. 47, Amer. Chem. Soc., Washington, D. C. (1965).
23. K. Kordesch and A. Marko, *This Journal*, **107**, 480 (1960).
24. E. J. Cairns and A. D. Tevebaugh, Saturated Hydrocarbon Fuel Cell Program, Technical Summary Report No. 3, Part I, Task IV, Jan. 1-June 30, 1963, Contract No. DA-44-009-ENG-4909, ARPA Order No. 247, U.S.A.E.R.D.L.
25. L. W. Niedrach and M. Tochner, *Electrochem. Tech.*, **5**, 270 (1967).
26. W. T. Grubb, *Nature*, submitted.
27. J. O'M. Bockris and S. Srinivasan, Proc. 19th Ann. Power Sources Conf., Atlantic City (May, 1965).
28. E. J. Cairns and D. C. Bartosik, *Electrochem. Tech.*, **111**, 1205 (1964).
29. R. P. Hamlen and E. J. Szymalak, *ibid.*, **4**, 172 (1966).
30. E. R. White and H. J. R. Maget, Proc. 19th Ann. Power Sources Conf., Atlantic City (May, 1965).

Complex Scale Formation on an Iron-18% Chromium Alloy

D. P. Whittle and G. C. Wood

Corrosion Science Division, Department of Chemical Engineering, University of Manchester Institute of Science and Technology, Manchester, England

ABSTRACT

The oxidation of a pure Fe-18.0% Cr alloy in oxygen at 1 atm pressure in the temperature range 800°-1200°C has been studied using thermogravimetry, metallography, and electron probe microanalysis. Chromium oxide, containing minor amounts of dissolved iron, is the only oxide formed at 800° and 1000°C. This oxide is also formed initially at 1200°C, but its subsequent mechanical failure permits rapid oxidation of the underlying chromium-depleted alloy. Three types of scale formation are found in this second oxidation stage on different regions of the specimen surface. Each of these types of scale contains alternate layers of chromium-rich and iron-rich oxides. Two of the scale types are eventually healed by formation of a basal Cr_2O_3-rich layer; the third, occurring at the edges of the specimens, grows unimpeded. The mechanism of formation of these stratified scales and, where relevant, their subsequent healing, is explained by a theory involving the variation of the mobilities of Fe^{3+}, Fe^{2+}, and Cr^{3+} ions with composition in the spinel, $FeFe_{(2-x)}Cr_{(x)}O_4$, $(O \leq x \leq 2)$.

When chromium-rich iron-chromium alloys are oxidized in oxygen in the range 800°-1200°C, they form almost pure chromium oxide (1, 2) (subsequently designated Cr_2O_3 because it contains only minor quantities of dissolved iron). More dilute alloys containing 14-25% Cr also form this oxide under all but the severest conditions (1, 3, 4), when failure of the Cr_2O_3 scale allows thick stratified scale to develop. The mechanism of protective scale failure, proposed earlier (1-5), is substantiated here.

The nature of the stratified scales formed on the second class of alloys depends on the surface chromium content of the alloy when it is exposed by the protective scale failure. This critical dependence is exemplified in the present paper by the scales on Fe-18% Cr which vary according to their location around the specimen surface. Generally this type of variation (4) is expected where the bulk alloy chromium content is close to the border-line between protective and nonprotective behavior; in more dilute alloys the situation is not as critical (2, 3), and only one type of stratified scale is produced. Also, with the more dilute alloys, breakthrough and stratified scale growth are disastrous, and complete destruction of the specimen occurs, whereas with the 18% Cr alloy some self-healing of the scale is observed.

Experimental

The Fe-18.0 w/o Cr alloy was made from a base of special Swedish iron and pure chromium by vacuum melting, and subsequent hot and cold rolling to strip 0.040 cm thick (1). The impurity content of a similar alloy of the same batch was: C 0.017, N 0.023, S 0.014, P 0.002, Mn 0.02, Si 0.08, O 0.023, Al 0.04, Ni 0.01, Sn <0.002, Nb <0.006, W <0.05, Ti <0.04, Cu <0.01, Mo <0.005, V <0.004, B <0.0015 w/o.

Specimens 2.5 x 0.5 x 0.040 cm were annealed *in vacuo* (10^{-5} Torr) for 5 hr at 1000°C in order to remove any residual stresses in the alloy and to give a starting material of approximately constant grain size. Immediately prior to oxidation, specimens were individually electropolished for a total time of approximately 3 min in a mixture of glacial acetic acid and perchloric acid (sp gr 1.72) in the ratio 20 parts to 1 by volume. During polishing the current density was maintained in the range 0.4-0.8 amp cm^{-2} and the electrolyte cooled to 15°C. Specimens were then given a minimum cathodic etch at 10 μa cm^{-2} for 90 sec in 4*N* HCl producing a slightly etched but "clean" surface.

After a standard time of 30 min the prepared coupon was rapidly located in the hot zone of a previously heated silica spring thermobalance (sensitivity ± 0.05 mg cm^{-2}) containing slowly flowing dry oxygen (O_2 99.5%, A 0.5%, CO_2 5 ppm, H_2 50 ppm, hydrocarbons 10 ppm, N_2 trace, CO nil, H_2O < 0.15 g^{-3}). Loss of a volatile chromium oxide species [probably CrO_3 (6)] from the oxidizing sample was minimized by surrounding it with a Cr_2O_3-coated crucible. Weight gains were measured within several minutes of exposure and were continued for periods up to 50 hr. At the termination of the run the specimens were cooled to room temperature over a period of about 15 min.

The oxidized specimens were examined in plan by optical microscopy and also in cross section after standard metallographic preparation.

The prepared cross sections, made conducting by a thin carbon film, were also studied in a Cambridge Mark II "Microscan" microanalyzer at 29 kv. The results are presented as scanning x-ray images or as ultra slow-scanning line concentration profiles. The individual points on these traverses indicate where absorption and fluorescence corrections have been made, rather than the location of static probe measurements. The latter were occasionally used to check results. Distances marked on the abcissae scales are measured from the scale/atmosphere interface.

Results and Interpretation

Oxidation kinetics.—The over-all oxidation behavior can be divided into three stages, as shown in Fig. 1 which gives the weight gain/time curves at 1200°C. These three stages are: (*a*) an initial protective stage, shown in detail in the inset of Fig. 1, (*b*) a period of very rapid, apparently linear, oxidation, and (*c*) a further period of slow protective oxidation.

(*a*) During this period at 1200°C there was generally good agreement between the weight gains of the various specimens and of the time taken to breakthrough, (typically 1 hr, although it varied between 45 min and 2 hr). The scale thickened at an approximately parabolic rate, the mean rate constant being 8 x 10^{-10} g^2 cm^{-4} sec^{-1}. This is only slightly higher than that for alloys richer in chromium at this temperature (1, 2).

At 800° and 1000°C only this oxidation stage occurs, at least up to 50 hr. Growth occurs reproducibly with only a slight negative deviation from the parabolic law, as has been observed for alloys richer in chromium (1, 2). At 1000°C, the parabolic rate constant is 4.3 x 10^{-11} g^2 cm^{-4} sec^{-1} compared with 5.8 x 10^{-11} g^2 cm^{-4} sec^{-1} for an Fe-28% Cr alloy of similar purity (1, 2). Corresponding rate constants at 800°C are 1.0 x 10^{-12} and 4.7 x 10^{-12} g^2 cm^{-4} sec^{-1}.

(*b*) The linear oxidation rate during the second

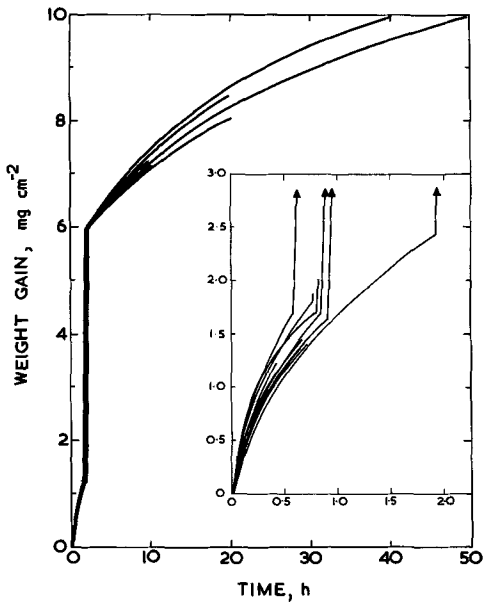

Fig. 1. Weight gain/time curves for the oxidation of Fe-18.0% Cr at 1200°C in oxygen.

stage was (5.1-6.5) x 10^{-6} g cm^{-2} sec^{-1}, corresponding approximately to a rate of increase in scale thickness of 0.6 μm min^{-1} which is considerably slower than the corresponding value for an Fe-14.0% Cr alloy (5 μm min^{-1}) (2). However, these rate constants carry very little meaning as they refer only to the very rapid localized nodular scale growth, as will be seen later. This stage of oxidation lasted in all cases until a weight gain of approximately 6.0 mg cm^{-2} had been obtained, this probably being when the whole specimen surface had been subjected to rapid oxidation.

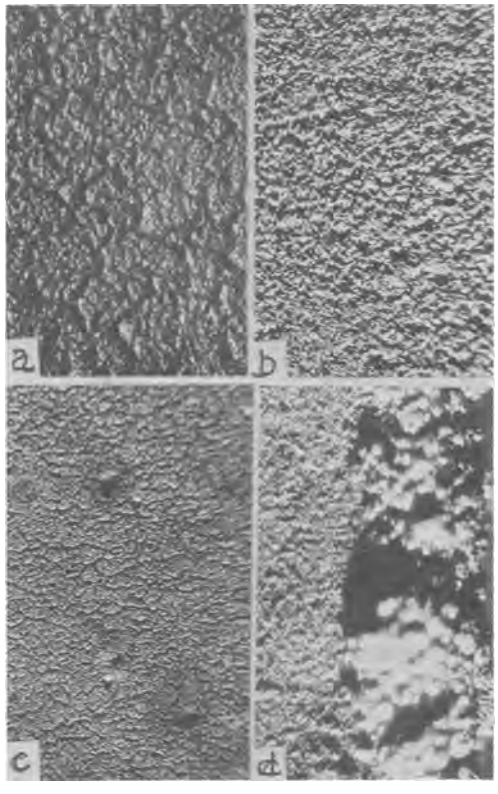

Fig. 2. Surface topography of scales formed on Fe-18.0% Cr; oblique illumination: a, 1 hr at 1000°C, magnification *ca.* 80X; b, 50 hr at 1000°C, magnification *ca.* 80X; c, 5 hr at 1200°C, magnification *ca.* 24X; d, 50 hr at 1200°C, magnification *ca.* 24X.

(c) During the final stage, the weight gain/time curves again apparently follow a parabolic law, with the parabolic rate constant slightly greater than that during the first stage. The absolute value of the rate constant is not important because the scale being formed shows marked differences around the specimen. However, metallographic examination shows later that a "healing" layer of Cr_2O_3 is growing over most of the surface, accounting for the similarity between the rate constant here and that during the first stage.

Surface metallography.—At 800° and 1000°C the superficial appearance of the scale was reasonably uniform except that the alloy grain boundaries were replicated in the scale, Fig. 2a. As oxidation proceeded, the scale surface became less angular in nature and the alloy grain boundaries were not observed, Fig. 2b; scales formed in the initial stages at 1200°C were similar. Occasionally, the scale formed at 1000°C showed nodular growths, Fig. 2c, approximately 50-80 μm in diameter and 10 μm high. This failure of the protective scale was always very localized and never showed any tendency to spread by disrupting adjacent areas of protective scale. Furthermore, nodular growth was always so slight at 1000°C as to be undetectable in the weight gain/time curves. At 1200°C, nodular growth was much more extensive and, once initiated, spread rapidly over the whole specimen. Generally, the scales at the edges of the specimen appeared much thicker than over the remainder of the surface and had a characteristic silvery appearance, Fig. 2d.

Metallography in cross section and electron probe microanalysis.—For ease of presentation this section is divided into three parts corresponding to the three stages noted in the oxidation kinetic curves at 1200°C.

Initial protective oxidation stage.—Only Cr_2O_3 was observed during this stage of the oxidation. However, the morphology of the scales formed at 800° and 1000°C was considerably different from that formed at 1200°C. At the lower temperatures, the Cr_2O_3 scale was a single layer and did not vary in thickness around the prepared cross section by more than about 30%. At 1200°C, the scale was highly irregular and contained many oxide balloons (Fig. 3). The extent to which the irregularities in the scale have been accentuated by the metallographic preparation and differential contraction between scale and alloy on cooling from the oxidation temperature is difficult to establish. The irregularity of the alloy/oxide interface is possibly indicative of scale lifting at temperature, but it is more likely to be due to plastic deformation of the alloy surface layers (7) by stresses in the specimen. In any event, the alloy/oxide interface was more rugged than that of other Fe-Cr alloys (27.4 and 59.5% Cr) when oxidized at this temperature (1, 2). Cracking at temperature of Cr_2O_3 scale lifted

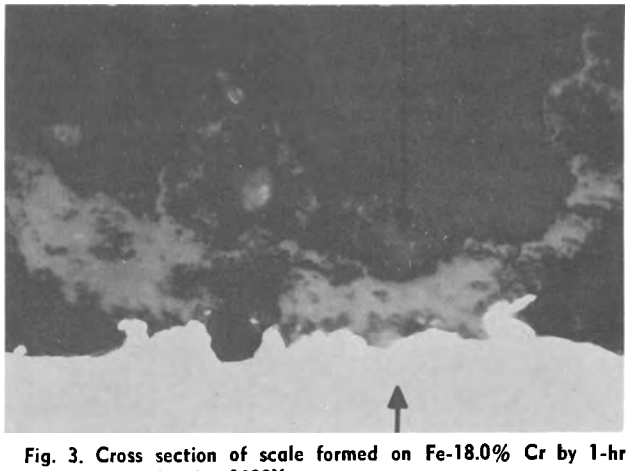

Fig. 3. Cross section of scale formed on Fe-18.0% Cr by 1-hr oxidation. Magnification 1000X.

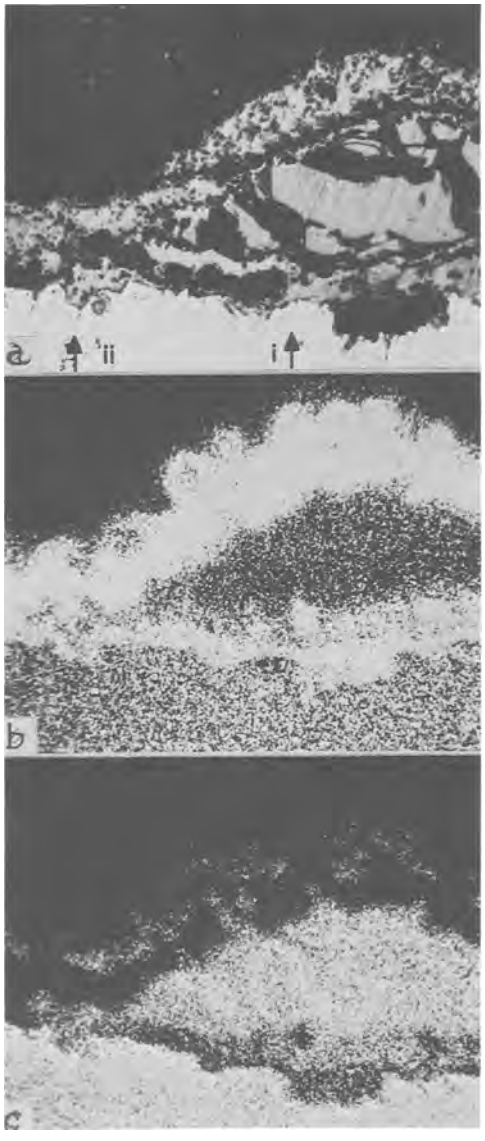

Fig. 4. Cross section of scale formed on Fe-18.0% Cr by 70-min oxidation at 1200°C: a, optical; b, KαCr image; c, KαFe image. Magnification *ca.* 400X.

from the alloy followed by re-formation of Cr_2O_3 is unlikely because the chromium concentration at the alloy/oxide interface is too low (5). Certainly the layered-type of Cr_2O_3 scales found on Fe-59.5% Cr oxidized at this temperature are absent (1, 2).

A typical electron probe microanalysis of a Cr_2O_3 scale formed after 50-hr oxidation at 1000°C gave 60.2% Cr and 1.5% Fe. These values can be normalized to a total metal content of 67.6% as most of the error is due to overlapping effects of the x-ray source in analyzing these thin films; normalized values are 65.9% Cr and 1.7% Fe. A similar analysis, 60.7% Cr and 1.1% Fe (normalized values 66.4% Cr and 1.2% Fe) was obtained for the scale formed for 1 hr at 1200°C.

The chromium concentration profile in the alloy, along the line shown in Fig. 3, indicates a relatively sharp decrease in chromium concentration near to the alloy/oxide interface down to a value of 9.5% Cr. Although not easily detectable in the microanalyzer the chromium-depleted zone should reach about 120 μm into the alloy because the alloy interdiffusion coefficient is relatively large (5).

Linear oxidation stage.—Generally, when the oxidation was terminated during this stage, there were areas of the specimen surface still covered by Cr_2O_3 and areas of fully developed stratified scale, described in the next section. As the linear oxidation stage proceeded, only the relative areas of the specimen surface covered by these two types of scale changed. The stratified scale must have grown extremely rapidly as it was very difficult to obtain examples of the scale at the start of its growth.

Figure 4a shows how the protective Cr_2O_3 separated away from the alloy surface and how stratified scale was formed beneath it. Other similar configurations of Cr_2O_3 and stratified scale are possible (1-4), but none shows the mechanism as clearly as Fig. 4a. The outer layer of Cr_2O_3 is visible over the whole field of view, Fig. 4b. At the left side of the micrograph, the Cr_2O_3 is adjacent to the alloy whereas over the remainder of the visible surface it is separated from the alloy by a mixed oxide nodule, Fig. 4b and 4c. The thickness of this outer Cr_2O_3 layer is independent of its position in the scale because it was formed during the first stage of oxidation. All the oxide layers are very porous, but this is largely connected with the poor metallographic preparation. The concentration profiles, Fig. 4d, across the line marked (i) in Fig. 4a confirm the general pattern of the elemental distribution shown in the x-ray images. The outer oxide is Cr_2O_3 as it contains 66.9% Cr and only 0.3% Fe. The remaining part of the scale is similar to the double layer scales observed on other alloys (1-3); an outer, almost pure iron oxide layer 30 μm thick, and inner, mixed layer containing undulating chromium and iron concentration profiles, also 30 μm thick. In order to identify these oxides completely, x-ray diffraction of the scales would be necessary. However, until a technique for microdiffraction becomes available, bulk analysis of scales stratified on such a fine scale is not very informative.

Traverses across lines such as (ii) in Fig. 4a show a simple Cr_2O_3 scale together with a chromium depletion in the underlying alloy.

Third stage of oxidation.—During this final stage, four general types of scale are found around the specimen cross sections: (i) over most of the specimen surface a stratified scale containing a chromium-rich layer at the alloy/oxide interface; (ii) a thicker stratified scale without the chromium-rich basal layer and usually confined to areas close to the specimen edges; (iii) a stratified scale intermediate between types (i) and (ii) also found near to specimen edges; and (iv) areas where the initial protective Cr_2O_3 scale still remained.

Figure 5a, together with its x-ray images 5b and c, shows a typical area where scales of type (i) and (iv) are adjacent. Clearly the thinner, protective oxide in these areas is Cr_2O_3 containing very little iron. The thicker, nodular oxide contains layers of chromium-rich and iron-rich oxides and is discussed more fully later.

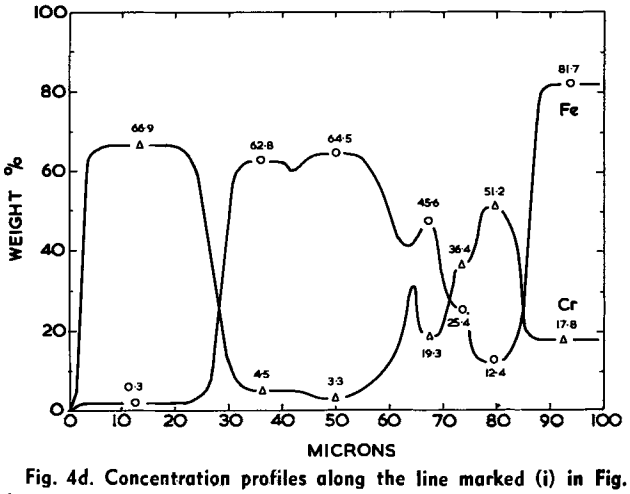

Fig. 4d. Concentration profiles along the line marked (i) in Fig. 4a.

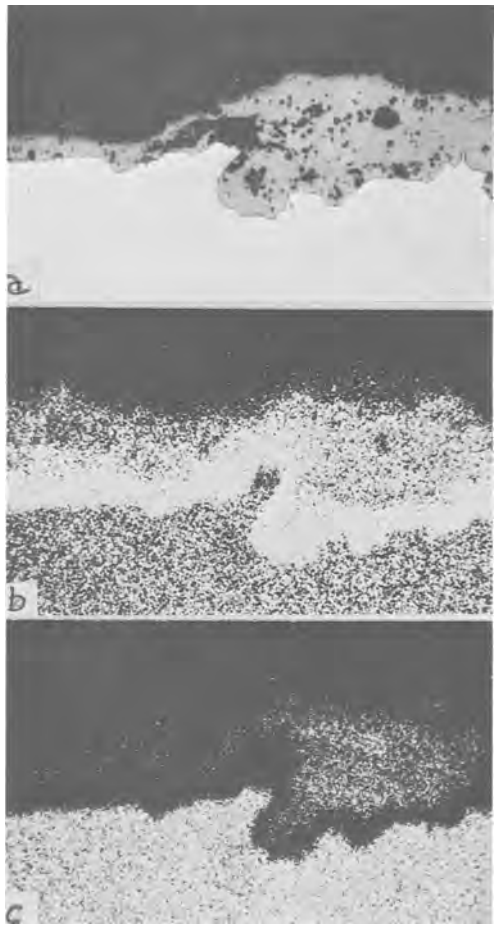

Fig. 5. Cross section of scale formed on Fe-18.0% Cr by 10-hr oxidation at 1200°C: a, optical, b, KαCr image; c, KαFe image. Magnification ca. 400X.

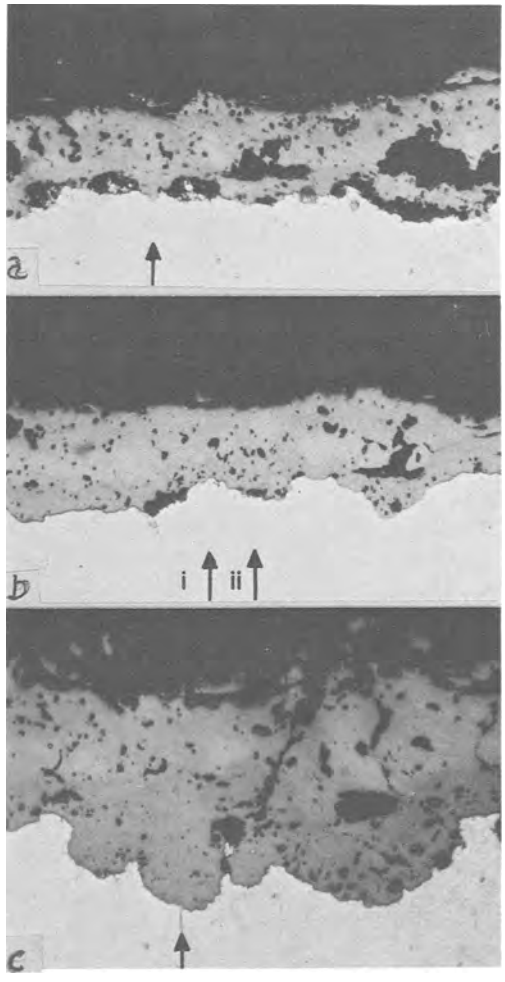

Fig. 6. Cross sections of scale formed on Fe-18.0% Cr by: a, 5-hr oxidation at 1200°C; b, 10-hr oxidation at 1200°C; c, 50-hr oxidation at 1200°C. Magnification ca. 400X.

Figure 6a, b, and c show the typical growth sequence of scales of type (i), these specimens having been oxidized for 5, 10, and 50 hr, respectively. The individual oxide layers are more easily distinguishable in the corresponding concentration profiles measured along the lines marked in Fig. 6a, b, and c and presented in Fig. 7a, b (i and ii) and c, respectively. Two traverses, (i) and (ii), are given in Fig. 7b corresponding to lines (i) and (ii) in Fig. 6b. In Fig. 7a two outer layers, not separable in the photomicrograph (Fig. 6a), are indicated, the outer one being richer in iron. Beneath these is an iron-rich, lighter-colored phase which does not form a continuous layer in the scale (Fig. 6a). The layer adjacent to the alloy/oxide interface is Cr_2O_3 and is approximately 3-4 μm thick. There is no internal oxide.

Scales of this type do not increase very greatly in thickness as oxidation proceeds. Figure 7b shows that all the increase in thickness after oxidation for 10 hr is associated with the thickening of the inner Cr_2O_3 layer, now 6-7 μm thick. The two traverses (i) and (ii) again show that the light-colored, iron-rich oxide does not form a continuous layer in the scale, being present in scan (i) but not in scan (ii). Furthermore, interdiffusion appears to have taken place between the two outer layers, although there is still an enrichment of iron at the scale/atmosphere interface.

After oxidation for 50 hr the inner Cr_2O_3 layer is about 30 μm thick (Fig. 6c). There is the expected distribution of iron and chromium across the scale (Fig. 7c) with interdiffusion between all the scale layers, except the innermost Cr_2O_3 layer, being well advanced. Again no internal oxide is present, although this is hardly surprising behind as stable an oxide as Cr_2O_3.

A typical scale of type (ii) which, as stated previously, occurs at the ends of the specimen cross sections, is presented in Fig. 8a. The darker colored oxide, typical of Fe_3O_4, is observed in these regions whereas it did not appear to be present in the other types of scales. Furthermore, this darker colored phase is surmounted by a lighter colored oxide, Fe_2O_3 while the inner scale is apparently porous. Reference to the x-ray images, Fig. 8b and c, indicates that there is no Cr_2O_3 layer at the base of this type of scale and as a result of this, the formation of internal oxide,

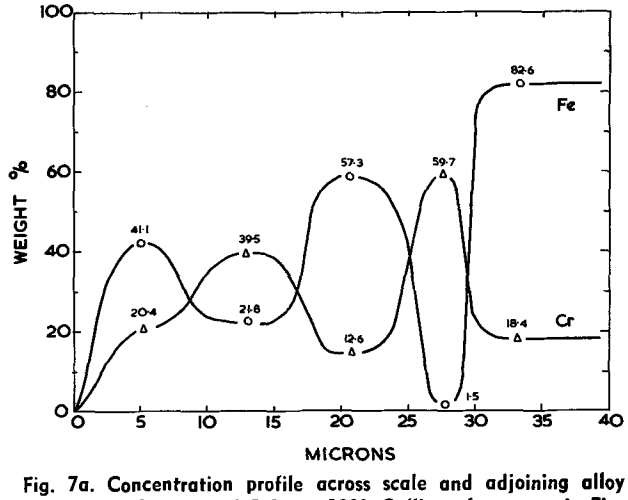

Fig. 7a. Concentration profile across scale and adjoining alloy for Fe-18.0% Cr oxidized 5 hr at 1200°C (line of traverse in Fig. 6a).

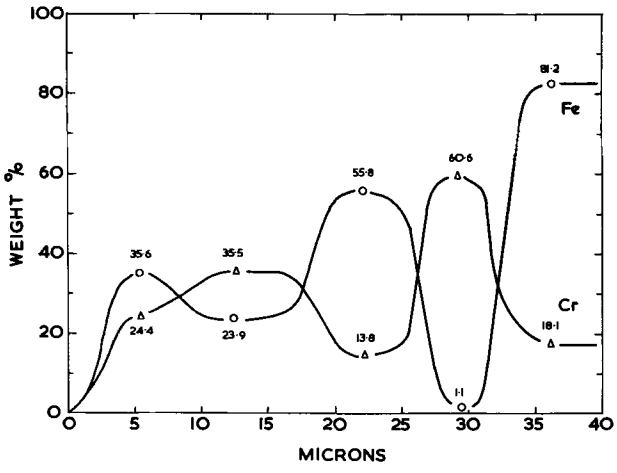

Fig. 7b (i). Concentration profile across scale and adjoining alloy for Fe-18.0% Cr oxidized 10 hr at 1200°C (line of traverse in Fig. 6b).

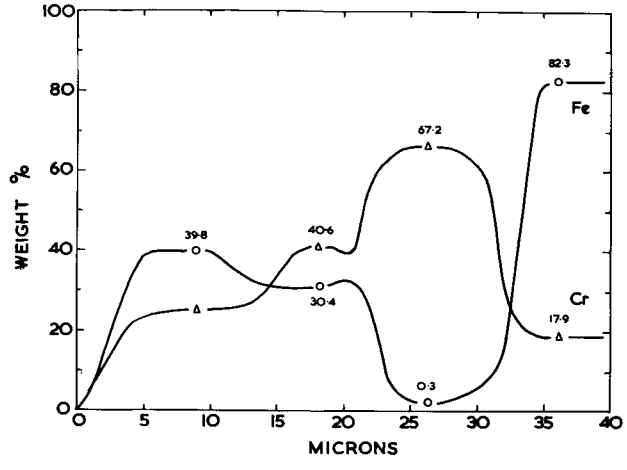

Fig. 7b (ii). Concentration profiles across scale and adjoining alloy for Fe-18.0% Cr oxidized 10 hr at 1200°C (line of traverse in Fig. 6b).

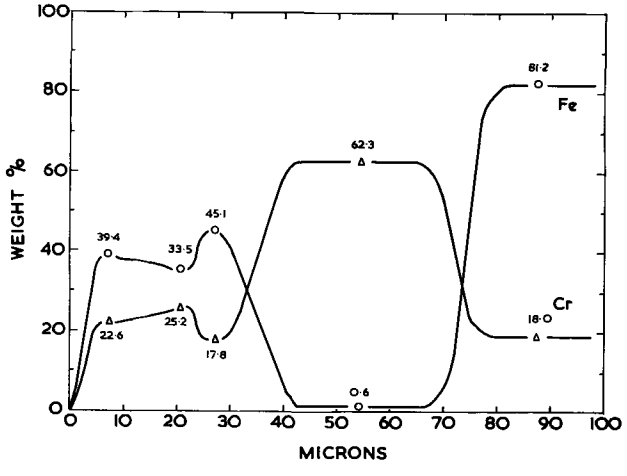

Fig. 7c. Concentration profile across scale and adjoining alloy for Fe-18.0% Cr oxidized 50 hr at 1200°C (line of traverse in Fig. 6c).

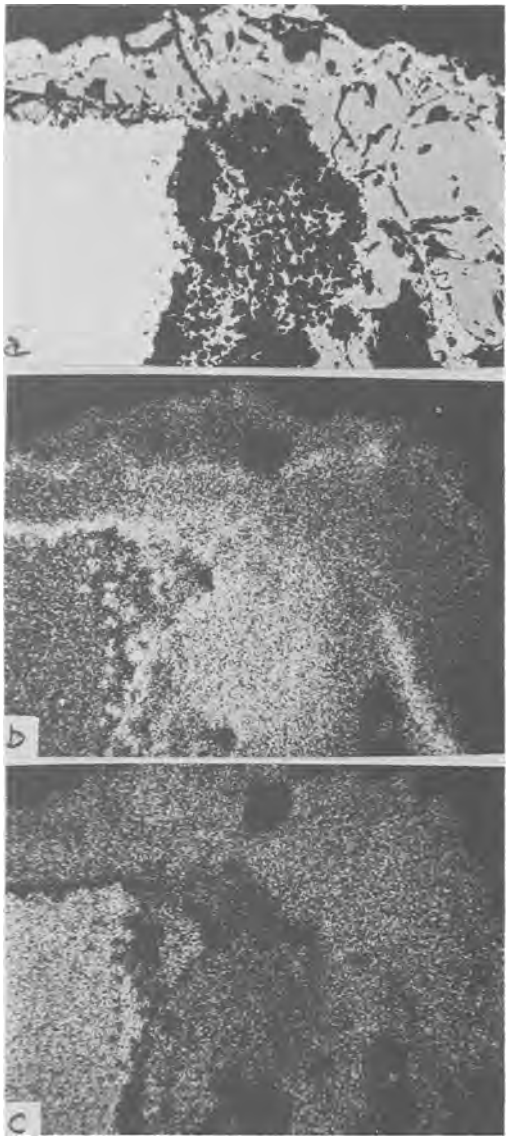

Fig. 8. Cross section of scale formed on Fe-18.0% Cr by 5-hr oxidation at 1200°C: a, optical; b, KαCr image; c, KαFe image. Magnification *ca.* 120X.

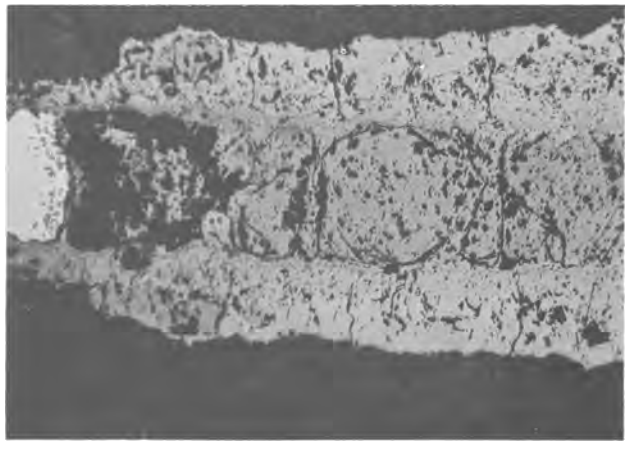

Fig. 9. Cross section of scale formed on Fe-18.0% Cr by 50-hr oxidation at 1200°C. Magnification 75X.

which is now possible, occurs. Figure 9 shows that the growth of type (ii) scale remains unchecked, causing the alloy to be completely converted into oxide. The inner region of this large nodule is again very friable and contains many pores. However, most of these are probably introduced during the metallographic preparation. Internal oxide particles do not appear to have increased in population with the increasing oxidation time.

Finally, the fourth type of scale, (iii), is shown in Fig. 10a, b, and c. The quantitative analyses of the scale (Fig. 10d) indicate the usual layered structure.

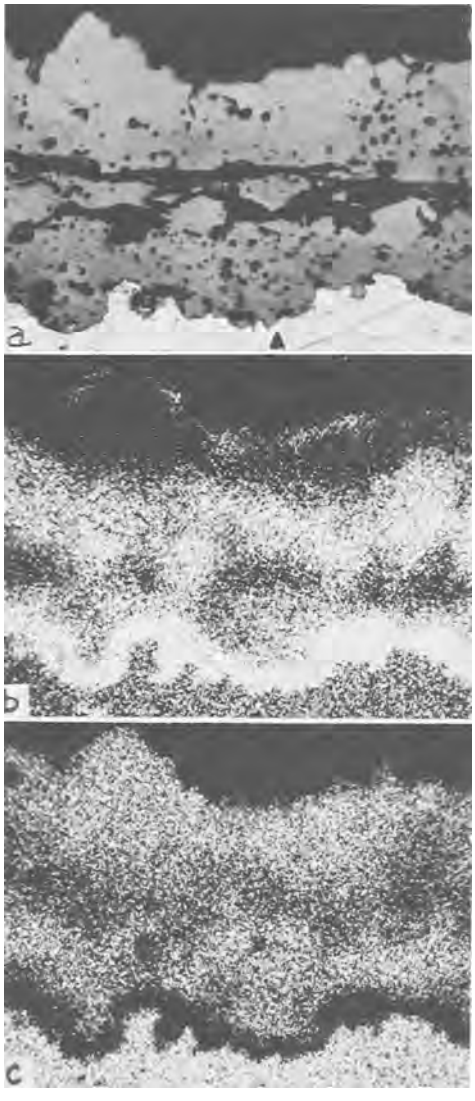

Fig. 10. Cross section of scale formed on Fe-18.0% Cr by 5-hr oxidation at 1200°C: a, optical; b, KαCr image; c, KαFe image. Magnification *ca.* 400X.

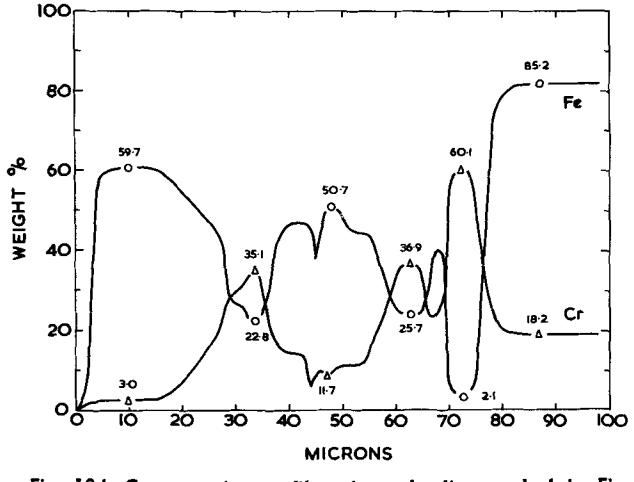

Fig. 10d. Concentration profiles along the line marked in Fig. 10a.

Comparison of these profiles with those for type (i) scale (Fig. 7a, b, or c) indicates a certain similarity. The three outer layers of type (i) scale appear in duplicate in this type (iii) scale, surmounting the usual Cr_2O_3 layer at the alloy/oxide interface. Again no internal oxide is present.

Discussion

Formation of the protective oxide Cr_2O_3.—The only oxide formed at 800° and 1000°C, and during the first stages of oxidation at 1200°C is Cr_2O_3. The growth mechanism of this oxide is presumably similar to that on alloys richer in chromium, namely, predominantly by cationic diffusion as discussed elsewhere (1, 2). Certainly, the parabolic rate constants are of a similar magnitude.

The iron content of the Cr_2O_3 scales was always small and decreased with time, the actual weight of iron in the scale remaining constant and equal to that present in the "initial film" as discussed previously (1, 2). No spinel, of the type $FeFe_{(2-x)}Cr_{(x)}O_4$ ($O \leq x \leq 2$), was ever observed metallographically, nor the associated higher iron contents by microanalysis. If this oxide were formed initially, then it must have been rapidly replaced by Cr_2O_3.

At 800° and 1000°C, there was in general no cracking of the protective oxide at temperature, no double layers of Cr_2O_3 were formed and very little roughening of the alloy/oxide interface occurred. At 1200°C, however, a roughened alloy/oxide interface was formed, and there was ballooning of the Cr_2O_3 scale, although this latter could have occurred on cooling the specimen from the oxidation temperature. When cracking of the Cr_2O_3 scale occurs at 1200°C, Cr_2O_3 is not re-formed as it is with alloys richer in chromium (1,2), because the chromium concentration at the alloy/oxide interface is too low (5). Instead rapid scaling or breakthrough occurs.

Mechanism of breakthrough.—At 1200°C, the end of the protective oxidation and commencement of rapid attack occurs at apparently random sites over the specimen surface. The suddenness of the onset of rapid oxidation, together with the observance of only protective Cr_2O_3 immediately prior to breakthrough, is indicative of a mechanical cracking mechanism (1, 3-5) rather than a "chemical mechanism" (8-10) for the transformation in oxidation rate. Providing that the Cr_2O_3 scale formed initially remains in contact with the alloy, or becomes detached without puncturing, there is no reason why it should not continue to grow. A simple calculation (5) shows that Cr_2O_3 is thermodynamically stable with an Fe-Cr alloy containing as little as 0.2% Cr at 1200°C. Calculated chromium concentration profiles (5) which, due to the assumptions made, give the minimum possible chromium concentrations, indicate that the interfacial chromium concentration at 1200°C increases from 4.8% after 10-min oxidation to 5.5% after 5-hr oxidation. Generally, experimentally measured values are not as low as this. Thus, the Cr_2O_3 scale formed at the start of oxidation never becomes thermodynamically unstable, and its subsequent failure is simply due to mechanical causes. This is further emphasized, in that at 1000°C where breakthrough does not generally occur, the chromium concentration at the alloy/oxide is calculated to be 2.5% after 10-min oxidation and 7.1% after 5 hr.

Apparently, the loosely attached protective scales balloon from the alloy surface before cracking open so that relatively large areas of the chromium-depleted underlying alloy are eventually exposed; rapid scaling through simple cracks in the protective scale would soon be stifled (1, 3). Presumably the punctured chromium oxide envelope is eventually lost completely from the specimen as it is never observed after breakthrough. In other instances it can stifle the growth of the stratified scale (4) or be slowly incorporated into the growing nodule (2).

Loss of the protective oxide need not occur simultaneously over the whole specimen surface. Cracking of one or two voids initially, followed by very rapid scaling there, would be sufficient to give the observed sudden increases in weight. Intermittent opening of other cavities in rapid succession would then result

in the smooth weight gain/time curves produced. Such failures would be expected randomly, but possibly the development of stratified scale in some places tends to disrupt the protective oxide in nearby locations. Overheating of the specimen may be important under catastrophic oxidation conditions.

It is extremely difficult to isolate one factor as the cause of the loss of protective scale, and probably it is a combination of factors: scale thickness, scale plasticity, alloy ductility, phase changes, adhesion between alloy and oxide and alloy and/or oxide grain growth. Detailed discussion of these factors is given elsewhere (1, 2).

Growth of stratified scale.—The scale formed at breakthrough depends implicitly on the chromium concentration at the surface of the underlying alloy when directly exposed to the atmosphere. Generally the higher the bulk alloy chromium content the higher is the chromium content at the alloy/oxide interface when it is exposed, although other factors, oxidation rate, alloy interdiffusion rate, time, are also important (5). Specimen geometry is also sometimes important because larger depletions of chromium are expected near to the specimen edges (chromium being used up from such regions by oxide growth on two or more nearby faces simultaneously) and at locations of thin section. With the present Fe-18% Cr alloy, the chromium concentration at the alloy/oxide interface when breakthrough occurs is near to the borderline between that for formation of type (i) and type (ii) scales. Thus, at the edges of specimens where lower chromium contents are likely type (ii) scales, typical of alloys of lower bulk chromium content, are formed. Over most of the remainder of the surface type (i) scales are formed, while at intermediate locations, type (iii) scales are formed.

At breakthrough, the chromium concentration at the alloy/oxide interface is never high enough for the immediate re-formation of a Cr_2O_3 scale as is observed for higher chromium alloys (1, 2) and a mixed iron and chromium oxide is formed. Whether this mixed oxide is the spinel, $FeFe_{(2-x)}Cr_xO_4$ ($O \leq x \leq 2$), or the rhombohedral oxide, $Fe_{(2-x)}Cr_xO_3$ ($O \leq x \leq 2$) or even mixtures of the two is relatively unimportant as both these oxides can vary continually with composition. For the purposes of this discussion, it is assumed that the spinel plays the major role in determining the subsequent oxidation behavior, particularly as this is the more favored phase at chromium levels of this magnitude (11).

Thus, the start of stratified scale growth is the formation of a spinel on the alloy surface exposed by the loss of protective Cr_2O_3. Initially the spinel is of uniform composition, but the chromium content of the spinel is dependent on the chromium concentration at the alloy surface when this is exposed; it is lower where type (ii) scales eventually develop than where type (i) scales are formed. The spinel produced in the chromium-rich areas may in fact be the normal spinel as evidenced by its composition (12). The situation at this stage is shown schematically in Fig. 11a, for scales of types (i) and (ii); type (iii) scales are similar to these and are discussed later.

Soon after the spinel is initiated, the faster diffusing iron ions start to segregate at the outer scale surface, leaving a chromium-rich region at the alloy/oxide interface (Fig. 11b), a distribution favored thermodynamically. If the scale is mainly spinel, then the value of x in the formula $FeFe_{(2-x)}Cr_xO_4$ varies through the scale, increasing as the alloy/oxide interface is approached (13). In general, the ionic mobilities in chromite spinels are lower than in ferrite spinels (14) making interdiffusion rates slower in type (i) scales than in type (ii) scales. Thus, in the former scales the segregation is not as complete as in type (ii) scales where the virtually pure spinel magnetite is formed at the surface of the scale, this being further oxidized to Fe_2O_3 in a manner similar

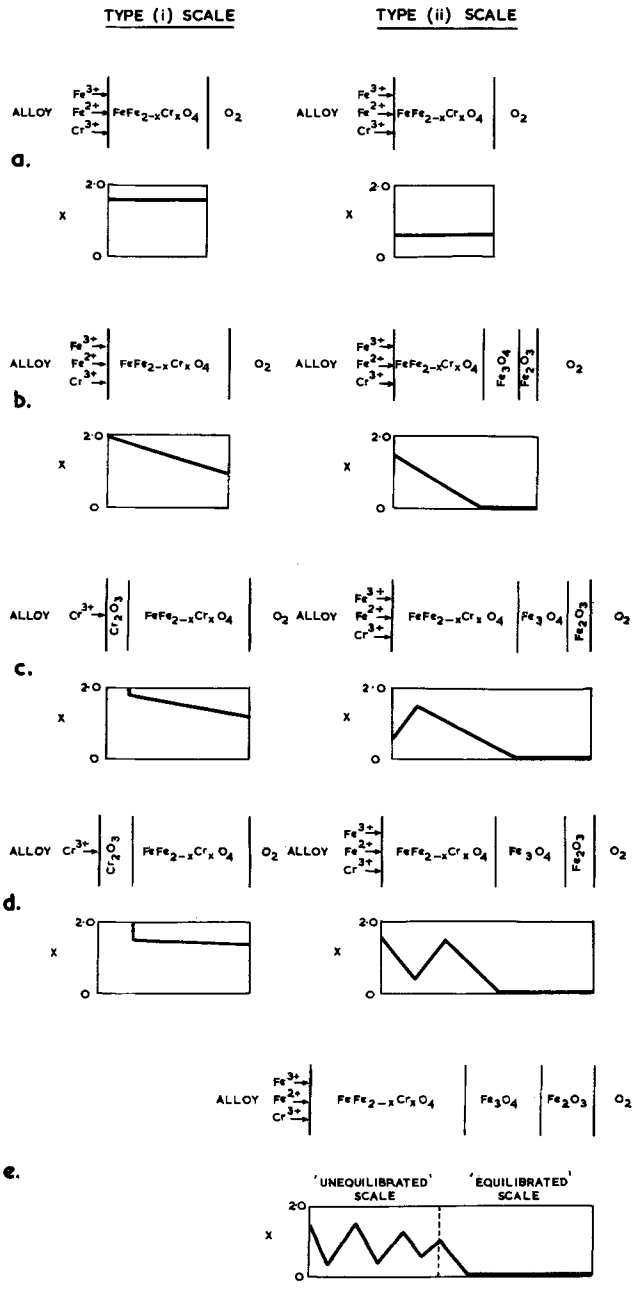

Fig. 11. Schematic diagram of the formation of scales of type (i) and (ii).

to that formed on pure iron. Clearly the over-all growth rate of type (ii) scales will be greater than the more chromium-rich type (i).

When the chromium content of the spinel in the vicinity of the alloy/oxide interface increases it acts as a partial barrier to the continued diffusion of iron ions to the outer scale layers. Consequently, a second iron-rich layer is formed beneath this barrier, resulting in a second chromium-rich barrier layer at the alloy/oxide interface. This is shown schematically for type (ii) scales in Fig. 11c and d. Further growth of type (ii) scales occurs by the continued formation of these iron-rich and chromium-rich oxides, resulting in the complex distribution of alternate iron-rich and chromium-rich layers found in these scales. With type (i) scales, the formation of the chromium-rich spinel at the alloy/oxide interface is closely followed by the formation there of the rhombohedral oxide, Cr_2O_3, containing only a very small amount of dissolved iron (Fig. 11c). Iron from the alloy cannot now enter this Cr_2O_3 layer at the base of the scale unless

the chromium concentration falls to about 0.2% at 1200°C (5), thus the supply of Fe^{2+} and Fe^{3+} ions to the outer scale layers is terminated. Further scale growth (Fig. 11d) of type (i) scale is, therefore, only the continued thickening of the Cr_2O_3 layer, the reaction at the Cr_2O_3/spinel interface being

$$3FeFe_{(2-x)}Cr_xO_4 + (6\square''' + 3\square'')_{spinel} = 4Cr_2O_3 + (8\square''')Cr_2O_3$$

where $(\square''')_{spinel}$, $(\square'')_{spinel}$, and $(\square''')_{CrO_3}$ represent trivalent and divalent cation vacancies in the spinel and trivalent cation vacancies in the rhombohedral oxide, respectively.

Scales of type (iii) are formed in an identical manner to those of type (ii) except that several pairs of iron-rich and chromium-rich layers are formed before the scale is healed by a Cr_2O_3 layer as described for type (i) scales. Further discussion of scale healing by Cr_2O_3 is reserved for the final section.

During later growth of all these scales the undulating chromium and iron concentration profiles tend to approach steady-state conditions. In type (i) scales this is seen in the sequence Fig. 7a-c where interdiffusion has reduced the compositional differences between the three layers. This process is essentially slow because ionic mobilities in the chromium-rich spinels are relatively low. However, it is assisted by the inner Cr_2O_3 layer preventing further thickening of the outer spinel layers. Possibly these outer spinel layers are oxidized further to the corresponding mixed rhombohedral oxide.

In type (ii) scales, the levelling out of the compositional differences between iron-rich and chromium-rich layers has to take place simultaneously with the continued growth of these layers. Thus, local activity gradients in the scale, which are not necessarily in the same direction as the over-all activity gradient, are gradually being removed as the scale grows under the over-all activity gradient between alloy and oxidizing atmosphere. Figure 11e shows this situation where the outer scale represents the steady state (a smooth activity gradient) and the inner scale the nonsteady state (an undulating activity gradient), the degree of "equilibration" decreasing as the alloy/oxide interface is approached.

Internal oxidation never occurs behind healed scales because the Cr_2O_3 at the alloy/oxide interface is thermodynamically very stable. In other instances, penetration of internal oxide particles into the alloy is never very great because the diffusion rate of oxygen into the alloy is not much faster than the rate of encroachment of the alloy/oxide interface. Incorporation of internal oxide particles into the surface scale would cause further stratification and local concentration gradients in the inner layers.

Mechanism of scale healing.—The reasons why stratified scale is healed along the sides of the specimen and not at the edges is not entirely clear. As soon as breakthrough occurs and rapid scaling starts, the chromium depletion established during the initial Cr_2O_3 formation is rapidly consumed. However, the alloy is not completely equilibrated as there is still a degree of selective oxidation of chromium during the rapid scaling.

Scale healing is associated with the formation of a continuous layer of the protective oxide, Cr_2O_3, in the present system, as opposed to a discontinuous layer or internal oxide of Cr_2O_3. After the start of rapid scaling, oxygen produced by dissociation of the surface scale at the alloy/scale interface diffuses into the alloy producing an internal oxide precipitate of Cr_2O_3. If the volume fraction of this internal oxide is above a certain critical level, then further formation of Cr_2O_3 will occur by sideways growth of the existing internal oxide particles (15). When the volume fraction is below the critical level, new Cr_2O_3 internal oxide precipitates are formed deeper in the alloy. Under the former conditions, continued sideways growth of the Cr_2O_3 particle results in a continuous "healing" Cr_2O_3 layer being formed, providing the rate of encroachment of the alloy/oxide interface is not so fast as to cause the Cr_2O_3 particles to be incorporated into the scale before they link up. Where continued nucleation of Cr_2O_3 particles occurs, a continuous layer will never be formed and scaling continues unchecked.

Factors governing the formation of this critical volume fraction of internal oxide include: (*a*) the chromium concentration profile in the alloy at the time of breakthrough; (*b*) the alloy interdiffusion coefficient which governs the flux of chromium atoms to the alloy/oxide interface; (*c*) the oxygen diffusion rate in the alloy; (*d*) the oxygen pressure at the alloy/external scale interface; and (*e*) the over-all oxidation rate. Comparing the edges of the specimens with the remainder of the surface, the interdiffusion coefficients, (*b*) and (*c*) above, will be the same. However, the other factors tend to favor healing along the sides of the specimens as compared to the edges of the specimens. Thus the lower local chromium concentrations at the edges of specimens, as discussed earlier, promote more iron-rich spinels in the external scale and therefore faster oxidation rates and higher effective oxygen pressures at the alloy/scale interface. Consequently Cr_2O_3 continues to be precipitated as internal oxide rather than form a continuous layer.

In order to understand more quantitatively the formation and healing of scales of this type, more information on diffusion and lattice defects in ternary oxides is required. Using thermodynamic and transport data it is possible at present to predict the final steady-state scaling conditions, but little can be said about the rate at which the steady state is approached or about the scaling behavior during the transient period. Presumably a more sophisticated theoretical approach will permit this.

Acknowledgments

The authors' thanks are due to Professor T. K. Ross for providing facilities and encouraging this study. They are also indebted to the Science Research Council for providing the electron probe microanalyzer and for a research studentship to one of them (D.P.W.) from October 1962 to September 1965.

Manuscript received May 15, 1967; revised manuscript received July 5, 1967.

Any discussion of this paper will appear in a Discussion Section to be published in the June 1968 JOURNAL.

REFERENCES

1. D. P. Whittle, Ph.D. Thesis, Univ. of Manchester (1965).
2. G. C. Wood and D. P. Whittle, To be published.
3. G. C. Wood and D. P. Whittle, *Corrosion Sci.*, **4**, 263, (1964).
4. G. C. Wood and D. P. Whittle, *ibid.*, **4**, 293 (1964).
5. D. P. Whittle, G. C. Wood, D. J. Evans, and D. B. Scully, *Acta Met.*, in press.
6. D. Caplan and M. Cohen, *This Journal*, **108**, 334 (1961).
7. D. Caplan, A. Harvey, and M. Cohen, *Corrosion Sci.*, **3**, 161 (1963).
8. G. Bandel, *Arch. Eisenhuttenw.*, **15**, 271 (1941/2).
9. J. O. Edström, *J. Iron Steel Inst.*, **185**, 450 (1957).
10. I. A. Menzies and D. Mortimer, *Nature*, **208**, 1307 (1965).
11. A. U. Seybolt, *This Journal*, **107**, 147 (1960).
12. H. J. Yearian, J. M. Kortwright, and J. Langenheim, *J. Chem. Phys.*, **22**, 1196 (1954).
13. H. J. Yearian, E. C. Randall, and T. A. Longo, *Corrosion*, **12**, 515t (1956).
14. C. E. Birchenall, *Met. Rev.*, **3**, 235 (1958).
15. C. Wagner, *Z. Elektrochem.*, **63**, 772 (1959).

Electron Diffraction Studies of Active, Passive, and Transpassive Oxide Films Formed on Iron

C. L. Foley, J. Kruger, and C. J. Bechtoldt

National Bureau of Standards, Washington, D. C.

ABSTRACT

Iron foil specimens were anodically polarized by means of a potentiostat in 1*N* H_2SO_4, 0.1*N* NaOH, and a sodium borate-boric acid solution (*p*H, 8.5). Both passive, active, and transpassive regions of the polarization curve were studied for each solution. The oxide films were examined while still in contact with the iron foil by selected area transmission electron diffraction. Five iron planes were studied: {100}, {110}, {111}, {210}, and {211}, and the epitaxial relationship of the oxide to the iron substrate determined. Evidence was found indicating that in all of the electrolytes used the passive film contained γ-Fe_2O_3, while the nonpassive films did not.

Of prime importance to our understanding of the nature of the phenomenon of passivity is a knowledge of the nature of the passive film. This includes its composition, structure, and relationship to the metal surface on which it was formed. There has not been a concentrated effort to discover the nature of the film, but there have been a few such studies (1-3) of the passive film on iron. Due to the thinness of the films, these studies have involved the use of electron diffraction. Two techniques, in particular, have been used. One is film stripping coupled with transmission electron diffraction; the other is reflection electron diffraction, leaving the film still in contact with the metal surface on which it was formed. The first technique has the advantage that the quality of the patterns obtained allows one to detect the weaker oxide reflections rather easily, but has the disadvantage that the film must be removed from the substrate under rather corrosive conditions. Mayne and Pryor (1) have evidence to show that the removal procedure does not chemically alter the film, although the possibility always exists that subtle changes may have occurred. Another problem associated with film stripping is that the film may change structurally during or subsequent to being detached from the metal surface. For example, stress existing in the film while it is attached to the metal may be relaxed upon stripping, thereby changing the lattice parameter and, as Mayne and Pryor (1) have suggested, may produce recrystallization of the film. The reflection technique, while it does look at films still in contact with the metal, is less able to detect weak oxide reflections because they may be hidden by the elongated stronger metal and oxide reflections.

This study attempts to combine the advantage of reflection diffraction (looking at the film while it is still on the metal) with that of transmission diffraction (greater sensitivity). This is accomplished by producing both passive and nonpassive oxide films on thin metal foils, of the type used so effectively in many recent transmission electron microscopy studies of metals (2). Selected area diffraction enables us to look at double layers of the film (one on each side of the foil) on metal grains of many different crystallographic orientations. The epitaxial relationships between the substrate iron and the film can thus be easily determined for many orientations without the necessity of using large iron single crystals. The film-metal-film "sandwich" doubles the amount of passive film studied and thus increases the possibility of detecting the weaker oxide reflections that are necessary to distinguish between Fe_3O_4 and γ-Fe_2O_3. This is of importance since a number of workers have indicated that the γ-Fe_2O_3 plays a role in passivity (3, 5). This "sandwich" would also increase the chances for double diffraction effects, but as will be mentioned later, this did not present a problem in our patterns. The technique now used suffers from the same disadvantage that is present with both of the aforementioned electron diffraction techniques, in that for examination the specimen must be removed from the environment where the film is formed. Thus, there is a possibility that the nature of the film itself has been altered by the time it is studied in the electron diffraction apparatus. Experiments described later indicate that this is not a serious difficulty.

These studies of films formed on pure iron foils have extended the range of systems studied by electron diffraction to include those formed in acidic and basic as well as neutral solutions. The prepassive and transpassive regions of the anodic polarization curve were studied, in addition to the passive region.

Experimental

The electrolytic cell used for polarizing thin foil specimens to selected potentials by means of a potentiostat is shown in Fig. 1. This cell enabled us to deaerate our solutions with Grade A, 99.99% helium during all experiments. Foil specimens were rolled to a thickness of 0.005 cm from an iron sample obtained

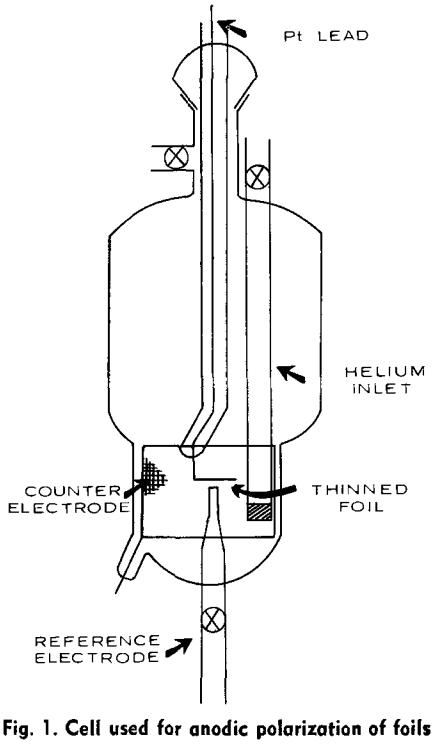

Fig. 1. Cell used for anodic polarization of foils

from the Battelle Memorial Institute.[1] After degreasing with ethanol and trichloroethylene, the foil was annealed for 1 hr at 1000°C in a hydrogen atmosphere. The foil specimens were thinned by the Bollman technique (2), using a mixture of one part 70% perchloric acid to twenty parts glacial acetic acid, for the electropolishing solution. Specimens were then rinsed in high-purity methanol and transferred immediately to the electrolytic cell. After 1 min of cathodic reduction to remove any oxide films, the specimen was brought to the desired potential and usually held at this potential for 2 hr. Longer exposures did not give significantly different results.

When the specimen was ready for inspection, it was rapidly removed from the cell, rinsed, and submerged in methanol. The foil was mounted for the electron microscope and selected area diffraction patterns were obtained at an operating voltage of 100 kv. In order to introduce as little contamination and heating into the specimens as possible, the diffraction patterns were taken, during the first 5 min of examination, then electron micrographs of the same area were made, if they were desired.

Three solutions were used in these experiments: a basic solution of 0.1*N* NaOH with a *p*H of 11.4, a nearly neutral solution, which we will refer to as "borate" consisting of 0.15*N* $Na_2B_4O_7 \cdot 10H_2O$ and 0.15*N* H_3BO_3 mixed in proportions giving a *p*H of 8.5, and an acidic solution of 1*N* H_2SO_4 with a *p*H of 1.1. Using each solution, there were four main groups of experiments: prepassive, passive, passive-decay (initially passive, but then driven potentiostatically to an active potential), and transpassive. The anodic polarization curves used to determine the potentials characteristic of these various regions were determined in a manner similar to that used by Nagayama and Cohen (3).

[1] Gaseous impurities (ppm): O_2 (vacuum fusion), 2.1; S (colorimetric), 4 ± 3; C (combustion-conductometric), 3 ± 3; N_2 (vacuum fusion), 0.5; H_2 (vacuum fusion), 0.3. Major metallic impurities (ppm): Al, 15; Cr, 5; Co, 5; Cu, 7; Ni, 20; P, 9; Si, 10.

The potentials used (*vs.* SCE) are listed in Tables I, II, and III.

A few studies were made on specimens that were formed by exposure to the inorganic passivating solution, 0.1*N* $NaNO_2$. Several other experiments were carried out using the borate and H_2SO_4 solutions containing chloride ions.

Results and Interpretation

The results of our study of oxide films formed in the acidic, basic, and neutral solutions for five of the iron planes are presented in Tables I, II, and III. Figure 2 shows that the patterns obtained for the passive films in the three solutions, plus $NaNO_2$, had the same geometric distribution and differed only in intensity. It should be noted that the observable differences in the patterns are due to the intensity distribution and the difference in thickness of the film. While this figure depicts one iron orientation, the relative quality was similar for all orientations studied.

Indexing and epitaxy.—The indexing of each negative plate was accomplished by the standard methods utilizing the sideline technique (6), the iron spots serving as an internal standard. As a check, the angles between various oxide spots were measured and compared with the standard cubic interplanar angles (7). Figures 3-7 show examples of both a passive and a nonpassive film for each plane listed in Tables I, II and III, with a corresponding indexed diagram. A comparison between the epitaxial relationships obtained in our work and other work done in this field is shown in Table IV. The comparison studies listed have all been concerned with films formed by gaseous oxidation.

There were some special problems associated with indexing. The principal one arises because the thickness of the oxide layer [≈ 30Å (8)], makes it possible for reciprocal lattice spikes (9) from more than one oxide layer to intersect the reflecting sphere. In fact,

Table I. Borate solution

		A	B	C	D	E
	Plane, Fe	{100}	{110}	{111}	{210}	{211}
1.	State and potential	Prepassive, −0.6v or open circuit				
2.	Oxide parameter, in Å	8.39	Not determined	Not determined	—	8.40
3.	Identification	Fe_3O_4	α-FeOOH	α-FeOOH	No oxide	Fe_3O_4
4.	Epitaxy					
	Oxide plane	$\{\bar{1}\bar{1}4\}$	—	—	—	$\{01\bar{1}\}$
	Oxide axes parallel to Iron axes	$[1\bar{1}0]$Ox ‖ [010]Fe [100]Ox ‖ [110]Fe				[011]Ox ‖ [111]Fe [111]Ox ‖ [011]Fe
5.	Remarks	No γ-Fe_2O_3	Rings	Rings	Clean	No γ-Fe_2O_3
6.	State and potential	Passive, +0.75v, +0.85v				
7.	Oxide parameter, in Å	8.3	8.32	8.29	8.33	8.31
8.	Identification	γ-Fe_2O_3	γ-Fe_2O_3	γ-Fe_2O_3	γ-Fe_2O_3	γ-Fe_2O_3
9.	Epitaxy					
	Oxide plane	$\{\bar{1}\bar{1}4\}$	$\{01\bar{1}\}$	$\{01\bar{1}\}$	{100}	$\{01\bar{1}\}$
	Oxide axes parallel to	[221]Ox ‖ [200]Fe	$[0\bar{1}1]$Ox ‖ [001]Fe	$[111]$Ox ‖ $[1\bar{1}0]$Fe	$[\bar{1}01]$Ox ‖ [001]Fe	Same as above,
	Iron axes	[100]Ox ‖ [110]Fe	$[\bar{2}11]$Ox ‖ [111]Fe	$[100]$Ox ‖ [011]Fe $[311]$Ox ‖ $[11\bar{2}]$Fe	$[11\bar{1}]$Ox ‖ $[2\bar{1}3]$Fe $[\bar{2}\bar{1}2]$Ox ‖ [100]Fe	E—4 plus, [100]Ox ‖ [110]Fe
10.	Remarks	Has γ-Fe_2O_3	Has γ-Fe_2O_3	Has γ-Fe_2O_3	Has γ-Fe_2O_3	Has γ-Fe_2O_3
11.	State and potential	Decay, to −0.6v				
12.	Oxide parameter, in Å	8.29	8.38	8.38	8.37	8.35
13.	Identification	γ-Fe_2O_3	Fe_3O_4	Fe_3O_4	γ-Fe_2O_3 or Fe_3O_4	γ-Fe_2O_3 or Fe_3O_4
14.	Epitaxy					
	Oxide plane	$\{\bar{1}\bar{1}4\}$	$\{11\bar{1}\}$	$\{01\bar{1}\}$	{100}	$\{01\bar{1}\}$
	Oxide axes parallel to Iron axes	Same as above A—9	$[101]$Ox ‖ [001]Fe $[\bar{2}10]$Ox ‖ $[11\bar{1}]$Fe	Same as above C—9	Same as above D—9	Same as above E—4
15.	Remarks	Some γ-Fe_2O_3	Some γ-Fe_2O_3	Some γ-Fe_2O_3	Some γ-Fe_2O_3	Some γ-Fe_2O_3
16.	State and potential	Transpassive, +1.25v				
17.	Oxide parameter, in Å	8.37	—	8.42	—	8.39
18.	Identification	Fe_3O_4	—	Fe_3O_4	—	Fe_3O_4
19.	Epitaxy					
	Oxide plane	$\{\bar{1}\bar{1}4\}$	—	$\{01\bar{1}\}$	—	$\{01\bar{1}\}$
	Oxide axes parallel to Iron axes	Same as above A—4		Same as above C—9		Same as above E—4
20.	Remarks	No γ-Fe_2O_3	No plates	No γ-Fe_2O_3	No plates	No γ-Fe_2O_3

Table II. H_2SO_4 solution

		F	G	H	I	J
	Plane, Fe	{100}	{110}	{111}	{210}	{211}
1.	State and potential		Prepassive, +0.2v			
2.	Oxide parameter, in Å	—	—	—	—	8.37
3.	Identification	No oxide	No oxide	Some with γ-FeOOH others clean	No oxide	Fe_3O_4
4.	Epitaxy					
	Oxide plane	—	—	—		$\{01\bar{1}\}$
	Oxide axes parallel to Iron axes					[011]Ox || [111]Fe [111]Ox || [011]Fe
5.	Remarks	Clean	Clean	Clean or rings	Clean	No γ-Fe_2O_3
6.	State and potential		Passive, +1.4v, + 1.6v			
7.	Oxide parameter, in Å	8.32	8.30	8.31	8.31	—
8.	Identification	γ-Fe_2O_3	γ-Fe_2O_3	γ-Fe_2O_3	γ-Fe_2O_3	γ-FeOOH
9.	Epitaxy					
	Oxide plane	$\{\bar{1}1\bar{4}\}$	$\{11\bar{1}\}$, $\{01\bar{1}\}$	$\{01\bar{1}\}$	{100}	—
	Oxide axes parallel to Iron axes	[221]Ox || [200]Fe [100]Ox || [110]Fe	Same as Table I B—9, B—14	Same as Table I C—9	Same as Table I D—9	
10.	Remarks	Has γ-Fe_2O_3	No γ-Fe_2O_3	Has γ-Fe_2O_3	Has γ-Fe_2O_3	Rings
11.	State and potential		Decay, open circuit			
12.	Spinel parameter	8.36	8.33	8.36	8.30	—
13.	Identification	γ-Fe_2O_3 or Fe_3O_4	γ-Fe_2O_3 or Fe_3O_4	γ-Fe_2O_3 or Fe_3O_4	γ-Fe_2O_3 or Fe_3O_4	—
14.	Epitaxy					
	Oxide plane	$\{\bar{1}1\bar{4}\}$	$\{11\bar{1}\}$, $\{01\bar{1}\}$	$\{01\bar{1}\}$	{100}	
	Oxide axes parallel to Iron axes	Same as above F—9	Same as Table I B—9, B—14	Same as Table I C—9	Same as Table I D—9	
15.	Remarks	Some γ-Fe_2O_3	No γ-Fe_2O_3	No γ-Fe_2O_3	Some γ-Fe_2O_3	No plates
16.	State and potential		Transpassive, +1.75v			
17.	Oxide parameter, in Å	8.40	8.39	—	8.37	—
18.	Identification	Fe_3O_4	Fe_3O_4	γ-FeOOH	Fe_3O_4	No oxide
19.	Epitaxy					
	Oxide plane	$\{\bar{1}1\bar{4}\}$	$\{11\bar{1}\}$	—	{100}	—
	Oxide axes parallel to Iron axes	Same as Table I A—4	Same as Table I B—14		Same as Table I D—9	
20.	Remarks	No γ-Fe_2O_3	No γ-Fe_2O_3	Rings	No γ-Fe_2O_3	Clean

Table III. NaOH solution

		K	L	M	N	O
	Plane, Fe	{100}	$\{\bar{1}10\}$	{111}	{210}	{211}
1.	State and potential		Prepassive, open circuit			
2.	Oxide parameter, in Å	8.27	8.40	—	8.40	—
3.	Identification	γ-Fe_2O_3	Fe_3O_4	No oxide or has α-FeOOH	Fe_3O_4	—
4.	Epitaxy					
	Oxide plane	$\{\bar{1}1\bar{4}\}$	$\{11\bar{1}\}$	—	{100}	—
	Oxide axes parallel to	[221]Ox || [200]Fe	[101]Ox || [001]Fe		Same as Table I	
	Iron axes	[100]Ox || [110]Fe	$[\bar{2}10]$Ox || [111]Fe		D—9	
5.	Remarks	Has γ-Fe_2O_3	No γ-Fe_2O_3 some rings	Clean or rings	No γ-Fe_2O_3	No plates
6.	State and potential		Passive, +0.5v			
7.	Oxide parameter, in Å	8.31	8.33	8.31	8.31	8.30
8.	Identification	γ-Fe_2O_3	γ-Fe_2O_3	γ-Fe_2O_3	γ-Fe_2O_3	γ-Fe_2O_3
9.	Epitaxy					
	Oxide plane	$\{\bar{1}1\bar{4}\}$	$\{01\bar{1}\}$	$\{01\bar{1}\}$	{100}	$\{01\bar{1}\}$
	Oxide axes parallel to Iron axes	Same as above K—4	Same as Table I B—9	Same as Table I C—9	Same as Table I D—9	Same as Table I E—4, E—9
10.	Remarks	Has γ-Fe_2O_3	Has γ-Fe_2O_3	Has γ-Fe_2O_3	Has γ-Fe_2O_3	Has γ-Fe_2O_3
11.	State and potential		Decay, to −1.0v			
12.	Oxide parameter, in Å	—	8.40	8.36	8.35	—
13.	Identification	—	Fe_3O_4	γ-Fe_2O_3 or Fe_3O_4	γ-Fe_2O_3 or Fe_3O_4	—
14.	Epitaxy					
	Oxide plane	—	$\{11\bar{1}\}$	$\{01\bar{1}\}$	{100}	—
	Oxide axes parallel to Iron axes		Same as above L—4	Same as Table I C—9	Same as Table I D—9	
15.	Remarks	No plates	No γ-Fe_2O_3	No γ-Fe_2O_3	No γ-Fe_2O_3	No plates
16.	State and potential		Transpassive, +1.0v			
17.	Oxide parameter, in Å	8.35	8.41	—	—	—
18.	Identification	Fe_3O_4	Fe_3O_4	No oxide	—	No oxide or has α-FeOOH
19.	Epitaxy					
	Oxide plane		$\{01\bar{1}\}$	—	—	—
	Oxide axes parallel to Iron axes	Same as Table I A—4	Same as Table I B—4			
20.	Remarks	No γ-Fe_2O_3	No γ-Fe_2O_3	Clean	No plates	Rings or clean

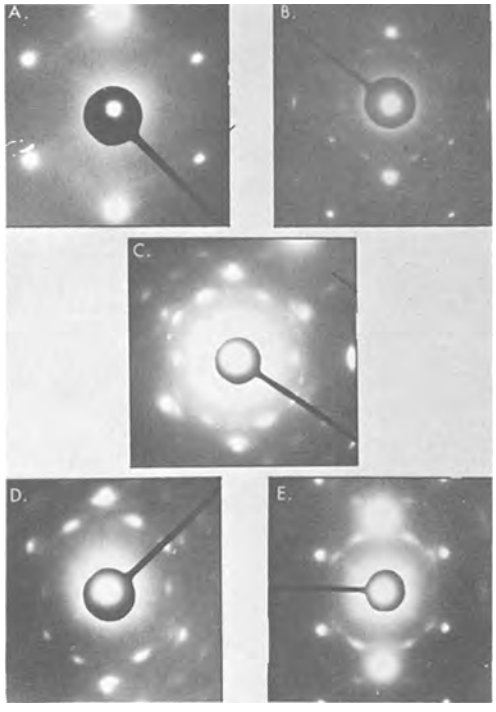

Fig. 2. Comparison of solutions: A, {111} plane shows no oxide after just submerging in borate; B, {111} plane, polarized at +0.75v in borate; C, {111} plane, polarized at +0.5 in NaOH; D, {111} plane, polarized at +1.4v in H_2SO_4; E, {111} plane, dipped in $NaNO_2$.

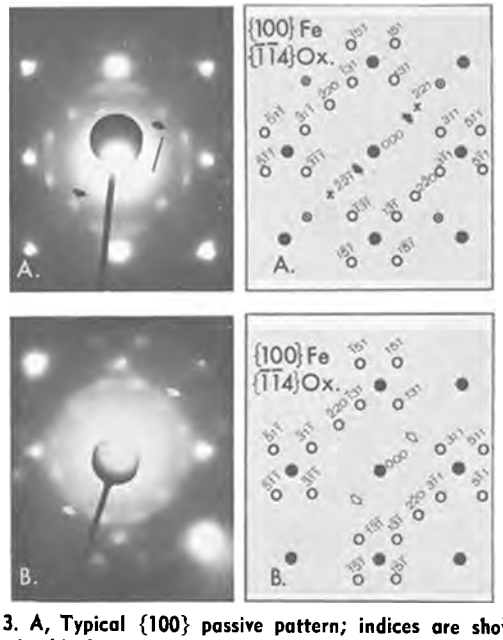

Fig. 3. A, Typical {100} passive pattern; indices are shown for oxide only; black arrows indicate γ-Fe_2O_3 reflections on a passive foil which disappear for nonpassive. B, Typical {100} nonpassive pattern; white arrows show sites where γ-Fe_2O_3 reflections have disappeared. Three oxide levels are represented in both A and B. Note: The oxide orientation is "nearly" $\bar{1}1\bar{4}$. It is composed of reflections on the zero level as well as reflections rel-rodded from above and below. Key: •, iron; ○, spinel Fe_3O_4 (or coincident γ-Fe_2O_3 spots in the passive case); X, γ-Fe_2O_3; ⊙, double diffraction.

a number of the patterns could be indexed only by taking this effect into account. An example of this can be seen for {210} iron, where three oxide levels are present (see Fig. 6). Some of the other planes are also interpreted in this manner.

Another difficulty was encountered in indexing films for the {100} substrate. As seen in Fig. 3 the passive

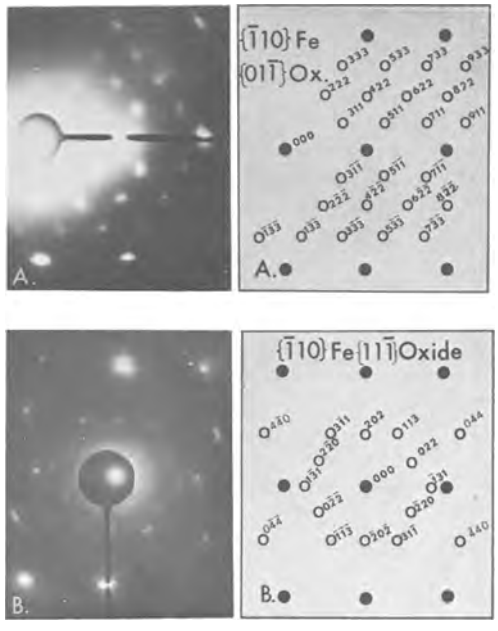

Fig. 4. A, Typical {$\bar{1}10$} passive pattern; only one oxide layer is represented. B, Typical {$\bar{1}10$} nonpassive pattern; again, the oxide is nearly {$11\bar{1}$}, being composed of reflections from more than one oxide layer. Key: •, iron; ○, spinel Fe_3O_4 (or coincident γ-Fe_2O_3 spots in the passive case).

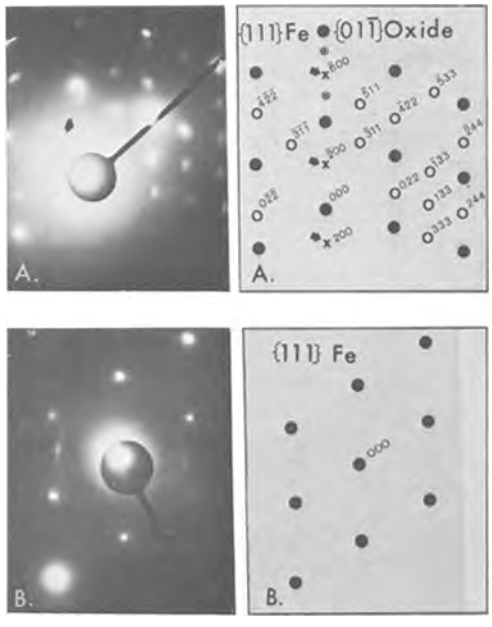

Fig. 5. A, Typical {111} passive pattern. B, The typical {111} nonpassive pattern showed either no oxide (as shown here), or a weaker version of the passive pattern, often incorporating oxide α-FeOOH rings. Only one oxide layer is represented in A. Key: •, iron; ○, spinel Fe_3O_4 (or coincident γ-Fe_2O_3 spots for the passive case); X, γ-Fe_2O_3.

film appears to have fourfold symmetry, indicating a {100} oxide orientation (this orientation was found in previous studies as indicated in Table IV). Nonpassive films for the {100} iron lose this symmetry, however. In order to explain the disappearance of only one pair of the center oxide spots (marked with arrows in Fig. 3), when the film became nonpassive, it was necessary to consider another orientation for the passive film. A close examination of the passive film pattern revealed a slight, but reproducible difference in the radial distances to the center oxide pairs. The closer pair, having a slightly higher d-value, could then be distinguished as a {221} reflection (d = 2.78), which

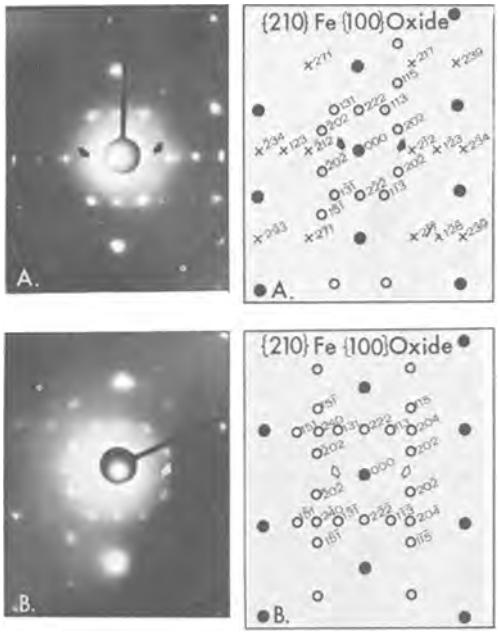

Fig. 6. A, Typical {210} passive pattern; black arrows indicate γ-Fe_2O_3 reflections. B, The {210} nonpassive pattern showed the same structure without the γ-Fe_2O_3 reflections (empty sites indicated by white arrows). Two oxide levels are represented in both A and B, thus the oxide orientation is "nearly" {100}. Key: •, iron; ○, spinel Fe_3O_4 (or coincident γ-Fe_2O_3 spots for the passive case); X, γ-Fe_2O_3.

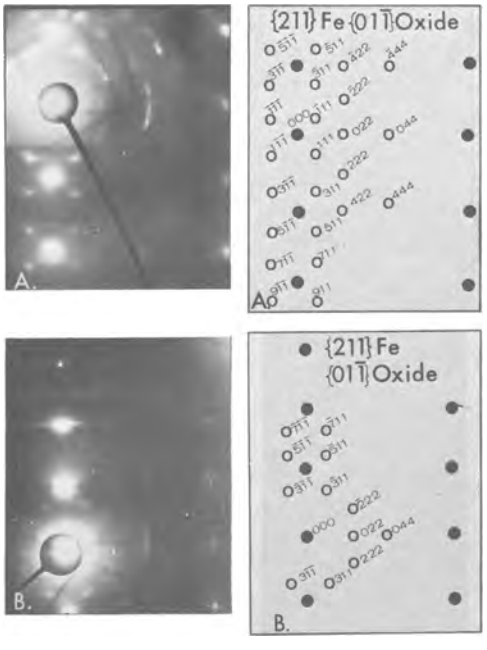

Fig. 7. A, Typical {211} passive pattern; and B, the weaker nonpassive version of the same structure. Only one oxide layer is represented. *Note:* This oxide relationship shows a resemblance to the super lattice reflections (27) perpetrated by partially coherent oxide precipitates. This particular oxide orientation consists of only one oxide level, however, while the super lattice reflections of this type will usually occur only when the foil is tipped a few degrees from a prominent matrix zone. Key: •, iron; ○, spinel Fe_3O_4 (or coincident γ-Fe_2O_3 reflections for the passive case).

would disappear when in the nonpassive state. This distinction between certain oxide reflections will be discussed further. When indexed in this manner, the oxide film orientation would be considered as {$\bar{1}\bar{1}4$} in both passive and nonpassive cases.

As seen in Table IV, our work showed the same oxide orientation for both passive and nonpassive films

Table IV. Epitaxial relationships

Reference	Parallel planes		Parallel axes	
	Iron	Oxide	Iron	Oxide
This work	{100}	{$\bar{1}\bar{1}4$} P	[200]	[221]
			[110]	[100]
	{100}	{$\bar{1}\bar{1}4$} NP	[010]	[$\bar{1}$10]
			[110]	[100]
Sewell, Cohen, Stockbridge (4)	{001}	{001}	[010]	[$\bar{1}$10]
Haase (6)	{001}	{001}	[110]	[100]
Boggs (7)	{001}	{001}	[010]	[011]
			[$\bar{1}$00]	[0$\bar{1}$1]
This work	{$\bar{1}$10}	{01$\bar{1}$} P	[001]	[0$\bar{1}\bar{1}$]
			[11$\bar{1}$]	[$\bar{2}$11], [2$\bar{1}\bar{1}$]
	{110}	{111} NP	[001]	[101]
			[11$\bar{1}$]	[$\bar{2}$10]
Sewell, Cohen, Stockbridge	{011}	{111}	[11$\bar{1}$]	[1$\bar{1}$0], [$\bar{1}$10]
Haase	{110}	{011}*	[111]	[11$\bar{2}$]
			[100]	[110]
Wagner, Lawless, Gwathmey (26)	{011}	{111}	100	[$\bar{1}$10]
Boggs	{011}	{111}	[$\bar{1}$11]	[$\bar{1}$01]
			[$\bar{1}$12]	[12$\bar{1}$]
This work	{111}	{01$\bar{1}$} P	[1$\bar{1}$0]	[111]
		{01$\bar{1}$} NP	[0$\bar{1}$1]	[100]
			[11$\bar{2}$]	[$\bar{3}$11]
Sewell, Cohen, Stockbridge	{111}	2 degrees of {210}	[1$\bar{1}$0]	[001]
Boggs	{111}	{1$\bar{1}$0}	[01$\bar{1}$]	[001]
	{111}	{$\bar{2}$10}	[01$\bar{1}$]	[00$\bar{1}$]
This work	{210}	{100} P	[001]	[$\bar{1}$01]
	{210}	{100} NP	[2$\bar{1}$3]	[11$\bar{1}$]
	{210}		[100]	[2$\bar{1}\bar{2}$]
No other studies published on this iron plane.				
This work	{211}	{01$\bar{1}$} P	[111]	[011]
			[011]	[111]
			[021]	[100]
	{211}	{01$\bar{1}$} NP	[111]	[011]
			[011]	[111]
Sewell, Cohen, Stockbridge	{112}	{110}	[$\bar{1}$11]	[1$\bar{1}$0]
Boggs	{112}	{011}	[111]	[3$\bar{1}$1]

* Determined by the authors from an indexed figure in ref. (6).

for all except the {$\bar{1}$10} substrate orientation. The problem of the {$\bar{1}$10} iron orientation will be discussed later, but it should be noted in Fig. 4 that there is a clear distinction between the passive film orientation and the nonpassive film orientation. This situation is not similar to the {100} substrate where, for reasons mentioned before, the difference between the passive and nonpassive patterns has not been ascribed to a difference in orientations.

Although other iron planes have been studied, *e.g.*, {113} and {301}, the results for these were not significantly different from those listed in Tables I, II, and III, and will not be given a detailed survey here in order to conserve space. The epitaxy for these two orientations is given in Table V.

Double diffraction.—Double diffraction effects from the iron were encountered only with the NaOH solution where films formed were relatively thick. The extraneous reflections due to this effect were easy to detect by the method mentioned by Hirsch *et al.* (10).

Table V. Epitaxy for the {113} and {301} iron orientations. These relationships hold for both the passive (P) and nonpassive (NP) cases.

{113} iron ||	{001} oxide P and NP
[$\bar{3}$01] iron	|| [111] oxide
[211] iron	|| [$\bar{3}$11] oxide
{301} iron ||	{100} oxide P and NP
[001] iron	|| [$\bar{1}$01] oxide
[312] iron	|| [$\bar{5}$11] oxide

The NaOH patterns were then used as a basis for determining all of the double diffraction reflections on each iron orientation. The double layer of oxide viewed (film-metal-film) did not seem to introduce extra reflections for the thinner oxide layers formed in neutral and acidic solutions since double diffraction was not detected for these films.

Lattice parameters.—The spinel lattice parameters for each negative were determined by using many d-values for different pairs of oxide spots and the parameter calculated for each. Many of the selected area diffraction patterns were found to suffer from a certain amount of pin-cushion distortion (11). In order to correct for the error in lattice parameter determinations introduced by this effect, we measured the degree of distortion using a Palladium standard and used the displacements calculated from this to determine the undistorted values of the radial distances for the oxides. These corrections were small (0-1.25%), but important in distinguishing between γ-Fe_2O_3 (8.32Å) and Fe_3O_4 [8.396Å (12)]. The "average" values of lattice parameters listed in Tables I, II, and III, represent values which have been "corrected" for the pin-cushion effect. A number of plates were used to determine each value. Since each oxide spot can be measured with the same absolute accuracy, it is necessary to weight any measurement error in the lattice parameter according to the value of $\sqrt{h^2 + k^2 + l^2}$. This practice has generally been neglected in previous error determinations of the lattice parameters in this system. (Note: A discussion of the structure of γ-Fe_2O_3 follows.) A statistical analysis of the lattice parameter data taking this weighting factor into account showed a maximum error of $\pm$ 0.02Å on the parameter values.[2]

It should be noted that, in general, the spinel parameters are much lower for the passive state (Tables I, II, and III, line 1) than for the transpassive or prepassive states. Whenever indications of γ-Fe_2O_3 have been found on most of the films for a particular group (see lines 5, 10, and 15), the lattice parameter is very near the γ-Fe_2O_3 value (8.32Å). Previous studies have verified this result for films formed in chromate solutions (1) and by gaseous oxidation (4).

The lattice parameters found for passive-decay films usually fall nearly midway between these for γ-Fe_2O_3 and Fe_3O_4, indicating a transition state. The decay patterns sometimes showed faint γ-Fe_2O_3 reflections, but not consistently.

Distinction between γ-Fe_2O_3 and Fe_3O_4.—The structures of the two oxides Fe_3O_4 and γ-Fe_2O_3 are closely related, γ-Fe_2O_3 being a pseudospinel probably having the lithium "spinel," $LiFe_5O_8$, type structure. γ-Fe_2O_3 has all of the reflections of the Fe_3O_4 spinel structure, plus additional reflections which probably result from ordered vacancies or ordered substitution of protons for ferrous ions in certain of the special positions, 16d, Fd3m of the spinel structure. This substitution has the effect of reducing the structure to primitive cubic and, as a result, introduces mixed even-odd indices reflections for the γ-Fe_2O_3 (12, 20). In some γ-Fe_2O_3 preparations (14, 15), including the standard sample used in this laboratory,[3] faint extra reflections can be detected which can be indexed using a tetragonal cell (with $c_o = 3\ a_o$, where a_o equals a_o of the cubic cell). However, the principal lines of this pattern occur in the order of magnitude one would expect for the $LiFe_5O_8$ type structure, and, therefore, a close relation is evident. Bloom and Goldenberg (21) claim that the tetragonal cell occurs with the incomplete removal by oxidation of ferrous ions. In this paper, γ-Fe_2O_3 is regarded as cubic. In addition to the additional mixed even-odd reflections the d-values and angles for γ-Fe_2O_3 reflections are sufficiently different from those of the nearby Fe_3O_4 reflections to be easily identified. The γ-Fe_2O_3 reflections obtained for our patterns were closely matched to the standard values (16) and were easily distinguished from the standard values for Fe_3O_4 (17). We would label the oxide film on a particular iron orientation as "γ-Fe_2O_3" only if it had these extra spots and a lower lattice parameter.

Validity of electron diffraction studies.—There have been objections raised to the study of passive films out-of-solution, no matter what the technique. The most serious of these involved the possibility that the films undergo chemical or structural changes in the interval between formation and observation.

For our work, this objection can be met in a number of ways. First, after a passive film has been formed by anodic polarization, the circuit can be open for a considerable length of time before the specimen's potential relative to SCE will drop below the value characteristic of the passive region. A series of experiments in H_2SO_4 showed a decay time of more than 7 min when left in an acidic environment. Since our specimens were removed from solution and mounted in an evacuated chamber within 5 min, it seems reasonable to assume that the passive film had remained intact. This hypothesis was checked by passivating a specimen, removing it from solution, treating it in the same manner as required for electron diffraction work, and then replacing it in solution: the potential still remained in the passive range.

Second, the films formed in NaOH were very thick and difficult to dissolve (as can be seen in the decay experiments for this group, Table III). Since the patterns found for foils prepared in H_2SO_4 and borate were similar to those for the NaOH prepared foils, it is again reasonable to assume that the passive condition exists for foils prepared in all three solutions when they are under examination.

Finally, prepassive and transpassive films gave different results from those observed for passive films. If the passive films were changed during handling and observation, it is most likely that they would have become nonpassive. This did not happen for any of the NaOH films and occurred only rarely for the other films.

The possibility that the γ-Fe_2O_3 is formed by exposure to air does not seem apparent here as the exposure of the specimens to air and the vacuum environment of the diffraction apparatus is not great enough to produce the sort of lattice parameter variations as noted by Sewell, Stockbridge, and Cohen (4). Since all of the specimens receive approximately equal exposure, the considerable lattice parameter variations found between passive and nonpassive films could not be explained in this manner.

Effect of chloride ions.—When chloride ions were added to the solutions used, rings were always detected in the diffraction patterns of the films formed. These rings were found to be due to γ-FeOOH, in agreement with the previous work of Mellors *et al.* (18) for passive films formed in the presence of chloride in inorganic inhibitor solutions. Table II indicates that γ-FeOOH was also detected in some cases when films were formed in the active region. Since the γ-FeOOH was randomly oriented, it seems likely that it formed by precipitation from the solution rather than by direct growth on the metal surface.

Discussion

This study shows that the structure and composition of the anodic passive film formed on iron is not dependent on the pH of the electrolyte, but only on the orientation of the surface on which it is formed. The

[2] The "weighting" factor is necessary since the lattice parameter is a function of $\sqrt{h^2 + k^2 + l^2}$ and the distortion is greater near the center and on the edges of the patterns. The negative plates were oriented and the same oxide and iron spots on each were used to approximate the actual distortion pattern. Then by casting an undistorted grid on the pattern, the percentage of "pull" on each spot could be calculated.

[3] This analysis was made from a sample kindly lent to the authors by Dr. M. C. Bloom, Naval Research Laboratory.

passive film gives electron diffraction patterns of γ-Fe_2O_3, whether it be formed by anodic polarization or by the use of an inorganic passivating solution and in each case shows the same epitaxial relationships to the iron substrate. Since the γ-Fe_2O_3 pattern contains all of the reflections of Fe_3O_4, it is possible that it is present along with the γ-Fe_2O_3. This assumption has its basis in the work of Nagayama and Cohen (2) who have suggested that it exists at the metal interface.

The interpretation of two oxide phases in the passive film is not new experimentally (1) nor is it unexpected theoretically (5). As was mentioned earlier, however, this study extends the *p*H range of the solutions studied from the neutral region of past studies to both the acidic and basic regions and shows that regardless of mode of formation, the nature of the film remains essentially the same.[4] More important, perhaps, than presenting evidence supporting the presence of γ-Fe_2O_3 in the passive film, are the results of this study obtained in the prepassive and transpassive regions showing the absence of γ-Fe_2O_3 and the presence of only Fe_3O_4. Had this not been found, the presence of γ-Fe_2O_3 in the passive film could be considered as only an interesting fact, but one not necessarily related to its being passive.

Since the presence of γ-Fe_2O_3 in the passive film appears related to the passive state of the metal, what special property does it have that differentiates it from the very similar Fe_3O_4 which we find in the nonpassive films? A recent suggestion has been made by Bloom and Goldenberg (21) who point out that a major difference between the two oxides is the great difference in their electrical conductivity, the Fe_3O_4 being a better conductor by many orders of magnitude. As Hoar (22) has pointed out, most current ideas concerning the conductivity of the passive film on iron consider it as being a good electrical conductor. This idea is mainly based on the fact that in going to the transpassive region large currents are easily passed, indicating a film of high conductivity. When the transpassive region is reached, this study shows that the film is no longer γ-Fe_2O_3, but is the relatively good conductor Fe_3O_4. In agreement with this we find that low conductivity γ-Fe_2O_3 is absent in these active films. Since γ-Fe_2O_3 is always associated only with a passive film, and it is a poor conductor, then passivity must require a film with an insulating outer layer if it has more than one layer. Recent kinetic studies from this laboratory (8) lend support to this hypothesis. However, no direct measurement, to our knowledge, has been made of the conductivity of the very thin outer γ-Fe_2O_3 layer in the passive film in order to settle this question. Another difference noted by Bloom and Goldenberg (21) is that γ-Fe_2O_3 does not have the formula, Fe_2O_3, but is probably similar to the lithium spinel $LiFe_5O_8$, the lithium being replaced by hydrogen to give HFe_5O_8. The structure of HFe_5O_8 can be derived from the Fe_3O_4 structure by systematically replacing four iron atoms in the special positions, 16d and Fd3m of the spinel structure with protons. The specific positions to be filled are: (5/8, 5/8, 5/8), (1/8, 7/8, 3/8), (3/8, 1/8, 7/8), and (1/8, 3/8, 7/8). These are the special positions 4b of the space group $P4_33$. The other positions of the spinel structure can be assigned to other sets of special positions of this space group (12). This revised structure would give, as does $LiFe_5O_8$, the extra reflections that were found in this study.

The other aspect of passivity dealt with in this study is the epitaxial relationship between films formed in the prepassive, passive, and transpassive regions of the anodic polarization curve and the iron substrate. The most unexpected finding is that a {110} iron surface bears a different epitaxial relationship to the film formed on it, depending on whether the film is passive or active. This is not true for any of the other substrate orientations studied, where both passive and nonpassive films gave the same epitaxial relationships. This special behavior of the {110} orientation agrees with previous studies which showed that, of all the other orientations studied, it exhibited greater pitting tendency (23) and that the passive films formed on it had larger numbers of breakdown sites (24). Both of these earlier findings also agree with the present result that the {110} plane showed a lesser tendency to retain the passive state on removal of the potential difference across the cell. This was usually not the rule for other substrate orientations, where the decay films would sometimes show similarities to the passive films.

The origin of this special behavior by the {110} plane (the closest packed plane in the bcc structure) is obscure. Attempts were made to establish any relationship between how well the metal ions in the oxide lattice matched the underlying atoms in the metal lattice and this change of orientation. Based on a simple matching of hard sphere crystal models, it appeared that the passive oxide orientation was a "better match" than the nonpassive. It is difficult, however, to relate the degree of misfit between oxide and substrate to film properties. This was shown by an investigation of the problem of misfit for another system (25), where it was not possible to relate the degree of oxide film-metal substrate misfit to protectiveness in a consistent manner. One would expect that the geometrical relationship between the film lattice and the metal lattice must determine the strain in the film and, hence, the grain size and the number and nature of imperfections. All of these will modify the intrinsic electrical characteristics of the film and determine the film's permeability to the movement of ions and, hence, its protective properties.

Conclusions

1. γ-Fe_2O_3 is present in all passive films independent of the *p*H of the solution in which the films are formed, or the orientation of the iron substrate.
2. Films formed in the prepassive or transpassive regions of the polarization curve contain the Fe_3O_4 spinel structure and not the γ-Fe_2O_3 structure.
3. The epitaxial relationships between spinel film and substrate on all the orientations studied are the same for both passive and nonpassive films, with the exception of the {110} plane, which has different oxide orientations for the two states.

Acknowledgments

The authors are grateful to D. Ballard for his help with the preliminary diffraction and to Mary Ann Giles who obtained the majority of the diffraction patterns used in this paper. They are also indebted to Brian Joiner for his aid in the statistical analysis of their data.

Manscript received Feb. 21, 1967.

Any discussion of this paper will appear in a Discussion Section to be published in the June 1968 JOURNAL.

REFERENCES

1. J. E. O. Mayne and M. J. Pryor, *J. Chem. Soc.*, **1949**, 1831.
2. P. B. Hirsch, A. Howie, R. B. Nicholson, D. W. Pashley, and M. J. Whelan, "Electron Microscopy of Thin Crystals," p. 32, Butterworths, London (1965).
3. N. Nagayama and M. Cohen, *This Journal*, **109**, 781 (1962).
4. P. B. Sewell, C. D. Stockbridge, and M. Cohen, *ibid.*, **108**, 933 (1961).
5. K. J. Vetter, *ibid.*, **110**, 597 (1963).
6. O. Haase, *Z. Naturforsch*, **11a**, 46 (1956).

[4] One study of films formed in very concentrated H_2SO_4 gives very different results. This work by Riggs (19) studying films thick enough to be detected by x-ray diffraction found them to be composed of various sulfates. Such layers are not the thin films usually referred to as passive. Their different composition is not surprising considering the unusual environment.

7. Hirsch, Howie, Nicholson, Pashley, and Whelan, *op cit.*, p. 112
8. J. Kruger and J. P. Calvert, *This Journal*, **114**, 43 (1967).
9. Hirsch, Howie, Nicholson, Pashley, and Whelan, *op. cit.*, p. 132.
10. *Ibid.*, p. 117.
11. C. E. Hall, "Introduction to Electron Microscopy," pp. 131-4 McGraw-Hill Book Co., New York (1953).
12. H. E. Swanson, H. F. McMurdie, M. C. Morris, J. H. DeGroot, E. H. Evans, S. J. Carmel, Standard X-Ray Diffraction Powder Patterns, NBS Report #9367 (1966).
13. R. W. G. Wyckoff, "Crystal Structures," Vol. 3, pp. 75-85, Interscience Publishers, Inc., New York, (1965).
14. D. R. Dasgupta, Geol. Survey, Calcutta, India.
15. Schrader and Buttner, *Z. anorg. u. allgem. chem.*, **320**, 205 (1963).
16. Haul and Shoon, *Z. Phys. Chem.*, **44**, 216 (1939).
17. E. Z. Basta, *Min. Mag.*, **31**, 431 (1957).
18. G. W. Mellors, M. Cohen, and A. F. Beck, *This Journal*, **105**, 322 (1958).
19. W. E. Boggs, *ibid.*, **114**, 32, (1967).
20. O. L. Riggs, Jr., *Corrosion*, **20**, 275t (1964).
21. M. C. Bloom and L. Goldenberg, *Corrosion Sci.*, **5**, 623 (1965).
22. T. P. Hoar, D. C. Mears, and G. P. Rothwell, *ibid.*, **5**, 279 (1965).
23. J. Kruger, *This Journal*, **106**, 763 (1959).
24. J. Kruger, *ibid.*, **110**, 654 (1963).
25. K. R. Lawless and A. T. Gwathmey, *Acta Met.*, **4**, 153 (1956).
26. J. B. Wagner, K. R. Lawless, and A. T. Gwathmey, *Trans. Met. Soc. AIME*, **221**, 257 (1961).
27. Hirsch *et al.*, op. cit. p. 323.

Passivation of Aluminum by Chromate Solutions

M. A. Heine and M. J. Pryor

Metals Research Laboratories, Olin Mathieson Chemical Corporation, New Haven, Connecticut

ABSTRACT

Passive films of γ-Al_2O_3 formed on aluminum by chromate solutions exhibit lower ionic resistance and higher electronic resistance than amorphous thermal films of the same thickness. The low ionic resistance is attributed to the formation of some crystalline γ-Al_2O_3 of very low ionic resistance at the oxide solution interface. The high electronic resistance is attributed to the inclusion of some protons in the passive film. A detailed mechanism for the passivation process is advanced.

Despite the numerous studies of the passivation of ferrous metals by chromate solutions, comparatively little has been published on the mechanism by which they inhibit the corrosion of aluminum. Mears and Brown (1) in an early study reported that chromates were effective in polarizing the local anodes on aluminum but did not specify a detailed mechanism. Later Edeleanu and Evans (2) suggested that chromate ions and aluminum underwent a redox reaction to form aluminum oxide and chromic ions. One of the authors (3) subsequently conducted an electrochemical-electronoptical study of inhibition of the corrosion of aluminum by sodium chromate solutions within the *p*H range of 2.5-9.5. The passive films were found to be somewhat thicker than the air-formed oxide film on aluminum and were duplex in nature, with an underlying layer of amorphous γ-Al_2O_3 being overlaid by a few angstroms of microcrystalline γ-Al_2O_3 exhibiting sharp spotty diffraction patterns.

It was deduced that passive films grew for a few hours on initially film-free aluminum with inverse logarithmic (or logarithmic) kinetics and thereafter thickened at a somewhat slower rate. This observation was considered to support a high field growth mechanism for the passive film with the enhanced field being supplied by the high adsorbed charge density in chromate solutions as compared with dry oxidation. Aluminum ions migrating to the oxide-solution interface were considered to be oxidized to γ-Al_2O_3, with the chromate ions being reduced to the trivalent condition. It was further suggested that passivation was a kinetic balance between film growth and film dissolution, the former being sensitive to chromate concentration and the latter to *p*H.

At the time when the former study (3) was conducted, techniques were not readily available to determine the ionic and electronic resistance of thin surface films on aluminum. Consequently, the earlier study was not able to throw light on any differences in conduction characteristics between passive (chromate) and amorphous thermal films of similar average thickness. In the intervening years such techniques have been developed in the writers' laboratory and chloride degradation of γ-Al_2O_3 films has been extensively studied (4-7). Accordingly, the primary purpose of the present work was to study the a-c resistance characteristics of passive films formed on aluminum by chromate solutions. The results have been compared with those obtained previously on thermal and barrier layer anodic films of similar thickness so that some more detailed view of the defect structure of passive films and its relation to the passivation process could be formed. The effects of chloride ions on the resistance of passive films has also been studied with a view to determining why chromates are so effective in preventing corrosion of aluminum by chloride ions.

Experimental

Materials.—The aluminum used was in the form of annealed 0.37 mm thick sheet having a purity of 99.997%. The impurities were 0.001% Cu, 0.001% Fe, 0.001% Si. All passivating chromate solutions were made up from A.R. grade chemicals and distilled deionized water and were adjusted to *p*H 6 by the addition of sodium dichromate unless otherwise indicated. All studies were carried out at 25° ± 0.05°C.

Experimental methods.—Passive films were mainly formed in 1.0M sodium chromate solution on aluminum specimens carrying an original air-formed oxide film and on caustic etched (and essentially film free) aluminum. The air-formed oxide films were formed by 24 hr exposure to dry air of 6 cm^2 aluminum specimens that had originally been etched in 0.5*N* NaOH solution at room temperature for 15 min followed by

less than 1 sec immersion in 50% nitric acid at 85°C. This surface pretreatment produces a slightly scalloped, reproducible, surface having a roughness factor of 1.2 and has been described in detail previously (8). The advantage of this particular surface is that reproducible, high resistance, contamination free, oxide films may be subsequently formed on it by a variety of oxidation processes. Essentially film-free aluminum surfaces were obtained as a starting condition by etching the specimens in 0.5*N* sodium hydroxide solution for 15 min, rapidly rinsing in distilled deionized water, and immediately inserting the specimens into the passivating chromate solution.

Film resistance studies were carried out at frequencies from 1-100 kc using a General Radio Type 716-C capacitance bridge and associated type 716-P4 guard circuit; the measurements were conducted in a separate solution of molar sodium chromate at *p*H 7 as has been described in earlier publications (6, 7). A 50 mv p-p signal was employed throughout with masked specimen areas of 0.02 cm². The neutral chromate solution will form thin films having a thickness greater than around 20-25Å (the passive film thickness) in a uniform manner, thereby permitting a-c resistance profiles to be obtained at various frequencies. In the case of passive films formed by simple immersion in 1.0M chromate solution, resistance profiles could not be obtained by this method because the initial films were already at their terminal passive thickness. Accordingly, after forming passive films by simple immersion for a period of 24 hr at 25°C they were thickened slightly by constant current anodizing in 1.0M sodium chromate solution at *p*H 6.0. Constant current anodizing was performed at 1 μa/cm². The potential of the specimen was monitored until the total film thickness was around 37Å. The times required to form the 37Å thick passive films varied between 45 and 90 min depending on the particular solution used and the surface condition prior to passivation. The additional passive film so produced was compact and quite dissimilar to the porous thick films produced at much higher voltages in chromates (3). Under no condition was the potential of the specimens during anodic polarization permitted to rise above +1.0v on the hydrogen scale. Such films could then be thinned back to around 20-25Å in 1.0M sodium chromate solution at *p*H 7, and resistance profiles developed for the exterior portions of the passive films. A simple analogue of a capacitor with a parallel resistance was used to represent the electrical behavior of the films. Corrections for solution resistance were made at all frequencies.

Some experiments were conducted on specimens carrying passive films that had not been thickened anodically. These films were formed in 1.0 and 0.01M sodium chromate both free from and containing one tenth and equal concentrations of sodium chloride solution. Passive films were formed on 6 cm² specimens carrying an original air-formed oxide film by simple immersion for 6 hr in the passivating chromate solution of varying chromate and chloride ion concentrations. The specimens were again masked to expose an area of 0.02 cm²; the thickness and a-c resistance of these films were determined at 1 kc only by immersion in fresh solutions of 1.0M sodium chromate solution at *p*H 6 since here, thinning rate of the films is at a minimum.

Results

Plots of parallel a-c resistance *vs.* thickness[1] at frequencies of 1, 10, and 100 kc are shown in Fig. 1-3. These results all pertain to passive films formed in 1.0M sodium chromate at *p*H 6 which had been subsequently thickened to around 37Å by constant current anodizing at 1 μa/cm². Each figure contains experimental points determined on quadruplicate specimens both freed from and carrying an original air-formed oxide film.

[1] From capacitance measurements at 1 kc.

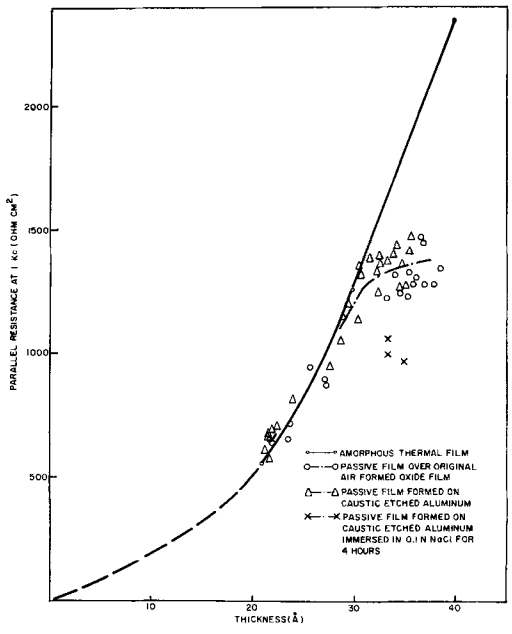

Fig. 1. Relation between parallel a-c resistance at 1 kc and thickness of an amorphous 350°C thermal film and of passive films formed on aluminum in 1.0M sodium chromate solution at *p*H 6 and at 25°C.

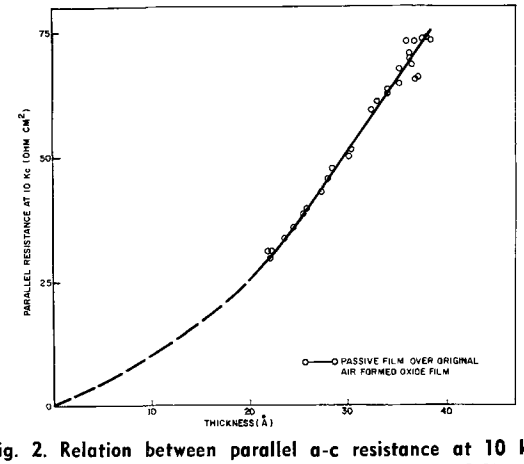

Fig. 2. Relation between parallel a-c resistance at 10 kc and thickness of passive films formed on aluminum in 1.0M sodium chromate solution at *p*H 6 and at 25°C.

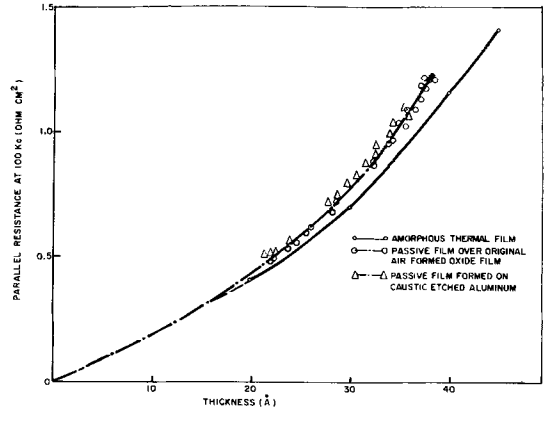

Fig. 3. Relation between parallel a-c resistance at 100 kc and thickness of an amorphous 350°C thermal film and of passive films formed on aluminum in 1.0M sodium chromate solution at *p*H 6 and at 25°C.

In Fig. 1 and 3 the parallel resistance results on the passive films are compared with previous results obtained on amorphous thermal films of the same average thickness (8) (350°C for 20 hr at P_{O_2} = 76 Torr). These in turn are identical to resistance results also obtained previously on amorphous barrier layer anodic films formed in neutral ammonium tartrate solution (6, 8). It may be seen from Fig. 1 that, at a frequency of 1 kc, the a-c resistance of the passive films is identical to that of thermal and barrier layer anodic films until a film thickness of around 30Å has been achieved; thereafter, and at higher thicknesses, the a-c resistance of the passive films becomes much less than that of amorphous thermal films. The resistance profile of passive films at 1 kc was not affected by whether the passivation was conducted on specimens carrying a 20Å air-formed oxide film or on essentially film-free aluminum. Also included in Fig. 1 are three points representing the total resistance of specimens carrying a 35Å thick passive film which has been formed as described above and which had then been immersed in 0.1M sodium chloride for 4 hr at 25°C. Such immersion is known to produce no change in the thickness, crystallographic structure or topography of γ-Al_2O_3 films on aluminum (5). A significant reduction in a-c resistance of the passive films at 1 kc was observed.

At the highest frequency studied in this work, *i.e.*, 100 kc, substantially different results were obtained (Fig. 3). Again, the results obtained on passive films were compared with results obtained previously on amorphous thermal films (8, 9) and on barrier films formed in neutral ammonium tartrate (6, 7). Figure 3 shows that the high-frequency a-c resistance of the passive films is significantly higher than that exhibited by amorphous thermal films. Again, the results in Fig. 3 are individual points from quadruplicate specimens with the two initial surface conditions. Also, the results obtained are independent of whether the passive films were formed on top of an original air-formed oxide film or on caustic etched aluminum. The experiment in which the passive film formed in 1.0M sodium chromate at pH 6 and the specimen then exposed for 4 hr to 0.1M sodium chloride solution at 25°C was repeated. At 100 kc, exposure to chloride solution produced no detectable lowering of film resistance.

At 10 kc (Fig. 2) the results on the passive films more closely parallel the results of 100 kc than at 1 kc. Such behavior has been noted previously in barrier layer anodic films exposed to sodium chloride solution (5).

It is also possible to obtain from the previous experiments information on the kinetics by which the various films are thinned by the 1.0M sodium chromate solution at pH 7.0 from their initial thickness of around 37Å to their terminal thickness of around 25Å. In such instances the measurement of capacitance as a function of time permits calculation of the average thickness of oxide removed at any interval of measurement. The thinning rates of the 350°C thermal film together with those of 37Å thick passive films grown on aluminum freed from and carrying an original air-formed oxide film are shown in Fig. 4.

A final series of experiments was conducted on passivation in 1.0 and 0.01M sodium chromate solutions at pH 6 with and without various additions of sodium chloride as described earlier. The a-c resistivity results on replicate specimens at 1 kc are shown in Fig. 5. In 1.0M sodium chromate solution at pH 6, the simultaneous presence of a chloride ion concentration of 0.1M resulted in, at best, a slight drop in film resistivity. A significant drop in film resistivity was observed when the chloride concentration in the chromate solution was increased to 1.0M. In all experiments, the aluminum remained passive throughout. In the absence of chloride the initial film resistivity in 0.01M sodium chromate was only around 70% of that in the 1.0M chromate solution. The presence of

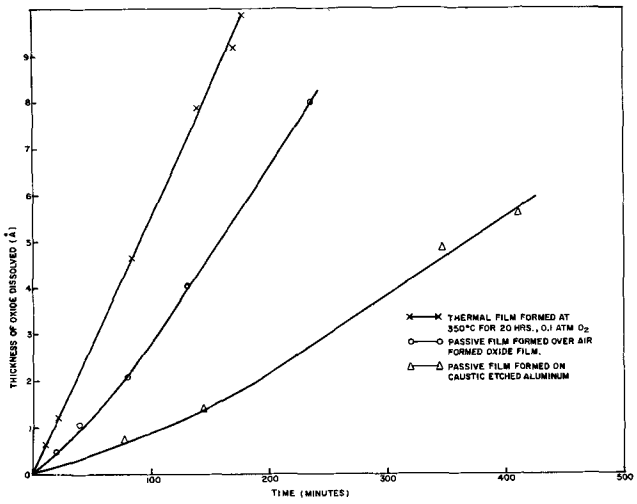

Fig. 4. Relation between time and average oxide thickness removed in 1.0M sodium chromate solution at pH 7 for an amorphous 350°C thermal film and for passive films formed in 1.0M sodium chromate solution at pH 6 on aluminum carrying and freed from its original air-formed oxide film.

chloride ions at a concentration in 0.001M resulted in no change in low-frequency film resistivity; further, the simultaneous presence of 0.01M sodium chloride resulted in a slight rise in film resistivity, although the magnitude of the rise is of somewhat dubious experimental significance. The addition of chloride to the passivating chromate solutions had no effect on film resistivity at 100 kc as had been observed in Fig. 3 and in past work (5-7).

Discussion

The primary objectives of the present work were: (*a*) to improve understanding of how chromate solutions alone passivate aluminum and (*b*) to obtain information on why chromate ions are so effective in preventing corrosion of aluminum by chloride solutions. The low-frequency (1 kc) a-c resistance profiles of passive films (Fig. 1) show that passive film resistance is identical to that of amorphous thermal films until the film thickness exceeds around 30Å. Thereafter and at higher thicknesses low frequency a-c resistance of passive films is substantially less than that of amorphous thermal and barrier layer anodic films. At best, at the natural passive film thickness of around 25Å a-c resistance at 1 kc can be no higher than that of the less protective thermal films and may well be less. Against this background it is not surprising that identical results were obtained at

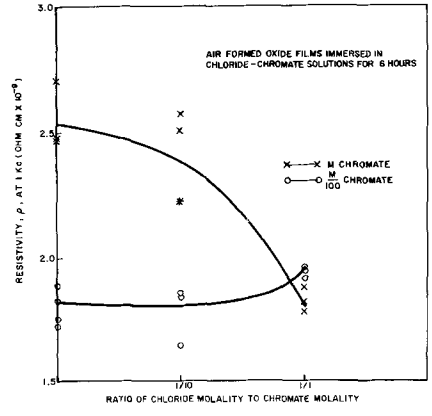

Fig. 5. Effect of chloride ion concentration on the parallel resistivity at 1 kc of passive films formed on aluminum by 1.0 and 0.01M sodium chromate solutions at pH 6.

1 kc irrespective of whether the aluminum specimens carried an air-formed oxide film or were initially freed from oxide by etching in caustic soda.

Very similar low-frequency resistance profiles have been observed previously on thermal films formed at high temperatures in excess of 450°C (8). A marked reduction in the slope of the resistance/thickness curves, almost identical to that in Fig. 1, occurred when well-defined crystals of γ-Al_2O_3 nucleated and grew at the amorphous oxide-metal interface. Electronoptical studies of the thermal γ-Al_2O_3 crystals (8) showed the presence of extensive faulting, and it was suggested that enhanced ionic conduction took place at these internal surfaces. Crystalline γ-Al_2O_3 also forms during passivation in chromates but at the oxide-solution interface. Figure 1 suggests that this crystalline oxide also has a very low resistivity at 1 kc compared with amorphous γ-Al_2O_3 and that a significant quantity in terms of average thickness must be present before it is easily detected by the capacitance-loss method. Since natural passive films, formed without auxiliary anodic polarization, also show crystals at the oxide-solution interface it is almost certain that these films do not have as high an a-c resistance at 1 kc as amorphous thermal films of identical thickness.

Considerable previous study has been devoted to clarifying the interpretation of the frequency dispersion of the a-c resistance of films of γ-Al_2O_3 (5-7). Most impurity defects in γ-Al_2O_3 appear to have characteristic relaxation times of around 10^{-4} sec (4). Accordingly, details in the a-c resistance *vs.* thickness curves seen at frequencies below 10 kc but not above 10 kc pertain to ionic relaxation effects and are related to d-c ionic conduction through the films. Details seen above 10 kc similarly are related to d-c electronic conduction through the films.

Against this background it appears that the amorphous part of the passive film has a virtually identical ionic resistance to that of a similar thickness of amorphous γ-Al_2O_3 formed thermally. When crystalline γ-Al_2O_3 forms at the outer surface of the amorphous film during passivation it exhibits much lower ionic resistance, similar to that of the crystalline portion of thermal films formed above 450°C and probably for the same reasons (8). This observation explains why a deviation from inverse logarithmic growth kinetics, calculated from potential data, was observed after a few hours in earlier work (3). The earlier corrosion potential measurement sensed ionic resistance of the film in a crude and approximate fashion (3). As long as the passive film grew by a high field mechanism and as long as the oxide so produced had ionic resistance characteristics similar to those of barrier layer anodic films, growth kinetics should be inverse logarithmic with time (10). However, as some crystalline oxide of much lower ionic resistivity was produced then the potential measurements will not sense this new oxide quantitatively and growth kinetics calculated from such electrochemical measurements will deviate from an inverse logarithmic law.

From the foregoing it is clear that considerations of ionic resistance alone provide no explanation for the unusually protective nature of passive films on aluminum. Indeed, the passive films will exhibit somewhat inferior ionic resistance to amorphous thermal films, the relative inferiority increasing with the proportion of crystalline γ-Al_2O_3 in the over-all passive film. However, Fig. 4 indicates one area of the complex process of passivation where the presence of crystalline γ-Al_2O_3 may be helpful. It may be seen that the dissolution rate of the outer crystalline portion of passive films formed on aluminum either carrying or freed from an original air-formed oxide film is much less than that of the underlying amorphous γ-Al_2O_3. Since passivation by chromates is believed to involve a kinetic balance between film formation and film dissolution (3) any factor that retards film dissolution should aid in increasing passive film thickness. Similar low dissolution rates of crystalline γ-Al_2O_3 have been observed previously in studies of duplex thermal films formed above 450°C and possible reasons for this behavior have been advanced (8). Similar reasons are believed to be valid for crystalline γ-Al_2O_3 formed during passivation. The linear slope of the dissolution curve for the passive film formed on aluminum carrying an original air-formed oxide film is only slightly less than that for the 350°C thermal film. The linear slope of the dissolution curve for the passive film formed on caustic etched (and essentially film-free) aluminum is much lower than either of the other two curves. No convincing explanation can be offered for this behavior at the present time. The effect cannot be related to an effect of surface preparation on the amount of crystalline phase because the low frequency resistance-thickness curves are identical for the two surface conditions (Fig. 1).

The high frequency (100 kHz) a-c resistance *vs.* thickness curves (Fig. 3) throw additional light on the reasons for the highly protective nature of passive films on aluminum. At all thicknesses studied a-c resistance at 100 kc was significantly higher for passive films formed in chromate solutions than for similar thickness amorphous films formed thermally at 350°C (8) or anodically in ammonium tartrate solution (6, 7). Crystalline γ-Al_2O_3 does not reduce high-frequency a-c resistivity of duplex thermal films formed above 450°C (8, 9) and from Fig. 3 exhibits similar behavior when formed in chromate solutions. Again no effect of initial surface condition was found in these experiments. The form of the a-c resistance *vs.* thickness curves at 100 kc for thermal and barrier layer anodic films is a very accurate parabola (9) for distances up to 90Å from the oxide-metal interface. At greater thicknesses the resistance is a linear function of thickness (6, 7). Heine and Sperry (9) interpreted these results as meaning that 90Å is the limit of thickness of γ-Al_2O_3 at which a conductivity effect due to excess metal arising from the proximity of the metal substrate disappears. At thicknesses lower than this value, conductivity is an inverse function of distance from the metal interface (on account of the parabolic nature of the R_p *vs.* thickness curve) and so the concentration of excess metal current carriers must also vary inversely with distance from the metal interface. Heine and Sperry (9) accepted the earlier model of Grunberg and Wright (11) for the probable defect structure in the vicinity of the oxide-metal interface, *i.e.*, an F′ center structure with excess metal existing as missing oxygen ions with two electrons trapped per oxygen vacancy. Since high-frequency a-c resistance singularities have been related to similar singularities in electronic d-c resistance (5-7) the foregoing implies that electronic conduction through these films to a thickness of 90Å is controlled primarily by the loosely bound electrons in the F′ center defect structure. The form of the 100 kc a-c resistance *vs.* thickness curve for passive films is also a parabola from Fig. 6 but with a greater slope than that for thermal films. This implies higher electronic resistance at any thickness due to the presence of somewhat fewer loosely bound electrons. Such defect structure could logically arise from the relatively uniform incorporation of some water or H^+ in the γ-Al_2O_3. γ-Al_2O_3 is a defect spinel with a close packed fcc oxygen lattice. The cation lattice is poorly understood, but could well contain a number of vacant sites. If a H^+ were to enter the oxide, either in one of the vacant cation sites or interstitially, one electron would have to be added for electrical neutrality and electronic resistance would decrease. Such is clearly not the case from Fig. 3. If however, a proton were to replace an aluminum ion, two electrons would have to be removed to maintain electrical neu-

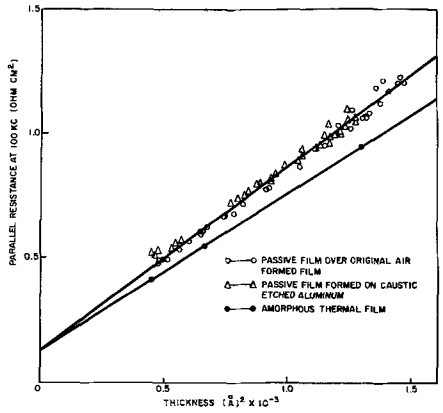

Fig. 6. Relation between parallel a-c resistance at 100 kc and (thickness)^2 of an amorphous 350°C thermal film and of passive films formed on aluminum in 1.0M sodium chromate solution at *p*H 6 and at 25°C.

trality, and electronic resistance would increase without any change in ionic resistance. This explanation is consistent with the experimental data in Fig. 1 and 3. Calculations from earlier data (4) would suggest a substituted H^+ concentration of around 1 pt in 10^5 or less. Similar explanations can be derived for the substitution of water, but the present work provides no means of distinguishing these alternatives.

From the foregoing considerations a more detailed mechanism for the passivation of aluminum by chromate solutions may now be advanced. First a redox reaction appears to be involved in passivation as suggested by Edeleanu and Evans (2). Chromate ions from solution are likely strongly and specifically adsorbed on the metal, if it is originally film free, or on an air-formed oxide film as is the more normal condition. This contention is supported by the earlier detection of Cr^{6+} on the surface of passivated iron (11). The adsorbed charge density from the small divalent $CrO_4^=$ ion should be higher than that pertaining during dry oxidation from the formation and adsorption of the energetically more probable O' ion. Accordingly, a higher than limiting field should exist across any pre-existing air-formed oxide film. Ionic migration will accordingly commence. As migrating aluminum ions arrive at the oxide-solution interface they become oxidized to γ-Al_2O_3 with Cr^{6+} ions becoming reduced to Cr^{3+} although the latter species has not been detected to date. The film will thicken until the limiting field of somewhat less than 10^7 v/cm is re-established. The amorphous portion of the passive film appears to be formed at field strengths significantly above the limiting field strength; the outer crystalline portion of the passive film appears to form at field strengths only slightly above or at the limiting field.

Because the passive film is duplex in nature the passivation reaction does not proceed in an identical manner to the more widely studied anodic film formation. During the time when the passive film is amorphous, electrochemical information indicates that the growth kinetics are logarithmic or inverse logarithmic, *i.e.*, in accord with a high field mechanism. The amorphous part of the passive film has the same ionic resistance at any thickness as a thermal or a barrier layer anodic film. Simultaneously it exhibits higher electronic resistance than comparable thermal films probably due to inclusion of small quantities of H^+ or water and so is more protective. As the low ionic resistance crystals appear at the outer surface of the passive film, electrochemical measurements do not sense the new low-resistance film adequately, and kinetics calculated from these measurements appear to deviate from the former growth law. However, the new crystalline film still contributes to the high electronic resistance of the passive film, being indistinguishable in this respect from the amorphous part of the passive film. It further dissolves in the passivating solution at a lower rate than the amorphous substrate and tends to protect against the competitive film dissolution process. Excellent evidence of this may be found from earlier work. Capacitance measurements (sensitive to the presence of both crystalline and amorphous γ-Al_2O_3) showed that passive film thickness was constant between *p*H 6 and 9 (6). Electrochemical measurements (3), not as sensitive to the presence of low ionic resistance γ-Al_2O_3 crystals, had been interpreted (erroneously) as meaning that passive film thickness is at a maximum at *p*H 6 and decreases with increasing or decreasing *p*H. These observations can now be reconciled as follows. Passive film thickness from capacitance measurements is not *p*H dependent between 6.0 and 9.0 (6). However, ionic resistance by electrochemical measurement (3) does decrease with increasing *p*H above 6.0. It appears that the proportion of low resistance crystalline γ-Al_2O_3 phase must be at a minimum at *p*H 6 and increases as the *p*H moves in the alkaline or acid direction. This contention is supported by earlier potential-time curves (3) which showed that serrated potential-time traces, characteristic of the formation of crystalline γ-Al_2O_3, initiated at lower potentials when *p*H was moved from 6.0 in either direction. Furthermore, the onset of these serrations (crystal formation) was dependent at constant *p*H on the chromate concentration, occurring at lower potentials as the chromate solution was diluted. Accordingly, the proportion of crystalline γ-Al_2O_3 in the film, being *p*H (minimum at *p*H 6.0) dependent and chromate concentration dependent (decreasing with increasing concentration) has a marked influence on the electrochemical properties of the over-all film. The proportion of crystals has little or no effect on the total thickness of film or on its very high electronic resistance both of which are important components of its unusual protective action. The proportion of crystalline phase profoundly modifies ionic resistance of the film which decreases with increasing proportion of crystals. This effects the electrochemical response of the passivated aluminum more than the protective action of the duplex film since an increasing proportion of crystalline γ-Al_2O_3 phase also implies a reduction of the rate of dissolution in the passivating medium.

Finally, there remains the question of the means by which chromate solutions prevent corrosion of aluminum by chloride ions in such an effective manner. The influence of chloride ions on aluminum covered with amorphous γ-Al_2O_3 has been studied in some detail earlier by the authors (5-7). In the absence of chromate, chloride ions can enter the γ-Al_2O_3 lattice, create cation vacancies and lower ionic (1 kc) resistance without changing electronic (100 kc) resistance. γ-Al_2O_3 containing small amounts of substituted Cl' also dissolves more rapidly in sodium chromate at *p*H 7 than unsubstituted γ-Al_2O_3. The effect of the simultaneous presence of chromate and chloride ions on aluminum is presented in Fig. 5 at chromate concentrations of 1.0 and 0.01M. The study was confined to one frequency (1 kc) which is sensitive to chloride inclusion in the film and to the natural passive film thickness (around 25Å in both solutions). First, it may be seen that the resistivity of the passive film in 0.01M chromate is only about 70% of that in 1.0M chromate. The passive film thicknesses are identical from capacitance measurements, and the difference in resistivity may be attributed to a higher proportion of crystalline γ-Al_2O_3 of low ionic resistance in the more dilute passivating solution. When the two chromate solutions contain sodium chloride at a concentration of one tenth the chromate concentration, *i.e.*, 0.1 and 0.001M, respectively, no significant change in passive film thickness or resistivity is seen at 1 kc. When passivation is conducted in the two chromate solutions with equal concentrations of sodium chloride (1.0 and 0.01M) the thickness of the

passive film again remains constant. However, passive film resistivity decreases in the concentrated (1.0M) solutions and remains essentially unchanged in the dilute (0.01M) solutions. The effects of the chloride in the simultaneous presence of chromate could be due to one of two causes: (*a*) a reluctance of chloride to enter the crystalline γ-Al_2O_3 and penetrate to the amorphous layer where its effect at 1 kc should be large. Such behavior has been noted in high-temperature crystalline γ-Al_2O_3 (8); and (*b*) an adsorption effect whereby chromate prevents simultaneous adsorption of chloride on the film surface. In the absence of specific adsorption of Cl' ions their entry into the γ-Al_2O_3 lattice is not considered possible.

In order to distinguish between these alternatives, passive films were formed in 1.0M chromate on aluminum as described earlier and thickened anodically to around 35Å thereby increasing the amount of crystalline γ-Al_2O_3. After this treatment the specimens were rinsed and immersed in chromate free 0.1M NaCl solution at *p*H6 for 4 hr. The low-frequency (1 kc) resistance of the total film was then measured in the standard manner at *p*H 6 in the absence of film thinning. The results in Fig. 1 show a marked decrease in ionic resistance for these specimens. If this result is compared with the fact that the same concentration of chloride (0.1M) when present in combination with 1.0M sodium chromate permitted growth of a passive film of undiminished resistivity at 1 kc (Fig. 5), it is clear that explanation (*a*) is untenable. Indeed the stability of passive film formed in the combined presence of chromate and chloride must be due to a relative adsorption effect whereby the chromate ions are specifically adsorbed on the growing oxide so strongly that they will displace chloride from the surface at least up to a certain critical concentration level. The fact that the relative critical chloride concentrations differ with the chromate concentration also supports such a view. This conclusion is consistent in part, with views expressed on chromate and chloride adsorption on passive iron by Matsuda and Uhlig (12). It receives direct experimental support from the zeta potential studies of O'Connor *et al.* (13) on corundum, γ-Al_2O_3 and Al·O·OH which indicated a much stronger specific adsorption for divalent CrO_4'' ions on these oxides. This conclusion also indicates that the protection against chloride corrosion is only obtained in the simultaneous presence of chromate and that once the latter is removed, film degradation by chloride ions can proceed in a normal fashion.

Acknowledgment

The authors wish to acknowledge, with thanks, the financial support of this work by the Aluminum Division of the Olin Mathieson Chemical Corporation and their permission to publish the results.

Manuscript received Nov. 3, 1966.

Any discussion of this paper will appear in a Discussion Section to be published in the June 1968 JOURNAL.

REFERENCES

1. R. B. Mears and R. H. Brown, *This Journal*, **97**, 75 (1950).
2. C. Edeleanu and U. R. Evans, *Trans. Faraday Soc.*, **65**, 683 (1949).
3. M. J. Pryor, *Z. Elektrochem.*, **62**, 782 (1958).
4. J. J. McMullen and M. J. Pryor, First International Congress on Metallic Corrosion, p. 52, Butterworths, London (1961).
5. A. F. Beck, M. A. Heine, D. S. Keir, D. van Rooyen, and M. J. Pryor, *Corrosion Sci.*, **2**, 133 (1962).
6. M. A. Heine and M. J. Pryor, *This Journal*, **110**, 1205 (1963).
7. M. A. Heine, D. S. Keir, and M. J. Pryor, *ibid.*, **112**, 24 (1965).
8. A. F. Beck, M. A. Heine, E. J. Caule, and M. J. Pryor, *Corrosion Sci.*, In press.
9. M. A. Heine and P. R. Sperry, *This Journal*, **112**, 359 (1965).
10. A. Guntherschulze and H. Betz, *Z. Physik*, **71**, 106 (1933).
11. N. Hackerman and R. A. Powers, *This Journal*, **100**, 314 (1953).
12. S. Matsuda and H. H. Uhlig, *ibid.*, **111**, 156 (1964).
13. D. J. O'Connor, P. G. Johansen, and A. S. Buchanan, *Trans. Faraday Soc.*, **52**, 229 (1956).

Theory of Organic Corrosion Inhibitors

II. Electrochemical Characteristics of Iron in Acidic Solutions Containing Ring-Substituted Anilines

Francis M. Donahue,[1] Akitane Akiyama,[2] and Ken Nobe

Department of Engineering, University of California, Los Angeles, California

ABSTRACT

The effect of aniline and aniline derivatives on the electrochemical characteristics of iron in H_2SO_4 has been studied using relaxation techniques. Armco iron corrosion was found to be inhibited primarily by an adsorption mechanism. However, evidence was noted which suggested a contribution from a "surface chelate." Evidence for surface chelation was more pronounced in the case of zone-refined iron which showed a transition from a nearly "pure adsorption" to a predominant surface chelation process. Subsequent loss of inhibition with time by some organics has been attributed to charge transfer processes associated with the surface chelate.

An understanding of the structure-corrosion inhibition relationship of organic compounds may be obtained by: (a) empirically correlating observed corrosion rates of metals in the presence of inhibitors with physico-chemical measurements or correlation parameters [e.g., see ref. (1-4)]; (*b*) a detailed study of the electrochemical behavior of inhibited metal dissolution (5, 6); and (c) measurement of adsorption properties of metal-solution interfaces (2, 7).

An unequivocal solution to the structure-corrosion inhibition relationship is not to be anticipated from any of these techniques alone. In fact, unless the nature of the dissolution reaction itself is well under-

[1] Present address: Department of Chemical and Metallurgical Engineering, The University of Michigan, Ann Arbor, Michigan.
[2] Permanent address: Department of Applied Electrochemistry, Tokyo Institute of Technology, Tokyo, Japan.

stood, very little of fundamental significance can be gained from studies of inhibition. Therefore, this laboratory has undertaken the task of simultaneously studying the inhibited and uninhibited behavior of iron in acidic solution. The first paper in this series (4) was concerned with correlation of adsorption and inhibition behavior of organic compounds with phenomenological constants derived from physical-organic chemistry. Another paper (8) is associated with the detection and role of intermediates in the dissolution process. This paper and the one to follow (9) are associated with the electrochemical characteristics of inhibited dissolution and a study of empirical correlations of inhibitor data, respectively. A "final" paper (10) is a study of the uninhibited kinetics of iron. It is the authors' purpose to investigate in a systematic manner with several electrochemical techniques the structure-corrosion inhibition relationship of a series of organic compounds on two different iron samples.

The present paper considers the effect of the addition of organic compounds on the observed electrochemical behavior of iron. Thus, observations of the open-circuit potential (corrosion potential), polarization behavior, and differential capacitance will be used in the manner described below to deduce the role of the organic in the inhibition process.

The various theories of inhibition by organic compounds have been adequately reviewed in the literature (11, 12) and, hence, are not considered here. Whereas chemisorption was assumed as the mode of inhibition in the "Theoretical" aspect of this series (4), no assumptions are made with respect to the mode of inhibition here.

Kaesche (5) has suggested that observations of the shift of the open-circuit potential in the presence of an inhibitor permits the specification of which partial process is influenced by the inhibitor. In summary, his postulates are these: (*a*) shifts of the open-circuit potential in the positive direction indicate predominant interference with the anodic partial process; (*b*) shifts in the negative direction, the cathodic partial process is affected; and (c) no shift in open-circuit potential, both processes are affected to the same extent. The analysis tacitly assumes near constancy of the respective Tafel slopes, *i.e.*, no change in mechanism of the partial processes in the presence of the inhibitor. Therefore, mere measurements of open-circuit potentials cannot describe unequivocally the interaction of the organic with the partial processes, and it is necessary to polarize the electrode to verify the Tafel slope constancy.

Bockris (13) has suggested the following mechanism for iron dissolution

$$Fe + OH^- \rightleftarrows (FeOH)_{ads} + e^- \quad [1]$$

$$(FeOH)_{ads} \rightarrow (FeOH)^+ + e^- \quad [2]$$

$$(FeOH)^+ \rightarrow Fe^{+2} + OH^- \quad [3]$$

where step [1] is in quasi-equilibrium, step [2] is rate limiting, and step [3] is fast. In the light of this mechanism and techniques which have recently been developed (8), the rate constants for step [1] may be calculated from anodic charging curves under certain circumstances, *e.g.*, Armco iron in 1N H_2SO_4, and the rate of disappearance of the adsorbed intermediate may be deduced from decay measurements. In this manner the question of "deactivation" of the metal surface may find a partial resolution (5). Thus, an inhibitor which "stabilizes" the iron atom in the lattice will cause a shift in the equilibrium given by [1] and, thereby, change the ratio of the rate constants. From the theoretical development given before (8), this effect should be characterized by a decrease in adsorption pseudocapacitance (*i.e.*, surface coverage of intermediate) and an alteration of the shape of the charging curve.

If the effect of the inhibitor is on the adsorbed intermediate, *e.g.*, some sort of chelation mechanism, the evaluation is less direct. Consider the following

$$(FeOH)_{ads} + n\,I \rightleftarrows [(FeOH) \cdot I_n]_{ads} \quad [1a]$$

$$[(FeOH) \cdot I_n]_{ads} \rightarrow [(FeOH) \cdot I_n]^+ + e^- \quad [1b]$$

In step [1a] the adsorbed intermediate interacts with n molecules of inhibitor I (at this point it is unnecessary to stipulate whether the inhibitor is adsorbed) to form a complex which is adsorbed on the surface. To the extent that the complex can undergo charge transfer, *i.e.*, step [1b], and desorb as a complex ion, a postulated inhibitor may in fact be an accelerator (see Experimental Results below). Likewise, the value of the equilibrium constant of [1a] ought to determine the extent of inhibition provided that the rate of [1b] is much slower than [2]. In addition, the values of the rate constants for [1a] should intimately affect the measured values of the rate constants for [1]. For example, should the rate constants for [1a] be much less than those of [1], then the anodic charging curve would be insensitive to the presence of the inhibitor. On the other hand, if the rate constants for [1a] (especially the forward constant) are equal to or greater than those of [1], then the charging curve should undergo a significant change in shape. Unfortunately, no theoretical analysis of the scheme suggested here has been worked out. However, such an alteration of the charging curve would be partial support for such a mechanism.

Since the rate-determining step for hydrogen evolution on Armco iron has been shown to be the first electron transfer step (14), such an analysis for the cathodic partial process is precluded. However, "deactivation" of the surface for hydrogen evolution would reveal itself in an alteration of the cathodic Tafel slope.

A simple blocking of the surface by adsorption of the inhibitor would decrease the area available to the respective partial processes and thereby decrease the apparent exchange currents in an identical fashion. Therefore, the open-circuit potential and Tafel slopes would remain unaltered. However, the adsorption pseudocapacitance would decrease linearly with increasing adsorption of the organic [provided the surface coverage of (FeOH) was less than 0.1 (8)]. In the same manner, the apparent double layer capacitance would also decrease on increasing adsorption of organic.

The foregoing discussion gives a rather qualitative picture of how one might attempt to ascertain information pertinent to the mode of inhibition of organic compounds using electrochemical techniques. In the text to follow an example of this approach is given.

Experimental

The details of the experimental equipment and the procedure are given elsewhere (10). The materials used were Armco iron and a sample of zone-refined iron which was donated by the American Iron and Steel Institute (designated as Bar 65A) and prepared in rod form by Battelle Memorial Institute. The electrodes were of cylindrical form and were rotated at constant speed.

The organic compounds were purified before use by distillation at reduced pressure in a nitrogen atmosphere or by recrystallization (p-Toluidine). Boiling point ranges were $\leq$ 2°C and the melting point of p-Toluidine was 42°-43.5°C.

The determination of the rate constants was by the technique previously described (8).

Results and Discussion

Figure 1 shows the effect of the addition of organic compounds on the open-circuit potential of Armco iron. The solid line shows behavior of uninhibited iron (10) for comparison. Aniline and p-Toluidine show deviation in the negative direction, while the remainder exhibit positive deviations. However, with the exception of p-Toluidine, the deviations are smaller

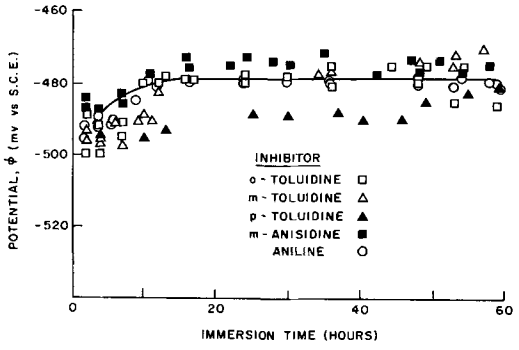

Fig. 1. Open-circuit potential of Armco iron in the presence of 0.3M aniline and ring-substituted anilines. The solid line describes the behavior of uninhibited iron (10).

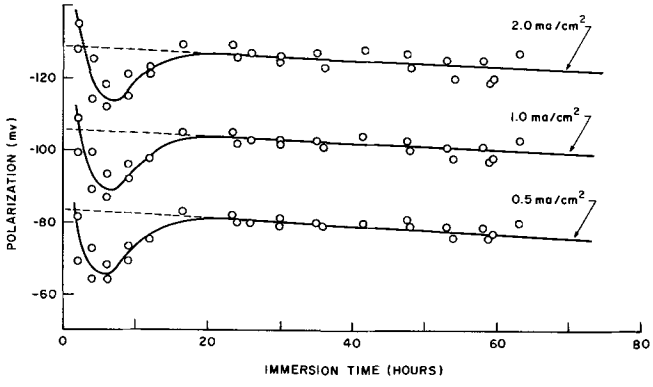

Fig. 2. Cathodic polarization behavior of Armco iron electrodes in the presence of 0.3M aniline.

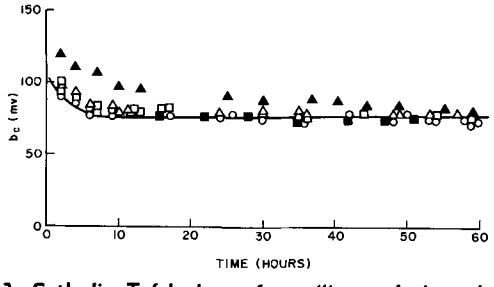

Fig. 3. Cathodic Tafel slopes for aniline and ring-substituted anilines as a function of time of immersion. Solid line shows the data for uninhibited iron (10). See Fig. 1 for designation of symbols.

than about 5 mv, which are smaller than those of Kaesche (5), and are not considered to be sufficient to permit ascribing any specific interaction with one or the other partial process.

Figure 2 shows the typical cathodic pulse polarization behavior observed for Armco iron. The minimum in polarization is characteristic of unannealed Armco iron electrodes (10) and does not reflect any effect of the inhibitor.

Figure 3 shows the variation of cathodic Tafel slope with time for inhibited Armco iron [again the solid line is presented to allow comparison with the uninhibited work (10)]. It can be seen that the inhibited samples (except p-Toluidine) follow the behavior of the uninhibited samples. This suggests that the cathodic partial process is essentially unaffected (in terms of reaction mechanism) by the presence of most of the organics. This is not true of p-Toluidine, which only approaches the uninhibited behavior as a limit at long immersion times. This behavior of p-Toluidine is consistent with other observations with this compound. Although it is chemically related to the other ring-substituted anilines, its behavior at the iron electrode seems to be quite anomalous.

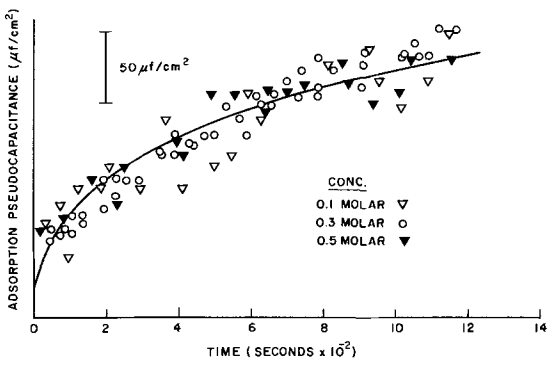

Fig. 4. Adsorption pseudocapacitance observed during anodic polarization of iron in the presence of aniline. Solid line is curve for uninhibited iron (8). Current density, 1 ma/cm².

One aspect of Fig. 3 which deserves comment at this time is the observation of rather low cathodic Tafel slopes. Values between 100 and 120 mv have been most frequently reported. In fact, previous work on this system (Armco iron/H_2SO_4) in this laboratory gave slopes of 100 mv (15). However, those experiments were usually completed within 2 hr after the samples were immersed. Those observations are in accord with the present work if one examines Fig. 3 at short times. Likewise, Kaesche (5) noted a range of Tafel slopes of 83-92 mv for uninhibited samples whose polarization data were obtained after 5 and 7 hr immersion time, again, in accord with the curve shown in Fig. 3. This underlines the need for investigators to stipulate at what time following immersion their data were obtained. Unless this is done, comparison of data among investigators may not be meaningful.

It has been shown elsewhere (8) that the slow achievement of a steady-state potential during anodic polarization is associated with the slow build-up of the surface concentration of the intermediate species (FeOH). It was also shown that an indirect measurement of this build-up could be made by determining the adsorption pseudocapacitance during the polarization by superimposing short galvanostatic pulses on the already existing signal. Figures 4 and 5 show the experimental results for aniline at three concentrations and some ring-substituted anilines, respectively. The agreement between the inhibited samples and their approximation to the uninhibited case is quite revealing as shown in Fig. 4 and 5. From this it may be surmised that the energetics of the initial electron transfer (see Eq. [1] above) seem to be independent of the presence of the organic or its chemical structure. Again it should be noted that p-Toluidine is an exception.

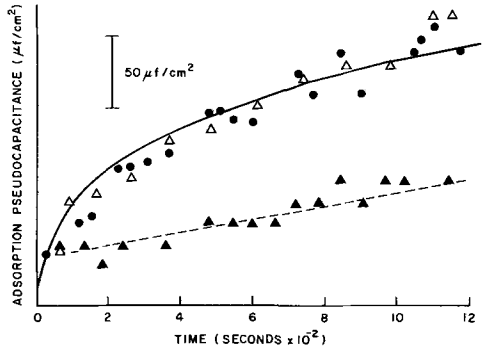

Fig. 5. Adsorption pseudocapacitance observed during anodic polarization of iron in the presence of some ring-substituted anilines. Solid line is curve for uninhibited iron (8). Current density, 1 ma/cm². Compounds are: 0.1M as-received aniline (●), 0.3M m-Toluidine (△), 0.3M p-Toluidine ▲.

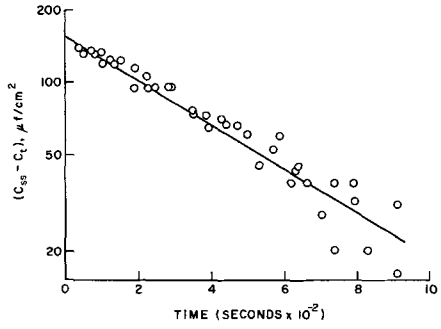

Fig. 6. Experimental test of Eq. (15), ref. (8) for an iron electrode in the presence of 0.3M aniline.

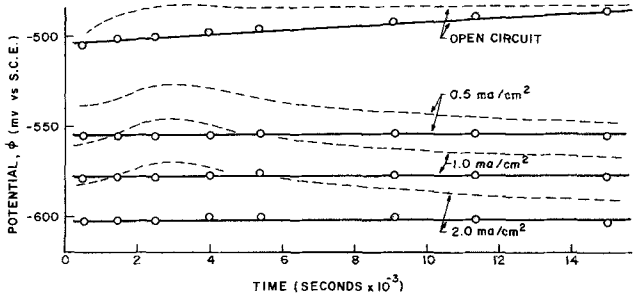

Fig. 7. Electrode potential (open circuit and cathodic pulse polarization) during the relaxation following anodic polarization. Inhibitor: 0.3M aniline. Dashed line shows the results for uninhibited iron (10).

From the comments in the preceding paragraph, it is anticipated that an estimation of the rate constants from the adsorption pseudocapacitance data would approximate that which has been found for the uninhibited case (8). Figure 6 shows the results which were obtained for two different Armco iron electrodes in the presence of 0.3M aniline. The slope of the line, *i.e.*, the sum of the rate constants of Eq. [1], was 2.1 x 10^{-3} sec^{-1}, which was within 10% of the average value obtained for the uninhibited samples (8).

Thus far all of the suggested electrochemical techniques have been able to supply answers to the specific questions which have been posed. In addition to the mere presentation of answers, the picture which the results suggest is self-consistent, *i.e.*, the open-circuit potential and both the anodic and cathodic polarization measurements suggest a nonspecific, "nondeactivating" mechanism for the effect of the organic on the electrochemical behavior of iron.[3] In addition, it has been possible to eliminate a fast "chelation" step (*e.g.*, see Eq. [1a]). However, the results have not been able to differentiate between a simple blocking mechanism such as might be envisioned in a chemisorption mechanism and a slow "chelation" step (Eq. [1a]).

The resolution of the problem is at least theoretically at hand. If the chelation process proceeds at a reasonable rate (from the rapid convergence of the inhibited and uninhibited cathodic Tafel slopes, it seems reasonable to assume that whatever process is operative it probably has a relaxation time which is less than an hour), then measurements of the decay of adsorption pseudocapacitance following the cessation of anodic polarization ought to show the presence of the chelate. Two pieces of information are available from the previous analysis for uninhibited iron (8): (*A*) The decay relaxation time is about an order of magnitude larger than the charging case; (*B*) the decay data are not as reproducible as charging data. The first observation suggests that it is possible to observe the equilibration of [1*a*] during decay even if we could not detect it during the charging process. The second observation suggests that at the present state of the experimental method one can, at best, only qualitatively evaluate the chelation effect. The experimental results obtained for the decay experiments [see Eq. (16) of ref. (8)] are not shown since the reproducibility was even poorer than those obtained in the uninhibited case (8) and would not lend anything to the discussion.

Another series of measurements are available during the decay process which has not been considered previously. Short (~5 sec) cathodic pulses can be applied to an electrode which is relaxing following the cessation of anodic polarization without perturbing the relaxation process and, thereby, determine the polarization characteristics during the relaxation (10). It has been suggested that (FeOH) catalyzes, *i.e.*, increases the apparent exchange current, the hydrogen evolution reaction (h.e.r.) (15). Since an electrode during the relaxation process has a varying amount of (FeOH) on its surface, the potential associated with a given current density should increase with decreasing (FeOH) if such an hypothesis is correct. On the other hand, if the (FeOH) does not catalyze the h.e.r. or is unavailable for such a catalysis, the potential for a given value of current density should remain constant. Figure 7 compares an uninhibited and an aniline-inhibited iron sample. In the uninhibited sample (dashed line) it can be seen that at times greater than 1 hr (the time corresponding to the achievement of a steady-state open-circuit potential) the previous hypothesis (15) finds experimental support, *i.e.*, the adsorbed (FeOH) affects the h.e.r. In the case of the inhibited sample, however, catalysis is essentially absent. It does not seem likely that such a result can be explained except in terms of a "surface chelation" process.

It was suggested at the outset that measurements of adsorption pseudocapacitance on open circuit should permit an estimation of the coverage of the inhibitor. However, capacitance measurements of Armco iron displayed a large intrinsic scatter from electrode to electrode which has tentatively been ascribed to "surface defects" (10). The same phenomena have been observed in the inhibitor study so that at present the capacitance technique is of no benefit in determining surface coverages of the inhibitor on unannealed Armco iron electrodes.

The zone-refined iron has not been considered in the preceding discussion. It has already been noted that the zone-refined sample undergoes a rather rapid equilibration of step [1], *viz.*, about 10^3 times more rapid than Armco iron (8). Therefore, it is not possible to evaluate the purer sample in the same manner as that given above.

It has been observed that zone-refined iron in 1*N* H_2SO_4 achieves a steady-state potential in less than 5 sec for anodic (8) and cathodic polarization (10). Therefore, in contrast to the Armco iron, it is possible to obtain steady-state polarization data for zone-refined iron with minimum perturbations of the quiescent (open-circuit) conditions of corrosion.

The open-circuit potentials of zone-refined iron were not as reproducible as those for Armco iron both in the presence and absence of aniline. However, in presence of aniline zone-refined iron was always more negative than in the uninhibited case. Consequently, from the analysis of Kaesche (5) it may be deduced that aniline affects the cathodic partial process more than the anodic partial process. This is a different result than had been obtained in the case of the Armco iron (see above).

Figure 8 shows the variation of cathodic Tafel slope for zone-refined iron in the presence and absence of aniline. At times greater than about 20 hr, the slope of the former deviates from that associated with the uninhibited case. Figure 9 shows the variation of the corrosion rate under the same circumstances. A com-

[3] These comments are not true for p-Toluidine, and for the present that compound will be omitted from any generalizations.

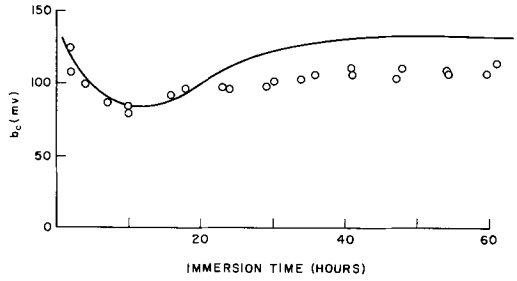

Fig. 8. Cathodic Tafel slope of zone-refined iron in the presence of 0.3M aniline. The solid line represents the behavior of the uninhibited iron (10).

parison of these two graphs is illuminating. In the vicinity of the deviation of cathodic Tafel slopes it is seen that the corrosion rate of uninhibited iron begins to "run away," *i.e.*, the shape of the curve for uninhibited iron in Fig. 9 suggests an autocatalytic process. Such a process and the conditions under which it could be realized have been considered elsewhere (10). Let it suffice here that inhibited iron behaves in a "regular" fashion, *i.e.*, at times beyond 20 hr it does not behave much differently than it did at shorter times, and that the "deviation" is more associated with uninhibited iron. Therefore, it is difficult to attempt to rationalize the significance of the Tafel slope deviations.

The rate-determining step for h.e.r. on high-purity iron in the absence of inhibitors has been shown to be slow discharge (16-18). If this is also the rate limiting step in the presence of the inhibitor (a question which remains unanswered), then an inhibitor which decreases the Tafel slope (see Fig. 8) and decreases the corrosion rate must simultaneously decrease the activation barrier and depress the exchange current. For the foregoing observations to prevail, the depression of the exchange current must be very large. An alternate possibility exists which is more intimately associated with the anodic partial process and, hence. will be considered further below.

The anodic Tafel slope for the uninhibited zone-refined iron has been found to be 47 ± 2 mv (10) while in the presence of 0.3M aniline, slopes of 55 ± 3 mv were obtained. This increase in Tafel slope suggests a mode of inhibition involving an interposition of organic into the charge transfer process for the anodic reaction. This is consistent with the mechanism suggested above if the equilibration of [1a] is fast and is shifted toward the right, *i.e.*, the surface concentration of free (FeOH) is low, and the bulk of the dissolution comes from [1b].

This suggestion of an interposition of the organic in the anodic charge transfer process may help clarify the observations of cathodic Tafel slope deviations and modes of inhibition. If one allows the possibility of the generation of surface sites, which are preferred for adsorption, during the natural corrosion process, then it does not seem unreasonable to suggest that the equilibrium by [1] will be adjusted such that the surface concentration of (FeOH) would increase. In turn the rate of the dissolution reaction would increase and, thereby, beget more surface sites, etc., until the process would tend toward autocatalytic behavior. Tentatively, the h.e.r. process has been neglected, but in fact its exchange current is also increased (10). Therefore, if one could introduce a species which could simultaneously trap the (FeOH) and consume the surface sites (by an appropriate adsorption mechanism) this "autocatalytic" process could be stifled. As was suggested above, the results indicate that the aniline does fill this dual role, *i.e.*, the aniline adsorbs on the surface and complexes with the (FeOH) on the surface.

In contrast to Armco iron, zone-refined iron has reproducible open-circuit capacitance behavior. Therefore, in the latter case, one may deduce the effective surface coverage of the inhibitor. If one assumes that the adsorption of the organic compound "insulates" that part of the metal-solution interface, then the relationship between the capacitance in the presence and absence of inhibitor and the surface coverage is

$$C_i = (1 - \theta)\, C_u \qquad [4]$$

where the subscripts i and u correspond to the inhibited and uninhibited cases, respectively, and θ is the surface coverage of inhibitor. Therefore, the ratio C_i/C_u is a measure of the surface coverage. If adsorption is the only mode of inhibition, then the ratio of the inhibited rate to the uninhibited rate (at any time) should be the same as that for the capacitance ratio.

The capacitance-time behavior of the inhibited zone-refined iron is shown in Fig. 10. It is seen that the capacitance of uninhibited iron has a higher C-t slope than inhibited iron. This is consistent with the suggestion that the inhibition process decreases the rate of appearance of the intermediate (FeOH).

Table I is a collection of data from Fig. 9 and 10 and provides an indication of the extent to which adsorption alone contributes to the inhibition. Considering the approximativeness of the numbers used in the calculation, the correspondence between the ratios of capacitance and corrosivity at times ≤ 20 hr is good and suggests a predominantly adsorption mechanism. However, at times greater than 20 hr, the differences between the two can be ascribed to surface chelation as described above.

A detailed tabulation of the observed corrosion rates with time for Armco iron as well as the LFER correlation of the data is given elsewhere (9). The data

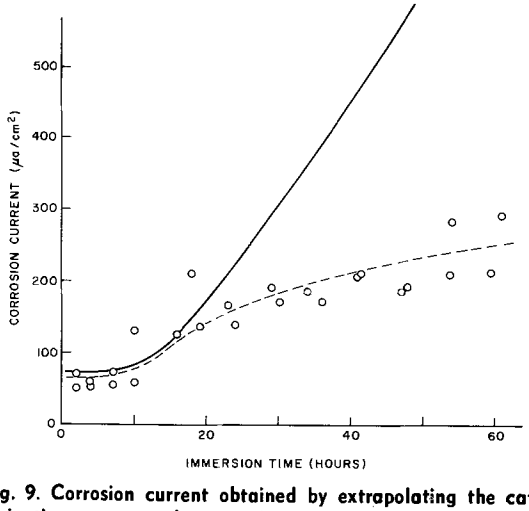

Fig. 9. Corrosion current obtained by extrapolating the cathodic polarization curve to the corrosion potential for zone-refined iron samples in the presence of 0.3M aniline. The solid line shows the behavior of the uninhibited iron (10).

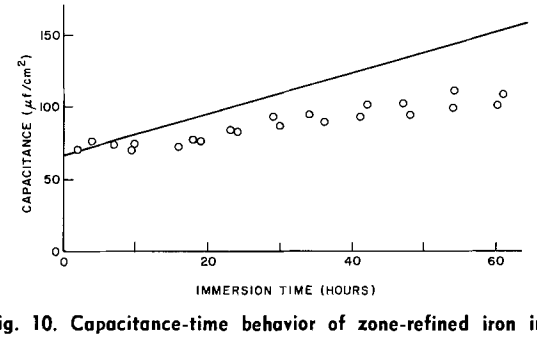

Fig. 10. Capacitance-time behavior of zone-refined iron in the presence of 0.3M aniline. The solid line represents the behavior of the uninhibited iron (10).

Table I. Comparison between the capacitance and corrosivity ratios for aniline-inhibited zone-refined iron

Time, hr	C_i/C_u*	r_i/r_u**	θ***
2	1.00	0.95	0.00
5	0.97	0.95	0.03
10	0.93	0.91	0.07
20	0.85	0.82	0.15
30	0.79	0.60	0.21
40	0.76	0.44	0.24
50	0.72	0.38	0.28
60	0.71	0.33	0.29

* Data from Fig. 10.
** Data from Fig. 9.
*** From Eq. [4].

showed that meta- and para-toluidine lost inhibition with time (para- before the meta-) until both were acting as accelerators. Mere loss of inhibition would derive from an exclusion of the organic from the surface; acceleration suggests a definitive role for the organic. These results may be explained in terms of reaction [1b] becoming the dominant dissolution reaction. The reason for the shift from [2] to [1b] is not clear, but is probably a complex interaction between the stability of the surface chelate and its oxidation propensity. This may be seen in Fig. 5 where the p-Toluidine is seen to deviate from the behavior of the other inhibitors and the uninhibited case. It is suggested that the rate of equilibration of [1] would be very slow due to the intervention of steps [1a] and [1b] to yield the complex ion with iron in the divalent state.

A final comment concerning purification of the organic should be made. During the course of this work, it was found that 0.1M aniline in the as-received state (brownish-colored liquid) gave nearly identical inhibition as 0.3M of the redistilled (clear) aniline. Therefore, it is suggested that only purified compounds should be used when studying the effect of organic compounds on electrochemical properties of metals.

Conclusions

The results of electrochemical measurements of Armco iron and zone-refined iron in the presence of aniline and its ring-substituted derivatives have shown that deactivation of the iron lattice (5) is not the model by which the anodic partial process is altered. Instead, there is an equilibrated "capture" of the monovalent intermediate, *i.e.*, (FeOH), in some sort of surface chelate. However, at low coverages of the intermediate, the inhibition is essentially a blocking (adsorption) mode.

The effect of aniline derivatives on the hydrogen evolution reaction is essentially an adsorption mode. In the case of the zone-refined iron the drastic alterations in h.e.r. exchange current were more associated with the absence of the intermediate (FeOH) due to the presence of surface chelate than any deactivation of the cathodic partial process, *per se*.

The work presented here shows the utility of the multifaceted electrochemical approach to the problems of ascertaining the effects of organics on the electrochemical properties of active metals. An analysis of the structure-inhibition relationship is given elsewhere (9).

Acknowledgment

This work has been supported by the Corrosion Research Council, Project 14. Partial support was received from the University of California Sea Water Desalination Program.

Manuscript received Sept. 6, 1966.

Any discussion of this paper will appear in a Discussion Section to be published in the June 1968 JOURNAL.

REFERENCES

1. R. C. Ayers and N. Hackerman, *This Journal*, **110**, 507 (1963).
2. H. F. Finley and N. Hackerman, *ibid.*, **107**, 259 (1960).
3. P. F. Cox, R. L. Every, and O. L. Riggs. *Corrosion*, **20**, 299t (1964).
4. F. M. Donahue and K. Nobe, *This Journal*, **112**, 886 (1965).
5. H. Kaesche and N. Hackerman, *ibid.*, **105**, 191 (1958).
6. R. R. Annand, R. M. Hurd, and N. Hackerman, *ibid.*, **112**, 144 (1965).
7. E. Blomgren, J. O'M. Bockris, and C. Jesch, *J. Phys. Chem.*, **65**, 2000 (1961).
8. F. M. Donahue and K. Nobe, *This Journal*, **114**, 682 (1967).
9. F. M. Donahue and K. Nobe, *ibid.*, **114**, 1012 (1967).
10. F. M. Donahue and K. Nobe, To be published.
11. N. Hackerman and A. C. Makrides, *I.E.C.*, **46**, 523 (1954).
12. N. Hackerman, Symposium Europeen sur les Inhibiteurs de Corrosion. Comptes Rendus. Universita Degli Studi Ferrara, Ferrara, 1961, p. 99.
13. J. O'M. Bockris, D. Drazic, and A. R. Despic, *Electrochim. Acta*, **4**, 325 (1961).
14. M. A. V. Devanathan and Z. Stachurski, *This Journal*, **111**, 619 (1964).
15. F. M. Donahue and K. Nobe, Proceedings of the Second International Congress on Metallic Corrosion, NACE, Houston, 1966, p. 916.
16. J. O'M. Bockris and D. Drazic, *loc. cit.*, **7**, 293 (1962).
17. J. O'M. Bockris and D. F. A. Koch, *J. Phys. Chem.*, **65**, 1941 (1961).
18. E. J. Kelly, *This Journal*, **112**, 124 (1965).

Corrections

The titles and authors of the following papers, "Effect of Hydrogen Absorbed by Electrode and Electrolyte on Hydrogen Coverage" by David J. Ben-Daniel and Fritz G. Will, pp. 909-915 and "Primary and Solvent Isotope Effects in the Anodic Evolution of Oxygen" by Mark Salomon, pp. 922-926 were inadvertently omitted from the Table of Contents of the September 1967 issue of the *Journal*.

Theory of Organic Corrosion Inhibitors

III. LFER Correlation of Inhibition of Armco Iron by Ring-Substituted Anilines

Francis M. Donahue[1] and Ken Nobe

Department of Engineering, University of California, Los Angeles, California

ABSTRACT

The corrosion rates of Armco iron in the presence of ring-substituted anilines were shown to obey a LFER predicated on inhibition by adsorption. Deviations from the adsorption correlation were shown for p-Toluidine at times greater than 20 hr and for m-toluidine in excess of 30 hr. These deviations tended toward an acceleration which has been attributed to an oxidative propensity of the "surface chelate." Since 0-Toluidine was found to follow the adsorption correlation, it was concluded that adsorption of the organic was parallel to the electrode surface. Adsorption data on Hg where the orientation was shown to be parallel to the electrode surface were also correlated by the LFER theory.

Recently, the authors have proposed a correlation between adsorption of and/or inhibition by organic compounds and physical-organic chemical substituent constants (1). Correlating such parameters was not completely new since Hackerman and Hurd (2) had plotted the degree of inhibition for ring-substituted N-methylanilines *vs.* the Hammett substituent constant as early as 1961. However, no previous formalism had been developed for plotting inhibition *vs.* substituent constants.

In essence, the "theory" states that, if inhibition (or adsorption) of organic compounds is determined by the electronic distribution in the "anchoring" group of the adsorbate, then it should be amenable to a "Linear Free Energy Relationship" treatment. The term "anchoring" has been placed in quotation marks here and previously (1) for two pragmatic reasons:

(*A*) If one is to investigate electron distributions in an organic molecule, he ought to focus his attention on one atom within that molecule and note variations in the electron density due to variations of a substituent elsewhere in the molecule. Therefore, the choice of the "marked" atom is somewhat arbitrary, although a certain atom in some molecules, *e.g.*, the nitrogen in alkyl substituted pyridines, suggests itself. In physical-organic chemistry the marked atom is invariably the reaction site.

(*B*) In studies of corrosion inhibition the term "anchoring" atom has been used extensively, and the authors feel that one may use such a term provided it is not taken literally [see Discussion, p. 888, of ref. (1)]. Therefore, to remove such an improper interpretation the quotation marks have been and will continue to be used.

Cox and co-workers (3) following the reasoning of Hackerman and Makrides (4) demonstrated a correlation between degree of inhibition for ring-substituted anilines and n.m.r. chemical shift for the amine hydrogens (a measure of the nitrogen electron density). This correlation should have lent considerable support to the authors' theory (1) since Suhr (5) and Dyall (6) had shown correlations between n.m.r. chemical shifts for amine hydrogens and the Hammett substituent constant. However, neither the corrosion inhibition data (3) using Eq. [15b] (1) nor the chemical shifts (3) were found to correlate with the substituent constants. Since Dyall (6) had studied six of the ring-substituted anilines which Cox (3) had observed, it is noteworthy that the results of the two investigators show essentially no correlation with each other. The difference in solvents between the two investigators is probably not the source of the discrepancy since Dyall's work in CCl_4 and acetonitrile gave good internal checks. Unfortunately, the authors cannot resolve the discrepancies in the n.m.r. work and, hence, will have to forego any further critique until more work in this interesting area is published.

However, the authors can address themselves to the corrosion inhibition data of Every and Riggs (7). The authors have observed previously that impure organics, *i.e.*, those used in the as-received state without further purification, yield misleading results (8). In neither the paper under discussion (7) nor in previous work by those investigators (9, 10) was mention made of purification of the organics prior to inhibition studies. Likewise, their representation of the degree of inhibition (7) is derived from an integral corrosion rate *i.e.*, the total weight loss after 24 hr in the presence of inhibitor is compared with the uninhibited weight loss for the same duration. Unless the weight loss-time curves have the same shape (an unsubstantiated assumption), such a measurement is not indicative of the over-all efficacy of the inhibitor. Consider Fig. 1 as an example. Using the integral corrosion rate technique, all three inhibitors (a, b, and c) show about a 25% protection at 24 hr. However, only "b" will show this degree at any other time while "a" will give a higher value of protection at longer times and "c" will soon be an accelerator.

From the previous derivation (1) the instantaneous rate, *i.e.*, the slope of the curves in Fig. 1 or the corro-

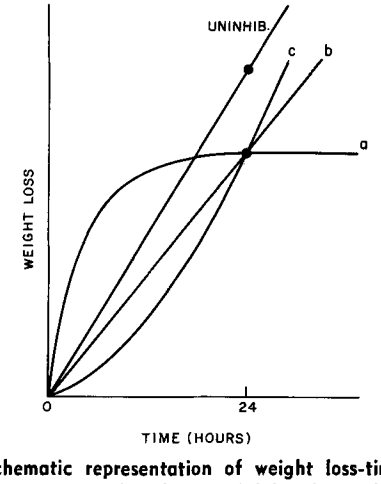

Fig. 1. Schematic representation of weight loss-time curves for three inhibitors compared with an uninhibited sample.

[1] Present address: Department of Chemical and Metallurgical Engineering, The University of Michigan, Ann Arbor, Michigan.

sion current from polarization measurements, should be correlated with the substituent constant. Consequently, simple weight loss measurements are an unsatisfactory method of testing the theory unless a sufficient number of data points can be obtained such that a differentiation of curves like those shown in Fig. 1 may be effected. Electrical resistance probes (11) can be used effectively for this purpose under certain conditions.

An important aspect of the proposed theory (1) has been questioned recently (12). Due to an apparent misunderstanding of the usage of "anchoring" group (see comments above), it was suggested by Annand that observations such as those by Blomgren and Bockris (13), who concluded from their results that the adsorption of ring-substituted anilines on mercury was parallel to the electrode surface and was attached to the surface by π-bonds from the aromatic nucleus, negated our entire analysis. On the contrary, Fig. 2 shows that Eq. [9c] (1) correlates the data of Blomgren (13) quite well when the organic was at the high concentration. The deviations at the lower concentration could be due to slow adsorption or just the intrinsic reproducibility of their measurements coupled with the nature of the ordinate of Fig. 2. The main point here is that for a case which had already been shown to proceed by parallel adsorption the theory prevails. The data followed the correlation because the conjugated system which interacted with the surface was composed of the six carbon atoms and the nitrogen atom. Therefore, the electron density at nitrogen was directly coupled to the density at the aromatic nucleus [see p. 526 of ref. (4)]. This strongly suggests that the organic which adsorbs is unprotonated in support of Hackerman's hypothesis (4) which has been questioned by Blomgren (13). The latter's comments were perhaps premature since dissociative adsorption, *i.e.*, fragmentation of the anilinium ion into free amine and proton at the surface, cannot be ruled out provided equilibrium is maintained with the anilinium ions in the double layer.

Results and Discussion

Table I shows the instantaneous corrosion rate of Armco iron specimens as a function of immersion time in solutions containing 0.3M organic in 1*N* H_2SO_4 (8). It may be seen that all of the organics show a minimum in corrosion rate in the region of 20-30 hr immersion. From the previous discussions (8) it can be seen that the inhibition process is a combination of a number of coupled chemical and electrochemical processes. It is not known at present why this coupling should be optimum after this period of immersion. However, it is noteworthy (although perhaps fortuitous) that this same time was observed for the

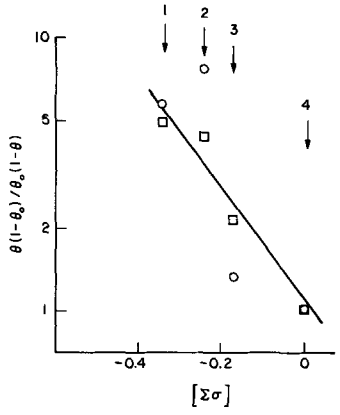

Fig. 2. Electrocapillary measurements of Blomgren (13) vs. substituent constants for substituted anilines. 1, 2,6-dimethyl-; 2, 2,3 dimethyl-; 3, O-Toluidine; 4, Aniline. Circles, 10^{-3} M; squares, 10^{-2} M.

Table I. Corrosion current (μa/cm^2) obtained from cathodic pulse polarization of Armco iron in 0.3M solutions of inhibitor in 1*N* H_2SO_4. Data are from previous work (8).

	Inhibitor					
Time, hr	None	Aniline	o-Toluidine	m-Toluidine	p-Toluidine	m-Anisidine
2	105	62	75	66	87	44
4	98	82	95	89	92	62
6	85	82	91	85	—	68
8	75	69	84	83	—	70
10	65	58	73	79	85	63
15	60	47	58	(60)	87	42
20	60	45	57	(58)	—	38
25	60	46	56	56	95	38
30	60	47	58	65	101	40
35	60	47	62	65	110	38
40	60	46	—	—	115	42
45	60	46	60	—	115	43
50	60	49	61	61	112	43
Symbol for figures	←	○	□	△	▲	■

( ) represents an estimate from an i_{corr}-t curve.

transition from adsorption to "chelation" control in the case of zone-refined iron (8).

The previously suggested processes associated with the effects of organic compounds on the electrochemical properties of iron will be repeated here with the same notations as before for the convenience of discussion (8).

$$Fe + OH^- \rightleftarrows (FeOH)_{ads} + e^- \quad [1]$$

$$(FeOH)_{ads} + n\,I \rightleftarrows [(FeOH) \cdot I_n]_{ads} \quad [1a]$$

$$I + S_{ads} \rightleftarrows I_{ads} + S \quad [1a']$$

$$(FeOH)_{ads} + n\,I_{ads} \rightleftarrows [(FeOH) \cdot I_n]_{ads} \quad [1a'']$$

$$[(FeOH) \cdot I_n] \rightarrow [(FeOH) \cdot I_n]^+ + e^- \quad [1b]$$

$$(FeOH)_{ads} \rightarrow (FeOH)^+ + e^- \quad [2]$$

$$(FeOH)^+ \rightarrow Fe^{+2} + OH^- \quad [3]$$

$$[(FeOH] \cdot I_n]^+ \rightarrow [FeI_n]^{+2} + OH^- \quad [3a]$$

Steps [1a'] and [1a"] have been added for completeness. The symbol S denotes the solvent or any specifically adsorbed electrolytic ions.

In the previous analysis (8), step [1a'] would be the mode of inhibition which has been designated as "blocking" or adsorption. Steps [1a] and [1a"] are the surface chelate modes. If the process described by [1a"] was the dominant mechanism for the production of chelate, then the formation of chelate would be enhanced by increased coverage of both adsorbed inhibitor and reaction intermediate. Since increased coverage of intermediate leads to product formation via step [2], the chelation process, *i.e.*, [1a"], must be fast or the surface coverage of adsorbed inhibitor must be high for inhibition to be maintained. Assuming the foregoing to be correct, *i.e.*, chelate forms by [1a"] and that the equilibria of [1] and [1a'] are shifted toward the right as adsorption sites are generated by dissolution (8), then the importance of chelation ought to increase with increasing immersion time. The extent to which [1] and [1a'] are shifted to the right relative to each other and the stoichiometry of [1a"], *i.e.*, whether $n \geqq 1$, will determine whether inhibition will increase, decrease, or remain constant. Thus, until one may ascertain the critical parameters associated with [1], [1a'], and [1a"], only a qualitative discussion of the causes of the observed phenomena can be made.

From the foregoing discussion, it should not be assumed that the mechanism given by [1a] has been ruled out. On the contrary, such a mechanism is still attractive since organic is more readily available from the solution than it would be via some sort of surface diffusion mechanism. On the other hand, the fact that adsorbed organic is indeed present and the organic

and intermediate are assumed to gravitate toward the same surface sites suggest a preference for [1a"].

In the previous study it was noted that both adsorption and surface chelate functioned in a more or less concerted manner to achieve inhibition (8). Likewise, it was suggested that acceleration of corrosion was associated with the oxidative propensity of the surface chelate. The theory which was previously derived (1) predated the experiments, and, hence, did not anticipate stability of surface chelates as playing a role in inhibition. Therefore, the analysis was proposed on the basis of only an adsorption mechanism. Consequently, the theory must be re-evaluated in the light of the experimental observations.

Although the bulk of the "theoretical" paper (1) was associated with adsorption phenomena, the actual applicability of the concept is more universal than might be thought initially. Little and co-workers (14) have shown correlations between chronopotentiometric quarter wave potentials for substituted phenylferrocenes and directly substituted ferrocenes and substituent constants. As noted in the previous paper (1), correlations have likewise been observed for the fifth wave oxidation potential for substituted anilines (15). Chen (16) has demonstrated a Linear Free Energy Relationship (LFER) between complex ions and the pK's of the liquids. The authors mentioned most of this work in passing (1); however, it did not seem important at that time to dwell on areas which then seemed unrelated to corrosion inhibition. The subsequent experimental work (8) showed this view to be short-sighted.

In a very naive sense, [1a] and [1a"] may be viewed as "two dimensional complex ions" or surface chelate (8). Consequently, the stability constant for the complex will be intimately related to the pK of the ligand (organic) provided the three-dimensional work of Chen may be translated to the surface chelate. The pK's of these compounds parallel the Hammett substituent constant. Therefore, the shift in equilibrium of [1a] or [1a"] should vary directly with the substituent constant. Since it was postulated above that inhibition was dependent on the stability of the surface chelate, by deduction it was again seen that inhibition is directly correlatable to a substituent constant.

Likewise, the oxidative propensity of the complex ion may be viewed in the light of Little's work (14). Here the iron of the complex undergoes a single electron oxidative transfer with retention of the structure of the complex. This is identical in form to [1b]. Consequently, extrapolating Little's results to the case under consideration, one deduces that the oxidative propensity of the complex ought to be a function of the substituent constant as well.

In summary, it can be seen [and experimentally demonstrated to an extent (8)] that an organic such as a ring substituted aniline compound is capable of performing the following functions at a corroding electrode: (*a*) chemisorbing on the surface; (*b*) forming a more or less stable complex with a corrosion intermediate and effectively removing the intermediate from the dissolution sequence; (c) formation of a complex as in (*b*) with a finite oxidative propensity. Each of these processes taken alone is theoretically capable of being correlated with a substituent constant with an unique value of ρ for each process. Since each of these separate functions derive their stability (or lack of it) from the electronic distribution throughout the molecule, it seems reasonable to suppose that as the electron density is varied in a family of molecules the relative contribution to each of these possibilities will change in a monotonic fashion. For example, a molecule with the greatest tendency for adsorption will probably have a small tendency for formation of the surface complex (one may view this molecule as being in a "stable" state while adsorbed) and, consequently, will have a negligible contribution to oxidation of the complex. On the other end of the spectrum one may envisage a molecule with a great affinity for the lattice ion, but a negligible tendency for long-lived adsorption. Such a molecule would function as an accelerator to corrosion. It would be fortuitous, indeed, if the ρ's for these respective procesess were identical.

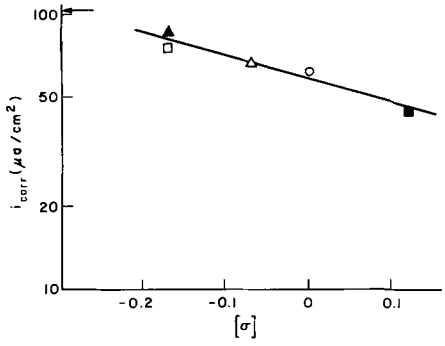

Fig. 3. Corrosion rate as a function of substituent constant for Armco iron electrodes after 2 hr immersion. Arrow denotes uninhibited rate. Symbols for compounds are given in Table I.

The comments immediately above suggest that attempts to formalize organic corrosion inhibitors in terms of a single correlation are not likely to succeed. Such a pessimistic outlook would be justified if the only data available to the investigator were the respective corrosion rates and correlation parameters. However, as was noted here and previously (8), each of these three functions, *viz.*, adsorption, complexation, and acceleration, can be determined to a degree by the supporting electrochemical measurements.

For electrodes in the solution for a short period of time, *e.g.*, 2 hr, it may be assumed that the adsorption step has essentially equilibrated. Since the results with most of the organics did not indicate a fast chelation process, even under conditions of high coverage as in the anodic charging experiments (8), it may be assumed that contributions from the chelate were minimal, thereby negating the oxidative mode as a contributor as well. Therefore, a LFER correlation under these conditions should describe the adsorption mode of inhibition and yield a value of ρ_{ads} for future use. Figure 3 is a correlation plot made under those conditions. It is noteworthy that the ortho substituent [a Taft σ^* was used for the correlation, see ref. (1)] obeys the adsorption LFER correlation. This rules out a perpendicular orientation with the nitrogen as the "anchoring" group. It suggests, but does not prove, a parallel orientation toward the surface.

Figure 4 shows a correlation plot for data after 25 hr immersion. This is the region where the minimum corrosion rate had been observed. The solid line, which was purposely drawn parallel to the line in Fig. 3, is meant to describe the adsorption "component" of the various functions described above. From the plot

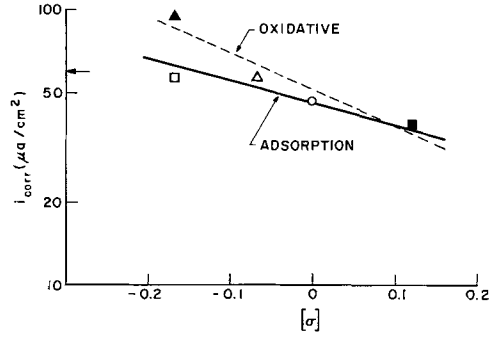

Fig. 4. Corrosion rate as a function of substituent constant for Armco iron electrodes after 25 hr immersion. Symbols for compounds are given in Table I.

it seems that an adsorption mode still describes the behavior of all the compounds except p-Toluidine which at this time is involved in an acceleration on the order of 50%. Therefore, it may be concluded that p-Toluidine is functioning in the oxidative mode. A second line (dashed) is drawn with the naive suggestion that this may describe the oxidative mode. However, such a correlation line cannot be drawn at this time. That adsorption is the main mode for the remaining organics corroborates the previous kinetic measurements (8).

Conclusions

The results presented herein show the validity of a LFER correlation for ring-substituted anilines in terms of corrosion inhibition. The results also demonstrated the necessity for supporting electrochemical measurements. This need was underlined when the analysis of the data suggested the existence of eight possible chemical and electrochemical reactions in the over-all scheme. Such a scheme could be deduced from corrosion rate measurements alone, but the supporting electrochemical measurements permitted definitive mechanisms to be ascribed to the various organics as a function of immersion time.

The observation that adsorption was the primary mode of inhibition by the organics studied lends support to an earlier hypothesis by Hackerman and Makrides (4); however, the results for the zone-refined iron in the presence of aniline (8) present a new challenge to this hypothesis which should be pursued further. The correlation of the work of Blomgren (13) with the current theory and the agreement of the O-Toluidine with the other compounds suggests parallel adsorption of free amine at the metal surface.

Acknowledgment

This work has been supported by the Corrosion Research Council, Project 14. Partial support was received from the University of California Sea Water Desalination Program.

Manuscript received Sept. 6, 1966.

Any discussion of this paper will appear in a Discussion Section to be published in the June 1968 JOURNAL.

REFERENCES

1. F. M. Donahue and K. Nobe, *This Journal*, **112**, 886 (1965).
2. N. Hackerman and R. M. Hurd, "1st Intl. Congr. on Metallic Corr. London," p. 166, Butterworths, London (1962).
3. P. F. Cox, R. L. Every, and O. L. Riggs, *Corrosion*, **20**, 299t (1964).
4. N. Hackerman and A. C. Makrides, *Ind. Eng. Chem.*, **46**, 523 (1954).
5. H. Suhr, *Z. Elektrochem.*, **66**, 466 (1962).
6. L. K. Dyall, *Australian J. Chem.*, **17**, 419 (1964).
7. R. L. Every and O. L. Riggs, *Materials Protection*, **3**, 46 (1964).
8. F. M. Donahue, A. Akiyama, and K. Nobe, *This Journal*, **114**, 1006 (1967).
9. O. L. Riggs and R. L. Every, *Corrosion*, **18**, 262t (1962).
10. O. L. Riggs and F. J. Radd, *ibid.*, **19**, 1t (1963).
11. A. J. Freedman, E. S. Troscinski, and A. Dravnieks, *ibid.*, **14**, 175t (1958).
12. Discussion of ref. (1) by R. R. Annand and the authors' reply, *This Journal*, **116**, 633 (1966).
13. E. Blomgren and J. O'M. Bockris, *J. Phys. Chem.*, **63**, 1475 (1959).
14. W. F. Little and others, *J. Am. Chem. Soc.*, **86**, 1376 (1964); *ibid.*, **86**, 1382 (1964).
15. I. Fox, R. W. Taft, and J. M. Schempf, Technical Report No. 22, Office of Naval Research, Contract Nour 656 (05) Project NRO55-328, June 1959.
16. Y. T. Chen, *Z. physik Chem.*, **220**, 231 (1962).

Mechanism of the Corrosion Inhibition of Stainless Steel in Sulfuric Acid by Sodium Molybdophosphate

E. A. Lizlovs

Research Laboratory, Climax Molybdenum Company of Michigan, Inc., A Subsidiary of American Metal Climax, Inc., Ann Arbor, Michigan

ABSTRACT

Sodium 12-molybdophosphate inhibits the corrosion of an actively corroding type 430 stainless steel sample in sulfuric acid by first polarizing the sample to the primary passivation potential. After this potential is reached, the stainless steel sample passivates spontaneously. From the potentiodynamic polarization curves it was deduced that the addition of sodium molybdophosphate to the sulfuric acid does not significantly alter the anodic characteristics of the type 430 steel in sulfuric acid. The experimental results were in agreement with the electrochemical theory for the passivator-type inhibitors.

The corrosion inhibiting properties of the molybdates are well known, and a considerable amount of research has been devoted to the subject. The inhibiting properties of the heteropolymolybdates, on the other hand, are far less known. Exploratory studies conducted at this Laboratory showed that sodium molybdophosphate or molybdophosphoric acid was an effective corrosion inhibitor for stainless steel in a sulfuric acid medium. In addition, the inhibition of corrosion of the actively corroding stainless steel sample was accompanied by the formation of the intensely blue reduced form of the molybdophosphate ion. Therefore, it was suspected that the molybdophosphates might be passivating-type inhibitors, the theory for which has been presented by Stern (1). Further work by Makrides and Stern (2) and by Makrides (3) demonstrated the validity of the theory for the inhibition of corrosion of type 410 stainless steel and pure iron by ferric sulfate. This investigation was undertaken to clarify the corrosion inhibition mechanism of the molybdophosphate ion.

Experimental Procedures

Commercial grade, type 430 stainless steel was used for all experiments. The construction and preparation of the electrodes is described elsewhere (4). All po-

tentials reported are for the saturated calomel electrode.

Two series of experiments were performed with type 430 stainless steel. One series consisted of the potentiodynamic polarization studies, and the other series was primarily concerned with the potential measurements of the corroding specimen.

Potentiodynamic studies were conducted in 1.05*N* H_2SO_4 containing 0.010, 0.100, 1.0, 3.0, and 6.0g of sodium 12-molybdophosphate ($Na_3PMo_{12}O_{40}\cdot nH_2O$) per liter of solution.[1] All experiments were performed in argon-purged solutions at 29.6°C, and the test solution was stirred magnetically. The potential scanning rate was approximately 0.15 mv/sec.

The minimum amount of the inhibitor necessary to passivate an actively corroding sample was determined by the slow addition of 1.05*N* H_2SO_4 solution containing 50 mg of $Na_3PMo_{12}O_{40}\cdot nH_2O$ per milliliter to 2100 ml of 1.05*N* H_2SO_4 test solution containing the corroding specimen. The potential of the sample was recorded on a strip-chart recorder. The transition from the active to the passive state was marked by a rapid and sharp potential rise from the active to the passive values.

The approximate amount of inhibitor necessary to maintain the passivity was established by passivating the type 430 electrode potentiostatically at +0.50v for 1, 10, and 60 sec, and 2 hr in a solution of 1.05*N* H_2SO_4 acid containing 0, 10, and 100 mg of the inhibitor per liter of solution. The potential decay was recorded after the discontinuation of passivation. The procedures for potentiostatic passivation and determination of the passive-film breakdown times are described elsewhere (4).

Results

The addition of sodium molybdophosphate to 1.05*N* H_2SO_4 resulted in a very pronounced change in the appearance of the potentiodynamic polarization curves for the type 430 stainless steel. The potentiodynamic curves for the pure 1.05*N* H_2SO_4 and for the sulfuric acid containing 0.100 and 6.0 g/l of sodium molybdophosphate are shown in Fig. 1 through 3. With an increased sodium molybdophosphate content, the oscillations in the polarization current became increasingly larger, the measured critical current density (I_{cr}') became smaller, and a progressively more extensive cathodic loop appeared on the polarization diagrams. For a sodium molybdophosphate concentration of 6 g/l, the measured polarization current remained negative up to the potential of +0.456v. The cathodic loop usually terminated at the equilibrium potential for the molybdophosphate/reduced molybdophosphate system, that is, at the potential exhibited by the platinum wire electrode in the test medium. This cathodic loop was due to the reduction of the molybdophosphate ion on the passive type 430 electrode. The oscillations in the cathodic current were dependent on the stirring rate of the solution. In stagnant solutions, no oscillations occurred and the current was considerably smaller.

The most striking feature of the polarization diagram was the presence of the anodic dissolution region even at the most concentrated solution used (Fig. 3). The increased amounts of sodium molybdophosphate depressed the anodic dissolution region; nevertheless, the height of this region was estimated as being unchanged and was approximately equal to that seen for pure sulfuric acid. The potentials (E_{pp}), corresponding to the measured critical current density, remained exactly the same for all concentrations of sodium molybdophosphate as for pure sulfuric acid. For the most concentrated solution (6 g/l of sodium molybdophosphate) no net anodic current was observed, and the measured critical anodic dissolution current was actually negative. The measured critical anodic current density and the corresponding primary passivation potentials are summarized in Table I. Average values are given when the current could not be determined exactly because of the oscillations.

The transpassive behavior of the type 430 stainless steel was not affected by the sodium molybdophosphate. The oxidation of the reduced molybdophosphate should occur in the transpassive region, but because of the small amount of the reduced form present, the oxidation current of this compound could not be de-

[1] Since the exact molecular weight of the $Na_3PMo_{12}O_{40}\cdot nH_2O$ is not known, the inhibitor concentrations are expressed in grams per liter rather than in molarity or normality. Approximate molarity can be calculated by assuming that the molecular weight of the $Na_3PMo_{12}O_{40}\cdot nH_2O$ is 2000 (see Table I).

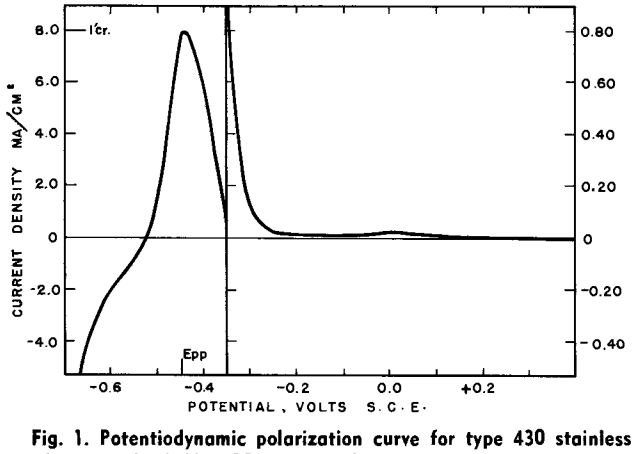

Fig. 1. Potentiodynamic polarization curve for type 430 stainless steel in stirred 1.05*N* H_2SO_4 at 29.6°C.

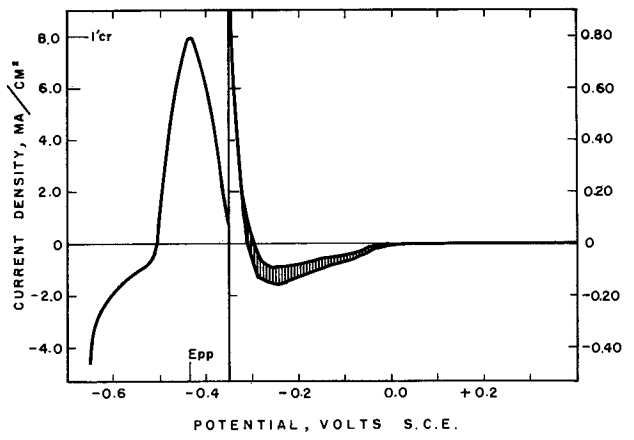

Fig. 2. Potentiodynamic polarization curve for type 430 stainless steel in stirred 1.05*N* H_2SO_4 containing 0.100 g/l of $Na_3PMo_{12}O_{40}\cdot nH_2O$ at 29.6°C.

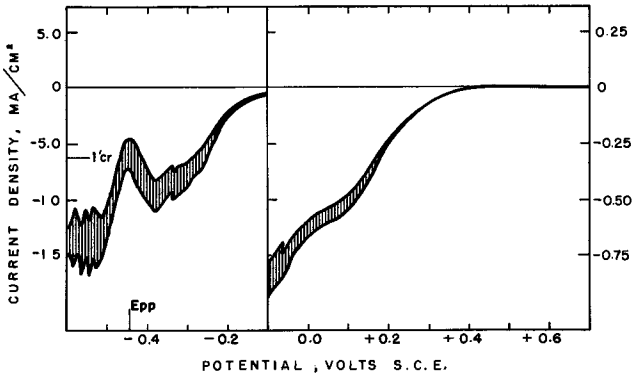

Fig. 3. Potentiodynamic polarization curve for type 430 stainless steel in stirred 1.05*N* H_2SO_4 containing 6.0 g/l of $Na_3PMo_{12}O_{40}\cdot nH_2O$ at 29.6°C.

Table I. Measured critical current densities and primary passivation potentials for various concentrations of $Na_3PMo_{12}O_{40} \cdot nH_2O$ in 1.05*N* H_2SO_4

Concentrations of $Na_3PMo_{12}O_{40} \cdot nH_2O$ g/l	Approximate molarity*	Measured critical current density, ma/cm²	Primary passivation potential, v SCE†
0	0	8.0	−0.440
0.010	5×10^{-6}	8.8	−0.440
0.100	5×10^{-5}	8.0	−0.435
1.0	5×10^{-4}	5.8	−0.435
3.0	1.5×10^{-3}	1.5	−0.435
6.0	3×10^{-3}	−5.8	−0.440

* Calculated assuming the approximate molecular weight of 2000.
† SCE is saturated calomel electrode.

tected in the presence of a much larger transpassive current.

Successive additions of sodium molybdophosphate to the 1.05*N* H_2SO_4 solution gradually polarized the corrosion potential of the freely corroding type 430 sample in the noble direction, until the critical potential was reached (Fig. 4). This critical potential was the same as the primary passivation potential determined by potentiodynamic studies, −0.440 to −0.435v. Once this potential was reached, passivation of the corroding electrode resulted. The passivation process was evident by a rapid change of the electrode potential from the active to passive values. The final potential of the electrode was about the same as the potential of a platinum electrode in the same solution, +0.492v. The minimum amount of sodium molybdophosphate needed to passivate freely corroding type 430 stainless steel in stirred 1.05*N* H_2SO_4 was determined to be 3.540 g/l (1.8×10^{-3}M). However, this amount was dependent on the stirring rate of the solution. In quiescent solutions the electrode continued to corrode even in solutions containing 6 g/l of sodium molybdophosphate.

The passive-film breakdown times for the type 430 stainless steel in 1.05*N* and in 1.05*N* H_2SO_4 containing sodium molybdophosphate are given in Table II. As Table II shows, the inhibitor concentration of 10 mg/l apparently represents the borderline concentration for maintenance of the passivity of type 430 steel after prior passivation. The experiments were not performed with more dilute solutions because of the increasing possibility of hydrolytic decomposition of more dilute solutions of molybdophosphate ion.

Discussion

The behavior of the type 430 stainless steel in sulfuric acid containing various amounts of sodium molybdophosphate is an agreement with Stern's electrochemical theory for the passivating-type inhibitors (Fig. 1 through 3). As the sodium molybdophosphate concentration is increased, the measured current becomes more negative because of the increased total reduction current. Nevertheless, the anodic dissolution region and the presence of the critical anodic current is clearly indicated even at sodium molybdophosphate concentrations of 6 g/l (Fig. 3), where the cathodic partial current at E_{pp} is greater than the critical anodic current, and consequently the total measured current is cathodic. The most striking feature is that E_{pp} remains unchanged for all concentrations of sodium molybdophosphate and is the same as for the pure sulfuric acid (—0.435v). The critical anodic current density can be estimated to be approximately the same in the presence of molybdophosphate as in the pure acid. Furthermore, the critical current densities for the two most dilute solutions, where the effect of the reduction current of the molybdophosphate is expected to be negligible at E_{pp}, are essentially the same as for the pure acid (Table I). Hence, it can be concluded that the anodic dissolution characteristics of type 430 stainless steel in 1.05*N* H_2SO_4 are not affected by the sodium molybdophosphate additions to the acid. The main function of the inhibitor is to polarize the steel until the corrosion potential coincides with the primary passivation potential. Further polarization then results in spontaneous passivation of the stainless steel sample (Fig. 4) with the final potential value being determined by the redox potential of the molybdophosphate/reduced molybdophosphate system. Thus, the molybdophosphate ion belongs to the passivating class of inhibitors. As the corrosion potential becomes more noble, corrosion rates increase until the critical value of 8.0 to 8.8 ma/cm² is reached. The corrosion rates at any corrosion potential up to E_{pp} in the presence of molybdophosphate ion should be the same as the corrosion rates at the corresponding potentials under potentiodynamic conditions in pure sulfuric acid. The corrosion rates of type 430 steel in the passive state are negligible as can be seen from the polarization diagram shown in Fig. 1, and these rates are also expected to be negligible in inhibited solutions.

According to well-known electrochemical principles, any corroding metal for which the measured critical current density is positive will corrode actively in that medium. On the other hand, if the measured critical current density is zero or negative, the metal will undergo spontaneously active-passive transition. Furthermore, if the potentiostatic (or potentiodynamic) polarization curve for a metal in a corrosive medium is characterized by a cathodic loop, a corroding metal can continue to corrode actively or remain passive, depending on the conditions under which it is exposed to the corrosive medium. No spontaneous transition from one state to the other can take place. The results from this investigation are again in agreement with the theoretical principles above. A spontaneous passivation occurred in a solution containing 6.0 g/l of molybdophosphate for which I_{cr}' is negative (Fig. 3). At the inhibitor concentration of 3.0 g/l no spontane-

Table II. Passive-film breakdown times for the type 430 stainless steel in 1.05*N* H_2SO_4

Passivation time	Concentration of $Na_3PMo_{12}O_{40} \cdot nH_2O$ mg/l	Passive-film breakdown times
1 sec	0	5-6.8 sec
	10	7-10 sec
	100	13.4 sec
10 sec	0	21-47 sec
	10	32-49 sec
	100	114 sec
1 min	0	2-5 min
	10	4-8 min
	100	No breakdown
2 hr	0	38-53.5 min
	10	38 min for one sample No breakdown for two other samples

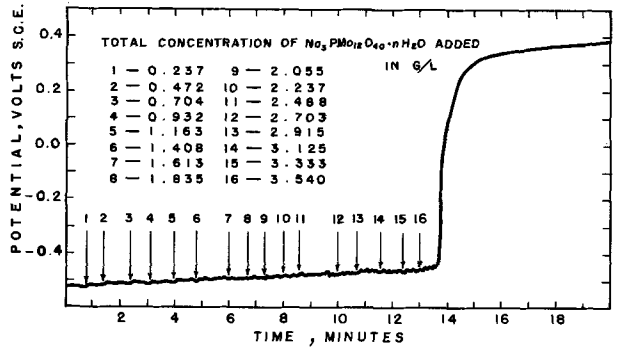

Fig. 4. Effect of successive additions of sodium molybdophosphate on the potential of actively corroding type 430 stainless steel in stirred 1.05*N* H_2SO_4 at 29.6°C.

ous passivation is expected; however, the value of I_{cr}' is close to zero (Table I), and small changes in experimental conditions can be expected to result in spontaneous passivation. Increase of sodium molybdophosphate concentration to 3.540 g/l indeed resulted in the spontaneous passivation (Fig. 4). No spontaneous passivation is expected for the 1.0 and 0.100 g/l concentrations, but if the sample were passivated in these solutions, a stable passive state should result because of the prominent cathodic loops present on the polarization curves for these solutions (Fig. 2). This conclusion was also verified by the experiments, and no breakdown of passivity was obtained in these solutions if the sample had been passivated. On the other hand, the specimen continued to corrode actively after cathodic activation and no repassivation occurred. The solution containing 0.010 g/l of the sodium molybdophosphate represents the borderline case. The potentiodynamic polarization curve has a cathodic loop, but this loop is not very pronounced. A small change in experimental conditions can be expected to result in the retention or loss of passivity after the passivation treatment. This again is in accord with experimental observations. In very dilute solution a partial hydrolytic decomposition of the molybdophosphate ion can be expected. Therefore, the retention of the passivity in a dilute solution such as 0.010 g/l (5×10^{-6}M) may be partially due to some form of molybdate ions.

The effectiveness of the molybdophosphate ion as a passivating agent depends on the ease of its reduction. Earlier observations in this Laboratory have shown that the molybdophosphate ion is very easily reduced to an intensely blue compound. Because of its ease of reduction it is quite corrosive to many metals, including molybdenum, tungsten, and copper. Because of the diffusion control of the reduction reaction in the important potential range around E_{pp}, the passivating process is drastically influenced by the rate of transport of the inhibitor to the surface of the corroding specimen. The minimum amount of the molybdophosphate necessary to passivate the specimen will therefore be strongly dependent on the hydrodynamic characteristics of the system. However, once the passivation occurs, the rate of mass transfer no longer has a significant effect and the passivity will be retained in quiescent solutions.

The minimum amount of molybdophosphate ion necessary to passivate any metal or alloy in acid solution, aside from the hydrodynamic considerations discussed above, will usually depend on the magnitude of the anodic critical current density. For stainless steels more alloyed than type 430, considerably smaller quantities of the sodium molybdophosphate will be needed for passivation. On the other hand, for metals with very large critical current requirements, no amount of the inhibitor will be sufficient to affect the active-passive transition, and the only effect will be the acceleration of the corrosion rate. Thus, for iron, which has a critical current density of about 600 ma/cm^2 in 1N H_2SO_4 (5), no amount of sodium molybdophosphate is expected to effect passivation. Exploratory studies showed that no passivation of iron electrode occurred in vigorously stirred 1.05N H_2SO_4 containing as high as 50 g/l of sodium molybdophosphate. The results from this investigation were in agreement with the results of Makrides and Stern, and Makrides for the ferric sulfate system (2, 3).

Manuscript received Nov. 17, 1966, revised manuscript received June 19, 1967. This paper was presented at the Philadelphia Meeting, Oct. 9-14, 1966.

Any discussion of this paper will appear in a Discussion Section to be published in the June 1968 JOURNAL.

REFERENCES

1. M. Stern, *This Journal*, **105**, 638 (1958).
2. A. C. Makrides and M. Stern, *ibid.*, **107**, 877 (1960).
3. A. C. Makrides, *ibid.*, **108**, 412 (1961).
4. E. A. Lizlovs, *Corrosion*, **22**, 297 (1966).
5. M. Prazak, V. Prazak, and Vl. Cihal, *Z. Elektrochem.*, **62**, 739 (1958).

The Nonelectrolytic Deposition of Titanium on Columbium Alloys from Fused Salts

J. B. Steinman, R. V. Warnock, C. G. Root, and A. R. Stetson

Solar Division, International Harvester Company, San Diego, California

ABSTRACT

A high-temperature cell was designed for deposition of metallic coatings on refractory alloy substrates. The deposition of titanium from fused chloride and fluoride salts onto columbium alloys was investigated at several temperatures from 800° to 1100°C. The as-deposited coatings were generally dense and adherent and exhibited excellent side-to-side and edge uniformity. An explanation of the driving force and a mechanism for nonelectrolytic deposition is proposed, and an activation energy for deposition is calculated.

Considerable work has been directed toward the development of a process for the production of high-purity titanium and, alternatively, toward deposition of a uniform titanium coating from a molten salt bath. Studies at the National Bureau of Standards (1) produced titanium coatings 0.001- to 0.002-in. thick by electrolysis of a fused salt bath containing $NaTiCl_4$, KCl, and LiCl. Current densities up to 200 amp/ft^2 were used and the deposit was largely dendritic. Using an all-fluoride bath, K_2TiF_6 and NaF, Stetson was able to deposit a fairly uniform titanium coating by the electrolytic method (2). However, electrolytic deposition of titanium from a fused salt bath has produced primarily dendritic growths rather than smooth coatings.

Gill, Straumanis, and Schlecten first observed the corrosion of titanium in NaCl to form "pyrosols," and the subsequent use of these sols in the titanium coating of steels, copper, nickel, and cobalt (3-5). Alpert used scrap titanium, a partially reduced $TiCl_3$-$TiCl_2$ mixture, and NaCl to produce a titanium bath which reportedly gave coatings up to 0.02-in. thick on nickel,

iron, and tantalum (6). Stetson and Moore (7) successfully plated titanium on the columbium alloys, D43 and B66, with a K_2TiF_6, NaCl, LiF, Ti bath. This bath was run nonelectrolytically between 1010° and 1093°C and gave 0.0007 in. of titanium alloy plate in 20 hr.

The nonelectrolytic deposition of chromium, aluminum, nickel, titanium, silicon, and vanadium has been observed by the authors to occur from fused salt baths.

In the present work, an investigation of nonelectrolytic titanium plating was conducted. All fluoride, K_2TiF_6-LiF-NaF-Ti and all chloride, $TiCl_3$-NaCl-$BaCl_2$-Ti baths were investigated at two active salt concentrations and two temperatures. Additional work has shown that the baths will plate well without the addition of K_2TiF_6 or $TiCl_3$; however, the equilibration period before acceptable deposits and deposition rates can be obtained is approximately three days compared with one day for the baths with active salt additions. Two additional temperatures were investigated with a 5 m/o (mole per cent) K_2TiF_6 bath in an effort to determine the activation energy for deposition. Smooth, uniform, titanium alloy coatings up to 0.007-in. thick were obtained in 16 hr at 1093°C.

A special plating cell was designed for use in this project, and provisions were made for control of the atmosphere above the baths at all times.

Materials

All chemicals used in this work were of reagent or better grade. The barium chloride was vacuum dried at 150°C to eliminate hydrated water. All other chemicals were used as supplied. Commercially pure titanium sheet was used to fabricate the cylindrical titanium source used in each bath.

Cb752 (Cb-10W-2.5Zr) and D43 (Cb-10W-1Zr-0.1C) were used as the substrate alloys. Both alloys were obtained as 0.020-in. thick sheet and were in the duplex heat-treated condition (solution treated, cold reduced 25%, and aged). Table I shows chemical analyses of the as-received columbium alloys.

Two bath concentrations were investigated in the fluoride system and one in the chloride system. The fluoride baths consisted of 5 m/o K_2TiF_6, (28.0 w/o K_2TiF_6, 34.6 w/o LiF, 37.4 w/o NaF) and 20 m/o K_2TiF_6 (65.1 w/o K_2TiF_6, 16.8 w/o LiF, 18.1 w/o NaF) dissolved in LiF-NaF eutectic. The chloride baths were prepared by dissolving 5 m/o $TiCl_3$ in a eutectic mixture of $BaCl_2$-NaCl to give a 6.4 w/o $TiCl_3$, 27.8 w/o NaCl, and 65.8 w/o $BaCl_2$ bath. Sufficient titanium metal, in the form of a cylinder, was provided to effect reduction of the baths and to maintain metallic titanium in contact with the bath at all times. The melts weighed approximately 1600g and gave a bath depth of approximately 8 in.

Equipment

A high-temperature plating cell was designed for deposition of metallic coatings on refractory alloy substrates. Provisions were made to ensure positive control of the argon inert atmosphere and to prevent atmospheric contamination of the bath during insertion and extraction of specimens. The cell was designed to operate in the temperature range 427°-1150°C (800°-2100°F) in a gas fired furnace with a temperature control of ± 5°C. A schematic diagram of the cell is shown in Fig. 1.

The bottom part of the cell is 0.125-in. Inconel 600 tube that has been aluminized. The upper chamber

Table I. Chemical analysis of the as-received alloys

Alloy	Oxygen, ppm	Hydrogen, ppm	Nitrogen, ppm	Carbon, ppm	Tungsten, w/o	Zirconium, w/o
D43	221	1	19	935	9.8	1.1
Cb752	52	6	42	10	9.97	2.5

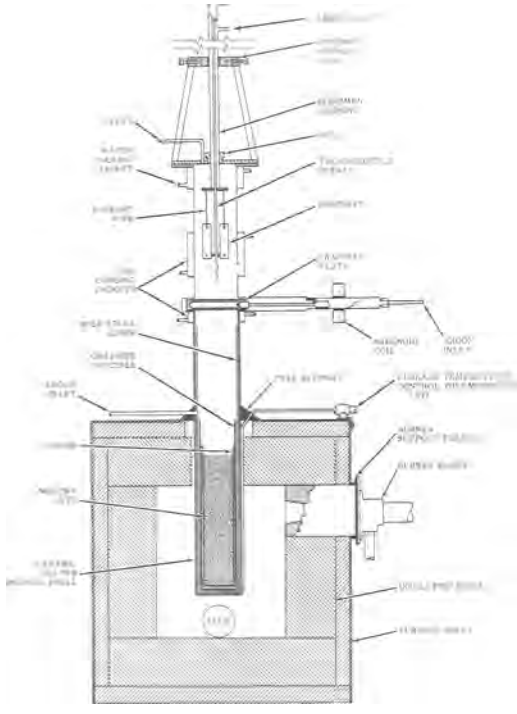

Fig. 1. Schematic diagram of fused salt plating cells

was fabricated from type 321 stainless steel and is separated from the lower bath chamber by a graphite gate valve actuated magnetically by a solenoid coil. This arrangement permits insertion and removal of specimens while continuously purging the lower chamber with argon.

The specimens, 2.0 x 0.5 x 0.020 in., are hung on tantalum wires welded to the Inconel specimen support rod which enters the cell through a Teflon compression seal. The cell top, through which the specimen support rod passes, is bolted to the upper chamber flange and is sealed with an O-ring.

The bath is contained in a National Carbon Company ATJ grade graphite crucible with an ID of 2.875 in. This grade of high-density graphite has proven impermeable to the salt mixtures at operating temperatures. The graphite crucible is placed in a mild steel liner which is, in turn, placed inside the Inconel retort. The bottom half of the crucible is wrapped in 0.002-in. molybdenum foil to prevent formation of the iron-carbon eutectic and subsequent fusion of the liner to the Inconel retort.

The furnace is gas fired using an Eclipse Tempered Air Burner. The temperature is controlled by a Barber-Coleman controller operating on the output of a chromel-alumel thermocouple in a protective sheath attached to the outside of the retort. The internal bath temperature is monitored by means of a tantalum-sheathed chromel-alumel thermocouple which enters the bath through the specimen support rod. Water and air cooling jackets are available for cooling the upper chamber but were not used in this work.

Procedure

The entire weighed salt mixture is placed in the graphite crucible into which has been inserted a cylindrical sheet of pure titanium (this is the titanium source in the deposition reaction). The molybdenum-wrapped crucible is then placed in a liner which is, in turn, placed in the cell. After assembly, the cell is purged with argon (99.997% argon) for 4 hr (the time required to decrease the oxygen level in the cell effluent to <5 ppm) with an argon flow of 8 cfh. The furnace is then fired and the cell temperature brought to about 450°C and held for 16 hr. This procedure permits elimination of volatile impurities present in the salt mixture. The temperature is brought to 1093°C

Table II. Titanium deposition on Cb752 from a 5 m/o K_2TiF_6 bath

Time, hr	Average weight gain in mg/cm²			
	799°C (1470°F)	872°C (1600°F)	982°C (1800°F)	1093°C (2000°F)
1	1.0	1.9	5.0	11.2
2	1.5	2.9	7.1	14.4
4	2.1	5.7	11.2	23.6
16	4.3	12.4	29.2	50.0

where the salt is fused and allowed to "equilibrate" (establish a uniform temperature, become homogeneous, and reach the proper valence state).

The bath preparation procedure is slightly modified in the case of the chloride baths. The anhydrous reagent grade $BaCl_2$ contains some water of hydration even after heating to 150°C in a vacuum drying oven. The remaining moisture is eliminated by heating the NaCl-$BaCl_2$ solvent to 1100°C in a stream of argon in the fused salt cell. The $TiCl_3$ is then added in a polyethylene bag suspended from the specimen support wires. The polyethylene decomposes and is vaporized.

To insert the specimens, the top of the cell is removed (with the gate valve closed). The specimens, hung on the tantalum support wires, are introduced into the upper chamber which is then sealed, and purged with argon for 15 min. The gate valve is then opened, and the specimens are lowered into the bath. For removal, the specimens are raised out of the bath into the upper chamber and the gate valve is closed. The specimens are allowed to cool in the argon atmosphere in the upper chamber for 5 min before the cell is opened and the specimens removed. The adherent salt is readily removed from the specimens after a short period of soaking in hot water.

Experimental Results

Titanium deposition studies were carried out in two different fused salt systems: the all-fluoride system and the all-chloride system. The carrier salt composition for a given system remained the same throughout the studies while the active salt percentage was varied.

The all-fluoride system.—A series of plating runs was made in both the 5 and 20 m/o K_2TiF_6 baths. Four temperatures were investigated in the case of the former and the two standard temperatures, 982° and 1093°C (1800° and 2000°F) for the 20 m/o bath. The temperatures studied in the 5 m/o bath included 799°, 872°, 982°, and 1093°C (1470°, 1600°, 1800°, 2000°F). The data from the runs in the 5 m/o K_2TiF_6 bath are shown in Table II and plotted in Fig. 2.

The series of plating runs in the 20 m/o K_2TiF_6 bath at 982° and 1093°C produced results very similar to those from the 5 m/o bath. The deposition ranged from a low of 4.4 mg/cm² in 1 hr at 982°C to a high of 80 mg/cm² in 16 hr at 1093°C. Both macroscopically and microscopically the coatings were similar to those deposited from the 5 m/o K_2TiF_6 bath.

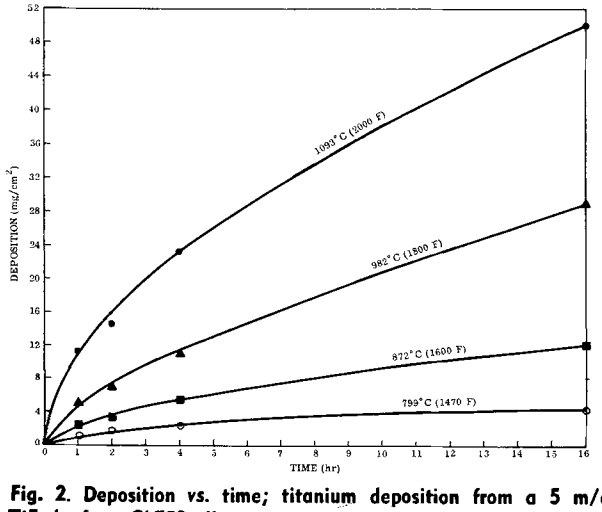

Fig. 2. Deposition vs. time; titanium deposition from a 5 m/o K_2TiF_6 bath on Cb752 alloy.

Table III. Titanium deposition on Cb752 from a 5 m/o $TiCl_3$ bath

Time, hr	Average weight gain (mg/cm²)	
	982°C (1800°F)	1093°C (2000°F)
1	2.5	6.5
2	4.5	8.4
4	7.5	14.9
16	16.6	36.0

Table IV. Titanium deposition on D43 alloy

Bath	Time, hr	Weight gain (mg/cm²)	
		982°C	1093°C
5 m/o K_2TiF_6	2	6.8	—
	4	7.6	—
5 m/o $TiCl_3$	2	4.7	6.3
	4	9.1	13.8

All-chloride system.—A 5 m/o $TiCl_3$ bath was investigated at 982° and 1093°C. A series of runs was completed at each temperature on the Cb752 alloy, and the data are presented in Table III and plotted in Fig. 3.

The deposition rate in this chloride bath was found to be somewhat lower than that found in the all-fluoride system.

Two- and four-hour runs were made in the baths studied using D43 specimens. Results are shown in Table IV.

Comparison of this data with that for Cb752 shows the rate of titanium alloy formation to be slightly higher on Cb752 in two of the three comparable cases. While substrate composition should have a considerable influence on diffusion controlled deposition, little substrate effect was seen in this case since the alloys are quite similar. There is a possible exception which might be caused by the only compositional difference in the alloys. This one notable difference is the carbon content of the D43 which makes this alloy precipitation hardened (ZrC precipitates). The carbon in the alloy could influence the initial titanium deposition rate because of the possible formation of TiC. However, this effect was not seen in the present work.

The deposition rate curves for all the baths are generally parabolic in shape and fit an equation of the form, $W^2 = kt$, where W is the weight gain, k is a rate constant, and t is the time. The rate constants are a function of temperature and for the 5 m/o K_2TiF_6 bath ranged from 1.1 at 799°C to 131 mg²/cm⁴ hr at 1093°C.

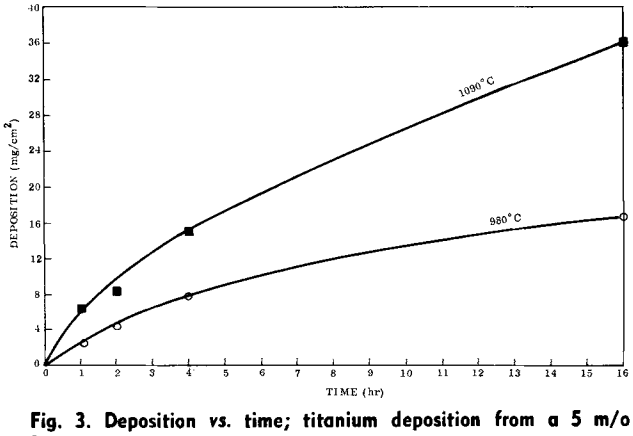

Fig. 3. Deposition vs. time; titanium deposition from a 5 m/o $TiCl_3$ bath on Cb752 alloy.

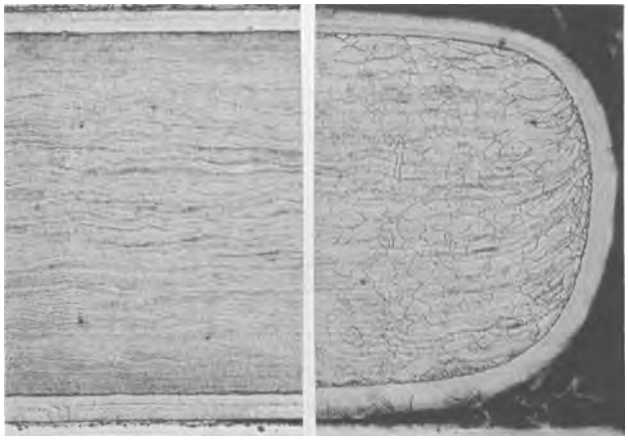

Fig. 4. Cb752 substrate (0.020 in.) with a titanium alloy coating applied in the all-fluoride bath at 1093°C (2000°F) in 4 hr: A (left), note the uniformity of thickness from side to side of the specimen; B (right), edge coating uniformity is shown. Magnification ca. 100X.

All of the deposits were smooth, adherent, and presented a shiny macroscopic appearance. Figure 4 shows a photomicrograph of a typical titanium-coated specimen. The side-to-side and edge uniformity should be noted.

Microhardness traverses were made on typical specimens from each of the baths studied in both fluoride and chloride systems. Results were similar for all baths, and a typical microhardness traverse is shown in Fig. 5. The average hardness of the as-received Cb752 alloy is 280 Knoop Hardness Number (50-g load).

A representative group of Cb752 specimens, coated with titanium in different baths, was subjected to bend ductility tests at minus 73°C. In all cases, the specimens bent without fracture or visible signs of cracking as did the uncoated standards. The titanium alloy coating remained intact.

As noted earlier, the baths were protected by an argon atmosphere at all times. It was found that any exposure of the bath to the air resulted in decreased plating rates. For example, exposure of the molten bath surface for less than 5 min resulted in as much as a 75% decrease in plating rates and a concomitant loss in coating quality. Shih and co-workers (8) claimed that the presence of oxygen in a Ti-NaCl or KCl bath was necessary for plating and indicated that poor coatings on iron resulted when no oxygen was present.

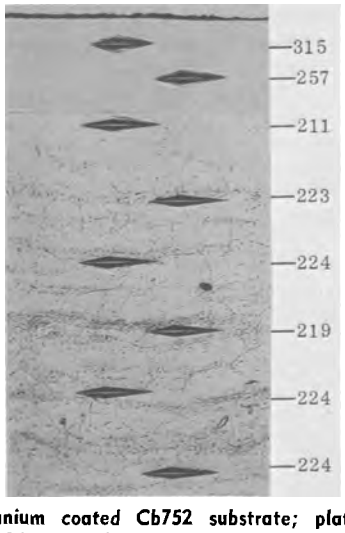

Fig. 5. Titanium coated Cb752 substrate; plated in 5 m/o $TiCl_3$ bath for 16 hr at 1093°C (2000°F). Magnification ca. 200X.

While it was not possible to completely exclude oxygen from the fused salt baths in this investigation, all practical precautions were taken to prevent its introduction. It should be noted that the titanium deposition rates in this study were two to four times greater than any reported in the literature.

Discussion of Results

The fused salt baths investigated in this work produced smooth, adherent titanium alloy deposits on both Cb752 and D43 alloys. Close examination of the specimen cross section seen in Fig. 4 shows two different structures. The single-phase region adjacent to the substrate is probably columbium-rich, beta titanium alloy. The outer, Widmanstatten-like structure is a very dilute solid solution of columbium in transformed beta titanium alloy and was not evident on thinner coatings which showed the single-phase, beta structure only.

The substrate was also affected by the coating treatment. Examination of the microhardness traverse in Fig. 5 shows a loss in substrate hardness. This loss, in all cases, was most pronounced in the area immediately adjacent to the coating and was as much as 25% in some cases. The decrease in hardness was greater at higher temperatures and longer times. This phenomena may be explained by the "interstitial sink effect" (9). This term is used to describe the potential for migration and the equilibrium partition of an interstitial element as a result of the difference in the partial molal free energies of the element in two adjacent metallic layers.

The Cb752 alloy is basically a solid solution strengthened alloy depending on oxygen in solution plus a small distribution of ZrO_2 precipitates. These precipitates are readily seen in the as-received alloy with the aid of electron microscopy. A similar examination of the titanium-coated alloy revealed a large reduction or complete elimination of this precipitate for varying depths below the coating-substrate interface depending on the coating time and temperature. The distribution of oxygen between columbium and titanium may be calculated by considering the partial molal free energies of solution. This partition at 1500 K (at equilibrium) in a titanium-coated Cb752 alloy is:

	Columbium	Titanium
Oxygen, ppm	1	1000

In an effort to fully characterize the plating chemistries, periodic chemical analyses were performed on the operating baths. Comparison of the observed data (weight per cent titanium in the bath) and theoretical weight per cents, as a function of oxidation state, gave an indication of the valence state of the titanium in a bath. Previous work reported in the literature (10, 11) indicated that the predominant reduction product in a K_2TiF_6 bath, similar to those used in this work, was Ti^{+3}. Analyses and calculations have shown the average valence in the fluoride baths to be generally between +2 and +3, while the predominant species in the $TiCl_3$ baths was found to have an average valence of +2.2. Kreye and Kellogg (12) reported Ti^{+2} as the dominant species in an NaCl-KCl-$TiCl_3$ melt at 760°C. They also observed a slightly lower Ti^{+2} concentration at 782°C with a corresponding increase in the Ti^{+3} species. These findings are in accord with the +2.2 average valence in the present work and might also explain the somewhat higher plating rates found in the K_2TiF_6 baths compared with the chloride system. With an average valence of +2.2, the chloride baths were not in as fully reduced a condition as were the fluoride baths when in the +3 or lower state.

The parabolic nature of the deposition rate indicates that the deposition is controlled by diffusion into the metal substrate. A diffusion controlled hypothesis is supported by considering the difference in chemical

activity between the titanium in the source and the titanium in solution in the columbium. The activity of the titanium in solution in the columbium is lower than the activity of the titanium in the source. The decrease in activity from the pure to the alloyed state is then the probable driving force for deposition. It was also noted that the deposition rate was highly temperature dependent, increasing with increasing temperature. This behavior would be expected in a diffusion-controlled reaction as the diffusivity increases with the temperature. Further, if the deposition were diffusion controlled, the rate constant, k, from the equation

$$W^2 = kt \quad [1]$$

could be described by the Arrhenius equation and expressed by:

$$k = A\ (\exp) -\frac{Q}{RT} \quad [2]$$

where A is a constant, Q might be called the "activation energy for deposition," R is the universal gas constant, and T is the absolute temperature. If the diffusion hypothesis is correct and Eq. [2] accurately describes the rate constant, an Arrhenius plot of ln k *vs.* $(1/T)$ should yield a straight line. Such a plot is shown in Fig. 6 for the 5 mole per cent K_2TiF_6 bath and is seen to be linear. An activation energy for deposition was determined graphically from Fig. 6 and is 46 kcal/mole. This may be compared to the activation energy for diffusion of titanium in columbium which ranges from about 61 kcal/mole in pure columbium to 39 kcal/mole in pure titanium (13) while the activation energy for diffusion of complex titanium ions in fused salt solutions is expected to be only 6-10 kcal/mole (14). This further supports the hypothesis that the rate-determining step is interdiffusion of the titanium and the basis metal.

Straumanis *et al.* (15) determined the activation energy for diffusion of titanium into an iron substrate. A value of 32 kcal/mole may be calculated from their reported data. This may be compared with the value of 46 kcal/mole determined in the present work and designated, "the activation energy for deposition." More precisely, the latter value, 46 kcal/mole, reflects the activation energy for diffusion of titanium in a columbium alloy, and a comparison of the two values indicates that a titanium alloy coating may be developed more easily on an iron substrate than a columbium substrate under similar conditions if nearly equal frequency factors (A) are assumed. Preliminary work was undertaken to substantiate this conclusion, and results are presented in Table V.

No runs were performed which lasted over 60 min; however, as might be expected, the initial titanium deposition rate is faster on iron than on columbium by a factor of 1.4 to 2. In general, diffusion activation energies of metals in substitutional solid solution are proportional to the melting point, and deposition rates should also be proportional to melting points. An approximately linear relationship between titanium deposition rate and substrate melting point has been observed (over an 1800°C substrate melting point range) in other work by the authors.

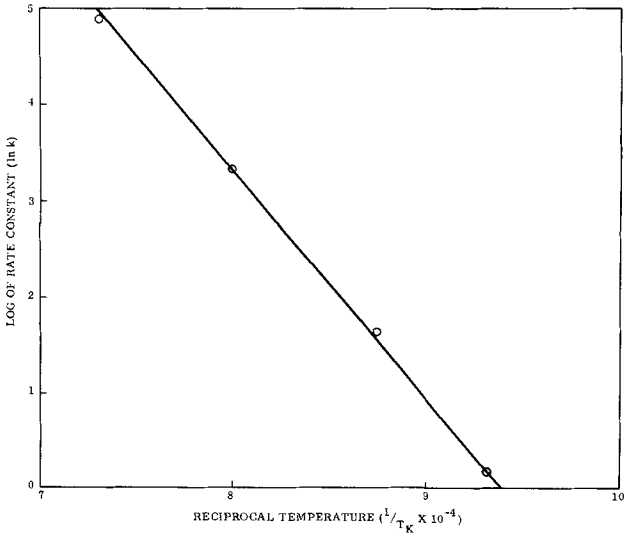

Fig. 6. Arrhenius plot ln k *vs.* reciprocal absolute temperature

Table V. Titanium deposition on 1010 steel from a 20 m/o K_2TiF_6 bath

Time, min	Average weight gain (mg/cm²) at 982°C
2	0.8
6	1.9
15	3.4
30	4.0
60	6.9

There are several possible mechanisms (of which three are most apparent) which could account for the deposition of titanium on columbium alloys with the subsequent formation of a titanium-rich titanium/columbium alloy at the specimen surface. One such mechanism is an oxidation reduction type in which reactions similar to the following might occur:

$$3Cb\ (\text{alloy}) + 5TiF_3 \rightarrow 3CbF_5 + 5Ti$$

or

$$2Cb\ (\text{alloy}) + 5TiCl_2 \rightarrow 2CbCl_5 + 5Ti$$

Interdiffusion of the titanium and columbium would then produce the observed alloy coating. The operation of this oxidation-reduction mechanism should result in a decreased substrate thickness, an over-all weight loss or slight weight gain (depending on the coefficients in the redox equation chosen), and the accumulation of columbium in the bath.

Another possibility is a disproportionation reaction leading to the production of titanium metal. A possible representation is:

$$Ti + 6F^- + 3TiF_6^{-2} \rightarrow 4TiF_6^{-3}$$

$$Cb + 4TiF_6^{-3} \rightarrow 3TiF_6^{-2} + 6F^- + (\text{Ti-Cb alloy})$$

This mechanism should be dependent on TiF_6^{-3} concentration and would presumably decrease to a negligible rate with decreasing temperature. As long as sufficient titanium is present to support the deposition rates observed, interdiffusion rates would still control the plating rate. It is possible that some TiF_4 would be lost from the bath as a gaseous species; however, it would more probably be retained as a complex F^- ion.

The remaining possible mechanism is the diffusion of dissolved or finely dispersed titanium in the melt into the columbium substrate; for example

$$Ti + Cb\ (\text{alloy}) \rightarrow TiCb\ (\text{alloy})$$

Again, the deposition rate should be a function of the ease of interdiffusion of titanium and the substrate material and should decrease with increasing alloy thickness. All of the suggested mechanisms would be temperature dependent.

The oxidation-reduction type mechanism can be eliminated because no decrease in substrate thickness occurs and a positive weight gain is always observed for a coated specimen.

Straumanis, Shih, and Schlecten (15) stated that they were able to differentiate between a disproportionation type reaction and one in which dispersed titanium metal or TiO_x reacted to form the alloy coating. They concluded that the coating was formed by direct impact of dispersed titanium or TiO_x particles in the melt with the surface to be coated.

When examining the possibility of the dissolved or finely dispersed titanium theory, it is interesting to note that recent work (16) has demonstrated the ex-

istence of true solutions of metals in their own halide salts at elevated temperatures. Although no data are available for solutions of titanium in titanium-fluoride or chloride melts, it is quite possible that such systems do exist. X-ray diffraction analysis of melt samples in the present investigation failed to show the presence of any free titanium or titanium oxides in the bath. This does not, though, eliminate the possibility of dissolved titanium metal.

Sufficient data are not available from the present work to determine whether disproportionation of a reduced titanium complex at the specimen surface or mechanical adherence of free titanium metal is the coating mechanism. Evidence for both mechanisms exist, and neither may be ruled out at this time.

Acknowledgments

The authors are indebted to Messrs. Warren Johnson and Gail Eichelman for helpful discussions and technical direction on this program. The work described was supported by the Chemical Engineering Branch (MATC), Manufacturing Technology Division, Air Force Materials Laboratory, Wright-Patterson Air Force Base, Ohio on Contract AF33(615)-3173.

Manuscript received Dec. 27, 1966; revised manuscript received May 18, 1967. This paper was presented at the Philadelphia Meeting, Oct. 9-14, 1966.

Any discussion of this paper will appear in a Discussion Section to be published in the June 1968 JOURNAL.

REFERENCES

1. G. B. Wood, P. A. Krasley, K. Schere, and A. Brenner, Electrodeposition of Titanium. U. S. Department of Commerce, National Bureau of Standards, ASTIA-AD 56206 (1 October 1954).
2. A. R. Stetson, U. S. Pat. No. 3,024,174.
3. C. B. Gill, M. E. Straumanis, and A. W. Schlecten, *This Journal*, **102**, 42 (1955).
4. *Ibid.*, 81.
5. M. E. Straumanis and A. W. Schlecten, *ibid.*, **102**, 131 (1955).
6. M. B. Alpert, U. S. Pat. No. 2,734,003 (Feb. 7, 1956).
7. A. R. Stetson and V. S. Moore, Technical Documentary Report No. RTD-TDR-63-4006, Part III (1965).
8. S. T. Shih, M. E. Straumanis, and A. W. Schlecten, *This Journal*, **103**, 395 (1956).
9. A. G. Metcalfe and J. S. Dunning, Solar Report RDR-1392 (July 1965).
10. J. G. Wurm, L. Gravel, and R. J. A. Potvin, *This Journal*, **104**, 301 (1957).
11. M. E. Siebert and M. A. Steinberg, *J. Metals*, **2**, (September 1956).
12. W. C. Kreye and H. H. Kellogg, *This Journal*, **104**, 504 (1957).
13. C. S. Hartley, J. E. Steedly, and L. D. Parsons, "Binary Interdiffusion in Body-Centered Cubic Transition Metals," Diffusion in Body-Centered Cubic Metals, ASM (1965).
14. S. Senderoff, and G. W. Mellors, *ibid.*, **113**, 66 (1966).
15. M. E. Straumanis, S. T. Shih, and A. W. Schlecten, *This Journal*, **104**, 17 (1957).
16. J. Lumsden, "Thermodynamics of Molten Salt Mixtures," Academic Press, London and New York (1966).

Electrolytic Reductive Coupling

XV. Electroreductions of Aqueous Concentrated Solutions of Diethyl Maleate in the Presence of Sodium or Tetraethylammonium Cations[1]

Manuel M. Baizer and John P. Petrovich

Central Research Department, Monsanto Company, St. Louis, Missouri

ABSTRACT

Concentrated solutions of diethyl maleate in dimethylformamide-water containing sodium or tetraethylammonium *p*-toluenesulfonate were electrolyzed at constant current. The yields of diethyl succinate and of tetraethyl butanetetracarboxylate were determined. At a given concentration of supporting cation and of bulk water less hydrodimer is formed in the presence of sodium than in the presence of tetraethylammonium cations. These results are related to previous suggestions concerning the influence of the degree of hydration of the supporting cations upon the nature of the electroreduction products.

It has been suggested (2) that during the electroreduction of concentrated aqueous solutions of acrylonitrile the presence of alkali metal cations (M^+), which are simultaneously discharged, leads to substantial yields of propionitrile [1] because of concomitant chemical reactions, whereas the replacement of M^+ by quaternary ammonium cations (R_4N^+), which are not discharged at the operating cathode potential, permits the attainment of very high yields of adiponitrile [2].

$$CH_2{=}CHCN + 2\bar{e} + 2H_2O \xrightarrow{M^+(H_2O)_x} CH_3CH_2CN + 2\,\overline{OH} \quad [1]$$

$$2CH_2{=}CHCN + 2\bar{e} + 2H_2O \xrightarrow{R_4N^+} NC(CH_2)_4CN + 2\,\overline{OH} \quad [2]$$

Recently Feoktistov and co-workers (3) and, independently, Gillet (4) have offered an alternate explanation for the change in the distribution of reduction products when one replaces supporting electrolytes containing M^+ by those containing R_4N^+. They have pointed out that alkali metal cations are hydrated while quaternary ammonium cations are not. As a consequence, Gillet has argued, when the acrylonitrile molecule, aligned with the β-carbon atom on

[1] For Part XIV see (1).

Table I. Electrolysis of 43.0g of diethyl maleate at a mercury cathode 20°-25°, 1.00 amp for 3 hr

Run	Catholyte			Esters recovered							Apparent losses	
	G salt	Ml H_2O	Ml DMF	G diethyl maleate	G diethyl succinate	Equiv. amp hr	Curr. eff, %	G hydrodimers*	Equiv. amp hr	Curr. eff, %	G diethyl maleate equiv.	Amp hr.
1	19.4A[a]	16	80	22.6	2.41	0.743	24.8	13.0	2.01	67.0	5.0	0.25
2	19.4A	22	74	21.2	4.96	1.53	51.0	10.7	1.67	55.5	6.1	−0.20
3	30.1B[b]	16	80	20.6	0.81	0.25	8.2	15.6	2.42	80.5	6.0	0.33
4	30.1B	22	74	22.4	2.16	0.67	22.2	14.6	2.27	75.5	3.8	0.06
5	15.5A + 6.0B	22	74	20.5	1.62	0.50	16.7	15.1	2.34	78.0	5.8	0.16
6	19.4A	30	66	25.0	5.33	1.64	54.9	8.84	1.37	45.7	3.8	—
7	30.1B	30	66	22.3	1.93	0.60	19.8	13.9	2.16	72.0	4.8	0.24
8[c]	36.1B	36	79	9.21[c]	3.51	1.18	36.2	10.3	1.59	53.0	4.8	0.23

[a] Sodium p-toluenesulfonate.
[b] Tetraethylammonium p-toluenesulfonate.
[c] Initially 5.0 ml of diethyl maleate was included in the catholyte. The remainder, to a total of 25.8g (0.15 mole), was added in the course of the run. Acetic acid had to be added dropwise to maintain the desired pH.
* Identified by comparison of vpc retention time with samples previously prepared (7). Two isomers in a ratio of *ca* 93/7 (presumably meso-/dl) were obtained.

the cathode surface, is being reduced[2] the final anionic intermediate which is just leaving the cathode surface has an opportunity to react at the β-carbon atom with water when $M^+(H_2O)_x$ is the counterion [1], whereas it has an overwhelming opportunity to react with a second acrylonitrile molecule when R_4N^+ $(H_2O)_o$ is the counterion.

The purpose of the work reported here was to test the effect of (supporting) cation hydration on the yield of hydrodimer prepared from an activated olefin whose electroreduction occurs at a cathode voltage at which simultaneous cation discharge is unambiguously avoided. While several monoactivated olefins CH_2= CHX (where X is an electron-withdrawing group) are available which reduce at a considerably more positive cathode voltage than is required for $Na^+(H_2O)_x$ discharge, they may, like methyl vinyl ketone, undergo under the conditions of electrolysis various chemical side reactions which complicate the interpretation of the results. Because its reduction occurs at a voltage at least 0.7v more anodic than that of $Na^+(H_2O)_x$, its polarography has been extensively[3] studied (6), its electrolytic hydrodimerization to tetraethyl butanetetracarboxylate has been reported (7), and its side reactions during reduction are minimal, diethyl maleate was chosen as the model activated olefin for this study.

Experimental

Reagents.—Diethyl maleate (Matheson Scientific, Superior) was used as received. Vpc and nmr analyses showed that it contained about 8% diethyl fumarate. Tetraethylammonium p-toluenesulfonate (Alfred Bader Company) was recrystallized from acetone and dried *in vacuo* at 60°. Sodium p-toluenesulfonate was prepared from the acid and base and dried as above. The dimethylformamide (DMF) was redistilled through a Vigreau column at atmospheric pressure.

Equipment.—The electrolysis cell and associated apparatus have been described (1). A mercury cathode, area 55 cm^2, was used throughout. Vpc analyses of the products obtained from the electrolyses were carried out using an F and M Model 300 instrument; the column contained 1% silver nitrate and 18% Carbowax 20M on 35-48 mesh Chromosorb W and was used at 125° (for "low boilers") and at 225° (for "high boilers").

Procedures.—The electrolysis data are summarized in Table I. The catholytes contained 43.0g (0.25 mole) of diethyl maleate, 0.10 mole of sodium (19.4g) or tetraethylammonium p-toluenesulfonate (30.1g), and 96 ml of a DMF-water mixture; the total volume was *ca.* 150 ml. The anolytes were saturated aqueous solutions of the same electrolyte present in the catholyte. The electrolyses were conducted at a constant current of 1.00 amp for 3 hr. The cathode voltage in the several experiments was −1.19 to −1.30v (SCE). Acetic acid was available for dropwise addition to the catholyte in order to maintain the pH at 7-8 (measured externally on Alkacid paper). Usually no acid addition was needed, indicating that saponification of the ester was rapid enough to provide a buffering effect. No hydrogen was evolved. At the end of the electrolysis the catholyte was separated from the mercury, diluted with 200 ml of ice water, and extracted with three 100 ml portions of methylene chloride. The combined extracts were washed with three 100 ml portions of water and dried over anhydrous magnesium sulfate. The filtered solution was heated on a water bath to remove methylene chloride and then fractionated through a 2-ft Vigreau column to a vapor temperature of 50° (18 mm) to remove the bulk of the residual DMF. The remaining crude mixture of esters was fractionated through a semimicro apparatus having a vacuum-jacketed 6-in. Vigreau column. The following fractions were collected: (*i*) to 115° (20 mm), (*ii*) 115°-118° (20 mm), (*iii*) to 153° (0.25 mm), (*iv*) 156°-161° (0.25 mm), (*v*) pot residue.[4] Each fraction[5] was analyzed by vpc first at 125° to determine DMF, diethyl maleate, diethyl succinate, and diethyl fumarate and then at 225° to determine tetraethyl butanetetracarboxylate and its ratio to the lower boiling components.

Discussion of Results

At a given level of proton donor (water) concentration in the catholyte, all other conditions being the same, more hydrodimerization occurs in the presence of tetraethylammonium than of sodium (run 3 *vs.* 1; run 4 *vs.* run 2). The hydrodimerization is less sensitive to increasing water concentration when tetraethylammonium is used than when sodium is used, *e.g.*, the yield of hydrodimer in run 7 is 89.5% of its value in run 3, whereas the yield in run 6 is only 68.3% of its value in run 1. Further the addition of tetraethylammonium to a catholyte containing sodium (run 5) is capable of elevating the yield of hydrodimer substantially. These results lend support to the proposal (3, 4) that, in effect, adsorption of tetraalkylammonium on the mercury cathode leads to the establishment of a water-poor zone close to the cathode surface.[6] The substantial yield of hydrodimer ob-

[2] In the over-all two-electron process the acrylonitrile may during the uptake of the first electron react simultaneously at the -CN or α-carbon atom with a molecule of water from the bulk of solution [5].
[3] Professor Wawzonek has pointed out that the polarography of diethyl maleate in tetralkylammonium electrolytes has not been previously reported. While this information will be later presented separately in a paper describing work which is currently in progress, it may be stated now that in aqueous dimethylformamide no significant differences were found in the polarographic behavior using sodium or tetraethylammonium supporting electrolytes.
[4] This was always negligible, indicating that no oligomers higher than the hydrodimer had been formed.
[5] This procedure gave more satisfactory results than the attempted vpc analysis of the crude mixture directly.
[6] This may likewise explain the reported excellent yield of adiponitrile from acrylonitrile in an amalgam reduction in the presence of aqueous acid and tetraethylammonium p-toluenesulfonate (8).

tained (run 8) even when the concentration of diethyl maleate in the catholyte at a given time is relatively low and the concentration of water relatively high emphasizes again the need for caution in predicting the products of an electrochemical reduction; this is particularly true when activated olefins are involved.

Since all runs were carried out at the same constant current density, the rates of generation of the reduced intermediates were the same. If formation of hydrodimer occurred *via* radical coupling of anion-radicals or (after neutralization with water) their derived radicals, the yield of hydrodimer should not be affected by the nature of the supporting cation nor by the relatively small over-all changes in water concentration. The experimental results are better accommodated by the proposal (9) that the coupling is the result of an anionic attack of a reduced species upon an unreduced molecule. Whether this is a two-step (9) or a concerted process (1) is still a moot question. It is also not known at present whether the hydrodimerization of 1,2-diactivated olefins proceeds by the same mechanism as the hydrodimerization of monoactivated olefins: this problem is under investigation in this Laboratory.[7]

Finally, it is instructive to examine (Table I) the apparent losses of diethyl maleate and to compare these with the coulombic input not accounted for in the form of reduced products isolated. In run 1, *e.g.*, the "missing" 0.25 amp hr is equivalent to 0.81g diethyl succinate or 1.61g hydrodimer. Assuming complete loss of these reduced esters through saponification[8] there is still considerable diethyl maleate to account for. The facile saponification of the latter ester is well known (6); it was of interest to be able to estimate whether part of the saponified maleate (as half-ester or diacid) was being reduced in the course of the electrolysis and was causing a shift of the cathode v to a more negative value than it would have had in the absence of saponification, or whether part of the diethyl succinate already formed was being later saponified. A study[9] of the kinetics of diethyl maleate/diethyl succinate[10] saponification showed a rate ratio of $k_m/k_s = 20$. Even if all the diethyl succinate had been present from the start (run 1) and the cathode surface had a pH of *ca.* 13, less than 0.2g of diethyl succinate would have been saponified in 3 hr; however, all of the unrecovered ester can be accounted for by saponification of diethyl maleate under the same conditions. Therefore, the "excess" current was most probably used in the reduction of ethyl hydrogen maleate.

Manuscript received March 29, 1967; revised manuscript received *ca.* June 12, 1967.

Any discussion of this paper will appear in a Discussion Section to be published in the June 1968 JOURNAL.

REFERENCES

1. J. P. Petrovich, J. D. Anderson, and M. M. Baizer, *J. Org. Chem.*, **31**, 3897 (1966).
2. M. M. Baizer, *This Journal*, **111**, 215 (1964).
3. L. G. Feoktistov, A. P. Tomilov, and I. G. Sevast'yanova, *Soviet Electrochemistry*, **1**, 1165 (1965).
4. I. E. Gillet, Abstracts 17th Meeting of CITCE, Tokyo-Kyoto, September 1966, p. XXV.
5. F. Beck, *Chem. Ing. Techn.*, **37**, 607 (1965).
6. P. J. Elving and C. Teitelbaum, *J. Am. Chem. Soc.*, **71**, 3916 (1949); R. Takahashi and P. J. Elving, *Electrochim. Acta*, **12**, 213 (1967).
7. M. M. Baizer and J. D. Anderson, *This Journal*, **111** 223 (1964); A. P. Tomilov and L. V. Kaabak, *Zhur. Obshchei Khim.*, **33**, 731 (1963).
8. F. Matsuda, *Tetrahedron Letters*, 6193 (1966).
9. M. M. Baizer, *ibid.*, 973 (1963).
10. G. C. Jones and T. H. Ledford, *ibid.*, 615 (1967).

[7] After this manuscript was submitted for publication, a possibly relevant paper appeared (10) concerning the participation of the α-carbon atom in electrolytic reductive couplings of activated olefins. In 1,2-bis-activated olefins the α-β-carbon atoms are of course equivalent.

[8] The half-ester or diacid would not have been extracted by methylene chloride from slightly alkaline solution.

[9] The rates of ester saponification were followed to > 50% reaction by vpc analysis using an XE-60 on Teflon column at 115°. In a typical experiment the appropriate ester and diphenylmethane, the vpc internal standard, were dissolved in a DMF solution containing 30g of tetraethylammonium *p*-toluenesulfonate and 30 ml of 10% aqueous tetraethylammonium hydroxide and diluted to 100 ml with DMF. The reaction flasks were thermostated at 25°. At appropriate times a 1 ml aliquot was removed, neutralized with acetic acid, and analyzed directly by vpc for unreacted diester. The second order rate constants obtained by this method for diethyl maleate and diethyl succinate were 2.1×10^{-3} and 1.0×10^{-4} liter mole^{-1} sec^{-1}, respectively. The estimated error in k is $\pm$ 0.2.

[10] It was assumed that the rate of saponification of the hydrodimer was too low to affect the conclusions.

Electrolytic Oxidation of Aromatic Amines

S. Wawzonek and T. W. McIntyre

Department of Chemistry, University of Iowa, Iowa City, Iowa

ABSTRACT

The electrolytic oxidation of anilines at a rotating platinum electrode in acetonitrile in the presence of pyridine involved a two electron change and formed azobenzenes. Evidence for the mechanism was the voltammetric behavior of hydrazobenzenes, *p*-phenylenediamine and 4,4'-dimethoxyazobenzene and the formation of azobenzenes in macroscale oxidations. The behavior of anilines in the absence of pyridine was more complex since the amine acted as a base and formed a salt which was not easily oxidized. Exceptions were the weakly basic *o*-nitroaniline, *p*-nitroaniline, 2,4-dinitroaniline and the reversible systems, o-phenylenediamine and *p*-phenylenediamine; two electrons were involved for these examples.

The electrolytic oxidation of aromatic amines was studied in acetonitrile at a microrotating platinum electrode to determine whether this reaction could be used to prepare azobenzenes on a macroscale.

Voltammetric studies of aromatic amines in acetonitrile have been carried out with aniline (1), 2-aminoanthracene, 2-fluorenamine, 1- and 2-naphthylamine (2), *p*-phenylenediamine (3, 4), 9-amino-10-phenylanthracene (5) and dimethylanilines (4, 6). A stepwise oxidation is reported for *p*-phenylenediamine (3) and a one-electron oxidation change is suggested for the dimethylanilines (4, 6) and 9-amino-10-phenylanthracene (5).

Large-scale oxidations of anilines have been carried out mainly in aqueous acid and basic media. The former usually leads to polymeric products or nitrogen free compounds, (7-10). In alkaline solution *p*-toluidine and 2,4-dimethylaniline gave the corresponding

azobenzenes at an iron anode (11). If one or both of the N-hydrogens are replaced by alkyl groups, dimeric products result (12, 13).

Experimental

Apparatus.—The voltammetric data were obtained with a Sargent Model XXI polarograph and were corrected for *iR* drop across the cell. All measurements were made in a water thermostat at 25° ± 0.1°.

Resistances were measured with a Wheatstone bridge circuit which contained an audio oscillator signal generator and a head set as a null indicator. A variable capacitor was placed in one arm of the bridge circuit to balance the capacitance effects of the cell. An input voltage of 1v (a.c.) and a signal of 1000 Hz was used.

The indicator electrode was a platinum bead electrode, which had an exposed area of 1.0 mm^2. This microelectrode was constructed by sealing a No. 20 platinum wire into a 6 mm glass tube parallel to the axis of rotation; the exposed wire was then fused flush with the glass surface. The platinum electrode was rotated at 600 rpm with a Sargent Synchronous Rotator and cleaned before each run by the procedure of Kolthoff and Coetzee (14).

The solutions (25 ml volumes were used) were studied in a cylindrical shaped cell with an external Ag/0.1M $AgClO_4$ reference electrode connected to the cell through a fine glass frit.

The large-scale electrolyses were carried out in two different cells. One cell was an H-cell, which had a medium glass frit separating the two compartments of equal volume (100 ml). One compartment contained a cylindrical platinum gauze anode, which could be rotated at high speed, and the other compartment contained a stirred mercury pool cathode. This cell was also provided with a compartment for a reference electrode for controlled potential electrolysis.

The second cell consisted of a tall beaker 14.5 cm high and 7 cm in diameter. A Coors porous cup (7.5 by 2.6 cm with a wall thickness of 2 mm) was placed inside as the cathode compartment.

A Heath-Kit IP-12 battery eliminator was used as a direct current source with a variable voltage range of 0-15v. For controlled potential electrolysis the manual apparatus described by Lingane (15) was used. An L&N Student Potentiometer was employed as the voltage measuring device.

Infrared spectra of cast films were recorded using a Perkin-Elmer spectrophotometer.

Chemicals. Acetonitrile was purified by method E of Coetzee *et al.* (16).

Pyridine was purified by refluxing with solid potassium hydroxide and fractionally distilling through a Fenske column; the center fraction (60%) was collected.

Lithium and sodium perchlorate (G. F. Smith and Company) were dried under vacuum at 80° and stored over phosphorous pentoxide.

The various anilines, hydrazobenzenes, and azobenzenes studied were either obtained commercially or synthesized by appropriate methods given in the literature.

Electrolytic oxidations.—p-Nitroaniline. p-Nitroaniline (1.0g)) was dissolved in 90 ml of acetonitrile (0.5*M* pyridine, 0.5*M* sodium perchlorate) and electrolyzed in the H-cell using a rotating platinum gauze anode and a mercury pool cathode. The solution was degassed with nitrogen before and during the electrolysis. At an applied potential of 10v, a current of 0.3 amp was obtained, which decreased to a final value of 0.05 amp in 4 hr. The anolyte was concentrated to 20 ml and 30 ml of water was added. The precipitated material was collected and extracted with 100 ml of cold acetone. The acetone was removed, and the residue was chromatographed on alumina in benzene-chloroform mixtures. The first fraction gave reddish brown crystals (0.26g, 39.2%), mp 220°-222°. The infrared spectrum was identical with that of an authentic sample of 4,4'-dinitroazobenzene. The second fraction from the column was *p*-nitroaniline.

p-Chloroaniline.—Oxidation of *p*-chloroaniline (1.0g) was carried out under conditions similar to those used for *p*-nitroaniline. At an applied voltage of 10v a current of 0.15 amp was obtained which decreased to a final value of 0.01 amp in 14 hr.

The anolyte was concentrated to 10 ml and poured into 500 ml of methylene chloride. The methylene chloride was filtered and extracted with two 100-ml portions of cold 5% hydrochloric acid solution. The aqueous extract was evaporated to dryness and 0.32g of *p*-chloroaniline was recovered as the hydrochloride. The methylene chloride extract was dried over anhydrous sodium sulfate, concentrated and chromatographed on alumina with benzene-chloroform mixtures. The first fraction contained 0.165g (24.3%) of 4,4'-dichloroazobenzene, which was identified by comparison of its infrared spectrum with that of an authentic sample. The melting point of the product after recrystallization from methanol was 185°-187°. The second fraction from the column gave 0.053g (7.8%) of a red crystalline compound, which had a melting point of 258°-260d° after recrystallization from toluene. This product produced a violet color when dissolved in concentrated sulfuric acid and gave a NH band in the 3200-3500 cm^{-1} region in the infrared region. These properties agree with those of 2,5-di-*p*-chlorophenylaminobenzoquinonedi-*p*-chlorophenylimine [tetra-*p*-chloroazophenine (I)] (17).

A similar electrolysis of *p*-chloroaniline in the absence of pyridine and using 0.5*M* lithium perchlorate gave an acidic anolyte at the conclusion of the reaction. Products isolated were starting material (20%) and tar.

2,4-Dichloroaniline.—The electrolysis was conducted at 10v using the beaker cell with a platinum anode and a copper cathode. The initial current of 0.25 amp decreased to 0.05 amp in 4 hr. During the electrolysis the anolyte turned reddish brown and the azo compound precipitated. The mother liquor was concentrated and poured into water. The resulting product was extracted with hot benzene (200 ml) and chromatographed on alumina. The first fraction consisted of azo compound and was combined with the precipitated fraction. Recrystallization from methanol gave 2,4,2'4'-tetrachloroazobenzene; mp 161°-162°; yield, 30.0%. The infrared spectrum was consistent with this structure.

p-Anisidine.—Oxidation was carried out in a similar fashion to that used for *p*-chloroaniline using 0.5*M* lithium perchlorate. The residue in benzene was chromatographed on alumina and gave 4,4-dimethoxyazobenzene (5.2% yield) which melted at 162°-163° after recrystallization from a benzene-(30°-60°) petroleum ether mixture. The infrared spectrum was identical with that of an authentic sample.

The second fraction gave an 8.6% yield of dark red crystals melting at 236°-237°. These crystals gave a red-violet color with concentrated sulfuric acid and had an NH band in the 3200-3500 cm^{-1} region of the infrared. These properties are in agreement with di-*p*-anisidinobenzoquinone-di-*p*-methoxyphenylimine (I) (tetra-*p*-methoxyazophenine) (18). The remaining oxidation products were resinous in nature.

Aniline and p-chloroaniline.—A solution of *p*-chloroaniline (0.5g) and aniline (3.0g) in 60 ml of acetonitrile and 10 ml of pyridine containing 0.5*M* sodium perchlorate was electrolyzed in a beaker containing a porous cup cathode compartment. The anode was a platinum screen and the cathode was a copper wire. The solution was purged with nitrogen and a potential of 8.0v was applied to the cell. The original current of 0.1 amp decreased to 0.05 amp after 4 hr. In this period the anolyte changed from an orange to a reddish-

brown color, and the anode became coated with a brown-black tar.

The anolyte was concentrated to 30 ml and poured into ether (30 ml). The ether solution was filtered, concentrated to 50 ml and chromatographed on alumina (grade I). The first fraction consisted of azo compounds which were rechromatographed. The second fraction gave a dark red solid (0.21g) which, on recrystallization from benzene, melted at 234°-236° and gave a violet color in concentrated sulfuric acid. This compound was halogen free and agreed in all respects with di-(phenylamino) benzoquinone-diphenylimine (azophenine) (19). The mixed azo compounds when rechromatographed twice on alumina using a 1:1 mixture of benzene-(30°-60°)petroleum ether gave azobenzene (0.243g) which melted at 68°-69° and *p*-chloroazobenzene (0.86g) melting at 88°-89° [ref. (20), 87.5°]. The infrared spectrum was similar to that for azobenzene and 4,4'-dichloroazobenzene.

p-Chloroaniline and 2,4-dinitroaniline.—A solution of p-chloroaniline (0.5g), 2,4-dinitroaniline (1.0g) in acetonitrile (80 ml) and pyridine (5 ml) containing 0.5*M* sodium perchlorate was electrolyzed under nitrogen in the H-cell at a controlled potential of +0.80v *vs.* the Ag/0.1*N* $AgClO_4$ electrode, using a rotating platinum anode and a mercury pool cathode. The initial current of 0.15 amp decreased to 0.05 amp in 8 hr. The anolyte was concentrated to 20 ml, poured into water (50 ml), and extracted with ether (500 ml). The ether extract was washed with 100 ml of 5% hydrochloric acid and 100 ml of water. The acid extract gave the hydrochloride of *p*-chloroaniline (0.11g). Removal of the ether gave a solid which was dissolved in a minimal amount of 1:1 benzene-chloroform mixture and chromatographed on alumina. The first fraction gave 4,4'-dichloroazobenzene (0.102g) melting at 184°-186°, and the second fraction gave 2,4-dinitroaniline (0.921g) melting at 178°-179° after crystallization from ethanol (92.1% recovery). No cross product was isolated.

p-Chloroaniline and p-nitroaniline.—This mixture was treated in a similar fashion to that described in the preceding paragraph using a controlled potential of +0.7v, 4,4-Dichloroazobenzene (22.8%) and *p*-nitroaniline (90%) were obtained together with resinous material.

Hydrazobenzene.—This compound (2.0g) was oxidized in a beaker (100 ml) containing a porous cup cathode compartment. The cell was wrapped with aluminum foil to keep out light, and the solution was deaerated during the electrolysis with nitrogen. The resulting solution when processed in the usual manner gave azobenzene (0.216g), dark brown polymeric material and a black crystalline residue similar to aniline black.

4,4-Dichlorohydrazobenzene.—The electrolysis was performed in a similar manner to that for hydrazobenzene. The anode solution gave an 82% yield of 4,4'-dichloroazobenzene.

4,4-Dimethoxyazobenzene.—The electrolysis and processing of the oxidation product was similar to the above procedure. The anolyte gave starting material (55%) and brown resinous material.

Results

The voltammetric behavior of various anilines in acetonitrile containing 0.5*M* sodium perchlorate in the presence and absence of pyridine is given in Table I. Half-wave potentials corrected for the *iR* drop are reported against an external silver 0.1*M* silver perchlorate reference electrode.

Most of the compounds exhibited normal S-shaped waves in the absence of pyridine. In the presence of this compound the curves reached a current plateau which decreased near the end of the voltage scan. This behavior is associated with film formation on the electrode surface for, if the current-voltage curve is retraced without cleaning the microelectrode, the limiting current is substantially reduced. Waves were also encountered as peaks and are probably caused by an immediate coating of the electrode. The decrease in current was not caused by the oxidation of pyridine since this compound when pure does not give an oxidation wave in acetonitrile. In order to evaluate the number of electrons involved in the oxidation, hydroquinone and bromide ion were studied under similar conditions, and the data are given in Table I.

To aid in formulating an electrode mechanism a series of hydrazobenzenes and azobenzenes was studied under similar conditions, and the data are given in Table II.

Table I. Voltammetric behavior of substituted anilines in acetonitrile containing 0.5M sodium perchlorate.[a] (vs. Ag/0.1N Ag^+)

Compound	Conc, millimolar	$+E_{1/2}$	I_l[d]	2mM $+E_{1/2}$	Pyridine I_l[d]
Aniline	0.43	0.54	10.1[b]	0.54	13.2[c]
o-Nitroaniline	0.23	1.07	15.0[b]	1.03	15.0[b]
p-Nitroaniline	0.40	1.03	14.2	0.95	16.9[b]
	1.00	0.97	7.0		
		1.14	7.0		
m-Nitroaniline	0.32	0.90	8.6	0.88	17.2[b]
p-Bromoaniline	0.33	0.61	8.3	0.62	17.5[b]
m-Bromoaniline	0.40	0.70	8.5[b]	0.64	8.5[c]
p-Chloroaniline	0.40	0.60	8.3	0.61	17.1[b]
o-Anisidine	0.62	0.34	8.7[b]	0.36	20.0[b]
p-Anisidine	0.23	0.26	6.5	0.24	7.1
				0.42	6.7
				1.03	7.6[b]
2,4-Dinitroaniline	0.35	1.48	18.8	1.41	18.7[b]
2,4-Dichloroaniline	0.50	0.78	8.6	0.74	16.7[b]
sym-Trichloroaniline	0.55	0.95	10.3	0.87	18.9
o-Phenylenediamine	0.82	0.08	7.2	0.09	25.8[c]
		0.76	7.8		
m-Phenylenediamine	0.40	0.26	7.0[c]	0.24	7.0
				0.41	5.1[c]
p-Phenylenediamine	0.44	−0.10	7.1	−0.10	7.1
		0.44	6.3	0.15	6.5
2,2'-Diaminobiphenyl	0.27	0.51	8.4	0.48	5.2[c]
		0.87	4.0[c]		
Ethylphenylamine	0.30	0.40	8.8	0.43	16.4[b]
N,N-diethylaniline	0.40	0.34	9.6	0.36	18.5
N,N-diethyl-p-chloroaniline	0.33	0.47	8.9	0.47	9.5
N,N-dimethylaniline	0.30	0.35	10.8	0.36	20.5
N,N-dimethyl-p-chloroaniline	0.64	0.49	10.4	0.48	13.4
				1.08	2.3
Hydroquinone	1.00	0.68	16.7	0.42	16.6
Tetra-n-butyl-ammonium Bromide	0.96	0.42	5.4		
		0.74	2.8		

[a] Normal S-shaped wave.
[b] Plateau followed by a decrease in current.
[c] Peak
[d] $I_l = i_l/C$.

Table II. Voltammetric behavior of azobenzenes and hydrazobenzenes in acetonitrile containing 0.5M sodium perchlorate[a] (vs. Ag/0.1N Ag^+)

Compound	Conc, millimolar	$+E_{1/2}$	I_l[d]	2 mM $+E_{1/2}$	Pyridine I_l[d]
Azobenzene	0.48	1.33	18.4	Coating[c]	
Hydrazobenzene	0.44	0.18	10.1	0.05	18.5
		1.35	7.7		
4,4'-Dichloro-azobenzene	0.21	1.44	17.4	Coating[c]	
4,4'-Dichloro-hydrazobenzene	0.46	0.26	11.0	0.16	19.2
		1.44	10.4		
4,4'-Dimethoxy-azobenzene	0.74	0.98	18.0	0.98	18.0
				1.25	25.8[b]
4,4'-Dinitro-azobenzene	0.29	No wave		No wave	
2,2',4,4'-Tetra-nitroazobenzene	0.34	No wave		No wave	
2,2'4,4'-Tetra-chloroazobenzene	0.21	1.59	17.8	Coating[c]	
sym-Hexachloro-azobenzene	0.29	1.63	17.8	Coating[c]	

[a] Normal S-shaped wave.
[b] Plateau followed by a decrease in current.
[c] Small bump in the c-v curve.
[d] $I_l = i_l/c$.

Table III. Large-scale electrolytic oxidations of primary aromatic amines[a] and hydrazobenzenes[a]

Compound	Supporting electrolyte, 0.5M	Products (per cent yield)
p-Nitroaniline	$NaClO_4$	4,4'-Dinitroazobenzene (39.2%)
p-Chloroaniline	$NaClO_4$	4,4'-Dichloroazobenzene (24.3%); tetra-p-chloroazophenine (7.8%)
p-Chloroaniline[b]	$LiClO_4$	Tar
2,4-Dichloroaniline	$NaClO_4$	2,2',4,4'-Tetrachloroazobenzene (30.1%)
p-Anisidine	$LiClO_4$	4,4'-Dimethoxyazobenzene (5.2%) tetra-p-methoxyazophenine (8.6%)
Aniline and p-Chloroaniline	$NaClO_4$	Azophenine (7.0%); azobenzene (8%); p-chloroazobenzene (83%)
Hydrazobenzene	$NaClO_4$	Azobenzene (10.8%)
4,4'-Dichlorohydrazobenzene	$NaClO_4$	4,4'-Dichloroazobenzene (82%)

[a] The electrolysis were run in a nitrogen atmosphere, and pyridine (0.1M) was added unless otherwise indicated.
[b] No pyridine was added.

In further studies of the mechanism of oxidation macroscale oxidations of several anilines were carried out in acetonitrile, and the results are reported in Table III.

Discussion of Results

Comparison of the limiting currents for the oxidation of the anilines in the presence of pyridine with that for hydroquinone and bromide ion indicates that the majority of the examples involve a two-electron change. The lower values observed for aniline, o-nitroaniline, m-bromoaniline, m-phenylenediamine, and 2,2'-diaminobiphenyl were caused by coating of the electrode.

The electrode reaction suggested by the two-electron change using aniline as an example is the following

(a) $C_6H_5NH_2 - e \rightarrow C_6H_5NH_2^{+\cdot}$

$C_6H_5NH_2^{+\cdot} + \text{pyridine} \rightarrow C_6H_5NH\cdot + C_5H_5NH^+$

(b) $2C_6H_5NH\cdot \rightarrow C_6H_5NHNHC_6H_5$

$2C_6H_5NHNHC_6H_5 - 2e + 2\text{ pyridines} \rightarrow C_6H_5N = NC_6H_5 + 2C_5H_5NH^+$

(c) $C_6H_5NH\cdot \leftrightarrow HN=$ 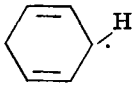

$C_6H_5NH\cdot +$ 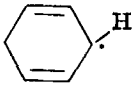

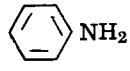

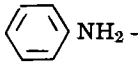

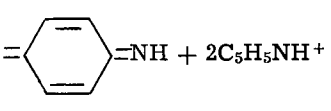

The extent to which reactions (b) and (c) occur will depend on the substituents present.

In agreement with this mechanism is the oxidation of hydrazobenzenes (Table II) and p-phenylenediamine (Table I) in the presence of pyridine at more negative potentials than those for the anilines, and the formation of azobenzenes and azophenines (I) in the macroscale oxidations (Table III)

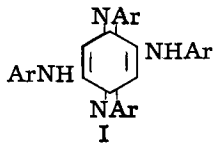

I

Further evidence is the appearance of a third wave in the oxidation of p-anisidine at approximately the same point as that for 4,4'-dimethoxyazobenzene. A similar wave was not observed for other azobenzenes because of coating of the electrode.

Diethylaniline and dimethylaniline in the presence of pyridine would involve coupling in the p-position in a manner to that suggested by Adams (6)

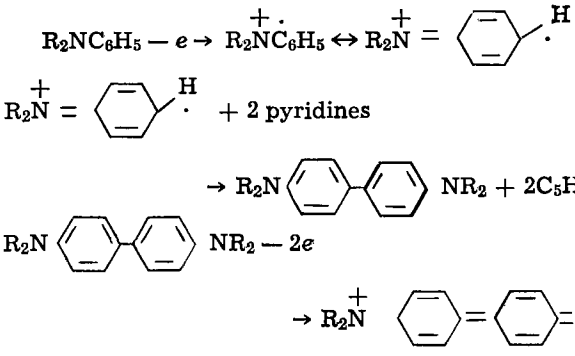

The oxidation of N-ethylaniline and N-p-nitrobenzylaniline could proceed in the same fashion or could give rise to a hydrazine which would be oxidized further. Large-scale oxidation of p-nitrobenzylaniline formed the hydrazine together with polymers (21).

p-Phenylenediamine and o-phenylenediamine which behave reversibly in aqueous medium are oxidized stepwise to the quinoneimine (3). In the presence of pyridine o-phenylenediamine behaves differently and shows an abnormally high wave. A similar behavior has been observed in aqueous acetate buffer solution (22) and has been ascribed to the formation of a diaminophenazine which is oxidized further. Another possible explanation is further oxidation of the resulting o-quinonediimine to muconitrile since

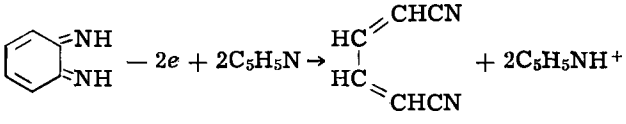

such a reaction is reported to take place in the oxidation of o-phenylenediamine by lead tetraacetate (23).

The oxidation of the anilines in the absence of pyridine is more complex. The aniline itself acts as a base and converts the cation radical into the free radical and a salt which would not be easily oxidized

$$ArNH_2 - e \rightarrow ArNH_2^{+\cdot}$$

$$ArNH_2^{+\cdot} + ArNH_2 \rightarrow ArNH\cdot + ArNH_3^+$$

Exceptions are the nitroanilines and are discussed later. The free radical thus formed would couple and form the corresponding hydrazobenzenes and N-arylphenylenediamines as mentioned earlier. The latter compound would lead to an N-arylquinonediimine which is considered to be the precursor of the varied products obtained in the oxidation of anilines (24). This formation of N-arylphenylenediamines may be favored in the absence of pyridine since tars were mainly formed on a large scale under these conditions.

Hydrazobenzenes (Table II) formed under these circumstances would be oxidized further to azobenzenes. This process occurs in the absence of pyridine by a two step process.

$$C_6H_5NHNHC_6H_5 - e \rightarrow C_6H_5\overset{+}{N}HNHC_6H_5$$

$$C_6H_5\overset{+}{N}HNHC_6H_5 - e \rightarrow C_6H_5N = NC_6H_5 + 2H^+$$

These reactions would be modified to a certain extent by the aniline and would give oxidation waves with unequal heights. The second wave which occurs at the same point as azobenzene is not caused by this compound since the addition of pyridine to the same solution gave one oxidation wave. Azobenzenes under similar circumstances caused coating of the electrode and gave no oxidation waves except for 4,4'-dimethoxyazobenzene. The oxidation products formed from azo compounds are unknown since large-scale oxidations in acetonitrile gave tars.

o-Nitroaniline, *p*-nitroaniline, and 2,4-dinitroaniline gave a two electron wave in the absence of pyridine. This behavior suggests that the cation radical, because of the decreased basicity of these compounds, loses a proton easily and forms the radical which dimerizes to the hydrazo compound.

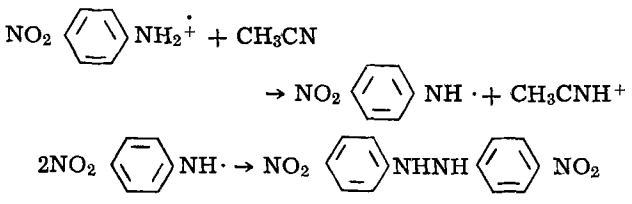

The latter would be oxidized further to the azo compound. A two-step process was actually observed with *p*-nitroaniline at higher concentrations.

Analyses of the current-voltage curves for *p*-bromoaniline and *p*-anisidine in the absence of pyridine gave values of 0.0645 and 0.049, respectively, for the slope which are in fair agreement with the initial one electron step postulated. The addition of pyridine causes the reaction to become more irreversible since *p*-bromoaniline gave a value of 0.0734. *p*-Anisidine is an exception under similar conditions since it gives a stepwise oxidation and a slope of 0.057 for the first wave. This value is in good agreement with the one-electron step involved.

Large-scale oxidations of the anilines at a platinum electrode in acetonitrile (Table III) were in agreement with the electrode mechanisms mentioned; azobenzenes, azophenines, and tars were obtained since the potential was not controlled. The potentials applied, however, gave similar initial currents to those obtained under controlled potential conditions.

Hydrazobenzenes on large-scale oxidation gave azobenzenes as expected. In the oxidation of hydrazobenzene itself, the product was accompanied by tar and aniline black since the potential was not controlled.

No products involving pyridine were isolated in the oxidation of the anilines, and this result eliminates the possible formation of a cation as the initial product

$$ArNH_2 - 2e \rightarrow ArNH^+ + H^+$$

Such an intermediate would be expected to react with pyridine, since pyridine is in excess, and form a hydrazonium salt. Further evidence against this cation is the crossed coupling of two anilines. A mixed azobenzene was obtained only with aniline and *p*-chloroaniline which are oxidized at approximately the same point. Mixtures of *p*-chloroaniline with *p*-nitroaniline and with 2,4-dinitroaniline when oxidized at controlled potential gave only 4,4'-dichloroazobenzene.

Acknowledgment

The authors wish to acknowledge the support of the U. S. Army Research Office under Contract DA-31-124-ARO-D-406, and Grant No. DA-ARO(D)-31-124-G351.

Manuscript received Feb. 20, 1967; revised manuscript received *ca.* June 12, 1967. This work was abstracted in part from the Ph.D. Thesis of T. W. McIntyre. February 1967.

Any discussion of this paper will appear in a Discussion Section to be published in the June 1968 JOURNAL.

REFERENCES

1. H. Lund, *Acta Chem. Scand.*, **11**, 1323 (1957).
2. E. S. Pysh and N. C. Yang, *J. Am. Chem. Soc.*, **85**, 2124 (1963).
3. M. T. Melchior and A. H. Maki, *J. Chem. Phys.*, **34**, 471 (1961).
4. A. Zweig, J. E. Lancaster, M. T. Negalia, and W. H. Jura, *J. Am. Chem. Soc.*, **86**, 4130 (1964).
5. G. Cauquis, J. Badoz-Lambling, and J. Billon, *Bull. Soc. chim. France*, **1965**, 1433.
6. E. T. Seo, R. F. Nelson, J. M. Fritsch, L. S. Marcoux, D. W. Leedy, and R. N. Adams, *J. Am. Chem. Soc.*, **88**, 3498 (1966).
7. F. Goppelsroeder, *Compt. rend.*, **81**, 408 (1875); **82**, 228, 1392 (1876).
8. L. Gilchrist, *J. Phys. Chem.*, **8**, 531 (1904).
9. J. W. Shipley and M. T. Rogers, *Can. J. Res.*, **B17**, 147 (1939).
10. T. Yasui, *Bull. Chem. Soc., Japan*, **10**, 306 (1935).
11. F. Goppelsroeder, *Compt. rend.*, **82**, 1199 (1876).
12. S. Goldschmidt and F. Nagel, *Ber.*, **64**, 114 (1931).
13. F. Fichter and E. Rothenberger, *Helv. Chim. Acta*, **5**, 168 (1922).
14. I. M. Kolthoff and J. F. Coetzee, *J. Am. Chem. Soc.*, **79**, 1852 (1957).
15. J. J. Lingane, "Electroanalytical Chemistry," p. 202, Interscience Publishers, Inc., New York (1953).
16. J. F. Coetzee, G. P. Cunningham, and D. K. McGuire, *Anal. Chem.*, **34**, 1139 (1962).
17. D. G. H. Daniels and B. C. Saunders, *J. Chem. Soc.*, **1953**, 822.
18. *Ibid.*, **1951**, 2112.
19. O. N. Witt and E. G. P. Thomas, *J. Chem. Soc.*, **43**, 112 (1883).
20. E. Bamberger, *Ber.*, **29**, 103 (1896).
21. S. Wawzonek, T. H. Plaisance, and T. W. McIntyre, *This Journal*, **114**, 588 (1967).
22. P. J. Elving and A. F. Krivis, *Anal. Chem.*, **30**, 1648 (1958).
23. K. Nakagawa and H. Onoue, *Chem. Commun.*, **1965**, 396.
24. S. Goldschmidt and B. Wurzschnitt, *Ber.*, **55**, 3216 (1922).

High-Temperature Oxidation

IV. Zirconium and Hafnium Carbides

Joan B. Berkowitz-Mattuck

Arthur D. Little, Inc., Cambridge, Massachusetts

ABSTRACT

The oxidation of ZrC was studied at temperatures of 1130°-2160°K and oxygen partial pressures around 3.9 and 20 Torr. The rate of oxidation was monitored with a thermal conductivity cell. Independent measurements were made of net weight gain and quantities of CO(g) and CO_2(g) evolved. Oxidation was shown to be nonpreferential, *i.e.*, zirconium was oxidized at the same rate as carbon. Gas phase diffusion control imposed by the experimental system was frequently encountered. Where it was possible to observe a true chemically controlled reaction rate, the kinetics appeared to be linear. Microscopic examination of the oxidized specimens revealed preferential oxidation along grain boundaries. Between 1130° and 1560°K this preferential oxidation resulted in intercrystalline fracture. At higher temperatures stresses were apparently sufficiently relieved so that the samples remained intact. The oxidation of HfC between 1790° and 2000°K, at oxygen pressures near 10 Torr, was also found to be linear and preferential along grain boundaries.

The oxidation of zirconium carbide was studied by Margrave and Kuriakose (1) at temperatures of 550°-650°C in oxygen at 1 atm. The oxidation was found to be linear, with an activation energy of 16.7 ± 1.7 kcal/mole.

Bartlett, Wadsworth, and Cutler (2) studied the weight gain of sized powders of zirconium carbide in air, oxygen, and oxygen-helium mixtures at temperatures of 450°-580°C, and oxygen pressures of 6.5 x 10^{-5} to 1 atm. Stoichiometric oxidation of ZrC to ZrO_2 and gaseous oxides of carbon was assumed. The data were interpreted on the basis of two parallel independent processes: a parabolic diffusion reaction involving the partial replacement of interstitial carbon in the ZrC lattice with oxygen, and a linear surface reaction occurring at the ZrC-ZrO_2 phase boundary. Both processes occur simultaneously, with the diffusion reaction predominating at short times and the surface reaction becoming rate controlling as oxidation proceeds. The activation energies were calculated as 53 kcal/mole for the diffusion process and 46 kcal/mole for the surface reaction. Water vapor, in the presence of oxygen, was found to accelerate the rate of the surface reaction while leaving its activation energy unchanged. The solid oxidation product was found to be cubic ZrO_2, a phase normally thought to be unstable, but which might be stabilized by small amounts of carbon.

Watt, Cockett, and Hall (3) made a single weight change measurement of 49.8 mg/cm² on a solid sample of ZrC of density 6.20 g/cc and 4.8% porosity, exposed to a stream of dry air flowing at 5.3 cm/sec, for 30 min at 800°C.

The present study was undertaken to investigate the oxidation of ZrC and the chemically related HfC at temperatures above 900°C.

Experimental Method

Cylindrical pellets of ZrC were cut from zone refined bars prepared as described by Westrum and Feick (4). The fabricated bars contained 11.2 w/o carbon. Hafnium carbide powder was prepared by the Carborundum Company from high-purity HfO_2 supplied by Wah Chang Corporation. The HfC powder was sintered into bars and arc-melted on a water-cooled copper hearth using a water-cooled tungsten electrode. In order to minimize loss of carbon during melting, the operation was conducted in an atmosphere of argon containing 3.14% of ethylene and 11.4% of hydrogen. The resulting material was carbon deficient, corresponding to a composition $HfC_{0.952}$ (5).

The anticipated products of the oxidation of ZrC and HfC were the permanent gases, CO(g) and CO_2(g), in addition to the refractory metal oxides. Due to the evolution of permanent gases, the thermal conductivity method described in previous publications (6-8) had to be modified to study the oxidation. A known mixture of helium and oxygen was passed through the reference side of a thermal conductivity cell (6) and over an inductively heated carbide pellet supported on ThO_2 fingers by three point contact. A portion of the oxygen in the gas stream reacted with the pellet to produce oxides of the metal and carbon. The effluent gas was therefore depleted in oxygen, but enriched in CO(g) and CO_2(g). The latter was removed by passage through a weighed Ascarite bulb, and the remaining mixture of CO(g), O_2(g), and He entered the sampling side of the thermal conductivity cell (6). Finally, the CO(g) was oxidized to CO_2(g) over copper oxide powder at 500°C, and the CO_2(g) produced was collected in a second weighed Ascarite bulb. The signal from the thermal conductivity cell in this case was therefore not directly related to the rate of oxygen consumption as in previously studied systems (6-8), but instead reflected the difference between the rate of total oxygen consumption and the rate of formation of CO(g). The calibration constant, relating the electrical signal to the difference in gas pressure on the two sides of the cell is the same for both CO and O_2 in He. Hence, evolution of CO depresses the signal, as compared to simple removal of oxygen.

Results

Zirconium carbide.—Oxidation kinetics.—The experimental data are summarized in Table I. The signal from the thermal conductivity apparatus was constant with time in every experiment. However, only in the case of experiment XII-1 did this reflect true chemically controlled linear oxidation kinetics. In the other experiments more than 90% of the oxygen passed over the carbide pellet reacted with it, and the controlling process was therefore probably the rate of arrival of oxygen gas at the sample surface. At higher pressures and/or higher gas flow rates, a greater proportion of the carbide would have been converted to oxides.

In Table I, the "initial" weights were taken after degassing at 2200°K in pure helium until the signal from the thermal conductivity cell indicated that no permanent gases were being evolved. The surface areas were calculated from micrometer measurements of the height and diameter of the cylindrical pellets. Temperatures were measured optically and corrected for an emissivity of 0.7, determined by comparing

Table I. Summary of experimental data on ZrC

Expt.	Initial weight, g	Geometric surf. area, cm^2	Temp, °K	Oxygen pressure, Torr	Exposure time, min	Net weight change W_o, (g)	CO formed W_{CO} (g)	CO_2 formed W_{CO_2} (g)	C consumed W_c (g)	Zr consumed W_{Zr} (g)	Zr/C
XII-8	0.446	1.103	1130	22.9	51	—	0.0001	0.0611	—	—	—
XII-5	0.5645	1.394	1260	20.4	128	—	—	0.0709	—	—	—
XII-3	0.6963	1.493	1560	21.2	62	—	0.0289	0.0399	—	—	—
X-31	0.5864	1.310	1860	9.1	129	0.0402	0.0438	0.0220	0.0248	0.1852	7.47
X-29	0.7073	1.450	1940	8.1	120	0.0366	0.0405	0.0145	0.0214	0.1652	7.72
XII-1	0.7051	1.500	1970	25.9	112	0.0851	0.0968	0.0356	0.0510	0.388	7.60
X-27	0.6361	1.252	2070	8.5	124	0.0389	0.0464	0.0175	0.0236	0.1780	7.55
X-16	0.6840	1.388	2070	8.5	119	0.0402	0.0540	0.0073	0.0252	0.1862	7.39
VII-8	0.6643	1.528	2100	3.0	180	0.0207	0.0242	0.0079	0.0126	0.0949	7.54
X-25	0.6812	1.371	2165	8.9	120	0.0356	0.0523	0.0072	0.0244	0.1710	7.01

surface temperatures with ultrasonically drilled black body cavity temperatures under oxidizing conditions. Oxygen partial pressures in helium are given; the total pressure was close to 1 atm in every experiment. The carrier gas flow rate was 58.6 cc/min in every experiment, corresponding to a linear flow velocity in the neighborhood of the sample of 1.9 cm/sec, except VII-8 where a flow of 51.5 cc/min was used.

From the measured net weight change of the carbide on oxidation, and the observed weight changes W_{CO_2} and W_{CO} in the Ascarite bulbs, the total amounts of carbon and zirconium consumed were readily calculated, on the assumption that the only oxidation products were $CO_2(g)$, $CO(g)$, and $ZrO_2(s)$. The formation of ZrOC(s) cannot be precluded, but since it is isostructural with ZrC, no positive evidence was obtained for its presence. The total weight of carbon consumed, W_c, is given by

$$W_c = \frac{[C]}{[CO_2]} \cdot W_{CO_2} + \frac{[C]}{[CO]} \cdot W_{CO} \qquad [1]$$

where the symbols in brackets represent molecular weights. The total weight of zirconium, W_{Zr}, that has been converted to oxide is calculated from the measured weight change, W_o, and the derived carbon consumption

$$W_{Zr} = \frac{[Zr]}{2[O]} (W_o + W_c) \qquad [2]$$

The ratio of the number of grams of zirconium consumed to the number of grams of carbon consumed during oxidation is shown in Table I to have an approximately constant value of 7.5 ± 0.2. Since the corresponding ratio in the ZrC starting material is 7.6, it would appear that the oxidation of ZrC is stoichiometric. That is, for each zirconium atom converted to oxide, a single carbon atom is also converted to oxide.

Structural changes during oxidation.—The reason that weight change data were not given for pellets XII-8, XII-5, and XII-3 is that at these relatively low temperatures the pellets were broken apart by the oxidation process. At the end of each experiment, the grain boundaries of the ZrC were seen to be outlined by a white material, identified by room temperature x-ray as monoclinic ZrO_2. The growth of the oxide in pre-existing cracks and grain boundaries of ZrC undoubtedly creates enough stress to fracture the carbide. At higher temperatures, as discussed below, significant grain boundary oxidation was observed, but stresses are apparently sufficiently relieved so that fracture does not occur.

Pellet XII-1 for which true kinetic data had been obtained was mounted and polished for metallographic examination.

Figure 1a shows the specimen at a magnification of ca. 4X. The gray outer rim is the oxide, and the inner white circular area is the surface of carbide. To the naked eye, the outer oxide coating looked white and chalky, and the inner surface from which the oxide coating was polished off, looked bright and metallic. A mottled rim is clearly visible along the oxide-alloy interface in the figure and the remaining photomicrographs focus on portions of this interface. In Fig. 1b, at a magnification of *ca.* 30X, the oxide fills the entire upper half of the photograph, and the alloy the lower. The oxide is obviously growing preferentially along grain boundaries in the carbide, and enveloping individual alloy crystallites. The structure of the bulk oxide is very different from that on ZrB_2 (8), although after cooling both showed only the x-ray lines for monoclinic ZrO_2. On ZrB_2 the oxide was seen to grow in a columnar structure; on ZrC, the ZrO_2 assumed an equiaxed grain structure very similar to that of the original alloy. Figures 1c and 1d show the oxide alloy interface at a still higher magnification, *ca.* 195X, and one sees even more clearly the preferential oxidation of grain boundaries, and the lateral fingerlike growth of oxide from the boundaries into the crystallite bulk. The reaction zone of intergranular attack was approximately 0.014 ± 0.002 cm in thickness. The outer oxide was about ten times thicker. The mechanism of oxide growth on ZrC at high temperatures appears to be rapid attack at grain boundaries, and slow oxidation of the alloy from the grain boundary surface inward. Figure 1e, at a magnification of *ca.* 345X, shows portions of the alloy completely enveloped by oxide. Finally, Fig. 1f is a view of the alloy surface at a magnification of *ca.* 345X. This surface had been covered with a dense oxide prior to polishing, and one sees here the penetration of the oxide into grain boundaries of the alloy. Between 1126° and 1559°K the grain boundary attack results in intergranular fracture of the alloy. Above 1580°K there is apparently enough plasticity in either alloy, oxide, or both, so that the sample remains intact during oxidation.

Hafnium carbide.—Oxidation kinetics.—The experimental data for HfC are summarized in Table II. Since the arc-melted samples were highly irregular in shape,

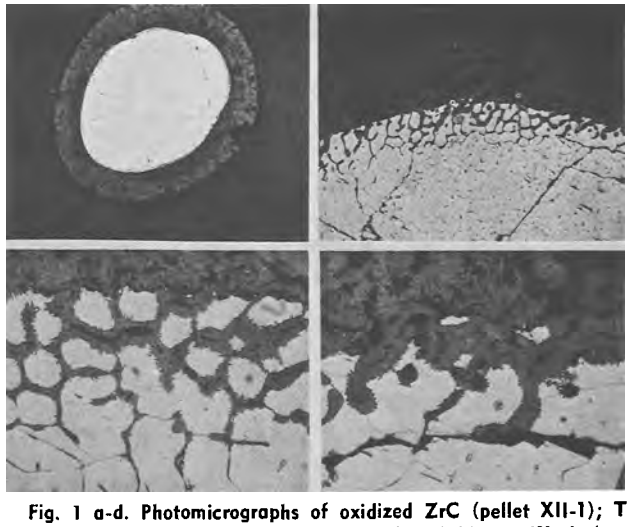

Fig. 1 a-d. Photomicrographs of oxidized ZrC (pellet XII-1); T 1960°K; P_{O_2} 25.9 Torr. Magnification: a (top left) ca. 4X; b (top right) ca. 30X; c (bottom left) ca. 195X; d (bottom right) ca. 195X.

Fig. 1 e-f. Photomicrographs of oxidized ZrC (pellet XII-1); T 196°K; P_{O_2} 25.9 Torr. Magnification: e (left) and f (right) ca. 345X.

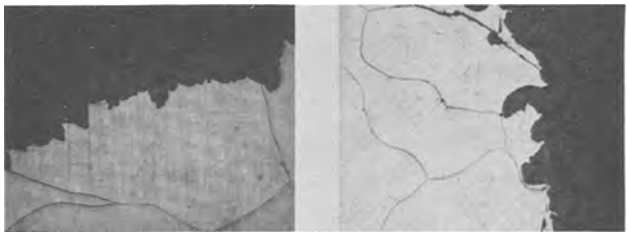

Fig. 2. Photomicrographs of oxidized hafnium carbide pellet XVI-19; temperature 1600°-2000°K; P_{O_2} 11.5 Torr. Magnification ca. 130X.

the geometrically calculated surface areas are only approximate. The surface oxide tended to flake and spall on removal of the sample from the apparatus; and, hence, the measured weight gains are minimum values. From the measured minimum net weight gains, and the weights of CO(g) and CO_2(g) in the product gas stream, the minimum ratio of hafnium to carbon oxidized can be calculated, as described above for the oxidation of ZrC. The experimental values of the ratio are given in Table II as 14.1, 10.1, and 15.9, to be compared to an Hf:C ratio in the original alloy of 15.6. Linear oxidation was observed in every case. Flow rates of 119 cc/min, approximately double those used for the ZrC experiments, were employed in order to maintain an adequate supply of oxygen.

At 1280°K in pure oxygen at 1 atm, a hafnium carbide specimen disintegrated into several pieces within 3 min in a manner very similar to that described above for zirconium carbide.

Metallographic examination of oxide films.—Pellet XVI-19 was imbedded in plastic and polished for microscopic observation. In the photomicrographs shown in Fig. 2, the oxide is seen to contain considerable porosity. As in the case of zirconium carbide, oxidation appears to be preferential along grain boundaries.

The photomicrograph in Fig. 3 is for a hafnium carbide pellet that had been exposed to a N_2-He mixture for an hour and a quarter at a temperature of 1960°K. The N_2 apparently contained a small quantity of oxygen, and white HfO_2(c) was identified on the surface of the sample by x-ray diffraction. The net weight change of the sample was 0.0024 g/cm², an order of magnitude less than that observed at an oxygen partial pressure of 11.5 Torr at about the same temperature. The oxidation rate was seen to decrease slightly with time, and, although grain boundary oxidation is

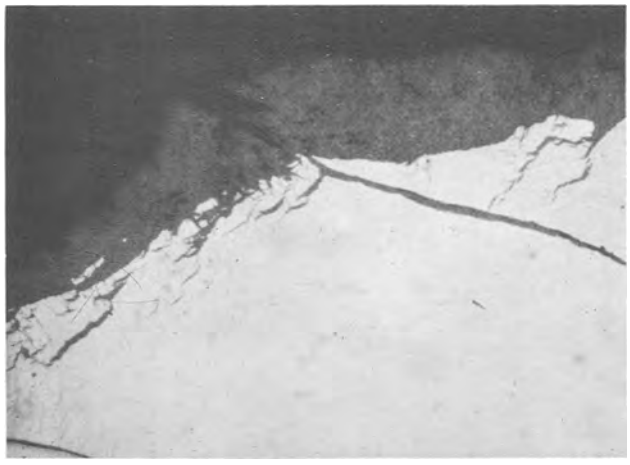

Fig. 3. Photomicrograph of oxidized hafnium carbide pellet XVI-22; temperature 1960°K, low oxygen pressure. Magnification ca. 230X.

apparent in Fig. 3, the oxide seems less porous than that shown in Fig. 2, for oxidation at a higher pressure.

Discussion

A recent report (9) suggests that grain boundary oxidation is characteristic of iron contaminated ZrC. For material with an impurity level about 1 v/o Fe_3C or about 1.1 w/o, the Fe_3C is found to be segregated at the grain boundaries, and to be oxidized at a much more rapid rate than the ZrC matrix.

A chemical analysis of the zone melted material used in the present study showed an iron contamination level of 0.07% by weight. In order to try to assess the possible influence of iron on the present results, the oxidized and polished ZrC sample shown in Fig. 1 was examined for iron with the electron probe.[1]

An $FeK_{\alpha 1}$ scanning image was taken of the sample, and iron was found to be concentrated in the small circular inclusions visible in Fig. 1, and inhomogeneously in the cracks. Point count analyses take in the inclusions, the cracks, the grain boundaries, and the matrix showed the presence of iron particles of less than 1μ in size distributed at random in the inclusions and cracks, but failed to reveal the presence of any iron at all in either the grain boundaries or the matrix. The preferential grain boundary oxidation observed in zirconium carbide, therefore, seems to be characteristic of the pure material.

Acknowledgment

It is a pleasure to thank John Engelke of Arthur D. Little, Inc., for his assistance in obtaining and interpreting the electron probe data, and to acknowledge the invaluable assistance of Richard F. Quigley and Walter Christensen with the experimental work.

Manuscript received Jan. 23, 1967; revised manuscript received May 31, 1967.

Any discussion of this paper will appear in a Discussion Section to be published in the June 1968 JOURNAL.

[1] The electron probe analysis was kindly supplied by Acton Laboratories, 531 Main Street, Acton, Massachusetts.

Table II. Summary of experimental data on HfC

Expt.	Initial weight, g	Area, cm²	Temp, °K	Pressure, Torr	Time, min	Minimum net weight change, g	CO formed, g	CO_2 formed, g	C consumed, g	Minimum Hf consumed, g	Hf/C min
XVII-4	0.5374	1.076	1790	11.5	85	0.021	0.0160	0.0254	0.0138	0.195	14.1
XVI-38	0.6544	1.241	1890	11.5	69	0.016	0.0232	0.0355	0.0196	0.199	10.1
XVI-36	0.7511	1.032	2005	11.5	43	0.022	—	0.0191			
XVI-19	0.6057	1.256	2000-1600 (continuous drop)	7.5	120	0.038	0.0340	0.0225	0.0207	0.328	15.9

REFERENCES
1. A. K. Kuriakose and J. L. Margrave, *This Journal*, **111**, 827 (1964).
2. R. W. Bartlett, M. E. Wadsworth, and I. B. Cutler, *Trans. AIME*, **227**, 467 (1963).
3. W. Watt, G. H. Cockett, and A. R. Hall, *Metaux*, **28**, 222 (1963).
4. E. F. Westrum, Jr., and G. Feick, *J. Chem. Eng. Data*, **8**, 176 (1963).
5. L. A. McClaine, Thermodynamic and Kinetic Studies for a Refractory Materials Program, 4th Semi-annual Progress Report (August, 1963), Contract No. AF 33(616)-7472.
6. J. B. Berkowitz-Mattuck, *This Journal*, **111**, 908 (1964).
7. J. B. Berkowitz-Mattuck and R. R. Dils, *ibid.*, **112**, 583 (1965).
8. J. B. Berkowitz-Mattuck, *ibid.*, **113**, 908 (1966).
9. K. R. Janowski, R. D. Carnahan, and R. C. Rossi, "Static and Dynamic Oxidation of ZrC," TDR-669(6250-10)-3, Aerospace Co., El Segundo, Calif., January, 1966.

Fundamental Limitations on the Low-Temperature Operation of Electrolytic Devices

C. A. Angell

Department of Chemistry, Purdue University, Lafayette, Indiana

ABSTRACT

A new approach to the understanding of transport behavior in concentrated electrolyte solutions requires the recognition at low temperatures of a liquid state limiting temperature which is a thermodynamic constant of any solvent-electrolyte solution. The value of this constant, which determines service limits, is a function of electrolyte concentration except at low concentrations where solvent structure may dominate. In this paper the results of workers investigating electrolyte solutions for low-temperature battery applications are used to emphasize the usefulness of the concepts underlying this approach to low-temperature electrolyte problems.

This article considers briefly some implications of recent developments in electrolyte solution transport theory to the practical problems encountered in the use of electrolyte solutions at low temperatures.

Temperature and concentration dependence of solution transport properties.—In recent papers (1-3) it has been shown that the temperature dependence and composition dependence of electrical (equivalent) conductance, Λ, and viscous flow, η, processes in various concentrated aqueous electrolyte solutions at low corresponding temperatures may be described by equations of the following form

constant composition

$$\Lambda_{(N)}, 1/\eta_{(N)} = A \exp \frac{-k}{T - T_o} \qquad [1]$$

constant temperature

$$\Lambda_{(T)}, 1/\eta_{(T)} = A \exp - \frac{k/Q}{N_o - N} \qquad [2]$$

where A, k, and T_o in Eq. [1] and A, k/Q, and N_o in Eq. [2] are constants; T and N are, respectively, the absolute temperature and the equivalent concentration.

A plausible theoretical interpretation discussed in detail elsewhere (1, 4, 5) may be given these equations in terms of the controlling influence on the transport processes, of the liquid configurational entropy content (6). The constants T_o and N_o in this case represent the temperature at fixed composition, and the equivalent concentration at constant temperature, respectively, at which the configurational entropy vanishes.

Significance of low-temperature electrolyte solution behavior.—An important result of this treatment which we wish to emphasize in this paper is the realization that, provided crystallization has not already occurred, any electrolyte solution will lose its liquid character and become a glass at a temperature ($\sim T_o$) which in general will be well above 100°K. Where the electrolyte property of interest depends on, or is related to, the fluidity of the substance, this temperature therefore places an absolute lower limit to the serviceability of the material.[1]

Furthermore, it is found that, for many electrolyte mixtures and solutions at temperatures not too far above T_o, T_o itself is the only important variable in the transport equation, so that the low-temperature transport properties of such liquids are to a large extent known once T_o is known (3). Thus, the scaling factor to be used in comparing a given property amongst different solutions is, from Eq. [1], $(T - T_o)$.

To illustrate the usefulness of this point, we take an example from the work of Garrett *et al.* (7) who were investigating various strong (presumed fully dissociated) electrolyte solutions for suitability in low-temperature battery applications. Their (uninterpreted) data on the viscosity of some solutions, relative to the viscosity of water at 25°C, are reproduced in Fig. 1(i). The striking feature of the data is, of course, the very rapid rise in solution viscosity at the lower temperatures. In Fig. 1(ii) we show how the use of a T_o value appropriate to each solution in the scaling factor $(T - T_o)$ reduces the data approximately to a single curve. The remaining minor differences seem to be due mainly to variations in the value of the preexponential term A, as seen in the following.

According to Eq. [1], the values of T_o which reduce the solution viscosities as in Fig. 1(ii), should yield a linear plot for the relative viscosities when log η/η_o, (or log η_o/η to maintain Eq. [1] signs) is plotted against $1/(T - T_o)$. The appropriate semilogarithmic plots are shown in Fig. 2. The various plots are now seen to be differentiated by small changes in the values of the parameter A, the plots being linear with essentially equal values of the slope k. It must be said, however, that the available data are not sufficiently

[1] The limiting temperature usually imposed by the crystallization temperature is not an absolute limit insofar as suitable additives can usually make crystal nucleation a very improbable process even when thermodynamically favored.

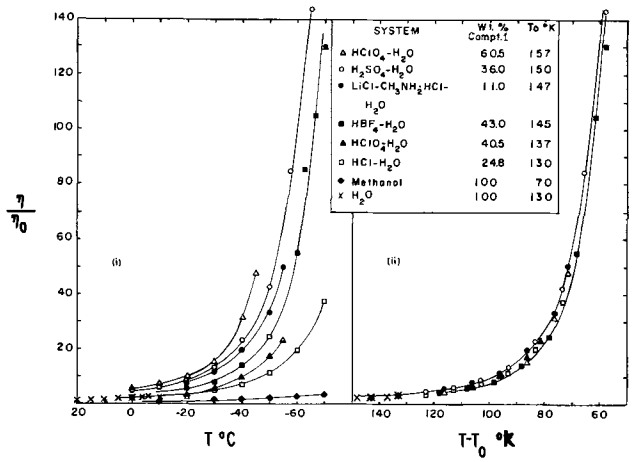

Fig. 1 (i). Viscosities of various electrolyte solutions relative to η_{H_2O} at 25°C (η_0) [after Garrett et al. ref. (7)]. Legend gives weight per cent (w/o) of the first component listed: in ternary system, weight per cent of $CH_3NH_2 \cdot HCl$ is 33%; Fig. 1 (ii). Data of (i) scaled by means of the vanishing entropy (S_c) temperature T_o [$S_c \rightarrow 0$ as $T \rightarrow T_o$, see ref. (5, 6)].

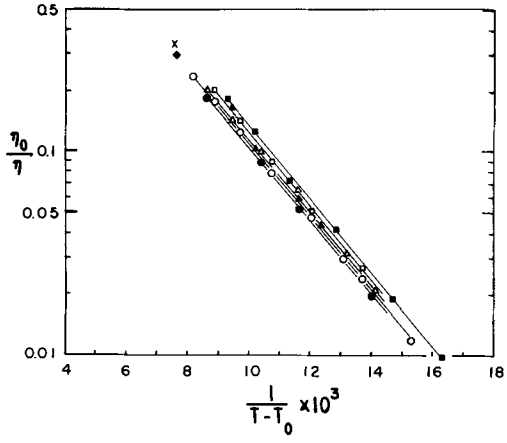

Fig. 2. Plot showing the linear dependence of log (relative viscosity) for the solutions of Fig. 1 on $1/(T-T_o)$ required by Eq. [1]. Points are identified in Fig. 1 legend.

accurate or extensive to conclude that k has the same value for each solution, though the differences apparently cannot be great.

Thus, the low-temperature electrolyte data of Fig. 1(i) are well accounted for by Eq. [1]; it follows that any theoretically guided quest for electrolytes serviceable to very low temperatures must focus attention on the property T_o of the material. We return to this matter shortly.

The Case of Specific Conductance

An interesting situation arises when the low-temperature property of interest is the electrical conductance. For the case of equivalent conductance, the viscosity and conductance at high concentrations follow essentially parallel paths except for small differences in the parameter k (2, 3). However, for practical applications it is the ability of a given volume of the electrolyte to conduct current which is of importance, and one is therefore concerned with the specific conductance, κ, which is related to the equivalent conductance by

$$\kappa = \frac{\Lambda N}{1000} \qquad [3]$$

whence, from Eq. [2],

$$\kappa = NA' \exp - \left(\frac{k/Q}{N_o - N} \right) \qquad [4]$$

Thus the equation for isothermal specific conductance contains the electrolyte concentration in both preexponential and exponential terms. The preexponential N leads to an increase in conductance with increasing N, due to the increase in number density of current carriers, while the exponential N opposes this increase, by raising the T_o value of the solution towards the isothermal temperature, T. Thus at $N = 0$, $\kappa = 0$, and eventually, as $N \rightarrow N_o$, $\kappa = 0$. Thus it is clear from Eq. [4] that the specific conductance must go through a maximum, provided the solubility limit of the salt is not first exceeded. The maximum in κ observed for many highly soluble salts is, of course, well known (8).

The not-so-obvious consequence of Eq. [4] which is of special interest to the present discussion, is the fact that since the influence of the preexponential N is independent of temperature (provided we are dealing with fully dissociated electrolytes) the maximum in the specific conductance isotherm must shift to lower concentrations at lower temperatures, since N_o decreases with decreasing temperature. Thus attempts to compensate for the low conductances encountered at the low temperatures by raising the electrolyte concentration, are increasingly frustrated the lower the temperature. To observe the effect of concentration on T_o, the data for the two compositions of perchloric acid treated in Fig. 1 and 2 may be referred to (see also Table I, discussed below). The effect of temperature on the specific conductance maximum is illustrated adequately by some data on zinc nitrate solutions due to Bak (9) shown in Fig. 3. The effect should be more dramatic at lower temperatures, but suitable data are not available to demonstrate this.

It should be pointed out, in view of the fact that most of the electrolyte solutions whose low-temperature properties were tested by Garrett and co-workers (7) were acids, that although the conductance exhibited is primarily proton conductance, the temperature dependence of the process should still be of the form of Eq. [1]. This will be true because proton conductance requires configurational freedom on the part of the water molecules (primarily freedom to rotate) which, like dielectric relaxation (10), requires an Eq. [1] type of description for the temperature dependence.

Factors Determining the Magnitude of T_o

The problem of what determines T_o is therefore fundamental to the question of low-temperature electrolytes. T_o is evidently a thermodynamic property of the material and a parameter of major importance to the understanding of liquid-solid relations. As discussed elsewhere (1) it appears to be the temperature

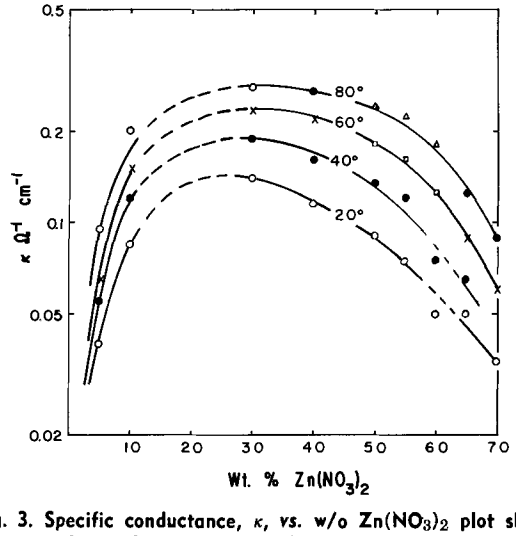

Fig. 3. Specific conductance, κ, vs. w/o $Zn(NO_3)_2$ plot showing movement of specific conductance maximum to lower concentrations as isotherm temperature decreases [after Bak, ref. (9)].

Table I.

Liquid		N equiv. l^{-1}, at $-70°C$[a]	T_0, °K
pure, w/o	H_2O	10^{-7}	130
40.5	$HClO_3$	5.5	137
43.0	HBF_4	7.2	145
24.8	HCl	8.0	130
36.0	H_2SO_4	9.9	150
60.5	$HClO_4$	10.1	157

[a] Values of N are calculated using the densities at $-70°C$ quoted in ref. (7).

at which the "ideal metastable amorphous solid" (11) phase commences to exchange vibrational for configurational degrees of freedom, but it is not clear that this implies a dependence only on bond strength, or cohesive energy, as the interpretation of Turnbull and Cohen (12) suggests. Since the vibration frequencies of the amorphous solid are apparently involved it seems reasonable to enquire about the possible effects of the mass of the constituent particles on T_0. Investigations of such possible factors are currently in progress.

Certainly the cohesion among the particles of the material must play a role, and in this connection the difference in T_0 values between H_2O and methanol deserves comment.[2] The higher value for H_2O is evidently to be attributed to the more strongly hydrogen-bonded structure of water. The so-called "structure-breaking" solutes may therefore tend to lower T_0 at least at low concentrations, while at the same time supplying current carriers. Such properties would seem desirable for low temperature applications, but unfortunately these salts do not produce low eutectic temperatures with water.

It is notable that 24.8% HCl has the same value of T_0 as that assigned to H_2O. The reason is probably that chloride ion, unlike the oxy- and fluoro-anions of the other acids, can only participate weakly in configuration restricting hydrogen bonding to the water molecules, so that increases in cohesion due to electrostatic effects are largely nullified by a net reduction in hydrogen bonding. HBr and HI solutions may therefore reach still lower T_0 values. Apart from HCl, the values of T_0 correlate (approximately) with the equivalent concentration, N, (Table I) as Eq. [2] predicts. The hydrogen bond contribution will vary from acid to acid and a quantitative correlation is not to be expected.

Figure 1 (i) and (ii) show that the difference in limiting service temperatures (*e.g.*, maximum permissible viscosity, resistance, or relaxation time) is effectively the difference in T_0 values. Accordingly, for very low-temperature work, solvents with T_0 values lower than that of H_2O would be required, and a non-hydrogen-bonded structure would seem necessary. This leads to something of an impasse however, since a nonhydrogen-bonded structure appears to conflict with the requirement of a dielectric constant high enough to promote electrolyte dissociation. There is room for further experimental work in this area, with systems such as the fluorosulfonic acids in nitrile and mixed alcohol solvents offering interesting possibilities.

[2] The assignment of T_0 values to these liquids (see legend Fig. 1) is only approximate because in neither case does the available transport data approach T_0 closely enough to permit a solution of Eq. [1] for T_0 with confidence. (Solutions of Eq. [1] for H_2O viscosities yield the result $T_0 = 150°K$ [F. Gutmann and L. M. Simmons, *J. Appl. Phys.*, **23**, 977 (1952); A. A. Miller, *J. Chem. Phys.*, **38**, 1568 (1963)].) The value, $T_0 = 130°K$ assigned to H_2O in this work is based mainly on the observation of the glass transition at 139°K for vapor-deposited vitreous ice [J. McMillan and S. C. Los, *Nature*, **206**, 806 (1965)], (recently confirmed in this laboratory [C. A. Angell, E. J. Sare, and R. D. Bressel, *J. Phys. Chem.*, **71**, 2759 (1967)], and the experience that the experimental glass transition is always observed at a temperature higher than T_0 by 5 – 30% dependent partly on molecular complexity. The estimate for methanol is based on the experimental value for the observed glass transition, 110°K [J. A. Faucher and J. V. Koleske, *Phys. Chem. Glasses*, **7**, 454 (1966)] and the known value $T_0 = 73.5°K$ for n-propanol [see ref. (10)] for which the measured glass transition temperature is also 110°K.

Manuscript received Nov. 2, 1966, revised manuscript received June 12, 1967.

Any discussion of this paper will appear in a Discussion Section to be published in the June 1968 JOURNAL.

REFERENCES

1. C. A. Angell, *J. Phys. Chem.*, **70**, 3988 (1966).
2. C. T. Moynihan, *ibid.*, **70**, 3399 (1966).
3. C. A. Angell, presented at 17th Meeting of the Comite Internationale de Thermodynamique et de Cinetique Electrochimique, Tokyo (CITCE), September (1966).
4. G. Adam and J. H. Gibbs, *J. Chem. Phys.*, **43**, 139 (1965); *J. Chem. Phys.*, **46**, (12) 4673 (1967).
5. C. A. Angell, *J. Phys. Chem*, **70**, 2793 (1966).
6. J. H. Gibbs and E. A. Dimarzio, *J. Chem. Phys.*, **28**, 373 (1958).
7. (a) A. B. Garrett, J. Welsh, S. Woodruff, R. Cooper, and J. Heiks, *J. Phys. Chem.*, **53**, 505 (1949); (b) A. B. Garrett and S. A. Woodruff, **55**, 477 (1951).
8. A. N. Campbell, A. P. Gray, and E. M. Kartzmark, *Can. J. Chem.*, **31**, 617 (1953).
9. B. V. Bak, *Zhur. Obsch. Khim.*, **16**, 395 (1946).
10. D. Davidson and R. H. Cole, *J. Chem. Phys.*, **19**, 1484 (1951).
11. D. Turnbull, "Physics of Non Crystalline Solids," p. 41, J. Prins, Editor, North-Holland Publishing Co. (1965).
12. D. Turnbull and M. H. Cohen, *J. Chem. Phys.*, **34**, 120 (1961).

A Generalized Expression for the Tafel Slope and the Kinetics of Oxygen Reduction on Noble Metals and Alloys

D. S. Gnanamuthu and J. V. Petrocelli

Applied Research Laboratory, Scientific Research Staff, Ford Motor Company, Dearborn, Michigan

ABSTRACT

The usually employed expression for the Tafel slope is modified to take into account the potential which is effective in charge transfer within the double layer. The exchange currents and cathodic Tafel slopes are obtained on noble metal electrodes having different number of holes in the d-band. Using the conventional and modified Tafel slopes, possible paths and rate-determining steps are suggested for the cathodic reduction of oxygen.

It has been well established that the oxygen electrode reaction

$$O_2 + 4H^+ + 4e = 2H_2O \quad \text{(acidic)}$$
$$O_2 + 2H_2O + 4e = 4\,OH^- \quad \text{(basic)}$$

is highly irreversible. In fact only a few investigators have been able to establish the thermodynamically reversible potential on the noble metals. In these cases the electrodes were pretreated by methods which produced oxide films on the surface (1-3).

It is very likely that much of the reported data on the cathodic reduction of oxygen and the anodic evolution of oxygen on the noble metals were obtained on oxide covered surfaces (1-5). Since the completion of this work Damjanovic *et al.* (6-8) have obtained cathodic Tafel lines on Pt and Rh. They report different Tafel slopes for prereduced and oxide covered surfaces.

The energetically unfavorable steps in the reduction of oxygen are the endothermic reactions, (*i*) breaking the oxygen bond which requires about 5 ev, and (*ii*) the addition of a second electron to an oxygen atom which requires about 7.0 ev (8a). Although the addition of the first electron to the oxygen atom is exothermic by 1.0 ev, it should be noted that this electronic level

$$O(g) + e \rightarrow O^-(g)$$

lies about 3-4 ev above the Fermi level, when the metal electrode is at equilibrium for the over-all reaction, with reactants and products in their standard states. The reaction path should be dictated by these energetic requirements, and it is reasonable to assume that the chemisorption of the proper species will play a large role in reducing the activation energy. The adsorption energy will, of course, depend on the bond strength and, whether we consider a valence bond or an electrostatic bond, the number of electrons in the d-levels may play an important role.

The object of this study was to determine the effect of the number of holes in the d-band of the electrode on the Tafel parameters and over-all activity for the reduction of oxygen. Since the presence of an oxide on the metal surface may well obscure any metallic electronic structure effects, the data was obtained on prereduced electrodes of Au, Pt, Pd, Ir, Rh, Os, Ru, Pt-Au, and Pd-Au alloys.

It may be noted that McDonald and Conway obtained Tafel slopes for oxygen evolution on a series of Pd-Au alloys, but concluded that any possible effects of d-band structure were probably obscured by the role of surface oxides (5).

Tafel Slopes

It is difficult, if indeed possible, to determine a unique reaction path by means of only Tafel parameters. However, if one reaction path is predominant and one of the elementary reactions (step) in the sequence of elementary reactions is rate determining, the Tafel slope, b_c, will be characteristic of the rate-determining step (rds).

The assumption usually made in obtaining the "expected slope" is that the symmetry factor for the rds is 0.5. Riddiford has shown that this assumption may not be in accord with the experimental facts (9). McDonald and Conway have pointed out the possible effect of oxide films on the symmetry factor (5).

We suggest that even if the symmetry factor of the rds is 0.5 and oxide films are absent, the expression generally used to obtain the "expected" Tafel slope (7-13)

$$-b_c = \frac{2.303\,\nu_j}{n_c + \beta_c\, n_j}\,\frac{RT}{\mathbf{F}} \qquad [1]$$

may not be correct in some cases. In this expression n_c is the total number of electrons transferred before the rds, n_j is the number transferred in the rds, β_c is the symmetry factor of the rds, and ν_j is the number of times that the rds must occur in order for the over-all reaction to take place once, usually designated the stoichiometric number of the rds.

Although this expression is usually employed, the derivation has not been given (7, 10). For purposes of clarity we shall designate this b_c as the "conventional expected" Tafel slope, (CTS) and present a derivation in order to indicate its limitations and finally derive a more general expression. The latter will be more satisfactory especially for some reaction paths which have been postulated for the oxygen reaction (7).

When the over-all reaction is governed predominantly by one reaction path, and one of the consecutive elementary reactions, a step, is rate determining, the slope may be obtained by assuming "quasi-equilibrium" for all reactions preceding the rds (12) or by considering the passage of the reactants over a series of energy barriers (11). We shall follow the latter approach.

If we have an over-all reaction

$$xX + bB^z + ne \rightarrow wW + cC^{(bz-n)/c} \qquad [2]$$

it is assumed that the completion of this over-all reaction requires the formation and decomposition of ν identical activated complexes A^*, where ν is an integer. The rate-determining reaction may then be written as

$$\frac{x}{\nu}X + \frac{b}{\nu}B^z + \frac{n}{\nu}e \rightarrow \frac{w}{\nu}W + \frac{c}{\nu}C^{(bz-n)/c} \qquad [3]$$

and ν is usually called the stoichiometric number of the reaction.

The four states to be considered are: the initial state *I*, the state immediately before the highest energy barrier *P*, the state immediately after this barrier, *Q*, and the final state *F*. A cross section of the energy surface indicating the reaction path is shown, schematically, in Fig. 1.

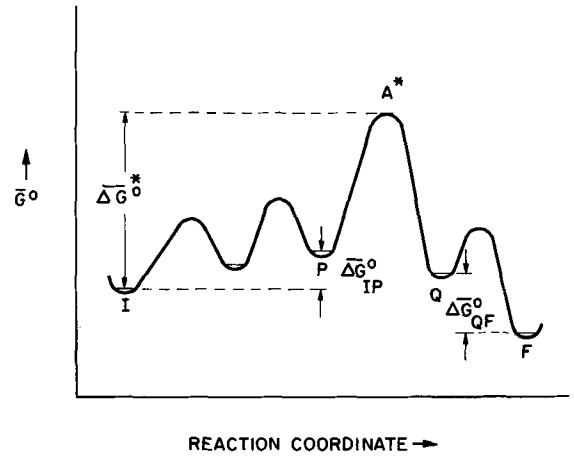

Fig. 1. Standard free energy change in a consecutive reaction path (schematic).

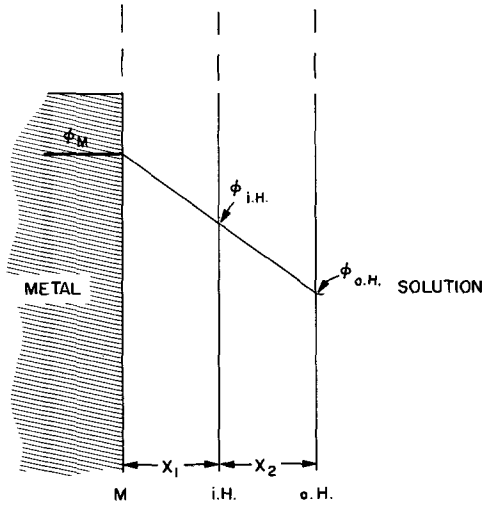

Fig. 2. Distribution of potential in the double-layer (schematic)

The electrical part of the standard free energy of activation in the forward direction is given by

$$\Delta G^{*o}_{Elec} = \sum_i Z_{IP} F \Delta\phi_{IP} + Z_{PQ} F \Delta\phi_{PA^*} \quad [4]$$

where Z_{IP} is the charge of a particle which is transferred from state I to P, $\Delta\phi_{IP}$ is the electrical potential difference through which the particle moves in going from I to P and the summation is over all charged particles i which react in order for the rds to occur once. Similarly the second term is for the charged particles which react to form the transition complex A^*.

If we let

$$\beta_c = \frac{\Delta\phi_{PA^*}}{\Delta\phi_{PQ}} \quad [5]$$

where β_c is the fraction of the potential difference between state P and Q which is effective for the activation of a charged particle i. We may write:

$$\Delta G^{*o}_{Elec} = \sum_i Z_{IP} F \Delta\phi_{IP} + Z_{PQ} F \beta_c \phi_{PQ} \quad [6]$$

β_c is then the conventional symmetry factor.

If we now identify the electric inner potentials which occur in the various states with those of the metal, ϕ_M, and the solution, ϕ_S, and consider only the transfer of electrons, we can write Eq. [6] as

$$\Delta G^{*o}_{Elec} = \frac{n_{IP}}{\nu_j} F [\phi_M - \phi_S] + \frac{n_{PQ}}{\nu_j} F \beta_c [\phi_M - \phi_S] \quad [7]$$

where effectively we assume that the electric potential difference across each barrier is that between the metal and the solution. n_{IP}/ν_j and n_{PQ}/ν_j are the number of electrons which are transferred from the metal to the solution prior to the rds and in the rds, respectively, in order for the rate-determining reaction, Eq. [3], to take place once.

For the complete reaction we have

$$\frac{n}{\nu_j} F [\phi_M - \phi_S] = \frac{n_{IP}}{\nu_j} F [\phi_M - \phi_S] + \frac{n_{PQ}}{\nu_j} F [\phi_M - \phi_S] + \frac{n_{QF}}{\nu_j} F [\phi_M - \phi_S] \quad [8]$$

The rate of the forward reaction in terms of current density is

$$i = \frac{n}{\nu} F\kappa \frac{kT}{h} a^{x'}{}_X a^{b'}{}_B e^{\frac{-\Delta G^{*o}_{Chem}}{RT}} e^{\frac{-\Delta G^{*o}_{Elec}}{RT}} \quad [9]$$

where

$$x' = \frac{x}{\nu} \text{ and } b' = \frac{b}{\nu}$$

which for a given reaction may be written as

$$\Delta G^{*o}_{Elec} = -RT \ln i + C \quad [10]$$

substituting Eq. [7] into [10] we obtain

$$\frac{n_{IP}}{\nu_j} F [\phi_M - \phi_S] + \frac{n_{PQ}}{\nu_j} F \beta_c [\phi_M - \phi_S] = -RT \ln i + C \quad [11]$$

and

$$-b_c = \frac{2.303\,\nu_j}{n_{IP} + \beta_c n_{PQ}} \frac{RT}{F} \quad [12]$$

which is identical with Eq. [1], the expression for the CTS.

It will be obvious that Eq. [11] and [12] are only true when the electrons or charges, are transferred from the metal to the solution or *vice versa*. This may not always be the case. In some of the elementary reactions, charges may not cross the total double layer. If the electrons are transferred from the metal to the adsorbed species and the ions are transferred from the adsorbed sites to the solution, or *vice versa*, the above equations must be modified.

Recalling the relative positions of the metal-plane, the inner Helmholtz plane, iH, and the outer Helmholtz plane, oH, shown schematically in Fig. 2, we may designate ϕ_M, ϕ_{iH}, and ϕ_{oH} as the inner electric potential of these planes (13-15). The diameter of an adsorbed radical or ion in the oxygen electrode reaction will be approximately equal to that of an oxygen atom or ion and will lie in the iH plane.

If we go back to Eq. [6] and substitute it into Eq. [10], the following general expression is obtained

$$\sum_i Z_{IP} F \Delta\phi_{IP} + Z_{PQ} F \beta_c \Delta\phi_{PQ} = -RT \ln i + C \quad [13]$$

Let

$$\Delta\phi_{IP} = f_{IP} \Delta\phi_{MS}$$
$$\Delta\phi_{PQ} = f_{PQ} \Delta\phi_{MS} \quad [14]$$

We have from Eq. [13] and [14]

$$-b_c = \frac{2.303}{\sum_i Z_{IP} f_{IP} + Z_{PQ} \beta_c f_{PQ}} \frac{RT}{F} \quad [15]$$

By this treatment we have retained the conventional definition and concept of the symmetry factor β_c as the portion of the change in the standard free energy of the rds which is effective in the activation process. The quantities f_{IP} and f_{PQ} then indicate the fraction of the total electrical potential difference at the metal-solution interface involved in the charge transfer process.

The transfer coefficient for the reaction will be given by

$$\alpha_c = \sum_i Z_{IP} f_{IP} + Z_{PQ} \beta_c f_{PQ} \quad [16]$$

As a first approximation we will let $\phi_{oH} = \phi_S$ (neglect p·d of the diffuse layer), take $\partial\phi/\partial X$ in the double layer as constant, and take the distance from the metal to the iH plane equal to that from the iH plane to the oH plane.

With these approximations and the usual reasonable assumption that $\beta_c = 0.5$, the "corrected" Tafel slopes, b'_c, have been calculated from Eq. [15] for the reaction paths given in Table I. Values of the "conventional" Tafel slopes, b_c, are included for comparison. The paths I through XIV have been listed by Damjanovic *et al.* (7); paths XV and XVI have been added.

Since Eq. [15] will yield the "conventional" slope when the values of f_{IP} and f_{PQ} are equal to unity, only paths VI, X, XI, XIII, XIV, XV, and XVI are affected.

To illustrate and clarify the concepts developed here, let us apply Eq. [15] to the Hoar's alkaline path, section VI in Table I, which has received support from Hoar (10) and Damjanovic *et al.* (7).

We assume that step 3 is rate determining so that $\nu_j = 2$. First it should be noted that since this step does not involve electron transfer, the conventional treatment assumes that this is not directly potential dependent. Yet the elementary reaction as written indicates the transfer of charge from the adsorbed site to the solution. Certainly this transfer should depend on $(\phi_{iH} - \phi_S)$, and Eq. [15] takes this into account.

The electrical part of the standard free energy of the various states *I*, *P*, *Q*, and *F* are

State	G°_{Elec}
I	$-2F\phi_M$
P	$-F\phi_{iH} - F\phi_M$
Q	$-F\phi_S - F\phi_M$
F	$-2F\phi_S$

The total electrical standard free energy change for the rate-determining reaction

$$\tfrac{1}{2}\,O_2 + 2e + H_2O \rightarrow 2\,OH^-$$

is

$$(\Delta G^\circ_{Elec})_{Total} = 2F\Delta\phi_{MS}$$

as it should be, and the electrical part of the standard free energy of activation for the forward reaction is

$$\Delta G^{*\circ}_{Elec} = F[\phi_M - \phi_{iH}] + F\beta_c[\phi_{iH} - \phi_S] = 0.5F\Delta\phi_{MS} + 0.25F\Delta\phi_{MS}$$

so that

$$\alpha_c = 0.75$$

$$-b'_c = 0.079V \text{ @ } 25°C$$

whereas the conventional slope = —0.059v.

If the reacting species are in fact adsorbed on the metal surface as indicated by the reaction equations, the conventional expected values of b_c used by investigators in their analysis would not yield a correct slope.

Experimental

The experiments were performed in highly purified solutions at 25°C. The techniques and methods of purification were similar to those described in the literature. Oxygen was maintained at unit pressure and at a constant rate of bubbling. Some data were obtained on rotating electrodes, but they were essentially the same as in the solutions stirred only by oxygen bubbling, except for larger limiting current densities in some cases.

The solutions were 1*N* H_2SO_4, 0.1*N* NaOH and various concentrations of Na_2SO_4 which were of constant ionic strength but various pH values by adding a few drops of diluted H_2SO_4 or NaOH.

Pt, Pd, and Au electrodes were 99.999% pure and the other electrodes were 99.9% pure. The Pd-Au and Pt-Au alloys were made in an induction furnace using recrystallized alumina crucible and helium atmosphere. They were cast and rolled to 50% reduction at room temperature, except for some of the Pt rich Au-Pt alloys which were rolled at 1100°C. All alloys

Table I. Oxygen reaction paths and cathodic Tafel slopes

			$-b_c$	$-b'_c$
I The "Oxide" Path				
1. $O_2 + 2M$	→	$2MO$	∞	∞
2. $MO + MH_2O$	→	$2MOH$	∞	∞
3. $MOH + H^+ + e$	→	$M + H_2O$	0.118	0.118
II The "Electrochemical Oxide" Path				
1. $O_2 + 2M$	→	$2MO$	∞	∞
2. $MO + MH_2O + H^+ + e$	→	$MOH + M + H_2O$	0.118	0.118
3. $MOH + H^+ + e$	→	$M + H_2O$	0.039	0.039
III The "Hydrogen Peroxide" Path				
1. $O_2 + M + MH_2O$	→	$MOH + MO_2H$	∞	∞
2. $MOH_2 + MO_2H$	→	$MOH + MH_2O_2$	0.059	0.059
3. $M + MH_2O_2$	→	$2MOH$	0.03	0.03
4. $MOH + H^+ + e$	→	$M + H_2O$	0.118	0.118
IV The "Metal Peroxide" Path				
1. $O_2 + M + MH_2O$	→	$MHO_2 + MOH$	∞	∞
2. $M + MHO_2$	→	$MO + MOH$	0.059	0.059
3. $MO + MH_2O$	→	$2MOH$	0.03	0.03
4. $MOH + H^+ + e$	→	$M + H_2O$	0.118	0.118
V The "Electrochemical Metal Peroxide" Path				
1. $O_2 + M + MH_2O$	→	$MOH + MHO_2$	∞	∞
2. $MHO_2 + H^+ + e$	→	$MO + H_2O$	0.039	0.039
3. $MO + MH_2O$	→	$2MOH$	0.03	0.03
4. $MOH + H^+ + e$	→	$M + H_2O$	0.071	0.071
VI Hoar Alkaline Path				
1. $M + O_2 + 2e$	→	MO_2^{-2}	0.059	0.118
2. $M + MO_2^{-2} + 2H_2O$	→	$2MH_2O_2^-$	0.03	0.059
3. $MH_2O_2^-$	→	$MOH + OH^-$	0.059	0.079
4. $MOH + e$	→	$M + OH^-$	0.039	0.039
VII Conway and Bourgault Reaction Path				
1. $M + MH_2O + O_2$	→	$MHO_2 + MOH$	∞	∞
2. MHO_2	→	$MOH + MO$	0.059	0.059
3. $MO + H^+ + e$	→	MOH	0.024	0.024
4. $MOH + H^+ + e$	→	$M + H_2O$	0.071	0.071
VIII Alternative Conway and Bourgault Reaction Path				
1. $M + MH_2O + O_2$	→	$MOH + MHO_2$	∞	∞
2. $MHO_2 + H^+ + e$	→	$MO + H_2O$	0.039	0.039
3. $MO + H^+ + e$	→	MOH	0.024	0.024
4. $MOH + H^+ + e$	→	$M + H_2O$	0.039	0.039
IX Riddiford Path				
1. $O_2 + MH_2O + H^+ + e$	→	$MHO_2 + H_2O$	0.118	0.118
2. $MHO_2 + H^+ + e$	→	$MO + H_2O$	0.039	0.039
3. $MO + MH_2O$	→	$2MOH$	0.03	0.03
4. $MOH + H^+ + e$	→	$M + H_2O$	0.039	0.039
X Krasilshchikov Path (Ni electrodes)				
1. $O_2 + 2M$	→	$2MO$	∞	∞
2. $MO + e$	→	MO^-	0.118	0.236
3. $MO^- + H^+$	→	MOH	0.059	0.079
4. $MOH + H^+ + e$	→	$M + H_2O$	0.039	0.039
XI Wade and Hackerman's Path				
1. $O_2 + 2e + 2M + MH_2O$	→	$2MOH^- + MO$	0.059	0.118
2. $MO + MH_2O + 2e$	→	$2MOH^-$	0.02	0.03
XII				
1. $O_2 + H^+ + e + M$	→	MO_2H	0.118	0.118
2. $MO_2H + H^+ + e$	→	$MO + H_2O$	0.039	0.039
3. $MO + H^+ + e$	→	MOH	0.024	0.024
4. $MOH + H^+ + e$	→	$M + H_2O$	0.017	0.017
XIII				
1. $M + O_2$	→	$2MO$	∞	∞
2. $MO + H_2O$	→	$MO - H - OH$	∞	∞
3. $MO - H - OH + e$	→	$MO - H - OH^-$	0.118	0.236
4. $MO - H - OH^- + H^+$	→	$MOH + H_2O$	0.059	0.079
5. $MOH + H^+ + e$	→	$M + H_2O$	0.039	0.039
XIV				
1. $O_2 + H^+ + e + M$	→	MHO_2	0.118	0.118
2. $MHO_2 + e$	→	$MO + OH^-$	0.039	0.039
3. $MO + H_2O$	→	$MO - H - OH$	0.03	0.03
4. $MO - H - OH + e$	→	$MO - H - OH^-$	0.024	0.026
5. $MO - H - OH^-$	→	$MOH + OH^-$	0.020	0.021
6. $MOH + H^+ + e$	→	$M + H_2O$	0.017	0.017
XV Hoare Path (2)				
1. O_2 (aq)	→	MO_2	∞	∞
2. $MO_2 + e$	→	MO_2^-	0.118	0.236
3. $MO_2^- + H^+$	→	MHO_2	0.059	0.079
4. $MHO_2 + e$	→	MHO_2^-	0.039	0.047
5. $MHO_2^- + H^+$	→	MH_2O_2	0.03	0.034
6. $2H_2O_2$	catalytic →	$2H_2O + O_2$ (ads)	0.03	0.03
XVI [Quoted by Ives (20)]				
1. $M + O_2 + e$	→	MO_2^-	0.118	0.236
2. $MO_2^- + H^+$	→	MO_2H	0.059	0.079
3. $MO_2H + e$	→	MO_2H^-	0.039	0.047
4. $MO_2H^- + H^+$	→	MH_2O_2	0.03	0.034
5. $MH_2O_2 + e$	→	$MOH + OH^-$	0.024	0.024
6. $MOH + e$	→	$M + OH^-$	0.017	0.017

were homogenized for 12 hr at the proper temperature and quenched in water to obtain a homogeneous, single phase solid solution. Au-Pt alloys having the following compositions were used (w/o Au): 4.72, 9.66, 17.35, 27.38, 37.25, 49.84, 60.35, 70.13, 80.03, and 89.64. Au-Pd alloys were of the following composition (w/o Au): 9.47, 23.96, 53.89, 67.06, 71.01, 76.90, and 85.8.

The alloy electrodes were cut from the inside of the specimen in order to avoid any possible surface inhomogeneity. The homogeneity of the surface was checked by the electron probe microanalyzer.

Electrodes were metallographically polished, thoroughly cleaned, rinsed, and dried. Acid pretreatments were omitted in order to avoid possible preferential dissolution of alloy constituents. Experiments on pure metals with and without acid treatment showed the same final results.

All the electrodes were prereduced at +0.20v in H_2SO_4 and —0.60v in NaOH for 15 min. Since the final results were the same whether the solutions were saturated with oxygen or nitrogen during the reduction, most prereductions were done in an oxygen saturated solution. After prereduction the circuit was opened and the electrode assumed an open-circuit potential, E_o, which became steady in about 10 min. The electrode was then cathodically polarized, galvanostatically, from low to high current densities, then from high to low current densities without opening the circuit.

Electrode potential values are given on the standard hydrogen electrode scale.

Results

Pure metals.—The η log i curves for oxygen reduction showed a reproducible Tafel relation for all the electrodes in H_2SO_4 and NaOH from about 10^{-6} amp/cm^2 to about 10^{-3} amp/cm^2. Concentration polarization became noticeable at these higher current densities under the stirring conditions used. The curves were the same whether obtained from low to high currents or *vice versa*.

Except for Au in H_2SO_4 the potential changed very little from the open-circuit value, E_o, until the current density reached about 10^{-6} amp/cm^2. The η-log i relation was not linear in this low current density range. The results for Pt, Pd, and Au are typical and are shown in Fig. 3.

The Tafel parameters are given in Table II. The reported values are the mean of at least six experiments. The values of the slope, b_c, were reproducible to better than ±0.005v for all metals in NaOH, to about the same value for Pt and Pd in H_2SO_4, and about ±0.01v for the other metals and alloys in H_2SO_4. The values of i_o could be reproduced by a factor of ten. Except for Au in H_2SO_4, E_o varied by about ±0.02v in H_2SO_4 and ±0.01v in NaOH. The E_o of Au varied by about ±0.05v in acid. The overpotential at 10^{-5} amp/cm^2, η^o, was chosen as a relative index of the "over-all activity" of the electrode for the reduction reaction.

Pt has the highest i_o and activity (lowest η^o) in both acid and alkaline solutions. Except for Pt, the activity of the metals is greater in NaOH. Since the values of i_o are all quite low, b_c plays the greater role in determining η^o.

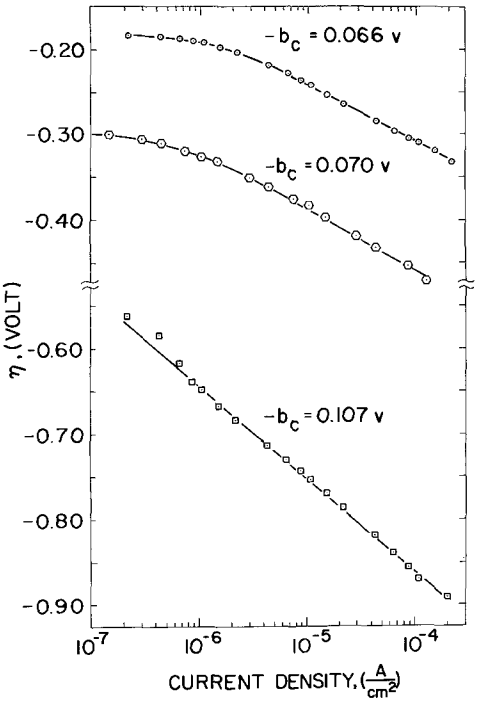

Fig. 3. Overvoltage, η — log i relationship in 1*N* H_2SO_4. ⊙ Pt; ⊙ Pd; ⊡ Au.

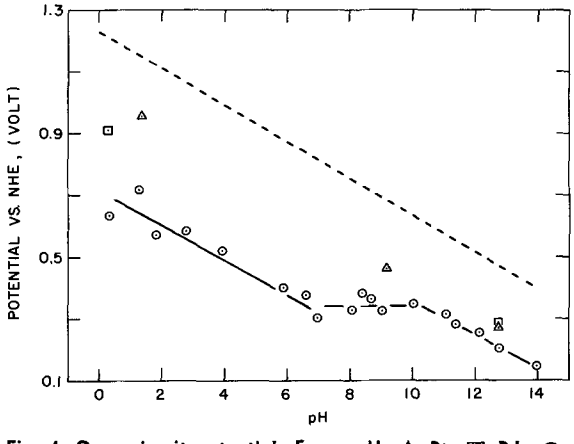

Fig. 4. Open-circuit potential, E_o vs. pH. △ Pt; ⊡ Pd; ⊙ Au. Dashed line indicates theoretical potential-pH relationship, calculated from the equation

$$E = 1.23 - \frac{RT}{4F} \ln \frac{(a_{H_2O})^2}{(a_{H^+})^4 (P_{O_2})}$$

Since the values of b_c and η^o for Au were significantly different in H_2SO_4 and NaOH, more detailed data were obtained for this metal with solutions of different pH values. The results are shown in Fig. 4, 5, and 6.

Alloys.—The data for the alloys are shown in Fig. 7, 8, and 9. These figures also include parameters of

Table II. Experimental Tafel parameters

Metal	No. of holes in d-band	$-b_c$,* volt		i_o, amp/cm^2		$-\eta^o$ [at 10^{-5} amp/cm^2], volt		E_o vs. NHE, volt	
		1*N* H_2SO_4	0.1*N* NaOH	1*N* H_2SO_4	0.1*N* NaOH	1*N* H_2SO_4	0.1*N* NaOH	1*N* H_2SO_4	0.1*N* NaOH
Au	0.0	0.10	0.047	10^{-13}	10^{-13}	0.74	0.35	0.70	0.21
Pt	0.58(21)	0.065	0.053	10^{-9}	10^{-10}	0.26	0.29	1.03	0.26
Pd	0.58(22)	0.070	0.046	10^{-11}	10^{-13}	0.39	0.30	0.90	0.28
Rh	1.7 (19)	0.12	0.048	10^{-11}	10^{-13}	0.60	0.37	0.83	0.12
Ir	1.7 (19)	0.09	0.040	10^{-11}	10^{-16}	0.47	0.41	0.91	0.18
Ru	2.2 (19)	0.08	0.051	10^{-12}	10^{-13}	0.55	0.35	0.82	0.21
Os	2.2 (19)	0.13	0.035	10^{-10}	10^{-15}	0.58	0.35	0.98	0.20

* — b_c reproducible to ± 0.005v in NaOH; ± 0.005v for Pt and Pd in H_2SO_4; ± 0.01v for others in H_2SO_4.

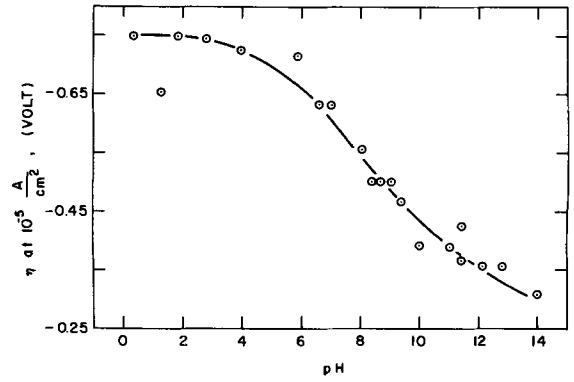

Fig. 5. Activity, η° *vs.* pH for Au

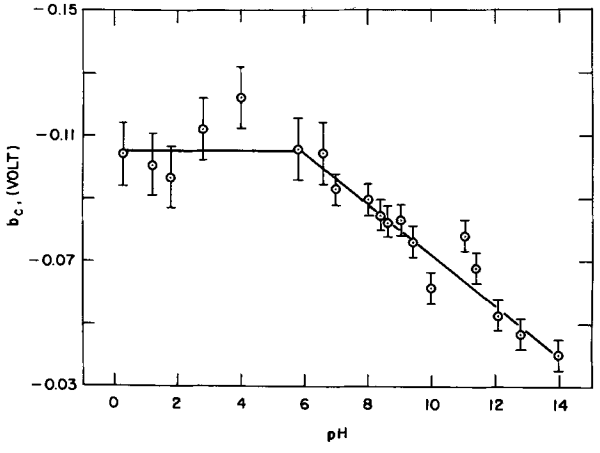

Fig. 6. Tafel slope, b_c *vs.* pH for Au

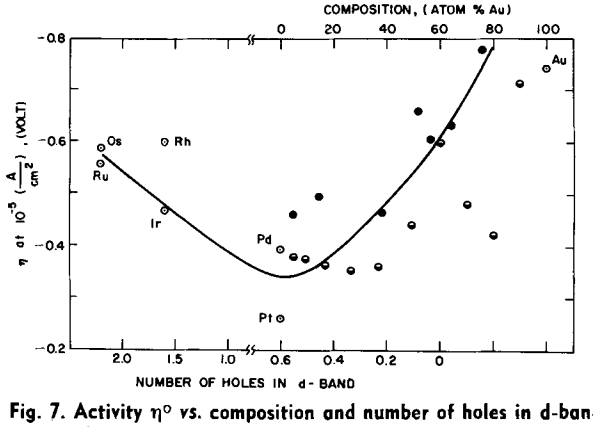

Fig. 7. Activity η° *vs.* composition and number of holes in d-band; in 1*N* H_2SO_4. ◒ Pt-Au alloys; ● Pd-Au alloys.

the pure metals in order to show the effect of the d-band structure as well as composition.

Pt-Au *alloys in* H_2SO_4.—E_o remains close to the value for Pt until about 85 a/o (atomic per cent) Au. The value of i_o remains close to that of Pt until about 60 a/o Au. Surprisingly, b_c changes to that of Au at only about 5 a/o Au. The net effect is a decrease of activity with Au content.

Pt-Au *alloys in* NaOH.—i_o decreases with Au content, while E_o remains close to that of Au for all compositions. η° and b_c do not vary with alloy composition.

Pd-Au *alloys in* H_2SO_4.—E_o remains close to that of Pd until about 70 a/o Au. The values of b_c, i_o, and η° change approximately linearly with Au content from the values of Pd to those of Au, with considerable scatter in the values.

Pd-Au *alloys in* NaOH.—E_o remains close to that of Pd until about 60 a/o Au. The values of b_c and η° are

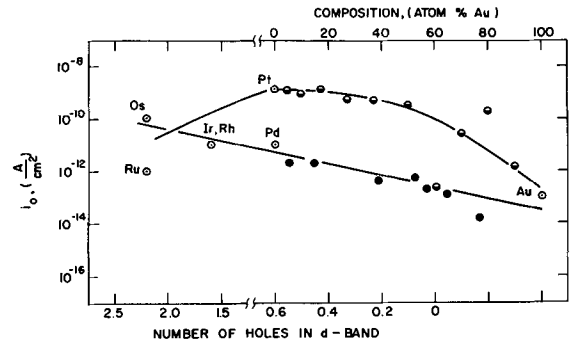

Fig. 8. Exchange current, i_o *vs.* composition and number of holes in d-band; in 1*N* H_2SO_4. ◒ Pt-Au alloys; ● Pd-Au alloys.

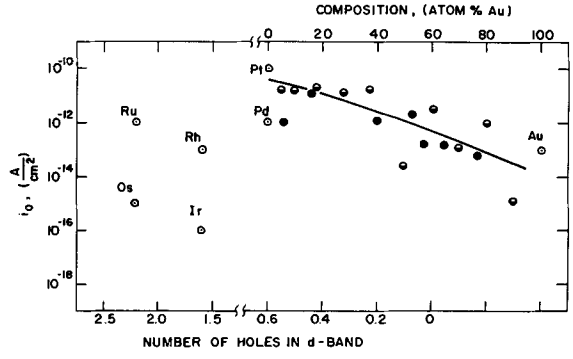

Fig. 9. Exchange current, i_o *vs.* composition and number of holes in d-band; in 0.1*N* NaOH, ◒ Pt-Au alloys; ● Pd-Au alloys.

about the same for the two pure metals and show no significant dependency on composition, considering the reproducibility. The i_o values for Pd and Au are about 10^{-12} amp/cm^2 and 10^{-13} amp/cm^2, respectively. The value for the alloys changes approximately linearly with Au content between these two limits.

Any effects due to the number of holes in the d-band (nhd) may be seen from Fig. 7, 8, and 9, by considering the data for the pure metals along with that for the alloys. The large scatter in the values does not allow precise evaluation, but certain consistent trends of the variation of the Tafel parameters η° and i_o are indicated. These trends are shown by the curves drawn in the figures. The trends are much more with the chemical composition-surface structure than with the nhd.

Discussion

Open-circuit potential.—The nonlinear character of η-log i and the very low rate of change of η with log i in the low current density range strongly indicates that the open-circuit potential is either a mixed potential with a "reaction current density" of about $10^{-6.5}$ amp/cm^2 or that it is a reversible potential for some reaction with an exchange current density of the same value. We believe that the former is the case, in agreement with Hoar and others (16, 16a).

Reaction mechanisms.—It is not possible to determine reaction mechanisms by means of b_c and i_o. Since the anodic reaction occurs on an oxide surface (5, 6), the anodic slope b_a and ν could not be obtained on prereduced surfaces. Moreover E_o is about 1V, and hence one cannot use the linear relation between η and i to calculate ν (11).

Values of b_c may be used to eliminate certain reaction paths and indicate possible paths. Many reaction paths can be devised for the oxygen electrode, but we will limit our discussion to those listed in Table I. Taking into account the variations in the reproducibility of the b_c values the possible paths for the metals are summarized in Table III.

Table III. Possible reaction paths and rate-determining steps corresponding to experimental b_c

No.	System	Possible paths and rds**	Remarks
1	Pt in H_2SO_4	III(2), IV(2), VI(2), VII(2), V(4),* VII(4)*	Damjanovic *et al.* (6) obtained 0.054v on oxide free Pt. Bianchi *et al.* (3) obtained 0.06v on oxide free Pt.
2	Pt in NaOH	III(2), IV(2), VI(2), VII(2), XV(4),* XVI(3)*	Damjanovic *et al.* (7, 8) obtained 0.065v on oxide covered Pt. Hoar (16) obtained 0.048v
3	Pd in H_2SO_4	V(4),* VII(4)*	
4	Pd in NaOH	XV(4),* XVI(3)*	
5	Au & Rh in H_2SO_4	I(3),* II(2),* III(4),* IV(4),* VI(1),* IX(1),* XII(1),* XIV(1)*	Damjanovic *et al.* (8) obtained 0.06v on reduced Rh and 0.06v on oxidized Rh at low current densities.
6	Au & Rh in NaOH	XV(4),* XVI(3)*	Hoar obtained 0.048v (16) on Au. Damjanovic *et al.* (8) obtained about 0.100v on oxidized Rh.
7	Os in H_2SO_4	Refer No. 5 above	
8	Os in NaOH	II(3),* V(2),* VI(4),* VIII(2),* VIII(4),* IX(2),* IX(4),* X(4),* XII(2),* XIII(5),* XIV(2),* XV(5), XVI(4), III(3), IV(3), V(3), IX(3), XIV(3), XI(2)*	
9	Ir in H_2SO_4	VI(3), X(3), XIII(4), XV(3), XVI(2)	Damjanovic *et al.* (8) obtained 0.100v on oxidized Ir.
10	Ru in H_2SO_4	VI(3), X(3), XIII(4), XV(3), XVI(2), V(4),* VII(4)*	
11	Ru in NaOH	Refer No. 6 above	

* In these steps electrons are transferred.
** Roman numeral indicates the reaction path and the numeral in parenthesis indicates the rds; refer to Table I.

The continuous variation of b_c with pH for Au is noteworthy. Although data were not obtained for Ru, Rh, Ir, and Os, which also show a fairly large change in slope from acidic to alkaline solutions, it is likely that a similar variation of b_c with pH occurs on these metals. The continuous variation in b_c with pH is very likely due to the presence of at least two alternate reaction paths whose rates are close in value with one path being pH dependent.

There is no apparent relationship of the number of holes in the d-band (nhd) with the activity in NaOH or with b_c in H_2SO_4 and NaOH. The exchange current density, i_o, does show a trend with nhd in H_2SO_4. It does not appear significant, however. The trend in NaOH is even less significant. The activity in H_2SO_4 does show a definite trend (Fig. 7), with a maximum activity (minimum η^o) at Pt and Pd. Our general conclusion is that composition, hence geometric and chemical factors, play the predominant role in this series of metals. These results and conclusions are not at variance with some current views on the role of electronic structure on catalysis (17). It is interesting to note that Brennan *et al.* found that the integral heat of adsorption for oxygen on Pt, Pd, and Rh varied almost linearly with atomic radii (18). On the other hand, Rao *et al.* have reported an increase in surface coverage of oxygen with an increase in the nhd for the same metals used in this work (19).

Acknowledgment

The authors wish to express their appreciation to the Ford Motor Company for permission to publish this work.

Manuscript received March 20, 1967. This paper was presented at the Dallas Meeting, May 7-12, 1967.

Any discussion of this paper will appear in a Discussion Section to be published in the June 1968 JOURNAL.

REFERENCES

1. J. O'M. Bockris and A.K.M.S. Huq, *Proc. Roy. Soc., London*, **A237**, 277 (1956); N. Watanabe and M.A.V. Devanathan, *This Journal*, **111**, 615 (1964).
2. J. P. Hoare, *ibid.*, **112**, 849 (1965).
3. G. Bianchi and T. Mussini, *Electrochim. Acta*, **16**, 445 (1965).
4. J. J. Lingane, *J. Electroanal. Chem.*, **2**, 296 (1961).
5. J. J. McDonald and B. E. Conway, *Proc. Roy. Soc.*, **A269**, 419 (1963).
6. A. Damjanovic and J. O'M. Bockris, *Electrochim. Acta*, **11**, 376 (1966).
7. A. Damjanovic, A. Dey, J. O'M. Bockris, *ibid.*, **11**, 791 (1966).
8. A. Damjanovic, A. Dey, and J. O'M. Bockris, *This Journal*, **113**, 739 (1966).
8a. D.F.C. Morris and H. N. Schmeising, *Nature*, **181**, 469 (1958).
9. A. C. Riddiford, *Electrochim. Acta*, **4**, 170 (1961).
10. T. P. Hoar, Proc. 8th Meeting CITCE, 1956, p. 439, Butterworths, London (1958).
11. R. Parsons, *Trans. Faraday Soc.*, **47**, 1332 (1951); G. H. Fraser and R. G. Barradas, *This Journal*, **112**, 462 (1965).
12. B. Lovrecek, *J. Phys. Chem.*, **24**, 817 (1956); J. O'M. Bockris, *ibid.*, **24**, 817 (1956); B. E. Conway, *Trans. Roy. Soc. Canada*, **54**, (111) 19 (1960).
13. R. Parsons, "Modern Aspects of Electrochemistry," Vol. I, J. O'M. Bockris and B. E. Conway, Editors, p. 103; Academic Press Inc., New York (1954).
14. P. Delahay, "Double Layer and Electrode Kinetics," Interscience Publishers, New York (1956).
15. J. R. Macdonald and C. A. Barlow, Jr., *This Journal*, **113**, 978 (1966); "Electrochemistry" (Proc. 1st Australian Conference), Pergamon Press, New York (1964).
16. T. P. Hoar, *Proc. Roy. Soc., London*, **A142**, 628 (1933).
16a. Giner, *Z. Elektrochem.*, **63**, 386 (1959); J. P. Hoare, *This Journal*, **109**, 858 (1962).
17. G. Ehrlich, "Proc. 3rd International Congress on Catalysis," p. 113; John Wiley & Sons, Inc., New York (1965).
18. D. Brennan, D. O. Hayward, and B. M. Trapnell, *Proc. Roy. Soc., London*, **A256**, 81 (1960).
19. M.L.B. Rao, A. Damjanovic, and J. O'M. Bockris, *J. Phys. Chem.*, **67**, 2508 (1963).
20. "Reference Electrodes—Theory & Practice," Edited by D. J. Ives and G. J. Janz, p. 365; Academic Press, New York (1961).
21. D. W. Budworth, F. E. Hoare, and J. Preston, *Proc. Royal Soc., London*, **A257**, 250 (1960).
22. F. E. Hoare and B. Yates, *ibid.*, **A240**, 42 (1957).

Technical Notes

The Kolbe Electrosynthesis of Polydifluoromethylene

Madeline S. Toy

Douglas Aircraft Company, Missile and Space Systems Division, Astropower Laboratory, Newport Beach, California

In general, dicarboxylic acids, such as malonic acid, do not undergo reactions of Kolbe type, but oxidize to degradation products at anode electrode in an alkaline medium. However, the alkaline salts of the monoester dicarboxylic acids have been reported to give Kolbe type reactions with products being higher dicarboxylic acid esters (1). The electrolysis of dibasic acids in methanol have been reported by Garrison (2) to form polymers, and Kolbe couplings of perfluorinated monobasic acids have been reported by Levin, Chechina, and Sokolov (3). A recent patent describes the production of long-chain perfluoromono- and perfluorodicarboxylic acid esters also through Kolbe couplings (4).

This note reports the anodic synthesis of polydifluoromethylene from a perfluorodicarboxylic acid. Polydifluoromethylene has been prepared by electrolysis of solutions of commercial perfluoroglutaric acid (mp 85°-90°C) with sodium in methanol. The temperature of the experiments ranged from 25° to 55°C and the monomer concentration in absolute methanol ranged from 5 to 25 w/o. The electrolytic cell was equipped with two smooth platinum electrodes. A typical run employed 10% monomer by weight, current density of 40 to 100 ma/cm², and applied voltage up to 40v (depending on the distance between the electrodes and salt concentration). A white loosely adhering coating was formed on the anode in 4 hr. The current density could not be maintained but gradually decreased. After a few hours of electrolysis, a small amount of white flocculent precipitate was observed around the anode. The flocculent precipitate can be slightly increased by occasionally reversing the polarity of the electrodes. The white solid scraped from the anode partially softened at 300°C and was insoluble in solvents, including hexafluorobenzene, chloroform, dimethyl formamide, dimethyl sulfoxide, concentrated sulfuric acid, while the small amount of white solid recovered from the suspension was partially soluble in concentrated sulfuric acid, but not in the other tested solvents. The very strong broad absorption band between 7.9 and 8.7μ (5) for "Teflon" (trademark of du Pont's polytetrafluoroethylene) is observed in Fig. 1. The anodically synthesized polydifluoromethylene also shows another strong absorption band at 5.6μ with a weak peak at 2.9μ, indication typical of COOH in fluorocarbons (6). The infrared spectrum (Fig. 1) and the absolutely insoluble characteristics of the white solid scraped from the anode indicate that the polymer is essentially a long perfluorocarbon chain as Teflon, but with carboxylic terminal groups. The estimated molecular weight is low at approximately one thousand by the relative intensities of the CF and CO groups in the infrared spectrum.

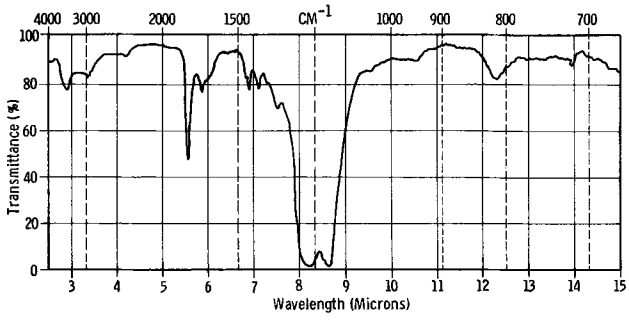

Fig. 1. Infrared spectrum of anodically synthesized polydifluoromethylene.

The mechanism of anodic synthesis of polydifluoromethylene from perfluoroglutaric acid appears to involve diradical couplings on the electrode surface.

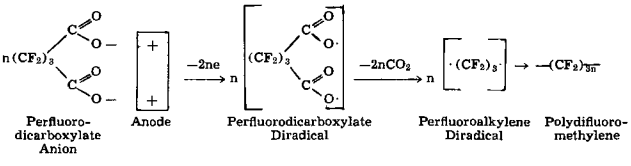

During electrolysis, the perfluorodicarboxylate anions are impelled to the anode, where they give up the ionic charges and possibly exist in a transient phase as a perfluorodicarboxylate diradical having an odd electron on both ends. This diradical at once loses carbon dioxide molecules and gives an equally transient trivalent carbon radical on both ends. This perfluoroalkylene diradical finally achieves stabilization by radical combinations with adjacent diradicals to form a polydifluoromethylene coating on the metal surface.

Manuscript received April 24, 1967; revised manuscript received *ca.* June 22, 1967.

Any discussion of this paper will appear in a Discussion Section to be published in the June 1968 JOURNAL.

REFERENCES

1. M. J. Allen, "Organic Electrode Processes," pp. 109-111, Reinhold Publishing Co., New York (1958).
2. W. E. Garrison, Jr., *Diss. Abstr.*, **20**, 77 (1959).
3. A. I. Levin, O. N. Chechina, and S. V. Sokolov, *Zh. Obshch, Khim.*, **35**, (10), 1778 (1965).
4. W. Bloechl and H. Kuckertz, German Pat. 1,231-679 (1967).
5. J. D. Simons, Editor, "Fluorine Chemistry," Vol. II, p. 497, Academic Press, New York, (1954).
6. M. I. Bro and C. A. Sperati, *J. Polymer Sci.*, **38**, 289 (1959).

Oxygen Reduction on a Partially Immersed Rotating Platinum Cathode

R. J. Roethlein and H. J. R. Maget

DECO Research & Development Laboratory, General Electric Company, West Lynn, Massachusetts

Reaction rates for an electrochemical process occurring on stationary electrodes in a diffusion controlled region having essentially the same interphase between the conducting electrolyte and the gas phase reactant have been shown by many authors to be associated with mass transport processes through thin electrolyte films (1-5). The reaction zone is confined to a small region near the film-meniscus interphase, and it is evident that these electrodes utilized only a fraction of the total electrode surface area. The bulk electrolyte presents a longer path for the mass transport of the reactant (gas) species to the electrode surface, and the reaction zone is further limited by the increased resistance to ionic flow encountered in the thin film region as the distance from the bulk electrolyte region increases. In order to facilitate a larger portion of the electrode surface area for mass transport processes a rotating electrode structure was investigated.

A circular hydrophobic electrode structure was rotated intermittently through an aqueous electrolyte and a depolarizing gas (oxygen). This procedure extends the region of thin film formation above the electrolyte level causing an increase in the total electrode current. Similar investigations have been carried out by Bonnemay *et al.* (6) in an attempt to separate adsorption from mass transport in electrochemical studies, and Weber *et al.* (7) have used a rotating copper electrode to investigate the mechanism of metal oxidation. The increased currents observed on partially immersed porous electrode has been employed by Bianchi (8) as a convenient basis for a comparative study of electrocatalytic activity of noble metals and for investigations of electrocatalytic processes of various reactant gases.

Therefore this novel electrode structure may not only provide higher diffusion controlled currents but also serve as an effective tool in catalyst evaluation. Further by variation of the rotational speed and depth of immersion this device could be used to determine the relative rates of:

1. The diffusion of a reactant gas across an electrolyte film.
2. Migration parallel to the electrolyte film.
3. Reaction and desorption of reactants into the electrolyte.
4. Adsorption on a dry surface or below the electrolyte film level.

Experimental

Experiments were carried out in a specially modified Pyrex glass test cell, which contained reference and counter electrode compartments separated from the study electrode section of the cell, Fig. 1. The counter electrode consisted of a large section of platinum black screen, and the reference system contained a dynamic hydrogen reference electrode, which maintained a steady potential near the reversible H^+/H_2 potential. The test electrode consisted essentially of a Teflon-bonded platinum black electrode (9) which was cut into a circular disk and then mounted on a tantalum shaft. The shaft was connected by means of an insulated bushing to a multi-speed transmission which has a 600 rpm reversible synchronous motor and a gear train with twelve steps of reduction. By the use of this motor various speeds of rotation could be imposed upon the

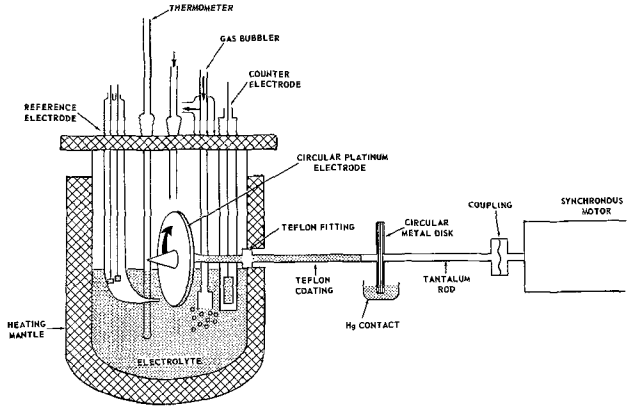

Fig. 1. Experimental apparatus

electrode. The study electrode was held vertical on the shaft with two circular Teflon disks which were threaded into the tantalum rod.

Electrical contact was accomplished by having a metal disk connected to the shaft outside of the test cell which then rotated through a pool of mercury. Teflon couplings mounted on the glass inlet port for the tantalum shaft prevented electrolyte leakage from the test cell, but still permitted the metal shaft to rotate freely. Temperature was maintained constant to within a few degrees by means of a variac controlled heating mantel. The study electrode was composed of the same materials generally employed in making Niedrach-Alford-type electrodes, nine parts platinum black to one part of weight of Teflon; pressed on platinum screening. The electrode was pressed at approximately 6200 psi at 700°F for a period of 7.5 min. A thin film of Teflon was sprayed on both sides of the electrode with an aqueous dispersion of (T-30). The actual electrode area on both faces of the disk was approximately 42 cm^2 with an average thickness of 10 mils. Measurements of the electrochemical reduction of oxygen were made in 10*N* H_2SO_4 at 25°C; both the electrolyte and surrounding atmosphere inside the test cell were kept completely saturated with oxygen gas. The electrolyte was presaturated with oxygen by means of the gas bubbler; however, during test the oxygen was admitted above the electrolyte level. Electrode potential was held constant by means of a Wenking potentiostat.

Results and Discussion

Performance studies were made of the rate of the electrochemical reduction of oxygen under various conditions. The electrode was held at a constant potential of +0.600v *vs.* H^+/H_2 and the current recorded for various conditions of electrode immersion and rotational speed. Figure 2 shows a plot of variation in current with the square root of rotational speed for six different immersion depths, 10, 15, 30, 50, 75, and 100% of the total electrode surface below the electrolyte level. When the electrode is totally immersed the electrochemical process is controlled by the bulk diffusion of oxygen through the electrolyte; hence only low currents are obtainable which show only slight increases with rotational speed. As

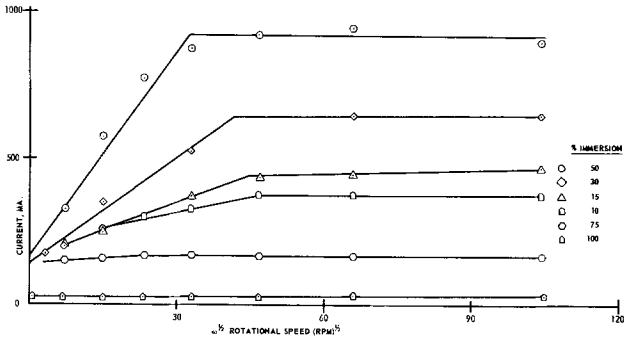

Fig. 2. Effect of rotational speed and immersion depth on electrode current. O_2 reduction; ion-H_2SO_4. 25°C; applied potential +0.600v vs. H^+/H_2.

the electrode is raised out of solution there is an immediate increase in current even while the electrode is at rest. This is due to the formation of a thin film of electrolyte in the exposed portion of the electrode matrix, which provides a shorter path for diffusion of oxygen molecules to the catalyst surface (10). Increasing the amount of exposed surface area has no substantial effect on the current while the electrode is at rest. This is due to the fact that the effective "active" area of the thin film portion of the electrode is virtually the same no matter how much of the total electrode surface is above the electrolyte level. The "active" length of the film is dependent mainly on the thickness of the electrolyte film which can produce large ionic resistance variations during current flow. At rest, gravitational forces will cause the liquid film to drain to a constant thickness which is independent of the amount of exposed surface area. When the electrode is rotated a linear increase in current is obtained with the square root of rotational speed up to an optimum value above which there is no subsequent current change with increasing rotational speed.

Observations made of the electrode surface at rest and during rotation show a distinctly hydrophobic surface in that the contact angle is greater than 90° and liquid does not cling to the exposed electrode surface during rotation. However the catalyst matrix beneath the Teflon film does wet, and rotating the electrode brings this wetted section above the electrolyte level. At this point electrolyte in the catalyst matrix drains downward, but has the immediate effect of providing an electrolyte film in the exposed section of the electrode above the level of the electrolyte. Increasing the speed of rotation will tend to counter balance the force of gravity providing a temporary greater film thickness in the region above the electrolyte level. Thus a larger portion of the thin film will be able to support current due to the decreased ionic resistance provided by the increase in film thickness. Eventually increasing the rotational speed will no longer have any effect on the film thickness and electrode current will reach a plateau.

Variations in the amount of electrode surface partially immersed reflect changes in the electrode current during rotation. There is a steady increase in current as the depth of immersion increases up to approximately 50% of the total electrode area; subsequent increases in the per cent of immersion produce a decrease in total electrode current. For immersion depths less than half of the total electrode area smaller portions of the outside perimeter of circular electrode surface are wetted by electrolyte during rotation. As the immersion depth increases the total current increase is due to a geometric increase in electrode area on which the active area of the thin film can be formed. The lower currents obtained for immersions depths greater than approximately 50% are caused by a decrease in the active area of the thin film region since a larger portion of the electrode surface is below the electrolyte level and bulk diffusion controlled.

Manuscript received May 8, 1967; revised manuscript received June 22, 1967.

Any discussion of this paper will appear in a Discussion Section to be published in the June 1968 JOURNAL.

REFERENCES

1. F. Will, *This Journal*, **110**, 152 (1963).
2. H. J. R. Maget and R. J. Roethlein, *ibid.*, **112**, 1034 (1965).
3. R. J. Roethlein and H. J. R. Maget, *ibid.*, **113**, 581 (1966).
4. D. N. Bennion and C. W. Tobias, *ibid.*, **113**, 589 (1966)
5. R. P. Icztowski, *ibid.*, **111**, 1078 (1964).
6. R. Bonnemay, Paris Meeting on Fuel Cells, February 1965.
7. H. C. Weber, H. P. Meissner, and D. A. Sama, *This Journal*, **109**, 884 (1962).
8. G. Bianchi, *ibid.*, **112**, 233 (1965).
9. L. W. Niedrach and H. R. Alford, *ibid.*, **112**, 117 (1965).
10. R. J. Roethlein and H. J. R. Maget, To be published.

Brief Communication

Conductivity of KOH and KOH-ZnO Electrolytes from 36° to -66°C

Charles T. Baker and Isaac Trachtenberg

Texas Instruments, Incorporated, Dallas, Texas

Currently, emphasis is being placed on the research of alkaline batteries using the negative zinc electrode, and more information is needed on the KOH and KOH-ZnO electrolyte systems which are used in such batteries. In this note data are presented on the specific conductivities of various KOH and KOH-ZnO solutions as a function of temperature between 36° and —66°C and on the solubility of ZnO in these KOH solutions. These latter data are in agreement with those of other investigators (1, 2).

All KOH and KOH-ZnO solutions were prepared using reagent grade KOH and ZnO and deionized water. During the preparation and utilization of these solutions, precautions were taken to prevent the introduction of CO_2. A Tenney, Jr., Environmental Chamber, Model TJR, was used to control the temperature of the experiments to ±0.5°C. The conductivity measurements were made with an L&N model 4805-50 conductivity cell assembly in conjunction with a General Radio Company impedance comparator, model 1605, using General Radio Company precision resistance and capacitance decade boxes. The cell constant for the conductivity cell was determined by using the solutions and data given by Jones and Bradshaw (3).

In the ZnO solubility studies, at each temperature the sample solution was agitated periodically by means of an ultrasonic bath over a three-day span in order to insure that equilibrium had been established. When samples were needed for analysis, the required amount of solution was extracted from the vessel in the environmental chamber by means of a reduced pressure system.

Results of the conductivity experiments are reported in Fig. 1 and Fig. 2 for 39, 34, 30, and 25% KOH and for 36.3% and 30% KOH saturated with ZnO at temperatures from 36° to —66°C. Both Dirkse (4) and Bodamer (1) have shown that for a particular KOH concentration and temperature, the specific conductivity decreases as the concentration of zinc in solution increases.

The conductivity data point out one major problem which must be considered in the use of alkaline batteries at low temperatures. There will be about a 100 fold change in the internal resistance of the battery which in itself can grossly affect the charge-discharge characteristics of the battery. For the pure KOH solutions, the 30% KOH solution exhibits the best behavior over the temperature range investigated. The 25% KOH solution is equally conductive at temperatures down to —23°C and is slightly more conductive for temperatures down to —36°C, but is limited by a freezing point in the neighborhood of —41°C. The conductivity data for the KOH solutions saturated with

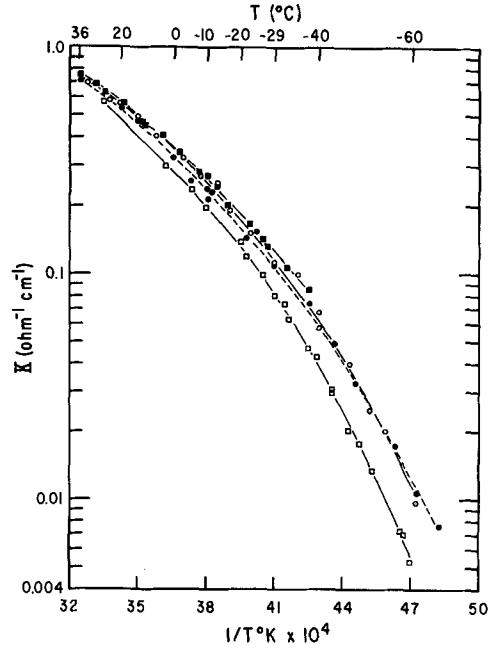

Fig. 1. Specific conductivity of KOH solutions as a function of temperature. ■ 25% KOH; O 30% KOH; ● 34% KOH; and □ 39% KOH.

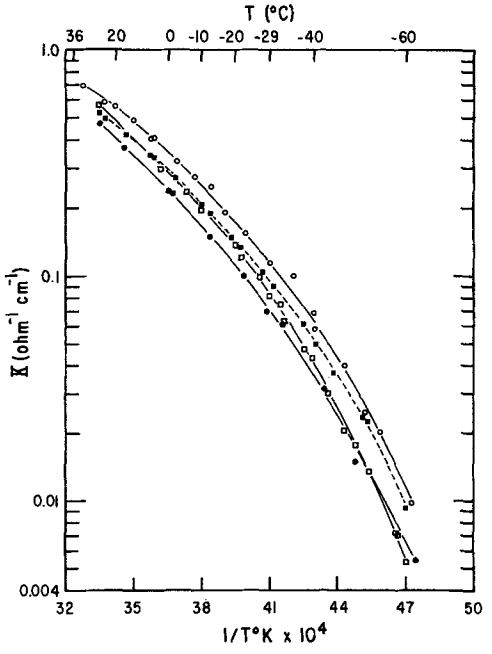

Fig. 2. Specific conductivity of KOH and KOH-ZnO solutions as a function of temperature. O 30% KOH; □ 39% KOH; ● ZnO saturated 36.3% KOH; and ■ ZnO saturated 30% KOH.

Table I. Solubility of ZnO in KOH at 25°C

% KOH (before saturation)	*M* Zn ions in solution
25 (5.5*M* KOH)	0.45
30 (6.9*M* KOH)	0.64
34 (8.1*M* KOH)	0.83
36.3 (8.7*M* KOH)	0.95

ZnO at these low temperatures are consistent with that reported by Bodamer at the higher temperatures. Addition of ZnO to a KOH solution decreases the conductivity of the solution.

Results of the solubility studies of ZnO in 25, 30, 34, and 36.3% KOH at 25°C are given in Table I and are in agreement with the values reported by Bodamer (1) and Dirkse (2). The effect of temperature on the solubility of ZnO in 36.3% KOH is shown in Table II. As the temperature decreases from 26° to −62°C, the solubility of ZnO appears to be invariant. Bodamer observed the same effect for temperatures between 10° and 95°C. Based on these two sets of data, the over-all heat of solution appears to be close to zero.

Manuscript received July 25, 1967.

Table II. Effect of temperature on the solubility of ZnO in 36.3% KOH

Temperature, °C	*M* Zn ions in solution
−62	0.92
−51	0.92
−30	0.95
−30	0.94
−26	0.97
−10	0.92
0	0.94
+26	0.97

Any discussion of this paper will appear in a Discussion Section to be published in the June 1968 JOURNAL.

REFERENCES

1. G. W. Bodamer, "Heat Sterilizable Impact Resistant Cell Development," Jet Propulsion Lab. Contract No. 951296.
2. T. P. Dirkse, *This Journal*, **106**, 154 (1959).
3. G. Jones and B. C. Bradshaw, *J. Am. Chem. Soc.*, **55**, 1780 (1933).
4. T. P. Dirkse, *This Journal*, **102**, 497 (1955).

Characterization of Energy Transfer Interactions between Rare Earth Ions

L. G. Van Uitert

Bell Telephone Laboratories, Incorporated, Murray Hill, New Jersey

ABSTRACT

Energy transfer studies employing the sodium rare earth tungstates (scheelite structure) indicate a number of modes of, and requirements for, nonradiative interaction. Direct dipole-dipole interactions are prevalent. However, dipole-quadrupole interactions are observed for the states of the larger rare earth ions that lie high in energy. The relation of lifetime (τ_e) to intensity changes with the mode of transfer. Phonon assisted transfer is enhanced by exchange coupling between rare earth ions in nearest or next nearest neighbor positions. Excitation may migrate between Tb ions in such positions when thermally activated and provided a suitable quenching center (*e.g.*, Nd, Eu) is present. Such migration appears to be directional in comparison to transfer by radiation reabsorption. The latter is essentially random. Methods for analyzing lifetime data for transfer interactions are also discussed.

Energy transfer between rare earth (RE) ions is a subject of appreciable current interest for practical as well as theoretical reasons. The use of rare earths for laser and colored television applications have stimulated a desire for a better understanding of transfer. Early work in this field has been discussed by Botden (1). More recent work has been summarized elsewhere (2). Much of the previous work has been limited to demonstrations that transfer does occur and general statements as to the probable mechanisms involved. In fact, however, a sufficiently strong theoretical basis exists for more exacting results to be obtained (3-6). The RE ions are particularly suitable for the study of energy transfer as the absorption and emission due to f-electrons is sharp and the associated oscillator strengths are weak.

Energy transfer is generally associated with multipolar interactions, radiation reabsorption, or exchange. These effects can be identified by examining intensity and lifetime data as a function of the excited (E) and/or the quenching (Q) ion concentration. Intensity values can be obtained by direct measurement under equilibrium conditions, but lifetime is obtained under transient conditions and is somewhat subject to interpretation. Procedures for analyzing lifetime data and the significance of various correlations of intensity and lifetime with E-ion and/or Q-ion concentration are discussed.

Materials and Measurements

Crystals of various members of the series $Na_{0.5}(Y,RE)_{0.5}WO_4$, where RE = Pr, Nd, Sm, Eu, Tb, Dy, and or Er in the combinations indicated in the accompanying figures, were grown from a $Na_2W_2O_7$ flux as described previously (7). The crystals have the scheelite ($CaWO_4$) structure; however, the Na, Y, and RE ions are distributed somewhat randomly over the dodecahedral sites normally occupied by Ca. The compositions were analyzed by x-ray fluorescence methods.

Intensity comparisons were obtained using a standard plaque technique. The intensity of emission of Pr (at 0.487μ for Pr^3P_0), of Sm (at 0.598μ for $Sm^4F_{5/2}$), of Eu (at 0.614μ for Eu^5Do), of Tb (at 0.544μ for Tb^5D_4), of Dy (at 0.574μ for $Dy^4F_{9/2}$) and of Er (at 0.552μ for $Er^4S_{3/2}$) was obtained under ~0.365μ excitation as provided by a CH4 spotlamp and CS7-54 longwave uv pass filter. The intensity of emission of Er (at 1.56μ for $Er^4/I_{13/2}$) or Nd (at 1.06μ for $Nd^4F_{3/2}$) was obtained under 0.43-0.62μ excitation isolated from the CH4 lamp by a CS3-72 cut-off filter and a $CuSO_4$ solution before the sample. A Gaertner high dispersion spectrometer equipped with an AMINCO microphotometer and S11 detector were employed to record data for the visible region. A Bausch and Lombe No. 33-86-03 monochromator, with a CS7-56 filter at the input, and S1 detector at the output, was used to record data at 1.06μ; and a Bausch and Lombe No. 33-86-04 monochromator, with a CS7-56 filter at the input, and a InAs detector at the output, was used to record data at 1.56μ.

Lifetime data were obtained employing a confocal ellipse laser housing with an EG&G FX12 flashlamp at one focus and the sample at the other. One side of the ellipse was slotted so that the output of the sample could be viewed. A Bausch and Lombe No. 33-86-02, -03 or -04 monochromator equipped with an S1, cooled S11 (~217°K), or cooled InAs (~77°K) detector and oscilloscope were used to obtain photographic recordings of the decay curves. A CS-7-54 filter was placed between the flashlamp and sample when obtaining data in the visible region. A CS-3-72 filter was placed between the lamp and sample in measuring at 1.06μ, but none was used in obtaining data at 1.56μ A CS-7-56 filter was placed in front of the monochromator for all infrared measurements.

Intensity and Lifetime

The emission spectra of RE ions change little with concentration provided that increasing substitution does not appreciably change the effective crystal field seen by the RE ions. This condition is satisfied when substituting RE ions for others of equivalent radius and valence in the sodium rare earth tungstates.

The probability for de-excitation of the E-species (P_3) is equal to the sum of the probabilities for emission (P_1) and nonradiative loss (P_2). Therefore emission per E-ion (I) relative to that obtained under dilute conditions (I_o) is

$$I/I_o = P_1/P_3 = P_1/(P_1 + P_2) \qquad [1]$$

If the nonradiative losses are attributable to multipolar transfer, $P_2 \propto (C/C^*)^{\theta/3}$ where C is the Q-ion concentration, C^* is the critical transfer concentration of Q-ions and θ = 6, 8, or 10 for dipole-dipole, dipole-quadrupole, or quadrupole-quadrupole interactions, respectively (3-6). Substituting into relation [1] and rearranging, one obtains

$$I/I_o = [1 + \beta(C/C^*)^{\theta/3}]^{-1} \qquad [2]$$

where β is a constant for each interaction.

Lifetime measurements are obtained under transient conditions and can involve various modes of decay that complicate their interpretation. When there is no interaction between RE ions, the emission decay curve is a single exponential. Lifetime can then be

taken to be the time (t) required for the transient intensity (Φ) to fall to 1/e (or 0.368) of the value it has at $t = 0$. This relation defines τ_e. If direct multipolar interactions quench the E-species, the decay curve is much more complex. τ_e/τ_o, where τ_o is the value of τ_e under dilute conditions, cannot then be substituted directly for I/I_o in relation [2]. However, this relation can be employed to define an arbitrary lifetime τ_a

$$\tau_a/\tau_o = [1 + \beta'(C/C^*)^{\theta/3}]^{-1} \qquad [3]$$

The relation of τ_e to τ_a and the procedure for determining a lifetime (τ_i) which approximates τ_a from the initial or early slope of the decay curve is discussed in the Appendix. Properly selected values of τ_i correlate with I and are therefore helpful in characterizing energy transfer interactions.

Interactions

Exchange is generally limited to interactions between RE ions in nearest neighbor (nn) or next nearest neighbor (nnn) dodecahedral sites in the scheelites. Six such interactions are permissible (8). Therefore, the fraction of RE ions which, in any event are little affected by exchange is $(1 - x)^6$, where x is the fraction of dodecahedral sites occupied by RE ions. Where RE ions that are exchange coupled (but no others) are quenched, intensity of emission per ion (I) will follow this relation and a peak in total emission will be obtained at $\sim x = 0.14$. When direct multipolar interactions are involved, quenching is generally more extensive and relations [2] and [3] tend to be obeyed (8-14). Quenching is even greater when excitation migrates over the E-ion set. If migration is rapid compared to direct transfer, quenching tends to be proportional to Q-ion concentration ($\theta = 3$), since transfer to Q-ions from close lying E-ions becomes the rate limiting step (8-14). Lifetime tends to be a single exponential, but decreases rapidly with Q-ion concentration under these conditions. If radiation reabsorption, self-quenching, or internal relaxation is strong, the foregoing intensity and/or lifetime relations can be altered significantly. Examples are cited under results.

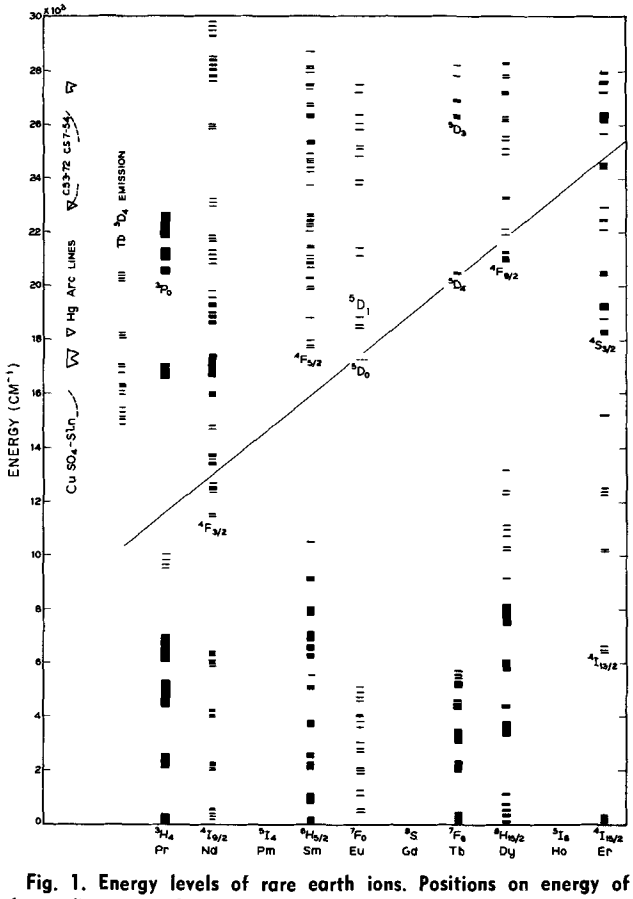

Fig. 1. Energy levels of rare earth ions. Positions on energy of the radiation peaks from the mercury arc source, of emission lines of Tb from Tb^5D_4, and of the cut-off frequencies for the CS7-54, CS3-72, and $CuSO_4$ solution filters are also indicated. The diagonal line is a somewhat arbitrary demarcation between manifolds which have been observed to participate in dipole-quadrupole interactions (upper part) and those for which only dipole-dipole interactions have been observed.

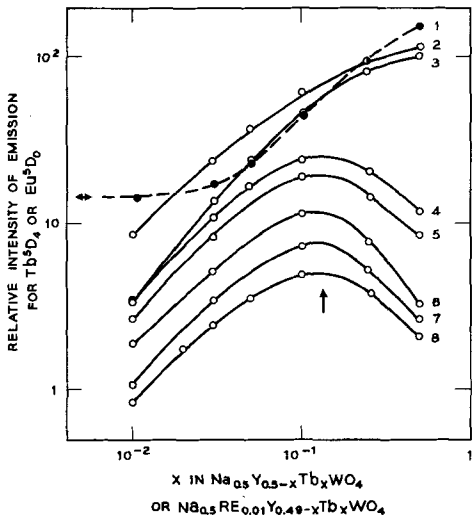

Fig. 2. Relative intensity of emission of Tb from Tb^5D_4 (O) at 295°K *vs.* Tb concentration for the following series: curve 3, $Na_{0.5}Y_{0.5-x}Tb_xWO_4$; curves 2, 4, 5, 6, 7, and 8, $Na_{0.5}RE_{0.01}Y_{0.49-x}Tb_xWO_4$ where RE = Dy, Eu, Pr, Sm, Nd, and Er respectively. Curve 1 represents emission from Eu^5D_0 (●) for series 4. The reference mark (↔) indicates the intensity of emission for Eu in $Na_{0.5}Eu_{0.01}Y_{0.49}WO_4$.

Results

The positions in energy of significant excited states of Pr, Nd, Sm, Eu, Tb, Dy, and Er in the tungstates are shown in Fig. 1. The energies of the spectral lines for emission from Tb^5D_4 and for emission from the CH4 Hg arc lamp and the cut-off frequencies of the CS7-54, CS3-72, and $CuSO_4$ solution filters employed are also indicated. The diagonal line represents a somewhat arbitrary demarcation between states that have been observed to participate in dipole-quadrupole ($\theta = 8$) interactions (upper part) and those for which only dipole-dipole ($\theta = 6$) interactions have been observed (see Discussion). The manifold designations are those given by Dieke for chlorides (15).

Intensity of emission from Tb^5D_4 at 295°K under 0.365μ excitation is shown *vs.* Tb concentration in various series in Fig. 2. All of the Tb intensity data is relative to 100 for $Na_{0.5}Tb_{0.5}WO_4$. Curve 3 is for the series $Na_{0.5}Y_{0.5-x}Tb_xWO_4$ and curves 2, 4, 5, 6, 7, or 8 are for the series $Na_{0.5}RE_{0.01}Y_{0.49-x}Tb_xWO_4$ where RE equals Dy, Eu, Pr, Sm, Nd, or Er, respectively. Dy transfers excitation from $Dy^4F_{9/2}$ (20,900 cm^{-1}) to Tb^5D_4 (20,500 cm^{-1}) and has little quenching effect on Tb^5D_4 for the indicated Dy concentration. This is shown by curve 2 lying above curve 3. Eu, Pr, Sm, Nd, and Er, however, increasingly quench Tb^5D_4 in the given order. If only direct Tb to Q-ion multipolar interactions occurred, curves 4-8 would all be parallel to curve 3 as the average distance from Tb to Q-ion is not dependent on Tb concentration. In general, the strengths of the multipolar interactions responsible increase with the overlap of Tb emission and RE absorption. However, discrepancies do occur (2, 12).

At high Tb concentrations, excitation may migrate from remote Tb ions to those that are close to Q-ions and thereby enhance the probability for transfer to the latter. This effect accounts for the increased displacement of curves 4-8 from curve 3 at high Tb concentrations. Although Eu, Pr, Sm, Nd, and Er are quite different in quenching power, curves 4-8 all peak at

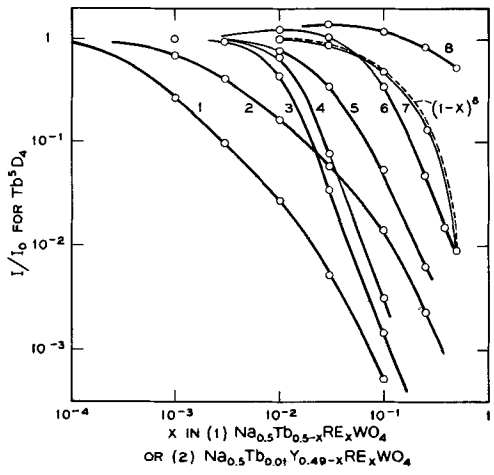

Fig. 3. Normalized emission *per* Tb (I/I_o) for emission from Tb^5D_4 *vs.* RE concentration for the series 1 $Na_{0.5}Tb_{0.5-x}RE_xWO_4$ and 2 $Na_{0.5}Tb_{0.01}Y_{0.49-x}RE_xWO_4$ where RE = Nd, Eu, or Dy. Curves 1 and 4 are for series 1 Nd at 295°K and 4.2°K, respectively. Curve 3 is for series 2 Nd at 295°K. Curves 2 and 5 are for series 1 Eu and series 2 Eu, respectively, at 295°K. Curve 7 represents both series 1 Eu and series 2 Eu at 4.2°K. The data for both of the latter series fit the relation $(1-x)^6$. Curve 6 represents both series 1 Dy and series 2 Dy at 295°K, and curve 8 represents the comparable data for Dy at 77°K (or 4.2°K).

$x \simeq 0.14$ indicating that the migration is dominated by exchange (8-13). That is, energy may move between Tb^5D_4 manifolds only when the Tb-ions are in nearest or next nearest neighbor dodecahedral sites in the tungstates and therefore the chances for such excitation migration depends directly on Tb concentration. When Eu is the Q-species, the excitation lost to Eu by Tb appears as emission from Eu^5D_0 (16). The effect on Eu emission is indicated by curve 1 of Fig. 2. Since multipolar transfer from Tb to $Eu_{0.01}$ is rather weak, the large increase in Eu emission at high Tb concentrations is almost entirely due to enhanced transfer due to migration between exchange coupled Tb ions.

I/I_o for emission *per* Tb from Tb^5D_4 under 0.365μ excitation is shown *vs.* RE concentration in Fig. 3 for the series 1 $Na_{0.5}Tb_{0.5-x}RE_xWO_4$ and 2 $Na_{0.5}Tb_{0.01}Y_{0.49-x}RE_xWO_4$ where RE = Nd, Eu, or Dy. Curves 1 and 4 are for series 1 where RE = Nd, 1 Nd, at 295°K and 4.2°K, respectively. Curve 3 is for series 2 Nd at 295°K, curves 2 and 5 are for series 1 Eu and series 2 Eu, respectively, at 295°K while curve 7 which fits the relation $(1-x)^6$, represents both series 1 Eu and series 2 Eu at 4.2°K. Curve 6 represents both series 1 Dy and series 2 Dy at 295°K, and curve 8 represents the comparable data for series 1 Dy and series 2 Dy at 77°K (or 4.2°K). The curves for RE = Nd, Eu, and Dy have been selected as representative of three different energy relations between the E- and Q-ions. For the first Q-species (Nd), there is an exact match between an emission transition of Tb and an absorption transition of Nd originating from the ground state. Therefore transfer from Tb to Nd is not dependent on temperature. The data of curve 3, for series 2 Nd, is fitted by a $\theta = 8$ relation showing that the transfer from Tb to Nd is dipole-quadrupole in character. Curve 1, for series 1 Nd at 295°K shows the additional quenching due to excitation migration between Tb ions in nn or nnn sites (2,12). This migration no longer occurs at 4.2°K as shown by the near coincidence of curves 3 and 4 of Fig. 3.

For the second Q-species (Eu), Tb emission overlaps Eu absorption at 295°K but not at 4.2°K. However, transfer can occur at the lower temperature through simultaneous interaction with the phonon spectrum. The data of curve 5 of Fig. 3, for series 2 Eu, is fitted by a $\theta = 6$ relation indicating that transfer from Tb to Eu is by dipole-dipole interactions at 295°K. Curve 2, for series 1 Eu, shows that excitation migration between Tb-ions is also prevalent at 295°K when Eu is the Q-ion species. At 4.2°K, however, the data for both series 1 Eu and series 2 Eu lie along curve 7 of Fig. 3. This curve follows the relation $(1-x)^6$, indicating that at 4.2°K transfer from Tb to Eu only occurs when these ions are in nn or nnn positions (9).

Dy, the third Q-ion, only acts as a quenching center for Tb^5D_4 when quenched itself. The receiving manifold ($Dy^4F_{9/2}$) lies $\sim$400 cm^{-1} above Tb^5D_4 (see Fig. 1). Emission from Tb^5D_4 to the ground state, the highest emission line in Fig. 1, can match an absorption transition to $Dy^4F_{9/2}$ when Dy (400 cm^{-1}) is thermally populated. This occurs at 295°K but not at 77°K. At low Dy concentrations, transfer is predominantly from $Dy^4F_{9/2}$ to Tb^5D_4, as indicated in connection with Fig. 2. However, at high Dy concentrations, where Dy is strongly self-quenched, the reverse transfer can be important. Lifetime data show that transfer from Tb^5D_4 to $Dy^4F_{9/2}$ is by dipole-dipole ($\theta = 6$) interactions (10). Curve 6, however, is altered by transfer from Dy to Tb for low Dy concentrations. The extent of this transfer is apparent from curve 8, which represents the data for series 1 Dy and series 2 Dy at 77°K where transfer from Tb to Dy is negligible. It is apparent that I/I_o is not dependent on Tb concentration when Dy is the Q-species, even at 295°K.

I/I_o for emission *per* E-ion is shown *vs.* concentration for self-quenching of $Dy^4F_{9/2}$, $Er^4S_{3/2}$, $Sm^4F_{5/2}$, $Nd^4F_{3/2}$, Pr^3P_o, and Tb^5D_3 by curves 1-6 of Fig. 4A, respectively (8-14). Similar curves for the quenching of Tb^5D_4 by multipolar interactions with Er, Sm, Pr, Nd, Eu, and Dy in the series $Na_{0.5}Tb_{0.1}Y_{0.4-x}RE_xWO_4$ are shown by curves 7-12 of Fig. 4B, respectively. Curve 12′ fits the data of curve 12 when the latter are corrected for Dy to Tb transfer (10). The data for curves 1, 2, 4, 7, 11, and 12′ are fitted by $\theta = 6$ relations indicating that the corresponding interactions are dipole-dipole in character. The data for the remaining curves are fitted by $\theta = 8$ relations, indicating that dipole-quadrupole interactions are responsible for transfer in these instances. Curve 2 deviates from a $\theta = 6$ relation toward $\theta = 8$ at high Er concentrations. This is attributable to the combined effects of radiation reabsorption and rapid internal relaxation (13).

Examples of the relation of τ_i/τ_o to I/I_o for emission per E-ion are given in Fig. 5. Curves 1 and 2 represent τ_i/τ_o and I/I_o, respectively, for emission from Tb^5D_4 in the series (*a*) $Na_{0.5}Tb_{0.1}Y_{0.4-x}Nd_xWO_4$ (for Tb^5D_4, τ_o = 565 μsec). Curves 3 and 4 represent I/I_o and τ_i/τ_o, respectively, for emission from Tb^5D_4 in the series (*b*) $Na_{0.5}Tb_{0.1}Y_{0.4-x}Eu_xWO_4$ and curves 5 and 6

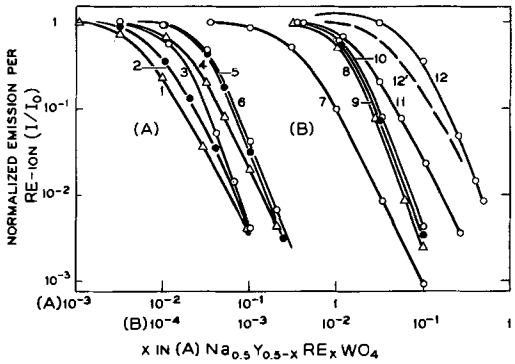

Fig. 4.(A) Normalized emission per E-ion (I/I_o) *vs.* E-ion concentration in series (A) $Na_{0.5}Y_{0.5-x}RE_xWO_4$. Emission is from $Dy^4F_{9/2}$, $Er^4S_{3/2}$, $Sm^4F_{5/2}$, $Nd^4F_{3/2}$, Pr^3Po, or Tb^5D_3 for curves 1-6, respectively. *(B)* Normalized emission *per* Tb (I/I_o) for emission from Tb^5D_4 *vs.* RE concentration for the series *(B)* $Na_{0.5}Tb_{0.1}Y_{0.4-x}RE_xWO_4$ where RE — Er, Sm, Pr, Nd, Eu, or Dy for curves 7-12, respectively.

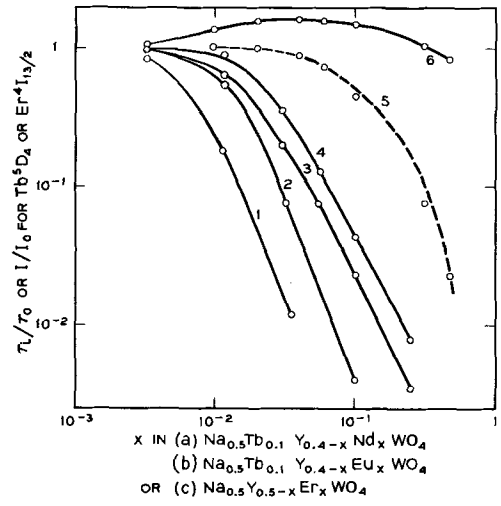

Fig. 5. Normalized initial lifetime (τ_i/τ_0) or normalized emission per E-ion (I/I_o) for emission from Tb^5D_4 or $Er^4I_{13/2}$ vs. Nd, Eu, or Er concentration. Curves 1 and 2 represent τ_i/τ_0 and I/I_o, respectively, for Tb emission from series (a). Curves 3 and 4 represent I/I_o and τ_i/τ_0 respectively for Tb emission from series (b) and curve 6 and the data following curve 5 are for τ_i/τ_0 and I/I_o respectively for Er emission from series (c). Curve 5 is the relation $(1-x)^6$.

approximate I/I_0 and τ_i/τ_o, respectively, for emission from $Er^4I_{13/2}$ in the series (c) $Na_{0.5}Y_{0.5-x}Er_xWO_4$. All data are for 295°K. Moderately high Tb concentrations were employed for series (*a*) and (*b*) to insure fast internal relaxation to Tb^5D_4 (11, 12, 17). Further, radiation reabsorption by Tb^5D_4 is minimal since less than 10% of the emission from Tb^5D_4 is to the ground state. Hence, the relations between τ_i/τ_0 and I/I_0 for these series [(*a*) and (*b*)] are relatively uncomplicated. It can be observed that τ_i/τ_0 falls outside I/I_o for series (b), which follows a $\theta = 6$ relation, and inside I/I_o for series (*a*), which follows a $\theta = 8$ relation.

All of the strong emission transitions of Er appear to be to the ground manifold. Further, the drain time from higher lying manifolds to $Er^4I_{13/2}$ is small compared to the lifetime of the latter (~4,500 μsec) (13). Hence, the prolonged lifetimes where $\tau_i/\tau_0 > 1$, indicated by curve 6 of Fig. 5, for intermediate values of Er in series (c), can be attributed to radiation reabsorption. The I/I_o data for series (c) follows the $(1-x)^6$ relation indicated by the broken line (curve 5). This indicates that quenching is associated with interactions between Er ions in nn or nnn positions. The quenching may involve nonradiative excitation migration between exchange coupled Er-ions to Q-ions present as impurities or it may be due to pairing enhancing interaction with the phonon spectrum. In either case, radiation absorbed by the paired Er-ions is not emitted and therefore beyond ~$Er_{0.1}$, the chances for absorption and re-emission of resonance radiation decreases with increasing Er concentration, resulting in a decline in τ_i/τ_0 back to ~1.0.

Discussion

The lifetime τ_a defined by relation [3] can be approximated by measuring τ_i from the initial or early slope of the decay curve for emission, as outlined in the Appendix. τ_i/τ_0 has the same dependence on C/C^* as the corresponding equilibrium intensity measurement I/I_o. However, for multipolar interactions where other things are equal τ_i/τ_0 lies at decreasing values of C/C^* relative to the comparable I/I_0 curve as θ increases (see Fig. 5). This displacement is consistent with the fact that, when quenching is strong, the fraction of the total emission yielded up to $t = \tau_e$ (or τ_i) changes from 0.28 to 0.10 to 0.045 on changing from a $\theta = 6$ to 8 to 10 mechanism. Quadrupole effects tend to shift τ_i/τ_0 to the inside of the comparable I/I_o curve while prolonged drain time to the emitting manifold or radiation reabsorption by this manifold have the opposite effect.

Multipolar interactions generally increase with the overlap of E-ion emission and Q-ion absorption. However, when the overlap is small, processes involving the simultaneous release of energy to the phonon spectrum become competitive. Single phonon processes, for energies up to that of the fundamental stretching frequency (~850 cm^{-1} in the tungstates), do not appear to have drastically reduced probabilities for transfer (12, 13). Further, these and more complex interactions can be facilitated by the mixing effects of exchange.

As shown in Fig. 1, the positions in energy of Eu^5D_1 and Eu^5D_0 and the emission lines originating from Tb^5D_4 are mismatched by ~100 cm^{-1}, with the closest emission lines lying below the Eu levels. The closest to a match for a Tb emission line that lies higher in energy than a Eu level (Eu^5D_0) is out by ~900 cm^{-1}. At 295°K, however, Eu^7F_1 (~500 cm^{-1}) is populated from Eu^7F_0, permitting a match of the Tb emission line at ~16,800 cm^{-1} to the Eu absorption transition Eu^5D_0 (17,300 cm^{-1}) ← Eu^7F_1 (~500 cm^{-1}). As a result, multipolar transfer takes place at this temperature (curve 5 of Fig. 3). However, at 4.2°K, Eu^7F_1 is not populated, and transfer requires the release of ~900 cm^{-1} to the phonon spectrum. I/I_o follows the relation $(1-x)^6$ under these circumstances, indicating that the mixing effects of exchange facilitate transfer from Tb to Eu (curve 7 of Fig. 3).

Excitation migration between Tb-ions in nn or nnn positions at 295°K is evident for series 1 Nd and series 1 Eu (curves 1 and 2 of Fig. 3, respectively) but not for series 1 Dy (curve 6 of Fig. 3). Nd and Eu can act as quenching centers as single Q-ions while Dy only does so when it, itself, is quenched. However, as Dy is self-quenched at intermediate concentrations (see curve 1 of Fig. 4) and, therefore, dissipates excitation received from Tb^5D_4 by multipolar transfer, it is evident that excitation migration does not occur, even at 295°K, unless a sink that acts directly is present. In contrast to the essentially random movement of excitation by emission and reabsorption, this implies that migration by nonradiative interactions can be directed toward the Q-ion promoting the transfer.

It is apparent from Fig. 4 that both $\theta = 6$ and $\theta = 8$ relations are observed for interactions between RE-ions in the scheelite structure. The manifolds Pr^3P_0, $Sm^4F_{5/2}$, Tb^5D_3 and Tb^5D_4 have been found to participate in dipole-quadrupole interactions. These lie above the diagonal in Fig. 1. The manifolds $Nd^4F_{3/2}$, Eu^5D_0, $Dy^4F_{9/2}$, and $Er^4S_{3/2}$ lie below the diagonal. So far the latter have only been found to participate in dipole-dipole transfers. Such interactions may be typical for smaller RE-ions and for the lower lying levels of the larger RE-ions. Dipole-quadrupole interactions seems more likely for the higher lying levels of the larger RE-ions. There seems to be an increased probability for quadrupole interactions when the states involved are strongly perturbed. Perturbation increases with the tightness of the fit of the rare earth into the site it occupies and with the proximity of the manifold involved to the continuum.

Acknowledgments

The author is indebted to J. E. Geusic and R. N. Thurston for helpful discussions.

APPENDIX

Analysis of Lifetime Data

The intrinsic lifetime for fluorescence (τ_0) of an excited E-ion state is equal to the time (τ_e) required for the transient intensity of emission (Φ) to decay to $1/e$ (or 0.368) of its initial value when there is no interaction between E-ions or with Q-ions by radiative or nonradiative means. When conditions are ideal, Ln Φ is linear with time (t). However, if multipolar transfer occurs τ_e will be less than τ_0 and, if emission, corresponding to transitions to the ground manifold of

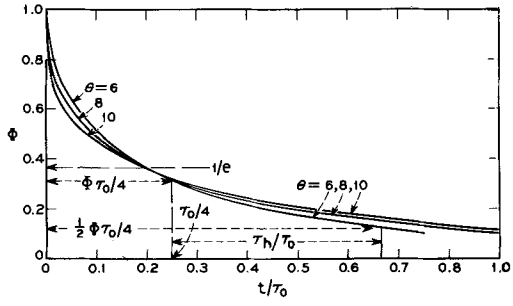

Fig. 6. Transient intensity (Φ) vs. normalized time (t/τ_o) for relation [5] when $C = C^*$ and θ is the value indicated. Markings relevant to determining τ_h/τ_o are also present.

the E-ion, is reabsorbed τ_e will tend to be greater than τ_o.

The probability for de-excitation of the E-species (P_3) is equal to the sum of the probability for emission (P_1) and the probability for nonradiative transfer (P_2)

$$P_3 = P_1 + P_2 \qquad [4]$$

P_1 is inversely related to τ_o (or $P_1 \propto 1/\tau_o$); $P_2 \propto (C/C^*)^{\theta/3}$ as indicated previously; and P_3 is inversely related to τ_a, the representative lifetime when both radiative and nonradiative de-excitation occurs. Substituting for P_1, P_2, and P_3 in relation [4] and rearranging, one obtains relation [3] which has the same form as that for intensity, relation [2]. θ and β/C^* can be determined from relation [2]. θ can also be determined from relation [3] provided one measures the proper lifetime, *i.e.*, τ_a.

θ and an independent value for C^* can be obtained by fitting accurately measured decay curves to the theoretical expression for decay given by Inokuti and Hirayama (6).

$$\Phi(t) = \exp\,[-t/\tau_o - \Gamma(1 - 3/\theta)\,(C/C^*)\,(t/\tau_o)^{3/\theta}] \qquad [5]$$

However, for most materials such a procedure would require greater measurement accuracy than can generally be relied on. Φ for relation [5] is plotted *vs.* t/τ_o in Fig. 6 for $C = C^*$ and $\theta = 6$, 8, or 10. The value of $\Gamma(1 - 3/\theta)$ is 1.77, 1.43, and 1.30, respectively, for these curves. The markings relating to $\tau_o/4$ and τ_h are discussed below. It can be seen that relatively small errors in measuring Φ can seriously affect one's ability to determine the correct value of θ. It is easier to determine θ from the concentration dependence of intensity by relation [2] or from the concentration dependence of lifetime by relations 3 or 5.

The dependence of τ_e/τ_o on C/C^* for $\theta = 6$, 8, or 10 is shown in Fig. 7 by set (A) curves 1, 2, and 3, respectively. The comparable relations for τ_a/τ_o (or I/I_o are shown by set (B), curves 4, 5, and 6, respectively. Curves 1, 2, and 3 were obtained from relation [5] by setting $\mathrm{Ln}\Phi = -1$.

$$\mathrm{Ln}\Phi = -1 = -t/\tau_o - \Gamma(1 - 3/\theta)\,(C/C^*)\,(t/\tau_o)^{3/\theta} \qquad [6]$$

while curves 4, 5, and 6 were obtained from relation

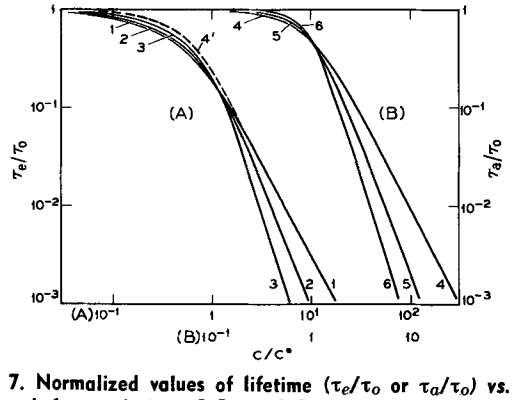

Fig. 7. Normalized values of lifetime (τ_e/τ_o or τ_a/τ_o) vs. C/C^* calculated from relations [6] or [3], respectively. Curves 1, 2, and 3 are for τ_e/τ_o for $\theta = 6$, 8, or 10, respectively, and curves 4, 5, and 6 are for τ_a/τ_o for $\theta = 6$, 8, or 10, respectively, when $\beta' = 1.0$. Curve 4' is obtained from relation (7). Normalized intensity I/I_o follows the τ_a/τ_o relation.

[3] by setting $\beta' = 1$. Curve 4' is curve 4 brought into coincidence with curve 1 (for $C > C^*$) by assigning $\beta' = 3.2$

$$\tau_a/\tau_o = [1 + 3.2(C/C^*)^2]^{-1} \qquad [7]$$

Curve 1, for τ_e/τ_o when $\theta = 6$, deviates up to 30% from curve 4', τ_a/τ_o for $\theta = 6$, over the first order of magnitude of quenching. However, for $C > C^*$, the slope of the curve for either τ_a/τ_o or τ_e/τ_o, from relation [3] or relation [5], respectively, is about equal to θ. For the first order of magnitude of quenching τ_e/τ_o can be corrected to τ_a/τ_o by comparing the above curves. For stronger quenching, where discrimination between θ values is much clearer, τ_e can be employed as a measure of τ_a. However, τ_e is difficult to determine directly in this region. Therefore, if intensity measurements are impractical, other methods for obtaining lifetime data at high Q-ion concentrations should be considered.

It can be seen from relation [6] that when $t < \tau_o$ and $C > C^*$ the second term of the exponent is dominant and the first can be ignored. Under these circumstances, if θ is fixed the decay curves for various C/C^* ratios can be reduced to a single representative curve by multiplying the values along the t/τ_o coordinate (see Fig. 6) by $(C/C^*)^{\theta/3}$. Such relations are shown by curves 4, 5, and 6 of Fig. 8.

Figure 8 has been constructed by plotting Φ from relation [5], on a logarithmic scale *vs.* $n(t/\tau_o)$, on a linear scale, where n is the scaling factor required to position $\Phi = 0.1$ at $n(t/\tau_o) = 1.0$. The parameter $n(t/\tau_o)$ is only used to graph the theoretical decay curves. In practice, the abscissa is t alone on a scale that suitably displays curve symmetry. Curve 1 is the exponential relation for $C/C^* = 0$. Curve 2 is for $C = 0.28C^*$ and $\theta = 6$, curve 3 is for $C = C^*$, and $\theta = 6$ and curves 4, 5, and 6 are representative for Q-ion concentrations where $C > 2C^*$ when $\theta = 6$, 8, or 10, respectively.

Lifetime calculated from the tangent (1, 2'-5' or 6') to the respective curve as drawn is equal in value to τ_a. This value also equals τ_e for 1, 4', 5', and 6'. It is 25% larger than τ_e for 2' and 20% larger than τ_e for 3'. In practice, for the first factor of 5 of quenching, τ_a can be estimated from τ_e by adding the correction indicated by superimposing the calculated relations between τ_e/τ_o and τ_a/τ_o. The corrections required are essentially independent of θ as τ_a/τ_o varies in the same manner as τ_e/τ_o with θ (see Fig. 7). However, if there is some question as to the value of Φ at $t = 0$, the decay curve can be plotted as in Fig. 8 and τ_a inferred from the proper tangent. For weak interactions (curves 1 and 2) the tangent required to obtain τ_a averages the points of the curve lying between 10 and

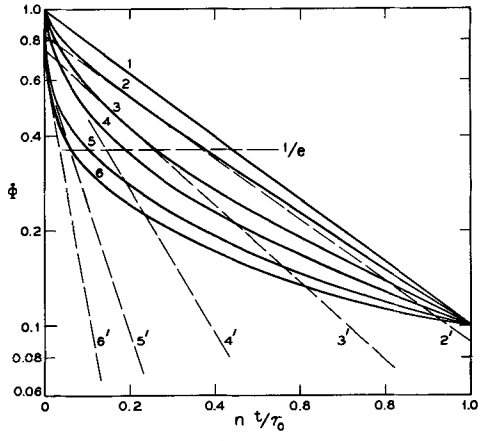

Fig. 8. Transient intensity (Φ) from relation [5] vs. adjusted time, $n(t/\tau_o)$, where n is the scaling factor required to position $\Phi = 0.1$ at $n(t/\tau_o) = 1.0$. Curve 1 is for $C/C^* = 0$; curve 2 is for $C = 0.28C^*$, $\theta = 6$; curve 3 is for $C = C^*$, $\theta = 6$; and curves 4, 5, and 6 are characteristic for $C > 2C^*$ for $\theta = 6$, 8, or 10, respectively. The tangents 2'-6' are drawn to indicate the correct value of τ_a. As an aid to reading the theoretical curves, it is noted that for the intercept of Φ with, i.e., $\tau_e/\tau_o = (1/n)[n(t/\tau_o)$ for the intercept] and for the tangents $\tau_a/\tau_o = [1/(2.3n)]n(t/\tau_o)_{10}$, where $n(t/\tau_o)_{10}$ is the time period elapsed for a tenfold decrease for the coordinate of the tangent along Φ.

30% of the way along the time coordinate to $\Phi = 0.1$. When quenching is by a factor greater than 5 (*i.e.*, $\tau_e/\tau_o < 0.2$ or $C > C^*$), Φ at $t = 0$ is generally so obscured by the excitation flash, or in some instances by the rise in Φ on excitation being prolonged by a finite drain time from higher lying states, that it is difficult to estimate its value accurately. Under these circumstances, the tangent to the initial measurable slope of the decay curve provides a good estimate of τ_e or τ_a as long as the lifetime for emission exceeds the decay time of the flash lamp. The symmetry of the appropriate curve of Fig. 8 should be kept in mind when choosing the tangent or otherwise estimating lifetime. The tangents shown in Fig. 8 indicate the slopes to measure to obtain τ_a in each case. The lifetime derived in this way from the early or initial slope of the decay curve, or by correcting τ_e, is termed τ_i and is the estimate of τ_a obtained by observing the foregoing procedures.

Other Measures of τ

As shown in Fig. 7 there is less than 5% difference in τ_e/τ_o for $\theta = 8$ and either the neighboring curve for $\theta = 6$ or for $\theta = 10$ over the first order of magnitude of quenching. Obviously it is difficult to characterize transfer interactions from such data alone. Further, even if τ_e or a comparable defined lifetime is accurately measured the results would be deceiving unless they were properly analyzed. For example τ_e values employed in place of τ_a values in relation [3] may indicate the wrong value of θ. As can be seen from Fig. 7, τ_e/τ_o for $\theta = 10$, indeed, lies closer to τ_a/τ_o for $\theta = 6$ than does τ_e/τ_o for $\theta = 6$ itself over the first order of magnitude of quenching.

Nakazawa and Shionoya employ a lifetime (τ_h) which is defined as the time (t) required for Φ to fall from its value at $\tau_o/4$ to one-half of that value, as illustrated for the $\theta = 6$ curve of Fig. 6 (18). This definition effectively limits measurement to the first order of magnitude of quenching. τ_h/τ_o bears a relation to I/I_o that is susceptible to analysis. However, the shape of the curve follows a $\theta = 3$ relation regardless of the actual mechanism of quenching. These results are quite similar to those obtained by taking lifetime from the tangent to the decay curve (Ln Φ *vs.* t) at a fixed value of t. As can be seen from relation [5], θ appears in the exponent of t/τ_o not C/C^*; hence, the curves obtained by plotting such data *vs.* C/C^* only change in displacement along the latter coordinate as θ changes.

Unfortunately, most of the literature concerning lifetime measurements connected with transfer interactions is not clear as to the actual procedure for analyzing data. It is therefore not easy to draw significant conclusions concerning the mechanism of energy transfer involved from such lifetime data alone.

Manuscript received May 1, 1967; revised manuscript received June 23, 1967. This paper was presented at the Dallas Meeting, May 7-12, 1967.

Any discussion of this paper will appear in a Discussion Section to be published in the June 1968 JOURNAL.

REFERENCES

1. F. J. Botden, *Philips Res. Rept.*, **6**, 425 (1951); **7**, 197 (1952).
2. L. G. Van Uitert and L. F. Johnson, *J. Chem. Phys.*, **44**, 3514 (1966).
3. D. L. Dexter, *ibid.*, **21**, 836 (1953).
4. D. L. Dexter and J. H. Schulman, *ibid.*, **22**, 1063 (1954).
5. D. L. Dexter, *Phys. Rev.*, **26**, 1962 (1962).
6. M. Inokuti and F. Hirayama, *J. Chem. Phys.*, **43**, 1978 (1965).
7. L. G. Van Uitert and R. R. Soden, *J. Appl. Phys.*, **31**, 328 (1960).
8. L. G. Van Uitert, E. F. Dearborn, and J. J. Rubin, *J. Chem. Phys.*, **45**, 1578 (1966).
9. L. G. Van Uitert, E. F. Dearborn, and H. M. Marcos, *Appl. Phys. Letters*, **9**, 255 (1966).
10. L. G. Van Uitert, E. F. Dearborn, and J. J. Rubin, *J. Chem. Phys.*, **46**, 3551 (1967).
11. L. G. Van Uitert, E. F. Dearborn, and J. J. Rubin, *J. Chem. Phys.*, In press.
12. L. G. Van Uitert, E. F. Dearborn, and J. J. Rubin, *J. Chem. Phys.*, **47**, 547 (1967).
13. L. G. Van Uitert, E. F. Dearborn, and J. J. Rubin, *J. Chem. Phys.*, In press.
14. L. G. Van Uitert, E. F. Dearborn, and J. J. Rubin, *J. Chem. Phys.*, **46**, 420 (1967).
15. G. H. Dieke, in "Advances in Quantum Electronics," J. A. Singer, Editor, p. 164, Columbia University Press, New York (1961).
16. L. G. Van Uitert and R. R. Soden, *J. Chem. Phys.*, **36**, 1289 (1962).
17. L. G. Van Uitert and R. R. Soden, *ibid.*, **32**, 1161 (1960).
18. E. Nakazawa and S. Shionoya, Preprints 9/70 International Conference on Luminescence, Budapest 1966.

Photovoltaic Behavior of the TCNE-THF Solution Charge-Transfer Complex

P. J. Reucroft, P. L. Kronick, and E. E. Hillman

Chemistry Department, The Franklin Institute Research Laboratories, Philadelphia, Pennsylvania

ABSTRACT

Reversible photoinduced electron transfer in solutions of tetracyanoethylene (TCNE) in tetrahydrofuran (THF) has been shown to lead to a voltaic effect. The photovoltage spectral response peaks at the absorption edge of the charge-transfer band, demonstrating that light capable of promoting charge-transfer must penetrate to the vicinity of the electrode. Maximum power output recorded is in the region of 10^{-10} watts for monochromatic light input intensity of 10^{-3} w/cm^2. A sublinear dependence of photovoltage on light intensity suggests a mechanism of photovoltage production whereby photogenerated ionic species distribute to give concentration gradients, or alternatively a process involving the preferential adsorption of the negative ion species.

The production of photovoltages in organic systems has been widely reported. Thin films of organic solid sandwiched between semitransparent layers of metal have been most commonly investigated (1g). Organic solids studied in this way include aromatic hydrocarbons (1a), organic dyes and pigments (1b, c) and organometallics (1d). Photovoltaic effects in organic crystals in contact with electrolyte solutions as electrodes have also been reported (1e). Photovoltages obtained in layers of electron-donor organic solids in contact with electron-acceptor organic solids have been attributed to photoinduced donor-acceptor interaction (1f). Photovoltages in these systems usually fall in the range 10^{-6} to 1v and power outputs in the range 10^{-8} to 10^{-17}w.

In order to explore more fully the role of donor-acceptor interaction in photovoltage production in organic systems and evaluate the potential of organic systems for significant power output, we have investigated the photovoltaic behavior of molecular complexes in solution. The present work deals with the photovoltaic behavior of solutions of tetracyanoethylene (TCNE) in tetrahydrofuran (THF). This system was chosen for the investigation as previous studies on photoinduced electron spin resonance (2a, b) and photoconduction (2b) have provided some understanding of the fundamental processes which take place on illumination. In addition, complicating photochemical reactions are minimal in this system (2c), the main effect of illumination being to promote a reversible photoinduced electron transfer from the electron-donor molecule (THF) to the electron-acceptor molecule (TCNE). Reversible photovoltaic effects were thus expected and were, in fact, found.

Experimental

Photovoltaic measurements were carried out by illuminating platinum electrodes immersed in the TCNE-THF solutions. A typical cell, used in initial studies, is shown in Fig. 1. The electrodes were constructed from platinum sheet, 0.5 mm in thickness, welded to 2 mm diameter platinum rod. The electrode area and spacing was 2 cm^2 and 1 cm, respectively. Solution was introduced into the cell and was in contact with platinum and glass only. After successive freeze-thaw cycles, evacuating after each freezing procedure, the cell was sealed off under a vacuum of 5 x 10^{-3} mm Hg. In later experiments, an all-glass cell was used to eliminate solvent attack on the O-ring.

THF, supplied by Matheson, Coleman, and Bell, was purified by distillation from a sodium dispersion under 1 atm of nitrogen. Eastman Kodak White Label TCNE was vacuum sublimed. All measurements were made on freshly prepared solutions.

The experimental arrangement for measuring photovoltage is shown in Fig. 2. A Keithley 610 electrometer, or a Cary vibrating-reed electrometer operating in the 31V mode, was used to measure the photoinduced voltages. Open-circuit photovoltages were usually measured. The power output of the photocell was determined by measuring the photovoltage across a series of shunt resistors, varied from 10^{11} to 10^2 ohms. An Osram 900-W or 150-W xenon light source was used for illumination. Monochromatic light could be obtained from these sources in conjunction with Bausch and Lomb monochromator gratings, Nos. 33-86-07 and 33-86-02. Illumination conditions were arranged so that one electrode received the full

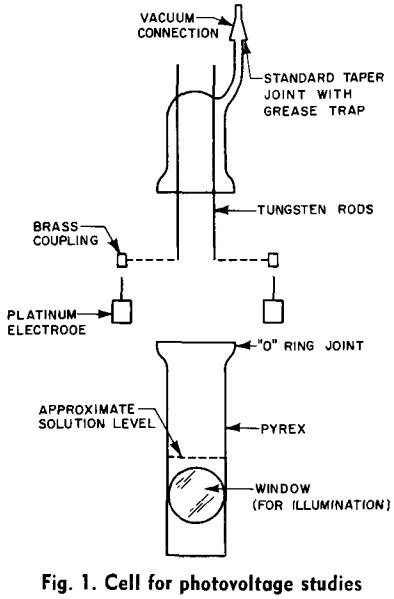

Fig. 1. Cell for photovoltage studies

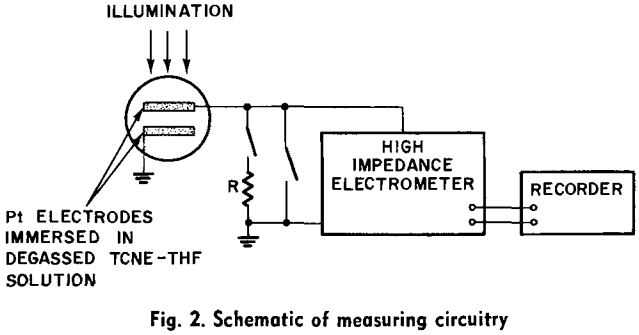

Fig. 2. Schematic of measuring circuitry

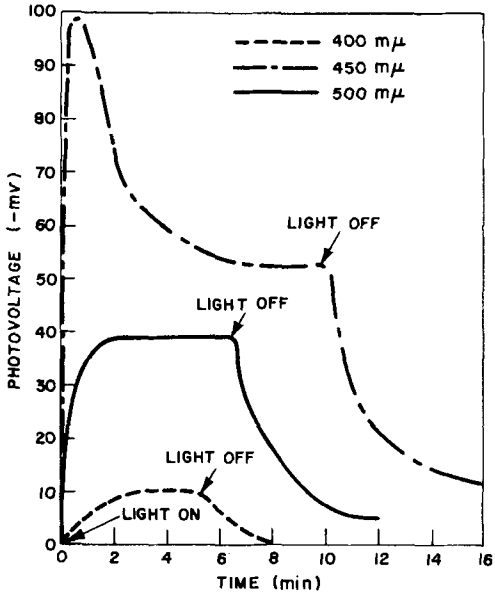

Fig. 3. Photovoltage response of 10^{-1}M TCNE-THF solution at various illuminating wavelengths.

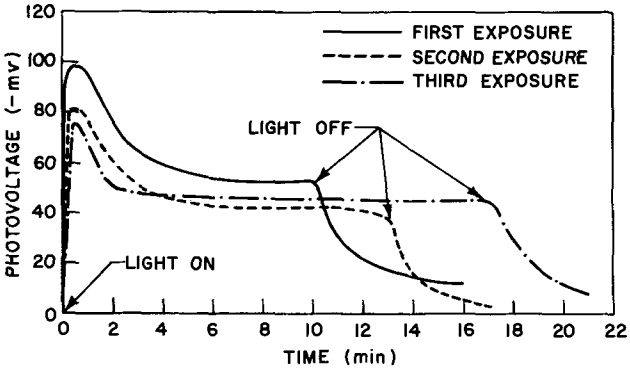

Fig. 4. Reproducibility of photovoltage response of 10^{-1}M TCNE-THF solution at 450 mμ.

illumination. Illumination intensities were measured by means of a bismuth-silver thermopile supplied by Eppley Laboratory Inc. Solution spectra were measured with a Cary 14R recording spectrophotometer.

Results

The photovoltage response is shown in Fig. 3 at three illuminating wavelengths for a 10^{-1}M solution of TCNE in THF. The fast rise observed at 450 and 500 mμ reflects the response time of the external circuit. A slower rise was observed at 400 mμ, however, which appears to be a property of the solution system. The electrode attached to the electrometer input (the illuminated electrode) always acquired a negative voltage. Reproducibility and reversibility of the photovoltage is illustrated in Fig. 4.

Similar results were obtained with 10^{-3} and 7 x 10^{-1}M solutions of TCNE in THF. The 10^{-3}M solution responded more slowly and required a dark period for regeneration.

The spectral dependence of the photovoltage for three solution concentrations is shown in Fig. 5. The photovoltage magnitude is corrected to a uniform incident light intensity throughout the spectral region. The absorption spectra of the various solutions is also shown in Fig. 5 illustrating that the photovoltage increases sharply with decreasing wavelength at the absorption edge for each solution. The absorption of TCNE-THF solutions in this spectral region is due to the TCNE-THF charge-transfer band (2b, c, 3). The maxima in the photovoltage curve for the more concentrated solutions demonstrate that light capable of producing charge-transfer must be able to penetrate to the vicinity of the electrode in order to promote photovoltage production. This is only possible at the absorption edge, in the case of concentrated solutions, since wavelengths at the absorption peak are completely absorbed by the solution and do not penetrate to the electrode region. Thus, the photovoltage spectrum decreases again at the onset of strong absorption, the peak photovoltage shifting to longer wavelengths as the concentration increases. The results for the 10^{-1} and 7 x 10^{-1}M solutions indicated that the peak voltage increases as the TCNE concentration decreases. The peak photovoltage in the case of the 10^{-3}M solution was not determined in view of experimental difficulties due to the reduced light output of the source below 380 mμ. A trend toward a peak voltage at least as high as the peak observed for the 10^{-1}M solution is suggested, however, from the data at wavelengths longer than 380 mμ.

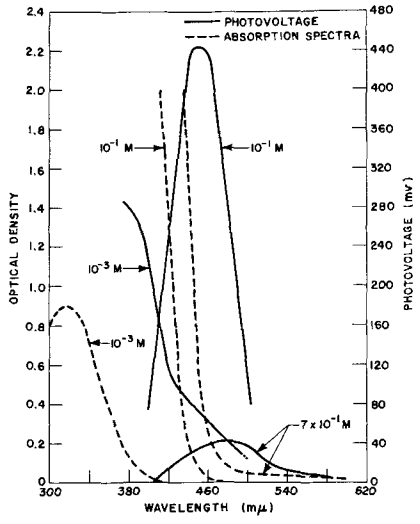

Fig. 5. Photovoltage spectral response and absorption spectra of TCNE-THF solutions (photovoltage corrected to incident light intensity 3.4 mw/cm^2).

Maximum power output was obtained from the 10^{-3}M solution at 1.6 x 10^{-10}w, illuminating with monochromatic light. Maximum power output from the 7 x 10^{-1}M solution with polychromatic light intensity 0.13w/cm^2 was 4 x 10^{-11}w. The photovoltage-current characteristic for a 10^{-3}M solution is shown in Fig. 6.

A sublinear dependence of photovoltage on light intensity was generally observed, *i.e.*, $V = K(I)^n$ where

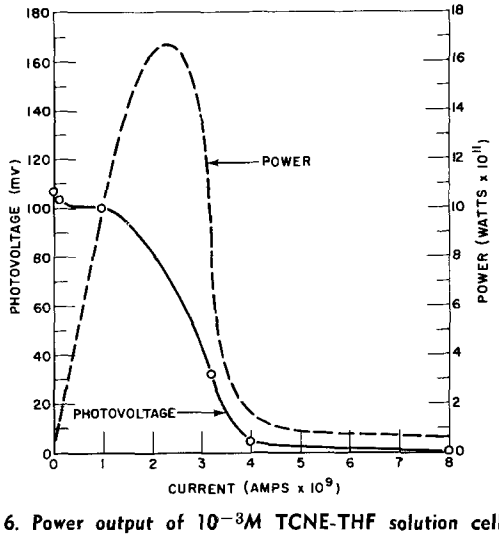

Fig. 6. Power output of 10^{-3}M TCNE-THF solution cell (illuminating wavelength 450 mμ; incident light intensity 1.7 mw/cm^2).

Table I. Effect of illumination intensity on photovoltage of 10^{-3}M TCNE-THF solution

Wavelength, mμ	Intensity, μw/cm²	Photovoltage, mv	Intensity, μw/cm²	Photovoltage, mv	Intensity ratio	Photovoltage ratio
375	—	(−) 40	202	(−) 70	—	1.7
400	54	(−) 70	832	(−) 115	15	1.6
425	112	(−) 54	1370	(−) 68	12	1.3
450	141	(−) 15	1662	(−) 58	12	3.8
475	204	(−) 10	2485	(−) 40	12	4.0
500	183	(−) 2	2080	(−) 18.5	11	9.2

$n < 1$. This is illustrated by the photovoltage data in Table I at two incident light intensities and the plot of photovoltage against incident light intensity shown in Fig. 7. In this plot $n = 0.62$.

Discussion

ESR and photoconductiviy studies have shown that the TCNE negative-ion radical and, presumably, the THF positive-ion radical are formed on illuminating TCNE-THF solutions in the TCNE-THF charge transfer band. The TCNE negative-ion radical was identified from the hyperfine splitting of the ESR signal. The positive-ion radical was not detected, possibly because hole migration from $THF^{+}\cdot$ to THF neutral species (present in large excess) leads to broadening of the ESR signal (4). Chemical reaction of $THF^{+}\cdot$ is unlikely, since no permanent changes are detected.

The present data suggest two possible explanations for the production of photovoltages in charge-transfer solutions. In one view the photogenerated ions distribute to give concentration gradients in the vicinity of a platinum electrode yielding a net emf which can be sensed by the electrode. Evidence for this was provided by measurements of photovoltages with the charge-transfer solution stirred and unstirred. An unstirred 10^{-3}M solution of TCNE in THF gave a photovoltage of 126 mv at 425 mμ. On commencement of stirring, with a Teflon-coated magnetic stirring bar incorporated in the cell, the voltage dropped immediately to 96 mμ and dropped almost to zero on increasing the stirring speed. Assuming that the photovoltage (V) follows the Nernst relation

$$V = A \log C + B \qquad [1]$$

where C is the concentration of ionic species and A and B are constants, then taking $C = K'(I)^{1/2}$ (2b, c), where I is the intensity of incident illumination, we have

$$V = \frac{A}{2} \log I + B' \qquad [2]$$

which is a sublinear dependence of photovoltage on illumination intensity. The observation of a sublinear dependence of photovoltage on illumination intensity is thus consistent with this picture, although the intensity data shown in Fig. 7 does not give a good fit to Eq. [2].

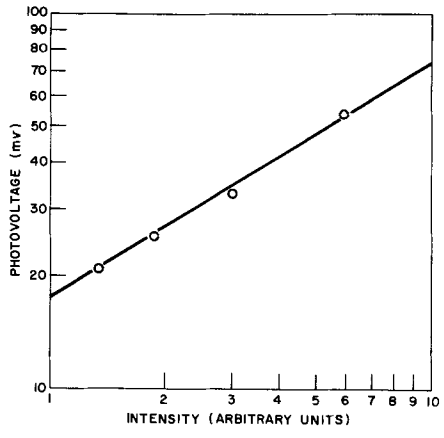

Fig. 7. Photovoltage-illumination intensity relationship for 10^{-1} TCNE-THF solution (illuminating wavelength 500 mμ).

Alternatively the photovoltage may arise from the preferential adsorption of one ionic species on the platinum electrode. This would explain the negative potential if it is assumed that the TCNE negative radical-ion is preferentially adsorbed. When light was confined to the solution between the electrodes, erratic results were obtained. This is further evidence that the interaction between the illumination and the charge-transfer species must take place in the vicinity of the electrode for photovoltage production.

Assuming that the photovoltage is directly proportional to the number of ions adsorbed and that Henry's law obtains, *i.e.*, number of ions adsorbed is directly proportional to the ionic concentration in solution, we have

$$V = K(I)^{1/2} \qquad [3]$$

An approximate fit to such a relationship is shown in Fig. 7. This model predicts a saturation effect with increased intensity as a monolayer of adsorbed ions is approached (Langmuir isotherm). Some evidence for this was found at the highest intensities with polychromatic light. The weight of evidence can thus be considered to favor the second explanation.

Further studies on the interaction of ion radical species with the electrode surface and measurements of photovoltages with reference electrodes are needed to settle some of these points, however.

Maximum power output of the TCNE-THF solution cell was on the order of 10^{-10}w, obtained with the 10^{-3}M solution. This value is on the upper limit of the range of values reported for organic solid photovoltaic systems (1) and suggests that organic solution systems may have more potential than organic solid systems for significant power output. Attempts were made to improve the power output by supplying ionic additives to the solution which would decrease the internal cell resistance without affecting the photovoltage magnitude or reversibility. This approach was largely unsuccessful.

Summary and Conclusions

Reversible photoinduced electron transfer in solutions of TCNE in THF leads to the production of voltages which can be sensed by platinum electrodes. The mechanism of photovoltage production is not well understood, but probably involves distribution of photogenerated ionic species leading to a voltaic cell effect, or an effect related to the adsorption of ionic species on the electrode.

Maximum power output from these systems is in the region of 10^{-10}w for monochromatic illumination intensities of 10^{-3} w/cm². This is an extremely low conversion efficiency compared to the values reported for the best inorganic photovoltaic devices (5). Power output is on the high range of values reported for organic systems, however. Solution photovoltaic cells of this type may thus have greater potential in the development of organic photovoltaic devices than the solid systems investigated previously.

Acknowledgments

Research reported in this publication was supported by the United States Air Force Cambridge Research Laboratories, Office of Aerospace Research, under Contract No. AF19(628)-5511.

Manuscript received May 26, 1967; revised manuscript received July 10, 1967.

Any discussion of this paper will appear in a Discussion Section to be published in the June 1968 JOURNAL.

REFERENCES

1. (a) H. Inokuchi, Y. Maruyama, and H. Akamatu in "Symposium on Electrical Conductivity

in Organic Solids," p. 69, H. Kallmann and M. Silver, Editors, Interscience Publishers, Inc., New York (1961).
(b) A. Terenin, *ibid.*, p. 39.
(c) B. Rosenberg, *ibid.*, p. 291.
(d) H. Meier and W. Albrecht, *Ber.*, **68**, 64 (1964).
(e) H. Kallmann and M. Pope, *J. Chem. Phys.*, **30**, 585 (1959).
(f) D. Kearns and M. Calvin, *ibid.*, **29**, 950 (1958).
(g) For a recent review see "Organic Semiconductors" by F. Gutman and L. E. Lyons, John Wiley & Sons, Inc., New York (1967).
2. (a) R. L. Ward, *J. Chem. Phys.*, **39**, 852 (1963).
(b) D. F. Ilten and M. Calvin, *ibid.*, **42**, 3760 (1965).
(c) D. F. Ilten, Ph.D. Thesis, University of California, Berkeley (1964).
3. R. Vars, L. A. Tripp, and L. W. Pickett, *J. Phys. Chem.*, **66**, 1754 (1962).
4. J. W. Eastman, G. M. Androes, and M. Calvin, *Nature*, **193**, 1067 (1962).
5. (a) P. Rappaport and J. J. Wysocki, *Acta Electronica*, **5**, 364 (1961).
(b) M. Wolf, *Proc. IRE*, **48**, 1246 (1960).
(c) P. Rappaport and J. J. Wysocki in "Photoelectronic Materials and Devices," p. 259, S. Larach, Editor, Van Nostrand Co., Inc., New York (1965).

Bismuth in Yttrium Vanadate and Yttrium Europium Vanadate Phosphors

R. K. Datta

Lighting Research Laboratory, General Electric Company, Cleveland, Ohio

ABSTRACT

Activation of rare earth vanadate by ions other than rare earths is successfully attempted in the present investigation. Bi^{+3} can be incorporated in the YVO_4 and $GdVO_4$ lattice by solid-state reaction. The phosphor $R_{1-x}Bi_xVO_4$ (R = Y,Gd), excited by cathode rays or uv radiation, shows luminescence with a continuous emission band extending from 4000 to 7000Å and peaking at 5670Å. Under 2537Å excitation, the energy is absorbed essentially by Y-O components of the matrix and transferred to the emission centers (Bi^{+3}). Under 3650Å excitation, energy absorbed by charge-transfer processes involving (V-O) and (Bi-O) components of the phosphor is transferred to the emission centers (Bi^{+3}). The transmission of energy from the absorption to the emission centers under 2537 and 3650Å excitations involved a radiationless process. The phosphor YVO_4:Bi can be modified by incorporating Eu^{+3} in the lattice. YVO_4:Eu:Bi, when excited by short- or long-wavelength uv radiation, shows emission spectra with sharp Eu^{+3} emission peaks. Under cathode-ray or 3650Å excitation, the Bi^{+3} emission is gradually quenched when Eu^{+3} is incorporated in the YVO_4:Bi lattice with a constant level of Bi^{+3} concentration; on the other hand, under 3650Å excitation, the Eu^{+3} emission is enhanced when Bi^{+3} is incorporated in the YVO_4:Eu lattice with a constant level of Eu^{+3} concentration. This indicates a radiationless transfer of energy from Bi^{+3} to Eu^{+3} under 3650Å radiation.

In recent years activation of yttrium vanadate (YVO_4) by various rare earth ions has become of considerable scientific (1-5) and technological (6-7) interest. The phosphor YVO_4:R (R = rare earth), when excited by cathode rays, 2537 or 3650Å radiation, shows a typical, narrow-band spectrum of the corresponding rare earth fluorescence. Datta (8) studied the mechanism of absorption and photoluminescence and postulated that YVO_4:Eu is a host-sensitized phosphor. The excitation of the phosphor by uv radiation is due to absorption by two separate processes in the matrix (YVO_4). The energy absorbed by the matrix is transferred by a resonance process to the activator (Eu^{+3}) which causes excitation of Eu^{+3} ions among levels of the $4f^6$ configuration and thence the final emission from them. O'Connor (5) investigated the laser properties of YVO:Nd^{+3} and suggested transfer of energy from the lattice (YVO_4) to Nd^{+3}. Although these investigations indicate that YVO_4 is a promising matrix which can be activated by various types of activator ions, published reports list phosphors where YVO_4 is activated by rare earth ions only. This is probably due to recent interest in color-television phosphor and solid-state laser studies. YVO_4:R shows fluorescence of rare earth ions where transitions among the $4f^6$-electron energy levels result in line emission because the shielding effects of outer electrons minimize the perturbing influence of the crystal field. However, possibilities of activating YVO_4 with activator ions involving s-, p-, or d-electrons, where considerable perturbation occurs resulting in broad emission bands, cannot be ruled out.

In the present investigation, Bi^{+3} among other trivalent activators (other than the rare earth ions) was substituted for Y^{+3} in the YVO_4 lattice in various concentrations. It has been found that YVO_4, $GdVO_4$, and their various solid solutions, when activated with Bi^{+3}, show a broad emission band under cathode-ray, short- and long-wavelength uv excitations. It has been observed that the function of Bi^{+3} in the phosphor is manifold. It acts as absorption and emission centers in the phosphor. In addition, when coactivated with Eu^{+3} in the YVO_4 or $GdVO_4$ matrix, Bi^{+3} acts as a sensitizer for Eu^{+3} emission.

This report (*i*) characterizes the phosphors YVO_4:Bi $GdVO_4$:Bi and YVO_4:Eu:Bi; (*ii*) qualitatively describes the general function of Bi^{+3} ions in terms of absorption, emission, and excitation of the phosphors under uv radiation with special emphasis on YVO_4:Bi and YVO_4:Eu:Bi.

Experimental Procedure

Sample preparation and composition.—The raw materials used in this investigation consisted of luminescent grade (99.99-99.999% pure) oxides, such as yttrium oxide, Y_2O_3, gadolinium oxide, Gd_2O_3, europium oxide, Eu_2O_3, bismuth oxide, Bi_2O_3, and vanadium pentoxide, V_2O_5. In order to obtain the optimum

brightness of luminescence and high reflectance in the visible region, the vanadate should preferably be of stoichiometric composition. The activator(s) was incorporated with Y_2O_3 (Gd_2O_3) by coprecipitation as the oxalate, which was ignited at about 830°C to form the oxide. This insured uniform distribution of the activators in the phosphor. This oxide and V_2O_5 were mixed essentially in stoichiometric proportion (1:1 mole ratio) and fired at about 1000°C for 1½ hr. Additional 1-2 m/o (mole per cent) of V_2O_5 in the mixture insures compensation of the loss of V_2O_5 due to volatilization during firing. After cooling, the mixture was ground and washed in an ammonia solution to remove any excess V_2O_5. The washed and dried phosphor was reheated at ~1100°C for 1 hr. The firings of the phosphors were done in silica crucibles, and the homogeneity of the final products checked by x-ray diffraction analysis. CuK_α reduction from a G.E. diffractometer with a nickel filter was used to investigate all compounds. For precise determination of the change of d-spacing with change in composition of the solid solution series of the system YVO_4-$BiVO_4$, diffraction patterns were run at high angle ($2\theta \sim 65°$) region at slow speed (¼ deg/min/in.). Reproducibility of measurement was within ±0.0125°. Composition of the finished phosphors were periodically analyzed by wet chemical method in order to determine the loss of bismuth during firing. The loss ranged from 2 to 6% of bismuth added in the starting compositions; the amount of bismuth in the phosphors described throughout this paper is based on the formulated compositions.

Spectroscopic measurements.—Diffuse reflectance spectra of the samples within the range 2500-7000Å were obtained by using CaF_2 [1] as standard in a Cary Recording Spectrophotometer, Model No. 14. The emission spectra and the intensity of emission (peak height) measurements were obtained with a direct recording spectroradiometer (10) with a grating monochromator with nearly constant dispersion. The details involved are described elsewhere (8). The excitation spectra were measured using sodium salicylate as standard.

Cathodoluminescence spectra were obtained using a demountable cathode-ray tube operating at a 20 kv anode potential at 17.5 μa beam current over a standard scan TV raster of 35 cm^2 area. Brightness and color points of emission under these conditions were measured using an eye-corrected Weston foot-Lambert meter and G.E. colorimeter (JB 1E), respectively.

Compositions of the phosphors studied.—Since the absorption and emission spectra of phosphors may not always be independent of the relative amounts of the activator and coactivator, phosphors with wide range of concentration of Bi^{+3} and rare earth ions were prepared. The compositions of the phosphors can be expressed by the general formula

$$Y_{1-(x+y)}Bi_xEu_yVO_4$$

x and y can vary from 0.000025 to 0.1 and 0 to 0.1, respectively.

The subsequent discussion on the properties of phosphors is generalized and does not pertain to one specific phosphor composition. The exact compositions of the phosphors are described in the text whenever such descriptions are necessary and meaningful. However, reflectance, emission, and excitation spectra are given along with the exact composition of the corresponding phosphor.

Results and Discussion

Phase equilibrium relationship.—Subsolidus studies showed at least 7 m/o of $BiVO_4$ can be dissolved in the YVO_4 lattice within the temperature range (830°-1100°C) of sample preparation. This is well within the range of activator concentration used in the present investigation.

Reflectance spectra.—(YVO_4:Eu:Bi).—Figures 1 and 2 show the effects of Bi^{+3} incorporation on the diffuse reflectance spectrum of the phosphor YVO_4:Eu. Except for the sharp Eu^{+3} absorption lines in the visible region, the diffuse reflectance spectra of YVO_4 and YVO_4:Eu are essentially alike. Figure 1 shows the reflectance spectra of samples having a constant concentration (5 a/o [atom per cent]) of Eu^{+3} but different amounts of Bi^{+3}, whereas Fig. 2 shows the reflectance spectra of samples having a fixed amount of Bi^{+3} (2 a/o) but different levels of Eu^{+3} concentration. These spectra show that the absorption of the phosphor YVO_4:Eu:Bi in the uv region is essentially independent of Eu^{+3} concentration. However, incorporation of Bi^{+3} enhances the absorption at long-wavelength uv radiation. On the basis of the spectra shown in Fig. 1, 2, and 3, it may be suggested that the mechanisms of absorption in the uv region by the phosphors YVO_4:Bi (discussed below) and YVO_4:Eu:Bi are essentially similar.

(YVO_4:Bi).—The diffuse reflectance spectra of some of the YVO_4:Bi samples studied are shown in Fig. 3. YVO_4 shows two absorption bands, namely, at 2500

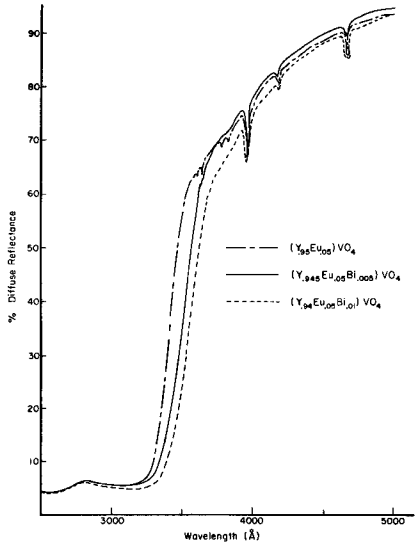

Fig. 1. Diffuse reflectance spectra of YVO_4:Eu:Bi samples (constant Eu content).

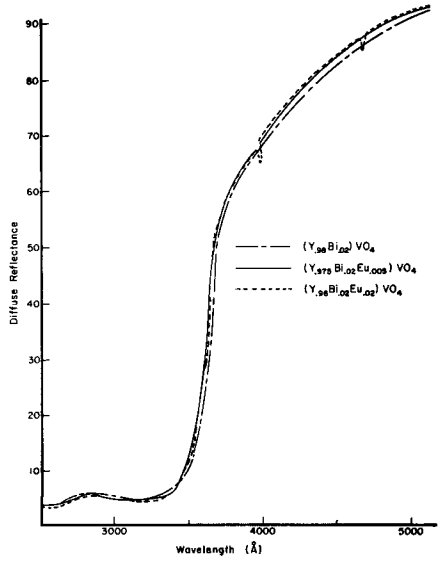

Fig. 2. Diffuse reflectance spectra of YVO_4:Eu:Bi samples (constant Bi content).

[1] In addition to higher reflectance in the region 2500-4000A, CaF_2 shows better chemical stability in room conditions than the usual reflectance standards, such as MgO, $MgCO_3$, which partly react with atmospheric moisture and lower their reflectance in the uv region even further (9).

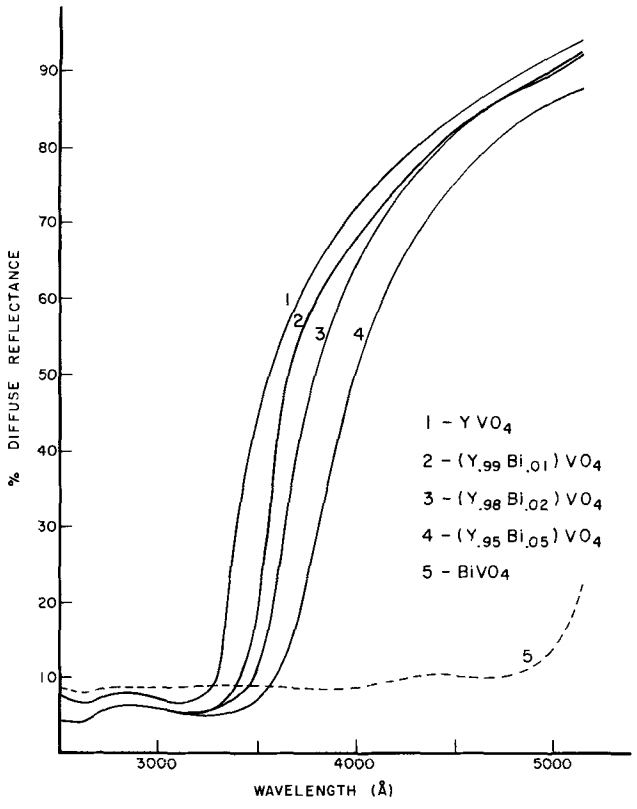

Fig. 3. Diffuse reflectance spectra of YVO_4:Bi samples

and 3200Å. These are attributed to charge transfer processes involving Y-O and V-O components of the matrix, respectively (8, 16). Addition of Bi^{+3} in YVO_4 shifts the absorption edge toward longer wavelength, whereas the absorption band at 2500Å region remains essentially unchanged. Pure YVO_4 shows an absorption edge at about 3200Å with about 60% absorption at 3400Å. Addition of 1 and 2 a/o of Bi^{+3} shifts the edge to 3300 and 3450Å and increases the absorption at 3400Å to about 85 and 90%, respectively (Fig. 3). From a study of the reflectance spectra of BiF_3 and Bi_2O_3, it has been shown (11) that the absorption of long-wavelength uv radiation due to incorporation of Bi^{+3} in an oxide matrix is mainly caused by charge-transfer states involving bismuth and oxygen. The shift in the absorption edge of YVO_4 to longer wavelength due to Bi^{+3} addition, as observed in the present investigation, may be ascribed to the absorption caused by charge-transfer states involving Bi^{+3} and the neighboring eight oxygen atoms of $(YBi)VO_4$ (12).

It can be summarized that YVO_4:Bi and YVO_4:Eu:Bi show strong absorption of short- and long-wavelength uv radiations. The absorption of short-wavelength uv radiation is due to a charge-transfer process involving the Y-O components (8), whereas the charge-transfer process involving Bi-O and V-O component (8) of the phosphor are responsible for absorption in the 3000-3400Å region. In addition, increase in Bi^{+3} content of the sample causes increased absorption at wavelengths about 3400Å and higher. For the sake of brevity, in the subsequent sections of this paper absorption due to charge-transfer processes involving the Bi-O components is referred to as Bi^{+3} absorption.

In the foregoing discussion little emphasis has been placed on the absorption of short-wavelength uv radiation by the Bi-O components of YVO_4:Eu:Bi and YVO_4:Bi. However, it is not suggested that such absorption by Bi^{+3} and/or Bi-O is either not taking place or is not important. On the contrary, the absorption of short-wavelength uv radiation by Bi^{+3} incorporated in the Y_2O_3 matrix is shown by the

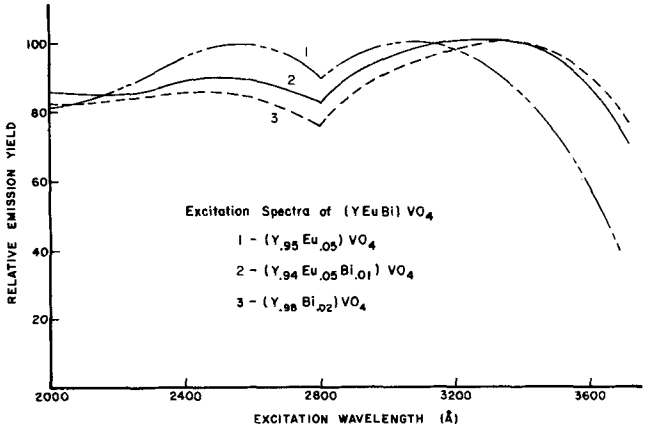

Fig. 4. Excitation spectra of $(YEuBi)VO_4$

diffuse reflectance spectra of Y_2O_3:Bi samples (11). The only suggestion made here is that although some (about 20%) absorption of short-wavelength uv radiation is probably caused by Bi and/or Bi-O, such process is not the underlying cause for high efficiency of the phosphor YVO_4:Bi under 2537Å excitation. This idea may be indirectly supported by the fact that as the concentration of Bi^{+3} in the phosphor YVO_4:Bi increases from 0.75 to 2 a/o, the absorption of the short-wavelength (2537Å) uv radiation and the intensity of emission under 2537Å remain essentially constant.

Excitation spectra.—Normalized excitation spectra of the samples YVO_4:Bi, YVO_4:Eu, and YVO_4:Eu:Bi are shown in Fig. 4. The emission spectra of samples with and without Eu^{+3} are quite different. Hence, their response to the photomultiplier tube used in obtaining excitation spectra are also different. Any quantitative comparison of the excitation spectra should be made after necessary correction. However, it may be generalized that these phosphors have continuous broad excitation spectra with two wide maxima at 2600 and 3200Å. These samples respond efficiently to 2537 and 3650Å excitations.

Emission spectra.—$(YVO_4:Bi)$.—When excited by cathode-rays, short (2537Å)- or long (3650Å)-wavelength uv radiations, Bi^{+3}-activated YVO_4 shows luminescence with an emission band extending from 4000 to 7000Å and peaking at 5670Å (Fig. 5). The present investigation does not include any quantitative measurement of the quantum efficiency of the phosphor under different excitations. However, a qualitative evaluation of the emission process can be attempted.

The band shape of the emission spectra of the phosphor YVO_4:Bi (Fig. 5) is independent of the exciting source and amount of Bi^{+3}. The question now arises whether the emission is from the lattice (YVO_4), Bi^{+3} ions or from the excited Bi-O components. The emis-

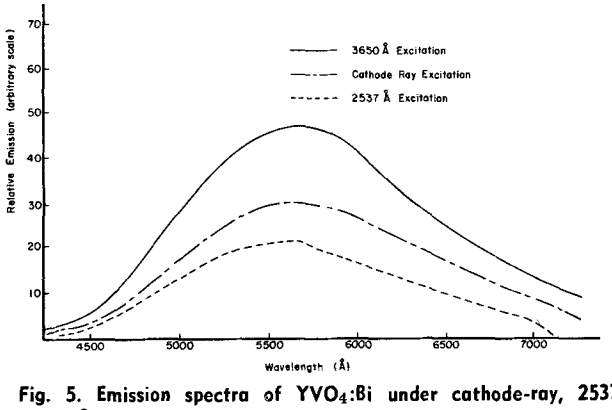

Fig. 5. Emission spectra of YVO_4:Bi under cathode-ray, 2537 and 3650Å excitations.

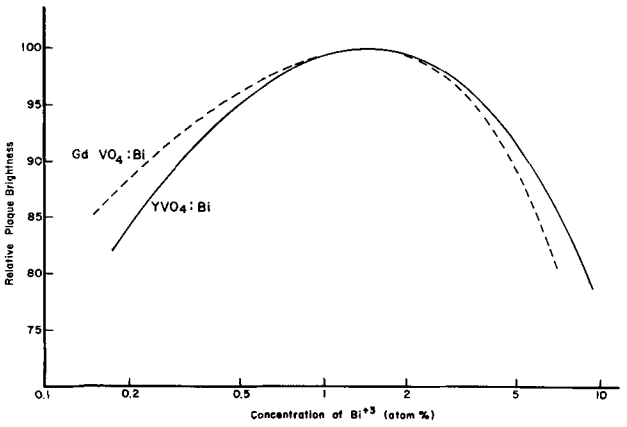

Fig. 6. Plaque brightness vs. activator concentration of RVO_4:Bi (R = Gd, Y), 2537Å excitation.

sion spectrum of pure YVO_4, excited by cathode rays, 2537 or 3650Å radiations, shows a broad weak emission extending from 4000 to 5500Å region and peaking at about 4375Å. The position of the peak of this emission spectrum is quite different from that of YVO_4:Bi. In addition, the intensity of emission of YVO_4:Bi is a function of Bi^{+3} concentration. Normalized plots of plaque[2] brightness against logarithm of Bi^{+3} concentration in YVO_4 and $GdVO_4$ under 2537Å excitation are shown in Fig. 6. When excited by uv radiation, the optimum concentration of Bi^{+3} is independent of the wavelength of the exciting source. The concentration of Bi^{+3} may be chosen within wide limits (1-10 a/o), the optimum being 1-3 a/o of bismuth substituted for Y or Gd in YVO_4 and $GdVO_4$, respectively. When excited under cathode rays, the optimum Bi^{+3} concentration ranges from 0.1 to 0.5 a/o. These indicate that the emission in YVO_4:Bi is not a matrix fluorescence; it is related to Bi^{+3} ions and/or Bi-O components.

Most of the Bi^{+3}-activated phosphors (sulfides, selenides, carbonates, oxides, silicates, etc.) emit in the blue region, although other emissions, such as green, yellow, red, etc., are known (13). The absorption and emission of trivalent metal ions of the sixth period with $^1S_0$ ($5d^{10}6s^2$) ground state have been discussed in considerable detail by McClure (14). However, no simple correlation between the Bi^{+3} emission and composition and structure of the matrix could be obtained from available literature. McClure (14) suggested a $6s6p \rightarrow 6s^2$ transition for Bi^{+3} fluorescence. These outer sp orbitals of post-transitional metal ions are also actual bonding orbitals. Hence, the energy levels of Bi^{+3} ions are highly perturbed by the anions (O^{-2}) of the matrix. In the subsequent discussion this emission is referred to as Bi^{+3} emission.

It should be noted that the emission spectrum of pure YVO_4 which extends from 4000-5500Å, is in part coincident with that of the phosphor YVO_4:Bi (4000-7000Å region), although their peak positions are different. From the symmetric nature of the emission spectrum of YVO_4:Bi, even when the concentration of Bi^{+3} is very low (about 0.7 a/o of yttrium), it can be suggested that the lattice emission (YVO_4) is essentially absent. Hence, it can be suggested that the excitation energy absorbed under short (2537Å)- or long (3650Å)-wavelength uv radiation is emitted mostly as Bi^{+3} fluorescence.

(YVO_4:Eu:Bi).—When Eu^{+3} is incorporated in the YVO_4:Bi lattice with a fixed concentration of Bi^{+3}, the broad Bi^{+3} emission under cathode rays, 2537 and 3650Å excitations is gradually quenched, and sharp, line emissions of Eu^{+3} appear. The relative intensity of these two emissions are dependent on the relative concentration of these two activators so that concentrations can be varied within a wide range depending on the nature of emission desired.

[2] Powdered samples tightly packed in a flat holder.

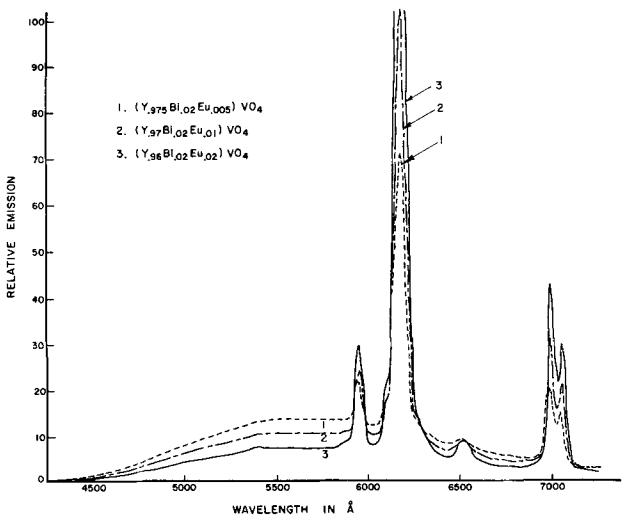

Fig. 7. Emission spectra of YVO_4:Eu:Bi under 2537Å excitation

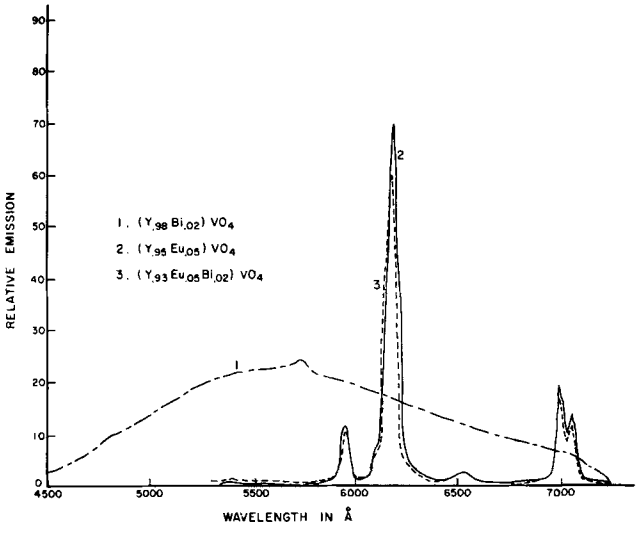

Fig. 8. Emission spectra of YVO_4:Eu:Bi under 2537Å excitation

The phosphor YVO_4:Eu:Bi behaves differently under different uv excitations, namely, 2537 and 3650Å radiations. These are discussed separately below.

2537Å *excitation.*—When Eu^{+3} concentration is gradually increased in the $Y_{0.95}Bi_{0.02}VO_4$ lattice, the broad Bi^{+3} emission under 2537Å excitation is gradually quenched without any change in the band shape of Bi-emission, and narrow-band Eu^{+3} emissions appear (Fig. 7). When Bi^{+3} is incorporated in the $Y_{0.95}Eu_{0.05}VO_4$ lattice, a very faint Bi^{+3} emission is noticed, and there is little effect on the intensity of Eu^{+3} emission (Fig. 8, 12). With further increase in Bi^{+3} concentration (above 2 a/o) the intensity of Eu^{+3} emission is gradually decreased without any enhancement of Bi^{+3} emission. At higher concentration, Bi^{+3} acts as "killer" for Eu^{+3} emission.

3650Å *excitation.*—When Eu^{+3} concentration is gradually increased in the $Y_{0.98}Bi_{0.02}VO_4$ lattice, the intensity of broad Bi^{+3} emission under 3650Å excitation is decreased, and narrow-band Eu^{+3} emissions appear (Fig. 9, 10). Even 0.5 a/o Eu^{+3} can considerably decrease Bi^{+3} emission of $Y_{0.98}Bi_{0.02}VO_4$ (curve 2, Fig. 10). However, Bi^{+3} emission is never completely quenched, even with Eu^{+3} concentration as high as 5 a/o (curve 5, Fig. 11). When Bi^{+3} is gradually incorporated in the $Y_{0.95}Eu_{0.05}VO_4$ lattice, the emission lines of Eu^{+3} show enhanced intensity, especially the main emission peak at 6190Å. The intensity of this peak shows an increase of almost 200% as Bi^{+3} content of $Y_{0.95}Eu_{0.05}VO_4$ is increased from 0 to

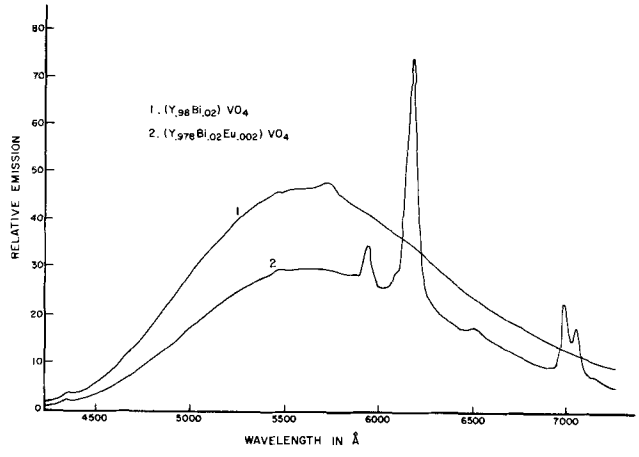

Fig. 9. Emission spectra of YVO_4:Eu:Bi under 3650Å excitation

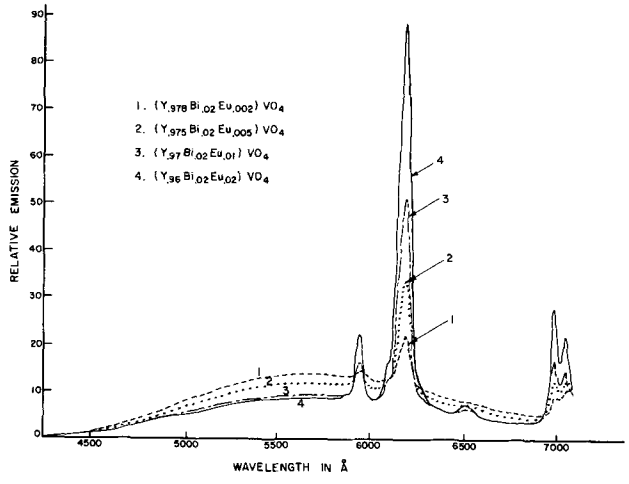

Fig. 10. Emission spectra of YVO_4:Eu:Bi under 3650Å excitation

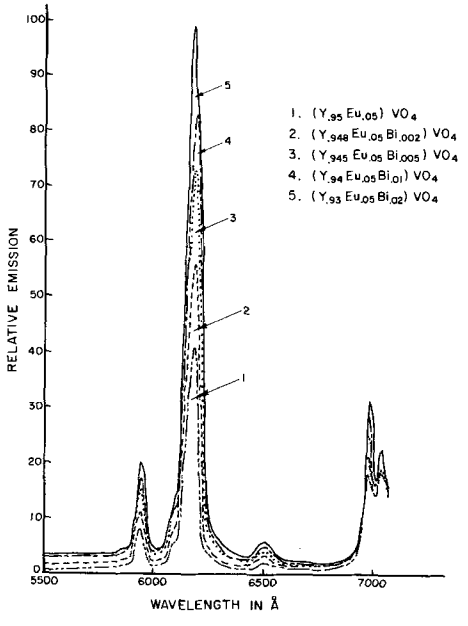

Fig. 11. Emission spectra of YVO_4:Eu:Bi under 3650Å excitation

2 a/o. That is, the composition of the phosphor is changed from $Y_{0.95}Eu_{0.05}VO_4$ to $Y_{0.93}Eu_{0.05}VO_4$ to $Y_{0.93}Eu_{0.05}Bi_{0.02}VO_4$ (Fig. 11). Figure 12 shows the effects on the main Eu^{+3} emission peak at 6190Å under 2537 and 3650Å excitations due to incorporation of Bi^{+3} in $Y_{0.95}Eu_{0.05}VO_4$. Because of the difference in

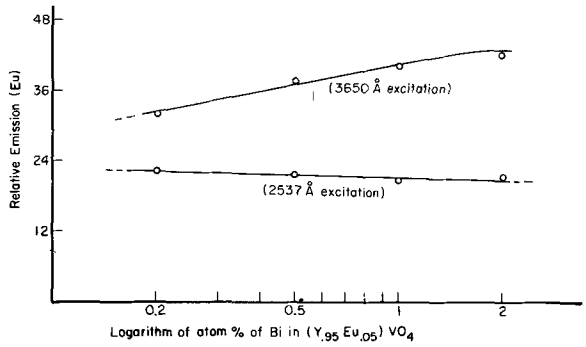

Fig. 12. Relative Eu^{+3} emission of YVO_4:Eu:Bi under 2537 and 3650Å excitations vs. Bi^{+3} content of the samples. (The emission is measured from the total area of the peak at 6190Å.)

the intensities of the two exciting sources used in the present investigation, the relative response of the phosphor, $(YEuBi)VO_4$ to these two excitations should not be deduced from Fig. 12 and compared with the data presented in Fig. 4.

Mechanism of Energy Transfer

It has been suggested in the reflectance spectra section of this paper that in the phosphors YVO_4:Bi and YVO_4:Eu:Bi the short-wavelength uv radiation is absorbed essentially by the lattice, whereas the long-wavelength uv radiation is absorbed jointly by the lattice (V-O components) and the impurity (Bi-O components) elements. The question now arises: What are the mechanisms involved in the transfer of energy from the absorber to the emitting centers, *i.e.*, Bi^{+3} and Eu^{+3} ions in YVO_4:Bi and YVO_4:Eu:Bi, respectively? Klick and Schulman (15) discussed two different methods by which energy from the absorbing components can be transferred to the emission centers in photoluminescent phosphors: (*i*) a radiative transfer of energy through the emission of photons from the absorbing matrix and reabsorption by the final emitter; (*ii*) a nonradiative or exchange process associated with resonance between the absorber and emitter.

In the former case, the absorbing species of the phosphor system must be a very good emitter, and the emitting species must be an efficient absorber. In addition, for any significant amount of energy transfer by the radiative process, the emission spectrum of the absorbing species must substantially overlap the absorption band of the emitting species.

In the phosphor YVO_4:Bi, the weak emission of the matrix (YVO_4) which extends from 4000-5500Å region under uv radiations does not overlap significantly the Bi^{+3} absorption band (3200-4200Å region) of the phosphor. In the phosphor YVO_4:Eu:Bi, the emission of YVO_4:Bi which extends from 4000 to 7000Å under uv excitations does not overlap the main absorption band (at about 2500Å) of Eu^{+3} ions. Hence, any substantial transfer of energy by a radiative process from YVO_4 and YVO_4:Bi to the emitting centers, such as Bi^{+3} and Eu^{+3} of the phosphor systems YVO_4:Bi and YVO_4:Eu:Bi, respectively, can be ruled out.

It may be emphasized that two steps are involved in case of energy transfer by a radiationless or resonance process in photoluminescent phosphors (16): (*i*) energy transfer through the matrix, *i.e.*, from one absorbing group to the other, and (*ii*) energy transfer from the absorbing groups to the activators or emitting centers. Dexter (17) studied the mechanisms and conditions required for a nonradiative transfer of energy through the matrix. The probability of such transfer is a function of the overlap of the wave functions of the absorbing groups and the overlap of the absorption and emission bands of the absorbing groups. It has been shown that such conditions are well satisfied in the YVO_4 matrix (16). Blasse (16) studied many host-sensitized Eu^{+3}-activated phosphors and suggested several requirements for energy transfer from

the matrix to the emitting centers (activators): (a) overlap between the orbitals of the central cation of the absorbing group and the neighboring activator ions, and (b) some overlap of the emission and absorption of the absorbing and emitting groups, respectively.

Blasse (16) further suggested that by virtue of the arrangements of the ions in the lattice, the requirement of orbital overlap betwen yttrium and vanadium is very well satisfied in YVO_4. As a result, YVO_4-based phosphors where part of the yttrium is randomly substituted by the activator ion show efficient energy transfer from the absorbing centers (VO_4^{-3}) to the emitters. In YVO_4:Bi a part of the emission spectrum of YVO_4 is overlapped by the absorption band of Bi^{+3}. Hence, in case of YVO_4:Bi, the short-wavelength (2537Å) uv radiation absorbed by the matrix (YVO_4) may well be transferred by a radiationless process (15, 17) to the emitting centers (Bi^{+3}) resulting in the excitation of Bi^{+3} ions and the final emission from them ($6s6p \rightarrow 6s^2$ transition). The mechanism of excitation of Bi^{+3} ions under 3650Å radiation is slightly different. In this case, in addition to the transfer of energy from the matrix to the activator centers (Bi^{+3}), Bi^{+3} ions themselves absorb the excitation energy and undergo excitation directly. In YVO_4:Eu:Bi, the requirement for energy overlap for the transfer of energy from the matrix to the emission centers is satisfied. This is because Eu^{+3} ions show small, sharp absorption lines within the region (4000-7000Å) of continuous emission spectrum of YVO_4:Bi under uv excitations. It can be recalled here that both YVO_4:Bi and YVO_4:Eu are essentially host-sensitized phosphors under 2537Å excitation. The energy absorbed by the matrix is transferred to the emission centers Eu^{+3} and Bi^{+3}. When these two activators are present together, as observed in the present investigation, energy absorbed by the matrix is transferred preferentially to Eu^{+3} ions which undergo excitation and the final emission. Since Eu^{+3} and Bi^{+3} ions randomly substitute part of yttrium in the YVO_4 lattice[3] and their probabilities of being near the absorption matrix are equal, it is not yet understood why only Eu^{+3} ions are excited. On the other hand, it could be a multistep transfer, *i.e.*, energy from the host is transferred to Eu^{+3} *via* Bi^{+3}. However, even with increased Bi^{+3} concentration very little energy absorbed by the matrix is emitted from Bi^{+3}.

The emission of YVO_4:Eu:Bi under 3650Å excitation is an example of simultaneous host- and impurity (coactivator)-sensitized luminescence (15). In case of impurity-sensitized phosphor, such as $CaSiO_3$:Pb:Mn, energy absorbed by Pb is transferred by a radiationless process to Mn^{++} which undergoes excitation and the final emission (18). In case of host-sensitized phosphors, such as YVO_4:Eu and Y_2WO_6:Eu, energy absorbed by the matrix (VO_4^{-3}, WO_6^{-6}) is transferred by a radiationless process to the emission centers (Eu^{+3}) (8, 19). In YVO_4:Eu:Bi, as observed in the present investigation, energy absorbed by the lattice (VO_4^{-3}) and the impurity centers (Bi-O) under 3650Å excitation is transferred to Eu^{+3} ions by a nonradiative or resonance process (15, 20). The idea of transfer of energy is supported by the following observations under 3650Å excitations: (*i*) The broad Bi^{+3} emission of $Y_{0.98}Bi_{0.02}VO_4$ is gradually quenched as Eu^{+3} concentration is increased in the lattice. (*ii*) The Eu^{+3} emission of $Y_{0.95}Eu_{0.05}VO_4$ is enhanced markedly with gradual increase in Bi^{+3} content.

Sensitization of Eu^{+3} emission by other rare earths, such as Tb, is known (21). YVO_4:Eu:Bi is probably the first phosphor reported where Eu^{+3} emission is sensitized by a nonrare earth ion (Bi^{+3}). This paper describes the photoluminescence of the phosphors YVO_4:Bi and YVO_4:Eu:Bi. However, for the sake of completeness, the effects of Bi^{+3} addition on color point and brightness of $Y_{0.95}Eu_{0.05}VO_4$ emission under cathode-ray excitation are shown (Table I). Although, because of instrumental limitations, no Bi^{+3} emission was detected in the emission spectra of (YEuBi)VO_4 under cathode-ray excitation, data in Table I are more consistent with the introduction of a Bi^{+3} emission (hence the color shift) with little effect on the Eu^{+3} emission intensity.

[3] X-ray diffraction patterns obtained with carefully prepared samples of YVO_4 and $Y_{1-(x+y)}Bi_xEu_yVO_4$ to avoid preferred orientation were compared. Absence of any additional reflection in the activated samples was interpreted as a lack of superlattice or long-range order of Bi-Eu or Bi-Y-Eu in $Y_{1-(x+y)}Bi_xEu_yVO_4$. However, short-range order, usually indicated by preferential increase or decrease of intensities of certain reflections over others in a randomly oriented sample, cannot be unequivocally ruled out due to very small concentration of Bi involved.

Table I. Cathode-ray brightness of YVO_4:Eu:Bi samples

Composition	A/O Eu	A/O Bi	Relative brightness	Color coordinates* X	Y
(YBi)VO_4	—	0.2	100	378	537
(YBi)VO_4		0.5	97		
(YBi)VO_4		1.0	87	380	545
(YEuBi)VO_4	5	—	100	655	336
(YEuBi)VO_4	5	0.1	126	636	351
(YEuBi)VO_4	5	0.2	129	637	352
(YEuBi)VO_4	5	0.5	130	625	361
(YEuBi)VO_4	5	0.7	132	618	367
(YEuBi)VO_4	2.5	0.1	110	630	349

* Based on 1931 CIE Chromaticity Diagram.

Summary and Conclusion

Yttrium vanadate (YVO_4) is a well-known matrix for fluorescence of rare earth ions. In the present investigation it has been activated with Bi^{+3}. YVO_4:Bi is a new phosphor with a broad excitation band extending from 2000 to 3600Å. The phosphor responds very well to cathode rays, 2537 and 3650Å excitation and emits a broad emission band extending from 4000 to 7000Å with a peak at 5670Å. Under 2537Å excitation, energy is absorbed by the Y-O components of the matrix and transferred to Bi^{+3} ions (emission centers) by a radiationless process. The emission of YVO_4:Bi is attributed to the $6s6p \rightarrow 6s^2$ transition of Bi^{+3} ions. These sp orbitals are also bonding orbitals. Hence, influence of the oxygen ions surrounding Bi^{+3} ions on emission cannot be ruled out. Under 3650Å excitation, energy is absorbed by charge-transfer processes involving the V-O and Bi-O components of the phosphor. The energy from the matrix (V-O) is transferred by a radiationless process to Bi ions resulting in their excitation and the final emission from them.

When Eu^{+3} is incorporated in the YVO_4:Bi lattice, the broad Bi^{+3} emission is gradually quenched under cathode rays, 2537 and 3650Å excitation, and the line emission of Eu^{+3} ions appears. With proper selection of concentration of Eu^{+3} and Bi^{+3}, the Eu^{+3} emission is enhanced under 3650Å excitation without showing any appreciable emission of Bi^{+3}.

On the basis of these observations, it can be suggested that the photoluminescence of YVO_4:Eu:Bi under 3650Å excitation is a result of host and impurity sensitization. The energy absorbed by the matrix (V-O) and the impurity centers (Bi-O) is transferred by a resonance process to the emission centers (Eu^{+3}) resulting in the excitation of Eu^{+3} ions among the energy levels of the $4f^6$ configuration and final narrow band emission from them with a peak at 6190Å involving mainly $^5D_0 \rightarrow {}^7F_2$ transition of Eu^{+3}. This investigation shows that Bi^{+3} in YVO_4:Eu:Bi and YVO_4:Bi acts as absorber, emitter, and sensitizer.

Acknowledgments

The author acknowledges the assistance of Dr. R. L. Brown, T. E. Lusk, and B. Walsh in obtaining emission and excitation spectra, of M. Brines and F. Geraghty who measured cathode-ray brightness. The author also wishes to express his thanks to L. S. Staikoff for x-ray measurements, to T. Luscher for preparing the phosphor and measuring uv brightness, and to Dr. E. F. Apple for many helpful discussions. Dr. T. S. Davis and

V. Thelian helped in preparing the manuscript in the final form.

Manuscript received May 23, 1967; revised manuscript received *ca.* July 3, 1967. This paper was presented at the Dallas Meeting, May 7-12, 1967.

Any discussion of this paper will appear in a Discussion Section to be published in the June 1968 JOURNAL.

REFERENCES

1. L. G. Van Uitert, R. C. Linares, R. R. Soden, and A. A. Ballman, *J. Chem. Phys.*, **36**, 702 (1962.).
2. A. Levine and F. C. Palilla, *Appl. Phys. Letters*, **5**, 118 (1964).
3. L. H. Brixner and E. Abramson, *This Journal*, **112**, 70 (1965).
4. F. C. Palilla, A. K. Levine, and M. Rinkevics, *ibid.*, **112**, 776 (1965).
5. J. R. O'Connor, *Appl. Phys. Letters*, **9**, 407 (1966).
6. A. K. Levine and F. C. Palilla, *Electrochem. Tech.*, **4**, 16 (1966).
7. F. C. Palilla and A. K. Levine, *Appl. Optics*, **5** 1467 (1966).
8. R. K. Datta, *Trans. Metal. Soc. AIME*, **239**, 355 (1967).
9. F. J. Studer, Personal communications.
10. R. L. Brown, *Illum. Engr.*, **61**, 230 (1966).
11. R. K. Datta, In press.
12. W. A. Runciman, *Proc. Phys. Soc.*, **A68**, 647 (1955).
13. F. A. Kroger, "Some Aspects of the Luminescence of Solids," Elsevier Publishing Co., Inc., New York (1948).
14. D. S. McClure, "Solid State Physics," Vol. 9, Academic Press, New York (1959).
15. C. C. Klick and J. H. Schulman, "Solid State Physics," Vol. 5, Academic Press, New York (1957).
16. G. Blasse, *J. Chem. Phys.*, **45**, 2356 (1966).
17. D. L. Dexter, *ibid.*, **21**, 836 (1953).
18. H. J. Schulman, R. J. Ginther, and C. C. Klick, *This Journal*, **97**, 123 (1950).
19. G. Blasse and A. Bril, *J. Chem. Phys.*, **45**, 2350 (1966).
20. P. G. Botden, *Philips Research Rept.*, **7**, 197 (1952).
21. L. G. Van Uitert and R. R. Soden, *J. Chem. Phys.*, **36**, 1289 (1962).

Ohmic Electrical Contacts to P-Type ZnTe and $ZnSe_xTe_{1-x}$

M. Aven and W. Garwacki

General Electric Research and Development Center, Schenectady, New York

ABSTRACT

Low resistance electrical contacts to p-type ZnTe and $ZnSe_xTe_{1-x}$ can be made by diffusing Li from a Li salt into the area of the crystal to be contacted and forming an electroless Au deposit on top of the Li-diffused area. The Li-Au contacts stay nearly ohmic down to 35°K and have been used on crystals having carrier concentrations below 10^9 cm^{-3}. It is suggested that the superior behavior of the Li-Au contacts arises from high concentrations of shallow acceptors in the Li-diffused region which narrows the potential barrier between the valence band of ZnTe and the filled band of the contacting material sufficiently to allow tunneling of carriers even at low temperatures.

Fundamental studies as well as device applications of II-VI compounds, particularly the Zn chalcogenides, have been seriously hindered by the difficulties in making low resistance, low noise, ohmic contacts to these materials. In a recent paper Blount *et al.* (1) have reviewed the requirements for obtaining such contacts. In brief, these requirements call for a material for the contact electrode which has a smaller work function than that of the semiconductor if the semiconductor is n-type or larger if the semiconductor is p-type, and which, when diffused into the semiconductor, will act as a dopant providing majority carriers.

Following these guidelines, satisfactory ohmic contacts can be produced to n-type CdS, CdSe, and CdTe by using In or Ga as the contact metal (2). The contacting of n-type ZnS and ZnSe, which have lower work functions (3) and show a greater tendency toward compensation is more difficult. Nevertheless, satisfactory ohmic contacts have been found for low and high resistivity ZnSe (4), low resistivity ZnS (5), and, more recently, even for high resistivity ZnS (1). Low resistivity p-type CdTe and ZnTe have been electroded with moderate success with electroless gold (6-7). The contacting of these compounds in high or even moderate resistivity form, however, has been very difficult. As a consequence, low-temperature electrical transport studies of these materials in high-purity p-type form are very scarce.

In this paper the authors wish to describe the preparation and some characteristics of Li-diffused contacts to high resistivity p-type ZnTe and $ZnSe_xTe_{1-x}$ crystals. Such contacts stay ohmic and noiseless to quite low temperatures and can be used on crystals having very low carrier concentrations.

Preparation

The crystal to be electroded is etched for 10 to 60 sec in boiling 50% NaOH, rinsed first with hot dilute NaOH, and then with hot distilled water. A small drop of $LiNO_3$ solution (10^{-4} mol/ml) is placed on the crystal in the desired electrode location while the crystal is heated to 40°C in air. The heating is not a necessary requirement, but promotes the evaporation of the solution to dryness. This is particularly useful when applying several electrodes to different sides of the crystal. The crystal is then slowly heated to 320°-350°C in H_2 and held there for 20 to 60 sec. As the crystal is heated, the dry $LiNO_3$ deposit melts at 250°C. At about 300°C the liquid melt suddenly reacts with the substrate and appears to penetrate into the crystal, leaving a barely visible gray spot on the surface. Lateral spreading causes the spot to increase to several times the size of the contact area of the original liquid salt droplet. After cooling to room temperature, the crystal is rinsed with distilled water, dried, and an electroless Au deposit is formed (6) on top of the Li-reacted area. If desired, wires can be soldered to the Au deposit with an In or In-Ag alloy, or fastened to it with silver paste.

In a few instances, while electroding very small bar-shaped ZnTe crystals for Hall effect measure-

ments, the lateral spread of the Li-diffused area or, possibly, a fine spray of droplets from the Li solution caused a partial shorting of some of the electrodes to each other. To safeguard against such low resistivity surface channels, the following procedure was adopted for crystals with closely-spaced (less than a few mm) contacts. After forming the Li-contacts, each was covered with a small drop of thermosetting resin (*e.g.*, GE 7031 "Adhesive and Insulating Varnish"). After the resin had set for 30 to 60 min, the crystal was etched for 30 to 45 sec in boiling concentrated NaOH. This removed some 20-50μ of material from the crystal surface in locations not covered by the resin. After rinsing, the resin was dissolved in a 1:1 mixture of ethyl alcohol and toluene, and a gold dot was deposited on each of the small Li-diffused mesas left by the etching of the surrounding areas. Crystals electroded in such fashion rarely showed any signs of interelectrode shorting. With contacts that were more than a few mm apart, this more complicated procedure was, in most cases, unnecessary.

Electrical Properties

Figure 1 shows a series of oscilloscope I-V traces obtained between a pair of Au and pair of Li-Au contacts on two ZnTe crystals from the same boule at several temperatures. The resistivity of the crystals was about 10 ohm-cm at room temperature and 200 ohm-cm at 55°K. It can be seen that whereas the Au contacts show a considerable contact resistance already at 300°K (note the different current scales for the Li-Au and the Au sequences), the Li-Au contacts

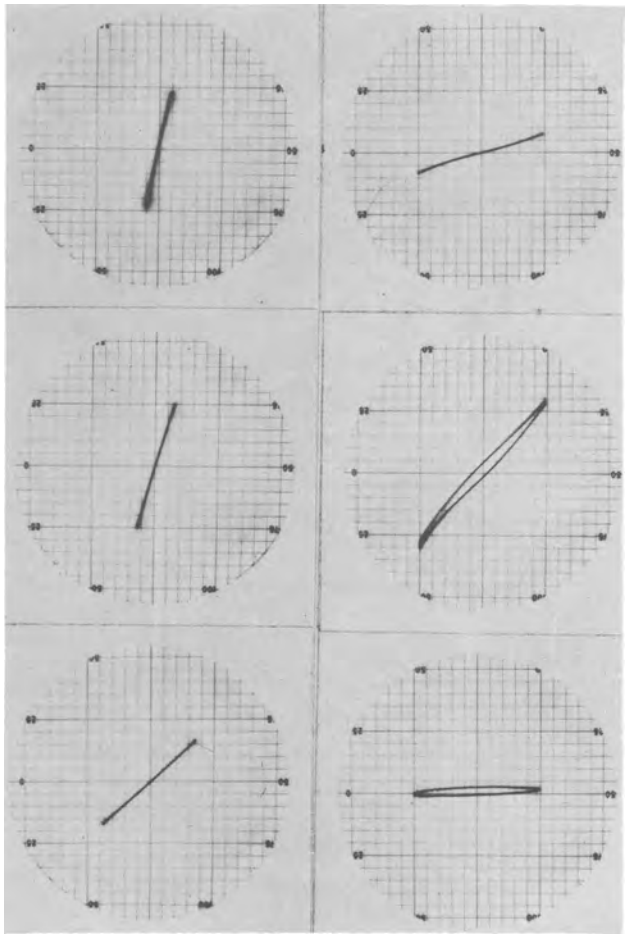

Fig. 1. Current-voltage characteristics obtained between a pair of Li-Au (left sequence) and a pair of Au (right sequence) contacts on ZnTe. Horizontal scale 1v/in. (1 in. corresponds to one large division). The temperatures and vertical scales are, from top to bottom: Li-Au sequence, 300°K, 10^{-3} amp/in.; 232°K, 10^{-3} amp/in.; 55°K, 10^{-6} amp/in.; Au sequence, 300°K, 10^{-4} amp/in.; 232°K, 10^{-5} amp/in.; 70°K, 10^{-7} amp/in.

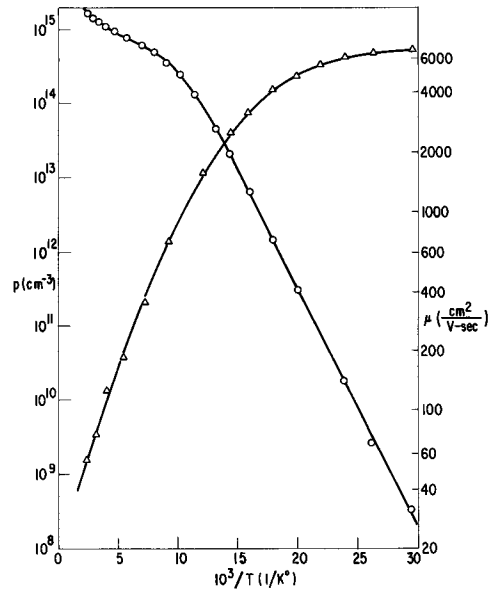

Fig. 2. Temperature dependence of the free hole concentration (circles) and of the Hall mobility (triangles) of an undoped ZnTe crystal.

stay relatively low resistance down to 55°K. At 70°K the contact resistance of the Au electrode is so high as to make the current through the crystal unobservably low on the scale employed. Frequently the Au contacts to ZnTe have displayed strongly nonohmic behavior even at room temperature. Investigation of the conditions which produce optimum room temperature Au contacts showed that a 60-sec heating period at 80°-100°C after the forming step led to best results. No heating or heating at higher temperatures produced much inferior contacts. However, Au contacts with even the best room temperature characteristics started rapidly deteriorating at about 150°C and were unusable for Hall effect measurements on high resistivity ZnTe crystals below liquid N_2 temperature. The significance of this finding is discussed below.

Figure 2 shows the temperature dependence of the free hole concentration and of the Hall mobility of an undoped p-type ZnTe crystal. Measurements of this type at temperatures below the liquid N_2 range have been very difficult before due to the unavailability of suitable contacts. The data in Fig. 2, obtained with a crystal with five Li-Au contacts, have enabled us, for the first time, to extend the measurements to about 35°K. On a reciprocal temperature scale this provides an additional range extending from about $10^3/T = 14$ (pumped N_2 temperature) to $10^3/T = 29$. As can be seen in the figure, this is the range in which the log p *vs.* $1/T$ relationship has become linear, and which, therefore, enables one to obtain the acceptor ionization energy with good accuracy. Hall mobility measurements between the liquid N_2 temperature and 35°K indicate increasing departure from pure LO phonon scattering (4). Mobility studies in this temperature range thus make it possible to investigate the scattering due to low concentrations of charged impurities.

The forward I-V characteristics at 77°K of a $ZnSe_{0.36}Te_{0.64}$ light emitting p-n junction diode (8) with an In-Hg electrode on the n-type side and either a Li-Au or a Au electrode on the p-type side of the diode are compared in Fig. 3. It can be seen that the Li-Au contact allows a substantially higher current to pass through the diode than the Au contact. The strongly nonideal I-V characteristic of this particular diode even with the Li-Au contacts is due to the high bulk resistance of the p- and n-type sides of the diode.

It has been reported (7) that originally low resistivity Li-doped ZnTe crystals gradually become high re-

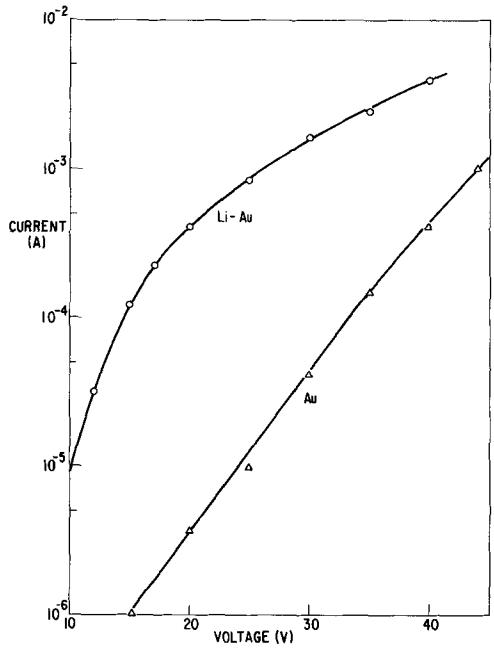

Fig. 3. Forward I-V characteristics of a $ZnSe_{0.36}Te_{0.64}$ light emitting p-n junction diode with an In-Hg electrode on the n-type side and either a Li-Au (circles) or a Au (triangles) electrode on the p-type side.

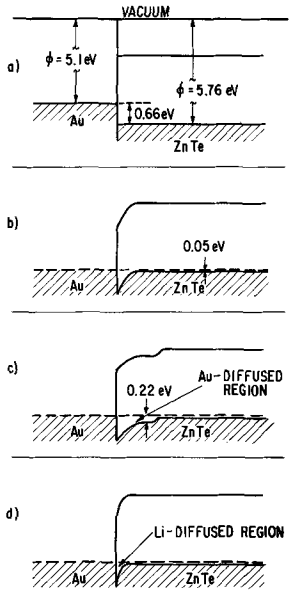

Fig. 4. Band structure of the Au-ZnTe contacts. (a) Relative positions of the Fermi levels in Au and ZnTe; (b) "Noninteracting" Au contact; (c) Au-diffused contact; (d) Li-diffused contact with Au overlay.

sistivity when annealed at even relatively low temperatures. The high ionic mobility of Li and its tendency to associate with other lattice defects in semiconductors is well known (9). In view of this a life test was conducted with a $ZnSe_{0.36}Te_{0.64}$ p-n junction diode in which the I-V characteristic was measured originally, and after (*a*) 264 hr in liquid N_2; (*b*) 312 hr at room temperature in vacuum; (c) 640 hr at room temperature in air; and finally (*d*) 93 hr at liquid N_2 temperature in vacuum, with 30v forward bias. The I-V characteristic was found to be essentially unchanged after each of the indicated periods, indicating the electrical stability of the Li-Au contacts under the test conditions employed.

Discussion

The shallow acceptor activity in undoped ZnTe and CdTe has generally been attributed to doubly ionizable Zn vacancies (4, 10, 11), which have their first charge state about 0.05 ev above the valence band edge. Acceptor states with ionization energies comparable to that of the Zn vacancy have been observed in Li- and Na-doped ZnTe and CdTe (7). The noble metals Ag, Cu, and Au, on the other hand, have been found to introduce deeper acceptor states, 0.11, 0.15, and 0.22 ev, respectively (4). Using this information in conjunction with the results of the present study leads to the following characterization of the Au and Au-Li contacts.

As shown in Fig. 4a the relative work functions of Au and ZnTe are such (3) as to suggest a barrier of about 0.66 ev between the Fermi level in Au and the valence band edge in ZnTe. Although the presence of surface contamination, surface states, etc., often does not allow one to rely on simple calculation of barrier heights from work function data, it has been shown by several workers (3, 12) that in the case of II-VI compounds this is often not a bad approximation. The band structure resulting from an essentially noninteracting contact (in the sense that the barrier shape and height depends only on the work function difference of Au and ZnTe and the charge density in ZnTe) on undoped ZnTe would then look as shown in Fig. 4b. Due to a moderate concentration of shallow Zn vacancy acceptor states, the barrier height and width are such as to allow a small but measurable current of holes from the metallic contact into the valence band of ZnTe, and *vice versa*, at room temperature. At low temperatures, however, the barrier becomes a serious obstacle to current passage, and the contact becomes high resistance. We believe that the Au contact on undoped ZnTe, processed under optimum conditions, comes close to this case. Figure 4c schematically represents an Au contact in which Au has diffused too far into the crystal and replaced the shallow Zn vacancy acceptors by the deep Au acceptors. In addition to the barrier one now has a high resistivity region under the contact. The structure of the Li-diffused contact is shown in Fig. 4d. Here the high concentration of shallow acceptors in the surface region significantly reduces the barrier width and allows a tunneling current of holes to pass from the external Au electrode into the valence band of ZnTe even at low temperatures. Gold contacts to Li, Na, or P-doped ZnTe work in a similar fashion, except that now the high p-type doping exists uniformly throughout the bulk of the ZnTe crystal rather than just in the Li-diffused surface region.

The external contacts of chemically deposited Au are much superior to simple mechanical electrodes such as silver paste, colloidal graphite, or tungsten wire even on Li-diffused areas on ZnTe crystals. This suggests that the chemical reaction between ZnTe and the solution used to form the electroless Au contacts ($HAuCl_4$ · aq) which consumes a small layer of the ZnTe crystal under the Au solution drop thereby effects a clean-up of the surface immediately beneath the Au deposit. Evidence of the etching action of $HAuCl_4$ · aq is revealed by microscopic examinations of Au-contacted ZnTe crystals, which show that the Au deposits reside in slightly depressed areas having the appearance of shallow negative mesas.

Conclusion

It has been shown that electrical contacts to ZnTe and $ZnSe_xTe_{1-x}$ crystals fabricated by a method in which Li is first diffused into the area to be contacted and then an electroless Au deposit is formed on top of the diffused area, are significantly superior to electroless Au contacts. Using the Li-Au electroding technique on undoped ZnTe crystals it has been possible to investigate the electrical transport properties of this material at considerably lower temperatures than has been done previously. $ZnSe_xTe_{1-x}$ p-n junction diodes

electroded with the Li-Au contact on the p-type side have been found to pass substantially higher current at comparable voltages than diodes electroded with the Au alone. It has been suggested that the low contact resistance of the Li-Au contacts arises from the highly Li-doped surface regions of the ZnTe crystals being electroded. In such regions the shallow acceptor concentration is considerably higher than in undoped ZnTe, and hence the barrier separating the valence band of ZnTe from the filled band of the external contacting material is much narrower. This allows a tunneling current to communicate between the crystal and the external electrode even at low temperatures.

Acknowledgments

The authors wish to thank R. K. Swank and H. H. Woodbury for the many helpful suggestions and stimulating discussions during the course of this work. Work on this paper was sponsored by the Air Force Cambridge Research Laboratories under Contract No. AF-19(628)-4976.

Manuscript received May 22, 1967.

Any discussion of this paper will appear in a Discussion Section to be published in the June 1968 JOURNAL.

REFERENCES

1. G. H. Blount, M. W. Fischer, R. G. Morrison, and R. H. Bube, *This Journal*, **113**, 690 (1966).
2. R. W. Smith, *Phys. Rev.*, **97**, 1525 (1955).
3. R. K. Swank, *ibid.*, **153**, 844 (1967).
4. M. Aven and B. Segall, *ibid.*, **130**, 81 (1963).
5. M. Aven and C. A. Mead, *Appl. Phys. Letters*, **7**, 8 (1965).
6. D. de Nobel, Thesis, University of Leiden (1958).
7. B. L. Crowder and W. N. Hammer, *Phys. Rev.*, **150**, 541 (1966).
8. M. Aven, *Appl. Phys. Letters*, **7**, 146 (1965).
9. See, *e.g.*, H. Reiss, C. S. Fuller, and F. J. Morin, *Bell Syst. Tech. J.*, **35**, 533 (1956).
10. D. G. Thomas and E. A. Sadowski, *J. Phys. Chem. Solids*, **25**, 395 (1963).
11. L. R. Shiozawa and J. M. Jost, Aeronautical Research Laboratory, USAF, Contract No. AF 33(657)-7399, Final Report, March 19, 1965.
12. C. A. Mead, *Appl. Phys. Letters*, **6**, 103 (1965).

The Effects of Double Insulating Layers on the Electroluminescence of Evaporated ZnS:Mn Films

M. J. Russ and D. I. Kennedy

Bowmar Canada Limited, Ottawa, Ontario, Canada

ABSTRACT

The performance of ZnS:Mn electroluminescent layers deposited between double SiO insulating films is described. The dependence of emission properties on SiO and ZnS film thickness and Mn content are outlined. The relatively bright (700 ft-L) and efficient (1 lpw) emission is interpreted in terms of excursions from equilibrium trap occupation under high field conditions.

A considerable number of investigations of EL (electroluminescence) in thin ZnS films have been carried out using direct contact between the ZnS films and the conducting electrodes. In some investigations a single thin insulating layer has been used between the films and one of the electrodes. In most of the cases the results have shown marked asymmetry with respect to changes in polarity of the applied voltage. This situation has frequently led to difficulties in interpretation of the results. The present experiments were designed to eliminate some of the complexity by using thin insulating layers on both sides of the ZnS films.

In the past there have been a number of reports (1-11) on a-c EL in ZnS thin films. These reports have covered a variety of preparation techniques. Halsted and Koller (1) prepared EL (electroluminescent) ZnS:Mn films by the vapor reaction technique of Studer and Cusano (12), whereas Thornton (2) used the diffusion method of Feldman and O'Hara (13) to prepare ZnS:Mn:Cl and ZnS:Cu:Cl films. Vlasenko and Popkov (4) prepared ZnS:Mn films by separate evaporation and subsequent high-temperature diffusion of the constituents. Using a technique of coevaporation on a heated substrate proposed by Koller and Coghill (14), Antcliffe (15) has prepared EL ZnS:Mn films. Apart from variations in methods of producing the phosphor layer, various types of composite device have been investigated. Several authors (4, 6) have utilized an insulating layer between the phosphor film and the metal electrode. Harper (6) has reported that improved efficiencies and over-all brightness levels can be obtained by the use of an SiO_2 film of thickness between 7 and 160Å in this position.

The technique of coevaporation of ZnS and Mn on a heated substrate was adopted for the present experiments because of the simple, one-stage process.

Film Preparation

High-purity ZnS in either single crystal or compressed polycrystalline form was used as source material and, in the majority of experiments, Mn powder was added to the ZnS crystals in a range of concentrations from 0.04 to 6.0 w/o. To maintain uniform conditions in successive depositions the accurately weighed charges were evaporated to completion.

It was found that in order to obtain high-brightness EL the deposition conditions were critical. Substrate temperatures had to be maintained in the range 250°-300°C. Above 300°C significant crystallization of the ZnS film occurred and this resulted in the formation of an opaque white layer. For substrates maintained at temperatures between 20° and 250°C, only low-level emission was obtained. The critical deposition rate was found to be 1000 Å/min at a pressure of 10^{-5} Torr. The source temperature required to maintain this deposition rate at a distance of 7 in. from the substrate was 1230°C as determined by an optical pyrometer. The use of a lower evaporation rate did not permit sublimation of the added Mn, and a higher rate led to poor incorporation of the Mn in the film. This latter condition resulted in the deposition of a film having a black metallic coloration.

When the critical deposition conditions were met it was possible to obtain emission from panels with a range of ZnS film thicknesses and Mn concentrations. In order to obtain panels with a usable brightness, however, it was necessary to control the latter parameters also.

Prior to deposition of the ZnS film a layer of SiO was evaporated onto the unheated tin-oxide coated glass substrate. SiO thicknesses which were varied from 600 to 5000Å were used. Subsequent to the deposition of the phosphor film a second SiO layer was evaporated and finally metal electrodes were deposited. The properties of devices made with this structure were found to be independent of the metal electrode used (Al, Au, and In were each investigated). The results are based on an evaluation of at least 36 devices for each experiment.

Results

The emission resulting from a-c excitation of the ZnS:Mn films was located in the same region of the spectrum as reported by previous authors. Using a DK-2A spectrophotometer it was found that the peak occurred at 5780Å and the half-width was 450Å.

On first application of voltage to these devices it was found that the emission would grow steadily to a uniform brightness over the active area. This behavior contrasted strongly with previous experiments carried out in this laboratory and elsewhere on structures with no insulating layers or a single such layer. In the latter cases it was found that a "forming" process, in which the phosphor was subjected to a critical near-breakdown electric field, was required to produce over-all luminescence. This "forming" process was attended initially by high currents without the presence of EL, and the emission appeared gradually as the currents fell to lower values. These processes have been discussed by Goldberg and Nickerson (16) and Cusano (17). The use of single insulating layers reduces the severity of the break-in process, and the double layers described in this report virtually eliminate the effect.

Effects of SiO *layers.*—Using the deposition conditions described above a 1000Å film of SiO was evaporated on tin-oxide coated glass followed by deposition of a 1.5μ ZnS:Mn film (Mn concentration in source of 0.6 w/o). This was followed by deposition of SiO stripes which increased in thickness in steps over the range from 220 to 5000Å. Metal electrodes of area 6 x 10^{-2} cm^2 were then evaporated to complete the devices.

Figure 1 shows the results obtained on a-c excitation of these films at a frequency of 13 kHz in terms of the dependence on surface brightness on the rms electric field applied across the ZnS film. (This latter parameter was estimated from the total applied voltage using measured results for the dependence of the dielectric constants of ZnS and SiO on film thickness at the frequencies used.) The brightness was measured using a Spectra-Spot brightness meter. All results show a marked dependence of brightness on SiO thickness. As the SiO thicknesses were gradually increased it was found that the observed emission for a given field across the ZnS layers passed through maxima and minima. Although the emission process may be influenced by SiO thickness to some extent, the oscillatory nature of the characteristics pointed strongly to the existence of optical interference effects in the composite structure.

To maximize the observed emission in the above structure it was necessary to use particular values of SiO layer thickness. Utilization of data similar to that shown in Fig. 1 for dependence of brightness on SiO thickness at fixed values of ZnS field showed that the maximum brightness is obtained for an SiO thickness of 650Å. This differs from the theoretical value of 730Å calculated from reported refractive indices for the various layers; the difference probably

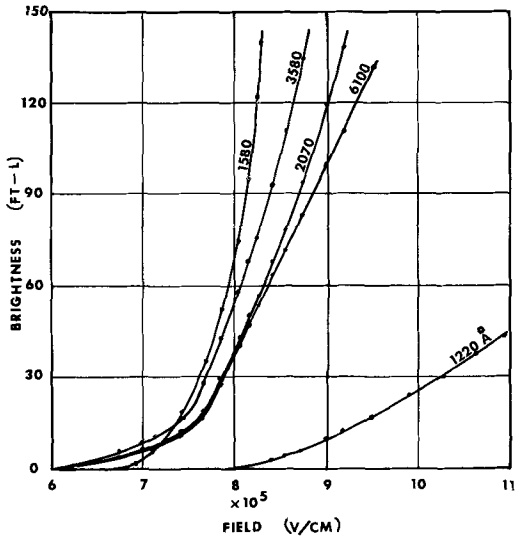

Fig. 1. Dependence of brightness on ZnS field at 13 kHz for various SiO layers. 1000Å SiO films were used between the ZnS and SnO_2 and thicknesses of 220-5100Å of SiO were used between the ZnS and Al.

results from the complex dependence of refractive index on film composition and thickness in the materials used. By varying the thickness of the SiO layer between the tin-oxide electrode and the ZnS film while maintaining the second SiO layer constant, it was possible to establish an optimum thickness value of 1300Å for the internal SiO layer. This value is in agreement with theory assuming $n_{SiO} < n_{SnO_2}$. A further increase in observed emission would be anticipated if the SiO or tin-oxide layers were replaced with materials with more ideally matched refractive indices.

It is interesting to note that the field strengths applied to the ZnS layers in our devices under routine operating conditions appear to be equal to or slightly higher than values normally used in this type of experiment and also than the reported dielectric breakdown strength for ZnS (4, 18). The calculated field strength values were obtained from separate measurements on SiO and ZnS layers of equivalent thicknesses and may not correspond exactly to the values which occur in composite structure. Nevertheless, the possibility exists that the double SiO layers eliminate one form of breakdown which occurs when direct metal/ZnS contact exists. The highest-efficiency EL in this work was observed when devices were operated in this field regime.

The dependence of brightness on frequency in the range from 1-20 kHz, showed, for all values of SiO thicknesses, a saturation effect above 8 kHz. As the frequency was increased above 13 kHz the average brightness at a given applied field decreased. Although this decrease may be associated with impedance effects in the various layers or with internal heating there is some evidence that it could be caused by failure of the excitation and recombination processes to reach completion within individual half cycles of the applied field.

Effect of manganese concentration.—There is little information in the literature on the dependence of ZnS film emission properties on Mn concentration. The majority of published work has been carried out on single values of Mn content in a range between 0.1 and 1 w/o. Vlasenko and Popkov (4) carried out experiments with several Mn concentrations and reported an optimum value of 0.6 w/o. In the present work a range of samples were prepared from sources containing from 0.04 to 6.0% Mn. In all cases the ZnS film thickness was maintained at 1.5μ, and a symmetrical structure with double SiO layers of 700Å thickness was used.

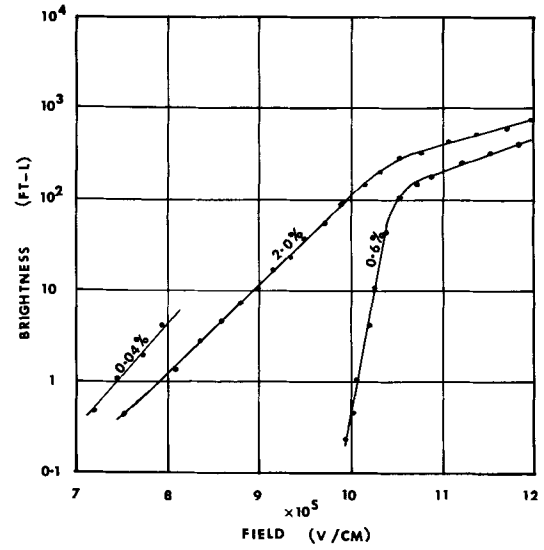

Fig. 2. Dependence of brightness on ZnS field at 13 kHz for various Mn concentrations. A ZnS thickness of 1.5μ was used in conjunction with double 700Å SiO layers.

Figure 2 shows the dependence of integrated brightness on the applied field at 13 kHz for three Mn concentrations. A considerable improvement in brightness levels was obtained as the Mn concentration increased. The maximum brightness for a phosphor containing 2 w/o Mn was in excess of 700 ft-L compared with 5 ft-L for a 0.044 w/o phosphor. If the Mn concentration was increased to 6%, the maximum brightness was reduced to 10 ft-L, and the panels were found to burn out at low applied voltages; this would appear to be due to the reduction in the resistivity of the phosphor with high Mn content. At 6 w/o Mn the films had a metallic black rather than yellow coloration. In the concentration range from 0.04 to 2.0 w/o the maximum brightness and discrimination ratio increased with increasing Mn content. Although 2% Mn was the maximum level of incorporation which led to repeatably good results using the described procedures it is felt that higher concentrations could be achieved using more sophisticated source materials and deposition procedures. In this case it should be possible to obtain even brighter emission from the devices. The present results are in agreement with Kodzhespirov *et al.* (8) who reported that emission intensities of ZnS:Mn devices increased with increasing Mn content. The maximum concentration used by these authors was 4.0 w/o and the ratio of emission intensity in the high-concentration devices to those with 0.04 w/o Mn was reported to be 10^3:1.

The dependence of the El output on frequency exhibited little variation as the Mn concentration was altered.

Effect of ZnS *thickness.*—There is little information in the literature on the effects of variation of phosphor film thickness on device performance. The results from the present work are shown in Fig. 3. In these experiments the concentration of Mn was maintained at 0.6 w/o, and the film was again sandwiched between 700Å SiO layers. The maximum obtainable brightness increased with ZnS thickness to 1.3μ, but did not increase appreciably thereafter. The discrimination ratio attained a maximum value for films in the region of 1.3μ in thickness. The figure also demonstrates that the field strength required to develop a given emission intensity falls towards a lower limit as the ZnS film thickness is increased. Vlasenko and Popkov (4) observed that emission intensity increased with increasing film thickness and the field strength at which emission was first discernible to the eye decreased with increasing thickness. The latter authors interpreted the results to be evidence

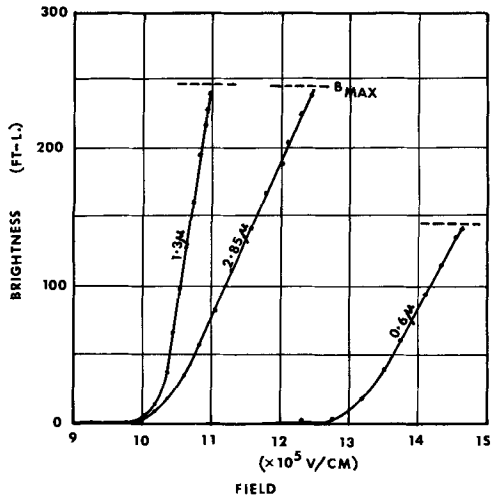

Fig. 3. Dependence of brightness on ZnS field at 13 kHz for various ZnS film thicknesses. A Mn concentration of 0.6 w/o was used and double 700Å SiO layers were employed.

of recombination throughout the bulk of the phosphor.

The dependence of electroluminescent output on frequency was found to saturate for all thicknesses of ZnS layers but, as the ZnS thickness was increased beyond 1.3μ, saturation occurred at successively lower frequencies.

In measurements of I-V curves on a number of panels over a brightness range from 1 to 700 ft-L it was found that the current increased linearly with voltage. As the SiO thickness was decreased or as the Mn content was decreased a given change in applied voltage would produce a greater change in current.

The relationship between brightness and rms applied voltage was measured for a number of films and was found to consist of two exponential regions. The curves, which are illustrated in Fig. 4 for several ZnS thicknesses, obey the following relation

$$B = B_1\left(\exp\frac{V}{V_1} - 1\right) + B_2\left(\exp\frac{V}{V_2} - 1\right)$$

where B is the surface brightness, V is the rms applied voltage, and B_1, B_2, V_1, and V_2 are constants. Kolomeitsev *et al.* (9) also found their results to obey this expression.

Efficiency-voltage characteristic.—Figure 5 shows the efficiency-voltage curves for several typical de-

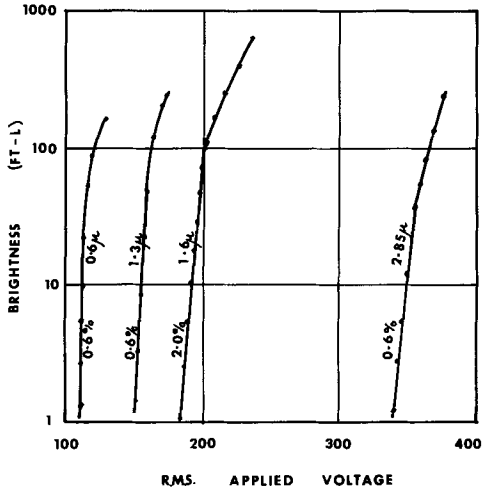

Fig. 4. Dependence on brightness on rms applied voltage for various ZnS film thicknesses and Mn concentrations using 700Å SiO layers.

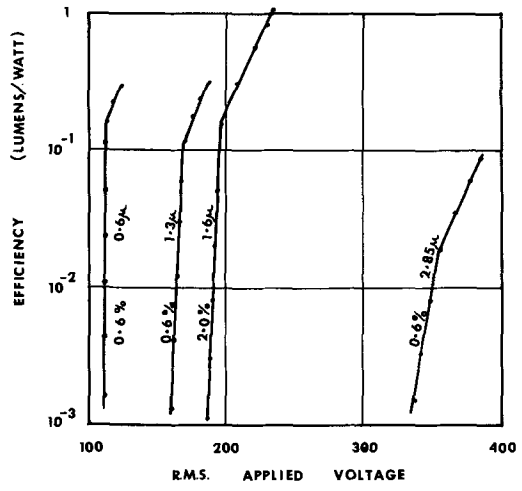

Fig. 5. Efficiency vs. rms applied voltage for various ZnS film thicknesses and Mn concentrations using 700Å SiO layers.

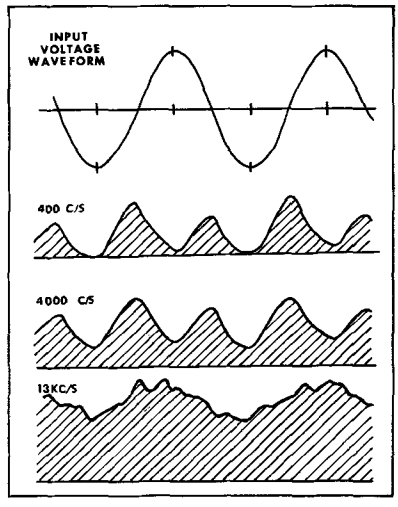

Fig. 6. Tracings of the emission waveforms obtained under sinusoidal excitation at several frequencies from a typical 2% Mn 1.6μ ZnS film.

vices. Once again double SiO layers were used and an excitation frequency of 13 kHz was employed. Emission efficiencies in the range from 0.1 to 1.0 lpw were regularly obtained; the higher efficiency results usually occurred when ZnS with 2 w/o Mn was evaporated, and the devices had the optimum SiO thicknesses for maximum emission.

The reduction in rate of increase of efficiency with applied voltage shown in Fig. 5 was also reported by Kodzhespirov and Kostylev (8). The dependence of efficiency on SiO thickness attained a maximum for values similar to those described in the section dealing with optical effects in these layers. Therefore, the improvement in efficiency can also be associated with these effects. The improvements in efficiency reported by Harper (6) for SiO_2 layers were associated with tunneling and accumulation effects in these layers; for these thin films (7-160Å) significant optical enhancement would not be anticipated.

In comparing the performance of thin-film and powder El phosphors it is significant that the efficiency of films increases with applied voltage whereas the efficiency of powder phosphors reaches a peak at approximately one-half of the desirable operating brightness and falls off with further increase of voltage. Although powder cells have exhibited maximum efficiencies of 14 lpw at low brightness, a value of 3 lpw is a more typical efficiency under normal operating conditions. The efficiency of thin-film panels of the type described here operating under similar conditions compares favorably with this value.

Emission characteristics under sinusoidal and pulsed excitation.—The shapes of the emission output waveforms were detected by a type 7625 photomultiplier and displayed on a Hewlett-Packard 175A dual-trace oscilloscope. Tracings of photographs of the waveforms obtained under sinusoidal excitation are shown in Fig. 6; the wavetrains progress from left to right of the diagrams. It was noted at low frequencies that there were two emission pulses per cycle of applied voltage and that the maximum emission lagged the maximum voltage for both polarities by 0.6 to 0.8 msec. At 400 Hz the two pulses were distinct but at 4 kHz the emission from a particular pulse did not decay to zero before onset of the succeeding pulse. At 13 kHz the emission pulses appeared only as a slight structure superimposed on a continuous level of emission.

It was found in a number of devices that, although similar time and frequency dependence of the emission peaks occurred, their amplitudes were not always equal. In these cases where the emission pulses were not equal in amplitude it was found that the light output corresponding to positive voltage applied to the tin oxide electrode could exceed the reverse case by up to 50%. Because of the similarity of behavior of the two peaks in all other aspects and because of the independence of results on the nature of the electrodes it is felt that the asymmetry results from nonuniform excitation or emission properties through the ZnS layer or at its interfaces with SiO. The nature of the device fabrication unfortunately introduces asymmetry in two respects. First, the distribution of Mn through the depth of the ZnS film may be nonuniform due to rapid depletion of Mn at the start of evaporation or deposit of an excess at the completion [in previous work (14) the Mn:Zn ratio has been shown to vary from 0.003 to 0.007 to 0.011 in subsequent 1-min deposition intervals]. A second factor arises from the sequential film deposition procedures which involve substrate heating during the ZnS evaporation. This process inevitably introduces inequalities in the properties of the initial and final SiO layers.

Figure 7 shows the response of a panel to symmetrical pulse excitation. Again two pulses per cycle were observed, and the maximum light emission lagged the voltage switching time by about 0.6 msec. Similar results were obtained for the cases where the tin-oxide electrode was pulsed positive and negative with respect to the metal electrode; the only slight distinction occurred in cases where the two emission

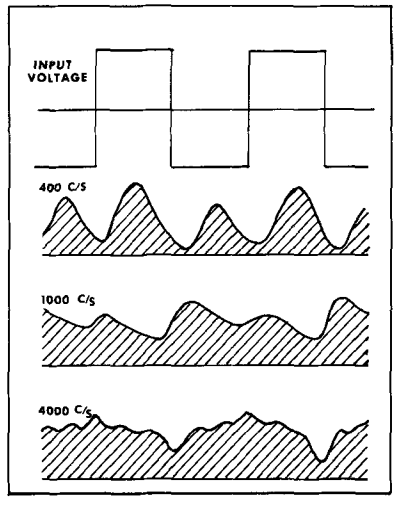

Fig. 7. Tracings of the emission waveforms obtained under symmetrical pulse excitation at several frequencies.

pulses were unequal in amplitude. In the latter case the larger pulse would occur when the tin-oxide layer was switched positive with respect to the metal electrode regardless of the potential at which the metal electrode was held (0 volts or full negative potential). At 400 Hz the two pulses per cycle were distinct but, as higher frequencies were applied, the light emission did not decay to zero between field reversals.

An interesting result was obtained by varying the mark: space ratio of the pulse waveform at a repetition rate in the region of 400 Hz, *i.e.*, below saturation frequencies. At a 50:50 duty cycle it was found that two approximately equal pulses per cycle were obtained, but as the ratio was moved to 85:15 the amplitude of one pulse decreased and the second pulse increased. At 85:15 only a single pulse occurred each cycle and this was approximately twice the size of its counterpart in the 50:50 duty cycle case. The single pulse was found to reach a peak approximately 0.6 msec after the termination of the 85% part of the cycle.

A series of experiments were performed in which the metal electrode was held at ground potential and the tin oxide was pulsed to full positive potential for 15% of each cycle. These experiments were repeated for the same pulse durations but with application of negative pulses to the tin oxide. Both sets of experiments were repeated using longer pulse durations so that the pulse occupied 85% of the cycle times. In all cases the results were similar, and the samples behaved as if the condition in which 85% of the time was spent was the equilibrium state and emission took place only after the applied voltage switched to the 15% state. Figure 8 illustrates two of these cases. It can be seen that the decay to zero emission following each light pulse takes several milliseconds.

Ageing.—One major disadvantage of thin-film El panels is their extremely rapid ageing characteristic. Apart from exceptional cases, thin films prepared by the above techniques show a reduction to half initial brightness within tens of operating hours. This figure is similar to values obtained by other authors. Ageing was accelerated by elevating the ambient temperature. It was noted, however, that the lifetime parameter showed distinct variations from one batch of devices to another prepared at a different time but in ostensibly the same manner, whereas from one device to another within any one particular batch there was consistency in ageing characteristics. There is evidence to suggest that this property is related to controlled and uniform manganese incorporation and that the use of more sophisticated material preparation and evaporation procedures may yield significant improvements. It was found that the lifetime of panels capable of several hundred foot-Lamberts could be extended by operation at lower brightness levels. The initial decay of brightness is not truly exponential, and a fast decay occurs during the application of the first few cycles of voltage. Because of this it is almost impossible to establish the true starting time for the decay process and therefore to state the true half-life. In our work we have taken the initial brightness as a value measured within the first minute of field application.

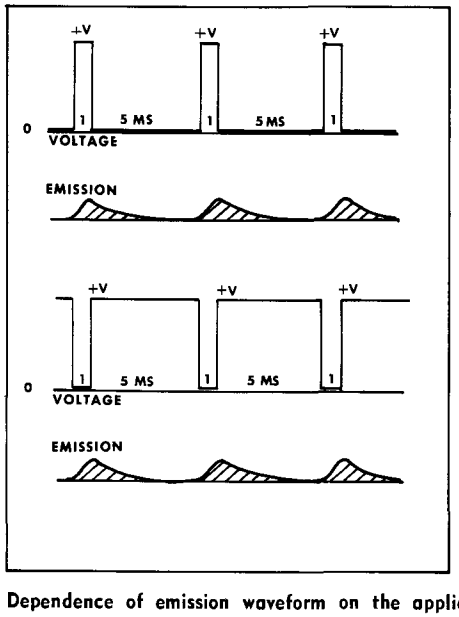

Fig. 8. Dependence of emission waveform on the applied pulse duty cycle.

Discussion

A great deal of controversy is apparent in recent published work on ZnS films. The majority of workers suggest that the best structure for obtaining efficient emission has a blocking layer at the positive metal electrode while others report that blocking contacts at the cathode are advisable [these points are reviewed in ref. (19)]. In the present work using relatively thick double insulating layers the emission was found in almost every case to be similar for both applied polarities regardless of the nature of the metal electrodes. This result implies that the metal/insulator interface properties are of secondary importance and that the carriers required for the recombination process originate either in the ZnS film itself or in the ZnS/SiO interface barriers, for example, in an accumulation layer of the type described by Harper (6).

The most favored mechanisms for explaining electroluminescence in Zns films include injection effects from adjacent layers (16, 20) or internal p-n junctions (5),and electronic impact ionization (6, 21). It is almost certain that light emission can and does result from these and other processes depending on the film preparation and contact properties. In the case of the present devices where average fields of 10^6 V/cm exist in the films under the optimum operating conditions one would anticipate a high-field mechanism to be operative. Impact excitation is likely to occur at these fields. The source of carriers for the emission process may be thermally generated electrons, but it is also possible that field effects lead to depopulation of traps in the various parts of the devices and that these could represent a significant contribution (23, 25). It should be noted that an average field of 8×10^5 V/cm was normally required for the efficient emission process in our layers and that the light output increased typically from 1 to 600 ft-L with a minor increase of field to 1.2×10^6 V/cm. Although inefficient emission was detected at lower fields its characteristics were different; the bright emission process appeared to have a definite field threshold. (Since there was evidence of space-charge effects in the devices it was possible that nonuniform field distribution occurred within the layers and that considerably higher than the average local fields may have been present.)

The emission from the films was similar to emission from a variety of ZnS:Mn devices and is believed to result from excitation of Mn centers by collision or resonance transfer. It is unlikely that direct field excitation of the Mn center itself occurred because of the high calculated field strength required for this process (22).

The emission waveform was considerably simpler than described results from ZnS films with other activator systems. The secondary peaks often described in work with other films were not observed in the present experiments. After a single step increment in voltage the emission was found to grow to a peak after 0.6 to 0.8 msec and then to decay over a considerably longer time interval. This behavior together with the observations under various applied waveforms could be explained in the following manner.

It is a well-established fact that ZnS films, interfaces, and oxide insulators possess a number of trapping levels with time constants ranging from microseconds to hours. The degree of occupation of these levels in structures such as the present panels is a complex function of applied voltage, ambient temperature, illumination, and past history. On changing the applied voltage a series of events occurs which leads to a new distribution of the carrier population throughout the devices. At first the free carriers and easily excited carriers flood toward their new positions and, more gradually, the deeper levels adjust in population according to a complex time dependence. Some of the adjustment occurs at a rate determined by thermal detrapping, but additional field-enhanced detrapping at fields as low as 5×10^3 V/cm could also occur (23). The internal field in each part of the structure cannot instantaneously acquire a new equilibrium value when the applied voltage is increased, but rather it will rise to a new value according to a time dependence determined by the level repopulation processes. Based on these premises it is tempting to conclude that it is this gradual field growth after a change in applied voltage which leads to the 0.6 msec delay before peak emission occurs. In other words the required field for the collision process does not appear across the total volume of the main emitting regions until 0.6 msec after application of the required voltage (the 0.6 msec time being a particular property of the present panels under these applied conditions).

As equilibrium is approached the flow of carriers diminishes and this leads to a gradual reduction in the number of excitations and recombinations. This is likely to be the explanation for the observed decay in emitted brightness after the peak value at 0.6 msec. A small residual light emission after equilibrium is established caused by thermally generated carriers entering the high-field regions might also be expected.

The above picture provides a simple and self-consistent explanation of the observed emission waveforms. Under sinusoidal or symmetrical pulse excitation there are equal excursions about each side of an average condition. This creates two major disturbances of equilibrium per cycle and could be expected to lead to two emission pulses per cycle. If the symmetry of the pulse excitation is altered to an 85:15 duty cycle, the equilibrium will be biased predominantly to the 85% condition. This being the case only one major excursion from equilibrium per cycle occurs. The excursion will be larger in magnitude than in the 50:50 duty cycle, and the result would be the observed single emission pulse of larger amplitude following the onset of the 15% parts of the waveform. This situation would occur regardless of the actual voltage experienced by the panel during the 85% part of the cycle.

The frequency dependence of the results is also explained. At high frequencies the 0.6 msec required by the present devices to reach full emission is not available. Instead the emission only grows to part of the maximum value. As the frequency is raised, however, the number of partial emissions per second is increased. These two effects counterbalance until, above 15 kHz the emission per pulse is so weak that the increased repetition rate no longer compensates and the output falls off. At low frequencies the growth of emission to a peak after 0.6 msec followed by a decay may be completed before the end of the applied voltage pulse. The total emission would in this case be simply determined by the pulse repetition rate. This linear emission fall off with reduced frequency was in fact observed.

With no applied field the distribution of occupied traps takes on its field-free form. Under sinusoidal or pulse excitation, parts of the ZnS films and adjacent layers become depopulated during a fraction of each voltage cycle and the population of deeper levels slowly adjusts to a value determined by the average occupation of the shallow levels. This operational equilibrium is different from the field-free case, and the transition from one situation to the other is believed to be responsible for the gradual build-up of emission during the first few cycles of voltage which is frequently described in the literature (26-28).

Conclusion

The experiments that have been reported have shown that the use of insulating layers on both sides of a ZnS:Mn film can lead to bright and relatively efficient electroluminescence (700 ft-L at 1 lpw). It is considered that the emission results from an impact excitation process which occurs when the various energy states in the device are disturbed from equilibrium under high-field conditions. It is also believed that the present efficient emission occurs in a regime of electric field in which the ZnS layer would normally experience breakdown if placed in direct contact with a metal electrode.

The proposed mechanism for the EL provides a consistent and straightforward explanation of the present observations, and it can also be shown to provide a simple alternative explanation of several other experiments which are described in the literature. The mechanism is amenable to experimental verification although the procedures are complex because of the small range of applied voltage during which the panels pass from 1 to 700 ft-L emission. A study of the time-dependence of the repopulation effects and their relation to ambient temperature, field, and illumination will clarify the situation.

The critical nature of the film deposition parameters required to produce efficient devices can be attributed to two factors. First, the required electrical properties of the ZnS layer are strongly dependent on the degree of crystallinity and the structural properties of the film. Second, the incorporation of high concentrations of Mn without serious disruption of the film must be achieved.

The brightness, efficiency, and ageing characteristics of the ZnS devices all appear to be related to the successful incorporation of Mn without film disruption. The present films improved in these characteristics as the Mn content in the source material was increased from 0.04 to 2.0 w/o. There is every reason to believe that further improvements will be possible when more sophisticated deposition techniques are used.

Acknowledgment

The authors would like to thank Mr. W. Carkner for his assistance in the fabrication of the ZnS devices and the Bowmar Instrument Corporation for permission to publish information contained in the First and Second Annual Research Reports on DIR Grant E54. The work was carried out as part of a research program jointly supported by Bowmar Canada Limited and the Defence Industrial Research Program operated by the Canadian Defence Research Board.

Manuscript received May 15, 1967; revised manuscript received June 12, 1967.

Any discussion of this paper will appear in a Discussion Section to be published in the June 1968 JOURNAL.

REFERENCES

1. R. E. Halsted and L. R. Koller, *Phys. Rev.*, **93**, 349 (1954).
2. W. A. Thornton, *J. Appl. Phys*, **30**, 123 (1959)
3. W. A. Thornton, *Phys. Rev.*, **116**, 893 (1959).
4. N. A. Vlasenko and Iu. A. Popkov, *Optics & Spectros*, **8**, 39 (1960).
5. W. A. Thornton, *This Journal*, **108**, 636 (1961).
6. W. J. Harper, *ibid.*, **109**, 103 (1962).
7. V. L. Bakumenko, G. S. Kojina, and V. N. Favorin, *Optics & Spectros*, **15**, 262 (1963).

8. F. F. Kodzhespirov and S. A. Kostylev, *Optics & Spectros*, **12**, 144 (1964).
9. F.I. Kolomoitsev, F. F. Kodzhespirov, and S. A. Kostylev, *ibid.*, **12**, 497 (1964).
10. A. G. Gol'dman, G. A. Zholkevich, and N. P. Lazar, *Soviet Phys., Doklady*, **10**, 1148 (1966).
11. V. A. Vlasenko and S. A. Zyn'o, *Zn. Priklad. Spectrosk (USSR)*, **5**, 67 (1966).
12. R. J. Studer and D. A. Cusano, *J. Opt. Soc. Amer.*, **42**, 878 (1952).
13. C. Feldman and M. O'Hara, *ibid.*, **47**, 300 (1957).
14. L. R. Koller and H. D. Coghill, *This Journal*, **107**, 973 (1960).
15. G. A. Antcliffe, *Brit. J. Appl. Phys.*, **16**, 1467 (1965).
16. P. Goldberg and J. W. Nickerson, *J. Appl. Phys.*, **34**, 1601 (1963).
17. D. A. Cusano, Doctoral Dissertation, Rensselaer Polytech. Inst. (Jan. 1959).
18. K. L. Chopra, *J. Appl. Phys.*, **36**, 655 (1965).
19. P. Goldberg in "Luminescence of Inorganic Solids," P. Goldberg, Editor, p. 408, Academic Press, New York (1966).
20. R. C. Jaklevic, D. K. Donald, J. Lambe, and W. C. Vassell, *Appl. Phys. Letters*, **2**, 7, (1961).
21. D. A. Cusano in "Luminescence of Organic and Inorganic Materials," H. P. Kallman and G. M. Spruch, Editors, p. 494, John Wiley & Sons, Inc. New York (1962).
22. W. W. Piper and F. E. Williams in "Solid State Physics," Volume VI, p. 96, Academic Press, New York (1958).
23. K. W. Boër and U. Kümmel, *Ann. Phys.*, **16**, 181 (1955).
24. G. F. Alfrey and J. B. Taylor, *Proc. Phys. Soc.*, **68B**, 775 (1955).
25. M. J. Russ, Ph.D. Thesis, University of Birmingham (1962).
26. S. Kawashima, *This Journal*, **113**, 1083 (1966).
27. H. F. Ivey in "Electroluminescence and Related Effects," p. 65, Academic Press, New York (1963).
28. H. K. Henisch in "Electroluminescence," MacMillan, New York (1962).

Technical Notes

(Cd,Zn)S Photoconductive Sintered Layer

Miyoshi Haradome and Hirokuni Kawashima

The Physical Science Laboratories, Nihon University at Narashino, Chiba-ken, Japan

As is widely known, light-sensitive sintered layers of CdS show a remarkable fall-off of photoconductive sensitivity in the spectral region below 520 mμ, because of surface recombination of carriers. In order to remove such a fault, one of the authors (1) previously examined the preparation of (Cd,Zn)S solid solution layers in the way similar to that for usual CdS layers (2). It must be noted, however, that such a conventional method was unsuccessful in producing satisfactorily adherent and uniform layers of recrystallized (Cd, Zn)S, especially in the Zn-rich region.

In the present study, the authors have succeeded in developing a new sintering technique for the (Cd, Zn)S, layer by making use of a high-temperature, high-pressure argon atmosphere and of NaCl solvent flux. The resultant product exhibits high sensitivity even in the spectral region from 520 down to 400 mμ.

Experimental

The sintering apparatus utilized in this work is shown schematically in Fig. 1. In a stainless steel tube an impurity protector and sample chamber both made of quartz are enclosed, and the whole system is put in a SiC resistance furnace for heat-treatment. The sample chamber is loosely sealed with a quartz cap. Fluorescent powder of (Cd, Zn)S solid solution activated with a small amount of Ag or Cu (product of the Dai-Nippon Paint Company, Ltd.) was used as starting material. A mixture of 3×10^{-2} mole of the fluorescent powder and 9×10^{-3} mole of high grade NaCl was blended with 3 cc of distilled water and was ground in a quartz mixer for 5 hr. This suspension was sprayed on the surface of high-purity alumina plates by a quartz spray-gun. The sprayed layer was dried for 2 hr at 80°C and was then enclosed in the stainless steel tube which was evacuated to 10^{-4} Torr. After introducing high-purity argon gas (oxygen content of 0.2 ppm) into the tube, the heat-treatment for sintering was started. It took about 20 min to raise the temperature to 1100°C, at which the sintering was most appropriately conducted.

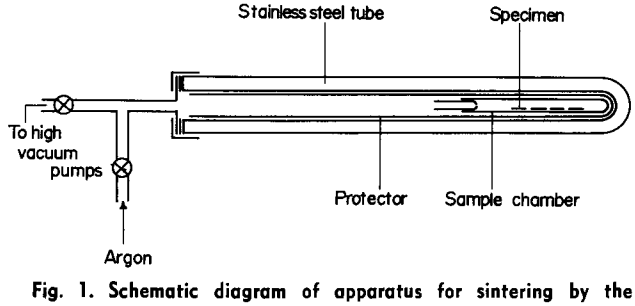

Fig. 1. Schematic diagram of apparatus for sintering by the high-pressure sintering method.

Results and Discussions

From grain size observation with an optical microscope, the average grain size of the (Cd, Zn)S solid solution layers prepared in the pressure range above 30 atm has been found to indicate a monotonic increase with increasing sintering temperature (1000°-1150°C) and time (0-100 min). It must be noted that the evaporation of the specimen takes place under pressures below 30 atm. It may be emphasized, in addition, that x-ray diffraction data indicate no change in composition of (Cd, Zn)S solid solutions if the sintering is done at temperatures below 1150°C, under pressures exceeding 30 atm, and within times less than 100 min.

Figure 2 gives the sintering temperature dependence of the photocurrent and dark current produced in

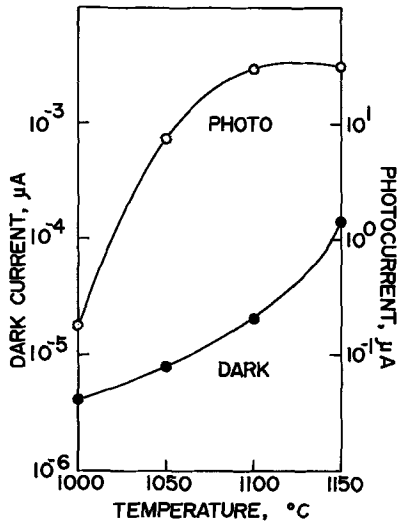

Fig. 2. Sintering temperature dependence of the photocurrent and dark current for the 30 m/o Zn, sintered for 60 min under 50 atm Ar.

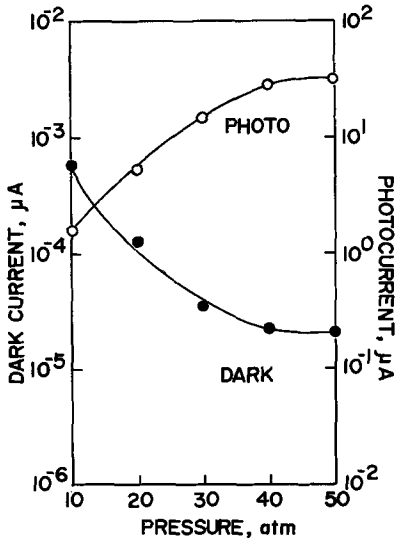

Fig. 3. Pressure dependence of the photocurrent and the dark current for the 30 m/o Zn, sintered for 60 min at 1100°C.

the specimens containing 30 m/o ZnS, while the sintering was done under a pressure of 50 atm for 60 min. A maximum of the photocurrent curve is found at 1100°C, making a sharp contrast to the monotonic increase of dark current. In Fig. 3 is presented the pressure dependence of the photocurrent and dark current for the specimen containing 30 m/o Zn when heat treated at 1100°C for 60 min. With increasing pressure, the photocurrent increases remarkably, while the dark current decreases, both showing leveling-off in the high-pressure range above 40 atm. The maximum position in the photoconductivity spectrum for a number of (Cd, Zn)S:Ag, Cl layers sintered at 1100°C for 60 min under 50 atm is shown schematically in Fig. 4. The shift of the photoconductivity peak with change in composition is almost parallel to that of the emission peak (3), which may suggest that composition of those (Cd, Zn)S layers has not changed during the heat-treatment. In Fig. 5, the decay time of the photocurrent when the same specimens were exposed to 100 Lx radiation is plotted against the composition. For the

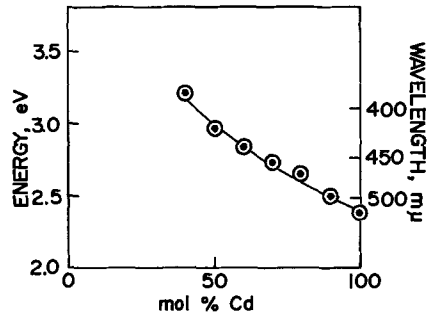

Fig. 4. Maximum of the photoconductivity spectrum of the (Cd,Zn)S:Ag, Cl solid solution sintered layers.

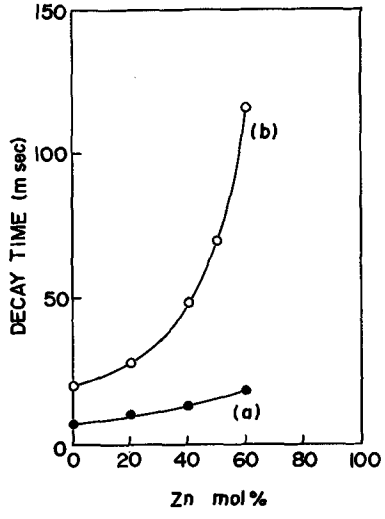

Fig. 5. Decay time of the photocurrent for the (Cd,Zn)S:Ag,Cl solid solution sintered layers. (a): high-pressure sintering method; (b) conventional sintering method.

sake of comparison, the behavior of specimens prepared by the conventional sintering method (1) is also shown in Fig 5. On the basis of these data, one can conclude that the much shorter decay times exhibited by the layers prepared at high pressures may be ascribed to the presence of fewer grain boundaries, causing less scattering of the photoconductivity carriers. On the other hand, the decay time is found to increase almost linearly with the content of Zn. Through a preliminary investigation of the behavior of thermally stimulated current and decayed thermally stimulated current, such an increase of the decay time has been concluded to arise from the increase of the density and depth of the electron traps.

Further studies, especially of electron and hole traps are being pushed forward and will be published in the not too far distant future.

Manuscript received June 12, 1967.

Any discussion of this paper will appear in a Discussion Section to be published in the June 1968 JOURNAL.

REFERENCES

1. Ryuichi Hioki, Miyoshi Haradome, and Hiroshi Kukimoto, *Japan. J. Appl. Phys.*, 2, (1963).
2. S. M. Thomsen and R. H. Bube, *Rev. Sci. Instr.*, 26, 664 (1955).
3. R. E. Halsted, M. Aven, and H. D. Coghill, *This Journal*, **112**, 177 (1965).

Cd_4SiS_6 and Cd_4SiSe_6, New Ternary Compounds

Synthesis, Photoconductive and Fluorescent Properties

E. Kaldis,[1] L. Krausbauer, and R. Widmer

Laboratories RCA Ltd., Zurich, Switzerland

In the course of a program aimed at the synthesis of new photoconductors and phosphors attempts were made to synthesize ternary cadmium and zinc chalcogenides with silicon and germanium. Accordingly the following systems were examined: Cd-Si-S, Cd-Si-Se, Cd-Si-Te, Zn-Si-S, Zn-Si-Se, Zn-Si-Te, Zn-Ge-S, Zn-Ge-Se, Zn-Ge-Te. Ternary phases could be found only in the first two of these systems. The compounds Zn_2GeS_4 and Zn_2GeSe_4 which have been reported in the literature (1) could not be synthesized.

Since the compound Cd_4GeS_6 had been found to be a good photoconductor (2-5), it could be expected that metal silicon chalcogenides might also show photoconduction. Due to the lighter atomic weight of silicon the peak sensitivity was expected to be at shorter wavelengths than in the corresponding metal germanium chalcogenides (6).

This paper deals with the synthesis, crystal growth, and preliminary measurements of the photoconductivity and fluorescence properties of Cd_4SiS_6 and Cd_4SiSe_6.

Cd_4SiS_6 was synthesized by reacting stoichiometric quantities of cadmium sulfide, silicon, and sulfur (5*N* purity, Light, England) in evacuated quartz tubes. The tube with the well mixed starting materials was put in a furnace with a flat temperature profile and was slowly heated up to 850°C within 2 days. This slow heating rate was necessary to avoid explosions.

Guinier powder diagrams showed that the reaction product was isomorphous to the germanium compound which a new chemical analysis (3) showed to have the formula Cd_4GeS_6. The latter was found to crystallize in the C_c space group with unit cell dimensions $a = 12.303$Å, $b = 7.056$Å, $c = 12.335$Å, and $\beta = 110°02'$ (4). The x-ray diagrams of Cd_4SiS_6 showed only the lines corresponding to those of Cd_4GeS_6. No additional lines could be detected. The angle β for Cd_4SiS_6 was measured with the optical goniometer to $\beta = 110°30'$.

The Cd_4SiS_6 powder synthesized as described above looks very homogeneous but has a light olive green color, although the fundamental absorption edge of the compound lies at 4300Å (see below). Material synthesized in the presence of iodine or crystals grown by iodine transport have a lemon yellow color. Also, the powder synthesied in the presence of excess of sulfur is yellow. All these materials have the same x-ray diagram. The yellow color could not be restored by adding small amounts of excess cadmium sulfide, silicon, or a mixture of silicon and sulfur to the starting material. Yellow crystals of Cd_4SiS_6 heated at 1250°C in a small evacuated quartz ampoule become greenish. In the presence of a partial sulfur pressure of 1 atm the color of the crystals remains yellow.

It is possible that the green color is the result of a slight decomposition taking place only at the surface of the powder. At 1250°C this decomposition can obviously be suppressed by 1 atm of sulfur pressure. A partial sulfur pressure which is probably high enough to prevent decomposition is also built up during the iodine transport.

Cd_4SiSe_6 was synthesized from the elements in the presence of iodine at 800°C in an evacuated quartz ampoule.

Crystals of Cd_4SiS_6 with dimensions up to 10 x 5 x 6 mm^3 were grown by iodine transport at 800°C in a closed system. The iodine concentration in the ampoules was 4 mg/cm^3. Using values of undercooling (4) between 5° and 30°C and growth times of two to ten days crystals with varying dimensions and highly reflecting natural faces could be grown.

Doped crystals were grown by mixing the starting materials with the dopant in the form of the metal iodides.

Black crystals of Cd_4SiSe_6 with dimensions of a few millimeters were grown by iodine transport at 800°C.

The optical measurements were made with conventional apparatus. For photoconductivity and absorption measurements in the visible part of the spectrum a xenon high-pressure lamp was used as light source in connection with a Leiss single prism monochromator and a Zeiss double prism monochromator, respectively. In the near uv a hydrogen lamp was used. A high impedance Keithley micromicroammeter in connection with a Moseley X-Y-recorder was used to register photocurrent *vs.* wavelength and current-voltage curves.

Reflectivity measurements were carried out with a tungsten or hydrogen lamp, a Bausch and Lomb grating monochromator, and a RCA 1P28 phototube as detector.

For luminescence measurements the samples were irradiated with the 3660Å-Hg-line, the luminescent light was focussed onto the entrance slit of a single prism Leiss monochromator. An RCA 7265 photomultiplier was used as detector of the light at the exit slit of the monochromator. The output of the photomultiplier was fed into a Varian chart recorder, the speed of which was synchronized with the prism rotation of the monochromator. The curves so obtained were corrected for the multiplier sensitivity and the dispersion of the prism to give the true spectrum in arbitrary units.

It was found that as-grown crystals were covered with an insulating surface layer. To remove this surface layer the crystals were washed immediately after they had been taken out of the ampoule, first with hot hexane to dissolve silicon iodide and then with alcohol to dissolve cadmium iodide. In cases where this treatment was not successful the insulating layer could be removed mechanically by grinding and polishing the crystal surface. After these treatments evaporated contacts of silver, cadmium, indium, gallium, and aluminum were found to be ohmic and to give the same wavelength dependence of the photocurrent. Throughout this work indium electrodes were used unless otherwise stated. The electrodes were evaporated in a vacuum of $5 \cdot 10^{-5}$ Torr, the electrode separation d being 0.3 to 0.8 mm.

Annealing experiments were made in air and hydrogen at different temperatures. For each experiment the crystals were kept at the annealing temperature for 30 min. All dark and photocurrent measurements were done at room temperature.

Results

Undoped Cd_4SiS_6 crystals without any heat-treatment show good photoconductive properties. Measurements with a thermoelectric tester (7) showed n-type conductivity, both in the dark and under illumination. The crystals have a dark conductivity between 10^{-12} and 10^{-10} ohm-cm^{-1}. A typical wavelength dependence of the photoconduction is shown in Fig. 1. There

[1] Present address: Laboratorium für Festkörperphysik, ETH, Zürich, Switzerland.

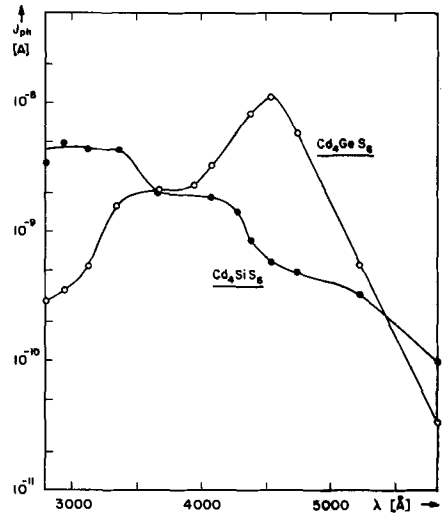

Fig. 1. Wavelength dependence of the photocurrent for unannealed Cd_4SiS_6 and Cd_4GeS_6 crystals. The photocurrent is corrected for equal numbers of incident light quanta under the assumption that $J_{Ph} \alpha B$ (B = light intensity).

are three regions in the response curve: All Cd_4SiS_6 crystals show a photoconductivity shoulder around 5000Å, another one at about 4200Å, and a third one around 3300Å. Typical values for the photoconductivity of Cd_4SiS_6 crystals at 4200Å with a light intensity of $N = 10^{12}$ quanta/cm^2 sec lie between 10^{-6} ohm-cm^{-1} and 10^{-7} ohm-cm^{-1}. At 3000Å and for the same light intensity the photoconductivity values vary between 10^{-7} and 10^{-5} ohm-cm^{-1}. The ratio of the photoconductivity to the dark conductivity lies between 10^3 and 10^4. The sensitivity defined by Bube (8) as $S = \Sigma_{Ph} \cdot d^2$/absorbed power ($\Sigma_{Ph} = I_{Ph}/U$, U = applied voltage) reaches values of 10^{-2} mho cm^2/w, which is of the same order of magnitude as the values for cadmium sulfide and Cd_4GeS_6. The Cd_4SiS_6 crystals show a gain of several hundreds for a field strength of 10^3 v/cm. The response time of these crytals is of the order of a few seconds for a light intensity of $N = 10^{12}$ quanta/cm^2 sec. It increases with decreasing light intensity.

Absorption measurements on Cd_4SiS_6 crystals showed the fundamental optical absorption edge to lie at about 4300Å. The absorption coefficient shows an exponential increase for wavelengths shorter than 4550Å and reaches a value of $k = 5 \cdot 10^3$ cm^{-1} for λ = 4360Å. We conclude therefore that the photoconductivity shoulder around 4200Å corresponds to the fundamental optical absorption edge and the shoulder around 5000Å is due to impurity photoconduction.

The question arises as to the origin of the third shoulder in the photoconductivity response around 3200Å. To our knowledge so far an increase in photoconductivity for energies higher than the fundamental absorption edge has only been observed for GaP (9). CdS and especially Cd_4GeS_6 do not show such an effect. (The fundamental absorption edge of Cd_4GeS_6 lies at about 4700Å). The increase in photoconductivity in the uv for Cd_4SiS_6 could be due to a change in the physical properties of Cd_4SiS_6 (absorption coefficient, mobility, carrier lifetime a.s.o.) as a function of light frequency or intensity, as is invoked to explain the anomalous photoresponse in GaP (9), or it could be due to a surface effect caused either by surface states, or by a surface of different chemical composition on top of the Cd_4SiS_6 crystals.

Reflectivity measurements have been made on a Cd_4SiS_6 and a Cd_4GeS_6 crystal from λ = 5000Å to 2200Å (Fig. 2). Both curves show a maximum at the fundamental optical absorption edge and a weak peak around 3400Å in the case of Cd_4SiS_6 and around 3300Å in the case of Cd_4GeS_6. Similar results are known for GaP (10). Therefore the uv photoresponse in Cd_4SiS_6 could be due to strong direct optical transitions similar to the explanation presented by Nelson *et al.* for GaP (9).

It might be worthwhile mentioning that the photoconductivity response for Cd_4GeS_6 also shows a shoulder for energies higher than the fundamental absorption edge (Fig. 1). Therefore similar transitions might occur in Cd_4GeS_6, but different surface states in this material might cause a decrease in the carrier lifetime and by this a decrease in photoconductivity.

It is generally known that silicon-sulfur compounds hydrolyze easily (11-13). A colorless insulating layer has been found on the surface of the as-grown crystals. Although the greater part of this layer is removed by chemical or mechanical means, in order to get ohmic contacts on the crystal, it is probable that a thin layer still exists on the surface of the crystals. However, this layer must inhibit further hydrolysis because the photoconductive properties of as-grown and ground Cd_4SiS_6 crystals do not change after a treatment with hot water (100°C, for 30 min). An amorphous, hydrolyzed surface layer on the Cd_4SiS_6 crystals could be responsible, either alone or in conjunction with the Cd_4SiS_6 lattice, for the observed high uv-sensitivity if one assumes a high absorption coefficient of this surface layer for wavelengths between 3000 and 4000Å. Bradford *et al.* (14) have found a fairly high absorption coefficient for SiO_{2-x} layers depending on the amount of oxygen and the degree of disorder of the layers. The higher the silicon to oxygen ratio or degree of disorder the higher the absorption coefficient around 3000Å was found to be.

Some indication for such an explanation of the uv photoconductivity can be found in annealing experiments in air and hydrogen. Annealing Cd_4SiS_6 crystals at 300°C in air, *e.g.*, decreases the uv sensitivity considerably whereas it is unchanged or increased for crystals annealed in hydrogen. In the first case the decrease of the uv sensitivity could be the result of a decrease of the silicon to oxygen ratio due to a partial surface oxidation which in its turn might lead to a decrease of the absorption coefficient. On the other hand annealing in hydrogen is not expected to decrease the silicon to oxygen ratio.

So far no final decision can be made about the origin of the uv photosensitivity of untreated Cd_4SiS_6 crystals. Further experiments are necessary to show if the uv photoresponse in Cd_4SiS_6 has a similar origin to that in GaP or to give direct evidence for the ex-

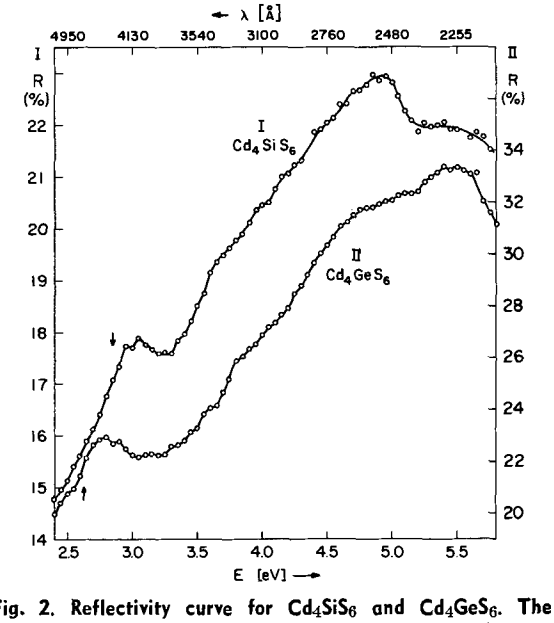

Fig. 2. Reflectivity curve for Cd_4SiS_6 and Cd_4GeS_6. The arrows indicate the approximate positions of the fundamental optical absorption edge.

Table I. Peak wavelengths and intensities of various Cd_4SiS_6 phosphors in comparison with the commercial RCA CdZnS : Ag phosphor

Sample No.	Composition	T = 300° λ_{max}	T = 300° I_{rel}, %	T = 77°K λ_{max}	T = 77°K I_{rel}, %
51	CdZnS : Ag	6800	100	6800	120
227	Cd_4SiS_6	7100	1.0	6500	30
125	+ Cu	7100	30	6900	36
127	+ Ag	7000	4	6600	11
231	+ Hg	7100	7	6700	37
131	+ Mn	—	—	6650	48
133	+ Ga	7100	1.5	6600	45
234	+ In	7100	1	6650	30
132	+ Tl	7300	1.2	6600	45
233	+ Nb	7000	2	6600	28
129	+ Nernst filament*	—	—	6600	60
232	+ Eu	6900	0.6	6600	27
126	+ U	—	—	6650	25
130	+ As	—	—	6600	46

* Consisting of 85% ZrO_2 and 15% Y_2O_3.

istence and eventually the composition of a surface layer.

Cd_4SiS_6 crystals annealed in cuprous sulfide for 3 and 6 hr show a broad photoconductivity response in the wavelength region from 4400 to 6200Å with a maximum photoconductivity of $\sigma_{Ph} = 4 \cdot 10^{-4}$ and $4 \cdot 10^{-5}$ ohm-cm^{-1}, respectively, but no uv sensitivity. No further annealing experiments have been made with these crystals.

Preliminary measurements on Cd_4SiSe_6 crystals showed that this material is a good photoconductor. The dark conductivity is similar to that of Cd_4SiS_6. The photoconduction *vs.* wavelength curve shows a broad region of photosensitivity from about 4000 to 7000Å. The photoconductivity reaches values of $\sigma_{Ph} = 3 \cdot 10^{-5}$ ohm-cm^{-1}, and the sensitivity is $S = 10^{-2}$ mho cm^2/w. No photoconductivity was observed for wavelengths shorter than 4000Å.

Undoped Cd_4SiS_6 crystals and those doped with copper, silver, mercury, gallium, indium, thallium, europium, arsenic, niobium, manganese, uranium, and mixed with a powdered Nernst filament (consisting of 85% zirconia and 15% yttrium oxide) were examined for their luminescence properties.

At room temperature, only copper-doped material showed a considerable red luminescence with a broad maximum peaking at 7200Å, the intensity of the peak wavelengths being about one-third of the red commercial RCA ZnCdS : Ag phosphor (33-Z-639*D*) at its peak wavelength (see Table I).

At liquid nitrogen temperature we found the results listed in Table I. All luminescence peaks are shifted to shorter wavelengths in comparison with the peaks at room temperature. Undoped material shows a broad luminescence peak at 6600Å with an intensity about one-third of the mentioned red RCA phosphor. In general the dopant material has only little influence on the luminescence properties of Cd_4SiS_6 at 77°K. Only mercury and copper shift the peak to longer wavelengths, by 200 and 400Å, respectively. The highest intensity is achieved by Cd_4SiS_6 doped with a powdered Nernst filament; the intensity is twice as high as that of the undoped material. Silver, on the other hand, decreases the luminescence intensity to about one-third.

Acknowledgment

The authors wish to thank Dr. G. Harbeke, Dr. H. Kiess, and Dr. R. Nitsche for stimulating discussions, and Mr. E. Meier for taking the reflectivity measurements.

Manuscript received June 22, 1967.

Any discussion of this paper will appear in a Discussion Section to be published in the June 1968 JOURNAL.

REFERENCES

1. H. Hahn, Paper given at the XVIIth IUPAC Congress, Munich, Germany, September 1959.
2. L. Krausbauer, F. Lappe, W. J. Merz, and R. Nitsche, *Physik. Verhandl.*, 366 (1962).
3. E. Kaldis and R. Widmer, *J. Phys. Chem. Solids*, **26**, 1697 (1965).
4. R. Nitsche, *Z. Krist.*, **120**, 1 (1964).
5. H. Kiess, *Helv. Phys. Acta*, **37**, 638 (1964). H. Kiess, To be published in *J. Phys. Chem. Solids*.
6. W. J. Merz, *Helv. Phys. Acta*, **35**, 274 (1962).
7. A. G. Fischer, J. N. Carides, and J. Dresner, *Solid State Comm.*, **2**, 157 (1964).
8. R. H. Bube, "Photoconductivity of Solids," p. 59, John Wiley & Sons, Inc., New York (1960).
9. D. F. Nelson, L. F. Johnson, and M. Gershenzon, *Phys. Rev.*, **135**, A1399 (1964).
10. R. Zallen and W. Paul, *ibid.*, **134**, A1628 (1964); E. F. Gross *et al.*, *Sov. Phys. - Dokl.*, **8**, 1103 (1964).
11. Gmelin's Handbuch der Anorganischen Chemie, Volume Silicon.
12. E. Zintl and K. Loosen, *Z. Phys. Chem.*, **A174**, 301 (1935).
13. A. Haas, *Z. angew. Chem.*, **77**, 1066 (1965).
14. A. P. Bradford, G. Hass, M. McFarland, and E. Ritter, *Appl. Optics*, **4**, 971 (1965).

Temperature Oscillations in Czochralski Crystal Growth

J. R. Carruthers[1]

Department of Metallurgy and Materials Science, University of Toronto, Toronto, Canada

Temperature fluctuations resulting from thermal convection during crystal growth are known to cause growth rate fluctuations and impurity microsegregation. These fluctuations are normally random in otherwise stationary liquids, although Hurle (1) reports regular periodicities near the surface of liquid gallium at low-temperature gradients. When a liquid with such temperature oscillations is spun about a vertical axis or subjected to a magnetic field (if conducting), additional stabilizing forces are provided which eliminate the oscillations and allow steady flow. With spin, this additional force is the Coriolis force which acts on particles having a horizontal velocity component.

Spin may have a second important effect in addition to the stabilization of flow. When instability does arise under spin, the consequent motion might be oscillatory rather than unidirectional. This type of instability has been termed "overstability" and occurs only in fluids with a low Prandtl number, N_{Pr}, where

$$N_{Pr} = \nu/K < 0.68 \text{ for overstability}$$

where ν is the kinematic viscosity and K the thermal diffusivity. This note reports the existence of overstable oscillations in rotating liquid silicon ($N_{Pr} \approx 0.088$) as observed from a fine set of growth striations appearing on the outer surface of nonrotated silicon crystals.

Chandrasekhar and Elbert (2) define a nondimensional frequency, σ, for overstable oscillations as

$$\sigma = \left[\frac{2}{1+2N_{Pr}}\right]^{1/2}\left[\frac{1+N_{Pr}}{N_{Pr}}\right]^{1/3}\left[\frac{\pi^2}{2}\right]^{1/3} N_{Ta}^{1/3}$$

where N_{Ta} is the dimensionless rotation rate given by

$$N_{Ta} = \frac{4\Omega^2 h^4}{\mu^2}$$

where Ω is the crucible rotation rate and h is the liquid depth. Substitution of N_{Pr} for liquid silicon gives

$$\sigma = 5.15\, N_{Ta}^{1/3}$$

Chandrasekhar and Elbert (2) write the oscillation period; τ, as

$$\tau = \frac{2\pi}{\Omega}\frac{N_{Ta}^{1/2}}{2\sigma}$$

Substituting for σ and using the crucible rotation rate, ω, in revolutions per minute gives

$$\tau = 5.82\,\frac{N_{Ta}^{1/6}}{\omega}\ \text{sec}$$

[1] Present address: Bell Telephone Laboratories, Inc., Murray Hill, New Jersey.

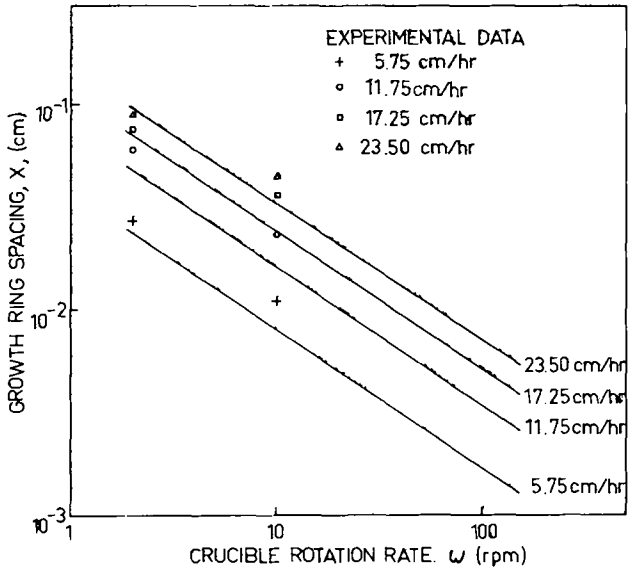

Fig. 1. Variations of growth rate fluctuation spacing caused by overstable oscillations in rotating liquid silicon.

The corresponding spacing period, x, (in growing crystals) of perturbations associated with overstable oscillations for a growth rate, R, will be

$$x = R\tau$$

This relation does not, of course, apply at very low crucible rotation rates. The spacing, x, is plotted as a function of ω for various growth rates, R, in Fig. 1 using $\nu = 0.0125$ cm^2/sec and $h = 4.1$ cm. Experimentally observed points for crystals grown with no crystal rotation are shown for the different growth rates. These crystals were supplied to the author by K. E. Benson of the Bell Telephone Laboratories Inc., The observed spacings were obtained by counting the number of outer growth rings contained in a 1-in. length of the crystal surface. The agreement between theory and experiment is reasonably close, although the slope appears to be somewhat in error. This discrepancy undoubtedly arises because the analysis ignores the additional fluid circulation generated by horizontal temperature gradients and the resultant damping of temperature oscillations.

Manuscript received May 19, 1967; revised manuscript received June 30, 1967.

Any discussion of this paper will appear in a Discussion Section to be published in the June 1968 JOURNAL.

REFERENCES

1. D. T. J. Hurle, *Phil. Mag.*, **13**, 305 (1966).
2. S. Chandrasekhar, and D. Elbert, *Proc. Roy. Soc. (London)*, **A231**, 198 (1955).

Epitaxial InAs on InAs Substrates

G. R. Cronin and S. R. Borrello

Texas Instruments Incorporated, Dallas, Texas

Halogen transport and vapor growth of InAs were first reported by Effer *et al.* (1, 2). Epitaxial deposition of pure InAs as well as GaAs-InAs mixed crystals on low resistivity GaAs substrates has also been described by Minden (3), but the net carrier concentration and mobility of the deposits were not reported. By depositing InAs on chromium doped semi-insulating GaAs substrates, electrical measurements on pure epitaxial InAs deposits have been made (4, 5). While these deposits compared favorably with melt grown material in terms of net carrier concentration and mobility at 77°K, electron mobilities at 300°K were on the average somewhat lower than those observed for melt-grown material.

Since defect free deposits were not generally obtained on GaAs substrates, the influence of these defects on electrical properties cannot be ignored. Furthermore, strains in the deposited layer arising from differences in lattice spacing and thermal expansion coefficients may also influence the electrical characteristics of these deposits (6).

In order to avoid these effects as much as possible in the present series of experiments, epitaxial InAs was deposited on undoped InAs substrates. In order to make electrical measurements on the epitaxial layers alone, the deposits were made thick enough (75-100μ) so that the substrates could be removed leaving the deposited layer intact.

The reactor and flow systems are the same as those described previously (4) using elemental indium and arsenic, 99.9999% pure.

InAs substrates were prepared from undoped pulled crystals cut on the (100) orientation. These crystals showed typical excess electron concentrations of 4-5 x 10^{16}/cm^3 at 300°K with dislocation densities ranging from high 10^3 to low 10^4/cm^2. Wafers cut 30 mils thick were chemically polished on a paper pad soaked with a solution of bromine in methanol, 0.5% by volume (7).

Under the operating conditions shown in Table I approximately 6 hr of deposition time are required for a layer of sufficient thickness for substrate removal. The surfaces of these deposits were quite smooth, shiny, and, in general, free of visible defects. In instances where surface imperfections were observed they were identical in appearance with those described previously for deposits on GaAs substrates (4).

Unlike deposition on GaAs where the interface between deposit and substrate is clearly visible due to a slight color difference, epitaxial layers on InAs substrates are virtually impossible to distinguish on a cleaved edge. Growth rates were therefore obtained by using partially masked substrates. Masking is achieved with an SiO_2 film deposited on a portion of the substrate using standard photolithographic techniques. Since no deposit is generally observed on the masked portion of the substrate, deposit thickness is conveniently measured by observing the "step height" revealed on the cleaved edge of the sample (Fig. 1).

Hall measurements were made by the van der Pauw (8) technique on cloverleaf shaped samples 6 mm in diameter. The substrate portion of the specimen was almost totally removed by wet lapping with 5μ alumina abrasive. When the total thickness of the sample (deposit plus substrate residue) measured 125-150μ, the remaining portion of the substrate was removed by etching the sample in a 5% bromine-methanol solution. Approximately 5 min etching time are required to remove 30-50μ of material.

Table I. Temperature and flow conditions for epitaxial InAs deposition

Item	Temperature, °C	Flow rate cc/min
Arsenic	400	15
Indium	870	100
Substrate	720	—
Excess hydrogen flush	—	5
As Cl_3 reduction furnace	880	—

Table II. Mobility and carrier concentration at 300° and 77° K of InAs crystals grown epitaxially to InAs

Crystal No.	Thickness, μ	Carrier concentration, x 10^{15}/cm^3 300°K	Carrier concentration, x 10^{15}/cm^3 77°K	Hall mobility, x 10^3 cm^2/v-sec 300°K	Hall mobility, x 10^3 cm^2/v-sec 77°K
474	100	15	12	30	69
475	70	6.2	5.3	31	98
476	125	9.5	8.6	30	73
477	95	12	10	29	71
485	110	15	14	28	65
489	80	16	15	28	65
491	94	26	22	25	53.2
492	85	14	11	28	67
493	90	33	31	27.5	47.5
494	95	34	31	26	44.6
505	75	17	15	30	61
507	75	17	14	28	61
513	100	4.9	3.7	30	112

The final thickness of the sample on which Hall measurements were made was usually about 75-100μ which corresponded to the minimum deposit thickness.

The electron mobility at 300°K for most of the epitaxial InAs crystals measured varies little from approximately 30,000 cm^2/volt-sec. Since the net carrier concentration varies as much as an order of magnitude, the results (see Table II) imply that the mobility at 300°K is probably limited by optical phonon scattering. At 77°K, however, the electron mobility is explicitly related to the carrier concentration (see Fig. 2) for both vapor deposited and melt grown InAs (9). The shift in data points in Fig. 2 represented by the GaAs substrates may be an indirect result of the 7% lattice mismatch between these two materials. The point which noticeably deviates from the best fit curves, we believe, represents rather closely compensated material.

The temperature variation of the electron mobility was determined for two epitaxial crystals and is shown in Fig. 3. These data can be fitted to a fair degree

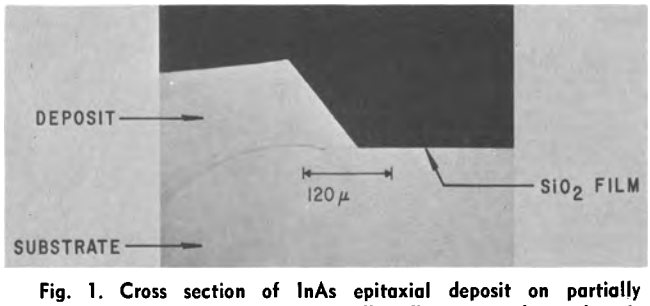

Fig. 1. Cross section of InAs epitaxial deposit on partially masked (SiO_2) substrate. Height of "step" corresponds to deposit thickness. Note also a small amount (approximately 45 μ) of overgrowth. The angle of growth between the surfaces of the masked substrate (100), and the epitaxial deposit corresponds closely to a (111) plane.

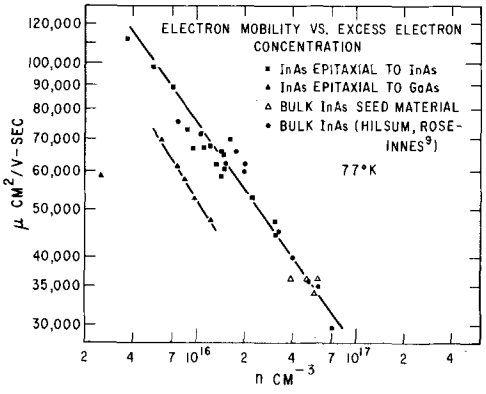

Fig. 2. Electron mobility vs. excess electron concentration for vapor grown and melt grown InAs.

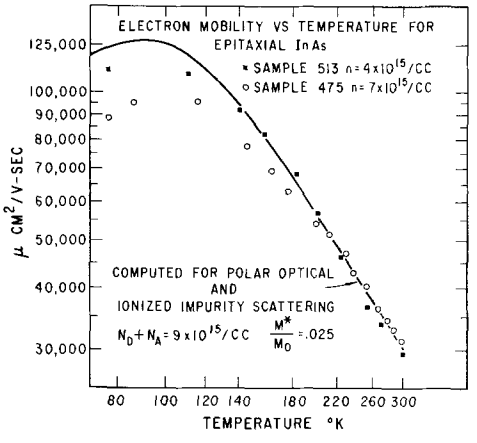

Fig. 3. Electron mobility vs. temperature for InAs epitaxial to InAs.

by a combination of polar optical (10) and ionized impurity (11) scattering and agree well with the results of Chasmar (12). An effective mass ratio of 0.025 and a donor plus acceptor concentration of 9 x 10^{15}/cm^3 were used to obtain the computed curve. The computed curve and the data are in close agreement from 300° to 130°K below which the deviations are less than 30%. Since the assumed value of 9 x 10^{15}/cm^3 for the total ionized impurity concentration produces a good fit for the temperature variation of the mobility and the net carrier concentration is measured at 3.7 x 10^{15}/cm^3, the donor concentration becomes approximately 6.5 x 10^{15}/cm^3 and the acceptor concentration 2.5 x 10^{15}/cm^3. The functional dependence of mobility on net carrier concentration as shown in Fig. 2 is consistent with the ionized impurity scattering model (11) implying that the excess electron concentration is large compared with the acceptor concentration.

The vapor-grown samples shown in Fig. 2 represent an improvement in properties over InAs deposited on GaAs substrates as well as melt grown material. In the former case, it seems reasonable to attribute the increase in mobility to a decrease in the defect density and strains in the deposited layer. In the latter case, it is possible that the impurity segregation coefficients are smaller in this particular vapor-solid growth mechanism than in the liquid-solid. The possibility also exists that the higher excess carrier concentrations normally observed in melt grown InAs are a result of a defect structure introduced at the solidification temperature. We have tried several etchants to reveal differences in the structure of the vapor-grown layer and the InAs substrate but, as yet, without result.

Acknowledgments

The authors acknowledge support of the Air Force Avionics Laboratory under Contract No. AF 33(615)-2913 for this work. They also thank W. L. Kriss for preparation of the samples, and H. Strack for helpful suggestions.

Manuscript received March 29, 1967; revised manuscript received June 22, 1967. This paper was presented at the Philadelphia Meeting. Oct. 9-14, 1967.

Any discussion of this paper will appear in a Discussion Section to be published in the June 1968 JOURNAL.

REFERENCES

1. D. Effer, *This Journal*, **112**, 1020 (1965).
2. G. R. Antell and D. Effer, *ibid.*, **106**, 509 (1959).
3. H. T. Minden, *ibid.*, **112**, 300 (1965).
4. G. R. Cronin, R. W. Conrad, and S. R. Borrello, *ibid.*, **113**, 1336 (1966).
5. J. P. McCarthy, Paper presented at Institute of Physics and Physical Society Conference on "The Physics of Semiconducting Compounds," Swansea, Sept., 1966.
6. R. W. Conrad, P. L. Hoyt, and D. D Martin, *This Journal*, **114**, 164 (1967).
7. C. S. Fuller and H. W. Allison, *ibid.*, **109**, 880 (1962).
8. L. J. van der Pauw, *Philips Research Repts.*, **13**, 109 (1958).
9. C. Hilsum and A. C. Rose-Innes, "Semiconducting III-V Compounds," Pergamon Press, New York (1961).
10. H. Ehrenreich, *J. Phys. Chem. Solids*, **12**, 97 (1959).
11. H. Brooks, *Advances in Electronics and Electron Physics*, **7**, 85 (1955).
12. R. R. Chasmar, *J. Phys. Chem. Solids*, **20**, 164 (1961).

Brief Communication

A Chemical Notation for Defect Solid State Chemistry

J. N. Ong, Jr.

College of Applied Science and Engineering and Laboratory for Surface Studies, University of Wisconsin-Milwaukee, Milwaukee, Wisconsin

Communication has been hindered among and between electrochemists, metallurgists, ceramists, and solid-state chemists and physicists, for lack of a consistent or standardized notation to describe chemical reactions in the solid state. This note demonstrates that normal chemical notation is adequate for most purposes and that existing notations are needlessly complicated.

Two familiar reactions are discussed, F-center formation and metal deficit nonstoichiometric oxide formation, (*a*) to illustrate the diversity of symbolism encountered in existing notations to describe vacancies (Schottky-Wagner defects) and charge carriers, (*b*) to suggest an alternate notation, (c) to demonstrate that one common adjustment to the existing notations renders their symbols for vacancies equivalent to each other and to normal chemical notation, and (*d*) to recommend alternate symbols for holes when used in chemical equations.

F-Center Formation

Some of the ways in which the reaction of sodium vapor with rock salt to produce F-centers has been symbolized are shown in Table I, reactions (B)-(E). Not shown are another building unit system of notation due to Schottky (2, 8) and a notation of Schmalzried's (9), typographically similar to that of Schottky (1) but considered a structure element system (10). The proponents of both the building unit system and structure element system have discussed their notations elsewhere at length (1, 3). For present purposes it is sufficient to remark that Kröger, Stieltjies, and Vink (3) point out that Schottky's F-center symbol $|Cl|$ in reaction (B) has the operational meaning "take away a chlorine atom" and is in the material balance sense a "negative mass" particle. Schottky (1) objects to the atomic notation because only virtual potentials, $\xi(Na_{Na})$ and $\xi(V_{Cl})$[1] may be assigned to the symbols Na_{Na} (sodium atom at a sodium site) and V_{Cl} (vacancy at a chlorine site).

On the other hand Anderson (11, 12) persists in the use of Rees' notation, reaction (D), even though it is less convenient for writing mass action expressions.

The ionic notation, reaction (E), presupposes purely ionic bonding in rock salt. However, the resulting symbol for F-center, $V^{-}{}_{Cl}-$ along with that of Rees, $e|\square-$ represents a more accurate physical picture of the location of the electron than that of Kröger and Vink (2), whose symbol, V_{Cl}, carries zero charge. For future reference and by comparison with Schottky's symbol, observe that the three F-center-symbols in reactions (C), (D), and (E) are essentially "zero mass" particles.

We may view reaction (A) in a more conventional sense and by so doing return to a simple notation, discover one point of difference between the notations, and indicate the procedure by which they may be reconciled on this point. Let us view the F-center as arising from the solution of sodium in NaCl and express the material balance as reaction (F), Table I. Since we know that a sodium atom in solution occupies a lattice site in NaCl normally occupied by sodium and that a chlorine atom is absent from its normal site we may, for purposes of convenience, convey such structural information within the symbol (6) as shown in reaction (G). [The subscripts identify the lattice sites and V denotes absence of matter (2)]. It is frequently desirable to convey polarization information within a symbol. In our example we know that the electron from the sodium atom is localized in the vicinity of the vacancy (6). We may then write the symbol in the form shown in reaction (H). These symbols, Na (identity), $(Na_{Na}V_{Cl})$ (structure) and $(Na^{+}{}_{Na}V^{-}{}_{Cl})$ (polarization) are directly comparable to conventional chemical symbols, for example H_2O,

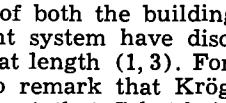

H, and

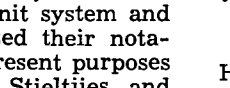

H, respectively. To complete the analogy, it is evident that we may solvate the solute atom to any convenient degree, reaction (I), and by incorporating the structure, polarization and solvation refinements to the basic symbol, Na (in solution), we finally arrive at the familiar schematic representation of the F-center (7) shown in reaction (J). In the chemical notation the F-center symbols are

Table I. Comparisons of various notations used to describe dilute solution formation in an ionic crystal

	Reaction	System of notation	Ref.
A.	Sodium vapor + rock salt = rock salt + F-centers	Verbal	
B.	$Na(g) = NaCl + \|Cl\|$	Building unit	(1)
C.	$Na(g) = Na_{Na} + V_{Cl}$	Structure element, atomic	(2-4)
D.	$Na(g) = Na^{+} \|\square\|^{+} + e\,\|\square\|^{-}$	Structure element, Rees	(2,5)
E.	$Na(g) = Na^{+}{}_{Na} + V^{-}{}_{Cl}$	Structure element ionic	(2)
F.	$Na(g) = Na$ (in solution)	Chemical	
G.	$Na(g) = (Na_{Na}\,V_{Cl})$	Chemical, with structure	(6)
H.	$Na(g) = (Na^{+}{}_{Na}\,V^{-}{}_{Cl})$	Chemical, with polarization	(6)
I.	$nNaCl + Na(g) = Na(NaCl)_n$ $Na^{+}\,Cl^{-}\,Na^{+}\,Cl^{-}$	Chemical, with solvation	(6)
J.	$nNaCl + Na(g) = Cl^{-}\,Na^{+} - Na^{+}$ $Na^{+}\,Cl^{-}\,Na^{+}\,Cl^{-}$	Chemical, with structure polarization and solvation	(6,7)

[1] We usually distinguish between chemical potentials (13) of neutral species, $\mu(i)$, whose values are normally experimentally accessible, and electrochemical potentials (13) of charged species (ions), $\mu_{+}(i)$ or $\mu_{-}(i)$, whose values are experimentally accessible only provided that their sum $\sum_j \nu_j\mu_{+} + \sum_k \nu_k\mu_{-}$ in any equilibrium equation is subject to the restriction of electrical neutrality, $\sum_j \nu_j z_j = 0$, where ν is the stoichiometric coefficient and z is the charge number of the appropriate species. Kröger's (3) virtual thermodynamic potentials (virtual potentials), $\xi(i)$, are analogous to electrochemical potentials. The condition that they be experimentally accessible is, however, subject not to electrical neutrality but to a constant ratio between different types of lattice sites. We will write all potentials as $\mu(i)$, $\xi(i)$, etc., instead of μ_i, ξ_i, etc. to avoid typesetting difficulties.

all "positive-mass" particles in contrast to the building unit and structure element symbols.

Mass action expressions relating defect concentrations to vapor pressure present another source of difficulty which is simplified by use of the conventional chemical notation. Experiment shows that the equilibrium number of F-centers formed is directly proportional to the sodium vapor pressure (6). We can obtain this relation by the usual procedure of equating chemical potentials. From reaction (G) for example we have

$$\mu(\mathrm{Na[g]}) = \mu(\mathrm{Na_{Na}V_{Cl}}) \quad [1]$$

from which we get the mass action expression (13)

$$K_G P_{Na} = a(\mathrm{Na_{Na}V_{Cl}}) \simeq [(\mathrm{Na_{Na}V_{Cl}})] \quad [2]$$

where K_G is the equilibrium constant, P_{Na} is the sodium vapor pressure, $a(\mathrm{Na_{Na}V_{Cl}})$ and $[(\mathrm{Na_{Na}V_{Cl}})]$ are the relative activity [ref. (13), p. 226] and concentration, respectively, of the F-center. The concentration is a good approximation to the relative activity when the solution is dilute.

If the same procedure is strictly followed with any of reactions (C), (D), and (E), (C) say, we may equate the chemical and virtual potentials according to

$$\mu(\mathrm{Na[g]}) = \xi(\mathrm{Na_{Na}}) + \xi(\mathrm{V_{Cl}}) \quad [3]$$

from which follows the relation

$$K_C P_{Na} = a(\mathrm{Na_{Na}})a(\mathrm{V_{Cl}}) \simeq [\mathrm{Na_{Na}}][\mathrm{V_{Cl}}] \quad [4]$$

relative activities $a(\mathrm{Na_{Na}})$ and $a(\mathrm{V_{Cl}})$ having been approximated by concentrations in the last term. Since there are equal numbers of excess[2] sodium atoms and vacancies, we have the additional restriction on Eq. [4] of

$$[\mathrm{Na_{Na}}] = [\mathrm{V_{Cl}}] \quad [5]$$

When Eq. [5] is substituted into Eq. [4], we obtain the result

$$(K_C P_{Na})^{1/2} = [\mathrm{V_{Cl}}] \quad [6]$$

which does not agree with experiment.

This conclusion may be avoided by arbitrarily assigning a value of unity to $a(\mathrm{Na_{Na}})$ in Eq. [4]. We may just as readily, and in many respects less arbitrarily, assign unit value to $a(\mathrm{V_{Cl}})$ and regard the changed properties of the crystal as arising from the activity of the excess sodium. A more satisfactory procedure is to regard the excess atom-vacancy pair as inseparable and its symbol accordingly associated, for example (NaCl+|Cl|) reaction (B),[3] ($\mathrm{Na_{Na}}+\mathrm{V_{Cl}}$) reaction (C), *etc.* It is clear from Table I that if the pairs of symbols on the right hand side of reactions (B) to (E) are combined as indicated above, they become equivalent in all but one respect to each other and to the symbols of reactions (F), (G), and (H), *i.e.*

$$(\mathrm{NaCl} + |\mathrm{Cl}|) \equiv (\mathrm{Na_{Na}} + \mathrm{V_{Cl}}) \equiv (\mathrm{Na^+}|\square_+ + \mathrm{e}|\square_-) \equiv$$
$$(\mathrm{Na^+{}_{Na+}} + \mathrm{V^-{}_{Cl-}}) \equiv \mathrm{Na(in\ solution)} \equiv$$
$$(\mathrm{Na_{Na}V_{Cl}}) \equiv (\mathrm{Na^+{}_{Na}V^-{}_{Cl}}) \quad [7]$$

With this one change, all the symbols become "positive mass" particles, all can be assigned normal chemical potentials and all the reactions will lead to the correct equilibrium relationship between vapor pressure and concentration, Eq. [2].

The only difference between symbols lies in the degree of polarization which is implied or assumed. Rather than assign virtual potentials to the separate symbols $\mathrm{Na_{Na}}$ and $\mathrm{V_{Cl}}$ with their respective effective charges, we may assign a chemical potential to the combined symbol ($\mathrm{Na_{Na}V_{Cl}}$) and account for polarization by including an appropriate term in the chemical potential which reflects the contribution to it, due to the presence of the sodium atom in an electric field [ref. (13), p. 415]

$$\xi(\mathrm{Na_{Na}}) + \xi(\mathrm{V_{Cl}}) = \mu(\mathrm{Na_{Na}V_{Cl}}) =$$
$$\mu^\circ(\mathrm{Na_{Na}V_{Cl}}) - \mu^E(\mathrm{Na_{Na}V_{Cl}}) \quad [8]$$

where $\mu^\circ(\mathrm{Na_{Na}V_{Cl}})$ denotes the value of $\mu(\mathrm{Na_{Na}V_{Cl}})$ at zero field strength and where $\mu^E(\mathrm{Na_{Na}V_{Cl}})$ is a function of electric field strength, molecular polarizability, electric moment, and temperature.

Regardless of the merits of the structure element notations for symbolizing polarization, for all other chemical purposes conventional chemical notation is preferable. These purposes include the performance of material balances and thermodynamic and kinetic analyses. The chemical notation can be used for solution, solvation, and ionization reactions, phase transformations or ordering phenomena, and half-cell, electrochemical, and oxidation-reduction reactions.

Table II summarizes the symbols, masses, and thermodynamic potentials associated with the most common defects in solid crystals; interstitial (Frenkel), substitutional, and Schottky-Wagner defects in the building unit, atomic, ionic, and chemical notations. Discussion of Table II is deferred until later.

Metal Deficit Nonstoichiometric Oxide Formation

Both vacancies and positive charge carriers form in some solids. An example, which has been symbolized in Table III in the various notations, is the reaction between cobaltous oxide and oxygen which produces a metal deficit nonstoichiometric p-conducting oxide containing cobalt vacancies. First, I show that the symbols for the vacancies should be modified in a way similar to the F-center example. Second, I point out the differences in and discuss the relative merits of the symbols for charge carriers in the building unit, atomic and Rees notations (holes) and in the ionic, and chemical notations (ions).

Let us reconsider the question of symbolism for vacancies. By arguments similar to those of the preceding section, it is clear that the expected one sixth power oxygen pressure dependency upon equilibrium vacancy concentration (14, 15) cannot be obtained from the structure element notations unless either unit activity is arbitrarily assigned to $a(\mathrm{O^=_O})$ (15), reaction (N) for example, or unless the excess oxygen ion-vacancy pair can be considered associated, $(\mathrm{V_{Co}} + \mathrm{O^=_O})$.

We obtain the proper equilibrium pressure dependency on excess oxygen ion concentration (vacancy concentration) by the normal procedure of equating the appropriate potentials, using reaction (O), say

$$2\mu_+(\mathrm{Co^{++}}) + (\tfrac{1}{2})\mu(\mathrm{O_2,(g)}) =$$
$$2\mu_+(\mathrm{Co^{+++}}) + \mu_-(\mathrm{O^=}) \quad [9]$$

From Eq. [9] we may write for the equilibrium constant, K_O, the expression

$$K_O = \mathrm{a_+{}^2(Co^{+++})\ a_-(O^=)/a_+{}^2(Co^{++})P^{1/2}{}_{O_2}} \quad [10]$$

where $\mathrm{a_+}$ and $\mathrm{a_-}$ are ion activities.

If we make the usual simplifying assumptions of $\mathrm{a_+(Co^{++})} = 1$ and for the mean ion activity coefficient $\gamma_+{}^2(\mathrm{Co^{+++}})\gamma_-(\mathrm{O^=}) \simeq 1$, for the limiting condition of a dilute solution, [ref. (13), Chap. 8], Eq. [10] reduces to

$$P_{O_2}{}^{1/2}K_O = [\mathrm{Co^{+++}}]^2[\mathrm{O^=}] \quad [11]$$

Finally, by noting that $[\mathrm{Co^{+++}}] = 2[\mathrm{O^=}]$, we obtain the correct pressure dependence on either excess

[2] This is clearly a consequence of the precise statement of reactions (C), (D), and (E). If we rewrite reaction (C), say, to include the rock salt: (*m*) NaCl + Na(g) = (*m*) NaCl + $\mathrm{Na_{Na}}$ + $\mathrm{V_{Cl}}$ where usually $m >> 1$, common amounts of NaCl cancel on both sides of the equation leaving only the excess Na on the right-hand side present in equal numbers to vacancies. Alternatively, the activity of the original crystal cancels in the corresponding mass action expression

$$K_C = a^m(\mathrm{NaCl})a(\mathrm{Na_{Na}})a(\mathrm{V_{Cl}})/a^m(\mathrm{NaCl})P_{Na}$$

[3] In the building unit notation, this operation should be regarded as purely formal. It is not to be construed that the notation is inconsistent.

Table II. Symbols, masses, and thermodynamic potentials of typical defects in solids in various notations

Type of defect and example		Notation: Building Unit	Atomic	Ionic	Chemical
Frenkel (Interstitial Zn in ZnO)	Symbol	Zn^x	Zn_i	Zn_i	Zn_i
	Mass	+	+	+	+
	Potential	$\mu(Zn^x)$	$\mu(Zn_i)$	$\mu(Zn_i)$	$\mu(Zn_i)$
Substitutional (Be in Ge)	Symbol	B|Ge|	B_{Ge}	B_{Ge}	B_{Ge}
	Mass	$-$ [a]	+	+	+
	Potential	$\mu(B) - \mu(Ge)$	$\mu(B_{Ge})$	$\mu(B_{Ge})$	$\mu(B_{Ge})$
Schottky-Wagner (F-center in NaCl)	Symbol	|Cl|	V_{Cl}	V^-_{Cl}	Na or $(Na^+_{Na}\ V^-_{Cl})$
	Mass	$-$	O	$O^{(b)}$	+
	Potential	$-\mu(\|Cl\|)$	$\xi(V_{Cl})$	$\xi(V^-_{Cl})$	$\mu(Na)$
Schottky-Wagner (Co vacancy in non-stoichiometric CoO)	Symbol	$\|Co\|''$	V''_{Co}	$V_{Co^{++}}$	O= or $(V_{Co}\ O_O)^=$
	Mass	$-$	$O^{(b)}$	O	+
	Potential	$2\mu_-(e) - \mu(Co)$	$\xi(V''_{Cl})$	$\xi(V_{Co^{++}})$	$\mu_-(O^=)$
Immobile charge carrier (Co^{+++} ion in non-stoichiometric CoO)	Symbol	$\|e\|^\bullet$	h	$Co^{+++}{}_{Co^{++}}$	Co^{+++} or $Co^{+++}{}_{Co}$
	Mass	$-$	$-$	+	+
	Potential	$\mu_+(Co^{+++}) - \mu_+(Co^{++})$	$\mu_+(Co^{+++}) - \mu_+(Co^{++})$	$\mu_+(Co^{+++}{}_{Co^{++}})$	$\mu_+(Co^{+++})$
Mobile charge carrier (Intrinsic conductivity in Si)	Symbol	$\|e\|^\bullet$	h	Si^+	Si^+ or $Si^+{}_{Si}$
	Mass	$-$	$-$	+	+
	Potential	$\mu_+(Si^+) - \mu(Si)$	$\mu_+(Si^+) - \mu(Si)$	$\mu_+(Si^+)$	$\mu_+(Si^+)$

Notes: (a) Mass can also be positive, *e.g.*, Ge|B|.
(b) Mass of electron or effective negative charge excluded.

oxygen ion (metal vacancy) concentration or Co^{+++} ion concentration

$$P^{1/2}{}_{O_2}K_O = 4[O^=]^3 = (1/2)[Co^{+++}]^3 \quad [12]$$

The notation and the thermodynamic formulation employed here is nothing more than that which is normal for strong electrolytes (12). For example, when the reaction is expressed in the form of reaction (Q), we see that the product can be considered a dilute solution of dissociated Co_2O_3 in a CoO solvent. To the extent that association tends to occur with increasing Co_2O_3 concentration, we may represent this by the sum of the association reactions $2(CoO)^+ + O^= = (CoO)^+ + (CoO_2)^-$, and $(CoO)^+ + (CoO_2)^- = Co_2O_3$ and the solvation reaction $Co_2O_3 + CoO = Co_3O_4$.

Because of the associating and solvating tendencies of solutions of this type of reaction, any attempt to relate a definite number of vacancies to the number of excess oxygen ions in solution at high concentrations appears at present to be problematical (12, 16). As before, this difference between the three structure element notations in Table III disappears when the excess ion-vacancy pairs are associated; $(V_{Co} + O_O)''$ (atomic), $(V_{Co^{++}} + O_{O^=})^=$ (ionic) *etc.*, provided, first, that the effective negative charge in the modified atomic notation is interpreted to be a real negative charge and equivalent to the real negative charge associated with the modified ionic and Rees symbols, and, second, that there is a direct correspondence between excess oxygen ions added and metal vacancies created in the crystal.

We now consider the charge carrier symbols. Recalling the equivalence of the vacancy symbols

$$(CoO + |Co|'') \equiv (O_O + V_{Co}'') \equiv (O^=|\square_- + \square_+) \equiv (O^={}_{O^=} + V_{Co^{++}}) \equiv O^= \equiv (V_{Co}O_O)^= \quad [13]$$

we may subtract reactions (K), (L), or (M) from (N), (O), or (P) to determine that the hole symbols, $|e|^\bullet$ and h, represent a difference of two chemical symbols

$$|e|^\bullet \equiv h \equiv (Co^{+++}{}_{Co} - Co^{++}{}_{Co}) \quad [14]$$

Furthermore, since the mass of Co^{++} is greater by one electron than Co^{+++}, holes in both the building unit and atomic notations are "negative mass" particles, and when used in chemical equations, have the operational meaning: "take away an electron" (3). When the thermodynamic potentials of holes are to be considered, Eq. [14] serves to stress that such potentials from a chemical point of view must be regarded as the difference of two potentials, Table II

$$\mu_+(|e|^\bullet) \equiv \xi(h) = \mu_+(Co^{+++}) - \mu_+(Co^{++}) \quad [15]$$

The chemical origin of the hole is frequently of incidental importance for many electrical purposes, and from the electrical viewpoint we can appreciate the practice of representing the charge carrier by a single symbol. Nevertheless distinctions are often made between intrinsic and extrinsic and mobile and immobile holes. In addition to the reactions of Table III which give rise to extrinsic immobile p-conduction due to nonstoichiometry we have, using the chemical notation, extrinsic immobile p-conduction due to impurities, *e.g.*, Fe in MgO

$$(1/2)O_2(g) + 2Fe^{++}{}_{Mg} = (V_{Mg}O_O)^= + 2Fe^{+++}{}_{Mg} \quad [16]$$

intrinsic mobile p-conduction, *e.g.*, Si ionization

$$Si_{Si} = e + Si^+{}_{Si} \quad [17]$$

and extrinsic mobile p-conduction, *e.g.*, B-doped Ge

$$B_{Ge} + Ge_{Ge} = B^-{}_{Ge} + Ge^+{}_{Ge} \quad [18]$$

The last term on the right of the above equations clearly identifies the chemically different charge carriers. On the other hand a single electrical symbol for a hole can represent at least four chemically different conditions

$$|e|^\bullet \text{ or } h = (Co^{+++}{}_{Co} - Co^{++}{}_{Co}) = (Fe^{+++}{}_{Mg} - Fe^{++}{}_{Mg}) = (Si^+{}_{Si} - Si_{Si}) = (Ge^+{}_{Ge} - G_{Ge}) \quad [19]$$

Equation [19] will permit more precise distinctions to be made in the character of the holes where necessary.

Listed in Table II for the various notations are the symbols, masses, and thermodynamic potentials of the defects discussed in this section.

Table III. Comparisons of various notations used to describe metal deficit nonstoichiometric oxide formation

	Reaction	System of Notation
K.	$(1/2)O_2(g) = CoO + \|Co\|'' + 2\|e\|^\bullet$	Building unit
L.	$(1/2)O_2(g) = O_O + V''_{Co} + 2h$	Structure element, atomic
M.	$(1/2)O_2(g) = O^=\|\square_- + \square_+ + 2h$	Structure element, Rees
N.	$2Co^{++}{}_{Co^{++}} + (1/2)O_2(g) = O^={}_{O^=} + V_{Co^{++}} + 2Co^{+++}{}_{Co^{++}}$	Structure element, ionic
O.	$2Co^{++} + (1/2)O_2(g) = O^= + 2Co^{+++}$	Chemical
P.	$2Co^{++}{}_{Co^{++}} + (1/2)O_2(g) = (V_{Co}\ O_O)^= + 2Co^{+++}{}_{Co}$	Chemical; with structure
Q.	$2CoO + (1/2)O_2(g) = O^= + 2(CoO)^+$	Chemical; solution and dissociation of Co_2O_3

Discussion

Two common solid-state reactions have been formulated using a variety of notations. The two reactions discussed were a simple solution of a polarizable sub-

stance (F-center formation, Table I), and an oxidation-reduction reaction (metal deficit p-conducting cobaltous oxide formation, Table III). One simplification of the notations results when properties of nonstoichiometric compounds usually attributed to the presence of vacancies in the lattice are attributed instead to the presence of the excess constituent giving rise to the vacancy. It is shown that structure element notations must be modified to produce correct thermodynamic relationships between the equilibrium concentrations of excess constituents in solution and their vapor pressures. When both building unit and structure element notations are modified in the same way, *e.g.*, Eq. [7] and [18], they become equivalent to each other and to conventional chemical notation in this respect. In the ionic and chemical notations, the identity of the positive charge carrier can be determined, whereas in the building unit, atomic, and Rees notations, which employ the hole symbol, this may not always be done.

Comparing notations in Table II it is important to note that in the chemical notation we may associate not only a positive mass with every symbol but also a single normal thermodynamic potential, a chemical potential for a neutral species and an electrochemical potential for a charged species. In these two crucial respects this notation is identical in form with all chemical notation. The building unit notation although formally correct has both positive and negative masses associated with the symbols and positive, negative, and differences of, thermodynamic potentials associated therewith. Unless one possesses an intimate knowledge of this notation, it is difficult to read and awkward to use (3). The ionic notation has positive and zero masses associated with its symbols. With only one modification, for the vacancy, it becomes equivalent to conventional notation. The symbols in the atomic notation have positive, zero and negative masses associated with them and consequently the gamut of normal, virtual, and differences of, thermodynamic potentials.

Recommendations.—Use the chemical notation to describe reactions in the solid state. No conceptual difficulties will be encountered by its use, and no thermodynamic or chemical confusion can result from its use from the symbols themselves.

If a selection among symbols is to be made, pick the simplest one that will fit your needs. In the F-center example, if the solubility of sodium in rock salt is under consideration, it is unnecessary to use a symbol more detailed than Na(in solution). On the other hand, if defect structure and polarization are under consideration, then use the symbol $(Na^{+}_{Na}V^{-}_{Cl})$. In the cobaltous oxide example the description of cation mobility, diffusivity and oxidation phenomena may require the use of the symbol $(V_{Co}O_O)^{=}$, in reaction (P). However, if the description of the positive charge carrier, Co^{+++} is under consideration, the description of the counter ion, $O^{=}$, need not necessarily convey any structural information.

The use of h (and $|e|^{\bullet}$) as a symbol for positive charge carriers is widespread and a change in usage is unlikely. However, when this symbol is used in chemical equations it is important to keep in mind that it is not a chemical symbol. It describes the operation "take away an electron" and should be represented chemically as a difference of two chemical symbols and thermochemically as a difference of two thermodynamic potentials. When in doubt it is recommended that the use of the symbol h in chemical equations be replaced by an appropriate difference in chemical symbols, Eq. [19].

Acknowledgment

This work was supported in part by the Independent Research Program of Lockheed Missiles & Space Co., Palo Alto, California.

Manuscript received May 5, 1967; revised manuscript received June 27, 1967.

Any discussion of this paper will appear in a Discussion Section to be published in the June 1968 JOURNAL.

REFERENCES

1. W. Schottky, in "Halbleiterprobleme, Band IV," p. 235, W. Schottky, Editor, F. Vieweg u. Sohn, Braunschweig (1958).
2. F. A. Kröger and H. J. Vink in "Solid State Physics," Vol. 3, F. Seitz and D. Turnbull, Editors, p. 307, Academic Press, Inc., New York (1956).
3. F. A. Kröger, F. H. Stieltjies, and H. J. Vink, *Philips Res. Repts*, **14**, 557 (1959).
4. F. A. Kröger, "The Chemistry of Imperfect Crystals," North Holland Publishing Co., Amsterdam (1964).
5. A. L. G. Rees, "Chemistry of the Defect Solid State," John Wiley & Sons, Inc., New York (1954).
6. N. F. Mott and R. W. Gurney in "Electronic Processes in Ionic Crystals," 2nd ed., Chap. 4, Oxford (1948).
7. C. Kittel, in "Introduction to Solid State Physics," p. 493, McGraw-Hill, New York (1956).
8. W. Schottky and F. Stockmann, in "Halbleiterprobleme, Band I," p. 80, W. Schottky, Editor, F. Vieweg u. Sohn (1954).
9. H. Schmalzried, in "Progress in Solid State Chemistry" Vol. 2, p. 265, Pergamon Press, New York (1965).
10. H. Schmalzried, Private communication.
11. J. S. Anderson in "High Temperature Technology," p. 285, Butterworths, Washington, (1964).
12. J. S. Anderson, *in* "Non-Stoichiometric Compounds," p. 1, Adv. in Chem. Series No. 391, Am. Chem. Soc., Washington, D. C. (1963).
13. E. A. Guggenheim, "Thermodynamics," p. 301, 304, North-Holland Publishing Co. Amsterdam (1959).
14. B. Fisher and O. S. Tannhauser, *This Journal*, **111**, 1194, (1964).
15. S. P. Mitoff, *J. Chem. Phys.*, **35**, 882 (1961).
16. W. L. Roth, *Acta Cryst.*, **13**, 140, (1960).

Low-Pressure Oxidation of Zirconium

J. Levitan, J. E. Draley, and C. J. Van Drunen

Argonne National Laboratory, Argonne, Illinois

ABSTRACT

Low-pressure oxidation of zirconium at high temperatures exhibited a pressure dependence, and several stages of oxidation could be distinguished: an initial period was followed by two periods with a linear rate dependence. Transition from the first linear period to the following linear period was accompanied by increase in oxidation rate. Surface reaction control is suggested for these periods. Linear oxidation was followed by a period when the rate was limited by a protective oxide film.

Low-pressure oxidation of transition metals is receiving increasing attention in connection with vacuum and space applications. There is rather a small number of systematic investigations in the field (2-5). Phenomena observed in low-pressure oxidation reflect specific conditions of lower reacting gas concentration and different sticking probability.

It has recently been reported (1) that the potential recorded across a growing scale on oxidizing zirconium exhibits a dependence on oxygen partial pressure (p_{O_2}) at pressures below 1 mm Hg, remaining constant at $p_{O_2} > 1$ mm. Since the unchanging electric field at $p_{O_2} > 1$ mm corresponds to oxidation kinetics independent of p_{O_2}, a study of low-pressure zirconium oxidation was initiated. Preliminary results (1) stimulated a modification of the existing experimental system in order to run constant pressure and volumetric experiments.

Experimental

The source of material was high-purity zirconium supplied by Materials Research, Inc. Impurity content of the batch, as found by spectrographic analysis was (in ppm by wt):

H	3.3	Al	3.0	Cl	2.0	Ti	1.0
B	0.005	Si	1.5	K	0.004	V	0.05
C	6	P	0.1	Ca	0.04	Cr	0.5
N	2.1	Ni	1.5	Hf	40.0	Fe	30.0
O	25	Cu	0.01				

Specimens were prepared from 1.6 mm thick sheet by punching out disks 12.7 mm diameter. These were wet ground and etched for 2 min at room temperature in a 45:5:50 (by volume) HNO_3 (70%) +HF (49%) + H_2O etchant.

An Ainsworth RV-AU-2S vacuum semimicrobalance (reproducibility ± 0.03 mg) was employed for continuous automatic recording of the weight changes. A Granville-Phillips automatic control valve was used in the experimental system (Fig. 1). Excellent pressure control in the 10^{-5} to 1 mm range was achieved. Pressure control was usually obtained within 1 to 1½ min from the beginning of the experiment and controlled with high precision during the whole run. Temperature was recorded from a thermocouple in a well close to the specimen; this was calibrated to provide actual specimen temperature (controlled to ± 1°C). Experimentally determined corrections were made for buoyancy and thermal convection. Research grade oxygen supplied by Matheson Company was used as-received, with less pure gas (and a desiccant) used for flushing and storage. Oxygen was supplied to the system from a storage vessel through the control valve. Recordings of pressure drop in the storage vessel provided the oxygen consumed in volumetric measurements. The system was built from 304 stainless steel, copper, and brass. Because of variability in initial oxygen adsorption in the system, volumetric results have been only confirmatory in the present study: gravimetric results have been used exclusively.

Results

Zirconium oxidation at different oxygen pressures in the 1 to 400 mm range was found to be essentially independent of p_{O_2}. This is in agreement with results reported by previous investigators (6-10). Slight disagreement with previous data from this laboratory (6) is probably explainable in terms of the degree of purity or of metallurgical history of specimen materials.

However, the oxidation rate exhibited a significant pressure dependence for pressures below 1 mm. This is shown in Fig. 2 for 700°C. Rate of weight gain (per unit area) were considerably lower than that for "standard"[1] oxidation for short times, then increased so that oxidation was more rapid than under standard conditions. Finally, the rate decreased at lower pressures more rapidly than at standard pressures, so that at 1100 min exposure, rates of weight gain were the same at the three lower pressures shown and only about 10% greater than that at 1 mm.

Also notable in Fig. 2 are periods when rates of weight gain remained constant for significant periods of time: the straight line portions such as during the interval 70-240 min at 3 x 10^{-3} mm oxygen pressure.

Behavior during early exposure is not shown clearly in Fig. 2. The weight gain of one specimen is shown on an expanded scale in Fig. 3. It is observed that preceding the linear portion previously noted there is an earlier linear portion at about 8 to 27 min, with a lower slope than that at about 51 to 127 min. This earliest straight line generally did not extrapolate to to origin, as indicated in Fig. 3. The earliest portion of the oxidation curve was rather short and the weight

[1] The term "standard" will be used to refer to oxidation at pressures 1 to 400 mm where oxidation behavior is independent of oxygen pressure.

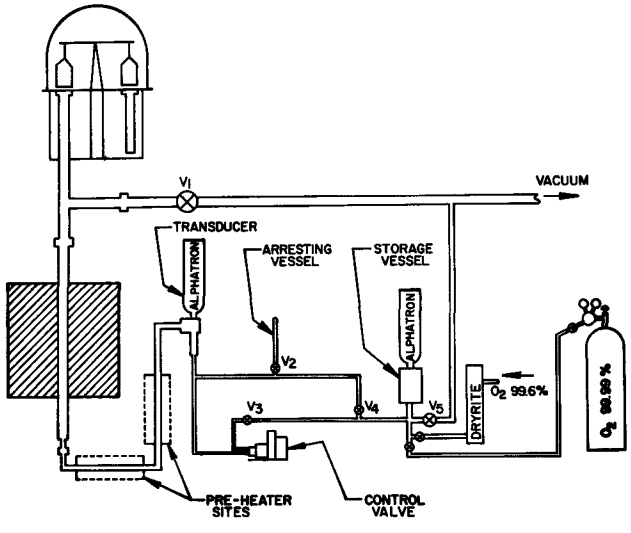

Fig. 1. Ainsworth balance system

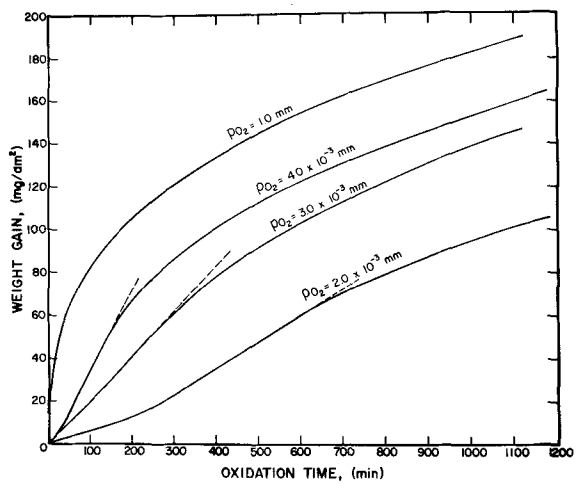

Fig. 2. Oxidation of zirconium at 700°C

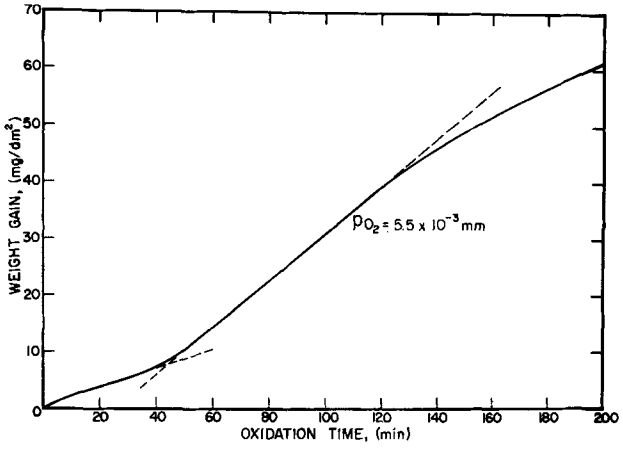

Fig. 3. Typical low-pressure zirconium oxidation at 700°C

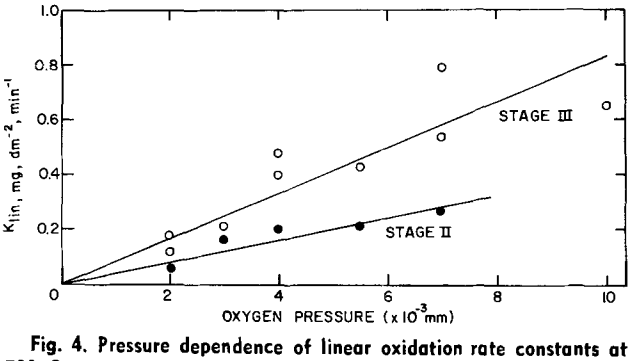

Fig. 4. Pressure dependence of linear oxidation rate constants at 700°C.

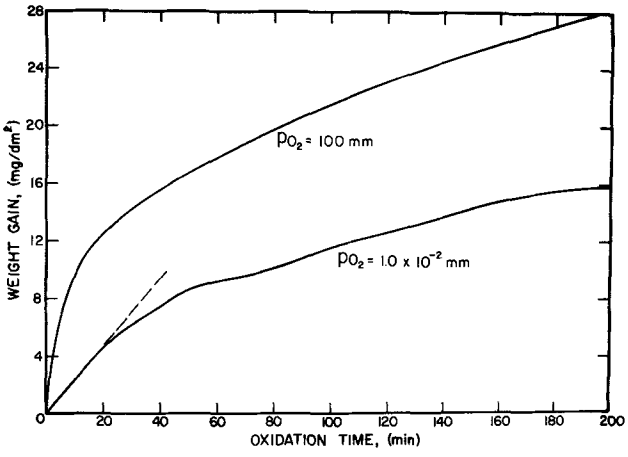

Fig. 5. Typical low-pressure zirconium oxidation at 550°C

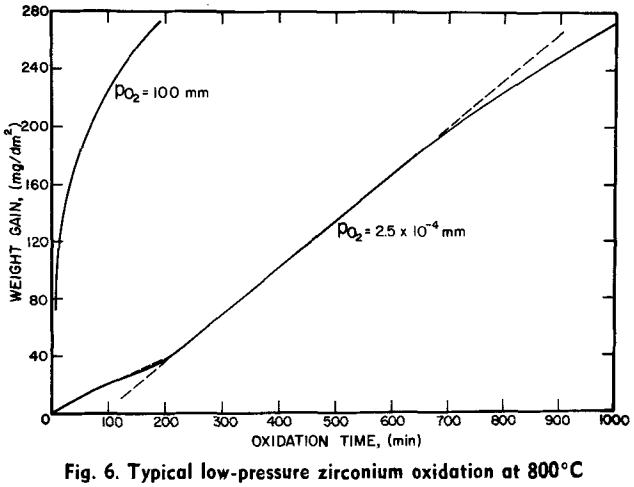

Fig. 6. Typical low-pressure zirconium oxidation at 800°C

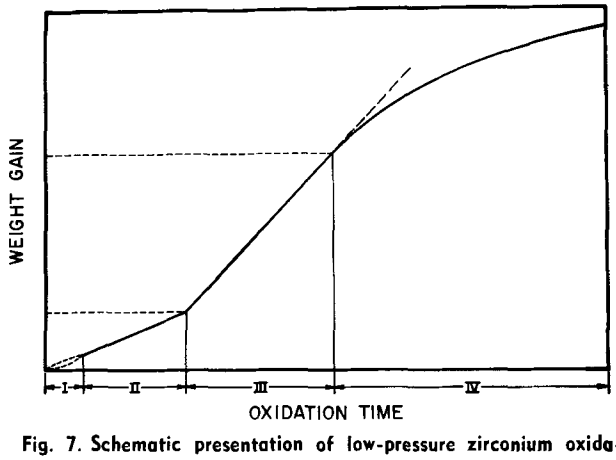

Fig. 7. Schematic presentation of low-pressure zirconium oxidation.

gains small, so that no accurate curve shape can be described. Generally, the rate decreased during this period.

As can be observed in Fig. 2, the rates of weight gain during the linear portions varied with oxygen pressure. The available linear rate constants are plotted in Fig. 4 as a function of oxygen pressure. (For some runs stage II was not sufficiently clear to justify estimating slopes.) A roughly linear dependence was exhibited both for the first (stage II) and second (stage III) linear portions. The least squares slopes were 42 and 83 mg, dm^{-2}, min^{-1}, $(mm\ Hg)^{-1}$. Their ratio, 2.0, shows the increase in rate which occurred in transition between the first and second linear reaction periods. Degree of reproducibility can be judged in the figure.

Similar behavior was exhibited at other temperatures. At 550°C, only the second linear portion was observed at the higher (than at 700°C) "low pressures" in which pressure sensitivity was evident (see Fig. 5). At 800°C lower "low pressures" were required to display pressure dependence; all stages in the oxidation curve were evident (Fig. 6).

Discussion

The low-pressure oxidation of zirconium can be divided conveniently into four stages as shown schematically in Fig. 7. During the first stage a decreasing rate of oxidation was generally (but not always) observed. During stage II weight was gained at a constant rate, which was approximately proportional to the oxygen pressure. The oxidation rate then increased by a factor of about 2.0, and during stage III

another period of constant oxidation rate was observed. Again the rate was approximately proportional to p_{O_2}. Finally, in stage IV the rate of oxidation continuously decreased with time.

The following explanation seems consistent with the known facts. Before the oxidation experiment, the specimen presumably formed (in air) an oxide film on a surface which was nearly clean (and in which it is hoped the metal structure was not seriously distorted in view of the metal removal during etching). It was then held at oxidation temperature at a pressure low enough for no discernible weight gain to occur. The air-formed oxide film very likely completely dissolved, considering the high rate of oxygen diffusion and the high solubility of oxygen in zirconium (12, 13).

During stage I oxidation, some kind of steady-state situation is being developed on the metal surface. Lack of reproducibility indicates a sensitivity to the original condition of the specimen (oxygen content and disorder in the surface layers of metal?). Perhaps some oxide nuclei form at most susceptible positions on the surface [as observed by Hart in other low-pressure studies (11)], but essentially all the oxygen is presumably dissolving in the metal. The rate of weight gain is substantially less than the expected rate of diffusion of oxygen inward from a saturated surface layer (12).

In stage II, the rate of oxygen uptake is apparently limited by the rate of chemisorption at the metal surface (not by the rate of arrival of oxygen at the surface, since this is calculated to be substantially greater than the oxidation rate). It is difficult to estimate the degree of coverage by oxygen molecules or atoms, but coverage by ions must be rather small because the rate of uptake is still lower than the expected rate of oxygen diffusion inward from a saturated surface. The pressure dependence of the rate is reminiscent of a Langmuir adsorption model. During this stage, local oxygen concentration in surface layers of the metal apparently builds up with time until, at the end of stage II, saturation occurs and surface oxide begins to form.

This surface oxide is not significantly protective; in fact the rate of oxygen uptake increases, perhaps because the ionic crystal surface is more favorable for the formation of adsorbed oxygen ions (as distinguished from uncharged species). As time goes on, more of the surface metal becomes saturated, and more of the surface becomes covered with oxide. Presumably, different grain surfaces become saturated at different times because of their different oxygen diffusion characteristics (12).

In due course the surface is covered with oxide and stage III begins (Table I). Prior to this time it can be expected that the concentration of the oxygen-diffusing species in the surface layers of metal would not have been constant with time, and therefore that the oxygen uptake at this point would be less than that expected if oxygen diffusion had been occurring from a saturated surface. However, during the period between stage II and stage III there often occurred an amount of oxidation which was substantial with respect to that which had occurred by the end of stage II. In order to aid in the development of a model for the processes actually occurring it was decided to compare the experimental results with those which would be anticipated if oxygen diffusion into the metal had been occurring from a saturated surface (such as an oxide-covered surface).

Using this model, the value of the weight gain (W) at the beginning of stage III might approximate $kt^{1/2}$, where k is the diffusion rate constant. Accordingly, the "least squares" optimum value of k was calculated for the nine available low pressure runs at 700°. A kind of rough correlation was observed, with calculated weight gains deviating by amounts up to 38% from those observed. The value of the diffusion rate constant was 1.55 mg dm^2 $t^{-1/2}$, as close to Pemsler's (12) value of 2.0 for polycrystalline zirconium as could be expected in this kind of analysis.

During stage III oxidation the rate is again controlled by the rate of chemisorption, and again Langmuir-like pressure dependence is observed. The oxide film is not thick enough to offer significant impediment to penetration by oxygen. The film continues to thicken, however, and eventually does exhibit protectiveness. Accordingly, the rate decreases (stage IV), slowly at first, and then more rapidly as the rate becomes more and more completely limited by the thickening oxide film. Reaction kinetics then become similar to what is observed in standard oxidation (a rather straight line on a log-log plot of W *vs.* t, with a slope somewhat less than ½).

As an approximation, it might be expected that the film would become significantly protective at about the same thickness (s) for different experiments. Under these circumstances the value of the weight gain at the end of stage III would be expected to equal $s + kt^{1/2}$, where k is again the rate constant for the diffusion of oxygen in zirconium. A least-squares fit provided values for s and k for the same 9 runs used previously. This time the fit was better, with an average deviation in W of 7% (see Table II).

The diffusion rate constant was 1.62, in good agreement with that calculated in connection with the start of stage III, and a bit closer to Pemsler's value for polycrystalline zirconium. At this time no particular significance can be ascribed to the thickness (apparently independent of oxygen pressure in the range studied) at which the oxide film becomes significantly protective. The value calculated was 23.4 mg oxygen/dm^2, or 1.51μ thickness.

Some time after the beginning of stage IV oxidation, the rate of oxidation appeared to be essentially independent of p_{O_2}. Even an oxygen pressure as high as 1 mm caused only about 10% decrease in rate (decrease, rather than increase, because the oxide thickness was greater). It is surprising that the rates were equal at the end of the three low-pressure runs of Fig. 2, although the pressure varied by a factor of 2.0, the weight gains showed about a 60% variation, and the

Table I. Comparison of calculated and observed values of weight gain at start of stage III. Zirconium in oxygen at 700°C

Run No.	p_{O_2}, mm Hg, × 10^3	t, min	W_{obs}, mg/dm^2	$W_{calc.}$ mg/dm^2 ($= 1.55t^{1/2}$)	% Deviation
215	10.0	18	6.4	6.6	+3
213	7.0	36	11.7	9.3	−21
218	7.0	19	10.9	6.8	−38
226	5.5	53	11.3	11.3	0
219	4.0	49	13.3	10.8	−19
222	4.0	48	10.0	10.7	+7
225	3.0	58	11.4	11.8	+4
220	2.0	286	21.2	26.2	+24
221	2.0	357	31.6	29.3	−7
				Average deviation	14%

Table II. Comparison of calculated and observed values of weight gain at end of stage III. Zirconium in oxygen at 700°C

Run No.	p_{O_2}, mm Hg, × 10^3	t, min	W_{obs}, mg/dm^2	W_{calc}, mg/dm^2 ($= 23.4 + 1.62t^{1/2}$)	% Deviation
215	10.0	55	30.7	35.4	+15
213	7.0	93	42.0	39.1	−7
218	7.0	49	35.0	34.8	−1
226	5.5	110	35.5	40.4	+14
219	4.0	130	45.5	41.9	−8
222	4.0	114	41.3	40.7	−1
225	3.0	279	56.9	50.5	−11
220	2.0	616	60.9	63.7	+5
221	2.0	510	58.9	60.1	+2
				Average deviation	7%

calculated oxide thicknesses varied by a factor of 2.3. Apparently the reaction rate at this time is limited by the oxide film, but is not in any simple way related to total oxide film thickness. An explanation is not now available.

It is felt that the new data reported here will probably prove valuable in interpreting oxidation mechanisms for zirconium. Certainly, a few new questions have been posed.

Manuscript received Feb. 16, 1967; revised manuscript received July 31, 1967. This work was performed under the auspices of the United States Atomic Energy Commission.

Any discussion of this paper will appear in a Discussion Section to be published in the June 1968 JOURNAL.

REFERENCES

1. J. Levitan, J. E. Draley, and C. J. Van Drunen, ANL-7272, Argonne National Laboratory, (Sept. 1966).
2. H. Inouye, "Columbium Metallurgy" AIME Metallurgical Society conferences, Vol. 10, pp. 649-664, Interscience Publishers, New York (1961).
3. P. Kofstad, *J. Less-Common Metals*, **7**, 241 (1964).
4. P. Kofstad and S. Espevik, *This Journal*, **2**, 153 (1965).
5. E. J. Delgrosso, J. S. Carta, and A. Ricard, "The Low Pressure Oxidation of Pure Columbium," PWAC-460 (Pratt and Whitney) (Sept. 1965).
6. D. H. Bradhurst, J. E. Draley, and C. J. Van Drunen, *This Journal*, **112**, 1171 (1965).
7. A. Guillet and A. M. Anthony, *Rev. Hautes Temp. Refr.*, **1**, 325 (1965).
8. H. A. Porte, V. G. Schnizlein, R. C. Vogel, and D. F. Fisher, *This Journal*, **107**, 506 (1960).
9. G. R. Wallwork, W. W. Smeltzer, and C. J. Rosa, *Acta Met.*, **12**, 409 (1964).
10. D. Cubiccioti, *J. Am. Chem. Soc.*, **72**, 4138 (1959).
11. R. K. Hart, Private communication.
12. J. P. Pemsler, *This Journal*, **6**, 315 (1958).
13. B. Holmberg and T. Dagerhamn, *Acta. Chem. Scand.*, **15**, 919 (1961).

The Oxidation Properties of a Zirconium-2.7 w/o Niobium Alloy in the Temperature Range 300°-500°C

M. G. Cowgill and W. W. Smeltzer

Department of Metallurgy and Materials Science, McMaster University, Hamilton, Ontario, Canada

ABSTRACT

The reaction kinetics and structures of the alloy/oxide composite system were determined for martensitic and several Widmanstatten-structured alloys oxidized at 300°, 400°, and 500°C in oxygen at 1 atm pressure. At 300° and 400°C, there was little difference between the oxidation rates of the differently structured alloys in the early stages of the reaction. Prolonged exposures illustrated the occurrence of two limiting oxidation curves: martensitic specimens oxidized most rapidly, the oxidation rate decreasing until a transition range was attained in which the rate subsequently increased to a maximum value associated with linear kinetics; on the other hand, Widmanstatten-structured specimens containing equilibrium amounts of proeutectoid alpha-zirconium from the quench temperature oxidized most slowly, the initial decreasing oxidation rates finally approximating to linear kinetics at long exposures. Specimens containing intermediate amounts of proeutectoid alpha-zirconium oxidized at rates between these two limiting cases. At 500°C, the initial oxidation rates for all alloys approximated to parabolic kinetics, the reaction rate constants being directly dependent on the volume fractions of martensite. The oxide was cracked in the range of linear kinetics, but the role of the film as a barrier to oxidation could not be determined. The formation of oxide pustules on martensitic specimens was the only distinct feature indicating a difference in the mode of oxide formation on differently structured alloys. The major product of the reaction at all temperatures irrespective of alloy structure was an oxide whose structure could be indexed as monoclinic zirconia.

Zirconium-niobium alloys containing 2-3 w/o niobium are being utilized in nuclear reactor technology for their desirable mechanical and low neutron absorption properties. A primary disadvantage of poor corrosion resistance for alloys in an appropriate martensitic structure for optimum mechanical behavior has been largely overcome by cold-working and tempering treatments. Dawson (1) has presented a review of the literature on this subject. Although there are many observations on the beneficial effects of tempering on decreasing the corrosion rates of dilute alloys in steam, air, and carbon dioxide atmospheres, studies have not been attempted of structural effects from a fundamental viewpoint. In this investigation, results are reported for the oxidation properties of a Zr-2.7 w/o Nb alloy in both martensitic and Widmanstatten structures exposed to pure oxygen at temperatures in the range 300°-500°C. Alloys of these structures could be readily obtained by vacuum annealing followed by quenching from temperatures in the β solid solution and in the $\beta + \alpha$ phase regions selected from the binary phase diagram (2, 3).

Experimental

The material was a zirconium-2.7 w/o niobium alloy received as 2 mm thick sheet. Analyses for impurities are presented in Table I. Specimens approximately 1 cm^2 were cut from this sheet and subjected to an appropriate annealing and quenching treatment. Several specimens of the above dimensions were received already in a martensitic structure following a vacuum anneal at 960°C for 10 min before water quenching. They were prepared directly for oxidation tests.

Specimens were prepared by annealing and quenching in an all-metal system capable of maintaining a vacuum of 10^{-6} Torr. In order to minimize contamination from residual gas, specimens were wrapped in

Table I. Analysis of impurity content of Zr-2.7% Nb

Element	ppm (max)	Element	ppm (max)
Al	52	Mo	<10
B	<0.2	N	24
C	100	Ni	50
Cd	<0.3	O	1100
Co	<5	Pb	<5
Cr	30	Si	100
Cu	35	Sn	<100
Fe	980	Ta	<200
H	5	Ti	20
Hf	76	V	<5
Mg	<10	W	<25
Mn	<10	Zn	<50

platinum foil. In all cases, heat-treatments were carried out by raising the furnace already at 1000°C over the annealing tube containing the specimen. The specimen was held at this β-solution temperature of the alloy for 1 hr, and, if the structure required was that of full martensite, it was then quenched into oil. Specimens were also quenched from 800°C, in which cases a specimen was furnace cooled from 1000° to 800°C, held at this temperature for a predetermined time, then quenched into oil.

The surfaces of specimens were prepared by abrasion on SiC papers from 240 through 600 mesh grit under water followed by polishing for several hours on napped cloths, impregnated with 6 and 1μ diamond paste, respectively, and lubricated with kerosene. Final polishing was obtained with a vibratory polisher using a suspension of 0.3μ alumina powder suspended in water. In addition, several specific preparations involving chemical etching and different types of abrasion treatments were employed to determine possible effects of surface preparation on the oxidation kinetics.

Oxidation kinetic experiments were carried out using a vacuum microbalance apparatus (4). These results were supplemented by a series of experiments in which the specimens were intermittently removed for weighing from a quartz reaction tube. Furnaces were controlled to ±2°C, and the oxygen pressure during reaction was 1 atm. Medical grade oxygen was used which was purified by passage through cupric oxide, phosphorous pentoxide, Linde 5Å molecular sieves, and a trap immersed in solid carbon dioxide to remove traces of hydrogen, water vapor, carbon monoxide, and carbon dioxide.

The surfaces of oxidized specimens were examined microscopically and subjected to nickel filtered copper radiation with a recording x-ray diffractometer in order to identify oxide constituents in the scales. Metallographic examinations were carried out on specimen cross sections mounted in bakelite (4). In some instances, it was possible to delineate the structure of two-phase alloys by relief polishing without etching. When an etchant was needed, the most successful was found to be an aqueous solution containing 30 v/o H_2SO_4, 30 v/o HNO_3, and 10 v/o HF at a temperature in the range 68°- 75°C. The volume fraction of proeutectoid α-Zr in a two-phase alloy structure was readily determined by projecting the microstructure on a calibrated objective screen of the microscope at a magnification in the range 200-600X.

Results

In order to determine the reproducibility of measurements and the influence of surface preparation on the reaction rates, several specimens were prepared with different structures and surface preparations for oxidation at 400°C (Fig. 1). Curves (a) and (b) illustrate the oxidation behavior of martensitic specimens subjected to metallographic and chemical polishes. These different preparations did not influence oxidation at long exposures since the rates were of the same magnitude after transition to linear kinetics. In the early stages of the reaction, a correlation was not found between the methods of surface preparation due to the irreproducibility of measurements. How-

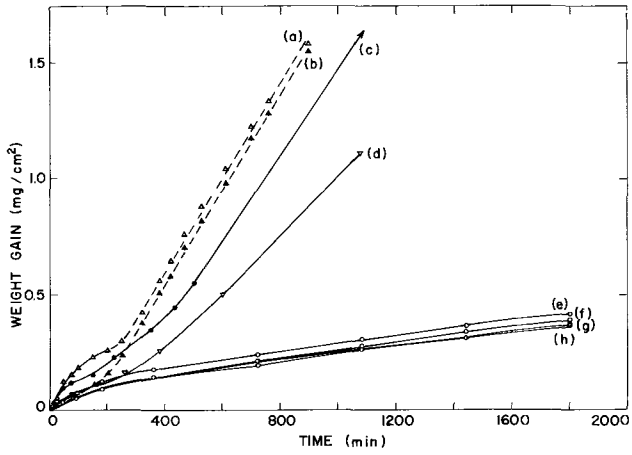

Fig. 1. Oxidation of Zr-2.7 w/o Nb alloy at 400°C in oxygen at 1 atm pressure. (a) anneal 10 min at 960°C, water-quenched, surface chemically polished; (b) anneal 10 min at 960°C, water-quenched, surface metallographically polished; (c) anneal 1 hr at 1000°C, water-quenched, surface metallographically polished; (d) anneal 1 hr at 1000°C, oil-quenched, surface metallographically polished; (e) and (g) anneal 1 hr at 1000°C and 1 hr at 800°C, oil-quenched, surface polished on 0.25μ diamond; (f) and (h) anneal 1 hr at 1000°C and 1 hr at 800°C, oil-quenched, surface polished on 0.3μ alumina.

ever, it was established that the martensitic specimens exhibited oxidation variations dependent upon the heat treatment conditions. This is illustrated by comparing the curves (b), (c), and (d) for specimens quenched into water after vacuum anneals for 10 min at 960° and 1 hr at 1000°C and for the specimen wrapped in platinum foil and quenched into oil after a vacuum anneal of 1 hr at 1000°C, respectively. These oxidation curves are of the same form with the latter specimen exhibiting the slowest rate. This behavior with the platinum-wrapped specimen would be associated with less impurity pickup from the residual gas or the slower rate of cooling during quenching. Martensitic specimens used in this investigation were prepared by both methods and are specified in the results.

Possible effects on the oxidation rate due to variations in the final stage of mechanical polishing were also investigated by oxidizing Widmanstatten structured specimens from the same batch heat-treatment (Fig. 1). Curves (e) and (g) were obtained from specimens after a polish with 0.25μ diamond paste on a selvyt cloth, whereas, curves (f) and (h) were obtained from specimens polished on a vibratory pol-

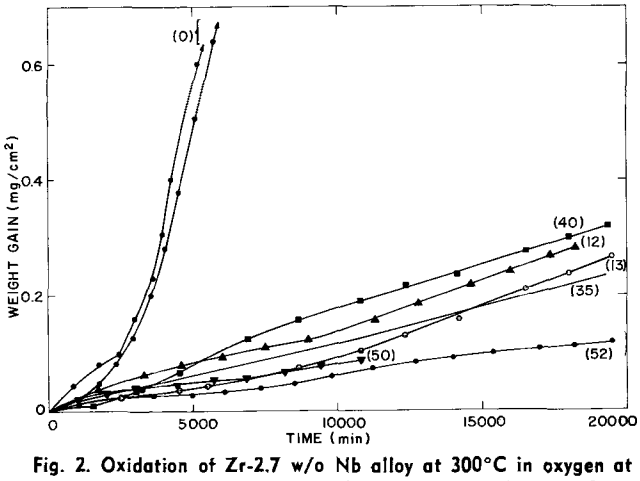

Fig. 2. Oxidation of Zr-2.7 w/o Nb alloy at 300°C in oxygen at 1 atm pressure. Figures in parantheses are approximate volume fractions of α-Zr in the alloys. Martensitic specimens water-quenched.

isher using a suspension of 0.3μ alumina in water. Apparently, the oxidation rate is not influenced by the type of abrasive employed in the final polishing stage.

Typical measurements of oxidation rates at 300°, 400°, and 500°C for various alloys prepared by metallographic polishing are shown in Fig. 2, 3, and 4. Although the kinetics were characterized by a certain degree of irreproducibility in the initial stages, the large variations in the oxidation rates could be correlated with the structures of the specimens. It is apparent from the volume fraction of α-Zr in the alloy listed with each kinetic curve that the oxidation rates at all investigated temperatures decrease with increasing amount of this phase.

Two examples of specimen microstructures obtained by quenching from 800° and oxidized at 400°C are shown in Fig. 5. If the anneal was carried out for only 5 min, structures containing 10-15 v/o α-Zr were obtained. Upon equilibrating an alloy at 800°C, the structure would contain about 50 v/o proeutectoid α-Zr. This condition was found after an anneal for 1 hr. Specimens containing contents of this phase between these two extremes were obtained by annealing within the above time periods.

The topography of an oxidized specimen was dependent on the alloy structure, the reaction temperature, and the time of exposure. A martensitic structured specimen, oxidized at 300° or 400°C, exhibited interference colors to film thicknesses of approximately 2000Å with color tints varying from grain to grain. At about the time of transition from an initial decreasing rate to a more rapid approximately linear rate, isolated growths of pustular shape were observed. The densities of these pustules varied with alloy grain orientations (Fig. 6a). These growths spread with lengthening exposure to cover most of the surface, although complete coverage was never observed in the exposure periods of the present experiments (Fig. 6b). On viewing the surface of a pustule at high magnification, fine cracks were observed which appeared to emanate from the tip. These pustules protruding above the main oxide surface only accounted for a relatively small amount of oxide as they were not observed at the surface of metallographic cross sections.

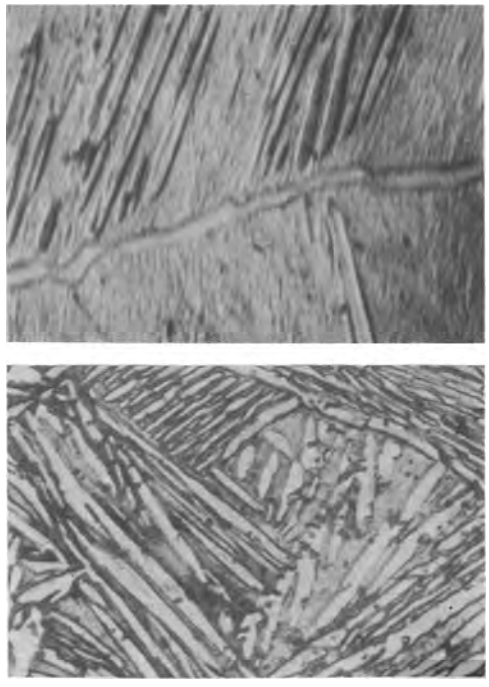

Fig. 5. Microstructures of two specimens quenched from 800° and oxidized at 400°C. a (top), volume fraction of proeutectoid α-Zr $\sim$ 15%; b (bottom), volume fraction of proeutectoid α-Zr $\sim$ 48%.

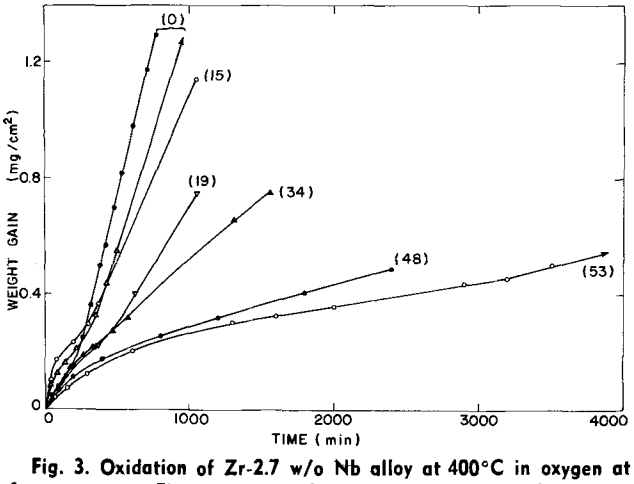

Fig. 3. Oxidation of Zr-2.7 w/o Nb alloy at 400°C in oxygen at 1 atm pressure. Figures in parantheses are approximate volume fractions of α-Zr in the alloys. Martensitic specimens water-quenched.

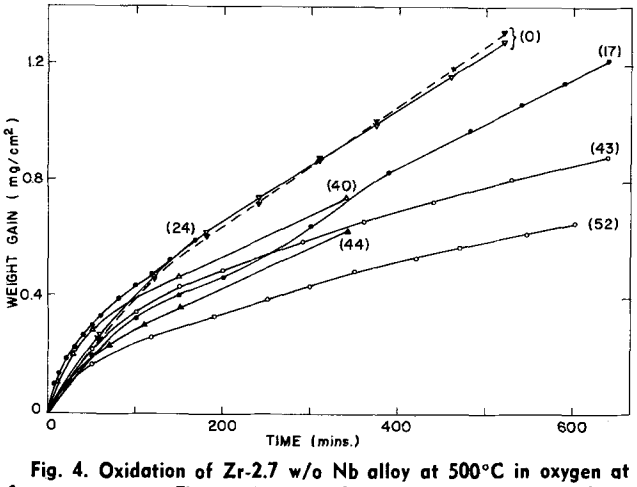

Fig. 4. Oxidation of Zr-2.7 w/o Nb alloy at 500°C in oxygen at 1 atm pressure. Figures in parantheses are approximate volume fractions of α-Zr in the alloys. Martensitic specimens oil-quenched.

Martensitic specimens oxidized at 500°C did not exhibit pustules even at brief exposures of 10 min. The oxidized specimens exhibited a gray rippled surface (Fig. 6c). This external appearance indicated that a very large number of small pustules had formed in close proximity without a large degree of lateral growth before their coalescence.

Oxidation of an alloy obtained by quenching from the (α + β) alloy region gave rise to rates of film growth dependent on the phase on which the oxide was growing. The growth of oxide on the α-Zr platelets was much less than on the α'-Zr regions. For the conditions and exposures examined, the former film never exhibited other than interference colors. The film on the α' structure gave rise initially to interference colors, but its growth rate was estimated to be at least triple that of the film on α-Zr. The film eventually became gray, and small cracks appeared running parallel to the direction of the α-Zr plates (Fig. 7a). Eventually, these cracks became more extensive and developed into intricate networks (Fig. 7b). Such observations applied to all specimens in this alloy condition, irrespective of the reaction temperature, when reaction had proceeded to linear kinetics. No oxide pustules were observed at any time for this alloy condition by light microscopy.

Cross sections of all oxidized specimens revealed an uneven metal/oxide interface. Martensitic-structured specimens exposed to the transition range for linear kinetics exhibited fine microscopic irregularities

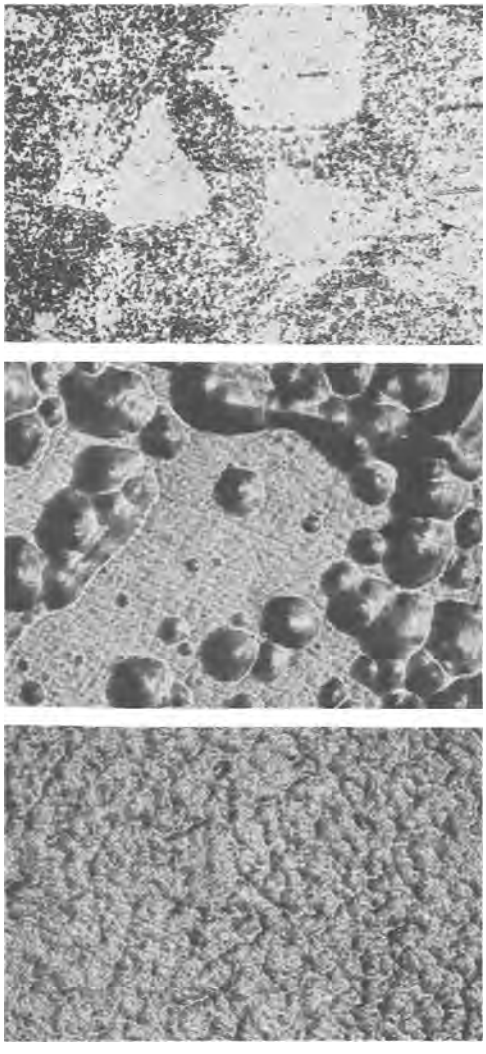

Fig. 6. Topographies of oxidized specimens with martensitic structure. a (top), 400 min at 400°C, oxygen uptake 0.07 mg/cm^2, magnification 150X; b (center), 1330 min at 400°C, oxygen uptake 1.9 mg/cm^2, magnification 100X; c (bottom), 300 min at 500°C, oxygen uptake 0.8 mg/cm^2; magnification 150X.

and also much larger undulations representing areas, rather than points, of larger oxide penetration (Fig. 8a). At long exposures, the larger variations almost disappeared to leave a relatively uniform thick scale containing cracks, many of which appeared to follow the contour of the metal/oxide interface (Fig. 8b).

The topographical observations on oxidized specimens in the two phase ($\alpha + \alpha' - Zr$) structure were confirmed by the examinations of cross sections (Fig. 9); that is, the rate of oxide growth was greater on the α' structure. This behavior was most vividly illustrated by specimens exposed for long times at 300°C where the oxide formed on the α'-regions had selectively penetrated to the extent that it appeared pinned by the unoxidized α plates (Fig. 9a). This degree of selective penetration became less pronounced with increasing temperature, and the oxide in the external film appeared less cracked at the highest temperature of 500°C (Fig. 9c).

Detailed examination of the metal/oxide interface of all specimens oxidized for relatively long time periods demonstrated that localized points of oxide penetration occurred at the lines of martensitic transformation in the α'-Zr microstructure. This is illustrated by the etched microstructure of the martensitic alloy (Fig. 10a), and by the Widmanstatten-structured alloys (Fig. 9a, 10b) where the fine degree of oxide penetrations into the martensitic structure between the α-Zr plates is readily apparent.

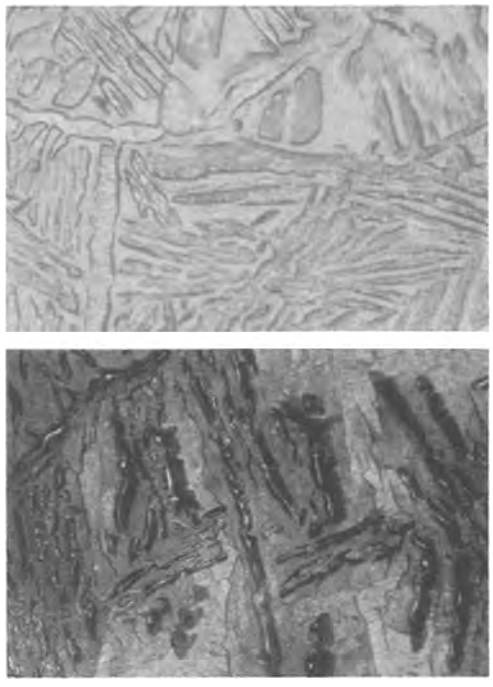

Fig. 7. Topographies of oxidized specimens with Widmanstatten structure. a (top), 10,800 min at 300°C, oxygen uptake 0.09 mg/cm^2; magnification *ca.* 680X; b (bottom), 485 min at 400°C, oxygen uptake 0.5 mg/cm^2; *magnification ca.* 460X.

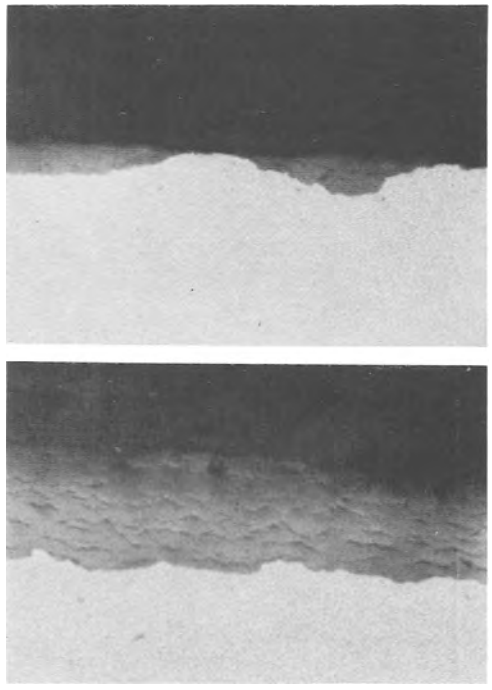

Fig. 8. Cross sections of oxidized specimens with martensitic structures. a (top), 1030 min at 400°C, oxygen uptake 1.1 mg/cm^2, magnification 675X; b (bottom), 1380 min at 500°C, oxygen uptake 2.0 mg/cm^2, magnification 675X.

X-ray analyses revealed that the major oxidation product could be indexed as monoclinic zirconia. Occasionally a weak reflection was observed which could be interpreted as either the cubic or tetragonal form of zirconia. Oxides of niobium were not detected. However, the technique is limited and monoclinic zirconia may not be the only reaction product.

Discussion

An attempt has been made to elucidate more fully the oxidation mechanisms of a Zr-Nb alloy by deter-

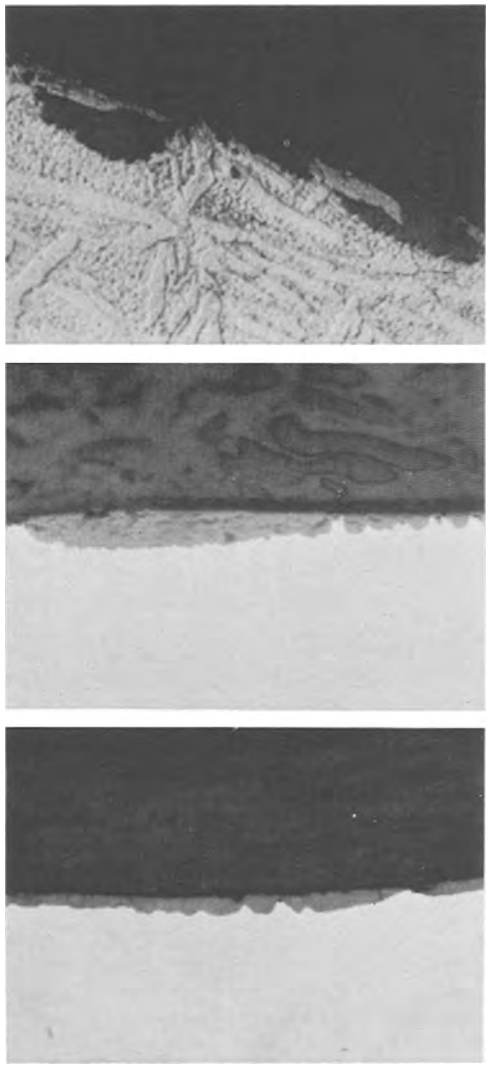

Fig. 9. Cross sections of oxidized specimens with Widmanstatten structures. a (top), 19,300 min at 300°C, oxygen uptake 0.23 mg/cm^2; b (center), 485 min at 400°C, oxygen uptake 0.5 mg/cm^2; c (bottom), 150 min at 500°C, oxygen uptake 0.5 mg/cm^2. Magnification 675X.

mining the effects of alloy structures on the oxidation kinetics. The results available at 300° and 400°C (Fig. 2 and 3) gave two limiting oxidation curves for the alloy under examination. A distinct transition was shown in the oxidation curves of the martensitic alloy, prepared by quenching from a β-solid solution temperature. The rate decreased until a transition range was attained in which the rate increased again to a maximum value associated with approximately linear kinetics. The other limiting oxidation curve was shown by alloys with Widmanstatten structures produced by quenching from 800°C and containing approximately 50 v/o proeutectoid α-Zr, the equilibrium amount for this temperature. These curves exhibited a decreasing rate, which, in the later stages, approximated to linear kinetics.

In the early stages of the reaction at 300° and 400°C, there was little difference between the oxidation rates for the two alloy structures. However, the reaction rate at long times of a Widmanstatten-structured alloy was much less than the linear rate of the martensitic alloy. Specimens with intermediate amounts of proeutectoid α-Zr exhibited oxidation rates between these two limiting cases, the over-all rate increasing with decreasing amount of α-Zr.

A direct relationship between the magnitude of the reaction kinetics and the amount of α-Zr in an alloy could not be demonstrated from the present results

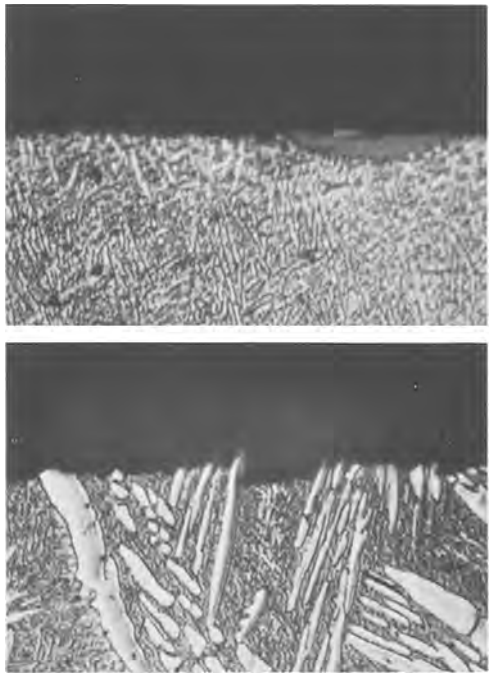

Fig. 10. Etched structures of oxidized specimens. a (top), martensitic structure, 7130 min at 300°C; b (bottom), Widmanstatten structure, 485 min at 400°C. Magnificaion 675X.

at 300° and 400°C. In the initial stages, the oxidation rate of α'-Zr was at least three times faster than α-Zr, while in the final stages of the exposures, the contribution of film growth on the α-Zr plates was of minor significance to the over-all film growth. Moreover, the oxide film on α'-Zr at long exposures was cracked and porous. These observations suggest that the linear oxidation kinetics at 300° and 400°C would be largely dependent on the amount of α'-Zr in the alloy.

Plots of the linear rate constants *vs.* the amount of α'-Zr are shown in Fig. 11 and 12. At 300°C, the kinetic curves were irregular and the rate constants are only approximations. The martensitic specimens reacted rapidly at this temperature, the rate decreasing markedly over the range to 85 v/o martensite. At 400°C, the decrease in rate was proportional to the amount of α'-Zr from full to approximately 80 v/o martensite. A smaller dependence of the oxidation rate on the contents of α'-Zr less than 80 v/o appeared to be associated with the morphological development of the oxide film.

Chemical composition is a major difference between martensite formed by quenching from 1000° and 800°C. α'-Zr formed under the latter condition would contain twice as much niobium. At small niobium contents, alloys with larger niobium concentration exhibit more rapid oxidation (5, 6). Thus, α'-Zr would possibly oxidize more rapidly in the specimens quenched from 800°C. The observations from this investigation do not support this consideration. Accordingly, any variations to be expected from increased niobium concentration in the martensitic phase were suppressed by possible variations in the structure of this phase or its mechanism of oxidation in the presence of proeutectoid α-Zr.

It has been shown that the oxide on the martensitic phase was subject to constraint by α-Zr plates and was pinned beneath the metal/oxide interface, Fig. 9(a). The oxide under such circumstances was less porous and the oxidation rate showed a smaller dependence on the amount of α'-Zr at percentages less than 80 v/o (Fig. 11 and 12). Thus, the over-all oxidation rate became dependent on two factors: the amount of α'-Zr and the penetration depth of oxide into the metal. With low percentages of proeutectoid

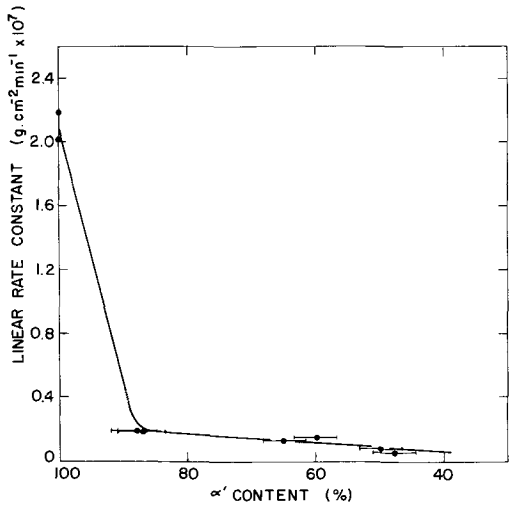

Fig. 11. Plot of linear oxidation rate constants vs. amount of α'-Zr at 300°C.

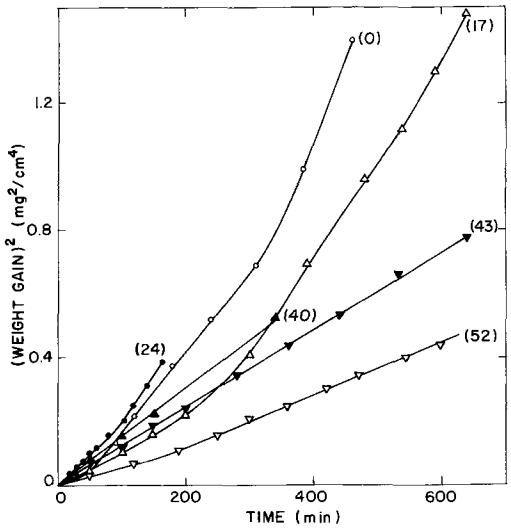

Fig. 13. Oxidation kinetics at 500°C represented by parabolic plots.

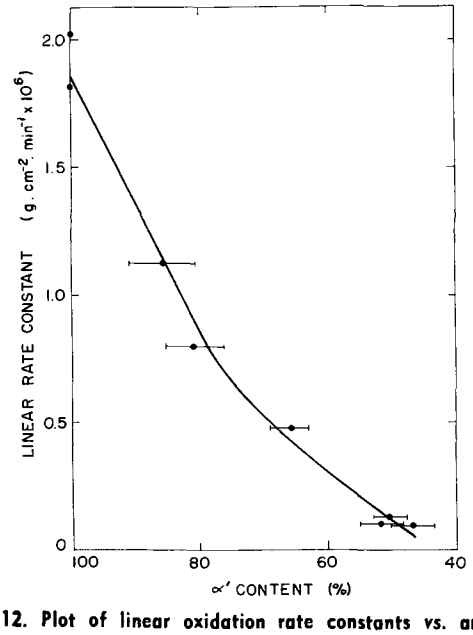

Fig. 12. Plot of linear oxidation rate constants vs. amount of α'-Zr at 400°C.

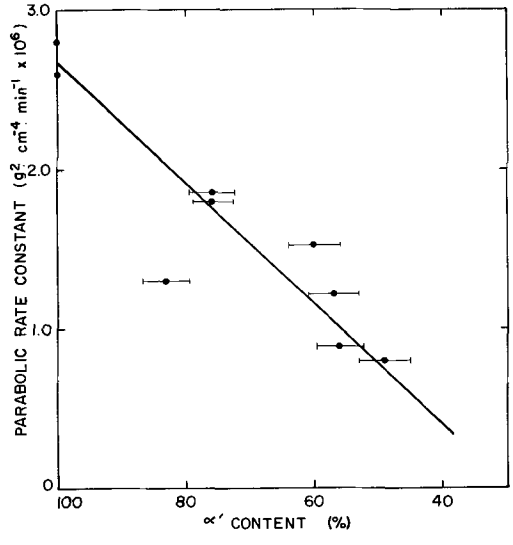

Fig. 14. Plot of parabolic oxidation rate constants vs. amount of α'-Zr at 500°C.

α-Zr, this latter factor was less important, and the over-all rate varied almost linearly with the amount of martensite. However, at large percentages of the proeutectoid phase, oxide on martensite penetrated selectively between plates of the former phase, and the oxidation rate was much slower than to be predicted by a direct proportionality between oxidation rate and amount of α'-Zr.

Oxidation curves at 500°C did not exhibit transitions to more rapid linear kinetics as observed at the two lower temperatures. Although the films on α-Zr were characterized by interference colors, those on the α'-phase were invariably gray at all observed times in contrast to results at the lowest temperatures. Though the oxidation properties were dependent on alloy structure at this highest temperature employed, the kinetics could be represented by parabolic plots for relatively long exposures (Fig. 13). Moreover, a plot of the parabolic constants *vs.* the amount of α'-Zr demonstrated a direct proportionality from full martensite to 50 v/o proeutectoid α-Zr (Fig. 14). This behavior appears reasonable since pronounced selective penetration of oxide between plates of this phase did not occur as at lower temperatures. Tempering of martensite occurs at this temperature and α-Zr would exhibit a larger niobium solubility. The influence of these parameters on oxidation processes in a manner not understood at present may account for the smaller degree of selective phase oxidation.

In view of the fact that the form of the oxidation curve is dependent on both alloy structure and temperature, conclusions drawn from comparisons of results obtained under different exposure conditions must be accepted tentatively. The major product of the reaction of all temperatures, irrespective of alloy structure, was an oxide whose structure could be indexed as monoclinic zirconia. However, it is interesting to compare the differences in surface topography and cross sections of oxidized specimens (Fig. 6-9). At 500°C and while the rate curve was parabolic, the gray oxide which formed did not exhibit cracks distinguishable by light microscopy. The oxidation rate would be possibly controlled by diffusion processes in the oxide film during this stage of the reaction. Cracking of such oxide, however, was noted at 300° and 400°C for all alloys in early periods of exposure at small film thicknesses and parabolic kinetics were not obeyed. On the other hand, the oxide was cracked in the range of approximately linear kinetics at all temperatures, but its role as a barrier to oxidation could not be interpreted by using standard metallographic techniques.

The formation of oxide pustules was the only distinct feature indicating a difference in the mode of oxide formation on different structured alloys. The pustules, moreover, were only observed at the temperatures 300° and 400°C on martensitic specimens and appeared on the surface during the transition to linear kinetics. These specimens were the only ones to exhibit the type of oxidation curve where there was a very pronounced transformation in the kinetics from a small initial rate to a much more rapid rate at long exposures. This behavior, involving pustule formation and cracking, may be associated with interfacial stress between the alloy and the oxide film. At 500°C, such stress might be relieved by tempering of the alloy at the reaction temperature and thus allow a more compact film to form. The presence of the proeutectoid α-Zr plates could similarly aid stress relief and so reduce the possibility of pustule formation, but no substantiating evidence could be found in the present results.

Acknowledgments

The authors were indebted to B. Cox for supplying the Zr-Nb alloy sheets and several specimens in prepared metallurgical structures. This research was completed under auspices of the Atomic Energy of Canada Limited and the Defence Research Board of Canada.

Manuscript received June 2, 1967. This paper was presented at the Chicago Meeting, Oct. 15-19, 1967.

Any discussion of this paper will appear in a Discussion Section to be published in the June 1968 JOURNAL.

REFERENCES

1. J. D. Dawson, U.K.A.E.A. Report AERE-R 4820 (1964).
2. H. Richter, P. Wincierz, K. Anderko, and U. Zeicker, *J. Less Common Metals*, **4**, 252 (1962).
3. G. T. Higgins and E. E. Banks, *Electrochem. Technol.*, **4**, 341 (1966).
4. R. J. Hussey and W. W. Smeltzer, *This Journal*, **111**, 564 (1964).
5. O. Zmeskal and M. L. Brey, *Trans. ASM*, **53**, 415 (1961).
6. R. S. Ambartsumjan, A. A. Kiselev, R. V. Grebenikov, V. A. Myshin, L. J. Tsuprun, and A. F. Nikulina, Proc. 2nd. U.N. Inter. Conf. Peaceful Uses of Atomic Energy, **5**, 12 (1958).

Electrochemical Reduction of Cyanoalkyldimethylsulfonium Ions

John H. Wagenknecht and Manuel M. Baizer

Central Research Department, Monsanto Company, St. Louis, Missouri

ABSTRACT

The polarographic and coulometric reduction of cyanomethyldimethylsulfonium ion (I) in anhydrous dimethylsulfoxide occurs in a single apparent one-electron reduction. Evidence from polarography in the presence of acetic acid and from macroelectrolyses leads to the interpretation that I probably actually undergoes a two-electron reduction to form the cyanomethyl anion which reacts at the electrode surface with a second parent ion. This result is another example of a concealed limiting current in the reduction of compounds $(LCH_2E)^+X^-$. Cyanoethyldimethylsulfonium ion and cyanopropyldimethylsulfonium ion each have an initial one-electron reduction wave followed at more negative potentials by reduction to form cyanoalkyl anions which react with the parent sulfonium ion. Products obtained from macroelectrolyses are consistent with those predicted from the mechanisms proposed from the polarographic data.

As part of a study of the follow-up reactions of species formed by the electrochemical reductive cleavage of compounds $[L(CH_2)_nE]^+X^-$ (when L is a "leaving group" and E is an electron-withdrawing group), we recently reported the electrochemical reduction at mercury of triphenylcyanoalkylphosphonium ions and the reaction of the cleaved cyanoalkyl groups with styrene (1). This paper is a report of the results of a similar study of cyanoalkyldimethylsulfonium ions, $(CH_3)_2S^+(CH_2)_nCN$ (n = 1, 2 or 3; I, II, and III, respectively).

Calculations based on polarography and coulometry of I in aprotic solvents give a value of $n = 1$. We report evidence which strongly suggests that a two-electron reduction is involved to form the cyanomethyl anion which then reacts with another I to form a nonreducible product.

The polarograms of II and III obtained in aprotic media contain an initial one-electron reduction wave followed by a maximum. The diffusion current is the same before and after the maximum. Evidence from polarograms of II and III obtained in the presence of phenol indicates that at the potential of the maximum a wave is repressed by reaction of the reduction product with the parent sulfonium ion. Previous reports on sulfonium ion reductions (2-8) have indicated only that various β-ketosulfonium ions have unusual maxima (4-7). These do not appear to arise from the same phenomena as those occurring in the polarograms of II and III.

Attempts to trap the electrochemically cleaved cyanoalkyl fragments by *in situ* reaction with styrene were of limited success, but the identification of the products obtained in the macro electrolyses was helpful in rationalizing the course of the electrochemical-chemical reactions.

Experimental[1]

The polarographic data were obtained using a Sargent Model XXI Polarograph. Electrode constants were m = 2.216 mg/sec, t = 3.43 sec, and $m^{2/3}t^{1/6}$ = 2.08 $mg^{2/3}t^{-1/2}$ at a mercury column height of 90 cm. The polarographic cell was immersed in a thermostated water bath at 25° ± 0.1°C. A Chemical Electronics Corporation (Newcastle, England) potentiostat and an electrometer operational-amplifier integrator[2] were used to obtain microcoulometric data. The coulometry was carried out on 0.1 to 0.2 mmole of sulfonium compound at a mercury pool cathode in a divided cell with a SCE reference electrode and silver wire secondary electrode. The solvent was dimethylsulfoxide containing 0.1*M* tetrabutylammonium bro-

[1] Boiling points are not corrected.
[2] Built by Dr. John M. Fritsch at our laboratories.

mide. Nuclear magnetic resonance analyses were carried out with a Varian A-60 n.m.r. spectrometer. Analytical gas chromatography was carried out with a F&M Model 300 Gas Chromatograph with 3m, ¼ in. columns packed with 18% Carbowax 20-1% $AgNO_3$ on Chromosorb W, 3% XE-60 on Teflon, 3% Flexol 8N8 on Teflon or silicone grease on Chromosorb W. Vpc analyses were obtained from two or more columns to insure the identity of the peaks.

The dimethylsulfoxide (Matheson, Coleman & Bell) was distilled at reduced pressure from a small amount of sodium hydride, bp 58°-60° (5 mm). The dimethylformamide (DMF) was distilled from barium oxide before use. Styrene (Eastman) was distilled *in vacuo* just before use and stabilized with hydroquinone. Tetra-*n*-butylammonium bromide (Eastman) was recrystallized from ethyl acetate before use. Tetraethylammonium *p*-toluenesulfonate (Alfred Bader Chemical Company) was recrystallized from acetone.

The electrolytic cell used for macro electrolyses has been described (9). The cathode potential was monitored with a SCE and vacuum tube voltmeter. The power supply was a Nobatron RC150-7.5, and the cell voltage was adjusted so that the cathode potential was near the first wave, half-wave potential of the compound being reduced. The cell voltage was manually controlled later in the run to prevent a large rise in cathode potential. The electrolysis was stopped when the cathode potential would no longer remain near the half-wave potential at a cell current of 0.25 amp indicating that nearly all of the starting material had been consumed. An Analytical Instruments, Inc. current integrator was used to determine the total amount of electricity passed.

The anolyte in each case was a solution of tetraethylammonium *p*-toluenesulfonate in DMF. Styrene was present in the catholyte in each case to trap reactive intermediates.

Macroelectrolysis of I.—The catholyte consisted of 20.5g (0.075 mole) of cyanomethyldimethylsulfonium *p*-toluenesulfonate (10), 200 ml of DMF, 30g of tetraethylammonium *p*-toluenesulfonate and 30 ml of styrene. The electrolysis was carried out at 10°-15°, 1.0-0.25 amp and a cathode voltage of —1.0 to —1.13v (*vs.* SCE). The total quantity of electricity was 0.096**F**. After the electrolysis, the solvent was removed from the catholyte by distillation at reduced pressure. The strong odor of dimethyl sulfide was present. Vpc analysis of the distillate showed the presence of 2.15g (70% based on starting material) of acetonitrile. The residue after solvent removal was extracted with ether. The residue after removal of the ether from the ether extract contained no 4-phenylbutyronitrile by vpc analysis. Traces of DMF were removed from the residue by distillation at 0.1 mm leaving a black, gummy residue.

A second electrolysis of I was carried out using a glass frit divided H cell with a 20 ml catholyte capacity. The cathode was a 2 cm diameter mercury pool. The anode was platinum foil. The catholyte consisted of 19 ml of 0.915*M* cyanomethyldimethylsulfonium *p*-toluenesulfonate in dimethylsulfoxide. The anolyte consisted of 27 ml of 1*M* tetra-*n*-butylammonium bromide in dimethylsulfoxide and 1.5 ml of cyclohexene. The catholyte was deaerated with N_2 before the electrolysis and then was sealed. The anolyte was swept with N_2 during the electrolysis. The cathode potential was not monitored. Only a thermometer was in contact with the catholyte. The catholyte was maintained at 20°C during the run by immersing the cell in an ice-water bath. The electrolysis was carried out at 50-60 ma until 8.7 m**F** of current was passed. After the electrolysis, polarographic analysis of the catholyte and anolyte[3] indicated 8.53 mmoles of I had been consumed. Vpc analysis of the catholyte showed the presence of 3.9 mmoles of acetonitrile (90% yield based on 2 **F**/mole).[4] No acetonitrile was detected in the anolyte.

Macroelectrolysis of II.—The catholyte was identical to the previous run except that the sulfonium salt (22g, 0.078 mole) was cyanoethyldimethylsulfonium *p*-toluenesulfonate. The electrolysis was carried out at 0°, 1.0-0.25 amp, and a cathode potential of —1.74 to —1.89v (*vs.* SCE).[5] The total quantity of electricity was 0.097**F**. The electrolysis was stopped at this point because more than 1**F** of electricity per mole had been passed, and it was suspected that II had been decomposed[5] to form acrylonitrile, the reduction of which would require 2**F**/mole. The workup was as described for the previous run and yielded 1.0g (37%) of propionitrile, 0.54g (21.6%) of acrylonitrile and a trace of adiponitrile (all by vpc analysis). No 5-phenylvaleronitrile or mercurials were detected.

A second electrolysis was carried out in a glass frit divided H-cell with a mercury pool cathode and platinum foil anode. The catholyte consisted of 150 ml of dimethylsulfoxide containing 0.1*M* tetra-*n*-butylammonium bromide, 40g (0.14 mole) of dimethylcyanoethylsulfonium *p*-toluenesulfonate, 30 ml of styrene, and a trace of hydroquinone. The anolyte was dimethylsulfoxide containing 0.1*M* tetra-*n*-butylammonium bromide and saturated with cyclohexene. The cell was maintained at 15° by a water bath. The electrolysis was carried out for 24.25 hr with a cell voltage of 150v, a curernt of 0.2 amp, and at a cathode potential of —1.6v (*vs.* SCE). A total of 0.167**F** of electricity was passed. The cathode potential did not increase as the 1**F**/mole of II point was passed, and it was again suspected that decomposition of II had occurred.

After the electrolysis, the catholyte was evacuated to 30 mm through a dry-ice, acetone-cooled trap overnight. The trap overnight collected about 1 ml of a mixture of acrylonitrile, propionitrile, and dimethylsulfide.

Attempts to get a quantitative analysis of acrylonitrile in the catholyte by vpc analysis were futile because II decomposes in the injection port to form acrylonitrile. Attempts to determine the amount of acrylonitrile present in the catholyte by polarography were also unsuccessful because the waves of it and II were too close together.

The catholyte was then mixed with 500 ml of water, and this mixture was extracted with three 200-ml portions of ether. The combined ether extract was back-extracted with water and dried over anhydrous magnesium sulfate. The ether solution was concentrated on a rotary evaporator. The concentrated solution was cooled in dry-ice whereupon 1.2g (5.5%) of biscyanoethylmercury, mp 46°-48° (17), precipitated.

The remainder of the ether was stripped from the solution, and the styrene was removed at reduced pressure (0.3 mm). The residue was distilled at 0.2 mm giving a single cut from 50°-80° (2.0g). Nmr analysis of this indicated 1.0g each of 3-thiomethylpropionitrile (7.1%) and methylcyanoethyl mercury (5.3%). Vpc analysis of the pot residue which contained all the hydroquinone used to prevent styrene polymerization showed the presence of 0.012g of 5-phenylvaleronitrile. (The standard sample of 5-phenylvaleronitrile was obtained from 5-phenylvaleric acid by the usual methods.)

The mixture of 3-methylthiopropionitrile and methylcyanoethyl mercury was redistilled in a micro apparatus. The 3-thiomethylpropionitrile distilled at 50°-60° at 0.2 mm. Two small cuts were then taken at 70° and 71°. The first was used for nmr analysis and

[3] A small amount of I had been forced by hydraulic pressure into the anode compartment.

[4] Due to decomposition of I in the vpc injection port to unknown products which emerge in the dimethyl sulfide region, it was impossible to determine dimethyl sulfide by this method. However, nmr analysis of the solution indicated the presence of 7.3 mmoles of dimethyl sulfide in the catholyte (168% base on 2 **F**/mole). See Discussion.

[5] This electrolysis was carried out at a lower temperature than the others, so that over the duration of the electrolysis (*ca.* 4 hr) the base catalyzed Hofmann elimination reaction of II could be minimized.

the second for mass spectral analysis of the methylcyanoethyl mercury.

The nmr spectrum of methylcyanoethyl mercury consists of a singlet at $\tau = 9.68$ for the methyl with its Hg^{199} side bands at $\tau = 8.75$ and 10.56. The triplets for the methylenes α and β to the mercury occur at $\tau = 8.92$ and 7.31, respectively. Hg^{199} side bands occur as triplets at $\tau = 6.51$ and 9.78 and a multiplet between the major α and β methylene triplets. The nmr spectrum contained small peaks due to thiomethylpropionitrile and 5-phenylvaleronitrile.

The vpc analysis of the second cut indicated the presence of small amounts of thiomethylpropionitrile and 5-phenylvaleronitrile along with what were probably decomposition products of the methylcyanoethyl mercury. Mass spectral analysis of this cut showed small parent ion peaks for thiomethylpropionitrile at $m/e = 101$ and 5-phenylvaleronitrile at $m/e = 159$. The parent ions for the methylcyanoethyl mercury were obtained in the correct ratios for all the naturally occurring mercury isotopes, the major ion being at $m/e = 271$ corresponding to the parent ion containing Hg^{202}, the major naturally occurring isotope.

The nmr spectrum of biscyanoethyl mercury consists of triplets for the methylene α and β to the mercury at $\tau = 8.64$ and 7.18, respectively. The Hg^{199} side bands occur as triplets at $\tau = 6.25$ and 9.55 and a multiplet between the major methylene triplets.

Macroelectrolysis of III.—The catholyte was identical with that used for I except that now the sulfonium salt was 30g (0.1 mole) of cyanopropyldimethylsulfonium p-toluenesulfonate. The electrolysis was carried out at 20°-25°, 1.0-0.25 amp, and a cathode potential of —1.90 to —2.05v (*vs.* SCE). The total quantity of electricity was 0.123F.

Vpc analysis of the catholyte indicated a trace of butyronitrile. The catholyte was then distilled at 5.0 mm to remove solvent (warning: dimethyl sulfide). The nmr spectrum of the material trapped in a dry ice-acetone cooled trap during the solvent removal distillation showed a singlet at $\tau = 9.82$ suggesting the presence of dimethyl mercury (11).

The residue remaining after the solvent was removed from the catholyte was treated with 250 ml water and extracted with dichloromethane. The dichloromethane was removed by distillation from the extract. A trace of 6-phenylcapronitrile was detected in the residue by vpc. Distillation of the residue at 0.005 mm gave three fractions (*a*) mostly DMF, bp < 25°, (*b*) 3.0g, bp 55°, (c) 3.1g, bp 145°-155°. Fraction (*b*) contained 4-methylthiobutyronitrile by vpc analysis. The nmr spectrum of fraction (*b*) suggested the presence of methyl-3-cyanopropyl mercury giving singlets at $\tau = 9.77$ and $\tau = 8.95$ and $\tau = 10.57$ (satellites due to Hg^{199} splitting) for the methyl group attached to mercury. Fraction (c) appeared to be nearly pure biscyanopropyl mercury by nmr analysis which showed a complex multiplet at $\tau = 7.85$ due to the methylenes alpha and beta to the nitrile and triplets at $\tau = 8.94$ and $\tau = 9.78$ due to the methylene alpha to the mercury and one of its Hg^{199} satellites. The area ratio was 2:1 for the multiplet and major triplet. A portion of fraction (c) was dissolved in ether and treated with anhydrous HCl. From this solution cyanopropylmercuric chloride crystallized. It was recrystallized from ether cooled in dry ice giving white crystals, mp 109°-110°.

Anal. Calcd. for C_4H_6ClHgN: C, 15.79; H, 1.99; Cl, 11.66; Hg, 65.95; N, 4.61. *Found*: C, 15.70; H, 2.04; Cl, 11.41; Hg, 66.19; N, 4.64.

The ether solution, after removal of the solid, was found by vpc to contain butyronitrile.

Preparation of cyanoethyldimethylsulfonium p-toluenesulfonate.—3-Methylthiopropionitrile (12) was quaternized with methyl p-toluenesulfonate at room temperature. Crops were removed from time to time. After four weeks, 78.5% of crude product was obtained which, after recrystallization from ethanol, melted at 110°-111°.

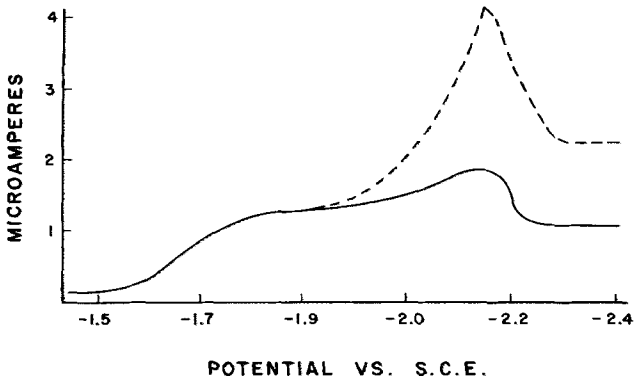

Fig. 1. Polarogram of cyanoethyldimethylsulfonium p-toluenesulfonate in dimethylsulfoxide containing 0.2M tetra-n-butylammonium bromide. Dashed line represents the effect of adding phenol to the solution.

Anal. Calcd. for $C_{12}H_{17}NO_3S_2$: C, 50.14; H 5.96; S, 22.32. *Found*: C, 50.12; H, 5.62; S, 22.43.

Preparation of dimethylcyanopropylsulfonium p-toluenesulfonate.—A mixture of 17.4g of sodium hydroxide in 200 ml of ethanol was saturated with methanethiol. To this solution was added 45g of 4-chlorobutyronitrile, and the solution was stirred for 2 hr at 10°C. The mixture was poured onto ice and then extracted with ether. Evaporation of the ether and distillation of the residue yielded 32g (64%) of 4-methylthiobutyronitrile, bp 85° (9 mm), $n^{25}D$ 1.4777. The 32g of thionitrile was mixed with 52g of methyl-p-toluenesulfonate and allowed to stand at room temperature. After 4 days, the mixture was filtered and the solid recrystallized from CH_3CN yielding 30g (36%) of dimethylcyanopropylsulfonium p-toluenesulfonate, mp 142.5°-144°.

Anal. Calcd. for $C_{13}H_{19}NO_3S_2$: C, 51.80; H, 6.35; N, 4.64; S, 21.28. *Found*: C, 51.96; H, 6.14; N, 4.43; S, 21.46.

Results and Discussion

The values of $E_{1/2}$ (*vs.* SCE) and I_d[6] (in parentheses) for I, II and III were —1.04 (1.04), —1.69 (1.08), and —1.76 (1.06), respectively, for 1 mm solutions in dimethylsulfoxide containing 0.2*M* tetra-n-butylammonium bromide. In addition, the polarograms of II and III each contain an unusual maximum (Fig. 1) occurring from —2.05 to —2.35v and —2.15 to —2.45v, respectively. Microcoulometry gave values of $n = 0.945$, 0.98, and 1.03 for I, II, and III, respectively, on exhaustive reduction at a potential just past the half-wave potential. By inference the values of I_d must correspond to a one-electron reduction when taken in conjunction with evidence from microcoulometry and comparison with values obtained with similar phosphonium ions (1). Dimethylsulfoxide was used for polarographic studies because traces of dimethylamine, which abstract a proton from I, could not be removed from DMF.

The addition of a small amount (less than 1%) of acetic acid[7] to the polarographic solution of I caused the value of I_d to double. Addition of more acetic acid caused no change. This parallels the behavior of triphenylcyanomethylphosphonium ion (1) and can be explained similarly. The reduction of I is most easily understood as a two-electron reduction (reaction [1]). In the absence of another proton source the cyano-

[6] $I_d = i_d/C_m^{2/3}t^{1/6}$.

[7] Phenol did not effect the polarogram. The phenol was apparently not acidic enough to compete effectively with the very acidic I for protonation of the cyanomethyl ion. The strong acidity of I is not surprising in view of the acidity of the methylene hydrogens in compounds such as cyanoacetic esters, malononitrile, etc.

methyl anion

$$\underset{\text{I}}{(CH_3)_2\overset{+}{S}CH_2CN} \xrightarrow{2e} (CH_3)_2S + (CH_2CN)^- \quad [1]$$

abstracts a proton from an unreduced I (reaction [2]). The

$$I + (CH_2CN)^- \rightarrow (CH_3)_2\overset{+}{S}-\overset{-}{C}HCN + CH_3CN \quad [2]$$

net result is that two electrons effectively consume two of the sulfonium ions giving an apparent one-electron reduction. However, when acetic acid is present, the cyanomethyl anions are protonated by the acetic acid and all the sulfonium ions that diffuse to the mercury drop are available for reduction, giving a two-electron reduction wave. Khaikin and Feoktistov (13) recently published a theoretical treatment of a general system which would include the above example.

Gerdil (14) recently reported that certain sulfides ($C_6H_5S\ CH_2X$, X = CN, $CO_2C_2H_5$, CO_2H) gave one-electron reduction polarograms in anhydrous DMF, but that the wave height doubled on addition of phenol. These results may also be explained by reaction of the anion formed with the depolarizer.

$$C_6H_5S\ CH_2X \xrightarrow{2e} C_6H_5\overset{+}{S}(-) + (-)CH_2X$$

$$C_6H_5S\ CH_2X + (-)CH_2X \rightarrow CH_3X + C_6H_5S\overset{(-)}{C}HX$$

The results of the macroelectrolyses of I give further evidence for the reactions shown in Eq. [1] and [2]. If the reduction of I were a true one-electron reduction, the products would be dimethylsulfide and cyanomethyl radicals. The reduction carried out in DMF in the presence of styrene would have been expected to give the product of attack on styrene by cyanomethyl radicals (reaction [3]).

$$\cdot CH_2CN + C_6H_5CH = CH_2 \rightarrow$$

$$C_6H_5\dot{C}H(CH_2)_2CN \xrightarrow{\text{solvent}} C_6H_5(CH_2)_3CN \quad [3]$$

No γ-phenylbutyronitrile was detected in the electrolysis products. The only products detected in either electrolysis were acetonitrile and dimethylsulfide.[8] It may be calculated from the yield of acetonitrile that about half the cyanomethyl anions formed in the electrolysis of I in DMF were protonated by sources other than I. Since the electrolysis was carried to completion, it is not surprising that as the concentration of I became lower other sources of protons such as water and dimethylamine could effectively compete with I to react with cyanomethyl anions.

The electrolysis of I in dimethylsulfoxide in the absence of styrene was carried to only about 50% completion. Since there was still a high concentration of I at the end of the run, little competition by other proton sources was observed. The values of 1.02 **F**/mole of I consumed and a 90% yield of acetonitrile based on 2 **F**/mole are in accord with reactions 1 and 2. The higher than theoretical yield of dimethylsulfide can be explained by the fact that the sulfur ylid decomposes to form dimethylsulfide.[9]

[8] The other product expected would be the sulfur ylid in reaction [2]. Since simple sulfur ylids are very reactive (16), the ylid shown presumably led to the intractible material formed in this electrolysis. Triphenylcyanomethylphosphonium ion behaves similarly to I, but in that case the more stable phosphorus ylid survived the electrolysis and reacted with water in the workup to give triphenylphosphine oxide which was isolated and identified (1).

[9] A 1*M* solution of cyanomethyldimethylsulfonium *p*-toluene-sulfonate in dimethylsulfoxide was treated with an equivalent amount of potassium *t*-butoxide in dimethylsulfoxide. The nmr spectrum of I in this mixture immediately disappeared and a small adsorption for dimethylsulfide appeared indicating that displacement of dimethylsulfide from I by nucleophilic attack by *t*-butoxide is not a major contributing reaction. Over a period of 6 hr the dimethylsulfide concentration increased at least tenfold; therefore, it must have arisen by decomposition of the sulfur ylid since no more I was present. No acetonitrile could be detected in the reaction mixture.

The first polarographic waves of II and III are not effected by the addition of phenol indicating a true one-electron reduction (reaction [4]). However, the addition of phenol does affect the unusual maximum for II or III

$$(CH_3)_2\overset{+}{S}(CH_2)_nCN \xrightarrow{1e} (CH_3)_2S + \cdot(CH_2)_nCN\ (n = 2 \text{ or } 3) \quad [4]$$

changing it to an ordinary maximum preceding a wave (Fig. 1). Since the second waves for II and III occur only in the presence of a proton donor, a reaction similar to that of I is suggested. Thus, at the potential of the second wave, a two-electron reduction occurs leading to the cyanoalkyl anion (reaction [5] or [6]).

$$(CH_3)_2\overset{+}{S}(CH_2)_nCN \xrightarrow{1e} (CH_3)_2S + \cdot(CH_2)_nCN \xrightarrow{1e^-} (-)(CH_2)_nCN \quad [5]$$

$$(CH_3)_2\overset{+}{S}(CH_2)_nCN \xrightarrow{2e} (CH_3)_2S + (-)(CH_2)_nCN \quad [6]$$

The reduction at the second wave may be a direct two-electron reduction (reaction [6]), or a one-electron reduction-disproportionation—one-electron reduction pathway (reaction [5]).

In the presence of phenol the cyanoalkyl anion is protonated by phenol, and both waves are observed. In the absence of phenol the second wave does not appear because the cyanoalkyl anion formed reacts with unreduced sulfonium ion (reaction [7] or [8]) so that two electrons effectively remove two sulfonium ions. This then gives the

$$(-)(CH_2)_nCN + \overset{+}{(CH_3)_2S}(CH_2)_nCN \rightarrow (CH_3)_2S + CN(CH_2)_{2n}CN \quad [7]$$

$$(-)(CH_2)_nCN + \overset{+}{(CH_3)_2S}(CH_2)_nCN \rightarrow CH_3(CH_2)_{n-1}CN + (CH_3)_2\overset{+-}{S}CH(CH_2)_{n-1}CN \quad [8]$$

same wave height as the original one-electron reduction. Although the diffusion current is prevented from increasing at the potential of the second wave by reaction [7] or [8], the maximum associated with the change in electrode mechanism still occurs giving the unusual polarogram. The maxima observed for β-ketosulfonium ions (4-9) have a similar appearance, but, since they occur in aqueous solution, they probably cannot be explained by similar reactions.

The macroelectrolysis of II was complicated by the ease of base catalyzed decomposition of II (reaction [9]).

$$(CH_3)_2\overset{+}{S}CH_2CH_2CN \xrightarrow{B:} (CH_3)_2S + CH_2 = CHCN + BH \quad [9]$$

It has been mentioned (15) that the region next to the cathode is very basic during electrolysis even if the bulk solution is neutral. It is not surprising then that the products obtained from the reduction of II in DMF appear to arise from the reduction of acrylonitrile. The products identified were acrylonitrile, propionitrile, and adiponitrile and are visualized as being formed by reactions [9]-[11].

$$CH_2 = CHCN \xrightarrow[2H+]{2e} CH_3CH_2CN \quad [10]$$

$$2CH_2 = CHCN \xrightarrow[2H+]{2e} CN(CH_2)_4CN \quad [11]$$

Since even traces of base can catalyze reaction [9], the second electrolysis of II was carried out in a more acidic medium, dimethylsulfoxide. In this run, tetra-*n*-butylammonium bromide was used so that bromine would be liberated at the anode. Cyclohexene was added to the anolyte to react with the bromine. This was done in an attempt to eliminate the possibility of acidic material formed at the anode from entering the cathode compartment. All the components of the catholyte were rigorously purified. These precautions, however, did not prevent the decomposition of II to acrylonitrile. However, it was possible in this case to reduce enough II to allow products of that reduction to be isolated. In addition to dimethylsulfide, acrylonitrile, and propionitrile there were also obtained thiomethylpropionitrile, methylcyanoethyl mercury, biscyanoethyl mercury, and 5-phenylvaleronitrile.

The products of the macroelectrolysis of III were butyronitrile, dimethylsulfide, thiomethylbutyronitrile, 6-phenylcapronitrile, and biscyanopropyl mercury, with evidence of dimethyl mercury and methylcyanopropyl mercury. The biscyanopropyl mercury was identified by its nmr spectrum (described in the experimental section) and its reaction with HCl to form butyronitrile and cyanopropylmercuric chloride (reaction [12]).

$$(CNCH_2CH_2CH_2)_2Hg + HCl \rightarrow CH_3CH_2CH_2CN + CNCH_2CH_2CH_2HgCl \quad [12]$$

The products from the reductions of II and III are visualized as being formed by the following scheme

$$\text{II or III} \xrightarrow{1e} (CH_3)_2\dot{S}(CH_2)_nCN \qquad (n = 2 \text{ or } 3)$$

(IV)

$$IV \rightarrow (CH_3)_2S + \cdot(CH_2)_nCN$$

$$IV \rightarrow CH_3S(CH_2)_nCN + \cdot CH_3$$

$$\cdot(CH_2)_nCN \xrightarrow{\text{Styrene}} C_6H_5\dot{C}H(CH_2)_{n+1}CN \xrightarrow{\text{Solvent}} C_6H_5(CH_2)_{n+2}CN$$

$$\cdot(CH_2)_nCN \xrightarrow{\text{Solvent}} CH_3(CH_2)_{n-1}CN$$

$$\cdot(CH_2)_nCN \xrightarrow{Hg} [\cdot Hg(CH_2)_nCN] \rightarrow \tfrac{1}{2}[CN(CH_2)_n]_2Hg + \tfrac{1}{2}Hg$$

$$\cdot CH_3 \xrightarrow{Hg} [\cdot HgCH_3] \rightarrow \tfrac{1}{2}(CH_3)_2Hg + \tfrac{1}{2}Hg$$

$$[\cdot HgCH_3] + [\cdot Hg(CH_2)_nCN] \rightarrow CH_3Hg(CH_2)_nCN + Hg$$

The electrolyses were carried out at the potential of the first wave in each case, and the products are those expected from a one-electron reduction. Compounds of the series $(CH_3)_2\overset{+}{S}(CH_2)_nCN$ fall into three categories: (*a*) $n = 1$, (*b*) $n = 2$, (*c*) $n = 3$ or greater. The primary chemical consequence of the electron transfer is cleavage of the starting material between the sulfonium group and the adjacent carbon. The —CN group has a decreasing influence on the fate of the cyanoalkyl fragment. When $n = 1$, further reduction of the initial cyanomethyl radical to the relatively stable cyanomethyl anion is a very favorable process. The relatively anodic cathode voltage required reflects this ease of reduction. The cyanomethyl anion abstracts a proton from the most acidic substrate present, namely I. When $n = 2$ or 3 the —CN group has a much weaker (inductive) stabilizing influence upon the cyanoalkyl fragment. Reduction to the cyanoalkyl carbanion is decreasingly favored, and reactions deriving from the initial cyanoalkyl radical predominate. When $n = 2$, further complications arise from the ease of decomposition of II in a Hofmann-type degradation to yield an additional electro-reducible material (acrylonitrile).

Manuscript received Dec. 27, 1966; revised manuscript received *ca.* July 24, 1967. This paper was presented at the Dallas Meeting, May 7-12, 1967.

Any discussion of this paper will appear in a Discussion Section to be published in the June 1968 JOURNAL.

REFERENCES

1. J. H. Wagenknecht and M. M. Baizer, *J. Org. Chem.*, **31**, 3385 (1966).
2. W. A. Bonner, *J. Am. Chem. Soc.*, **74**, 5078 (1952).
3. E. L. Colichman and D. L. Love, *J. Org. Chem.*, **18**, 40 (1953).
4. S. Tang and P. Zuman, *Collection Czech. Chem. Commun.*, **28**, 1526 (1963).
5. P. Zuman and S. Tang, *ibid.*, **28**, 829 (1963).
6. J. M. Saveant, *Compt. Rend.*, **257**, 448 (1963).
7. J. M. Saveant, *ibid.*, **258**, 585 (1964).
8. A. Luttringhaus and H. Machatzke, *Ann.*, **671**, 165 (1964).
9. M. M. Baizer, *This Journal*, **111**, 215 (1964).
10. M. M. Baizer, *J. Org. Chem.*, **31**, 3847 (1966).
11. M. D. Rausch and J. R. Van Wazer, *Inorg. Chem.*, **3**, 761, (1964).
12. C. D. Hurd and L. L. Gershbein, *J. Am. Chem. Soc.*, **69**, 2328 (1947).
13. B. I. Khaikin and L. G. Foektistov, *Russ. J. Phys. Chem.*, **38**, 294 (1964).
14. R. Gerdil, *J. Chem. Soc.*, (B), **1966**, 1071.
15. M. R. Ort and M. M. Baizer, *J. Org. Chem.*, **31**, 1647 (1966).
16. E. J. Corey and M. Chaykovsky, *J. Am. Chem. Soc.*, **84**, 3782 (1962).
17. A. P. Tomilov, Yu. D. Smirnov, and S. L. Varshavskii, *J. Gen. Chem. USSR*, **35**, 390 (1964).

Correction

Captions to Fig. 2 and 3 in the Technical Note by N. A. Hampson and D. Larken "The Double Layer Capacitance in Aqueous Solution," pp. 933-935, September 1967 issue should read:

Fig. 2. Differential capacity curves and their frequency dependence in aqueous $NaClO_4$; electrolytic etch, 25°C: A, 1M $NaClO_4$ 2 kHz; B, 0.001M $NaClO_4$ 2 kHz; C, 0.01M $NaClO_4$ 103 Hz; D, 0.01M $NaClO_4$ 400 Hz; E, 0.01M $NaClO_4$ 2 kHz.

Fig. 3. Differential capacity curves in aqueous KCl; electrolytic etch 25°C, 2 kHz, • 1M KCl; ○ 0.001M KCl.

Nuclear Activation Technique for Detecting Nitrogen-15 Tracer in Solids

Ralph H. Condit, J. Birch Holt, and Lawrence Himmel

Lawrence Radiation Laboratory, University of California, Livermore, California

ABSTRACT

A technique for studying the transport of nitrogen in solids is described which makes use of the nuclear activation, $N^{15}(\alpha,n)F^{18}$. The radioactivity of the product, F^{18}, can be used to deduce the location of the original N^{15} tracer by autoradiographic methods. Requirements for the success of this technique are discussed, and its application to the study of nitrogen diffusion in uranium mononitride is outlined. Other possible uses, *i.e.*, the analysis for nitrogen or the identification of nitride inclusions in solid, are also mentioned.

Radiotracers have proven useful in many areas of solid-state research, particularly in diffusion and other material transport studies. Unfortunately, two of the most important elements, oxygen and nitrogen, do not have radioisotopes with convenient half-lives, and for them it has usually been necessary to use stable isotope techniques which employ sources of the elements enriched in one of their less abundant species, O^{17}, O^{18}, or N^{15}. These have generally involved a procedure wherein a solid specimen is annealed in a gaseous environment containing the isotopically enriched element, and the depletion of this enrichment in the gas has been followed by mass spectrometric analysis. Alternatively, the solid may be sectioned and the sections subjected to atomic mass analysis. These two methods have been compared (1). Interpretation of the data in order to derive values for the diffusion within the solids in these ways is often obscured by (*a*) uncertainties regarding the surface exchange rate between gas and solid, (*b*) the possibility of diffusion along defects such as grain boundaries or dislocation lines, and (*c*) the frequent need for fine particle materials to insure sufficient area of solid for adequate exchange, because determination of the surface area requires an added experimental step. Special techniques such as internal friction (2) or nuclear magnetic resonance (3) have been used to give an indirect indication of diffusion coefficients, but these are often limited to special crystallographic species such as the bcc metals for internal friction or special isotopes for NMR. With radiotracers, however, it is possible to use autoradiography which has proven versatile in pin-pointing the location of a tracer in solid specimens. This can reveal segregation at microinclusions of an impurity or preferential diffusion along grain boundaries.

We have previously described a means for circumventing this problem in the case of oxygen (4). This involves the proton bombardment activation of O^{18} according to the nuclear reaction, $O^{18}(p,n)F^{18}$, leading to the production of a radioisotope of fluorine in those areas in which the oxygen tracer had migrated. This means that one can make use of O^{18} almost as if it were a radiotracer. The only difference from the usual radiotracer experiment is that the O^{18} is made radioactive after the experiment rather than having been active from the start. In locating the F^{18}, we have relied on autoradiography which provides an indication of the distribution of O^{18} at the surface of the irradiated specimen.

This technique has been used in the study of oxygen diffusion along dislocations and microcracks (5) and grain boundaries (6) in MgO, and marker-type experiments have been carried out with O^{18} tracer used in the reaction between CoO and Al_2O_3 (7). It is currently being used in studies of the mechanism of iron oxidation (8). A related technique has been developed to study silicon self-diffusion (9), the stable isotope, Si^{30}, being allowed to penetrate into silicon and then subsequently being activated by neutron irradiation to give 2.6-hr Si^{31}. However, we are using charged-particle irradiations rather than neutrons. A general review of charged-particle activation techniques has been prepared by Tilbury (10). It is the purpose of this paper to describe an ion bombardment procedure for following the nitrogen isotope, N^{15}, which makes such studies as those in oxides also possible in nitrides.

Experimental Requirements

For the nuclear activation of stable isotopes to be of practical interest in transport studies in solids, it is necessary that the following conditions be met:

1. The necessary stable isotopes must be available in sufficient degree of enrichment over the natural concentration. This is clearly essential if self-diffusion measurements are contemplated.

2. The activation reaction must give enough activity for it to be measurable by counting methods or autoradiographic procedures.

3. Nuclear reactions involving other elements must not give rise to the same radioisotope as does the element of principal interest, and other radioactive species which are produced must not interfere with the detection of the principal one. Additionally, secondary reactions between constituents of the material under study and the products of the primary reaction, such as neutrons produced by (p,n) or (α,n) reactions, must not yield interfering activities.

4. The specimen must be able to withstand the irradiation conditions. In the case of ion bombardment this will normally mean some increase in temperature under vacuum conditions, although setups usually can be designed to avoid this.

5. The activity must be produced in the same position as that occupied by the tracer. The product radioisotope must not recoil appreciably from the point of reaction, and it must not diffuse away before its position is determined.

6. The resolution of the detector, such as autoradiographic emulsions or counters, must be adequate for the purposes of the experiment.

7. It must be possible to relate some measurement of activity to the amount of stable tracer present. This means that there must be control over the homogeneity of flux of the bombarding particles and their energy. Given a homogeneous beam, the effect on nuclear reaction rates of variations in density and crystal orientation must be understood, because these affect the depth of penetration of the beam. There must also be a relatively simple relationship between the geometry of the product activity and the detector, and it must be possible to calibrate the detector so that its response can be related to the activity.

Experimental Results

The ways in which α-particle irradiation of N^{15} can be used to satisfy the above conditions are described in the following sections:

1. Nitrogen-15 is present in 0.37% concentration in natural nitrogen and can be purchased in enrichments up to 99%, a factor of almost 270. Under α-particle bombardment, it is converted to fluorine-18 via the nuclear reaction $N^{15}(\alpha,n)F^{18}$. The radioactive F^{18} has a half-life of 110 min (11) and decays with the emission of a 0.6-Mev positron but without any accompanying nuclear γ-ray. This means that γ-spectroscopy cannot be usefully employed to distinguish this isotope from others which might also be produced.

2. The cross section of the $N^{15}(\alpha,n)F^{18}$ reaction has not been measured experimentally, but the energy has been calculated as —6.41 Mev (12), *i.e.*, it is endothermic and this energy is required to drive the reaction. Therefore, taking into account the momentum correction for the participants $(15 + 4)/15$, the threshold energy for the reaction should be about 8.1 Mev. In a preliminary attempt at estimating the cross section, we have irradiated specimens of uranium nitride with 9.6-, 10.4- and 12.9-Mev α-particles and have then removed a series of parallel slices by grinding and taking counts of residual fluorine-18 activity remaining after each slice. The observed activity density increases to a peak at a point below the surface and then falls off to zero at the depth into the UN specimen where the energy of the α-particles had been reduced to 8.1 Mev (see Fig. 1). On the basis of this measurement, it appears that there is a resonance peak in the cross section between 9.5 and 10.0 Mev.

The cross section at the resonance peak can be estimated as being roughly 100 mb on the basis of the radiochemical yield of fluorine-18. The amount of activity produced in a specimen is about 3×10^5 disintegrations per minute for each minute of irradiation with a 1-μa bombardment current. Even so, during a 10-min irradiation, only about one N^{15} atom in 3×10^6 undergoes reaction, so that chemical alteration of the sample is negligible. Any further reaction between this product isotope and the bombarding α-particles can also be neglected. In a 10-min irradiation with a current of 1 μa over a square centimeter area, a generous amount of activation is obtained with a pure N^{15} target; exposures of less than a minute with Kodak Autoradiographic Plate, Type A, or 20 min with Kodak AR-10 stripping emulsion will give images of good film density. Of course, this is equally true for small amounts of tracer concentrated at a few points. More dilute tracer requires longer irradiation, and times up to about one half-life of the F^{18} may prove worthwhile.

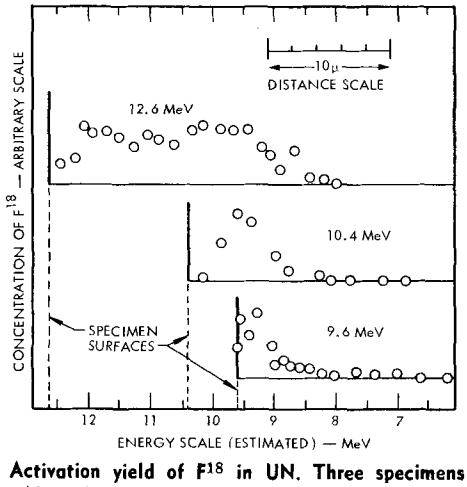

Fig. 1. Activation yield of F^{18} in UN. Three specimens of UN containing N with natural isotopic abundance were bombarded with α-particles having energies of 9.6, 10.4, and 12.6 Mev. The density of F^{18} produced from N^{15} as a function of depth below the surface was determined by sectioning the specimens. Yields are shown as a function of energy, i.e., the initial surfaces are displaced so as to align the three yield curves as a function of energy. Near-surface values are normally suspect because of slight surface roughness of about 1 μ.

3. The activation of elements other than N^{15} has not been found to be serious with most materials we have studied thus far. However, unwanted activation is more frequent than for the corresponding $O^{18}(p,n)F^{18}$ activation method mentioned above. Our usual bombardment energy of 10 Mev is relatively low as far as reactions involving α-particles are concerned, because the doubly charged α-particle must overcome the electrostatic repulsion of the target atom. This means that most reaction cross sections under our bombardment conditions should fall off quite rapidly after atomic number 40, and become negligible after number 50. Among the majority of those elements which can be activated with 10-Mev α-particles, the resultant half-lives will either be short compared with the 110-min half-life of F^{18}, so that these unwanted products can be allowed to decay away before analyzing a sample, or the half-lives are relatively long; in this case, the specific activity will be low compared with that of the F^{18}, and the autoradiographic exposures of less than a few hours will not register them strongly.

To obtain a rough measure of interferences to be expected from various elements, a number of targets have been irradiated and counted with an end-window β counter. The activities in these targets 1 hr after irradiation with 10-Mev alphas are compared in Table I with that of a pure nitrogen target of natural isotopic composition. The activation ratios have been normalized so that they correspond to equivalent irradiations. Product isotopes have been identified in most cases from an analysis of their half-lives. The activation ratios listed in Table I should be used only for rough comparison because they do not take into account such important variables as differences in sensitivity of different detectors, *i.e.*, film *vs.* counters, and the effect of target density on the depth of activation. Also, the ratio is a function of time after irradiation and, indeed, on the duration of the irradiation. In summary, it appears that there is no nitrogen compound in which nitrogen diffusion could not be studied by this activation technique, provided high enrichments, greater than about 50% of N^{15} were used.

The product neutrons carry off several Mev energy, and the secondary reactions produced by them may have to be considered in some experiments. The lowest energy neutrons produced by this reaction still have energies above 1 Mev when α bombardment energies are just above the threshold for reaction and the cross sections for most elements with such neutrons are generally small. Thus, a typical 0.1-barn cross section in a 0.3-cm-thick specimen will give 0.1% of the activity which one would obtain in a target of a nitride of pure N^{15} or 1/3 of that produced in a target of natural nitrogen composition.

4. Under ion bombardment the specimen must be protected against heating. A 10-Mev, 1-μa beam delivers 10w, or 2.4 cal/sec. Therefore, the specimen must be mounted on a cooled support. We have normally employed a water-cooled target specimen holder and have placed a thin layer of a nonvolatile, heat-resistant silicone grease between the back of our specimens and the holder as an aid to heat conduction from the specimen. On the basis of the thermal conductivity of a material such as uranium nitride, 0.17 w/cm/°C (13), having 0.3 cm thickness and an area of 1 cm^2, one would expect to impose a temperature differential of 18°C. In other materials with lower conductivities the surface temperature will be greater, and fracturing of a specimen under the temperature gradient may occur. The fact that such heating takes place in the vacuum of the cyclotron or Van de Graaff beam pipe may result in the deterioration of the specimen by vaporization or pyrolysis when less stable

Table I. Ratio of activity produced in elements under α bombardment to that produced in nitrogen of natural isotopic abundance (0.37% N^{15})

Element	Z	Remarks	Activity ratio (measured 1 hr after bombardment)
H	1		0*
He	2		0*
Li	3		0
Be	4		0
B	5	Rich yield of N^{13}, $t_{1/2}$ = 10 m.	0
C	6		0
N	7		1.00
O	8		0
F	9	Rich yield of Na^{22}, $t_{1/2}$ = 2.6 y.	0.2
Ne	10		0*
Na	11		0
Mg	12		0
Al	13	Rich yield of P^{30}, $t_{1/2}$ = 2.6 m.	0
Si	14		0
P	15	Cl^{34}, $t_{1/2}$ = 32 m, to be expected	>1*
S	16	Ar^{37}, $t_{1/2}$ = 34 d., to be expected	1*
Cl	17		0
Ar	18		0*
K	19	Good yield of Sc^{44}, $t_{1/2}$ = 3.9 h.	20
Ca	20	Good yield of Ti^{45}, $t_{1/2}$ = 3.1 h.	0.3
Sc	21	V^{48}, $t_{1/2}$ = 16 d, to be expected	<1
Ti	22	Rich yield of Cr^{49}, $t_{1/2}$ = 42 m.	40
V	23		0
Cr	24	Good yield of Fe^{53}, $t_{1/2}$ = 8.4 m.	1
Mn	25	Fair yield of Co^{58m}, $t_{1/2}$ = 9 h.	0.1
Fe	26	Fair yield of Ni^{57}, $t_{1/2}$ = 37 h.	0.1
Co	27	Fair yield of Cu^{62}, $t_{1/2}$ = 10 m.	1
Ni	28	Good yield of Cu^{61}, $t_{1/2}$ = 3 h.; Zn^{63}, $t_{1/2}$ = 38 m.	20
Cu	29	Good yield of Ga^{68}, $t_{1/2}$ = 68 m.; Ga^{66}, $t_{1/2}$ = 10 h.	30
Zn	30	Mixed products	1
Ga	31	As^{72}, $t_{1/2}$ = 26 h., to be expected	<1*
Ge	32	Some yield of Sc^{73m}, $t_{1/2}$ of 44 m.	0.3
As	33	Br^{76}, $t_{1/2}$ = 64 m., to be expected	0.0*
Se	34	Mixed products to be expected	1*
Br	35	Fair yield of Rb^{84m}, $t_{1/2}$ = 21 m.	0.3
Kr	36	Mixed products to be expected	10*
Rb	37	Y^{88}, $t_{1/2}$ = 105 d, to be expected	0.01*
Sr	38	Mixed products to be expected	0.1*
Y	39		.00
Zr	40	Small yield of Mo^{93m}, $t_{1/2}$ = 6.9 h.	0.01
Nb	41	Fair yield of Tc^{96m}, $t_{1/2}$ = 52m.	0.01
Mo	42	Small yield of Ru^{95}, $t_{1/2}$ = 1.7 h.	0.05
Tc	43		—
Ru	44	Mixed products to be expected	1*
Rh	45	Good yield of Ag^{106m}, $t_{1/2}$ = 24 m.	5
Pd	46	Fair yield of Cd^{105}, $t_{1/2}$ = 55 m.; Cd^{107}, $t_{1/2}$ = 6.7 h.	0.2
Ag	47	Mixed products	0.2
Cd	48	Mixed products	0.05
In	49	Sb^{118}, $t_{1/2}$ = 5 h., to be expected	1*
Sn	50	Mixed products	0.03
....	....		....
Hf	72	Activities probably due to impurities	0.01
Ta	73		0.05
W	74		0.05
Re	75		0.05

* Estimated ratios not based on actual measurements.

compounds are studied. Protective foil coverings are possible, provided the beam energy is boosted to compensate for its energy degradation in the foil. This procedure may give unwanted neutrons, however.

5. The excess energy of the nuclear reaction, that is, the bombardment energy minus 6.41 Mev, appears afterward as kinetic energy of the two products. It is divided between the F^{18} atom and the neutron roughly in the ratio 1:18, depending on the directions in which they recoil. The few hundred kilovolt F^{18} recoil distance will be less than a few tenths of a micron in typical solids (14), a distance smaller by at least a factor of ten than the resolving power of standard autoradiographic techniques.

It should be recognized that the F^{18} may be able to diffuse in the target material at the temperature to which it is heated in the beam. We have not checked this in the case of F^{18} in UN, but it seems improbable that diffusion over measurable distances will occur at temperatures below the few hundred degrees to which a specimen may be heated if a 10-μa beam is used or if the specimen is not perfectly cooled.

6. Although the most sophisticated autoradiography which makes use of the electron microscope to examine the photographic emulsion may give resolutions of the order of 0.1μ (15), resolutions of little better than 10μ can normally be expected with commercially available stripping films (16, 17).

7. The α-particle beam may not be homogeneous over the 1 cm^2 circular target area which we generally employ. However, the shape of the beam normally remains fairly constant with time and the beam homogeneity can be checked with a fluorescent quartz disk (available in many irradiation facilities). Alternatively, a standard target having a uniform distribution of N^{15} may be irradiated and autoradiographed to serve as a reference against which other specimens can be compared. Then the concentration of N^{15} at one point can be related to that at another in a straightforward way if the material is chemically and physically homogeneous. For determining the amount of nitrogen in solution in a specimen the absolute amount of bombardment must be known, and the total charge of α particles injected can usually be measured within a few per cent by current integration.

One precaution which should be observed in ion bombardment activation is to check the effect of crystal orientation. The bombarding ions travel in closely parallel paths, and entry into a crystal along certain low-index crystallographic directions may permit channeling through lines of interstitial sites which do not block the ions in the usual way (18). The activation in such cases might be expected to be significantly different from that in randomly oriented crystals.

A unique feature of ion bombardment activation is that, unlike neutron or γ-activation, the nuclear reactions take place within a region close to the surface rather than throughout the volume of the specimen. The range of penetration of 10-Mev α-particles in UN may be 25μ, but they only have sufficient energy to induce the reaction with N^{15} to a depth of about 9μ (Fig. 1). If the target specimen were to be mounted so that a beam strikes the surface at a shallow or grazing angle, the depth of activation could easily be reduced to about 1μ.

Production of such a thin active layer can serve the same purpose as does the thinning of metallurgical specimens before an autoradiograph is taken, and makes it possible to achieve maximum resolution of features of activity at or near the surface (19). The distance within which a flux of F^{18} positrons in UN would drop to $1/e$ would be close to 100μ. Therefore, if F^{18} were present throughout the sample, subsurface activity would tend to obscure surface details. In thicknesses of a few microns, on the other hand, the flux from one point as measured at another on the surface falls off as the reciprocal of distance squared. Therefore, ion bombardment activation combined with autoradiography can almost be thought of as metallographic technique for looking at details of a surface. This can be important in measuring the diffusion coefficient if the mean penetration of N^{15} is small. Variations in activity as revealed from densitometer scans of the autoradiograph can then be related to variations in surface concentration of the N^{15} tracer. The photographic emulsion can be calibrated by making a series of different exposures with the same sample so that the characteristic curve, *i.e.*, the optical density of the film *vs.* exposure time, can be used to translate film density into specimen activity.

Discussion of Applications

We have been applying these techniques in the study of the diffusion of nitrogen in uranium mononitride. In our exploration of the use of this activation technique we have used UN, because (*a*) its preparation and properties have been described (13); (*b*) it is suitable for our purposes because it is available in dense, coarse-grained form; (c) there are no competing reactions under our α bombardment energies; and (*d*) the rate of diffusion of nitrogen in the material has been measured previously by gas exchange (20).

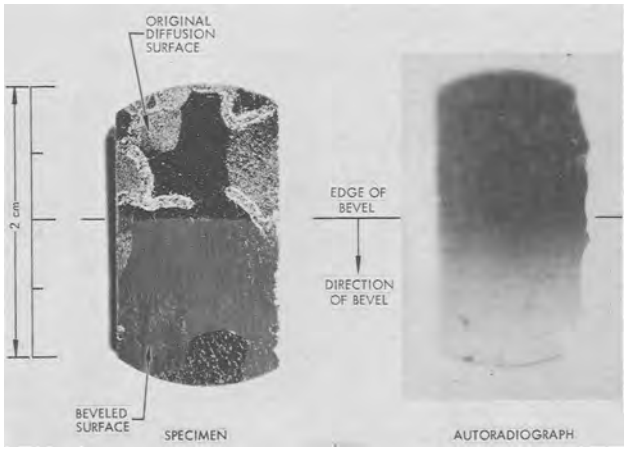

Fig. 2. Beveled UN and autoradiograph. A specimen after a diffusion anneal in enriched N^{15} gas as described in the text was beveled, the surface irradiated with α-particles, and an autoradiograph taken. Note the decreased concentration of N^{15} with depth below the original surface as revealed in the autoradiograph. Note, also, the preferential diffusion along grain boundaries.

Specimens were prepared by hot-pressing UN, obtained by arc-melting metallic uranium in a nitrogen atmosphere. The material had a density about 97% of theoretical, and average grain diameter of about 2 mm. Porosity visible under the microscope was confined mostly to grain boundaries (see Fig. 2), and there did not seem to be many open connecting pathways between the pores. The specimen surfaces were ground flat and parallel, and one surface was polished through 4/0 emery paper. The sample was then annealed in an atmosphere of nitrogen enriched to 35% N^{15} at a pressure of 129 Torr for 23.6 hr at 1792°C.

After this diffusion anneal, the specimen was prepared for irradiation by grinding a shallow bevel on the previously polished surface of the material, so as to spread out the view of the region below the original interface as one scans away from the intersection of the bevel plane with the original surface plane. In the specimen shown (Fig. 2), this was a 16-μ increase in depth per millimeter of traverse. The specimen was then irradiated for 40 min in a 1.0-μa beam of 10-Mev α-particles. Within an hour after irradiation an autoradiograph was taken, with a 6-min exposure on autoradiographic plate type A (Eastman Kodak Co.). This autoradiograph shows the activity due to F^{18}. The activity, which can be taken proportional to the N^{15} concentration at the surface, falls off from the original diffusion interface as shown in the densitometer trace (Fig. 3). Comparison with the grain structure (Fig. 2) shows that this corresponds to bulk penetration of the nitrogen. On the basis of the anneal time and the penetration as determined from the calibration of this autoradiograph, the diffusion coefficient of N in UN at 1792°C is approximately 8.1 x 10^{-11} cm²/sec. This is smaller than the value measured by Sturiale and De Crescente (20) who monitored the isotopic content of the gas phase as it exchanged with a UN specimen by diffusion. The apparent discrepancy between the two sets of measurements will not be discussed here, since our diffusion work will be reported in detail at a later time. However, it is possible that grain-boundary diffusion may have been an important but neglected factor in the earlier study. It can be seen in Fig. 2 that enhanced penetration has occurred at the boundaries. Some of the rapid diffusion paths are actual cracks while others appear to be microscopically sound boundaries. Apart from trying to decide at this time the exact nature of the preferred paths of penetration, the importance of this observation to the present discussion is that such paths can be made apparent by this activation and autoradiographic detection technique.

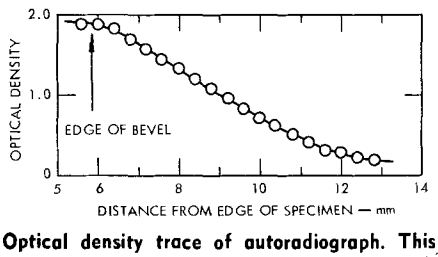

Fig. 3. Optical density trace of autoradiograph. This measurement of the optical density of the autoradiograph, Fig. 2, was obtained in the direction of the bevel. From this, a calibration of the film density in terms of activity and a relationship between distance along the surface of the specimen and depth below the original diffusion interface (16μ increase in depth per mm of traverse) it is possible to obtain the N^{15} penetration profile.

The N^{15} activation procedure may also find other applications. It can serve as an analytical tool for determining nitrogen in solids due to the 0.37% of N^{15} present in the natural element. Of course, this is only possible for those materials for which the activity ratio (Table I) is not much greater than 1.0, or unless the half-lives are clearly separable. Even the high Z elements, for which this method is attractive, are likely to contain impurities which could give a mixed yield of half-lives, thereby obscuring the F^{18} activity. However, taking a favorable element, hafnium, with an apparent activity ratio of 0.01, it would appear possible to detect 1% natural nitrogen. If one wished to carry out solubility studies using 100% N^{15} it should be possible to detect about 40 ppm N.

For the purpose of identifying nitride inclusions in a metal it is necessary that the irradiation be followed by taking an autoradiograph on the specimen. This should prove successful if

$$\frac{E\,d^2}{RS^2} > 1$$

where E is the atomic fraction of nitrogen in the inclusion (normally about 0.5), d is the diameter of the inclusion, R is the activation ratio, and S is the minimum distance resolvable by the film. With films having resolutions of 10μ it should therefore be possible to identify nitride particles in hafnium having diameters of 1-2μ, provided they are separated by distances greater than the film resolution. This is a sensitivity which is comparable with standards achieved with the electron beam microprobe. If studies were to be carried out with enriched N^{15} and high-resolution autoradiographic techniques, much greater sensitivity and resolution would be possible.

Conclusion

The activation reaction, $N^{15}(\alpha,n)F^{18}$ appears to have significant potential value in the study of nitrogen self-diffusion in nitrides and other solids, for the identification of nitride inclusions in a number of materials, and the analysis for nitrogen in solids. The ion bombardment with α-particles can be designed to yield activity within a micron of the surface of a specimen, and therefore this activation, when coupled with autoradiography of the irradiated surface, can serve as a technique for resolving features of the distribution of the nitrogen-15 tracer.

Acknowledgments

The authors are indebted to Dr. Charles Engelmann at the Center for Nuclear Studies, Saclay, France, for suggesting the use of the α activation of N^{15}. The irradiations were carried out with the staff of the 90-in. cyclotron at the Lawrence Radiation Laboratory, Livermore. Mr. Frank Vanderhoofven and Mrs. Marcia Almassy carried through several of the experimental steps.

This work was performed under the auspices of the United States Atomic Energy Commission.

Manuscript received May 15, 1967.

Any discussion of this paper will appear in a Discussion Section to be published in the June 1968 JOURNAL.

REFERENCES

1. L. A. Simpson and R. E. Carter, *J. Am. Ceram. Soc.*, **49**, 139 (1966).
2. R. Gibala and C. A. Wert, in "Diffusion in Body-Centered Cubic Metals," Metals Park, Ohio (1965).
3. M. Eisenstadt and A. G. Redfield, *Phys. Rev.*, **132**, 635 (1963).
4. R. H. Condit and J. B. Holt, *This Journal*, **111**, 1192 (1964).
5. J. B. Holt and R. H. Condit, in "Materials Science Research," Vol. 3, p. 13-29. W. W. Kriegel and Hayne Palmour III, Editors, Plenum Press, New York (1966).
6. D. R. McKenzie, Influence of Iron on Oxygen Grain Boundary Diffusion in Periclase Crystals (1965). Report UCRL-14215, Lawrence Radiation Laboratory, Univ. of California, Livermore.
7. J. B. Holt, To be published in *Materials Science Research*, Vol. 4.
8. L. Himmel and J. B. Holt, Abstract Bull. Institute of Metals Div., AIME, **1(2)**, 38 (1966).
9. R. N. Goshtagore, *Phys. Rev. Letters*, **16**, 890 (1966).
10. R. S. Tilbury, "Activation Analysis with Charged Particles," Nat. Acad. Sci.-Nat. Research Council, Nuclear Science Series, NAS-NS3110. (1966) (Available from Clearinghouse for Federal Scientific and Technical Info., NBS, U.S. Dept. Commerce, Springfield, Va.).
11. J. D. Mahony and S. S. Markowitz, *J. Inorg. Nucl. Chem.*, **26**, 907 (1964).
12. V. J. Ashby and H. C. Catron, "Tables of Nuclear Reaction Q Values," ASAEC Report UCRL-5419 (1959). Available from OTS, Dept. of Commerce, Washington, D. C.
13. R. W. Endebrock, E. L. Foster, Jr., and D. L. Keller, Battelle Memorial Institute Report BMI-1690, Preparation and Properties of Cast UN, (1964).
14. B. G. Harvey, in "Annual Review of Nuclear Science," Vol. 10, p. 235-258 (1960).
15. C. B. Gilpin, D. H. Paul, S. K. Asunmaa, and N. A. Tiner, in "Advances in Electron Metallography," Spec. Tech, Publ., p. 396, Amer. Soc. Testing Materials (1966).
16. R. H. Herz, *Lab. Investigation*, **8**, 71 (Jan.-Feb. (1959).
17. R. G. Ward, in "The Physical Examination of Metals," B. Chalmers and A. G. Quarrel, Editors, p. 825-852, Edward Arnold, London (1962).
18. B. W. Farmery, R. S. Nelson, R. Sizmann, and M. W. Thompson, *Nuclear Instruments and Methods*, **38**, 231 (1965).
19. F. Barigozzi and P. L. Lensi, La Metallurgia Italiana, **55**, 129 (1963). (Available in English translation, NP-TR-1150, U.K.A.E.A., Harwell, England.)
20. T. J. Sturiale and M. A. DeCrescente, Pratt-Whitney Aircraft Co., Middletown, Conn. Report PWAC-477 (1965).

Impurity Effects in the Pre-Electrolysis of Caustic Electrolytes

Paul Malachesky, Raymond Jasinski, and Brian Burrows

Tyco Laboratories, Inc., Waltham, Massachusetts

ABSTRACT

Pre-electrolysis is a common purification technique for aqueous solutions. However, detectable quantities of dissolved anode metal are found in caustic electrolytes, if one of the pre-electrolysis electrodes is allowed to reach the oxygen evolution potential. The reduction of O_2 on oxidized cadmium and the displacement of the H_2 evolution potential on gold are useful tests for this phenomenon. Holding the Pt anode at +500 mv (*vs.* DHE) or less prevents dissolution. Significant purification is accomplished on a high surface area platinum fuel cell electrode held $\leq$ +300 mv (*vs.* DHE). Some of the impurities adsorbed by the electrode are desorbed at +500 mv. In the purified electrolyte little activity for oxygen reduction was found on oxidized cadmium; the reaction on reduced cadmium is diffusion limited.

It is well established that aqueous solutions of high purity must be employed when studying charge transfer processes on smooth electrodes. A common *in situ* purification technique is pre-electrolysis between "inert" noble metal electrodes, primarily platinum. The beneficial effects of this technique on the H_2 oxidation reaction on platinum has been recently discussed in some detail by Kronenberg (1). This approach to purification is not without its pitfalls, however. Although impurities are indeed removed, it is also possible simultaneously to contaminate the electrolyte. Such effects have been observed, for example, by Giner (2) in acid solutions. This paper discusses a similar contamination problem in caustic electrolytes, particularly with regard to the oxygen reduction reaction on cadmium.

Experimental

2*N* KOH was made up from Baker Analyzed Reagent pellets and triply distilled water. Most of the electrolysis experiments were carried out in an L&N coulometry cell (No. 7961). This cell had a Teflon cover which was attached to a 100 ml Pyrex tall-form beaker by a polyethylene ring. Openings of various sizes in the cell cover allowed the insertion of electrodes and a gas bubbling tube. A 100 ml capacity cell, with ground glass connections, was used for experiments requiring more efficient exclusion of atmospheric impurities. Argon was used to purge the system; the residual oxygen concentration in the gas was given by the manufacturer as 0.1-0.5 ppm. All potentials were measured *vs.* the dynamic hydrogen electrode (DHE) (3). The DHE electrodes were enclosed in a glass shield. This device successfully inhibited diffusion of soluble platinum from the anode of the DHE couple to the test electrode.

A Wenking potentiostat was used to obtain current-time curves. For the galvanostatic charging experiments, the potential step sequence for the electrode cleaning was obtained from the "set" and "output"

positions of a laboratory constructed, step function generator. Switching from potentiostatic to galvanostatic operation was carried out with a mercury relay (Potter-Brumfield). A battery pack (90v) with appropriate resistors was used to supply the constant current pulse. Potential-time curves were photographed on a Tektronix Type 651A oscilloscope equipped with a Type 2A63 differential amplifier and a Type 2B67 time base.

Purity monitoring techniques.—The purity monitoring techniques can be broadly classified into two categories: (*i*) methods which are sensitive to the presence of electroactive organic compounds, dissolved oxygen, and heavy metal ions, and (*ii*) methods which are selectively sensitive to the presence of trace noble metals.

In the first category are the following: (*a*) residual currents, (*b*) the stability of hydrogen oxidation on platinum, (c) the stability of O_2 reduction on platinum or gold, and (*d*) galvanostatic charging. The residual, or background current method is probably the least sensitive; furthermore, it is affected by residual oxygen, which is not of particular concern in this study. The H_2 oxidation method has been described by Kronenberg (1); the O_2 reduction method is similar in concept. A recent paper indicated that organic rather than inorganic impurities altered the oxygen reduction activity of a noble metal probe electrode (4).

The galvanostatic charging method (5-9) assumes the formation of a monolayer of atomic hydrogen (or oxygen) on a platinum electrode before molecular hydrogen (or oxygen) is evolved. The predominant face on polycrystalline platinum is the (100) plane which adsorbs 1.3 x 10^{15} atoms/cm^2 or 210 μcoulombs/cm^2 in the deposition of a monolayer of H atoms or 420 μcoulombs for a monolayer of O atoms. In the presence of an absorbate, these sites are "poisoned," and the charge required for the formation of the Pt-H monolayer (Q_H) or the Pt-O monolayer (Q_O) decreases in proportion to the surface coverage. In addition, if the absorbate itself is oxidizable, it can cause an apparent increase in Q_O.

The two methods used to detect the presence of trace noble metals are based on (*a*) O_2 reduction on cadmium and (*b*) H_2 evolution on gold. The cadmium was used as a rotating disk electrode in a solution saturated with oxygen. These results are discussed in detail below.

Results and Discussion

It was observed that pre-electrolysis of 2*N* KOH at *ca.* 10 ma/cm^2, in the usual manner (1, 10) removed impurities as judged by the monitoring techniques described above. However, it was also found that O_2 reduction activity was induced on an oxidized cadmium electrode. Curve A of Fig. 1 is a slow sweep (100 mv/min) cyclic voltammogram of such an electrode immersed in a nitrogen-saturated solution; curve B is for an oxygen saturated solution. Negligible activity for the reduction of oxygen at positive potentials was obtained; the reaction on cadmium metal is diffusion limited. Pre-electrolysis with Teflon-bonded platinum fuel cell electrodes led to a substantial increase in O_2 reduction activity on oxidized cadmium (Fig. 2).

This activated cadmium electrode was then removed from solution, washed thoroughly with distilled water, and placed in fresh, nonelectrolyzed electrolyte saturated with oxygen. The results were identical to those shown in Fig. 2. Thus the electrode had been permanently altered by the pre-electrolysis procedure. The same phenomenon was observed when palladium, gold, or silver were used as pre-electrolysis electrodes, but not when cadmium itself was used. Traces of platinum and silver added to the electrolyte in the form of chloroplatinic acid or silver oxide also induced oxygen reduction activity.

Another technique sensitive to the presence of trace platinum is the potential of the H_2 evolution reaction

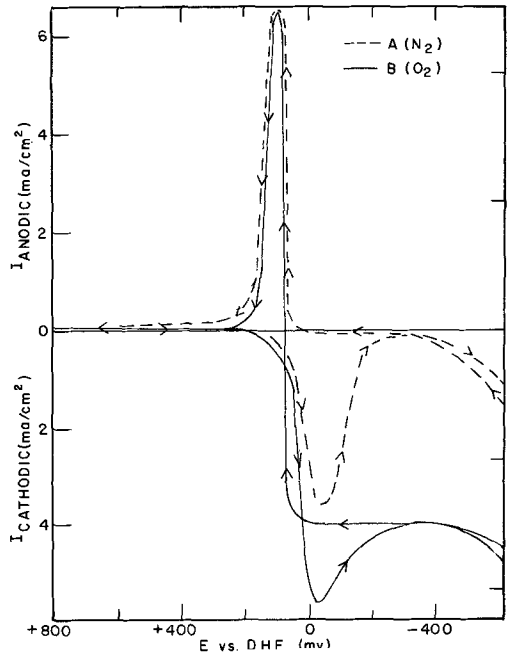

Fig. 1. Cyclic voltammograms (100 mv/min) of a rotating cadmium disk electrode in nonpre-electrolyzed 2*N* KOH under N_2 (curve A) and O_2 (curve B).

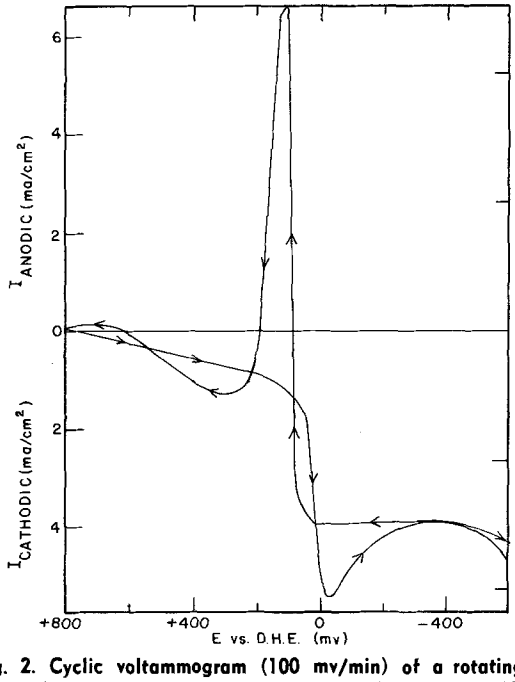

Fig. 2. Cyclic voltammogram (100 mv/min) of a rotating cadmium disk electrode in Pt electrode pre-electrolyzed 2*N* KOH under O_2.

on gold. Brummer (11) has observed, when working with acid solutions, that if a platinum counter electrode was used in conjunction with a gold working electrode, the gold electrode became covered with what appeared to be a monolayer of platinum. Giner has observed similar effects in studies of H_2 oxidation on gold in dilute acid (2). Apparently the same phenomenon can take place in aqueous caustic. Figure 3 shows results for hydrogen evolution on gold before and after pre-electrolysis with platinum. There is little doubt that trace noble metals can be introduced into a caustic electrolyte after conventional pre-electrolysis. However, as will be shown, this effect is potential dependent and, if proper precautions are ob-

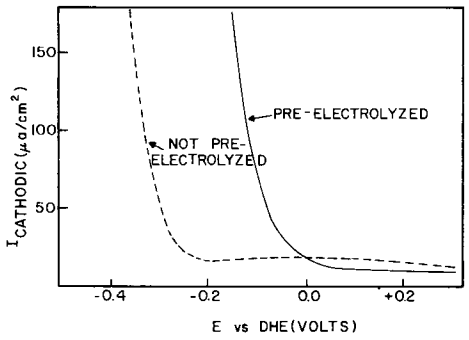

Fig. 3. Variation of the potential of H_2 evolution on a gold electrode in Pt-electrode pre-electrolyzed and nonpre-electrolyzed 2N KOH.

served, significant purification can be obtained without simultaneous contamination.

High surface area, electroplated platinum electrodes have often been used for pre-electrolysis. Teflon-bonded platinum fuel cell electrodes are more convenient and were used in the experiments described below. Some success has been achieved with this configuration in acid electrolytes as well (2).

The specific criteria of purity were the stability of the H_2 oxidation reaction on platinum in 2N KOH and the value of Q_H as a function of time. The criteria for contamination of the solution by dissolved platinum was the activity of anodized cadmium electrode toward oxygen reduction. The platinum test electrode was a wire of fixed area; the same electrode was used throughout the experiments reported below. Its real area, based on 210 μcoul/cm^2 for Q_H, was approximately 0.25 cm^2.

In an unpurified solution the value of Q_H on the probe is as shown in Table I. The test electrode was first cleaned by holding at +1.35v and taken to the potential of interest. The oxide formed at +1.35v is reduced within the first 10 msec. After holding for the time specified, the electrode is pulsed to hydrogen evolution and the quantity of hydrogen deposited on the surface during this pulse computed.

Purification was first carried out with a platinum fuel cell electrode at approximately +1200 mv *vs.* DHE. Although the solution was purified, this procedure was unacceptable because significant noble metal contamination took place as judged by oxygen reduction on oxidized cadmium. The effectiveness of purification at less positive potentials was then explored.

The platinum fuel cell electrode was taken to +300 mv and held for 24 hr to allow adsorption of impurities. A cathodic current was observed during this time. The palladium counter electrode, previously charged with hydrogen, was at +500 mv, where presumably the oxidation of adsorbed hydrogen took place. The quantity of hydrogen then adsorbed on the platinum probe at +300 mv was 38.5 ± 1.2 μcoul at t = 3 sec and 32.7 μcoul at 300 sec. Thus considerable improvement on the untreated solution was noted. Trace noble metals were not present as indicated by the Cd/O_2 test. A triangular voltage sweep on a cadmium electrode operated in the purified electrolyte gave curves essentially as shown in Fig. 1.

Table I. Platinum in untreated 2N KOH at 25°C

E of adsorption (mv *vs.* DHE)	Q_H* (μcoul)
+500	35.9
+400	23.0
+300	17.3
+200	9.7

* Measured with t_{adsp} = 3 sec.

Table II. Platinum charging in purified 2N KOH at 25°C

t (sec) at +300 mv	Q_H (μcoul)
2	45.5
5	44.6
10	40.3
30	41.4
60	
120	39.8
300	39.2
	$\overline{Q_H}$ ave = 41.3 ± 1.6

Considerable purification can in fact be achieved without pre-electrolysis. A platinum black electrode immersed in the solution will adsorb impurities extensively as shown by the following results. A Teflon-bonded fuel cell electrode was immersed in a hydrogen saturated, 2N KOH solution for 24 hr. The dissolved hydrogen maintained the electrode potential at +55 mv *vs.* DHE. Cathodic galvanostatic charging curves were then carried out on the platinum wire probe and Q_H determined for E = +300 mv *vs.* DHE. The results are shown in Table II. The current-time curves for the oxidation of H_2 on the probe in untreated electrolyte and after purification by adsorption on Pt are shown in Fig. 4. Obviously, a significant amount of impurity has been removed from the electrolyte.

The same fuel cell electrode was then held potentiostatically at +500 mv for 24 hr in the purified solution now saturated with argon. A small anodic current was observed; the Pt counter electrode was at +35 mv *vs.* DHE. After this period Q_H on the probe at t = 300 sec was 24 ± 0.5 μcoul, a marked decrease from its previous value of 39.2 μcoul. Thus, some of the impurities adsorbed by the platinum electrode can apparently be desorbed at +500 mv.

Summary

The presence of trace platinum in the electrolyte induces O_2 reduction on cadmium hydroxide and decreases the overpotential for H_2 evolution on gold. Conventional pre-electrolysis between platinum, palladium, gold, or silver electrodes introduces detectable quantities of metals into a 2N KOH electrolyte. Noble metal dissolution occurs at high positive potentials; it can be avoided by holding the platinum electrodes at lower potentials. At 500 mv, dissolution does not take place but there is no purification. At ≤300 mv, there is no dissolution and considerable purification of the caustic solution.

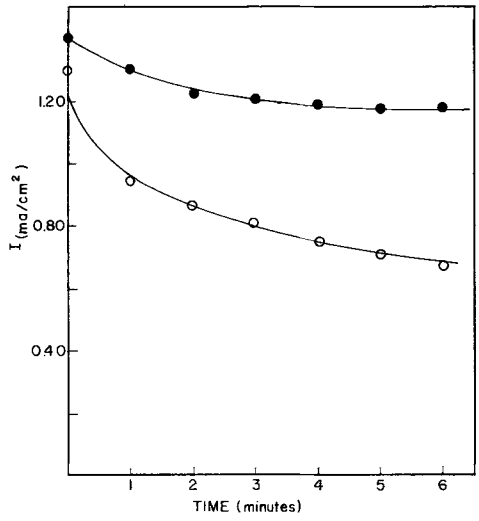

Fig. 4. Time dependence of the H_2 oxidation current in the activation-controlled region in untreated (○) and "adsorption" purified (●) 2N KOH.

An oxidized cadmium electrode in a purified, 2*N* KOH electrolyte is not active for O_2 reduction. Oxygen reduction on Cd metal is diffusion limited.

Acknowledgments

The authors wish to acknowledge the helpful suggestions of Dr. J. Giner, the assistance of Miss Susan Carroll, and the support of the U.S. Navy Air Systems Command (NOw 66-0621-c).

Manuscript received July 7, 1967.

Any discussion of this paper will appear in a Discussion Section to be published in the June 1968 JOURNAL.

REFERENCES

1. M. L. Kronenberg, *J. Electroanal. Chem.*, **12**, 122 (1966).
2. J. Giner, Private communication.
3. J. Giner, *This Journal*, **111**, 376 (1964).
4. A. Damjanovic, M. A. Genshaw, and J. O'M. Bockris, *ibid.*, **114**, 466 (1967).
5. S. B. Brummer and J. I. Ford, *J. Phys. Chem.*, **69**, 1355 (1965).
6. S. B. Brummer, J. I. Ford, and M. J. Turner, *ibid.*, **69**, 3424 (1965).
7. A. Hickling, *Trans. Faraday Soc.*, **41**, 333 (1945).
8. J. Butler, "Electrical Phenomenon at Interfaces," Macmillan Co., New York (1951).
9. A. Slygin and A. Frumkin, *Acta Physiochim. USSR*, **3**, 791 (1935).
10. A. Damjanovic, A. Dey, and J. O'M. Bockris, *Electrochim. Acta*, **11**, 791 (1966).
11. S. B. Brummer, *This Journal*, **112**, 633 (1965).

The Mechanism of Oxygen Reduction at Platinum in Alkaline Solutions with Special Reference to H_2O_2

A. Damjanovic, M. A. Genshaw, and J. O'M. Bockris

The Electrochemistry Laboratory, The University of Pennsylvania, Philadelphia, Pennsylvania

ABSTRACT

A rotating disk electrode with a concentric ring has been used to determine the role of hydrogen peroxide in the reduction of oxygen at platinum electrodes in alkaline solution. Oxygen reduction proceeds along two parallel reaction paths with comparable rates. In one of the paths, hydrogen peroxide is a reaction intermediate which is partially reduced to water. In the other, oxygen reduces to water without hydrogen peroxide as an intermediate. In the path with hydrogen peroxide intermediate, the first part of the probable sequence of reaction steps is shown to be

$$O_2 + e^- \rightleftarrows O_2^-$$

$$O_2^- + H_2O \rightarrow HO_2^- + OH$$

$$OH + e^- \rightleftarrows OH^-$$

The peroxide anion is thereafter reduced to water in a path which does not involve an electron transfer before or in the rate-controlling step. Possible paths for oxygen reduction to water without peroxide intermediates are discussed in the light of already proposed mechanisms for the reduction at prereduced and preoxidized electrodes.

It has often been reported that H_2O_2 is formed in O_2 reduction at platinum electrodes in alkaline solutions (1-12). It was not clear, however, whether H_2O_2 is an intermediate in a reaction path and reduces further to water or a product in a reaction path parallel to that in which oxygen is reduced to water without hydrogen peroxide as an intermediate. The rotating disk electrode with a concentric ring proved to be suitable for detecting H_2O_2 formed in a reaction path (13). Using a diagnostic equation, which was previously developed to distinguish between reaction intermediates and products in a parallel reaction (14), it has recently been shown that in oxygen reduction at oxide free platinum in acid (H_2SO_4) solution no H_2O_2 forms either as a reaction intermediate in the over-all reduction to water or as a product in a parallel path, providing the solution is sufficiently "pure" and electrode potential is anodic to 0.15v in respect to the hydrogen electrode in the same solution. In impure or in insufficiently purified solution H_2O_2 is formed in a reaction path parallel to that in which oxygen is reduced to water without H_2O_2 as an intermediate (15).

In this paper, the role of H_2O_2 in the reduction of oxygen at Pt electrodes in alkaline solution is analyzed. The mechanism of O_2 reduction is discussed in the light of the available experimental data.

Experimental

The cell is shown in Fig. 1. It is the same cell used in a previous study (15). It consists of a spherical main compartment with a side compartment for a hydrogen reference electrode. Between experiments the cell was washed with a mixture of HNO_3 and H_2SO_4. The details of the cell and of the rotating disk electrode with the concentric ring are given in a previous paper (15).

KOH solutions (0.1*N*) were prepared from Baker Analyzed Reagent grade KOH and conductance water. Solutions were not purified by electrochemical means as no time dependent effects on electrodes were observed attributable to the residual impurities in the solutions. This is a notable contrast to the behavior in sulfuric acid solutions where the current is strongly time dependent (15).

The electrode was washed with acetone, conductance water, concentrated sulfuric acid, and again with conductance water. To remove $SO_4^=$, the electrode was then immersed for 15 min in the KOH solution used

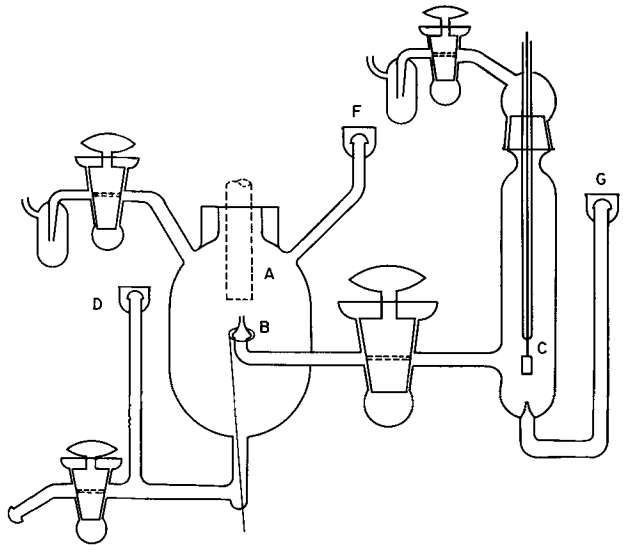

Fig. 1. Drawing of the cell: A, position of the rotating disk electrode; B, counter electrode and Luggin capillary; C, reference electrode; and D, F and G, gas inlets.

in the measurements. Measurements were taken by increasing electrode potentials in steps starting from 0.00v at which potential[1] the electrode was kept for 1 min before the measurement. These electrodes are called here prereduced. In some experiments, measurements are taken by decreasing electrode potential in steps starting from the rest potential (not prereduced electrodes).

Electrical circuit and the procedure of measurements were the same as described in an earlier paper (15). For any given potential of the disk electrode, currents both at the disk and the ring electrodes were measured. To ensure that all hydrogen peroxide which diffuses from the disk electrode to the ring electrode is oxidized and hence detected, the ring electrode is kept at 1.4v.

Results

Potential-current relationships are shown in Fig. 2. At high potentials, Tafel slope is close to 0.06v either for prereduced or not prereduced electrodes. The same value of the slope was previously reported by other workers (2, 5, 10, 16, 17). The average exchange current density from 6 measurements is 5 x 10^{-11} amp/cm^2.

A second Tafel region with a slope of $2RT/F$, which has not previously been reported in alkaline solution, appears at more cathodic potentials. To eliminate the effect of mass transfer so that Tafel lines at higher current densities can be obtained, plots (18) of $1/J$ *vs.* $\omega^{-1/2}$ were extrapolated to $\omega \to \infty$. Here, ω is the rate of disk rotation, and J is the total (current) flux of oxygen reacting at the electrode. To make this plot, the flux of oxygen is obtained from measured currents at the disk and ring electrodes.

The flux to the disk electrode is given by

$$J = I_1 + I_2 + I_3 + I_4 \qquad [1]$$

where I_1 is the partial current due to the reduction of oxygen to water in the path without peroxide intermediate, I_2 is the partial current due to the reduction to hydrogen peroxide, I_3 is the partial current for the further reduction of hydrogen peroxide to water, and I_4 is the flux of hydrogen peroxide, expressed as current, which diffuses away from the disk electrode. Now, with (14)

$$I_1 + I_2 + I_3 = I_d \qquad [2]$$

and with (14)

$$I_4 = I_r/N \qquad [3]$$

the flux to the disk electrode becomes

$$J = I_d + I_r/N \qquad [4]$$

Here I_d is the current at the disk electrode, I_r is the current at the ring electrode, and N the geometric factor of the electrode which depends on the radii of the disk and ring electrodes (19, 20).

The linearity of the $1/J$ *vs.* $\omega^{-1/2}$ plot (Fig. 3) with the slope predicted from the mass transfer considerations (18), indicates that the reaction is first order in oxygen.

In Fig. 4 and 5, the dependence is given of I_d/I_r *vs.* $\omega^{-1/2}$ for the prereduced electrodes. For a given electrode potential, I_d/I_r is linearly dependent on $\omega^{-1/2}$. In the potential range 0.30-0.60v, the slopes of the I_d/I_r lines increase with increasing potential. Above about 0.60v, they decrease. The intercept of these lines with the I_d/I_r axis cluster around the value of 10 (*cf.* Fig. 4 and 5).

The dependence of I_d/I_r on $\omega^{-1/2}$ for the not prereduced electrodes at potentials cathodic to about 0.65v is basically the same as for the prereduced electrodes. The intercepts with the I_d/I_r axis are again close to

[1] All potentials are given with respect to the reversible hydrogen electrode in the same solution.

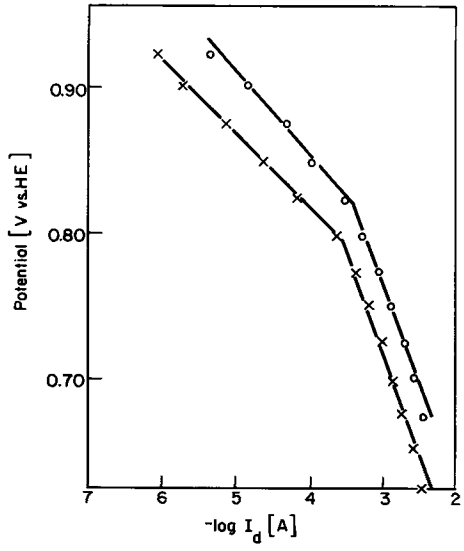

Fig. 2. Current at the disk electrode. o, prereduced Pt electrode; x, not prereduced Pt electrode. The area of the disk electrode is 0.18 cm^2.

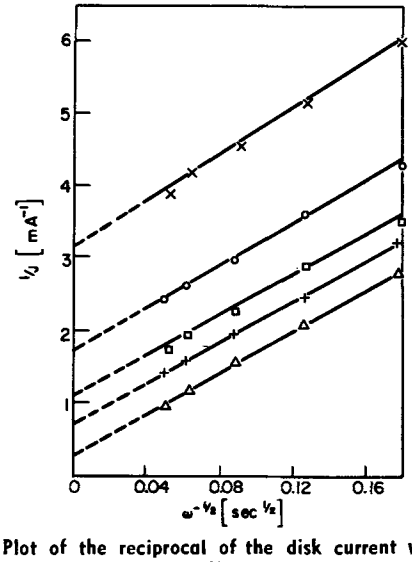

Fig. 3. Plot of the reciprocal of the disk current *vs.* reciprocal of the rate of disk rotation, $\omega^{-1/2}$. Potential of the disk electrode: x, 0.875v; o, 0.800v; □, 0.775v; +, 0.750v; and △, 0.725v (*vs.* HE).

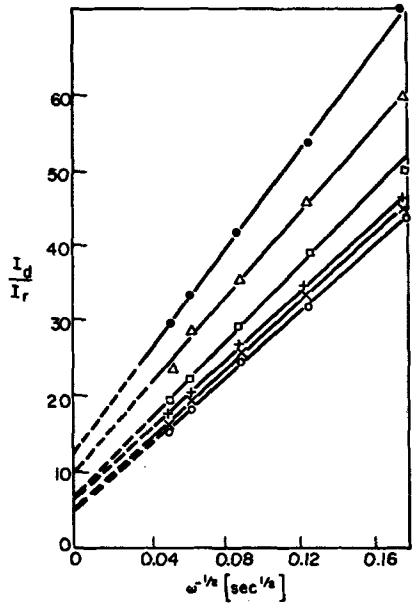

Fig. 4. Plot of I_d/I_r *vs.* $\omega^{-1/2}$. Potential of the disk electrode: x, 0.35v; o, 0.40v; +, 0.45v; □, 0.50v; △, 0.55v. and •, 0.60v (*vs.* HE). Electrode is prereduced.

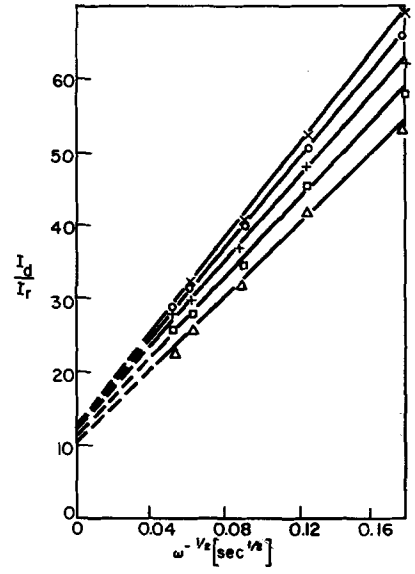

Fig. 5. The same as in Fig. 4. x, 0.62v; o, 0.65v; +, 0.67v; □, 0.70v; and △, 0.725v (*vs.* HE).

10. At higher potentials (Fig. 6), the intercepts are less than 10.

Discussion

It is possible to distinguish whether in the electrode reduction of oxygen, hydrogen peroxide is an intermediate in a single reaction path, or it is a product in a path parallel to the main path in which oxygen is reduced to water without hydrogen peroxide as an intermediate. For this distinction the equation (14)

$$\frac{I_d}{I_r} = \frac{x+1}{N} + \frac{x+2}{N}\,\frac{1.61\,k_3\nu^{1/6}}{D^{2/3}\,\omega^{1/2}} \qquad [5]$$

is used. In this general equation, I_d and I_r have the same meanings as given above, N is a calculable geometric factor for the given electrode assembly (19, 20), k_3 is the rate constant for the further reaction of an intermediate at the disk electrode, ν is the kinematic viscosity, and D is the diffusion coefficient of the intermediate. The ratio of the current at the disk electrode due to the reaction which does not result in the

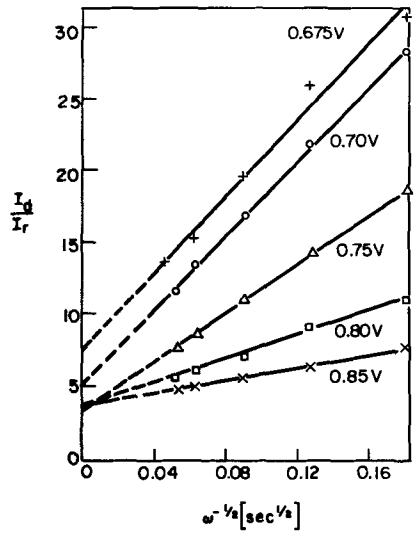

Fig. 6. Plot of I_d/I_r *vs.* $\omega^{-1/2}$. Pt electrode is not prereduced. Potentials of the disk electrode are marked in the figure.

formation of intermediates, to the current at the same electrode due to the formation of intermediates is given by x. From the intercept of an I_d/I_r *vs.* $\omega^{-1/2}$ line with the I_d/I_r axis, x can be obtained. From the slope of this line, k_3 can be calculated.

For oxygen reduction, the intercept of straight lines in the plots of I_d/I_r *vs.* $\omega^{-1/2}$ is given by

$$\text{intercept } \frac{x+1}{N} = \frac{I_{H_2O}/I_{H_2O_2}+1}{N} \qquad [6]$$

Here, I_{H_2O} is the partial current at the disk, due to the reduction of oxygen to water in a path without hydrogen peroxide as an intermediate, and $I_{H_2O_2}$ is the partial current at the same electrode due to the reduction of oxygen to hydrogen peroxide. For the present electrode assembly, N is 0.38, as calculated from the dimensions of the electrodes (21), and checked by a redox reaction ($Fe^{+++} \rightarrow Fe^{++}$).

The intercepts of the plots of I_d/I_r *vs.* $\omega^{-1/2}$ are all greater than $1/N = 2.6$. Thus $x > 0$, and two paths of oxygen reduction must be present, with hydrogen peroxide produced as an intermediate in one of them.

Rates for individual reaction paths.—For each potential of the disk electrode, the individual rates of the two partial reactions, I_{H_2O} and $I_{H_2O_2}$, can be obtained from the disk and ring currents if the value of x can be obtained with sufficient accuracy [*cf.* Eq. (19) and (20) of ref. (14)]. For the prereduced electrodes the dependence of these partial currents on potential are given in Fig. 7. For the not prereduced electrode, in the Tafel region x is less than 1, and the separation

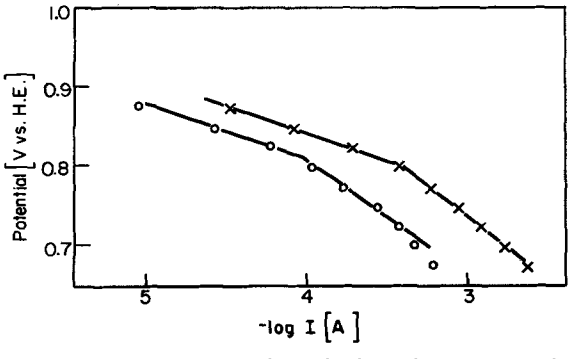

Fig. 7. Partial currents at the disk electrode. o, current due to the formation of hydrogen peroxide; x, current due to the reduction of oxygen to water without peroxide intermediate. Prereduced electrode. The area of the electrode is 0.18 cm^2.

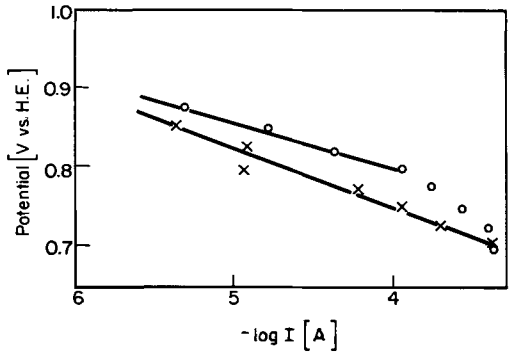

Fig. 8. Same as in Fig. 7, but electrode is not prereduced

of partial currents I_{H_2O} and $I_{H_2O_2}$ is rather uncertain. Nevertheless, from the best estimated values of x, these partial currents are calculated (Fig. 8).

For the prereduced electrode (Fig. 7), the slope of the log $I_{H_2O_2}$ — V line is about 0.070v at higher, and 0.140v at lower potentials. For I_{H_2O}, the corresponding slopes are 0.070 and 0.150v.

For the not prereduced electrode (Fig. 8), the slope for the log $I_{H_2O_2}$ line is about 0.050v, and it increases at higher cathodic overpotentials. The slope of the log I_{H_2O} line is 0.070v. Here, no change in the slope with potential is observed. $I_{H_2O_2}$ appears to be independent of the electrode pretreatment, while the I_{H_2O} changes with the pretreatment by about factor 10. being larger at the prereduced electrodes.

The change in the rate of oxygen reduction (Fig. 2, 6, and 7) with electrode pretreatment is not surprising, as the amount of oxides at the surfaces of these two electrodes are probably very different. Ellipsometric studies (22) in sulfuric acid solutions have shown that an air oxidized electrode is covered by an oxide layer of average thickness of ~6Å. It has also been shown that in sulfuric acid solutions the kinetics and the mechanism of oxygen reduction at the bare and oxide covered Pt surfaces are different (17, 23, 24), the activity at the bare electrodes, at 0.9v for instance, being higher than at an oxide covered electrode by more than a factor 10. A similar situation exists in alkaline solutions; activity at bare electrodes (17) is about a factor 10 higher than at oxide covered electrodes (24). Thus, an increase in the reaction rate by an order of magnitude when the oxides at the Pt surface are reduced is expected.

Reaction path followed in oxygen evolution.—Since for the same electrode, two paths for oxygen reduction are found, the question arises: "Which path is followed in oxygen evolution?" Tafel lines for oxygen evolution and reduction at oxide covered[2] Pt electrodes intersect at the reversible potential (16, 24, 25), and thus a common path is probably followed for the evolution and reduction reactions at these electrodes. A simple argument is presented here to show that the path with the hydrogen peroxide intermediate is not involved in oxygen evolution, and hence also in the reduction at oxide covered electrodes at potentials close to the reversible oxygen potential.

Were H_2O_2 an intermediate, then at the reversible oxygen potential the oxygen electrode reaction is in equilibrium. The rate of each stage of the reaction must be equal to or greater than the (observed) exchange current density ($\sim 10^{-10}$ amp/cm^2). For the stage of reduction of hydrogen peroxide to water, the rate of the reaction may be written as

$$i = nFkc_{H_2O_2} \geqq i_o \sim 10^{-10} \text{ amp/cm}^2 \qquad [7]$$

The concentration of hydrogen peroxide, $c_{H_2O_2}$, at the electrode surface as calculated from the Nernst's equation for two electron reduction of oxygen is 10^{-21} moles/cm^3. Substituting this value into [7], it is found that

$$k \geqq 10^6 \text{ cm/sec} \qquad [8]$$

This rate constant is 8 orders of magnitude larger than that experimentally observed for the reduction of H_2O_2 to H_2O in the potential range 0.90-0.00v (see later). It is unlikely that the rate would increase so greatly when the potential is made 0.30v more anodic (from 0.9 to 1.2v). Also, the anodic reaction would have to occur with an equal rate constant. From experimental data on hydrogen peroxide oxidation (26, 27), the rate constant at 1.23v is about 10^{-2} cm/sec. It is much lower than that required for the model in which, at potentials close to the reversible oxygen electrode potential hydrogen peroxide is an intermediate in a reaction path. Hence, the path which does not have hydrogen peroxide intermediate must predominate near the reversible potential and in oxygen evolution.

The mechanism in the path with peroxide intermediate.—For analyses of this path, the following diagnostic data are available. The Tafel slope is $-RT/F$ at low overpotentials and changes to $-2RT/F$ at more cathodic potentials. Under Langmuir conditions of adsorption[3]

$$b_c = -\frac{\nu RT}{(n_c + \beta n^*)F} \qquad [9]$$

where b_c is the cathodic Tafel slope, ν the stoichiometric number, n_c is the total number of electrons transferred before the rate-controlling step, β is the symmetry factor ($= \frac{1}{2}$), and n^* is the number of electrons transferred in the rate-controlling step. With $b_c = -RT/F$ for low current density region

$$n_c + \beta n^* = \nu \qquad [10]$$

Thus, since

$$n_c + n^* \leqq 2 \qquad [11]$$

either

$$n_c = 1,\ n^* = 0,\ \text{and}\ \nu = 1 \qquad [12]$$

or

$$n_c = 0,\ n^* = 2,\ \text{and}\ \nu = 1 \qquad [13]$$

or

$$n_c = 2,\ n^* = 0,\ \text{and}\ \nu = 2 \qquad [14]$$

Since a simultaneous transfer of two electrons ($n^* = 2$) is improbable, the second case may be rejected. The third case requires two identical species for the rate-determining step. This would require a dissociation of the oxygen-oxygen bond followed by a recombination in the rate-determining step which is highly improbable. Thus, the path must consist of an electron transfer step followed by a rate-controlling step which does not involve an electron transfer.

Two such paths may be suggested. The first is

$$O_2 + e^- \rightleftarrows O_2^- \qquad [15]$$

$$O_2^- + H_2O \rightarrow HO_2^- + OH \qquad [16]$$

$$OH + e^- \rightleftarrows OH^- \qquad [17]$$

The second is

$$O_2 + H_2O + e^- \rightleftarrows HO_2 + OH^- \qquad [18]$$

$$HO_2 + H_2O \rightarrow H_2O_2 + OH \qquad [19]$$

$$OH + e^- \rightleftarrows OH^- \qquad [20]$$

These mechanisms may be distinguished by their different pH dependences. In respect to a potential of a pH independent electrode, the first is pH independent, while the second has the dependence given by $\partial V/\partial \text{pH} = -RT/F$. The experimental pH dependence of —26 mv/pH for the prereduced electrodes in alkaline solution (28) reflects most probably the dependence on pH of the parallel reaction leading to H_2O without peroxide intermediate. This is because the rate of the reaction for the latter path is higher by at least a factor 3 than that for the path in which

[2] In evolution, a Pt electrode is expected to be oxide covered.

[3] See ref. (17) and (25).

peroxide in an intermediate. Hence, a clear distinction between the proposed reaction paths may not be made.

The region of Tafel slope of $-2RT/F$ is consistent with either path and corresponds to a change of the rate-controlling step to the first, charge transfer step (Eq. [15] or [18]). A point in favor of the first path ([15], [16], and [17]) is that this is the path followed in the reduction of oxygen to peroxide at gold electrodes, which behaves kinetically, in the $-2RT/F$ Tafel region, like platinum (29)

A possible path with a peroxide intermediate under Temkin conditions.—If the rate-controlling step is

$$O_2 + e^- \rightarrow O_2^- \qquad [21]$$

the rate expression under Temkin conditions of adsorption is

$$i = k[O_2] \exp(-\beta VF/RT) \exp[-\beta f(\theta)] \qquad [22]$$

With (15)

$$f(\theta) = VF/RT - \ln [H^+] \qquad [23]$$

and $\beta \approx \frac{1}{2}$, the rate expression becomes

$$i = k[O_2][H^+]^{1/2} \exp(-VF/RT) \qquad [24]$$

At higher cathodic overpotentials, $\theta \rightarrow 0$ and Temkin conditions no longer hold. Then, the rate expression becomes

$$i = k[O_2] \exp(-\beta VF/RT) \qquad [25]$$

and the Tafel slope for the same rate-controlling step changes from $-RT/F$ for Temkin to $-2RT/F$ for Langmuirian conditions.

Thus, the experimental results are consistent with either Temkin or Langmuirian conditions. However, a similar behavior of platinum, and gold, in respect to oxygen reduction in alkaline solution (29), favors the interpretation in terms of Langmuirian conditions with the same path followed at these electrodes. This is because at gold the adsorption must be Langmuirian as coverage by oxygen is low.

The mechanisms in the paths with no hydrogen peroxide as an intermediate.—For the parameters available in the literature ($\partial V/\partial \ln i \approx +RT/F$ and $-RT/F$, for anodic and cathodic reaction at low overpotentials (16, 24), respectively, and $+2RT/F$ for high anodic overpotentials (24), and for (24) $\partial \log i/\partial \log p_{O_2} \approx 0.5$), two paths were suggested in the literature for the reduction at preoxidized electrodes. These are first path (30)

$$O_2 \rightleftarrows 2\,O \qquad [26]$$

$$2(O + e^-) \rightleftarrows 2\,O^- \qquad [27]$$

$$2(O + H_2O) \rightleftarrows 2(OH^- + OH) \qquad [28]$$

$$2(OH + e^-) \rightleftarrows 2\,OH^- \qquad [29]$$

and second path (24)

$$O_2 \rightleftarrows 2\,O \qquad [30]$$

$$2(O + H_2O) \rightleftarrows 2\,O\text{-}H\text{-}OH \qquad [31]$$

$$2(O\text{-}H\text{-}OH + e^-) \rightleftarrows 2\,O\text{-}H\text{-}OH^- \qquad [32]$$

$$2(O\text{-}H\text{-}OH^-) \rightleftarrows 2(OH + OH^-) \qquad [33]$$

$$2(OH + e^-) \rightleftarrows 2\,OH^- \qquad [34]$$

In the first path, step [28] is the rate-controlling at low overpotentials with step [27] and [29] becoming the rate-controlling at high cathodic and anodic overpotentials, respectively. In the second path, which is basically a hydrated version of the first path, step [33] is rate-controlling at low overpotentials with [32] and [34] becoming rate-controlling at more cathodic and anodic overpotentials, respectively.

It is suggested that at the not prereduced electrodes of the present work, which are likely to be partially oxide covered, the mechanism for oxygen reduction to water is as that for the preoxidized electrodes.

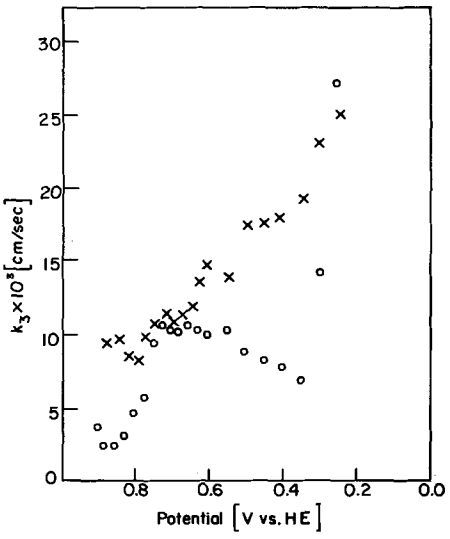

Fig. 9. Plot of the rate constant for hydrogen peroxide reduction, k_3, vs. disk potential. Two measurements.

The kinetics at the prereduced electrodes of the present work corresponds to that at the oxide free electrodes for which the mechanism has recently been discussed in some details (17). For these prereduced electrodes, oxygen partial pressure ($\partial V/\partial \log p_{O_2} \approx RT/F$) and pH dependence ($\partial V/\partial pH \approx -RT/2F$) were accounted for if Temkin conditions of adsorption by intermediates are considered. The rate-controlling step was suggested (17) to be the first discharge according to either [15] or [18]. The observed order of the reaction with respect to O_2 of the present work[4] is in agreement with this mechanism.

The change of slope from $-RT/F$ at low overpotentials to $-2RT/F$ at high overpotentials, as observed in the present work, is then accounted for by the change of the conditions for adsorption of intermediates from Temkin, at low overpotentials, to Langmuirian at high overpotentials.

The situation in which for oxide free electrodes Langmuirian conditions are favored for the path in which peroxide is an intermediate, and Temkin (at low overpotentials, at least) for the path in which no peroxide is formed, is not an impossible one. Thus, this situation may arise whenever there is a heterogeneity of the electrode surface. If, for instance, a part of the surface is still covered by oxides, these may serve as sites at which reduction occurs under Langmuirian conditions while at oxide free electrode Temkin conditions may prevail with a different reaction path. It seems probable that the O_2^- in a hydrogen peroxide path is not chemisorbed at the electrode surface. This view lends support from an analysis that in acid solution H_2O_2 appears to form only at sites at which residual impurities from the solution are already adsorbed (15), and, hence no chemisorption of O_2^- at these sites is possible.

The reduction of hydrogen peroxide.—From the diagnostic Eq. [5], the slope of I_d/I_r *vs.* $\omega^{-1/2}$ plots is given by (14)

$$\text{slope} = \frac{(x+2)}{N} 1.61\, D^{-2/3} \nu^{1/6} k_3 \qquad [35]$$

From this relationship, the rate constant for the further reduction of hydrogen peroxide to water, k_3, is obtained for each electrode potential (Fig. 9). The change in k_3 is less than two orders of magnitude for the potential change of 0.9v. In Fig. 10, the log of k_3 is plotted as a function of potential. If a straight line were drawn through the points, the slope would be about 0.6v. This unusually high slope probably indi-

[4] For these prereduced electrodes the observed order of the reaction corresponds to the path in which O_2 is reduced to water.

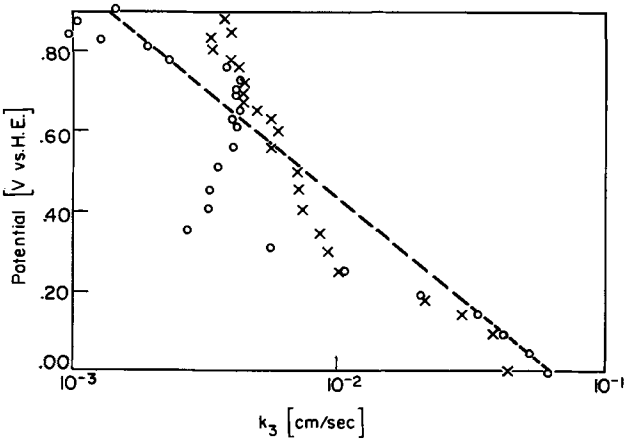

Fig. 10. Same as in Fig. 9, but with k_3 on a log scale

cates that the reduction of hydrogen peroxide is controlled by a chemical step, rather than a step involving an electron transfer.

The value of k_3 was previously determined by Muller and Nekrasov (31) to be $8.9 \pm 0.8 \times 10^{-2}$ cm/sec at 0.5v, and $3.6 \pm 0.5 \times 10^{-2}$ cm/sec at 0.1v. Jacq and Bloch (8) have determined the rate constant in 1*N* KOH to be 2.3×10^{-2} cm/sec at platinized platinum at −0.5v *vs.* NHE. These values are somewhat higher than those in Fig. 9. Considering the differences in the techniques used, the agreement of three independent sets of data for the rate constants of the reduction of hydrogen peroxide is good.

The mechanism of hydrogen peroxide reduction at platinum.—The rate constant for the reduction of hydrogen peroxide shows only a small dependence on potential between 0.90 and 0.00v (*cf.* Fig. 10). Since in this potential region, the coverage by OH and hydrogen varies from zero to appreciable values without a major change in the reaction rate, Temkin kinetics will not be considered.

Several paths for hydrogen peroxide reduction, which do not involve electron transfers before or in the rate-controlling step, have been proposed. In the path (32)

$$H_2O_2 + OH \rightarrow HO_2 + H_2O \qquad [36]$$

$$HO_2 + H_2O_2 \rightarrow O_2 + H_2O + OH \qquad [37]$$

oxygen is formed which is then reduced to hydrogen peroxide.

In another path hydrogen peroxide is dissociated in the rate-controlling step which is then followed by a charge transfer (33)

$$H_2O_2 \rightarrow 2\,OH \qquad [38]$$

$$OH + e^- \rightleftarrows OH^- \qquad [39]$$

Finally, in the path (34)

$$H_2O_2 + Pt \rightarrow PtO + H_2O \qquad [40]$$

$$PtO + H_2O + 2e^- \rightleftarrows Pt + 2\,OH^- \qquad [41]$$

hydrogen peroxide is decomposed into water and an oxygen atom which then reduces to OH^-.

Since the coverage with adsorbed OH is known to be potential dependent, it seems unlikely that the path according to [36] and [37] can be followed. The other two paths involve dissociation of hydrogen peroxide. No distinction between these paths by electrochemical methods can be made.

Acknowledgments

The authors wish to thank the sponsor of this work, the U.S. Army Electronics Materials Laboratory, Fort Monmouth, N. J. (Contract No. DA-36-039-Sc88921) for financial support, and Dr. H. F. Hunger and Mr. J. Wynn for their advice during this work. They also thank Mr. O. Shannon for machining the disk electrode assembly, and Mr. J. Dawson for glassblowing the cell.

Manuscript received Dec. 7, 1966; revised manuscript received July 21, 1967.

Any discussion of this paper will appear in a Discussion Section to be published in the June 1968 JOURNAL.

REFERENCES

1. H. A. Laitinen and I. M. Kolthoff, *J. Phys. Chem.*, **45**, 1061 (1941).
2. T. N. Belina and A. I. Karsil'shchikov, *Zhur. Fiz. Khim.*, **28**, 1286 (1954).
3. D. Winkelmann, *Z. Elektrochem.*, **60**, 731 (1956).
4. W. Vielstich, *Z. physik. Chem. (Frankfurt)*, **15**, 409 (1958).
5. D. T. Sawyer and R. J. Day, *Electrochim. Acta*, **8**, 589 (1963).
6. L. N. Nekrasov and L. Muller, *Doklady Akad. Nauk SSSR*, **149**, 1107 (1963).
7. L. Muller and L. N. Nekrasov, *Electrochim. Acta*, **9**, 1015 (1964).
8. J. Jacq and O. Bloch, *ibid.*, **9**, 551 (1964).
9. V. A. Shepelin, Ts. I. Zalkind, and V. I. Veselovskii, *Zhur. Fiz. Khim.*, **38**, 2098 (1964).
10. A. Kozawa, *J. Electroanal. Chem.*, **8**, 20 (1964).
11. A. N. Frumkin, E. I. Khrusheva, M. R. Tarasevich, and N. A. Shumilova, *Elektrokhimiya*, **1**, 17 (1965).
12. L. Muller and V. V. Sobol, *ibid.*, **1**, 111 (1965).
13. A. N. Frumkin, L. N. Nekrasov, V. G. Levich, and Yu. B. Ivanov, *J. Electroanal. Chem.*, **1**, 84 (1959).
14. A. Damjanovic, M. A. Genshaw, and J. O'M. Bockris, *J. Chem. Phys.*, **45**, 4057 (1966).
15. A. Damjanovic, M. A. Genshaw, and J. O'M. Bockris, *This Journal*, **114**, 466 (1967).
16. T. P. Hoar, *Proc. Roy. Soc. (London)*, **A142**, 628 (1933).
17. A. Damjanovic and V. Brusic, *Electrochim. Acta*, **12**, 615 (1967).
18. A. C. Riddiford, "Advances in Electrochemistry and Electrochemical Engineering," Vol. 4, p. 96, P. Delahay, Editor, Interscience Publishers (Wiley), New York (1966).
19. V. G. Levich, "Physicochemical Hydrodynamics," p. 327, Prentice-Hall, Inc., Englewood Cliffs, N. J. (1962).
20. W. J. Albery and S. Bruckenstein, *Trans. Faraday Soc.*, **62**, 1946 (1966).
21. S. Bruckenstein, Private communication.
22. M. A. Genshaw, Thesis, University of Pennsylvania (1966).
23. A. Damjanovic and J. O'M. Bockris, *Electrochim. Acta*, **11**, 376 (1966).
24. A. Damjanovic, A. Dey, and J. O'M. Bockris, *ibid.*, **11**, 791 (1966).
25. T. P. Hoar, Proc. Meeting Intern. Comm. Electrochem. Thermodyn. Kinet., 8th, (1956), Butterworths, (London), 439.
26. J. Giner, *Z. Elektrochem.*, **64**, 491 (1960).
27. A. Hickling and W. H. Wilson, *This Journal*, **98**, 425 (1951).
28. K. M. Wong, Private communication.
29. M. A. Genshaw, A. Damjanovic, and J. O'M. Bockris, *J. Electroanal. Chem.*, in press.
30. A. I. Krasilshchikov, *Zhur. Fiz. Khim.*, **37**, 531 (1963).
31. L. Muller and L. N. Nekrasov, *J. Electroanal. Chem.*, **9**, 282 (1965).
32. F. Haber and J. Weiss, *Proc. Roy. Soc. (London)*, **A147**, 332 (1934).
33. J. O'M. Bockris and L. F. Oldfield, *Trans. Faraday Soc.*, **51**, 249 (1955).
34. G. Bianchi, F. Muzza, and J. Mussini, *Electrochim. Acta*, **7**, 457 (1963).

The Electrochemical Activation of Platinum Electrodes

S. D. James[1]

Brookhaven National Laboratory, Upton, New York

ABSTRACT

The various mechanisms proposed for the electrochemical activation of platinum electrodes are reviewed. Experimental results are described showing impurity desorption to be by far the most important result of conventional brief activation treatments. Literature evidence is cited for the view that a second type of activation exists produced by prolonged preoxidation and characterized by an exceptionally stable activity. This latter activation is probably associated with an oxide quite distinct from that formed in conventional brief anodizations.

It is well known that an electrical oxidation-reduction (anodization-cathodization, A-C) pretreatment applied to smooth Pt electrodes in aqueous solution usually causes a marked improvement in the reversibility and reproducibility of electrode processes subsequently studied at the electrode. Equally well known is the fact that this increase in electrode activity is only transitory and decays at rates varying widely according to experimental conditions. This appears to have been first noticed by Hammett (1) who observed that the activation effect was obtained even if a long time separated "A" from "C" but that it disappeared quickly after "C" (2). Various explanations have been advanced for these observations. The impurity theory (3-7) supposes that the A-C treatment causes desorption of adsorbed surface-active contaminants which were poisoning the electrode. These impurities may be traces of organic matter or of certain cations which, at sufficiently negative potentials, are very strongly adsorbed on Pt (6). Desorption might be effected either by the surface disruption involved in the formation and dissolution of the oxide film or by the general tendency of organic or cationic adsorbates to be desorbed during large positive excursions from the potential of zero charge ($\approx +0.2$v, NHE for Pt in 1M $HClO_4$ or H_2SO_4). In addition, destructive oxidation of organics might produce simpler and less adsorbable products. The initially high activity then decays as fresh contaminant adsorbs on the electrode.

The platinization theory (8-13), on the other hand, attributes the increased activity to a change in the nature of the surface layers of Pt consequent on the successive formation and reduction of a superficial oxide. Anson regards the A-C treatment as effecting a light platinization of the electrode. This is supported by the fact that the surface texture is visibly coarsened by repetitive A-C treatments (11, 14). One hundred such cycles removed the luster from a bright Pt electrode in 1M H_2SO_4 and 600 cycles resulted in a dark surface resembling that of a conventionally platinized electrode (11). According to Will and Knorr (9) the A-C procedure results in the formation of a very thin layer of unstable atoms having a high electrochemical activity. This activity is supposed to decay as the active disturbed structure gradually relaxes into a relatively stable and inert state.

A third interpretation of the effect of A-C treatments on electrode activity was given by Feldberg *et al.* (15). From their measurements in $HClO_4$ they inferred that a fully oxidized Pt surface suffered cathodic reduction (at constant current) rapidly to a half-reduced state but only very slowly beyond this to the fully reduced state. They imply that the half-reduced state is produced under the conditions of most A-C treatments and that this state is one of very high electrochemical activity. However this explanation is untenable because (a) a rapid decay in activity can be observed at a potential of about +0.8v, NHE [cf. Fig. 1 referring to Fe(II)-(III) in 1M $HClO_4$] where, on their own testimony, the half-reduced state should be quite stable and (b) under appropriate conditions, quite long-lived activations of the hydrogen evolution reaction can be obtained, at 0v, NHE in acid where the half-reduced state should be quite unstable. These arguments also dispose of the basically similar mechanism proposed by Davis (16), *viz.*, that the A-C treatment gives rise to a partially reduced oxide film which facilitates electron transfer *via* oxygen bridges between electrode and reactant.

A special mechanism, sometimes invoked for the hydrogen electrode, is related to the so-called "hydrogen poisoning" effect. It has been observed [see ref. (17) for summary] that hydrogen electrodes are subject to fatigue on prolonged cathodization or exposure to hydrogen. It is postulated that this decay in activity is associated with a slow attainment of equilibrium adsorption of atomic hydrogen into the bulk platinum (18). Anodization, according to this idea, activates the electrode by stripping the surface layers of dissolved hydrogen.

Time variations, after activation, in the activity of smooth Pt cathodes reducing O_2 in acid solutions have been attributed to progressive deactivation by adsorption of anions (19). This correlates with a pronounced shift in $E_{1/2}$ for O_2 reduction towards negative values in the series $HClO_4 < H_2SO_4 < HCl < HBr$, *i.e.*, the shift increases with anion adsorbability (20-22).

The present study indicates clearly that the removal of adsorbed impurities is by far the most important result of conventional brief activation treatments.

Since one of the major themes of this article is the overriding importance of solution purity in solid-electrode studies, a brief discussion of this subject is in order.

Workers in Frumkin's laboratory (23, 24) first realized the significance of capillary-active poisons under conditions of low electrode-area to solution-volume ratio and long electrode-solution contact time. The effect of these contaminants is minimized at the DME by the short ($\approx$4 sec) contact time. However, at a hanging drop or small area solid electrode, removal of adsorbable impurities is of paramount importance in obtaining reproducible and meaningful results. In some cases Frumkin utilized platinized platinum as a purifying adsorbent. Bockris and Conway (25) recommended preelectrolysis on auxiliary platinum electrodes as a method for cleaning a solution. However as Barker pointed out (26) preelectrolysis on an auxiliary cathode, while capable of removing reducible impurities like oxygen or some of the metal ions, leaves organic contaminants virtually untouched. Furthermore, exhaustive preelectrolysis at an auxiliary Pt anode is likely to do more harm than good, since oxidized Pt is quite inert as a material for the electrooxidation of most organic compounds over a wide range of potentials (27) while, during the preelectrol-

[1] Present address: Electrochemistry Division, Chemistry Research Department, United States Naval Ordnance Laboratory, White Oak, Maryland.

ysis, appreciable amounts of Pt can leave the anode and deposit on other cell surfaces. This can be a fruitful source of confusion, especially when electrode materials other than Pt are under study (28). Vahramian (29) showed that impurities responsible for the passivation of silver electrodes in $AgNO_3$ solutions could be eliminated by bubbling oxygen through for 2 hr at 60°C in the presence of platinized platinum. Vermilyea (30) confirmed this and established that both platinized platinum and O_2 were necessary for the cleansing effect. No effect was obtained with Pt alone, or with activated carbon or alumina, with or without oxygenation, *i.e.*, the effect was primarily one of oxidation rather than adsorption of impurities. In a study of the $Cu\text{-}Cu^{2+}$ reaction by an impedance technique in molar KNO_3, Hillson (31) found that it was impossible, by repeated recrystallizations, to purify his reagent-grade salts sufficiently to prevent electrode contamination during the course of an experiment. He eliminated surfactants and obtained stable impedances by a batch treatment of his 200-ml cell solutions with 5g of λ, a chromatographic alumina adsorbent. Although quite effective in this case the procedure in general is severely limited by the unacceptable solubility levels of high-area alumina in many aqueous solutions.

In connection with his studies on single-drop polarography, Barker (26) developed an adsorption purification technique, a simplified version of which was used in the present work. In view of the effectiveness and versatility of this method and the relative inaccessibility of the original publication (26), this work will be briefly described. The adsorbent column used contained a mixture of active charcoal and silica gel. The charcoal was purified by extraction for several weeks in a Soxhlet apparatus, first with 2*N* HCl and then with water. Granulated silica gel, formed by treating sodium silicate solution with dilute HCl, was washed repeatedly with water. Before use both materials were roasted in air then boiled with water to ensure thorough wetting. The small adsorbent column containing 5g of charcoal-silica mixture was an integral part of the polarographic cell and, in the *in situ* purification, a nitrogen lift circulated the cell solution (≈100 ml) through this column for about an hour. An additional effort to eliminate reducible cations involved circulating the solution for 15 hr past a 30-cm^2 Hg pool cathode maintained at —0.8v, NHE.

By following the double-layer capacity of a Hg drop formed in his solutions (molar KCl, analytical reagent) Barker was able to demonstrate the radical improvement effected by his cleansing procedure. In a cleansed solution the high initial capacity after drop formation was maintained with a fall of <1% in 24 hr. On the other hand, in untreated KCl, the capacity had fallen to 40% of the high value only 4 min after drop formation, due to the adsorption of surface-active impurities. Barker's method of solution purification, although used in British electrochemistry laboratories for over a decade (32) still appears relatively unknown in the United States. This is unfortunate as the method seems unrivalled in its general efficacy, *e.g.*, Parsons (33) obtained stable impedances in a study of V^{3+}/V^{2+} at a hanging Hg drop only in charcoal-treated solutions. Other standard purification techniques like distillation, recrystallization, and preelectrolysis proved quite unsatisfactory. The charcoal adsorbent is inexpensive and chemically resistant to all but the most strongly oxidizing solutions.

Experimental

Solution cleansing.—To cleanse solutions from surfactants, Barker's method was subjected to a drastic simplification. Both the silica half of the adsorption treatment and the preelectrolysis at a Hg cathode were dispensed with, and solutions were merely passed through a column of purified active charcoal. The charcoal employed was Nuchar C-115 (granular), a

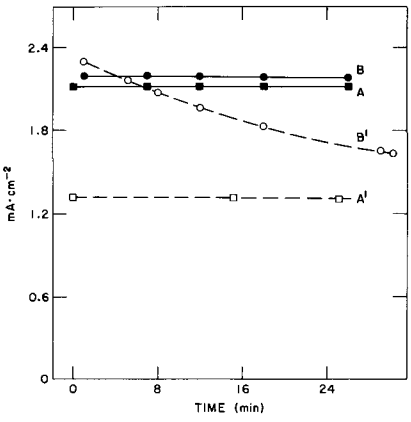

Fig. 1. Effect of A-C pretreatment (1 min at 2.34 then 1 min at 0.1v, NHE) on current-stability during the anodic oxidation of Fe(II) at a constant voltage of 30 mv applied to a Pt rde. All curves in 1M $HClO_4$, 1.06 x 10^{-2}M in Fe(II) and (III) and at 1500 rpm. A and B: Before and after A-C in charcoal-cleansed solution; A' and B': before and after A-C in uncleansed solution.

decolorizing carbon from the West Virginia Pulp and Paper Company, having a specific surface of 800 m^2 (BET). This carbon was sieved, retaining the 16-40 mesh particles which constituted about 70% of the whole. After boiling with water for about 2 hr, that portion still floating was discarded and purification commenced in an extra large Soxhlet apparatus. The ground surfaces of the large (103/60) tapered joint in this apparatus were coated with a thin Teflon layer to prevent freezing and a special Pyrex, fritted extraction thimble was made, capable of holding nearly 1000 ml of carbon. Extraction with constant boiling HCl (6*N*) was carried out for 2 weeks using successive charges of fresh HCl for 2-, 4-, and 8-day periods. Drainage of HCl from the thimble occurred every 30 min. Before the first and second changes of HCl the boiler solution had a strong green and a pale green color, respectively, while at the end of the extraction this solution was quite colorless. After the HCl extraction, the whole apparatus, including carbon, was rinsed with twice-distilled water and then a similar water-extraction was done with daily charges of fresh water. Extraction for 5 days sufficed for the complete removal of HCl (boiler solution tested with $AgNO_3$). The purified carbon was stored under distilled water in Pyrex jars. Solutions to be cleansed (about 300 ml in volume) were percolated at 3 ml/min through a 2.4 x 18-cm column of charcoal (this 80 ml of column contained 20g of dry carbon[2]) *via* a ground joint directly into the Pyrex electrochemical cell which was continuously purged with pure N_2.

In the case of the Fe(II)-(III)-$HClO_4$ system the solution was percolated as Fe(II)-1M $HClO_4$, since Fe(III) was very strongly adsorbed by the charcoal. After percolation, half of the Fe(II) was anodically oxidized *in situ* at a 40-cm^2 Pt electrode. For the study of the hydrogen evolution reaction, no such problem existed, and 2*N* H_2SO_4 was filtered directly into the cell.

The effectiveness of the charcoal treatment is obvious in Fig. 1 from the complete elimination of current-instability (at ≈0.8v, NHE) following the A-C treatment. The charcoal used to cleanse this solution had been purified the previous week. After a year of storage under distilled water, some of this carbon was lent to a colleague who had found it impossible to reproduce voltammograms for $Ag^+ \rightarrow Ag$ at a rotating

[2] This amount of carbon has a BET surface area of ≈2 × 10^6 cm^2, i.e., monolayer adsorption would involve 10^{-2} to 10^{-1} moles of a molecule occupying say 50A^2. This is 10^6-10^9 times the amount of contaminant likely to exist in 1 liter of, *e.g.*, reagent grade H_2SO_4 solution which is thought to contain about 10^{-7} M of impurity (34-36). Thus, even allowing for the specificity of adsorption and a wide heterogeneity of adsorption sites, it seems likely that such a column could be re-used many times to cleanse solutions of normal, reagent-grade purity.

disk electrode. After charcoal-cleaning the molar $HClO_4$ supporting electrolyte, his scans (between 0.8 to 0.5v, NHE) became quite reproducible (37). Thus the year's storage under water had left the charcoal's cleansing ability unimpaired. The charcoal used to cleanse the H_2SO_4 used for Fig. 4 (h.e.r. at Pt) had been stored under water for 2 years. Comparing curves A and C, it is clear that, while considerably reducing current-instability, the charcoal treatment by no means eliminated it. That the residual instability was still largely due to solution impurities is shown by its pronounced dependence on rpm. It is probable that the smaller success of charcoal cleansing in stabilizing the h.e.r. is connected with an inherently greater sensitivity of this reaction to impurities rather than with a degradation of the carbon during storage. This greater sensitivity may be linked with the relative rational potentials (ϕ = deviation of electrode potential from its zero charge value) in the different systems. The potential of zero charge for Pt in H_2SO_4 or $HClO_4$ is about +0.2v, NHE (38) and that for Ag in $HClO_4$ is probably close to +0.05v, NHE (39). Thus, in Fig. 1, $\phi \approx +0.6$v; for the $Ag\text{-}Ag^+$ study mentioned above, ϕ was between +0.75 to 0.45v whereas in the h.e.r. study, $\phi \approx -0.2$v. Figure 2 reveals, as is discussed below, that on Pt at 0v, NHE, there is a wide spectrum of adsorbed impurities which are progressively removed at increasingly positive potentials. Thus, because of the more positive ϕ's in the first two systems, even at open circuit, they are already activated relative to the hydrogen electrode in that they are sensitive to a smaller range of impurities. The few direct measurements made, *e.g.*, for Cd^{2+} and Tl^+ (40), support the expectation that, at least in this range of potential, the adsorbability of cations on Pt falls as ϕ rises. Also, as a general rule, ions are not well adsorbed on activated charcoal (41). Hence it is likely that the impurities responsible for the instability of current in Fig. 4 are metallic cations which passed through the charcoal column.

Thus it appears that purified charcoal may be stored for long periods under water with little or no loss in effectiveness and is therefore always ready for immediate use. While excellent for the removal of organic contaminants it appears much less so for metallic cations and where sensitivity to cations is anticipated (at low values of ϕ) it should be supplemented by cathodic preelectrolysis at Hg, as recommended by Barker (26). Actually, for Pt electrode studies the simplest way to clean a solution involves prolonged exposure to a large-area auxiliary Pt electrode held at the most negative potential of the projected study (34). A periodic brief anodic cleaning of this auxiliary electrode in another solution would enhance its effectiveness.

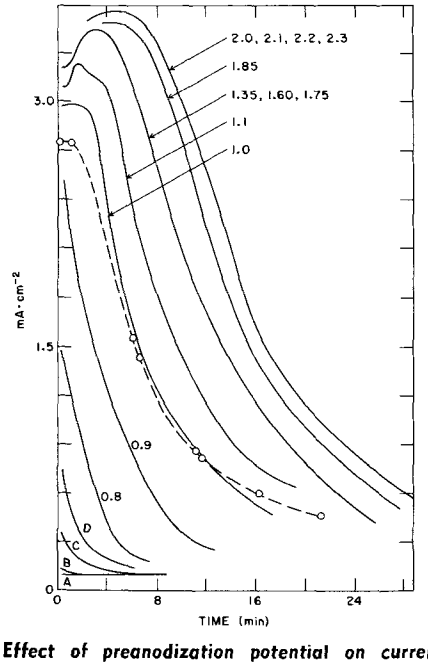

Fig. 2. Effect of preanodization potential on current-stability for h.e.r. at Pt rde. All curves at 1200 rpm in uncleansed 2N H_2SO_4 and constant cathodic applied voltage of 14.7 mv, RHE. Each curve labelled with potential (vs. RHE) of its 1 min (1200 rpm) pre-anodization except curves A, B, C, and D where these potentials were 0.0, 0.25, 0.5 and 0.7v, RHE, respectively. Broken curve: see text.

Apparatus and procedure.—Electrode activity was followed by recording the current at a given small overpotential under well-defined and constant mass-transfer conditions. This latter situation was achieved at a rotating disk electrode of Pt ($\approx$0.03-cm^2 area) spinning at a constant rpm ($\pm$1%) in an all-glass air-thermostatted cell at 25° $\pm$ 1°C. This apparatus has been described elsewhere (42).

In the case of the Fe(II)-Fe(III) system, voltages of $\pm$10 and $\pm$30 mv (constant and reproducible to within 0.1 mv) were applied between the rde and a large (40 cm^2) unpolarized Pt counter electrode in oxygen-free molar $HClO_4$, equimolar in Fe(II) and (III) at about 10^{-2}M. The general procedure was as follows. After the rde had been quiescent in the solution, under pure nitrogen, for a few hours or more, a small constant voltage was applied at 1500 rpm and the resulting current recorded for about 20 min. Then the still spinning electrode was given an A-C activation comprising 1 min at +2.34v, NHE (plating out oxygen at 120 ma · cm^{-2}) and 1 min at +0.1v, NHE. After 1 min at open-circuit the current was again recorded at the same rpm and applied voltage. All these electrical operations were done with a Sargent model XXI polarograph and potentials are given on the Stockholm sign convention. The results of the above procedure were compared in two different solutions. The first solution contained chemicals of the reagent-grade purity customary in most electrochemical studies. The second solution employed the same source of Fe(II) and $HClO_4$, but it was cleansed from surface-active contaminants by the charcoal treatment described above. The unpurified solution was made up with Fe(II) and (III) equimolar at 1.06 x 10^{-2}M in 1M $HClO_4$. From limiting currents at the rde in this solution, diffusion coefficients of 6.12 and 4.66 x 10^{-6} $cm^2 \cdot sec^{-1}$ at 25°C were calculated for Fe(II) and (III), respectively. Using these data, by a reverse process, the composition of the purified solution after half-oxidation was calculated as 1.32 x 10^{-2}M for both ferrous and ferric in molar $HClO_4$. Currents observed in the purified solution were multiplied by 0.80 to allow for this concentration difference and facilitate the comparison, in Fig. 1, of behavior in the two solutions.

In the h.e.r. study illustrated in Fig. 2 to 4, the same Pt rde was used in N_2-saturated molar H_2SO_4. However, this time, the counter and reference electrode was a reversible hydrogen electrode in the same solution separated from the main compartment by a fine frit. During these hydrogen deposition experiments, H_2 formed at the Pt disk was continually swept by the motion of the rde into a fringe of bubbles on the Teflon nonworking surface leaving the Pt surface perfectly bright. At rpm's above 1500 these H_2 bubbles were swept entirely away from the rde. The time-zero in Fig. 2 to 4 coincides with the end of the preanodization. Although the results of Fig. 2 to 4 were all obtained at the same constant applied voltage of about 14.6 mv, RHE, a substantially varying iR drop (R = 65 ohm) is included in this figure. For instance, in curve A of Fig. 2, η = 14.5 mv, RHE, whereas at the highest i in this figure, η = 5.5 mv. This fact, while causing the curves of Fig. 2 to 4 significantly to understate both the initial activation levels achieved and the rate of their decay, does not vitiate the discussion, in which only the relative shapes of these curves are invoked.

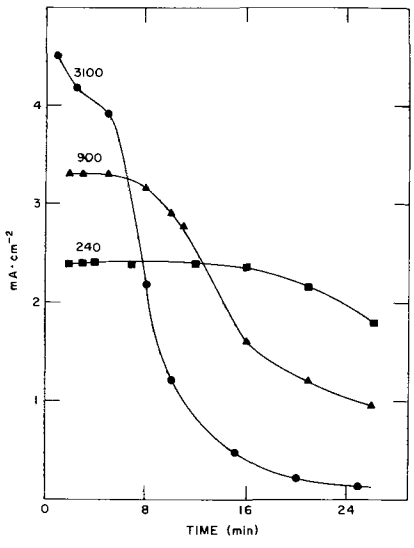

Fig. 3. Effect of stirring-rate on current-stability for h.e.r. at Pt rde. All curves, at labelled rpm's, in uncleansed 2N H_2SO_4 and constant cathodic applied voltage of 14.6 mv, RHE, were preceded by 1 min of preanodization at 2.0v, RHE (at 1200 rpm).

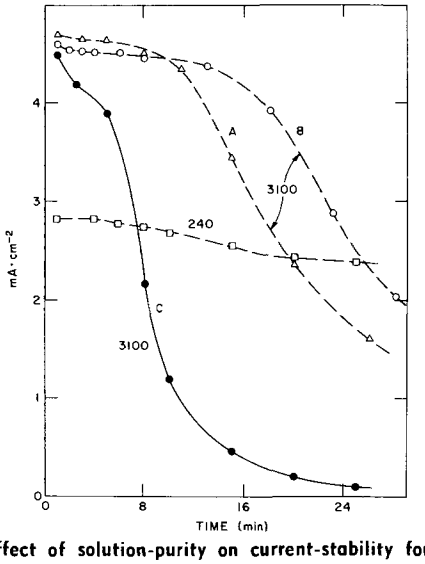

Fig. 4. Effect of solution-purity on current-stability for h.e.r. at Pt rde. All curves, at labelled rpm's and constant cathodic applied voltage of 14.6 mv, RHE, were preceded by 1 min of anodization at 2.0v, RHE (at 1200 rpm). Broken curves in charcoal-cleansed 2N H_2SO_4. Curve C in uncleansed 2N H_2SO_4. Before B, solution subjected to additional cleaning described in text.

Results and Discussion

Ferrous-Ferric.—Figure 1 shows the effect of the A-C treatment on current and its time-dependence for the oxidation of Fe(II) at the rde. (After correction for iR drops, the actual anodic η operating in this case was 27.4 mv and at 2.1 ma · cm^{-2}, the anodic i was about 40% of its limiting value.) In the unpurified solution (A', B') the A-C treatment caused an initial boost of about 70% in the current which then sank back quite rapidly toward its original level. On the other hand, in the purified solution (A, B) the A-C treatment raised i by only about 3%, and this increase took hours to recede. A' and B' were only approximately reproducible, but A and B in the purified solution were precisely reproducible, *e.g.*, even after eight days at open-circuit under pure N_2 curves A and B could be duplicated exactly.

Comparable behavior to that illustrated in Fig. 1 was obtained for both anodic and cathodic currents at ±10 and ±30 mv applied voltage. Thus the charcoal-cleansing treatment of the solution virtually nullified the effect of an A-C pretreatment on electrode activity. The "active-electrode" behavior obtained initially in B' following the A-C treatment was produced in A, B merely by the cleansing procedure. This is conclusive evidence for the impurity theory as opposed to the other theories concerning the mechanism of electrochemical activation. The 3% increase in current following A-C in the purified solution may arise from the presence of residual surfactants or from a small "platinization" effect.

Hydrogen evolution.—Figure 2, referring to uncleansed molar H_2SO_4, illustrates the activation levels achieved and their stability as a function of the potential (E_A) of the 1-min preanodization. All preanodization and the subsequent recording of current were done at 1200 rpm. Prior to curve A, the stationary rde was shorted to the reversible hydrogen electrode for 2 hr with N_2 bubbling through the solution. Then the other curves were obtained after 1-min anodizations at the potentials listed. The maximum activation effect, both in terms of the initial current and its stability, was achieved after E_A = 2.0v, RHE. Raising E_A to 2.3v, RHE, effected no greater activation. Taking rough account of the differing η's prevailing in the two cases, the initial current after E_A = 2.0v, RHE, was about one hundredfold greater than that after prolonged maintenance at the equilibrium potential (curve A). This is a much greater effect than the 70% increase in current observed in the Fe(II) $\rightleftarrows$ (III) system. As discussed in the experimental section, this is probably caused by the much lower (by 0.8v) rational potential in the h.e.r. study and its consequently greater sensitivity to surfactants in general and metal cations in particular. A significant feature of Fig. 2 is the fact that substantial levels of activation were attained even when $E_A < 0.9$v, RHE, where it is quite unlikely that the Pt surface is oxidized to any appreciable extent (43-45). The unlabeled broken curve of Fig. 2 is also relevant to this point. The pretreatment here was 24-hr soaking of the previously reduced rde in the cell at open-circuit under flowing N_2. The equilibrium potential just before recording of the curve was 0.95v, RHE. Since a 24-hr soaking in molar H_2SO_4 has been employed to completely free Pt electrodes from surface oxides (46), it is obvious that the recent reduction of a surface oxide had nothing to do with the considerable activation evident in this broken curve. Thus the platinization theory of activation is untenable for this system.

In the subsequent work illustrated in Fig. 3 and 4 a 1-min preanodization at 2.0v, RHE, was invariably used as this achieves maximum activation without an inconveniently high anodic current (actual anodic $i \approx 5$ ma · cm^{-2}). Employing this 1-min prepolarization at 1200 rpm, Fig. 3 shows the rpm dependence of current-stability for h.e.r. in uncleansed molar H_2SO_4. The radically faster decay at higher rpm shows the deactivation to be largely caused by mass transfer controlled adsorption of solution impurities and hence the activation must have been due mainly to the reverse process, *viz.*, impurity desorption. It is difficult to imagine how any structural change in the electrode surface, *e.g.*, recrystallization or oxide reduction could be affected by angular velocity of the electrode. Also, at this large concentration of H_2SO_4 (2*N*) adsorption of ions from H_2SO_4 could not be limited by mass transfer, *i.e.*, the gradual deactivation is not related to anion adsorption from the supporting electrolyte. The large increase in initial current with rpm, evident in Fig. 3, shows considerable control of the h.e.r. by concentration polarization of dissolved H_2. The polarization resistance R_η for the over-all process of hydrogen evolution, calculated from the initial current at 3100 rpm was ≈0.9 ohm · cm^2 (i = 4.5 ma · cm^{-2} at η = 4.0 mv). This would be somewhat lower after correction for residual concentration polarization, and thus the electrode is quite active (47). As the current diminished, during deactivation, so also did its rpm

dependence which eventually changed sign, *e.g.*, at the end of the 3100-rpm curve of Fig. 3; when i, η had changed from their initial values of 4.5 ma · cm^{-2} at 4.0 mv to 0.125 ma · cm^{-2} at 14.5 mv, lowering rpm from 3100 to 1200 boosted i to 0.2 ma · cm^{-2}, *i.e.*, nearly 100% increase. Obviously, the deactivation had caused a change in mechanism of the h.e.r. It is well-known that, at contaminated Pt electrodes, the combination of adsorbed H is inhibited, *e.g.*, (18b). Hence it seems possible that, at the deactivated (contaminated) electrodes, electrochemical desorption becomes rate-limiting, *viz.*, $H_{ads} + H^+ + e \rightarrow H_2$. An increase of stirring, by tending to clear the surface of H_{ads}, might then cause a decrease in current.

Figure 4 shows the effect of solution purity on the stability of the h.e.r. current after a 1-min (1200 rpm) preanodization at 2.0v, RHE. A greatly enhanced stability in the charcoal-cleansed solution (broken curves) is further support for the idea that the activation effect is primarily one of impurity desorption. That the residual instability in the cleansed solution is still largely due to solution impurities is shown by its pronounced dependence on rpm. Curve B, like A, was in a charcoal-cleansed solution at 3100 rpm but, before B, the solution was given an additional cleansing as follows. As an integral part of the cell it contained a 40 cm^2 auxiliary smooth Pt electrode which, during every curve of Fig. 2-4 excepting B of Fig. 4, was standing idle in the solution at an open-circuit potential of $\approx$ + 0.9v, RHE. However, before B, this large electrode was shorted to the RHE for 40 min with N_2 bubbling through the solution. Since Fig. 2 showed that Pt is very much more heavily contaminated at 0.0v than at 0.9v, RHE, it was anticipated that this procedure would significantly improve solution cleanliness. The higher stability of current in B shows this was true although not quite to the extent hoped for. (The open-circuit potential of the large electrode rose slowly during the recording of B, but even at the end of B it was only $\approx$0.1v, RHE.)

Thus, Fig. 2 to 4 show that, at least in 2*N* H_2SO_4, the decay in activity of Pt electrodes for h.e.r., following activation, is due mainly to the readsorption of solution impurities, not to the relaxation of a disturbed structure in the Pt surface, to the readsorption of anions from H_2SO_4, nor to a gradual "hydrogen poisoning" effect. H_2SO_4 contains a wide spectrum of surface-active poisons which are progressively desorbed with increasing potential between 0.0 to 2.0v, RHE.

Oxygen reduction.—The present study of electrochemical activations was about to be concluded by examining oxygen reduction in acid when this was made unnecessary with the publication of the work of Damjanovic, Genshaw, and Bockris (34). They investigated O_2 reduction in 0.1*N* H_2SO_4 at a Pt rde. After an activation treatment comprising 1.4 and 0.0v, RHE, for 1 min each, it was found that, while potentiostatting at potentials <0.8v, RHE, the cathodic current decayed at a rate which increased greatly with rpm but was greatly lessened (by × 10-100) after purifying the solution. The purification involved circulating the solution for 5 to 10 hr through a platinized Pt gauze adsorbent maintained at 0.3v, RHE. Thus their activation effects were caused mainly by impurity desorption. They also found that, at potentials anodic to 0.15v, RHE, H_2O_2 was produced only in a dirty solution. In a purified solution at these potentials, O_2 was reduced wholly to H_2O, the limiting current being attained at 0.5v.

In unpurified solutions, after activation, scanning at constant rpm cathodically from 0.9v, RHE, produced a maximum current at 0.6v, RHE, in their manual voltammograms. With further cycling of potential between 0.9 and 0.0v, the height of this maximum fell radically as time elapsed, *e.g.*, 20 min after the activation the maximum current was only 7% of its initial value. They associated the maximum with the idea that, as the potential falls during a cathodic scan, a progressively more extensive contamination of the electrode occurs producing a type of site where O_2 is reduced only as far as H_2O_2 (at least if $E > 0.15$v, RHE). They also postulated that the reduction to water occurs on a different type of site, not subject to the influence of contaminants and does not have H_2O_2 as an intermediate. Apart from the inherent improbability of these postulates, if this latter type of site is uninfluenced by contaminants then contamination can reduce the current only insofar as O_2 reduction is diverted to the 2-electron process at the contaminated sites, *i.e.*, a maximum lowering of 50% as compared with the factors of 10 or more by which currents in the later stages of their Fig. 5 differ from those immediately following the activation.

There seems no justification for their identification of impurities as exclusively or even mainly organic in character. After activation at 1.4v, RHE, the gradual diminution of current during successive cycles between 0.9 and 0.0v could, as they say, be due to the partial oxidation of organic impurities to even more tenaciously adsorbable products. However their alternative explanation, in terms of a wide spectrum of impurities, a fraction of which desorbs only above 0.9v, seems just as cogent. If, after an activation at 1.4v, the potential is not allowed to exceed 0.9v, then this fraction will gradually readsorb in a pseudoirreversible manner causing the gradual reduction in peak current which they obtained. They advance no reason why various metallic cations could not form part of this spectrum of impurities.

Thus, for the three electrode reactions described in this paper it has been shown that impurity desorption is by far the most important result of brief electrochemical activations. Other effects like the creation of a disturbed Pt surface, the desorption of ions derived from the supporting electrolyte, or, in the case of the h.e.r., the stripping of absorbed H from surface layers may quite possibly be present but appear inconsequential to the electrode kinetics.

Activations involving protracted preanodizations.—In contrast to the conclusion, expressed in the preceding paragraph, that brief activations act merely by impurity desorption, the work of Shibata (12) contains evidence linking activations produced by protracted preanodization with a change in structure of the superficial layers of Pt atoms, and this work merits further discussion. He found that, although a wide variety of preoxidation treatments resulted in the same high, initial value of electrode activity for H^+ reduction, the stability of this activity differed profoundly according to the nature and duration of the pre-oxidation procedure. Assuming that each preoxidation completely desorbed impurities and that electrode activation was due solely to this desorption, he reasoned that a similar time-decay of activity should be observed, as contaminant readsorbs from bulk solution, irrespective of the detailed nature of the preoxidation. Hence he discarded the impurity theory and supposed the activation to originate in a superficial structural change whose lifetime increased with severity of the preoxidation. Shibata's quite complicated pretreatments, applied to a number of 1-cm^2 Pt foil electrodes included aging for 2 weeks in a hydrogen atmosphere at room temperature followed by a preoxidation (*a*) by soaking in chromic acid at 80°C for 1, 15, or 60 min, or (*b*) by anodization in 1*N* H_2SO_4 at 100 ma·cm^{-2} for 0.25, 1, or 28 hr. After washing in water followed by cathodization at 20 ma·cm^{-2} for 200 sec, the electrodes were placed in H_2-saturated 1*N* HCl for a definite time before measuring their activity in this solution.

In all cases the electrode activity fell off with time from roughly the same initial high value. The various preoxidations yielded activities increasing in stability along the series listed above. In the least stable case, after chromic acid pretreatment for 1 min, the activity

in HCl dropped a hundredfold in 3 hr. At the other extreme, 28 hr of preanodization produced a high activity that had diminished only 10 to 20% after 30 hr in HCl. His initial activity corresponded to an over-all R_η for h.e.r. at 15°C in 1*N* HCl of ≈50 ohm·cm². This relatively large value [cf. ref. (47)] is probably due, not to a relative inactivity of Shibata's electrodes but to the fact that his measurements were made in unstirred, H_2-saturated solution, *i.e.*, the 50 ohm·cm² figure must contain a large contribution arising from concentration polarization of dissolved H_2. Considering the fact that his solutions were not particularly pure with respect to surface-active material (no preelectrolysis or adsorption technique was used) the activation produced by his extended anodization was unprecedentedly stable.

Another striking feature of Shibata's results are the two arrests in cathodic chronopotentiograms of his anodically activated electrodes. The first arrest at 0.6v, NHE, corresponded to a surface charge of 4 mC·cm^{-2}. Similarly high charges have been observed previously at this potential (43, 48). The second arrest at 0.3v, NHE, lengthened with duration of the preanodization (after an induction period of about 30 min) and was 36 mC·cm^{-2} for an electrode which had been preanodized at 0.1 amp·cm^{-2} for 28 hr. The only arrest previously described in the literature at this potential is that caused by monolayer hydrogen adsorption, accounting for 0.5 mC·cm^{-2} at the most (49). $i\tau$ for the second arrest was independent of cathodic i over at least 10 to 600 μa·cm^{-2} (50) and this arrest thus arises in a surface film of some kind. Even allowing a roughness factor of 2.5 (49) a film equivalent to 36 mC·cm^{-2} corresponds to associating 40 oxygen atoms with each surface Pt. Shibata attributed the second arrest to the reduction of such a "thick" surface oxide and the stable high activity persisting after this reduction to residual strain remaining in the surface layers. If the temperature of Shibata's preanodizations was <21°C, irrespective of the severity or duration of the anodic treatment, the second arrest was never observed in subsequent cathodic chronopotentiograms (50). Shibata's discovery of this low-potential arrest during the reduction of Pt electrodes subjected to excessive prior anodization was confirmed and extended by Kozawa (20b). After constant current anodization in 1*N* H_2SO_4, Kazawa recorded voltammograms in N_2-saturated 1*N* H_2SO_4 from 0.9 to 0.0v, NHE. As well as the normal cathodic peak at 0.6v he got a second peak at 0.2v the height of which increased with the duration, current-density, and temperature of the anodic pretreatment. As in Shibata's experiments, the charge corresponding to this low-potential peak, under extreme conditions, greatly exceeded that of the first peak. During anodization at 300 ma·cm^{-2} at 40°C in 1*N* H_2SO_4 a Pt anode acquired, after 3 hr, a yellow film whose color deepened with continued electrolysis.

This Japanese work, indicating as it does the existence of an electrochemically well-differentiated second oxide formed at very severely oxidized Pt, is very interesting and appears to be unique. The latter is certainly due to the fact that with the notable exception of the persulfuric acid manufacturers, extended anodization of Pt is rarely practiced by electrochemists. In view of the innumerable papers published on the 0.6v oxide, the deafening silence with which electrochemists have greeted the 0.2v oxide is surprising.

The work of Hoare (51, 52) has some similarity to that of Shibata in that an extended period of preoxidation was employed resulting in a stable high activity. After preoxidation by immersion in concentrated HNO_3, Hoare measured the activity of an electrode by its ability to retain an open-circuit potential of 1.229v, NHE, in oxygen-saturated acid solution (51), or to catalyze the reduction of oxygen in acid (52). Hoare's activities were significantly less stable than Shibata's probably because of the greater severity of the latter's preoxidations. An important feature of Hoare's results is the fact that the development of a stable activity depended on an immersion in HNO_3 for a minimum of about 50 hr, a much greater time than that needed to free the electrode surface from adsorbed contaminants. This fact argues for Hoare's contention that his activation was caused by some change extending several monolayers into the platinum. He identifies this change with the formation of a "Pt-O alloy" layer (53). Cathodic chronopotentiograms on Hoare's activated electrodes revealed only the single arrest customarily obtained at about 0.7v, NHE, in acid (54). However, in acid solution swept with H_2 gas, Hoare's activated electrodes took about 40 min to arrive at the same potential as reduced platinum compared to 4 min for electrodes oxidized by conventional anodization (51, 53). Assuming that Hoare had carefully removed adsorbed nitrogeneous species after the HNO_3-soaking, this would indicate that the HNO_3-soaking yielded an oxide more stable or more extensive than that obtained conventionally. This then is another significant similarity to Shibata's results as opposed to those normally obtained.

To sum up, both Hoare and Shibata activated platinum electrodes under conditions which appear to exclude impurity desorption as the cause of activation. Both employed protracted preoxidations and attributed the resulting activation to the presence (Hoare) and recent presence (Shibata) of a surface oxide qualitatively different from that rapidly reduced at 0.6v, NHE, in acid solution. It appears likely therefore that the electrochemical activation of platinum electrodes must be divided into two classes: (*a*) conventional anodizations of the order of a minute in duration which merely clean the electrode surface by desorbing impurities, and (*b*) severe oxidations extending over periods of many hours which appear to effect a more penetrating oxidation and an activation which is very stable, even in solutions not particularly clean with respect to adsorbable impurities.

Apart from the work of Shibata and Kozawa already cited, other evidence exists for postulating a qualitative change in the nature of the anodic film on Pt under extreme conditions of oxidation. For instance, several workers (43-45) have found definite changes in slope in plots of mC·cm^{-2} *vs.* *E* at about 1.8v, NHE, in acid solution. (mC·cm^{-2} is the charge required for the galvanostatic reduction of an electrode after its potentiostatic oxidation at potential *E*.) Mayell and Langer (43) observed a distinct maximum in such plots at 1.8v followed by a plateau. These authors proposed a series of platinum-oxygen couples culminating in a "tight" platinum oxide at potentials above 1.8v. Also, in Tafel plots for the oxygen evolution reaction at Pt in $HClO_4$ or H_2SO_4, a rapid transition toward higher overvoltages is observed at high current densities (55). This transition is associated with the incipient participation of anions in the electrode reaction caused perhaps by a qualitative change in the nature of the oxide film. It is relevant here to mention that, in 1922, by fusing $NaNO_3$ with chloroplatinic acid, Voorhees and Adams (56) arrived at a platinum oxide which is readily reduced by hydrogen giving a Pt black of unprecedentedly high and reproducible activity. This Pt black is still the best Pt catalyst available to the organic chemist for hydrogenations (57). In view of all the foregoing, it does not seem unlikely that the prolonged maintenance of platinum electrodes in a severely oxidizing environment might produce the more penetrating oxidation envisaged by Shibata and Hoare and hence a type of activation quite distinct from that associated merely with "anodic cleaning" of electrodes.

Manuscript received Feb. 1, 1967; revised manuscript received June 22, 1967. This work was performed under the auspices of the United States Atomic Energy Commission. The paper was presented at the Dallas Meeting, May 7-12, 1967.

Any discussion of this paper will appear in a Discussion Section to be published in the June 1968 JOURNAL.

REFERENCES

1. L. P. Hammett, Dissertation, Columbia University, 1923.
2. H. T. Beans and L. P. Hammett, *J. Am. Chem. Soc.*, **47**, 1215 (1925).
3. E. Wieke and B. Weblus, *Z. Electrochem.*, **56**, 159 (1952).
4. E. Yeager, T. S. Oey, and F. Hovorka, *J. Phys. Chem.*, **57**, 268 (1953).
5. J. O'M. Bockris, I. A. Ammer, and A. K. M. S. Huq, *ibid.*, **61**, 879 (1957).
6. G. C. Barker, *This Journal*, **113**, 1024 (1966).
7. S. Gilman, *J. Phys. Chem.*, **67**, 78 (1963).
8. J. A. V. Butler and G. Armstrong, *J. Chem. Soc.*, **1934**, 743.
9. F. G. Will and C. A. Knorr, *Z. Elektrochem.*, **64**, 258, 270 (1960).
10. F. C. Anson, *Anal. Chem.*, **33**, 934, 939 (1961).
11. F. C. Anson and P. M. King, *ibid.*, **34**, 362 (1962).
12. S. Shibata, *Bull. Chem. Soc. Japan*, **36**, 525 (1963).
13. H. Dietz and H. Göhr, *Electrochim. Acta*, **8**, 343 (1963).
14. S. Shibata, *J. Chem. Soc. Japan, Pure Chem. Sec.*, **79**, 239 (1958); **80**, 453 (1959).
15. S. W. Feldberg, C. G. Enke, and C. E. Bricker, *This Journal*, **110**, 826 (1963).
16. D. G. Davis, *Talanta*, **3**, 335 (1960).
17. G. J. Hills and D. J. G. Ives, in *"Reference Electrodes,"* p. 90, Academic Press, New York and London (1961).
18. (a) St. von Naray-Szabo, *Z. Physik. Chem.*, **178**, 355 (1937); (b) E. Gileadi, M. A. Fullenwides, and J. O'M. Bockris, *This Journal*, **113**, 926 (1966).
19. V. S. Bagotskü, L. N. Nekrasov, and N. A. Shumilova, *Russian Chemical Revues* (English Translation), **34**, 717 (1965).
20. A. Kozawa, (a) *This Journal*, **110**, 174C (1963); (b) *J. Electroanal. Chem.*, **8**, 20 (1964)
21. V. N. Modestova, *Zhur. Fiz. Khim.*, **25**, 1138 (1951).
22. G. Bianchi and T. Mussini, *Electrochim. Acta*, **10**, 445 (1965).
23. S. Levina and V. Sarinsky, *Acta Physicochim., URSS*, **6**, 475, 491 (1937).
24. B. Ershler and M. Proskurnin, *ibid.*, **6**, 195 (1937).
25. J. O'M. Bockris and B. E. Conway, *Trans. Faraday Soc.*, **45**, 989 (1949).
26. G. C. Barker, *"Square Wave Polarography,"* Part 3, A.E.R.E., Harwell, England, C/R 1563, 1957.
27. Yu. B. Vasil'ev and V. S. Bagotskii, "Fuel Cells, Their Electrochemical Kinetics," p. 77, Consultants Bureau, New York, 1966. (Translated from Russian edition, Nauka Press, Moscow, 1964).
28. J. D. E. McIntyre, Private communication.
29. A. Vahramian, *Acta Physicochim., URSS*, **19**, 148 (1944).
30. D. A. Vermilyea, *This Journal*, **105**, 286 (1958).
31. P. J. Hillson, *Trans. Faraday Soc.*, **50**, 385 (1954).
32. J. E. B. Randles, in "Transactions of the Symposium on Electrode Processes," E. Yeager, Editor, p. 366, John Wiley & Sons, Inc., New York (1961).
33. K. M. Joshi, W. Mehl, and R. Parsons, *ibid.*, p. 249.
34. A. Damjanovic, M. A. Genshaw, and J. O'M. Bockris, *This Journal*, **114**, 466 (1967).
35. A. M. Azzam, J. O'M. Bockris, B. E. Conway, and H. Rosenberg, *Trans. Faraday Soc.*, **46**, 918 (1950).
36. S. Gilman, *Electrochim. Acta*, **9**, 1025 (1964).
37. P. W. Carr, Private communication.
38. A. N. Frumkin, *This Journal*, **113**, 1011 (1966).
39. *idem., Z. Elektrochem.*, **59**, 807 (1955).
40. A. D. Obrucheva, *Doklady Akad. Nauk SSSR*, **141**, 1413 (1961).
41. J. W. Hassler, "Activated Carbon," 2nd ed., p. 32, Chemical Publishing Co., New York-London (1963).
42. S. D. James, *Electrochim. Acta*, **12**, 939 (1967).
43. J. S. Mayell and S. H. Langer, *This Journal*, **111**, 438 (1964).
44. S. Gilman, *Electrochim. Acta*, **9**, 1025 (1964).
45. M. Becker and M. W. Breiter, *Z. Elektrochem.*, **60**, 1080 (1956).
46. J. J. Lingane and P. J. Lingane, *J. Electroanal. Chem.*, **5**, 411 (1963).
47. *e.g.*, A. N. Frumkin in "Advances in Electrochemistry and Electrochemical Engineering," Vol. 3, p. 341, P. Delahay Editor, Interscience Publishers (Wiley) New York (1963).
48. W. Visscher and M. A. V. Devanathan, *J. Electroanal. Chem.*, **8**, 127 (1964).
49. *e.g.*, F. Will, *This Journal*, **112**, 451 (1965).
50. S. Shibata, Private communication.
51. J. P. Hoare, *This Journal*, **110**, 1019 (1963).
52. *Ibid.*, **112**, 849 (1965).
53. J. P. Hoare, S. G. Meibuhr, and R. Thacker, *ibid.*, **113**, 1078 (1966).
54. J. P. Hoare, Private communication.
55. P. Delahay, "Double Layer and Electrode Kinetics." p. 269, Interscience Publishers (Wiley) New York (1965).
56. V. Voorhees and R. J. Adams, *J. Am. Chem. Soc.*, **44**, 1397 (1922.)
57. J. H. Wolfenden, *J. Chem. Educ.*, **44**, 299 (1967).

Correction

The following corrections are indicated for "Electrochemical Reduction of Aromatic Hydrocarbons in Ethylenediamine" by H. W. Sternberg, R. E. Markby, I. Wender, and D. M. Mohilner, **143**, 1060-1062 (1966).

In the text to Fig. 3, ref. (6) and (10) should be replaced by (1) and (3).

The subscripts s in e^-_s should be omitted in the equations on the second column of page 1062. If any subscript is to be used, it should indicate the phase in which the electron occurs. For example, e^-_{pt} indicates the electron in the platinum. The equations should read

$$\begin{array}{rl} Li^o_s = Li^+_s + e^-_{pt} & E_i = 1.1 \\ B_s + e^-_{pt} = B^-_s & E_i = -1.4 \\ \hline B_s + Li^o_s = Li^+_s + B^-_s & E_o = -0.3 \end{array}$$

Li^o_s stands for $Li^+ \ldots e^-_s$ and e^-_s signifies the solvated electron in contrast to the electron in the platinum e^-_{pt}.

A simpler and perhaps more informative formulation would be the following

$$\begin{array}{rl} e^-_s = S + e^-_{pt} & E_i = 1.1 \\ B_s + e^-_{pt} = B^-_s & E_i = -1.4 \\ \hline B_s + e^-_s = S + B^-_s & E_o = -0.3 \end{array}$$

Here S indicates the solvent molecules required to solvate an electron.

On the Activity of Platinum Catalysts in Solution

I. Effects of Thermal Treatment and Chemical Etching on the Pt-O/Hydrogen Specific Reaction Rate

Theodore B. Warner, Sigmund Schuldiner, and Bernard J. Piersma[1]

Naval Research Laboratory, Washington, D. C.

ABSTRACT

The effects of thermal treatment and chemical etching of platinum on the specific rate of the chemical reaction of chemisorbed oxygen with hydrogen were determined. The hydrogen was present in electrochemically clean 1M H_2SO_4 and in the derma of the metal. On successive thermal treatments of bright Pt beads, which were heated to the melting point and then slowly recrystallized under high temperatures, the specific rate varied randomly from trial to trial. Where heating was more uniform, and the cooling rate slower, reaction of hydrogen with Pt-O was usually faster. Repeated aqua regia etching of a given Pt bead caused monotonic improvement until a rate between 0.014 and 0.021 amp/cm^2 was attained. Rates on Pt wire electrodes, which probably differed from the flame-formed Pt beads both in average crystallite size and in number of defects (created by the drawing process and only partially removed by subsequent annealing), were highly variable, but considerably lower than on beads. Surfaces whose activity for the Pt-O/hydrogen reaction differed manyfold showed no differences in anodic charging curves nor did electrochemical rates of water oxidation at +0.617 and +0.587v (NHE) or reduction of hydrogen ions at +0.300v differ. It appears that many electrochemical reactions are insensitive to these differences in surface condition. Because of its great sensitivity to catalyst pretreatments, the Pt-O/hydrogen reaction is identified as a "demanding reaction," especially useful for identifying and examining certain variables affecting contact catalysis in solution. Since impurity sorption is one such variable, the rate of this reaction is one of the most responsive cleanliness tests available.

Boudart *et al.* (1) have pointed out that the rates of some catalyzed reactions are much more sensitive to subtle nonuniformities of solid surfaces than others. They suggested that it may be important to distinguish between these different types of reactions, and proposed the terms "demanding" and "facile" reactions. They define a facile reaction as one for which the specific activity of the catalyst is practically independent of its mode of preparation. The selection and use of demanding reactions to monitor effects of changes in catalysts should offer considerable advantages in precision and discrimination.

It was previously found (2) that the rate of chemical reaction of oxygen chemisorbed on a smooth platinum electrode with hydrogen present both in 1M H_2SO_4 solution and dissolved in the electrode was very sensitive to changes in the composition of the surface. In particular, absorption of a monolayer of oxygen atoms in the top few atomic layers of the metal caused a change in the reaction mechanism and a sixfold reduction in rate, *i.e.*, the Pt catalytic activity depended on the amount of dermasorbed oxygen, even when the amounts were much less than a monolayer. This reaction rate could be measured simply, quickly, and fairly precisely by observing the time required for potential decay after depositing known amounts of adsorbed and/or dermasorbed oxygen with an anodic current pulse. It appeared to be a demanding (1) reaction, well suited to the study of other factors important in catalysis.

A study of catalysis must have as one prerequisite a way to eliminate effects due to impurity sorption. The responsiveness of the rate of the Pt-O/hydrogen reaction to surface variations made it more sensitive to trace impurities than any other rapid test we have had available, and accordingly the investigation was divided into two main sections. First, the effects of varying degrees of solution and metal cleanliness on rate were examined to determine under what conditions platinum could be considered sufficiently clean so that changes in catalytic behavior due to metallic factors were not obscured. The usefulness of this reaction rate as a cleanliness test was concurrently examined. Second, having established these criteria and while maintaining the necessary conditions, the effect on rate of changing the atomic arrangement and/or the surface condition of the metal was determined. This study was not designed to identify which types of surface conditions are the most active, although inferential evidence was obtained, but rather to demonstrate that subtle metal phase changes in a clean catalyst surface can have large effects on some reaction rates. The sensitivity of the studied reaction makes it a particularly useful experimental probe. Finally, the question was examined, will surface morphology changes that affect the catalytic activity for this chemical reaction necessarily cause changes in electrochemical reaction rates?

Apparatus and General Procedure

The gas-tight electrochemical system, He and H_2 purification trains, solutions, and general procedures were essentially the same as previously used (2, 3). The cell contained a large platinum gauze counter electrode (about 80 cm^2 wetted geometric area), a Pt wire reference electrode 0.064 cm diameter extending about 3 cm into the solution, a miniature glass reference electrode, and two bright Pt bead working electrodes with areas about 0.1 cm^2. The beads were formed by melting the end of 99.99% pure Pt wire. One bead was mounted by sealing the wire into a Pyrex tube, the other was mounted in a Teflon tube and sealed with molten polyethylene. True electrode areas were determined from the amount of oxygen deposited in an anodic charging curve (3) and all areas given are true areas unless otherwise specified. The oscilloscope was a Tektronix Type 547 with Type 1A1 preamplifier; the electrolyte was 1M H_2SO_4

[1] National Academy of Sciences Postdoctoral Resident Research Associate at NRL. Present address: Eastern Baptist College, St. Davids, Pennsylvania.

at 25° ± 1°C, and all potentials are given *vs.* the normal hydrogen electrode.

The cell was cleaned at different times in two different ways. The first method (5) was with hot HNO_3 followed by numerous rinses with triply distilled water. In the second method, the reference electrode and polyethylene-sealed bead were removed, and after cleaning with hot nitric acid the cell and remaining electrodes were steamed for several days while carrying the condensate out a side arm in a constant stream of purified H_2. Periodically the cell was allowed to fill; on one such filling, NaOH was added to make hot 1M NaOH and the cell was soaked for 1 hr, and then rinsed by further steaming. Finally, condensate was again allowed to collect and concentrated reagent grade H_2SO_4 was added to make up the electrolyte. In this cleaning technique, the cell is isolated from the room atmosphere at all times except when adding the NaOH or H_2SO_4, or when replacing the electrodes. Laboratory air was continuously purified (4).

Solutions were cleaned by electrolysis under H_2 or He at 50 to 250 ma with the Pt wire electrode as cathode and all other electrodes as anodes, the wire subsequently being cleaned with HNO_3 and an H_2/O_2 flame. Any electrode removed was rinsed with concentrated HNO_3 and water before reinsertion.

Electrodes in the cell were cleaned by one or more of the following anodic treatments, listed in order of increasing severity and effectiveness: level 1, single anodic pulses just up to O_2 evolution region, as in Fig. 1; level 2, multiple pulses as in 1 with partial recovery of potential between pulses; level 3, d-c anodization at 3 amp/cm²; level 4, repeated (200/min) 7 amp/cm² pulses for periods of 1 to over 10 min.

Two classes of impurities could be distinguished by their influence on charging curves and by the difficulty of their removal from an electrode surface or from solution. Their exact natures are unknown; they will be defined as "readily oxidizable" or "difficultly oxidizable" impurities as follows. The first category could be removed from an electrode by level 1 or 2 anodization and could be removed from solution by extended electrolysis. The "difficulty oxidizable" could be removed slowly and sometimes only partially with level 3 or 4 treatment, and they could not be removed from solution by electrolysis; they could be eliminated by cleaning the cell and charging with fresh solution.

The strength of the bond between a foreign substance and a platinum lattice may vary continuously from weak physisorption to lattice incorporation. Impurities will be arbitrarily and operationally divided into those removable by the cell and cleaning techniques used, and those not, with the former being called "sorbed impurities" and the latter "lattice impurities." It should be understood that under this division a sufficiently tightly sorbed species could be classed as a lattice impurity and would be experimentally indistinguishable from one.

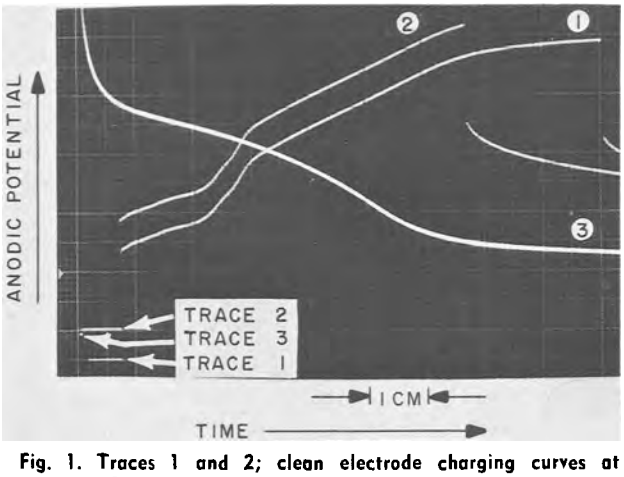

Fig. 1. Traces 1 and 2; clean electrode charging curves at 2.3 amp/cm², 25°C; time = 50 μsec/cm, voltage = 0.5 v/cm. Trace 1 shows a full charging curve up to and into the O_2 evolution region, used to determine how much charge was required to deposit a monolayer of Pt-O. Trace 2 represents the pulse, adjusted in length such that just one monolayer of Pt-O was deposited, whose decay time was subsequently measured. Trace 3 is the subsequent decay curve; time = 5 msec/cm, voltage = 0.2 v/cm. Decay time ≈ 30 msec. The starting point of each trace is 0.000v. The end point of trace 2 is 1.68v, just below the 1.76v normally associated with the beginning of the O_2 evolution region (3).

Measurement of Decay Times

The Pt electrode was exposed to one-atmosphere hydrogen-saturated electrolyte until an equilibrium H^+/H_2 potential was reached. The electrode was then anodized with a single constant-current pulse such that just one monolayer of atomic oxygen was deposited. Current densities of 2.5 to 7.0 amp/cm² were used to avoid dermasorption of oxygen in the metal lattice. Also, because of these high current densities and since the pulses were terminated before the O_2 evolution region was reached, an insignificant amount of O_2 was formed. At pulse cut-off, the electrode potential became less positive as Pt-O was reduced by reaction with hydrogen. The time required for the potential to drop to a plateau at about 0.3v is defined as the decay time. At 0.3v, the electrode is virtually free of O_{ad} and significant H sorption commences. Figure 1 shows a typical display; for details see ref. (2). In ref. (2) varying amounts of oxygen q_o were deposited on the electrode, and the observed decay times t_{decay} were converted to reaction rates i_r where

$$i_r(\text{amp/cm}^2) = \frac{q_o(\text{coul/cm}^2)}{t_{decay}\ (\text{sec})} \qquad [1]$$

In this study, the t_{decay} resulting during removal of one monolayer of oxygen (420 μcoul/cm²), deposited on the electrode in the manner described above, was defined as t_o and reaction rates are frequently discussed in terms of the corresponding t_o. This procedure eliminates need for *a priori* knowledge of electrode area; it measures a quantity related to specific reaction rate, automatically adjusted for surface area changes. In these terms, the i_r previously found for a clean system of 0.014 amp/cm² [from Fig. 4a of ref. (2); blank correction requires that ordinate values of Fig. 4 and 5 be divided by 2] is equivalent to a monolayer decay time, t_o, of 30 msec.

During pulse cut-off and potential decay, the impedance between the working electrode and any other cell component must be high enough so that an insignificant current flow results. This is achieved by using a 10 megohm probe [for circuit see Fig. 3, ref. (3)] and adding blocking diodes to the pulse generator output to impede back flow of current after the pulse terminates [as in Fig. 2, ref. (6)]. Long decay times of over 100 msec that later decrease with additional purification are excellent evidence for the absence of significant current leakage. Absence of long t_o in less active systems would indicate undetected leakage paths.

Previous results (2) showed that decay times in clean solutions are not a function of hydrogen stirring rate from 0 to 560 ml/min, nor of current density in the range used. The t_o values are independent of soak time (time elapsed since last polarizing pulse) from 1 min to many days; temperature is not important, nor is hydrogen partial pressure (although longer soak times are required at lower partial pressures).

Cleanliness Criteria

For the purposes of this paper an electrode or a solution has been called clean if the following criteria were met. These criteria were monitored during the course of the experiments and were also used to estimate relative amounts and types of contaminants, when present.

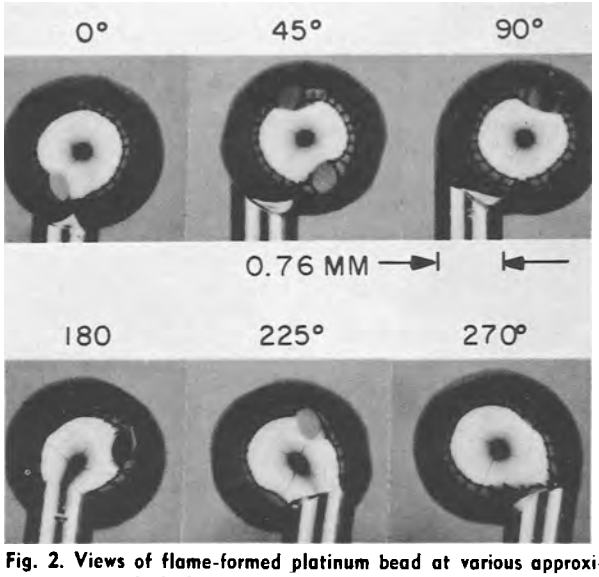

Fig. 2. Views of flame-formed platinum bead at various approximate amounts of clockwise rotation. Magnification ≈ 12X. Photos by A. C. Simon.

Hydrogen electrode potentials.—For a clean system, at $P_{H_2} = 1$ atm, the potentials of the four smooth platinum electrodes differed by no more than 0.1 mv.

Current-voltage relations.—Recent (7) measurements in He-saturated solution in a separate "improved gas-tight system" showed that in that system the rate of electrode recontamination with oxidizable or reducible species was no more than one millionth of the surface area per second, roughly equivalent to contamination rates in a 10^{-12} Torr vacuum system. Further, there was no indication of the presence of any nonoxidizable electrode poisons. Certain of the present experiments were carried out in this improved gas-tight system immediately after termination of the previous work (7).

Anodic charging curves.—Figure 1 represents curves typical of a clean system (8). They show detail in the hydrogen region, a small plateau in the double layer region, and a linear oxygen region. To test system cleanliness with charging curves, it is first left under flowing hydrogen at open circuit for extended periods (usually 16-64 hr, sometimes longer). Polarization resulting from the very first pulse applied is photographed. After several intermediate charging curves to clean the surface, followed by a soak time of no less than 4 min, an additional pulse is photographed without changing trace position. If the two superimposed traces are essentially the same, and if they meet the above criteria concerning shape, the system is judged clean. If the pulses do not coincide, the differences in pulse shapes when correlated with soak time can give information on the type and amounts of contaminants present.

Decay time.—In the course of this work it was found that a low decay time together with a linear O_{ad} formation region is a dependable measure of cleanliness of an electrode and its associated electrolyte. Whenever possible, one electrode with a t_o below 30 msec was obtained and used as a probe for solution condition while the other electrode was treated in varying ways. So long as the solution probe electrode retained its t_o, short and unchanging, the solution was considered clean and unchanging.

Results

Effects of impurities.—Decay times are directly related to solution and/or platinum cleanliness. Given an imperfectly cleaned solution, as shown by charging curve tests, newly prepared Pt electrodes generally showed relatively high t_o of over 100 msec. This initial value was dependent on a number of variables. Repeated solution and electrode cleaning caused a steady reduction of t_o to some limiting value, which will be called the "base value" of t_o. When this base value was reached, further cleaning of solution and electrode had no effect on t_o, and unchanged values of t_o could then be observed over time periods of many weeks. When a base value was attained, other tests indicated a clean solution. Base values attained on different electrodes differed considerably, ranging from 25 to over 100 msec.

Factors other than solution or platinum cleanliness influence decay times. Two Pt electrodes, nominally the same and in the same solution at the same time usually showed different initial values of t_o, differing on occasion by almost two orders of magnitude. Extended cleaning generally yielded base values of t_o that also differed, a typical pair being 32.7 ± 3.2 and 100 ± 15 msec (all errors given for t_o are standard deviations). Previous work[2] indicated that t_o of 29.6 ± 3.0 msec could be attained in clean solution, so that Pt with a significantly higher t_o was assumed to be capable of increased catalytic activity. Of the pair of electrodes mentioned above, the one with an invariant t_o of 33 msec indicated that the solution was clean and unchanging. The other was unaffected by any of the above cleaning techniques up to and including level 4 anodization while simultaneously boiling the solution. Other tests gave no evidence of impurity present. It was concluded that some factor other than solution cleanliness or undesired sorbed species also influenced t_o. In a series of experiments, the higher base value t_o of a given pair was independent of type of electrode mounting (glass or Teflon-polyethylene) eliminating that variable. The two-electrode studies described above also showed, that given a clean solution, as indicated by the solution probe electrode, a newly prepared Pt electrode could be inserted into the cell without detectable solution contamination. This result was a necessary precondition to experiments described below. Such a newly inserted electrode would sometimes have sorbed impurity on it, as indicated by high initial t_o, that could be removed by the cleaning techniques used. The resulting base value t_o varied over wide limits.

Decay time on "active" platinum in a clean solution increases on introduction of impurities to the solution. Active Pt is here defined as that with $t_o < 35$ msec in clean solution. The amount of impurity required to cause a detectable change in t_o is related to the base value of t_o originally shown; the lower the base value t_o, the more sensitive it is to traces of impurities. Clean solutions containing two active electrodes were observed over long periods under conditions, such as frequent opening of the cell for short periods to insert or remove one electrode, where gradual solution recontamination from impurities in the room atmosphere was expected to occur. The presence or absence of impurity was estimated from charging curves, the relative amounts of impurity from amount accumulated in a given soak time. Simultaneously, the base values of t_o were monitored as well as the amount and level of electrode cleaning required to reattain the base value after long times on open circuit.

In solutions believed to be very clean, the decay time from the very first charging curve applied after 12 days soak time was the same as the base value. With continued use, however, the "first decay time" after a given soak time became higher and higher and successively more severe electrode cleaning was required to bring t_o back to the base value. Finally, the original base value became unattainable, and "apparent base values" were observed that rose as more impurity collected in solution. These apparent base values were unaffected by electrode cleaning up to level 4, or by extended preelectrolysis of solution. Under these conditions, both the solution probe

[2] Data taken from that used in ref. (2), Fig. 4a, and i_r values converted to corresponding t_o.

electrode and the working electrodes would show similar rises in apparent base value t_o, that is, they both appeared to be controlled by some external factor and took essentially the same value as they slowly rose together.

Rising apparent base values were connected with difficultly oxidizable impurities described more fully below. The point in this sequence at which such an impurity could be observed on the electrode using the charging curve test was highly variable, but, in general, first decay times observed after a few minutes soak that were higher than the base value would signal the presence of difficultly oxidizable impurity under conditions where a charging curve after 8 to 24 hr frequently would not. On the other hand, when impurity level in the solution was high enough to cause apparent base values to rise, its presence could be confirmed *via* charging curves after 8-hr soak periods.

This difficultly oxidizable impurity had a number of interesting properties. It was classed as difficultly oxidizable because it could not be removed from solution by extended electrolysis, and because, when present in sufficient concentrations, it could not be removed from the electrode by anodization, as indicated by charging curves and by the rising apparent base values. Yet after long standing in H_2-saturated solutions, charging curves showed a species on the electrode surface that was oxidized at about 1v. After this readily oxidizable species was removed, the electrode still had impaired catalytic activity, yet charging curves gave no indication of any remaining impurity. It was tentatively concluded that this was some nonvolatile, oxidized form of an impurity that could interact only slowly with H_2 to give an oxidizable product on the electrode surface yet was itself not removed with anodic treatment. Note the interesting similarities between this substance and CO_2, which, when present in solutions containing H_2 also causes anodic charging curves showing something being oxidized at around 1v (9).

The importance of these observations is that difficultly oxidizable impurities might accumulate in any real system under prolonged use. Even if the amount of surface covered with these impurities were too small to influence charging curves, demanding reactions such as the Pt-O/hydrogen reaction could be affected. Hence, to study such demanding reactions the usual kinds of anodic cleaning may not suffice.

The above results indicated that the increasing t_o were due to impurity sorption. However, it was also possible that some other process, such as a slow change in the catalyst lattice, could be affecting the base t_o. If the increase in t_o had been due to sorption of some impurity very resistant to removal by anodic polarization, then recleaning the solution and cell should cause the original value of t_o to be regained. These treatments would not affect a changed catalyst structure, however. Experimentally, the original base value could be regained by recleaning the cell, recharging with fresh solution, and again cleaning solution and electrodes *in situ*. In a typical case, the initial base value was 23 msec, the highest apparent base value was 55 msec, and the regained base value after recleaning was 25 msec. It might be argued that the solution electrolysis following recleaning of the cell would once again modify the base lattice to make it active again; however, the results in the paragraphs on Thermal Annealing below show that anodization of a surface is not a necessary prerequisite for an active surface, and further, that anodization of an inactive but clean surface will not affect its activity in the least.

Behavior of platinum with high t_o in clean solutions.—If under the treatments described, the only variable causing changes in t_o were sorbed impurity, and if a system were sufficiently clean initially, then the initial value t_o should be the same as the base value. It was desirable to obtain evidence in a system whose cleanliness was measured by an independent method. The improved gas-tight system (7) was such a system. The initial value of t_o was 270 msec; it was unaffected by increasingly severe anodic treatment up to level 4 while simultaneously boiling the solution.

Variables intrinsic to platinum.—Different Pt electrodes, nominally the same, showed widely differing t_o even when clean and in clean solutions. The variables that could affect the catalytic activity for the Pt-O/hydrogen reaction five or tenfold appeared to be fixed in the platinum when the electrodes were frozen. The following experiments were primarily designed to show that this was the case. The Pt surfaces were rearranged by remelting and by different heat-treatments, and the effect on decay time was observed. Surfaces were also etched with aqua regia. In the following work, unless otherwise specified, solutions were clean as indicated by an active solution probe electrode with unvarying decay time, usually less than 25 msec, as well as all other tests. Effects due to impurities introduced into the cell on a newly inserted electrode were eliminated, and all t_o under these conditions are necessarily base values.

Thermal annealing.—Platinum beads were melted and recrystallized repeatedly with determination of t_o between subsequent treatments. They had highly variable decay times on successive trials. Figure 2[3] shows typical appearance of a well-annealed Pt bead before mounting. It is nominally spherical with a number of well-developed flat regions that may have crystallographic significance. Not only are the developed flats regularly arrayed, but emerging flat regions are also part of the pattern, for example, the emerging regions at 2 and 8 o'clock in the 45° view are spaced between the large flats at 11 and 5 o'clock. A similar emerging flat can be seen in the 225° view. Under proper conditions, an entire bead could be held molten for as long as desired in a relatively large flame whose temperature was adjusted by changing the H_2/O_2 ratio. By reducing temperature gradually the bead could also be kept indefinitely just below the crystallization temperature and then slowly cooled from there. Beads so formed had variable t_o ranging from 20 to over 100 msec; they were highly reflective and, in general, would have no visible (10X optical) surface irregularities other than the flats. Beads made with smaller flames or cooled rapidly from a molten condition frequently showed fissures due to contraction on cooling, and flats were neither so numerous nor well-formed. Their t_o were also variable on repeating reforming of the same bead; they were frequently much higher, a typical series being 550, 200, 600, and 650 msec.

Typically, on inserting a newly formed bead, it was repeatedly anodized to oxygen evolution (in such a way as to introduce dermasorbed O) to remove surface impurities. Usually this caused t_o to fall to a value lower than the initial value. It was possible that the repeated introduction of oxygen into the lattice followed by its removal with hydrogen was alternately expanding and contracting the Pt surface layers and that this was the essential process in changing t_o. However, on several occasions, the initial t_o before any anodic polarization other than the single charging curve was less than 30 msec and was also the base value, *i.e.*, heavy anodic polarization in clean solutions is not a prerequisite for low t_o. Furthermore, heavy anodization of an originally clean electrode does not affect t_o even when it is as high as 270 msec (cf. section on behavior of Pt with high t_o in clean solutions, above). Anodization is presumed to reduce t_o primarily by removing sorbed species.

Chemical etching.—Decay time on a given Pt bead decreased monotonically with time etched in hot aqua

[3] Photographs were obtained by surrounding the bright, reflective bead with a white right circular cylinder marked with a black grid of parallel lines. Illumination was projected downward through a translucent planar surface, also marked with a rectangular grid, that appears as a bright circle in the photographs.

regia until a t_o was reached matching that of the solution probe electrode (between 20 and 30 msec). Further etching caused no change in t_o, and it would then remain unchanged as long as the solution remained clean. Since it remained unchanged over long periods it was concluded that contamination by Cl_2 or Cl^- had been avoided. Microscopic examination showed that etching occurred first in the regions between flats and, as etching continued, less and less area was unattacked, but the centers of many of the flats remained bright even after 15 min etching. Since attack is expected to take place at the most highly strained areas first, this supported the hypothesis that the flats might be crystallographically significant.

Platinum wires vs. platinum beads.—If the structural form of the underlying crystal lattice is significant, then rates on wires should be different from rates on beads, for the drawing process introduces large numbers of defects and possibly also surface impurities that can only be removed partially by annealing. Furthermore, a wire is unquestionably composed of many small crystallites. Wire electrodes under extended aqua regia treatment could not be brought down to active bead values; the lowest wire decay time achieved was 120 msec.

Electrochemical rates on different Pt electrodes.—Previous measurements in this laboratory of hydrogen overvoltage, anodic charging curves, etc., have not shown any detectable variation when measured on different electrodes, yet the foregoing indicates that substantial differences in catalytic activity for the chemical Pt-O/hydrogen reaction are the general rule. This suggested that these electrochemical reactions may be facile reactions, *i.e.*, independent of Pt pretreatment.

Rates of oxidation and reduction of water were measured in an improved gas-tight system (7) with a t_o = 270 msec electrode. Brief aqua regia treatment reduced t_o to 50 msec, and three representative points were redetermined. Data are shown in Table I; the currents were measured under He stirring rates of 350 ml/min, and the currents given for the t_o = 270 msec electrode are mean values taken from Fig. 1 of ref. (7). Current uncertainty at a given potential is about ±30%. Etching the Pt bead did not affect these rates within experimental error, although it increased the rate of the Pt-O/hydrogen chemical reaction involved in the decay fivefold.

Discussion

The results show that each Pt electrode as formed has some intrinsic activity for the chemical reaction

$$Pt\text{-}O_{ad} + \text{hydrogen} = Pt + H_2O \qquad [2]$$

Hydrogen is available from solution as H_2 and from the Pt metal as dermasorbed H. The intrinsic activity, that is, the catalytic activity of the clean metal, varied widely depending on how the metal was originally crystallized, worked after crystallizing, or etched. These treatments should affect the state of the surface, possibly by changing the type and number of grain boundaries exposed at the surface, by changing the number and distribution of crystal defects at or near the surface, or by changing the number and distribution of impurity atoms in the lattice and exposed at the surface. Carbon is one such impurity persistently present in trace amounts in platinum, and the platinum atoms surrounding such an impurity are expected to be quite different energetically. Previous work (2) indicated that oxygen present as an impurity in the lattice would change activity. Which are the more important variables cannot be established on the basis of these experiments.

Table I. Reaction rates on different electrodes

Potential in volts *vs.* NHE	Current amp/cm² t_o = 50 msec	Current amp/cm² t_o = 270 msec
+0.617	$+2.0 \times 10^{-8}$	$+2.0 \times 10^{-8}$
+0.587	$+1.2 \times 10^{-8}$	$+1.2 \times 10^{-8}$
+0.300	-4.5×10^{-8}	-6.0×10^{-8}

Since the detailed mechanisms of the chemical Pt-O/hydrogen reaction and of the electrochemical reactions investigated are not known, it is not possible to establish why the former should be so sensitive to surface changes while the latter are unaffected. However, it may be suggested that one way that these reactions differ is in the extent that surface diffusion of reactant is rate limiting. Notwithstanding the many differences between gas and solution phases, diffusion over the surface of a metal is expected to be very sensitive to structural differences. For example, in the gas phase, Ehrlich and Hudda (10) observed that surface diffusion of tungsten adatoms on tungsten occurred at different rates on different single crystal planes, that migrating atoms were reflected at boundaries of certain planes, and that in some planes motion along atomic rows was favored over diffusion across lattice steps. The thermal and chemical treatment used could act in a way to remove barriers to rapid surface diffusion. It was previously concluded (1) that the probable rate-determining process in the decay reaction was diffusion of either O_{ad} or H_{ad} over the surface to an active site.

It is not appropriate to speak in general about active or inactive electrodes, for one may be more active than the other for a demanding reaction, but both be equivalent and as active as possible for a facile reaction. If the reaction that defines the activity is explicitly given, then such ambiguity is avoided. This obviously also applies to such terms as electrode activation. One aspect of this investigation should be stressed. Anodic pretreatment of clean electrodes, for extended periods at up to 7 amp/cm², changes neither the surface area nor the Pt activity for the $Pt\text{-}O_{ad}/H_2$ reaction. If, however, Pt electrodes have impurities sorbed on them, anodization can improve such activity. Platinum electrodes equal in activity to the best obtained could be achieved with no initial anodic treatment. Such active surfaces stay active and unchanged indefinitely on open circuit, as long as they remain clean.

The combination of a charging curve and its subsequent decay curve gives extensive information concerning solution and electrode cleanliness. Charging curves are extremely sensitive to chemisorbed oxidizable substances (9) whereas this work shows that they may fail to signal presence of traces of difficulty oxidizable impurities. On the other hand, decay curves may not be influenced by trace amounts of easily oxidized species, which would tend to be removed by the preceding charging curve, but they are dependably influenced by difficultly oxidizable species present in quantities too small to be detected by any other technique. Experience indicates that these difficultly oxidizable impurities are more prevalent than heretofore expected and, while they require demanding reactions to detect when present in trace amounts, they can seriously affect catalysis. Experience also suggests, however, that the electrochemical reactions previously studied in this laboratory to date are relatively facile and unaffected by Pt surface structure.

Conclusions

The specific rate of the chemical reaction of oxygen chemisorbed on platinum with hydrogen is particularly sensitive to metallic pretreatment. Under clean conditions, certain thermal, chemical (etching), and physical treatments can modify this rate manyfold while several electrochemical reaction rates monitored concurrently are unchanged.

This demanding reaction is proposed as especially useful for identifying and examining certain variables affecting catalysis. Because impurity sorption is one

such variable, the rate of this reaction is one of the most responsive cleanliness tests available. It is quickly and easily applied and is a convenient way to monitor solution purity.

Anodization of a platinum surface is not a necessary prerequisite for maximizing its catalytic activity either for the Pt-O/hydrogen reaction or for the electrochemical reactions investigated. Under clean conditions, anodization of Pt that has low activity for this reaction does not affect its activity in the least. When sorbed impurities are present, anodic treatment can improve activity by removing these sorbed species, but such anodization cannot do more than bring activity up to that intrinsic to the clean metal itself.

Acknowledgments

The authors wish to thank Mr. A. C. Simon for devising the technique and obtaining the photographs shown in Fig. 2, and to thank him, Mrs. J. B. Burbank, and Dr. R. L. Jones for fruitful discussions concerning crystallography.

Manuscript received April 24, 1967; revised manuscript received July 11, 1967. This paper was presented at the Dallas Meeting, May 7-12, 1967.

Any discussion of this paper will appear in a Discussion Section to be published in the June 1968 JOURNAL.

REFERENCES

1. M. Boudart, A. Aldag, J. E. Benson, N. A. Dougharty, and C. Girvin Harkins, *J. Catalysis*, **6**, 92 (1966).
2. S. Schuldiner and T. B. Warner, *This Journal*, **112**, 212 (1965).
3. S. Schuldiner and R. M. Roe, *ibid.*, **110**, 332 (1963).
4. T. B. Warner and S. Schuldiner, *ibid.*, **112**, 853 (1965).
5. S. Schuldiner, B. J. Piersma, and T. B. Warner, *ibid.*, **113**, 573 (1966).
6. S. Schuldiner and C. H. Presbrey, Jr., *ibid.*, **111**, 457 (1964).
7. S. Schuldiner, T. B. Warner, and B. J. Piersma, *ibid.*, **114**, 343 (1967).
8. S. Schuldiner and T. B. Warner, *J. Phys. Chem.*, **68**, 1223 (1964).
9. B. J. Piersma, S. Schuldiner, and T. B. Warner, *This Journal*, **113**, 1319 (1966).
10. G. Ehrlich and F. G. Hudda, *J. Chem. Phys.*, **44**, 1039 (1966).

Electrochemical Formation and Dissolution of Different Types of Copper Layers on Platinum

M. W. Breiter

General Electric Research and Development Center, Schenectady, New York

ABSTRACT

The formation of adsorbed layers of Cu atoms and of thin and thick copper patches was studied at constant potential between 0.6v and 0.1v on smooth platinum in acidic solutions containing between 10^{-5}M to $5 \cdot 10^{-4}$M $CuSO_4$. After an activation procedure copper deposition was allowed for different times up to 1600 sec. The copper layers were characterized by the waves in the current-potential curves during their anodic stripping by a linear potential sweep at 30 mv/sec. Adsorbed layers alone are produced between 0.6 and 0.4v. Sites for weakly and strongly bonded Cu atoms may be distinguished as for H adsorption. At potentials between 0.4 and 0.1v the adsorbed layer is formed first, followed by the formation of thin and thick copper patches. The production of thin patches that do not yet possess the bulk properties of thick patches could be investigated at 0.3v. The extent of the formation of thin patches is small.

The first studies (1-4) of the deposition and dissolution of very small amounts of metals on inert electrodes were made with radioactive tracers. In general, deposition of fractions of monolayers was observed to occur at a certain "undervoltage" with respect to the equilibrium potential of the reaction

$$M^{z+} + 2e^- = M \qquad [1]$$

Here, M^{z+} designates the metal ion, and M, the metal atom in a lattice position.

It was recognized (3) that the undervoltage results energetically from the contribution of the heat of adsorption of the metal atoms on the inert metal surface to the energy of activation of the discharge reaction. Electrochemical studies of undervoltage phenomena were carried out with different trace metals on electrodes of Au (5), Ag (5-7), and Pt (8). A comprehensive paper involving Au, Ag, Cu, Bi, Pb, and Sn as inert electrodes and Bi, Pb, Sn, Tl, and Cd as deposited atoms was published (9) recently. Adsorption of polarized adatoms or adions is widely assumed (10, 11) to play an important role in the deposition of metal ions on electrodes of the same metal.

The decrease of hydrogen adsorption on smooth platinum in the presence of traces of copper ions was studied previously (12). The present investigation is much more comprehensive. It was carried out for three reasons. First, the properties of the platinum surface have been characterized by extensive studies (13) of the adsorption of H atoms. Sites for the adsorption of weakly bonded H-atoms may be easily distinguished (14-16) from sites on which H atoms are strongly bonded. It was of interest to see if two types of sites are involved in the adsorption of Cu atoms.

Second, the transition from the formation of an adsorbed layer to the formation of thick copper layers may be investigated in a simple way. The growth of thick layers need not be uniform across the surface. Thin layers ($\leq$20Å) of oxides or metals do not yet possess (17) the properties of the bulk phase. The free energy of formation approaches (17) that of the bulk phase with increasing layer thickness. Thus the initial formation of thin copper layers may be expected at potentials more anodic than the equilibrium potential of reaction [1], but less anodic than the potentials at which adsorbed layers are produced. Ex-

perimental evidence for the behavior of thin layers is scarce. The deposition and dissolution of small amounts of metals on inert electrodes seems to offer an opportunity to find out if and to what extent thin films exist as an intermediate stage in metal deposition in these systems.

Third, the formation of the described layers, especially of the adsorbed layer of Cu atoms should depend strongly on potential. It is the purpose of the paper to establish this dependence for the system Pt/Cu.

Experimental

The experiments were made in a Pyrex glass vessel of standard design at 20° ± 1°C. The electrolytic solutions (XM $CuSO_4$ + 0.5M H_2SO_4 or XM $CuSO_4$ + 1M $HClO_4$, $X = 10^{-5}$ to $5 \cdot 10^{-4}$M) were prepared from double distilled water and Analytical Reagent chemicals. Purified helium was used to remove molecular oxygen from the solutions and for stirring. The glass vessel was in an atmosphere of nitrogen inside a plastic dry box. The electrode potential, U, was measured *vs.* a hydrogen electrode in 0.5M H_2SO_4 or 1M $HClO_4$, respectively.

The following procedure which is similar to procedures (18) for the study of the adsorption of organic species on platinum was adopted. The platinum wire electrode (0.5 cm^2 geometric surface area) was kept for 5 min under He stirring at 1.4v. The stirring was stopped. Two minutes later, the electrode potential was switched potentiostatically to the desired potential ($0.1v \leq U \leq 0.6v$). The oxygen layer is reduced rapidly at these potentials. Deposition of copper atoms was allowed for different times up to 1600 sec. Subsequently, the copper layers were removed by anodic potential sweeps of 30 mv/sec. In a given solution, the copper deposition was carried out for different times at 0.5v first, then at 0.4, 0.3, 0.2v, and finally at 0.1v. The subsequent series of runs was made in a fresh solution with increased copper sulfate concentration.

The Wenking potentiostat 6 IRS, the Type 255 Function Generator of Exact Electronics, a Western Electric 275C Relay, and suitable potentiometers formed the electronic circuit. The current, I, was measured as voltage drop across standard resistors. The voltammetric I-U curves were recorded by the Varian F 80 X-Y recorder or the Tetronix 502 Oscilloscope. Cyclic I-U curves were also taken under different experimental conditions.

Results

Anodic I-U curves that were obtained after different times of deposition at 0.5v in 10^{-5}M $CuSO_4$ + 0.5M H_2SO_4 are replotted in Fig. 1. The curves are shifted against each other. A wave that is absent in 0.5M H_2SO_4 appears between about 0.6 and 0.9v. It was

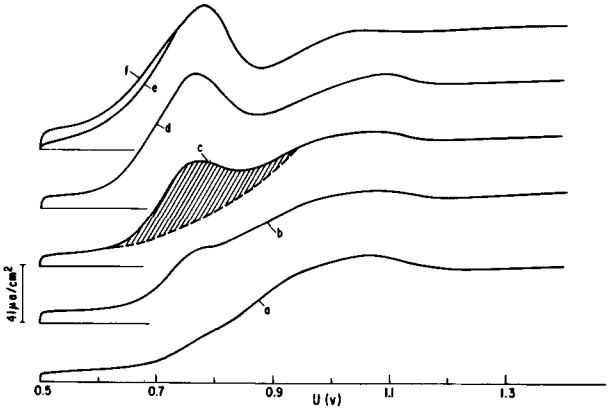

Fig. 1. Anodic I-U curves at 30 mv/sec after different times of copper deposition at 0.5v in 10^{-5}M $CuSO_4$ + 0.5M H_2SO_4: a, 50 sec; b, 100 sec; c, 200 sec; d, 400 sec; e, 800 sec; f, 1600 sec.

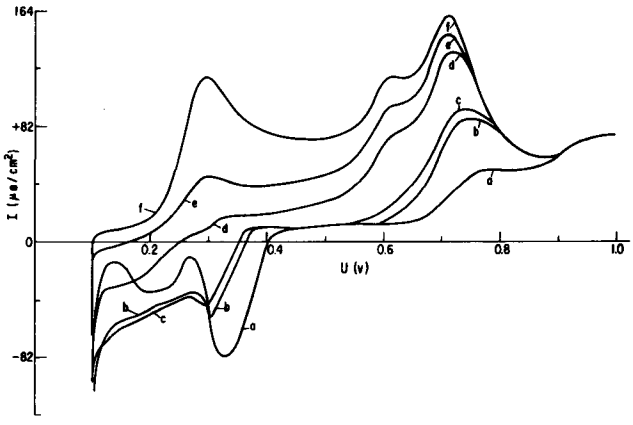

Fig. 2. Anodic I-U curves at 30 mv/sec after different deposition times at 0.1v in 10^{-5}M $CuSO_4$ + 0.5M H_2SO_4: a, 50 sec; b, 100 sec; c, 200 sec; d, 400 sec; e, 800 sec; f, 1600 sec.

verified by the corresponding experiments in 0.5M H_2SO_4 alone that this wave is not due to the slow adsorption of traces of organic impurities. The height of the wave increases with time. It tends to a limiting value in Fig. 1 after 1000 sec. The charge equivalent used up by the process that causes the appearance of the wave may be estimated by integrating the dashed area (sec curve c) between the I-U curves with and without this wave. It was 0.16 mcoul/cm^2 for curve c. As will be discussed later in detail, the wave is attributed to the anodic removal of adsorbed Cu atoms. The deposition of Cu atoms on a Rh electrode has been postulated (19) previously at potentials $U \leq 0.4v$ on the basis of the inhibition of the anodic dissolution of molecular hydrogen in 0.5M H_2SO_4 in the presence of traces of copper ions.

The I-U curves taken after different deposition times at 0.1v in 10^{-5}M $CuSO_4$ + 0.5M H_2SO_4 are replotted in Fig. 2. Curve a exhibits two minima of the cathodic current between 0.1 and 0.3v and the above described anodic wave between 0.6 and 0.9v. The two minima of the cathodic current are due to the superposition of the partial anodic current of reaction [2]

$$H_{ad} = H^+ + e^- \qquad [2]$$

to the limiting diffusion current of copper ions between 0.1 and 0.3v at small coverage with Cu atoms. The agreement of each of the potentials of the two minima with the corresponding potentials of the hydrogen peaks in 0.5M H_2SO_4 [see Fig. 1 in ref. (15)] demonstrates this. While the H layer is formed rapidly at 0.1v, only a small amount of Cu atoms is deposited in 50 sec because of mass transport control. The increase of the height and the broadening of the anodic wave between 0.6 and 0.9v is paralleled in curves b and c by a decrease of the partial anodic currents of reaction [2]. It is concluded that H atoms are replaced by Cu atoms that are more strongly bonded than hydrogen atoms.

Two new features are observable in curves d, e, and f. The broadening of the anodic wave between 0.6 and 0.9v leads to the appearance of another peak. The two peak potentials differ by about 0.1v. Simultaneously, an additional anodic wave with the peak at about 0.3v increases in height with time. The development of the described features is accompanied by the disappearance of hydrogen adsorption. It will be shown in the discussion that the wave with peak at about 0.3v may be ascribed to the anodic dissolution of thick copper patches.

While it is possible to determine the charge equivalent of the wave between 0.6 and 0.9v (compare curve c in Fig. 1) for $U \geq 0.4v$ at deposition times up to 1600 sec, the curves in Fig. 2 are an example for the fact that the integration can only be made with certainty at shorter times for $U \leq 0.3v$. The overlapping

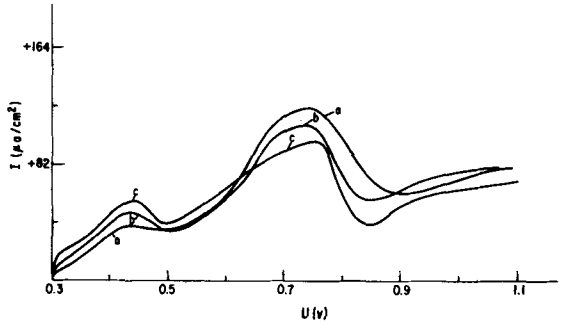

Fig. 3. Anodic *I-U* curves at 30 mv/sec after 1600 sec at 0.3v in XM $CuSO_4$ + 0.5M H_2SO_4: a, $X = 10^{-5}$M; b, $X = 3 \cdot 10^{-5}$M; c, $X = 10^{-4}$M.

of the different waves makes it difficult to find the integration limits at larger times. There is also the possibility that an additional anodic wave which is masked by overlapping effects exists between 0.35 and 0.55v in curves d, e, and f of Fig. 2. The actual presence of this wave is demonstrated by the *I-U* curves in Fig. 3. These curves were taken after a deposition of 1600 sec at 0.3v in *X*M $CuSO_4$ + 0.5M H_2SO_4 ($X = 10^{-5}$M, $3 \cdot 10^{-5}$M, 10^{-4}M). The wave with the peak potential at about 0.43v increases only slightly in height with the concentration of copper ions. It could not be detected after deposition at potentials $U \geqq 0.4$v.

The expected influence of mass transport processes is demonstrated by the cyclic *I-U* curves of Fig. 4 in XM $CuSO_4$ + 1M $HClO_4$ ($X = 4 \cdot 10^{-5}$M, 10^{-4}M, $5 \cdot 10^{-4}$M). Stirring increases the height of the anodic wave between 0.6 and 0.9v (compare curves a and a'). The wave between 0.35 and 0.55v appears in addition to the adsorption wave at $X = 10^{-4}$M in curve b'. An increase of the sweep rate has the same effect as a decrease of the rate of stirring, *i.e.*, the height of the waves decreases (compare curve b with b' and c with c'). All three waves are present in curve c'. The splitting of the adsorption wave is visible in curves b' and c'.

Discussion

Conclusions on electrode reactions from the formation of thick films.—The thermodynamic aspects and steady-state kinetics of the copper electrode have been discussed (20) recently. Three electrochemical net reactions, the standard potentials (21) U_o of which are given on the side of the equations, have to be considered

$$Cu^+ + e^- = Cu \qquad U_o = 0.522\text{v} \quad [3]$$

$$Cu^{++} + 2e^- = Cu \qquad U_o = 0.346\text{v} \quad [4]$$

$$Cu^{++} + e^- = Cu^+ \qquad U_o = 0.170\text{v} \quad [5]$$

Thick copper layers could be built up by three different mechanisms (a) by reaction [3]; (b) by reaction [4]; (c) by a net local cell represented by reactions [1] and [2]. The contribution of reaction [3] is negligible because of the small concentration of Cu^+. The thermodynamics demonstrate that the formation of thick layers according to reaction [4] is not feasible at $U \geqq 0.20$v for $X = 10^{-5}$M and at $U \geqq 0.23$v for $X = 10^{-4}$M. The results in Fig. 5 suggest that only reaction [4] contributes to the formation of thick copper layers because of the occurrence of a peak at 0.3v in the region of correct thermodynamics for Eq. [4] and by its absence when the thermodynamics indicate that reaction [4] will not go.

Curve d taken after 1600 sec of deposition at 0.1v and $X = 10^{-4}$M coincides practically with curve c between 0.23 and 0.30v. The peak of curve d appears at a more positive potential than that of curve c. This is interpreted as a combined influence of activation polarization and resistance overvoltage during the final depletion of the thick copper layer. Curves b, c, and d show the presence of the wave between 0.6 and 0.9v, in spite of the considerable charge equivalent corresponding to the dissolution of the thick layer. This is considered experimental evidence that the thick layer grows nonuniformly in patches on the Pt surface.

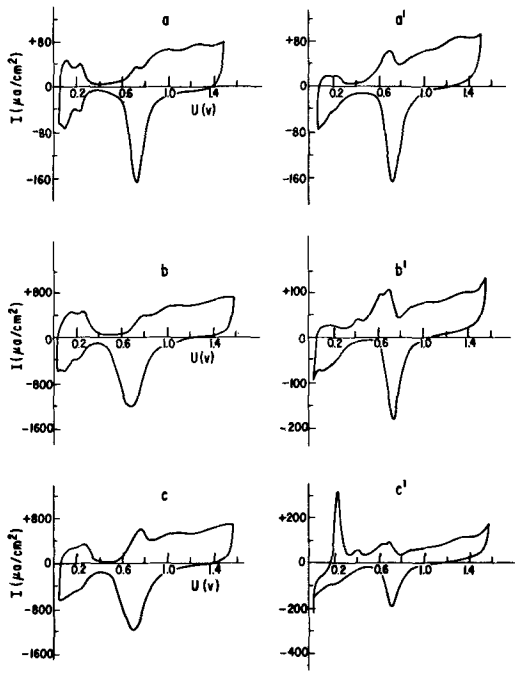

Fig. 4. Cyclic *I-U* curves at 30 mv/sec (a, a', b', c') or 300 mv/sec (b, c) in unstirred (a, b, b', c, c') and stirred (a') solutions of XM $CuSO_4$ + 1M $HClO_4$: a, a', $X = 4 \cdot 10^{-5}$M; b, b', $X = 10^{-4}$M; c, c', $X = 5 \cdot 10^{-4}$M.

Curves a, b, c and d in Fig. 2 demonstrate that the formation of the adsorbed layer takes place first at 0.1v. After nearly a monolayer exists, the other copper layers begin to form. The same statement holds for deposition at 0.2v.

Formation of thin layers.—After deposition at 0.3v the small wave between 0.35 and 0.55v is found for

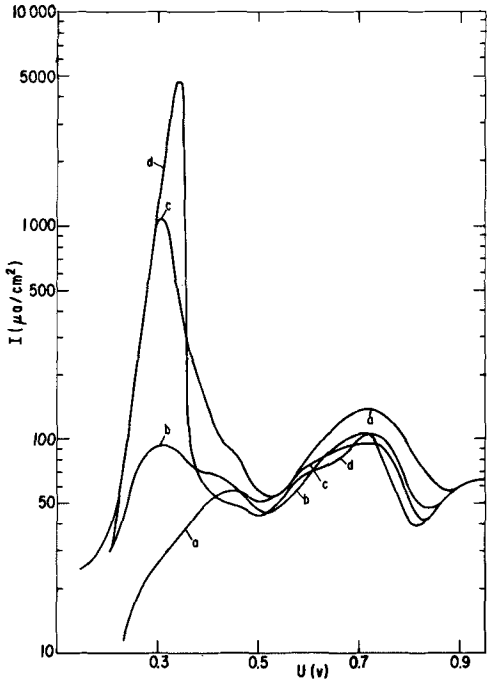

Fig. 5. Anodic *I-U* curves at 30 mv/sec after 1600 sec at 0.2v (a, b, c) or 0.1v (d) in XM $CuSO_4$ + 0.5M H_2SO_4: a, $X = 10^{-5}$M; b, $X = 3 \cdot 10^{-5}$M; c, $X = 10^{-4}$M; d, $X = 10^{-4}$M.

deposition times larger than 400 sec at $X = 10^{-5}$M, than 200 sec at $X = 3 \cdot 10^{-5}$M, and than 100 sec at $X = 10^{-4}$M. In contrast, the wave between 0.6 and 0.9v is largely developed when the small wave begins to appear. This result and the value of the peak potential of the small wave suggest that a few patches of thin films with intermediate behavior between adsorbed layers and thick layers are formed. Weak adsorption of Cu atoms in a second layer on top of the first layer might be another interpretation of the origin of the small wave. However, a larger dependence of the height of the small wave on the concentration of Cu^{++} than that in Fig. 3 would be expected in this case.

Curve a in Fig. 5 shows that the small wave is also present after deposition at 0.2v if the concentration of Cu^{++} is sufficiently small to rule out the formation of thick layers. Humps in curves b, c, and d of Fig. 5 indicate the existence of the wave in the presence of thick patches. It appears that the thin patches have not been converted into thick patches under the given conditions.

A simple calculation demonstrates that the small wave cannot result from the formation of a few thick patches according to reaction 3. In this case the concentration of Cu^{+} ions would have to be $1.6 \cdot 10^{-4}$M at least. This is not possible for curves a and b in Fig. 3 with $X = 10^{-5}$M and $3 \cdot 10^{-5}$M, respectively.

Formation of adsorbed layers.—The wave between 0.6 and 0.9v can only be attributed to the removal of adsorbed Cu atoms. Deposition of Cu atoms, according to reactions 3a and 4a

$$Cu^{+} + e^{-} = Cu_{ad} \qquad [3a]$$

$$Cu^{++} + 2e^{-} = 2Cu_{ad} \qquad [4a]$$

may occur at potentials more positive than the equilibrium potentials of reaction [3] and [4] at $X \leq 10^{-4}$ M, since the free energy of activation of reactions [3a] and [4a] is smaller than that of reactions [3] and [4] because of the influence of the free energy of adsorption. The situation is similar to that of reaction [2] for which the effect of the free energy of hydrogen adsorption has been discussed (22) in detail.

The charge equivalent ${}_sQ_H$ corresponding to a monolayer of H atoms was determined from *I-U* curves in 0.5M H_2SO_4 at the beginning of each series of deposition runs in the usual way (23). It was found to decrease slowly with the number of runs. The charge equivalents Q_{Cu} of the anodic wave between 0.6 and 0.9v were obtained for deposition at 0.4, 0.5, and 0.6v in the way shown for curve c in Fig. 1. Table I contains ${}_sQ_H$, Q_{Cu}, and $\theta_{Cu} = Q_{Cu}/2 \cdot {}_sQ_H$ at a deposition time of 1600 sec for the different concentrations.

The error in the determination of ${}_sQ_H$ and Q_{Cu} is estimated as 5% leading to an error of about 10% in θ_{Cu}. Overlapping prevents a reliable determination of θ_{Cu} for $U \leq 0.4$v.

In agreement with the results on the formation of thick layers, it had been assumed in the definition of θ_{Cu} that reaction [4a] is involved in the formation of the adsorbed layers of Cu atoms. The θ_{Cu} values in Table I support this assumption since θ_{Cu} is larger than 0.5 at 0.4v. The results in Table I demonstrate that the adsorption depends strongly on potential. As for the adsorption of organic substances (18, 24), the coverage decreases at constant bulk concentration in the potential region of oxygen adsorption on platinum. Oxygen atoms are more strongly bonded than Cu atoms. Monolayer formation is not yet achieved at 0.4v in 10^{-4}M $CuSO_4$ + 0.5M H_2SO_4 according to Table I. The appearance of a second peak in the desorption wave is just noticeable after deposition at 0.4v and $X = 10^{-4}$M.

Table I. Characteristic values for adsorption of Cu atoms at 0.4, 0.5, and 0.6v

	${}_sQ_H$ mcoul/cm²	0.4v Q_{Cu} mcoul/cm²	0.4v θ_{Cu}	0.5v Q_{Cu}	0.5v θ_{Cu}	0.6v Q_{Cu}	0.6v θ_{Cu}
10^{-5}M $CuSO_4$	0.59	0.66	0.56	0.42	0.36	0	0
$3 \cdot 10^{-5}$M $CuSO_4$	0.52	0.60	0.60	0.41	0.39	0.05	0.05
10^{-4}M $CuSO_4$	0.46	0.64	0.64	0.38	0.41	0.11	0.12

The anodic removal of Cu_{ad} occurs in a potential region of about 0.35v. This width corresponds approximately to that of the ionization of H_{ad} on smooth platinum in 0.5M H_2SO_4 at room temperature. Similarly, the desorption wave consists of two overlapping waves (see curves d to f in Fig. 2). A distinction between loosely and strongly bonding sites may be made for Cu_{ad} as well as for H_{ad}. However, while the number of strongly and weakly bonding sites is approximately equal for H_{ad} in 0.5M H_2SO_4, there are more strongly bonding sites than weakly bonding sites for Cu_{ad}. Since the adsorption experiments with H_{ad} and Cu_{ad} involve the same anions and the same concentration of anions, the latter difference is attributed to the specific influence of the adsorbed species on the surface states in the sense of an induced effect.

Comparison of the preceding conclusions with the results of cyclic voltammetry.—The conclusions on the formation of thick and thin copper layers and of adsorbed layers of Cu atoms are confirmed by the results obtained by cyclic voltammetry. Deposition of Cu atoms starts during the cathodic sweep after the oxygen layer has been reduced.

The hydrogen waves are well pronounced in curve a of Fig. 4, and the desorption wave of Cu atoms is small in unstirred $4 \cdot 10^{-4}$M $CuSO_4$ + 1M $HClO_4$. Stirring of the solution decreases the thickness of the diffusion layer. More Cu atoms were deposited in the case of curve a' than in curve a. The desorption wave is large. The cathodic current of Cu^{++} deposition is superimposed to that of the deposition of the H layer during the cathodic sweep. This effect is clearly pronounced for curve a' taken in the stirred solution. Owing to blocking of sites for H adsorption by adsorbed Cu atoms, the hydrogen wave is small in curve a'. The sweep rate and the concentration of Cu^{++} are such that formation and removal of only the adsorbed layer are observable.

The desorption wave of Cu atoms is small in curve b of Fig. 4 because of the short deposition time at a sweep rate of 300 mv/sec. At 30 mv/sec monolayer formation can be considered complete as indicated by the presence of the two peaks of the desorption wave. The small wave at the foot of the desorption wave shows that a few patches of thin films are dissolved there.

As to be expected the height of the desorption wave in curve c' increases with the Cu^{++} ion concentration above the height of the corresponding wave in curve b. Simultaneously hydrogen adsorption decreases. The relatively large cathodic current between 0.4 and 0.05v in curve c' indicates that formation of the thick layer occurs in $5 \cdot 10^{-4}$M $CuSO_4$ + 1M $HClO_4$ at 30 mv/sec. The presence of the first anodic wave confirms this conclusion. In addition, the waves corresponding to the removal of the thin layer and of the adsorbed layer are well pronounced.

It is clear from the preceding discussion that the same conclusions that were obtained in a quantitative manner from the results in Fig. 1 to 3 may be drawn in a qualitative manner from the curves in Fig. 4.

Manuscript received March 22, 1967; revised manuscript received *ca.* June 29, 1967. This paper was presented in part at the Dallas Meeting, May 7-12, 1967.

Any discussion of this paper will appear in a Discussion Section to be published in the June 1968 JOURNAL.

REFERENCES

1. M. Haissinsky, *J. Chim. Phys.*, **30**, 27 (1933).
2. L. B. Rogers and A. H. Stehney, *J.* (*and Trans.*) *Electrochem. Soc.*, **95**, 25 (1949).

3. J. T. Byrnes and L. B. Rogers, *ibid.*, **98**, 457 (1951).
4. M. Haissinsky, *Experientia*, **8**, 125 (1952).
5. T. Mills and G. M. Willis, *This Journal*, **100**, 452 (1953).
6. E. Schmidt and H. R. Gygax, *Helv. Chim. Acta*, **48**, 1178 (1965).
7. E. Schmidt and H. R. Gygax, *ibid.*, **48**, 1584 (1965).
8. B. J. Bowles, *Electrochim. Acta*, **10**, 731 (1965).
9. E. Schmidt and H. R. Gygax, *J. Electroanalyt. Chem.*, **12**, 300 (1966).
10. M. Fleischman and H. R. Thirsk, "Advances in Electrochemistry and Electrochemical Engineering," Vol. 3, Chap. 3, P. Delahay and C. Tobias, Editors, Interscience Publishers, New York (1962).
11. J. O'M. Bockris and A. Damjanovic, "Modern Aspects of Electrochemistry, "Vol. 3, Chap. 4, J. Bockris and B. Conway, Editors, Butterworths, Washington (1964).
12. M. Breiter, C. A. Knorr, and W. Völkl, *Z. Elektrochem.*, **59**, 681 (1955).
13. A. N. Frumkin, "Advances in Electrochemistry and Electrochemical Engineering," Vol. 3, Chap. 8, P. Delahay and C. Tobias, Editors, Interscience Publishers, New York (1962).
14. A. Eucken and B. Weblus, *Z. Elektrochem.*, **55**, 114 (1951).
15. M. Breiter, C. A. Knorr, and H. Kamermaier, *ibid.*, **60**, 37 (1956).
16. M. W. Breiter, *J. Phys. Chem.*, **68**, 2249 (1964).
17. K. G. Weil, *This Journal*, **110**, 640 (1963).
18. M. W. Breiter and S. Gilman, *ibid.*, **109**, 622 (1962).
19. M. Breiter and F. G. Will, *Z. Elektrochem.*, **61**, 1177 (1957).
20. V. Bertocci, *Electrochim. Acta*, **11**, 1261 (1966).
21. W. M. Latimer, "The Oxidation States of the Elements and Their Potentials in Aqueous Solutions," Prentice Hall, New York (1938).
22. R. Parsons, *Trans. Faraday Soc.*, **54**, 1053 (1958).
23. W. Böld and M. Breiter, *Z. Elektrochem.*, **64**, 897 (1960).
24. M. W. Breiter, *Electrochim. Acta*, **8**, 447 (1963).

Brief Communications

Use of Nonlinear Circuits for the Acquisition of Electrode Kinetic Data

S. D. James[1]

Brookhaven National Laboratory, Upton, New York

A wide variety of relaxation methods has been devised to measure the parameters characterizing the kinetics of electrode processes. The usual single-pulse techniques involve recording transient i, η, or Q (charge) *vs.* time, immediately following the imposition of a galvanic step-function to the cell (1-5) or recording η *vs.* t after the completion of a very abrupt increment in electrode charge density (6, 7).

In the potential-step (1), potential-step-integral (2), voltage-step (3), and small amplitude current-step or galvanostatic (4) methods, the required parameters are obtained from the slope and intercept of plots of i, η, or Q *vs.* $t^{1/2}$. In the charge-step method (6) and its derivative current-impulse method (7), η is abruptly changed with a slug of charge. The double layer then relaxes by discharging through the electrode reaction, and kinetic parameters are extracted from plots of ln η *vs.* t. In the large amplitude current-step or chronopotentiometric method (5) the required plot is η *vs.* ln $(1 - At^{1/2})$, where $A = \tau^{-1/2}$, τ = transition time.

It appears that much more attention has been paid to the imposition of the electrical perturbation than to the read-out of cell response (8). The usual data acquisition method in these studies has been to photograph an oscilloscopic record of the electrical variable *vs.* time and then replot the data in the form designed to achieve linearity. Apart from the time consumed (especially in chronopotentiometry) and the errors introduced by this replotting, the experimentation lacks fluency, punctuated as it is by hiatuses for the replotting. This is especially true in the η or i *vs.* $t^{1/2}$ experiments where the linearity with $t^{1/2}$ is often rather brief and elusively sandwiched between the decay of capacitative current on the one hand and the onset of pure diffusion control on the other. The examination of a few time scales is always desirable to locate the one best displaying the linear region. In the opinion of the present author, these difficulties may, at least in part, explain the relative paucity of applications of these methods (9).

The use of nonlinear circuits is recommended for the direct display of the desired linear relations. Devices possessing a logarithmic response have been on the market for about five years and appear well adapted for the direct display of ln η *vs.* t curves (6, 7) by interposition between the cell output and the y-plates of the CRO. About three years ago many other nonlinear devices became available in the form of plug-in units which can perform a broad spectrum of mathematical operations on an electrical signal (these devices are the building bricks of the more advanced analogue computers). There seems no reason why a direct read-out of, *e.g.*, the chronopotentiometric linearity between η and ln $(1 - At^{1/2})$, could not be obtained with a combination of four of these devices: a quadratic for $t^{1/2}$, linear for A, differential amplifier to get $(1 - At^{1/2})$, and finally a logarithmic device.

Of particular use in electrochemical kinetics is the square-rooting circuit or "quadratic transconductor," which can convert an input V into an output proportional to $V^{1/2}$. By diverting the ramp voltage which drives the time base of an oscilloscope through one of these circuits, the time base can be made to displace

[1] Present address: Electrochemistry Division, Chemistry Research Department, U. S. Naval Ordnance Laboratory, White Oak, Maryland.

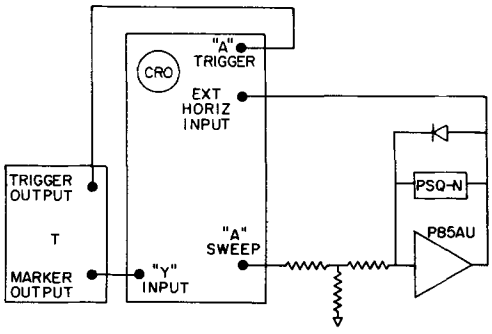

Fig. 1. Circuit designed to illustrate square-rooting of CRO time base. T, Time mark generator Tektronix 180A; CRO, Tektronix 547; PSQ-N and P85AU, quadratic transconductor and differential operational amplifier, respectively, of Philbrick Researches Inc.

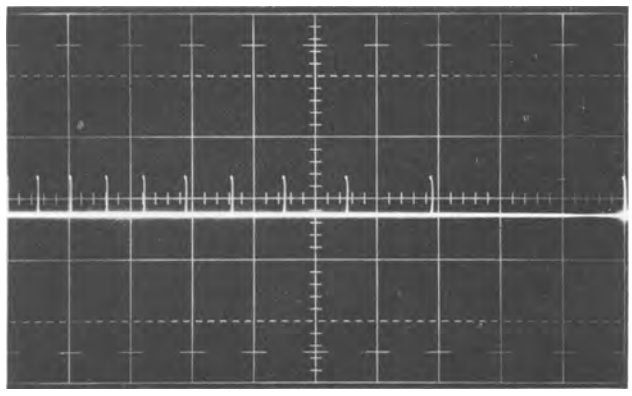

Fig. 2. Photograph illustrating square-rooting of CRO time base. Total time interval of 10 msec starting from the right. Markers at 1-msec intervals.

according to $t^{1/2}$ instead of t. Thus a direct display of the commonly useful $t^{1/2}$ linearity is secured. A circuit designed to effect and illustrate the square-rooting of an oscilloscope's time base is shown in Fig. 1. PSQ-N is the quadratic device. Its input is 0-10v, and the accuracy of the square-rooted output is 0.1% of full scale. The response, in terms of a settling-time to within 10% of its final value, is 1 μsec. Thus it is already suitable for most applications and further improvement in both accuracy and response time is to be expected. Figure 2 is a photograph of 1-msec markers on a total time-base interval of 10 msec. The time base was square-rooted with the circuit of Fig. 1. If a cell output instead of the time markers were applied to the y-plates, a direct recording of output *vs.* $t^{1/2}$ would be obtained with an abscissa dimension of 10^{-2} $sec^{1/2}/cm$.

Acknowledgment

The author is grateful to Robert P. Ducey for his assistance with the instrumentation. This work was performed under the auspices of the United States Atomic Energy Commission.

Manuscript received July 31, 1967.

Any discussion of this paper will appear in a Discussion Section to be published in the June 1968 JOURNAL.

REFERENCES

1. M. Fleischmann and H. R. Thirsk, *Trans. Faraday Soc.*, **51**, 71 (1955); H. Gerischer and W. Vielstich, *Z. Physik. Chem.*, **3**, 16 (1955); *ibid.*, **4**, 10 (1955).
2. J. H. Christie, G. Lauer, and R. A. Osteryoung, *J. Electroanal. Chem.*, **7**, 60 (1964).
3. W. Vielstich and P. Delahay, *J. Am. Chem. Soc.*, **79**, 1874 (1957).
4. T. Berzins and P. Delahay, *ibid.*, **77**, 6448 (1955).
5. *Ibid.*, **75**, 2486 (1953).
6. P. Delahay, *J. Phys. Chem.*, **66**, 2204 (1962); W. H. Reinmuth, *Anal. Chem.*, **34**, 1159 (1962).
7. W. D. Weir and C. G. Enke, *J. Phys. Chem.*, **71**, 275, 280 (1967).
8. Cf., *e.g.*, Symposium on Operational Amplifiers in Analytical Instrumentation, *Anal. Chem.*, **35**, 1770 (1963).
9. N. Tanaka and R. Tamamushi, *Electrochim. Acta*, **9**, 963 (1964).

Charge-Transfer Coefficients for Aqueous Cd (II) Evaluated by Large Amplitude A-C Polarography

J. D. McLean and Andrew Timnick

Department of Chemistry, Michigan State University, East Lansing, Michigan

This article is an extension of the initial work on large amplitude a-c polarography of aqueous Cd(II) (1). The purpose of this work is to test the extent of applicability of existing equations developed for low amplitude a-c polarography by determining the effect of large amplitudes of the applied a-c potential on experimentally determined charge-transfer coefficient (α) values for Cd(II) in aqueous solutions.

The solutions and chemicals employed in this work were described previously, as well as the instrumentation and experimental techniques (1).

Charge-transfer coefficients can be evaluated from cot ϕ *vs.* $\omega^{1/2}$ plots of a-c polarographic data, where ϕ is the corrected phase-angle between the applied a-c potential and the measured a-c current from the polarographic cell, and ω is the angular frequency of the applied a-c potential. The phase-angles are corrected for uncompensated solution resistance and double-layer charging current of the supporting electrolytes according to the method of Bauer and Elving (3). The experimental constants necessary for these corrections are listed in Table I. To calculate values for α, it is necessary to obtain the slopes of cot ϕ *vs.* $\omega^{1/2}$ plots evaluated at two different d-c potentials. The following equation is used for this calculation (2)

$$\alpha = \frac{2.303}{(j_2 - j_1)} \left\{ \log \left(\frac{1 + e^{j_2}}{1 + e^{j_1}} \right) - \log \left(\frac{\text{slope 1}}{\text{slope 2}} \right) \right\} \quad [1]$$

where

$$j_1 = \frac{n\mathbf{F}}{RT} (E_{\text{d.c.1}} - E_{1/2^R}) \quad [2]$$

$$j_2 = \frac{n\mathbf{F}}{RT} (E_{\text{d.c.2}} - E_{1/2^R}) \quad [3]$$

In these equations the subscripts, one and two, refer to the two d-c potentials, $E_{\text{d.c.1}}$ and $E_{\text{d.c.2}}$, respectively, and $E_{1/2^R}$ is reversible half-wave potential. The slopes listed in Tables II and III are the least squares slopes of cot ϕ *vs.* $\omega^{1/2}$ plots evaluated at 15 frequencies be-

Table I. Experimental constants for the correction of the phase-angle for various supporting electrolytes

Supporting electrolyte	$E_{1/2}{}^R$ vs. SCE v^a	$E_{1/4}$		$E_{1/2}{}^R$		$E_{3/4}$	
		$c_{d.l.}$, μf	R_t ohms	$c_{d.l.}$, μf	R_t ohms	$c_{d.l.}$, μf	R_t ohms
1.0M Na_2SO_4	−0.606	0.844	78.7	0.834	78.7	0.816[b]	74.3[b]
1.0M H_2SO_4	−0.597	0.966	56.0	0.956[b]	60.4[b]	0.912	56.0

[a] $E_{1/4}$ and $E_{3/4}$ were displaced 14 mv from $E_{1/2}{}^R$ in all media.
[b] Determined with a second D.M.E.

Table II. Variation of the charge-transfer coefficient with changing amplitude of applied a-c potential for 5.0 x 10^{-4}M Cd(II) in 1.0M Na_2SO_4

Δ^Ep − p, mv	Slope × 10^2 at $E_{1/4}$	Slope × 10^2 at $E_{1/2}{}^R$	Slope × 10^2 at $E_{3/4}$	α^a	α^b
10	1.77	2.69	3.15	0.24	0.24
20	1.50	2.28	2.58	0.25	0.25
30	1.48	2.40	2.69	0.23	0.25
40	1.45	2.24	2.55	0.24	0.24
50	1.59	2.26	2.73	0.25	0.25
60	1.55	2.21	2.60	0.26	0.26
70	1.49	2.20	2.42	0.28	0.28
80	1.52	2.14	2.43	0.28	0.28
90	1.49	2.03	2.32	0.30	0.30
100	1.62	2.13	2.41	0.32	0.32

[a] Obtained from ratio of slopes at $E_{3/4}$ and $E_{1/4}$, see Eq. [1].
[b] Obtained from an average of α's evaluated from the ratio of slopes at $E_{1/2}{}^R$ and $E_{1/4}$ and at $E_{3/4}$, and $E_{1/2}{}^R$, see Eq. [1].

Table III. Variation of the charge-transfer coefficient with changing amplitude of applied a-c potential for 5.0 x 10^{-4}M Cd(II) in 1.0M H_2SO_4

Δ^Ep − p, mv	Slope × 10^3 at $E_{1/4}$	Slope × 10^2 at $E_{1/2}{}^R$	Slope × 10^2 at $E_{3/4}$	α^a	α^b
10	8.71	1.32	1.57	0.23	0.22
20	8.29	1.35	1.58	0.20	0.21
30	8.00	1.45	1.46	0.22	0.20
40	8.21	1.38	1.59	0.20	0.20
50	8.26	1.37	1.54	0.21	0.22
60	8.27	1.30	1.58	0.20	0.20
70	8.37	1.21	1.54	0.22	0.22
80	8.23	1.26	1.40	0.25	0.26
90	8.31	1.21	1.39	0.26	0.26
100	7.76	1.06	1.38	0.23	0.24

[a] Obtained from ratio of slopes at $E_{3/4}$ and $E_{1/4}$, see Eq. [1].
[b] Obtained from an average of α's evaluated from the ratio of slopes at $E_{1/2}{}^R$ and $E_{1/4}$ and at $E_{3/4}$, and $E_{1/2}{}^R$, see Eq. [1].

tween 30 and 1100 Hz, at d-c potentials of $E_{1/4}$, $E_{1/2}{}^R$ and $E_{3/4}$. The various supporting electrolytes were used to obtain a range of values for the apparent heterogeneous rate constant (k_h) since the accuracy of the determination of α depends on the magnitude of k_h.

Table II lists the variation of values of α with increasing amplitude of the applied a-c potential for Cd(II) in 1.0M Na_2SO_4, for which k_h = 0.06 cm/sec. Table III lists similar variations of α for Cd(II) in 1.0M H_2SO_4 for which k_h = 0.14 cm/sec. From Tables II and III it is apparent that α values, as determined by the low amplitude equation, do not vary markedly up to an amplitude of 80 mv peak to peak. Although the α values show good agreement, some deviations in the plots become apparent above 40 mv. These deviations occur as a distinct falling off from linearity in the cot ϕ *vs.* $\omega^{1/2}$ plots at frequencies above 600 Hz, with the magnitude of the error increasing directly with the frequency. For typical plots, see Fig. 1 of the previous paper (1). In all of these plots the intercept is one on the cot ϕ axis at zero frequency, as predicted by low amplitude theory.

The changes in the slope of the cot ϕ *vs.* $\omega^{1/2}$ plots with increasing amplitudes are smaller at $E_{1/4}$ and $E_{3/4}$ than at $E_{1/2}{}^R$. This leads to the conclusion that acceptable values of α can be evaluated at large amplitudes even though α is more sensitive to changes in the slope of these plots, than is k_h. Smith's (4) theoretical plots of cot ϕ *vs.* $E_{d.c.}$ for a hypothetical system at amplitudes of 10, 40, 60, and 80 mv peak to peak, predict smaller slope changes at $E_{1/4}$ and $E_{3/4}$ than at $E_{1/2}{}^R$, in agreement with the results obtained in this study.

The conclusions of this study are only valid for charge-transfer coefficients for systems having apparent heterogeneous rate constants in the range 0.01 to 0.20 cm/sec, as is the case for Cd(II) in the various sulfate media. When employing large amplitudes, charge-transfer coefficients should only be evaluated with low amplitude equations at potentials near $E_{1/4}$ and $E_{3/4}$ or from averages of data obtained at $E_{1/4}$ and $E_{1/2}{}^R$ and at $E_{1/2}{}^R$ and $E_{3/4}$, since the larger variations in the slopes of cot ϕ *vs.* $\omega^{1/2}$ plots at $E_{1/2}{}^R$ are eliminated in this manner.

Transfer coefficients for Cd(II) in 1.0M KNO_3 could not be evaluated due to the large value of the heterogeneous rate constant of 0.67 cm/sec. This caused the ratio of the uncertainties in the slopes of cot ϕ *vs.* $\omega^{1/2}$ plots to become competitive with the values of the ratio of the slopes.

The results obtained for the aqueous Cd(II) system indicate that, if the apparent heterogeneous rate constant for electron transfer is between 0.05 and 0.20 cm/sec, low amplitude equations can be used to calculate α values for applied a-c potentials of up to 80 mv peak to peak, which is considerably beyond the previously predicted limit of 16/n mv which would be 8 mv for Cd(II).

Acknowledgment

The authors are grateful to The Electrochemical Society for the partial support of this work.

Manuscript received July 31, 1967.

Any discussion of this paper will appear in a Discussion Section to be published in the June 1968 JOURNAL.

REFERENCES

1. J. D. McLean and A. Timnick, *This Journal*, **114**, 239 (1967).
2. J. K. Frischmann and A. Timnick, *Anal. Chem.*, **39**, 507 (1967).
3. H. H. Bauer and P. J. Elving, *J. Am. Chem. Soc.*, **82**, 2091 (1960).
4. D. E. Smith, "Electroanalytical Chemistry," Vol. I, Chap. I, A. J. Bard, Editor, Marcel Dekker, Inc., New York (1966).

Gas Phase Anodization of Tantalum

T. A. Jennings and W. McNeill
Frankford Arsenal, Philadelphia, Pennsylvania
and R. E. Salomon
Department of Chemistry, Temple University, Philadelphia, Pennsylvania

ABSTRACT

The anodic oxidation of tantalum in the gas phase was studied using an electromagnetic ion cathode. The anodic films were prepared at constant current densities of 1.0 and 2.0 ma/cm^2. The growth characteristics of anodic tantalum oxide films, in the gas phase, were found to be similar to films prepared in liquid electrolytes. A comparison is made between the results of this study and other reported gas phase reactions with various anode surfaces. The tantalum oxide growth, for the experimental conditions reported here, is shown to be linearly dependent on the total charge passed in the anode circuit during the reaction up to a formation voltage of 200v.

Tantalum oxide films prepared by anodic reactions in aqueous and nonaqueous electrolytes have been shown to contain impurities from the solution (1-3). Anodic oxide films prepared in an oxygen discharge (4-7) have been found to exhibit physical and electrical properties analogous to those found with films formed in liquid electrolytes. Certain aspects of the growth of films by anodization in liquid electrolytes are similar to those observed during gas phase anodization. Examples are the relationship between thickness and the formation voltage and the current decay at constant voltage.

Some authors (5) report the presence of a large electron population in the gaseous electrolyte and anode temperatures as high as 200°C during anodization. This paper reports the use of an electromagnetic ion cathode which was designed to limit the electron and positive ion concentration in the gaseous electrolyte. Separation of the ion cathode from the anode reduces heating effects of the anode and allows for the observation of the anode reaction without the masking effects of a general discharge. Results are compared with anodic oxidation of tantalum in aqueous electrolytes and with gas phase anodization of various materials as reported by others.

Experimental

The gas phase electrochemical cell is illustrated in Fig. 1. Part of the cell (see Fig. 2) consists of an electromagnetic ion cathode. The primary function of the ion cathode is to serve as a source of negative charge carriers. The ion cathode consists of a permanent magnet (1400 gauss), a tantalum cylinder which serves as a cathode, and a tungsten coil which serves as a positive electrode. The tantalum cylinder (cathode) was held at 500 to 1000v negative with respect to ground while the tungsten coil was maintained at ground potential. The magnetic field served to restrict the motion of the electrons to the space defined by the tungsten coil and thereby enhance the probability of electron capture by the oxygen. The oxygen is introduced at the base of the ion cathode through a variable leak.[1]

The anode consisted of a tantalum sheet, 0.010 in. thick, which was connected to an electrically insulated lead. The tantalum anodes were constructed from metallurgical grade (99.90% min) tantalum sheet supplied by the Fansteel Metallurgical Company. The anodes were prepared by cleaning in a hot detergent solution for several hours, followed by rinsing in freshly distilled water. After drying, an anode area of 3.6 cm^2 was defined by masking the rest of the anode with vinyl insulating tape. Electrical contact to the anode was made by contacting a wide strip of thin tantalum sheet to the back of the anode to serve as a low resistance contact. Only the 3.6 cm^2 anode area was exposed to the gas electrolyte.

The pressure of the cell, determined by a discharge gauge located in the base plate, was first reduced to 5 x 10^{-5} Torr and was maintained at this pressure for less than 1 hr in order to limit possible contamination due to backstreaming of the diffusion pump oil. The cell was then backfilled with oxygen to a pressure of 70 mTorr.

One of the operating characteristics of our gas phase anodizing cell was that no significant anode current was measured when the anode was negative with respect to ground. This was taken as evidence for a low concentration of positive ions leaving the ion cathode. The presence of positive ions in the gas phase cell was investigated using a probe fashioned after that described by Barnes (8). Positive ions were

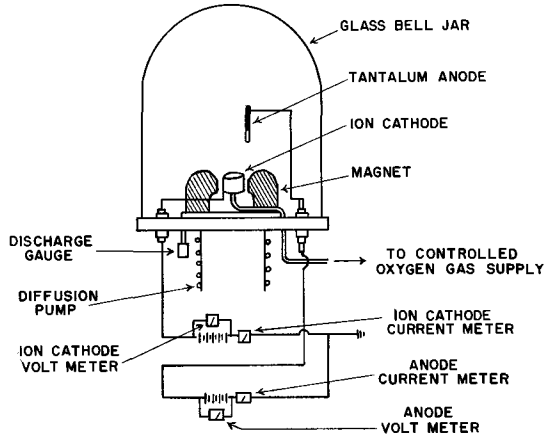

Fig. 1. Gas phase anodization apparatus

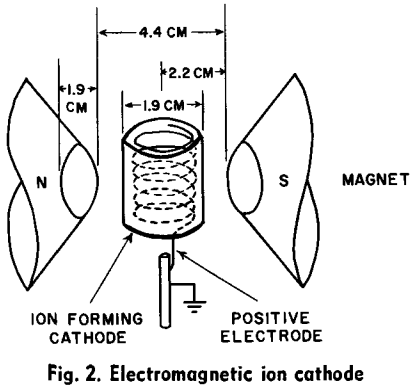

Fig. 2. Electromagnetic ion cathode

[1] Vactronic variable leak, model number VVS-50W.

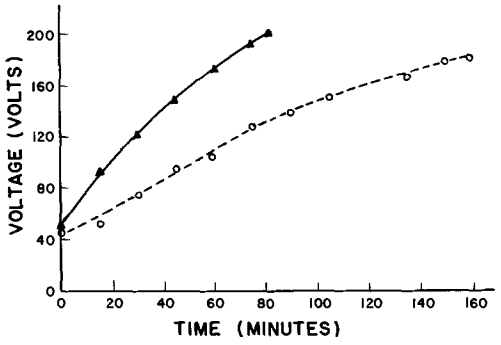

Fig. 3. Chronopotentiograms for constant current density. ○, 1.0 ma/cm², 40°C; ▲, 2.0 ma/cm², 70°C, ion cathode voltage ~750v, current 25 ma; oxygen pressure, 70 mTorr.

detected only when the anode was positive with respect to ground and only when the probe was in a zone characterized by a pale green glow immediately adjacent to the anode surface.

Anodic reactions were carried out at anode current densities of 1.0 and 2.0 ma/cm². The anode temperature, which was measured by a thermocouple attached to the metal back of the anode, did not exceed 40°C for the anodic reactions performed at 1.0 ma/cm² and 70°C for reactions at 2.0 ma/cm².

All films were grown at a constant current density and to a predetermined voltage. This voltage is defined as the formation voltage and is measured between ground and the metal anode. Figure 3 illustrates the voltage-time dependency for films formed at current densities of 1.0 and 2.0 ma/cm². It will be noted that in Fig. 3 the voltage-time curves do not intersect the ordinate at zero time. This is because it was observed experimentally that in a time of about 1 sec or less the anode voltage would rise to about 45-50v for current densities of 1.0 and 2.0 ma/cm²

In Fig. 4, the anode current is plotted as a function of time for a 100v gas phase anodic Ta_2O_5 film. It is seen that the relationship is nonlinear, while the reciprocal current-time function is linear.

Figure 5 is a plot of the anode current in the gas electrolyte as a function of the applied anode voltage for a constant film thickness. In order to study this effect a 100v film was first prepared by gas phase anodization at a constant current density of 2.0 ma/cm². The applied voltage was reduced to zero and then increased in small increments. The current was measured after each increment. Since there was no noticeable change in the interference color of the film it is assumed that there was not a significant increase in the film thickness. Figure 5 reveals a relationship between the anode current density and the applied voltage which is probably due to simultaneous changes in the electrical characteristics of both the gas electrolyte and the oxide film. It is of interest to note that the steep rise in the current density between 32

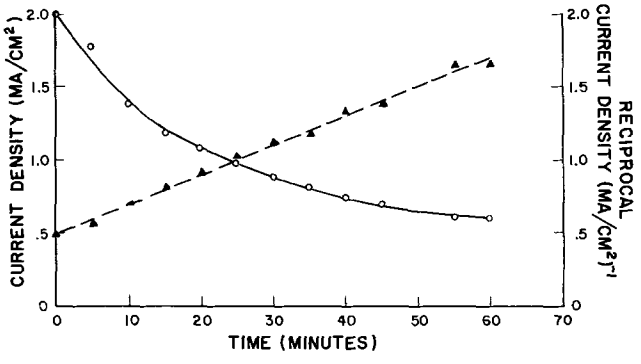

Fig. 4. Time dependence of anode films form at a constant formation voltage. ○, current density vs. time; ▲, reciprocal current density vs time.

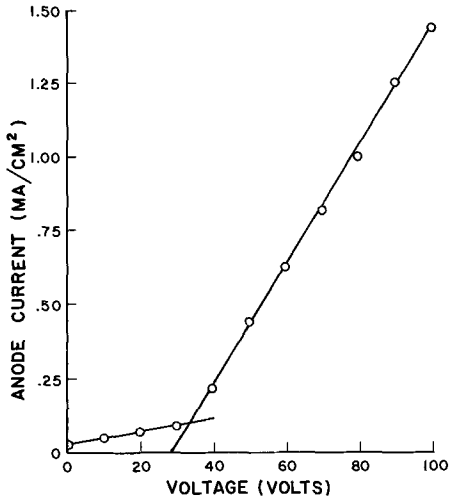

Fig. 5. Anode current as a function of anode voltage at constant film thickness.

and 50v is in the same region as that where film growth begins.

Film thickness was determined by capacitance measurements and by comparison with an optical step gauge. In the capacitance measurements eighteen gold contacts, measuring approximately 0.020 cm², were deposited on the oxide film. Electrical contact to the gold film was made with a smaller spot of conductive silver paint. After the silver paint had dried, the capacitance of the films was measured using a type 716-C General Radio Capacitance Bridge. Capacitance values measured at 1 kc/sec are shown in Table I. Thicknesses were calculated assuming a dielectric constant of 27.6 (9). The possible presence of αTa_2O_5, which Pavlovic (10) showed to have a much larger dielectric constant, was discounted by the observation that the capacitance and the dissipation factor of our films remains nearly constant from 77° to 300°K, while the dielectric properties of αTa_2O_5 are reported to be strongly temperature dependent.

Thickness measurements were also made by comparison with an optical step gauge (11). The gauge was prepared by anodization of a chemically polished strip of tantalum in a 0.1 w/o solution of Na_2SO_4 at 48°C. Anodization was carried out in 15v steps, and for each increase in voltage a portion of the tantalum strip was removed from the solution. The current density was 2.0 ma/cm² maximum and was allowed to decay to 0.1 ma/cm² which was used as the end point for each step. The films prepared by gas phase anodization were compared with the step gauge, and by matching the number of fringes and the color it was possible to estimate film thickness.

The thickness-voltage values determined by both the capacitance and optical techniques are plotted in Fig. 6. One should note that the voltage-thickness plots are linear for our gas phase films and have slopes close to that reported by Vermilyea (11) for

Table I. Capacitance and dissipation factors for Ta_2O_5 films measured at 1 kc/sec

Anode	Current density, ma/cm²	Anode voltage, v	Mean capacitance, μf/cm²	Mean dissipation factor
1	1.0	75	0.2563 ± 0.03*	0.048 ± 0.007*
2	1.0	100	0.1742 ± 0.01	0.045 ± 0.007
3	1.0	150	0.1129 ± 0.003	0.025 ± 0.004
4	1.0	200	0.0807 ± 0.006	0.011 ± 0.002
5	2.0	75	0.4289 ± 0.03	0.051 ± 0.005
6	2.0	150	0.1322 ± 0.008	0.018 ± 0.004
7	2.0	200	0.0944 ± 0.008	0.035 ± 0.008
8	2.0	250	0.0725 ± 0.008	0.013 ± 0.002

* Standard deviation.

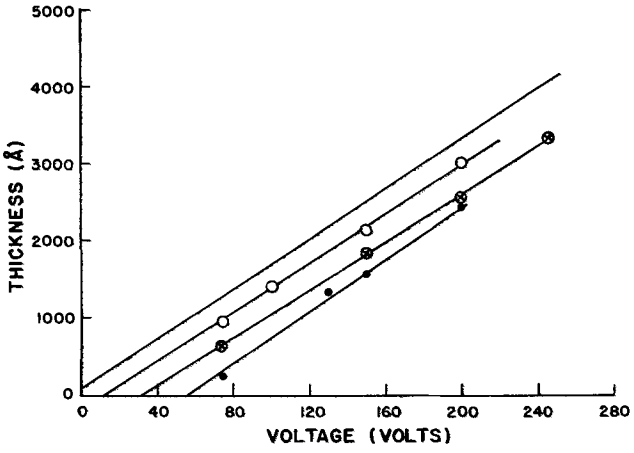

Fig. 6. Thickness as a function of voltage at a constant current density. ———, data from ref. (11); ○, 1.0 ma/cm², thickness determined by capacitance; ⊗, 2.0 ma/cm², thickness determined by capacitance; ●, 1.0 ma/cm², thickness determined by optical step gauge.

Ta_2O_5 films grown in liquid electrolytes. The slopes for the gas phase film grown at 1.0 ma/cm² is 16.5 Å/v and for the 2.0 ma/cm² films it is 15.7 Å/v. There are differences due to measurement techniques and anodization conditions. However, a strong similarity between the thickness-voltage relationship for the liquid and gas phase films is evident. It is also noted that extrapolation to zero thickness leads to voltage intercepts that are larger than zero.

The efficiency of film growth was determined by calculating the mass of the Ta_2O_5 produced for each set of anodization conditions and comparing them with the quantity of charge that had passed through the anode circuit. For these calculations a density of 8.0 g/cm³ was assumed for Ta_2O_5 (12). The Faraday efficiency calculated for films grown at applied anode voltages of 200 or less is 17%. Figure 7 is a plot of the measured thickness values as a function of the total charge that passed through the anode circuit. Although there is a difference between the intercepts of the plots from the capacitance and the optical data (the latter are believed to be more accurate and have a slope of 256 Å/coul/cm²), both are linear for films grown up to 200v. It is also evident that film growth efficiency is independent of the current density and anode temperature in the limited range of the variables studied, since the points for 1.0 and 2.0 ma/cm² films fall on the same line. The extrapolation of the optical plot in Fig. 7 to zero charge leads to an intercept on the ordinate that corresponds to a film thickness of 57Å.

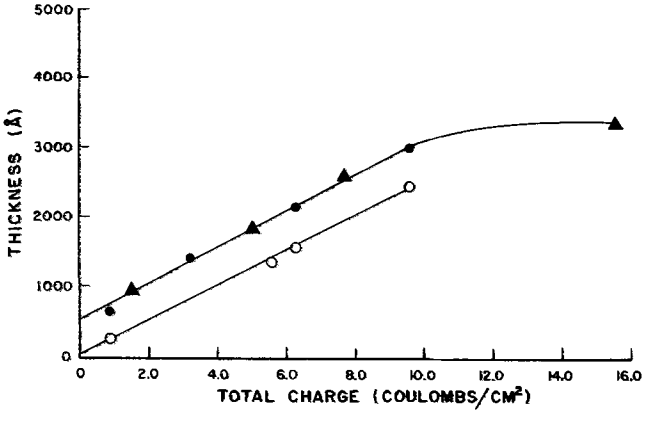

Fig. 7. Total charge dependence of total film thickness. ●, film formed at 1.0 ma/cm², thickness determined by capacitance; ▲, films formed at 2.0 ma/cm², thickness determined by capacitance; ○, films formed at 1.0 ma/cm², thickness determined by comparison of interference colors with an optical step gauge.

The results of the x-ray diffraction studies on the gas phase anodic films did not indicate the presence of crystalline Ta_2O_5. A vacuum fusion analysis was conducted on both anodized and unanodized tantalum. The results of these analyses showed a significant increase in the oxygen concentration and no significant increase in the hydrogen and nitrogen concentration as a result of the gas phase anodization of tantalum. These results indicate that the film was free from hydrocarbon contamination due to the vinyl tape and the diffusion pump oil.

Discussion

The nature of the interference colors, the apparent temperature independent dielectric constant, the low dielectric loss of the films, and the fact that these films were insoluble in all common acids and alkali, except HF, is in accord with the assumption that the composition of these gas phase anodic films is Ta_2O_5.

It is of interest to compare the growth characteristics of the films formed by the gas phase and by liquid phase anodization of tantalum.

The voltage-time curves shown in Fig. 3 for the gas phase anodization exhibit similarities to those for liquid phase anodization (11) except for a brief initial period in which the voltage rise is exceptionally rapid in the gas phase process.

The thickness-voltage relationship for gas phase anodic Ta_2O_5 films plotted in Fig. 6 is not only a straight line, but matches very closely the slope of the plots for comparable films grown in liquid solutions (11). The intercepts on the voltage axis are substantially above zero.

The decay of the anode current measured as a function of time at constant current voltage is nonlinear and, in addition, the plot of the reciprocal current *vs.* time (Fig. 4) is linear and agrees with the experimental observations by Dreiner (13) for anodic Ta_2O_5 films grown in liquid electrolytes.

The current-voltage relation for a film pre-formed at 100v is more complex than that for film growth in liquid electrolytes. It can be represented as two straight lines intersecting at about 32v. This voltage value is near the point at which film growth appears to begin in the plot of Fig. 3 and also coincides with the region of the voltage intercepts in Fig. 4. These results suggest that there may be an induction period required before Ta_2O_5 film growth can proceed in the gas phase system. This latter observation may well be associated with the build-up of reactive species in the vicinity of the anode or may be due to the initial presence of a thin oxide film on the anode surface as in Vermilyea's experiments and as suggested by the plot of our data in Fig. 7. The localization of reactive species in the vicinity of the anode is consistent with the observation of a glow near the anode, but further experimental work will be required to determine adequately the composition of the gaseous electrolyte.

It is also of interest to compare our results with those of Miles and Smith (4), Tibol and Hull (5), Ligenza (6), and Weinreich (7), who have investigated gas phase anodic processes with various materials.

Miles and Smith (4) and Tibol and Hull (5) observed a linear dependence of film thickness on applied voltage with aluminum anodes. The latter also reported a nonlinear decay of the anode current with time at constant anode voltage, but their results for aluminum differ from ours for tantalum in that a plot of the reciprocal of the current *vs.* time for aluminum is nonlinear.

The maximum applied anode voltage in this work was 250v while in Miles and Smith's paper the maximum voltage reported is 9v for aluminum, and in the work of Tibol and Hull the maximum is 90v for aluminum. Ligenza (6) reports a maximum voltage of 90v for silicon anodes and Weinreich (7) reports a

maximum voltage of 50v for GaAs anodes. Ligenza (6) and Miles and Smith (4) also noted that oxide films grew on their anode surfaces when no voltage was applied, and this is probably due to the presence of high energy species in the gaseous electrolyte.

Ligenza reported a white glow on the surface of the anode during anodization. We also observed a glow, which was, however, pale green. In both cases the intensity of the glow was associated with an increase in the rate of oxide formation.

In summary, we have investigated the gas phase anodization of tantalum and observed that films obtained in this manner bear a close similarity in growth characteristics and optical and dielectric properties to those films obtained by anodization in the liquid electrolyte. We believe that this observation is made possible by the design of the anodization cell in which the anode surface is not exposed to the high energy species present in the conventional discharge. It is furthermore considered significant that the quantity of Ta_2O_5 produced in the gas anodization process is a linear function of the charge passed through the anode surface up to a formation voltage of 200v.

We suggest that the gas phase anodization process described here offers a means of preparing Ta_2O_5 films which are comparable to those obtained in liquid systems, but which are free of impurities deposited from the solution.

Manuscript received Dec. 8, 1966; revised manuscript received May 29, 1967. This research was supported by the U. S. Army Research Office, Durham, North Carolina, Intra-Army Order No. ARO-D-7 and is part of a dissertation submitted by one of the authors (T.A.J.) to Temple University Graduate Board in partial fulfillment of the requirements for the M.A. degree.

Any discussion of this paper will appear in a Discussion Section to be published in the June 1968 JOURNAL.

REFERENCES

1. W. McNeill and L. Gruss, *This Journal*, **110**, 863 (1963).
2. F. H. Godsey, Jr., *Trans. Electrochem. Soc.*, **61**, 515 (1932).
3. R. B. Mason, *This Journal*, **102**, 671 (1955).
4. J. L. Miles and P. H. Smith, *ibid.*, **110**, 1240 (1963).
5. G. J. Tibol and R. W. Hull, *ibid.*, **111**, 1368 (1964).
6. J. R. Ligenza, *J. Appl. Phys.*, **36**, 2703 (1965).
7. O. A. Weinreich, *ibid.*, **37**, 2924 (1966).
8. B. T. Barnes, *ibid.*, **37**, 694 (1966).
9. L. Young, "Anodic Oxide Films," p. 82, Academic Press, New York (1961).
10. A. S. Pavlovic, *J. Chem. Phys.*, **40**, 951 (1964).
11. D. A. Vermilyea, *Acta Meta.*, **1**, 282 (1953).
12. A. J. Schrijner and A. Middelhoek, *This Journal*, **111** 1167 (1964).
13. R. Dreiner, *ibid.*, **111**, 1350 (1964).

Luminescent Behavior of Bismuth in Rare-Earth Oxides

R. K. Datta

Lighting Research Laboratory, General Electric Company, Cleveland, Ohio

ABSTRACT

Activation of rare-earth oxides by ions other than rare earths is successfully attempted in the present investigation. Bi^{+3} is incorporated in yttrium, gadolinium, and lanthanum oxides by solid state reaction. Probably a charge-transfer mechanism involving bismuth and oxygen introduces an absorption band at about 3200Å region. Under 3650Å radiation R_2O_3:Bi (R =Y, Gd, La) shows Bi^{+3} emission (blue) with a broad-band spectrum extending from 4500 to 6000Å and peaking at 5000Å. When incorporated in R_2O_3:Eu phosphors, Bi^{+3} acts as a sensitizer for Eu^{+3} emission under 3650Å radiation. Energy absorbed by bismuth-oxygen component is transferred by a radiationless process to Eu^{+3} resulting in the final emission from excited Eu^{+3} ($^5D_0 \rightarrow {}^7E_2$). However, under 2537Å radiation Bi^{+3} in R_2O_3:Bi acts as a "killer." Among the three oxide matrices studied, the fluorescence of Bi has been found to be most efficient in Y_2O_3 host. Reflectance, emission, and excitation spectra of the phosphors are discussed with special reference to Y_2O_3:Bi and Y_2O_3:Eu:Bi.

Activation of rare-earth oxides by various rare-earth ions has drawn much attention in recent years. The phosphor R_2O_3:Eu (R = Y,Gd) (1) shows narrow-band, Eu^{+3} emissions in the region 5900-7000Å, a very strong maximum occurring at about 6100Å. Although efficient under cathode-ray and short wavelength (2537Å) u.v. excitations, this phosphor has very poor response to long wavelength (3650Å) u.v. radiation. Borchardt (2) studied the mechanism of absorption and emission in Y_2O_3:Eu from empirical observations. Wickersheim *et al.* (3) studied the same phosphor and interpreted its photoluminescence in terms of crystal-field theory. Ropp (4) studied different rare-earth oxide phosphors activated by rare-earth ions and generalized that except for Gd_2O_3, where special stability of Gd^{+3} is obtained due to half-filling of inner 4f shell, fluorescence occurs only in those oxides where the cation possesses no unpaired electron, *i.e.*, in Y_2O_3 and La_2O_3. Although various rare-earth ions are used to activate these oxides and other rare-earth compounds (5), only one published report (6) has come to the present author's attention where ions other than rare earths have been used to activate rare-earth compounds, especially the oxides. Bi^{+3} ion is well known as an activator and sensitizer in several particular phosphors (7). In addition, on the basis of ionic size Bi^{+3} (radius = 0.96Å)[1] is very close to Y^{+3} (r = 0.92Å), Gd^{+3} (r = 0.97Å), and La^{+3} (r = 1.14Å). On the basis of these arguments, Bi^{+3} is used in an attempt to activate Y_2O_3, Gd_2O_3, La_2O_3 (the most promising rare-earth oxide matrices known) and various solid solutions of these oxides. It has been found in the present investigation that Bi^{+3} can activate Y_2O_3, Gd_2O_3, La_2O_3, and sensitize the Eu^{+3} emission of Y_2O_3:Eu, Gd_2O_3:Eu, and La_2O_3:Eu phosphors under 3650Å excitations and possibly under cathode-rays. Thus, two different groups of phosphors are obtained. (*i*) R_2O_3:Bi (R = rare earth, Table I) and (*ii*) R_2O_3:Eu:Bi. R_2O_3:Bi shows weak blue emission under cathode rays and 3650Å radiation, whereas R_2O_3:Eu:Bi phosphor shows strong red Eu^{+3} emission under cathode rays, 2537 and 3650Å excitations.

[1] Ahrens revised figure (1953).

It should be noted that the former group does not show any Bi^{+3} fluorescence under 2537Å excitation, and although sensitized Eu^{+3} emission is observed in the latter group of phosphors under 3650Å excitation, only usual unsensitized Eu^{+3} fluorescence is shown under 2537Å radiation.

This paper describes the mechanism of photoluminescence in terms of absorption, emission, and excitation of the phosphors with special emphasis on Y_2O_3:Bi and Y_2O_3:Eu:Bi.

Experimental Procedure

Sample preparation and composition.—The raw materials used in this investigation consisted of luminescent grade (99.99-99.999% pure) oxides, such as yttrium oxide, Y_2O_3, gadolinium oxide, Gd_2O_3, lanthanum oxide, La_2O_3, europium oxide, Eu_2O_3, and bismuth trioxide, Bi_2O_3.

Appropriate amounts of Y_2O_3, Eu_2O_3, and Bi_2O_3 were mixed together and dissolved in dilute nitric acid. Eu and Bi were incorporated in yttrium (gadolinium, lanthanum) oxide by co-precipitation as the oxalates from the nitrate solution. The oxalate was ignited to oxide at temperatures from 900° to 1000°C[2] for 1 or 2 hr depending on the size of the charge. The firings of the phosphor were done in covered, fused-silica containers. Samples consisting essentially of Gd_2O_3 required a second firing at about 650°C for complete conversion to the low temperature, cubic form which is the most efficient matrix among Gd_2O_3 polymorphs.

Samples having general composition $(R_{1-y}Bi_y)_2O_3$ and $(R_{1-x-y}Eu_xBi_y)_2O_3$ with x and y varying from 0.005 to 0.06 and 0.001 to 0.02, respectively, were synthesized. Composition of the finished phosphors were periodically analyzed by wet chemical method in order to determine the loss of bismuth during firing. A loss of 2-6% of Bi was noticed in the analyzed samples; however, the amount of bismuth in the phosphor described throughout this report is based on the formulated compositions.

To assure that all bismuth-activated compositions studied in the present investigation were single phases, the preliminary step involved in activating rare-earth oxides was to study the solubility of Bi_2O_3 in the rare-earth oxide lattices. Bi_2O_3 has two stable polymorphs. The high temperature cubic form shows a reversible transition to the low temperature monoclinic form at 730°C. Levin and Roth (8) studied the phase equilibrium relationship of the bismuth-rich side [100-85 m/o (mole per cent) of Bi_2O_3] of the systems Bi_2O_3-M_aO_b (M stands for cations having charge from one to five). Since a detailed study of the phase equilibrium relationships between the rare-earth oxides and Bi_2O_3 is beyond the scope of the present program, only the subsolidus solubility of Bi_2O_3 in the rare-earth oxide lattices at 1050°C was studied. It has been found that at least 50, 35 and 15 m/o of Bi_2O_3 is soluble in Y_2O_3, Gd_2O_3, and La_2O_3, respectively, at 1050°C. These amounts are well beyond the range of concentration of activators in usual phosphors. Nevertheless, phase purity of the phosphors prepared was checked by x-ray diffraction analysis. CuKα radiation from a G. E. diffractometer with a nickel filter was used to investigate all compounds.

Spectroscopic measurements.—Diffuse reflectance spectra of the samples within the range 2500-7000Å were obtained using CaF_2 as standard in a Cary Recording Spectrophotometer, Model No. 14. The emission spectra from phosphor plaques, excited under different u.v. sources, were obtained by a direct-recording spectroradiometer (9) adapted with a grating monochromator with nearly constant dispersion. Maximum sensitivity in the spectral region from 2500-7000Å was obtained with a quartz-windowed, S-20 response photomultiplier. The total band pass was kept about 30Å. The spectra were calibrated against a standard tungsten filament lamp reflected from a magnesium-oxide plaque. Photoluminescent-brightness data given throughout this report were measured from the height of the main peak (in case of narrow emission), or from the area (in case of broad emission) of the emission spectra. The excitation spectra were measured using sodium salicylate as standard.

Cathodoluminescence spectra were obtained using a demountable cathode-ray tube operating at 20 kv anode potential at 17.5μ a beam current over a standard scan TV raster of 35 cm^2 area. Brightness and color points of emission under these conditions were measured using an eye-corrected Weston foot-Lambert meter and G. E. colorimeter (JB1E), respectively.

Results and Discussions

The subsequent discussion on optical properties will pertain to the optimized phosphors, *i.e.*, $(Y_{0.995}Bi_{0.005})_2O_3$ and $(Y_{0.946}Eu_{0.05}Bi_{0.004})_2O_3$, unless otherwise stated. However, spectra of phosphors having other compositions are presented in many figures to emphasize the role of Bi.

Excitation spectra.—The excitation spectra of Y_2O_3:Bi (Fig. 1) and Y_2O_3:Eu:Bi (Fig. 2 and 3) are shown.

Y_2O_3:Bi has a spectrum with narrow responses at about 2000 and 3650Å regions. Y_2O_3:Eu:Bi has a broad excitation spectrum with responses to 2000, 2537, and 3650Å excitations. This spectrum, divided into two parts, is shown in Fig. 2 and 3. Y_2O_3:Eu has a very poor response to 3650Å excitation. However, incorporation of Bi enhances its response to 3650Å excitation markedly with a simultaneous, but small decrease in its response to both 2000 and 2537Å radiations. The

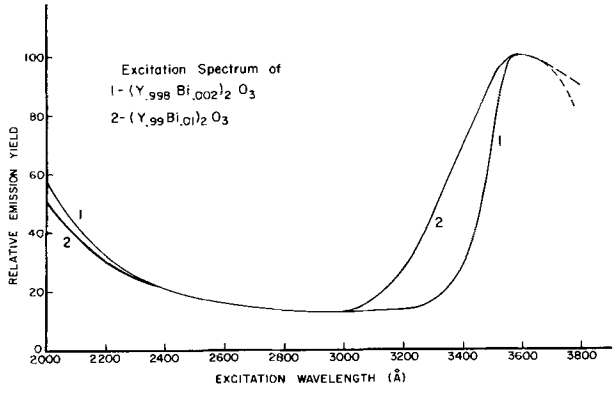

Fig. 1. Excitation spectrum of Y_2O_3:Bi

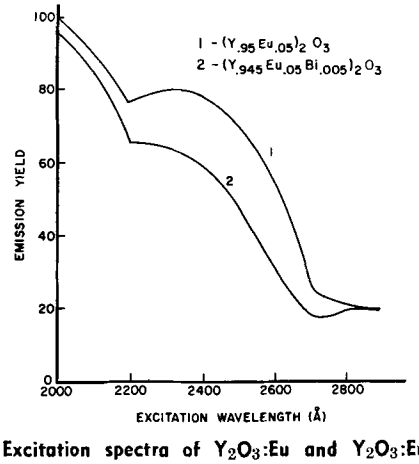

Fig. 2. Excitation spectra of Y_2O_3:Eu and Y_2O_3:Eu:Bi (2000-2800Å).

[2] Commercial grade Y_2O_3:Eu phosphor is usually fired at about 1200°C or higher. The lower temperature of firing, as followed in the present investigation, was necessitated due to high volatility of Bi_2O_3. This low temperature of firing also explains the lower brightness of the standard sample (see Tables II and III).

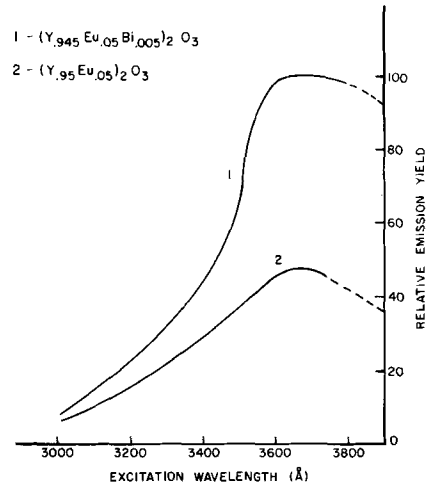

Fig. 3. Excitation spectra of Y_2O_3:Eu and Y_2O_3:Eu:Bi (3000-3800Å).

implication of these excitation data will be discussed later in conjunction with emission and reflectance spectra.

Emission spectra and plaque brightness.—Bi^{+3} activated rare-earth oxides do not show any emission under 2537Å radiation (Table I). However, when excited by 3650Å radiation, they emit broad-band spectra in the region of 4500-6000Å with a peak at about 5000Å. Most of the Bi^{+3}-activated phosphors (sulfides, selenides, carbonates, oxides, silicates, etc.) emit in the blue region, although other emissions, such as green, yellow, red, etc., are known (7). No simple correlation between the Bi^{+3} emission and composition and structure of the matrices could be obtained. Bi^{+3} fluorescence is suggested to be due to $6s6p \rightarrow 6s^2$ transition (10). These outer sp orbitals of Bi^{+3} ions are also actual bonding orbitals which are influenced by the neighboring anions. It may be generalized that in all these phosphors Bi^{+3} ions act as emission centers, although the nature of the emission is highly influenced by the environment of Bi^{+3} ion. Pure rare-earth oxides, such as Y_2O_3 and Gd_2O_3, do not show any emission under cathode-ray and u.v. excitations. Hence, on the basis of their blue emission under cathode-ray and 3650Å excitations, it may be postulated that Bi^{+3} ions in R_2O_3:Bi act as primary activators, although indirect involvement of oxygen ions in the emission process cannot be ruled out.

The emission spectra of Y_2O_3:Bi under 3650Å excitation are shown in Fig. 4. Normalized plots of plaque brightness against logarithm of Bi^{+3} concentration in Y_2O_3 and Gd_2O_3 are shown in Fig. 5. The optimum ranges of concentration of Bi^{+3} in Y_2O_3 and Gd_2O_3 are found to be about 0.5-2 and 0.5-1 m/o, respectively, of total yttrium (gadolinium) and bismuth present.

Table I. Visible* Bi^{+3} fluorescence in rare-earth oxide matrices

Composition	Brightness under excitation, 3650Å	Cathode ray brightness	Body color	Structure**
$(Y_{0.999}Bi_{0.001})_2O_3$	w	—	White	Cubic
$(Y_{0.998}Bi_{0.002})_2O_3$	m	m	White	Cubic
$(Y_{0.995}Bi_{0.005})_2O_3$	m	m	White	Cubic
$(Y_{0.99}Bi_{0.01})_2O_3$	m	—	White	Cubic
$(Y_{0.98}Bi_{0.02})_2O_3$	m	—	Pale gray	Cubic
$(Y_{0.96}Bi_{0.04})_2O_3$	w	—	Yellow	Cubic
$(La_{0.999}Bi_{0.001})_2O_3$	w	—	White	Hexagonal
$(La_{0.99}Bi_{0.01})_2O_3$	w	w	White	Hexagonal
$(La_{0.98}Bi_{0.02})_2O_3$	w	w	White	Hexagonal
$(Gd_{0.999}Bi_{0.001})_2O_3$	w	—	White	Cubic
$(Gd_{0.998}Bi_{0.002})_2O_3$	m	m	White	Cubic
$(Gd_{0.995}Bi_{0.005})_2O_3$	m	m	White	Cubic
$(Gd_{0.99}Bi_{0.01})_2O_3$	m	w	White	Cubic
$(La_{0.1}Y_{0.895}Bi_{0.005})_2O_3$	w	—	White	Cubic
$(La_{0.1}Y_{0.89}Bi_{0.01})_2O_3$	w	—	Gray	Cubic
$(La_{0.05}Gd_{0.945}Bi_{0.005})_2O_3$	w	—	White	Cubic
$(La_{0.9}Y_{0.095}Bi_{0.005})_2O_3$	w	—	Gray	Hexagonal
$(La_{0.9}Gd_{0.095}Bi_{0.005})_2O_3$	w	—	Gray	Hexagonal
$(Y_{0.5}Gd_{0.445}Bi_{0.005})_2O_3$	m	w	White	Cubic
$(Y_{0.9}Gd_{0.095}Bi_{0.005})_2O_3$	m	—	White	Cubic
$(Gd_{0.9}Y_{0.095}Bi_{0.005})_2O_3$	m	m	White	Cubic

* w = weak; m = medium; s = strong.
** As indicated by x-ray diffraction.

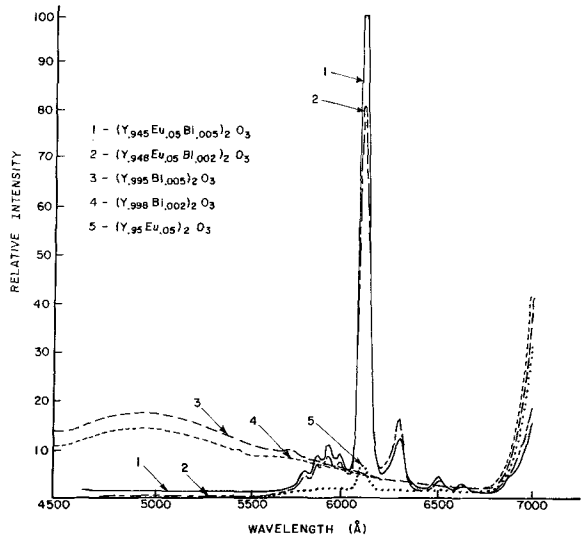

Fig. 4. Emission spectra of $(YEuBi)_2O_3$ under 3650Å excitation

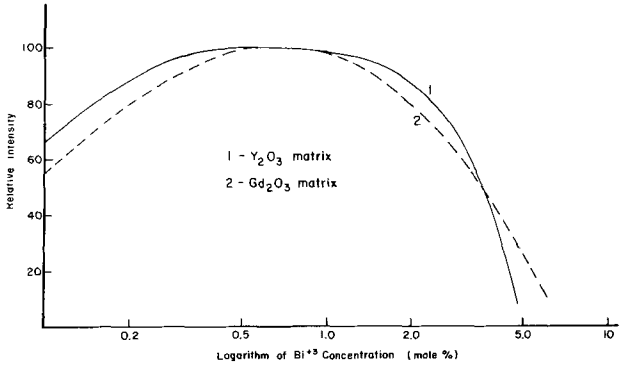

Fig. 5. Plaque brightness vs. Bi^{+3} concentration in Y_2O_3 and Gd_2O_3 (3650Å excitation).

Y_2O_3:Eu:Bi samples show essentially Eu^{+3} emission under cathode rays (Fig. 6), 2537Å (Fig. 7), and 3650Å radiations (Fig. 4). Under 2537Å radiation, as Bi^{+3} is added to Y_2O_3:Eu, the plaque brightness gradually decreases, whereas under 3650Å excitation the brightness shows a sharp rise with increase in Bi^{+3} content (Fig. 8, Table II). This is also demonstrated in the emission spectra of the samples.

Under 3650Å excitation Y_2O_3:Eu has very weak emission. As Bi^{+3} is incorporated in the lattice, the narrow-band Eu^{+3} emission with a maximum at 6110Å ($^5D_0 \rightarrow {}^7F_2$ transition) is enhanced considerably. On the other hand, the band shape of the Bi^{+3} emission in Y_2O_3:Bi is generally unchanged, although the intensity of the luminescence of Bi^{+3} is strongly quenched by incorporating europium in the phosphor (Fig. 4). This indicates that Bi^{+3} is acting as a sensitizer for Eu^{+3} emission and the major portion of the energy, which would have otherwise been emitted as Bi^{+3} emission (as in Y_2O_3:Bi), is transferred by a radiationless process (11) to Eu^{+3} resulting in excitation of the latter among levels of the $4f^6$ configuration. The final emission originates from these excited Eu^{+3} ions. The situation is quite different under 2537Å excitation. Bi^{+3} in Y_2O_3:Bi does not show any emission, whereas Y_2O_3:Eu shows Eu^{+3} emission corresponding to $^5D_0 \rightarrow {}^7F_2$ transition. As Bi^{+3} is gradually

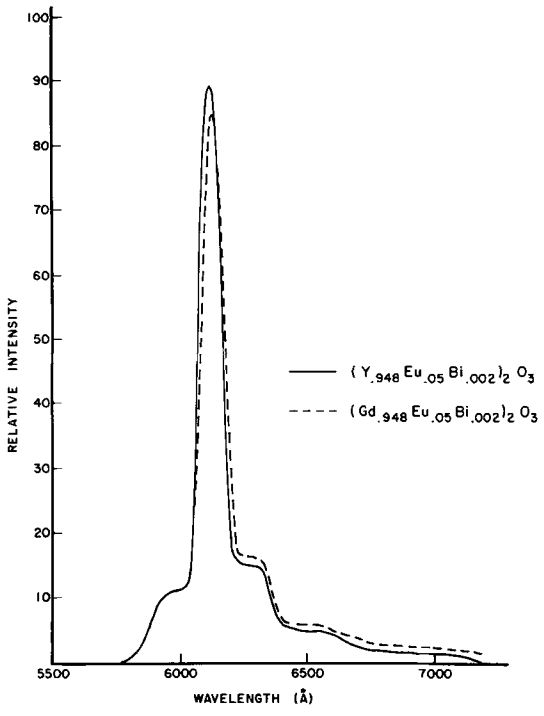

Fig. 6. Emission spectra of R_2O_3:Eu:Bi phosphors (R= Gd, Y); cathode ray excitation.

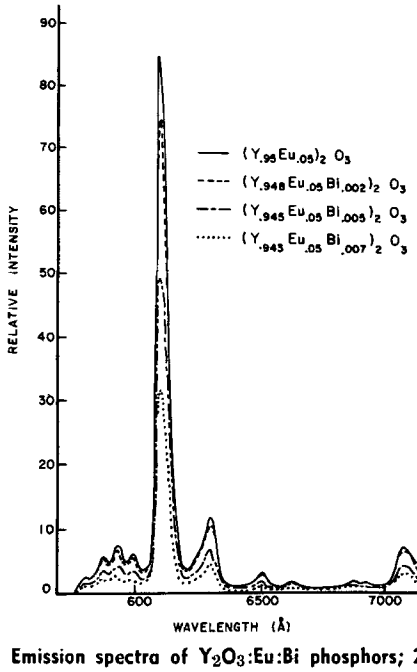

Fig. 7. Emission spectra of Y_2O_3:Eu:Bi phosphors; 2537Å excitation.

incorporated in Y_2O_3:Eu, Eu^{+3} emission is gradually reduced without any noticeable emergence of Bi^{+3} emission.

These observations indicate that Bi^{+3} in Y_2O_3:Eu:Bi acts as "killer" and sensitizer for Eu^{+3} emission under 2537 and 3650Å excitation, respectively.

The cathode ray brightness of Y_2O_3:Eu:Bi as function of Bi^{+3} concentration is shown in Fig. 9. Because of instrumental limitations, the cathode-ray spectra (Fig. 6) could not detect any Bi^{+3} emission. However, weak Bi^{+3} emission under cathode-ray excitation, as indicated by shift in color point (Table III) with increase in Bi^{+3} content, is inferred. This bismuth emission, although undetected, may also explain the increased brightness of the phosphor Y_2O_3:Eu:Bi with

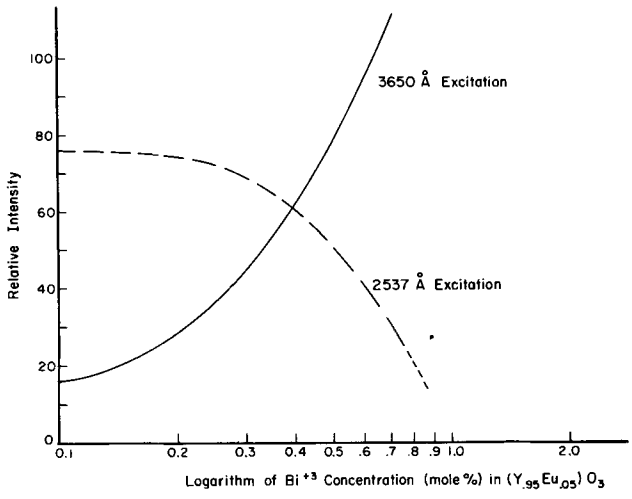

Fig. 8. Plaque brightness vs. Bi^{+3} concentration in Y_2O_3:Eu:Bi

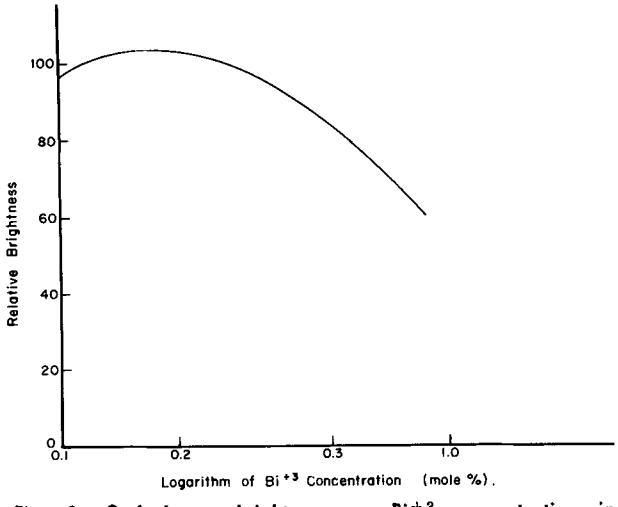

Fig. 9. Cathode-ray brightness vs. Bi^{+3} concentration in Y_2O_3:Eu:Bi.

very litle change in the Eu^{+3} emission peak under cathode-ray excitation.

Reflectance spectra.—Y_2O_3:Bi.—The reflectance spectra of the Y_2O_3:Bi samples studied are shown in Fig. 10. Gd_2O_3, Y_2O_3, and La_2O_3 show broad u.v.-absorption bands at wavelengths less than 2300Å. Addition of Bi^{+3} to these oxides introduces two broad absorption bands, namely, at 2500 (or lower wavelengths) and 3200Å regions. Pure Y_2O_3 has about 90 and 100% re-

Table II. Plaque brightness of R_2O_3:Eu:Bi phosphors (R = Gd, Y, La)

Composition	Relative brightness under u.v. excitation 2537A	3650A	Body color
$(Y_{0.95}Eu_{0.05})_2O_3$	85.0	5.0	White
$(Y_{0.940}Eu_{0.05}Bi_{0.001})_2O_3$	73	17	White
$(Y_{0.948}Eu_{0.05}Bi_{0.002})_2O_3$	75	27	White
$(Y_{0.945}Eu_{0.05}Bi_{0.005})_2O_3$	50	81.5	White
$(Y_{0.943}Eu_{0.05}Bi_{0.007})_2O_3$*	32.2	108	White
$(Gd_{0.95}Eu_{0.05})_2O_3$	80.7	4.5	White
$(Gd_{0.940}Eu_{0.05}Bi_{0.001})_2O_3$	69.5	20.3	White
$(Gd_{0.945}Eu_{0.05}Bi_{0.005})_2O_3$*	40.2	77.0	White
$(La_{0.95}Eu_{0.05})_2O_3$	47.0	5	White
$(La_{0.940}Eu_{0.05}Bi_{0.001})_2O_3$	31	12	White
$(La_{0.945}Eu_{0.05}Bi_{0.005})_2O_3$*	25	35	White
$(La_{0.1}Y_{0.845}Eu_{0.05}Bi_{0.005})_2O_3$	35	60	White
$(Gd_{0.45}Y_{0.495}Eu_{0.05}Bi_{0.005})_2O_3$	51	75	White
Commercial grade YVO_4:Eu	100	100	

* These samples show both Bi^{+3} and Eu^{+3} emissions under 3650Å radiation.

Table III. Cathode-ray brightness of Y_2O_3:Eu:Bi

Compositions	Per cent brightness	Color coordinates* x	y
$(Y_{0.95}Eu_{0.05})_2O_3$	96.4	0.636	0.347
$(Y_{0.940}Eu_{0.05}Bi_{0.001})_2O_3$	98.4		
$(Y_{0.948}Eu_{0.05}Bi_{0.002})_2O_3$	103.4	0.640	0.354
$(Y_{0.945}Eu_{0.05}Bi_{0.005})_2O_3$	86.2	0.640	0.354
$(Gd_{0.948}Eu_{0.05}Bi_{0.002})_2O_3$	104.1	0.643	0.357
Commercial grade Y_2O_3:Eu	100.0	0.637	0.360

* Based on 1931 CIE Chromaticity Diagram.

flectance at 2500 and 3600Å, respectively, whereas $(Y_{0.995}Bi_{0.005})_2O_3$ has about 20 and 60% reflectance at the corresponding wavelengths. The u.v.-absorption bands (below 2300Å) of pure rare-earth oxides are attributed to charge-transfer absorption states involving the rare-earth ion and oxygen (2). A similar absorption band is seen in Bi_2O_3, except that it extends to longer wavelength (to 4200Å) as shown in Fig. 11. Absorption of u.v. radiation due to charge-transfer processes involving Bi^{+3} is known (10). The question now arises if Bi^{+3} is excited directly, or bismuth-oxygen states are involved during such absorption. The reflectance spectrum of a non-oxidic bismuth compound, such as BiF_3 (Fig. 11), shows absorption around 2500Å only. This suggests that u.v.-absorption of Y_2O_3:Bi at about 3200Å may well be due to charge-transfer states involving bismuth and oxygen, whereas the absorption at about 2500Å is caused by excitation of Bi^{+3} ion.

The essential mechanism of fluorescence in Y_2O_3:Bi under 3650Å excitation is, therefore, suggested to be absorption of long wavelength (3650Å) u.v. radiation by the bismuth-oxygen component resulting in the excitation of charge-transfer states and the final emission from such excited states. The excitation band of Y_2O_3:Bi at around 2000Å (Fig. 1) may be due to fundamental absorption by Y_2O_3. The failure of Y_2O_3:Bi to emit under 2537Å excitation, in spite of its high absorption of this radiation, is not understood yet.

Y_2O_3:Eu:Bi.—Y_2O_3:Eu has about 15 and 95% reflectance around 2500 and 3600Å, respectively, and it shows strong Eu^{+3} emission under short wavelength (2537Å) u.v. radiation. From a study of the reflectance and excitation spectra of many Eu^{+3}-activated phosphors,

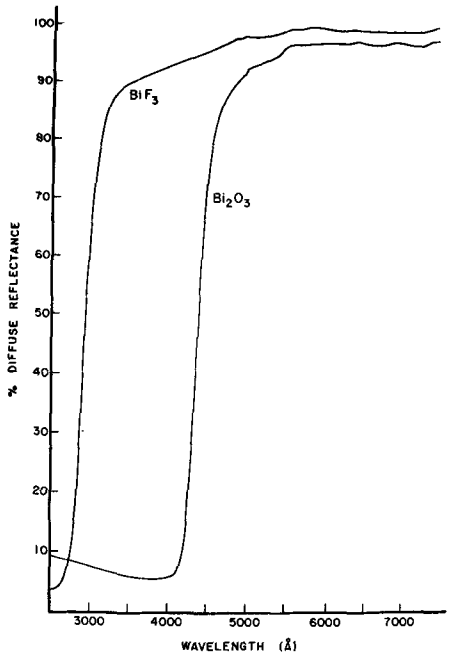

Fig. 11. Diffuse reflectance spectra of BiF_3 and Bi_2O_3

Borchardt (2) suggested that excitation is due to charge-transfer absorption involving Eu-O components, and wavelengths anywhere below 2800Å would cause such absorption and efficiently excite Eu^{+3} ions to fluoresce.

When Bi^{+3} is incorporated in Y_2O_3:Eu, a new, broad absorption band is introduced at about 3200Å, although little change in absorption at about 2500Å is observed. The band extends well up to 4000Å, and incorporation of 0.5 m/o of Bi^{+3} in $(Y_{0.95}Eu_{0.05})_2O_3$ causes a reflectance of about 60% at 3650Å, whereas $(Y_{0.95}Eu_{0.05})_2O_3$ with no Bi^{+3} has a reflectance of about 95% at the same wavelength (Fig. 12). This new absorption, on the basis of arguments presented earlier, might well be due to absorption by bismuth-oxygen components of the phosphor. Furthermore, this new absorption band is responsible for the enhanced Eu^{+3} emission of Y_2O_3:Eu:Bi under 3650Å excitation. It

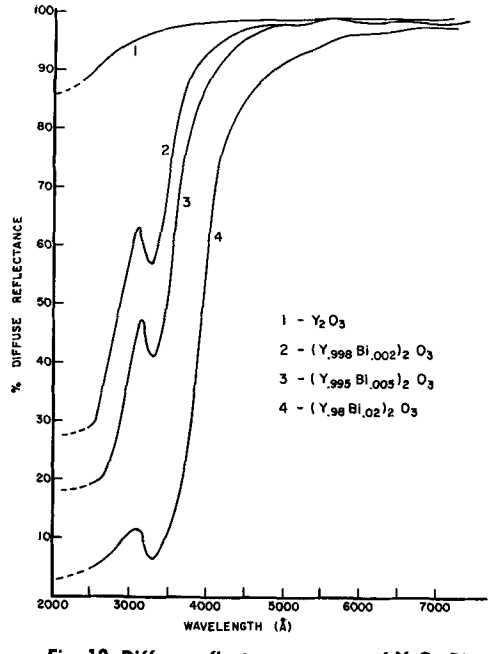

Fig. 10. Diffuse reflectance spectra of Y_2O_3:Bi

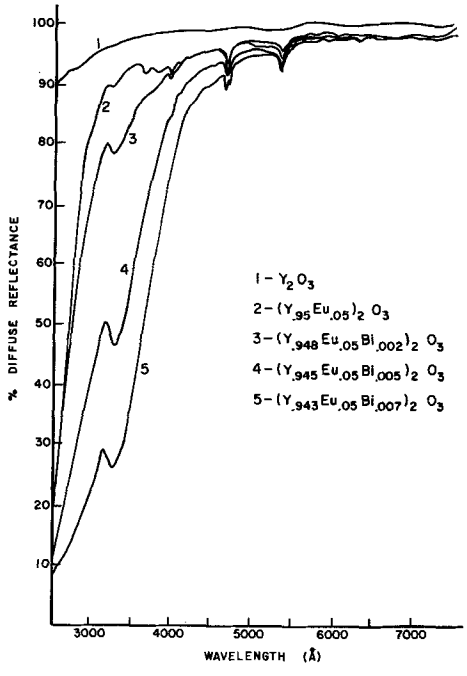

Fig. 12. Diffuse reflectance spectra of Y_2O_3:Eu:Bi

may be recalled here again that under 3650Å excitation Y_2O_3:Eu:Bi phosphor shows Eu^{+3} emission much more intensely than that shown by Y_2O_3:Eu under similar conditions. This contradicts Borchardt's (2) suggestion that the minimum energy required for Eu^{+3} fluorescence in any host is about 2800Å radiation. His observation is true in cases where absorption is caused essentially by Eu-O components of the phosphors.

The inferences drawn from the emission and reflectance spectra can be combined and the postulated mechanism of fluorescence in Y_2O_3:Eu:Bi restated. Eu^{+3} emission of Y_2O_3:Eu:Bi under 3650Å excitation is due to charge-transfer absorption involving Bi-O components of the phosphor resulting in the excitation of charge-transfer states, relaxation of these giving rise to Bi^{+3} in the excited states, transfer of energy from Bi^{+3} to Eu^{+3} and the final emission from the excited states of Eu^{+3} among levels of the $4f^6$ configuration. Although incorporation of Bi^{+3} does not decrease the absorption of Y_2O_3:Eu around 2500Å region, Eu^{+3} emission of Y_2O_3:Eu is gradually reduced under 2537Å excitation as Bi^{+3} is gradually incorporated in the lattice (Fig. 7). Probably, under 2537Å radiation Bi^{+3} acts as a "killer" in the phosphor Y_2O_3:Eu:Bi.

Summary

Oxides of yttrium, gadolinium, and lanthanum show extensive solid solution with Bi_2O_3. However, when incorporated in small amounts (0.1-2 m/o) in these oxides, Bi^{+3} introduces broad absorption bands at about 3200Å. By analogy, as well as by independent evidence, this absorption band is attributed to charge-transfer states involving bismuth and oxygen. By virtue of such broad absorption, R_2O_3:Bi (R = Y, Gd, La) show Bi^{+3} emission (blue) under 3650Å excitation. When incorporated in R_2O_3:Eu phosphor, Bi again introduces a new absorption band around 3200Å which extends well up to 4000Å. This enhances the Eu^{+3} emission of R_2O_3:Eu:Bi under 3650Å radiation; on the other hand, the emission under 2537Å excitation is reduced. Bi^{+3}, therefore, acts as a sensitizer and "killer" for the Eu^{+3} emission in R_2O_3:Eu:Bi under 3650 and 2537Å, respectively. In the former case, energy absorbed by bismuth-oxygen component is transferred by a radiationless process to Eu^{+3} resulting in the sensitization of Eu^{+3} ions and their excitation between states of the $4f^6$ configuration. Final emission takes place from the excited Eu^{+3} ion ($^5D_0 \rightarrow {}^7F_2$).

Of the three oxide matrices studied, Y_2O_3 has been found to be the most suitable matrix for Bi^{+3} activation.

Acknowledgment

The author acknowledges the assistance of Dr. R. L. Brown in obtaining emission and excitation spectra, of Miss M. Brines and F. Geraghty who measured cathodoluminescent properties. The author also wishes to express his thanks to L. S. Staikoff for x-ray measurements, to T. Luscher for preparing the phosphor and measuring u.v. brightness and to Dr. E. F. Apple for many helpful discussions. The quantitative analyses of Bi in the samples were done by N. Braun.

Manuscript received April 27, 1967; revised manuscript received July 17, 1967.

Any discussion of this paper will appear in a Discussion Section to be published in the June 1968 JOURNAL.

REFERENCES

1. N. C. Chang, *J. Appl. Phys.*, **34**, 3500 (1963).
2. H. J. Borchardt, *J. Chem. Phys.*, **39**, 504 (1963).
3. K. A. Wickersheim and R. A. Lefever, *This Journal*, **111**, 47 (1964).
4. R. C. Ropp, *ibid.*, **111**, 311 (1964).
5. G. H. Dieke and R. Sarup, *J. Chem. Phys.*, **36**, 371 (1962).
6. R. A. Lefever and K. A. Wickersheim, General Telephone and Electronics Lab., U. S. Pat. 3,291,747, Dec. 13, 1966.
7. F. A. Kroger, "Some Aspects of the Luminescence of Solids," Elsevier Publishing Co., Inc., New York (1948).
8. E. M. Levin and R. S. Roth, *J. Research, Natl. Bur. Standards*, **68A** [2], 200 (1964).
9. R. L. Brown, *Illum. Eng.*, **61**, 230 (1966).
10. D. S. McClure, "Solid State Physics," vol. 9, pp. 399-525, Academic Press, New York (1959).
11. C. C. Klick and J. H. Schulman, "Solid State Physics," vol. 5, pp. 97-172, Academic Press, New York (1957).

The Role of Copper in the Transformation of Hexagonal Zinc Sulfide

Gleb Gashurov[1] and Ephraim Banks

Department of Chemistry, Polytechnic Institute of Brooklyn, Brooklyn, New York

ABSTRACT

The mechanism of the copper-induced transformation of hexagonal zinc sulfide was investigated. High-temperature x-ray studies and rate experiments suggest that the transformation is characterized by a one-dimensional recrystallization process, initiated by nuclei of cubic ZnS which precipitate from a solid solution of ZnS in cuprous sulfide under gross isothermal conditions. This solid solution is formed at elevated temperatures, and at 800°C the concentration of ZnS that can be dissolved in cuprous sulfide lies in the neighborhood of 8 mole per cent.

Well crystallized hexagonal ZnS is known to be exceptionally stable toward the transformation to its cubic modification. The temperature of transition between hexagonal ZnS (high temperature form) and cubic ZnS is around 1020°C (1, 2), but highly perfect crystals of hexagonal ZnS show no change in structure even after annealing at 975°C for 504 hr (3).

When hexagonal ZnS (wurtzite) is fired in the presence of small amounts of copper, the transformation to the cubic phase (sphalerite) is found to begin at a temperature as low as 350°C (4). It appears that there exists a minimum concentration of copper that will initiate the wurtzite-sphalerite transformation at a given temperature within a reasonable period of time. Nickerson, Goldberg, and Baird (5) found that when a given hexagonal ZnS:Cu,Cl sample was fired in H_2S, above its critical temperature, appreciable amounts of both copper and chloride were ejected from the ZnS lattice. They speculate that the H_2S serves to remove copper as copper sulfide, and that it is the physical presence of copper sulfide as a separate phase that triggers the observed transformation. This hypothesis is strongly supported by their experiments in which a small amount of copper sulfide was added to samples containing certain amounts of incorporated copper. Complete transformation occurred at a temperature 100°-200° below the temperature at which the transformation would occur without additional copper. These samples showed no significant changes in incorporated copper content.

Aven and Parodi (6) have also proposed that the hexagonal to cubic transformation of ZnS:Cu is initiated by the formation of a separate phase of copper sulfide. They observed that, in ZnS:Cu samples synthesized at 1100°C in H_2S and then cooled to room temperature, the wurtzite-sphalerite transition become detectable when the concentration of incorporated copper was increased to about 5×10^{-4} atom fraction. However, in the presence of small amounts of aluminum, which has been shown to increase the solubility of copper in ZnS (7), a higher concentration of copper was necessary to trigger the transformation. In fact, the change became appreciable when the Cu-concentration in excess of that of aluminum was about 5×10^{-4} atom fraction.

The effect of copper on the transformation of hexagonal ZnS has also been discussed by Ballentyne (8), Gobrecht *et al.* (4), and by Presland *et al.* (9).

The experiments by Nickerson *et al.*, as well as those by Aven and Parodi, indicate then that it is the external (unincorporated) copper sulfide phase that initiates the ZnS transition. It was decided therefore to carry out a detailed study of the zinc sulfide-copper sulfide interaction. Particular emphasis was placed on a high temperature x-ray study of the system. The investigation also included a study of the kinetics of the copper-induced ZnS transformation.

Experimental

Materials.—Hexagonal ZnS was prepared by firing ZnS precipitate in an atmosphere of hydrogen sulfide at 1200°C for 2 hr. The resulting hexagonal ZnS showed no detectable transformation to the cubic phase when fired at 800°C for 2 hr in H_2S,N_2, vacuum or sulfur vapor. $Cu_{1.8}S$ was prepared in two steps. Spectroscopically pure copper was fired in H_2S at 800°C for 1 hr. Chemical analysis showed its copper content to be 78.36% by weight (the theoretical content is 79.88%). This impure $Cu_{1.8}S$ was then fired in a sealed, evacuated vial containing a small amount of CuS at 800°C for 4 hr. (CuS was separated from $Cu_{1.8}S$ by means of a quartz partition as shown in Fig. 1). The x-ray pattern of the resulting sulfide was in excellent agreement with that of Djurle's $Cu_{1.8}S$ (10). The preparation of Cu_2S was also carried out in two steps. First, CuS was fired in nitrogen at 800°C for 1 hr. This treatment produced $Cu_{1.96}S$ together with a small amount of Cu_2S. The mixture was then fired in a sealed, evacuated vial containing a small amount of copper (Fig. 1) at 800°C for 4 hr. The resulting material was examined with x-rays and found to be essentially pure Cu_2S with a trace of $Cu_{1.96}S$. Single crystals of zinc sulfide were kindly supplied by Dr. H. Samelson of General Telephone & Electronics Laboratories. The preparation of these crystals is described in ref. (11).

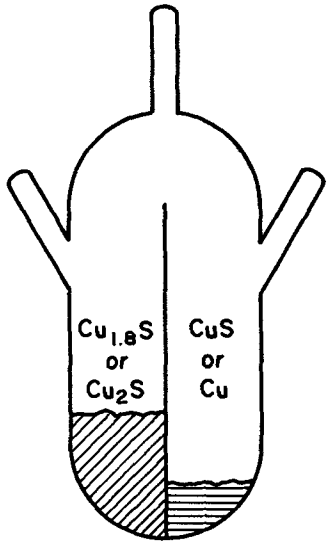

Fig. 1. Quartz vial used for preparation of cuprous sulfides

[1] Present address: General Telephone & Electronics Laboratories, Incorporated, Bayside, New York.

X-ray measurements.—X-ray measurements were made on a Philips wide range goniometer using a Geiger tube as a detecting source. The degree of the ZnS conversion was calculated by measuring the integrated intensity of the (200) cubic reflection and normalizing it with respect to the intensity for a completely converted sample. The (200) peak was chosen because it is the strongest cubic reflection which is not overlapped by hexagonal peaks. The (200) peak was scanned at the rate of 1/8°/min using a time constant of 4 sec. To minimize preferred orientation, the following technique was used. Specimens were moistened with a dilute solution of castor oil in xylene and gently pressed into the specimen holder which was in the form of a machined recess in an aluminum disk. The specimen was then rotated about an axis at right angles to the diffractometer axis and normal to the plane of the specimen. This technique reduced the mean deviation in the (200) integrated intensity to a few per cent. In those cases where only a qualitative x-ray identification was desired, the scanning speed was increased to 1°/min. Nickel filtered CuKα was used in all x-ray measurements.

High temperature x-ray measurements were made in a special high temperature diffractometer attachment (model X-86G, MRC Corporation) used with a Philips wide-range goniometer. The specimen stage in most experiments was a Pt-40% Rh ribbon which also served as a heating element, with a Pt/Pt-13% Rh thermocouple welded to the specimen stage. High temperature runs were made in a nitrogen atmosphere. The zero positioning in the attachment is possible only by using actual Bragg reflections as a gauge. The Bragg reflections of the powder specimen were determined at room temperature prior to the high temperature measurements. The room temperature reflections served as the basis for correcting the high temperature peaks.

Results

According to Djurle (10) there are four compositional forms of copper sulfide: Cu_2S, $Cu_{1.96}S$, $Cu_{1.8}S$, and CuS. Since preliminary experiments showed that firing of hexagonal ZnS with CuS produces no detectable transformation in the ZnS phase until CuS is decomposed into cuprous sulfide, investigation of the relative efficiencies of copper sulfides in transforming hexagonal ZnS was limited to cuprous sulfides.

First, experiments were carried out to determine conditions under which firing of ZnS with cuprous sulfides produces no change in the copper sulfide phase. ZnS was mixed with $Cu_{1.8}S$ (in the ratio of 2 to 1 by weight) and fired in a sealed, evacuated quartz vial containing a small amount of CuS (not in physical contact with the mixture) at 800°C for 1 hr.[2] A similar experiment was carried out with a mixture of ZnS and Cu_2S, except that in this case copper metal was used instead of CuS. In both cases ZnS was completely converted to the cubic form but no changes could be detected in the copper sulfides. These experimental conditions appear then to preserve the identities of copper sulfides. Next, ZnS was fired in sealed vials at 800°C for 1 hr with 1% by weight of Cu_2S or $Cu_{1.8}S$ under conditions stabilizing the respective cuprous sulfides. Conversion was found to be complete in the case of ZnS-$Cu_{1.8}S$, and nearly complete in the case of ZnS-Cu_2S. Similar firings were carried out at lower temperatures (700° and 600°C). In all cases the degree of transformation was only slightly higher for the ZnS-$Cu_{1.8}S$ combination. Similar experiments were carried out with ZnS-$Cu_{1.96}S$. Unfortunately, attempts to prepare pure $Cu_{1.96}S$ (free of Cu_2S) were not successful. Experiments with cuprous sulfide consisting of predominantly $Cu_{1.96}S$ (with some Cu_2S) showed that this mixture was essentially as effective as pure Cu_2S. One may conclude, then, that at least when present in amounts exceeding 1%, all forms of cuprous sulfide, namely, Cu_2S, $Cu_{1.96}S$, and $Cu_{1.8}S$, are nearly equally effective agents in ZnS transformation.

[2] In this experiment as well as in all experiments except the high temperature x-ray studies, samples were cooled by removing the combustion tube from the furnace. This resulted in a cooling time of about 5 min.

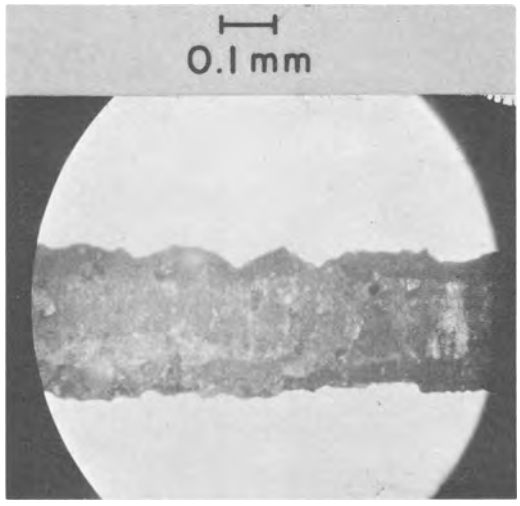

Fig. 2. Photomicrograph of ZnS single crystal treated with CuS at 800°C.

In the course of studies with single crystals, it was found that heat treatment of ZnS single crystals embedded in copper sulfide leaves marked signs of chemical attack on ZnS. For example, a "thick" crystal of hexagonal ZnS (3 mm long and 0.2 mm thick) was fired together with two "thin" ZnS crystals (2 mm long and slightly less than 0.1 mm in thickness) in H_2S at 800°C for 1 hr. The crystals were embedded in CuS powder. After the treatment, the thin crystals could not be detected; microscopic examination of the thick crystal (after KCN-washing) showed that the crystal had been heavily attacked by CuS as can be seen in Fig. 2. A rotation photograph of this crystal was that of a heavily faulted cubic ZnS with just a trace of coherent hexagonal ZnS. In addition, a polycrystalline pattern of cubic ZnS was superimposed on the single crystal photograph.

Additional single crystal experiments gave similar results. Of particular interest is the experiment in which two single crystals of hexagonal ZnS were placed on a pressed pellet of $Cu_{1.8}S$ and fired in H_2S at 900°C for 1 hr. Figure 3 shows the photographs of one of the crystals before and after firing. One can see that as a result of this treatment, the ZnS crystal has been covered with a very thick coating of $Cu_{1.8}S$ (the cross-section has increased by a factor of almost two). The crystal was then treated with KCN solution for a few minutes and photographed again. In Fig. 3c small ZnS crystallites are seen dispersed in $Cu_{1.8}S$. Complete KCN treatment left only polycrystalline ZnS together with a very thin ZnS plate containing fairly large portions of monocrystalline cubic ZnS. The plate was found below the original ZnS crystal and since its dimensions were longer than the cross-section of the original crystal, it is possible that it crystallized on cooling.

A possible explanation for the result of the above experiments is that zinc sulfide and copper sulfide interact to form a compound or a solid solution. X-ray examination of quenched ZnS-CuS samples showed no phases other than those of pure ZnS (hexagonal or cubic) and cuprous sulfide. It was decided therefore to use high temperature x-ray techniques in our further study of the ZnS-copper sulfide interaction.

High temperature x-ray studies.—The following experiment shows a typical course of the ZnS-CuS interaction at elevated temperatures. A 1 to 1 mixture (by weight) of ZnS and CuS was x-rayed in N_2 atmosphere on a high-temperature diffractometer. The temper-

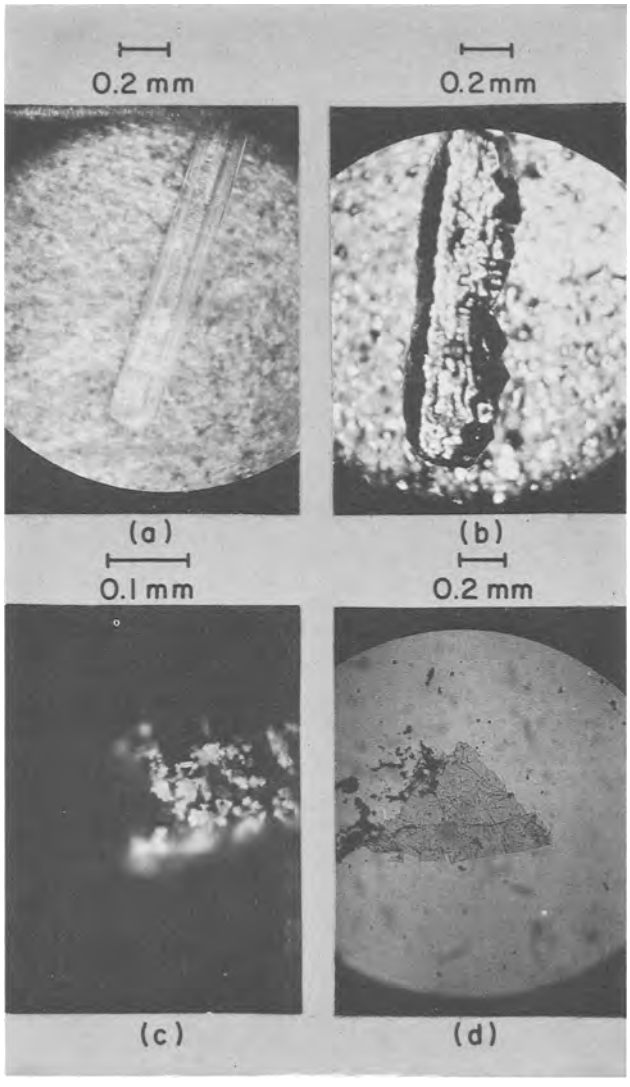

Fig. 3. Photomicrograph of ZnS single crystal treated with cuprous sulfide: (a) before copper treatment, (b) after copper treatment, (c) copper treated crystal after KCN etching, (d) ZnS plate (see text).

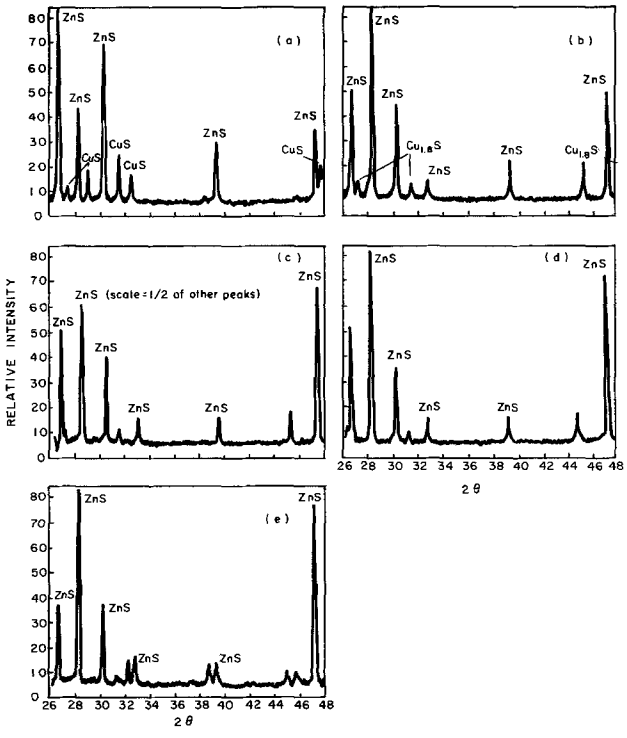

Fig. 4. High temperature diffractometer traces of ZnS + CuS: (a) at 300°C, (b) at 350°C, (c) at 350°C, (d) at 400°C, (e) at room temperature following high temperature run.

ature was raised from room temperature to 300°C within 15 min, and 30 min later an x-ray trace was taken. The x-ray pattern, Fig. 4a, is that of well-crystallized hexagonal ZnS and CuS. The temperature was raised to 350°C, and a few minutes later an x-ray trace was taken. CuS was found to be converted to $Cu_{1.8}S$, while a substantial fraction of the ZnS was transformed to the cubic form (Fig. 4b). The temperature was kept constant, and 30 min after the first run at 350°C a second trace was taken. As can be seen from Fig. 4c, the ratio of cubic to hexagonal ZnS increased still further. A slight shift may be detected in the cuprous sulfide peaks indicating transition from $Cu_{1.8}S$ toward $Cu_{1.96}S$. The temperature was next raised to 400°C, and after about 20 min an x-ray trace was taken. Figure 4d shows that the cubic to hexagonal ratio increased still further, while the cuprous sulfide peaks diminished slightly in intensity (the intensity decrease in cuprous sulfide peaks has been found to be quite general for the ZnS-cuprous sulfide system at elevated temperatures). The temperature was lowered to room temperature within a few minutes. Apart from a slight thermal shift, the ZnS pattern can be seen to be essentially unchanged as compared with that at 400°C. The cuprous sulfide is found to consist of low-temperature forms of $Cu_{1.96}S$ and $Cu_{1.8}S$ (Fig. 4e).

In some high temperature experiments the conversion of CuS has been found to precede the transformation of ZnS. The temperature of the incipient ZnS transformation was usually around 350°-400°C. Certain important facts emerge from these experiments. First, the conversion of ZnS occurs at the firing temperature and not during the cooling process. Also the transformation of ZnS appears to be preceded by the conversion of CuS. It appears then that copper sulfide must be in the form of the high temperature modification of cuprous sulfide in order to exert its catalyzing effect.

Experiments were then carried out to determine changes in lattice constants of ZnS and Cu_2S. The lattice determination of the high temperature Cu_2S form was based on its (220) peak since this is the strongest peak of high Cu_2S and, except for the (311) peak [which is only 4° above the (220) peak], is the peak with the highest θ value. For the sake of consistency, the lattice determination of ZnS was also based on its (220) peak, both (220) of ZnS and (220) of Cu_2S occurring in the 22°-24° θ range. Since in the high temperature diffractometer the flat surface of the specimen did not usually pass through the rotation axis of the instrument, the following procedure was adopted. The pure samples of ZnS and Cu_2S were first run on the regular wide range diffractometer at room temperature, and the (220) peak of ZnS (cubic), as well as the (3.12.0) peak of room temperature Cu_2S, was calibrated against the (220) peak of a National Bureau of Standards silicon sample. The difference between the correct value of the peak (of either ZnS or Cu_2S) and the room temperature value of the same peak recorded on the high temperature diffractometer was used to correct the high temperature (220) peaks of both ZnS and Cu_2S. This procedure is permissible since all the pertinent peaks occur in the 22°-24° θ region. The angular shift due to displacement of the sample from the instrument axis is proportional to $\cos\theta$ (12), and this means that in the 22°-24° region the shift varies by less than 1.4%.

Table I gives the calculated lattice parameters for ZnS and Cu_2S. The values were based on three independent runs. According to Djurle (10) the value of a for Cu_2S is 5.735 ± 0.010Å at 500°C which is seen to

Table I. Lattice parameters of ZnS and Cu_2S

Sample	a, Å
Pure ZnS at 500°C	5.434 ± 0.010
ZnS in ZnS + Cu_2S mixture at 500°C	5.437 ± 0.010
Pure ZnS at 800°C	5.448 ± 0.010
ZnS in ZnS + Cu_2S mixture at 800°C	5.450 ± 0.010
Pure Cu_2S at 500°C	5.725 ± 0.010
Cu_2S in ZnS + Cu_2S mixture at 500°C	5.720 ± 0.010
Pure Cu_2S at 800°C	5.762 ± 0.010
Cu_2S in ZnS + Cu_2S mixture at 800°C	5.736 ± 0.010

be quite close to the value obtained in our investigation, 5.725. If one assumes a linear relation between unit cell parameter and concentration, one obtains a value of 8 m/o (mole per cent) of ZnS in Cu_2S at 800°C. The lattice parameter of ZnS, in the presence of Cu_2S at high temperatures, seems to show a slight trend indicating solid solution of Cu_2S in ZnS. However, these shifts are within experimental error. No such apparent shift was detectable in ZnS at room temperature. In all cases, analysis of cooled and cyanide washed samples showed retained copper concentrations of the order of a few hundred parts per million.

The results of the experiments described so far point very strongly to the existence of a solid solution between ZnS and cuprous sulfide. These results are thus in basic agreement with those of Novoselov (13). Novoselov's value for the concentration of ZnS dissolved in Cu_2S at 800°C is about 12 m/o (as estimated from his diagram). His results were obtained by means of differential thermal analysis.

Experiments were carried out to obtain additional evidence for solid solution formation between ZnS and Cu_2S.

A mixture of 0.95 mole of Cu_2S and 0.05 mole of cubic ZnS was deposited on Pt-Rh holder. The temperature was raised quickly (2 to 3 min) to 800°C. The (111) peak of cubic ZnS could not be detected. The 30°-28° region was scanned for 38 min more but no indication of the (111) peak was obtained. The temperature was then lowered to 500° and a small though rather broad (111) peak was recorded. This peak became sharper with time at 500°C, indicating a crystallization process of ZnS. The temperature was raised to 800°C again and the (111) peak disappeared. A similar experiment was made with a mixture containing 8 m/o of cubic ZnS. The results were essentially the same as in the preceding experiment. In a mixture containing 15 m/o of ZnS, however, the ZnS phase could be detected at both 500° and 800°C.

The last three experiments allow one to set approximate limits on the solid solubility at 500° and 800°C. The ZnS phase in the 5% ZnS mixture was detectable at 500°C. The ZnS concentration in Cu_2S is therefore less than 5 m/o at 500°C. At 800°C the ZnS phase disappears in both 5 and 8% ZnS mixtures. It is significant that in the 8% mixture the position of the (200) Cu_2S peak reached what appears to be an equilibrium 2θ value at 800°C. The ZnS concentration at 800°C then does not exceed 8 m/o.

The following experiment is quite indicative of solid solution formation. A layer of hexagonal ZnS was deposited on a Pt-Rh strip and Cu_2S was then placed on top of the ZnS. The diffractometer trace taken at room temperature showed weak reflections of hexagonal ZnS. This probably indicates that the Cu_2S layer was not thick enough to stop the x-ray radiation used. The temperature was raised to 800°C and the scanning of the 31-28 2θ region was begun. The x-ray trace showed no hexagonal ZnS. The cubic (111) peak was initially quite broad; it grew steadily with time, reaching what appeared to be an equilibrium intensity after about 80 min at 800°C. At no time was the hexagonal phase detectable. It appears that hexagonal ZnS forms a solid solution with Cu_2S and the cubic ZnS precipitates in the cooler portion of the layer.

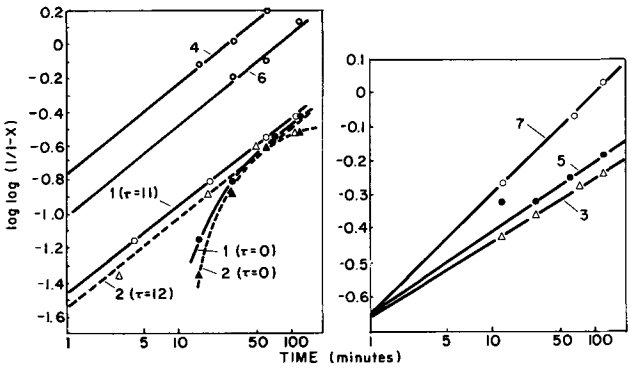

Fig. 5. Plot of log log (1/1—x) against log t. Sample numbers refer to Table II.

Rate experiments.—In these experiments two different preparations of hexagonal ZnS and two CuS reagents were used. CuS was used, rather than any form of cuprous sulfide because the former was available as very fine powder, while the Cu_2S prepared here was very coarse-grained. To have ground the Cu_2S materials might have introduced unwanted contamination. The crystallite size in both CuS reagents was about the same (below 1μ); however, in CuS-2 the crystallites were frequently sintered together, forming somewhat coarser particles than in CuS-1. All experiments in this section were carried out by mixing 4 parts of hexagonal ZnS and 1 part of CuS and firing the mixture in nitrogen atmosphere for various periods of time. It was found that the above ratio of the reactants was sufficient to provide intimate contact between the reacting particles and that no change in the ZnS transformation rate would result on increasing the CuS to ZnS ratio. The degree of conversion to the cubic form of ZnS was determined on the basis of the integrated intensity of the cubic (200) ZnS peak, measured at room temperature.

The experimental data have been found to fit the so-called sigmoidal rate equation.

$$x = 1 - \exp(-bt^n)$$

where x is the fraction of the transformed phase, t the total transformation time, n a constant determined by the shape of the growing particle, and b is a constant related to the rate constant.

In numerous instances the sigmoidal equation has been found to describe the kinetics of various phase changes (14). A plot of ln ln(1/1—x) against ln t should yield a straight line, and Fig. 5 shows that good straight lines are indeed obtained for the data of our experiments. The failure to obtain a straight line relation between ln ln(1/1—x) and ln t for samples fired at 500°C indicates that at this temperature the induction period, τ, is relatively long. In this case ln ln(1/1—x) was plotted against ln(t—τ) for a series of τ values, and the value of τ which gave a straight line was taken as the induction period.

Table II lists the values of the constants n and b, as well as the rate constants $k = nb$ obtained from Fig. 5.

Table II shows that for samples treated with CuS-1, as well as for samples fired at 500°C (with either CuS-1 or CuS-2), the value of n is very nearly 1/2.

Table II. Rate parameters of ZnS transformation

	Series	Temp, °C	n	b	k (min^{-n})
1	(ZnS-2 + CuS-2)	500	0.51	0.078	0.040
2	(ZnS-1 + CuS-1)	500	0.53	0.064	0.034
3	(ZnS-2 + CuS-2)	600	0.205	0.51	0.10
4	(ZnS-2 + CuS-1)	600	0.54	0.39	0.21
5	(ZnS-2 + CuS-2)	700	0.225	0.51	0.11
6	(ZnS-1 + CuS-1)	700	0.54	0.22	0.12
7	(ZnS-2 + CuS-2)	800	0.325	0.51	0.17

A departure from $n = 1/2$ is observed for samples fired with CuS-2 at temperatures above 500°C. This may be attributed to the fact that, owing to the coarser particles of CuS-2, an appreciable number of ZnS crystallites may have escaped attack by CuS. This effect, however, would be of relatively minor importance at 500°C where the transformation rate is not fast. Also it may be noted that the two preparations of ZnS transformed at different rates; this may be attributed to slight differences in their stoichiometry or crystalline perfection.

Discussion

It has been shown that the copper phase effecting the ZnS transformation is the high temperature modification of cuprous sulfide and that, at least when present in sufficiently large amounts (1% or more), all compositional forms of cuprous sulfide, *i.e.*, Cu_2S, $Cu_{1.96}S$, and $Cu_{1.8}S$, are nearly equally effective at elevated temperatures. It has also been shown that at elevated temperatures ZnS and cuprous sulfide interact to form a solid solution having a composition in the neighborhood of 8 m/o ZnS at 800°C. The high temperature x-ray evidence for the solid solution is based on experiments involving Cu_2S. Other forms of cuprous sulfide, in particular $Cu_{1.8}S$, undoubtedly form solid solutions also, as has been shown in experiments with single crystals. This is understandable since the high temperature modifications of all cuprous sulfides appear to be isostructural (10). In this structure the sulfur atoms form a close-packed cubic arrangement, and the copper atoms are statistically distributed in the tetrahedral sites (15). The structure of high cuprous sulfide is thus seen to be related to that of cubic ZnS, in which the positions of the sulfur atoms are also those of face-centered cubic close packing with the zinc atoms occupying one-half of the tetrahedral holes. It appears that it is the structural similarity between cubic ZnS and high cuprous sulfide that enables the two sulfides to form solid solution. The (Cu,Zn)S solid solution cannot be preserved by quenching to room temperature, and this again is understandable since on cooling the high temperature form of the cuprous-sulfides is transformed into low symmetry structures (10).

One may assume then that the first step in the ZnS transformation (copper induced) is formation of the (Cu,Zn)S solid solution. The high temperature x-ray results show that in a thoroughly mixed sample of ZnS and cuprous sulfide (containing comparable amounts of both sulfides) this process is quite rapid at 800°C. The rapid rate of the solid solution formation is illustrated by the fact that the shift in the (220) peak of Cu_2S in ZnS-Cu_2S mixture appears to reach an equilibrium value within the first 1 or 2 min at 800°C (with a total heating-up period of only 2-3 min). At this temperature then, solid solution formation is not a rate determining step. The fact that the transformation rates are quite close in the 600°-800°C range suggests that all the steps in the transformation, including that of solid solution formation, are rapid in the 600°-800°C range.

There is no direct evidence on which one could draw conclusions regarding the rate of nucleation, but the kinetic data suggest that, in the 600°-800°C range, nuclei are formed in a time that is negligible compared to the time required for particle growth. Rapid nucleation rates have been established (by inference from over-all rate) in a number of precipitation reactions (14), as well as in many recrystallization processes (16). It is reasonable to assume then that in the 600°-800°C range the formation of ZnS nuclei is not a rate determining process.

The over-all transformation rate of ZnS has been found to obey the sigmoidal rate equation

$$\frac{dx}{dt} = k(1-x)\ t^{n-1}$$

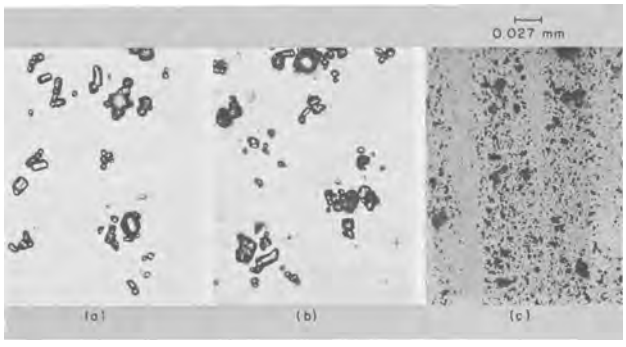

Fig. 6. Photomicrographs of (a) starting hexagonal ZnS, (b) hexagonal ZnS treated with CuS at 800°C (after KCN wash), (c) precipitated ZnS fired at 800°C.

with n lying in the neighborhood of 1/2. This value of n may be explained either in terms of a one-dimensional growth mechanism which is determined only by processes occurring at the interface of the growing phase, or in terms of a one-dimensional precipitation model proposed by Roberts *et al.* (17). The essential difference between these two models lies in the fact that in the latter model (precipitation) the growth of the particle is diffusion controlled. It has been shown by Zener (18) that the rate of linear growth in this case is proportional to $(Dt)^{1/2}$, where D is the diffusion coefficient of the diffusing species. Assuming a linear concentration gradient, it is then easy to show (17) that the growth rate of a particle in one dimension (*e.g.*, a platelet which thickens with time) should be proportional to $t^{-1/2}$.

If one assumes that the growth of cubic ZnS is diffusion controlled, it follows that the ZnS transformation proceeds by dissolution of hexagonal ZnS in Cu_2S, followed by precipitation and subsequent crystallization of cubic ZnS. In Fig. 6 are shown photomicrographs of the starting hexagonal ZnS, hexagonal ZnS treated with CuS at 800°C for 1 hr, and ZnS precipitate crystallized for 1 hr at 800°C. It is seen that the copper-treated sample (which was almost completely converted to the cubic form) is essentially similar to the starting hexagonal ZnS. Crystallization of ZnS precipitate, on the other hand, yielded crystallites considerably smaller in size. Crystallization of ZnS precipitate at temperatures lower than 800°C would be expected to produce even smaller crystallites, yet the crystal size of ZnS samples treated with CuS even at 350°C shows no detectable difference from that of the starting material (although considerable conversion to the cubic form may be achieved after 1 hr at 350°C). One may then reject the diffusion-controlled mechanism, though as pointed out earlier it has been found operative under certain conditions.

We shall now examine a one-dimensional growth mechanism which is controlled primarily by processes occurring at the phase interface. It may be recalled that the ZnS structure can be regarded as being composed of ZnS layers stacked in the direction normal to the layer plane. The forces holding each layer together are apparently considerably stronger than those holding the separate layers together. This is evidenced by the fact that the mechanical or thermal treatment very often produces one-dimensional faulting, but there is no detectable sign of disorder within individual layers. It is significant that mechanical or thermal treatment of hexagonal ZnS (without copper) produces usually little or no coherent cubic ZnS. For example, Smith and Hill (19) found that impact comminution of hexagonal ZnS results in a heavily faulted structure which is neither coherent cubic nor coherent hexagonal. They obtained similar results for thermally treated ZnS (prolonged sintering with NaCl at 850°-970°C). Short and Steward (20) describe similar experiments on grinding hexagonal ZnS. They report a

decrease in the proportion of hexagonal stacking as the grinding time is increased. However, there is no evidence in their paper for the appearance of a coherent cubic phase, as can be seen from the absence of any intensity in the cubic (200) reflection. Extensive faulting with little or no coherence in either cubic or hexagonal phases was reported in the case of thermally treated hexagonal ZnS in the absence of copper (21). In the single crystal experiments carried out as part of this investigation it was also observed that in the absence of copper, thermal treatment produces faulting but little or no coherent cubic ZnS.

The theory of one-dimensional disorder, as developed by Wilson (22) and Jagodzinski (23), which proved to be successful in interpreting stacking fault disorder in certain layer structures (cobalt, graphite, ZnS, etc.), assumes that whenever growth or deformation faulting occurs, the position which will be taken by a given layer depends on the positions of the preceding layers. In Wilson's theory the "sphere of influence" was restricted to two preceding layers. This model proved to be inadequate in certain cases (including ZnS) and better agreement with experiment was achieved by extending the sphere of influence to 3 layers (23). A more adequate description of one-dimensional disorder would probably have to extend the interaction range to more layers (24).

It is proposed that the failure of thermal treatment (no copper) to transform hexagonal ZnS into coherent cubic phase lies in the fact that for such transformation to occur one needs nuclei of coherent cubic ZnS which could guide the transformation wave. Such nuclei appear to form in copper-treated ZnS as a result of precipitation of cubic ZnS from the (Cu,Zn)S solid solution. When the nucleus attains a certain critical size (perhaps a few tens of layers thick), it may start to reorder the hexagonal layers, provided the nucleus happens to grow on certain specific hexagonal faces, for example, (0002). The transformation of hexagonal ZnS may then be characterized by a progressive movement of the hexagonal-cubic interface, the driving force being a decrease in the free energy associated with the transition to the stable cubic phase. In this case the transformation mechanism amounts to a one-dimensional growth process. Now, assuming that the linear growth rate is proportional to $t^{-1/2}$, which according to Loria *et al.* (16) appears to hold for many recrystallization processes, and further assuming that the nucleation period is negligible compared with the time required for growth (which also seems to be a very reasonable assumption) (16), one may set the over-all transformation rate proportional to $t^{-1/2}$. Making allowance for mutual interference of growing domains by introducing a factor $(1-x)$, one obtains

$$\frac{dx}{dt} = k(1 - x)t^{-1/2}$$

which is the rate equation describing our kinetic data.

Acknowledgment

The authors are indebted to the following staff members of General Telephone & Electronics Laboratories: H. Samelson for the generous supply of ZnS single crystals; R. Weberling and J. Cosgrove for performing copper analyses; and to F. C. Collins and B. Post of the Polytechnic Institute of Brooklyn for valuable discussions. The authors would also like to acknowledge the aid of General Telephone & Electronics Laboratories, Inc. for the use of their laboratory facilities for this investigation.

Manuscript received June 12, 1967; revised manuscript received July 19, 1967. This paper was abstracted in part from a dissertation submitted by one of the authors (G.G.) in partial fulfillment of the requirements for the PhD. degree in chemistry at the Polytechnic Institute of Brooklyn, June 1966.

Any discussion of this paper will appear in a Discussion Section to be published in the June 1968 JOURNAL.

REFERENCES

1. E. T. Allen and J. L. Crenshaw, *Am. J. Sci.*, **34**, 341 (1912).
2. V. N. Nesterov and V. D. Ponomarev, *Tr. Vses. Soveshch. Sverdlovsk*, 1960, 439 (*C.A.* 57 15891 d).
3. A. Addamiano and M. Aven, *J. Appl. Phys.*, **31**, 36 (1960).
4. H. Gobrecht, H. Nelkowski, and P. Albrecht, *Z. Naturforsch.*, **16a**, 857 (1961).
5. J. Nickerson, P. Goldberg, and D. H. Baird, *This Journal*, **110**, 1228 (1963).
6. M. Aven and J. A. Parodi, *J. Phys. Chem. Solids*, **13**, 56 (1960).
7. H. C. Froelich, *This Journal*, **100**, 280 (1953).
8. D. W. G. Ballentyne, *J. Phys. Chem. Solids*, **10**, 242 (1959).
9. M. J. Presland, R. Marshall, and J. Franks, *This Journal*, **111**, 168 (1964).
10. S. Djurle, *Acta Chem. Scand.*, **12**, 1415 (1958).
11. H. Samelson and V. A. Brophy, *This Journal*, **108**, 150 (1961).
12. G. M. Brindley, in "X-ray Diffraction By Polycrystalline Materials," H. S. Peiser, H. P. Rooksby, and A. J. C. Wilson, Editors, pp. 145-175, J. Wright & Sons Ltd. (1955).
13. S. Novoselov, *Tsvetn, Metal*, **28**, 15 (1955).
14. D. Turnbull, *Solid State Phys.*, **3**, 225 (1956).
15. N. Morimoto and G. Kullerud, *Am. Mineralogist*, **48**, 110 (1963).
16. E. A. Loria, K. Detert, and J. G. Morris, *Acta Met.*, **13**, 929 (1965).
17. C. S. Roberts, B. L. Averbach, and M. Cohen, *Trans. Am. Soc. Metals*, **45**, 576 (1953).
18. C. Zener, *J. Appl. Phys.*, **20**, 250 (1949).
19. F. G. Smith and V. G. Hill, *Acta Cryst.*, **9**, 821 (1956).
20. M. A. Short and E. G. Steward, *Z. Phys. Chem.*, **13**, 298 (1957).
21. T. Peters, J. Singer, V. A. Brophy, and J. L. Birman, *J. Appl. Phys.*, **34**, 2210 (1963).
22. A. J. C. Wilson, *Prov. Roy. Soc. A*, **180**, 277 (1942).
23. H. Jagodzinski, *Acta Cryst.*, **2**, 208 and 298 (1949).
24. R. Gevers, *ibid.*, **7**, 337 (1954).

Influence of Carbon Transport Kinetics on Solution Growth of β-Silicon Carbide Crystals

R. W. Bartlett, W. E. Nelson, and F. A. Halden

Stanford Research Institute, Menlo Park, California

ABSTRACT

Twinned β-silicon carbide platelets with a (111) habit were grown from the walls of graphite crucibles in liquid silicon solutions with carbon concentrations below 0.1 a/o (atomic per cent). The observed crystal growth effects resulting from increasing the carbon solute transport rate by stirring the solution are described and correlated with boundary layer theory. Both forward growth of platelets into the solution and lateral growth of platelets were accelerated by stirring. However, crystal growth in the forward direction was eventually limited by a boundary layer region, beyond which the solution was no longer supersaturated. Because of the decrease in boundary layer thickness with increasing stirring speed, the terminal lengths of silicon carbide platelets decrease with increasing stirring speed.

Cubic β-silicon carbide crystals have been grown from carbon-saturated liquid silicon solutions (1, 2). These crystals normally occur as vicinal platelets with a (111) habit. They nucleate on walls of the graphite crucible and extend into the solution with their major faces normal to the wall. The crystals are usually twinned on the (111) planes (3), and the twin plane re-entrant edge formed when at least two (111) twin planes occur in the crystal is believed to cause more rapid growth at the edge of these platelets than in a direction normal to their habit faces (4, 5). This anisotropy in growth kinetics accounts for the platelet morphology. However, modifications in this general form have been observed under different growth conditions. Stirring the solution causes a reduction in platelet length and an increase in platelet thickness, and rapid stirring leads to approximately equidimensional twinned crystals (see Fig. 1 where cross sections of partially leached crucibles are shown). Untwinned crystals are also polyhedral and quite small unless the solution is rapidly stirred to increase the rate of transport of carbon across the boundary layer.

Although there is considerable experimental evidence to support the twin plane re-entrant edge mechanism of platelet crystal growth for silicon carbide (see Fig. 2) there are no data on the kinetics of solute attachment to the crystal (sticking coefficients) as a function of crystal habit that would permit an analytical treatment of this aspect of the crystal growth rate. It would be exceedingly difficult, if not impossible, to devise suitable experiments to secure these data because of the high crystal growth temperatures and highly reactive growth environment. Consequently, the present study was confined to an analysis of carbon transport in the solution adjacent to the growing crystal platelet and the effect of carbon transport on crystal growth rates. Both forward, <110>, and lateral, [111], growth directions of platelets were considered, but primary attention was placed on the forward growth rate.

Experimental

The method of growing β-silicon carbide from solution in a molten silicon solvent has been described previously (1, 2). Silicon is melted in a graphite crucible and is held in a thermal gradient, which permits solution of carbon at the upper walls and growth of silicon carbide crystals on the base and lower walls of the crucible. The solubility of carbon in liquid silicon (6) is only about 0.03 a/o at 1600°C. Carbon transport

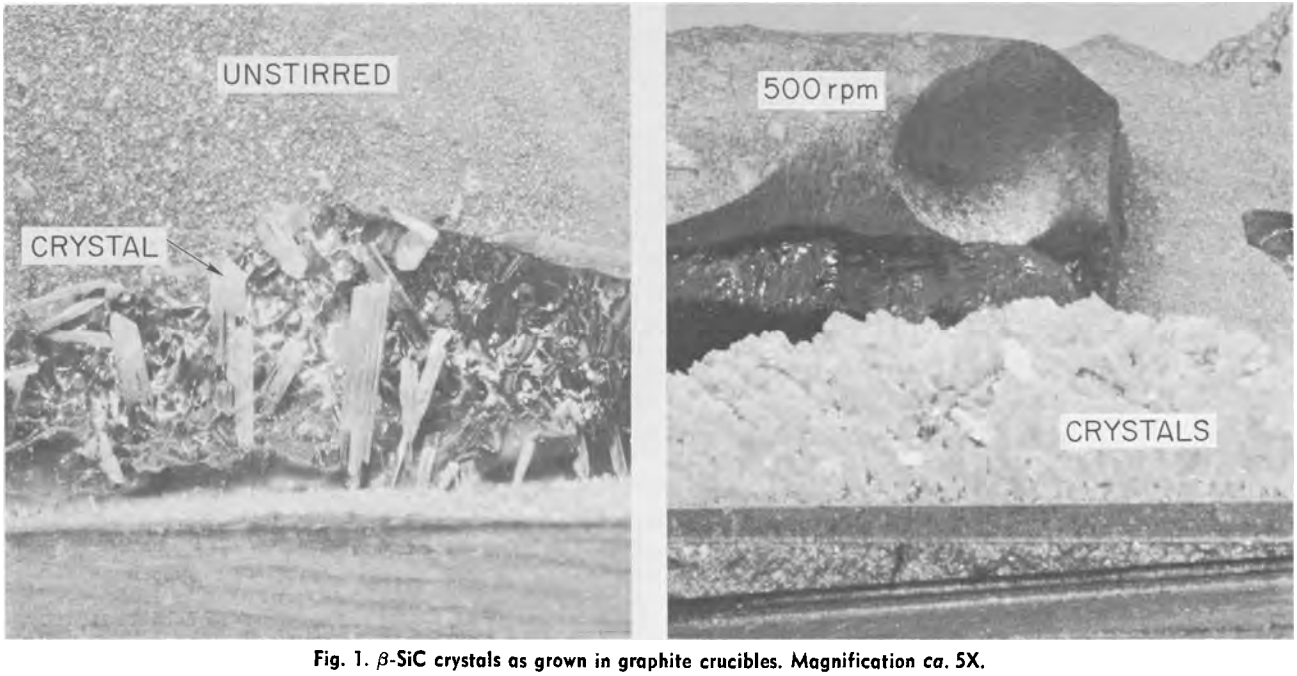

Fig. 1. β-SiC crystals as grown in graphite crucibles. Magnification *ca.* 5X.

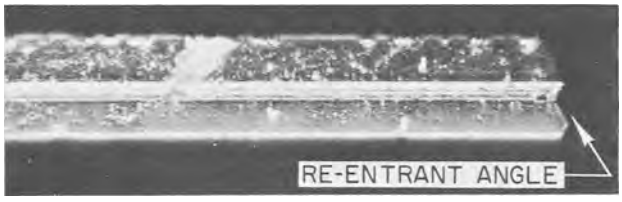

Fig. 2. Edge view of twinned β-silicon carbide crystal showing the re-entrant angle. Magnification 235X.

within the solution normally occurs by free convection and diffusion. In the present study, carbon transport was accelerated by stirring the solution with a graphite impeller. The crucible diameter was 50 mm and the impeller diameter was 38 mm. The impeller was separated 15-20 mm from the crucible base. Crystal growth experiments were conducted at impeller speeds varying from 0 to 500 rpm.

Although more crystals were formed with increasing impeller speed, platelet length decreased. The terminal length of platelets grown in 24 hr decreased from 8-10 mm to about 1 mm as the stirring speed was increased from 0 to 500 rpm (see Fig. 1). Platelet thickness increased with stirring speed, and at 500 rpm crystal thickness approached crystal length.

Theory

Latent heat effect.—The effect of the latent heat of formation of the growing silicon carbide crystals on the growth mechanism is insignificant. This fact can be confirmed by examining the diffusion-controlled rate of growth of silicon carbide in a perfectly quiescent solution with the following typical experimental conditions: a temperature difference ΔT of 100°C and a carbon mole fraction difference $X_{c_\infty} - X_{c0}$ of 2 x 10^{-4} (2 x 10^{-2} a/o) from source to sink, and a distance Δy of 3 cm between the source and sink. $T_\infty - T_0$ and $X_{c_\infty} - X_{c0}$ correspond to a growth temperature of 1530°C and a source temperature of 1630°C, based on Scace and Slack's data (6) for carbon solubility in silicon.

For steady-state diffusion, the carbon flux J (moles cm^{-2} sec^{-1}) is given by

$$J = C_0 D(X_{c_\infty} - X_{c0})/\Delta y \qquad [1]$$

where C_0 is the total molar concentration of the dilute solution (0.0768 mole cm^{-3}), and D is the diffusivity of carbon in the solution. The physical properties of liquid silicon $\overline{C}_p$, D, K_L, μ, and ρ, required for this and subsequent analyses are listed in Table I. Estimates were made for μ, K_L, and D. The diffusion coefficient for carbon, D = 1.7 x 10^{-4} cm^2 sec^{-1}, was estimated using the generally accepted empirical equation for self-diffusion in liquids shown in Table I. The growth rate $\dot{y}$ is related to the carbon flux in solution by the expression

$$\dot{y} = J(M/\rho)_{SiC} = 12.5J \qquad [2]$$

Table I. Properties of liquid silicon

Property	Value
Specific heat, $\overline{C}_p$	0.182 cal g^{-1} $°C^{-1}$
Viscosity, μ	1 x 10^{-2} poise (est.)*
Thermal conductivity, K_L	0.08 cal sec^{-1} cm^{-1} $°C^{-1}$ (est.)*
Density, ρ	2.55 g cm^{-3}
Diffusion, D	1.7 x 10^{-4} cm^2 sec^{-1}†
Kinematic viscosity, $\nu = \mu/\rho$	3.92 x 10^{-3} cm^2 sec^{-1}
Prandtl number, $Pr = \overline{C}_p\mu/K_L$	0.023
Schmidt number, $Sc = \mu/\rho D$	23

* Liquid silicon is metallic rather than semiconducting; estimates for thermal conductivity and viscosity are based on values for other liquid metals, particularly tin.

† Diffusion coefficient calculated from liquid silicon properties using the following formula

$$D = (kT/2\pi\mu)(N_0\rho/M)^{1/3}$$

For the selected conditions previously mentioned, $\dot{y}$ = 8.3 x 10^{-3} mm/day, or conversely, 121 days are required to increase the crystal length by 1 mm.

The heat flux q_f associated with this simple diffusion-controlled growth can be calculated from the heat of formation of silicon carbide from liquid silicon saturated with carbon

$$q_f = \dot{y}\rho(-\Delta H_f) \qquad [3]$$

where ΔH_f is the heat of formation of SiC at 1580°C; ΔH_f = −1470 cal/g (−59,000 cal/mole). The heat flux transferred through the liquid solution, q_L, is given for the convectionless case

$$q_L = K_L(T_\infty - T_0)/\Delta y \qquad [4]$$

The ratio q_f/q_L is the ratio of heat flux originating from crystallization to heat flux arising from transfer through the solution. This ratio is very small for the selected condition, q_f/q_L = 1.6 x 10^{-5}, and consequently the heat of crystallization will not significantly affect heat transfer or temperature distribution within the solution or at the crystal solution interface. Stirring the solution will increase both q_f and q_L, but the ratio q_f/q_L will remain negligibly small for the growth of silicon carbide.

Boundary layer profiles.—Boundary layer theory (7, 8) is used to describe the silicon solution adjacent to the crucible wall under defined stirring conditions. This analysis proceeds as follows. Dimensionless profiles of the mass (carbon concentration), fluid velocity, and temperature are calculated as functions of a dimensionless distance from the cold wall. These calculations are made without regard to the presence of silicon carbide crystals, which are considered to be too few in number to alter the boundary layer profiles. Physical constants for liquid silicon or estimated physical constants based on properties of other similar liquid metals are used. The thermal boundary layer is much thicker than the mass boundary layer, leaving a supersaturated region near the cold wall, even if equilibrium is attained at the cold wall surface. The converse is true near the hot wall, where an undersaturated region will be found even though equilibrium with respect to carbon solubility is attained at the hot wall. These results are a consequence of the thermal diffusivity being much larger than the mass diffusivity. The situation is shown schematically in Fig. 3. The linear gradients in this figure represent molecular diffusion and thermal conduction in a quiescent liquid.

Consider solution flow around a flat disk that rotates about an axis perpendicular to its plane with uniform angular velocity ω in a fluid otherwise at rest. Because of friction, a boundary layer of fluid is carried by the disk and thrown outward by centrifugal forces. This flow is compensated for by an influx of fluid in the axial direction toward the disk. The axial and radial flow are shown in Fig. 4. This case permits a solution

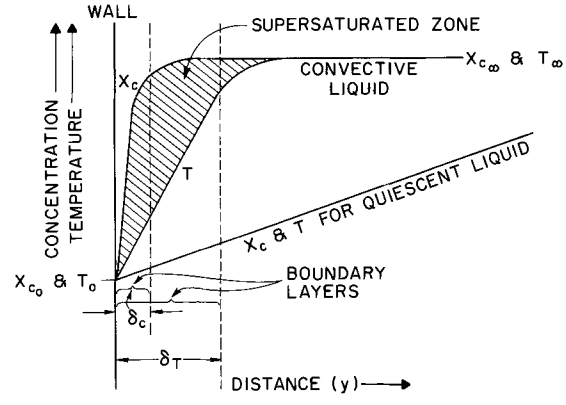

Fig. 3. Schematic diagram comparing the temperature and carbon mole fraction profiles near the crucible cold wall.

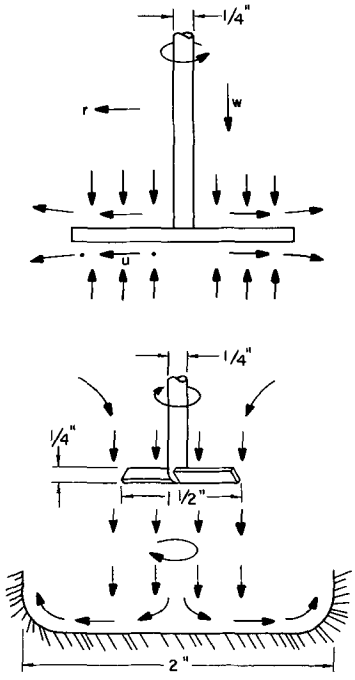

Fig. 4. Axial and radial fluid flow for a rotating flat disk in an otherwise quiescent liquid and for a crucible base in a stirred liquid.

of the Navier-Stokes equations for flow (7) and, with some modification, provides a good analogue of the conditions existing at the bottom of an impeller-stirred crucible. The thickness δ of the layer carried by the disk is

$$\delta \cong (\nu/\omega)^{1/2} \quad [5]$$

Dimensionless velocity profiles for tangential (circumferential), radial, and axial flow are shown in Fig. 5(a) as functions of a dimensionless distance ξ from the disk, where $\xi = y/(\nu/\omega)^{1/2}$. The actual velocities, v in the tangential direction, u in the radial direction, and w in the axial direction, are obtained from the dimensionless velocities by the following defining equations

$$G = v/r\,\omega\,\xi \quad [6]$$

$$F = u/r\,\omega\,\xi \quad [7]$$

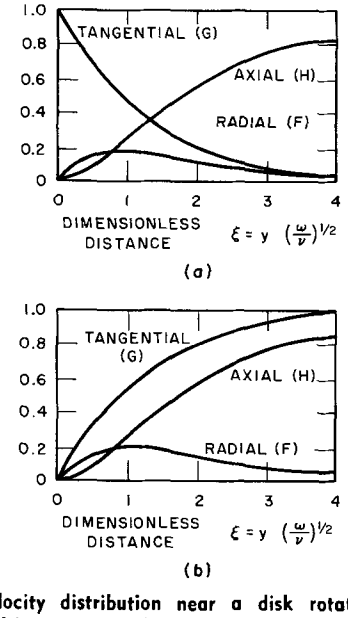

Fig. 5. Velocity distribution near a disk rotating in a fluid at rest (a) and in a rotating fluid near a disk at rest (b).

$$H = w/(\nu\,\omega\,\xi)^{1/2} \quad [8]$$

where r is the local radius of the disk where the velocity values are being determined. The velocity profiles for a stationary disk, *e.g.*, with the reference coordinates rotating with the disk, are shown in Fig. 5(b). The tangential flow is zero at the surface and increases in the direction away from the surface. This situation corresponds closely with that in the base of a stirred crucible when the impeller forces fluid down onto the crucible base. The curves of Fig. 5 are for an infinite disk, but they are not altered for a finite disk, or a finite crucible diameter, provided that the disk or crucible radius $R >> \delta$. The tangential velocity for rotating coordinates is defined as

$$|G| = 1 - (v/r\omega\,\xi) \quad [9]$$

Although the axial flow component is essential for permitting the introduction of enriched solution into the boundary layer, it is not significant in terms of flow over the surface of a platelet protruding into or through the boundary layer. This is because of the much smaller absolute magnitude of the axial flow compared with tangential flow, *i.e.*, $r > (\nu/\omega)^{1/2}$ and therefore $v >> w$ at all but very small values of r, $(r \to 0)$. Furthermore, the region beyond the velocity boundary layer $y > (\nu/\omega)^{1/2}$, is of primary interest because the thermal boundary layer is much thicker than the velocity boundary layer. Since flow in the radial direction does not increase beyond $y = (\nu/\omega)^{1/2}$, flow past a platelet growing in the region to the limit of the thermal boundary layer (supersaturated region) can be described to a good approximation with only the tangential velocity component.

The temperature and mass (carbon) boundary layer thicknesses depend on the velocity boundary layer, δ. Figure 5(b) shows that an exact definition of δ is impossible, because the velocity is a continuous function of y. Boundary layer theory can be used to calculate the temperature and concentration profiles as functions of η, where $\eta = y/\delta$. These dimensionless temperature and concentration profiles also depend on the Prandtl (Pr) and Schmidt (Sc) numbers, respectively (see Table I). In the limit as the net mass transfer rate approaches zero, which is a valid approximation because of the slow growth of silicon carbide, the profile equations are

$$\frac{T - T_0}{T_\infty - T_0} = \frac{\int_0^\eta \exp(-1.328Pr\,\eta^3/3!)\,d\eta}{\int_0^\infty \exp(-1.328Pr\,\eta^3/3!)\,d\eta} \quad [10a]$$

$$\frac{X_c - X_{c0}}{X_{c_\infty} - X_{c0}} = \frac{\int_0^\eta \exp(-1.328Sc\,\eta^3/3!)\,d\eta}{\int_0^\infty \exp(-1.328Sc\,\eta^3/3!)\,d\eta} \quad [10b]$$

For a derivation of these equations, the reader is referred to Bird *et al.* (8), chap. 4 and 19, or to Schlichting (9), chap. 7.

The general profile from Eq. [10] is plotted in Fig. 6, which is taken from Bird *et al.* (8). By letting $\delta = 1.3\ (\nu/\omega)^{1/2}$, the curve of Fig. 6 fits well with the tangential curve of Fig. 5(b). In effect, curve fitting has been used to select the constant, 1.3, in Eq. [5] in order to match all of the profiles appropriately. Using the values for Sc and Pr listed in Table I and the curve from Fig. 6, the temperature and carbon concentration dimensionless profiles were calculated and plotted in Fig. 7. It is readily seen that the mass transfer boundary layer is thinner than the velocity boundary layer and very much thinner than the temerature boundary layer. Since equilibrium (carbon-saturated solution) occurs in the silicon solution beyond the boundary layers, a supersaturated region must occur within the thermal boundary layer. Crystal growth is enhanced in this region in direct proportion to the separation between the mass transfer profile

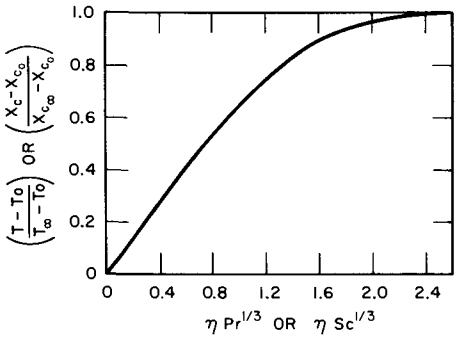

Fig. 6. Temperature or concentration profiles for high Prandtl or Schmidt numbers.

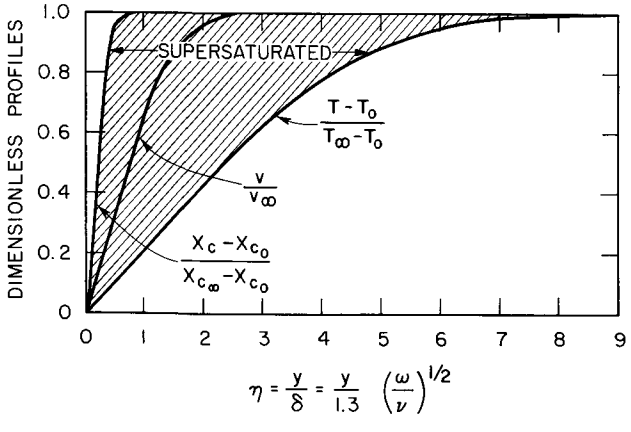

Fig. 7. Dimensionless temperature, velocity, and carbon mole fraction profiles in a stirred crucible of liquid silicon.

and the temperature profile, since this is a measure of the degree of supersaturation. The boundary layer thickness is proportional to $(\omega^{-1/2})$ (see Eq. [5] and Fig. 7).

This pronounced difference in profiles is a direct consequence of the disparity in Schmidt and Prandtl numbers; more particularly, the thermal diffusivity, $K_L/\rho\overline{C_p}$, is very much higher than the mass diffusivity, D. Thus, mass transport is very dependent on stirring, whereas thermal transport is always rapid and is accelerated only slightly by stirring.

Calculated platelet growth rate.—Calculation of the platelet growth rate involves two major terms: (*i*) the excess carbon mole fraction, $\overline{\Delta X_c}$, in the supersaturated (boundary layer) region, and (*ii*) an appropriate mass transfer coefficient, k_m. The velocity profiles for the silicon carbide growth conditions have been described and used to determine temperature and concentration profiles that define the supersaturated region. Over all of this region, except very close to the wall, the carbon mole fraction X_c is equal to the level within the solution, $X_c \approx X_{c_\infty}$, and the tangential fluid velocity v is equal to the velocity of the bulk of the solution, v_∞. Consequently, the critical carbon mole fraction $\overline{\Delta X_c}$ in excess of equilibrium is a function of distance into the boundary layer, y, as follows

$$\overline{\Delta X}_{c(y)} = \left[1-\left(\frac{T-T_0}{T_\infty-T_0}\right)\right]_{(y)} (X_{c_\infty}-X_{c0}) \quad [11]$$

where $(T-T_0)/(T_\infty-T_0)$ is given by Fig. 7.

The carbon flux J to the surface and the reaction rate to form silicon carbide, assuming a sticking coefficient $\sigma = 1$, are proportional to the carbon mole fraction in excess of equilibrium $\overline{\Delta X}_{c(y)}$ as follows

$$J_{(y)} = k_m \overline{\Delta X}_{c(y)} \quad [12]$$

where k_m is the mass transfer coefficient, which will now be discussed.

In general, k_m is a function of the fluid properties and velocity of flow. The Nusselt number (Nu_m) for mass transfer, which is a dimensionless group defined as

$$Nu_m = k_m d/C_0 D \quad [13]$$

where d is a characteristic dimension of the system, is often used in treating mass transfer problems in fluid systems. Empirical correlations have been made to evaluate the Nusselt numbers for forced flow around a few simple shapes. The tangential flow of silicon over the tip of a platelet affects its forward growth rate. Flow over the minor dimension (thickness) of a platelet can be approximated by viscous flow around a submerged rod (transverse direction) or sphere. The resulting Nusselt numbers using the sphere correlation differ little from the Nusselt numbers for the rod. The calculated Nusselt numbers for rods or spheres of the same diameter in identical fluids and flow velocities are usually within 20% of each other, which is adequate for our purpose. Adopting the simple sphere correlation (10)

$$Nu_m = 2.0 + 0.6\, Re^{1/2}\, Sc^{1/3} \quad [14]$$

where Re is the Reynolds number for flow over the tip of the platelet

$$Re = d\, r\omega/\nu \quad [15]$$

In Eq. [15] d is the minor dimension (thickness) of the platelet, and r is the radial distance from the center of the crucible to the platelet. From Eq. [13] and [14] the mass transfer coefficient is

$$k_m = (C_0 D/d)\,(2.0 + 0.6\, d^{1/2}\, r^{1/2}\, \omega^{1/2}\, \nu^{-1/2}\, Sc^{1/3}) \quad [16]$$

Combining Eq. [2], [11], [12], [13], and [14] yields the following relation for the rate of forward platelet growth (sticking coefficient $\sigma = 1$)

$$y = (M/\rho)_{SiC}\,(C_0 D/d)\,(2.0 + 0.6\, d^{1/2}\, r^{1/2}\, \omega^{1/2}\, \nu^{-1/2}\, Sc^{1/3}) \left[1-\left(\frac{T-T_0}{T_\infty-T_0}\right)\right]_{(y)} (X_{c_\infty}-X_{c0}) \quad [17]$$

where $[1-(T-T_0/T_\infty-T_0)]_{(y)}$ is a function of y determined from Fig. 7. Because of this term the growth rate $\dot{y}$ decreases as y increases.

The effects of the radial location of the platelet in the crucible, r, and the minor dimension, d, of a platelet on forward growth velocity and terminal thickness of the platelet are also obtained from Eq. [17], or the Reynolds number. Increasing r increases the growth velocity, but does not affect terminal length. The growth rate decreases slightly as d increases (decrease in aspect ratio).

Results and Discussion

Equation [17] was integrated by successive approximations to obtain growth curves for SiC platelets at various stirring speeds. The following parameters were used in Eq. [17]: the minor platelet thickness, d, is 10^{-2} cm (typical of observed values of d); $(X_{c_\infty}-X_{c0}) = 1 \times 10^{-4}$; and the radial platelet location is $r = 3$ cm. The calculated growth curves are shown in Fig. 8. Results of crystal growth experiments for $(X_{c0}-X_{c_\infty}) = 1 \times 10^{-4}$ are also presented in Fig. 8 as bars. The number adjacent to each data bar indicates the stirring speed, in rpm rather than ω, associated with the crystal lengths observed in that run. The data consensus of more than 30 unstirred experiments is shown as a dashed zone. The terminal crystal lengths are in good agreement with observed values for various stirring speeds, except at the lowest stirring speed, 1 rpm. Crystals longer than 10 mm are usually thin whiskers, and none greater than 15 mm has been grown. Several factors, in addition to some lack of precision in determining the boundary layer thickness, may contribute to this small discrepancy: (*A*) A stirring speed of 1 rpm is very slow, and free convection in an unstirred nonisothermal solution

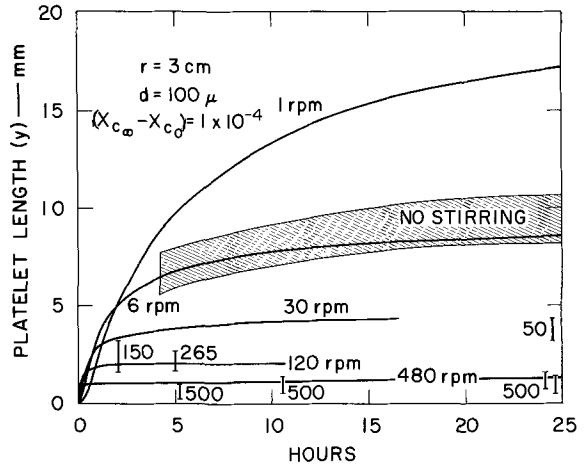

Fig. 8. Calculated growth (length) of silicon carbide platelets at various stirring speeds.

may actually provide more mixing than is secured from stirring at this speed, and consequently may reduce the boundary layer thickness. (*B*) The sticking coefficient in the forward growth direction may be less than $\sigma = 1$. (*C*) As growth progresses, impurities may strongly adsorb on the surface, blocking reactive sites and slowing or even halting further growth. Support for impurity poisoning is found in the fact that crystals longer than a few millimeters have only been obtained in an environment without nitrogen or oxygen. Iron and other metals, when added to the solution in sufficient quantity, have been observed to repress the forward growth of platelets.

Thus far no attempt has been made to analyze the free convection situation where fluid motion is induced because of gravitational forces and the differential specific gravity of a nonisothermal solution. The results in Fig. 8 indicate that free convection mixing is approximately equivalent to stirring at 5 rpm.

The lateral growth direction, [111], of β-silicon carbide can be discussed only qualitatively. The sticking coefficient on the (111) habit is undoubtedly $\sigma << 1$, and because surface active sites for carbon attachment are probably kinks, edges, or other surface anomalies, the effective sticking coefficient probably varies with the surface roughness. Considerable variation in thickness of crystals within a single melt has been observed. Nevertheless, the effect of stirring on the relative rate of lateral growth is of interest because significantly thicker crystals are obtained as a result of stirring. The mass transfer coefficient for growth in the lateral direction can also be expressed as a function of an appropriate Nusselt number, and it can be shown by dimensional analysis that $Nu_m = f(Re^n)$. For simple shapes $n \approx 0.5$. Thus the lateral growth velocity ($\dot{z}$) is a function of stirring velocity, $\dot{z} = f(\omega^n)$. Assuming n = 0.5, untwinned polyhedral crystals grown at a stirring speed of 480 rpm should be 22 times larger than untwinned crystals grown at 1 rpm over the same growth period. A marked increase in the size of untwinned crystals was observed as a result of stirring the solution.

Summary

The case of a rotating impeller inside a large crucible has been treated using boundary layer theory for laminar flow, and the calculated crystal growth results are similar to experimental results obtained using a crucible stirred with a thin impeller. Stirring creates a region of quasi-uniform temperature and carbon concentration throughout most of the solution. However, near the cold base of the crucible where growth occurs, the solution temperature, carbon concentration, and the fluid velocity decrease as the crucible wall is approached. Within this gradient zone, or boundary layer, supersaturation and crystal growth occur. At higher stirring velocities, crystal growth is more rapid, but the boundary layer is also thinner. Consequently, growth in the forward direction quickly terminates at a shorter total platelet length than is eventually attained by slower growing crystals in less rapidly stirred solutions. Growth in the lateral direction, [111], which is the slow-growth direction, is increased by stirring and proceeds without impediment until, given sufficient time, adjacent crystals come in contact. Because higher stirring speeds cause greater supersaturation at the crucible wall, the number of stable nuclei is probably increased by stirring. At higher stirring speeds, these phenomena, coupled with the greater lateral growth velocity of twinned crystals, eventually produce a compact mass of adjacent, approximately equidimensional crystals, rather than the widely separated platelets obtained at low stirring speeds, or without stirring. The agreement between calculated and observed lengths for twinned crystals is satisfactory at all stirring speeds. Agreement is poorest at low velocities: at 1 rpm, the calculated platelet lengths obtained in 24-48 hr are about twice the maximum observed length.

In a perfectly quiescent solution there is no boundary layer limit on the crystal length, but the rate of growth becomes extremely slow. In reality, a quiescent solution is never attained, even without stirring, because of the free convective mixing of the nonisothermal solution. A description of free convection in a hot-top, cold-bottom large crucible has not been attempted. This situation causes much less mixing than the opposite thermal gradient, but the problem is too complex for analysis at this time. The modest free convective mixing obtained in large crucibles, such as those used currently, is probably a good compromise between adequate growth velocity and adequate terminal length of the crystals.

Acknowledgments

The research reported in this paper was sponsored by but does not necessarily constitute the opinion of the Air Force Cambridge Research Laboratories, Office of Aerospace Research, under contract AF 19(628)-4190.

The authors wish to acknowledge Dr. W. A. Tiller of Stanford University for many helpful discussions and Mr. Friedel Knemeyer for assistance with the crystal growth experiments.

Manuscript received April 13, 1967; revised manuscript received July 27, 1967.

Any discussion of this paper will appear in a Discussion Section to be published in the June 1968 JOURNAL.

NOMENCLATURE

C_o	Total solution concentration
C_p	Specific heat of solution
d	Minor dimension of silicon carbide platelets and characteristic dimension for definition of Nu_m
D	Solution diffusion coefficient (carbon)
F	Radial dimensionless fluid velocity
G	Tangential dimensionless fluid velocity
H	Axial dimensionless fluid velocity
ΔH_f	Heat of formation of silicon carbide from solution
J	Carbon flux in solution
k	Boltzmann's constant
k_m	Mass transfer coefficient
K	Thermal conductivity
M	Molecular weight
N_o	Avogadro's Number
q	Heat flux
r	Radial location of platelet in crucible ($0 \leq r \leq R$)
R	Crucible radius
T	Temperature
u	Radial fluid velocity
v	Tangential fluid velocity
w	Axial fluid velocity
X_c	Carbon mole fraction in solution

$\overline{\Delta X}_{c(y)}$ Carbon mole fraction in excess of equilibrium value (a function of y given by Fig. 7 and equation (11))
y Distance in forward growth direction (normal to crucible wall)
$\dot{y}$ Growth velocity in the forward direction
z Distance in lateral growth direction, [111]
δ Boundary layer thickness
η Corrected dimensionless distance
μ Viscosity of solution
ν Kinematic viscosity (μ/ρ)
ξ Dimensionless distance, uncorrected (Note: $\xi \approx \eta$)
ρ Density
σ Sticking coefficient
ω Angular velocity
Nu_m Nusselt dimensionless group for mass transport
Pr Prandtl dimensionless group
Re Reynolds dimensionless group
Sc Schmidt dimensionless group

Subscripts

f Property based on heat of formation of silicon carbide
L Solution property
o Evaluated at crystal surface
∞ Evaluated beyond the boundary layer

REFERENCES

1. F. A. Halden, "Silicon Carbide: High Temperature Semiconductor," J. R. O'Connor and J. Smiltens, Editors, p. 115, Pergamon Press, New York (1960).
2. W. E. Nelson, F. A. Halden, and A. Rosengreen, *J. Appl. Phys.*, **37**, 333 (1966).
3. J. A. Kohn and D. W. Eckart, *Am. Mineral.*, **47**, 1005 (1962).
4. R. S. Wagner, *Acta. Met.*, **8**, 57 (1960).
5. J. W. Faust and H. F. John, *Trans. Met. Soc. AIME*, **233**, 230 (1965).
6. R. I. Scace and G. A. Slack, *J. Chem. Phys.*, **30**, 1551 (1959).
7. H. Schlichting, "Boundary Layer Theory," pp. 75-77, McGraw-Hill Book Co., New York (1955).
8. R. B. Bird, W. E. Stewart, and E. N. Lightfoot, "Transport Phenomena," Chap. 4.4 and 19.3, John Wiley & Sons, New York (1960).
9. H. Schlichting, "Boundary Layer Theory," chap. 7, McGraw-Hill Book Co., New York (1955).
10. W. E. Ranz and W. R. Marshall, Jr., *Chem. Eng. Progr.*, **48**, 141, 173 (1952).

Behavior of Large-Scale Surface Perturbations during Silicon Epitaxial Growth

W. R. Runyan and Earl G. Alexander

Texas Instruments Incorporated, Dallas, Texas

and S. E. Craig, Jr.

Arizona State University, Tempe, Arizona

ABSTRACT

The behavior of relatively large surface depressions and protrusions was studied as a function of various epitaxial growth parameters. It is shown that at high concentrations of silicon-bearing species, surface stability occurs which cannot be explained solely on the basis of gas phase diffusion and capillarity.

The effects of various process variables on the growth rate of silicon over large relatively flat areas have been studied extensively and are reasonably predictable. The differences to be observed between the infinite plane case just mentioned and one in which only small areas of silicon are exposed has also been treated (1, 2). In addition, the general problem of the stability of very small surface perturbations during diffusion controlled growth was examined in terms of the relative effects of the diffusion gradient and capillarity (3-5). The behavior of rather large individual surface depressions or protrusions during vapor phase growth is also of considerable importance and is the subject of the present investigation. It will be shown that, by the proper choice of gas stream composition, large initial variations in the surface contour can be made to disappear, remain, or grow in amplitude.

This particular study was initiated originally because of the possibility of studying growth rates as a function of orientation by examining the behavior of different sides of small holes. Initial work, however, showed that in the silicon system other features of the deposition process were usually dominant and should be further investigated. From a more practical standpoint, the desire to construct commercial semiconductor devices which require far more complex structures than the original n on n+ material has added considerable impetus to confined growth. As examples of structures requiring this type of growth there are field effect transistors using channels etched and refilled, the polycrystalline silicon deposition required in making dielectric isolation networks, the n- and p-type local areas used for complementary structures in p-n junction isolated integrated circuits, and the etch-refill process often used in conjunction with dielectric isolation. Even though the results have not been fully verified for other systems (such as germanium and gallium arsenide), it is felt that the study and interpretation of such confined growth can materially aid in the understanding of vapor deposition processes.

Experimental

While the majority of the data taken related to silicon, the $GeCl_4$-H_2 system was briefly examined and found to behave in a roughly analogous manner.

The experimental arrangement used for the silicon growth studies has been described previously in some detail (6). Substrates of single crystal (111) oriented silicon approximately 2.5 cm in diameter were first polished chemically to produce damage-free planar surfaces. One side of each slice was then selectively masked and further etched to produce hills or holes approximately 125 μm in diameter and 25 μm deep spaced

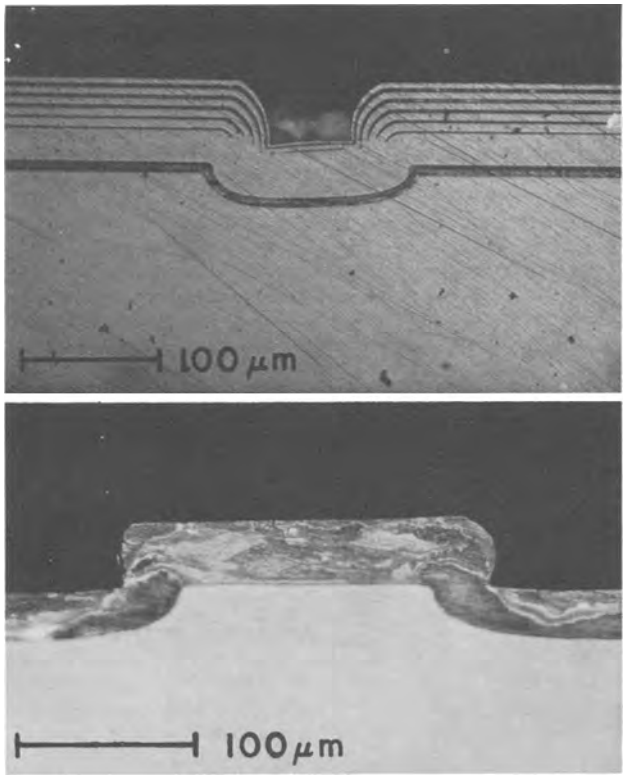

Fig. 1. Cross section of a depression and a hill overgrown at 1270°C while using a mole fraction of 0.006 $SiCl_4$ in hydrogen. During growth in the depression, alternate p- and n-type dopants were introduced at equal time intervals. This produced, after subsequent staining, the banding visible in the photograph.

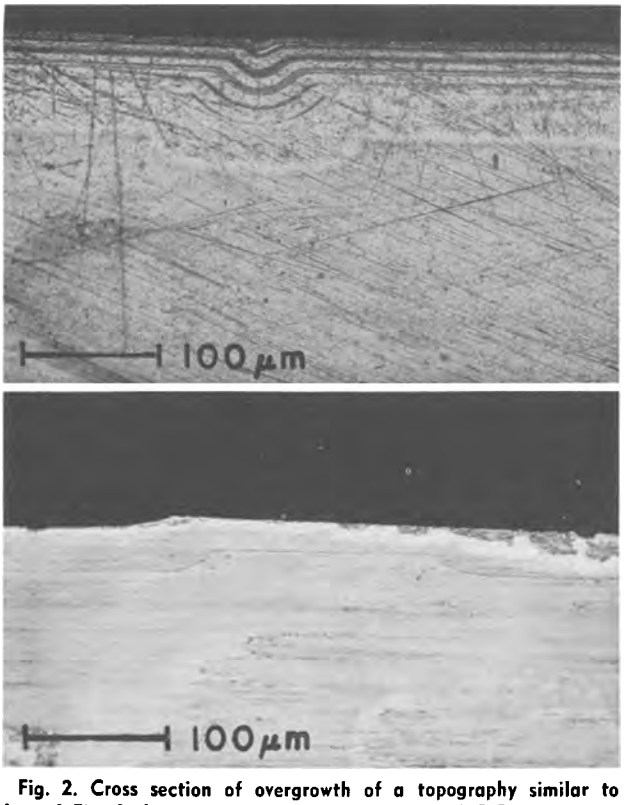

Fig. 2. Cross section of overgrowth of a topography similar to that of Fig. 1, but using a mole fraction of 0.06 $SiCl_4$ in hydrogen (growth at 1270°C).

on 1.25 mm centers, after which the masking material was removed. Reactant gases were fed through a conventional flow system and delivered at atmospheric pressure to a single-slice, vertical-flow epitaxial reactor. The surface was *in situ* vapor etched and the silicon grown epitaxially by either the hydrogen reduction of $SiCl_4$ or by the pyrolysis of silane diluted with hydrogen. During growth, p- and n-type dopants were sometimes alternately introduced so that by staining a perpendicular section, the growth interface at any given time could be approximately determined. The germanium was deposited via the hydrogen reduction of $GeCl_4$ at 900°C onto (111) oriented, *in situ* vapor etched germanium substrates.

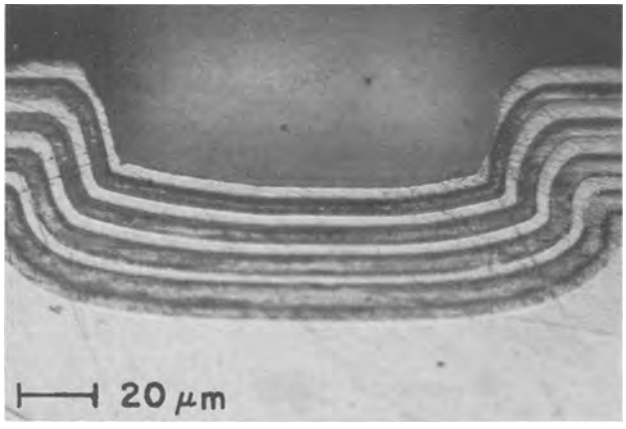

Fig. 3. Detail of the overgrowth of a hole using a $SiCl_4$ mole fraction of 0.01 (growth at 1270°C). Time dependence of the growth interface is revealed by staining the layers of alternating dopant types.

The photographs of Fig. 1-3 are typical of the behavior observed during the silicon deposition from $SiCl_4$ at temperatures of 1270°C. Figure 1 is a cross section of a hole and a hill overgrown while using a mole fraction of 0.006 $SiCl_4$ in H_2. These are the conditions often used during silicon growth and are the ones which give unstable growth.[1] Figure 2, which shows silicon grown using a mole fraction of 0.06 $SiCl_4$ in H_2 (which produces, on a flat surface, the same deposition rate as the 0.006 $SiCl_4$ case), represents a stable system, *i.e.*, the holes fill up and the hills level out. Comparable experiments using the silane-hydrogen system failed to show any region of stability. Detail of the growth interface, as delineated by the alternating dopant technique, is shown in Fig. 3 for the intermediate mole fraction of 0.01 $SiCl_4$ in H_2.

Figure 4a plots the observed growth rate *vs.* mole fraction $SiCl_4$ for a flat surface at both 1130° and 1270°C. In Fig. 4b the ratio of the growth rate on the perturbation (hill or hole) to that on the flat surface is plotted as a function of y, the reactant gas stream mole fraction of $SiCl_4$ in hydrogen. Since the rate on the perturbation is time-dependent, the numbers presented are estimated initial rates. Figure 5 shows germanium growth cross sections for $GeCl_4$ mole fractions 0.0005 and 0.005, respectively. Figure 6, analogous to Fig. 4, shows that for germanium the conversion from unstable to stable growth occurs before the maximum deposition rate, whereas for silicon, the transition appears quite close to the maximum.

Discussion

Because of the observations just mentioned, it is tempting to postulate a mechanism based on simple diffusion through a boundary layer of thickness w over the unperturbed portion of the slice. Then, if a small depression of depth δ occurs, in that depression the boundary layer thickness will be approximately $w + \delta$, and the rate will be correspondingly reduced since all silicon-bearing species are required to diffuse through a larger distance. If growth conditions are such that the deposition rate J decreases as the gas stream concentration y increases (*i.e.*, $\partial J/\partial y$ is negative), increasing the layer width might lead to an

[1] A stable system is defined as one in which the amplitude of surface discontinuities decreases with time.

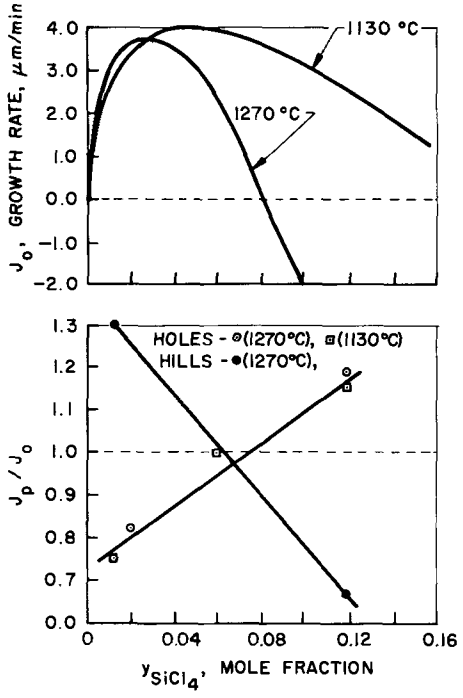

Fig. 4a. (top) Observed silicon growth rate for a flat surface versus mole fraction $SiCl_4$ (growth at 1130° and 1270°C). Fig. 4b. Ratio of silicon growth rate on the perturbation (J_p) to that on the flat surface (J_o) as a function of mole fraction of $SiCl_4$ in hydrogen.

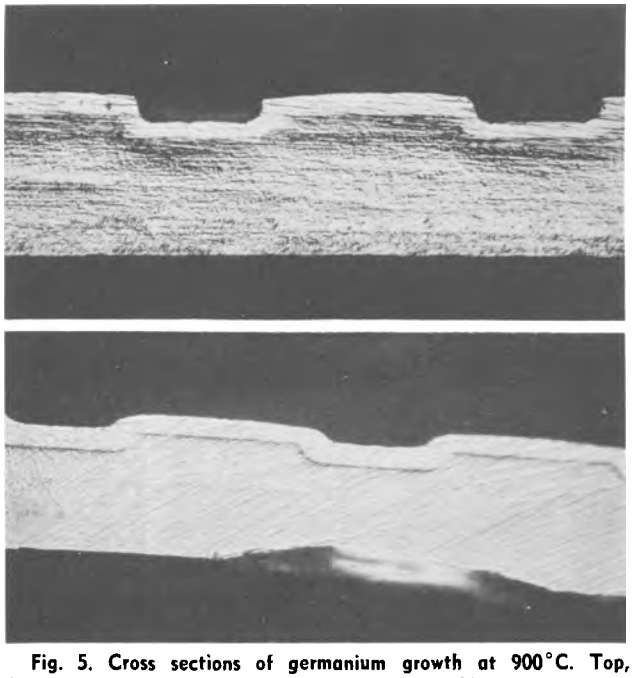

Fig. 5. Cross sections of germanium growth at 900°C. Top, 0.0005 mole fraction $GeCl_4$ in H_2; bottom, 0.005 mole fraction $GeCl_4$ in H_2. Hole diameters are 200 μm.

increased deposition rate in the hole. Such an argument is difficult to deal with even qualitatively because of the inability to actually determine whether or not a change in y occurred. Despite the previous discussion it cannot be said that the surface concentration changed since there appears to be considerable evidence that very close to the surface, equilibrium occurs [*e.g.*, (7, 8)]; surface concentration is thus independent of local diffusion layer thickness. Similarly, the inlet gas stream concentration is clearly independent of surface fluctuations.

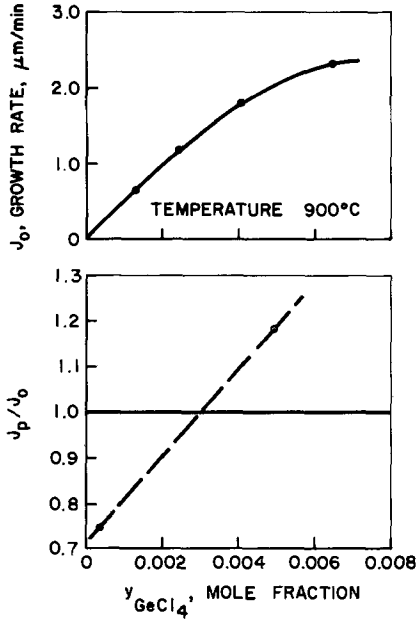

Fig. 6. Observed germanium growth rate for a flat surface vs. mole fraction $GeCl_4$. Growth at 900°C.

There are actually several formulations of J *vs.* y, depending on the assumptions made and boundary conditions chosen. The growth rate may be considered in terms of thermodynamics, surface kinetics, mass transport, or a combination of these concepts (*9*). The mass transport formulation can in general be reduced to the form

$$J = k(y - y_o^*) \qquad [1]$$

where k is a mass transfer coefficient (which involves appropriate diffusion coefficients and is inversely dependent on the boundary layer thickness), y is the summation of the mole fractions of all silicon-containing species (*i.e.*, SiH_4, $SiCl_4$, $SiCl_2$, etc.) in the bulk gas, and y_o^* is the value at equilibrium with a flat surface. From this,

$$dJ = dk(y - y_o^*) + k dy - k dy_o^* \qquad [2]$$

If surface energy effects are neglected, dy and dy_o^* are zero as the surface is traversed. A depression will cause an increase in the boundary layer thickness and dk will be negative. The consequent negative dJ leads to a hole deepening for all values of y. The inclusion of surface energy terms changes the equilibrium surface concentration y_o^* to y^* at the perturbation, given by

$$y^* = y_o^* (1 + \Gamma K) \qquad [3]$$

where K is the curvature determined by the geometry of the hole or hill, $\Gamma = (\gamma\Omega/RT)$, γ is the surface energy, Ω is the molar volume of the solid, and RT is the gas constant times absolute temperature. The curvature is positive for a convex surface (hill) and negative for a concave surface (hole). With this addition, Eq. [1] becomes

$$J = k\,[y - y_o^* (1 + \Gamma K)] \qquad [4]$$

and

$$dJ = [y - y_o^* (1 + \Gamma K)]\, dk - k\Gamma y_o^* dK \qquad [5a]$$

or

$$\Delta J = J_p - J_o = (y - y_o^*)\,(k_p - k_o) - y_o^*\,\Gamma k_p K_p \qquad [5b]$$

since dy, dy_o^*, $d\Gamma$,[2] and $K_o = 0$. The subscript p denotes in the perturbation and the subscript o denotes on the flat surface.

Note in Eq. [5b] the term involving the surface energy is negative while the term involving Δk, *i.e.*, $(k_p$

[2] $d\Gamma$ is probably not zero since γ is orientation dependent. However, the change should be small and can be neglected as a first approximation.

$- k_o$), is positive. Note also that Δk and K have the same sign (positive quantities for a hill, negative for a hole). Thus, if Γy_o^* is sufficiently large, the system is stable. For the silane system y_o^* is extremely small over the useful range of inlet silane concentrations. No range of stability would then be expected, and as previously indicated none was observed. The behavior of the silicon tetrachloride-hydrogen system is decidedly different however, in that as the inlet $SiCl_4$ concentration increases, so does y_o^* [see *e.g.*, Fig. 7 and ref. (10)].

This fact does provide for a range of stability, but the formulation is not completely satisfactory because a substitution of appropriate numbers does not agree well with measured dJ's. This can most easily be shown by examining Eq. [5b] for the case of the hole neither deepening nor filling. Thus,

$$y - y_o^* = \frac{y_o^* \Gamma k_p K_p}{k_p - k_o} \qquad [6]$$

Unstable growth should result if the right-hand side of Eq. [6] is smaller than the left. Conversely if the right-hand side is larger than the left, the growth should be stable.

From Eq. [1], values of k_o and k_p may be calculated for the case of small y (and accordingly, small y_o^*). y_o^* can be obtained from Fig. 7, which was plotted from Lever's data (10). The curvature term K_p may be estimated from the appropriate photograph, and from Fig. 4b the value of y for $\Delta J = 0$ can be determined. Alternatively, the average value of the ratio of transport coefficients may be obtained from the boundary layer theory as

$$\frac{k_p}{k_p - k_o} = -\frac{w}{\delta} \qquad [7]$$

while the average K may be obtained from the definition $K_{avg} = (dA/dV) \cong 4/D$, where A is the surface area, V is the volume of solid, and D is the perturbation diameter. The parameter Γ, involving the surface tension γ, is the only term not experimentally observable, but by substitution of the values into Eq. [6], γ must be at least 20,000 ergs/cm^2, as compared to a reported value of 1230 ergs/cm^2.

While some uncertainties exist in the values of K, k, y_o^*, and γ, these uncertainties cannot explain the discrepancies noted above. Also, two-dimensional computer solutions and three-dimensional electrical analog solutions of the diffusion equation were obtained which confirmed the general finding that, for gas phase diffusion to explain the observed phenomena, the surface energy of silicon would need to be at least an order of magnitude greater than its known value.

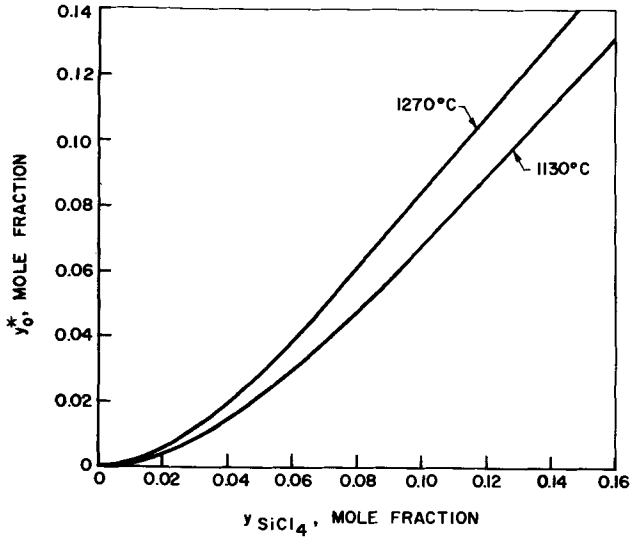

Fig. 7. Equilibrium surface concentration of silicon-containing species, y_o^*, as a function of mole fraction of $SiCl_4$ in incident reactant gas stream, y.

The diffusion equation assumes a stagnant film through which mass is transported and this certainly is not true. However, the concentration field in the gas is distorted by the perturbations for only a very small distance into the gas as compared to the total apparent film thickness. In this distorted region the velocities are very low and the standard diffusion equations should be an excellent approximation. We are strengthened in this conclusion by noting that the deposit shapes and local deposition rate around the perturbation are not a function of the direction of flow.

Departures of the gas phase concentrations from the equilibrium values of y_o^* exist, but these cannot explain the observed results. Since all areas of the sample surface are undergoing deposition, the concentrations must be equal to or greater than the values given by the equilibrium equation corrected for capillarity in order to have the small positive δy's required for a driving force. One would expect these δy's to be generally proportional to rate of growth. Therefore, such δy's would be in the wrong direction to explain the observed results. Also in cases where the perturbation bottoms (or tops) remain flat and grow at the same rate as the main flat surface, δy in the center of the perturbation should equal δy on the main flat surface, and any deviations from equilibrium would cancel.

Diffusion of possible unknown species in the gas phase has already been taken into consideration in our development. We have added the gradients of all silicon-containing gas species to obtain the total gradient of silicon in the gas phase. We have assumed that all gas phase species have the same diffusivities and have neglected the total flow of gases away from the surface. This treatment may result in an error of a few per cent, but cannot result in an error of a size needed to explain the observed results.

It appears that theory based on gas phase diffusion and capillarity cannot be used alone to explain the details of growth on perturbed surfaces of silicon. An additional mode of mass transport of silicon is required. Since volume diffusion of solid silicon is extremely slow, the only possibility seems to be surface diffusion. If this is true, several conclusions can be drawn about the diffusing surface specie. First and most obvious is that such a specie is not silicon adatoms. The concentration of silicon adatoms on the surface is believed to be mainly a function of temperature, growth rate, and crystal orientation. However, deposits which have approximately the same concentration of adatoms have growth characteristics that differ widely. Also, the surface species cannot be composed of only silicon and hydrogen, for the sample deposited from silane would then be expected to exhibit the same type growth phenomena as that observed for $SiCl_4$ reduction. It is concluded therefore that the species diffusing on the surface must also contain chlorine. They may be chemically adsorbed $SiCl_4$, $SiHCl_3$, or $SiCl_2$, etc., or perhaps an adsorbed radical such as SiCl.

Conclusions

While most of the studies reported were for the specific case of silicon, and while explanations of the observations are not complete, the results should be directly applicable to systems which exhibit a y_o^* that varies appreciably with inlet gas concentration. If a substrate etch is used which produces surface asperities, growth conditions can be chosen to eliminate them. This explanation could, for example, be applicable to GaAs where the vapor etching prior to deposition often produces a rough surface which after deposition is again found to be smooth. However, if

a faithful replica of the original surface is desired, this can also be approximated.

It is observed that even if the system is unstable, *i.e.*, a hole gets deeper, the walls often gradually close in. If small areas are initially masked, perhaps by unintentional foreign matter, a well may be formed which can close over to give a continuous surface with holes beneath. It is suggested that this is the mechanism which gave rise to the interface voids observed during some of the early work with silicon and germanium epitaxy. Even though such a system is not desirable, it may still be preferable to one which allows direct overgrowth of the impurity with the attendant high probability of polycrystalline growth.

Finally, it should be remembered that while all of the discussion has been based on single crystal growth, most of the observations should apply directly to polycrystal growth as well. For the specific case of silicon we have verified that the polycrystalline filling or deepening of holes directly parallels the single crystal behavior.

Acknowledgments

The authors wish to thank E. C. Teague for the germanium data and O. J. Lewis for sectioning, staining, and photography.

Manuscript received Feb. 8, 1967; revised manuscript received July 24, 1967. Much of this paper was presented at the Gordon Conference on Chemistry and Metallurgy of Semiconductors, Proctor Academy, Andover, New Hampshire, July 1965.

Any discussion of this paper will appear in a Discussion Section to be published in the June 1968 JOURNAL.

REFERENCES

1. E. G. Alexander and W. R. Runyan, *Trans. Met. Soc. AIME*, **236**, 284 (1966).
2. W. G. Oldham and R. Holmstrom, *This Journal*, **114**, 381 (1967).
3. W. W. Mullins and R. F. Sekerka, *J. Appl. Phys.*, **34**, 323 (1963).
4. W. W. Mullins and R. F. Sekerka, *ibid.*, **35**, 444 (1964).
5. F. A. Nichols and W. W. Mullins, *ibid.*, **36**, 1826 (1965).
6. E. G. Alexander, paper presented at the Dallas Meeting of the Society, May 1967; Extended Abstract No. 105, Electronic Division.
7. W. Steinmaier, *Philips Res. Repts.*, **18**, 75 (1963).
8. T. O. Sedgwick, *This Journal*, **111**, 1381 (1964).
9. J. O. Oxley, "Transport Processes," in "Vapor Deposition," C. F. Powell, J. O. Oxley, and J. M. Blocher, Editors, John Wiley & Sons., Inc., New York (1966).
10. R. F. Lever, *IBM J. Res. & Develop.*, **8**, 460 (1964).

Some Properties of Vapor Deposited SiC

Kenneth E. Bean and Paul S. Gleim

Texas Instruments Incorporated, Dallas, Texas

ABSTRACT

A process for the vapor deposition of silicon carbide films on silicon substrates using the hydrogen reduction of silicon tetrachloride and the pyrolysis of a hydrocarbon such as toluene was developed. At the optimum deposition temperature of 1075° ± 10°C, the deposition rate using 0.89% silicon tetrachloride and 0.18% toluene was 1.6 μ/min. Films deposited at less than 0.18% toluene, with a fixed silicon tetrachloride concentration of 0.89%, were attacked by "Planar etch," while those deposited at or above 0.18% toluene were not; the electrical resistance decreased, however. When the silicon tetrachloride concentration was varied from 0.7 to 0.9% at 0.18% toluene, the electrical resistance of the films was greater than one hundred megohms. The thermal coefficient of expansion was tailored to be less than, equal to, or greater than that of silicon by changing the concentration of silicon tetrachloride from 0.6 to 1.2% at 0.18% toluene. The refractive index of the films also changed with the change in silicon tetrachloride concentration. Infrared transmission data on films deposited at 0.18% toluene and 0.89% silicon tetrachloride were identical to those for bulk silicon carbide. X-ray diffraction studies showed that the films were normally polycrystalline and consisted of both alpha and beta phases, however, epitaxial silicon carbide was observed in some cases.

Considerable work has been done on the growth of SiC crystals for various purposes. Also, work has been reported both in the open literature and in government reports on the vapor deposition of thin SiC films (1-10). The work to be discussed in this paper covers the vapor deposition of polycrystalline SiC films which were very hard, had high electrical resistivity, and were chemically resistant to standard silicon etchants.

The process used was the hydrogen reduction of silicon tetrachloride and the pyrolysis of a hydrocarbon. The flow system employed was a conventional vapor deposition unit. Silver palladium purified hydrogen was used as the reducing agent for the silicon tetrachloride and as the carrier gas for the silicon halide and the hydrocarbon, toluene. Other hydrocarbons, both liquid and gaseous, were also used successfully. Constant temperature baths were used to control the vapor pressure of the silicon halide and hydrocarbon. A liquid nitrogen trap was employed to prevent back streaming of the hydrocarbon into the pure hydrogen source. Anhydrous hydrogen chloride was used for *in situ* vapor etching (11) of the substrates prior to silicon carbide film deposition. Forming gas was used as the purge gas. The reactor was a horizontal, resistance-heated, cold-wall unit utilizing a water cooled quartz reaction chamber. Water cooled Hastelloy B electrodes were used to carry current to the silicon carbide (TI-Kote)®[1] coated graphite strip heater. The deposition temperature was monitored and controlled by a radiation detector and feedback controller.

The substrates used for film deposition were single crystal silicon. The (111), (110), and (100) orientations (both on and 1½° off) were examined. Very

[1] (R) U.S. Patent Office.

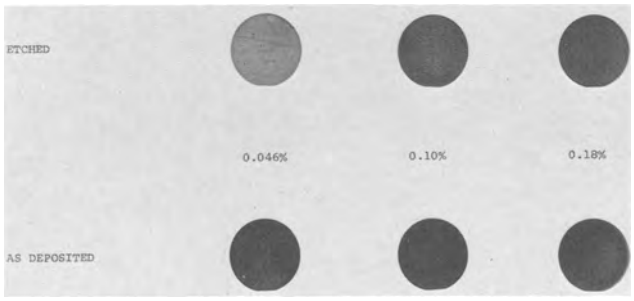

Fig. 1. SiC etch resistance vs. per cent toluene in source

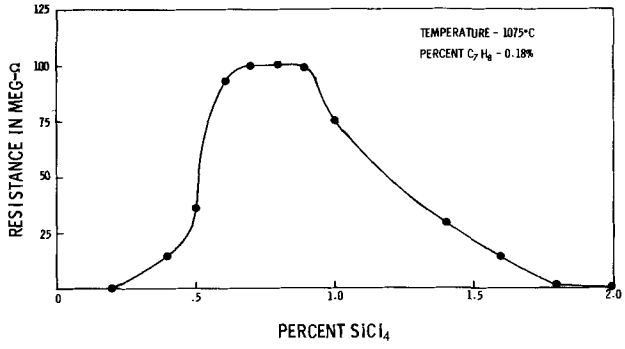

Fig. 2. Electrical resistance vs. per cent silicon tetrachloride

little difference in film quality was observed, however, films deposited on substrates oriented 1½° off the (110) were consistently haze free and had mirror like surfaces. It should be noted that the visual appearance of the film is also dependent on substrate surface preparation.

Experimental

Experiments were carried out to determine the optimum deposition temperature to give the desired film characteristics. Investigations were made at 25° increments between 800° and 1300°C. The optimum temperature for producing films that had mirror-like planar surfaces was found to be 1075° ± 10°C.[2] At this temperature, the deposition rate was 1.6 μ/min at 0.89% silicon tetrachloride and 0.18% toluene.

Silicon carbide films were deposited on silicon substrates (in groups of two) at a constant temperature of 1075°C, 0.89% silicon tetrachloride and a total flow rate of 50 l/min. The per cent toluene was varied from 0.046 to 0.28%. One slice from each group was subjected to a planar etch[3] while the other was kept as a standard. Figure 1 is a photographic comparison of the slices. As is evident from the figure the films deposited at less than 0.18% toluene were attacked (note discoloration) by planar etch while those deposited at or above 0.18% toluene were inert to planar etch. Films deposited at 0.28% toluene and 0.89% silicon tetrachloride were completely inert to planar etch but had an electrical resistivity substantially below that of films deposited at 0.18% toluene.

To determine the effect of changing the concentration of silicon tetrachloride on the film's electrical resistance and resistivity, the silicon tetrachloride concentration was varied from 0.2 through 2.0%. Resistance measurements were made by a two-point probe technique on 20.0μ films on silicon substrates. The relative values obtained are plotted in Fig. 2. The resistance of the films from 0.7 to 0.9% was at least one hundred megohms, which is the upper limit of the test equipment used. Resistance values of films deposited with silicon tetrachloride concentrations below 0.7 and above 0.9% drop off markedly perhaps due to a change in the stoichiometry of the films. Evidence of this change, which produces a silicon rich or carbon rich film is apparent from the data in Fig. 1, 3, and 5. For example in Fig. 1, as the toluene concentration is decreased below 0.15% a silicon rich film results which is more soluble in the common silicon etchants. Resistivity measurements were made by Hall mobility studies using low resistivity silicon as contacts and values of approximately 6000 ohm-cm were obtained. Resistivity values on samples deposited with different concentrations of silicon tetrachloride were calculated from sheet resistance measurements on thick films (> 20 mils) using a four-point probe and values of approximately 8000 ohm-cm were obtained. This resistivity is adequate for the isolation of components in some integrated circuits.

The reported value for the thermal coefficient of expansion of SiC (4.4×10^{-6}) (20) closely matches that of silicon (4.2×10^{-6}) (12, 13) (see Table I). A series of runs was conducted to determine the effect of varying the concentration of silicon tetrachloride in the reactant gases on the thermal coefficient of expansion of the deposited films. Films 50.8μ thick were deposited with silicon tetrachloride concentrations from 0.6 to 1.2% on 1 in. diameter, 14 mil thick silicon substrates. The relative change in the thermal coefficient of expansion was determined by measuring the amount of curvature[4] of the silicon slice after film deposition. These measurements were made by using a Taylor-Hobson Talysurf and the data are shown in Fig. 3. From the data it may be observed that the coefficient of thermal expansion of the SiC films can be changed or tailored to be equal to, greater than, or less than that of silicon by changing the per cent silicon tetrachloride in the reactant gas stream.

An experiment was conducted to compare the curvature of like silicon substrates having silicon carbide films with those having silicon dioxide films. Silicon carbide films 10.0μ thick were deposited (one side only) at 1075°C with a deposition rate of 1.6 μ/min on 1-in. diameter 14 mil thick silicon substrates, using 0.89% silicon tetrachloride and 0.18% toluene. Films of SiO_2

[2] Optical pyrometer.
[3] Planar etch, 15-HNO_3, 5-HAc, 2-HF.
[4] Curvature is defined herein as the variation from planarity across a 1 in. diameter substrate and is expressed in mils.

Table I. Some properties of Si, SiC, Si_3N_4, and SiO_2

	Si	SiC	Si_3N_4	SiO_2
Thermal expansion	4.2×10^{-6}/°C (0-1000°C) (13)	4.8×10^{-6}/°C (2) α 4.3×10^{-6}/°C (20) β 4.5×10^{-6}/°C (20) (0-1000°C)	α : 2.87×10^{-6}/°C β : 2.25×10^{-6}/°C (25-1000°C) (19)	(Fused silica) 0.58×10^{-6}/°C (0-1200°C) (15)
Thermal conductivity	0.30 cgs @ 20°C (12)	1.17 cgs @ 20°C (21)	0.035 cgs (22)	0.0021 cgs @ 20°C (23)
Resistivity @ 25°C	$>10^5$ ohm-cm (12)	$6\text{-}8 \times 10^3$ ohm-cm (text, also) (see Fig. 4)	$>10^{13}$ ohm-cm (25) 5×10^{14} ohm-cm (24)	10^{15}-10^{17} ohm-cm (27)
Dielectric constant	11.7 @ 5×10^2 to 3.0×10^7 cps (12)	10.0 (long wavelengths) (18)	4.2 @ 1×10^3 cps (29)	3.78 @ 10^2 to 10^{10} cps (28)
Index of refraction	4.05 @ 5461Å (16)	2.6 @ 5461Å (18)	2.05 @ 5461Å (26)	1.47 @ 5461Å (16)
Young's modulus	27.6×10^6 psi [111] direction (12)	56×10^6 psi (30)	13×10^6 psi (31)	10.4×10^6 psi (fused) (33)
Hardness				
Knoop	950-1150	2500-2550 100g	3000 8g (26)	710-790 100g (32)
Vickers	1000	3000-3500 25 g		1103-1260 50g (32)
Mohs	7 (12)	9.2 (30)	>9 (31)	4.9 (fused) (33)

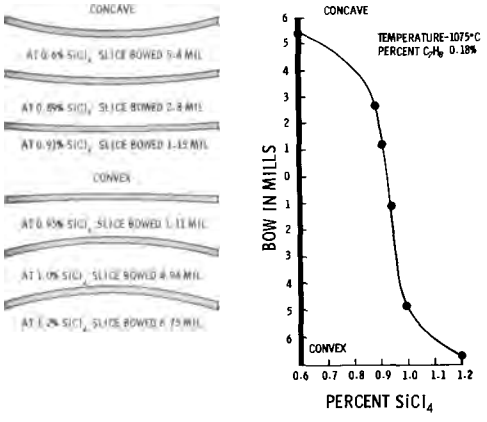

Fig. 3. Slice curvature vs. per cent silicon tetrachloride

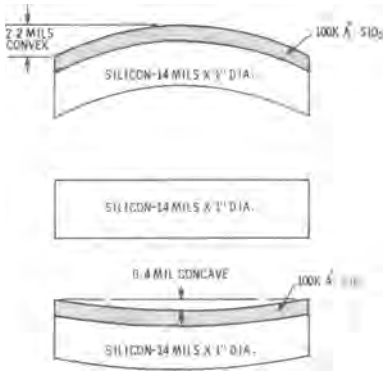

Fig. 4. Curvature of silicon slice, with SiO_2 vs. SiC film

(10.0μ thick) were deposited from silicon tetrachloride, CO_2 and H_2 at 1250°C with a deposition rate of 0.34 μ/min. The SiC films produced a 10.0μ curvature, concave to the top or SiC surface. The SiO_2 films produced a 56.0μ curvature, convex to the top or SiO_2 surface. This indicates a 5.5 times greater bowing or curvature in the opposite direction in the case of the SiO_2 films (see Fig. 4). The reported thermal coefficient of expansion of fused silica (SiO_2) is 0.58 x 10^{-6}/°C (14).

A series of runs was made, varying the per cent silicon tetrachloride, to determine the refractive index of the deposited films as a function of per cent silicon tetrachloride in the reactant gas stream. The per cent toluene was 0.18 and the deposition temperature was 1075°C. These data were taken at 5461Å using the ellipsometer technique (15, 16) and are plotted in Fig. 5. It should be noted from Fig. 5 that the curve passes through 2.6, the reported value (17) for the index of refraction of SiC, at approximately 0.9 and again at approximately 0.15% silicon tetrachloride.

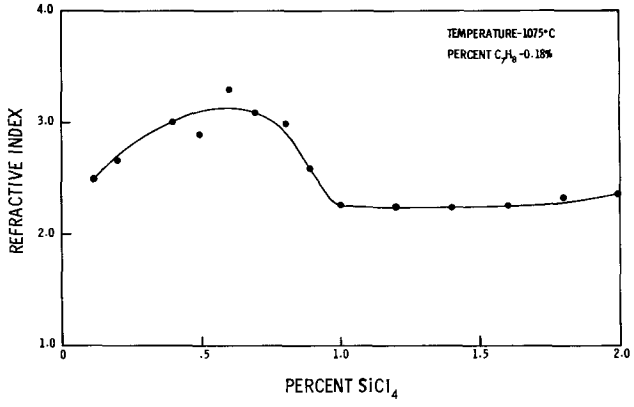

Fig. 5. Refractive index vs. per cent silicon tetrachloride

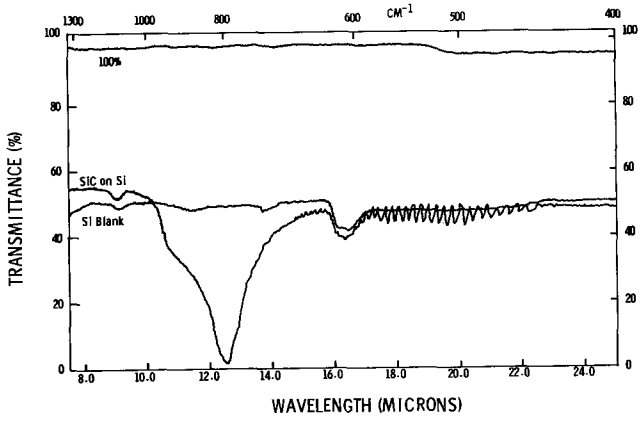

Fig. 6. Infrared transmission curve for SiC on silicon

Infrared transmission data were obtained on films deposited at 1075°C with a toluene concentration of 0.18% and silicon tetrachloride concentration of 0.89%. These data show the transmission of the films is the same as for bulk SiC (18). The infrared transmission curve for a SiC film on silicon is shown in Fig. 6.

Attempts to measure hardness as a function of the per cent toluene in the gas stream are incomplete; however, from observations during sawing, lapping, and polishing of the films, the hardness increases with increasing toluene.

X-ray diffraction studies show the films are alpha and beta SiC. Single crystal epitaxial SiC was observed in some cases but the growth of very hard, chemically stable, high resistivity films was the objective of this program.

Summary and Applications

The chemical, physical, and optical properties of silicon carbide films can be tailored by changing the deposition temperature, volume per cent silicon tetrachloride and or toluene. The optimum conditions for deposition were 1075°C at 0.89% silicon tetrachloride and 0.18% toluene in hydrogen with a total flow of 50 l/min. At these conditions a deposition rate of 1.6 μ/min was obtained. Infrared transmission data on the polycrystalline (alpha and beta) films agree with that reported for bulk silicon carbide.

The films were used as the isolation medium in dielectric isolation type structures. They are superior to SiO_2 films from the standpoint of hardness or abrasive resistance thus providing an excellent lap stop or wear resistant surface. They are also superior to SiO_2 films with respect to etch resistance thus providing an excellent etch stop. The thermal conductivity of silicon carbide (see Table I) is much greater than that of silicon dioxide and other common insulating materials. In general the dielectric properties of the films are inferior to those of SiO_2. However, a thin oxide or nitride film can be used in conjunction with the SiC film to give good dielectric isolation.

Acknowledgments

The authors wish to thank W. R. Runyan, Marion W. Johnson, Marvin L. Morris, Jimmie B. Sherer, Richard L. Yeakley, and Steven P. Emmons of the Semiconductor Research and Development Laboratory and Charlie E. Jones, Jr., A. Ray Hilton, and James A. Arnold of the Central Analytical Facility.

Manuscript received Nov. 7, 1966; revised manuscript received July 13, 1967. This paper was presented at the Cleveland Meeting, May 1-6, 1966.

Any discussion of this paper will appear in a Discussion Section to be published in the June 1968 JOURNAL.

REFERENCES

1. J. R. O'Connor and J. Smiltens, "Silicon Carbide," Proc. of Conference on Silicon Carbide, Boston, Mass., Pergamon Press, April 23, 1959.

2. G. J. Caras, "Silicon Carbide for Semiconductors," RSIC-381, Redstone Scientific Information Center (1965).
3. J. W. Mellor, "A Comprehensive Treatise on Inorganic and Theoretical Chemistry," Vol. 8, Longmans, Green and Co., (1953).
4. A. R. G. Brown, "Silicon Carbide-A Review," Royal Aircraft Establishment (Aug. 1960).
5. D. M. Jackson and R. W. Howard, *Trans. Met. Soc. AIME*, **233**, 468 (1965).
6. N. C. Tombs *et al.*, "Solid State Electronics," **8**, 839-842, Pergamon Press (1965).
7. R. B. Campbell and T. L. Chu, *This Journal*, **113**, 825 (1966).
8. L. J. Kroko, *ibid.*, **113**, 801 (1966).
9. V. J. Jennings, A. Sommer, and H. C. Chang, *ibid.*, **113**, 728 (1966).
10. D. M. Jackson, Jr., and B. VanPul, Government Report Contract No. AF 19(628)-4802, Report No. 1, Oct. 1965.
11. K. E. Bean and P. S. Gleim, *This Journal*, **110**, 265C (1963).
12. W. R. Runyan, "Silicon Semiconductor Technology," McGraw-Hill Book Co. (1965).
13. M. R. Holter *et al.*, "Fundamentals of Infrared Technology," Table 6-4, 148, The MacMillan Co., (1962).
14. Handbook of Chemistry and Physics, 43rd Edition, p. 2279, Chemical Rubber Publishing Co. (1961-1962).
15. R. J. Archer, *J. Optical Soc. Am.*, **52**, 970 (1962).
16. F. L. McCrackin, E. Passaglia, R. R. Stromberg, and H. L. Steinberg, *J. Research Natl. Bur. Standards*, 67A, No. 4 (July-August 1963).
17. Handbook of Chemistry and Physics, 43rd Edition, p. 646, Chemical Rubber Publishing Co. (1961-1962).
18. W. G. Spitzer *et al.*, "Silicon Carbide," J. R. O'Connor and J. Smiltens, Editors, Pergamon Press (1960).
19. O. H. Krikorian, "Thermal Expansion of High Temperature Materials," UCRL, 6132 (1960).
20. W. B. Pearson, "A Handbook of Lattice Spacing and Structure of Metals and Alloys," Pergamon Press (1958).
21. G. A. Slack, *J. Appl. Phys.*, **35**, 3460 (1964).
22. Ceramic Materials for High Temperature, Alfred University Progress Report, No. 237, 21, (1956).
23. W. G. Bradshaw, and C. O. Mathews, "Properties of Refractory Materials: Collected Data and References," LMSD-2466 (1958).
24. N. C. Tombs *et al.*, "A New Insulated-Gate Silicon Transistor," *Proc. IEEE*, 87 (1966).
25. S. M. Hu, "Properties of Amorphous Silicon Nitride Films," *This Journal*, **113**, 693 (1966).
26. K. E. Bean, P. S. Gleim, W. R. Runyan, and R. L. Yeakley, *ibid.*, **114**, 733 (1967).
27. R. P. Donovan, "Formation and Properties of Oxides on Silicon," Proc. 4th Annual Microelectronics Symposium, p. 4A-16 (1965).
28. State of the Art Report, "Optical Materials for Infrared Instrumentation," Report No. 238-11-S, Table 3-1, 13 (1959).
29. C. Feldman and M. Hocskay, *Rev. of Sci. Instr.*, **33**, 1459 (1962).
30. P. T. B. Shaffer, No. 1 Materials Index, Handbook of High Temperature Materials, p. 108, Plenum Press (1964).
31. *Ibid.*, p. 284.
32. *Ibid.*, p. 353.
33. Table of Physical Properties of Clear Fused Quartz General Electric Data Form Q8B, July 1962.

The Ga-P-Te System

Morton B. Panish

Bell Telephone Laboratories, Incorporated, Murray Hill, New Jersey

ABSTRACT

Differential thermal analysis, x-ray, and electron beam microprobe studies of melts cooled from the liquid in the Ga rich region of the Ga-P-Te system have been done, and a part of the ternary condensed phase diagram has been drawn on the basis of the experimental data. GaP does not form continuous or extensive solid solutions with Te containing phases. The possible existence of a ternary compound in the P rich region is discussed.

This work is part of a series of studies of the phase systems and phase fields encountered when GaAs or GaP are present in equilibrium with other phases containing elemental impurities which are of general interest in semiconductor studies.

The most extensive work with III-V-VI systems has been done for the $A^{III}B^{V}$—$A_2^{III}C_3^{VI}$ binary systems (1) where there is particular interest in the $A_2^{III}C_3^{VI}$ compounds, which crystallize in a tetrahedral lattice with built-in vacancies. These compounds might be expected to have extensive solid solubility with $A^{III}B^{V}$ compounds. In addition to solid solution formation, III-V-VI systems are likely to be complicated by ternary compound formation such as has been suggested by Hahn and Thiele (2) for In_2AsSe and demonstrated for $InAs_3S$ by Luzhnaya *et al.* (3). Liquid immiscibility has been observed in the InSb-InSe system by O'Kane and Stemple (4). The Ga-P-Te system appears to be most closely related to the Ga-As-Te system which was recently studied in this laboratory (5).

In this work we have observed thermal effects by differential thermal analysis when cooling several molten mixtures through phase transitions. Compositions were along selected cuts in the ternary system. Because of the high pressure and temperatures encountered in this system we were able to study in detail only mixtures with compositions in the gallium rich region of the ternary.

Samples obtained after cooling ternary mixtures from the melt were examined by electron beam microprobe and x-ray techniques.

Experimental

Semiconductor grade Te with purity better than 99.999% and reclaimed Ga and GaP with purities better than 99.99% were used in this work. The use of GaP rather than the elements was necessary in order to prevent explosions resulting from the exothermal reaction of the elements.

Fused silica capsules with a volume of about 2 cc which were about 2/3 filled with melt were used for the differential thermal analysis experiments. The experimental details are very similar to those which have already been described for the study of the Ga-As-Zn ternary (6) and several other systems

Table I. DTA, x-ray, and microprobe data

a/o Ga	a/o P	a/o Te	T_1	T_2	T_3	Phases (x-ray & microprobe)	Cut
70	10	20	1247	740	—	— —	A
50	5	45	—	832	(770)	GaP††, GaTe†‡	B
50	5	45	1222	829	(785)	GaP††, GaTe†‡	B
50	10	40	1290	821	(740)	— —	B
50	10	40	—	840*	—	— —	B
50	10	40	—	855*	—	— —	B
40.5	2.5	57.0	1101	802	(795)	GaP††, Ga_2Te_3†‡	C
41.0	5.0	54.0	1171	798	774	GaP††, Ga_2Te_3†‡	C
41.5	7.5	51.0	—	None obtained	—	GaP††, Ga_2Te_3†‡	C
42.0	10.0	48.0	—	802	770	GaP††, Ga_2Te_3†‡	C
33.0	17.0	50.0	1158	415**	390**	GaP††, Ga_2Te_3†‡, ?	D
20	20	60	—	None obtained	—	GaP††, Ga_2Te_3††, P‡, ?	E
30	30	40	—	None obtained	—	GaP††, Ga_2Te_3††, ?	E

* Heating. † X-ray. ( ) Very small effect.
** Extensive supercooling. ‡ Microprobe.

(5, 7). The precision to which thermal effect temperatures are reported is about ±5°K.

For all of the runs it was necessary to heat the cells above 1250°C and in some cases to about 1350°C. These temperatures are above the softening point of fused silica and in general the cells expanded. Expansion of the DTA cell resulted in poorer contact of the liquid to the thermopile well. The precision of the temperature-thermal effect data in these studies is therefore somewhat poorer than in previous studies. In some cases only the highest temperature transition could be obtained before the cell became useless. In these cases other transitions were obtained by heating the cell to 1200°-1250°C and then allowing it to cool without attempting to study the first transition.

X-ray analysis of the DTA samples was done by standard powder techniques, and electron beam microprobe analyses were obtained for several of the samples.

For several compositions along the GaP-Te cut at which we were unable to obtain DTA curves, mixtures were heated in heavy (1/8 in.) walled fused silica capsules which were only about 1/5 filled with the molten mixture. These samples were heated very slowly to about 1250°C and then allowed to cool at about 1°C/min.

The Binary Phase Systems

Ga-P.—Gallium and phosphorus form a single congruently melting compound GaP, with a melting point of 1465°C (8). Thurmond (9) has utilized the solubility data of Rubenstein (8) and Hall (10) along with an adaptation of the regular solution treatment of Vieland (11) to construct the binary phase diagram.

Ga-Te.—Gallium and tellurium form two congruently melting compounds, GaTe and Ga_2Te_3. The melting point of Ga_2Te_3 has been reported as 792°C (12) and 790°C (13) and that of GaTe as 835° (12) and 824°C (13). In recent work on the Ga-As-Te system (5) the melting points of Ga_2Te_3 and GaTe were found to be 789° ± 3°C and 827° ± 3°C, respectively. Two other tellurides, Ga_3Te_2 and $GaTe_3$, have been suggested on the basis of thermal analysis studies (12). These compounds were reported to decompose below their melting points. A phase corresponding to $GaTe_3$ has been identified in a metallographic study (14), but in the same study Ga_3Te_2 was not identified. A region of liquid immiscibility on the gallium rich side of the binary phase diagram has been reported but not confirmed (12).

Te-P.—There is no phase information available for the Te-P system. One compound, P_2Te_3, has been reported (15).

Results

The temperatures at which thermal effects were observed and the phases obtained when various compositions were cooled are given in Table I, and some of the data are plotted in Fig. 1 and 2.

In each case T_1 represents the temperature at which the surface of primary crystallization was reached, and T_2 represents the temperature of the first appearance of a second phase. GaP was found by powder

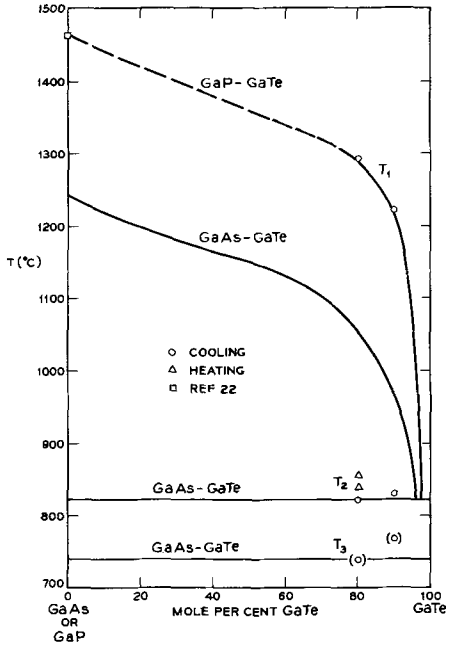

Fig. 1. Thermal effects for samples with composition along cut B (the GaP-GaTe cut) of Fig. 3.

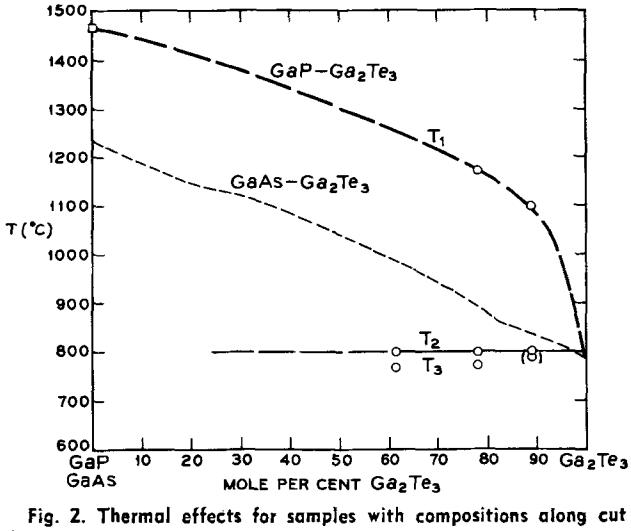

Fig. 2. Thermal effects for samples with compositions along cut C (the GaP-Ga_2Te_3 cut) of Fig. 3.

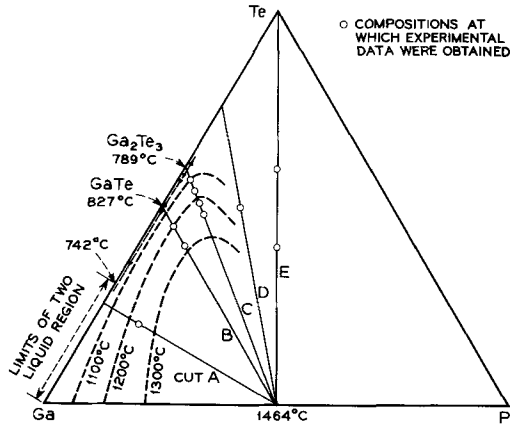

Fig. 3. Portion of the Ga-P-Te ternary phase diagram. Compositions are in atom per cent.

x-ray and microprobe studies to be present in all samples. By analogy with the Ga-As-Te system we take this to indicate that, since GaP is the highest melting compound in the system and since T_1 is quite high in all cases, all the mixtures studied were in the GaP primary phase field.

The x-ray patterns for GaP were sharp and unshifted. This indicates that GaP crystallized in this system did not form extensive solid solutions with Te.[1]

Cut A.—Only one experimental point was obtained along cut A of Fig. 3. Except for the higher value of T_1, the DTA and the x-ray data are essentially identical with the data from a similar point in the Ga-As-Te system (5). When cooling, GaP precipitates first; then as the liquid composition moves along cut A toward the Ga-Te binary, a two liquid region is encountered (no thermal effect observed) and finally at 740°C GaTe precipitates.

Cut B (the GaP-GaTe *system).*—Several DTA runs with samples at two compositions on this cut were done. As above, except for the higher temperature of the T_1 transition, the DTA data and the x-ray data are similar to the data previously obtained in the Ga-As-Te system (5). The suggested liquidus curve is given in Fig. 1 along with that for the GaAs-GaTe cut for comparison. The T_2 and T_3 transitions obtained when cooling are at approximately the same temperature as transitions obtained in the Ga-As-Te system. Several DTA points for T_2 were obtained from slow heating cycles and yielded a somewhat higher temperature. It is not clear whether T_2 is a eutectic or peritectic transition from this data. As with the GaAs-GaTe system, the occurrence of the T_3 transition, which in this case is very slight, is an indication that the liquid has reached the composition of the start of the two liquid region and therefore that the GaTe phase precipitating must be somewhat rich in Te.

Cut C (the GaP-Ga_2Te_3 *cut).*—Transitions observed by DTA for two compositions along this cut are shown in Fig. 2. The suggested liquidus curve is shown along with that for the GaAs-Ga_2Te_3 cut for comparison. Examination of the cooled samples with the electron beam microprobe showed large crystals of GaP present, and this is again interpreted to show that GaP is present as the primary phase formed at T_1. X-ray and microprobe examination showed the second phase (which we suggest starts to precipitate at T_2) to be Ga_2Te_3. In contrast to the GaAs-Ga_2Te_3 cut, in this case the x-ray lines from the Ga_2Te_3 phase are moderately sharp and unshifted. Since T_2 is above the melting point of pure Ga_2Te_3 it appears that as in the GaAs-Ga_2Te_3 case a solid solution containing excess P, and Te is found, but to a much more limited extent, and below the limits of detectibility (~5-10 a/o P) in the x-ray powder photographs.

Unfortunately, the second order L_{β_1} line of Te interferes with $K\alpha_1$ line of P and therefore reduces the sensitivity of the electron beam microprobe to P in the presence of Te. It was therefore not possible to determine the amount of P in the Ga_2Te_3 phase. Goryunova and Radautsan (16) have, however, reported an approximate solubility of about 6 a/o P in Ga_2Te_3.

The T_3 transition is interpreted here as a ternary eutectic or peritectic which occurs near the Ga-Te binary between the GaTe and Ga_2Te_3 compositions.

Cut D.—DTA, x-ray, and electron beam microprobe data have been obtained for one point along cut D of Fig. 3. Again the high T_1 value and the presence of large crystals of GaP are taken to show that the over-all composition is in the GaP primary phase field. The T_2 and T_3 transitions are due to the formation of phases in the Te rich portion of the phase diagram.

It is instructive to inspect three electron beam microprobe photographs of the surface of a polished sample from the DTA run of cut D taken by scanning the fluorescence radiation from each of the elements (Fig. 4). Several features of this system are demonstrated. There is a large region (lower left corner) of GaP and a large region which is high in Te as shown by the Te fluorescence photograph but which contains at least three different intensities of Ga fluorescence radiation. The P fluorescence radiation photograph contains an over-all haze of interference from the Te second order L_{β_1} line as mentioned above, but also has a few bright zones in the Te rich region. It thus appears that there are at least two tellurium containing phases other than the Ga_2Te_3 phase identified by the x-ray powder patterns. The bright regions on the P photograph indicate that at least one of these Te containing phases may be associated with P, and there is some x-ray evidence that one of the phases may be principally Te. The powder patterns for this sample were too complicated, however, to permit definite identification of anything other than the GaP and Ga_2Te_3 phases.

Cut E (the GaP-Te *pseudobinary).*—Only x-ray and electron beam microprobe studies were done with mixtures with compositions on this cut. DTA studies

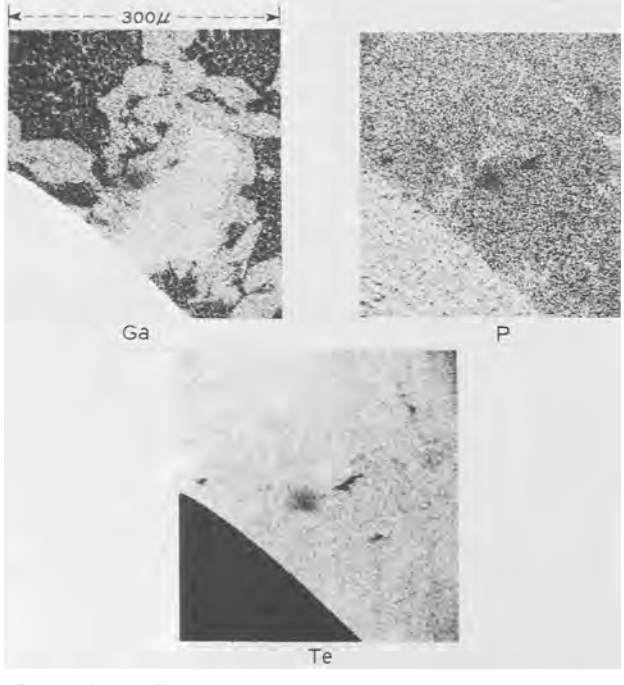

Fig. 4. X-ray fluorescence photographs of a sample from cut D of Fig. 3.

[1] It should be noted that the precision of the powder x-ray data is such that solid solutions with less than several per cent of impurity would not be detected.

were attempted but the relatively thin walled (1 or 2 mm) fused silica cells charged with Te and GaP always exploded during the heat-up period. Explosions occurred at temperatures as low as 800°C if the cells were heated at about 5°C/min and in the 1200°C range when heated much more slowly.

It was possible to prepare molten mixtures which were then slow cooled for subsequent examination by using relatively large heavy walled cells which were only about 1/5 filled with the mixture. These cells also exploded occasionally at about 800°C during the heat up, and on several occasions cells exploded at about the same temperature on cooling when too full or when too rapidly cooled.

The x-ray and microprobe examinations both revealed the presence of GaP and Ga_2Te_3 in addition to other phases. Again, the x-ray patterns were too complicated to permit identification of the other phases, and the Te interference with the P radiation prevented accurate analysis for P. There is, however, at least one phase containing Ga other than Ga_2Te_3. Furthermore, there is evidence for a phase very rich in P (probably elemental P) from the microprobe studies. In Fig. 5 the Ga, P, and Te radiation photographs of a small region of the sample containing 60 a/o Te are shown. Figure 5 shows a dendrite like structure which is essentially all P in a matrix which is principally Ga_2Te_3 with some small areas containing a phase with Te and probably some P.

On the basis of the small amount of data obtained for this cut, it appears that the primary phase is GaP at the compositions studied. The explosion of cells at about 800°C on heating indicates that an exothermic reaction (probably occurring suddenly due to a phase change in a protecting layer) occurred to form an unknown new phase. The presence of elemental phosphorus can be explained if we assume that a compound or compounds decomposed at a ternary peritectic at a relatively low temperature. [This is reminiscent of the Ga-As-Te system (5) in which there was evidence that a ternary compound decomposed at a low temperature (~340°C) to yield elemental arsenic and a phase based on the Ga_2Te_3 structure.]

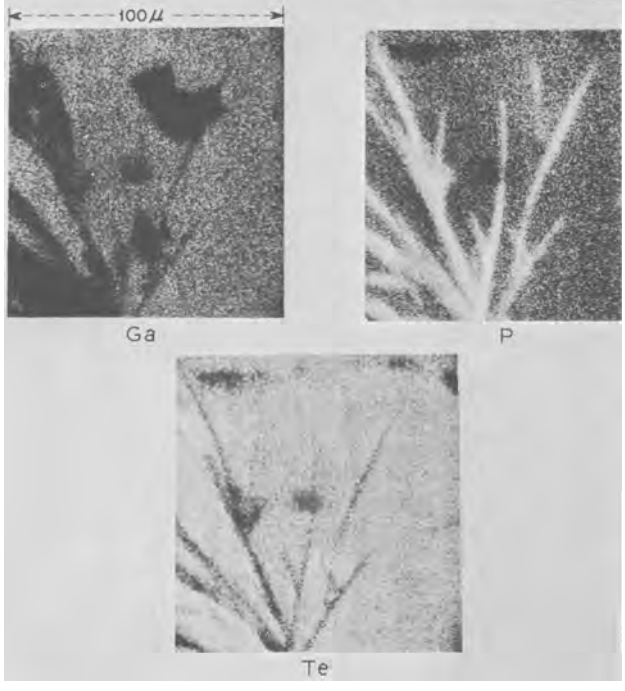

Fig. 5. X-ray fluorescence photographs of a sample from cut E of Fig. 3.

The ternary phase diagram.—The ternary diagram (Fig. 3) is drawn in such a manner as to be consistent with the DTA, x-ray, and microprobe data for the cuts indicated. No data were obtained in the Te and P rich regions of the system.

Conclusion

Part of the condensed ternary phase diagram for the Ga-P-Te system has been constructed on the basis of data obtained from differential thermal analysis, x-ray, and electron beam microprobe studies. Unlike several other III-V-VI systems (17-21), no regions of extensive solid solubility of tellurium in GaP or GaP in Ga_2Te_3 were observed. The gallium rich part of the phase diagram appears to be similar to that found earlier for the Ga-As-Te system (5) except that the primary phase formation of GaP occurs at higher temperatures than the formation of GaAs, as would be expected from the higher melting point of GaP.

DTA data were not obtained for mixtures on the GaP-Te cut. X-ray and microprobe data for samples prepared along this cut yield data which indicate that a ternary compound may exist in the P rich region which decomposes to yield P and Ga_2Te_3 on cooling.

Acknowledgments

The author would like to acknowledge useful discussions with C. D. Thurmond. H. Schreiber performed the electron beam microprobe analyses and aided in their interpretation. Powder x-ray analyses were done by M. Leung. S. Sumski prepared the DTA samples.

Manuscript received May 26, 1967.

Any discussion of this paper will appear in a Discussion Section to be published in the June 1968 JOURNAL.

REFERENCES

1. J. C. Woolley, "Compound Semiconductors", Chap. 3, Reinhold Publishing Corp., New York (1962).
2. H. Hahn and D. Thiele, *Z. anorg. Chem.*, **303**, 147 (1960).
3. N. P. Luzhnaya, G. K. Slovnova, Z. S. Medvedeva, and A. A. Eliseev, *Russian J. Inorg. Chem.*, **9**, 642 (1964).
4. D. F. O'Kane and N. R. Stemple, *This Journal*, **113**, 289 (1966).
5. M. B. Panish, *This Journal*, **114**, 91 (1964).
6. M. B. Panish, *J. Phys. Chem. Solids*, **27**, 291 (1966).
7. M. B. Panish, *J. Less Common Metals*, **10**, 416 (1966).
8. M. Rubenstein, Electrochem. Soc., Extended Abstracts, Electronics Div., **11**, 129 (1962).
9. C. D. Thurmond, *J. Phys. Chem. Solids*, **26**, 785 (1965).
10. R. N. Hall, *This Journal*, **110**, 385 (1963).
11. L. Vieland, *Acta Meta.*, **11**, 137 (1963).
12. P. C. Newman, J. C. Brice, and H. C. Wright, *Philips Res. Rept.*, **16**, 41 (1961).
13. W. Klemm and H. U. Vogel, *Z. anorg. Chem.*, **219**, 45 (1964).
14. J. R. Dale, *Nature*, **197**, 242 (1963).
15. E. Montignie, *Bull. Soc. Chim. France*, **9**, 658 (1942).
16. N. A. Goryunova and S. I. Radautsan, Soviet Research in New Semiconductor Materials, D. N. Nasledov and N. A. Goryunova, Editors, Kartya Moldovenyaské, Kishinev, 1964; translated by Consultants Bureau, 1965.
17. J. C. Woolley and B. A. Smith, *Proc. Phys. Soc. (London)*, **72**, 867 (1958).
18. N. A. Goryunova and V. S. Grigoreva, *Zhur. Tekh. Fiz.*, **26**, 2157 (1956).
19. J. C. Woolley and P. M. Keating, *J. Less Common Metals*, **3**, 194 (1961).
20. N. A. Goryunova and S. I. Radautsan, *Dokl. Akad. Nauk. SSSR*, **121**, 848 (1958).
21. N. A. Goryunova and S. I. Radautsan, *Zhur. Tekh. Fiz.*, **28**, 1917 (1958).
22. D. Richman, *J. Phys. Chem. Solids*, **24**, 1131 (1963).

Properties of Gold Doped MOS Structures

S. F. Cagnina and E. H. Snow

Research and Development Laboratory, Fairchild Semiconductor, Palo Alto, California

ABSTRACT

The theoretical capacitance-voltage characteristics of gold-doped metal-oxide-silicon structures have been calculated and compared with experiment for both the high and the low frequency cases. It is found that gold diffused from the back side causes a negative interface charge Q_{Au} in addition to the usual positive Q_{ss}. Evidence is presented to show that the gold responsible for Q_{Au} is located in the silicon very near the oxide silicon interface. Gold diffused from the top side (through the oxide) results in a positive Q_{Au} indicating that gold in the oxide near the interface is positively charged. Temperature-bias tests showed that Q_{Au} was stable under conditions which mobile alkali ions such as sodium drift rapidly. In addition, an MOS capacitance-voltage method is described for determining diffusion coefficients and solid solubilities in the oxide layer. Values of $D \cong 3 \times 10^{-3}$ μ^2/hr and $N \cong 3 \times 10^{18}$ cm^{-3} were obtained for gold in SiO_2 at 1100°C.

The introduction of gold into silicon devices is an effective and commonly used method for controlling minority carrier lifetime. Because of this practical application, the properties of gold in bulk silicon have been studied extensively (1). It has been found that gold diffuses rapidly in silicon, but that its diffusion depends in a complicated way on the defect structure of the crystal (2, 3). It has also been found that each gold atom in a substitutional site gives rise to two energy levels located within the silicon forbidden band: one of these is a donor level 0.35 ev above the valence band edge; the other is an acceptor level located 0.54 ev below the conduction band edge (4).

Because of the current importance of planar silicon technology, a knowledge of the effects of gold on oxidized silicon surfaces would be desirable. Such surfaces can be studied effectively using the capacitance-voltage characteristics of metal-oxide-semiconductor (MOS) structures. Theoretical C-V characteristics have already been calculated for nongold doped devices and successfully compared with experiment (5). The most important conclusion of these studies is that the oxidized silicon surface is characterized by a fixed positive surface-state charge Q_{ss} which tends to deplete or invert p-type silicon and accumulate n-type silicon. These theoretical C-V characteristics, however, are valid only for the case of silicon doped with shallow donors or acceptors such as phosphorus and boron for which complete ionization throughout both the neutral semiconductor and the surface space-charge region can be assumed. The charge state of the deep gold levels, on the other hand, will depend strongly on the electrostatic potential within the silicon. Thus, before one can effectively study the surface characteristics of gold doped silicon, the corresponding theoretical C-V characteristics must be developed. In the following sections these characteristics are calculated for both the high and the low frequency cases and are compared with experimental measurements. Such comparisons reveal the presence of an excess interface charge in addition to the normal Q_{ss}. The interface charge density is determined for various gold diffusion conditions and an attempt is made to determine the physical location of the gold responsible for the excess charge. Finally, the MOS method is used in a novel way to determine the diffusion coefficient and solid solubility of gold in SiO_2.

Theory

We shall now proceed to calculate the theoretical capacitance-voltage characteristics of gold doped MOS capacitors using the same procedure and notation as were used in ref. (5) for the nongold doped case.

The introduction of gold into the silicon substrate will affect the C-V characteristic because of the presence of the gold energy levels lying deep within the forbidden gap, the charge state of which will depend on the potential within the depletion region. Thus the space-charge density and hence the depletion region width and the resultant high frequency capacitance will be dependent on the gold concentration. At sufficiently low measurement frequencies, the charge in the gold levels will also respond to the a-c signal, giving an additional contribution to the semiconductor capacitance (6).

The charge state of a gold atom in silicon is not related to the potential by the usual Fermi factor because each gold atom introduces both a donor level and an acceptor level and the two are not independent; *i.e.*, a gold atom cannot be both a positively charged donor and a negatively charged acceptor at the same time. Taking this into account, the expressions for the concentration of gold atoms in each charge state become (2, 7)

$$N_{Au-} = \frac{N_{Au}}{1+2\exp(u_F+u-u_{Au-})\,[1+\tfrac{1}{2}\exp(u_F+u-u_{Au+})]} \quad [1]$$

$$N_{Au+} = \frac{N_{Au}}{1+2\exp(u_{Au+}-u_F-u)\,[1+\tfrac{1}{2}\exp(u_{Au-}-u_F-u)]} \quad [2]$$

where N_{Au} is the total gold concentration, u_{Au-}, and u_{Au+} are the potentials of the gold acceptor and donor levels, respectively, u_F is the Fermi potential in the bulk and u is the electrostatic potential or band bending.[1] Note that when the Fermi level lies above the gold acceptor level most of the gold atoms are negatively charged; when the Fermi level is between the two gold levels most of the gold atoms are neutral; and when the Fermi level is below the gold donor level most of the gold atoms are positively charged.

Potential and charge distributions in the vicinity of an inverted n-type silicon surface are shown in Fig. 1 and 2. The band diagrams are drawn to scale and were obtained from a computer solution to Poisson's equation, which will be described in detail later. Figure 1 corresponds to a sample doped with 1.0×10^{16} shallow donors/cm^3 and shows the usual uniform charge distribution and parabolic potential distribution within the depletion region. Figure 2 shows the same sample but with the addition of 0.98×10^{16} gold atoms/cm^3 to the silicon. Note that the bulk Fermi level has moved toward midgap due to compensation by the gold atoms. Note also that the depletion region is considerably wider and no longer contains a uni-

[1] All potentials are measured in units of kT/q with the potential at the intrinsic Fermi level in the bulk of the semiconductor taken as reference. Note that the energy levels in the lower half of the band gap correspond to positive potentials while energy levels in the upper half of the band gap correspond to negative potentials.

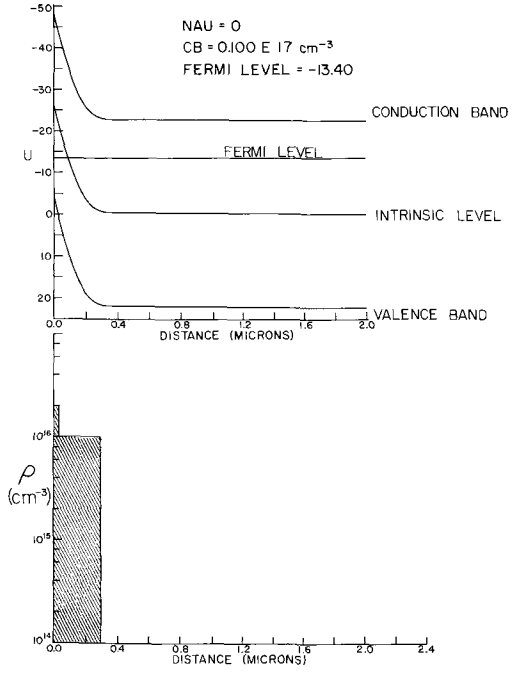

Fig. 1. Approximate charge density ρ (electronic charges/cm^3) and energy band diagram near an inverted n-type silicon surface ($N_D = 1.0 \times 10^{16}$ cm^{-3}, $u_S = -26.8$). The charge in the depletion region consists of positively charged ionized donors. The thin layer of added charge at the surface is due to accumulated minority carriers (holes).

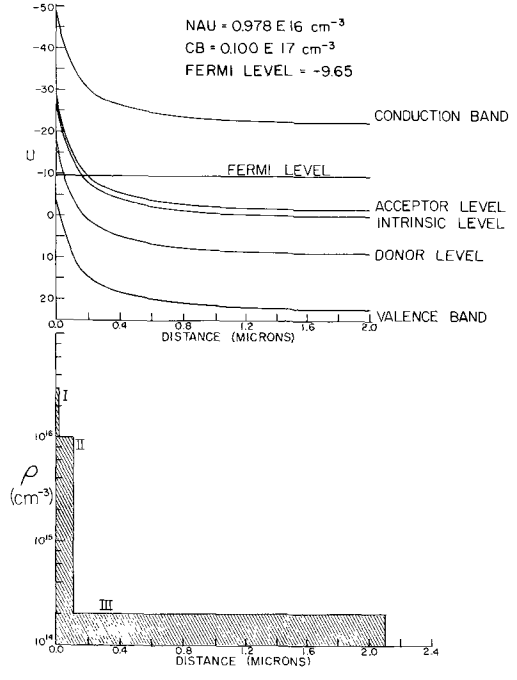

Fig. 2. Approximate charge density ρ (electronic charges/cm^3) and energy band diagram near an inverted surface of gold-doped n-type silicon ($N_D = 1.0 \times 10^{16}$ cm^{-3}, $N_{Au} = 9.8 \times 10^{15}$ cm^{-3}, $u_S = -26.8$). The charge in region I consists of minority carriers (holes) plus positively charged ionized donors plus positively charged gold atoms. The charge in region II consists of positively charged ionized donors (the gold is neutral). The charge in region III consists of positively charged ionized donors plus negatively charged gold atoms.

form charge density. In fact the depletion region can be divided into three regions corresponding to the three charge states of the gold. In region I the charge density is given approximately by $q(N_D+N_{Au})$, in region II by qN_D and in region III by $q(N_D-N_{Au})$. It is because of the charge compensation in region III that the band bending extends farther into the silicon than in the nongold doped case. This is true for all gold concentrations $N_{Au} \leqq N_D$. For gold concentrations substantially above N_D, the gold donor ions in region I will contribute approximately N_{Au} positive charges whereas the compensation effect in region III will diminish because the Fermi level will lie close to (or even below) the gold acceptor level.[2] The silicon depletion region will then consist of two regions: one of charge density $N_{Au} + N_D$ and the other of density $\sim N_D$. Effectively, the silicon will have an average donor concentration greater than N_D, thereby resulting in a smaller maximum depletion region width than is obtained on the nongold doped case [see ref. (5)].

The above figures and discussion were based on the calculated variation of the space charge in the silicon with potential. We shall now discuss these calculations using gold-doped n-type silicon as an example. The theory applies equally well for p-type silicon, but different characteristics are obtained because of the asymmetry of the gold levels about the center of the forbidden band. The charge density in the silicon is given by

$$\rho = q(p - n + N_D - N_A + N_{Au+} - N_{Au-}) \quad [3]$$

where p and n are the equilibrium electron and hole concentrations, N_D and N_A are the densities of shallow level donor and acceptor impurities, and N_{Au+} and N_{Au-} are the densities of charged gold atoms in donor and acceptor states respectively as given by [1] and [2]. Assuming that the semiconductor is nondegenerate, the carrier concentrations are given by

$$p = n_i \exp(u_F - u)$$

and

$$n = n_i \exp(u - u_F) \quad [4]$$

The Fermi potential is determined from the condition of charge neutrality in the bulk (far from the surface); there $u = 0$ and

$$n + N_{Au-} + N_A = p + N_{Au+} + N_D \quad [5]$$

In terms of the normalized potential u, Poisson's equation is given by

$$\frac{d^2u}{dx^2} = \frac{-q\rho}{kTK_S\epsilon_0} \quad [6]$$

Substituting [3] into [6], defining the intrinsic Debye length

$$L_D \equiv \left(\frac{kTK_S\epsilon_0}{2q^2n_i}\right)^{1/2}$$

and noting that

$$\frac{d^2u}{dx^2} = \frac{du}{dx}\frac{d}{du}\left(\frac{du}{dx}\right) = \frac{1}{2}\frac{d}{du}\left(\frac{du}{dx}\right)^2 \quad [7]$$

we obtain

$$\frac{d}{du}\left(\frac{du}{dx}\right)^2 = \frac{2}{L_D^2}\left\{\sinh(u-u_F) - (N_D - N_A)/2n_i - \frac{N_{Au}/2n_i}{1+2\exp(u_{Au+}+u-u_F)[1+\frac{1}{2}\exp(u_{Au-}+u-u_F)]} + \frac{N_{Au}/2n_i}{1+2\exp(u_F-u_{Au-}-u)[1+\frac{1}{2}\exp(u_F-u_{Au+}-u)]}\right\} \quad [8]$$

The above expression can be integrated in closed form from $u = 0$ (far in the bulk) to $u = u_s$ (at the silicon surface). The net charge per unit area in the silicon is then given by

$$Q_S = \frac{kT}{q}K_S\epsilon_0\left.\frac{du}{dx}\right|_{x=0} \quad [9]$$

[2] Adding gold to n-type silicon will progressively move the Fermi level toward the center of the band gap and will ultimately assume a position midway between the two gold levels.

This charge is made up of two parts: (*i*) minority carriers (holes) in a narrow inversion layer near the surface, and (*ii*) ionized gold and shallow donor and acceptor ions within a depletion region of width x_d. The part of Q_s which is due to holes in the inversion layer can be calculated from

$$Q_p \equiv q\int_0^{x_d} p(x)\,dx = q\int_{u_s}^{0} \frac{p(u)}{du/dx}\,du \qquad [10]^3$$

Similarly, that part of Q_s which is due to uncompensated ions within the depletion region may be calculated from

$$Q_B = q\int_0^{x_d} [N_{Au^+}(x) - N_{Au^-}(x) + N_D - N_A]dx$$

$$= q\int_{u_s}^{0} \frac{[N_{Au^+}(u) - N_{Au^-}(u)]}{du/dx}\,du + q(N_D - N_A)x_d \qquad [11]$$

where x_d is the effective depletion region width. This useful quantity may be determined from the relation

$$Q_s = q\int_{u_s}^{0} \frac{p(u)}{du/dx}\,du + q\int_{u_s}^{0} \frac{[N_{Au^+}(u) - N_{Au^-}(u)]}{du/dx}\,du + q(N_D - N_A)x_d \qquad [12]$$

Once a surface is strongly inverted, x_d rapidly approaches a maximum value with further increase in surface potential, corresponding to the fact that the added potential variation causes a very large increase in Q_p without substantially affecting Q_B.

In an MOS capacitor, the gate voltage V_G applied to the metal electrode is related to the silicon surface potential ϕ_s and the net charge in the silicon Q_s by (5)

$$V_G - \Phi_{MS} + Q_{ss}/C_o = \phi_s - Q_s/C_o \qquad [13]$$

where Φ_{MS} is the metal-semiconductor work function difference, C_o is the oxide capacitance per unit area, and Q_{ss} is the surface-state charge density which for nongold doped samples was shown to be independent of surface potential over the observable range.

If the charge in surface states is independent of surface potential, the small signal MOS capacitance per unit area can be calculated from the relation

$$C = \frac{1}{(1/C_o) + (1/C_s)} \qquad [14]$$

where $C_o = K_o\epsilon_o/x_o$ is the oxide capacitance per unit area and C_s is the silicon space charge capacitance per unit area. The latter must be calculated separately for the two cases of high and low measurement frequency. At sufficiently low frequencies, the minority carriers, the majority carriers, and the charge on the gold atoms within the space-charge region can follow the applied a-c measurement signal and contribute to the capacitance. The silicon capacitance can thus be determined from the relation

$$C_s = -\frac{dQ_s}{d\phi_s} = -\frac{d}{d\phi_s}\int_o^{\infty} \rho(x)\,dx = -\frac{d}{d\phi_s}\int_{\phi_s}^{0} \frac{\rho(x(\phi))}{d\phi/dx}\,d\phi = \frac{\rho(x=0)}{\left.\frac{d\phi}{dx}\right|_{x=0}} \qquad [15]$$

where the surface charge density $\rho(x = 0)$ is given by Eq. [3] evaluated at $u = u_s$, and the potential gradient at the surface follows directly from the first integration of Poisson's equation [8].

[3] Though the inversion layer does not, of course, extend throughout the depletion region, the expression for $p(u)$ decreases exponentially and the integral may be extended to $u = 0$ without serious error.

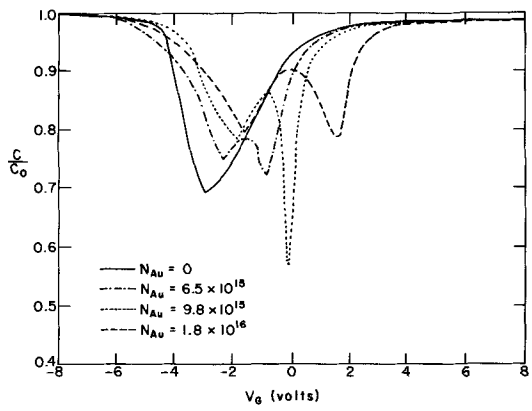

Fig. 3. Theoretical low frequency MOS C-V curves for a constant donor density of 1 x 10^{16} cm^{-3} and various gold concentrations ($x_o = 0.2\mu$).

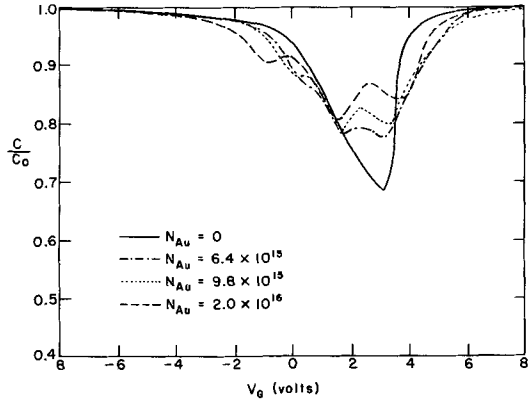

Fig. 4. Theoretical low frequency MOS C-V curves for a constant acceptor density of 1 x 10^{16} cm^{-3} and various gold concentrations ($x_o = 0.2\mu$).

For particular values of $N_D - N_A$, various Fermi levels were fed into an IBM 1130 computer. Gold concentrations were calculated for each Fermi level from the equation of charge neutrality [5]. For each gold concentration, the silicon capacitance C_s was computed for values of surface potential spanning most of the band gap. The MOS capacitance was then determined as the series sum of the oxide and silicon capacitances [14]. Finally, each surface potential was related to the effective applied gate voltage $V_G - \Phi_{MS} + Q_{ss}/C_o$ by Eq. [13]. Families of calculated C-V curves for 10^{16} doped n-type and 10^{16} doped p-type material with gold concentration as a parameter are shown in Fig. 3 and 4. These particular curves are for an oxide thickness of 0.2μ.

The presence of gold within the depletion region results in a peak in the C-V curve in the depletion-inversion range of the characteristic. This peak is similar to what would be obtained if surface states localized in energy within the forbidden band could follow the a-c measurement signal and contribute to the capacitance. As an example, a low-frequency MOS C-V characteristic was calculated for the case of nongold doped n-type silicon in the presence of 5 x 10^{10} cm^{-2} fast donor states located 8.88 kT units below the intrinsic level and 5 x 10^{10} cm^{-2} fast acceptor states located 1.54 kT units above the intrinsic level, corresponding to the energy levels of gold. The doping was chosen such that the Fermi level was the same as that for the sample, doped with 9.8 x 10^{15} gold atoms/cm^{-3}, whose C-V characteristic is shown in Fig. 3. The results are shown in Fig. 5, where two sharp peaks can be seen in the depletion-inversion region, corresponding to the Fermi level crossing each of the surface state levels. In the case of gold-doped silicon, those gold atoms that are located at the point where either

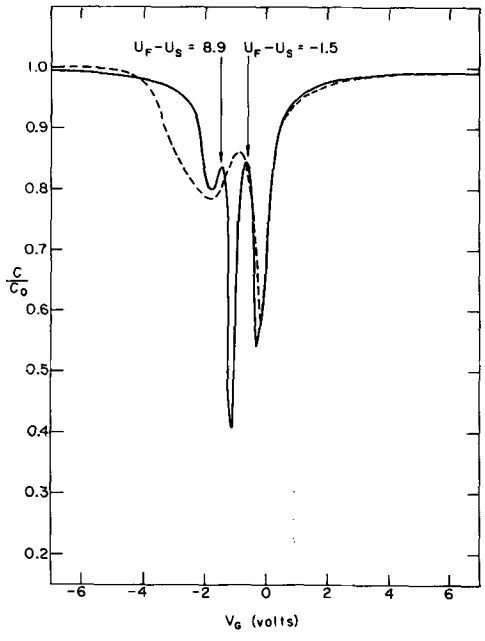

Fig. 5. Comparison of the effects of surface states and deep bulk levels on low frequency MOS C-V characteristics. The solid line corresponds to the case of 5 x 10^{10} cm^{-2} fast acceptor states at $u = -1.5$ and 5 x 10^{10} cm^{-2} fast donor states at $u = +8.9$. The dotted line corresponds to gold doped silicon (N_{Au} = 9.8 x 10^{15} cm^{-3}). In each case N_D = 1 x 10^{16} cm^{-3} and x_o = 0.2μ.

gold level crosses the Fermi level will contribute to the capacitance in the same way. However, the gold will continue to contribute even after the gold levels at the surface cross the Fermi level, since the crossover point then simply moves back into the bulk with increasing surface potential. Thus, the discrete gold levels behave qualitatively like fast surface states that are distributed in energy, resulting in a smearing of the two peaks into the single broader peak which is actually obtained.

At sufficiently high frequencies only the majority carriers can respond to the a-c signal; the minority carriers and the charge on the gold within the depletion region do not contribute to the capacitance. For this case the silicon capacitance is obtained by differentiating Eq. [12] keeping the first two terms on the right constant. This results in

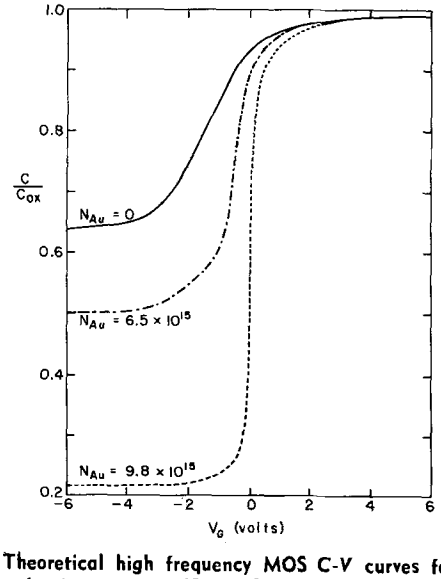

Fig. 6. Theoretical high frequency MOS C-V curves for a constant donor density of 1 x 10^{16} cm^{-3} and various gold concentrations (x_o = 0.2μ).

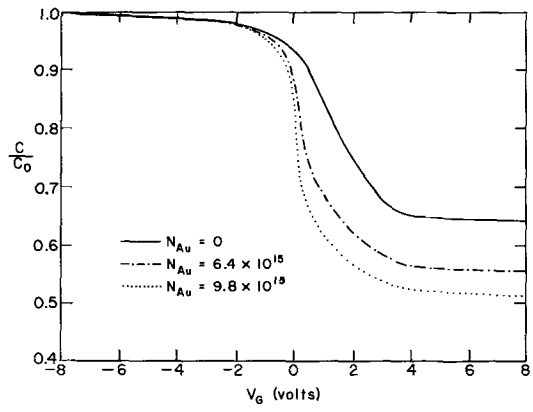

Fig. 7. Theoretical high frequency MOS C-V curves for a constant acceptor density of 1 x 10^{16} cm^{-3} and various gold concentrations (x = 0.2μ).

$$C_s = q(N_A - N_D)dx_d/d\phi_s \quad [17]$$

where $dx_d/d\phi_s$ can be calculated on the basis of the idealized charge distribution shown in Fig. 2. This results in

$$C_s = K_s\epsilon_o/x_d \quad [18]$$

Thus for each value of surface potential, an x_d, and hence a C_s, is obtained. C_s is related to the MOS capacitance by Eq. [14] and surface potential is related to gate voltage by Eq. [13], as in the low frequency case.

High frequency curves for n-type ($N_D = 10^{16}$ cm^{-3}) and p-type ($N_A = 10^{16}$ cm^{-3}) silicon doped with varying amounts of gold are shown in Fig. 6 and 7. Note that the MOS capacitance levels off at a minimum value in the inversion range corresponding to a maximum value for x_d. We shall refer to this limiting value of the effective space-charge width as x_{dmax}. The effect of increasing gold concentration on x_{dmax} is shown in Fig. 8. Here the calculated ratio of x_{dmax} with gold to the corresponding value without gold is shown as a function of normalized gold concentration.

Comparison of Experimental and Theoretical Characteristics

Gold doped MOS capacitors were fabricated in order to compare the calculated C-V characteristics with experiment. n-type units were made using (100) surface oriented silicon wafers doped with 1.0 x 10^{16} phosphorus atoms/cm^3. The wafers were chemically polished to 150μ and oxidized in dry O_2 to form a 0.2μ thick oxide layer. The oxide was then removed from one side; 500Å of gold was deposited on this side and then diffused for 1.5 hr at 1000°C in a nitrogen ambient. Aluminum was then evaporated onto the oxide

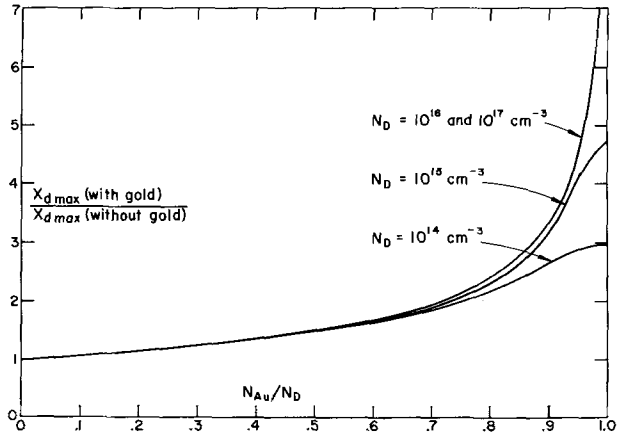

Fig. 8. Theoretical gold concentration N_{Au} (normalized to N_D) as a function of x_{dmax} (normalized to x_{dmax} without gold) for various values of N_D.

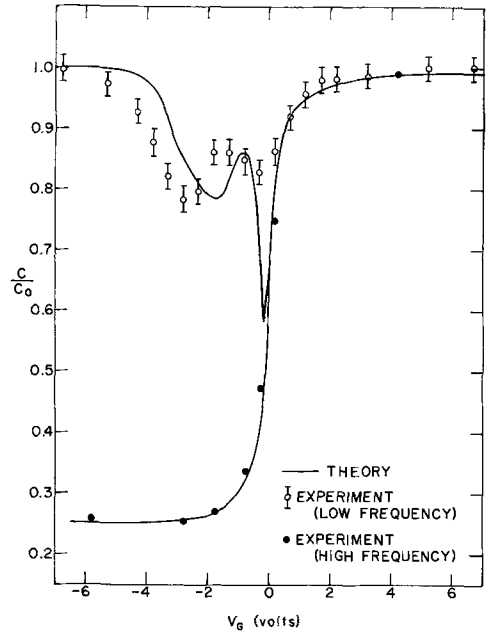

Fig. 9. Comparison between theoretical and experimental MOS C-V characteristics for n-type silicon gold-diffused at 1000°C ($x_o = 0.2\mu$, $N_D = 1 \times 10^{16}$ cm^{-3}, and $N_{Au} = 9.8 \times 10^{15}$ cm^{-3}, low frequency: 73 Hz, high frequency: 100 kHz). Experimental curves are shifted to the left to account for a fixed negative interface charge.

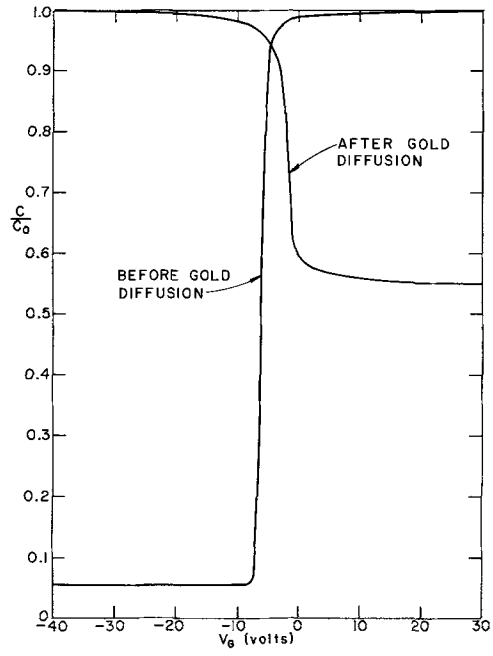

Fig. 10. Experimental C-V characteristic of a lightly doped n-type sample overcompensated with gold (gold diffused 40 min at 1200°C). Also shown is the C-V characteristic on the same sample before gold diffusion.

side and etched to form the field plates of MOS capacitors. Finally, the sample was heat treated at 565°C in nitrogen.[4]

High frequency C-V characteristics (100 kc/sec) were obtained using a Boonton model 74C-S8 capacitance bridge, and low frequency characteristics (73 Hz) were obtained using a Wayne-Kerr model B221 bridge. The transition between high and low frequency type characteristics [see Ref. (5)] was about 100 Hz for these devices. The results for a typical device are shown as the data points in Fig. 9. Reproducibility of both high and low frequency characteristics from device to device was good. The theoretical characteristics (solid lines), to which the experimental points are compared, were chosen so as to match the minimum capacitance of the high frequency measurements. The theoretical curves thus obtained correspond to a gold concentration of 9.8×10^{15} cm^{-3}, a value in good agreement with the solid solubility of gold at the 1000°C diffusion temperature. Agreement between theoretical and experimental curve shapes is excellent in the high frequency case and fairly good in the low frequency case.[5]

The possibility of over-compensation of n-type material with gold was also demonstrated using the MOS technique. For this purpose MOS capacitors were fabricated with starting material phosphorus doped to a concentration of only 10^{13} cm^{-3} and with gold diffusion taking place at 1200°C. Controls were fabricated similarly but without the gold diffusion step. High frequency (100 kHz) capacitance-voltage measurements made on the resulting devices are shown in Fig. 10. Note that the characteristic of the gold-diffused device corresponds to a p-type silicon substrate. Although the silicon substrate is nearly insulating (the Fermi level is a few kT units below the intrinsic level), the minimum-to-maximum capacitance ratio corresponds to a relatively large substrate impurity concentration. As the bands are bent downward (corresponding to a positive voltage on the gate electrode), the gold acceptor level is brought below the Fermi level and hence the gold near the surface becomes negatively charged. Thus, the charge density in the surface space-charge region is equal to the gold concentration which is $\sim 10^{16}$ cm^{-3} in this case.

[4] The above MOS processing was used throughout the course of this work unless otherwise noted.

[5] For this comparison the experimental characteristics were shifted horizontally along the voltage axis by a constant amount ΔV to bring them into alignment with the theoretical curves. The magnitude of ΔV can be used to calculate interface charge densities, as will be described in the next section.

Interface Charge Densities

The surface-state charge density Q_{ss} of oxidized silicon can be evaluated from capacitance-voltage characteristics by comparing an experimental plot of C *vs.* V_G with a theoretical plot of C *vs.* $V_G - \Phi_{MS} + Q_{ss}/C_o$. If Φ_{MS} is known, the displacement between the two curves yields Q_{ss}. For nongold doped silicon, Q_{ss} is normally positive and of the order of several times 10^{11} electronic charges per cm^2, its exact value depending on orientation (8) and on oxidation and annealing conditions (9). In the present study, high frequency capacitance-voltage characteristics were measured on both control and gold diffused samples and were compared with the appropriate theoretical curves. The controls yielded Q_{ss} values in general agreement with those previously reported, but the apparent Q_{ss} of the gold-diffused samples was less positive than that of the controls and in many cases it was actually negative. This indicates the presence of a gold-related effective interface charge in addition to the normal Q_{ss}. We shall refer to the density of this gold related interface charge as Q_{Au}. Thus the displacement ΔV between theoretical and experimental C-V curves is given by $\Delta V = Q_{ss}/C_o - \Phi_{MS}$ for the control samples and by $\Delta V = (Q_{ss} + Q_{Au})/C_o - \Phi_{MS}$ for the gold diffused samples. After back side gold diffusion, Q_{Au} was always negative. Its magnitude increased with diffusion time reaching a steady state value after about 10 min at 1000°C. To assure that this steady state had been reached, standard diffusion times of 1 hr were used for comparing samples processed in various ways. In each case it was demonstrated that Q_{Au} was stable under fields of ± 50 v/μ at 250°C, a condition under which mobile oxide impurities such as sodium migrate rapidly (10).

Effect of doping and conductivity type.—Negative Q_{Au} shifts are observed on both p- and n-type silicon; neither type nor doping seem to have an important

Table I. Values of Q_{ss} and Q_{Au} for a set of n- and p-type samples

Doping	$(Q_{ss} + Q_{Au})$/(gold)	Q_{ss}/q (control)	Q_{Au}/q
5×10^{15} cm^{-3}, n	-3×10^{11} cm^{-2}	2×10^{11} cm^{-2}	-5×10^{11} cm^{-2}
1×10^{17} cm^{-3}, n	-1.5×10^{11} cm^{-2}	2×10^{11} cm^{-2}	-3.5×10^{11} cm^{-2}
1×10^{16} cm^{-3}, p	-3×10^{11} cm^{-2}	3×10^{11} cm^{-2}	-6×10^{11} cm^{-2}

Table II. Values of Q_{ss} and Q_{Au} for (100) and (111) orientations

Orientation	$(Q_{ss} + Q_{Au})/q$ (gold)	Q_{ss}/q (control)	Q_{Au}/q
(100)	-1×10^{11} cm^{-2}	1×10^{11} cm^{-2}	-2×10^{11} cm^{-2}
(111)	-3×10^{11} cm^{-2}	3×10^{11} cm^{-2}	-6×10^{11} cm^{-2}

effect. Values of -5×10^{11} electronic charges/cm^2 are typical for both p- and n-type samples of (111) orientation which have been diffused 1 hr at 1000°C. Values of Q_{ss} and Q_{Au} for a set of n- and p-type samples with 0.2μ oxides and various doping concentrations are shown in Table I.

Effect of orientation.—There appears to be a definite orientation effect on the magnitude of the gold-related interface charge. Values of Q_{ss} and Q_{Au} for (100) and (111) orientations are shown in Table II. All were n-type ($\sim 10^{16}$ cm^{-3}) with 0.2μ oxide and were gold diffused for 1 hr at 1000°C.

Effect of dislocation density.—To determine the effect of dislocation density on Q_{Au}, the following experiment was performed. Three different sets of wafers, one with low dislocation count (<100 cm^{-2}), another with intermediate dislocation count ($\sim$3000 cm^{-2}), and the third with high dislocation density (>10,000 cm^{-2}) were gold diffused 1 hr at 1000°C in N_2. Control samples were fabricated similarly but without the gold diffusion step. In agreement with an earlier study (11) the controls all showed identical Q_{ss}, approximately 2.5×10^{11} cm^{-2} independent of dislocation count. The gold diffused samples all showed negative Q_{Au} of about -6.0×10^{11} cm^{-2}, independent of dislocation density.

Effect of ambient.—To ascertain the effect of the diffusion ambient, Q_{Au} was compared for samples gold diffused at 1000°C in nitrogen and in oxygen. The sample that had been oxygen diffused was subjected to an initial 15 min in nitrogen to ensure that a sufficient quantity of gold entered the silicon before an oxide layer began to form on the back side. Capacitance-voltage measurements revealed Q_{Au}/q values of -5×10^{11}/cm^2 on both samples, suggesting that the negative shift due to gold is independent of the gaseous ambient (inert or oxidizing) in which the gold diffusion takes place.

Physical location of the negative interface charge.—In this section we describe experiments that are aimed at locating the region of the oxide-silicon system that is responsible for the negative Q_{Au} observed after back-side gold diffusion.

In the first of these experiments, gold diffused wafers and controls were split into three groups. Group A received no additional treatment. The existing 2000Å of thermal oxide was etched off group B and 2000Å of SiO_2 was vapor deposited by reacting SiH_4 and O_2 at $\sim$400°C. The deposition time was about 20 sec. In the case of group C, the thermal oxide was etched off and, in addition, the silicon surface was given a light etch to remove $\sim 1\mu$ of silicon. A 2000Å film of SiO_2 was then vapor deposited on these samples also. The average Q_{ss} and Q_{Au} values and the spreads in each group are shown in Table III. Although the Q_{Au} values in this experiment are smaller than typical values, they are clearly evident. Note that approximately the same Q_{Au} is observed on all three groups, indicating that the gold responsible for the shift either is not located within the oxide or it diffuses back into the new oxide during the short heat treatments at 400° and 565°C that occur during processing.

Table III. Average Q_{ss} and Q_{Au} values in gold diffused wafers

Group	$(Q_{ss} + Q_{Au})/q$ (gold)	Q_{ss}/q (control)	Q_{Au}/q
A	$0.9 \pm 0.2 \times 10^{11}$ cm^{-2}	$3.1 \pm 0.5 \times 10^{11}$ cm^{-2}	-2.2×10^{11} cm^{-2}
B	$1.7 \pm 0.3 \times 10^{11}$ cm^{-2}	$3.8 \pm 0.1 \times 10^{11}$ cm^{-2}	-2.1×10^{11} cm^{-2}
C	$1.5 \pm 0.1 \times 10^{11}$ cm^{-2}	$2.9 \pm 0.6 \times 10^{11}$ cm^{-2}	-1.4×10^{11} cm^{-2}

Radiotracer studies have shown that back-side gold diffusion results in a large gold concentration (in excess of the solid solubility in silicon) at the Si-SiO_2 interface (12). Since the observed negative Q_{Au} could be related to this interfacial gold, an experiment was performed in which an attempt was made to introduce gold only at the interface but not in the bulk silicon or in the oxide. Chemically polished n-type ($\sim 10^{16}$ cm^{-3}) silicon wafers were subjected to the following treatment: A thin layer of gold was evaporated onto the top surface and the wafers were heated for 10 min at 565°C in nitrogen. They were then immersed in an aqua regia bath to remove any unalloyed metallic gold from the surface. After this treatment the surface had lost its initially shiny appearance and appeared dull. A 0.2μ film of SiO_2 was then vapor deposited on the surface. C-V measurements revealed very large negative Q_{Au} values for the gold-alloyed samples (from about -1.5×10^{12} cm^{-2} and upward in magnitude), whereas the control sample had a Q_{ss} value of approximately $+8 \times 10^{11}$ cm^{-2}. From the capacitance minimum of the gold-alloyed samples, a bulk doping value was calculated which agreed well with the known initial resistivity of the n-type wafer. This shows that negligible gold was present within most of the depletion region of the MOS devices ($x_{dmax} = 0.3\mu$).

The above two experiments show that the gold responsible for the negative Q_{Au} is at or near the interface. Also, they indicate that the negatively charged gold atoms probably reside in the silicon. If the species causing the negative Q_{Au} is in the silicon, then it should be possible to obtain gold-induced C-V shifts on MOS structures using dielectrics other than SiO_2. For this reason, a third experiment was performed in which gold was diffused for 1 hr at 1000°C into silicon upon which a layer of silicon nitride had been previously deposited in place of the usual thermally grown SiO_2. The silicon nitride was deposited on n-type ($N_D = 5 \times 10^{15}$ cm^{-3}) silicon slices at 900°C utilizing an ammonia and silicon tetrachloride process. Capacitance-voltage measurements on control samples showed large positive Q_{ss}/q values of about 10^{12} cm^{-2}. However, in every case, negative Q_{Au} shifts of about -6×10^{11} cm^{-2} were obtained for the gold-diffused samples. This value of Q_{Au} is very typical of what is observed on oxidized samples for the same gold diffusion temperature and time.

Gold Diffusion through SiO_2

In this section we describe the results of experiments to determine the charge state of gold in SiO_2, and a novel method for determining the diffusivity and solid solubility of gold in the oxide. These experiments were performed as follows: n-type silicon was initially oxidized to form oxide layers 0.1, 0.2, and 0.5μ thick. A single dot of gold approximately 0.75 cm^2 in area was then evaporated onto the oxide. The back side was covered by a thicker oxide to ensure that any gold "breaking through" the oxide and entering the silicon during diffusion had entered through the top oxide layer. The samples were diffused in nitrogen for varying lengths of time at temperatures between 800° and 1100°C.

Q_{Au} shifts.—Positive Q_{Au} shifts were observed after gold diffusion through the oxide, corresponding to the apparent introduction of positive charges into the

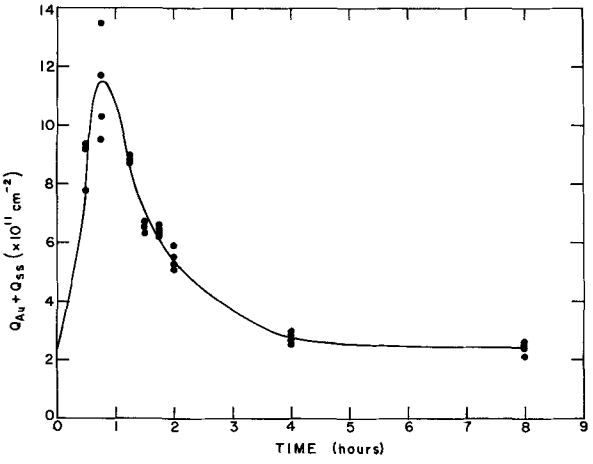

Fig. 11. Total interface charge $Q_{Au} + Q_{ss}$ vs. top side gold diffusion time [(111) surface oriented sample, $N_D = 2 \times 10^{15}$ cm^{-3}, $x_o = 0.2\mu$].

oxide. Temperature-bias tests (10) were used to demonstrate that these positive shifts were stable and were not due to contamination by mobile alkali ions.

The Q_{Au} shift at first increases with diffusion time, reaching a maximum value of about 10^{12} electronic charges/cm^2. It then decreases with longer diffusion time and approaches zero. An example of the time dependence is shown in Fig. 11 for the case of diffusion at 1000°C. That this type of behavior is due to evaporation of the gold from the wafer is considered unlikely, since a layer of gold remained atop the oxide surface after all high temperature treatments.

In an effort to determine the charge distribution in the oxide, the excess charge induced in the silicon due to gold (Q_s') was measured as a function of oxide thickness as the oxide was etched away in steps [see ref. (9)]. After each etching step, C-V curves were measured using a mercury probe as the metal electrode. The excess charge per unit area induced in the silicon Q_s' was determined from the relation

$$Q_s' = \Delta V \cdot C_o \qquad [19]$$

where ΔV is the voltage shift between the C-V characteristics of the gold-diffused and nongold-diffused devices and C_o is the oxide capacitance per unit area. Samples of 0.5μ oxide thickness, diffused varying lengths of time, were etched to as thin as 0.15μ, and 0.2μ samples were etched to about 0.12μ. No decrease in Q_s' was observed. This indicates that most of the positive charge Q_{Au} is located within 500Å of the interface and is not distributed throughout the oxide.

Diffusion coefficient of gold in SiO_2.—In addition to the positive Q_{Au} shifts, it was observed that after a sufficiently long diffusion time the capacitance minimum decreased over the entire gold-covered area. This is interpreted as being due to gold which had diffused through the oxide into the silicon so as to compensate the original n-type doping. C-V characteristics or oxides gold-diffused at 1000°C in a nitrogen ambient for 2 and 4 hr, respectively, are shown in Fig. 12(a) and (b)

The diffusion of gold through a film of SiO_2 is analogous to the permeation of a gas through a membrane. The solution to the latter problem is available in the literature (13). If the diffusivity of gold in the silicon is much larger than in the oxide (an assumption which we shall verify) and the gold concentration in the silicon remains smaller than the solid solubility limit, it can be shown that the concentration of gold in the silicon (N_{Au}) as a function of time is given by

$$N_{Au} = \frac{D_o N_o t}{W x_o} + \frac{2N_o x_o}{\pi^2 W} \sum_1^\infty \frac{(-1)^n}{n^2} \left[1 - \exp\left[-\left(\frac{n\pi}{x_o}\right)^2 D_o t\right]\right] \qquad [20]$$

In this expression D_o is the diffusivity of gold in the oxide, N_o is the gold concentration at the outer surface of the oxide (presumed equal to the solid solubility), x_o is the oxide thickness, and W is the silicon wafer thickness. For times sufficiently large, this expression reduces to (13)

$$N_{Au} \cong \frac{D_o N_o t}{W x_o} - \frac{N_o x_o}{6W} \qquad [21]$$

Equation [21] can be rearranged and put in the form

$$\frac{x_o^2}{6t^*} = \frac{D_o}{(1 + 6N_{Au}^* W/N_o x_o)} \qquad [22]$$

where t^* represents the time required for the gold concentration in the silicon to reach its minimum detectable value ($N_{Au}^* \sim 10^{14}$ cm^{-3} in our experiment). If $N_o x_o >> 6N_{Au}^* W$, then $x_o^2/6t^*$ will be independent of x_o and just equal to D_o.

In Fig. 13, measured values of $x_o^2/6t^*$ for various oxide thicknesses are shown (all samples diffused at

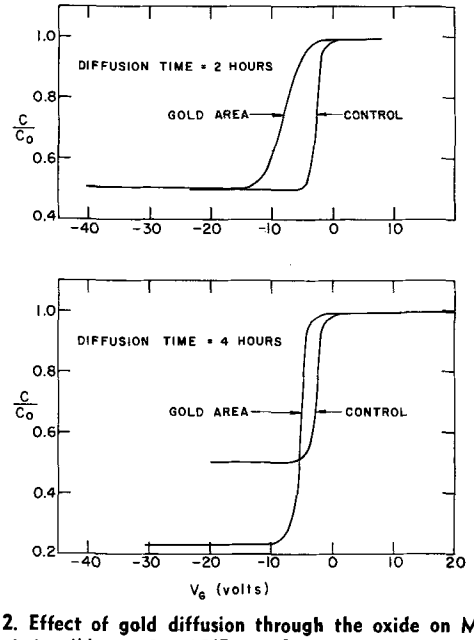

Fig. 12. Effect of gold diffusion through the oxide on MOS C-V characteristics ($N_D = 2 \times 10^{15}$ cm^{-3}, $x_o = 0.2\mu$, diffusion temperature = 1000°C). Breakthrough occurs between 2 and 4 hr as is evident from the change in capacitance minimum.

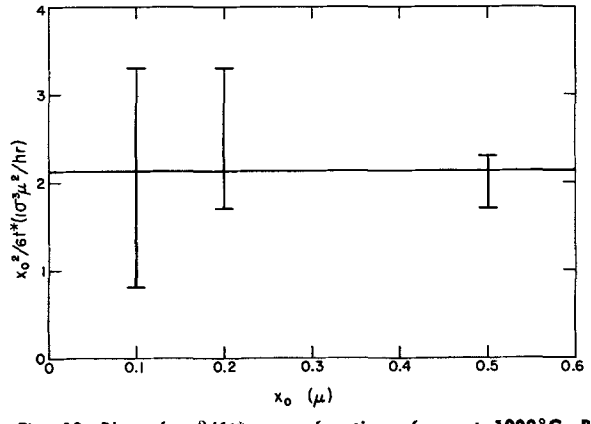

Fig. 13. Plot of $x_o^2/6t^*$ as a function of x_o at 1000°C. Best fit appears to be a horizontal line (independent of x_o) corresponding to a diffusivity $D_o \simeq 2 \times 10^{-3}$ μ^2/hr.

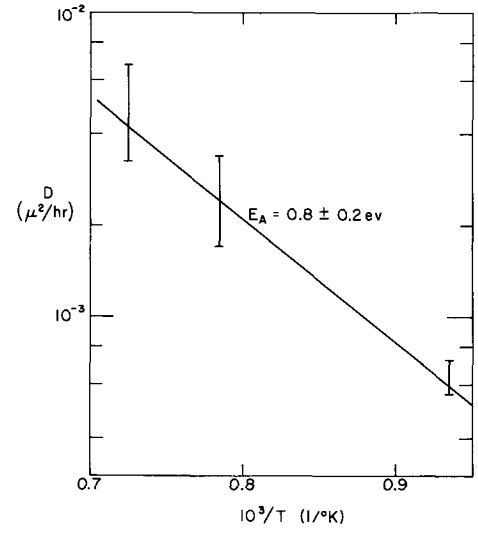

Fig. 14. Gold diffusivity in SiO_2 as a function of temperature

1000°C). The best line fit through the data appears to be horizontal, corresponding to a diffusivity $D_o \cong 2 \times 10^{-3}$ μ^2/hr and placing a lower bound on the solid solubility of gold in SiO_2 of about $N_o \gtrsim 10^{18}$ cm^{-3} at this temperature.

Data on gold diffusivities at 800° and 1100°C were also determined for 0.1μ oxide films, using the expression $D_o \cong x_o^2/6t^*$. These data are plotted in Fig. 14 as a function of reciprocal temperature. An activation energy of 0.8 ± 0.2 ev is indicated.

From Eq. [21] it can be seen that a plot of N_{Au} *vs.* diffusion time should be a straight line with intercept on the N_{Au} axis proportional to N_o and slope proportional to both N_o and D_o. Thus by plotting the gold concentration as a function of time after the breakthrough time t^*, it is possible to determine the gold solubility N_o and the diffusivity D_o independently. Such a plot is shown in Fig. 15 for the case of gold diffusion at 1100°C. In this case the oxide thickness was 0.1μ and the silicon wafer thickness was 150μ. The best straight line through the data points indicates a solubility of $N_o \simeq 3 \times 10^{18}$ cm^{-3} and a diffusivity $D_o \simeq 3 \times 10^{-3}$ μ^2/hr.

Collins, Schroder, and Sah (14) have inferred diffusivity values for gold in Si and SiO_2 from their measurements of the dependence of Q_{Au} on gold diffusion time. Their analysis was based on several assumptions including the supposition that the gold in the oxide is negatively charged. Since this is in conflict with the present findings, it is not surprising that their results ($D_o = 4.8 \times 10^{-4}$ μ^2/hr at 1100°C and $E_a = 2.14$ ev) are in substantial disagreement with ours.

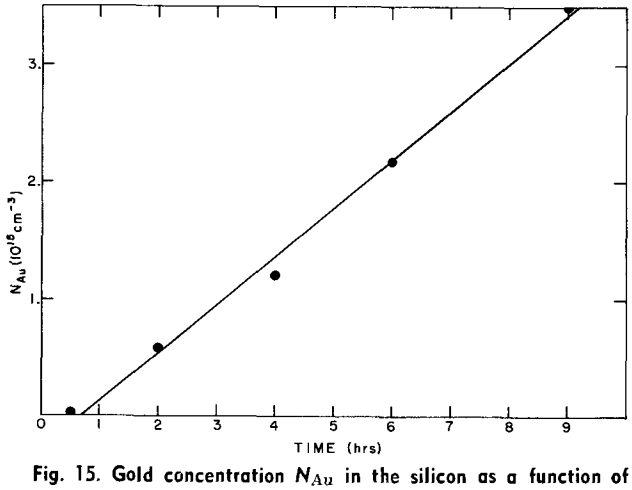

Fig. 15. Gold concentration N_{Au} in the silicon as a function of total diffusion time through the oxide ($x_o = 0.1\mu$, $T = 1100$°C). These data indicate a diffusivity $D_o \simeq 3 \times 10^{-3}$ μ^2/hr and a gold solubility in the oxide $N_o \simeq 3 \times 10^{18}$ cm^{-3}.

Conclusions

The theory of the MOS capacitance-voltage method has been extended to the case of gold-doped silicon and has been verified experimentally. Using this method, it was shown that back-side gold diffusion into an oxidized silicon wafer causes an apparent negative shift in the interface charge density. A series of special experiments indicated that this negative charge is localized in the silicon very near the oxide-silicon interface.

Why such interfacial gold should have a fixed negative charge is not understood. It is known that substitutional gold in the silicon bulk gives rise only to the pair of deep levels discussed previously (4). However, it has also been reported that gold piles up at the oxide-silicon interface reaching concentrations far in excess of the solid solubility (12). One can speculate that this excess interfacial gold has energy levels quite different from those of the bulk substitutional gold. A high concentration of shallow acceptor levels localized at the interface could account for the observed results.

Gold diffused into an MOS structure from the top side through the oxide gives a positive contribution to the interface charge density indicating that gold in the oxide near the interface may be positively charged as is sodium (10). However, it is immobile at temperatures ~250°C at which sodium drifts rapidly under an applied field.

Finally, the MOS method has been used to measure the diffusion coefficient and solid solubility of gold in SiO_2. This method should be applicable to many other impurities. It is as sensitive as the p-n junction method which has been used for phosphorus (15), boron (16), and gallium (17) and it has the additional advantage that it can be used with impurities such as gold which do not form p-n junctions in silicon, but merely compensate the initial doping.

Acknowledgments

The authors wish to thank K. M. Cooper for his assistance with the measurements and A. S. Grove for many stimulating and helpful discussions throughout the course of the work.

Manuscript received May 19, 1967; revised manuscript received July 12, 1967.

Any discussion of this paper will appear in a Discussion Section to be published in the June 1968 JOURNAL.

REFERENCES

1. For a recent review, see W. M. Bullis, *Solid-State Electronics*, **9**, 143 (1966).
2. B. I. Boltaks, G. S. Kulikov, and R. S. Malkovich, *Soviet Physics-Solid State*, **2**, 2134 (1961).
3. W. R. Wilcox and T. J. LaChapelle, *J. Appl. Phys.*, **35**, 240 (1964).
4. C. B. Collins, R. O. Carlson, and C. J. Gallagher, *Phys. Rev.*, **105**, 1168 (1956).
5. A. S. Grove, B. E. Deal, E. H. Snow, and C. T. Sah, *Solid-State Electronics*, **8**, 145 (1965).
6. C. T. Sah and V. G. K. Reddi, *IEEE Trans. on Electron Devices, ED-11*: 7, 345 (1964).
7. A. G. Samoilovich and L. L. Korenblit, *Uspekhi Fiz. Nauk*, **57**, 577 (1955).
8. P. Balk, P. J. Burkhardt, and L. V. McGregor, *Proc. IEEE*, **53**, 2133 (1965).
9. B. E. Deal, M. Sklar, A. S. Grove, and E. H. Snow, *This Journal*, **114**, 266 (1967).
10. E. H. Snow, A. S. Grove, B. E. Deal, and C. T. Sah, *J. Appl. Phys.*, **36**, 1664 (1965).
11. B. E. Deal, Private communication.
12. J. W. Adamic and J. E. McNamara, Paper presented at the New York Meeting of the Society, Sept. 29-Oct. 3, 1963, Abstract No. 149.
13. W. Jost, "*Diffusion*," Vol. 1, 42-45, Academic Press, Inc., New York (1960).

14. D. R. Collins, D. K. Schroder, and C. T. Sah, *Appl. Phys. Letters*, **8**, 323 (1966).
15. C. T. Sah, H. Sello, and D. A. Tremere, *J. Phys. Chem. Solids*, **11**, 288 (1959).
16. S. Horiuchi and J. Yamaguchi, *Jap. J. Appl. Phys.*, **1**, 314 (1962).
17. A. S. Grove, O. Leistiko, and C. T. Sah, *J. Phys. Chem. Solids*, **25**, 985 (1964).

Chemistry and Electrical Properties of the Interface Between ZnSe and an Electrolyte

Richard Williams

RCA Laboratories, Princeton, New Jersey

ABSTRACT

The interface between n-type ZnSe and electrolyte solutions has been investigated. A summary discussion of the properties of a Schottky barrier under these conditions has been given with reference to the experiments which are reported here. For the interface, ZnSe: 1.0M HCl, barrier height is from 2.0 to 2.6 ev for different crystals. These results are obtained from capacitance measurements and compared with photovoltage measurements. Current-voltage curves for forward and reverse bias are shown. For forward bias the current-voltage curve for the hydrogen evolution reaction has been measured. Results emphasize the difficulty of distinguishing between cases where the current is controlled by the properties of the Schottky barrier and those where it is controlled by the electrochemical kinetics. With high electric fields there is electron multiplication in the ZnSe. An efficient photochemical decomposition of the ZnSe is observed in which the net reaction is to deposit free selenium on the surface of the crystal and to liberate Zn^{++} ions into the solution.

The interface between a semiconductor and an electrolyte combines the behavior of electrochemical and semiconductor systems. The special features of such an interface are emphasized when the semiconductor has a high band gap. With high band gap materials electrolyte contacts have provided a unique tool for studying surface properties and obtaining high electric fields in the semiconductor (1-7). In addition, study of the photochemical decomposition of binary compounds in contact with an electrolyte (8) shows an important link between structure, charge transport, and chemical reaction. In this article a summary discussion is given of the semiconductor-electrolyte interface for high band gap materials. Emphasis is on physical concepts rather than detailed theory and equations are given which are applicable to the experimental results of this study. Use is made of the simple diode rectifier theory which has been applied to metal-semiconductor contacts (9). Experimental results are reported which give a survey of the general properties of the interface between ZnSe and an electrolyte.

Semiconductor-Electrolyte Interface

Reviews of the semiconductor-electrolyte interface have been given by Dewald (10), Green (11), and Gerischer (12). In general there is separation of charges at equilibrium and corresponding potential differences develop in both semiconductor and electrolyte. For high band gap materials it is common for a Schottky barrier to form in the semiconductor, within which there is a space charge of ionized donor or acceptor ions. If the band gap is 2 ev or more, minority carriers are present in concentrations too small to be significant through most of this barrier region. The thickness of the barrier region is typically around 1μ. By way of contrast the Helmholtz layer, the corresponding region in the electrolyte in which charge separation and space charge are important, has a thickness of several angstroms. Hence the capacitance of these two regions in series is effectively the capacitance of the Schottky barrier alone. Measurement of the small signal a-c capacitance of the barrier as a function of d-c bias voltage gives information about bending of the bands in the semiconductor at the interface. An ideal Schottky barrier for an n-type semiconductor is one in which the donors are completely ionized and uniformly distributed, and in which the minority carrier concentration is small compared to the donor concentration. For this system the relation (9) between the carrier capacitance, C, the ionized donor concentration, N, the dielectric constant, ϵ, the diffusion voltage, V_d, and the applied voltage, V, is

$$\frac{1}{C^2} = \frac{8\pi(V_d + V)}{\epsilon e N} \qquad [1]$$

This can be put into practical units, using the value (13) of 9.1 for the dielectric constant of ZnSe. Equation [1] becomes

$$\frac{1}{C^2} = 1.9 \times 10^7 (V_d + V)/N \qquad [2]$$

Here C is in pF/cm^2, N in cm^{-3}, V and V_d in volts. The sign convention used is that V has positive values for reverse bias and negative values for forward bias. Measurements of C as a function of V can be plotted to give a straight line. The slope of the line gives N and the intercept with the horizontal axis gives V_d.

An alternative formulation of Eq. [2] has been given (14) which takes account of the reserve region at the inner edge of the barrier where ionization is incomplete. This gives a correction of kT/e or 0.026 ev at room temperature to the voltage sum in [2]. This has not been used in the present work but can easily be used wherever the barrier is low or the accuracy of the measurements warrants. It will be emphasized in what follows that, for the electrolyte-semiconductor system, capacitance measurements can give values for V_d which include a contribution from two electrolyte half-cells in series with the barrier. When this is the case, as it is in this work, the capacitance measurements give a value of V_d which is not a fundamental property of the semiconductor. In this it differs fundamentally from the metal-semiconductor system.

The relation between current and applied voltage may be determined by the transport of electrons to or from the surface or, alternatively, by the electrochemical reaction which is going on. Since charge transport in the semiconductor is entirely electronic and that in the electrolyte is entirely ionic there must be a change in the mechanism of transport at the interface. Whether transport to the interface or the reaction at the interface is slower depends on the details of the reaction and the supply of carriers. It is conceivable that, for a given system, charge transport is dominant at one current density and electrochemical reaction at a different current density. For a Schottky barrier, transport of carriers to the surface is most simply described by the diode rectifier theory. This is oversimplified for many systems but its simplicity commends it for describing the general properties which are the subject of this article. A band picture diagram for a Schottky barrier at the interface between an n-type semiconductor and a high work function metal is shown in Fig. 1. At equilibrium, equal and opposite exchange currents, j_o, flow over the barrier between metal and semiconductor. These are thermionic emission currents due to electrons having energies equal to or greater than the barrier energy, $\Delta\phi$, above the Fermi level. The magnitude of j_o is related (9, 15) to the effective mass, m^*, electron charge, e, absolute temperature, T, Boltzmann constant, k, and Planck's constant, h.

$$j_o = \left(\frac{4\pi m^* ek^2T^2}{h^3} \right) e^{-\Delta\phi/kT} \qquad [3]$$

In practical units, for room temperature, this becomes

$$j_o = 1.0 \times 10^7 \ (m^*/m) \times 10^{-17\Delta\phi} \text{ amp/cm}^2 \qquad [4]$$

$\Delta\phi$ is in ev.

For the current-voltage relation the diode theory gives

$$j = j_o \ (1 - e^{-eV/kt}) \qquad [5]$$

This has been put into a form which is consistent with the convention introduced. Reverse bias voltages are taken as positive. This governs the transport of electrons to and from the surface. For reverse bias when the barrier voltage is more than a few times kT/e (26 mv at room temperature) the current is equal to j_o, independent of voltage. For forward bias voltages greater than several times kT/e, j becomes

$$j = j_o \, e^{-eV/kT} = j_o \times 10^{17 \ {}^{V}f} \text{ amp/cm}^2 \qquad [6]$$

Here the last expression is in practical units for room temperature; ${}^{V}f$ is the absolute magnitude of the forward bias voltage. The minus sign has been dropped for simplicity. It is often found in practice that the exponential relation of Eq. [6] is obeyed but the factor multiplying the voltage is not 17. The equation in this case is commonly written as

$$j = j_o \times 10^{17 \ {}^{V}f/\beta} \qquad [7]$$

β is independent of voltage and is usually between 1 and 2. Typical experimental values are given in ref. (15).

Equations [6] and [7] are valid as long as the current flow across the interface is limited by the transport of carriers up to the interface. In the metal-semiconductor system the density of unoccupied electron states in the metal is comparable to that in the semiconductor at the same energy and does not limit transport of electrons across the interface. Replacing the metal by an aqueous solution may provide a smaller density of states. This would limit transport and may be a factor in the current-voltage curve for forward bias which departs appreciably from Eq. [6].

As long as the electrochemical reaction is using up electrons as fast as they arrive at the surface then Eq. [6] will give the current-voltage relation, subject to a possible restriction by the density of states. This means that the potential across the Helmholtz layer

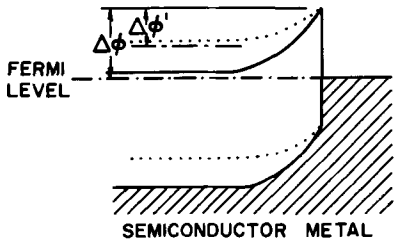

Fig. 1. Energy band diagram for the interface between a metal and an n-type semiconductor with high band gap. Solid lines indicate the energy band edges in the dark with no applied voltage. The dotted lines show the band edges under illumination with a high resistance external circuit.

does not depart significantly from its open circuit value for which there is no current flow. Under these conditions there is no significant departure from equilibrium of the concentrations of any charged species on the surface. If the discharge of such species becomes the rate limiting step then the rate of their arrival at the surface determines the current and the voltage dependence of this rate determines the current-voltage curve.

A specific example of such a process is the transfer of a surface electron, e_s, to an adsorbed hydrogen ion, $H^+(s)$.

$$e_s + H^+(s) \rightarrow H(s)$$

This would give a current-voltage relation determined by the rate of formation of $H^+(s)$. The Tafel equation (16) is appropriate for an electrode reaction under these conditions. In a clearcut case it may be possible to infer from the experimental current-voltage relation whether it is transport of electrons to the surface or reaction at the surface which determines the current. The Tafel equation has the form

$$j = j_o \, e^{e\alpha\eta/kT} = j_o \times 10^{17\alpha\eta} \qquad [8]$$

Here η is the overpotential, *i.e.*, the departure of the potential drop in the electrolyte from the equilibrium potential drop, and α is the fraction of the overpotential which assists the forward reaction. The proper experimental determination of α and η is complicated for a semiconductor system and will not be taken up here. We wish to note here only the similarity between Eq. [7] and [8] and to emphasize the difficulty in assigning unique values to the constants involved from the analysis of experimental current-voltage data.

A useful tool for determining properties of a Schottky barrier is the photovoltaic effect. Consider the band picture diagram of Fig. 1. The metal-semiconductor interface is illuminated with light which is absorbed near the interface, producing hole-electron pairs. The barrier field separates the pairs drawing the holes into the metal and the electrons through the barrier in the opposite direction. If the diode is short circuited there is a current, $j(I)$ which is proportional to the light intensity, I. The number of electrons flowing per unit time is equal to the number of photons absorbed per unit time, providing the quantum yield for creation of hole-electron pairs is unity. If the diode is operating under open circuit conditions the electrons which flow to the left and the holes which flow to the right do not recombine through the external circuit. Instead the separated charges create a field that opposes the barrier field. This is equivalent to applying forward bias from an external voltage supply. As a result there is a current, j, of electrons from left to right. When equilibrium is reached there is no net flow of charge and

$$j = j(I) \qquad [9]$$

Using Eq. [7] we see that this happens when

$$j_o \times 10^{17 \ {}^{V}f/\beta} = j(I) \qquad [10]$$

Since $j(I)$ is directly proportional to I Eq. [10] gives the logarithmic relation between photovoltage and light intensity which is commonly observed. (The observed photovoltage will be ^{V}f). It is not usually possible to use a light intensity high enough to flatten the bands in the semiconductor. It is possible to estimate the total barrier height without flattening the bands from the following argument. Consider the open circuit photovoltage produced by a light of intensity, I, which gives the value, $j(I)$, for the short circuit current. At open-circuit equilibrium the forward bias current of electrons toward the metal must be equal to the current, $j(I)$, of electrons away from the metal. This is just the thermionic emission current over that part of the barrier, $\Delta\phi'$, which still remains at the given level of illumination. This is the j_0 of Eq. [4] for a barrier equal to $\Delta\phi'$. If a photovoltage, V_{ph}, is measured for a light intensity given a short circuit current, $j(I)$, then $\Delta\phi'$ is obtained by equating the right side of Eq. [4] to $j(I)$. The total barrier in the diode at equilibrium in the dark is then $(V_{ph} + \Delta\phi'.)$ Similar considerations hold for the Schottky barrier in a semiconductor in contact with an electrolyte. This method will be used here for estimating the total barrier height, as a check on the barrier height determined from capacitance measurements. This assumes that the photovoltage is a semiconductor property and not an electrochemical property. The chemical properties of the electrode are not irrelevant, however, They may determine whether a given semiconductor undergoes dissolution in the dark or only under illumination. The foregoing is a summary of basic relations for the simplest possible model for the semiconductor electrolyte interface.

Experimental

The crystals of ZnSe used were grown by Fischer and DeMeis in this laboratory, using a vapor growth technique (17). To obtain n-type conductivity they were doped after growth with aluminum under excess zinc pressure at 1030°C, followed by quenching. Before use, the crystals were etched in hot concentrated KOH solution to remove about 0.1 mm of the surface. Ohmic contacts of indium were applied by heating in nitrogen atmosphere to 300°C. The final specimens had dimensions of about 5 x 5 x 1 mm. In one specimen the area in contact with the electrolyte contained a twin boundary. The others were single crystal. Crystals were mounted as shown in Fig. 2. A round hole was drilled in the bottom of a small lucite box and the crystal cemented over this polystyrene cement. The working electrode in the electrolyte was a sheet of platinum with a geometric area of 2 cm² which had been sandblasted to increase its effective surface area. Preliminary experiments with two such platinum electrodes in 1.0M HCl solution showed that there is no significant cathodic polarization up to currents of 10^{-4} amp and no significant anodic polarization up to currents of 10^{-6} amp. For all experiments shown except that in Fig. 7 the working platinum electrode is not polarized and the voltages shown are the externally applied voltages. This gives potentials at the ZnSe electrode relative to the potential in the dark with no externally applied voltage. For the data of Fig. 7 a saturated calomel reference electrode was used to obtain potential differences.

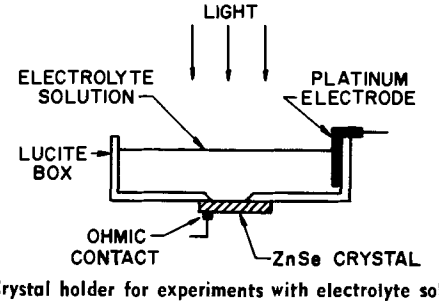

Fig. 2. Crystal holder for experiments with electrolyte solutions.

The potential difference between the ohmic contact on the ZnSe and the calomel reference electrode was measured as a function of current using a Keithley 610B electrometer. The platinum still served as a working electrode. Potentials were plotted relative to that with no externally applied voltage, as was done for the other data.

Measurements of the small signal a-c capacitance were made as a function of d-c bias using a Boonton 74D bridge in which the measuring signal has a frequency of 100 kHz. Photovoltage and current measurements were made with a Keithley electrometer.

General Behavior

The general behavior of the system ZnSe-1.0M HCl is that to be expected for a Schottky barrier in an n-type semiconductor, according to the discussion given above. The following observations are consistent with the energy diagram of Fig. 1. There is a high degree of rectification for current flow in the dark. The polarity for easy current flow is with the ZnSe negative. On illumination a photocurrent and photovoltage are generated for which the direction of electron flow is from the surface of the ZnSe crystal toward the interior.

Figure 3 shows current-voltage curves for forward and reverse bias. Reverse bias is with the ZnSe positive. Under illumination there is a saturation current for reverse bias, independent of voltage but proportional to light intensity. This is due to collection of all hole-electron pairs by the barrier field. Similar reverse saturation currents have been reported by Brattain and Garrett (18) for the germanium electrode in KOH solution, by Beck and Gerischer (19) for germanium in various electrolytes and by the author (8) for CdS in KCl solution. For the ZnSe the reverse bias dark current is very small. At 2v, for example, the dark current is 2×10^{-11} amp/cm². For forward bias the magnitude of the current grows rapidly with increasing voltage.

The spectral response data for the back bias saturation current support the idea that the current is due to the collection of free hole-electron pairs by the barrier field. Figure 4 shows the current per incident photon as a function of photon energy for a back bias of 1v. The current is excited almost exclusively by light of energies greater than 2.6 ev. The band gap (20) of ZnSe is 2.6 ev so the exciting light is restricted to energies sufficient to create hole-electron pairs.

Capacitance Measurements

Figure 5 shows capacitance as a function of d-c bias for four crystals, plotted in the form, $1/C^2$ *vs.* V, suggested by Eq. [2]. The intercept, on the voltage axis, of the extrapolated straight line gives an experimental value of V_d. These vary over a range of more than 1v. Values for N, the ionized donor concentra-

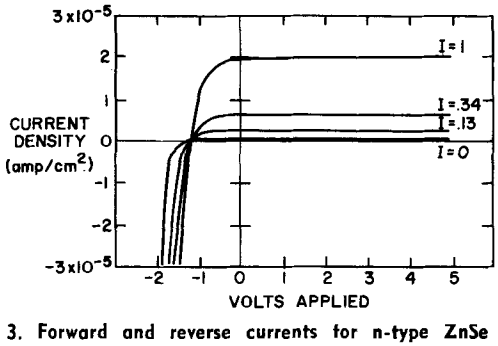

Fig. 3. Forward and reverse currents for n-type ZnSe crystal in 1.0M HCl solution. The relative light intensity is indicated for each curve. As an example of the magnitude of the reverse dark current, the current at 2v in the dark is 2×10^{-11} amp/cm². Positive values of voltage mean that the positive terminal of the external voltage source goes to the ZnSe crystal.

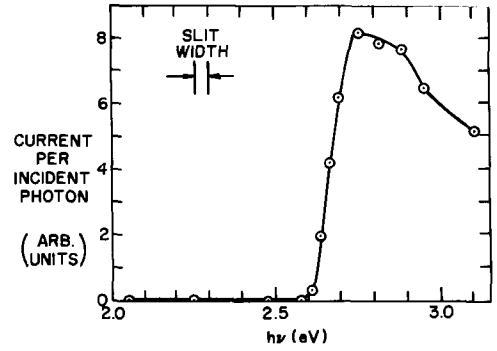

Fig. 4. Spectral response of the saturation photocurrent: 1v reverse bias. The band gap for ZnSe is 2.6 ev.

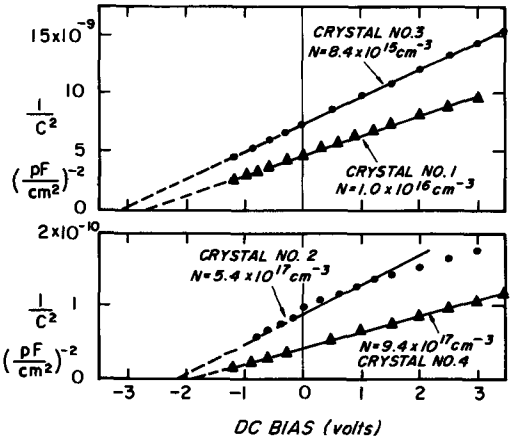

Fig. 5. $1/C^2$ vs. d-c bias voltage for four different crystals. Note that the voltage scale is the same for both parts of the figure.

tions, obtained from the slopes of the lines, are shown for each crystal. V_d decreases monotonically as N increases. For crystals 1 and 3, V_d is larger than the band gap of ZnSe. This never happens at a metal-semiconductor interface but can take place at a semiconductor-electrolyte interface under certain conditions which seem to be fulfilled here. There must be an electrochemical reaction at the semiconductor-electrolyte interface and the dark resistance of the barrier must be very high. The half-cell formed at the semiconductor-electrolyte interface can act together with the half cell at the platinum electrode as a battery in series with the ZnSe crystal. The dark current through the ZnSe barrier at low applied voltages is of order 10^{-11} amp/cm^2 so that a very slow electrode reaction is sufficient to build up a charge on the surface faster than it can leak through the barrier. Since, under these conditions the barrier region is acting as a capacitor, the charge builds up a voltage. This is equivalent to putting a battery in series with a metal-semiconductor Schottky barrier. Thus we may anticipate that, for a semiconductor-electrolyte interface, the band bending under short-circuit conditions may exceed the band gap by as much as 1v or so. An example of an appropriate electrochemical reaction would be the reaction described below for the photochemical dissolution of ZnSe. This might go fast enough, even in the dark, to maintain a significant potential difference across the Schottky barrier. It is emphasized that the amount of reaction required is very small. To maintain a potential difference in this way across a barrier in which the leakage current is 10^{-11} amp/cm^2 requires the dissolution of about one monolayer of the surface per month. To summarize the capacitance results, apparently the barrier height under short circuit conditions depends significantly on both an electrochemical cell of which the crystal forms one half-cell and all the normal

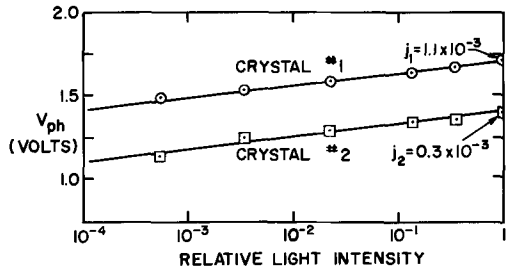

Fig. 6. Open circuit photovoltage as a function of relative light intensity for two crystals with 1.0M HCl solution. Short circuit current is indicated for the highest light intensity in each case. Note that the vertical scale does not begin at zero.

semiconductor interface properties which ordinarily determine the barrier height in nonelectrolyte systems.

Photovoltaic Effect

Analysis of photovoltage and photocurrent measurements confirms that barriers are high but the barrier heights obtained in this way are not as high as those obtained with capacitance measurements. The difference, apparently, is that photovoltage measurements are made under open circuit conditions as opposed to the closed circuit conditions used for capacitance measurements. The battery effect described in the preceding section is not operating here. A battery in series with a Schottky barrier does not establish any potential difference across the barrier if there is an open circuit. For this reason the barrier heights estimated by the photovoltage method do not exceed the band gap of the ZnSe. Figure 6 shows typical photovoltage data for two of the crystals used to obtain Fig. 5. The data give straight lines on a logarithmic plot and the slope in each case is 78 mv/decade. This gives a value of 1.3 for β in Eq. [7]. The short-circuit currents for the highest light intensity were used to estimate the remaining barrier height, $\Delta\phi'$, at this light intensity. This is added to the photovoltage at this light intensity to obtain the total equilibrium barrier height for open-circuit conditions. This is compared with the barrier heights for the capacitance measurements in Table I. The consistently higher values obtained from capacitance data are apparently a result of the battery effect.

Forward I-V Curve and Hydrogen Evolution

Due to the limited number of crystals available the electrochemical data are necessarily of a preliminary nature. The current-voltage relation has been measured over 8 orders of magnitude in current for ZnSe in 1.0M HCl. At the higher current densities, the electrode reaction is clearly hydrogen evolution. The similarity between the Tafel equation, [8], describing electrochemical reaction, and the diode rectifier equation, [7], describing charge transport in a Schottky barrier has been pointed out. The difficulty of determining which of these equations is appropriate may be seen by examining the data of Fig. 7. Here V is the potential of the ohmic contact of the ZnSe relative to its potential when the cell is short circuited

Table I. Crystal measurements and concentration

Crystal No.	$\Delta\phi$ (ev) capacitance measurements*	$\Delta\phi$ (ev) photovoltaic measurements	N (cm^{-3}) ionized donor concentration
3	3.1	2.2	8.4×10^{15}
1	2.7	2.3	1.0×10^{16}
2	2.2	2.0	5.4×10^{17}
4	1.9	2.2	9.4×10^{17}

* This is the energy difference between the conduction band edge in the interior of the crystal and that at the surface. This differs from $\Delta\phi$ defined in Fig. 1 by the difference between the Fermi level and the conduction band edge in the interior of the crystal which is of order 0.1 ev.

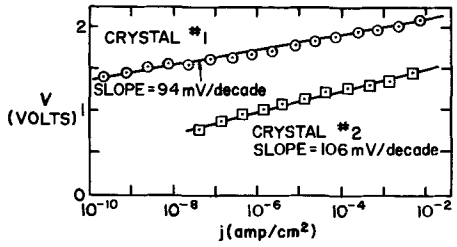

Fig. 7. Dark current for forward bias for ZnSe in 1.0M HCl on a logarithmic plot.

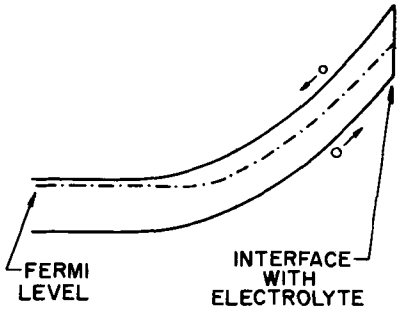

Fig. 8. Band diagram for Schottky barrier and electrolyte contact with high reverse bias. The variation of the Fermi level from the interior of the crystal, which is field free, to the interface is shown. The Fermi level in the barrier region is determined by thermally generated hole-electron pairs.

(*i.e.*, zero applied voltage). The corresponding dark current densities for cathodic bias fall on a straight line on the logarithmic plot. The data fall on two separate lines. These are separated on the voltage axis by 0.6 to 0.7v. This is comparable to the difference in barrier heights in going from one crystal to another. However, the slopes are different from those obtained by the photovoltage technique. This fact suggests that the slopes in Fig. 7 may be determined by electrochemical considerations and that these are Tafel plots. It is also possible that the current is actually limited by transport in the Schottky barrier, though neither case is proven at this point. We stress that in a system of this kind additional evidence other than current-voltage data is probably necessary to analyze the electrochemical reaction.

High Electric Fields and Electron Multiplication

At high reverse bias the region of the semiconductor including the Schottky barrier becomes a layer of insulating material. To the extent that no electrons are injected from the electrolyte (perfect blocking contact) the only carriers in the barrier region are those thermally generated. This means that electrons and holes are present in equal numbers and the Fermi level is in the middle of the forbidden gap.[1] This is illustrated in the band diagrams of Fig. 8. Hence, by application of modest voltages it is possible to obtain very high fields in the barrier region. Quantitatively the field may be obtained from the capacitance as follows. The capacitance, C, in pF/cm^2 is related to d, the thickness of the barrier in centimeters, by the equation

$$C = 1.1\ (\epsilon/4\pi d) \qquad [9]$$

$$Cv = 1.1\left(\frac{\epsilon}{4\pi}\right)\left(\frac{V}{d}\right) \qquad [10]$$

$$v = V + V_d = E_{av}\, d \qquad [11]$$

E_{av} is the average field in the barrier since it is the total voltage drop across the barrier divided by the total thickness. In a Schottky barrier the field is a linear function of distance increasing from zero at the inner face of the barrier to a maximum value, E_{sur}, at the surface next to the electrolyte. $E_{sur} = 2E_{av}$. Hence

$$E_{sur} = 2.5\ Cv \qquad [12]$$

The value of the dielectric constant for ZnSe has been put into Eq. [12].

[1] This idea about the location of the Fermi level was suggested during conversation by A. Rose.

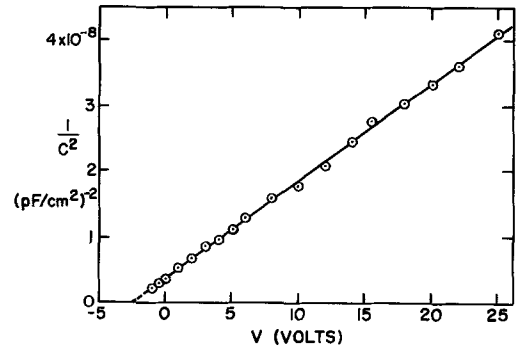

Fig. 9. Capacitance-voltage plot for voltages up to that where there is dielectric breakdown, crystal No. 1.

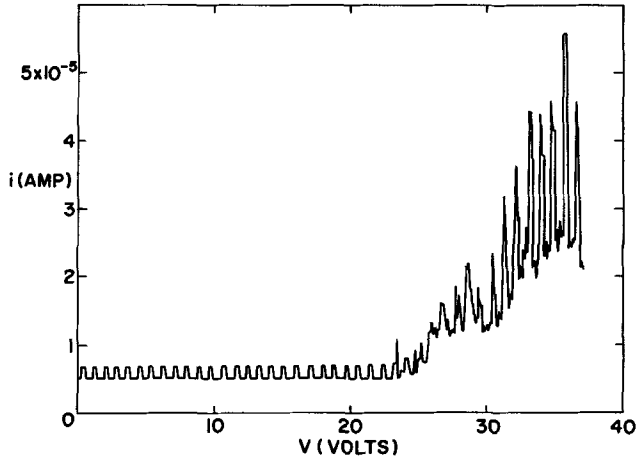

Fig. 10. Recorder tracing showing a long region of saturated photocurrent followed by multiplication of the carriers which are injected by the light. Intermittent light is obtained with a 1 cps chopper. Voltage is increased smoothly with a motor driven Helipot potentiometer. Multiplication of about 15 is seen at the highest voltage. The light was strongly absorbed blue light obtained from a W lamp and Corning 5-58 filter. Note that the current zero is displaced from the horizontal axis so that it may be seen clearly.

A plot of $1/C^2$ *vs.* V up to high reverse bias is shown in Fig. 9 for crystal 1. It is seen that the Schottky relation is maintained over a wide range of voltage. The voltage is indicated where E_{sur} becomes equal to 1 x 10^5 v/cm. At higher fields there is electron multiplication in the barrier due to impact ionization. This is shown by the recorder tracing of Fig. 10. Here a back biased ZnSe crystal is illuminated with strongly absorbed light, made intermittent by interposing a 1 Hz mechanical chopper between light source and crystal. The photocurrent and dark current are displayed alternately on the vertical channel of a pen recorder. At the same time the applied voltage is increased steadily by a motor driven potentiometer and this voltage drives the horizontal channel of the recorder. Thus at low voltages the photocurrent has a constant magnitude, independent of voltage. After a long range of constant photocurrent there is a noisy but steeply increasing photocurrent beyond about 23v. This shows that the carriers injected by the light are being multiplied by impact ionization in the high field of the barrier. From the capacitance data it is inferred that impact ionization begins when E_{sur} reaches 2.5 x 10^5 v/cm. This experiment provides direct support for the mechanism advanced by Fischer (21-23) for electroluminescence in ZnSe. This mech-

anism is based on the creation of hole-electron pairs by impact ionization of free carriers in a high electric field with subsequent recombination through luminescent centers.

It is interesting to note that attempts to observe electron multiplication in CdS by this technique have given negative results and it has been concluded that the ultimate dielectric breakdown in CdS is due Zener tunneling of electrons from valence band to conduction band (24). The band gap and electron mobility for CdS (2.5 ev and 300 cm^2/v-sec) are remarkably similar to those for ZnSe (2.6 ev and 260 cm^2/v-sec). Hence the difference in high field behavior must reflect some more subtle aspect of electron transport.

Photochemical Dissolution of ZnSe

The photochemical dissolution of ZnSe follows an interesting pattern which has been found earlier for CdS. In the cell shown in Fig. 2, short circuited, behavior in light and dark were compared. In the dark, in contact with an inert solution such as 0.1M KCl, ZnSe does not undergo any visible reaction even after standing for days. It does not appear to be attacked even by concentrated HCl at room temperature. In light there is a rapid photochemical reaction. After several minutes of illumination by a tungsten microscope lamp the surface is noticeably changed. After about half an hour of illumination there is a layer of a deep red solid on the surface of the crystal. This solid is readily soluble in CS_2. From this (25) it is concluded that the red material is elemental selenium, probably amorphous. At the same time that selenium is depositing on the surface, zinc ions are going into solution. A ZnSe crystal was mounted in contact with 0.1M KCl acidified with a drop of HCl solution to avoid possible precipitation of Zn^{++}. The solution was allowed to stand in contact with the crystal for 1 hr in the dark. There was no visible decomposition of the crystal. The solution was removed and replaced by another solution. This was allowed to stand for 1 hr in contact with the crystal under illumination. The light intensity was not high enough to raise the temperature of the crystal significantly above room temperature. The photovoltaic current was measured as a function of time. The total charge flowing during 1 hr was 1.5×10^{-2} coulomb. After this time the characteristic deposit of selenium was on the surface of the crystal. The solution was removed and, both this and the above solution analyzed by emission spectroscopy for zinc. In the solution which stood in the dark the zinc content was less than the limit of detectability which was 0.5 μg. In the solution which stood in the light the zinc content was (4.0 ± 1.2) μg. If one zinc ion requires two electrons then 1.5×10^{-2} coulombs should give 4.9 μg zinc in the solution. Thus, within the limits of error of the analysis, the photovoltaic current is accompanied by the dissolution of one zinc ion for every two electrons which flow in the external circuit. Rough estimates of the amount of selenium deposited are consistent with the interpretation that to within an order of magnitude, one selenium is deposited for each two electrons flowing in the external circuit.

This reaction is similar to the photochemical decomposition of CdS under similar circumstances. The mechanism can be understood from Fig. 11. Here the band structure is shown. For ionic crystals such as alkali halides the conduction band can be identified with the positive ions and the valence band with the negative ions (26). This is less true for materials such as ZnSe which are not strongly ionic but appears to retain some validity as a qualitative guide (8). A possible mode of dissolution of such a crystal is the unsymmetric one in which a zinc ion goes into solution as Zn^{++}, leaving a negatively charged $Se^{=}$ attached to the crystal. The resulting separation of charge prevents any appreciable amount of dissolution unless the excess negative charge on the selenium ions can be transported out of the crystal and through the external circuit. For an n-type semiconductor this provides difficulties because the charge is at an energy near that of the valence band and can be transported out of the crystal only through the conduction band, which lies 2.6 ev higher in energy. Thermal excitation is too slow to support significant reaction at room temperature. Optical excitation greatly speeds up reaction by providing hole-electron pairs. The holes come to the surface and neutralize the excess charge on the $Se^{=}$ and the electrons leave through the external circuit. In this way the excess charge is removed and further reaction can take place. According to this mechanism the passage of two electrons through the external circuit should be accompanied by the deposition of one selenium atom on the surface and the passage of one Zn^{++} into the solution in agreement with the observations. This appears to confirm the connection between semiconductivity type and photochemical reaction which has been suggested earlier (8).

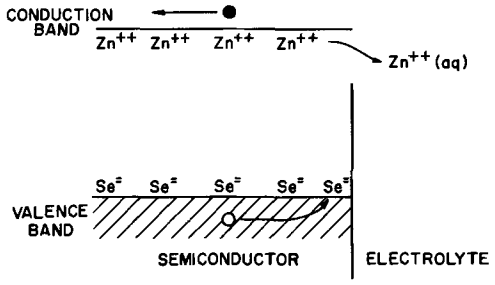

Fig. 11. Illustration of the mechanism suggested to explain the photochemical decomposition of ZnSe in solutions of inert electrolytes such as 0.1M KCl. The conduction band is associated with Zn^{++} ions and the valence band with $Se^{=}$ ions. A Zn goes into solution as Zn^{++} (aq) leaving a negative charge behind on a $Se^{=}$ at the surface. To remove this excess charge from the crystal requires light which produces a hole-electron pair. The hole neutralizes the charge on $Se^{=}$ and the electron goes through the external circuit to complete the electrochemical reaction. For simplicity the Schottky barrier field at the surface has not been indicated in this diagram though it is essential for efficient utilization of hole-electron pairs in this way.

Summary

Several properties of the ZnSe-electrolyte interface have been examined experimentally. Capacitance measurements, which are, of necessity, done under short-circuit conditions, show that the barrier height for these conditions is determined by both the semiconductor properties and by an electrochemical half-cell at the interface. It is possible for the band bending at the interface to be larger than the band gap under short-circuit conditions. Photovoltage measurements, which are ordinarily done under open-circuit conditions, give lower values for the barrier height which are not larger than the band gap. The general features of the current-voltage data for forward and reverse bias can be explained by the diode rectifier model. For the hydrogen evolution reaction there is ambiguity and it cannot be stated with certainty whether the current-voltage relation is determined by electrochemical kinetics or by electron transport to the surface. Multiplication of electrons by impact ionization was observed in high electric fields and provides direct confirmation for the mechanism which has been proposed by Fischer for electroluminescence in ZnSe. There is an efficient photochemical decomposition of ZnSe in contact with an electrolyte. The over-all reaction is

$$ZnSe(s) \xrightarrow{h\nu} Zn^{++}(aq) + Se(s) + 2e$$

Acknowledgment

The author is indebted to A. G. Fischer, W. M. DeMeis, and R. A. Kauffunger for growing and doping the ZnSe crystals and for providing much helpful advice during the course of this work.

Manuscript received May 18, 1967; revised manuscript received July 2, 1967.

Any discussion of this paper will appear in a Discussion Section to be published in the June 1968 JOURNAL.

REFERENCES

1. K. L. Shaklee, F. H. Pollak, and M. Cardona, *Phys. Rev. Letters*, **15**, 883 (1965).
2. A. Many, *J. Phys. Chem. Solids*, **26**, 587 (1965).
3. W. Mehl and W. Büchner, *Z. Physik. Chem. (Frankfurt)*, **47**, 76 (1965).
4. P. Mark and W. Helfrich, *J. Appl. Phys.*, **33**, 205 (1962).
5. R. Williams, *Phys. Rev.*, **117**, 1487 (1960).
6. R. Williams, *ibid.*, **123**, 1645 (1961).
7. R. Williams, *J. Phys. Chem. Solids*, **22**, 129 (1961).
8. R. Williams, *J. Chem. Phys.*, **32**, 1505 (1960).
9. H. K. Henisch, "Rectifying Semiconductor Contacts," pp. 196-203, Oxford University Press, New York (1957).
10. J. F. Dewald in "Semiconductors," pp. 727-752, N. B. Hannay, Editor, Reinhold Publishing Co., New York (1959).
11. M. Green in "Modern Aspects of Electrochemistry," pp. 343-407, J. Bockris, Editor, Academic Press, New York (1959).
12. H. Gerischer in "Advances in Electrochemistry and Electrochemical Engineering," Vol. 1, pp. 139-232, P. Delahay, Editor, Interscience Publishers, New York (1961).
13. D. Berlincourt, H. Jaffe, and L. R. Shiowaza, *Phys. Rev.*, **129**, 1009 (1963); see also M. Aven, D. T. F. Marple, and B. Segall, *J. Appl. Phys.*, Suppl. Vol. **32**, 2261 (1961).
14. J. F. Dewald, *Bell System Tech. J.*, **39**, 615 (1960).
15. A. M. Goodman, *Surface Science*, **1**, 54 (1964).
16. E. C. Potter, "Electrochemistry," p. 128. Cleaver-Hume Press Ltd., London (1956).
17. W. M. DeMeis and A. G. Fischer, *Materials Res. Bull.*, April 1967.
18. W. H. Brattain and C. G. B. Garrett, *Bell System Tech. J.*, **34**, 129 (1955).
19. F. Beck and H. Gerischer, *Z. Elektrochem.*, **63**, 943 (1959).
20. R. H. Bube, "Photoconductivity of Solids," p. 233, John Wiley and Sons, New York (1960).
21. A. G. Fischer, Proc. 7th Intern. Conf. on the Physics of Semiconductors, Dunod, Paris, 1965 p. 259.
22. A. G. Fischer in "Luminescence of Inorganic Solids," p. 580-588, S. Larach, Editor, Academic Press, New York.
23. A. G. Fischer, *This Journal*, **110**, 733 (1963).
24. R. Williams, *Phys. Rev.*, **125**, 850 (1962).
25. W. F. Linke, "Solubilities, K-Z," Vol. 2, pp. 1444-1445, Fourth Ed., American Chemical Soc., Washington, D. C. (1965).
26. N. F. Mott and R. W. Gurney, "Electronic Processes in Ionic Crystals," pp. 69-74, Oxford University Press, New York (1960).

Thermodynamic and Transport Properties of Stoichiometric and Nonstoichiometric Nickel Oxide

S. Pizzini and R. Morlotti

Electrochemistry Group, Euratom C.C.R., Ispra, Italy

ABSTRACT

Electrical conductivity and emf measurements on polycrystalline NiO, as functions of the partial pressure of oxygen, at temperatures ranging between 800° and 1100°C, are used to study some transport and thermodynamic properties of nearly stoichiometric and nonstoichiometric NiO. Due to the localized character of electrons in ionic, hopping-type semiconductors, results are discussed with a chemical approach, in terms of the dependence of the activation enthalpy for the electrical conductivity and of the activity coefficients of Ni^{3+} on the partial pressure of oxygen. A defect model for nonstoichiometric NiO is given, which involves the presence of defect clusters (microdomains) with an inverse spinel structure. Furthermore, electrical conductivity results in nearly stoichiometric NiO are presented and discussed, which show straightforward evidence of the influence of iron doping in the range 100-500 ppm on the "intrinsic" character of the electrical conductivity.

Nickel oxide is a well-known metal-deficit semiconductor. Since the pioneering work of Baumbach and Wagner (1) a great deal of information has been obtained on its defect structure, the type of electrical conductivity (it is well established that the charge transport in NiO, as in other transition metal oxides, is of the thermally activated hopping-type and electron holes are localized at cation lattice sites), and the influence of different dopants on electrical and galvanomagnetic parameters (2-22).

The present investigation deals with results of electrical conductivity and emf measurements on solid galvanic couples of nearly stoichiometric and nonstoichiometric NiO. It is intended primarily as a contribution to the knowledge of the interactions between points and electronic defects within the lattice and their influence on the thermodynamic and transport properties of NiO. In addition we consider the nature of defect clusters and complexes in metal-deficit NiO, as well as the role of specific impurities, which are shown to influence remarkably the activation enthalpy for the electrical conductivity of the nearly-stoichiometric NiO.

Experimental Procedures

NiO *sample preparation.*—The preparation of NiO samples has been carried out according to standard ceramic procedures. Manyfold recrystallized reagent grade pure $Ni(NO_3)_2$ [1] has been used as the starting material. Nickel oxalate was first precipitated from nitrate solutions, decomposed at about 450°C, and finally fired at 700°-1200°C to yield a rather active, green NiO. The oxide was first pressed to pellets 12 mm diameter, 2-4 mm thick at a pressure of about 10 metric tons/cm^2 at room temperature and then sintered in air at 1500°C in a Superkanthal furnace.

[1] (Cl 30 ppm, SO_4 100 ppm, Cu 20 ppm, Fe 50 ppm, Co 100 ppm, Zn 50 ppm).

Table I. Density, impurity content, preparation characteristics, and relevant electrical properties of NiO samples

Sample	% th. density	Ni (met.)	Impurity content, ppm Cr	Fe	Al	Co	Li	Na	K	Firing temp, °C	Sintering temp, °C	Annealing temp, °C	Activation energy E, ev
C_{1A}	86.0	n.d.	—	150*	—	—	—	—	—	1200 (air)	1200	1050	3.62
C_1	—	15%	—	150 ± 50*	—	—	—	—	—	—	1150 (vacuum)	—	3.62
C_2	86.0	n.d.	44 ± 4Δ	504 ± 10Δ	100*	88 ± 0.5Δ	33 ± 2Δ	26 ± 2Δ	15Δ	1200 (air)	1500 (air)	1050	3.62
C_4	86.0	n.d.	50*	100*	100*	—	—	—	—	1200 (air)	1500 (air)	1050	3.36
C_5	86.0	n.d.	50*	100*	100*	—	—	—	—	1200 (air)	1500 (air)	1050	3.36
C_6	86.0	n.d.	50*	504 ± 10Δ 100*	100*	—	33 ± 3Δ	—	—	1200 (air)	1500 (air)	1050	3.36
C_7	97.6	n.d.	50*	100*	500*	—	—	—	—	600°C	1600 (air)	1050	2.55
C_8	91.8	n.d.	44 ± 4	<60Δ	105 ± 3Δ	<1Δ	18.6 ± 1Δ	<3Δ	<38Δ	300°C	1600 (air)	1050	1.62

n.d. Not detected.
* X-ray fluorescence.
Δ Neutron activation analysis.
— Not analyzed for.

In the powders obtained by decomposing and firing in air at temperatures lower than 700°C, nickel metal at concentrations between 10-40% was found which, however, disappears during the sintering process. Nickel metal is also present in pellets sintered in vacuum at temperatures of 1100°-1200°C.

Table I shows the relevant characteristics of different samples which have been prepared and tested for impurity content and density. Density has been measured by means of a mercury pycnometer.

Furnace and cell for electrical conductivity measurements.—The furnace used is of the resistance type and was supplied with rectified current. Figure 1 shows the furnace and the measuring cell. A NiO pellet is pressed between two spectropure Pt-13% Rh electrodes. The electrodes are arranged at the ends of two vertical silica tubes. The tube at the bottom of the cell is externally supported by a clamp, the upper one is held in position by spring pressure. The measuring Pt, Pt-10% Rh thermocouple is placed very near the pellet (0.5 mm) and the temperature is continuously recorded by means of a potentiometric recorder.

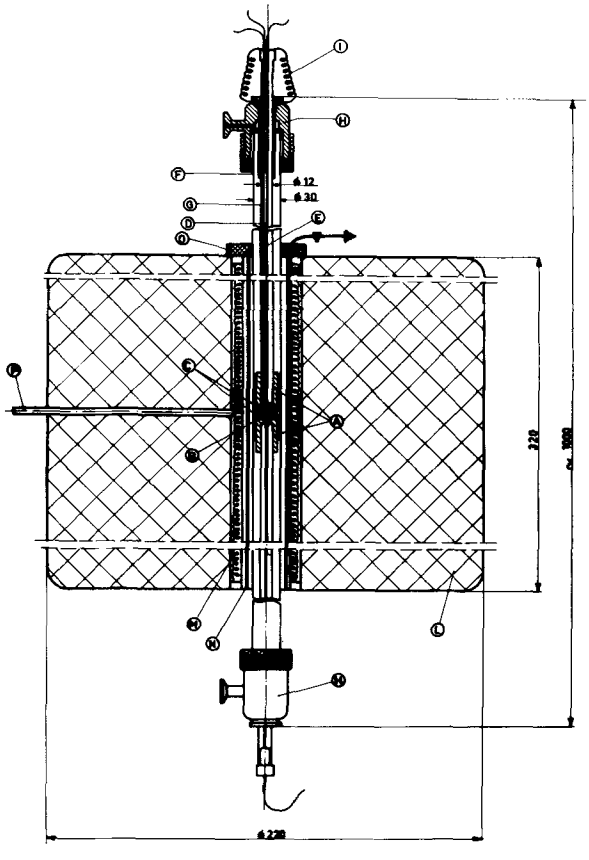

Fig. 1. Assembly of oven and cell for electrical conductivity measurements. A, fused silica holders; B, sample; C,Pt-13% Rh electrodes; D, Pt, Pt-10% Rh thermocouple for temperature measurement; E, leads from the electrode; F, outer silica tube; G, silica pressing tube; H, Inox cover; I, springs; L, furnace; M, resistance heaters; N, platinum tube; O, refractory cover; P, Pt, Pt-10% Rh thermocouple for temperature control.

Oxygen-free nitrogen or nitrogen-oxygen mixtures are allowed to flow through the silica tube at a rate of few cubic centimeters per minute. A slight overpressure is maintained in the cell, and partial pressures of oxygen are varied by varying the oxygen and nitrogen flows, measured with conventional laboratory rotameters. Mass spectrometrically standardized O_2-N_2 mixtures have been used as well. Thermal diffusion effects have been calculated to be negligibly small, and no correction due to these effects has been applied to the measured values of gas composition.

NiO pellets, to be used for electrical conductivity measurements, were coated with a thin Au or Pt layer to avoid contact resistances and to insure that the measurements give results significant for volume conductivity. The Au was evaporated and the Pt was sputtered in a conventional high vacuum evaporation unit. Direct-current resistance measurements have been carried out with the two terminal method. In order to tell whether contributions by Seebeck voltages due to small temperature gradients across the pellet were present, readings were also taken with voltage or current flow reversed.

A platinum tube inside the furnace acts as an electrostatic shield to avoid spurious stray-voltage effects when measurements were made on very high resistance samples. No such contributions were found. Moreover no significant polarization effects have been observed on imposing a total potential drop across the pellet as high as 1.35v over the whole experimental temperature range.

Furnace and cell for emf measurements.—The same type of furnace and shielding has been used for emf measurements as for conductivity measurements.

The cell, which may be represented as

$$Pt/NiO(p'_{O_2})/ZrO_2 + CaO/NiO(p''_{O_2})/Pt$$

consists essentially of a zirconia tube (Zr 23 Degussit), to the bottom of which a pellet of ZrO_2-18% CaO is sealed with a high-temperature ceramic cement, obtained from Melpar Inc. Two oxide electrodes are in contact with the faces of the zirconia pellet, the electrical contact being ensured by means of Pt-30% Rh electrodes. The arrangement is shown in Fig. 2. The oxide electrodes (in the present case two NiO pellets) are kept under different oxygen partial pressures by sweeping gas mixtures of known oxygen content through each compartment by means of Vycor tubes. Temperature is measured by means of Pt, Pt-10% Rh thermocouples, placed very near the Pt electrode. Failures due to imperfect tightness of the ceramic seal are easily monitored by the sudden change in the emf of the cell, which drops to zero, when there is a leak.

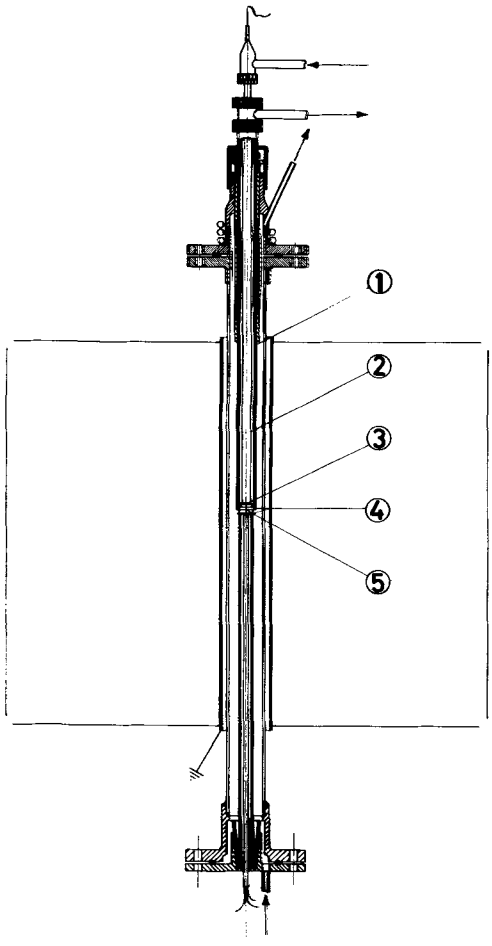

Fig. 2. Assembly of oven and cell for EMF measurements. 1. Zirconia tube; 2, silica electrode holder; 3, NiO pellet; 4, intermediate electrolyte; 5, NiO pellet.

The electrolyte has been previously tested for 100% ionic conductivity by using it for the emf determination of the solid galvanic cell

$$Pt/Fe/w\ddot{u}stite/ZrO_2 + CaO/NiO,Ni/Pt$$

the emf of which is well known from the literature (23). Results of this test are given in Fig. 3, which indicates the correct working of the electrolyte.

Results

Electrical conductivity of NiO *samples in inert gas atmosphere.*—Electrical conductivity measurements have been carried out under inert gas atmospheres

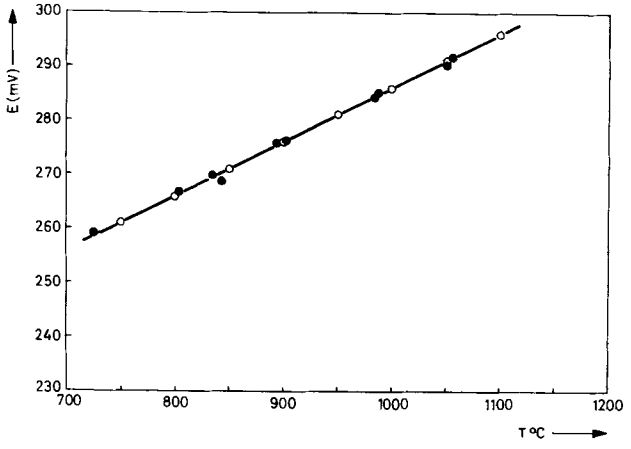

Fig. 3. EMF of the cell Pt Fe/wüstite ZrO_2 + CaO/NiO, Ni/Pt. ● Present results; ○ Kiukkola and Wagner (23).

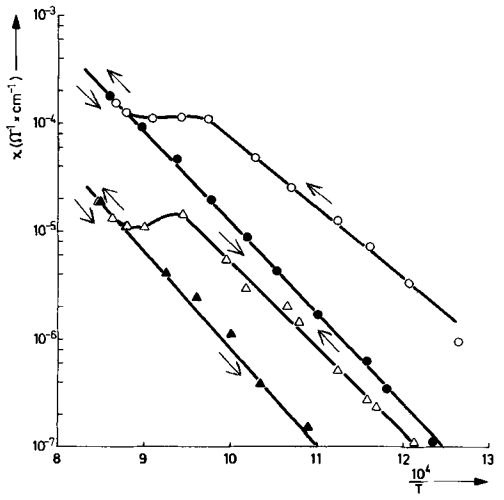

Fig. 4. Results of two typical experiments showing the effect of annealing processes on the electrical conductivity of NiO.

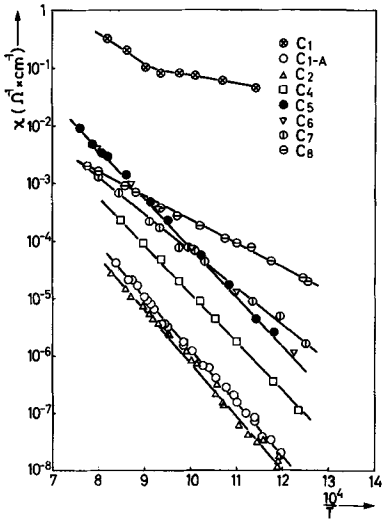

Fig. 5. Electrical conductivity χ of different NiO samples as a function of the temperature (see Table I).

(oxygen-free argon or nitrogen)[2] on samples C_1 to C_8 of Table I (where preparation and analytical data are summarized). The samples were subjected to a high-temperature anneal to remove the excess oxygen dissolved in the samples during the preparation processes.

Figure 4 shows the effect of annealing with stepwise increasing temperatures; the break at about 850°C is taken to indicate the evolution of the excess oxygen. When the annealing is carried out carefully at temperatures higher than 850°C the break is no longer observed during successive cooling and heating cycles.

For each homogeneous sample a linear relationship is obtained by plotting the logarithm of the experimental d-c conductivity χ *vs.* $1/T$ as shown in Fig. 5. Breaks in the curves log χ *vs.* $1/T$ are, however, observed when Ni metal is present as a second phase (see sample C_1).

In Table I the values of the slope of the curves of log χ *vs.* $1/T$ are reported as "activation energy" values, as calculated from the relationship $\chi = \chi^\circ \exp -(E/2\,kT)$. It can be deduced from the table that there is a certain relationship between the activation energy, the firing temperature, and the iron content of the samples.

[2] The residual partial pressure of oxygen is of the order of 10^{-6} atm, as determined by mass spectrometric analysis, and it has been demonstrated that, within the limits of experimental accuracy, variation of p_{O_2} in this range does not affect the experimental results.

Electrical conductivity of NiO in oxygen atmosphere.—Electrical conductivity measurements have been carried out on samples C_6, C_7, and C_8 (see Table I) at partial pressures of oxygen ranging between 10^{-3} and 1 atm. Results are given in Fig. 6, 7, and 8 in log χ *vs.* $1/T$ plots.

In agreement with the results of Mitoff (6), Herbst (15), Thorton (16) and Snowden (17), experiments carried out at temperatures lower than 750°C show that the equilibration time is very long (hours or days) and that breaks appear in the curves log χ *vs.* $1/T$.

Moreover the temperature of the break, which should represent the lowest temperature at which thermodynamic equilibrium is established between the gaseous atmosphere and the crystal, depends on the cooling and heating rate of the sample. In the present experimental temperature range (800°-1050°C) the equilibration times are orders of magnitude lower than those measured at low temperature, and the electrical conductivity is a function of the temperature and partial pressure of oxygen, according to the relationship (5, 6)

$$\chi = \chi^{\circ}\, p_{O_2}^{1/n} \exp -\left(\frac{\Delta H}{RT}\right) \qquad [1]$$

where ΔH is the over-all activation enthalpy.

In Fig. 9, 10, and 11, log χ *vs.* log p_{O_2} plots are presented, from the slopes of which values of n can be derived, assuming the activation energy in the exponential term of Eq. [1] does not depend on the partial pressure of oxygen. At partial pressures of oxygen $<10^{-1}$ atm a value of n close to 6 is obtained ($5.7 \leq n \leq 6.4$).

In Fig. 12, 13, and 14, where the present experimental results are plotted in terms of resistivity, ρ *vs.* $p_{O_2}^{1/6}$, it is apparent that, within the limits of the experimental accuracy, Eq. [1] is satisfied for an n value of 6 up to partial pressures of oxygen of about 10^{-1} atm, where a remarkable deviation from linearity is observed.

EMF measurements.—Emf measurements have been carried out on low-density NiO samples for ensuring better and faster equilibration with the external atmosphere. As reference pressure a partial pressure of oxygen not lower than 10^{-3} atm has been chosen to avoid complications due to iron contamination which, as will be shown in the following discussion, has a noteworthy influence on the Ni^{3+} concentration at very low partial pressures of oxygen.

Five isotherms are shown in Fig. 15. The electrochemical "n" value, as determined from the slope of

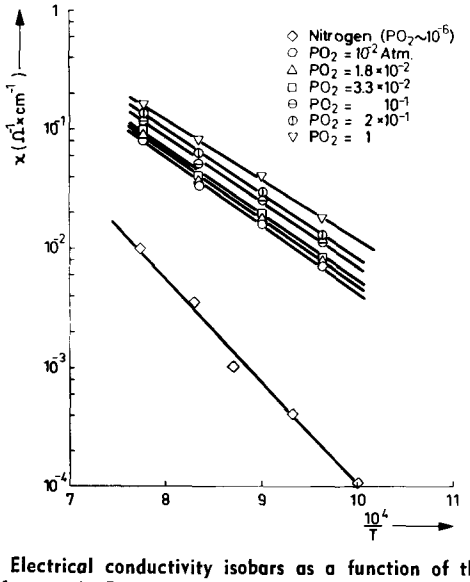

Fig. 6. Electrical conductivity isobars as a function of the temperature for sample C_6.

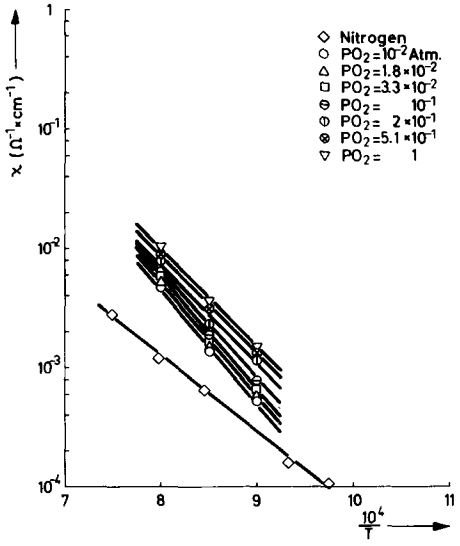

Fig. 7. Electrical conductivity isobars as a function of the temperature for sample C_7.

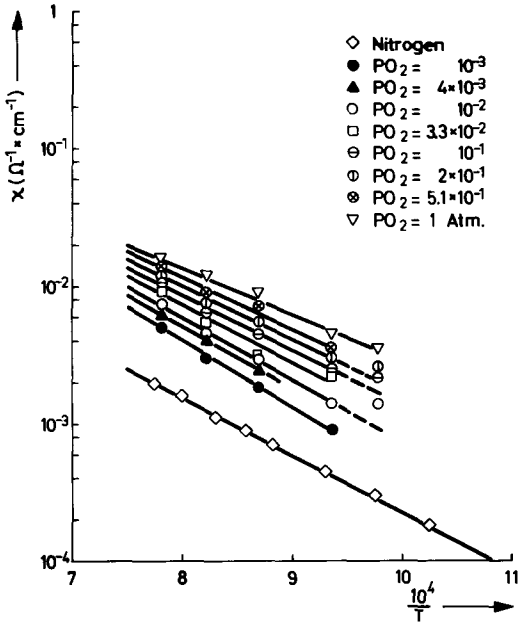

Fig. 8. Electrical conductivity isobars as a function of the temperature for sample C_8.

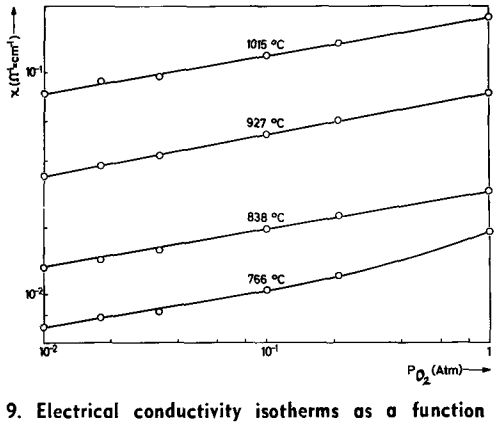

Fig. 9. Electrical conductivity isotherms as a function of the partial pressure of oxygen for sample C_6.

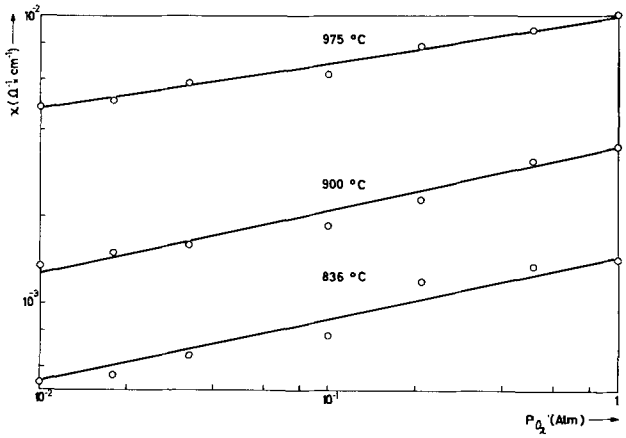

Fig. 10. Electrical conductivity isotherms as a function of the partial pressure of oxygen for the sample C_7.

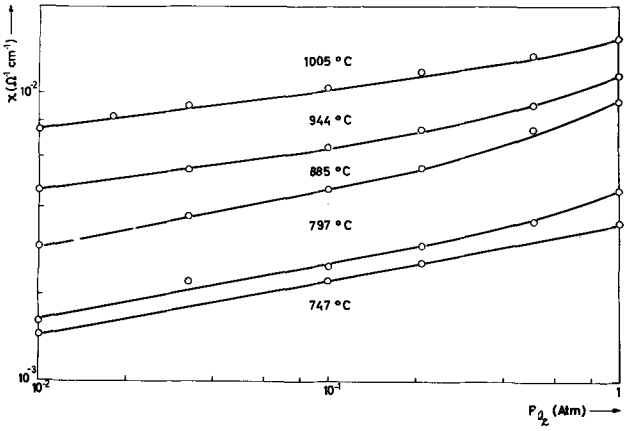

Fig. 11. Electrical conductivity isotherms as a function of the partial pressure of oxygen for the sample C_8.

the linear part of the E *vs.* log p'_{O_2}/p''_{O_2} plots according to the relationship

$$E = \frac{RT}{n\mathbf{F}} \ln \left(\frac{p'_{O_2}}{p''_{O_2}} \right) \qquad [2]$$

is shown in Fig. 16. It can be seen that n depends strongly on temperature, shifting continuously from 2 to 6 as temperature increases.

Since in the case of an oxygen cell we should observe slopes which equal $RT/4\mathbf{F}$, the emf of the cell

$$\mathrm{Pt} \mid \mathrm{Ni}_{1-x}\mathrm{O}(p'_{O_2}) \mid \mathrm{ZrO_2} + \mathrm{CaO} \mid \mathrm{Ni}_{1-y}\mathrm{O}(p''_{O_2}) \mid \mathrm{Pt} \qquad [3]$$

reflects, under equilibrium conditions, the changes in activity of electron-holes localized at cationic sites (*i.e.*, the activity of Ni^{3+}) as a function of the oxygen pressure.

In fact, NiO is a metal-deficient p-type semiconductor for which the electron-hole concentration is dependent on the partial pressure of oxygen (see below) according to the relationship[3]

$$\tfrac{1}{2}\,O_2 \rightleftarrows O_O + 2h^{\bullet} + V''_{Ni} \qquad [4]$$

By assuming the activity of oxygen ion in the anionic sublattice is constant and independent of the partial pressure of oxygen (it is generally recognized that ionic defects occur almost exclusively in the cationic sublattice), the electrode reaction at the metal (I) NiO(II) phase boundary is

$$_{II}Ni^{3+} + {}_{I}e \rightleftarrows {}_{II}Ni^{2+} \qquad [5]$$

[3] The Kröger and Vink symbols will be used throughout in this paper.

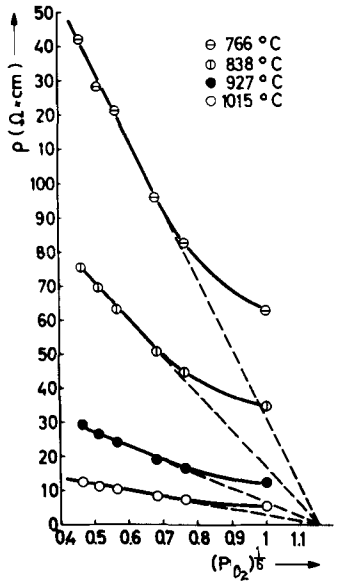

Fig. 12. Electrical resistivity isotherms for the sample C_6 as a function of the sixth root of the partial pressure of oxygen.

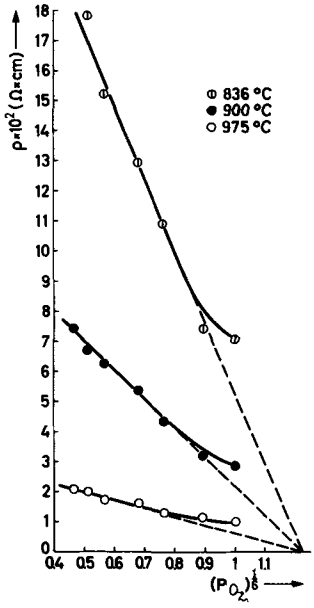

Fig. 13. Electrical resistivity isotherms for the sample C_7 as a function of the sixth root of the partial pressure of oxygen.

and that at the oxide (II)-zirconia (III) phase is

$$_{II}O^{2-} \rightleftarrows {}_{III}O^{2-} \qquad [6]$$

where CaO-doped ZrO_2 works, as is well known, as a purely anionic membrane ($t_{O^{2-}} = 1$).

From the condition of electrochemical equilibrium between phases of different composition we obtain

$$_{I}\tilde{\mu}_e = {}_{II}\tilde{\mu}_h \qquad [7]$$

$$_{I}\phi - {}_{II}\phi = \frac{1}{\mathbf{F}} ({}_{I}\mu_e + {}_{II}\mu_h) \qquad [8]$$

and

$$_{II}\tilde{\mu}_{O^{2-}} = {}_{III}\tilde{\mu}_{O^{2-}} \qquad [9]$$

$$_{II}\phi - {}_{III}\phi = g_{II,III} = \frac{1}{\mathbf{F}} ({}_{III}\mu_{O^{2-}} - {}_{II}\mu_{O^{2-}}) \qquad [10]$$

where $\tilde{\mu}_i$ is the electrochemical potential of the i^{th}

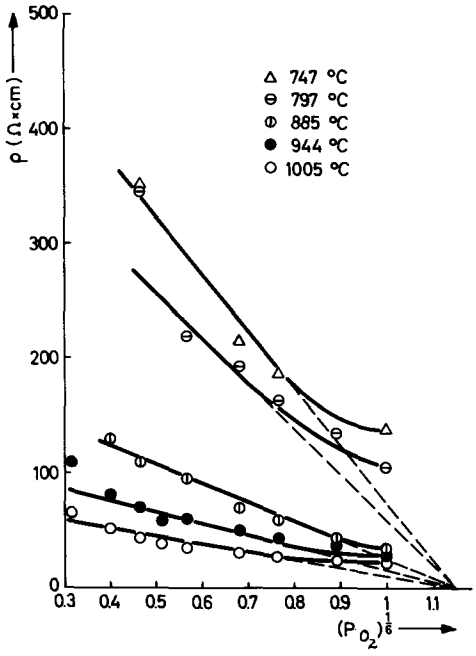

Fig. 14. Electrical resistivity isotherms for the sample C_8 as a function of the sixth root of the partial pressure of oxygen.

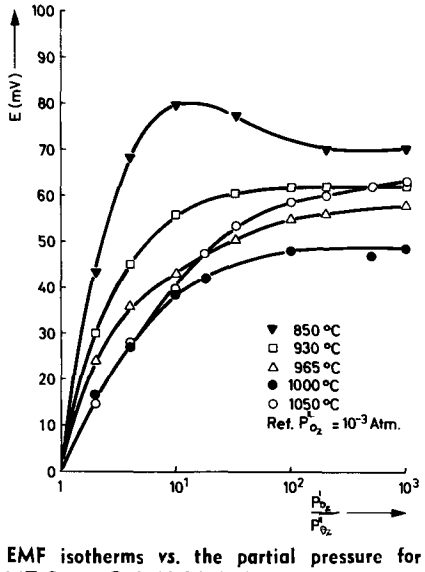

Fig. 15. EMF isotherms vs. the partial pressure for the cell: $Pt/NiO(p'_{O_2})/ZrO_2 + CaO/NiO(p''_{O_2})/Pt$.

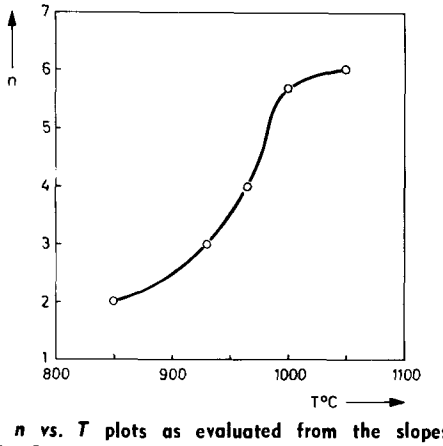

Fig. 16. n vs. T plots as evaluated from the slopes of the curves of Fig. 15 at very low partial pressures of oxygen.

species in the α phase and is defined as

$$\tilde{\alpha\mu_i} \equiv \alpha\mu_i + \mathbf{F}\phi \qquad [11]$$

$\alpha\mu_i$ is the chemical potential of the i^{th} species in the α phase, ϕ is the internal potential of the phases and g is the Galvani potential difference.

Moreover, since the chemical potential of O^{2-} in the NiO phase is independent of the oxygen partial pressure, we can write

$$g_{II,\,III} - g_{III,\,II} = 0 \qquad [12]$$

and the emf of the cell [3] may be written

$$E = {}_I\phi' - {}_I\phi'' = \frac{1}{\mathbf{F}}({}_I\mu''_e - {}_I\mu'_e = \frac{1}{\mathbf{F}}({}_{II}\mu'_h - {}_{II}\mu''_h) \qquad [13]$$

where the symbols (') and (") refer to the left-hand and right-hand compartments of cell [3]. Equation [13] reduces to the explicit equation

$$E = \frac{RT}{\mathbf{F}} \ln \frac{a'_{Ni3+}}{a''_{Ni3+}} \qquad [14]$$

when the emf of the cell is expressed in function of Ni^{3+}.

Discussion

Electric conductivity of NiO *in inert gas atmosphere.*—In spite of the fact that a great deal of experimental and theoretical information is available on charge transfer processes in both stoichiometric and nonstoichiometric NiO, it seems questionable if one could succeed in measuring the properties of pure and stoichiometric NiO. We shall indeed restrict our discussion to the influence of the environmental conditions and the impurity content of NiO on the activation energy for the conductivity, which is generally assumed to represent a bulk property of a material, even when measured in polycrystalline samples. In the present case it is well to emphasize that the excellent agreement of our results with those obtained by different authors on single crystals indicates a negligible effect of surface conductivity on the measured activation energy.

The accurate determination of the impurity content of sample C_2 (which is representative of samples from C_1 to C_6) and of sample C_8 has been carried out by means of neutron activation analysis and is reported in Table I. It is apparent that the alkali metal content is very low and comparable in both series and that the samples differ mainly in the iron content. The chromium and aluminum contents remain low and constant in all the samples, apart from the case of sample C_7.

Insofar as the nickel metal content is considered, sample C_1, the only one which has a rather high nickel metal content, exhibits an anomalous behavior. Moreover, electron microprobe experiments on samples where x-ray powder diffraction measurements did not reveal the presence of nickel metal seem to indicate no apparent segregation of minute amounts of nickel metal at the grain boundaries. However, these experiments are not conclusive, as the resolution power of the electron microprobe used is relatively low (about 2μ).

The experimental activation energies, as calculated from the slopes of the log χ *vs.* $1/T$ diagrams (see Fig. 5 and Table I) indicate that samples from C_1 to C_6 exhibit very large values of activation energy, as compared with those of ref. (3-5, 17), whereas the values for samples C_7 and C_8 are in satisfactory agreement.

According to Van Houten (8) Mitoff (6), and Morin (4b) an activation energy of about 2 ev (from a slope $E/2k$) as we observe in samples C_7 and C_8, is to be accounted for by an extrinsic conduction process, which is associated with the change of carrier concentration due to the excess oxygen dissolution.

According to the results of the investigations of Newman and Chrenko (24) and, more recently, of Ksendzov and Drabkin (25) on epitaxially grown NiO single crystals, the optical absorption spectrum and the dependence of the photocurrent on the incident radiation energy, indicate that the wide absorption band observed at 4 ev (24) is associated with a photoionization process and that the energy gap calculated from the slope $E/2k$ [for the relationship between thermal and optical activation energies, see ref. (26)] of a log χ *vs.* $1/T$ plot agrees well with the red edge value of the photocurrent, which lies at 3.7 ev. This indicates that we are dealing with intrinsic behavior.

Results of experiments on samples C_{1A}, C_2, C_4, C_5, and C_6 indicate that the values of the activation energy obtained from electrical conductivity measurements in inert gas with an oxygen partial pressure less than 10^{-5} atm, agree within a few 0.1 ev with those of Ksendzov and Drabkin, as is shown in Table I. We might assume as did Ksendzov and Drabkin that samples from C_1 to C_6 exhibit intrinsic behavior. Our results indicate, however, that by greatly improving the purity of the samples (Fe $\leq$ 100 ppm) the activation energy drops to values which are well accounted for by an extrinsic conduction process (see Eq. [18] and [19]).

We would like to stress, however, that at constant temperature and partial pressure of oxygen (*i.e.*, at a certain fixed electron-hole and vacancy concentrations) the equilibrium involving a redox impurity such as iron

$$Fe^{2+} + Ni^{3+} \rightleftarrows Fe^{3+} + Ni^{2+} \qquad [15]$$

is strongly shifted to the right [from the difference in the third ionization potentials of Ni and Fe, which equals 5.5 ev (27)]. The resulting situation can be described according to the following equations

$$\mu^\circ_{Fe^{2+},Fe^{3+}} + RT \ln \frac{a_{Fe^{3+}}}{a_{Fe^{2+}}} = \mu^\circ_{Ni^{2+},Ni^{3+}} + RT \ln \frac{a_{Ni^{3+}}}{a_{Ni^{2+}}} \qquad [16]$$

and

$$\mu^\circ_{Ni^{2+},Ni^{3+}} >> \mu^\circ_{Fe^{2+},Fe^{3+}} \qquad [17]$$

(where μ° redox are the standard chemical potentials for the redox couples Fe^{3+}/Fe^{2+} and Ni^{3+}/Ni^{2+}, which are identical with the electronic energy levels generally used in discussing the properties of semiconductors).

If holes at localized iron extra levels are to be considered as trapped holes, then at a particular temperature, oxygen partial pressure, and iron concentration, the concentrations of holes and electrons provided by intrinsic ionization predominate, and we have

$$n \simeq p$$

Moreover, if the difference between the value of the μ's (μ° Fe^{2+}, Fe^{3+} — μ° Ni^{2+}, Ni^{3+}) is greatly in excess of the difference in the chemical potentials of oxygen obtained by varying the oxygen pressure over few orders of magnitude, it is apparent that the value of the ratio $(a_{Ni^{3+}})/(a_{Ni^{2+}})$ is practically unaffected by the partial pressure of oxygen, as long as the concentration of the excess holes introduced by oxygen dissolution is lower than, or, in the limiting case, equal to the iron content.

It has been tacitly assumed that conditions of complete equilibrium with the gas phase exist, but it is apparent that Eq. [15] and [16] hold even when only internal electronic equilibrium exists between the iron impurities and defects frozen in the lattice.

In strong support of this suggestion, we quote the results of Richards *et al.* (27) who demonstrated that the high diffusivity of iron in NiO (which is appreciably greater than that of Ni) could be accounted for, by realizing that, while the total concentration of vacancies and holes is fixed at constant temperature and p_{O_2}, the specific concentration of Fe^{3+} (bound holes) would always be higher than that of Ni^{3+} (quasi-free holes) because of its lower ionization potential.

As to the influence of monovalent impurities, it is apparent that, at sufficiently high temperatures, doping in the ppm range is of little significance. Recent investigations (13-29) demonstrated the restricting role of steric parameters on the solubility of several monovalent oxides in NiO, such as K_2O and Na_2O, which seem to be almost insoluble.

Electrical conductivity measurements in oxygen atmosphere.—The plots of Fig. 9, 10 and 11, which show the log χ *vs.* p_{O_2} relationships and those of Fig. 12, 13, and 14 which show the ρ *vs.* $p_{O_2}^{1/6}$ relationships, indicate that, at least at pressures lower than 10^{-1} atm, the value of n equals 6 over the whole experimental temperature range.

This value of n reflects, in good agreement with the results of Mitoff (6), Petitt (7), and Herbst (15), the presence of doubly ionized cation vacancies at a concentration largely in excess over that of singly ionized ones. Each atom of oxygen in stoichiometric excess introduces a cation vacancy and two electron holes, according to the following equations

$$\tfrac{1}{2}\, O_2 \rightleftarrows O_o + 2h^\bullet + V''_{Ni} \qquad [18]$$

or

$$\tfrac{1}{2}\, O_2 + 2Ni_{Ni} \rightleftarrows O_o + 2Ni^\bullet_{Ni} + V''_{Ni} \qquad [19]$$

where electron holes in their state of lower energy are localized at lattice sites (*i.e.*, corresponding to Ni^{3+} at octahedral sites); the cation vacancies bear a $-2e$ charge.

$$K_1 = \frac{a^2_{Ni^\bullet_{Ni}}\, a_{V''_{Ni}}}{P_{O_2}^{1/2}}$$

is the equilibrium constant of Eq. [19] and

$$a_{Ni^\bullet_{Ni}} = a_{h^\bullet} = K_1^{1/3} p_{O_2}^{1/6} \qquad [20]$$

The electron hole concentration is of course fully determined by the electroneutrality requirements within the crystal.

Trivalent nickel ions may be localized at interstitial positions as well, just as in the case of trivalent iron in ferrous oxide, according to Roth's paper (30) on neutron diffraction of $Fe_{0.87}O$. When this is the case, we should express the equilibrium between Ni^{3+} at octahedrally and tetrahedrally coordinated sites by the following equations

$$V''_{Ni} + Ni^\bullet_{Ni} + V_i^* \rightleftarrows (V_{Ni}\, Ni_i\, V_{Ni})' \qquad [21]$$

and

$$\tfrac{1}{2}O_2 + 2Ni_{Ni} + V_i^* \rightleftarrows Ni^\bullet_{Ni} + (V_{Ni}\, Ni_i\, V_{Ni})' + O_o \qquad [21']$$

and we remark, according to Anderson (31) that the defect complex $(V_{Ni}\, Ni_i\, V_{Ni})'$ and its immediate environment (which includes one Ni^{3+} in octahedral position) behaves like a microdomain of inverse-spinel structure, with 0.5 of the total Ni^{3+} at octahedral positions and 0.5 at tetrahedral sites. We assume on steric grounds that positive holes are trapped at tetrahedrally coordinated sites (31). It appears that the microdomain behaves as a neutral species and that its activity a^* depends on the partial pressure of oxygen as

$$a^* = K_2\, p_{O_2}^{1/2} \equiv a_{Ni^\bullet_{Ni}} \equiv a_{h^\bullet} \qquad [22]$$

where K_2 is the equilibrium constant of reaction [21']

By considering that only holes at octahedral positions behave as free current carriers, we obtain

$$\chi = \overline{K_2}\, p_{O_2}^{1/2} \qquad [22']$$

It is well to emphasize that we assume here that the defect complex $(V_{Ni}\, Ni_i\, V_{Ni})'$ of Eq. [21] can never trap a second hole according to the equation

$$(V_{Ni}\, Ni_i\, V_{Ni})' + h^\bullet \rightleftarrows (V_{Ni}\, Ni_i\, V_{Ni})^* \qquad [23]$$

inasmuch as this process of trapping requires the stability of singly ionized vacancies, whereas, in the temperature range here considered, doubly ionized vacancies are shown to be largely in excess of the singly ionized ones.

Deviations of conductivity isotherms from the theoretical plot should indeed indicate that the reaction [21] participates or is predominant in determining the concentration of the free-current carriers. The isotherms of Fig. 12, 13, and 14 suggest a significant contribution of reaction [21] only at high partial pressures of oxygen and at temperatures lower than about 1200°K. At higher temperatures, deviations from the theoretical plot (indicated by a dotted line) are negligibly small at the higher partial oxygen pressures too.

The plots of Fig. 6, 7, and 8 have been used for the evaluation of the activation enthalpy for the conductivity and its dependence on the partial pressure of oxygen. In order to discuss the experimental results, we will use the equation

$$\chi = (C/T)x \exp - (\Delta G/RT) \qquad [24]$$

where (C/T) is nearly a constant, x is the concentration of current carriers, ΔG is the free energy of activation, and the other symbols have their usual significance. This is the same equation Heikes and Johnson (5) used for discussing the electrical conductivity in transition metal oxides. If, now the concentration x which enters Eq. [24] is expressed as a function of the partial pressure of oxygen, according to Mitoff (6), we obtain, by assuming [19] to be the predominant contribution

$$\chi = (\overline{C}/T)\ p_{O_2}{}^{1/6} \exp - \left(\frac{\Delta H^{\neq}}{RT} + \frac{\Delta H_f}{3RT} \right) \qquad [25]$$

In this equation the ΔG terms are split in their enthalpy and entropy contribution and ΔS terms are included in the preexponential $(\overline{C}/T)$. ΔH_f is the enthalpy of formation for the reaction of Eq. [19] and $\Delta H^{\neq}$ is the activation enthalpy for the mobility.

The calculation of the enthalpy of formation has been accomplished according to Mitoff by assuming that the activation enthalpy $\Delta H^{\neq}$ is constant and independent of the partial pressure of oxygen, *i.e.*, independent of the composition. The results are given in Table II. It is apparent that the over-all activation enthalpy and therefore the enthalpy of formation is a function of the partial pressure of oxygen, as also results from the data of Takeuchy and Igaky (22) and as has been recently demonstrated for CoO as well (32).

By assuming for $\Delta H^{\neq}$ a value of 5500 cal/mole as used by Mitoff (6) or of 6900 cal/mole as used by Herbst (15) the values of the enthalpy of formation of defects have been calculated and are reported also in Table II. It results that the ΔH_f values for sample C_6 are very near to the Mitoff values (measured at 1 atm O_2) whereas those for sample C_8 are in very good agreement with the Herbst results. (Results for sample C_7 are not reported, as it is apparent that spurious contributions due to the high aluminum content lead to anomalously high ΔH_f values. Results for sample C_6 should be treated carefully, as the iron content of the sample could be of significant importance). Mitoff reports that the sample used was of reagent grade purity, *i.e.*, about 1000 ppm total impurities, and quotes the lithium content as below the limits of detection. Herbst's data for impurity content closely approach those of our sample C_8.

It appears however, that the above mentioned arguments give only a fictitious solution of the problem. If we assume that $\Delta H^{\neq}$ remains constant (and independent of the concentration of current carriers) and if we used a value of $n=6$, the ΔH_f values are unambiguously determined. Nevertheless, we cannot suppose that the activation enthalpy for the mobility $\Delta H^{\neq}$ remains constant unless the carrier concentration changes negligibly with the partial pressure of oxygen. As the dependence of the activation enthalpy for the mobility on the carrier concentration is known from the literature for Li-doped NiO, the results from such experiments may be compared with the results on samples C_6 and C_8, and those of Takeuchy and Igaky (22), if the Li_2O concentration scale is arbitrarily related to the p_{O_2} scale. We observe that at pressures between 10^{-2} and 10^{-1} atm. the slope changes, namely, if b_1 is the slope at high pressures and b_2 is the slope at low pressures:

$$b_2 = 1/3\ b_1$$

In order to account for this change of slope, we recall the dependence of carrier concentration on the partial pressure of oxygen for Ni^{3+} in lattice positions alone and for holes distributed over both lattice and interstitial positions (see Eq. [19] and [21'])

$$x_{h^{\bullet}} = K_1{}^{1/3}\, p_{O_2}{}^{1/6} \qquad [20]$$

$$\frac{\partial \Delta H}{\partial \ln x} = 6 \frac{\partial \Delta H}{\partial \ln p_{O_2}} \qquad [26]$$

$$x_{h^{\bullet}} = K_2\, p_{O_2}{}^{1/2} \qquad [22]$$

$$\frac{\partial \Delta H}{\partial \ln x} = 2 \frac{\partial \Delta H}{\partial \ln p_{O_2}} \qquad [27]$$

when electron holes are distributed across lattice and interstitial nickel sites and, as before, holes at tetrahedral nickel positions behave as bound-holes.

It appears that the change of slope observed in Fig. 17 only reflects the transition from Eq. [19] to Eq.

Table II. Experimental ΔH values and calculated ΔH_f values for the reaction of Eq. [19]; n is taken to be equal to 6

Sample	ΔH°,*** kcal/mole	$\Delta H = \left(\Delta H^{\neq} + \frac{\Delta H_f}{n/2} \right)$, kcal/mole							
		10^{-3}	4×10^{-3}	10^{-2}	3.3×10^{-2}	10^{-1}	2.0×10^{-1}	5.1×10	1 atm
C_6	38.91	—	—	25.98	25.53	24.91	24.42	—	23.08
C_7	29.41	—	—	43.76	43.33	41.54	37.36	37.45	38.96
C_8	18.7	23.22	22.59	22.24	20.21	17.63	18.48	16.62	14.80
Sample	$\Delta H^{\neq}$, kcal/mole	ΔH_f, kcal/mole							
C_6	6.9*	—	—	57.27	55.26	54.09	51.11	—	48.48
C_7	5.5**	—	—	61.47	59.46	58.29	55.31	—	52.68
	—	—	—	—	—	—	—	—	—
C_8	6.9	48.96	47.07	46.05	39.94	32.19	34.73	29.17	23.70
	5.5	53.16	51.28	50.23	44.14	36.39	38.94	33.37	27.90

* Herbst's value ΔH_f (1 atm O_2) = 31.2,
** Mitoff's value ΔH_f (1 atm O_2) = 53.40.
*** As obtained from the expression $\chi = \chi_0 \exp - (\Delta H/RT)$ from measurements in inert gas (see Table I).

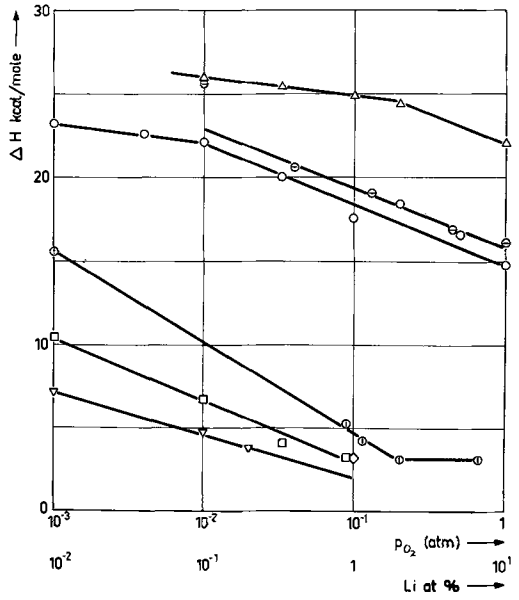

Fig. 17. Activation energy (over-all) *vs.* the partial pressure of oxygen or the Li concentration for metal-deficient and Li-doped NiO: △ authors' results exp. C_6; ○ authors' results exp. C_8; ⊖ Takeuchi and Igaki (22); ◇ Thistlethwaite, *et al.* (34); ▽ Van Houten and Bosman (33); □ Heikes and Johnson (5); ⓘ Koide (21).

[21'] due to the different dependence of the free carrier concentration on the partial pressure of oxygen. Unfortunately, as is shown in the same figure, it seems to be rather difficult to correlate the Li_2O concentration dependence of the ΔH of lithium doped NiO with our results, as the slopes obtained from the literature values are not very consistent. Moreover, as Van Houten and Bosman (33) observed, it is not certain that the activation energy for the jumping of a hole around a lithium ion is the same as for the hopping of a free hole through the NiO lattice, although the difference is not expected to be very large. Nevertheless, Koyde's data (21) express a slope b which is approximately twice the slopes observed by us (or deduced from the Takeuchy data) at high partial pressures of oxygen.

It results that the experimental dependence of the over-all activation enthalpy on the partial pressure of oxygen roughly corresponds to the dependence of the activation enthalpy for the mobility of the current carriers on the concentration of the free carriers over the whole concentration range considered.

EMF measurements.—Due to the composite character of the electrical conductivity as a function both of the concentration and of the mobility of the current carriers, only indirect evidence has been drawn from the dependence of the electrical conductivity or of its activation energy on the partial pressure of oxygen about the occurrence of defect association reactions in nonstoichiometric NiO.

In the absence of direct structural information, emf measurements, which allow the measurement of the activity of Ni^{3+} introduced by excess oxygen dissolution in the NiO lattice, should be used to test the validity of the defect model proposed with Eq. [21] and [21'], involving interstitial nickel at the higher oxygen partial pressures.

We will choose as an ideal solution model that solution where Ni^{3+} behaves as a free, independent ion [*i.e.*, the partial molar enthalpy of mixing or, according to Guggenheim (35) the interchange energy w, equals zero] and in which the concentration (= activity) of Ni^{3+} depends on the partial pressure of oxygen according to the formal equilibrium constant

$$K_1 = \frac{a_{Ni^{3+}}\, a_{V''_{Ni}}}{p_{O_2}{}^{1/2}}$$

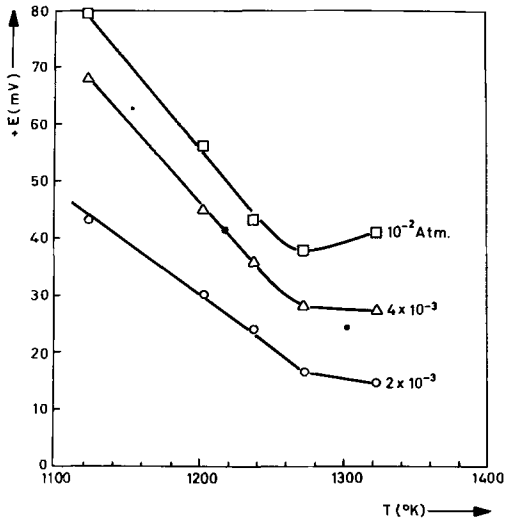

Fig. 18. EMF isobars as a function of the temperature for the cell: $Pt/NiO(p'_{O_2})/ZrO_2 + CaO/NiO(p''_{O_2})/Pt$ at low oxygen pressures.

and

$$a_{Ni^{3+}} = K_1{}^{1/3}\, p_{O_2}{}^{1/6} \qquad [20]$$

Since it would be unnecessarily restrictive, we will not consider here the condition of undistinguishability of Ni^{3+} and Ni^{2+} (35) that could be supposed to hold, due to the continuous exchange of electrons between altervalent metal ions (36). We have first to remark that the isotherm at 1323°K of Fig. 15 fits this model quite well at least at pressures lower than about 10^{-2} atm. Furthermore, from the isobars of Fig. 18, we observe that a kink is present at 1273°K in the E *vs.* T plots, in a range of pressures where the isotherms of Fig. 15 indicate the presence of a purely monophasic system. Finally, it is worthwhile to remark that, the E *vs.* p_{O_2} plots indicate, at temperatures lower than 1273°K and at pressures higher than about 5 x 10^{-2} atm, the existence of a two-phase system (from the constancy of the chemical potential of Ni^{3+}).

The segregation of a second phase could be easily accounted for by considering that the occurrence of reaction [21'] involves the presence of microdomains of the inverse spinel Ni_3O_4, which apparently is soluble in the NiO phase only to a very limited extent at temperatures lower than 1273°K, which can be considered as the temperature of critical mixing (35). Above this temperature, the emf isotherms indicate the presence of a purely monophasic system up to the higher pressures; therefore the discontinuity at 1273°K in the emf *vs.* T plot indicates also an order-disorder transition which reflects the randomization of the point and electronic defects within the crystal.

From the difference between the experimental (E) and the theoretical ($E°$) emf of the cell

$$Pt/NiO(p'_{O_2})/ZrO_2 + CaO/NiO(p''_{O_2})/Pt \qquad [3]$$

we calculated the activity coefficients of Ni^{3+}

$$E - E° = \frac{RT}{F} \ln \left(\frac{\gamma C_{Ni^{3+}}}{C_{Ni^{3+}}} \right)_{p'_{O_2}} = \frac{RT}{F} \ln (\gamma)_{p'O_2} \qquad [28]$$

where the $E°$ values have been calculated according to the following equation

$$E° = \frac{RT}{6F} \ln \frac{p'_{O_2}}{p''_{O_2}} = \frac{RT}{F} \ln \frac{C'_{Ni^{3+}}}{C''_{Ni^{3+}}} \qquad [29]$$

assuming that at the reference pressure ($p'' = 10^{-3}$ atm) the solution is nearly ideal. The latter is a very crude approximation, which nevertheless is helpful in the evaluation of the activity coefficients as well as of the enthalpies of mixing.

Experimental values are reported in Table III. It may be stated that at temperatures lower than 1273°K

Table III. Activity coefficient values as obtained from emf measurements on cell of Eq. (3)

p_{O_2}, atm	E, mv	E^0, mv	T, °K	log γ	γ
2×10^{-3}	43.5	11.20	1123	0.145	1.397
4×10^{-3}	68.0	22.30	1123	0.205	1.604
10^{-2}	79.5	37.12	1123	0.190	1.549
3.3×10^{-2}	77.5	56.36	1123	0.095	1.245
10^{-1}	72.0	74.24	1123	0.009	1.023
2×10^{-3}	30.0	11.97	1203	0.075	1.191
4×10^{-3}	45.0	23.94	1203	0.088	1.225
10^{-2}	56.0	39.76	1203	0.068	1.170
3.3×10^{-2}	60.5	60.35	1203	0.006	1.014
10^{-1}	62.0	79.52	1203	0.073	1.185
2×10^{-3}	24.0	12.32	1238	0.047	1.117
4×10^{-3}	35.5	24.64	1238	0.044	1.108
10^{-2}	43.0	40.92	1238	0.008	1.019
3.3×10^{-2}	50.5	62.12	1238	0.047	1.116
50^{-1}	55.0	81.84	1238	0.109	1.286
1×10^{-3}	16.5	12.67	1273	0.015	1.030
4×10^{-3}	27.0	25.34	1273	0.006	1.016
10^{-2}	38.5	42.09	1273	0.014	1.034
3.3×10^{-2}	45.0	63.89	1273	0.075	1.189
10^{-1}	48.0	84.18	1273	0.143	1.390
2×10^{-3}	14.5	13.16	1323	0.005	1.013
4×10^{-3}	28.0	26.33	1323	0.006	1.015
10^{-2}	40.0	43.73	1323	0.014	1.033
3.3×10^{-2}	53.5	66.38	1323	0.048	1.119
10^{-1}	58.5	87.46	1323	0.110	1.290

the activity coefficients are well accounted for only in the range of compositions corresponding to the solid solution. At higher concentrations their value is only fictitious. It is nevertheless quite evident that at temperatures < 1273°K γ diverges rapidly from 1 at pressures slightly increasing from the reference one, whereas at higher temperatures the deviations from ideality are also relatively low at the higher pressures.

As this behavior (at temperatures lower than that of critical mixing) reflects the properties of a regular solution (35) we may calculate the partial molar enthalpy of mixing of Ni_3O_4 in NiO, $\Delta\bar{H}$, from the temperature dependence of the activity coefficients of Ni^{3+} at 2×10^{-3} atm and at 4×10^{-3} atm according to the relationship

$$\ln \gamma = -\frac{\Delta \bar{H}}{RT} \qquad [30]$$

which describes the ln γ *vs.* $1/T$ plots of Fig. 19.

We thereby obtain a value for the partial molar enthalpy of mixing equal to 5.46 kcal/g ion at $p_{O_2} = 2 \times 10^{-3}$ and 7.46 kcal/g ion at 4×10^{-3} atm; thus, indeed, the solution cannot be considered as a strictly regular one (35).

Conclusions

1. Intrinsic semiconductivity has been observed in fully compensated polycrystalline NiO. The activation energy for the intrinsic process corresponds to half of the energy gap value as obtained from optical measurements. It seems moreover that surface conductivity does not affect our results in the temperature range of our experiments.

2. Nickel vacancies are fully ionized over the entire experimental temperature range. Literature data which indicate the existence of partially ionized vacancies suffer from errors attributed to the effect of unknown impurities.

3. In nonstoichiometric (metal deficit) NiO a second phase segregates at temperatures lower than 1300°K which has an inverse spinel structure. The existence of inverse spinel microstructures has been tentatively inferred, at partial pressures of oxygen lower than that corresponding to the segregation of a second phase, from the dependence of the activation energy for the conductivity on the partial pressure of oxygen.

4. From emf measurements the activity coefficients of Ni^{3+} and the partial molar heat of mixing of Ni_3O_4 in NiO have been calculated and an order-disorder transition temperature of 1273°K has been inferred.

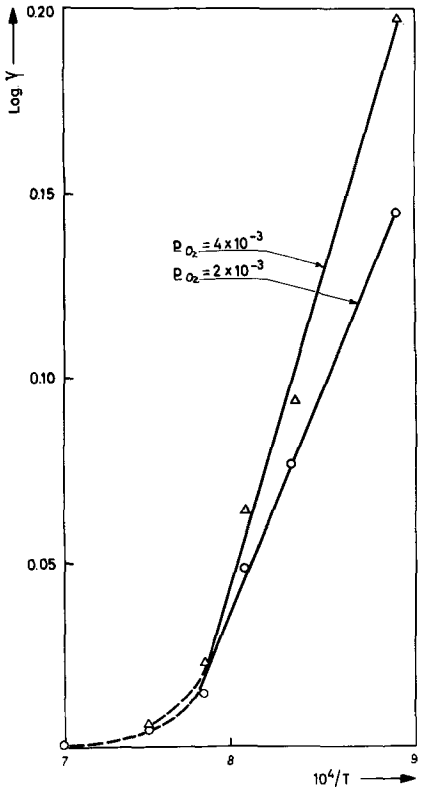

Fig. 19. Log γ *vs.* $1/T$ plot for the activity coefficients γ as obtained from Eq. [17] at 2×10^3 and 4×10^{-3} atm of oxygen.

Acknowledgment

The authors are greatly indebted to Mr. C. Geel for the preparation of samples, to Dr. Vos and Mr. Toussaint of the Analytical Chemistry Group, and to Dr. Girardi and Mr. Sabbioni of the Nuclear Chemistry Group for their analytical support, and to Dr. R. Kelly of the Solid State Physics Group for helpful discussions. They would like, moreover, to acknowledge Dr. J. H. Westbrook, who substantially improved the text and to Dr. N. Hackerman and Mrs. R. G. Sterns for their helpful suggestions.

Manuscript received April 10, 1967; revised manuscript received June 28, 1967.

Any discussion of this paper will appear in a Discussion Section to be published in the June 1968 JOURNAL.

REFERENCES

1. H. H. Baumbach and C. Wagner, *Z. Phys. Chem.*, **B24**, 59 (1934).
2. E. J. W. Verwey, P. W. Haaijman, F. C. Romeijn, and G. W. v. Oosterhout, *Philips Research Repts.*, **5**, 173 (1950).
3. R. W. Wright and J. P. Andrews, *Proc. Phys. Soc. London*, **62A**, 446 (1949).
4a. F. T. Morin, *Phys. Rev.*, **93**, 1199 (1954).
4b. "Semiconductors," N. B. Hannay, Editor, Reinhold Publishing Co., New York (1960).
5. R. R. Heikes and N. D. Johnson, *J. Chem. Phys.*, **26**, 582 (1957).
6. S. P. Mitoff, *ibid.*, **35**, 882 (1961).
7. F. S. Petitt, *This Journal*, **113**, 1249 (1966).
8. S. v. Houten, *J. Phys. Chem. Sol.*, **17**, 7 (1960).
9. M. I. Klinger, *Phys. Stat. Sol.*, **11**, 499 (1965).
10. J. Appel, *Phys. Rev.*, **141**, 506 (1966).
11. G. L. Sewell, *ibid.*, **129**, 597 (1963).
12. A. J. Bosman and C. Crevecoeur, *ibid.*, **144**, 763 (1966).
13. G. M. Schwab and H. Schmid, *J. App. Phys.*, **33**, 426 (1962).
14. K. Hauffe and J. Block, *Z. Phys. Chem.*, **196**, 438 (1950).
15. R. J. Herbst, Univ. Microfilms (Ann Arbor, Mich.) No. 64-6077.
16. H. R. Thorton, Univ. Microfilms (Ann Arbor, Mich.) No. 64-2979.

17. D. P. Snowden, E. Saltsburg, and J. Pereue, *J. Phys. Chem. Sol.*, **25**, 1099 (1964).
18. M. G. Harwood, N. Herzfeld, and S. L. Martin, *Trans. Faraday Soc.*, **46**, 650 (1950).
19. J. G. Austin, A. J. Springthorpe, and B. A. Smith, *Phys. Letters*, **21**, 20 (1960).
20. H. J. Van Daal and A. J. Bosman, *Physics Letters*, **23**, 525 (1966).
21. S. Koide, *J. Phys. Soc. Japan*, **20**, 123 (1965).
22. S. Takeuchi and K. Igaki, *J. Japan Inst. Metals*, **148**, 10 (1950).
23. K. Kiukkola and C. Wagner, *This Journal*, **104**, 379 (1957).
24. R. Newman and R. M. Chrenko, *Phys. Rev.*, **114**, 1507 (1959).
25. Ya. M. Ksendzov and I. A. Drabkin, *Sov. Phys. Sol. St.*, **7**, 1519 (1965).
26. N. F. Mott and R. W. Gurney, "Electronic Processes in Ionic Crystals," Clarendon Press, Oxford (1957).
27. W. Finkelnburg and W. Humbach, *Naturwiss.*, **42**, 35 (1955).
28. K. J. Richards and F. E. Wagstaff, *J. Phys. Chem.*, **70**, 1553 (1966).
29. A. Bielanski and J. Deren, *Trans. Faraday Soc.*, **58**, 166 (1962).
30. W. L. Roth, *Acta Cryst.*, **13**, 140 (1960).
31. J. S. Anderson, "Nonstoichiometric Compounds," Advances in Chemistry Series No. 39, Am. Chem. Soc., Washington (1963).
32. B. Fischer and D. S. Tannhauser, *J. Chem. Phys.*, **44**, 1663 (1966).
33. S. Van Houten and A. J. Bosman, Int. Proc. Buhl. Conf., p. 123, E. R. Schetz, Editor, New York (1964).
34. P. J. Thistlethwaite, K. R. Turnbull, P. J. Fensham, "Proc. 1° Australian Conference on Electrochemistry," Pergamon Press, Oxford (1963).
35. E. A. Guggenheim, "Mixtures," Clarendon Press, Oxford (1952).
36. G. G. Mikhailov and V. A. Kozhenrov, *Russ. J. Phys. Chem.*, **39**, 408 (1965).

Technical Note

The Si-WSi_2-Si Epitaxial Structure

Norikazu Hashimoto and Yasushi Koga

Central Research Laboratory, Hitachi Ltd., Kokubunji, Tokyo, Japan

Chemical vapor deposition of metals on single crystal silicon has received increasing attention in the fabrication of devices with a metal-semiconductor contact, such as the Schottky barrier diode. There are the following problems: (*a*) morphology and crystallinity of the deposited metal layer, and (*b*) silicide formation at the interface between the deposited metal and the silicon substrate.

Deposition of molybdenum on silicon has been reported by Casey *et al.* (1) and Lindmayer (2). The latter author reported that 100Å thick molybdenum layers on silicon were not single crystals. Kano *et al.* (3) have studied the molybdenum-silicon Schottky barrier formed by chemical vapor deposition in which a special technique (preactivation of reaction) was employed to prevent the formation of the silicide. Crowell *et al.* (4) have reported deposition of polycrystalline tungsten layers on silicon, germanium, and gallium arsenide substrates. Deposition of vanadium on silicon has been reported by Miller *et al.* (5) where no evidence of the silicide formation was observed.

Very recently, the silicide formation on deposition of molybdenum has been reported by Casey *et al.* (6). The orientations of molybdenum silicides with respect to the silicon substrates have been determined to (001) $MoSi_2$ // (100) Si with (110) $MoSi_2$ // (010) Si and (110) Mo_3Si // (111) Si with [335] Mo_3Si // [$10\bar{1}$] Si.

This paper reports on deposition of tungsten and the formation of its silicide layer by hydrogen reduction of the hexachloride on single crystal silicon substrates. The orientation relations between the silicide layer and the substrate are analyzed by electron diffraction and x-ray diffraction. Furthermore, we are concerned with epitaxial growth of the silicon layer on the grown silicide layer.

Experimental

Materials.—Commercial tungsten hexachloride, WCl_6 (99% min) was purified by sublimation. The resultant impurity contents in the chloride (in weight per cent) were as follows: Ca, Mg, and Cu 1 — 5 × 10^{-4}; Al 1 — 5 × 10^{-3}; Fe and Si 5 — 10 × 10^{-3}. Tungsten oxychlorides ($WOCl_4$, WO_2Cl_2) were eliminated by preliminary sublimation.

Hydrogen (99.9%) used as a carrier gas was passed through a "Deoxo" and then through a two-stage liquid nitrogen trap.

The silicon substrates used were circular slices, 25 mm diameter, 0.2 mm thickness, with (111), (110), and (100) faces.

Apparatus.—The apparatus used for deposition is shown schematically in Fig. 1. It consisted of a hydrogen purifier, quartz evaporator, and a quartz reaction chamber. A high-frequency induction heater was used.

Operation.—The substrate was etched with HF (46%) for 1 min and then set on the silicon pedestal. After preliminary purge of the reaction chamber with hydrogen gas, the substrate surface was treated with hydrogen stream at *ca.* 1200°C. A gaseous mixture of WCl_6 and hydrogen was produced by passing dry hy-

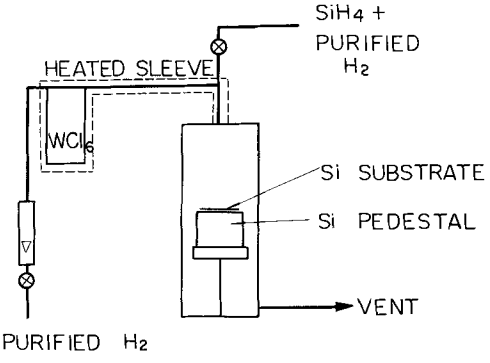

Fig. 1. Schematic diagram of the vapor deposition apparatus

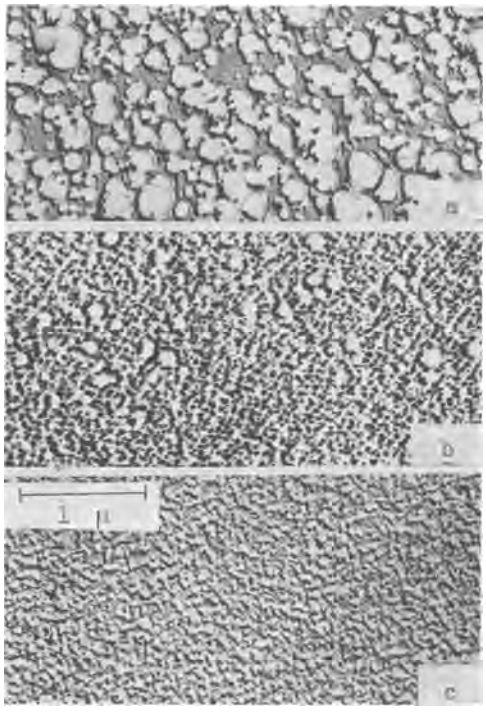

Fig. 2. Replica electron micrographs of the tungsten surfaces deposited (a) at 650°C, (b) at 750°C, and (c) at 840°C.

drogen at a flow rate of 5 l/min over the solid chloride heated at 200°C in the evaporator and was introduced into the chamber. The chloride was reduced and tungsten was deposited onto the substrates which had been heated to a temperature in the range from 650° to 1250°C.

Presence of oxygen in the deposition system resulted in formation of oxides on the silicon substrate. Since this affects deposition processes markedly, care should be taken to remove trace amount of oxygen.

In the case of silicon deposition on the silicide layer, the reaction chamber was first purged with hydrogen. The monosilane gas was then introduced directly into the hydrogen stream, and silicon was deposited on the silicide by thermal decomposition of the gas.

Results and Discussion

Deposition of W *on* Si, *and formation of* WSi_2—Figures 2a, b, and c illustrate typical deposits of the polycrystalline tungsten on the single crystal silicon at 650°, 750°, and 840°C, respectively. The surfaces become smoother on increasing the deposition temperature.

According to the measurements of the photoelectric response, the barrier height between the deposited tungsten and n-type silicon was higher than that of tungsten and n-type silicon which was formed by vacuum deposition by about 0.20 ev. This result has been attributed to the existence of tungsten silicides between the deposited tungsten and the silicon substrate; nevertheless the deposition temperatures are 400°C or more lower than the W-Si eutectic temperature (4, 7).

Compositions of the deposited tungsten layers at higher temperatures were determined by electron diffraction and x-ray diffraction analyses. Results are given in Table I. The deposition time was 5 min. With electron diffraction, we can observe thin surface films, because penetration of the electron beam is slight. On the other hand, the main composition of the deposited layer can be determined with x-ray diffraction. At 1065° and 1087°C, the thin surface films of the deposited layer were polycrystalline tungsten, although the main composition was tungsten disilicide (WSi_2). The deposited layers at 1120° and 1180°C were WSi_2 throughout. The thickness of the WSi_2-layer was estimated by the angle lapping method as about 5000Å.

Table I. Analyses of deposited layers on Si substrates by hydrogen reduction of tungsten hexachloride

Substrate temperature, °C	Electron diffraction analysis	X-ray diffraction analysis
1065	W	WSi_2
1087	W	WSi_2
1100	W or WSi_2	WSi_2
1120	WSi_2	WSi_2
1180	WSi_2	WSi_2

The growth of WSi_2-layer with respect to time followed to the well-known parabolic relationship, and the activation energy for the growth was 22 kcal/mole (8). This indicates that WSi_2-layer growth is controlled by a solid-state diffusion mechanism.

Epitaxial growth of WSi_2 *on* Si *substrates.*—At higher deposition temperatures, orientation of the grown silicide layers were found by reflection electron diffraction analysis. Figure 3 shows the electron micrograph of the grown layer on the (110) Si surface at 1200°C. One of electron diffraction patterns showing the WSi_2 (110) plane parallel to the Si (110) substrate plane are shown and analyzed in Fig. 4. Patterns for WSi_2 crystal grown on Si (111) and Si (100) planes are shown in Fig. 5 and 6. The extra spots in the patterns which are not explained as due to the orientated WSi_2 crystals probably come from multiple twins in the WSi_2 crystals or other tungsten silicides on the surface.

Epitaxial Si *growth on the grown* WSi_2*-layer on* Si. —Silicon was deposited on the epitaxially grown WSi_2-layer by the thermal decomposition of monosilane (SiH_4). The epitaxial growth of silicon was achieved at 1100°-1150°C with a mole ratio of SiH_4/H_2 of 0.0001-0.001.

Figure 7 shows the reflection electron diffraction pattern and the replica electron micrograph of the epitaxially grown Si-layer on the WSi_2-layer which has

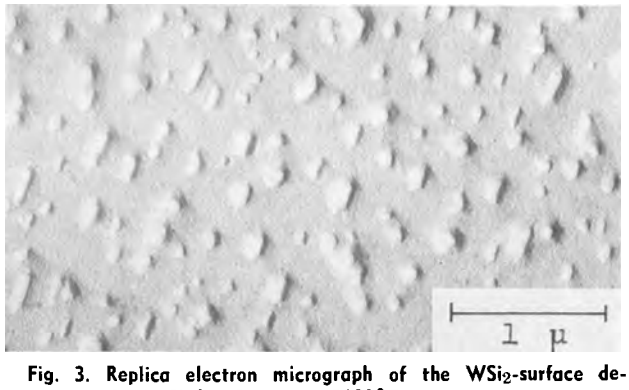

Fig. 3. Replica electron micrograph of the WSi_2-surface deposited on the (110) Si substrate at 1200°C.

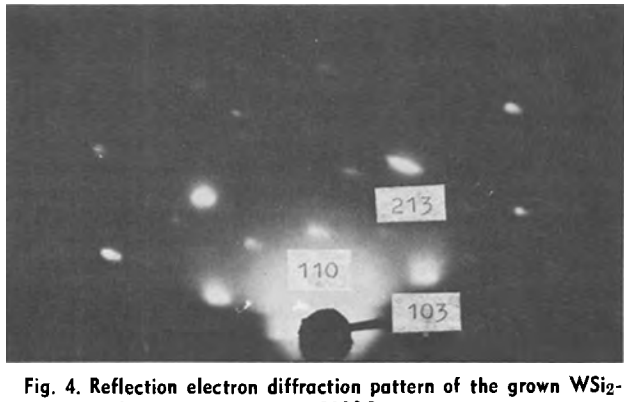

Fig. 4. Reflection electron diffraction pattern of the grown WSi_2-layer on the Si (110) substrate at 1200°C.

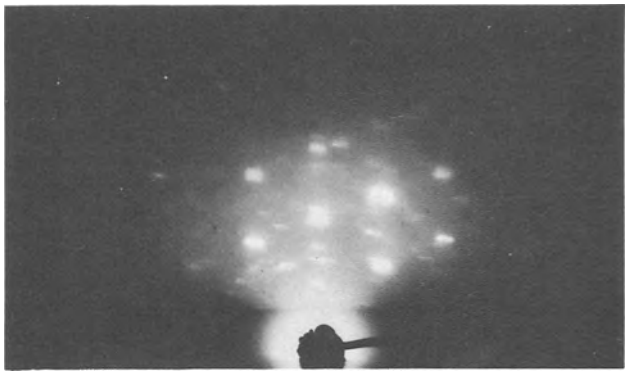

Fig. 5. Reflection electron diffraction pattern of the grown WSi_2-layer on the Si (111) substrate at 1200°C. WSi_2(101) is parallel to Si (111).

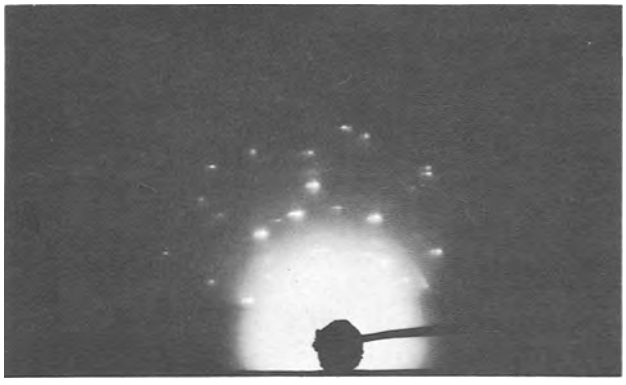

Fig. 6. Reflection electron diffraction pattern of the grown WSi_2-layer on the Si (100) substrate at 1200°C. WSi_2 orientation can not be determined.

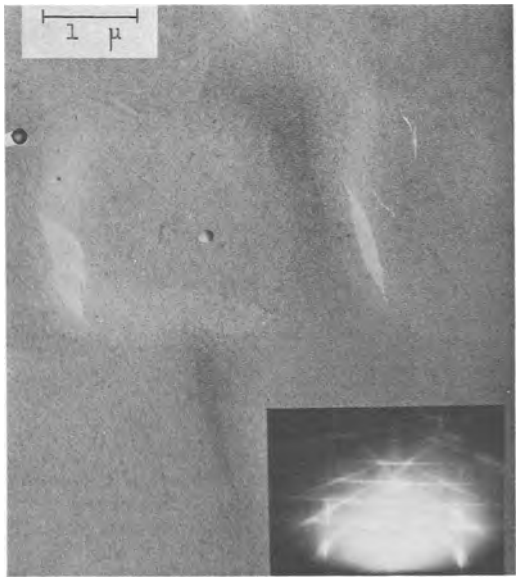

Fig. 7. Replica electron micrograph and reflection electron diffraction pattern of epitaxially grown Si-layer on the WSi_2-layer which has been grown on the Si (110) substrate.

been epitaxially grown on the (110) Si substrate. The Kikuchi lines appear clearly in the diffraction pattern.

On measurement of tungsten silicide and n-type Si barriers, aluminum films of approximately 1000Å were evaporated in a vacuum on the WSi_2-layers. When the WSi_2-layers are fragmentary, Al films become ohmic contacts to the substrate. The WSi_2-layer between the thin deposited Si-layer and the substrate was confirmed by x-ray diffraction analysis and the existence of a Schottky-type metal-semiconductor barrier (9). The epitaxy of the second Si-layer may

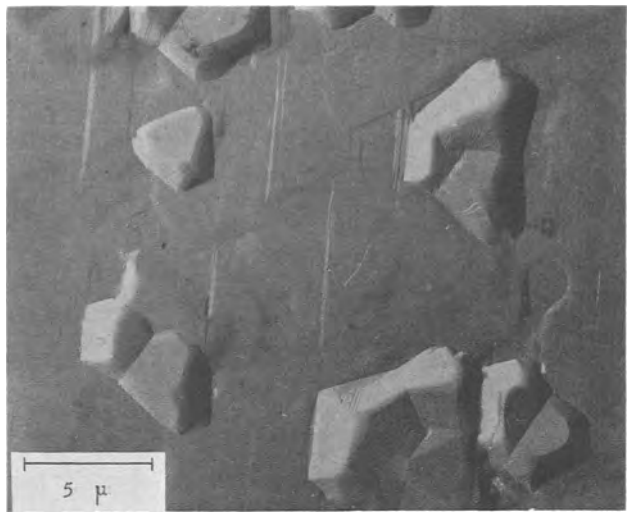

Fig. 8. Replica electron micrograph of epitaxially grown Si-layer on the WSi_2-layer which has been grown on the Si (111) substrate.

not raise direct nucleation on exposed Si substrate at holes in the WSi_2-layer.

The epitaxial relationships for the "three-layer" structures such as the above were found to be (110) Si // (110) WSi_2 // (110) Si substrate and (111) Si // (101) WSi_2 // (111) Si substrate from electron diffraction patterns and photomicrographs of the deposited Si-layer.

At higher temperature and the thicker deposited Si-layer the deposited silicon atoms diffuse into the orientated WSi_2 substrate during the deposition and so the WSi_2-layer deteriorates. On the other hand, lower temperatures generally increase the nucleation rate of the deposit and hence cause the growth of polycrystalline silicon.

The crystallographic texture of silicon was more evident in deposits on thicker ($>$ *ca.* 1μ) WSi_2-layers. Tripyramids on an epitaxial (111) Si-layer are shown in Fig. 8.

When the WSi_2-layer was very thin ($<$ *ca.* 0.1μ), however, single crystal silicon grew epitaxially on the WSi_2-layer as well as on the Si substrate, although the epitaxial Si-layer had many faults. The fact indicates that a continuous WSi_2-layer free of microholes cannot be formed when the WSi_2-layer is thin. These holes may become preferred or nonpreferred sites for the nucleation of deposited silicon close to the substrate silicon and act as the origin of many faults.

Acknowledgments

The author would like to thank Y. Itoh and Dr. T. Inoue for their valuable discussions.

Manuscript received April 17, 1967; revised manuscript *ca.* July 18, 1967.

Any discussion of this paper will appear in a Discussion Section to be published in the June 1968 JOURNAL.

REFERENCES

1. J. Casey, R. Garnache, J. Lindmayer, and J. L. Sprague, Paper presented at the Pittsburgh Meeting of the Society, April 15-18, 1963.
2. J. Lindmayer, *Proc. IEEE*, **52**, 1751 (1964).
3. G. Kano, I. Inoue, J. Matsuno, and S. Takayanagi, *J. Appl. Phys.*, **37**, 2985 (1965).
4. C. R. Crowell, J. C. Sarace, and S. M. Sze, *Trans. Met. Soc. AIME*, **233**, 478 (1965).
5. K. J. Miller, M. J. Grieco, and S. M. Sze, *This Journal*, **113**, 902 (1966).
6. J. J. Casey, R. R. Verderber, and R. R. Garnache, *ibid.*, **114**, 201 (1967).
7. Y. Itoh and N. Hashimoto, *J. Appl. Phys.*, **38**, 899 (1967).
8. N. Hashimoto, *Trans. Met. Soc. AIME*, **239**, 1109 (1967).
9. Y. Itoh and N. Hashimoto, To be published.

Brief Communication

Infrared Spectra of Silicon Nitride Deposited on Gallium Arsenide

R. S. Levitt[1] and W. K. Zwicker

Philips Laboratories, Briarcliff Manor, New York

Considerable interest exists (1) in using silicon nitride (Si_3N_4) films as a passivating or protective insulating coating for semiconductor surfaces and devices. We have been investigating methods of preparation of such films, using various techniques to characterize their properties. In this note we report on the infrared transmission spectra of a mechanically good Si_3N_4 film deposited on a gallium arsenide substrate which exhibits several characteristics of "pure" (nonoxygen contaminated) nitride.

The characteristic infrared absorption of Si_3N_4 occurs in the 8-14μ wavelength region (2, 3). In order to be able to record definitive spectra in this region it is best to use as a substrate a material which is both optically nonabsorbing and chemically stable. The most useful semiconductor, silicon, unfortunately fails the first criterion, having a complex spectrum of lattice absorptions throughout this region. Only with careful optical compensation can good spectra be recorded. (Germanium, while better satisfying the first criterion, its lattice absorption spectrum starts at 11.5μ, appears to be severely attacked during the deposition process.) Gallium arsenide (GaAs) more particularly high resistance GaAs, however, appears to be an excellent substrate material. The normalized infrared "transmission" spectrum through a 25 mm path length of high resistivity GaAs is shown in Fig. 1. Absorption due to free carriers is almost completely absent, and the transmittance is constant out to at least 12μ. The lattice band absorptions which occur toward longer wavelengths can be nicely balanced out by simply inserting a similar plate of equal path length in the reference beam of our double-beam, ratio-mode spectrometer, the details of which have been described elsewhere (4). The normalized transmittance (I/I_o) through the ~1 mm thick plate of high resistivity GaAs which was subsequently used as the substrate is also shown in Fig. 1.

The substrate was mechanically polished on all surfaces and carefully cleaned prior to deposition. The silicon nitride film was deposited pyrolytically by the reaction of silicon tetrachloride with ammonia. The apparatus for this deposition was very similar to that generally used for silicon epitaxial growth. The deposition was performed in a quartz reaction chamber. The sample was heated to 700°C by being placed on a quartz pedestal which enclosed an RF heated high-purity graphite core. The reaction was completed in only a few minutes resulting in a film ~1250Å thick, pale bluish-green in color.[2] The film appeared to be adherent, uniform, continuous, and nonporous over the entire exposed surface of the sample. It was subsequently found that the film was much more slowly attacked by concentrated hydrofluoric acid than the GaAs substrate. It was therefore necessary to remove by mechanical means the imperfect and nonuniform

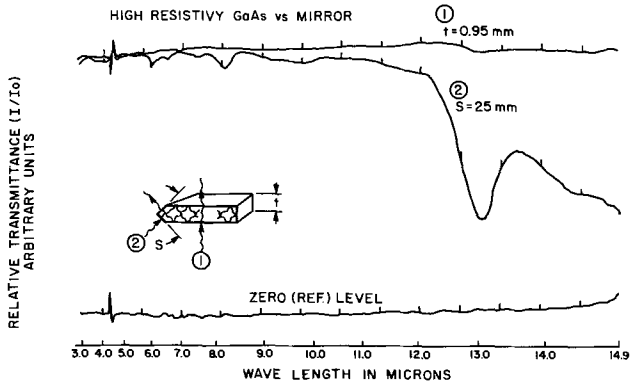

Fig. 1. Infrared optical absorption characteristics of high resistivity GaAs used as substrate material. Curve 1 refers to transmission transversely through a 0.95 mm plate. Curve 2 refers to transmission via internal reflections through the same plate but with a path length of 25 mm. In both cases reflection off of a highly polished mirror constituted the reference beam.

film from the surface which was in contact with the quartz pedestal. The refractive index of the film was determined by the liquid immersion method (5) and found to be 1.98 ± 0.02. The refractive index determined by the ratio of optical thickness to actual thickness (interferometrically determined) is in excellent agreement with this value.

The transmission spectrum of this film is shown in Fig. 2.[3] (With the double-beam, ratio-mode technique reflection and insertion losses are automatically compensated so that what is recorded is I/I_o *vs.* λ. This is shown schematically in the insert.) A second trace is also shown which was obtained by increasing the gain by a factor of 3 and suppressing the zero by a like amount. The characteristic heavy, broad absorption centered about 11μ is easily observed. At 11.35μ we determine the absorption coefficient to be 1.7×10^4 cm^{-1}. The asymmetry of the line and the suggestion of structure on both the short and long wavelength shoulders are to be noted.

Several observations lead us to conclude that this film is relatively uncontaminated by oxygen. The high value of refractive index we measure is characteristic of the "pure" silicon nitride. It is our experience that the refractive index is greatly influenced by the presence of oxygen, and that films with a refractive index as high as this are not easily prepared consistent with the difficulty of excluding oxygen from the system. Even the native oxide film on the substrate surface is a source of oxygen contamination. The use of GaAs

[1] Present address: Amperex Electronics Corp., EOD Division, Providence Pike, Slatersville, Rhode Island.

[2] The optical thickness of the film determined from its color is 2500Å (±10%). Optical thickness is the product of actual thickness and refractive index of the medium.

[3] Internal reflection spectra (6) could not be satisfactorily recorded due to the unexplained appearance after deposition of a large number of "scratches" and other imperfections on the GaAs surface under the Si_3N_4 film. These gave a large scattering loss at short wavelengths and severely distorted the internal reflection spectrum at longer wavelengths so as to make a quantitative interpretation impossible.

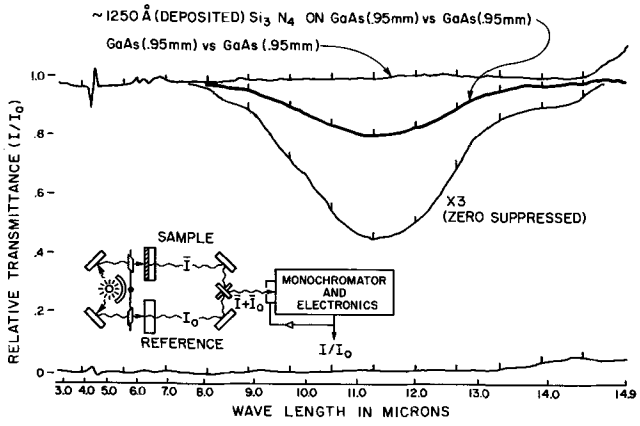

Fig. 2. Infrared transmission spectrum of vapor deposited silicon nitride film on GaAs substrate. The upper curve which represents 100% transmission, neglecting reflectance losses, was obtained prior to the deposition by placing the uncoated plate in the sample beam (I). For the lower curve the gain is increased 3-fold and the zero suppressed an equal amount. In all cases the reference beam (I_0) was transmitted through a GaAs plate of the same thickness. A schematic of the double-beam, ratio-mode, constant energy infrared prism spectrometer is shown in the insert.

should have eliminated this source. Further evidence is the lack of any observable SiO_2 structure in the transmission or internal reflection spectra. The high resistance to etching by HF is also typical of films with low oxygen contamination. Based on these optical and chemical properties of this film, we feel that Fig. 2 represents the characteristic spectrum of relatively uncontaminated, deposited silicon nitride.

Acknowledgment

The authors wish to acknowledge the assistance of Steve Baumann in the preparation of the film and Donald Fisher in the optical measurements.

Manuscript received June 14, 1967; revised manuscript received Aug. 21, 1967.

Any discussion of this paper will appear in a Discussion Section to be published in the June 1968 JOURNAL.

REFERENCES

1. V. Y. Doo, D. R. Nichols and G. A. Silvey, *This Journal*, **113**, 1279 (1966).
2. H. F. Sterling and R. C. G. Swann, *Solid-State Elec.*, **8**, 653 (1965).
3. Spectra #Y383S, Si_3N_4, Sadtler Research Laboratories, Inc., Philadelphia, Pennsylvania.
4. N. J. Harrick, "Internal Reflection Spectroscopy," Interscience Publishers Inc., New York (1967). See Fig. 13 of chap. 6.
5. A. E. Lewis, *This Journal*, **111**, 1007 (1964).
6. N. J. Harrick and F. K. du Pré, *Appl. Optics*, **5**, 1739 (1966).

Silver Oxide Electrode Processes

Thedford P. Dirkse, David DeWit, and Richard Shoemaker

Calvin College, Grand Rapids, Michigan

ABSTRACT

The cathodic and anodic overvoltages at a silver electrode were measured in a range of KOH concentrations of 20-45%. The values of these overvoltages undergo a change in 30-35% KOH. Similar changes or maxima or minima have been observed for other phenomena in KOH solutions, *e.g.*, double layer capacitance. An attempt to account for these changes is made in terms of ion-pair association in concentrations greater than 35% KOH. This association is due to insufficient solvent for the normal hydration of the ions.

Occasionally, in studying various phenomena taking place in alkaline solutions, it has been observed that these phenomena have a maximum or a minimum value at about 30-35% KOH. For example, the hydrogen overvoltage at a zinc electrode shows a minimum at about 10M in both KOH and NaOH (1); the parameters associated with the anodic passivation of zinc have a maximum at about 9M KOH (2); and the rate of decomposition of silver oxide dissolved in KOH solutions has a minimum at 7-9M KOH (3). Sometimes these maxima or minima can be explained in terms of the net effect of increasing OH^- ion concentration and increasing viscosity (or decreasing mobility) as the KOH or NaOH concentration increases. However, this does not offer a satisfactory explanation for all these phenomena. Consequently, the work reported here was undertaken with a twofold objective: (*a*) to see whether any silver electrode processes exhibited maxima or minima; and (*b*) to seek an explanation for any such phenomena. Similar work on the zinc electrode is also in progress at our Laboratory.

Experimental

The method selected to look for maxima and minima involved the use of the sine wave tester described by Kordesch and Marko (4). The IR-free overvoltage of the silver electrode was measured as the current was increased anodically and then as it was increased cathodically. The silver electrode was a piece of silver foil of which only a circular area of 0.32 cm^2 was exposed to the electrolyte. The counter electrode was a sintered Ag-Ag_2O plate, 4 x 5 cm; the reference electrode in most runs was $Hg/HgO/OH^-$. The OH^- concentration was the same in the cell as in the reference electrode.

Readings were taken at 1-min intervals during each run. A typical set of results is given on Fig. 1. The anodic run was carried out first. Then the electrode was allowed to remain on open circuit for about an hour before the cathodic run was made. During the open-circuit period some of the AgO may have decomposed to Ag_2O, and some Ag_2O may have dissolved off the electrode. Figure 2 shows the pattern of the open-circuit voltage after the anodic run was terminated. The voltage holds at the AgO/Ag_2O level for some time and then, because of decomposition of at least the surface layer of AgO, falls to the Ag_2O/Ag level. The cathodic run was begun only after the open-circuit voltage had fallen to that of the Ag_2O/Ag level.

Results and Discussion

In analyzing the results, emphasis was placed on changes rather than absolute values because the values obtained are, to some extent, time dependent. Consequently, only comparisons are significant. In the anodic process three values were compared: (*a*) the overvoltage at the Ag_2O/Ag level at 1.3 ma/cm^2; (*b*) the overvoltage at the AgO/Ag_2O level at 9.5 ma/cm^2; (*c*) the current density at which the voltage changes from the lower to the higher value. A summary of these three values is given on Fig. 3. Each point is the average of at least two runs. Of interest is the fact that the overvoltage at the Ag_2O/Ag level increases much more slowly beyond 30% KOH than in more dilute solutions; the overvoltage at the AgO/Ag_2O level has a maximum at about 35% KOH, and the current density at which the voltage transition occurs decreases rapidly beyond 30% KOH. Qualitatively, this last phenomenon can be accounted for by the increased viscosity of the KOH solutions as the concentration increases beyond 30%. This reduces the mobility of the OH^- ions markedly and the anodic processes do require these ions, *e.g.*

$$2Ag + 2\,OH^- \rightarrow Ag_2O + H_2O + 2e$$

Cathodically, the points of interest are: (*a*) the overvoltage at the Ag_2O/Ag level at 1.3 ma/cm^2, and (*b*) the current density at which the overvoltage decreases rapidly. A summary of the cathodic results is given on Fig. 4. Again the current density falls rapidly beyond 30% KOH while the overvoltage has a minimum at about 35% KOH. The current density

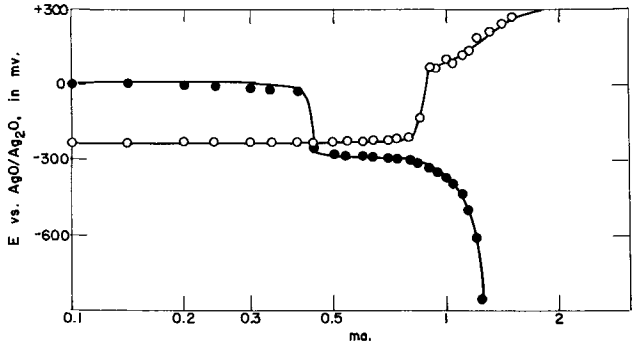

Fig. 1. Current-voltage curve for a silver electrode in 20% KOH at room temperature. The reference electrode is AgO/Ag_2O; ○ anodic; ● cathodic.

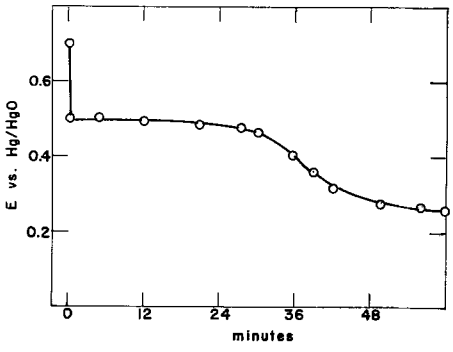

Fig. 2. Open-circuit voltage of a silver electrode after anodic treatment in 30% KOH at room temperature. Reference electrode is HgO/Hg.

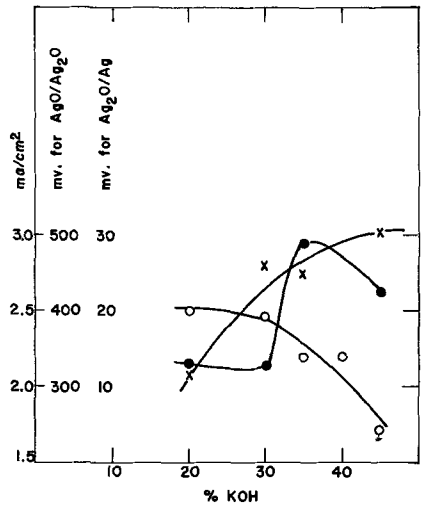

Fig. 3. Values for anodic silver electrode processes at room temperature. ○ current density at which voltage transition occurs; ● overvoltage at the AgO/Ag_2O level; X overvoltage at the Ag_2O/Ag level.

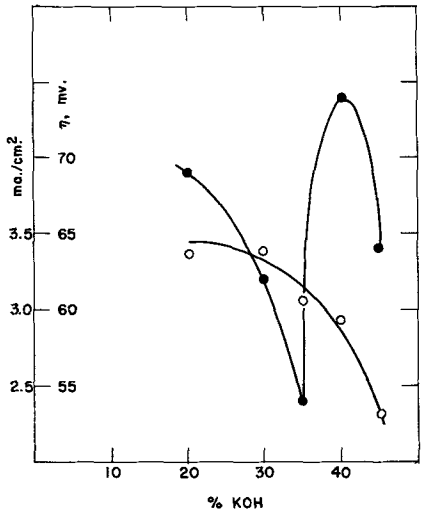

Fig. 4. Values for cathodic silver electrode processes at room temperature. ○ current density at which voltage drops rapidly; ● overvoltage at the Ag_2O/Ag level.

variation can perhaps be accounted for in terms of the increasing viscosity of the more concentrated KOH solutions, but this does not account for the overvoltage behavior. While the line drawn for overvoltages on Fig. 4 connects all the data points, this line does not necessarily give a complete description of the overvoltage behavior between 35 and 45% KOH. More data would be needed for this. But the data do show a minimum in the vicinity of 35% KOH.

Double Layer Capacitance.—The foregoing results suggested that with some of the silver electrode processes in alkaline solution, a change takes place as the concentration of the KOH solutions becomes about 35% or 8.5M. Consequently, still further work was attempted. Because these processes are associated with an electrode, it is possible that changes in the processes could be due to changes in the adsorption at the electrode-electrolyte interphase or in the composition of the double layer. One way to determine this is to measure the differential double layer capacity (dlc) of the electrode and note any changes in it. This measurement is made from the slope of the voltage-time curve during the charging of the double layer. This requires a constant current density, and here one encounters difficulty with the silver electrode. The current can be kept constant, but because the electrode is active, it undergoes a chemical change which changes the surface area and, consequently, the current density. Furthermore, the current may be used to bring about chemical change as well as to charge the double layer.

With these difficulties in mind, attempts were still made to get some sort of value for this double layer capacity. Because of this difficulty, only changes, and not absolute values, were considered significant. In the first attempt, the method of McMullen and Hackerman (5) was used. The counter electrode was a 3 x 6 cm platinized platinum screen. The reference electrode, kept in a separate compartment, was a partially charged cadmium electrode, and the silver electrode was either a 0.3 cm^2 circular area of a silver foil, or a half of a small bead of silver with about 0.1 cm^2 area exposed. The silver electrode was placed against the capillary from the reference electrode. The frequency of the square wave was 20 or 50 kHz.

In each run the silver electrode was cleaned by dipping it in dilute HNO_3, then in dilute NH_4OH, and then rinsing in deionized water. This electrode was allowed to stand in the cell for about an hour before any runs were made. During this time, the potential of the silver electrode became constant. The potential of the electrode was always allowed to reach a constant value before any measurements were made. The results were surprisingly reproducible. A representative set of results is given on Fig. 5. Similar results were obtained in 30, 35, and 45% KOH. The sudden drop in the "capacitance" is attributed to the formation of an oxide layer. (The terms capacitance or dlc refer to the calculated values. They are not intended to mean actual double layer capacitance values.)

For purposes of comparison, the dlc at 1.0-1.1v was considered to be that of the silver surface before any appreciable oxide formation took place. This value, it was found, does vary with KOH concentration, Fig. 6. The value is high at 35% KOH and decreases on either side of this concentration. No attempt will be made here to give a mechanistic interpretation of Fig. 6, but the results do show that some type of change occurs at the electrode surface at about 35% KOH. This same behavior was noted a year earlier by another student in connection with another research project.

In order to verify the relationships described above, the differential double layer capacity and the over-

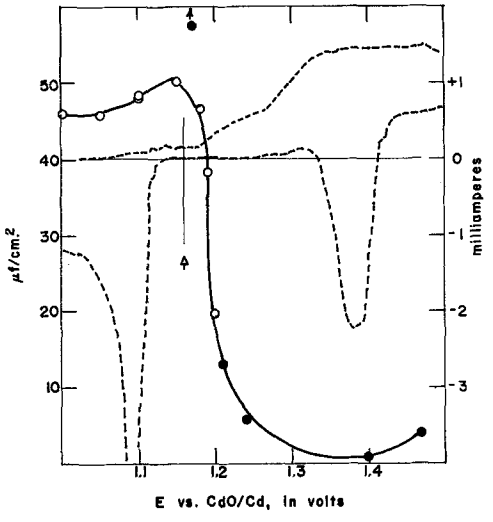

Fig. 5. "Double layer capacitance" (solid line) of silver electrode in 40% KOH at room temperature. The different symbols refer to two different runs and electrodes. The dashed line is the voltage-current (right hand scale) plot obtained with the voltage sweep technique at a rate of 20 mv/sec. The arrow points to the open-circuit voltage of the Ag_2O/Ag electrode.

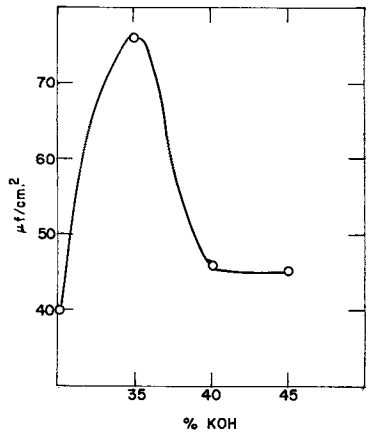

Fig. 6. Variations of dlc of a silver electrode with KOH concentration.

voltage for the anodic process were measured using the single pulse technique described by Hoare (6). The silver electrode was a circular area, 0.32 cm^2, of a silver foil, the counter electrode was a commercial sintered AgO electrode, and the reference electrode was Hg/HgO having the same KOH concentration as that being used in the cell. All runs were made at room temperature and, unless otherwise noted, only anodic pulses were used. In one series of runs the electrode was treated anodically until its potential, compared to the reference electrode, was 0.55v, including IR drop. At this point the voltage was rising from that of the Ag_2O/Ag level to the AgO/Ag_2O level. By treating all the electrodes this way it was assumed that the surface condition and area would be fairly similar in all runs. The electrode was then given a single pulse and the voltage-time curve was photographed from an oscilloscope.

In another series of runs, the silver electrode was treated anodically for varying lengths of time before it was subjected to the single pulse. All overvoltages reported are corrected for IR drop.

Figure 7 shows a typical set of results for an electrode that was charged to 0.55v with respect to Hg/HgO before measurements were made. The calculated dlc does vary with the current density of the anodic pulse used, but appears to approach a constant value as the current density increases. A comparison of the values at two current densities is shown on Fig. 8. Again there is evidence of a maximum in these values for the Ag_2O electrode. Because of uncertainties with respect to the surface, however, this comparison is, at best, qualitative in nature.

That the nature of the surface has a definite bearing on the dlc is well known and is illustrated on Fig.

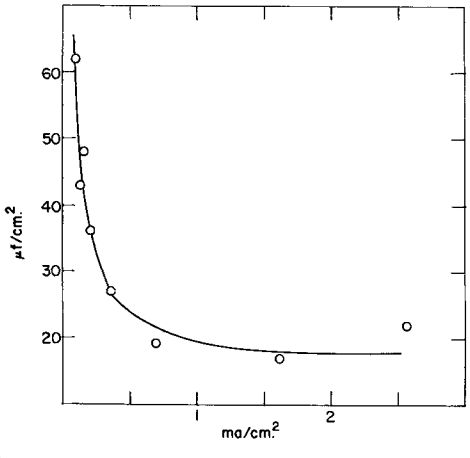

Fig. 7. Double layer capacitance calculated for silver electrode in 30% KOH at room temperature.

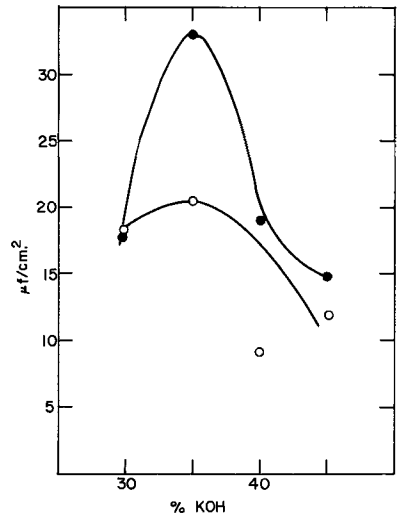

Fig. 8. Variation of dlc of an Ag_2O electrode with KOH concentration. ○ current density of 2 ma/cm^2; ● current density of 1 ma/cm^2.

9. Here the silver electrode was treated anodically for different lengths of time, or to different voltages with respect to the reference electrode. The higher the voltage reached, the more current has been passed, and the thicker the Ag_2O coating produced. The electrode was then subjected to an anodic pulse of 2 ma/cm^2 and the dlc was calculated from the voltage-time trace. The dlc decreases rapidly as the thickness of the Ag_2O layer increases and again appears to approach a limiting value. The overvoltage increases as the Ag_2O layer increases.

Exchange Current.—In the course of this work with the single pulse technique, the activation overvoltages were measured. These, however, could not be measured with a great degree of accuracy because of the uncertainty in estimating the IR drop. No Tafel slopes were drawn because the overvoltages used (< 40 mv) are not beyond the limits where the cathodic process can be neglected in the general current-overvoltage equation. Instead, since the overvoltages are small, the approximate form of the equation can be used

$$\frac{\eta}{i} = \frac{RT}{i_0 F}$$

A plot of overvoltage *vs.* current is given on Fig. 10. The slope of this line gives a value of 2 ma/cm^2 for

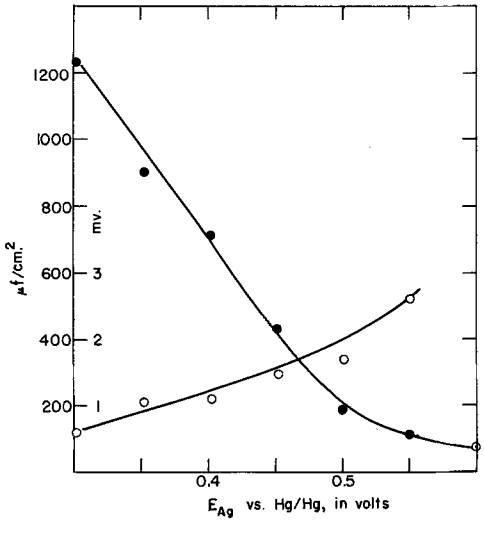

Fig. 9. Values for an Ag_2O electrode in 35% KOH as a function of the thickness of the Ag_2O layer. ○ overvoltage; ● dlc.

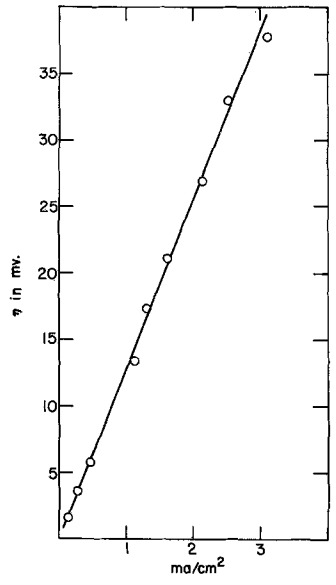

Fig. 10. Overvoltage-current curves for the anodic treatment of an Ag_2O electrode at room temperature in 35% KOH.

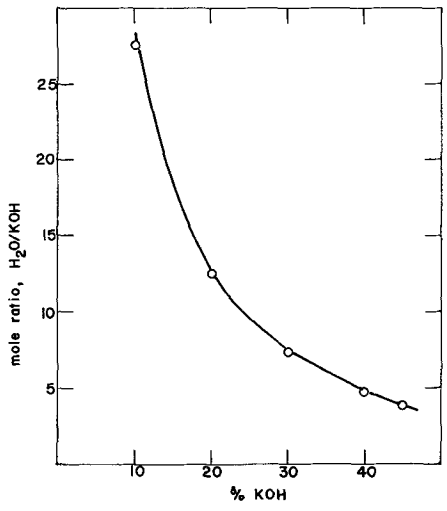

Fig. 11. Mole ratio of H_2O/KOH in aqueous KOH solutions

i_O. Others (7) have determined i_O for the cathodic process and obtained a value of 50 ma/cm². Considering the difficulties involved in either case, the agreement is reasonably good. In our work we made only a few cathodic pulse measurements, but they are unsuitable for calculating i_O.

All these results show that several values associated with the silver electrode processes have a maximum, a minimum, or undergo some alteration at about 35% KOH. Probably the most significant of these is the differential double layer capacity. It too shows a maximum at this KOH concentration both for a silver electrode and an electrode having a layer of Ag_2O. Regardless of the precise physical significance of these results, they suggest some change in electrode behavior and/or double layer composition. It is possible that this factor may account for the maxima and minima that cannot be explained in terms of the trade-off between increasing OH^- ion concentration and decreased mobility as the KOH concentration increases.

Effect of Electrolyte.—A possible interpretation of the variations noted in Fig. 6 and 8 follows. In a water solution, water molecules cover the surface of the electrode. As the KOH concentration increases, these are replaced by OH^- ions which are attracted to the electrode (positive charge) and increase the dlc. [At the potentials used here the silver electrode is almost 1v anodic to its potential of zero charge (8).] The OH^- and the K^+ ions are hydrated. It has been estimated that the K^+ ions have 4 water molecules associated with them (9). The OH^- ions may have 1 or 2 water molecules of hydration. Thus, hydration of the ions requires about 5 or 6 moles of water per mole of KOH. This is the ratio that prevails in about a 35% KOH solution, Fig. 11. Therefore, in KOH solutions more concentrated than 35% there is insufficient water for normal hydration of ions. This leads to a competition for water molecules and perhaps the OH^- ions at the electrode surface are, in effect, neutralized by ion-pair formation with K^+ ions. This could occur by means of bridging water molecules. As a result, the dlc decreases again. The possibility of ion pair formation in these solutions has also been suggested recently by Lander (10).

Electrode processes.—If this explanation is correct, then it should also be applicable to the overvoltage behavior observed in this work. Anodically the overvoltage increases rapidly at about 30-35% KOH, Fig. 3. A possible explanation is that the OH^- ions needed for the anodic process are then more closely bound to the K^+ ions and hence more energy is needed to pry these OH^- ions away.

An alternate explanation assumes that these silver electrode reactions proceed by way of a species in solution (11, 12), *e.g.*,

$$Ag(s) \rightarrow Ag^+_{sol'n} + e \quad [1]$$

$$Ag^+_{sol'n} + OH^- \rightarrow \tfrac{1}{2}Ag_2O(s) + \tfrac{1}{2}H_2O \quad [2]$$

In the anodic process the OH^- ions are needed to react with the Ag^+ ions in solution. However, the overvoltage then is that of reaction [1] and would likely be due to concentration polarization of the Ag^+ ions in solution. An increase of 20 mv in the overvoltage would correspond to a Ag^+ ion concentration of about 2M. This seems inordinately high in view of the relative insolubility of Ag_2O even though this would be but a local interfacial concentration. The OH^- concentration in this area would then be of the order of 10^{-4}M.

Cathodically, there is a lowering of the overvoltage in 35% KOH, Fig. 4, *i.e.*, the process takes place more easily in this concentration of KOH. This is consistent with a proposed mechanism suggested earlier (13). Hydrated K^+ ions are involved in this process. As the concentration of these ions increases, the process proceeds more easily (overvoltage decreases). But beyond 35% KOH, the incipient ion-pair formation changes this relationship and the OH^- ions in solution now also compete for the water of hydration of the K^+ ions. As a result, the overvoltage for the reduction of silver oxide increases.

A somewhat similar explanation has been offered for the minimum in the hydrogen overvoltage curve at a zinc electrode (1). It was suggested that beyond about 35% KOH there is a decrease in cation hydration in the double layer. These less-hydrated cations then have a greater screening effect on the electrical force lines, making it more difficult for the water molecules to discharge.

It is also possible to assume that the cathodic process proceeds by way of a species in solution, *e.g.*,

$$Ag_2O(s) + 2\,OH^- + H_2O \rightarrow 2Ag(OH)_{2(sol'n)}^- \quad [3]$$

$$2Ag(OH)_{2(sol'n)}^- + 2e \rightarrow 2Ag + 4\,OH^- \quad [4]$$

Again the overvoltage and its changes would likely be due to the concentration of $Ag(OH)_2^-$ and this would be governed by the availability of both H_2O and OH^- ions to dissolve the Ag_2O. However, other evidence suggests that it is more likely that the cathodic process takes place on the electrode (13).

The dlc data on Fig. 5 have a close resemblance to similar data obtained for the cadmium electrode (14). Superimposed on Fig. 5 is a part of the voltage-cur-

rent trace obtained by using a sweeping voltage technique at a rate of 20 mv/sec. The current becomes anodic at potentials cathodic to the $Ag_2O/Ag/OH^-$ electrode in that solution. The beginning of this anodic current coincides with the slight rise in the dlc. It may be associated with the formation of a strongly adsorbed layer of OH^- ions or of OH radicals (14), but not with the formation of Ag_2O (15). As the potential increases anodically, the anodic current also increases, corresponding to the formation and growth of the Ag_2O layer. The dlc then also decreases because this film or layer of Ag_2O introduces a parallel capacitance at the electrode-electrolyte interphase (14).

If this model has any validity, then it should also be applicable to other electrode processes occurring in KOH solutions. Further work is now in progress to make this test of the model.

Acknowledgment

This work was performed under contract with the United States Office of Naval Research.

Manuscript received May 1, 1967; revised manuscript received Aug. 16, 1967.

Any discussion of this paper will appear in a Discussion Section to be published in the June 1968 JOURNAL.

REFERENCES

1. N. G. Bardina and Z. A. Iofa, *Izv. Vysshikh Uchebn. Zavedenii, Khim. i Khim. Teknol.*, **5**, 916 (1962).
2. N. A. Hampson and M. J. Tarbox, *This Journal*, **110**, 95 (1963).
3. T. P. Dirkse, D. Vander Hart, and J. Vriesenga, *J. Inorg. Nucl. Chem.*, **27**, 1779 (1965).
4. K. Kordesch and A. Marko, *This Journal*, **107**, 480 (1960).
5. J. J. McMullen and N. Hackerman, *ibid.*, **106**, 341 (1959).
6. J. P. Hoare, *Electrochim. Acta*, **9**, 599 (1964).
7. L. G. Austin and H. Lerner, "Review of Fundamental Investigations of Silver Oxide Electrodes," Report No. 1 on Contract DA49-186-AMC-197(D), October 1965, Pennsylvania State University, University Park, Pa.
8. D. D. Bode, Jr., T. N. Andersen, and H. Eyring, *This Journal*, **114**, 72 (1967).
9. G. W. Brady and J. T. Krause, *Norelco Reporter*, **5**, 111 (1958).
10. J. J. Lander and J. A. Karella, "Silver-Zinc Electrodes and Separator Research," 2nd Quarterly Report of 15 January 1967 on Contract No. AF 33(615)-3487, Delco-Remy, Anderson, Ind.
11. M. Fleischmann and H. R. Thirsk, "Advances in Electrochemistry and Electrochemical Engineering," Vol. 3, p. 193, Interscience Publishers, Inc., New York (1963).
12. T. P. Dirkse, *This Journal*, **111**, 629 (1964).
13. T. P. Dirkse, *ibid.*, **107**, 859 (1960).
14. M. W. Breiter and J. L. Weininger, *ibid.*, **113**, 651 (1966).
15. T. P. Dirkse and D. B. DeVries, *J. Phys. Chem.*, **63**, 107 (1959).

Low-Temperature Intermediate pH Fuel Cell Electrolytes

M. Beltzer

Esso Research and Engineering Company, Linden, New Jersey

ABSTRACT

Expressions are developed to compare the efficiency of buffers with strong acids or bases in minimizing concentration polarization. The effect of electrode structure on electrolyte efficiency is also considered. The expressions are tested experimentally. In certain cases, practical current densities can be obtained with buffer electrolytes at sufficiently low concentration polarizations. It is possible therefore to supplant, *e.g.*, strong acids in some fuel cell systems. Unlike acid electrolytes, the performance of buffers is markedly dependent on electrode structure.

Sulfuric and phosphoric acid electrolytes are frequently used in fuel cells because these systems reject carbon dioxide, have high ionic conductivity, minimize concentration polarization, and allow attainment of high activity levels. The corrosiveness of these acids, however, restricts choice of electrode catalysts to noble metals. Auxiliary cell components must also be composed of noble metals or expensive nonnoble corrosion resistant metals such as tantalum. The use of noble metal catalysts and costly cell components constitutes the major obstacle to the development of a practical economical fuel cell.

One approach to this problem would be to investigate inexpensive alloys which would be acid resistant and possibly catalytic. An alternative approach, which will be the theme of this article, is the use of less corrosive electrolytes to replace sulfuric acid in low-temperature fuel cells.

Acids can be conveniently grouped into three types according to how they partake in the corrosion reaction (1). There are strong acids such as sulfuric and hydrochloric acids, weak acids such as acetic acid, and oxidizing acids such as nitric acid. Excluding oxidizing acids, hydrogen ion is the principal and most universal factor in corrosion phenomenon. Alkaline electrolytes are, therefore, not nearly as corrosive as acids. When corrosion does occur in alkaline electrolytes, it is usually the result of particular reactions such as formation of anionic metal complexes. Although it is difficult to generalize about the corrosiveness as a function of electrolyte *p*H, neutral and alkaline *p*H electrolytes are normally not as corrosive as acids (1,2). The requirement that the electrolyte reject carbon dioxide sets an upper limit to the alkalinity. Accordingly, a study was undertaken to determine if electrolytes in the neutral to weakly alkaline *p*H range would be suitable as fuel cell electrolytes. The potentials of the electrodes are *p*H dependent which means that any electrolyte used in a fuel cell must have buffering action.

Invariance Requirement Sets Upper pH Limit of Buffer System

The necessity for electrolyte invariance sets the upper limit to the *p*H range and, therefore, the buffer systems that can be used. Whether a buffer system or electrolyte in general is carbon dioxide rejecting or not depends on the extent of the reaction

$$CO_2 + H_2O + 2H_{N-1}A^{-(M+1)} \rightarrow 2H_NA^{-M} + CO_3^{-2} \quad [1]$$

where $H_{N-1}A^{-(M+1)}$ is an anionic basic buffer component and H_NA^{-M} the anionic acidic buffer component. Anionic buffer components were chosen for illustration simply because the components of the so-called practical buffer systems are anions, *e.g.*, as in phosphate and carbonate buffers. All charge types of course are possible.

The equilibrium constant for the reaction with carbon dioxide is

(III)
$$\begin{cases} H_{N-1}A^{-(M+1)}{}_{\{\text{bulk solution}\}} \xrightarrow[\text{Diffusion, Migration, Convection}]{\text{Slow}} H_{N-1}A^{-(M+1)}\ (\text{electrode}) + H_2O \\ H_NA^{-M}{}_{(\text{electrode})} \xrightarrow[\text{Diffusion,Migration}]{\text{Slow}} H_NA^{-M}\{\text{bulk solution}\} \end{cases}$$

$$K = \frac{[H_NA^{-M_2}]^2[CO_3^{-2}]}{[H_{N-1}A^{-(M+1)}]^2[CO_2]} = \frac{K_1K_2}{K_A^2} \qquad [2]$$

where K_1 and K_2 are the first and second ionization constants of carbonic acid, and K_A the ionization constant of the buffer acid (H_NA^{-M}). It can readily be shown that carbonate formation becomes appreciable when K_A is of the order of 10^{-10} for finite carbon dioxide partial pressures. Extensive formation of carbonate means that the buffer has been quantitatively converted to its acid form and therefore no longer can function as a buffer.

The resultant electrolyte reacts further with carbon dioxide as shown below

$$H_2O + CO_2 + CO_3^{-2} \rightarrow 2\ HCO_3^{-1} \qquad [3]$$

The equilibrium constant for the above reaction is K_1/K_2. This is also the equilibrium constant when the buffer system is a carbonate-bicarbonate buffer, *i.e.*, $H_NA^{-M} = HCO_3^{-1}$, $H_{N-1}A^{-(M+1)} = CO_3^{-2}$ and $K_A = K_2$. It has been shown that at the contemplated fuel cell conditions, in particular the operating temperatures and carbon dioxide partial pressures, the equilibrated carbonate-bicarbonate mixture will be constituted so that it is capable of functioning as a buffer (3, 4). Complete conversion of carbonate to bicarbonate would result in a solution of low buffering capacity. If this occurred, then the upper pH limit of suitable fuel cell electrolyte would be less than pK_2; *i.e.*, only a buffer whose pK_A was one to two units lower than pK_2 would be suitable. The carbonate-bicarbonate carbon dioxide equilibrated electrolyte is a buffer system because conversion is not complete. Consequently, no buffer system whose acid component is a weaker acid than bicarbonate ion can be an invariant electrolyte. Thus, the upper pH limit for electrolyte invariance is approximately equal to pK_2.

Theoretical

Buffers are the only possible substitute electrolytes for fuel cells if it is desirable not to use either strong acids or bases. It is therefore of interest to compare the efficiency of buffers with that of acids and bases in minimizing electrolyte concentration polarization. It is also of interest to determine the effect of electrode structure on the ability of the buffers to support practical current densities. To this end it was necessary to develop the expressions for concentration polarizations incurred with buffers as a function of their mass transfer characteristics.

Consider a fuel cell operating in a neutral Na_2SO_4 electrolyte. When current is drawn, anodically produced hydrogen ions cause a precipitous pH decrease at the anode. At the cathode a large pH increase occurs simultaneously due to hydroxide ion production. To prevent the occurrence of large pH changes at the electrodes, agents are needed to remove anodically produced hydrogen ion and cathodically produced hydroxide ion. These agents are the basic and acidic components of what constitutes a buffer system.

The sequence of reactions occurring at an anode of fuel cell employing a buffer electrolyte is given below.

(I) $$\tfrac{1}{2}\ H_2 + H_2O \xrightarrow[\text{Discharge}]{\text{Anodic}} H_3O^+ + E^-$$

(II) $$H_{N-1}A^{-(M+1)}{}_{(\text{electrode})} + H_3O^+{}_{(\text{electrode})} \xrightarrow[\text{Recombination}]{\text{Fast}} H_NA^{-M}\ (\text{electrode})$$

Hydrogen ions produced by the anodic current are removed by reaction with the basic buffer component. It is well known that the recombination steps are very rapid and many have recently been measured (5). The rate-limiting steps are replenishment of the basic component in the unstirred layer from the bulk electrolyte by diffusion and migration, and mass transfer of the acidic buffer component out of this region.

If a linear concentration gradient for each species is assumed to exist across the boundary layer, and if Fick's law is applicable to each diffusing species, the steady-state concentration of the buffer components at the electrode electrolyte boundary can be calculated. In turn, the change in pH at the boundary and, therefore, the concentration polarization as a function of the current density, can be calculated.

At steady state, consumption of the basic component is equal to the rate at which it is replaced by mass transfer.

$$\frac{I}{\mathbf{F}} = D_B\frac{(C^o_B - C_B)}{\delta} + t_B\frac{I}{\mathbf{F}} \qquad [4]$$

Here C^o_B is the bulk concentration of the basic component in eq/cm^3, C_B the concentration at the electrode due to a current density I (amp/cm^2), t_B and D_B the transference number and diffusion coefficient, respectively, of the basic component, and δ the boundary layer thickness. Rearrangement of the above expression gives the limiting anodic current density I_{LA}

$$\frac{C_B}{C^o_B} = 1 - \frac{I(1-t_B)\delta}{C^o_B D_B \mathbf{F}} = 1 - \frac{I}{I_{LA}};$$

$$I_{LA} = \frac{D_B \mathbf{F} C^o_B}{(1-t_B)\delta} \qquad [5]$$

By similar reasoning, the concentration at steady state of the acidic component at the electrode can be calculated where the

$$\frac{I(1+t_A)}{\mathbf{F}} = \frac{D_A(C_A - C^o_A)}{\delta} \qquad [6]$$

subscripts refer to the acid component and its parameters. The concentration of the acidic buffer component may also be cast in terms of a limiting current by appropriate rearrangement.

$$\frac{C_A}{C^o_A} = 1 + \frac{I(1+t_A)\delta}{C^o_A D_A \mathbf{F}} = 1 + \frac{I}{I_{LC}} \qquad [7]$$

That $I_{LC} = D_AC^o_A\mathbf{F}/(1+t_A)\delta$ is the limiting cathodic current density will be shown when considering concentration polarization at the cathode.

When the relative concentrations of the basic and acid components are such that the electrolyte acts as a buffer, the pH of the solution may be expressed by the Henderson-Hasselbach approximation

$$pH = pK_A + \log\frac{C^o_B}{C^o_A}$$

The pH change at the electrode-electrolyte boundary may be calculated by appropriate substitution into this equation. Thus, the pH change due to current at the anode is

$$\Delta pH_{Anode} = \log \frac{[1 - I/I_{LA}]}{[1 + I/I_{LC}]} \quad [8]$$

The anodic concentration polarization is simply

$$\eta_{Anode} = -2.3 \frac{RT}{F} (\Delta pH) \quad [9]$$

At the cathode, the hydroxide ions produced are removed by reaction with the acidic buffer component. Here too, mass transfer of the buffer components into and out of the boundary layer is rate determining.

The concentration of the acidic buffer component at the electrode-electrolyte boundary can be calculated in a similar manner as shown at the anode, where I_{LC} is the limiting cathodic current density.

$$\frac{I(1 + t_A)}{F} = \frac{D_A(C^o_A - C_A)}{\delta} \quad [10]$$

$$\frac{C_A}{C^o_A} = 1 - \frac{I}{I_{LC}} \quad [11]$$

The basic buffer component concentration at the electrode is similarly calculated.

$$\frac{I}{F} = \frac{D_B(C_B - C^o_B)}{\delta} + t_B \frac{I}{F} \quad [12]$$

$$\frac{C_B}{C^o_B} = 1 + \frac{I(1 - t_B)_\delta}{D_B F C^o_B} = 1 + \frac{I}{I_{LA}} \quad [13]$$

The pH change at the cathode due to current flow is

$$\Delta pH_{cathode} = \log \frac{\left[1 + \frac{I}{I_{LA}}\right]}{\left[1 - \frac{I}{I_{LC}}\right]} \quad [14]$$

and the polarization,

$$\eta_{cathode} = 2.3 \frac{RT}{F} [\Delta pH \text{ cathode}] \quad [15]$$

Comparison of buffers with strong acids and bases.— Williams and Gregory (6) have shown that, in strong acids, limiting current densities are encountered at the cathode. Cathodic current decreases the hydrogen ion concentration at this electrode and since the concentration cannot drop below zero, a limiting current will be attained. The limiting current expressed in amp/cm^2 is given by the expression

$$I_{LC(acid)} = \frac{D_{H+} C^o_{H+} F}{(1 - t_{H+})\delta} \quad [16]$$

where t_{H+}, C^o_{H+}, and D^o_{H+} are the transport number, bulk concentration, and diffusion coefficient of hydrogen ion.

In strong base, hydroxide ion is decreased at the electrode-electrolyte boundary of the anode so that it is at this electrode that limiting currents are attained. The limiting current in base is given by the expression

$$I_{LA(base)} = \frac{D_{OH-} C^o_{OH-} F}{(1 - t_{OH-})\delta} \quad [17]$$

where t_{OH-}, C^o_{OH-}, and D_{OH-} are the equivalent parameters for a strong base.

As shown previously, buffers exhibit limiting currents at both electrodes due to decrease of the basic component at the anode and of the acidic component at the cathode. In addition to exhibiting limiting currents at both electrodes, the limiting currents in buffer are considerably less than those attained in acid and base. The limiting current ratios are given below

$$\frac{I_{LC(acid)}}{I_{LC(buffer)}} = \left(\frac{D_{H+}}{D_A}\right)\left(\frac{C^o_{H+}}{C^o_A}\right)\left[\frac{(1 + t_A)}{(1 - t_{H+})}\right] \quad [18]$$

$$\frac{I_{LA(base)}}{I_{LA(buffer)}} = \left(\frac{D_{OH-}}{D_B}\right)\left(\frac{C^o_{OH-}}{C^o_B}\right)\left[\frac{(1 - t_B)}{(1 - t_{OH-})}\right] \quad [19]$$

A sample calculation using reasonably accurate values for diffusion coefficients and transference numbers would show that the limiting current densities attainable in acids or bases are much larger than what can be attained in buffer. Using the literature values given below, plus some reasonable estimates where data are not available, shows that the limiting cathodic current density in acid is more than 40 times greater than that in buffer

$$D_{HCl} \simeq 4 \times 10^{-5} \text{ cm}^2 \text{ sec}^{-1} \quad 7$$

$$t_{H+} \simeq 0.8 \quad 8$$

$$D_{NaH_2PO_4} \simeq 0.5 \times 10^{-5} \text{ cm}^2/\text{sec} \quad 8$$

$$t_{H_2PO_4} \simeq 0.1 \text{ (estimated)}$$

$$\frac{I_{LC(acid)}}{I_{LC(buffer)}} \simeq 44, \text{ for } C^o_{H+} = C^o_A$$

The abnormally high ionic diffusivities and mobilities of hydrogen and hydroxide ion allow much greater limiting currents to be reached. This does not mean that buffers are unsuitable. The limiting current in 3M strong acid for example assuming a boundary layer thickness of 10^{-2} cm is about 6000 ma/cm^2. This means that in the practical current density range, *i.e.*, 100-400 ma/cm^2, concentration polarization in acid would not be discernible. In buffer, the limiting current density would be about 120 ma/cm^2 which is in the range of practical fuel cell loads.

It can be shown that the concentration polarization with a buffer electrolyte at less than the limiting current densities is much greater than what would be incurred using an acidic or basic electrolyte, at identical current densities. A comparison can be readily made by using the expanded form of logarithm in Eq. [8] or [14] and neglecting the higher order terms.

$$\underset{(buffer)}{\Delta pH_{anode}} \simeq -0.43I\left[\frac{1}{I_{LA(buffer)}} + \frac{1}{I_{LC(buffer)}}\right] \simeq -\underset{(buffer)}{\Delta pH_{cathode}} \quad [20]$$

Assuming that $I_{LA(buffer)} \simeq I_{LC(buffer)}$

$$\Delta pH_{anode} \simeq -2(0.43)\frac{I}{I_{LA(buffer)}} \quad [21]$$

The following expression is obtained

$$\underset{(base)}{\Delta pH_{anode}} \simeq -0.43\frac{I}{I_{LA(base)}} \simeq \frac{-0.43(I)(1 - t_{OH-})\delta}{D_{OH-} C^o_{OH-} F} \quad [22]$$

by expanding the logarithm of the expression for concentration polarization in strong base (6).

Comparing concentration polarization at the anode for example in buffer and in base at the same current density

$$\frac{\underset{(buffer)}{\Delta pH_{anode}}}{\underset{(base)}{\Delta pH_{anode}}} = 2\frac{I_{LA(base)}}{I_{LA(buffer)}} = 2\frac{(C^o_{OH-})D_{OH-}(1 - t_B)}{(C^o_B)D_B(1 - t_{OH-})} \quad [23]$$

As the pH changes vary inversely with the limiting current density, it is obvious that concentration polarization in buffers will be considerably greater than that incurred in acids or bases.

If we consider the case of a buffer system equimolar in each component having a stoichiometric concen-

tration equal to the hydroxide ion concentration, the ratio of the pH changes becomes

$$(4)\quad \frac{D_{OH^-}\,(1-t_B)}{D_B\,(1-t_{OH^-})} = \frac{\eta\text{anode(buffer)}}{\eta\text{anode(base)}} \qquad [24]$$

The factor 4 reflects the fact that the maximum buffering capacity of a buffer solution, one containing equimolar amounts of each component, is only ¼ that of a solution of strong base or acid having a hydroxide or hydrogen ion concentration equal to the stoichiometric buffer concentration.[1] Thus, completely exclusive of mass transfer considerations, the lower inherent buffering capacity of buffers means that greater pH changes would occur with this electrolyte than with strong acids or bases. It is the cooperative coupling of the greater inherent buffer capacities of strong acids and bases with the abnormally high mobilities of hydrogen and hydroxide ion that make these markedly superior electrolytes in minimizing concentration polarization.

A sample calculation shows that if an electrode exhibited a concentration polarization of, *e.g.*, 50 mv in buffer, the same electrode in base would be polarized about 1 mv.

Using $t_{OH^-} = 0.74$ and $D_{KOH} = 2.2 \times 10^{-5}$ cm^2 sec^{-1} and the appropriate values for the buffer system

$$\frac{\Delta pH_{\substack{\text{anode}\\(\text{buffer})}}}{\Delta pH_{\substack{\text{anode}\\(\text{base})}}} = 4\,\frac{(2.2)\times 10^{-5}\,(1-0.3)}{(0.5)\times 10^{-5}\,(1-0.74)}$$

$$\simeq 50 = \frac{\eta\text{anode(buffer)}}{\eta\text{anode(base)}}$$

Tests were conducted on platinum electrodes using hydrogen as the test reactant because of its negligible activation polarization. Galvanostatic performance curves were obtained using a Kordesch-Marko bridge (9). Consequently, the measured polarization under load is strictly concentration polarization. Because of the necessity for maintaining an interface to insure an unimpaired supply of hydrogen, it is not possible to use the idealized electrode model of the calculation. This structure can be approached by using an extremely thin porous electrode such as that manufactured by the American Cyanamid Company (10). It has been shown that practically all of the electrode catalyst surface area is available for reaction. As these electrodes are too porous to maintain a stable interface, it was necessary to clad the electrodes. The cladding material was a Gelman Acropor Battery Separator (11) which has microscopic porosity ($\sim 0.5\mu$).

A material of microscopic porosity rather than submicroscopic porosity was chosen to simulate more closely, the situation where the electrode is wetted by a stagnant film that is in contact with a bulk electrolyte, *i.e.*, the Nernst boundary layer conditions.

Comparison of the hydrogen performances in phosphate and carbonate buffers, with that in sulfuric acid and potassium hydroxide, Fig. 1 shows that the results are in good agreement with what Eq. [18], [19], and [25] predicted.

It is readily seen that there is no sensible polarization in 3M KOH or 30% H_2SO_4 at 100 ma/cm^2, for example, as opposed to 40 mv in buffer. The fact that no polarization occurs in base or acid is taken to mean that these electrode structures are not hydrogen limited and that the polarization in the buffer systems is due to ionic mass transfer limitations. Although finite polarizations occur with buffers, practical current densities can be attained.

Effect of electrode structure.—It is of interest to determine if buffers are suitable electrolytes for the electrode structures commonly employed in fuel cells.

[1] Buffer capacity is defined as the number equivalents of strong base or acid per liter required to produce a unit change of pH in the solution.

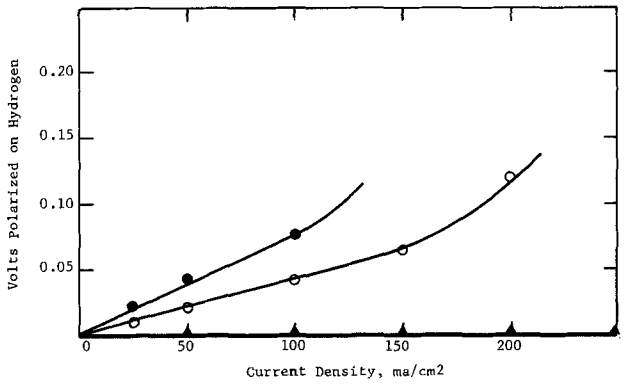

Fig. 1. Unlike strong acids and bases, buffers exhibit finite concentration polarizations at practical current densities. Temperature 80°C, Electrode type AA-1 Cyanamid clad with Gelman Acropor membrane. ● 1M each KH_2PO_4, K_2HPO_4; ○ 2M each RbH_2PO_4, Rb_2HPO_4; ▲ 30% H_2SO_4 or 3M KOH.

For example, fuel cell electrodes using gaseous reactants cannot have the active catalytic surface in direct contact with the bulk electrolyte and attain adequate performance levels. If the dissolved gas molecules are forced to diffuse through a thick liquid interface to reach the catalyst surface, the supply of reactant to the electrode will be insufficient to maintain the electrochemical reaction, and thereby become rate controlling. Only if very thin electrolyte films wet the catalyst surface can this rate limitation be removed, *i.e.*, the electrode must be interface maintaining. It will be shown, however, that with buffer electrolytes, practical current densities cannot be attained at the usual interface maintaining electrode structures without incurring large ionic concentration polarizations.

An example of an interface maintaining a structure is the membrane electrode (12). This generally consists of thin electrode bonded to a membrane. The membrane is a thin sheet or film having submicroscopic pores and is usually organic in nature. The electrode cladding the membrane may be powdered metal directly bonded, or may consist of catalyst and binder spread uniformly on to a metal gauze which in turn is bonded to the membrane.

As used in most applications, the uncatalyzed side of the membrane contacts the bulk electrolyte. Electrolyte is imbibed by the membrane although bulk flow through the membrane does not occur because it is a structure of submicroscopic porosity. The electrolyte layer on the catalyzed side of the membrane is regulated by the properties of the membrane as well as being stabilized at the junction between a fine pore layer and a coarse pore layer of the catalyst. Teflon may also be mixed with the catalyst to regulate the gas-electrolyte interface further.

In the following discussion, it will be assumed that the membrane electrode is planar, that all fluxes are normal to the electrode, and that the steady state can be attained. A membrane electrode as now constituted can be considered to consist of three barriers to ion transport either toward or away from the electrode surface. The sequence of these barriers considering ionic mass transfer from the bulk of solution through the membrane to the electrode surface are as follows; the stagnant electrolyte film on the side of the membrane contacting the electrolyte, the membrane, and the electrolyte film wetting the catalyst.

When a steady-state current is attained, the value of each ionic flux across all planes parallel to the interfaces is constant. It is assumed that a linear concentration gradient exists across each barrier. In addition, the membrane is assumed to be uncharged so that the distribution coefficient of both electrolytes and nonelectrolytes is unity. This coefficient is defined as the ratio of the concentration of a species in the membrane to that in the external solution at equilibrium.

The concentration of the buffer components at the electrode electrolyte interface is calculated from the flux equations. Thus for a membrane electrode functioning as an anode, the interfacial concentration of the basic component C'''_B is

$$C'''_B = C^o_B - \frac{I}{\mathbf{F}}\left[\frac{(1-t_{B1})\delta_1}{D_{B1}} + \frac{(1-t_{B2})\delta_2}{D_{B2}} + \frac{(1-t_{B3})\delta_3}{D_{B3}}\right] \quad [25]$$

Where D_{B1}, D_{B2}, and D_{B3}, are the diffusion coefficients of the basic buffer component in the stagnant electrolyte film, the membrane and the electrolyte film wetting the electrode, respectively. The corresponding transport numbers in each phase are t_{B1}, t_{B2}, and t_{B3}; δ_1, etc., the corresponding diffusion barrier thicknesses and C^o_B has its previous meaning.

This may be generalized for both components in an n-barrier system so that

$$C_B{}^{n'} = C^o_B - \frac{I}{\mathbf{F}}\sum_{i=1}^{n}\frac{(1-t_{Bi})\delta i}{D_{Bi}}, \text{ and}$$

$$C_A{}^{n'} = C^o_A + \frac{I}{\mathbf{F}}\sum_{i=1}^{n}\frac{(1+t_{Ai})\delta i}{D_{Ai}} \quad [26]$$

The concentration polarization at the anode is given by the equation

$$\eta\text{anode} = \frac{2.3\,RT}{\mathbf{F}}\log\left[\frac{1-\frac{I}{C^o_B\mathbf{F}}\sum_{i=1}^{n}\frac{(1-t_{Bi})\delta i}{D_{Bi}}}{1+\frac{I}{C^o_A\mathbf{F}}\sum_{i=1}^{n}\frac{(1+t_{Ai})\delta i}{D_{Ai}}}\right] \quad [27]$$

and the limiting current density by

$$I_{LAM} = \frac{\mathbf{F}C^o_B}{\sum_{i=1}^{n}\frac{(1-t_{Bi})\delta i}{D_{Bi}}} \quad [28]$$

Similar equations are obtained for the case of a membrane electrode cathode.

It has been generally assumed that material transport across a membrane resembles diffusion in bulk solutions with the following differences. Only the void volume, *i.e*, that volume not occupied by the membrane matrix, is available for solute transport. The tortuosity of the pores makes the average distance traveled by the ions in traversing the membrane greater than the average distance traveled in crossing the same thickness of pure water by random Brownian displacements. In addition, the actual mobility of the diffusing species may be reduced by interactions with the pore walls. The retarding effect of the membrane matrix can be taken into account by using an effective membrane diffusion coefficient $\overline{D}$ which must obviously be lower than the diffusion coefficient $\overline{D}$ of the species in free solution. Thus, $\overline{D}$ refers to both D_{A2} and D_{B2}.

There are various models which attempt to relate the diffusion coefficient in the absence of a matrix with that of the effective intra-particle diffusion coefficient of the species in an ion exchange particle (12, 13). These treatments can be applied to diffusion through porous membranes. Helfferich (14) has estimated $D/\overline{D}$ as approximately 5. Most membranes are thicker than the adherent film wetting their external surfaces. The quotient $D\delta_2/\overline{D}\delta_1$, where δ_2 is the membrane thickness, δ_1 that of the adherent film, ranges from 10 for very thick membranes to 200 for a relatively thick one, *e.g.*, 0.1 cm. Consequently, it would be expected that even with very thin membranes, the membrane will determine the over-all rate of transport.

Therefore, the anodic concentration polarization is given by the expression

$$\eta\text{anode} = \frac{2.3\,RT}{\mathbf{F}}\log\frac{\left[1-\frac{2I\delta_2(1-t_{B2})}{C^oD_{B2}\mathbf{F}}\right]}{\left[1+\frac{2I\delta_2(1-t_{A2})}{C^oD_{A2}\mathbf{F}}\right]} \quad [29]$$

and the limiting anodic current density by

$$I_{LAM} \simeq \frac{C^oD_{B2}\mathbf{F}}{\delta_2(1-t_{B2})} \quad [30]$$

The limiting current density (I_{LAM}) at a membrane electrode is therefore only about 1/10 to 1/200 that which can be obtained in the absence of a membrane since, *e.g.*,

$$\frac{I_{LAM}}{I_{LA}} \simeq \frac{D_{A1\,2}}{D_{A2\,1}}$$

Since the range of the buffer region is inversely proportional to the limiting current density, Eq. [21], it follows that the buffer range with a membrane electrode is so compressed as to make this structure entirely unsuitable for use in a practical fuel cell.

Using the same experimental set up previously described, membrane electrode systems were tested with hydrogen in phosphate buffer, carbonate buffer, sulfuric acid, and potassium hydroxide. The membrane used was a Nalfilm D-30 membrane made by the National Aluminate Company. A description of its properties is available (15). This membrane has a fractional void volume as measured by water content of 65% and pores ranging from 30 to 60Å in diameter; too small to allow convection. Figure 2 shows that the retarding effect of the membrane matrix is to reduce severely the limiting current density attainable with phosphate buffers to impractically low levels. Similar results were obtained with carbonate buffers and with both buffers on various types of porous diffusion electrodes.

No structure effect is evident with sulfuric acid or potassium hydroxide. This is because the high efficiency of hydrogen ion and hydroxide ion in minimizing concentration polarization obliterate the effect of structure at practical current densities. Thus for example, if the effect of a membrane is to reduce the limiting current density in acid by a factor of 10, it would still be as high as 600 ma/cm^2 based on previous calculations. Consequently, in the practical current density range of 100-400 ma/cm^2 concentration polarization would still be small.

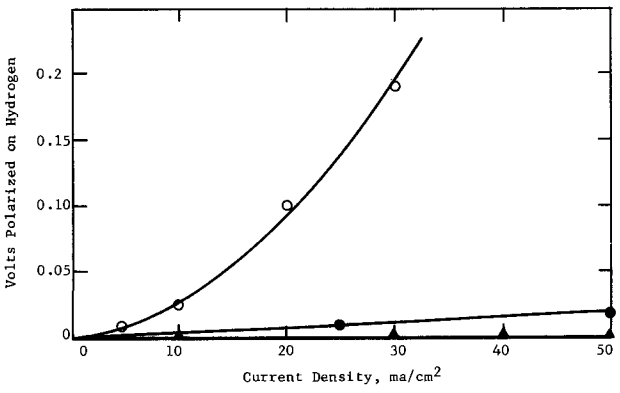

Fig. 2. Dependence of buffer efficiency on electrode structure. Temperature 60°C, Electrode type AA-1 Cyanamid; ○ Electrode clad with Nalfilm D-30 in 1M each KH_2PO_4, K_2HPO_4 buffer; ● electrode clad with Gelman Acropor battery separator in phosphate buffer; ▲ electrode clad with either backing material in 30% H_2SO_4 or 3M KOH.

Electrode structure is, therefore, critical only when the electrolyte is a buffer. Strong acids and bases can be used with a variety of structures because of their high buffering capacity and abnormally high ionic mobilities. Concentration polarization with buffer systems is markedly sensitive to electrode structure because they do not have these rather unique properties of acids and bases.

Buffers and electrolyte soluble fuel systems.—With an electrode that does not have to maintain an interface, a more favorable situation for buffer ion mass transport exists. For example, when a soluble fuel such as methanol is oxidized, a relatively nonporous electrode structure can be used. The working area of the electrode is immersed in and completely wetted by the fuel containing electrolyte. The active electrode areas are subject to natural convection which would be augmented by carbon dioxide evolution, when the electrode is under load.

Methanol runs were carried out using platinum black anodes. The catalyst was made by reduction of chloroplatinic acid with potassium borohydride. Electrodes were fabricated by pressing the freshly precipitated platinum into 80-mesh platinum or gold support screens. Anodic activity runs were obtained in neutral phosphate and in weakly alkaline carbonate buffers, each 1M in each buffer component and containing 1M in each buffer component and containing 1M methanol. Steady-state current-voltage curves were obtained with quiescent solutions, and with the electrolytes stirred magnetically at 200 rpm.

Suppression of ionic concentration polarization by stirring allows a more accurate measurement of the true catalytic activity, as well as a way to measure the major portion of the concentration polarization itself. At 60°C for example, stirring either buffer solution produces a polarization decrease of 50 mv when the anode is operating at 100 ma/cm^2. That the reductions in anode polarization obtained by stirring are solely that due to lowering of ionic concentration polarization, and not to fuel transport limitations can readily be shown.

It is known that stirring sulfuric acid solutions containing 1M methanol has no effect on anode performance (16). Studies have also shown that with methanol concentrations as low as 0.1M, identical steady-state current-voltage curves are obtained in quiescent as well as stirred solutions in strong acid (16) and strong base electrolytes (17). The difference between the results obtained in strong acids or bases and buffers can, therefore, be only due to the concentration polarization in buffers. The use of buffer solutions of increased capacity would, as expected, lower concentration polarization still further. This can be accomplished by simply increasing the buffer concentration, or without changing concentration, employ buffers that are salts of polybasic acids having successive ionization constants that overlap sufficiently so that they do not differ appreciably in magnitude.

Methanol performances were obtained in stirred and unstirred solutions of 2M each RbH_2PO_4, Rb_2HPO_4, and 1M each $K_3HP_2O_7$, $K_4P_2O_7$ solution as an example of the latter system. The performance improvements obtained in the unstirred higher capacity buffer solutions were similar to those obtained by stirring the more dilute buffer systems. Consequently, agitating the higher buffer capacity solutions had little influence on activity. The comparative results showing the decreased effect of stirring with increased buffering capacity is given in Table I, demonstrating the virtual elimination of concentration polarization.

Figures 3 and 4 show that methanol activity on platinum in the intermediate pH range is comparable to or considerably better than that exhibited in strong acid medium. That there is a pH effect on activation polarization can be readily seen by the markedly superior activity in carbonate bicarbonate buffer. The influence of pH on activation polarization will not be considered in this communication, however. In all cases, carbon dioxide evolution was observed in the buffer electrolytes at current densities as low as 5 ma/cm^2. This is also about the lowest current density at which evolution can be visually ascertained in acid electrolytes. No electrolyte pH changes were observed despite high loads sustained for time intervals of sufficient length to alter the electrolyte composition if it was not invariant.

Table I. Effect of stirring and buffer capacity on anode performance

Current density, ma/cm^2	Reduction of polarization (volts) at 60°C by stirring		
	1M KH_2PO_4 1M K_2HPO_4	2M RbH_2PO_4 2M Rb_2HPO_4	1M $K_3HP_2O_7$* 1M $K_4P_2O_7$
25	0.020	0.010	0.010
50	0.040	0.010	0.015
100	0.050	0.015	0.015
150	0.050	0.015	0.015

* Pyrophosphate hydrolyzes to phosphate, but at 60°C and neutral pH, hydrolysis is slow enough that steady-state current-voltage data can be obtained with negligibly low conversions to orthophosphate.

Conclusions

Compared to strong acids and bases buffers are inferior fuel cell electrolytes. They exhibit considerably greater concentration polarizations than, *e.g.*, acids and cannot be used with typical interface maintaining fuel cell electrodes. Limiting current densities are exhibited at both anode and cathode, unlike acids or bases. As buffer ions do not have the high conduc-

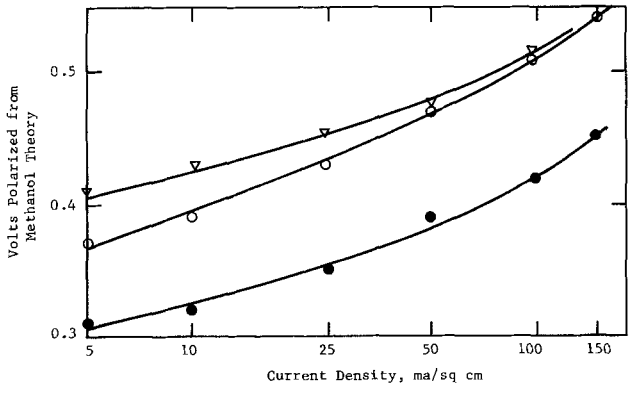

Fig. 3. Methanol performance on platinum catalyst in phosphate buffer (1M each KH_2PO_4, K_2HPO_4, pH = 6.6 at 25°C). Methanol concentration, 1M. Electrolyte stirred at 200 rpm, ○ = 60°C run, ● = 80°C run, ▽ = 1M methanol in 30% H_2SO_4 at 60°C, no stirring.

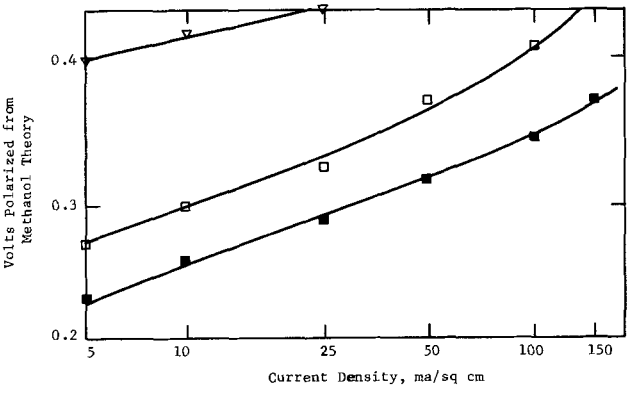

Fig. 4. Methanol performance on platinum catalyst in carbonate buffer (1M each $KHCO_3$, K_2CO_3, pH = 10.2 at 25°C). Methanol concentration, 1M. Electrolyte stirred at 200 rpm, □ = 60°C run, ■ = 80°C run, ▽ = 1M methanol in 30% H_2SO_4 at 60°C, no stirring.

tivities of hydrogen or hydroxide ion, ohmic losses would be higher in a buffer fuel cell. Where electrode structure is unimportant, as in the case of electrolyte soluble fuels, buffers are comparable to strong acids or bases.

Practical current densities have been attained however at novel interface maintaining electrode structures with finite but tolerable concentration polarizations. The justification for buffer systems is that cheaper nonnoble catalysts unstable in acid can be assessed for activity in less corrosive media. Buffers therefore present the opportunity to construct practical economical fuel cells.

Acknowledgment

A portion of this work was supported by the Advanced Research Projects Agency through the United States Army Electronics Laboratories.

Manuscript received June 9, 1967. This paper was presented at the Philadelphia Meeting, Oct. 9-14, 1966.

Any discussion of this paper will appear in a Discussion Section to be published in the June 1968 JOURNAL.

REFERENCES

1. R. K. Swandby, "Corrosion Resistance of Metals and Alloys," pp. 45-56, ACS Monograph No. 158, F. L. LaQue and H. R. Capson, Editors, Reinhold Publishing Co., New York (1963).
2. M. Pourbaix, Atlas D'Equilibres Electrochimiques á 25°C, Gauthier-Villars and Co., Paris (1963).
3. J. S. Tosh, J. H. Field, *et al.*, Bureau of Mines Report of Investigations 5484 (1959).
4. H. F. Benson *et al.*, *Chem. Eng. Prog.*, **50**, 356 (1959).
5. M. Eigen, *Angewandete Chem.*, **75**, 489 (1963).
6. K. R. Williams and D. P. Gregory, *This Journal*, **110**, 209 (1963).
7. B. E. Conway, "Electrochemical Data," Elsevier Publishing Co., New York (1952).
8. R. Parsons, "Handbook of Electrochemical Constants," Academic Press (1959).
9. K. E. Kordesch and A. Marko, *This Journal*, **107**, 480 (1960).
10. R. G. Haldeman, W. P. Colman, et al., "Fuel Cell Systems," Advances in Chemistry Series, No. 47, pp. 106-115, American Chemical Society, Washington, D. C. (1965).
11. Gelman Instrument Company, Product Bulletin No. 122.
12. J. S. Mackie and P. Meares, *Proc. Roy. Soc. (London)*, **A232**, 498 (1955).
13. J. A. Lane and J. W. Riggle, *Chem. Engr. Prog. Symp. Ser.*, **55**, 127 (1959).
14. F. Helffrich, "Ion Exchange," p. 348 McGraw-Hill Book Co., New York, (1962).
15. M. Mindick and R. Oda, Nalco Reprint No. 77.
16. J. M. Matsen and D. G. Levine, *Electrochem. Tech.*, **5**, 266 (1967).
17. R. G. Gentile, F. B. Lietz, *et al.*, U.S. Govt. Report AD272352 (1960).

The Kinetics of the Fluorination of Beryllium

Patricia M. O'Donnell

National Aeronautics and Space Administration, Lewis Research Center, Cleveland, Ohio

ABSTRACT

The kinetics of the reaction of sheet beryllium and gaseous fluorine to form beryllium fluoride were studied by means of the pressure drop method over the temperature range of 125°-775°C and at pressures from 20 to 700 Torr. The reaction followed the parabolic rate law. Parabolic rate constants were calculated, and activation energies are given. The pressure dependence is approximately first order with respect to the fluorine pressure. A change of slope in the plot of the rate constant against reciprocal temperature suggests a change in the nature of the reaction near 525°C. Above 525°C the crystal structure of the film changes from α-quartz hexagonal to rhombic tridymite. Beryllium is identified as the diffusing species.

Beryllium, because of its light weight, high-temperature strength, thermal conductivity, and neutron-moderating characteristics, is of interest for application in reactors, satellites, and future supersonic aircraft. The beryllium-oxygen reaction has been extensively studied, and it involves the outward diffusion of beryllium ions (1). At high temperatures the initially protective oxide film is no longer protective (2) because of the onset of breakaway oxidation. Several other beryllium-gas reactions have been investigated (3) including the reactions of beryllium with carbon monoxide and with carbon dioxide (4). Although data appear in the literature (5, 6) concerning the thermodynamic properties of beryllium fluoride, little is reported on the kinetics of the beryllium fluorine reaction. This work presents the kinetics of the reaction of fluorine with beryllium and the effect of temperature and pressure on the reaction rate.

Experimental

The experimental apparatus and the procedure used to measure the rate of fluorination are described in (7). The high-purity beryllium test pieces were strips measuring 1.27 x 15.24 x 0.012 cm with a 0.5 cm diameter hole drilled in one end for handling. The strips were treated with a solution of $HF\text{-}HNO_3$ during manufacture by the supplier. Immediately before being inserted into the fluorine system the strips were washed with detergent (8), distilled water, and finally an acetone rinse. This procedure was followed as a safety measure in order to avoid any possibility of contamination. The strips were preheated for 0.5 hr at 525°C. After reaction the products were characterized by x-ray diffraction and cross-section metallography.

Results and Discussion

In Fig. 1 and 2 the reaction is shown to follow the parabolic rate law $y^2 = kt$, where y is the amount of fluorine consumed (at STP) per unit area of beryllium surface (ml/cm^2), k is the parabolic rate constant, and t is the time (min). All the data over the temperature and pressure ranges studied can be described by this parabolic rate law. Solid symbols represent duplicate runs and show the reproducibility of the data. A reaction similar to breakaway oxidation was not found with fluorine; the film continued to be protective.

The values of the parabolic rate constants are listed in Table I. The parabolic rate constant is plotted as a

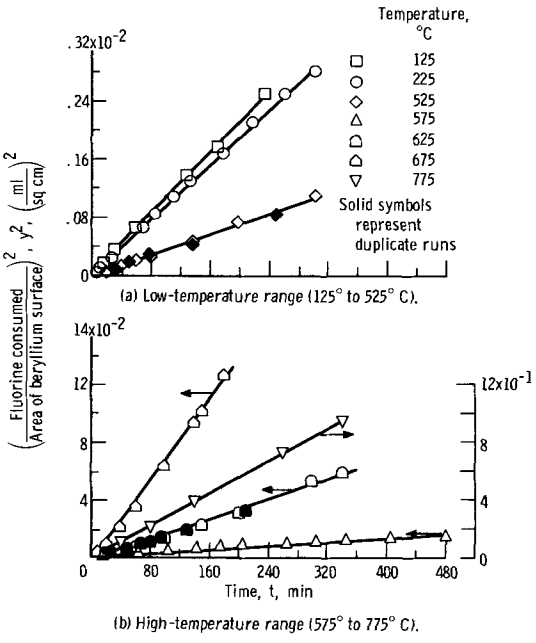

Fig. 1. Effect of temperature on fluorination of beryllium. Pressure, 200 Torr.

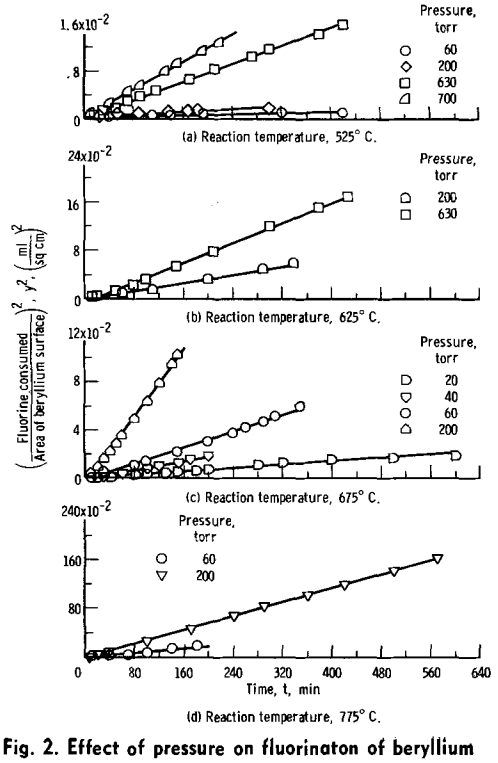

Fig. 2. Effect of pressure on fluorinaton of beryllium

function of temperature at a pressure of 200 Torr in Fig. 3. In this figure the rate of reaction shows a negative temperature dependence in the low-temperature range. This behavior is not unique because in heterogeneous systems where the rate of reaction is determined by diffusion in a solid layer a simple temperature dependence of the net process is not always found. Reactions of this type are complex processes involving the diffusion of at least one ion and electrons across the film through accessible diffusion sites. The number and accessibility of these sites can change at different temperatures; thus, the rate of reaction can decline with rising temperature. The effect shown in this region is not due to the experimental error. A variation of this amount in k would represent greater than a 60% error in determining the amount of fluorine consumed. This is far outside the precision of

Table I. Summary of temperature and pressure conditions and calculated parabolic rate constants

Temperature, °C	Pressure, Torr	Parabolic rate constant, k, $(ml/cm^2)^2/min$
125	200	1.05×10^{-5}
225	200	0.94×10^{-5}
525	60	0.20×10^{-5}
	200	0.69×10^{-5}
	630	3.77×10^{-5}
	700	5.70×10^{-5}
575	200	3.30×10^{-5}
625	200	17.0×10^{-5}
	630	41.0×10^{-5}
675	20	4.03×10^{-5}
	40	9.70×10^{-5}
	60	16.30×10^{-5}
	200	69.20×10^{-5}
775	60	130×10^{-5}
	200	280×10^{-5}

the determination. From duplicate runs in the low-temperature region the average deviation in k is (0.03 x 10^{-5} $ml/cm^2)^2/min$. There are many examples in the literature where oxidation rates have been found to decrease with increasing temperature so that the equation $k = a \exp-(\Delta H/RT)$ yields an apparent negative activation energy. A good explanation for this is not available. It could be suggested that the effect is due to changes brought about possibly by ageing or sintering of the reaction film. A break in the curve appears at 525°C. At this point the activation energy (ΔH_a) changes from —0.8 kcal/mole at the low temperatures to 8 kcal/mole at the high temperatures. Although this value for the activation energy appears low when compared to oxidation reactions it is not low when compared to the ΔH_a values of other fluorination reactions reported in the literature. An example is the fluorination of nickel with a reported activation energy of 5 kcal/mole (9). The following equations define the variation of the rate constant in the two temperature ranges

$$k = .0.4\text{x}10^{-5} \exp(800/RT) \quad (ml/cm^2)^2/min \text{ for } 125°—525°C \quad [1]$$

$$k = 1.5\text{x}10^{-2} \exp(-8000/RT) \quad (ml/cm^2)^2/min \text{ for } 525°—775°C \quad [2]$$

where k is the rate constant, R is the gas constant, and T is the absolute temperature.

A log-log plot of the rate constant as a function of the fluorine pressure is shown in Fig. 4. The reaction is approximately first order with respect to the fluorine pressure. The values are $k = 7.404\text{x}10^{-9}\ P^{1.3}$ at 525°C and $k = 1.019\text{x}10^{-6}\ P^{1.2}$ at 675°C.

The low-temperature film is identified as α-quartz hexagonal BeF_2, and the high-temperature film is

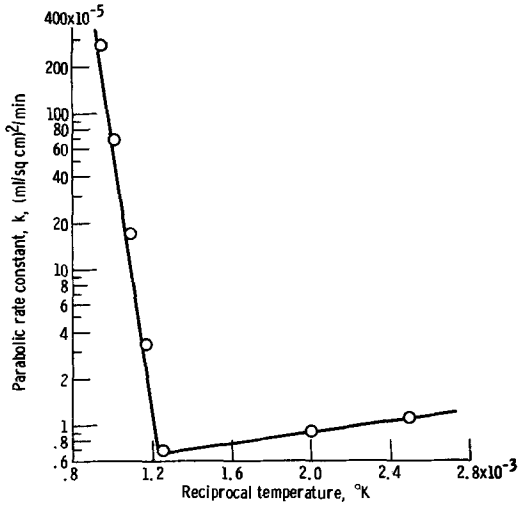

Figure 3. - Effect of temperature on parabolic rate constant. Pressure, 200 torr.

Fig. 3. Effect of temperature on parabolic rate constant. Pressure, 200 Torr.

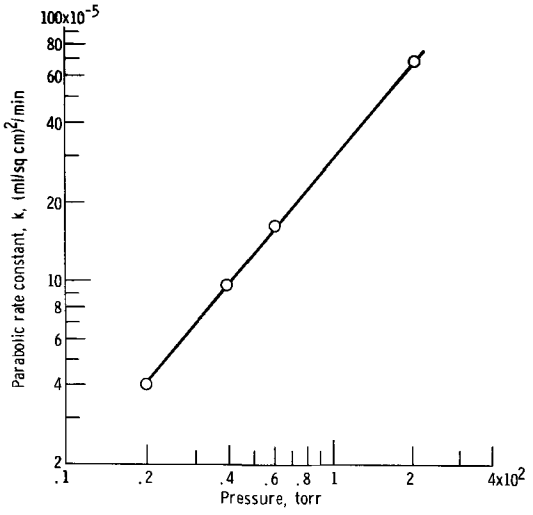

Fig. 4. Effect of pressure on parabolic rate constant. Temperature, 675°C.

identified as rhombic tridymite BeF_2 (10). A study was made of the reaction of α-quartz BeF_2 with fluorine gas at a temperature of 675°C and a fluorine pressure of 200 Torr. No apparent change was observed in that no rhombic tridymite form was found. This observation would lead to the assumption that for the high-temperature reactions the α-quartz hexagonal BeF_2 is not formed first and then converted to the tridymite form but that the tridymite BeF_2 is formed directly. Films formed at low temperatures were dull, nonreflecting surfaces, while those produced at high temperatures resembled shiny mirrors. Reacted metal strips are shown in Fig. 5 and 6. Figure 5 shows a reacted metal strip after fluorine exposure at a temperature of 625°C and a pressure of 630 Torr.

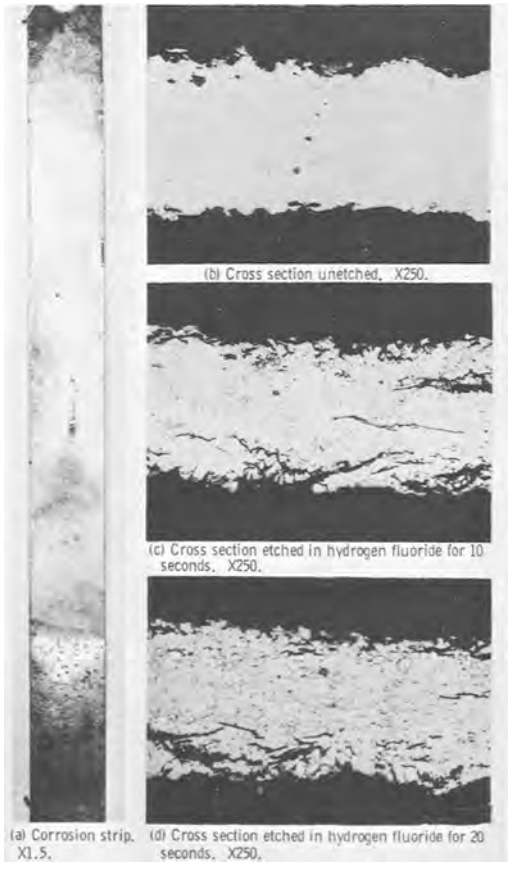

Fig. 5. Reacted metal strip after fluorine exposure. Temperature, 625°C; pressure, 630 Torr. (Reduced 40% in printing.)

Fig. 6. Cross section showing beryllium fluoride coating. X500. (Reduced 50% in printing.)

Etched cross sections of the strip show that the reaction is not a grain boundary attack but is a transgranular attack. The photomicrograph in Fig. 6 is a cross section showing the BeF_2 coating. The boundary between the beryllium and the BeF_2 is not well defined, but beryllium is seen as light areas extending into the film. If the gas was the primary diffusing species, one would expect a sharp, well-defined interface as was observed previously in the fluorination of iron (11). The appearance of Be in the film could suggest that outward diffusion of beryllium is taking place. Another experimental technique used to determine which species, metal or nonmetal, was the principal diffusing species was to determine whether two films of the same material, beryllium fluoride in this case, growing toward each other would fuse into one continuous film or whether there would be an interface formed between the films (12). If the metal were the principal diffusing species and the reaction site was at the gas/film interface, the two surfaces would fuse together as the metal species from one film migrated into the other film. If however the nonmetal were the principal migrating species, the two films would come together but would not fuse resulting in an interface between the two films. Two beryllium strips were clamped together along the 1.27 cm side with a 0.012 cm thick Monel ribbon inserted between the plates to form a small wedge angle. The sample was fluorinated at 675°C at 400 Torr. Figure 7 shows a cross section of the polished sample which reveals that the surfaces have fused together, suggesting that the metal rather than the nonmetal is diffusing during fluorination at high temperature. The approximate first order pressure relationship associated with a parabolic rate law is unusual and could be explained by suggesting that the diffusing species is an interstitial fluorine molecule; however, present experimental evidence does not indicate this.

Manuscript received April 5, 1967; revised manuscript received July 28, 1967. This paper was presented at the Philadelphia Meeting, Oct. 9-14, 1966.

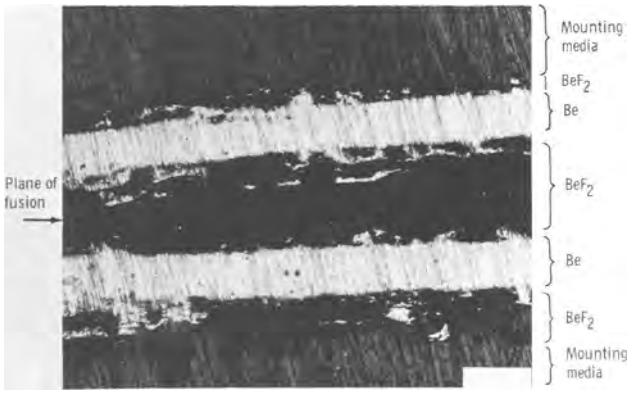

Fig. 7. Cross section showing that surfaces have fused together. X75. (Reduced 55% in printing.)

Any discussion of this paper will appear in a Discussion Section to be published in the June 1968 JOURNAL.

REFERENCES

1. W. B. Jepson, *Research*, **15**, 288 (1962).
2. W. D. Alymore, S. J. Gregg, and W. B. Jepson, *J. Nuclear Materials*, **2**, 169 (1960).
3. J. P. Pemsler and R. W. Anderson, Nuclear Metals Inc., No. 9805 (1961).
4. S. J. Gregg, R. J. Hussey, and W. B. Jepson, *Nature*, **186**, 468 (1960).
5. A. R. Taylor, Jr., Proceedings of the Second Meeting of the Applied Physics Lab. working group on thermochemistry, Virginia, 1, (1964).
6. M. A. Greenbaum, J. N. Foster, *et al.*, *J. Phys. Chem.*, **67**, 36 (1963).
7. P. M. O'Donnell and A. E. Spakowski, *This Journal*, **111**, 633 (1964).
8. W. W. Beaver, and A. J. Stonehouse, Brush Beryllium Co. TR 329, (1963).
9. Stephan Lawroski, Argonne National Lab. rept. no. 5924 (1958).
10. Yu. M. Korenev, *Akad. Nauk. Doklady.*, **147**, 846 (1962).
11. P. M. O'Donnell, *This Journal*, **114**, 218 (1967).
12. J. G. Schnizlein, J. D. Woods, J. D. Bingle, and R. C. Vogel, *ibid.*, **107**, 783 (1960).

Infrared Studies of Protective Films Formed by Acetylenic Corrosion Inhibitors

G. W. Poling

Research and Technical Department, Texaco Inc., Beacon, New York

ABSTRACT

Infrared spectra of surface films formed on iron and steel mirrors by propargyl alcohol. acetylene, and ethynyl-cyclohexanol acid corrosion inhibitors were recorded using a multiple reflectance technique. These spectra showed that the acetylenic molecules reacted at the metal surfaces in HCl solutions to produce protective polymer film coatings. Corrosion protection increased markedly as the polymer coatings grew from nearly two-dimensional, adsorbed layers to films 20°-200A° thick. Saturated hydrocarbon material composed the majority of these films. Hydrogen evolved by the acid corrosion reaction probably participated in hydrogenating adsorbed acetylenic species. The polymer also contained several polar species including hydroxyl and carbonyl groups. Increased carbonyl content appeared to decrease the protectiveness of these films.

Acetylenic alcohols effectively inhibit the acid corrosion of metals such as iron, aluminum, and zinc. The carbon-carbon triple bond has been shown (1) to act as the focal point in the inhibiting action of acetylenic derivatives. Several investigators (1-3) have proposed that the acetylenic molecules chemisorb on the metal surface to form a protective film one monolayer thick. This chemisorption is believed to involve sharing of π electrons in the triple bond with metal atoms at the surface. Recent studies have indicated that the protective films may instead consist of products of the reaction of these inhibitors at the metal-acid interface. Duwell, Todd and Butzke (4) found hydrogenation and dehydration reaction products in heptane extracts of acid-iron powder-ethynylcyclohexanol ($C_6H_{10}OHC{\equiv}CH$) reaction mixtures. Putilova, Rudenko, and Terentev (5) used a similar solvent extraction technique to show that acetylene reacted at iron-HCl interfaces to form thick polymolecular films on the iron. Electrochemical studies by Duwell (3) and Froment and Desestret (6) indicate that acetylenic compounds act primarily as cathodic inhibitors in acid solutions. Opposing results have been published by Okamoto *et al.* (7) who found that propargyl alcohol inhibited primarily the anodic reaction of steel in HCl solutions.

This paper describes an infrared study of the surface films formed by propargyl alcohol ($HC{\equiv}CCH_2OH$), acetylene ($HC{\equiv}CH$) and 1-ethynylcyclohexan-1-ol ($C_6H_{10}OHC{\equiv}CH$) inhibitors on iron and steel mirrors in HCl solutions. A multiple reflectance technique has been used so that spectra of films left intact on acid-exposed metal mirrors could be recorded. These spectra have provided direct evidence on the composition, structure, and thickness of the protective films. Determinations of mirror corrosion rates have enabled correlation of the infrared data with corrosion inhibition efficiencies. Our results indicate that acetylenic inhibitors react at iron or steel-HCl interfaces to form polymer film coatings that can grow to several hundred angstroms thickness. The protectiveness of these films increased markedly as they grew in thickness.

Experimental

Recording infrared spectra.—Figure 1 shows a schematic drawing of the multiple reflectance accessory that was used with a Beckman IR-12 spectrophotometer to record the spectra of thin films formed on two metal-mirror corrosion test specimens, M_4 and M_5.

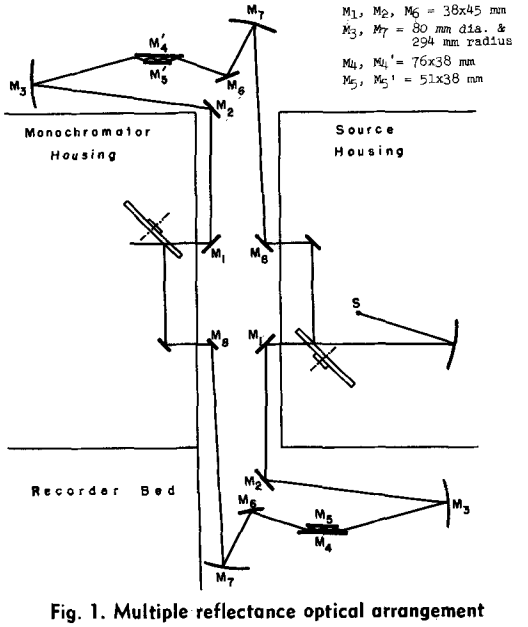

Fig. 1. Multiple reflectance optical arrangement

This accessory produced seven reflections at 73° incidence from the two metal sample mirrors. All other mirrors in the sample beam path were front-surfaced aluminum. Mirror-imaged but otherwise identical optics were provided in the reference beam path to maintain optical balance in the double-beam spectrophotometer. Spectra of surface films formed on the two sample mirrors M_4 and M_5 were, therefore, recorded differentially to two similar reference mirrors M_4' and M_5'. These reference mirrors were maintained in their freshly polished condition throughout the experiments. The reflectance accessory was enclosed in a plexiglas cover so that the entire optical path could be purged free of interfering water vapor using dry air or nitrogen. The accessory was designed to enable the IR-12 to record spectra of surface films as thin as one monolayer on sample mirrors that had sometimes become slightly roughened due to their exposures to the test solutions. Achieving monolayer-detecting sensitivity also required the installation of an efficient infrared polarizer in the monochromator section of the IR-12. Use of ordinate scale expansion facilities up to 20X expansion was also necessary. Details of the theory and practice of the multiple reflectance infrared technique have been clearly presented in papers by Francis and Ellison (8) and by Greenler (9).

Multiple reflectance spectra could not be recorded while the sample mirrors M_4 and M_5 were immersed in the acidic test solutions due to intense absorption of the infrared light by such solutions. Instead spectra from these mirrors were recorded before and after their exposure to the inhibited acid test solutions. Differences between these spectra were due mainly to absorption of the infrared light by thin surface films that the acetylenic inhibitors had formed on the sample mirrors. The ability to record spectra of films as thin as one monolayer was demonstrated by recording a recognizable spectrum of a single monolayer of barium stearate. This monolayer film had been deposited on two aluminum sample mirrors using the Langmuir-Blodgett technique.

Materials and procedures.—Two Armco iron or mild steel (1020) sample mirrors (3 x 1½ in. and 2 x 1½ by ⅛ in. thick) were used in each inhibitor test. Mirrors were prepared from metal plates either by mechanical lap polishing, using αFe_2O_3 polishing grit or by electropolishing (10), in a 20/1 glacial acetic acid to 70% perchloric acid solution.

Propargyl alcohol and acetylene were obtained from Matheson, Coleman and Bell. The acetylene was purified before use by passing it through H_2SO_4 and then through a column of activated alumina. 1-ethynylcyclohexan-1-ol was obtained from Air Reduction Company. No significant impurities were detected in the infrared spectra of these pure inhibitors.

Multiple reflectance spectra of freshly polished sample mirrors were first recorded to serve as background spectra. These were flat and featureless since spectra of the two sample mirrors were recorded differentially to two similarly prepared reference mirrors. The two sample mirrors were then immersed in the inhibited acid test solution in a 1-liter Pyrex reaction flask. All joints to this flask used Viton-A O-ring seals. A bubbler-tube extended to the bottom of the flask for purging the solution. The solution was magnetically stirred. Normal use of 500 ml of acid solution provided 4.6 ml acid/cm² of exposed metal specimen.

Most inhibitor tests were conducted in 10% HCl (3.3*N*) at 65° ±2°C with the solutions deaerated by continuously purging with helium or argon. Exposure times varied from a few minutes to several days. Inhibitor concentrations of *ca.* 9 x 10^{-2}M were generally used. In testing acetylene as an inhibitor, the acid was maintained saturated with this gas. After the desired exposure, the sample mirrors were removed from the flask, immediately rinsed in distilled water, and dried at room temperature. Their multiple reflectance spectrum was then recorded and compared with the original background spectrum to detect any organic film formation.

In most tests, corrosion by the inhibited HCl was so uniform that the sample mirror reflectivities were practically unaffected by exposures lasting several hours. When the mirror surfaces were roughened, increased light scattering caused loss of infrared energy over the entire spectral region (4000-400 cm^{-1}). This energy loss was more pronounced at the higher frequencies (cm^{-1}) which was characteristic of a light scattering phenomenon. These energy losses were therefore readily distinguished from the sharp absorption bands due to an organic film on the mirrors. The spectra presented in this paper were replotted to subtract spectral changes due to increased light scattering.

Corrosion rates of the metal mirrors were determined by periodical removal of 3-5 ml aliquots of the acid solution for atomic absorption spectroscopic analysis for iron.

Inhibitor tests were also made at other than the "standard" conditions cited above. These included HCl concentrations from 1.7 to 12N, temperatures from 22° to 93°C, and exposure of the acid solution to air.

Film thickness calculations have been based on application of the Beer-Lambert law to the measured intensity of the C-H stretching bands in the organic films. Estimation of appropriate absorption coefficients were derived from Greenler's (8) data. Random orientation of the C-H groups, with respect to the incident and reflected infrared beam, was assumed. Even if the C-H groups were preferentially oriented with respect to the metal surfaces, microroughness of these surfaces would probably produce random orientation with respect to the infrared beam.

Results

Propargyl alcohol inhibitor.—Spectra of films.—Figure 2A shows an infrared spectrum of pure liquid propargyl alcohol inhibitor together with assignments (11) of its major absorption bands. Figure 2B shows a spectrum of the film formed on Armco iron mirrors during their 23-hr exposure to helium purged 3.3*N* HCl solution at 65°C containing 8.7 x 10^{-2}M propargyl alcohol. The zero absorbance level in this figure represents the initial "background" spectrum of the mirrors prior to their test exposure. Spectrum B is typical of many spectra that resulted from similar tests of propargyl alcohol for exposure times ranging from 15 min to several days. Absorption band intensities, which were directly proportional to film thicknesses, increased with the length of the exposure. Based on the intensity of the 2930 cm^{-1} CH_2 band in spectrum

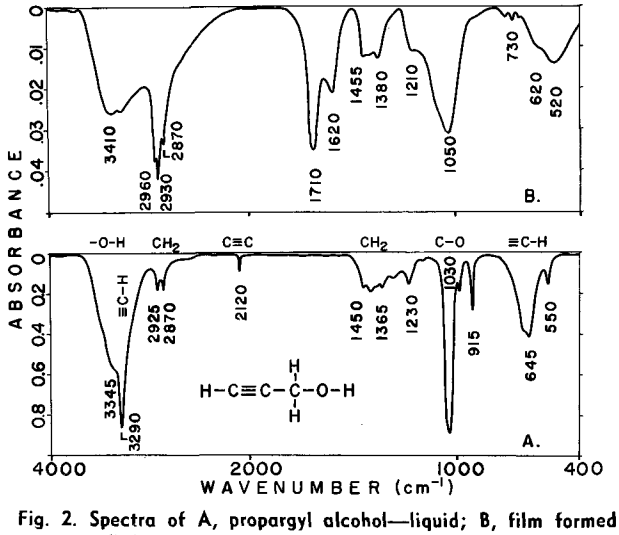

Fig. 2. Spectra of A, propargyl alcohol—liquid; B, film formed on iron in HCl by propargyl alcohol.

B, this organic film was calculated to be about 60Å thick. This would be equivalent to nearly 15 monolayers thickness of the added inhibitor molecules.

Direct comparison of spectra A and B of Fig. 2 indicates that the organic film consisted of reaction products of propargyl alcohol rather than chemisorbed inhibitor molecules. Acetylenic (H—C≡C—) groups were not present in the film as evidenced by absence of characteristic bands at 3290, 2120, and 645 cm^{-1}. In addition, the film exhibited bands that were not present in the spectrum of the inhibitor (A). These new bands and their assignments are as follows

2960 cm^{-1}	— CH_3 stretch (11)
1710 cm^{-1}	— $\geq C=O$ stretch
~1620 cm^{-1}	— overlapping { $\geq C=C\leq$ stretch; H—O—H bend; COOFe stretch
520-620 cm^{-1}	— Fe—O stretch

The above assignments are based on reference to characteristic group frequencies (11) and on the following tests of the films. Reacting amines with the films decreased the intensity of the 1710 cm^{-1} band and confirmed its assignment to carbonyl groups; *i.e.*, $\geq C=O+H_2NR \rightarrow \geq C=NR+H_2O$. Contribution of a small amount of residual olefin ($\geq C=C\leq$) to the ~1620 cm^{-1} band was indicated by the observation that exposure to ozone decreased the 1620 cm^{-1} band intensity while the ~1710 cm^{-1} carbonyl band was markedly enhanced, *i.e.*, 3 [$\geq C=C\leq$] + 2 $O_3 \rightarrow$ 6($\geq C=O$). Evidence for contribution of iron carboxylate (—COOFe) groups to the ~1620 cm^{-1} band is presented later. Assignment of the 520-620 cm^{-1} bands to Fe-O stretching modes is based on reference to spectra (12) of iron oxide compounds.

Physical properties of films.—Protective films formed by propargyl alcohol on iron proved to be highly insoluble, nonvolatile, and strongly adhering. Solvents tested included n-heptane, benzene, acetone, chloroform, pyridine, and 3.3*N* HCl solution. Of these, only acetone and chloroform dissolved appreciable film material. These solvents were able to extract only about one-third of the film. A 1-hr exposure of film-covered mirrors to uninhibited 3.3*N* HCl at 22°C did not remove appreciable film material. No significant evaporation of film material to vacuum was detected below a temperature of approximately 250°C. At 350°C most of the film was removed within 1 to 2 hr. The small amount of residual film exhibited broad bands at 1, 1590 cm^{-1}, 2, 1430 cm^{-1}, 3, 1070 cm^{-1}, and 4, 400-600 cm^{-1}. Bands 1 and 2 are characteristic of iron carboxylate (—COOFe) species. Band 3 is believed due to C-O stretch in iron alkoxide groups (—COFe) (13). Bands in the 400-600 cm^{-1} region are ascribed to Fe-O stretching modes in iron alkoxide and iron oxide groups. These stable species thus appear to have been concentrated at the organic film-iron (iron oxide) interface.

The film coated iron mirrors were observed to be hydrophobic on their removal from the helium purged HCl test solutions. After a short rinse in distilled water, the mirrors became hydrophilic even though the organic film persisted on the mirror surfaces. This indicated that air oxidation could have caused this conversion by the production of polar groups at the surface of the organic films. To test this theory, an experiment was conducted in which air contact of the mirrors was eliminated. The acid-exposed mirrors were transferred from the reactor flask to an infrared gas cell within a helium-filled dry box. The spectrum of this film was similar to that shown in Fig. 2B (which was recorded in air) except that the 1710 cm^{-1} carbonyl band was about 50% less intense. Subsequent addition of oxygen to the gas cell, containing the iron mirrors, resulted in an immediate 50% increase in the intensity of the carbonyl band. The spectrum did not change further on exposing the mirrors to air for several days. This experiment indicated that approximately one-third of the carbonyl content of films that were exposed to air was probably due to air oxidation reactions.

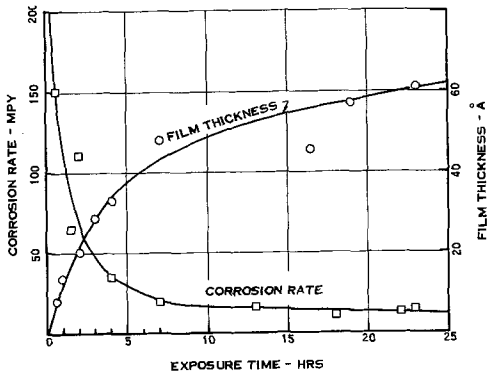

Fig. 3. Time dependence of protective film growth and corrosion rates, for iron in 10% HCl at 65°C with 8.7 X 10^{-2}M propargyl alcohol.

Corrosion rate vs. film thickness.—Figure 3 shows how the corrosion rate decreased as the thickness of an organic film formed by propargyl alcohol increased. A replot of these curves has shown that the logarithm of the corrosion rate exhibited a linear dependence on film thickness up to 50Å which was near the limiting film thickness. Under similar conditions (helium purged 3.3*N* HCl at 65°C) but with no inhibitor present, the corrosion rate steadily increased with exposure time. A rate of 10,000-12,000 mils per year (mpy) was attained within a few hours exposure of the "blank" iron specimens.

Figure 4 shows how the corrosion protection increased as the organic film grew in thickness.

$$\text{Per cent protection} = 100\left(\frac{\text{uninhibited rate-inhibited rate}}{\text{uninhibited rate}}\right)$$

Results are shown for tests of propargyl alcohol in both helium purged and air-exposed 3.3*N* HCl solutions. These curves show that the organic films became highly protective (*i.e.*, >99%) only after they had grown to thicknesses equivalent to many molecular layers. Near one monolayer thickness, the films appeared to confer 80-90% protection. Figure 4 illustrates that, at equal thicknesses, films formed in air-exposed HCl solutions were less protective than those formed in solutions free of oxygen. Differences in the compositions of these films are described in the following section.

Effects of varying exposure conditions.—Acid exposure conditions such as concentration, temperature, and oxygen availability have been varied to study their effect on the composition, growth rate, and pro-

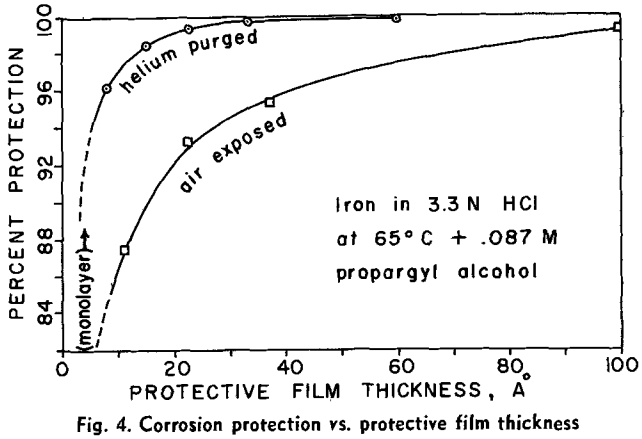

Fig. 4. Corrosion protection vs. protective film thickness

Table I. Results of varying exposure conditions on corrosion inhibition by propargyl alcohol (8.7×10^{-2}M) in HCl solutions

Test	Metal mirror composition	Exposure conditions: Acid conc, %	Temp, °C	Solution purge	Exposure time, hr	I.R. spectra of films: Film thickness, Å	Remarks on I.R. spectra	Corrosion rate, mpy	Inhibitor % protection
1	Armco iron mechanically polished	10	65	Helium	19	57	As shown in Fig. 2B	11	99.9
2	Armco iron mechanically polished	10	22	Helium	16	8	Very similar to Fig. 2B	3	94.0
					38	24		2	96.0
3	Armco iron mechanically polished	15	93	Helium	1¼	35	Very similar to Fig. 2B	180	— [a]
4	Armco iron mechanically polished	10	65	Air	17	100	Similar to Fig. 2B except 1710 cm^{-1} C=O band ca-3X as intense	83	99.1
5	Armco iron electropolished	10	65	Helium	13	56	Very similar to Fig. 2B	16	99.9
6	1020 steel mechanically polished	10	65	Helium	19	48	Very similar to Fig. 2B	9	99.9

[a] Uninhibited corrosion rates were not determined for these conditions.

tectiveness of the organic films. Results have also been obtained using both mechanically and electrolytically polished Armco iron and mild steel sample mirrors. Table I summarizes these results. Typical data for the standardized exposure conditions (test 1 of Table I) are included for comparative purposes. The growth rates of the films were highly dependent on the exposure conditions. Film compositions were found to be relatively independent of changing conditions. Test 4, with the HCl test solution exposed to the air, was the exception. The films from this test exhibited considerably higher carbonyl content than those formed in oxygen-free solutions. In spite of the fact that the test No. 4 film grew to be thicker than the others, it was less protective as shown in Fig. 4.

Acetylene inhibitor.—Infrared analyses of films formed on iron by acetylene in HCl solutions were made to help elucidate the film formation mechanisms. Figure 5 (A and B) shows spectra of the acetylene gas that was used as an inhibitor. The three major bands in these spectra are due to ≡C-H stretching and bending modes in the C_2H_2 molecule. Exposure of Armco iron mirrors to an acetylene saturated, 5% HCl solution (~1.7*N*) for 4¼ hr at 47°C followed by an additional 1¼ hr at 57°C produced a film which exhibited spectrum C of Fig. 5. This film was calculated to be about 40Å thick.

The differences between the spectra of the acetylene inhibitor and the film that it formed on iron are very striking. There is, however, a close similarity between the spectrum of the acetylene-formed film (Fig. 5C) and the spectrum of the film formed from propargyl alcohol (Fig. 2B). Comparison of these spectra shows differences only in relative band intensities. This indicates that the compositions of the films formed by these two inhibitors were very similar, *i.e.*, both films contained the following groups: —OH (3410 cm^{-1}); CH_3 (2960 cm^{-1}); CH_2 (2930 and 2870 cm^{-1}); >C=O (1705 cm^{-1}); —COOFe (~1600 cm^{-1} shoulder); —C—O—Fe (1010-1100 cm^{-1}) and Fe-O (400-600 cm^{-1}).

Benzene extraction of the organic film succeeded in removing about one half of the original film material. No appreciable decrease in bands attributed to iron carboxylate (~1600 and 1430 cm^{-1}), iron alkoxide (1000-1100 cm^{-1}) or iron oxide (400-600 cm^{-1}) resulted from this extraction.

In the 47°C exposure described above, the iron mirrors corroded at a rate of 12 mpy. The subsequent 10°C temperature rise to the 57°C exposure did not alter this corrosion rate.

Ethynylcyclohexanol inhibitor.—Films formed on iron by this cyclic acetylenic alcohol were much more readily extracted by solvents than those previously mentioned. By observing the infrared spectra of the residual films after successive extractions, we have obtained information on variations of composition through the film. Figure 6 presents typical spectral results. Spectrum A is that of the pure ethynylcyclohexanol inhibitor. The films, formed by exposing two mechanically polished Armco iron mirrors for 16 hr to an oxygen-free 3.3*N* HCl solution at 65°C with 7.2×10^{-2}M ethynylcyclohexanol, exhibited spectrum B. This film was calculated to be about 470Å thick.

Comparison of spectra A and B of Fig. 6 indicates that the relatively thick organic films consisted of products of the reaction of ethynylcyclohexanol at the surface. Similarity of the C-H stretching bands (2940 and 2860 cm^{-1}) and C-H bending bands (1450-900 cm^{-1}) in these two spectra suggested that the cyclohexyl ring structure was retained in the organic film. Apart from this feature and the absence of CH_3 groups

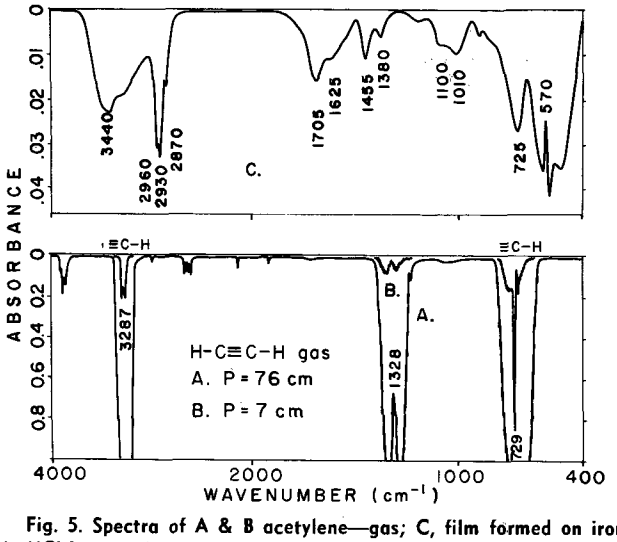

Fig. 5. Spectra of A & B acetylene—gas; C, film formed on iron in HCl by acetylene.

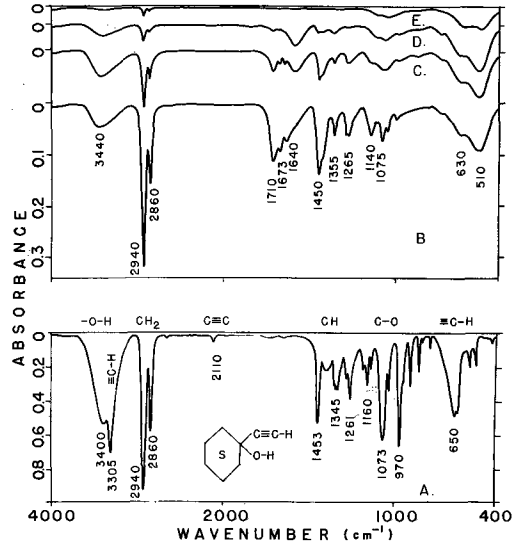

Fig. 6. Spectra of A, ethynylcyclohexanol—liquid; B, film formed on iron in HCl by ethynylcyclohexanol; after extraction by C, heptane, D, acetone; E, 10% HCl.

Table II. Spectral data on solvent extractions of protective film formed by ethynylcyclohexanol on iron in HCl solution

Spectrum	Band position, cm^{-1} / Band assignment	3400 —OH	2940 CH_3	2860 CH_2	1710 >C=O	1673 C–C	1640 C–C	1580 —COOFe	1450 CH_2 —COOFe	1075 COFe	510 Fe—O
B	Initial film band absorbances	0.045	0.32	0.16	0.11	0.09	0.07	~0.04	0.14	0.07	0.10
C	After heptane extr. % original intensity	100	34	32	36	33	30	100	39	50	90
D	After acetone extr. % original intensity	56	9	9	~9	~9	10	100	10	43	90
E	After HCl extr. % original intensity	—	5	5	—	—	—	—	—	29	40

(no bands at 2960 and 1370 cm^{-1}), the composition of these films appears similar to those formed by propargyl alcohol (Fig. 2B) and by acetylene (Fig. 5C).

Spectra C, D, and E of Fig. 6 were exhibited by residual films after successive extractions in n-heptane, acetone and 10% HCl solutions, respectively. Spectra C and D were recorded after the mirrors had been immersed in each organic solvent until no further dissolution occurred at 22°C. Exposure to 10% HCl (at 22°C) lasted 10 min. Table II summarizes the results of these extractions. The tabulation of spectrum C shows that n-heptane removed about two thirds of the C–H, C=C, and C=O content of the original film. The bands attributed to —OH, —COOFe, —COFe, and Fe-O were relatively unaffected. After the acetone extraction, the film was only about one tenth of its original thickness of 470Å. Again the four bands just mentioned were left relatively unaffected. The HCl treatment left a film only about 25Å thick based on the residual 2940 cm^{-1} CH_2 band in spectrum E. The C-H, C-O, and Fe-O bands retained in spectrum E are believed due to several monolayers of iron alkoxide (RCOFe) on a thin layer of iron oxide that was retained on the iron surface. The above results indicated that the composition of the organic film was uniform throughout its thickness apart from concentration of iron carboxylate and iron alkoxide species at the organic film/iron oxide interface.

Discussion

Structure and properties of protective films.—These infrared studies have shown that the acetylenic corrosion inhibitors propargyl alcohol, acetylene, and ethynylcyclohexanol reacted at HCl-exposed iron and steel surfaces to form organic film coatings. These surface reactions were not limited to the formation of "adsorbed layers" since the organic films grew to thicknesses equivalent to many molecular layers.

The films were composed primarily of fully saturated hydrocarbon material. Hydroxyl, carbonyl, carboxylate, and alkoxide groups were also present in all films studied. The —OH content, which varied considerably, is believed due mainly to retention of absorbed water and to presence of hydrated or hydroxylated iron oxide species. Even in the films formed by acetylenic alcohols (Fig. 2B and 6B) the OH bands did not appear to be due to retained —C—O—H groups. This was indicated by the fact that the relative intensities of the —C—O (~1070 cm^{-1}) and —O—H (~3400 cm^{-1}) bands varied widely (see for example Table II). Therefore these bands could not have been due to one species. These results indicate that the acetylenic alcohol inhibitors must have been dehydrated at the surface. Most of the carbonyl content of films formed in absence of oxygen is believed to have resulted from hydration of the acetylenic bond followed by isomerization. This is discussed in the following section. Some carbonyl also originated from air oxidation after the films were formed, as described above. Evidence has been presented (*i.e.*, in Table II) that the carboxylate and alkoxide groups were concentrated at the organic film-iron oxide interface. These stable species probably contributed to strong adhesion of the organic film to the iron.

The infrared spectra, low solubility, low volatility, and high thermal stability of these organic films indicate that they were composed of polymeric material. Spectra of the films formed by propargyl alcohol (Fig. 2B) and by acetylene (Fig. 5C) are similar to spectra (14) of oxidized polyethylenes, for example. The films exhibiting these particular spectra were about 60 and 40Å thick, respectively. Much weaker but otherwise similar spectra were recorded when these films were of the order of one monolayer thick. Therefore, even in the early stages of growth, the films are best described as being nearly two dimensional or adsorbed polymer layers. A simplified model of the structure of the protective films formed by acetylenic inhibitors is presented in Fig. 7. In films formed by ethynylcyclohexanol, the hydrocarbon would consist primarily of cyclohexyl rings instead of as shown in Fig. 7.

Film forming reactions.—Polymerizations of acetylenic hydrocarbons are common reactions, particularly when they are surface catalyzed. For example, infrared studies (15) (16) of surface species resulting from hydrogenation of acetylene adsorbed on nickel, palladium, and copper metals have shown that polymerization produced n-alkyl hydrocarbons. A reaction involving hydrogenation and dehydration of acetylenic alcohols has been used in the commercial production of 1,3-butadiene and buna rubber (17). The iron-HCl-acetylenic inhibitor system offers the possibility for similar surface catalyzed reactions for the formation of protective polymer films. Hydrogen evolution from the acid-exposed metal surface was found to be necessary for the formation of polymer films by these inhibitors. Polymer films did not form on copper, silver, and platinum in 3.3*N* HCl at 65°C, where no hydrogen was evolved. When the HCl concentration was increased to greater than 6.7*N* (>20%) so that hydrogen was evolved from copper, the acetylenic inhibitors then formed relatively thick polymer films on this metal. Apparently, hydrogenation of adsorbed acetylenic inhibitor species by cathodically liberated hydrogen participated in the polymer film formation.

Some of the oxygenated groups found in films formed in oxygen-free acid solutions probably resulted from the following types of reactions:

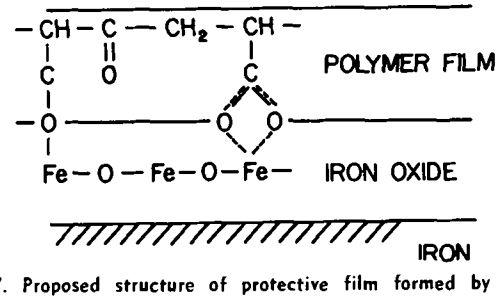

Fig. 7. Proposed structure of protective film formed by acetylenic inhibitors.

1. *Hydration of the C≡C*

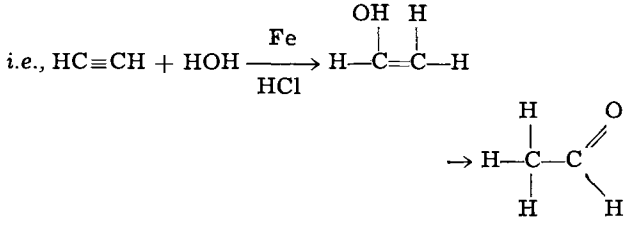

In a similar process, used for the commercial production of acetaldehyde, formation of tarry condensation products are troublesome. Similar condensation products probably contribute to polymer film formation in use of acetylenics as corrosion inhibitors. The strongest evidence for this type of reaction comes from the composition of the films formed by acetylene (Fig. 5C). Although this inhibitor contained no oxygen and the acid was well purged with helium, the polymer films exhibited a strong carbonyl band at 1705 cm^{-1}. Most of this carbonyl content probably derived from hydration of the C≡C.

2. *Formation of Alkoxides and Carboxylates*

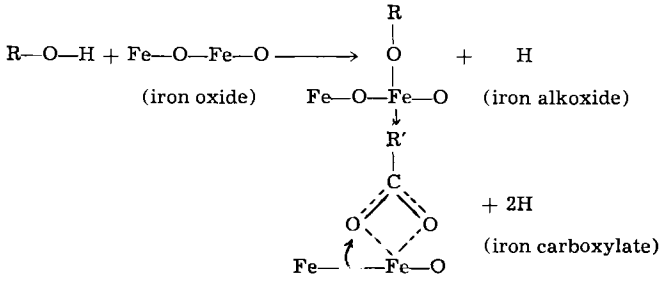

Adsorption of alcohols on Al_2O_3 was shown to result in the formation of similar aluminum alkoxide and carboxylate species (18). The alcohol for the above reaction could be an acetylenic alcohol inhibitor or it could be the intermediate product in hydration of C≡C groups as shown above. Hydrogen released by the above reactions could have participated in the hydrogenation of acetylenic species or it could have been evolved as a gas. According to the above reactions, alkoxide and carboxylate species would be formed only at the surface of an iron oxide film on the iron or steel specimens. Our infrared results agree with this mechanism since these species were found concentrated at the organic film-iron oxide interface.

Corrosion inhibition mechanisms.—Acetylenic corrosion inhibitors effectively prevent the acid corrosion of iron and steel by the formation of polymer film coatings on the exposed metal surface. The protection afforded by these films increased markedly as they grew from near two-dimensional, adsorbed polymer networks (~4A° thick) to films of up to several hundred angstroms thickness. This is illustrated in Fig. 4 for films formed by propargyl alcohol inhibitors. Similar results have been obtained from our study of other acetylenic inhibitors including acetylene, 1-ethynylcyclohexan-1-ol, 1-hexyn-3-ol, and 2-butyn-1,4-diol. Production of polymer film coatings, therefore, appears to be the general mode-of-action of acetylenic corrosion inhibitors. Rapid chemisorption of these inhibitors to form metal-acetylene surface complexes is probably a crucial step in initiating the formation of protective polymer films. The ability of acetylene to act as an efficient inhibitor provides indirect evidence of this mechanism. Films in the chemisorbed or monolayer thickness range appeared capable of decreasing the uninhibited acid corrosion rate by about 10 times (*i.e.*,~90% protection). This rapid reduction in corrosion rate probably enabled subsequent growth of relatively thick polymer films that remained strongly adhering to the surface. These thicker films often resulted in 1000 times reduction of the uninhibited corrosion rate (*i.e.*, ~99.9% protection).

The protectiveness of the polymer films depended on both the thickness and composition of the polymer films as indicated in Fig. 4. In general, the corrosion rate was found to vary linearly with the exponential of the film thickness (*i.e.*, mpy=exp. $K \times$ Å thickness $+C$). This relationship was often obeyed from the monolayer stage to bulk films approaching limiting thicknesses. Therefore, the protective mechanism did not appear to change markedly throughout this film growth interval. Availability of oxygen resulted in growth of a thicker film (*i.e.*, 100Å in Fig. 4) than in its absence (*i.e.*, 60Å in Fig. 4), but the thicker film was less protective. The thicker film contained about three times as much carbonyl content as the thinner film. This increase in content of polar carbonyl species could have facilitated charge transfer through the film and thus decreased its protectiveness. Studies are planned to correlate infrared structural studies of films with electrochemical polarization data to help elucidate the effects of composition and thickness on the rate controlling corrosion reactions.

Acknowledgments

The author expresses appreciation to H. Macy and D. Bauer for help with the experimental work, to R. P. Eischens, B. C. Lippens, and L. C. Roess for stimulating discussions and helpful suggestions and to the management of Texaco Inc. for support of this research.

Manuscript received April 21, 1967; revised manuscript received Aug. 24, 1967. This paper was presented at the Dallas Meeting, May 7-12, 1967.

Any discussion of this paper will appear in a Discussion Section to be published in the June 1968 JOURNAL.

REFERENCES

1. G. L. Foster, B. D. Oakes, and C. H. Kucera, *Ind. Eng. Chem.*, **51**, 825 (1959).
2. J. G. Funkhouser, *Corrosion*, **17**, 283t (1961).
3. M. Froment and A. Desestret, Comptes Rendus Symposium Europeen sur les Inhibiteurs de Corrosion, Ann. Univ. Ferrara, Sez 1, 223 (1966).
4. E. J. Duwell, J. W. Todd, and H. C. Butzke, *Corrosion Sci.*, **4**, 435 (1964).
5. I. N. Putilova, N. V. Rudenko, and A. N. Terentev, *Russ. J. Phys. Chem.*, **38**, 263 (1964) (in English).
6. E. J. Duwell, *This Journal*, **109**, 1013 (1962).
7. G. Okamoto, M. Nagayama, J. Kato, and T. Baba, *Corrosion Sci.*, **2**, 21 (1962).
8. S. A. Francis and A. H. Ellison, *J. Opt. Soc. Amer.*, **49**, 131 (1959).
9. R. G. Greenler, *J. Chem. Phys.*, **44**, 310 (1966).
10. P. B. Sewell, C. D. Stockbridge, and M. Cohen *Can. J. Chem.*, **37**, 1813 (1959).
11. L. J. Bellamy, "The Infrared Spectra of Complex Molecules," John Wiley & Sons, Inc., New York (1962).
12. Unpublished results.
13. G. Blyholder and W. V. Wyatt, *J. Phys. Chem.*, **70**, 1745 (1966).
14. L. H. Cross, R. B. Richards, and H. A. Willis, *Discussion Faraday Soc.*, **9**, 235 (1950).
15. W. A. Pliskin and R. P. Eischens, *J. Chem. Phys.*, **24**, 482 (1956).
16. L. H. Little, N. Sheppard, and D. J. C. Yates *Proc. Roy. Soc.*, **A259**, 242 (1960).
17. J. S. Reppe, "Acetylenic Chemistry," Charles Mayer, New York (1949).
18. R. G. Greenler, *J. Chem. Phys.*, **37**, 2094 (1962).

Oxidation of Nickel by Carbon Dioxide

J. E. Antill and J. B. Warburton

Metallurgy Division, Atomic Energy Research Establishment, Harwell, Berkshire, England

ABSTRACT

Two studies have been carried out, one to determine the conditions for the equilibrium between nickel, nickel oxide, carbon dioxide, and carbon monoxide, and the second to determine the kinetics of the oxidation of nickel in carbon dioxide and in CO_2/CO mixtures. The equilibrium conditions determined over the temperature range 580°-1016°C are given by the equation

$$\log_{10}\left(\frac{p_{CO}}{p_{CO_2}}\right) = -\frac{2381}{T} - 0.025$$

The kinetic study covered the behavior of pure nickel, commercial impure nickel, and nickel dispersion strengthened with alumina or thoria within the temperature range 700°-1100°C. The reaction rates were significantly reduced by the normal impurities in commercial nickel and by water vapor in the carbon dioxide. It was deduced that the oxidation rate was at least partially governed by a reaction at the oxide/gas interface and that considerable plastic flow occurred in the oxide scales.

The present paper covers the oxidation of nickel and oxide dispersion strengthened nickel by carbon dioxide and CO_2/CO mixtures at elevated temperatures. Examination of the relevant thermodynamic data reveals that the concentration of carbon monoxide necessary to prohibit the formation of nickel oxide in CO_2/CO mixtures is small, but considerable scatter exists in the values which can be calculated or have been determined directly for this concentration. The first studies in the present work involved therefore an accurate determination of the conditions for equilibrium between nickel, nickel oxide, carbon dioxide, and carbon monoxide

$$Ni + CO_2 \rightleftarrows NiO + CO$$

These studies were followed by kinetic studies of the oxidation of four grades of nickel, including oxide dispersion strengthened nickel, in primarily carbon dioxide over the temperature range 700°-1100°C, although some work was also carried out with CO_2/CO mixtures and oxygen. By comparison with previous work the exposure times were long (*e.g.*, 1000 hr). The data obtained in the equilibrium studies were in the midst of most of those published previously, while the kinetic studies extended previous work.

Thermodynamic Study

The conditions for the equilibrium have been studied previously by four major groups of workers (1-4) and may be calculated from a summary of the thermodynamic data (5) for the four components. The various sets of work are not in good agreement as the values for the ratio of the partial pressures of the two gases at equilibrium at a given temperature can vary by up to a factor of 10. In the present work the equilibrium was studied directly over the temperature range 580°-1016°C.

Experimental

A standard technique was used in which a CO_2/CO gas mixture was circulated round a closed loop containing a heated mixture of nickel and nickel oxide. When equilibrium was established samples of the gas mixture were taken and analyzed by two methods, one in which the total pressure and the carbon monoxide partial pressure were measured manometrically and with a McLeod gauge, respectively, and the other using the tracer ^{14}C in the gas and a Geiger-Mueller end window counter attached to the gas circuit. In both methods the carbon monoxide partial pressure was measured after the carbon dioxide had been removed by a small liquid nitrogen trap, but the trap and the size of the sample were different in the two cases. The second method had the advantage that erroneous results could not arise from the inadvertent presence of an inert gas such as nitrogen. The p_{CO}/p_{CO_2} ratios obtained by the two methods agreed to within 4%. The total pressure varied during the series of experiments within the range 0.34-0.66 atm. The temperature of the solid mixture was measured with a Pt/PtRh thermocouple in a pocket in the reaction tube adjacent to the mixture. The values were accurate to ±3°C. The solid mixture weighed approximately 5.5g and consisted of equal amounts of an intimate mixture of nickel and nickel oxide powders.

The nickel and nickel oxide were spectrographically standardized and obtained from Johnson Matthey Company. The major impurities were 75 ppm carbon, 2 ppm silicon, and 1 ppm iron in the nickel, and 60 ppm carbon, 5 ppm silicon, 3 ppm iron, and 1 ppm magnesium in the nickel oxide. The initial charge of gas was spectrographically standardized carbon dioxide supplied by BOC to which was added some $^{14}CO_2$ made from barium carbonate. It was dried over phosphorous pentoxide before use.

Results

The results are summarized in Fig. 1 and by the equation

$$\log_{10}\left(\frac{p_{CO}}{p_{CO_2}}\right) = -\frac{2381}{T} - 0.025 \quad \ldots [1]$$

The experimental values for the p_{CO}/p_{CO_2} ratio agree with Eq. [1] to within ±3%. The gas flow rate for the majority of the experiments was 220-240 cm^3/min. It was shown that there was no thermal segregation of the gases or cooling of the solid mixture as the p_{CO}/p_{CO_2} ratio at equilibrium was unaffected by flow rate over the range 100-500 cm^3/min. Also the results were unaffected by the direction from which the equilibrium was approached. However it is noteworthy that reproducible results could not be obtained until the solid mixture had been outgassed at 900°-1000°C; the reason for this behavior is not known. Fricke and Weitbrecht (4) have reported complications arising from the deposition of carbon by the Boudouard reaction

$$2CO \rightarrow C + CO_2$$

but this reaction did not occur in the present work as the carbon content of the nickel-nickel oxide mixture at the end of the experiments was only 30-100 ppm, and hence comparable with the initial content.

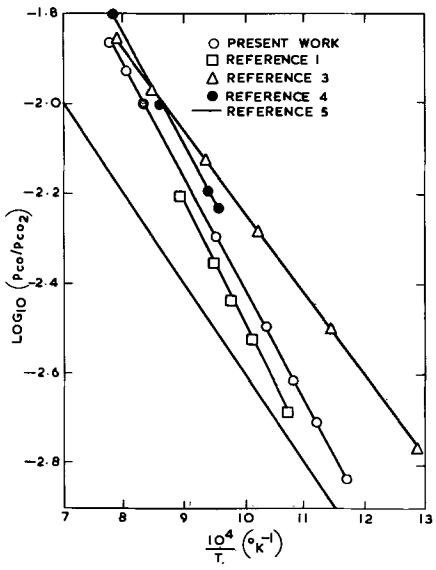

Fig. 1. Summary of thermodynamic data

Discussion

The data obtained in the present work are compared with the results of three of the direct studies (1,3,4) carried out previously and the compiled data of Kubaschewski, Evans, and Alcock (5) in Fig. 1. The compiled data used the standard free energy equations for the reactions

$$Ni + \tfrac{1}{2}O_2 \rightarrow NiO \quad (a)$$
$$C + \tfrac{1}{2}O_2 \rightarrow CO \quad (b)$$
$$C + O_2 \rightarrow CO_2 \quad (c)$$

Other thermodynamic data obtained for these reactions have not been included because direct studies of the equilibrium are of most interest and the compilation of data for several reactions leads to comparatively large limits of error. The data from the direct study by Kapustinsky and Silberman (2) have not been included in Fig. 1 because the equilibrium p_{CO}/p_{CO_2} ratios differ markedly from the other values, being greater than those obtained in the present work by at least a factor of five.

The agreement with the data of Watanabe (1) and of Fricke and Weitbrecht (4) is good especially as the small discrepancies with the German work could be due to the better precautions taken in the present work against separation of the gases by thermal diffusion. No firm explanation can be offered for the significant disagreement with Bogatski's data at low temperatures although it is noteworthy that the purity of the nickel and nickel oxide used in the present work was superior to that used by Bogatski (3) or any of the other workers.

The free energy equation obtained from Eq. [1] for the formation of nickel oxide from carbon dioxide

$$Ni + CO_2 \rightarrow NiO + CO$$

is

$$\Delta G^\circ = 10890 + 0.11T \text{ cal/mole } (853°\text{-}1289°K) \quad \ldots [2]$$

The free energy values obtained from Eq. [2] are within 2 kcal/mole of the compiled data of Kubaschewski, Evans, and Alcock (5) which is within the limits of error given for this data, the limits being ±2 kcal/mole for reaction (*a*) and ±1 kcal/mole for reactions (*b*) and (*c*).

When Eq. [2] is combined with the data of Kubaschewski, Evans, and Alcock (5) for reactions (*b*) and (c) the following equation is obtained for the free energy of formation of nickel oxide from oxygen [reaction (*a*)]

$$\Delta G^\circ = -56600 + 20.9T \text{ cal/mole } (853°\text{-}1289°K)$$

Kinetic Study

The oxidation behavior of nickel and thoria dispersion strengthened nickel has been covered by several previous publications. Most of the studies have been concerned with oxidation by oxygen (6-16) although two pieces of work have covered carbon dioxide and CO_2/CO mixtures (16, 17). While the subject has received considerable attention several complicating features have not been fully explained, and the rate-determining processes have not been clearly identified. In oxygen at temperatures of 500°-1400°C the over-all attack may be approximated to a parabolic law although deviations are in general obtained with the nickel oxide being either more or less protective than required by the law. Cation diffusion via cation vacancies in the nickel oxide is normally accepted as the rate-determining process. Consistent with this view, the parabolic rate constant is increased by impurities in the metal such as iron, manganese, and chromium and is proportional to $p_{O_2}^{1/4}$ up to an oxygen pressure of 1 atm. Complicating features are that the parabolic rate constant is independent of the pressure of oxygen above 1 atm, that in one study on thoria dispersion strengthened nickel it was deduced that some control of the oxidation rate was exercised at 950°-1000°C by a surface reaction at the oxide/gas interface (14), and that the oxide film may consist of two layers with markers positioned within the scale between the two layers. The inner oxide layer is porous and is usually assumed to grow with the transfer of oxygen gas across the pores. The formation of the two oxide layers is facilitated by the presence of impurities in the metal.

The two previous studies (16, 17) with carbon dioxide and CO_2/CO mixtures were carried out at temperatures of 900°-1300°C. A linear rate law was obeyed initially, and this was followed by a period in which the rate continuously decreased according approximately to a parabolic law. It was deduced that during the linear period the rate of oxidation was controlled by the dissociation of carbon dioxide on the surface of the nickel oxide while latterly ionic diffusion was rate controlling. However the dependence of the linear rate constant on the carbon monoxide concentration did not agree with theoretical predictions which held in the case of the analogous oxidation of iron (18). In contrast to the behavior for oxygen only one layer was observed in the oxide film with markers being situated at the oxide/metal interface.

Experimental

Four types of nickel were investigated, spectrographically standardized pure metal from Johnson Matthey Company, an impure commercial grade containing appreciable amounts of manganese and iron, and metal dispersion strengthened with approximately 2 vol % of either alumina or thoria from Henry Wiggins Company and E. I. du Pont de Nemours & Co., respectively. Detailed analyses are given in Table I. The particle sizes of the oxide in the alumina and thoria strengthened materials were 500-5000 and 100-400Å, respectively. The first three types were tested in the form of 500μ thick sheet while the last was as sections of tube 1.5 cm diameter with a wall thickness of 750μ. Before testing all the specimens were annealed for 15 min at 900°C and then pickled in a mixture of nitric, sulfuric, orthophosphoric, and acetic acids to obtain a bright smooth surface. The carbon dioxide and oxygen were the spectrographically standardized grades supplied by BOC. They were dried over phosphorus pentoxide before use.

Oxidations were carried out on vacuum microbalances by a procedure described previously (19). Specimens were outgassed at room temperature and then at the reaction temperature before the admission of the reactant gas. There was no carrier gas or continuous gas flow through the apparatus. Carbon monoxide formed by the oxidation with carbon dioxide was continuously reconverted to carbon di-

Table I. Analyses of materials used in the kinetic study

	Al_2O_3, %	ThO_2, %	Fe, ppm	Si, ppm	Mg, ppm	Al, ppm	Cu, ppm	Mn, ppm	Li, ppm	Ti, ppm	Co, ppm	Cr, ppm	C, ppm	O_2, ppm	N_2, ppm
Pure metal	—	—	2	3	2	<1	<1	—	—	—	—	—	—	—	—
Impure metal	—	—	600	<700	400	300	100	1200	<5	<300	600	100	65	250	<50
Al_2O_3 strengthened	0.9	—	<100	<500	<100	—	<100	<100	<10	<200	<200	<100	—	4100	200
ThO_2 strengthened	—	2.6	300	<500	<100	200	<100	<100	<10	<200	<200	<100	58	2400	100

oxide by two beds of cupric oxide, one in the reaction vessel beneath the specimen and one in a thermal convection loop attached to the balance. The temperature of the beds was 350°-400°C for all the experiments. Analysis of the gas at the end of the experiments established that the beds worked efficiently and the final carbon monoxide pressure in the apparatus was $<10^{-5}$ atm. The experiments with the CO_2/CO mixtures were carried out in a gas circuit similar to that used for the thermodynamic study but containing a microbalance and a bed of nickel and nickel oxide powders, the temperature of which fixed the p_{CO}/p_{CO_2} ratio.

Information on the mechanisms of oxide film growth was obtained from marker studies employing platinum deposits on preoxidized surfaces, and the alumina particles in the alumina dispersion strengthened material. The deposits were prepared from a product supplied by Engelhard Industries containing a platinum compound in a hydrocarbon solvent. The specimen was painted with the product and then given the normal high-temperature outgassing treatment on a microbalance to decompose the platinum compound and thereby produce a fine dispersion of metallic platinum.

Results

The primary experiments were carried out in carbon dioxide at 0.1 atm pressure at 700°, 800°, 900°, 1000°, and 1100°C. All four batches of metal were tested at the four latter temperatures, but only the pure nickel was investigated at 700°C. As the results from these experiments were in some respects unexpected, further experiments were carried out with pure nickel in oxygen at 0.1 atm and in carbon dioxide at 1 atm to provide reference data which overlapped published work. Experiments were also carried out with the pure nickel in CO_2/CO mixtures at 0.1 atm at 900° and 1000°C.

With carbon dioxide and CO_2/CO mixtures the kinetics were complex and varied to a significant extent in duplicate runs but allowed firm conclusions to be reached. The weight gain-time curves for carbon dioxide are given for the four higher temperatures and a gas pressure of 0.1 atm in Fig. 2-5, respectively. The degree of irreproducibility is demonstrated in the figures by duplicate runs for pure nickel. The initial rate of oxidation decreased and then became linear or continued to decrease. After very long exposures a linear rate would change to a steadily decreasing rate. At 700°C the oxidation of the pure metal was very slight with the weight gain amounting to only 0.1 mg/cm² after 1000 hr exposure. With oxygen the rate steadily decreased during the course of the experiment. Decreasing rates obeyed in general a parabolic law as demonstrated by the data for carbon dioxide at 1000°C in Fig. 6. The parabolic rate constants obtained initially for the pure metal in carbon dioxide and oxygen are summarized together with those for the relevant published data in Fig. 7. The following conclusions were drawn from an analysis of the results:

(*A*) The data for carbon dioxide at 1 atm and for oxygen are in good agreement with the comparable published data.

(*B*) With a pressure of 0.1 atm the extent of the oxidation by carbon dioxide is almost independent of temperature over the range 900°-1100°C and is decreased by the impurities in commercial nickel. This latter conclusion is in general supported by the results of the dispersion strengthened materials.

(*C*) An increase in the gas pressure from 0.1 to 1 atm increases significantly the oxidation by carbon dioxide particularly at the higher temperatures of 1000° and 1100°C.

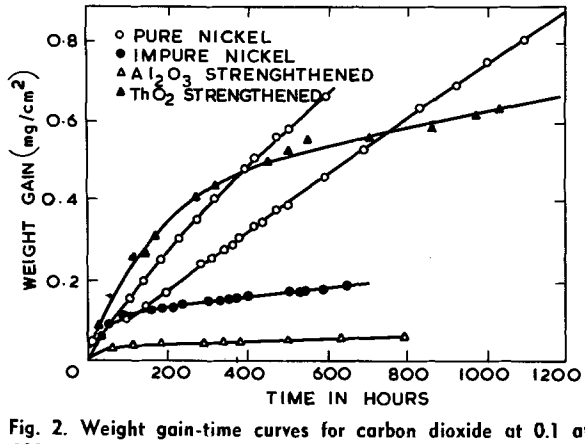

Fig. 2. Weight gain-time curves for carbon dioxide at 0.1 atm at 800°C.

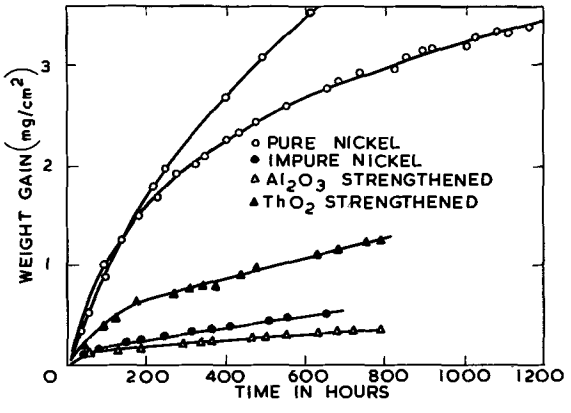

Fig. 3. Weight gain-time curves for carbon dioxide at 0.1 atm at 900°C.

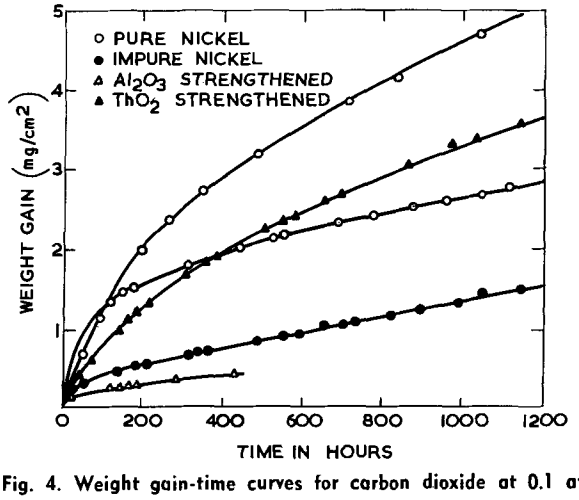

Fig. 4. Weight gain-time curves for carbon dioxide at 0.1 atm at 1000°C.

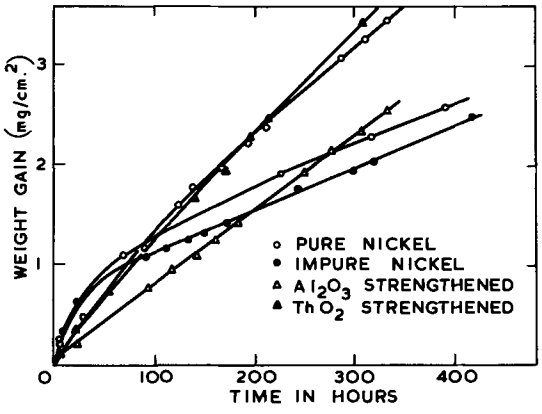

Fig. 5. Weight gain-time curves for carbon dioxide at 0.1 atm at 1100°C.

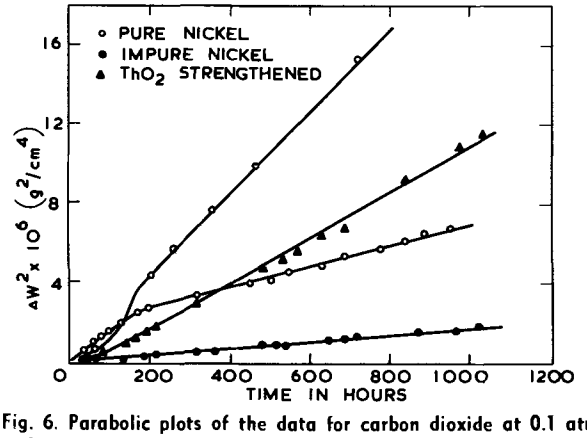

Fig. 6. Parabolic plots of the data for carbon dioxide at 0.1 atm at 1000°C.

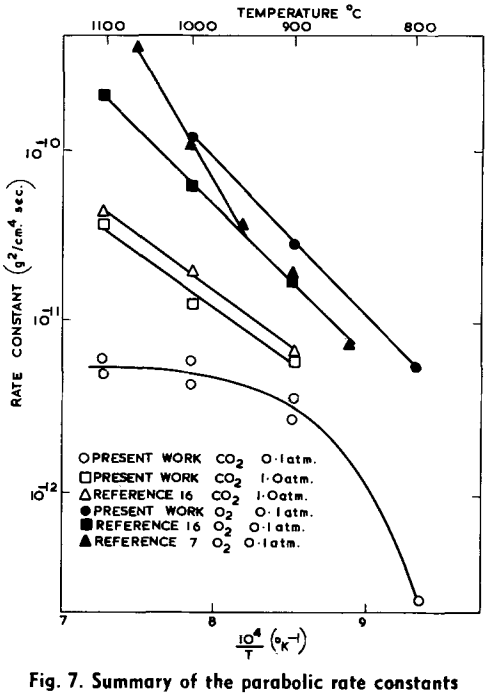

Fig. 7. Summary of the parabolic rate constants

The addition of carbon monoxide to the carbon dioxide at 0.1 atm pressure decreased the extent of the oxidation. At 900°C a linear law was obeyed after the initial oxidation, and a series of experiments was carried out on one specimen in which the carbon monoxide level was varied over the range 0.16-0.7% such that a rate constant was determined for each of 5 carbon monoxide concentrations. The results are summarized in Fig. 8 which shows the rate constant varied linearly with the percentage of carbon monoxide in the gas. At 1000°C two experiments were carried out with 0.91 and 0.94% carbon monoxide. In both cases a parabolic law was obeyed over the 300-1200 hr exposure period, the respective rate constants being 2.1×10^{-13} and 4.9×10^{-13} g²/cm⁴ sec.

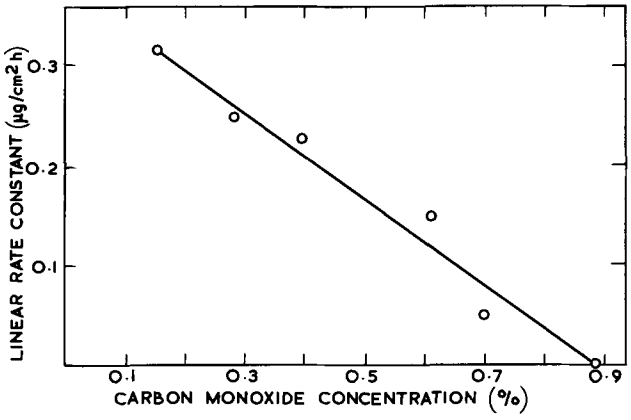

Fig. 8. Influence of carbon monoxide on the linear rate constant for CO_2/CO mixtures at 0.1 atm at 900°C.

Metallographic examination of the specimens established that for the pure and impure grades of metal the extent of the attack differed on different metal grains at 700° and 800°C and for some but not all specimens at 900°C. This phenomenon was obtained also for pure nickel in oxygen at 700° and 900°C but was absent for oxygen at 800°C and for both carbon dioxide and oxygen at temperatures ≧ 1000°C. During the oxidation of the pure metal in carbon dioxide pores were formed on grain boundaries within the metal at 700° and 800° and in some specimens at 900°C, but not at higher temperatures or in oxygen at any temperature. With the impure nickel, pores were not formed within the metal, but internal oxidation was obtained at all test temperatures; this oxidation was more pronounced the higher the temperature and resulted in the formation of oxide particles primarily on the grain boundaries but also within the grains at the higher temperatures. Electron microprobe analysis showed that the internal oxide was enriched in manganese. Internal oxidation was not obtained for any other metal-environment combination other than for one anomalous pure metal specimen oxidized in carbon dioxide at 1 atm at 1000°C. With the two oxide dispersion strengthened materials there was no pore formation within the metal or internal oxidation although the oxide/metal interface was very uneven at the higher experimental temperatures, indicating preferential attack of certain grains. The oxide scales formed on all, but possibly one specimen, were single layered and contained pores of various sizes (Fig. 9); these pores appeared closed and hence did not provide access for the gas to the oxide/metal interface. The possible exception was the alumina strengthened material oxidized in carbon dioxide at 1000°C, which had an outer dense layer and an extremely porous inner oxide with a pronounced tendency to separate from the metal substrate on cooling of the specimen.

All the experiments with a platinum marker were carried out at 1000°C and with the surface of the metal slightly preoxidized in carbon dioxide at 1000°C before application of the marker. The preoxidation amounted to a weight gain of 18-30 μg/cm² and stopped interaction of the marker with the metal. A separate experiment in which the marker was applied to a heavily oxidized specimen which was subsequently heat-treated *in vacuo* at 1000°C for 478 hr confirmed that the marker did not interact with the oxide. Three experiments were carried out with pure nickel for varying oxidation times. The majority of

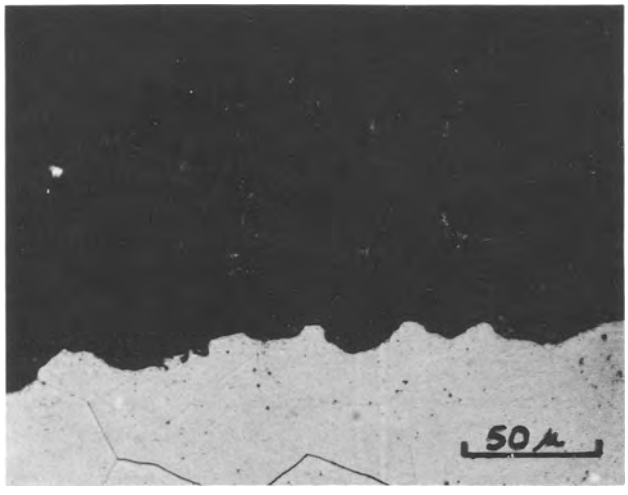

Fig. 9. Section of the scale formed on pure nickel after 6000 hr oxidation in carbon dioxide at 1 atm at 1000°C.

the platinum was found in approximately the middle of the scale although appreciable amounts were distributed randomly throughout the oxide between the two interfaces (Fig. 10). One experiment was carried out on the alumina strengthened material and the majority of the platinum was found at the boundary between the dense and porous regions of the scale, although in contrast electron probe analysis of this and other alumina strengthened specimens indicated that little or no alumina was incorporated into either region of the oxide, instead there was an accumulation of alumina at the oxide/metal interface.

Discussion

For the experiments with carbon dioxide, the oxygen potential of the gas should have been determined by the experimental temperature according to the equilibrium

$$CO_2 \rightleftarrows CO + \tfrac{1}{2} O_2 \qquad \ldots [d]$$

but as the partial pressures of carbon monoxide and oxygen will have been low consideration should be given to the effects of carbon monoxide produced by the oxidation of the metal. First, it may be deduced that changes in the carbon monoxide content of the main gas stream could not have invalidated the essential kinetic results for temperatures of 900°-1100°C as (*a*) reaction rates differed considerably between the different batches of metal; (*b*) there was only a slight effect of temperature on the kinetics with a total pressure of 0.1 atm; (*c*) there was only a slight effect of total pressure on the kinetics at 900°C, the temperature within the 900°-1100°C range at which the maximum effect of carbon monoxide should be obtained at 0.1 atm from considerations of the reaction rates and carbon monoxide contents produced by reaction [*d*].

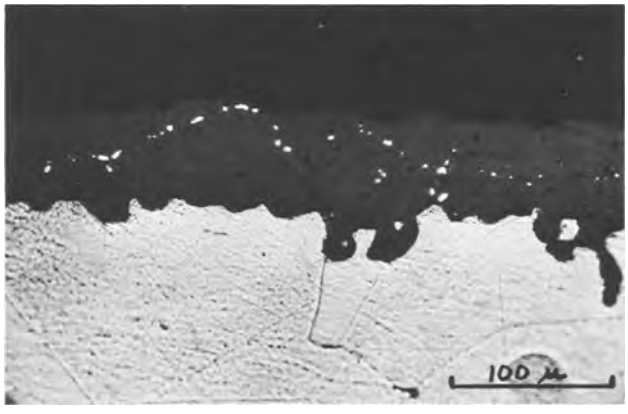

Fig. 10. Platinum marker in oxide formed on pure nickel after 1500 hr oxidation in carbon dioxide at 0.1 atm at 1000°C.

Regarding points (*b*) and (*c*), if the CO_2/CO ratios had been altered significantly by the oxidation, high reaction rates would have been expected at 1100°C 0.1 atm and 900°C 1 atm by comparison with 900°C 0.1 atm because the proportionate contributions to the carbon monoxide content of the gas from the oxidation would have been greatly reduced in the former instances. Also with particular relevance to the data for 1000°-1100°C the carbon monoxide pressures produced by the oxidation were shown at the end of the experiments to be $< 10^{-5}$ atm, a pressure comparable with or less than that obtained from reaction [*d*] at temperatures $\geq$ 1000°C. It may be deduced that the oxidation had no significant influence on the CO_2/CO ratios below 900°C because at these temperatures the decrease in the reaction rate with temperature was greater than that for the carbon monoxide produced by reaction [*d*]. Further to the above points interdiffusion rates between carbon dioxide and carbon monoxide are fast by comparison with the reaction rates from which it may be shown that changes in carbon monoxide concentration across a diffusion barrier layer next to the metal would have been small. Considerations of the kinetic data and the thermodynamics of reaction [*d*] show that the maximum effect of the barrier layer would have been obtained at 900°C with a total pressure of 0.1 atm. With the maximum reaction rate obtained initially at 900°C, an interdiffusion coefficient of 1 cm^2/sec and a barrier layer thickness of $<$ 1 mm it may be calculated that the change in carbon monoxide concentration across the barrier layer would have been $< 1.5 \times 10^{-6}$ atm. By comparison the carbon monoxide concentration in the main gas stream at 900°C and 0.1 atm total pressure according to reaction [*d*] was 1.2×10^{-6} atm. Under the worst possible conditions, therefore, the oxidation of the metal could have only doubled the carbon monoxide content of the gas next to the metal. This increase would have only decreased the cation defect concentration in the oxide at the oxide/gas interface by 30% assuming the defect concentration is proportional to $p_{O_2}^{1/4}$. Also it would have been unlikely to have affected surface reaction rates appreciably, and therefore it is concluded that the carbon monoxide produced by the oxidation had no significant influence.

Nickel oxide is a p-type semiconductor from which it is assumed throughout the remainder of this discussion that nickel is the predominant diffusing ion in the oxide and that the position of markers within the oxide scale in both this and other work must be explained by mechanisms other than the diffusion of oxygen ions. The temperature dependence of the kinetic data for pure nickel in carbon dioxide clearly indicates that the oxidation rate was at least partially governed by a process other than the diffusion of nickel across the oxide scale. At 0.1 atm pressure the parabolic rate constant was almost independent of temperature over the range 900°-1100°C and at 1 atm pressure the activation energy was only 29 kcal/mole. In contrast the activation energy for reaction by oxygen was 42 kcal/mole and the values reported for the diffusion of nickel in nickel oxide are within the range 44-62 kcal/mole (13). For pure diffusion control the activation energy for oxidation by carbon dioxide should be slightly greater, not less than these values because the oxygen potential of the environment rises with temperature according to reaction [*d*]. As already discussed the kinetics cannot be explained in terms of the carbon monoxide produced by the oxidation but instead it is considered that the oxidation rates are at least partially governed by a surface reaction at the oxide/gas interface. This view is supported by a linear rate law being obeyed in several instances. In particular the data obtained for the CO_2/CO mixtures at 900°C obey an equation shown by Pettit *et al.* (18) to hold when a linear rate law

is obeyed and reaction is controlled by the dissociation of adsorbed carbon dioxide, namely

$$\overset{o}{n} = k'P'(1 + K)[N'_{CO_2} - N'_{CO_{2(equil)}}] \quad \ldots [3]$$

where $\overset{o}{n}$ = number of equivalents of oxide formed/sec/cm² area; k' = rate constant of the phase boundary reaction; P' = total pressure; K = equilibrium constant between metal, metal oxide, and gas mixture; N'_{CO_2} = mole fraction of carbon dioxide in gas; and $N'_{CO_{2(equil)}}$ = mole fraction of carbon dioxide in CO_2/CO gas mixture in equilibrium with metal and oxide. In contrast this relationship did not apply to the data of Fueki and Wagner (17) for temperatures within the range 1100°-1300°C.

In addition to the linear regions, interface control is believed to apply to at least a limited extent during periods in which the reaction rate continuously decreases with time, thereby explaining the low activation energies for the parabolic rate constant for carbon dioxide at both 0.1 and 1 atm pressure. Also it could explain the pronounced pressure dependence of the parabolic rate constant at 1000°-1100°C. For example at 1100°C oxidation controlled by cation diffusion should result in the rate constant being increased by a factor of 1.5 for a total pressure increase from 0.1 to 1.0 atm assuming the rate constant is proportional to $p_{O_2}^{1/4}$, while in fact the constant increased by a factor of 6.4. Interface control could apply during an extended period in which the over-all reaction rate was decreasing if it was assumed that the interface reaction was linked to the diffusion of nickel in the oxide and decreased with time, with for example the rate of the interface reaction being coupled to the defect concentration of the nickel oxide at the oxide/gas interface. A mechanism consistent with the data would be that the rate of adsorption or dissociation of carbon dioxide decreased as the concentration of cation vacancies increased. By such a mechanism both the interface and diffusion processes would be linked to give a continuously decreasing over-all rate of oxidation, and the concentration of cation vacancies at the oxide/gas interface would gradually increase. Thickening of a thin oxide film initially in equilibrium with the metal would increase the diffusion path for nickel ions and thereby tend to increase the concentration of nickel ion vacancies at the oxide/gas interface, but this would be partially counteracted by a slowing of the interface reaction. For pure diffusion control the oxide at the oxide/gas interface would be in equilibrium with the gas while for complete interface control this oxide would be in equilibrium with the metal; it follows that in the present case an intermediate situation is envisaged in which the oxide at the interface is in equilibrium with neither the underlying metal nor the gas.

The proposed mechanism would be consistent with the low rates of oxidation obtained for the impure nickel, the impurities in which should increase the concentration of nickel ion vacancies as shown by the high rates of attack obtained in oxygen with metal contaminated with iron and manganese (15), the main impurities in the commercial grade of metal. Also it is consistent with the work of Jones and Westerman (14) on the reaction of TD nickel with oxygen in that these workers deduced that the partial interface control for this reaction resulted from the adsorption of oxygen (reaction [e]) being decreased by the

$$O_2 + \text{site} + 4e^- \rightarrow 2\,O^{--}\ (\text{ads}) \quad \ldots [e]$$

presence in the oxide of foreign cations with a valency > 2 (*i.e.*, thorium).

Further support for interface control was obtained from experiments aimed at explaining the significant irreproducibility in the kinetics by determining the influence of water vapor in the carbon dioxide. The experiments were carried out at 800°, 900°, and 1000°C with a total pressure of 0.1 atm. Oxidation started in dry carbon dioxide, water vapor at a pressure of 3.5 x 10^{-2} atm was subsequently added, and then finally the water vapor was removed and the oxidation concluded in dry carbon dioxide. The results demonstrated that at the three temperatures water vapor inhibited the reaction. Results for 900° and 1000°C are summarized in Fig. 11. The free energies of formation of carbon dioxide and water vapor at these temperatures are such that the water vapor could not have significantly altered the oxygen potential of the gas, and hence diffusion rates in the nickel oxide, and therefore the results can only be explained by the water vapor modifying the surface reaction and being adsorbed in preference to carbon dioxide. It is relevant to note that the water vapor exerted its effect at 800°C, although the preferential attack of certain metal grains obtained at this temperature would indicate that processes at the metal/oxide interface were of prime importance.

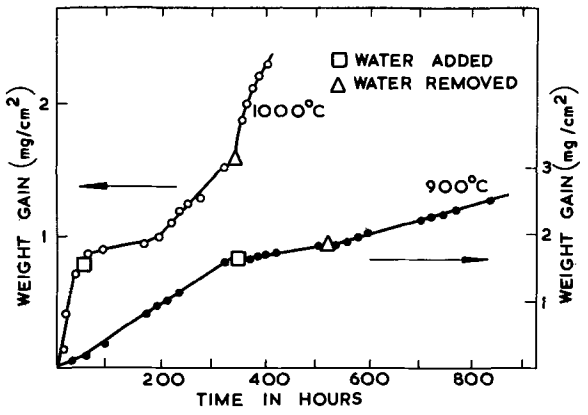

Fig. 11. Influence of water vapor on oxidation of pure nickel by carbon dioxide at 0.1 atm at 900° and 1000°C.

Consideration of the parabolic rate constants obtained for oxygen and CO_2/CO mixtures at 1000°C showed that the rate constant was proportional to $p_{O_2}^{1/4}$, but in view of the influence of interface control for pure carbon dioxide no conclusions can be drawn from this relationship as to the defect structure or diffusion processes in the nickel oxide. The observance of a parabolic law is therefore considered incidental and of no particular significance.

As in other work it was observed that the color of the oxide could vary considerably from bright green to black. Films which were black in reflected light were shown to be green in transmitted light, and therefore in contrast to previous work (8) it was concluded that the color was not dependent on the composition of the oxide, but rather was a measure of the surface roughness and the proportion of transmitted light reaching the eye. Also supporting experiments could obtain no correlation between color and stoichiometry.

The metallographic examination clearly established that the internal oxidation was associated with impurities in the metal. The one anomalous result, with internal oxidation of a pure nickel specimen at 1000°C, is not understood, but may have resulted from surface contamination during specimen preparation. The pores formed in pure nickel are believed to have resulted from the condensation of vacancies produced by the outward diffusion of nickel ions through the oxide film. The penetration of the vacancies was reduced by high temperatures and by the presence of the alumina and thoria particles, or the fine grain size resulting from the particles in the oxide dispersion strengthened materials. These factors would have facilitated the nucleation and growth of the pores at the oxide/metal interface. The absence of pores in the impure nickel specimens is probably due to the internal oxide facilitating condensation of vacancies as in the dispersion strengthened materials and to the reverse process of embryo pores acting as nuclei for internal oxidation

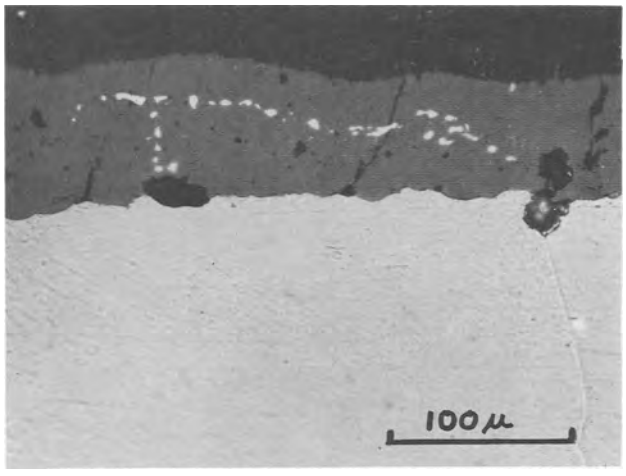

Fig. 12. Platinum marker neighboring a pore in a scale formed on pure nickel after 1500 hr oxidation in carbon dioxide at 0.1 atm at 1000°C.

such that oxide fills the vacancies as they condense. The pores within the oxide scale could have been formed by a variety of mechanisms which cannot be discussed profitably on the basis of the available data. However, it should be noted that the distribution of the pores was random.

With one possible exception the double layered scales obtained in previous studies with oxygen were not obtained. In particular the scales formed on impure nickel in carbon dioxide were single layered. To ensure consistency on this subject with previous work additional experiments were carried out with the impure nickel in oxygen at 1100°C. In agreement with the previous work the impurities led to the formation of a double layered oxide at a weight gain similar to that for the single layered scale formed in carbon dioxide (6 mg/cm^2). Double layered scales appear therefore to be associated with a high oxygen potential in the environment or the associated fast growth rates as well as impurities. Also in agreement with other work these experiments demonstrated that the impurities enhanced the attack in oxygen as distinct from carbon dioxide.

Considerable plastic flow of the oxide caused by pore formation and/or other factors was deduced from the photomicrographs. In particular the platinum markers were broken up and distributed across the oxide scale and the oxide usually kept in close contact with uneven metal surfaces (Fig. 9 and 10) resulting from preferential attack of certain regions (*e.g.*, grain boundaries). The behavior of the platinum adjacent to pores was consistent with considerable flow (Fig. 12) in these regions which would be expected as flow should be accentuated by the pores acting as barriers to ionic diffusion in the oxide, thereby tending to produce a scale of uneven thickness. The behavior of the platinum will have been facilitated by placing it on a preoxidized surface. In contrast, with the alumina strengthened material, the alumina did not pass into the oxide confirming that little or no diffusion of oxygen ions occurred in the nickel oxide and indicating that flow of the oxide did not extend to the oxide/metal interface.

The notable disagreements with previous work arise from the work of Fueki and Wagner (17) in that Eq. [3] was obeyed at 900°C although it should be noted that the other work referred to 1100°-1300°C, and in that partial interface control was believed to apply in carbon dioxide at 1 atm as well as at lower pressures. Also partial interface control is believed to apply in many instances over protracted periods when the reaction rate continuously decreases. In other respects the data are in good agreement with the previous work and extend previous knowledge in the areas covering in particular the influence of impurities in the metal, of water vapor in the gas, and the physical structure of the oxide scale.

Manuscript received April 14, 1967; revised manuscript received Sept. 5, 1967.

Any discussion of this paper will appear in a Discussion Section to be published in the June 1968 JOURNAL.

REFERENCES

1. M. Watanabe, *Sci. Rep. Tohoku Imp. Univ.*, **22**, 436 (1933).
2. A. F. Kapustinsky and A. Silberman, *Acta Physicochim., URSS*, **5**, 605 (1936).
3. D. P. Bogatski, *Metallurg.*, **13**, 18 (1938).
4. R. Fricke and G. Weitbrecht, *Z. Elektrochem.*, **48**, 87, 389 (1942).
5. O. Kubaschewski, E. Ll. Evans, and C. B. Alcock, "Metallurgical Thermochemistry," 4th ed., pp. 421, 422, 426, Pergamon Press, London (1967).
6. E. A. Gulbransen and K. F. Andrew, *This Journal*, **101**, 128 (1954).
7. E. A. Gulbransen and K. F. Andrew, *ibid.*, **104**, 451 (1957).
8. J. A. Sartell and C. H. Li, *J. Inst. Metals*, **90**, 92 (1961-62).
9. B. M. Vasyutinskiy and G. N. Kartmazov, *Fiz. Metal Metalloved*, **15**, 132 (1963).
10. J. P. Baur, R. W. Bartlett, J. N. Ong, Jr., and W. M. Fassell, Jr., *This Journal* **110**, 185 (1963).
11. W. L. Phillips, *ibid.*, **110**, 1014 (1963).
12. F. S. Pettit and E. J. Felten, *ibid.*, **111**, 135 (1964).
13. G. C. Wood *et al.*, *Corrosion Sci.*, **5**, 645 (1965).
14. D. A. Jones and R. E. Westerman, *Corrosion*, **21**, 295 (1965).
15. O. Kubaschewski and B. E. Hopkins, "Oxidation of Metals and Alloys," 2nd ed., p. 243, Butterworths London (1962).
16. K. Fueki and J. B. Wagner, *This Journal*, **112**, 384 (1965).
17. K. Fueki and J. B. Wagner, *ibid.*, **112**, 1079 (1965).
18. F. Pettit *et al.*, *Acta Met.*, **8**, 617 (1960).
19. W. B. Jepson *et al.*, *Brit. Corrosion J.*, **1**, 15 (1965).

Correction

To avoid confusion, please note that Fig. 1 of the paper by T. Biegler and D. F. A. Koch "Adsorption and Oxidation of Methanol on a Platinum Electrode" on page 905 of the September 1967 issue of the *Journal* is printed upside down.

The Effect of Anodic Films on the Gaseous Oxidation of Tantalum

II. Films Formed in Phosphoric Acid Solutions

R. E. Pawel

Metals and Ceramics Division, Oak Ridge National Laboratory, Oak Ridge, Tennessee

ABSTRACT

The high-temperature oxidation characteristics of tantalum specimens anodized in phosphoric acid solutions were studied. The anodic oxide films containing phosphorus were found to be considerably more effective in limiting oxygen access to the metal and in postponing breakaway oxidation than phosphorus-free anodic films of the same thickness. Thickness-voltage calibrations were obtained for anodization in 0.9M and 14M H_3PO_4 electrolytes allowing quantitative measurements and comparisons of oxidation behavior to be made with that previously found for plain tantalum and for tantalum specimens anodized in dilute aqueous solutions.

In a previous paper (1) it was indicated that thin anodic films can exert a significant influence upon the subsequent gaseous oxidation characteristics of tantalum. Briefly, at temperatures up to about 600°C, the anodic films were observed to decrease the oxygen consumption rate and to postpone the occurrence of the "breakaway" increase in the oxidation rate common to this metal. While during the protective stage of oxidation the amorphous anodic films passed oxygen to the metal at a rate inversely proportional to their thickness, they appeared not to change in thickness or to crystallize. Loss of the protective properties of the films was associated with the formation of crystalline oxides, proposed to originate at the anodic oxide-metal interface, which physically ruptured the overlying film at isolated points. The purpose of the present paper is to present and discuss some of the differences in these effects when the anodic films are formed in phosphoric acid solutions rather than in dilute aqueous solutions of Na_2SO_4 and KF.

Many effects on the formation characteristics and film properties associated with anodizing in concentrated and nonaqueous electrolytes have been reported in the literature (2). In particular, anodization in phosphoric acid solutions has produced some interesting results. Vermilyea (3) concluded from his experiments that films formed in phosphoric (or sulfuric) acid electrolytes consist of two layers: a layer of normal Ta_2O_5 next to the metal and a layer of unspecified composition having different properties next to the electrolyte. Randall *et al.* (4) investigated quantitatively the composition of the films formed over a wide range of conditions. By a radiotracer technique, they confirmed the "two-layer" model, showing that the inner layer (approximately half the total thickness except for those formed in concentrated acid) was essentially stoichiometric Ta_2O_5, with the outer layer containing up to about 18 mole % phosphorus depending on the phosphoric acid concentration of the electrolyte. The relative thickness of the phosphorus-rich layer increased with increasing current density and electrolyte concentration. Smyth and his coworkers (5, 6) have made extensive measurements of the dielectric behavior of such films, particularly after mild heat-treatments, and found significant differences from those properties exhibited by phosphorus-free anodic films. The irregular distribution of phosphorus in the anodic film was found to become still more irregular upon annealing. For 1-hr anneals in air at 500°C, the "interface" separating the two layers of film moved away from the tantalum, resulting in a large phosphorus concentration increase in a narrow zone within the phosphorus-containing layer. In addition, Smyth reported several observations which indicated that mass transport, particularly of oxygen, is more difficult in phosphorus-containing anodic Ta_2O_5 films, a behavior consistent with that observed for several other metal-oxide systems where phosphorus is involved. It is also interesting to note that thin phosphide layers, formed by holding specimens in phosphorus vapor, have been reported to decrease the rate of high-temperature (800°C) oxidation of several refractory metals (7, 8).

Since the early stages of gaseous oxidation of tantalum involve the dissolution of comparatively large quantities of oxygen with the attendant development of both stress and mechanical-property gradients in addition to oxide formation, it is anticipated that devices which decrease oxygen access to the metal through decreasing oxygen mobility in oxide films might be especially effective in combating otherwise poor oxidation resistance. Therefore, the extent of protection during subsequent oxidation afforded by anodic films formed in phosphoric acid was studied and compared with the previous results on tantalum anodized in dilute aqueous solutions. The manner in which the films eventually break down during oxidation was also investigated.

Experimental Procedure

The tantalum[1] specimens were prepared from 0.020- and 0.050-in. sheet in the form of 1- × 2-cm coupons. The coupons were annealed in vacuum at 1600°C for 2 hr, mechanically polished through 0.3-μ alumina, and electropolished in a 90% H_2SO_4-10% HF solution. A short length of 0.010-in. electropolished tungsten wire was spot welded to the specimen to serve as electrical contact and support during anodization. The electropolished tungsten did not interfere with the anodization of the tantalum and, during oxidation, proved to be more "inert" than fine tantalum wire which sometimes exhibited premature breakdown of the anodic film.

Since the H_3PO_4-anodized specimens oxidized very slowly compared to unanodized tantalum, it was important to reduce spurious oxygen consumption sources to a minimum in order for the kinetic studies to be meaningful. The specimens were carefully electropolished to avoid as much as possible physical surface flaws such as pits or fine scratches which serve as sources for breakdown. The 0.050-in.-thick specimens appeared to exhibit less severe edge and corner effects, perhaps due to the rounding that occurred at these

[1] Nominal analysis is 99.7-99.8% Ta with Nb, Fe, W, and Si being major metallic impurities; interstitial content after vacuum anneal is 200-300 ppm.

points during extended electropolishing, and most of the data presented in this paper were obtained on such specimens.

The specimens were anodized at room temperature to a given voltage in a simple cell in which the initially high rates of film formation were limited by a variable series resistor. The series resistance was reduced to zero and the specimen held at full voltage for a "standard" time, in this case 2 min, such that the final thickness was relatively insensitive to small differences in the anodization sequence or time.

The specimens were heated quickly in dry oxygen to the desired reaction temperature in a high sensitivity manometric oxidation rate apparatus, and the rate of oxygen consumption was followed as a function of time. Specimens for metallographic examination were similarly oxidized for various times in a quartz apparatus.

Results and Discussion

Film formation.—Generally, the anodic films formed on electropolished tantalum surfaces in dilute electrolytes are of very uniform thickness and consist of amorphous layers or very small crystallites of material having pentoxide stoichiometry. The anodization efficiency is virtually 100%, and suitable thickness-voltage calibrations can be obtained with a simple constant-voltage power supply using the procedures outlined above. The measurement of the weight changes of a 450 cm^2 tantalum sheet specimen during stepwise anodization in 0.2% KF to 200v resulted in a linear relationship between weight gain and voltage of 0.2399 $\mu g/cm^2$-v. Recent measurements (9, 10) indicate that the density of the amorphous oxide formed under these conditions is approximately 8.03 g/cm^3, which leads to an oxide thickness calibration value of 16.5 Å/v.

Anodizing tantalum in phosphoric acid solutions also produces uniform amorphous layers of oxide; however, the effect of included phosphorus on the physical properties of these layers is not well established. The problem is magnified because of the apparent duplex nature of the films, and an accurate thickness-voltage calibration in this case is difficult to obtain. In Fig. 1, the weight gain as a function of applied voltage is presented for anodization in 0.9M and 14M H_3PO_4. These data were obtained with a standard laboratory microbalance using polished tantalum sheet specimens having surface areas of approximately 500 and 600 cm^2, respectively. In 0.9M H_3PO_4, the tantalum anodized very much in the same manner as in dilute solutions: that is, a critical examination of interference colors, weight gain data, and electrical breakdown voltages is necessary to distinguish this film from one formed, for example, in 0.2% KF. On the other hand,

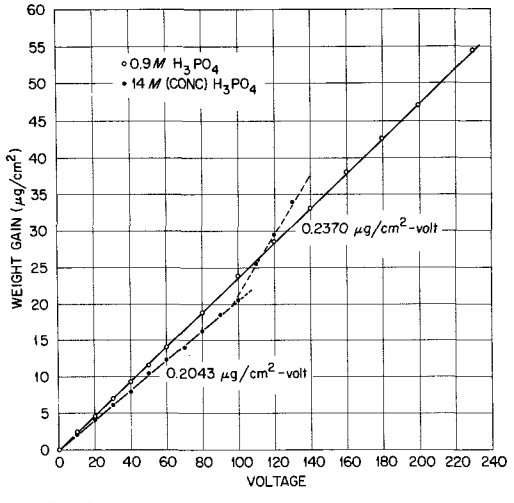

Fig. 1. Anodization of tantalum in H_3PO_4 solutions. ○ 0.9M H_3PO_4; ● 14M H_3PO_4.

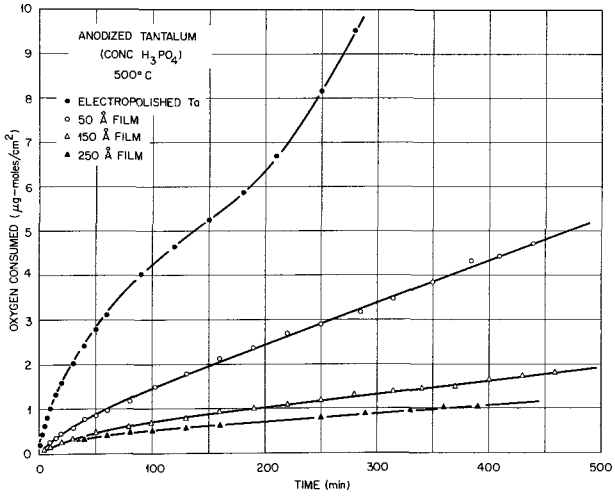

Fig. 2. Effect of anodic film thickness on the oxidation rate of polycrystalline tantalum at 500°C. Electropolished tantalum anodized in concentrated (14M) H_3PO_4 electrolyte. ● plain electropolished tantalum; ○ 50Å anodic film; △ 150Å anodic film; ▲ 250Å anodic film.

in the case of concentrated (85.3%, 14M) H_3PO_4, it is much more obvious that the process results in films of different properties.

The weight gain data of Fig. 1 are well described by a linear function of the voltage up to the breakdown voltage for each of the electrolytes. In 0.9M H_3PO_4, the specimen gained weight at a rate of 0.2370 $\mu g/cm^2$-v which was very close to that measured for tantalum in dilute KF, 0.2399 $\mu g/cm^2$-v. However, for our anodization procedures, about 10-12% additional voltage was required for 0.9M H_3PO_4 electrolytes to match interference colors with films formed in the dilute electrolytes. The breakdown voltage in this electrolyte was in excess of 220v.

In 14M H_3PO_4, the rate of weight gain of the specimen with voltage was appreciably less, 0.2043 $\mu g/cm^2$-v. The film suffered a self-healing dielectric breakdown and partial crystallization at about 95v resulting, among other things, in an increase in the rate of weight gain. In the concentrated acid, about 50% higher voltage was required to produce the same interference color as that formed in the dilute solution: for example, 49.5v films in 0.2% KF matched those formed to 75v in 14M H_3PO_4.

In order to establish a suitable thickness-voltage calibration for the phosphorus-containing films, it would be desirable to have an estimate of the density or at least information regarding the composition, structure, and refractive index of the films. While only limited direct data are available, some indirect measurements permitted a reasonable value to be estimated from the weight gain measurements. As indicated in detail in the Appendix, the most probable values were determined to be 13.2 Å/v for 14M H_3PO_4, and 15.7 Å/v for 0.9M H_3PO_4.

Kinetics.—Electropolished tantalum specimens anodized to a given film thickness in concentrated phosphoric acid (14M) were found more resistant to subsequent gaseous oxidation at elevated temperatures than specimens anodized in dilute aqueous solutions. While there were differences in the degree of protection depending on the phosphoric acid concentration of the electrolyte, the maximum effect seemed to occur for specimens anodized in the concentrated acid, and these results only will be considered in this paper.

The oxidation kinetics of plain tantalum and several anodized specimens[2] during the early stages of oxidation at 500°C are shown in Fig. 2. At this temperature,

[2] The thickness of the anodic films reported in Fig. 2-5 were calculated on the basis of a 14.0 Å/v calibration and are thus considered to be an upper limit of the actual thickness (see Appendix).

compared to the plain tantalum specimen, the anodized specimens consumed oxygen at a much slower rate: films as thin as 50Å exerted a considerable effect; films thicker than 250Å reduced the oxidation rate to very small values. By comparison with our previous work (1) it was apparent that these films were considerably more efficient in reducing the oxidation rate than those formed in dilute electrolytes. Smyth *et al.* (5, 6) previously reported that the over-all oxygen uptake of anodized tantalum while being annealed in air was less for the phosphorus-containing films. Smyth also concluded that the mobilities of the diffusing species, both high-temperature and field-driven, were decreased by the presence of phosphorus.

As further discussed below, the rate of oxygen permeation through the films was found to be inversely proportional to their thickness. This indicated that, as in the case of films formed in dilute electrolytes, oxygen diffused through the film and dissolved in the metal without an appreciable change in the film thickness. After a period of time in which oxygen solution in the metal was the primary event, the oxidation rate suddenly increased in a manner similar to the "breakaway" observed in the case of pure metal. The effect of temperature on the oxidation kinetics of tantalum specimens anodized in 14M H_3PO_4 to film thicknesses of 250 and 1000Å is shown in Fig. 3 and 4. The behavior was qualitatively the same as that shown previously (1) for conventional anodic films. However, for a given film thickness and temperature, the oxidation rate and time-to-breakaway were greatly different. It should be pointed out that the occurrence of breakaway of the oxidation rate curves for anodized specimens usually represents the start of film breakdown on an extremely local scale and not a general degradation of the protective properties of the film.

It was also possible to compare quantitatively the oxygen flux through these films with the corresponding flux observed during oxidation of tantalum specimens anodized in dilute solutions. The oxygen flux or permeation rate was taken as the slope of the almost-straight-line portion of the oxidation rate curve which existed immediately prior to the breakaway inflection. In order to check our results and to make use of some improvements in technique, our measurements for specimens anodized in 0.5% Na_2SO_4 solution were repeated and extended to higher temperatures. Figure 5 is a plot of the permeation rate as a function of reciprocal temperature for the four sets of specimens having two different film thicknesses. The data for 250 and 1000Å films formed in the dilute Na_2SO_4 solution are slightly higher than those presented in our earlier work (1); however, within experimental error the slopes of the lines describing the present data are the same as those found previously.

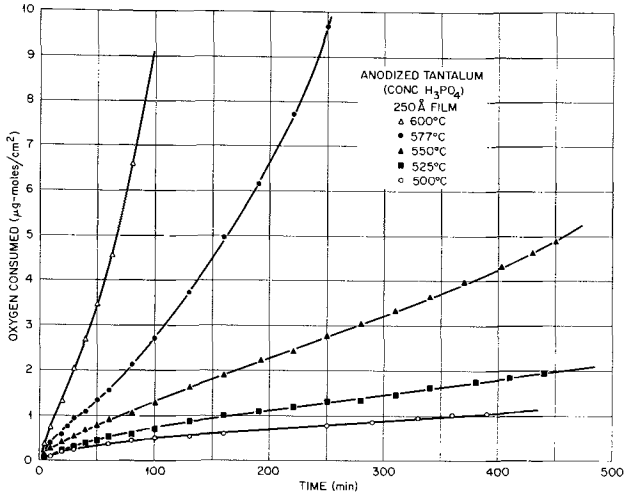

Fig. 3. Effect of temperature on the oxidation rate of anodized polycrystalline tantalum. Specimens anodized in concentrated (14M) H_3PO_4 to a film thickness of 250 Å. ○ 500°C; ■ 525°C; ▲ 550°C; ● 577°C; △ 600°C.

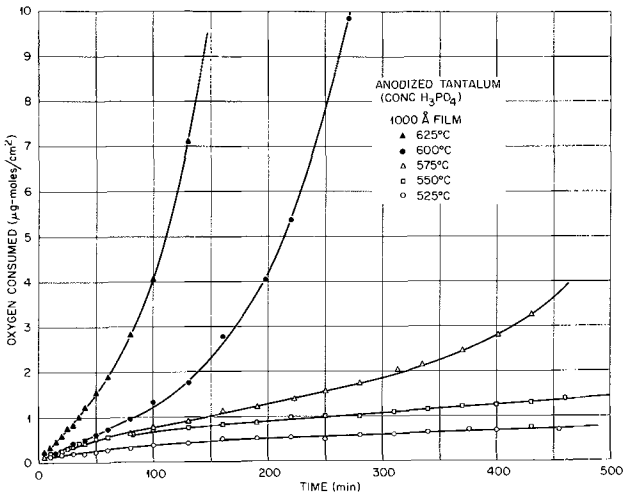

Fig. 4. Effect of temperature on the oxidation rate of anodized polycrystalline tantalum. Specimens anodized in concentrated (14M) H_3PO_4 to a film thickness of 1000 Å. ○ 525°C; □ 550°C; △ 575°C; ● 600°C; ▲ 625°C.

The data of Fig. 5 show that at a given temperature the oxygen permeation rates through films formed in dilute Na_2SO_4 were roughly five times greater than those for films of equivalent thickness formed in concentrated H_3PO_4. For films formed in either electrolyte, the permeation rates were inversely proportional to the film thickness, indicating that transport within the film was rate controlling. The activation energies for oxygen transport in both types of films, determined from the slopes in Fig. 5, were only slightly different: about 43 kcal/mole for plain Ta_2O_5 and about 46 kcal/mole for the phosphorus-containing films. Obviously, the error limits of these values overlap so it is impossible to tell unequivocally if the differences in rate were simply due to differences in activation energy

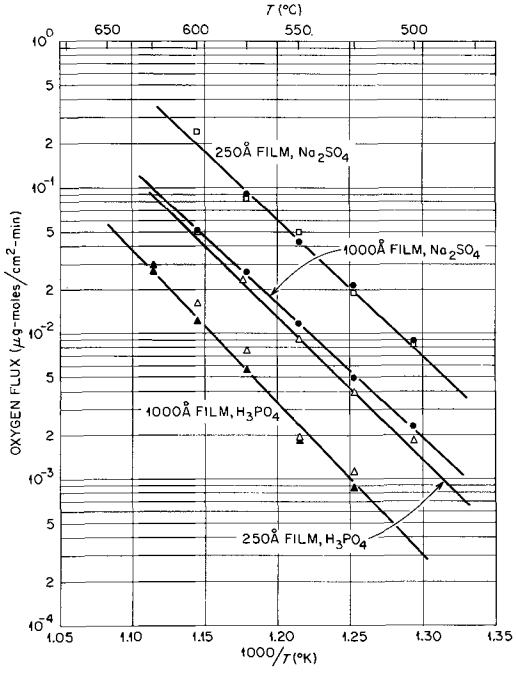

Fig. 5. Oxygen permeation rates through anodic films on polycrystalline tantalum. ● and ▲ specimens prepared from 0.050-in. Ta sheet. □ and △ specimens prepared from 0.020-in. Ta sheet. Anodic film thickness and electrolyte specified on figure.

rather than concentration differences or preexponential factor effects. However, a difference of this magnitude in activation energy could indeed account for the observed difference in rate in this temperature range.

Breakdown of the films.—Visual and microscopic observations of the topography of anodized specimens during oxidation emphasized, perhaps even more than the oxidation rate curves, the differences in protection afforded by the anodic oxide films. For all tantalum specimens anodized in concentrated H_3PO_4 (with the possible exception of specimens having film thicknesses of 150Å or less) virtually no changes in surface topography of the oxide were observed until localized regions of accelerated attack appeared. The onset of this localized attack correlated well with the beginning of the "breakaway" stage of oxidation as indicated by the oxidation rate curve. As in the case of the type of film breakdown reported for plain anodic films (1), it appears that the oxygen content in the metal at the anodic oxide-metal interface increased until crystalline oxide formed which in turn physically disrupted the overlying anodic film or promoted its crystallization. The presence of flaws in the anodic oxide films such as those described by Vermilyea (11) would probably determine to a large extent the limit of protection afforded by an anodic film of a given thickness and also account for the local nature of the accelerated attack, particularly at the higher temperatures. It may be that the role of phosphorus in increasing the over-all oxidation resistance is to change the nature of the flaws as well as to decrease the rate of oxygen permeation. It is also tempting to speculate that an unusual rearrangement of the available phosphorus, such as that described by Smyth (6), may be responsible for the large effects. Obviously, considering the film to be of uniform composition is a dangerous oversimplification.

A comparison of the topography of plain and anodized tantalum after oxidation is presented in Fig. 6-11. Figure 6 shows the oxide texture on plain electropolished tantalum after 4 hr in oxygen at 500°C. Oxidation has proceeded into the breakaway stage, and the surface has become at least partially covered with the crystalline pentoxide. In contrast, Fig. 7 shows that a similar specimen, anodized to a film thickness of only 250Å in dilute KF, was virtually unchanged by 8-hr exposure. However, 48 hr at 500°C produced serious breakdown over most of the specimen. Figure 8 shows the type of breakdown which occurred: the dark regions in the micrograph are areas exhibiting high oxidation rates where voluminous crystalline pentoxide existed; the light regions are areas still protected by the anodic oxide film. That there was an orientation effect on the morphology of film breakdown at least for the thinner films is obvious from the figure. It is possible that this is caused by the fact that formation of one or more of the suboxides of tantalum which may develop prior to the breakdown of the overlying amorphous film is orientation dependent. As these high-rate regions grew in size, the measured oxidation rate continued to increase, and "breakaway" was thus rather sluggish compared to that for plain tantalum.

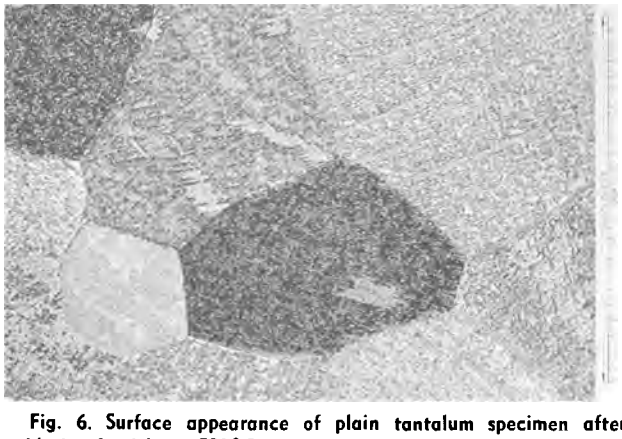

Fig. 6. Surface appearance of plain tantalum specimen after oxidation for 4 hr at 500°C.

Fig. 7. Surface appearance of anodized tantalum specimen after oxidation for 8 hr at 500°C; 0.5% Na_2SO_4 electrolyte; 250Å film thickness.

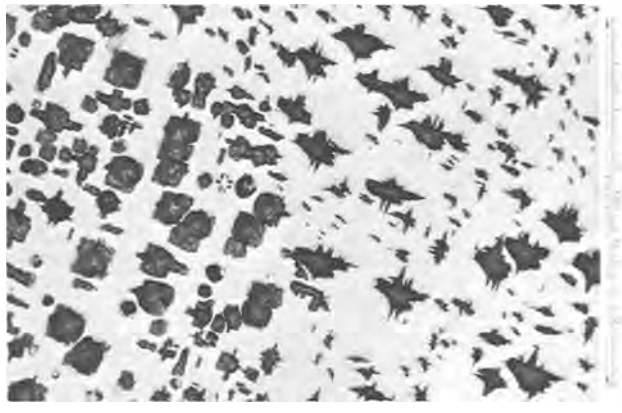

Fig. 8. Surface appearance of anodized tantalum specimen after oxidation for 48 hr at 500°C; 0.5% Na_2SO_4 electrolyte; 250Å film thickness.

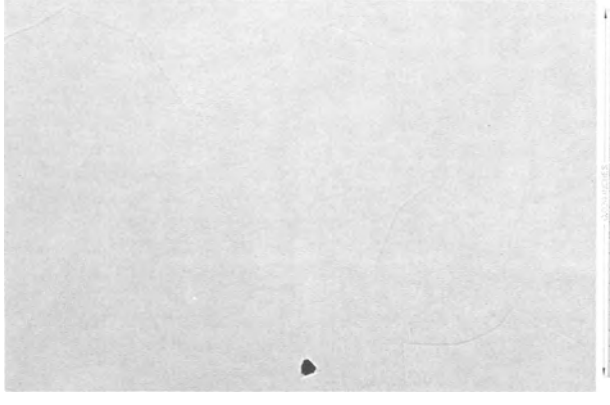

Fig. 9. Surface appearance of anodized tantalum specimen after oxidation for 48 hr at 500°C; 14M H_3PO_4 electrolyte; 250Å film thickness.

On the other hand, films of a given thickness formed by anodizing in H_3PO_4 were considerably more resistant to this sort of breakdown than those formed in dilute solutions. For example, Fig. 9 shows the surface of a specimen anodized to a film thickness of 250Å after 48 hr at 500°C in oxygen. The film was still protective to the extent that the observation of a small "breakdown" area such as that seen in the figure was a rare event. Specimens anodized to this film thickness were held in oxygen for over 100 hr at 500°C

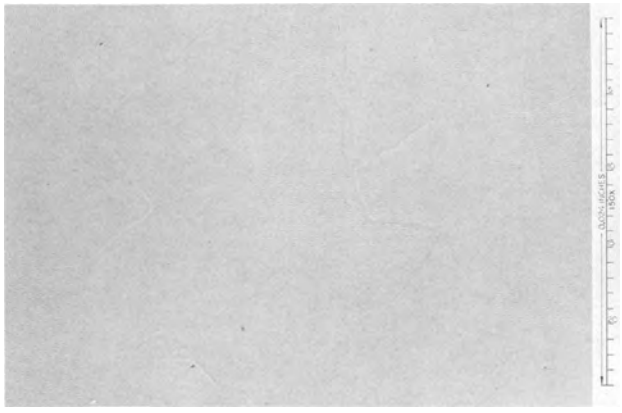

Fig. 10. Surface appearance of anodized tantalum specimen after oxidation for 6 hr at 600°C; 14M H_3PO_4 electrolyte; 1000Å film thickness.

with only few such areas observed. Even after 500 hr, large areas of film were still protective on an otherwise heavily attacked specimen. Thicker anodic films furnished an increased degree of efficiency in postponing breakaway. Figure 10 shows a typical surface area showing no breakdown of a 1000Å phosphorus-containing film after 6 hr in oxygen at 600°C, a rather severe oxidation treatment for tantalum. Of course, when a flaw in the film breaks down when the oxidation temperature is 600°C, the result is catastrophic. Figure 11 shows such a surface region from the same specimen as that of Fig. 10. The large, thick oxide patch has resulted from the consumption of practically the entire thickness of the metal at that point. While perhaps 1 or 2% of the surface area is oxidizing at a rate comparable to that of the plain metal, the rest is still being well protected by the film. The high degree of physical distortion of the film and metal around the oxide patch suggests that stresses associated with the volume change when tantalum is converted to oxide may play an important role in the lateral propagation of the fast-rate regions.

Conclusions

Anodic oxide films formed on electropolished tantalum specimens serve as protective oxide films during subsequent gaseous oxidation in the sense that they decrease the early-stage oxygen consumption rate and postpone the breakaway increase in oxidation rate associated with voluminous pentoxide formation. In agreement with the observations of Smyth *et al.* (5, 6), the presence of phosphorus in the anodic films, brought about by anodizing the specimens in phosphoric acid electrolytes, was shown to be especially effective in increasing the protective properties of the films. Compared to the behavior exhibited by films formed in dilute electrolytes, the oxygen permeation rates through films formed in concentrated phosphoric acid were shown to be decreased by a factor of five; however, the data were not sufficiently accurate to ascertain if the indicated increase in the activation energy for oxygen transport were solely responsible.

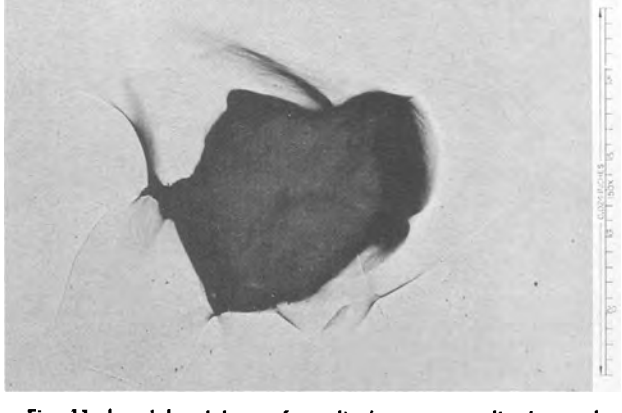

Fig. 11. Local breakdown of anodic layer on anodized tantalum specimen oxidized for 6 hr at 600°C; 14M H_3PO_4 electrolyte; 1000Å film thickness.

The characteristics of the eventual breakdown of the phosphorus-containing anodic films were shown to be similar to that observed for films formed in dilute solutions (1). Breakdown appeared to be initiated at isolated points in the film. At these points, which may be associated with any of several types of flaws in the anodic films, it appeared that crystalline oxide is nucleated either via oxidation of the metal or crystallization of the amorphous layer, or both. The resulting physical disruption of the film leads to a locally high oxidation rate. The density of activated flaws seemed to depend particularly on film thickness. For specimens with thick anodic films oxidizing at high temperature, oxidation generally proceeded from a small number of fast-oxidizing regions which consumed the specimen mainly by lateral growth.

Acknowledgments

The author is indebted to J. V. Cathcart for his helpful suggestions during the course of this work and preparation of the manuscript. Thanks are also extended to D. M. Smyth at Sprague Electric Company for communicating some of his results prior to publication, and to J. J. Campbell for a large contribution to the experimental work. Research on this paper was sponsored by the United States Atomic Energy Commission under contract with the Union Carbide Corporation.

Manuscript received June 7, 1967. A portion of this paper was presented at the Philadelphia Meeting, Oct. 9-14, 1966.

Any discussion of this paper will appear in a Discussion Section to be published in the June 1968 JOURNAL.

APPENDIX

Establishment of the Thickness-Voltage Relationship for Tantalum Films Formed in Phosphoric Acid Solutions from the Weight Gain Measurements

On the assumption that the film is amorphous, stoichiometric Ta_2O_5 only, having a density of 8.03 g/cm³ (9, 10), the thickness-voltage relationship is given by

1. for anodization in 14M H_3PO_4

$$0.2043 \frac{\mu g O_2}{cm^2 - v} \times \frac{441.76}{80} \frac{g Ta_2O_5}{g O_2} \times \frac{1}{8.03} \frac{cm^3 Ta_2O_5}{g Ta_2O_5} \times 10^8 \frac{Å}{cm} = 14.05 \frac{Å}{v}$$

2. for anodization in 0.9M H_3PO_4, $0.2370 \frac{\mu g O_2}{cm^2 - v}$, the above expression yields 16.30 Å/v.

We can make the assumption that the film is a uniform layer of PTa_9O_{25}. According to Roth and his coworkers (12, 13), this compound is tetragonal. A theoretical density of 7.424 g/cm³ can be calculated on the basis of the x-ray data. Thus, if this assumption is correct, the thickness-voltage relationship is

1. for anodization in 14M H_3PO_4:

$$0.2043 \frac{\mu g (O_2 + P)}{cm^2 - v} \times \frac{2058.9}{431} \frac{g PTa_9O_{25}}{g (O_2 + P)} \times \frac{1}{7.424} \frac{cm^3 PTa_9O_{25}}{g PTa_9O_{25}} \times 10^8 \frac{Å}{cm} = 13.16 \frac{Å}{v}$$

2. for anodization in 0.9M H_3PO_4, $0.2370 \frac{\mu g (O_2 + P)}{cm^2 - v}$, the above expression yields 15.25 Å/v.

We could also make the assumption that phosphorus is included in the film so that the general formula $P_xTa_{2-x}O_5$ is applicable. The criterion that phosphorus

substitute for tantalum in the amorphous pentoxide without a volume change leads to a density for PTa_9O_{25} of 7.485 g/cm³. This figure is in reasonable agreement with that calculated for the crystalline material, and gives an additional degree of credence to this method of estimating the density. It is significant also to note that the density of oxide formed in 50% H_2SO_4 has been determined as 7.87 g/cm³ (9). The mole ratio of phosphorus to tantalum in the outer part of the anodic layer has been found (4) to be about 0.18 and 0.09 for 14M and 0.9M H_3PO_4 solutions, respectively. The effective density of the films can then be calculated as 7.59 and 7.79 g/cm³ corresponding to the compositions $P_{0.16}Ta_{1.84}O_5$ and $P_{0.09}Ta_{1.91}O_5$. These compositions approximate the average composition expected in the films. Therefore, on the above basis, the thickness-voltage relationship becomes

1. for anodization in 14M H_3PO_4:

$$0.2043 \frac{\mu g(O_2 + P)}{cm^2 - v} \times \frac{417.8}{85} \frac{gP_{0.16}Ta_{1.84}O_5}{g(O_2 + P)} \times \frac{1}{7.59} \frac{cm^3 P_{0.16}Ta_{1.84}O_5}{gP_{0.16}Ta_{1.84}O_5} \times 10^8 \frac{Å}{cm} = 13.23 \frac{Å}{v}$$

2. for anodization in 0.9M H_3PO_4

$$0.2370 \frac{\mu g(O_2 + P)}{cm^2 - v} \times \frac{428.3}{82.8} \frac{gP_{0.09}Ta_{1.91}O_5}{g(O_2 + P)} \times \frac{1}{7.79} \frac{cm^3 P_{0.09}Ta_{1.91}O_5}{gP_{0.09}Ta_{1.91}O_5} \times 10^8 \frac{Å}{cm} = 15.74 \frac{Å}{v}$$

Randall *et al.* (4) report a decrease of about 24% in the dielectric constant for the phosphorus-rich portion of the anodic film formed in 14M H_3PO_4 solutions. This change implies a decrease in the index of refraction and, all other things being equal, an increase in the thickness at which a given interference color appears.

The thickness, t, at which destructive interference of a wavelength, λ, occurs due to multiple reflection from a film-covered metal surface at near-normal incidence is

$$t = (2m - 1) \frac{\lambda}{4n} + C$$

where m = 1,2,3, ---, n = refractive index of the film, and C a constant reflecting the difference in the phase retardation at the metal-film interface from π. Young (14) reported that C varies from —100 to —200Å; our data favor the latter value for C for λ near 6500Å.

For two films, A and B, which exhibit the same interference color (in the same order) the following expression is applicable

$$t_B = \frac{t_A - C_A}{n_B/n_A} + C_B$$

By noting that a film anodized by the procedure outlined in the text to 75v in concentrated H_3PO_4 exhibited a color identical to that of a specimen anodized to 49.5v in dilute KF (817Å), an additional means to estimate the film thickness is obtained. Since $C_A \cong C_B$ for the films under consideration, a lower limit (when $n_A = n_B$) for the thickness-voltage ratio is found to be 10.9 Å/v. How much higher the actual value will be depends on how much the refractive index has been changed. If it is assumed that the ratio of the refractive indices of films A and B is equal to the square root of the ratio of their dielectric constants, about 0.88, (an assumption requiring that the frequency dependence of the dielectric constant of each be similar), a value of 12.8 Å/v is obtained for films formed in the concentrated acid.

Despite the various assumptions made in the above calculations, the range of values obtained for the thickness-voltage relationship is relatively narrow. For anodization in concentrated H_3PO_4 and 0.9M H_3PO_4, 13.2 and 15.7 Å/v, respectively, have been chosen as the "best" values based on present information.

REFERENCES

1. R. E. Pawel and J. J. Campbell, *This Journal*, 113, 1204 (1966).
2. See L. Young, "Anodic Oxide Films," Academic Press, New York (1961) and pertinent references contained therein.
3. D. A. Vermilyea, *Acta Met.*, 2, 482 (1954).
4. J. J. Randall, W. J. Bernard, and R. R. Wilkinson, *Electrochim. Acta*, **10**, 183 (1965).
5. D. M. Smyth, T. B. Tripp, and G. A. Shirn, *This Journal*, **113**, 100 (1966).
6. D. M. Smyth, *ibid.*, **113**, 1271 (1966).
7. C. G. Kirkpatrick, Refractory Intermetallic Compounds RC-195, Research Chem. Div., Nuclear Corp. of America (1962).
8. J. H. Witte and H. A. Wilhelm, USAEC Research and Development Report, IS-854, Ames Laboratory, Iowa State Univ. (1964).
9. A. J. Schrijner and A. Middelhoek, *This Journal*, **111**, 1167 (1964).
10. J. Klerer, *ibid.*, **112**, 896 (1965).
11. D. A. Vermilyea, *ibid.*, **110**, 250 (1963).
12. J. L. Waring and R. S. Roth, *Acta Cryst.*, **17**, 455 (1964).
13. R. S. Roth and A. D. Wadsley, *ibid.*, **18**, 643 (1965).
14. L. Young, *Proc. Roy. Soc.*, A244, 41 (1958).

Crystal Morphology and Mechanisms of Growth of Alpha-Fe_2O_3 Whiskers on Iron

Richard L. Tallman and Earl A. Gulbransen

Westinghouse Electric Corporation, Research and Development Center, Pittsburgh, Pennsylvania

ABSTRACT

The morphology of α-Fe_2O_3 whiskers formed on iron at 400°-500°C in dry oxygen was studied. Diffraction patterns of individual whiskers and texture patterns of oxidized surfaces showed the whisker axis to be $[\bar{1}\bar{1}20]$. The axial rotation indicated by the pattern is that resulting from an axial twist. This is good evidence that the most simple oxide whiskers have a single axial screw dislocation. Arguments are presented for the view that growth of the whisker occurs by diffusion of iron atoms or ions through the dislocation and reaction with oxygen at the tip.

When iron is heated in oxidizing atmospheres, localized oxide growths form on the oxidized iron surface (1-3). The crystal habit of these oxide growths and the extent of oxide growth depend on many factors, including temperature, time of reaction, internal or external stress, impurities in the metal, pretreatment of the metal, and the composition of the oxidizing atmosphere (3).

Oxide whiskers formed on pure annealed iron at 400°-500°C in dry oxygen have diameters of about 150Å or more, lengths up to 4 x 10^5Å, and whisker densities on the surface up to $10^8/cm^2$ (3). Electron diffraction studies show that the most simple whiskers are single crystals of α-Fe_2O_3.

This paper presents: (*i*) new selected area electron diffraction studies on single iron oxide whiskers formed during the oxidation of iron in dry oxygen, (*ii*) morphological evidence for screw dislocations in oxide whiskers, and (*iii*) a growth mechanism for oxide whiskers on iron.

Experimental

A large file of carefully oxidized pure iron wires were available from earlier studies (3). Before oxidation, the iron wires had been carefully annealed and cleaned. The iron wires were then oxidized in dry and purified oxygen under controlled temperature and time conditions.

An RCA EMU-3D electron microscope with selected area diffraction was used at 100 kv electron energy. The relative rotation of the selected area electron diffraction pattern was determined by use of the selected area images and the selected area diffraction patterns of asbestos fibers.

Structural Information

α-Fe_2O_3 crystal structure.—Pauling and Hendricks (4) determined the crystal structure to be trigonal or rhombohedral, space group R $\bar{3}$ c. This structure was confirmed by Blake *et al.* (5) in 1966. The latter authors give the following structural hexagonal dimensions: $a = 5.038 \pm 0.002$Å, $c = 13.772 \pm 0.012$Å, and $c/a = 2.733 \pm 0.015$Å. We have calculated the corresponding structural rhombohedral dimensions to be $a = 5.469$Å and $\alpha = 55°13.9'$. The natural hematite used contained, with lesser impurities, sufficient aluminum to fill 2.8 ± 0.6% of the iron positions. The dimensions we have chosen (6) are sufficiently accurate for this work.

Unit cells and indices.—Figure 1 shows top and front views and dimensions (6) for the unit cells for α-Fe_2O_3 and its isomorphs. Four unit cells are in common use. The conventional structural hexagonal and rhombohedral unit cells are shown at the left. Four indices are used to describe a set of lattice planes in terms of the hexagonal cell. The conventional morphological rhombohedral unit cell is shown at the right. The face-centered rhombohedral F unit cell has an *a* value of twice that for the conventional morphological rhombohedral unit cell. This cell is shown at the center. The rhombohedral F cell angle α is nearly 90°. It is this relationship to the face-centered cubic cell which makes the rhombohedral F cell convenient for indexing. Directions are nearly normal to lattice planes with the same indices. This cell is used in indexing all of our selected area diffraction patterns and is referred to wherever the unit cell is not identified. Conventional structural hexagonal and rhombohedral indices are also given.

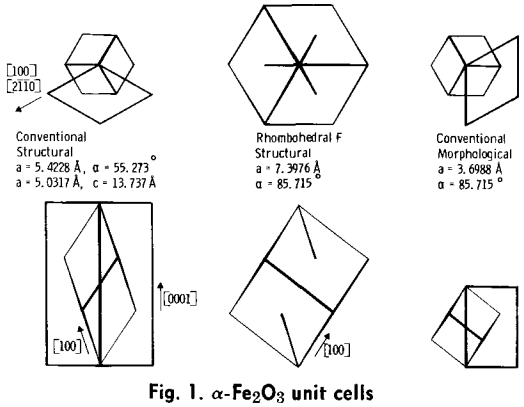

Fig. 1. α-Fe_2O_3 unit cells

Results and Discussion

Figure 2 shows a selected area electron diffraction pattern from an iron oxide whisker measuring 1.5μ in the selected area image. Indexing was made using the rhombohedral F unit cell. The orientation of the projection of the axis of the whisker lies normal to the layer lines of the pattern shown in Fig. 2, *i.e.*, in the [$\bar{2}$20] direction. This whisker axis is [$1\bar{1}$20] and [$\bar{1}$01] in the conventional structural hexagonal and structural rhombohedral indices, respectively.

An analysis of the diffraction spots in Fig. 2 shows two nets, the first is a net normal to the [111] direction and the second is a net normal to the [110] direction. The angles between rows of spots are within 1° of the angles between rows of index points in the reciprocal lattice of α-Fe_2O_3. The sections of whisker giving the two reciprocal lattice nets lie at 32.4° to one another.

Both nets of Figure 2 include the origin, $\bar{2}$20, and 220. We conclude, therefore, that the rotation axis of the pattern is [$\bar{2}$20]. The same conclusion results from the fact that the spots of each layer line are indexed by points in a corresponding reciprocal lattice net normal to [$\bar{2}$20].

Two additional oxide whiskers which have been studied satisfactorily by selected area electron diffraction are of interest. In one, two new nets of spots, normal to the [001] and [$\bar{1}\bar{1}$2] directions, respectively, were found. The rotation axis of the oxide whisker was [$\bar{2}$20]. The whisker axis was proved to be the rotation axis as follows: The whisker axis lies in a plane normal to the pattern of the second oxide whisker different from the plane of the whisker axis for the whisker giving the pattern shown in Fig. 2. These two planes intersect in the [$\bar{2}$20] rotation axis.

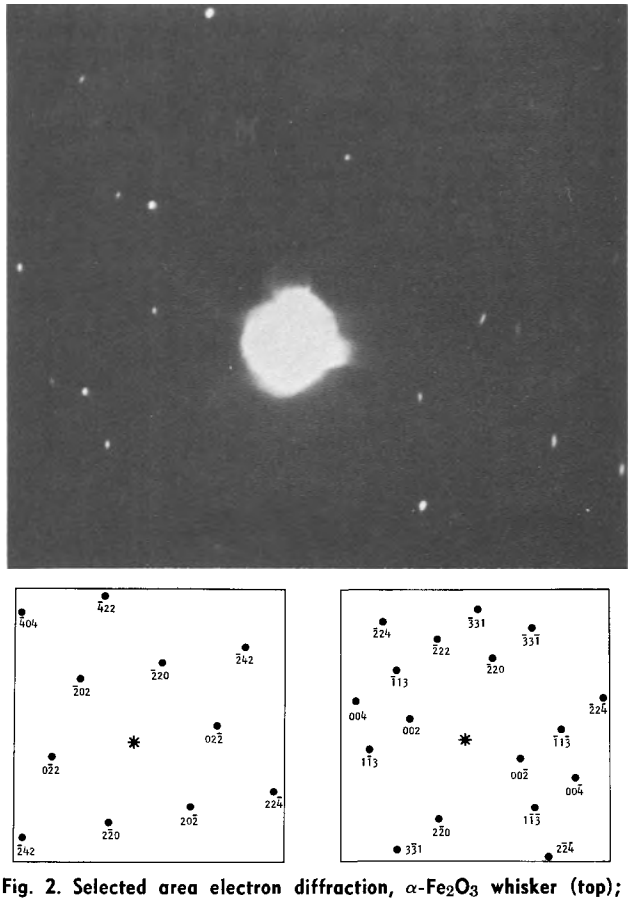

Fig. 2. Selected area electron diffraction, α-Fe_2O_3 whisker (top); 1.5μ long, 10^{-15}g; indexed with a face-centered rhombohedron, $\alpha = 85.7°$. Nets normal to [111] and [110] included (bottom).

If the whisker axis is the same in the two cases, it is $[\bar{2}20]$.

For the third indexed pattern, the same rotation axis was found, but not close to 90° to the beam direction. Again the projections of the whisker and rotation axes coincide in the pattern. This is a more common type of diffraction pattern than that shown in Fig. 2. Bent, kinked, and apparently multiple whiskers introduce further complications.

The three different selected area patterns which were indexed include very weak extra anomalous diffraction spots on the layer lines. Some of the spots correspond in position in the pattern to the systematically absent diffraction from planes of the form $\{11\bar{1}\}$, but most of the spots could not be indexed. The anomalous spots were also found by Takagi (2).

Since the whisker axis and the rotation axis coincide we are led to hypothesize that the whisker is twisted. This is consistent with the diffraction patterns of individual whiskers, in that they show a limited rotation by including diffraction represented by appropriately limited sectors of the reciprocal lattice. All of the selected area diffraction patterns of individual whiskers obtained for this work, about forty, are composed of rows of spots (layer lines) normal to the projection of the whisker axis. It appears certain that axial twist was at least common to whiskers sufficiently long to be selected separate from other whiskers.

Since no grain boundaries are commonly revealed by diffraction contrast in the micrographs, any grain boundaries which may exist must be such that the contrast is difficult to observe. The probability that a small number of untwisted crystals might lie in the special orientations in the beam indicated by the diffraction patterns of individual whiskers is negligible.

In addition to evidence in the selected area diffraction patterns of individual whiskers, we find evidence of axial twist in the electron diffraction patterns of whiskers growing from a surface. These patterns contain long, straight streaks which include elongated spots on arcs of several rings of the pattern between 400 and $42\bar{0}$, ($02\bar{2}4$ and $12\bar{3}2$ in structural hexagonal indices).

The angles of the streaks on the pattern and the positions of the spots on the streaks show that each streak is the second layer line for limited rotation about the whisker axis. That is, the streaks correspond to diffraction represented by the plane of the reciprocal lattice normal to the whisker axis, $[\bar{2}20]$, and passing through $\bar{2}20$ (or $2\bar{2}0$). The rotation of the crystal about $[\bar{2}20]$ is evidenced further by the continuity of the streaks, as follows: the intensity between the spots results from integration over the sector of the reciprocal lattice plane by rotation through the reflecting sphere.

Axial Twist Calculations

The axial twist α can be calculated from an equation given by Eshelby (7), $\alpha = K\,b/A$. Here b is the length of the Burgers vector, A is the cross section area, and K is a constant which depends on the shape of the cross section. $K = 1$ for an elliptical cross section with central dislocation. If we approximate the cross-sectional area A with the area of a circle of the whisker image diameter, we can calculate the axial twist and compare this with the observed twist. The full length of whisker in the selected area image for the pattern of Fig. 2 was 1.5μ. The diameter, including contamination, was about 300Å. Assuming the smallest Burgers vector, *i.e.*, the minimum repeat distance along the whisker axis, 5.03Å, the axial twist is calculated to be 41°/μ. The sections of whisker giving the two reciprocal lattice nets of Fig. 2 are at 32.4° to one another by rotation about the whisker axis. If at most these two sections lie at the ends of the 1.5μ whisker section, the axial twist is not less than 22°/μ; thus the 5.03Å Burgers vector is likely.

There are many reasons for a discrepancy between the calculated and observed axial twist: (*i*) both the cross section and the axial twist were difficult to determine; (*ii*) the elastic anisotropy of α-Fe_2O_3 may be important and should be included in the theory; (*iii*) the dislocation strain may have a planar character which would alter the strain distribution near the core; (*iv*) the discrete atomic structure and the decreased stress at high strain near the dislocation may result in a smaller twist than that calculated by the simple formula of Eshelby (7); and (*v*) surface stresses may decrease the axial twist.

Comparison with Previous Morphological Studies

Miyake (8) reported in 1937 a preferred orientation in the electron diffraction pattern of α-Fe_2O_3 formed on an oxidized iron specimen. He stated that the $(10\bar{1})$ structural rhombohedral plane was parallel to the surface. Apparently, lack of knowledge of the existence of oxide whiskers precluded a complete interpretation. The $(10\bar{1})$ structural rhombohedral plane given by Miyake is normal to the whisker axis we have determined.

Takagi (2) determined the growth axis of localized α-Fe_2O_3 growths using diffraction patterns of individual growths. That Takagi's work preceded the general recognition of axial twist apparently explains his failure to recognize the rotation pattern. Takagi oxidized pure iron in flowing dry oxygen, but not so dry as to prevent the formation of oxide platelets. He observed that whiskers and sometimes smaller blades grew from broken bases of blades. This and other observations suggested that growth is from the top. Takagi postulated a screw dislocation mechanism for the localized growths. He considered surface diffusion to provide the transfer of metal.

Bigot (9) and Talbot and Bigot (10) failed to analyze correctly their selected area electron diffraction patterns of α-Fe_2O_3 whiskers and platelets. They give no indexing for their whisker rotation patterns. Instead they determine the whisker axis on the basis that the most intense spots are aligned parallel to the smallest dimension of the crystal. They give incorrectly the structural hexagonal direction $[10\bar{1}0]$ as the whisker axis without supporting data. The most intense arc in the fiber texture pattern for whiskers on an oxidized iron surface is at 90° to the surface in the $11\bar{2}0$ ring. This results from the preferred orientation of the $(11\bar{2}0)$ planes, which are normal to the $[11\bar{2}0]$ whisker axis. Thus, the most intense arc is on a normal to the $[10\bar{1}0]$ direction, but this is not the whisker axis.

Transport Mechanisms of Whisker Growth

Three mechanisms have been put forward for the growth of oxide whiskers: (*i*) surface diffusion to the tip of the whisker, (*ii*) extrusion from the oxide, and (*iii*) growth by internal diffusion in a hole or screw dislocation.

The possibility that α-Fe_2O_3 whiskers result from some extrusion process seems unlikely because the growths are so uniform and are apparently of high crystalline perfection.

It is also unlikely that α-Fe_2O_3 whiskers could grow by a surface transport mechanism as suggested by Takagi (2) from a surface with competing α-Fe_2O_3 surface growth mechanisms. The hypothesis of a surface growth mechanism would require that other growth mechanisms or the existence of α-Fe_2O_3 crystals growing by only mechanisms other than the mechanism of whisker tip growth be very limited. The existence of species and mechanisms for surface transport of iron sufficient to produce the rapid growth rates and the extreme lengths of the α-Fe_2O_3 whiskers is not known and is unlikely because of the stability of

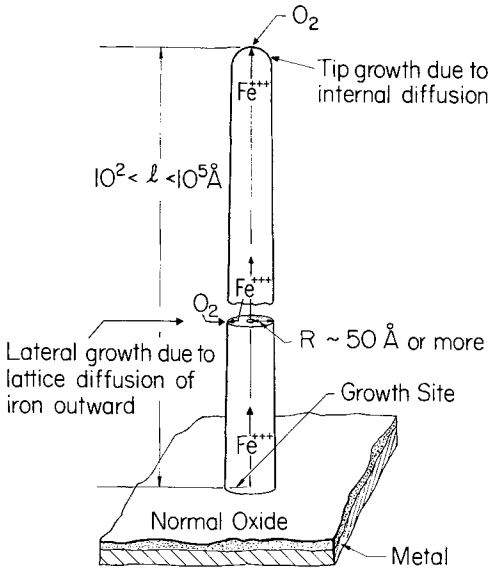

Fig. 3. Model of whisker growth during oxidation of iron, 400°C, dry O_2.

the Fe_3O_4 from which the iron would be transported. Furthermore, the nucleation of α-Fe_2O_3 on Fe_3O_4 is a common phenomenon and involves only a change from cubic close-packing to a distorted hexagonal close-packing of oxygen in the α-Fe_2O_3 lattice together with a change in the iron positions. One cannot readily propose that the driving force for rapid diffusion to the α-Fe_2O_3 whisker tips can be provided by high concentrations of iron species mobile on the Fe_3O_4 surfaces.

Gulbransen (11) has proposed a model for the growth of oxide whisker assuming the whiskers are hollow or contain a screw dislocation at the center. The essential feature of this model is that this internal defect allows rapid diffusion of iron to occur compared to normal lattice diffusion. The morphological studies presented demonstrate that oxide whiskers are single crystals of high crystalline perfection and show axial twist. The latter property is strong evidence for a screw dislocation at the center of the whisker.

Figure 3 shows a model for the whisker growth on iron. The whisker contains an internal hole or screw dislocation where dislocation core or internal surface diffusion of iron occurs along a gradient in chemical potential.

Most of the growth occurs by reaction with oxygen atoms or ions at the tip of the whisker. Since the diameter is nearly uniform during growth it follows that cationic mobility is much smaller in the lattice than along the dislocation.

Good measurements of the growth rates of oxide whiskers are not yet available. Pease and Ploc (12) have observed initial growth rates at 500°C of over 0.2 μ/min, an average rate over 5 min. Takagi (2) observed growth rates up to 2 μ/min at 700°C in the first minute. Whether the growth observed in these cases should be classified as whiskers or platelets cannot be determined from the information given.

The structures of the sections where the cation diffusion rate is high cannot be given at this time. It may be that information on these structures is contained in the anomalous diffraction. The structure in the immediate vicinity of the screw dislocation must show ions either displaced by the strain into some distortion of the α-Fe_2O_3 structure, or otherwise positioned, possibly in some disordered structure. In either type of structure, diffusion coefficients would be expected to be different from those in the much less distorted structure of more than half of the cross section of the whisker. This outer region probably exhibits the bulk or lattice ionic diffusion coefficients.

Acknowledgment

This work was accomplished with the support of the Office of Naval Research under Contract No. Nonr-4949(00).

Manuscript received Jan. 16, 1967; revised manuscript received Aug. 4, 1967.

Any discussion of this paper will appear in a Discussion Section to be published in the June 1968 JOURNAL.

REFERENCES

1. G. Pfefferkorn, *Naturwiss.*, **40**, 551 (1953).
2. R. Takagi, *J. Phys. Soc. Japan*, **12**, 1212 (1957).
3. E. A. Gulbransen and T. P. Copan, *Discussions Faraday, Soc.*, **28**, 229 (1959).
4. L. Pauling and S. B. Hendricks, *J. Am. Chem. Soc.*, **47**, 781 (1925).
5. R. L. Blake, R. E. Hessevick, T. Zoltai, and L. W. Finger, *Am. Mineralogist*, **51**, 123 (1966).
6. ASTM X-ray Powder Data File, Card 13-534 (1964), Aravindakshan and Ali.
7. J. D. Eshelby, *Phil. Mag.*, **3**, 440 (1958).
8. S. Miyake, *Inst. Phys. and Chem. Res. (Japan)*, **31**, 161 (1937).
9. J. Bigot, *Mem. Sci. Rev. Met.*, **60**, 5 (1963).
10. S. Talbot and J. Bigot, *ibid.*, **62**, 261 (1965).
11. E. A. Gulbransen, *ibid.*, **62**, 253 (1965).
12. R.F.W. Pease and R. A. Ploc, *Trans. Met. Soc. AIME* **233**, 1949 (1965).

The Chemical Vapor Deposition of Titanium Carbide Coatings on Iron

Takehiko Takahashi, Kohzoh Sugiyama, and Kensuke Tomita

Department of Applied Chemistry, Faculty of Engineering, Nagoya University, Nagoya, Japan

ABSTRACT

When titanium tetrachloride carried by argon is reduced by titanium sponge and the product flows over a carbon steel at 850°-1000°C, a titanium carbide film is formed on the steel surface, and the thickness can be related linearly with the square root of time. If a mixture of hydrogen and propane is used as carrier, the carbide film grows linearly with time. Pre-electrodeposition of cobalt on low carbon steel is effective to obtain good titanium carbide coatings.

Titanium carbide is known as a refractory, very hard, and corrosion resistant material. If titanium carbide coating could be deposited on various materials, the coated materials would be widely used. Titanium carbide has been plated on graphite at 1200°-1300°C (1) and also on carbon or tungsten

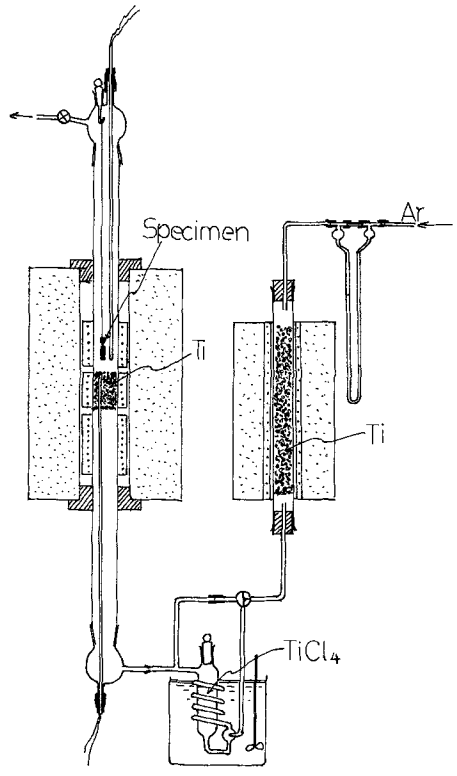

Fig. 1. Apparatus for the vapor plating with titanium sponge as reductant.

filament from a gas mixture of hydrogen, hydrocarbon, and titanium tetrachloride at temperatures between 1300°-1700°C (2-4). Ruppert and co-workers reported on titanium carbide coated on carbon and/or chromium containing iron at above 800°C (5-8). Semenova and Minkevich have investigated titanium carbide coatings on 12% chromium steel at 1100°C (9). When the base material is iron, especially, thick coatings of titanium carbide may spall off for the thermal expansion coefficient of titanium carbide is much smaller than that of iron. Further it would be advantageous to cover iron with a thick titanium carbide layer without restriction of the composition of the base material.

Apparatus and Experimental

In the present work, two kinds of experiments have been carried out. In the first, carbon was supplied from high carbon steel substrate, and titanium sponge was used as reductant of titanium tetrachloride. In the second experiment, carbon was supplied by gaseous hydrocarbons, and hydrogen was chosen as reductant and carrier gas.

The apparatus used for the first kind of experiment is shown in Fig. 1. Argon, the carrier gas, was flowed through a deoxygenerator filled with titanium sponge heated up to 800°C, before bubbling into the titanium tetrachloride saturator, then passing into the quartz tube reactor, 27 mm ID, for which three zones, each of which were 80 mm long, were provided for preheating and for heating the titanium sponge and specimen. The temperatures of these three zones were controlled independently. The specimens were connected to the top of the quartz tube by means of a platinum or high carbon steel wire. After a certain time, the gas stream was changed to pure argon, then the specimen was raised to the upper cool part of the tube where it was cooled, thereafter taken out, and washed with ether. The specimen was of cylindrical shape, 3 mm OD and 20 mm long. The carbon content of the specimen was 0.80 w/o (weight per cent), and α-iron structure was confirmed by the x-ray diffraction pattern.

In the experiment, the growth rate of titanium carbide was too low to coat iron with a thick film. For this reason, in the second experiment, carbon was supplied by gaseous hydrocarbons, and the reductant was changed to hydrogen. The apparatus is shown in Fig. 2. The coating chamber was quartz tube, 220 mm long and 27 mm ID. Three iron specimens, 20 x 10 x 1 mm^3, were connected to a balance. The carbon content in the specimen was 0.035%. In this case, the direct coating of titanium carbide on low carbon steel was found to be hopeless due to severe weight loss of iron and its cementation both of which cause weakening of the adherence of titanium carbide on iron. Preplating of the low carbon steel with a cobalt layer was found to be of use to suppress the weight loss of iron.

Results and Discussion

Type 1 experiment (carbon supplied by the base).—Changes in weight of the specimen.—In the preliminary experiments, the weight changes of various materials were measured with no titanium sponge layer in the reactor. Titanium, wrought iron, platinum, copper, and quartz underwent considerable weight loss, but with the high carbon steel the decrease was relatively slight. From these facts, it is concluded that the titanium tetrachloride stream causes a loss of base materials probably due to the formation of chlorides of the respective metals. The small change in weight of high carbon steel suggests the formation of corrosion resistant surface film. When titanium sponge was used as shown in Fig. 1, the weight of the specimen increases with time. Based on x-ray analysis, this weight increase was attributed to the formation of titanium carbide film on the specimen.

Dependence of the growth rate.—The temperature of titanium sponge and of the titanium tetrachloride saturator and the flow rate of argon showed minute effects, but the temperature of the specimen was the dominant factor for the deposition of titanium carbide layers. Weight increase was observed at above 800°C.

Figure 3 shows the relation between the titanium carbide thickness and the square root of time at various temperatures. In this experiment, the temperatures of titanium sponge and of the titanium tetrachloride saturator were held at 900° and 40°C, respectively, and the flow rate of argon was 5 cc/sec. The titanium carbide thickness was calculated from the weight increase considering the specific gravity of

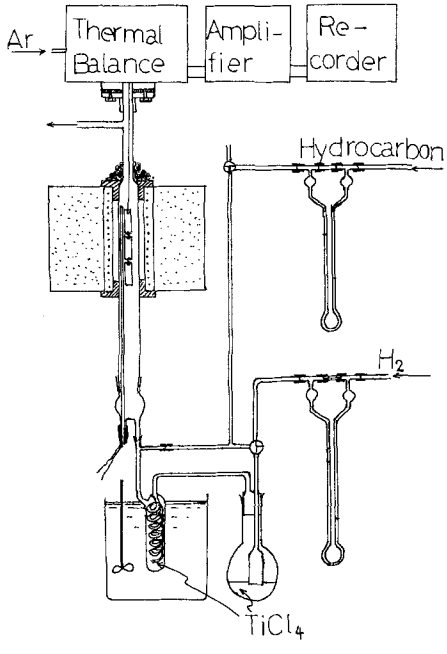

Fig. 2. Apparatus for the vapor plating with hydrocarbon feeder

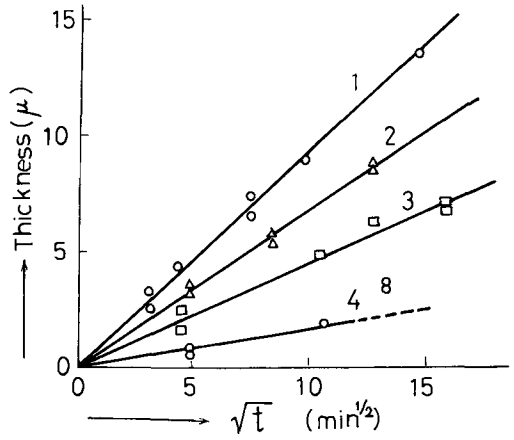

Fig. 3. Relation between the thickness of the coatings and the square root of time. 1, 1000°C; 2, 950°C; 3, 900°C; 4, 850°C.

titanium carbide layer to be 4.94. The linear relation between the thickness of the titanium carbide layers and the square root of time suggests the rate-determining process is not the surface reaction but a diffusion process in the titanium carbide layer or in the base. From a plot of the logarithm of the gradient at various temperatures against the reciprocal absolute temperature, the activation energy was calculated to be 48 kcal/mole, which is supposed to be that for carbon diffusion in titanium carbide (10).

Microstructure of the titanium carbide coatings.—Figure 4 shows the cross section of titanium carbide coated on iron. The middle layer consists of titanium carbide which was applied at 900°C in 170 min. The upper layer is copper plated for protection of the edge break while being polished. A tight and nonporous titanium carbide layer is seen in this figure.

Figure 5 shows a cross section through a titanium carbide coating which was deposited at 1000°C in 225 min. The higher the temperature the looser the contact between the titanium carbide layer and the high carbon steel. Titanium carbide formed at 1000°C was gray colored and had a metallic luster, but below 900°C a blue-black-colored dull surface was obtained.

Interdiffusion between titanium carbide layers and iron.—Figure 6 shows the profiles obtained by means of an electron-probe microanalyzer at the interface of iron and titanium carbide formed at 900° and 1000°C. The intensities of titanium correspond roughly with those of pure titanium carbide. In the profile, the carbon intensities are recorded by two magnifications, and the proportionality of the carbon concentration to that of titanium can be seen; however, the absolute carbon concentration cannot be estimated because the neighboring atoms show the high extinction coeffi-

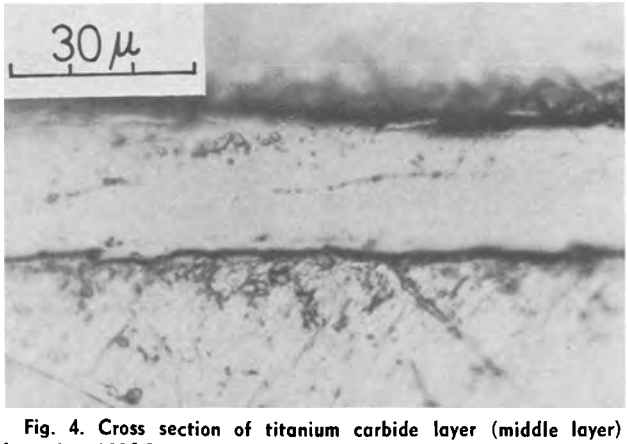

Fig. 4. Cross section of titanium carbide layer (middle layer) formed at 900°C in 170 min.

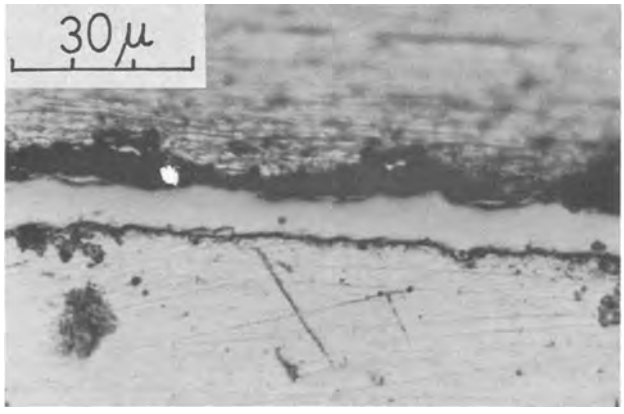

Fig. 5. Cross section of titanium carbide layer formed at 1000°C in 225 min.

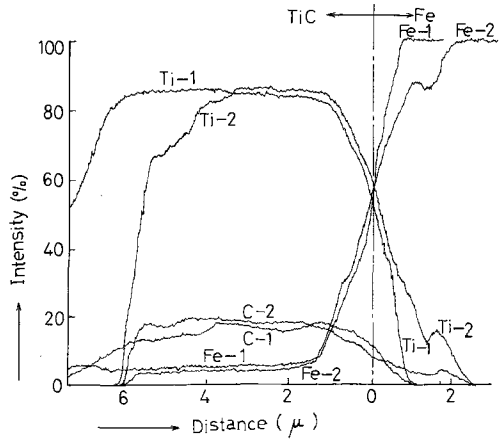

Fig. 6. Concentration profiles at the interface obtained by electron probe microanalyzer. 1, 900°C, 170 min.; 2, 1000°C, 60 min.

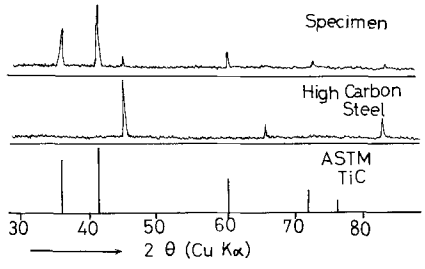

Fig. 7. X-ray diffraction pattern of a specimen coated with titanium carbide at 1000°C in 225 min.

cient of carbon Kα x-ray. The concentration of iron in the titanium carbide layer amounts to 2-7%, the value of which depends on the thickness of titanium carbide layer and the coating temperature.

Figure 7 shows the x-ray diffraction profiles of titanium carbide deposited onto iron at 1000°C in 225 min. The peaks obtained are in accord with the superposition of those of titanium carbide (11) and α-iron. The intensity of {200} plane is relatively high. The lattice constant was calculated as $a = 4.33$Å from the 2θ value.

Type 2 experiment (carbon supplied by hydrocarbons).—Dependence of weight increase on time.—Cobalt was plated from a sulfate bath at 25°-40°C, and at a current density of 4 amp/dm², within 40 min. The bath contained in 1 liter solution; 450g $CoSO_4 \cdot 7H_2O$, 32g H_3BO_3 and 13g NaCl. Figure 8 shows the sum of the weight increases of three specimens. The temperature of the titanium tetrachloride was 60°C. The flow rate of propane and hydrogen were 0.08 and 2.80 cc/sec, respectively. These curves show a linear

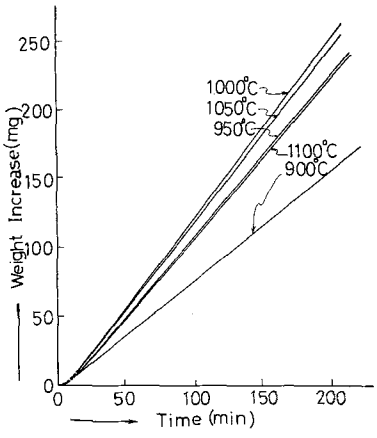

Fig. 8. Relation between the weight increase and the plating time

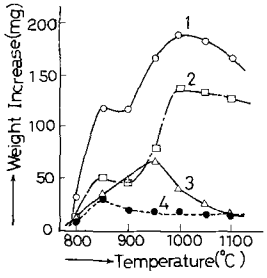

Fig. 9. Effect of the specimen position on the weight increase. 1, sum of the weight increase of three specimens; 2, 3, and 4, weight increase of the specimen at the lower, the middle, and the upper positions, respectively.

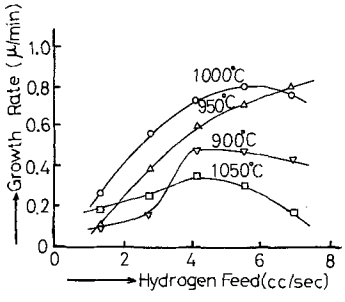

Fig. 10. Effect of hydrogen feed rate on growth rate

relation between the weight increase and time; the highest increase was found at 1000°C.

Dependence of weight increase on the position of specimen.—Figure 9 shows the influence of the specimens position (as illustrated in Fig. 2) on weight increase. The coating time is 150 min. The total weight increase has a maximum at 1000°C, while the weight increase of the specimens at the upper, middle, and lower position have the maxima at 850°, 950°, and 1000°C, respectively. The temperature at the upper position was nearly equal to that of the middle position, while the temperature of the lower position was somewhat less than that of the middle position. The influence of position may be attributed to variations of titanium subchlorides, or to the state of unstable hydrocarbons or of soot formed by thermal decomposition of propane.

Dependence of growth rate on hydrogen supply and on temperature.—In Fig. 10 a relation between the growth rate and the rate of hydrogen supply is shown. The maximum growth rate was obtained at 1000°C, while at the higher flow rate of hydrogen, it was obtained at 950°C. The propane flow rate was held at 0.08 cc/sec. The maximum of growth rate was 0.8 μ/min. Figure 11 shows the relation between the

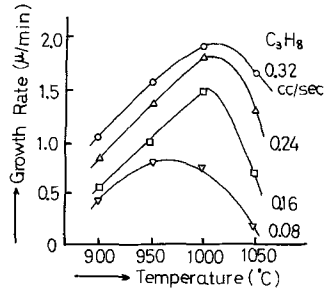

Fig. 11. Relations between growth rate and temperature as a parameter of hydrocarbon feed rate.

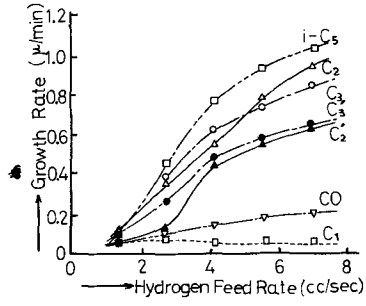

Fig. 12. Dependence of growth rate on the kinds of hydrocarbons

growth rate and the coating temperature with the flow rate of propane as a parameter. The hydrogen feed was held at 7 cc/sec. The higher the propane feed rate, the higher the growth rate. A saturating tendency was found at 0.32 cc/sec where the atomic ratio of titanium in titanium tetrachloride carried by hydrogen to carbon in propane was roughly unity.

Surface appearance.—The surface appearance of the specimen formed by high feed rate of propane was black and coarse which suggests that the saturating tendency arises from the covering by soot.

Effect of hydrocarbon species.—Figure 12 shows the effect of hydrocarbon species. The coating temperature is 950°C. In the figure, x in C_x and C_x' is the carbon number of paraffins and olefins, respectively. From the results obtained, it may be derived that paraffins such as i-pentane, propane, and ethane show high coating growth rate up to 1 μ/min on the average of three specimens, but methane and carbon monoxide show very low rates, and olefins such as propylene and ethylene are placed on intermediate positions between the former two groups. These relations are in accord with the thermal stabilities of the respective hydrocarbons. In other experiments, interruption of titanium carbide growth was observed when the surface was covered with soot. Therefore it is considered that solid carbon may react with titanium chloride to form titanium carbide only at relatively high temperatures, such as 1300°-1700°C, which were chosen by other investigators. Hydrocarbons are considered to decompose to hydrogen and soot at the surface of specimen or at the wall of the reactor. Only the atomic carbon formed at the titanium carbide surface may react to form titanium carbide crystals at relatively low temperature. The soot which has been deposited cannot react in accessible rate, but it interferes with the adsorption and desorption of titanium subchlorides.

Microstructure and microhardness of the titanium carbide coatings.—The microscopic cross section of a cobalt-titanium carbide double layer is seen in Fig. 13. The starting thickness of the cobalt layer was 8.5-10μ and that of titanium carbide was about 17μ. This coating was deposited at 950°C in 35 min. The upper layer is titanium carbide under which the cobalt interlayer is unified with the base material. Figure 14 shows the surface appearance of titanium carbide formed at

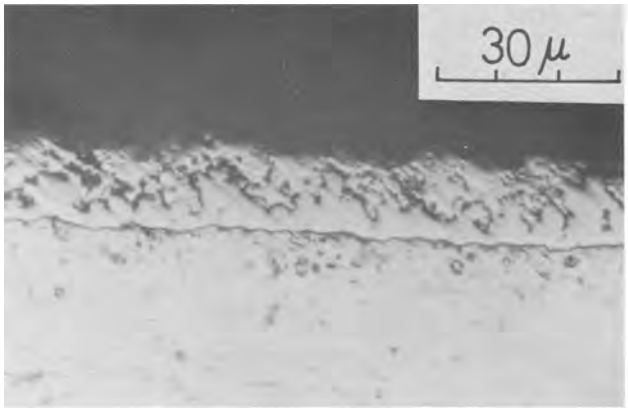

Fig. 13. Micrograph of the cross section of the specimen obtained at 950°C in 35 min. The thickness of the precoated cobalt layer, 8.5 — 10μ.

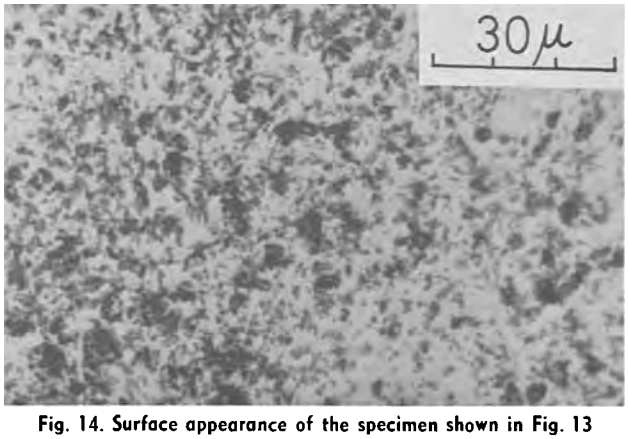

Fig. 14. Surface appearance of the specimen shown in Fig. 13

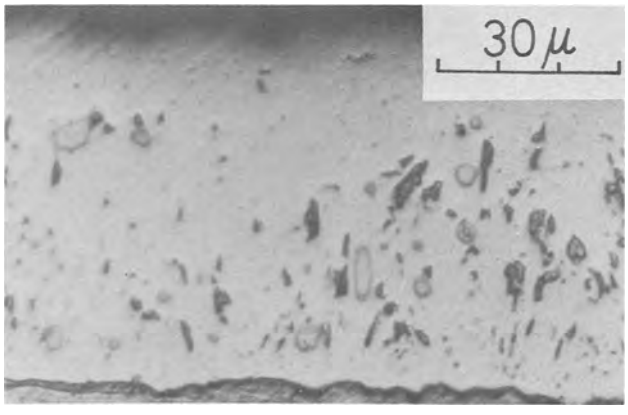

Fig. 15. Profile of the cross section of the specimen deposited at 1100°C in 160 min.

950°C. Micropores can be seen. Figure 15 shows the cross section of a titanium carbide coating applied at 1100°C in 160 min. The thickness is about 80μ.

The microcrystalline coating in Fig. 16 was deposited at 950°C while holding the temperature of titanium tetrachloride at 90°C. The crystal size was roughly estimated to be 4-6μ. Figure 17 shows the cross section.

Microhardness measurements were carried out using a load of 50g. The values are gathered in Table I. The high hardness values are nearly equal to that of pure titanium carbide (12). The hardness of the thin titanium carbide layers seems to be lower than that of the thick coatings. This is probably not due to an influence of the cobalt layer.

Figure 18 shows the effect of the thickness of cobalt on the x-ray diffraction patterns. Titanium carbide was deposited at 950°C in 72-92 min under the flow

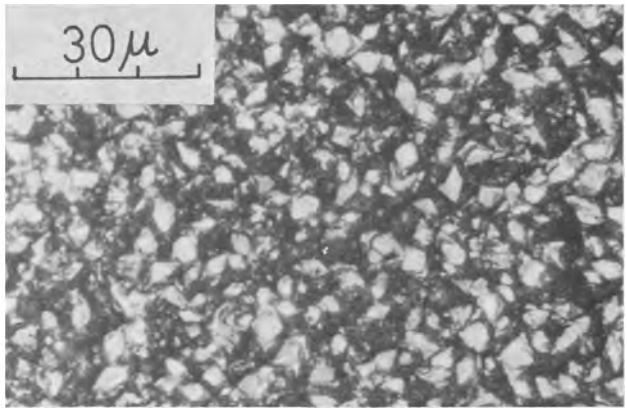

Fig. 16. Microcrystalline coating obtained under a partial pressure of $TiCl_4$ of 0.24 atm at 950°C.

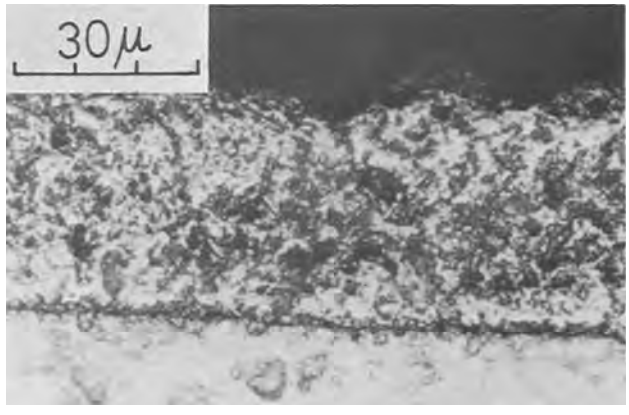

Fig. 17. Micrograph of the cross section of the specimen in Fig. 16.

rates of 2.8 cc/sec for hydrogen and of 0.08 cc/sec for propane, the partial pressure of titanium tetrachloride being 0.079 atm. Peaks of titanium carbide and α-iron diffractions can be seen, if the thickness of cobalt interlayer was only 4-5μ. In case of the thicker cobalt layers, the peaks of α-iron were weakened, and those of titanium carbide were sharpened. If the thickness of cobalt was 33-40μ, γ-Co-Fe phase appeared, and that of titanium carbide was weakened.

The crystallization of titanium carbide which was deposited above 950°C can be estimated from Fig. 19. The crystal grain size did not change much at 950°C. The two profiles at the bottom of the figure are those of titanium carbide for keeping the temperature of titanium tetrachloride at 90° and 75°C. The abnormal growth of {220} and {111} planes can be seen.

Table I. Microhardness

Specimen	TiC plating conditions: Temperature, °C	Partial pressure of $TiCl_4$, atm	Plating time, min	Thickness of TiC layer, μ	Microhardness, kg/mm²
Cobalt plated on iron	—	—	—	—	220
TiC plated on cobalt layer (thickness of cobalt layer; 20μ)	900	0.079	205	11	145
	950	0.079	170	35	2400
	950	0.14	200	24	2300
	950	0.24	220	33	3200
	1050	0.079	142	67	3300
	1100	0.079	160	64	3700

Specimen	TiC plating time, min	Thickness of cobalt layer, μ	Thickness of TiC layer, μ	Microhardness, kg/mm²
TiC plated at 950°C and under the partial pressure of $TiCl_4$ of 0.079 atm	72	4-5	17-20	147
	80	8.5-10	17-20	1470
	92	13-15	22-25	1040
	78	33-40	17-20	1380

(50g load)

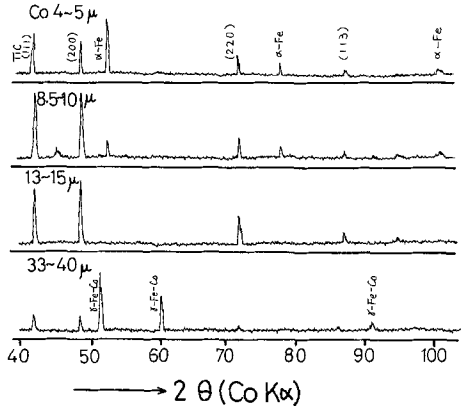

Fig. 18. X-ray diffraction patterns for the specimens precoated with cobalt in various thickness.

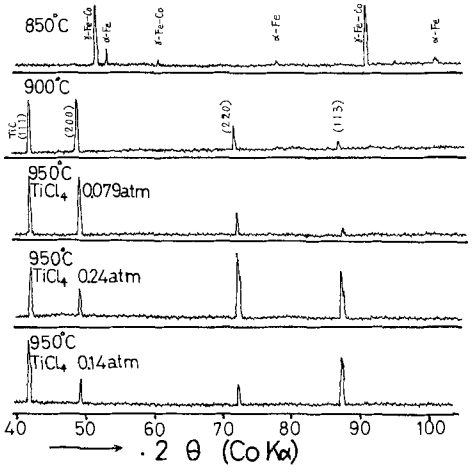

Fig. 19. X-ray diffraction patterns for the specimens obtained at various temperatures and under various partial pressures of $TiCl_4$.

Solid phase reaction at the interfaces.—Figure 20 shows the microanalyzer profiles of titanium carbide coated on the cobalt interlayer of 4-5 and 33-40μ. The cobalt contents at the interface are 58% for thin cobalt interlayers and 82-90% for thick cobalt interlayers. The diffusion layer thicknesses at thin and thick cobalt interlayers were 2.0 and 10-12μ, respectively. The iron and cobalt contents in the titanium carbide layer at a distance of 17-20μ from the TiC-Co alloy interface are 0.65 and 0.23 w/o for thin cobalt interlayer and 0.29 and 0.34 w/o for thick cobalt.

Conclusions

From these results, it is concluded that thick cobalt layer, transformed to γ-Co-Fe phase by the interdiffusion of cobalt and iron, and the thin cobalt interlayer favor the formation of α-Fe solid solution in spite of taking an arrangement of γ-phase at coating temperature.

Up to present, the effects of cobalt layer are considered to improve the adherence of the titanium carbide layer to iron and to suppress the interdiffusion

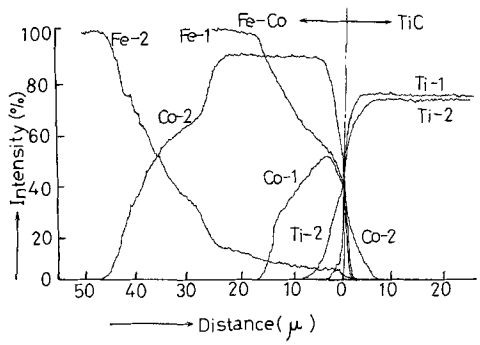

Fig. 20. Profiles of the concentration of iron, cobalt, and titanium obtained by electron probe microanalyzer. The thickness of precoated cobalt: 1, 8.5 — 10μ; 2, 33 — 40μ.

of iron and carbon. The former effect appears to arise from the affinity of cobalt to titanium carbide as is known from the sintered carbide alloys which consist of titanium carbide powder and cobalt binder. The reason for the good adherence of titanium carbide layers to the base, in spite of the large difference between their coefficients of expansion, cannot be explained here. However the titanium carbide layers sometimes spalled off at the part of edge, especially from those specimens which were coated at high growth rates. Annealing of the contact layer might improve the adherence of the coatings, and it is now under investigation. Materials other than cobalt have also been sought, but no further favorable material has yet been found.

Acknowledgment

The authors wish to acknowledge the assistance of Katsuhiko Kitagawa with the experimental work.

Manuscript received May 1, 1967; revised manuscript received Aug. 2, 1967. This paper was presented at the Dallas Meeting, May 7-12, 1967.

Any discussion of this paper will appear in a Discussion Section to be published in the June 1968 JOURNAL.

REFERENCES

1. C. F. Powell, J. H. Oxley, and J. M. Blocher, Jr., "Vapor Deposition," p. 368, John Wiley & Sons, New York (1966).
2. W. Burgers and J. Basart, *Z. anorg. u. allgem. Chem.*, **216**, 209 (1934).
3. F. H. Pollard and P. Woodward, *Trans. Faraday Soc.*, **46**, 190 (1950).
4. K. Moers, *Z. anorg. u. allgem. Chem.*, **198**, 243 (1931).
5. A. Münster and W. Ruppert, *Z. Elektrochem.*, **57**, 564 (1953).
6. A. Münster and K. Sagel, *ibid.*, **57**, 571 (1953).
7. W. Ruppert, *Metalloberfl.*, **14**, 193 (1960).
8. H. Wiegend and W. Ruppert, *ibid.*, **14**, 229 (1960).
9. G. A. Semenova and A. N. Minkevich, *Izv. Vysshikh Uchebn. Zavedenii Chern. Met.*, **8**, 168 (1965).
10. A. V. Shcherbedinskaya and A. N. Minkevich, *Izv. Vysshikh Uchebn. Zavedenii Tsvetn. Met.*, **1965**, 123.
11. J. V. Smith *et al.*, "Index to the Powder Diffraction File," American Society for Testing Materials, Philadelphia (1964), Card No. 6-0614.
12. Kirk-Othmer; "Encyclopedia of Chemical Technology," **14**, 80 (1955).

Torsion-Effusion and Torsion-Langmuir Studies of Zinc Telluride

William T. Lee and Zuhair A. Munir

Department of Materials Science, School of Engineering, San Jose State College, San Jose, California

ABSTRACT

The vapor pressure of polycrystalline zinc telluride was measured by the torsion-effusion and torsion-Langmuir methods. The pressure, in atmospheres, measured by the torsion-effusion method between 888° and 1150°K is given by the equation: $\log P = 6.18 - 1.065 \times 10^4/T$. Third-law calculations of the heat of sublimation for the reaction 2 ZnTe (s) = 2 Zn (g) + Te_2 (g) gave a value of $\Delta H°_{298} = 156.3 \pm 3.0$ kcal. The free-surface vapor pressure, in atmospheres, measured by the torsion-Langmuir method between 800° and 1015°K is given by the expression: $\log P = 7.89 - 1.283 \times 10^4/T$. The energy of activation for this sublimation process, $\Delta H^{\ddagger}_{298}$, was calculated to be 178.6 ± 4.2 kcal, and the evaporation coefficient, α, was found to vary from 0.155 at 807°K to 0.294 at 953°K.

Thermodynamic properties of zinc telluride were first investigated by McAteer and Seltz (1) by the application of reversible galvanic cells. Korneeva *et al.* (2) made vapor pressure measurements on zinc telluride at relatively high temperatures. More recently, Goldfinger and Jeunehomme (3) made rather extensive vaporization studies of Group IIB-VIA compounds by mass spectrometric and Knudsen-cell methods. Their work showed that the vaporization process of ZnTe is

$$2ZnTe\ (s) = 2Zn\ (g) + Te_2\ (g) \qquad [1]$$

The existence of such gaseous diatomic molecules in the sublimation products has been shown to give rise to a slow step in the sublimation mechanism and, hence, low apparent vapor pressure (4, 5).

The use of the torsion-Langmuir method (4) has provided an effective way for apparent pressure measurements, and, when combined with Knudsen-cell techniques, values of accommodation coefficients can be determined.

None of the vapor pressure studies of zinc telluride has incorporated both torsion-effusion and torsion-Langmuir experiments. Free-surface evaporation studies to establish activation energies and sublimation coefficient as a function of temperature are therefore highly desirable.

Apparatus

The torsion-effusion method has been described in several publications (4-7).

Figure 1 shows a schematic diagram of the torsion apparatus. The lower portion of the apparatus consists of a stainless steel vacuum chamber 35.6 cm in diameter and 45.7 cm high. Situated in the center of this chamber is an 11.4 cm diameter and 17.8 cm high cylindrical tungsten mesh heating element. Several layers of curved tantalum radiation shields are wrapped around the oustide of the heating element to insure black body conditions. Mounted within the heating element and close to its center is a graphite "dummy" cell identical to the cell used for measurements. A 10v secondary of a 50 kva transformer supplies power to the heating element. Water cooled, heavy-walled 0.64 cm copper tubing carries power to the heating element.

The upper portion of the torsion apparatus consists of a Pyrex glass housing 10.2 cm in diameter and 91.5 cm long. This detachable glass tubing is joined to the vacuum chamber by two rubber O-rings. At the top of this tube, a goniometer acts as the anchor point for the entire suspension system by means of a 0.64 cm diameter copper rod which enters the top of the Pyrex tubing through an O-ring joint to insure a good vacuum. Attached to the end of the copper rod is a 2 mil diameter annealed tungsten wire, approximately 35.6 cm long. From the other end of the tungsten wire, a 0.64 cm diameter aluminum rod is suspended. To this rod is glued a 1.27 cm diameter circular mirror which during operation hangs directly behind an optically flat window in the vertical glass tube. A circular aluminum disk 4.75 cm in diameter and 0.64 cm thick attached to the rod about 7.62 cm below the mirror serves as a damper when a permanent magnet is placed near it outside the glass housing. The lower part of the suspension system is a 0.25 cm diameter, 33.0 cm long tantalum wire which is attached to the aluminum rod below the mirror. The torsion cell, made of National Carbon ZT101 grade graphite, is fastened to the lower end of this tantalum rod. During a run, the torsion cell hangs free in the center of the heating element about 1.9 cm above the dummy cell.

Torsion cells are made from cylindrical pieces of graphite approximately 4.5 cm long and 2.5 cm in diameter. Sample cavities were drilled into both ends of the cell and tightly fitting lids were used to seal off the sample cavities. One of the cells used in this investigation was tested for leakage before its effusion holes were drilled. No deflections were observed while heating tin samples over the entire experimental temperature range. Effusion holes drilled at diagonally opposite locations into the sample cavities had diameters ranging from 1 to 3 mm for various cells.

The torsion-Langmuir cells used in this work were made of graphite blocks. Two wells 1.27 cm in diameter and 0.32 cm deep were drilled into opposite sides of these blocks. Sample wafers, 0.16 cm thick, were

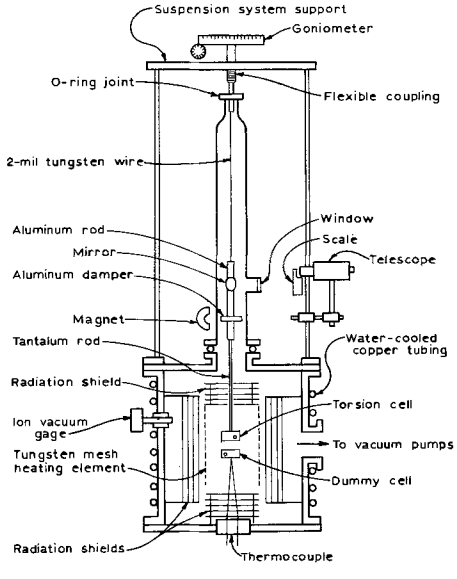

Fig. 1. Schematic diagram of torsion apparatus

placed inside these recessions and were secured there by specially designed graphite washers. Each washer had one flat surface that fit snugly against the sample wafer, with a concave surface on the other side. When the washer was in place, the effective sublimation area of the sample was defined by the 0.64 cm diameter opening through each washer. To prevent vapor that sublimed from the rear faces of the wafers from escaping in a manner that might contribute to the torque, a pair of holes were drilled on top of the cell into cavities behind the two samples. Due to relatively large sizes of the holes (3 mm in diameter), any vapors subliming from the rear face of a sample would escape through the holes in the top of the cell and give rise to no angular deflection.

Vacuum was maintained by a duo-seal Welch forepump and an NRC H56-1500 oil diffusion pump with 300 liter per second capacity placed beneath a liquid nitrogen cold trap. A CVC Phillips ionization gauge was used to measure pressure below one micron. During any run a background pressure of less than 2×10^{-5} Torr was maintained in the chamber.

Temperatures were measured by means of a calibrated 20 mil Pt/Pt-10% Rh thermocouple. Calibration of the couple was accomplished by measuring the apparent melting points of copper, gold, silver, aluminum, and zinc inside the dummy cell. The thermocouple leads were inserted in a small hole in the bottom of the dummy cell. Temperature was measured using an L&N potentiometer, Model 8662.

Methods of Operation

Torsion-effusion.—After loading about 1.5g of ZnTe 99.99% pure) powder in each sample compartment, the torsion cell was attached to the suspension system. With the torsion cell hanging free in the middle of the heating element, the system was closed and pumped. Power was introduced when the ambient pressure had reached 2×10^{-5} Torr or lower. Vapor pressure measurements were made only after the system had come to an equilibrium condition, as indicated by the constancy of temperature as a function of time. The temperature in the torsion cell was assumed to be equal to that in the dummy cell, which was read from the potentiometer during each torsion run. This assumption is based on findings which will be discussed later.

The torque resulting from the effusion of vapor through the cell orifices was determined from the angle through which the wire had twisted. Angles of deflection were determined by returning the suspension system to its original (null) position. Proper alignment was ascertained by viewing through the telescope on the mirror, which reflects a scale placed outside the vacuum system. Vapor pressure values were then calculated from deflection angles.

Torsion-Langmuir.—Deflection measurements were made in a similar fashion to those described above. Readings were taken at progressively higher temperatures until deflections began to decrease either with further increase in temperature or with increased time at constant temperature. Examination of the wafers after apparent pressures had departed from the straight line portion of a plot of log P *vs.* $1/T$ always revealed that holes had developed completely through one or both wafers in at least one region. Only those points measured before the apparent pressures began to decrease systematically with time were used in the calculations of apparent pressures, since the rest represented deflection due to sublimation from a surface with an unknown area.

X-ray analysis.—To determine the congruency of the evaporation of zinc telluride crystals, two samples, one before and one after heating in vacuum at 1160°K for 30 min in a graphite torsion cell with an orifice of 3 mm, were analyzed by the Debye-Scherrer powder method, using Cu K_α radiation with an Ni-filter. The power setting (in G.E. XRD-6) used was 30 kv and 18 ma, and the exposure time was 5 hr for each film.

Results

Congruency of sublimation.—X-ray patterns of the heated samples were compared to those of the unheated sample. All lines of the heated sample corresponded to those of the unheated zinc telluride. Furthermore, the lines of the heated sample were compared to those of zinc, tellurium, zinc oxide, and tellurium dioxide with negative results of correspondence.

Torsion-effusion studies.—Vapor pressures were calculated from the torsion-effusion and torsion-Langmuir data by means of the equation

$$P = 2D\phi/(f_1 q_1 a_1 + f_2 q_2 a_2) \qquad [2]$$

where P is the pressure in atmospheres, D is the torsion constant of the wire in dyne-centimeter per radian, ϕ is the angle of deflection of the cell in radians, q_1 and q_2 are perpendicular distances in centimeters from the center of the effusion holes to the axis of rotation, a_1 and a_2 are the areas of the effusion orifices in square centimeters, and f_1 and f_2 are Searcy's force correction factors (8, 9).

The vapor pressure of tin (99.99% pure) was measured as a check on the validity of the experimental results obtained with this apparatus. Tin was chosen as the calibration material because previous investigations (7, 10, 11) indicated it to be a well-behaved and uncomplicated material. Vapor pressure values from 1.1×10^{-6} to 6.3×10^{-5} atm were obtained from the temperature range 1378°-1640°K. From these measurements the third-law heat of sublimation at 298°K was found to be 72.8 kcal/mole compared to 72.2 kcal/mole calculated by Hultgren *et al.* (12) from results of earlier studies.

The results of the torsion-effusion studies on zinc telluride are plotted in Fig. 2. Figure 2 also shows previous results obtained by Goldfinger and Jeunehomme (3). All calculated thermodynamic functions were based on the reaction $2ZnTe\ (s) = 2Zn\ (g) + Te_2(g)$. Calculations of the heat of sublimation are tabulated in

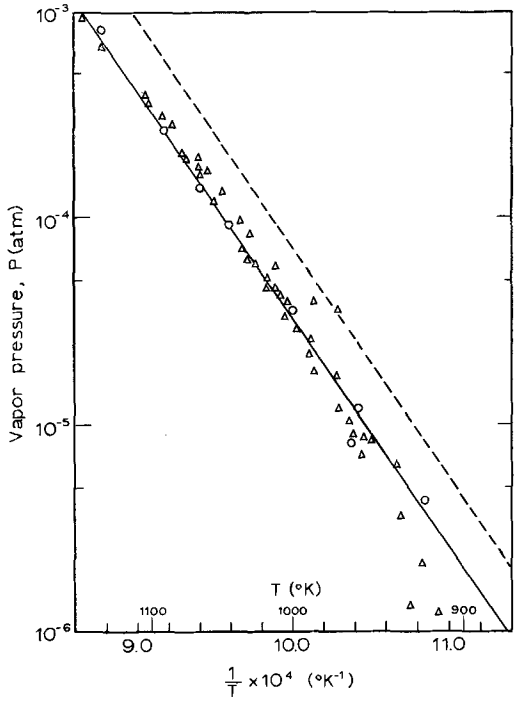

Fig. 2. Vapor pressure of zinc telluride (s), torsion-effusion method: △, this work, orifice $d \simeq 2$ mm; o, this work, orifice $d \simeq 1$ mm; —, this work, least-square fit; . . ., Goldfinger and Jeunehomme (3).

Table I. Third-law heats of sublimation of
$2ZnTe\ (s) = 2Zn\ (g) + Te_2\ (g)$

T, °K	−log P	−[fef] ZnTe (s)	$\Delta H°_{298}$ kcal	T, °K	−log P	−[fef] ZnTe (s)	$\Delta H°_{298}$ kcal
888	6.8325	94.18	155.80	1019	5.6781	94.99	156.32
915	6.0828	94.20	157.90	1028	5.7860	95.07	156.39
921	6.6335	94.24	155.80	1030	5.9165	95.08	156.20
925	6.3222	94.28	155.50	1033	5.9859	95.10	156.30
931	5.1189	94.33	155.94	1033	5.8312	95.10	156.30
935	6.5557	94.38	155.80	1033	5.7753	95.10	156.30
952	6.9258	94.50	156.10	1033	5.7899	95.10	156.40
958	6.9340	94.53	156.20	1043	5.9528	95.17	156.60
958	6.8179	94.53	156.20	1044	5.9614	95.19	156.20
962	5.3160	94.57	156.28	1050	4.1206	95.22	156.32
963	6.9430	94.59	156.40	1053	4.0663	95.24	156.21
965	6.9085	94.61	156.40	1058	4.2201	95.27	156.20
965	5.0043	94.61	156.40	1063	4.2019	95.33	156.30
970	5.5700	94.64	156.10	1063	4.2851	95.33	156.70
973	5.0722	94.65	156.30	1064	4.2355	95.33	156.68
978	5.2279	94.68	156.10	1067	4.2095	95.34	156.30
986	5.5911	94.76	156.40	1073	4.2878	95.40	156.58
988	5.2577	94.77	156.30	1077	4.2988	95.41	156.58
988	5.2900	94.77	156.40	1078	4.2967	95.44	156.57
988	5.2455	94.77	156.40	1083	4.4487	95.47	156.20
990	5.3424	94.79	156.40	1090	4.4281	95.50	156.59
999	5.4579	94.86	156.38	1092	4.5051	95.52	156.58
1005	5.4997	94.89	156.38	1103	4.5988	95.62	156.45
1010	5.7520	94.92	156.27	1103	4.5843	95.62	156.60
1011	5.5809	94.92	156.28	1105	4.5888	95.62	156.60
1013	5.6469	94.96	156.39	1142	4.9138	95.88	156.60
1018	5.6590	95.00	156.39				

Table I. From this table an average of $\Delta H°_{298}$ of 156.3 ± 3.0 was obtained.

A least-square fit of the data gives an equation for log P at any temperature between 800° and 1150°K for the sublimation of zinc telluride

$$\log P = 6.18 - 1.065 \times 10^4/T \qquad [3]$$

From the second-law method, the heat of sublimation of zinc telluride at 298°K, $\Delta H°_{298}$, was found to be 150.4 ± 1.0 kcal.

Torsion-Langmuir studies.—Figure 3 shows a plot of the logarithm of the free-surface vapor pressure of polycrystalline zinc telluride *vs.* $1/T$. When experimental total pressures were expressed in the form $\log P = a + (b/T)$ with the aid of the least-square method, the following expression for the free-surface sublimation resulted

$$\log P = 7.89 - 1.283 \times 10^4/T \qquad [4]$$

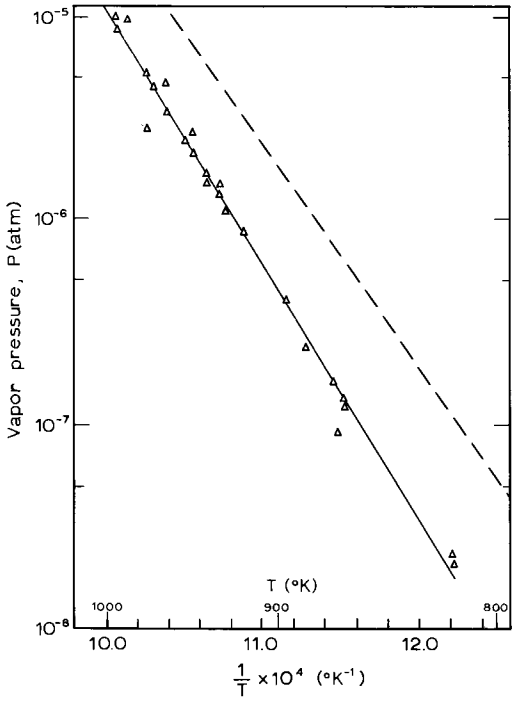

Fig. 3. Vapor pressure of zinc telluride (s), torsion-Langmuir method: △, this work; —, this work, least-square fit; . . ., this work, torsion-effusion method.

where P is the free-surface vapor pressure of zinc telluride in atmospheres between 810° and 1013°K.

By defining $K = (P_{Zn})^2(P_{Te_2})$, where K is the apparent equilibrium constant of the dissociation, Eq. [4] can be expressed

$$\log K = 22.78 - 3.849 \times 10^4/T \qquad [5]$$

From Eq. [4] the second-law heat of actiyation at 298°K was calculated to be 178.6 ± 4.2 kcal.

Discussion

X-ray analysis of zinc telluride samples heated in vacuum at 1160°K for 30 min showed no change in composition. Therefore, it was concluded that the sublimation of zinc telluride is congruent. No diffraction lines belonging to zinc, tellurium, zinc oxide, or tellurium dioxide were observed. Hence, the sublimation of zinc telluride could have occurred by means of one of the following evaporation processes

$$ZnTe\ (s) = ZnTe\ (g) \qquad [6]$$

$$2ZnTe\ (s) = 2Zn\ (g) + Te_2(g) \qquad [1]$$

Mass spectrometric studies have confirmed that the reaction defined by Eq. [1] is predominant for the sublimation of zinc telluride (3).

Nearly all of the torsion-effusion data for zinc telluride were obtained using a 2-mm diameter orifice. A torsion-effusion cell with 1-mm orifice gave vapor pressure data in line with those obtained previously with the 2-mm orifice cell, thus indicating that the assumption of the existence of equilibrium conditions inside the cell with a 2-mm orifice is valid.

The value for the heat of sublimation of zinc telluride polycrystal calculated by the second-law method from torsion-effusion studies is $\Delta H°_{298}$ = 150.4 ± 1.0 kcal. This value is in good agreement with 151.8 kcal reported by Goldfinger and Jeunehomme (3). However, it is somewhat lower than the value of 154.2 kcal calculated by Goldfinger and Jeunehomme when their data were combined with those of McAteer and Seltz (1). Based on Cp data estimated by Goldfinger and Jeunehomme using Kubaschewski's procedure (13), third-law calculations of $\Delta H°_{298}$ gave a value of 156.3 ± 3.0 kcal. This value is in reasonable agreement with the second-law value given above.

Thermodynamic calculations were made to determine the entropy of sublimation for zinc telluride. The second-law entropy was found to be 83.9 ± 1.4 eu at 298°K, which is in reasonable agreement with the value $\Delta S°_{950}$ = 86.2 eu reported by Goldfinger and Jeunehomme (3).

Temperature measurements have been a source of conflict between investigators working in this area. The present research uses a thermocouple calibrated *in situ* using the fusion points of several metals as standard points. Furthermore, with a similar torsion-effusion apparatus, Munir and Searcy (4, 6) have shown that the temperature of the dummy cell is the same as that of the effusion cell for a given power input to the heating element.

From apparent pressure measurements obtained by the torsion-Langmuir method, the free-surface activation energy for the sublimation of polycrystalline zinc telluride was calculated to be 178.6 ± 4.2 kcal at 298°K. The apparent equilibrium constant for the dissociation reaction of Eq. [1] was calculated to be K = 4.62 x 10^{-16} at 1000°K as compared to 3.5 x 10^{-15} at 1000°K obtained by the torsion-effusion method. This difference between the apparent equilibrium constants for sublimation measured under Langmuir conditions and those measured in Knudsen cells demonstrates the existence of free energy barrier to the sublimation process. The evaporation coefficient of zinc telluride appears to vary from α = 0.298 at 953°K to α = 0.155 at 807°K if the Langmuir data are compared to the pressures measured with the torsion-effusion cell.

Since the composition of solid zinc telluride is not changed by heating, therefore it would seem that solid-state diffusion is not a necessary step in the process. Accordingly, the free-energy barrier must be imposed either by a step involved in the transfer of Zn and Te atoms from lattice positions in the surface layers to adsorption sites on the surface, by the desorption of Zn atoms, or by the step of formation and desorption of Te_2 molecules from two adsorbed tellurium atoms.

Acknowledgments

The authors extend their appreciation to Mr. Dennis W. De La Roca for his help in the computation of some of the data and to Mr. Walter Mounts for his technical assistance. Special thanks are extended to Dr. Alan W. Searcy who provided valuable counsel.

Manuscript received May 12, 1967; revised manuscript received Aug. 1, 1967.

Any discussion of this paper will appear in a Discussion Section to be published in the June 1968 JOURNAL.

REFERENCES

1. J. H. McAteer and H. Seltz, *J. Am. Chem. Soc.*, **58**, 2081 (1936).
2. I. V. Korneeva, A. V. Belyaev, and A. V. Novoselova, *Zhur. Neorg. Kh.*, **5**, 3 (1960).
3. P. Goldfinger and M. Jeunehomme, *Trans. Faraday Soc.*, **59**, 2851 (1963).
4. Z. A. Munir and A. W. Searcy, *J. Chem. Phys.*, **42**, 4223 (1965).
5. B. A. H. Blank, Ph.D. Thesis, Univ. of Calif., Berkeley, April 23, 1965 (UCRL-16018).
6. Z. A. Munir and A. W. Searcy, *This Journal*, **111**, 1170 (1964).
7. D. A. Schultz, Ph.D. Thesis, Univ. of Calif., Berkeley, 1961 (unpublished).
8. R. D. Freeman and A. W. Searcy, *J. Chem. Phys.*, **22**, 762 (1954).
9. D. A. Schultz and A. W. Searcy, *ibid.*, **36**, 3099 (1962).
10. R. E. Honig, *ibid.*, **21**, 573 (1953).
11. L. Brewer, "The Chemistry and Metallurgy of Miscellaneous Materials," McGraw-Hill Book Co., Inc., New York (1950).
12. R. Hultgren, R. L. Orr, P. D. Anderson, and K. K. Kelley, "Selected Values of Thermodynamic Properties of Metals and Alloys," John Wiley & Sons, Inc., New York (1963).
13. O. Kubaschewski, E. Evans, and C. B. Alcock, "Metallurgical Thermochemistry," Pergamon Press Ltd., Oxford (1967).

Performance of Silver-Palladium Alloys in a Concentrated Caustic Electrolyte

Paul Malachesky and Raymond Jasinski

Tyco Laboratories, Inc., Waltham, Massachusetts

ABSTRACT

The anodic oxidation of silver and a series of palladium-silver alloys, all in the form of smooth rotating disk electrodes, has been studied in 36% KOH. The total charge accepted by silver and the alloys is a pronounced function of current density. Charge acceptance at the Ag(I) level is enhanced with the palladium-silver alloys in agreement with existing data on porous electrodes. Maximum charge acceptance on the first cycle was accomplished with the 1% Pd-Ag alloy. Cycling increased both charge acceptance capacity and surface roughness (as measured by double layer capacitance), being more pronounced for the alloys than for pure silver. However, the increase in surface roughness (area) did not lead to a totally commensurate increase in the total charge accepted with all materials studied.

One approach to altering the charge acceptance properties of silver is to modify the electronic conductivity of Ag_2O. This can be done by alloying silver with minor impurities. Addition of metals of the same group as Ag (*e.g.*, Cu) or of anions (*e.g.*, $S^=$) can promote vacancy formation, presumably due to the lowering of the energy necessary for the creation of vacancies. Impurities which change the concentration of holes in the oxide crystal are metals to the left of silver in the periodic table (*e.g.*, Pd) or metals of high ionization potentials (*e.g.*, Au).

Indeed, the use of palladium as an additive to the silver plate has been reported to increase charge acceptance, particularly at the Ag(I) level (1). Some problems are also reported for electrodes of this type. For example, these same plates did not accept charge efficiently at the Ag(II) level (2). Studies of separator deterioration in cells containing Pd additions showed significant amounts of this additive in the separators (3). The concentration of Pd in positive plates of this type appeared to stabilize at 0.1-0.2%. Generally, cells designed to operate at the Ag(I) level containing such additives had good recharge properties, but discharge characteristics were poor, especially with respect to initial capacity and capacity maintenance (4).

The experiments described in this paper are concerned with changes in the charge acceptance of silver resulting from alloying with varying amounts of palladium. Smooth electrodes were used in order to avoid the complications of mass transport processes within porous plate structures.

Experimental

The palladium-silver alloys (10, 1, and 0.1 a/o) were prepared by direct fusion of the elements. All alloys, in the form of cylinders, were mounted by threading onto a ¼ in. metal shaft. The cylinder sides were coated with Kel-F wax so that only the cylinder face was exposed; the metal shaft was encased in heat-shrinkable Teflon tubing. A Sargent synchronous motor was used to rotate the electrode at 30 rps. All potentials are reported with respect to the dynamic hydrogen electrode (DHE) (5). All runs were made in N_2-saturated 36% KOH at 35° ± 2°C.

A freshly coated and polished (with successively finer alumina powders) electrode was used for the determination of the charge-discharge curves on the first charging cycle. The electrodes were cathodized to H_2 evolution before taking measurements in order to reduce any surface oxide formed during handling.

On successive cycling some etching occurred at the edges of the disk electrodes causing minor leakage between the cylinder sides and the wax. This contribution to an increase in effective electrode area generally proved to be negligible in comparison with that resulting from oxide formation and dissolution on the surface disk. However at low current densities (*i.e.*, longer charge-discharge periods) on the single cycle experiments, this erratic leakage effect did cause some scatter in the charge acceptance capacities. The data reported are the averages of 3-6 determinations made at each current density.

A possible experimental complication in studies using rotating disk electrodes is that of unequal current distribution across the surface of the disk (6). This effect could, in principle, give rise to premature oxygen evolution before the disk electrode was completely charged at the Ag(II) level. Experimentally, it was observed that rotating the electrode had no effect on the observed charge acceptance values and, when charging was continued into the O_2 evolution plateau, no additional oxide was formed. Thus at the beginning of the O_2 evolution potential step the silver electrode had accepted its maximum charge.

Potential-time curves were recorded on a Houston Instruments X-Y recorder (x-axis on time base) or a Tektronix type 561A oscilloscope with a type 2A63 differential amplifier and a type 2B67 time base. An operational amplifier-based voltage follower was used as an impedance matching device in the potential measuring circuit. A Wenking potentiostat operated in the galvanostatic mode or an Electronic Measurements and Control constant current power supply was used as the current source.

The double layer capacity measurements were made using the method of Will and Knorr (7), employing a triangular wave of 100 Hz and an amplitude of *ca.* 25 mv (*i.e.*, a sweep rate of 5 v/sec), biased by a d-c voltage.

Results

The data for the initial charge-discharge cycle will be considered first, followed by the effects of cycling.

The total charge accepted (Q_T) as a function of current density for silver and the palladium alloys is plotted in Fig. 1. The scatter in data can be due in part to the leakage effect described above. Some "natural" scatter is also to be expected due to the inherent irreproducibility of the oxidation of metals. This has been attributed to the erratic or irreproducible creation of grain and strain points in the metal lattice during the working of these metals (8, 9). Because of the pronounced sensitivity of Q_T to current density, slight uncontrolled variations in charging current could also result in scatter of the data.

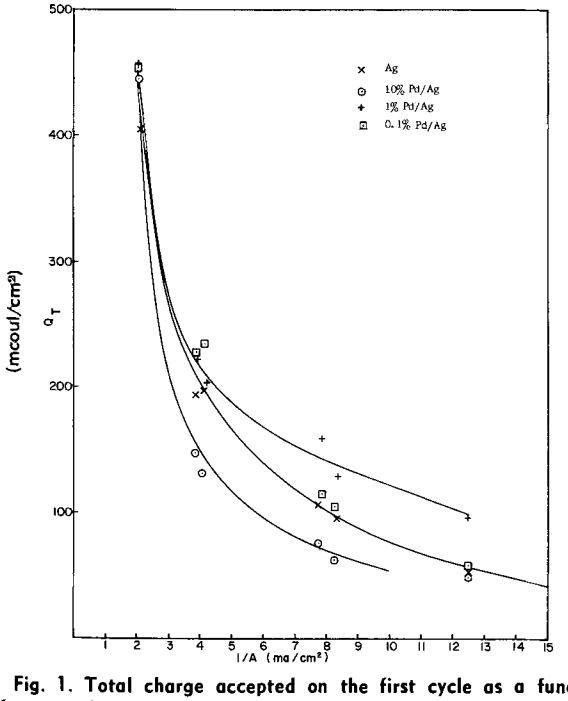

Fig. 1. Total charge accepted on the first cycle as a function of current density for silver and silver palladium alloys.

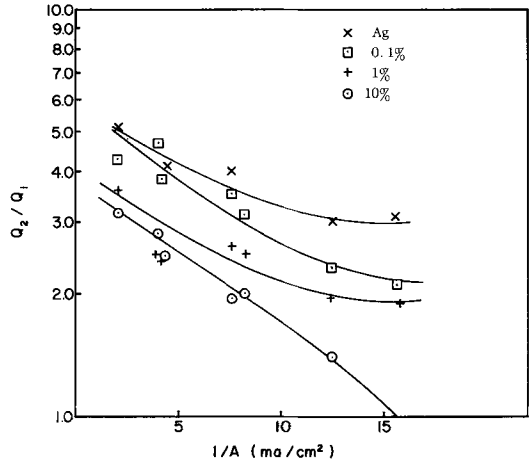

Fig. 2. Ratio of the charge passed at the Ag_2O/AgO potential level (Q_2) to that passed at the Ag/Ag_2O level (Q_1) on the first charge cycle as a function of current density.

At all current densities, the charge accepted on the first cycle by silver and the 0.1% alloy are only marginally different. The sensitivity of Q_T to charging rate at the lower current densities obscures the effect of alloy composition. At high current densities (> 4 ma/cm²) maximum charge acceptance was accomplished with the 1% alloy. This is in agreement with data on porous battery structures (1). No difficulty was experienced in charging to the Ag(II) level, in contrast to data in the literature (2).

The ratio of the charge accepted at the AgO potential level (Q_2) to that passed at the Ag_2O potential level (Q_1) on the first cycle is plotted in Fig. 2 as a function of current density. As can be seen, this ratio (Q_2/Q_1) decreases with increasing current density and also with increasing palladium content. This dependence on composition is consistent with results reported on porous electrodes (1). The charge passed to the Ag_2O/AgO potential is given in Table I for silver and the alloys.

Discharges of the electrodes were carried out at the same current density as used in the charging cycle. The discharge efficiencies were in the range of 90-95%. The ratio Q_1/Q_2 for the first discharge cycle is plotted as a function of current density in Fig. 3.

On cycling, the charge accepted and delivered by all materials increases. The total charge acceptance, at a constant current density of 3.87 ma/cm², is plotted *vs.* the number of cycles in Fig. 4. The ratio of charge accepted at the AgO potential level to that accepted at the Ag_2O level decreases as the electrodes are cycled (Fig. 5); the ratio Q_2/Q_1 on discharge is essentially independent of cycling. The relative change in double layer capacitance is shown in Table II. There is a significant increase in all cases; eventually a leveling off is approached.

The ratios of total charge accepted (Q_T) to the double layer capacitance (C_{dl}), as measured at +300

Table I. Charge passed to the Ag_2O/AgO potential (mcoul/cm²)

I/A, ma/cm²	Ag	0.1% Pd-Ag	1% Pd-Ag	10% Pd-Ag
2.08	57 ± 3	88 ± 8	103 ± 9	105 ± 6
3.87	45 ± 8	41 ± 6	63 ± 4	40 ± 3
4.17	31 ± 6	50 ± 4	60 ± 7	35 ± 2
7.75	21 ± 2	28 ± 4	47 ± 2	25 ± 2
8.35	15 ± 1	27 ± 5	37 ± 6	23 ± 10
12.50	15 ± 1	20 ± 2	32 ± 5	21 ± 1
15.50	—	17 ± 1	33 ± 1	24 ± 2

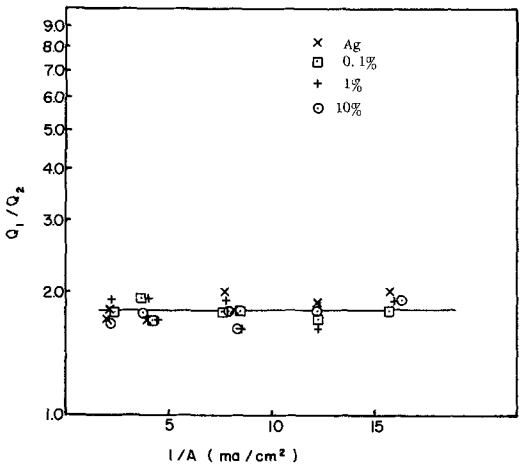

Fig. 3. Ratio of the charge passed at the Ag/Ag_2O level (Q_1) to that passed at the Ag_2O/AgO potential level (Q_2) on the first discharge cycle as a function of current density.

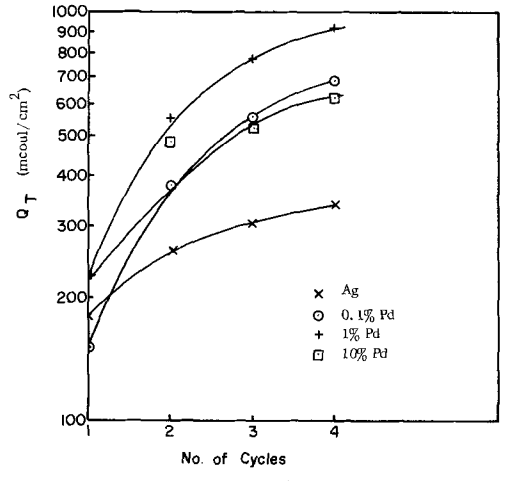

Fig. 4. Total charge accepted at 3.87 ma/cm² as a function of cycle number.

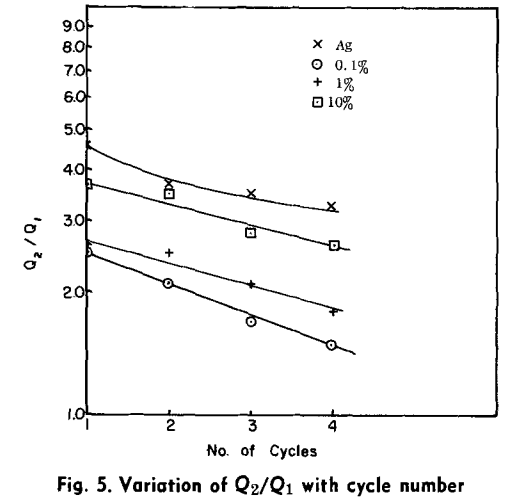

Fig. 5. Variation of Q_2/Q_1 with cycle number

mv, before each charging cycle are plotted in Fig. 5 for Ag and the 1% Pd alloy at 2.08 ma/cm².

Discussion

As shown in Fig. 1, the total charge accepted on the first cycle is a pronounced function of current density for all materials, particularly at the lower charging rates. These results are similar in form to those obtained by Wales (10) on porous battery electrodes. This improved charge acceptance at low rates was attributed (10) to greater time for diffusion of electrolyte into the pores of the electrode and reaction of the divalent silver with metallic Ag according to

$$AgO + Ag \rightarrow Ag_2O$$

Since the electrode is oxidized more completely before barrier layers are formed, the lower charging rates are more effective.

This bulk diffusion explanation is inconsistent with the present measurements on smooth rotating disk electrodes since no macropore structure exists. Furthermore, the results were relatively independent of stirring rate. However, it is not possible on the basis of those results to discount diffusion phenomenon within the micropores, *i.e.*, the volume of electrolyte between the crystallites of oxide within the diffusion layer.

The discharges were all 90-95% efficient. Essentially all charge delivered to the electrode was recoverable; the slight deviation from 100% can be explained in terms of solubility of the oxides in the large volume of bulk electrolyte.

Consider next the distribution of charge between divalent and monovalent silver. The ratio of the coulombs passed into the two silver plateaus (Q_2/Q_1) on charge is dependent on current density, alloy composition and the number of cycles, while the ratio (Q_1/Q_2) for the discharge process is independent of these variables.

As shown by Langer and Patton in a coulogravimetric study of a sintered silver electrode (11), both Ag_2O and AgO are formed at the Ag(II) plateau on charge. The x-ray diffraction study of Wales and Burbank (12) indicated that a similar situation prevailed on discharge, *i.e.*, the lower potential discharge plateau arises from AgO as well as Ag_2O. The constancy of Q_1/Q_2 on discharge, in the present work, implies either that the high potential discharge plateau arises solely from the total discharge of AgO or, to be consistent with ref. (12), that the discharge of AgO at the higher potential level comprises a constant fraction of the total discharge capacity. It is not possible, at this time, to suggest a simple mechanism other than coincidence for the constant fraction interpretation of the constancy of Q_1/Q_2 with current density and with alloy composition.

The alloys are all more effective than silver in charge acceptance and delivery of the Ag(I) level, 1% Pd/Ag showing the largest value (103 mcoul/cm²), (Table I). With this alloy, at 2.08 ma/cm, an additional 107 mcoul/cm² of Ag_2O is formed at the Ag(II) level. Thus a possible procedure to obtain the maximum charge of Ag_2O in a working plate is to charge fully and then bleed off the AgO charge (13).

The anomalous behavior of the 10% Pd alloy in total charge accepted may be explained in terms of a passivating oxide film. With the 10% Pd-Ag alloy, the contribution of a lower palladium oxide on discharge at +700 mv was particularly evident. In addition, the formation of a higher oxide of palladium at $E \cong +1600$ mv *vs.* DHE must also be considered (14). The palladium oxides formed on charge are apparently 3-10 monolayers thick. Silver, on the other hand, forms oxide layers of approximately 300 monolayers at 2.08

Table II. Relative double layer capacitances*

Cycle No.	Ag 91 μf/cm²	0.1% Pd 100 μf/cm²	1% Pd 98 μf/cm²	10% Pd 110 μf/cm²
0	1	1	1	1
1	3.8	2.5	4.1	1.45
2	3.6	7.0	7.9	9.1
3	3.8	5.8	11.5	8.5
4	3.8	6.8	11.5	8.5
5	4.3	6.6	12.2	

* Cycling carried out at 2.08 ma/cm².

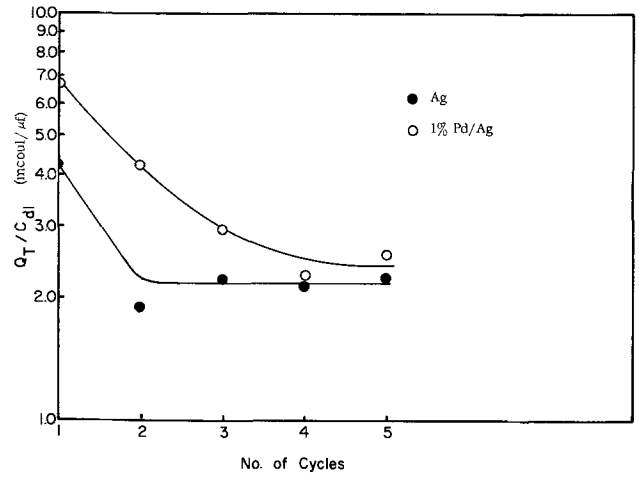

Fig. 6. Ratio of the total charge accepted (Q_T) to the double layer capacitance (C_{dl}) as measured before each charging cycle.

ma/cm^2. This lower depth of oxidation of palladium thus can result in the formation of thin, isolated palladium oxide deposits on the alloy surface, obscuring some silver from the charging reaction. A very similar explanation has been advanced (15) in the high-temperature oxidation of alloys containing a solute which has less affinity for oxygen than the solvent metal.

Cycling the electrodes increased substantially the quantity of charge accepted. As shown in Table II, the double layer capacity of all the electrodes also increased with cycling. Since C_{dl} is proportional to surface roughness, this implies that the increase in capacity is due primarily to an increase in the area of the electrode accepting charge. In Fig. 6 the ratio of the total charge accepted to C_{dl} is plotted as a function of cycles for Ag and 1% PdAg. A decrease is observed rather than an increase, *i.e.*, the surface appears to roughen faster than the coulombic capacity increases. As shown in Fig. 2, the ratio of the amount of charge accepted on the first cycle at the Ag_2O/AgO potential level to that at the Ag/Ag_2O level increased with decreasing current density. However, on cycling, this ratio decreased with increasing double layer capacitance values, *i.e.*, decreasing real current densities. Therefore, as implied by the double layer data, the effect of cycling on charge acceptance is not solely a matter of decreasing the effective current density.

There are at least two alternative explanations: (*i*) part of the roughened surface, as measured by C_{dl}, is not available to the charging reaction or (*ii*) the crystal structure of the surface of the electrode is different from that of the smooth electrode, alloy or silver. (Such a change could also affect C_{dl}.)

It is not possible with the present data to resolve these alternatives. The fact that there is a second alternative is based on the work of Wales and Burbank (12), who observed that prior to cycling, a smooth rolled silver sheet showed a strong preferred orientation. On cycling x-ray diffraction patterns revealed a gradual increase in the amount of randomly oriented polycrystalline silver, as well as surface roughness.

Conclusions

1. The total charge acceptances for silver and palladium-silver alloys are all a pronounced function of current density. Differences between materials at low current densities are obscured by this high sensitivity to charging rate. Since this effect, first reported for porous electrodes, is also observed on smooth electrodes, the mechanism must involve processes taking place at or near the electrode surface, rather than diffusion into and out of large pores.

2. No difficulty was experienced in introducing charge at the Ag(II) level in palladium-silver alloys, contrary to data reported for porous electrodes.

3. While palladium-silver alloys may accept more charge at the Ag/Ag_2O potential level, the relative amount of charge delivered at the two discharge potential levels after a complete charge is constant and independent of current density and alloy composition.

4. The total charge accepted and the double layer capacitance (proportional to surface roughness) for the palladium-silver alloys increase more with cycling than for pure silver, accounting for most of the improvements noted in charging cells containing palladium as an additive. The double layer capacitance of all electrodes increased on cycling, but this increase does not result in a completely proportional increase in total charge accepted. Thus, some other factor besides surface area and/or surface orientation is probably involved in the charging process.

Acknowledgments

The authors wish to acknowledge the assistance of Miss Susan Carroll in carrying out the experimental work and the support of the U.S. Naval Air Systems Command (Contract No. W66-0621-C).

Manuscript received Aug. 1, 1967.

Any discussion of this paper will appear in a Discussion Section to be published in the June 1968 JOURNAL.

REFERENCES

1. a, J. Lander and J. Keralla, Report ASD-TDR-62-668, June 1962; b, J. Lander *et al.*, U.S. Pat. 3,212,934, October, 1965; c, M. Sulkes and G. Dalin, Report No. 4, Contract No. DA-36-039-AMC-02238(E) (July 1964) AD453792.
2. M. Sulkes and G. Dalin, Report No. 6, Contract No. DA-36-039-AMC-02238(E) (Jan. 1965) AD464470.
3. M. Sulkes, Report No. 7, Contract No. DA-36-039-AMC-02238(E) (April 1965) AD621583.
4. J. Goodkin, Report No. 5, Contract No. AF33(615)-2615 (Sept. 1966) AD802355.
5. J. Giner, *This Journal*, **111**, 376 (1964).
6. J. Newman, *This Journal*, **113**, 1235 (1966).
7. F. Will and C. A. Knorr, *Z. Elektrochem.*, **64**, 258 (1960).
8. U. R. Evans, "The Corrosion and Oxidation of Metals," Edward Arnold Ltd., London (1960).
9. E. A. Butler and A. U. Blackham, Report No. 1, Contract NAS7-100 (July 1966) NASA CR-80126.
10. C. P. Wales, *This Journal*, **108**, 395 (1961).
11. A. Langer and J. T. Patton, *ibid.*, **114**, 113 (1967).
12. C. P. Wales and J. Burbank, *This Journal*, **112**, 13 (1965).
13. A. M. Chreitzberg, U.S. Pat. 3,118,100.
14. A. Hickling and G. Vrjosek, *Trans. Faraday Soc.*, **57**, 123 (1961).
15. J. C. Scully, "The Fundamentals of Corrosion," Pergamon Press, London (1966).

Electrochemical and Related Phenomena under Weightless Conditions

I. Flowing Electrolyte Thermocells

Minas Ensanian

Physical Chemistry Group, Textron's Bell Aerosystems Company, Buffalo, New York

ABSTRACT

A flowing electrolyte thermogalvanic cell (Cu, $CuSO_4$) has been studied under weightless conditions via drop-tower experiments. Unexplained perturbations have been observed in the output potential in both the time-dependent (emf build-up) and quasi-stationary state regions over a wide range of experimental conditions. Exhaustive control experiments as well as the general and over-all reproducibility of perturbations *per se* in a large number of trials rule out oscillations in the hydraulic system as well as random transients as factors responsible for the observed phenomena. Stationary electrolyte systems including thermocells, concentration cells, and a Daniell cell, exhibited similar perturbations during the 1-*g* to 0-*g* transition.

The addition of urea was found to dampen the marked oscillations normally shown by a copper thermocell at the same output potential. The result is important in view of the known decreased ultrasonic attenuation and increased sound velocity caused by urea addition to water. At ambient temperatures the electrolytic conductivity of freshly prepared urea-cupric sulfate solutions gradually increases and in subsequent drops the zero-gravity induced oscillations reappear.

Copper thermocells utilizing nonaqueous solvents (acetonitrile or absolute methanol) exhibit a voltage decrease (several millivolts) but the time/potential curve continues on its original course after impact. The potential of concentration cells (with linear and nonlinear gradients) increases (several millivolts in 0.7 sec), then decays to its initial value prior to impact; cells with linear gradients exhibit relatively larger changes. Inversion tests are also described. Daniell cells (1.09v at 20°C) show a similar behavior except that the voltage increase is about 40 mv.

To understand better the influence of the 1-*g* to 0-*g* transition on physicochemical processes, the electrochemical measurements were supplemented (with the appropriate controls) by a study of diffusional phenomena, heterogeneous and homogeneous chemical reactions. In all cases increased rates were observed and are attributed to enhanced ion mobility during weightlessness. On the basis of these experiments it must be concluded that an interaction exists between chemically reacting systems and gravitational fields.

In recent years the question of an interaction between gravitational fields and chemically reacting systems (1) has become increasingly important. From the experimental viewpoint, the unevacuated drop tower conveniently provides a weightless environment for periods of 1 or 2 sec.

This paper reports the results obtained in the first of a series of studies concerned with the behavior of flowing and stationary electrolyte thermocells (including nonaqueous systems), concentration cells, and galvanic cells during the 1-*g* to 0-*g* transition.[1]

In a previous communication (2) it was reported that partially frozen thermocells exhibited oscillations and a potential decay with the reduction of gravity. A similar "zero-gravity effect" has now been observed in a thermocell in which the electrolyte is under forced flow during the free fall period.

The results which demonstrate the perturbation of an electrochemical system with the sudden removal of the gravity field are of considerable interest in view of the reported physiological effects of weightlessness during space flight (3, 4), the theory of coupled transport processes (5, 6), and theoretical electrochemistry (7).

Concurrently, the effects of free fall on the boundary between concentrated copper sulfate solutions and water, the solubility of copper sulfate crystals in water, the reaction between triphenylchloromethane (in benzene) and a zinc surface, the stress corrosion of Plexiglas by a (KI, I_2, $ZnCl_2$, HCl) reagent, and the rate of the "iodine clock reaction" were investigated.

These studies were initiated in order to gain insight on the influence of a weightless environment (and or memory) on diffusion, wetting, heterogeneous and homogeneous reactions. Although some of the work reported here is preliminary in nature, the indications are nevertheless, that the zero gravity drop tower may become an important tool for electrochemical investigations.

Experimental

Flowing electrolyte thermocells.—The effect was demonstrated and studied in the apparatus (8) shown in Fig. 1. The inflation of a collapsed bottle against the sides of the reservoirs (T_1 and T_2) forces electrolyte past the electrodes into the containers (R_1 and R_2) below. The electrical circuit is completed via a pinhole (1 mm diam) located an inch below the tips of the electrodes.

The reservoirs and containers (500 ml polyethylene bottles, squeeze type with screw caps) are connected by 3/16 in. ID Tygon tubing (1/16 wall) 25 in. in length properly aligned and taped at the position indicated. The electrodes are a 4 mm OD coil of copper wire (B & A reagent, B & S No. 24) 1 in. long (10 turns/in.) having a geometrical surface area of 0.361 in.^{2} and located midway along the Tygon tubes. After degreasing they were immersed for several hours in

[1] As used here the term (1-*g* to 0-*g* transition) or simply the transition means going from a state of rest (normal gravity) to free fall (reduced gravity).

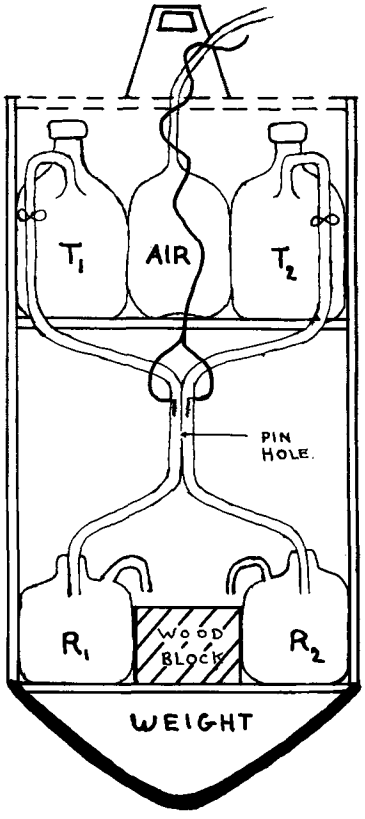

Fig. 1. Schematic diagram of flowing electrolyte thermocell and Zero Gravity Drop Capsule. The usable time of cell depends on the volume of fluid that can be discharged as well as the rate. The single air bottle (actually lying on its side) shown can discharge up to 250 ml from each of the 500 ml reservoirs at rates up to 25 ml/sec. Three or four smaller bottles (500 ml) inserted symmetrically enable 350 ml at rates up to 35 ml/sec. When the warmer reservoir is properly wrapped with rubber tape, the amounts of fluid released by the reservoirs will normally differ by less than 20 ml. Pressures within the bottles (2-10 psig). Cell continues to operate after impact.

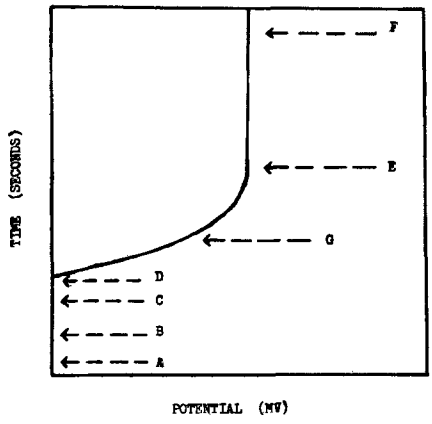

Fig. 2. The experimental sequence shown in terms of the time/potential profile. A—recorder chart on, B—pressure adjustment begun, C—pinch clamps opened, and D—electrolyte flows past the pinhole region. The regions D-E and E-F represent time dependent and stationary states respectively, and cell behavior during the reduction of gravity was studied in both of these regions. Practical limitations prevent a drop test before the point G has been reached. As used here, output voltage refers to the emf at drop-time, *e.g.*, the points G or F. The polarity of the cold electrode is negative with respect to the potentiometer terminal.

hot electrolyte (cupric sulfate, Baker reagent) of identical composition to that found in the reservoirs prior to their being used.

Shielded lead wires (30 ft long) attached to the electrodes and taped to the rubber hose were connected to a recorder which had a balancing and chart speed of 1-sec and 24 in/min. The hose (30 ft of 5 mm ID blk gum rubber) attached to the air bottle (1 liter) was connected to a source of compressed gas (N_2) and the pressure monitored by a Will (15292) regulator.

Two drop capsules (I and II) were used (constructed of wood/plastic) having aerodynamic cross-sections of 113 and 50 in.^{2} and weighing 13 and 15 lb, respectively. In view of drag forces, the attainment of true zero gravity (10^{-3}-10^{-5}-g) for durations of 1 to 2 sec can only be achieved in an evacuated tower or by means of the encapsulated cell method (9). An unguided capsule dropped through air requires a high ratio of weight to frontal area ($\sim$ 1 to 2 psi) in order to overcome this resistance (10, 11). The preliminary work was done with the lighter capsule and the second used in an attempt to amplify the discovered effect.

The experimental procedure is as follows; after the capsule is positioned (17 ft above a sand pit), the electrical circuit is checked, and the reservoirs nearly filled with cold (T_1) and hot (T_2) electrolyte and temperature readings taken, whereupon they are filled to overflow and the screw caps replaced and taped. Some gas is then introduced into the air bottle ($<$ 1 psig) causing electrolyte to flow past the upper pinch clamps which are then closed, thus permitting an opportunity to inspect the system, making minor adjustments, as well as putting the release mechanism (essentially a wire cutting tool) in the "on" position. The drop capsule was released in less than 2 min after temperature readings were taken. The recording chart is turned "on," the gas pressure is rapidly adjusted to the desired value as the clamps are opened, and after a short count-down (during which the flow system is still under visual observation) the capsule is released. The sequence is shown in Fig. 2.

Control experiments fell into three main categories, viz., mechanical, electrical, and chemical. In the mechanical tests the electrolyte flow rate was varied, pulsated, restricted, and reversed, and as in all control tests effects on the time/potential curves were noted. Beginning with a gravity flow of 9 ml/sec the gas pressure could be adjusted to enable flow rates in excess of 30 ml/sec. In the pulsated flow tests a rate in the above range was selected and one or both of the Tygon tubes at a point midway between the electrodes and the upper reservoirs was manually constricted once or twice a second. Restricted flow refers to closing the pinch clamps when they are positioned between the electrodes and the lower reservoirs. In the reverse flow tests the fluid in one of the tubes was flowing in the normal direction while in the other tube it was being forced to flow at the same rate in the opposite direction, thus changing the vorticity in the pinhole.

Vibration, impact, and rotation tests were made on a loaded capsule to ascertain the effects (if any on the output potential) of handling and minor changes in capsule orientation during flight.

In the electrical category the following tests were made; swinging and twisting of the lead wires, controlled streams of air bubbles of various sizes being forced over the electrode surfaces as well as through the pinhole, and eliminating the pinhole and allowing the liquids to empty onto a common surface (8) or into a single reservoir.

In the chemical tests, thermal and concentration shock experiments were performed, *i.e.*, in the flowing electrolyte thermocells and the more recently studied flowing electrolyte concentration cells (to be discussed in another report), precise amounts (Cornwall syringe) of hot or cold electrolyte of identical composition, or in the case of the concentration cells at the same temperature but different concentration, were injected at definite intervals at distances of 0.75-1.5 in. upstream from the electrodes as well as through the pinhole area and the response noted.

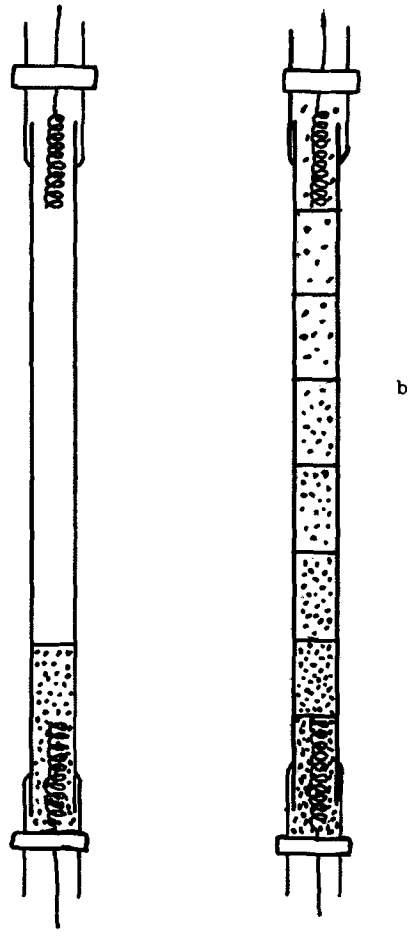

Fig. 3. Concentration cells with nonlinear (a) and linear (b) gradient used in this study. Cells (a) and (b) are made from glass and Tygon tubing, respectively. Cell (b) can also be made from glass which means either a very long tube in order to accommodate a certain amount of uncontrollable mixing or successively freezing each addition in the tube which may not always be practical. In cell (a) the height of the 1.0M cupric sulfate solution (dotted region) can be varied at will provided the lower electrode is completely covered. Tygon tubing is attached to the ends of the cells which are sealed by means of pinch clamps. The polarity of the lower electrodes is positive with respect to the potentiometer terminals. Concentration cells with membranes have also displayed perturbations and will be considered in another report.

Finally, the behavior of a flowing electrolyte system was observed (during free fall) when there was no temperature difference (No, dT) between the fluids in the reservoirs (T_1 and T_2), in other words, identical solutions. The output voltages observed under these conditions are due to microscopic differences (surface conditions, stored energy, etc.) between the electrodes.

Stationary electrolyte thermocells and concentration cells.—The thermocells (not shown) and concentration cells with nonlinear gradients (Fig. 3a) were made by inserting the coiled wire electrodes through Tygon attached to the ends of a Pyrex tube and sealed by means of a pinch clamp. In the case of the thermocell the tube was filled to overflow with a homogeneous solution of 0.005M cupric sulfate. Urea-cupric sulfate electrolyte was prepared by adding 1g of urea (Baker reagent, mp 132°-133°C used without further purification) to 50 ml of 0.005M cupric sulfate, mixed and poured immediately into the cell.

Thermocells were also made with nonaqueous electrolytes, 0.5g of $CuCl_2 \cdot H_2O$ (Baker reagent, as received) was dissolved in 25 ml of acetonitrile (Fisher reagent, bp 81.5°-82.0°C) or 40 ml of absolute methanol (Baker reagent, 99.8% purity).

Concentration cells with multiple lines of demarcation, *i.e.*, with a linear gradient (Fig. 3b) were made by taking a Tygon tube (8 mm ID) with a sealed electrode at the bottom and pouring in as many as eight different concentrations (equal volume) of decreasing strength by pinching the plastic tubing just above the last entry and pouring in the next volume of electrolyte and releasing the pressure and carefully allowing the fluids to come into contact. The following values refer to the ratio (in milliliters and beginning from the bottom of the cell) of 1.0M cupric sulfate to water in eight stock solutions used to prepare a typical gradient: 50/0,43/7,36/14,29/21,22/28,15/35,8/42, and 1/49. The total length of the tube was 63.5 cm and each of the eight additions was approximately 3.8 ml. The interelectrode distance (tip to tip) was 58 cm. These cells exhibit remarkable stability, however, they are supported (jacketed) before being placed into the drop capsule.

The voltage of a cell depends on its construction, for example, in the nonlinear case on the respective heights of the 1.0M cupric sulfate and the water above it, and likewise, in the linear case on (dc/dx). These factors can be varied at will, provided both electrodes are covered by a homogeneous phase.

In addition to drop tests the cells were also subjected to inversion tests, *i.e.*, rotating the cell 180° (in a time of the same duration as free fall).

Diffusion.—The effect of weightlessness on ion diffusion was investigated by measuring the optical density across an aqueous interface in a column of fluid before and after free fall and by observing the output potential of a concentration cell or a Daniell cell (Fig. 4) during the 1-*g* to 0-*g* transition. Fifteen milliliters of 1.0M cupric sulfate was pipetted into a 12 mm ID Pyrex tube and 55 ml of distilled water carefully added so as to obtain a clear line of demarcation and the system sealed by means of Tygon tubing and a pinch clamp. The tubes were then dropped from a height of about 22 ft and scanned in a photometer developed in this laboratory. Stationary control tubes were subjected to simulated impact by means of a spring-driven sandbucket propelled upward toward the tubes (equal penetration depth) and were likewise scanned. The drop-tower and photometer reading room temperatures were 15° and 20°C, respectively.

In a single low temperature experiment (no controls) of another type (Liesegang phenomena) concentrated solutions of KI and $CuSO_4 \cdot 5H_2O$ (1 gram each in 10 ml of water) were very carefully placed in the positions shown (Fig. 5) and covered with dilute starch solution and the system sealed. The tube was then dropped nine times at intervals of 2 min from a height of 24 ft (drop-tower temperature 9°C) and was then set aside in a room where the temperature varied from 15° to 21°C.

At a higher temperature a total of six tubes have been evaluated including two sets of controls, viz., simulated impact and those left alone. The drop-tower temperature was 21°C while the room temperature averaged 25°C.

Solubility.—Crystals of cupric sulfate (Fisher Tech. Crystal) weighing approximately 1.30g were wrapped in cotton cloth and suspended a distance of 3.75 cm from the top of 38 cm Pyrex tubes. The cloth passed through a small piece of Tygon tubing which again was sealed by a pinch clamp. Eight pairs of crystals (a drop and a control) were selected and the individual volumes noted by immersion in acetone at 20°C. The tubes (12 mm ID) were dropped 3 times from 22 ft and photometer readings taken after each drop. The reference point was 11 cm from the lower end of the tube. The drop-tower and photometer reading room temperatures were 15° and 20°C, respectively.

Adsorption.—Triphenylchloromethane (Fisher reagent) was dissolved in carbon dioxide saturated benzene (Baker reagent) and the solution poured into a Pyrex tube into which was placed a mirror-like sheet of zinc (ribbon, Baker reagent) and the system hermetically sealed. The drop samples and controls

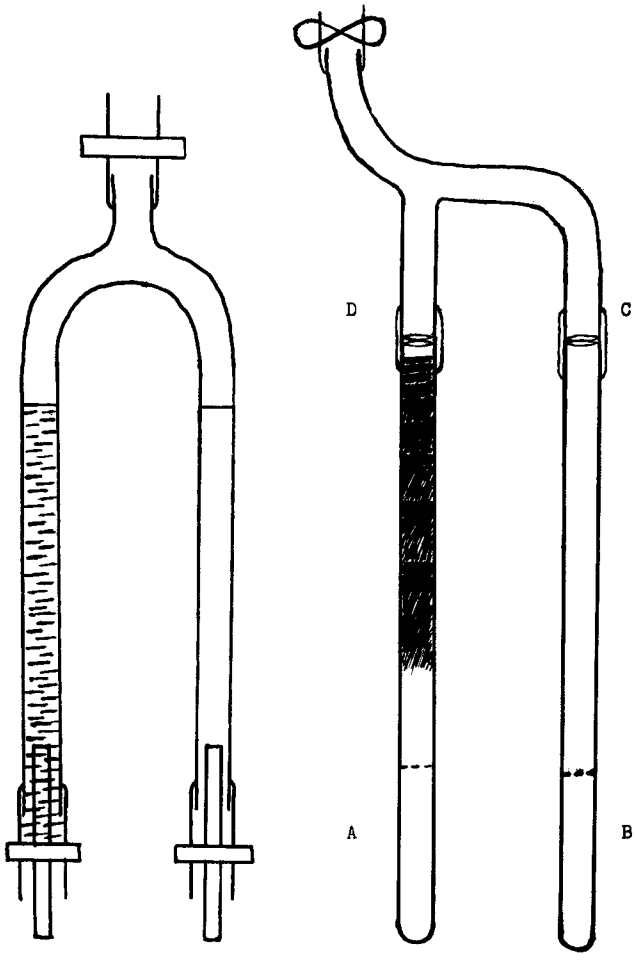

Fig. 4 (left). Daniell cell used for zero-gravity investigations. Several cells of this type were constructed and showed a very large perturbation (40 mv) of the type shown in Fig. 7 during free fall. 1.0M solutions of cupric sulfate (dotted region) and zinc sulfate are introduced to the levels shown and the remaining volume carefully filled to overflow with distilled water. The electrodes are made from thin sheets of copper and zinc and held in position by means of pinch clamps as shown. The emf of the cell is about 1.09v at 20°C. In work of this kind Tygon tubing is a very useful material for making impact proof seals.

Fig. 5 (right). Glass apparatus used to demonstrate Liesegang bands in an aqueous system. Solutions of potassium iodide and cupric sulfate are contained in tubes (A) and (B) respectively at the levels indicated by the broken lines which are 11 cm from the bottom. Arm (A) is 44.5 cm long and the parallel tubes (8 mm OD) are 4 cm apart. After 32 days (in the low temperature experiment) a purple color began to develop in the region shown (tube containing the potassium iodide) and by the 41st day 9 distinct bands or rings had formed. It required 72 days before the liquid in region (C) assumed a light blue color. Eventually, the darkest color developed in the region (D). Although at higher temperatures ring formation is much more rapid it is not as well defined. The tubes were connected by Tygon at the positions shown.

were compared with regard to the golden color of the triphenylmethyl free radical which develops on the zinc surface. A total of eight tubes were evaluated, each being dropped 5 times from a height of 22 ft. The drop-tower temperature was 15°C. The reduction of gravity in the solubility and adsorption studies was estimated at 10^{-3}-*g*.

Stress corrosion.—The corrosive reagent consisted of 4g of potassium iodide, 1g of iodine, 25 g of zinc chloride, 25 ml of HCl and 50 ml of water, mixed and stored in a glass stoppered bottle. Plexiglas samples 62 mm in length and 17 mm wide were bent in a wooden vise to an angle of about 44° and the vise placed in a small plastic box which served as the drop capsule. One drop of the reagent was then placed at the point of greatest tension (eyes must be protected) and followed by a small pinch of zinc dust (12). The box was then closed and dropped from a height of about 24 ft and subsequently the time to failure noted. A clearly visible iodine stain marks the initial position of the drop and the effects of minor variations in the amounts of zinc are negligible. Thirty samples (0-*g*) were dropped and 30 others (static) acted as controls. This work was preceded by an exploratory investigation during which over a hundred test specimens were evaluated. Every attempt was made to duplicate in the controls everything which a dropped sample experienced except the momentary reduced gravity state. This included impact, the spreading, and rolling, etc. of the corrosive droplet. The drop-tower temperature was 9°C.

Homogeneous reaction.—Fresh iodic acid solution was prepared by dissolving 5g of iodine pentoxide (K & K crystal) in one liter of triple distilled water; iodine pentoxide is a powerful oxidizer and must be kept away from flammable vapors, etc. Five milliliters of water was saturated (slow bubbling) for 10 min with anhydrous sulphur dioxide from a Matheson cylinder and then added to a liter of water. The starch solution was prepared by making a paste of 12.2g (Baker reagent) with chilled water and then adding one liter of boiling water.

Fifty milliliters of the iodic acid solution was poured into a beaker and 15 ml of starch solution added; 50 ml of the sulfurous acid solution was poured into a beaker and enough water added to make 300 ml of solution. Water was also added to the iodic acid starch mixture to give a final volume of 300 ml. Both solutions were stirred and then poured into a 2000 ml beaker and the reaction mixture stirred for 15 sec. Each of eight 2-oz bottles were then filled in two steps in a sequence that was empirically determined to insure standardization.

In order to keep the temperature as uniform as possible during the experiments, the solutions as well as the reaction mixtures were prepared near the drop tower where temperatures averaged 9°C. The 2-oz vessels were filled to overflow and attempts were made to minimize the entrapment of air bubbles which were measured and recorded after the experiment and subsequently taken into consideration.

A photometer was constructed which contained two chambers that could accommodate four bottles each and the photometric readings were an indication of the average radiant energy (light) that was transmitted through the row of four bottles simultaneously. The light source was a 150w 120v flood lamp (Sylvania) and the radiation intensity measured by two calibrated Soligor meters which were found to be satisfactory. Although the geometry of the system was rigid and the bottles locked in numbered positions, the positions of the meters as well as the bottles (rows) were switched separately during the course of the investigation and the results were found to be nearly identical.

The reaction is very concentration dependent and reaction time is defined as the interval between the initial mixing and when the bottles first begin to turn blue. In addition to the bottles that were dropped there were two sets of controls; one set was left alone after the bottles were closed and the other was subjected to simulated impact at the same time the zero-gravity bottles were dropped. All bottles were, at all times, exposed to the same amount of light. The experimental procedure was as follows: A total of four drops were made from a height of 24 ft, viz., at 3 min and 40 sec (after mixing), 4 min, 4 min and 20 sec, and 4 min and 40 sec. The four drop bottles as well as the four simulated impact bottles were always placed into the photometer at 5 min and 10 sec and the flood lamp turned on at 7 min and 30 sec. The distance between the lamp and the lightmeters was

Table I. Flowing electrolyte thermogalvanic cell stationary state potentials

Molar conc.	Temp, °C T_1	Temp, °C T_2	Flow rate, ml/sec	Potential, mv
		Gravity flow		
0.005	7	30	9	17
0.01	7	30	9	20
		Forced flow		
0.005	7	30	12	18
			21	21
			30	27
0.01	7	30	12	21
			21	27
			30	29
	10	52	21	35
	5	58	21	45

67 cm. Two sets of experiments were done (the only alternative would have been to build a photometer with three chambers in order to accommodate the twelve 2-oz bottles) viz., where the simulated impact set was compared with the initial controls as well as those which experienced free fall. The reduction of gravity was estimated at 10^{-3}-*g*.

Results

Flowing electrolyte thermogalvanic potentials are difficult to reproduce, *e.g.*, if a dozen or more cells are constructed in identical detail and evaluated and, although each produces a curve similar to that shown in Fig. 2, nevertheless, the range of their respective voltages at point F may be as high as 10 mv or more. Some data are shown in Table I, and the values represent the average of four experiments.

The apparatus can easily be converted into a flowing electrolyte concentration cell (also exhibit zero-gravity oscillations) and by proper adjustments of concentration differences, flow rate, and cell temperature a wide range of reasonably controllable voltages can be obtained and will be discussed in another report.

During the course of 107 drop tests (with flowing electrolyte thermocells), three general types of zero-gravity effects (Fig. 6) have been observed over a wide range of conditions; concentrations (0.005-0.35M) ΔT (T_1 from 2 to 13; T_2 from 25° to 65°C), flow rates (from 12 to 30 ml/sec), and output voltages (from 10 to 70 mv); viz., oscillations (6a, 6c), potential decay (6b) and combinations (6d) in both the time dependent (D — E) and stationary state (E — F) regions.

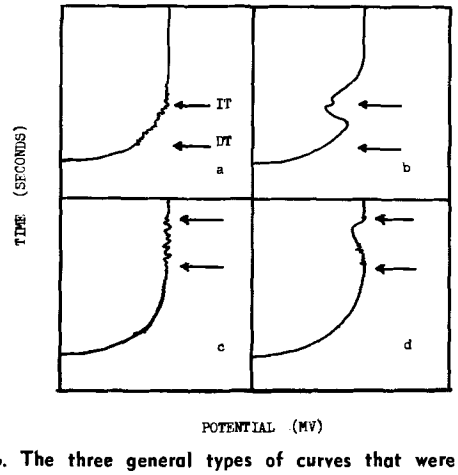

Fig. 6. The three general types of curves that were observed over a wide range of experimental conditions. The oscillatory curves exhibited as many as nine deflections during the free fall interval and whose amplitude varied as much as ± 1 mv. Potential decays of 4 mv have been seen with a semblance of recovery prior to impact. Curve 6b appears at 0.01M, when $T_1 < 10$°C, $\Delta T > 47$°C and the output voltage > 35 mv, at a flow rate of 21 ml/sec when a preliminary study was made of the time dependent region (D-E). DT and IT refer to drop time and impact time, respectively.

A large number of experiments would be required to characterize these curves and, although the evidence is limited, an output voltage of 35 mv in the time dependent region appears to be a transition range, *i.e.*, below this value we see curve 6a and above it curve 6b.

The control experiments showed that the observed effect was due to the sudden reduction in gravity and in particular those concerned with pulsated or variable flow rates, proved that the perturbations cannot be due to oscillations in the hydraulic system, in fact, on the basis of their frequency alone it is a physical impossibility with the apparatus shown. The only way to change the potential of a flowing electrolyte thermocell or concentration cell in this manner is to either suddenly and completely restrict all fluid flow or attempt to rapidly increase the air bottle pressure and even then there is a lag-time of at least 0.6 sec before a smooth transition is registered by the recorder. Streams of bubbles (some as large as the coils) passing through the electrodes or the pin-hole region had no effect on the potential either under gravity or forced flow in a normal 1-*g* environment. No perturbations were observed during the thermal and concentration shock experiments.

In the (No, dT) experiments, at very low flow rates, there are oscillations in polarity, but as soon as the flow rate increases (5-30 ml/sec) one of the electrodes becomes anodic and the other cathodic. At various times and under different conditions during the course of this investigation, 18 drop tests have been made with electrolyte concentrations of 0.005, 0.01, 0.1, and 0.3M cupric sulfate and at temperatures ranging from 17° to 34°C. In spite of the fact that comparisons are difficult in view of varying temperatures, flow rates, etc., the following conclusions can nevertheless be drawn. The potential increases with time, in other words, there is a build-up curve (Fig. 2) and output voltages range from 0.5 to 11 mv, although one occasionally observes higher potentials momentarily and the lower concentrations give higher output potentials. In all cases during free fall the cells exhibited perturbations and continued to operate after impact.

In marked contrast to the behavior of partially frozen (upper electrode) thermocells previously reported (2), when the upper electrode region is heated with air instead of being frozen, pronounced saw-toothed oscillations are observed during weightlessness with the time/potential curve resuming its initial course after impact. It has been found that the addition of urea substantially dampens the zero-gravity induced perturbations when the cell is dropped at the same output potential. The electrolytic conductivity of freshly prepared urea-cupric sulfate solutions gradually increases (at ambient temperatures) and in subsequent drops (after 3-4 sec of weightlessness, corresponding to a drop-tower operating time of about 25-35 min) the zero-gravity induced oscillations reappear. The principle characteristic of the time/potential curves of thermocells employing acetonitrile or absolute methanol, is potential decay during the 1-*g* to 0-*g* transition. However, as in all decay curves under these circumstances some type of oscillation (spiked or smooth) is always present.

During the course of about 70 experiments it has been observed (at least in 50% of the cases) that the output voltage (cells shown in Fig. 3) will increase during free fall (otherwise some type of perturbation is observed, oscillations or potential decay), *e.g.*, if the initial emf is 28 mv (in a cell with a linear gradient) it may increase as much as 2.5 mv during weightlessness in the manner shown in Fig. 7. In some cases a cell will show a similar but weaker increase when dropped a second or third time. If instead of dropping a cell it is rotated 180° (inversion test)[2] in a time of the same duration as free fall, then,

[2] In inversion tests the recorder chart is left on until zero output potential.

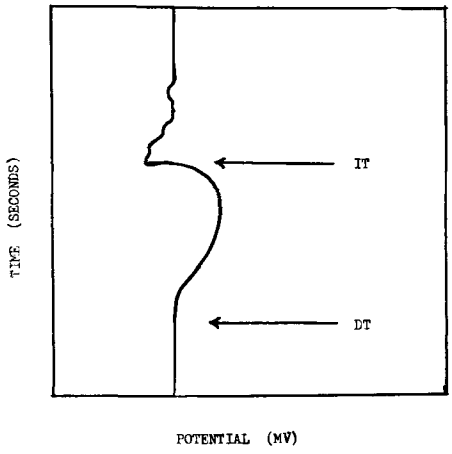

Fig. 7. A time/potential curve of the type frequently observed with the cells shown in Fig. 3. Cells with linear gradients show a larger potential increase during the free fall period. Cells that are rotated 180° (turned upside down) display similar behavior however, there is a lag-time of about a second or more after the cell is in the new orientation before a potential change is indicated; the voltage increments, however, are similar, viz., 0.5-2.5 mv. Although the evidence is limited since almost all of this work has been done with coiled wire electrodes, the indications are that electrodes made from metal sheet will behave in a like manner. Concentration cells (Fig. 3b) of identical construction but slightly different emf's have been connected in series and parallel and in both cases have acted as expected. They have exhibited a small increase in emf when dropped.

for reasons as yet unknown to the author, one may either see a brief increase in the emf before potential decay or an immediate decay, in either case the curves are smooth.

Some preliminary work has been done with nonlinear gradient concentration cells where the internal diameter of the tubes varied from 2 to 25 mm with cell length from 12 to 36 in. On a relative basis for example, if a 2 mm ID cell is rotated 180°, depending on the initial gradient, it may take 30 sec or more before there is any indication of potential change and as may be expected, this type of cell did not exhibit any perturbations during the first second of free fall. However, in subsequent drops the same cell exhibited perturbations, an indication of an additive or memory effect. The ratio of the inversion time to 0-g time, for indications of potential change, (neglecting any contributions due to impact) can be used to obtain a rough estimate of diffusion rates under weightless conditions and the calculations show it to be four to six times faster. Contributions due to impact could be readily determined experimentally. If the glass wall near the lower electrode of the cell shown in Fig. 3a is uniformly heated, a smooth non-oscillatory voltage build-up will be observed.[3] Conversely, if the upper electrode area is warmed, there will be a smooth potential decay, nevertheless, under either condition, the cell exhibits oscillations and potential decay during free fall. The curves are shown in Fig. 8 and 9. The diffusion experiments have shown that during weightlessness the line of demarcation (now faint but still visible) between the colored and colorless solution (cupric sulfate/water) has advanced about 0.70 cm while that of a control (as nearly well-defined as before) has only advanced about 0.25 cm. Some typical curves are shown in Fig. 10 and 11.

The results of the Liesegang experiments are interesting but complicated, suggesting a large number of trials before the zero-gravity samples and the controls can be characterized and compared. However, in spite of the limited evidence the following observations have been made. Two kinds of rings or bands are formed, viz., horizontal and inclined (~45°), the latter are formed first and, although all tubes have one or two such rings, the simulated impact samples have the most. Rings eventually grow into one another and disappear. The zero-gravity samples display more even spacing as well as the greater ring stability and

[3] The experiment is important in that it offers another method of studying the effects of weightlessness on build-up and decay curves. The potential increase or decrease continues on its original course after impact indicating that heat losses during the course of the experiment are unimportant.

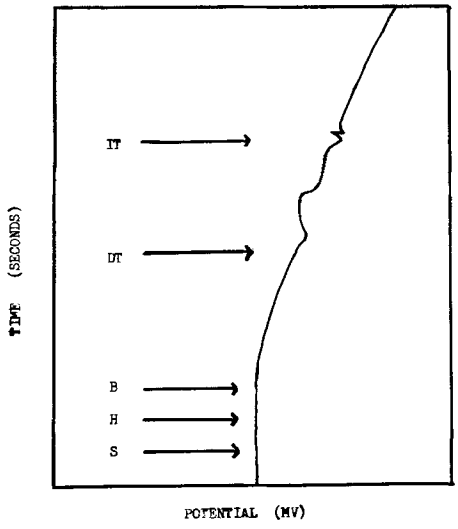

Fig. 8. A typical time/potential curve for a concentration cell of the type shown in Fig. 3a (nonlinear gradient) when the region at the lower electrode is heated with air at 78°C. S—steady state potential, H—warm air applied to glass wall near electrode, B—beginning of build-up curve. In the systems studied the average time between points H and B was 6.53 sec and the voltage increment between point B and drop time, 7 mv. The rate of change was 0.27 mv/sec. Although only four cells of identical construction have been evaluated, the zero-gravity perturbations of these systems are remarkably reproducible in general detail. The system is referred to as a delta "T" concentration cell, (ΔT, ΔC).

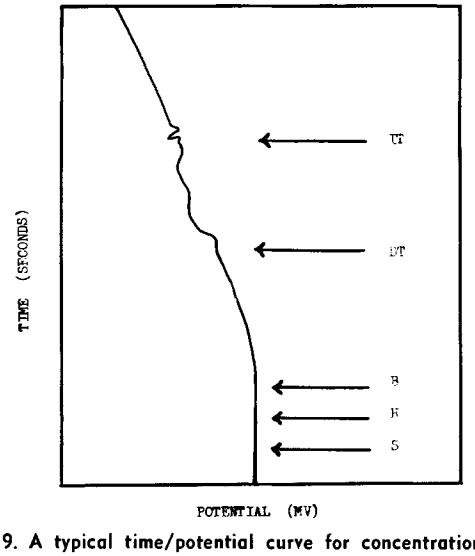

Fig. 9. A typical time/potential curve for concentration cell of the type shown in Fig. 3a (nonlinear gradient) when the region at the upper electrode is heated with air at 78°C. S—steady state potential, H—warm air applied to glass wall near electrode, B—beginning of the decay curve. The average time between points H and B was 5.56 sec and the potential decrease between point B and drop time, 7 mv. The rate of voltage decay was 0.62 mv/sec. These systems likewise exhibit nearly reproducible curves during the brief period of weightlessness and merit serious consideration. The electrodes were made from coiled copper wire (4 mm OD and previously described) and the initial cell temperature and voltage (point S) were 20° and 44 mv, respectively. The effective cell length (6 mm ID Pyrex) was 42 cm and the tubes filled to the 13 cm level with 1.0M cupric sulfate. The interelectrode distance (tip to tip) was 33 cm.

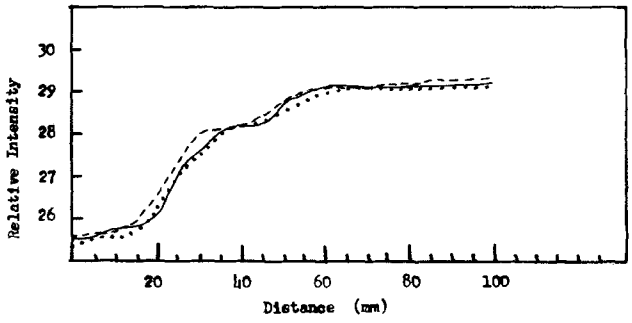

Fig. 10. Photometric curves showing the relative amount of light from a tungsten lamp passing through a 12 mm ID Pyrex tube containing 15 ml of 1.0M cupric sulfate and 55 ml of distilled water when the tube which has been subjected to simulated impact is lowered through the instrument in 5 mm increments. The solid line refers to initial conditions and the dot and dash lines to conditions following the first and second simulations (impact), respectively.

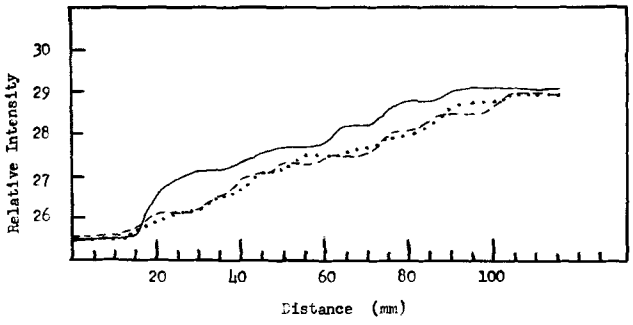

Fig. 11. Photometric curves showing the relative amount of light passing through a 12 mm ID Pyrex tube containing 15 ml of 1.0M cupric sulfate and 55 ml of distilled water when the tube which has been subjected to weightlessness (22 ft drop) is lowered through the instrument in 5 mm increments. The solid line refers to initial conditions and the dot and dash lines to conditions following the first and second weightless periods respectively. The nonsuperimposition of the solid lines of Fig. 10 and 11, of little consequence here, reflects, nevertheless, the inherent experimental difficulty and or limitations in attempting to reproduce gradients. The air drag on the drop capsule was estimated to be between 10^{-2} and 10^{-3}-g.

increased rates of diffusion, *e.g.*, the diffusion of the iodide ion and or the rate of formation of the blue color in the arm (Fig. 5) containing the cupric sulfate. The average number of rings formed in the 6 tubes was seven. These experiments are best performed at lower temperatures (15°C or less) where individual ring formation can be more easily followed. There is no immediate explanation for the greater ring stability of the samples with a weightless memory.

The indications are that, although polycrystalline material was evaluated (and thus the crystals differed in weight, volume, shape, and structure), weightlessness enhances the rate of crystal solubility. The zero-gravity samples dissolved approximately 1.5 times faster than the controls. In a similar vein drop tests indicated that the golden color of the triphenylmethyl free radical which develops on the zinc surface (adsorption experiments) is more intense than for the controls.

Concerning the free fall stress corrosion studies the statistics are as follows: average angle of the drop samples, 43.5°, static samples, 43.8°. The average thicknesses were the same, viz., 1.42 mm. The average time for failure was 67.4 sec for the zero-gravity samples and 82.9 sec for the controls. The average place of failure (see Fig. 12) for the dropped samples were 2.3 and 2.5 for the controls.

A total of 109 experiments were performed during the study of the "iodine clock reaction," although the reported averages concern only 60 of the trials. The

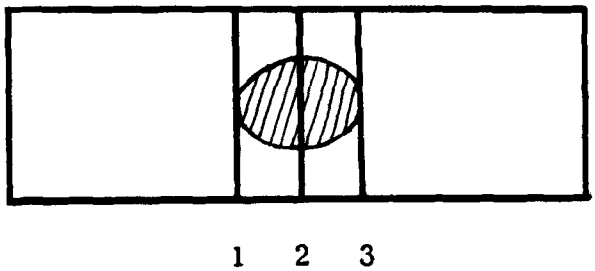

Fig. 12. Plexiglas sample used in the zero-gravity stress corrosion study showing the regions relative to the liquid where the specimen could fail. A drop of the corrosive liquid was placed at the point of greatest tension as shown. The zero-gravity samples and the controls failed at the positions 2.3 and 2.5, respectively, indicating more extensive wetting near the plane of greatest tensile strain in the samples subjected to weightlessness.

reaction time for the zero-gravity bottles was found to be 13.8 min compared to 14.6 min for the simulated impact bottles. Likewise, the latter differed by about 3.5 sec (earlier) from the initial controls.

It was of considerable interest to notice that, although in all cases the zero-gravity bottles had a shorter reaction time than either set of controls, nevertheless, with respect to the time required to reach maximum color intensity once the bottles began to change color, the initial controls reached maximum intensity in less time than the bottles experiencing weightlessness.

Discussion

The main observation on the time/potential curves of flowing electrolyte thermocells due to the sudden reduction of gravity has been the appearance of oscillations. Except for an earlier paper (2) the literature concerning the behavior of electrochemical systems during the 1-g to 0-g transition is essentially nonexistent and since this is the first paper in a long range study a detailed analysis would be premature, however, in view of the concurrent studies, there is some basis for speculation and it may be helpful in some cases to indicate a possible explanation. In essence the concurrent studies suggest that ion mobility is enhanced under these conditions.

In the thermocell shown (Fig. 1) there are three regions that may possibly be influenced by the transition, viz., the electrode surface, the bulk electrolyte, and the liquid-liquid interface within the pinhole region. With respect to the latter, regardless of the initial vorticity, and in view of the existence of quasi-stationary or slow moving layers of fluid, there is the remote possibility of perturbing mass transport through this region during the sudden transition. However, in the control experiments bubbles of air were forced through the pinhole region and which obviously changed the vorticity, likewise, concentrated solutions of copper sulfate as well as water were forced through this region, again with no observable effect on the output potential of the cell. If the reservoirs (R_1 and R_2) and the pinhole are removed and the streams of electrolyte allowed to impinge or mix above or upon a flat glass surface 5 or 6 in. below, there are no effects; the same holds true if the Tygon tubes are separately or simultaneously rotated or swung back and forth like a pendulum. These experiments appear to rule out any contributions from this source.

Although the question of dissolved gases in the electrolyte being adsorbed or the expansion or contraction of gas films on the electrode surface during weightlessness cannot be answered at this time, it is doubtful the oscillations could be explained on this basis.

The behavior of various electrochemical systems during the 1-g to 0-g transition is summarized in Table II and in those cases where the data is preliminary and work is currently in progress it is so indicated. Turning our attention to the electrode surface, one

Table II. Behavior of various electrochemical systems during the 1-*g* to 0-*g* transition

Cell type					Electrodes Upper	Lower	Principle change in potential
Thermogalvanic	Static				Frozen	Ambient	Decay†
					Hot	Ambient	Oscillations
		Urea*			Hot	Ambient	Dampened oscillations
		Nonaqueous solvents*			Hot	Ambient	Decay
	Flowing			No ΔT			Oscillations
				ΔT			Oscillations/decay††
Concentration	Static	Linear gradient			Dilute	Conc.	Increase
		Nonlinear gradient			Dilute	Conc.	Increase
					Ambient	Hot	Oscillations
					Hot	Ambient	Oscillations
			Capillary		Dilute	Conc.	None**
			Membrane*		Conc.	Dilute	Oscillations
	Flowing*			Ambient			Oscillations

† Ref. (2).
* Will be discussed more fully in another report.
†† EMF in time-dependent region > 35 mv.
** During the first second of free fall.

may expect a gravitational field effect even in a dynamic system (fluid flow) for the following reasons. When a body is being acted upon by the earth's gravitational field, there is no weakening of the field in the region of this body at any time, in other words, the process is void of energy transfer and is the only known interaction of this kind, therefore, whether we have a rotating disk in a fluid or a fluid flowing over a plate, there are in either event quasi-stationary fluid layers near the solid surface and if these encompass the reaction zone, then a true gravitational field effect would be independent of fluid motion.

In a discussion of periodic processes, Frank-Kamenetskii (13) points out that besides purely kinetic oscillations, there is the possibility of a periodic course of a chemical reaction due at the same time to both the kinetics of the reaction and to the evolution and removal of the heat and refers to this kind of oscillation as thermokinetic.

Returning to the flowing thermocells and neglecting any effects associated with enhanced wetting, the hydration and dehydration of ions at electrode surfaces involves the evolution and adsorption of heat, and one might envision the oscillations as being due to a Lotka-Volterra (14, 15) type mechanism (ecological oscillation)[4]; in other words, we assume that the sudden zero gravity induced increase in the mobility of ions gives rise to a situation where the interaction of the three principle rates, viz., arrival, departure, and change within the reaction zone, is such that the time/potential curve becomes periodic[5]. However, to draw upon such an analogy, *e.g.*, the Ross malaria equation (14) touches upon a fundamental question, viz., that such systems operate without benefit of the principle of microscopic reversibility.

With regard to the bulk electrolyte, it is not possible at this time in the absence of significant experiments to speculate on internal changes within a flowing electrolyte during the 1-*g* to 0-*g* transition, however, this is not the case for cells with stationary fluids.

Although the theory of the liquid state (structure of pure liquids and solutions) is incomplete, it is generally assumed (with the exception of the hydrogen and hydroxyl ions) that ions pass through a liquid (the solvent is not a continuous medium) by jumping from one hole to another.

The dampening of the oscillations by urea additions is important and deserves serious attention, *e.g.*, Hammes and Schimmel (17) have reported decreased ultrasonic attenuation and increased sound velocity as a result of urea additions to water, and is thought to be due to an increase in the population of unbonded water molecules which pack more tightly than molecules which are hydrogen bonded in the water clusters. In the present work the reappearance of the zero gravity induced oscillations is due to the chemical degradation of the urea (conversion to ammonium cyanate) and efforts are presently being made to determine if the reappearance of the oscillations coincides (time-wise) with any significant change in the slope of the conductivity curve.

Although a limited number of thermocells have been made with nonaqueous solvents, the observed potential decay curves somewhat resemble in form and magnitude the curve shown in Fig. 7, (but going in the opposite direction) *i.e.*, with a semblance of recovery prior to impact. It is not known whether the cooperative relaxation of the nonaqueous solvent (during the transition) can momentarily trap or retard any of the migrating ions[6].

The question of a change in the structure of a solvent during the transition is presently being considered by two types of studies, viz., a straightforward electrical conductivity measurement and the transmission or scattering of polarized light. Theoretically, in a weightless environment temperature is the driving force for molecular distribution since molecular matter has an equal probability of distributing in one direction as in another; thermal and concentration gradients in static systems are expected to be perturbed during free fall.

Finally, with regard to the observed increase in ion mobility in the various concurrent studies the possibility arises that the cooperative relaxation of the solvent (aqueous solutions) during the transition could momentarily reduce the frictional force on the ions. On this basis one would expect the conductance at high dilution to increase during the transition since the asymmetry and electrophoretic retarding effects under these conditions are at a minimum and the remaining retardive influence, viz., the frictional force of the solvent, may be further reduced by the 1-*g* to 0-*g* transition. Efforts in this direction are currently in progress.

Conclusion

The following conclusions are based on the observed behavior of flowing and stationary electrolyte electrochemical cells and a number of physicochemical systems during and after the 1-*g* to 0-*g* transition.

1. An interaction exists between chemically reacting systems and gravitational fields.

2. Ion mobility increases suggesting structural changes within the solvent. Further work is indicated, *e.g.*, electrical conductivity measurements on pure solvents and very dilute electrolytes, systems with nonaqueous solvents and in aqueous systems the utiliza-

[4] The relationship between chemical mechanisms and kinetic oscillations has recently been reviewed by Higgins (16).

[5] The observation that an output potential of 35 mv may be a transition point in going from oscillations to potential decay in the time-dependent region is important, however, more experimentation is necessary.

[6] Theoretically a local interaction of this kind could give rise to a space charge.

tion of structure-forming and structure-breaking additives.

3. Oscillatory time/potential curves may be due to the mechanics of energy dissipation processes at the electrodes initiated by increased ion mobility. Other possibilities that may explain zero-gravity induced perturbations concern the disruption of thermal and concentration gradients and interrupted ion transport through the bulk electrolyte.

4. These experiments suggest that the behavior of electrochemical systems during the transition is a manifestation of relaxational forces and indicate that the Zero Gravity Drop Tower can be utilized for fundamental investigations in electrochemistry.

Acknowledgment

The author wishes to thank his colleagues in the Engineering Laboratories and the Chemistry Section for their encouragement and generous cooperation, in particular G. Kappelt, W. C. Schulte, M. Taylor, and H. Ph. Heubusch.

He also thanks B. N. Ensanian and A. O. Ensanian for their assistance in the construction of the drop-capsules and numerous cells and E. Rogers for several useful suggestions.

Thanks also are due to J. W. Useller, W. J. Masica, and E. L. Corpas of the NASA-Lewis Zero Gravity Research Facility for a penetrating discussion of zero-gravity phenomena and assistance in calculating gravitational accelerations, the staff of the Bell Technical Library for their generous assistance as well as the Leeds & Northrup Company, The Falls Welding and Supply Company, and the Great Lakes Plastics Company for supplying instrumentation and materials.

Manuscript received March 22, 1967; revised manuscript received July 5, 1967.

Any discussion of this paper will appear in a Discussion Section to be published in the June 1968 JOURNAL.

REFERENCES

1. M. Ensanian, Proceedings of the Fourth Space Congress, Canaveral Council of Technical Societies, Cocoa Beach, Florida, p. 1-20, Scholarly Publications, Sun Valley (1967).
2. M. Ensanian, *This Journal*, **113**, 5 (1966).
3. N. M. Sisakyan, O. G. Gazenko, and V. V. Antipov, "Satellite Biological Experiments - Major Results and Problems," in Life Sciences and Space Research III, Fifth International Space Science Symposium, Florence 12-16, May (1964), North Holland, Amsterdam, p. 185 (1965); N. M. Sisakyan, Editor, Problemy Kosmicheskoy Biologii, tom IV, Moskva, Izd-vo "Nauka," p. 715 (1965).
4. P. L. Altman and D. S. Dittmer, "Environmental Biology," Federation of American Societies for Experimental Biology, Bethesda, Maryland, p. 264 (1966).
5. L. Onsager, *Phys. Rev.*, **37**, 405 (1931): **38**, 2265 (1931).
6. R. C. L. Bosworth, "Transport Processes in Applied Chemistry," pp. 88-114, John Wiley & Sons, Inc., New York (1956).
7. M. Ensanian, Aerospace Medicine, To be published.
8. M. Ensanian and R. T. Foley, Unpublished research, Melpar, Inc., 1962.
9. W. J. Masica and D. A. Petrash, NASA TN D-3005, Sept. (1965); H. Cohan and M. Rogers, Editors, "Fluid Mechanics and Heat Transfer under Low Gravity," DDC- AD 633580 (1966).
10. E. T. Benedikt and R. Lepper, "Weightlessness-Physical and Biological Effects," E. T. Benedikt, Editor, p. 56, Plenum Press, New York (1961).
11. G. F. Cooper, *J. Spacecraft*, **3**, 6 (1966).
12. M. Ensanian, *Nature*, **193**, 4811 (1962).
13. D. A. Frank-Kamenetskii, "Diffusion and Heat Exchange in Chemical Kinetics," Transl. by N. Thon, p. 350, Princeton Univ. Press (1955).
14. A. Lotka, "Elements of Mathematical Biology," Dover (1956).
15. V. Volterra, "Leçons sur la Théorie Mathematique de la Lutte pour la Vie," Gauthier-Villars, Paris (1931).
16. J. Higgins, *Ind. & Eng. Chem.*, **59**, 5 (1967).
17. G. G. Hammes and P. R. Schimmel, *J. Am. Chem. Soc.*, **89**, 2 (1967).

Catalytic Decomposition and Anodic Current-Potential Characteristics of Methanol on Active Palladium in Alkaline Solution

Tsutomu Takamura and Fusako Mochimaru

Central Research Laboratory, Tokyo Shibaura Electric Company, Ltd., Komukai, Kawasaki-shi, Japan

ABSTRACT

Methanol was found to decompose into hydrogen and CO_3^{2-} on active palladium immersed in alkaline solution containing methanol. The hydrogen evolution rate was examined by using a hydrogen permeating foil electrode. From the concentration dependency of the evolution rate, the catalytic decomposition was found to proceed through the reaction, $CH_3OH + 2\,OH^- \rightarrow CO_3^{2-} + 6H_{ad}$ (liquid-solid interface) and $2H_{ad} \rightarrow H_2$ (gas-solid interface). The current-potential characteristics during anodic polarization recorded in the low current-density region showed two steps, which could be elucidated by taking the above mechanism into consideration. Decomposition mechanism also dealt with standard potential.

Recent studies of the electrocatalytic oxidation of methanol at platinum electrode have been concentrated in acidic media (1-4). Podlevchenko and Gorgonova pointed out that methanol in acidic media adsorbs on Pt/Pt surface and decomposes into adsorbed hydrogen and a fragment such as COH, which are then oxidized into H_2O or CO_2 during anodization (1).

On the other hand, a few papers have treated the surface fragment formed during the electrooxidation of methanol in alkaline media (5, 6). During the course of the present study, Pringent and Bloch reported on the hydrogen evolution of Raney nickel powder immersed in methanolic alkaline solution at about 120°C (7). In connection with the results of

anodic oxidation, they showed that the hydrogen evolution proceeds through Eq. [1]

$$CH_3OH + 2\,OH^- \rightarrow CO_3^{2-} + 3H_2 \qquad [1]$$

but their conclusion does not seem to be on the quantitative analysis of reaction mechanism.

The anodic oxidation of methanol on palladium in alkaline solution was investigated by one of the present authors who suggested that the reaction involves a formation of intermediates such as $(H)_{ad}$ and $(CO_2^-)_{ad}$ (6). Since palladium, like Raney nickel, has considerable affinity for hydrogen, it is plausible that the palladium takes hydrogen away from the methanol molecule which is going to be oxidized. Experimental indication of this reaction has been observed for the metal at higher temperature. The initial open-circuit voltage at active palladium in methanolic solution was about —0.75v *vs.* HgO electrode, while it shifted gradually to a more negative value and finally reached a saturation value of about —0.85v which is close to the hydrogen potential at the electrode. The reversible potential calculated for the over-all oxidation, Eq. [2], is —0.99v *vs.* HgO electrode, which is higher than the observed value.

$$CH_3OH + 8\,OH \rightarrow CO_3^{2-} + 6H_2O + 6e \qquad [2]$$

The actual initial voltage is considered to be controlled by some rate-determining reactions, and the final higher negative voltage would depend on the amount of the adsorbed hydrogen formed by a catalytic decomposition of methanol at palladium. In the present investigation, the rate of hydrogen formation was determined quantitatively by the method in which the hydrogen was taken into a vacuum cell through a thin palladium plate electrode, one side of which was contacted with the solution. The evolution rate was observed to depend on both methanol and alkali concentrations, respectively, the reaction being confirmed to proceed through reaction [1].

Experimental

All the reagents used and the method of measurements of the current-voltage curve were the same as described in a previous paper (6), but care was taken to measure the very low current density region.

Measurement of the rate of hydrogen evolution.— Hydrogen formed by the decomposition of methanol at the solution side of palladium plate was taken through the plate into a vacuum compartment, and the evolution rate was measured as a pressure increase. An outline of the measuring cell is sketched in Fig. 1. A thin palladium plate (0.1 mm thick, 3 cm diameter) was soldered to cover one end of a Kovar ring, and the other end was air-tightly joined to a glass tube. An ionization gauge was attached to the tube which was connected to a vacuum line through a stopcock. The palladium plate was palladized electrolytically on both sides. Lead wires were soldered at an appropriate position of the Kovar ring the outer bare part of which was coated with polyethylene. The cell was immersed in the electrolyte solution, and the pressure inside the cell was read with an ionization gauge. Electrolytic voltage was read by referring to HgO electrode through a Luggin capillary. The counter electrode for applying the anodizing voltage to the Pd electrode was faced through a cylindrical separator. Total volume inside the cell (to the stopcock) was about 400 ml. Galvanostatic potential transient was traced on a Toshiba oscilloscope, the constant current being supplied from a high potential source.

Results and Discussion

Current-voltage characteristic at 60°C is shown in Fig. 2, where each point was read 10 min after the setting at the desired current. At room temperature a stable voltage more negative than —0.75v was hard to obtain whereas at 60°C, high negative value of —0.85v could be obtained easily.

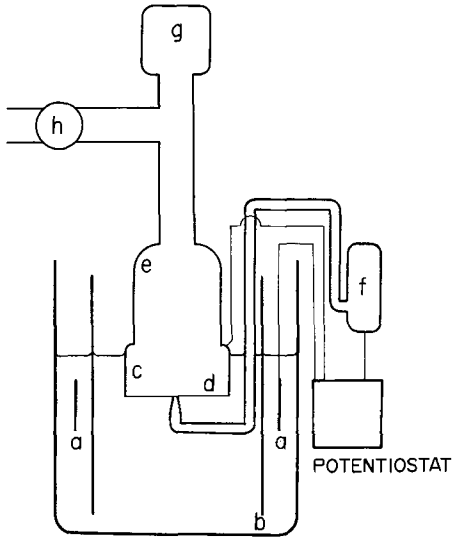

Fig. 1. Cell for measuring the rate of catalytic formation of hydrogen at Pd electrode: a, Pt counter electrode; b, glass cylindrical separator; c, Kovar tube; d, Pd foil electrode; e, glass tube; f. HgO reference electrode; g, ionization gauge; h, vacuum stopcock.

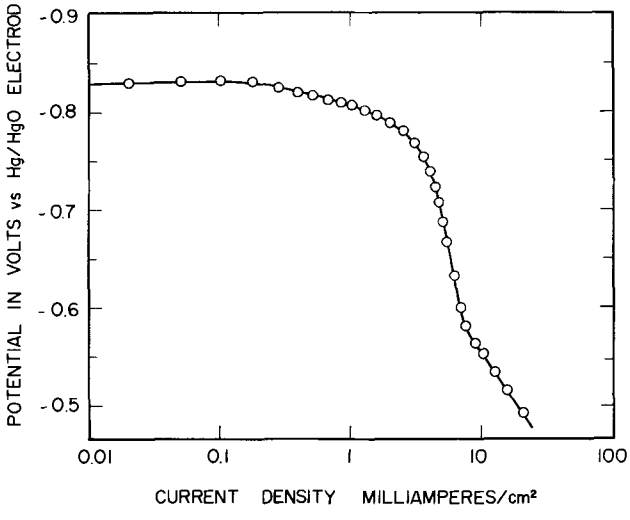

Fig. 2. Anodic current-voltage characteristic for Pd immersed in the alkaline solution in the presence of CH_3OH. [KOH] = 1.6M, [CH_3OH] = 3M, 60°C.

At high temperature the initial open-circuit voltage of a newly immersed test electrode was about —0.75v, and the voltage shifted gradually to a more negative value, reaching a final limiting value of —0.86v within 10 min. In the very low current density region of the polarization curve, the voltage was found to be independent of the current density giving a flat characteristic. In the region of more increased current density, slow increase in current gave a gentle downward slope where the voltage was unstable and shifted very slowly to a positive side during the measurement. After this slope, the curve falls rapidly to about —0.6v where direct electrooxidation of methanol begins to take place and the current-voltage relation fell on the Tafel line.

Since the high negative voltage at very low current density region nearly coincides with the reversible hydrogen potential at the electrodes, methanol is supposed to decompose adsorbed hydrogen. The current-voltage characteristics can be elucidated with this assumption. At constant temperature and at fixed concentrations of all species the rate of the hydrogen formation reaction will reach a stationary state because the formed hydrogen will be absorbed into a large reservoir of palladium lattice without remain-

ing at the surface site. When the rate of oxidation of hydrogen due to anodic polarization is slow compared with the catalytic formation rate of hydrogen, the observed potential will be constant irrespective of anodic current density because the exchange current density for the hydrogen oxidation is sufficiently high at the electrode.

On the other hand, when the increased anodic current overcomes the rate of the hydrogen formation, the electrode potential will shift to the positive side. The observed slow downward region will correspond to this situation. The rate of anodic oxidation of methanol in this region, however, is still not as rapid as that of hydrogen oxidation. The limiting current in the downward region is explained by the restricted supplying rate of hydrogen. Under the sufficient overvoltage thus reached, the rate of direct anodic oxidation of methanol becomes fast enough to fall on the Tafel line.

The evidence of hydrogen formation was found as a pressure increase in the cell shown in Fig. 1. In the absence of methanol, the alkaline solution gave no pressure increase in the room separated from a pumping line by a closed stopcock. This indicates no observable gas leakage through any connection or palladium foil. Some 10 min after methanol was added to the solution, the pressure began to increase, the increasing rate being slow at first but more rapid with the lapse of time. But this increased pressure was found to decrease under anodic polarization at about —0.4v, where the formed hydrogen was consumed at the electrode before being absorbed. Contrary to this, even in the absence of methanol, the pressure increase was found when the electrode was polarized cathodically.

The dependency of the rate of this catalytic hydrogen formation reaction on the concentration of reacting species was examined by varying the concentrations of methanol and hydroxyl anion. As shown in Fig. 3, the rate was proportional to the concentration of methanol at fixed hydroxyl concentration. On the other hand, increased concentration of hydroxyl at fixed methanol concentration resulted in the rate increase depending on the square of hydroxyl concentration, which is given in Fig. 4.

Galvanostatic traces were obtained for two cases: the one was traced in the base solution with the palladium containing absorbed hydrogen; the other was traced with the test electrode immersed for sufficient time in methanolic alkaline solution. Two traces are depicted in Fig. 5 (curves a and b), which shows the two traces are identical in feature and give a wave at

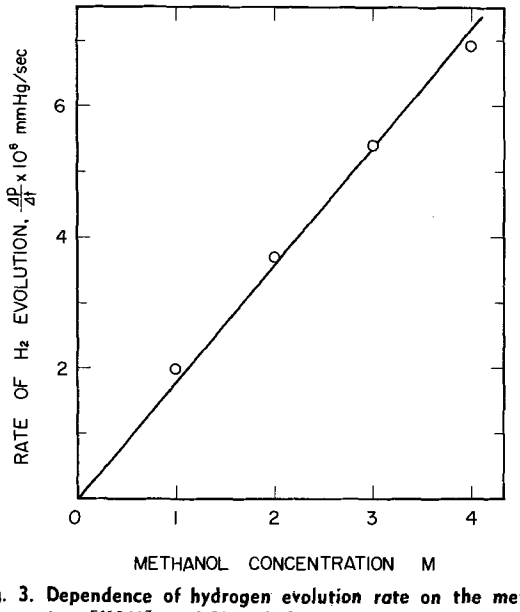

Fig. 3. Dependence of hydrogen evolution rate on the methanol concentration. [KOH] = 1.0M, 60°C.

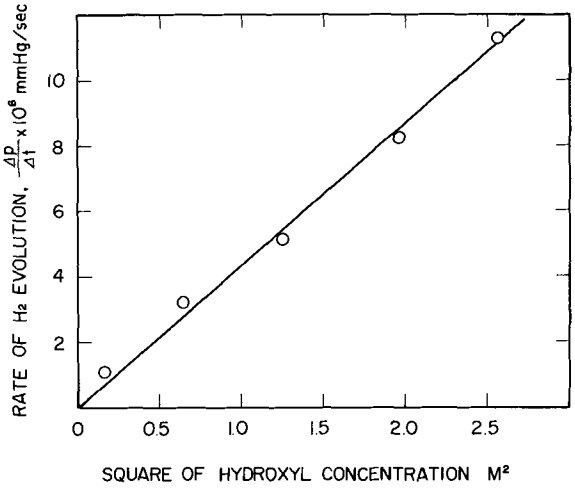

Fig. 4. Dependence of hydrogen evolution rate on the hydroxyl concentration. [CH_3OH] = 3.0M, 60°C.

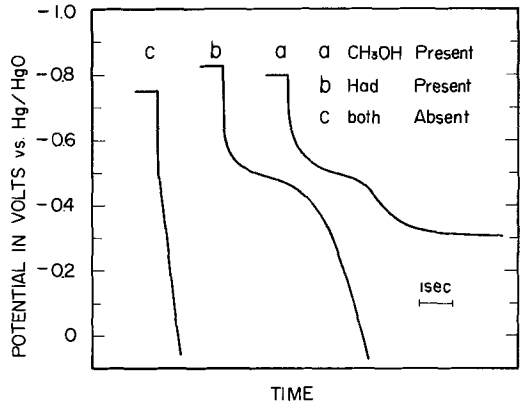

Fig. 5. Galvanostatic transients obtained during anodic polarization for Pd in alkaline solution. [KOH] = 2.0M.

—0.48v due to the oxidation of absorbed (or adsorbed) hydrogen. A trace immediately after the first trace, however, gave no indication of hydrogen wave, (Fig. 5, curve c). The amount of surface hydrogen estimated from the transition time for the two cases was far less than the value expected for full coverage. This indicates that the amount of hydrogen staying at the surface is very small, and a major part of hydrogen formed at the surface is immediately absorbed in the palladium lattice. Consequently the rate of the hydrogen formation reaction of methanol is difficult to estimate from the galvanostatic trace. The increasing rate of hydrogen pressure in the gas phase of the cell was far slower than the diffusing rate of methanol to the electrode in solution (see later). Accordingly, the adsorption of methanol (methoxyl) or hydroxyl ion at the electrode surface would be in an adsorption equilibrium. If the equilibrium amount of adsorption were near the saturation and accordingly, the amount is independent of concentration, the rate of hydrogen evolution is expected to be independent of the concentrations. The experimental rate, however, was proportional to the methanol concentration and to the square of hydroxyl concentration, respectively, indicating the actual amounts of adsorption to be far from the saturated amounts. These features may be written as follows.

$$[CH_3OH_{ad}] = K_1\,[CH_3OH] \qquad [3]$$

$$[OH^-{}_{ad}] = K_2[OH^-] \qquad [4]$$

$$\frac{dp_{H2}}{dt} = k[CH_3OH_{ad}][OH_{ad}{}^-]^2 \qquad [5]$$

$$= k\,K_1K_2[CH_3OH][OH^-]^2 \qquad [6]$$

where [ad] denotes surface amount of adsorption, K_1 and K_2 the equilibrium constants of adsorption, dp_{H_2}/dt the rate of hydrogen pressure increase, and k the appropriate rate constant. When active palladium was immersed in the test solution which contained barium hydroxide, a white precipitate of barium carbonate was found to be formed on the palladium as the hydrogen gas evolution proceeded. On the other hand, if we use formate or formaldehyde instead of methanol, the more rapid hydrogen evolution accompanied by the formation of carbonate can be observed at the elevated temperature. These findings indicate that the decomposition product of methanol is not the species like formaldehyde or formate but carbonate. Although the quantitative coulometry for the formation of carbonate was failed because of its very small amount, we infer that the decomposition of methanol proceeds through the reaction [1] which contains two steps

$$CH_3OH + 2\,OH^- \rightarrow CO_3^{2-} + 6H_{ad} \text{ (liquid solid interface)} \quad [7]$$

and

$$2H_{ad} \rightarrow H_2 \text{ (gas solid interface)} \quad [8]$$

Open-circuit voltage at room temperature was about —0.75v, and it was not possible to shift the voltage to the higher negative value of hydrogen equilibrium potential which could easily be realized at higher temperature. The rate of hydrogen evolution reaction [5] was evaluated in two different ways; from the observed dp_{H_2}/dt and from a limiting current in the flat region of high negative voltage in the current-voltage curve. The estimated rates at 60°C by the two ways coincided, and it was about 10^{-9} mol/sec cm^2, showing that the rate at room temperature would be too slow to give a hydrogen equilibrium potential in the presence of some species having inhibit action.

Several electrode reactions which give a equilibrium potential of —0.75v were examined by considering the conception given by Spiro and Ravno (8). Formation reaction of formaldehyde and water such as

$$CH_3OH + 2OH^- \rightarrow HCHO + 2H_2O + 2e \quad [9]$$

gives a higher negative value than —0.75v *vs.* HgO electrode. Similar results are given for the formations of formate or carbonate.

On the other hand, formation reaction of adsorbed hydrogen may be classified into three possible categories. The first is related to the formation of $(CO_2^-)_{ad}$ such as

$$CH_3OH + l\,OH^- \rightarrow (CO_2^-)_{ad} + (6-l)H_{ad} + (l-1)H_2O + (l-1)e \quad [10]$$

where $l = 2$ to 5.

The second is related to the formation of $(CO)_{ad}$ like

$$CH_3OH + mOH^- \rightarrow (CO)_{ad} + (4-m)H_{ad} + mH_2O + me \quad [11]$$

where $m = 1$ to 3.

The third is related to the formation of $(CO^-)_{ad}$ like

$$CH_3OH + nOH \rightarrow (CO^-)_{ad} + (4-n)H_{ad} + nH_2O + (n-1)e \quad [12]$$

where $n = 2$ and 3. In these three mechanisms, $(CO_2^-)_{ad}$, $(CO)_{ad}$, and $(CO^-)_{ad}$ are supposed to be chemisorbed species like

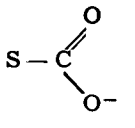

, S = C = O and S = C — O$^-$,

respectively, where S denotes surface site.

In order to calculate standard potentials for these reactions, we should know the values of free energy of formation of all the species appearing in the reaction. Since we have no data for $(CO_2^-)_{ad}$, $(CO)_{ad}$, and $(CO^-)_{ad}$, tabulated values of similar stable species were used as substitutes: As a rough approximation, we assumed that the binding energy of C-Pd bond in the adsorbed form does not differ seriously from that of C—H bond. Then for $(CO_2^-)_{ad}$, the value of HCO_2^-, for $(CO)_{ad}$, that of formaldehyde, and for $(CO^-)_{ad}$, that of CH_3O^- in aqueous solution were used, respectively. The free energy of formation of CH_3O^- was evaluated from that of CH_3OH in aqueous solution and pk_a of it (9). The free energy of H_{ad} was estimated experimentally. If the test electrode is cathodically polarized in alkaline solution in the absence of alcohol and is brought to $\alpha\beta$ coexistence phase, the open-circuit voltage will give the value in question, since the voltage is due to the reaction [13].

$$H_{ad} + OH^- \rightarrow H_2O + e \quad [13]$$

The actual value was —0.87v *vs.* HgO electrode, from which standard free energy of formation of H_{ad} was calculated to be —1.3 kcal/mole. The standard free energy of formation of stable species used for calculation were of the values cited in Latimer's text book (10). All the equilibrium potential calculated for various cases are very high negative values except for reaction [11] with $m = 1$ and 2 whose $E°$ are —0.63 and —0.75v *vs.* HgO electrode, respectively. If the surface concentrations of $(CO)_{ad}$ and H_{ad} can be assumed to be far lower than those of reactant species, the mechanism of $m = 1$ is more probable. This mechanism agrees with the mechanism proposed by the present author (6) in which three H_{ad} are formed from one mole of methanol, but differs in the contribution number of hydroxyl ion. In the previous paper, the author mistook the rate-determining mechanism to be reaction [14].

$$CH_3O\cdot + 2\,OH \rightarrow (CO_2^-)_{ad} + 3H_{ad} + H_2O + e \quad [14]$$

with the assumption that equilibrium exists between methanol and methoxyl anion from which $CH_3O\cdot$ is formed. In this equilibrium one hydroxyl takes part, and accordingly, concentration of $CH_3O\cdot$ will be represented by the product of original methanol and hydroxyl concentrations, respectively. Therefore the electrochemical reaction order for OH^- in reaction [14] is not 2/3 but 1 as represented by reaction [10] with $m = 3$. But this mechanism is rejected in the present consideration on the basis of equilibrium potential. The reaction order of OH^- for the accepted present mechanism [11] is 1/3, which differs from the preceding observed value of 2/3. Precise reinvestigation should be carried out to explain this point.

Manuscript received Dec. 6, 1966; revised manuscript received Sept. 1, 1967.

Any discussion of this paper will appear in a discussion Section to be published in the June 1968 JOURNAL.

REFERENCES

1. B. I. Podlevchenko and E. P. Gorgonova, *Doklady Phys. Chem.*, **1964**, 548.
2. S. Gilman, *J. Phys. Chem.*, **68**, 70 (1964).
3. J. A. Chropshire, *This Journal*, **112**, 465 (1965).
4. M. W. Breiter, *ibid.*, **110**, 449 (1963).
5. L. A. Mirkind and M. Ya Foioshin, *Doklady Phys. Chem.*, **154**, 177 (1964).
6. T. Takamura and K. Minamiyama, *This Journal*, **112**, 333, (1965).
7. M. Prigent and O. Bloch, *Compt. rend.*, **260**, 909 (1965).
8. M. Spiro and A. B. Ravno, *J. Chem. Soc.*, **1965**, 38.
9. E. J. King, "Acid Base Equilibria," p. 293, Pergamon Press Ltd., Oxford (1965).
10. W. N. Latimer, "The Oxidation States of the Elements and their Potentials in Aqueous Solutions," pp. 39, 128, 176, Prentice-Hall, Inc., Englewood Cliffs, N. J. (1956).

Technical Notes

Electrolytic Reduction of Acrylonitrile to Allylamine

Tsutomu Nonaka and Kiichiro Sugino

Department of Applied Electrochemistry, Tokyo Institute of Technology, Tokyo, Japan

The electrolytic reduction of acrylonitrile in sulfuric acid[1] was found to occur smoothly at a lead cathode, for example, when the cathode potential reached — 1.3 ~ 1.5v (*vs.* SCE). In this case, the reduction product consisted mainly of allylamine. A small amount of propylamine was produced as by-product, but formation of secondary amines was present only in trace amounts if at all. The current efficiency for allylamine was above 50%. Cadmium and zinc were found to be effective but at lower efficiency. On the other hand, mercury was seen to be inefficient for this reduction as was palladium. The latter fact indicated that the nature of the reduction is not a catalytic one.

It is interesting to note that the selective reduction of the nitrile group in acrylonitrile could be performed in acidic medium. The detailed results of the electrode process will be reported later.

Experimental

An H-type cell, similar to that described earlier (2), was used with a sintered glass diaphragm. Cathode was lead (treated with dilute nitric acid); area, 12.0 cm^2; anode, platinum disk. The electrolysis was carried out by controlling the cathode potential at —1.45v (*vs.* SCE). The electrolysis conditions were: catholyte, 10g acrylonitrile, 25 cc methanol, 50 cc 10% sulfuric acid; anolyte, 10% sulfuric acid; amperage, 1.30 ~ 0.27 amp; cathodic current density, 12 ~ 2 amp/dm^2 (average, 3.9 amp/dm^2); temperature, about 20°C; amount of current, 3.99 amp hr (about 20% of the theoretical amount for allylamine).

After the reduction, the catholyte was neutralized with a 50% solution of sodium hydroxide in water. The resulting solution was extracted with ether. The ether extract was analyzed by gas chromatography for propionitrile and unreacted acrylonitrile. The aqueous solution was evaporated to dryness at reduced pressure, and the residue was thoroughly extracted with ethanol. The ethanol extract was evaporated to dryness at reduced pressure leaving pale yellow hygroscopic crystals. These were found to consist mainly of allylamine sulfate as described below: mp 230°-235°C (after purification); analysis, calculated for $C_3H_7N \cdot \frac{1}{2}H_2SO_4$; N, 13.2; SO_4, 45.3; found: N, 12.4; SO_4, 45.3. By paper chromatography of the crystals[2] only two spots corresponding to allylamine and propylamine were obtained. No spot was found for secondary amines. Using this information, the amount of allylamine in the crystals was determined by titration with a mixed solution of potassium bromide and potassium bromate in the presence of sulfuric acid. Secondary amines could hardly be obtained even from a large amount of samples obtained by a separate run. Also, it should be noted that polymerization of acrylonitrile itself could hardly occur during the electrolysis.

The amounts of products identified were as follows: allylamine, 1.16g; propylamine, 0.18g; ammonia,[3] 0.12g; propionitrile, 0.07g; hydrogen, 58 cc. Current efficiency was 55% for allylamine and 13% for propylamine. The formation of propionaldehyde was also confirmed.

Identity was then confirmed by the preparation of several compounds from free amine which was obtained by distillation of the sulfate with alkali. Crude allylamine thus obtained boiled at 52°-55°C (3), its hydrochloride and picrate melted at 105°-110°C (4), and at 140°-141°C (5), respectively. It gave propylamine, which was identified as N-n-propylbenzamide, mp 83°-84°C (6) and picrate, mp 132°-134°C (7), by catalytic hydrogenation over nickel catalyst in acetic unhydride at 50°-60°C under 100 atm. Bromination of the crude allylamine in hydrobromic acid gave 2,3-dibromopropylamine hydrobromide as precipitate, mp 164°-165°C (8). After removal of the precipitate, the mother liquor was distilled with alkali to obtain propylamine which was identified as picrate, mp 132°-135°C (7).

These compounds were further identified by IR spectroscopy and also by a mixture melting point test with authentic sample.

A scale-up preparative study was made by using forty times the amount of sample for the run and using lead. This gave almost the same result as in the small scale experiment. Thus: catholyte, 400g acrylonitrile, 2000 cc 10% sulfuric acid, 1000 cc methanol [during the electrolysis four portions (50 cc each) of 50% sulfuric acid were added]; anolyte, 1600 cc 10% sulfuric acid; cathode, lead (treated with dilute nitric acid); anode, lead; amperage, 55 amp; cathodic current density, 5.8 amp/dm^2; temperature, 20°C; amount of current, 247 amp hr (30% of the theoretical amount for allylamine).

The products obtained (current efficiency) were: allylamine sulfate 137g (56%), propylamine sulfate 31g (19%), ammonium sulfate 30g (10%), propionitrile 2.4g (1%).

Acknowledgment

This investigation was promoted by a grant for fundamental and developmental scientific research from the Ministry of Education of Japan and also a grant from Nippon (Japan) Carbide Industries Inc., for which the authors wish to express their deep appreciation.

Manuscript received July 10, 1967; revised manuscript received Sept. 12, 1967. This paper was presented at the Annual Meeting of the Chemical Society of Japan, Tokyo, March 31-April 4, 1967.

Any discussion of this paper will appear in a Discussion Section to be published in the June 1968 JOURNAL.

[1] At about the same time that the authors conducted their research, S. L. Varshavskii *et al.* (1) also carried out the same investigation and obtained allylamine.

[2] Before use, the original sulfate was converted to hydrochloride.

[3] This might result from the hydrolysis of a reduction intermediate, $CH_2 \cdot CH_2 \cdot CH{=}NH$, taking the formation of propionaldehyde into consideration.

REFERENCES
1. S. L. Varshavskii *et al.*, *Obraztsy Tovarnye Znaki*, **43** [10], 31 (1966); *C. A.*, **66**, 2679 (1967).
2. K. Sugino, K. Shirai, and T. Nonaka, *Bull. Chem. Soc. Japan*, **37**, 1895 (1964).
3. W. H. Perkin, *J. Chem. Soc. London*, **55**, 680 (1889).
4. M. Delépine, *Bull. soc. chim.*, [3] **17**, 296 (1897).
5. S. Gabriel and G. Eschenbach, *Ber.*, **30**, 1125 (1897).
6. F. E. Gould, G. S. Johnson, and A. F. Ferris, *J. Org. Chem.*, **25**, 1658 (1960).
7. M. F. Chancel, *Bull. soc. chim.*, [3] **7**, 405 (1892).
8. C. Paal and H. Hermann, *Ber.*, **22**, 3076 (1889).

On the Ratio Method of Analysis of Potentiostatic Current-Time Curves for Planar Electrodes

Charles A. Johnson and Sidney Barnartt

E. C. Bain Laboratory for Fundamental Research, United States Steel Corporation, Monroeville, Pennsylvania

Potentiostatic current-time curves for a simple first-order electrode reaction of the type: $O^{z+} + ne^- = R^{(z-n)+}$, coupled with semi-infinite linear diffusion, are described by the theoretical equation (1)

$$i_{(t)}/i_{(t=0)} = \exp(\lambda^2 t)\ \mathrm{erfc}\ (\lambda\sqrt{t}) \qquad [1]$$

Here $i_{(t)}$ is the current at time t, and the initial current $i_{(t=0)}$ is the desired charge-transfer current corresponding to the applied potential step. λ is a diagnostic constant, dependent on the charge-transfer mechanism as well as on reactant concentrations and diffusivities; we need not know its components for the purpose of this note.

At short times such that $1 > i_{(t)}/i_{(t=0)} > 0.85$, Eq. [1] reduces to

$$i_{(t)}/i_{(t=0)} = 1 - \frac{2}{\sqrt{\pi}}\lambda\sqrt{t} \qquad [2]$$

so that $i_{(t=0)}$ is readily obtained by linear extrapolation of an $i - \sqrt{t}$ plot back to zero time. For cases where experimental data are not available at such short times, we have proposed (2) a simple "ratio method" of analyzing the longer-time data. This utilizes the ratio

$$R = \frac{i_{(t)}}{i_{(4t)}} = \frac{\exp(\lambda^2 t)\ \mathrm{erfc}\ (\lambda\sqrt{t})}{\exp(4\lambda^2 t)\ \mathrm{erfc}\ (2\lambda\sqrt{t})} \qquad [3]$$

From the "master" curve of R against $\lambda\sqrt{t}$, the value of $\lambda\sqrt{t}$ corresponding to any measured R may be read. This value yields λ, and then Eq. [1] gives $i_{(t=0)}$. Methods of obtaining the charge-transfer parameters from λ and $i_{(t=0)}$ have been described (1-3) and will not be repeated here.

The master curve of R *vs.* $\lambda\sqrt{t}$ has been published (2), and this curve is adequate for approximate analyses. For accurate analyses, a numerical table of the function exp (x^2) erfc (x) given to at least four significant figures and at intervals $\Delta x \leq 0.01$ is required. Such an extensive table of this function is not generally available. We have succeeded, however, in obtaining a sufficiently precise and useful analytical relation between R and $\lambda\sqrt{t}$, such that tables of the function exp (x^2) erfc (x) are no longer required. Our relation gives $\lambda\sqrt{t}$ as the rational polynomial

$$\lambda\sqrt{t} = \frac{a_0(R-1) + a_1(R-1)^2}{1 + a_2(R-1)} \qquad [4]$$

$$a_0 = 0.8827,\ a_1 = -0.45387,\ a_2 = -0.907113$$

For $1.15 < R < 1.67$, which covers the range $0.14 < \lambda\sqrt{t} < 1$, Eq. [4] yields $\lambda\sqrt{t}$ with an accuracy better than ±0.05%. The current-time curve beyond $\lambda\sqrt{t} \simeq 1$ contains no appreciable kinetic information (1, 3) and therefore is not considered in the present analysis.

Table I. Analysis of data by Gerischer (4) in the intermediate-time range

t, (sec) × 10^3	$i(t)/i(4t)$	λ, $(\mathrm{sec})^{-1/2}$	$i_{(t=0)}$*
0.25	1.22_9	14.3	8.28
0.50	1.33_2	15.6	8.55
0.75	1.39_6	15.9	8.63
1.00	1.44_5	16.0	8.66
1.25	1.48_3	16.1	8.69
1.50	1.51_5	16.2	8.73
1.75	1.54_6	16.4	8.80
2.00	1.56_2	16.1	8.71
2.25	1.58_0	16.0	8.67
	Mean :	16.1	8.70
	σ :	0.16_3	0.05_4

* Unit current is one division of the ordinate scale, Fig. 6 of ref. 4.

A good illustration of the precision obtainable using this ratio method is afforded by experimental data of Gerischer (4) for potentiostatic deposition of cadmium from cyanide solution. In this paper Gerischer proposed an analytical procedure based on the measured slope of the current-time curve, but his procedure gave scattered results. Oldham and Osteryoung (3) devised an improved method also based on the slope of the current-time curve, which was applied to a particular experimental curve from Gerischer's paper and yielded $i_{(t=0)}$ with a standard deviation $\sigma = 4\%$. We have now applied our ratio method to the same experimental curve and the results (5), which span the entire experimental curve, are listed in Table I. The standard deviation[1] is less than 1% in $i_{(t=0)}$; the mean value and standard deviation exclude the data for $t \leq 0.5$ msec, since Gerischer noted that the currents at such short times included spurious transient components.

Table I illustrates both the high precision obtainable with the ratio method of analysis, and the good conformity of Gerischer's experimental current-time curve with Eq. [1].

Manuscript received July 19, 1967; revised manuscript received Aug. 22, 1967.

Any discussion of this paper will appear in a Discussion Section to be published in the June 1968 JOURNAL.

REFERENCES
1. H. Gerischer and W. Vielstich, *Z. physik. Chem. (Frankfurt)*, **3**, 16 (1955).

[1] As pointed out by a referee: (*a*) this is not strictly the standard deviation, but an estimate of it determined from seven trials; (*b*) a better statistical description is obtained by giving the 95% confidence limits of the mean values, namely $\lambda = 16.1 \pm 0.15$, $i_{(t=0)} = 8.70 \pm 0.05$.

2. C. A. Johnson and S. Barnartt, *J. Phys. Chem.*, **71**, 1637 (1967).
3. K. B. Oldham and R. A. Osteryoung, *J. Electroanal. Chem.*, **11**, 397 (1966).
4. H. Gerischer, *Z. Elektrochem.*, **64**, 29 (1960).

5. Each of the present authors independently read a set of current values from an enlarged photograph of Gerischer's published curve, and the mean curve was used to obtain the ratios listed in Table I.

Glass-Membrane Potentials in Mixed Anion Melts

Kurt H. Stern

Electrochemistry Section, National Bureau of Standards, Washington, D. C.

In a previous study of membrane potentials (1) at molten salt-fused silica interfaces it was shown that the emf of the cell

$$\text{Ag}|\text{AgCl, NaCl}|\text{glass}|\text{AgBr, NaBr}|\text{Ag} \qquad (A)$$

could be calculated by a straight-forward thermodynamic method if it was assumed that the only equilibrium at the glass-melt interface involved sodium ions. The cell reaction then is

$$\text{AgBr} + \text{NaCl} = \text{AgCl} + \text{NaBr} \qquad [1]$$

Calculated and experimental results were in good agreement when $X_{AgCl} = X_{AgBr} = 0.99$, $X_{NaCl} = X_{NaBr} = 0.01$. For equal sodium concentrations below ~1 m/o (mole per cent) the emf depends only on the $E°$ values of the above four salts and is independent of the concentration. (However, the emf can neither be calculated nor measured for zero sodium concentration since there would then exist no equilibrium at the glass-melt interface.) Since no extrathermodynamic assumptions about anion-glass interactions were made in the derivation of the cell emf it was tentatively assumed that such interactions were absent.

Nevertheless, it seems that mixed anion cells might offer a more sensitive tool for detecting possible anion-glass interactions, particularly since sulfate and nitrate ions have been found to inhibit the potential response of the glass to changes in sodium ion concentrations (1, 2). Moreover, the thermodynamic interpretation of such cells is of some interest. The mixed chloride-bromide analog to cell (A) was therefore studied. Since the thermodynamic derivation of the cell has not previously been worked out it is presented first.

Consider the concentration cell

$$\underset{\text{I}}{\text{Ag}|\text{Ag}^+, \text{Na}^+, \text{Cl}^-, \text{Br}^-|\text{glass}|\text{Ag}^+, \text{Na}^+, \text{Cl}^-, \text{Br}^-}\underset{\text{II}}{|\text{Ag}}$$

Since only the cations are involved in the cell reaction this can be written as

$$\text{Ag}^+(\text{II}) + \text{Na}^+(\text{I}) = \text{Ag}^+(\text{I}) + \text{Na}^+(\text{II}) \qquad [2]$$

However, the corresponding E or ΔG can only be expressed in terms of the thermodynamic components (cation-anion pairs) of the reciprocal salt system. Writing the cell in this manner gives

$$\underset{\text{I}}{\text{Ag}|\text{AgBr}(X_\text{I}), \text{AgCl}(X'_\text{I}), \text{NaCl, NaBr}|\text{glass}|}$$
$$\underset{\text{II}}{\text{AgBr}(X_\text{II}), \text{AgCl}(X'_\text{II}), \text{NaCl, NaBr}|\text{Ag}} \qquad [3]$$

Since activity coefficients of all the components are not known over the entire concentration range we restrict the derivation to the case $X_{Na+} << X_{Ag+}$. We now assume that the chemical potentials are additive functions in the mole fractions of the components. For example,

$$\mu_{\text{Ag}^+(\text{I})} = X_\text{I}\,\mu_{\text{AgBr(I)}} + X'_\text{I}\,\mu_{\text{AgCl(I)}} \qquad [3a]$$

$$\mu_{\text{Na}^+(\text{I})} = X_\text{I}\,\mu_{\text{NaBr(I)}} + X'_\text{I}\,\mu_{\text{NaCl(I)}} \qquad [3b]$$

The Gibbs energy change for reaction [2] then is

$$\begin{aligned}\Delta G = (\mu_{\text{Ag}^+(\text{I})} + \mu_{\text{Na}^+(\text{II})}) - (\mu_{\text{Ag}^+(\text{II})} + \mu_{\text{Na}^+(\text{I})}) \\ = [X_\text{I}(\mu°_{\text{AgBr}} + RT\ln a_{\text{AgBr(I)}}) \\ + X'_\text{I}(\mu°_{\text{AgCl}} + RT\ln a_{\text{AgCl(I)}}) \\ + X_\text{II}(\mu°_{\text{NaBr}} + RT\ln a_{\text{NaBr(II)}}) \\ + X'_\text{II}(\mu°_{\text{NaCl}} + RT\ln a_{\text{NaCl(II)}})] \\ - [X_\text{II}(\mu°_{\text{AgBr}} + RT\ln a_{\text{AgBr(II)}}) \\ + X'_\text{II}(\mu°_{\text{AgCl}} + RT\ln a_{\text{AgCl(II)}}) \\ + X_\text{I}(\mu°_{\text{NaBr}} + RT\ln a_{\text{NaBr(I)}}) \\ + X'_\text{I}(\mu°_{\text{NaCl}} + RT\ln a_{\text{AgCl(I)}})] \qquad [4]\end{aligned}$$

Combining terms and using $\Delta G = -n\mathbf{F}E$, $n = 1$, gives

$$\begin{aligned}E = [(X_\text{I} - X_\text{II})\,E°_{\text{AgBr}} + (X'_\text{I} - X'_\text{II})\,E°_{\text{AgCl}} \\ + (X_\text{II} - X_\text{I})\,E°_{\text{NaBr}} + (X'_\text{II} - X'_\text{I})\,E°_{\text{NaCl}}] \\ + RT/\mathbf{F}\left[X_\text{I}\ln\frac{a_{\text{AgBr(I)}}}{a_{\text{NaBr(I)}}} + X'_\text{I}\ln\frac{a_{\text{AgCl(I)}}}{a_{\text{NaCl(I)}}}\right. \\ \left. + X_\text{II}\ln\frac{a_{\text{NaBr(II)}}}{a_{\text{AgBr(II)}}} + X'_\text{II}\ln\frac{a_{\text{NaCl(II)}}}{a_{\text{AgCl(II)}}}\right] \qquad [5]\end{aligned}$$

Since the melts are very dilute in Na^+ we assume

$$a_{\text{NaCl}} = X_{\text{Na}^+}\,X_{\text{Cl}^-} = X_{\text{Na}^+}\,X_{\text{AgCl}} \qquad [6a]$$

$$a_{\text{NaBr}} = X_{\text{Na}^+}\,X_{\text{Br}^-} = X_{\text{Na}^+}\,X_{\text{AgBr}} \qquad [6b]$$

where X_{Na+} is the cation fraction of Na^+. Substituting [6] into [5] and rearranging gives

$$\begin{aligned}E = [(X_\text{I} - X_\text{II})\,(E°_{\text{AgBr}} - E°_{\text{NaBr}}) \\ + (X'_\text{I} - X'_\text{II})\,(E°_{\text{AgCl}} - E°_{\text{NaCl}})] \\ + RT/\mathbf{F}\ln[X_\text{I}\ln\gamma_{\text{AgBr(I)}} + X'_\text{I}\ln\gamma_{\text{AgCl(I)}} \\ - X_\text{II}\ln\gamma_{\text{AgCl(II)}} - X_\text{II}\ln\gamma_{\text{AgCl(II)}} \\ + (X_\text{II} + X'_\text{II} - X_\text{I} - X'_\text{I})\ln X_{\text{Na}^+}] \qquad [7]\end{aligned}$$

where the activity coefficient $\gamma_i = a_i/X_i$. If the sodium concentrations on both sides of the membrane are equal the last term in the second bracket becomes zero. The entire second bracket is a correction term for the nonideality of the AgCl-AgBr solutions. For the limiting case $X_\text{I} = 1$, $X'_\text{I} = 0$, $X_\text{II} = 0$, $X'_\text{II} = 1$ Eq. [7] reduces to the equation derived previously for the cell Ag|AgCl, NaCl|glass|AgBr, NaBr|Ag. For very low and equal concentrations of sodium on both sides of the membrane the entire second bracket becomes zero and the cell emf then depends only on the relative chloride-bromide composition. Since the activity coefficients of all the components in Eq. [5] are not known over the entire range of composition the experiments were restricted to cells in which the cation fraction of sodium was 10^{-2} in each compartment. It was then assumed that the activities of AgCl and AgBr in the resulting solution are the same as in the absence of sodium and could be obtained from the data of Murgulescu and Marchidan in AgCl-AgBr mixtures (3). The general experimental procedures have been described previously (1).

Experimental.—In order to ensure that the mixed melts would retain equal sodium ion concentration 1 m/o NaCl in AgCl and 1 m/o NaBr in AgBr melts were prepared first and subsequent melt compositions made by mixing these.

Table I. Experimental and calculated emf's for cell (B) at 525°C

X_I	X'_I	X_{II}	X'_{II}	$-E_{calc.}$ (mV)	$-E_{exp}$ (mV)
0.490	0.500	0.489	0.501	0	4
0.454	0.536	0.489	0.501	9	10
0.407	0.583	0.489	0.501	16	30
0.367	0.623	0.489	0.501	30	26
0.331	0.659	0.489	0.501	37	37
0.293	0.697	0.489	0.501	46	49
0.263	0.727	0.489	0.501	53	56
0.263	0.727	0.515	0.475	53	55
0.263	0.727	0.560	0.430	60	62
0.263	0.727	0.596	0.394	67	70
0.263	0.727	0.630	0.360	73	78
0.263	0.727	0.660	0.330	79	87
0.263	0.727	0.700	0.290	87	92
0.263	0.727	0.726	0.264	92	100
0.263	0.727	0.757	0.233	99	107
0.263	0.727	0.791	0.199	107	117

In contrast to experiments in which the new equilibrium potential is established almost immediately after the addition of a sodium salt to a silver halide, in the present case steady potentials were obtained much more slowly, frequently several hours after a change in melt composition. In every case steady emf's were eventually obtained, however. Two runs were made. In the first of these, at 525°C, both compartments initially contained a nearly equimolar AgCl-AgBr mixture. The composition of the compartments was then altered by increasing the AgCl concentration of one, and the AgBr concentration of the other.

Results

Table I shows the comparison of the experimental results with those calculated from Eq. [7]. The term in the second bracket is small ($\leq$3 mv) compared to the first. The source of the $E°$ values has been discussed elsewhere (1).

Since $E_{calc.}$ is essentially equal to the first bracket of Eq. [7] which consists of a small difference between two large terms (and thus is very sensitive to small changes to the choice of the $E°$'s and small errors in concentration) the agreement between calculated and experimental values must be considered excellent. Except for four points agreement is within 5 mv.

The second experiment was similar except that one compartment initially contained only the AgCl-NaCl mixture and the AgBr-NaBr mixture was added to it. Results were similar but ($E_{calc.} - E_{exp}$) was somewhat larger, ~15 mv.

In view of these results it appears that Eq. [7] correctly gives the emf of cell B and that the assumption implicit in Eq. [3] is justified.

Acknowledgment

The author is indebted to Dr. H. A. Øye for helpful discussion.

Manuscript received July 27, 1967.

Any discussion of this paper will appear in a Discussion Section to be published in the June 1968 JOURNAL.

REFERENCES

1. K. H. Stern, To be published.
2. K. H. Stern, Unpublished results.
3. I. G. Murgulescu and D. I. Marchidan, *Rev. de Chimie, Acad. Rep. Pop. Roumaine*, **3**, 1 (1958).

Performance of a Silver-Gold (10%) Alloy in a Concentrated Caustic Electrolyte

Paul Malachesky and Raymond Jasinski

Tyco Laboratories, Inc., Waltham, Massachusetts

Silver oxide, Ag_2O, is a p-type semiconductor of low electronic conductivity, ~10^{-8} ohm^{-1} cm^{-1} (1). In principle, this conductivity can be increased by the addition of minor impurities which change the concentration of holes or which promote the formation of vacancies. Impurities of the former type are metals to the left of silver in the periodic table (*e.g.*, Pd) or metals of high ionization potential (*e.g.*, Au). An increase in electrical conductivity of Ag_2O can be expected to result in an improvement in the charge acceptance characteristics of silver when anodized in a concentrated caustic electrolyte. The performance of silver-palladium alloys has been discussed elsewhere (2). This paper is concerned with the electrochemical characteristics of an Ag/10% Au alloy. The oxidation behavior of a 2% gold-silver alloy has been reported, but no quantitative data were given (3).

Experimental

The apparatus and approach employed to investigate this effect, have already been described (2). Briefly, the system consists of a polished gold-silver alloy electrode mounted in a rotating disk assembly. The electrolyte was 35% KOH saturated with nitrogen. The electrode was cathodized before using and freshly polished between each galvanostatic charging experiment.

The electrode was anodized at varying current densities, and the charge accepted on the Ag (I) and Ag (II) plateaus was measured. During cycling, the double layer capacity was measured after each total discharge step. Details are given elsewhere (2).

The data on charge acceptance and delivery on all cycles are the average of at least triplicate runs. The total charge accepted in millicoulombs/square centimeters is designated as Q_t; the charge accepted on the Ag (I) level and the Ag (II) level are designated as Q_1 and Q_2, respectively.

Results and Discussion

The total charge accepted by the 10% Au sample is compared in Fig. 1 with the charge acceptance for silver. The form of the curve is identical for both materials and for silver-palladium alloys as well (2). The quantity of total charge accepted is particularly sensitive to current density at and below 3 ma/cm^2. At all current densities the alloy shows a greater charge acceptance than pure silver.

Also significant is the difference between the alloys in the quantity of charge accepted on the Ag (I) plateau. As shown in Fig. 2, the alloy will accept approximately 2.5 times as much charge at this level as will silver itself. Furthermore, this effect is maintained over the entire current density range surveyed.

The ratio of charge accepted on the Ag (II) level to that on the Ag (I) level is shown is Fig. 3 for the 10% Au alloy. As observed with silver and silver-palladium alloys (2), there is a relative increase in the Ag (I) plateau with increasing current density. Comparing this curve with Fig. 1 implies that de-

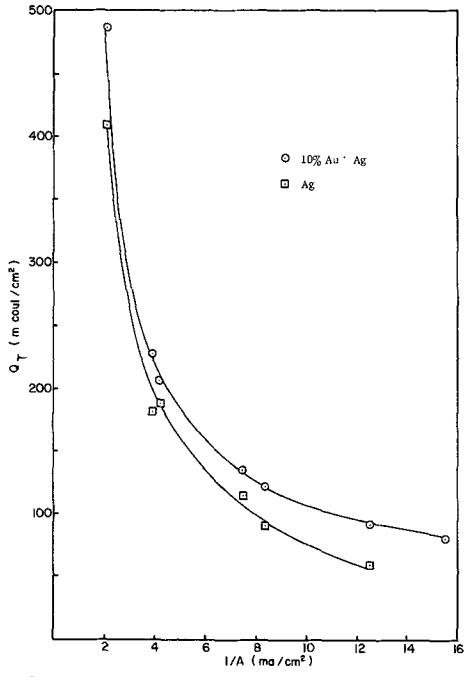

Fig. 1. Total charge accepted (Q_T) on the first cycle as a function of current density for pure silver and the 10% Au-Ag alloy.

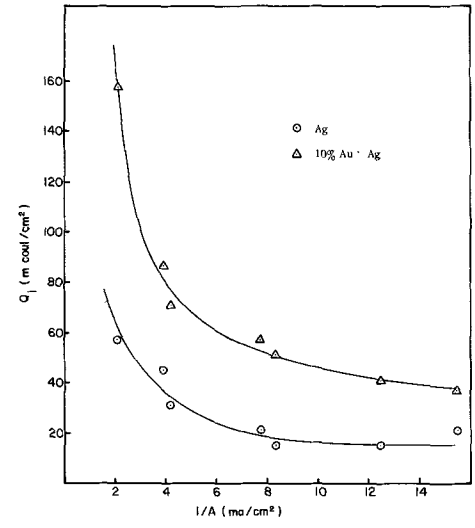

Fig. 2. Charge accepted at the Ag/Ag_2O potential level (Q_1) as a function of current density for silver and the 10% Au-Ag alloy.

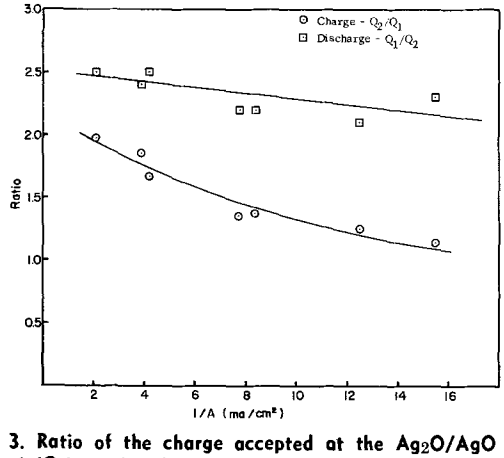

Fig. 3. Ratio of the charge accepted at the Ag_2O/AgO potential level (Q_2) to the charge accepted at the Ag/Ag_2O level (Q_1) as a function of current density, on the first charge-discharge cycle.

Table I. Relative variation in C_{dl}* on cycling at 2.08 ma/cm²

Cycle	Ag, 91 μf/cm²	Ag/10% Au, 100 μf/cm²
0	1	1
1	3.8	3.2
2	3.6	3.9
3	3.8	4.3
4	3.8	4.0
5	4.3	4.2

* Normalized to C_{dl} before cycling.

creasing current density will increase charge acceptance at both oxide levels, although Q_2 increases somewhat more rapidly than Q_1.

The inverse ratio (Q_1/Q_2) is also shown for the discharge of this alloy at the same current density as the charging process. There is a slight dependence on current density, as the relative length of the Ag (II) plateau increases with increasing current density.

This electrode was then cycled at a number of current densities. The relative change in double layer capacitance (C_{dl}) is shown in Table I for silver and the 10% Au alloy cycled at 2.08 ma/cm².

The higher charge acceptance of the alloy on the first cycle does not appear due to a higher roughness factor. Although it is not possible to deduce values rigorously for the initial surface roughness from the double layer capacitances, the values observed, 91 μf/cm² for Ag and 100 μf/cm² for Au, imply that the alloy does not have a markedly greater roughness than silver. The variation of C_{dl} on cycling is most likely due to surface roughening. Thus, for both materials there is a significant change in electrode surface area for the first two cycles, approaching a steady state of about 4/1. The change in total charge acceptance on the first five cycles for silver and the 10% Au alloy is shown in Fig. 4 at a current density of 4.2 ma/cm². Similar data for the alloy up to 15 cycles are presented in Fig. 5. The effect of cycling on the ratio Q_2/Q_1 is shown in Fig. 6.

The charge acceptance curves show the same general features as the C_{dl} data of Table I. Q_t for the alloy reaches a relatively constant value after the first two cycles, while the charge accepted by the silver electrode continues to increase slowly as, apparently, the surface continues to roughen. The change of Q_t for the 10% Au alloy after 10 cycles is believed due to leakage about the Kel-F seal on the rotating disk electrode.

The relative quantity of charge accepted at the Ag (I) level is higher for the alloy initially and after the fourth cycle. As shown in Fig. 6 the curves for the two materials are parallel after these few cycles, showing no tendency to approach one another.

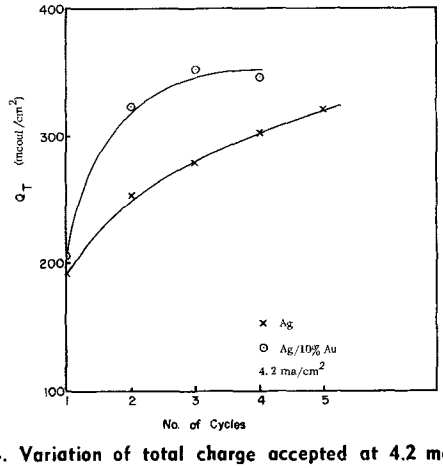

Fig. 4. Variation of total charge accepted at 4.2 ma/cm² with cycle number for silver and the gold-silver alloy.

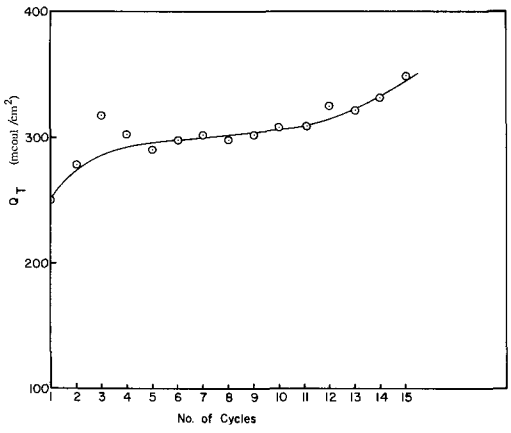

Fig. 5. Variation of the total charge passed for the gold-silver alloy with cycle number on extended cycling at 3.9 ma/cm^2.

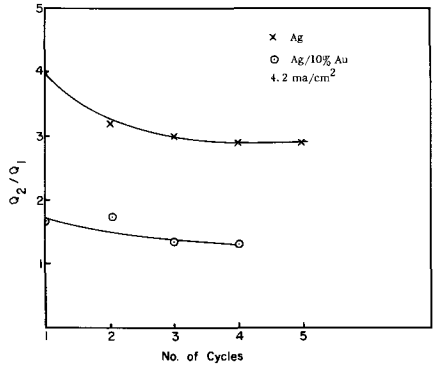

Fig. 6. Variation of Q_2/Q_1 on charging with cycle number

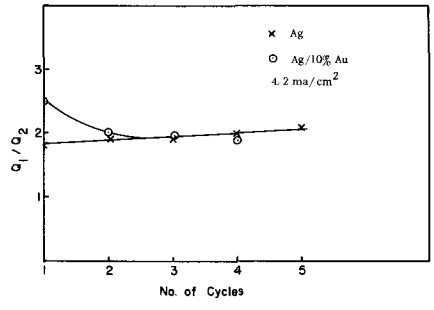

Fig. 7. Variation of Q_1/Q_2 on discharge with cycle number

This relative increase in Q_1 on cycling (Fig. 6) must involve more than a decrease in current per real surface area. As shown in Fig. 3 for charge acceptance as the first cycle, a decrease in current density decreases the relative amount of Q_1. A similar effect was noted for the Pd/Ag alloys (2).

The electrodes were discharged at the same current density as used in the charging portion of the cycle. The Q_t-cycle curves parallel the charge acceptance curves. In Fig. 7 is shown the variation of Q_1/Q_2 on discharge at 4.2 ma/cm^2. After this first discharge, both materials discharge with the same relative lengths of Ag (I) and Ag (II) plateaus. This characteristic was also noted for silver-palladium alloys (2).

Discharge efficiencies for the Au-Ag alloy were 80-85% in comparison to the value to 90-95% observed for silver and silver-palladium alloys (2). On stand at full charge for 5 min, efficiency was reduced to 62% for the Au-Ag alloy in comparison to a decrease in efficiency to 83% for a fully charged silver electrode over the same time period. The AgO plateau on discharge for the gold alloy became much shorter than usual. The length of the Ag (I) plateau remained essentially unchanged. This behavior can be explained in terms of the corrosion of AgO to Ag_2O; the anodic reaction is the gold catalyzed evolution of oxygen.

This decomposition of AgO to Ag_2O on the gold-silver alloy can explain the small decrease in Q_1/Q_2 with increasing current density (decreasing charging time) in Fig. 3. Similar data for pure silver showed no such variation in Q_1/Q_2 (2). The effect of this decomposition process on the charging data is less clear since both silver and the gold alloy show a decrease in Q_2/Q_1 with increasing current density. Thus, since the relative amount of decomposition is small during the duration of the experiments, the data for Q_t *vs.* current density (Fig. 1) probably represent true differences in the charge acceptance properties of silver and the silver-gold alloy.

Conclusions

1. The Ag/10% Au alloy will accept more charge than pure silver over the current density range studied.
2. The relative amount of charge accepted on the Ag (I) level is substantially greater for the alloy than for pure silver.
3. Both materials show a pronounced dependence of charge acceptance on current density.
4. Both materials show an increase in total charge acceptance on cycling. However, this increase is not commensurate with the increase in surface roughness as measured by double layer capacitance. The gold alloy reached a steady state after two cycles; the silver alloy continued to roughen on repetitive cycling.
5. After the first cycle, both materials discharged with the same relative lengths of the Ag (I) and Ag (II) plateaus.
6. The presence of gold apparently accelerates the decomposition of AgO; the charge delivered at the Ag_2O/Ag level was unaffected.

Acknowledgments

The authors wish to acknowledge the assistance of Miss Susan Carroll in carrying out the experimental work and the support of the United States Naval Air Systems Command (Contract No. W66-0621-C).

Manuscript received Aug. 1, 1967.

Any discussion of this paper will appear in a Discussion Section to be published in the June 1968 JOURNAL.

REFERENCES

1. B. D. Cahan, J. B. Ockerman, R. F. Amlie, and P. Rüetschi, *This Journal*, **107**, 725 (1960).
2. P. Malachesky and R. Jasinski, *ibid.*, **114**, 1239 (1967).
3. S. Yoshizawa and Z. Takehara, *Denki-Kagaku*, **32**, 197 (1964).

Brief Communication

Area Changes of a Smooth Platinum Electrode

T. Biegler

Division of Mineral Chemistry, Commonwealth Scientific and Industrial Research Organization, Port Melbourne, Victoria, Australia

The problem of whether or not a smooth platinum electrode maintains a constant "real" surface area has arisen mainly in connection with studies of the nature of the process of activation of such electrodes by anodic-cathodic pretreatment [see *e.g.*, (1) and (2) and references therein]. Since areas are measured by means of an electrode reaction (generally deposition or ionization of a monolayer of hydrogen atoms), which must be sensitive to contamination of the surface, there is no immediate way of separating "area" and "activity" effects without establishing independent criteria. However, there is a good deal of evidence that activation by the usual means is essentially a cleaning procedure (2, 3) and that the platinized active surface state proposed by Anson (4) is simply a clean surface. French and Kuwana (1), who supported Anson's concept of a distinct surface state, found that deactivation obeyed first order kinetics with a half-life of 46 min. In contrast, Bagotskii and Vasil'ev (5) reported that they could maintain a fully active electrode surface for at least 20 min in 1*N* H_2SO_4. Gilman (3) was able to reproduce the hydrogen area of an electrode over several weeks' use and concluded from this and from stirring effects that deactivation is a result of adsorption of impurities. On the other hand, modifications of platinum electrode surfaces have been observed (6-8) under sufficiently severe conditions. Blackening of the surface was found (6, 7) when electrodes were polarized with a.c. into the oxygen evolution region. Gilman (8) showed that at 120°C in 85% phosphoric acid the surface area of a smooth electrode was modified by treatments involving formation and reduction of an oxide layer.

This communication describes observations of what are believed to be true area changes found during a study of adsorption of methanol on a smooth platinum electrode (9). Area changes were also noted with two other platinum electrodes used in this work, but these were not followed systematically. Full details of the types of experiments carried out with the electrode will be found in ref. (9). Briefly, current/time curves for adsorption of methanol from 1M H_2SO_4 were determined by the potential step technique described earlier (10). Charges needed to oxidize layers of chemisorbed methanol were measured by a technique in which methanol was adsorbed, the solution was replaced by supporting electrolyte, and the adlayer stripped off during a linear anodic potential sweep. During use, the electrode potential was normally within the range 0.04-1.55v *vs.* reversible hydrogen electrode in 1M H_2SO_4; occasionally a potential of 1.8v was used for vigorous anodic cleaning. Between runs the electrode was stored in distilled water. No significant area changes were observed in the periods between sets of experiments (up to two weeks). Each series of runs was preceded by a period of anodic-cathodic cleaning in 1M H_2SO_4, using pulses and/or sawtooth scanning between 0.08 and 1.55v. Since the changes in surface properties described below were of a long term nature there was no problem in judging

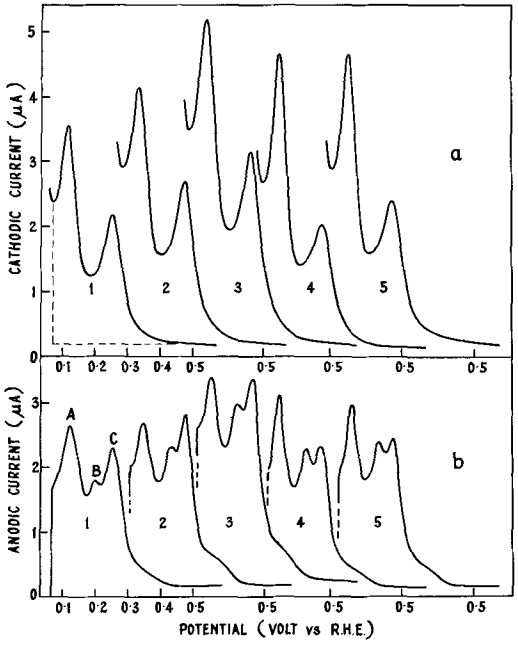

Fig. 1. Current-voltage curves (a, cathodic, b, anodic) in the hydrogen region for a platinum electrode at various stages of its life (see text). Solution, 1M H_2SO_4. Curves displaced horizontally for clarity. Broken lines on curve 1a indicate limits for integration to obtain $Q_H{}^S$. Sweep rate 37 mv/sec.

electrode cleanliness from the reproducibility of successive area determinations and anodic scans in the oxide region. Experiments were carried out at 22° ±2°C.

Figure 1 shows anodic and cathodic sweeps for 1M H_2SO_4 in the hydrogen region at various stages of the life of the electrode (34 gauge Pt wire, geometric area 0.042 cm^2). Anodic sweeps were obtained by cleaning the electrode with anodic pulses from 0.08 to 1.55v, then holding at 0.08v for 10 sec before starting the anodic scan. For the cathodic curves, cleaning was achieved by anodic pulses between 0.58 and 1.55v, the potential was held at 0.58v for 10 sec, and the cathodic sweep started. These curves were integrated according to Gilman's procedure (3) in order to obtain the saturation hydrogen coverage, $Q_H{}^S$. The solution was unstirred during these measurements. Sweep rate was 37 mv/sec.

The history of this electrode is as follows. After sealing into soft glass it was washed in cleaning solution, rinsed, and set up in the cell with degassed 1M H_2SO_4. Repetitive sawtooth scanning between 0.08v 1.55v was then commenced. Voltammegrams assumed the shape expected for a clean, active electrode after about 60 cycles [*cf.* (2)] when $Q_H{}^S$ was 10.7 μcoul. Curves 1a and b were taken after some 1700 cycles

and are qualitatively much the same as those after 60 sweeps; Q_H^S had, however, increased by 6%.

The electrode was then put into use for the methanol adsorption experiments. Curves 2a and b were obtained after a number of such runs by which time Q_H^S had increased to 14.8 μcoul. The electrode area continued to increase steadily with use and when the series of experiments with methanol was completed curves 3a and b were recorded. Q_H^S was now 19.2 μcoul, almost double the original value. It was then decided to examine the effects of further prolonged cycling in 1M H_2SO_4 and curves 4a and b were obtained after about 5900 sawtooth sweeps between 0.08v and 1.55v. There was a dramatic fall in Q_H^S to 13.4 μcoul as well as a marked change in the shapes of the curves. At this point, the solution was replaced with 0.5M methanol in 1M H_2SO_4 and 2200 cycles over the same potential range were applied, after which Q_H^S had increased to 15.2 μcoul (curves 5a and b). Only a slight change in the shapes of the curves accompanied this increase.

From the above, it appears that area changes occurred more rapidly during methanol stripping runs than in the separate experiment in which cycling in 0.5M methanol, 1M H_2SO_4 was carried out for an extended period. Quantitative comparison is difficult because no record was kept of the number of anodic excursions of the electrode during the methanol adsorption experiments. However, to give a rough comparison, in runs on a single day during which an estimated total of 600 potential steps and sweeps (mainly the former) was applied, Q_H^S increased by 23%. This compares with the 13% increase found after 2200 cycles in 0.5M methanol. Although we cannot explain the dependence of rate of area change on the type of experiment, it seems clear that the presence of methanol is necessary for the large area increases observed.

Comparison of the curves in Fig. 1 with the work of Will (11) strongly suggests that the present results reflect changes in the platinum surface structure. Will used linear sweep voltammetry to study hydrogen adsorption on platinum single crystal electrodes cut to expose each of the three low index crystal planes. Three peaks for anodic sweeps over the range 0.05-0.4v were found for each face and these were attributed to adsorption of hydrogen on the three crystal planes. The relative peak heights depended on the face used and Will concluded (11) that his technique had produced polycrystalline electrodes with a predominance of the nominal crystal face. Furthermore, he found that triangular cyclic voltammetry (0.05-1.55v) with a freshly cut face resulted in an over-all change in electrode area together with a change in relative peak heights. Will interpreted these effects as indicating etching of the surface and development of facets during repeated anodic-cathodic cycling.

There is a sufficient analogy between Will's observations (11) and the present results to indicate that the surface structure of a polycrystalline platinum electrode has been influenced by the electrode reactions which occurred on it during the course of this work. Accepting Will's assignment of the peaks in the anodic scans,[1] one concludes that the experiments with methanol caused a small decrease in the [110] plane (peak A) relative to the [111] (peak B) and [100] (peak C) planes which retained about the same relation to each other; at the same time there was an overall increase in area. After cycling in sulfuric acid, Q_H^S fell, peak A became predominant, and the heights of the other two peaks were now equal. It is a striking result that curves 2 and 4, representing similar electrode areas, indicate such different surface structures. Here, curve 2 was recorded before maximum expansion of the surface had occurred and curve 4 after it had been returned to around its former area. The surface changes are clearly not reversible.

A few general conclusions can be drawn from the few results available. We have found that a platinum surface is slowly altered by electrochemical processes occurring on it at ambient temperatures. This response depends on the nature of the reaction and the history of the electrode. Thus, examples have been found of both an increase and a decrease in Q_H^S after cycling in 1M H_2SO_4, *i.e.*, the same electrode reactions (hydrogen adsorption/desorption, oxide formation/dissolution) cause different effects depending on electrode prehistory. The observed changes in the electrode surface are considered to result from an increase in surface mobility of platinum atoms brought about by formation of bonds between surface atoms and chemisorbed reactants, with a consequent weakening of adjacent Pt-Pt interactions. In this connection, structural changes have been reported (12) for evaporated silver films on which formic acid vapor has been decomposed catalytically, but conclusive evidence that the catalyzed reaction is solely responsible does not appear to be available.

Manuscript received July 31, 1967.

Any discussion of this paper will appear in a Discussion Section to be published in the June 1968 JOURNAL.

REFERENCES

1. W. G. French and T. Kuwana, *J. Phys. Chem.*, **68**, 1279 (1964).
2. M. W. Breiter, *Electrochim. Acta*, **11**, 905 (1966).
3. S. Gilman, *J. Phys. Chem.*, **67**, 78 (1963).
4. F. C. Anson, *Anal. Chem.*, **33**, 934 (1961).
5. V. S. Bagotskii and Yu. B. Vasil'ev, *Electrochim. Acta*, **11**, 1439 (1966).
6. F. C. Anson and D. M. King, *Anal. Chem.*, **34**, 362 (1962).
7. J. P. Hoare, *Electrochim. Acta*, **9**, 599 (1964).
8. S. Gilman, *J. Electroanal. Chem.*, **9**, 276 (1965).
9. T. Biegler, *J. Phys. Chem.*, Submitted for publication.
10. T. Biegler and D. F. A. Koch, *This Journal*, **114**, 904 (1967).
11. F. G. Will, *ibid.*, **112**, 451 (1965).
12. J. Bagg, H. Jaeger, and J. V. Sanders, *J. Catalysis*, **2**, 449 (1963).

[1] Note that cathodic scans have only two peaks so that factors other than the reversible adsorption equilibrium of hydrogen must influence the current-voltage curves, *e.g.*, molecular hydrogen forms slowly and leaves the surface by diffusion in this potential region. The electrode at any potential therefore "sees" a different H_2 concentration depending on the direction of scan and this factor could possibly account for the observed difference. Association of peaks with crystal faces must be considered tentative.

DISCUSSION SECTION

This Discussion Section includes discussion of papers appearing in the *Journal of The Electrochemical Society*, Vol. 113, No. 8 and 11 (August and November 1966) and Vol. 114, No. 1 and 3 (January and March 1967).

Studies of the Electrochemical Kinetics of Indium, III. Systems In + $InCl_3$ and In + Combined Sulfate-Chloride Electrolyte

V. Markovac and B. Lovrecek (pp. 838-841, Vol. 113, No. 8)

G. A. Wright[1]: Steady-state Tafel lines for the polarization of the indium amalgam electrode have been obtained by using galvanostatic pulses. Markovac and Lovrecek have interpreted the Tafel slopes by using the following equations for cathodic and anodic reactions, respectively.

$$\frac{\partial \log_{10} i_-}{\partial V} = -\frac{z\mathbf{F}}{2.303\,RT}(n_c^* - \alpha) \qquad [1]$$

$$\frac{\partial \log_{10} i_+}{\partial V} = \frac{z\mathbf{F}}{2.303\,RT}(n_a^* - 1 + \alpha) \qquad [2]$$

n_c^* and n_a^* are the ordinal numbers of the slowest reaction steps for cathodic and anodic polarization, $(1 - \alpha)$ and α are the transfer coefficients for the cathodic and anodic reactions, and z is the number of electrons transferred in the rate-determining step. Other symbols have their usual meanings.

These formulas are incorrect and should be replaced by

$$\frac{\partial \log_{10} i_-}{\partial V} = -\frac{\mathbf{F}}{2.303\,RT}(n + z - \alpha z) \qquad [3]$$

$$\frac{\partial \log_{10} i_+}{\partial V} = \frac{\mathbf{F}}{2.303\,RT}(n + \alpha z) \qquad [4]$$

Here n is the number of electrons involved in a rapid equilibrium which precedes the rate-determining step, and the other symbols have the same meaning as before. The derivation of these equations is quite straightforward.[2] Thus for a cathodic reaction

$$0 + ne^- = \mathrm{P}, \text{ equilibrium}$$

$$\mathrm{P} + ze^- \rightarrow \mathrm{R}, \text{ rate determining}$$

the first step is an electrochemical equilibrium

$$a_p = \mathrm{K}\, a_o \exp\left[-\frac{n\mathbf{F}V}{RT}\right] \qquad [5]$$

The second step obeys the usual rate equation of electrode kinetics

$$i_- = (n + z)\mathbf{F}\, k\, a_p \exp\left[-\frac{z(1-\alpha)\,\mathbf{F}V}{RT}\right] \qquad [6]$$

$$= (n + z)\mathbf{F}\, k K\, a_o \exp\left[-\frac{(n + z - \alpha z)\mathbf{F}V}{RT}\right] \qquad [7]$$

This leads directly to Eq. [3]. Lovrecek[3] originally derived Eq. [1] and [2] by considering only 1-electron steps, and the correct result was obtained for that case. Generalization of his result for reaction steps with more than 1-electron has led to the error.

The difference between the equations can be seen by considering the following hypothetical mechanism of cathodic reduction of the indium ion.

$$\mathrm{In}^{3+} + e^- = \mathrm{In}^{2+} \quad \text{equilibrium}$$

$$\mathrm{In}^{2+} + 2e^- \rightarrow \mathrm{In} \quad \text{rate determining}$$

Equation [1] predicts $\partial \log_{10} i_-/\partial V = -(4 - 2\alpha)/0.059$ v^{-1} at 25°C, whereas the correct result from Eq. [3] is $-(3 - 2\alpha)/0.059$ v^{-1}. It is however fortunate that for all the mechanisms proposed by Markovac and Lovrecek, Eq. [1] and [2] yield the same parameters as would be obtained from Eq. [3] and [4]. Thus the tables of transfer coefficients are consistent with the mechanisms proposed, and the same is true for an earlier paper in this series.[4]

I would also like to point out that the use of Tafel slopes as a criterion of mechanism can be ambiguous, even when supported by additional evidence as discussed by Markovac and Lovrecek. In the case of the anodic dissolution of indium amalgam in a chloride electrolyte, it was found that $\partial \log_{10} i_+/\partial V = 11.95\ \mathrm{v}^{-1}$. Markovac and Lovrecek propose that the rate-determining step is $\mathrm{In} \rightarrow \mathrm{In}^+ + e^-$ with $\alpha = 0.69$. But the same Tafel slope is consistent with $\mathrm{In} \rightarrow \mathrm{In}^{2+} + 2e^-$ with $\alpha = 0.35$, and this rate-determining step seems to be equally probable.

V. Markovac and B. Lovrecek: Actually Eq [1] and [2] from the quoted paper are valid generally in case of electrode reactions with 1-electron steps. In the case of a rate-determining step with more than 1 electron they will hold only if the first reaction step is rate determining. All our results and kinetic parameters really relate to the above cases.

Formulas given by Wright, [3] and [4] are certainly correct. (We would only suggest the form

$$\frac{\partial \log_{10} i_-}{\partial V} = -\frac{\mathbf{F}}{2.303\,RT}(n_c^* - 1 + z - \alpha z)$$

and

$$\frac{\partial \log_{10} i_+}{\partial V} = \frac{\mathbf{F}}{2.303\,RT}(n_a^* - 1 + \alpha z)$$

with usual meaning of symbols.)

As to the question of ambiguity of Tafel slopes as a criterion for mechanism it would certainly be wrong to claim its absolute validity in every case. But in many cases, cautiously applied it can give suggestions on mechanism, especially if combined with other evidences.

Some Problems in Electrodeposition

J. A. Harrison, S. K. Rangarajan, and H. R. Thirsk (pp. 1120-1133, Vol. 113, No. 11)

B. Behr, W. Kemula, and J. Taraszewska[5]: At the Symposium on Electrode Processes held in Cleveland in May 1966 an interesting discussion followed this paper. The important points of this discussion, concerning the mechanism of the anodic oxidation of mercury in the presence of chloride ions, were the following:

(A) Which stage of the process of calomel-layer formation corresponds to the "induction time" determined ellipsometrically by Bockris *et al*?[6]

(B) Which is the primary product of anodic oxidation of mercury?

[1] Department of Chemistry, University of Auckland, Auckland, New Zealand.
[2] B. E. Conway, "Theory and Principles of Electrode Processes," p. 115, Ronald Press Co., New York (1965).
[3] B. Lovrecek, *J. Phys. Chem.*, 63, 1795 (1959).
[4] V. Markovac and B. Lovrecek, *This Journal*, 112, 520 (1965).
[5] Institute of Physical Chemistry, Polish Academy of Sciences, Warszawa, Poland.
[6] J. O'M. Bockris, M. A. V. Devanathan, and A. K. N. Reddy, *Proc. Roy. Soc.*, A279, 327 (1964).

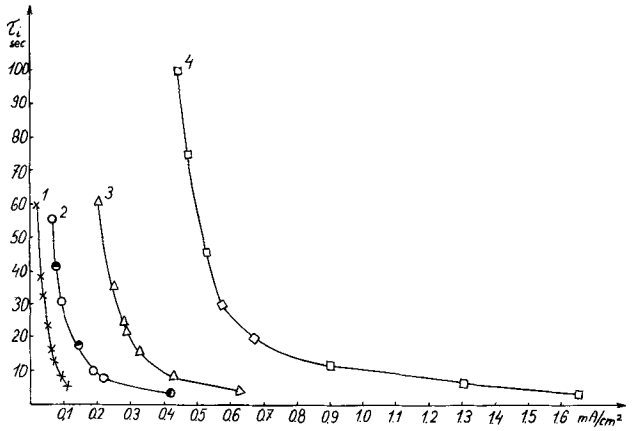

Fig. 1. Induction times measured in KCl solutions by the method of reducing the volume of the mercury drop, in dependence on current density: 1-0.1M, 2-1.0M, 3-1.5M, 4-2.0M. Black points taken from Bockris et *al.*[6]

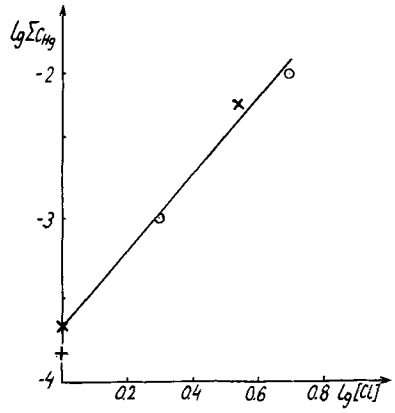

Fig. 2. X, Total mercury concentration in equilibrium with Hg and Hg_2Cl_2, determined polarographically; +, from the data of Sillen;[10] o, the concentration of electroactive species calculated by Armstrong, et *al.*, [11] from the Warburg impedance.

The first question is important because of its relation to the mechanism of calomel crystallization: is calomel the primary product of the electrode reaction or a secondary product formed by crystallization from the solution? In view of the high-sensitivity of the ellipsometric method Bockris *et al.* assumed that the induction time corresponds to the first moment of crystallization of calomel. However it was generally agreed during the discussion that this should be checked also with another method. Some of our experiments[7] may be helpful in discussing this question.

Our results were obtained as follows: we have measured under galvanostatic conditions the shortest time τ_i after which a calomel layer can be detected on the hanging mercury drop electrode. This can be made simply by reducing the volume of the mercury drop electrode by taking most of mercury back into the capillary and observing the shape of the drop showing the formation of the stiff layer.[8] The results obtained by this method (Fig. 1) in the case of 1M KCl solution, are identical with the induction times determined ellipsometrically by Bockris *et al.*[6] Our measurements of the potential-time relationship confirmed also the results of these authors. Investigating the 0.1M KCl solution we have recorded oscillographically similar potential-time curves as described by Ives *et al.*,[9] and we were able to correlate the induction times measured by us with the results of the authors. The induction time always corresponded to a point well after the hump on the V-t curve. According to the microscopic observations of Ives *et al.*[9] crystals of calomel could be seen on the electrode surface when the hump was reached. This may be considered as an argument against the supposition of Bockris *et. al.*[6] that before the induction time is reached there exists no precipitate at the electrode surface.

A similar conclusion (also for 1M KCl solution) could be obtained by considering the equilibria between mercury electrode and all soluble mercuric species formed as a result of electrolysis and their diffusion rate toward the bulk of the solution. We have calculated the minimal quantity of mercury in the calomel layer formed by subtracting the maximal quantity of mercuric species which could diffuse away from the electrode till the induction time was reached from the total quantity of mercury being oxidized galvanostatically.

The participation of the diffusion of mercuric species in studied processes has been calculated as follows. The actual surface concentration of dissolved mercuric ions was estimated using the V-t curves and equilibrium data. The equilibrium concentrations of chloromercuric complexes formed in the presence of Hg and Hg_2Cl_2 in a solution of ionic strength of 0.5 are given by Sillen.[10] Polarographic determination of total concentration of mercury (II) in the bulk of solution being in equilibrium with Hg and Hg_2Cl_2 was done for 1M and also for saturated KCl (Fig. 2). Our result for 1M KCl was slightly higher than that of Sillen. We assumed that for 1M KCl solution the surface concentration of the potential-determining species corresponding to the experimentally found overvoltage of 14 mv is equal to thrice of the equilibrium value. Thus, we have used for calculating the diffusion of mercuric species from the electrode, the total mercury surface concentration as equal to $3x2.2x10^{-4} = 6.6x10^{-4}$M. From thermodynamic considerations it is impossible to expect that higher concentrations of soluble species are formed at the electrode surface. The maximal possible charge transported from the electrode into the solution by soluble mercuric species formed has been calculated by integrating over the induction time the equation for linear diffusion at a constant potential and applying the value of the diffusion coefficient equal to 10^{-5} $cm^2\ sec^{-1}$ and $n=2$ (practically only the Hg^{II} complexes are formed). The quantities thus obtained and the resulting minimal values of charge consumed in formation of the calomel layer are presented in Table I. The real value of the charge corresponding to the calomel layer formed, would be higher if there were any slow homogeneous reaction in solution.

The large amount of soluble mercuric complexes in the solution which may correspond to a threefold supersaturation with calomel (η = 14 mv) may produce significant contribution to further calomel growth after switching off the current. This effect should not

[7] B. Behr and W. Kemula, *J. Taraszewska.* In preparation.
[8] W. Kemula, Z. Kublik, and J. Taraszewska, *Bull. Acad. Polon. Sci. Ser. Sci. chim.*, **8**, 269 (1960).
[9] D. C. Cornish, S. N. Das, D. J. G. Ives, and R. W. Pittman, *J. Chem. Soc.*, **A281**, 111 (1966).
[10] L. G. Sillen, *Acta Chem. Scand.*, 3, 539 (1949).

Table I

i $\mu a/cm^2$	τ_i sec	q_{τ_i} $\mu C/cm^2$	$q^{max}_{diff.}$ $\mu C/cm^2$	q^{min}_{layer} $\mu C/cm^2$
		0.1M KCl		
115	5	575	8	567
90	8	720	10	710
40	32	1280	20	1260
22	60	1320	26	1294
		1.0M KCl		
220	7.5	1650	1120	530
188	9.5	1790	1270	520
150	16	2400	1640	760
66	55	3630	3050	580

be observed in 0.1M KCl. As follows from our calculations based on equilibrium concentrations given by Sillen, the contribution of the diffusion process is in this case insignificant, amounting only to a few per cent of the total charge. Therefore we could expect that the induction time in this case will be independent of stirring, contrary to the 1M KCl solution. This conclusion has been confirmed experimentally.

The results given above may be regarded as an evidence that the induction time, measured both ellipsometrically and determined by reducing the mercury drop volume, corresponds to some particular stage in the crystallization process at which the average thickness of the layer is already polymolecular. In view of microscopic observations of Ives *et al.*,[9] it may be the stage of secondary growth of calomel crystals.

It seems that the problem of the primary electrode reaction cannot be solved at present owing to the lack of necessary additional information. There is no evidence for any slow homogeneous reaction occurring in solution. Our considerations based on equilibrium data are rather consistent with the model in which the overvoltage observed during the galvanostatic process is due to crystallization only. Also the concentrations of the electroactive form present in solution calculated from the impedance data by Armstrong *et al.*[11] in 2M and 5M HCl are consistent with experimental equilibrium concentrations obtained by us as is shown in Fig. 2. This only means that there exists an equilibrium between the mercury electrode and the soluble mercuric species and not that the $HgCl_4^{2-}$-ion is the primary product of the electrode reaction.

Studies of Hydrocarbon Fuel Cell Anodes by the Multipulse Potentiodynamic Method, III. Behavior of Saturated Hydrocarbons on Conducting Porous Teflon Electrodes with a Phosphoric Acid Electrolyte

L. W. Niedrach and M. Tochner (pp. 17-22, Vol. 114, No. 1)

J. A. Shropshire[12]: I think the authors are to be commended for having turned their attention to the study of a catalyst and electrode system which bear some relationship to a realistic fuel cell electrode. Although the MPP technique falters somewhat in the face of the high surface area catalyst, the comparison of the C_1-C_4 paraffins is still of considerable interest.

In the discussion, the authors repeatedly state that the initial adsorption rates of the paraffin fuels are: butane>propane>ethane. This is not at all clear from the data available in the paper. For instance, in their Fig. 11, if one takes the (low coverage) 15-sec adsorption, the accumulated charge ($Q_{E_{tot}}$) is exactly what one expects for equal moles of the various fuels having adsorbed on the surface. Thus, the accumulated charge ratios (at 15 sec) are approximately

$$C_3/C_2 = 1.45; \quad C_4/C_2 = 1.84; \quad C_4/C_3 = 1.27$$
(measured from graph)

If one assumes oxidation to CO_2, the ratios of the required number of electrons per mole for the three fuels are

$$C_3/C_2 = 1.43; \quad C_4/C_2 = 1.86; \quad C_4/C_3 = 1.30$$

a remarkable agreement under the circumstances.

Since according to the authors' data, the steady-state oxidation current at $U = 0.3$v (the potential of the above measurements) is relatively minor, the above values should represent a fairly realistic relative accumulation rate. On this basis then the adsorption rates appear to be substantially equal for the three fuels.

L. W. Niedrach and M. Tochner: We appreciate Dr. Shropshire's communication and agree that we have overstressed the relative order of the initial adsorption rates for ethane, propane, and butane. Actually, as emphasized in the paper, it was not possible to perform measurements at short enough equilibration times to obtain highly accurate estimates for the adsorption rates on the clean surface. In addition, such estimates are further complicated by the presence of several species in the ad layer. In any event we agree with Dr. Shropshire that the three adsorption rates are of the same order of magnitude, and indeed quite close.

With regard to the remarkable agreement among the accumulated charge ratios at 15 sec and the electron ratios for oxidation of the individual fuels, this must be considered fortuitous in the light of the variety of derived species that are present on the surface. Further, the accumulated charge ratios change considerably with the time of the equilibrations. For the precise relationships quoted by Dr. Shropshire to have direct meaning, it would be necessary to assume physical adsorption of the fuel entities themselves, although one or two site attachment through dissociative adsorption would not markedly affect the ratios. This appears quite unreasonable in the light of available evidence concerning the ad layer. That it consists of a variety of species including an appreciable fraction of partially oxygenated material as well as alkyl radicals is adequately supported by many investigations.[13-17] It should also be noted that although the steady-state currents in our experiments at 0.3v were small, sizable currents did flow during the initial stages of adsorption. These currents were, of course, associated with the oxidation of dissociated hydrogen as well as the formation of the partially oxidized species.

That the rates of adsorption of these saturated hydrocarbons are not markedly different undoubtedly reflects the structural similarity among them and hence a similarity of behavior in the adsorption step itself. Coupled with this would be regular, but small, trends among solubilities and diffusion coefficients, both of which control mass transport to an electrode. These are undoubtedly important during the early stages of adsorption. Some suggestions bearing on these latter points have been discussed recently.[18]

Ellipsometric-Potentiostatic Studies of Iron Passivity, I. Anodic Film Growth in Slightly Basic Solutions

J. Kruger and J. Calvert (pp. 43-49, Vol. 114, No. 1)

H. H. Uhlig[19]: The results presented by the authors eloquently describe the process of film growth on iron anodically polarized in a buffered borate solution. They demonstrate and further confirm that the ellipsometric technique is a sensitive method for studying growth of films *in situ*. Unfortunately, ellipsometry inherently provides no information regarding the composition and structure of such films. Hence it is not clear whether the anodic films measured in the authors' experiments are ferrous or ferric hydroxide, ferrous borate, or indeed anhydrous iron oxides as they hypothesize.

It is also not clear whether such films, the thickness of which they report, are justifiably called passive films. For example, it has been established by previous investigators that several metals in the passive state are often covered by films which are equivalent to no more than a monolayer of oxygen. On the other hand, many metals in the active state, including iron, which do not show passive behavior may be covered by adherent oxide films 30-100Å thick. Discussions

[11] R. D. Armstrong, M. Fleischman, and H. R. Thirsk, *Trans. Faraday Soc.*, 61, 2238 (1965).
[12] Esso Research and Engineering Company, Linden, N. J.
[13] S. Gilman, *Trans. Faraday Soc.*, 61, 2546, 2561 (1965).
[14] L. W. Niedrach, *et al.*, *This Journal*, 112, 1161 (1965); 113, 645 (1966).
[15] S. B. Brummer, 154th Meeting Am. Chem. Soc., Chicago, Ill., Preprints of Fuel Cell Symposium, 11, No. 3, 178 (1967).
[16] J. Giner, 15th Meeting CITCE, London and Cambridge, September 21-26, 1964, summaries of papers, p. xxix.
[17] W. T. Grubb and M. E. Lazarus, *This Journal*, 114, 360 (1967).
[18] E. J. Cairns, *Science*, 155, 3767 (1967).
[19] Department of Metallurgy, Massachusetts Institute of Technology, Cambridge, Massachusetts.

along these lines are of long standing. U. R. Evans[20] in 1927 succeeded in isolating thin oxide films from passive iron, but significantly he also succeeded in isolating similar oxide films from active iron.[21]

It is perhaps relevant to any discussion of passivity to remind ourselves of certain properties that apply to passive but not to other-type films on iron. (A) Thermally produced films of Fe_3O_4, or duplex Fe_2O_3 overlying Fe_3O_4 films on iron do not result in any of the usual passive film characteristics, no matter how thin or how thick such films may be. (B) The potential of iron in equilibrium with any of the known iron oxides is about 0.6v too active to account for observed passive potentials. Hypothesizing a cation-defect iron oxide, as was done by Nagayama and Cohen[22] in order to bridge the gap, is hardly acceptable because any such defect oxide would by definition allow rapid ion diffusion and would be a relatively poor diffusion barrier film in a corrosive environment. Alternatively, the hypothesis of a potential drop through an insulating iron oxide runs into the serious problem that no insulator could readily sustain the required potential gradient. Even if all of the film thickness (30Å), as measured by the present authors, were insulating (which passive film conductivity measurements contradict) an over-all potential of 0.6v requires a potential gradient of 2×10^6 v/cm, which value can be compared with the dielectric breakdown of glass equal to 0.7 to 1.5×10^6 v/cm or of mica equal to $1.5\text{-}2.2 \times 10^6$ v/cm. The potential gradient in an insulating film thinner than 30Å, as would be required by any oxide model, would exceed 2×10^{-6} v/cm. (C) The passive film on iron is able to oxidize chromites to chromates[23] in accord with 3 O (in passive film) + Fe + OH^- + CrO_2^- + $H_2O \rightarrow CrO_4^{--}$ + $Fe(OH)_3$. Passive iron which has been activated by mechanical shock does not have similar oxidizing properties. None of the known iron oxides is able thermodynamically to effect the above reaction, hence it is not likely that the usual iron oxides can in fact constitute the passive film.

Present viewpoints on structure of the passive film on *e.g.*, iron, nickel, chromium, and the stainless steels usually resolve themselves into two categories: *i.e.*, the passive film is either (a) an ion diffusion barrier or (b) it acts instead to increase anodic overvoltage for metal dissolution (decreases the exchange current density i_0 in the Tafel equation). Difficulties in the way of successfully assuming an ion diffusion barrier for iron are contained in some of the points raised above. In addition the observed limited dimensions of passive films suggest that they are protective by some other mechanism. Air-formed films on iron, as measured by ellipsometry,[24] in time reach 30Å or more, but these films are not protective to chemical environments and hence are not the same as the passive films. On the other hand, anodic overvoltage for metal dissolution can in principle be raised appreciably by oxygen adsorbed on the metal surface, and an assumed passive film of this kind also meets other requirements. Such a film by increasing the activation energy for hydration and ionization of metal atoms (or ions), parallels the well-known properties of many adsorbed organic and some inorganic species to increase either hydrogen or anodic overvoltage at metal electrodes. Oxygen is one of the most effective substances able to chemisorb on transition metals, but other compounds like CO (on stainless steels) and in some cases iodine (on iron in H_2SO_4) can also do so, and they similarly increase corrosion resistance in aggressive media.

Low energy diffraction data of metals like Ni[25] have disclosed that the first-formed chemisorbed layer of oxygen is extremely stable, resisting thermal decomposition even up to the melting point of Ni (1450°C). Multiple adsorbed layers which may form by anodic polarization at noble potentials, are less energetically bonded to the surface than is the first layer and are easier reduced. Depending on the metal, they may reduce more readily than the metal oxide (*e.g.*, Fe_3O_4). Hence adsorbed films of this kind, either easier or more difficult to reduce than the metal oxide depending on structure and thickness, and perhaps not easy to detect by ellipsometry, more readily fit the description of films accounting for passive phenomena. Such adsorbed films slow down corrosion processes but the rate of chemical reaction remains finite nevertheless, particularly in aqueous media or at elevated temperatures. Thick oxide films eventually grow which may behave as diffusion barrier layers, but their protective qualities, in aqueous media at least, remain inferior to the first-formed passive films at the immediate metal surface.

The thicker films described by the authors, if the above viewpoint has any merit, are probably iron compounds of unspecified composition which grow on top of the passive film. These thicker films presumably confer secondary protective qualities; but acting alone they would not be expected to account for recognized passive properties (*e.g.*, resistance to concentrated HNO_3).

In this connection, R. Frankenthal,[26] employing quantitative coulometry, has recently demonstrated that a primary passive film first forms on a 24% Cr-Fe alloy which is less than an equivalent monolayer of close-packed oxygen ions. This film itself in H_2SO_4 accounts for observed very low anodic current densities in the passive potential range. He finds a secondary thicker film to form subsequently at more noble potentials, which perhaps is constituted of hydrous metal oxides. The hydrous oxide film, however, has little or no influence on the passive current density (and hence on corrosion rate) in H_2SO_4. If the situation is similar for iron, as seems likely from the accumulated evidence, the primary passive film is the first-formed adsorbed structure. This film remains thin, being followed by a thicker stoichiometric iron compound film which grows on top of the passive film, the latter however having only secondary protective qualities.

J. Kruger and J. P. Calvert: We appreciate Professor Uhlig's interest in our paper. The main gist of his arguments is that the origin of the passivity of iron resides in a very thin film, presumably a chemisorbed monolayer of oxygen, next to the metal surface, and that any films that may be detected above this thin film are incidental to the phenomenon of passivity.

It is difficult to understand how this can be the correct picture of passive film on iron, when one considers, for example, the recent work by Nagayama and Cohen[27], using the same borate solutions as we do. (Some recent results of ours which are to be published as Part II of the series of which the paper under discussion is part, provide ellipsometric verification for their coulometric measurements.) These results show that when one reduces the outer layer of the passive film, the one that Professor Uhlig feels is incidental to the phenomenon of passivity, one then has a surface which exhibits an active potential and is no longer passive. However, at this point in the process, Nagayama and Cohen and our own work show that there still exists a film on the iron surface. Therefore, it is difficult to understand how Professor Uhlig's picture can be correct, because his picture would require that when the metal surface becomes active, the all-important oxygen monolayer slips out from between the metal surface and the oxide. This seems highly unlikely.

[20] U. R. Evans, *J. Chem. Soc.*, 1927, 1022.
[21] U. R. Evans, Discussion Section. *Trans. Electrochem. Soc.*, 79, 124 (1941).
[22] M. Nagayama and M. Cohen, *This Journal*, 109, 781 (1962).
[23] H. Uhlig, *Z. Elektrochem.*, 62, 626 (1958); (with T. O'Connor) *This Journal*, 102, 562 (1955).
[24] A. Winterbottom, *J. Iron and Steel Inst.*, 165, 9 (1950).
[25] A. MacRae, *Science*, 139, 379 (1963); *Surface Science*, 1, 319 (1964).
[26] R. Frankenthal, *This Journal*, 114, 542 (1967).
[27] M. Nagayama and M. Cohen, *This Journal*, 109, 781 (1962).

That there is indeed an oxide film on the iron surface, even in the active region, and that this film is as shown by others[27] Fe_3O_4, is further supported by electron diffraction studies.[28] These studies, moreover, show that when one forms a passive surface, besides Fe_3O_4 there are found extra spots due to γ-Fe_2O_3. In other words, when a passive potential is observed, both Fe_3O_4 and γ-Fe_2O_3 are present. At an active potential, only Fe_3O_4 spots are observed. Does it not then seem more reasonable to associate passivity with an outer layer and an active surface with Fe_3O_4 alone?

The fact that "thermally produced films of Fe_3O_4 or duplex Fe_2O_3 overlying Fe_3O_4" do not result in the usual passive film characteristics, really has no relevance to the present argument. The Fe_2O_3 in films formed at temperatures a few hundred degrees above room temperature is α-Fe_2O_3 and not γ-Fe_2O_3 Also, recent work of Okamoto[29] on passivation of stainless steel in aqueous solutions and our own on iron[30] indicate that hydrogen may play a role in the formation of a passive film. This is explained in a paper by Bloom and Goldenberg[31] as being due to the difficulty of obtaining γ-Fe_2O_3 without having hydrogen present in the lattice. Thus, some sort of aqueous environment may be necessary to form passive films on iron. Interestingly enough, films formed on iron at room temperature in oxygen containing small traces of water do indeed produce films that have different characteristics from those formed in pure oxygen alone.[32]

The important point to make here, however, is that one should not compare the film formed in aqueous solution with that formed in gaseous environments, even though we may nominally have the same kind of oxides from a bulk standpoint. Also, oxide in the form of very thin films may have quite different properties than bulk oxides because of the big influence of small amounts of impurities such as hydrogen, or because of a nonstoichiometry that may exist which produces cation or anion defects. The new thin film electronic devices depend on the very fact that large changes in properties can be produced by fantastically small changes in composition. It is for this reason, also, that one should not make predictions as to what potential the iron should exhibit in equilibrium with known iron oxides, because only the known bulk values for the iron oxides can be used, while thin film oxides may give entirely different values. Thus, one does not really know that a potential calculated using bulk values is "0.6 volts too active to account for observed passive potentials," when very thin films are involved. If one wants to hypothesize, one can by suitable models using the properties of bulk oxides, as Vetter[33] has done, account for the passive potentials. We think this is a dangerous game to play, however.

Likewise, it is difficult to predict what the breakdown potentials of these films are and, hence, to say that it is not possible to have the kind of potential drop that we speculate about in the paper. Whitehead's monograph[34] on dielectric breakdown of solids makes the point that as a film gets thinner, the electric strength can actually increase. He quotes breakdown values for some oxide films that are much higher than those given in our paper, thereby making our values quite possible. By the same token, one cannot assume that the oxidation of chromite to chromate can or cannot occur on the surface of thin oxide films from thermodynamic considerations because the thermodynamic data for the oxides (as very thin films) are not known.

[28] C. L. Foley, J. Kruger, and C. J. Bechtoldt, *This Journal*, 114, 994 (1967).
[29] G. Okamoto and T. Shibata, *Nature*, 206, 1350 (1965).
[30] H. T. Yolken, J. Kruger, and J. P. Calvert, To be published.
[31] M. C. Bloom and L. Goldenberg, *Corrosion Science*, 5, 623 (1965).
[32] J. Kruger and H. T. Yolken, *Corrosion*, 20, 29t (1964).
[33] K. J. Vetter, *This Journal*, 110, 597 (1963).
[34] S. Whitehead, "Dielectric Breakdown of Solids," p. 88, Oxford University Press, London (1951).

We fail to see the relevance of low energy electron diffraction data for a metal like nickel on a discussion of the passivity of iron. Granted that the monolayer formed on nickel may be quite stable; this may not say anything about such a monolayer formed on iron. Assuming that the results for Ni are relevant, the films formed by gas-metal reaction must also start with this very stable initial monolayer. If this monolayer were the passive film, are room temperature formed films, which start with this monolayer, passive? You cannot have it both ways. You cannot have a film formed by gaseous oxidation in a low energy electron diffraction experiment be passive, while one formed by gaseous oxidation in a non-low energy electron diffraction experiment, not be passive.

Just as one cannot extrapolate gas-metal results to aqueous solution, one cannot take the data of an entirely different kind of material, such as 24% chromium-iron alloy, and expect that the results found there are applicable to pure iron. Thus, the results of Frankenthal may or may not be relevant. An indication that this is so can be found from some of our own work[35] that indicates that at 24% chrome-iron concentration, the film formed on such an alloy does not exhibit any crystallinity; it is amorphous. Our own work shows that, although optically we can detect films that are as thick as 20Å at a concentration of 18% chromium, an amorphous film is observed. Surely such a film can be expected to behave differently than the highly crystalline film that one observes on passive iron[27,28]. Hence, one cannot argue that because one kind of film found in the case of chromium-iron alloys may exhibit passivity, that such a film is responsible for the passivity of iron.

Surface Roughness Effects in the Electrodeposition of Copper in the Limiting Current Range

N. Ibl and K. Schedegg (pp. 54-57, Vol. 114, No. 1)

R. Piontelli, B. Mazza, and P. Pedeferri[36]: This paper gives very interesting information on some of the problems involved by the formation of powdery deposits.

The authors[37] consider the decisive condition to be that of reaching the limiting current of mass transport. As a matter of fact this is often a sufficient condition. It does not appear, however, to be a necessary one. Moreover, the mere statement that in the limiting current range, powdery deposits are often encountered, does not appear to throw sufficient light on the mechanism of the phenomena itself. Like the whole field of electrocrystallization this problem is still wanting a satisfactory solution.

Some suggestions arising from the systematic work carried out in this laboratory[38] on the powdery-deposits formation from sulfamate baths[39] may be recalled here. The incoherent deposits of the various classes (spongy, coarse-powdery, blacks) are formed in any case, starting from tridimensional nuclei, mutually independent and in respect to the basis metal.

The possibility of formation and the kind of the incoherent deposit depends on the relative formation rate of the nuclei themselves, which must be high enough, and on the distribution in space of their

[35] J. Kruger, C. L. Foley, and J. P. Calvert, To be published.
[36] Institute for Electrochemistry, Physical Chemistry and Metallurgy, Milan Polytechnic, Milan, Italy.
[37] See also N. Ibl, "Advances in Electrochemistry and Electrochemical Engineering," P. Delahay and C. W. Tobias, Editors, Vol. 2, pp. 49-143, Interscience Publishers, New York (1962).
[38] B. Mazza, P. Pedeferri, R. Piontelli, and F. Siniscalco, *Electrochimica Metallorum*, 1, 441 (1966); *ibid.*, 1, 449 (1966); see also "Proceedings of the Symposium on Sulfamic Acid and its Electrometallurgical Applications (Milan, May 1966); Associazione Italiana di Metallurgia, Editor; Milan (1967).
[39] Also in this field the sulfamate baths appear to be especially interesting in view of their versatility and capacity to give powders (of Cu, Ag, Zn, Cd, Ni, Co, Pb, Sn and others) free from inclusions and contamination.

growth rate, which must be tendentially isotropic.[40]

In this sense a very essential role is played by the throwing power at the microscopic scale, largely decided by the rate of change of the overvoltages with current density, the contribution of the concentration polarization included. In this general frame the importance of the limiting current conditions, in view of the separation of powdery deposits, may find a reasonable interpretation, when one considers that everywhere the ratio: current density/activity of the metal ions attains high enough values; also the ensuing concentration polarization may be sufficient to deviate the cathodic metal separation, thus promoting a tendentially isotropic growth.

On the other hand also the intervention of factors, which appear to be rather underestimated by the "limiting current theory" of the powdery deposits formation, must be taken into account. This, especially in view of the study of the formation conditions of powdery deposits from complex-salt baths or from melts, and of explaining the transition from dendritic or spongy to powdery-deposits.

Among these factors one may recall: (A) the nature of the metal, as far as the exchange overvoltages, their dependence law on current density, the influence of the lattice forces on the properties and behavior of nuclei are concerned; (B) factors influencing the secondary inhibition effects by hydrogen, colloidal products, but also by anions, secondary constituents of the baths, *etc.;* and (C) the physical and mechanical conditions (also apart from their direct influence on the mass transfer).

As in many other fields of the theory of electrode processes, the models which do not explicitly acknowledge the direct influence of the nature of the metal and of the bath constituents, are at least incomplete.

N. Ibl[41]: The remarks of Piontelli *et al.*, are very pertinent. Reaching the limiting current is indeed in general a sufficient, but not always a necessary condition for the formation of a very rough or powdery deposit. We have discussed this question in more detail in a previous review paper[42]. Powdery or spongy deposits can be obtained well below the limiting current. A well-known case is the formation, at lower currents, of spongy Zn or Cd deposits from nonacidified sulfate solutions, a phenomenon which is very probably not due to mass transfer effects[42]. However, if no other causes of powder formation are operative at lower currents, the deposit, as a rule, becomes very rough or powdery when the limiting current is reached.

But the properties of the powders obtained at the limiting current are also affected by other factors[42] beside mass transport. For instance, we have found that copper powder deposited from a nonacidified copper sulfate solution containing gelatin is very finely divided and almost black, whereas the powder obtained without addition of gelatin is much coarser and reddish in color.[43] But in both cases powder formation starts at the limiting current. As pointed out by the authors, the structure of electrodeposits depends in general on a number of factors and their interaction. One of these factors is mass transport. Its role can be more or less important, depending on the circumstances. Sometimes it is negligible, but in certain cases it is predominant.

Undoubtedly, many factors finally contribute to shape the structure and the properties of an electrodeposit, but the main fact which I would like to point out here is that we can visualize a pure transport mechanism which should, in a very general way, cause the formation of a very rough deposit, at the limiting current as a rule, and, under certain circumstances, already below the limiting current. The leading ideas, which have been developed in more detail in a recent review paper[44], are as follows:

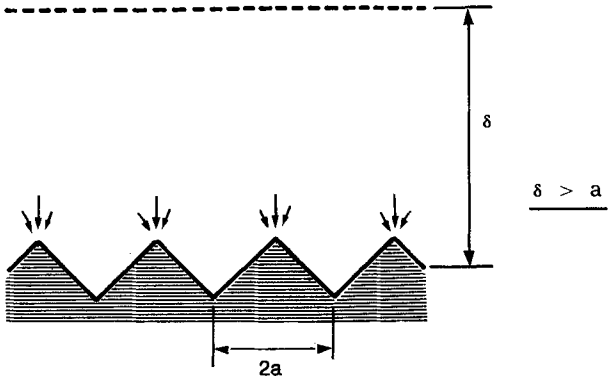

Fig. 1.

Let us consider a metal surface which has some initial roughness, with small crests and recesses, as shown schematically in Fig. 1. We will now discuss the question under which conditions certain factors tend to enhance the irregularities of the surface, and how they operate. This is a problem of current density distribution.

If the characteristic length a of such a profile is small as compared to the thickness of the diffusion layer δ (Fig. 1), the crests of the profile are privileged from the viewpoint of mass transport, because the free cross section for diffusion increases with increasing distance from the crest: the crest is more accessible for mass transfer than a recess. However, this does not yet mean that the local current density is necessarily larger at the crest, because the current density distribution depends not only on the transport of mass but also on the transport of charges through the solution and through the electric double layer at the interface, *i.e.,* it also depends on electric quantities (conductivity of the solution, overvoltage). Depending on the conditions, the current distribution is governed mainly by the transport of mass, or of charge, or by both simultaneously to a comparable degree.

Let us now consider the simple case that the current distribution is given solely by the geometry of the system and by the conductivity of the solution. We then have what is called in plating primary current distribution. Under these conditions, the local current density is larger at a crest than in a recess because the crest is privileged from the viewpoint of the transport of charges through the solution: the lines of electric flux converge toward the crest (Fig 1). Now, if we take into account overvoltage, the situation is changed: the overvoltage tends to make the current distribution more uniform (secondary current distribution). The decisive quantity is the polarization parameter P defined as the product of the specific conductivity of the solution κ and the slope of the current voltage curve, $d\eta/di$: $P = \kappa d\eta/di$. If P is large as compared to the characteristic length a of the profile, the current distribution is virtually uniform over the profile[45], in spite of the influence of the serrated geometry. This can be interpreted, at least qualitatively, in a simple manner. Along the interface, between crest and recess (Fig. 1), there is, in the solution, an ohmic potential drop ΔE_R, which must be compensated by the difference $\Delta\eta$ between the overvoltage at the crest and in the recess

$$\Delta E_R + \Delta\eta = 0 \qquad [1]$$

[40] A predominating growth-rate parallel to the basis metal may lead to compact deposits, while one normal to the cathode enhances the dendritic or acicular growth.

[41] Department of Industrial and Engineering Chemistry, Swiss Federal Institute of Technology, Zurich, Switzerland.

[42] N. Ibl, "Advances in Electrochemistry and Electrochemical Engineering," P. Delahay and C. W. Tobias, Editors, Vol. 2, p. 49. Interscience Publishers, New York (1962).

[43] N. Ibl, *Helv. Chim. Acta.*, 37, 1149 (1954).

[44] N. Ibl, Proceedings of the International Conference, "Protection against Corrosion by Metal Finishing," Basle, Switzerland, November 1966, p. 48, Forster Verlag, Zurich, Switzerland.

[45] C. Wagner, *This Journal*, 98, 116 (1951).

If the overvoltage η increases rapidly with increasing current density i ($d\eta/di$ large), a negligible increase in current at the crest will be enough to create an increase in overvoltage which is sufficient to compensate ΔE_R, and the current density is virtually the same at the crest and in the recess.

Let us now consider separately concentration and activation overvoltage, which we denote by η_c and η_a, respectively; we therefore split the total overvoltage difference $\Delta\eta$ in two parts, $\Delta\eta_c$ and $\Delta\eta_a$, which correspond to concentration and activation overvoltage, respectively. Equation [1] thus takes the form

$$\Delta E_R + \Delta\eta_c + \Delta\eta_a = 0 \qquad [2]$$

In this equation, $\Delta\eta_c$ and $\Delta\eta_a$ have not the same sign. This can be seen as follows. If the current distribution is virtually uniform, the lines of the electric flux and those of the flux of mass do not converge toward the crests as indicated in Fig. 1, but are essentially parallel, vertical lines. The concentration c_i of the metallic cations at the interface electrode-solution is then larger at the crest than in the recess; the difference Δc_i between the interfacial concentration at the crest ($_cc_i$) and in the recess ($_rc_i$) is given by

$$\Delta c_i = {}_cc_i - {}_rc_i = h\, dc/dy \qquad [3]$$

where h is the vertical distance between crest and recess and dc/dy the concentration gradient in the vertical direction[46]. We see that the concentration overvoltage is larger in the recess than at the crest; therefore, $\Delta\eta_c$ is of the same sign as ΔE_R but has the opposite sign of $\Delta\eta_a$. We thus come to the important conclusion that only activation overvoltage necessarily tends to flatten the current distribution; in the case of a microprofile ($a<\delta$), concentration overvoltage cannot contribute to making the current distribution more uniform than would correspond to primary current distribution; to the contrary, it counteracts the equalizing action of activation overvoltage and tends to make the current distribution nonuniform. The extent of the departure from an even distribution depends on the relative values of ΔE_R, of $\Delta\eta_c$ and of $d\eta_a/di$, *i.e.*, of the variation of the activation overvoltage with current density. If $\Delta\eta_c$ is large, the current distribution will be nonuniform even if the slope of the current voltage curve, $d\eta/di$, is large. An extreme case is that of the limiting current. It can be easily shown that $\Delta\eta_c$ is proportional to $\ln({}_cc_i/{}_rc_i)$; at the limiting current, or close to it, $_rc_i$ tends to zero, whereas $_cc_i$ is still finite; the value of $\Delta\eta_c$ thus tends to be exceedingly large. Under these conditions, the influence of concentration overvoltage is overwhelming and the current distribution is controlled by mass transport. Since the crests of a microprofile are privileged from the viewpoint of diffusion, under mass transport control, the local current density is larger on a crest than in a recess. Geometric irregularities of the surface will then tend to grow.

The surface of a polycrystalline metal is usually heterogeneous. This causes local variations of the activation overvoltage, and therefore of the current density, which are, in general, randomly distributed, both in location and in time. There is thus a natural tendency for the formation of small, geometric irregularities in the deposit. Below the limiting current, the concentration overvoltage changes only slowly, and the influence of activation overvoltage on the current distribution at a microprofile is often predominant. If the polarization parameter P is sufficiently large, the small protuberances of the surface, randomly distributed in space and in time, are, on the average, not privileged; the local current density tends to be the same on the crests and in the recesses and, on the time average, peaks do not grow faster than the rest of the deposit. At the limiting current, however, the situation is very different. According to the above discussion, the current distribution is mass transport controlled and the current density is larger at the peaks, which thus grow faster; the irregularities of the surface are strongly amplified: there is, at the limiting current, a sort of instability with respect to small protuberances present by chance on the surface, and a very rough or dendritic deposit results.

Let us note that, under certain circumstances, a similar situation prevails even below the limiting current, or at least already when the limiting current is being approached. The essential condition is that the rate of change of activation overvoltage with current density, $d\eta_a/di$, is sufficiently small. If this is the case, the current distribution over a microprofile is nonuniform, and the deposit tends to become very irregular even at low currents. The activation overvoltage is usually very small in the deposition of metals from fused salts, because the high temperatures involved much accelerates the ion exchange at the interface. But it is sometimes also very low at room temperature in aqueous solutions, for instance, in the deposition of Ag from aqueous $AgNO_3$. It is well known that it is indeed very difficult to get even deposits in molten salt electrolysis, and that metals of an irregular, dendritic form are usually obtained. Similarly, in the deposition of silver from an aqueous $AgNO_3$– solution there is a marked tendency for the formation of long dendrites and needles which grow outward into the solution. This is in qualitative agreement with the above discussion.

Generally speaking, the formation of very rough or dendritic deposits is necessarily linked with nonuniform current distribution. It is therefore to be expected that the factors which govern current density distribution (conductivity of the solution, overvoltage, and mass transport) have a very great influence on the structure of electrodeposits. It was the main purpose of the paper under discussion, and of some of our earlier articles, to stress these aspects which have been hitherto rather neglected in the literature. Undoubtedly, factors such as the formation of new nuclei and the rate of growth of already existing crystals play an eminent role in electrocrystallization. But they have been already studied by quite a number of authors.

[46] A more quantitative treatment along these lines has been developed and compared with experiment (unpublished calculations of J. Levkov and N. Ibl). The results will be published later.

Surface Tensions of Co-Ce and Pu-Co-Ce Alloys as Determined from Frozen Menisci

J. C. Biery (pp. 225-231, Vol. 114, No. 3)

P. D. Ownby and B. C. Allen[47]: Interest in Biery's surface-curvature technique of measuring surface tensions was generated when his first paper[48], which forms the basis of his present one, appeared.

There is some similarity between his technique and that used recently at the Columbus Laboratories of Battelle Memorial Institute[49,50] to determine the surface tension of reactive materials. Chromous iodide[49] and boron triiodide [50] have been allowed to rise in 0.02 to 0.2-cm ID capillary tubes in evacuated quartz or Pyrex containers. The liquid surface tension, γ_{LV} was determined from the capillary-rise height, h, using the capillary-rise equation

$$\gamma_{LV} = \frac{g\rho_L r h}{2\cos\theta}$$

[47] Battelle Memorial Institute, 505 King Avenue, Columbus, Ohio 43201.

[48] J. C. Biery and J. N. Oblak, *Ind. Eng. Chem. Fundamentals*, 5, 121 (1966).

[49] C. M. Jackson, B. C. Allen, and R. D. Gretz, Unpublished work. See also Ph.D. dissertation by C. M. Jackson, The Ohio State University (1966).

[50] P. D. Ownby and R. D. Gretz, *Surface Science*, To be published. See also Ph.D. dissertation by P. D. Ownby, the Ohio State University (1967).

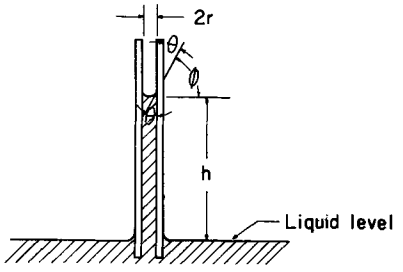

Fig. 1. Schematic diagram of capillary and height of rise measured to determine surface tension.

where g = 981 cm/sec^2, ρ_L = liquid density, r = capillary radius, and θ = contact angle (Fig. 1).

In the case of CrI_2, where the quartz view window was clouded, h was measured by radiographic methods. In the case of BI_3, h could be viewed and measured directly and/or photographed. Both contact angles used in Eq. [1] were determined independently by the sessile-drop method *in vacuo*. In an attempt to compare the results of the two techniques, a photograph[50] of the 0.052-cm ID capillary containing BI_3 was enlarged, and the Biery technique applied to the meniscus shape.[51] Although the photograph was grainy, a modification of the technique described was reported to correlate favorably[51] with the surface-tension value obtained by the capillary-rise technique. However, the contact angle determined by the Biery technique was 52°. The sessile-drop method yielded a contact angle less than 5°, and 0° was used in the capillary-rise calculation

In an attempt to resolve this discrepancy, the question of capillary-diameter measurement arose. It was found that diameter measured by viewing through the capillary wall was somewhat larger than that measured from the capillary cross section. That is, a magnification effect enlarged the apparent capillary diameter when viewed through the capillary. This same effect distorted the apparent meniscus shape, so that the angle obtained by smoothing or extrapolation to the wall was consistently larger than the actual value. This can be seen by referring to Biery's data[48] on water, where "the sine of the outside angle at contact" ϕ, or the cosine of the contact angle θ (see Fig. 1) was between 0.50 and 0.65. This gave a contact angle of 30°-40°. The contact angle for water in preliminary experiments using the capillary-rise technique was found to be ~0°.[50] Using a zero contact angle, the surface tension of water by capillary-rise was found to correlate with the accepted value of 72 dynes/cm at 25°C.[52]

Biery's method of photographing meniscus shapes through a glass tube inaccurately determines the contact angle, and the shape itself appears distorted because of the lens effect. Because the lens effect is one dimensional, no distortion of the capillary-rise height is experienced in either photographing or radiographing the liquid. Therefore, Biery's complex calculations seem to have little advantage over the more straightforward and reliable capillary-rise technique.

In his present paper, Biery has presented surface-tension results on alloys that have not been studied previously. Except for one capillary-rise value, there are no standards with which to compare his elevated-temperature results. Since surface contours of a solidifying metal distort by differential contraction or expansion, curvature measurements based on solidified metals are not recommended.[53] In fact, the resulting surface tensions can be 50-70% low.[54] In spite of the methods presented for arbitrary mathematical selection of solidified menisci, the validity of the reported surface tensions appears questionable. It seems as though the results would be greatly enhanced by (*a*) correlation with a metal of known surface tension, using similar experimental techniques; (*b*) measurements on unalloyed cerium to provide base-line surface-tension data for the alloys; and (*c*) correlation with radiographs taken with the alloy liquid.

The computational method is presented as being capable of determining contact angle as well as surface tension. In the capillary-rise result presented for 57.7 w/o Pu-9.4 w/o Co-32.8 w/o Ce, a contact angle of 0° was assumed. It would be enlightening to see an explicit comparison between the assumed value and that observed and/or calculated from menisci shape.

It appears that the "usual methods of determining surface tension" would be applicable to plutonium alloys. For example, a simple technique could involve the capillary-rise method [49,50] in an inert atmosphere, since a nonreactive capillary material, tantalum, is available. Small-diameter tantalum capillaries could be tack welded to the inside of the tube containing the alloy. When melted, the alloy would form a reservoir on the bottom and rise up the tubes. A radiograph at temperature would provide an accurate measure of capillary-rise height. Values of the height from radiographs in the solidified alloy could then be calibrated and used for most of the determinations.

J. C. Biery: The surface tension generation technique as outlined in footnote 55 was applied by the author to the BI_3 meniscus of Ownby and Allen. However, the method was found to be unworkable with such a meniscus formed in a capillary rise experiment where the meniscus rise height was very small as compared to the capillary rise itself. The shape of the meniscus did not vary sufficiently with changes in surface tension in this case to overcome the inaccuracies and distortions involved in photographing the meniscus.

The technique that was utilized was a new one[56] which the author derived by assuming a mathematical form for local sections of the meniscus. Parameters in the assumed equations, when utilized with the Laplace-Young equation and physical data from the meniscus, generated surface tensions as a function of radius. An interesting result from this development was that $\sin\theta$, where θ was the angle between a horizontal line and a line tangent to the meniscus curve, was a linear function of the radius when the capillary rise was many times greater than the height of the meniscus. Thus, in principle, the contact angle at the wall of a capillary rise experiment could be obtained by making a linear extrapolation of the $\sin\theta$ data obtained from a photograph of the meniscus. This procedure was followed with the BI_3 meniscus of Ownby and Allen, and the $\sin\theta$ at the wall was found to be 0.62 and θ to be 38° (the contact angle as normally defined was then 52°).

As indicated by the communication of Ownby and Allen, the 52° angle did not agree with the 5° angle that they measured from sessile-drops. Three possibilities exist to explain the discrepancy. (A) The actual contact angle in the capillary tube was not the same as the sessile-drop contact angle. The change in angle could result from impurities and contamination on the inside of the capillary. In capillary rise experiments, the contamination of the inside surface is a common malady. (B) The distortion from the curvature of the glass tube in a small capillary may have made the photograph unusable for determination of the $\sin\theta$ versus radius curve. (C) In the work done in footnote 55 and the present article, the menisci were magnified approximately 20x while

[51] J. C. Biery, Private communication.
[52] "Handbook of Chemistry and Physics," 32nd ed., p. 1815, C. D. Hodgman, Editor. The Chemical Rubber Publishing Co., Cleveland, Ohio (1950).
[53] W. D. Kingery, "Property Measurements at High Temperatures," p. 376, John Wiley & Sons Inc., New York (1959).
[54] W. D. Kingery and M. Humenik, Jr., *J. Phys. Chem.*, 57, 359 (1953).
[55] J. C. Biery and J. N. Oblak, *Ind. Eng. Chem. Fundamentals*, 5, 121 (1966).
[56] J. C. Biery, Manuscript in preparation.

the BI_3 capillary meniscus had to be enlarged 260x. The large magnification definitely produced additional uncertainty. In the BI_3 case, there was no positive check as to which of the three possibilities was causing the disagreement. Possibly, all factors were contributing. Further work with liquids of known surface tension is required to define the causes for disagreement between the two contact angle procedures.

Distortion near the tube wall was very evident in the photographs of the water and mercury menisci formed in glass tubes which were analyzed and reported in footnote 55. Because of this distortion, as noted in that paper, the full meniscus up to the wall could not be utilized. As a result, $\sin\theta$ at the outside of the meniscus section studied was not the sine of the tangent angle at the wall. Therefore, the statement made by Ownby and Allen about water contact angles at the wall has no validity since contact angles at the wall were not determined in the work presented in footnote 55. Also, in that work the $\sin\theta$ data could not be linearly extrapolated to the wall since the capillary rise was small as compared to the rise in the meniscus.

The comments of Ownby and Allen concerning the use of the solidified menisci and the possible distortions involved are well taken. The procedure developed in footnote 55 and used in the paper under question was designed to detect distortion. Still the possibility exists that distortion which changed the meniscus to another mathematically consistent meniscus shape would not be detected by the procedure. To check data from this procedure, data from other methods certainly are necessary. However, because of the check with the one capillary rise experiment, and also because of the fine agreement of the surface tensions of the same alloy in containers of different diameters where distortion effects should have been considerably different, the author believes that the data presented for Pu-Co-Ce and Co-Ce do give good indications of the surface tensions of the alloys at their freezing points.

In reference to their comment about use of radiographs of the liquid, some work with radiographs of liquid menisci has been done. The menisci in all cases were too fuzzy to produce good data with this technique. To be successful, very sharp radiographs of the meniscus must be made.

Ownby and Allen raised the question of contact angles for the Pu-Co-Ce and Co-Ce alloys. Both alloy systems completely wet the insides of the capsules above the meniscus. This creeping phenomenon would indicate a 0° contact angle at the wall. Also, the computational method indicated $\sin\theta = 1.0$ or 0° wall contact angles for menisci analyzed. Figures 5 and 6 of the article being considered show $\sin\theta$ equal to 1.0 at the outside of the 25th increment which in these cases was coincident with the wall.

Hydrogen Absorbed by Clean Platinum Electrodes

Fritz G. Will and David J. BenDaniel

General Electric Research and Development Center, Schenectady, New York

Rebuttal on Comments by S. Schuldiner (Vol. 114, 916 (1967))

In a paper published in the September issue of this *Journal* (1), we presented a mathematical analysis of the effect of hydrogen absorbed by electrode and electrolyte on the hydrogen surface coverage as determined by nonsteady-state methods. Using reliable experimental values of the hydrogen diffusivity and solubility in platinum, we were both able (*i*) to establish systematic errors in the widely used charging curve and sweep methods due to these effects, and (*ii*) to show quantitative agreement between predictions of our analysis and other workers' measurements of surface coverage on platinum. In a comment published in the same issue of the *Journal*, S. Schuldiner attacked our analysis on a variety of points. We present now a point-for-point reply to those comments in sufficient detail such as to prevent any ambiguity from existing with respect to our work.

We quote our critic on his major objections.

1. "Slow phase boundary reactions cannot be ignored for studies of the permeation rates of hydrogen through metals."
2. "BenDaniel and Will cannot assume that slow phase boundary reactions did not affect the H permeation rate found by Vetter and Knaack, or that the Vetter and Knaack Pt electrode was clean."
3. "On a clean Pt surface hydrogen diffusion through Pt is immeasurable."
4. "BenDaniel and Will confuse the issue of electrode cleanliness and activity for hydrogen permeation."
5. "The assumption used by BenDaniel and Will that the rate of diffusion through a Pt electrode is dependent on the square root of the hydrogen partial pressure in the gas phase above the solution is not applicable to a polarized electrode."
6. ". . . the solubility and diffusion coefficients for hydrogen in Pt by BenDaniel and Will are much larger than would be reasonably expected."

In summary of our comments to be presented below, we find that the overwhelming evidence in the literature establishes the inapplicability of each of these criticisms.

1. Regarding his first and main objection, that slow phase boundary reactions cannot be ignored in H permeation studies, our critic cites only a single reference (2), and this single reference is misinterpreted.[1] On the other hand, we wish to point out that the fast rate of phase boundary reactions on clean, active platinum electrodes has been well documented (3-10). These rates are by 3 to 5 orders of magnitude larger than the permeation rates of H through Pt found by Vetter and Knaack and other authors. Thus, Bodenstein (11) found a permeation rate of $1.1 \cdot 10^{-12}$ moles H/cm/sec at 40°C, Vetter and Knaack (12) found $6.6 \cdot 10^{-13}$ at 25°C, and Gileadi *et al.* (13), on Pt intentionally poisoned with As_2O_3, found a rate of $3.5 \cdot 10^{-14}$ at 70°C. Note that the current density, equivalent to a permeation rate of $6.6 \cdot 10^{-13}$ moles H/cm/sec is only 22 μa/cm^2 for a 30μ thick Pt foil (12), while the equilibrium rates of the H discharge and the H_2 dissociation on active Pt are several hundred milliamperes per square centimeter (3-6) and several milliamperes per square centimeter (7-9), respectively. It is evident from a comparison of these numbers that for active surfaces the diffusion of H through Pt solely determines the over-all permeation rate, *i.e.*, phase boundary reactions have no effect on the permeation rate.

Furthermore, there is ample experimental evidence that, even for the H-Pd system with its large permeation rates [$4 \cdot 10^{-9}$ (14) to $1.2 \cdot 10^{-8}$ (15) and $1.6 \cdot 10^{-8}$ (16) moles H/sec/cm, *i.e.*, about 4 orders of magnitude larger than for H-Pt], the effect of phase boundary reactions has been successfully eliminated, for example, by "activation" of the surface by oxidation and subsequent reduction (17). Nevertheless, with such high permeation rates, as for H-Pd, one has to be careful to obtain results which are free of the effects of the processes occurring on the phase boundary or in the electrolyte.[2]

2. With regard to our critic's second assertion, we can verify in a straightforward and well-known way that the H-permeation rate found by Vetter and Knaack (12) was indeed not affected by slow phase boundary reactions. The permeation transients obtained by these authors uniquely meet the two sufficient criteria for diffusion through the metal as determining the over-all permeation rate, *i.e.*, (*i*) the diffusion distances (membrane thicknesses) are proportional to the square root of the diffusion times, and (*ii*) the steady-state permeation rates are inversely proportional to the diffusion distances.

Incidentally, we did not assume in our analysis, as asserts our critic, that the Pt electrode of Vetter and Knaack was particularly "clean." The 0.12v slope on the polarization side of their electrode signifies that H_2 diffusion in the electrolyte was not rate determining; in fact, it shows that the H^+ discharge determined the rate of the hydrogen evolution on their Pt electrode. However, since the rate of H diffusion through Pt was much slower than any of the processes on the polarization side, the question which one of these determined the rate of H_2 evolution is irrelevant. Moreover, while the Pt electrode of Vetter and Knaack was not very "active," it was clean enough to establish the reversible hydrogen potential.

3. We now concern ourselves with our critic's third claim, that no H permeates through clean Pt or that the surface has to be poisoned to observe permeation. We find that contrary to his claim, it was not demonstrated in the two references cited by him (13, 19) that the surfaces were free of adsorbed impurities, *i.e.*, clean. Hence, we are inclined rather to accept the evidence of the overwhelming majority of investigators who were able to demonstrate H permeation into Pt, without finding it necessary to poison their Pt surfaces intentionally (11, 12, 20-23) [compare also Smith (24) and more references cited there].

Parenthetically, in a later paper (25) our critic himself provided convincing experimental evidence that hydrogen is absorbed by

[1] It suffices to say that Ash and Barrer (2) present a theory in which they merely show how the permeation rate would be affected if phase boundary reactions were slow.

[2] Thus, Schuldiner *et al.* (18) obtained permeation data which are about an order of magnitude lower than those by Wicke *et al.* (15) and Barrer (16) and which fail to show the inverse proportionality between permeation rate and membrane thickness characteristic for slow diffusion through the solid. Indeed, LaPietra (14) showed that Schuldiner's data were affected by slow transport of the ceric-cerous couple in solution.

Pt whose surface was proven to be clean by showing H coverage to the extent of a full monolayer. In fact, it was this very paper we used to verify successfully our analysis. Conversely, the fact that the experimental results follow the predictions of our diffusion analysis for current densities from 0.78 to 203 ma/cm^2 is clear evidence in itself that H diffusion into clean Pt occurs and that phase boundary reactions are not rate determining in this range of currents.

Last, it is also interesting to note that with his third assertion our critic directly refutes own statements in the mentioned paper (25) in which he writes, and we quote, "that platinum electrodes in sulfuric acid solution can absorb considerable quantities of oxygen and hydrogen."

4. Our critic states that we "confuse electrode cleanliness and activity for H permeation." However, established views of permeation and adsorption clearly favor such "confusion." It is well documented that (i) adsorption is a prerequisite for permeation (26), and (ii) commonly adsorbed impurities interfere with H adsorption (10). In other words, the cleaner and more active the Pt electrode, the more it will favor H permeation.

Further, we find our critic's claim "that for clean Pt electrodes with high activity for H_2 evolution, the H-permeation is negligible" plainly incompatible with a later statement in the same Comments "that the atomic hydrogen activity on the . . . electrode surface is the primary factor controlling the rate of solution and migration of H through the metal."

5. Our critic also believes that we set the rate of H diffusion through Pt proportional to the square root of the H_2 partial pressure above the solution and argues that we should have used the "effective H_2 partial pressure" instead. But, in fact, this is exactly what we have done (compare Eq. [3a] and [4] in our analysis).[3]

6. Our critic states that our values for the diffusivity ($3\cdot10^{-8}$ cm^2/sec) and solubility $2.2\cdot10^{-5}$ moles H/cm^3) derived from Vetter and Knaack (12) are "much larger than would be reasonably expected."

Again, he bases this opinion on two obviously inapplicable studies while not quoting the work of a larger number of investigators whose values are comparable with ours. Our critic quotes data obtained by Sieverts (27) at temperatures between 409° and 1342°C. If one would extrapolate Sievert's data, one would find a solubility of 10^{-16} moles H/cm^3 at 25° (and 10^{-14} at 70°C). These values are clearly much too low to be reasonable. In fact, they are by 8 orders of magnitude lower than even the values obtained in the second study, quoted by our critic (13), which was done on Pt intentionally poisoned by As_2O_3. Obviously, we favored the values of Vetter and Knaack which were obtained on Pt that established the reversible hydrogen potential. Furthermore, Vetter's permeation rates at 25°C agree well with data of Bodenstein (11), who found rates twice as large at 40°C. Also, careful studies by Graham (20) and Thiel *et al.* (21) result in solubilities of $4.9\cdot10^{-4}$ and $7.9\cdot10^{-4}$ mole H/cm^3 both at 25°C. Their Pt electrodes had been thoroughly outgassed by heating *in vacuo*, then cathodically polarized for several hours, and finally heated *in vacuo* again to remove and measure all of the absorbed hydrogen. If, as our critic recommends, one applies Gileadi's *et al.* (13) finding that only 5-15% of this hydrogen is "free to move" at ordinary temperatures, the solubilities of mobile hydrogen in Graham's and Thiel's studies would be $2.4\cdot10^{-5}$ to $1..2\cdot10^{-4}$ moles H/cm^3. The lower of these values agrees very well with Vetter's value.

Finally, the diffusivities of hydrogen in metals in general make it clear that our value for the diffusivity in Pt is well in order. Thus, by extrapolation of Eichenauer's *et al.* data obtained between 200° and 900°C we find H diffusivities of $2.4\cdot10^{-9}$ cm^2/sec for Al (28), $1.0\cdot10^{-5}$ for α-Fe (20), $2.3\cdot10^{-9}$ for Cu (28), $9.8\cdot10^{-9}$ for Ag (29), and $4.5\cdot10^{-8}$ for Au (30), all at 25°C. Diffusivities of H in Pd measured near room temperature by three investigators are $2.4\cdot10^{-7}$ cm^2/sec at 37°C (16), $2.7\cdot10^{-7}$ (16), $2.2\cdot10^{-7}$ (14), and $1.6\cdot10^{-7}$ (15), all at 25°C.

In conclusion, the assumption in our diffusion analysis that the rate of the phase boundary reactions is fast compared to the rate of permeation into the metal is fully justified in the case of hydrogen diffusing into clean platinum and beyond that, is expected to hold in a variety of other cases. The values by Vetter and Knaack on the diffusivity and solubility of hydrogen in platinum, which we use in our analysis, are valid and reliable. They were clearly obtained under conditions of diffusion control through the platinum. These values compare favorably with values obtained by other authors on platinum and on a variety of other metals. Our quantitative interpretation of recent transient measurements on evidently clean Pt electrodes, based on the simple and sole process of diffusion, is sufficient proof in itself for the applicability of our analysis. We feel that the burden of proving otherwise now falls on the proponent of the unusual hypothesis of "dermasorption" which has recently been invoked (31).

[3] One could, however, argue that the use of a square root relationship in itself is not a good approximation in the limiting case of large surface coverages.

REFERENCES

1. D. J. BenDaniel and F. G. Will, *This Journal*, **114**, 909 (1967).
2. R. Ash and R. M. Barrer, *Phil. Mag.*, **4**, 1197 (1959).
3. P. Dolin and B. Ershler, *Acta Physicochim. URSS*, **13**, 747 (1940).
4. K. Rozental, P. Dolin, and B. Ershler, *ibid.*, **21**, 213 (1946).
5. M. Breiter, H. Kammermaier, and C. A. Knorr, *Z. Elektrochem.*, **60**, 37 (1956).
6. R. Parsons, *Trans. Faraday Soc.*, **54**, 1053 (1958).
7. A. N. Frumkin and E. Aikasjan, *Doklady Akad. Nauk SSSR*, **100**, 315 (1955); *Izvest. Akad. Nauk*, 202 (1959).
8. M. Breiter, C. A. Knorr, and R. Meggle, *Z. Elektrochem.*, **59**, 153 (1955).
9. L. Nekrasov, *Vestnik Moskov. Univ. Ser.* **II**, 19 (1960).
10. A. N. Frumkin, "Advances in Electrochemistry," Vol. 3, pp. 287-392, P. Delahay, Editor, John Wiley & Sons, New York (1963).
11. M. Bodenstein, *Z. Elektrochem.*, **28**, 517 (1922).
12. K. J. Vetter, "Elektrochemische Kinetik," p. 495, Springer, Berlin (1961). M. Knaack, Ph.D. thesis, Technical University, Berlin (1957).
13. E. Gileadi, M. A. Fullenwider, and J. O'M. Bockris, *This Journal*, **113**, 926 (1966).
14. A. LaPietra, Ph.D. thesis, The Catholic University of America (1961).
15. E. Wicke, A. Küssner, and K. Otto, Actes Internation. Congress Catalyse, 2, Paris (1960), **1**, pp. 1035-1044.
16. R. M. Barrer, *Trans. Faraday Soc.*, **36**, 1235 (1940).
17. A. Farkas, *ibid.*, **32**, 1667 (1936).
18. S. Schuldiner and J. P. Hoare, *This Journal*, **103**, 178 (1956).
19. J. P. Hoare and S. Schuldiner, *ibid.*, **103**, 237 (1956).
20. Th. Graham, *Pogg. Ann.*, **134**, 321 (1868).
21. A. Thiel and W. Hammerschmidt, *Z. anorg. Chem.*, **132**, 15 (1924).
22. G. C. Schmidt and Th. Luecke, *Z. Phys.*, **8**, 152 (1922).
23. R. Koehler, *Z. phys. Chem.*, **135**, 369 (1928).
24. D. P. Smith, "Hydrogen in Metals," p. 79, University of Chicago Press, Chicago (1948).
25. S. Schuldiner and T. B. Warner, *This Journal*, **112**, 212 (1965).
26. C. J. Smithells, "Gases in Metals," p. 156, Chapman & Hall, Ltd., London (1937).
27. A. Sieverts and E. Jurisch, *Ber.*, **45**, 221 (1912).
28. W. Eichenauer and A. Pebler, *Z. Metallkunde*, **48**, 373 (1957).
29. W. Eichenauer, H. Kuenzig, and A. Pebler, *ibid.*, **49**, 220 (1958).
30. W. Eichenauer and D. Liebscher, *Z. Naturforsch.*, **17a**, 355 (1962).
31. T. B. Warner and S. Schuldiner, *This Journal*, **112**, 853 (1965).

Hydrogen Evolution on Single Crystal GaAs Electrodes

Kathleen D. N. Brummer

Tyco Laboratories, Inc., Waltham, Massachusetts[1]

ABSTRACT

Hydrogen evolution from 0.1*N* $HClO_4$ at 23°C on the Ga (111) and As ($\bar{1}\bar{1}\bar{1}$) faces of single crystals of GaAs has been studied using current-potential curves, differential capacity measurements and anodic charging curves. The irreproducible results frequently found are shown to be the result of surface corrosion, and it is shown that great care must be taken to preserve the crystal surface. A freshly etched and washed electrode can be taken from −1.2v to −0.3v (*vs.* RHE), and reproducible hydrogen evolution measurements can be obtained at both Ga and the As faces. Current-potential curves on the Ga face show two regions: positive to ~ −0.6v (*vs.* RHE) the current is almost independent of the potential; negative to ~ −0.6v, Tafel behavior is found with a slope of 180-200 mv/decade; n-type and p-type electrodes show similar behavior, and there are no photoeffects.

Differential capacities on the Ga face indicate substantial space charge effects at potentials positive to −0.7v, but suggest degeneracy at more negative potentials. A substantial frequency dispersion is found in the range 0.5-20 kHz and is shown to originate from surface states. The variation of the surface state contribution with potential suggests that some of them arise from adsorbed hydrogen. After allowance for space charge effects, made from the differential capacity data, the Tafel slope for the reaction in the region above −0.6v is shown to be $\leq 2\ RT/\mathbf{F}$.

Anodic charging curves show a change from high to low hydrogen coverage at ~0.7v.

It is suggested that the reaction path is discharge ($H^+ + e \rightarrow H_{ads}$) followed by recombination ($2H_{ads} \rightarrow H_2$) where discharge is rate limiting over the range investigated, −0.4 to −1.2v. This mechanism is quantitatively consistent with all the experimental data.

The object of the work reported in this series of papers was to investigate the hydrogen evolution reaction on a number of single crystal III-V semiconductors with a view to understanding the properties of the electrode material which determine the kinetics of electrochemical processes.

The hydrogen evolution reaction was chosen for this study, partly because of its relative simplicity and partly because it should be possible to study it on these electrode materials without undue competition from corrosion reactions. III-V semiconductors, *e.g.*, gallium arsenide, were chosen for this purpose because of their unusual crystal structure. Gallium arsenide, a typical III-V semiconductor, crystallizes in the zinc blende structure, so that each atom is surrounded tetrahedrally by four atoms of the other kind (1). Each (111) crystal surface comprises atoms of entirely one kind or the other. It follows that atoms of gallium exposed at the arsenic surface by the removal of the surface atoms are unstable. So too are atoms of arsenic exposed at the gallium surface by the removal of the surface atoms. This description of the crystalline properties of III-V semiconductors is idealized in that there is probably minor surface faceting on the atomic level. Nevertheless a series of III-V semiconductor electrodes offers an opportunity to compare an electrochemical reaction at each of the (111) surfaces of such a compound with the same reaction at the surface of each constituent pure element.

Because of their unusual structure, these compounds have been the subject of a number of investigations. Their etching behavior (2) and anodic dissolution (3, 4) have been studied in detail. The hydrogen evolution reaction at the surface of single crystal samples of gallium arsenide has been investigated by Harvey (4), Pleskov (5), and Gerischer and Mattes (6).

Pleskov (5) found that for strongly doped materials there was substantially no difference in behavior between p-type and n-type electrodes. In the range 10^{-4} to 5×10^{-2} amp/cm^2, he found Tafel behavior with a slope of 0.12 v/decade in *N* H_2SO_4. Below 10^{-4} amp/cm^2, he found a "knee' which was attributed to semiconductor properties of the electrode. This knee was unstable and the H_2 overpotential tended to become larger with time in this region. Considerable hysteresis between ascending and descending (cathodic) current regimes was reported.

The results of Gerischer and Mattes (6) are in sharp contrast to the results of Pleskov. They did find a limiting current for H_2 evolution on p-type electrodes. This limiting current increased with illumination. These observations suggested that the reaction consumes electrons from the conduction band. On n-type electrodes in 2*N* H_2SO_4, Gerischer and Mattes found a Tafel slope of ~200 mv/decade. Thus a considerable part of the p.d. across the interface must be across the Helmholtz double layer rather than across the space charge in the electrode. They were unable to decide whether the electron transfer is rate limiting, however. They found AsH_3 in the gas phase during H_2 evolution and suggested that the surface is saturated with hydride. Cyclic voltammetry indicated an approximate monolayer of this material ($\equiv H_{ads}$). They did not report any hysteresis effects nor whether they distinguished the crystal faces.

Harvey (4) reported considerable hysteresis between increasing and decreasing cathodic currents. This he attributed to changes in surface condition. His cathodic curves were obtained after anodic polarization thus the hysteresis may relate to changes in the surface produced both by this treatment and also by subsequent treatment at very cathodic potentials; the latter particularly on the As ($\bar{1}\bar{1}\bar{1}$) face. Indeed, Harvey reported great sensitivity of his cathodic data to the anodic pretreatment. He carefully distinguished between the Ga (111) and the As ($\bar{1}\bar{1}\bar{1}$) faces, but found no difference either in NaOH or in $HClO_4$. He also found no difference between n-type and p-type electrodes and, specifically, found no limiting current

[1] Present address: 31 Oak Hill Road, Wayland, Massachusetts.

for the latter out to 100 ma/cm^2. With repetitive anodic-cathodic cycles, the surface condition of the electrode was modified such that the hysteresis effects disappeared; then, he found a Tafel slope of 300 mv/decade.

It is clear from the above that considerable disagreement and uncertainty exists about the H_2 evolution reaction on GaAs. In particular, the effects of prior anodic treatment and of careful orientation have not always been appreciated. Because of this uncertainty, there is very little evidence concerning the mechanism of the reaction. In the present investigation, it was desired to carry out experiments bearing these factors in mind in order to clarify the mechanism of the reaction. This paper describes procedures which were developed to investigate the H_2 reaction on the faces of single crystals of GaAs while preserving their chemical identities. In this context, a detailed study of the mechanism of the reaction on the Ga (111) face was carried out. In a further paper (7), we have compared the H_2 reaction on a number of III-V semiconductor electrodes.

Experimental

Electrodes.—Single crystal samples of gallium arsenide, cut into flat plates along the (111) crystal surface, were obtained from Monsanto Chemical Company, St. Louis, Missouri. The plates were about 0.5 cm^2 in area and about 0.1-0.2 cm thick, the resistivity of different samples was: 1.1 ohm cm and 0.0075 ohm cm for n-type material and 0.004 ohm cm for p-type. Each sample was soldered to the end of a steel rod, with which it made ohmic contact, and with the flat area parallel to the axis of the rod. The reason for this was to hold the electrode vertically in the cell. The steel rod was then inserted in a glass tube, which was ground on the outside, and sealed at the ends with a tapered Teflon stopper similar to that described in ref. (8). The soldered joint between the rod and sample and the edges of the sample were sealed with Kel-F wax. Only one side of the sample was therefore exposed to the solution. The exposed electrode surface was chemically polished in a 4:3:1 mixture of distilled water, nitric acid and hydrofluoric acid (2) and then washed in distilled water.

The cell.—Measurements were made in a conventional, three electrode cell. The center compartment, which contained the gallium arsenide electrode, was made so that the ground glass tube of the electrode fitted through a long tube at the top of this compartment. At the top of this tube there was a cup, which was filled with electrolyte, to make an air-tight seal. The purpose of the long tube was to allow the electrode to be raised and lowered in and out of the electrolyte, without breaking the air-tight seal. During the measurements the working electrode was clamped close to the Luggin capillary. The counter electrode, a large platinized wire, was separated from the working electrode by a glass frit, and a copious supply of hydrogen was maintained in this compartment to ensure that the current could be carried by the hydrogen reaction at a voltage close to the reversible potential. This was done to ensure that no platinum dissolved from the counter electrode, as it might have been plated out on the working electrode.

Solutions and cleaning procedures.—Measurements were taken in 0.1*N* perchloric acid, obtained by diluting 70% acid with triple distilled water (one distillation from alkaline permanganate) at room temperature (23° ± 2°C).

Since it was desired to measure the capacity at the GaAs electrode, special solution-cleaning procedures were adopted. Each experiment was preceded by prolonged electrolysis with a platinized platinum electrode, and a hydrogen lift pump was included in the cell.[2] By means of this, the electrolyte was percolated through platinum black for several hours to remove adsorbable impurities. This procedure was repeated periodically during the course of each experiment. The platinum black for the lift pump was first cleaned in a Soxlet distillation apparatus with hydrochloric acid for two days to remove base metal impurities and then with distilled water for at least a week. As an example of the effect of this treatment, the electrode capacity at 10 kHz between —0.80 and —1.00v was 20-50 μF/cm^2 with the lift pump and 8 μF/cm^2 without it. The reproducibility of the capacity was 10-15% in any one experiment, over a period of several days, and within a factor of two between different experiments.

Measurement procedures.—Most of the measurements were made potentiostatically using a Wenking "fast rise" potentiostat. Some experiments were carried out galvanostatically, and the constant current pulses were obtained using a high voltage battery with a bank of resistors. Current-time traces were recorded on a Sargent S. R. recorder *via* a high input-impedance amplifier.

Capacity measurements were made by balancing the impedance of the electrode solution interface against a variable capacity and resistance in series, using a bridge similar to that described by Parsons (9). The galvanostatic circuit was used for these measurements.

The reference electrode was a reversible hydrogen electrode, and the data are reported with respect to the hydrogen electrode.

The reproducibility of the measurements varied with the circumstances of the experiment, as is discussed below. It was found (see below) to be necessary to put the gallium arsenide electrode into the solution at a certain cathodic potential, and the following procedure was therefore adopted for the final measurements: The cell was cleaned and assembled and the electrode lowered through the neck in the cell to a position above the electrolyte. The cup was then filled with electrolyte to make an air seal. Hydrogen was then bubbled through all three cell compartments for an hour to remove oxygen and to bring the reference electrode to the required potential. The connections were then made to the potentiostat, which was set at —1.20v. At this point the gallium arsenide electrode was lowered into the electrolyte to its position near the Luggin capillary, thus completing the circuit.

Results and Discussion

Establishment of conditions for preserving the crystal surfaces.—The hydrogen overvoltage has been measured at both the gallium and the arsenic (111) surfaces of gallium arsenide. The measurements taken initially were very irreproducible, and it was observed that the behavior of the electrode was complicated by its corrosion. At potentials more positive than —0.24v the electrode dissolves as an anodic current is measured. However, since this is a mixed potential between hydrogen evolution and electrode dissolution, the latter process must also occur at more negative potentials than —0.24v.[3] After allowing some electrode dissolution, a different hydrogen overvoltage was observed. A systematic investigation was carried out of these effects. The results for the two (111) faces were very different and are discussed separately.

[2] The H_2-lift pump comprised a special side-compartment of the cell. This consisted of a glass tube (12 mm OD) with a fritted disk at the bottom containing platinum black. A narrow glass tube looped from the bottom of this chamber and re-entered it at the top. H_2 was admitted near the bottom of this narrow tube and each gas bubble, as it rose, drew solution from the main compartment of the cell and dropped it into the Pt. The use of this device was suggested by Dr. R. Payne.

[3] It is not certain at what potentials gallium and arsenic dissolve from gallium arsenide. The standard potentials have been calculated (4) as +0.11 and −0.05v for gallium arsenide and the trivalent gallium ion and as −0.69 and −1.47v for gallium arsenide and arsine. The standard potentials of the pure elements are −0.46v for gallium and its trivalent ion, and −0.60v for arsenic and its hydride (10).

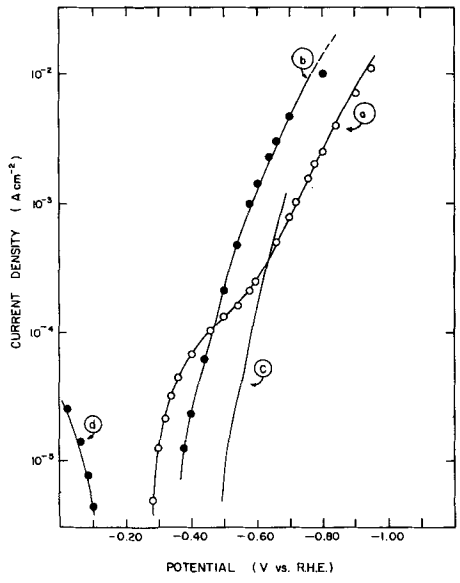

Fig. 1. Current *vs.* potential in 0.1N $HClO_4$ at: curve a, the gallium face of single crystal gallium arsenide; curve b, an electroplated gallium surface; curve c, pure liquid gallium, in H_2SO_4 (11); curve d, anodic current at gallium arsenide electrode.

The gallium (111) face.—The gallium surface was investigated first, the results are shown in Fig. 1; two extreme situations are given in curves a and b. Curve a was obtained in the following manner. A freshly polished and washed electrode was lowered into the electrolyte at a potential of —1.20v, as described in the experimental section. No solution of the electrode was allowed, and the current quickly reached a steady value. The overpotential curve was then measured at successively less negative potentials. The current at each potential showed no tendency to drift, and at potentials more negative than —0.60v the line a was reproducible to ±10 mv from one experiment to another. In this straight line portion of a the Tafel slope was 0.19 ± 0.01v, and the line could be reproduced on increasing or decreasing the potential. Anodic to —0.60v, the overvoltage curve a showed a knee, where the current was larger than would have been expected from the results at more negative potentials. These results were less reproducible than those obtained below —0.60v, by about a factor of two, i.e., ±20 mv. The current did not drift with time, however.

The rest potential occurred at —0.24v and at less negative potentials than this the anodic current represented by line d was obtained. This represents electrode dissolution. Having undergone anodic dissolution, this electrode was then taken back gradually to —1.20v. At each potential more negative than about —0.20v a much larger cathodic current was observed than in line a. This current decreased rapidly at first and then more slowly and did not become steady, even after an hour at a given potential. These high currents were as much as fifty times greater than those represented in line a. At —1.20v, the current became sensibly steady after about 2 hr, and subsequently, on increasing the potential, line b was obtained. These measurements did not vary with time and were reproducible to within ±20 mv from sample to sample; the rest potential occurred at —0.35v. Line b could be repeated with this electrode for measurements made at succesively increasing potentials, as before. In order to obtain line a again, the electrode was removed from the cell, repolished and washed and then returned to the cell at —1.20v, as described above.

Intermediate treatment of the electrode produced measurements intermediate between lines a and b; that is to say an electrode could be taken down line a to some point just above —0.60v, say to —0.50v, and subsequently, on decreasing the potential, a large but decreasing current was observed. This settled down to a steady value after the electrode was kept for some time at —1.20v. Then, on increasing the potential again, a line between lines a and b was obtained. Above —0.60v a knee occurred, smaller than in line a, and the rest potential of the electrode (a mixed potential of course) was between —0.24 and —0.35v. The longer the electrode was kept at a less negative potential than —0.60v and/or the more positive the potential to which the electrode was taken, the nearer the measurements came to line b.

The following interpretation of these differences in the hydrogen overvoltage is suggested. Line a corresponds to hydrogen evolution on the gallium face of gallium arsenide, but line b and the curves intermediate between lines a and b correspond to hydrogen evolution on a partly dissolved and subsequently gallium-plated surface. That is, at relatively anodic potentials, greater than —0.60v, the electrode dissolved. Then, as the potential subsequently decreased, some replating of one or both of the constituent elements occurred, and a steady state for hydrogen evolution was not obtained. At high negative potentials the replating process was more or less completed. Both elements could have been plated on the electrode, but it appeared probable that any arsenic plated out would have been reduced to the hydride, so that whatever actually occurred initially, a plated gallium surface remained on the electrode. Line b therefore, represents the hydrogen overvoltage on plated gallium. The results intermediate between lines a and b were obtained on a partially gallium plated electrode.

Two tests were made to corroborate this picture. First, the results of Sabo and Bagotskaya (11) were plotted for comparison in Fig. 1, line c. Their results were made in sulfuric acid using a liquid gallium electrode. The difference in roughness between a solid plated surface and liquid surface may account for some of the observed difference in the results represented by lines b and c, and therefore the comparison is not entirely conclusive. However we note that there is no knee in either line b or c. In order to make a better comparison, a freshly etched and washed gallium arsenide electrode was cathodized at —1.20v, for 5 to 10 min in a solution of gallium ions in perchloric acid in a separate cell from the one used in the overpotential experiments. This electrode was then washed and put into the other cell at —1.20v. Then a curve indistinguishable from line b, to within ±20 mv, was obtained. It is concluded from this that line a represents the hydrogen overvoltage on the gallium face of gallium arsenide and that line b, like line c, represents the hydrogen overvoltage on pure gallium.

The arsenic (111) face.—Measurements made of the hydrogen overvoltage at the arsenic surface of gallium arsenide were more complex, Fig 2. When the hydrogen reaction was measured at a freshly polished electrode, beginning at the open-circuit potential and decreasing the potential to more negative values, line c was obtained. The current first became unsteady at —0.58v, when it oscillated slowly between the two currents shown at this, and more negative potentials. There was no over-all increase nor decrease with time, just an oscillation.

The hydrogen evolution reaction was also measured, as before, beginning at —1.20v and proceeding to less negative potentials. The results shown in line a of Fig. 2 were obtained. The currents at potentials positive of —0.80v fluctuated, but no long term increase nor decrease with time was observed. Line a was reproducible, even after the electrode was kept as long as 10 min at —0.35v. This is in sharp contrast to the corresponding results at the gallium surface, see line a of Fig. 1, and probably reflects the fact that gallium from solution is not plated out onto the arsenic surface at —1.20v as it was onto the gallium surface.

Different results were obtained after holding the electrode at a very negative potential, *e.g.*, —2.00v for

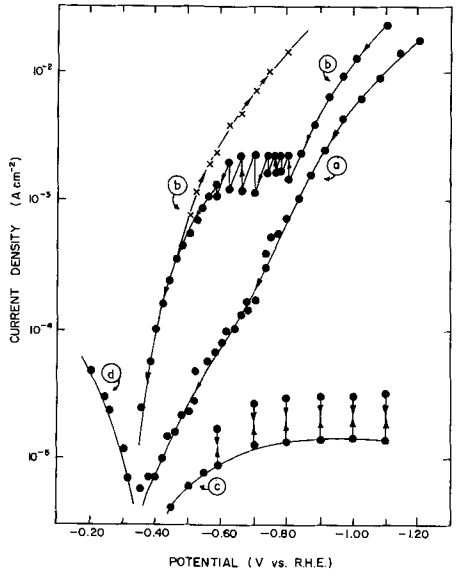

Fig. 2. Current *vs.* potential in 0.1*N* $HClO_4$ at the arsenic face of gallium arsenide: curve a, potential increasing from —1.20 to —0.30v; curve b, potential increasing from —1.20v after being held at —2.00v, and subsequently decreasing as indicated; curve c, potential decreasing from —0.40v; curve d, anodic current at gallium arsenide electrode.

about an hour, line b. Then, at potentials increasing from —1.20 to —0.80v, the current was steady, but higher than that represented in the same potential region by line a. Between —0.80 and —0.58v the current changed with time as indicated. The current did not fluctuate erratically in this potential region, but systematically. An increase in potential produced an initial decrease in the current, and a larger increase in potential produced a larger initial decrease in the current. However, after each change in potential, the current then increased slowly to a constant value independent of time and potential, taking about 10 min after a 40 mv increase in potential and about 5 min after a 20 mv increase in potential. Above —0.58v the current potential curve was closely similar to that of the hydrogen reaction at an electroplated, pure gallium surface. If the potential were then made more negative, after being above —0.58v, the experimental points again followed the curve representing the hydrogen reaction at a pure gallium surface, that is line b of Fig. 1. The lines b of Fig. 2 were only obtained after the electrode was held for some time at a high negative potential (—2.00v). If the electrode were held at —1.20v, even overnight (about 16 hr) line a was still obtained.

These results are rather unusual, but were obtained repeatedly, with various samples. All the reported features of them were reproducible at least to 20 mv, but the sections of lines b and c where the current oscillated were only reproducible to within about 50 mv. Also lines a above —0.80v was only poorly reproducible.

The objective as before had been to measure a steady hydrogen evolution curve, but at the arsenic surface of gallium arsenide and to define the conditions necessary for keeping the surface constant. In view of the possibility of hydride formation from arsenic below —0.69v [3] the measurements were first made beginning at the rest potential and proceeding to more negative potentials, line c. This was clearly unsatisfactory as the measurements were unsteady. Instead the current potential curve was started at —1.20v in an analogous manner to that for the gallium face; line a was obtained. This was reproducible, within the limits given above, and it was concluded that the results represent the hydrogen evolution reaction at the arsenic face. Analysis of the effluent gases showed no evidence of hydride formation, nor was there any undue corrosion of the surface.

Hydride formation evidently occurs only at much more negative potentials, *e.g.*, —2.00v, for the results in line b are probably the results on a surface which has undergone cathodic corrosion. A suggested interpretation of line b is as follows. At a large negative potential the hydrides of both gallium and arsenic may be formed. These hydrides are both volatile. The corroded surface must then consist of gallium and arsenic patches no longer part of an orderly crystal structure. Line b, between —0.80 and —1.20v, represents the hydrogen reaction on a mixed polycrystalline surface. Since the section of line b obtained after taking the electrode to more positive potentials than —0.58v is very close to the results obtained at a gallium plated electrode, we must conclude that the section of line b between —0.58 and —0.80v represents the region where the patches of arsenic are removed, leaving a disordered gallium surface.

We can see that in order to measure meaningful H_2-evolution rates on the single faces of GaAs, great care must be taken to avoid corrosion of the surface. This can occur at low cathodic potentials, near to the rest potential, and at high cathodic potentials, for example at —2.0v. Thus the data must be taken, at each electrode, by changing the potential from a large cathodic value of about —1.20v to the rest potential at —0.20 to —0.30v, but not in the reverse direction. Particular care must be taken to avoid redeposition of the dissolved Ga after any corrosion has been allowed. In these circumstances, both the Ga (111) and As ($\bar{1}\bar{1}\bar{1}$) faces of GaAs give reproducible behavior.

Further studies to elucidate the mechanism of the H_2 evolution reaction were carried out on the Ga (111) face of the crystals.

Current-potential curves on the Ga(111) *face of* GaAs.—Details of the current potential curve for hydrogen evolution on GaAs are shown in Fig. 1. The main features, as indicated, are that negative to $\sim$ —0.6v a stable and reproducible (<10 mv) current-potential curve is found with a Tafel slope of 180-200 mv/decade. Positive to —0.60v, the Tafel slope is much less steep (350-420 mv/decade). In this region the current at a fixed potential tends to decay because of destruction of the surface. The rest potential is $\sim$ —0.3v.

These current-potential curves are similar in general shape to those reported by Pleskov (5). The Tafel slope in the high overpotential region is similar to that found by Gerischer and Mattes (6) on n-type material although the overpotential is about 0.3v less here. The present overpotentials are, however, fairly close to those reported by Harvey (4) in the same current range.

Similar features were found for both p-type and n-type samples (Fig. 3), and no significant difference in behavior was ever found between p-type and n-type materials except perhaps in the region of the knee positive to —0.6v. Here, currents for p-type were possibly a little higher than for n-type (Fig. 3). This observation of similarity for the two conductivities and the failure to observe a limiting current for p-type material agrees with the observations of Pleskov (5) and Harvey (4) but disagrees with Gerischer and Mattes (6).

One possibility to account for the absence of a limiting current with p-type electrodes is to assume that H_2 evolution generates holes in the valence band rather than consuming electrons from the conduction band. Gerischer and Mattes' (6) observations show quite clearly, however, that the reaction must occur *via* the conduction band. It is evident then that their material was more perfect, *i.e.*, had fewer generation and recombination centers, than that used in this investigation. Finding a similarity of behavior between p-type and n-type suggests that the present samples

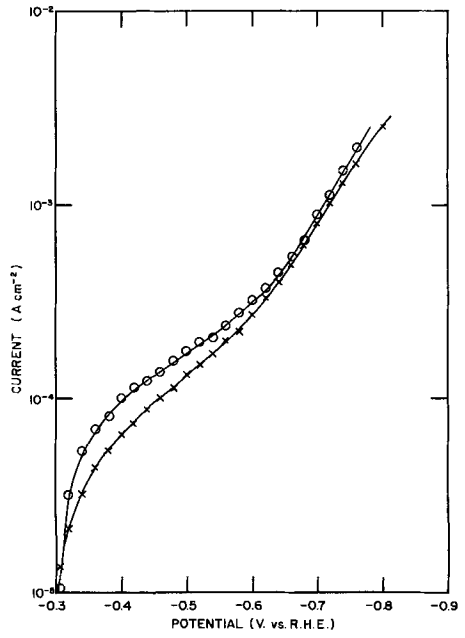

Fig. 3. Comparison of Tafel plots for p-type and n-type GaAs. x, 1.1 ohm cm n-type; O, 0.004 ohm cm p-type.

were more or less degenerate, certainly in the more cathodic region.

This conclusion is reinforced by the absence of a photoeffect on the H_2 evolution rate and by the differential capacity data presented later. We will proceed on the basis that below ~ —0.6v the semiconductor properties are not important and that the electrode is essentially a metal, *i.e.*, the space-charge region in the electrode is inconsequential in magnitude or at least independent of applied potential.

According to the analysis of Parsons (12), the following mechanism could lead to a Tafel slope of ~180 mv on a metallic electrode

$$H^+ + e \rightarrow H_{ads} \quad [1]$$

$$2H_{ads} \rightarrow H_2 \quad [2]$$

Here, H^+ discharge is followed by atom combination and the discharge is rate limiting. The combination step is not in equilibrium and the H_{ads} coverage, θ, is in the middle range of coverage, *i.e.*, Temkin (13) adsorption conditions apply. Then the Tafel slope is

$$b = \frac{RT}{\mathbf{F}}\left(\frac{2\gamma + \alpha}{2\alpha\gamma}\right) \quad [3]$$

Here α is the transfer coefficient of the discharge step and γ that of the combination step, if we take $\alpha = \gamma = 0.5$, b is $3RT/\mathbf{F}$, *i.e.*, 177 mv at 25°C.

If θ is small at low overpotentials, as is likely since reaction [1] will be relatively slower than reaction [2], this mechanism predicts that b should become smaller. In the limit of $\theta \rightarrow 0$, b should tend to $RT/\alpha\mathbf{F}$, *i.e.*, 118 mv if $\alpha = 0.5$. The mechanism also predicts that there should be pseudocapacity since θ changes with potential. In order to obtain evidence for this mechanism, the differential capacity of the electrode was investigated as a function of potential.

Differential capacity data on the Ga (111) *face of* GaAs.—The impedance of the electrode was measured with a series combination of resistance (R_s) and capacitance (C_s). Results are shown in Fig. 4 and 5. The most remarkable feature of the results is the large frequency dispersion. Thus the resistance part of the impedance increases from a limiting value of ~80 ohms (~ the solution resistance) at 20 kHz and —1.0v to ~700 ohms at 2 kHz and —0.45v. Similarly, the capacity increases from about 0.25 μF/cm² at 20 kHz and —0.46v to about 300 μF/cm² at 0.5 kHz and —0.62v. As

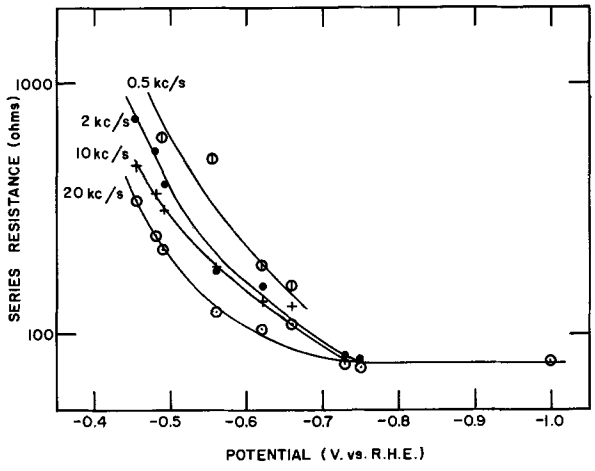

Fig. 4. Series resistance as a function of the frequency and the potential.

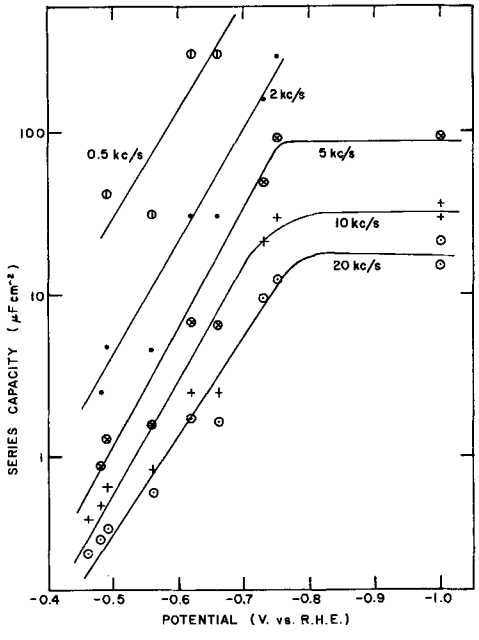

Fig. 5. Series capacity as a function of the frequency and the potential.

an example of the effect of frequency at a single potential, we note that C_s increases from 0.36 to 42 μF/cm² at —0.49v when the frequency decreases from 20 to 0.5 kHz.

The capacity of GaAs electrodes has been investigated also by Birintzewa and Pleskov (14). Their studies were mostly carried out in 1M KOH, and they also found considerable frequency dispersion which they attributed to Faradaic effects.

The large frequency dispersion suggests the possibility of the presence of the large adsorption capacity required by the postulated mechanism, reactions [1] and [2]. Thus the equivalent circuit for the Faradaic reaction might, following Parsons (9), be depicted by the circuit shown in Fig. 6(a). Here, R_e is the solution resistance, C_d the capacity of the double layer, R_r the reaction resistance, and C_a the postulated pseudocapacity. W is the Warburg diffusional impedance, negligible in this instance. In the limit of high frequency, the series capacitance and resistance elements should approximate R_e (~80ω) and C_d (~20 μF/cm²).

The data of Fig. 4 indicate that even at 20 kHz the resistance at low overpotentials is considerably higher than the solution resistance (*viz.*, 350ω at —0.46v). With any "normal" (*e.g.*, ~20 μF/cm²) value of C_d this is unlikely. This is because the impedance

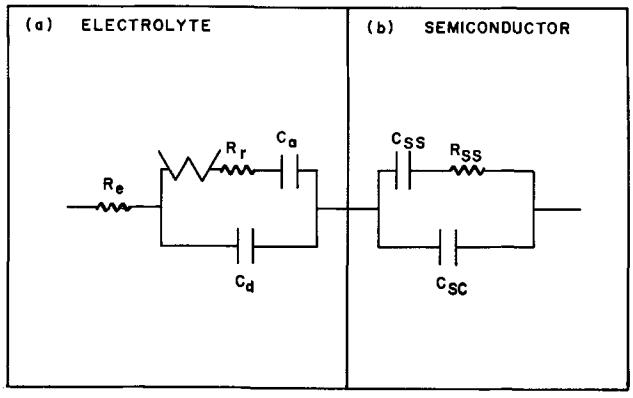

Fig. 6 (a). Equivalent circuit of the H_2 evolution reaction after Parsons (9). Fig. 6 (b). Equivalent circuit of semiconductor with surface states, after Gerischer (15). Combination of (a) and (b) is the postulated electrode-solution interface.

of such a value of C_d at this frequency is only about 0.5ω, which would shunt out R_r. Even more significant, the high-frequency values of C_s, particularly at less cathodic potentials, are already much too low to be equal to C_d. Thus at —0.46v, C_s is only 0.25 μF/cm^2 at 20 kHz. Yet even this low value is higher than the infinite frequency value.

These low values of C_s suggest that certainly at less cathodic potentials we may not treat the semiconductor electrode as a metal. The capacity in this region is apparently largely determined by the space charge in the semiconductor. If this is so, it is impossible to find the large values of C_{sc} that we do find at lower frequencies solely as a result of a series combination of the space charge capacity, C_s, and any capacity on the solution side of the interface, say C_a. This is because in these circumstances

$$\frac{1}{C_s} = \frac{1}{C_a} + \frac{1}{C_{sc}} \qquad [4]$$

and C_s would always be lower than either C_{sc} or C_a.

It follows that at low frequencies there must be an admittance parallel to C_{sc} on the semiconductor side of the interface. Such an admittance could be contributed by surface states (15). An equivalent circuit, after Gerischer (15), for such surface states is represented in Fig. 6b. The surface states contribute a relaxation term, C_{ss}, and a resistance term, R_{ss}. At low frequencies the large value of C_{ss} provides a path for charge redistribution at the interface as the potential is altered. At very high frequencies the surface states cannot follow potential changes and the charge variations we see are distributed *via* C_{sc}. The analogy with the solution side of the interface is plain.

So the frequency dependence of the observed capacity must originate largely on the semiconductor side of the interface and gives little information about the H_2 evolution reaction directly. It may be argued that the surface states originate (at least partly) from H-atoms adsorbed on the surface, but this is somewhat speculative since we do not know exactly how GaAs interacts chemically with aqueous solutions. Gerischer and Mattes (6) reported some AsH_3 evolution from their samples and suggested that the surface is saturated with AsH_3. This gas could contribute surface states although in the present work very careful examination showed that no AsH_3 is evolved out to —1.2v from the Ga (111) face. Thus the presently found surface states might originate from H_{ads}, but there is no evidence that they are from AsH_3.

We may note that the frequency dispersion is still large in the very cathodic region where the capacity is reasonably high and fairly independent of potential (Fig. 5). In this potential region, the capacity-potential relation suggests that the surface has become degenerate, as assumed in the previous section, *i.e.*, the surface charge density has become almost independent of the applied potential. It is likely that the frequency dependence in this region arises substantially from adsorbed H effects.

Important evidence that some of the observed surface states are associated with H_{ads} was obtained from anodic charging curves.

Anodic charging curves on the Ga (111) *face of* GaAs.—Anodic galvanostatic transients were applied to the electrode to analyze for the removal of H_{ads}. The electrode was potentiostated at —1.00v before application of each anodic pulse. A typical chronopotentiogram is shown in Fig. 7. We see that the potential increases rapidly until at ~0.7-0.55v, depending on the current density, there is a plateau. The anodic process involved in this plateau consumes about 2 x 10^{-4} coulombs cm^{-2} (Fig. 8). After this plateau, the potential increases again until it reaches a second plateau region in which much more charge is consumed than in the first plateau. Finally, the potential reaches a steady value corresponding to steady-state dissolution of the GaAs.

It is postulated that the first plateau corresponds to the oxidation of H_{ads} while the later processes correspond to electrode oxidation. We may note that the first plateau occurs at just about the region where the knee in the current-potential relation starts (Fig. 1 and 3). The charge consumed in the plateau is of the

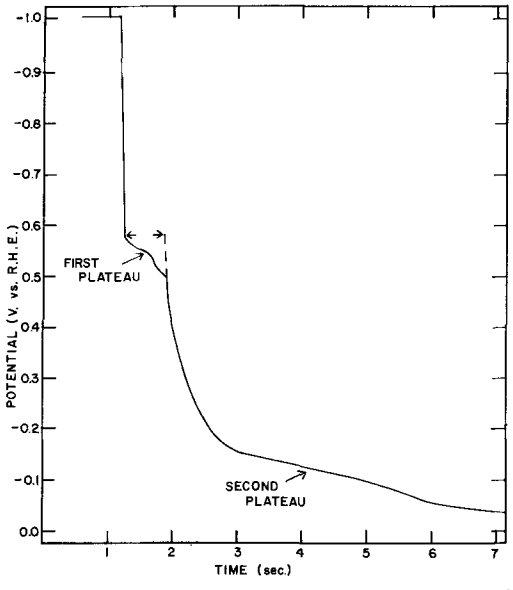

Fig. 7. Typical anodic charging curve taken from —1.00v vs. RHE on a p-type sample at 1.3 x 10^{-4} amp/cm^2.

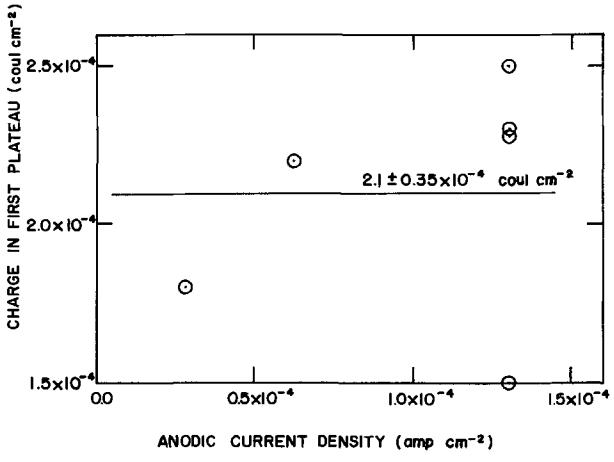

Fig. 8. Charge in the first plateau in the anodic charging curves as a function of anodic current density.

order of monolayer. It is possible that this plateau does in fact correspond to some kind of electrode oxidation. It seems unlikely, however, that such a clean separation between the two plateaus would be found in that case. Gerischer and Mattes (6) have also reported an extra charge in this potential region during an anodic sweep. This they also attributed to oxidation of about a monolayer of adsorbed H atoms or hydride.

The interpretation of these data then is that below $\sim$ —0.7v the electrode is covered with a substantial amount of adsorbed hydrogen. Above —0.7v the electrode is thought to be virtually bare. Further qualitative evidence for this latter view can be found from further consideration of the differential capacity curves.

Potential distribution in the electrode.—In the discussion of the current-potential data, it was assumed that the electrode could be treated as a metal. That is to say that there is either no space charge or a constant space charge, independent of applied potential. The evidence for this followed from the similarity between p- and n-type electrodes (Fig. 3) and the absence of a photoeffect. Further evidence that this is reasonable in the far cathodic range follows from the capacity data which show typical degenerate behavior in this region (Fig. 5).

However, these same capacity data indicate that positive to $\sim$ —0.6v it is not possible to treat the electrode as having no space charge since the low values of C_s at high frequencies must be associated with space charge effects. Indeed the region of high Tafel slope in the current-potential curves could be associated with the space charge. This is particularly probable since a similar, almost symmetrical potential-independent region was found for the anodic dissolution of the electrode. It is of some interest then to estimate the space charge potential from the capacity data.

In the absence of surface states, for space charge potentials with respect to the electrode bulk $>3RT/\mathbf{F}$, we may approximate C_{sc} for an n-type semiconductor as (15)

$$C_{sc} \simeq A \exp (\psi_s \mathbf{F}/RT)^{1/2} \quad [5]$$

where A is a constant and ψ_s is the potential drop across the space charge. Experimentally (Fig. 5), at high frequencies where the contribution of surface states to the measured capacity is small, we find that

$$C_s \simeq B \exp (-E\mathbf{F}/2.7RT) \quad [6]$$

Here B is a constant and E is the measured potential *vs.* RHE. Equating C_s with C_{sc} and taking $\exp(\psi_s \mathbf{F}/RT) >> 1$, we obtain

$$-2.7 \frac{RT}{\mathbf{F}} \ln \frac{A}{B} = \text{const} = 1.35\, \psi_s + E \quad [7]$$

However

$$E = \eta - \psi_s \quad [8]$$

where η is the potential available to drive the reaction. Hence we obtain the desired relationship between observed potential, E, and the driving potential η

$$\eta = \text{const} + 0.26E \quad [9]$$

Using Eq. [9], we can allow for the space charge potential in the region above —0.60v. Experimentally, above 0.60v for n-type material, we find approximately a 340 mv slope, *i.e.*

$$i = \text{const} \exp \left(- \frac{E\,\mathbf{F}}{5.75\,RT} \right) \quad [10]$$

Using [9] and [10], the relationship i and η is

$$i \simeq \text{const} \exp \left(- \frac{\eta\,\mathbf{F}}{0.24 \times 5.75\,RT} \right) = \text{const} \exp \left(- \frac{\eta\,\mathbf{F}}{1.4\,RT} \right) \quad [11]$$

For p-type, with a 450 mv slope

$$i \simeq \text{const} \exp \left(- \frac{\eta\,\mathbf{F}}{1.9\,RT} \right) \quad [12]$$

In either case, the important point is that this approximate calculation of ψ_s gives a lower Tafel slope between i and η than that found in the more cathodic region. This is expected from the mechanism of reactions [1] and [2] if the coverage is low at potentials positive to —0.6v. These calculations substantiate in some measure the requirement of the mechanism particularly in conjunction with the anodic charging data.

Further evidence on the hydrogen coverage in the region above —0.6v can be found from reconsideration of the capacity data. Ignoring the solution side of the interface and assuming that $R_{ss} < 1/\omega\, C_{ss}$, we may write the capacity as

$$C_s = C_{sc} + C_{ss} \quad [13]$$

Thus in the region near the space charge minimum, C_s will be given essentially by C_{ss}. We will consider a low frequency, say 0.5 kHz, where the impedance of R_{ss} is less significant. Since C_s at this frequency is much lower at —0.46v than at more cathodic potentials, it follows that C_{ss} increases sharply as we go more cathodic. Such an increase must be associated with increase in the number of surface states as we go cathodic and presumably this results from an increase in θ. The degeneracy exhibited below —0.75v would on this view, reflect saturation coverage with H_{ads}, although other explanations are possible (16).

Summary and Conclusions

1. Meaningful H_2 evolution rates at the Ga (111) and As ($\bar{1}\bar{1}\bar{1}$) faces of single crystals of GaAs may be obtained if care is taken to avoid corrosion of the surface. This corrosion can occur either at relatively anodic potentials or under very cathodic conditions. Most of the previously reported hysteresis is the result of changes of the condition of the surface due to corrosion and replating processes following corrosion. The procedure for preserving the chemical integrity of the faces is never to allow the electrode to rest at potentials more positive than $\sim$ —0.3v or at very negative potentials. It is safe to work as low as —1.2v. Satisfactory data are then obtained by raising the potential from —1.2v in the positive direction.

2. The current-potential curves for H_2 evolution from 0.1*N* $HClO_4$ on the Ga (111) face of single crystal GaAs show two distinct regions: At potentials positive to $\sim$ —0.6v *vs.* RHE, the current is almost independent of potential. More negative than $\sim$ —0.6v, Tafel behavior with a slope of 180-200 mv/decade is found.

3. Similar behavior is found on n-type and p-type samples and no limiting current is found on the latter. No photoeffect on the rate of H_2 evolution was found. These results suggest that the space charge regions in the electrodes are not important and that they can be treated as metals for purpose of mechanistic analysis of the reaction.

4. Differential capacity measurements indicate substantial space charge effects at potentials positive to $\sim$ —0.7v, however. They confirm degenerate behavior at more negative potentials.

5. A large frequency dispersion is shown to arise from the contribution of surface states to the bulk properties of the semiconductor. The variation of these surface states with potential suggests that some of them originate from adsorbed hydrogen.

6. Further evidence for considerable hydrogen adsorption is found from anodic charging curves. They indicate a transition from high coverage to low coverage at about —0.7v.

7. The following mechanism is suggested

$$H^+ + e \xrightarrow{\text{slow}} H_{ads} \quad [1]$$

$$2H_{ads} \rightarrow H_2 \qquad [2]$$

Here discharge is rate limiting over the whole range from —0.4 to —1.2v. This mechanism is consistent with the current-potential behavior and with the coverage data.

Manuscript received April 11, 1967; revised manuscript received Aug. 24, 1967.

Any discussion of this paper will appear in a Discussion Section to be published in the June 1968 JOURNAL.

REFERENCES

1. E. Parthé, "Crystal Chemistry of Tetrahedral Structures," Gordon & Breach, New York (1964).
2. H. C. Gatos and M. C. Lavine, *J. Phys. Chem. Solids*, **14**, 169 (1960).
3. H. Gerischer, *Record Chem. Progr.*, **23**, 135 (1962); *idem.*, *Z. Naturforsch*, **19a**, 553 (1964); idem., *Ber. Bursenges Physik. Chem.*, **69**, 578 (1965).
4. W. W. Harvey, *This Journal*, **114**, 472 (1967).
5. Yu. V. Pleskov, *Dokl. Akad. Nauk.*, **143**, 1399 (1962).
6. H. Gerischer and I. Mattes, *Z. Physik. Chem.*, **49**, 112 (1966).
7. K. Brummer, To be published.
8. A. C. Makrides and M. Stern, *This Journal*, **107**, 782 (1960).
9. R. Parsons, *Trans. Faraday Soc.*, **56**, 1340 (1960).
10. W. M. Latimer, "The Oxidation States of the Elements and Their Potentials in Aqueous Solution," 2nd. ed., Prentice Hall, New York (1952).
11. K. Sabo and I. A. Bagotskaya, *Dokl. Akad. Nauk. SSSR*, **149**, 139 (1963).
12. R. Parsons, *Trans. Faraday Soc.*, **54**, 1053 (1958).
13. M. I. Temkin, *Zhur. Fiz. Khim.*, **15**, 296 (1941).
14. T. P. Birintzewa and Yu. V. Pleskov, *Izv. Akad. Nauk. SSSR, Chem. Ser.*, **2**, 251 (1965).
15. H. Gerischer, "Semiconductor Electrode Reactions," in "Advances in Electrochemistry and Electrochemical Engineering," P. Delahay, Editor, vol. 1, p. 139, Interscience Publishers, New York (1961).
16. Thus, we expect degeneracy on increasingly high cathodic polarization irrespective of H_{ads}. See, for example, results of J. F. Dewald *Bell System Tech. J.*, **39**, 615 (1960), for cathodic polarization of ZnO.

Phase Equilibria in the Zinc-Tellurium System

Richard A. Reynolds,[1] David G. Stroud,[2] and David A. Stevenson

Materials Science Department, Stanford University, Stanford, California

ABSTRACT

The Knudsen effusion cell method was used to determine the free energy of formation of subliming ZnTe between 650° and 830°C. The values of $\Delta H°$ and $\Delta S°$ for the reaction $ZnTe_{(s)} = Zn_{(g)} + \frac{1}{2}Te_{2(g)}$ were found to be 79.1 kcal/mole and 45.0 e.u., respectively. The calculated minimum total vapor pressure over congruently subliming ZnTe using these data is significantly lower than the values calculated from earlier vapor pressure data. The solubility of Te in liquid Zn was measured in the temperature range 500°-900°C using weight loss and chemical methods. The mole fraction of Te in the Zn-rich liquidus is given by

$$\log N_{Te(l)} = \frac{-3320 \pm 738}{T°K} - 0.67 \pm 0.50$$

A pressure-temperature diagram showing the range of stability of solid ZnTe was constructed using the vapor pressure data and the temperature-composition diagram for ZnTe. The pressure-temperature diagram and the measured solubility of Te in liquid Zn were used to calculate the activity coefficient of Te in liquid Zn. At 1000°K the calculated activity coefficient is 10^{-2}, the small value being due to a large, negative deviation from ideality in the Zn-Te binary system. The compositional limits of the ZnTe phase field were calculated using the pressure-temperature diagram and data giving the high temperature conductivity of ZnTe in Zn vapor. The calculations suggest the existence of a retrograde solubility of a native double acceptor defect on the Te rich side of the ZnTe phase field.

The point defect concentrations in solid crystalline compounds are significantly influenced by the high temperature equilibrium between the solid and the vapors of its components. These defects in turn are important in controlling the physical properties of the compounds. A quantitative description of the high temperature solid-vapor equilibrium, therefore, is significant in describing the variation in physical properties of compounds treated in different crystal environments. In addition, such information is valuable in selecting the optimum conditions for crystal growth and also in the calculation of the standard free energy, enthalpy and entropy of formation of the compound.

Zinc telluride (ZnTe) is a II-VI compound of interest for its potentially useful electrical and optical properties. The solid-vapor equilibrium, which has been shown to influence the high temperature defect equilibrium (1), has been the subject of two previous investigations. Korneeva *et al.* (2) have measured the decomposition pressure from 518° to 715°C using a free sublimation method; occasional reference points using a Knudsen cell were obtained to determine the evaporation coefficient. In interpreting their results, they assumed that the vapor was exclusively molecular ZnTe. Goldfinger *et al.* (3) determined the decomposition pressure of ZnTe from 553° to 837°C using a Knudsen cell technique, and in their study, the vapor species were identified by mass spectrometric techniques and found to be predominantly Zn and Te_2; no significant amount of the molecular species ZnTe was observed. The absence of molecular vapor species such as ZnTe is general of all the II-VI compounds and is further evidenced by the vapor transport characteristics of the II-VI compounds (4). The two investigations are not in satisfactory agreement, even when the results of Korneeva *et al.* are recalculated

[1] Present address: Texas Instruments, Dallas, Texas.
[2] Present address: Physics Department, Harvard University, Cambridge, Massachusetts.

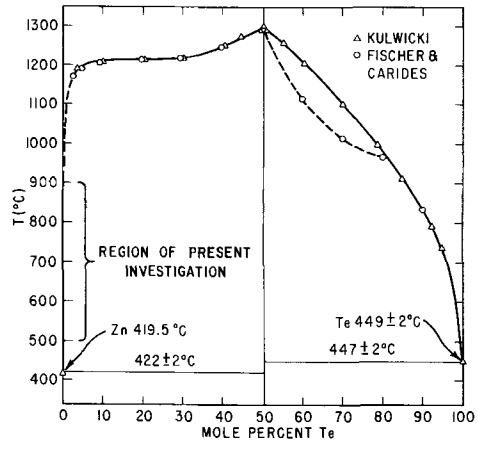

Fig. 1. Temperature-composition (T-X) diagram for the Zn-Te alloy system as determined by Kulwicki (6) and Carides and Fischer (7). The region investigated in this work is indicated.

(5) using the observed vapor species. As a consequence, additional experimental information is needed.

The present work describes investigations of the solid-vapor equilibrium of ZnTe from 650° to 830°C using a Knudsen cell technique and of the solubility of ZnTe (or Te) in liquid Zn between 500° and 900°C. The Knudsen effusion data were used to calculate the enthalpy and entropy of formation of ZnTe and to calculate the pressure-temperature diagram for ZnTe by using the existing information concerning the temperature-composition diagram and the thermodynamic properties of the elements. The total pressure over congruently subliming ZnTe reported here is lower than that found in the previous studies (2, 3), and the range of component pressures over which solid ZnTe is stable is calculated to be greater than expected on the basis of previous studies.

The liquidus of the Zn-Te system has recently been redetermined by means of DTA calorimetry by Kulwicki (6) and by Carides and Fischer (7). Their results are shown in Fig. 1. In the region of low tellurium concentration, the dashed line represents an estimate of the liquidus curve. Since the liquidus curve in this region is important for estimating the pressure-temperature diagram, an experimental determination of this line was made for the temperature range of 500°-900°C. The data giving the solubility of ZnTe in liquid Zn and the pressure-temperature diagram were combined to calculate the activity coefficient of Te, γ_{Te}, along the Zn-rich liquidus line. At 1000°K, γ_{Te} is about 10^{-2}, this small value being due to the large, negative deviation from ideality in the Zn-Te system.

Finally, the compositional limits of the ZnTe phase field were calculated using a model of the dominant defect in ZnTe (a Zn vacancy or Te interstitial acceptor defect), data giving the high temperature conductivity of ZnTe in Zn vapor (1), and the pressure-temperature diagram. Results of this calculation suggest that the Te-rich composition limit is nearly independent of temperature and that a retrograde solubility of Te in ZnTe may occur at 800°-900°C. The Zn-rich composition limit shows a continuously increasing solubility of Te in ZnTe as the temperature is increased.

Experimental Procedure and Results

Vaporization of ZnTe.—The ZnTe used for this study was synthesized from the pure elements (purity of 99.999% or better) and the resulting compound was sublimed in a dynamic vacuum for further purification and compositional control. Optical microscopic examination and x-ray diffraction analyses confirmed that the ZnTe was single phase and contained no voids, precipitates, or inclusions of Zn or Te. Mass and emission spectrographic analyses showed that the total impurity content was about 1 x 10^{17}/cm^3 to 5 x 10^{17}/cm^3 with the principal impurities being Si, Fe, and Cu.

The Knudsen cell method is described in detail elsewhere (8). In the present study, a graphite cell was used and a molybdenum jacket served as a thermal mass around the cell to minimize temperature gradients. The radius of the orifice of the cell was measured with a traveling microscope to be 0.052 cm, and the thickness of the orifice was measured with a micrometer to be 0.122 cm. The cell and its molybdenum jacket were contained in a quartz tube which was heated by a resistance furnace. The temperature of the cell was measured with a chromel-alumel thermocouple in a well which protruded into the cell. The measuring thermocouple was periodically calibrated with a platinum-platinum + 13% rhodium thermocouple calibrated by the National Bureau of Standards. The background pressure of the system was kept between 10^{-5} and 10^{-6} Torr during effusion. During heating of the cell, however, the system was backfilled with argon to minimize weight loss prior to the effusion measurement.

The mass of the ZnTe efflux was determined by two methods: direct weight loss of the cell, and the measurement of the Zn^{65} radioactive tracer activity of the entire efflux from a radioactive ZnTe source. The former method is discussed in detail elsewhere (8). The latter method was particularly sensitive and was used for the lower temperature measurements. A liquid nitrogen cooled stainless steel cup was used to collect the efflux, which was then dissolved in nitric acid, and the resulting solution was evaporated until a convenient volume was obtained for counting. In order to determine the weight of ZnTe in the efflux, the solution was placed in the well of a gamma ray spectrometer and the activity of the 1.1 Mev $Zn^{65}\gamma$ radiation was compared with that of a standard ZnTe sample having the same specific activity as the ZnTe contained in the cell.

In all cases the efflux was assumed to be stoichiometric for purposes of calculating the pressures of Zn and Te_2. In order to verify this assumption, and to compare the results obtained from the weight loss and tracer methods, the following experiment was performed. An effusion experiment which produced a large, easily measured weight loss was done using radioactive ZnTe. The Zn tracer activity was determined in the usual manner and converted into a weight of Zn. The weight of Te in the efflux was then taken as the difference between the total weight loss and the weight of the Zn calculated from the Zn tracer activity. The efflux was found to be stoichiometric and the vapor pressure determined by the two methods agreed within the experimental scatter of 5%. It should be emphasized that this is not a check on the precise stoichiometry related to the concentration of defects, but rather a justification of assuming stoichiometry for relating weight loss to the effusion pressure of Zn and Te.

The Knudsen effusion weight loss is related to the pressure of the vaporizing species i by the equation

$$P_i = Z_i\,(M_iT)^{1/2}/(44.33\,W_o \cdot A \cdot t) \qquad [1]$$

where P_i is the pressure of species i in atm, Z_i the efflux of i in moles, M_i the molecular weight of species i, T the absolute temperature, W_o the Clausing factor (calculated to be 0.48 from the orifice dimensions), A the orifice area in cm^2, and t the time in seconds. This representation of P_i is appropriate as long as the mean free path of the gas molecules is large compared to the orifice dimensions. The vaporization reaction is

$$ZnTe_{(s)} = Zn_{(g)} + \tfrac{1}{2}\,Te_{2(g)} \qquad [2]$$

for which the vaporization constant is

$$K = P_{Zn}\,P_{Te_2}^{1/2} \qquad [3]$$

Table I gives the experimental data and the cor-

Table I. Data on effusion runs

Symbols: T, temp °K; Tr, tracer analysis, WL, weight loss measurement in mg; Time in sec × 10^3; pressures in atm; $K = p_{Zn}p_{Te_2}^{1/2}$.

T	Method	WL (mg)	Time	P_{Zn}	P_{Te_2}	K	$10^4/T$	ln K
918	Tr	1.31	9.10	1.05×10^{-6}	1.04×10^{-6}	1.07×10^{-9}	10.89	−20.655
947	Tr	3.44	8.76	3.03	3.00	5.25	10.55	−19.065
948	Tr	2.95	6.90	3.17	3.14	5.62	10.54	−18.997
962	Tr	4.77	7.74	4.57	4.53	9.73	10.40	−18.448
987	Tr	10.97	8.40	9.68	9.59	2.98×17^{-8}	10.12	−17.328
1010	WL	19.5	10.62	1.36×10^{-5}	1.35×10^{-5}	5.00	9.90	−16.811
1023	WL	20.5	7.44	2.05	2.03	9.25	9.77	−16.196
1050	WL	60.0	9.90	4.57	4.53	3.08×10^{-7}	9.52	−14.992
1064	WL	23.0	3.24	5.38	5.33	3.93	9.40	−14.748
1066	WL	44.8	5.22	6.40	6.34	5.10	9.38	−14.488
1095	WL	47.0	2.94	1.24×10^{-4}	1.23×10^{-4}	1.36×10^{-6}	9.13	−13.514

responding calculated values of P_{Zn}, P_{Te_2}, and K. Figure 2 shows a plot of log K *vs.* $1/T$ for the results reported here as well as those of Korneeva *et al.* (2) [recalculated (5) assuming the vapor species to be Zn and Te_2], and of Goldfinger and Jeunehomme (3). A least squares fit of our data gives

$$\log K\ (\text{atm}^{3/2}) = \frac{-17{,}270}{T_{°K}} + 9.84 \qquad [4]$$

Possible sources of error in our measurements are in the (*i*) weighing and/or radiotracer counting procedures, (*ii*) temperature measurement, and (*iii*) Clausing factor calculation. The agreement between the data of the weight loss method and that of the radioactive tracer method suggests that the first source of error is not larger than about 5% in this study. We believe the uncertainty of the temperature inside the effusion cell is the largest source of error. Since the collection cup above the Knudsen cell was at liquid nitrogen temperature for runs using radioactive ZnTe, temperature gradients within the cell were likely. A conservative estimate of the temperature error, however, would not exceed 5°C. This error in temperature would not cause an error of greater than 30% in the value of pressure calculated from the least squares fit of the experimental data.

Finally, in order to verify the Clausing factor and to check the apparatus, an effusion experiment was performed at 1051°K with KCl and the results compared with previous work. A value for the vapor pressure of KCl of 0.36 Torr was obtained from the present work (assuming the vapor to be 100% KCl molecules). This may be compared with 0.41 Torr obtained from the equation of Treadwell and Werner (9), 0.46 Torr from the equation of Zimm and Mayer (10) and 0.48 Torr from the equation of Pugh and Barrow (11). This corresponds to a difference of approximately 15-25%, suggesting that in our measurements errors from all sources were in the range 15-30% at a maximum.

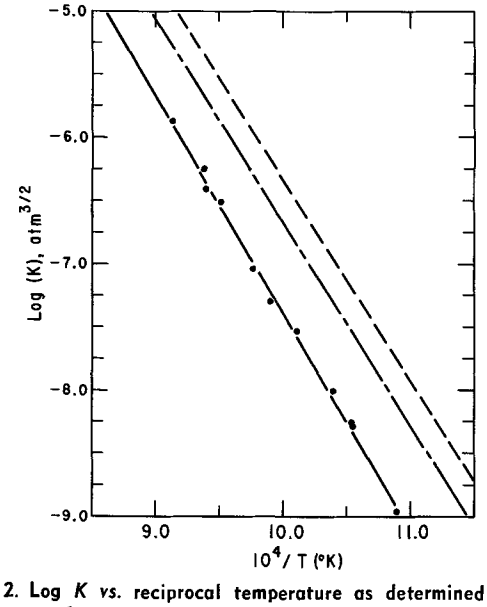

Fig. 2. Log K *vs.* reciprocal temperature as determined in this work (———O———); by Korneeva *et al.* (2) (- - - -); and by Goldfinger and Jeunehomme (3) (——— — ———).

Determination of the Zn-ZnTe *liquidus in the 500°-900°C range.*—A determination of the liquidus composition was made by equilibrating zinc telluride crystals with liquid zinc followed by separation of the solid and liquid at temperature. The liquidus composition was then determined in two ways: chemical analysis of the material that was liquid at temperature; and measurement of the weight loss of the solid crystals.

Quartz ampules (17 mm diameter and containing two doubly connected compartments) were charged with approximately 20g of zinc shot (purity of 99.999% or better) and 0.5g of a zinc telluride crystal, evacuated to 5×10^{-6} Torr and sealed. Initial weights of Zn and ZnTe were measured to ± 12 and ± 3 μg, respectively, with a Mettler microbalance. The ampules were annealed in a resistance wound furnace. A nickel jacket minimized temperature gradients and the samples were rotated during annealing to speed the attainment of equilibrium. Temperature was controlled to within ± 1/2°C with a Barber-Coleman 293C controller and temperature was monitored with a chromel-alumel thermocouple that was periodically compared with a thermocouple calibrated by the National Bureau of Standards.

At the end of the annealing time, the ampules were tilted and shaken to separate the solid from the liquid at temperature and then quenched. The portion of the sample that was liquid at temperature was analyzed for tellurium content gravimetrically. The remaining ZnTe crystals were etched with HCl to remove excess zinc (HCl attacks ZnTe at a rate negligible compared to that for Zn metal), reweighed, and the solubility computed from the weight loss.

The experimental results are summarized in Table II. As is evident from the data, there is rather poor agreement between the weight loss points and the results obtained from chemical analysis. For dilute solutions such as the liquidus in this region of the T-X diagram, one expects Henry's law to apply and the liquidus composition to follow the relation

$$\ln X_{Te}^{L} = \frac{m}{T} + b \qquad [5]$$

where X_{Te}^{L} is the mole fraction of Te in the liquid, T the temperature of the liquid, and m and b are constants. Treating the present data, one obtains

$$\ln X_{Te}^{L} = -\frac{7.63 \times 10^3}{T} - 1.55 \qquad [6]$$

with the probable error values of m and b of ± 1.16 x 10^3 and ± 1.16, respectively. While these error values are large in comparison to m and b (15% and 75%, respectively), they are not unreasonable in view of the small solubilities measured. The data are useful for semiquantitative estimates (as below); however,

Table II. Solubility of tellurium in liquid zinc

i	°C	X (atm frac units) × 10^{+5}	(°K)$^{-1}$ × 10^{+4}
1	512	3.29	12.7
2	512	2.69	12.7
3	580	7.15	11.7
4*	580	1.03	11.7
5	641	10.23	10.9
6*	641	1.54	10.9
7	649	12.81	10.8
8*	649	1.54	10.8
9	698	8.98	10.2
10*	698	3.07	10.2
11	772	13.01	9.5
12*	772	8.20	9.5
13	796	18.47	9.3
14*	796	6.15	9.3
15*	812	6.66	9.2
16	819	25.26	9.1
17*	819	16.40	9.1
18	855	36.35	8.8
19*	855	34.85	8.8
20	876	43.00	8.7
21	908	63.53	8.4
22	910	71.99	8.4
23*	910	87.16	8.4

* Denotes a result obtained through chemical analysis; all others obtained by weight-loss methods.

Table III. Standard enthalpy and entropy for the reaction $ZnTe_{(s)} = Zn_{(g)} + \frac{1}{2} Te_{2(g)}$

Reference	$\Delta H°$, kcal/mole	$\Delta S°$, e.u.
This work (650°-830°C)	79.1	45.0
2 (518°-715°C)	73.0	44.0
3 (553°-837°C)	73.6	43.1

they are not adequate for obtaining excess heats and entropies of solution.

Discussion

Enthalpy and entropy of formation of ZnTe.—The vaporization constant (Eq. [3]) is related to the change in standard enthalpy ($\Delta H°$) and entropy ($\Delta S°$) for the vaporization of ZnTe by the equation

$$R \ln K(T) = \frac{-\Delta H°(T)}{T} + \Delta S°(T) \qquad [7]$$

For the temperature ranges covered by the three vaporization studies the dependence of $\Delta H°$ and $\Delta S°$ on temperature may be neglected[3] so that $\Delta H°$ and $\Delta S°$ can be calculated directly from the analytical expressions for K. Table III lists the values of $\Delta H°$ and $\Delta S°$ calculated from our results and from the results of Korneeva *et al.* and of Goldfinger and Jeunehomme. The differences in the values of ΔH and $\Delta S°$ listed in Table III are small, but they result in significant differences in the calculated total pressure over congruently subliming ZnTe. At 1000°K, for example, the calculated pressures are 1.6 x 10^{-2} Torr, 9 x 10^{-2} Torr, and 5 x 10^{-2} Torr using our data, the data of Korneeva, *et al.*, and the data of Goldfinger and Jeunehomme, respectively. The differences in the calculated pressures are due to differences of the same magnitude in the experimental values of the vapor pressure.[4] Considering the major sources of experimental error, those in the weighing and/or counting operations would be random, and any error in the Clausing factor would be constant, independent temperature, and hence neither would influence the calculated enthalpy. An error in temperature, however, would probably be systematic and result in an error in the enthalpy. Since the data of each investigation are self-consistent but there exist small but significant differences in the enthalpy values, an error in the measurement of temperature is probably the major reason for the discrepancies between the present study and previous investigations. As discussed above, a conservative estimate of the error in pressure due to the experimental error in temperature in the present study is placed at 30% which is less than the observed differences.

The values of $\Delta H°$ and $\Delta S°$ for the reaction

$$Zn_{(s)} + Te_{(s)} = ZnTe_{(s)} \qquad [8]$$

have been determined at lower temperatures by McAteer and Seltz (13) and by Pool (14). Values of $\Delta H°$ and $\Delta S°$ for the vaporization of ZnTe can be calculated from these data and compared with the values determined from the vapor pressure studies. Because of the large temperature difference between these investigations and the vaporization investigations one must estimate ΔC_P for Eq. [2] and also insure that the standard state of the ZnTe is the same in all the investigations. An estimate of C_P for ZnTe can be made using the empirical methods discussed by Kubaschewski and Evans (15) and gives

$$C_P(\text{ZnTe}) = 11.5 \text{ cal/°K mole} + 2.8 \times 10^{-3} T \qquad [9]$$

Other required values of C_P are in the literature (16-18). The standard state chosen for ZnTe is the pure, stoichiometric compound, and since the phase field of ZnTe is very narrow, it is assumed that negligible deviation from this standard state can be achieved experimentally. In other words, it is assumed that the phase field of ZnTe is so narrow in terms of its composition limits that the difference between the free energies of formation of ZnTe saturated with Zn and ZnTe saturated with Te cannot be detected experimentally. This assumption has been shown to be valid for CdTe as discussed by Brebrick and Strauss (12).

McAteer and Seltz (13) used a reversible galvanic cell to study the reaction of Eq. [8] and found $\Delta H°$ = — 28.2 kcal/mole and $\Delta S°$ = —2.9 e.u. at an average temperature of 658°K (385°C). Pool (14) used tin solution calorimetry to determine $\Delta H°_{273°K}$ for the same reaction and obtained a value of —28.5 kcal/mole. Since ΔC_P is expected to be negligible for Eq. [8] [Neumann and Kopp's law (16)], the agreement between these two values of $\Delta H°$ is expected despite the difference in temperatures of measurement. Combining these data with the thermodynamic data for the vaporization of a solid Zn and Te (17) and the heat capacities of $Zn_{(s)}$(18), $Te_{(s)}$(15), $Zn_{(g)}$(17) and $Te_{2(g)}$(17) enables one to calculate $\Delta H_{658°K}$ = 79.1 kcal/mole and $\Delta S°_{658°K}$ = 51.3 e.u. for the dissociation of ZnTe into $Zn_{(g)}$ and $Te_{2(g)}$ (Eq. [2]). Using the estimated heat capacity of ZnTe, one calculates further that ΔC_P for Eq. [2] is —2.5 cal/mole °K, leading to $\Delta H°_{1000°K}$ = 77.6 kcal/mole, and $\Delta S°_{1000°K}$ = 49.5 e.u. These values are in good agreement with those derived from the vapor pressure studies (Table III) when one considers the approximations and extrapolations required for the calculation. Previously, Kröger (19) has concluded that the data of McAteer and Seltz yielded calculated vapor pressure values in conflict with those measured directly and with the maximum melting point (6, 7) of ZnTe (Kröger's Figure I indicates a $\Delta H°$ derived from data of McAteer and Seltz which is about 25% larger than those determined by vapor pressure measurements).

Pressure-reciprocal temperature diagram.—The pressure-reciprocal temperature (P-1/T) diagram for compounds describes the component pressures along the liquidus line of the temperature-composition (T-X) diagram and shows the range of component pressures at a given temperature for which the solid

[3] In the present and two previous studies a plot of $\ln(K)$ *vs.* $1/T$ is well represented by a straight line, indicating that a Σ function analysis over these temperature ranges is not necessary. Furthermore, the estimated value of ΔC_P of —2.5 cal/mole °K for the reaction in Eq. [2] (see below) would produce a change of less than —1.0 kcal/mole in $\Delta H°$ and less than 1.0 e.u. in $\Delta S°$ between the minimum and maximum temperatures of each investigation.

[4] The composition of ZnTe inside the effusion cell is very near that of congruently subliming ZnTe (12). Hence, the measured vapor pressures are very near the minimum total vapor pressure, which occurs over congruently subliming ZnTe.

phase is stable. The (P-1/T) diagram is used to determine the range of component pressures under which the compound can be annealed without melting, and to predict the extrema in defect concentrations for those crystalline defects in equilibrium with the external component pressures.

An experimental determination of the (P-1/T) diagram for the Zn-Te system has not been made; however, one can construct a diagram by combining the vapor pressure data with the T-X diagram which was recently redetermined by two investigators (6, 7) and is shown in Fig. 1. Studies of the P-T-X diagrams for the Cd-Te (20), Cd-Se (21), and Hg-Te (22) systems show that Raoult's law can be applied to liquids except for compositions in the region of the compound. Assuming that Raoult's law also may be applied to liquids in the Zn-Te system, the partial pressures of Zn over the Zn rich liquidus and of Te over the Te rich liquidus are given by

$$P_{Zn} = P^{\circ}_{Zn} N_{Zn(l)} \qquad [10]$$

and

$$P_{Te_2} = P^{\circ}_{Te_2} N^2_{Te(l)} \qquad [11]$$

respectively, where P°_i is the vapor pressure of pure Zn or Te, and N_i is the mole fraction of Zn or Te in the liquidus composition at temperature T as shown by the T-X diagram.[5] The vapor pressures of Zn over the Te rich liquidus and of Te over the Zn rich liquidus can be calculated from the vaporization constant of ZnTe (Eq. [3]) and the vapor pressure of the major component in the liquid phase, if it is again assumed that the phase field of ZnTe is so narrow that free energy of formation (*i.e.*, the vaporization constant) of ZnTe is independent of changes in the solid composition. A P-1/T diagram constructed in this manner is shown in Fig. 3 using the values of the vaporization constant from this work. Both the Zn and Te vapor pressures are shown in Fig. 3 in order to emphasize that over the Zn rich liquidus the Zn pressure is orders of magnitude higher than the Te_2 pressure, and that over the Te rich liquidus the Te_2 pressure is orders of magnitude higher than the Zn pressure. Consequently there exists a composition of solid ZnTe between those corresponding to saturation with Zn or Te whose total vapor pressure has a minimum value. The solid composition having the minimum total vapor pressure is known as the congruently subliming composition because it and its equilibrium vapor have precisely the same composition (which may also be a function of temperature). Deviations from stoichiometry in ZnTe are small, however, so that both the congruently subliming solid and its equilibrium vapor may be considered to be stoichiometric for purposes of chemical analysis. The total vapor pressure over congruently subliming ZnTe is related to the vaporization constant by (4)

$$P_T(\text{Torr}) = 3/2^{2/3} K^{2/3} \times 760 \qquad [12]$$

and is also shown in Fig. 3. Due to the lack of sufficient thermodynamic data at temperatures above about 1000°C for extrapolation purposes, the portion of the P-1/T diagram above this temperature must be considered to be approximate.[6]

[5] A significant discrepancy exists between the two experimental Te-rich liquids lines above 1000°C (Fig. 1). The causes of this discrepancy are not readily apparent, especially since the data agree well along the Zn-rich liquidus where pressures are higher and the DTA experimentation more difficult. Average values for $N_{Te_{(l)}}$ were used to calculate the P-1/T diagram above 1000°C, since the major sources of error in the calculation at these temperatures are in the use of Raoult's law and the lack of experimental values of C_p for ZnTe.

[6] In Fig. 3 the liquidus lines near the maximum melting point have been constructed so that the maximum melting composition also sublimes congruently (*i.e.*, $P_{Zn} = 2P_{Te_2}$ at T_{max}). This assumed coincidence has not been demonstrated experimentally.

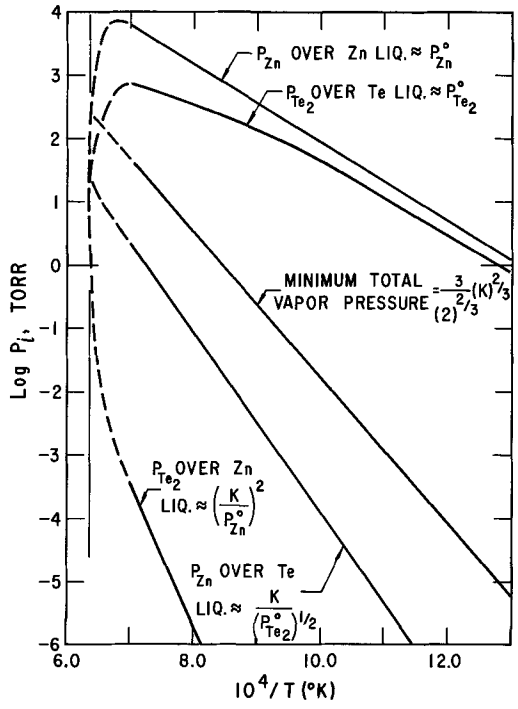

Fig. 3. Pressure-reciprocal temperature diagram showing the Zn and Te_2 partial pressures along the liquidus of the T-X diagram (Fig. 1), and the minimum total vapor pressure over congruently subliming ZnTe. Above about 1000°C the diagram is tentative because of the lack of heat capacity data for proper extrapolation of the vapor pressure of ZnTe, and possible deviations from ideality in the liquid phase.

Activity coefficient of Te *in liquid* Zn.—An estimate of the activity coefficient of Te in liquid Zn can be made by combining the data giving the solubility of Te (or ZnTe) in liquid Zn with the vapor pressure of Te_2 over ZnTe saturated with Zn, which is given by the P-1/T diagram of Fig. 3.

The activity coefficient γ_{Te} of Te in liquid Zn-Te alloys is given by

$$\gamma_{Te} = \frac{1}{X_{Te(l)}} \left(\frac{P_{Te_2}}{P^{\circ}_{Te_2}} \right)^{1/2} \qquad [13]$$

where $X_{Te(l)}$ is the mole fraction of Te in the liquid, P_{Te_2} is the vapor pressure of Te_2 over the liquid, and $P^{\circ}_{Te_2}$ is the vapor pressure of pure Te. The value of $P_{Te_2}{}^{1/2}$ is given by

$$P_{Te_2}{}^{1/2} = \frac{K}{P_{Zn(l)}} \qquad [14]$$

where K is the dissociation constant for ZnTe and $P_{Zn(l)}$ is given by Eq. [10]. Using Eq. [6] for $X_{Te(l)}$, the vapor pressures of pure Zn and Te, and our vaporization constant for ZnTe to evaluate Eq. [13] gives

$$\log \gamma_{Te} = -4800/T + 2.86 \qquad [15]$$

where γ_{Te} is explicitly for the Zn-rich liquidus. The calculated value of γ_{Te} is 10^{-2} at 1000°K and 6 x 10^{-2} at 1173°K. These small values arise due to the large, negative deviation from ideality in the Zn-Te system. They can be compared to the value of 5 x 10^{-4} calculated (21) for Se along the Cd rich liquidus of Cd-Se alloys between about 1200° and 1400°K. Since the melting points and free energies of formation for CdSe and ZnTe are very comparable (3, 21), one might expect that the activity coefficients of the group VI elements would be of more comparable magnitudes in these two alloy systems.

Compositional limits of the ZnTe *phase field.*—Undoped ZnTe is a p-type semiconductor, presumably

due to the presence of a native defect which acts as a double acceptor. The defect is believed to be due to the incorporation of excess Te and generally has been attributed to be a zinc vacancy (1, 24, 25). Self-diffusion data (26) for Zn and Te, however, suggest that the acceptor defect is an interstitial Te atom. Thomas and Sadowski (1) have measured the high temperature hole concentration in ZnTe as a function of temperature and zinc partial pressure and found that

$$p \propto (P_{Zn})^{-n} \quad [16]$$

where n varied from 0.44 at 700°C to 0.30 at 950°C. Thomas and Sadowski interpreted their data to show that doubly ionized zinc vacancies dominate the defect equilibria at high temperatures according to the reaction

$$Zn_{(ZnTe)} = Zn_{(g)} + V_{Zn}^{-2} + 2p \quad [17]$$

where V_{Zn}^{-2} is a doubly ionized Zn acceptor vacancy. This reaction and the presumed charge neutrality condition of

$$p = 2[V_{Zn}^{-2}] \quad [18]$$

predict that

$$p \propto P_{Zn}^{-1/3} \quad [19]$$

which approximates the experimental results at the higher temperatures. The double acceptor model would predict the same electrical behavior regardless of whether the defect was assumed to be a zinc vacancy or an interstitial Te atom.

If one combines the experimental data of Thomas and Sadowski, an appropriate model of the defect equilibria, and the P-$1/T$ diagram previously constructed for the Zn-Te system, it is possible to calculate the compositional limits of the ZnTe phase field. The composition limits on the zinc rich side of the ZnTe phase field are determined by extrapolating the data of Thomas and Sadowski to zinc pressures corresponding to zinc saturation, while the composition limits on the Te rich side are determined by extrapolating their data to the zinc pressures corresponding to Te saturation, as read from the P-$1/T$ diagram. The double acceptor defect model described above has been used by Reynolds (27) and Kroger (19) to calculate the limits of the ZnTe phase field. Both authors assumed that the acceptor defect was doubly ionized for all relevant values of temperature and Zn partial pressure; hence, their calculations of the Te-rich boundary of the ZnTe phase field employs an extrapolation of the hole concentration at all temperatures on the basis that $p \propto P_{Zn}^{-1/3}$. However, if the acceptor defect were singly ionized for some values of temperature and Zn pressure, the defect model would predict $p \propto P_{Zn}^{-1/2}$. The data of Thomas and Sadowski, which give $p \propto P_{Zn}^{-0.44}$ at 700°C and $p \propto P_{Zn}^{-0.38}$ at 750°C, indicate that this is the case. Both lower temperatures and lower Zn partial pressures will favor single over double ionization of the defect. Even at a constant temperature the defect may become singly instead of doubly ionized as the Zn pressure is reduced because the crystal is becoming more p-type (Fermi level of energy moving closer to the valence band). Hence isotherms giving the hole (or defect) concentration as a function of Zn partial pressure may be analytically complex and show some "irrational" average dependence on Zn pressure lying between $P_{Zn}^{-1/3}$ and $P_{Zn}^{-1/2}$. In order to demonstrate the effect of the possible change in charge state on the calculated limits of the ZnTe phase field, Fig. 4 shows the Te-rich limit calculated using both Eq. [19] and the experimental pressure dependencies for extrapolation purposes. A decrease in hole concentration with increasing temperature at low temperatures is suggested when the experimental hole concentration-P_{Zn} relations are used. This tendency would be reduced if the data at the higher temperatures were extrapolated according to $P_{Zn}^{-1/3}$ near Zn saturation and according to $P_{Zn}^{-1/2}$ near Te saturation, due to a decrease in charge of the acceptor defect as the Zn pressure is reduced. Nevertheless, the use of the experimental pressure dependencies would suggest that the Te-rich solidus is nearly temperature independent and perhaps exhibits a retrograde solubility limit. In fact, the suggestion of retrograde behavior persists even using the pressure dependence of $P_{Zn}^{-1/3}$. The temperature range over which the retrograde behavior is suggested is in qualitative agreement with the range suggested by the theory of Miller and Komarek (28) which (for the Zn-Te system) relates the temperature of the maximum in the retrograde solubility to the temperature of the inflection in the Te-rich liquidus line in the T-X diagram (Fig. 1). Further evidence suggesting retrograde behavior is the pronounced precipitation which occurs in ZnTe crystals annealed at high temperatures in Te-rich atmospheres (26, 29). Finally, a nearly temperature independent Te-rich solidus is in agreement with the Hall effect measurements of Larsen (30) who found that the net acceptor concentration in ZnTe annealed in excess Te was nearly independent of annealing temperature (the net concentration in crystals annealed in excess Zn increased rapidly as the annealing temperature was increased).

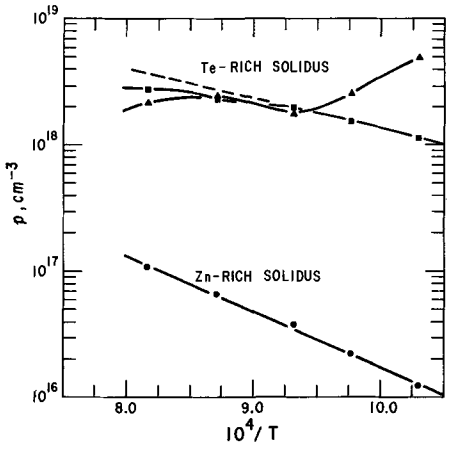

Fig. 4. Free hole concentration in ZnTe vs. reciprocal temperature for the conditions of Zn saturation (1) (———●———); for Te saturation as calculated using the P-$1/T$ diagaram (Fig. 3) and Eq. [19] for extrapolation (———■———); and for Te saturation as calculated using the P-$1/T$ diagram and the experimentally determined hole concentration vs. P_{Zn} relations (———▲———). The dotted line is a straight line extrapolation using the three low temperature points at Te saturation as computed assuming Eq. [19].

An alternative defect model which also would predict that $p \propto P_{Zn}^{-1/2}$ at the lower temperatures postulates that charge neutrality is given by

$$\tfrac{1}{2}[A^{-2}] = [D^{+}] \quad [21]$$

where A^{-2} is the double ionized acceptor native defect and D^{+} is a donor impurity. When the temperature is made sufficiently high the thermally generated concentration of A^{-2} would exceed the concentration of D^{+} and the charge neutrality condition would become that given in Eq. [19] so that $p \propto P_{Zn}^{-1/3}$. Analysis of the data of Thomas and Sadowski using this model of the defect equilibria would suggest that their crystals contained about $5 \times 10^{16}/cm^3$ donor impurities. This model, however, is difficult to reconcile with the good reproducibility from crystal to crystal observed by Thomas and Sadowski because it infers all crystals have the same donor content.

Acknowledgments

The authors thank Ronald R. Royce for performing experimental portions of the study of the solubility of

Te in liquid Zn. This research was partially supported by the Advanced Research Projects Agency through the Center for Materials Research at Stanford University and the Atomic Energy Commission under Contract AT(04-3)-283.

Manuscript received April 24, 1967; revised manuscript received July 25, 1967.

Any discussion of this paper will appear in a Discussion Section to be published in the June 1968 JOURNAL.

REFERENCES

1. D. G. Thomas and E. A. Sadowski, *J. Phys. Chem. Solids*, **25**, 395 (1964).
2. I. V. Korneeva, A. V. Belyaev, and V. Novoselova, *Russian J. Inorg. Chem.* (English translation), **5**, 1 (1960).
3. P. Goldfinger and M. Jeunehomme, *Trans. Faraday Soc.*, **59**, 285 (1963).
4. D. deNobel, *Phillips Research Repts.*, **14**, 361 (1959).
5. A. S. Pashinkin, *Russian J. Inorg. Chem.* (English translation), **7**, 1367 (1962).
6. B. M. Kulwicki, Ph.D. Thesis, Univ. of Mich. School of Engineering, p. 74 (July 1963).
7. J. Carides and A. G. Fischer, *Solid State Comm.*, **2**, 217 (1964).
8. An. N. Nesmeyanov, "Vapor Pressure of the Elements," Academic Press, New York (1963).
9. W. D. Treadwell and W. Werner, *Helv. Chim. Acta*, **36**, 1436 (1953).
10. B. H. Zimm and J. E. Mayer, *J. Chem. Phys.*, **12**, 362 (1944).
11. A. C. P. Pugh and R. F. Brown, *Trans. Faraday Soc.*, **54**, 671 (1958).
12. R. F. Brebrick and A. J. Strauss, *J. Phys. Chem. Solids*, **25**, 1441 (1964).
13. J. H. McAteer and H. Seltz, *J. Amer. Chem. Soc.*, **58**, 2081 (1936).
14. M. J. Pool, *Trans. Met. Soc. AIME*, **233**, 1711 (1965).
15. O. Kubaschewski and E. L. Evans, "Metallurgical Thermochemistry," p. 180, Pergamon Press, New York (1951).
16. *Ibid.*, p. 185.
17. D. R. Stull and G. C. Sinke, "Thermodynamic Properties of the Elements," Amer. Chem. Soc., Washington, D. C. (1956).
18. K. K. Kelly, U. S. Bureau of Mines Bull. No. 476, 1949.
19. F. A. Kröger, *J. Phys. Chem.*, **69**, 3367 (1965).
20. M. R. Lorenz, *J. Phys. Chem. Solids*, **23**, 939 (1962).
21. R. A. Burmeister and D. A. Stevenson, *This Journal*, **114**, 394 (1967).
22. R. F. Brebrick and A. J. Strauss, *J. Phys. Chem. Solids*, **26**, 989 (1965).
23. L. R. Shiozawa *et al.*, Final Report, Contract AF 33(616)-6865, June 1962. Research performed at Electronics Research Laboratories, Clevite Corp., Cleveland, Ohio.
24. M. Aven and B. Segall, *Phys. Rev.*, **130**, 81 (1963).
25. G. Mandel, *ibid.*, **134**, 1073 (1964).
26. R. A. Reynolds, Ph.D. Thesis, Stanford University Dept. of Materials Science, Nov. 1965; *Bull. Am. Phys. Soc.*, **11**, 178 (1966).
27. R. A. Reynolds, Thesis Prog. Rept. No. 3 "Preparation and Properties of ZnTe," June 1964, Dept. of Materials Science, Stanford Univ.
28. E. Miller and K. L. Komarek, *Trans. Met. Soc. AIME*, **236**, 832 (1966).
29. R. T. Lynch, D. G. Thomas, and R. E. Dietz, *J. Appl. Phys.*, **34**, 706 (1963).
30. T. L. Larsen, Materials Science Department, Stanford University. Private communication.

Formation of Precipitates in Gold Diffused Silicon

E. D. Wolley and R. Stickler

Westinghouse Electric Corporation, Research and Development Center, Pittsburgh, Pennsylvania

ABSTRACT

Gold was diffused into silicon wafers with a variety of surface treatments and doping conditions by a sealed tube $AuCl_3$ process. Transmission electron microscope examinations of the wafers showed that precipitates were formed at or near dislocations, at loop-type defects, and at the $Si-SiO_2$ interface. In one case of a slow-cooled diffusion run very large precipitates which were formed at the $Si-SiO_2$ interface were identified as Au_2P_3.

Wilcox, LaChapelle, and Forbes (1) found that the increase in resistivity of uniformly gold diffused silicon was not as much as expected from the gold concentration determined by tracer techniques. These results lead to a conclusion that not all of the gold is present as substitutional atoms in the silicon lattice but that some gold may be present as precipitates. These investigators also found that the solubility and diffusion constant of gold were higher in silicon which was highly doped with phosphorus. They concluded that one possible explanation of these results was the formation of a gold phosphide compound Au_2P_3. Sprokel and Fairfield (2) showed by means of autoradiographs that the concentration of gold was increased in regions of high phosphorus concentration. By x-ray diffraction microscopy these investigators also found precipitates in highly phosphorus-doped silicon samples which had been gold diffused (3). Joshi and Dash (4) recently reported transmission electron microscope observations on the precipitation of a not-further-identified "Au-Si-P" compound in gold- and phosphorus-diffused silicon.

All these investigators used elemental gold deposited on silicon surfaces as diffusion sources. In the present investigation silicon wafers were gold diffused by using a volatile gold compound as a diffusion source. The diffusion was carried out in a sealed tube process with small amounts of $AuCl_3$ as a source.

We have examined the gold diffused silicon wafers by transmission electron microscopy (TEM) and electron diffraction (ED) in order to ascertain if any precipitation does occur and to identify the precipitate, if present. Precipitation was observed, and some of these precipitates have been identified as gold phosphide, Au_2P_3 (5). The Au_2P_3 was observed at or near the silicon-silicon dioxide interface. Other precipitated particles were also detected which could not be identified because they were too sparse and electron diffraction patterns were inconclusive. Some of these particles could be gold. On some specimens a finely dispersed surface precipitate could be identified as SiC.

Experimental Procedures

Materials and wafer preparation.—Wafers of 250 μm (1 μm = 10^{-6} m) thick silicon of several different resistivities both n-type (phosphorus-doped) and p-type (boron-doped), as well as relatively perfect and highly imperfect material were diffused. The material,

Table I. Experimental data for gold diffusion

Group No.	Cond. type	Dopant	Resistivity (ohm cm)	Prediffusion treatment	Gold diffusion temp, °C	Diffusion time, hr	Cooling rate
1	n	P	20	Mixed acid polished[f]	1235	2	Fast[b]
	n	P	20	Mixed acid polished[f]	1235	2	Slow[e]
2	n	P	20	Deformed[a]	1235	2	Fast
	n	P	20	Deformed[a]	1235	2	Slow
3	n	P	20	Lapped[c]	1235	2	Fast
	n	P	20	Lapped[c]	1235	2	Slow
4	n	P	150	Lapped[c]	1235	2	Slow
	n^+	P	0.06	Lapped[c]	1235	2	Slow
	p^+	B	0.08	Lapped[c]	1235	2	Slow
5	p	B	20	Mixed acid polished Phos. diffused[d]	1235	2	Slow
	p	B		Mixed acid polished	1235	2	Fast (P_2O_5 gettered)
6	See Table III			Mixed acid polished	1235	2	Fast
	See Table IV			Mixed acid polished	885	31	Fast

Notes: (See text for complete description of notes):
[a] Lightly deformed by heat-treating to 1275°C with strain (2×10^5 dislocation/cm^2).
[b] Quenched.
[c] Heavily dislocated by lapping (10^9 dislocations/cm^2).
[d] Two-step phosphorus diffusion, 1100°C for 1 hr, 1200°C for 4 hr.
[e] Slow cooled to 400°C (see text).
[f] Wafers as received < 100 dislocations/cm^2.

treatment before diffusion, and diffusion conditions are listed in Table I.

The wafers referred to in the table as "Deformed" were slightly deformed in a quartz tube so that the wafers were suspended on the edges by the tube walls. A quartz rod was placed on top of the wafers, the tube was evacuated to 10^{-5} Torr, back-filled to 1/5 atm with argon, and sealed off. Then the tube was heated at 1275°C for 24 hr. Only 2×10^5 dislocations cm^{-2} were introduced by this treatment, however.

Since a relatively high dislocation density ($> 10^6$ cm^{-2}) is required in order to observe dislocations readily by TEM, wafers of the two subsequent gold diffusions were lapped with 600 mesh Al_2O_3 and given only a light polish with 0.25 μm diamond powder before diffusion. This treatment is referred to in Table I as "lapped." The dislocations were introduced by the abrasion treatment and rearranged during heat-treatment by the relief of lapping stress (6).

Gold diffusion.—The Si wafers were oxidized in wet argon at 1200°C to produce surface oxide films ranging from 7000 to 12,000Å in thickness. Prior to the Au-diffusion treatment, the oxide was removed from one side of the wafers, and the wafers were sealed in quartz tubes (20-60 cm^3 volume) together with approximately 0.1 mg of $AuCl_3$ (supplied by Engelhard Industries). The $AuCl_3$ was held at a low temperature during pump-down to 10^{-5} Torr and seal-off to prevent decomposition. The $AuCl_3$ is somewhat hygroscopic with the result that a small amount of H_2O and perhaps other adsorbed gases might have been introduced into the diffusion tube. The diffusions were carried out at 885°C for 16 hr or at 1235°C for 2 hr. For these diffusion conditions, the distribution of gold through the 250 μm samples should have been relatively uniform at the end of the diffusion time. Wafers were both slow cooled and fast cooled from the diffusion temperature. For the slow cooled wafers the average cooling rates were 10°C/min to 1000°C, 5°/min to 800°C, and 1°C/min to 400°C. Fast cooling was accomplished by removing the diffusion tube from the furnace and placing it under running tap water. The time required to cool the tube to room temperature was 5-10 sec.

During the sealed-tube gold diffusions, a thin oxide layer of a thickness varying from a few to several hundred Angstroms formed on the side from which the thick oxide film had been removed. Nevertheless, in the following this side will be called the "free" surface and the side with 7000 to 12,000Å the "oxidized" surface.

Transmission electron microscope examinations.—After gold diffusion the wafers were divided into pieces small enough to be mounted on the specimen stage of the electron microscope. They were chemically thinned from one or both sides, to obtain areas transparent to the electron beam (6). Both the free and the oxidized sides of the wafers were examined. When the samples were examined near the surface region by thinning from one side only, they were examined first through the oxide and the silicon. Then, the oxide was removed in HF and the Si samples were re-examined.

Determination of electrically active gold.—In order to compare the amount of the electrically active gold obtained by the $AuCl_3$ sealed tube diffusion process to that obtained by other investigators by the use of deposited gold sources, the change in resistivity of various silicon wafers after the gold diffusion was determined.

Since gold introduces both a deep donor and acceptor (7) in silicon, it decreases the net carrier concentration in both p-type and n-type material. Thus the amount of electrically active gold introduced by diffusion can be determined by measuring the change in resistivity in either p-type or n-type material. Several resistivities in both conductivity types covering a range of concentrations from 3×10^{15} to 6×10^{17} cm^{-3} were diffused with gold at 1235° and 885°C for 2 and 31 hr, respectively. The diffusion time was presumably long enough to diffuse completely through the wafers, and hence a relatively uniform distribution of gold was obtained. After diffusion the wafers were fast cooled to prevent appreciable redistribution or precipitation of the gold.

The resistivities and conductivity type of the wafers were measured before and after diffusion. The carrier concentrations were determined from the resistivities and the data of Irving (8).

Results

Electrical data.—The results of the 1235 and 885°C diffusions are given in Table II and Table III, respectively. From Table II it is apparent that the amount of electrically active gold which was obtained at 1235°C is approximately 1×10^{16} cm^{-3}. Note that for concentrations above 10^{16} cm^{-3} the change in resistivity corresponded to an active Au concentration of about 1×10^{16} cm^{-3}. For concentrations below 1×10^{16} cm^{-3} the resistivity became very large as a result of complete compensation. This value of 10^{16} cm^{-3} is less than the solid solubility of gold in silicon reported by Collins *et al.* (9), who reported a value of about 10^{17} cm^{-3} at 1235°C. The concentration of gold in the gaseous phase in our diffusion experiments was of the order of 10^{15} cm^{-3} which probably accounts for the value lower than the solid solubility.

From Table III it appears that the amount of gold diffused at 885°C depended on the concentration in

Table II. Change in resistivities of silicon wafers gold diffused at 1235°C

Type	Before, ohm-cm	N, cm^{-3}	Type	After, ohm-cm	N, cm^{-3}	Change N, cm^{-3}
N	0.106	8×10^{16}	N	0.115	7×10^{16}	1×10^{16}
P	0.09	5.7×10^{17}	P	0.089	5.7×10^{17}	—
P	0.43	5×10^{16}	P	0.496	4×10^{16}	1×10^{16}
N	0.55	1.1×10^{16}	—	>200	—	—
N	1.02	5.5×10^{15}	—	>200	—	—
N	1.82	2.8×10^{15}	—	>200	—	—

Table III. Change in resistivities of silicon wafers gold diffused at 885°C

Type	Before, ohm-cm	N, cm^{-3}	Type	After ohm-cm	N, cm^{-3}	Change N, cm^{-3}
P	0.491	4.3×10^{16}	P	0.490	4.3×10^{16}	—
N	0.699	8.2×10^{15}	N	0.758	7.5×10^{15}	7×10^{14}
N	1.01	5.4×10^{15}	N	1.16	4.6×10^{15}	8×10^{14}
N	1.81	2.8×10^{15}	N	2.24	2.1×10^{15}	7×10^{14}
N	11.5	4.2×10^{14}	N	21.8	2.2×10^{14}	2×10^{14}
P	21.9	6×10^{14}	P	26.8	5×10^{14}	1×10^{14}

the starting material. Other investigators have found that the diffusion rate and the solubility of gold in silicon depends on the quantity and type of impurities present in the silicon (1, 2).

Electron microscope examinations.—Description of the results of electron microscopic examinations will be made of the groups of diffusions listed in Table I in the order in which they appear in the table.

Float-zone material (Group 1).—Figure 1 is composed of TEM's taken about 100 μm below the surface. Figure 1a is a TEM of a typical undiffused starting wafer showing loop-type features (10, 11), which are often found in starting material. In the gold diffused and fast-cooled wafer from group 1 the loops remained substantially unchanged. In the slow cooled specimen shown in Fig. 1b, there is evidence of precipitate formation or change in the nature of the loop-type features. An ED pattern could not be obtained from these precipitates.

Deformed material (Group 2).—As stated above, this material was only slightly deformed so that the effect of deformation was not apparent in the TEM's. These wafers were, however, substantially different from those of group 1. Figure 2a shows the surface region of a fast cooled wafer with the oxide film removed in HF. There are more small precipitates near the surface than were evident in the fast-cooled wafers of group 1. A TEM of a slow cooled specimen is shown in Fig. 2b.

The large regular-shaped particles were located near the silicon-silicon dioxide interface. A spotted ED ring pattern was obtained from these particles. The d-spacings determined from the ED pattern did not match those of Au which lead us to postulate the precipitate was a gold-phosphide compound. However,

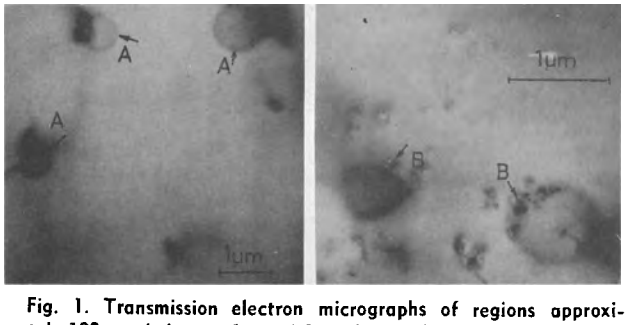

Fig. 1. Transmission electron micrographs of regions approximately 100 μm below surface of Si-wafers: a (left) untreated wafer, 20 ohm-cm, n-type, loop-type defects (A); b (right) portion of same wafer, Au-diffused at 1235°C for 2 hr and slow cooled, formation of precipitate near loop-type defects (B).

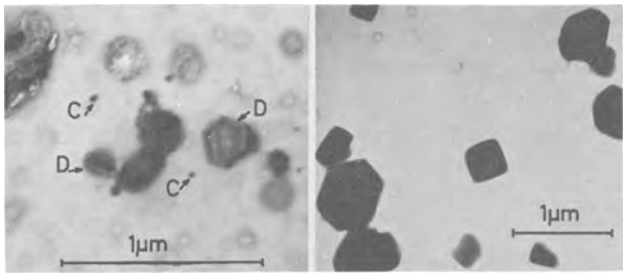

Fig. 2. Transmission electron micrographs of surface regions of Si-wafers (20 ohm-cm, n-type) heat-treated at 1275°C for 2 hr in vacuum prior to Au-diffusion at 1235°C for 2 hr: a (left) wafer fast cooled after diffusion treatment, surface oxide film removed with HF, fine precipitated particles (C) and thin plate-like precipitate (D); b (right) wafer slow cooled after diffusion treatment, oxide film removed with HF, massive particles identified as Au_2P_3.

there is little crystallographic data on gold-phosphide compounds. In order to obtain accurate structural data on Au_2P_3, a 40 a/o (atom per cent) gold, 60 a/o phosphorus alloy was prepared as follows. Gold powder was put into a Vycor glass ampoule, the P was placed upright in the glass ampoule in a small quartz phial (10% over the stoichiometric amount). Thus, only P vapor could reach the Au powder. The ampoule was then evacuated to better than 10^{-5} Torr, sealed off, and placed in a furnace. After several hours heating at 600°C the ampoule was removed and allowed to cool to room temperature. The reaction product appeared as a dark gray powder. Unreacted P was driven off by gently heating the sample by flaming the ampoule with a Bunsen burner, while cooling the other end of the ampoule. The tube was then opened. A chemical analysis of the reaction product revealed a P content of 60.4 a/o which is very close to the stoichiometric composition of Au_2P_3. X-ray diffraction data were obtained from Debye-Scherrer patterns; the measured d-values are listed in Table IV and compared with electron diffraction data obtained from

Table IV. Comparison of d-spacings of bulk prepared Au_2P_3 and the precipitates in Au diffused wafers

d-Spacings (Å) determined from the electron diffraction pattern of precipitates on Au diffused wafer	d-Spacings (Å) determined from the x-ray diffraction data of bulk Au_2P_3*
14.08	12-13
7.6	7.6
—	7.2
—	6.1
—	5.85
—	5.7
5.00	5.2
4.87	—
3.80	3.85
3.71	3.79
—	3.65
3.46	3.48
3.12	3.09
3.04	3.05
—	2.96
2.82	2.79
2.76	2.78
—	2.68
—	2.60
2.53	2.56
—	2.41
—	2.37
—	2.30
—	2.22
—	2.20
—	2.17
—	2.09
2.06	2.07
1.94	1.93
1.88	1.90
—	1.855
—	1.84
—	1.82
—	1.807

* Structure of the bulk Au_2P_3 was determined to be hexagonal, a_o = 6.13 Å, Co = 11.08 Å (5).

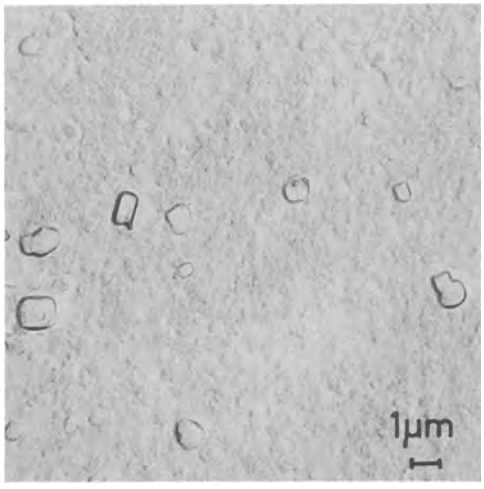

Fig. 3. Electron micrograph of direct-C replica of surface of same wafer as shown in Fig. 2b after extended etching in HF.

the precipitate by electron diffraction. The crystal structure has been reported elsewhere (5). Electron microscope examination of the bulk prepared Au_2P_3 showed it to be unstable in the vacuum under intense electron beam irradiation, leaving Au as residue after a short time exposure in the electron beam. A similar instability was noted also for the precipitate in the diffused wafers.

In addition, the bulk prepared Au_2P_3 and the precipitates both were soluble in HF. The similarity in decomposition under electron irradiation and the dissolution in HF and, particularly, the similarity of the d-spacing as shown in Table IV in the bulk prepared Au_2P_3 and the precipitates of Fig. 2b indicate that these precipitates are indeed Au_2P_3.

Further evidence that these precipitates were located near the Si-SiO_2 interface is that on extended etching in HF the particles disappeared leaving depressions in the silicon. Most of the precipitates consisted of platelets, as is evident from the carbon replica which was made of the surface after the particles were removed on extended etching in HF, Fig. 3.

Lapped material (Group 3).—The TEM's of the fast cooled wafer, Fig. 4, show tangles or networks of dislocations. ED patterns sometimes show extra diffraction spots; however, no positive identification of any other phase was possible. Small precipitated particles can be seen at some dislocation lines, especially close

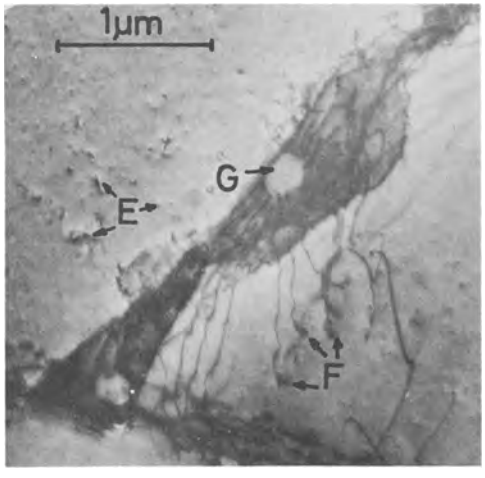

Fig. 4. Transmission electron micrograph of surface region of "damaged" Si-wafer, Au-diffused at 1235°C for 2 hr and fast cooled. Fine precipitate at E could be identified as SiC. Small particles at the emergence points of dislocations (F) and massive particles within dislocation networks (G) could not be identified.

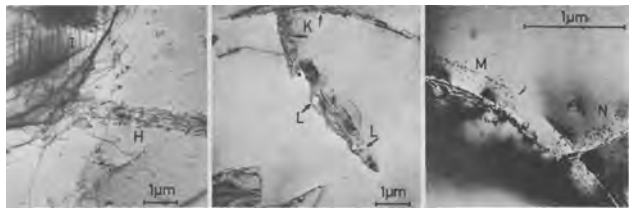

Fig. 5. Transmission electron micrographs of surface regions of damaged Si-wafers, Au-diffused at 1235°C for 2 hr and slow cooled: a (left) high phosphorus doped Si, 0.06 ohm-cm, note precipitated particles in dislocation network intersecting the wafer surface (H), while no precipitate is evident in the dislocation networks parallel to the wafer surface (I); b (center) low phosphorus doped Si, 150 ohm-cm, note precipitate in dislocation networks intersecting the wafer surface (K) and in the oxide platelets (L); c (right) high boron doped Si, 0.08 ohm-cm, note precipitate in regions close to dislocation network (M) and crack (N).

to the wafer surface. Some dislocation lines appear as broad bands of different contrast. Fine particles are distributed all over the surface, which yield a sharp electron diffraction ring pattern for cubic SiC.

Heavily damaged material with high doping (Group 4).—In order to observe the effect of high phosphorus and boron doping on the gold diffusion, the wafers of group 4 were prepared and examined. TEM's typical of the samples from this group are shown in Fig. 5. In the phosphorus-doped specimens of both high and low concentrations, Fig. 5a and b, precipitates were found at dislocations inclined to the surface while there was little or no precipitation evident at dislocation networks parallel to the surface. Precipitation was also observed near or at the oxide platelets shown in Fig. 5b. The formation of these oxide platelets has been described by Stickler and Booker (6).

Many fine particles were observed near dislocation networks inclined to the silicon surface and near cracks in the wafer with high boron doping as is shown in Fig. 5c. Although the gold diffusion was the same there was a striking difference in the highly boron-doped and phosphorus-doped specimens. In the boron-doped silicon the precipitates were formed not only in the dislocation networks but also in the bulk near these networks. In the phosphorus-doped wafers precipitates occurred only at the dislocation networks. The precipitates in either the boron-doped or the phosphorus-doped samples could not be identified.

Phosphorus diffused material (group 5).—Wafers of group 5 were phosphorus diffused in order to obtain higher doping than was available in the uniformly doped material in group 4 and to make a preliminary investigation of the mechanism of P_2O_5 gettering. TEM examination of the phosphorus diffused material showed the diffusion induced dislocation networks (12), but relatively few precipitates, none of which could be conclusively identified.

Figures 6a and b are TEM's of the gold diffused and P_2O_5 gettered material. These TEM's are of the surface region and were taken through the thin phosphosilicate glass. The dislocation network induced by the shallow phosphorus diffusion which occurs during the gettering is evident. Numerous small dark particles between the dislocation network and larger geometrically shaped particles can be seen in Fig. 6b. An identification of these precipitates could not be made by the transmission electron diffraction technique.

Discussion

By TEM methods not much difference in the Au-diffused wafers was observed in the appearance of the free surface and the oxidized surface. This is understandable, since the gold diffusion times and temperatures were such that the gold should have diffused all the way through the wafers. The free surface, furthermore, was always covered with a thin

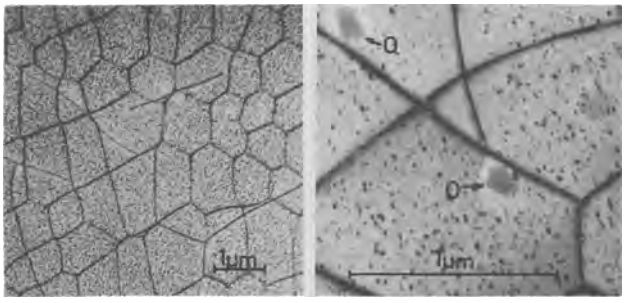

Fig. 6. Transmission electron micrographs of surface region of Si-wafer Au-diffused at 1235°C for 2 hr, fast cooled, and P_2O_5-gettered at 1040°C for 15 min: a (left) dislocation network generated during gettering step; b (right) same area at higher magnification, note fine precipitated particles (small black dots) and massive precipitate (O).

oxide layer (100-1000Å) after the gold diffusion. Thus, there was on both sides of the wafer a Si-SiO_2 interface at which precipitation could occur, and a relatively equal concentration of gold near these surfaces may be expected. This thin oxide layer apparently is formed from traces of H_2O introduced with the $AuCl_3$. Variation in thickness of the oxide, amount of thermal etching, and perhaps the formation of SiC may be due to variations in the residual gas atmosphere.

Most of the investigations were made in the region comprised of the SiO_2 film, the Si-SiO_2 interface, and a Si layer about 0.5 μm thick. The Au_2P_3 precipitates identified in group 2 wafers were found to be present at or near the Si-SiO_2 interface. It is likely that, during the slow cooling from the diffusion temperature, the gold diffused out of the silicon toward the surface, reacted with phosphorus, and precipitated at the interface. The redistribution of appreciable quantities of gold to the surface can be understood in view of the decreased solubility with decreasing temperature, the relatively high diffusion coefficient at temperatures as low as 750°C, and the deactivation of Au by the formation of Au_2P_3. However, an approximate calculation shows that insufficient phosphorus was present in the starting material to account for the amount of the precipitate observed. It is possible that these group 2 wafers were accidentally phosphorus contaminated during the heat-treatment employed to produce dislocations. Phosphorus contamination from certain lots of quartz tubing has been observed in our laboratory.

Precipitates were also observed in all other groups at the Si-SiO_2 interface and at or near the oxide platelets extending into the heavily damaged material. They were also observed at or near dislocations and cracks, predominantly at those intersecting the surface. Some effects of the diffusion treatment could also be observed in the bulk at the loop-type defects. These precipitates could not be identified because there was not enough material to produce an ED pattern. Only SiC near the surface especially in the wafers of groups 3 and 4 could be positively identified. The presence of SiC in these groups may be a result of the reaction of the silicon with residual oil vapors from the seal-off system.

The unidentified precipitates are likely to be gold or gold compounds since they occur only after the gold diffusion. They are more pronounced in the slow-cooled wafers. In the slow-cooled wafers the gold has time to diffuse to defects, interfaces, and to form precipitates.

We have been unable to reproduce the conditions for the formation of the large precipitate in subsequent experiments. Precipitates were formed in other phosphorus doped specimens (Fig. 6a) but these were small, presumably because of a greater number of dislocation sites for precipitation. They could not be identified. Wafers of 0.01 ohm-cm phosphorus doped silicon with all surface damage removed by polish etching were gold diffused at 1235°C for 2 hr and slow cooled. Large precipitates were observed but not nearly as bulky as those seen in Fig. 2c and again they could not be identified from the few diffraction spots obtained. Although we have been unable to reproduce the conditions for formation of the massive, identifiable Au_2P_3 precipitate as formed in the one experiment in several wafers, it may be present in other specimens in smaller quantities and crystal sizes.

Both in the heavily dislocated wafers of groups 3 and 4 and in the gettered wafers of group 5 precipitates were prominent at dislocations which intersected the surface. Since diffusion proceeds faster along dislocations, these dislocations may provide a convenient "exit" for the gold during the slow cooling or gettering and precipitates may form at or near their terminus.

The precipitation of gold is expected to affect the determination of gold solubility and the determination of the electrical effects in silicon devices. Most determinations of the solubility of gold in silicon have been performed by tracer or activation analysis. These techniques determine the total amount of gold in the silicon and do not differentiate between the electrically active and precipitated gold. Thus, when the change in resistivity of gold diffused silicon is calculated from the total amount of gold as Wilcox, LaChapelle, and Forbes (1) have done, agreement between calculated and measured values need not exist. On the other hand, Bemski (7) and Collins *et al.* (9) both found agreement between electrically determined values of gold concentration and concentrations determined by neutron activation analysis and radioactive tracer analysis, respectively.

Our value for concentration of electrically active gold obtained at 1235°C corresponds more closely with that calculated from the change in resistivity data of Wilcox *et al.* (1) than with that of Collins *et al.* (9). However, our diffusions were from a gaseous source with a concentration of 10^{15} cm^{-3} rather than from a solid. The limit of solid solubility of gold in silicon may not have been reached in our experiments and, consequently, only a relatively small fraction of the gold may have been available for precipitation.

Summary and Conclusions

Precipitates occur in silicon wafers which are gold diffused at 1235°C for 2 hr and either fast or slow cooled. These precipitates are more prevalent in slow-cooled than in fast-cooled wafers. The precipitates occur mainly at or near defects, including dislocations and loop-type features, and at the Si-SiO_2 interface. In one group of wafers large regular-shaped precipitates at the Si-SiO_2 interface were identified as Au_2P_3 by a comparison of ED patterns from the precipitates and x-ray diffraction patterns from Au_2P_3 prepared in bulk in the laboratory. The conditions under which large Au_2P_3 precipitates are formed in silicon are not yet fully explored. The electrically active concentration of gold introduced by our diffusions at 1235°C for 2 hr was about 10^{16} cm^{-3}. The $AuCl_3$ diffusion process can be used to obtain gold concentrations less than those obtained by elemental diffusion methods.

Acknowledgment

The authors wish to thank H. F. John for suggesting this investigation, W. C. Hughes for help with the electron microscope work, C. G. Beck for help with the electron diffraction and x-ray diffraction work, and L. S. Saxon for help with the gold diffusions and electrical measurements.

This work was supported in part by the George C. Marshall Space Flight Center, Huntsville, Alabama, under Contract NAS8-11432.

Manuscript received Sept. 8, 1966; revised manuscript received Aug. 29, 1967. This paper was presented at the San Francisco Meeting, May 9-13, 1965.

Any discussion of this paper will appear in a Discussion Section to be published in the June 1968 JOURNAL.

REFERENCES

1. W. R. Wilcox, T. J. LaChapelle, and D. H. Forbes, *This Journal*, **111**, 1377 (1964).
2. G. J. Sprokel and J. M. Fairfield, *ibid.*, **112**, 200 (1965).
3. J. M. Fairfield and G. J. Sprokel, Paper presented at the San Francisco Meeting of the Society, May 1965, Abstract 126.
4. M. L. Joshi and S. Dash, *J. Appl. Phys.*, **37**, 2453 (1966).
5. C. G. Beck and R. Stickler, Paper presented at the Pittsburgh Diffraction Conference, 3, November 1965, to be published.
6. G. R. Booker and R. Stickler, *Phil. Mag.*, **8**, 859 (1963).
7. G. Bemski, *Phys. Rev.*, **111**, 1515 (1958).
8. J. C. Irving, *BSTJ*, **41**, 387 (1962).
9. C. B. Collins, R. O. Carlson, and C. J. Gallagher, *Phys. Rev.*, **105**, 1168 (1957).
10. A. N. Knopp and R. Stickler, *Electrochem Technol.*, **5**, 367 (1967).
11. H. F. John, J. W. Faust, Jr., and R. Stickler, *IEEE Transactions on Parts, Materials and Packaging*, **PMP2**, 51 (1966).
12. E. D. Wolley, R. Stickler, and T. L. Chu, Recent News Paper presented at the Buffalo Meeting of the Society, October 1965.

The Occurrence and Identification of Precipitates in Zinc-Diffused GaAs

J. F. Black

The Bayside Laboratory, research center of General Telephone & Electronics Laboratories Incorporated, Bayside, New York

ABSTRACT

Both submicroscopic and microscopically visible precipitates in zinc-diffused GaAs have been studied by means of conventional optical microscopy of etched samples, infrared transmission microscopy of polished samples, and electron probe microanalysis. The microscopically visible precipitates were discrete particles located principally at grain boundaries in polycrystalline samples and at subgrain structures in "single" crystals, and they were identified as zinc rich by the electron probe. The submicroscopic precipitates were concluded to be zinc rich by arguments based on the existence of zones depleted of these precipitates around the larger visible particles. Samples in which part of the diffused zinc was present as submicroscopic precipitates were found to cause attenuation of IR far greater than that caused in samples in which all of the zinc was in solution.

It has recently been established (1, 2) that the diffusion of zinc into GaAs can, under certain conditions, cause the appearance of submicroscopic precipitates. It was, however, not possible from the evidence presented to establish that these precipitates were zinc rich. This is important because the occurrence of zinc-diffusion-induced precipitation in GaAs cannot be completely understood until these precipitates have been identified. There is yet no direct proof of the precipitation of zinc in GaAs, nor for that matter in any other III-V compound, as a result of diffusion with zinc. Although Gershenzon and Mikulyak (3) and others (4) have reported the formation of "zinc" precipitates in III-V compounds, their identifications were based on circumstantial evidence.

The current work was intended to provide direct proof of the major presence of zinc in precipitates induced in GaAs by the indiffusion of zinc. By means of the electron probe microanalyzer, visible precipitate particles formed in GaAs by the indiffusion of zinc were positively identified as zinc-rich. In addition, infrared (IR) transmission microscopy of precipitate structures and the study of etch figures developed by a dislocation etchant provided confirming evidence that the submicroscopic precipitation was also zinc-rich. Finally it was demonstrated that, for equal zinc concentrations, samples containing part of their zinc in the form of submicroscopic precipitates were much more effective in attenuating IR radiation than samples in which the zinc was present only as dissolved ionized acceptors.

Experimental Procedures

Because precipitates formed at grain boundaries are usually larger and therefore easier to observe and identify than those formed within single crystals the bulk of the data presented herein were obtained on polycrystalline GaAs. This polycrystalline material was undoped n-type with n $\sim 5\times10^{17}/cm^3$. The single crystals used in this investigation were Cd-doped with a resistivity of $\sim$ 1 ohm·cm (p $\sim 5\times10^{16}/cm^3$) and a dislocation density of 10,000-50,000/cm^2. P-type crystals were used for simplicity in making Hall effect measurements after zinc diffusion (5), for later comparisons with chemical (zinc) analysis. Cadmium-doped material was selected since the Cd diffusion coefficient was sufficiently small compared with that of zinc to preclude any change in the background p-doping during the indiffusion of zinc. Prior to diffusion, wafers were ground and lapped flat and parallel with No. 600 alumina grit and then carefully polished with 0.3 and 0.05 micron alumina to remove the damage introduced by the diamond wafering saw. Single crystal test samples processed by this technique and annealed at 1000°C for 2 hr showed no significant increase in dislocations as determined by etch pit counting. The final thickness of both single crystal and polycrystal samples was 0.030 $\pm$ 0.002 in. Diffusion was carried out in evacuated sealed quartz capsules of 50 cm^3 volume containing 10-50 mg of pure zinc and 1g of finely powdered GaAs.

Diffusion was conducted at fixed temperatures ranging from 900° to 1100°C. Unless otherwise indicated, all diffusions were terminated by slowly withdrawing the capsule from the furnace over a period of 2 min and then immersing it in a bucket of water. Care was taken during the diffusion cycle to keep the end of the capsule containing the zinc at a temperature at least 10°C below that of the samples and the powdered GaAs.

Samples diffused at the upper extremes of temperature and zinc vapor concentration usually showed clear evidence of surface melting, especially in polycrystalline samples. The surface melting was spotty and in polycrystalline samples showed a strong preference for the grain boundaries. Cross sectioning of samples showed that even in the worst cases (50 mg Zn at 1100°C) surface melting penetrated no more than 5μ at grain boundaries and less than 2μ elsewhere beneath the original surface of the sample.

After diffusion, samples to be viewed in a direction normal to the plane of diffusion were lapped so that the surface of section was approximately in the center plane of the original sample. During final polishing a slowly rotating lap was used with 0.05μ alumina in order to keep as few precipitate particles as possible from being swept away by the lapping action.

IR transmission microscopy was generally performed on polished samples, since etching enhanced surface features such as scratches and produced grooves at grain boundaries which interfered with the study of the subsurface precipitate structures. Samples were examined under transmitted IR illumination by means of an IR image converter adapted to the ocular of an inverted stage metallographic microscope. Observations of IR transmission through polished profile sections were made with the aid of slotted masks positioned and fixed under the IR microscope so that only the diffused region of the sample was exposed to the illumination. Without the use of a mask, IR radiation passing through the relatively transparent undiffused portion of the section made it difficult to assess the true optical character of the diffused layer. Infrared photomicrographs were obtained with Eastman Kodak Type I-M Spectroscopic Plates.

P-n junctions were revealed by swabbing samples with a freshly prepared solution of 1 part HF, 5 parts HNO_3, 3 parts 1% $AgNO_3$ solution for 10 to 30 sec, quickly followed by a rinse in deionized water. In addition to p-n junctions, this etch revealed grain boundaries and p + p junctions. An NaOH-H_2O_2 etchant which was specific to a {111} Ga surface was also used (1 part 30% H_2O_2-5 parts 2% NaOH solution). Previous investigation (1) has shown that in the presence of submicroscopic precipitation in zinc-diffused GaAs the NaOH-H_2O_2 solution develops a {111} Ga etch structure of densely packed (10^7/cm^2 and higher) shallow triangular etch pits (see Fig. 1).

Experimental Results and Discussion

Optical effects of the submicroscopic precipitates.— It was found that for a given zinc content, diffused samples containing submicroscopic precipitates caused IR attenuation far greater than that which could be caused by free-carrier absorption alone. Figure 1a is a photomicrograph of an etch structure typical of a diffused sample in which precipitation has occurred. In Fig. 1b the same region is shown by transmitted infrared (0.9-1.2μ) where the thickness of the section is 75μ. Figure 1c shows a typical zinc concentration profile determined by electron probe microanalysis.[1] Note that the boundary of the layer containing the submicroscopic precipitation (see Fig. 1a) coincides with the boundary of the IR opaque layer (Fig. 1b), and note also that the diffusion profile in Fig. 1c shows that the critical zinc concentration for precipitation is about 1x10^{19} atoms/cm^3. The dashed line at the tail end of the zinc profile in Fig. 1c is the zinc concentration gradient estimated from the probe analysis. However, because the zinc concentration in this region was close to the limit of the probe sensitivity (which was about 5x10^{18} zinc atoms/cm^3), the dashed line is probably not the true zinc profile. Measurements of p+p and p-n junctions in diffused n-type

[1] The penetration profile of Fig. 1 is convex toward the origin rather than concave as is generally the case for zinc in GaAs. Convex profiles, which have been observed before at very high zinc concentrations (1a) suggest that the diffusion coefficient is decreasing with increasing zinc concentration. See ref. (12) for a more complete discussion.

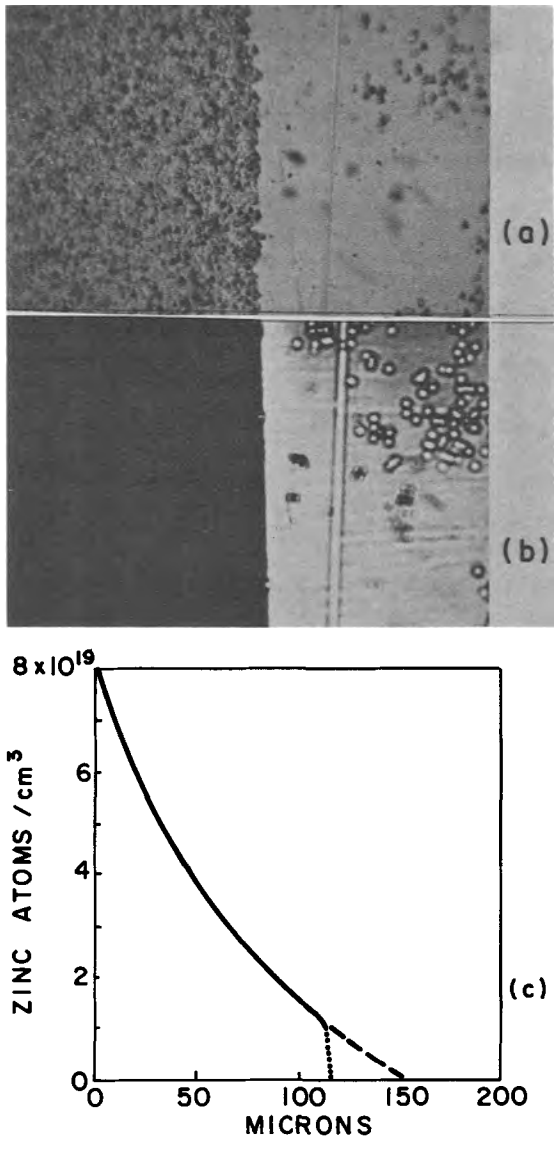

Fig. 1. GaAs single crystal diffused at 900°C for 2 hr from 10 mg zinc (see text for details of diffusion): (a) (111) Ga, plane of cross section viewed by conventional optical microscopy after etching with NaOH-H_2O_2; (b) same area viewed under transmitted IR; (c) zinc penetration profile of the diffused layer determined from point by point Zn$K\alpha_1$ scan. The dashed line and the dotted line are explained in the text.

samples suggest that the dotted line is closer to the actual shape of the zinc profile in this region. The high attenuation of IR shown in Fig. 1b was not caused by scattering of IR from the densely packed etch pits, since the sample was just as opaque to IR in its polished condition. The etched sample is shown instead of the polished sample because the etching provides convenient fiducial marks to correlate the two photographs; for instance the scratch mark and the array of etch pits (the pits appear as small dark halos in Fig. 1b).

For purposes of comparison, a sample of zinc-(melt)-doped GaAs of the same thickness as the slice of Fig. 1b but doped to 3.7x10^{19} zinc atoms/cm^3 (free hole concentration 4.0x10^{19}/cm^3) was examined under the same incident IR intensity using the masking technique described under Experimental Procedures. It was expected that the melt-doped sample would be quite opaque to IR because of its high doping level (high free-carrier absorption) compared to the diffused sample; instead it was moderately transparent.

From the known absorption coefficient of the zinc-melt-doped sample (which was about 500 cm^{-1}

averaged over 0.9-1.2μ), the "absorption" coefficient at the boundary of the diffused region in Fig. 1b was determined to be larger than 500 cm^{-1}. If only free-carrier absorption were acting, a zinc concentration of $1x10^{19}$ atoms/cm^3 (the boundary concentration) would have produced GaAs with $\bar{\alpha}$ of only 100 cm^{-1} or so (6). Thus it appears that the precipitation present at the boundary of the diffused layer is sufficient to cause excess attenuation amounting to 400 cm^{-1}.

It is clear that the IR attenuation of the thin section shown in Fig. 1b does not follow the zinc concentration profile, *i.e.*, the IR attenuation appears just as strong at $1x10^{19}$ atoms/cm^3 (the boundary concentration) as it does at $8x10^{19}$ atoms/cm^3 (the surface concentration). If the submicroscopic precipitates were zinc rich, one would expect that the amount of precipitate present, and hence the degree of IR absorption, would increase at the higher zinc concentrations. Such an increase in IR absorption could, however, only have been observed if the sample were thin enough so that at least part of it, presumably that part near the boundary, transmitted some IR. Even when the profile section was thinned to a few hundredths of a millimeter, the diffused portion was still completely opaque to IR. For the amount of zinc contained near the boundary of the diffused region [$1x10^{19}$ atoms/cm^3 $\equiv$ 0.02 w/o (weight per cent) Zn] such strong attenuation (absorption + scattering) is surprising and implies at least a very fine particle size for the precipitate well dispersed throughout the matrix.

The optical properties of the diffused layer have important consequences relative to the fabrication of injection electroluminescent devices. The presence of a highly attenuating layer such as shown in Fig. 1b can seriously reduce the external quantum efficiency and radiant power output of the electroluminescent diodes. On the other hand such a layer can be useful in absorbing emissions from p-n junctions in optoelectronic devices to keep such emissions from affecting other light-sensitive parts of the device.

Identification of the visible precipitates.—The chemical identification of precipitates in solids is currently most conveniently accomplished by *in situ* analysis with the electron probe microanalyzer (7). To execute the analysis it is necessary to develop precipitate structures with particles large enough to be seen under the microscope and large enough to be seen and analyzed by the electron probe. In practice it was found that particles a few microns in diameter were of sufficient size for these purposes.

Extended diffusion of polycrystalline wafers of GaAs caused them to become saturated with zinc, producing submicroscopic precipitation throughout the sample as well as causing discrete microscopically visible precipitate particles to appear along grain boundaries or twin boundaries. Figure 2 shows a series of photomicrographs of one of a number of areas found in a polycrystalline wafer saturated with diffused zinc. This particular area was selected because it contained a number of discrete precipitate particles at two grain boundaries, and a grain whose surface of section was close enough to a {111} Ga plane to allow the study of defect etch structures developed by the NaOH-H_2O_2 etchant. Figure 2a is a photomicrograph of the as-polished sample, showing particles up to several microns in diameter strung out along two of three intersecting boundaries. All or part of the many particles have been swept away during polishing, and this is the reason for the dark appearance of particles. Figure 2b is an electron probe topograph of the same area, showing the ZnKα_1 characteristic x-ray emissions excited by the focused (about one micron diameter) electron beam. Figure 2c is the same area as Fig. 2a and 2b but a higher magnification, after etching the sample with NaOH-H_2O_2 solution. A comparison of Fig. 2a and 2b shows that without doubt the precipitate particles are zinc rich. Note that one of the

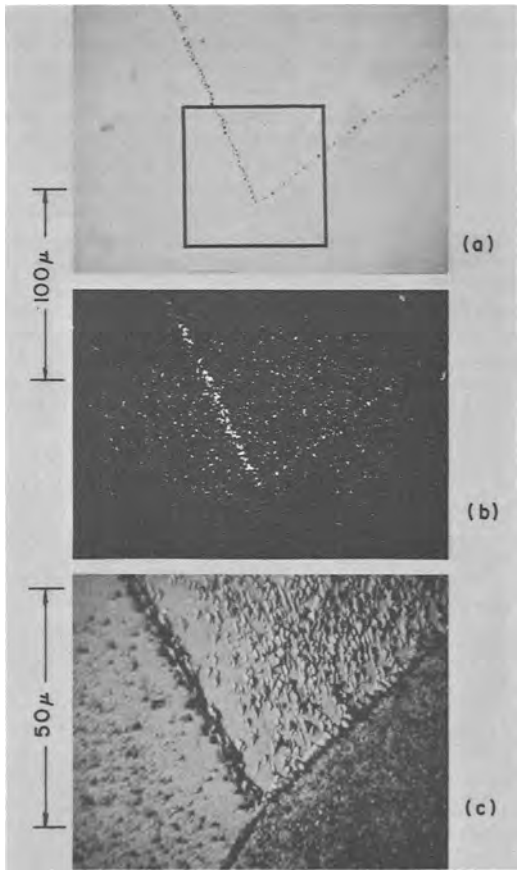

Fig. 2. Cross section of polycrystalline GaAs diffused from 10 mg of zinc at 900°C for 48 hr: (a) as-polished sample; (b) same area shown by CRT display of electron probe scan for ZnKα_1 radiation. The white spots not in the V represent the electronic noise background during this scan; (c) area outlined in (a) after etching with NaOH-H_2O_2.

three grain boundaries is not seen in Fig. 2a or 2b because it is free of visible precipitates and note also that of the other two boundaries the one on the left is definitely more heavily decorated. This marked difference in the amount of precipitation between the three grain boundaries is consistent with the different degrees of mismatch in the contiguous lattices along each of these boundaries (8), indicated by the distinctly different etch figures in each grain.

The etch structure of Fig. 2c is of particular interest. The grain at the top shows a triangular pit etch structure which is typical of submicroscopic precipitation. Because the surface of section is about 10° from the <111> Ga direction, the etch pits in this grain appear as strongly skewed triangles. Notice that there is a corridor along the grain boundary at the upper left that is relatively free of etch pits. The significance of this etch pit free corridor will be discussed in detail later.

Prolonged diffusion with zinc resulted in larger and more readily characterized particles. These particles were best observed in nearly single crystals, *i.e.* crystals with small-angle grain boundaries. Large precipitate particles formed in a region of small angle-grain boundaries in an otherwise single crystal are shown in Fig. 3. Instead of comparing an optical photomicrograph with the ZnKα_1 scan, as in Fig. 2, we compare a backscattered electron topograph (Fig. 3a) with the ZnKα_1 scan (Fig. 3b). The backscattered electron topograph of Fig. 3a reveals structural details of the kind that would be shown by a reflection optical micrograph. In this case we have much stronger patterns to compare than before (notice that the magnification is the same as in Fig. 2a and 2b). Once again the correspondence of zinc-rich regions with

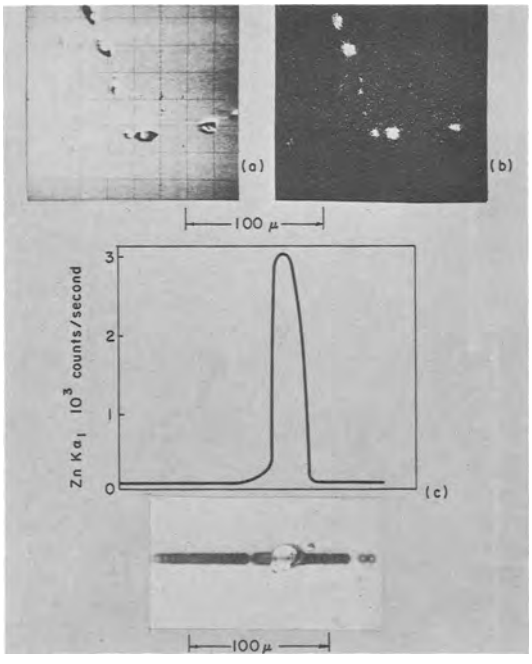

Fig. 3. Precipitates in region of small angle grain boundaries of "single" crystal GaAs diffused for 16 hr at 1100°C from 50 mg of zinc. Sample is sectioned in plan view, i.e., parallel to plane of diffusion, and the surface viewed is approximately coincident with midplane of original sample. (a) Area shown by backscattered electrons; (b) same area shown by CRT display of ZnKα_1 scan; (c) point by point ZnKα_1 scan of large precipitate particle, the dark circular spots, most of which overlap, mark the course of the electron beam.

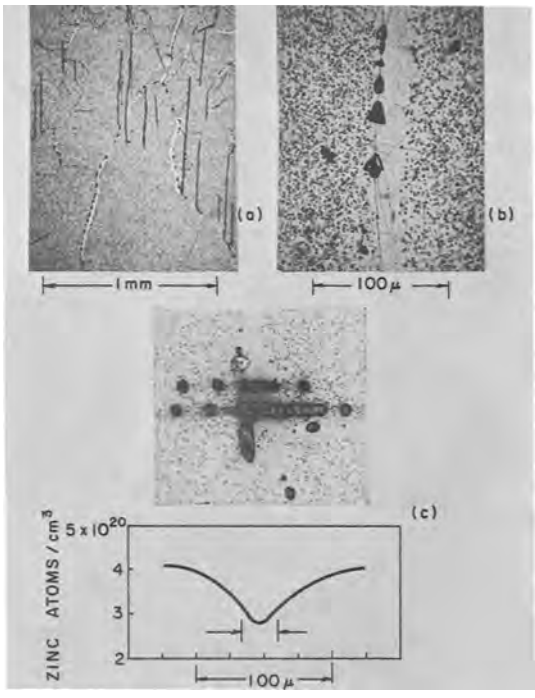

Fig. 4. Precipitates along small angle grain boundaries in a GaAs crystal diffused for 16 hr at 1100°C from 50 mg of zinc; sample has been etched with NaOH-H_2O_2. (a) View at low magnification; (b) high magnification view of one of the boundaries showing details of the structure; (c) zinc concentration profile of boundary determined by point to point ZnKα_1 scan.

visible discrete precipitate particles is unmistakable. A point-by-point ZnKα_1 scan made across an especially large particle is shown in Fig. 3c. Note the sharp and considerable increase in zinc counting rate that was recorded as the particle was scanned by the electron beam. By comparing the counts obtained on a pure zinc standard (5200 counts/sec) with counts obtained on these visible precipitates (3000 counts/sec), it was established that although the precipitates were not pure zinc, they were composed of major proportions of zinc. Electron probe scans for arsenic and for gallium showed these elements to be present, but at relatively low levels compared with the surrounding GaAs matrix.

The photomicrographs of Fig. 4 show small-angle grain boundaries in a zinc-diffused "single" crystal of GaAs. This crystal was oriented in the <111> direction, and the surface observed is a {111} Ga plane parallel to the plane of diffusion. The sample has been etched with NaOH-H_2O_2 solution, producing the triangular pit etch structure indicative of submicroscopic precipitation. Besides the small densely packed etch pits, the etchant has also produced many dark voids along the grain boundaries. These dark voids are the regions formerly occupied by the visible precipitates which etched away faster than the surrounding zinc diffused GaAs. (The size and shape of these voids has been exaggerated by the etchant.) Notice the corridors essentially free of etch pits running along many of the boundaries, especially those which contained appreciable numbers of discrete particles. Note also the similarity of the corridor in Fig. 4b to the one in Fig. 2c.

Figure 4c shows an area of the sample that has been analyzed by the electron probe. This analysis was performed after the sample has been repolished and lightly etched since the relatively heavy etching shown in 4a and 4b would have produced undesirable scattering in the analytical results. A region free of visible precipitates was chosen to avoid the possibility that precipitate voids or residual pockets of zinc rich precipitate would interfere with the analysis. Figure 4c shows that the boundary of the etch-pit-free corridor corresponds to a zinc concentration of about $3x10^{20}$ atoms/cm^3, while in the corridor itself the concentration is only slightly less. The zinc concentration in the surrounding grain is about $4x10^{20}$/cm^3. Thus only a small part of the diffused zinc appears to be tied up as submicroscopic precipitates; a result which is in agreement with other studies of zinc-diffused GaAs(1,9).

Identification of the submicroscopic precipitates.— The following argument is presented, along with substantiating evidence, to show that the existence of etch-pit-free zones immediately adjacent to zinc-rich microscopically visible precipitate particles is strong evidence that the submicroscopic precipitation in diffused single crystals is zinc rich.

In a given polycrystalline solid solution the formation of precipitates proceeds in two stages (8): (*i*) rapid nucleation of precipitates at grain boundaries, initially forming submicroscopic particles but very soon producing relative large particles; (*ii*) slow nucleation and growth of submicroscopic precipitates in the rest of the system. It is well-established that, in a given solid system, at fixed temperature, whenever chemically identical precipitates exist with widely different particle sizes, one of which is very fine (submicroscopic), the larger particles grow at the expense of the smaller particles (10). The driving force is the excess energy of the fine particles due to their high surface-to-volume ratio.

Since the densely packed etch pits in zinc-diffused GaAs are associated with submicroscopic precipitation (1), the disappearance of the etch pits must therefore mean the disappearance or dissolution of the precipitates. The submicroscopic precipitates shed their excess energy by dissolving and, in so doing promote, the growth of the visible grain boundary precipitates. Then, since the visible precipitates are zinc rich, it follows that the submicroscopic precipitation is also zinc rich. The tendency of internal crystal boundaries

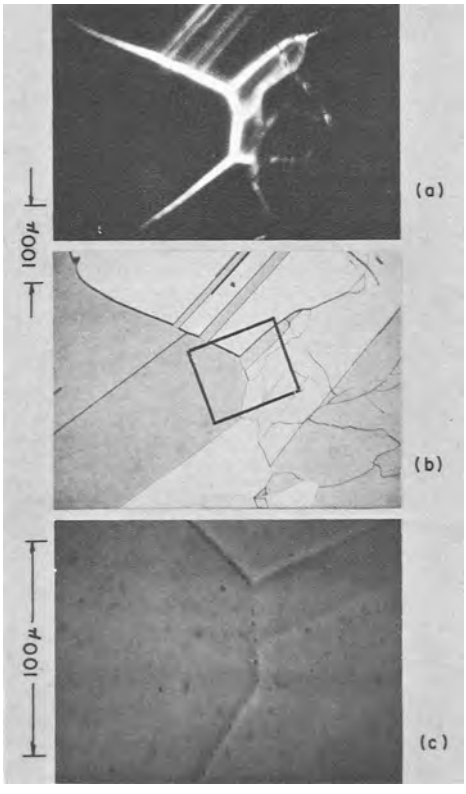

Fig. 5. Polycrystalline GaAs diffused for 7 days at 900°C from 10 mg of zinc; (a) grain boundaries revealed by transmitted IR; (b) same area viewed by conventional optical microscopy after etching with NaOH-H_2O_2; (c) area outlined in (b) after repolishing to show the discrete precipitate particles.

to "absorb" precipitates from the bulk of the crystal is well known in solid-state science (8).

It was noticed that the grain boundaries, along with their precipitates, were sometimes located near the center of the etch pit free corridors, but they were more often located toward one side of the corridor as in Fig. 4b. This type of grain boundary precipitate structure indicates that many of the grain boundaries have moved during the course of precipitation (11). This is very interesting because it implies Ga and As diffusion rates that are several orders of magnitude higher than the accepted values for pure GaAs (12).

If the submicroscopic zinc-rich precipitates are dissolving and promoting the growth of visible grain boundary precipitates, as has been postulated above, then a corridor of IR transparent material, corresponding to the corridor free of etch pits, should appear along the grain boundaries. (Recall the relative IR transparency of precipitate-free zinc doped GaAs discussed earlier, with regard to Fig. 1b.) Such an IR transparent corridor is seen in one of the series of photomicrographs of Fig. 5. These photos show a region of a polycrystalline sample diffused with zinc at 900°C for 7 days. Figure 5a is a view of the polished sample under transmitted IR radiation, and Fig. 5b shows the grain boundary structure of this same region. Figure 5c is a view, at high magnification, of the region enclosed by the square in Fig. 5b, after repolishing to show the precipitate particles. The structure shown in Fig. 5a was recorded after the sample had been thinned to a few hundredths of a millimeter. To make sure that the transmitted light was not due to cracking of the sample at the grain boundaries, a separate exposure was made using photographic plates sensitive to the visible spectrum only (Eastman Kodak Type IF). No transmission structure could be seen in these plates, confirming that the structure of Fig. 5a was due to the selective IR transparency of the grain boundary region. None of the grains in the area shown in Fig. 5 had orientations close enough to a <111> Ga orientation to develop the etch structure associated with submicroscopic precipitation, so it was not possible to correlate etch pit free corridors with IR transparent corridors in this sample. Nevertheless it is clear from the evidence presented so far that the correlation exists.

Gershenzon and Mikulyak (3) have described IR structures similar to Fig. 5a in zinc-diffused GaP which, after diffusion, had been annealed at high temperatures in evacuated capsules. They attributed their structures to preferential out-diffusion of zinc along grain boundaries. In the present case, however, the IR transparent grain boundaries cannot be attributed to the out-diffusion of zinc since a zinc atmosphere was maintained throughout the entire diffusion period.

Concluding Remarks

The results of this investigation lead to the conclusion that the submicroscopic precipitation that has been found to occur in heavily zinc diffused GaAs (1) is zinc rich. If this conclusion is to be accepted, however, some interesting questions are raised. For example, how can the existence of zinc-rich precipitates in GaAs diffused with $1x10^{19}$ zinc atoms/cm^3 be reconciled with prior investigations which appear to show that zinc is soluble, *i.e.*, gives one free-charge carrier for every zinc atom present (5, 13) at zinc concentrations much greater than $1x10^{19}$ atoms/cm^3? Recently, comparisons of the free-carrier concentration and the zinc concentration in diffused samples containing intense submicroscopic precipitation have shown that in many samples the amount of zinc tied up as precipitates may not be more than 10% of the total amount of zinc indiffused (1, 9). In this case precipitation would escape detection by the comparison of chemical analysis and free-carrier concentration (Hall effect) of the usual accuracy and precision. In fact, were it not for the studies of etch structure, IR transmission, and x-ray (anomalous) transmission, such as are reported in this and other recent publications (1-4), the existence of precipitates in zinc-diffused GaAs would still be suspect. If, however the precipitates constitute only a small fraction of the indiffused zinc, it is difficult to understand the very strong IR attenuation they cause.

In addition, it is important to note that these zinc-rich precipitates have not been observed in crystals doped from the melt; they have been found to appear only on the introduction of zinc into GaAs by diffusion. This implies that diffusion induced dislocations might be necessary for precipitation. In spite of some evidence to the contrary (1), it is this mechanism that is most consistent with all of the experimental facts.

Stresses due to the presence of precipitates usually cause an enhancement of diffusion rates. If, in addition, the precipitate contains the diffusant as a major constituent, the effect on diffusion rates becomes even more complicated. None of the accepted theories of zinc diffusion in GaAs are based on experiments in which it was established that the samples were free of diffusion induced precipitates. Thus it would appear that the current theories (12) should be re-examined. On the other hand, the excellent agreement between current theory and extensive quantitative studies of the diffusion of zinc into GaAs constitutes a strong argument against precipitates having a significant effect on the diffusion process. These conflicting viewpoints could be resolved if the diffusion induced precipitates were not present during the diffusion period. If precipitation occurred onto diffusion induced dislocations only during cooling (or quenching) or afterward then the precipitates would have no effect, unless the sample were re-diffused.

Acknowledgments

The author is indebted to W. Sutkowski for the electron probe analyses, to J. Hurley for his assistance

in some of the experimental work and to Dr. L. Bodi and Dr. J. Bilello for helpful suggestions in reviewing this manuscript.

Manuscript received May 5, 1967; revised manuscript received Aug. 9, 1967. This paper was presented at the Cleveland Meeting, May 1-6, 1966.

Any discussion of this paper will appear in a Discussion Section to be published in the June 1968 JOURNAL.

REFERENCES

1. J. F. Black and E. D. Jungbluth, *This Journal*, **114**, 181 (1967); **114**, 297 (1967).
1a. D. B. Wittry, J. M. Axelrod, and J. O. McCaldin, "Properties of Elemental and Compound Semiconductors," H. C. Gatos, Editor, p. 89, Interscience Publishers, New York (1960).
2. J. F. Black and E. D. Jungbluth, *This Journal*, **114**, 188 (1967).
3. M. Gershenzon and R. M. Mikulyak, *J. Appl. Phys.*, **35**, 2132 (1964).
4. M. S. Abrahams and C. J. Buiocchi, *ibid.*, **37**, 1973 (1966); H. R. Winteler and A. Steinemann, *Helv. Phys. Acta*, **39**, 182 (1966).
5. J. F. Black, *This Journal*, **108**, 178C (1961); **111**, 924 (1964).
6. D. E. Hill, *J. Appl. Phys.*, **36**, 3405 (1965).
7. "The Electron Microprobe," T. D. McKinley, K. F. J. Henrich and D. B. Wittry, Editors, John Wiley & Sons Inc., New York (1966).
8. "Metal Interfaces," p. 269 The American Society for Metals (1952).
9. J. F. Black, To be published.
10. "Physical Metallurgy," Chap. 8, Bruce Chalmers, John Wiley & Sons, Inc., New York (1959); Ekstrom and J. F. Dismukes, *J. Phys. Chem. Solids*, **27**, 857 (1966).
11. M. F. Ashby and I. G. Palmer, *Acta Met.*, **15**, 420 (1967); E. F. Kock and K. T. Aust, *ibid.*, 405.
12. For a review of the theories of zinc diffusion in GaAs see "Diffusion in III-V Compounds with Particular Reference to Self-Diffusion in Indium Antimonide" by D. L. Kendall, Doctoral Dissertation, Dept. of Materials Science, Stanford University SU-DMS Report No. 65-29.
13. R. A. Ruehrwein and A. S. Epstein, *This Journal*, **109**, 68C (1962); J. O. McCaldin, *J. Appl. Phys.*, **34**, 1748 (1963).

Impurity Redistribution in a Semiconductor during Thermal Oxidation

Wen H. Chen[1]

Hughes Aircraft Company, Culver City, California

and Wen S. Chen

Boeing Scientific Research Laboratory, Seattle, Washington

ABSTRACT

A general review of mathematical treatments on this redistribution phenomena has been made and discussed. A series method is developed and exact solutions describing the redistributed impurity concentration profiles in both the oxide and the semiconductor can be given. Boundary conditions of diffusion equations are discussed according to different physical situations. Special cases are treated for three initial impurity concentration profiles in silicon: Gaussian, complementary error function, and uniform. Experiments were performed on boron-doped silicon by wet oxygen at 1200°C. The initial concentration profile was a Gaussian, and the segregation coefficient was found to be about 1.8.

It is well known that impurities will be redistributed near the oxide-semiconductor interface during the thermal oxidation process. A model of the redistribution process was developed by Atalla and Tannenbaum (1). Their model was based on the case where the diffusion coefficient of impurities in the oxide was negligibly small. A solution of the diffusion equation for uniformly doped silicon thas been given by Cooper, Doucette, and Mehnert (2). Leuenberger (3) has shown that boron is depleted in the silicon near the oxide-silicon interface after the redistribution process and that a p-n junction is formed in boron-phosphorus, compensated, p-type silicon. Grove, Leistiko, and Sah (4) and Ku (5) treated this problem with consideration of diffusion of impurities in both the oxide and silicon. Grove *et al.* assumed that impurity concentration was kept constant at the outer oxide surface during the redistribution process. Their solution agrees with that of case II in Ku's study where the same boundary condition was assigned. Ku, in his case I, assumed that the outer oxide surface was impermeable. The result he obtained using this boundary condition, is the same as the one obtained by Cooper *et al.* (2). Mathematical treatment for a case of nonuniformed doped silicon was first made by Kato and Nishi (6). The impurity profile before redistribution was a complementary error function. An analytic solution to describe the redistributed concentration profile was given approximately in an integral form by means of the method of Green's function. Cave (7) simplified the problem by assuming that the oxide growth is linear instead of parabolic and the initial profile was a simple exponential function of coordinate. Both Cave and Kato utilized Atalla's model in which the diffusion in the oxide was assumed to be negligibly small and therefore the redistribution process in oxide and the boundary condition at the outer oxide surface were completely neglected in their mathematical formulation. In general, the diffusion process in the oxide and the boundary condition at the outer oxide surface are factors which affect the redistribution of impurities in the semiconductor, especially when the diffusion coefficient in the oxide is not negligibly small.

This paper develops a series method to obtain the exact solutions of the diffusion equations with appropriate boundary and initial conditions which describe

[1] Formerly with Boeing Company, where most of this work was done. Present address: United Aircraft Research Laboratories, East Hartford, Conn.

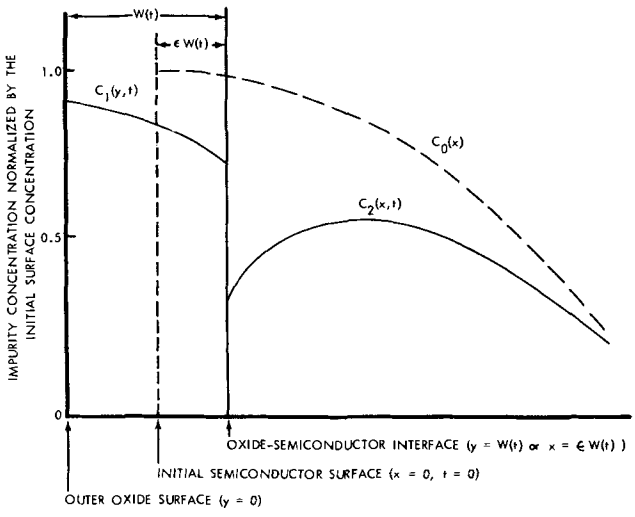

Fig. 1. Diagram of impurity-concentration profiles following the thermal-oxidation process and the oxide layer thickness and location of the oxide-semiconductor interface with respect to the initial silicon surface at time t. $C_0(x)$ is the initial impurity concentration profile in the semiconductor, $C_1(y, t)$ is the impurity concentration profile in the oxide layer at time t, and $C_2(x, t)$ is the impurity concentration profile in the semiconductor at time t.

the redistribution process. Various boundary conditions at the outer oxide surface have been assigned and discussed according to different physical situations. Solutions which describe the redistributed impurity concentration profiles in the oxide and semiconductor will both be given. The initial profile before the redistribution is a constant or a Gaussian or a complementary error function. When boundary conditions consistent with those of Grove *et al.* and Ku and an initial uniform impurity concentration are used, the solution obtained agrees with those of Grove *et al.* and Ku.

Experiments were performed by wet oxidizing at 1200°C boron-doped silicon slices that had Gaussian impurity distributions. The impurity profile obtained after oxidation was found to agree closely with the profile predicted from the theory when a segregation coefficient of 1.8 was used.

Mathematical Formulation

The model for the redistribution of impurities in a semi-infinite semiconductor during thermal oxidation, is shown in Fig. 1. At $t = 0$, the semiconductor surface of one end is at $x = 0$ and the concentration profile is $C_0(x)$. At a time t later the oxide thickness is $W(t)$. The corresponding thickness of semiconductor material used in producing the oxide layer is $\epsilon W(t)$, where ϵ is a constant. In a silicon silicon-dioxide system, ϵ is about 0.41 to 0.44 for an amorphous oxide (1, 5). The concentration profile in the oxide is described by $C_1(y,t)$ and in the semiconductor by $C_2(x,t)$, where $C_1(y,t)$ and $C_2(x,t)$ are solutions of the diffusion equations[2]

$$\frac{\partial C_1}{\partial t} = D_1 \frac{\partial^2 C_1}{\partial y^2} \quad 0 < y < W \qquad [1]$$

and

$$\frac{\partial C_2}{\partial t} = D_2 \frac{\partial^2 C_2}{\partial x^2} \quad \epsilon W < x \qquad [2]$$

where D_1 and D_2 are diffusion coefficients of the impurity in the oxide and the semiconductor, respectively.

During the redistribution process, the outer oxide surface and oxide-semiconductor interface move, and the location of the interface is at $x = \epsilon W(t)$ or $y = W(t)$. The impurities will then be redistributed such that a discontinuity in concentration may exist at the oxide-semiconductor interface. This discontinuity is described by a segregation coefficient η, defined as

$$\frac{C_1(W, t)}{C_2(\epsilon W, t)} = \eta \qquad [3]$$

where η is a constant. A set of values of η for different elements in silicon and germanium have been estimated by Thurmond (8). This equation also defines one of the boundary conditions at the oxide semiconductor interface. Another boundary condition at the interface is that of the conservation-of-impurity during oxidation[3]

$$[C_1(W, t) - \epsilon C_2(\epsilon W, t)] \frac{dW}{dt} = -D_1 \left(\frac{\partial C_1}{\partial y} \right)_{y=W} + D_2 \left(\frac{\partial C_2}{\partial x} \right)_{x=\epsilon W} \qquad [4]$$

Two possibilities for the boundary condition at the outer oxide surface have been considered and are discussed below.

(*A*) The impurity concentration in the ambient gas is such that the oxide surface impurity concentration reaches the equilibrium value C_s instantly and remains constant throughout the growth of the oxide layer. This condition is expressed as

$$C_1(0, t) = C_s \qquad [5]$$

(*B*) If the impurity concentration in the ambient gas is such that an appreciable time is required for the equilibrium impurity concentration, C_s, to be established at the oxide surface, the rate of loss or gain of impurities through the outer oxide surface can be assumed proportional to the difference between the surface impurity concentration, $C_1(0,t)$ at any time t in the oxide, and the equilibrium concentration C_s.

This condition is expressed as

$$-\left(\frac{\partial C_1}{\partial y} \right)_{y=0} = g[C_s - C_1(0, t)] \qquad [6]$$

where g is a constant. Equations [5] and [6] with $g \neq 0$, describe the boundary condition when there is impurity transport either in or out across the outer oxide surface. Equation [6] with $g = 0$ (Ku's case I) means the outer oxide surface is impermeable that there is no impurity transport across this surface. It is interesting to note that the solution of the diffusion equation, with the boundary condition described by Eq. [6] and g large, approaches the same solution as when the boundary condition is described Eq. [5]. The two solutions approach each other at $g \to \infty$ because the boundary conditions themselves approach each other. In other words as $g \to \infty$, $C_1(0,t) \to C_s$ in Eq. [6] since the flux must remain finite.

The oxide thickness is a parabolic function of time (1)

$$W(t) = kt^{1/2} \qquad [7]$$

where k is a constant.

The importance of these boundary conditions is determined largely by the value of D_1 and k. If $(D_1 t)^{1/2}$ is small with respect to $kt^{1/2}$, the influence of the boundary condition at the outer oxide surface on the impurity profile in the silicon will be negligible. The influence will also be small on the impurity distribution in the oxide at distances greater than $(D_1 t)^{1/2}$ from the surface. Thus, if $(D_1 t)^{1/2}$ is small with respect to $kt^{1/2}$, then g in Eq. [6] can be assumed to be zero.

The initial conditions are defined by

$$C_2(x, 0) = C_0(x) \qquad [8]$$

[2] They are described by two independent coordinates x and y. They also can be described in one coordinate system, see ref. (1) and (5).

[3] See Eq. [13] of ref. (4) and Eq. [4] of ref. (1) with $D_1 = 0$ and $D_2 = D$.

where $C_0(x)$ can be a Gaussian, a complementary error function, or a constant.

Equations [1] and [2] with conditions described by [3], [4], [5], [6], [7], and [8] can be solved by letting

$$u_1 = y/2\,(D_1 t)^{1/2} \quad [9]$$

and

$$u_2 = x/2\,(D_2 t)^{1/2} \quad [10]$$

The solutions can then be written as[4]

$$C_1(u_1, t) = \sum_{n=0}^{\infty} (D_1 t)^{n/2} [a_n h_n(u_1) + A_n i^n \operatorname{erfc} u_1] \quad [11]$$

and

$$C_2(u_2, t) = \sum_{n=0}^{\infty} (D_2 t)^{n/2} [b_n h_n(u_2) + B_n i^n \operatorname{erfc} u_2] \quad [12]$$

where a_n, A_n, b_n, and B_n are constants determined from the initial and boundary conditions and the functions $h_n(u)$ and $i^n \operatorname{erfc} u$ are defined below.

$$h_n(u) = j^{3n} H_n(ju)$$

$$= (2u)^n + \frac{n!}{(n-2)!}(2u)^{n-2} + \frac{n!}{(n-4)!2!}(2u)^{n-4} + \cdots + \begin{cases} \dfrac{n!}{3![(n-3)/2]!}(2u)^3 + \dfrac{n!}{[(n-1)/2]!}(2u) & \text{for odd } n, \\ \dfrac{n!}{2![(n-2)/2]!}(2u)^2 + \dfrac{n!}{(n/2)!} & \text{for even } n, \end{cases}$$

$$n = 0, 1, 2, 3 \ldots \quad [13]$$

where $j = \sqrt{-1}$ and $H_n(ju)$ is the n^{th} Hermite polynomial of an imaginary argument. The term $i^n \operatorname{erfc} u$ is an integral of the complementary error function (12, 14), defined as

$$i^n \operatorname{erfc} u = \int_u^{\infty} i^{n-1} \operatorname{erfc} \xi d\xi \quad n = 0, \pm 1, \pm 2, \ldots \quad [14]$$

and

$$i^{-1} \operatorname{erfc} u = \frac{2}{\sqrt{\pi}} e^{-u^2}$$

$$i^0 \operatorname{erfc} u = \operatorname{erfc} u \quad [15]$$

Some properties of these functions are given in Appendix I.

Each term of the series in Eq. [11] and [12] can be an individual solution of the diffusion equation, and they are described in ref. (10). The first part of C_1 and C_2 series with coefficients a_n and b_n has been called the double power series solutions in ref. (10), and they are described in terms of the Hermite polynomials in this paper. At $t = 0$, the series A_n or B_n coefficients will vanish. For a case there is no oxide at $t = 0$, coefficients b_n can be evaluated from the initial condition alone by equating like power of x between $C_2(x,0)$ and $C_0(x)$. Coefficients a_n, A_n and B_n are then determined from the boundary conditions described in Eq. [3], [4] and either [5] or [6]. Derivations of Eq. [16] and [17] are given in Appendix II. Equations [19]-[22] can be obtained by similar derivations.

Equation [12] can be interpreted in a simple way. The first part of C_2, the series with b_n coefficient represents diffusion of the initial profile $C_2(x,0)$ if no oxide were grown because the first part is not related with the oxide growth. The second part of C_2 is a correction due to the oxide growth. An example for a Gaussian profile is presented in Appendix III.

The series in Eq. [11] and [12] may converge very slowly so that numerical analysis is tedious. The complexity of the coefficients and the amount of work required for an accurate solution is materially reduced if g can be taken as zero in the boundary condition (B). In some cases, D_1 is so small that $g = 0$ is a good approximation.

Only solutions for the boundary condition (B), when $g = 0$ and the initial profile is (a) Gaussian, (b) a complementary error function, or (c) a constant, are given below. The first part of C_2, the series with b_n coefficients has been represented in a compact form. The derivations are in Appendices III and IV.

(A) When the initial concentration profile is Gaussian, $C_0(x) = \alpha \exp(-\beta^2 x^2)$

$$C_1 = \sum_{n=0}^{\infty} (-1)^n \frac{\alpha \beta^{2n}}{n!}\left(\frac{D_2}{D_1}\right)^n \times \frac{h_{2n}(S_2)\,\eta\,(H_2^{2n-1} + I_2^{2n-1})}{h_{2n}(S_1)\,(\eta H_1^{2n-1} + I_2^{2n-1})} (D_1 t)^n h_{2n}(u_1) \quad [16]$$

$$C_2 = \frac{\alpha}{(1 + 4\beta^2 D_2 t)^{1/2}} \exp\left(-\frac{\beta^2 x^2}{1 + 4\beta^2 D_2 t}\right) + \sum_{n=0}^{\infty} \left[(-1)^n \frac{\alpha \beta^{2n}}{n!} \frac{h_{2n}(S_2)}{i^{2n} \operatorname{erfc} S_2} \times \frac{(H_2^{2n-1} - \eta H_1^{2n-1})}{(\eta H_1^{2n-1} + I_2^{2n-1})} (D_2 t)^n i^{2n} \operatorname{erfc} u_2\right] \quad [17]$$

where $S_1 = k/2\,D_1^{1/2}$ and $S_2 = \epsilon\, k/2\,D_2^{1/2}$.

$$I_a^m = \frac{1}{2 S_a} \frac{i^m \operatorname{erfc} S_a}{i^{m+1} \operatorname{erfc} S_a} - 1 = \frac{(m+2)(i^{m+2} \operatorname{erfc} S_a)}{S_a (i^{m+1} \operatorname{erfc} S_a)} \quad \text{(see [A8])}$$

and

$$H_a^m = \frac{m+1}{S_a} \frac{h_m(S_a)}{h_{m+1}(S_a)} + 1 = \frac{h_{m+2}(S_a)}{2 S_a h_{m+1}(S_a)} \quad \text{(see [A5])} \quad [18]$$

where $a = 1$ or 2, and $m = -1, 0, 1, 2, \ldots$.

(B) When the initial concentration profile is an error function complement, $C_0(x) = \alpha \operatorname{erfc} \beta x$,

$$C_1 = \frac{\alpha \eta (1 + I_2^{-1})}{\eta + I_2^{-1}} + \sum_{n=0}^{\infty} \left\{(-1)^{n+1} \frac{2 \alpha \beta^{2n+1}}{\sqrt{\pi}(2n+1)n!} \times \frac{(D_2/D_1)^{(2n+1)/2} h_{2n+1}(S_2)\,\eta\,(I_2^{2n} + H_2^{2n})}{2^{2n+1}(2n+1)!\,(I_2^{2n} - \eta I_1^{2n})\, i^{2n+1} \operatorname{erfc} S_1 + h_{2n+1}(S_1)\,(I_2^{2n} + \eta H_1^{2n})} \times [(D_1 t)^{(2n+1)/2} h_{2n+1}(u_1) + 2^{2n+1}(2n+1)!\,(D_1 t)^{(2n+1)/2} i^{2n+1} \operatorname{erfc} u_1]\right\} \quad [19]$$

[4] This series has been introduced by the author in *Proc. IEEE*, 55, 101 (1967). Detail of the individual term can be seen in ref. (10), p. 52, Eq. [10] and [13] and the footnote in the same page, also ref. (11), p. 1566, for relations with the Weber function.

$$C_2 = \alpha \operatorname{erfc}\left(\frac{4\beta^2 D_2 t u_2^2}{1+4\beta^2 D_2 t}\right)^{1/2} + \frac{\alpha(1-\eta)}{(\eta + I_2^{-1})\operatorname{erfc} S_2}\operatorname{erfc} u_2 + \sum_{n=0}^{\infty}\left[(-1)^{n+1}\frac{2\alpha\beta^{2n+1}}{\sqrt{\pi}(2n+1)n!}\frac{h_{2n+1}(S_2)}{i^{2n+1}\operatorname{erfc} S_2}\right.$$
$$\times \frac{2^{2n+1}(2n+1)!\,(H_2^{2n}+\eta I_1^{2n})\,i^{2n+1}\operatorname{erfc} S_1 + h_{2n+1}(S_1)\,(H_2^{2n}-\eta H_1^{2n})}{2^{2n+1}(2n+1)!\,(I_2^{2n}-\eta I_1^{2n})\,i^{2n+1}\operatorname{erfc} S_1 + h_{2n+1}(S_1)\,(I_2^{2n}+\eta H_1^{2n})}$$
$$\left.\times (D_2 t)^{(2n+1)/2}\, i^{2n+1}\operatorname{erfc} u_2\right] \qquad [20]$$

(*C*) Where the initial concentration profile is a constant, $C_0(x) = \alpha$. C_1 and C_2 can be obtained immediately by letting $\beta = 0$ in (*A*) and (*B*) above.

$$C_1 = \frac{\alpha\eta(1+I_2^{-1})}{\eta + I_2^{-1}} \qquad [21]$$

$$C_2 = \alpha + \frac{\alpha(1-\eta)}{(\eta + I_2^{-1})\operatorname{erfc} S_2}\operatorname{erfc} u_2 \qquad [22]$$

Note that C_1 is constant in Eq. [21] and independent of D_1, while C_2 in Eq. [22] is the same as the result of Ku (5) and Cooper *et al.* (2), and is also independent of D_1. Recall that their mathematical models to describe the redistribution process were different. Their results agree with each other because, as shown in Eq. [21] and [22] C_1 and C_2 are not functions of D_1. The theoretical model with $g = 0$ (*i.e.*, the outer oxide surface is impermeable) must satisfy the condition that impurity atoms are conserved in the oxide and the semiconductor, that is

$$\int_0^W C_1(y,t)\,dy + \int_{\epsilon W}^{\infty} C_2(x,t)\,dx = \int_0^{\infty} C_0(x)\,dx$$
(a constant independent of t) [23]

This statement can be proved by direct integration.

Solutions for boundary conditions described in Eq. [5] and [6] can be also obtained by directly applying the series method in the diffusion equations. Coefficients of the series will be evaluated by the initial and boundary conditions. In many cases, a recurrence formula for coefficients will appear. A case with $g \neq 0$ is given in Appendix V.

Experimental Results

Two different rates of growing thermal oxides on silicon slices with Gaussian impurity distributions were used in the studies. Boron was deposited on n-type wafers (background phosphorus concentration 1.3 x 10^{16}/cm^3) in an open tube furnace at 930°C for 15 min. The boron glass, formed on the surface of the wafers during the deposition, was etched off. This procedure formed a shallow diffused layer with an abrupt junction about 0.2μ below the silicon surface. The wafers were then placed back in a furnace at 1200°C for 1 hr, and nitrogen gas (dried by passing through liquid nitrogen) was passed through the tube. The boron distribution after this diffusion procedure was assumed to be Gaussian.[5] The surface concentration was measured and found to be approximately 1.0 to 1.1 x 10^{19} atoms/cc.

The thermal oxidation was carried out in an open tube furnace (temperature 1200°C), with water vapor carried by nitrogen gas bubbled through hot water. Water temperature was 82°C for case (*A*), 92.5°C for case (*B*). A curve was obtained for each of the following two cases.

(*A*) The initial concentration profile was $C_0(x) = 1.0 \times 10^{19} \exp(-5.14 \times 10^7 x^2)$. Oxidation time was 1 hr and a 5600Å-thick oxide was produced.

(*B*) The initial concentration profile was $C_0(x) = 1.1 \times 10^{19} \exp(-5.14 \times 10^7 x^2)$. Oxidation time was 0.5 hr and a 5100Å-thick oxide was produced.

[5] The actual profile, measured in a separate experiment, was close to Gaussian.

The oxide thickness was measured with an interferometer. After the oxide layer was removed, the concentration profile of the redistributed boron was determined by four-point probe measurement and thin layer etch technique (15). The values of $\epsilon = 0.44$ and $D_2 = 1.35 \times 10^{-12}$ cm^2/sec have been used for the calculation. The value of D_2 was obtained from the work of Kurtz and Yee (16), and the value of D_1 was obtained from the work of Yamaguchi and Horiuchi (17) which showed that $(D_2/D_1)^{1/2}$ was approximately equal to 58. The experimental results along with calculated curves, are shown in Fig. 2 and 3.

The calculated curves used to fit the data of Fig. 2 and 3 were obtained from Eq. [7]. The segregation coefficient (η) was used as an adjustable parameter to fit the experimental results. The best fit was obtained using the value $\eta \approx 1.8$.

This value is somewhat smaller than the value of 3.1 obtained by Grove *et al.* (4). However, when the difference in initial conditions is considered, the results are in reasonable agreement. The difference may be due to a concentration dependence of η.

The values of that can be determined accurately by

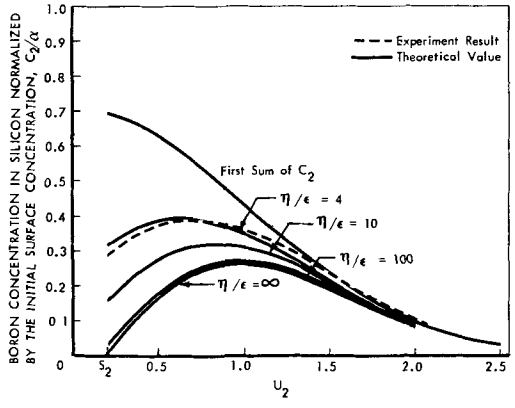

Fig. 2. Concentration profile of boron in silicon after an oxide layer has been grown at the surface under condition A. Theoretical curves for several values of η are also shown.

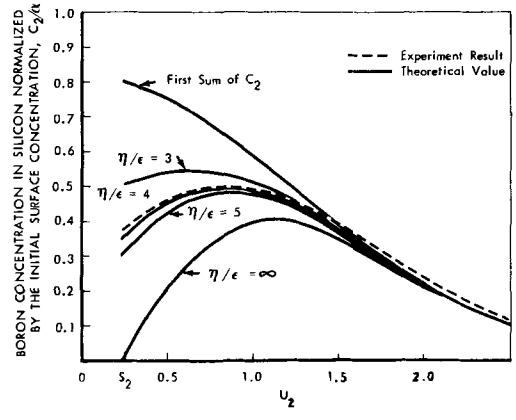

Fig. 3. Concentration profile of boron in silicon after an oxide layer has been grown at the surface under condition B. Theoretical curves for several values of η are also shown.

curve fitting are limited to values between $\approx$ 0.1 and 10. For values larger than $\approx$ 10 and smaller than 0.1, the curves are insensitive to η.

Summary

The analysis presented a mathematical treatment of the impurity redistribution phenomena during thermal oxidation. Exact solutions of diffusion equations can be obtained for many cases when the initial and boundary condition have been well defined as Eq. [3] and [8]. Application of this series can be extended to solve many diffusion and heat conduction problems, *e.g.*, diffusion or heat conduction through different media, or with moving boundaries, double diffusions, *etc.*

Good agreement was found between the theory and the experimental results when $\eta = 1.8$ was used for the segregation coefficient. This agrees reasonably well with the value of 3.1 obtained by Grove *et al.* (4).

Acknowledgments

The authors wish to express their gratitude to G. S. Horsley and D. W. Nichol for their stimulating discussions and encouragement, to L. R. Kolb, P. A. LaClaire, R. A. Jacomb, and H. R. Arrowood for their help in carrying out these experiments, and to L. E. Spanel and R. W. Cunningham for their help in the preparation of this paper.

Manuscript received April 3, 1967; revised manuscript received Aug. 9, 1967.

Any discussion of this paper will appear in a Discussion Section to be published in the June 1968 JOURNAL.

REFERENCES

1. M. M. Atalla and E. Tannenbaum, *Bell System Tech. J.*, **39**, 933 (1960).
2. H. W. Cooper, E. I. Doucette, and R. A. Mehnert, Paper presented at Chicago Meeting of the Society, May 1-5, 1960, abstract No. 104.
3. F. Leuenberger, *J. Appl. Phys.*, **33**, 2911 (1962).
4. A. S. Grove, O. Oeistiko, Jr., and C. T. Sah, *ibid.*, **35**, 2695 (1964).
5. H. Y. Ku, *ibid.*, **35**, 3391 (1964).
6. T. Kato and Y. Nishi, *Jap. J. Appl. Phys.*, **3**, 377 (1964).
7. K. J. S. Cave, *Solid-State Electronics*, **8**, 991 (1965).
8. C. D. Thurmond, "Properties of Elemental and Compound Semiconductors," p. 121, Interscience, New York (1960).
9. J. Crank, "The Mathematics of Diffusion," p. 34 and Fig. 3, 4, Oxford at the Clarendon Press (1956).
10. H. S. Carlaw and J. C. Jaeger, "Conduction of Heat in Solid," 2nd ed., p. 52, Oxford University Press (1959).
11. P. M. Morse and H. Feshback, "Method of Theoretical Physics," pp. 784-787, McGraw-Hill Book Co., New York (1953).
12. O. S. Berlyand, R. I. Gavrilora, and A. P. Prudnikov, "Table of Integral Error Function and Hermite Polynomials," English edition translated by Prasenjit Basu, A Pergamon Press Book, the MacMillan Co., New York (1962).
13. D. R. Hartree, *Mem. and Proc. Manchester Lit. and Phil. Soc.*, **80**, 85 (1935).
14. J. Kay, *J. Math. and Phys.*, **34**, 119 (1955).
15. E. Tannenbaum, *Solid State Electronics*, **2**, 123 (1960).
16. A. D. Kurtz and R. Yee, *J. Appl. Phys.*, **31**, 303 (160).
17. J. Yamaguchi and S. Horiuchi, *Japan J. Appl. Phys.*, 1, 314 (1962).

APPENDIX I

Functions $h_n(u)$ and i^n erfc u, defined in Eq. [13] and [14], have the following properties

(Unless otherwise indicated, n is an integer ≥ 0.)

$$h_{2n}(0) = (2n)!/n! \qquad [A1]$$

$$h_{2n+1}(0) = 0 \qquad [A2]$$

$$\frac{d}{du} h_n(u) = 2n\, h_{n-1}(u) \quad (n \geq 1) \qquad [A3]$$

$$h_{2n+1}(u) = 2(2n+1) \int_0^u h_{2n}(\xi)\, d\xi \qquad [A4]$$

$$h_{n+1}(u) = 2u\, h_n(u) + 2n\, h_{n-1}(u) \quad (n \geq 1) \qquad [A5]$$

$$i^n \text{ erfc } 0 = \frac{1}{2^n \Gamma\left(\frac{n}{2} + 1\right)} \qquad [A6]$$

$$\frac{d}{du} i^n \text{ erfc } u = -\, i^{n-1} \text{ erfc } u \qquad [A7]$$

$$2(n+1)\, i^{n+1} \text{ erfc } u = i^{n-1} \text{ erfc } u - 2u\, i^n \text{ erfc } u \qquad [A8]$$

$$H_n(u) = (-1)^n e^{u^2} \frac{d^n}{du^n} (e^{-u^2}) \qquad [A9]$$

$$i^{-n} \text{ erfc } u = \frac{2}{\sqrt{\pi}} e^{-u^2} H_{n-1}(u) \quad (n \geq 1) \qquad [A10]$$

$$H_{2n}(u) = \frac{(-4)^n n!}{\Gamma(n + 1/2)} L_n^{-1/2}(u^2) \qquad [A11]$$

$$H_{2n+1}(u) = \frac{2(-4)^n n!}{\Gamma(n + 3/2)} u\, L_n^{1/2}(u^2) \qquad [A12]$$

where $L_n^a(u)$ are Laguerre polynomials with the following generating function

$$\frac{1}{(1-t)^{a+1}} \exp \frac{-ut}{1-t} = \sum_{n=0}^{\infty} \frac{t^n}{\Gamma(n + a + 1)} L_n^a(u) \qquad [A13]$$

Additional details are contained in ref. (10) through (14).

APPENDIX II

In this appendix, a process to determine the redistributed impurity profiles C_1 and C_2 (Eq. [16] and [17]) are given. The case discussed in the following is for a semi-infinite semiconductor. At $t = 0$, there is no oxide at one end (at $x = 0$), and the initial impurity profile is a Gaussian, *i.e.*

$$C_0(x) = \alpha \exp(-\beta^2 x^2) = \alpha \sum_{n=0}^{\infty} (-1)^n \frac{(\beta x)^{2n}}{n!} \qquad [A14]$$

The impurity will be redistributed during a thermal oxidation. The boundary conditions for the diffusion equation during this process are described in Eq. [3], [4], and [6] with $g = 0$. After a certain time t, the redistributed impurity profiles in the oxide and the semiconductor are described by C_1 and C_2, respectively.

Coefficients b_n in C_2 can be easily determined by the initial profile. At $t = 0$, C_2 (u_2, 0) is a simple power series in x, *i.e.*

$$C_2(u_2, 0) = \sum_{n=0}^{\infty} b_n x^n \qquad [A15]$$

and all terms with coefficients B_n vanish. By equating like powers of x between Eq. [A14] and [A15], b_n are determined as

$$\left.\begin{aligned} b_{2n} &= (-1)^n \frac{\alpha \beta^{2n}}{n!} \\ b_{2n+1} &= 0 \end{aligned}\right\} \qquad [A16]$$

where n is a nonnegative integer and remains so through this appendix. According to the boundary condition at the outer oxide surface described by Eq. [6] with $g = 0$, we can obtain

$$\sum_{n=0}^{\infty} \left[a_{2n} (D_1 t)^n \frac{(2n+1)!}{n!} - \frac{A_{2n+1}}{2} (D_1 t)^n\, i^{2n} \text{ erfc } 0 - \frac{A_{2n}}{2} (D_1 t)^{(2n-1)/2}\, i^{2n-1} \text{ erfc } 0 \right] = 0 \text{ for all } t > 0 \qquad [A17]$$

where i^{2n} erfc $0 = 1/2^{2n}n!$ (Eq. [A6]). In Eq. [A17], the coefficient of each individual term of the like power t should vanish, therefore,

$$\left.\begin{aligned} A_{2n} &= 0 \\ A_{2n+1} &= 2^{2n+1}\,(2n+1)!\,A_{2n+1} \end{aligned}\right\} \quad [A18]$$

Similarly, the following relations can be obtained from Eq. [3] and [4], the boundary conditions at the oxide-semiconductor interface

$$a_{2n+1}\,h_{2n+1}\,(S_1) + A_{2n+1}\,i^{2n+1}\,\text{erfc}\,S_1 = \eta\left(\frac{D_2}{D_1}\right)^{(2n+1)/2} B_{2n+1}\,i^{2n+1}\,\text{erfc}\,S_2 \quad [A19]$$

$$a_{2n}\,h_{2n}\,(S_1) = \eta\left(\frac{D_2}{D_1}\right)^{n}\left[b_{2n}\,h_{2n}\,(S_2) + B_{2n}\,i^{2n}\,\text{erfc}\,S_2\right] \quad [A20]$$

and

$$a_{2n+1}\,D_1{}^n\left[\frac{k}{2}\,D_1{}^{1/2}\,h_{2n+1}\,(S_1) + (2n+1)\,h_{2n}\,(S_1)\right] + A_{2n+1}\,D_1{}^n\left[\frac{k}{2}\,D_1{}^{1/2}\,i^{2n+1}\,\text{erfc}\,S_1 - \frac{1}{2}\,i^{2n}\,\text{erfc}\,S_1\right] + B_{2n+1}\,D_2{}^{n+1}\left[-\frac{k}{2}\,\epsilon D_2{}^{1/2}\,i^{2n+1}\,\text{erfc}\,S_2 + \frac{1}{2}\,i^{2n}\,\text{erfc}\,S_2\right] = 0 \quad [A21]$$

$$a_{2n}D_1{}^n\left[\frac{k}{2}\,h_{2n}(S_1) + 2nD_1{}^{1/2}\,h_{2n-1}\,(S_1)\right] + b_{2n}D_2{}^n\left[-\frac{k}{2}\,\epsilon h_{2n}\,(S_2) - 2nD_2{}^{1/2}\,h_{2n-1}\,(S_2)\right] + B_{2n}D_2{}^n\left[-\frac{k}{2}\,\epsilon i^{2n}\,\text{erfc}\,S_2 + \frac{1}{2}\,D_2{}^{1/2}\,i^{2n-1}\,\text{erfc}\,S_2\right] = 0 \quad [A22]$$

The values of a_{2n+1}, A_{2n+1}, and B_{2n+1} can be determined immediately by Eq. [A18], [A19], and [A21]

$$a_{2n+1} = A_{2n+1} = B_{2n+1} = 0 \quad [A23]$$

The values of a_{2n} and B_{2n} can be determined by Eq. [A16], [A20], and [A22]

$$a_{2n} = (-1)^n\,\frac{\alpha\beta^{2n}}{n!}\,\frac{D_2{}^n\,h_{2n}(S_2)\,\eta[H_2{}^{2n-1} + I_2{}^{2n-1}]}{D_1{}^n\,h_{2n}(S_1)\,[\eta H_1{}^{2n-1} + I_2{}^{2n-1}]} \quad [A24]$$

$$B_{2n} = (-1)^n\,\frac{\alpha\beta^{2n}}{n!}\,\frac{h_{2n}\,(S_2)\,[H_2{}^{2n-1} - \eta H_1{}^{2n-1}]}{i^{2n}\,\text{erfc}\,S_2\,[\eta H_1{}^{2n-1} + I_1{}^{2n-1}]} \quad [A26]$$

where $H_1{}^{2n-1}$, $H_2{}^{2n-1}$, $I_1{}^{2n-1}$, $I_2{}^{2n-1}$ are defined in Eq. [18], the first part of C_2, the series with b_n coefficient, can be put into a compact form. The derivation is in the Appendix III. Equations [16] and [17] will follow after the substitution of Eq. [11] and [12] with the values of their coefficients.

APPENDIX III

The following example shows the first part of C_2 in Eq. [12] and proves that the series with the b_n coefficient is a solution of the diffusion equation having the same initial conditions but no oxide grown on the surface.

Assume that a slice of silicon has an initial impurity concentration profile of

$$C_0(x) = \frac{Q}{(\pi\,D_2t_0)^{1/2}}\exp\left(-\frac{x^2}{4\,D_2t_0}\right) \quad [A26]$$

where Q is the total quantity of impurity in the slice. The slice is heated so that the impurities are diffused deeper with the diffusion coefficient D_2 and no impurity loss at the surface. No oxide is grown on the slice. After time t the concentration profile will be

$$C(x,t) = \frac{Q}{[\pi\,D_2\,(t+t_0]^{1/2}}\exp\left[-\frac{x^2}{4\,D_2(t_0+t)}\right] \quad [A27]$$

Assume that another slice, with an initial concentration profile described by Eq. [A26], is diffused. The diffusion coefficient remains unchanged, but an oxide layer is grown on the surface. After time t the concentration profile in the semiconductor will be described by $C_2(x,t)$ in Eq. [12]. The b_n coefficient in Eq. [12] is evaluated using the initial condition

$$\left.\begin{aligned} b_{2n} &= (-1)^n\,\frac{\alpha\beta^{2n}}{n!} \\ b_{2n+1} &= 0 \quad n = 0, 1, 2, 3 \ldots \end{aligned}\right\} \quad [A28]$$

where $\alpha = Q/(\pi\,D_2t_0)^{1/2}$ and $\beta^2 = 1/4\,D_2t_0$. Using Eq. [A11] and [A13] and the definition of $h_{2n}\,(u_2)$ in (13), the first sum of $C_2\,(x,t)$ (the series with the b_n coefficient) can be written in this compact form

$$\sum_{n=0}^{\infty}(-1)^n\,\frac{\alpha\beta^{2n}}{n!}\,(D_2t)^n\,h_{2n}\,(u_2) = \sum_{n=0}^{\infty}(-1)^n\,\frac{\alpha\beta^{2n}}{n!}\,(D_2t)^n\,(-1)^n\,H_{2n}\,(ju_2) = \sum_{n=0}^{\infty}(-1)^n\,\frac{\alpha\beta^{2n}}{n!}\,(-D_2t)^n\,\frac{(-4)^n\,n!}{\Gamma(n+1/2)}\,L_n{}^{-1/2}\,(-u_2{}^2) = \alpha\sum_{n=0}^{\infty}\frac{(-4\,\beta^2\,D_2t)^n}{\Gamma(n+1/2)}\,L_n{}^{-1/2}\,(-u_2{}^2) = \frac{\alpha}{(1+4\,\beta^2\,D_2t)^{1/2}}\exp\left(-\frac{4\,\beta^2\,D_2\,tu_2{}^2}{1+4\,\beta^2D_2t}\right) = \frac{\alpha}{(1+4\,\beta^2\,D_2t)^{1/2}}\exp\left(-\frac{\beta^2\,x^2}{1+4\,\beta^2\,D_2t}\right) \quad [A29]$$

Equations [A27] and [A29] are identical when the values for α and β have been inserted.

APPENDIX IV

The following process is used to obtain the first part of C_2 in Eq. [12] and to transform the series into a compact form for the case where the initial distribution is a complementary error function.

From the initial condition

$$C_0(x) = \alpha\,\text{erfc}\,\beta x = \alpha\left[1 - \frac{2}{\sqrt{\pi}}\sum_{n=0}^{\infty}\frac{(-1)^n\,(\beta x)^{2n+1}}{(2n+1)\,n!}\right]$$

the b_n coefficient is determined as

$$b_0 = \alpha$$
$$b_{2n} = 0 \text{ for } n > 0$$
$$b_{2n+1} = (-1)^{n+1}\,\frac{2\alpha}{\sqrt{\pi}}\,\frac{\beta^{2n+1}}{(2n+1)\,n!}, \quad n = 0, 1, 2, \ldots$$

The first part of C_2, $C_2{}^{\text{I}}$, in Eq. [12] can be written as

$$C_2{}^{\text{I}} = \alpha - \sum_{n=0}^{\infty}(-1)^n\,\frac{2\alpha}{\sqrt{\pi}}\,\frac{\beta^{2n+1}}{(2n+1)\,n!}\times(D_2t)^{(2n+1)/2}\,h_{2n+1}\,(u_2)\,.$$

Using Eq. [A4] and [A17], $C_2{}^{\text{I}}$ can be written as

$$C_2{}^{\text{I}} = \alpha\left\{1 - \frac{4\beta\,(D_2t)^{1/2}}{\sqrt{\pi}}\int_0^{u_2}\sum_{n=0}^{\infty}\left[(-1)^n\,\frac{\beta^{2n}}{n!}\,(D_2t)^n\,h_{2n}\,(\xi)\right]d\xi\right\} = \alpha\left[1 - \frac{4\beta\,(D_2t)^{1/2}}{\sqrt{\pi}}\int_0^{u_2}\frac{1}{(1+4\,\beta^2\,D_2t)^{1/2}}\exp\left(-\frac{4\,\beta^2\,D_2t\,\xi^2}{1+4\,\beta^2\,D_2t}\right)d\xi\right] = \alpha\left[1 - \text{erf}\left(\frac{4\,\beta^2\,D_2t\,u_2{}^2}{1+4\,\beta^2\,D_2t}\right)^{1/2}\right] = \alpha\,\text{erfc}\left(\frac{4\,\beta^2\,D_2t\,u_2{}^2}{1+4\,\beta^2\,D_2t}\right)^{1/2} \quad [A30]$$

APPENDIX V

This appendix discusses the case where impurities are redistributed in a semiconductor during thermal oxidation using [6] as the boundary condition at the outer oxide surface and assuming that $C_s = 0$. This corresponds to the physical condition where the environment contains no impurities and the loss due to evaporation at the surface is linearly proportional to the instantaneous concentration at the surface (9). The initial concentration profile is assumed to be Gaussian, *i.e.*, $C_0(x) = \alpha \exp(-\beta^2 x^2)$. The b_n coefficient is determined as Eq. [A16] by employing the initial conditions. After the b_n coefficient has been determined, a set of equations for a_n, A_n, and B_n can be obtained by using the boundary conditions and equating the like powers of t as follows

$$A_0 = 0 \qquad [A31]$$

$$A_{2n+2} + 2g\,A_{2n+1} = 0 \qquad [A32]$$

$$-(2n)!\,g\,a_{2n} + (2n+1)!\,a_{2n+1} - 2^{-2n}\,g\,A_{2n} - 2^{-(2n+1)}\,A_{2n+1} = 0 \qquad [A33]$$

$$h_{2n}(S_1)\,a_{2n} + (i^{2n}\operatorname{erfc} S_1)\,A_{2n} - \eta\left(\frac{D_2}{D_1}\right)^n (i^{2n}\operatorname{erfc} S_2)\,B_{2n} = (-1)^n \frac{\alpha\beta^{2n}}{n!}\left(\frac{D_2}{D_1}\right)^n \eta\,h_{2n}(S_2) \qquad [A34]$$

$$h_{2n+1}(S_1)\,a_{2n+1} + (i^{2n+1}\operatorname{erfc} S_1)\,A_{2n+1} - \eta\left(\frac{D_2}{D_1}\right)^{n+1/2} (i^{2n+1}\operatorname{erfc} S_2)\,B_{2n+1} = 0 \qquad [A35]$$

$$h_{2n+1}(S_1)\,H_1^{2n}\,a_{2n+1} - (i^{2n+1}\operatorname{erfc} S_1)\,I_1^{2n}\,A_{2n+1} + \left(\frac{D_2}{D_1}\right)^{n+1/2} (i^{2n+1}\operatorname{erfc} S_2)\,I_2^{2n}\,B_{2n+1} = 0 \qquad [A36]$$

$$h_{2n}(S_1)\,H_1^{2n-1}\,a_{2n} - (i^{2n}\operatorname{erfc} S_1)\,I_1^{2n-1}\,A_{2n} + \left(\frac{D_2}{D_1}\right)^{n} (i^{2n}\operatorname{erfc} S_2)\,I_2^{2n-1}\,B_{2n} = (-1)^n \frac{\alpha\beta^{2n}}{n!}\left(\frac{D_2}{D_1}\right)^n h_{2n}(S_2)\,H_2^{2n-1} \qquad [A37]$$

where I_1^{2n}, H_1^{2n}, etc., are defined as in Eq. [18]. By eliminating a_{2n}, a_{2n+1}, B_{2n}, and B_{2n+1} in Eq. [A33] through [A37] a recurrence formula for A_n's can be obtained as

$$A_0 = 0,\ A_{2n+2} + 2\,g\,A_{2n+1} = 0,\ \left[\frac{2^{2n+1}(2n+1)!\,(i^{2n+1}\operatorname{erfc} S_1)\,(I_2^{2n} - \eta\,I_1^{2n})}{h_{2n+1}(S_1)\,(I_2^{2n} + \eta\,H_1^{2n})} + 1\right]A_{2n+1} + 2g\left[1 - \frac{2^{2n}(2n)!\,(i^{2n}\operatorname{erfc} S_1)\,(I_2^{2n-1} - \eta\,I_1^{2n-1})}{h_{2n}(S_1)\,(I_2^{2n-1} + \eta\,H_1^{2n-1})}\right]A_{2n} = (-1)^{n+1}\,2\,g\,\frac{\alpha\beta^{2n}}{n!}\left(\frac{D_2}{D_1}\right)^n \frac{2^{2n}(2n)!\,h_{2n}(S_2)\,\eta\,(I_2^{2n-1} + H_2^{2n-1})}{h_{2n}(S_1)\,(I_2^{2n-1} + \eta\,H_1^{2n-1})} \qquad [A38]$$

from which all the A_n's will be obtained. Then a_{2n}, a_{2n+1}, B_{2n}, and B_{2n+1} will be solved in terms of A_{2n} and A_{2n+1} from Eq. [A33] through [A37].

The Preparation and Properties of Large, Solution Grown GaP Crystals

T. S. Plaskett, S. E. Blum, and L. M. Foster

IBM Watson Research Center, Yorktown Heights, New York

ABSTRACT

A method of growing large crystals of GaP from solution, similiar to that of Broder and Wolff in which a zone of liquid gallium saturated with GaP is passed upward through a GaP ingot, is investigated. With this method, all the advantages of a solution growth process are retained, *i.e.*, low temperature, and therefore low phosphorus pressure, and minimum contamination from container materials. In order to grow large crystals it was found necessary to initiate growth on a twinned seed crystal, with all of the twin planes parallel, and parallel to a <211> growth direction. The effect of repeated zone passes through the same ingot on the purity and electrical properties is presented.

Gallium phosphide has emerged over recent years as a potentially useful electroluminescent material. Its exploitation has been deterred, however, by the lack of suitable procedures for controlled growth of bulk single crystal. Crystals of GaP can be prepared easily by precipitation from gallium or other metal solvents in which it has an appreciable solubility. However, the crystals produced in this way are usually in the form of thin dendritic platelets of various sizes and morphologies(1-5), and it is difficult to form reproducibly large, uniformly doped platelets that are essential for device applications and physical characterization studies. Nevertheless, solution growth processes in general offer distinct advantages for the growth of GaP and similar high melting, unstable compounds because of the low temperatures that can be employed for off-stoichiometric growth [stoichiometric GaP melts at 1467°C under about 35 atm of phosphorus pressure (6)]. Chief among these are the minimal equipment requirements because of the greatly reduced pressure and the lessening of contamination from container materials. With Ga as a solvent, for example, the solubility of GaP at 1220° is about 15% by weight and the P pressure is only 0.02 atm(7, 8). At this temperature there is a choice of several possible container materials, including quartz, boron

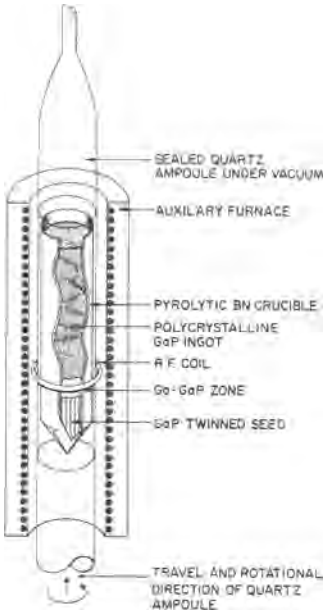

Fig. 1. Cut-away drawing of the solution zoning apparatus

nitride, and graphite. A secondary advantage of solution growth is the purification that can result simply by dilution of impurities in the large volume of solvent.

One method of growing a large bulk crystal of GaP by a solution growth process was described by Broder and Wolff(9). In their method a high-temperature, saturated Ga-GaP zone is passed through a composite of liquid Ga and solid GaP. By dissolution of GaP at the leading edge of the zone and precipitation at the trailing edge, a solid ingot with large grains was produced. In this paper, an extension of their process, in which large monocrystalline sections are produced, is described, together with some electrical and chemical properties of the product.

Experimental Technique

In Fig. 1 is shown a schematic drawing of the essential features of the apparatus. At the start, the layer of Ga, approximately ¼ in. thick, is placed between the seed and polycrystalline ingot of GaP, all of which are contained in a pyrolytic BN crucible.[1] The loaded crucible is then sealed under vacuum in a quartz tube with a minimum of free space. The zone of Ga is heated to about 1160°C by the single turn RF coil. At this temperature the zone dissolves about 10% of its weight of GaP, taking the material initially from both the seed and ingot surfaces. [The Ga temperature is actually estimated by its GaP content, determined after completion of an experiment, and the use of published solubility data(7, 8)].

The auxiliary furnaces, located above and below the coil, control the shape of the solid-liquid interface and provide the required temperature profile along the axis of the system. The rate of zone travel upward through the ingot is about 4 mm/day. The tube is also rotated in the coil at about 8 rpm to smooth out radial temperature nonuniformities. The mechanical motions and the RF heating are obtained by modifying a commercial Lepel, Model FLZ-100 float zone silicon refiner.

For the successful passage of the liquid zone it was found that an essentially nonporous ingot had to be employed as the feed; otherwise a void would accumulate above the gallium and eventually isolate it from the feed. Completely sound, single-phase polycrystalline ingots were synthesized for this purpose from Ga and phosphorus by the vertical Bridgman technique, with the phosphorus source controlled to give approximately 10 atm pressure. The synthesis was

[1] Obtained from the High Temperature Materials Division of the Union Carbide Corporation.

Fig. 2. Typical crystal grown by solution zoning technique. Seeding occurred at the 2 cm position. The button at the 6 cm position is what is left of the unzoned ingot. The Ga-GaP zone has been removed by acid leaching.

carried out in a BN crucible of the same dimensions as the one subsequently used for the travelling solvent regrowth. This synthesis is described by Blum and Chicotka (10).

Results and Discussion

Nature of the regrown crystal.—A typical crystal grown by this technique is shown in Fig. 2. The remaining unzoned feed material is also shown at the position approximating that during growth. Seeding occurred in this instance at about the 2-cm position. The growing interface at the last to freeze is slightly convex. This represents the actual growing interface since the termination of a run occurred by abruptly turning off the rf power and auxiliary furnaces. The GaP precipitating during cooling under this condition is as fine platelets surrounded by Ga, and any adhering to the crystal is easily removed during the acid leach to dissolve away the Ga. A convex interface was required to prevent polycrystalline growth around the periphery of the crystal.

At a growth rate of about 4 mm/day and with the precipitating surface considerably colder than the dissolution surface, the zone travelled through the polycrystalline ingot with no visible entrapment of the Ga solvent. The actual temperature gradient could not be measured but the top auxiliary furnace was run at about 1000°C and the lower furnace at 800°C. The temperature of the zone as mentioned previously was estimated to be about 1160°C.

Initially, an attempt was made to seed onto a large grain ingot, as shown in Fig. 3a, but it was not successful. Instead of the large grains propagating, the small twinned grain shown in the seed began to predominate, as shown in Fig. 3b after about 4 cm of growth. After about 6 cm of growth the whole cross section consisted of this one twinned crystal (Fig. 3c). This length of growth was obtained in three separate experiments, with the last part of one ingot used as the seed for the next one. (To make an additional zone pass it was necessary to open the system, cut the crystal at the seed, and insert a new zone of gal-

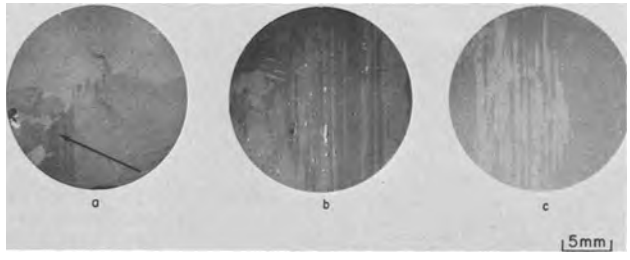

Fig. 3. Cross section of GaP crystals grown by the solution zoning technique (a) initial seed, arrow marks the twin crystal which propagated, (b) after 4 cm of growth and, (c) after 6 cm of growth.

lium.) The twin structure was observed to be a consistent pattern; that is, regardless of the size and orientation of the grains in the seed, the structure that soon developed and propagated up the ingot consisted of lamellar twins whose growth direction was parallel to the travel of the zone. Since there were no seeds available initially to directly initiate that type of growth, they had to be generated in the program; the best section of a regrown ingot would be retained as seed for subsequent experiments.

The concentration and nature of impurities in the feed ingot seemed to have an effect on the quality of the regrown crystal, although their role has not been definitely established. Generally, regrowth was better when the seed and feed ingot were n-type, indicating a predominance of nonmetallic impurities. These typically have high distribution coefficients and therefore would be readily incorporated in the crystal rather than accumulate at the interface where they may inhibit further nucleation and growth.

The structure of the twinned regrown crystal, and the structure desired for a seed to initiate such growth, is one in which the twin planes are parallel to each other and parallel to a <211> growth direction. The leading edges of two such adjacent twins intersect at indestructible grooves which present favorable sites for nucleation and growth. The same growth mechanism applies to the growth of dendritic GaP platelets from dilute gallium solutions(4). A model of an idealized seed structure is shown in Fig. 4. In some experiments seeds with large untwinned areas, as shown in Fig. 3c, were used to determine if an untwinned crystal would propagate. Usually, however, the twinned area increased at the expense of the untwinned. The exact reason for the large area free of twins shown in Fig. 3c is not known.

A macrograph of a lapped cross section is shown in Fig. 5a. A longitudinal section taken parallel to the (111) twin planes from the same crystal and through the untwinned portion, as indicated by the above cross section, is shown in Fig. 5b. The twinned structure is apparent in the cross section but in the longitudinal section the structure appears polycrystalline because it lacks the straight line twin boundaries. However, an x-ray examination of the grains showed all to have (111) surfaces but with a 60° rotation to each other

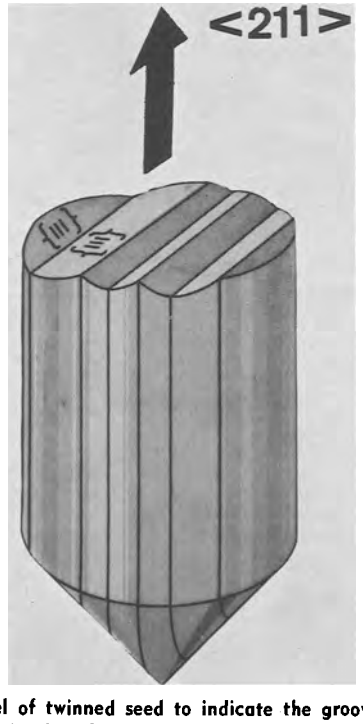

Fig. 4. Model of twinned seed to indicate the grooved nature of solid-liquid growing interface.

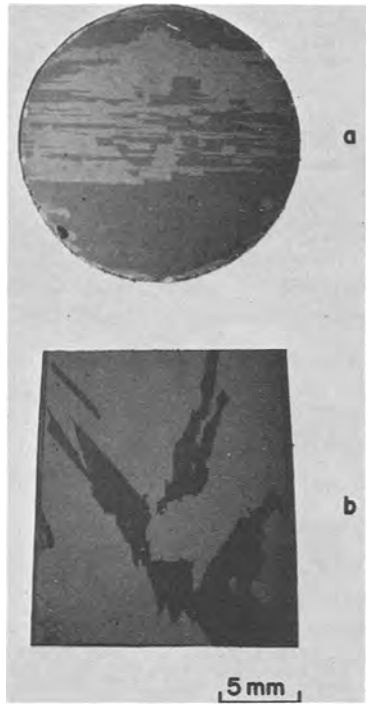

Fig. 5a. Transverse and Fig. 5b longitudinal sections of a solution zoned crystal.

normal to the longitudinal surface. This means that the only twin planes, as suggested by the model shown in Fig. 4, are those parallel to the growth axis. However, since more than one grain is evident in a longitudinal section, this indicates that the twin planes are not flat but may jog in a step-wise manner or else terminate and new parallel twin planes start elsewhere.

Twinning in GaP should not detract from its usefulness in electroluminescence studies. If the twins in the material are confined to those described above (first-order), then the twin boundaries would not perturb the electrical transport across them. Moreover, a common method of forming the p-n junction in GaP for the production of light emitting diodes employs a solution over-growth process onto (111) oriented substrates (11). Such substrates are obtained by cutting longitudinal slabs parallel to the twin planes.

Chemical and electrical properties.—The feed ingots as synthesized were generally p-type as determined by point contact rectification. On occasion they were n-type, however. In these cases analysis generally indicated higher silicon contamination during synthesis. If the feed ingot was p-type, it remained p-type after the passage of the zone. The acceptors have not been clearly identified. Table I shows emission spectroscopic analysis of a p-type starting feed ingot and the same ingot after one and two zone passes. The entries are order of magnitude figures. "Less than" a given concentration means that a line was seen on the plate but adequate calibration had not been carried out to provide narrower sensitivity limits. The analyses

Table I. Emission spectrochemical analysis (ppm by wt)

	Starting		1st pass		2nd pass	
Element	Bottom	Top	Bottom	Top	Bottom	Top
Ca	<10	<10	<10	<10	<10	<10
Si	3-10	1-3	3-10	3-10	<3	<3
Mg	0.3-1.0	0.3	0.3	0.3-1.0	0.3-1.0	0.3
Fe	10-30	3-10	<3	<3	N.D.	<3
Al	<3	<3	<3	<3	<3	<3
Cu	<1	<1	N.D.	N.D.	N.D.	N.D.
B	N.D.	N.D.	N.D.	<3	N.D.	N.D.

Table II. Electrical properties

Sample description	298°K			77°K		
	Resistivity, ohm-cm	Hall mobility, $cm^2/v\text{-}sec$	Carrier concentration, cm^{-3}	Resistivity, ohm-cm	Hall mobility, $cm^2/v\text{-}sec$	Carrier concentration, cm^{-3}
After two passes through a p-type ingot	0.29 (p-type)	100	2.2×10^{17}	1.04	960	6.3×10^{15}
After one pass through a n-type ingot	0.26 (n-type)	142	1.6×10^{17}	232	340	7.8×10^{13}

show a reduction in the silicon and iron content with the additional zone passes.

Table II shows Hall data, provided by J. F. Woods of this Laboratory, after two zone passes through a p-type ingot and one zone pass through an n-type ingot. The Hall specimens were ultrasonically cut bars with three pairs of Hall probes which also served as resistance probes. Ohmic contacts were made to n-type material with Au-Sn and to p-type material with Au-In alloys.

Improved purity of the regrown ingots would undoubtedly result from the use of a larger gallium zone in which to further dilute the impurities. This is impractical in the present system. A more effective way of upgrading the purity is to use higher purity feed ingots. This approach is being pursued.

Conclusions

This initial investigation has shown the feasibility of producing large, solution grown GaP crystals by a travelling solvent method. The success of the process is to a large extent dependent on the orientation and twinned structure of the seed. There is no evidence of contamination of an ingot during the regrown process. Rather, appreciable purification results from passage of the molten zone. Material of sufficient purity can be made by the present practice for doping studies to be undertaken in the mid 10^{17} cm^{-3} range, either by adding the dopant to the gallium zone or by predoping the feed ingot during synthesis. Higher purity regrown ingots are expected from the use of purer feed ingots.

Acknowledgment

The authors are grateful to Messrs. A. H. Parsons and B. K. Bischoff for assistance in the experimental part; to J. Grandia and W. A. Kahn for construction of the apparatus; and to Dr. W. Reuter for the chemical analyses.

Mansucript received June 28, 1967; revised manuscript received Aug. 23, 1967. This paper was presented at the Dallas Meeting, May 7-12, 1967. This work was supported in part by the U.S. Army Engineering Research and Development Laboratory, Fort Belvoir, Virginia, Contract #DA-44-009-AMC-1674(X).

Any discussion of this paper will appear in a Discussion Section to be published in the June 1968 JOURNAL.

REFERENCES

1. G. A. Wolff, P. H. Keck, and J. D. Broder, *Phys. Rev.*, **94**, 753 (1954).
2. H. G. Grimmeiss and H. Scholz, *Phys. Rev. Letters*, **8**, 233 (1964).
3. D. G. Thomas, M. Gershenzon, and F. A. Trumbore, *Phys. Rev.*, **133**, A269 (1964).
4. L. M. Foster, T. S. Plaskett, and J. E. Scardefield, *IBM J. Res. and Develop.*, **10**, 114 (1966).
5. J. W. Faust, Jr., and H. F. John, *J. Phys. Chem. Solids*, **25**, 1407 (1964).
6. D. Richman, *ibid.*, **24**, 1131 (1963).
7. R. N. Hall, *This Journal*, **110**, 385 (1963).
8. M. Rubenstein, Society Electronics Division Extended Abstracts, **11**, 129 (1962).
9. J. D. Broder and G. A. Wolff, *This Journal*, **110**, 1150 (1963).
10. S. E. Blum and R. J. Chicotka, Paper presented at the Dallas Meeting of the Society, May 1967.
11. M. R. Lorenz and M. Pilkuhn, *J. Appl. Phys.*, **37**, 4094 (1966).

Technical Notes

Fluorescence of Rhodium-Activated Aluminum Oxide

G. Blasse and A. Bril

Philips Research Laboratories, N.V. Philips' Gloeilampenfabrieken, Eindhoven-Netherlands

In his survey of phosphors Kröger (1) mentions the red fluorescence of Al_2O_3:Rh. It seemed interesting to study this phosphor in more detail.

Samples were prepared by firing intimate mixtures of aluminum- and rhodium hydroxide in oxygen at 1350°C. The rhodium concentration was 0.1-1.0 a/o (atomic per cent). The reaction products had a light-yellow body color and showed an orange-red fluorescence under long-wave uv and cathode-ray excitation. Samples prepared from the same aluminum hydroxide without rhodium did not show fluorescence. The performance of the optical measurements has been described previously (2).

Figure 1 shows the spectral energy distribution of the fluorescence of Al_2O_3:Rh under long-wave uv excitation, the excitation spectrum of the fluorescence and the diffuse reflection spectrum. The fluorescence shows a pronounced temperature dependence: the light output under long-wave uv excitation at room temperature is about 60% of that at liquid nitrogen temperature. At about 450°K the fluorescence is completely quenched. The radiant efficiency for cathode-ray excitation of our samples is 2% at room temperature. In view of the weak uv absorption no measurements of the efficiency for uv excitation were performed. The decay time of the fluorescence of Al_2O_3:Rh under

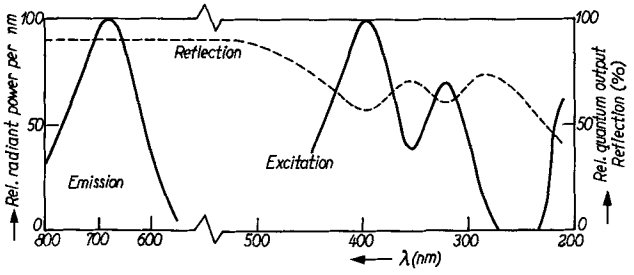

Fig. 1. Left-hand side: spectral energy distribution of Al_2O_3:Rh under cathode-ray excitation. Right-hand side: relative excitation spectrum of the emission of Al_2O_3:Rh. The broken line is the diffuse reflection spectrum of Al_2O_3:Rh. Note the change in the wavelength scale between 500 and 600 nm.

cathode-ray excitation is 0.6 msec at room temperature and 1.6 msec at liquid nitrogen temperature.

The Rh^{3+} ion ($4d^6$) occupies (irregular) octahedral sites in the corundum structure of α-Al_2O_3 and will be in the nonmagnetic low-spin state (t^6_{2g}, $^1A_{1g}$). The lowest excited configuration is $t^5_{2g}e_g$, which is split in the states $^3T_{1g}$, $^3T_{2g}$, $^1T_{1g}$, $^1T_{2g}$. The spin-forbidden transitions $^1A_{1g} \rightarrow {}^3T_{1g}$ and $^3T_{2g}$ were not observed by us, but the two absorption (and excitation) bands located at 25,400 and 31,200 cm^{-1} are undoubtedly due to the transitions $^1A_{1g} \rightarrow {}^1T_{1g}$ and $^1T_{2g}$. According to Jørgensen (3) the wave numbers of these transitions are given to a good approximation by

$$\sigma(^1A_{1g} \rightarrow {}^1T_{1g}) = \Delta - 4B + 86B^2/\Delta$$

and

$$\sigma(^1A_{1g} \rightarrow {}^1T_{2g}) = \Delta + 12B + 2B^2/\Delta$$

Here Δ is the cubic crystal field splitting and B the electrostatic interaction parameter. The last term of these formulas accounts for the off-diagonal elements of the electron repulsion matrix. It is assumed that the electrostatic interaction parameter C equals $4B$. From our experimental data we find that $\Delta = 26{,}400$ cm^{-1} and $B = 400$ cm^{-1}. The value of B for the free ion is 720 cm^{-1} (3). The low value of B for the Rh^{3+} ion in Al_2O_3 points to strong delocalization of the d-electrons of Rh^{3+} in Al_2O_3. For comparison we also give the values of Δ and B for $Rh^{3+}(H_2O)_6$ (27,000 and 510 cm^{-1}) and for $Rh^{3+}(Cl^-)_6$ (20,300 and 350 cm^{-1}) (3).

At higher wave numbers the excitation and reflection spectra show another band, which is not present in the case of undoped Al_2O_3. The peak of this band is beyond the limit of our apparatus, but is estimated to be located at approximately 50,000 cm^{-1}. It seems probable that this band corresponds to a charge-transfer transition in the $Rh^{3+}(O^{2-})_6$ complex. For $Rh^{3+}(Cl^-)_6$ such a band is found at 39,200 cm^{-1} (3).

The fluorescence emission of Al_2O_3:Rh consists of one broad band in the far red (680 nm), which is probably due to the spin-forbidden $^3T_{1g} \rightarrow {}^1A_{1g}$ transition, in agreement with the relatively long decay time.

We have also studied some other Rh^{3+}-activated aluminates, viz., $YAl_3B_4O_{12}$, $Li_{0.5}Al_{2.5}O_4$, and $Y_3Al_5O_{12}$. The photoluminescence of these materials is, however, very weak and the radiant efficiency for cathode-ray excitation less than 0.5%.

Manuscript received Aug. 7, 1967.

Any discussion of this paper will appear in a Discussion Section to be published in the June 1968 JOURNAL.

REFERENCES

1. F. A. Kröger, "Some Aspects of the Luminescence of Solids," Elsevier Publishing Company, Inc. (1948).
2. A. Bril and W. L. Wanmaker, *This Journal*, **111**, 1363 (1964).
3. C. K. Jørgensen, "Structure and Bonding," Springer Verlag, **1**, 3 (1966).

Evaluation of Electronic Grade Silicon and Trichlorosilane by a Frozen Drop Method

F. Hubbard Horn

General Electric Company, Research and Development Center, Schenectady, New York

The evaluation of silicon and its precursors for electronic purposes presents problems to both suppliers and users. In the case of silicon, it is clear that electrical resistivity alone does not uniquely specify the purity since the number of carriers measured is a net number, which in the worst situation may result from a near compensation of a relatively high concentration of both donors and acceptors. In the case of chemicals such as trichlorosilane used to prepare silicon either as massive crystals or for epitaxy, sufficiently sensitive tests for all of the impurities and particularly boron have not been developed.

Evaluation methods have been devised to meet some of these problems. The zone refining of test rods of silicon has been in most common use for both crystalline silicon and for silicon-bearing chemicals after deposition of silicon on a test rod. Electrical resistivity and resistivity profiles are used in conjunction with information on impurity segregation to determine the background concentration of boron and the concentration of some of the other possible impurities. Zone refining for such analytical purposes must be performed with great care and control and requires considerable time.

The same kind of analytical information as is obtainable from zone refining may be obtained by a frozen drop method, which requires less material and may be conducted more rapidly. Use is made of the fact that the surface tension of silicon will support a molten drop of sufficient length for significant electrical resistivity measurement. The progressive freezing of the molten drop from the supported end can give a unique and simple distribution of impurities according to their segregation coefficients. In the case of evaluating a silicon-bearing chemical, silicon is deposited on the bottom of a rod of silicon of known purity, a drop is formed from the deposited silicon, and refrozen for evaluation.

The steps that need to be considered in the application of the frozen drop method for silicon and trichlorosilane are: (*i*) formation of frozen drop and evaluation of silicon or silicon "seed" crystal; (*ii*) deposition of silicon from trichlorosilane on evaluated "seed" silicon; (*iii*) formation of frozen drop from silicon deposit and application of corrections; (*iv*) evaluation of silicon deposit from frozen drop. These steps will be discussed sufficiently to describe a general procedure; there is room for individual preference

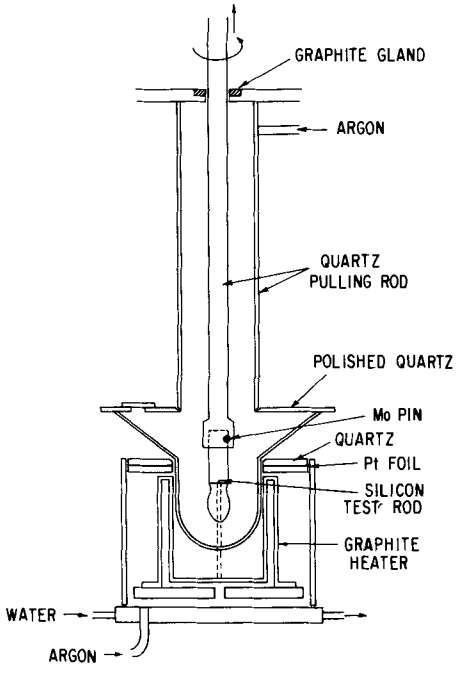

Fig. 1. Schematic drawing of furnace used to form a frozen drop from silicon rod.

in the choice of apparatus or measuring equipment used.

Formation of Frozen Drop from Silicon

A ⅜ in. diameter rod of silicon will support a molten drop about ¾ in. long. This length of refrozen crystal is sufficient for evaluation. A rod of single crystal silicon grown of appropriate known diameter or cut, centerless ground, and etched clean is mounted in a crystal-growing apparatus of the type shown in Fig. 1.[1] All parts are carefully etched clean and dried beforehand, and pure argon is allowed to flow slowly through the apparatus. The furnace is brought to a temperature sufficient to melt silicon. The silicon rod, originally held such that the bottom of the rod is above the crucible, is lowered part way into the crucible. As melting of the rod tip starts and proceeds, the rod is further lowered until the molten drop shows a necked-in region close to the liquid-solid interface. After allowing time for stabilization, *i.e.*, complete melting through the drop, the rod is withdrawn from the furnace or the furnace temperature reduced slightly such that freezing of the drop takes place from the rod downward to the tip. Typical frozen drops of varying length are shown in the photograph of Fig. 2. Freezing should be performed slowly in order that near equilibrium conditions are obtained. It is possible to control the freezing rate to about 1 mm/min. After cooling, the rod and frozen drop are removed. The frozen drop is cut from the rod at least several mm above the point at which recrystallization took place. Bars of uniform cross section 2-2.5 mm are cut longitudinally. These are lapped and the cross section measured for use in computing the electrical resistivity from electrical resistance measurements.

Procedure for Evaluating Silicon Using Frozen Drop

The central bar of approximately square cross section, cut from the frozen drop and some of the original crystal, is lapped and mounted for electrical resistance measurement in equipment such as illustrated by Fig. 3. The traveling probe is made to traverse the bar quickly in a search for p-n junction.[2] These are recognized as steps in the trace of the voltage-drop *vs.*

[1] High frequency (4 mc) may be used to form a frozen drop; however, it is more difficult to control the rate of freezing and to assure that freezing proceeds entirely from the rod-drop boundary. The drop shape also is affected by the method of formation.

[2] A thermoelectric probe is also useful for this purpose.

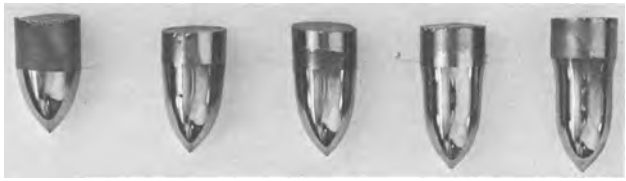

Fig. 2. Photograph of frozen drops of silicon from ⅜-in. diameter silicon rod.

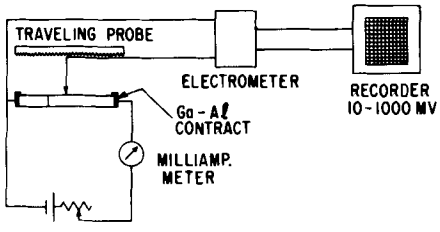

Fig. 3. Schematic electrical circuit for resistivity measurement of sections of frozen drop.

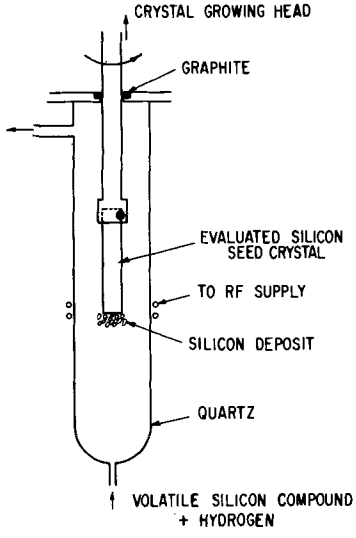

Fig. 4. Schematic drawing of apparatus used to decompose trichlorosilane for silicon evaluation.

position. Note is made of the position on the test bar at which a junction first appears. For electrical resistivity measurements, the electrical contacts should be made such that the current path is through silicon of the same type. The voltage drop through the sample is then measured as a function of position using the slow traverse traveling probe. The rate of movement of the paper in the recorder is fixed for a known rate of movement of the traveling probe. The electrical resistivity of any point in the bar is determined from the slope of the voltage-position curve since the measuring current and cross section of the test bar are known.[3]

Procedure for Evaluating Silicon from Trichlorosilane

A weighed rod of silicon previously evaluated by the frozen drop method to determine purity is mounted in an apparatus, such as shown schematically in Fig. 4, suitable for decomposing trichlorosilane to silicon. The apparatus is purged with pure hydrogen, the bottom tip of the rod brought to a temperature of about 1250°C, and the trichlorosilane to be tested then admitted from a weighed source. The decomposition is allowed to proceed until an appropriate amount of silicon is deposited on the rod. After stopping the flow of TCS, the power to heat the rod is turned off and the apparatus allowed to cool. The rod with silicon deposit is transferred to the furnace previously described

[3] The rate of change of voltage drop may also be obtained directly by the appropriate circuit to differentiate.

(Fig. 3) and a frozen drop formed. After cooling, the rod and frozen drop are weighed to determine the amount of silicon deposited. The length of the frozen drop from the refreeze position to the sprout is measured. These values are necessary to determine the concentrations of boron and phosphorus originally present in the trichlorosilane. Although the yield of silicon from trichlorosilane is low, it is substantially the same as will be encountered in the use of trichlorosilane to produce silicon. One does not thus really arrive at concentrations of impurities in the trichlorosilane; one obtains a measure of the impurities that will be present in silicon derived from trichlorosilane. This is no different from the problem encountered with deposition and zone refining for evaluation in general practice. Comparisons between zone refining and the frozen drop method have shown agreement to within less than 0.1 ppb in 40% of the cases and within 0.1 ppm in the other 60%.

Analysis of Data

The use of the electrical resistivity *vs.* position on the drop for determining the concentrations of boron and phosphorus present initially in the silicon rod or deposit (that is, what they were before making a frozen drop) requires several types of corrections. First, account must be taken of the redistribution of boron (p-type) and phosphorus (n-type) during formation of the frozen drop. Second, there are corrections that depend on the size and shape of the drop. In addition, in the case of evaluating silicon from trichlorosilane, a correction is required for dilution of the deposited silicon by some of the seed rod.

The ability to analyze for impurities in silicon is based on the fact that the two most important ones, boron and phosphorus, have slightly different segregation coefficients, both of which are much larger than the coefficients for all other impurities. Although the segregation coefficient for arsenic is nearly that for phosphorus, arsenic is not generally present in concentrations approaching that for phosphorus. For this reason, the donor impurity will be treated as being phosphorus. Boron ($K_B = 0.8$) and phosphorus ($K_P = 0.35$) and other impurities ($K \lesssim 0.01$) will be distributed in the frozen drop according to the laws of normal freezing. In normal freezing, the initial concentration of an impurity, C_i, before redistribution is given by

$$C_i = \frac{C_g}{K(1-g)^{K-1}} \qquad [1]$$

where C_g is the concentration of the impurity after redistribution, at some point in the crystal expressed as g, the fraction of crystal solidified. Since the conductivity type of boron (p-type) and phosphorus (n-type) is opposite, a crystal containing these two impurities will have an electrical conductivity governed by their algebraic sum. Thus, if the electrical resistivity ρ_o is measured at (near) $g = 0$, the net carrier concentration C_{net} is obtained from

$$\underset{g=0}{C_{net}} = \frac{1}{\rho_o e \mu} \qquad [2]$$

But from [1]

$$\underset{g=0}{C_{net}} = C_B - C_P = K_B C_{Bi} - K_P C_{Pi} \qquad [3]$$

where C_{Bi} and C_{Pi} are the initial concentrations of boron and phosphorus in the silicon before forming a frozen drop.

Similarly, from the electrical resistivity ρ_g measured at a known value for g, the net carrier concentration at position g after redistribution of the impurities can be obtained. Thus, from ρ_g one obtains

$$C_{net_g} = K_B C_{Bi}(1-g)^{K_B-1} - K_P C_{Bi}(1-g)^{K_P-1} \qquad [4]$$

in terms of C_{Bi} and C_{Pi}. Rather than solve for C_{Bi} and C_{Pi} simultaneously from Eq. [3] and [4], it is found more convenient to work through the ratio

$$\frac{C_{Pi}}{C_{Bi}} = R \qquad [5]$$

and to identify three regimes in which the ratio is obtained conveniently. Once the ratio is known, C_{Pi} and C_{Bi} are evaluated using Eq. [3].

The three operational regimes for evaluating R in [5] are: (*i*) that there are electrical junctions for values of g less than 0.85, (*ii*) that a junction appears for g greater than 0.85, and (*iii*) there are no junctions present. The latter case may arise either because there are virtually no n-type impurities present or because the ratio $C_{Pi}:C_{Bi}$ is greater than 2.3 in which case the entire frozen drop is n- rather than p-type. This case can be treated, but it has not been here.

In Fig. 5 are plotted the curves for the distribution of boron and phosphorus in a frozen drop. Position in the drop is in terms of g, the fraction of crystal solidified. It is observed that when the initial concentrations of boron or phosphorus are equal, their concentrations will again be equal after redistribution at $g = 0.85$. Conversely, if in the drop their concentrations are equal at $g = 0.85$, their initial concentrations before forming the drop were equal. Under such conditions $C_{net} = 0$ and an electrical junction is formed since the type changes at such a point. In Fig. 6 is plotted the position of a junction in terms of g as a function of the ratio C_{Pi}/C_{Bi}. This has been obtained from Eq. [4] setting $C_{net} = 0$ and calculating g for arbitrary values of C_{Pi}/C_{Bi}. The position of a junction can be used

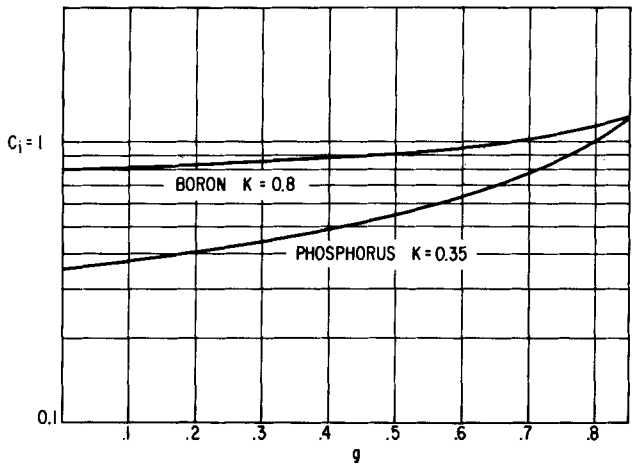

Fig. 5. Ideal distribution of boron and phosphorus in frozen drop

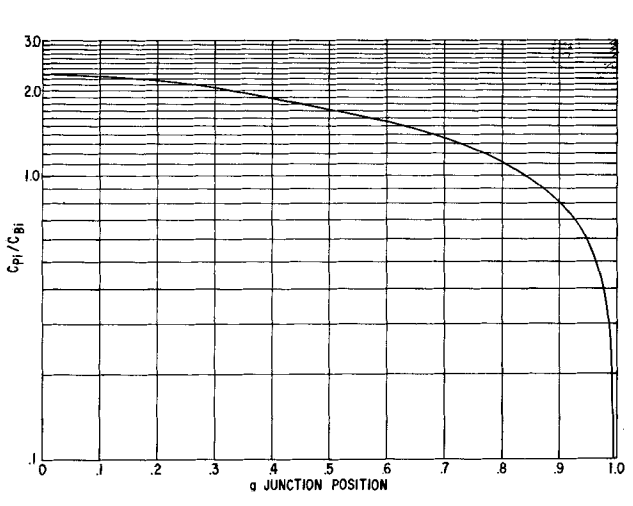

Fig. 6. Ratio of initial phosphorus to boron concentrations as a function of junction position on frozen drop. Position expressed as g, the fraction recrystallized.

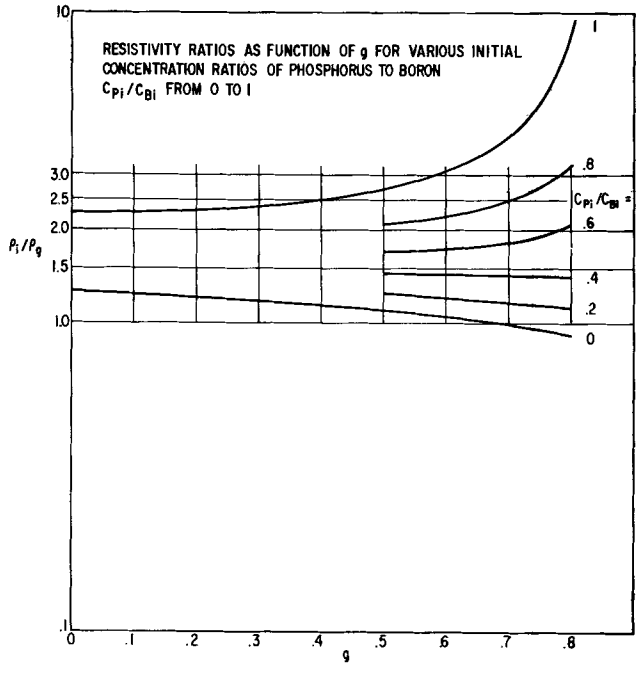

Fig. 7. Ratio ρ_i/ρ_g as a function of g, the fraction of drop crystallized for different initial concentration ratios of phosphorus to boron (C_{Pi}/C_{Bi}).

therefore to obtain the $C_{Pi}:C_{Bi}$ ratio from which C_{Pi} or C_{Bi} can be calculated from Eq. [3]. This step, which requires knowing the relation between the measured length and the fraction crystallized, g, will be discussed later.

If the ratio of C_{Pi}/C_{Bi} is less than unity, the junction is found at a value of g too close to the sprout for accurate measurement, and the ratio of the electrical resistivity at two known points on the crystal rather than the position of junctions should be used. This may be developed numerically each time; however, in order to make possible the use of a simple chart later, it will be presented graphically here. In Fig. 7 are plotted different resistivity ratios ρ_i/ρ_g where ρ_i is the resistivity of the sample before forming a frozen drop and after forming a drop, ρ_g is the resistivity at a point given in terms of g for various initial ratios of phosphorus to boron concentrations from 0 to 1. From these curves, one observes that sensitivity is lost for small values of g, and unjustified high resistivity is generated for large values of g and ratios approaching unity. Values for g of 0.6 or 0.7 offer a compromise. In Fig. 8, therefore, are plotted curves relating ρ_o/ρ_g

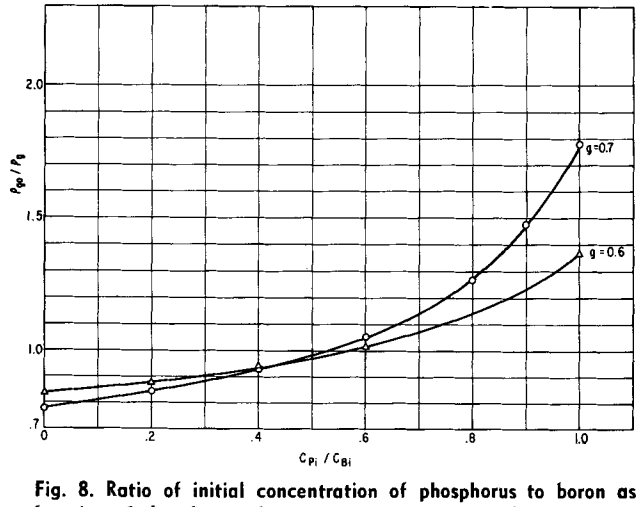

Fig. 8. Ratio of initial concentration of phosphorus to boron as a function of the electrical resistivity ratios at $g = 0$ to $g = 0.6$ and 0.7.

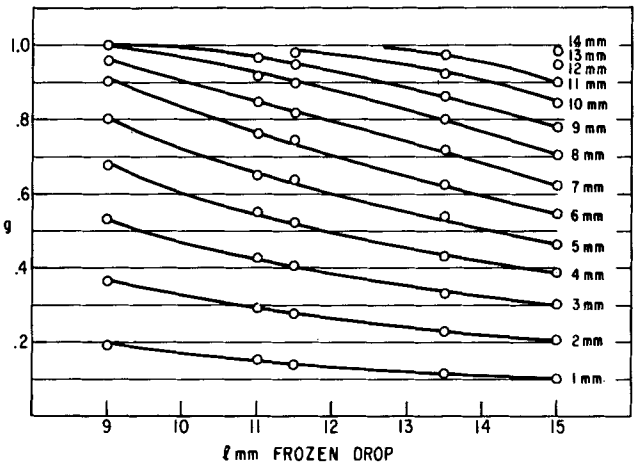

Fig. 9. Equivalent of each millimeter of length on frozen drop to g, fraction solidified, as a function of length of frozen drop.

(where ρ_o is the resistivity measured at $g = 0$ on a frozen drop) to the ratio C_{Pi}/C_{Bi} for values of $g = 0.6$ and 0.7. Thus, from the ratio of the measured resistivities at $g = 0$ to, say $g = 0.6$ one may obtain the C_{Pi}/C_{Bi} ratio necessary to calculate the original concentrations of boron and phosphorus.

The use of the ratio C_{Pi}/C_{Bi} depends on knowing g, the fraction of crystal solidified as a function of position along the test bar. For a crystal of uniform dimensions, g is related linearly to distance along the crystal. Frozen drops are not of uniform dimension, and some means must be found to relate position along the crystal (test bar) to the fraction of crystal solidified. This has been done for frozen drops formed on a 0.375-in. diameter rod by making enlarged shadow images of the drops. From these, assuming circular symmetry, one can measure the diameter at equal small distances along the image and calculate the volume per unit of distance. The change in volume (fraction solidified) as a function of length for drops of different length made on 0.375-in. diameter rod and calculated in the above manner are plotted in Fig. 9. From such a plot, knowing the length of the drop and the electrical resistivity trace as a function of distance from the drop-rod interface, it is possible to obtain the electrical resistivity corresponding to a particular value of g for a junction or for $g = 0.6$ or 0.7 needed for computing the impurity concentrations. The shapes of drops depend on the rod diameter and the process used to form them. The data presented here apply only to drops formed on a ⅜ in. diameter rod in a static system. A relation between g and distance along the crystal should be obtained for the particular system used. Drops formed using high-frequency heating differ also depending on whether the rod is moved or the power reduced during freezing.

When the ratio C_{Pi}/C_{Bi} has been obtained either from the position of junctions or from the resistivity ratios in terms of g, Eq. [3] may be solved and either the boron or phosphorus concentration calculated. This solution is presented graphically for boron in Fig. 10, where concentration is expressed in parts per billion atomic as is done in the industry. The constants used are mass, 22.08: density, 2.33 g/cm^3; μ, 480 cm^2/volt sec (hole mobility). The mobility is assumed to be constant. Thus, from the resistivity ρ_o and the ratio C_{Pi}/C_{Bi} obtained as explained above, the initial concentration of boron may be read directly from the graph of Fig. 10. The initial phosphorus concentration is of course obtained in the same units (ppb) from the product of the known boron concentration and the ratio C_{Pi}/C_{Bi}.

In the case of evaluating a drop formed primarily from silicon deposited from trichlorosilane on a rod, allowance must also be made for dilution by the silicon of the rod. To make this correction, one needs to

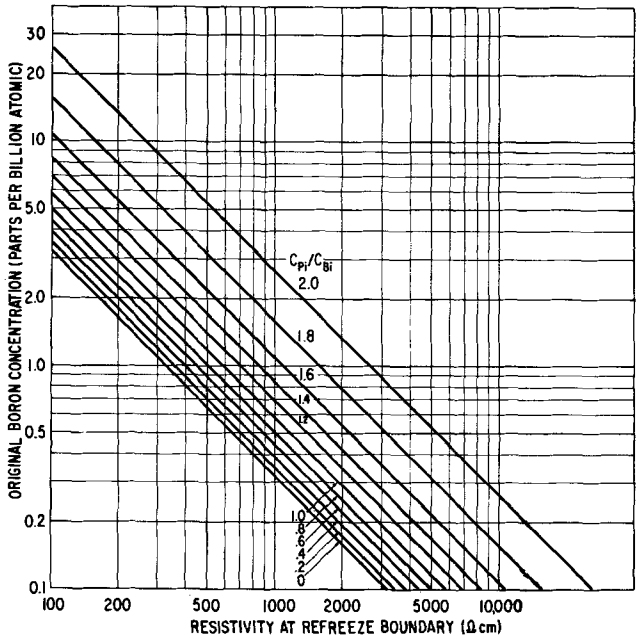

Fig. 10. Original concentration of boron in parts per billion as a function of electrical resistivity at $g = 0$ at refrozen boundary of frozen drop.

know the concentrations of boron and phosphorus initially present in the rod. These are obtained from analysis of a frozen drop made from the rod. If the same rod is weighed prior to and after depositing silicon, the weight of silicon deposited is readily obtained. In order to prevent contamination, the rod and deposit are weighed after the drop has been formed rather than before. It has been observed that for a given rod diameter, the weight of the frozen drop formed is a reproducible function of the length of the drop for a particular method of formation. Use is made of this to obtain the dilution factor. Results for the weight of drop as a function of length for drops made on ⅜-in. diameter rod are given in Fig. 11 from which, knowing the length of the drop, the corresponding weight of the drop is obtained. The weight of rod making up the drop is obtained from the difference between the weight of the drop and the weight of the deposit. Straightforward dilution rules can be applied to determining the original concentration in the deposit since one knows concentrations of impurities in the original rod and the frozen drop and knows the weights of silicon in the deposited silicon, the frozen drop, and rod silicon in the frozen drop. The more nearly comparable the purity of the rod and deposited silicon, the less important becomes the dilution correction.

Other Impurities

The sprout of the frozen drop is useful to determine the presence of certain other impurities, since in the sprout have been highly concentrated those impurities with very small segregation coefficients that may

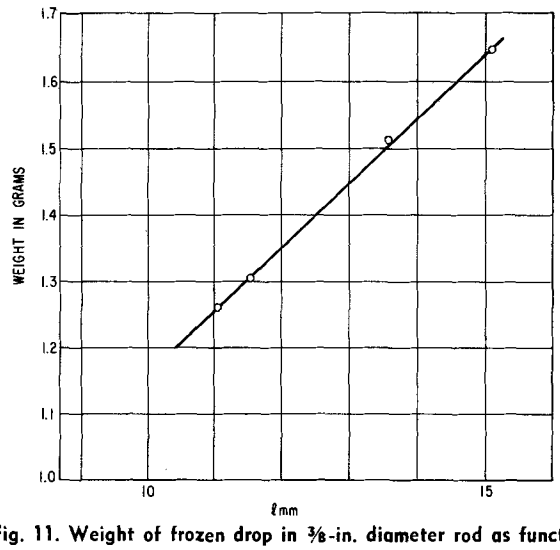

Fig. 11. Weight of frozen drop in ⅜-in. diameter rod as function of length of drop.

have been present in very small initial concentrations in the silicon. Solid source mass spectroscopy or x-ray emission analysis of the sprouts can frequently identify the presence of such impurities as Fe, Ni, Cr known to be deleterious in very low concentrations in electronic applications. This is particularly valuable information in evaluating trichlorosilane for use in epitaxial processes where subsequent melting and regrowth of crystal for eliminating impurities will not be possible.

Summary

A method is described for analyzing crystals for impurities whose segregation coefficients are known, and the method is applied to the determination of impurities of concern in electronic applications in silicon and trichlorosilane. The method depends on forming a molten drop and allowing it to freeze such that a "normal" freezing redistribution of impurities occurs. Analysis for boron and phosphorus is achieved by a proper use of electrical resistivity measurements on bars cut from the frozen drop. Additional information on impurities is obtained by analysis of the sprout by other than electrical means.

Acknowledgments

The author gratefully acknowledges the contributions from many others in helping to apply this frozen drop method. Dr. A. Torkelson of the Silicone Products Department was particularly instrumental in successfully applying the method to evaluating trichlorosilane. Max Tochner, Lloyd Keifer, and Robert Haislip made many valuable contributions in refining the technique to make it useful in routine evaluations. The work has benefited also from discussions with Dr. R. N. Hall.

Manuscript received June 9, 1967; revised manuscript received Aug. 17, 1967.

Any discussion of this paper will appear in a Discussion Section to be published in the June 1968 JOURNAL.

Twin Configurations in FCC Dendrites

J. W. Faust, Jr.

The Pennsylvania State University, University Park, Pennsylvania

and Fielding Ogburn, Daniel Kahan, and A. W. Ruff, Jr.

National Bureau of Standards, Washington, D.C.

Long ribbons of germanium have been grown from a supercooled melt by Bennett and Longini (1). These ribbons were shown to have two or more closely spaced parallel twin planes (2-4), which afforded indestructible re-entrant edges at which nucleation could more easily occur. Ribbons and webs of other

diamond type materials have also been grown (5-7) from the melt. Faust and John showed that this mechanism (*i.e.*, growth by two or more closely spaced parallel twin planes) could be made operative in growth from molten metal solutions for diamond type and zinc blende materials (8) and for fcc metals (9). They went on to show that parallel twin planes play a role in the dendritic growth of fcc metals by electrodeposition (10, 11), as did Ogburn *et al.* (12, 13).

Several workers (8, 14-20) have reported that under certain growth conditions fcc metals and semiconductors contain five twin planes intersecting at a common line. From the morphology, it is evident that the five intersecting twin planes played a major role during growth. Summing the angles for five twin planes in the fcc and zinc blende structure show that 7°20′ of arc are unaccounted for. There is no agreement on how this mismatch is taken up. Some authors believe it is taken up by strain, while others believe a mismatch boundary is present. A new symmetry group was even suggested that contains no twin planes (21). Faust and John suggested a number of other intersecting twin plane structures that may be found to operate in crystal growth. They went on to show experimental evidence for several of these.

It is the purpose of this paper (*a*) to show that some of the models of Faust and John were incorrect and to give the corrections, (*b*) to give additional models, and (c) to give experimental evidence for one more model.

Discussion of Results

We are dealing with two or more twin (composition) planes intersecting along a line in the body of the dendrite, which is parallel to the [110] growth axis of the dendrite. The orientations of adjacent twin crystals must be mirror images of each other across the twin plane. Since the twin planes in an fcc structure are of the type {111}, the angle of intersection between two of these twin planes must be either 70°32′ or 109°28′.

These restrictions require that wherever two or more twin planes intersect there must be a mismatch boundary. This is seen by inspection of the possible configurations. For example, let us consider the structure (shown in Fig. 1a) in which the solid lines are composition planes and the dashed lines are traces of {111} planes. In Fig. 1, II is a twin of I, and III is a twin of I. Further, II and III must be two different crystals since their {111} traces are not parallel. The two are not in a twin relation and, hence, their common boundary must be a mismatch, as is shown by the dotted line. Our general conclusion is that wherever two or more twin planes intersect, there will be a mismatch boundary or boundary region.

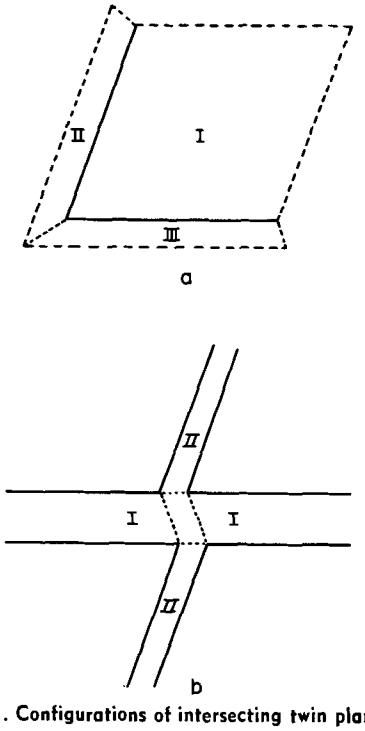

Fig. 1. Configurations of intersecting twin planes

Faust and John (8) in their Fig. 8a and g, and 9a, b, c, d, e, and f (and associated discussion) show configurations with intersecting twin planes, but do not include the required mismatch boundaries. Figure 8e of Faust and John has the mismatch boundary, but a twin plane was inadvertently omitted. With the twin plane the configuration would be essentially that of their Fig. 8b. Other configurations of intersecting twin planes in crystals with a <110> growth direction are theoretically possible using the 109°28′ angle between {111} planes on the {110} surface as the central angles.

In a configuration such as Fig. 9a of Faust and John (shown here as Fig. 1b) there are four pairs of intersecting twin planes. There will be a mismatch boundary ending at each of the four intersections within the intersecting lamallae. Three cases seem possible: (*i*) both of the I and II dotted lines will be mismatch boundaries; (*ii*) either dotted lines I or II (but not both) can be twin boundaries while the other pair must be mismatch boundaries; and (*iii*) either dotted lines I or II do not occur, while the remaining pair must be mismatch boundaries. Experimental evidence for the configuration of case (*ii*) has recently been obtained.

A silver dendrite, electrodeposited from a silver nitrate solution[1], was observed to have two planar arms extending out from the growth axis. A back-reflection Laue x-ray diffraction pattern indicated[1] that the dendrite was a single crystal with a <110> growth axis. The dendrite was mounted and sectioned normal to the growth axis for microscopic examination. The sectioned surface was chemically polished (2 ml 5% HCl; 24g CrO_3; 20 ml H_2O) and etched (2.5g KCN; 2.5g $(NH_4)_2S_2O_8$; 95 ml H_2O) to reveal the microstructure. Figure 2a shows a composite optical micrograph of one such section from the dendrite. In Fig. 2a, both planar arms are seen to contain lamellae extending along their length. The encircled portion in the micrograph is additionally enlarged, making the details somewhat more discernible. The narrowness of the lamellae, the fact that they occupy such a small fraction of the volume of the dendrite, explains the absence of their reflections in the x-ray diffraction pattern. The angle included between arms was about 70°, suggesting that {111} twinning was possibly involved in these features.

In order to verify the nature of the intersecting boundaries and their relationships, an electron-optical examination of the sections was undertaken. Under suitable etching conditions, the lattice relationships across the boundaries should be revealed. Palladium-shadowed plastic replicas were obtained and examined in an electron microscope. Figure 2b is an electron micrograph of the areas under consideration, showing the boundary intersection details. Measurements of the angular rotation of the etched microstructure across the various boundary lines shown here were always consistent with a mirror-plane relation, except for the two shortest boundary lines. Further, the main lamellae intersected each other at an angle of about 70° and the narrow lamellae were mirror-reflected on intersecting the other. We conclude that these lamellae are narrow twins intersecting in this dendrite. All the boundaries except for the two shortest sections (arrows) are twins. These two short mismatch boundaries are required for continuity. In addition, the lamellae can apparently thicken during growth as is shown in this figure at two locations (arrows) of

[1] The dendrite was grown by J. P. Young; the x-ray examination was done by C. J. Bechtoldt.

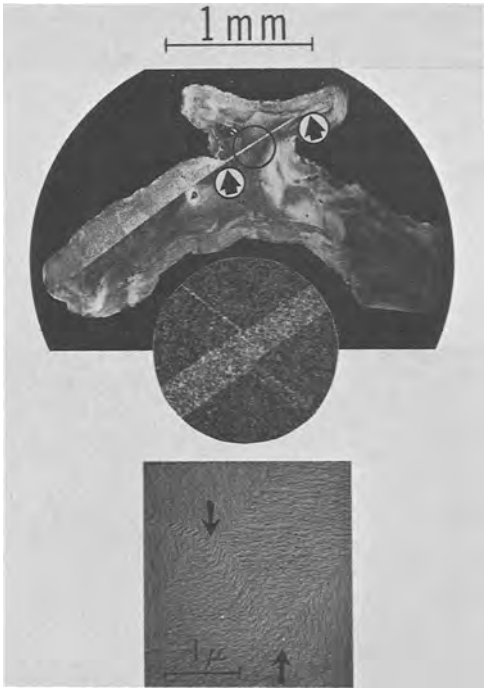

Fig. 2a (top). Optical micrograph from transverse section of silver dendrite showing twin lamellae in growth arms; the inset from the encircled region is magnified additionally by x 12; Fig. 2b (bottom) Electron micrograph of twin intersection region. The lattice relationships across the boundaries are shown by the etched structures. Arrows indicate mismatch boundaries.

the wide lamella. The importance of twin lamellae in influencing the external crystal habit is suggested in Fig. 2a.

Manuscript received Nov. 30, 1966; revised manuscript received Sept. 6, 1967.

Any discussion of this paper will appear in a Discussion Section to be published in the June 1968 JOURNAL.

REFERENCES

1. A. I. Bennett and R. L. Longini, *Phys. Rev.*, **116,** 53 (1959).
2. R. S. Wagner, *Acta Met.*, **8,** 57 (1960).
3. D. R. Hamilton and R. S. Seidensticker, *J. Appl. Phys.*, **31,** 1165 (1960).
4. J. W. Faust, Jr., and H. F. John, *This Journal*, **108,** 855 (1961).
5. S. N. Dermatis and J. W. Faust, Jr., *ibid.*, **112,** 792 (1965).
6. H. Nicholson and J. W. Faust, Jr., *ibid.*, **110,** 940 (1965).
7. S. M. Dermatis and J. W. Faust, Jr., *Trans. IEEE on Communication and Electronics*, **65,** 94 (1963).
8. J. W. Faust, Jr., and H. F. John, *J. Phys. Chem. Solids*, **25,** 1407 (1964).
9. J. W. Faust, Jr., and H. F. John, *Trans. AIME*, **233,** 230 (1965).
10. J. W. Faust, Jr., and H. F. John, *This Journal*, **108,** 109 (1961).
11. J. W. Faust, Jr., and H. F. John, *ibid.*, **110,** 463 (1963).
12. F. Ogburn, *ibid.*, **111,** 870 (1964).
13. F. Ogburn, C. Bechtoldt, J. B. Morris, and A. Pekoranyi, *ibid.*, **112,** 574 (1965).
14. F. Ogburn, B. Paretzkin, and H. S. Peiser, *Acta Cryst.*, **17,** 774 (1964).
15. M. A. Gedwill, C. J. Altstetter, and C. M. Wayman, *J. Appl. Phys.*, **35,** 2266 (1964).
16. A. J. Melmed and D. O. Hayward, *J. Chem. Phys.*, **31,** 545 (1959).
17. D. C. Skillman and C. R. Berry, *Photographic Sci. and Engr.*, **8,** 65 (1964).
18. R. W. DeBlois, *J. Appl. Phys.*, **36,** 1647 (1965).
19. R. L. Schwoebel, *ibid.*, **37,** 2516 (1966).
20. R. H. Wentorf, Jr., in "The Art and Science of Growing Crystals," J. J. Gilman, Editor, p. 192, John Wiley & Sons, New York (1963).
21. B. G. Bagley, *Nature*, **208,** 674 (1965).

DISCUSSION SECTION

This Discussion Section includes discussion of papers appearing in the *Journal of The Electrochemical Society*, Vol. 114, No. 3 and 4 (March and April 1967).

Physical Description of the Anisotropic Stress Effect in the Silicon P-N Junction Cantilever Transducer

L. K. Russell and W. H. Legat (pp. 277-285, Vol. 114, No. 3)

J. J. Wortman[1] and **J. R. Hauser**[2]: In the theoretical discussion of the ASE in p-n junctions, the authors treat the electrical current which results from generation-recombination in the space charge region. This current is not only related to junction width and lifetime as the authors consider but is also directly proportional to the intrinsic carrier density, n_i, of the material. The authors fail to consider any stress dependence on n_i. It has been shown that in fact variations in n_i due to stress induced band structure changes can explain the observed changes in generation-recombination current.[3,4]

[1] Research Triangle Institute, Research Triangle Park, North Carolina.
[2] Electrical Engineering Department, North Carolina State University, Raleigh, North Carolina.
[3] J. J. Wortman and J. R. Hauser, *J. Appl. Phys.*, 37, 3527 (1966).
[4] H. Kressel and A. Elsea, *Solid State Electronics*, 10, 213 (1967).

The 30% changes induced in lifetimes by stress that are given in ref. (23,24 of the paper under discussion) are doubtful. For example, it is pointed out in the discussion of ref. 23 that the method used to estimate the lifetime may not apply since a negligible lifetime is required in the stressed region. The 10-30% changes cited in ref.(23) are the combined effects of the small stressed area and the much larger unstressed area. In ref. (25), which the authors used but failed to mention in the text, approximately an order of magnitude change in lifetime with stress in germanium is shown to occur. This data is for near intrinsic material in which log $(1/\tau_\sigma)$ is linearly related to stress. Such a dependence on stress naturally leads one to suspect a shift of the recombination energy level with stress rather than a reversible change in the density of the recombination centers. From considerations of changes in energy level with stress one would expect lifetime in intrinsic material to be much more sensitive to stress than that in extrinsic material such as used in p-n junctions.

In conclusion, we feel that the major features of the reversible results reported can be explained in terms of shifts of the energy band edges and the recombination levels with stress. The sensitizing of

the junction probably introduces generation-recombination centers which are electrically active. The induced centers may be annealed out with time and temperature but for short time periods probably appear to be stationary.

A Method of Growing CuCl Single Crystals with Flux

Minoru Soga, Rikizo Imaizumi, Yoshihiro Kondo, and Takahiro Okabe (pp. 388-390, Vol. 114, No. 4)

H. Jaffe[5]: This paper is a most welcome contribution for the description of a method for growth of good CuCl crystals as well as the presentation of new data on the electro-optic Pockels effect. To the writer's knowledge these are the first quantitative data since the original work of West[6] which was of a preliminary nature. For a comparison it is, however, necessary to know the orientation of the CuCl crystal rods used by Soga *et al.* The transverse effect observed by them can be obtained either with electric field in the [111] direction and light propagation normal thereto, or with the field in a [110] direction with light propagation along the [110] direction. In the former orientation the effect is smaller by a factor $2/\sqrt{3}$ than in the latter. If Soga *et al.* used the [111] arrangement their results is in good agreement with West's, taking the difference in wavelength of the two measurements into account. If however Soga used the [110] bar his retardation values are about 20% lower than would have been expected from West.

[5] Clevite Corp., Electronic Research Division, 540 East 105th Street, Cleveland, Ohio 44108.

[6] West, Am. Inst. Phys., Handbook, McGraw-Hill Publishing Co., 1957, pp. 6-97.

Minoru Soga, Rikizo Imaizumi, Yoshihiro Kondo, and Takahiro Okabe: As for the orientation of the particular crystal rods used in our experiment, our laboratory note records of etch pit observation indicate that electric field was in the [111] direction and light was propagating perpendicular to it, as Mr. Jaffe pointed out. Possible misalignments were a few tenth of a degree for the crystal grown with $BaCl_2$ (Δ in Fig. 3) and 3~4 degrees for the crystal grown with $SrCl_2$ (O in Fig. 3).

Apart from the above discussion, we would like to add an information which may be useful: CuCl single crystals grown with $BaCl_2$ and $SrCl_2$ (about 1.5 mole % each) did not show adherence to the quarts crucible.